JOURNAL OF THE ELECTROCHEMICAL SOCIETY

ELECTROCHEMICAL SCIENCE

JANUARY 1971

ES

Transport Properties of Silver Beta Alumina

M. Stanley Whittingham*
Department of Materials Science, Stanford University, Stanford, California 94305

and Robert A. Huggins*[1]
Advanced Research Projects Agency, Washington, D. C. 20000

ABSTRACT

The total electrical conductivity and the electronic conductivity in silver beta alumina have been determined between 23° and 800°C over a wide range of oxygen partial pressure using a-c and d-c techniques. The ionic transference number was found to be very close to unity under all conditions. Comparison of these measurements with tracer diffusion studies shows that the diffusion of silver ions takes place by an interstitialcy mechanism.

Previously reported measurements (1-3) of the ionic conductivity and the diffusion coefficient of monovalent ions, M, in materials of the beta alumina structure, represented by the general formula $MAl_{11}O_{17}$, have indicated that this phase might prove to be very useful as a solid electrolyte or transducer element in electrochemical cells.

In order to evaluate materials for such purposes, however, knowledge must be obtained about the transference numbers of both ionic and electronic species as well as the total electrical conductivity over broad ranges of temperature and other thermodynamic variables. Widely useful materials should have low values of electronic conductivity and relatively rapid ionic transport under conditions whereby they might be applied. It is not enough to have this information for only a limited set of experimental circumstances.

Information concerning the electrical conductivity of single crystals of beta alumina containing silver as the monovalent cation is presented in this paper. In this case simple (silver) metallic electrodes could be used which are essentially reversible to both M ions and electronic species over wide ranges of both temperature and oxygen partial pressure. In addition to standard a-c and d-c measurements, the Wagner asymmetric polarization technique (4-8) was used to investigate the electron and hole conductivities. Experiments were conducted from 23° to 800°C, and over a range of oxygen partial pressures, from 0.2 to 10^{-24} atm.

Experimental and Results

Preparation and analysis of samples.—Batches of single crystals of sodium beta alumina were obtained from the Carborundum Company, and crystals which were optically free of a second phase were selected for study. Samples of silver beta alumina were prepared from the sodium beta alumina starting material by immersion in pure silver nitrate at a temperature slightly above its melting point (1). However, in this case, elemental silver was also present in the bath, so that the silver activity was maintained at unity. A process of solid-state ion exchange takes place by chemical diffusion among the monovalent cations in the beta alumina structure, with the sodium ions being replaced by silver ions. After equilibration (about 24 hr) the samples were removed, washed, and weighed to indicate the amount of exchange, and replaced in a fresh batch of silver nitrate so that the sodium activity was again reduced to a very low value. This process was repeated until no further detectable weight change occurred. Except in the case of large crystals, this normally involved only one exchange. Completeness of the exchange of the monovalent ions was checked by arc spectrographic techniques. In all cases, the residual sodium content was found to be less than 0.1% by weight; the other major impurities present were silicon (0.1%), calcium (0.03%), and iron (0.02%).

The assumption that only the identity of the monovalent cations was being changed by this process was investigated by similar reconversion of samples to sodium beta alumina. Weight measurements indicated that this assumption was justified, as complete reversibility was found.

In all cases, an excess of the monovalent cation concentration was found, relative to the stoichiometric formula $MAl_{11}O_{17}$. Expressing the composition as $Ag_{1+x}Al_{11}O_{17}$, the value of x was found to be 0.158 ± 0.004 for eight different samples.

X-ray diffraction experiments of the samples containing silver showed that they had the same structure as that reported (9-11) for sodium beta alumina, but with lattice parameters of $a_o = 5.596$Å and $c_o = 22.47$Å. These agree well with the results of Yao and Kummer (1), who found the values of 5.594 and 22.498Å, for a_o and c_o, respectively. Analysis of the intensities of the various diffraction lines indicated that they could be best explained by assuming the presence of 15-20% excess silver ions residing in the secondary (alternative) monovalent cation site in the loosely packed layer in this structure (10). The site geometry within this bridging layer, which is adjoined by blocks having the spinel structure of $MgAl_2O_4$, the Mg^{2+} sites also being occupied by Al^{3+} ions, is indicated in Fig. 1.

Measurements of the total electrical conductivity.—Crystals about 5 mm square and 1 mm thick were

[1] On leave from Stanford University.
* Electrochemical Society Active Member.
Key words: silver diffusion in beta alumina, electrical transport, solid electrolyte.

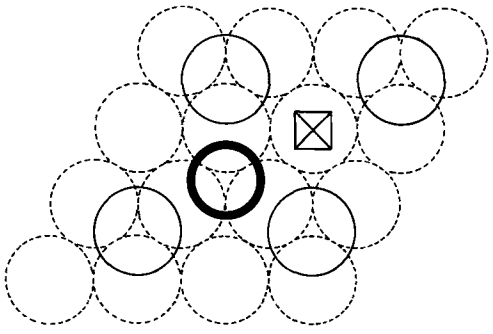

Fig. 1. Ionic arrangement in loosely packed layer of beta alumina. ⬭ Oxygen ions above and below plane of paper; ○ oxygen ion in plane of paper (aluminum ions are in the tetrahedral sites above and below these ions). ○ M ion in plane of paper on normal lattice site; ⊠ interstitial site in plane of paper.

mounted between silver electrodes in a quartz cell assembly in which the oxygen partial pressure could be controlled. The c-axis was perpendicular to the large faces, and the electrodes were placed so that conduction was measured parallel to the a-axis. The nature of the crystal structure is such that highly anisotropic behavior is expected, with very much slower transport in the c-direction. Contact to the solid silver electrodes was enhanced by coating the appropriate edges of the crystals with Engelhard silver resinate solution, which was baked at 500°C to give a coherent film of silver metal. Excess silver was removed by nitric acid, and the electrodes attached by the application of more resinate solution and baking the whole assembly. A small amount of mechanical force was applied by an external steel spring to press the electrodes and sample together. This procedure gave excellent mechanical and electrical contact.

In order to remove spurious effects due to the presence of residual silver ions from the resonate solution on the crystal surface, samples were annealed for 12 hr at 800°C prior to conductivity measurements. The measuring cell was contained in a furnace, whose temperature control and stability were better than 0.5°C.

The use of elemental silver electrodes fixed the chemical activity of the silver in the beta alumina at unity; however, in such a ternary system the activity of one of the other components must also be controlled in order to properly define the thermodynamic state of the sample. In this case the oxygen partial pressure was controlled by the use of a flowing gas system. Helium was used as the flowing gas and its oxygen content was controlled by passage over hot titanium or calcium chips; the gas was subsequently dried by passage through liquid nitrogen. The oxygen partial pressure in the helium was monitored continuously by the use of the solid-state electrochemical transducer technique (8, 12-14) with a stabilized zirconia tube and air at the reference electrode.

The total a-c conductivity was measured by use of a General Radio Type 1608A impedance bridge and an external oscillator. No frequency dependence was observed over the span 10^2-10^5 Hz at any combination of temperature and oxygen partial pressure within the range investigated. Measurements made under d-c conditions also gave the same values of conductivity if the value of total current was maintained less than about 5 mA/cm² (at high temperatures). At higher current fluxes the apparent conductivity was found to decrease gradually, possibly because of void formation at the interface between the crystal and the silver source electrode or polarization at this interface.

Measurements of both a-c and d-c conductivity were obtained for five crystals; results are shown in Fig. 2 for a typical sample. It is seen that the data produce a linear relation between the logarithm of conductivity-temperature product and the reciprocal of the absolute

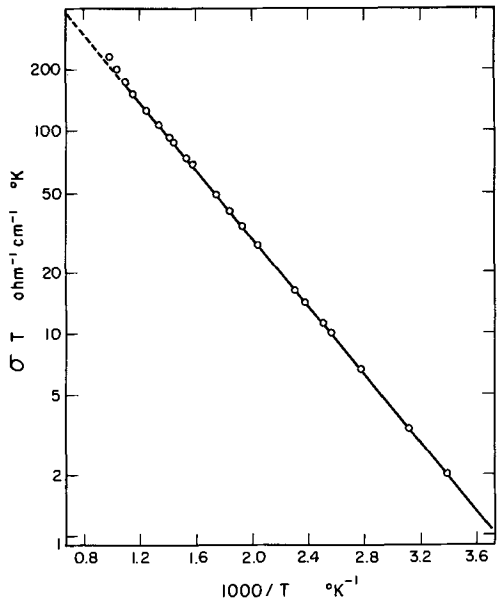

Fig. 2. Total conductivity of silver beta alumina

temperature from room temperature to above 650°C, as expected from the general relation

$$\sigma = (\sigma_0/T) \exp(-Q/RT) \quad [1]$$

The origin of the positive deviation from this relation at higher temperatures, which was observed for all samples, is not definitely known but may be due to a change in the diffusion mechanism.

The apparent activation energy Q for the linear range was found to have the value 3.98 ± 0.08 kcal/mole. The conductivity at 23°C was (6.41 ± 0.30) x 10^{-3} (ohm-cm)$^{-1}$.

Attempts to measure the oxygen partial pressure dependence of the total conductivity resulted in the conclusion that the dominant conduction process is essentially independent of oxygen partial pressure over the range from that of air to about 10^{-24} atmospheres. Experiments from 600° to 800°C showed an effect of less than 5%, which is deemed to be within experimental error.

Measurements of the electronic contribution to the conductivity.—Following the method of Wagner (4-7), the electronic conductivity of silver beta alumina has been deduced from current-potential curves for the cell

$$-\text{Ag/AgAl}_{11}\text{O}_{17}\text{/Pt} + \quad (\text{I})$$

On applying a potential below the decomposition voltage of silver beta alumina to the cell (I) with the negative pole on the left silver ions will tend to flow to the left and electrons to the right. However there is no source of silver ions at the right electrode, so the crystal will become depleted in silver at this electrode which will cause silver to flow toward this end under a chemical concentration gradient. At equilibrium the flow of silver ions due to the electrical gradient will equal the flow due to the chemical gradient, and the total current will be carried solely by electrons and positive holes.

This current in a cationic conductor is given by

$$I = (RT/LF)[\sigma_e(1 - \exp[-EF/RT]) + \sigma_h(\exp[EF/RT] - 1)] \quad [2]$$

where I is the current, L the cell constant which is determined by the crystal geometry, σ_e and σ_h the electron and hole conductivities, respectively, and E the applied potential difference. This may be rearranged (7) to give the more experimentally useful expression

$$I/[\exp(EF/RT) - 1] = RT/LF[\sigma_e \exp(-EF/RT) + \sigma_h] \quad [3]$$

Thus the value of σ_e may be obtained from the slope of a plot of $I/[\exp(EF/RT) - 1]$ against $\exp(-EF/RT)$ and σ_h from the intercept on the $I/[\exp(EF/RT) - 1]$ axis.

For this set of experiments a crystal was prepared as described above for the total conductivity measurement except that platinum resinate solution was used to form one of the electrodes. The sample was suspended in the furnace by means of wires attached to the electrodes so that there was no possibility of a sample holder short-circuiting the specimen. In all cases it was found necessary to keep the cell at about 800°C for several days, with an applied voltage across it to prevent the migration of silver across the surface. After this treatment the current attained a steady low value which was much less than originally observed. Subsequently when the applied potential was changed, polarization occurred fairly rapidly and the equilibrium current was usually attained within an hour. Measurements of the current using a Cary 401 electrometer were made on cell (I) between 555° and 790°C over a wide range of oxygen partial pressure. Figure 3 shows the results obtained at 790°C.

The intercept on the potential axis is influenced by two (extraneous) different effects. In cell (I) the oxygen activity at the platinum electrode is fixed by the surrounding oxygen partial pressure; however at the silver electrode the silver activity is fixed at such a high value that the oxygen activity will be very low, and so only at very low oxygen partial pressures will the activity of the oxygen at both electrodes be equal. Thus there will be an oxygen concentration gradient across the beta alumina causing a potential drop across the sample opposite in sign to the applied potential. In agreement with the experimental observations, this potential decreases with decrease of ambient oxygen partial pressure, however the curves still do not go through the origin at very low pressures.

The silver activity at the platinum interface is described by $a_{Ag} = \exp(-EF/RT)$, and as silver is soluble in platinum (15) there will be a flow of silver into the platinum which will create a silver ion current in the beta alumina. This current which may be large at low potentials will cause the measured current to fall to zero at some positive potential as observed. Figure 4 shows the effect of these different behaviors on the measured current-potential curve at 790°C where the oxygen partial pressure was 0.2 atm. Similar behavior has been reported for AgBr (16) and AgCl (17).

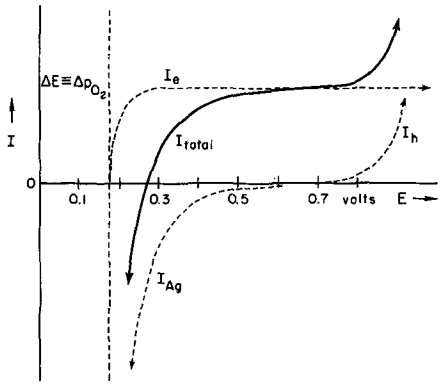

Fig. 4. Contributary and total current-potential curves at 790°C for $p_{O_2} = 0.2$ atm.

As Eq. [3] can clearly not be used when there is an appreciable silver ion current, which varies with the applied potential, the electron conductivity was calculated from the current plateau using the expression

$$\sigma_e = ILF/RT \qquad [4]$$

which is simply Eq. [2] with no positive hole conduction. These results are given as a function of temperature in Fig. 5. Satisfactory results could not be obtained at lower temperatures because of both long equilibration times and as no plateau was reached in the current-potential curve although one was obviously being approached. This latter behavior was undoubtedly due to the silver ion contribution to the total current. In no case was any positive deviation from the current plateau observed, indicating that the positive hole conductivity was at least three orders of magnitude less than the electron conductivity.

Replacement of the platinum in cell (I) by graphite, in which silver is not expected to be soluble, gave current-potential curves which appeared to go through the origin as expected from the above theory. However this cell could not be used for quantitative measurements as the results obtained were unreproducible and were accompanied by a large amount of "noise" of the kind described by Van der Meulen and Kröger (17). For platinum this noise was completely eliminated by the initial high-temperature anneal, but such a treatment had no effect on the graphite cell. This noise is most probably due to poor interface contact at the blocking electrode.

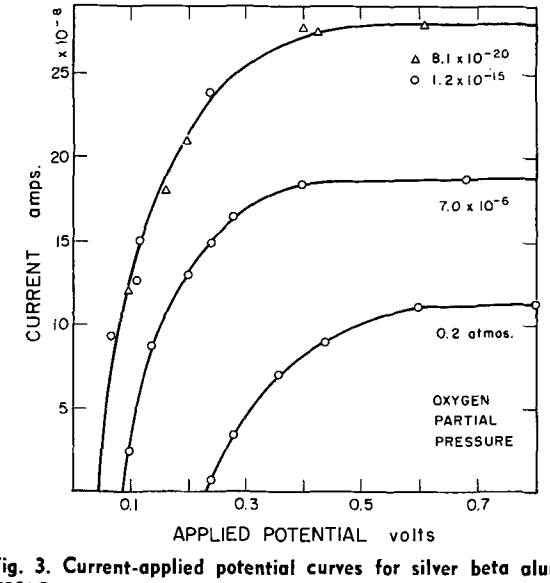

Fig. 3. Current-applied potential curves for silver beta alumina at 790°C.

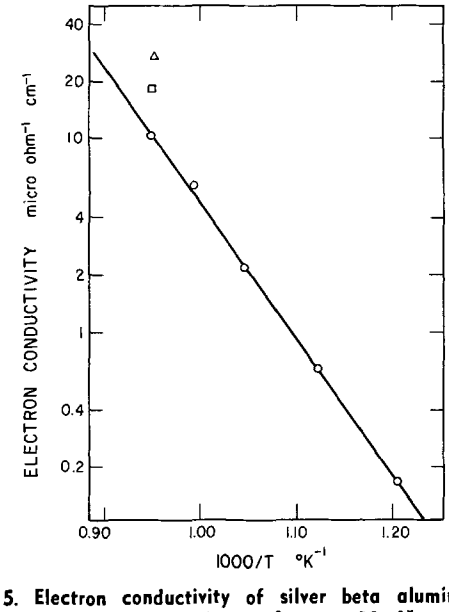

Fig. 5. Electron conductivity of silver beta alumina. Oxygen partial pressure: ○, 0.2; □, 7 x 10^{-6}; Δ, $\lesssim 10^{-15}$ atm.

Discussion

Defect structure of beta alumina.—Silver beta alumina was shown above to contain a considerable excess of the monovalent ion, silver. It may thus be described as a highly defective nonstoichiometric compound. As none of the ions show any polyvalent character and the electronic conductivity is so low, it is highly probable that the excess silver ions are charge balanced by other lattice defects rather than by electronic defects. As mentioned earlier, the crystal structure of beta alumina is made up of cubic close-packed blocks, four layers thick, of oxygen ions in which the aluminum ions take up both the magnesium and the aluminum positions of the spinel $MgAl_2O_4$; these blocks are held together by a loosely packed layer containing Al-O-Al bridging groups and silver ions. The arrangement in this layer was shown in Fig. 1. It is clear that extra ions can be readily accommodated in this layer.

X-ray studies (10) on the silver and thallium beta aluminas indicate that the excess monovalent ions, M, are present as interstitials, M_i, on the interstitial site indicated in Fig. 1. These may be charge balanced either by addition of negative charge in the form of interstitial oxygen ions, O''_i, or by removal of positive charged aluminum ions giving aluminum vacancies, V'''_{Al}. A third possibility is the replacement of some of the aluminum ions by divalent cations. However there were not enough such impurity ions present to compensate the observed silver excess. Impurity effects will therefore be ignored. X-ray data have not yet been able to distinguish between the first two models as they involve low defect concentrations of poor x-ray scatterers, *e.g.*, in the second case, aluminum vacancies on less than 0.5% of the total aluminum sites would compensate a 15% excess of M. It is most probable that such aluminum vacancies or replacement ions will be in the region of the bridging layers so as to be close to the defects they are compensating. Excess oxygen ions could reside upon a number of positions, *e.g.*, some of the oxygen ions on the normal lattice sites might be displaced slightly to give small regions of the magnetoplumbite structure (18), or they might displace some of the M ions from their lattice sites. It is unlikely that oxygen ions would reside on the interstitial sites suggested for the excess silver ions as this would involve placing an oxygen ion between two other oxygen ions which would be energetically unfavorable.

The effect of the oxygen partial pressure on the concentrations of defects in the first two models, and hence on their electrical conductivity, will now be discussed. In both cases it is assumed that the concentrations of electrons and positive holes are small compared to those of the lattice defects of the same charge; this is consistent with the known ionic conductivity of these materials. At high oxygen pressures the predominant defects are likely to be cation interstitials, $M^{\bullet}_i$, and its compensating defect, either V'''_{Al} or O''_i, whereas at low oxygen pressures the compensating defect is more likely to be a cation vacancy, V'_M. The latter is simply Frenkel disorder in the M lattice. Figures 6 and 7 show the results of calculations based on these defect models, and using the experimental data at 550°C with the assumption that the electron and hole mobilities are unity.

Both these models suggest that at high oxygen pressures the concentrations of interstitial cations and electrons, $[M^{\bullet}_i]$ and [e'], should depend on the oxygen partial pressure. This was not found to be the case experimentally and suggests that either (*i*) all oxygen pressures investigated were within the lower range, (*ii*) the defect models considered are incorrect, or (*iii*) the silver beta alumina samples were not in equilibrium with the environment. As the models considered here seem to be the most feasible, and no

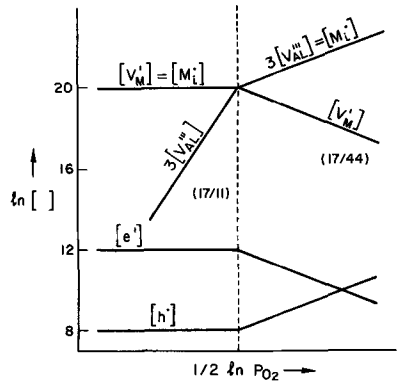

Fig. 6. Defect equilibrium diagram where V'''_{Al} is predominant at high p_{O_2}. |Slopes| are given in ( ).

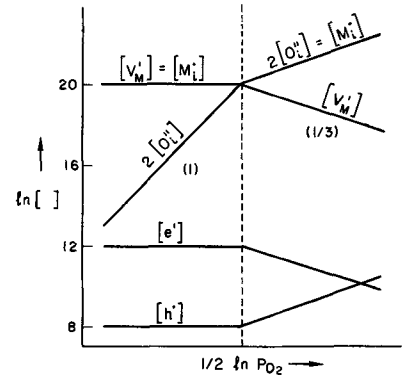

Fig. 7. Defect equilibrium where O''_i is predominant at high p_{O_2}. |Slopes| are given in ( ).

excess of M is expected in the lower oxygen pressure range, the possibility of nonequilibrium with the environment is the most likely. The sodium beta alumina from which these samples were obtained was crystallized from the melt at about 2000°C; at no subsequent time were the samples raised to such temperatures. It is thus possible that if one of the compensating defects were frozen in on cooling from this temperature the silver concentration would reflect the thermodynamic condition (and sodium content) expected at that high temperature rather than of the temperature at which it was prepared by the ion exchange technique or present during the subsequent measurements. This assumption leads to a differentiation between the two proposed compensation mechanisms. If compensation were by means of oxygen interstitials then there is no *a priori* reason why these defects should not show a reasonably high diffusion coefficient and be able to come to equilibrium with the environment at 800°C considering the open nature of the planes containing these ions. However, if the compensating defect were an aluminum vacancy, then it could be frozen into any part of the close-packed blocks or in the bridging groups; in either case it would be expected to have a much lower diffusivity than the oxygen interstitial. It is therefore suggested that the compensation mechanism for the excess M ions in the beta alumina structure involves aluminum vacancies and that for all practical purposes these vacancies should be considered frozen into the lattice at the temperatures of these experiments.

Mechanism of diffusion of silver in beta alumina.—The diffusion coefficients for silver diffusion in silver beta alumina, obtained from the conductivity data of Fig. 2 using the Nernst-Einstein relationship

$$D = \sigma RT/cq^2 \qquad [5]$$

and from the tracer diffusion studies of Yao and Kummer (1), are compared in Fig. 8. The concentra-

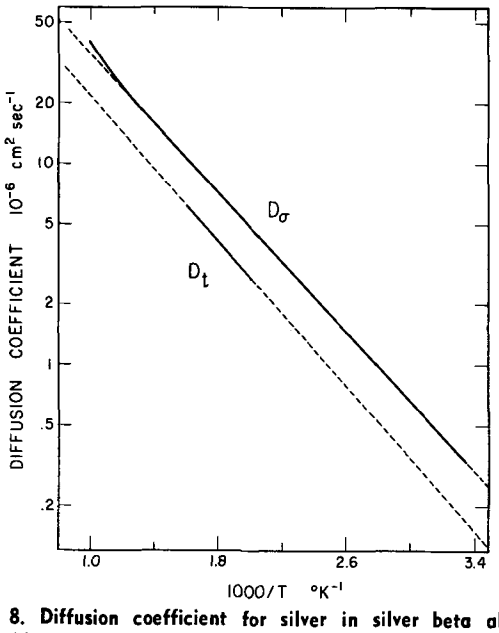

Fig. 8. Diffusion coefficient for silver in silver beta alumina. ——— Measured, - - - - - extrapolated.

tion of silver ions, c, was taken as equal to that of the stoichiometric compound, which is 5.453 x 10^{-3} moles/cc. The conductivity results show that in the equation

$$D = D_o \exp(-Q/RT) \quad [6]$$

D_o and Q have the values of 2.55 x 10^{-4} cm^2 sec^{-1} and 3.98 kcal/mole, as compared with tracer diffusion values (1) of 1.65 x 10^{-4} cm^2 sec^{-1} and 4.05 kcal/mole. The value of D_σ/D_t at 280°C, the center of the measured temperature range, is 1.64. This suggests that diffusion does not take place by an interstitial mechanism. Inspection of Fig. 9 shows that an interstitialcy mechanism is the most probable; it may also be noted that the structure precludes the possibility of a collinear interstitialcy mechanism. Theoretically (19) for the interstitialcy mechanism the correlation factor, f, is given by

$$D_\sigma/D_t = 1/f = (a_i/a_t)^2/2(1 + \overline{\cos\theta}) \quad [7]$$

where a_i is the effective jump distance of an interstitial ion, a_t is the jump distance of the tracer, and θ is the angle between a tracer jump from an interstitial site to a normal lattice site and the next jump from the normal site to an interstitial site. In this case, a_i is the distance between two interstitial sites and a_t the distance between an interstitial and a normal lattice site. For this structure $(a_i/a_t)^2 = 3$ and the value of $1 + \overline{\cos\theta}$ has been calculated, by direct summation of the jumps of an interstitial, to be 0.898 ± 0.002 assuming no interaction between interstitials and only completely free silver ions on normal and interstitial sites. This gives $D_\sigma/D_t = 1.67$ in excellent agreement with experiment. It should be remembered however that there is a 15% occupancy of the interstitial sites. This has been ignored in the above treatment, but is expected to reduce the value of D_σ slightly, thus decreasing the ratio D_σ/D_t, and raise the value of f.

The linear variation of log (σT) with $1/T$ in Fig. 2 is in accordance with a model in which there is a large number of charge carriers, which does not change appreciably with temperature. The small positive deviation at the higher temperatures may be associated with excitation of some of the silver ions from normal lattice sites to interstitial sites thus creating a larger number of charge carriers. It may also be due to an actual change in the diffusion mechanism, *e.g.*, to a multiple jump mechanism.

Comparison with other fast ionic conductors.—The ionic conductivities of several "good" electrolytes are compared in Fig. 10. Only two, AgI and $RbAg_4I_5$, have appreciably higher conductivities than $AgAl_{11}O_{17}$, and the difference between these two can be accounted for by the difference in silver concentration. It is interesting to consider why there is such a large difference in the conductivity [6.4 x 10^{-3} and 2.1 x 10^{-1} (ohm-cm)$^{-1}$, respectively, at 23°C] between $AgAl_{11}O_{17}$ and $RbAg_4I_5$, when the crystal structure of beta alumina is so open. In $RbAg_4I_5$ all the silver ions are on equivalent sites (25) so that they are all equally capable of diffusing in a potential field; however, in beta alumina the silver ions are on two different sites and because of the diffusion mechanism the "effective number" of mobile ions is equal to the concentration of occupied interstitial sites. Thus the number of charge carriers, n, is 1.13 x 10^{22} cm^{-3} for $RbAg_4I_5$ and about 15% of 3.28 x 10^{21} or 4.92 x 10^{20} cm^{-3} for $AgAl_{11}O_{17}$.

Using the common expression, $\sigma = nq\mu$, the mobility, μ, of the silver ion in beta alumina is found to be 70% of that in the rubidium iodide. It is clear that the main reason for the conductivity difference does not lie in the ionic mobility but in the number of ions available for conduction. The conductivity of beta alumina might thus be improved by increasing the number of interstitial ions, *e.g.*, by doping with a divalent metal such as magnesium which will reside on an aluminum site. There should be no difficulty in doing this as the block structure of beta alumina is that of the spinel $MgAl_2O_4$ and replacement of only 4.5% of the aluminums by magnesium will increase the silver content to

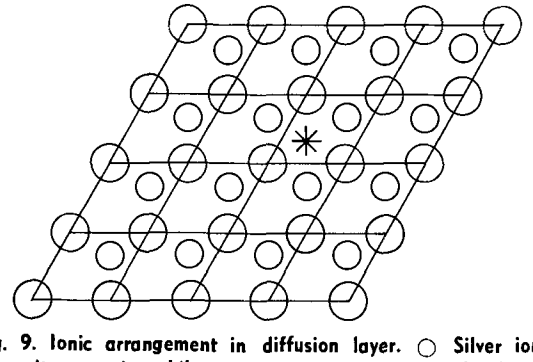

Fig. 9. Ionic arrangement in diffusion layer. ○ Silver ion on lattice site; ⊗ immobile oxygen ion; ✳ interstitial silver ion.

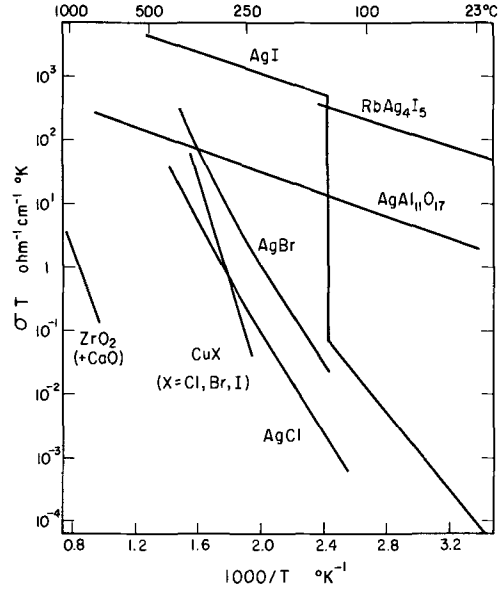

Fig. 10. Conductivity of some highly conducting solid electrolytes. ZrO_2(7), CuX(6), AgBr(20), AgCl(21), AgI(22, 23), $RbAg_4I_5$(24).

50% over stoichiometric and thus the present interstitial concentration by more than a factor of three. However, the diffusion mechanism will probably change at some value of the interstitial concentration when the assumption that the interstitial ions are independent of one another breaks down.

Inspection of the tracer diffusion data of Yao and Kummer (1) shows that the sodium ion in the beta alumina has a mobility about double that of the silver ion. Sodium beta alumina is thus expected to have the highest known mobility of any known solid electrolyte at ambient temperature, and suitable doping of the alumina matrix as discussed above should be capable of producing values of ionic conductivity comparable in magnitude with that of $RbAg_4I_5$.

The structure of sodium beta" alumina (10, 11, 26) is very similar to that of beta alumina, but it contains about twice the concentration of sodium ions, all of which are thought to be in identical sites. The diffusion mechanism may then be similar to that in the two highly conducting silver iodides so that all the sodium ions participate in the diffusion process.

To be useful as an electrolyte in batteries or solid-state cells a material must exhibit rapid ionic transport of one or more species, and at the same time have a very low electronic transference number over wide ranges of temperature and partial pressures of the components. Silver beta alumina clearly fulfills these criteria. From the data of Fig. 2 and 5 the electron transference number can be found as a function of temperature. Results are shown in Fig. 11. These values of the transference number for electronic carriers are lower than the measured values of any of the other solid electrolytes shown in Fig. 10, several of which are being used as electrolytes in batteries and other solid-state cells. It has the added advantage that it appears be be unaffected by light contrary to the behavior of some other silver compounds. Thus silver beta alumina appears to be a very interesting solid electrolyte for both technological and scientific uses.

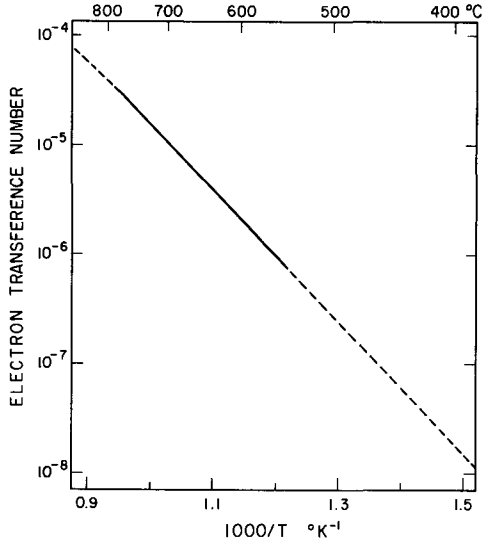

Fig. 11. Electron transference number of silver beta alumina. ——— Measured, – – – – – extrapolated.

Acknowledgment

The authors would like to thank Douglas Clark and Robert Helliwell for many fruitful discussions. This work was supported by the Office of Naval Research through Contract N0014-67-0112-0020 and by the Advanced Research Projects Agency through the Center for Materials Research at Stanford University.

Manuscript submitted April 27, 1970; revised manuscript received *ca.* Aug. 27, 1970.

Any discussion of this paper will appear in a Discussion Section to be published in the December 1971 JOURNAL.

REFERENCES

1. Y. Y. Yao and J. T. Kummer, *J. Inorg. Nucl. Chem.*, **29**, 2453 (1967).
2. N. A. Toropov and M. M. Stukalova, *Comp. Rend. Acad. Sci. URSS*, **24**, 459 (1939).
3. N. A. Toropoy and M. M. Stukalova, *ibid.*, **27**, 974 (1940).
4. C. Wagner, *Z. Elektrochem.*, **60**, 4 (1956).
5. C. Wagner, *Proc. Int. Comm. Electrochem. Thermo. Kinetics (CITCE)*, **7**, 361 (1957).
6. J. B. Wagner and C. Wagner, *J. Chem. Phys.*, **26**, 1597 (1957).
7. J. W. Patterson, E. C. Bogren, and R. A. Rapp, *This Journal*, **114**, 752 (1967).
8. L. Heyne, "Mass Transport in Oxides," J. B. Wachtman and A. D. Franklin, Editors, NBS Special Publication, **296**, 149 (1968).
9. C. A. Beevers and M. A. Ross, *Z. Krist.*, **97**, 59 (1937).
10. M. S. Whittingham and R. A. Huggins, To be published.
11. G. Yamaguchi and K. Suzuki, *Bull. Chem. Soc. Japan*, **41**, 93 (1968).
12. J. Weissbart and R. Ruka, *Rev. Sci. Instr.*, **32**, 593 (1961).
13. H. Schmalzried, *Z. Elektrochem.*, **66**, 572 (1962).
14. D. Yuan and F. A. Kröger, *This Journal*, **116**, 594 (1969).
15. A. Schneider and U. Esch, *Z. Elektrochem.*, **49**, 72 (1943).
16. D. O. Raleigh, *J. Phys. Chem. Solids*, **26**, 329 (1965).
17. Y. J. van der Meulen and F. A. Kröger, *This Journal*, **117**, 69 (1970).
18. V. Adelskold, *Arkiv Kemi*, **12A**, No. 29, (1938).
19. K. Compaan and Y. Haven, *Trans. Faraday Soc.*, **54**, 1498 (1958).
20. R. J. Friauf, *Phys. Rev.*, **105**, 843 (1957).
21. W. D. Compton and R. J. Maurer, *J. Phys. Chem. Solids*, **1**, 191 (1956).
22. K. H. Lieser, *Z. Physik Chem. N.F.*, **9**, 302 (1956).
23. A. Kvist and A. Josefson, *Z. Naturfors.*, **23A**, 625 (1968).
24. B. B. Owens and G. R. Argue, *Science*, **157**, 308 (1967).
25. H. Wiedersich and S. Geller, "The Chemistry of Extended Defects in Non-metallic Solids," L. Eyring and M. O'Keefe, Editors, pp 629-650, North-Holland Publishing Co., Amsterdam (1970).
26. M. Bettman and C. R. Peters, *J. Phys. Chem.*, **73**, 1774 (1969).

The Microstructure of Sintered Silver Electrodes

III. Ag_2O Formation during Charges

Charles P. Wales*

Electrochemistry Branch, Naval Research Laboratory, Washington, D. C. 20390

ABSTRACT

Ag electrodes were charged at the 20-hr rate of constant current and discharged at the 1-hr rate in 35% KOH solution at 25°C. Cross sections of samples cut from the electrodes during charges at cycles 1-30 were examined. Almost all Ag particles had a visible coating of Ag_2O when an electrode was charged for half the capacity accepted at the Ag/Ag_2O potential plateau. The electrode surface had the same structure as the interior. In a cycled electrode approximately 60% of the Ag had been oxidized to Ag_2O when the potential peak separating the Ag/Ag_2O and Ag_2O/AgO plateaus was reached.

The present paper describes structural changes in Ag electrodes as Ag_2O was formed in an alkaline solution. The Ag electrodes were of the type used in Ag-Zn and Ag-Cd storage batteries.

There have been two previous papers in this series concerning the microstructure of sintered Ag electrodes. The first paper described the structures present as charged electrodes were being reduced during discharges (1). The second described the structures present at the end of a series of complete discharges (2). The formation of AgO will be the subject of a later paper. The electrodes in this series of investigations were always discharged at the 1-hr rate and charged at the 20-hr rate of constant current in 35% KOH solution.

When Ag electrodes are discharged in a KOH solution at a high current density for a series of cycles the electrode capacity is maintained at a higher value than when a low discharge C.D. is used. This difference in capacity results from changes in the microstructure of the electrodes. The microstructure of a cycled electrode depends partly on the discharge C.D. that is used. A discharge at the relatively fast 1-hr rate results in formation of small Ag particles, many having a size on the order of 1μ. Particles of this size oxidize readily during the next charge. When the slow 20-hr discharge rate is used, however, most of the Ag particles that form are 10-25μ (3).

Particles of Ag larger than 4 or at most 5μ do not oxidize completely during a charge. Oxidation usually stops before an oxide layer reaches a thickness of 2μ. As a result, the central portion of large particles remains as metallic Ag at the end of a charge instead of being oxidized. Once large particles form in an electrode during a slow discharge, the original discharge capacity is not regained readily. When slow discharges are used, the capacity decreases so rapidly that by cycle 3 the electrodes always discharged at the 20-hr rate give less capacity than electrodes always discharged at the 1-hr rate. This occurs despite the fact that approximately 10% of the oxide remains at the end of a fast discharge, and almost all of the oxide is reduced during a slow discharge.

Experimental Procedure

Only a brief account of the experimental procedure will be given here, because it has already been described (1). Sintered Ag electrodes were cycled individually in an excess of 35% KOH solution at 25°C. The Ag electrodes were charged using constant current at the 20-hr rate until oxygen began to evolve. Electrodes were discharged using constant current at the 1-hr rate. These currents were not based on theoretical capacity of the electrodes but were the currents that actually resulted in a charge reaching oxygen evolution in 20 hr and a discharge reaching the cutoff potential in 1 hr. Discharges were ended at a potential of −500 mV *vs.* the Ag/Ag_2O reference electrode, the equivalent to approximately 1.0V for a typical Ag-Zn cell. Electrodes were given up to 30 charge-discharge cycles.

Samples for microscopic examination were cut from the Ag electrodes at various times during charges. After a sample had been washed and dried, it was impregnated with an epoxy resin while under a vacuum. Then a cross section of the sample was prepared by grinding and polishing. Finally a sample was examined with a metallurgical microscope and the appearance of significant areas recorded by photography.

Results

Oxidation of Ag to Ag_2O.—A small area of an electrode that had been partly charged at the Ag/Ag_2O potential plateau is shown in Fig. 1. All photographs in this paper are of cross sections through electrodes. The photographs, therefore, also show cross sections

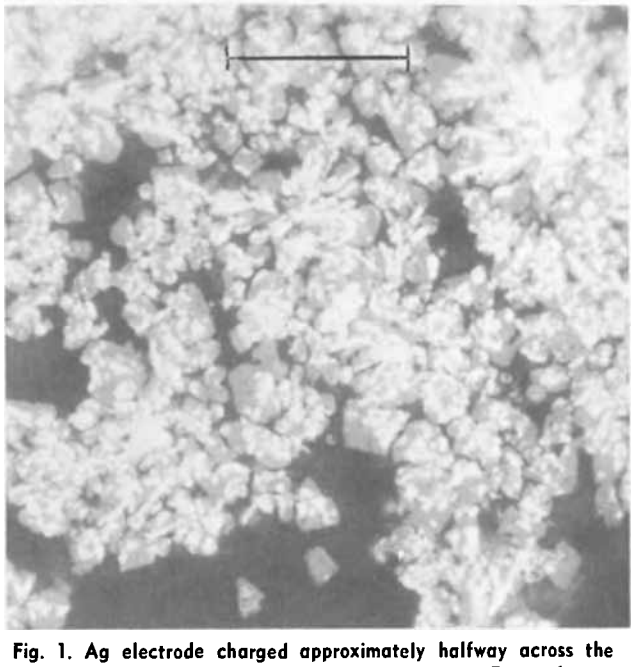

Fig. 1. Ag electrode charged approximately halfway across the Ag/Ag_2O potential plateau at cycle 6 in 35% KOH. Electrode was given 19% of average charge acceptance. Metallic Ag particles are the lightest shade in the photograph. Ag_2O that formed during the charge is medium gray. Void areas are the darkest shade. Marker indicates 15μ.

* Electrochemical Society Active Member.

Key words: silver electrode, silver oxidation, silver oxide, electrode structure.

through the individual crystals in the active material of an electrode. This sample was taken from an electrode during cycle 6 charge. The electrode had always been charged at the 20-hr rate and discharged at the 1-hr rate.

The electrode shown in Fig. 1 had been given half the capacity this electrode would accept during a charge at the Ag/Ag_2O potential plateau. The partial charge amounted to approximately 19% of the capacity usually accepted before oxygen evolution began. The surface of this electrode had the black color of Ag_2O. Microscopic examination showed that the surface had the same structure as the interior. The reaction was uneven in the electrode, however, with a greater amount of Ag_2O having formed in some areas than in others.

The small Ag particles within the Ag_2O of Fig. 1 were the unoxidized remainder from Ag particles that formed during the previous discharge. Most of the Ag in a discharged electrode was present as small particles or needles. Some larger Ag particles were also present. These larger particles of Ag were residual from the particles present in the unused electrode. Small Ag particles and needles of Ag are visible in the partly charged electrode shown in Fig. 1. Only 5% of a typical unused electrode consisted of particles over 15μ in size. The area shown in Fig. 1 did not include any of these large Ag particles.

A definite Ag_2O coating had formed on most of the Ag particles during the partial charge given the electrode shown in Fig. 1. Based on the weight of Ag present in the unused electrode (excluding the grid of expanded sheet Ag) the partial charge at the Ag/Ag_2O potential had oxidized approximately 28% of the Ag to Ag_2O. If the charge had not been interrupted the amount of Ag_2O in the electrode would have doubled before charge potential rose sufficiently that AgO could begin to form. Only a very small proportion of the Ag had no visible Ag_2O coating.

Ag_2O and AgO appear as different shades of gray when unpolarized light is used and under most conditions can be distinguished from each other readily. Identification may be less certain when using unpolarized light if only one of the oxides is present, but under polarized light Ag_2O and AgO have quite different colors. Under polarized light the crystals in Fig. 1 were definitely identified as being Ag_2O and not AgO crystals.

Figure 2 shows an electrode charged until potential rose to the peak that ends the Ag/Ag_2O potential plateau. The area shown includes some of the larger Ag particles present in an electrode. Comparison with Fig. 1 shows changes that took place as Ag_2O was forming. Ag particles had decreased in size as the result of additional oxidation of their surfaces. Very few of the needlelike particles of Ag remained in electrodes charged to the end of the Ag/Ag_2O plateau.

The oxidation did not take place evenly throughout an electrode. Figure 3 shows another area of the same electrode already shown in Fig. 1 but after the electrode was charged twice as much. Based on the weight of Ag present in this electrode, the charge had oxidized approximately 60% of the Ag to Ag_2O. In the area shown in Fig. 3, an area of very small Ag particles, 80-90% of the Ag had been oxidized. In some other areas where larger Ag particles were present, less than 50% of the Ag had been oxidized to Ag_2O.

Small Ag particles were still present within almost all of the Ag_2O in an electrode charged to the end of the Ag/Ag_2O potential plateau. A few individual crystals or small clumps of Ag_2O crystals not containing metallic Ag were also found. Although Ag_2O from the surfaces of adjacent Ag particles tended to grow together, many small voids remained in the Ag_2O. The Ag_2O did not form into large solid masses in the way that AgO formed later in a charge. No AgO formed before the potential peak was reached.

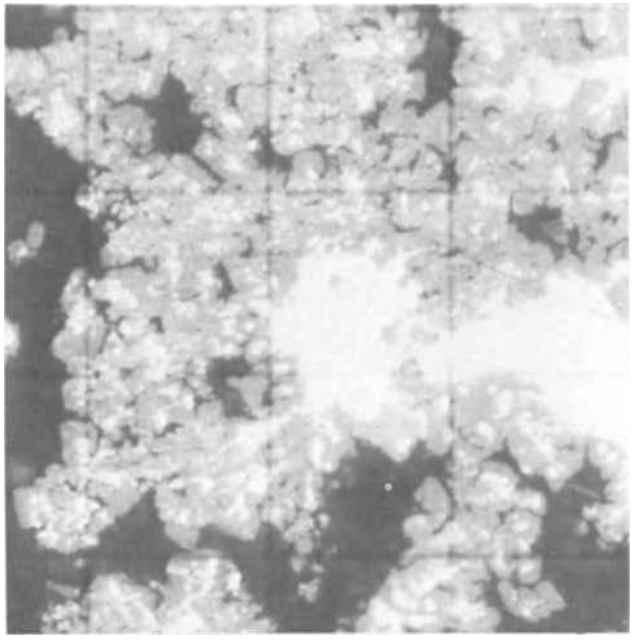

Fig. 2. Ag electrode charged at cycle 2 until potential reached the peak that ends the Ag/Ag_2O plateau. Lines forming squares are 15μ apart, same magnification as Fig. 1.

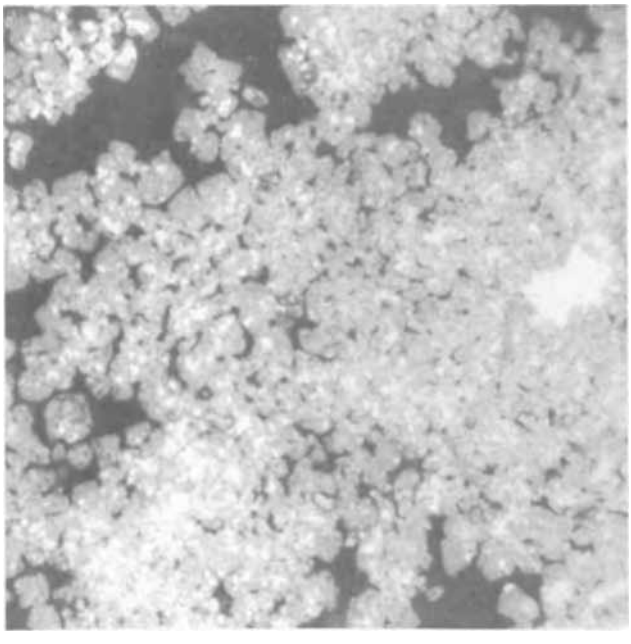

Fig. 3. Ag electrode charged at cycle 6 until potential rose at the end of the Ag/Ag_2O potential plateau. Electrode was given 39% of average charge acceptance. Small Ag particles in the area shown had largely oxidized to Ag_2O. Same magnification as Fig. 1 and 2.

A lower magnification view of Ag_2O formation is given in Fig. 4. This electrode, charged at cycle 2 until potential rose to the peak that ends the Ag/Ag_2O potential plateau, is the same electrode shown in Fig. 2. Magnification is one-fourth as much as was used in Fig. 1-3. The lower magnification emphasizes the fact that the active material was in clumps.

Part of the expanded metal grid and a few of the larger Ag particles are included in Fig. 4. The large particles were distributed randomly in an electrode at cycle 2. Ag_2O had formed on the surface of the Ag particles as well as on the grid. The surface of the grid in an unused electrode was comparatively smooth. Penetrating attack was already noticeable on the grid surface shown in Fig. 4. The large Ag particles had the same amount of surface attack as did the grid. Thicker

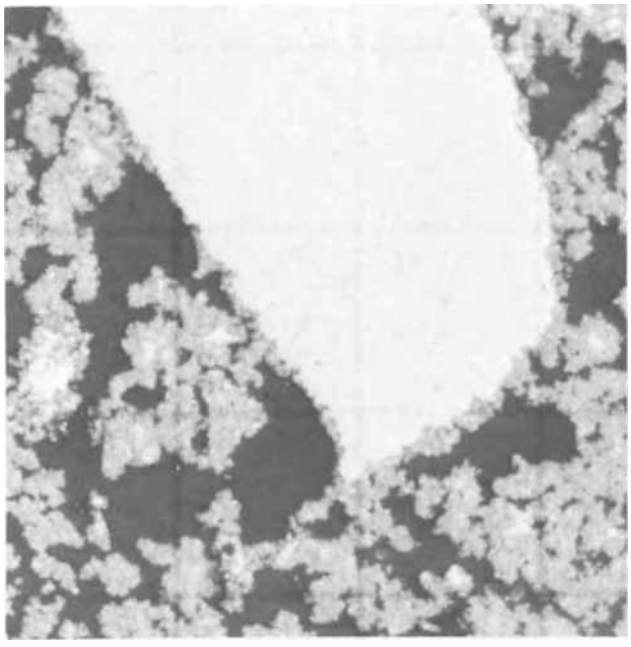

Fig. 4. Ag electrode charged at cycle 2 until potential rose at the end of the Ag/Ag_2O potential plateau, showing typical Ag_2O formation found in early cycles. Large white object is part of the Ag grid. Lines forming squares are 60μ apart.

Ag_2O layers had formed on the grid and on the large Ag particles of this partly charged electrode at cycle 2 than had formed during the first charge. The Ag_2O layer was thickest on the small Ag particles.

Effects of current density and cycling.—The amount of Ag_2O that formed during a charge was strongly influenced by the conditions used for the previous cycles. When electrodes were always discharged at the relatively fast 1-hr rate, the charge acceptance at the Ag/Ag_2O potential plateau increased during the first few charges. Consider cycle 2, for example. The electrode shown in Fig. 2 had been charged to approximately 22% of theoretical capacity. This means that an estimated 44% of the Ag had been oxidized to Ag_2O by the time that potential reached the peak that separates the Ag/Ag_2O and Ag_2O/AgO plateaus. Charge acceptance at the Ag/Ag_2O plateau had increased at cycle 6. Approximately 60% of the Ag had oxidized to Ag_2O in the electrode shown in Fig. 3. As charge acceptance at the Ag/Ag_2O plateau increased, charge acceptance at the Ag_2O/AgO plateau had decreased proportionately. Total capacity accepted before oxygen evolution began was relatively constant in this period. The electrodes shown at cycles 2 and 6 had accepted 33% and 39% of total capacity, respectively, when charge potential reached the peak.

Figure 5 gives the charge capacity that Ag electrodes accepted before their potential reached the peak ending the Ag/Ag_2O plateau. Each of the four electrodes whose capacity is shown had close to the same capacity acceptance during the first charge. All the electrodes were charged at the 20-hr rate. Two were discharged at the 1-hr rate and the other two at the 20-hr rate. The changes in discharge capacity when these four electrodes were cycled have been shown in Fig. 6 of reference (2).

All electrodes given the same cycle treatment tended to accept approximately the same amount of charge at the Ag/Ag_2O potential. After the first few cycles, electrodes always discharged at the relatively fast 1-hr rate formed approximately three times as much Ag_2O as did electrodes always discharged at the slow rate (Fig. 5). When the 1-hr discharge rate was used, the charge accepted at the Ag/Ag_2O level at cycle 1 was 33-39% of the capacity of the following discharge. From cycles 3 to 30 the charge was usually in the range of 37-46% of discharge capacity.

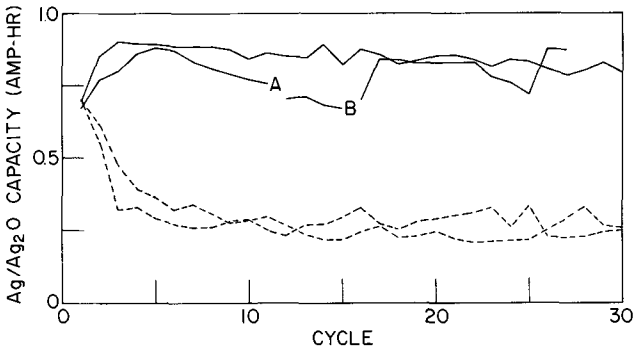

Fig. 5. Charge capacity accepted at Ag/Ag_2O level when electrodes were charged at the 20-hr rate in 35% KOH at 25°C. Solid lines are for two Ag electrodes always discharged at the 1-hr rate. Dashed lines are for two electrodes always discharged at the 20-hr rate. At point A one cell stood discharged 74 days and at point B the electrolyte in this one cell was replaced.

A larger discharge capacity was obtained at cycle 1 when the 20-hr discharge rate was used than when the 1-hr rate was used. The charge accepted at the Ag/Ag_2O level at cycle 1 was 27-32% of capacity of the following discharge when the discharge was done at the 20-hr rate. The charge at the Ag/Ag_2O level decreased for the next few cycles and then from cycle 5 to cycle 30 was usually in the range 15-22% of the capacity of the slow discharges.

Replacing the old electrolyte with fresh 35% KOH made a noticeable difference in charge acceptance. Electrolyte was replaced in one cell at point B of Fig. 5. The charge acceptance at the Ag/Ag_2O level was somewhat larger after the electrolyte was replaced, but the total discharge capacity had increased by a greater proportion.

Changes in structure after repeated cycling.—The average size of Ag particles in an electrode tended to increase as an electrode was cycled using fast discharges. Figure 6 illustrates an electrode charged at cycle 28 for half the capacity the electrode would accept at the Ag/Ag_2O potential plateau. Most of the Ag particles were covered with a layer of Ag_2O. Ag_2O coatings were the same on particles at the surface of

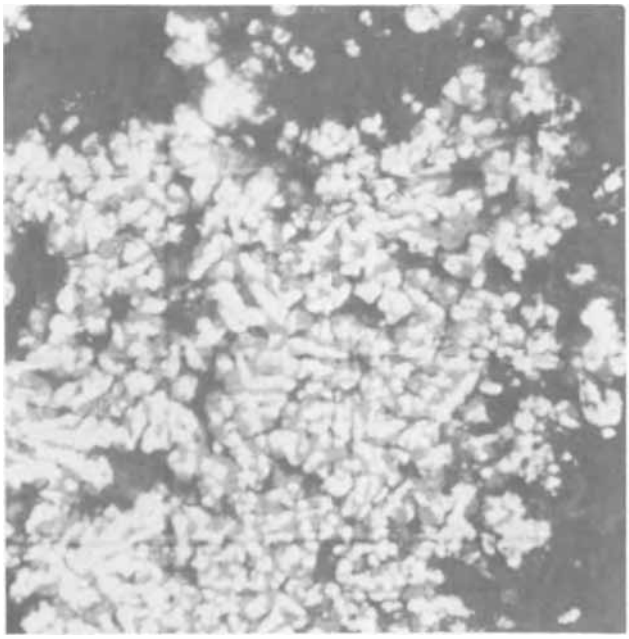

Fig. 6. Ag electrode charged approximately halfway across the Ag/Ag_2O potential plateau at cycle 28. The surface of the electrode is included at the right of this photograph. Compare with Fig. 1 to see changes in particle size that gradually took place as electrode was cycled. Lines forming squares are 15μ apart.

the electrode as in its interior. A small proportion of the particles had no Ag_2O coating visible at the magnifications used (up to 1600X). Many Ag particles larger than those shown here were present in other areas of the electrode.

When the charge of this electrode was continued until potential rose to the peak that ends the Ag/Ag_2O potential plateau, additional Ag_2O formed as shown in Fig. 7. The area shown in Fig. 7 included larger Ag particles than were shown in Fig. 6. The changes to be noted are the decrease in size of the small Ag particles and increase in Ag_2O thickness. Based on the weight of Ag in the unused electrode, 27% and 52% of the Ag had been oxidized to Ag_2O in the electrodes shown in Fig. 6 and 7, respectively. The size of typical Ag particles was larger at cycle 28 than at cycles 2 and 6. This can be seen by comparison of Fig. 6 with Fig. 1, and also by comparison of Fig. 7 with Fig. 2 and 3.

When an electrode was cycled repeatedly the distribution of the large Ag particles became uneven. The large Ag particles had a marked tendency to form in the interior of an electrode rather than in areas near a surface (2). The small Ag particles became less common as the large particles developed. Many of the smallest Ag particles present at the beginning of cycle 28 charge had already been oxidized to Ag_2O before the state of charge shown in Fig. 7 was reached, because the current oxidized small particles in preference to large particles. Figure 7 was typical of the structure at the end of the Ag/Ag_2O potential plateau at cycle 28, although a few areas similar to the one shown in Fig. 3 were still present. Individual isolated crystals of Ag_2O or groups of these crystals had been found in the early cycles but were rare at cycle 28. Almost all clumps of Ag_2O contained metallic Ag.

The active material gradually clumped as an electrode was cycled. Figure 8 gives a lower magnification view of another part of the electrode shown in Fig. 7. Comparison of Fig. 8 with Fig. 4 shows that the active material was in larger clumps at cycle 28 than in cycle 2. The Ag_2O still formed as a quite porous mass, much as in the early cycles. As the clumps of active material became larger, the distribution of void space worsened and large voids formed in the electrode.

A small number of clumps of particles had become oriented parallel to each other as an electrode was cycled. An example of particles in clumps parallel to other clumps is shown at the right side of Fig. 8. These oriented clumps were not common. They were found most often at the surfaces of the electrodes, with the clumps aligned at right angles to the electrode surface.

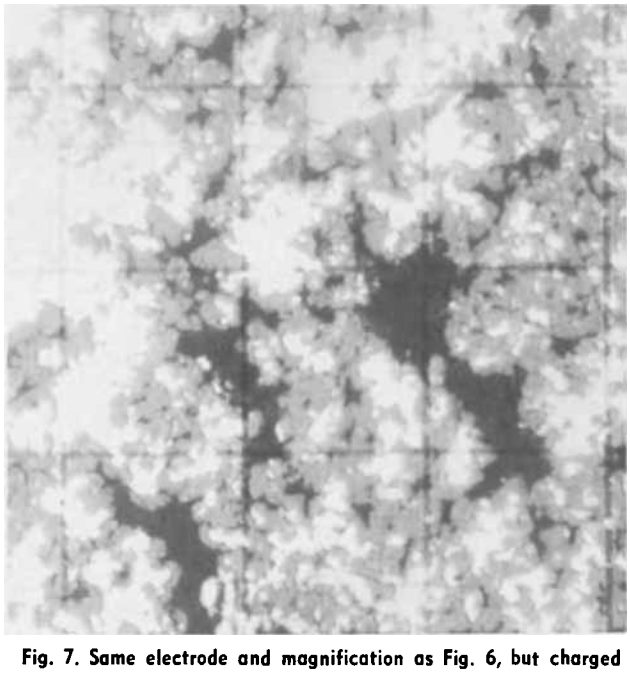

Fig. 7. Same electrode and magnification as Fig. 6, but charged until potential rose at the end of the Ag/Ag_2O potential plateau at cycle 28. Compare with Fig. 2 and 3 for changes with cycling.

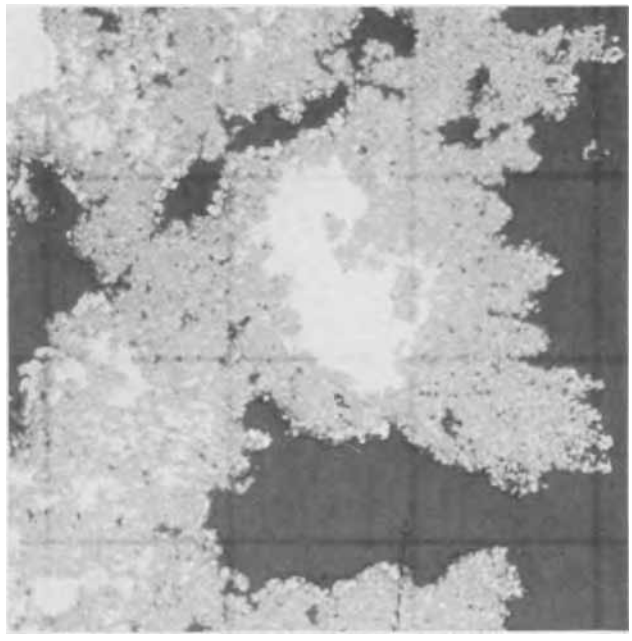

Fig. 8. Another area of the electrode shown in Fig. 7, but at lower magnification with lines forming squares being 60μ apart. Electrode surface is at the right. Comparison with Fig. 4 shows that active material had clumped as electrode was cycled.

Discussion

Anodic formation of Ag_2O.—It has been established that the anodic oxidation of Ag to Ag_2O in an alkaline solution takes place through two mechanisms (4-6). When a bare Ag surface is anodically oxidized, the initial reaction is Ag going into solution, probably as the ion $Ag(OH)_2^-$. The solution becomes supersaturated in the early part of a charge (7). Dissolved Ag precipitates on the Ag surface as Ag_2O. Through this process the amount of Ag in a particle can increase or decrease as the Ag is oxidized. In practice, little or no change in average particle size was observed during a charge. The oxidation mechanism changes after a layer of Ag_2O has deposited on Ag and then Ag_2O forms directly at crystallization centers. Obviously the number of crystallization centers present in the sintered electrode was very large. This was evident from the fact that almost all individual Ag particles had a coating of Ag_2O before the formation of Ag_2O was half completed. The formation and growth of Ag_2O crystals on smooth Ag has been studied by electron microscopy of surface replicas by Yoshizawa and Takehara (8) and in more detail by Briggs *et al.* (9). Although most of the present work was not directly comparable with this electron microscopy, the results agreed in general. The present work differed in using cross sections of porous electrodes and in viewing these at a much lower magnification. The fact that particles near the surface of porous electrodes differed from the interior after cycling indicated that conditions in sintered Ag particles can be significantly different from those on smooth Ag.

Measurements have shown no appreciable photochemical decomposition of Ag_2O under ordinary conditions (10). When anodic current is being passed, illumination can result in nonequilibrium conditions at the surface of the electrode, resulting in lowered resistance and AgO forming at potentials lower than usual (11-13). This process can take place only near the surface where light penetrates and probably had no effect on the present work using relatively thick electrodes which were never illuminated strongly. The experimental cell was exposed to some room light during daytime, but light reaching the electrode was

limited by the translucent polyethylene cell case and also by the opaque separator material which was wrapped around the electrode.

There are indications that Ag_2O and AgO are not the only oxides of silver. For example, Vol and Shishakov heated thin films of Ag at 100°-200°C in O_2 near atmospheric pressure and detected by electron diffraction what they considered to be a thin surface peroxide film of "AgO_2" having a cubic structure with a = 5.52 ± 0.02Å (14). Later Gossner and Polle used electron diffraction and detected a surface oxide which they call "AgO_x" when Ag reacted with H_2O_2 or when Ag was anodically oxidized in 0.1M NaOH (15). This oxide was reported to have a cubic structure with a = 5.55 ±0.01Å and is obviously the same material found earlier (14). No chemical analyses have been reported for this AgO_2 or AgO_x.

More recently Gossner *et al.* studied the anodic oxidation of Ag in 0.01M NaOH and claim that this AgO_x always forms as an intermediate between Ag_2O and AgO (16). They reported that after a coating of Ag_2O has formed on the surface of Ag under constant current conditions, then AgO_x forms in place of the Ag_2O as potential rises toward the peak at the end of the Ag/Ag_2O plateau, and no Ag_2O remains on Ag at the potential peak. AgO is then formed from the AgO_x. They find the same formation sequence under potentiostatic conditions.

If it is assumed that Ag_2O is entirely converted to some other oxide such as AgO_x before potential reaches the peak, then the photographs in the present work should show this other oxide and not Ag_2O. However, there actually is no valid reason for believing that any oxide except Ag_2O is shown in the photographs. When earlier work is considered, it becomes obvious that the statements of Gossner *et al.* (16) cannot be accepted as universally true. For example, the results of x-ray diffraction performed while Ag was being anodically oxidized in 8.4M KOH showed the presence of only Ag_2O and Ag as potential approached and reached the peak (17). The Ag_2O diffraction pattern did not broaden or shift as Ag_2O was then oxidized to AgO. Obviously all Ag_2O had not been converted to a material such as the proposed AgO_x before AgO formed. In fact, if any AgO_x was present under these conditions it must have been present in only such a small amount or such a thin layer that AgO_x was undetectable by x-ray diffraction.

Perhaps the difference between much of the literature concerning the anodic oxidation of Ag and the results of Gossner *et al.* comes from the weakly alkaline solution they used (16) in contrast to the strongly alkaline solutions more often used. However, even in 1*N* KOH Briggs *et al.* found only Ag_2O in samples oxidized anodically up to the potential peak (9). There is no reason to doubt that in the present work when an electrode was oxidized to the potential peak the oxide was mostly or entirely Ag_2O and not AgO_x.

Oxidation of Ag in porous electrodes.—Ag_2O occupies a greater volume than does metallic Ag, per atom of Ag. Void space between particles of Ag decreased, therefore, as Ag_2O was formed during a charge. This change can be seen by comparing Fig. 1 with Fig. 2 and 3. It can also be seen by comparing Fig. 6 with Fig. 7.

Although the oxidation of Ag did not take place simultaneously in all areas of the porous electrodes used in the present work, Ag_2O had formed on most of the Ag particles before an electrode was 20% charged. Approximately 40% of the active material in a cycled electrode still remained as metallic Ag when potential reached the peak between the Ag/Ag_2O and Ag_2O/AgO plateaus. Most of this Ag consisted of the larger Ag particles in the electrode, particles that did not oxidize completely during a charge. The smaller Ag particles had been oxidized to a greater extent, and only small remnants of these remained as Ag metal (Fig. 2, 3, 7).

Approximately one-tenth of the silver oxide in a charged electrode was not reduced during a discharge at the 1-hr rate, but still remained when potential reached the cutoff value and discharge ended. The amount of oxide remaining gradually increased as the electrolyte aged, apparently the result of carbonate concentration slowly becoming larger while KOH concentration decreased proportionately. An increase in capacity was obtained by replacing the electrolyte with fresh KOH solution. Part of this increase is indicated in Fig. 5 by the increased amount of Ag_2O which formed in cycles after point B.

Changes in structure after repeated cycling.—The charge capacity that an electrode accepted at the Ag/Ag_2O potential depended on whether large or small Ag particles had been formed during the preceding discharge. There was a large change in the structure of Ag electrodes during their first discharge, with the change depending on the discharge C.D. As mentioned, during a fast (1-hr) discharge Ag formed as particles having a size on the order of 1μ. These particles were smaller than those in the unused electrode. On the other hand, Ag particles ten times larger than those in the unused electrode had formed during the first slow (20-hr) discharge. Most Ag particles that form during a slow discharge are in the range of 10-25μ in size. During cycle 2 charge an increased amount of Ag_2O formed from electrodes containing small particles, while a decreased amount of Ag_2O formed from the large particles. An example of the large Ag particles that formed during slow discharges is given in Fig. 9. Since the large particles were only oxidized to a depth of 1-2μ at their surfaces, approximately 82% of the Ag remained in the metallic state in the electrode shown in Fig. 9. The effect of C.D. on particle size is reflected in Fig. 5 by the rise in the solid lines and fall in the dashed lines during the first few cycles.

After electrodes that always used fast discharges were given a number of cycles, the average size of Ag particles had increased. Despite this increased size the Ag particles were still much smaller after 27 cycles than after 5 cycles using slow discharges. This can be seen by comparing Fig. 6 and 7 with Fig. 9, all at the same magnification. Only a small proportion of par-

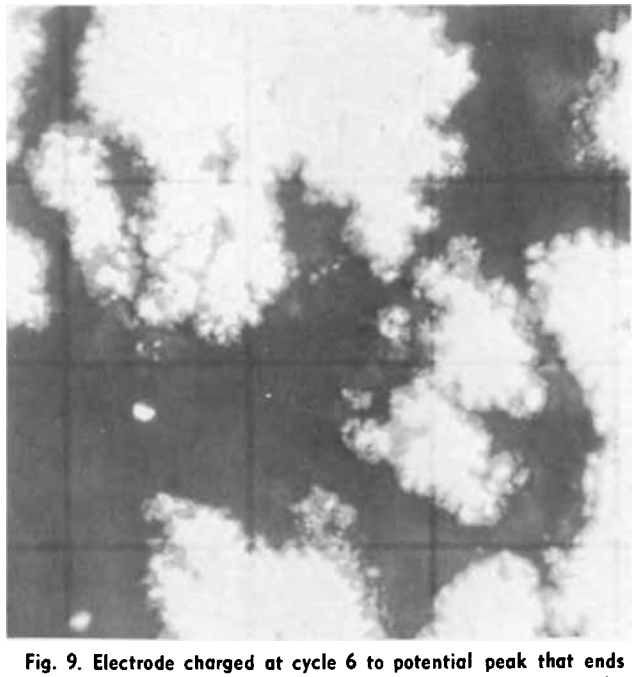

Fig. 9. Electrode charged at cycle 6 to potential peak that ends the Ag/Ag_2O plateau. This electrode was always discharged at the 20-hr rate, in contrast with other photographs where the 1-hr rate was always used. Comparison with Fig. 3 and 7 shows effect of discharge rate on subsequent formation of Ag_2O. Lines forming squares are 15μ apart.

ticles were larger than 5μ in an electrode never given slow discharges.

Although the proportion of particles having a particular size changed with cycling, the range of particle sizes and shapes did not change. When an electrode was viewed at high magnification (800X or higher), areas could be found in a well-cycled electrode that closely resembled areas in an electrode after only 1 or 2 cycles. The changes that took place during a particular charge as Ag particles were oxidized to Ag_2O were usually best observed at high magnifications.

Lower magnifications (100X to 400X) were useful for studying changes in structure that took place gradually over a series of cycles, such as changes in sizes of voids and of clumps of active material, as well as changes in the proportion of active material having a given structure. The clumping of active material during cycling can be seen by comparing Fig. 4 and 8 for electrodes at cycles 2 and 28. Clumping can also be seen, but less readily, by comparing Fig. 1 and 6. The clumping of active material resulted in large voids developing while small voids decreased in number. The active material tended to clump around large Ag particles and around the Ag grid. A study of the changes during cycles 1 and 2 indicated that probably all this deposition of active material on large Ag particles and on the grid took place during discharge and probably none during charge.

Conductivity must have been good because examination of these electrodes in various states of charge and discharge did not indicate that reactions took place at the grid (Fig. 4) in preference to the remainder of the electrode. Particles or groups of particles that appeared to be isolated reacted to the same extent as particles obviously touching each other. There must have been connections between the particles that were above or below the planes where the electrodes had been cut to reveal the cross sections. Many Ag particles that remained at the end of a charge, particularly the larger particles, served as parts of a conductive network together with the grid. During a fast discharge groups of small Ag particles formed on the Ag of the conductive network.

Even at the end of cycle 1 charge, before active material had clumped, adjacent crystals of AgO were often found touching each other. Since the oxides were slightly soluble in the KOH solution, oxides close to conducting particles could be reduced on these particles. In this way the deposit of small dendritic Ag particles gradually thickened on larger particles and on the grid as an electrode was cycled (compare Fig. 4 and 8). As a result the active material came to be present in increasingly large clumps of particles. At the same time voids between the clumps grew in size. The clumping and development of voids was the same whether the electrode was given fast or slow discharges.

The small Ag particles that deposited near the large Ag particles and near the grid during a fast discharge were of suitable size to be oxidized completely during the next charge. Thus the oxide layers in charged electrodes gradually became thicker with cycling. It was pointed out earlier that the small Ag particles oxidized before the grid surface and formed a coating protecting the grid from serious attack, in contrast with the large Ag particles which formed during slow discharges (2).

The fact that a few groups of particles developed an alignment at right angles to the electrode surface (right side of Fig. 8) suggests that formation of these groups was connected with either current paths or diffusion in the electrolyte. The aligned groups shown in Fig. 8 must have been present at the end of the previous discharge, because Ag particles were visible within the Ag_2O. A few similarly oriented groups of AgO were found at the end of a charge. It is not known whether the alignment of particles took place during charges or discharges.

Conclusions

1. Ag_2O formed on Ag particles at the surface and interior of electrodes without preference during a charge, but more Ag_2O formed in some areas than in others.
2. Most of the Ag particles had a definite Ag_2O coating before the Ag/Ag_2O potential plateau was half completed. Very few particles were completely oxidized to Ag_2O when the potential peak ending the Ag/Ag_2O plateau was reached.
3. Ag_2O did not form into large solid masses but contained many small voids. Void space within an electrode decreased during a charge, however, because Ag_2O occupied a greater volume than did Ag.
4. Electrode capacity was definitely related to the microstructure. Charge acceptance at the Ag/Ag_2O potential plateau increased during the first few charges following discharges at the 1-hr rate. In contrast, charge acceptance decreased following discharges at the 20-hr rate until only one-third as much Ag_2O formed. The difference resulted from small Ag particles forming during fast discharges while large particles formed during slow discharges
5. Conductivity was good within the electrode, apparently because many Ag particles served as parts of a conductive network together with the grid. Nearby oxides could be reduced on the conducting particles during discharges. As a result, during a series of cycles the active material gradually clumped around large Ag particles and around the grid.
6. Fast discharges repeated for many cycles resulted in changes within an electrode, but little change at the surfaces. It can, therefore, be misleading to draw conclusions about structure after examining only the surfaces of an electrode.

Manuscript submitted July 8, 1970; revised manuscript received Sept. 15, 1970. This was Paper 56 presented at the Atlantic City Meeting of the Society, October 4-8, 1970.

Any discussion of this paper will appear in a Discussion Section to be published in the December 1971 JOURNAL.

REFERENCES

1. C. P. Wales, *This Journal*, **116**, 729 (1969).
2. C. P. Wales, *ibid.*, **116**, 1633 (1969).
3. C. P. Wales and A. C. Simon, *ibid.*, **115**, 1228 (1968).
4. B. N. Kabanov and D. I. Leikis, *Z. Elektrochem.*, **62**, 660 (1958); G. L. Vidovich, D. I. Leikis, and B. N. Kabanov, *Dokl. Akad. Nauk SSSR*, **124**, 855 (1959); *ibid.*, **142**, 109 (1962).
5. M. J. Dignam, H. M. Barrett, and G. D. Nagy, *Can. J. Chem.*, **47**, 4523 (1969).
6. R. D. Giles, J. A. Harrison, and H. R. Thirsk, *J. Electroanal. Chem.*, **22**, 375 (1969).
7. B. Miller, *This Journal*, **117**, 491 (1970).
8. S. Yoshizawa and Z. Takehara, *J. Electrochem. Soc. Japan*, **31**, 91 (1963).
9. G. W. D. Briggs, M. Fleischmann, D. J. Lax, and H. R. Thirsk, *Trans. Faraday Soc.*, **64**, 3120 (1968).
10. T. P. Dirkse, D. Vander Hart, and J. Vriesenga, *J. Inorg. Nucl. Chem.*, **27**, 1779 (1965).
11. A. A. Yakovleva, T. I. Borisova, and V. I. Veselovskii, *Zh. Fiz. Khim.*, **16**, 1426 (1962).
12. H. Göhr and A. Breitenstein, *Elektrochim. Acta*, **11**, 1377 (1968).
13. R. Memming, F. Möllers, and G. Newmann, *This Journal*, **117**, 451 (1970).
14. Yu. Ts. Vol and N. A. Shishakov, *Izv. Akad. Nauk SSSR, Otd. Khim. Nauk*, **1962**, 586; *ibid.* **1963**, 1920.
15. K. Gossner and H. Polle, *Z. Physik. Chem. (Frankfurt)*, **54**, 93 (1967).
16. K. Gossner, Th. Eftychiadis, and D. Körner, *Z. Naturforsch.*, **24a**, 807 (1969); *ibid.* **24a**, 813 (1969).
17. C. P. Wales and J. Burbank, *This Journal*, **112**, 13 (1965).

Electrodissolution Kinetics of Iron in Chloride Solutions

Part I. Neutral Solutions

S. Asakura* and Ken Nobe*

School of Engineering and Applied Science, University of California, Los Angeles, California 90024

ABSTRACT

Anodic dissolution of iron in unbuffered neutral chloride solutions has been investigated by transient polarization techniques. A new method to correct for the ohmic potential drop has been proposed. It has been observed that the anodic Tafel slopes were 40 mV/decade for fast polarization and 80 mV/decade for slow or steady-state polarization. Steady-state anodic characteristics of iron have been studied by superimposing short cathodic potential and current pulses. At steady-state anodic polarization a Tafel relation was obtained between the cathodic potential (ϕ_c) and the cathodic current (i_c) with a Tafel slope of about 120 mV/decade for both potentiostatic and galvanostatic pulses. The difference in anodic Tafel slopes has been interpreted in terms of the formation of a hydroxochloro-iron complex, $[Fe(OH)_m(Cl)_n]^{2-m-n}$. The cathodic pulse polarization results indicate that $m = 1$.

Numerous studies of the anodic dissolution of iron in acidic chloride solutions have been carried out. There have not been as many studies of iron in neutral solutions in spite of their practical importance. Hoar and Farrer (1) studied the anodic polarization of mild steel in dilute neutral chloride solution and obtained Tafel slopes of about 60 mV. Stern (2) observed marked hysteresis for iron in 4% NaCl solutions of pH 1-4. Stern and Roth (3) indirectly deduced the anodic Tafel slope of iron in this solution as 78 or 68 mV. On the other hand, Hurlen (4) obtained reproducible Tafel lines with slopes of 30 mV for iron in acidic KCl solutions. He observed deviations from the Tafel line at high current densities and at high pH. Based on extensive experiments, Bockris, Drazic, and Despic (5) obtained anodic Tafel slopes of 40 mV for iron in acidic sulfate and chloride solutions.

Nobe and Tobias (6) observed that the anodic polarization of iron in H_2SO_4 in the active state was not appreciably affected by chloride ions. Podesta and Arvia (7) found that the steady-state anodic polarization of iron yielded Tafel slopes of 32-54 mV (2M NaCl) and 37-61 mV (0.2M NaCl) for solutions of various pH values.

Ross, Wood, and Mahmud (8) studied the anodic behavior of iron in flowing solutions of HCl and H_2SO_4. While no effect of flow was observed at low current densities, polarization decreased as the flow rate increased at high current density. They ascribed the latter to the formation of a porous surface compound formed at high current densities. Foroulis (9) observed considerable hysteresis in HCl solutions and surmised that this hysteresis was due to adsorption of Cl^- and subsequent complex formation. Complex formation of this kind had been previously proposed by Schottky (10). Morozumi and Posey (11) applied the pH-stat technique (12) to the detection of an iron complex. Florianovich, Sokolova, and Kolotyrkin (13) have suggested the formation of an iron-sulfate complex.

In this work, the anodic dissolution of iron in unbuffered neutral solutions has been investigated by transient techniques.

Experimental

The electrolyte used was 1*N* potassium chloride solution, deaerated with purified nitrogen. The test specimen was Ferrovac E iron with a purity of 99.91%. The 1 cm diameter rod was sealed in Teflon such that only one cross-sectional surface was exposed to the electrolyte. This surface was polished by 2/0 emery paper. The electrode was degreased with detergent and rinsed several times with distilled water and benzene. When surface roughing became pronounced during an experiment, the electrode was repolished, degreased, and rinsed again in the same manner. Electrical signals were generated by combining the potentiostat (response time, 1 μsec) with function generators and pulse generators. The responses were recorded on either an oscilloscope or an X-Y recorder. The electrochemical cell was constructed of Pyrex and was the common three-electrode type cell. The temperature was maintained at 25° ± 1°C.

Results

Steady-state anodic polarization.—The open triangle in Fig. 1 shows the apparent potential (E_a)-current (i_a) relation under steady-state anodic polarization. While the plot follows Tafel behavior at low current density, the deviation is considerable at high current density due to the ohmic potential drop. The potential after the subtraction of the ohmic drop from the apparent potential is plotted as closed circles. The solution resistance was determined by the pulse technique.

The electrode potential was also measured by the current-interrupting method. Current was interrupted for 120 μsec. The interruption was repeated at intervals of 10 Hz. The open circles represent the potential immediately after interrupting the current. The plots, after correction for the ohmic drop, show Tafel behavior with a slope of about 80 mV/decade up to 200 mA/cm^2.

Linear anodic potential sweep polarization.—The linear potential sweep method was used to obtain the anodic polarization behavior under transient conditions. The potential sweep in the anodic direction was started at the open-circuit potential (E_o). The open-

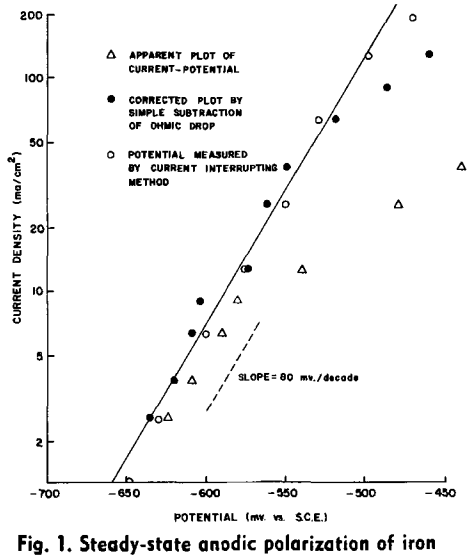

Fig. 1. Steady-state anodic polarization of iron

* Electrochemical Society Active Member.

Key words: corrosion, anodic behavior, transient behavior.

circuit potential was around −780 mV *vs.* SCE. At high sweep rates, the charging current for the double layer capacitance, *i.e.*, nonfaradaic current, was dominant in the low current density region. However, at high current densities the ohmic drop became considerable. Therefore, in order to obtain the faradaic current at fast potential sweeps the ohmic drop must be eliminated.

The tangent method has been developed to eliminate the ohmic drop. The procedure is as follows. As illustrated in Fig. 2, a line tangent to a point on the apparent potential-current curve is drawn and extrapolated to zero current. The intercept of the tangent line with the potential axis ($i_a = 0$) is an important parameter as shown below.

The apparent potential (E_a) is equal to the sum of the electrode potential (ϕ_a) and the ohmic drop $R_s i_a$

$$E_a = \phi_a + R_s i_a \qquad [1]$$

where R_s is the solution resistance. The line tangent to the curve at (i_{al},E_{al}) is expressed by

$$E_a = \left[\left(\frac{\partial \phi_a}{\partial i_a} \right)_{i_a = i_{al}} + R_s \right] (i_a - i_{al}) + E_{al} \qquad [2]$$

The potential of the intercept, E_{ax}, is obtained by putting $i_a = 0$

$$E_{ax} = \phi_a - i_{al} \left(\frac{\partial \phi_a}{\partial i_a} \right)_{i_a = i_{al}} \qquad [3]$$

Equation [3] does not include the term for the ohmic potential drop given in Eq. [1]. In other words, E_{ax} is only a function of ϕ_a. The solution of the differential Eq. [3] with respect to ϕ_a is shown in Eq. [4].

$$\phi_a = i_{al} \int_{i_{al}}^{\infty} (E_{ax}/i_a^2)\, di_a \qquad [4]$$

Thus, the electrode potential ϕ_a, which does not include the ohmic potential drop, can be deduced from the intercept E_{ax}. For the special case where ϕ_a obeys the Tafel equation

$$\phi_a = a + b \log i_a \qquad [5]$$

E_{ax} can be expressed by

$$E_{ax} = a - b/2.3 + b \log i_a \qquad [6]$$

Equation [6] indicates that a plot of E_{ax} *vs.* log i_a is a straight line with the slope b. Therefore, ϕ_a is determined from

$$\phi_a = E_{ax} + b/2.3 \qquad [7]$$

An example of a plot of ϕ_a *vs.* log i_a is shown in Fig. 3 and compared with the apparent Tafel plot. At low current densities, E_a and ϕ_a show good agreement because of the negligible ohmic potential drop. At high current densities, E_a deviates from the straight line, while ϕ_a still follows the linear relationship. The plots of ϕ_a *vs.* log i_a were determined for various sweep rates. At high sweep rates these plots were still linear in the high current density region. The Tafel slopes thus obtained are shown in Fig. 4. The Tafel slope was found to change from 80 to 40 mV/decade with increase in sweep rate. Limitations of the function generator precluded results at higher sweep rates.

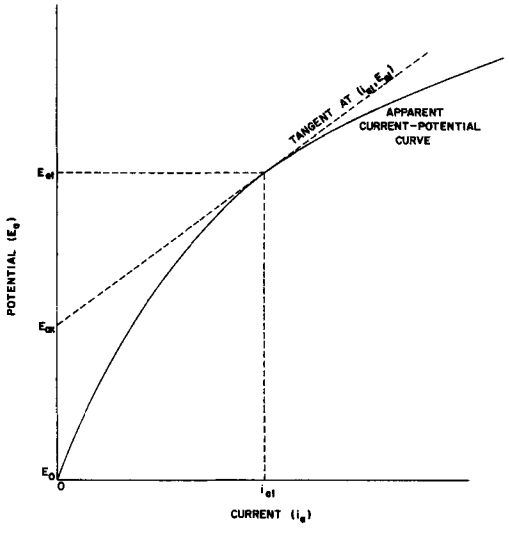

Fig. 2. Illustration of the tangent method

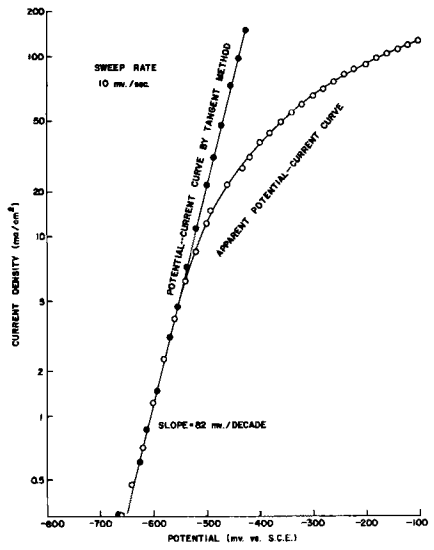

Fig. 3. Comparison of polarization curves obtained directly and by the tangent method.

Potentiostatic anodic pulse polarization.—A short single potential pulse was imposed on the electrode at the open-circuit potential, as shown in Fig. 5. An analysis of the responding current yields the polarization behavior corrected for the ohmic potential drop. The

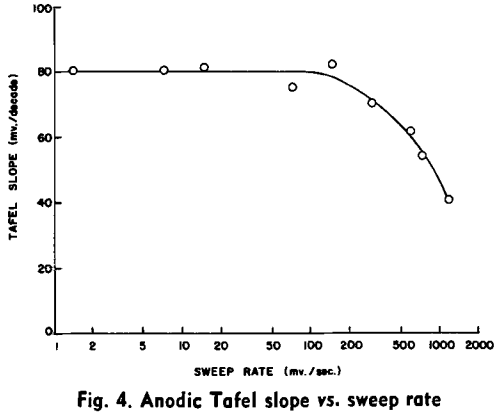

Fig. 4. Anodic Tafel slope *vs.* sweep rate

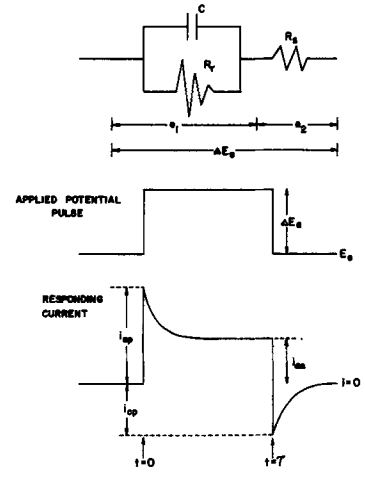

Fig. 5. Transient behavior during pulse polarization

principle is as follows. The equivalent circuit of the electrode is given by the top figure in Fig. 5. The applied potential pulse ΔE_a can be divided into the change in the electrode potential, e_1 and the ohmic potential drop, e_2, *i.e.*

$$\Delta E_a = e_1 + e_2 \qquad [8]$$

Immediately after ΔE_a is imposed, e_1 is zero due to the double layer capacitance C_{dl}. Therefore

$$e_2 = \Delta E_a \text{ at } t = 0 \qquad [9]$$

Then, the current i_{ap} at $t = 0$ is

$$i_{ap} = \Delta E_a / R_s \qquad [10]$$

After C_{dl} is charged, the current reaches a constant value, i_{as}. At this stage

$$e_1 = \phi_a - E_o \qquad [11]$$

$$e_2 = R_s i_{as} \qquad [12]$$

where ϕ_a is the electrode potential, exclusive of the ohmic potential drop.

When the pulse is shut off at $t = \tau$ ($\Delta E_a = 0$), e_1 still follows Eq. [11]. Then, i_{cp}, the current at $t = \tau$ is related to ϕ_a by

$$\phi_a = R_s \mid i_{cp} \mid + E_o \qquad [13]$$

Thus, ϕ_a can be determined because of the existence of the double layer capacitance. Experimentally, the double layer charging was completed within 1 msec. R_s was determined from the plot of i_{ap} *vs.* ΔE_a. By substituting R_s, thus obtained, into Eq. [13], ϕ_a can be determined. ϕ_a is plotted *vs.* log i_{as} in Fig. 6. The plots show straight lines up to high current densities in spite of the large ohmic drops. When ΔE_a is small, the points for short pulses deviated from these plots due to the nonfaradaic current. Tafel slopes were about 40 mV/decade for short pulses, while it was about 80 mV/decade for long pulses.

Potential pulse reduction of an anodized electrode.— An anodically polarized electrode at a steady state was periodically reduced by short constant cathodic potential pulses. The potential pulse width was 5 msec and the time interval between pulses was 0.5 sec. The duration of the potential pulse was so short that the anodic process can be considered to be maintained at steady-state conditions. Figure 7 shows an example of the current transient (i_c) due to a reducing cathodic potential pulse. The plot is shown as the logarithm of $|i_c|$ *vs.* time (t). A slow linear decrease in log current is observed after a sharp decrease which corresponds to the charging of the double layer capacitance. The plots of the current (i_{ci}) at $t = 0$ *vs.* the applied pulse potential give straight lines as shown in Fig. 8.

Since a double layer capacitance exists between the electrode and solution as shown in Fig. 5, the electrode

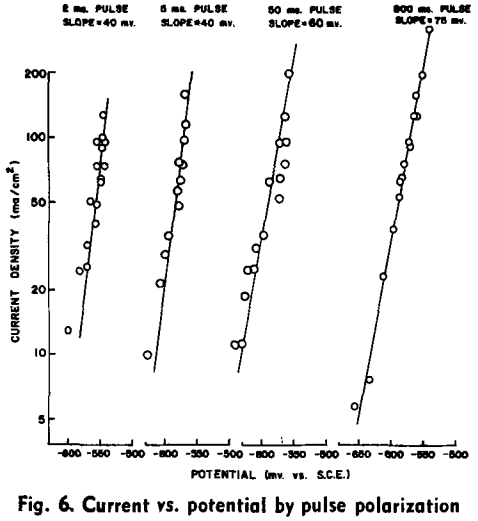

Fig. 6. Current *vs.* potential by pulse polarization

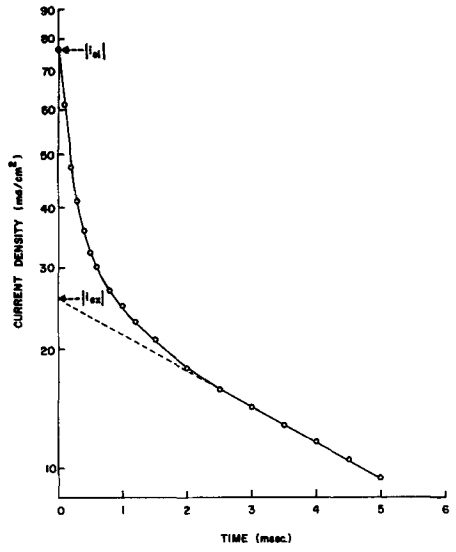

Fig. 7. Current transient of a cathodic potential pulse during anodic polarization of iron.

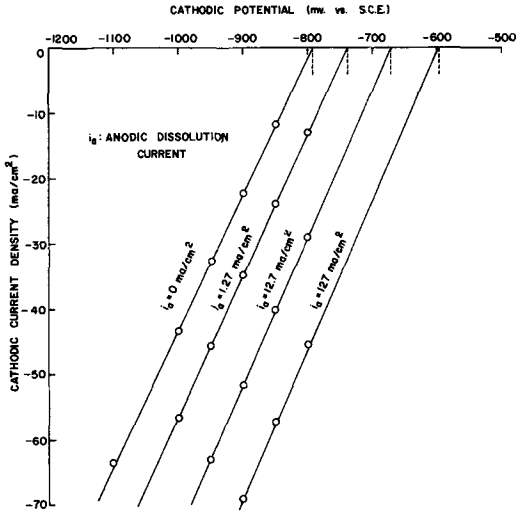

Fig. 8. Plots of i_{ci} *vs.* the cathodic potential pulse

potential at steady-state anodic polarization, ϕ_a, is still maintained at $t = 0$. Then, the relation

$$i_{ci} = (E_c - \phi_a)/R_s \qquad [14]$$

is obtained, where E_c is the applied cathodic pulse potential. Therefore, the slopes of the lines in Fig. 8 express the solution conductance $1/R_s$ and the extrapolation of these lines to zero current gives, ϕ_a, the steady-state anodic potential exclusive of the ohmic potential drop. The anodic electrode potential, ϕ_a, thus obtained, is plotted against the logarithm of the anodic current, i_a, in Fig. 9. The Tafel slope of this line is about 80 mV/decade.

$$\partial \phi_a / \partial \log i_a = 80 \text{ mV/decade} \qquad [15]$$

This value is in good agreement with that obtained from the direct steady-state anodic polarization data discussed above. Thus, the anodic Tafel slope of iron in neutral chloride solutions for steady-state polarization has been confirmed by another method. Morozumi (14) reported nearly the same value for iron in neutral sodium chloride solutions.

The slow decrease in the log $|i_c|$ probably results from a change in the surface state of iron. The extrapolation of the linear portion of the curve in Fig. 8 to zero time would give the cathodic current, i_{cx}, at conditions where the iron surface and its environment have not changed appreciably from that at steady-state anodic polarization. The charging current is only

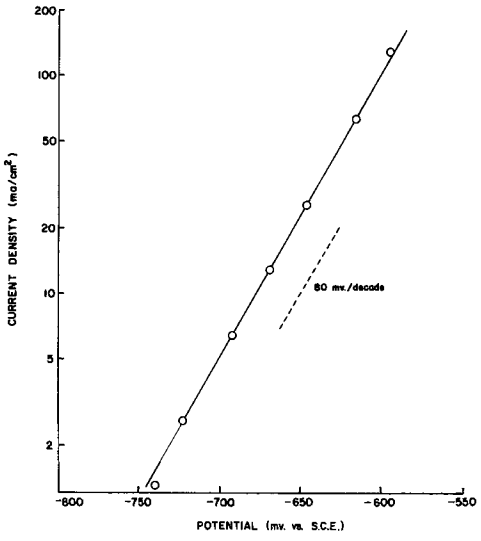

Fig. 9. Steady-state anodic Tafel plot obtained by the cathodic potential pulse method.

a negligible part of i_{cx}. The logarithm of $|i_{cx}|$ is plotted in Fig. 10 against ϕ_c which is the cathodic potential exclusive of the ohmic potential drop. The slope of the plots was about −120 mV/decade

$$\left(\frac{\partial \phi_c}{\partial \log |i_{cx}|}\right)_{i_a} \approx -120 \text{ mV/decade} \qquad [16]$$

Figure 11 shows the dependence of the cathodic current i_{cx} on the steady-state anodic current, i_a. It is found that log $|i_{cx}|$ is linearly related to log i_a with the slope of about 1

$$\left(\frac{\partial \log |i_{cx}|}{\partial \log i_a}\right)_{\phi_c} \approx 1 \qquad [17]$$

Galvanostatic pulse reduction of an anodized electrode.—A short cathodic current pulse, i_c, was superimposed on the constant anodic current. The cathodic current pulse width and time interval between pulses were 5 msec and 0.5 sec, respectively. The anodic process was maintained at steady state. The potential transient for a reducing cathodic current pulse is shown in Fig. 12. At $t = 0$, the potential abruptly drops to E_{ci} due to the ohmic potential drop followed by a gradual decrease. The linear part of the curve is extrapolated to $t = 0$ and the intercept is defined as E_{cx}. Both E_{ci} and E_{cx} include the ohmic potential drop, $R_s i_c$, *i.e.*

$$E_{ci} = \phi_a + R_s i_c \qquad [18a]$$

$$E_{cx} = \phi_{cx} + R_s i_c \qquad [18b]$$

where ϕ_{cx} is the cathodic potential, exclusive of the ohmic potential drop.

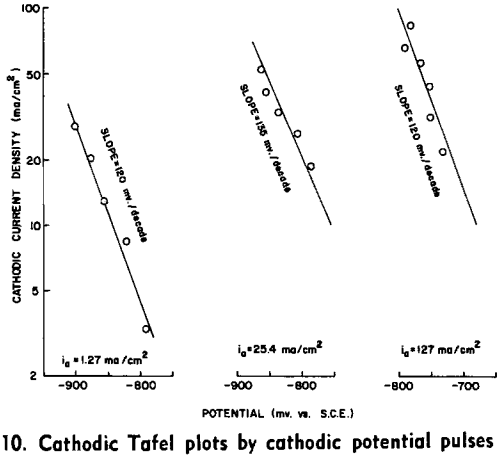

Fig. 10. Cathodic Tafel plots by cathodic potential pulses during anodic polarization.

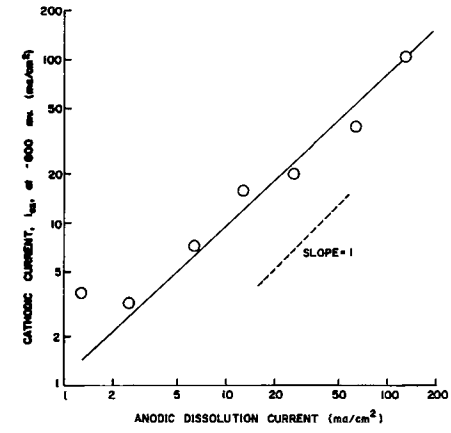

Fig. 11. Extrapolated cathodic current (i_{cx}) vs. the steady-state anodic current.

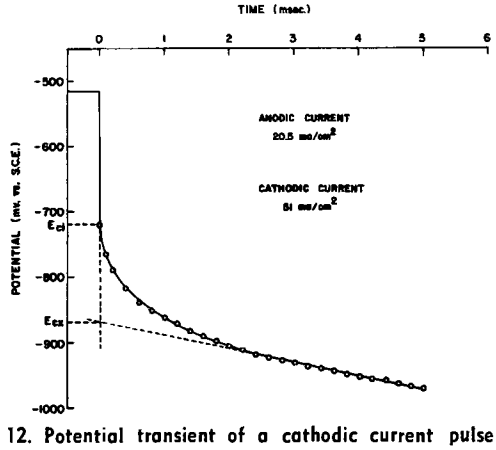

Fig. 12. Potential transient of a cathodic current pulse during anodic polarization of iron.

Therefore

$$E_{ci} - E_{cx} = \phi_a - \phi_{cx} \qquad [19]$$

and does not include the ohmic potential drop. Since ϕ_a is independent of i_c, the following relation holds

$$\left(\frac{\partial (E_{ci} - E_{cx})}{\partial \log |i_c|}\right)_{i_a} \approx -\left(\frac{\partial \phi_{cx}}{\partial \log |i_c|}\right)_{i_a} \qquad [20]$$

The plots of log $|i_c|$ *vs.* $(E_{ci} - E_{cx})$ are shown in Fig. 13. These plots exhibit straight lines with slopes of about 120 mV/decade. Therefore, the following relation is obtained

$$\left(\frac{\partial \phi_{cx}}{\partial \log |i_c|}\right)_{i_a} \approx -120 \text{ mV/decade} \qquad [21]$$

The plots of E_{cx} *vs.* log i_a at constant i_c are shown in Fig. 14. A linear relation is observed with slopes of

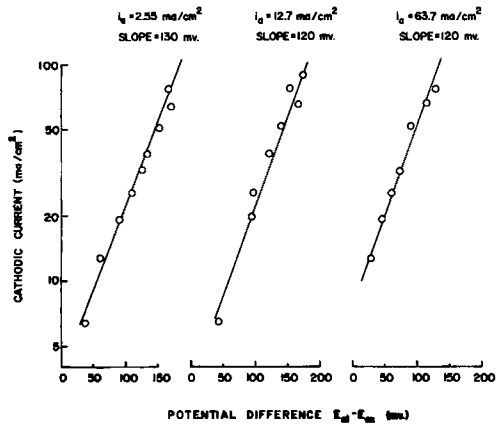

Fig. 13. Cathodic Tafel plots by cathodic current pulses during anodic polarization of iron.

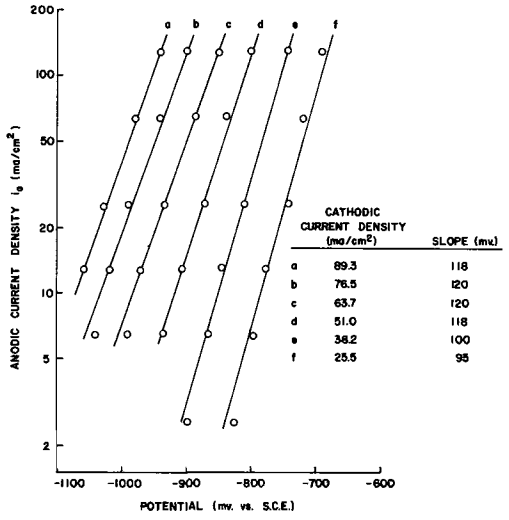

Fig. 14. Plots of the extrapolated cathodic potential (E_{cx}) vs. log i_a at constant cathodic current.

between 120 to 95 mV/decade, *i.e.*

$$\left(\frac{\partial E_{cx}}{\partial \log i_a}\right)_{ic} = 120 \text{ to } 95 \text{ mV/decade} \qquad [22]$$

By introducing Eq. [18b], Eq. [22] becomes

$$\left(\frac{\partial \phi_{cx}}{\partial \log i_a}\right)_{ic} = 120 \text{ to } 95 \text{ mV/decade} \qquad [23]$$

Discussion

As mentioned above, the anodic Tafel slopes were about 40 mV/decade for fast polarization and about 80 mV/decade for slow or steady-state polarization. The Tafel slope for fast polarization is consistent with that deduced from the Bockris mechanism. Akiyama *et al.* (15) reported the same value for iron in 1*N* H_2SO_4 under steady-state polarization. It is evident that the *p*H at the electrode is much different from that of the bulk solution in unbuffered neutral solutions. In this experiment, the anodic passivation was not observed even at a current density of 200 mA/cm². The critical current density for the neutral solutions in the absence of chloride ions has been reported to be less than 100 μA/cm² (16). In acidic solutions, *e.g.*, 1*N* H_2SO_4, the critical current is about 200 mA/cm² in the absence of chloride ions (17). The absence of passivation even at high current densities and Tafel behavior in the entire range indicate the probable formation of a soluble iron complex with chloride ions. The existence of an iron complex with chloride ions has been suggested previously by Schottky (10) and Foroulis (9). Therefore, it seems reasonable that the results of this work can be interpreted by assuming the formation of a hydroxochloro-iron complex and the consequent *p*H change at the electrode surface. In addition, the Bockris mechanism (5) with low coverage of reaction intermediate, Fe(OH), is assumed.

Reaction mechanism.—The Bockris mechanism (5) for iron dissolution is as follows

$$Fe + OH^- = (FeOH)_{ads} + e \qquad [24a]$$

$$(FeOH) \xrightarrow{RDS} FeOH^+ + e \qquad [24b]$$

$$FeOH^+ = Fe^{++} + OH^- \qquad [24c]$$

In addition, the reaction for the formation of the complex is assumed to be at equilibrium

$$Fe^{++} + mH_2O + nCl^- = [Fe(OH)_m(Cl)_n]^{2-n-m} + mH^+ \qquad [24d]$$

Therefore, the over-all reaction can be expressed by

$$Fe + mH_2O + nCl^- = FeX + mH^+ + 2e \qquad [24e]$$

where FeX represents the complex ion, $[Fe(OH)_m(Cl)_n]^{2-n-m}$. According to Eq. [24e] the solution at the electrode becomes more acidic as the reaction proceeds. When step [24b] is rate determining and the hydrogen ion concentration at the electrode surface is $(a_{H^+})_{x=0}$

$$i_a = k_a(a_{H^+})^{-1}_{x=0} \exp(1+\beta)\mathbf{F}\phi_a/RT \qquad (25)$$

where k_a and β are the rate constant and the transfer coefficient, respectively. It has been assumed that the surface coverage of FeOH is low and that the Langmuir isotherm is valid.

Fast anodic polarization.—The concentration of H^+ at the electrode can remain nearly constant during polarization because the amount of H^+ produced by reaction [24d] is not appreciable. Therefore

$$\frac{\partial \phi_a}{\partial \ln i_a} = RT/(1+\beta)\mathbf{F} \qquad [26]$$

The Tafel slope corresponding to this equation is 40 mV/decade for $\beta = \frac{1}{2}$ at 25°C. This value is consistent with that obtained experimentally.

Steady-state anodic polarization.—At steady state, the H^+ and FeX produced must diffuse away continuously. Also the current is proportional to the diffusion rates of H^+ and FeX. The relation can be expressed by

$$i_a = -2\mathbf{F}D_{FeX}\left(\frac{\partial a_{FeX}}{\partial x}\right)_{x=0} = \frac{-2\mathbf{F}D_{H^+}}{m}\left(\frac{\partial a_{H^+}}{\partial x}\right)_{x=0} \qquad [27]$$

Application of diffusion layer theory simplifies Eq. [27]. Also, $(a_{H^+})_{x=0}$ is assumed to be much larger than the activity of H^+ in the bulk solution. Then

$$i_a = 2\mathbf{F}D_{H^+}(a_{H^+})_{x=0}/m\,\delta = 2\mathbf{F}D_{FeX}(a_{FeX})_{x=0}/\delta \qquad [28]$$

where δ is the diffusion layer thickness. Insertion of $(a_{H^+})_{x=0}$, thus obtained, into Eq. [25] gives

$$i_a^2 = \frac{2\mathbf{F}k_aD_{H^+}}{m\delta}\exp[(1+\beta)\mathbf{F}\phi_a/RT] \qquad [29]$$

that is

$$i_a = \sqrt{2\mathbf{F}k_aD_{H^+}/m\delta}\exp(1+\beta)\mathbf{F}\phi_a/2RT \qquad [30]$$

Therefore

$$\partial\phi_a/\ln i_a = 2RT/(1+\beta)\mathbf{F} \qquad [31]$$

The Tafel slope corresponding to Eq. [31] is 80 mV/decade. Thus, the difference in the Tafel slopes can be interpreted on the basis of *p*H changes at the iron surface. As discussed above, a number of authors have reported irreproducibility and deviation from anodic Tafel behavior at relatively high *p*H. At least part of these complications are the result of the *p*H change at the electrode surface.

Potential pulse reduction of an anodized electrode.—Since the complexation reaction is assumed to be at equilibrium, the following equation holds for a large excess of chloride ions

$$\frac{a_{FeX}a^m_{H^+}}{a_{Fe^{++}}} = K \qquad [32]$$

where K is the equilibrium constant. Equations [28] and [32] give

$$(a_{Fe^{++}})_{x=0} = K^{-1}(a_{FeX})_{x=0}(a_{H^+})^m_{x=0} = K'i_a \cdot i_a^m = K'i_a^{m+1} \qquad [33]$$

where

$$K' = \frac{mK^{-1}}{D_{H^+}D_{FeX}}\left(\frac{\delta}{2\mathbf{F}}\right)^2$$

When Eq. [24b] is also rate determining for the cathodic deposition reaction, the faradaic cathodic current is expressed by

$$i_{cx} = -k_c(a_{Fe^{++}})_{x=0}(a_{OH^-})_{x=0}\exp -(\beta'\mathbf{F}\phi_c/RT) \qquad [34a]$$

or

$$i_{cx} = -k'_c(a_{Fe++})_{x=0}(a_{H+})^{-1}{}_{x=0}\exp -(\beta'\mathbf{F}\phi_c/RT) \quad [34b]$$

where k_c and k'_c are rate constants and β' is the transfer coefficient corresponding to the reverse reaction of Eq. [24b]. Combining Eq. [34b] with [28] and [33], the cathodic current for conditions where the electrode surface and its environment are at the steady-state anodic polarization is obtained

$$i_{cx} = -k''_c i_a{}^{m+1} i_a{}^{-1}\exp -(\beta'\mathbf{F}\phi_c/RT)$$
$$= -k''_c i_a{}^m \exp -(\beta'\mathbf{F}\phi_c/RT) \quad [35]$$

where k''_c is a constant.

From Eq. [35], the following relation can be deduced

$$\left(\frac{\partial \phi_c}{\partial \log |i_{cx}|}\right)_{i_a} = \frac{-2.3RT}{\beta'\mathbf{F}} \quad [36]$$

$$\left(\frac{\partial \log |i_{cx}|}{\partial \log i_a}\right)_{\phi_c} = m \quad [37]$$

From Eq. [36]

$$\left(\frac{\partial \phi_c}{\partial \log |i_{cx}|}\right)_{i_a} = -120 \text{ mV/decade}$$

for $\beta = \frac{1}{2}$ at 25°C.

This is consistent with the values obtained from Eq. [16] and [21]. A comparison of Eq. [37] with Eq. [17] gives $m = 1$. This result can also be determined from the galvanostatic reduction experiments. In this case, Eq. [35] is transformed to

$$i_c = -k''_c \exp\left[-\frac{\beta'\mathbf{F}}{RT}\left(\phi_{cx} - \frac{RT}{\beta'\mathbf{F}} m \ln i_a\right)\right] \quad [38]$$

Therefore, when i_c is constant, the following relation is obtained

$$\left(\frac{\partial \phi_{cx}}{\partial \log i_a}\right)_{i_c} = \frac{2.3RT}{\beta'\mathbf{F}} m \quad [39]$$

By inserting Eq. [23], m is obtained as

$$m = 0.8 \text{ to } 1$$

Thus, the pulse reduction studies of anodized electrode have been shown to be consistent with the Bockris mechanism of iron electrodissolution, the formation of a hydroxochloro-iron complex, $[Fe(OH)_m(Cl)_n]^{2-n-m}$, $m = 1$ and the related pH change at the electrode surface.

Acknowledgment

This work was supported by a grant from the Office of Saline Water, U. S. Department of the Interior.

Manuscript received Jan. 8, 1970; revised manuscript received *ca.* Aug. 20, 1970.

Any discussion of this paper will appear in a Discussion Section to be published in the December 1970 JOURNAL.

LIST OF SYMBOLS

a	constant in Eq. [5]
a_{Fe++}	activity of hydrogen ions
a_{FeX}	activity of hydroxochloro-iron complex
$(a_{Fe++})_{x=0}$	activity of ferrous ions at iron surface
$(a_{FeX})_{x=0}$	activity of FeX at iron surface
a_{H+}	activity of hydrogen ions
$(a_{H+})_{x=0}$	hydrogen ion activity at iron surface
a_{OH-}	activity of hydroxyl ion
b	constant in Eq. [5]
C_{dl}	capacitance of electrical double layer
D_{FeX}	diffusion coefficient of FeX
D_{H+}	diffusion coefficient of hydrogen ions
E_a	apparent anodic potential, mV *vs.* SCE
E_{ax}	anodic potential as shown in Fig. 2
E_{al}	apparent anodic potential at point 1 on potential-current curve
E_c	applied cathodic potential pulse, mV
E_{ci}	cathodic potential as shown in Fig. 12, mV *vs.* SCE
E_{cx}	cathodic potential as shown in Fig. 12, mV *vs.* SCE
E_o	open circuit potential, mV *vs.* SCE
e_1	potential difference as shown in Fig. 5
e_2	potential difference as shown in Fig. 5
$\mathbf{F}$	Faraday's constant
i_a	steady-state anodic current density, mA/cm²
i_{ap}	current change as shown in Fig. 5
i_{as}	current change as shown in Fig. 5
i_{al}	anodic current at point 1 on potential-current curve
i_c	cathodic current density, mA/cm²
i_{ci}	cathodic current as shown in Fig. 7, mA/cm²
i_{cp}	current change as shown in Fig. 5
i_{cx}	cathodic current as shown in Fig. 7, mA/cm²
K	equilibrium constant as defined in Eq. [32]
K'	constant defined in Eq. [33]
k_a	constant in Eq. [25]
k_c	constant defined in Eq. [34a]
k'_c	constant defined in Eq. [34b]
k''_c	constant defined in Eq. [35]
m	ligand number for hydroxide
n	ligand number for chloride
R	gas constant
R_r	reaction resistance
R_s	solution resistance
T	absolute temperature, °K
t	time after imposition of pulse
x	distance in electrolyte from iron surface
β	transfer coefficient in Eq. [25]
β'	transfer coefficient in Eq. [35]
ΔE_a	applied anodic potential pulse, mV
δ	diffusion layer thickness
ϕ_a	anodic electrode potential (corrected for *IR* drop), mV *vs.* SCE
ϕ_c	cathodic electrode potential (corrected for *IR* drop), mV *vs.* SCE
ϕ_{cx}	cathodic electrode potential as defined in Eq. [18b], mV *vs.* SCE
τ	time period as shown in Fig. 5

REFERENCES

1. T. P. Hoar and T. W. Farrer, *Corrosion Sci.*, **1**, 49 (1961).
2. M. Stern, *This Journal*, **102**, 609 (1955).
3. M. Stern and R. M. Roth, *ibid.*, **104**, 390 (1957).
4. T. Hurlen, *Acta Chem. Scand.*, **14**, 1533 (1960).
5. J. O M. Bockris, D. Drazic, and A. R. Despic, *Electrochim. Acta*, **4**, 325 (1961).
6. K. Nobe and R. F. Tobias, *Corrosion*, **20**, 263t (1964).
7. J. J. Podësta and A. J. Arvia, *Electrochim. Acta*, **10**, 171 (1965).
8. T. K. Ross, G. C. Wood, and I. Mahmud, *This Journal*, **113**, 334 (1966).
9. Z. A. Foroulis, *ibid.*, **113**, 532 (1966).
10. W. F. Schottky, *Halbleiterprobleme* Bd. II, p. 255 (1955).
11. T. Morozumi and F. A. Posey, *Denki Kagaku*, **35**, 633 (1967).
12. F. A. Posey, T. Morozumi, and E. J. Kelly, *This Journal*, **110**, 1183 (1963).
13. G. M. Florianovich, L. A. Sokolova, and Ya. M. Kolotyrkin, *Electrochim. Acta*, **12**, 879 (1967).
14. T. Morozumi, *Bull. Fac. Eng., Hokkaido Univ.*, (Sapporo, Japan), **41**, 309 (1966).
15. A. Akiyama, R. Patterson, and K. Nobe, *Corrosion*, **26**, 51 (1970).
16. M. Nagayama and M. Cohen, *This Journal*, **109**, 781 (1962).
17. U. F. Franck, *Z. Electrochem.*, **55**, 154 (1951).

Electrodissolution Kinetics of Iron in Chloride Solutions

Part II. Alkaline Solutions

S. Asakura* and Ken Nobe*

School of Engineering and Applied Science, University of California, Los Angeles, California 90024

ABSTRACT

The anodic behavior of pure iron in alkaline chloride solution was studied by potential sweep and galvanostatic methods. For active dissolution anodic Tafel slopes of 65 and 66 mV/decade were obtained from the galvanostatic and potential sweep experiments, respectively. These values can be interpreted in terms of the Bockris mechanism with Temkin adsorption. Passivation was also observed. The peak current or critical current which appeared in the potential-current curve obtained by potential sweeps was proportional to the square root of the sweep rate. The potential associated with the peak current varied linearly in the anodic direction as the log of the sweep rate with a slope of 33 mV/decade. The square root of the passivation time obtained from galvanostatic polarization was inversely proportional to the current. These results were interpreted by assuming that passivation occurred when the iron chloride complex attained its solubility limit.

Comparatively few studies have been reported previously of iron in alkaline chloride solutions. Kabanov, Burstein, and Frumkin (1) found that the rate of anodic dissolution was not affected by the concentration of chloride ions ranging from 0.01 to 4*N* in 0.01*N* NaOH. They concluded that Cl^- did not actually participate in the anodic process. Hurlen (2) carried out some galvanostatic experiments in alkaline potassium chloride solutions. His chronopotentiograms showed active dissolution and passivation behavior. Shepherd and Schuldiner (3) studied the potentiostatic behavior of iron in a closed, high-purity alkaline system. They showed that iron acted like an inert noble metal but with addition of chloride ions extensive iron corrosion occurred; however, passive behavior as shown in potential-current curves was observed.

The complexation of iron in alkaline chloride solutions could play an important role in the iron dissolution processes. The importance of the formation of iron chloride complexes has been pointed out previously by Schottky (4) and Foroulis (5). Recently, Ogura, Haruyama, and Nagasaki (1) studied the open-circuit potential decay of passivated iron in neutral solutions containing chloride ions. They interpreted their results by assuming the formation of the complex FeOCl, which had been suggested previously by Schottky (4).

In this paper the anodic behavior of iron in an alkaline chloride solution was investigated by potential sweep and galvanostatic methods. The results have been interpreted in terms of the formation of an iron chloride complex, as proposed in a previous paper (7), and its precipitation on the electrode.

Experimental

A 1*N* potassium chloride and 0.1*N* potassium hydroxide solution was used as the electrolyte. The solution was deaerated with prepurified nitrogen. The test specimen was Ferrovac E iron with a purity of 99.9%. The temperature was maintained at 25° ± 1 C°. The electrical signals were generated by a potentiostat and function generators. The electrical responses were recorded by an X-Y and ordinary pen recorders.

Results

The electrode was reduced at about −1.5V (*vs.* SCE) and then left at open-circuit conditions until the electrode potential reached a constant value. After this treatment, the electrical signals were imposed on the electrode.

Potential sweep experiments.—The potential sweeps in the anodic direction were started from the open-circuit potential. Examples of the potential-current curves are shown in Fig. 1. Passivation behavior was observed, and it is seen that the shape of the curves was affected by the sweep rate (λ). The logarithm of the peak current (i_p) is plotted against log λ in Fig. 2. The log i_p was found to be linearly related to log λ with the slope of 1/2. Hence, the following relation was obtained

$$i_p = k_1\sqrt{\lambda} \qquad [1]$$

where k_1 is a constant. The primary passivation potential (E_p), *i.e.*, the potential associated with the peak current is plotted *vs.* log λ in Fig. 3. The slope of the linear relationship was 33 mV/decade

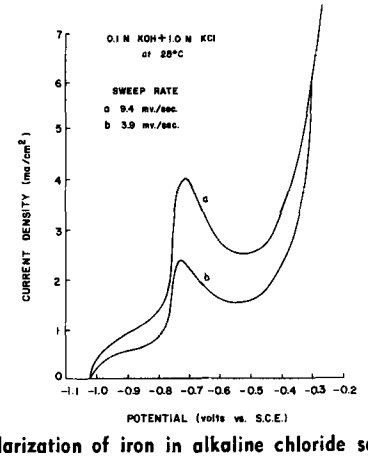

Fig. 1. Polarization of iron in alkaline chloride solutions by the potential sweep method.

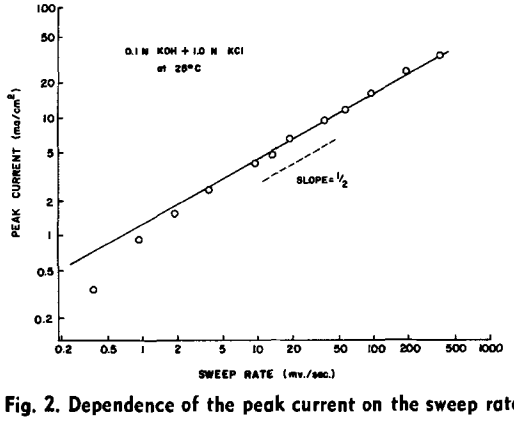

Fig. 2. Dependence of the peak current on the sweep rate

* Electrochemical Society Active Member.
Key words: corrosion, passivation, anodic behavior.

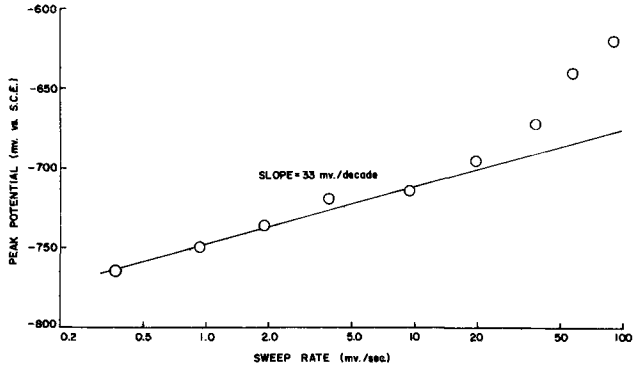

Fig. 3. Dependence of the peak potential on the sweep rate

$$\frac{\partial E_p}{\partial \log \lambda} = 33 \text{ mV/decade} \qquad [2]$$

The nonlinearity of the plot at high sweep rates was probably due to the ohmic potential drop.

Galvanostatic experiments.—A typical chronopotentiogram is shown in Fig. 4. There is a potential arrest at E_a and then a subsequent increase in potential. E_a can be regarded as the active potential corresponding to the applied current (i_a).

E_a is plotted against log i_a in Fig. 5. The Tafel slope was about 65 mV/decade

$$\frac{\partial E_a}{\partial \log i_a} = 65 \text{ mV/decade} \qquad [3]$$

The passivation time (t_p) was determined in the manner shown in Fig. 3. The plot of log t_p *vs.* log i_a is given in Fig. 6. A linear relation is obtained with the slope of −2 giving the following relation

$$i_a\sqrt{t_p} = k_2 \qquad [4]$$

where k_2 is a constant.

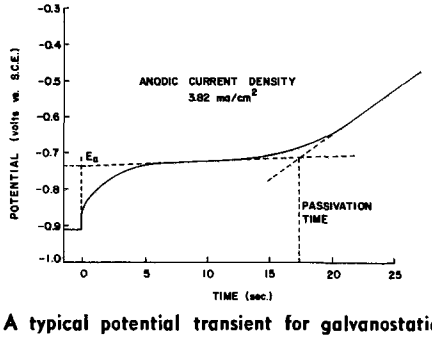

Fig. 4. A typical potential transient for galvanostatic polarization.

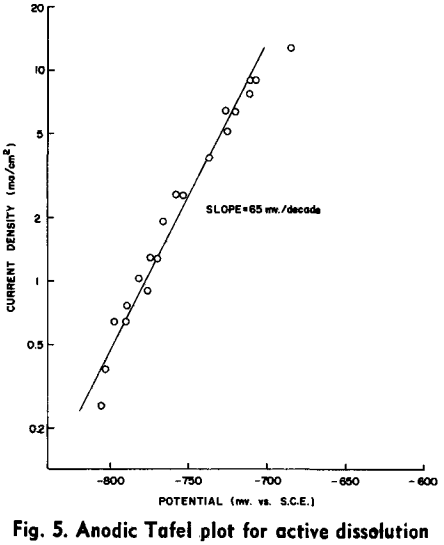

Fig. 5. Anodic Tafel plot for active dissolution

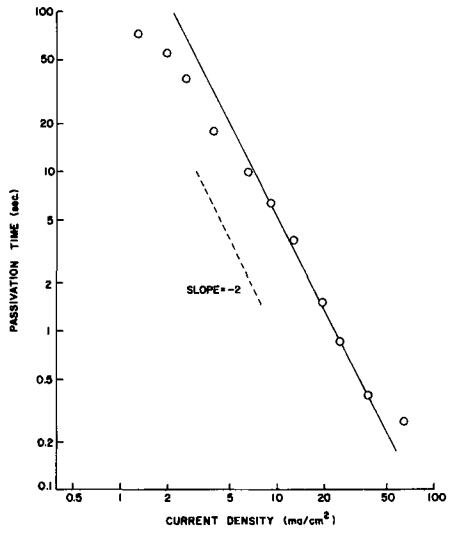

Fig. 6. Dependence of passivation time on the current

Discussion

In the previous paper (7) the dissolution kinetics of iron in neutral chloride solutions was interpreted in terms of the Bockris mechanism with the additional consideration of the formation of an iron chloride complex. The present results can also be interpreted on the same basis.

The Bockris mechanism (8) is as follows

$$\mathrm{Fe} + \mathrm{OH^-} = \mathrm{Fe(OH)} + e \qquad [5a]$$

$$\mathrm{FeOH} \xrightarrow{\text{RDS}} \mathrm{Fe(OH)^+} + e \qquad [5b]$$

$$\mathrm{Fe(OH)^+} = \mathrm{Fe^{++}} + \mathrm{OH^-} \qquad [5c]$$

The complexation reaction of iron in alkaline chloride solutions is

$$\mathrm{Fe^{++}} + m\mathrm{OH^-} + n\mathrm{Cl^-} = [\mathrm{Fe(OH)}_m\ (\mathrm{Cl})_n]^{2-m-n} \qquad [6]$$

Then, the over-all reaction is

$$\mathrm{Fe} + m\mathrm{OH^-} + n\mathrm{Cl^-} \rightarrow \mathrm{FeX} + 2e \qquad [7]$$

where FeX represents the complex ion

$$[\mathrm{Fe(OH)}_m\ (\mathrm{Cl})_n]^{2-m-n}$$

In alkaline solutions, the reaction mechanism would differ from that in neutral solutions as follows: (*A*) The surface coverage of the reaction intermediate Fe(OH) is considerably larger due to the high concentration of OH^-. (*B*) The change of *p*H at the electrode surface is not appreciable. (*C*) The nature of the complex FeX in alkaline solutions is different than in neutral solutions.

Anodic Tafel slope.—The Bockris mechanism (8) predicts the anodic Tafel slope of iron in acidic solutions as 40 mV/decade. In acidic solutions, the surface coverage of the reaction intermediate FeOH is assumed to be very low. Therefore, the Langmuir isotherm was applicable. This assumption was shown to be also valid for iron dissolution in neutral solutions (7). However, in alkaline solutions, the coverage of FeOH should be much greater. Therefore, the Temkin isotherm would be more appropriate than the Langmuir isotherm. The rate equations of reaction [5a] for Temkin adsorption can be written as (9)

$$r_a = k_a\,(1-\theta)\,[\mathrm{OH^-}]\exp(\beta E\mathbf{F}/RT)\exp(-\alpha f\theta) \qquad [8a]$$

$$r_{-a} = k_{-a}\,\theta\exp[-(1-\beta)E\mathbf{F}/RT]\exp[(1-\alpha)f\theta] \qquad [8b]$$

where, r_a and r_{-a} = the rate of the forward and backward reactions; k_a and k_{-a} = rate constants of the forward and backward reactions; β = symmetry factor;

E = potential; α = proportionality constant ($0 < \alpha \leqq 1$); f = Temkin free energy parameter; θ = coverage of FeOH.

Since θ is in the range $0.2 < \theta < 0.8$, in the case of Temkin adsorption, Eq. [8] can be approximated as follows

$$r_a = k_a [OH^-] \exp(\beta EF/RT) \exp(-\alpha f\theta) \quad [9a]$$

$$r_{-a} = k_{-a} \exp[-(1-\beta) EF/RT] \exp[(1-\alpha) f\theta] \quad [9b]$$

Since Eq. [5a] is at equilibrium

$$r_a = r_{-a} \quad [10]$$

Then, $f\theta$ can be obtained as

$$f\theta = \ln\left[\left(\frac{k_a}{k_{-a}}\right)[OH^-] \exp(FE/RT)\right] \quad [11]$$

Now, the rate equation for Eq. [5b] can be written as

$$r_b = k_b \theta \exp(\gamma FE/RT) \exp(\epsilon f\theta) \quad [12]$$

where k_b, γ, and ϵ are the rate constant, the symmetry factor, and the proportionality constant for reaction [5b], respectively. Equation [12] is simplified to

$$r_b = k'_b \exp(\gamma FE/RT) \exp(\epsilon f\theta) \quad [13]$$

Finally, the reaction rate can be obtained by inserting Eq. [11] into Eq. [13]

$$i_a = k''_b [OH^-]^\epsilon \exp[(\gamma + \epsilon) FE/RT] \quad [14]$$

where k''_b is a constant.

Usually, ϵ is equal to $(1 - \gamma)$ and γ is 1/2. Therefore, the actual rate equation can be given by

$$i_a = k''_b \sqrt{[OH^-]} \exp[FE/RT] \quad [15]$$

The Tafel slope is obtained as

$$\frac{\partial E}{\partial \log i_a} = \frac{2.3\,RT}{F} \quad [16]$$

This value is 60 mV/decade at 25°C, which is in good agreement with the result of active dissolution of iron given by Eq. [3].

Interpretation of passivation phenomena.—The passivation phenomena can be interpreted based on the following assumptions: (*I*) Active dissolution proceeds until passivation occurs. (*II*) When the concentration of FeX attains the solubility limit, passivation occurs. (*III*) The equilibrium constant of the complexation process, Eq. [6], is sufficiently large, *i.e.*, $[Fe^{++}] << [FeX]$.

The concentration, C, of FeX can be obtained by solving the diffusion equation

$$\frac{\partial C}{\partial t} = D\frac{\partial^2 C}{\partial x^2} \quad [17]$$

where, D = diffusion coefficient of FeX
t = time after the imposition of the electrical signals
x = the distance from the electrode surface.

Since the concentration of FeX in the bulk solution is negligible, the following conditions apply

$$C(\infty, t) = 0 \quad [18]$$

$$C(x, 0) = 0 \quad [19]$$

According to assumption (*III*), the current is related to the concentration of FeX in the following manner

$$-D\left(\frac{\partial C}{\partial x}\right)_{x=0} = i_a/2F = F(t) \quad [20]$$

Laplace transformation can be utilized to solve the above differential equations (10). Equations [17], [18], and [20] are transformed with respect to time

$$su(x,s) = D\frac{d^2u(x,s)}{dx^2} \quad [21]$$

$$u(\infty,s) = 0 \quad [22]$$

$$-D\left(\frac{du(x,s)}{dx}\right)_{x=0} = f(s) \quad [23]$$

where s is the Laplace parameter and $u(x,s)$ which satisfied Eq. [21], [22], and [23] is

$$u(x,s) = \sqrt{\frac{1}{Ds}} f(s) \exp\left(-\sqrt{\frac{s}{D}}x\right) \quad [24]$$

Applying the convolution theorem, the inverse transform of Eq. [24] can be obtained

$$\mathcal{L}^{-1}u(x,s) = \frac{1}{\sqrt{D}}\mathcal{L}^{-1}f(s) * \mathcal{L}^{-1}\left[\frac{1}{\sqrt{S}} \exp\left(-\sqrt{\frac{s}{D}}x\right)\right] \quad [25a]$$

Equation [25a] can be transformed to

$$C(x,t) = \frac{1}{\sqrt{\pi D}}\int_0^t F(t-\tau)\frac{1}{\sqrt{\tau}}\exp\left(\frac{-x^2}{4D\tau}\right)d\tau \quad [25b]$$

Finally, the concentration of FeX at the electrode surface is given by

$$C(0,t) = \frac{1}{\sqrt{\pi D}}\int_0^t F(t-\tau)\frac{1}{\sqrt{\tau}}d\tau \quad [26]$$

In accord with assumption (*II*) passivation occurs when $C(0,t)$ attains the solubility limit, C_s

$$C(0,t_p) = C_s \quad [27]$$

where t_p is the passivation time. In the case of galvanostatic polarization, $F(t)$ is constant

$$F(t) = F_o \quad [28]$$

Then, t_p is given by

$$C_s = \frac{2F_o}{\sqrt{\pi D}} \cdot \sqrt{t_p} \quad [29a]$$

Introducing Eq. [20], i_a is related to t_p

$$i_a\sqrt{t_p} = FC_s\sqrt{\pi D} = \text{constant} \quad [29b]$$

Thus, the empirical relation of Eq. [4] has been deduced theoretically.

In the case of the potential sweep experiments, $F(t)$ is given by the Tafel relation for active dissolution, according to assumption (*I*). When the potential sweep starts from the open-circuit potential, $F(t)$ is expressed by

$$F(t) = k \exp(E/K) \quad [30]$$
$$E = \lambda t + E_o$$
$$K = b/2.3$$

where, k = a rate constant
b = Tafel slope
λ = sweep rate
E_o = open circuit potential

The insertion of Eq. [30] into Eq. [27] gives

$$C_s = \frac{k}{\sqrt{\pi D}}\exp(Ep/K)\int_0^{t_p}\frac{\exp(-\lambda\tau)}{\sqrt{\tau}}d\tau \quad [31]$$

where $E_p = \lambda t_p + E_o$.
Putting $y = \lambda t/K$, Eq. [31] becomes

$$\sqrt{\frac{D\lambda}{K}}C_s = k\exp(E_p/K) \cdot \frac{1}{\sqrt{\pi}}\int_0^{(E_p-E_o)/K}\frac{\exp(-y)}{y}dy \quad [32]$$

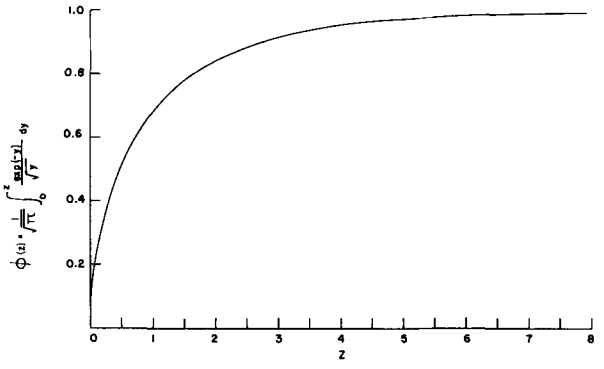

Fig. 7. ϕ (z) vs. z plot

The function

$$\phi(z) = \frac{1}{\sqrt{\pi}} \int_0^z \frac{\exp(-y)}{\sqrt{y}}\, dy \qquad [33]$$

is plotted in Fig. 7. For $z > 4$, $\phi(z)$ is almost unity

$$\phi(z) \approx 1, \quad z > 4 \qquad [34]$$

In the present experiments, $(E_p - E_o)$ is greater than 250 mV and b is about 60 mV/decade. Therefore, the approximation of Eq. [34] is valid for this experiment. Equation [32] is simplified to

$$C_s \sqrt{\frac{D\lambda}{K}} = k \exp(E_p/K) \qquad [35]$$

Since the peak current is expressed

$$i_p = 2\mathbf{F} \cdot \mathbf{F}(t_p)$$

the combination of Eq. [35] with Eq. [30] gives

$$i_p = 2\mathbf{F}k \exp[E_p/K] = 2\mathbf{F}C_s \sqrt{\frac{D\lambda}{K}} \qquad [36]$$

As C_s and D are constant, i_p is proportional to $\sqrt{\lambda}$. Thus, Eq. [1] can be derived theoretically. Also, E_p can be deduced from Eq. [35] as follows

$$E_p = \frac{K}{2} \ln \lambda + \ln 2\mathbf{F}C_s \sqrt{\frac{D}{K}} \qquad [37]$$

Therefore

$$\frac{\partial E_p}{\partial \log \lambda} = \frac{b}{2} \qquad [38]$$

The Tafel slope can be obtained by inserting the experimental value of Eq. [2]. The anodic Tafel slope, b, thus calculated is 66 mV/decade. This value is in approximate agreement with that obtained from the galvanostatic experiments, Eq. [3], and also with that derived theoretically, Eq. [16].

Acknowledgment

This work was supported by a grant from the Office of Saline Water, U.S. Department of the Interior.

Manuscript submitted Feb. 24, 1970.

Any discussion of this paper will appear in a Discussion Section to be published in the December 1971 JOURNAL.

REFERENCES

1. B. Kabanov, R. Burstein, and A. Frumkin, *Discussions, Faraday Soc.*, **1**, 259 (1947).
2. T. Hurlen, *Electrochim. Acta*, **8**, 609 (1963).
3. C. M. Shepherd and S. Schuldiner, *This Journal*, **115**, 1124 (1968).
4. W. Schottky, *Halbleiterprobleme*. Bd. 2, 255 (1955).
5. Z. A. Foroulis, *This Journal*, **115**, 532 (1966).
6. K. Ogura, S. Haruyama, and Nagasaki, *J. Electrochem. Soc. Japan*, **37**, 102 (1969).
7. S. Asakura and Ken Nobe, *ibid.*, **118**, 13 (1971).
8. J. O'M. Bockris, D. Drazic, and A. R. Despic, *Electrochim. Acta*, **4**, 325 (1961).
9. E. Gileadi and B. E. Conway, "Modern Aspects of Electrochemistry," No. 3, p. 347, J. O'M. Bockris and B. E. Conway, Editors, Butterworths, London (1964).
10. R. V. Churchill, Operational Mathematics," McGraw-Hill Book Co., Inc., New York (1958).

Anodic Polarization Behavior of 25% Chromium Ferritic Stainless Steels

E. A. Lizlovs* and A. P. Bond*

Research Laboratory, Climax Molybdenum Company of Michigan, Ann Arbor, Michigan 48106

ABSTRACT

Potentiodynamic polarization curves in 1*N* H_2SO_4 and in 1*N* HCl were obtained for 25% Cr ferritic stainless steels containing 0-5% Mo and 0-4% Ni. High-purity alloys and alloys containing the usual commercial levels of C, N, Si, and Mn were investigated. The critical current density was decreased by molybdenum and molybdenum-nickel additions in both acids. All the high-purity 25% Cr steels containing 3.5 or 5% Mo were immune to pitting corrosion and highly resistant to crevice corrosion at 25°C in 1*N* HCl and in 0.33M $FeCl_3$. Alloys containing commercial levels of impurities, on the other hand, were all subject to pitting attack in 1*N* NaCl solution under potentiodynamic conditions and in immersion testing in ferric chloride solution. The relative pitting resistance, however, was still improved by molybdenum additions.

The engineering applications of the austenitic stainless steels are sometimes limited by stress-corrosion cracking in chloride-containing media. The ferritic stainless steels, *e.g.* Types 430 and 434, are immune to stress-corrosion cracking (1), but their use is limited by their comparatively poor resistance to general corrosion. It is therefore of interest to investigate the possibility of improving the general corrosion resistance of ferritic stainless steels by increasing their alloy content, while preserving their good resistance to stress-corrosion cracking.

Molybdenum and nickel were the two additional alloying elements selected for this study on improving the general corrosion resistance of the iron-chromium

* Electrochemical Society Active Member.

Key words: corrosion, potentiodynamic polarization, molybdenum, pitting, sulfuric acid, hydrochloric acid.

Table I. Chemical compositions of the 25% Cr ferritic stainless steels

Steel	Composition, %								
	C	Cr	Mo	Ni	Mn	Si	P	S	N
High-purity steels									
25% Cr	0.002	25.66	0.002	0.13		NA[a]	NA	NA	NA
25% Cr-2% Mo	0.002	25.26	2.05	0.13		NA	NA	NA	0.017
25% Cr-3.5% Mo	0.002	25.28	3.49	0.13		NA	NA	NA	NA
25% Cr-5% Mo	0.002	25.25	5.24	0.13		0.019	0.012	0.002	0.013
25% Cr-3.5% Mo-1% Ni	0.002	25.32	3.49	1.14		NA	NA	NA	NA
25% Cr-3.5% Mo-2.5% Ni	0.002	26.54	3.50	2.56		NA	NA	NA	NA
25% Cr-3.5% Mo-4% Ni	0.002	26.35	3.54	3.91		NA	NA	NA	NA
Commerical-purity steels									
25% Cr	0.035	24.24	0.046	0.12	0.59	0.23			0.046
25% Cr-1% Mo	NA	NA	0.97	NA	NA	NA			NA
25% Cr-2.5% Mo	NA	NA	2.37	NA	NA	NA			NA
25% Cr-3.5% Mo	NA	NA	3.52	NA	NA	NA			NA
25% Cr-5% Mo	0.033	24.19	4.94	NA	NA	NA			0.043

[a] NA = not analyzed, but assumed to be similar to analyzed values for other materials of similar major alloy content.

alloy. The 25% Cr alloy was selected as the base composition since it, in combination with molybdenum, was expected to retain a ferritic structure with nickel contents, as high as 4%. The choice of the base ferritic alloy composition studied was supported by the work of Harada *et al.* (2). These authors conducted polarization experiments in 5% H_2SO_4 at 70°C and at the boiling point with an extensive series of 25% Cr stainless steels alloyed with nickel and molybdenum, and their experiments suggest that such alloys should possess good general corrosion resistance.

This study was conducted in two steps: first, high-purity, vacuum-melted alloys were investigated; then, alloys containing the usual commercial levels of C, Si, N, and Mn were studied. Since even high-purity nickel-containing alloys were shown to be susceptible to stress-corrosion cracking (3), no nickel alloys of commercial purity were investigated.

Experimental Procedures

Materials.—The chemical compositions of the high-purity and commercial-purity ferritic stainless steels studied are given in Table I. The high-purity heats were vacuum melted using Plastiron, low-carbon ferrochromium, nickel-shot, and molybdenum pellets. Commercial-purity alloys were melted from Armco iron, pure molybdenum chips, ferrochromium, ferromanganese, ferrosilicon, and graphite, and were prepared by melting in argon and casting in air. The split-heat technique (3) was used for both series of alloys. The ingots were hot forged and hot rolled to strips 0.76 cm (0.3 in.) thick and then cold rolled to a 0.38 cm (0.15 in.) thickness.

High-purity alloys were heated at 980°C (1800°F) for 1 hr and water quenched. Micrographic examination showed that 980°C was the minimum temperature that insured the absence of a second phase in the high-purity high-molybdenum alloys. The commercial-purity alloys were heated at 1095°C (2000°F) for 1 hr and water quenched, then heated at 705°C (1300°F) for 1 hr and water quenched. The 1095°C treatment was used to minimize the presence of the second phase in high-molybdenum alloys, and the lower temperature (705°C) treatment to minimize the sensitization to intergranular corrosion resulting from the high-temperature treatment. In contrast to high-purity alloys, the sensitization caused by high-temperature heat treatment is expected for the commercial-purity alloys because of the higher carbon and nitrogen levels (4).

Polarization experiments.—The electrodes for the potentiodynamic polarization studies were mounted in acrylic plastic, the exposed surface (0.5 by 0.6 cm) always being a longitudinal section parallel to the rolled surface. The exposed surface was polished using standard metallographic techniques, ending with a distilled water slurry of 0.3μ alumina. For the pitting potential measurements, the fine crevices between plastic and alloy were masked by Glyptal or the electrode surface was masked with electroplater's tape (Scotch 470), except for a circular area 0.36 cm in diameter. Masking of the electrodes was undertaken to prevent crevice corrosion of the electrode in chloride media.

The potentiodynamic polarization experiments were performed using standard equipment and techniques. Potentials were measured with respect to a saturated calomel electrode. The experiments were performed in 1*N* H_2SO_4, 1*N* HCl, and 1*N* NaCl saturated with prepurified nitrogen at 29.8°C. The potential scanning rate was 0.15 mV/sec.

Potentiostatic experiments were performed in 1*N* HCl with the materials that did not undergo pitting under potentiodynamic polarization conditions. For the potentiostatic experiments, the electrode was first activated and then the potential of the electrode was abruptly changed from the natural corrosion potential to the selected passive potential by switching the potentiostat on with a potential preset at the desired value. The polarization current and potential were recorded by a two-pen strip chart recorder. The electrode was usually kept overnight (over 16 hr) at the desired potential.

Potentiostatic holding experiments at −0.250V were also performed with all commercial-purity materials in 1*N* HCl. Since these experiments were designed to determine the mode of attack in hydrochloric acid in a near-passive range, the electrodes were not masked for these experiments.

Immersion tests.—Both the high-purity and commercial-purity materials were tested in acidified (*p*H 2) 0.33M $FeCl_3$. High-purity materials were also tested in oxygen-saturated 1*N* H_2SO_4 and nitrogen-saturated 1*N* HCl. Test coupons for the latter experiments were activated by touching with a magnesium rod immediately after immersion in acid. All immersion tests were performed at room temperature, 25° ± 1°C.

Results

Polarization behavior in the active-passive transition region.—Typical potentiodynamic polarization curves in the active-passive transition region in 1*N* H_2SO_4 for high-purity alloys are shown in Fig. 1 and 2. Molybdenum additions to both series of alloys caused a decrease in critical current density.[1] This decrease in critical current with increasing Mo content was more pronounced for high-purity alloys than for the commercial-purity steels. In addition, the critical current density for the commercial-purity 25% Cr steel

[1] Terms "critical current density" and "primary passivation potential" are defined in Ref. (5).

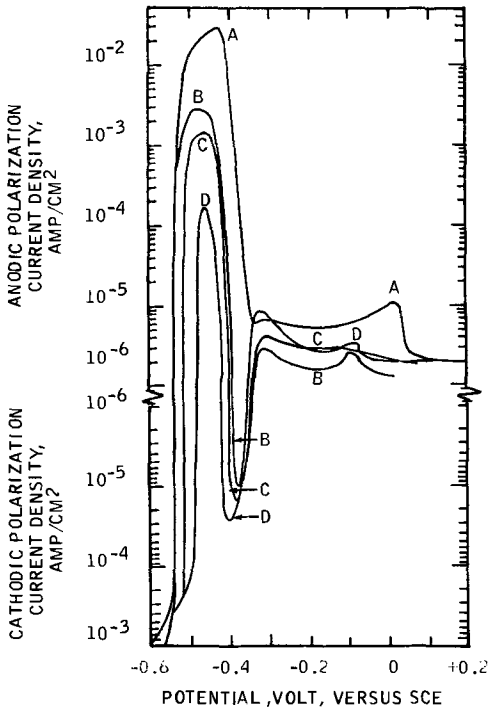

Fig. 1. Potentiodynamic polarization curves for the high-purity 25% Cr stainless steels in 1*N* H_2SO_4 at 29.8°C. Curve A, 25% Cr; curve B, 25% Cr-2% Mo; curve C, 25% Cr-3.5% Mo; curve D, 25% Cr-5% Mo.

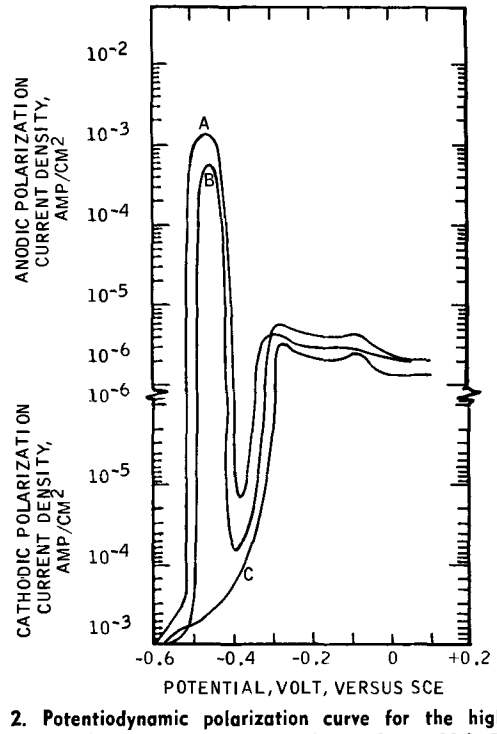

Fig. 2. Potentiodynamic polarization curve for the high-purity 25% Cr-3.5% Mo stainless steels in 1*N* H_2SO_4 at 29.8°C. Curve A, 25% Cr-3.5% Mo; curve B, 25% Cr-3.5% Mo-1% Ni; curve C, 25% Cr-3.5% Mo-2.5% Ni.

was considerably lower than for the high-purity 25% Cr alloy (Fig. 3). In the 25% Cr-3.5% Mo steels, nickel lowered the critical current density in 1*N* H_2SO_4. The increase in nickel content from 1 to 2.5% decreased the critical current density in 1*N* H_2SO_4 to such an extent that local action cathodic current was larger than the critical current and, as a result, the critical behavior could not be observed and was marked only as some deviation from the expected cathodic polarization curve (Fig. 2).

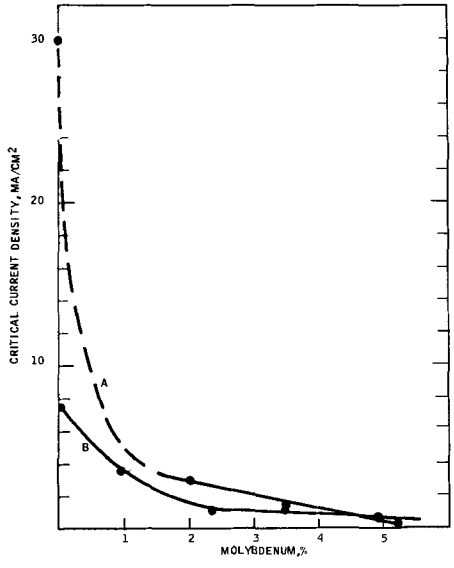

Fig. 3. Dependence of critical current density on molybdenum content for the 25% Cr stainless steels in 1*N* H_2SO_4 at 29.8°C. Curve A, high-purity alloys; curve B, commercial-purity alloys.

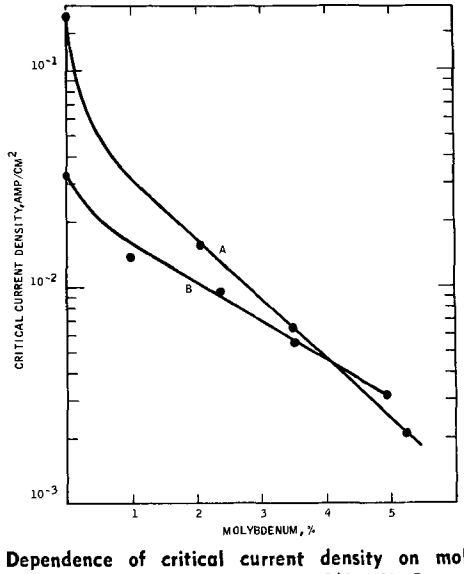

Fig. 4. Dependence of critical current density on molybdenum content for the 25% Cr stainless steels in 1*N* HCl. Curve A, high-purity alloys; curve B, commercial-purity alloys.

The decrease of critical current density with molybdenum content was also observed in 1*N* HCl. In general, the critical current densities were considerably higher in 1*N* HCl (Fig. 4) than in 1*N* H_2SO_4. Again, the decrease in critical current density was more pronounced for high-purity materials than for commercial-purity alloys, and the 25% Cr high-purity alloy had considerably higher critical current density than the 25% Cr commercial-purity alloy (Fig. 4). Nickel additions also decreased the critical current density in the high-purity 25% Cr-3.5% Mo alloys in 1*N* HCl (Fig. 5).

The effect of alloying elements on the primary passivation potential is shown in Fig. 6. Primary passivation potentials for the pure 25% Cr alloy were considerably more noble than corresponding primary passivation potentials for commercial-purity alloys in 1*N* H_2SO_4 and in 1*N* HCl. For the pure alloys, the addition of 2% Mo to the base composition resulted in significantly more active primary passivation potentials in 1*N* H_2SO_4 and in 1*N* HCl. Further increases in molybdenum content rendered primary passivation potentials slightly more noble in 1*N* H_2SO_4 for both series of alloys. Increasing amounts of molybdenum

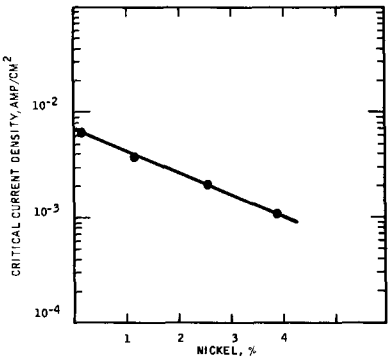

Fig. 5. Dependence of critical current density on nickel content for the high-purity 25% Cr-3.5% Mo stainless steels in 1*N* HCl at 29.8°C.

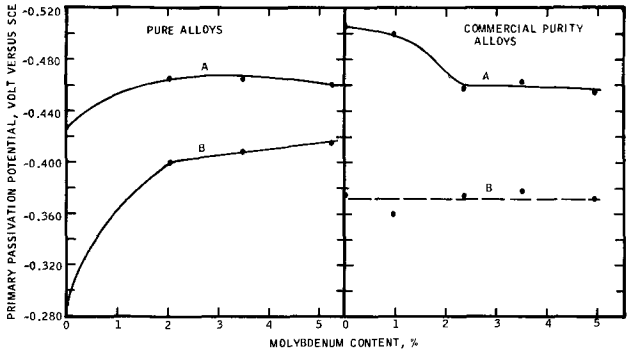

Fig. 6. Dependence of primary passivation potentials on molybdenum content for the 25% Cr stainless steels (A) in 1*N* H_2SO_4 and in (B) 1*N* HCl at 29.8°C.

in pure alloys rendered primary passivation potentials more active in 1*N* HCl, but no definite molybdenum effect was observed in commercial-purity materials. In general, primary passivation potentials for pure alloys in 1*N* HCl were more active than for commercial-type steels. In the pure 25% Cr-3.5% Mo series of steels, nickel rendered the primary passivation potentials more noble in both acids.

With the exception of the molybdenum-free alloy, all the pure alloys displayed a cathodic loop on polarization curves in 1*N* H_2SO_4, indicating that a stable passive state is possible in a given medium. Only the 25% Cr-3.5% Mo and 25% Cr-5% Mo steels of the commercial-purity series displayed a cathodic loop on the polarization curve in 1*N* H_2SO_4. The extent and the maximum value of the cathodic loops increased with alloying content (Fig. 1). Cathodic loops were never obtained in polarization experiments in 1*N* HCl.

Polarization behavior in sulfuric acid in the passive range.—The passive range for all materials in 1*N* H_2SO_4 terminated at the expected transpassive transition range, *i.e.* +0.85 to +0.95V. The passive potentiodynamic polarization curves above 0.1V were uneventful. The passive current densities under continuous potential scanning conditions were of the order of 1 x 10^{-6} A/cm² for all the high-purity materials. Under potentiostatic conditions, current densities even at the threshold of the transpassive transition range (0.80V) gradually decreased to the order of 1 x 10^{-7} A/cm², and possibly even lower, so that no true dependence of passive current density on the potential or alloy composition was observed for high-purity stainless steels. For the commercial-purity steels, the lowest passive current densities were observed with 25% Cr and 25% Cr-1% Mo alloys. Increases in molybdenum content resulted in increased passive currents with the 25% Cr-5% Mo steel having the highest current densities of all materials. This steel had a passive current density of the order of 10^{-5} A/cm² even under potentiostatic conditions at +0.60V.

Polarization behavior in hydrochloric acid in the passive range.—The current density for the 25% Cr, high-purity alloy in 1*N* HCl decreased very sharply after reaching the critical value. However, the current density beyond the primary passivation potential did not decrease below 2.7 mA/cm². Furthermore, the polarization current increased as the electrode potential was scanned toward more noble values. Similar behavior was also observed with the pure 25% Cr-2% Mo steel, except that the minimum polarization current was about two orders of magnitude lower than that of the 25% Cr steel. A potentiostatic-holding experiment with the high-purity 25% Cr alloy at −0.10V showed that it suffered general etching at this potential in 1*N* HCl. The masked 25% Cr-2% Mo electrode, on the other hand, could be passivated in 1*N* HCl when its potential was jumped from the active corrosion potential to +0.80V, and passivity could be maintained potentiostatically at this potential for more than 16 hr with the final polarization current of the order of 1 x 10^{-7} A/cm². Hence, the relatively high current densities in the passive range observed with unmasked electrodes of the above alloys would correspond to general corrosion for the 25% Cr steel and only to crevice corrosion for the 25% Cr-2% Mo steel.

The remaining high-purity alloys, *i.e.* all the 3.5 and 5% Mo alloys, exhibited complete passivity up to the normal transpassive transition potentials. Polarization current densities under potentiodynamic conditions were of the order of 1 x 10^{-6} A/cm² and were comparable to passive current densities in 1*N* H_2SO_4. Furthermore, all the high-purity 3.5 and 5% Mo steels completely passivated in 1*N* HCl when the potential of the unmasked electrode was jumped from the corrosion potential to +0.80V, and the passivity could be maintained at this potential for over 16 hr with no indication of any tendency of the passive polarization current to increase at the end of the experiment. The final polarization current density at +0.80V was of the order of 1 x 10^{-7} A/cm² and was the same as the current density in 1*N* H_2SO_4 under the same conditions.

For all the commercial-purity steels, current densities beyond the critical peak in 1*N* HCl first decreased to some minimum value, then increased again with an increase in potential. The lowest current densities in the passive state were observed for the 25% Cr-3.5% Mo and 25% Cr-5% Mo alloys. For the 25% Cr-5% Mo steels, current densities from 0 volt to transpassive transition potentials remained between 7 x 10^{-4} and 3.6 x 10^{-4} A/cm². The drastic differences in passive polarization behavior between high-purity and commercial-purity alloys in 1*N* HCl are illustrated in Fig. 7, which shows polarization curves for 25% Cr-5% Mo alloys. Potentiostatic-holding experiments showed that all commercial-purity materials suffered general etching at −0.250V. Hence, high current densities in the passive range in 1*N* HCl for commercial-purity alloys would correspond not only to crevice corrosion but to general corrosion as well. In no case was pitting observed for any of the materials in 1*N* HCl.

Experiments with a masked high-purity 25% Cr electrode showed that a complete passive range could be obtained in 0.1*N* HCl under potentiodynamic polarization conditions. However, passivity could not be potentiostatically maintained at +0.80V for a prolonged time. On the abrupt potential change from the corrosion potential to a selected potential in the passive range, the masked 25% Cr electrode would passivate in 0.1*N* HCl at +0.40V but would pit at +0.50V.

Polarization behavior in 1N NaCl.—Potentiodynamic polarization experiments in 1*N* NaCl solution were designed to obtain pitting potentials. Definite pitting potentials for commercial-purity alloys were only obtained for the two lowest alloyed materials, *i.e.* the

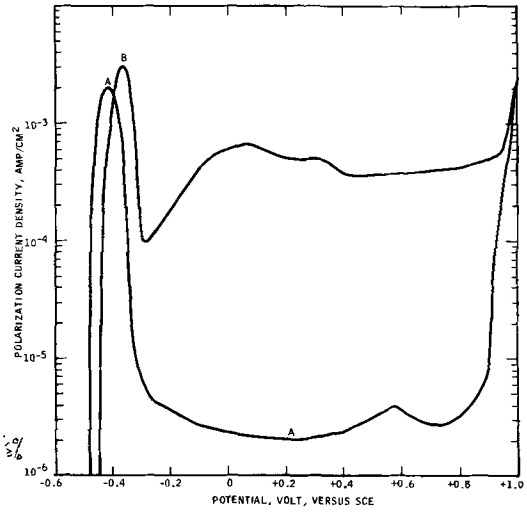

Fig. 7. Anodic potentiodynamic polarization curves in 1N HCl at 29.8°C for 25% Cr-5% Mo alloys. Curve A, high-purity alloy; curve B, commercial-purity alloy.

25% Cr and 25% Cr-1% Mo alloys. The 25% Cr alloy pitted at +0.15V and the 25% Cr-1% Mo alloy pitted at +0.16V. For the materials of the higher molybdenum content, current in the passive state was irregular and gradually increased. For the 25% Cr-3.5% Mo and 25% Cr-5% Mo steels, current remained at relatively low values (10^{-6} to 10^{-5}A) throughout the passive range up to the normal transpassive transition range. While no definite potential could be assigned to the onset of pitting, microscopic examination revealed some small pits and localized etching. The pure 25% Cr alloy pitted in 1N NaCl solution under potentiodynamic polarization conditions only at 0.79V.

Immersion tests in ferric chloride.—Corrosion rates in 0.33M $FeCl_3$ solution are given in Table II. The high-purity alloys, with the exception of the 25% Cr steel, did not pit. All the commercial-purity alloys were pitted. The most severe pitting was sustained by the 25% Cr and the 25% Cr-1% Mo steels. The 25% Cr-5% Mo alloy was the least pitted. Pitting occurred over all surfaces of the coupon.

Immersion tests in sulfuric acid and hydrochloric acid.—Corrosion rates in 1N H_2SO_4 and 1N HCl at room temperature (25°C) are given in Table III. Molybdenum additions decreased the corrosion rates in both media. An especially dramatic decrease in corrosion rate was observed between the 25% Cr and the 25% Cr-2% Mo alloys. The 25% Cr-3.5% Mo and 25% Cr-5% Mo alloys repassivated in 1N H_2SO_4 after activation with magnesium and they remained passive for the duration of the test (6 days). In no case was pitting observed and any corrosion was uniform.

Discussion

The materials that show a passive range up to normal transpassive transition potentials in 1N HCl with masked electrodes under potentiostatic conditions could be considered to be immune to pitting corrosion at the given chloride ion concentration and temperature. It follows that all molybdenum-bearing, high-purity 25% Cr steels are immune to pitting corrosion in 1N HCl at 29.8°C. The molybdenum-free 25% Cr steel could be pitted under potentiodynamic conditions in 1N NaCl at the potential close to the transpassive transition (+0.79V) and under the potential-jumping conditions in 0.1N HCl. These data indicate that molybdenum-free 25% Cr steel could pit under some circumstances when exposed to chloride media. The ferric chloride test verified this prediction. Only the 25% Cr steel of the high-purity series was pitted when immersed in 0.33M $FeCl_3$. The immersion in $FeCl_3$ solution would approximate the conditions of potential-jumping experiments in HCl.

Some qualitative conclusions concerning the susceptibility of stainless steels to crevice corrosion could be deduced from the passive polarization behavior of unmasked electrodes in hydrochloric acid. It has been found that susceptible alloys always display a rise in current within the normal passive region at potentials more active than the pitting potential, indicating that unmasked electrodes prepared by the techniques used always contain unintentional crevices (6, 7). Thus, since all the high-purity 25% Cr steels containing 3.5% or more molybdenum with or without nickel do not display any unusual current rise in the passive range up to transpassive transition in 1N HCl, these alloys should be highly resistant to crevice corrosion under experimental conditions. In another investigation employing a special crevice corrosion cell, it was shown that 25% Cr-3.5% Mo indeed is immune to crevice corrosion in 1N Cl^- concentration at room temperature (8).

The detrimental effects of impurities on the corrosion resistance of 25% Cr steels already manifested themselves in the passive state in 1N H_2SO_4. Passive polarization densities for 2.5-5% Mo steels were higher than for the corresponding pure alloys under comparable experimental conditions. In 1N HCl, the current densities in the passive state of commercial-purity alloys were several orders of magnitude higher than for the pure alloys and etching actually occurred at passive potentials. Furthermore, all the commercial-type steels were subject to pitting corrosion and, while crevice corrosion was not specifically studied, there is little doubt that all the commercial-purity 25% Cr steels would be subject to crevice attack in chloride media.

The deleterious effects of impurities on the resistance to pitting corrosion are probably due to the presence of carbide and nitride precipitates. Furthermore, metallographic examination showed that 2.5-5% Mo alloys of commercial purity contained an intermetallic phase, presumably chi-phase (9). While it was possible to bring this second phase into solution by a heat treatment at 1095°C, a desensitizing treatment at 705°C resulted in the reappearance of the second phase. Thus, there exists a dilemma with respect to heat treatment of commercial-purity alloys. Since, according to the previous experience in this Laboratory, ferritic stainless steels that have been

Table II. Corrosion rates in 0.33M $FeCl_3$ solution at 25°C

Steel	High-purity alloys[a] Exposure, days	High-purity alloys[a] Corrosion rate, mdd	Commercial-purity alloys[b] Exposure, days	Commercial-purity alloys[b] Corrosion rate, mdd
25% Cr	7	40	1	1,224
25% Cr-1% Mo			1	3,112
25% Cr-2% Mo	31	Nil		
25% Cr-2.5% Mo			1	855
25% Cr-3.5% Mo	31	Nil	1	558
25% Cr-5% Mo	31	Nil	1	324

[a] Tested at pH 1.
[b] Tested at pH 2.

Table III. Corrosion rates of high-purity alloys at 25°C

Steel	Corrosion rate, mdd, after 24-hr exposure: 1N H_2SO_4 O_2-saturated	1N HCl N_2-saturated
25% Cr	20,000	39,400
25% Cr-2% Mo	2,450	1,260
25% Cr-3.5% Mo	Nil[a]	556
25% Cr-5% Mo	Nil[a]	307

[a] Six-day exposure.

sensitized to intergranular corrosion have much poorer resistance to pitting corrosion than in the desensitized condition, all the alloys were tested in the desensitized state with an intermetallic phase present for the high-molybdenum steels. It is possible that the presence of a second phase was detrimental to the stability of the passive state, as indicated by relatively high passive current densities in sulfuric acid and general etching in the passive region in hydrochloric acid of 2.5-5% Mo alloys. No such effects were observable for comparable high-purity alloys.

A very strong effect of molybdenum was observed on active corrosion rates of pure alloys in 1*N* H_2SO_4 and 1*N* HCl at room temperature (Table III). With an increase in molybdenum content from 0 to 2%, corrosion rates were reduced approximately by a factor of 10 in 1*N* H_2SO_4 and by a factor of 30 in HCl. For 3.5 and 5% Mo alloys in oxygenated 1*N* H_2SO_4, repassivation occurred and corrosion rates were consequently nil. Apparently, the critical current density for these materials was sufficiently small so that the oxygen reduction current could polarize these alloys beyond the critical peak. Sharp reduction of active corrosion rates for pure 25% Cr alloys with additions of molybdenum in 1*N* H_2SO_4 was also reported by Chernova and Tomashov (10).

The observed decrease in critical current density with an increase in molybdenum content in 25% Cr stainless steel was in accord with the results from previous work with 17% Cr steels (7, 11) and the results of other investigators on a variety of stainless steels (10, 12-15). Of special interest, however, is the large difference in critical current density between the commercial-purity and high-purity 25% Cr steels, commercial-purity material having the lower critical current density. A similar difference in critical current density in 5% (1*N*) H_2SO_4 was observed earlier between the high-purity 17% Cr alloy and its commercial counterpart Type 430 steel (11, 16). In the present case, the elements that are present in considerably larger amounts in commercial-purity materials than in high-purity materials are C, N, Si, and Mn. Silicon already has been shown to have no significant effect on critical current density (11). The effect of manganese is not well known; however, it has been shown by other investigations to have an effect of increasing critical current density to some extent for Type 304 steel (17) and 200 series (Cr-Ni-Mn) stainless steels (18). Thus, the sharp lowering of the critical current density for commercial-type ferritic stainless steels as compared to high-purity counterparts most probably is the combined effect of residual carbon and nitrogen. Carbon has been shown by Wilde and Greene to lower the critical current density very considerably for Type 304 stainless steel (17). The effect of nitrogen on critical current density, however, is not known. Further work is needed to clarify the effect of nitrogen and also the effect of carbon on critical current density for ferritic stainless steels.

The analysis of the critical current density data showed some interesting correlations with the molybdenum or nickel content. The decrease in critical current density in sulfuric acid was linear with increase in molybdenum content from about 2% for pure alloys and from about 2.4% for commercial-purity alloys (Fig. 3). For the commercial-purity steels, the slope of the linear portion was quite small, so that the effect of molydenum additions on critical current density was less pronounced than for high-purity alloys. The linear relationship between molybdenum content and critical current density in 1*N* H_2SO_4 obtained in this investigation is in agreement with the results of Chernova and Tomashov (10). Their investigation showed that the addition of even 0.5% Mo to the 25% Cr, high-purity alloy results in a sharp reduction of the critical current density in 1*N* H_2SO_4 and that further reduction is linear up to a molybdenum content of 3%. The dashed portion in Fig. 3 refers to the estimated portion of the critical current density curve based on the similar curve given by Chernova and Tomashov. The decrease of critical current density in 1*N* HCl was logarithmic with an increase in the molybdenum content from about 1 to 5% for both series of alloys (Fig. 4). The logarithmic relationship was also observed for the decrease of critical current density in 1*N* HCl for 25% Cr-3.5% Mo alloys with an increase in the nickel content (Fig. 5).

It should be noted that, while commercial-type alloys had critical current densities either lower than or comparable to the pure alloys, their corrosion properties were inferior to those of pure alloys. Thus, the lowering of the critical current density by alloying additions cannot always be taken as a sole characteristic parameter for improving the corrosion resistance of stainless steel, especially for the alloys containing appreciable amounts of precipitates and second phase. There appears to be no simple connection between the magnitude of the critical current density and stability of the passive state. The lowering of the critical current density predicts only the ease of transition from an active to a passive state and only for the alloys of similar composition and structure.

The 25% Cr-3.5% Mo steels alloyed with nickel showed some desirable corrosion properties: the absence of an active region in 1*N* H_2SO_4 indicated that these materials should remain passive in dilute sulfuric acid, and the passive range up to normal transpassive transition in 1*N* HCl indicated that excellent pitting and crevice corrosion resistance of the 25% Cr-3.5% Mo alloy is not adversely affected by alloying with nickel. However, the usefulness of the nickel-containing ferritic stainless steels is very seriously limited by their susceptibility to stress-corrosion cracking (3).

Of all the effects of molybdenum on the corrosion properties of ferritic stainless steels discussed above, the most remarkable is the increase of the strength of the passive film with the increase of molybdenum content. Assuming that the strength of the passive film will be reflected in the density of the polarization current in the passive region in hydrochloric acid as well as in the pitting potential and relative resistance to breakdown of passivity within a crevice, the relative strength (or stability) of the passive film of various stainless steels can be inferred from the polarization diagrams in 1*N* HCl. Comparison of the polarization behavior of 17% Cr steels (7) and 18% Cr-16% Ni steels (6) in 1*N* HCl and the results of this investigation of 25% Cr steels indicate that the degree of the passive film stability achieved by a certain amount of molybdenum is dependent on the chromium content. Thus, it is the chromium-molybdenum combination that primarily determines the stability of the passive film toward the chloride ions in particular and, probably, toward aggressive ions in general.

Conclusions

Molybdenum and nickel additions lowered the critical current density of 25% Cr stainless steels in 1*N* H_2SO_4 as well as in 1*N* HCl. The critical current density for commercial-purity 25% Cr steel was considerably lower and the primary passivation potential more active than for the high-purity 25% Cr alloy in both 1*N* H_2SO_4 and 1*N* HCl. This phenomenon is most probably due to the combined effect of higher carbon and nitrogen levels in commercial-type alloys.

All the high-purity alloys containing molybdenum were immune to pitting in 1*N* HCl under potentiostatic conditions and in acidified 0.33M $FeCl_3$ solution at room temperature. The high-purity alloys containing 3.5% Mo or more were also highly resistant to crevice corrosion under potentiostatic conditions in 1*N* HCl.

The commercial levels of carbon and nitrogen were detrimental to the pitting corrosion resistance of 25% Cr steels; all the commercial-purity 25% Cr materials were pitted in 0.33M $FeCl_3$ solution.

Manuscript submitted April 27, 1970; revised manuscript received ca. Sept. 12, 1970. This was Paper 85 presented at the Detroit Meeting of the Society, Oct. 5-9, 1969.

Any discussion of this paper will appear in a Discussion Section to be published in the December 1971 JOURNAL.

REFERENCES

1. A. P. Bond, J. D. Marshall, and H. J. Dundas, ASTM STP 425, 116 (1967).
2. K. Harada, M. Sugimato, and Y. Kamada, *Nippon Kinzoku Gakkaishi*, **29**, 367 (1965).
3. A. P. Bond and H. J. Dundas, *Corrosion*, **24**, 344 (1968).
4. A. P. Bond, *Trans. AIME*, **245**, 2127 (1969).
5. N. D. Greene, *Corrosion*, **18**, No. 9, 136t (1962).
6. A. P. Bond and E. A. Lizlovs, *This Journal*, **115**, 1130 (1968).
7. E. A. Lizlovs and A. P. Bond, *ibid.*, **116**, 576 (1969).
8. E. A. Lizlovs, *ibid.*, **117**, 1335 (1970).
9. S. G. McMullin, S. F. Reiter, and D. G. Ebeling, *Trans. ASM*, **46**, 799 (1954).
10. G. P. Chernova and N. D. Tomashov, *Korroziya, Metallov i. Splavov*, Sb. 2 (Moscow), 7 (1965).
11. E. A. Lizlovs, *Corrosion*, **22**, 297t (1966).
12. M. Prazak and V. Cihal, *Corrosion Sci.*, **2**, 71 (1962).
13. M. Prazak, *Corrosion*, **19**, 75t (1963).
14. N. A. Bozin and M. M. Kurtepov, *Russ. J. Phys. Chem.*, **35**, 71 (1961).
15. G. J. Biefer and J. G. Garrison, "Mines Branch Technical Bulletin TB90," Dept. of Energy, Mines, and Resources, Ottawa, Dec 1967.
16. E. A. Lizlovs, *This Journal*, **114**, 1015 (1967).
17. B. E. Wilde and N. D. Greene, *Corrosion*, **25**, 300 (1969).
18. I. G. Murgulescu and O. Radovici, "First International Congress of Metallic Corrosion," p. 109, Butterworths, London (1962).

Effects of Amides on the Passivation of Iron

Keh-Chi Tsai and Norman Hackerman[1,] *

Department of Chemistry, The University of Texas at Austin, Austin, Texas 78712

ABSTRACT

The passivation of iron in acidic mediums with and without added amides has been studied by the steady-state polarization method. An empirical equation for the dissolution of iron was obtained from the polarization curves. A mechanism, based on the competitive adsorption by amides and the inhibiting species, $Fe(OH)_2$, for the anodic process is proposed. Assuming that the Langmuir adsorption isotherm is followed for this mechanism, a series of equations were derived for the surface coverages by $Fe(OH)_2$, θ_1, and by amides, θ_2, as well as the formation constant of $Fe(OH)_2$, K_1, and the adsorption constants of amides, K_2. These equations have been verified by experiments. K_1 was calculated by varying pH in a given system and K_2 by varying the amide concentration at a given pH. Linear relationships between the critical overpotentials and pH, as well as the logarithm of critical current densities and pH, were all obtained from this derivation and confirmed by the experiments. The surface coverage by amide reveals that the adsorption and desorption processes depend on the applied potential, since a surface coverage maximum is always observed in the $E_{crit} \sim E_p$ region. In the active region, the adsorption of amide is predominant and reversible. However, beyond the critical potentials, the formation of inhibiting species is predominant and is irreversible in the passive region.

There is some agreement that the initiation of passivation is associated with the appearance of a monolayer or less of inhibiting species (1, 2). In the case of iron, these inhibiting species are believed to be FeO or its hydrated species, $Fe(OH)_2$ (3, 4). A recent study by Pigeaud and Kirkpatrick (5) strongly supported this point of view. If this is so in steady-state measurements, the most likely electrochemical reaction for this precursory process for the passivation of iron in acidic mediums can be regarded as (1, 6, 7)

$$Fe(H_2O)_2 \rightleftarrows Fe(OH)_2 + 2H^+ + 2e^- \qquad [1]$$

Smialowski (8) has studied the effect of acids on the passivation of steel and concluded that the fatty acid anions reduced the number of active sites on the surface of iron and hence facilitated its passivation. From the adsorption theory of passivity (9), it is expected that the adsorption of organic species and the inhibiting species [*i.e.*, $Fe(OH)_2$] on the metal surface are competing processes.

This paper presents an attempt to elucidate the kinetic cause for the passivation of iron in acidic mediums in the presence of organic materials. A series of amides were chosen for this study because of their chemical and electrochemical stabilities (10) which restricts these organic species to a simple adsorption process and avoids complications arising from the anodic oxidation of these organic species as can be the case (8).

Experimental

All chemicals used were analytical reagent grade. The solutions were all 0.10M in K_2SO_4, were made from triple-distilled water, and were deaerated by bubbling through He. The He gas was purified and deoxygenated with activated copper. The pH values were measured with a Beckman expandomatic pH meter and adjusted with 2M H_2SO_4 to the range 1.1-4.9. The reaction vessel was thermostated at 5°C. The working electrodes were made of zone-refined iron (99.995% of Fe by weight, supplied by Battelle Memorial Institute and said by them to have no more than 45 ppm impurities). They were about 4 mm diameter rods which were inserted into a cylindrical Teflon plug, leaving one flat edge exposed. The plug was mounted in a glass support with a brass center rod screwed into the Teflon plug and the iron rod to provide good electrical contact. Immediately before use, the exposed

[1] Present address: Department of Chemistry, Rice University, Houston, Texas 77001.
* Electrochemical Society Active Member.
Key words: surface coverage, inhibition, polarization.

face of the electrode was abraded with 0 and 4/0 emery papers, degreased with acetone and pentane, and finally electropolished in 4 volumes of 70% $HClO_4$ to 1 of glacial CH_3COOH. A $Hg-Hg_2SO_4$ half cell was used as the reference electrode. A large platinum mesh cylinder was built in the reaction vessel and used as the counterelectrode. Electrode potentials were measured using a Luggin capillary and were converted to the hydrogen scale by adding 0.64V to measured values.

A Model 610B Keithley Electrometer was used to measure the rest potential and a Model 61RS Wenking Potentiostat was used to obtain anodic polarization curves. An ultrasensitive d-c microammeter (RCA) was used for current measurements in the passive region. Each potential setting was controlled manually and the current readings were taken at 50 mV intervals, except near the critical potential where 10 mV intervals were used.

The amides (11) listed in Table I were obtained from Eastman Organic Chemicals. The DMF, DMA, and NMP were vacuum distilled at less than 1 mm Hg. The other liquid amides were used as received. The purity of these amides was checked by conductivity measurements (12) which showed a specific resistance of at least 5 x 10^6 ohm-cm at 24°C for all. The solid amides, A, NMA, and P, were recrystallized from 50:50 acetone:chloroform (13) and vacuum dried.

Results and Discussion

Mechanism of the anodic process.—Empirical equation for iron dissolution at high overvoltage.—It is observed from the anodic polarization curves shown in Fig. 1 that at high overpotentials (*e.g.*, $\eta > 300$ mV) the slope $d\eta/d \log i$ is greater than the usual reciprocal Tafel slope. These slopes extend over 300-500 mV, depending on pH, and their magnitude depends on pH but not on the presence or absence of amide. The corresponding values of these slopes at various pH's, together with some electrochemical data obtained from Fig. 1, are given in Table II, where E_R is the rest potential and E_P is the passivation potential.

From Table II, it is found that the anodic reciprocal slopes at high overpotentials (*i.e.*, concentration polarization region) are related to pH by

$$d\eta/d \log i = 2.54 - 0.45\,pH \qquad [2]$$

Integration of Eq. [2] with η from 0 to η and i from i_0 to i gives

$$i = i_0 \exp\left(\frac{2.303\,\eta}{2.54 - 0.45\,pH}\right) \qquad [3]$$

Equation [3] gives the dissolution rate of iron at high overpotentials in the active polarization region.[2]

From Table II it is seen that the current density at $\eta = 0$, i_0, is related to pH as

$$i_0 = k\,[H^+]^\gamma \qquad [4]$$

in which $k = 10^{2.48}$ (mA/cm²) is the dissolution rate constant for iron in the concentration polarization region at pH 0 and $\gamma = 0.456$. Substituting Eq. [4] into Eq. [3] gives the expression for dissolution of iron in the concentration polarization region, *i.e.*

$$i = k\,[H^+]^\gamma \exp\left(\frac{2.303\,\eta}{2.54 - 0.45\,pH}\right) \qquad [5]$$

Formation of inhibiting species, $Fe(OH)_2$, on metal surface.—When the applied potential reaches the Flade arrest, E_F, it is believed that kinetically it is possible for an oxygen-metal ion complex to be formed due to the adsorption of oxygen on the metal surface (1, 4). However, this is offset by the chemical dissolution of this species. The detailed mechanism for the $Fe(OH)_2$ formation reaction is still controversial but, under the steady-state condition in the active polarization region, this reaction is generally regarded as

$$Fe(H_2O)_2 \rightleftarrows Fe(OH)_2 + 2H^+ 2e^- \qquad [1]$$

Anodic processes for amide adsorption.—The addition of amides to the solutions would be expected to cause change in passivation mechanism in two ways: (*a*) The amide may form complex compounds with ferrous ions in the metal surface which would accelerate the anodic dissolution reaction and thus be detrimental to the formation of passive films. (*b*) A competitive adsorption between amides and H_2O (or $SO_4^=$) on the active sites of metal could result in the inhibition of iron corrosion and facilitate the passivation. There was no experimental evidence found for process (*a*) since

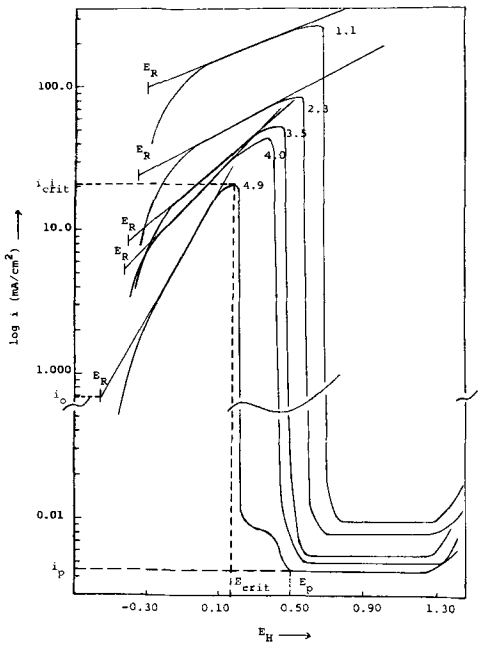

Fig. 1. Anodic polarization curves at different pH's in K_2SO_4 + H_2SO_4 solution.

Table I. Symbols and physical properties of amides*

Compound	Symbol	M.P. (°C)	B.P. (°C)	Density (g/ml)
Formamide	F	2.57	218	25° 1.1292
N-methylformamide	NMF	−5.4	180-185	21° 0.9961
N,N-dimethylformamide	DMF	−61	153	25° 0.9445
Acetamide	A	81.5	221.5	105° 0.980
N-methylacetamide	NMA	29.5	206	30° 0.9503
N,N-dimethylacetamide	DMA	−20	165	25° 0.9366
Propionamide	P	79	213	25° 1.042
N-methylpropionamide	NMP	−43	146/90 mmHG	25° 0.9304
N,N-dimethylpropionamide	DMP	−45	175.5/765 mmHG	25° 0.9203
N,N-dimethylbutyramide	DMB	−40	124.5/100 mmHG	25° 0.9064

* Data from Ref. (10), (11), and (23).

Table II. Some electrochemical data from Fig. 1

pH	E_R (mV)	E_{crit} (mV)	i_o (mA/cm²)	i_{crit} (o) (mA/cm²)	$d\eta/d \log i$ (mV/decade)
1.1	−300	670	100	260	2100
2.3	−350	560	24	86	1500
3.5	−400	450	8.2	52	980
4.0	−420	400	5.2	42	750
4.9	−560	200	1.6	21	420

i_{crit}(o) is the critical current density with no amide in the solution; i_o is the extrapolated current density from the anodic reciprocal slopes at $\eta = 0$; E_{crit} is the critical potential (see Fig. 1 with pH 4.9 as example).

[2] In the polarization curve, the potentials between E_R and E_{crit} are defined as active polarization region.

all the corrosion rates decreased in the presence of amides. The decrease of the corrosion rates were proportional to the increase of the amide concentrations. The reciprocal anodic slopes at high overvoltage show no change with respect to the values listed in Table II. Therefore, a mechanism based on the competitive adsorption between amide and water (or $SO_4^=$) on the active iron surface was considered to be a proper mechanism in the anodic process for this system.

From the values of the acidity constant ($K_a \sim 10^{-16}$) and the basicity constant ($K_b \sim 10^{-15}$), it is believed that amides, unlike amines, will remain neutral or hydrated species in aqueous solution within a certain pH range (14).

Previous workers (1, 7, 15, 16) proposed that the active iron surface is $FeOH^o$ and not Fe by virtue,

$$Fe\ (H_2O) \rightleftarrows FeOH^o + H^+ + e^- \qquad [6]$$

and the adsorption mechanism of polar organic inhibitors of Hackerman and Makrides (17) suggest the most likely mechanism for the adsorption of amides on the iron surface to be

$$FeOH\cdot OH_2 + A \rightleftarrows FeOH\cdot A + H_2O \qquad [7]$$

In steady-state measurements, the over-all adsorption process for these organic species would include Eq. [6] and [7]. Therefore, the over-all adsorption reaction is

$$Fe(H_2O) + A \rightleftarrows FeOH\cdot A + H^+ + e^- \qquad [8]$$

where A represents amide.

It must be emphasized that in Eq. [8] the chemisorbed site of the amide molecule in the metal surface is considered to be by means of the oxygen atom and not the nitrogen atom, since the structures of amides are best described as resonance hybrids of the primary structures

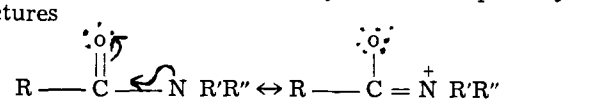

where R, R', and R'' = H, CH_3, C_2H_5, and C_3H_8 for the different amides in this study. Thus, electrostatically, the electron-rich oxygen atom would be favored for adsorption on the metal surface. Furthermore, it has been proved from infrared spectra that all amide complexes are coordinated with the metal through the oxygen rather than the nitrogen atom (18).

Over-all mechanism of the anodic process.—Following the discussion of the sections under Results and Discussion, we may obtain the most probable mechanism for the electrochemical reactions of iron in the presence of amides in $K_2SO_4 + H_2SO_4$ solutions in the concentration polarization region as

$$\underset{(1-\theta)}{Fe(H_2O)} + A \overset{K_2}{\rightleftarrows} \underset{\theta_2}{FeOH\cdot A} + H^+ + e^- \qquad [8]$$

$$\Big\downarrow k \qquad + H_2O \overset{K_1}{\rightleftarrows} \underset{\theta_1}{Fe(OH)_2} + 2H^+ + 2e^- \qquad [1]$$

$$Fe^{++} + 2e^- \qquad [9]$$

in which Eq. [9] is the final expression for iron dissolution reaction. In the above mechanism, θ_1 and θ_2 are the surface coverages of the metal surface by $Fe(OH)_2$ and amides, respectively. K_1 is the formation constant of $Fe(OH)_2$ and K_2 the adsorption constant for amides; k is the dissolution rate constant defined by Eq. [4]; and $\theta = \theta_1 + \theta_2$ is the total surface coverage.

It is observed from all the polarization measurements that the total surface coverage, θ, on the electrode surface is always small ($\theta < 0.1$) in the active polarization region. Therefore, before a detailed discussion of the various surface coverages, θ, θ_1, and θ_2, is given, a Langmuir type isotherm (19) (*i.e.*, the free energy of the active site surface will not be affected by the surface coverage, *etc.*) is considered for this mechanism and the following derivation is deduced, based on this isotherm.

Both Eq. [1] and [8] comprise the transport of protons and electrons. Although the high transport number of protons and the high applied field in the anodic process will tend to remove protons from the electrode, the rate of these transports is still very small compared to the charge transfer reaction of Eq. [9] in the active polarization region. The choice between passivation and continuous dissolution therefore appears to depend on the comparative ease with which protons and ferrous ions (or Fe^{++} complexes) pass through the interface.

Below the oxygen reversible potential, reaction [1] cannot proceed continuously and a quasi-equilibrium will obtain in which θ_1 will be potential dependent according to the electrochemical isotherm.

$$\frac{\theta_1 [H^+]^2}{1-\theta} = K_1 \exp\left(2\,(E_H - E_R)\mathbf{F}/_{RT}\right) = K_1 \exp\left(2\,\eta\mathbf{F}/RT\right)$$

$$\frac{\theta_1}{1-\theta} = K_1 e^{2x} [H^+]^{-2} \qquad [10]$$

where $\eta = E_H - E_R$, $x = \eta\mathbf{F}/RT$.

Equation [8] is the adsorption reaction of amides on the iron surface comprising one charge only. A quasi-equilibrium is considered in which θ_2 is dependent on potential according to the relation

$$\frac{\theta_2 [H^+]}{(1-\theta)\,[A]} = K_2 e^x$$

$$\frac{\theta_2}{1-\theta} = K_2 e^x [A]\,[H^+]^{-1} \qquad [11]$$

From Eq. [10] and [11]

$$1 - \theta = \frac{[H^+]^2}{[H^+]^2 + K_1 e^{2x} + K_2 e^x [A]\,[H^+]} \qquad [12]$$

which corresponds to the active surface area for the anodic dissolution reaction of Eq. [9]. Equations [10] and [11] also suggest that the corresponding surface coverages for the chemisorbed species, $FeOH\cdot A$, and the inhibiting species $Fe(OH)_2$, are

$$\theta_2 = \frac{K_2 e^x [A]\,[H^+]}{[H^+]^2 + K_1 e^{2x} + K_2 e^x [A]\,[H^+]} \qquad [13]$$

$$\theta_1 = \frac{K_1 e^{2x}}{[H^+]^2 + K_1 e^{2x} + K_2 e^x [A]\,[H^+]} \qquad [14]$$

and the total surface coverage

$$\theta = \theta_1 + \theta_2 = \frac{K_1 e^{2x} + K_2 e^x [A]\,[H^+]}{[H^+]^2 + K_1 e^{2x} + K_2 e^x [A]\,[H^+]} \qquad [15]$$

Under Langmuir isotherm conditions and in terms of the absolute rate theory (19), the final expression for the dissolution rate of iron in the presence of adsorption species for this system at high overpotentials is

$$i = k\,[H^+]^\gamma\,(1-\theta)\exp\left(\frac{2.303\,\eta}{2.54 - 0.45\,pH}\right) \qquad [16]$$

From Eq. [12], Eq. [16] reads

$$i(A) = \frac{K[H^+]^{2+\gamma}}{[H^+]^2 + K_1 e^{2x} + K_2 e^x [A]\,[H^+]} \exp\left(\frac{2.303\,\eta}{2.54 - 0.45\,pH}\right) \qquad [17]$$

If the system does not contain amides, the active corrosion current density will be

$$i\,(o) = \frac{k[H^+]^{2+\gamma}}{[H^+]^2 + K_1 e^{2x}} \exp\left(\frac{2.303\,\eta}{2.54 - 0.45\,pH}\right) \qquad [18]$$

The formation constant and the coverage of $Fe(OH)_2$ in the active polarization region.—Should the active anodic polarization curves follow Eq. [17] and [18], then the following properties will be observed from the experiments:

$$\text{At } E_H = E_{crit}, \left.\frac{di}{d\eta}\right|_{pH} = 0,$$

$$\text{where } \eta = E_H - E_R \text{ and } \frac{dx}{d\eta} = \frac{F}{RT}$$

The result for Eq. [18] will be

$$K_1 e^{2x}{}_{crit} = \frac{[H^+]^2}{91.2 - 16.2\,pH} \qquad [19]$$

The coefficient $2F/2.303\,RT = 36.3\ V^{-1}$ has been included in the denominator of Eq. [19]. The critical current density can be expressed in the form

$$i_{crit}(o) = \frac{k[H^+]^\gamma\,(2.51 - 0.45\,pH)}{2.54 - 0.45\,pH} \exp\left(\frac{2.303\,\eta_{crit}}{2.54 - 0.45\,pH}\right) \qquad [20]$$

From Eq. [19] the formation constant of $Fe(OH)_2$, K_1, can be calculated for various pH values and is given in Table III. K_1 at pH 0 is calculated from the extrapolated η^o_{crit} in which $\eta^o_{crit} = E^o_{crit} - E^o_R$ and $x^o_{crit} = F/RT\ \eta^o_{crit}$. The average K_1 is 4.8×10^{-40}. The small formation constant reveals that the formation of the inhibiting species in the active corrosion region of the polarization curve is not important. This effect should become noticeable at higher overpotential, especially when $\eta \rightarrow \eta_{crit}$.

The location of the Flade arrest has not always been a matter of agreement between investigators (4, 20, 21). This disagreement becomes even greater at pH ~ 7.0 (21). The Flade arrest is related to pH for passivity decay by

$$E_F = E_F{}^o - \frac{2.303\,RT}{zF} \cdot pH$$

This relation was first observed by Franck (22) for iron in sulfuric acid solutions. According to the adsorption theory of passivity, E_F is the potential at which oxygen begins to adsorb on the metal surface. However, the adsorption of oxygen is restricted either by the dissolution of metal or by the chemical dissolution of the inhibiting species resulting from the oxygen adsorption. The kinetics of the chemical dissolution of the inhibiting species in the passivation process is still unknown. Therefore, a theoretical attempt to explain the linear relationship between E_F and pH or the slope, $2.303\,RT/\eta F = 59$ mV at 25°C for iron in the potentiostatic polarization curves is almost impossible. However, an attempt based on the previous derivation to correlate η_{crit} rather than E_F with pH is possible.

Based on Eq. [14], there is a tendency to form the inhibiting species even at the corrosion potential (E_R) in the anodic process. This tendency becomes significant only when the metal surface is highly saturated with metal ions. At the critical potential, E_{crit}, the acceleration of metal dissolution *via* Eq. [9], along with the chemical dissolution of $Fe(OH)_2$, becomes equal to the acceleration process of protective film formation according to Eq. [1]. Following Eq. [19], a linear relation between the critical overpotential, η_{crit}, and pH can be obtained for this system, *i.e.*

$$\eta_{crit} = \eta^o_{crit} - b\,pH \qquad [21]$$

where

$$\eta^o_{crit} = \frac{2.303\,RT}{2F} \log \frac{4}{91.2K_1} \text{ and } b = \frac{2.303\,RT}{2F}\ (1.92)$$

in which a simplification has been made such as

$$\ln(1 + x) \approx +x \text{ for } |x| << 1$$

and is only valid at low pH (acidic mediums). With $K_1 = 4.8 \times 10^{-40}$, the calculated $\eta^o_{crit} = 1.029$ (volts) and $b = 0.053$ (volts).

This behavior has been verified from experiments, and it is shown in Fig. 4 that

$$\eta_{crit} = 1.025 - 0.054\,pH \qquad [22]$$

which is very close to the calculated values.

From Eq. [20] and [21] it can be further shown that

$$i_{crit}(o) = K[H^+]^\lambda \qquad [23]$$

where $K \doteqdot 10^{2.80}$, $\lambda \doteqdot 0.284$. These calculated values are valid only at pH < 5.0.

The experimental pH dependence of $i_{crit}(o)$ is shown in Fig. 2. This gives the relation

$$i_{crit}(o) = 10^{2.72}\,[H^+]^{0.286}$$

in fair agreement with the calculated values.

Coverage by the $Fe(OH)_2$, θ_1, can be calculated from Eq. [10] in which

$$\theta_1 = \frac{K_1 e^{2x}}{[H^+]^2 + K_1 e^{2x}} \qquad [24]$$

Experimentally, coverage by $Fe(OH)_2$ can be obtained from the simple expression obtained from Eq. [5] and [16], namely

$$\theta_1 = \frac{i_a - i(o)}{i_a} \qquad [25]$$

Here $i(o)$ is the actual measured current density in the absence of amides and i_a is determined from Fig. 1 by extrapolation of the logarithmic active metal dissolution section up to the given potential. The active metal dissolution in the concentration polarization region is expressed by Eq. [5] and not by the usual Tafel relation. However, as seen from Fig. 1, the current difference between i_a and $i(o)$ is too insensitive to be detected from the experiment in the active polarization region. At the critical potentials, the calculated surface coverages by the inhibiting species, θ_1, for pH = 1.1, 2.3, 3.5, 4.0, and 4.9 are 0.027, 0.045, 0.075, 0.110, and 0.145, respectively.

Table III. Calculated formation constant of $Fe(OH)_2$, K_1, from different pH

pH	η_{crit} (mV)	$e^{-2x_{crit}}$	$K_1 \times 10^{-40}$
0	1025	$10^{-37.73}$	2.1
1.1	970	$10^{-35.21}$	5.2
2.3	910	$10^{-33.03}$	4.4
3.5	850	$10^{-30.85}$	4.0
4.0	820	$10^{-29.76}$	6.6
4.9	760	$10^{-28.31}$	6.6

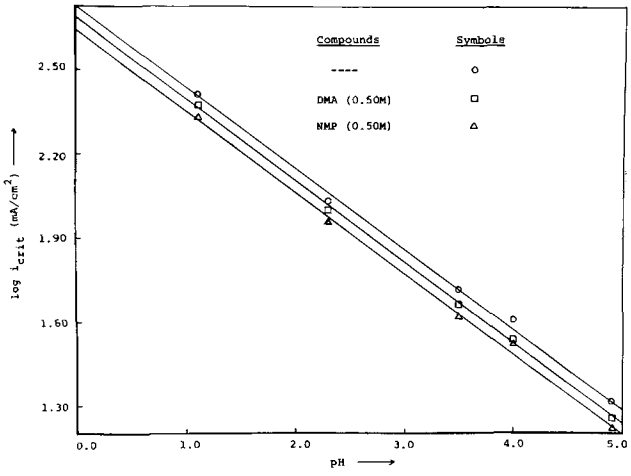

Fig. 2. Variation of log i_{crit} with pH

Table IV. Critical current densities, i_{crit} (A) (mA/cm^2), at different concentrations of F, NMP, DMA, and DMF at various pH's

Compound	pH \ Conc (m)	0	0.10	0.30	0.50	0.70	1.00
F	1.1	260	255	245	236	226	119
	2.3	86	84	80	77	73	71
	3.5	52	50	47	45	43	41
	4.0	42	40	38	35	33	32
	4.9	21	20	18	17	16.5	15
NMP	1.1	260	255	243	230	217	208
	2.3	86	83	78	72	68	63
	3.5	52	50	46	42	40	37
	4.0	42	40	37	33	31	30
	4.9	21	20	18	16	14.5	14
DMA	1.1	260	256	245	240	230	225
	2.3	86	84	80	77	75	71
	3.5	52	51	48	46	45	42
	4.0	42	40.5	38	36	34	32
	4.9	21	20.5	19	17.5	16.5	15.5
DMF	1.1	260	258	245	241	235	226
	2.3	86	85	81	78	75	73
	3.5	52	51	49	47	44	43
	4.0	42	40.5	39	36	34	33
	4.9	21	20.5	19	17	16.5	15

Adsorption constants of amides and the competitive surface coverages by $Fe(OH)_2$ and amides in the active polarization region.—The polarization curves in the presence of amides look very much like those without amides. Some important features which have been observed are: (*a*) the rest potentials and critical potentials show no change with respect to the previous study; (*b*) at potentials near the E_{crit}, iron dissolution rate decreases with increasing amide concentration. Therefore, a relation between η_{crit} and pH can also be described by Eq. [21].

Table IV shows the concentration effects of four amides on the critical current density at various pH's. It is seen from this table that i_{crit} (A) is related to pH by

$$i_{crit}(A) = K'[H^+]^{\lambda} \qquad [26]$$

which is similar to Eq. [23]. This equation is derived from Eq. [17] and [21] following the same argument given previously for the system without amides and is confirmed by experiments (shown in Fig. 2). The experimental values of K' for 0.50M DMA and NMP found in Fig. 2 are $10^{2.68}$ and $10^{2.64}$, respectively.

Table V lists the critical current densities, $i_{crit}(A)$, for 0.10M amides at various pH's. It is obvious that the addition of amides decreases the critical current density, thus decreasing the dissolution rate of iron at the critical potential. The adsorption of amides on the metal surface therefore decreases the active sites of the surface for metal dissolution which in turn decreases the dissolution of the metal in the active corrosion region.

Although the change of dissolution rate due to the adsorption of amide is small in all cases, a detailed study of the polarization curves provides evidence that amides with higher dielectric constants adsorb on the iron surface more effectively than do the lower ones. From Fig. 2 and Table IV, the relative adsorption effect for the four amides is NMP > F > DMA > DMF. This is also the order of decreasing dielectric constant for these compounds (10, 23, 24). In other words, the higher dielectric amides are better inhibitors than those amides with lower dielectric constants.

In general, the adsorption constant of the amide, K_2, can be obtained from polarization studies by varying the amide concentration in a given system.

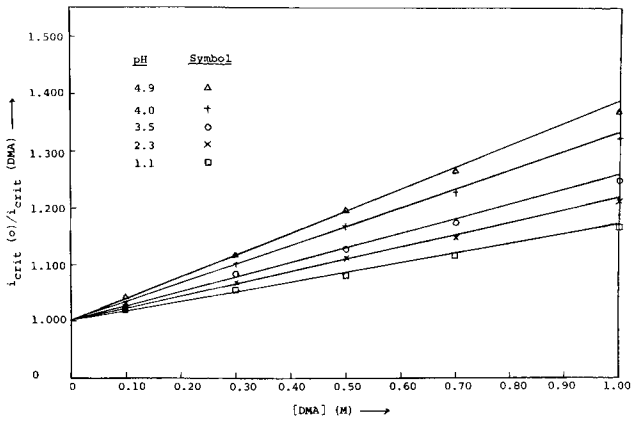

Fig. 3. A plot of $i_{crit}(o)/i_{crit}(DMA)$ vs. [DMA]

At η_{crit}, the ratio of the uninhibited and inhibited critical current densities from Eq. [17] and [18] is

$$\frac{i_{crit}(o)}{i_{crit}(A)} = 1 + \frac{K_2 e^{x_{crit}}[H^+]}{[H^+]^2 + K_1 e^{x_{crit}}} \cdot [A]$$

From Eq. [19], this ratio becomes

$$\frac{i_{crit}(o)}{i_{crit}(A)} = 1 + \rho[A] \qquad [27]$$

in which

$$\rho = K_2 \frac{2.51 - 0.45\,pH}{2.54 - 0.45\,pH} \cdot \frac{e^{x_{crit}}}{[H^+]}$$

Experimentally, ρ is obtained from a plot of $i_{crit}(o)/i_{crit}(A)$ *vs.* the concentration of amide, $[A]$. A typical plot based on Table IV is shown in Fig. 3 for dimethylacetamide. Fairly straight lines were obtained for each pH and it was observed that a relatively large slope was obtained at higher pH. According to the proposed mechanism, as shown in Eq. [8], the adsorption of amides is accompanied by proton transport from the metal surface into the solution. This proton transport will be smaller at lower pH due to the retardation of this process by hydronium ions in the solutions which, in turn, will result in a smaller adsorption of amides and therefore a smaller slope.

The adsorption constant, K_2, can be obtained directly from Eq. [27] in the form

$$K_2 = \left(\frac{2.51 - 0.45\,pH}{2.54 - 0.45\,pH} \cdot \frac{e^{x_{crit}}}{[H^+]} \right)^{-1} \cdot \rho \qquad [28]$$

Based on Table IV, different plots similar to Fig. 3 can be obtained for DMF, F, and NMP. These plots give different slopes, ρ, which enable us to calculate the adsorption constants of amides, K_2, by using Eq. [28]. Table VI gives the various slope values, ρ, and the calculated adsorption constants, K_2, for F, NMP, DMA, and DMF. It is seen that, for each amide, the adsorption constant is independent of pH. The average K_2 for F, NMP, DMA, and DMF is 5.5 x 10^{-20}, 7.8 x 10^{-20}, 4.7 x 10^{-20}, and 4.4 x 10^{-20}, respectively. A higher K_2 indicates a better inhibitor.

Relating Eq. [13], [17], and [18], we are able to find a simple expression for the surface coverage, θ_2, by amide at any given potential, *i.e.*

$$\theta_2 = \frac{i(o) - i(A)}{i(o)} \qquad [29]$$

Table V. Critical current densities, i_{crit} (A), for 0.10M amides at various pH's

pH \ Compound	F	NMF	DMF	A	NMA	DMA	P	NMP	DMP	DMB	—
1.1	255	252	258	260	255	256	259	255	254	260	260
2.3	84	82	85	86	82	84	87	83	84	82	86
3.5	50	49	51	53	49	50	52	50	51	51	52
4.0	40	39	40.5	41	39.5	40.5	42	40	41	40	42
4.9	20	19	20.5	21	19	20.5	21	20	21	20.5	21

Table VI. Various slopes and calculated adsorption constants for F, NMP, DMA, and DMF

pH	$\left(\frac{2.51-0.45\,pH}{2.56-0.45\,pH} \times \frac{e^{\beta}\,crit}{[H^+]}\right)^{-1}$	F		NMP		DMA		DMF	
		ρ	$K_2 \times 10^{20}$	ρ	$K_2 \times 10^{20}$	ρ	$K_2 \times 10^{20}$	ρ	$K_2 \times 10^{20}$
1.1	$10^{-18.6980}$	0.208	4.2	0.300	6.0	0.175	3.5	0.172	3.5
2.3	$10^{-18.8067}$	0.266	4.2	0.390	6.0	0.220	3.4	0.210	3.3
3.5	$10^{-18.9180}$	0.295	3.6	0.440	5.4	0.260	3.2	0.255	3.1
4.0	$10^{-18.8050}$	0.395	5.4	0.545	6.8	0.335	4.6	0.320	4.4
4.9	$10^{-18.6549}$	0.462	10.0	0.680	14.7	0.390	8.6	0.350	7.7

A plot based on Eq. [29] and [13] for DMA at pH 4.0 with three different concentrations is given in Fig. 4 as an example of the adsorption of amides. The relative surface coverage by this amide changes drastically with respect to the potential change. It is important to note also that the critical overpotenial which corresponds to the maximum dissolution rate of iron in a given system is not synonymous with the maximum surface coverage by the organic species. This is also true for the coverage of $Fe(OH)_2$ (see Fig. 5). As can be seen in Fig. 4, θ_2 increases continuously beyond $\eta_{crit} = 820$ mV. Therefore, from the experimental observation, it is apparent that the quasi-equilibrium reactions of Eq. [1] and [8] will proceed at the potential beyond the critical potential, E_{crit}. A detailed discussion on the surface coverages in the potential region $E_{crit} - E_p$, where $E_p > E_{crit}$, is presented in the next section.

Figure 5 shows the competitive surface coverages by $Fe(OH)_2$, θ_1, and by DMA at 0.50M, θ_2. This figure shows that the surface coverage by amide is always greater than the coverage of inhibiting species in the active polarization region. It is obvious from this that the adsorption of amide plays a predominant role on the total surface coverage at any given potential in this region.

Adsorption process in the $E_{crit} \sim E_p$ region.—In the potential region immediately more noble than the critical potentials, the anodic currents flowing at a given potential decrease with time, eventually reaching a low steady value. With amides added in the solution, the time required to obtain the steady value is longer. This shows that the passivating film is gradually becoming more protective. However, the film is not completely protective against metal dissolution since a quasi-equilibrium reading of current (constant reading within a certain period of time) can still be obtained at a given potential until a certain potential (E_p), considerably more positive than the critical potential, is reached. In general, it is difficult to identify from the anodic polarization curves obtained in this investigation, a marked discontinuity which could be definitely associated with the iron surface becoming completely protective by the passive film. This is a phenomenon observed by many other investigators (25-28) also. The potential corresponding to the completely protected passive film is known as the passivation potential and is represented as E_p (Fig. 1).

Normally, as can be seen from Fig. 1, the potential range of $E_{crit} \sim E_p$ extends from about 50 mV (for pH 1.1) to 300 mV (for pH 4.9), depending on pH. At lower pH, the potential range is narrower and reveals the ease of onset of the complete protective film. At pH 4.9, this range extends approximately 300 mV, revealing the difficulty of onset of complete protection by the passive film.

The onset of complete passivity, E_p, represents the complete coverage of the electrode surface with the inhibiting species. This potential also corresponds to the reversible minimum for Eq. [1], the $Fe(OH)_2$ formation reaction. An approximate evaluation of this portion of the electrode surface covered by a surface film, θ, at any given potential between E_{crit} and E_p can be obtained from the relation

$$\theta = \frac{i_a - i(A)}{i_a}, \quad \theta = \theta_1 + \theta_2 \qquad [30]$$

which is equivalent to Eq. [25] except that the measured current density is $i(A)$ instead of $i(o)$. A more precise polarization measurement (a potential step of 10 mV instead of the 50 mV used in most of this investigation) in this portion, $E_{crit} \sim E_p$, reveals the possibility of calculating the coverage by $Fe(OH)_2$, θ_1,

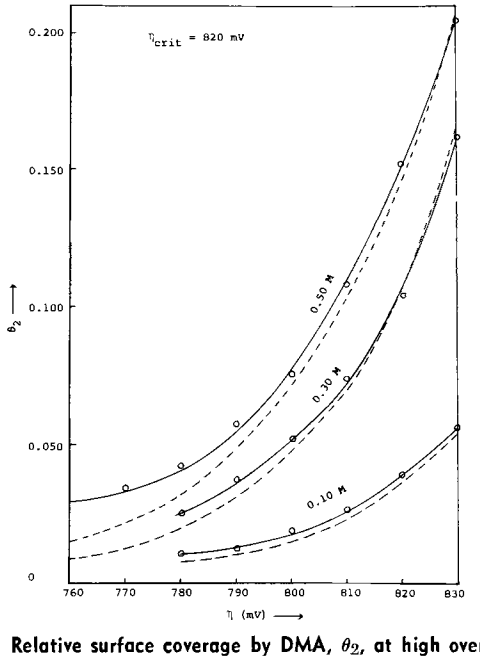

Fig. 4. Relative surface coverage by DMA, θ_2, at high overpotentials at pH 4.0 with concentrations of 0.10, 0.30, and 0.50M: ——— experimental (by Eq. [29]), - - - - - - - - - - calculated (by Eq. [13]).

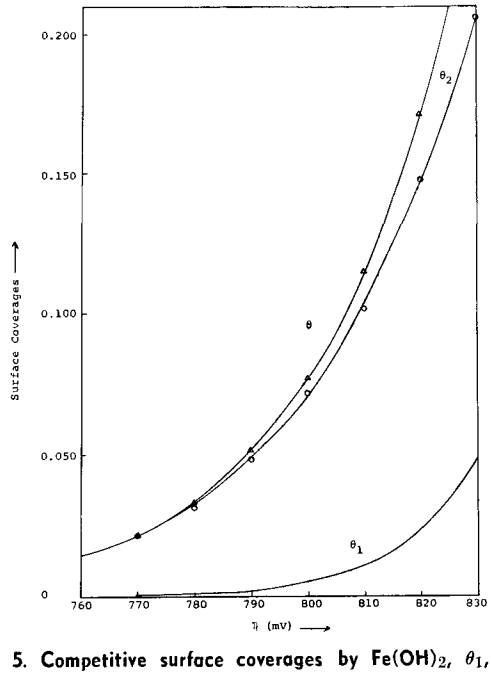

Fig. 5. Competitive surface coverages by $Fe(OH)_2$, θ_1, and by DMA (0.50M), θ_2, at pH 4.0; $\theta = \theta_1 + \theta_2$.

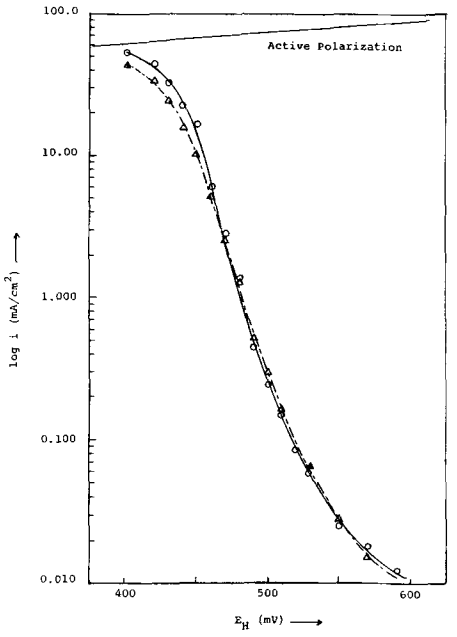

Fig. 6. Anodic polarization curves in the region E_{crit} — E_p at pH 3.5: ——— without amide, - - - - - - - - - - with [DMF] = 0.30M.

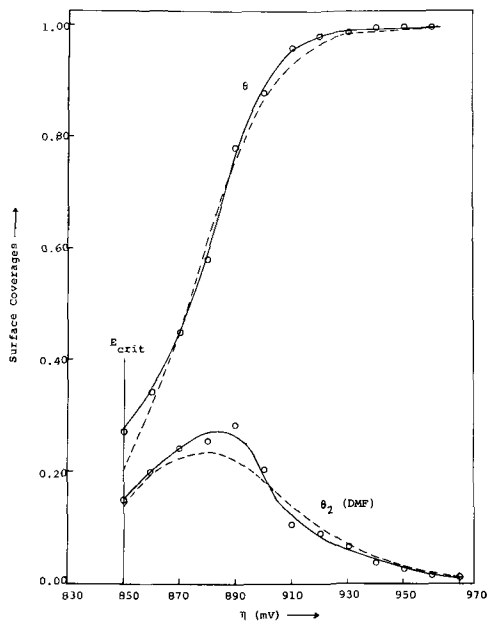

Fig. 8. Total surface coverage, θ, and the surface coverage by DMF (0.30M) in the E_{crit} — E_p region at pH 3.5: ——— experimental, - - - - - - - - - - calculated.

as well as the surface coverage by amide, θ_2. Figure 6 shows the polarization curves with and without DMF at pH 3.5. The upper straight line is the extrapolation of the logarithmic active metal dissolution governed by concentration polarization. Figure 7 shows the comparison of the calculated coverage by $Fe(OH)_2$ using Eq. [24] with the experimental values using Eq. [25] based on Fig. 6. It is seen that the coverage of $Fe(OH)_2$ changes drastically with respect to a small change of applied potential. Figure 8 shows the total surface coverage, θ, using Eq. [30] and the coverage by DMF, θ_2, using Eq. [29]. The calculated curves using Eq. [15] for θ and Eq. [13] for θ_2 are also given in this figure for comparison.

These figures show that the coverage of $Fe(OH)_2$ is a continuous process before the onset of the complete protection at E_p. However, the surface coverage by amide reveals that the adsorption and desorption processes depend on the applied potential since an adsorption maximum exists in the $E_{crit} \sim E_p$ region. In

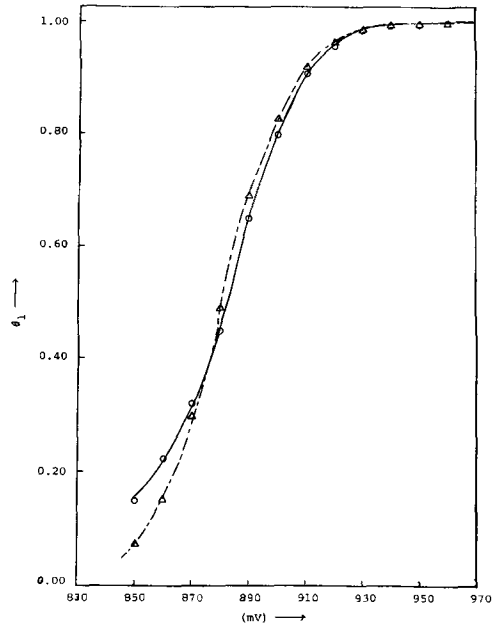

Fig. 7. The coverage of $Fe(OH)_2$, θ_1, in the E_{crit} — E_p region at pH 3.5: ——— experimental, - - - - - - - - - - calculated.

Fig. 8 it is seen that θ_2 at the potential near E_p is negligible compared to θ_1. This is to be expected if the proposed mechanism is correct since it can be assumed that, under quasi-equilibrium conditions, the adsorption of amide and the $Fe(OH)_2$ formation are competitive reactions. Beyond the critical potential, the $Fe(OH)_2$ formation is predominant and desorption of amide occurs. This desorption continues until the potential reaches E_p at which the active electrode surface is essentially completely covered by the inhibiting species. Beginning at E_p, the adsorption of amide must take place on the passive metal surface material rather than on the active surface. A detailed discussion on the amide adsorption in the passive region is given in the next section.

Effect of amide adsorption in the passive region.— Beginning at the onset of the complete passivity, E_p (Fig. 1), the rate of anodic process is independent of potential. The reason for this constant rate of anodic process is still controversial (1, 9). According to the adsorption theory, the anodic reaction on a passive metal, as on an active metal, consists of the transfer of lattice cations into the bulk solution. Passivation is due to an increase of the overvoltage of this transfer which is the result of some changes in the properties of the adsorbing oxygen on the metal surface. The mechanism of these changes is not clear. The oxide film theory explains that the constant current of the anodic process is due to the chemical dissolution of the passivating oxide, not to the formation of hydrated cations. The cations arrive in the solution as the result of the subsequent dissociation of this oxide and is considered to be an ordinary electrically neutral chemical reaction (29).

These two theories must work from the same conclusion that metal cations appear in the solution and their formation is governed by Faraday's laws. With an increase in the anodic potential and the electrical field in the film, the rate of the penetration of metal ions from the active metal surface through the protective film in the opposite direction increases, resulting in protective film thickening. Therefore, the oxide film thickness is directly dependent on the applied potential (30).

Although it is generally agreed that the initiation of passivation before E_p is associated with the appearance of a monolayer or less of an "adsorbed" inhibiting species (2, 3), the entity of this "species" has not been fully understood. In the case of iron, the adsorbed in-

Table VII. Passivation current densities, i_p (μA/cm^2), of 0.10M amides at different pH's

pH \ Compound	—	F	NMF	DMF	A	NMA	DMA	P	NMP	DMP	DMB
1.1	9.6	7.2	7.6	8.8	8.0	7.6	9.0	8.4	6.4	7.8	7.4
2.3	7.9	5.6	5.8	7.6	5.9	6.0	7.5	6.8	4.0	7.2	6.5
3.5	5.6	4.2	4.0	4.9	5.0	4.6	4.9	4.6	3.8	5.1	4.0
4.0	5.0	4.0	3.6	4.2	4.5	3.5	4.4	4.4	2.9	4.4	3.3
4.9	4.4	3.2	3.0	3.8	3.6	2.8	3.6	4.0	2.6	3.0	2.5

hibiting species is believed by some to be FeO or its hydrated species, $Fe(OH)_2$. The alternate oxide species, Fe_3O_4, is also possible since ferrous hydroxide may decompose to a mixture of magnetite and iron (21, 31).

$$4\,Fe(OH)_2 \rightarrow Fe_3O_4 + Fe + 4\,H_2O$$

Beginning at E_p, a more protective oxide film other than $Fe(OH)_2$ is formed on the metal surface (1, 4). From electron diffraction (32) and chemical analysis (27) of this oxide film, the passive film of iron is said to consist of γ-Fe_2O_3 and Fe_3O_4. The dissolution species in the passive state, no matter whether it is coming from the corrosion of the active metal surface or the dissolution of oxide film, is ferric ions instead of ferrous ions (21).

Table VII lists the passivation current densities, i_p, with and without 0.10M amides at various pH's. Each i_p is the average of three experiments.

Table VIII shows the concentration effect of four amides on the passivation current density. The current densities decrease with increase of concentration at a given pH. If we regard the passivation current density as the dissolution rate of the passive state, then it is clear that amides will behave as an inhibitor on the passive iron. Comparing Tables IV and VIII, the inhibiting effect of the organic material is seen to be much more effective in the passive than in the active region. Unless a fully detailed chemical analysis of the oxide film is carried out, it is very difficult at this stage to guess whether the amides will be incorporated in the oxide film growth. It seems likely that the effects of amides on the passivation current densities are associated with their strong adsorption on the passive metal surface. This adsorption should lead to decreased ionic conductivity in the passive film.

The marked inhibition effect of amides on the passive state as compared to that for the active state is probably due to the interference by metal dissolution in the latter. The large dissolution rate of iron in the active polarization region suggests a less competitive adsorption of these organic species on the active metal surface, while the small and constant dissolution rate of oxide film should permit a more competitive adsorption of amides on the passive metal surface.

Table VIII. Passivation current densities, i_p, at different concentrations of F, NMP, DMA, and DMF at various pH's

Compound	pH \ Conc (M)	0	0.10	0.30	0.50	0.70	1.00
F	1.1	9.6	7.2	3.6	2.4	1.9	1.9
	2.3	7.9	5.6	3.2	1.8	1.5	1.1
	3.5	5.6	4.2	2.1	1.8	1.5	1.2
	4.0	5.0	4.0	2.5	1.3	0.8	0.6
	4.9	4.4	3.2	1.6	1.0	0.6	0.3
NMP	1.1	9.6	6.4	4.2	1.2	0.6	0.4
	2.3	7.9	4.0	1.2	0.8	0.5	0.5
	3.5	5.6	3.8	1.4	0.6	0.6	0.2
	4.0	5.0	2.9	2.1	0.9	0.4	0.3
	4.9	4.4	2.6	1.2	0.4	0.2	0.2
DMA	1.1	9.6	9.0	6.9	6.2	6.0	4.4
	2.3	7.9	7.5	6.9	6.0	5.2	3.8
	3.5	5.6	4.9	4.3	4.5	3.2	2.5
	4.0	5.0	4.4	3.8	3.0	2.3	2.1
	4.9	4.4	3.6	2.6	2.2	1.6	1.9
DMF	1.1	9.6	8.8	7.4	6.4	6.1	4.9
	2.3	7.9	7.6	6.4	5.3	5.2	3.8
	3.5	5.6	4.9	5.3	4.5	2.9	2.5
	4.0	5.0	4.2	4.2	3.4	2.6	2.3
	4.9	4.4	3.8	2.9	2.6	2.0	1.4

Acknowledgments

The financial support by the Robert A. Welch Foundation of Houston, Texas, is gratefully acknowledged. The authors are also indebted to the Battelle Memorial Institute, Columbus, Ohio, for the generous supply of zone-refined iron.

LIST OF ABBREVIATIONS

V	volts
mV	millivolts
mA	milliamperes
μA	microamperes
E_H	measured potential with respect to hydrogen scale
E_R	rest potential or corrosion potential
E_{crit}	critical potential
E_p	passivation potential
E_F	Flade arrest
i	current density (mA/cm^2)
i_{crit}	critical current density
i_p	passivation current density
$i(o)$	current density in the absence of amide
$i(A)$	current density in the presence of amide
i_o	current density at $\eta = 0$
i_a	extrapolated active metal dissolution current density
i^o	current density at pH 0
η	overpotential, $= E_H - E_R$
η_{crit}	critical overpotential, $= E_{crit} - E_R$
η^o_{crit}	critical overpotential at pH 0
k	dissolution rate constant
K_1	oxygen-ion complex formation constant
K_2	adsorption constant of amide
θ_1	surface coverage by inhibiting species
θ_2	surface coverage by amide
θ	over-all surface coverage, $= \theta_1 + \theta_2$
A	abbreviation for amide
γ	constant, $= -\partial \log i_o/\partial$ pH
x	$= \eta F/RT$
λ	constant, $= -\partial \log i_{crit}/\partial$ pH
K, K'	proportional constants for $i_{crit}(o)$ and $i_{crit}(A)$

Manuscript submitted June 2, 1970; revised manuscript received *ca.* Aug. 24, 1970.

Any discussion of this paper will appear in a Discussion Section to be published in the December 1971 JOURNAL.

REFERENCES

1. N. Hackerman, *Z. Elektrochem.*, **62**, 632 (1958).
2. Ya. M. Kolotyrkin, *ibid.*, **62**, 664 (1958).
3. P. V. Popat and N. Hackerman, *J. Phys. Chem.*, **65**, 1201 (1961).
4. N. D. Tomashov and G. P. Chernova, "Passivity and Protection of Metals Against Corrosion," Plenum Press, New York (1967).
5. A. Pigeaud, and H. B. Kirkpatrick, *Corrosion*, **25** (5), 209 (1969).
6. G. H. Cartledge, *Brit. Corrosion J.*, **1**, 293 (1966).
7. B. Kabanov, R. Burstein, and A. Frumkin, *Disc. Faraday Soc.*, **1**, 259 (1947).
8. M. Smialowski and Z. Szklarska-Smialowski, "2eme Symposium Europeen sur les Inhibiteurs de Corrosion," pp. 22-24, Ferrara (Italie) (1965).
9. V. M. Novakowskii and Yu. A. Likhachev, *Zashchita Metallov*, **1** (1), 13 (1965).
10. D. S. Reid and C. A. Vincent, *J. Electroanal. Chem.*, **18**, 427 (1968).
11. Beilsteins Handbuch, Band IV, Erster Teil, S. 1-1094.
12. H. C. Eckstrom, Djong-gie Oei, and L. R. Dawson, *J. Phys. Chem.*, **67**, 2804 (1963).
13. J. F. O'Donnel and C. K. Mann, *J. Electroanal. Chem.*, **13**, 157 (1967).

14. J. D. Roberts and M. C. Caserio, "Basic Principles of Organic Chemistry," W. A. Benjamin, New York (1964).
15. K. E. Heusler, *Z. Elektrochem.*, **62**, 582 (1958).
16. E. J. Kelly, *This Journal*, **112**, 124 (1965).
17. N. Hackerman and A. C. Makrides, *Ind. Eng. Chem.*, **46** (3), 523 (1954).
18. W. E. Bull, S. K. Madan, and J. E. Willis, *Inorg. Chem.*, **2**, 303 (1963).
19. B. E. Conway, "Theory and Principles of Electrode Processes," The Ronald Press Co., New York (1965).
20. H. H. Uhlig, *This Journal*, **108** (4), 327 (1961).
21. K. J. Vetter, "Electrochemical Kinetics," Academic Press, New York (1967).
22. U. F. Franck, *Z.. Naturforschung*, **4A**, 378 (1949).
23. R. M. Meighan and R. H. Cole, *J. Phys. Chem.*, **68**, 503 (1964).
24. S. J. Bass, W. I. Natham, R. M. Meighan, and R. H. Cole, *ibid.*, **68**, 509 (1964).
25. D. M. Brasher and A. D. Mercer, *Proc. Int. Congr. Metallic Corrosion, 3rd, Moscow* (1966).
26. J. G. N. Thomas and T. J. Nurse, *Brit. Corrosion J.*, **2**, 13 (1967).
27. M. Nagayama and M. Cohen, *This Journal*, **109**, 781 (1962); **110**, 670 (1963).
28. R. P. Frankenthal, *ibid.*, **114**, 542 (1967).
29. T. P. Hoar, "New Problems of Electrochemistry," II, J. O'M. Bockris, Editor, Moscow (1962).
30. K. Kudo, T. Shibata, G. Okamoto, and N. Sato, *Corrosion Sci.*, **8**, (11), 809 (1968).
31. J. M. West, "Electrodeposition and Corrosion Process," D. Van Nostrand Co., London (1965).
32. J. E. O. Mayne and J. W. Menter, *J. Chem. Soc.*, **99**, 103 (1954).

Crystallographic Factors in High-Rate Anodic Dissolution of Copper

D. Landolt*,[1], R. H. Muller,* and C. W. Tobias*

Inorganic Materials Research Division, Lawrence Radiation Laboratory and Department of Chemical Engineering, University of California, Berkeley, California 94720

ABSTRACT

Surface textures resulting from the anodic dissolution of polycrystalline and single crystal copper at 50 A/cm^2 in 2M KNO_3 have been studied. Electrolyte flow velocities of 2500 and 400 cm/sec have been used for dissolution in the active and transpassive mode. Results obtained by light and electron microscopy show that surface topography resulting from active dissolution depends on crystal orientation. Flow streaks appear in transpassive dissolution. Transpassive pitting was observed in polycrystalline samples only.

An important problem in the process of electrochemical machining is the control of the resulting surface finish. In previous studies of high-rate anodic metal dissolution (1-3), it has been shown that the surface finish resulting from the anodic dissolution of copper in a given electrolyte depends both on flow velocity and current density. The micrographs shown in Fig. 1 exhibit a transition from etching to polishing dissolution along a line running approximately from the upper left to the lower right of the array. Below this line, the surface appears etched and dull; above it, smooth and bright, with pits increasing in prominence with the separation from the transition region. The transition in surface finish coincides with the transition from a low voltage dissolution mode, which we have termed active, to a high voltage mode, which we call transpassive. It is to be expected that structural factors of the anode material also affect the resulting surface finish. In the present study, the surface topography resulting from the high-rate anodic dissolution of copper specimens has been investigated under active and transpassive dissolution conditions in 2 molar potassium nitrate solution. Polycrystalline samples of variable grain size and single crystals of different orientations have been used.

Experimental

The flow system and the electrical circuit employed have been described before (1). Two flow rates have been employed, 2500 cm/sec for dissolution in the active mode and 400 cm/sec for dissolution in the passive mode. Electrolysis was conducted at a constant current of 50 A/cm^2 with a stainless steel cathode of 3 mm diam positioned 0.5 mm from the anode. During each experiment, a charge of 25 coulombs/cm^2 was passed, which corresponds to an average dissolution depth of 10μ (based on the formation of Cu^{++}).

Disk anodes of 1.5 mm diam and 45 mm length, embedded in cylindrical polypropylene holders of 5 mm diam, were used. They were prepared from 99.999% copper rod (Cominco Co., Spokane, Washington). Polycrystalline specimens were used as received or were annealed (1750°F, 4 hr in argon, after 7.5% diam reduction). Single crystals were grown from the same material in induction-heated graphite molds, using spherical seed crystals. The surfaces of the embedded electrodes were gently polished over extended periods (6-30 hr) with 1 and 0.5μ chromium oxide abrasive. Structural damage due to this treatment was sufficiently shallow that it was not visible in the x-ray diffraction pattern of single crystals. In order to put a limit on the depth of lattice damage expected to be still present on the surface (without affecting the x-ray diffraction pattern), experiments were performed to determine the thickness of distorted copper necessary to obliterate the diffraction from an underlying single crystal. Cold-rolled copper foils of different thicknesses were attached to the surface of a (100) oriented crystal. No discernible diffraction pattern was obtained with a 10μ thick foil and a greatly attenuated one resulted from 5μ, independent of the closeness of contact of the copper foil. These results indicate that surface damage due to polishing extended to a depth of much less than 5μ, and the anodic dissolution indeed proceeded into the undisturbed crystal. The smoothness and flatness of the polished electrode surface was ascertained by interference microscopy. Deviation from flatness over the

[1] School of Engineering and Applied Science, University of California, Los Angeles, California 90024.
* Electrochemical Society Active Member.
Key words: electrochemical machining, copper dissolution, single crystal dissolution.

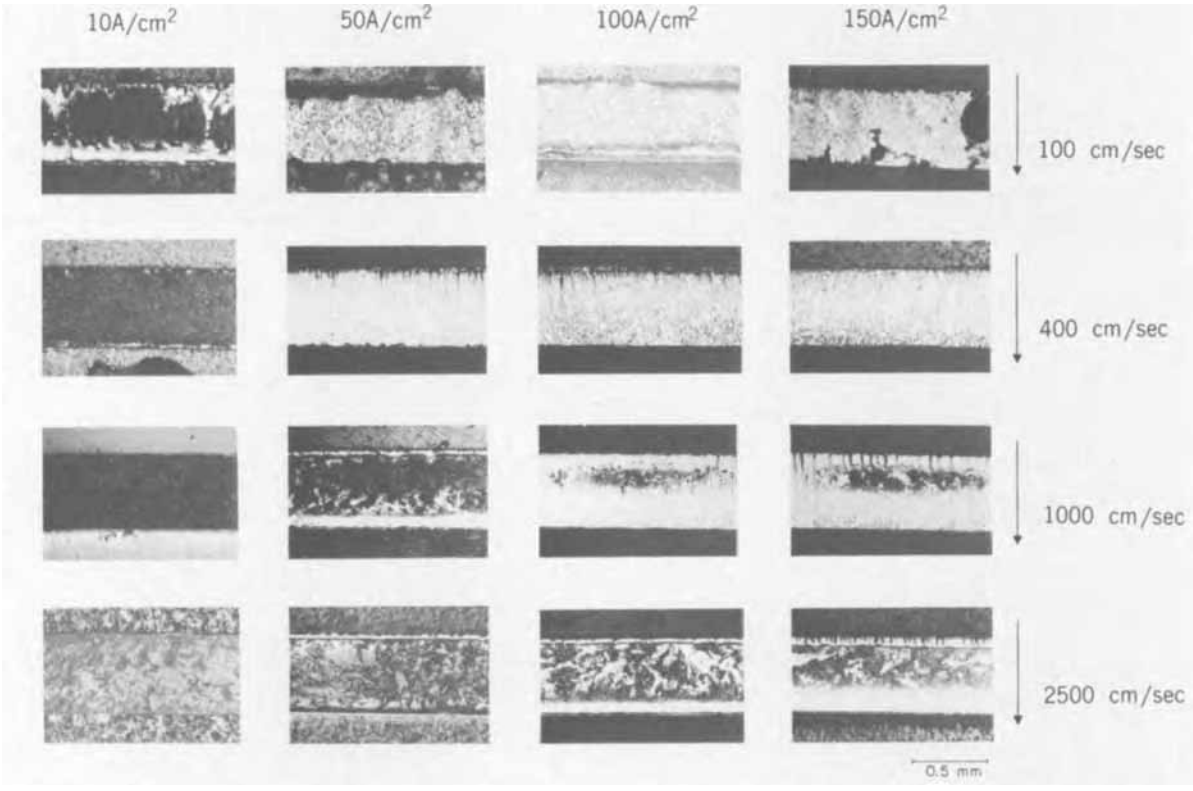

Fig. 1. Polycrystalline copper surfaces after dissolution in 2M KNO_3 at different current densities and flow velocities. Optical micrographs

entire surface was usually less than 2μ as illustrated in Fig. 2. Residual polishing marks were at most 0.05μ deep (Fig. 3).

Before use, the electrodes were cleaned with acetone and detergent and subjected to cathodic hydrogen evolution in 1M NaOH (100 mA/cm², 3 min). After the dissolution experiment, the electrodes were immediately removed from the flow channel cell, rinsed with distilled water, and dried with acetone. Without delay, they were examined by optical microscopy and interference microscopy. From some surfaces, plastic-carbon replicas were prepared for transmission electron microscopy; others were examined in the scanning electron microscope.

Active Dissolution

Figure 4 shows the surface of an annealed polycrystalline electrode after dissolution in the active mode. The exhibition of individual grains, similar to chemical etching, suggests that anodic attack depends on crystallographic orientation. The same surface viewed at higher magnification (Fig. 5) demonstrates that the different appearance of grains is due to the development of ridges and shallow etch pits, whose orientation and shape vary among adjacent grains. Still higher magnification reveals that ridges and etch

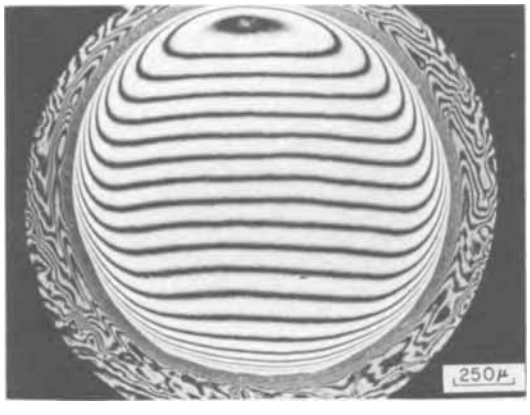

Fig. 2. Low-power interference micrograph of polished copper single crystal electrode surface 10° off (110) orientation. Maximum deviation from flatness, 2μ.

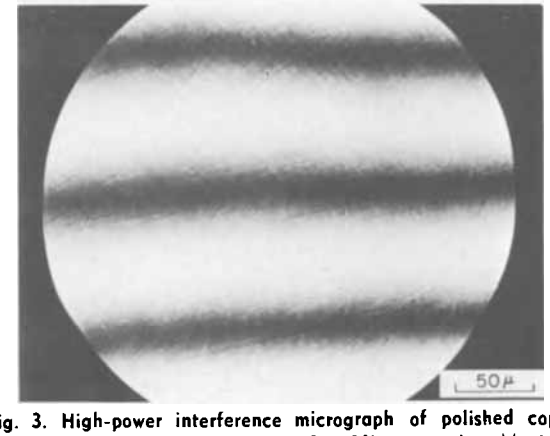

Fig. 3. High-power interference micrograph of polished copper single crystal electrode surface 10° off (110) orientation. Maximum depth of residual polishing marks 0.05μ.

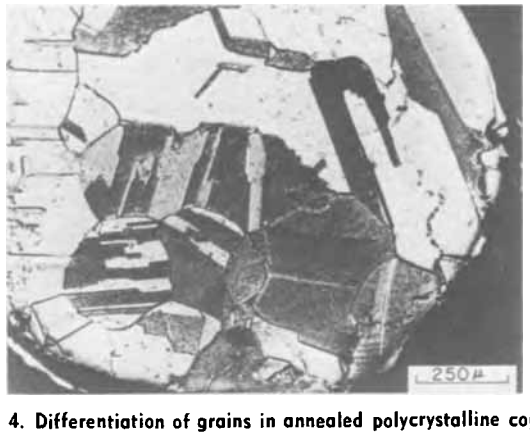

Fig. 4. Differentiation of grains in annealed polycrystalline copper after active dissolution. Optical micrograph.

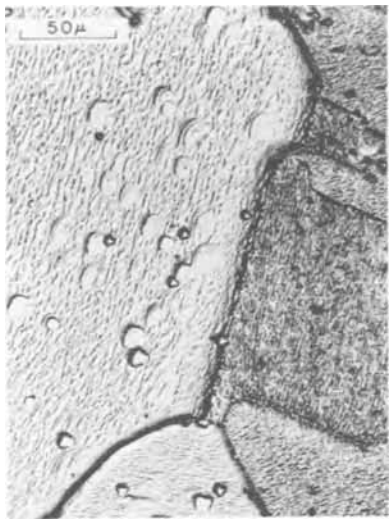

Fig. 5. Ridges and etch pits on different grains after active dissolution. Same specimen as in Fig. 4.

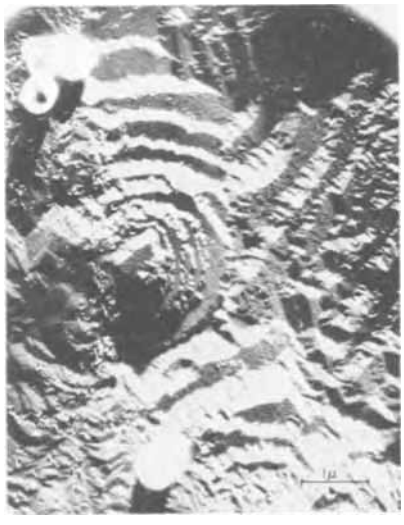

Fig. 6. Submicroscopic steps in a grain of polycrystalline copper after active dissolution. Electron micrograph of two-stage carbon replica. Diameter of latex spheres 0.5μ.

pits are composed of submicroscopic steps (Fig. 6). These observations are similar to those reported from electrocrystallization and vaporization studies. They can be related to the mechanism of removal of atoms from the crystal lattice which can be described by the movement of atomic ledges across close-packed lattice planes.

In order to investigate the effect of crystal orientation, experiments were also carried out with single crystal electrodes. Contrary to the polycrystals which exhibited a dull appearance after active dissolution, single crystal surfaces of low index orientation remained bright without visible etching. This difference is illustrated in Fig. 7 which may be compared with Fig. 5 taken at the same magnification. The (110) face employed in Fig. 7 shows surface texture at the limit of optical resolution. On the (100) face, only the electron microscope revealed shallow crystallographic etch patterns. The (111) face (even at that resolution) was almost featureless, as shown in Fig. 8. These results seem to support a dissolution mechanism involving the motion of monatomic ledges on tightly packed lattice planes (6). These observations are also consistent with those of Hulett and Young (7) who found the formation of etch pits on (111) copper faces in HCl at low current densities only after the addition of HBr

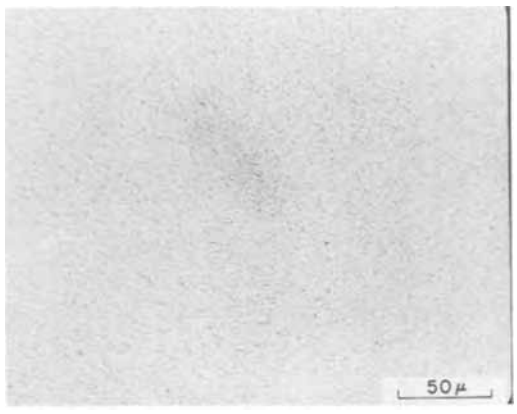

Fig. 7. (110) single crystal surface with barely visible texture after active dissolution. Optical micrograph.

Fig. 8. Smooth copper (111) surface after active dissolution. Latex sphere of 0.53μ diam provides scale for direction and length of shadows. Electron micrograph of two-stage carbon replica.

which acted as a poison for ledge motion. No such poisoning appears to have occurred under the present dissolution conditions. According to the ledge motion mechanism, dissolution starting with a high index crystal plane (comparable to the random orientation of grains in polycrystalline material) is expected to result in a faceted surface. Such facets have been observed on several randomly oriented crystals. A typical example is shown in Fig. 9. This surface texture is similar to the one reported for iron cathodically deposited at high (150-200 mV) overvoltage (8). The surface textures resulting from active dissolution indicate that dissolution at very high rates does not proceed by a basically different mechanism from that at low rates, provided that removal of reaction products from the surface by convective diffusion and migration is sufficiently fast.

Transpassive Dissolution

Figure 10 illustrates a polycrystalline surface after transpassive dissolution. In contrast to the appearance of the same specimen after active dissolution (Fig. 4), the surface now is bright and differences between individual grains are barely discernible at the optical level of resolution. A large number of round, deep pits, some arranged in rows, are distributed over the surface. Streaks in the flow direction, due to a waviness of the surface, extend from the leading edge over most of the specimen. Bright and pitted surfaces, resulting from dissolution in the presence of an anodic passivating layer, have also been reported for electropolishing at much lower current densities (9). Brightness is due

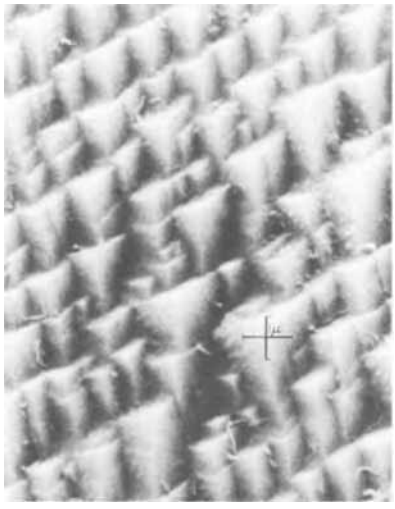

Fig. 9. Copper single crystal surface, oriented 10° off (110) direction after active dissolution. Scanning electron micrograph. tilted 30°.

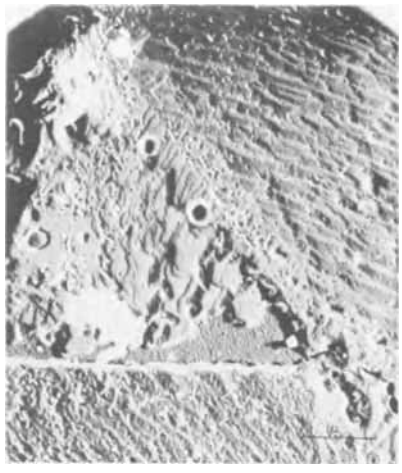

Fig. 11. Surface texture of neighboring grains of annealed, fine grain polycrystalline copper after transpassive dissolution. Electron micrograph of two-stage carbon replica.

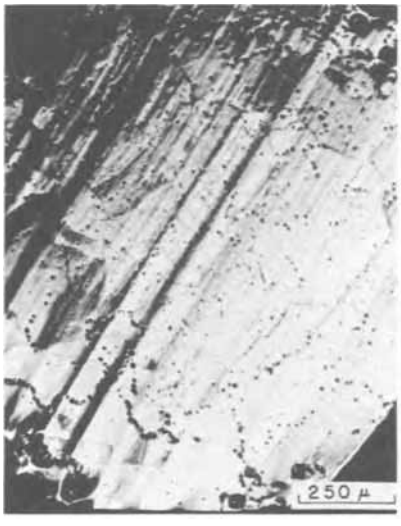

Fig. 10. Bright, pitted surface with flow streaks. Annealed polycrystalline copper after transpassive dissolution. Optical micrograph. Flow direction from lower left to upper right.

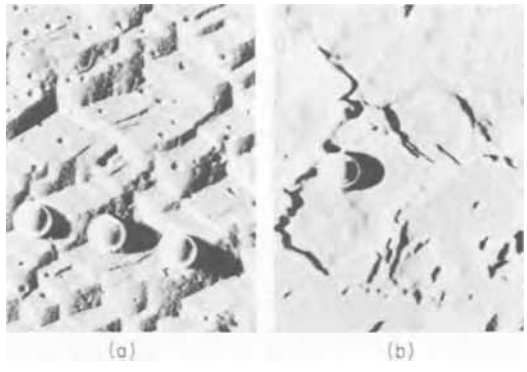

Fig. 12. Microtexture of copper single crystal oriented 10° off (110): (a) after active dissolution, (b) after transpassive dissolution, same magnification. Electron micrographs of two-stage carbon replicas, diameter of latex spheres 0.53μ.

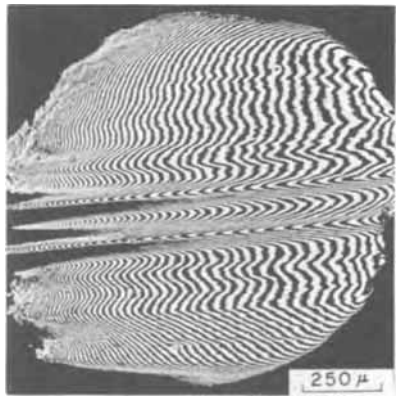

Fig. 13. Flow streaks resulting from transpassive dissolution of (100) single crystal face. Interference micrograph. Flow direction from left to right.

to a greatly reduced micro-roughness, and the even attack on differently oriented grains has been explained by the equalizing effect of an oxide layer (10). At much higher resolution, differences in surface texture between neighboring grains occasionally become visible. The electron micrograph, Fig. 11, illustrates one of the most pronounced microtextures observed after transpassive dissolution. Compared with the surface resulting from active dissolution shown in Fig. 6 at the same magnification, the roughness is an order of magnitude lower.

The difference in microtexture between active and transpassive dissolution is particularly pronounced with a randomly oriented single crystal. The electron micrographs in Fig. 12 illustrate this situation for a surface oriented 10° off the (110) plane. Interestingly enough, no pitting has been observed on any of the single crystals studied. Flow streaks appeared on single crystals in transpassive dissolution similar to the ones observed on polycrystalline specimens. The interferogram, Fig. 13, shows the associated macroscopic waviness of the surface. Typically these profiles are 0.1 mm wide and a few microns deep and they become shallower and wider downstream. Flow streaks observed under technical ECM conditions have been attributed to cavitation effects. In the present study, flow streaks have not been observed in active dissolution, where cavitation is more likely, due to the higher flow rates (2500 cm/sec active, 400 cm/sec transpassive).

Conclusions

1. The present study shows that crystallographic factors influence the surface texture resulting from high-rate anodic dissolution of copper in the active mode. Transpassive dissolution proceeds in the pres-

ence of anodic layers, which diminish the effect of crystal orientation and lead to brightening.

2. In the active mode, submicroscopic facets lead to the development of ridges, which give the surface an etched appearance. This appearance depends on crystallographic orientation and results in a differentiation between grains in polycrystalline material. Active dissolution of (100) and (111) faces has not resulted in the formation of facets. These observations are in agreement with a dissolution mechanism based on the motion of atomic ledges on tightly packed lattice planes.

3. Flow streaks are associated with transpassive dissolution, while the surface resulting from active dissolution is independent of flow direction.

4. Transpassive pitting is linked to metallurgical factors not present in the single crystals studied.

Acknowledgment

The authors wish to thank Mr. W. T. Giba for the preparation of electron microscope replicas and for other valuable assistance in this investigation. This work was conducted under the auspices of the U.S. Atomic Energy Commission.

Manuscript received Sept. 30, 1970. This was Paper 219 presented at the Atlantic City Meeting of the Society, October 4-9, 1970.

Any discussion of this paper will appear in a Discussion Section to be published in the December 1971 JOURNAL.

REFERENCES

1. D. Landolt, R. H. Muller, and C. W. Tobias, *This Journal*, **116**, 1384 (1969).
2. D. Landolt, R. Acosta, R. H. Muller, and C. W. Tobias, *ibid.*, **117**, 839 (1970).
3. K. Kinoshita, D. Landolt, R. H. Muller, and C. W. Tobias, *ibid.*, **117**, 1246 (1970).
4. J. O'M. Bockris and G. A. Razumney "Fundamental Aspects of Electrocrystallization," Plenum Press, New York (1967).
5. R. W. Mar and A. W. Searcy, *J. Chem. Phys.*, in press.
6. R. Kaischew and E. Budevski, *Contemp. Phys.*, **8**, 489 (1967).
7. L. D. Hulett, Jr., and F. W. Young, Jr., *J. Phys. Chem. Solids*, **26**, 1287 (1965).
8. K. E. Heusler and R. Knoedler, *Electrochim. Acta*, **15**, 243 (1970).
9. T. P. Hoar and G. P. Rothwell, *ibid.*, **9**, 135 (1964).
10. T. P. Hoar, *Corrosion Sci.*, **7**, 341 (1967).
11. T. P. Hoar, D. C. Mears, and G. P. Rothwell, *ibid.*, **5**, 279 (1965).
12. J. Bayer, M. A. Cummings, and H. V. Jollis, TID Report ML TDR 64313, General Electric Co. (1964).
13. R. R. Cole and Y. Hopenfeld, *Trans. ASME Ser. B*, **85**, 395 (1963).
14. S. Maeda, N. Saito, and S. Arai, Technical Report, Nagoya Works, Mitsubishi Electric Corp., Aug. (1963).

Anode Potentials in High-Rate Dissolution of Copper

D. Landolt,*,[1] R. H. Muller,* and C. W. Tobias*

Inorganic Materials Research Division, Lawrence Radiation Laboratory, and Department of Chemical Engineering, University of California, Berkeley, California 94720

ABSTRACT

A constant current interrupter technique was employed in the experimental determination of anode potentials during high-rate anodic dissolution of copper. The influence of ohmic voltage drops in the solution on measured overvoltage has been compensated by electronic means. For short electrolysis times, dissolution proceeds in the active mode; in sulfuric acid, Tafel behavior was observed up to the highest current densities employed (100 A/cm^2). Passivation effects may lead to significantly higher anodic potentials.

In electrochemical machining (ECM), metals are dissolved anodically at current densities of many amperes per square centimeter. In order to get a better understanding of electrochemical factors governing metal dissolution proceeding at such high rates, meaningful anode potential measurements are needed. Potential measurements performed at high current densities with rapidly dissolving anodes pose many problems (1), and anode potential data reported for technical ECM conditions appear to be of questionable value (2, 3). The anodic dissolution of copper has been chosen in this laboratory for the study of some fundamental aspects of ECM (1, 6-8). For high-rate anodic dissolution of copper, abrupt potential changes of many volts have been found, coinciding with a change from an active to a transpassive dissolution mode (1). However, the experimental techniques employed did not allow for the subtraction of ohmic voltage drops from the potential values measured. Electrode potential data obtained at low current densities have been extrapolated by Hoare *et al.* to predict high current density behavior of ECM electrolytes (4, 5). In view of many unknowns inherent in ECM it appeared desirable, however, to develop experimental procedures that allow direct potential measurements over a wide range of current densities. In the present paper, a galvanostatic interrupter technique is described which was applied to the determination of anode potentials prevailing under conditions of high-rate dissolution of copper in sulfate electrolytes. Experiments were performed under free as well as under forced convection conditions.

* Electrochemical Society Active Member.
[1] School of Engineering and Applied Science, University of California, Los Angeles, California 90024.
Key words: electrochemical machining, copper dissolution.

Experimental

Two cell types were employed, each assuring fast electrical response through low capacitance and careful exclusion of ground loops. Cell I (Fig. 1) was of cylindrical geometry, thus providing for even current distribution. No external convection was employed. A 10 mil diam, 6.3 mm long 99.999% copper wire served as anode, providing a surface area of 5 mm^2. Since, due to dissolution, considerable loss of diameter resulted during experiments, it was necessary to replace the anode frequently. This was accomplished by simply advancing the continuous wire (A) by approximately ½ in. During experiments, the anode was sealed by two Teflon compressible inserts (E) which were held tight by means of nylon screws (G). The anode was

ence of anodic layers, which diminish the effect of crystal orientation and lead to brightening.

2. In the active mode, submicroscopic facets lead to the development of ridges, which give the surface an etched appearance. This appearance depends on crystallographic orientation and results in a differentiation between grains in polycrystalline material. Active dissolution of (100) and (111) faces has not resulted in the formation of facets. These observations are in agreement with a dissolution mechanism based on the motion of atomic ledges on tightly packed lattice planes.

3. Flow streaks are associated with transpassive dissolution, while the surface resulting from active dissolution is independent of flow direction.

4. Transpassive pitting is linked to metallurgical factors not present in the single crystals studied.

Acknowledgment

The authors wish to thank Mr. W. T. Giba for the preparation of electron microscope replicas and for other valuable assistance in this investigation. This work was conducted under the auspices of the U.S. Atomic Energy Commission.

Manuscript received Sept. 30, 1970. This was Paper 219 presented at the Atlantic City Meeting of the Society, October 4-9, 1970.

Any discussion of this paper will appear in a Discussion Section to be published in the December 1971 JOURNAL.

REFERENCES

1. D. Landolt, R. H. Muller, and C. W. Tobias, *This Journal*, **116**, 1384 (1969).
2. D. Landolt, R. Acosta, R. H. Muller, and C. W. Tobias, *ibid.*, **117**, 839 (1970).
3. K. Kinoshita, D. Landolt, R. H. Muller, and C. W. Tobias, *ibid.*, **117**, 1246 (1970).
4. J. O'M. Bockris and G. A. Razumney "Fundamental Aspects of Electrocrystallization," Plenum Press, New York (1967).
5. R. W. Mar and A. W. Searcy, *J. Chem. Phys.*, in press.
6. R. Kaischew and E. Budevski, *Contemp. Phys.*, **8**, 489 (1967).
7. L. D. Hulett, Jr., and F. W. Young, Jr., *J. Phys. Chem. Solids*, **26**, 1287 (1965).
8. K. E. Heusler and R. Knoedler, *Electrochim. Acta*, **15**, 243 (1970).
9. T. P. Hoar and G. P. Rothwell, *ibid.*, **9**, 135 (1964).
10. T. P. Hoar, *Corrosion Sci.*, **7**, 341 (1967).
11. T. P. Hoar, D. C. Mears, and G. P. Rothwell, *ibid.*, **5**, 279 (1965).
12. J. Bayer, M. A. Cummings, and H. V. Jollis, TID Report ML TDR 64313, General Electric Co. (1964).
13. R. R. Cole and Y. Hopenfeld, *Trans. ASME Ser. B*, **85**, 395 (1963).
14. S. Maeda, N. Saito, and S. Arai, Technical Report, Nagoya Works, Mitsubishi Electric Corp., Aug. (1963).

Anode Potentials in High-Rate Dissolution of Copper

D. Landolt,*,[1] R. H. Muller,* and C. W. Tobias*

Inorganic Materials Research Division, Lawrence Radiation Laboratory, and Department of Chemical Engineering, University of California, Berkeley, California 94720

ABSTRACT

A constant current interrupter technique was employed in the experimental determination of anode potentials during high-rate anodic dissolution of copper. The influence of ohmic voltage drops in the solution on measured overvoltage has been compensated by electronic means. For short electrolysis times, dissolution proceeds in the active mode; in sulfuric acid, Tafel behavior was observed up to the highest current densities employed (100 A/cm^2). Passivation effects may lead to significantly higher anodic potentials.

In electrochemical machining (ECM), metals are dissolved anodically at current densities of many amperes per square centimeter. In order to get a better understanding of electrochemical factors governing metal dissolution proceeding at such high rates, meaningful anode potential measurements are needed. Potential measurements performed at high current densities with rapidly dissolving anodes pose many problems (1), and anode potential data reported for technical ECM conditions appear to be of questionable value (2, 3). The anodic dissolution of copper has been chosen in this laboratory for the study of some fundamental aspects of ECM (1, 6-8). For high-rate anodic dissolution of copper, abrupt potential changes of many volts have been found, coinciding with a change from an active to a transpassive dissolution mode (1). However, the experimental techniques employed did not allow for the subtraction of ohmic voltage drops from the potential values measured. Electrode potential data obtained at low current densities have been extrapolated by Hoare *et al.* to predict high current density behavior of ECM electrolytes (4, 5). In view of many unknowns inherent in ECM it appeared desirable, however, to develop experimental procedures that allow direct potential measurements over a wide range of current densities. In the present paper, a galvanostatic interrupter technique is described which was applied to the determination of anode potentials prevailing under conditions of high-rate dissolution of copper in sulfate electrolytes. Experiments were performed under free as well as under forced convection conditions.

* Electrochemical Society Active Member.
[1] School of Engineering and Applied Science, University of California, Los Angeles, California 90024.
Key words: electrochemical machining, copper dissolution.

Experimental

Two cell types were employed, each assuring fast electrical response through low capacitance and careful exclusion of ground loops. Cell I (Fig. 1) was of cylindrical geometry, thus providing for even current distribution. No external convection was employed. A 10 mil diam, 6.3 mm long 99.999% copper wire served as anode, providing a surface area of 5 mm^2. Since, due to dissolution, considerable loss of diameter resulted during experiments, it was necessary to replace the anode frequently. This was accomplished by simply advancing the continuous wire (A) by approximately ½ in. During experiments, the anode was sealed by two Teflon compressible inserts (E) which were held tight by means of nylon screws (G). The anode was

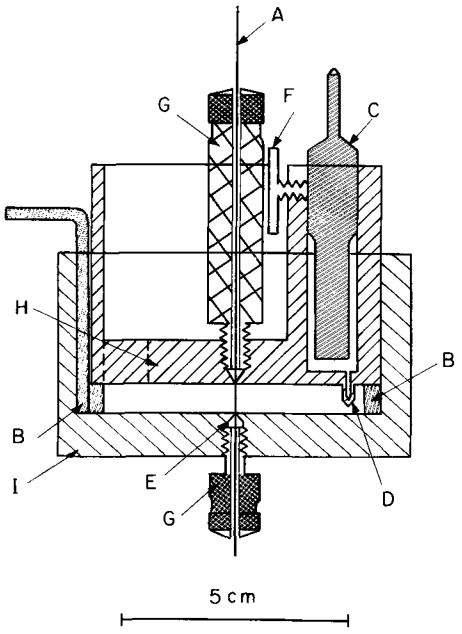

Fig. 1. Cross section of cell I for studies under free convection conditions: A, copper wire anode; B, cylindrical copper cathode; C, reference electrode; D, capillary; E, Teflon inserts; F, set screw; G, nylon screws; H, Lucite cell cover; I, Lucite cell body.

surrounded by a circular counterelectrode made of copper (B). The whole interelectrode space was filled with liquid. Holes drilled in the cell cover (H) near the cathode provided for escape of cathodically evolved gas. The reference electrode (C), made of copper, was connected to the cell compartment by capillary D, positioned at a distance of 24 mm from the center. The cylindrical geometry of the cell allowed one to calculate the ohmic voltage drop between capillary and anode. No provision for excluding oxygen was made, since at the high current densities employed here its effect on the dissolution kinetics was considered negligible. On the other hand, the presence of oxygen might influence the potential of the reference electrode by establishing a mixed potential. Numerical estimation showed, however, that this effect was always much smaller than 10 mV and, hence, could be neglected within the accuracy of the present study. Before insertion in the cell, the copper electrodes were cleaned in nitric acid and rinsed with distilled water. Several short anodic current pulses were applied before the start of measurements.

Cell II (Fig. 2) was a rectangular flow channel (E) through which the electrolyte was moved by means of a piston pump (C). A Teflon piston was advanced at constant, preset rate in a PVC cylinder, sweeping out a volume of 400 cm^3. At the end of each stroke, the motion of the piston was stopped by means of microswitches. The direction of rotation of the motor was then reversed to refill the cylinder with electrolyte. An electrolyte reservoir of 2 liters was employed. Except for the electrodes, no metal parts were in contact with the solution.

The 0.5 x 3 mm copper anode was cast into epoxy, and its short length was positioned parallel to the flow direction. A copper counterelectrode of the same surface area was used. The distance between anode and cathode was 0.5 mm, fixed by the thickness of a Teflon spacer into which a 3-mm wide slot—the flow channel—was cut. The cell was sealed by pressing the flat anode epoxy cast against the Teflon spacer by means of 4 knurled screws.

Linear flow velocities at the electrodes up to 10 m/sec were used, corresponding to a minimum discharge time of the pump of 25 sec. In order to reach such high velocities without requiring excessive inlet pressures, the distance between cell inlet and anode was kept short (1.5 cm). Thus, the hydrodynamic conditions in

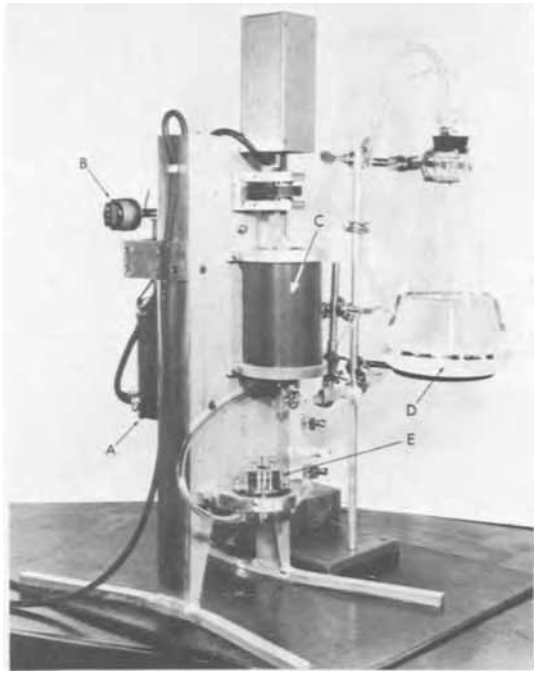

Fig. 2. Flow channel apparatus for studies under forced convection conditions: A, motor drive; B, dial indicator for setting flow rate; C, piston pump; D, electrolyte reservoir; E, flow channel cell (cell II).

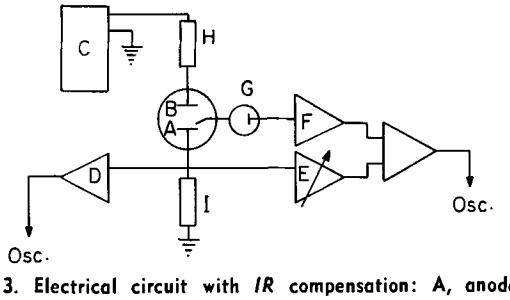

Fig. 3. Electrical circuit with *IR* compensation: A, anode; B, cathode; C, pulse generator; D, current measuring preamplifier; E, preamplifier with variable gain; F, preamplifier for reference electrode signal; G, reference electrode; H, series resistor; I, 5 ohm resistor.

the present cell were not as well defined as those in previous experiments (1, 6). In the present study, using transient techniques, it was considered more important, however, to achieve a compact design which allowed one to keep electrical connections to the cell short and which made it possible to avoid any metallic contact other than the electrodes with the electrolyte solution. In addition, the present design permitted the achievement of high flow velocities at the electrodes without requiring large electrolyte volumes. A copper reference electrode was located in the cell wall upstream from the cathode. All experiments were carried out at room temperature.

A galvanostatic pulse method was chosen for this study because it offers the most convenient technique for the elimination of large ohmic voltage drops inherent in high current density potential measurements. The electrical circuit is given schematically in Fig. 3. Current was drawn from a pulse generator[2] capable of providing square-pulses of up to 100V and 2A with rise time < 15 nsec. Pulse duration was varied between 10 μsec and 10 msec. Constant current through the cell was established by means of a series resistance (H). The current was measured in each experiment over a 5 ohm resistance (I) and displayed on a dual beam oscilloscope.[3]

[2] Model 214A Hewlett Packard.
[3] Model 555 Dual Beam Tektronix.

Two types of potential measurements were performed. On the one hand, the over-all behavior of potential transients was determined on a millisecond time scale. These experiments yielded information on relative potential changes associated with passivation phenomena. On the other hand, potential decay upon switching off the current was measured on a microsecond time scale. These experiments allowed for estimates of the nonohmic part of anode potentials in both the active and transpassive dissolution mode. Electronic compensation of ohmic voltage drops between capillary and anode surface was necessary in these experiments. This was achieved by means of variable gain preamplifier (E), the output signal of which was subtracted from the output signal of amplifier (F) connected to the reference electrode (G). A commercial amplifier unit[4] was used in this procedure. The difference signal was displayed on the dual beam oscilloscope together with the current signal and recorded on Polaroid film. Among several compensation procedures investigated, the following was found to give most satisfactory results. Low current density pulses, typically in the order of 20 mA/cm^2, were applied to the cell in order to determine the ohmic resistance between capillary and anode. Double layer charging was sufficiently slow under these conditions to allow for easy separation of the ohmic and the nonohmic part of the charging transient. The cell was then disconnected and replaced by an ohmic resistance of accurately known value, usually lower than the measured resistance between capillary and anode. The gain of amplifier (E) was adjusted to provide compensation equal to the value of the inserted resistance. The cell was then reconnected for the experiment while keeping the gain of (E) to the adjusted value. The use of a fixed compensating resistance of well-known value, together with variable amplifier gain, allowed for frequent and easy recheck of the accuracy of compensation. Partial, rather than full, compensation of the ohmic electrolyte resistance was used in order to avoid saturation of the differential amplifier. The uncompensated part of the ohmic electrolyte resistance was subtracted from the decay transient in a conventional way.

Active Dissolution

At high flow rates or very short experimental times, copper dissolves anodically in sulfate solutions in the active dissolution mode (1). Experiments were performed here to investigate the validity of extrapolating Tafel behavior found at low current densities (9) to high currents. For this purpose, anode potentials as a function of current density were determined from decay transients. The length of the applied current pulse was kept short enough to avoid any significant influence of concentration polarization effects on the anode potentials measured. On the other hand, pulse lengths were long enough to completely charge the electrical double layer. Depending on current density, pulse duration was between 10 μsec and several milliseconds.

Results obtained in cell I with a 1M sulfuric acid solution containing 0.1 mole per liter copper sulfate are given in Fig. 4. Within the accuracy of the measurements, Tafel behavior is observed up to the highest current density studied (39 A/cm^2). The accuracy of the data at high current densities is limited mainly by two factors: the *IR* drop in the solution and the rate of double layer discharge. The influence of the latter may be estimated by setting for the rate of change of overvoltage η after current switch-off

$$\frac{-d\eta}{dt} = \frac{|i_F|}{C} \qquad [1]$$

with i_F = Faradaic current density, C = double layer capacitance. For constant C and Tafel kinetics the solution of Eq. [1] becomes (10)

$$\eta_{t=0} - \eta = b \log \left(1 + \frac{2.3\,|i|\,t}{bC}\right) \qquad [2]$$

where i = applied current density.

Due to limitations in the frequency response of the amplifiers, η cannot be determined experimentally exactly at $t = 0$. One expects, therefore, that measured η values are lower than the true overvoltage prevailing at current switch-off. The possible magnitude of this error was estimated by inserting typical numerical values into Eq. [2]. From oscilloscope traces, it was estimated that in present experiments, potential readings were possible within at least 0.5 μsec after switch-off. Decay traces suggested that a reasonable value for C was 50 μF/cm^2. (Experimentally determined C values showed large scatter, and the value given has to be regarded as an order of magnitude estimate only.) The value of b was determined from Fig. 4 to be 40 mV. With these numerical values, one calculates $\eta_{t=0} - \eta_{t=0.5\,\mu sec}$ = 21 mV at 4 A/cm^2 or 55 mV at 40 A/cm^2. The resulting uncertainty in potential measurements is indicated in Fig. 4 by the dotted line.

Large ohmic voltage drops exist between capillary and anode as illustrated by Fig. 5 in which measured *IR* drops and anode potentials for the experiments of Fig. 4 are plotted on a linear scale. At the highest current density of 39 A/cm^2, the ohmic voltage drop is approximately 28 times larger than the actual anode potential. From the measured slope, one calculates a conductivity of 0.364 ohm^{-1} cm^{-1} at 24°C, in good agreement with the value one obtains at 25°C by using the estimation formula given by Hsueh (11), 0.379 ohm^{-1} cm^{-1}. By employing optimum compensation conditions as described above, it was estimated that the value of the nonohmic decay potential could be measured to ±1% of the *IR* drop corresponding to the current density of the measurements. The resulting uncertainty in measured anode potentials is indicated by the dashed line in Fig. 4. A least square fit of the measured points in Fig. 4 yielded a Tafel slope of 40 mV, coinciding with the value reported by Mattson and Bockris (9) for copper dissolution in highly purified sulfuric acid electrolytes at low current densities under exclusion of oxygen. Tafel parameters for anodic copper dissolution in sulfuric acid as well as values from the literature are summarized in Table I. Present

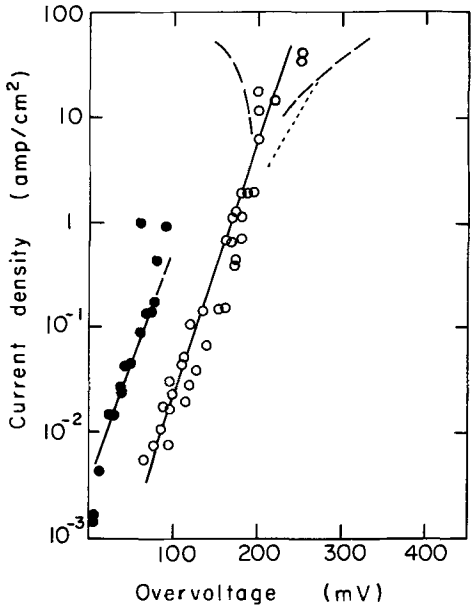

Fig. 4. Anode potential vs. current density for active dissolution of copper in sulfuric acid solution: ○, data obtained in cell I in 1M H_2SO_4, 0.1M $CuSO_4$; - - - -, uncertainty calculated from Eq. [2]; — — — —, uncertainty due to *IR* subtraction; ●, data from Ref. (9) for 0.5M H_2SO_4 0.075 $CuSO_4$.

[4] Model 1A1 Tektronix.

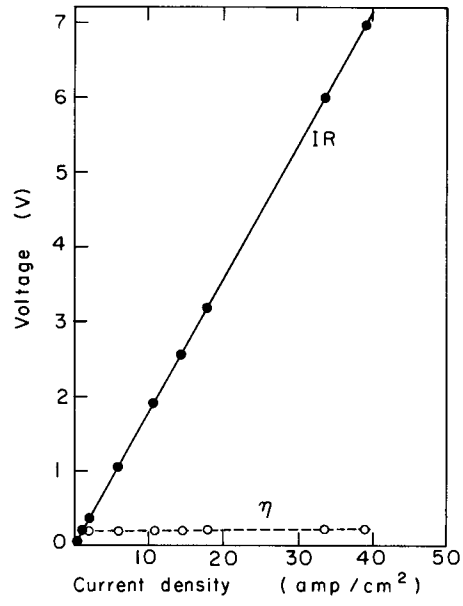

Fig. 5. Measured ohmic drop (*IR*) and anode overvoltage (η) in cell I, 1M H_2SO_4 0.1M $CuSO_4$.

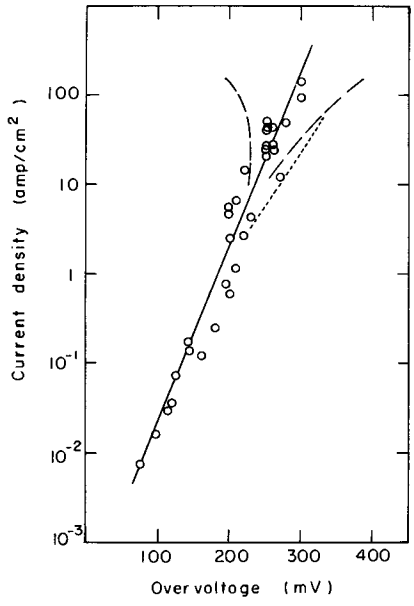

Fig. 6. Anode potential vs. current density for active copper dissolution in 1M H_2SO_4 0.1M $CuSO_4$ in flow channel cell (cell II). Flow rate, 140 cm/sec; - - - -, uncertainty according to Eq. [2]; — — — —, uncertainty due to *IR* subtraction.

results extend the previously reported Tafel region to higher current densities by two orders of magnitude.

At high current densities, uncertainties associated with fast double layer discharge and ohmic compensation become increasingly more important. The indicated Tafel behavior up to 40 A/cm² has, therefore, to be considered as an approximation rather than an exact representation of real behavior. Indeed, a deviation from the given Tafel slope of 40 mV at high enough current density is to be expected if the two-step charge transfer mechanism suggested by Mattson and Bockris prevails

$$Cu \overset{\text{fast}}{\rightleftarrows} Cu^+ + e \qquad (I)$$

$$Cu^+ \overset{\text{slow}}{\rightleftarrows} Cu^{2+} + e \qquad (II)$$

The species Cu^+ is considered adsorbed on the surface, its surface concentration depending on potential. Assuming no loss of Cu^+ due to diffusion, the current for such a two-step charge transfer process can be expressed (12) by

$$i = 2\frac{\exp[-(\alpha_1+\alpha_2)f\eta] - \exp[(2-\alpha_1-\alpha_2)f\eta]}{\frac{1}{i_{01}}\exp[(1-\alpha_2)f\eta] + \frac{1}{i_{02}}\exp(-\alpha_1 f\eta)} \qquad [3]$$

where α_1 and α_2 are the charge transfer coefficients for steps I and II, i_{01} and i_{02} are the respective exchange current densities. Following the assumption usually made, one may set $\alpha_1 = \alpha_2 = \alpha = 0.5$. For the case of $i_{01} >> i_{02}$ and intermediate overvoltage η, the first terms in the numerator and denominator can be neglected and Eq. [3] reduces to

$$i = -2\,i_{02}\exp[(2-\alpha)f\eta]\left(1 << f\eta << \ln\frac{i_{01}}{i_{02}}\right) \qquad [4]$$

This equation predicts a Tafel slope of 39 mV. At high values of η, the limiting value of Eq. [3] is

$$i = -2\,i_{01}\exp[(1-\alpha)f\eta]\ (f\eta \to \infty) \qquad [5]$$

corresponding to a Tafel slope of 118 mV. Since we do not know the value of i_{01}, no quantitative test of the above relationships is possible. A slight deviation from the slope of 40 mV consistent with the prediction of Eq. [4] cannot be excluded at the highest current density, but the measured results seem to fit Eq. [4] much better than Eq. [5]. No further mechanistic interpretation of results is justifiable here.

Table I. Tafel parameters for anodic copper dissolution in sulfuric acid

H_2SO_4 (M)	Electrolyte $CuSO_4$ (M)	Current density (A/cm²)	Cell	Ref.	*a* (mV)	*b* (mV)
1	0.1	5×10^{-3} to 39	I	present	171 ± 16	40 ± 15
1	0.1	8×10^{-3} to 140	II	present	184 ± 21	51 ± 16
0.5	0.5	—		(9)	81,† 82	40 ± 6,† 36 ± 10
0.5	0.075	5×10^{-3} to 0.2*		(9)	93,† 113	44 ± 4,† 45 ± 4
0.5	0.011	—		(9)	100	41 ± 4

* The range of current density in which Tafel behavior was observed was estimated from two figures given in Ref. (9).

† First value for He annealed copper, second for electrodeposited copper. The standard deviation of the results given in Ref. (9) was multiplied by two to get a 95% confidence limit. The values of *a* were calculated from i_0 values given in Ref. (9).

Flow channel cells have been used previously for studying high-rate metal dissolution under forced convection conditions (1, 6-8). Their advantage lies in the control of mass transfer and temperature effects. On the other hand, current distribution is inhomogeneous in such cells. To investigate experimentally the error that might be introduced in potential measurements performed under nonideal current distribution conditions, the same experiments described above were performed with cell II, the geometry of which resembled that of previously used flow channel cells.[5] Results comparable to those given in Fig. 4 are indicated in Fig. 6. The least square fit yielded a slope of 50 mV which is somewhat higher than the 40 mV obtained with cell I having cylindrical geometry. The scattering of data did not allow a quantitative analysis of this difference. Some qualitative comments may be appropriate, however. Upon current switch-off, two discharge processes may proceed now. Aside from the Faradaic current, a current may flow in the solution between differently charged regions of the double layer. The second effect will be larger when the current distribution is more nonuniform. In the case of Tafel kinetics and in the absence of concentration polarization, the uniformity of current distribution is characterized by the magnitude of the parameter $K = \kappa b/li$,

[5] Since experimental times were kept short in the present experiments, convection did not influence these results.

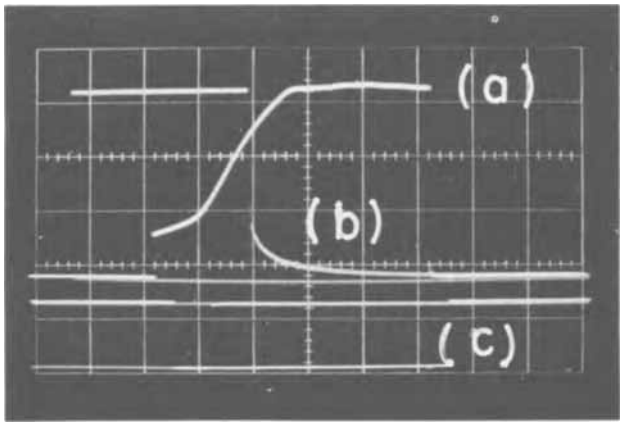

Fig. 7. Transpassive behavior of copper in 1M H_2SO_4 + 0.1M $CuSO_4$, Cell II. Current density, 77 A/cm^2; flow velocity, 140 cm/sec; no *IR* compensation. Trace a: over-all potential transient; anode potential, 10 V/div; time, 1 msec/div. Trace b: decay transient after current switch-off; anode potential, 10 V/div; time, 5 μsec/div. Trace c: current transients; 5 V/div.

where l is a characteristic length, i the current density, κ the electrolyte conductivity, and b the Tafel slope. Primary current distribution prevails for $K << 1$; secondary current distribution, for $K >> 1$. In our case $\kappa = 0.38$ ohm^{-1} cm^{-1}, $l = 0.5$ mm, $b = 40$ mV. One may, therefore, assume primary current distribution for $K \leq 0.1$ or $i \geq 3$ A/cm^2 and secondary current distribution for $K \geq 10$ or $i < 30$ mA/cm^2. In the intermediate region, a gradual change from secondary to primary current distribution occurs with increasing current, *i.e.* the current density at the edge of the electrode will increase more than the average current density. The ohmic part of the measured decay transient, on the other hand, is independent of current distribution (14). Therefore, in the intermediate region $0.1 < K < 10$, one would expect that the measured nonohmic part of the anode potential increases faster with current density than that corresponding to the true Tafel slope. This is qualitatively consistent with the observed behavior of Fig. 6. It appears that, in the case of active copper dissolution in acid sulfate solutions, the anodic behavior at high current densities can be described adequately by extrapolating Tafel kinetics valid for low current density. For many electrochemical machining purposes, possible inaccuracies in anodic overvoltage measurements resulting from a nonuniform current distribution can be neglected.

Transpassive Dissolution

At sufficiently high current densities and longer experimental times, solid anodic layers may be formed which lead to a sharp rise in measured anode potentials. The behavior is illustrated by Fig. 7, trace a. The measurement was performed in cell II at a flow velocity of 140 cm/sec and a current density of 77 A/cm^2. The electrolyte was 1M H_2SO_4 + 0.1M $CuSO_4$; no *IR* compensation was employed. An increase in over-all measured anode potential by 25V takes place 1 msec after start of the galvanostatic run.[6] It has been shown previously that dissolution in the high voltage mode proceeds with different stoichiometry (7) and leads to a different surface texture (1). The transition between the two dissolution mechanisms, active and transpassive, is mass transfer controlled (1). In the present study, experiments were performed aimed at further characterizing the current voltage behavior of copper anodes dissolving in the transpassive mode. This included the study of the influence of flow rate and of current density on the measured voltage rise and the measurement of decay potentials in the transpassive region.

Optical observation of anodically dissolving copper electrodes in acidic sulfate solutions suggested that relatively thick loosely adherent oxide layers are formed upon passivation (8). One would expect that their thickness and, hence, their effect on measured over-all anode potential would strongly depend on the prevailing hydrodynamic conditions; at high flow velocities, the loosely adherent deposits would be washed away from the anodes much more easily, and the extent of the voltage rise upon passivation ought to be reduced. Figure 8 gives five superimposed transients measured at 89 A/cm^2 with flow rates ranging from 65 to 1000 cm/sec. Qualitatively, the expected decrease in measured voltage with increasing flow rate is indeed observed, but the effect is small; for example, the difference between initial voltage (which represents mostly the *IR* drop in the solution) and maximum voltage is $\Delta E = 26$V at 65 cm/sec and $\Delta E = 23$V at 1000 cm/sec. This indicates that the observed voltage increase is caused by a tightly adherent layer rather than by the loosely adherent solids observed visually. The magnitude of the observed voltage increase cannot be explained by the formation of insulating solid dissolution products which block the anode surface and thereby increase the effective ohmic resistance. Figure 8 shows a 25-V potential increase taking place within a time interval of approximately 2 msec during which a charge of 154 mcoulomb/cm^2 is passed. The thickness of a compact cuprous oxide layer formed at 100% current efficiency during this time would be 3.8×10^{-5} cm. So as to explain the observed voltage drop across such an insulating layer by electrolytic conduction in pores, a porosity in the order of 10^{-4} would have to be postulated.

Other observations lead to a similar conclusion. A change in specific electrolyte conductivity by approximately a factor of two had no measurable effect on the voltage rise ΔE. Furthermore, a large fraction of ΔE was found to be nonohmic as indicated by trace b in Fig. 7, which represents the potential decay after current interruption (time resolution 5 μsec/div) for the same electrolysis conditions under which charging trace a was observed.

The above discussion suggests that during transpassive dissolution the anode potential is determined by the presence of a thin compact layer. It can be speculated that dissolution occurs through this layer by solid-state conduction, although no experimental proof for this view exists at present. An increase in ionic conductivity of an anodic layer with increasing current density due to heating effects is qualitatively

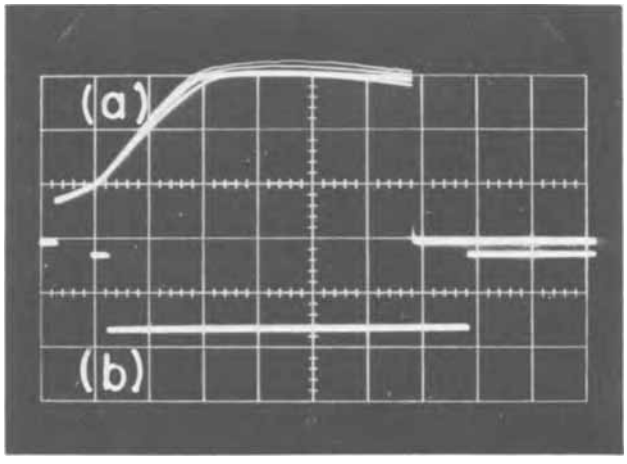

Fig. 8. Effect of flow rate on anodic transients in transpassive region. Current density (b), 89 A/cm^2; time, 1 msec/div; anode potential (a), 10 V/div. Flow rate for transients from top to bottom: 65 cm/sec, 140 cm/sec, 370 cm/sec, 610 cm/sec, and 1000 cm/sec.

[6] Potential time transients of the type given exhibit a maximum before steady state is reached. This does not show here because of the short pulse length employed. The indicated voltage increase upon layer formation is therefore larger than the steady-state voltage difference across the layer.

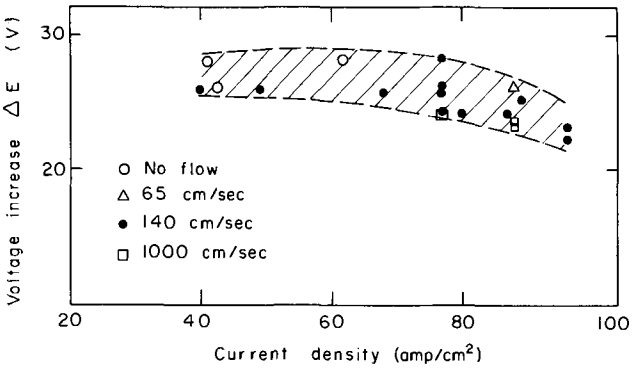

Fig. 9. Voltage increase upon anodic layer formation in function of current density. ΔE, peak voltage minus initial voltage.

consistent with the results shown in Fig. 9. The voltage rise is almost independent of current density, which indicates that the effective resistance of the layer decreases strongly with increasing current density (and hence increasing power dissipation). It is possible that, as a result of the heating effect, stresses are generated within the layer, which lead to its periodic rupture during the anodic dissolution process.

A more detailed understanding of the nature of the anodic layers present is necessary to determine the sequence of events in transpassive dissolution. Kinoshita *et al.* (7, 8) analyzed solid reaction products during copper dissolution in sulfate media by x-ray diffraction. The products were sampled continuously downstream from the anode. Cuprous oxide which may disproportionate into copper ion and metallic copper was found to be a major constituent. The direct analytical study of anodic layers is complicated, however, by the fact that upon current switch-off their nature may be changed within a matter of milliseconds. This is evidenced by the experiments illustrated in Fig. 10 and 11. Two identical current pulses were applied to the anode in time intervals ranging from a fraction of a millisecond to several milliseconds. The shape of the second pulse then depended strongly on the elapsed time between the two pulses (Fig. 10). The time interval necessary for the second pulse to become identical with the first pulse was considered equivalent to the time necessary for removal of the anodic layer after current switch-off. In Fig. 10, this corresponds to approximately 6 msec. The time for removal depended on the flow rate as well as on the current density at which the layer had been formed. This is evidenced by Fig. 11 in which the difference between the initial voltage of the second pulse and that of the first pulse, as determined from transients similar to those given in Fig. 10, is plotted as a function of the elapsed time

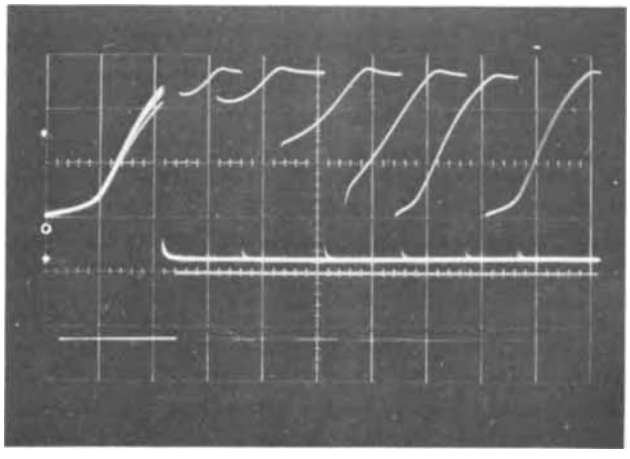

Fig. 10. Double pulses applied at different time intervals. Current density, 77 A/cm²; flow rate, 1000 cm/sec; anode potential traces, 10 V/div, time scale, 1 msec/div.

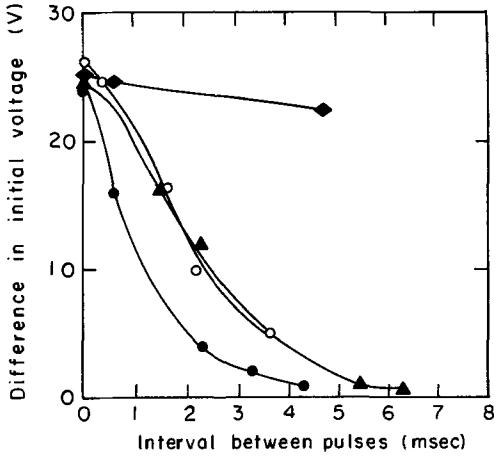

Fig. 11. Difference in initial voltage between first and second pulse as a function of time interval between pulses: ●, 93 A/cm² at 1000 cm/sec; ○, 46 A/cm² at 1000 cm/sec; ▲, 93 A/cm² at 140 cm/sec; ◆, 50 A/cm² at 140 cm/sec.

between two consecutive pulses. The layers formed at high current density appeared to be removed faster than those formed at lower current density. Increasing flow rate also accelerated removal. The latter effect is not unexpected; it may be related to an enhancement of either mechanical removal of solid products or to an increase in rate of mass transport of dissolved products. It is to be noted, however, that layer removal took somewhat longer than layer formation (Fig. 10). Since layer formation is initiated by a mass transport limited process (1), it appears that removal is not entirely governed by a simple mass transport process. Accelerated layer removal with higher formation current density may be due to higher local temperatures of the surface which speed up chemical dissolution, or to larger concentrations of hydrogen ions accumulated at the surface under conditions of high formation current density.

Summary and Conclusions

Galvanostatic transient techniques have been used for the study of current voltage relationships characterizing anodic copper dissolution at current densities of up to more than 100 A/cm². With the possible accuracy of high current density potential measurements, results for active dissolution obtained in the present study were consistent with the Mattson-Bockris mechanism. Presence of oxygen and preelectrolysis of the solution apparently have little influence on measured anodic Tafel slopes at high dissolution rates.

Potential current relationships for active dissolution obtained in a flow channel cell were little different from those measured in a cylindrical cell. This indicates that the error introduced into transient measurements by the nonideal geometry of the flow channel was small, and it appears that such cells are well suited for the study of active as well as transpassive metal dissolution under controlled flow conditions.

Dissolution in the transpassive mode proceeds by a different mechanism at much higher anode potential. Experimental results and numerical estimations show that the observed high values of the anode potential in the transpassive mode are due to a thin, well-adhering layer. Since earlier studies showed that loose solid reaction products are generated during transpassive dissolution, it has to be assumed that the anodic layer has a dual structure, consisting of a thin compact layer in contact with the metal and loose material (mostly cuprous oxide) sitting on top of it. The loose material has little influence on observed galvanostatic transient behavior which is governed by the properties of the adherent layer. The effective resistance of this layer was shown to decrease with increasing current density, an effect which is attributed to local heating. Quantitative models for the description of the dy-

namics of transpassive dissolution have not been developed so far.

Acknowledgment

The authors are greatly indebted to Prof. H. Gerischer, who actively participated in the initial phase of this study. This work was conducted under the auspices of the United States Atomic Energy Commission. One of the authors (D. L.) also received partial support from the U. S. Office of Naval Research under Contract N00014-69-A-0200.

Manuscript received Oct. 2, 1970. This was Paper 225 presented at the Atlantic City Meeting of the Society, October 4-9, 1970.

Any discussion of this paper will appear in a Discussion Section to be published in the December 1971 JOURNAL.

REFERENCES

1. D. Landolt, R. H. Muller, and C. W. Tobias, *This Journal*, **116**, 1384 (1969).
2. R. R. Cole and Y. Hopenfield, *Trans. ASME Ser. B*, **85**, 395 (1963).
3. J. Bayer, M. A. Cummings, and H. U. Jollis, Tech. Doc. Rept. No. ML-TDR-64-313, General Electric Co. (1964).
4. J. P. Hoare, *This Journal*, **117**, 142 (1970).
5. J. P. Hoare, M. A. LaBoda, M. L. McMillan, and A. J. Wallace, *ibid.*, **116**, 199 (1969).
6. D. Landolt, R. Acosta, R. H. Muller, and C. W. Tobias, *ibid.*, **117**, 839 (1970).
7. K. Kinoshita, D. Landolt, R. H. Muller, and C. W. Tobias, *ibid.*, **117**, 1246 (1970).
8. K. Kinoshita, Ph.D. Thesis, University of California, Berkeley, UCRL-19051, Sept. (1969).
9. E. Mattson and J. O'M. Bockris, *Trans. Faraday Soc.*, **55**, 1586 (1959).
10. K. Vetter, "Electrochemical Kinetics," Academic Press, New York (1967).
11. L. Hsueh, Ph.D. Thesis, University of California, Berkeley, UCRL-18597, Dec. (1968).
12. P. Delahay, "Double Layer and Electrode Kinetics," Interscience Pubs. (1965).
13. H. S. Mickley, T. K. Sherwood, and C. E. Reed, "Applied Mathematics in Chemical Engineering," 2nd Ed., p. 97, McGraw-Hill (1957).
14. J. Newman, *This Journal*, **117**, 507 (1970).

The Anodic Oxidation of Platinum: Evidence for a High-Field Ionic Conduction Mechanism

J. L. Ord* and F. C. Ho†

Department of Physics, University of Waterloo, Waterloo, Ontario, Canada

ABSTRACT

The anodic oxidation of platinum in 1*N* H_2SO_4 is studied by using open-circuit transients to determine Tafel slopes and by following film growth optically with an ellipsometer. The Tafel slope values are found to be proportional to the film thicknesses measured with the ellipsometer. This result is interpreted in terms of an ionic conduction model in which the overpotential appears across the anodic oxide film, and the logarithm of the ionic current density is proportional to the field in the oxide. The results are compared with the results of similar measurements on iron and tantalum. Although platinum, iron, and tantalum have quite different chemical properties, and their oxides span a thickness range from a monolayer to several thousand angstroms, it is concluded that the same basic process is responsible for the anodic oxidation of the three metals.

The formation of anodic oxide films on metals is a process for which no particular model is usually applied to more than a small class of similar metals. For valve metals such as tantalum, it is agreed that the electric field in the layer limits the process, and, although no single model is universally accepted, all models used to describe the formation of anodic oxides on these metals consider ionic transport in a high electric field to be rate limiting. The passive metals such as iron form another class of similar metals for which models describing the formation of anodic oxide films have been proposed. There is no general agreement on the rate-limiting step in the case of the passive metals, and, as a result, the models proposed have virtually nothing in common.

The studies of anodic oxidation carried out in our laboratory have attempted to determine whether anodic oxidation is really a process which changes markedly from metal to metal and electrolyte to electrolyte, or whether one model can account for the basic features of the process on a variety of quite different metals. We found that remarkably similar results were obtained when the same measurements were made on iron and tantalum (1, 2), and we concluded that a high-field ionic conduction model could be used to account for the growth of anodic oxide films on both metals. To account for all the features of the anodic behavior of iron, a dissolution reaction competing with oxide film formation at low potentials, and an electronic tunneling current above the oxygen-evolution potential must be added to the basic model.

In this paper we present the results obtained when platinum is used as a substrate in the experiments whose results on iron and tantalum form the basis for the high-field model. Platinum is an ideal metal on which to study anodic oxidation because it is possible to study the process from its initiation on a bare surface, through partial surface coverage, to growth beyond monolayer thickness. It is a simpler metal to study than either iron or tantalum in that its anodic oxide is reducible and no dissolution reaction precedes oxide formation, but the narrow potential region over which oxide is formed before oxygen is evolved restricts the film thicknesses to very low values. The three metals have one feature common to their anodic behavior: under galvanostatic oxidation the potential increases linearly with time across the layer growth region. In the case of platinum this is one of the criteria used to test for cleanliness of the system (3). This behavior is required by a field-limited model, and without it such a model could be rejected for the anodic oxidation of platinum without further study.

* Electrochemical Society Active Member.
† Electrochemical Society Student Member.
Key words: anodic oxidation, platinum, ellipsometry.

In principle, it is a straightforward matter to determine whether the field or the potential drives an activation-controlled process. The Tafel slope expresses the change in overpotential required to produce a specified (usually tenfold) change in the current density. If the change in the current density is produced by a change in the field in the layer, then the measured Tafel slope must be directly proportional to the layer thickness ($V = D\,E$, hence $\Delta V = D\,\Delta E$); otherwise the Tafel slope should be independent of the layer thickness. Hence simultaneous Tafel slope and layer thickness measurements can provide direct evidence enabling field-limited processes to be distinguished from potential-limited processes.

In practice, values obtained for Tafel slopes on oxide-covered electrodes often depend on the experimental technique used in their determination (1, 2, 4, 5). This difficulty arises because the Tafel slope is defined as the partial derivative of the overpotential with respect to the logarithm of the current density, and it is difficult to select experimental conditions to measure this partial derivative without making a basic assumption about the nature of the process under study. We choose to measure Tafel slopes by analyzing open-circuit transients using a technique similar to that proposed by Grahame in his paper on the current-interrupter method (6). We feel that a measurement of this type disturbs the system only slightly, and as a result provides a value for the Tafel slope which comes close to being a true partial derivative.

Experimental

In situ optical measurements were made during anodic oxidation using a following ellipsometer. Two following ellipsometers have been built in our laboratory, and their construction, operation, and performance have been described in the literature (7, 8). They differ from conventional ellipsometers in that they can be nulled in less than 1 sec with 0.01° resolution, and hence can make null measurements on surfaces covered by films which are growing at slow to moderate rates. The data presented in this paper illustrate this performance and show how the accuracy of the measurements (as indicated by the scatter in the data) compares with the resolution of the instrument. A small helium-neon gas laser is used as a light source, and all our refractive index values were determined at its wavelength, 6328Å.

The cells used with the ellipsometer are constructed for a specified angle of incidence. Angles of incidence of both 60° and 75° were used in this study, but only data obtained at 60° are presented here. The 60° cells consist of hollow glass equilateral prisms with standard taper joints in the top for mounting the electrode, platinum counterelectrode, mercurous sulfate reference electrode (with 0.1*N* K_2SO_4 salt bridge), and gas dispersion tube. The cell used for 75° measurements has a separate compartment in which the electrode is mounted. An angle of incidence of 60° was chosen for sets of measurements where a reproducibility from run to run of ± 0.01° was required because the 60° cells have a better geometry for sweeping out the trace amounts of hydrogen and oxygen which are evolved even in experiments designed to minimize evolution of these gases. The cell is bubbled with argon for a day prior to an experiment, and the bubbling is continued throughout the experiment, keeping the cell at a slight excess pressure of argon and minimizing the leakage of oxygen into the cell through the Teflon-sleeved standard-taper joints. All experiments were performed at room temperature (23°C).

A major factor influencing reproducibility of the optical data from run to run is the roughness of the surface. A study of the smoothing and roughening of the single-crystal platinum surface was carried out using a variety of electrolytes, and conditions were determined under which a series of experiments could be carried out with no change in the roughness factor of the surface. The study of the effect of varying surface roughness on optical measurements was too extensive for a description of the experiments to be included here.

The platinum sample used in the experiments was a single crystal which was clamped between Teflon washers in a glass electrode holder exposing a cylindrical surface of 1.2 cm^2 area to the electrolyte. A flat on one side of the cylinder was used for the optical measurements, although the laser source and double-pinhole lens-free optics of the ellipsometer enable measurements to be made on cylindrical surfaces. The electrolyte used in all the experiments was 1*N* H_2SO_4 prepared from high-purity sulfuric acid purchased in 10*N* concentration. Measurements of the steady-state current density gave values comparable to those obtained by other workers using closed systems (9). A Tafel slope is often used to express the potential dependence of this steady-state current density, and we would like to emphasize that this Tafel slope is in no way related to the Tafel slope for anodic oxidation which we study in this paper. The steady-state current is the residual current which flows after the anodic oxidation process has slowed to an imperceptible rate, and as such it is very sensitive to trace impurities in the system. The current whose potential dependence we express using a Tafel slope is the current flowing when the anodic oxidation reaction is proceeding at an appreciable rate. We measure this Tafel slope over a range of current density during the open-circuit self-discharge transient, but all current densities in this range (typically 1-10 $\mu A/cm^2$) are well in excess of the steady-state current density at the same potential. Our measured Tafel slope values are not strongly affected by the cleanliness of the system, and we find that greater care is required to achieve reproducibility in the optical data than in the electrical data.

The electrical circuitry uses high-impedance operational amplifiers for a galvanostat, potentiostat, potential sweep circuit, and follower. The potential is monitored on a strip chart recorder in the laboratory, but the transients from which Tafel slopes are determined are recorded using the A/D converter of the IBM 1710 process control computer, The computer sets a latching contact to open a relay in the cell circuit, then samples the potential at fixed time intervals (every 4.8 msec) and stores data at specified potential intervals. The recording of data in this manner provides a set of results directly suited to a least squares analysis of potential *vs.* log *t*. The computer carries out this analysis and prints out the Tafel slope and an estimate of its standard deviation.

The capacitance can be determined from the open-circuit transient analysis, however the curve-fitting procedure is less sensitive to capacitance errors than it is to Tafel slope errors. We can monitor the capacitance continuously during an experiment by adding an a-c component to the current from the galvanostat. A lock-in amplifier detects the component of the a-c voltage 90° out of phase with the current, and the output of the lock-in amplifier is plotted *vs.* potential on an X-Y recorder.

Results and Discussion

A typical anodic oxidation transient is shown in Fig. 1. The platinum electrode is held initially at a potential of +0.27V (on the hydrogen scale). At point A the electrode is switched to the galvanostat set for a current density of 10 $\mu A/cm^2$. The potential rises rapidly at first, then increases linearly with time along BC. At point C (1.37V) the galvanostat is switched to −10 $\mu A/cm^2$, and the potential traces out the s-shaped reduction curve to point D at which the electrode is switched back to its initial potential, +0.27V. A series

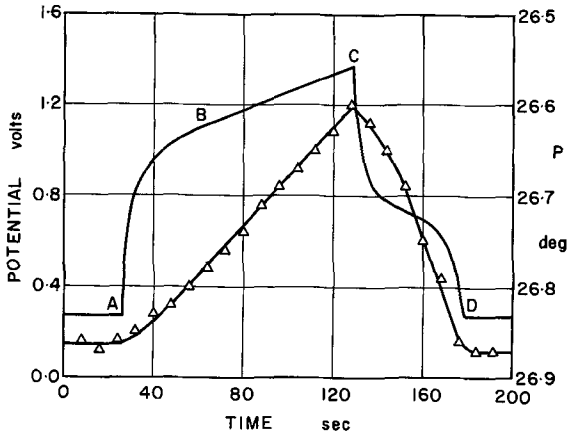

Fig. 1. Variation of potential (solid curve) and polarizer null reading (triangles) for galvanostatic oxidation (ABC) and reduction (CD) at 10 $\mu A/cm^2$ of a platinum electrode in 1*N* H_2SO_4.

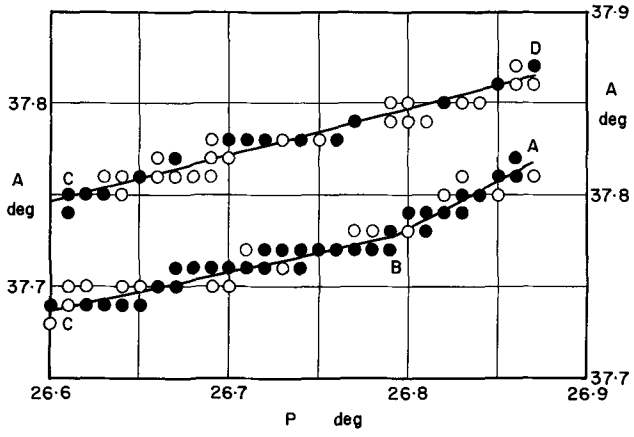

Fig. 3. *P-A* plot of the optical data recorded during the galvanostatic transient plotted in Fig. 1. To avoid overlap, different A scales are used for the oxidation data (ABC, right A scale) and the reduction data (CD, left A scale). Open circles show points which were recorded once only; solid circles show points recorded two or more times.

of polarizer and analyzer null readings are recorded by the following ellipsometer as the transient is swept out. The polarizer null readings (P) at 8 sec intervals are plotted *vs.* time along with the potential in Fig. 1. P changes linearly with time in the region BC in which the potential increases linearly with time, and returns to its initial value at point D after cathodic reduction. The over-all change in P is only 0.27°, and hence the accuracy and reproducibility of the data are very important. The narrowness of the range of variation of P made it necessary to carry out a study of the effect of variation in surface roughness on reversibility and reproducibility of the data. Under the experimental conditions used to obtain the data in Fig. 1, the optical data can be reproduced in a succeeding run to within ± 0.01°. The accuracy of the data is not apparent in Fig. 1 in which points at 8-sec intervals are plotted. In Fig. 2 the section of Fig. 1 from $t = 50$ to $t = 100$ sec is plotted on an expanded time axis. The data points show very little scatter; in fact, in the latter half of the time interval, no scatter is detectable, and the only deviation from linearity is produced by 0.01° resolution of the instrument. Fifty-nine data points were recorded in this 50-sec interval, but only 53 distinct points appear in the figure because only two of the 18 printer columns were used to record time, and the data have a limited 1-sec time resolution. As a result, in two instances two values of P appear as distinct simultaneous points, and 6 other points overlap the plotted points.

In Fig. 1 and 2, P is used to represent the optical data, but an actual optical measurement includes the analyzer null reading, A, also. The optical results can be displayed conveniently on an X-Y plot of P vs. A. This is the form in which the data are monitored during an experiment, and the same form is used when fitting the data using a graphic display computer terminal. Figure 3 is a *P-A* plot of the optical data

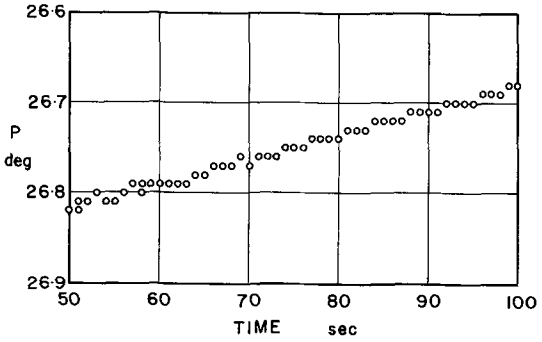

Fig. 2. Complete polarizer null data for a segment of the transient plotted in Fig. 1.

recorded during the transient plotted in Fig. 1. The points A, B, C, and D in the figure are the points so identified in Fig. 1. The optical data show a slight inflection at point B during anodic oxidation, but show no inflection along CD during cathodic reduction. The lines AB (47 points, slope 0.509 with standard deviation 0.026), BC (75 points, slope 0.215 with standard deviation 0.021), and CD (58 points, slope 0.254 with standard deviation 0.006) were fitted to the data using least squares. The inflection during anodic oxidation occurs at a potential of 1.1V, and the change in slope is statistically significant.

The changes in P and A produced by growth of a uniform film depend on both the complex refractive index of the film, $n - ik$, and its thickness, D. For thin films the locus traced out in the *P-A* plane as D increases with n and k constant is simply a straight line whose slope depends on n and k, and whose length is proportional to D. The data in Fig. 3 fall on three lines of significantly different slope and hence cannot be generated by a process in which only D is varying. The inflection at point B can be accounted for either by the growth of a second layer with different index on top of the initial layer grown from A to B, or by a progressive change in the refractive index as the layer continues to grow beyond the 1.1V potential. (A structure of this type would not be produced by the growth of a monolayer whose effective index varies with surface coverage, followed by growth beyond a monolayer at constant index; such behavior would require A, B, and C to be co-linear points, BC to be a straight line, and AB to deviate from linearity.) The fact that the data fall on one line of intermediate slope as the layer is removed by cathodic reduction suggests that only one layer is present on the surface at point C, and hence favors a model in which the film index changes progressively as the potential increases beyond 1.1V. A detailed analysis to determine the refractive index of the layer at point C is presented in the Appendix. A unique value cannot be determined for the layer index or the absolute thickness. A reasonable estimate of the calibration factor relating changes in P to changes in film thickness is found to be 10-20 Å/deg P with higher values possible. This gives a range of 0.8-1.6Å for the thickness at B, and 2.7-5.4Å at C.

A set of Tafel slopes can be determined at points along the transient plotted in Fig. 1 by opening the circuit briefly at selected points and recording potential-time data for Tafel slope analysis. The parameter we use to designate the point at which the Tafel slope is measured is the potential reached just prior to

opening the circuit. We refer to this potential as the formation potential, V_f. The Tafel slope expresses the dependence of current density on overpotential and is not itself a function of overpotential, but it may depend on the state of the electrode surface, and this state may be specified uniquely in these experiments by two parameters: the formation potential and the formation current density (the value set on the galvanostat).

The Tafel slopes obtained at a formation current density of 10 μA/cm^2 are plotted *vs.* formation potential in Fig. 4 along with the corresponding values of (P_o-P). For values of V_f above 1.1V, the Tafel slope increases linearly with formation potential, whereas below 1.1V the Tafel slope remains approximately constant at 19 mV. (P_o-P) also increases linearly with V_f above 1.1V. The linear portions of the (P_o-P) and Tafel slope plots both extrapolate to zero at 0.975V, and hence the Tafel slope is proportional to (P_o-P) over the region in which both increase linearly with V_f. We would prefer to plot film thickness rather than (P_o-P) in Fig. 4, but this is not possible. If we ignore the variation in refractive index above 1.1V, the curve ABC in Fig. 4 can be considered a plot of relative thickness *vs.* V_f, and we can conclude that the Tafel slope is proportional to the thickness of the film. If the slight variation in index above 1.1V is taken into account, the relative film thickness plot will still be a curve similar to ABC, but the section BC may be rotated slightly about B. A rotation about B will shift the intercept away from D, but, since BD is short compared with BC, a slight variation in index will not invalidate our conclusion that the Tafel slope for anodic oxidation is proportional to the thickness of the oxide film, and hence the process is limited by the field in the film.

The extrapolation of the Tafel slope plot to intersect the formation potential axis at 0.975V determines the zero of overpotential for the anodic oxidation process. In a series of potentiostatic measurements, Reddy, Genshaw, and Bockris (10) found that a film formed suddenly when the potential crossed 0.98 $\pm$ 0.01V. Our value for the zero of overpotential is consistent with their measurements.

The abrupt change in the slope of V_o curve in Fig. 4 at $V_f = 1.1$V, and the slight inflection in the *P-A* plot in Fig. 3 at the same potential, lead us to conclude that this is the point at which the surface is covered by a monolayer of oxide. Below this value of V_f the Tafel slope retains a value proportional to the thickness of the layer partially covering the surface, whereas the optical measurements involve an average over the bare and covered portions of the surface. The optical estimate of the monolayer thickness, 0.8-1.6Å or higher, is not unreasonable when compared with the ionic radii of platinum and oxygen, 0.5 and 1.4Å. The progressive change in layer index above 1.1V suggests that PtO can be formed as a monolayer, but, as the oxide grows beyond monolayer thickness, there is a tendency for its oxidation state to rise.

The value of the capacitance whose self-discharge is studied during an open-circuit transient is determined by the analysis used to obtain the Tafel slope. In addition, the a-c voltage at a phase angle of 90° to a superimposed a-c current can be plotted *vs.* formation potential. The a-c measurement is displayed directly in a convenient form, whereas the results from open-circuit transients are obtained only after a least squares analysis, but the interpretation of the a-c measurements is less direct. The reciprocal capacitance values from open-circuit transients are plotted in Fig. 5 along with a tracing of the a-c voltage for a 10 μA/cm^2 50 Hz a-c current density superimposed on a 40 μA/cm^2 formation current density. For this frequency and formation current density, the a-c impedance at 90° phase angle is not just $1/\omega C$, but the dependence of the a-c voltage on V_f will be due mainly to the dependence of $1/C$ on V_f.

The two sets of data plotted in Fig. 5 show a consistent dependence on V_f, but this dependence is not the simple linear dependence found in Fig. 4 for the Tafel slope, although in any simple high-field model both parameters should be proportional to film thickness. The failure of the $1/C$ values to increase with formation potential beyond 1.2V is probably related to the progressive change in the refractive index which we have attributed to the raising of the oxidation state of the layer. The same type of dependence of Tafel slope and reciprocal capacitance on formation potential was found by DeSmet (11) in his work on the anodic oxidation of nickel, another metal whose anodic oxide can be raised to a higher oxidation state. Although the capacitance measurements can be made consistent with a high-field model, they cannot be claimed to provide direct support for such a model.

The high-field model can be used to predict the dependence of layer thickness on formation potential at higher potentials where oxygen evolution becomes important. Even if other processes are going on, the ionic current is determined by the field in the film, and the growth rate of the film is proportional to the ionic current. The model considers oxygen evolution to be due to an electronic tunneling current which flows through the layer to the metal once its potential exceeds the oxygen evolution potential. The total current flowing through the layer therefore consists of an electronic component and a field-limited ionic component. In the layer growth region below oxygen evolution (region BC in Fig. 1) a linear potential

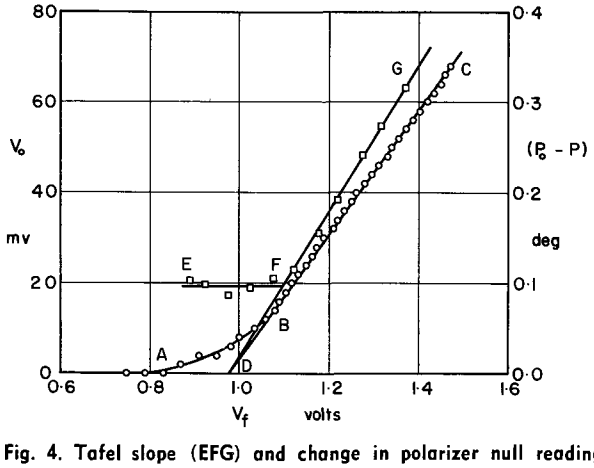

Fig. 4. Tafel slope (EFG) and change in polarizer null reading (ABC) plotted as a function of formation potential for a formation current density of 10 μA/cm^2.

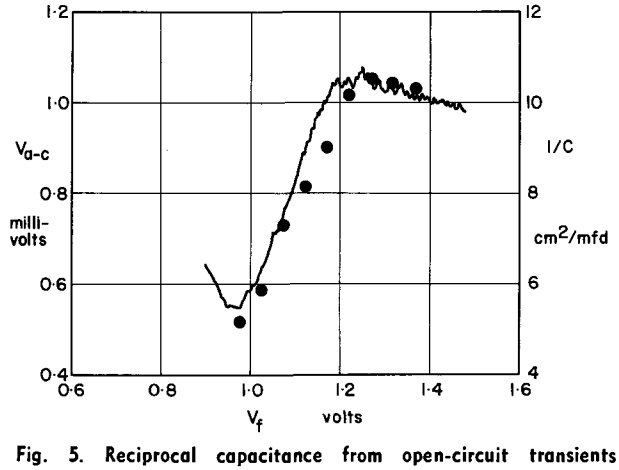

Fig. 5. Reciprocal capacitance from open-circuit transients (circles) and a-c voltage 90° out of phase with a 50 Hz a-c current of 10 μA/cm^2 superimposed on a d-c current of 40 μA/cm^2, both plotted as a function of formation potential.

sweep and a constant current are equivalent, but once oxygen evolution begins the two experimental conditions are quite different and result in different dependences of layer thickness on formation potential.

In a galvanostatic experiment the total current is fixed, and hence an increase in the electronic component can only result from a decrease in the ionic component caused by a decrease in the field in the layer. This drop in the field shows up in a plot of layer thickness *vs.* formation potential as an increase in the slope once the oxygen evolution potential is crossed. (Although layer thickness increases more slowly with time once oxygen evolution begins, it increases more rapidly with formation potential.) The (P_o-P) measurements from a galvanostatic experiment at a current density of 40 μA/cm^2 trace out the curve RST in Fig. 6 when plotted *vs.* V_f. The predicted increase in slope is found as the oxygen evolution potential is crossed.

In a linear potential sweep experiment, the ionic and electronic currents would seem to be independent, but actually they are coupled. The coupling arises because the currents are not driven by the same overpotential: the overpotential across the layer sets up the field which drives the ionic current, but the electronic current results from a reaction controlled by an overpotential across the double layer in electrolyte (*i.e.*, the tunneling process is not rate determining). These overpotentials are in series, and the constraint that their sum increase linearly with time couples the ionic and electronic processes. Once the formation potential includes an increasing series component across the double layer, the slope of the (P_o-P) *vs.* V_f graph decreases. The results from an experiment in which the potential is swept linearly at 10.8 mV/sec appear in Fig. 6 plotted along XYZ. The predicted decrease in slope is observed as the oxygen evolution potential is crossed.

The above discussion, although qualitatively correct, is not complete. The two effects which produce deviations in opposite directions from a linear (P_o-P) *vs.* V_f plot, the reduced ionic current and the reduced overpotential across the layer, are both present whenever the potential exceeds the oxygen evolution potential. A more detailed discussion could show that the reduced ionic current effect dominates in a galvanostatic transient, whereas the reduced overpotential effect dominates in a potential sweep transient. The results plotted in Fig. 6 are of some importance because they show that the high-field model can be used to predict the results of more than just the Tafel slope experiments from which the model was derived.

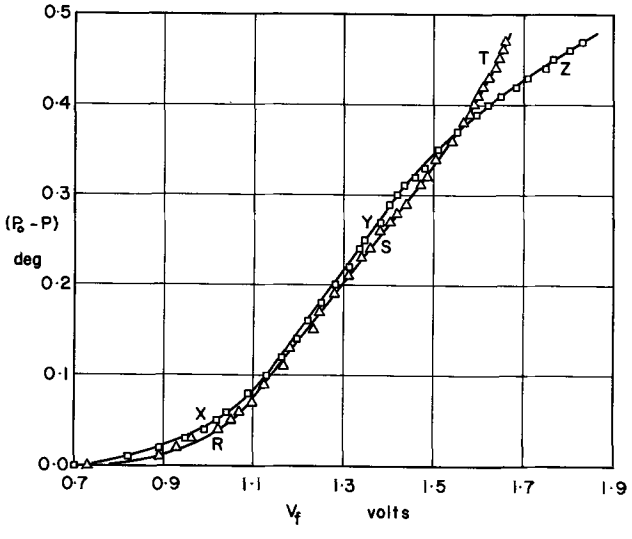

Fig. 6. Polarizer null data for transients extending into the oxygen evolution region; RST, galvanostatic oxidation at 40 μA/cm^2; XYZ, potential sweep at 10.8 mV/sec.

Conclusions

We have shown that the anodic oxidation of platinum meets the basic requirements for a process limited by the field in the oxide layer, and hence we conclude that the anodic oxidation of platinum and tantalum are governed by the same general laws. We do not expect this conclusion to be accepted universally by workers studying anodic processes on platinum, for the very good reason that the oxide film and the potential across it have virtually no effect on reactions for which the platinum electrode acts simply as a sink for electrons. The tunneling process will not itself be rate determining, and the potential of importance in tunneling will be the potential of the platinum electrode, not the potential of the oxide surface.

Our conclusion says considerably more about the anodic oxidation process than it does about the anodic behavior of platinum. If the same basic laws govern the anodic oxidation of metals as dissimilar as platinum, iron, and tantalum over a range of oxide film thicknesses from monolayer coverage on platinum to thousands of angstroms on tantalum, then any meaningful theory of anodic oxidation must not be overly sensitive to either the chemistry of the metal or the structure of the oxide.

Acknowledgment

The authors would like to acknowledge the help given by Dr. F. G. Will in a discussion of the feasibility of these experiments on platinum and gold substrates. This work was supported in part by the National Research Council of Canada under Grant No. A-1151.

Manuscript submitted April 13, 1970; revised manuscript received *ca.* Aug. 24, 1970.

Any discussion of this paper will appear in a Discussion Section to be published in the December 1971 JOURNAL.

APPENDIX

The bare surface measurement at 60° incidence, $P_o = 26.86°$, $A_o = 37.81°$, gives a value of 2.32-5.14*i* for the refractive index of platinum at 6328Å. As is usual with very thin films, a unique value cannot be determined for the refractive index of the oxide. The set of n-ik values which give layer growth curves with slopes $\Delta A/\Delta P$ equal to the slope of the experimental curve AC in Fig. 3 can be displayed as a curve in the n-k plane. This curve is plotted in Fig. 7 and has two segments, AB and CD. Any point on either segment

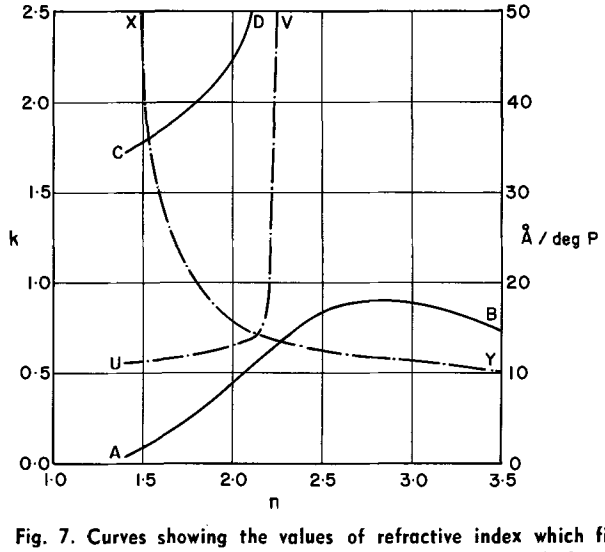

Fig. 7. Curves showing the values of refractive index which fit the experimental data (AC in Fig. 3), and the absolute thickness calibration factors. The index values are represented in the n-k plane by AB and CD, and the corresponding calibration factors are plotted *vs.* n along XY and UV.

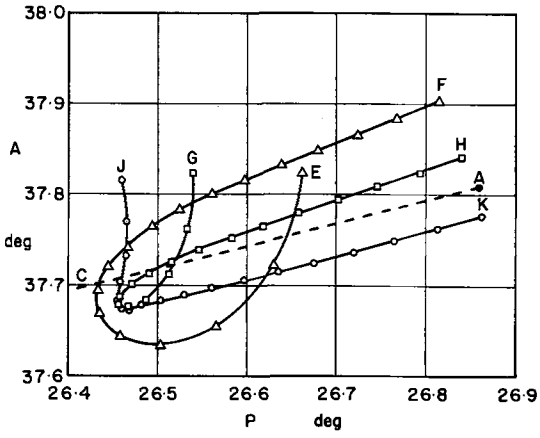

Fig. 8. Theoretical curves showing the loci traced out when k is incremented from 0.0 to 5.1 in 0.3 steps for a film with a thickness of 5Å and real index component of 1.7 (EF), 2.1 (GH), and 2.5 (JK). Point A is the bare substrate reading, and the dashed line AC shows the slope of the experimental curve generated as the layer is removed from the surface.

represents a possible value of the refractive index of the layer. The absolute thickness calibration factor, in Å/deg P, depends on the value chosen for the layer index, and is plotted *vs.* n in Fig. 7. This curve also has two segments, XY and UV, corresponding to the segments AB and CD of the refractive index curve.

Three theoretical curves are plotted in Fig. 8 to indicate how Fig. 7 is generated, and why it has two segments at low n. The bare surface measurement is plotted at point A, and the dashed line AC shows the slope of the experimental curve AC in Fig. 3. Curve EF is the locus traced out in the P-A plane as k is varied in 0.3 steps from 0.0 at E to 5.1 at F for a layer of fixed $n = 1.7$ and $D = 5$Å. The curve EF intersects AC at two points corresponding to $k = 0.2$ and $k = 1.9$. The $k = 0.2$ value lies on AB in Fig. 7, and the 1.9 value lies on CD. The thickness calibration factor depends on the distance from A to the intersection of AC with EF, and hence its two values at $n = 1.7$ differ by about a factor of two.

For values of n equal to 2.1 and 2.5, curves GH and JK are traced out as k goes from 0.0 to 5.1 for $D = 5$Å. AC intersects GH at two points giving two values for k and two nearly equal values for the thickness calibration factor. AC intersects JK at only one point, and hence only one value of k is possible for $n = 2.5$.

The shape of the curves in Fig. 7 is quite sensitive to the slope AC which in turn depends on V_f (due, we concluded, to the raising of the oxidation state as V_f increases). In particular, it is apparent from Fig. 8 that if the slope of AC is increased somewhat, it will no longer intersect GH, and hence 2.1 will not be a possible value of n for any value of k. Our index values are not inconsistent with the value quoted by other workers (10) for $\lambda = 5461$Å, but the sensitivity to the slope AC and the wavelength difference make a direct comparison impossible.

REFERENCES

1. J. L. Ord, *This Journal*, **113**, 213 (1966).
2. J. L. Ord and D. J. DeSmet, *ibid.*, **116**, 762 (1969).
3. M. Rosen, D. R. Flinn, and S. Schuldiner, *ibid.*, **116**, 1112 (1969).
4. J. L. Ord, *ibid.*, **112**, 46 (1965).
5. N. Sato and M. Cohen, *ibid.*, **111**, 512 (1964).
6. D. C. Grahame, *J. Phys. Chem.*, **57**, 257 (1953).
7. J. L. Ord and B. L. Wills, *Appl. Opt.*, **6**, 1673 (1967).
8. J. L. Ord, *Surface Sci.*, **16**, 155 (1969).
9. S. Schuldiner, T. B. Warner, and B. J. Piersma, *This Journal*, **114**, 343 (1967).
10. A. K. N. Reddy, M. Genshaw, and J. O'M. Bockris, *J. Electroanal. Chem.*, **8**, 406 (1967).
11. D. J. DeSmet, Thesis, University of Illinois (1967).

The Effect of Superimposed A.C. on D.C. in Electrodeposition of Ni-Fe Alloys

Zlata Kovac* [1]

IBM Thomas J. Watson Research Center, Yorktown Heights, New York 10598

ABSTRACT

The effect of superimposing a sinusoidal alternating current on a direct current during electrodeposition of Ni-Fe alloys is discussed in terms of the following factors: (*a*) maintaining the *p*H at the electrode equal to that of the bulk electrolyte, (*b*) ionic diffusion processes, and (*c*) chemical processes in solution prior to electrochemical reduction. The effect of frequency, amplitude, and the ratio of a.c. to d.c. on the composition of electrodeposited alloy are given for acid solutions of different *p*H and for alkaline solutions of metallic complexes with a variable concentration of complexing agent. The behavior observed can be explained in terms of the factors listed above. In particular, it is shown that by proper choice of conditions, electrodeposited Fe-Ni alloys can be prepared with a uniform composition throughout their thickness.

Alternating current has a significant influence on many electrode processes and is widely used in such electrochemical investigations as the study of electrical double layers (1-3), the kinetics of the formation and dissolution of oxide films (4), fast electrode reactions (5, 6), and in the electrodeposition and dissolution of metals (7, 8).

Vagramyan and Sutyagina (9) reported that alternating current can effect the grain size, brightness, and porosity of electrodeposited metals. Marchese (10) showed that the superposition of a.c. on d.c. reduces internal stresses in electrodeposited nickel. The magnetic properties of electroplated Ni-Co films could also be improved by superimposing a.c. on d.c. during their codeposition (11).

Our interest was to find what effect a.c. (of variable frequency and amplitude) has on the composition and uniformity of electrodeposited Ni-Fe alloys.

First, let us examine ways in which superimposed alternating current can affect the electrodeposition process. We will consider the cases where:

[1] Present address: PPG Industries, Inc., Springdale, Pennsylvania.
* Electrochemical Society Active Member.
Key words: electrodeposition, alloys, permalloy, Ni-Fe films, a-c, d-c.

1. For some portion of each cycle, the a-c component converts the electrode from cathode to anode.
2. Current is controlled by ionic diffusion in the electrolyte.
3. Deposition at the electrode is preceded by a chemical reaction in the solution.

Case 1

During electrodeposition of most metals, discharge of H_3O^+ or H_2O occurs concurrently with pH changes in the vicinity of the electrode surface. For metals with small hydrolysis constants this alkalization will be reflected in the formation of metallic hydroxides, which subsequently can be incorporated into the deposit, thus causing nonuniformity. In the codeposition of two or more metals this phenomenon can cause preferential deposition of one metal, so-called anomalous codeposition (12), and a concentration gradient across the deposit thickness (13), which will be the most pronounced in the first 500Å.

If one superimposes a.c. on d.c. during electrodeposition of such metals, then during the time for which the electrode is the anode, oxidation of adsorbed hydrogen formed in the cathodic cycle will take place according to

$$H^+ + e^- \underset{\text{anod.}}{\overset{\text{cath.}}{\rightleftarrows}} H_{ads}$$

In the ideal case of balancing the rate of cathodic discharge of H^+ ions with its rates of oxidation and diffusion from solution, one can achieve control of pH on the surface such that pH (surface) → pH (bulk). Hence, the above-mentioned difficulties should be minimized if not completely eliminated. Mathematically, this presents a complex problem. However, experimentally one can easily find the condition where there is no preferential deposition of one of the metals and where there is no composition gradient in the deposit, *i.e.*, the condition of constant pH.

Case 2

Passage of either direct or alternating current through an electrolytic cell will produce concentration changes, which are susceptible to mathematical treatment. Sand (14) solved the diffusion equation for the case of electrolysis with a constant direct current and Warburg (15) and Kruger (16) for the case of sinusoidal alternating current. Both treatments start from Fick's second law

$$\frac{\partial c}{\partial t} = D\frac{\partial^2 c}{\partial x^2} \qquad [1]$$

where c is the concentration of one ionic species, D is its diffusion coefficient, and x is the distance from the electrode into the solution.

Both d-c and a-c currents have the same boundary conditions, namely

$$c_{x=0} = c_{x=\infty} \text{ for } t = 0$$

and

$$\frac{\partial c}{\partial x} = 0 \text{ for } x \to \infty \text{ and } t > 0$$

Here, $c_{x=0}$ is the concentration at the electrode surface and $c_{x=\infty}$ is the bulk concentration.

The solution of Eq. [1] for constant d.c. is

$$c_{(0,t)} = c_\infty - \frac{2i}{n\mathbf{F}}\sqrt{\frac{t}{\pi D}} \qquad [2]$$

where i is the current density, t is time, n is the number of electrons involved in the electrode reaction, and $\mathbf{F}$ is Faraday's constant. For steady-state conditions

$$c_0 - c_\infty = -\frac{i\delta}{n\mathbf{F}D} \qquad [3]$$

or

$$\Delta c = Ki\delta$$

where δ is the thickness of the diffuse layer, and K includes all constant terms.

For sinusoidal a.c. the solution of Eq. [1] is (15, 16)

$$c_{(0,t)} = c_\infty - \frac{I}{n\mathbf{F}\sqrt{D\omega}}\exp\left(-\sqrt{\frac{\omega}{2D}}\cdot x\right) \cdot \sin\left(\omega t - \sqrt{\frac{\omega}{2D}}x - \frac{\pi}{4}\right) \qquad [4]$$

where I is the amplitude of the current density, and $\omega = 2\pi f$ where f is the a-c frequency.

At the electrode surface where $x = 0$, Eq. [4] becomes

$$\Delta c = -\frac{I}{n\mathbf{F}\sqrt{D\omega}}\sin\left(\omega t - \frac{\pi}{4}\right) \qquad [5]$$

or

$$\Delta c = \frac{A}{\sqrt{\omega}}\sin\left(\omega t - \frac{\pi}{4}\right)$$

where $A/\sqrt{\omega}$ is the amplitude of concentration wave.

If both currents act simultaneously on the system, then the net concentration changes can be obtained by adding together the concentration change that would be produced by each current taken separately (17) (since the sum of a number of solutions of a linear differential equation is likewise a solution). Thus

$$\Delta c = -\left[i\delta + I\sqrt{\frac{D}{\omega}}\sin\left(\omega t - \frac{\pi}{4}\right)\right] \Big/ n\mathbf{F}D \qquad [6]$$

Suppose one electrodeposits a binary alloy, with one of the depositable metal ions under diffusion control and the other under charge transfer control. In such a case Eq. [6] is applicable to only one constituent of the alloy, and the other constituent will be deposited as if the a.c. were not present, since a.c. does not effect charge transfer reactions.

Now, let us examine the conditions under which a.c. and d.c. have comparable effect on concentration change of Fe, which is deposited under diffusion control (13). For a 10^{-3}M Fe solution and a total direct current density of 2 mA cm^{-2}, the partial current for discharge of Fe is found to be 0.32 mA cm^{-2}, which from Eq. [3] gives $\Delta c = 8.5 \times 10^{-6}$M cm^{-3}. Suppose we take I to be 15 mA cm^{-2}, then the amplitude of the concentration wave from [5] is 2.6×10^{-6} and 0.37×10^{-6}M cm^{-3} for a frequency of 20 and 1000 Hz, respectively. In other words, a.c. of low frequency produces 30% and of high frequency 4% of the total concentration change. If the d.c. is increased, then the effect of a.c. becomes even smaller (2% for 1000 Hz and $i_{d\text{-}c}$ of 4 mA cm^{-2}). Clearly the effect of diffusion becomes progressively smaller with increasing frequency. Theoretically (Eq. [5]), one can increase the effect of a.c. by increasing its amplitude. Practically, however, it is not desirable to go too high into the anodic region, where dissolution of the alloy and oxide formation can take place.

Case 3

If electrodeposition is carried out from a solution of complex ions, then a reduction to the metallic state can take place either directly from the complex ion or this electrochemical step can be preceded by a chemical step or several steps in series (18, 19).

If one assumes that electrochemical reduction is preceded by a homogeneous chemical reaction of a type

$$M_mC_n^{(z_1+z_2)} \underset{k_b}{\overset{k_f}{\rightleftarrows}} mM^{z_1} + nC^{z_2}$$

then the rate of formation of the metallic ions is

$$v = k_fC_{MC} - k_b\,(c_M)^m\,(c_C)^n \qquad [7]$$

where k_f is the rate constant for dissociation of the

complex and k_b that for the recombination, and c_{MC}, c_M, c_C are the concentrations of metallic complex, metal ion, and complexing agent, respectively. Equation [7] can be written as

$$v = v_o - kc_M^p \quad [8]$$

where v_o is the reaction exchange rate, $k = k_b c_C$ is the reaction rate constant, and p is the reaction order.

As a result of diffusion and chemical reaction the change of concentration with time and distance at the surface of electrode can be represented by Fick's second law in extended form

$$\frac{\partial c}{\partial t} = D\frac{\partial^2 c}{\partial x^2} + v \quad [9]$$

Equation [9] applies to both direct and alternating currents. The direct current due to the deposition of metal with a slow chemical step and $p = 1$ is (20)

$$i = -n\mathbf{F}\sqrt{v_o c_M D}\sqrt{1 + \frac{1}{2}\left(\frac{c_s}{c_M}\right)^2 - 2\frac{c_s}{c_M}} \quad [10]$$

where c_M is equilibrium concentration of metal ions determined by $c_M = Kc_{MC}/c_C$, K being the stability constant for a given complex. When the concentration of metal ions at the surface, c_s, becomes zero, a limiting reaction current i_r is reached, given by

$$i_r = -n\mathbf{F}\sqrt{v_o c_M D} \quad [11]$$

and from its value one can calculate v_o and k (since at equilibrium $v = 0$ and v_o becomes equal to $k \cdot c_M$). The reaction exchange rate is also related to the thickness of the reaction layer, δ_i, by the following equation

$$\delta_i = \sqrt{\frac{Dc_M}{v_o}} \quad [12]$$

Passage of a.c. through a system where chemical reaction occurs prior to charge transfer will produce concentration changes which depend not only on $\omega^{-1/2}$ but also on k.

Vetter (21) [who simplified Gerischer's original derivation (22)] gave the concentration change as a difference of ohmic and capacitive components of the electrolyte, both of which are function of $\omega^{-1/2}$ and k/ω. The concentration wavelength as well as penetration depth are also dependent on the same parameters. This derivation is valid only for very small differences between c_M and c_s. Furthermore, the a-c and d-c solutions of the differential equation cannot be added in this case, since the differential equation is nonlinear. A quantitative treatment has therefore not been attempted. Qualitatively, however, one would expect that at a low frequency the concentration wave will be able to follow the slowly varying current, and that the penetration depth would be of the same length as d-c reaction layer thickness. At higher frequencies, the formation and decomposition of metal complexes will be increasingly less important, since they cannot follow fast changes of current. In addition the penetration depth of the concentration wave will become smaller. For both these reasons, it is to be expected that at high frequencies the d-c behavior will dominate.

When two or more metallic complexes are present in the system, a-c will effect them differently depending upon the value of k/ω for each complex. Hence by superimposing a.c. on d.c. one can affect the deposition kinetics of alloys in a very practical way.

Experimental Procedure

Experiments were performed in two compartment cells. The cathode was Cu-sheet or evaporated Ag on glass (2 x 2 cm), placed horizontally in one compartment of the cell. The back of the electrode was masked, so that electrodeposition was carried out on one side only. A Pt-mesh auxiliary electrode was placed ~2 cm above the working electrode. The reference electrode

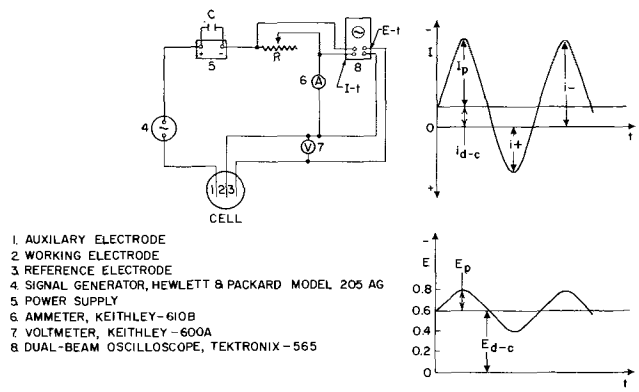

Fig. 1. Electrical arrangement for electrodeposition with combined d.c. and a.c. On the right-hand side are shown the net current and potential curves.

compartment (SCE) was connected with the main compartment through a Luggin capillary carefully bent to avoid any shielding effect.

The electrical circuit [similar to one used by Marchese (10)] is shown in Fig. 1. Current-time and potential-time curves were recorded simultaneously on a dual-beam oscilloscope (Tektronix Model 565). It is important that one records the potential, since this provides a means of determining the region in which the oxidation of hydrogen takes place by a method which minimizes dissolution of alloy and avoids its oxidation.

Experiments were carried out in acid and alkaline solutions. The acid solutions had the following compositions (23): "low Ni": 0.024M $NiSO_4$, 0.006M $FeSO_4$, 0.035M $NaKC_4O_4O_6$, pH = 3 or 4.6. The molar ratio of (Fe/Ni) in solution was 20/80. "High Ni": as above, but with 0.114M $NiSO_4$ and pH = 3, 3.8, or 4.6. Here, the (Fe/Ni) ratio in solution was 5/95. The alkaline solutions were ammoniacal-citrate solutions (24), the compositions of which were: "high citrate": 0.125M $NiCO_3$, 0.032M Fe dust, 0.301M $C_6H_8O_7$, 0.332M $(NH_4)_2HC_6H_5O_7$ and NH_4OH for pH = 9.25. The "low citrate" solution had the same pH and concentration of Ni and Fe, but it contained 0.127M $C_6H_8O_7$ and 0.137M $(NH_4)_2HC_6H_5O_7$. The molar ratio of (Fe/Ni) in solution was 20/80.

The solutions were made of ACS grade chemicals and deionized water. The citrate solutions were prepared according to Stephan's patent (25).

After electroplating, the samples were cut into 1.5 x 1.5 cm squares and analyzed by the x-ray fluorescence method for weight per cent Fe (accuracy ± 1 w/o) and thickness (accuracy ± 150 Å).

Results

In the first series of experiments we examined the effect of frequency on the rate of deposition and on the composition of the deposited alloy. In Fig. 2 and 3 are shown the rate and per cent Fe as a function of log frequency in low and high nickel solutions, respectively, for conditions of constant pH, i_{d-c} and I_{peak}. On the left-hand sides are given values for direct current plating only.

As was mentioned earlier, one expects a diminishing effect of a.c. with increasing d.c. in the system. This prediction is clearly seen from Fig. 4. With d_{d-c} of 2 mA cm^{-2} the Fe content varies from 9.5 to 30%, but changes only from 15.2 to 18% with i_{d-c} of 5 mA cm^{-2} at constant I_{peak} and pH (3.8).

Figure 5 shows a log i-E plot for the high citrate solution. It can be seen that for high values of total current, i_{Fe} reaches a limiting value, which is taken as the limiting reaction current according to Vetter's criteria (21). In Fig. 6 and 7 are given the deposition rates and per cent Fe as a function of log frequency for two values of direct current density.

The variation in composition with the density of direct current at constant frequency and amplitude of

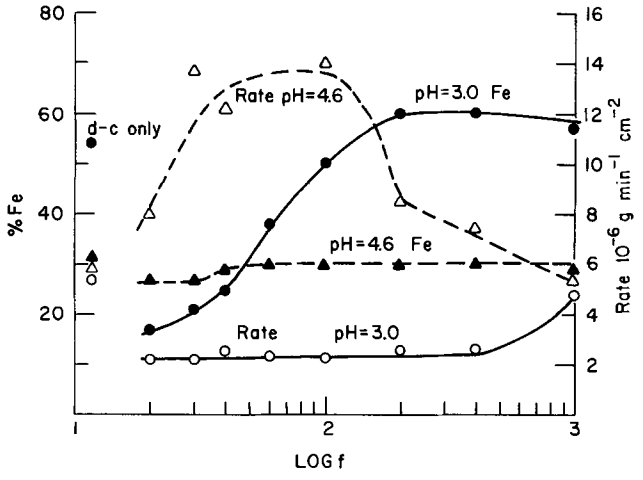

Fig. 2. Fe content and the rate of alloy deposition as a function of log f in low nickel solutions of pH = 3.0 and pH = 4.6. $(Fe/Ni)_{sol}$ = 20/80, with i_{d-c} = 2 mA cm^{-2} and i_p = 13.7 mA cm^{-2}.

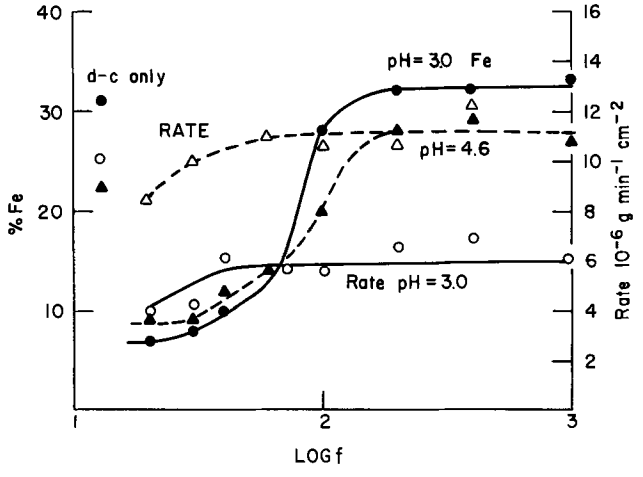

Fig. 3. Fe content and the rate of alloy deposition as a function of log f in high nickel solution of pH = 3.0 and 4.6, $(Fe/Ni)_{sol}$ = 5/95, i_{d-c} = 2 mA cm^{-2}, I_p = 13.75 mA cm^{-2}. Data in the left corner with d.c. alone.

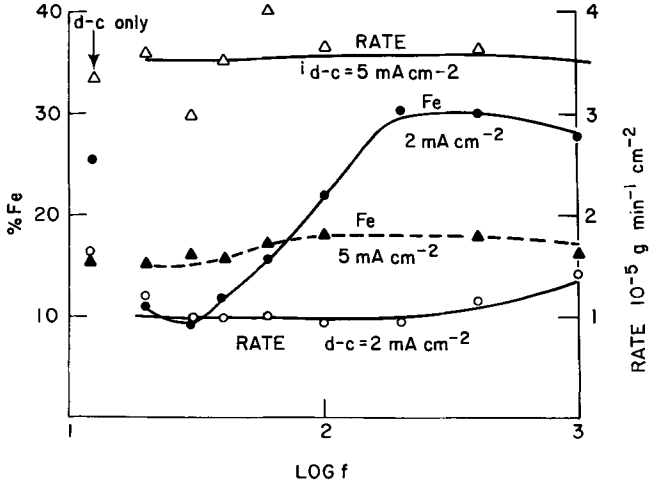

Fig. 4. Fe content and the rate of alloy deposition in high nickel solution of pH = 3.8 with i_{d-c} of 2 mA cm^{-2} and 5 mA cm^{-2} and I_p = 13.75 mA cm^{-2}.

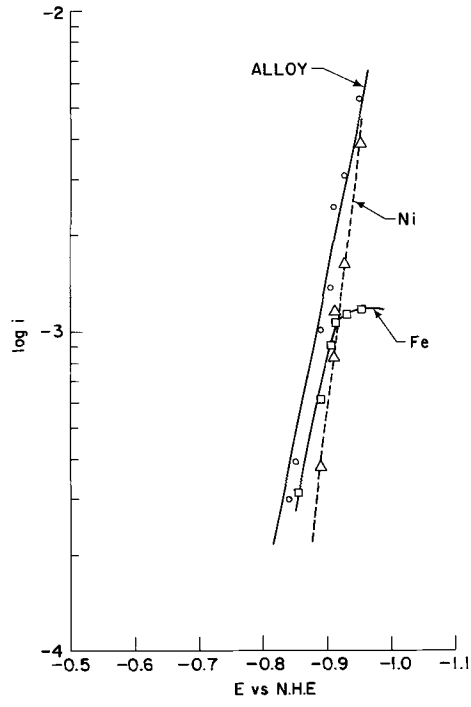

Fig. 5. Log direct current density vs. potential in high citrate solution of pH = 9.25.

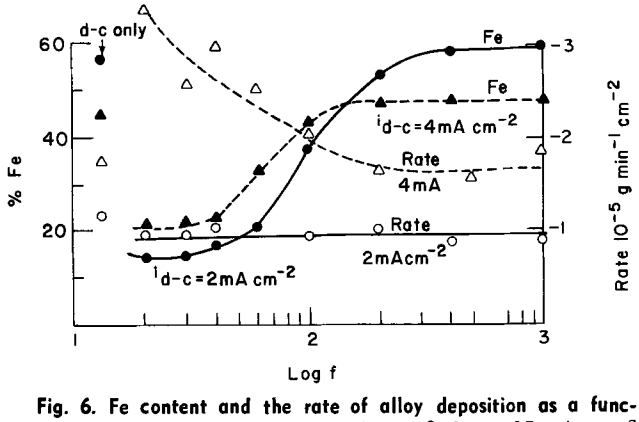

Fig. 6. Fe content and the rate of alloy deposition as a function of log f with i_{d-c} of 2 and 4 mA cm^{-2}, I_p = 15 mA cm^{-2} and $(Fe/Ni)_{sol}$ = 20/80. Data in left corner are the values of d.c. alone.

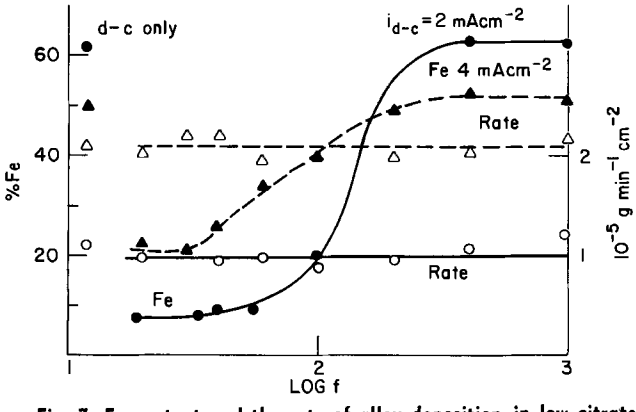

Fig. 7. Fe content and the rate of alloy deposition in low citrate solution of pH = 9.25, $(Fe/Ni)_{sol}$ = 20/80 with i_{d-c} of 2 and 4 mA cm^{-2} and I_p = 15 mA cm^{-2}.

alternating current is given in Fig. 8 and 9 for acid and alkaline solutions, respectively. For the purpose of comparison, data for d-c plating alone are also given and designated as f = 0.

From Eq. [5] one expects that the amplitude of the diffusion concentration wave to increase with increasing I_{peak}, and hence that the iron content of both the surface electrolyte and the deposit should decrease. This indeed can be seen from Fig. 10.

Since temperature affects the equilibrium constant for the dissociation of metallic complexes, it can be expected to exert an influence on the deposition rate.

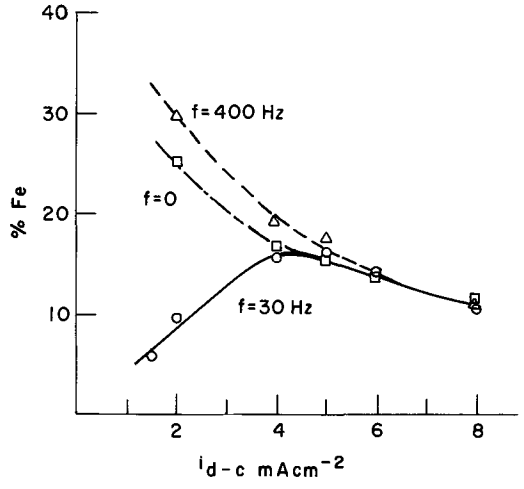

Fig. 8. Fe content as a function of direct current density for f = 0, 30, and 400 Hz with I_p = 13.75 mA cm^{-2}, (Fe/Ni)$_{sol}$ = 5/95 and pH = 3.8.

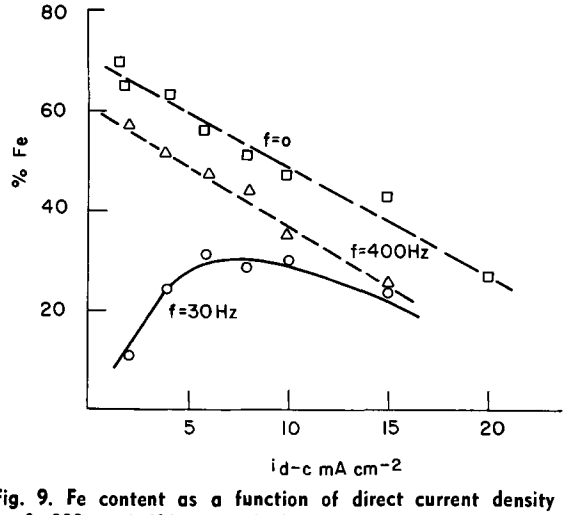

Fig. 9. Fe content as a function of direct current density for f = 0, 300, and 400 Hz in high citrate solution of pH = 9.25 and (Fe/Ni)$_{sol}$ = 20/80, I_p = 16.7 mA cm^{-2}.

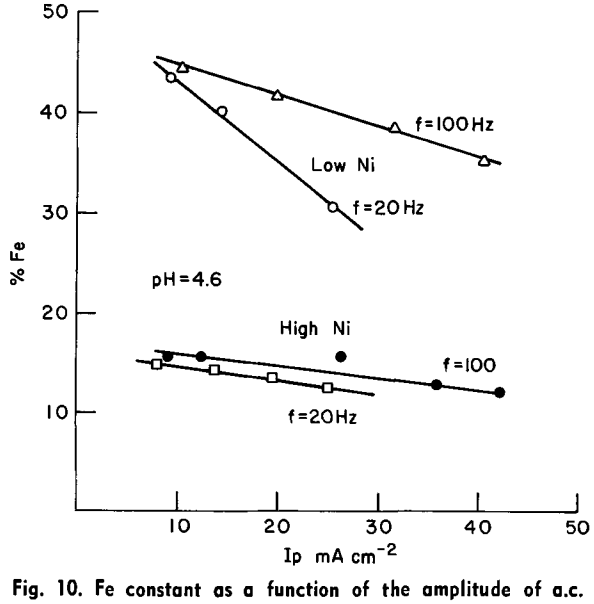

Fig. 10. Fe constant as a function of the amplitude of a.c. in low nickel, (Fe/Ni)$_{sol}$ = 20/80 and high nickel solution, (Fe/Ni)$_{sol}$ = 5/95 for f = 20 and 100 Hz and pH = 4.6.

In Fig. 11 are given rates and per cent Fe for the high citrate solution as a function of frequency for temperatures of 25° and 40°C. At higher temperatures the

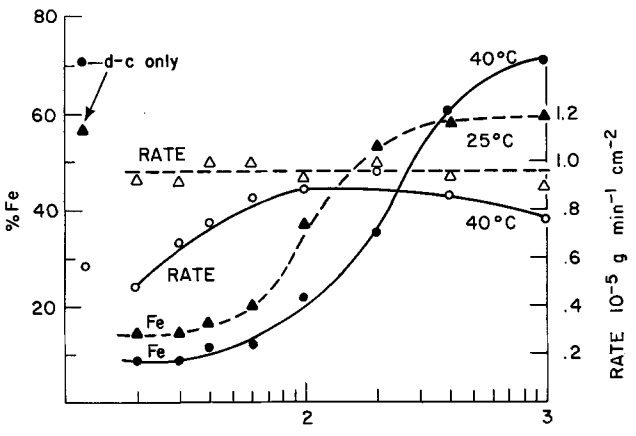

Fig. 11. Fe content the rate of alloy deposition as a function of log f in high citrate solution, with i_{d-c} = 2 mA cm^{-2}, I_p = 15 mA cm^{-2} for T = 25° and 40°C.

corrosion rate of the alloy becomes too large for meaningful study.

Discussion

From Fig. 2, 3, 4, 6, 7, and 11 one can clearly see to what a large extent the composition of the deposit is influenced by frequency. Since the percentage of one metal is a function both of its deposition rate and of the total rate of metal deposition, it is more meaningful to examine how the iron rate alone varies with frequency. The diffusion law predicts a linear dependence on $\omega^{-1/2}$, *c.f.*, Eq. [6]. From the plots given in Fig. 12-14 it can be seen that the rate of Fe deposition is indeed linearly dependent on $\omega^{-1/2}$, approaching its d-c value at high frequencies, where the contribution from the a-c component becomes negligible. However, there

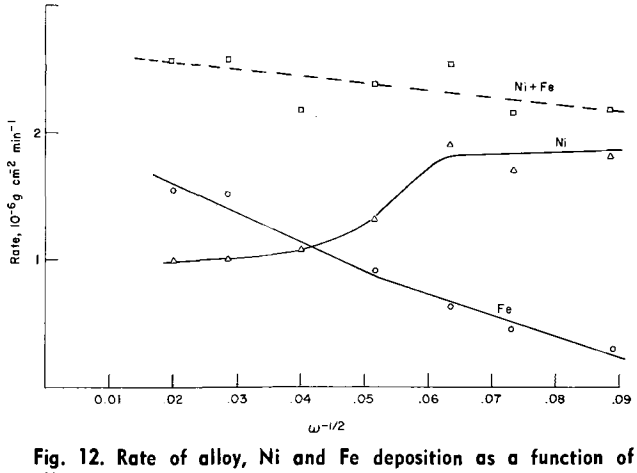

Fig. 12. Rate of alloy, Ni and Fe deposition as a function of $\omega^{-1/2}$ in low nickel solution, (Fe/Ni)$_{sol}$ = 20/80 and pH = 3.00, i_{d-c} = 2 mA cm^{-2}, I_p = 13.75 mA cm^{-2}.

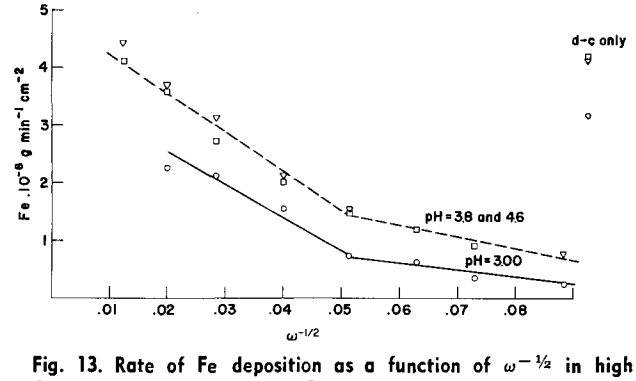

Fig. 13. Rate of Fe deposition as a function of $\omega^{-1/2}$ in high nickel solution, (Fe/Ni)$_{sol}$ = 5/95 at pH = 3, 3.8 and 4.6, i_{d-c} = 2 mA cm^{-2}, I_p 13.75 mA. Data in the right corner are the values for d.c. alone.

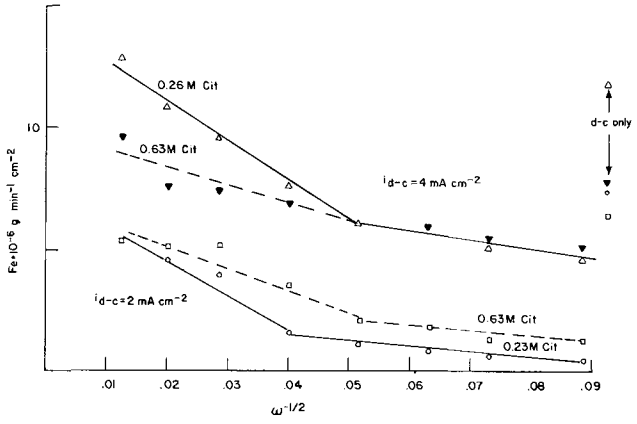

Fig. 14. Rate of Fe deposition as a function of $\omega^{-1/2}$ at i_{d-c} of 2 and 4 mC cm^{-2} in low and high citrate solution.

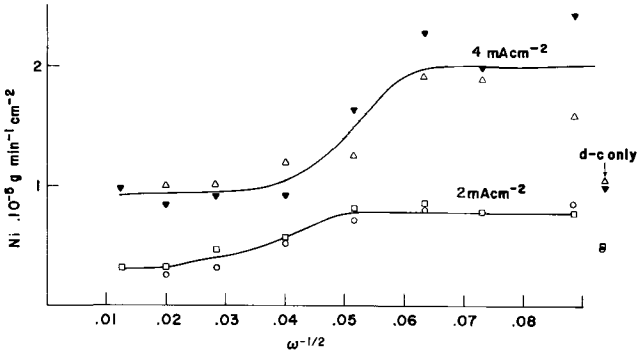

Fig. 15. Rate of Ni deposition as a function of $\omega^{-1/2}$ at 2 and 4 mA cm^{-2} in low (○, △) and high citrate solutions (□, ▼).

are two regions, one being that of low frequency, *i.e.*, 20-100 Hz, and the other from 100 to 1000 Hz for which the slope of the line has different values, being smaller at lower frequencies. The explanation of this behavior is discussed separately below for the two different types of solutions employed.

Deposition from acid solutions.—In the solution of pH = 3, the rate of alloy deposition is lower under a.c. plus d.c., than under d.c. alone. This indicates that some dissolution of alloy is taking place. One can argue that Fe dissolves faster than Ni, hence there is less Fe present in a deposit. However, there is no trend in the variation of alloy deposition rate with frequency. Furthermore, in the solutions of pH = 4.6, the total rate is not affected with a.c., but the Fe rate is lower and shows the same clearly defined two regions of different dependence on frequency. In the region of low frequency the contribution of a.c. is twofold. First, its effect on diffusion is the largest, and second, there is an effect on the surface pH. For, when the potential is varied slowly, the electrode remains in the anodic region sufficiently long to allow oxidation of adsorbed hydrogen on its surface (26). Hence, $pH_{surface}$ is brought back to its original value for the next cathodic cycle. If $pH_{surface}$ does not increase, the formation of hydroxides does not occur, hence there is no anomalous deposition of iron and the Ni deposition is not suppressed. This can be clearly seen from Fig. 12. With increasing frequency, the electrode spends less and less time in the anodic region, and the kinetic processes apparently cannot follow such rapid changes. As a result, $pH_{surface}$ increases sufficiently to cause the formation of iron hydroxide, which prevents the discharge of Ni. It is interesting to note that already at 100 Hz Ni and Fe deposit with the same rate, *c.f.*, Fig. 12, in spite of the fact that the bulk concentration of Ni is four times higher than that of Fe. Above 100 Hz Fe deposits with a higher rate than Ni. In Fig. 13 are shown the rates of Fe deposition for three values of bulk pH. Within the experimental error, Fe deposits from the solutions of pH = 3.8 and pH = 4.6 with the same rate, indicating that a.c. produced the same surface pH.

With increasing bulk pH, or by increasing the d-c level, the a-c component becomes less effective in controlling the pH of the surface (*c.f.*, Fig. 2, 3, and 4). It should be pointed out that according to Bockris *et al.* (25), the Fe rate, *i.e.*, partial current density for iron deposition, is closely connected with pH through the following relationship $(\partial \ln i_{Fe}/\partial \log c_{OH^-}) = 1$.

Examining Fig. 2, one can see that in the low Ni solution of pH = 4.6, the rate of alloy deposition is higher under a.c. plus d.c. then under d.c. alone. If adsorbed hydroxides block the surface, then a hydrogen evolution reaction from the rather dilute bath might be kinetically the most favorable reaction. With a.c. present adsorption of hydroxides does not occur, and hence the rate is higher.

Deposition from complex solutions.—As was mentioned earlier, deposition of the alloys from complex solutions with superimposed a.c. on d.c. presents a rather interesting problem on account of the dependence on the k/ω ratio. Furthermore, in such systems the two currents are more comparable since the reaction layer thickness for d.c. is approximately the same as the penetration depth for a.c. ($\sim 7.5 \cdot 10^{-5}$ cm). From Fig. 6 and 7 it can be seen that just by varying frequency one can vary the Fe content from 14-59%, or, by decreasing the concentration of complexing agent for Fe, from 8-63%.

In Fig. 14 are given the rates of Fe deposition as a function of $\omega^{-1/2}$ for two values of d.c. and two concentrations of citrate ions. At i_{d-c} = 2 mA cm^{-2} a quite surprising effect is found, namely, Fe deposits with a higher rate from the solution containing more of its complexing agent. When i_{d-c} is increased to 4 mA cm^{-2}, Fe deposits with the same rate from both citrate solutions in low-frequency region. However, at higher frequencies the situation becomes "normal," *i.e.*, with more complexing agent there are less Fe ions available for deposition. This "abnormality" can be explained if one compares the values of the rate constant for low and high citrate solution.

The reaction exchange rate, v_o, can be calculated from Eq. [11] if the limiting reaction current, i_r, is determined experimentally. For the high citrate solution i_r = 1.54 mA cm^{-2}, giving $v_o = 2.06 \cdot 10^{-4}$. For the low citrate solution i_r = 2.02 mA cm^{-2} and $v_o = 1.37 \cdot 10^{-4}$ mole cm^{-3} sec^{-1}. From these v_o values k was calculated to be $4.63 \cdot 10^3$ and $1.19 \cdot 10^3$ sec^{-1} for high and low citrate, respectively. It has been pointed out earlier that the rate depends not only on $\omega^{-1/2}$ but also on the ratio of k to ω. This ratio varies from 37 to 0.74 in the high citrate solution, but only from 9.5 to 0.19 in the low citrate, when f is varied from 20 to 1000 Hz. The rate constant is equal to ω at 740 and 190 Hz for high and low citrate, respectively. Since k is an order of magnitude larger than ω at low frequencies in the high citrate solution, Fe deposits with a higher rate than from low citrate solution where k and ω are of the same order of magnitude. At 1000 Hz the ratio of k/ω in both solutions are of same magnitude (0.74 and 0.19), hence there is very little difference in Fe rates (*c.f.*, left side of Fig. 14).

By increasing i_{d-c} more material is required according to Faraday's law, and therefore the effect of d.c. becomes more pronounced. When the frequency is increased the effect of a.c. is still further diminished, hence the transition to "normal" behavior is observed.

If the concentration of citrate ions is changed, one would not expect to see any changes in Ni rate, since Ni is present in solution as the $[Ni(NH_3)_n]^{++}$ complex. Experimental data given in Fig. 15 clearly bear out this expectation.

By superimposing a.c. on d.c. one expects that variation in Fe composition on the surface and consequently in the deposit will take place within the time of one cycle, *i.e.*, $\sim 10^{-2}$ sec. On a microscopic scale this means uniform composition, which is indeed observed experi-

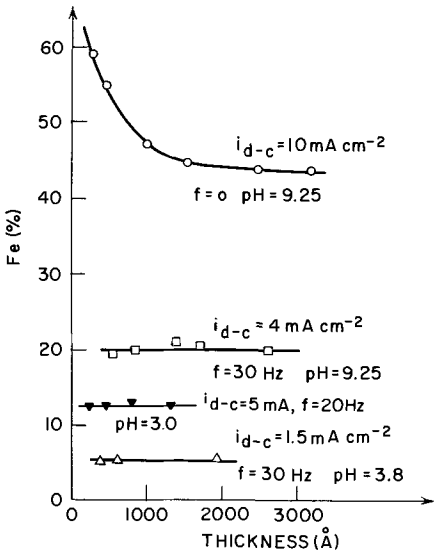

Fig. 16. Fe content as a function of film thickness in acid and alkaline solutions.

mentally, as shown in Fig. 16. The line at the bottom of the graph represents per cent Fe obtained from the solution with molar ratio of Fe/Ni = 5/95. Note that the composition of the solution is reflected exactly in the deposit throughout its thickness.

Conclusions

By superimposing a.c. on d.c. during the electrodeposition of alloys

1. One can diminish if not completely eliminate anomalous codeposition. Furthermore, inclusion of hydroxides into deposits can be excluded. This regulation can be used not only for iron group metals, but in all cases where one deals with metal ions which readily form hydroxides (Zn, In, Cd).
2. From the same solution the composition of an alloy can be varied in a rather wide region (8-60% Fe) merely by varying the frequency. This method could be usefully applied in studies of physicochemical properties (such as stress, morphology of a deposit, grain size, etc.) as a function of composition at constant d.c.
3. Deposits of uniform composition can be obtained.

Acknowledgments

Grateful acknowledgment is given to Mrs. Judith Olsen for her skillful, enthusiastic and patient experimental assistance. Thanks are due to Doctors B. Berry, I. M. Croll, J. F. Freedman, and L. T. Romankiw for helpful discussions.

Manuscript submitted April 20, 1970; revised manuscript received Aug. 28, 1970.

Any discussion of this paper will appear in a Discussion Section to be published in the December 1971 JOURNAL.

REFERENCES

1. Wien, *Ann. Phys. Leipzig*, **58**, 815 (1896).
2. D. C. Graham, *J. Am. Chem. Soc.*, **63**, 1207 (1941); **68**, 301 (1946).
3. M. A. Proskurin and A. N. Frumkin, *Trans. Faraday Soc.*, **31**, 110 (1935).
4. B. V. Ershler, *Trans. 2nd Meeting on Metal Corrosion, Acad. Sci., U.R.S.S.*, **2**, 52 (1943).
5. P. I. Dolin and B. V. Ershler, *Acta Physicochim.*, **13**, 747 (1940).
6. J. E. B. Randles, *Discussion Faraday Soc.*, **1**, 11 (1947).
7. A. T. Vagramyan and Z. A. Soleveva "Technology of Electrodeposition," p. 95, Robert Draper Ltd., Teddington (1961).
8. K. M. Gorbunova and A. A. Sutyagina, *J. Phys. Chem.*, **3**, 542 (1955).
9. A. T. Vagramyan and A. A. Sutyagina, *Izv. Akad. Nauk SSSR, Otd. Khim Nauk*, **3**, 410 (1952).
10. V. J. Marchese. *This Journal*, **99**, 39 (1952).
11. P. P. Zapponi, U. S. Pat. 2,619,454.
12. A. Brenner, "Electrodeposition of Alloys," Vol. 1, p. 84, Academic Press, New York (1963).
13. H. Dahms and I. M. Croll, *This Journal*, **112**, 771, (1965).
14. Sand, *Phil. Mag.*, **1**, 45 (1901).
15. E. Warburg, *Wied. Ann.*, **67**, 493 (1899).
16. F. Kruger, *Z. Phys. Chem.*, **45**, 1 (1903).
17. T. R. Roseburgh and W. L. Miller, *J. Phys. Chem.*, **14**, 816 (1910).
18. L. Gierst and A. Juliard, *Proc. Intern. Comm. Electrochem. Thermodynam. and Kinet.*, Milan, 1950, pp. 117, 279.
19. P. Delahay, "New Instrumental Methods in Electrochemistry," p. 215, Interscience Publishers, Inc., New York (1966).
20. H. Gerisher and K. J. Vetter, *Z. Physik Chem.*, **197**, 92 (1951).
21. K. J. Vetter, "Electrochemical Kinetics," p. 253, Academic Press, New York (1967).
22. Gerischer, *Z. Physik Chem.*, **198**, 286 (1951).
23. J. M. Brownlow, *J. Appl. Phys.*, **38**, 140 (1967).
24. J. H. Stephen, London Pat. 925, 144.
25. J. O'M. Bockris, D. Drazic, and A. Despic, *Electrochim. Acta*, **4**, 325 (1961).
26. K. Vetter, "Electrochemical Kinetics," p. 581, Academic Press, New York (1967).

The Effect of Molecular Structure on the Electrode Kinetics of Aminoquinones and Quinone Thioethers

Jeffrey L. Huntington and Donald G. Davis*

Department of Chemistry, Louisiana State University in New Orleans, New Orleans, Louisiana 70122

ABSTRACT

The electrochemistry of a number of aminoquinones and quinone thioethers has been investigated in aqueous-ethanol solutions. Half-wave potentials as a function of pH have been measured polarographically and heterogeneous rate constants for several of the compounds have been determined by cyclic voltammetry. The $E_{1/2}$'s and the $k_{s,h}$'s have been compared with hyperfine splitting constants determined by ESR spectrometry and conclusions arrived at as to the effect of spin density on electrochemical parameters.

A substantial number of naturally occurring quinones have been shown to be essential to life. Many of these are involved in the transport of electrons in biological systems (1). Also, it has been reported that menadione is an effective sensitizer in the radiotherapy of certain types of cancer (2). The effectiveness of menadione has been attributed to its ability to react with thiol groups such as cysteinyl residues in proteins

* Electrochemical Society Active Member.
Key words: ESR, cyclic voltammetry, heterogeneous rate constants, polarography.

(3). Because of these facts, we decided to investigate the reactions of quinones with thiol and amine groups and to study the electrochemistry and ESR spectra of the resultant products. In this way it was hoped that a better understanding of the biochemistry of quinones would result.

Simple quinones have been studied electrochemically by many workers but only recently has the biologically important ubiquinone-6 been studied comprehensively (4). The first report of an ESR spectrum of an aminoquinone appeared in 1960 (5). Russell *et al.* have published the spectrum of 2,5-bis (t-butylamino) benzoquinone in DMSO and some work with aminoquinones in acetonitrile has also been reported (6).

For this work we chose 50% ethanol in water because this solvent allows good solubility of quinones. The hyperfine splitting constants reported in nonaqueous solvents (6, 7) are roughly proportional to ours in aqueous ethanol but are only about two thirds as large.

The syntheses of the various aminoquinones and thioethers used in this study are reported elsewhere (8). Table I shows the structures of the various quinones studied. The same number is used to designate the quinone, semiquinone, or hydroquinone in any state of protonation. When a proton is spoken of as being α, β, or γ, the proton in question is attached to the α, β, or γ carbon, respectively, in the side chain or ring connected to the quinone moiety by the heteroatom.

Table I. Number assignments of quinones studied

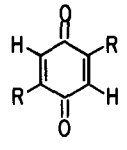

R	NO.	R	NO.
Me	1	$NHCH_2CH=CH_2$	10
t-Bu	2	$NHCH_2CO_2H$	11
OH	3		12
NHMe	4	SEt	13
NHEt	5	S-t-Bu	14
NH-n-Pr	6	SCH_2Ph	15
NH-i-Pr	7	S-i Pr	16
NH	8	SPh	17
NH-t-Bu	9	$SCH_2CH_2CO_2H$	18

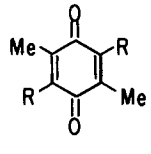

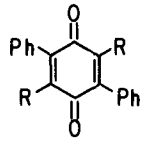

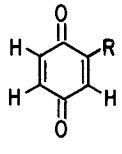

R	NO.	R	NO.	R	NO.
Me	19	NH-i-Pr	22	t-Bu	24
NH-n-Pr	20	S-i-Pr	23	CO_2Me	25
NH-i-Pr	21				

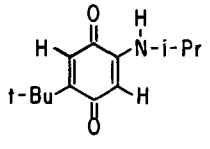

26

Experimental

The measurement of the ESR spectra of the quinones listed in Table I and a number of others has been previously reported (8), as have the syntheses, analyses, and NMR spectra. The solvent chosen for the ESR and electrochemical studies was "50% ethanol" prepared by mixing equal volumes of 100% ethanol and distilled water. In a number of cases it was found necessary to add a few per cent of chloroform to the "50% ethanol" to increase the solubility of the quinone. This practice had little effect on the ESR spectra (see compounds 8 and 13 in Table II) or the electrochemistry.

Reagents and buffers were generally the best commercial grade available and were used without further purification. Solutions were deaerated as necessary with prepurified nitrogen.

No system of "pH" measurement for nonaqueous solvents is universally employed (9). The "pH" values reported here are operationally defined. The procedure was simply to measure the pH with a glass electrode after standardization with aqueous buffer, even though pH values in ethanolic solutions tend to be lower than found in an aqueous solution of the same buffer (9). The pH readings were generally quite reproducible.

Coulometry, polarography, cyclic voltammetry, electrogeneration of radicals, and chronopotentiometry, all with three electrodes, were carried out by means of an operational amplifier, multipurpose electrochemical instrument, and triangle wave generator described elsewhere (10). Complete plans for this instrument are also available (11). The readout devices were a Hickock Model DMS-3200 digital voltmeter, a Houston Instruments HR-95 X-Y recorder, or a Tektronix Model 564 and/or Model 561A oscilloscopes with appropriate plug-in amplifiers and time bases.

Electrochemical cells were of local design and were constructed completely of Pyrex. The hanging mercury drop electrode used in many of the studies was supplied by Brinkmann Instruments and consisted of a stainless steel micrometer which extruded mercury from a Lucite reservoir through a glass capillary.

A dropping mercury electrode was constructed in these laboratories, entirely of glass. The mercury in a 2 mm capillary standpipe was supported by compressed air in a chamber above the mercury reservoir. The mercury column was pumped to the desired height by squeezing a pipette bulb. After closing the stopcock the mercury head would remain constant to within a few millimeters for a matter of hours. A second stopcock led from the reservoir to a full-length Sargent capillary (2-5 sec.) A platinum wire sealed through the glass just above the capillary made electrical contact, obviating the long lead which could be a source of excess noise.

The various electrochemical techniques were applied in the usual ways. Cyclic voltammetry was used to measure heterogeneous rate constants as proposed by Nicholson (12). Some of the details of this application are discussed below.

Results and Discussion

Controlled potential coulometry.—In various solvents, quinones have been reported to undergo one- (13), two- (7), or four-electron reduction (14) so it was necessary to establish the number of electrons transferred for representative quinones upon reduction in 50% ethanol at moderate pH. The reduction of compound **21** at a mercury pool in a pH 5 buffer consumed 1.98 electrons per molecule at $E = 0.50$V *vs.* SCE. Reoxidation at $E = 0.20$V recovered 1.8 electrons. Reduction of **7** under the same conditions consumed 2.09 electrons of which 2.01 were recovered on reoxidation. Evidently, reduction of aminoquinones in acidic solution is an over-all two-electron process and is not accompanied by decomposition.

Polarography.—Aminoquinones and quinone thioethers gave reversible or quasi-reversible polarographic waves except that both classes of compounds often exhibited large maxima. In solutions of *p*H 5 or above, the maxima disappeared spontaneously over the period of an hour or less. Quinone thioethers decompose sufficiently rapidly at *p*H 8 or above to prevent the gathering of useful data except for approximate half-wave potentials. For this reason the following discussion is concerned primarily with aminoquinones.

For quinones and aminoquinones, polarographic limiting currents are proportional to the square root of the mercury head, and the half-wave potentials do not depend on the drop time, the state of oxidation, or the supporting electrolyte concentration. The temperature coefficients of the $E_{I/2}$'s (including the effects of temperature on *p*H and junction potentials) are small, about −1 mV/°C, so it may be concluded that the waves are under diffusion control. Whereas the theoretical value of $dE/d \log [i/i_d - i]$ is 30 mV for a reversible two-electron wave at 25°C, the experimental is 32 mV for **21** and 34 mV for **7**. By way of comparison, the slope is 34 mV for duroquinone, **19**. The plots of log $[i/i_d - i]$ *vs.* *E* are linear, and the $E_{1/2}$ does not depend on quinone concentration, which implies that the electrode process is essentially reversible and does not involve a dimerization.

The less soluble compounds, such as **12**, frequently gave abnormally steep or otherwise misshapen waves, particularly below room temperature. That the difficulty here is insolubility is corroborated by the normal appearance of the waves upon warming to 50°C. This encouraged us to attempt to improve the electrochemistry by adding chloroform to improve the quinone solubility. This approach achieved a measure of success at chloroform concentrations of around 2%. Above 5%, however, the aminoquinone waves became increasingly irreversible, the $E_{1/2}$'s shifted cathodically, and the drop time became erratic. This is presumably a surface effect, but why only 5% of so innocent a solvent as chloroform should have such an adverse influence remains unexplained. Adding as much as 10% chloroform did not noticeably mitigate the enormous maxima observed at *p*H 5 and below.

The equilibrium constants for the formation of aminosemiquinones by disproportionation are far too small in aqueous solution to influence the shape of the polarographic wave. Alkylthiosemiquinones are stable enough at high *p*H to be studied electrochemically, but the rapid decomposition of the parent quinones makes precise measurements nearly impossible.

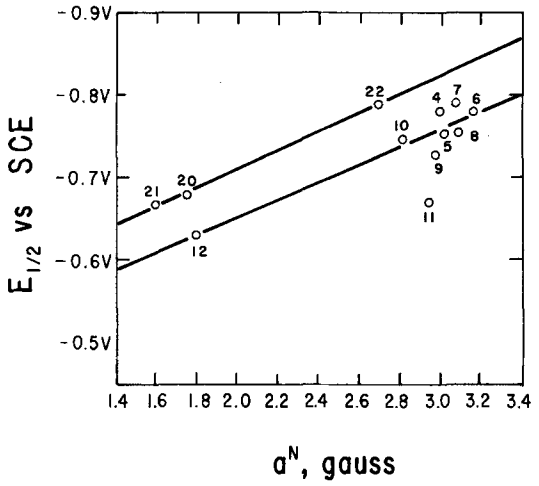

Fig. 1. Dependence of polarographic half-wave potential on aminosemiquinone nitrogen splitting constant: *p*H 11.0 glycinate buffer, 50% ethanol, 0.20*M* $NaClO_4$. Numbers beside experimental points refer to Table I.

Diffusion coefficients at 24°C in 50% ethanolic *p*H 11 glycine buffer containing 2.0 moles of $NaClO_4$ per liter were calculated from the Ilkovic equation to be 2.70 x 10^{-6} cm^2 sec^{-1} for **21**, and 2.82 x 10^{-6} cm^2 sec^{-1} for **8**. Duroquinone, **19**, gave a diffusion coefficient of 3.52 x 10^{-6} cm^2 sec^{-1} under the same conditions. These values are a little smaller than would be predicted for molecules of like size in aqueous solution, but the higher viscosity of 2.0*M* $NaClO_4$ in 50% ethanol makes them seem reasonable (11).

Table II is a compilation of the results of ESR studies on the compounds of interest to this work.

Despite the scatter in the data, it is obvious from Fig. 1 that half-wave potentials of bis(alkylamino) benzoquinones shift cathodically roughly in direct proportion to the hyperfine splitting constant of the semiquinone amine nitrogen. There are two principal trends: the compounds lacking substituents in the 3 and 6 positions fall on a line of slope −200 mV/G, and the ortho-disubstituted aminoquinones fall on a higher line with a somewhat shallower slope. It appears that the splitting constant of the semiquinone amine nitrogen is a measure of the ability of the nitrogen to donate electrons to the ring by resonance. Inductive and resonant effects of other groups must be considered, however, and those compounds with 3 and 6 position substituents must again be treated separately.

Table II. ^1H and ^{14}N hyperfine splitting constants of semiquinone, aminosemiquinone, and thioethersemiquinone radical anions

All spectra observed at approximately 3350 gauss, all splitting constants in gauss, listed without sign.

No.	HH a(ring)	$H(CH)_3$ a(ring)	H a_α	N a	H aNH	H $a$other	Line width (mg)	Spectrum width	*p*H	% $CHCl_3$	*E* cell *vs.* SCE
4	0.77		3.47	3.00	2.20		85	38.7	11	25	−1.00
5	0.77		3.46	3.02	2.30		200	32.0	11	5	−0.83
6	0.80		3.17	3.17	2.35[b]		400	31.78	11	5	−0.81
	0.775		3.20	3.25	2.36	0.1[c,d]	280	32.12	13	2	−0.80
7	0.77		2.31	3.08	2.31		200	23.08	11	10	−1.0
8[a]	0.8		2.3	3.1	2.3		500	23.08	10	25	−1.5
9	0.76		—	2.982	2.44	0.05[c,e]	350	18.33	11	20	−1.2
	0.777		—	3.05	2.55	0.05[c,e]	350	18.83	13	2	−0.8
10	0.79		2.83	2.82	2.10	0.05-0.1[c,e]	200	28.36	11	10	−1.2
11	0.6-0.7		0	2.95	2.35		120	16.95	13	0	−1.2
12	0.1		1.5	1.8			800	14.1	13	5	−0.60
20[a]		0.15	0.87	1.748	0.87		350	10.49	13	25	−1.10
21		0	0.27	1.60	0.87		150	8.70	11	10	−1.2
22			1.00	2.70	1.62	0	220	16.05	13	5	−1.4

[a] Poorly resolved.
[b] Confirmed by deuteration.
[c] Estimated by line broadening.
[d] γ-Proton.
[e] β-Proton.
[f] Electrolysis potential.

Allylamine would be expected to be a superior electron donor, and the $E_{1/2}$ of compound **10** does appear more cathodic than the main line. It may be seen in Table II that 2,5-bis(N-glycyl) benzoquinone, **11**, was anomalous in having no measurable α-proton splitting constant. Whether this lack of delocalization accounts for the position of **11** anodic of the trend is difficult to say. The inductive effect of a carboxylate anion ought in any case to be electron releasing rather than withdrawing. It also may be that compounds **12**, **20**, and **21** are set apart from the rest due to steric hindrance of their substituents which may force a nonplanar configuration of the radical and a lowering of a^N.

The ortho-substituted aminohydroquinones are stronger reductants than would be predicted from resonant electron release alone, as judged from a^N. This may be due in part to a decrease in steric repulsion when the rigidly planar hydroquinone is converted to the slightly more flexible cross-conjugated quinone. Probably more important is the increased ability of the nitrogens to donate electrons inductively when the net positive charge on the nitrogen due to conjugative electron release is lessened.

At the present level of precision, there is not a significant correlation between $E_{1/2}$ and a^{H}_{α} or a^{H}_{ring}. Because a^{H}_{NH} is approximately proportional to a^N, much the same correlation with $E_{1/2}$ is found with either.

Table III is a compilation of half-wave potentials as a function of substituents and pH. The cathodic shift upon thioether substitution is only 100-280 mV. The typical bis (alkylthio) quinone is then comparable in oxidizing strength to 2,5-dimethyl benzoquinone (compound **1**) and is actually stronger than 2,5-diethyoxy-benzoquinone (15). This indicates that electron release by the formation of π bonds involving sulfur is of less consequence than π bonding between an etheral oxygen and the quinone ring. This is supported by the facts that the ring proton hyperfine splitting constants of 2,5-dialkoxysemiquinones are smaller, and the α-proton splittings larger, than the corresponding 2,5-bis (alkylthio) benzoquinone (16).

It is apparent from Table III that the $E_{1/2}$ of a representative 2,5-bis(alkylamino)benzoquinone is 500 mV more cathodic at pH 11 than the $E_{1/2}$ of 2,5-dimethylbenzoquinone, **1**. Eleven or 12 kcal worth of electron release by the amino substituent (per mole) bespeaks very extensive conjugation of the nitrogen to the ring, as predicted from the substantial nitrogen hyperfine splitting constants.

Linear free-energy relationships in monoaminoquinones and monoamino-p-phenylenediamines have been developed with fair success (17). Those diamino- and dihydroxy-compounds which have been studied, however, generally show nonadditivity of Hammett or Taft parameters, which has been attributed to various ortho effects. Whereas nonadditivity of $E_{1/2}$ shifts upon multiple methyl- or chloro-substitution are manifested in a decreasing effect per substituent as the number of substituents increases, two nitrogen or oxygen substituents oriented para to each other may give more than twice the shift of a single substituent.

We observe such an instance in 2-isopropylamino-5-t-butylbenzoquinone, **26**, whose $E_{1/2}$ at pH 11 is 157 mV more cathodic than t-butylbenzoquinone, **24**, but 252 mV more anodic than 2,5-bis(isopropylamino)-benzoquinone. The comparison is not quite straightforward, because of the loss of inductive electron release by the t-butyl group, but the inference seems safe that two isopropylamino groups oriented para to one another are each more electron releasing than a single isopropylamino group para to a t-butyl. Rather than a peculiarity of the ortho relationship between carbonyl and amine, this would be better described as a "para effect," due to the increased resonant interaction between the two amine groups. The EPR spectrum of the monoaminoquinone, **26**, shows an a^N of 2.05G, very significantly smaller than the a^N of 3.08G found in the bis(amino)quinone, **7**. Rather than the second amine group pirating spin from the first, the two interact synergistically to increase their spin densities at the expense of the rest of the molecule. Such a large increase in a^N in the face of an increase from one nitrogen to two predicts a large cathodic shift in $E_{1/2}$ according to Fig. 1, which is exactly what is found.

The most serious impediment to comparison of quinone, aminoquinone, and quinone thioether half-wave potentials is the difference in pH dependence shown in Fig. 2. In the reduction $Q + ne^- + p(H^+) \rightarrow QH_p^{(p-n)+}$, the formal potential will shift cathodic by 59 p/n mV per pH unit at 25°C (18). Quinones and hydroquinones are very weak acids and bases

Table III. Polarographic half-wave potentials of quinones, aminoquinones, and quinone thioethers at pH 5, 8, and 11

pH buffer is 0.2*M* acetate, pH 8 buffer is 0.2*M* tris(hydroxymethyl)-aminomethane, pH 11 buffer is 0.2*M* glycinate. All buffers are 0.20*M* $NaClO_4$ in 50% ethanol. The reference electrode is a saturated calomel electrode.

Compound No.	$E_{1/2}$ pH 5	pH 8	pH 11
1			−0.267
2	−0.010		−0.445
3		−0.50	−1.03
4			−0.762
5		−0.56	−0.751
6		−0.56	−0.780
7	−0.318	−0.574	−0.790
8		−0.60	−0.755
9			−0.728
10			−0.746
11	−0.32		−0.67
12	−0.127	−0.345	−0.628
13			−0.295
14	+0.005		
15		−0.29	
16	+0.055	−0.120	−0.293
17	−0.12		
18	+0.064		
19			−0.462
20			−0.678
21		−0.485	−0.688
22			−0.788
23			−0.279
24			−0.381
25			−0.11
26			−0.538

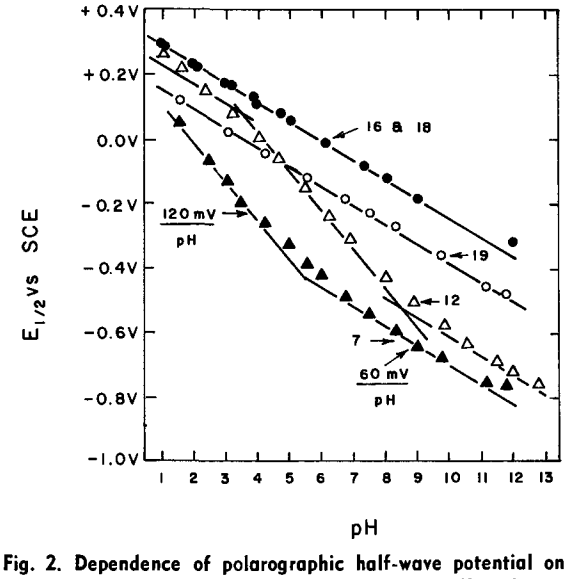

Fig. 2. Dependence of polarographic half-wave potential on pH for 2,5-bis(isopropylthio)benzoquinone (**16**), 2,4-bis(2-carboxyethylthio)benzoquinone (**18**), tetramethylbenzoquinone (**19**), 2,5-bis(1-piperidinyl)benzoquinone (**12**), and 2,4-bis(isopropylamino)benzoquinone (**7**). Glycine, citrate, imidazole, and tris(hydroxymethyl)-aminomethane buffers, 50% ethanol, 0.50M $NaClO_4$. 25° ± 2°C. The interpolated lines are of either 60 mV/pH or 120 mV/pH slope; the fit to the experimental points of compound **12** is arbitrary.

(although semiquinones are not) (19), and both species are generally neutral from pH 1 to about pH 10-13. Since both p and n equal 2, the plot of $E_{1/2}$ *vs.* pH is a straight line with slope 59 mV/pH. Duroquinone, bis(isopropylthio)-benzoquinone and bis(carboxyethylthio)benzoquinone live up to this expectation admirably. Bis(isopropylamino) benzoquinone, however, shows a region of 120 mV slope, a region of about 60 mV slope, and the curve shows signs of leveling off as the pH exceeds 11. A 120 mV slope means the consumption of four protons during the reduction, so the product must be the diprotonated hydroquinone. The intersection of the extrapolated 60 and 120 mV regions lies between pH 5.5 and 6, so the first two pK_a's of this diprotonated hydroquinone must lie near 5.5 or 6. Lack of protonation of the nitrogen of the quinone form at low pH's may be due to their amide character (8).

The $E_{1/2}$ of bis(1-piperidyl)benzoquinone, **12**, shifts with varying slopes as the pH is changed. There is a variety of excuses for such behavior in systems which are irreversible, proceed by complex mechanisms, or involve species highly charged and therefore liable to "double-layer effects," but that is not the case at hand. If the mechanism is single step, and n is 2, the implication that $p = 3$ or 4 is inescapable. It would come as quite a surprise that 2,5-bis(1-piperidyl)-hydroquinone would be a strong enough base to be protonated at pH 8 or above. Even at high pH's the semiquinones appear to be too unstable to effect these results.

It does not seem plausible to attribute the strange acid-base behavior of **12** to the effects of adsorption at the electrode surface; dialkyl- and tetra-alkylbenzoquinones apear to be even more strongly adsorbed (20), and the $E_{1/2}$ *vs.* pH diagram of duroquinone **19** is normal. To insure that the readings were not influenced by changes in junction potentials, duroquinone was present in solution with the aminoquinones as a "chaperon" and its $E_{1/2}$ was checked against previously determined values at each pH.

Measurement of heterogeneous electron transfer rates.—Substituent effects on electrochemical thermodynamics are well documented (13, 17) but the effects of substituents on electrochemical kinetics through stabilization of the transition state are much less understood. The suspicion that the electronic structures of free radicals should bear strong analogies to the electronic structures of excited states prompted us to search the semiquinone ESR spectra for clues to elucidating the dependence of aminoquinone electrode kinetics on structure.

There were several difficulties in obtaining kinetic data. Radical anions could be studied only in basic solution so it seemed fitting to study electrode kinetics in basic solution as well. However, most of the quinones decompose in basic solution and thus cause problems with kinetic studies. For this reason heterogeneous rate constants were measured at pH 8 where the quinones were found to be stable. The solutions contained 1% chloroform. Adsorption at the electrode surface also rendered attempts to measure $k_{s,h}$ invalid for a number of compounds so that electrode kinetics could be accurately measured only for seven different quinones.

Of the many techniques for measuring electrode kinetics, cyclic voltammetry was selected because it is applicable to a wide range of rate constants (12, 21), problems with adsorption are immediately apparent from the experimental data (22), and diagnostic criteria exist for multistep electrode mechanisms, with or without homogeneous complications (21, 22).

If the scan rate is sufficiently slow, the electron transfer process will be rapid compared to the time scale of the experiment and "reversible" behavior will be observed. As the scan rate increases, the assumption of reversibility fails and the peak separation increases beyond $57/n$ mV. Nicholson has published solutions to equations describing the dependence of peak potential on electrode kinetics, scan rate, *etc.* (12). Nicholson's derivation assumes that $\alpha = 0.50$. Fortunately, the calculation is very insensitive to α and the experimenter need satisfy himself only that α is between 0.3 and 0.7. For compounds **7** and **9** we obtained values of α between 0.4 and 0.6 which are sufficiently close to 0.5 to justify using Nicholson's Table (12). The α values were measured from a plot of the logarithm of the peak current *vs.* the peak separation (21).

It should be remembered that Nicholson's solution is for a single-step process and is not explicitly applicable to quinone systems since two electron transfers and two protonations are involved. If, however, the activation energies for the rate-controlling steps for the forward and reverse processes are the same, it ought to be possible to use the single-step model. This work rests on this assumption and thus the rate constants reported are to be considered apparent ones, recognizing that other factors beside electron transfer rates may influence the peak separation.

At the hanging mercury drop electrode, it was possible to obtain meaningful heterogeneous rate constants ($k_{s,h}$) at pH 8 (50% ethanol) for six bis(alkylamino)benzoquinones and for 2,5-bis(isopropylamino)-3,6-dimethylbenzoquinone. The measured rates at 25°C were:

Compound	$k_{s,h}$, cm sec^{-1}
4	0.32
5	0.24
6	0.13
7	0.011
9	0.035
10	0.32
21	0.0030

These values were for the first scan at a fresh drop. At high scan rates, the inability to compensate completely for ohmic potential drops causes the cyclic voltammogram to be distorted and the peak separation to become large regardless of the rate constant of the couple under study. The so-called "uncompensated resistance" was electronically corrected for by means of positive feedback (10). The feedback was adjusted by increasing it just to the point of oscillation and then reducing it by the equivalent of 1 ohm. Full compensation within an ohm or two was achieved up to scan rates of about 500 V/sec. No quantitative data were collected above this rate. On the other hand, rate constants can be calculated only when the scan rate is fast enough to cause a peak separation measurably larger than the reversible 30 mV, which required scan rates of about 50 V/sec for compound **4**. The larger rate constants could be measured only over a single decade of scan rates and the precision of the $k_{s,h}$ values above 0.1 cm sec^{-1} is about 20%. Smaller rate constants are precise to about 10%.

Some of the rate constants could also be measured at pH 11 (50% ethanol) and were not greatly different from those at pH 8. The $k_{s,h}$'s for **4** and **10** were about 0.3 cm sec^{-1} and the $k_{s,h}$ for **21** remained about 3×10^{-3} cm sec^{-1}.

Correlations between $k_{s,h}$ *and structure.*—Hyperfine splitting constants are a measure of spin densities at the nuclei in question, which are a function of the electronic energy levels of the radicals' diamagnetic precursers; hfs constants in radicals should therefore give some information about reactivity and kinetics of diamagnetic molecules. Latta and Taft (23) used hfs constants of N,N-dimethylaniline cation radicals to calculate Tafy σ-parameters for various substituents, which could then be applied to kinetic and thermodynamic linear free-energy relationships. Poole and Griffith (24) found a better correlation between re-

activity toward nitration at various sites in phenanthrene and hfs constants of protons at those positions in the phenanthrene radical than any reactive index calculated from molecular orbital considerations. The logarithm of the homogeneous rate constant for nitration at a particular position varied linearly with proton hfs constant at that position over nearly a decade of rate constants.

Peover and Powell (25) have published the only known direct correlation between hfs constants and electrode kinetics. The logarithms of the standard rate constants for the one-electron reduction of ten nitrated hydrocarbons in DMF varied linearly with the nitrogen hyperfine splitting constants in the same solvent. As the absolute value of $a^{N_{NO_2}}$ increased, log $k_{s,h}$ increased. On the assumption that charge distribution in radical anions parallels spin distribution, this behavior is explained in terms of the influence of excess charge at the nitro group on the solvation energy of the radical anion. The more the odd electron is localized on the nitro-group, the higher the energy of the transition state and the slower the reaction.

The linear dependence of log $k_{s,h}$ on the hyperfine splitting constant of the α-protons is shown in Fig. 3. Various other correlations were attempted but this proved to be the only fit. Compounds **4**, **5**, **6**, and **7** form an homologous series and are used to define the straight line. Compound **9** has no α-protons and thus cannot be plotted on Fig. 3 but its rate constant is somewhat larger than **7**. Compound **10** has two vinyl groups not present in any other compound, so any conjugative influence on kinetics should be emphasized. Compound **21**, unlike the others in Fig. 3, is substituted in the 3 and 6 position. This evidently indicates **21** must be considered as belonging to a different series (see also Fig. 1).

That the logarithm of the standard rate constant increases monotonically and linearly with $a^H\alpha$, implies that the spin distribution in the radical is a measure of the substituent influences on the energy of the electrochemical transition state. This might be due to stabilization of the paramagnetic species by delocalization of the unpaired electron onto the carbons. Release or withdrawal of charge can also accompany hyperconjugation, and the resulting charge delocalization might lower the solvation energy of the transition state enough to increase the rate of electron transfer appreciably.

The free energy of the electrode process can be estimated from absolute reaction rate theory according to

$$k_{s,h} = \frac{kt}{h} p \exp(-\Delta G^*/RT)$$

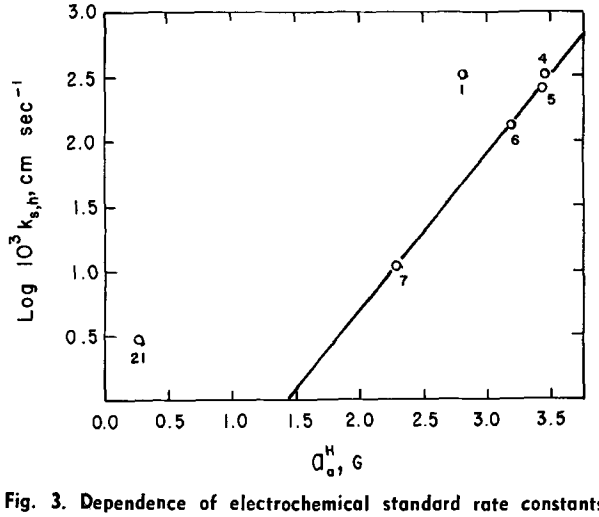

Fig. 3. Dependence of electrochemical standard rate constants for aminoquinones on aminosemiquinone α-proton hyperfine splitting constants. See text for definitions and explanation.

Where ΔG^* is the Gibbs free energy of activations of either the cathodic or anodic reaction at $E = E'_0$, and p is a parameter needed to correct the homogeneous collision number to heterogeneous units (26). In this equation, k is the Boltzmann constant, and h is Planck's constant. The magnitude of p is usually taken to be of the order of 10^{-8} cm, which implies a heterogeneous collision number of about 10^4 cm/sec (27). The ΔG^* for **21**, the slowest bis(alkylamino)-benzoquinone measured, is then around 8-9 kcal mole^{-1}. The semiquinone anions in solution are so unstable that it is hard to see how they could be of lower energy than the transition state and therefore be a candidate for a discrete intermediate. However, the energy of a paramagnetic species at the electrode surface could be substantially lowered by electron delocalization through overlap with the electrode (28). If the electrode mechanism were a simple two-electron transfer (and we have no evidence to the contrary for aminoquinones), acceptance of a single electron could occur at the high point on the reaction coordinate diagram. The transition state could thus have a structure analogous to that of the semiquinone anion without necessarily being at the same energy.

Acknowledgments

This investigation was supported by the National Science Foundation (GP-8565) and by the Cancer Association of Greater New Orleans.

Manuscript submitted Feb. 23, 1970; revised manuscript received *ca.* Aug. 28, 1970. This was Paper 312 presented at the Los Angeles Meeting of the Society, May 10-15, 1970.

Any discussion of this paper will appear in a Discussion Section to be published in the December 1971 JOURNAL.

REFERENCES

1. G. E. W. Wolstenholm and C. M. O'Conner, Editors, "Quinones in Electron Transport," Churchill, London (1961).
2. R. A. Morton, Editor, "Biochemistry of Quinones," Academic Press, London (1965).
3. F. E. Knock, "Anticancer Agents," C. C. Thomas, Springfield, Ill. (1967).
4. F. L. O'Brien and J. W. Olver, *Anal. Chem.*, **41**, 1810 (1969).
5. Y. Matsunaga and C. McDowell, *Can. J. Chem.*, **38**, 1167 (1960).
6. G. A. Russell, R. Konaka, E. T. Strom, W. C. Danen, K-Y. Chang, and G. J. Kaupp, *J. Am. Chem. Soc.*, **90**, 4646 (1968).
7. R. L. Hansen, *J. Org. Chem.*, **33**, 3968 (1968).
8. J. L. Huntington and D. G. Davis, *J. Mag. Reson.*, To be published.
9. O. Popovych and A. J. Dill, *Anal. Chem.*, **41**, 456 (1969).
10. J. L. Huntington and D. G. Davis, *Chem. Inst.*, **2**, 83 (1969).
11. J. L. Huntington, Ph.D. Dissertation, Louisiana State Univ. in New Orleans (1969).
12. R. S. Nicholson, *Anal. Chem.*, **37**, 1351 (1965).
13. O. Ryba, J. Pilar, and J. Petranek, *Coll. Czech. Chem. Comm.*, **33**, 26 (1968).
14. H. Berg and K. H. Konig, *Anal. Chim. Acta*, **18**, 140 (1968).
15. J. B. Conant and L. F. Fieser, *J. Am. Chem. Soc.*, **46**, 1858 (1924).
16. Y. Matsunaga and C. A. McDowell, *Can. J. Chem.*, **38**, 1158 (1960).
17. P. Zuman, "Substituent Effects in Organic Polarography," Chap. 8, Plenum Press, New York, (1967).
18. W. M. Clark, "Oxidation-Reduction Potentials of Organic Systems," Chap. 4, The Williams and Wilkins Co., Baltimore, Md. (1960).
19. Isao Yamazaki and L. H. Piette, *J. Am. Chem. Soc.*, **87**, 986 (1965).
20. W. Lorenz and U. Gaunitz, *Coll. Czech. Chem. Commun.*, **31**, 1389 (1966).
21. I. Shain and R. S. Nicholson, *Anal. Chem.*, **36**, 706 (1964).

22. R. H. Wopschall and I. Shain, *ibid.*, **39**, 1527 (1967).
23. B. M. Latta and R. W. Taft, *J. Am. Chem. Soc.*, **89**, 5172 (1967).
24. C. P. Poole, Jr., and O. F. Griffith, III, *J. Phys. Chem.*, **71**, 3672 (1967).
25. M. E. Peover and J. S. Powell, *J. Electroanal. Chem.*, **20**, 427 (1969).
26. P. Delahay, "New Instrumental Methods in Electrochemistry," p. 42, Interscience, New York (1954).
27. R. A. Marcus, *Disc. Faraday Soc.*, **45**, 7 (1968).
28. R. A. Marcus, *J. Phys. Chem.*, **67**, 853 (1963).

Polarographic Estimation of Ion-Solvent Interaction of the Alkali Metal Ions in Water and Other Solvents

John Broadhead and Philip J. Elving*

The University of Michigan, Ann Arbor, Michigan 48104

ABSTRACT

The half-wave potentials and diffusion current constants of all five of the alkali metal ions have been measured for the first time in wholly aqueous solution in a related series of experiments. A significant relationship has been shown to exist between the diffusion current constant and the Jones-Dole *B* value for each ion, where the *B* value is a measure of the solvent structure-making properties of the ion. The half-wave potential and diffusion current constant data for the alkali metal ions in water and thirteen other solvents are compared, together with other pertinent data where available, *e.g.*, heterogeneous rate constants and spectroscopic measurements; the relative half-wave potentials are best interpreted on the basis of ion-solvent interaction. Such comparison of the electrochemical data illuminates the nature of the electrode processes involved and allows postulation of the forms of the ion-solvent complex for the different solvents.

Despite the common occurrence of the alkali metal ions and their general analytical importance, the polarographic parameters in wholly aqueous media have never been measured for all of the ions in a single study. The scarcity of data for aqueous solutions has resulted in use being made, when comparing data in different solvent media, of "aqueous" data obtained in water-organic solvent mixtures. In connection with the present comparative study of the polarographic behavior of the alkali metal ions, all of them were examined in aqueous solution.

A recent comparison (1) on the rubidium scale (2, 3) of the half-wave potentials of the alkali metal ions in pyridine showed that the reduction of lithium(I) occurs at considerably more negative potential than that of other members of the series; further, the electrochemical data (polarography, cyclic voltammetry, coulometry) generally demonstrated the complicated nature of the Li(I) reduction. In the present study, analogous approaches, including consideration of kinetic and spectroscopic data, are used to analyze the voltammetric data for water and thirteen other solvents in order better to correlate the mechanistic reduction paths as reflected in the potential data. In particular, it is shown that the half-wave potentials of the alkali metal cations in different solvents are best compared on the basis of ion-solvent interactions. For example, a provocative linear relationship was found for the alkali metal cations in water between the diffusion current constant and the *B* term of the Jones-Dole equation (4), which is a measure of solvent structure making and breaking properties of the ion.

Experimental

Reagents.—Reagents were prepared as previously described (1).

Apparatus.—The instrumentation and cell have been described (1). The reference electrode was a calomel electrode with 0.1*M* tetraethylammonium chloride substituted for 0.1*M* KCl. A 0.1*M* tetraethylammonium perchlorate (TEAP)/agar plug and glass frit separated the reference and working compartments. The Sargent S-29417 mercury capillary used (mercury head = 54.1 cm) gave dropping mercury electrode (DME) capillary constants on open circuit in 0.1*M* TEAP of $t = 5.20$ sec and $m = 1.21$ mg sec^{-1}.

Procedure.—All test solutions were prepared by dissolving TEAP and electroactive species in the requisite quantity of water. The solution in the polarographic cell was deoxygenated with argon and a stream of argon was passed over the solution during experiments. Mean diffusion currents were determined by measuring the distance from the mid-point of the current oscillations on the plateau to the background current. Drop-times were measured at the same potential as that used for current measurement. Cyclic voltammograms were recorded on a hanging mercury drop electrode (HMDE) formed by collecting two mercury drops from the polarographic capillary.

Results.—The alkali metal ions gave well-defined polarograms in water, which did not exhibit maxima or abnormalities (*cf.* Fig. 1 and 2). Table I summarizes the polarographic results for aqueous solutions of the alkali metal ions.

All of the alkali metal ions exhibited redox couples on cyclic voltammetry. The peak potential separations for Na(I) through Cs(I) are essentially the same; for K(I), it is typically 0.37V (0.23V, when corrected for background current). However, Li(I) shows an anodic peak only when lithium is accumulated in the HMDE by holding the potential at −2.64V for 10 sec. These results are in accord with the work of Imai and Delahay (5) who found heterogeneous rate constants for the alkali metal ions in the range of (2 to 9) x 10^{-3} cm sec^{-1}, when corrected for double layer effects.

Comparative Polarographic Data

The excellent review by Takahashi (6) provides a useful starting point for the collation of the polarographic data on inorganic ions in nonaqueous solvents

* Electrochemical Society Active Member.

Key words: alkali metal ions, cesium, ion-solvent interaction, lithium, nonaqueous solvents, polarography in nonaqueous solvents, potassium, potential dependence on solvent, rubidium, sodium, solvation of alkali metal ions, solvents.

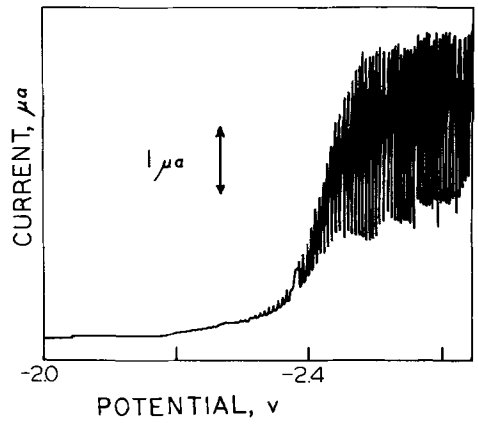

Fig. 1. D-C polarogram at the DME of 1.06 mM Li(I) in aqueous 0.1M TEAP solution.

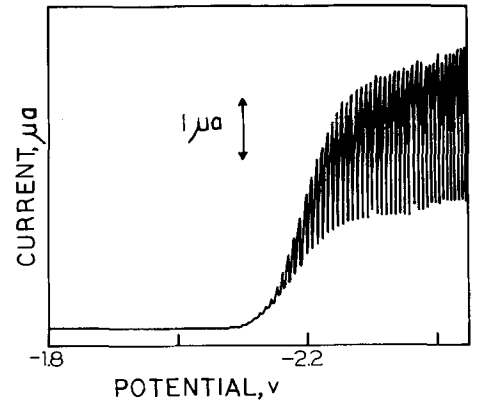

Fig. 2. D-C polarogram at the DME of 0.93 mM Na(I) in aqueous 0.1M TEAP solution.

available up to 1965. Several bases have been used in correlating the potential data. Thus, the half-wave potentials of the alkali metal ions in different solvents have been compared with the donor numbers of these solvents (7, 8); however, this type of comparison is arbitrary and severely limited by the lack of donor number values. Comparisons have also been based on the variation in dielectric constant of the solvents (9, 10). Since the dielectric constant is a macroscopic manifestation of a microscopic property, it is considered more meaningful to correlate half-wave potentials with the structural characteristics of the solvent, which affect the state of the ion in solution.

Table I. Polarographic data for the alkali metal ions in water (0.1M TEAP) at 25°

Ion[a]	$-E_{1/2}$,[b] V	I[c]	Wave slope[d]
Li(I)	2.41 ± 0.01	1.8 ± 0.1	47
Na(I)	2.20 ± 0.01	2.2 ± 0.1	53
K(I)	2.22 ± 0.01	2.6 ± 0.1	55
Rb(I)	2.22 ± 0.01	2.8 ± 0.1	50
Cs(I)	2.19 ± 0.01	3.3 ± 0.1	48

[a] The ionic concentration range is 0.1 to 2.0 mM.
[b] Data given represent the mean and average deviation of eight to twelve measurements at 25°C. The reference electrode is described in the text.
[c] Diffusion current constant, I = μA mM^{-1} $mg^{-2/3}$ $sec^{1/2}$.
[d] Calculated from relation, $E_{1/4} - E_{3/4}$ = slope.

Potential variation.—Table II summarizes the $E_{1/2}$ data for the alkali metal ions in fourteen solvents on the rubidium scale of potential (2, 3). The solvents are arranged in order of negativity of the lithium $E_{1/2}$ because this ion shows the greatest characteristic interaction with the solvent. [In the similar comparison by Gutmann *et al.* (7), the references to polarographic measurements in water, acetonitrile, and benzonitrile should include the work of Coetzee *et al.* (11).] In connection with Table II, it should be noted that some degree of irreversibility is shown by Li(I) in dimethylsulfoxide, dimethylacetamide, dimethylformamide [via ref. (20) but not according to ref. (10)], pyridine, water, isobutyronitrile, propylene carbonate, sulfolane, and acetonitrile. Cs(I) shows some indication of irreversibility in isobutyronitrile.

The polarographic reduction of lithium(I) in dimethylsulfoxide (DMSO) (12, 13) and dimethylacetamide (DMA) is difficult, *i.e.*, $\Delta E_{1/2}$ is large and negative [the data in ref. (13) only give values of $E_{1/2}$ for Li(I), Na(I), and K(I); the values of $\Delta E_{1/2}$ on the K(I) scale agree to within 30 mV with those in ref. (12)]. In truly anhydrous DMA, Li(I) is irreducible; reduction only occurs when 3% of water is present (14). In anhydrous DMSO, the Li(I) reduction is slow; the heterogeneous rate constant is of the order of 3 x 10^{-5} cm sec^{-1} (15).

In ethylenediamine (EDA) (16), dimethylformamide (DMF) (10, 13, 17), and pyridine (1), Li(I) is reduced at less negative potentials than in DMSO or DMA [the data on DMF in ref. (17) agree with those of ref. (10) to within 20 mV, but there is disagreement between ref. (10) and (13); data in Table II are taken from ref. (14)].

In water (no organic solvent present), the polarographic reduction of Li(I) appears reversible (18) with a $\Delta E_{1/2}$ of −0.19V, but cyclic voltammetry at the

Table II. Polarographic half-wave potentials of the alkali metal ions compared to rubidium ($\Delta E_{1/2}$) in various solvents[a]

Solvent:[b]	DMSO	DMA	EDA	DMF	Pyr	H_2O	Morph
ϵ:	46.7	37.8	12.9	36.7	12.3	78.5	7.3
Reference:	(12)	(14)	(16)	(10)	(1)	(18)	(19)
Li(I)	−0.39	−0.34	−0.30	−0.29	−0.26	−0.19	−0.13
Na(I)	−0.01	−0.02	0.14	−0.01	0.02	0.02	0.01
K(I)	−0.05	−0.04	0.11	−0.03	0.00	0.00	0.01
Rb(I)	0.00	0.00	0.00	0.00	0.00	0.00	0.00
Cs(I)	0.03	0.01	−0.04	−0.01	0.02	0.03	—

Solvent:	IBN	PC	Sulf[c]	PN	CH_3CN	BN	PAN
ϵ:	20.4 (24°)	69	43.2 (30°)	27.2	37.5	25.2	18.7
Reference:	(21)	(22)	(25)	(26)	(27)	(26)	(26)
Li(I)	−0.11 (−0.13)[d]	−0.02	0.00	0.01 (−0.10)[d]	0.03 (−0.10)[d]	0.06 (−0.08)[d]	0.06 (−0.06)[d]
Na(I)	0.02	0.01	0.11	0.11	0.13	0.14	0.12
K(I)	0.02	0.13	0.01	—	0.02	—	—
Rb(I)	0.00	0.00	0.00	0.00	0.00	0.00	0.00
Cs(I)	−0.01	0.00	0.01	—	0.01	—	—

[a] $\Delta E_{1/2}$ = ($E_{1/2}$ for ion) − ($E_{1/2}$ for Rb(I)). Dashes indicate data are not available.
[b] Solvents: DMSO, dimethylsulfoxide; DMA, dimethylacetamide; EDA, N,N'-ethylenediamine; DMF, N,N'-dimethylformamide; Pyr, pyridine; Morph, morpholine; IBN, isobutyronitrile, PC, propylene carbonate; Sulf, sulfolane; PN, propionitrile; BN, benzonitrile; PAN, phenylacetonitrile. The reference for the data on the particular solvent is given in parentheses underneath the dielectric constant, ϵ.
[c] Data recorded at 30°C.
[d] $\Delta E_{1/2}$ calculated on the Na(I) scale.

HMDE does not show a cyclic couple. An anodic Li(0) oxidation wave is only observed when Li(0) is accumulated in the mercury drop before the reverse sweep to positive potential is started, *i.e.*, it is seen only by stripping voltammetry.

The Li(I) reduction in morpholine (19) occurs at a relatively small $\Delta E_{1/2}$ (*cf.* pyridine).

Before considering the nitrile solvents, the Rb(I) half-wave potentials in these solvents should be examined. Since the solubility of rubidium perchlorate in nitrile solvents is extremely low, Coetzee *et al.* (11) measured the $E_{1/2}$ of rubidium iodide in tetrabutylammonium iodide solutions of these solvents and attempted to correct the measured potentials to "hypothetical" $RbClO_4$ values in tetraethylammonium perchlorate solution. The latter calculation involved estimation of the change in ion association from a study of the anion effect on the "comparable" Na(I) system and estimation or neglect of the change in liquid junction potential. The correction often shifted the Rb(I) potentials by as much as 100 mV. Because of the assumptions and approximations involved in this approach, it is proposed that a secondary reference potential be used. McMasters *et al.* (20) have used the Na(I) as a pilot reference ion. Although this ion may not be quite as "ideal" as Rb(I), the data in Table II for DMSO through morpholine indicate that had a Na(I) $E_{1/2}$ reference been used, the Li(I) potentials would be shifted by 20 mV or less (with the notable exception of EDA). Upon this basis, another $\Delta E_{1/2}$, based on Na(I), has been calculated for Li(I); these values, enclosed in parentheses, are also shown in Table II.

On the basis of the Na(I) standard, isobutyronitrile (21) has a $\Delta E_{1/2}$ for Li(I) similar to that of morpholine. Propylene carbonate (PC) (22) and sulfolane (Sulf) (23-25), however, would be reordered to follow the nitriles in the potential series. Li(I) is polarographically reduced at the same potential in propionitrile (26) and acetonitrile (27) and at less negative potentials in benzonitrile (26) and phenylacetonitrile (26).

Current magnitudes.—Diffusion current constant (I) data for the alkali metal ions in several of the solvents are summarized in Table III; the values of $I\eta^{1/2}$ in the table compensate for the different solvent viscosities. Because the I values are proportional to $D^{1/2}$, the corrected I data are, therefore, diagnostic of the size of the diffusing species and, together with the $\Delta E_{1/2}$ values, can be used to examine the nature of the ion-solvent complex.

Discussion

Review of the relative half-wave potentials of the alkali metal ions shows, as already mentioned, that only in the case of Li(I) does $\Delta E_{1/2}$ vary significantly from one solvent to another; EDA is probably the only exception to this generalization. Consequently, the subsequent discussion is mainly concerned with the variation in nature of the Li(I) solvation. Where supplementary spectroscopic or thermodynamic data are not available, there is some speculation concerning the nature of the Li(I)-solvent bond.

Dimethylsulfoxide.—Although cyclic voltammetric data are not available for the reduction of Li(I) in DMSO, the $\Delta E_{1/2}$ of −0.39V suggests a strong association between solvent and Li(I), which strong interaction is confirmed by NMR and thermodynamic studies (28-30); the relatively small heterogeneous rate constant of 3×10^{-5} cm sec^{-1}, observed for Li(I) reduction in DMSO (15), also suggests a strong solvent-solute linkage. However, recent data on diffusion current constants (13) disagree with the preceding; the relatively large values of I reported would indicate the presence of a small (relatively unsolvated) diffusing species. Further consideration of these I values is included with the DMF discussion. If the solvation bonding is between Li(I) and the oxygen of DMSO, the methyl groups of the latter will be outermost in the solvation shell and reduction of either the complex or the Li(I) through an electron bridge formed by the solvent molecules would be difficult because of the nonpolar nature of the methyl groups.

Dimethylacetamide.—In anhydrous DMA, the solvation of Li(I) is such that the complex entity is irreducible. If complexation is due to bonding between the nitrogen and Li(I), an array of methyl groups will be present on the outside of the solvation species forming an even more complete sheath of methyl groups than with the DMSO-Li(I) complex. Furthermore, I for the reduction of Li(I) (unfortunately in a 3% water-DMA mixture) indicates a bulky diffusing species. In a 3% H_2O-DMA solution (1.6*M* H_2O), hydrolysis of an amide group in the lithium solvation sheath may occur via hydrolytic attack of the C-N bond, which is weakened by the close proximity of the Li(I) ion. This process would momentarily leave the Li(I) entity open to reductive attack and would explain the formation of the lithium amalgam claimed by Gutmann *et al.* (14).

Ethylenediamine.—EDA is the only solvent in which there is a significant variation in $\Delta E_{1/2}$ for all of the alkali metals. This separation in potential may be due to the selective chelating property of this solvent. Na(I) and K(I) are probably chelating by the normal mechanism, thus promoting reduction via a $-NH_2$ bridging group. Li(I), however, being a small ion, may not form a stable chelate and may only solvate with EDA in an end-on position, leaving a less favorable path for electron transfer via a N-C-C-N bridge. Such end-on or monodendate complexation has been observed in the complexes of Ag(I) with EDA (31, 32). Cs(I) and Rb(I) probably do not form either type of complex and are not solvated to any appreciable extent.

Table III. Polarographic diffusion current constants for the alkali metal ions[a]

Solvent:[b]	DMSO	DMA	DMF	DMF	Pyr[c]	H_2O	IBN	PC	Sulf[d]	CH_3CN
η:	1.96	0.92	0.796	0.796	0.945 (20°)	0.8937		3.37[e]	10.29 (30°)	0.345
Reference:	(13)	(14)	(10)	(13)	(1)	(18)	(21)	(22)	(25)	(27)
Li(I)	1.61	0.95	1.09	1.92	1.29	1.8	1.83	0.97	0.78	2.56
	(2.25)	(0.91)	(0.97)	(1.71)	(1.2)	(1.7)		(1.78)	(2.50)	(1.50)
Na(I)	1.42	1.28	1.61	1.80	1.57	2.2	1.98	1.09	0.72	3.22
	(1.99)	(1.23)	(1.44)	(1.61)	(1.4)	(2.1)		(2.01)	(2.31)	(1.89)
K(I)	1.42	1.43	1.63	1.78	1.51	2.6	—	1.32	0.79	3.25
	(1.99)	(1.37)	(1.45)	(1.58)	(1.4)	(2.5)		(2.43)	(2.54)	(1.98)
Rb(I)	1.43	1.53	1.68	1.80	1.56	2.8	—	1.30	0.80	3.25
	(2.00)	(1.47)	(1.50)	(1.61)	(1.4)	(2.7)		(2.39)	(2.57)	(1.91)
Cs(I)	—	1.56	1.98	—	1.44	3.3	—	1.26	0.82	—
		(1.50)	(1.77)		(1.3)	(3.1)		(2.32)	(2.63)	

[a] Data in parentheses are for $I\eta^{1/2}$: product of the diffusion current constant and the square root of the viscosity. The diffusion current constant is in units of $\mu A\ mM^{-1}\ mg^{-2/3}\ sec^{1/2}$; the viscosity is in centipoise.
[b] Solvent abbreviations are given in Table I.
[c] $I\eta^{1/2}$ values are quoted to two significant figures because the viscosity of pyridine is given for 20°C. For the calculation, a "25°C" value of η was used by assuming a 2% per degree temperature coefficient.
[d] Data for 30°C; I values are calculated from current values at maximum drop size.
[e] Recently, the viscosity of propylene carbonate has been reported (41) to be 2.48 centipoise. Use of this value would change the $I\eta^{1/2}$ products for this solvent by 0.86.

Dimethylformamide.—The $\Delta E_{1/2}$ and I values for DMF given by Brown *et al.* (10) and Headridge *et al.* (17) and the $\Delta E_{1/2}$ values of Humar and Pantony (13) are consistent; there is solvation of Li(I). The latter (13), however, report very large I values which are in poor agreement with the other data; the discrepancy may lie in the method of measurement of the diffusion current. The solvation complex, which is probably formed between the nitrogen of DMF and Li(I), is not as resistant to reduction as the corresponding complex with DMA. This slightly enhanced activity may well be related to the presence of an H—C(=O)— group in the cluster of methyl groups. The diffusion current constant suggests that the complex is similar in bulk to the Li(I)-DMA entity.

Pyridine.—Li(I) forms a stable complex with pyridine (33) and there is strong evidence to suggest that electroreduction involves fission of a C-N bond in one of the pyridine molecules attached to the lithium ion (1). When small amounts of water are present, another process apparently is observed whereby a pyridine ring, which is hydrogen bonded through a water molecule to Li(I), also is opened by reductive fission, *e.g.*, two reduction peaks are observed when water is present.

Water.—Reduction of Li(I) in water proceeds to the amalgam, although cyclic voltammetry and stripping voltammetry indicate that the generation is not quantitative. However, the aquo solvation does not appear to hinder reduction to the degree observed with the previously discussed solvents. The faradaic rectification technique used by Imai and Delahay (5) shows a slightly lower corrected heterogeneous rate constant for the electroreduction of Li(I) than for the other alkali metal ions ($k^t_{Li(I)} = 0.002$; $k^t_{Na(I)} = 0.009$; $k^t_{K(I)} = 0.005$ cm sec^{-1}). Although there is little variation in $\Delta E_{1/2}$ for the other alkali metal ions in water, there is a marked trend in the corrected I values, which may well be linked to the abnormal structure of water. Because water is strongly hydrogen bonded with regions of crystalline regularity (ice-like and "quartz-like" structures), the solvation of an ion is much more long range in its effect, *i.e.*, the solvent structure well beyond the first solvation sheath has a measurable influence on the transport rate (34). Because of this long range influence, there is a much more pronounced degradation in solvation from Li(I) through Cs(I) in the case of water, as can be seen from the change in the B coefficient of the Jones-Dole equation (4), which describes the relative viscosity of an ionic solution in terms of the expansion

$$(\eta/\eta_0) = 1 + AC^{1/2} + BC \qquad [1]$$

where η is the viscosity of the salt solution of concentration C, η_0 is the viscosity of water, and A and B are coefficients. The B coefficient is a measure of the ion-solvent interaction and the solvent structure-making or structure-breaking properties of the ion; a large positive value [0.150 for Li(I)] indicates strong ion-solvent interaction and a negative value [−0.045 for Cs(I)] a weak interaction (structure-breaking).

The approximately linear relationship between diffusion current constant (related to diffusion coefficient), I, and B coefficient (Fig. 3) suggests that the variation in I is related to the characteristic change in viscosity of water and hence to the change in structural parameters of ionic aqueous solution. Indeed, it has been proposed that negative values of B indicate a negative solvation of the ionic species (35, 36). The individual I values for each metal ion in water are, however, all larger than the corresponding values in most other solvents. In addition to the structure-breaking properties of the large alkali metal cations, the abnormal proton jump and hydrogen bond exchange mechanisms in water effectively reduce the friction coefficient between ion and solvent below that for ion-nonaqueous systems.

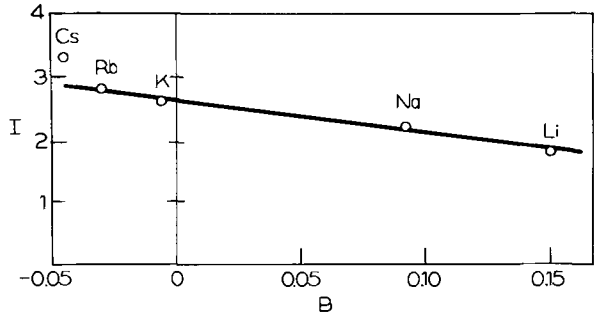

Fig. 3. Dependence of the diffusion current constant, *I*, for the alkali metal cations in aqueous solution on the Jones-Dole *B* coefficient (4). *I* is in μA mM^{-1} mg$^{-2/3}$ sec$^{1/2}$ and *B* is in l mole^{-1}.

The close agreement between Debye-Hückel theory and the solubilities of K(I), Rb(I), and Cs(I) perchlorates in aqueous solution over a range of ionic strength has been interpreted as indicating the virtual absence of ion-pairing (37).

Since factors other than ion solvation can influence the half-wave potential at mercury electrodes, *e.g.*, the free energies of amalgamation and of formation of the alkali metals, the values of such thermodynamic quantities are tabulated in Table IV for comparison with the polarographic data of Table I. The factors involved are discussed by Davies, Schwartz, Yeager, and Hovorka (38).

Morpholine.—In morpholine, the $\Delta E_{1/2}$ values are all very small or zero, except for Li(I), indicating that the lone pair of electrons on either the oxygen atom or the nitrogen atom of the molecule is sufficiently active for morpholine to solvate Li(I) strongly. The corrected I value for Li(I) confirms the bulkier nature of this species.

Nitriles.—The nitrile solvents are considered as a group because the —C≡N group appears to be the dominant influence in electrochemistry in these solvents. It is not clear whether donation from the solvent to the metal ion occurs from the π-bonds of the —C≡N linkage or from the lone pair on the nitrogen atom. However, the π-bonding electrons of the nitrile group form a relatively easy bridge for electroreduction of Li(I), especially in benzonitrile and phenylacetonitrile (least negative $\Delta E_{1/2}$ of the nitrile series), where the π-bonding of the benzene ring probably contributes to the electroreduction mechanism.

Propylene carbonate and sulfolane.—In PC and sulfolane, the small or zero $E_{1/2}$ for the reduction of Li(I) suggests that steric hinderance of solvent molecules prevents the strong solvation which is normally exhibited by this small ion. Of the data on sulfolane (23-25), only the work by Coetzee *et al.* (23) is quoted here since the other two investigations report measurements either at 40°C or at temperatures below the natural freezing point of the solvent. The large I values for Li(I) in both PC and sulfolane further support the

Table IV. Potential and thermodynamic data for alkali metal amalgams (38)

Ion	$-E_o$,[a] V	D_2[b] × 10^5, cm sec^{-1}	ΔH, kcal/mole	ΔG, kcal/mole	ΔS, eu
Li(I)	2.43	1.10	−19.8	-19.3_0	−1.7
	2.44[c]				
Na(I)	2.20	0.90	-19.9_7	-19.9_7	−8.3
K(I)	2.21	0.77	-26.5_1	-21.9_7	−15.2
Rb(I)	2.10[d]		−27.6	-21.8_9	−18.7
Cs(I)	2.11[e]	0.52	−38.6	−23.1	−53

[a] These potentials for the alkali metal amalgams were converted from values *vs.* NHE to values *vs.* SCE by adding 0.242V.
[b] Diffusion coefficient in the amalgam.
[c] From ref. (42).
[d] From ref. (43).
[e] *Vs.* mercuric oxide electrode.

notion that only small or negligible solvation occurs in these two inert solvents.

The presence of water in PC gives rise to a peak on cyclic voltammetry; a plot of the limiting value of $i_p/v^{1/2}$ *vs.* concentration of water yields a straight line from 50 to 600 ppm of water (39). The same workers showed that water can be determined chronopotentiometrically and inferred that an insoluble porous film of LiOH was formed over part of the electrode as a result of proton reduction. A similar effect was also noted by Dey (40).

Acknowledgment

The authors thank the National Science Foundation and the Petroleum Research Fund, which helped support the work described.

Manuscript submitted April 20, 1970; revised manuscript received *ca.* Aug. 20, 1970.

Any discussion of this paper will appear in a Discussion Section to be published in the December 1971 JOURNAL.

REFERENCES

1. J. Broadhead and P. J. Elving, *Anal. Chem.*, **41**, 1814 (1969).
2. V. A. Pleskov, *Usp. Khim.*, **16**, 254 (1947).
3. V. A. Pleskov, *Zh. Fiz. Khim.*, **22**, 351 (1948).
4. G. Jones and M. Dole, *J. Am. Chem. Soc.*, **51**, 2950 (1929).
5. H. Imai and P. Delahay, *J. Phys. Chem.*, **66**, 1683 (1962).
6. R. Takahashi, *Talanta*, **12**, 1211 (1965).
7. V. Gutmann, G. Peychal-Heiling, and M. Michlmayr, *Inorg. Nucl. Chem. Letters*, **3**, 501 (1967).
8. V. Gutmann, "Coordination Chemistry in Non-aqueous Solutions," pp. 33 *et seq.*, Springer-Verlag, New York (1968).
9. D. B. Bruss and T. De Vries, *J. Am. Chem. Soc.*, **78**, 733 (1956).
10. G. H. Brown and R. Al-Urfali, *ibid.*, **80**, 2113 (1958).
11. J. F. Coetzee, D. K. McGuire, and J. L. Hedrick, *J. Phys. Chem.*, **67**, 1814 (1963).
12. G. Schoeber and V. Gutmann, "Advances in Polarography," pp. 940 *et seq.*, I. S. Longmuir, Editor, Pergamon, London (1960).
13. G. P. Kumar and D. A. Pantony, *J. Polarog. Soc.*, **15**, 84 (1969).
14. V. Gutmann, M. Michlmayr, and G. Peychal-Heiling, *Anal. Chem.*, **40**, 619 (1968).
15. D. R. Cogley and J. N. Butler, *J. Phys. Chem.*, **72**, 4568 (1968).
16. W. B. Schaap, R. E. Beyer, J. R. Siefker, and F. C. Schmidt, "Advances in the Chemistry of Coordination Compounds," pp. 447 *et seq.*, Macmillan, New York (1961).
17. J. B. Headridge, M. Ashraf, and H. L. H. Dodds, *J. Electroanal. Chem.*, **16**, 116 (1968).
18. Data taken from measurements reported in this publication.
19. V. Gutmann and E. Nedbalek, *Monatsh. Chem.*, **88**, 320 (1957).
20. D. L. McMasters, R. B. Dunlap, J. R. Kuempel, L. W. Kreider, and T. R. Shearer, *Anal. Chem.*, **39**, 103 (1967).
21. J. F. Coetzee and J. L. Hedrick, *J. Phys. Chem.*, **67**, 221 (1963).
22. V. Gutmann, M. Kogelnig, and M. Michlmayr, *Monatsh. Chem.*, **99**, 693 (1968).
23. J. B. Headridge, D. Pletcher, and M. Callingham, *J. Chem. Soc.*, **1967**, 684.
24. J. Desbarres, P. Pichet, and R. L. Benoit, *Electrochim. Acta*, **13**, 1899 (1968).
25. J. F. Coetzee, J. M. Simon, and R. J. Bertozzi, *Anal. Chem.*, **41**, 766 (1969).
26. R. C. Larson and R. T. Iwamoto, *J. Am. Chem. Soc.*, **82**, 3239, 3526 (1960).
27. I. M. Kolthoff and J. F. Coetzee, *ibid.*, **79**, 870 (1957).
28. B. W. Maxey and A. I. Popov, *ibid.*, **90**, 4470 (1968).
29. B. W. Maxey and A. I. Popov, *ibid.*, **91**, 20 (1969).
30. M. Salomon, *This Journal*, **117**, 325 (1970).
31. P. Job, *Compt. Rend.*, **176**, 442 (1923).
32. P. Job, *ibid.*, **184**, 1066 (1927).
33. W. K. Thompson, *J. Chem. Soc.*, **1964**, 4028.
34. K. G. Breitschwerdt, H. Kistenmacher, and K. Tamm, *Phys. Letters*, **24A**, 550 (1967).
35. O. Y. Samoilov, "Structure of Aqueous Electrolyte Solutions and Hydration of Ions," pp. 74 *et seq.*, Consultants Bureau, New York (1965).
36. E. R. Nightingale, "Chemical Physics of Ionic Solutions," pp. 87 *et seq.*, B. E. Conway and R. G. Barradas, Editors, John Wiley & Sons, Inc., New York (1966).
37. W. B. Guenther, *J. Am. Chem. Soc.*, **91**, 7619 (1969).
38. M. O. Davies, E. Schwartz, E. B. Yeager, and F. Hovorka, "The Physical and Chemical Properties of Dilute Alkali Amalgams," U.S. Clearinghouse AD 138849 and AD 609294.
39. B. Burrows and S. Kirkland, *This Journal*, **115**, 1164 (1968).
40. A. N. Dey, *ibid.*, **114**, 823 (1967).
41. J. M. Sullivan, D. C. Hanson, and R. Keller, *ibid.*, **117**, 779 (1970).
42. R. Huston and J. N. Butler, *J. Phys. Chem.*, **72**, 4263 (1968).
43. G. N. Lewis and W. L. Argo, *J. Am. Chem. Soc.*, **37**, 1983 (1915).

Mass Transfer to a Rotating Disk

B. T. Ellison[1] and I. Cornet*

Department of Mechanical Engineering, University of California, Berkeley, California 94720

ABSTRACT

Experimental rates are reported for oxygen mass transfer to a disk rotating in 3½% (0.6M) aqueous NaCl. Average Sherwood numbers, $\overline{Sh}$, were obtained over a range of temperatures from 0.6°C (33°F) to 100°C (212°F), a range of Reynolds numbers, Re, from 10^4 to 1.18 x 10^7, and a range of Schmidt numbers, Sc, from 34 to 1400. The laminar flow results agree with generally accepted theories such as the Newman extension of the Levich theory, Sparrow and Gregg, and Gregory and Riddiford. Transition from laminar to turbulent flow was found to occur at $Re = 3.0 \times 10^5$. A least squares analysis indicates that the turbulent flow results for $8.9 \times 10^5 < Re < 1.18 \times 10^7$ and $34 < Sc < 1400$ can be correlated by

$$\overline{Sh} = 1.17 \times 10^{-2} Re^{0.896} Sc^{0.249} \quad \text{(I)}$$

with a standard error of the estimate of ±8.9%. For $3.0 \times 10^5 < Re < 8.9 \times 10^5$, Eq. (I) requires modification because there are significant contributions (over 10%) to the average Sherwood number due to laminar flow in the center. The experimental average Sherwood numbers agree well with friction analogy theories using either the Tien, Wasan, and Wilke or the Deissler eddy diffusivity profiles.

The present investigation is concerned primarily with mass transfer characteristics by induced flow about a disk rotating at very high Reynolds number in turbulent flow.

Heat, mass, and momentum transfer by flow about a rotating disk have been studied extensively in recent years not only because of their importance in practical applications but also because the disk is a convenient experimental tool for the study of three-dimensional boundary layers. Work on transport about a rotating disk is summarized by Kreith (1), Dorfman (2), Riddiford (3), and Levich (4). Laminar flow heat and mass transfer to a rotating disk has been studied extensively, and generally good agreement between theory and experiment has been recorded, *e.g.*, Cobb and Saunders (5), Riddiford (3), Tien and Campbell (6), Newman and Hsueh (7), Daguenet (8), Kreith *et al.* (9). Some semitheoretical and approximate theories have been developed for turbulent flow about a rotating disk by Kreith *et al.* (9), Davies (10), Dorfman (11), Levich (4), and Hartnett *et al.* (12). There have been several experimental investigations of heat or mass transfer to a rotating disk in induced turbulent flow by Kreith *et al.* (9), Tien and Campbell (6), Daguenet (8), Cornet and Kaloo (13), and Cobb and Saunders (5); however, these investigations have generally covered a limited range of Reynolds numbers.

Previous investigations have shown that when a rotating disk induces turbulent flow, the central portion of the fluid will be in laminar flow up to a local Reynolds number of about 2.5 x 10^5, depending on surface roughness, Cornet *et al.* (14). For a disk rotating at a Reynolds number below 10^6 and at Schmidt numbers below 1000, there are significant contributions to the average Sherwood number from the fluid in laminar flow. The maximum Reynolds numbers obtained in previous investigations were 7 x 10^5 (5, 6, 9), 10^6 (13), and 1.4 x 10^6 (8). It is difficult to ascertain from such data the behavior of the fully turbulent portion of the fluid, because the laminar portion accounts for more than 10% of the average Sherwood number. One objective of the present work was to obtain mass transfer data for Reynolds number $>10^6$, where the contributions to the average Sherwood numbers from the laminar portion of the fluid are negligible.

[1] Present address: Shell Development Company, Emeryville, California.

* Electrochemical Society Active Member.

Key words: corrosion, turbulence, cathodic protection, oxygen reduction.

Preliminary Considerations

Typically mass transfer rates for flow about a rotating disk are presented in the form of local or average Sherwood number as a function of the local or over-all Reynolds number and the Schmidt number. The local Sherwood number is defined as

$$Sh = N\, r/(D\, \Delta C) \quad [1]$$

where, N = mass flux to the disk
r = local radius
D = diffusion coefficient
ΔC = concentration difference between bulk and surface

The average Sherwood number is defined as

$$\overline{Sh} = \overline{N}\, r_o/D\, \Delta C \quad [2]$$

where

$$\overline{N} = 2r_o^{-2} \int_0^{r_o} N\, r dr$$

The local mass transfer rate to a rotating disk in the laminar regime is given as

$$Sh_{lam} = C_1\, Re^{1/2}_{local}\, Sc^{1/3} \quad [3]$$

where C_1 is specified for high Schmidt numbers by Levich (15), for Schmidt numbers greater than 100 by Newman (16), and for Schmidt numbers lower than 100 by Sparrow and Gregg (17). The local Sherwood number in turbulent flow is given by

$$Sh_t = C_2\, Re^m_{local}\, Sc^n \quad [4]$$

where m has been given as 0.8 by various investigators (9-12), but as 0.9 by Levich (4). Values proposed for n have ranged between ¼ and 1. Equations [3] and [4] can be integrated to give

$$\overline{Sh}_{lam} = C_1\, Re^{1/2}\, Sc^{1/3} \quad [5]$$

or

$$\overline{Sh}_t = C_3\, Re^m\, Sc^n \quad [6]$$

The average Sherwood number for a disk with the outside flow turbulent and center in laminar flow can be expressed as

$$\overline{Sh} = r_c/r_o\,[\overline{Sh}_{lam,c} - \overline{Sh}_{t,c}] + \overline{Sh}_t \qquad [7]$$

where c denotes that the Sherwood number is evaluated at the radius at which transition from laminar flow begins. For Reynolds numbers $>10^6$ and Schmidt numbers >34, accepted correlations show

$$\overline{Sh} \simeq \overline{Sh}_t$$

within 10%. Equation [6] then is an asymptote which has been approached by previous investigators and reached for a short Reynolds number span by Cornet and Kaloo and by Daguenet.

Equipment and Procedure

Mass transfer rates were measured by determining the current required to reduce oxygen arriving at the surface of a rotating disk in 3½ weight per cent (w/o) aqueous sodium chloride solution.

The over-all electrochemical reaction may be considered to be

$$O_2 + 2H_2O + 4e^- \leftrightarrow 4\,OH^- \qquad [8]$$

Under limiting current conditions the oxygen concentration at the cathode solution-metal interface may be taken as zero.

Equipment is shown schematically in Fig. 1. The cathode was a 24.8 cm (9¾ in.) diameter monel 400 alloy (ASTM B16.4 Class A) disk insulated on the back and outer edges. The disk rotated in a 64.5 cm (24 in.) diameter, 78.6 cm (31 in.) long, steel pressure vessel coated with coal tar epoxy on the inside to prevent corrosion. The anode was a titanium disk 38.1 cm (15 in.) in diameter with strips of platinum foil 64.5 cm^2 (10 $in.^2$) in area attached to the titanium by spot-welding. The anode was bolted to the back head of the pressure vessel and insulated from it. The reference electrode was 99.99% silver, partially coated with silver chloride, immersed in the 3½% aqueous NaCl. This electrode was insulated by a glass tube, inserted through the back head and through an opening in the anode, so that about 0.63 cm (¼ in.) of the electrode extended beyond the glass tube, to within 2.54 cm (1 in.) of the cathodic disk.

The disk was driven by either a 3 or a 15 hp motor, at speeds ranging from 10 to 2500 rpm. Temperatures between 0.6°C (33°F) and 100°C (212°F) were obtained by circulating the fluid between experiments through an outside heat exchanger. Oxygen concentration in solution was determined by Winkler analysis (18). Additional details of equipment and procedure are available (19).

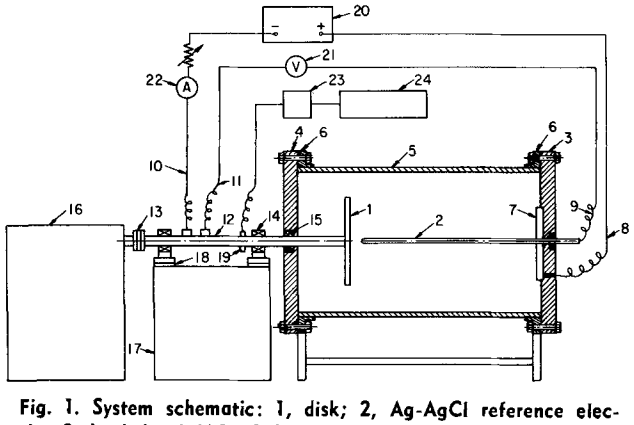

Fig. 1. System schematic: 1, disk; 2, Ag-AgCl reference electrode; 3, back head (ASA 250 lb standard blind flange); 4, front head (ASA 250 lb standard blind flange); 5, shell (24 in. dia. ½ in. wall SA-53); 6, 2—ASA 250 lb standard slip-on welding flanges; 7, platinum titanium anode; 8, anode lead wire (insulated from head); 9, probe lead wire; 10, current supply; 11, potential measuring contact; 12, shaft; 13, insulating coupling; 14, 2—bearings; 15, packing gland; 16, 15 hp motor Varidrive; 17, bearing support table; 18, insulating block; 19, 60-tooth gear and induction pickup; 20, regulated power supply; 21, high impedance voltmeter (Hewlett Packard 412A); 22, ammeter (Weston 430); 23, pulse amplifier; 24, counter.

Results and Discussion

A typical set of polarization curves is shown in Fig. 2. The mass transfer limiting current, *i.e.*, the mass flux of oxygen to the surface of the disk when the concentration of oxygen on the surface is zero, was chosen as the point of inflection on the polarization curves. From the limiting current data of Fig. 2, it is possible to evaluate Sherwood number, $Sh = qr/n\mathbf{F}D\Delta C$ at a given Reynolds number $Re = r^2\omega/\nu$. The diffusion coefficient for oxygen, D, was obtained by applying a temperature correction, after Wilke (20), to values from the International Critical Tables.

Typically the limiting current could be determined from the point of inflection to within ± 5%. In Fig. 2 some of the curves at similar rpm's represent differing oxygen concentrations, so the agreement in mass transfer is better than the curves might imply.

The experimental average Sherwood numbers for laminar flow are shown in Fig. 3 and 4 as a function of Reynolds number for Schmidt numbers of 53, 110, 400, and 1400, which correspond to electrolyte temperatures of 82°C (180°F), 54°C (130°F), 24°C (75°F), and 0.6°C (33°F). It is seen that the experimental data agree with well-known theoretical predictions within 5%, except for the lowest Reynolds numbers where free convection may be contributing substantially to the mass transfer. Agreement with conventional heat and mass transfer correlations is obtained by assuming four electrons are transferred per molecule of oxygen in the mass transfer limited cathodic reduction.

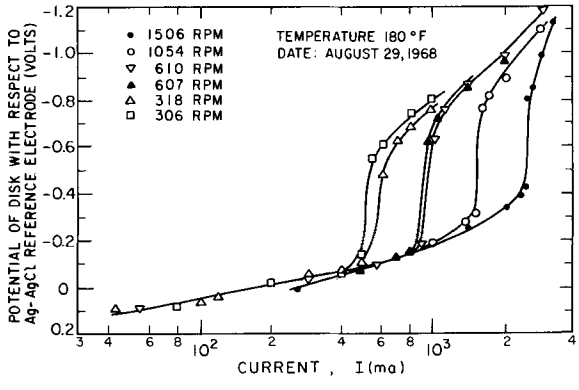

Fig. 2. Polarization curves

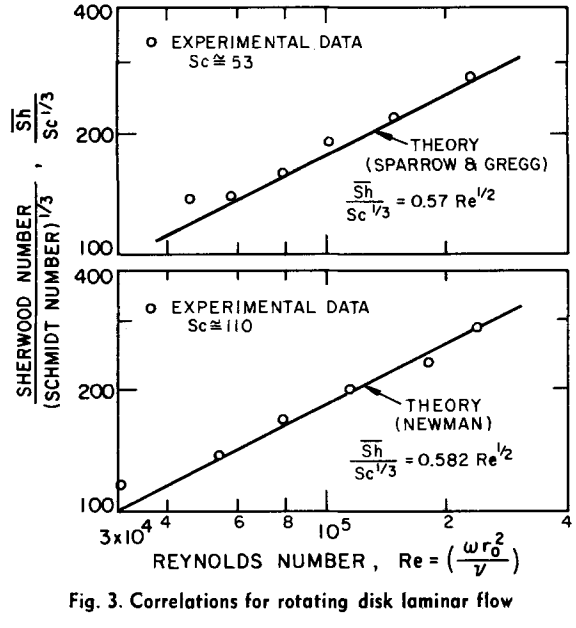

Fig. 3. Correlations for rotating disk laminar flow

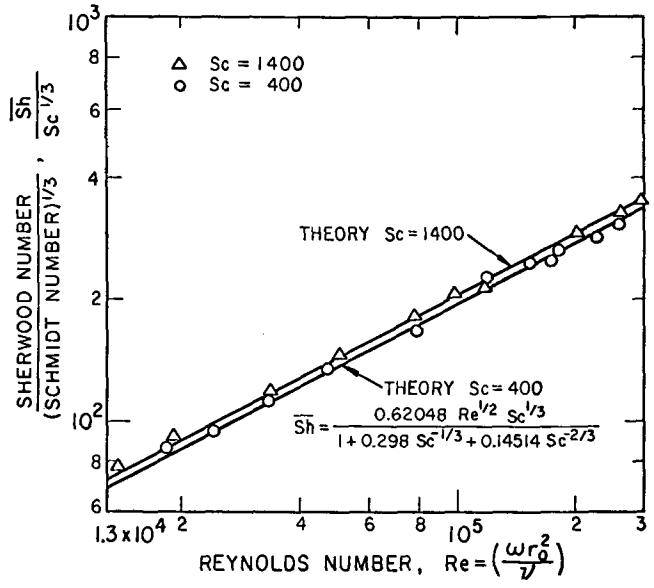

Fig. 4. Rotating disk laminar flow (theory after J. S. Newman)

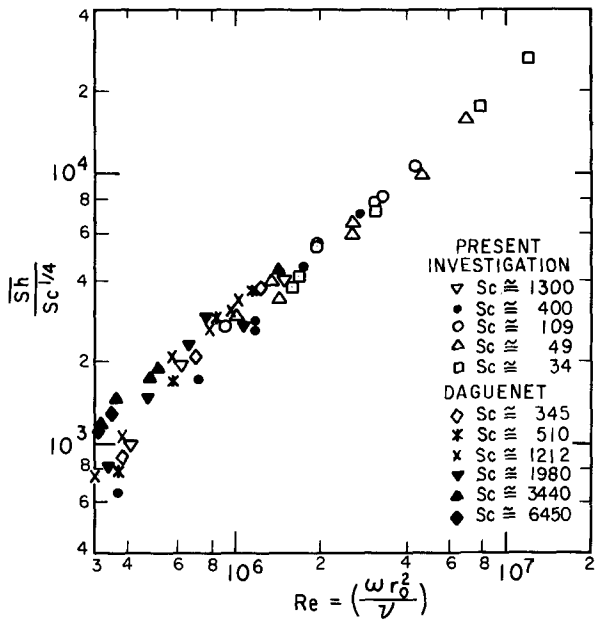

Fig. 6. Rotating disk turbulent flow

There was some variation of temperature between several experimental runs so that the actual value of the Schmidt number may differ by as much as 7% from the mean value reported; however, the actual value of the Schmidt number was used to calculate the ratio $\overline{Sh}/Sc^{1/3}$ for the plotted experimental points.

Transition from laminar to turbulent flow was found to occur at $Re = 3.0 \times 10^5$.

Figure 5 is a plot of $\overline{Sh}/Sc^{1/4}$ *vs.* Re for turbulent flow with Schmidt numbers of 34, 49, 109, 400, and 1300. Note that most of the data presented are for Reynolds numbers above 10^6 and that the highest Reynolds number attained was 1.18×10^7, which is almost an order of magnitude higher than previous published heat or mass transfer data.

Above a Reynolds number of 8.9×10^5 a straight line can be passed through the data. A least squares analysis indicates that the equation of the best straight line through the data is

$$\overline{Sh} = 1.17 \times 10^{-2}\ Re^{0.896}\ Sc^{0.249} \qquad [9]$$

with a standard error of the estimate of ± 8.9%.

Figure 6 is a plot of the present data and the high Schmidt number electrochemical mass transfer data of Daguenet. There is considerable scatter in the data at low Reynolds numbers. As the Schmidt number changes, the extent of the laminar contribution to the over-all Sherwood number changes. It is seen, however, that as the Reynolds number increases the scatter decreases, until at a Reynolds number above 8.0×10^5 Daguenet's and the present data are in reasonable agreement.

Figure 7 is a plot of the present data and representative points from Kreith, Taylor, and Chong (9), and Tien and Campbell (6) for the mass transfer of naphthalene ($Sc = 2.4$) as well as the heat transfer data of Cobb and Saunders (5) for $Pr = 0.72$. The ratio $\overline{Sh}/Sc^{1/4}$ is slightly lower for the naphthalene mass transfer than the present results and considerably lower for the heat transfer results. The reason for this is that as the Prandtl or Schmidt number decreases both the laminar and turbulent flow asymptotes decrease (17, 21).

Previous theories except for Levich's (4) do not agree with the data since their forms are

$$\overline{Sh_t} = C_3\ Re^{0.8}\ Sc^n \qquad [10]$$

The Levich theory with its unspecified constant fits the

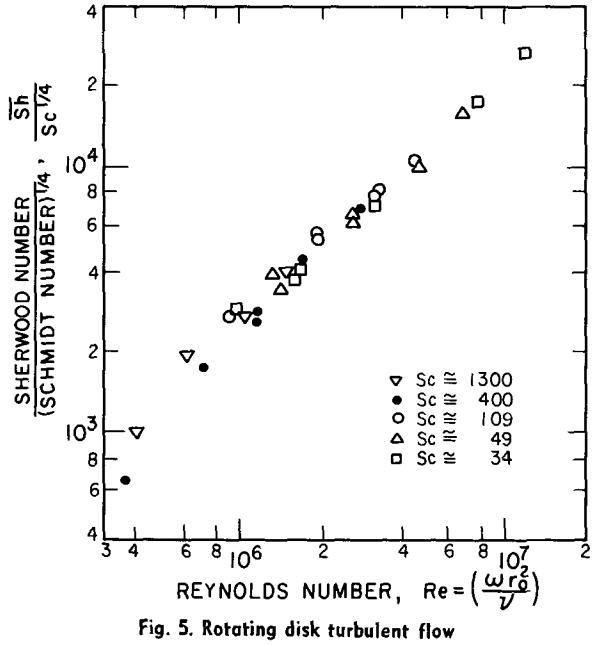

Fig. 5. Rotating disk turbulent flow

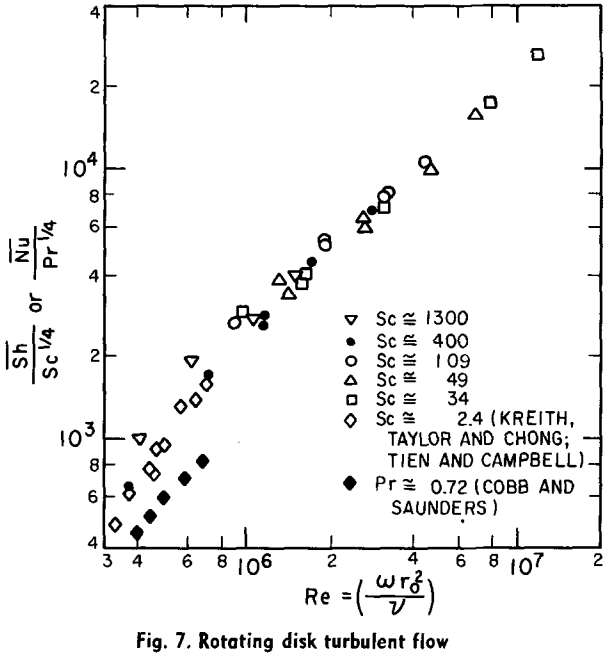

Fig. 7. Rotating disk turbulent flow

data since it predicts approximately the right power of the Schmidt and the Reynolds numbers.

$$\overline{Sh}_t = C_3\, Re^{0.9}\, Sc^{1/4} \qquad [11]$$

Previous theories except for Levich do not agree too closely with the present experimental data since they were developed for low Schmidt number flows. At low Schmidt numbers, the Sherwood number is proportional to the Reynolds number times the friction factor, whereas for high Schmidt numbers the Sherwood number is usually considered to be proportional to the Reynolds number times the square root of the friction factor (21-23).

Using Kreith's technique (9), but with a friction factor after Dorfman (2) and with eddy diffusivity profiles of either Deissler (21) or Tien, Wasan, and Wilke (22, 23) two equations have been derived which closely fit the present experimental results. Dorfman's friction factor (2) was chosen because it agrees more closely with the drag data than the previous theories of von Kármán (24) or Goldstein (25). The correlation based on the Deissler eddy diffusivity profile yields for the average Sherwood number

$$\overline{Sh}_t = 1.12 \times 10^{-2}\, Re^{0.91}\, Sc^{0.25} \qquad [12]$$

The Tien, Wasan, and Wilke correlation yields

$$\overline{Sh}_t = 5.93 \times 10^{-3}\, Re^{0.91}\, Sc^{0.34} \qquad [13]$$

Both of the above correlations are approximations valid for high Schmidt numbers. The Deissler high Schmidt number approximation predicts Sherwood numbers about 8% too high (when compared to Deissler's exact solution) at a Schmidt number of 34. The high Schmidt number approximation of the Tien, Wasan, and Wilke theory predicts values of the Sherwood number about 1% too high.

Both theories predict that the power of the Reynolds number is 0.91 as compared to the experimental value of 0.896. The Deissler theory more closely predicts the experimental value of the power of the Schmidt number, 0.249, than does the Tien, Wasan, and Wilke theory. Figure 8 shows a representative plot of average Sherwood number as a function of Reynolds number for constant Schmidt number, as well as the predictions of Eq. [12] and [13]. From Fig. 8 it is seen that the Eq. [12] based on a Deissler eddy diffusivity profile is almost an upper bound for the experimental data and that Eq. [13], based on a Tien, Wasan, Wilke eddy diffusivity profile is almost a lower bound on the data.

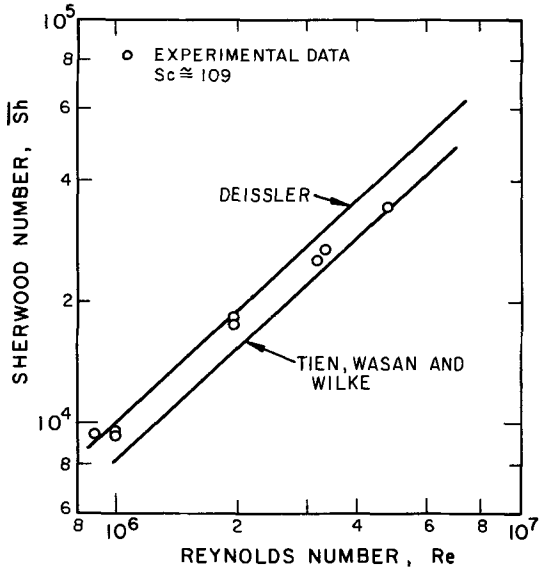

Fig. 8. Sherwood number vs. Reynolds number for Schmidt number ≃ 109.

It is remarkable that the above two equations fit the experimental results so closely. They are based on eddy diffusivity profiles which were developed for pipe flow data, where the only mean velocity component is along the axis of the pipe; in contrast, the rotating disk has a three-dimensional boundary layer with mean velocity components in the radial, circumferential, and axial directions.

Conclusions

It can be concluded from the experimental results that for Reynolds numbers between 8.9 x 10^5 and 1.18 x 10^7 and for Schmidt numbers between 34 and 1300 the mass transfer rate to a rotating disk can be represented by

$$\overline{Sh} = 1.17 \times 10^{-2}\, Re^{0.896} Sc^{0.249}$$

Furthermore, this correlation may be closely approximated from a friction analogy, using either the Deissler or Tien, Wasan, and Wilke diffusivity profiles.

Acknowledgment

The authors acknowledge with appreciation the partial support of this research by the Office of Saline Water, United States Department of the Interior, Grants number 14-01-0001-671 and 14-30-2545.

Manuscript submitted July 1, 1970; revised manuscript received *ca.* Sept. 13, 1970.

Any discussion of this paper will appear in a Discussion Section to be published in the December 1971 JOURNAL.

LIST OF SYMBOLS

ΔC	difference in concentration of oxygen between bulk of solution and metal-fluid interface, g moles/cm³
C_1, C_2, C_3	constants
$C_3 = \frac{2}{1+2m} C_2$	an integration constant
D	diffusion coefficient, cm²/sec
$\mathbf{F}$	Faraday's constant, 96,500 coulomb/g equivalent
m, n	exponential constants
n	number of electrons transferred in electrochemical reaction, in $Sh = qr/n\mathbf{F}D\Delta C$
N	mass flux to the disk, g moles/(cm² sec)
$\overline{N}$	average mass flux to the disk
q	current density, A/cm²
r	local radius, cm

Subscripts

c	critical radius at which transition from laminar flow begins
lam	laminar
o	outside
t	turbulent

Greek Symbols

ω	angular velocity, radians/sec
ν	kinematic viscosity, cm²/sec

Dimensionless groups

Re	Reynolds number, $r^2\omega/\nu$
Sc	Schmidt number, ν/D
Sh	local Sherwood number, $Nr/(D\Delta C)$
$\overline{Sh}$	average Sherwood number

REFERENCES

1. F. Kreith, "Convection Heat Transfer in Rotating Systems," in Advances in Heat Transfer," Vol. 5, pp. 129-246, J. Hartnett and T. Irvine, Editors, Academic Press, New York (1968).
2. L. A. Dorfman, "Hydrodynamic Resistance and the Heat Loss of Rotating Solids," pp. 77-101, Oliver and Boyd, Edinburgh (1963).
3. A. C. Riddiford, "The Rotating Disk System," in "Advances in Electrochemistry and Electrochemical Engineering," Vol. 4, pp. 47-117, Paul Delahay, Editor, Interscience Publisher, New York (1966). *See* also D. P. Gregory and A. C. Riddiford, *J. Chem. Soc.*, **1956**, 3756.

4. V. G. Levich, "Physicochemical Hydrodynamics," pp. 144-159, 231-367, Prentice-Hall, Englewood Cliffs, New Jersey, (1962).
5. E. C. Cobb and O. A. Saunders, *Proc. Roy. Soc.*, **A236,** 343 (1956).
6. C. L. Tien and D. T. Campbell, *J. Fluid Mechanics*, **17**, 105 (1963).
7. J. Newman and L. Hsueh, *Electrochim. Acta*, **12**, 417, (1967).
8. M. Daguenet, *Int. J. Heat Mass Transfer*, **11**, 1581 (1968).
9. F. Kreith, J. H. Taylor, and J. P. Chong, *Trans. ASME, J. Heat Transfer*, **81**, 95 (1959).
10. D. R. Davies, *Quat. J. Mechanics Appl. Math*, **8**, Part 2, 211 (1959).
11. L. A. Dorfman, *op. cit.*, p. 90.
12. J. P. Hartnett, S. H. Tsai, and H. N. Jantscher, *Trans. ASME, J. Heat Transfer*, **87**, 362 (1965).
13. I. Cornet and U. Kaloo, "Temperature and Velocity Effects on the Cathodic Protection of a Steel Disk Rotating in Salt Water," Third International Congress on Metallic Corrosion, *Extended Abstracts of Papers Presented*, 1966, pp. 213-214.
14. I. Cornet, W. N. Lewis, and R. Kappesser, *Trans. Instn. Chem. Engrs.*, **47**, T222 (1969).
15. V. G. Levich, *Acta Physicochim.*, **15**, 257 (1942).
16. J. Newman, *J. Phys. Chem.*, **7**, 1327 (1966).
17. E. M. Sparrow and J. L. Gregg, *Trans. ASME, J. Heat Transfer*, **81**, 249 (1959).
18. W. W. Scott, "Standard Methods of Chemical Analysis," Vol. 2, 5th ed., pp. 2079-2081, Van Nostrand, New York.
19. B. T. Ellison, "Mass Transfer to a Rotating Disk" Ph.D. Thesis, University of California, Berkeley, September 1969.
20. C. Wilke, *Chem. Engrg. Prog.*, **45**, 219 (1949).
21. R. G. Deissler, *NACA Report 1210*, pp. 69-82 (1955).
22. D. T. Wasan, C. L. Tien, and C. R. Wilke, *AIChE J.*, **9**, 567 (1963).
23. D. T. Wasan and C. R. Wilke, *Int. J. Heat Mass Transfer*, **7**, 87 (1964).
24. Th. von Kármán, *Z. Angew. Math. Mech.*, **1**, 365 (1921).
25. S. Goldstein, *Proc. Cambridge Phil. Soc.*, **31**, 232 (1935).

The Transient Behavior of Graphite-Silver Iodide and Platinum-Silver Iodide Interfaces in a Solid-State System

Michael N. Hull* and Arthur A. Pilla*

ESB Inc. Research Center, Yardley, Pennsylvania 19067

ABSTRACT

The electrochemical characteristics of the interface formed by solid silver iodide in contact with either platinum or graphite have been studied by linear sweep voltammetry, chronopotentiometry, and the potential and current step techniques. The results indicate that the graphite-silver iodide interface exhibits pure double-layer behavior over the potential range of -0.03 to $+0.46$V (*vs.* Ag/AgI), with no frequency dispersion effects observed up to approximately 1 MHz. In contrast, pure double-layer behavior could not be isolated for the platinum-silver iodide case under the same conditions. It is suggested that, for cathodic potentials, this is due to the rapid discharge of silver atoms onto the platinum surface at subunit activity, and at anodic potentials to liberation of iodine. Comparison of the two electrode systems in terms of recent ideas concerning molten salt double-layer behavior indicates that in both of these systems, the double layer is essentially determined by the structure of solid AgI. The graphite interface behaves very much in an ideally polarized manner while the platinum interface behaves very much as an ideally reversible system because of the rapid faradaic reactions prevalent throughout the entire accessible potential range.

In recent years there has been a growing reawakening of interest in the use of solid electrolytes in power sources. This has been primarily due to the discovery of a family of compounds of general formula M Ag_4I_5 (where M = K, Rb, or NH_4) which have an ionic conductivity of comparable magnitude to that normally associated with good liquid electrolytes (1-11). In these compounds, and also in the parent compound, silver iodide, conduction occurs solely by the movement of silver entities through the crystal lattice. It is therefore both of theoretical and practical interest to begin to obtain more basic information on the nature and kinetics of electrochemical processes which can occur in solid-state systems.

One of the major questions to be answered is that concerning the structure of the solid electrolyte-electrode interface. This is particularly so in view of the considerable theoretical and experimental work which has been reported (12-23) concerning space charge polarization in solid and liquid systems. These studies, which actually involve diffuse double-layer behavior, have attempted to explain the frequency dispersion noted when, *e.g.*, a solid electrolyte in contact with an ideally polarizable electrode is perturbed using a-c or transient techniques. The exact manner in which the diffuse double layer responds as a function of the frequency of a low level perturbation is still somewhat unclear (23). It is, however, certain that as charge is injected onto an ideally polarizable electrode, it is possible for a static concentration gradient of an ionic species of given sign to be established which extends to a significant extent into the bulk electrolyte. This phenomenon is, of course, well known in dilute aqueous electrolytes (24-26). However, it has also been observed in solid electrolytes (27) and suspected in molten salts (21). In a typical study of solid electrolytes (16), the a-c impedance of Ag/AgBr/Ag and Au/AgBr/Au arrays at temperatures of 200°-300°C was determined. Frequency dependent resistance and capacitance effects, with the latter having values of the order of 100 $\mu F \cdot cm^{-2}$, were observed. The interpretation of these and other similar studies is open to some doubt since, although no steady state faradaic current can flow through an array such as Au/AgBr/Au within the potential limits of stability

* Electrochemical Society Active Member.

Key words: double layer, solid electrolyte, silver iodide, frequency dispersion.

of the electrolyte, a transient faradaic current is possible as will be seen below. More recent work (28, 29) has pointed out that the study of such arrays can be placed on a more thermodynamically reasonable basis if one of the electrodes is reversible to one of the electrolyte components while the other electrode is inert. At the inert electrode, there again will exist a potential range over which no steady-state current will flow, but a transient faradaic current is possible which, according to the Nernst equation, will tend to readjust the activity of each of the electrolyte components at the inert electrode according to the applied d-c potential. For example, in the system Ag/AgI/M, where M is an electrode having no common ion with the electrolyte, the activity, a, of Ag and I_2 at the M/AgI interface is given by, for Ag

$$a_{Ag} = \exp - \frac{FE}{RT} \quad [1]$$

and for I_2

$$a_{I_2} = \exp - \frac{2F(E_D - E)}{RT} \quad [2]$$

where E_D is the decomposition potential of the electrolyte, E the potential of M with respect to Ag/AgI; the other terms have their usual significance. For a given change in the inert electrode potential, E, both a_{Ag} and a_{I_2} undergo a readjustment by faradaic processes, the rates of which are, of course, not predicted by Eq. [1] and [2]. It is expected, however, that the ease with which, *e.g.*, an M-Ag bond forms determines to a great extent these rates as has been shown in recent work concerning the Pt/Cu and Pt/Bi systems (30).

An interesting recent study (28) examined the double-layer behavior of the interface formed between a single crystal of silver bromide with single and polycrystalline graphite, platinum and gold electrodes at temperatures of 244°-292°C. This investigation showed that the response of such interfaces to potential step perturbations could not be represented by a simple RC series network as would be expected for pure double-layer behavior (17, 31), but that the cell response consisted of a mixture of several time constants. This behavior was suggested to be analogous to the frequency dependence of the a-c capacitance which is observed in aqueous systems at many solid electrodes (32, 33). Electrode capacitance values, calculated by dividing the total charge transferred during the repolarization of the interface by the magnitude of the potential step, gave values of several hundred $\mu F \cdot cm^{-2}$ for platinum electrodes and values approximately one order of magnitude smaller with graphite. However, the high temperature of these systems most probably resulted in relatively high rates for the faradaic processes, rendering the separation from double layer charging difficult.

The work described here examines the properties of the interface formed between a polycrystalline electrolyte and two polycrystalline electrodes at room temperature, thus keeping the faradaic reaction rate as low as possible. The system Ag/AgI/M where M is graphite or Pt was examined, silver iodide was chosen as the electrolyte in view of its relatively high ionic conductivity (0.0001 mho-cm^{-1}) at room temperature compared to other simple solid electrolytes. It may be noted that the intrinsic conductivity of AgI at room temperature is $\sim 10^{-8}$ ohm^{-1} cm^{-1}, but higher values are observed where grain boundary conduction predominates as is the case for the polycrystalline material utilized in this study.

Experimental

The experimental cell, which consisted of a silver counterelectrode, silver iodide electrolyte in which a small silver wire was imbedded to act as a reference electrode, and a platinum or graphite working electrode, was assembled by compressing the various constituents together in a steel die under a pressure of 40,000 psi to produce a pellet of 1.27 cm diameter and 0.2 cm thick. The procedure followed before pressing the pellet was as follows: 0.4g of powdered silver was placed in the die and pressed lightly to give a smooth, compacted surface. On top of this, 0.4g of powdered silver iodide was evenly spread and lightly compacted followed by a 2.0 cm length of 0.0122 cm diameter silver wire which was positioned for a portion of its length along the circumference of the die. Another 0.4g portion of the silver iodide was then added and again gently compacted to give a flat surface on top of which 0.05g of either powdered platinum black or powdered pyrolytic graphite was spread. The die contents were then compressed at the designated load. After removal of the pellet from the press, it was carefully sanded along the edge to reveal the wire reference electrode which was then pulled out at right angles to the cell as shown in Fig. 1. The cell was clamped between Teflon blocks, electrical contact being made to the counter and working electrodes by means of "plastic carbon" disks interposed between each of the Teflon blocks and the corresponding electrode. The complete experimental cell is shown in Fig. 1. Due to the fact that cumulative effects of repeated experimental runs on any one cell were not negligible, a fresh pellet was used for each run of each type of experiment. In this way, excellent reproducibility of the system response was obtained.

Anodic and cathodic potential and current perturbations were applied to the study electrode as shown in Fig. 2 and 3. For the potentiostatic experiments (see Fig. 2), a fast-rise Tacussel PIT 20-2X Potentiostat (A, Fig. 2) was programmed from a Tacussel GITP Pulse Generator (G, Fig. 2) for the step experiments or a Tacussel GSTP-2 Function Generator (G, Fig. 2) for linear sweep studies. For galvanostatic measurements, the potentiostat was employed in the mode shown in Fig. 3. In this, a resistor, R, (Fig. 3) two orders of magnitude greater than that of the ohmic resistance of the cell was placed in series with the latter. In addition, the feedback arrangement was such that a potential step could be applied across both R and the cell allowing the potentiostat (A, Fig. 3) to operate in its fastest mode (34).

Because of the large electrolyte resistance ($\approx$ 300 ohms) and the high electrode capacitances encountered

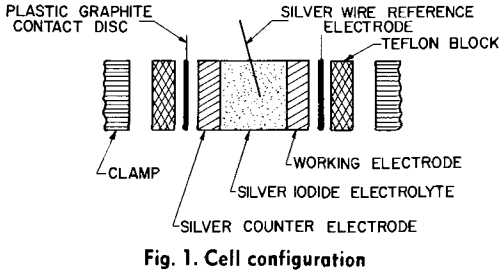

Fig. 1. Cell configuration

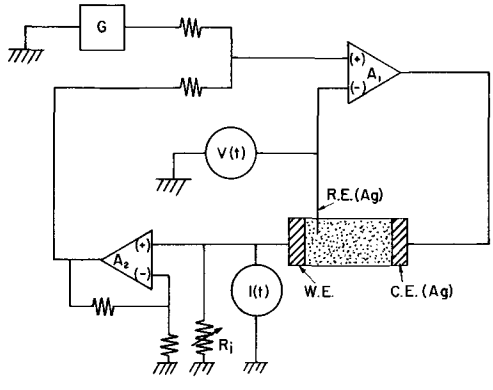

Fig. 2. Block diagram of the circuit employed for potentiostatic experiments with IR compensation.

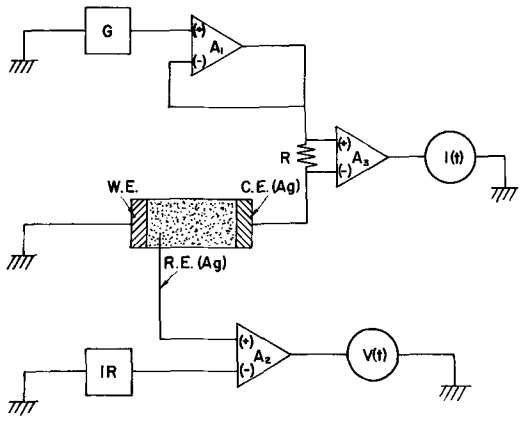

Fig. 3. Block diagram of the circuit employed for galvanostatic experiments with IR compensation.

(up to several thousand $\mu F/cm^2$), it was necessary in both potentiostatic and galvanostatic studies to introduce ohmic drop compensation. In the former case, (see Fig. 2), this was accomplished by reinjecting (via A_2, Fig. 2) a signal proportional to the magnitude of the current flowing through the cell back into the noninverting input of the potentiostat. Details of this circuitry have been published elsewhere (34). This mode of operation allows a critically damped current response having a minimum time constant (τ_{min}), beyond which the system exhibits damped oscillations (34), approximately two orders of magnitude lower than that of the uncompensated system to be readily achieved.

For galvanostatic studies, the ohmic component of the voltage response was removed by employing a high-speed differential probe (Tektronix P6046, A_2 Fig. 3) arranged as shown in Fig. 3. It can be seen that by applying a d-c voltage (IR, Fig. 3) to the inverting input of the differential probe of magnitude equal to that of the observed IR component appearing at the noninverting input, the ohmic-free voltage response of the electrode is obtained. All current and voltage functions were displayed on a Tektronix 565 dual beam, dual time base oscilloscope (V(t) and I(t), Fig. 2 and 3) utilizing type 3A7 differential input preamplifier plug-ins (A_3, Fig. 3).

Results

Linear sweep voltammetry and chronopotentiometry. —The over-all electrochemical behavior of each array was investigated by sweeping the potential of the study electrode in both the anodic and cathodic directions from an initial starting potential of +0.46V (*vs.* Ag/AgI). This value was chosen since platinum cells exhibited an open-circuit potential of +0.46V within several minutes of their construction. (Initially, the open-circuit potential of the array is zero since the cell is in a shorted state until it is removed from the steel die.) As Eq. [1] and [2] show, a potential of +0.46V corresponds (for $E_D = 0.68V$) to that at which the activity of silver and iodine at the platinum-silver iodide interface are equal (and, therefore, minimum). In contrast, graphite cells maintained an open-circuit voltage of zero after construction. However, this electrode could be polarized to any potential between approximately −0.03 and +0.5V, and the imposed voltage would be retained under open circuit conditions indefinitely. Thus the graphite-silver iodide interface appears to be an example of an ideally polarized interface (35) in a solid-state system.

As may be seen from Fig. 4, no appreciable faradaic current is observed to flow across a graphite-silver iodide interface as the potential is swept cathodically (region A-B) until an electrode potential of approximately −0.03V is attained, at which point silver deposition commences abruptly. This type of behavior indicates that Eq. [1] is not obeyed in the graphite case within the time scale of the experiments described here and that there is therefore no silver on the surface initially even at a potential of zero corresponding to an activity of unity. After the sweep direction is reversed at C, silver deposition occurs at potentials below the initial starting point, B. This shows that further deposition onto the electrode is occurring at those sites which are already covered with a layer of deposited silver and that this process can continue at a lower overvoltage than that required for deposition onto the silver-free sites. Between D and A, the deposited silver is removed from the surface and the current passes through a peak at about 0.1V.

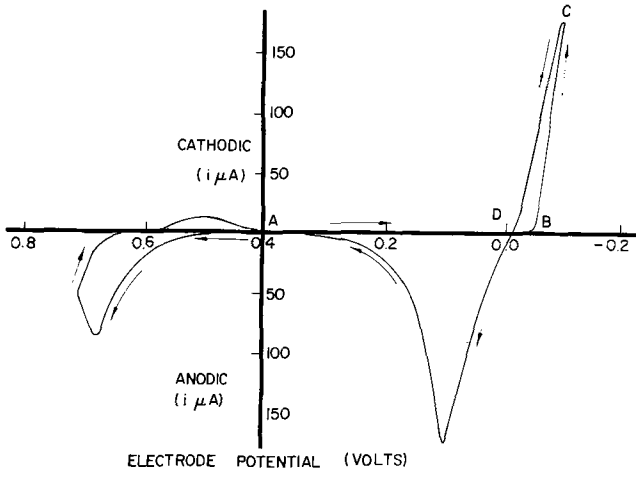

Fig. 4. Current-potential behavior of a graphite electrode recorded at a sweep rate of 5 mV-sec^{-1}.

The above behavior may be contrasted to that exhibited by platinum cells as shown in Fig. 5. One may see that, in this case, an increasingly larger amount of current flows through the system at all potentials cathodic to the cell open-circuit potential of +0.46V. This type of behavior suggests that silver deposition is taking place on the platinum electrode at subunit activity according to the dictates of Eq. [1]. After sweep reversal, an anodic peak due to the removal of silver from the surface is again observed similar to that in the graphite case. This is to be expected since silver is being removed from silver in both cases.

The liberation of free iodine occurs at approximately +0.5V for graphite and +0.46V for platinum electrodes during an anodic potential sweep as can be seen from Fig. 4 and 5. The liberated iodine, in each case, gives rise to a broad reduction peak on the return sweep.

Chronopotentiometric studies were conducted using various cathodic currents with the study electrodes at

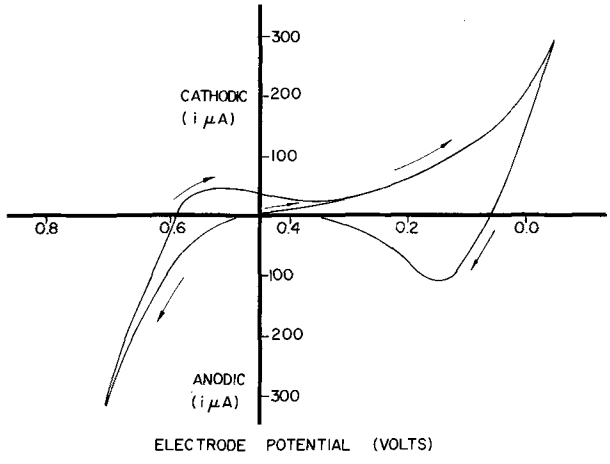

Fig. 5. Current-potential behavior of a platinum electrode recorded at a sweep rate of 5 mV-sec^{-1}.

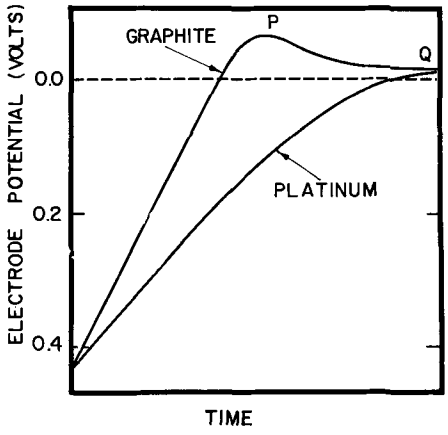

Fig. 6. Schematic illustration of the differences in chronopotentiometric behavior between graphite and platinum electrodes.

an initial potential of +0.46V similar to the linear voltage sweep studies. The general behavior exhibited by each electrode is shown schematically in Fig. 6. It can be seen that the potential of a graphite electrode underwent a linear increase with time until the abrupt onset of silver deposition at P. The potential then decreased to a steady-state value at Q. This potential overshoot which corresponds to the behavior exhibited using linear sweep conditions (see BCD Fig. 4) reflects the gradual transition from silver deposition on graphite to that of silver deposition on silver as a monolayer of silver is built up on the electrode surface. On the other hand, the corresponding response of a platinum electrode did not exhibit linearity, and the approach of the final steady-state value required an order of magnitude longer time than graphite and was not preceded by any "overshoot" region. The above patterns of behavior closely parallel those of the graphite-silver bromide and the platinum-silver bromide interfaces whose behavior at somewhat higher temperatures (244°-292°C) was reported earlier (28).

Both the linear voltage sweep and the chronopotentiometric studies show that there exists a range of potentials from approximately +0.5 to −0.03V for graphite arrays within which no appreciable faradaic reaction occurs and within which one should be able to observe solely the charging of the double layer on application of an appropriate low level perturbation. At potentials more negative than −0.03V and more positive than +0.5V, faradaic processes due to the deposition of silver and the liberation of free iodine, respectively, occur. In contrast, it appears that there is no potential range within which the platinum-silver iodide interface behaves as ideally polarized. The measurement of the double-layer capacitance of this interface could thus be expected to be complicated in all potential regions by faradaic processes associated with either the discharge of silver onto the electrode surface at subunit activity or the liberation of iodine by electrolyte decomposition.

Potential and current step studies.—Potential steps of low amplitude (<5 mV) were applied to each interface with various degrees of ohmic drop compensation. This was achieved by setting the degree of positive feedback, as determined by the value of R_i (Fig. 2), such that either the fastest stable response (τ_{min}) or some fraction of τ_{min}, *e.g.*, 90%, was obtained. In practice, the degree of compensation was adjusted using a "sacrificial" cell which was then replaced by a freshly prepared array for the experimental measurement. All of the results reported here were obtained from the first pulse applied to a new cell.

In Fig. 7, two representative response curves for the graphite-silver iodide interface are presented in semilogarithmic form. These were recorded at + 0.41V (*i.e.*, within the potential range for which no transient

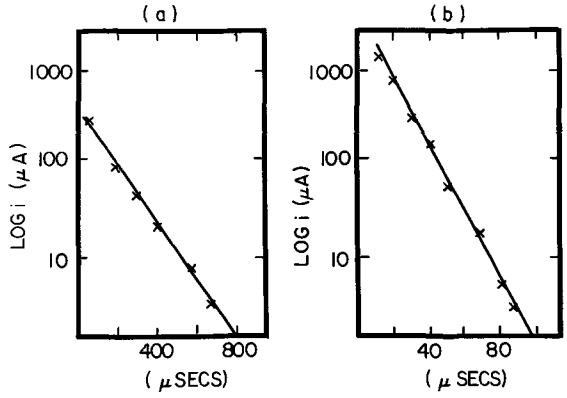

Fig. 7. Semilogarithmic plots of the response of a graphite electrode to a 5 mV potential step for differing degrees of IR compensation: (a) 90% τ_{min}; (b) τ_{min}.

faradaic reaction can occur) and with different degrees of positive feedback. As a first point, it may be noticed that both plots of log *i* *vs.* *t* are completely linear over the whole of the time scale of the charging process as one would expect for a system behaving as a simple RC series circuit. Thus for the cell configuration employed in this investigation, the capacitative properties of these interfaces may be studied without complications of the cell response by frequency dispersion effects. This single time constant behavior exhibited by the graphite-silver iodide interface was observed for times extending to seconds if the degree of IR compensation was sufficiently reduced and may be contrasted to that of the platinum-silver iodide interface for a similar potential step perturbation within the potential region for which no steady-state current can flow but which is active under transient conditions (see Fig. 5). Figure 8 shows the semilogarithmic current-time response curves for a platinum electrode at two different electrode potentials and with 90% τ_{min}. It may be seen that in this case there is no region of the response curve within which linearity of the functions plotted is observed even for times as long as several seconds after application of the potential step, although more recent studies (36) indicate that compensation in the presence of rapid faradaic reactions may be relatively difficult to interpret. Further, the amount of charge required to repolarize the interface is several orders of magnitude larger than that required for repolarization of the graphite-silver iodide interface under identical conditions indicating again that processes in addition to those associated with charging of the double layer are taking place.

In view of the above behavior, galvanostatic studies of the platinum electrode were conducted since IR

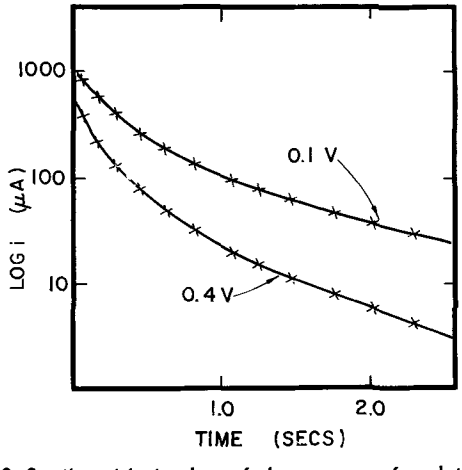

Fig. 8. Semilogarithmic plots of the response of a platinum electrode to a 5 mV potential step at 90% τ_{min}.

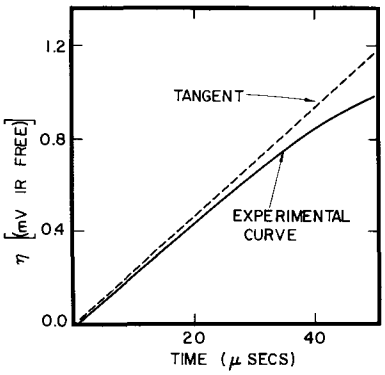

Fig. 9. IR free overvoltage response of a platinum electrode potentiostatted at an initial potential of +0.41V during a cathodic galvanostatic pulse of 780 μA.

free measurements could be made at shorter times than those employing compensated potential steps. It was believed that this procedure would increase the possibility of isolating the double layer parameters in this case. The response of this electrode to a 780 μA cathodic galvanostatic pulse applied at an initial starting potential of +0.41V is shown in Fig. 9. It is evident that even for times of the order of a few microseconds, the potential-time relationship is not linear as would be expected if the system were exhibiting simple RC behavior. A similar form of response curve is observed at all potentials within the studied range. These results indicate that the process giving rise to deviations from simple RC series behavior is still playing a predominant role at these short times. Galvanostatic studies of the graphite-silver iodide interface gave results identical to those observed in potentiostatic studies.

Discussion

One of the advantages of studying the double-layer behavior of a solid electrolyte is the absence of any effects associated with the presence of a solvent. However, although a one-component system should be inherently simple in its behavior, one suffers from the disadvantage that each ion in the double layer is a potentially electroactive species. Thus the problem of achieving an experimental separation between nonfaradaic and faradaic processes might be expected to be greater than for the case in aqueous layer studies where the majority of the ions in the double layer are inert in many cases (37).

The criterion that ideal double-layer charging is being observed has been shown to be the presence of a single time constant over a sufficiently large time range (at least one order of magnitude) from the shortest experimentally accessible times (31). Thus for a potential step experiment in which the rise-time of the step is much shorter than the electrode time constant(s), the double layer capacitance may be calculated from the equation

$$i(t) = \frac{V_o}{R_e} \exp - \frac{t}{R_e C_D} \qquad [3]$$

where V_o is the magnitude of the potential step, R_e the electrolyte resistance, and C_D the total double-layer capacitance. For the galvanostatic case, the equation

$$V(t) = i_o R_e + \frac{i_o t}{C_D} \qquad [4]$$

may be employed where i_o is the magnitude of the current step.

In the graphite case, these equations were found to be obeyed over the whole time range of the electrode response at each potential within the range +0.50 to −0.03V (see Fig. 7). This indicates that in this case, all of the charge accepted by the interface in the above potential range is utilized in solely a nonfaradaic process. In addition, it is evident that for the cell configuration utilized in these studies, as has been pointed out earlier, there is no frequency dispersion of the measured capacitance. This is in contrast to the behavior reported for the graphite-silver bromide interface at temperatures close to the melting point of the electrolyte (28).

Note that in view of the fact that graphite acts as an ideally polarized electrode over the potential range +0.46 to −0.03V, it might be expected that a diffuse double-layer effect would be observed as the potential becomes more cathodic than +0.46V due to the necessary accumulation of positive charge from Ag^+ ions at the interface. The effect of the presence of a diffuse double layer is generally considered to be simply a capacitance one. In other words, it is presumed to be a capacitance, C_d, in series with the inner layer capacitance, C_i, such that $1/C_D = 1/C_i + 1/C_d$, indicating that C_d is a lumped parameter showing no spatial dependence (25). It might therefore be assumed that the series RC model for which Eq. [3] and [4] hold is valid whether or not the diffuse layer capacitance contributes significantly to the measured C_D. This model, however, must inherently be wrong since the very existence of a diffuse double layer presupposes a concentration (and potential) gradient extending into the bulk electrolyte (25). It is thus surprising that the majority of studies concerning the a-c behavior of the diffuse double layer result in an equivalent electric circuit with lumped parameters (23). Exceptions to this are the work of Ferry (12), Anson (20), and Barker (19) who implicitly assume a distributed parameter system for the equilibrium diffuse double-layer structure. Presently work is being conducted in this laboratory to confirm the expected spatial dependence of both the diffuse double layer and the electrolyte resistance (39).

The above discussion indicates that the presence of a diffuse double layer would be expected to result in frequency dispersion with respect to a simple RC series circuit model. However, in order to observe this effect at presently available frequencies, it is necessary that both the total C_d (which can be evaluated from classical diffuse layer theory) be of the same order of magnitude or smaller than C_i, and that the extent to which the concentration (potential) gradient extends into the bulk electrolyte be significant. The second condition results from the conclusion that, in most cases, a simple finite RC transmission line is adequate to describe the spatial dependence of the diffuse double layer (12, 19, 20, 39). Since the line is finite, its behavior, under the boundary conditions present in this problem, will reduce to that of a simple RC series circuit at a frequency depending on the length of the line for a given system. If, in addition, the total impedance of the line is much less than that of C_i, which would tend to be the case if the total C_d, as obtained from the line, is much larger than C_i, it is then virtually impossible to isolate the frequency dependence of the transmission line from that of C_i. Classical diffuse layer theory (24) predicts that, except possibly for potentials very close to the point of zero charge, C_d is much greater than C_i, thus allowing only C_i to be observed.

In the case of solid AgI electrolyte in contact with graphite, the following will show that the spatial dependence of C_d is not likely to be observed. The total charge injected into the graphite/AgI system to move the potential 0.5V cathodic with respect to a potential of +0.46V is 4 μC cm^{-2}. Since solid AgI is a close-packed structure of I^- with highly mobile Ag^+ ions, it appears reasonable to assume that, in order to satisfy this charge requirement, more Ag^+ ions move into the double layer area. A simple calculation based upon the fact that 10^5 coulombs represent 6.23 x 10^{23}

Ag^+ ions shows, however, that there are more than enough Ag^+ ions (by one order of magnitude) in the first layer (of 1 cm^2) adjacent to the electrode to satisfy the 4 μC charge requirement assuming that there is one Ag^+ in each 10 $Å^2$ of a plane parallel to the electrode surface. Based on the above, it appears reasonable to assume that a concentration (potential) gradient of Ag^+ extending into the bulk is virtually nonexistent and, therefore, the diffuse double layer should act as a lumped parameter in the over-all series RC equivalent circuit.

The capacitance values for the graphite electrode which can now be considered as those of the true inner layer capacitance, in view of the above observations, are plotted in Fig. 10 as a function of potential. It can be seen that, within the potential range mentioned above, C_i is invariant and has a value of 8.0 $\mu F\ cm^{-2}$. Beyond these potential limits, the onset of the relatively rapid faradaic reaction corresponding to the discharge of either silver or iodine gives rise to additional time constants which mask the measurement of the double-layer capacitance in this region. The capacitance values plotted in these latter regions were those calculated from the tangent of the initial portion of the response curves to a galvanostatic step at the shortest accessible times. The values obtained, therefore, contain a contribution to the true value of C_i from the impedance associated with the particular faradaic process occurring.

It is interesting to speculate on the origin of the relatively low and invariant value of C_i observed in this case. To do this, reference may be made to recent work (40) concerning the double-layer structure of molten salts which indicates that to a very good approximation, this quantity is in large part determined by the structure of the particular molten salt. These studies have shown that the inner layer is present as a simple parallel plate capacitor and that it is essentially in series with another capacitor whose value is determined by the degree of long range order in the molten electrolyte which tends to prevent the formation of a very compact inner layer. In the case of solid AgI, the I^- ions are hexagonal close packed (41) at room temperature, and the bulk electrical properties are ohmic in nature. Similar to molten salts, it is to be expected (even more so in the case of a solid since it is difficult to visualize how the structure can become more compact) that this structure will predominate up to the inner layer region. This region, however, is far from ohmic and exhibits, as shown earlier, simple capacitive behavior. As a first approximation, the parallel plate capacitor model might then predict the observed value of C_i. This is given by

$$C_i = \frac{K_D \epsilon_0 A}{d} \qquad [5]$$

where K_D is the dielectric constant, ϵ_0 the permittivity of free space, d the distance between the capacitor plates, and A is the surface area. Since Ag^+ ions are relatively mobile with respect to I^- ions in the solid structure, it is to be expected that the Ag^+ ion population in a plane parallel to the graphite surface acts as the electrolyte side of the parallel plate capacitor model. The microscopic structure of the inner layer is thus most probably a plane of free electrons in the graphite extending to its surface, which is parallel to and opposite a plane of positive charges consisting of Ag^+ ions. For this model, d would then be expected to be given by the ionic radius of Ag^+ (1.2Å). The proposed inner layer structure also supposes that, in contrast to aqueous solution and molten salts (although the value of K_D for the inner layer may be a wrong assumption in this case) free space exists between the two capacitor plates in which case, $K_D = 1$. Substitution of the above values of d and K_D in [5] results in an inner layer capacitance of 7.4 $\mu F\ cm^{-2}$ in good agreement with the observed value of 8.0 $\mu F\ cm^{-2}$.

Application of Eq. [3] and [4] in the determination of the double-layer capacitance of the platinum electrode was not possible at even the shortest time ranges experimentally accessible at any electrode potential. This is well illustrated in Fig. 9 for the galvanostatic case where it is obvious that at short times, a deviation from the expected linearity (Eq. [4]) occurs. It may therefore be seen from a comparison of the behavior of both electrode systems that, although for each change of the electrode potential, Eq. [1] and [2] require that the activity of the silver and iodine at the interface should readjust to new equilibrium values by charge transfer, no such process appears to occur in the graphite case in the region of ideal polarizability within the time range of the above experiments. On the other hand, in the platinum case a rapid readjustment does occur involving, for example, the discharge of a finite quantity of silver onto the platinum surface for a cathodic potential step. That this readjustment does involve the formation of submonolayer quantities of deposited silver atoms and not adsorbed silver ions as has been suggested previously for the platinum-silver bromide case (28) has been proven by examining platinum electrodes with an electron microprobe after they had been potentiostatted at various positive electrode potentials. Clear proof of the presence of deposited silver on the platinum surface at such potentials was obtained (42). In view of the very rapid faradaic process occurring at the platinum-silver iodide interface, it is useful to consider the potential dependence of the total capacitance as determined by integration of the total charge passed during a 5 mV potential step. This dependence is shown in Fig. 11 where in the potential region for

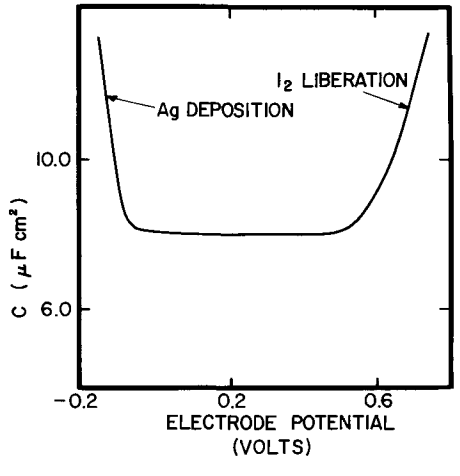

Fig. 10. Potential dependence of the capacitance of a graphite electrode determined from galvanostatic measurements recorded at microsecond times.

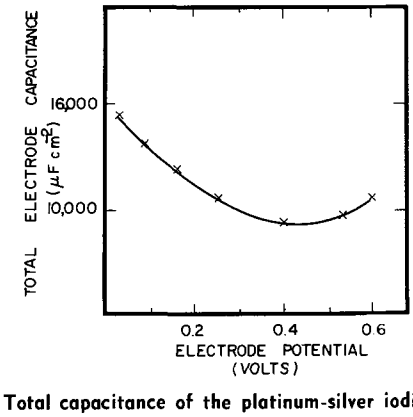

Fig. 11. Total capacitance of the platinum-silver iodide interface as a function of the electrode potential.

which no steady-state faradaic current flows (~0.0 to 0.5V), the form of the capacity-potential curve increases monotonically in either direction from the minimum at ~0.46V.

It is interesting to note that the form of the capacitance-potential curve shown in Fig. 11 is similar to that exhibited by liquid metal-molten alkali systems (40), where it has already been suggested that the high values of capacitance and its rapid increase as the potential becomes anodic or cathodic to the point of zero charge is due to contributions from the reversible faradaic reactions occurring at the interface (43). As stated earlier, faradaic complications are not present in the graphite case. It might thus be expected that the true double-layer capacitance of the platinum-silver iodide interface should exhibit a functional relationship with potential similar to that of graphite. This is particularly so since, as shown earlier, the capacitance of the double layer is predominantly determined by the ionic structure of the solid electrolyte and to a much lesser degree, by the nature of the particular electrode employed. Approximate evaluations of electrode capacitance at microsecond times obtained from results such as those shown in Fig. 9 yield substantially lower capacitance values (40-400 μF cm^{-2}). These measurements indicate that the true value of C_D might be obtainable if data could be gathered at times as short as several nanoseconds. This is possible through the use of the recently developed Transient Impedance Technique (31) which will be employed in future work on these systems.

In view of the difficulty in achieving an experimental separation of faradaic and nonfaradaic processes in the platinum system at room temperature and of the recently published (40) ideas concerning regions of ideal polarizability and ideal reversibility in molten salt systems, it appears important to exercise extreme caution in the interpretation of such experimentally measured capacitance values in terms of the structure of the interface and its eventual influence on electrode kinetics.

Acknowledgments

The authors wish to thank Dr. K. Doblhofer for many discussions concerning this work.

Manuscript submitted July 17, 1970; revised manuscript received *ca.* Sept. 8, 1970.

Any discussion of this paper will appear in a Discussion Section to be published in the December 1971 JOURNAL.

REFERENCES

1. J. N. Bradley and P. D. Greene, *Trans. Faraday Soc.*, **62**, 2069 (1966); **63**, 424 (1967).
2. B. B. Owens and G. R. Argue, *Science*, **157**, 308 (1967).
3. G. R. Argue, I. J. Groce, and B. B. Owens, Sixth International Power Source Symposium, Brighton, Sept. 1968.
4. J. N. Mrgudich, *This Journal*, **107**, 475 (1960).
5. M. N. Hull, Proceedings 22nd Annual Power Sources Conference, p. 106, PSC Publications Committee, Red Bank, N. J. (1968).
6. M. N. Hull, *Adv. Energy Conv.* (1970), in press.
7. R. T. Foley, *This Journal*, **116**, 13C (1969).
8. D. O. Raleigh, in "Progress in Solid State Chemistry," Vol. 3, pp. 83-134, H. Reiss, Editor, Pergamon Press, New York (1967).
9. S. Geller, *Science*, **157**, 310 (1957).
10. J. L. Weininger, *This Journal*, **105**, 439 (1958); **106**, 475 (1959).
11. J. N. Mrgudich, P. J. Bramhall, and J. J. Finnegan, *IEEE Trans.*, **AES-1**, 290 (1965).
12. J. D. Ferry, *J. Chem. Phys.*, **16**, 737 (1948).
13. J. R. Macdonald, *Phys. Rev.*, **92**, 4 (1953).
14. G. Jaffé, *Ann. Phys.*, **16**, 217 (1933); *Phys. Rev.*, **85**, 354 (1952).
15. H. Chang and G. Jaffé, *J. Chem. Phys.*, **20**, 1071 (1952).
16. R. J. Friauf, *ibid.*, **22**, 1329 (1954).
17. D. C. Grahame, *J. Am. Chem. Soc.*, **68**, 301 (1946).
18. J. H. Beaumont and P. W. M. Jacobs, *J. Phys. Chem. Solids*, **28**, 657 (1967).
19. G. C. Barker, *J. Electroanal. Chem.*, **12**, 495 (1966).
20. F. C. Anson, *J. Phys. Chem.*, **71**, 3605 (1967).
21. C. G. J. Baker and E. R. Buckle, *Trans. Faraday Soc.*, **64**, 469 (1968).
22. R. P. Buck, *J. Electroanal. Chem.*, **23**, 219 (1969).
23. J. R. Macdonald, *Trans. Faraday Soc.*, **66**, 943 (1970).
24. D. C. Grahame, *J. Chem. Phys.*, **21**, 1054 (1953).
25. D. M. Mohilner, in "Electroanalytical Chemistry" A. Bard, Editor, Vol. 1, p. 306, Marcel Dekker, New York (1966).
26. P. Delahay, "Double Layer and Electrode Kinetics," p. 33, John Wiley & Sons, Inc., New York (1965).
27. S. V. Karpachev and A. T. Filyaev, *Elektrokhimiya*, **2**, 617 (1966); **4**, 498 (1968).
28. D. O. Raleigh, *J. Phys. Chem.*, **70**, 689 (1966); **71**, 1785 (1967).
29. J. B. Wagner and C. Wagner, *J. Chem. Phys.*, **26**, 1597 (1957).
30. B. J. Bowles, *Electrochim. Acta*, **15**, 589 (1970); **15**, 737 (1970).
31. A. A. Pilla, *This Journal*, **117**, 467 (1970).
32. V. I. Melik-Gaikazyan and P. I. Dolin, *Dokl. Akad. Nauk SSSR*, **66**, 409 (1949).
33. D. I. Leikis and B. N. Kabanov, *Trudy Inst. Fiz. Khim. Akad. Nauk SSSR*, **6**, 5 (1957).
34. A. A. Pilla, *This Journal*, **116**, 1105 (1969).
35. D. C. Grahame, *Chem. Rev.*, **41**, 441 (1947).
36. A. A. Pilla, Paper 310 presented at the Los Angeles Meeting of the Society, May 10-15, 1970.
37. M. N. Hull, Paper 260 presented at the New York Meeting of the Society, May 4-9, 1969.
38. D. O. Raleigh, Paper 333 presented at the Los Angeles Meeting of the Society, May 10-15, 1970; D. O. Raleigh and H. R. Crowe, *This Journal*, **118**, 79 (1971).
39. A. A. Pilla, K. Doblhofer, and M. N. Hull, To be published.
40. A. D. Graves and D. Inman, *J. Electroanal. Chem.*, **25**, 357 (1970).
41. T. Takahashi, K. Kuwabara, and O. Yamamoto, *This Journal*, **116**, 357 (1969).
42. M. N. Hull, Unpublished results.
43. G. J. Hills and P. D. Power, *Trans. Faraday Soc.*, **64**, 1629 (1968).

Electrochemical Studies in Liquid and Solid AgBr

D. O. Raleigh and H. R. Crowe

Science Center, North American Rockwell Corporation, Thousand Oaks, California 91360

ABSTRACT

The comparative electrochemical properties of Pt electrodes have been studied in liquid AgBr at 429°C and solid AgBr at 300°-417°. At all temperatures, a significant time range of ideal polarization kinetics was observed. The intrinsic AgBr|Pt double-layer capacitance is the same for liquid and solid AgBr and is constant over the solid-state temperature range investigated. In addition, the principal characteristics of Ag submonolayer deposition are the same above and below the AgBr melting point. The results indicate the electrochemical properties are determined by an interfacial ion layer whose characteristics are independent of the state of the electrolyte. Decreasing double-layer charging rates were observed with decreasing solid-state temperature and are attributed to interface strain due to differential thermal contraction.

In a brief communication (1), the authors previously reported the achievement of ideal polarization kinetics at the AgBr|Pt solid-solid interface. While these findings were felt to be of special interest with regard to a previous body of literature on polarization capacitance in ionic solids (2), they were partial results of a more broadly based study to determine intrinsic electrode properties in a typical solid-electrolyte system. The purpose of the present publication is to present the full results of the study and give a better account of the experimental techniques involved.

Several previous studies (3) in our laboratory with the solid electrolyte AgBr were directed primarily toward determining the magnitude of its differential double-layer capacitance against various electrode materials at temperatures (>250°C) where it possesses good ionic conductivity. With polarizing d-c biases (Ag side negative) on solid-state cells of the type Ag|AgBr|(Pt or C), voltage steps were applied and the capacitances obtained by current integration. Static capacitance of order 25-45 $\mu f/cm^2$ were found against graphite, which could be attributed to a diffuse space charge layer in the AgBr. With platinum electrodes, minimal capacitances an order of magnitude larger were attributed to charge storage by an Ag^+ ion layer on the Pt surface. In addition, as the electrode voltage approached the silver potential, a large pseudocapacitance was observed, which could be attributed to the gradual buildup of an Ag monolayer on the Pt by Ag^+ ion discharge.

An additional item of interest in this previous work was the kinetics of interface charging. In contrast to the behavior expected for ideal polarized electrodes, plots of log i *vs.* t in response to the voltage steps were not linear. Their course suggested charging with a mixture of time constants, but the exact curve shapes showed some run-to-run variability, so effects involving the electrode contact were suspected. These cells consisted of cylindrical AgBr pellets spring-loaded between smoothed electrode faces, with contact made either by 1-hr annealing just below the AgBr melting point, or by briefly heating the cell above the melting point to flash-melt the electrode regions.

A principal objective of the present study was to reinvestigate the charging kinetics of the AgBr|Pt interface with a cell arrangement that permitted a more controlled method of forming the solid-solid interface. The cell employed consisted of a cylindrical Ag metal cup filled with fused AgBr, into which was lowered a centered Pt wire. The solid-solid interface was formed by slow cooling through the melting point. Because of the relatively large area of the Ag electrode, its impedance could be ignored. Since the arrangement also permitted electrochemical studies in the liquid state, a second objective of the experiments was to compare electrode characteristics in liquid and solid AgBr. Initial experiments were carried out at 429° and 417°, corresponding to several degrees on each side of the melting point (423°C), and later experiments explored the effect of cooling to 350° and 300° in the solid state.

Key words: solid electrolyte, AgBr electrochemistry, AgBr double layer.

Experimental

Cylindrical crucibles of 1 in. height, ½ in. ID, and ⅛ in. walls were machined from high-purity ¾ in. silver rod stock and cleaned in KCN and HBr solutions. For the melt loads, ½ in. cylinders of 99.95% AgBr single crystal rod stock, obtained from Semi Elements Inc., were used. Heating was carried out in a temperature-controlled Marshall furnace, using a vertical quartz furnace tube and a purified flowing argon atmosphere. Rubber tubing was avoided because of possible sulfur contamination. A stainless-steel-sheathed chromel-alumel thermocouple in the silver crucible wall served as an electrode lead and temperature indicator. The platinum electrode was attached to a coaxially mounted support rod which could be raised and lowered via a Pyrex sleeve seal.

Thermocouple-grade 20-mil Pt wire was generally employed for the working electrode. In one run, a 20-mil single-crystal Pt wire obtained from the Aremco Corporation was used. No observable difference in electrochemical properties was seen. Prior to their use, these wires were electropolished in fused NaCl-KCl as described previously (3b). In later runs, this operation was followed by an overnight anneal at 1550°C in air. Before immersion of the working electrode, a sacrificial Pt electrode was placed in the melt for several days at 0.2V (positive) to oxidize photolytic silver and help remove any melt impurities. In most runs, the AgBr was kept in the molten state for less than a week in all, in order to avoid extensive dendritic recrystallization of the Ag crucible walls.

On completion of electrochemical operations in the melt, the cell was cooled through the freezing point at about 2°C/hr. On freezing, the Pt electrode immersion remained the same, with a small contraction "pipe" forming at one side of the solidified melt. Electrochemical properties showed good reproducibility on cycling through the melting point and on cooling to room temperature and reheating. In the absence of other electrochemical operations, an 0.2V polarizing d-c bias was maintained on the cell.

The electrochemical operations carried out on the cell were cyclic voltammetry, a-c impedance measurements, galvanostatic chronopotentiometry, and potentiostatic chronocoulometry. The potentiostatic and galvanostatic operations were carried out essentially as described previously (3b). Series a-c resistance and capacitance were measured with a standard Wheatstone bridge arrangement (4) employing Gen-

eral Radio Company decade resistance and capacitance boxes, oscillographic nulling, and a 10-20 mV a-c signal amplitude. The frequency range was limited to 0.1 to 10 kHz because of the small resistance and large capacitances generally involved. Cyclic voltammetry was carried out with a standard arrangement.

Results

Steady-state cell current.—Solid-state cells of the type Ag|AgBr|Pt, which consist of a reversible and a more noble "inert" electrode, have been termed "polarization cells" (5) because of their ability to completely block steady-state ionic current over a wide range of applied d-c bias. In the appropriate bias range, the inert electrode functions as a capacitor toward ionic current and the only d-c cell current observed (in the absence of accidental depolarization effects) is a small electronic current. This current flows under field-free conditions, being due to an electron concentration difference at the two electrodes. In the present case, the current is given by (5, 6)

$$i_e = \frac{RT}{GF}\sigma_e^0 (1 - e^{-\epsilon F/RT})$$

where ϵ is the d-c bias, σ_e^0 is the local electronic conductivity at the interface with the reversible electrode, and G is the cell constant. Such cells have, in fact, been used to measure low-level electronic conductivity in predominantly ionic-conducting solids (6). Analogous experiments, however, have not been carried out with the same electrolyte in the liquid state.

At solid-state temperatures, steady-state cell currents <10 μA were obtained which showed the expected bias dependence and agreed well with previous data (7). In the liquid state at 429°, the current was 6-8 times as large as at 417°. The same bias dependence was observed, but the current level showed day-to-day drifts and agreed only approximately among various cells. It appears that an electronic current is still involved. Where the solid-state current, however, is strictly a diffusional current, it seems likely that at least some of the enhancement in the liquid state is due to convection. Thus, liquid-state cells, at least in the present configuration, do not seem especially suited to electronic conductivity measurements. Since such currents are in any event small and reasonably constant in the short term, their effects can be ignored in electrochemical measurements by instrumentally compensating for them in potentiostatic measurements and by using relatively large currents in galvanostatic ones. At 350° and 300°C these currents were small enough to neglect completely. In a-c impedance measurements, they represent a high-resistance parallel circuit path that can be ignored.

Cyclic voltammetry.—To obtain an over-all picture of the electrode behavior throughout the polarizing range, cyclic voltammagrams were carried out at all four temperatures. Figure 1 shows comparative sweep curves at 429° and 417°, corrected for steady-state cell current. The solid-state curve shows a broad range of purely capacitative charging. As the Ag potential is approached, a current attributed to gradual Ag monolayer deposition (3) is observed, with the start of the reverse sweep corresponding to monolayer stripping. Above 0.6V, effects attributable to a mixture of electronic hole current and Br_2 discharge are observed.

In the liquid state, the low-bias behavior is similar, but an apparent redox process appears above 0.4V and limits the range of liquid-state polarizability. Pt bromides at these temperatures are not stable in their standard states (8), but one expects bromination in the melt to be favored by halogen complex formation and melt dilution. In solid AgBr, it is unlikely that Pt halogen complexes could form in the crystal lattice and equally unlikely for Pt ions to have appreciable mobility. This seems the most likely explanation for the significant difference in electrochemical behavior observed here with the liquid and solid electrolytes.

Cyclic voltammagrams at 300° and 350°C were similar to one another and differed mainly from the 417° curves in the low-bias region. Figure 2 shows comparative curves at 417° and 350° in this region. The main difference is an apparent delayed monolayer stripping peak at 417°. When sweeps at 417° were made at successively more rapid rates, the delay shortened and eventually became negligible. It appears that the diffusion coefficient of Ag in Pt is large enough at the two highest temperatures to permit some in-diffusion of the monolayer during slow sweep cycles, resulting in a stripping delay. This and related effects will be discussed more extensively in subsequent sections.

A-C cell impedance.—The first a-c impedance measurements taken were series resistance and capacitance as a function of frequency at several fixed cell biases. The biases chiefly used were 0.05 and 0.25V to correspond to regions of the faradaic monolayer process and double-layer charging, respectively. In the molten state, impedances at 0.05V showed reasonable stability and run-to-run reproducibility, but early measurements at 0.25V gave considerable problems in this respect. Figure 3 shows a collection of capacitance-frequency results in the double-layer charging region at 429° from various runs. In addition to considerable day-to-day drift and irreproducibility in capacitance values, large low-frequency series resistances (up to 80 ohms at 0.1 kHz) were observed. These were electrode resistances, since the bulk (high-frequency limit) cell resistance at 429° was ~1 ohm.

A number of attempts were made to achieve more ideal capacitative charging behavior. These involved melt pretreatment, Pt electrode preparation, and cycling through the electrolyte melting point. In Fig. 3, a single data set (run 5, 4th cycle) gave a virtually frequency-independent capacitance associated with a

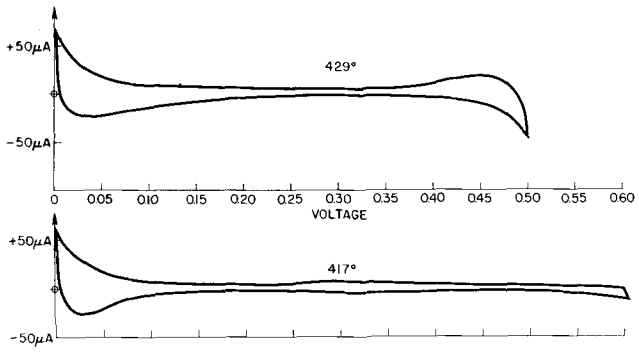

Fig. 1. Cyclic voltammagrams, Pt electrode in AgBr, 429° and 417°, sweep rate 35 mV/sec, sweep direction counterclockwise.

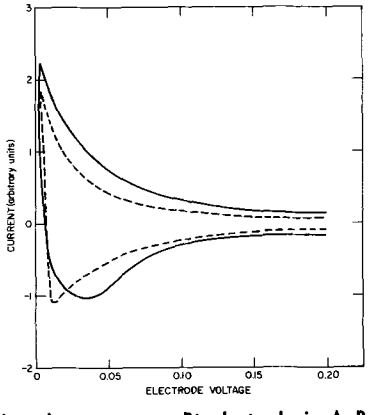

Fig. 2. Cyclic voltammagrams, Pt electrode in AgBr, low voltage segments, 417° (solid) and 350° (dotted), sweep rate 35 mV/sec, sweep direction counterclockwise.

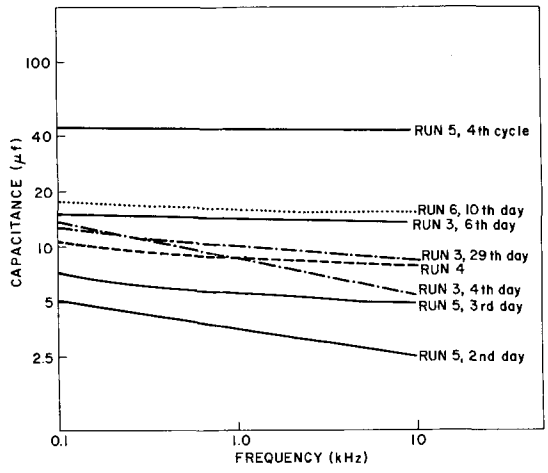

Fig. 3. A-C capacitance of Pt electrode in AgBr(l) at 429° and 0.25V as function of frequency (various runs).

very low (0.5 ohm) electrode resistance. This behavior was finally reproduced and stable, reproducible impedances obtained by the use of melt pretreatment with one or more sacrificial Pt electrodes, and the previously described Pt electropolishing and annealing procedures. With these precautions, the capacitance at 0.25V varied as little as 1% per decade of frequency and agreed to within 5% among various runs. It is felt that adsorbable melt impurities and electrode surface irregularities were chiefly responsible for the previous nonideal behavior.

When ideal capacitative charging (frequency-independent capacitance, low series electrode resistance) was achieved, the first operation was to monitor the a-c capacitance at 0.25V and 1 kHz during a slow cooling through the electrolyte melting point. On freezing, no change whatever was observed. Figure 4 shows the capacitance at 1 kHz as a function of cell voltage (potential with respect to the Ag electrode) at 429° and 417°. Above 0.4V, the curves diverge, presumably because of the Pt oxidation indicated in the cyclic voltammetric studies. At lower potentials, however, the curves are virtually congruent. It would appear, then, that the kinetics and magnitude not only of double layer charging but of the faradaic monolayer process are essentially identical in liquid and solid AgBr. We may anticipate somewhat our discussion of this result by recalling that we had previously (3) attributed the large double layer capacitance of AgBr on Pt to charge storage by a layer of adsorbed electrolyte ions. Our results would then indicate that the nature of this layer is independent of the state of the electrolyte.

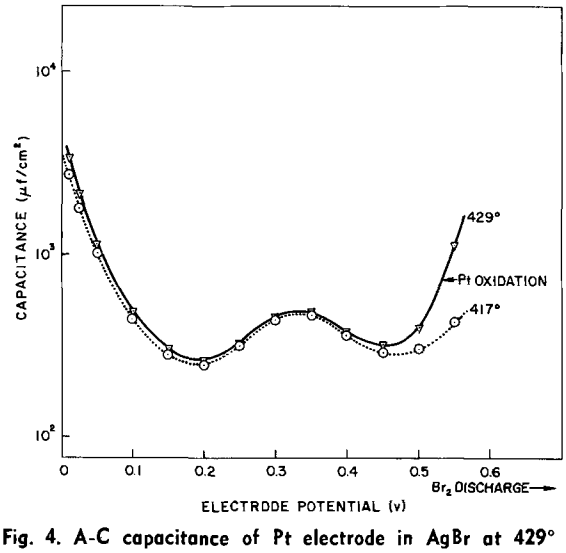

Fig. 4. A-C capacitance of Pt electrode in AgBr at 429° and 417° at 1 kHz as function of cell voltage.

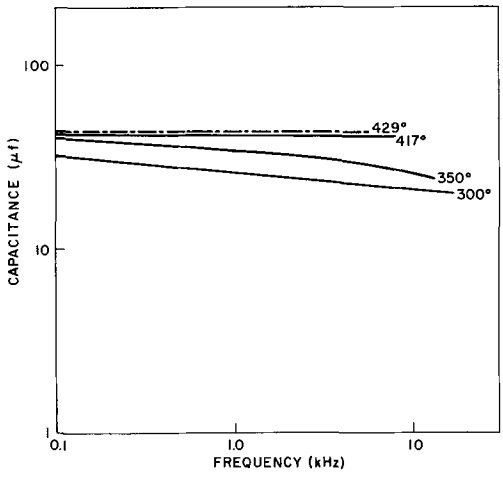

Fig. 5. A-C capacitance of Pt electrode in AgBr at 0.25V as function of frequency and temperature.

At 350° and 300°, capacitance values were smaller and more frequency-dependent. Figure 5 shows the frequency dependence in the double-layer region at the four temperatures. Capacitance-voltage curves at 1 kHz showed the same shape as the 417° curve of Fig. 4, being displaced downward by a more or less constant fraction. This and the appearance of Fig. 5 suggested the onset of finite charging kinetics with decreasing temperature, rather than a change in the intrinsic interface capacitance. Subsequent data confirmed this picture.

In the faradaic region, a-c capacitances were higher and generally more frequency dependent. Figure 6 shows the relative frequency dependences of the electrode capacitance in the double layer and faradaic regions at 429° and 300°C. In the 0.05V case, the "capacitance" is properly a pseudocapacitance. Its frequency dependence appears to reflect a finite rate for the monolayer faradaic process. With decreasing temperature, the magnitude of the pseudocapacitance decreased, but its frequency slope remained relatively unchanged. The result is that the frequency dependences at 0.05V and 0.25V were roughly the same at 300°. No attempt was made to fit the faradaic pseudocapacitance to a reaction model. As we shall see, more direct evidence on the nature of the faradaic process was provided by potentiostatic coulometry measurements.

Potentiostatic coulometry (capacitative region).—We noted above that Fig. 5 and the shapes of a-c capacitance-bias curves at 350° and 300° suggested the onset of finite double-layer charging kinetics at these temperatures rather than a change in the intrinsic capacitance. This was verified by preliminary potentiostatic coulometry measurements with an X-Y

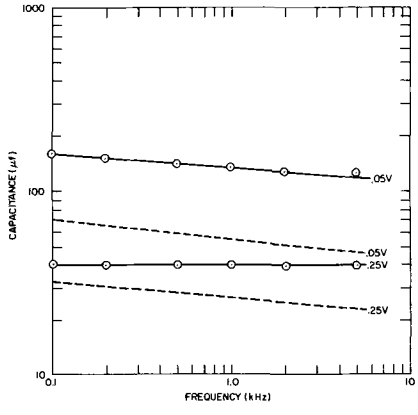

Fig. 6. A-C capacitance of Pt electrode in AgBr at 429° (solid) and 300° (dotted) in faradaic (0.05V) and capacitative (0.25V) voltage regions as a function of frequency.

recorder, which showed that the total (static) differential capacitance at these temperatures was the same as the a-c capacitance at 417° and 429°. The same measurements, however, showed the total capacitance at 417° and 429° to be significantly greater than the a-c capacitance. To clarify the situation, d-c voltage steps were applied in the capacitance charging region at all four temperatures and $Q(t)$ monitored continuously over the time range 0.1 msec to several hundred seconds by a combination of oscillographic and recorder displays.

Figure 7 shows a $Q(t)$ curve at 417° for the voltage step 0.20-0.25V. Qualitatively similar curves were seen elsewhere in the capacitative region at 417° and 429°. Two distinct charge transfer processes, well separated in time scale, appear to be involved. The capacitance corresponding to the first plateau was the same at all four temperatures, was well reproduced from run to run, and matched the a-c capacitance data at 417° and 429°. This was taken to be the intrinsic interface capacitance.

The capacitance corresponding to the slow second charge transfer process was significant only at 417° and 429°, was generally different at these temperatures, and varied by up to a factor of two among various runs. It was first thought to correspond to slow double-layer relaxation involving ion redistribution about irregularities on the electrode surface. Its magnitude, however, was too large for this. Its most likely source was indicated from the results of $Q(t)$ *vs.* $t^{1/2}$ plots. Figure 8 shows such a plot for the Fig. 7 data in the time range 10 msec to 225 sec. A linear variation is seen for times up to 90 sec, corresponding to a time range of almost four orders of magnitude. It appears that a diffusion-limited impurity current is involved; the $t = 0$ intercept gives the intrinsic capacitance. The fact that the charge transfer terminates indicates simply that the impurity "reservoir" is of finite extent. Since the total amount of impurity charge involved throughout the capacitative voltage range is only of order one monolayer, it seems pointless to guess as to the nature of the specific impurity or mixture of impurities.

Figure 9 shows the effective capacitance from $Q(t)$ curves at all four temperatures. The voltage step in question is 0.225 → 0.275V, so corresponds to the capacitance at or near 0.25V. At 429° and 417°, the effective capacitance was augmented at long times by the above-described impurity diffusion, which effect was essentially absent at 350° and 300°. At the short-time end, the intrinsic charging kinetics at 429° are apparently too fast to be observed as a finite charging rate. Supplemental oscillographic

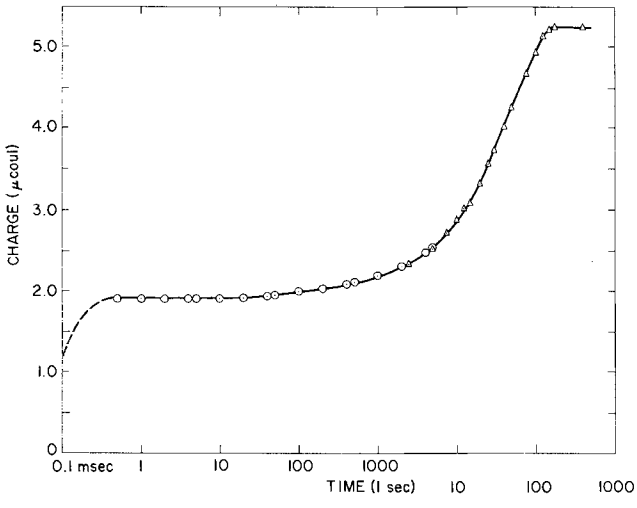

Fig. 7. Chronocoulometric curve for Pt electrode in AgBr(s) at 417° for voltage step (0.20-0.25V) in capacitative charging region. Open circles indicate oscillographic data; triangles are X-Y recorder data.

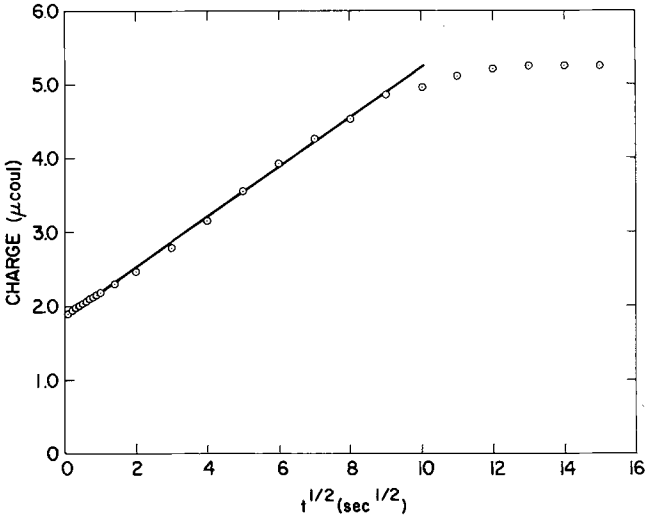

Fig. 8. Data of Fig. 7 replotted as function of $t^{1/2}(sec^{1/2})$ in time range 10 msec to 225 sec.

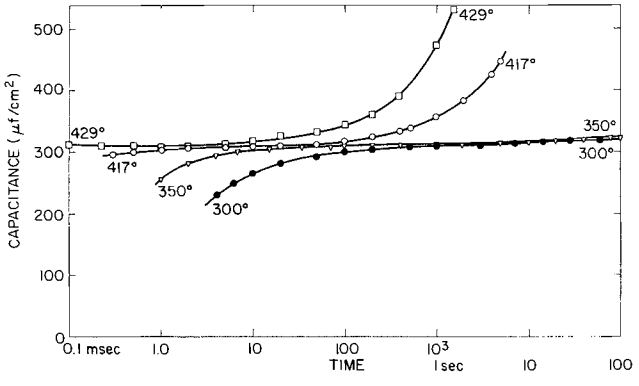

Fig. 9. Effective capacitance of Pt electrode in AgBr at 0.25V in liquid (429°) and solid electrolyte states from coulometric charging data.

sweeps showing charge and voltage rise times indicated no charging lag down to 20 μsec. At 417°, evidence of finite charging kinetics appears. The effect is more pronounced at 350° and still more pronounced at 300°. Since coulometrically determined capacitances are only valid for times at least several times as large as the intrinsic RC charging time of the cell, the curves shown here are for t such that $(1 - e^{-t/RC})$ is at least 0.98. Here, R is the cell resistance and C is the plateau-level capacitance. The start of the curve shifts to successively longer times at lower temperatures because of increasing electrolyte resistance (~40 ohm at 300°). The curves, then, show the relative interface charging kinetics at the four temperatures.

The principal result of the Fig. 9 curves is to define a single temperature-independent intrinsic interface capacitance. Similar sets of curves were obtained at other voltages in the capacitative charging region, the range of which is estimated to be about 0.15V to 0.55V. In this range, plateau-level capacitances from $Q(t)$ curves with various cells, voltages, and temperatures agreed with the Fig. 4 values to an average of 5%. Thus, the 417° curve of Fig. 4 in this region gives the intrinsic interface capacitance of AgBr against Pt to solid-state temperatures at least as low as 300°. In the temperature range investigated, corresponding to a factor of 40 change in electrolyte conductivity, the capacitance appears to depend solely on the electrode potential.

A further matter of interest in this voltage region was that $Q(t)$ curves in the neighborhood of the capacitance maximum (~ 0.33V) showed several distinct differences from $Q(t)$ curves at the minima on

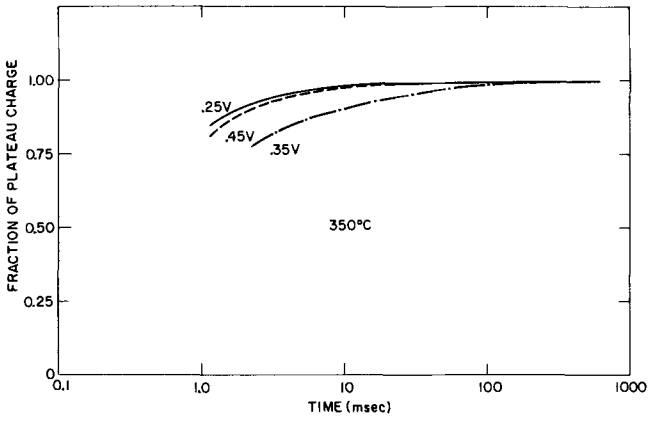

Fig. 10. Initial portions of chronocoulometric curves from 0.225-0.275V, 0.325-0.375V, and 0.425-0.475V voltage steps at 350°C, expressed as fraction of plateau-level charge.

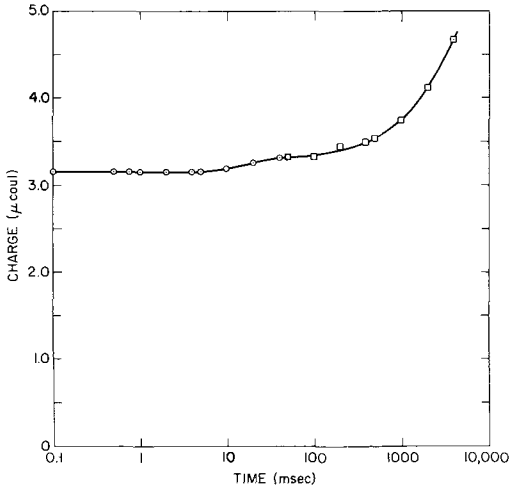

Fig. 11. Coulometric curve at 429° for voltage step (0.30-0.35V) in neighborhood of capacitance maximum. Open circles indicate oscillographic data; squares are X-Y recorder data.

either side. First, at temperatures where finite interface charging kinetics were observed, charging was several times slower at the capacitance maximum. This is shown in Fig. 10 for 350°C data, which indicates a factor of three slower charging time at the maximum. In addition, the full charging curves for voltage steps in the maximum region showed an unusual sigmoidal feature. This feature, seen in the time range 5-50 msec in Fig. 11, was most readily visible at 429° and 417°C, was partially observed at 350°, and was not seen at 300° because of masking due to decreasing interface charging rates at the lower temperatures. Both this and the decreased charging kinetics in the maximum region suggest structural characteristics of the interface double layer which will be discussed.

Potentiostatic coulometry (monolayer faradaic region).—We have already mentioned that a-c impedance measurements showed generally slower kinetics for the monolayer faradaic process than for capacitative charging. It was of interest to see what further information on the faradaic process could be obtained coulometrically. Earlier work (3) showed that submonolayer electrodeposition in response to an appropriate voltage step occurred more slowly than the stripping process due to the reverse step. Since this effect presumably involves steric factors in the process of depositing a uniform monolayer, it was felt that more basic information could be obtained from studying the stripping process.

A cell was equilibrated at 0.002V to achieve nearly complete monolayer coverage at a polarizing bias and the voltage then stepped to 0.200V to achieve

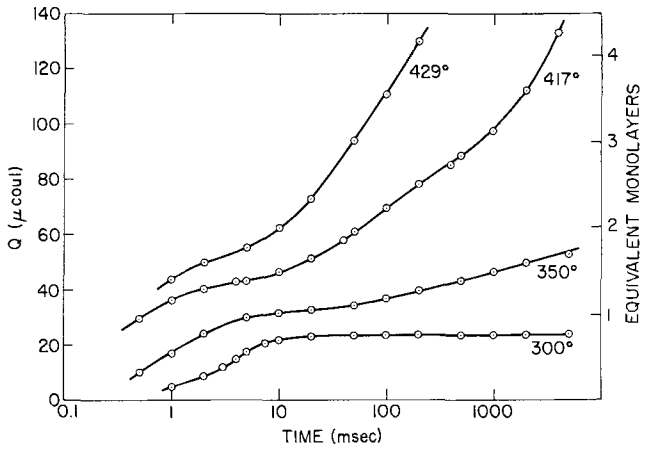

Fig. 12. Coulometric stripping curves corresponding to voltage step 0.002-0.200V. Right-side ordinate gives equivalent number of monolayers corresponding to charge values on left side.

nearly complete stripping. Figure 12 shows the $Q(t)$ curves at all four temperatures. Although not shown here, and although often obscured by slow drifts in the steady-state cell current, the curves were generally observed to level out to show completed charge transfer in the time range of several hundreds of seconds.

Only at 300°C was a clean coulometric stripping curve obtained in the subsecond region. The higher temperatures appear to show a rapid primary stripping process mixed with an increasing contribution from one or more slower faradaic processes. We noted earlier (Fig. 2) that cyclic voltammagrams indicated Ag diffusion into Pt at the two highest temperatures during a cyclic sweep. Accordingly, it was expected that the primary stripping process in Fig. 12 was being augmented by outdiffusion of Ag that had entered the Pt during the previous equilibration at 0.002V.

Figure 13 shows the data for the three highest temperatures in Fig. 12 replotted as $Q(t)$ *vs.* $t^{1/2}$ in the time range 0.5 msec to 4.0 sec. At each temperature, a curve with two linear regions is obtained, possibly indicating outdiffusion by a mixture of mechanisms. In any event, the curves permit a clean separation of kinetics presumably associated with diffusion and with the primary stripping process, allowing extrap-

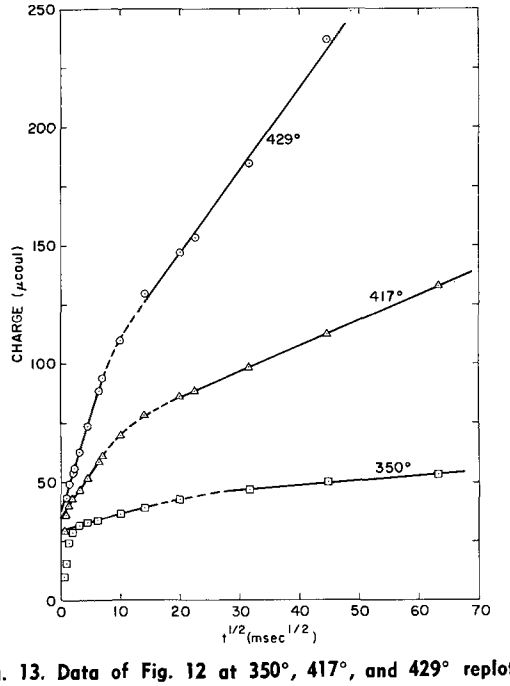

Fig. 13. Data of Fig. 12 at 350°, 417°, and 429° replotted as Q *vs.* $t^{1/2}$.

olation to $t = 0$ to obtain the charge associated with the latter process.

To obtain the monolayer coverage from the $t = 0$ intercepts, it was necessary to correct for double layer charging and incomplete monolayer stripping. An admittedly arbitrary double layer correction was made by assuming that the minimum capacitance of 0.19V from the 417° curve of Fig. 4 applied across the monolayer voltage region. Galvanostatic monolayer coverage curves from the present and previous (3) work indicate that the coverage at the 0.002V initial voltage for the stripping step is close to 94% complete and that, at 0.200V, stripping is essentially complete. The double-layer corrected $Q(t = 0)$ values were thus divided by 0.94 in calculating the number of monolayers coverage. Table I gives the coverage data for a particular run, along with galvanostatically derived coverage values.

At 417° and 429°C, the total charge transfer, obtained with charge integration times of several hundreds of seconds, was considerably greater than the "fast" monolayer charge. At these temperatures, charge values varied a good deal from run to run, showing a range of 5 to 20 equivalent Ag monolayers. Integrations carried out step wise over the voltage range 0-0.2V showed the same general voltage dependence pattern as the a-c capacitance in this range. Thus, it was felt that Ag metal, rather than an impurity, was involved. With sufficiently long waits, the slower charge transfers corresponding to (reverse polarity) monolayer buildup voltage steps approached those obtained with stripping steps. From this and the fact that completed charge transfer was generally observed in the long-time limit, it appeared that the presumed Ag diffusion processes involved a porous surface layer on the Pt, backed up by relatively impermeable bulk Pt.

Galvanostatic chronopotentiometry.—Previous chronopotentiometric studies (3) on the AgBr(s)|Pt(s) system had been carried out at 250° and 300°C to determine the nature of Ag electrodeposition on bare Pt and obtain data on the fractional monolayer coverage as a function of Ag activity. The present galvanostatic work was carried out in much the same way, with the objectives of extending the previous studies to higher solid-state temperatures and to the liquid state.

In these measurements, the cell is abruptly (~4 msec) switched from a polarizing bias well outside the monolayer range (*e.g.*, 0.3V) to a constant-current mode which passes Ag^+ ions toward the Pt, and the voltage is monitored oscillographically. The voltage trace is initially approximately linear, corresponding to double-layer charging. As the theoretical Ag(s)|AgBr(s) potential (zero volts) is approached, the trace rounds off and approaches it asymptotically, indicating gradual submonolayer deposition and the absence of any appreciable overpotential. By extrapolating the initial linear part, one can correct the total charge ($Q = it$) at any time t for the double-layer charging contribution, to obtain the faradaic charge as a function of voltage. If matching data are obtained at various current levels, the iR-corrected voltage may be assumed to be the equilibrium electrode voltage and, accordingly, data on fractional ideal monolayer coverage obtained as a function of Ag activity.

The present sweeps were carried out at at least 7.5 mA/cm² so that the electronic cell current at 429° would be relatively negligible, *i.e.*, ionic current would predominate. At these current levels, coverage is completed in at least 50 msec, so that contributions from Ag diffusion into the Pt should be minor. Comparisons of 7.5 and 15 mA/cm² sweeps on the basis of total charge passed as abscissa showed excellent congruence. Figure 14 shows an activity-coverage plot at 429° and 7.5 mA/cm² current level. As before, linear log-log plots were obtained through most of the submonolayer region. Deviations at low activities probably represent a systematic extrapolation error in the double layer charge at the low charge levels involved. The slight superunit Ag activity in the postmonolayer region was independent of the current level and is again (3b) attributed to some variety of relaxable stress in the monolayer. Extrapolation of the sub- and postmonolayer trace portions permits determination of an effective monolayer coverage.

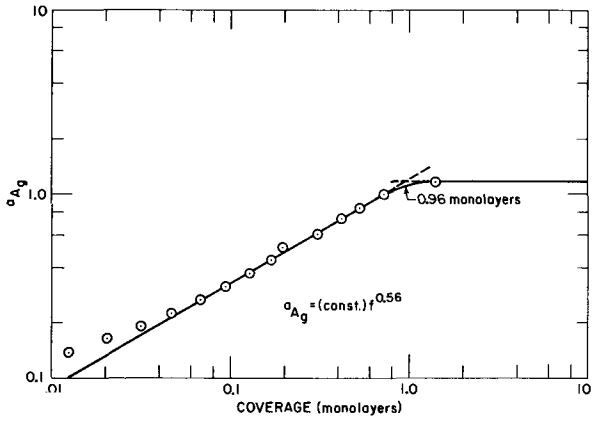

Fig. 14. Silver metal activity at AgBr|Pt interface vs. fraction of ideal monolayer coverage, from galvanostatic data at 429°C and 7.5 mA/cm².

Activity-coverage slopes, representing n in the empirical relationship $a_{Ag} = (\text{const})\ f^n$, averaged 0.60. These ranged 0.55 to 0.65 more or less randomly, showing no temperature dependence. The average value is in good agreement with that from the previous work (0.57). Thus, the activity-coverage power-relationship is not a function of the temperature or state of the electrolyte. The monolayer coverage values for a given run are shown in Table I, along with those from the potentiostatic data. The range of coverages is about the same by the two methods. The galvanostatic determinations, however, involve more random error, as seen by the scatter of n values and the smoother temperature dependence of the potentiostatic coverages. Because of this, as well as unknown contributions from Ag diffusion and monolayer buildup steric effects in the galvanostatic process, the potentiostatic coverages are felt to be more reliable.

Table I. Fractional Ag monolayer coverage at unit activity from coulometric and galvanostatic data

	429°C	417°C	350°C	300°C
Coulometric	1.09	0.97	0.82	0.58
Galvanostatic	0.96	0.80	0.60	0.65

Discussion

Two results are of special interest. First, of course, is success in preparing a solid-solid interface with a time range of electrochemically ideal polarization behavior. This behavior is manifested as a range of frequency-independent a-c capacitance and as an appreciable time range of completed charge transfer in $Q(t)$ plots. Solid-solid interfaces are, needless to say, a relatively unexplored area. The present results indicate it is indeed possible to prepare such interfaces in a sufficiently reproducible manner to obtain properties characterizable as "intrinsic." In the case of the interface between an ionic and an electronic conductor, electrochemical techniques provide a sensitive, sophisticated means of interface characterization.

In the present system, however, it is perhaps equally interesting that, with the exception of Pt oxidation in the melt above 0.45V, there was little if any basic difference in interface behavior with the electrolyte in liquid and solid forms. We already noted from the impedance data that, in the neighborhood of the electrolyte melting point, the kinetics and magnitude

of both double-layer charging and the monolayer faradaic process are essentially the same. Such variations in electrochemical properties as were observed were more a matter of the temperature than the state of the electrolyte.

One might expect that the electrochemical processes most influenced by whether the electrolyte is liquid or solid would be those whose rate was at least partially determined by transport in the electrolyte. In the present case, AgBr is a good ionic conductor on both sides of its melting point; the conductivity rises only severalfold on melting. Since no supporting electrolyte is involved, polarization in the electrolyte can only be ohmic and, in the present case, ohmic effects were small. Also, as we have stated, the size of the double-layer capacitance of AgBr against Pt requires it to involve charge storage in a compact ion layer. Thus, the electrolyte in the present case enters the picture only as one member of a phase boundary at which the natures of the electrochemical processes of interest are determined. The present results indicate that the nature of the first ion layer on the Pt and of a partially deposited Ag monolayer are independent of whether the electrolyte is liquid or solid. It is perhaps reasonable, then, to think of the electrolyte as no more than a mobile transport medium for supplying ions to an interface layer which has its own structural characteristics.

For the source of the large double-layer capacitances, we postulate a considerable variability in the composition of the interface ion layer with changing voltage. For the maximum charge storage capability, we visualize the extremes of a close-packed layer of purely cations and purely anions at the ends of the electrode potential range corresponding to Ag and Br_2 deposition. Such a layer would presumably involve chemisorptive bonding to the platinum and be thought of as distinct from the AgBr crystal lattice behind it. Because of the virtually, identical structures and lattice parameters of Ag and Pt, a layer of close-packed Ag^+ ions on Pt should represent the same charge as a single lattice layer of Ag metal; about 240 μcoul/cm^2. If we assume the Br^- ion coverage to be reduced by the square of the Ag^+:Br^- ionic radius ratio (0.42), the maximal Br^- coverage contributes 100 μcoul/cm^2 for a total of 340 μcoul/cm^2.

It is of interest to compare this figure with an estimate from Fig. 4 of the total double-layer charge over the full electrode potential range for AgBr. From galvanic cell measurements of Yushina *et al.* (9), the full electrode potential range, *i.e.*, the AgBr decomposition potential, is about 0.81V near the AgBr melting point. Earlier, we estimated the double-layer capacitance in the faradaic region of Fig. 4 to be given by the capacitance minimum at 0.19V. In fact, it would be more realistic to assume that the capacitance from the above type of ion-layer charge storage model would drop to zero at the two ends of the voltage range (corresponding to complete anion or cation coverage) and rise to a maximum at an intermediate potential. With this assumption, we estimate crudely from Fig. 4 that the total double-layer charge in the voltage range zero to 0.81V is about 175 μcoul/cm^2, or roughly half the maximal theoretical value. Thus, the ion layer model provides sufficient charge storage capability without the necessity of assuming full ionic coverage at the ends of the potential range. We feel this model best accounts for the large, reproducible capacitances of AgBr on Pt observed with both single-crystal and polycrystalline electrodes and with a number of different interface preparation techniques.

In this respect, two points seem significant. First, there is a considerable literature on double-layer capacitance in fused salts (10). Several double-layer models have been proposed, but these were developed to account for parabolic-shaped experimental capacitance-voltage curves with relatively small (20-40 μf/cm^2) and sharp capacitance minima. Moreover, these models dealt rather specifically with the liquid state. The totally different qualitative and quantitative aspects of the present results required a substantially different model, equally applicable to the liquid and solid states. The model proposed, however, is in line with the general observation in a recent review (10) that the double-layer capacitance in fused salts is most likely a special property of the melt structure at the interface.

Second, although the results reported in the present and previous (3) work allow one to characterize distinct voltage regions in terms of a predominant faradaic process and predominant double-layer charging, it is reasonable to inquire whether a faradaic component might nonetheless be partially responsible for the large apparent double-layer capacitances. Galvanostatic data, such as shown in Fig. 14, indicate negligible Ag monolayer coverage above 0.15V. Capacitances are frequency-dependent below 0.15V and frequency-independent above this voltage. The monolayer coverage, as well as apparent long-time impurity and diffusion effects (Fig. 8, 13) were temperature-dependent, while the presumed intrinsic capacitance is not. A possibility worth considering is that of a residual "tail" of low-activity metallic Ag in the double-layer region, rather more tightly bonded to the Pt than the bulk of the Ag monolayer. Such a faradaic component, however, should monotonically diminish with increasing potential, where, in fact, we see a capacitance maximum at 0.33V. Moreover, a frequency-independent faradaic capacitance above 0.15V would require faster reaction kinetics for the "residual" Ag than for the bulk monolayer. This seems unlikely for more tightly bonded Ag. The good run-to-run reproducibility of the presumed intrinsic capacitance tends to rule out fast faradaic impurity reactions. In sum, significant faradaic contributions seem unlikely.

The ion layer capacitance model provides a basis for interpreting the observed decrease in the capacitative charging rate with decreasing temperature, as well as the unique kinetics effects associated with the capacitance maximum. Regarding the former, it seems likely that interface strain induced by different thermal expansion rates of the solids in question is an inevitable property of solid-solid interfaces. At the melting point, the interface is presumably formed in a strain-free condition. On cooling to 300°C, the linear contraction in AgBr is about 1.3% (11); in Pt, it is about one-tenth this value. Thus, significant strain can be expected. The result may be that work is required to exchange Ag^+ ions between the interface region and the bulk electrolyte, resulting in decreased charging kinetics. In the present cell configuration, the interface region would be compressively strained. Other strain and resultant kinetic effects might be expected with other configurations.

The ion layer model implies that the capacitative charging in Fig. 4 involves cations at low biases, anions at high biases, and possibly a mixture of them in the neighborhood of the maximum. (It should be remarked here that anion layer formation with a cation-conducting electrolyte can be readily imagined in terms of removal of cations from a normal lattice layer.) In fact, the decreased charging kinetics and development of charge relaxation behavior (Fig. 10 and 11) in the neighborhood of the capacitance maximum suggests some manner of ordering or layer structure in this voltage range. This might be expected with a mixture of anions and cations in the layer, though its structure and composition might be quite different from a normal lattice layer of AgBr. In any event, an ordered structure might well involve decreased charging kinetics for steric reasons and might involve rearrangement from a "fast" initial configuration. It is perhaps appropriate at this time to note that the capacitance maximum was well reproduced with a number of different cells and that no peak lags were observed in cyclic voltammetric sweeps. Thus, it seems likely

to be a double-layer effect rather than to have resulted from an impurity redox reaction.

A number of characteristics of the monolayer faradaic reaction were ascertained. From the relative frequency slope of a-c capacitances at 0.05V and 0.25V (Fig. 6), it appears that the double-layer charging process is considerably faster at 429°, but that the rates of the two processes are about the same at 300°. Much the same picture is indicated by the potentiostatic coulometry data. Since both processes involve ion migration, to or from the electrode surface, the comparison at 429° would indicate a finite rate for the electron transfer step. With decreasing temperature, the decreasing rate for the charging process indicates both processes become rate determined by ion transport into or out of the interface region.

We have previously discussed galvanostatic monolayer coverage results for Ag on Pt in some detail (3b). In the present work, it was possible to extend the data to higher solid-state temperatures and to the liquid state. In addition, the potentiostatic coulometry measurements provided independent coverage data and supplied information as to the role of Ag diffusion into the Pt. The observed effect of increasing temperature was to increase the total coverage without changing the power dependence of the activity-coverage relationship, *i.e.*, to shift the Fig. 14 type curve to the right. The total coverage is envisioned here as the "surface solubility" or absorptivity of metallic Ag on Pt, which is about one full monolayer at the upper temperatures and decreases with decreasing temperature. The constancy of the activity-coverage slope indicates that it essentially involves the thermodynamics of the Ag-Pt system, irrespective of the temperature and state of the electrolyte.

Finally, we consider some aspects of Ag diffusion in the Pt. We have already noted that the leveling out of faradaic $Q(t)$ curves in the long time limit of several hundred seconds, as well as approximate agreement of indiffusion and outdiffusion charge values, indicates the Pt consists of a relatively porous surface layer backed up by relatively impermeable bulk Pt. Possible sources of the surface porosity are microcracks, dislocations, and a high concentration of point defects (*e.g.*, vacancies) near the surface.

The existence of two linear regions in the Q *vs.* $t^{1/2}$ plots of Fig. 13 suggests a combination of porosity types, but another explanation is also possible. Since defects such as microcracks and dislocations are scattered about in specific locations on the electrode surface, diffusion in them should also involve lateral diffusion in the interface. In this case, the over-all diffusion rate should be limited by interface diffusion at short times and diffusion in the electrode at long times. We have already indicated that interface strain in the solid state reduces ion mobility in the interface, as suggested by the decrease of capacitative charging kinetics with decreasing temperature. This may help explain the considerable reduction in the extent of diffusion at the lowest temperatures. A similar explanation may, in fact, apply to the previously observed impurity currents (Fig. 8) in the capacitative charging region.

Manuscript submitted July 28, 1970; revised manuscript received *ca.* Sept. 16, 1970.

Any discussion of this paper will appear in a Discussion Section to be published in the December 1971 JOURNAL.

REFERENCES

1. D. O. Raleigh and H. R. Crowe, *Solid State Comm.*, **8**, 955 (1970).
2. D. O. Raleigh, *J. Phys. Chem. Solids*, **29**, 261 (1968).
3. D. O. Raleigh, (a) *J. Phys. Chem.*, **70**, 689 (1966); (b) *ibid.*, **71**, 1785 (1967).
4. See, for instance, D. C. Grahame, *J. Am. Chem. Soc.*, **68**, 301 (1946).
5. C. Wagner, *Proc. Int. Comm. Electrochem. Thermo. Kinetics (CITCE)*, **7**, 361 (1957); *Z. Elektrochem.*, **60**, 4 (1956).
6. D. O. Raleigh, "Progress in Solid State Chemistry," Vol. 3, chap. 3, pp. 104-7, H. Reiss, Editor, Pergamon Press, Oxford (1967).
7. B. Ilschner, *J. Chem. Phys.*, **28**, 1109 (1958).
8. C. E. Wicks and F. E. Block, *U.S. Bur. Mines Bull.* **605**, pp. 91-2 (1963).
9. L. D. Yushina, S. F. Palguev, and S. V Karpachev, *Russ. J. Phys. Chem.*, **35**, 165 (1961).
10. For a recent review of this area, see A. D. Graves and D. Inman, *J. Electroanal. Chem.*, **25**, 357 (1970).
11. A. W. Lawson, *Phys. Rev.* **78**, 185 (1950).

Technical Notes

Electrochemical Properties of $RbAg_4I_5$ Solid Electrolyte

I. Conductivity Studies

Bruno Scrosati,* Giovanni Germano, and Gianfranco Pistoia

Universita' di Roma, Rome, Italy

The recent discovery of highly conductive electrolytes of the MAg_4I_5 type (1-5) has stimulated renewed interest in solid electrolytes, particularly in view of the development of solid-state batteries with high current capabilities.

The most stable of these electrolytes is the rubidium salt on which, consequently, the attention has been mainly focused. Nevertheless relatively few studies on the chemical and electrochemical properties of $RbAg_4I_5$ as well as on the electrochemical characteristics of cells containing this electrolyte have been so far reported.

The crystal structure of $RbAg_4I_5$ has been studied by Bradley and Greene (4) and by Geller (6). The distribution of 16 Ag^+ ions over 56 available interstitial sites per unit cell explains the high mobility of the Ag^+ ions and the high entropy of the compound. The physical properties of $RbAg_4I_5$ are summarized in Table I.

From the data of Table I a particular disagreement in the reported $RbAg_4I_5$ a-c specific ionic conductivity data is obvious. Bradley and Greene found a value of

* Electrochemical Society Active Member.
Key words: solid electrolyte, silver rubidium iodide, conductivity.

Table I. Physical properties of $RbAg_4I_5$ at 25°C

Free energy of formation	-142.3 ± 0.1 kcal/mole	(8)
Entropy	~20 cal/deg. mole	(4)
Density	5.38 g/cm³	(5)
Transport number of Ag^+	1.00 ± 0.01	(7, this work)
Silver diffusion coefficient	2.10^{-6} cm²/sec	(9)
Electronic specific conductivity	$<10^{-11}$ ohm^{-1} cm^{-1}	(7)
Decomposition potential	0.67 ± 0.01V	(10)
Ionic specific conductivity (Flat silver electrodes)	0.124 ohm^{-1} cm^{-1}	(2)
Mixtures of electrolyte and powder silver electrodes)	0.210 ohm^{-1} cm^{-1}	(5)
Mixtures of electrolyte and powder silver electrodes)	0.170 ohm^{-1} cm^{-1}	(11)
(Amalgamated silver electrodes)	0.250 ohm^{-1} cm^{-1}	(10)
(Electrodes not reported)	0.260 ohm^{-1} cm^{-1}	(7, 13)

0.124 ohm^{-1} cm^{-1} at 20°C, using flat silver electrodes (2), Argue and Owens a value of 0.210 ohm^{-1} cm^{-1} at 20°C, using a mixture of powdered silver and $RbAg_4I_5$ as electrodes (5), Takahashi and Yamamoto, using the same kind of electrodes, a value of 0.170 ohm^{-1} cm^{-1} at 25°C (11), and De Rossi, Scrosati, and Pistoia a value of 0.250 ohm^{-1} cm^{-1} at 25°C, using amalgamated silver electrodes (10). Finally Oxley and Humphrey reported a $RbAg_4I_5$ conductivity value of 0.260 ohm^{-1} cm^{-1} at room temperature but without describing the type of electrodes used in their studies (7).

In this paper a detailed study of the $RbAg_4I_5$ ionic conductivity is reported, particularly regarding contact resistance problems and reproducibility, in order to clarify the reason for the scattering in the reported values of the solid electrolyte ionic conductivity.

Experimental Section

The preparation of $RbAg_4I_5$ has been described already (10). The final product was compressed under vacuum into pellets for the experiments using a press of the Beckman RIIC type. The average density of the pellets, determined by weighing a known volume, was 5.40 g/cm³ at 25°C. Conductivity measurements have been performed by the use of a cell made of two amalgamated silver disks in contact with the electrolyte pellet. A-c conductivity was determined at 800 Hz by a Yokogawa Kohlrausch bridge K-IA type using a 545 B Tektronix oscilloscope as null detector.

The Ag^+ transport number in $RbAg_4I_5$ at 25°C has been determined by passing a known amount of charge through a cell made of two silver electrodes in contact with a solid electrolyte pellet and comparing the corresponding coulombs with those obtained by measuring the loss in weight of the anode. The transport number of Ag^+, as an average of 10 determinations, was 1.00 ± 0.01 in agreement with the value reported by Oxley and Humphrey (7).

Results and Discussion

As shown in Table I, there is a certain scattering among the ionic conductivity values. The relatively low value found by Bradley and Greene (2) may be explained in terms of contact resistance. In fact Mrgudich has shown that the use of flat silver electrodes in measuring the conductivity of solid electrolytes results in severe contact polarization effects which can be overcome using amalgamated silver electrodes (12).

With this type of electrode the conductivity of $RbAg_4I_5$ has been found in our laboratory to be of the order of 0.250 ohm^{-1} cm^{-1} at room temperature. Contact polarizations have also been overcome using a mixture of powdered silver and $RbAg_4I_5$ as electrodes, as shown by Owens and Argue (5). No discussion of the 0.260 ohm^{-1} cm^{-1} found by Oxley and Humphrey at room temperature (7) is possible since the technique used for the conductivity measurements is not described in their report.

Undoubtedly contact polarizations and, consequently, the type of electrodes used in the measurements, play an important role in the conductivity determination of $RbAg_4I_5$ solid electrolyte, as shown in Table II: amalgamated electrodes definitely behave better than the flat silver ones and than those formed by compressing powdered silver directly on the surfaces of the electrolyte pellets. An attempt to vapor deposit silver on the pellet has also been made but without success. The electrolyte assumed a green-brownish color, the silver layer a yellowish color, and the conductivity of the assembly was very poor and not reproducible. This effect, which has been previously noticed by Bentle (9), is not very easily explained, and it is still under study.

Table II. Ionic a-c specific conductivity of $RbAg_4I_5$ measured at 25°C with several types of electrodes. (Compression pressure of the electrolyte pellet 1200 kg/cm²)

Type of electrodes	Conductivity (ohm^{-1} cm^{-1})
Amalgamated silver	0.243 ± 0.007
Mixture of $RbAg_4I_5$-Ag (1:1 in weight)	0.200 ± 0.007
Flat silver	0.090 ± 0.007
Compressed silver	0.096 ± 0.008
Evaporated silver	Not successful

It is also possible that the discrepancies in the reported values of the conductivity may be explained not only in terms of physical contact problems but also in terms of differences in the compression of the electrolyte pellet. To check this effect, a-c conductivity of different pellets prepared by different compression pressures, has been measured. The results, reported in Table III and Fig. 1, show that the $RbAg_4I_5$ ionic conductivity indeed depends to a certain extent on the pressure at which the pellet is compressed. Measurements were made after the source of pressure was removed. The conductivity, measured with amalgamated silver electrodes, reaches maximum values for compression pressures of the order of 1200 kg/cm². The decrease in conductivity at higher compression pressure could be associated with a certain decomposition

Table III. Ionic specific conductivity of $RbAg_4I_5$ as a function of compression pressure at 25°C (amalgamated silver electrodes).

Compression pressure, kg/cm²	Pellet thickness, cm	Pellet surface, cm²	Conductivity, ohm^{-1} cm^{-1}	Average value, ohm^{-1} cm^{-1}
400	0.113	1.26	0.203 ± 0.005	
400	0.114	1.26	0.209 ± 0.009	
400	0.123	1.26	0.202 ± 0.008	0.200 ± 0.006
400	0.055	1.26	0.197 ± 0.009	
400	0.176	1.26	0.192 ± 0.006	
800	0.098	1.26	0.228 ± 0.007	
800	0.110	1.26	0.229 ± 0.006	
800	0.122	1.26	0.224 ± 0.005	
800	0.178	1.26	0.220 ± 0.003	
800	0.329	1.26	0.206 ± 0.008	0.220 ± 0.003
800	0.303	1.26	0.219 ± 0.004	
800	0.147	1.26	0.219 ± 0.004	
800	0.196	1.26	0.217 ± 0.003	
1200	0.223	5.06	0.245 ± 0.006	
1200	0.234	5.06	0.243 ± 0.006	
1200	0.085	5.06	0.240 ± 0.017	0.243 ± 0.007
1200	0.210	1.26	0.243 ± 0.007	
1200	0.205	1.26	0.238 ± 0.003	
1600	0.115	1.26	0.240 ± 0.009	
1600	0.165	1.26	0.220 ± 0.007	
1600	0.245	1.26	0.230 ± 0.006	0.231 ± 0.007
1600	0.128	1.26	0.235 ± 0.005	
2000	0.110	1.26	0.228 ± 0.006	
2000	0.183	1.26	0.212 ± 0.003	
2000	0.148	1.26	0.224 ± 0.004	0.217 ± 0.008
2000	0.145	1.26	0.214 ± 0.004	
2000	0.152	1.26	0.206 ± 0.004	
2400	0.155	1.26	0.204 ± 0.003	
2400	0.193	1.26	0.211 ± 0.003	
2400	0.144	1.26	0.218 ± 0.004	0.211 ± 0.005
2400	0.172	1.26	0.212 ± 0.003	
4000	0.166	1.26	0.192 ± 0.003	
4000	0.213	1.26	0.205 ± 0.002	0.199 ± 0.007
5600	0.206	1.26	0.169 ± 0.004	0.169 ± 0.004

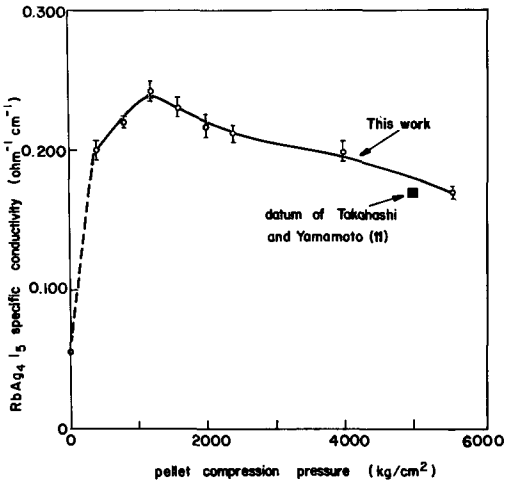

Fig. 1. Specific conductivity of $RbAg_4I_5$ pellets as a function of the compression pressure at 25°C (amalgamated silver electrodes).

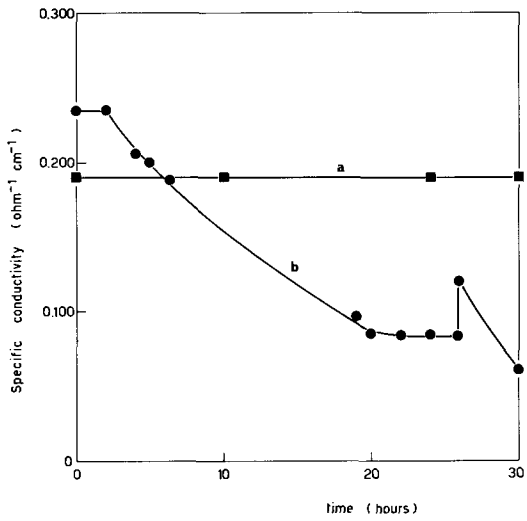

Fig. 2. Specific conductivity of $RbAg_4I_5$ as a function of time at 25°C (pellet compression pressure 1600 kg/cm²) where curve b refers to amalgamated silver electrodes and curve a to $RbAg_4I_5$-Ag mixture (1:1 ratio in weight) electrode determinations.

of the electrolyte or to possible phase changes. An x-ray study of $RbAg_4I_5$ pellets, compressed at pressures higher than 1200 kg/cm², could give a definite explanation of this effect. Such a study, however, is beyond the scope of this work which has been mainly intended as limited to a detailed conductivity study in order to try to find an explanation of the discrepancies existing in the literature on the $RbAg_4I_5$ ionic conductivity determinations.

The relatively lower conductivity observed for the pellets at low compression could be explained by the fact that at low pressures a complete uniformity of the pellet itself could not be achieved. Grain boundary and other similar effects, which should increase in extent when the compression pressure decreases, should accordingly hinder the silver ion mobility through the electrolyte and, therefore, lower its ionic conductivity. This explanation is supported by the fact that the ionic conductivity of powdered $RbAg_4I_5$, just slightly compressed between two amalgamated silver electrodes, is of the order of 0.055 ohm^{-1} cm^{-1}, as reported in Fig. 1.

On the basis of differences in compression pressure the relatively low (0.170 ohm^{-1} cm^{-1}) conductivity value found by Takahashi and Yamamoto (11) may find its explanation. These authors have reported that the pellets utilized in their solid state cells were pressed at 5 tons/cm², and it seems reasonable to believe that also the pellets for the conductivity measurements were compressed at the same pressure. With this assumption, the Takahashi and Yamamoto value is reported in Fig. 1. The agreement with the data found in this work at the same pressure is quite satisfactory.[1]

The conductivity measurements, reported in Table II, have been obtained with pellets of different dimensions and the results show that, for a given pellet-compression pressure, the $RbAg_4I_5$ specific conductivity is independent of pellet thickness and surface, *i.e.*, that it obeys Ohm's law in the dimension range examined.

From all the evidence so far discussed the beneficial effect of the amalgamation on the minimization of contact polarization effect and, consequently, on the $RbAg_4I_5$ ionic conductivity is clear. Nevertheless some disadvantages are associated with the use of this kind of electrode with the solid electrolyte. The most serious among them is the fact that mercury seems to slowly react with the electrolyte to form a definite compound which is less conductive than $RbAg_4I_5$. In Fig. 2 is shown the trend of the $RbAg_4I_5$ conductivity, measured with amalgamated silver electrodes, as a function of time. Conductivity remains constant for about 2 hr and then slowly decreases with time to reach a constant value which depends on the amount of mercury used for the amalgamation of the electrodes. The break in the curve corresponds to a time at which the cell was disconnected. The mercury was clearly transferred from the electrodes to the electrolyte whose color changed from white to yellow. When the electrodes were reamalgamated and the cell assembled again, the decrease in conductivity was sharper due to the new amount of mercury supplied.

The phenomenon is general and takes place any time mercury comes in contact with the electrolyte. An $RbAg_4I_5$ sample was left for a week in contact with an excess of mercury. The color of the electrolyte turned from white to yellow, and its specific conductivity, using a pellet compressed at 1200 kg/cm², was 0.006 ohm^{-1} cm^{-1} at room temperature.

Since the conductivity, measured with amalgamated silver electrodes, remains constant for about 2 hr and then decreases due to the presence of the unknown $RbAg_4I_5$ decomposition product, and the periods of time for the measurements reported in Fig. 1 are far smaller than 2 hr, the behavior reported in this figure is undoubtedly related simply to $RbAg_4I_5$ and not to the decomposition product.

Conclusion

The dependence of the a-c conductivity of $RbAg_4I_5$ pellets on the compression pressure and resistance effects at the boundary between electrodes and electrolyte may well explain the scattering in the solid electrolyte ionic conductivity values reported in literature.

Amalgamated silver electrodes behave quite well for a-c conductivity measurements of $RbAg_4I_5$. On the other hand these determinations are not reproducible with time since mercury slowly reacts with the electrolyte.

During the revision of the manuscript the authors became aware of work by Raleigh on ionic conductivity of single-crystal and polycrystalline $RbAg_4I_5$ (14), in which it is stated that variations in pressing conditions do not affect the $RbAg_4I_5$ polycrystalline conductivity, reported as 0.28 $(ohm\ cm)^{-1}$ at 25°C. On the other hand it is not clearly reported in the paper which was the pressure range in which the conductivity was tested and the precision of the polycrystalline conductivity data. Apparently, the measurements were done over a range of 1500 to 3000 kg/cm² and, since it is stated that the results compare both with a 0.26 and a 0.22 $(ohm\ cm)^{-1}$ previously reported values, one

[1] Note added in proof: Recently Takahashi reported that his conductivity data were indeed obtained with pellets compressed at 5000 kg/cm² (15).

could assume a precision of ± 0.06 (ohm cm)$^{-1}$. If this is the case then Raleigh's data also agree with those reported in the present work, according to which the conductivity varies from 0.24 to 0.21 (ohm cm)$^{-1}$ in the pellet compression range of 1500 to 3000 kg/cm^2.

Furthermore, in Raleigh's paper it is reported that a contact of 1 hr with mercury gives $RbAg_4I_5$ a yellowish coloration but not resistance changes. These findings are in perfect agreement with the observations reported in this work where resistance changes were observed at times exceeding two hours.

Acknowledgment

This work was sponsored by the Consiglio Nazionale delle Ricerche.

Manuscript submitted March 26, 1970; revised manuscript received Aug. 25, 1970.

Any discussion of this paper will apear in a Discussion Section to be published in the December 1971 JOURNAL.

REFERENCES

1. J. N. Bradley and P. D. Greene, *Trans. Faraday Soc.*, **62**, 2069 (1966).
2. *Ibid.*, **63**, 424 (1967).
3. *Ibid.*, **63**, 1023 (1967).
4. *Ibid.*, **63**, 2516 (1967).
5. B. B. Owens and G. R. Argue, *Science*, **157**, 308 (1967).
6. S. Geller, *ibid.*, **157**, 310 (1967).
7. J. E. Oxley and J. R. Humphrey, Atomics Int., Final Report, July 22—Oct. 22, 1968.
8. L. F. Topol and B. B. Owens, *J. Phys. Chem.*, **72**, 2103 (1968).
9. G. G. Bentle, *J. Appl. Phys.*, **39**, 4036 (1968).
10. M. De Rossi, G. Pistoia, and B. Scrosati, *This Journal*, **116**, 1964 (1969).
11. T. Takahashi and O. Yamamoto, *ibid.*, **117**, 1 (1970).
12. J. N. Mrgudich, *ibid.*, **107**, 475 (1960).
13. L. D. Fullmer and M. A. Hiller, *J. Crystal Growth*, **5**, 395 (1969).
14. D. O. Raleigh, *J. Appl. Phys.*, **41**, 1876 (1970).
15. T. Takahashi, *This Journal*, **117**, 1533 (1970).

Ellipsometry of Anodic Oxide Films on GaAs

C. J. Dell'Oca,[1,*] G. Yan, and L. Young[**]

Department of Electrical Engineering, The University of British Columbia, Vancouver, British Columbia, Canada

The growth of anodic oxide films on GaAs is of current interest in connection with several potential device applications. The oxide may be used as a dopant diffusion mask or as a dielectric (1).[2] Anodization could be used for the controlled thinning (*e.g.*, profiling) of GaAs. Oxide films of appropriate optical thickness could be used to increase the external efficiency of GaAs light-emitting diodes. Little published information is as yet available on the anodization of GaAs. In a patent application (1), GaAs was anodized in an aqueous solution of boric acid and sodium tetraborate. Revesz and Zaininger (2) anodized GaAs wafers in acetic anhydride saturated with potassium nitrate. They reported that the anodic oxide seemed uniform but its refractive index could not be determined due to severe pitting of the substrate during anodization because of dissolution of GaAs. In another paper, Zaininger and Revesz (3) determined the refractive index of GaAs to be 3.923-j0.304 by obtaining the asymptotic values of Δ and ψ of the GaAs surface which has been successively etched. Weinreich (4) reported a refractive index of 1.78 ± 0.02 for GaAs oxides grown in an oxygen plasma. Navratil (5) obtained a refractive index of 1.55 for thermally oxidized GaAs. In the present work we report an ellipsometric investigation of the properties of anodic oxides made in dilute aqueous ammonium pentaborate solution. This gave uniform oxides, provided the anodization period was short.

Experimental Procedure

The GaAs specimens, about 1 x 1 x 0.2 cm^3, were abraded, mechanically polished with 0.3 μm alumina powder, cleaned in boiling trichlorethylene, boiling acetone, and propanol, and then treated for 1-2 min in $7H_2SO_4(98\%):H_2O_2(30\%):H_2O$ at 80°C. A eutectic composition of gold-germanium was evaporated onto the reverse side of each GaAs mirror and later alloyed in a hydrogen atmosphere (6). This procedure has been found to produce ohmic contacts. In some experiments it was found convenient to use tantalum wire point-contacts as used for silicon anodization (7) (the tantalum is anodized and no stop-off is required). Specimens were normally mounted (using Silastic and Koldmount) in a recess in a Teflon plate (Fig. 1) such that only the polished surface was exposed to the electrolyte during anodization. A groove on the Teflon plate allowed the Teflon-coated wire to be brought out above the electrolyte. The Teflon plate was mounted on a holder which can be set at a fixed position with respect to the ellipsometer. Ellipsometry measurements were made on the unanodized GaAs and at intervals during anodization. Alignment was maintained in repeated anodization steps and ellipsometry measurements by transferring the entire unit (Teflon plate and holder) between the ellipsometer and the anodization bath. After each anodization the specimen was immediately rinsed in distilled water and carefully dried with lint-free paper. Anodization was carried out in subdued light in a solution of 2 g/liter ammonium pentaborate in water kept at 25°C. The anodization circuit was closed as soon as the specimen was immersed in the solution, a switch operated by the weight of the specimen assembly being used to facilitate this. A thin tantalum wire served as the cathode. The voltage between the cathode and the anode was measured using a Fluke Model 881AB differential voltmeter. The ellipsometer and the method used in taking

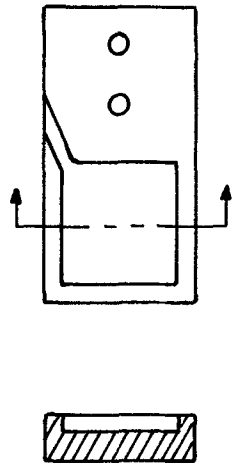

Fig. 1. Teflon-plate sample holder for specimens

* Electrochemical Society Student Associate Member.
** Electrochemical Society Active Member.
[1] Present address: Fairchild Research and Development Laboratories, Palo Alto, Calif.
[2] We thank Dr. W. W. Harvey for pointing out this reference to us.

Key words: dielectric films, passivation, semiconductor devices.

ellipsometry measurements have already been described (8).

Results

Figures 2 and 3 show ellipsometry data for anodized polycrystalline and single-crystal n-type GaAs, respectively. The respective room-temperature resistivities of the GaAs specimens were 3.8 x 10^{-3} and 0.07 ohm-cm. They were anodized at a constant current density of 1 mA/cm^2. The ellipsometric readings were taken with 5461Å light at a 70° angle of incidence. The

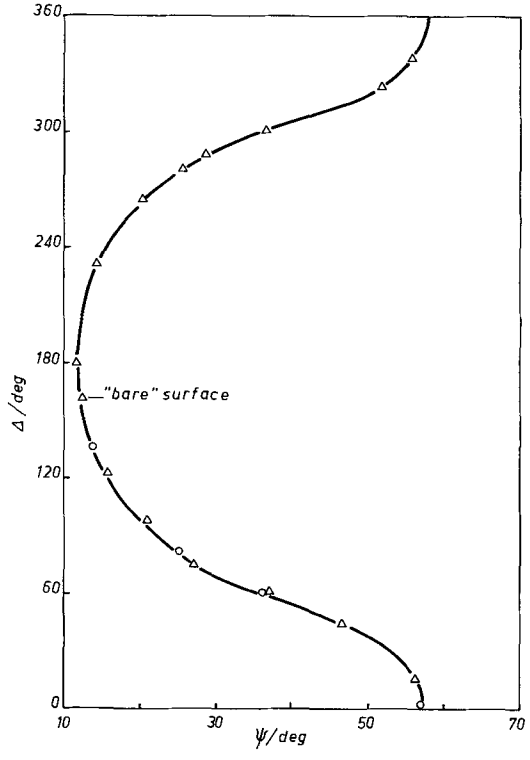

Fig. 2. Ellipsometry data for anodized polycrystalline GaAs. The curve is calculated with $n_1 = 1.82$, $n_2 = 4.00 - j0.307$. △, First cycle; ○, second cycle.

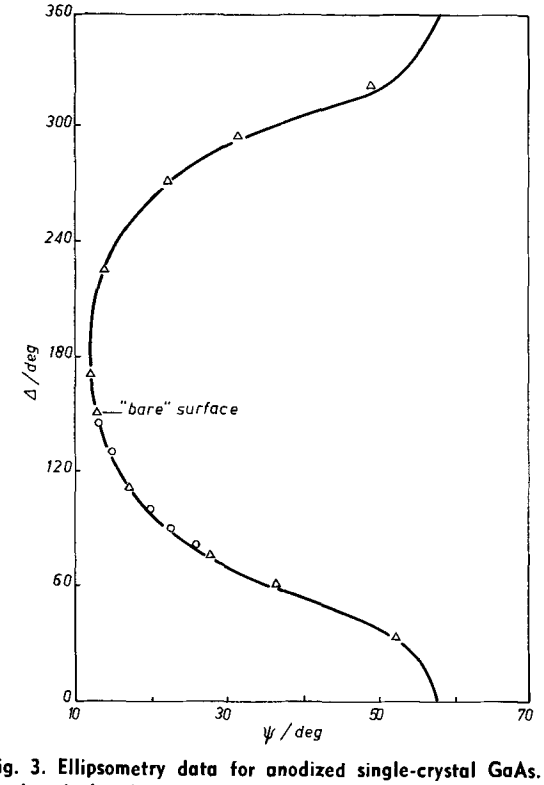

Fig. 3. Ellipsometry data for anodized single-crystal GaAs. The curve is calculated with $n_1 = 1.82$, $n_2 = 4.00 - j0.300$. △, First cycle; ○, second cycle.

Table I

GaAs substrates	n_1	n_2	$\langle\sigma_\psi\rangle$	$\langle\sigma_\Delta\rangle$	Total No. of points	Final oxide thickness
Polycrystal	1.82	4.00-j0.307	0.22	0.95	19	2395Å
Single crystal	1.82	4.00-j0.300	0.25	2.00	15	2150Å

refractive indexes of the oxide films and the GaAs substrates were obtained by curve fitting the experimental points using a computer program (8, 9). A best fit was obtained by varying the refractive indexes of the film and substrate such that mean square deviation between computed and experimental points was a minimum. The ellipsometry data shown in Fig. 2 and 3 are in good agreement with the computed curves for uniform, nonabsorbing films. Table I contains the fitted values of the refractive indexes of the oxide and the substrate (n_1 and n_2, respectively) and the mean standard deviation $\langle\sigma_\psi\rangle$ and $\langle\sigma_\Delta\rangle$ between computed and experimental results for ψ and Δ, respectively. The index of refraction of the film and the real and imaginary part of n_2 were varied in sequence and the fit to the experimental results was detectably worse for variations of ±0.02 in n_1 and ±0.03 $\pm j0.005$ in n_2 from the values in the table.

The oxide is amorphous. Electron reflection diffraction at 50 and 100 kV produced patterns which showed only very diffuse halos. The oxide was slowly dissolved by the forming solution and by distilled water. The interference colors, on a sample that was anodized at constant current to 50V and then left immersed in the solution for about 5 hr with no voltage applied, disappeared indicating that the oxide was being dissolved. Ellipsometry indicated that a 2000Å thick oxide was dissolved away from a sample after it had been in water for 2 days. Because the dissolution tends to be nonuniform, formation at constant voltage will in general lead to films of nonuniform thickness. For example, if an oxide is grown to 90V at 1 mA/cm^2 and then held at this voltage, the current then decays with time and a uniform increase in oxide thickness takes place at first. However, a time is reached when the current becomes almost constant (at 90V this is about 0.3 mA/cm^2) which probably corresponds to a rough equivalence between film growth and dissolution and the oxide becomes nonuniform. The film uniformity can be restored by increasing the voltage to produce an increase in current or growth rate. No changes in the ellipsometric readings were measured in an oxide held in air for about 15 hr, indicating a stable oxide. Growth at constant current gives results typical of anodic oxide growth on valve metals. That is the voltage and thickness increase linearly with time corresponding to a linear dependence of voltage on thickness with a zero film thickness intercept typically of about −2V. A typical dependence of voltage on thickness is shown in Fig. 4. The electric field in the oxide as esti-

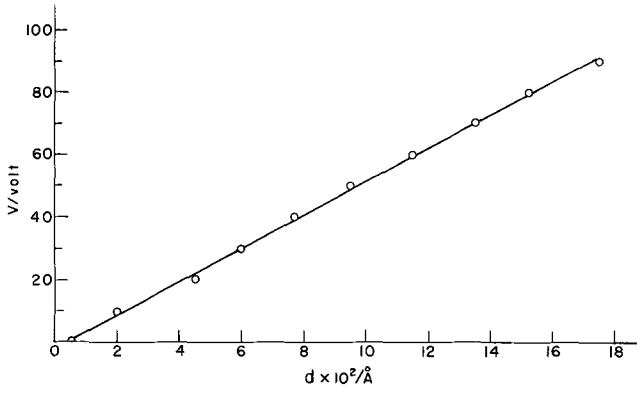

Fig. 4. Typical dependence of voltage on oxide thickness under anodization at constant current of 1 mA/cm^2.

mated from dV/dd was 5 x 10^6 V/cm both for polycrystalline and single-crystal material under growth at 1 mA/cm^2 (not corrected for leakage or dissolution) at 25°C. This field value is somewhat lower than for the same total current density applied to tantalum in dilute electrolytes at 25°C.

Acknowledgments

The authors thank the National Research Council of Canada and Sprague Electric Company for their support in this work.

Manuscript submitted July 6, 1970; revised manuscript received *ca.* Aug. 20, 1970.

Any discussion of this paper will appear in a Discussion Section to be published in the December 1971 JOURNAL.

REFERENCES

1. E. W. Durham and D. P. Holmes, Brit. Pat. 1,041,314, Sept. 1966.
2. A. K. Revesz and K. H. Zaininger, *J. Am. Ceram. Soc.*, **46**, 606 (1963).
3. K. H. Zaininger and A. K. Revesz, *J. Phys. Radium*, **25**, 208 (1964).
4. O. A. Weinreich, *J. Appl. Phys.*, **37**, 2924 (1966).
5. K. Navratil, *Czech. J. Phys.*, **B18**, 266 (1968).
6. N. Braslau, J. B. Gunn, and J. L. Staples, *Solid-State Electron.*, **10**, 381 (1967).
7. L. Young and F. G. R. Zobel, *This Journal*, **113**, 278 (1966).
8. C. J. Dell'Oca and L. Young, *Surface Sci.*, **16**, 331 (1969).
9. C. J. Dell'Oca, Ph.D. Thesis, Dept. of Electrical Engrg., Univ. of British Columbia (1969).

Relaxation of Internal Stresses in Electrodeposits during Stress Measurement by Null-Deflection Methods

J. M. Sykes and G. P. Rothwell

University of Cambridge, Department of Metallurgy, Cambridge, England

In most of the methods used to measure stress in electrodeposits, a thin metal strip is plated on one side only and the deflection produced, or the force required to prevent that deflection is measured (1-7). From these measurements the stress in the deposit may be calculated. The principal criticism of methods in which a deflection is measured is that in the tests relaxation of the internal stresses in the deposit will occur as the strip bends, whereas in practice the substrate is usually too thick to be deformed by stresses in the deposit. Although one can often calculate what the original stress must have been, relaxation can affect the behavior of subsequent layers of deposit. For instance, relaxation can prevent cracking of a brittle deposit. To prevent this kind of effect, null-deflection methods have been developed, such as the Hoar-Arrowsmith balance (7), in which the restoring force needed to prevent deflection is measured.

We show below, however, that if the restoring force is applied to the end of the strip, even if the whole length of the strip is plated, the resultant bending moment will not be zero along the whole length of the strip. The bending moment caused by the deposit will be the same at any point along the strip, but that due to the restoring force will be proportional to the distance from the point of application of the force, so that curvature of the strip will result. This leads to a new formula relating the restoring force to the stress in the deposit and allows the curvature of the strip to be compared with that of an unrestrained strip.

Another effect that has not been thoroughly investigated is relaxation of stress in the direction perpendicular to that in which the strip is restrained. This causes a decrease in elastic strain across the strip and will lead to a similar reduction in the elastic strain along the length of the strip, with a consequent reduction in the measured stress, determined by Poisson's ratio for the deposited metal. It will be shown that this is comparable with the relaxation which would occur in unconstrained bending and that it cannot be eliminated by suitable choice of dimensions for the test strip.

Calculation

In the simplest case, where the substrate and deposit have the same Young's modulus, E, and the thickness of the deposit, d, is small compared with that of the substrate, t, the bending moment, M_S, at any point in the strip due to a mean stress S in the deposit is given by (8)

$$M_S = \frac{Sb\,td}{2} \qquad [1]$$

where b is the width of the strip.

If this couple causes the beam to bend to a radius of curvature r, the elastic resistance of the combined beam will generate a bending moment M_e given by (8)

$$M_e = \frac{E(t+d)^3 b}{12r} \qquad [2]$$

If the strip, of length l, is fixed at one end and a restoring force, F, is applied at the other, a bending moment, M_F, will be generated at any point in the strip, which will be dependent on x, the distance from the fixed end. This moment is given by (9)

$$M_F = (l-x)F \qquad [3]$$

If the strip is in equilibrium the resultant of these three bending moments must be zero at all points in the strip.

$$M_S + M_e + M_F = 0,$$

$$\frac{Sbtd}{2} + \frac{E(t+d)^3 b}{12r} + (l-x)F = 0 \qquad [4]$$

Thus, the curvature

$$\frac{1}{r} = -\frac{12}{E(t+d)^3 b}\left[\frac{Sbtd}{2} + (l-x)F\right] \qquad [5]$$

But

$$\frac{1}{r} = -\frac{d^2y}{dx^2}$$

where y is the deflection of the strip at a distance x from the fixed end (9). Therefore

$$\frac{d^2y}{dx^2} = \frac{12}{Eb(t+d)^3}\left[\frac{Sbtd}{2} + F(l-x)\right] \qquad [6]$$

and by integration

$$\frac{dy}{dx} = \frac{12}{Eb(t+d)^3}\left[\frac{Sbtdx}{2} + F\left(lx - \frac{x^2}{2}\right)\right] + A \qquad [7]$$

Key words: mechanical properties, electroplating, Stresometer.

Because $dy/dx = 0$ for $x = 0$, the integrating constant $A = 0$. Further integration yields

$$y = \frac{12}{Eb(t+d)^3}\left[\frac{Sbtdx^2}{4} + F\left(\frac{lx^2}{2} - \frac{x^3}{6}\right)\right] + B \quad [8]$$

Because $y = 0$ for $x = 0$, the integrating constant B is also zero.

Now in null-deflection methods the value of F is fixed so that $y = 0$ for $x = l$.

Therefore

$$\frac{12}{Eb(t+d)^3}\left[\frac{Sbtdl^2}{4} + \frac{Fl^3}{3}\right] = 0$$

and

$$F = -\frac{3}{4}\frac{Sbtd}{l} \quad [9]$$

[The formula normally used (7) gives

$$F = -\frac{1}{2}\cdot\frac{Sbtd}{l}. \ ]$$

Substituting the value of F (Eq. [9]) into Eq. [5]

$$\frac{1}{r} = \frac{3\,Std(3x - l)}{El(t+d)^3} \quad [10]$$

From this equation we may obtain the curvature at particular points. Thus, for $x = l/3$, $1/r = 0$ (no curvature). Elsewhere, the strip will be curved, and maximum curvature occurs for $x = l$, when

$$\frac{1}{r} = \frac{6\,Std}{E(t+d)^3} \quad [11]$$

At this point the applied force has no bending moment (Eq. [3]) and the curvature will be approximately the same as that for an unrestrained strip (8). Maximum negative curvature occurs for $x = 0$, when

$$\frac{1}{r} = -\frac{3\,Std}{E(t+d)^3} \quad [12]$$

half the value for an unrestrained strip.

In summary, at the point at which the force is applied the relaxation of the internal stress will be the same as that for an unrestrained strip but will decrease toward the point of zero curvature, where there will be no relaxation. Along the final third of the length the stress in the deposit will become increasingly higher than its true (zero curvature) value as the support is approached.

By substitution from Eq. [9], Eq. [8] becomes

$$y = \frac{3}{2}\cdot\frac{Stdx^2(x - l)}{El(t+d)^3} \quad [13]$$

from which it may be shown that the maximum deflection of the strip occurs at $x = 2l/3$.

Let us now consider bending across the width of the strip. Where the strip is fixed to its support there can be no bending, but this constraint will be reduced further along the strip. For a long, thin strip at a sufficient distance from the support there will be virtually no constraint. Brenner and Senderoff (8) show that for an unconstrained strip the radius of curvature is given by

$$r = \frac{Et(t+d)}{6Sd} \quad [14]$$

The strip will describe an arc of a circle subtending a small angle θ at the center, such that $w = r\theta$ where w is the width of the strip. The mean radius of curvature for the deposit, r', will be given by

$$r' = r - \frac{t}{2}$$

Therefore the width of the deposit after contraction, $w' = r'\theta = (r - t/2)w/r$.

The contraction due to bending, $\Delta w = w - (r - t/2)w/r$. Thus

$$\Delta w = wt/2r \quad [15]$$

Strain in deposit

$$\Delta w/w = t/2r$$

But

$$r = \frac{Et(t+d)}{6Sd}$$

so that

$$\frac{\Delta w}{w} = \frac{3Sd}{E(t+d)} \quad [16]$$

If Poisson's ratio for the deposit is ν

$$\frac{\Delta l}{l} = \nu\cdot\frac{\Delta w}{w} = \frac{3\nu Sd}{E(t+d)} \quad [17]$$

Therefore the relaxation in the measured stress ΔS is given by

$$\Delta S = E\frac{\Delta l}{l} = \frac{3\nu Sd}{(t+d)},$$

$$\frac{\Delta S}{S} = \frac{3\nu d}{(t+d)} \quad [18]$$

This relaxation depends only on Poisson's ratio and the ratio of deposit thickness to total thickness, and not as has been suggested (7, 11) on the length/width ratio of the specimen. This is in agreement with Arrowsmith's observation (10) that the measured stress is independent of the length/width ratio over a wide range of values. If we put values into Eq. [18] above, for example: $\nu = 0.4$ for nickel, $d = 10^{-3}$ mm, $t = 10^{-1}$ mm

$$\frac{\Delta S}{S} = \frac{0.4\cdot 3\cdot 10^{-3}}{10^{-1}} \approx 1.2\times 10^{-2}$$

$$= 1.2\%$$

Thus for small thicknesses this effect may be disregarded, but we may note that this relaxation is of the same order of magnitude as the relaxation in an unrestrained strip and will increase as the deposit thickness increases.

Conclusions

We have shown that even in null-deflection methods there will be some stress relaxation due to bending of the test strip and that because of this bending the stress should be calculated using the formula

$$S = \frac{4}{3}\cdot\frac{Fl}{btd}$$

Similarly there will be some relaxation because constraint is not applied across the strip, but for thin deposits this will only lead to a small decrease in measured stress. The only method that rigorously simulates true plating conditions is clamping the specimen completely flat during plating and measuring curvature upon subsequent release (3). For continuous measurements some stress relaxation in the deposit has to be tolerated.

Manuscript submitted June 29, 1970; revised manuscript received Sept. 17, 1970.

Any discussion of this paper will appear in a Discussion Section to be published in the December 1971 JOURNAL.

REFERENCES

1. G. G. Stoney, *Proc. Roy. Soc. (London) Ser. A*, **82**, 172 (1909).
2. R. H. Barklie and J. J. Davies, *Proc. Inst. Mech. Eng.*, **731** (I, 1930).
3. A. W. Hothersall and C. J. J. Leadbetter, *J. Electrodepositors' Tech. Soc.*, **14**, 207 (1938).
4. K. G. Soderberg and A. K. Graham, *Proc. Am. Electroplaters' Soc.*, **34**, 74 (1947).
5. A. Brenner and S. Senderoff, *J. Res. Nat. Bur. Stand.*, **42**, 89 (1949).

6. J. B. Kushner, *Plating*, **41**, 1146 (1954).
7. T. P. Hoar and D. J. Arrowsmith, *Trans. Inst. Metal Finishing*, **34**, 354 (1957).
8. A. Brenner and S. Senderoff, *J. Res. Nat. Bur. Stand.*, **42**, 105 (1949).
9. S. Timoshenko, "Strength of Materials," Vol. 1, p. 243, Van Nostrand, New York (1930).
10. D. J. Arrowsmitn, Thesis, Univ. Cambridge (1957).
11. D. R. Gabe and J. M. West, *Trans. Inst. Metal Finishing*, **40**, 6 (1963).

Electroless Deposition of Certain Metal Oxides

II. Tl_2O_3, MnO_2

W. Mindt*[1]

Bell Telephone Laboratories, Incorporated, Murray Hill, New Jersey 07974

The object of this study is the deposition of metal oxides through surface catalyzed oxidation of metal ions from aqueous solutions by an oxidizing agent. In part I (1) deposition of α-PbO_2 was described. The electrochemical mechanism of this process was found to be analogous to electroless metal plating, being a mixed electrolytic reaction with superposition of anodic and cathodic partial currents according to the classical concept of Wagner and Traud (2). In general, the process can be described by the two partial reactions.

$$mMe^{z+} + nH_2O \rightarrow Me_mO_n + 2nH^+ + (2n - mz)e^- \quad [1a]$$

$$(2n - mz)(Ox + e^- \rightarrow Red^-) \quad [1b]$$

where Me^{z+} is a metal ion which can be oxidized to a higher oxide, and Ox and Red^- the oxidized and reduced species of a redox system.

The conditions under which electroless deposition of a metal oxide is possible have been outlined previously (1). In the present paper, deposition of two other oxides is reported under experimental conditions similar to those used for PbO_2.

Reactions of the type studied here may be valuable in cases in which an easy, room temperature deposition method of an electrically conductive metal oxide film is desired. An important feature of the method is that deposition on rough surfaces or in the pores of porous material may be possible. Two of the oxides (MnO_2 and PbO_2) are of interest for use as counterelectrodes in solid valve metal oxide capacitors (3-5). Other applications in thin-film devices may be limited by the chemical instability that is exhibited by most of the higher metal oxides for which this deposition technique would be applicable.

Experimental

As oxidizing agent, ammonium persulfate was used as described in part I. All experiments were carried out in a supporting electrolyte of M ammonium acetate. Tl_2O_3 and MnO_2 electrodes were prepared in two different ways: (*i*) by electrodeposition on platinum anodes—deposition of a 0.5μ thick layer was carried out in the same electrolyte used for the current potential measurements described below by applying an anodic current density of 0.5 mA/cm^2, and (*ii*) by chemical precipitation on glass substrates (1 × 3 in. slides)—the substrates, without special pretreatment, were immersed in a solution containing ammonium acetate, thallous or manganous acetate, ammonium persulfate, and silver nitrate as a catalyst for the persulfate oxidation. Precipitation of the metal oxide in the solution started after an induction time of several minutes. The substrates were left in the solution until a several hundred Angstrom thick layer of the oxide was formed. In the case of Tl_2O_3 a pH of 8.0 and for MnO_2 a pH of 5.0 proved to be optimal for this purpose. The platinum substrate electrodes were used for the current potential measurements; the weight gain measurements were carried out with electrodes prepared in both ways.

It should be noted that precipitation of the metal oxide in the solution did not occur during the experiments described below in which $AgNO_3$ was not added; the thallium baths remained clear for several days. In the manganese baths, precipitation of MnO_2 usually started after 10 to 30 min; the solution was then exchanged for a freshly prepared one.

The current potential measurements were carried out potentiostatically, using a platinum counterelectrode and an normal calomel reference electrode. Stationary conditions were achieved after several seconds at higher current densities and after a few minutes at current densities below 10 μA/cm^2.

The reagents used were analytical reagent grades of $TlC_2H_3O_2$, $Mn(C_2H_3O_2)_2$, $AgNO_3$, $(NH_4)_2S_2O_8$, and $NH_4C_2H_3O_2$ (prepared from glacial acetic acid and 30% NH_4OH). The pH of the solutions was adjusted by addition of NH_4OH. The electrolyte was agitated. All experiments were carried out at 25°C.

Results and Discussion

In Fig. 1, stationary current voltage curves of Tl_2O_3 electrodes are shown which were obtained in a solution of 50 mM thallous acetate in M ammonium

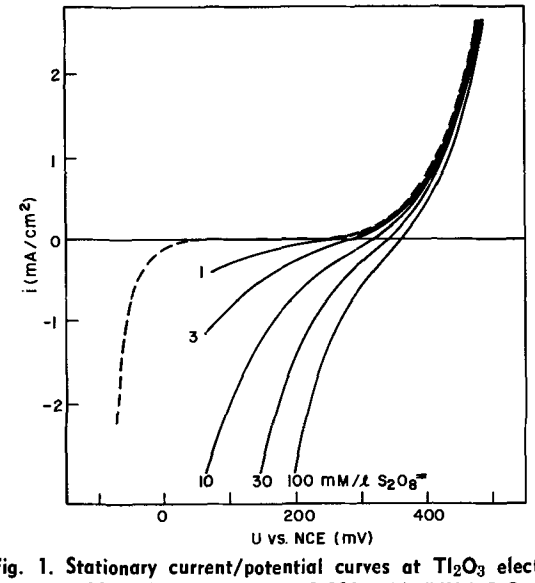

Fig. 1. Stationary current/potential curves at Tl_2O_3 electrodes. Electrolyte: 50 mM $TlC_2H_3O_2$ + 1-100 mM $(NH_4)_2S_2O_8$ in M $NH_4C_2H_3O_2$ at pH 10. Dashed line: without $(NH_4)_2S_2O_8$.

* Electrochemical Society Active Member.
[1] Present address: F. Hoffmann-La Roche and Company, Basel, Switzerland.
Key words: electroless deposition, oxide films, manganese dioxide, thallic oxide.

acetate at different concentrations of ammonium persulfate. In this solution the anodic reaction is

$$2Tl^+ + 3H_2O \rightarrow Tl_2O_3 + 6H^+ + 4e^- \quad [2]$$

In the presence of persulfate, the net current results from superposition of reaction [2] and reduction of $S_2O_8^=$

$$S_2O_8^= + 2e^- \rightarrow 2SO_4^= \quad [3]$$

At zero current, *i.e.*, under open-circuit conditions, deposition of Tl_2O_3 occurs at a rate given by the current density of the anodic partial reaction (dotted line) at the open-circuit potential. This was confirmed by weight gain measurements under open-circuit conditions at different $S_2O_8^=$ concentrations.

The situation in the case of MnO_2 (Fig. 2) is somewhat different because the zero current plateaus in the absence of persulfate (dotted lines) corresponding to the reaction

$$Mn^{++} + 2H_2O \rightarrow MnO_2 + 4H^+ + 2e^- \quad [4]$$

are not as well defined as for Tl_2O_3. One can recognize, however, the effect of the addition of persulfate. The curves were not as reproducible as those of Tl_2O_3; however, weight gain measurements at open circuit gave the expected growth rate within errors of ± 30%.

Properties of the films.—The deposits obtained on glass substrates were continuous and of uniform thickness. No pores could be seen by light microscopy. Good adherence was achieved up to a thickness of about 10μ with Tl_2O_3 and up to about 0.5μ with MnO_2. X-ray studies showed sharp lines of the cubic Tl_2O_3. No patterns were observed in MnO_2. The electrical resistivity of Tl_2O_3, determined by the four-point method, was 5×10^{-4} ohm-cm. The resistivity of MnO_2 depended on the pH of the electrolyte, *e.g.*, values of 4×10^2 ohm-cm and 2×10^4 ohm-cm were obtained at pH values of 8 and 6.3, respectively. These lie within the range of resistivities found for pyrolytic material.

Thermodynamic remarks.—The equilibrium potentials of both reactions [2] and [4] depend on the pH of the electrolyte. Thus, the current potential curves shift with pH as was seen in Fig. 2 with MnO_2. This results in a pH dependence of the growth rate. In addition, there exist some other pH dependent thermodynamic equilibria which may interfere with the deposition process. These are summarized in Fig. 3 and 4. The potentials are calculated from free energy data (6-8) for concentrations of 50 mM in Tl^+ and Mn^{++}.

Since only one lower oxide of thallium (Tl_2O) exists, the conditions are easy to survey in this case.

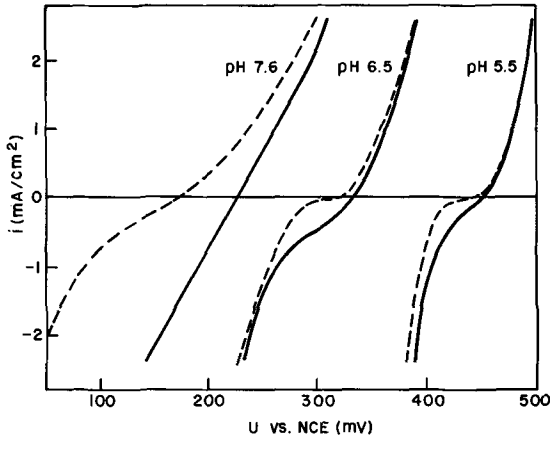

Fig. 2. Stationary current/potential curves at MnO_2 electrodes. Electrolyte: 50 mM $Mn(C_2H_3O_2)_2$ + 0.5M $(NH_4)_2S_2O_8$ in M $NH_4C_2H_3O_2$ at pH 5.5, 6.5, and 7.6. Dashed lines: without $(NH_4)_2S_2O_8$.

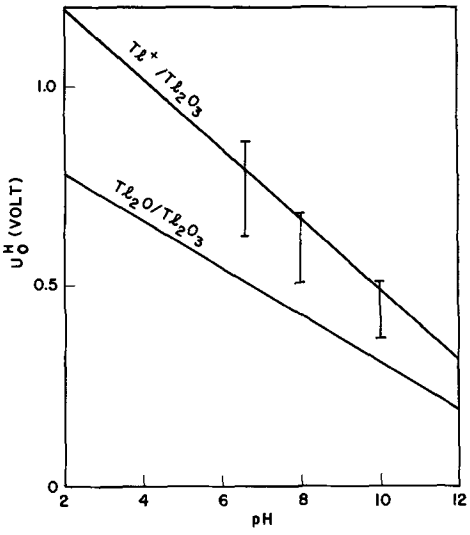

Fig. 3. Equilibrium potentials of reactions [2] and [5], calculated from thermodynamic data (6, 8), vs. pH. Bars show zero current plateaus at Tl_2O_3 electrodes measured in a solution of 50 mM $TlC_2H_3O_2$ in M $NH_4C_2H_3O_2$.

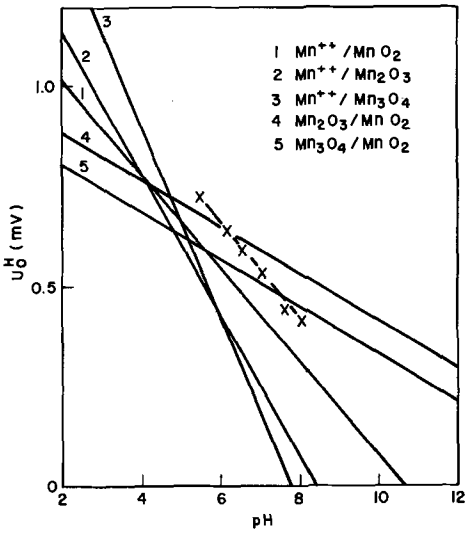

Fig. 4. Equilibrium potentials of reactions [4], [6]-[9], calculated from thermodynamic data (6,7), vs. pH. Crosses show open-circuit potentials of MnO_2 electrodes measured in a solution of 50 mM $Mn(C_2H_3O_2)_2$ in M $NH_4C_2H_3O_2$.

The equilibrium potentials of the reaction

$$Tl_2O_3 + 4H^+ + 4e^- \rightleftarrows Tl_2O + 2H_2O \quad [5]$$

are well below those of reaction [2] in the studied pH range. An influence due to this equilibrium at anodic currents is unlikely to occur. With cathodic currents, reduction of Tl_2O_3 to Tl_2O becomes possible. The potential range in which a zero current plateau is observed is shown in Fig. 3. However, since no activity coefficients and liquid junction potentials have been taken into account, this comparison gives only a rough confirmation that Tl_2O is not involved.

The situation in the case of MnO_2 is more complex, since equilibria of Mn^{++} and MnO_2 with lower oxides of manganese are thermodynamically possible. The equilibrium potentials of the following reactions (together with [4]) are plotted in Fig. 4

$$2Mn^{++} + 3H_2O \rightleftarrows Mn_2O_3 + 6H^+ + 2e^- \quad [6]$$

$$3Mn^{++} + 4H_2O \rightleftarrows Mn_3O_4 + 8H^+ + 2e^- \quad [7]$$

$$Mn_2O_3 + H_2O \rightleftarrows 2MnO_2 + 2H^+ + 2e^- \quad [8]$$

$$Mn_3O_4 + 2H_2O \rightleftarrows 3MnO_2 + 4H^+ + 4e^- \quad [9]$$

The experimentally observed open-circuit potentials are also shown. The equilibrium potentials of reactions [6] and [7] cross that of reaction [4] between pH 4 and 5. It is interesting to note that at pH values lower than 5 the electrical resistivity of the electrodeposited films becomes very high, so that finally deposition is no longer possible. This may indicate the beginning of co-deposition of an insulating lower oxide. The question of how much the equilibria [8] and [9] interfere with reaction [4] cannot be answered here. It appears, however, that at higher pH the cathodic parts of the current potential curves in Fig. 2 are determined by these reactions, since cathodic passivation occurs.

Acknowledgments

The author wishes to thank P. C. Milner for helpful discussions and interest in this work. He is also indebted to G. W. Kammlott for carrying out the x-ray studies.

Manuscript received July 29, 1970.

Any discussion of this paper will appear in a Discussion Section to be published in the December 1971 JOURNAL.

REFERENCES

1. W. Mindt, *This Journal*, **117**, 615 (1970).
2. C. Wagner and W. Traud, *Z. Elektrochem.*, **44**, 391 (1938).
3. R. W. Berry, P. H. Hall, and M. T. Harris, "Thin Film Technology," D. van Nostrand Co., Inc., Princeton (1968).
4. P. Robinson, U.S. Pat. No. 3,066,247, Nov. 27, (1962).
5. W. Mindt and G. I. Parisi, Patent pending.
6. NBS Circular 500, Part 1, "Selected Values of Chemical Thermodynamic Properties."
7. W. M. Latimer, "Oxidation Potentials," Prentice-Hall, Inc., Englewood Cliffs, N. J. (1952).
8. L. Brewer, *Chem. Rev.*, **52**, 1 (1953).

Anodic Oxidation of Carbohydrates and Related Compounds in Neutral Saline Solution

A. J. Appleby* and C. Van Drunen

Institute of Gas Technology, Chicago, Illinois 60616

In a previous communication (1) the oxidation of glucose and derivatives at platinum black electrodes in pH 7.4 saline solution isotonic with human plasma was discussed with the objective of determining the feasibility of consuming such materials in an implantable energy conversion device. Small versions of a fuel cell of this type (power ~100 μW) are capable of supplying electrical energy to a heart pacemaker, urinary stimulator, or physiological monitor device. Larger versions (power 4.5W or more) are potentially capable of supplying sufficient power for a prosthetic heart device. In each case the anodic process would be oxidation of carbohydrates at an electrode with an associated diffusion membrane to prevent contact with blood or intercellular fluid, and the cathodic process would be reduction of oxygen derived either from intercellular fluid (for the smaller devices) (2) or from the air via a percutaneous lead (for the prosthetic heart power source) (3).

In the present communication the catalytic effects of different electrode materials on the anodic oxidation process are discussed along with the order of reaction and probable kinetic rates that may be obtained with currently available catalytic materials at workable overpotentials.

Apparatus

The apparatus used was a conventional glass and Teflon 3-compartment cell with platinum counterelectrode and saturated calomel reference electrode. The electrolyte was Ringer's phosphate buffer solution of physiological strength and pH. A supply of electrolyte (about 500 ml) containing the required concentration of carbohydrate was deaerated using nitrogen in a spiral deoxygenator (4), where it could be stored under nitrogen until required. Electrolyte could be transferred directly under nitrogen from the deoxygenator to the cell. The whole apparatus was maintained at 37°C in a water bath.

A potentiostatic pulsing technique was used to prepare reproducible electrode surfaces. Polarization results, however, were obtained using a conventional galvanostatic circuit.

* Electrochemical Society Active Member.

Key words: biochemical fuel cells, catalytic oxidation, pacemaker energy source.

Electrocatalysis Experiments

Electrodes consisted of Pt and Au foils, and Ir, Ru, Rh, and Pt/Rh alloy plates cut from small rods or castings using a diamond saw. Areas varied from 0.51 to 2.0 cm^2. All were ground and polished, welded to gold wires, degreased, and washed in concentrated HCl and conductivity water. Preliminary experiments established that gold is a very poor catalytic surface for carbohydrate oxidation (see below); hence the presence of gold suspension wires will not be expected to affect data. In addition, a number of experiments were conducted on 1-cm^2 gold foils electroplated with Pt and Rh blacks. Areas were measured using the chronocoulometric hydrogen stripping method in dilute sulfuric acid.

Experiments were conducted in physiological strength (0.005N) glucose solution. Each bright electrode was first given an anodic and cathodic pulse treatment to ensure a reproducible clean surface. The electrode was first pulsed to 700 mV *vs.* calomel (1390 mV *vs.* hydrogen at the same pH), then given a reductive pulse to −900 mV *vs.* calomel, after which it was left on open circuit for 2 min to allow any hydrogen formed during the cathodic pulse to dissipate and to give sufficient time to allow glucose adsorption. A small anodic current was then applied, and the polarization measured after 2 min.

Initial open-circuit potentials on all electrodes were in the range from −610 to −626 mV *vs.* calomel (from +80 to +64 mV *vs.* hydrogen in the same solution). Decay on open circuit was very small (1 mV or less) during the initial period of rest. After this period a small anodic current was applied to the electrode, and the polarization measured after 2 min. The pulsing procedure was repeated before each current density was applied.

Current densities quoted for each electrode in Table I represent values where the onset of poisoning phenomena was considered to occur. Poisoning in this context is defined as rapid positive movement of potential (on the order of 5 mV or more in 2 min) that is irreversible so that the electrode does not return to the initial open-circuit value when the polarizing current is removed.

Table I. Current densities at which poisoning occurred on smooth electrodes

Electrode	Current density, $\mu A/cm^2$
Pt	0.5-1.0
Rh	5.0-7.0
Ir	2.0-3.0
Ru	0.5
Au	0.5
Pt-8 a/o Ru	2.0-3.0
Pt-18 a/o Ru	4.0
Pt-40 a/o Ru	3.0-5.0
Pt-60 a/o Ru	5.0

In all cases the potential at which poisoning became apparent was in the range from −605 to −610 mV *vs.* calomel (from +85 to +80 mV *vs.* hydrogen in the same solution).

It is evident that rhodium, closely followed by platinum-ruthenium alloys, gives the best catalytic performance of the materials studied. Platinum-ruthenium alloys have been shown in other contexts to be effective oxidation catalysts for organic fuels in energy-conversion devices and are known to be resistant to poisoning effects in the oxidation of carbonaceous compounds (5).

In view of the above conclusion, further work was conducted on rhodium black electrodes. Platinum black electrodes were simultaneously used as a standard of comparison.

Oxidation on Black Electrodes

Experiments were conducted on glucose oxidation using 1-cm^2 gold foil electrodes plated with rhodium (area roughness factors 167 and 26.7) and with platinum (area roughness factor 2.9). Black electrodes were given a pulsing treatment for initial surface activation similar to that for bright electrodes but were then left on open circuit for 10 min, followed by polarization at a given current density for 10 min.

Results were obtained in 0.005, 0.001, and 0.0002 M glucose solutions. Open-circuit potentials are given in Table II.

Overnight open-circuit values refer to electrodes left 16 hr in the solution after pulsing. Although there is a slight tendency for the initial open-circuit value on Pt to fall with decreasing glucose concentration, the opposite is the case for electrodes left overnight in the solution. Open-circuit values on Rh electrodes are essentially concentration independent. Smooth Rh and Pt electrodes had overnight open-circuit voltages ~300 mV NHE, and showed more rapid decay.

Initial polarization behavior on the 167-cm^2 Rh black electrode is illustrated in Fig. 1. On this electrode, poisoning was not apparent below 20 $\mu A/cm^2$, which on a real area basis is 0.12 $\mu A/cm^2$. Polarization curves for the three glucose concentrations studied as shown. In addition, a polarization plot for the 0.001M solution after the electrode had been allowed to stand for 1 hr after activation is shown (dashed line). The other group of polarization plots refers to the three solutions for electrodes that had been allowed to stand 16 hr after pulsing. It can be seen that the effect of glucose concentration is small, except at high current density where mass transport effects may start to predominate. In general the slow change in potential at constant current density (on a geometric-area basis) was much less on electrodes of high specific area, but

Table II. Open-circuit potentials on black electrodes

	Rhodium open circuit		Platinum open circuit	
	Initial	Overnight	Initial	Overnight
Glucose M	mV *vs.* calomel			
0.005	626-630	572	639-641	510
0.001	641-640	575-578	633-637	
0.0002	629-634	572	617-629	523

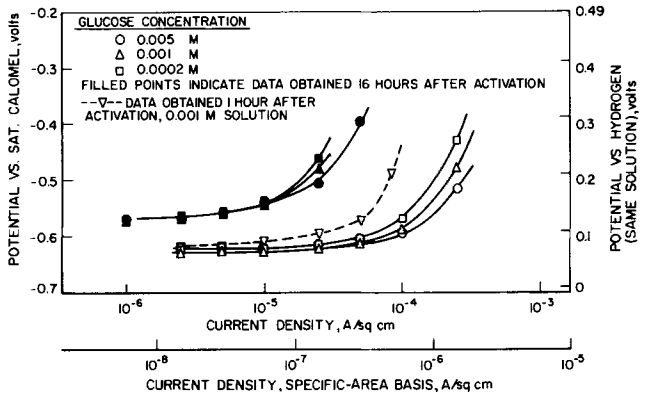

Fig. 1. Oxidation of glucose on rhodium black in Ringer's phosphate buffer (roughness factor 167) at 37°C.

these were not as good as smooth electrodes on a specific-area basis from the initial polarization point of view. This can be attributed to difficulty of diffusion of poisoning products within the porous structure, and perhaps to pH changes in the pore structure if local production of $[H^+]$ exceeds the buffering capacity of the electrolyte.

A series of tests similar to the above was carried out in 0.005, 0.001, and 0.0002M gluconic acid and glucosamine solutions. On the low-specific-area Rh black electrode (26.7 cm^2), polarizations of 23, 13, and 18 mV, respectively, were noted in the three glucose solutions at a geometric-area current density of 5 $\mu A/cm^2$ 10 min after activation. Open-circuit voltages were 628-632 mV *vs.* calomel. In glucosamine solutions, open-circuit potentials were 10-15 mV more negative, and corresponding polarizations were ~1, 4, and 4 mV only at 5 $\mu A/cm^2$ under the same conditions. Gluconic acid solutions gave open-circuit potentials ~15 mV more positive than glucose, and very large polarizations were recorded at 5 $\mu A/cm^2$ after 10 min (99 mV at 0.005M, 58 mV at 0.001M, and 23 mV at 0.0002M). The latter results are interesting in that they show a negative reaction order. Results on Pt black electrodes were similar with low apparent reaction orders for glucose and glucosamine. Again glucosamine showed the lowest and gluconic acid the highest polarizations, although the differences were not so marked as in the case of rhodium (~40 and 27 mV polarization for 0.005M and 0.0002M glucose; ~20 and ~30 mV, respectively, for similar glucosamine solutions; and ~40 and 50 mV for similar gluconic acid solutions at a geometric-area current density of 5 $\mu A/cm^2$).

Oxidation of a typical polysaccharide was studied using a 0.02% chondroitin sulfate solution. Preliminary results established initial polarization behavior to be midway between that for glucose and gluconic acid on both platinum and rhodium black electrodes. After allowing steady state to be reached (after about 16 hr in the solution) a Tafel plot on a platinum black electrode shows a slope of about 100 mV/decade (Fig. 2).

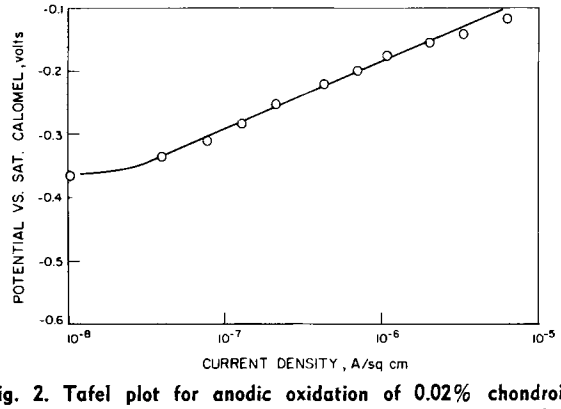

Fig. 2. Tafel plot for anodic oxidation of 0.02% chondroitin sulfate solution in Ringer's phosphate buffer on rhodium black (roughness factor 26.7) at 37°C.

Tafel plots of slope approaching $2RT/F$ are also given by glucose and gluconic acid solutions on poisoned electrodes (1).

Conclusions

Results obtained indicate that rhodium and Pt-Ru alloy electrodes are more effective than platinum for glucose oxidation, although gluconic acid is more effectively oxidized on platinum. Rate constants for gluconic acid oxidation appear to be lower than those for glucose in the +50 to +250 mV range *vs.* hydrogen in the same solution, in agreement with Rao and Drake's conclusions (6). Electrodes show a time-dependent rate constant due to poisoning effects. Reaction orders for glucose, gluconic acid, and glucosamine oxidation are low, and Tafel slopes approach $2RT/F$ for all the carbohydrate compounds studied when measurements are taken after a sufficiently long time. This suggests that the mechanism of carbohydrate oxidation is similar to that reported for ethylene and other organic compounds (5, 7) with the production or reaction of adsorbed OH as the rate-determining step, depending on the substrate.

The polarization data obtained in this work will be used in a mathematical model of a glucose diffusion anode for use in a proposed fuel cell for prosthetic heart propulsion.

Acknowledgment

We wish to thank Doctors S. K. Wolfson, Jr., and D. Y. C. Ng for helpful discussions.

Manuscript received Aug. 14, 1970.

Any discussion of this paper will appear in a Discussion Section to be published in the December 1971 JOURNAL.

REFERENCES

1. S. J. Yao, A. J. Appleby, A. Geisel, H. R. Cash, and S. K. Wolfson, Jr., *Nature*, **224**, 921 (1969).
2. S. K. Wolfson Jr., S. L. Gofberg, P. Prusiner, and L. Nanis, *Trans. Amer. Soc. Artificial Intern. Organs*, **14**, 198 (1968).
3. A. J. Appleby, D. Y. C. Ng, S. K. Wolfson, Jr., and H. Weinstein, Proceedings of the 4th Annual IECEC Meeting, 346.
4. D. Gilroy and J. E. O. Mayne, *J. Appl. Chem.*, **12**, 382 (1962).
5. J. O'M. Bockris and H. Wroblowa, *J. Electroanal. Chem.*, **7**, 428 (1964).
6. M. L. B. Rao and R. F. Drake, *This Journal*, **116**, 334 (1969).
7. A. T. Kuhn, H. Wroblowa, and J. O'M. Bockris, *Trans. Faraday Soc.*, **63**, 1458 (1967).

Nomographs for the Diffusivities of Salts, Acids, and Bases in Very Dilute Water Solutions

Adam Zanker

Kiriat-Jam "G," Haifa, Israel

Two nomographs were constructed in order to predict and calculate the diffusivity of electrolyte molecules in very diluted water solutions. As a basis for these nomographs, the following equations were chosen: (*i*) the Nernst equation, which allows calculation of the diffusivity at a certain temperature when the required conductivities are known (1); and (*ii*) the Reid and Sherwood equation, which allows prediction and calculation of the diffusivity at various temperatures when only a diffusivity at 25°C is known (2). These equations were chosen for two reasons: first, they give relatively good results, in many cases very close to the measured values; and second, they are in nomographable form.

The maximum discrepancies between calculated and measured values are as follows (in per cent) (3)

Molecule type \ Concentration of electrolyte in water	up to 0.001M, %	up to 0.01M, %
Molecules of 1:1 type (such as NaCl, KNO_3)	3	8
Other types of molecules	10	15

In the majority of cases the calculated results are much closer to the measured values so that the use of these nomographs gives quick and relatively reliable results. The equations used are:

1. *The Nernst Equation*

$$D_{25} = 8.931 \times 10^{-10} \times T \cdot \frac{(L_+^\circ \times L_-^\circ)}{(L_+^\circ + L_-^\circ)} \cdot \frac{(Z_+ + Z_-)}{(Z_+ \times Z_-)}$$

where: D_{25} = diffusivity of the molecule, cm²/sec (at 25°C)

Key words: graphical calculations (in chemistry), ionic conductance (at infinite dilutions), electrolyte solutions, temperature-diffusivity relationships, mobility of ions.

I_+° = cationic conductance at infinite dilution cm² · ohm⁻¹/equiv (at 25°C)
I_-° = anionic conductance at infinite dilution cm² · ohm⁻¹/equiv (at 25°C)
T = absolute temperature, in °K (taken as constant, T = 298°K = 25°C)
Z_+ = absolute valency of cation (without sign)
Z_- = absolute valency of anion (without sign)

2. *The Reid and Sherwood Equation*

$$D_T = D_{25} \cdot \frac{T}{334 \cdot \mu_T}$$

where: D_T = diffusivity of molecule, cm²/sec, at temp. T °K
D_{25} = diffusivity of molecule, cm²/sec, at 25°C (298°K)
T = required temperature, in °K
μ_T = viscosity of water, at temp. T °K, in cP.

In order to facilitate use of the nomographs, several values of anionic and cationic conductances at 25°C were plotted on suitable scales (4, 5). Both nomographs are based on the above equations, but it was found more useful to construct two separate nomographs, one for salts only and the other for acids and bases.

Due to the large difference between the conductance of H^+ and OH^- ions, and other cations and anions, a nomograph covering the full range of ionic conductances turned out to be very inaccurate in the conductance of salts. The possiblity of plotting a number of values of cationic and anionic conductances was also limited.

Use of the nomographs is as follows:

(*a*) The known values of anionic and cationic conductances, plotted on a suitable scale, have to be con-

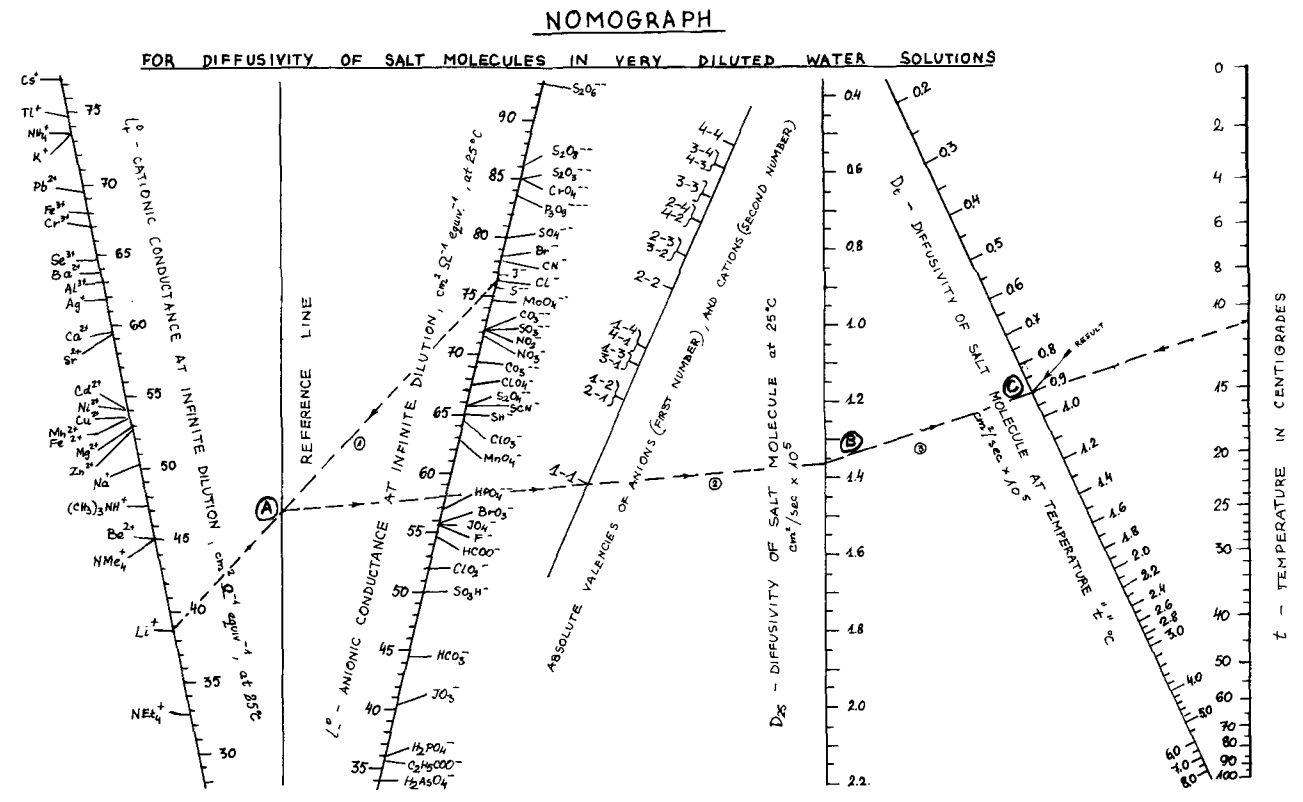

Fig. 1. Nomograph for diffusivity of salt molecules in very diluted water solutions

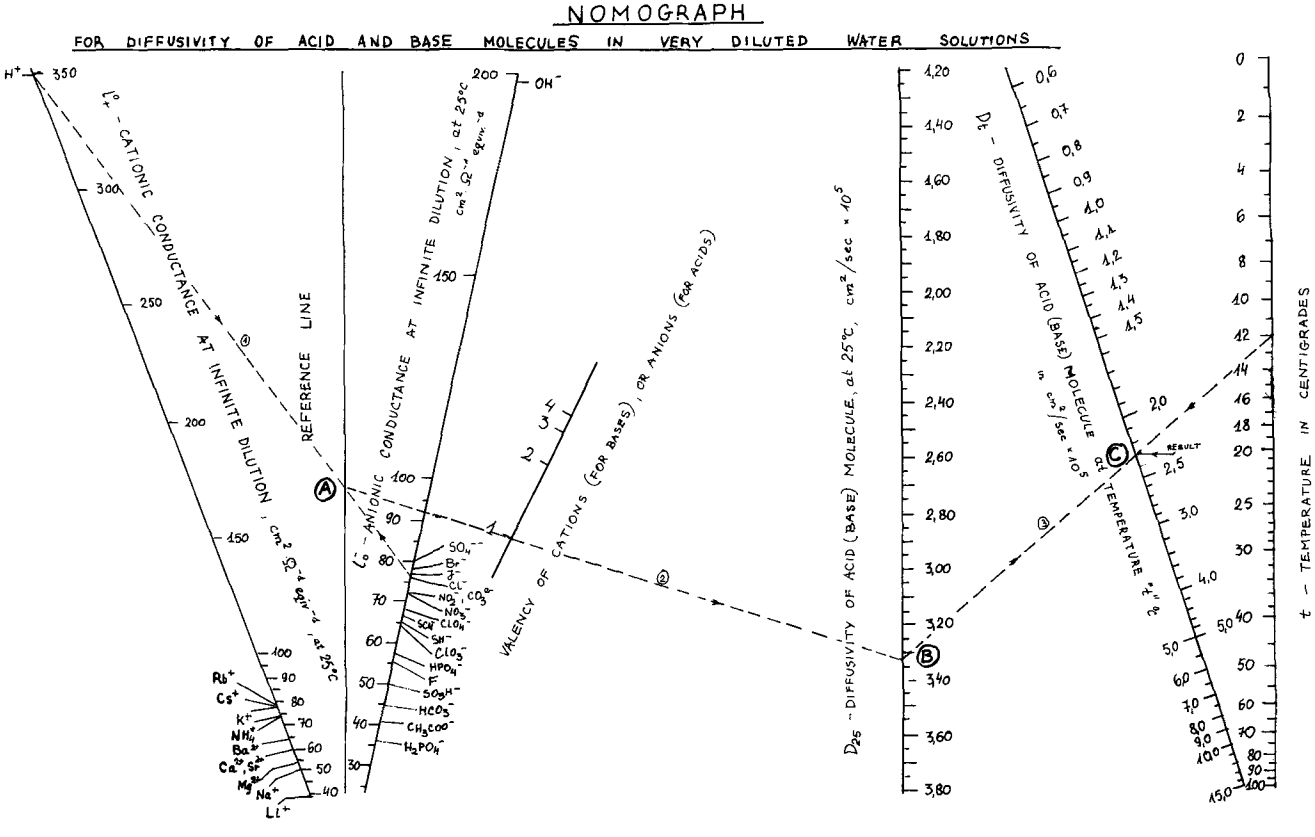

Fig. 2. Nomograph for diffusivity of acid and base molecules in very diluted water solutions

nected with a ruler. The intersection point of the ruler with the "reference line" gives the first auxiliary point, A.

(b) Point A has to be connected with a ruler with a suitable point on the scale which gives "valencies of the cations and the anions." This line has to be extended to the intersection point with the scale marked "diffusivity of molecule at 25°C," point B. This point gives the intermediate result, D_{25}.

(c) If it is desired to learn the diffusivity at a temperature other than 25°C, the value of D_{25} is to be connected with a ruler with the required temperature (t = °C) on the t scale. The intersection of the ruler with the D_t (oblique) scale gives the final result. In

order to illustrate use of the nomograph, an example is drawn, with a dotted line, on each of the nomographs shown.

Example 1. Nomograph for Diffusivity of Salts

What will be the diffusivity of diluted (0.01*N*) LiCl solution at 11°C? The conductance of Li^+ is 38.6 $cm^2 \cdot ohm^{-1}$/equiv at 25°C, and the conductance of Cl^- is 76.35 $cm^2 \cdot ohm^{-1}$/equiv at 25°C. Both values are plotted on suitable scales, and both values have to be connected with a ruler and the intersection point A with the reference line has to be found (dotted line 1).

The valencies of both cation and anion are 1 and 1. The point marked 1-1 on the valency scale is to be connected with the previously found point A, and the line extended up to the D_{25} scale (the dotted line 2 and point B). The value found is $D_{25} = 1.37\ 10^{-5}$ cm^2/sec. [The measured value is $1.313 \cdot 10^{-5}$ cm^2/sec (6).]

Point B should then be connected to a temperature of 11°C on the temperature t scale (dotted line 3 on the nomograph). The final result is found on the D_t scale (point C). The result is $D_t = 0.90 \cdot 10^{-5}$ cm^2/sec at 11°C. [The measured value is $0.93 \cdot 10^{-5}$ cm^2/sec (7).]

Example 2. Nomograph for Diffusivity of Acids and Bases

What will be the diffusivity of diluted (0.01*N*) HCl solution at 12°C? The conductance of H^+ is 349.8 $cm^2 \cdot ohm^{-1}$/equiv at 25°C and the conductance of Cl^- is 75.35 $cm^2 \cdot ohm^{-1}$/equiv at 25°C. Both values are plotted on suitable scales. Connect both values and find the intersection point A on the reference line (dotted line 1).

The valency of the cation is 1. The previously found point A has to be connected with the value 1 on the valency scale, and this line has to be extended up to the intersection with the D_{25} scale, pointed B (dotted line 2). The intermediate result is $D_{25} = 3.33 \cdot 10^{-5}$ cm^2/sec. [The measured value, graphically interpolated is $3.18 \cdot 10^{-5}$ cm^2/sec (8).]

The intermediate result, point B, has to be connected with the temperature 12°C on the temperature t scale (dotted line 3). The final result is then found on point C of the D_t scale and is $D_t = 2.3 \cdot 10^{-5}$ cm^2/sec at 12°C. [The measured value is $2.38\ 10^{-5}$ cm^2/sec (9).]

Manuscript submitted Aug. 5, 1970; revised manuscript received Sept. 7, 1970.

Any discussion of this paper will appear in a Discussion Section to be published in the December 1971 JOURNAL.

REFERENCES

1. R. A. Robinson and R. H. Stokes, "Electrolytic Solutions," p. 288, Butterworths (1959).
2. R. C. Reid and T. K. Sherwood, "The Properties of Gases and Liquids," p. 386, McGraw-Hill Book Co., New York (1958).
3. R. A. Robinson and R. H. Stokes, *ibid.*, p. 513.
4. R. A. Robinson and R. H. Stokes, *ibid.*, pp. 463, 465, 329, 289.
5. St. Bretsznajder, "The Properties of Gases and Liquids," pp. 706, 707, WNT—Warsaw, 1962.
6. R. A. Robinson and R. H. Stokes, *ibid.*, p. 289.
7. International Critical Tables, V, p. 65.
8. R. A. Robinson and R. H. Stokes, *ibid.*, p. 515.
9. International Critical Tables, V, p. 65.

Brief Communication

Note on the Electrodeposition of Magnesium from an Organic Solution of a Magnesium-Boron Complex

Abner Brenner*

National Bureau of Standards, Washington, D. C., 20234

Thus far no successful method of electrodepositing magnesium from a solution operated at room temperature has been published. Magnesium is too active a metal to be electrodeposited from aqueous solutions and electrolysis of various Grignard solutions has not yielded sound, coherent deposits of magnesium. The cathode deposits are mossy, dark in color, and obviously contaminated. I have reviewed the unsatisfactory situation pertaining to the electrodeposition of magnesium (1).

I have developed an organic plating bath, which deposited smooth, white, somewhat ductile coatings of magnesium. It was obtained by reactions involving decaborane, $B_{10}H_{14}$.

The first step in the preparation of the bath is the preparation of a lithium derivative of decaborane with a solution of lithium methyl in ether.[1] Lithium methyl in diethyl ether (25 ml of a commercial 1.7M solution) was introduced into an oxygen-free vessel through which pure argon flowed. Decaborane, 1g, dissolved in 10 ml of terahydrofuran (THF) was slowly added. The THF needs to be anhydrous.[2] With each addition of the decaborane solution a vigorous effervescence occurred, which probably represented the evolution of methane. A heavy, yellow layer separated out which contained most of the lithium.[3] On electrolysis of this two-phase solution at 0.1 to 1.0 A/dm^2, lithium deposited on the cathode but in much greater quantity from the lower layer which obviously had much greater conductivity.[4] At high current density, the lithium deposited as dendrites from the lower layer instead of as a smooth deposit.[5]

To the two-layer system of lithium-decaboron complex, 25 ml of a saturated solution of anhydrous magnesium chloride in THF was added. The system

* Electrochemical Society Active Member.

Key words: magnesium—electrodeposition of, decaborane, organometallic compound, nonaqueous electroplating, lithium deposition.

[1] Both materials are commercially available. Decaborane at the moment costs about $3 a gram, and, therefore, a research chemist might prefer to spend his money on platinum. However, with boric acid priced at about five cents a pound, there is no inherent reason why decaborane should not be produced more cheaply.

[2] The distillation with lithium aluminum hydride, so frequently described in the literature, is quite unnecessary. It is sufficient to add a sodium hydride suspension, a commercial 50% suspension of NaH in mineral oil, in small quantities to several hundred milliliters of THF until the gassing ceases, let stand until the excess NaH settles out, and then decant off the THF as needed.

[3] This lower layer had much higher conductivity than the supernatant liquid.

[4] This electrolysis contrasts with the initial solution of lithium methyl which scarcely conducts at all and from which lithium does not deposit.

[5] In some cases needles so fine as to be scarcely visible grew with great rapidity, for example, 1 cm in a minute, and shorted out the cell.

became homogeneous forming the plating bath.[6] The conductivity of the resulting solution was much higher than that of the lithium-decaboron solution from which it was formed. The magnesium complex in the solution appeared to be soluble at least to the extent of 1 mole per liter. The resulting solution on electrolysis yielded smooth, white, sound deposits of magnesium. The bath may be operated at current densities between 0.1 and 1.0 A/dm^2. The cathode and anode efficiencies were approximately 100%. With further development the process should be on a par with the hydride-ether aluminum plating process.

The bath can be prepared directly from a Grignard reagent and decaborane, for example, by mixing 60 ml of a THF solution of magnesium ethyl chloride (commercially obtainable) with a gram of decaborane and adding some magnesium chloride-THF solution. This bath was not as satisfactory as the one derived from the lithium complex, but with further investigation it might be improved.

The magnesium bath was prepared with rigid exclusion of oxygen, but after preparation it was stable on exposure to dry air. Moisture would undoubtedly decompose the magnesium complex. The bath is stable. A bath, which had evaporated to about half-volume during a six-month storage period, again became operative after THF was added to bring the bath up to volume together with some additional magnesium chloride in THF.

[6] Magnesium chloride dissolves slowly in THF and may at first give the appearance of low solubility, but the saturated solution has a concentration of about 0.75 molar. The salt and the THF may need to stand for several days or be stirred a number of hours. On long standing (some weeks or months) the saturated solution fills with a mass of colorless crystals of the THF etherate.

The deposit has not been quantitatively analyzed, but the indications are that it may contain a small amount of boron, perhaps below 1%. Tubes of magnesium were electroformed by depositing the metal on thin-walled aluminum tubing, serving as a master, which was subsequently dissolved out with caustic soda.

A beryllium analog of the magnesium bath is under investigation, but it does not yield as yet satisfactory deposits.

The compound present in the decaborane magnesium bath is probably not $Mg \cdot B_{10}H_{12} \cdot 2Et_2O$, which was prepared by N. N. Greenwood and N. F. Travers (2) by the reaction of diethyl magnesium with decaborane in a solution of diethyl ether. Their compound was prepared at $-78°$ and was described as being rapidly decomposed in air and insoluble in all common organic solvents, a behavior quite at variance with the stability and solubility of the magnesium complex in the plating bath.

Manuscript submitted July 13, 1970; revised manuscript received Sept. 4, 1970.

Any discussion of this paper will appear in a Discussion Section to be published in the December 1971 JOURNAL.

REFERENCES

1. Abner Brenner, in "Advances in Electrochemistry and Electrochemical Engineering," Vol. 5, p. 215, C. W. Tobias, Editor, Interscience Publishers, New York (1967).
2. N. N. Greenwood and N. F. Travers, *J. Chem. Soc. A* **1968** (1), 15.

JOURNAL OF THE ELECTROCHEMICAL SOCIETY

SOLID STATE SCIENCE

JANUARY 1971

Kinetics of the High-Temperature Phosphidation of Nickel

Yoshinori Sasaki, Akemi Kato, and Shiro Ueda

Department of Synthetic Chemistry, Faculty of Engineering, Chiba University, Yayoi-cho, Chiba, Japan

ABSTRACT

A study has been carried out on the kinetics of phosphidation of nickel sheets exposed to phosphorus vapor of 1 Torr to 2 atm at temperatures from 400° to 600°C by means of a sealed-tube method. The phosphidations were revealed to follow parabolic behavior. The values of the rate constant K_p at 2 atm have fallen into the category of order of 10^{-6} to 10^{-8} g^2/cm^4-min, whose Arrhenius plot yielded the activation energies of 15 ± 2.5 and 33 ± 3.5 kcal/mole for 400°-500° and 500°-600°C, respectively. The pressure dependence of K_p resulted experimentally in the expression $K_p \propto P^{0.055\sim0.109}$ at 500°C, which could be interpreted in terms of the mass action law. X-ray powder diffraction patterns indicated the phosphides to be composed mainly of Ni_2P, and an electron microprobe analysis showed that the phosphide layer in contact with nickel phase is Ni_2P. Metallographic observations showed the phosphidation to progress generally with formation of phosphide mounds, and sometimes with growth of whiskers and platelets.

The phosphides of nickel have extensively been studied by many groups of workers. Konstantinow (1) determined the phase diagram of the nickel-phosphorus system up to 36 atomic per cent (a/o) phosphorus, showing the existence of the phases Ni_3P, Ni_5P_2, and Ni_2P. X-ray investigations by Nowotny and Henglein (2) showed that in the same range of phosphorus concentration a compound Ni_7P_3 exists in addition to the above. Thermal decompositions and x-ray investigations of nickel-phosphorus compounds by Biltz and Heimbrecht (3) indicated the existence of NiP_3, NiP_2, and Ni_6P_5 as higher phosphides.

The heats of formation (4) and magnetic properties (5-7) of nickel phosphides have also been investigated. Recently the phase diagram (8) and the crystal structures of Ni_3P (9), Ni_5P_2 (10), $Ni_{12}P_5$ (11), Ni_2P (5, 12), Ni_5P_4 (13), NiP_2 (6, 14), and NiP_3 (7) have been studied in detail.

However, the investigation on the reactivity of nickel with phosphorus has not been extended beyond that on the reactivity which was estimated by measuring the variation in electric resistance of a technical nickel wire specimen exposed to phosphorus vapor (15). Especially, no reports dealing quantitatively with the rate of reaction of nickel with phosphorus have appeared up to the present.

In a previous paper (16), the rate of reaction of copper with phosphorus vapor was determined using a quartz helix method. The present study was undertaken to determine the rate of reaction between a nickel sheet and phosphorus vapor by means of an evacuated- and sealed-tube method, described below, in the temperature region 400°-600°C at phosphorus pressures ranging from 1 Torr to 2 atm. The phosphides obtained were identified by comparing their x-ray diffraction patterns with those of known phosphides. In addition, observations were metallographically made of surfaces and cross sections of the phosphidized specimens, and the distributions of phosphorus in the phosphide layers were also surveyed.

Key words: nickel phosphides—formation of Ni_2P, nickel phosphides—formation of NiP_2.

Experimental

Materials.—Nickel sheet 0.25 mm thick was cut into coupons of approximately 7 by 25 mm. According to an analysis supplied by the manufacturer, the amounts of main impurities in the nickel sheet are as follows: Co < 0.25; Mn, 0.03; Fe, 0.03; and Cu, 0.01 weight per cent (w/o). The coupons were abraded through 0/5-0/9 emery papers, degreased in trichloroethylene, and vacuum-annealed for 1 hr at 650°C. After these treatments the specimens to be phosphidized were chemically polished for 40 sec at about 90°C in a solution composed of 10 parts by volume 95% H_2SO_4, 10 parts 85% H_3PO_4, 30 parts 60% HNO_3, and 50 parts glacial acetic acid. The polished specimens then were rinsed in distilled water and subsequently in acetone.

Purification of red phosphorus is similar to that described in the previous paper (16).

Preparation of the sealed tube containing the sample nickel sheet and white phosphorus.—After an appropriate amount of the refined red phosphorus was introduced into a one-side-closed Pyrex or silica tube (inside diameter: 7 mm) and some clean glass wool was packed, the nickel specimen was put in this tube. This tube, including the specimen and the red phosphorus, was evacuated to 10^{-2} Torr at room temperature, then was filled to 1 atm with argon gas purified by passing through phosphorus pentoxide and heated active copper, and finally was reevacuated. The evacuating and the filling were repeated five times at 200°C in order to remove moisture, oxygen, and other gaseous impurities adsorbed on the red phosphorus, the glass wool, and the inner wall of the tube. In this case, only the nickel specimen placed near the entrance end of the tube was not heated. After these operations this tube was sealed under vacuum.

It seems reasonable for red phosphorus with a variety of structures not to give constant phosphorus

vapor pressures. Therefore, a conversion from red to white phosphorus is necessary to secure the more stable pressures of phosphorus vapor in the closed system. In this study, prior to the run, the phosphorus vapor that evolved by heating the red phosphorus in the sealed tube was condensed into white phosphorus by water cooling in the neighborhood of the packed glass wool.

Apparatus and procedure.—A schematic drawing of a phosphidation apparatus employed is represented in Fig. 1. It consists simply of two furnaces, in which each temperature was regulated individually by two automatic regulators within temperature variations of less than 3°C. A phosphorus vapor pressure is governed by the minimum temperature in the closed system. The phosphidation temperatures were given by one furnace, whereas the minimum temperature in the neighborhood of the contact part of the two furnaces was controlled by adjustment of the temperature of the other furnace.

The white phosphorus vapor pressure, P_{Torr}, is given as a function of the absolute temperature, T, as follows (17): $\log P_{Torr} = 7.808 - 2.729 \times 10^3/T$, 349.6° (1 Torr) $\leq T \leq$ 553°K (760 Torr). A temperature of 320°C gives 2 atm for the phosphorus vapor pressure (18). The above equations were used to obtain the desired phosphorus pressures.

Since the gaseous phosphorus molecule in the form of symmetrical p_4 tetrahedra scarcely dissociates into P_2 molecules at temperatures below 800°C, the phosphorus vapor can be regarded as consisting of P_4 molecules over the temperature region of 400°-600°C employed in this work.

After the desired period of time of phosphidation, the tube was taken out of the furnace and immediately the end of the tube opposite the specimen was quenched to avoid the condensation of the phosphorus vapor on the phosphidized specimen. No appreciable attack on the Pyrex and silica tubes was detected. After the phosphidized specimen was removed from the sealed tube and weighed, its surfaces were observed using a microscope. Distributions of phosphorus in the phosphide films were also surveyed with an electron microprobe (AKASHI Tronalyser TRA-25). The compositions of the obtainable phosphides were confirmed with x-ray diffraction patterns.

Experimental Results

Kinetics.—It is impossible to measure continuously the weight change, being caused by phosphidation, of a sample sheet *vs.* time by means of the sealed-tube method employed in this study.

Kinetic results are shown in Fig. 2 on phosphidation of the nickel sheets exposed to phosphorus vapor of 2 atm at temperatures from 400°-600°C. It should be noted that each data point represented here was obtained by phosphidizing a distinct specimen. The rate of the nickel phosphidation increases obviously with

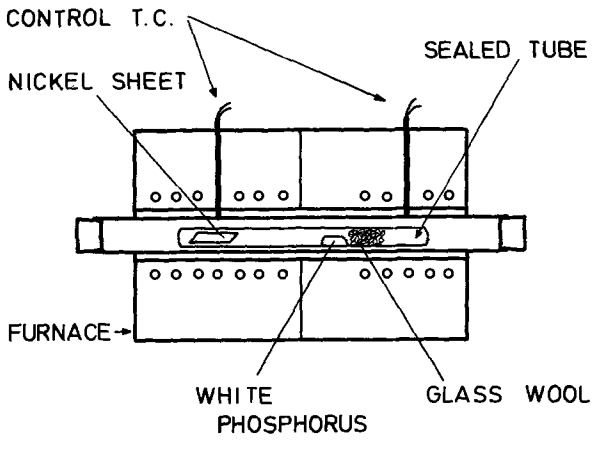

Fig. 1. Schematic drawing of apparatus

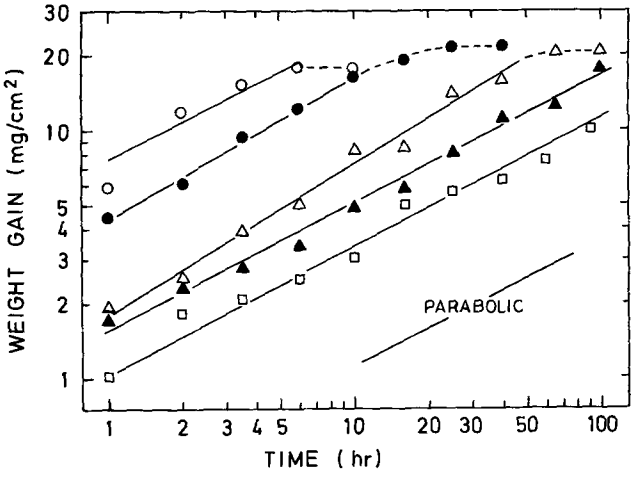

Fig. 2. Phosphidation of nickel at a phosphorus pressure of 2 atm: ○ 600°; ● 550°; △ 500°; ▲ 450°; □ 400°C.

an increase of temperature at a phosphorus vapor pressure of 2 atm.

Although these log-log plots are somewhat scattered, they yield straight lines with a slope equal to one-half. Therefore, the phosphidation may be regarded to follow a parabolic rate law based on a diffusion process.

After extended periods, the appearance of saturation curves in the phosphidations at 500°, 550°, and 600°C means the nickel sheets to have completely become the phosphides. This was determined from microscopic observations of the cross sections of these phosphidized specimens, and in this case their average compositions were estimated to be $NiP_{0.6}$, obtained by weight calculations.

Figure 3 gives results of phosphidation of nickel at 500°C under phosphorus pressures of 1, 4, and 20 Torr, and shows that each phosphidation obeys parabolic behavior. Consequently, it is concluded that the parabolic rate law governs the nickel phosphidation in the pressure range 1 Torr to 2 atm at 500°C.

From the above we conclude that an interface or adsorption reaction is distinctly faster than a diffusion process; hence, diffusion control predominates throughout the reaction time.

Values of the parabolic rate constants, K_p, obtained from the weight gain-time relationships are summarized in Table I.

X-ray diffraction.—Figure 4 illustrates the results of x-ray diffraction patterns taken at room temperature, employing nickel-filtered copper radiation. A broad division can be made between results of pulverized phosphides and those of the surface of the phosphide films. The diffraction pattern of powder reflects the bulk of phosphide scaling layers.

The resulting powder diffraction patterns (Fig. 4A) reveal the products to consist mainly of Ni_2P. For comparison, known patterns of nickel phosphides are illustrated in the same figure. Any peaks of NiP_3, NiP_2, and Ni_6P_5 have seldom been observed.

In diffraction patterns of the surface, however, the inherent peaks of NiP_2 appear for the specimens which were phosphidized in 2 atm phosphorus at 400°, 1 hr; 500°, 100 hr; and 550°C, 25 hr. Consequently, it may be emphasized that NiP_2 as higher phosphide is formed

Table I. Parabolic rate constants for the phosphidation of nickel

Temp, °C	Pressure	$K_p \times 10^8$ g²/cm⁴-min
400	2 atm	1.8 ± 0.2
450	2	4.0 ± 0.2
500	2	8.5 ± 2
550	2	38.0 ± 2
600	2	97.0 ± 15
500	20 Torr	5.3 ± 0.3
500	4	4.8 ± 0.2
500	1	4.2 ± 0.2

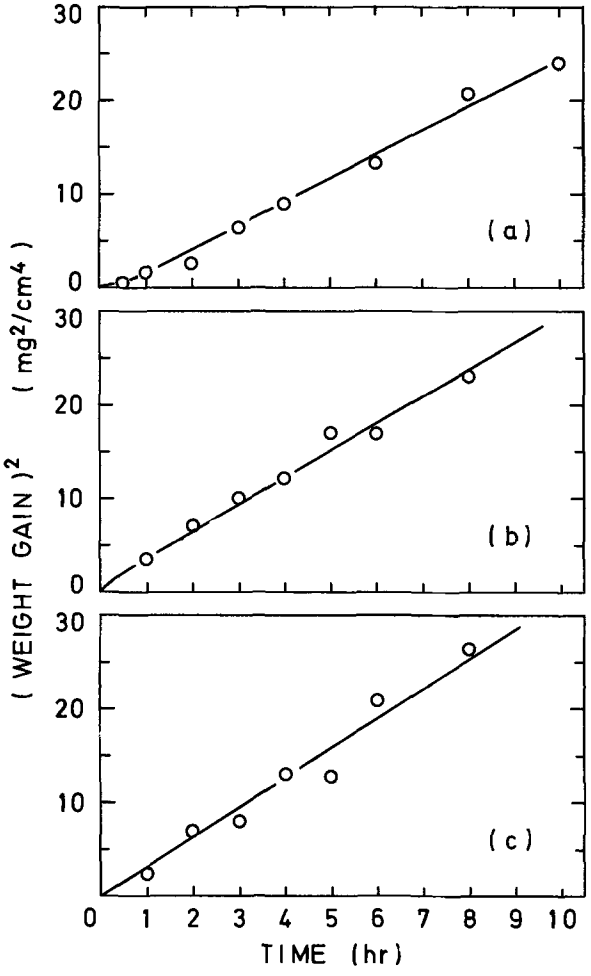

Fig. 3. Phosphidation of nickel at 500°C under various phosphorus pressures: (a)-1, (b)-4, (c)-20 Torr.

at relatively low temperatures and at early periods of phosphidation. It is also noteworthy to see that the weight increases obtained under the experimental conditions of "500°C 2 atm 100 hr" and "550°C 2 atm 25 hr" are just on the saturation curves shown in Fig. 2. Diffraction patterns at 400°C and 450°C in 2 atm of phosphorus for long periods of time were similar to their patterns for 6 hr, and the patterns at 500°, 550°, and 600°C have hardly varied with phosphidation time.

The diffraction patterns of the reverse sides of phosphide scaling films are in close agreement with that of Ni_2P (Fig. 4B). This fact is very important from the viewpoint that the formation of Ni_2P is found to take place at the phosphide/nickel interface. A large number of faceted crystals have grown on the surfaces at 500°C at 1 Torr for 4 and 8 hr. The x-ray diffraction pattern showed distinctly these faceted crystals to be Ni_2P (Fig. 4C). Under the experimental conditions employed, the existence of Ni_7P_3 and Ni_5P_2 as lower phosphides could be seldom detected from the x-ray diffractions. These results are important, suggesting one side of a characteristic feature of the nickel phosphidation mechanism.

Distribution of phosphorus.—Distribution of phosphorus in the phosphide scaling films, obtained by an electron microprobe, is shown in Fig. 5. This figure shows that the content of phosphorus in the phosphide films decreases toward inner scaling layers.

The nickel diphosphide already has been indicated to be present in the outer layer. It must be noted that plateaus having a certain constant content of phosphorus appeared in the bulk phosphide. The compositions of these plateaus have been assured to consist of Ni_2P from the x-ray diffraction patterns. It is worth giving special attention to the fact that no phosphides which are more rich in nickel than Ni_2P have been

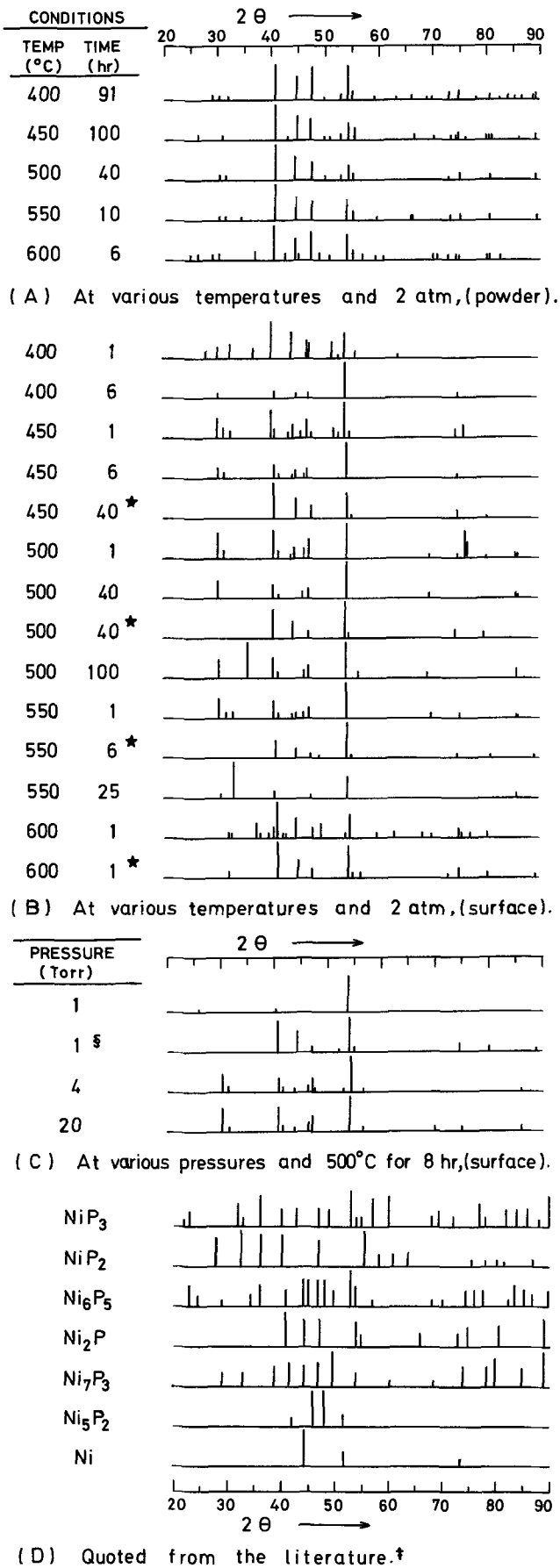

Fig. 4. X-ray diffractograms of the nickel phosphides obtained, employing Ni-filtered copper radiation. (θ: diffraction angle)
*The reverse side of the phosphide film,
§Faceted crystal,
†NiP_3 (3); NiP_2 (6); Ni_6P_5 (3); Ni_2P, Ni_7P_3 (2); Ni_5P_2 (10); Ni (19).

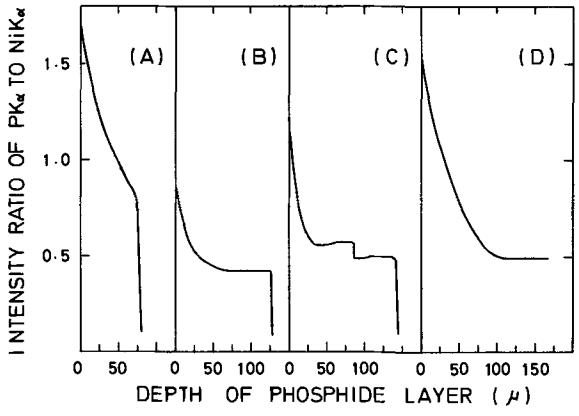

Fig. 5. Distributions of phosphorus in the phosphide scaling layers: (A)-400°, 60 hr; (B)-450°, 65 hr; (C)-500°, 40 hr; (D)-600°C, 10 hr.

formed. The upper step in the plateau in Fig. 5C suggests the presence of a phase other than Ni_2P, and corresponds reasonably to higher phosphide than Ni_2P.

Figure 5 suggests that the phosphorus dissolution and the phosphide formation occur simultaneously. Consequently the rate of phosphidation under the experimental conditions employed is expected to be controlled by the transport properties of the well-defined layer of phosphide in contact with the metal phases, that is, the rate is determined by a lattice-diffusion process at the Ni_2P/Ni interface.

Microscopic observation.—The phosphidation has generally progressed with growth of mounds of nickel phosphides, which seem to be related to the reaction velocity. For example, a micrograph of the surface of the specimen phosphidized for 16 hr at 450°C under 2 atm of phosphorus is shown in Fig. 6. This surface is covered all over with phosphide mounds of various sizes. Under the experimental conditions employed, in general, phosphide surfaces slowly became relatively flat with the lapse of time, and phosphide scales were generally very adherent to the metallic nickel even at room temperature.

An interesting phenomenon is the dapple aspect, shown in Fig. 7, of the phosphide surface which formed in comparatively early stages. Figure 8 is also a micrograph of the nickel substrate surface after removal of the phosphide film which formed for 3 hr at 500°C and 20 Torr. An aspect similar to that in Fig. 7 appears. These features suggest that phosphides have been formed with dependence on each crystal grain of the metallic nickel.

Growth of phosphide needles or whiskers were found in 2 atm of phosphorus over the entire temperature range employed and sometimes in the lower phosphorus pressures. An example is shown in Fig. 9, which is a micrograph of the phosphide needles or whiskers

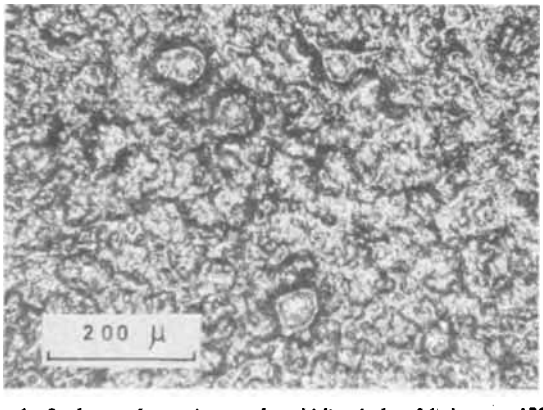

Fig. 6. Surface of specimen phosphidized for 16 hr at 450°C and 2 atm phosphorus.

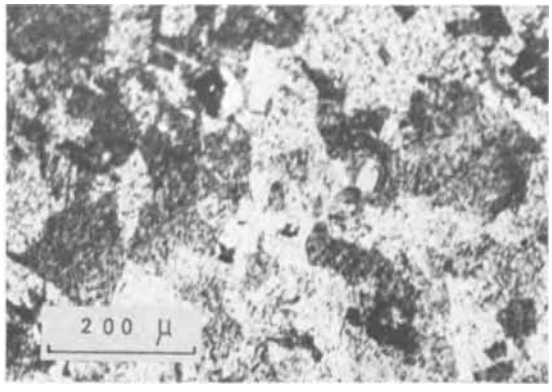

Fig. 7. Surface of specimen phosphidized in 2 atm of phosphorus at 500°C for 2 hr.

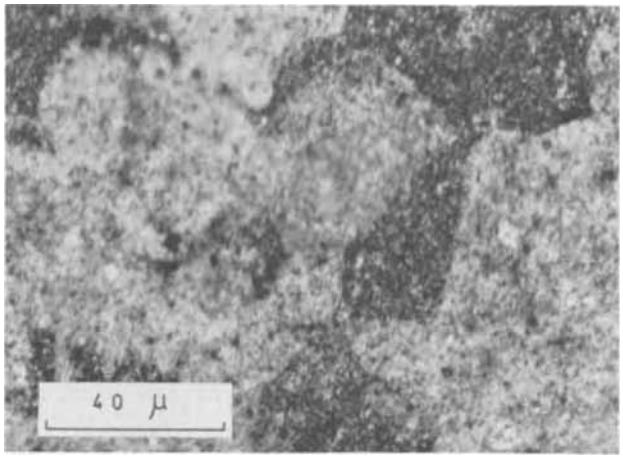

Fig. 8. Surface of nickel substrate after removal of the phosphide scale. Sample phosphidized at 500°C and 20 Torr phosphorus for 3 hr.

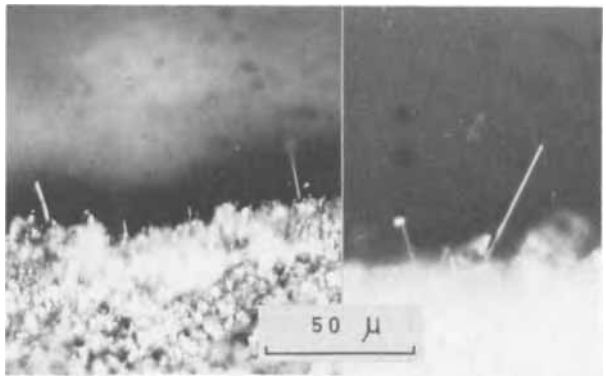

Fig. 9. Phosphide whiskers grown on the surface. Sample phosphidized at 500°C for 25 hr in 2 atm of phosphorus.

grown in spots and local areas on the surface of the specimen phosphidized at 500°C and 2 atm for 25 hr.

The phosphide appeared in the form of a large number of platelets lying more or less normally to the phosphide/metal interface at 500°C under the lower pressures such as 20, 4, and 1 Torr phosphorus. A view of numerous platelets grown on the surface is illustrated in Fig. 10, which refers to the specimen phosphidized for 3 hr at 550°C and 4 Torr phosphorus. In Fig. 10, platelets with corner of angle of 120° are also seen. Platelets were found alone or in combination with whiskers of phosphide.

Wrinkle-like phosphide surfaces were partly found at 500°C at 1 Torr for 0.5 and 1 hr. Faceted crystals also were sometimes observed at 500°C and 1 Torr, and the explanation on its x-ray patterns was discussed previously.

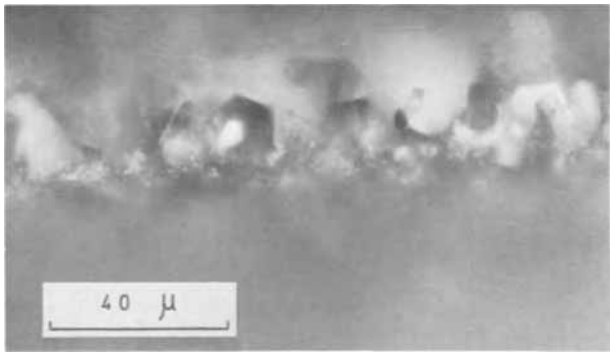

Fig. 10. Phosphide platelets grown on the surface of specimen phosphidized at 500°C for 3 hr in 4 Torr of phosphorus.

At low temperatures and low pressures the diffusion rate is so slow that the growth of various phosphide crystals seems to have become the predominant feature of the phosphidation.

There were voids in the bulk of almost all the scales produced.

Discussion

The temperature dependence of K_p at 2 atm is plotted in Fig. 11. The relationship gives two straight lines. Activation energies were evaluated to be 15 ± 2.5 kcal/mole for the temperature range 400°-500°C and 33 ± 3.5 kcal/mole for 500°-600°C. The discrepancy in activation energy between the higher and the lower temperature regions results presumably from differences in phosphidation products and in nucleation and growth of nickel phosphides.

A log-log plot of K_p at 500°C against the phosphorus vapor pressure is shown in Fig. 12, giving a straight line, whose slope coresponds to 0.082 ± 0.027.

It was ascertained from the x-ray diffraction patterns that the Ni_2P formation takes place in the interface between metallic nickel and the resulting phosphide layer. It is assumed that the lattice defect equation for high temperature is written as follows

$$1/4\,P_4(g) \rightleftarrows Ni_2P + 2(Ni\square''\cdot n\oplus) + 2(2-n)\oplus$$

where n has values of 0-2, and $Ni\square''$ and $(Ni\square''\cdot n\oplus)$ stand for a cation vacancy and a cation vacancy with n trapped electron holes $\oplus$, respectively. The $n = 0$ means the electron holes to be completely dissociated from the cation vacancies.

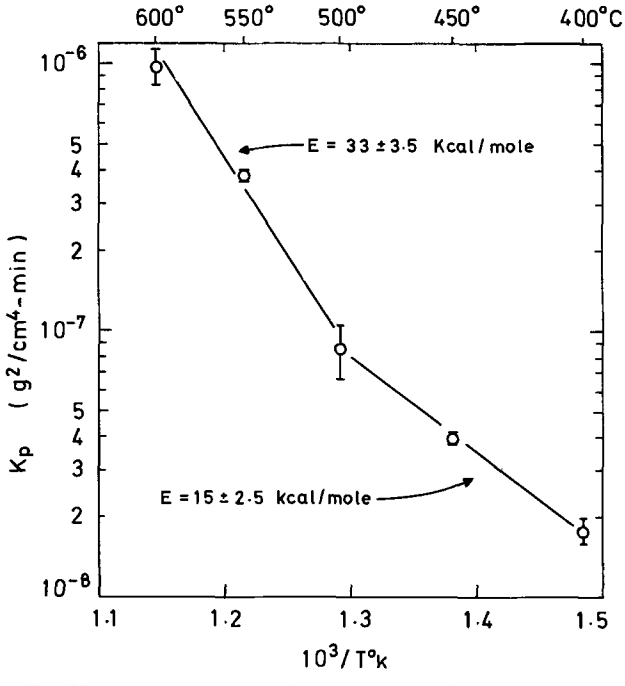

Fig. 11. Temperature dependence of the parabolic rate constant for the nickel phosphidation between 400° and 600°C.

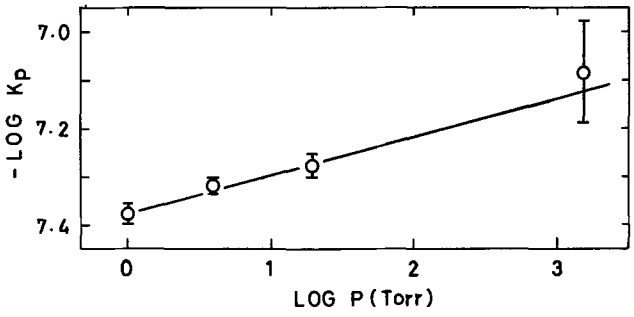

Fig. 12. Phosphorus-vapor-pressure dependence for the parabolic rate constant of phosphidation of nickel at 500°C.

The mass action law under ideal conditions similar to the ideal state in very dilute electrolytes is expressed as

$$X_{\oplus}^{2(2-n)}\cdot X^2_{(Ni\square''\cdot n\oplus)} = KP^{1/4}$$

where X denotes the respective concentrations and P is the pressure of the phosphorus vapor consisting of P_4 molecule. The phosphorus pressure dependence of the lattice defect concentration—with the electrical neutrality condition $X_{\oplus} = (2-n)X_{(Ni\square''\cdot n\oplus)}$—may be found

$$X_{\oplus} = (2-n)X_{(Ni\square''\cdot n\oplus)} = \text{const}\,P^{\frac{1}{8(3-n)}}$$

When $n = 0$, $X_{\oplus} = 2X_{Ni\square''} = \text{const}\,P^{0.0417}$, and when $n = 1$, $X_{\oplus} = X_{Ni\square'} = \text{const}\,P^{0.0625}$.

A parabolic rate constant seems to be proportional to $X_{\oplus}$ or $X_{Ni\square''}$. The above consideration in the case of $n = 1$ is in agreement with the experimental result $K_p \propto P^{0.055\sim0.109}$ obtained in this study.

In the nickel-phosphorus system a series of stepwise decompositions have been found as shown below (3).

$$4NiP_3 \rightleftarrows 4NiP_2 + P_4;\qquad \log P_{Torr} = -9340/T + 12.865$$

$$24/7NiP_2 \rightleftarrows 4/7Ni_6P_5 + P_4;\qquad \log P_{Torr} = -12430/T + 14.315$$

$$2Ni_6P_5 \rightleftarrows 6Ni_2P + P_4;\qquad \log P_{Torr} = -13740/T + 14.951$$

where P_{Torr} and T stand for the partial pressures of P_4 vapor and the absolute temperature, respectively.

Figure 13 shows the chemical potential diagram of the nickel-phosphorus system obtained from these

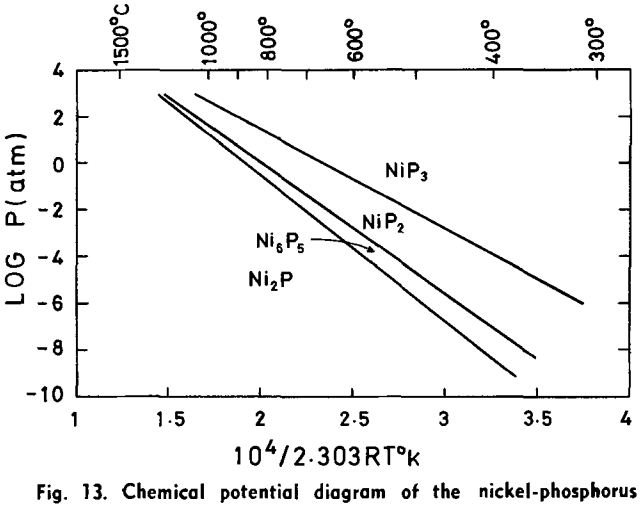

Fig. 13. Chemical potential diagram of the nickel-phosphorus system.

relations. If the reaction is controlled by a diffusion in the scaling film, the phosphorus potential in the film decreases toward the metallic nickel substrate. The stable phosphide phases corresponding to the phosphorus potential can be obtained from Fig. 13 so that the phosphide layer structure becomes $NiP_3/NiP_2/Ni_6P_5/Ni_2P$.

The formation of NiP_2 for short periods of time at relatively lower temperatures and that of NiP_2 on the saturation curves of weight gain *vs.* time at higher temperatures can be explained in terms of this thermodynamic consideration.

The interpretation of the phosphidation mechanism is complicated by many difficult factors such as the competition between phosphide film formation and phosphorus dissolution in the metal, and the correlation between the morphology of the reaction products and the associated rate curves, and other factors.

Conclusions

Experimentally it has been found that:

1. Phosphidations of nickel by phosphorus vapor follows parabolic behavior under the experimental conditions employed, *viz.* in 2 atm phosphorus at temperatures from 400°-600°C, and under the phosphorus pressures of 1 Torr to 2 atm at 500°C.

2. All of the parabolic rate constants, K_p, obtained have fallen into a category of order of 10^{-6} to 10^{-8} g^2/cm^4-min, as listed in Table I. The K_p increased with an increase of temperature between 400° and 600°C at 2 atm.

3. The activation energies were estimated to be 15 ± 2.5 and 33 ± 3.5 kcal/mole for the temperature regions 400°-500° and 500°-600°C, respectively.

4. The correlation between K_p and phosphorus pressure P was experimentally expressed as $K_p \propto P^{0.055 \sim 0.109}$ at 500°C, which could be explained in terms of the mass action law.

5. The x-ray diffraction patterns of the powdered phosphides showed the products to consist mainly of Ni_2P generally, and those of surfaces of specimens phosphidized at relatively lower temperatures showed the presence of NiP_2 as well as Ni_2P.

6. An electron microprobe analysis of the cross sections of specimens phosphidized has shown the content of phosphorus to decrease from the outer to inner scaling layers over the entire temperature range employed. It was also evident in combination with the x-ray diffraction work that Ni_2P forms at the phosphide/nickel interface, and that no phosphides richer in nickel than Ni_2P were formed.

7. Morphological observations showed the phosphidation to proceed with dependence on each crystal grain of nickel, generally with growth of phosphide mounds, and sometimes with growth of platelets and needles or whiskers, especially in comparatively lower pressures.

Acknowledgments

The authors wish to thank Mr. T. Hase for the use of electron microprobe facilities of the Tokyo Institute of Technology and for this measurement, and Mr. J. Mochinaga for helpful advice on this analysis.

Manuscript received April 27, 1970; revised manuscript received *ca.* Sept. 3, 1970.

Any discussion of this paper will appear in a Discussion Section to be published in the December 1971 JOURNAL.

REFERENCES

1. N. Konstantinow, *Z. Anorg. Allgem. Chem.*, **60**, 405 (1908).
2. H. Nowotny and E. Henglein, *Z. Physik. Chem.*, **B40**, 281 (1938).
3. W. Biltz and M. Heimbrecht, *Z. Anorg. Allgem. Chem.*, **237**, 132 (1938).
4. F. Weibke and G. Schrag, *Z. Elektrochem.*, **47**, 222 (1941).
5. R. Fruchart, A. Roger, and J. P. Senateur, *J. Appl. Phys.*, **40**, 1250 (1969).
6. P. C. Donohue, T. A. Bither, and H. S. Young, *Inorg. Chem.*, **7**, 998 (1968).
7. S. Rundqvist and N. O. Ersson, *Arkiv Kemi*, **30**, 103 (1968).
8. E. Larsson, *ibid.*, **23**, 335 (1965).
9. S. Rundqvist, E. Hassler, and L. Lundvik, *Acta Chem. Scand.*, **16**, 242 (1962).
10. G. S. Saini, L. D. Calvert, and J. B. Taylor, *Can. J. Chem.*, **42**, 1511 (1964).
11. S. Rundqvist and E. Larsson, *Acta Chem. Scand.*, **13**, 551 (1959).
12. S. Rundqvist, *ibid.*, **16**, 992 (1962).
13. M. Elfström, *ibid.*, **19**, 1694 (1965).
14. S. Rundqvist, *ibid.*, **15**, 451 (1961).
15. H. J. Booss, *Metall* (Berlin), **21**, 28 (1967).
16. S. Ueda, Y. Sasaki, M. Matsuura, and S. Nishimura, *This Journal*, **117**, 84 (1970).
17. D. R. Stull, *Ind. Eng. Chem.*, **39**, 540 (1947).
18. L. Gmelin, "Gmelins Handbuch der Anorganischen Chemie," 16, Phosphorus(B), p. 221, Verlag-Chemie, Weinheim, Germany (1964).
19. ASTM X-Ray Powder Data File, Card 4-0855 (1965).

Selective Growth of Epitaxial Silicon and Gallium Arsenide

P. Rai-Choudhury* and D. K. Schroder

Westinghouse Research Laboratories, Pittsburgh, Pennsylvania 15235

ABSTRACT

Homoepitaxial layers of silicon and gallium arsenide are grown selectively from a number of processes, namely, silane-hydrogen, silane-argon, silicon tetrachloride-hydrogen chloride-hydrogen, and trimethyl gallium-arsine-hydrogen systems. Silicon dioxide is used as the primary masking material. The thermodynamic considerations of the processes are in general agreement with the experimental results. The general conclusion is that in order to achieve selective growth it is either necessary for the masking material to react with the depositing or arriving atoms to form volatile products such as SiO, Ga_2O, etc., or to introduce into the system additional species, such as HCl gas, which will prevent adsorption of reactants preferentially on the mask. Preferential epitaxial growth using a SiO_2 mask is carried out most effectively in the presence of controlled amounts of HCl gas.

Preferential or selective growth of epitaxial layers, such as those of silicon and gallium arsenide, has many applications in integrated circuits. For example, it allows the use of SiO_2 masked regions as isolation walls between components of a circuit. It can also serve to produce elevated electrodes for the silicon photodiode array (1).

Generally, the method consists of the deposition of an epitaxial layer on selected areas of the substrate which are exposed via windows etched through a protective insulating film, *e.g.*, SiO_2, Si_3N_4, Al_2O_3, etc. In the H_2-$SiCl_4$ system (2-4), the selective growth is effected by injecting a stream of HCl gas which prevents growth on the masking film. When pyrolysis of SiH_4 is used for the epitaxial growth, it is necessary to establish a balance between the SiH_4 partial pressure and deposition temperature (5). In the growth of GaAs epitaxial layers from elemental sources using H_2 and HCl carrier gases, preferential growth through a SiO_2 mask can also be achieved (6).

The major problem in the preferential epitaxial growth, however, has been effectively and reproducibly to prevent nucleation and growth on the surface of the masking material. Since, under normal circumstances, hardly any surface exists in the real world which does not have heterogeneous nucleation sites, it is not likely to be rewarding to seek a clean and defect-free surface of the masked region. Also, a highly passive masking material may not be effective in preventing growth over the mask, because any arriving atom may remain on the surface unconsumed or unreacted. In such a case it is necessary to use additives, such as HCl gas, which prevent growth on the insulating layer, *e.g.*, Si_3N_4, by some unknown mechanism. If the insulator, *e.g.*, SiO_2, reacts with the deposits, *e.g.*, Si, forming a volatile compound, *e.g.*, SiO, then a delicate balance of reaction temperature and reactant partial pressures is necessary to prevent growth there. Another possibility which may exist with SiO_2 masks is the formation of an oxygen deficient surface (7) when heated in H_2 carrier gas. An arriving Si atom could then attach itself to a surface Si atom without significant steric hindrance from neighboring oxygen atoms. If this model is valid, then it may be possible to grow epitaxial Si selectively in the unmasked areas from pyrolysis of SiH_4 in an inert carrier gas.

In this investigation selective growth of Si on Si and GaAs on GaAs are studied under different conditions with the aim of improving the technology and better understanding of the various processes.

* Electrochemical Society Active Member.

Key words: epitaxial, silicon, gallium arsenide, thermodynamics, silane, chlorides, hydrogen, argon.

Thermodynamic Considerations

In a relatively simple system, such as the pyrolysis of SiH_4 in a H_2 carrier gas, the possible interaction with the SiO_2 layer may be represented by the following reactions

$$SiO_2(s) + Si(s) = 2SiO(g) \quad [1]$$

$$SiO_2(s) + H_2(g) = SiO(g) + H_2O(g) \quad [2]$$

Reaction [1] takes place between the depositing Si atoms and the surface layers of the SiO_2 as well as between the substrate Si atoms and the SiO_2 surface in contact with the substrate. Hence, if it proceeds too rapidly, it might result in blistering or lifting of the entire SiO_2 mask. Reaction [2] is likely to proceed only in H_2 carrier gas. Figure 1 represents the equilibrium partial pressure of SiO as a function of temperature for these two reactions. It is apparent that reaction [1] is much more likely than reaction [2] and, by selecting proper growth conditions, could be utilized to prevent growth on the SiO_2 film.

In the $SiCl_4$-H_2 system the process is considerably more complicated. Since preferential epitaxy using this system has been successful only through the in-

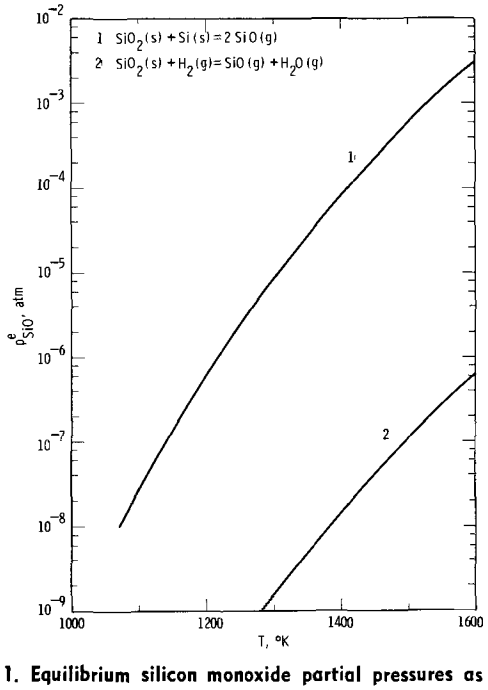

Fig. 1. Equilibrium silicon monoxide partial pressures as a function of temperature from reactions of silicon dioxide with silicon and hydrogen.

jection of appropriate amounts of HCl gas, the reactions involving HCl are considered now

$$SiO_2(s) + 4HCl(g) = SiCl_4(g) + 2H_2O(g) \quad [3]$$

$$SiO_2(s) + 2HCl(g) + H_2(g) = SiCl_2(g) + 2H_2O(g) \quad [4]$$

Reaction [3] is not favorable since the equilibrium $SiCl_4$ partial pressure is about 7×10^{-7} atm at 1500°K while the inlet $SiCl_4$ partial pressure is usually of the order of 10^{-2} atm. Figure 2 shows the equilibrium partial pressure of $SiCl_2$ as a function of temperature for reaction [4] at three levels of HCl partial pressures. This is also not a likely reaction under normal growth conditions, since the equilibrium $SiCl_2$ partial pressure from this reaction is orders of magnitude less than that from the $SiCl_4$-Si interactions. Further, HCl is known to prevent growth on Si_3N_4 masks (4) which is considerably more inert toward HCl. One likely explanation is that HCl prevents adsorption of reactant species on only the masked area while the unmasked areas remain active. The bond energies of adsorbed reactants to the surface atoms are likely to be weaker on an oxide or nitride surface than on a bare silicon surface. Possibly HCl may have an etching action which is sufficient to remove any adsorbed reactant species from the masked area.

During the growth of GaAs through windows etched in SiO_2 in the absence of HCl, any GaAs deposited on the mask could react as follows

$$SiO_2(s) + GaAs(s) = SiO(g) + \tfrac{1}{2}Ga_2O(g) + \tfrac{1}{2}As_2(g) \quad [5]$$

If this reaction proceeds at a suitable rate, growth on the masked area can be prevented. In the presence of HCl gas a mechanism similar to that operating in the selective growth of Si with HCl is probably effective.

Experimental Procedure

Chemical-mechanical polished silicon substrates, oriented in the (100) and 2° off from the (111) plane, were thermally oxidized in wet oxygen at 1100°C to produce an oxide layer of about 10,000Å thickness. On some of the wafers, 1700-2500Å films of silicon nitride were deposited from a SiH_4-NH_3-Ar system at about 850°C. GaAs used was of (100) orientation, semi-insulating and chem-mechanically polished. A 4000Å film of SiO_2 was deposited on these GaAs substrates from a SiH_4-O_2-Ar system at about 600°C. Windows, 9-20μ in diameter, were then etched through these masks using photolithographic techniques and appropriate etchants. Epitaxial layers were grown in a conventional horizontal quartz reactor, having a SiC-coated graphite susceptor, heated externally by an rf coil. Epitaxial layers of Si were grown in the exposed areas by a number of processes, namely, pyrolysis of SiH_4 in H_2, pyrolysis of SiH_4 in Ar, and from the $SiCl_4$-H_2 system with HCl injection. Provisions for doping with B_2H_6 and/or AsH_3 were also made. Epitaxial layers of GaAs were deposited from the trimethyl gallium (TMG)-AsH_3-H_2 system as well as from the $AsCl_3$-Ga-H_2 system.

The layers were evaluated by light microscopy and scanning electron microscopy (SEM) for growth morphology, and by electron microscopy for the quality of the deposited layer. A high resolution spreading resistance technique (8) was used to measure the impurity profile of the epitaxial silicon layers. Resistivity, net carrier concentration, and mobility of the gallium arsenide films were measured by the van der Pauw technique (9), using test slices where the epitaxial layers were deposited on a substrate without an insulating film.

Results

Selective growth of Si.—As mentioned earlier, selective growth of Si was carried out by three methods, namely, pyrolysis of SiH_4 in H_2, pyrolysis of SiH_4 in Ar, and from the $SiCl_4$-H_2 system with HCl injection. In the SiH_4-H_2 system, it was necessary to use a relatively high deposition temperature (>1200°C) in order to prevent growth on the SiO_2 mask. Figure 3 shows a scanning electron micrograph of a 5μ thick layer grown at 1220°C using a SiH_4 partial pressure of 1.0×10^{-3} atm. As can be seen from the micrograph, the masked regions are free from Si deposits. Reflection electron diffraction patterns from these layers were indicative of good quality epitaxial Si. Considerably more growth islands were observed on accompanying Si_3N_4-coated wafers. Also, frequent appearance of microcracks in the nitride film during epitaxial growth was noted whenever the nitride film was 2000Å or thicker. Thus prevention of growth on SiO_2 masks, when a SiH_4-H_2 system is used, is probably the result of reaction [1]. When higher deposition temperatures

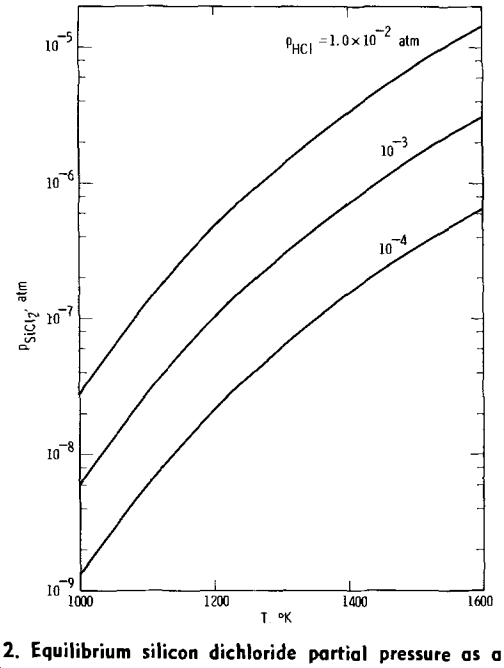

Fig. 2. Equilibrium silicon dichloride partial pressure as a function of temperature at various hydrogen chloride partial pressures from the reaction $SiO_2(s) + 2HCl(g) + H_2(g) = SiCl_2(g) + 2H_2O(g)$.

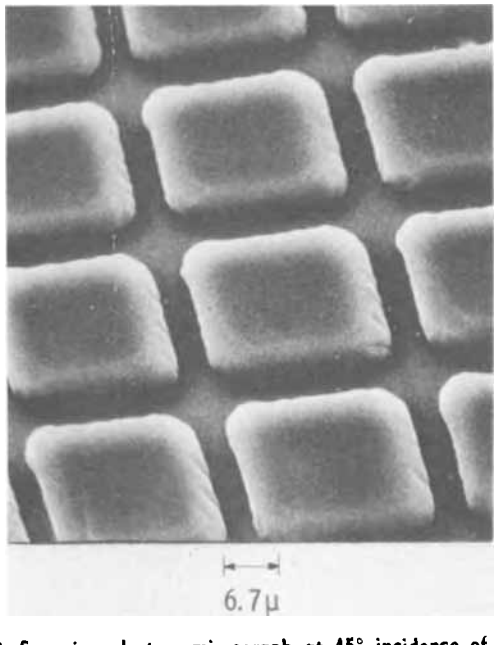

Fig. 3. Scanning electron micrograph at 45° incidence of selectively grown silicon in square windows etched through thermally grown SiO_2 using the silane-hydrogen system at 1220°C for 5 min; growth rate 1 μ/min.

(>1270°C) were used, the SiO_2 mask frequently lifted, probably due to the increased rate of reaction [1] at the substrate-oxide interface. It seems, therefore, that preferential growth from the SiH_4-H_2 system is rather sensitive to the growth conditions.

The possibility of Si nucleation or growth on an oxygen deficient surface of SiO_2 was tested by making runs in argon carrier gas, which should prevent the reduction of the oxide. Scattered deposits of Si on the oxides were generally observed and the results were considerably inferior to those shown in Fig. 3. This was not surprising since thermodynamic considerations indicate reaction [2] to be unlikely anyway. Use of ultrahigh-purity Ar instead of the usual palladium-purified H_2 possibly introduced a few impurities which may have caused the deposits to be less preferential relatively.

Experiments with the $SiCl_4$-H_2 system gave good results when a controlled amount of HCl was injected during the growth of the layers. Interaction of HCl gas with the SiO_2 was first tested to determine the extent of reactions [3] and [4]. In all cases no measurable change in the oxide thickness was noticeable as a result of HCl treatment at 1270°C. However, frequently the oxide lifted because of the HCl attack of the Si substrate surface through pinholes in the insulator. Thus it was confirmed that reactions [3] and [4] are not significant. Figure 4 shows a scanning electron micrograph of a 5μ layer grown at 1120°C in the $SiCl_4$-H_2 system at $SiCl_4$, HCl, and B_2H_6 partial pressures of 7.4×10^{-3}, 5.5×10^{-3}, and 9.7×10^{-8} atm, respectively. The doping level of the grown layer was 2×10^{17} at./cm^3, and the concentration profile as measured by the spreading resistance technique indicated normal, good quality epitaxial silicon having a very sharp substrate-epitaxial interface.

The growth rate of the silicon islands shown in Fig. 4 was about 1 μ/min whereas on the accompanying unmasked silicon wafer it was only 0.4 μ/min. Such increase in growth rate in the presence of a mask was also observed by Dumin (5) using a SiH_4-H_2 system and is confirmed in the present studies. It is interesting to note this common feature of two epitaxial systems of considerably different chemistry. The atomistics of this enhanced growth process is rather complex, and any model to explain the results could, at best, be a speculation. An explanation from a macroscopic point of view might be that, given the conditions which prevent reaction on the SiO_2 surface, the effective concentrations of the reactants are increased with a decrease in the reactive surface, namely, the unmasked region. Another noteworthy feature of the $SiCl_4$-H_2-HCl process of selective growth is that, unlike the SiH_4-H_2 system, it is considerably less sensitive to variations in reactant concentrations and growth temperature. For example, results comparable to those shown in Fig. 4 were obtained at 1220°C without the need to adjust any of the reactant partial pressures.

Selective growth of GaAs.—In previous investigations (6) on selective epitaxial growth of gallium arsenide, HCl was introduced either as a reactant or as a reaction product from the H_2 reduction of $AsCl_3$. To test the importance of HCl in the selective growth of gallium arsenide it was necessary to use a system free from any HCl gas. Epitaxial layers were deposited from the TMG-AsH_3-H_2 system on GaAs substrates of (100) orientation through a 4000Å SiO_2 mask. The quality of the grown layer from this system has been described elsewhere (10). Figure 5 shows a scanning electron micrograph of a 6μ layer grown through masked GaAs substrates where the exposed regions were squares 20 x 20μ with 2.5μ of SiO_2 separating the squares. The layer was grown at 700°C and partial pressures of TMG and AsH_3 of 6.5×10^{-4} atm and 1.2×10^{-2} atm, respectively. The high ridges on the micrograph represent growth on the SiO_2 mask whereas the pits or craters represent growth on unmasked regions. It appears that when growth occurs on the insulator the amount of deposit on the oxide exceeds that on the unmasked regions. This is also what is observed in the case of Si growth from the SiH_4-H_2 system. The rate of growth of the polycrystalline silicon on the masked regions is found to be greater than that of single crystal silicon through the windows. The reflection electron diffraction pattern from GaAs grown through the SiO_2 mask gave only a single crystal pattern with some twins. However, the transmission electron microscopic examination of the sample indicated the growth on top of the oxide to be highly disturbed, polycrystalline material which etched considerably more rapidly than the GaAs grown in the windows. In order to eliminate growth on the SiO_2 mask, an attempt is being made in which controlled

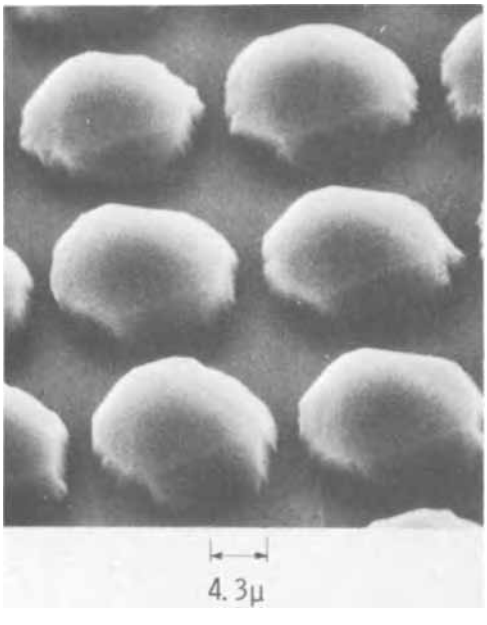

Fig. 4. Scanning electron micrograph at 45° incidence of selectively grown silicon in circular windows etched in thermally grown silicon dioxide using the $SiCl_4$-HCl-H_2 system at 1120°C for 5 min; growth rate 1 μ/min.

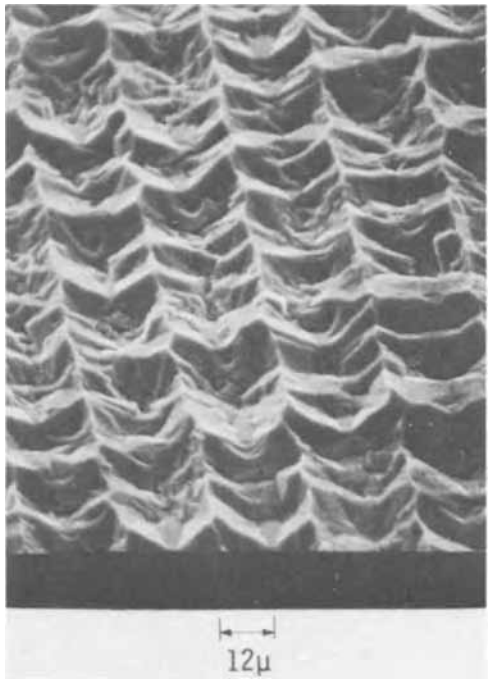

Fig. 5. Scanning electron micrograph at 40° incidence showing growth morphology of GaAs deposited from TMG-AsH_3-H_2 system onto GaAs substrate with SiO_2 mask.

amounts of HCl gas are injected into the main stream. The results of using an HCl-free system, namely, TMG-AsH_3-H_2, to grow GaAs selectively indicate that reaction [5] is not very effective in preventing growth on the SiO_2 mask under present experimental conditions. From these results, together with those from systems containing HCl gas (6), it is apparent that HCl is playing a significant role in preventing growth on the SiO_2 mask. Results identical to those shown in Fig. 4 were obtained using the $AsCl_3$-Ga-H_2 system.

Summary

Epitaxial silicon was grown selectively at about 1200°C using the SiH_4-H_2 system. The process was found to be relatively sensitive to growth temperature and reactant concentrations. For the $SiCl_4$-H_2 system, the epitaxial silicon growth through windows etched in a masking SiO_2 layer proceeds more effectively and also at lower temperatures than in the SiH_4-H_2 system. Growth on the masked regions is prevented by injecting appropriate amounts of HCl gas. The growth rate in the windows was approximately 1 μ/min. HCl is also important in preventing growth of GaAs on SiO_2 masks. Whenever conditions are such that GaAs growth does take place on the SiO_2 mask, the resulting deposition rate of polycrystalline material on the mask is higher than the rate of single crystal growth rate through windows etched into the SiO_2 mask.

Acknowledgment

The authors would like to thank W. Cifone for assistance with the experimental work, Dr. A. J. Noreika and J. Rieger for assistance with the electron microscopic evaluation of the samples and F. Berish for taking the scanning electron micrographs.

Manuscript submitted Aug. 5, 1970; revised manuscript received *ca.* Aug. 31, 1970.

Any discussion of this paper will appear in a Discussion Section to be published in the December 1971 JOURNAL.

REFERENCES

1. W. E. Engeler, M. Blumenfeld, and E. A. Taft, *Appl. Phys. Letters*, **16**, 202 (1970).
2. E. G. Alexander and W. R. Runyan, *Trans.* AIME, **236**, 284 (1966).
3. E. Sirtl and H. Seiter, International Symposium on Silicon Material Science and Technology, New York, 1969, p. 189.
4. M. Nomura, Paper 181 presented at the Detroit Meeting of the Society, Oct. 5-9, 1969.
5. D. J. Dumin, *J. Crystal Growth* (to be published).
6. D. W. Shaw, R. W. Conrad, E. W. Mehal, and O. W. Wilson, Proceedings of the International Symposium of the Institute of Physics and Physical Society, Conference Series No. 3, Reading, September 1966, p. 10.
7. R. W. Bicknell, J. M. Charig, B. A. Joyce, and D. J. Stirland, *Phil. Mag.*, **9**, 965 (1964).
8. R. G. Mazur and D. H. Dickey, *This Journal*, **113**, 332 (1964).
9. L. J. van der Pauw, *Philips Res. Repts.*, **13**, 1 (1958).
10. P. Rai-Choudhury, *This Journal*, **116**, 1745 (1969).

Facets Formed by Hydrogen Chloride Vapor Etching on Silicon Surfaces through Windows in SiO_2 and Si_3N_4 Masks

Katsuro Sugawara

Semiconductor and Integrated Circuits Division, Hitachi, Ltd., Kodaira, Tokyo, Japan

ABSTRACT

Selective etching of silicon by HCl gas through windows in SiO_2 and Si_3N_4 masks was investigated on silicon surfaces with nine different orientations on the [110] zone, including (001), (111), and (110). In the etched holes {111}, {311}, and {110} facets were observed, depending on the specimen orientation. For specimens with Si_3N_4 films, facets were developed directly below the film as well as on the periphery of the bottom of the etched area. For specimens with SiO_2 films, however, few facets could be found directly below the film. This difference might be explained by assuming that, in the case of SiO_2 film, the reaction of Si-SiO_2, which is dominant at higher temperature as indicated by thermodynamic calculations, occurs at the periphery of the etched hole, giving rise to faces without facets.

Selective epitaxial growth of desired dimensions, conductivity, and impurity concentration in desired locations is demanded both from a clarification of the crystal growth mechanism and from the formation of special integrated circuits for practical use. In fact, several papers on Si (1-9) and GaAs (10-13) already have been published. The author and his collaborators (14) have examined vapor etching by HCl as a first step toward this epitaxial growth and observed in the etched hole facets characteristic of the surface orientations of the silicon substrates. They also found a difference in the appearance of the facets between SiO_2 and Si_3N_4 films used as a mask for vapor etching. In this paper crystals of additional orientations were selected and details of the facet appearance were further investigated. Also, since examinations of the cause of differences in the facet appearance between SiO_2 and Si_3N_4 films have been conducted, the results are reported herein.

Key words: selective vapor etching, Si-SiO_2 reaction, SiO_2-coated Si surface, Si_3N_4-coated Si surface.

Experimental

As stated in a previous paper (14), a normal horizontal epitaxial reactor was used, and vapor etching was performed on an R.F. heated SiC-coated graphite susceptor.

Boron-doped (110) single crystals with resistivity of about 5 ohm-cm were grown by the Czochralski method. Crystals of nine orientations, (001), (711), (511), (311), (211), (111), (331), (551), and (110) on the [1$\bar{1}$0] zone were cut. The specimen orientations, (001), (511), (311), (211), (111), (311), and (110) were confirmed to agree with an accuracy of one degree or less by x-ray diffraction. Since the diffraction of other surfaces was weak, the (110) surface taken out on the

side was used as the standard, and seeking the angle formed with each surface, slicing was done. Even the crystal surface sliced in this manner is considered to be within 2°.

SiO_2 and Si_3N_4 films were formed on the mirror-polished wafers. An oxidized SiO_2 film of about 7000Å in thickness was formed in a wet oxygen atmosphere. Using the SiH_4-NH_3 system, a Si_3N_4 film of about 3000Å was deposited at 880°C. Ten holes, the diameters of which were arranged between 50 and 500μ at an interval of 50μ, were made on these wafers at a regular spacing of 1 mm by the usual photolithographic technique. Standard conditions for vapor etching consist of a temperature of 1250°C (corrected for emissivity), a mole fraction of HCl to H_2 of 0.025, and an etching time of 60 sec. The orientation of facets were determined by a goniomicroscope and/or 60° angle lapping.

Results

Facet appearance on (001) surface.—Figure 1 represents photographs of the facets as seen through the window opened in an SiO_2 film. The upper half of Fig. 1(a) is focused on the facets, while the lower half is a cross-sectional view of 60° angle lapping. The figure represents a synthesis of these two photos. As visible from the cross-sectional photo, the characteristic of the slope in the hole is a comparatively mild incline directly below the film. No facet is observed on this part, but at the bottom of the hole, a mildly inclined facet of (311) can be observed. Figure 1(b) is a synthesis of photographs of the facets (upper half) and of directly below the SiO_2 film (lower half). From the lower half of the photograph, it can be seen that by utilizing the above-mentioned etching conditions, the initial hole in the SiO_2 film expands but

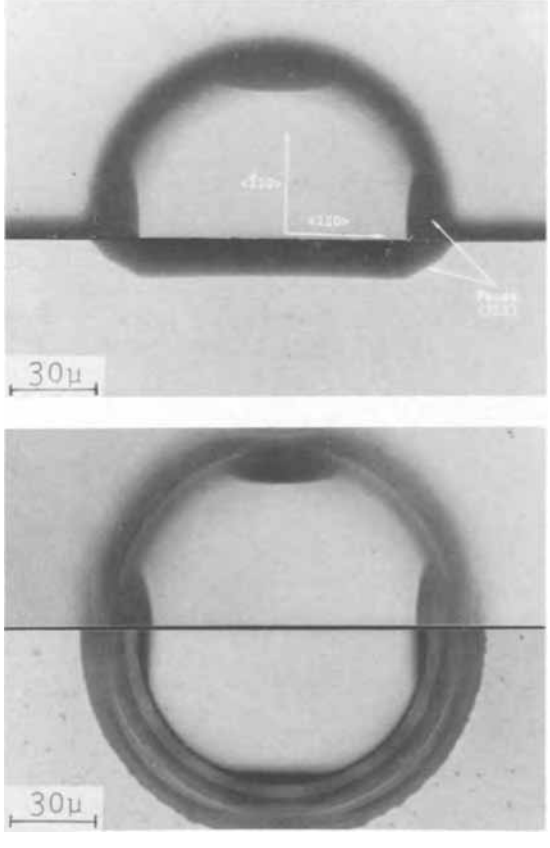

Fig. 1. Facets revealed on (100) surface when etched through a window of 100μ diameter in SiO_2 mask. Fig. 1 (a) (top) Upper half is the facets and the lower half is the cross section after 60° angle lapping; Fig. 1 (b) (bottom) Lower half shows directly below the SiO_2 film.

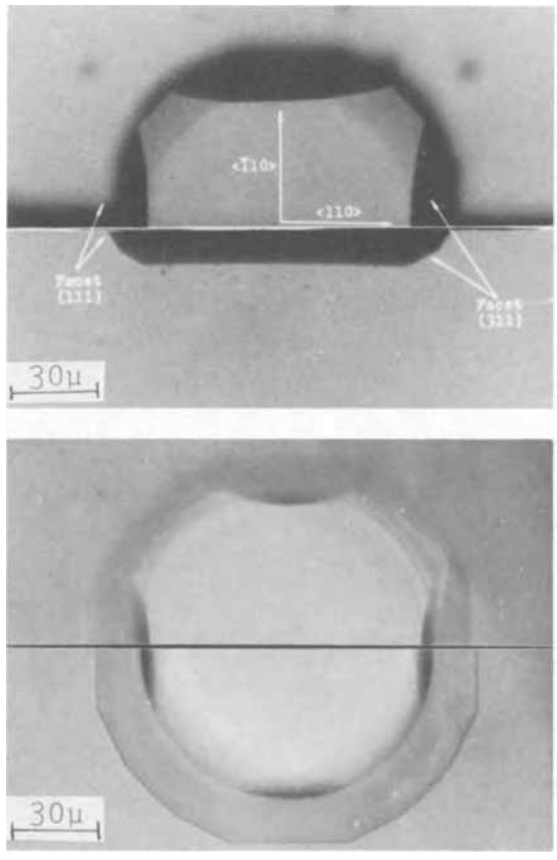

Fig. 2. Facets revealed when etched through Si_3N_4 mask: Fig. 2(a) (top) and 2(b) (bottom) correspond to Fig. 1(a) and 1(b) for SiO_2 film, respectively.

maintains its initial contour of a round shape during vapor etching. Figure 2(a) and 2(b) for Si_3N_4 film correspond to Fig. 1(a) and 1(b) for SiO_2 films. In Fig. 2(a), as steep (111) facets appear in the window, observation of the facets from directly above is rather difficult. The facets develop from under the film [Fig. 2(a)], and the etched shape is exhibited in a polygonized form [Fig. 2(b)]. At the bottom of the etched hole, mildly inclined (311) facets can be seen as in the case of the SiO_2 mask.

SiO_2 films of 5000, 8000, and 13,000Å and Si_3N_4 films of 400, 950, and 2000Å in thickness were made, and similar experiments were carried out, but no difference in the facet appearance due to film thickness was observable. In addition to thermally oxidized SiO_2 films, tetraethyl orthosilicate pyrolytic decomposition films at 760°C and SiH_4-O_2 vapor-grown films at 350°C were made and similar experiments were performed, but no difference in the facet appearance could be observed.

Crystal orientation and facet appearance.—Schematic illustrations of the facet appearance on the surface of various crystal orientations are given in Table I for SiO_2 film and Table II for Si_3N_4 film. The tables are arranged according to crystal orientations along the $(\bar{1}10)$ zone from (001) to (110). The asterisks in the tables indicate those facets that have appeared in common for both SiO_2 and Si_3N_4 films. The fourfold symmetry of (001) changes as the orientation changes to (117), showing the threefold symmetry of (111), and finally becomes the twofold symmetry of (110). Outstanding features evident from the two tables are as follows:

1. With SiO_2 films, few facets generally develop directly under the film; facets existing at a comparatively deeper bottom are observable.

2. With Si_3N_4 films, facets appear directly under the film. For this reason, polygons are formed mostly.

Table I. Facet appearance through windows in SiO_2 masks The asterisks (*) indicate facets that appeared common for both SiO_2 and Si_3N_4 masks

Crystal orientation	Appearance of facets	Angle between facets and specimen surface
(001)	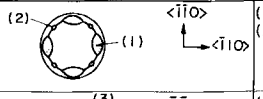	(1)(311)* 25.2° (2)(110)* 45.0°
(117)	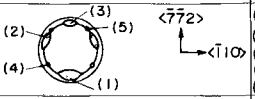	(1)(311)* 13.8° (2)(311)* 27.6° (3)(311)* 36.7° (4)(110)* 37.6° (5)(110)* 53.6°
(115)	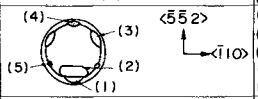	(1)(110)* 38.9° (2)(311)* 9.5° (3)(311)* 29.5° (4)(311)* 41.1° (5)(110)* 35.3°
(113)	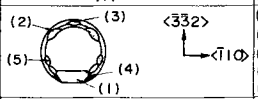	(1)(111)* 29.5° (2)(311)* 35.1° (3)(311)* 50.5° (4)(311)* 50.5° (5)(110)* 31.5°
(112)	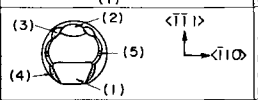	(1)(111)* 19.5° (2)(311)* 10.0° (3)(311)* 42.4° (4)(311)* 42.4° (5)(110) 30.0°
(111)	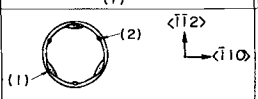	(1)(311)* 29.5° (2)(110) 35.3°
(331)	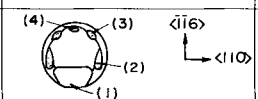	(1)(111)* 22.0° (2)(311)* 26.0° (3)(311)* 40.5° (4)(110) 13.3°
(551)	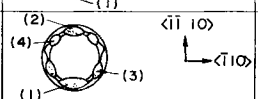	(1)(111)* 27.2° (2)(111)* 43.3° (3)(311)* 27.6° (4)(311)* 36.7°
(110)	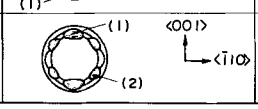	(1)(111)* 35.3° (2)(311)* 31.5°

3. Facets that appear near the periphery of the hole are common both for SiO_2 and Si_3N_4 masks.

4. Only {111}, {311}, and {110} planes appear as facets.

5. When any specific facet becomes anomalously large, facets that should appear may be hidden from view, as in the case of the (110) facets near the (111) facet of (331) orientation in SiO_2 mask.

Discussion

Difference in the facet appearance between SiO_2 *and* Si_3N_4 *coated specimens.*—As can be seen from Tables I and II, there is a marked difference in the appearance of facets directly under the film surfaces. Under the circumstances, the difference was considered to be due to a difference in chemical reaction between Si-SiO_2 and Si-Si_3N_4 films during vapor etching, and the following investigations were made:

Reaction between Si *and films.*—According to Alexander (4), the following are conceivable as the reactions between Si and SiO_2.

$$Si + SiO_2 = 2SiO \qquad [1]$$

$$K_1 = (P_{SiO})^2 \qquad [1a]$$

$$Si + H_2O = SiO + H_2 \qquad [2]$$

$$K_2 = \frac{P_{SiO} \cdot P_{H_2}}{P_{H_2O}} \qquad [2a]$$

$$SiO_2 + 2H_2 = Si + 2H_2O \qquad [3]$$

$$K_3 = \frac{(P_{H_2O})^2}{(P_{H_2})^2} \qquad [3a]$$

$$SiO_2 + H_2 = SiO + H_2O \qquad [4]$$

Table II. Facet appearance through windows in Si_3N_4 masks

Crystal orientation	Appearance of facets	Angle between facets and specimen surface
(001)	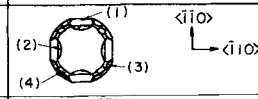	(1)(111) 54.7° (2)(311)* 25.2° (3)(311) 72.5° (4)(110)* 45.0°
(117)	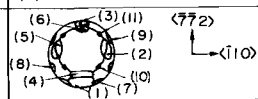	(1)(111) 43.3° (7)(311) 62.3° (2)(111) 55.6° (8)(311) 67.7° (3)(111) 66.2° (9)(311) 77.8° (4)(311)* 13.8° (10)(110)* 37.6° (5)(311)* 27.6° (11)(110)* 53.6° (6)(311)* 36.7°
(115)	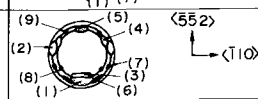	(1)(110)* 38.9° (6)(311) 58.7° (2)(111) 56.3° (7)(311) 66.0° (3)(311)* 9.5° (8)(110)* 35.3° (4)(311)* 29.5° (9)(110) 57.0° (5)(311)* 41.1°
(113)	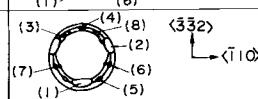	(1)(111)* 29.5° (6)(311) 63.0° (2)(111) 58.5° (7)(110)* 31.5° (3)(311)* 35.1° (8)(110) 64.8° (4)(311)* 50.5° (5)(311)* 50.5°
(112)	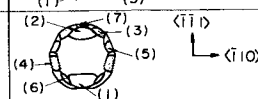	(1)(111)* 19.5° (6)(311)* 42.4° (2)(311)* 10.0° (7)(311) 60.5° (3)(311)* 42.4° (4)(311) 60.5° (5)(111) 61.9°
(111)	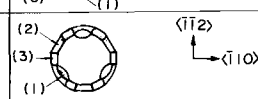	(1)(311)* 29.5° (2)(111) 70.5° (3)(311) 58.5°
(331)	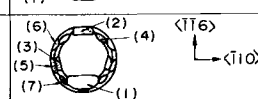	(1)(111)* 22.0° (6)(311) 69.8° (2)(111) 48.5° (7)(110) 49.5° (3)(311)* 26.0° (4)(311)* 40.5° (5)(311) 61.0°
(551)	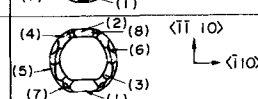	(1)(111)* 27.2° (6)(311) 67.7° (2)(111)* 43.3° (7)(110) 53.6° (3)(311)* 27.6° (8)(110) 66.7° (4)(311)* 36.7° (5)(311) 62.3°
(110)	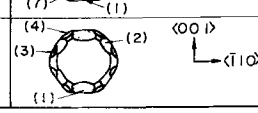	(1)(111)* 35.3° (2)(311)* 31.5° (3)(311) 64.8° (4)(110) 60.0°

$$K_4 = \frac{P_{SiO} \cdot P_{H_2O}}{P_{H_2}} \qquad [4a]$$

P_i and K_i are a partial pressure of each substance and an equilibrium constant of each reaction, respectively. With Si_3N_4 films, on the other hand, there are no data available for nitrides of a composition other than this chemical formula, and consequently, no reaction with silicon is conceivable.

Etching reaction of silicon.—The following reactions were considered, taking into account the thermodynamic analysis of the Si-HCl system reported by Lever (15), Shepherd (16), and Seki *et al.* (17).

$$Si + 4HCl = SiCl_4 + 2H_2 \qquad [5]$$

$$K_5 = \frac{P_{SiCl_4} \cdot (P_{H_2})^2}{(P_{HCl})^4} \qquad [5a]$$

$$Si + SiCl_4 = 2SiCl_2 \qquad [6]$$

$$K_6 = \frac{(P_{SiCl_2})^2}{P_{SiCl_4}} \qquad [6a]$$

$$Si + 3HCl = SiHCl_3 + H_2 \qquad [7]$$

$$K_7 = \frac{P_{SiHCl_3} \cdot P_{H_2}}{(P_{HCl})^3} \qquad [7a]$$

The equilibrium constant of each reaction was calculated from Janaf's thermochemical tables (18).

The total pressure P_{tot} in connection with vapor etching can be expressed as

$$P_{tot} = P_{H_2} + P_{HCl} + P_{SiCl_4} + P_{SiCl_2} + P_{SiHCl_3} = 1 \text{ (atm)} \qquad [8]$$

The mole fractions 0.025 (standard experimental condition), 0.05 and 0.1 of the initial HCl are included,

and the partial pressure of each gas component is calculated by a computer with Eq. [6a], [7a], [8a]. Then, when the partial pressure $(P_{Si})_I$ of the hypothetical Si to be vapor etched is calculated, the equations obtained are

$$(P_{Si})_I = P_{SiCl_4} + P_{SiCl_2} + P_{SiHCl_3} \quad [9]$$

Using the HCl/H_2 mole fraction as a parameter, Fig. 3 shows the temperature dependence of hypothetical partial pressure (P_{Si}).

Meanwhile, it can be seen from the equilibrium constants that between Si and SiO_2, reactions [1] and [2] are liable to occur at around 1250°C. However, as the dew point of H_2 carrier gas is limited to below −70°C, the H_2O gas contained in H_2 gas from the beginning need not be considered in the reaction of Eq. [2]. Oldham (7) claims that Eq. [3] and [4] need not be considered since the reactions are slow, but if it is assumed that the total H_2O arising in Eq. [3] and [4] causes the reaction of Eq. [2], the hypothetical Si partial pressure $(P_{Si})_{II}$ due to such reactions can be expressed as

$$(P_{Si})_{II} = (P_{Si})_1 + (P_{Si})_2 = \frac{\sqrt{K_1}}{2} + K_2 \frac{P_{H_2O}}{P_{H_2}} \quad [10]$$

Figure 3 shows $(P_{Si})_{II}$ also. According to the above hypothesis, the contribution of $(P_{Si})_2$ from Eq. [2] is small compared with $(P_{Si})_1$ from [1]. As these partial pressures of hypothetical Si are considered proportional to the etching rate, Fig. 3 shows the relative extent of reaction between vapor etching and Si-SiO_2 film.

What can be seen from Fig. 3 is that $(P_{Si})_I$ undergoes practically no change due to reaction temperature and is close to the trends of Shepherd's calculations and experiment in value (16). However, the Si-SiO_2 reaction rate is highly dependent on the reaction temperature. The fact that the vapor etching rate is dependent on orientation can be seen from the formation of facets. With Si_3N_4 films, vapor etching alone occurs, and the facets appear from directly under the film surface, thus forming an angular shape such as shown in Fig. 2(b). On the other hand, since the Si-SiO_2 reaction is not dependent on orientation the facets directly under the film do not appear so easily with SiO_2 films. Items that support this reasoning are:

1. This trend was recognized by examining the etching rate of Si through windows in SiO_2 and Si_3N_4 films etched simultaneously. The etching rate parallel to the specimen surfaces was obtained from the distance between the initial film surface and the part where no facet appeared with Si_3N_4 films. The etching rate normal to the surfaces was obtained from the distance between the film surface and the spot where the etching was deepest. The etching rate parallel to the specimen surfaces is clearly greater with SiO_2 films, as can be seen in Fig. 4.

2. If the mole fraction of HCl/H_2 is increased, the facet appearance even with SiO_2 films approaches that of Si_3N_4 films, as seen in Fig. 5. The same phenomenon was observable with ribbon oxide (19), the effective mole fraction of which changes within a single wafer.

3. Similarly, when the reaction temperature is lowered, the appearance with SiO_2 film approaches that with Si_3N_4 film. While Fig. 6 shows the facets etched at 1150°C, a part of them displays an angular shape, unlike the shape shown in Fig. 1(b).

4. The result of heating without vapor etching in H_2 is shown in Fig. 7(a) for SiO_2 film and shown in Fig. 7(b) for Si_3N_4 film. It is clearly observable that with SiO_2 film, reaction is taking place below the film and the initial round part is enlarged. On the other hand, no reaction is observable with Si_3N_4 film.

Facet appearance by other etchant.—Hays (20) has reported that vapor etching on the silicon surface by SF_6 was nonpreferential and did not reveal the facets. Besides HCl, vapor etching by HBr was tried. In the case of SiO_2 mask, sizes of facets were larger and the facets were easily observed. There was no large difference in the case of Si_3N_4 film. Dependence of the

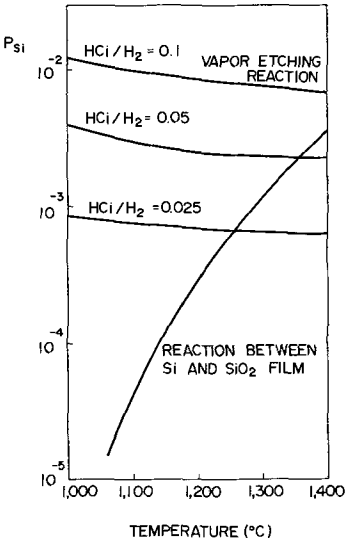

Fig. 3. Temperature dependence of hypothetical partial pressure of silicon P_{Si} to be etched off in the vapor etching reaction and in the reaction between Si and SiO_2 film.

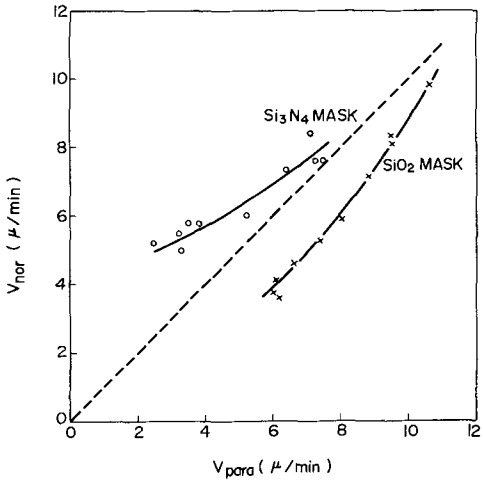

Fig. 4. Etching rate parallel to specimen surfaces, V_{para} and that normal to the surfaces, V_{nor}.

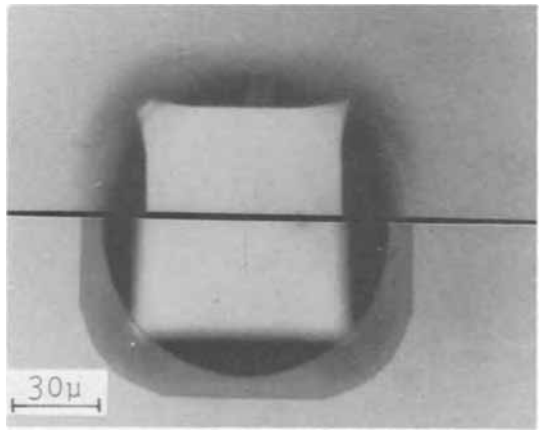

Fig. 5. Etching pattern through the window in SiO_2 mask at a larger mole fraction: mole fraction HCl/H_2 = 0.05, crystallographic orientation = (100), and etching temperature = 1250°C.

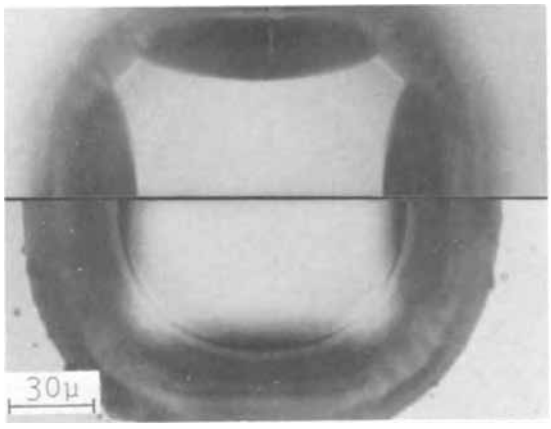

Fig. 6. Etching pattern at a lower etching temperature: mole fraction = 0.025 and etching temperature = 1150°C.

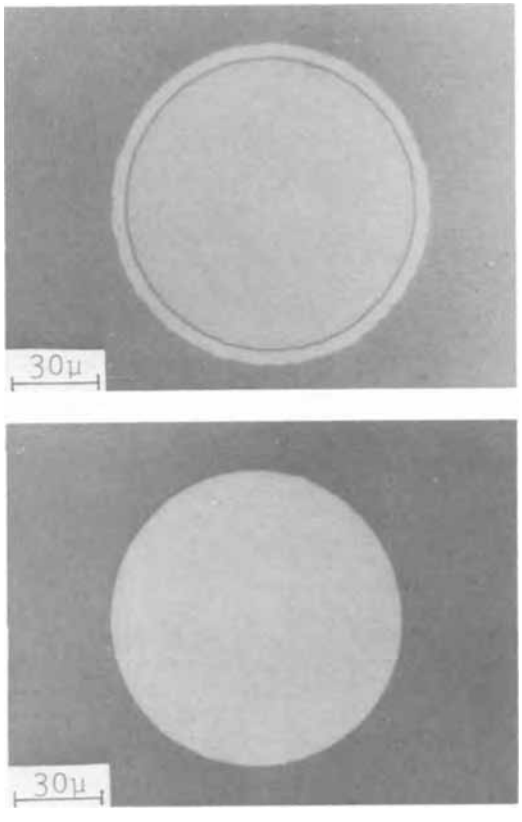

Fig. 7. Patterns after heating for 60 sec at 1250°C in H_2 without vapor etching: (a) (top) through the window of 100μ diameter in SiO_2 mask; (b) (bottom) through the window in Si_3N_4 mask.

etching rate on orientation seemed to differ little from that of HCl.

Conclusions

Silicon wafers with nine different orientations on the [110] zone, including (001), (111), and (110) were vapor etched by HCl through the windows made in SiO_2 and Si_3N_4 films. The results are summarized as follows:

1. Facets were identified to be {111}, {311}, and {110}. The mode at which the facets appeared, depended on the surface orientations.
2. When etching was carried out through a window made in SiO_2 film, the facets appeared only at the periphery of the bottom of the etched area, but when Si_3N_4 film was used, facets appeared directly under the film as well as at the periphery of the bottom. The shape of the holes directly under the film was almost circular for SiO_2 film but become angular for Si_3N_4 film.
3. Differences in the facet appearance between SiO_2 and Si_3N_4 films consisted of an occurrence of Si-SiO_2 reaction at the periphery of the etched hole besides HCl etching in the case of SiO_2 film, and should this reaction have no dependence on orientation, a qualitative explanation for the differences is possible.

Acknowledgments

The author expresses his grateful appreciation to Dr. S. Tauchi and Dr. Y. Sugita for helpful discussion and encouragement during this experiment and to Y. Nakazawa and H. Tochikubo for assistance in the experimental work.

Manuscript submitted May 13, 1970; revised manuscript received ca. Aug. 31, 1970.

Any discussion of this paper will appear in a Discussion Section to be published in the December 1971 JOURNAL.

REFERENCES

1. B. D. Joyce and J. A. Baldrey, *Nature*, **195**, 485 (1962).
2. M. Takabayashi *et al.*, *Toshiba Rev.*, **19**, 1279 (1964). (in Japanese).
3. D. M. Jackson, Jr., *Trans. Met. Soc. AIME*, **233**, 596 (1965).
4. E. G. Alexander and W. R. Runyan, *ibid.*, **236**, 284 (1966).
5. B. D. Joyce, N. P. Formigoni, C. C. Roe, and F. Schliesing, *Electrochem. Technol.*, **4**, 482 (1966).
6. G. L. Schnable, W. J. Hillegas, Jr., and C. G. Thornton, *ibid.*, **4**, 485 (1966).
7. W. G. Oldham and R. Holmstrom, *This Journal*, **114**, 381 (1967).
8. E. Sirtl and H. Seiter in "Semiconductor Silicon," p. 189, R. R. Haberecht and E. L. Kern, Editors, The Electrochemical Soc. Inc., New York (1969).
9. M. Nomura, Paper 181 presented at the Detroit Meeting of the Society, Oct. 5-9, 1969.
10. D. W. Shaw, *This Journal*, **113**, 904 (1966).
11. D. W. Shaw, *ibid.*, **113**, 958 (1966).
12. W. von Munch *et al.*, *Solid State Electronics*, **9**, 826 (1966).
13. F. W. Tausch Jr., and A. G. Lapierre, III, *This Journal*, **112**, 706 (1965).
14. K. Sugawara, Y. Nakazawa, and Y. Sugita, *Electrochem. Technol.*, **6**, 295 (1968).
15. R. F. Lever, *IBM Jour. Res. and Develop.*, **8**, 460 (1964).
16. W. H. Shepherd, *This Journal*, **112**, 988 (1965).
17. H. Seki and H. Araki, *Denki-kagaku*, **34**, 397 (1966) (in Japanese).
18. D. R. Stull, Janaf Thermochemical Tables, Clearinghouse, Washington, D. C. (1965).
19. R. M. Burger and R. P. Donovan, "Fundamentals of Silicon Integrated Device Technology," Vol. 1, p. 449, Prentice-Hall, Inc., Englewood Cliffs, N. J. (1967).
20. R. G. Hays, Recent News Paper 226 presented at the Detroit Meeting of the Society, Oct. 5-9, 1969.

The Effect of Growth Orientation on the Crystal Perfection of Horizontal Bridgman Grown GaAs

T. S. Plaskett,* J. M. Woodall,* and A. Segmüller

IBM Thomas J. Watson Research Center, Yorktown Heights, New York 10598

ABSTRACT

The crystalline perfection of Sn-doped GaAs crystals grown by the horizontal Bridgman technique was found to be dependent on the crystal growth direction. The highest perfection occurred for crystals grown near the <013> direction. Portions of both seeded and unseeded doped crystals grown in this direction were found to be dislocation-free. Also, undoped crystals seeded in the <013> direction were dislocation-free.

Steinemann and Zimmerli (1) have grown dislocation-free undoped crystals of GaAs by the Czochralski technique by maintaining careful control of the stoichiometry of the melt composition and of the temperature gradients in the solid. In this paper we report the growth of dislocation-free undoped and heavily Sn-doped GaAs crystals by the sealed horizontal Bridgman technique. The advantage of the horizontal Bridgman technique is that heavily doped crystals grown by this method are more homogeneous than doped crystals grown by the Czochralski technique. For device applications, crystals of high perfection and chemical homogeneity are required.

Experimental Technique

The crystals were grown in a sealed quartz system in quartz boats. Synthesis was performed from the elements *in situ* prior to growth. A schematic diagram of the apparatus and temperature profile used for the experiments is shown in Fig. 1. Two important features of the apparatus are (*a*) the zirconia tube located in the core of the melt control furnace which tends to reduce local radial and axial thermal variations and also retards the rate of devitrification of the sealed quartz system and (*b*) the use of Fiber-Fax insulating board between the two furnaces to produce a sharp temperature gradient. For the growth of the Sn-doped crystals, the Sn/Ga weight ratio in the melt was 3.3×10^{-2}. This amount gives between 2 to 5 x 10^{18} atoms/cm^3 in the first half of the crystal. The effective distribution coefficient for Sn, which was determined by fitting the dopant profile to a normal freeze curve, was found to be about 3.5×10^{-3} for this growth system. The dopant profile was determined from radiochemical analysis and electrical measurements. The growth was performed at a constant As pressure by controlling the coldest portion of the ampoule at 614° ± 0.2°C. This As pressure is nominally about 1 atm. At this pressure the melt is essentially at the stoichiometric composition.

It was found that unseeded crystals did not grow along any of the major axes. Therefore, in order to study crystalline perfection for growth along these axes, it was necessary to grow seeded crystals. Seeding of the melt was performed in specially designed quartz crucibles as shown in Fig. 2. The inside of the crucible was sand blasted to prevent wetting. The seed was placed in the end of the crucible with the small rectangular cross section. To ensure that seeding occurred, about one-half of the seed was allowed to melt back before growth commenced. A typical crystal grown by this technique is shown in Fig. 3. The sealed ampoule was moved through the furnace with a precisely controlled furnace gradient at a rate of about 0.85 cm/hr. Except for differences in growth direction, all crystals were grown under the same conditions.

* Electrochemical Society Active Member.
Key words: crystal growth, GaAs, crystal perfection.

The degree of perfection of a crystal was determined on chemically polished (111) or (100) wafers cut from the positions shown in Fig. 3. Metallographic examination for dislocation etch pits and other structures was performed on the (111) wafers. X-ray transmission topographs, using the scanning oscillatory technique of Schwuttke (2), were taken on either (111) or (100) wafers that were first chemically

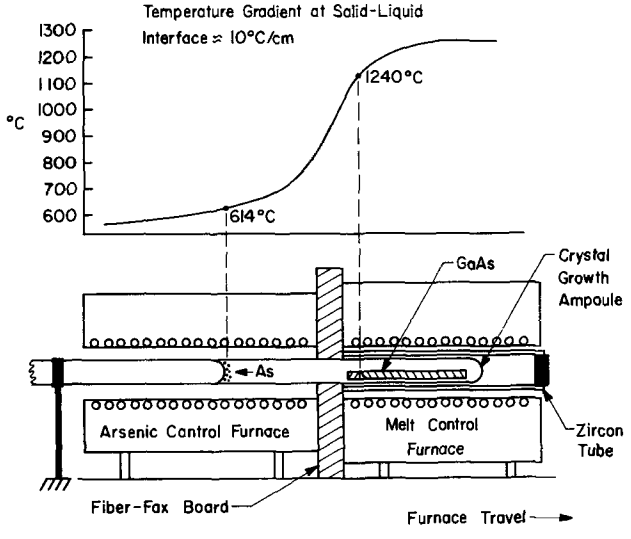

Fig. 1. Schematic drawing of the growth apparatus and furnace temperature profile.

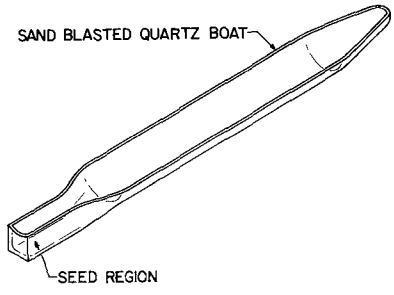

Fig. 2. Schematic drawing of the quartz boat used for seeding of the melt.

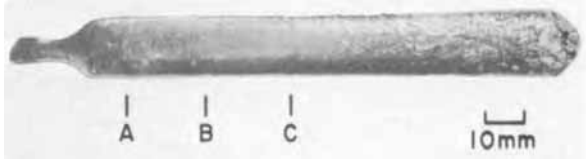

Fig. 3. Typical seeded crystal. A, B, and C indicate positions where wafers were cut for the defect examinations.

thinned to about 0.05 mm using the technique of Reisman and Rohr (3).

Results

The various growth orientations that were investigated for the Sn-doped crystals are shown in Fig. 4. (This is a double stereographic triangle which is required because of the polar nature of GaAs.) The crystalline perfection level observed for each orientation is indicated by the symbols. Around the major axes the crystals were grossly imperfect, with dislocation densities greater than 10^4 lines/cm^2 and with some dislocations aligned to form low-angle boundaries; *i.e.*, lineage structure as shown in Fig. 5b. In the central area of the double triangle the only defect structures that were observed were dislocations with densities less than 10^4 lines/cm^2 (Fig. 5a). The highest crystalline perfection occurred around the <013> direction and the dislocation densities were less than 10^3 lines/cm^2. Some portions were essentially free of dislocations. An x-ray transmission topograph taken from a Sn-doped crystal grown in this direction is

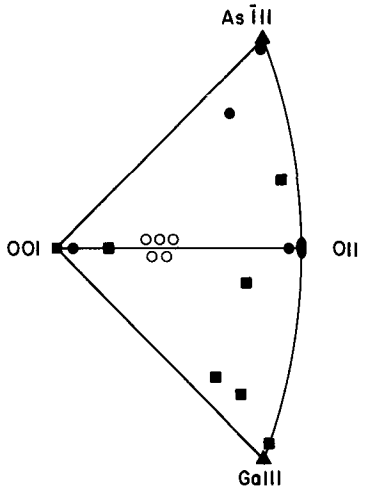

Fig. 4. Crystalline perfection for the various growth orientations investigated. ● grossly imperfect, ■ dislocated with densities between 10^3 and 10^4 lines/cm^2. ○ dislocated with densities less than 10^3 lines/cm^2 and with some positions dislocation-free.

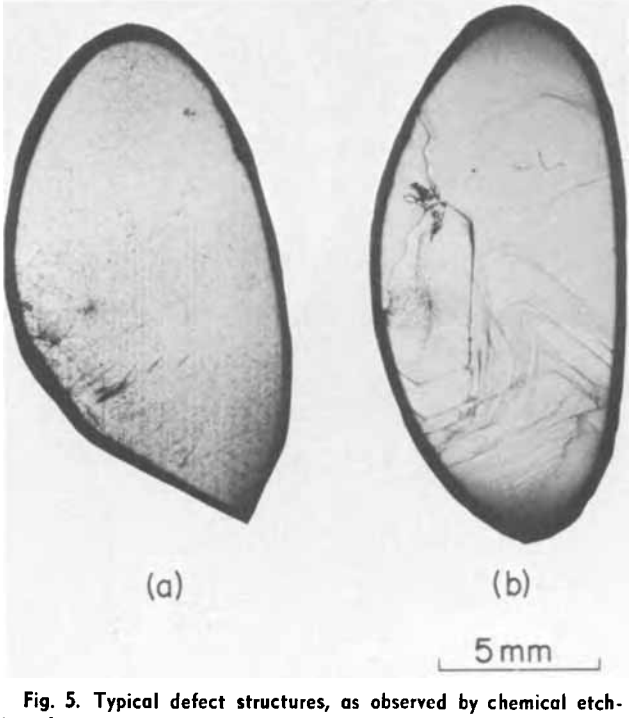

Fig. 5. Typical defect structures, as observed by chemical etching, for a crystal with the growth axis (a) away from the major axes and (b) near the major axes.

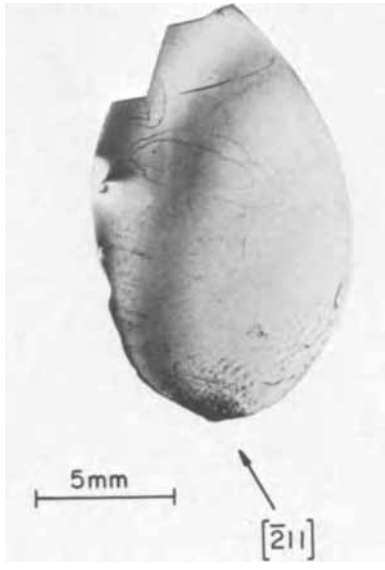

Fig. 6. X-ray topograph of a wafer from a crystal grown in <013> direction. A few dislocation loops are evident in the plane of the wafer. The broad dark band is a "Pendellösung" fringe due to the wedge shape of the wafer. The arrow denotes the diffraction vector. The Burgers vector of the two large loops is parallel to their long axis, a [1̄10] direction.

shown in Fig. 6. A few dislocations are evident as slip lines on the top free surface. At the edges of the wafer the dislocation density is higher. Two or three dislocation loops are evident in the plane of the wafer and are clearly resolved. This perfection level is typical for position A, B, and sometimes position C (see Fig. 3) for crystals grown in the <013> direction. At the lower edge of the wafer shown in Fig. 6 some cellular structure is evident. This is the only indication of chemical inhomogeneity present in this region of this doped crystal. More typically at position C the amount of cellular structure increased slightly from that shown in Fig. 6. Beyond position C the cross section shows both the cellular structure and two-phase growth. No striae were detected by etching or by infrared transmission microscopy in the first half of the crystal.

For Sn-doped crystals it was found that for all the orientations studied the highest crystal perfection occurred in crystals grown along the <013>. This is true for nonseeded Sn-doped crystals and for Sn-doped crystals seeded in the specially designed boat. However, when Sn-doped crystals were seeded with seeds having the same cross section as the bulk of the crystal and grown along the <013>, the resulting crystals exhibited dislocation densities $>10^4$ lines/cm^2. In addition several undoped crystals were seeded and grown in the <013> in the specially designed boat and were found to be nearly dislocation-free.

Except for the grossly imperfect crystals, the dislocations were generated by plastic deformation resulting from thermal stresses as evident from the slip line pattern shown in the etched sample in Fig. 5b and in the x-ray topograph in Fig. 7. The deformation undoubtedly occurred at elevated temperatures where GaAs is ductile. From the analysis of the slip line patterns of the sample, which showed only one set of slip lines, it was determined that the thermal stresses were uniaxial.

Discussion

Since the dislocations were generated by plastic deformation, the dependence of the dislocation density on growth orientation must be related to the high temperature strength of the crystal. The higher the strength, the less mobile are the dislocations, and therefore the greater are the stresses required to generate them. A mechanism whereby the crystal is

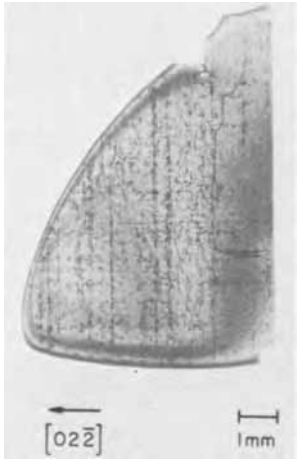

Fig. 7. X-ray topograph of a dislocated wafer. Most of the dislocations lie in slip planes which indicates that they were generated by plastic deformation. The arrow denotes the diffraction vector.

strengthened by the alloying action of the Sn dopant seems unlikely since the Sn concentration profile did not vary with orientation and <013> seeded undoped crystals could also be produced nearly dislocation-free. Also, the differences in the resolved shear stress to which the crystal was subjected during growth for the various growth directions cannot account for the orientation dependence; calculation of the resolved shear stresses of the <110> {111} type dislocation showed that the <013> growth direction had the highest relative value, although the differences in values for the various low-index growth directions were small.

The Dash (4) model may in part explain the growth of the dislocation-free seeded crystals. In the Dash technique initial growth conditions are provided which cause the dislocations to form in simple lines. These dislocations will then eventually grow out to a surface and be eliminated if the line of the dislocations is at some angle to the growth axis. In GaAs the axis of the most common dislocation is the <110> direction. The <013> growth direction makes an angle of about 27° to the axis of the line dislocations. This Dash type of dislocation behavior occurs when there are no radial or transverse thermal gradients. For the Czochralski technique this condition is met by necking the crystal down to a small diameter after seeding. In the present study it was found that the seed must have a smaller cross-sectional dimension than the crystal to be grown, which is equivalent to the necking down of the Czochralski crystals.

If conditions for the Dash model were the only criteria then the <111> and <100> would also be preferred directions. However, this was not found to be the case and this would indicate that other parameters are important.[1] Moreover, the Dash model does not explain why nonseeded doped crystals which grew in the <013> direction were dislocation-free right from the start. It is apparent, therefore, that further studies must be performed in order to completely understand the orientation effect observed.

Conclusions

From this investigation it was shown that it is possible to grow homogeneously doped and undoped GaAs crystals with a high crystalline perfection by the horizontal Bridgman technique. Crystals properly seeded in the <013> or unseeded Sn doped crystals which grew in this direction were of the highest perfection with portions of the crystal being dislocation-free.

Acknowledgments

The authors are grateful to Messrs. A. H. Parsons and W. C. Wuestenhoefer for assistance in the experimental part.

Work performed by J. M. Woodall was sponsored in part by the U. S. Army Electronics Command under Contract DA-28-043-02510(E), Fort Monmouth, New Jersey.

Manuscript submitted May 14, 1970; revised manuscript received *ca.* Sept. 1, 1970.

Any discussion of this paper will appear in a Discussion Section to be published in the December 1971 JOURNAL.

[1] One of the reviewers of this paper suggested that the reason the <111> and <100> are not preferred directions may be explained by the considerations of Sangster, who proposed that <311> to <511> should be preferred growth directions since none of the major axes offer an ideal combination of nucleation ease, surface stoichiometry, surface packing, and surface planarity. Growth directions such as the <311> (or <013>) which combine the favorable properties of the {100}, {110}, and {111} surfaces are, therefore, expected to produce crystals of higher perfection. [R. C. Sangster, "Model Studies of Crystal Growth Phenomena in the III-V Semiconducting Compounds," in "Compound Semiconductors," Vol. 1, R. K. Willardson and H. L. Goering, Editors, Reinhold Publishing Corp., New York (1963).]

REFERENCES

1. A. Steinemann and U. Zimmerli, "Crystal Growth," p. 81, H. S. Peifer, Editor, Pergamon Press Ltd. (1967).
2. G. H. Schwuttke, *J. Appl. Phys.*, **36**, 2712 (1965).
3. A. Reisman and R. L. Rohr, *This Journal*, **111**, 1425 (1964).
4. W. C. Dash, *J. Appl. Phys.*, **29**, 736 (1958).

Preferential Etching and Etched Profile of GaAs

Yasuo Tarui, Yoshio Komiya, and Yasoo Harada[1]

Electrotechnical Laboratory, Tanashi, Tokyo, Japan

ABSTRACT

The Br_2-CH_3OH system has been found to give good results for preferential etching of GaAs. The etch rates for the low-index planes of GaAs in this system have been investigated as a function of Br_2 concentrations in CH_3OH. The order of the etch rate at 1% Br_2 by weight has been found to be {110} $\gtrsim$ B{111} $\gtrsim$ {100} > A{111} where the A{111} planes have been only slightly etched. The A{111} planes have played an important role for the etched profiles produced by this etching system. A V-shaped groove, a reverse mesa-shaped structure, and a triangular prism-shaped "bridge" have been formed by channels being etched on the {100} planes. The sizes of the V-shaped groove and the "bridge" have been controlled by the width of the opening in the oxide mask. A channel etched groove in the B{111} planes has also exhibited crystal habit. Interesting etched profiles which are applicable for the design and fabrication of device structures are described.

The III-V intermetallic compounds with the zinc blende structure exhibit polarity along the <111> directions. Consequently, this structure has two types of the {111} planes designated as the A{111} planes or A planes and the B{111} planes or B planes. Regarding the difference in the etching behavior between the A{111} and B{111} planes, it has been proposed that the B{111} planes are chemically very reactive because of having an unshared pair of electrons, but the A{111} planes have not (1, 2). Br_2-CH_3OH (3) or H_2SO_4-H_2O_2 systems have usually been employed as the etchants which are capable of producing highly polished surfaces on GaAs. For silicon, the design and fabrication of device structures by means of preferential etching have been reported (4-6). However, for GaAs there has been no report on device shaping by using preferential etching.

In the present paper, we show preferential etching characteristics of GaAs in the Br_2-CH_3OH system and then demonstrate geometrically etched profiles produced in the B{111} and {100} planes by employing this system. Special emphasis has been placed on the unique device structures which are produced by the difference in the etch rate between the A{111} planes and the other low-index planes of the intermetallic compounds.

Experimental Procedure

Sample.—The wafers employed were slices of the low-index planes cut from GaAs single crystals (Te doped, carrier concentrations ranging from 5.3 to 15 x 10^{17} cm^{-3}), *i.e.* the A{111}, B{111}, {110}, and {100} planes, with an uncertainty of 1° or less. The surfaces of these wafers were lapped and polished with fine abrasive alumina (0.05-0.1μ particle size). After being degreased and rinsed with deionized water (ρ > 5 meg ohms), they were chemically polished in a slowly stirred solution of 5 H_2SO_4-1 H_2O_2-1 H_2O for 4 min at 50°-55°C.

Masking pattern.—The method selected for preparing the mask and determining the directions of the masking pattern was as follows.

1. The surfaces of the wafers, except for a portion near the corner, were coated with black wax.
2. The uncoated surfaces were etched in a solution of one volume of 33 w/o (weight per cent) CrO_3 aqueous solution–two volumes of 46 w/o HF (Sirtl etch) for 4 min at room temperature. The etched figures produced by this process are employed in the following photoetching process for the purpose of orientation alignment.
3. The wafers were degreased and rinsed with deionized water after removing the black wax. Then, their surfaces were masked with a 0.3-0.5μ thick Al_2O_3 layer by electron beam evaporation. The source was Al_2O_3 (99.999%).
4. The photoengraving process was carried out.
5. Heated phosphoric acid was employed to etch the Al_2O_3 film.

Etch solution.—The preferential etchant employed was Br_2-CH_3OH and etching experiments were carried out at room temperature. The Br_2 concentrations in CH_3OH were varied up to 5.0% Br_2 by weight. A large quantity of solution (~300 ml) was prepared to prevent the etching temperature from elevating and the etch composition from varying during the experiments (Br_2 purity ≥99.0%, CH_3OH purity ≥99.5%).

Etch rate determination.—The step heights etched were measured using a microscope after obtaining the etched cross sections of the samples by appropriate cleavage. The smallest step heights measured were about 0.5μ, where the accuracy of the microscope measurement was about 0.2μ.

Results and Discussion

Etch figures.—Schematic diagrams and photographs of the etch figures produced on the B{111} and {100} planes of GaAs in the CrO_3-HF system are shown in Fig. 1. The etch figures on the B{111} planes revealed an equilateral triangle as well known for silicon. However, the figures on the {100} planes of GaAs did not show a square as produced on silicon but indicated a rectangle because of the polarity along the <111> directions.

Br_2 *concentration dependence of the etch rate.*—Figure 2 shows the average Br_2 concentration dependence of the etch rate for 10 min on the A{111}, B{111} and {100} planes of GaAs, and the etch ratio B{111}/A{111}. The etch rates on these planes increased with Br_2 concentrations up to at least 5.0% Br_2 by weight. The ratio gives a minimum near 3.0% Br_2 by weight. This result indicates that, at the lower Br_2 concentrations, etching is more preferential; the B{111} planes of GaAs are very chemically reactive compared with the A{111} planes. Consequently, when a suitable etchant such as this system is employed, the etch rate on the A{111} planes is slower than on the B{111} planes (1, 2).

Orientation dependence of the etched depth.—Figure 3 shows the linearity between the etch depth and etch time with 5 min intervals for the low-index planes of GaAs at 1.0% Br_2 by weight. The order of magnitude of the etch rate was {110} $\gtrsim$ B{111} $\gtrsim$ {100} > A{111}, and the etch rate on the A{111} planes was very slow.

[1] Permanent address: Research and Development Center, Sanyo Electric Co., Ltd., Hirakata, Osaka, Japan.

Key words: polarity of zinc blende structure, etching rate, Br_2-CH_3OH system, Gunn effect device.

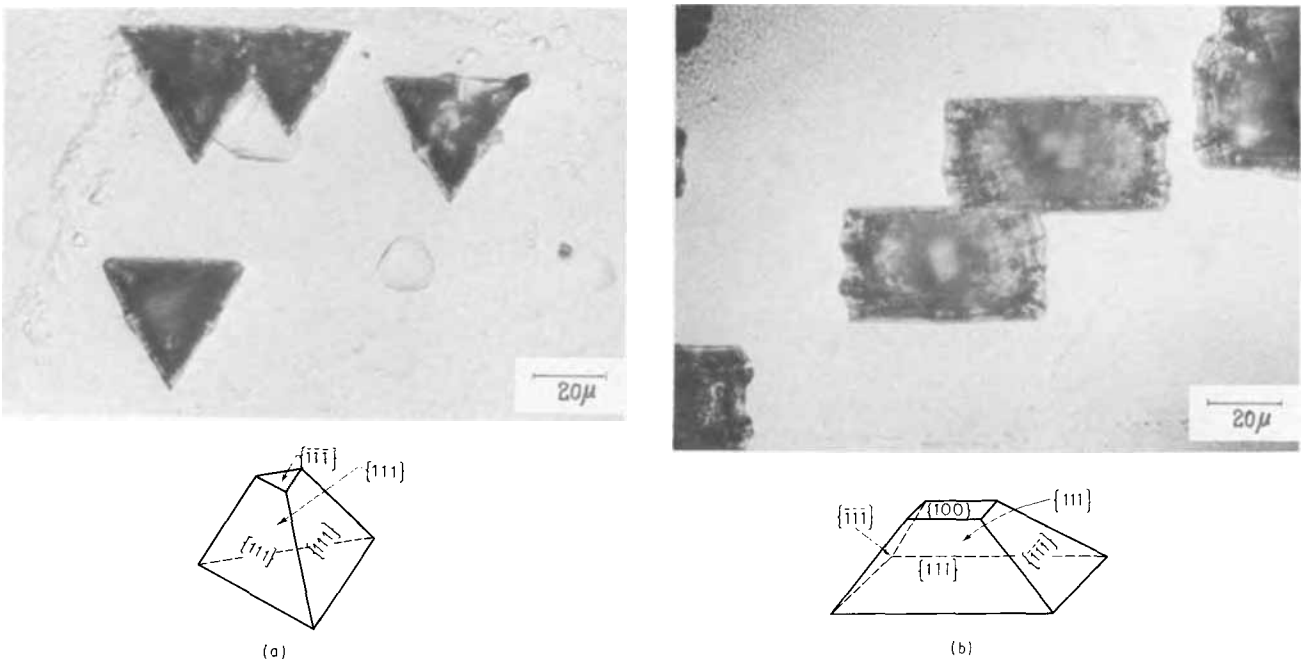

Fig. 1. Etch figures produced on B{111} and {100} planes of GaAs in CrO_3-HF system (room temp, 4 min) and schematic diagram of individual etch figures: (a) and (b) = etch figure on B{111}, {100}, respectively, and schematic diagram of individual etch figure (approx 300X).

When the B{111}, {110}, or {100} planes of GaAs which intercept the A{111} planes are employed as preferential etching surfaces, the etched grooves exhibiting crystal habit are formed because the etching stops at the A{111} planes, where the etch rate is slowest. These results suggest that the orientation effects produced by this system could be utilized in the design and fabrication of certain device structures.

Cross section of etched channels.—The cross sections of channels etched in the {100} and B{111} planes of GaAs are demonstrated in Fig. 4 and 5, respectively. Figure 4(a) shows the cross section of channels etched parallel to the short sides of the etch figures revealed in Fig. 1(b). The etched profile was a reverse mesa-shaped structure which exhibited crystal habit, while cross sections of channels etched parallel to the long sides of the rectangular figures in Fig. 1(b) were V-shaped as demonstrated in Fig. 4(b). This etched profile also exhibited crystal habit. Figures 5(a) and (b) show, respectively, cross sections of channels

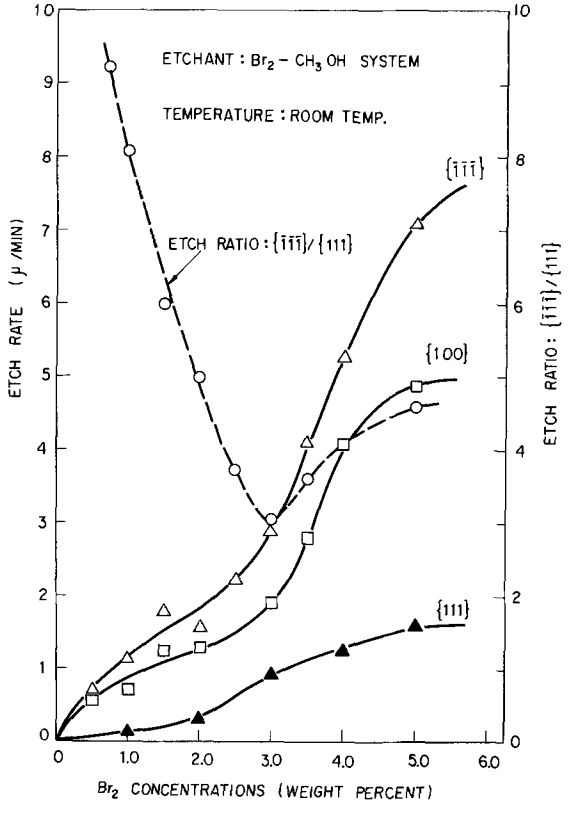

Fig. 2. Br_2 concentration dependence of the etch rate and etch ratio B{111}/A{111}: △, □, ▲ = etch rate on B{111}, {100}, A{111}, respectively; ○ = etch ratio B{111}/A{111}.

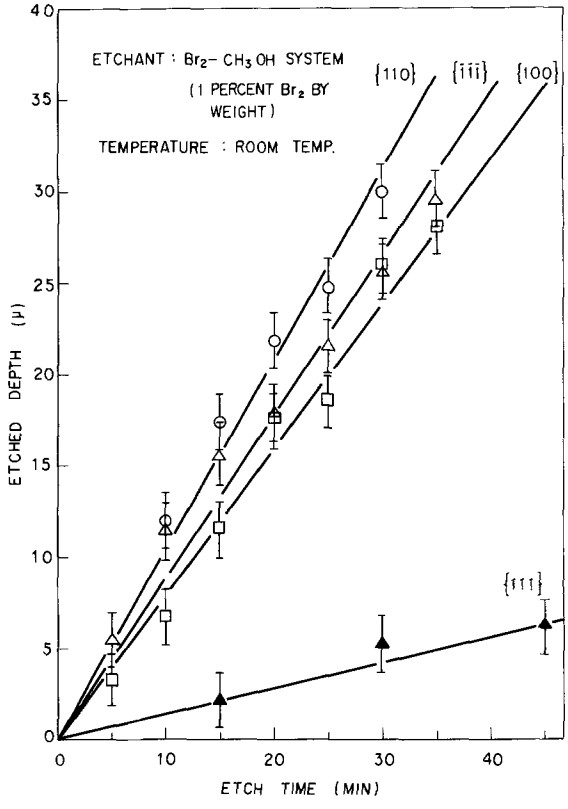

Fig. 3. Orientation dependence of the etched depth at 1% Br_2 by weight: ○, △, □, ▲ = etch rate on {110}, B{111}, {100}, A{111}, respectively.

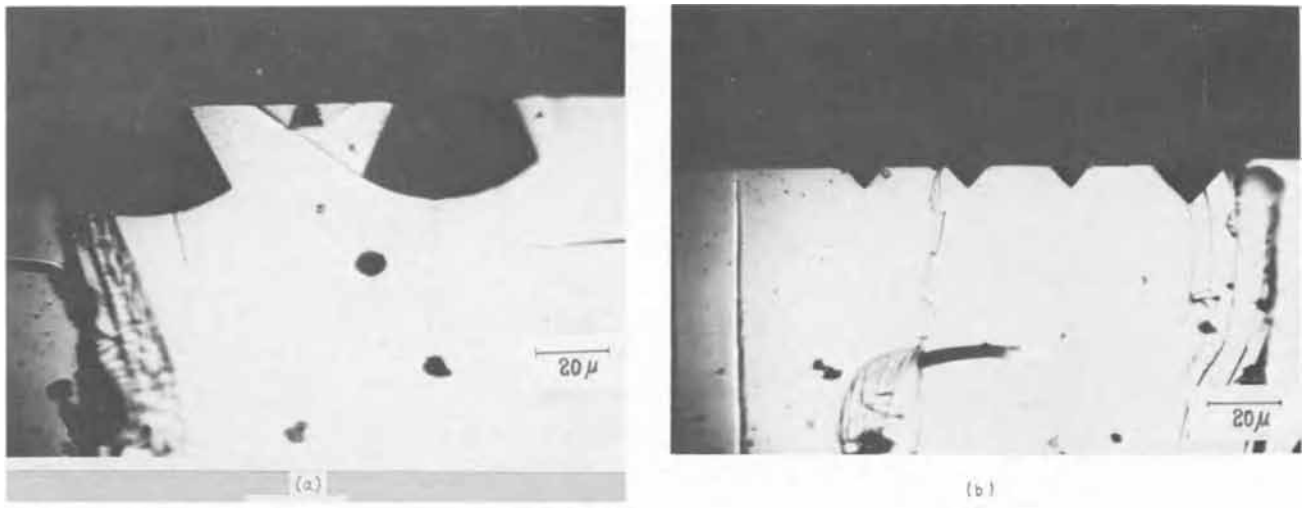

Fig. 4. Cross section of channels etched in {100} planes of GaAs and relation between a rectangular etch figure shown in Fig. 1(b) and the directions of a channel etching on {100} planes: (a) = cross section of channels etched parallel to the short side of etch figure at 1% Br_2 by weight for 10 min; (b) = cross section of channels etched parallel to the long side of etch figure at 4.8% Br_2 by weight for 10 min; (c) = relation between etch figure and the directions of channels being etched (approx 300X).

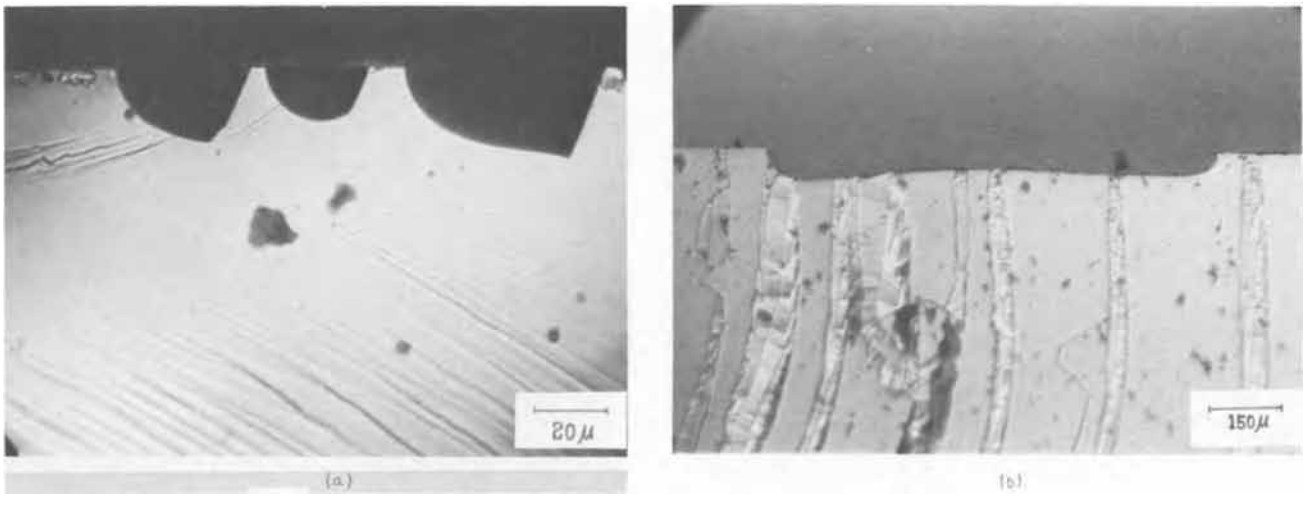

Fig. 5. Cross section of channels etched in B{111} planes of GaAs and relation between a triangular etch figure revealed in Fig. 1(a) and the direction of channels being etched on B{111} planes: (a) = cross section of channels etched parallel to one side of etch figure at 1% Br_2 by weight for 30 min (approx 300X); (b) = cross section of channel etched perpendicular to the one side of etch figure at 4.8% Br_2 by weight for 10 min (approx 90X); (c) = relation between etch figure and the direction of channel being etched.

etched parallel and perpendicular to the one side of the triangular figures shown in Fig. 1(a).

An etched groove demonstrated in Fig. 5(a) exhibited crystal habit but an etched one in Fig. 5(b) did not. The etched profile obtained in Fig. 4(a) is associated only with the intermetallic compounds, but the profile demonstrated in Fig. 4(b) is the same as for silicon (5, 6). This unique profile is formed because of the difference in the etch rate between the A{111} planes and the other low-index planes. Furthermore, we obtained a triangular prism-shaped "bridge," demonstrated in Fig. 6, by continuing the etching further in the case of Fig. 4(a). As shown by these results, when the direction of channels being etched on the {100} planes of GaAs is adjusted to the proper orientation, a V-shaped groove, a reverse mesa-shaped structure, and a triangular prism-shaped "bridge" as illustrated in Fig. 7 can be formed with Br_2-CH_3OH system.

Schematic diagrams of the etched cross section for the zinc blende structure are shown in Fig. 8 and 9 by perspective drawing through the {110} planes. Figures 8(b) and (c), respectively, show cross sections of a channel etched parallel to the $[0\bar{1}\bar{1}]$ and $[01\bar{1}]$ orientation in the (100) plane.

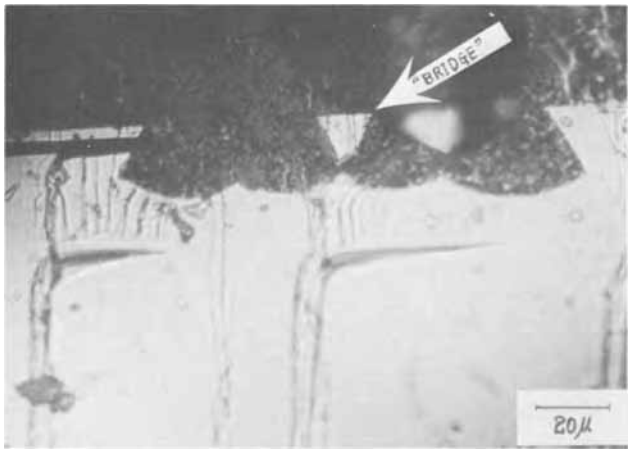

Fig. 6. Cross section of a triangular prism-shaped "bridge" obtained in {100} planes of GaAs by the Br_2-CH_3OH system (4.8% Br_2 by weight, 10 min) (approx 300X).

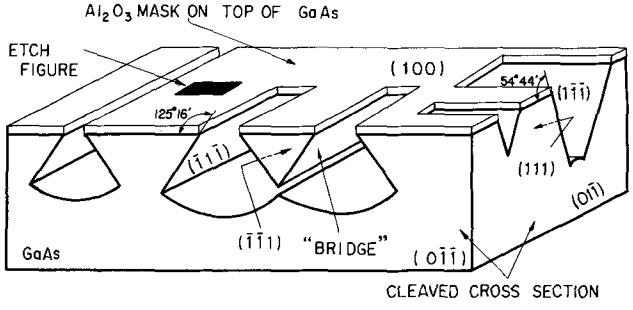

Fig. 7. Etched profile produced in {100} planes of GaAs by the Br_2-CH_3OH system.

There is twofold symmetry of the A{111} or B{111} planes intersecting the {100} planes as illustrated in Fig. 8(a). In Fig. 8(b), the $[\bar{1}1\bar{1}]$ and $[\bar{1}11]$ orientations intersect the [100] orientation at 125°16′, respectively, and, on the other hand, in Fig. 8(c), the $[1\bar{1}1]$ and [111] orientations intersect the [100] orientation at 54°44′, respectively. The $(\bar{1}1\bar{1})$ and $(\bar{1}11)$ planes are perpendicular to the $(0\bar{1}\bar{1})$ plane [Fig. 8 (b)] and also the $(1\bar{1}\bar{1})$ and (111) plane intersect the $(01\bar{1})$ plane at right angles [Fig. 8 (c)].

In the case of preferential etching in the [100] direction, the side etching proceeds up to the A{111} planes, *i.e.* the $(\bar{1}1\bar{1})$, $(\bar{1}11)$, $(1\bar{1}\bar{1})$, and (111) plane, while the etch rates on the B{111}, {110}, and {100} planes are much faster than the A{111} planes. Consequently a V-shaped and a reverse mesa-shaped profile are obtained whose sides form, respectively, an angle of 54°44′ and 125°16′ with respect to the (100) surface. The "bridge" can also be obtained whose sides form an angle of 125°16′ with respect to the (100) surface.

As schematically shown in Fig. 9(a), both the A{111} and B{111} planes form tetrahedrons having as all four sides either only the A{111} or only the B{111} planes. In one case, the insides of tetrahedrons are composed of only the A{111} planes and the outsides are surrounded by only the B{111} planes [Fig. 9 (a)]. In the other case, the insides are the B{111} planes and the outsides are the A{111} planes. Consequently, the $[\bar{1}\bar{1}\bar{1}]$ orientation intersects the $[1\bar{1}\bar{1}]$ orientation at 70°32′ and the $(1\bar{1}\bar{1})$ plane is perpendicular to the $(1\bar{1}0)$ plane as shown in Fig. 9 (b), which shows the cross section of a channel etched parallel to the $[1\bar{1}0]$ orientation in the $(\bar{1}1\bar{1})$ plane alone. When the channel of the mask pattern is aligned perpendicular to one side of the triangular etch figures, the etched cross section does not reveal crystal habit as shown in Fig. 5(b).

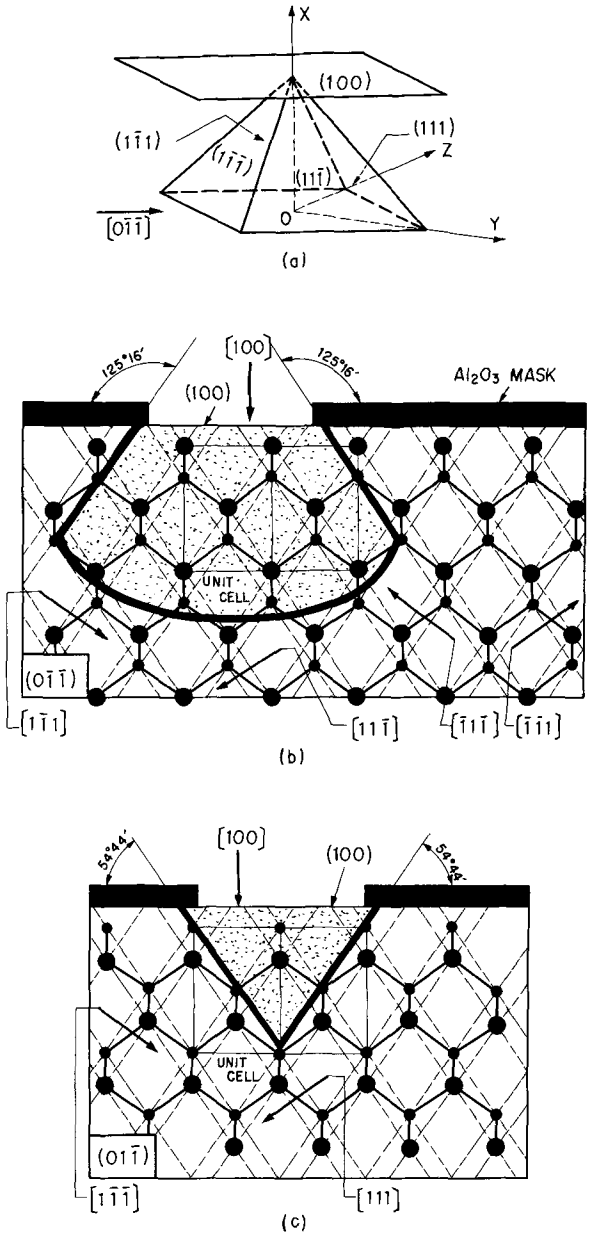

Fig. 8. Schematic diagrams of cross sections etched in {100} planes for zinc blende structure by perspective drawing through {110} planes and of relation between {100} and A{111} or B{111} planes: ○ = group III; ● = group V atoms; (a) = relation between {100} and A{111} or B{111}; (b) = cross section of a channel etched parallel to $[01\bar{1}]$ in (100); (c) = cross section of a channel etched parallel to $[0\bar{1}\bar{1}]$.

These results indicate that a triangular cone-shaped groove will be formed in the B{111} planes when a triangular mask pattern is aligned parallel to each side of the etch figures shown in Fig. 1(a).

Mask size and etched profile.—The sizes of a V-shaped groove, a triangular prism-shaped "bridge," and a triangular cone-shaped groove all can be controlled by the width of the opening in the oxide mask, since these geometric shapes are found to be surrounded by the A{111} planes. The similar, but unsymmetrical, etched profiles can be also formed by employing the higher index planes, *i.e.* {211}---, as the etching surfaces.

Proposed device structures.—We can widely apply the etched profiles described to the design and fabrication of device structures. Especially, the unique "bridge" structure shown in Fig. 6 and 7 has the advantage that the "bridge" is isolated by air and its size can be controlled by the window width of the

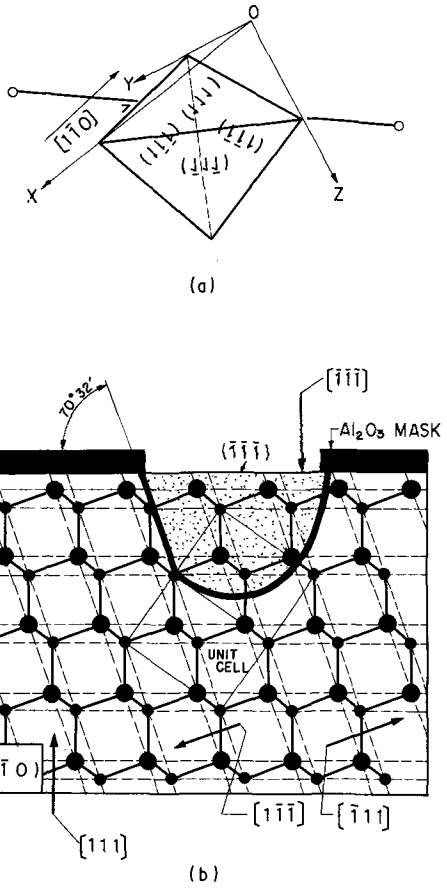

Fig. 9. Schematic diagrams of cross sections etched in B{111} planes for zinc blende structure by perspective drawing through {110} planes and of geometric tetrahedrons composed of only A{111} planes, *i.e.* (111), ($\bar{1}\bar{1}1$), ($1\bar{1}\bar{1}$), ($\bar{1}1\bar{1}$), or of only B{111} planes, *i.e.* ($\bar{1}\bar{1}\bar{1}$), ($11\bar{1}$), ($1\bar{1}1$), ($\bar{1}11$): • = group III; ● = group V atoms; (a) = insides of tetrahedrons are composed of (111), ($\bar{1}\bar{1}1$), ($\bar{1}11$), and ($1\bar{1}\bar{1}$); (b) = cross section of a channel etched parallel to [$1\bar{1}0$] in ($\bar{1}\bar{1}\bar{1}$).

oxide mask. By using the technology of semiconductor integrated circuits, we can monolithically fabricate the device structures composed of lots of the elements which are isolated by air and have small, geometric cross sections.

In the case of operating Gunn effect devices (7, 8) by utilizing the "bridge" structure, we can suppress the Gunn oscillation because the "bridge" section is small (9). Moreover, the problem of heat emission due to the power consumption of Gunn effect devices or luminescent devices will be much improved when the grooves around the "bridge" are refilled with a material of efficient heat conduction. These structures make the devices work at higher power. When we fill the grooves around the "bridge" with material which has a dielectric constant different from that of the semiconductor substrates used, we can control the state of the Gunn oscillation (10).

Field effect devices can be designed such that the structures with P-N junctions or Schottky contacts are fabricated on the upper surface of the "bridge." Gunn effect devices or luminescent devices with such a field effect structure can be modulated by the gate signal.

Conclusion

The Br_2-CH_3OH system gives good results for preferential etching of GaAs. Below 3% Br_2 by weight, the lower the Br_2 concentrations, the more preferential the etching behavior. The slowest etching planes are the A{111} planes, which play an important role for the etched profiles produced by this system. When the mask pattern is aligned in the proper orientation, an etched groove having crystal habit can be formed with this system. V-shaped grooves and triangular prism-shaped "bridge" structures can be fabricated, with sizes controlled by the width of the opening in the mask. These shaping methods give much flexibility to device fabricators.

Acknowledgments

The authors wish to thank Mrs. F. Hayashi and Mr. Y. Hayashi for their helpful suggestions and Mr. M. Yamanaka for assisting with experiments.

Manuscript submitted April 9, 1970; revised manuscript received Sept. 14, 1970.

Any discussion of this paper will appear in a Discussion Section to be published in the December 1971 JOURNAL.

REFERENCES

1. H. C. Gatos and M. C. Lavine, *J. Phys. Chem. Solids*, **14**, 169 (1960).
2. H. C. Gatos and M. C. Lavine, *This Journal*, **107**, 427 (1960).
3. C. S. Fuller and H. W. Allison, *ibid.*, **109**, 880 (1962).
4. R. M. Finne and D. L. Klein, *ibid.*, **114**, 965 (1967).
5. D. B. Lee, *J. Appl. Phys.*, **40**, 4569 (1969).
6. K. E. Bear and P. S. Gleen, *Proc. IEEE*, **57**, 1469 (1969).
7. J. E. Gunn, *IBM J. Res. Dev.*, **8**, 141 (1964).
8. J. A. Copeland, *J. Appl. Phys.*, **38**, 3096 (1967).
9. G. S. Kino and P. N. Robson, *Proc. IEEE*, **56**, 2056 (1968).
10. S. Kataoka, H. Tateno, and M. Kawashima, *Electronics Letters*, **5**, 48 (1969).

Studies of the Defect Structure of Nonstoichiometric Cerium Dioxide[1]

R. N. Blumenthal, P. W. Lee,[2] and R. J. Panlener

Metallurgy and Materials Science, College of Engineering, Marquette University, Milwaukee, Wisconsin 53233

ABSTRACT

The electrical conductivity of sintered specimens of $Ce_{1+y}O_2$ was measured over the temperature range 800°-1500°C and from 1 to 10^{-21} atm of oxygen. Based on the agreement between these experimental data and theoretically derived relations obtained using the law of mass action, the nonstoichiometric defect structure of $Ce_{1+y}O_2$ was interpreted in terms of a defect structure consisting of triply and quadruply ionized cerium interstitials and localized electrons. The standard enthalpies of formation for the following defect reactions in $Ce_{1+y}O_2$ were determined

(a) $V_i + 5Ce_{Ce} + 2\,O_o = Ce_i^{\cdots\cdot} + 4Ce'_{Ce} + O_2(g)$; $\Delta H_a^o = 10.4\text{ eV} \pm 0.3$

(b) $V_i + 4Ce_{Ce} + 2\,O_o = Ce_i^{\cdots} + 3Ce'_{Ce} + O_2(g)$; $\Delta H_b^o = 8.5\text{ eV}$[3]

(c) $Ce_{Ce} + Ce_i^{\cdots} = Ce_i^{\cdots\cdot} + Ce'_{Ce}$; $\Delta H_c^o = 1.9\text{ eV}$[3]

Nonstoichiometric cerium dioxide, $Ce_{1+y}O_2$, has been the subject of several x-ray (1-3), thermodynamic (4-6), and electrical conductivity investigations (7-12). Based on these experimental observations, $Ce_{1+y}O_2$ may be classified as a metal-excess, n-type semiconductor. Such a metal excess may arise from the presence of a defect structure involving anion vacancies or cation interstitials in the crystal. However, in spite of all this scientific interest in $Ce_{1+y}O_2$, there has been no conclusive experimental evidence to indicate which of the above defect models predominates.

Brauer and Gingerich (3, 4) studied the influence of temperature on the cerium oxide system by measuring the oxygen dissociation pressure in the region CeO_2-$Ce_{1.33}O_2$, from 600° to 1000°C, and by high-temperature x-ray powder-diffraction analysis in the region CeO_2-$Ce_{1.11}O_2$ over the temperature range 20°-1050°C. From the results of their investigation, it can be concluded that, above 800°C, a homogeneous cubic solid solution extends from CeO_2 to about $Ce_{1.20}O_2$ and, from $Ce_{1.20}O_2$-$Ce_{1.33}O_2$, a two-phase region exists.

Kuznetsov *et al.* (5) utilized both a galvanic cell technique and a gas equilibrium method to obtain the thermodynamic properties of cerium oxide over the composition range $Ce_{1.26}O_2$ to $Ce_{1.02}O_2$. The results of their investigation indicate the existence of a single-phase region between $Ce_{1.20}O_2$ and $Ce_{1.02}O_2$ above 700°C. Bevan and Kordis (6) measured the oxygen dissociation pressure of $Ce_{1+y}O_2$ and found that a single-phase region exists between CeO_2 and $Ce_{1.16}O_2$ at all temperatures above 685°C. Thus the phase field limits of $Ce_{1+y}O_2$ determined by high-temperature x-ray and thermodynamic measurements appear to be in good agreement.

More recently, Kofstad and Hed (13) have interpreted the thermodynamic data obtained by Bevan and Kordis in terms of a defect model involving singly and doubly charged interstitial cations and electrons localized at cerium ions on normal lattice sites. Atlas (14) has proposed a statistical model to account for partial ordering of anion vacancies and reduced cations in a hypostoichiometric fluorite type metal oxide. Although $Ce_{1+y}O_2$ is thermodynamically stable (4-6) over a wide range of P_{O_2} and temperature (*e.g.*, $Ce_{1+y}O_2$ is thermodynamically stable to values of P_{O_2} as low as 10^{-20} atm at 1023°C) most of the electrical conductivity (7-10) investigations on $Ce_{1+y}O_2$ have been limited to the oxygen pressure region 1 to 10^{-4} atm.

Rudolph (7) measured the electrical conductivity of $Ce_{1+y}O_2$ as a function of P_{O_2} at only one temperature, 987°C, and found

$$\sigma \sim P_{O_2}{}^{-1/5.7}$$

Greener *et al.* (8), using a two-probe method, measured the electrical conductivity of $Ce_{1+y}O_2$ in the temperature range 650°-1400°C and from 0.006 to 1 atm of oxygen. They found that their experimental data could be represented by the following relation

$$\sigma_T = \sigma_{Od} \exp\frac{(-2.2)}{kT} P_{O_2}{}^{-1/5} + \sigma_{Oi} \exp\frac{(-1.45)}{kT}$$

They interpreted their results in terms of a defect structure involving either quadruply ionized cerium interstitials or completely ionized oxygen vacancy pairs.

Kevane (9) analyzed the conductivity data of Greener *et al.* (8) and the gravimetric data of Bevan and Kordis (6) and concludes that it is possible to interpret these results for $Ce_{1+y}O_2$ on the basis of an oxygen vacancy model.

The results of these conductivity measurements over a very limited range of P_{O_2} have not provided an unambiguous determination of the defect structure in $Ce_{1+y}O_2$. Thus, in order to help elucidate the defect structure in $Ce_{1+y}O_2$, work was initiated in this laboratory on the electrical conductivity of $Ce_{1+y}O_2$ as a function of temperature and oxygen partial pressure from 800° to 1500°C and from 10^{-17} to 1 atm of oxygen.

The initial results of this investigation were reported recently by Blumenthal and Laubach (12). Based on the observed curve fit between the theoretically derived relation

$$\sigma^3 = (A\sigma + B) P_{O_2}{}^{-1/2}$$

and the experimental conductivity data from 1000° to 1500°C, in the "high" and "intermediate" oxygen pressure region, they interpreted the nonstoichiometric defect structure of $Ce_{1+y}O_2$ in terms of a defect model involving quasi-free electrons and both singly and doubly ionized oxygen vacancies. At the lower oxygen pressure regions in the range 1200°-1500°C, the electrical conductivity of $Ce_{1+y}O_2$ appeared to be relatively insensitive to oxygen pressure. This region was qualitatively interpreted as possibly due to degenerate semiconducting behavior because of a large departure from stoichiometry.

There appear to be at least two major difficulties with the above defect model:

[1] Supported by the U.S. Atomic Energy Commission. This is AEC report COO-1441-6.

[2] This paper is based in part on a thesis submitted by P. W. Lee in partial fulfillment of the requirements for the M.S. degree, Marquette University, August 1968.

[3] Approximate values.

Key words: electrical conductivity, defect structure, electron mobility.

1. The expression relating σ and P_{O_2} was derived assuming that $Ce_{1+y}O_2$ was in a region close to stoichiometry (*i.e.*, assuming unit activity for the cerium and oxygen atoms on the normal occupied lattice sites).

2. The assumed defect model could not quantitatively account for the relative insensitivity of σ to P_{O_2} in the low oxygen pressure region.

The purpose of this investigation was to eliminate these difficulties by obtaining additional conductivity data over a larger oxygen pressure region and by attempting a more comprehensive analysis of the conductivity data particularly in regions which show a significant departure from stoichiometry.

Theory

The metal excess nature of nonstoichiometric $Ce_{1+y}O_2$ may arise from the presence of a defect structure involving either anion vacancies or cation interstitials. For electronic conduction, the electrical conductivity is proportional to the concentration of electrons and the electron mobility. If the mobility is assumed to be temperature dependent only, then using the law of mass action in combination with the assumed defect reaction and the appropriate simplified electroneutrality equations, theoretical expressions can be derived relating the electrical conductivity to the partial pressure of oxygen.

Thus, if the metal excess behavior arises from a defect reaction involving cerium interstitials in a single state of ionization, the theoretical pressure dependence of the electronic conductivity may be expressed as (8, 12)

$$\sigma \sim P_{O_2}^{-1/m} \qquad [1]$$

where m represents the extent of ionization (m = 2,3,4, or 5 for a singly, doubly, triply, and quadruply ionized cerium interstitial, respectively). Similarly, for a defect reaction involving oxygen vacancies in a single state of ionization, the theoretical pressure dependence of the electronic conductivity may be expressed by the same relationship with m = 4 or 6 for singly and doubly ionized oxygen vacancies, respectively.

Blumenthal and Laubach (12) have extended the above mass action approach by considering an electroneutrality condition involving two states of ionization. For example, the electroneutrality condition for triply and quadruply ionized cerium interstitials is

$$[e'] = 3[Ce_i^{\cdots}] + 4[Ce_i^{\cdots\cdot}]$$

where $[e']$, $[Ce_i^{\cdots}]$, and $[Ce_i^{\cdots\cdot}]$ are the concentrations of electrons, triply ionized interstitials, and quadruply ionized interstitials, respectively. Using the above relation the electronic conductivity may be expressed as

$$\sigma^5 = (D\sigma + E)P_{O_2}^{-1} \qquad [2]$$

where D and E are constants related to the mass action constants, the electronic charge, and the electronic mobility.

Similarly, for a defect structure involving singly and doubly ionized oxygen vacancies, the electroneutrality condition is

$$[e'] = [V_o^{\cdot}] + 2[V_o^{\cdot\cdot}]$$

where $[V_o^{\cdot}]$ and $[V_o^{\cdot\cdot}]$ are the concentrations of singly and doubly ionized oxygen vacancies, respectively. The electronic conductivity may be expressed as

$$\sigma^3 = (A\sigma + B)P_{O_2}^{-1/2} \qquad [3]$$

where A and B are constants similar to D and E.

The above expressions relating the electronic conductivity to the partial pressure of oxygen were derived using the following assumptions:

(*a*) Only defects arising from nonstoichiometric defect reactions were considered. The concentration of defects created by thermal disorder and foreign impurities were assumed to be small compared to the concentration of nonstoichiometric defects.

(*b*) The possibility of associated defects was excluded because only atomic defects with like charges were considered. It was assumed, on the basis of coulombic interaction, that these defects would tend to repel one another.

(*c*) Henry's law was valid for the defects (*i.e.*, the activity coefficients are independent of defect concentration).

(*d*) An activity of one was assumed for the normal cerium and oxygen atoms, and also for the vacant interstitial sites (*i.e.*, Raoult's law was assumed to be valid for these species and $Ce_{1+y}O_2$ was assumed to be in a composition region close to stoichiometry).

In this paper, the same assumptions were made with the exception of (*d*). Instead of unit activities, the cerium, oxygen, and vacant interstitial site activities were equated to the fraction of the available sites occupied. These fractions may differ significantly from one because cerium dioxide is stable over a wide range of nonstoichiometry (*e.g.*, CeO_2-$Ce_{1.20}O_2$). Also in this analysis a first-order attempt, similar to that used by Kofstad and Hed (13), is employed to account for interaction between defects on near neighbor sites. Thus, for a defect structure involving quadruply ionized cerium interstitials and localized electrons (13, 15), the following reaction may be written

$$V_i + 5Ce_{Ce} + 2\,O_o = Ce_i^{\cdots\cdot} + 4Ce'_{Ce} + O_2(g) \qquad [4]$$

where V_i is a vacant interstitial site, Ce_{Ce} and O_O are cerium and oxygen ions, respectively, on their normal lattice sites, $Ce_i^{\cdots\cdot}$ is a quadruply ionized cerium interstitial, and Ce'_{Ce} is an electron localized at a cerium ion on a normal cerium site. Applying the law of mass action yields

$$K_1 = \frac{[Ce_i^{\cdots\cdot}][Ce'_{Ce}]^4 P_{O_2}}{[V_i][Ce_{Ce}]^5[O_o]^2} \qquad [5]$$

where K_1 is the mass action constant and the square bracketed terms represent the number of a given species divided by the number of sites available for that species.

Since the oxygen sublattice is unaffected by the interstitial defect, $[O_o] = 1$. The concentration of normal cerium sites, however, should be corrected for the occupancy of some sites by localized electrons. Kofstad and Hed (13) have also proposed that an ionized interstitial may block the six neighboring normal cerium ions from electron occupation. The number of interstitial sites in $Ce_{1+y}O_2$ is equal to the number of normal cation sites. Thus

$$[Ce_{Ce}] = 1 - [Ce'_{Ce}] - 6(1-\alpha)[Ce_i^{\cdots\cdot}] \qquad [6]$$

where α is the relative probability of a neighboring Ce_{Ce} site being occupied by an electron.

In addition, each ionized cerium interstitial may block the 12 nearest neighboring interstitial sites from occupation because of coulombic repulsion. Thus

$$[V_i] = 1 - [Ce_i^{\cdots\cdot}] - 12(1-\beta)[Ce_i^{\cdots\cdot}] \qquad [7]$$

where β is the relative probability of occupation of interstitials in neighboring interstitial sites.

Assuming the predominant atomic defect is $Ce_i^{\cdots\cdot}$, then $y = [Ce_i^{\cdots\cdot}]$ and the electroneutrality relation is $[Ce'_{Ce}] = 4[Ce_i^{\cdots\cdot}]$. Combining these relations with Eq. [6] and [7], Eq. [5] can be written as

$$K_1 = \frac{4^4 y^5 P_{O_2}}{[1 - y(13 - 12\beta)][1 - y(10 - 6\alpha)]^5} \qquad [8]$$

or

$$K_1' = \frac{\sigma^5 P_{O_2}}{\mu^5[1 - (c\sigma/\mu)(13 - 12\beta)][1 - (c\sigma/\mu)(10 - 6\alpha)]^5} \qquad [9]$$

since

$$y = \frac{c\sigma}{\mu} \qquad [10]$$

where c is assumed to be a constant and μ is the electron mobility.

A quantitative analysis of the conductivity data using Eq. [9] would require knowledge of the temperature and composition dependence of the electron mobility. Since only the temperature dependence of the electron mobility (15) in the range 800°-1200°C is currently available, Eq. [9] has been closely approximated by

$$\sigma^5 = (E - E_1\sigma)P_{O_2}^{-1} \quad [11]$$

to facilitate quantitative analysis. Equation [11] was derived as described below. The denominator of Eq. [8] was calculated as a function of y from $y = 0.0$ to $y = 0.14$, which is approximately the maximum value of y according to existing thermodynamic data (6). These results are shown in Fig. 1 for the four combinations corresponding to the limiting values (*i.e.*, 0 and 1) of α and β. Three of the four curves go to zero and become negative before the maximum value of y is attained. This behavior is inconsistent with the above defect model. It appears that, in the region where the quadruply ionized cerium interstitial predominates, α and β are both closer to one than to zero. Thus, as a first approximation, only the fourth curve was considered, where $\alpha \simeq \beta \simeq 1$. In addition, it was found that this curve could be approximated by a linear function in y from $y = 0.0$ to $y = 0.05$ with less than 7% error for all points where $y < 0.04$ and less than 15% error for $y < 0.05$.

With this motivation, Eq. [8] is written as

$$K_1 = \frac{y^5 P_{O_2}}{a - by} \quad [12]$$

where a and b are constants. The justification for Eq. [12] lies in that only a few of the data points to be analyzed here fall beyond the limiting value of y (*i.e.*, $y \simeq 0.05$) and therefore the error introduced due to these points in using Eq. [12] will be small. Equation [11] can then be obtained by combining Eq. [10] and [12]

$$\sigma^5 = (E - E_1\sigma)P_{O_2}^{-1} \quad [11]$$

where

$$E = K_1 a \mu^5 / c^5 \quad [11a]$$

$$E_1 = K_1 b \mu^4 / c^4 \quad [11b]$$

For a defect structure involving a predominance of triply ionized cerium interstitials, the following expression can be derived (16)

$$\sigma^4 = (D - D_1\sigma)P_{O_2}^{-1} \quad [13]$$

where D and D_1 are parameters similar to E and E_1.

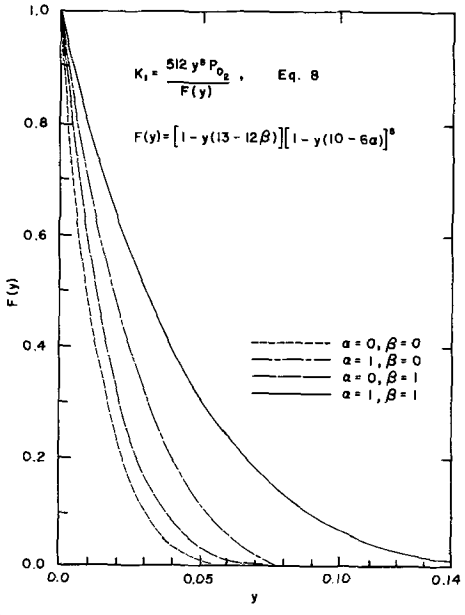

Fig. 1. The relation between $F(y)$ and y for $Ce_{1+y}O_2$

Similarly, for a defect structure involving singly ionized oxygen vacancies the following expression can be obtained (16)

$$\sigma^2 = (A - A_1\sigma)P_{O_2}^{-1/2} \quad [14]$$

For a defect structure involving doubly ionized oxygen vacancies, the following expression can be derived (16)

$$\sigma^3 = (B - B_1\sigma)P_{O_2}^{-1/2} \quad [15]$$

Since the electronic conduction mechanism is a "hopping type" process (15), the temperature dependence of the mobility may be expressed by the well-known relation

$$\mu = \mu_0 \exp(-\Delta E/kT) \quad [16]$$

If the defect model employed in obtaining Eq. [11] is valid, then the activation energy, ΔE, can be determined from the temperature dependence of the parameters E and E_1 as follows

$$E/E_1 \propto \mu \quad [17]$$

From Eq. [16]

$$E/E_1 \propto \exp(-\Delta E/kT) \quad [18]$$

Therefore

$$\Delta E = -k\frac{d[\ln(E/E_1)]}{d(1/T)} \quad [19]$$

The standard enthalpy of formation for a nonstoichiometric defect reaction is related to the mass action constant, K, by the well-known expression

$$K \propto \exp(\Delta S^\circ/k) \exp(-\Delta H^\circ/kT) \quad [20]$$

All of the above electrical conductivity models contain parameters that are proportional to the electronic mobility and to the mass action constants corresponding to particular defect reactions. Thus, since the temperature dependence of the electronic mobility has been determined (15), the standard enthalpy of formation of the defect reaction can be determined from the temperature dependence of the corresponding parameter.

Experimental

Specimen preparation.—The conductivity specimens were prepared by cold pressing and sintering CeO_2 powder obtained from the American Potash and Chemical Company (12, 16). Specimens 1 and 2 were made from 99.999%[4] and specimen 3 from 99.9999%[4] minimum purity CeO_2 powder. The results of a mass spectrographic analysis of a sintered specimen prepared from 99.999% type CeO_2 powder is shown in Table I.

The electrical conductivity measurements of $Ce_{1+y}O_2$ as a function of P_{O_2} in the temperature range 800°-1500°C were made in a molybdenum wound resistance furnace. A standard four-probe d-c technique was employed for the electrical conductivity measurements. The experimental apparatus employed was essentially the same as that described in an earlier publication (18).

Oxygen partial pressures were achieved by means of two methods. For pressures from 1 to 10^{-4} atm, premixed and analyzed O_2-Ar mixtures at 1 atm total pressure were used in the study. Controlled oxygen partial pressures in the low-pressure region were obtained by introducing known mixtures of CO and CO_2 at 1 atm total pressure. The well-known free energy values for the CO/CO_2 reaction were then used to calculate the oxygen partial pressure. A linear flow rate of 0.9 cm/sec was maintained for all gas mixtures used in this investigation to avoid errors arising from thermal diffusion (19). Isothermal electrical conductivity measurements at 100° intervals between 800° and 1500°C were made for both increasing and decreasing partial pressures of oxygen. Since the composition of $Ce_{1+y}O_2$ has a unique equilibrium value for each oxygen partial pressure and temperature, the above

[4] Purity designation with respect to rare earth impurities only.

Table I. Mass spectrographic analysis of a typical sintered specimen of CeO_2 (ppmw)

Element		Element	
Li	0.3	Ag	≦0.2
Be	<0.01	Cd	<0.2
B	≦7.0	In	<0.1
F	20.0	Sn	0.2
Na	15.0	Sb	<0.2
Mg	2.0	Te	<0.3
Al	15.0	I	<0.1
Si	20.0	Cs	<0.06
P	2.0	Ba	<1.0
S	7.0	La	<0.5
Cl	10.0	Ce	—
K	15.0	Pr	10.0
Ca	300.0	Nd	10.0
Sc	<0.1	Sm	<1.0
Ti	2.0	Eu	10.0
V	≦0.03	Gd	<5.0
Cr	0.2	Tb	2.0
Mn	0.2	Dy	1.0
Fe	6.0	Ho	≦0.3
Co	0.4	Er	≦0.5
Ni	20.0	Tm	<0.1
Cu	0.2	Yb	≦1.0
Zn	1.0	Lu	≦0.3
Ga		Hf	2.0
Ge	<0.2	Ta	≦3.0
As	<0.02	W	<0.2
Se	<0.4	Re	<0.3
Br	<0.3	Os	<1.0
Rb	<1.0	Ir	<0.2
Sr	0.2	Pt	<0.4
Y	0.5	Au	<0.4
Zr	10.0	Hg	<0.4
Nb	<0.02	Tl	<0.2
Mo	<0.07	Pb	1.0
Ru	<0.1	Bi	<0.1
Rh	<0.02	Th	50.0
Pd	<0.2	U	<0.06

procedure insures the measurement of equilibrium values of the conductivity, because the equilibrium state was approached from both higher and lower compositions of oxygen.

Results and Discussion

The electrical conductivity of sintered specimens of $Ce_{1+y}O_2$ was measured isothermally at 100° intervals between 800°-1500°C and from 1 to 10^{-21} atm of oxygen. The results of the conductivity measurements for specimen 1 (83% theoretical density) from 800° to 1100°C and specimen 2 (85% theoretical density) from 1200° to 1500°C are shown in Fig. 2. A check of the absolute magnitude of the conductivity of each specimen was performed at 1100°C and good agreement was observed over the entire oxygen pressure region investigated. The results of the conductivity measurements on specimen 3 (70% theoretical density) are shown in Fig. 3.

The values of m calculated from Eq. [1] depend on both the temperature and the partial pressure of oxygen. Thus, for the purpose of convenience of discussion, the conductivity data are divided into four regions as shown in Fig. 2 and 3.

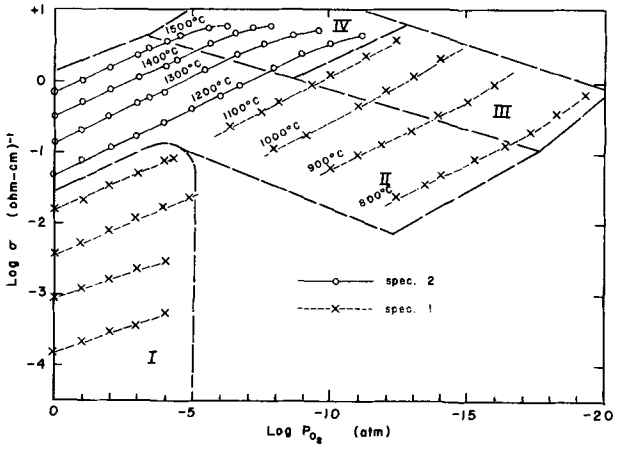

Fig. 2. Isothermal relation between the electrical conductivity of $Ce_{1+y}O_2$ and oxygen partial pressure for sintered specimens 1 and 2.

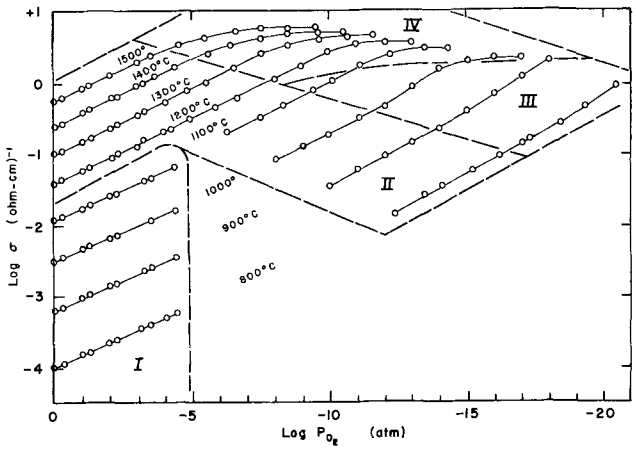

Fig. 3. Isothermal relation between the electrical conductivity of sintered $Ce_{1+y}O_2$ and oxygen partial pressure for specimen 3.

A qualitative explanation of the observed electrical conductivity data in terms of the four regions of m is described as follows:

1. The values of m in region I decrease from about 7.5 to 5.4 with increasing temperature as shown in Fig. 2. This can be interpreted in terms of the decreasing influence of impurities on the conduction process with increasing temperature. In Fig. 3, the values of m vary differently from Fig. 2, probably because the type and concentration of impurities were different.

2. In region II between 800° and 1100°C, m was approximately equal to 5. Above 1100°C, m increases to 5.3 at 1500°C. This region may be characterized by a predominance of quadruply ionized cerium interstitials or a combination of singly and doubly ionized oxygen vacancies.

3. In region III, m is approaching a value of 4. This can be interpreted as a defect model involving primarily either triply ionized cerium interstitials or singly ionized oxygen vacancies (18).

4. In region IV, the conductivity appears to be relatively insensitive to oxygen pressure. Blumenthal and Laubach (12) have qualitatively interpreted this insensitivity as due to degenerate behavior of the electron because of the large concentration of electronic defects. Another possible explanation for this behavior is that $Ce_{1+y}O_2$ exhibits a large departure from stoichiometry (6, 20). Thus, the assumption of unit activity for the cerium and oxygen atoms on normal lattice sites and the unoccupied interstitial sites may no longer be valid.

In order to obtain a quantitative explanation of the oxygen partial pressure dependence of the conductivity, the various equations corresponding to the aforementioned defect models were tested with a nonlinear curve fitting technique using a digital computer. Since region I was interpreted as an impurity controlled region, no attempt was made to analyze this region in terms of nonstoichiometric defect models.

A defect model involving quadruply ionized cerium interstitials

$$\sigma = EP_{O_2}{}^{-1/5} \qquad [1]$$

was tested using the conductivity data in region II. Below 1000°C, the result was in good agreement with the experimental data. Above 1100°C, this model did not provide a good fit of the data because the value of m in Eq. [1] is 5, whereas the value of m calculated from the data was greater than 5.

A curve fit of the conductivity data in regions II and III ($4 \leq m \leq 5$) was then attempted using each of the following equations which represent nonstoichiometric defect models involving defects with two states of ionization

$$\sigma^5 = (D\sigma + E)P_{O_2}{}^{-1} \qquad [2]$$

for triply and quadruply ionized cerium interstitials

and

$$\sigma^3 = (A\sigma + B)P_{O_2}^{-1/2} \quad [3]$$

for singly and doubly ionized oxygen vacancies. A good fit of the conductivity data was obtained for Eq. [2] or [3] at low temperatures (below 1100°C for specimen 1 and below 1000°C for specimen 3).

It is interesting to note that region III decreases in size with increasing temperature and does not appear to exist above 1200°C. Equation [2] does not provide a good fit of the conductivity data for region II above 1200°C because the maximum value of m is 5, whereas the value of m calculated from the experimental data was greater than 5. Equation 3, however, does provide a good fit of the conductivity data in this region because the value of m may vary between 4 and 6.

Although the singly and doubly ionized oxygen vacancy model provides a good curve fit of the conductivity data in regions II and III, it does not fit the data in region IV. The values of m calculated from the experimental data in region IV are greater than the maximum value of 6 allowed by Eq. [3] and increase with decreasing P_{O_2}.

On the basis of the thermogravimetric studies of $Ce_{1+y}O_2$ by Bevan and Kordis (6) and Balser (20), region IV corresponds to a region where the departure from stoichiometry is large (*i.e.*, $y > 0.02$). An attempt was made to analyze the conductivity data in regions II and IV between 1200° and 1500°C using Eq. [11], [13], [14], and [15]. These equations represent nonstoichiometric defect reactions where the departure from stoichiometry is large and account for the dependence of the activity for the cerium and oxygen atoms on the normal occupied lattice sites and vacant interstitial sites on defect concentration. All of the conductivity data in regions II and IV between 1200° and 1500°C, except the data points where the conductivity was independent of oxygen pressure, were analyzed for specimens 2 and 3. Only Eq. [11], which is based on a defect model involving a predominance of quadruply ionized cerium interstitials, provided a good fit of the conductivity data. The curve fit of Eq. [11] is shown in Fig. 4 where log σ is plotted as a function of log P_{O_2} for specimen 3.

The question arises whether a defect model with a predominance of triply ionized cerium interstitials and with values of the parameter α and β less than one would also fit the conductivity data in these regions. This possibility may be eliminated for the following reason. In region II below 1200°C the departure from stoichiometry is small. Thus the curve fit of any of the aforementioned defect models is independent of the values used for α and β. The only interstitial defect model which fits these data is one involving a predominance of quadruply ionized cerium interstitials. The same argument applies for most of the data in region II above 1200°C

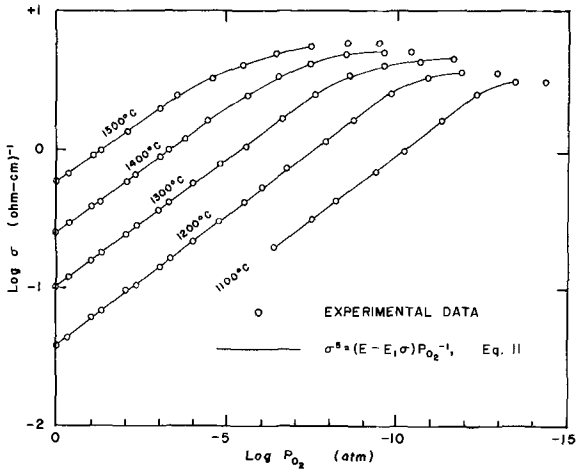

Fig. 4. A comparison of the curve fit of the quadruply ionized cerium interstitial model (Eq. [11]) with the experimental conductivity data as a function of oxygen partial pressure for specimen 3.

It should be noted, however, that in region IV where large departures from stoichiometry are encountered the possibility may exist that the concentration of triply ionized cerium interstitials is significant. The presence of triply ionized cerium interstitials should have the effect of increasing the dependence of the conductivity on the oxygen pressure (*i.e.*, a steeper slope should be observed such as shown in region III). This effect, however, may be masked in region IV for the following reasons:

(*a*) For large departures from stoichiometry, the decrease of available sites coupled with interactions described by α and β has the effect of decreasing the dependence of the conductivity on oxygen pressure.

(*b*) The electronic mobility which is a hopping type conduction process (15) should decrease with increasing defect concentration; *i.e.*, the concentration of normal cerium sites available for electron occupation, $[Ce_{Ce}]$, decreases with increasing departure from stoichiometry. To a first-order approximation, the compositional dependence of the mobility may be written as

$$\mu \propto \{1 - 4y - 6(1 - \alpha)y\} \quad [21]$$

Thus, in order to obtain a more comprehensive analysis of the conductivity than the analysis presented here, the following would be required:

(*a*) Eliminate the linear approximation used for the denominator in Eq. [11].

(*b*) Allow the parameters α and β to vary between 0 and 1.

(*c*) Allow the atomic defect to exist in more than one state of ionization when the departure from stoichiometry is large.

(*d*) Consider the compositional dependence of the electronic mobility. However, the results of such an analysis would be questionable until more information is obtained concerning both the nature of the nonstoichiometric defects and the compositional dependence of the electron mobility at large departures from stoichiometry.

In summation, based on the analysis of the conductivity presented here, the only defect model which is consistent with the experimental data over a wide range of temperature oxygen partial pressures is a nonstoichiometric defect structure involving triply and quadruply ionized cerium interstitials and localized electrons.

The standard enthalpy of formation for the nonstoichiometric defect reaction corresponding to the defect reactions can be calculated as discussed under Theory. For the defect reaction

$$V_i + 5Ce_{Ce} + 2\,O_o = Ce_i^{\cdots\cdot} + 4Ce'_{Ce} + O_2(g) \quad [4]$$

$\Delta H_a^\circ = 10.3 \pm 0.3$ eV was calculated using Eq. [2], [11], and [20] and the temperature dependence of E, which is shown in Fig. 5 for specimens 1 and 2 as log E *vs.* $1/T$. A correction has been made for the experimental activation energy of the mobility (15). The tolerance quoted is based on a 95% confidence limit corresponding to the over-all temperature dependence of E. Good agreement was obtained for the value of $\Delta H_a^\circ = 10.5 \pm 0.3$ eV calculated for specimen 3.

The values of E shown in Fig. 5 correspond to two different equations. Equation [2] was used to analyze the conductivity data in regions II and III between 800° and 1100°C. Between 1200° and 1500°C, Eq. [11] was used where only regions II and IV were observed. Since the values of E in Fig. 5 lie on essentially the same straight line, it appears that Eq. [2] and [11] are consistent with the assumed defect model.

In a similar manner, the standard enthalpy of formation, ΔH_b°, for the defect reaction

$$V_i + 4Ce_{Ce} + 2\,O_o = Ce_i^{\cdots\cdot} + 3Ce'_{Ce} + O_2(g) \quad [22]$$

was found to be equal to 8.4 and 8.6 eV for specimens

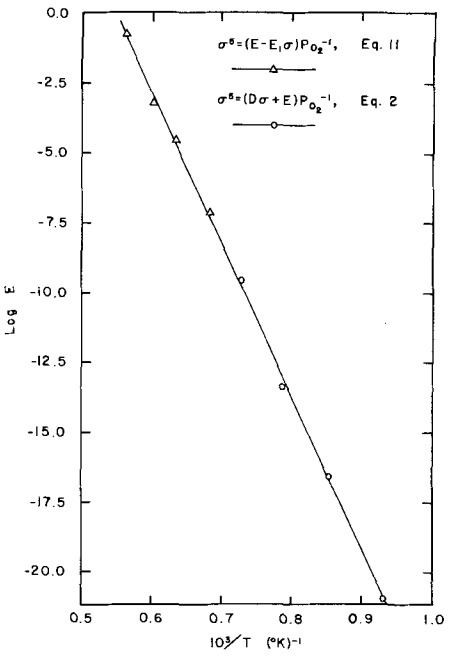

Fig. 5. A plot of the logarithm of E vs. $1/T$ for specimens 1 and 2 in the temperature range 800°-1500°C.

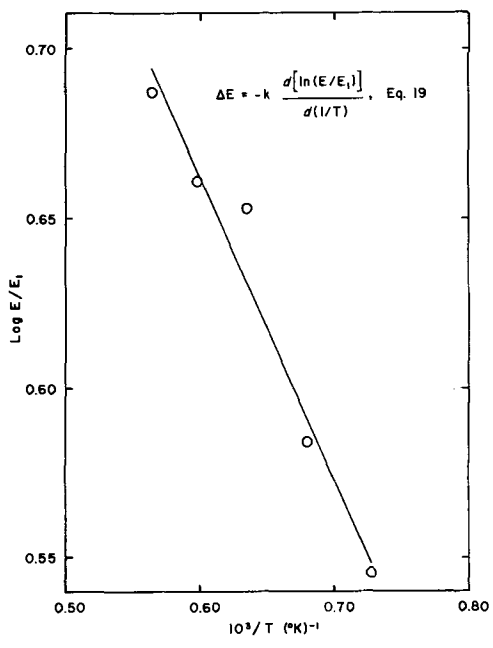

Fig. 7. A plot of the logarithm of E/E_1 vs. $1/T$ for specimen 3 in the temperature range 1100°-1500°C.

1 and 3, respectively. This result was obtained from the temperature dependence of D which is shown in Fig. 6 as log D vs. $1/T$ and correcting for the temperature dependence of the mobility. A calculation of tolerance is not meaningful in this case because of the relatively small number of data points.

Therefore, the standard enthalpy for the defect reaction

$$Ce_{Ce} + Ce_i^{\cdots} = Ce_i^{\cdots\cdot} + Ce'_{Ce}; \quad \Delta H_c^o = 1.9\ eV \quad [23]$$

calculated from the relation

$$\Delta H_c^o = \Delta H_a^o - \Delta H_b^o \quad [24]$$

should be regarded as an approximate value.

It is interesting to note that the differences in standard enthalpy of formation of the defect reactions for specimens 2 and 3 were in agreement within 4% even though the densities of these specimens differed by more than 20%. Thus it appears that, although the measured value of the conductivity depends on the density, the calculated values of the enthalpy of formation of the defect reaction are relatively insensitive to density.

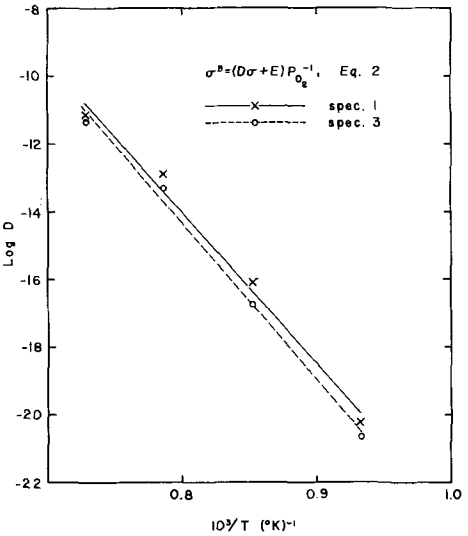

Fig. 6. A plot of the logarithm of D vs. $1/T$ in the temperature range 800°-1100°C for specimens 1 and 3.

Kofstad and Hed (13) have interpreted the thermodynamic data of Bevan and Kordis (6) in terms of a defect structure involving singly and doubly ionized cerium interstitials. Most of the data obtained by Bevan and Kordis were at temperatures and oxygen pressures lower than the conductivity data in this investigation. However, in the region that does overlap (*i.e.*, region III below 1100°C), we have interpreted the predominant defect reaction as involving triply ionized cerium interstitials rather than doubly ionized cerium interstitials as Kofstad and Hed have.

It is interesting to note, however, that ΔH_b^o is approximately equal to the value of $\Delta H_1 = 7.9$ eV calculated by Kofstad and Hed for the defect reaction corresponding to the formation of doubly ionized cerium interstitials.

A thermodynamic study of the composition of cerium dioxide over larger oxygen pressure and temperature regions is currently in progress in this laboratory to independently test the validity of the defect model proposed in this investigation.

Since the conductivity data were obtained using sintered specimens and accurate thermodynamic data over the entire oxygen pressure region were not available, an accurate determination of the absolute magnitude of the mobility could not be obtained. However, since the electronic conduction mechanism is a "hopping type" mechanism (15), the experimental activation, ΔE, may be obtained from the temperature dependence of the ratio, E/E_1, if Eq. [11] is valid. $\Delta E = 0.18$ eV was calculated from Eq. [19] and the slope of the line shown in Fig. 7 where log E/E_1 is plotted as a function of $1/T$. Although this result is in good agreement with the recently reported value, $\Delta E = 0.14$ eV (15), it nevertheless may be fortuitous. The exact interpretation of the parameter E_1 depends on the validity of Eq. [11] at relatively large departures from stoichiometry. And, as previously mentioned, this would be difficult to ascertain from this type of analysis.

Manuscript submitted May 16, 1969; revised manuscript received Aug. 25, 1970.

Any discussion of this paper will appear in a Discussion Section to be published in the December 1971 JOURNAL.

REFERENCES

1. G. Brauer and H. Gradinger, Z. *Anorg. Allgem. Chem.*, **277**, 89 (1954).
2. D. J. M. Bevan, *J. Inorg. Nucl. Chem.*, **1**, 49 (1955).

3. G. Brauer, K. A. Gingerich, and U. Holtzschmidt, *J. Inorg. Nucl. Chem.*, **16**, 77 (1960)
4. G. Brauer and K. A. Gingerich, *ibid.*, **16**, 87 (1960).
5. F. A. Kuznetsov, V. I. Beliy, and T. N. Rezukhina, *Doklady Akad. Nauk SSR, Fiz-Khim.*, **139**, No. 6, 1405 (1961).
6. D. J. M. Bevan and J. Kordis, *J. Inorg. Nucl. Chem.*, **26**, 1509 (1964).
7. J. Rudolph, *Z. Naturforsch.*, **14**, 727 (1959).
8. E. H. Greener, J. M. Wimmer, and W. M. Hirthe, "Rare Earth Research II," Edited by Karl S. Vorres, p. 539, Gordon and Breach, New York (1964).
9. C. J. Kevane, *Phys. Rev.*, **133**, A1431 (1964).
10. C. J. Kevane, E. L. Holverson, and James B. Armstrong, Paper presented at the Fifth Rare Earth Research Conference, Ames, Iowa, Aug. 1965.
11. I. V. Vinokurov, Z. N. Zonn, and V. A. Ioffe, *Soviet Phys.-Solid State (English Transl.)*, **9**, 2659 (1968).
12. R. N. Blumenthal and J. E. Laubach, "Anisotropy in Single-Crystal Refractory Compounds," Vol. 2, p. 137, Plenum Press, New York (1968).
13. P. Kofstad and A. Z. Hed, *J. Am. Ceram. Soc.*, **50**, 681 (1967).
14. Leon M. Atlas, *J. Phys. Chem. Solids*, **29**, 91 (1968).
15. R. N. Blumenthal and R. J. Panlener, *ibid.*, **31**, 1190 (1970).
16. P. Lee, M.S. Thesis, Marquette University, Milwaukee, Wis. (1968).
17. R. N. Blumenthal, Atomic Energy Commission, Technical Progress Report, COO-1441-1.
18. R. N. Blumenthal, J. Coburn, J. Baukus, and W. M. Hirthe, *J. Phys. Chem. Solids*, **27**, 643 (1966).
19. L. S. Darken and R. W. Gurry, *J. Am. Chem. Soc.*, **67**, 1398 (1945).
20. J. D. Balser, M.S. Thesis, Marquette University, Milwaukee, Wis. (1967).

The Effects of Epoxy Encapsulant Composition on Semiconductor Device Stability

R. C. Olberg*

Research and Development Laboratory,
Fairchild Camera and Instrument Corporation, Palo Alto, California 94304

ABSTRACT

This paper describes the effects of various ingredients in an epoxy resin formulation on the electrical stability of encapsulated transistors with only thermal oxide passivation. The type and level of ionic impurities and/or polar contaminants in a completely formulated epoxy resin, which affect the electrical characteristics of transistors, are discussed with specific reference to the nature of the epoxy, hardener, promoter, filler, and other ingredients used. Although the study was directed toward the development of improved epoxy resins for semiconductor applications, the principles involved are applicable to other organic or inorganic dielectric materials.

A plastic material suitable for encapsulation of semiconductors must perform many functions: It must provide protection against the ambient to which the device is likely to be exposed (*e.g.*, high humidity and various chemical agents), as well as wide temperature fluctuations and mechanical shock. It must provide such protection with a minimum of effect on device parameters over an extended period of time, and be relatively inexpensive and easy to process.

Although many thermosetting resins have been evaluated for this application, only epoxies, silicones, and phenolics have been used extensively. Initially, the resins chosen were formulated to meet the requirements of other end uses. Hence, proper care in the selection of raw ingredients by the formulator was not considered. As a consequence, semiconductor devices encapsulated in these resins exhibited poor reliability, and producers and consumers of semiconductor devices alike concluded that plastic packaging was synonymous with poor reliability. However, over the past few years, the resin suppliers have improved the electrical properties of their resins to the point where plastic packaged integrated circuits and discrete devices are presently exhibiting a reliability approaching that of the so-called hermetically packaged devices under most ambient conditions.

Little has been published concerning the effect of the composition of encapsulating resins on the electrical parameters of the devices. Lee, Licari, and Valles (1) reported the adverse effects of ammonia in phenolic molding powders. The ammonia originates from the decomposition of hexamethylene tetramine used as the cross-linking agent. They further disclosed a correlation between the elevated temperature resistivities of various coating materials with the performance of these materials as encapsulants. Licari and Browning (2) disclosed the dependence of stoichiometry and purity of the ingredients in an epoxy resin on the reverse current leakage of microdiodes at elevated temperatures, but did not identify the ingredients most responsible for the observed results.

In the present work we have attempted to identify those ingredients and/or impurities in a formulated epoxy resin that are most responsible for the degradation of the electrical stability of thermal oxide passivated semiconductor devices.

Factors Influencing Reliability of an Epoxy Resin

The reliability of an epoxy resin for semiconductor use is dependent upon its composition which, in turn, is directly related to the bulk electrical and physical properties of the cured resin. Therefore, in formulating an epoxy for semiconductor use, our main concern is the nature and purity of the epoxy resin, hardener, promoter, and other ingredients in the formulation, the ratio of reactants employed, the polarity of the ingredients, the concentration and type of ionic contaminants, and the completeness of the cure. All these affect the electrical and physical properties. Although many of these properties are interrelated, the specific properties of interest are listed separately, as follows.

Electrical properties:

Stability of transistor under high-temperature reverse bias due to electrical characteristics of the epoxy[1]
Volume resistivity at elevated temperature
Dielectric constant and dissipation factor
Conductance of aqueous extract of cured epoxy

* Electrochemical Society Active Member.
Key words: epoxy ingredient effect on semiconductors.

[1] Used principally in this paper for evaluation of various epoxy formulations.

Physical properties:

Moisture absorption and permeation
Adhesion
Thermal expansion
Thermal conductivity
Heat distortion temperature: second-order transition temperature
Tensile-elongation
Viscosity-flow
Cure shrinkage
Thermal stability
Cosmetic appearance

Epoxy resins.—Although there are literally dozens of epoxy resins available commercially, those in widest use in casting and molding formulations are diglycidyl ethers of bisphenol-A (BPA resins), epoxy novolacs, and aliphatic or cycloaliphatic epoxy resins. Examples of these are shown in Fig. 1. The BPA resins are most common and least expensive. The value of n is low, approaching zero for the low viscosity grades, and one for the more viscous grades. When n is greater than one, the resins are brittle solids. The epoxy novolac resins also vary from highly viscous liquids to brittle solids, but have a functionality greater than two. Because of this, they are used frequently where high-temperature properties are required. The aliphatics or cycloaliphatics made by the peracetic acid oxidation of the corresponding olefins are usually low in viscosity; for this reason they are frequently used as reactive diluents and have outstanding electrical properties and tracking resistance. Their bulk physical properties normally are not as outstanding as the BPA or epoxy novolac resins.

Hardeners.—Polyfunctional aliphatic amines, di- or polyfunctional anhydrides, and Lewis acids or bases are among the most common hardeners used for curing epoxy resins. However, the anhydrides are preferred for semiconductor application since they give better high-temperature and electrical properties than amine cured systems.

A large number of anhydrides are available, ranging from low viscosity liquids to high melting solids. Frequently, mixtures are used to tailor properties for a specific end use. Examples of some typical anhydride hardeners include dodecenylsuccinic anhydride, which is a liquid; hexahydrophthalic anhydride, which is a low melting solid; and phthalic anhydride and benzoylphenone tetracarboxylic dianhydride, which are high melting solids. Structures are shown in Fig. 2.

Promoters.—Although the more highly functional anhydrides produce cured resins without the use of promoters, most require tertiary amines or metal-

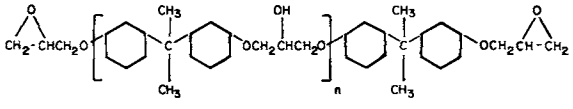

Diglycidyl ether from epichlorohydrin and bisphenol A (BPA Resins)
Simplest and purest member obtained when n = o (distilled product).

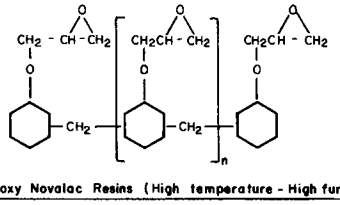

Epoxy Novolac Resins (High temperature - High functionality)

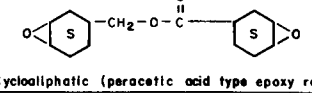

Cycloaliphatic (peracetic acid type epoxy resin)

Fig. 1. Typical epoxy resins

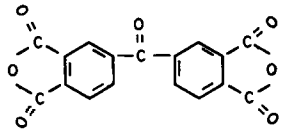

Sym. Benzoylphenone-tetracarboxylic acid dianhydride (BTDA)

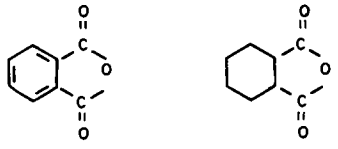

Phthalic Anhydride (PA) Hexahydrophthalic Anhyride (HHPA)

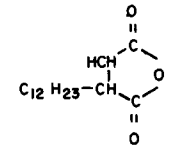

Dodecenyl Succinic Anhyride (DDSA)

Fig. 2. Typical anhydride hardeners

organic salts to promote the cure. The stoichiometry of the reactants is greatly affected by the nature of the promoter, and the effectiveness of various promoters is likewise associated with the type of epoxy and hardener employed.

Fillers.—Since fillers frequently comprise a high proportion of the total epoxy resin formulation, they exert a major influence on the final properties. Those most commonly used in epoxies for semiconductor application include silica, alumina, barium sulfate, and antimony oxide. The latter, when used in conjunction with a bromine substituted epoxy, confers flame-proofing properties to the epoxy. Fillers are used to modify the physical properties of the epoxy. They lower the cure shrinkage, the exotherm, and the thermal expansion coefficient of an epoxy formulation; they raise the thermal conductivity and the viscosity; and they act as reinforcing agents, particularly those in fiber form. The hydrated silicas are frequently employed to confer thixotropic properties to the formulation. Fillers also affect the electrical properties of the formulated epoxy. Ionic contamination and polar or polarizable groups in the filler contribute to a lowering of the electrical stability of the resin, particularly under high humidity and/or under electrical bias.

Other ingredients.—Other ingredients that may be present in a formulated epoxy resin included reactive diluents, plasticizers or flexibilizers, pigments, flow control agents, and mold release agents. A single formulation will seldom contain all of the above secondary ingredients. The end use determines the number needed in addition to those discussed above. Although a mold release agent is necessary in a molding powder formulation to aid in the release of the device from the mold, normally it is not used in a casting formulation.

Although the present investigation does not include an evaluation of the other ingredients, the conclusions regarding their nature and purity are applicable.

Experimental Procedures

npn Transistors (Fairchild TXB-1250 HB) packaged in standard TO-18 metal cans were used for evaluating the various casting resins. After removal of the metal tops from the cans, the resins were cast into the cavity and cured. The low heat distortion temperature formulations were cured for 2 hr at 90°C and 22 hr at

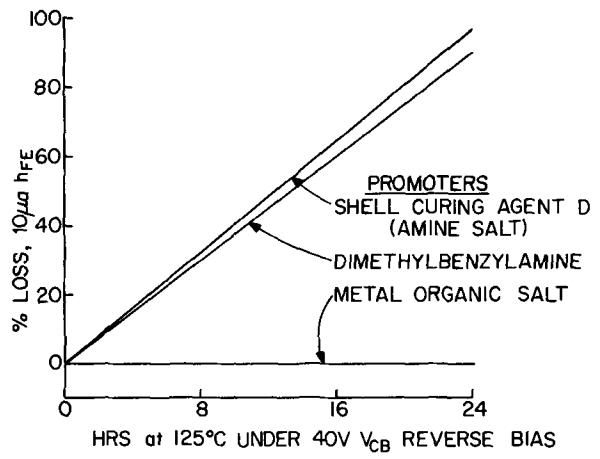

Fig. 3. Influence of the chemical nature of the promoter in an epoxy resin on the electrical stability of the encapsulated device.

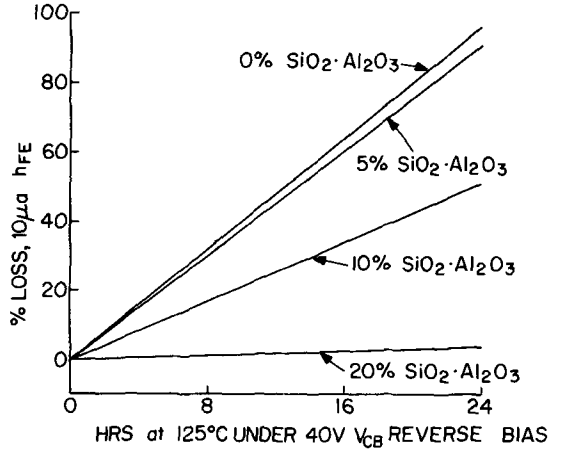

Fig. 4. Use of an acidic filler to neutralize the deleterious effect of an amine promoter.

150°C; the high heat distortion temperature formulations were cured at 175°C for 16 hr, and in some cases, followed by 200°C for up to 4 hr.

A Fairchild tester, Model 500, was used to determine the following electrical parameters of the encapsulated devices: I_{CBO} at 25V; I_{EBO} at 4V; I_{CEO} at 10V; BV_{CBO} at 10 μA; BV_{EBO} at 10 μA; BV_{CES} at 500 μA and 2 mA; $V_{CE,SAT}$ 1/0.1; and h_{FE} at 10V and 10 μA, 500 μA, and 10 mA. After the initial readout the units were subjected to 40V reverse bias at 125°C or 150°C with periodic readouts for up to 1000 hr. In each case, the units were cooled to room temperature under bias before the readout. Normally, 10 to 30 units were employed with each casting resin.

Of the above electrical parameters, the 10 μA beta was found to be the most sensitive to compositional variations in the encapsulant. Therefore, in this investigation the average loss in beta under reverse bias was used for comparing the stability of various epoxy formulations. However, increases in leakage currents could have been used and would have led to similar conclusions. Catastrophic failures due to shorts and opens under stressing were also noted.

The flatband voltage shift, at various current densities under reverse bias and at elevated temperatures, on a gate-controlled npn test device was also used in one instance for screening epoxies.

Results and Discussion

Effect of promoters.—As mentioned previously, when an anhydride is used to cure an epoxy resin, the reaction usually requires a promoter. Anhydride-cured epoxies are preferred for semiconductor application because of their superior electrical properties. Tertiary amines, tertiary amine salts, or metal-organic salts are commonly used to promote the reaction. Figure 3 compares the low current beta stability of transistors encapsulated in epoxy formulations utilizing the various promoters when subjected to 40V V_{CB} reverse bias at 125°C. The epoxy resin (DER 332)[2] and anhydride hardener (hexahydrophtalic anhydride, *HHPA*)[3] used were common to each formulation. Both the amine (dimethylbenzylamine) and amine salt (Shell curing agent D)[4] promoted epoxies caused over 90% loss in the 10 μA h_{FE} in 24 hr, while the metal-organic salt (DB VIII)[5] caused essentially no change in beta under the same conditions. No fillers were incorporated in these formulations.

Further evidence for the effect on device stability of the nature of the promoter used in an epoxy composition was obtained by the following flatband voltage shift of encapsulated gate-controlled npn test devices under high-temperature reverse bias (HTRB) at 125°C for 200 hr. The amine promoted epoxy formulation gave ΔV_{FB} of 25V compared to 9V for the metal-organic salt promoted formulation. The latter was similar to that of the metal can control device.

Effect of fillers.—The mechanism by which amines and other polar organic ingredients cause loss in beta under high temperature reverse bias is not fully understood. It appears to be a surface effect (3, 4). The extent of the degradation increases with time under bias. This suggests migration of polar groups to the surface of the device and alignment of polarizable groups in an electric field. When the field is removed at elevated temperatures, a random thermal scattering of the polar groups leads to partial recovery of beta, but the recovery is not complete. If the polar groups are alkali metal ions that can diffuse through the oxide, the effect is not reversible. Furthermore, the alkali content of the tertiary amine promoters is as low or lower than that in the epoxy resins (~1 ppm), and represents a minor portion of the over-all formulation. In order to gain further insight into the degradative mechanism, 5-20% filler containing Lewis acid sites (silica-alumina cracking catalyst) was added to the above formulation promoted with N, N-dimethylbenzylamine. The results, illustrated in Fig. 4, support the view that when the amine promoter is immobilized by the acidic filler, the stability of the epoxy on the surface of the transistor is indeed improved. Further, it was observed that the presence of the acidic filler had no effect on the rate and extent of the cure of the epoxy resin; the amine promoter was just as effective in the presence of the acidic filler.

Although fillers can improve stability by adsorption of polar impurities from the resin, they can also degrade the stability of the resin. An example is Minusil 10,[6] a 10μ precipitated silica. Formulated resins containing 50% by weight of untreated Minusil 10 silica cause rapid loss in low current beta under HTRB at 125°C. However, if the silica is first washed thoroughly with hot deionized water, the stability of the formulated resin is equivalent to that of resins containing naturally occurring sand filler (Clemcosil 325 mesh silica).[7] This is illustrated in Fig. 5.

The conductivity of the water extract is indicative of the soluble salts removed from the filler during washing; that from Minusil 10 was 1.7×10^{-3} *vs.* 6.4×10^{-4} mhos/cc from Clemcosil. The residue recovered during evaporation of the water extract from Minusil 10 was double that obtained from the Clemcosil silica, in agreement with the higher conductivity observed. However, the compositions of the two residues were quite similar; they consisted mainly of alkali and alkaline earth metals. Whether or not this similarity extends to the nature of the original soluble salts extracted from each silica is unknown. Qualitatively, we

[2] Dow Epoxy Resin 332, Dow Chemical Company, Midland, Michigan.
[3] Allied Chemical Corporation, Plastics Division, Morristown, N. J.
[4] Shell Chemical Company, Plastics and Resins Division, New York, N. Y.
[5] A proprietary salt obtained from Argus Chemical Co., Brooklyn, N. Y.
[6] Pennsylvania Glass Sand Corporation, Pittsburgh, Pa.
[7] Clementina Sand Company.

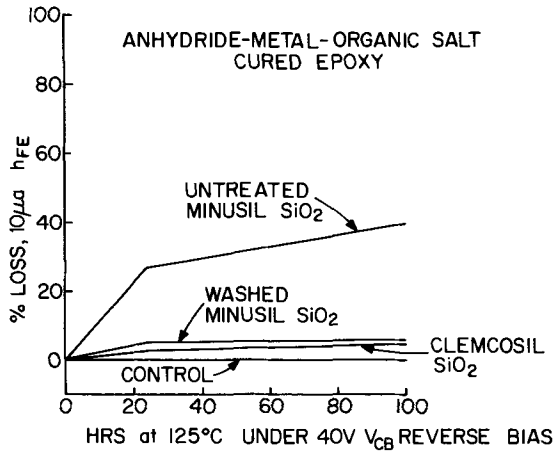

Fig. 5. The effect of adsorbed soluble salts in silica fillers incorporated in epoxy resins on the electrical stability of the encapsulated device.

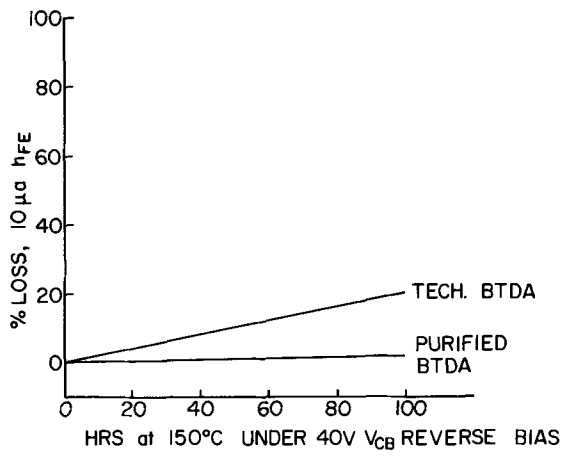

Fig. 7. The effect of the purity of the anhydride hardener component in an epoxy resin on the electrical stability of the encapsulated device.

observed that a heavy precipitate of silver halide resulted from the addition of silver nitrate to the aqueous extract from Minusil 10, while only a trace of precipitate was observed with the Clemcosil extract, which suggests a higher concentration of halide anion in the Minusil 10 silica.

Effect of epoxy resin purity.—The low hydrolyzable chloride, DER 332LC epoxy resin, is more stable than the less pure DER 332 resin, although the difference in the stability is not marked; a higher temperature is required to distinguish between them. The improvement in the stability is not traceable to lower sodium content, since the flame spectral analysis indicated 1 ppm sodium in the DER 332LC resin *vs.* 0.8 ppm in the DER 332 resin. This is illustrated in Fig. 6

Effect of anhydride purity.—The purity of the anhydride hardener likewise affects the electrical stability of the resin as shown in Fig. 7. Tetrafunctional benzophenone tetracarboxylic dianhydride (BTDA)[8] was employed in this study because the reactivity associated with high functionality precluded the use of promoters, thereby making the results less ambiguous. It was further demonstrated that the very high-temperature properties attainable in these highly cross-linked epoxy systems correlate with electrical stability on the surface of a transistor.

Effect of added impurities.—In order to determine the specific impurities that can lead to high failure rates, we undertook a study whereby certain polar organic compounds and inorganic salts were added to a stable, high-purity epoxy formulation (75 parts HHPA in 100 parts DER 332). The loss of 10 μA beta under HTRB at 125°C was followed as a function of time. The impurities selected were mainly ones that can arise either from the method of preparation or the initial purity of the ingredients from which the epoxy or anhydride is synthesized, or the source and purity of the filler and the nature of the promoter. Thus, the bisphenol A and epichlorohydrin impurities can arise from their incomplete reaction in the synthesis of the BPA epoxy resin. Glycidyl chlorohydrin can result from incomplete dehydrochlorination and sodium chloride from incomplete removal of the salt formed during the dehydrochlorination process. Certain alcoholic groups are formed during the curing reaction; glycols are sometimes used to accelerate cure. The results of this study are shown in Fig. 8 and 9.

[8] Obtained from Gulf Oil Corporation, Chemical Department, and purified by washing with dry acetone and dry isopropyl alcohol until filtrate is clear.

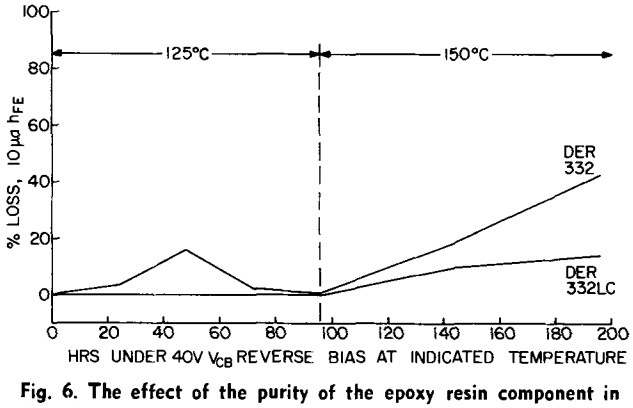

Fig. 6. The effect of the purity of the epoxy resin component in a formulated resin on the electrical stability of the encapsulated device.

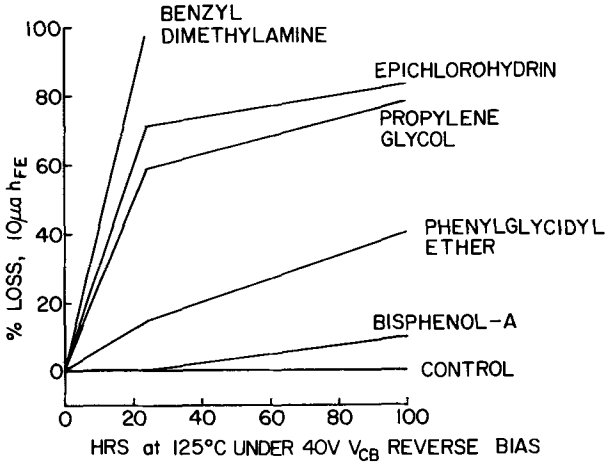

Fig. 8. The effect of various added organic impurities in an epoxy resin on the electrical stability of the encapsulated device.

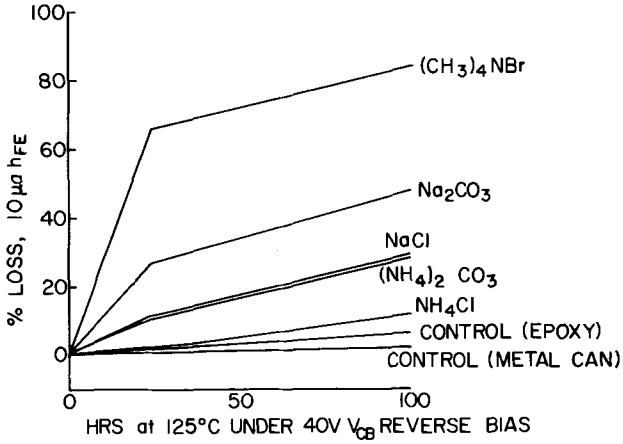

Fig. 9. The effect of various added inorganic impurities in an epoxy resin on the electrical stability of the encapsulated device.

An unfilled resin system was used for the organic contaminant study, since the compounds are completely soluble and therefore uniformly incorporated. They were added at a ratio of 1 part per 100 parts resin. However, because the volatility of epichlorohydrin required a lower gelation temperature to prevent excessive loss, it was run separately along with a control containing no contaminant. In spite of this, extensive volatilization occurred during the cure cycle. Following are the conclusions of this study:

1. The polar glycols and epichlorohydrin, which are capable of polarizing in an electric field, lead to extensive loss in low current beta.
2. The phenolic hydroxyls in bisphenol-A are more reactive and presumably are consumed during the cure; therefore, they cause very little loss in beta.
3. Phenylglycidylether is likewise consumed, but leads to partial loss in beta due to the excess epoxy groups which upset the stoichiometry and lower the heat distortion temperature.
4. The basic dimethylbenzylamine is the most deleterious ingredient added.
5. Volatile impurities such as epichlorohydrin can lead to degradation of uncontaminated units occupying the same cure oven. This was indicated by the excessive loss exhibited by control units compared to the epoxy control units run with the less volatile organic and inorganic contaminated devices. Apparently, epichlorohydrin vapor diffuses rapidly into the uncontaminated epoxy control units. This indicates a potential problem and the need for maintaining uncontaminated ovens.

With respect to the added inorganic contaminants, the following conclusions can be drawn:

1. The relative degradation effect exhibited may be more a reflection of the solubility than the nature of the impurity, since saturated solutions of the various salts in the epoxy resin were employed.
2. Although it is not shown in Fig. 9, sodium-containing impurities result in lower initial beta than the ammonium salts even though in some cases the loss in beta under HTRB is lower. This suggests that whenever the sodium ion contacts the surface of the device, rapid diffusion into the oxide occurs. On the other hand, the ammonium ion at the surface does not diffuse into the oxide; since the initial concentration is low, the effect is not seen until migration occurs under bias.

Conclusions

Both the polar organic groups and inorganic salts cause rapid degradation of the electrical parameters of devices in contact with them. The extent of degradation increases with time and temperature under bias. This suggests migration of the polar groups to the surface of the device and alignment of polarizable groups in an electric field. This is supported by the fact that the rate of degradation is increased by lowering the heat distortion temperature of the epoxy (lowering the cross-link density). Also, when the surface of the device is covered with a pure silicone, degradation will still occur with increased time, and the rate is still dependent on the level of contaminants in the epoxy external coating. Furthermore, as indicated previously, partial recovery of beta occurs on heating the devices in the absence of an electric field, presumably due to the random thermal scattering of polar groups.

The mechanism by which amines and other polar ingredients cause loss in beta is still undefined. The application of an image charge through the thermal oxide is one possibility. However, a thin film of silicon nitride over the oxide appears to give adequate protection. Another possibility is electron transfer. Experiments are under way to assess these hypotheses.

Acknowledgments

I wish to take this opportunity to express my deepest appreciation to Edward Martich who carried out most of the experimental work, to Eugene Held and Jose Rios who assisted with the electrical testing, and to Drs. Harry Sello and Bruce Deal whose encouragement and counsel have been invaluable.

Manuscript submitted April 22, 1970; revised manuscript received *ca.* Sept. 2, 1970. This was Paper 101 presented at the Detroit Meeting of the Society Oct. 5-9, 1969.

Any discussion of this paper will appear in a Discussion Section to be published in the December 1971 JOURNAL.

REFERENCES

1. J. J. Licari, S. M. Lee, and A. G. Valles, *Physics of Failure in Electronics*, **4**, 464 (1965), M. Goldberg and J. Vaccaro, Editors, RADC Series on Reliability (1966).
2. J. J. Licari and G. V. Browning, *Electronics*, **40**, 101 (1967).
3. G. A. Katsev, V. A. Presnov, E. N. Batueva, Y. G. Katsev, and L. A. Lyuze, V. V. Kuibyshev-State University, Tomsk, USSR, p. 151, from a compilation of translation of Russian papers entitled "Surface Properties of Semiconductors," A. N. Frumkin, Editor, Consultants Bureau (1964).
4. V. A. Presnov and L. L. Lyuze, *ibid.*, p. 156.

Phase Relationships in the In-S System

H. G. Ansell and R. S. Boorman

Materials Section, Research and Productivity Council, Fredericton, New Brunswick, Canada

ABSTRACT

Three binary compounds, In_2S_3, In_6S_7, and InS are stable in the In-S system. Solid solution was found only in In_2S_3, which contains up to 1.0 m/o (mole per cent) more indium than does stoichiometric In_2S_3. A rapid decrease in indium solubility, probably due to the inversion of tetragonal $In_{2+x}S_3$ to isometric symmetry, occurs at 837°C. A high-temperature form of InS may be present in the temperature range 657°-679°C. The compounds In_3S_4 and In_3S_5, noted in previous studies, were not found. The electrical properties of In_2S_3 are probably strongly affected by the deviation from stoichiometry as outlined in this study.

Although several studies have been made in the In-S system (1-3), parts of the phase diagram are ambiguous. The compound In_3S_4 is still considered a stable phase despite having been discredited (2), and several phase boundaries have not been closely investigated. As a result, during our work on ternary sulfide systems containing indium, we considered it necessary to re-examine portions of the In-S binary. These data were required both for our work on

Key words: indium sulfides, sulfides In system.

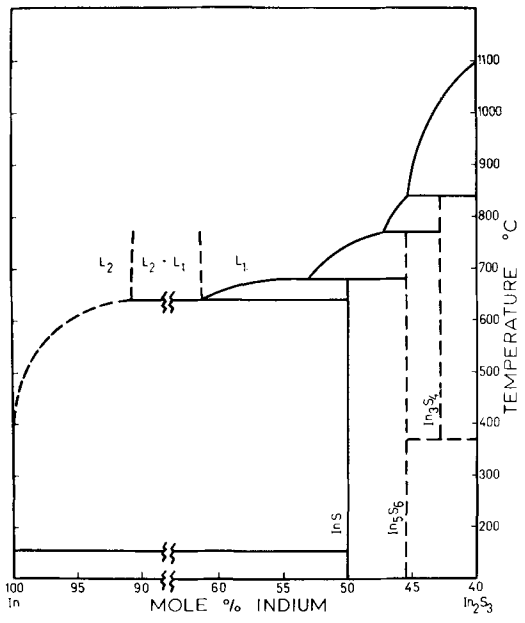

Fig. 1. Phase diagram of the In-In_2S_3 join, after Stubbs *et al.* (3).

natural systems containing indium and for materials application studies on indium sulfides.

Previous Work

Stubbs *et al.* (3) reported four indium sulfides, InS, In_5S_6, In_3S_4, and In_2S_3, to be stable between 150° and 1100°C (Fig. 1). The composition of In_5S_6 has since been shown to be In_6S_7 (5). Miller and Searcy (2) reported that the $InS_{1.12}$ (In_6S_7) phase had a solid solution field of 3.3 ± 0.4 a/o (atomic per cent) at 600°C which decreased to 0.8 ± 0.1 a/o at 664°C. Stubbs *et al.* (3) and Duffin and Hogg (1) were unable to synthesize In_3S_4. The possibility of it being present as an unquenchable phase has been discounted by Miller and Searcy (2). Zargarova and Gamidov (4) recently claimed to have synthesized In_3S_4 and a phase, In_3S_5, which is more sulfur-rich than In_2S_3 (Table I). Rooymans (6) has shown that the low-temperature In_2S_3 identified by Hahn and Klingler (7) is a poorly crystallized form of their high-temperature phase, rather than a distinct In_2S_3 polytype.

Experimental Procedure

Approximate phase boundaries were established from a series of furnace runs, the products of which were analyzed by x-ray diffraction. Starting mixtures were prepared from weighed amounts of indium metal (99.999+ %, ASARCO) and precipitated In_2S_3. Preparation of the In_2S_3 has been described previously (9).

All furnace charges were sealed in evacuated Vycor glass tubes and placed in electrically heated horizontal tube furnaces controlled to ±5°C. Runs were allowed to equilibrate over periods of 1-5 days. All charges were quenched to room temperature either in air or in cold water, and the products were examined under binocular and reflected light microscopes. An electron microprobe was used to determine the limits of solid solution fields.

Accurate delineation of phase boundaries was accomplished by differential thermal analysis. The work was carried out on a R. L. Stone Model 202 DTA system, using a platinum sample holder with post-type thermocouples. Two operative methods were used to ensure that no oxidation took place. In one series of runs, the sample was placed in platinum cups, the sample chamber was evacuated and then flooded with argon or nitrogen. With the second method, the sample was sealed under vacuum in specially prepared Vycor tubes. In each case, the sample was ground to −100 mesh and heated at a rate of 5°C/min.

Table I. Phases in the In-S system

Phase	Composition m/o In	Crystallography			Ref.
In_2S_3	40.0	Tetragonal,	$I4_1/amd$	$a = 7.623$Å $c = 32.36$	(6, 8)
In_6S_7	46.2	Monoclinic,	$P2_1/m$	$a = 9.090$Å $b = 3.887$ $c = 17.705$ $\beta = 108.20°$	(1, 5)
InS	50.0	Orthorhombic,	Pmnn	$a = 3.994$Å $b = 4.447$ $c = 10.648$	(1)
In_3S_4*	42.9	Hexagonal		$a = 9.86$Å $c = 20.5$	(4)
In_3S_5*	37.5	Hexagonal		$a = 7.59$Å $c = 20.3$	(4)

* Not confirmed by present study.

Results

No compounds other than In_2S_3, In_6S_7, and InS were synthesized (Fig. 2, Table II). In furnace runs containing more than 60 m/o sulfur, the only phases present in the charge tubes were In_2S_3, sulfur vapor, and condensed sulfur. The phase In_3S_5 described by Zargarova and Gamidov (4) was not found. No optical or x-ray evidence was found for the existence of In_3S_4 in the compositional range between In_6S_7 and In_2S_3.

All charge products were crystalline, fine-grained, and generally less than 0.1 mm in size, although a few large crystals of each indium sulfide were synthesized. The InS occurred as elongated red prisms up to 1 mm long, or as granular masses of smaller reddish-brown crystals. Crystals of In_6S_7 were black and acicular, up to several millimeters long. When coarsely crystalline, In_2S_3 occurs as dark red crystals with pyramidal faces and distinctive twinning, as described in detail by Goodyear and Steigmann (10). In polished section,

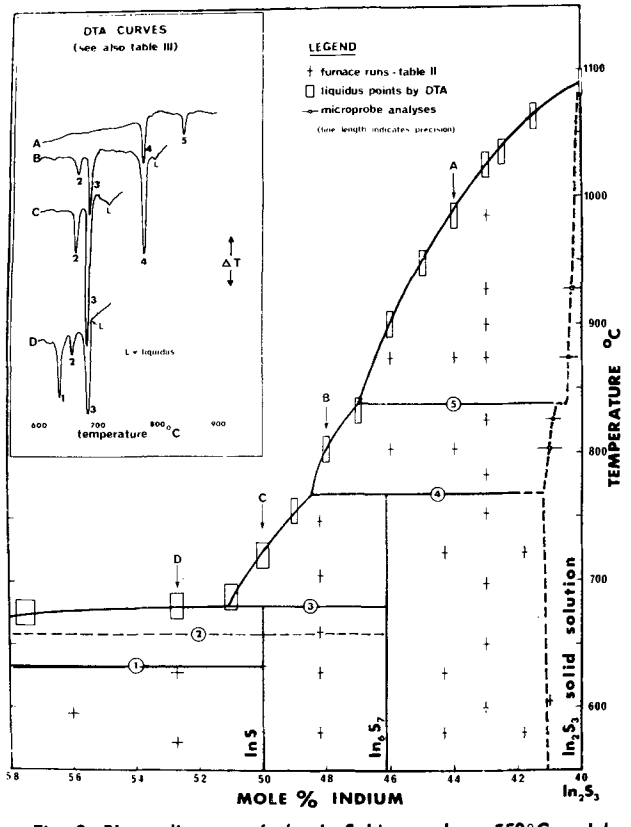

Fig. 2. Phase diagram of the In-S binary above 550°C and between 40 and 58 m/o indium. Numbers 1 through 5 refer to DTA reactions listed in Table III. These are illustrated in DTA curves at compositions A through D in the upper left-hand corner.

Table II. Furnace runs

Composition m/o In	Temperature °C	Hours	Phases present
37.5	702	132	In_2S_3 + S
37.5	900	120	In_2S_3 + S
41.0	618	112	In_2S_3
41.8	581	90	In_2S_3 + In_6S_7
41.8	722	75	In_2S_3 + In_6S_7
43.0	600	168	In_2S_3 + In_6S_7
43.0	650	168	In_2S_3 + In_6S_7
43.0	698	66	In_2S_3 + In_6S_7
43.0	752	66	In_2S_3 + In_6S_7
43.0	782	66	In_2S_3 + L
43.0	826	66	In_2S_3 + L
43.0	874	92	In_2S_3 + L
43.0	899	66	In_2S_3 + L
43.0	928	45	In_2S_3 + L
43.0	984	77	In_2S_3 + L
44.0	803	98	In_2S_3 + L
44.3	581	90	In_2S_3 + In_6S_7
44.3	627	88	In_2S_3 + In_6S_7
44.3	722	75	In_2S_3 + In_6S_7
46.0	803	98	In_2S_3 + L
46.0	874	92	In_2S_3 + L
48.2	581	90	In_6S_7 + InS
48.2	627	88	In_6S_7 + InS
48.2	659	75	In_6S_7 + InS
48.2	704	112	In_6S_7 + L
48.2	747	112	In_6S_7 + L
52.7	572	90	InS + In
52.7	627	75	InS + In
56.0	595	95	InS + In
60.0	595	95	InS + In

InS is strongly anisotropic from deep blue to pale yellow, with vivid red internal reflections. In contrast, In_6S_7 has weaker anisotropism and lower reflectivity, while In_2S_3 appears isotropic with faint red internal reflections. Indium metal polishes poorly and appears as grainy light orange patches under reflected light.

The unit cell of In_2S_3, when in equilibrium with In_6S_7, decreases with increasing temperature. A minimum is reached at the In_6S_7 breakdown temperature at 768°C (Fig. 2). At 752° and 782°C the lattice parameters are $a = 7.585 \pm 0.005$Å and $c = 32.20 \pm 0.03$Å. Above 768°C, where In_2S_3 coexists with an indium-rich melt, the cell size increases slightly at first, then sharply at 837°C to a value approximating that of the stoichiometric In_2S_3 cell ($a = 7.623$Å, $c = 32.36$Å) (8). The decrease in the In_2S_3 cell size is related to an increase in indium solubility, shown by microprobe analyses to reach an approximate maximum of 41.0 ± 0.4 m/o indium. Stoichiometric In_2S_3 has a composition of 40.0 m/o In. Electron microprobe analyses of co-existing phases showed no measurable solid solution (±0.4 m/o indium) for either In_6S_7 or InS.

Six different endothermic reactions were obtained by differential thermal analysis (Table III). The reaction at 893°C was obtained only sporadically and with runs in which the sample was flooded with argon gas. When the sample was heated in evacuated Vycor tubes, no reaction was recorded at that temperature. For the peaks at 633°, 657°, 679°, and 768°C (peaks 1-4, Fig. 2), maximum heat absorbed (ΔH max in Table III) was found to be at >60, 50, 50, and 47 m/o indium, respectively. No definite maxima were obtained for the reactions at 837° and 893°.

X-ray diffraction analyses of samples after DTA confirmed that InS and In_6S_7 break down at 679° and 768°C, respectively. The 657° endotherm appears to be closely related to the compound InS, since the maximum heat transfer occurs consistently at 50 m/o indium. At least three lines (d = 5.85, 5.13, 3.79Å) that are not present in the x-ray diffraction pattern for InS below 657° appear in the pattern for the material quenched from between 657° and 679°C. Rapid quenching of runs above 837° revealed, in some cases, that the moderately strong diffraction peak, d = 5.11Å, for tetragonal In_2S_3 was absent.

Table III—DTA results

Reaction	T°C mean	Standard deviation T°C	No. of runs	Compositional range, m/o In	Position of ΔH max, m/o In
Monotectic, appearance of L_1	633.1	2.7	8	50.0->60	>60
Inversion (?) of InS	657.2	1.2	20	46.5->60	50
InS ≒ In_6S_7 + L_1	679.2	1.4	20	46.5->60	50
In_6S_7 ≒ In_2S_3 + L_1	767.5	2.8	33	41.7-48.3	47
Inversion (?) of In_2S_3	837.3	2.3	24	41.0-47.0	?
?*	893.4	3.0	12	41.0-46.0	?

* Not obtained within evacuated Vycor tubes.

Discussion

Although the thermal reaction at 837°C (peak 5, Fig. 2) corresponds to the breakdown temperature of In_3S_4 proposed by Stubbs *et al.* (3), their lower stability limit at 370° was not recorded in this study. Also, the event at 768° marking the breakdown of In_6S_7 was noted in runs of bulk composition 41.8 m/o indium (Table III). This is well within the mutual stability field of In_3S_4 and In_2S_3 on the Stubbs *et al.* phase diagram (Fig. 1). Runs above the In_6S_7 decomposition temperature with bulk compositions between 40 and 48 m/o indium produced only In_2S_3 and a melt, even with very rapid quenching. Thus we suggest that In_3S_4 is not a stable phase in this system.

The reaction at 837°C could mark a structural inversion in In_2S_3. This "inversion" probably results from excess indium in the tetragonal lattice, because the thermal reaction at 837°C is not found in the stoichiometric compound. Inversions from tetragonal to isometric symmetry are common and often unquenchable. For example, the stable form of chalcopyrite ($CuFeS_2$) at 700°C is isometric. Inversion to the low-temperature tetragonal form occurs when chalcopyrite of maximum sulfur content with a Cu/Fe atomic ratio of approximately 1 is cooled, even rapidly, from 700° (11). The possibility of a similar inversion occurring in In_2S_3 is supported by x-ray diffraction evidence. The absence of the 5.11Å line in some high-temperature In_2S_3 makes it possible to index the remaining reflections as isometric, with a cell edge of approximately 10.78Å.

The erratic occurrence and magnitude of the thermal reaction at 893°C suggests that it may not be significant in terms of In-S phase relationships and that it may be related to the presence of argon in the sample chamber, or caused by reaction of the sample with the platinum cup.

Miller and Searcy (2) note that two crystallographic modifications of InS may exist and our differential thermal analysis tends to support this. An endothermic reaction was obtained at 657°C, below the breakdown of InS at 679°. Also, x-ray diffraction patterns for InS above and below 657° differed slightly. The few additional reflections noted may belong to a high-temperature modification of InS.

Rehwald and Harbeke (13) demonstrated that single crystals of In_2S_3 have n-type conductivity with a range of more than six decades in resistivity and Hall coefficient at room temperature. They attributed this wide range to a deviation from In_2S_3 stoichiometry. The main effect on concentration and sign of charge is due to a sulfur deficiency. Therefore indium substitution may be the factor controlling the inherent semiconductor properties of In_2S_3. Increased amounts of indium in the indium sulfide lattice will produce a surplus of interstitial cations which should strengthen the n-type conductivity. The thermal reaction at 837°C (Fig. 2) may be of special importance is this respect. The sharp drop in indium solubility above the In_2S_3 inversion could result in a marked increase in resistivity approaching p-type conductivity.

Conclusions

In_2S_3 is the only indium sulfide with measurable solid solution (approximate maxium 1.0 m/o indium). The thermal reaction at 837°C, previously attributed

to the breakdown of In_3S_4 by Stubbs *et al.* (3), could mark an inversion of tetragonal $In_{2+x}S_3$ to a higher symmetry form, possibly isometric. In order to establish the effect of the inversion on the electrical properties of In_2S_3, conductivity measurements are needed on crystals synthesized above and below 837°C. A high-temperature modification of InS may exist in the temperature range 657°-679°C. No evidence was found to support the existence of either In_3S_4 or In_3S_5.

Manuscript submitted April 8, 1970; revised manuscript received *ca.* Aug. 27, 1970.

Any discussion of this paper will appear in a Discussion Section to be published in the December 1971 JOURNAL.

REFERENCES

1. W. J. Duffin and J. H. C. Hogg, *Acta Cryst.*, **20**, 566 (1966).
2. A. R. Miller and A. W. Searcy, *J. Phys. Chem.*, **69**, 3826 (1965).
3. M. F. Stubbs, J. A. Schufle, A. J. Thomson, and J. M. Duncan, *J. Am. Chem. Soc.*, **74**, 1441 (1952).
4. M. I. Zargarova and R. S. Gamidov, *Izv. Akad. Nauk SSSR, Neorg. Mater.*, **3**, 1085 (1967).
5. J. H. C. Hogg and W. J. Duffin, *Acta Cryst.*, **23**, 111 (1967).
6. C. J. M. Rooymans, *J. Inorg. Nucl. Chem.*, **11**, 78 (1959).
7. H. Hahn and W. Klingler, *Z. Anorg. Chem.*, **260**, 97 (1949).
8. G. A. Steigmann, H. H. Sutherland, and J. Goodyear, *Acta Cryst.*, **19**, 967 (1965).
9. R. S. Boorman and J. K. Sutherland, *J. Materials Science*, **4**, 658 (1969).
10. J. Goodyear and G. A. Steigmann, *Proc. Phys. Soc.*, **78**, 491 (1961).
11. R. A. Yund and G. Kullerud, *J. Petrology*, **7**, 454 (1966).
12. A. R. Miller and A. W. Searcy, *J. Phys. Chem.*, **67**, 2400 (1963).
13. W. Rehwald and G. Harbeke, *J. Phys. Chem. Solids*, **26**, 1309 (1965).

Technical Notes

Energy Levels of Divalent Manganese in ZnS

Anjani Mehra

College of Environmental Sciences, University of Wisconsin, Green Bay, Wisconsin 54305

Manganese doped ZnS is well known for its interesting luminescence properties. A clear understanding of the mechanism of these phosphors requires a knowledge of energy levels of ions in the crystal. In spite of extensive optical studies (1-6) of Mn^{2+} doped ZnS, the assignments of various bands to intercombination transitions within the d^5 configuration of Mn^{2+} are still not well understood. Present study of the energy levels of Mn^{2+} ion in T_d symmetry of ZnS was undertaken to resolve this uncertainty.

The theory of d^5 configuration in octahedral (O_h) symmetry is well established (7-9). The crystal field energy matrices and energy level diagrams have been calculated by Tanabe and Sugano (7) and Orgel (8). Goode (9) has discussed the relative intensities of transitions to various quartet and doublet levels. Orgel (8) has discussed the bandwidths. Since the d^5 configuration is its own hole equivalent, the energy matrices and energy level diagram for it remain unaffected by the change of sign of Dq between O_h and T_d coordinations, and, therefore, one expects the general features of the spectra in the two cases to be quite similar. However, the magnitude of Dq in T_d complexes is found to be much smaller than that in O_h complexes, and it is found that this can result in different order for the levels and the corresponding bands in the spectra of two types of complexes.

Experimental energies of the observed band maxima and the assignments of the bands are listed in Table I. The band positions are taken from McClure's (1) data. The absorption spectrum consists of five main absorption bands. We shall first discuss the spectrum qualitatively with the help of the energy level diagram shown in Fig. 1. The spectra of transition metal ions could be discussed in both strong field or weak field schemes but for small Dq values as those of T_d complexes, it is more convenient to employ the weak field terminology which is adopted in the present work.

Key words: manganese, crystal field, optical absorption, zinc sulfide.

The two lowest energy bands at 18,850 and 20,100 cm^{-1} should be assigned to the two lowest levels $^4T_1$ (G) and $^4T_2$ (G) arising from the ^4G level of the free ion. The remaining two levels arising from ^4G level are $^4A_1$ and ^4E which should be degenerate in a simple cubic approximation, but in practice the degeneracy is removed due to several perturbations although the levels still lie quite close to within 300 cm^{-1} (10). These two states should be contained in the 21,555 cm^{-1} band and its associated structure.

The main problem is the assignment of next two bands at 23,000 and 25,700 cm^{-1}. Three quartet levels $^4T_2$ (D), ^4E(D), and $^4T_1$(P) are expected to lie in this region. In O_h complexes ^4E band is found to be sharper than the $^4T_2$ and $^4T_1$ bands which lie on its lower and higher energy sides, respectively. On examining the 23,000 and 25,700 cm^{-1} bands, it is found that the 25,700 cm^{-1} band has sharper structure and hence is more likely to involve the ^4E(D) state. Moreover, the assignment of 23,000 cm^{-1} band to ^4E(D) level was found to lead to unrealistic values for the crystal field parameters B and C. $^4T_2$ and ^4E levels arise from the ^4D level of the free ion, and the separation between them increases with increase in Dq value, but the $^4T_2$

Table I. Experimental and calculated band energies of Mn^{2+} in ZnS. Calculated energies are for $B = 780$, $C = 2400$, $Dq = 320$, and $\alpha = 76$ cm^{-1}.

Transition $^6A_1(^6S)$	Observed[a] energy in cm^{-1}	Calculated energy in cm^{-1}
$^4T_1$(G)	18,850	18,875
$^4T_2$(G)	20,100	20,973
$^4A_1$(G), ^4E(G)	21,270	21,320
	21,555	
$^4T_1$(P)	23,300	24,699
$^4T_2$(D)	25,374	25,176
^4E(D)	25,700	25,716

[a] Taken from ref. (1).

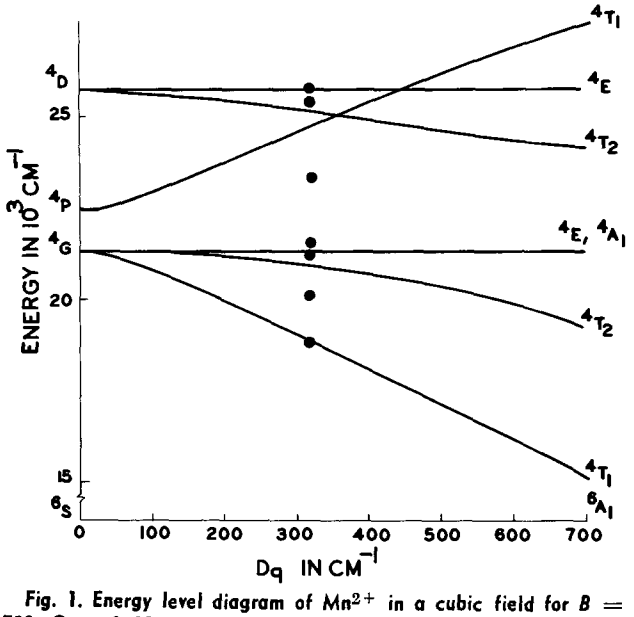

Fig. 1. Energy level diagram of Mn^{2+} in a cubic field for B = 780, C = 2400, α = 76 cm^{-1}. The observed band energies of Mn^{2+} in ZnS are marked ●. Crystal field levels arising from the ^4F level of the free ion are not shown.

level always lies lower to ^4E in energy. If one assigns the 23,300 cm^{-1} band to $^4T_2$ level (3), it is found that the separation of 2400 cm^{-1} between the so assigned $^4T_2$ and ^4E levels is larger than the corresponding separation of 1900 cm^{-1} observed in MnF_2 (10) which has near O_h symmetry. Because of the expected lower Dq in the present case, this separation should also be less, and hence it is unlikely that 23,300 cm^{-1} may correspond to $^4T_2$ level. In our view, this level should be contained in the structure of 25,700 cm^{-1} band, and the 23,300 cm^{-1} band should involve the other electronic state $^4T_1(P)$.

The only other possibility is the assignment of 23,300 cm^{-1} band to $^2T_2$ (^2I) level (2). This doublet level lies lowest among the doublet levels and ultimately becomes the ground state of the ion in the high field, low spin case. Its position is markedly dependent on the Dq value and goes down in energy for increase in Dq value. Theoretically calculated position (11) of this level in MnF_2 is around 29,000 cm^{-1}, and it is unlikely that it may come down to 23,300 cm^{-1} in the present case. Moreover, the intensity of 23,300 cm^{-1} band is of the same order as the intensities of the other bands which are transitions to the quartet levels, whereas the intensity of transition to a doublet level should have been much less than the intensities of transitions to the quartet levels (9). Thus we feel justified in assigning the 23,300 cm^{-1} band to $^4T_1(P)$ level on the basis of only the qualitative arguments. It is interesting to note that according to present assignment this level lies lower than ^4E level as against the reversed order of the levels found in O_h complexes.

In the calculation of energy levels, we employed a set of four parameters B, C, Dq and α in the weak field scheme. This set of parameters has been found quite suitable for Mn^{2+} spectra (11-13). The Trees correction parameter α was as usual fixed at the free ion value of 76 cm^{-1}. Parameters B and C were determined from the Dq independent [$^4A_1(G)$, $^4E(G)$] and $^4E(D)$ states and the values obtained are 780 and 2400 cm^{-1}, respectively. A Dq value of 820 cm^{-1} was chosen to fit the $^4T_1(G)$ level which is most sensitive to changes in Dq value. The calculated levels are given in Table I. The calculated energy of the other well assigned transition to $^4T_2(G)$ state is found to be in excellent agreement with the observed energy which justifies the choice of parameters. As expected, the calculated separation of about 550 cm^{-1} between $^4T_2(D)$ and $^4E(D)$ states is quite small and makes the assignment of 23,300 cm^{-1} band to $^4T_2(D)$ state very unlikely. The structure of 25,700 cm^{-1} band extends over 1000 cm^{-1}, and it is possible that it may contain both the electronic states. We have chosen a prominent line at 25,374 cm^{-1} as belonging to $^4T_2(D)$ state whose energy is quite close to the calculated one, but this assignment is by no means very certain. However, while analyzing the structure of this band, the presence of both the electronic states should be taken into account.

Although the agreement for $^4T_1(P)$ level is not very good, it at least supports the argument in this paper that this level could lie below $^4E(D)$ level. An inspection of the energy level diagram shows clearly that $^4T_1(P)$ level lies lower than the ^4E level on the low Dq side, but because of its large dependence on Dq it goes above ^4E on the high Dq side. In the free ion (10) too the parent level ^4P of this level lies lower than the parent level ^4D of the ^4E level. In octahedral complexes the Dq value is large and $^4T_1(P)$ level lies higher than the $^4E(D)$ level while in T_d complexes where the Dq value is small $^4T_1(P)$ can be expected to lie lower than the $^4E(D)$ level, as in the present case.

The degeneracy of $^4A_1(G)$ and $^4E(G)$ is not removed within the present calculations, and hence no separate assignment for the two is tried although two prominent lines at 21,270 and 21,555 cm^{-1} are mentioned and approximately the mid position is taken as the degenerate position. It may be mentioned that we have used the band maxima in our calculations to avoid the uncertainty associated with the location of zero phonon lines and also to keep the present parameters in line with the literature where the parameters have been mostly evaluated from the band maxima. Considering the appreciable amount of covalent bonding (14) in ZnS the usefulness of simple crystal field approach is quite satisfactory.

The Dq value obtained here is of the same order as obtained in other transition metal doped ZnS crystals. The reported Dq values (15) in Co^{2+} and Ni^{2+} doped ZnS are 375 and 475 cm^{-1}. Slack, Ham, and Chrenko (16) have obtained a value of 340 cm^{-1} for Fe^{2+} in ZnS. Koda *et al.* (5) find a value of 410 cm^{-1} for Dq for Mn^{2+} in ZnS from their pressure studies on the luminescence. Ikeda, Itoh, and Sato (17) have studied Mn^{2+} in CdS and have estimated $Dq \sim 490$ cm^{-1}. It is interesting to note that in spite of the low Dq value for the crystal, a comparatively large ground state splitting of about 23 x 10^{-4} cm^{-1} is observed in the paramagnetic resonance (18) of Mn^{2+} in ZnS. The calculated splitting in the ionic model using the parameters obtained from the optical spectrum should be less than 10^{-4} cm^{-1}, which is more than an order of magnitude smaller than the observed splitting. The presence of appreciable amounts of covalent bonding in the crystal is perhaps responsible for this discrepancy. However, a quantitative estimate of the effect of covalent bonding on the ground state splitting is not possible at present. In the optical studies the presence of covalent bonding is evident from the large reduction in the values of B and C from the free ion values of 910 and 3270 cm^{-1}, respectively (11).

Manuscript submitted May 4, 1970; revised manuscript received *ca.* Sept. 4, 1970.

Any discussion of this paper will appear in a Discussion Section to be published in the December 1971 JOURNAL.

REFERENCES

1. D. S. McClure, *J. Chem. Phys.*, **39**, 2850 (1963).
2. D. W. Langer and S. Ibuki, *Phys. Rev.*, **138A**. A809 (1965).
3. H. E. Gumlich, R. L. Pfrogner, J. C. Shaffer, and F. E. Williams, *J. Chem. Phys.*, **44**, 3929 (1966).
4. D. W. Langer and H. J. Richter, *Phys. Rev.*, **146**, 554 (1966).

5. T. Koda, S. Shionoya, M. Ichikawa, and S. Minomura, *J. Phys. Chem. Solids*, **27**, 1577 (1966).
6. A. K. Ryskin, G. I. Khilko, B. I. Maksakov, and K. K. Dubenskii, *Opt. i Spektroskopiya*, **16**, 274 (1964); Eng. Trans. *Optics and Spect. USSR*, **16**, 149 (1964).
7. Y. Tanabe and S. Sugano, *J. Phys. Soc. Japan*, **9**, 753, 766 (1954).
8. L. E. Orgel, *J. Chem. Phys.*, **23**, 1004 (1955).
9. D. H. Goode, *ibid.*, **43**, 2830 (1965).
10. J. W. Stout, *ibid.*, **31**, 709 (1959).
11. W. Low and G. Rosengarten, *J. Mol. Spectry.*, **12**, 319 (1964).
12. A. Mehra and P. Venkateswarlu, *J. Chem. Phys.*, **47**, 2334 (1967).
13. A. Mehra, *ibid.*, **48**, 4384 (1968).
14. J. L. Birman, *Phys. Rev.*, **109**, 810 (1958).
15. H. A. Weakliem, *J. Chem. Phys.*, **36**, 2117 (1962).
16. G. A. Slack, F. S. Ham, and R. M. Chrenko, *Phys. Rev.*, **152**, 376 (1966).
17. M. Ikeda, K. Itoh, and H. Sato, *J. Phys. Soc. Japan*, **25**, 455 (1968).
18. R. S. Title, *Phys. Rev.*, **131**, 623 (1963).

Silicon Impurity Distribution as Revealed by Pulsed MOS C-V Measurements

W. van Gelder* and E. H. Nicollian*

Bell Telephone Laboratories, Inc., Allentown, Pennsylvania 18103 and Murray Hill, New Jersey 07974

The purpose of this work is to discuss the application of the pulsed MOS C-V method (11) and its limitations in measuring doping profiles in silicon.

Several methods of measurement have been reported. Grove *et al.* (1) measured the redistribution of acceptor and donor impurities during thermal oxidation of silicon using an incremental capacitance-voltage technique on shallow (0.2μ) diffused p-n junctions. Theory and practice of the p-n junction dC/dV technique can be found in refs. (2) through (5). A variation of the junction dC/dV technique is described by Meyer and Gulbrandsen (6) who apply a sine wave to the junction and then measure the ratio k_2 of the second harmonic voltage to the first harmonic voltage generated by the diode. They showed that doping concentration as a function of depth is proportional to C^2V_1/k_2 where C is measured capacitance and V_1 is applied alternating voltage. Another elegant variation of the junction technique which makes direct plotting of the inverse doping profile possible was recently published by Copeland (7). Deal *et al.* (8) measured the redistribution of impurities due to thermal oxidation using the MOS structure. They measured maximum and minimum high-frequency capacitance and calculated doping concentration at the surface by applying a depletion approximation. Other workers have reported the same MOS C_{max}/C_{min} technique using essentially the same depletion approximation (9, 10).

Both the junction dC/dV and the MOS C_{max}/C_{min} method have their disadvantages. The diffusion of the p-n junction may alter the doping profile to be measured and the depth of the junction inherently prevents measurement close to the surface. Schottky barrier diodes would help in measuring closer to the surface, but fabrication of either a p-n junction or a Schottky barrier is destructive when these devices are not desired in later processing. The MOS C_{max}/C_{min} method can be considered nondestructive because the metal field plate can be easily removed from the oxide layer. The MOS C_{max}/C_{min} method cannot, however, measure a profile because it measures an undefined average over a maximun depletion width which in itself is a function of the doping concentration. As mentioned by Deal *et al.*, the method is based on a theory which assumes doping uniformity whereas that very method is used in the determination of a deviation from this condition (8).

The pulsed MOS C-V method is of interest because it not only is nondestructive but it also can be used to measure a true point-to-point doping profile over a greater distance into the silicon than the MOS C_{max}/C_{min} method. Its theory is remarkably similar to the one used for the step junction dC/dV method.

* Electrochemical Society Active Member.

Key words: pulsed MOS measurements, silicon impurity distribution, pulsed C-V measurements, impurity profile.

Theory

Consider a MOS capacitor which can be driven into deep depletion by the application of pulse bias (11). Only the depletion region of the capacitor characteristics will be treated here, and it will be assumed that interface states have a negligible influence.

A small increase in applied voltage dV is equal to

$$dV = dV_o + d\phi = dQ_{sc}/C_o + d\phi \quad [1]$$

where V_o = voltage drop across the oxide
ϕ = silicon surface potential
C_o = oxide capacitance/unit area
Q_{sc} = space charge density/unit area.

The increase of charge in the depletion layer causes an increase in the electric field

$$dE = dQ_{sc}/\epsilon_s \quad [2]$$

in which ϵ_s is the dielectric permittivity of silicon. The corresponding increase in surface potential is approximately

$$d\phi = W dE \quad [3]$$

Substituting [2] and [3] into [1]

$$dV = dQ_{sc}\,(1/C_o + 1/C_s) = dQ_{sc}/C_m \quad [4]$$

where C_m is total measured capacitance, $C_s = \epsilon_s/W$, and W is space charge width. Using the relation $dQ_{sc} = q\,N(W)dW$ in [4], where $N(W)$ is the doping concentration as a function of W, we get

$$dV = q\,N(W)\,dW/C_m \quad [5]$$

But,

$$dW = \epsilon_s\,d(1/C_s) = \epsilon_s\,d(1/C_m) \quad [6]$$

as $1/C_s = 1/C_m - 1/C_o$. Substituting [6] into [5] and solving for $N(W)$, we get

$$N(W) = 2(q\epsilon_s\,d(1/C_m^2)/dV)^{-1} \quad [7]$$

This equation shows that the doping concentration $N(W)$ can be calculated from the slope of the $1/C^2$ *vs.* V curve.

Other authors have mentioned that the impurity concentration can be measured from the slope of the $1/C^2$ *vs.* V curve (11, 12). However, these authors dealt exclusively with an integrated version of [7] which can be written as

$$C_o/C_m = (1 + 2C_o^2(V_G - V_{FB})/(q\epsilon_s N))^{1/2} \quad [8]$$

where V_{FB} = flatband voltage. Equation [8] cannot be simply differentiated to give [7] because [8] is normally derived with the assumption that N is not a function of W. Note that [7] is the same equation as used in the step junction dC/dV method given by Grove (13). The only difference is that C_m in [7] includes C_s and C_o in series while in the junction dC/dV method C_s is measured directly.

Limitations

Equation [7] is valid even when interface states are present provided they do not follow either the a-c measuring signal or the pulse. In practice, for typical pulse widths of several milliseconds and a-c signal frequencies of about 1 MHz, interface states follow neither the a-c signal nor the pulse over most of the deep depletion range because interface state time constants are too large. In this range [7] is valid. The time constants become smaller when the depletion depth is decreased. This happens when the applied bias is changed towards the flatband voltage. Interface states begin following first the pulse and then the a-c signal. When this happens, the slope of the $1/C^2$ *vs.* V curve is modified giving erroneous values of $N(W)$ from [7].

The space charge width at which interface state influence becomes important will depend on doping density as well as a-c frequency and pulse width. The value of W at which interface state influence becomes a factor can be roughly estimated by measuring an admittance *vs.* d-c bias curve at a frequency corresponding to a reciprocal pulse width. This value of W will occur when the equivalent parallel conductance becomes appreciable. Experience has shown that this occurs at a surface potential of around 0.4V or so, which corresponds to $W = 0.7$ μm for $N = 10^{15}$ cm^{-3} and $W = 0.2$ μm for $N = 10^{16}$ cm^{-3}.

The range of W over which interface state influence is negligible can be extended, of course, by using higher a-c frequencies ($>$ 500 kHz) and smaller pulse widths ($<$ 6 msec) than the ones used in this work.

Even if interface states are completely absent, [7] is not valid at the flat band condition where majority carrier density becomes comparable to space charge density. The limiting surface potential is in this case a few kT/q which at room temperature amounts to ~0.05V. In practice, this limitation is of no interest because the interface state effect is dominant.

The largest distance into the silicon at which [7] can be used is at the onset of breakdown either by avalanche for low doping density or by tunneling for high doping density. A basic limitation, characteristic for all C-V profile measurements, is the fact that higher doping levels require higher voltage to measure at a certain desired depth while the breakdown voltage decreases with increasing doping level.

Limitations pointed out by Kennedy *et al.* (15) concerning the fact that the junction dC/dV measurement establishes the distribution of majority carriers rather than the distribution of impurity atoms are of equal validity for the pulsed MOS case and should be taken into account when an attempt is made to measure the impurity distribution with either technique.

Apparatus and Measurement Technique

Apparatus and measurement technique used were identical to those outlined by Goetzberger and Nicollian (11). Signal frequency was 500 kHz, pulse width 6 msec, and duty cycle 6%.

Sample Preparation

MOS capacitors were made on <100> oriented silicon slices cut from Sb doped pulled crystals with $N_D \approx 10^{15}$ cm^{-3}. The slices were ~ 8 mil thick, lapped on both sides, and polished on one side. The metal field plate was filament evaporated aluminum. Contact was made to the back of a slice by evaporated aluminum and a vacuum chuck. A total of three slices were oxidized, each one in a different manner to produce a different "redistribution" of impurities at the surface. Before oxidation the four point probe resistivity was measured. Prior to each application of the aluminum field plate the slices were baked in N_2 at 1100°C for 25 min to assure a moderate interface state density.

The first oxidation of the three slices took place in separate runs in a tube furnace at 1100°C in wet O_2 (oxygen bubbled through 80°C water.) Oxide thickness was ~ 1200Å.

Table I shows the four-point probe N_D before oxidation and the N_D at the surface as measured from MOS C_{max}/C_{min} after oxidation. Note that slice 3 was oxidized together (in one run) with six N^+ phosphorous diffused bulk silicon slices. The N^+ diffused slices were prepared from slices similar to the 3 samples by subjecting them to a one-step phosphorous prediffusion deposition at 900°C for 20 min and then removing the phosphorous glass. The N_D from MOS C_{max}/C_{min} was measured according to the method of Deal *et al.* (8). Apparently, the presence of the N^+ slices during oxidation caused a large increase in N_D. [Evidence of this kind of phosphorous N-skin formation on silicon by vapor transport was recently reported by Edwards (14).] Apart from slice 3 the difference in N_D in row 1 and row 3 could be explained by the "pile-up" effect or "redistribution" during oxidation (8).

Table I. Sequence of process steps and measurements

		Slice No. 1	Slice No. 2	Slice No. 3
1	Initial four-point probe N_D, cm^{-3} × 10^{15}	0.75	0.50	0.89
2	Process	Wet O_2 oxidize 1100°C, 1200A	Wet O_2 oxidize 1100°C, 1200A	Wet O_2 oxidize 1100°C, 1200A with 6 N^+ slices
3	MOS C_{max}/C_{min} N_D, cm^{-3} × 10^{15}	1.05	0.61	69.2
4	Process	Strip oxide Steam oxidize 1100°C, 6000A	—	—
5	Process	Strip oxide Wet O_2 oxidize 1100°C, 1200A	—	—
6	MOS C_{max}/C_{min} N_D, cm^{-3} × 10^{15}	3.45	—	—
7	Process	Si etch left half Strip oxide Wet O_2 oxidize 1100°C, 1200A	—	—
8	MOS C_{max}/C_{min} N_D, cm^{-3} × 10^{15}	Left 2.17 Right 4.32	—	—
9	Pulsed MOS measurements	See Table II and Fig. 1	See Table II and Fig. 1	See Table II and Fig. 1
10	Final four-point probe N_D, cm^{-3} × 10^{15}	Left 0.80 Right 0.80	0.51	1.01

Slice No. 1 was further treated as follows (see Table I). (Read this table from top to bottom to get the proper sequence of operations.) The Al dots and the SiO_2 were stripped in boiling HCl and HF, respectively, and the slice was oxidized in 100% steam at 1100°C to an SiO_2 thickness of 6000Å (~ 60 min). This oxide layer was stripped again in HF and the slice was oxidized again in wet O_2 at 1100°C to a thickness of ~ 1200Å SiO_2. Al dots were reapplied and the N_D from MOS C_{max}/C_{min} was 3.45 x 10^{15} cm^{-3}. This amounted to a large increase in N_D compared to the previous MOS measurement of 1.05 x 10^{15} cm^{-3} or the initial four-point probe value of 0.75 x 10^{15} cm^{-3}. The increase was too large to be explained by the "redistribution" effect. To investigate further the depth of this increase the aluminum and the oxide were stripped again but only from the left half of the slice. The slice was then etched in a silicon etch (5 HNO_3:4.4 acetic acid: 1 HF saturated with iodine) for 12 sec, and 1.1 μm of silicon was removed from the left half. The oxide on the right half was only slightly attacked by the etch. This oxide was removed and the whole slice was oxidized again in wet O_2 at 1100°C to form 1200Å of oxide. Aluminum dots were again evaporated over the whole slice. At this point the 3 slices were subjected to the pulsed MOS C-V measurements. After these measurements the slices were stripped and four-point probe measured. Row 10 shows the final four-point probe N_D. It is clear from these values, especially in the case of slice 3, that the MOS-measured increase in N_D was confined to a thin layer at the surface. The purpose of the pulsed MOS measurements was thus twofold: first, to determine if such measurements are practical and, second, to confirm the evidence from the four-point probe measurements that the large build-up of N_D at the surface as measured by MOS C_{max}/C_{min} is indeed confined to a thin layer at the surface.

Results of Pulsed MOS C-V Measurements

Measurements are summarized in Fig. 1 where $(1/C_m)^2$ is plotted against $V_A - V_{FB}$. A least square straight line was fitted as indicated. The slope of the straight line gave calculated values of N_D using [7]. Depth of measurement can be read from the right-hand ordinate. This ordinate is strictly valid for only one value of C_o = 2.5 x 10^{-8} F/cm² which was the oxide capacitance of slices 1 and 3. The C_o for slice 2 was 2.08 x 10^{-8} F/cm² and the W scale in Fig. 1 is therefore not strictly valid for slice 2, although it is a good approximation.

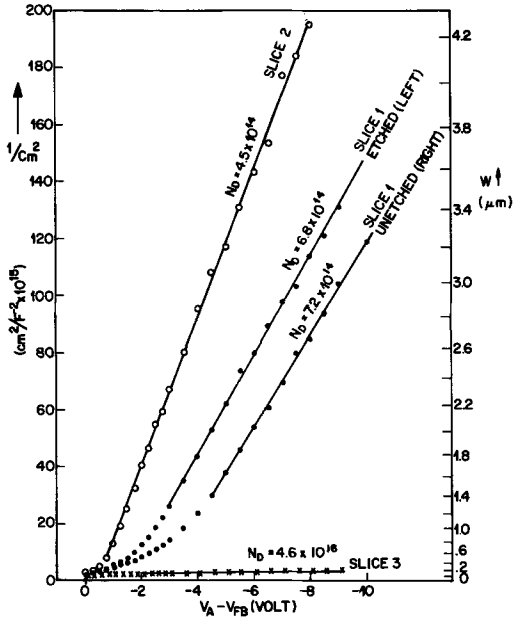

Fig. 1. Plots of $1/C_m^2$ vs. the applied voltage minus flatband voltage ($V_A - V_{FB}$). The right-hand ordinate indicates the depth (W) of the measurement below the Si surface (see Table II).

Table II. Calculated values of W and N_D corresponding to the points plotted in Fig. 1

V_A-V_{FB}, volt	Slice 1 Etched half W, μm	Slice 1 Etched half N_D, cm^{-3} x 10^{15}	Slice 1 Unetched half W	Slice 1 Unetched half N_D	Slice 2 W	Slice 2 N_D	Slice 3 W	Slice 3 N_D
−0.25	0.15	5.1	0.13	6.1	0.15	2.8	0.03	83
−0.50	0.21	3.6	0.19	4.7	0.31	0.96	0.03	88
−0.75	0.29	3.0	0.25	4.2	0.56	0.55*	0.04	65
−1.00	0.37	2.4	0.30	3.9	0.82	0.50↓	0.04	55
−1.25	0.46	2.0	0.36	3.4	1.06	0.49	0.05	61
−1.50	0.56	1.6	0.43	3.3	1.28	0.42	0.06	42
−1.75	0.68	1.1	0.49	2.9	1.50	0.37	0.06	45
−2.00	0.81	1.1	0.55	2.4	1.69	0.50	0.07	52*
−2.25	0.94	0.86	0.63	2.0	1.87	0.33	0.08	47↓
−2.50	1.07	0.84	0.71	1.9	2.02	0.73	0.08	55
−2.75	1.20	0.80	0.79	1.7	2.15	0.38	0.09	56
−3.00	1.42	0.63*	0.92	1.4	2.36	0.45	0.10	46
−3.50	1.67	0.70↓	1.10	1.2	2.62	0.38	0.11	48
−4.00	1.90	0.62	1.30	0.90	2.87	0.46	0.13	44
−4.50	2.11	0.66	1.52	0.75*	3.05	0.63	0.14	49
−5.00	2.33	0.51	1.73	0.76↓	3.22	0.44	0.15	48
−5.50	2.50	0.90	1.94	0.70	3.41	0.49	0.17	41
−6.00	2.66	0.62	2.11	0.84	3.57	0.56	0.18	45
−6.50	2.82	0.69	2.28	0.69	3.80	0.25	0.19	48
−7.00	2.93	1.20	2.47	0.58	4.00	0.83	0.20	40
−7.50	3.06	0.54	2.61	1.11	4.11	0.58	0.22	49
−8.00	3.20	0.84	2.74	0.65	4.18	0.33	0.23	45
−8.50	3.34	0.56	2.91	0.58			0.24	41
−9.00								

* From these points on a straight line was fitted as shown in Fig. 1.

Table II gives the correct relation between W and N_D for all slices. Values of W in this table were calculated by taking the average of each two neighboring $(1/C_m)^2$ values and then correcting for C_o. Each corresponding N_D value was calculated from the slope of the straight line between the points in Fig. 1.

Discussion of Results

The straight line portions of the curves in Fig. 1 yield N_D values that correspond well with the initial and final four-point probe values in Table I except for slice 3. Apparently the depth of measurement was large enough for slices 1 and 2 to reach into the undisturbed region of bulk doping. The largest value of W was ~ 3 μm for slice 1 and ~ 4 μm for slice 2. Slice 3 however did not go deeper than 0.24 μm although the applied maximum voltage was the same. This points out a basic limitation in all C-V profile measurements as discussed in the section on limitations. The higher doping levels require higher voltage to measure at the same depth, but the breakdown voltage, which limits the maximum applicable voltage, is lower for higher N_D. In the case of slice 3 the N_D value from Fig. 1 corresponds more to the MOS C_{max}/C_{min} value of Table I than to the initial or final four-point probe. The measurement apparently did not reach deep enough to reveal the bulk N_D.

The N_D value for slice 2 (Table II) becomes equal to the bulk N_D at $W \geqq 0.5\mu$. It is interesting to note how high N_D is for $W = 0.15\mu$. (see section on limitations.)

As expected, slice 1 unetched differs in profile from slice 1 etched. The difference is shown in Fig. 2.

It appeared that the repeated process sequence of oxidation-oxide strip caused an increase in N_D at the surface after each oxidation and that this "build-up" can be removed by etching the silicon. The exact reason for and mechanism of this phenomenon is unknown.

Remarks and Conclusion

The amount of experimental data in this communication is limited to three silicon slices because the measurements are meant merely to illustrate the cor-

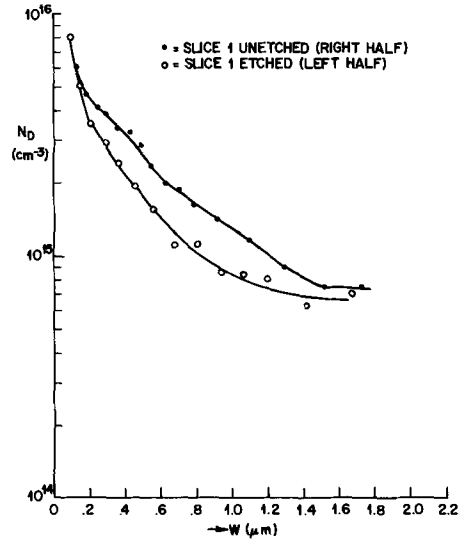

Fig. 2. Difference in N_D vs. W of slice 1 unetched and slice 1 etched.

rectness of theory and practicality of method. The measurements in addition dealt with an actual problem in device fabrication whereby an anomalously high increase in doping occurs at the surface of an n-type silicon slice. With these remarks in mind it is concluded that the pulsed MOS C-V technique can be a useful tool in revealing impurity profiles in silicon. The pulsed MOS technique has been used successfully to confirm 4-point probe evidence that an impurity increase due to repeated oxidation and stripping of the oxide is confined to a thin layer of ~ 1 μm at the surface.

Manuscript submitted May 4, 1970; revised manuscript received ca. Aug. 28, 1970.

Any discussion of this paper will appear in a Discussion Section to be published in the December 1971 JOURNAL.

REFERENCES

1. A. S. Grove, O. Leistiko, Jr., and C. T. Sah, *J. Appl. Phys.*, **35**, 2695 (1964).
2. J. Hilibrand and R. D. Gold, *RCA Rev.*, **21**, 245 (1960).
3. C. O. Thomas, D. Kahng, and R. C. Manz, *This Journal*, **109**, 1055 (1962).
4. I. Amron, *Electrochem. Technol.*, **12**, 327 (1964).
5. D. R. Decker, *This Journal*, **115**, 1085 (1968).
6. N. I. Meyer and T. Guldbrandsen, *Proc. IEEE*, **51**, 1631 (1963).
7. J. A. Copeland, *IEEE Trans. Electr. Devices ED*, **16**, 445 (1969).
8. B. E. Deal, A. S. Grove, E. H. Snow, and C. T. Sah, *This Journal*, **112**, 308 (1965).
9. C. Jund and R. Poirier, *Solid State Elec.*, **9**, 315 (1966).
10. D. C. Gupta and N. G. Anantha, *Proc. IEEE*, June *1967*.
11. A. Goetzberger and E. H. Nicollian, *J. Appl. Phys.*, **38**, 4582 (1967).
12. M. Zerbst and H. E. Longo, *Z. Angew. Physik*, **19**, 85 (1965).
13. A. S. Grove, "Physics and Technology of Semiconductor Devices," John Wiley & Sons Inc., New York (1967).
14. J. R. Edwards, *This Journal*, **116**, 866 (1969).
15. D. P. Kennedy, P. C. Murley, and W. Kleinfelder, *IBM J. Res. Develop.*, 399 (Sept. 1968).

Use of HCl Gettering in Silicon Device Processing

P. H. Robinson* and F. P. Heiman[1]

RCA Laboratories, Princeton, New Jersey 08540

It is well known that metals such as gold, copper, and iron severely degrade the minority carrier lifetime in silicon by forming recombination centers in the forbidden gap (1-4). These contaminants are generally present in most diffusion and oxidation furnaces, and it is common practice to getter them from the silicon after device processing (5-7). One gettering technique involves a long bake at 800°-1000°C with a phosphorus glass in contact with the silicon surface.

Transmission electron microscopy and infrared microscopy have been used to verify this gettering action by observing the disappearance of copper precipitates on dislocations after treatment (3, 8).

Another troublesome metallic impurity is sodium, which introduces unstable positive charge into the silicon dioxide layer (9). This has generally been avoided in silicon processing by ultraclean techniques, but most devices which are sensitive to sodium contamination (*e.g.*, MOS transistors) incorporate a phosphorus glass layer or silicon nitride layer to prevent contamination during metallization and subsequent handling.

The idea for using HCl as the gettering agent for sodium and other contaminants was first demonstrated by using a mixture of hydrochloric acid and distilled wafer as the source of steam for oxidation (14). Oxides were produced with essentially zero oxide charge using this technique even though the starting wafers were contaminated with sodium.

We reproduced this experiment but found no improvement in minority carrier lifetime. We reasoned that dry oxidation containing gaseous HCl would be more suitable for forming volatile metallic chlorides; the water vapor might favor the formation of involatile metal oxides. Indeed, most metals oxidize more rapidly in water vapor than in dry O_2.

Measurements of minority carrier lifetime using silicon films grown on both spinel and sapphire have yielded values of the order of 10^{-10}-10^{-9} sec. Bipolar transistors fabricated in these low lifetime films required very narrow base regions which in turn lead to many emitter-to-collector shorts, as well as low current gains (10). An improvement in minority carrier lifetime through use of the gettering technique described herein facilitated device processing and resulted in significantly higher performance. The procedure developed is described below.

Experimental Procedure

Systems for HCl processing in dry oxygen with either rf heating or resistance furnace heating were used for these studies and the procedure often included HCl etching of the silicon surface prior to high temperature HCl oxidation. This technique has yielded excellent results for preserving as well as recovering minority carrier lifetime in bulk and thin-film silicon. The procedure is only a minor modification of standard device processing; *i.e.* the inclusion of 0.5-1.0% HCl by volume into the oxygen gas stream. HCl cannot be used with other gases because the silicon will be etched in a nonoxidizing ambient. The furnace

* Electrochemical Society Active Member.
[1] Present address: Princeton Electronic Products, Incorporated.
Key words: gettering, minority carrier lifetime, thin film silicon, transient response MOS.

exhausts into a hood and plastic or glass tubing is used throughout. Termination of oxidation in an oxygen ambient will result in positive oxide charge (11). A 5 min anneal in an inert atmosphere at oxidation temperature will remove this charge.

Results on Bulk Silicon

Using the above technique, zero oxide charge has been reproducibly obtained in thermally grown oxide as determined by the capacitance-voltage curves and very high lifetime has been observed from the transient response of the MOS capacitor (12). Sodium, copper, and gold, *etc.* form highly volatile metal chlorides at elevated temperature and are presumably removed from the chamber as a gas. In addition, any of the metal impurities present in the silicon can be gettered during this oxidation step.

Typical results obtained with 8 ohm-cm N-type and P-type silicon wafers are as follows: (a) a steam-oxidized wafer exhibited an effective lifetime of 0.3 μsec. After 16 hr at 1200°C in 1% HCl/O_2 mixture, the minority carrier lifetime increased to 100-300 μsec, (b) one hour oxidation at 1100°C in 1% HCl/O_2 was found to preserve the minority carrier lifetime of 10-40 μsec which was measured before heat treatment, (c) increasing the HCl content to 10% by volume resulted in the formation of water (hydrochloric acid) in the cold parts of the furnace tube. The silicon wafer was badly pitted. HCl concentration below 1% does not affect the oxidation rate and it is presumed that very little water is formed.

A word is in order concerning the measurement technique. Lifetime is measured by observing the rate at which the inversion layer forms under an MOS capacitor after the application of a large depleting voltage (12). The generation rate in the depletion region, g, is related to minority carrier lifetime, τ, by

$$g = \frac{n_i}{2\tau} \qquad [1]$$

where n_i is the intrinsic carrier density. This expression is accurate if electron hole capture cross sections are equal, and all traps are locked at the center of the forbidden energy gap. It can be shown (13), however, that the generation out of traps located a distance ΔE from the center of the gap is reduced by exp $(\Delta E/kT)$. Thus, only those traps near the center are important in this process. This means that determination of lifetime by measuring the generation rate always results in a value $\geq$ the photoconductive lifetime. However, values taken before and after gettering are indicative of a change in impurity concentration and relate directly to the change in leakage current of diodes fabricated in the material.

Typical results are shown in Fig. 1 and 2. In Fig. 1, we see the transient response of an MOS capacitor whose oxide was grown in steam at 1100°C. Anneal in H_2 at 500°C for 30 min assures a low density of

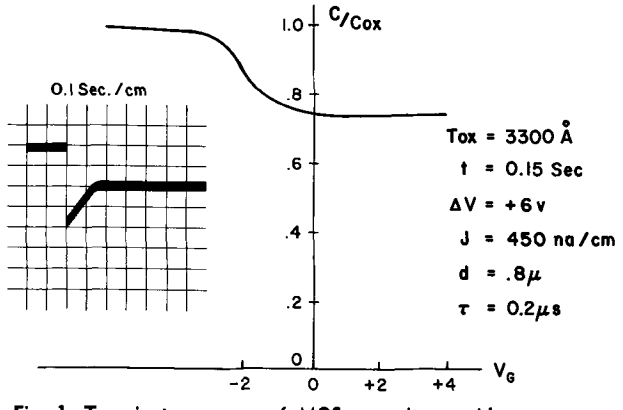

Fig. 1. Transient response of MOS capacitor; oxide was grown in steam at 1100°C.

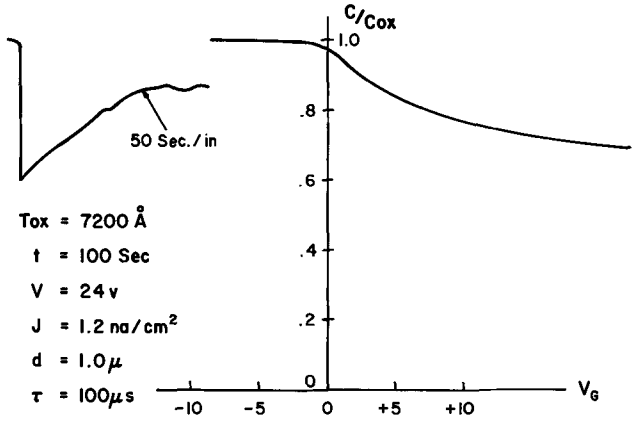

Fig. 2. Transient response of MOS capacitor; steam oxide was gettered in HCl/O_2 atmosphere at 1200°C for 16 hr.

interface states.[2] The total transient time is about 0.15 sec which corresponds to an average of 450 nA/cm^2. The capacitance measurement indicates an average depletion region depth of 0.8μ which yields a lifetime of 0.2 μsec. The transient response shown in Fig. 2 depicts the situation after gettering in 1% HCl/O_2 at 1200°C for 16 hr. A similar analysis yields a value for lifetime of 100 μsec.

Results with Thin-Film Silicon Grown on Insulators

Several experiments were performed using 2μ thick silicon-on-sapphire films. Measurement of lifetime in films before gettering resulted in values of 0.5 to 1 nsec. However, a 1 hr oxidation at 1100°C in HCl as described previously resulted in a lifetime of 3 nsec. Gettering for 16 hr increased this lifetime to over 13 nsec.

Lifetime measurements were also made on 2μ silicon films grown on aluminum-rich spinel obtained from Germany, having an Al_2O_3:MgO ratio of 3.3 to 1. The measured lifetimes were determined to be quite poor ($\approx$ 0.1 nsec) even though the films had essentially bulk mobilities. HCl gettering at 1100°C for 15 min did not improve the lifetime. Higher temperatures were not used due to the exsolution problem associated with Al rich spinel. Either this spinel is an infinite source for lifetime-killing impurities or the impurities which are affecting the lifetime are not being gettered. Additional experiments are being planned to determine why lifetime in silicon grown on this kind of spinel is so poor.

Some preliminary experiments on the growth of silicon-on-sapphire by the pyrolysis of silane in helium (15) at temperatures ranging from 800° to 1000°C have begun. Single crystal silicon films as determined by electron diffraction patterns were obtained at growth temperatures of 880°C and above. Films obtained at 925°C at a growth rate of ¼ μ/min were N-type with a resistivity of 2 ohm-cm. Hall measurements made at room temperature gave an electron mobility in the range of 450-500 cm^2/V-sec. Hall mobility *vs.* temperature was measured and results indicate that a negligible amount of aluminum is present in the silicon films.

Lifetime measurements were made on the helium grown silicon films without gettering. Values of 14 nsec were obtained on several films. These were then oxidized at 1200°C in the presence of HCl and lifetime increased to 43 nsec.

Several other silicon-on-sapphire films were grown by the pyrolysis of silane in helium at 1050°C. These films were 2μ thick, P-type with a resistivity of 0.5 ohm-cm. Mobility *vs.* temperature measurements indicated that these films were Al-doped presumably due to the higher growth temperature and a hole mobility of 125 cm^2/V-sec was determined.

[2] The authors have analyzed the effect of surface generation on the results. This can be separated out by careful waveform analysis and does not affect the values given in this report.

Lifetime measurements, however, resulted in very low minority carrier lifetimes of 0.5 nsec, and no significant improvement was found after HCl oxidation-gettering. This result suggests that Al present in the silicon films or aluminum-oxygen conglomerates after oxidation could be affecting the thin-film silicon lifetime.

Conclusions

We have observed that a small amount of dry gaseous HCl introduced into the gas during oxidation can significantly reduce the generation rate in silicon. This is presumed due to the gettering of metallic impurities from the silicon through the formation of volatile metal chlorides. HCl gettering processes are being used in the fabrication of silicon-on-sapphire bipolar transistors and complementary MOS transistor circuits.

Further work is underway to investigate, in detail, the time-temperature dependence of the process.

Acknowledgments

The authors would like to thank J. Jaklik and R. O. Wance for processing the devices and R. Ronen and E. Moonan for results obtained with silicon-on-sapphire bipolar transistors.

Research was sponsored in part by the USAF Avionics Laboratories under Contract F33615-68-C-1368.

Manuscript submitted March 12, 1970; revised manuscript received ca. Aug. 19, 1970.

Any discussion of this paper will appear in a Discussion Section to be published in the December 1971 JOURNAL.

REFERENCES

1. A. Goetzberger and W. Shockley, *J. Appl. Phys.*, **31**, 1821 (1960).
2. R. N. Hall and J. H. Rocette, *J. Appl. Phys.*, **35**, 379 (1964).
3. J. E. Lawrence, *This Journal*, **112**, 796 (1965).
4. W. M. Bullis, *Solid-State Electron.*, **9**, 143 (1966).
5. S. W. Ing, Jr., R. E. Morrison, L. L. Alt, and R. W. Aldrich, *This Journal*, **110**, 533 (1963).
6. E. J. Mets, *ibid.*, **112**, 420 (1965).
7. M. Walder and L. Sivo, *ibid.*, **107**, 298 (1960).
8. J. E. Lawrence, *Trans. Met. Soc.*, **242**, 484 (1968).
9. For a good bibliography of this subject see: E. S. Schlege, *IEEE Trans. Electron Devices*, **ED-14**, 728 (1967).
10. H. P. Heiman and P. H. Robinson, *Solid-State Electron.*, **11**, 411 (1968).
11. B. E. Deal, A. S. Grove, and E. H. Snow, *This Journal*, **114**, 266 (1967).
12. F. P. Heiman, *IEEE Trans. Electron Devices*, **ED-14**, 781 (1967).
13. C. T. Sah, R. N. Noyce, and W. Shockley, *Proc. IRE*, **45**, 1228 (1957).
14. A. Mayer, Private communication.
15. D. Richman and R. H. Arlett, *This Journal*, **116**, 872 (1969).

Influence of Silicon Slice Curvature on Thermally Induced Stresses

H. R. Huff,* R. C. Bracken,* and S. N. Rea

Texas Instruments Incorporated, Dallas, Texas 75222

The generation of thermally induced dislocations in silicon slices has been investigated recently for both diffusion furnace and epitaxial reactor geometries (1-3). It has further been shown that the detailed method of slice preparation can exert a considerable influence on the dislocation generation (4-8). For example, conventionally prepared 2-in. diameter silicon slices are observed by Talysurf measurements to exhibit curvatures up to several mils (5). This curvature arises from both the sawing operation and subsequent mechanical processing. The contribution of each to the slice curvature is a function of the particular processing technique utilized. Although curve-free slices can be prepared utilizing extreme care in performing each processing step, conventionally prepared slices do exhibit curvature.

In the present note, we will illustrate the influence of slice curvature as a mechanism for generating thermal stresses in slices placed on a uniformly heated susceptor. It is shown that these stresses may be of sufficient magnitude to activate residual surface dislocation sources and cause their propagation throughout the initially dislocation-free slice volume[1] (see Fig. 1). The dislocations thereby generated should be especially detrimental in that subsequent high-temperature processing may lead to their multiplication as well as their interaction with various types of point and higher-order defects (9).

A bowed slice sitting on a uniformly heated susceptor exhibits a temperature variation across its radius because of the variation in thermal coupling between slice and susceptor. The slice is heated by the susceptor through both conduction and radiation while it loses heat primarily by radiation. At points of maximum separation between slice and susceptor, the heat transport by conduction across the gaseous interface is substantially lower than at contact points. Therefore, that portion of the slice in intimate contact with the susceptor attains a temperature near that of the susceptor while the slice portion bowed away from the susceptor attains some lower temperature. The presence of thermal radiation introduces a strong nonlinearity in the differential equation governing slice

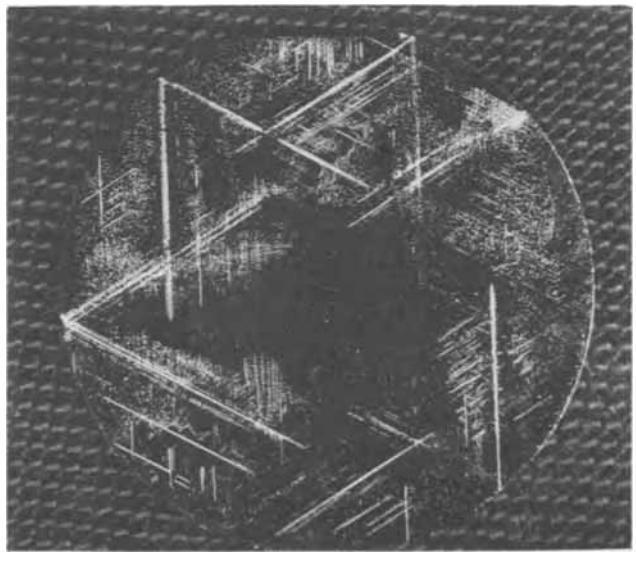

Fig. 1. Epitaxially processed slice after subsequent Sirtl etching

* Electrochemical Society Active Member.

Key words: epitaxy, dislocations, computer simulation.

[1] Determined by Sirtl etching.

temperature and necessitates computer solution. A finite-element computer model was used following standard procedures (10). This involved dividing the slice into many small elements (nodes), performing an energy balance on each node, and, through a relaxation scheme, determining the temperature distribution across the slice. The slice was assumed to be in a hydrogen atmosphere.

Calculated temperature distributions for such curved slices, as shown in Fig. 2, indicate that radial temperature variations on the order of 20°C are possible in 8-mil thick, 2-in. diameter slices, depending on the amount and sign of curvature. A perfectly flat slice exhibits a negligible temperature variation. The radial temperature distribution is fairly insensitive to slice thickness. Calculated temperature distributions for 4, 8, and 16-mil thick, 2-in. diameter slices were virtually identical.

The silicon slice is represented as a thin, circular disk of radius R with a radially symmetric temperature distribution about the center. By neglecting the stress component normal to the surface,[2] the stress tensor may be written in cylindrical coordinates as

$$\sigma = \begin{pmatrix} \sigma_r & 0 & 0 \\ 0 & \sigma_\theta & 0 \\ 0 & 0 & 0 \end{pmatrix} \quad [1]$$

with (11)

$$\frac{\sigma_r}{\alpha E} = \frac{1}{R^2}\int_0^R T(r)\,r\,dr - \frac{1}{r^2}\int_0^r T(r)\,r\,dr$$

$$\frac{\sigma_\theta}{\alpha E} = -T(r) + \frac{1}{R^2}\int_0^R T(r)\,r\,dr + \frac{1}{r^2}\int_0^r T(r)\,r\,dr \quad [2]$$

where, for an isotropic solid, α is the linear thermal expansion coefficient, E is Young's modulus, and $T(r)$ is the radial temperature distribution.

Once the radial (σ_r) and tangential (σ_θ) stresses are determined from Eq. [2], the maximum shear stress ($\tau_{s,max}$) may be determined through the Mohr circle procedure as

$$\tau_{s,max} = \tfrac{1}{2}\,|\,\sigma_r - \sigma_\theta\,| \quad [3]$$

We have estimated whether the resulting shear stress is sufficient to produce yielding by employing the maximum shear-stress criterion (12). That is, yielding occurs when the maximum shear stress equals the value it has when yielding occurs in the tensile test (taken as one-half the upper yield point, σ_{uyp})

$$\tau_{s,max} = \tfrac{1}{2}\,\sigma_{uyp} \quad [4]$$

[2] Calculated results indicate that temperature variations across the slice thickness are negligible.

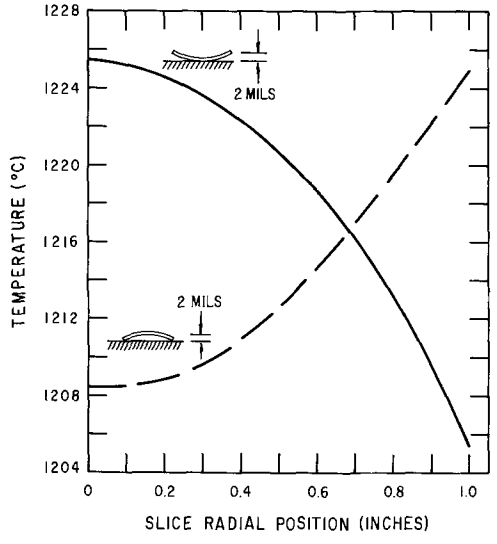

Fig. 2. Theoretical radial temperature distributions in a 2-in. diameter, 8-mil thick slice, susceptor temperature 1230°C.

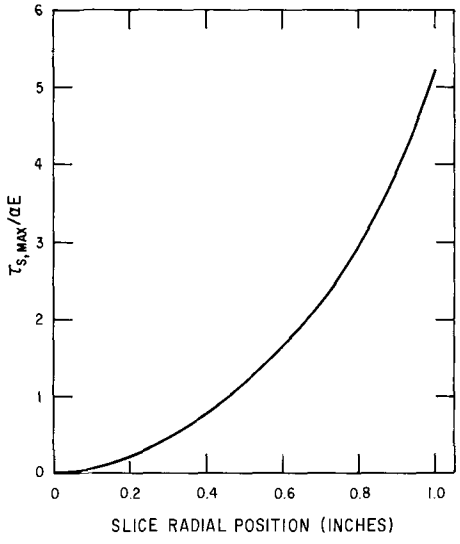

Fig. 3. Theoretical maximum shear stress variation in a 2-in. diameter, 8-mil thick concave slice (2-mil curvature).

The variation of $\tau_{s,max}/\alpha E$ as a function of radius was obtained by numerical integration of Eq. [2] and application of Eq. [3]. Figure 3 presents results based on the concave slice of Fig. 2 (solid line). The maximum shear stress at the slice periphery is estimated to be 21% of the upper yield point at 1200°C by taking $\sigma_{uyp} = 2 \times 10^8$ dynes/cm^2 (13), $\alpha = 4 \times 10^{-6}$ (°C)$^{-1}$ (14), and $E = 1.9 \times 10^{12}$ dynes/cm^2 (14). Since dislocations are observed in germanium at approximately 25-30% of the upper yield point (15) at 515°C (788°K or 64% of the melting point), the development of dislocations in silicon at 1200°C (1473°K or 87% of the melting point) is not unexpected. Thus, it appears that the thermal stress developed from typical slice curvatures may be sufficient to cause the activation of residual surface dislocation sources.

It should be noted, however, that the upper yield point is an extremely structure-sensitive property and is strongly dependent on whether surface or bulk sources are dominant (16-18). Furthermore, Young's modulus data at epitaxial temperatures are not available, although there are indications that it may be as much as 50% lower than the room temperature value.

A uniformly heated susceptor was assumed in the foregoing calculations. In practice, the susceptor itself can exhibit a substantial temperature variation which, coupled with the slice curvature effects, might more readily activate residual surface dislocation sources.

Acknowledgments

The authors wish to express their appreciation to Mrs. Betty Purkey for her assistance with the computer programming, and to Dr. L. D. Dyer for his constructive comments.

Manuscript submitted April 27, 1970; revised manuscript received Aug. 10, 1970.

Any discussion of this paper will appear in a Discussion Section to be published in the December 1971 JOURNAL.

REFERENCES

1. S. M. Hu, *J. Appl. Phys.*, **40**, 4413 (1969).
2. P. Rai-Choudhury and W. J. Takei, *ibid.*, **40**, 4980 (1969).
3. Y. Seki, K. Tanno, J. Matsui, and T. Kawamura, "Semiconductor Silicon," p. 653, R. R. Haberecht and E. L. Kern, Editors, ECS Softbound Symposium Series, New York (1969).
4. K. Morizane and P. Gleim, *J. Appl. Phys.*, **40**, 4104 (1969).
5. H. R. Huff and R. C. Bracken, "Semiconductor Silicon," p. 610, R. R. Haberecht and E. L. Kern, Editors, ECS Softbound Symposium Series, New York (1969).

6. H. R. Huff and C. M. Skooglund, AIChE MESD Biennial Conference Preprint Volume, 122 (1970).
7. B. G. Cohen and M. W. Focht, *Solid State Electronics*, **13**, 105 (1970).
8. J. R. Dale, "Semiconductor Silicon," p. 622, R. R. Haberecht and E. L. Kern, Editors, ECS Softbound Symposium Series, New York (1969).
9. H. J. Queisser, "Semiconductor Silicon," p. 585, R. R. Haberecht and E. L. Kern, Editors, ECS Softbound Symposium Series, New York (1969).
10. G. M. Dusinberre, "Heat-Transfer Calculations by Finite Differences," International Textbook Co., Scranton, Pa. (1961).
11. S. Timoshenko and J. N. Goodier, "Theory of Elasticity," p. 406, McGraw-Hill Book Co., New York (1951).
12. S. H. Crandall and N. C. Dahl, "An Introduction to the Mechanics of Solids," p. 199, McGraw-Hill Book Co., New York (1959).
13. W. D. Sylwestrowicz, *Phil. Mag.*, **7**, 1825 (1962).
14. W. R. Runyan, "Silicon Semiconductor Technology," McGraw-Hill Book Co., New York (1965).
15. J. R. Patel and A. R. Chaudhuri, *Phys. Rev.*, **143**, 601 (1966).
16. A. R. C. Westwood, "Chemistry and Physics of Interfaces," E. Gushee, Editor, p. 159, American Chemical Society Publications, Washington, D.C. (1965).
17. H. Alexander and P. Hansen, "Solid State Physics," F. Seitz, D. Turnbull, and H. Ehrenreich, Editors, Vol. 22, p. 27, Academic Press, New York (1968).
18. J. R. Patel and A. R. Chaudhuri, *J. Appl. Phys.*, **34**, 2788 (1963).

Silicon Optical Constants in the Infrared

P. A. Schumann, Jr.,* W. A. Keenan,* A. H. Tong,* H. H. Gegenwarth, and C. P. Schneider

IBM Components Division, East Fishkill Laboratory, Hopewell Junction, New York 12533

The optical constants of semiconductors, primarily silicon, are becoming increasingly important because of the emphasis on optical measurement techniques. These techniques are very promising, being in general nondestructive and contactless (1). At present they all require some knowledge of the optical constants primarily due to free carriers. The most important of the optical measurement techniques now used in the semiconductor industry are infrared interference for the measurement of epitaxial layer thickness (2-7), substrate carrier concentration (8, 9) and part of the outdiffused profile (10, 11), plasma resonance for measurement of high carrier concentration (12-14) and diffusion surface concentration (15-18), total internal reflection techniques for the measurement of the carrier concentration of the epitaxial layer (19, 20), pseudo-Brewster angle for the measurement of carrier concentration and diffusion surface concentration (21), and direct measurement of the absorption coefficient to determine carrier concentration. In addition, there are many infrared absorption techniques for impurities such as carbon and oxygen in silicon (22) and cryogenic absorption for other impurities.

All the measurements were made at room temperature with a Perkin-Elmer Model 621 spectrophotometer utilizing their Micro Specular Reflectance Accessory for reflectance. Reflectance and transmittance were measured and reduced to the optical constants using the technique previously reported (23, 24). For normal incidence, the reflectivity R of a semi-infinitely thick sample is (24)

$$R = \frac{(n-1)^2 + k^2}{(n+1)^2 + k^2} \qquad [1]$$

where n is the index of refraction, and k is the extinction coefficient.

The extinction coefficient k is related to the absorption coefficient α by the equation

$$k = \frac{\alpha\lambda}{4\pi} \qquad [2]$$

where λ is the wavelength in vacuum.

The transmission through a sample of finite thickness d is

$$T = \frac{(1-R)^2 e^{-\alpha d}}{1 - R^2 e^{-2\alpha d}} \qquad [3]$$

The measured reflectivity r for a sample of finite thickness d is (25)

$$r = R(1 + T e^{-\alpha d}) \qquad [4]$$

The simultaneous solution of Eq. [3] and [4] yields α and R; n and k can then be calculated from Eq. [1] and [2].

Carrier concentration was measured by determination of resistivity and utilization of Irvin's curves (26). These results were checked where possible by use of the plasma resonance minimum, in which the published calibration curves (14) were used. The average difference in the two techniques was 12% for n-type and 34% for p-type silicon. Thirty-five samples were measured with carrier concentrations between 8.6×10^{14} and 6.2×10^{19} cm^{-3} in the wavelength range from 2.5 to 40 μm. An intrinsic sample was also measured to study the lattice absorption bands; these absorption data were then compared with the previous data of Collins and Fan (27), as shown in Fig. 1. As can be

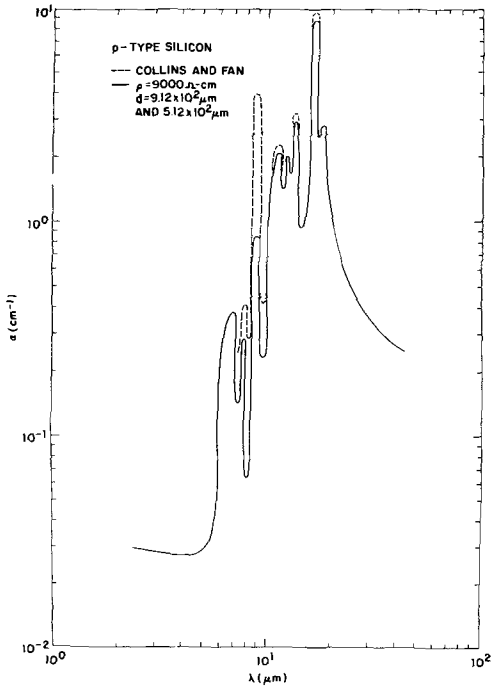

Fig. 1. Absorption coefficient α as a function of wavelength λ in micrometers for near intrinsic silicon.

* Electrochemical Society Active Member.

Key words: absorption coefficient, index of refraction, carrier concentration, extinction coefficient, plasma resonance.

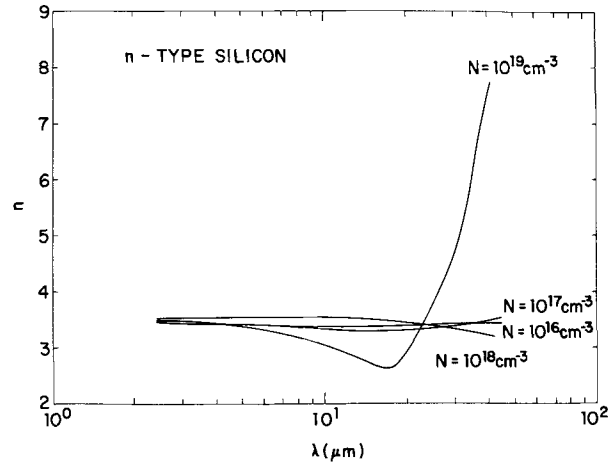

Fig. 2. Index of refraction n as a function of wavelength λ in micrometers for n-type silicon with various carrier concentrations.

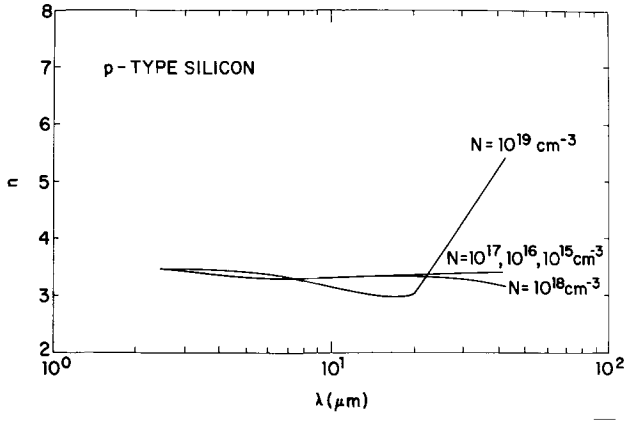

Fig. 3. Index of refraction n as a function of wavelength λ in micrometers for p-type silicon with various carrier concentrations.

seen, the agreement between the two sources of data is excellent.

Direct determination of the optical constants from the reflectance and transmittance is very sensitive to experimental variation in these quantities. A smoothing procedure was adopted to reduce the effects of this variation. After lattice absorption was subtracted from the reflection and transmission data, the optical constants were calculated by the technique above. The optical constants were first plotted as a function of concentration for the various wavelengths.[1] Smooth curves were hand-drawn through these data points. Values were then taken from these smooth curves and used to construct the optical constant *vs.* wavelength curves for various concentrations shown in Fig. 2-5.

Most of the published work on the optical constants reports only the absorption coefficient. The absorption coefficient has thus been chosen to compare previously published experimental data, this work, and theoretical calculations from a semiclassical free carrier absorption model (13). Representative curves are shown for n- and p-type silicon. Figures 6-9 are plots of the absorption coefficient as a function of carrier concentration, indicating both experimental and theoretical data. The dotted line is a hand-drawn estimate of the experimental data.

Figure 6 shows the data of Spitzer and Fan (23), Vavilov (28), Ukhanov (29), Spitzer, Gobeli, and Trumbore (30), and the authors for n-type silicon at a wavelength of 5 μm. The agreement between the experiment and theory is good. Figure 7, however, which shows the data of Vavilov (28), Hara and Nishi (31), and the authors for p-type silicon at the same wavelength, indicates even better agreement between theory and experiment.

At a wavelength of 40 μm the agreement is not good, as shown in Fig. 8 and 9. The data of Walles (32), and Walles and Boija (33) are given in Fig. 9. For n-type silicon the theory misses the experimental data completely. For p-type silicon, the theory crosses the experimental data and thus represents a better fit, pos-

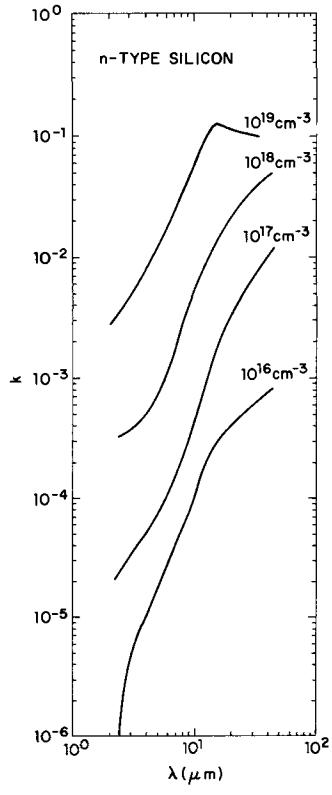

Fig. 4. Extinction coefficient k as a function of wavelength λ in micrometers for n-type silicon with various carrier concentrations.

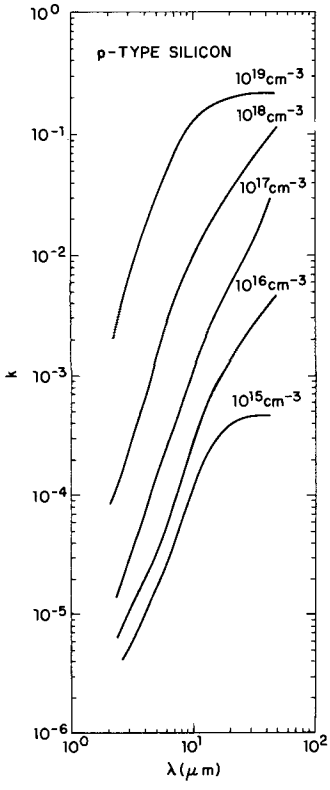

Fig. 5. Extinction coefficient k as a function of wavelength λ in micrometers for p-type silicon with various carrier concentrations.

[1] A complete set of data and curves is available on request from the authors: TR 22.1008.

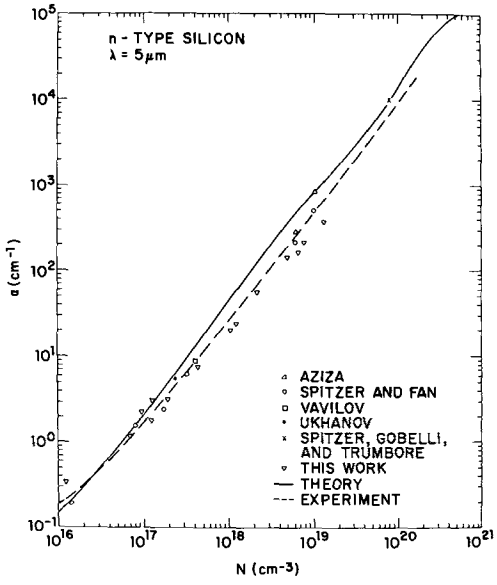

Fig. 6. Absorption coefficient α as a function of carrier concentration for n-type silicon at a wavelength of 5 μm.

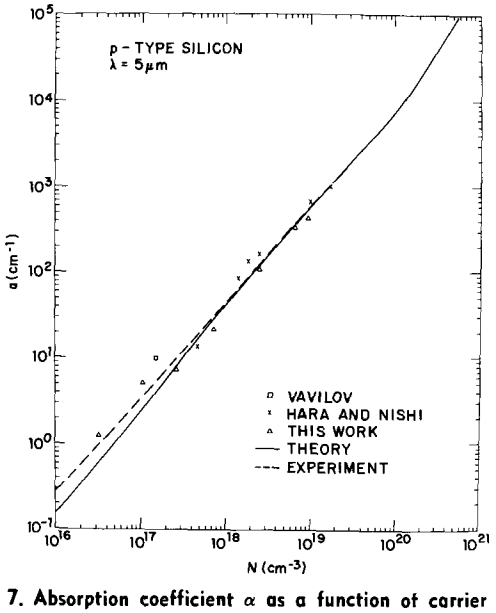

Fig. 7. Absorption coefficient α as a function of carrier concentration for p-type silicon at a wavelength of 5 μm.

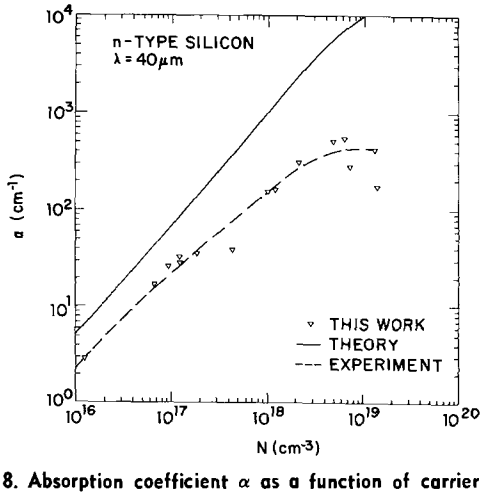

Fig. 8. Absorption coefficient α as a function of carrier concentration for n-type silicon at a wavelength of 40 μm.

sibly. In all cases, the authors' experimental data agree very well with the previously published data, thus offering for the first time a wide range of optical constants as a function of carrier concentration and wavelength.

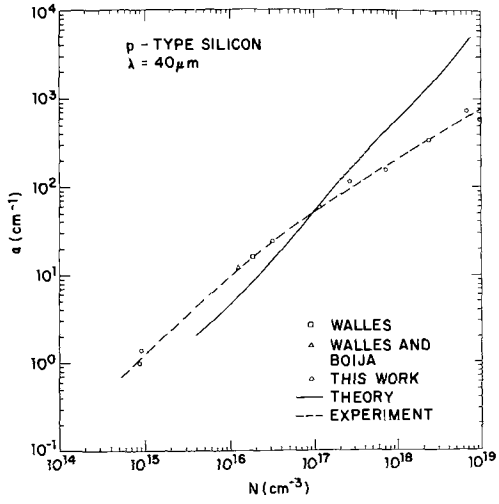

Fig. 9. Absorption coefficient α as a function of carrier concentration for p-type silicon at a wavelength of 40 μm.

The theoretical model used to calculate the optical constants appears to fit the experimental data well at short wavelengths, but the longer wavelength fit is not successful. It would appear necessary therefore to alter the theoretical model or improve it to better fit the long wavelength optical constants.

Manuscript submitted June 1, 1970; revised manuscript received ca. Sept. 10, 1970.

Any discussion of this paper will appear in a Discussion Section to be published in the December 1971 JOURNAL.

REFERENCES

1. P. A. Schumann, Jr., "Semiconductor Silicon," p. 662, R. R. Haberecht and E. L. Kern, Editors, ECS Symposium Soft Bound Series (1969).
2. W. G. Spitzer and M. Tannebaum, *J. Appl. Phys.*, **32**, 744 (1961).
3. M. P. Albert and J. F. Combs, *This Journal*, **109**, 709 (1962).
4. P. A. Schumann, Jr., R. P. Phillips, and P. J. Olshefski, *ibid.*, **113**, 368 (1966).
5. T. Abe and T. Kato, *Japan J. Appl. Phys.*, **4**, 742 (1965).
6. K. Sato, Y. Ishikawa, and K. Sugawara, *Solid-State Electron.*, **9**, 771 (1966).
7. P. A. Schumann, Jr., *This Journal*, **116**, 409 (1969).
8. P. A. Schumann, Jr., and C. P. Schneider, Submitted for publication.
9. A. H. Tong, P. A. Schumann, Jr., and W. A. Keenan, Paper 165 presented at the Atlantic City Meeting of the Society, Oct. 4-8, 1970.
10. P. A. Schumann, Jr., Paper presented at Conference on Silicon Processing, NBS, June 1969.
11. V. Tsunoda and O. Mori, *J. Phys. Soc. Japan*, **27**, 1077 (1969).
12. L. E. Howarth and J. F. Gilbert, *J. Appl. Phys.*, **34**, 236 (1963).
13. P. A. Schumann, Jr., and R. P. Phillips, *Solid-State Electron.*, **10**, 943 (1967).
14. P. A. Schumann, Jr., *Solid-State Tech.*, January, 1970, p. 50.
15. I. Kudman, *J. Appl. Phys.*, **34**, 1826 (1963).
16. H. D. Riccius and G. Ulbricht, *Z. Angew. Phys.*, **19**, 203 (1965).
17. E. E. Gardner, W. Kappallo, and C. R. Gordon, *Appl. Phys. Letters*, **9**, 432 (1966).
18. T. Abe and Y. Nishi, *Japan J. Appl. Phys.*, **7**, 397 (1968).
19. T. G. R. Rawlins, *This Journal*, **111**, 810 (1964).
20. D. C. Gupta, Paper 101 presented at the New York Meeting of the Society, May 4-9, 1969 (Extended Abstracts, p. 235).
21. W. A. Keenan and P. A. Schumann, Jr., Paper 117 presented at the Los Angeles Meeting of the Society, May 10-15, 1970.
22. J. A. Baker in "Semiconductor Silicon," p. 566, R. R. Haberecht and E. L. Kern, Editors, ECS Symposium Soft Bound Series (1969).

23. W. G. Spitzer and H. Y. Fan, *Phys. Rev.*, **106**, 882 (1957).
24. H. Y. Fan, The Physical Society Reports on Progress in Physics, **19**, 107 (1956).
25. Alfred Kahan, Government Research Report, AD 435620 (1963).
26. J. C. Irvin, *Bell System Tech. J.*, **41**, 387 (1962).
27. R. J. Collins and H. Y. Fan, *Phys. Rev.*, **93**, 674 (1954).
28. V. S. Vavilov, *Sov. Phys.—Solid State*, **2**, 346 (1960).
29. V. I. Ukhanov, *ibid.*, **4**, 2010 (1963).
30. W. G. Spitzer, G. W. Gobelli, and F. A. Trumbore, *J. Appl. Phys.*, **35**, 206 (1964).
31. H. Hara and Y. Nishi, *J. Phys. Soc. Japan*, **21**, 1222 (1966).
32. S. Walles, *Arkiv Fysik*, **25**, 33 (1963).
33. S. Walles and S. Boija, *J. Opt. Soc. Am.*, **54**, 133 (1964).

Brief Communications

Luminescence of Bi^{+3}-Activated LaOCl under X-Ray Excitation

P. Y. Simons

E. I. du Pont de Nemours & Co., Inc., Photo Products Department, Parlin, N. J. 08859

The luminescence of Bi^{+3}-activated LaOCl over a narrow bismuth composition range under ultraviolet, cathode ray, and x-ray excitation has been reported by Swindells (1). Blasse and Bril (2) in their investigation of Bi^{+3}-activated phosphors report on LaOCl activated with 1 a/o (atomic per cent) bismuth.

This present work concerns a study of the luminescence properties of Bi^{+3}-activated LaOCl over a wide composition range under x-ray excitation.

Experimental

A series of Bi^{+3}-activated phosphors were prepared by dissolving the appropriate amounts of La_2O_3 (99.99%) and reagent grade Bi_2O_3 in distilled water and HCl, evaporating to dryness, and firing the residue ($LaCl_3$ nH_2O) in air overnight at 600°C in porcelain crucibles. An additional firing in air at 1000°C for 3 hr was performed to increase phosphor crystallinity. All samples were checked by powder x-ray diffractometry and only single-phase LaOCl was found.

The emission spectra were recorded on a spectroradiometer system[1] with the x-ray excitation from a Faxitron[2] x-ray unit. The apparatus consists of a quartz prism monochromator[3] coupled to a photomultiplier microphotometer employing a 1P28 photomultiplier which in turn was coupled to a strip chart recorder. Automatic scanning was obtained by connecting a reversible motor to the micrometer which drove the monochromator. Since the output is a nonlinear wavelength *vs.* light intensity peak, all spectra were replotted in a linear scale and the intensity corrected for the detector system response.

The x-ray beam was collimated to reduce stray radiation in the x-ray chamber, and the powdered sample was completely immersed in x-rays during excitation. All spectra were taken at room temperature with the unfiltered tungsten target operating at 80 kVp and 3 mA. The dose rate at the sample position was about 1.7 roentgen/sec as measured with an ionization roentgen meter.[4]

Results and Discussion

Under x-ray excitation Bi^{+3}-activated LaOCl is characterized by broad-band emission at 365 nm and 450 nm (measured at peak half height). At all bismuth compositions below 25% the 365 nm is the more intense. Blasse and Bril (2) also observed these emissions in LaOCl:Bi(0.01) under ultraviolet excitation. The dependency of the emission on increasing bismuth content is given in Fig. 1, and the emission spectra of LaOCL doped with 10 and 25 m/o (mole per cent) bismuth are given in Fig. 2.

The 365 nm emission intensity reaches a maximum at a bismuth concentration of 10 m/o, and with

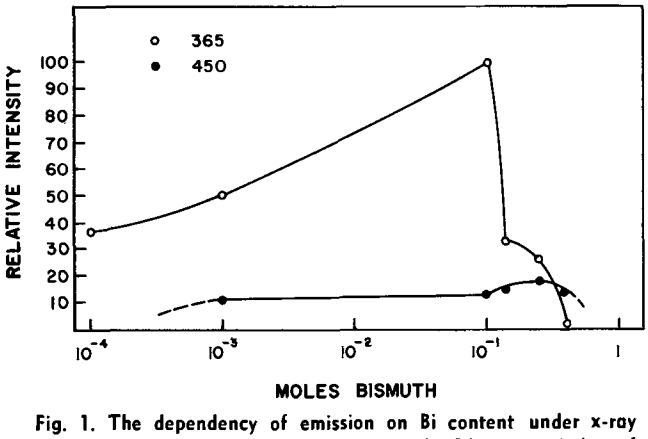

Fig. 1. The dependency of emission on Bi content under x-ray excitation. The intensity is normalized for the 365 nm emission of LaOCl:Bi(0.10) equal to 100.

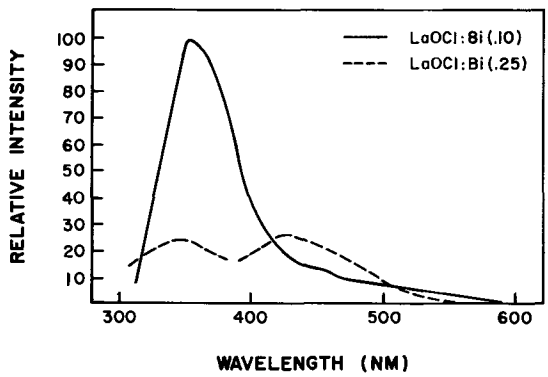

Fig. 2. Emission spectra of LaOCl:Bi(0.10) and LaOCl:Bi(0.25) under x-ray excitation.

Key words: luminescence spectra, phosphors, x-ray excitation, lanthanum oxychloride-bismuth oxychloride solid solutions, lanthanum oxychloride, bismuth oxychloride.

[1] International Light, Inc., Newburyport, Mass. 01950.
[2] Field Emission Corp., McMinnville, Oreg. 97128.
[3] Schoeffel Instrument Corp., Westwood, N. J. 07675.
[4] Victoreen Instruments, Cleveland, Ohio 44104.

increasing bismuth this emission is severely quenched. On the other hand, the 450 nm emission intensity appears to reach a maximum at 25% bismuth. Note that while the 365 nm emission is being quenched the 450 nm band intensity increases. A weak emission at 500 nm is also observed in the LaOCl:Bi spectrum. This band is due to impurities in the starting material. Undoped samples of LaOCl prepared from La_2O_3 gave this weak emission, whereas undoped LaOCl prepared from $La(NO_3) \cdot 5H_2O$ did not emit at 500 nm although it had weak bands at other wavelengths. BiOCl was also prepared but it did not luminesce under x-ray excitation.

The nature of the emission centers in Bi^{+3}-activated phosphors is not completely understood. Emissions have been assigned to electronic transitions between s^2-sp states or activator-matrix states (2). Emission in Y_2O_3:Bi has been attributed to bismuth occupying two centers in the host (3). Without excitation spectra the assignments of the transitions responsible for emissions in this system cannot be determined. However, based on the assignment of the $1P_1 \rightarrow 1S_0$ transition for the Bi^{+3} emission in YOCl:Bi^{+3} by Blasse and Bril (2) it appears reasonable to assign this transition to the 365 nm emission in LaOCl:Bi. It may also be reasonable to assume that the 450 nm emission is due to the $3P_1 \rightarrow 1S_0$ transition because this is the only other allowed transition of an ion with a s^2-sp excited configuration. However, this assignment cannot be made unequivocally without a detailed study of the absorption and excitation spectra of LaOCl:Bi emissions.

Manuscript received Aug. 18, 1970.

Any discussion of this paper will appear in a Discussion Section to be published in the December 1971 JOURNAL.

REFERENCES

1. F. W. Swindells, *This Journal*, **101**, 414 (1954).
2. G. Blasse and A. Bril, *J. Chem. Phys.*, **48**, 217 (1968).
3. S. Z. Toma and D. T. Palumbo, *This Journal*, **117**, 236 (1970).

Inhibition of Silicon Growth Rate During the Deposition of Arsenic-Doped Epitaxial Silicon Layers on Silicon by Pyrolysis of Silane

R. F. C. Farrow and J. D. Filby

Ministry of Technology, Royal Radar Establishment, Malvern, Worcestershire, England

The production of epitaxial layers of silicon by the pyrolysis of silane (SiH_4) on silicon substrates is well known (1, 2) to offer several advantages over present methods which involve hydrogen reduction of trichlorosilane ($SiHCl_3$) or silicon tetrachloride ($SiCl_4$). In the course of investigations into the effect of group III and V dopants on the epitaxial growth of silicon on silicon by pyrolysis of a molecular beam of silane, we have observed that silane pyrolysis on a (111) silicon substrate is inhibited by the presence of arsine at the surface. Since this inhibition implies a reduction in the growth rate of arsenic-doped epitaxial silicon layers using pyrolysis of silane we have examined the effect in some detail and report here our preliminary findings.

The system used in our investigations is shown schematically in Fig. 1. A molecular beam of silane is formed in a triple aperture, ultra-high vacuum system and impinges on the (111) face of a heated silicon specimen in a target chamber. The target and collimation chambers are each pumped by oil diffusion pumps fitted with molecular sieve traps and thermoelectrically cooled chevron baffles to prevent back diffusion of silicone oil. Gas species scattered from the silicon specimen are detected by a quadrupole residual gas analyzer. The entire system is baked at 350°C prior to each run, and base pressures in the region of 10^{-10} Torr in all parts of the system are achieved. Residual carbon and oxygen contamination of the surface is removed by heating the specimen to 1250°C for 5 min (3) before exposing it to the molecular beam. Group III or V dopants are introduced by adding the appropriate helium diluted dopant gases, *e.g.*, diborane, phosphine, arsine, to the silane beam.

The kinetics of pyrolysis of silane and arsine were studied by monitoring gas species desorbed from the (111) silicon surface as a function both of beam intensity and substrate temperature. It was found that the onset of pyrolysis of both silane and arsine was marked by a rapid increase in the flux of H_2 desorbed from the surface as a function of temperature. From a plot of the logarithm of the fractional increase in the H_2 signal as a function of reciprocal of absolute temperature (Arrhenius plot) activation energies of 10 ± 1 kcal/mole and 12 ± 1 kcal/mole were derived for pyrolysis of silane and arsine, respectively, on a clean (111) silicon surface. Furthermore, it was found that the fractional increase in the H_2 signal was linearly proportional to the beam intensity for both silane and arsine pyrolysis, *i.e.*, the production of H_2 by pyrolysis of silane and arsine is a first order reaction.

In addition to studying the kinetics of pyrolysis of arsine and silane separately, the effect on silane pyrolysis of the introduction of arsine to the silane beam was also investigated. It was found that the introduction of arsine led to an inhibition of the silane pyrolysis. This effect is shown in Fig. 2 in which the ratio of the H_2 signal for a given incident flux of silane molecules with arsine present to the H_2 signal for the same incident flux of silane molecules without arsine is plotted as a function of time for three different

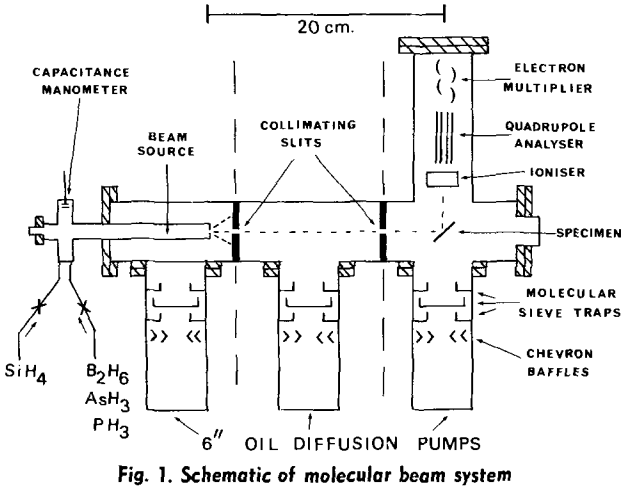

Fig. 1. Schematic of molecular beam system

Key words: surface reaction kinetics, pyrolysis.

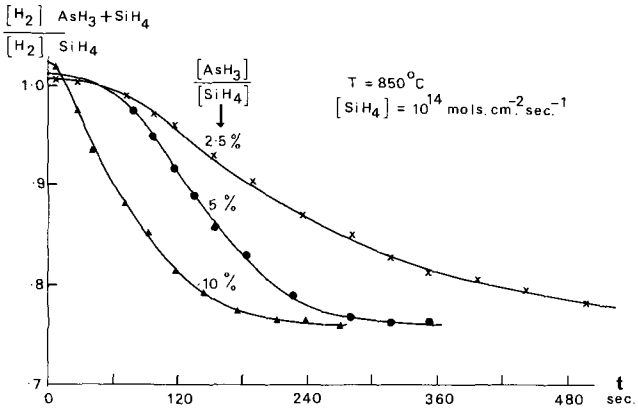

Fig. 2. Inhibition of hydrogen production during pyrolysis of a molecular beam of arsine + silane.

concentrations of arsine in the beam. The time zero represents the instant at which the arsine is added to the silane beam. It is seen that initially the H_2 signal with arsine present is greater than with only silane present due to the contribution of arsine pyrolysis to the H_2 signal. However, with increasing time the H_2 production is progressively inhibited and approaches a lower limit at which the H_2 signal is only 7% greater than the H_2 signal at ambient temperature. (The H_2 signal at ambient temperature is due to cracking of silane in the quadrupole residual gas analyzer.) This corresponds to an 80% reduction in the rate of silane pyrolysis. It can also be seen that increasing the concentration of arsine in the beam leads to a more rapid approach to the lower limit of the pyrolysis rate but does not affect this limiting rate. Moreover, by recording corresponding data to that shown in Fig. 2 for various specimen temperatures it was found that the activation energy for silane pyrolysis was increased to 14 ± 1 kcal/mole in the presence of arsine.

On the basis of these experimental facts, the most likely explanation for the inhibition of silane pyrolysis is that as arsenic is produced at the silicon surface it becomes strongly bound to certain surface sites which are active in inducing silane pyrolysis, thus preventing access of impinging silane molecules to these sites. At the present time the nature of these active sites is not clear although one possibility is that they are sites at the edge of atomic steps which are known to exist on thermally cleaned (111) silicon surfaces (4) and on the surface of silicon layers deposited on (111) silicon substrates under ultra-high vacuum conditions (5).

The preceding suggestion that arsenic "poisons" active sites on the silicon surface is supported by the fact that arsenic is well known as a catalyst poison in other chemical reactions, notably in the case of SO_3 production from SO_2 and O_2 in which traces of arsenic are sufficient to poison a platinum catalyst. Additional support for the observation of inhibition of silane pyrolysis by arsine is provided by the work of Eastwood *et al.* (6) who found that the deposition rate of arsenic doped SiO_2 layers (on silicon substrates) formed by pyrolysis of a gaseous mixture of silane, oxygen, and arsine decreased with increasing arsine concentration.

Table I. Thickness and resistivity of silicon layers

$\frac{[AsH_3]}{[SiH_4]}$ %	Thickness, μ	Resistivity, ohm-cm	Carrier concentration, cm^{-3}
0	12	20	$3 \cdot 10^{14}$
1	6	0.010	$5 \cdot 10^{18}$
2.5	2.4	0.007	$9 \cdot 10^{18}$
5	1.8	0.006	$1.1 \cdot 10^{19}$
10	1.2	0.005	$1.5 \cdot 10^{19}$

We have confirmed by measurement of the thickness of epitaxial silicon layers deposited using a conventional ultra-high vacuum system that the presence of arsine does indeed inhibit the silicon growth rate. This can be seen from Table I which summarizes the thickness and resistivity of layers grown in 60 min at 850°C with a silane pressure of 0.1 Torr.

It should be pointed out that inhibition of silane pyrolysis by arsine may prove a practical limitation only at high arsine concentrations where inhibition takes place in a time shorter than the time required for deposition of the epitaxial layer. At arsine concentrations below 0.1% we have found that the inhibition takes several hours to reach its maximum effect. This would explain why no inhibition of growth rate was reported either by Swanson and Tucker (7) or Richman and Arlett (2) who investigated the arsenic doping of epitaxial (111) silicon layers grown by pyrolysis of silane. The ratio of arsine to silane used in their work did not exceed 0.04%, and their layers were deposited in less than 1 hr.

Acknowledgment

The authors are grateful for helpful discussions with Dr. R. M. Logan and Dr. W. Bardsley.

This paper is published with the permission of the Controller H.B.M. Stationery Office.

Manuscript received Aug. 18, 1970.

Any discussion of this paper will appear in a Discussion Section to be published in the December 1971 JOURNAL.

REFERENCES

1. D. C. Gupta and R. Yee, *This Journal*, **116**, 1561 (1969).
2. D. Richman and R. H. Arlett, "Semiconductor Silicon," R. R. Haberecht and E. L. Kern, Editors, p. 200, Electrochemical Society, New York (1969).
3. B. A. Joyce, J. H. Neave, and B. E. Watts, *Surface Sci.*, **15**, 1 (1969).
4. B. E. Watts, Private communication.
5. H. C. Abbink, R. M. Braidy, and G. P. McCarthy, *J. Appl. Phys.*, **39**, 4673 (1968).
6. R. Nuttall, Private communication.
7. T. B. Swanson and R. N. Tucker, *This Journal*, **116**, 1271 (1969).

Isothermal Solution Mixing Growth of Thin $Ga_{1-x}Al_xAs$ Layers

J. M. Woodall*

IBM Thomas J. Watson Research Center, Yorktown Heights, New York 10598

Since the development of the liquid phase epitaxial growth of $Ga_{1-x}Al_xAs$ electroluminescent devices (1, 2), this method has been used to realize considerable improvements in threshold current densities for injection lasers. These improvements are due to the use of GaAs and $Ga_{1-x}Al_xAs$ heterojunction structures (3-5). The most recent optimization (6) employs a 1μ thick Si doped p-type GaAs layer sandwiched between an n-type and a p-type $Ga_{1-x}Al_xAs$ layer with $0.2 \leq x \leq 0.5$. Further improvement could be expected

* Electrochemical Society Active Member.
Key words: crystal growth, thin layers, $Ga_{1-x}Al_xAs$.

if the thickness of the p-type GaAs layer could be reduced even more. Previously, layers 1μ thick were grown using a specially designed apparatus (6) in which melts of different composition were brought into contact with the surface of a layer which was mechanically wiped clean of the previous melt. In order to avoid the possibility of mechanically damaging the surface of a thin layer during wiping, a new technique for heterojunction growth has been developed which is reported in the present communication. This method promises to have the capability for growing multilayered structures with thicknesses $<<$ 1μ. The purpose of this report is to describe the method, the apparatus, and some preliminary results.

A photograph of the apparatus used for isothermal solution mixing (ISM) is shown in Fig. 1. The main features of this apparatus are a cylindrical substrate holder and a partitioned crucible which can contain two melts. All parts are made of high-purity, high-density graphite. The substrate can be brought into contact with either melt by a rotation of the holder such that the substrate is aligned with one of the windows on the inner wall of the crucible. This apparatus can be used in either the normal liquid phase epitaxial growth mode or the ISM growth mode or both. For the ISM mode of growth a certain amount of one melt is trapped in the holder as it is rotated into the other melt. This trapped melt becomes supersaturated as it mixes with the other melt, causing crystal growth.

Melt preparation procedures are similar to those reported previously (7, 8). However, a notable difference in procedure for this method is the vacuum baking at 200°C of the system and substrate and the subsequent back filling by hydrogen which is purified by means of a palladium diffuser. This process step has notably improved the wetting of the substrate by the melt during the initial stages of growth. A Ga-Al melt is saturated with As using a rectangular bar of undoped GaAs with a mass in excess of that required for saturation. Using this procedure it is important to allow sufficient time for complete saturation to occur before rotating the substrate into the melt. This time is usually 1 hr and 15 min at 830°C. Bringing the substrate into contact with the melt before this time can result in complete dissolution of the substrate.

The composition profiles along the growth axis for two types of growth procedure are shown in Fig. 2 and 3. Figure 2 shows the profile of a layer which was grown from two different melts at a growth rate of 0.1°C/min. The layer was grown on the (100) face of an undoped GaAs substrate. The first part of the layer was grown from an As saturated melt containing 30g Ga with an Al/Ga weight ratio of 3 x 10^{-3}, and cooled from 862° to 852°C. The substrate was then rotated into a melt containing 30g Ga with an Al/Ga weight ratio of 5 x 10^{-3}, and cooled between 852° and 842°C. It should be noted that the composition profile is very flat for that part of the growth occurring in each melt. The decrease in Al concentration occurring near the end of the profile is due to fast freezing of the melt

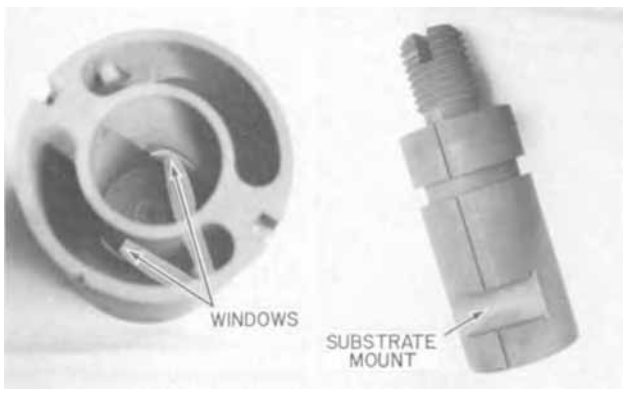

Fig. 1. Apparatus for isothermal solution mixing growth

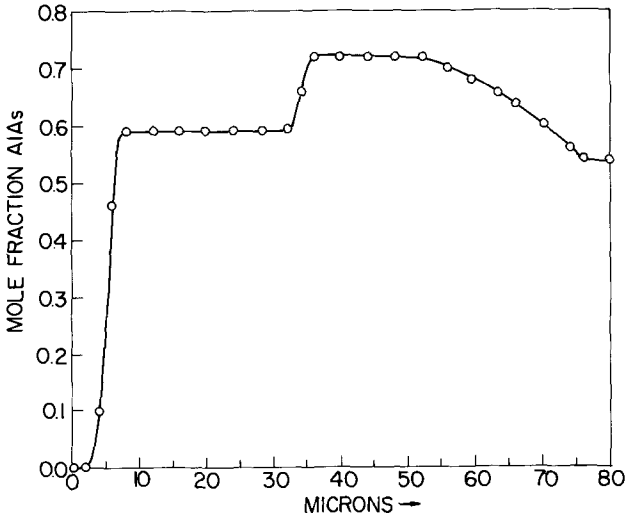

Fig. 2. Composition profile for layer growth by 0.1°C/min cooling and single rotation between two melts.

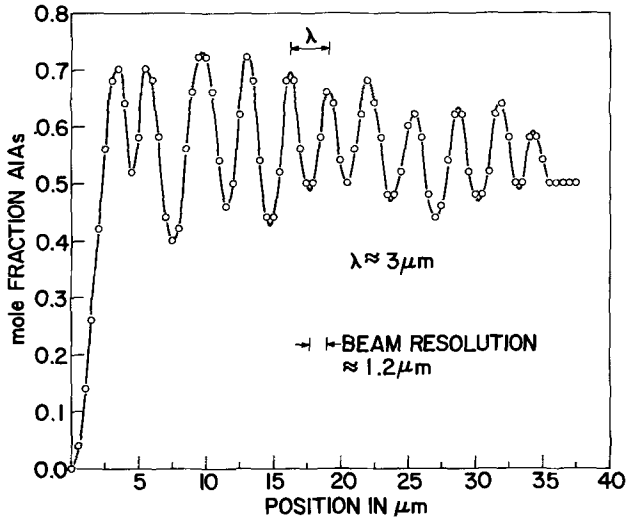

Fig. 3. Composition profile for layer growth by 0.1°C/min cooling and 23 melt changes.

which is trapped in the holder when the furnace is turned off.

Figure 3 shows the composition profile of a layer grown in the ISM mode by many rotations between two melts. It is seen that the layers show a periodic variation in Al concentration along the growth axis and that there is an over-all decrease in amplitude along the growth axis. The period is about 3μ, and hence each sublayer is about 1.5μ thick. One melt had an Al/Ga ratio of 10^{-3} and the other had a ratio of 5 x 10^{-3}. Rotation was done by rotating within a 2-sec time period from one melt to another and holding for 3 min. It was found that the thickness and spacing of the sublayer structure was independent of cooling rates between 0.03° and 0.1°C/min and rotation cycle time of 3 min/melt and 30 sec/melt. This appears to be good evidence that the growth of the substructure is due to the supersaturation which occurs during the mixing of the trapped melt which is brought over by the holder with the other melt.

The ISM epitaxial growth can be explained by the isothermal phase boundary-composition relations in the $Ga_{1-x}Al_x$ system (7, 9). A close examination of the Ga rich portion of this system shows that a solid-liquid phase boundary exists over a large composition range, and that the isothermal liquidus curve is such that when two melts having different composition on the liquidus line are mixed, the mixed melt will be supersaturated and hence crystallization can occur. This effect is shown in Fig. 4 which schematically rep-

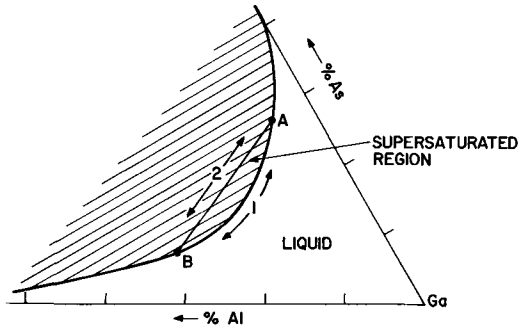

Fig. 4. Schematic Ga-Al-As-phase diagram at Ga rich corner

resents the Ga-Al-As liquidus line at constant temperature T at the Ga rich corner of the phase diagram. Points A and B represent two melts of different composition at solid-liquid equilibrium. Under equilibrium conditions the composition of the liquid melt can change along path 1 between A and B. When the melts are mixed the final composition of the mixed melt will lie at some point along path 2, the actual point depending on the volume ratio of the two melts. However, any point along path 2 at T except for points A and B lies in a region of supersaturation. This supersaturation is relieved by the growth of $Ga_{1-x}Al_xAs$ crystal.

The volume ratio of the melt compartment to the melt trapped in the holder of the apparatus in Fig. 1 is 25. It should be possible by the proper selection of this volume ratio, as well as the growth temperature and melt volume, to grow any desired thickness of such a sublayered structure. We have successfully employed this apparatus to grow a heterojunction layer structure (6) in which the $Ga_{1-x}Al_xAs$ layers are 1μ thick and the GaAs p-type layer is 1μ. This structure has produced lasing thresholds as low as 3600 A/cm^2 for a 75μ x 300μ Fabry-Perot cavity at room temperature.

Acknowledgments

The author wishes to thank R. M. Potemski and J. Grandia for technical assistance in the crystal growth experiments and contributions to the apparatus design; J. D. Kuptsis for electron beam probe measurements; and A. Benoric for preparing the laser devices.

Manuscript received Aug. 20, 1970.

Any discussion of this paper will appear in a Discussion Section to be published in the December 1971 JOURNAL.

REFERENCES

1. H. Rupprecht, J. M. Woodall, and G. D. Pettit, *Appl. Phys. Letters*, **11**, 81 (1967).
2. H. Rupprecht *et al.*, *IEEE J. Quantum Electron*, **QE-4**, 35 (1968).
3. I. Hayashi, M. B. Panish, and O. W. Foy, *ibid.*, **QE-5**, 211 (1969).
4. M. B. Panish, I. Hayashi, and S. Sumski, *ibid.*, **QE-5**, 210 (1969).
5. H. Kressel and H. Nelson, *RCA Rev.*, **30**, 106 (1969).
6. M. B. Panish, I. Hayashi, and S. Samski, *Appl. Phys. Letters*, **16**, 326 (1970).
7. M. H. Panish and S. Sumski, *J. Phys. Chem. Solids*, **30**, 129 (1969).
8. J. M. Woodall, H. Rupprecht, and W. Reuter, *This Journal*, **116**, 899 (1969).
9. M. Illegems and G. L. Pearson, 1968 Symposium on GaAs, Dallas, Texas.

JOURNAL OF THE ELECTROCHEMICAL SOCIETY

ELECTROCHEMICAL TECHNOLOGY

JANUARY 1971

Nonaqueous Batteries with $LiClO_4$-Ethylene Carbonate as Electrolyte

Gianfranco Pistoia

Istituto Chimico, Università di Roma, Rome, Italy

ABSTRACT

An evaluation of the use of ethylene carbonate as a solvent for high-energy nonaqueous batteries has been performed. The results are compared with those obtained for propylene carbonate. A 1.0M $LiClO_4$-EC solution has higher conductivity, lower viscosity, and lower influence on the polarization of Li, CuF_2, and NiS electrodes than an analogous $LiClO_4$-PC solution. Discharge curves at 1.0 and 2.4 mA/cm^2, obtained under the same conditions in 1.0M $LiClO_4$-EC and PC solutions for Li-CuF_2 and Li-NiS cells, gave better results when EC was used. A test cell Li/1.0M $LiClO_4$-EC/CuF_2, capable of providing about 200 Whr/kg (outside casing excluded) when discharged at 1.0 mA/cm^2 at 30°C, has been fabricated.

Research on the development of high-energy nonaqueous batteries has been focused mostly on propylene carbonate (PC) electrolytic solutions.

In 1964, Elliott *et al.* (1) pointed out that addition of ethylene carbonate (EC) to such solutions improved the system by increasing the dielectric constant, decreasing the viscosity, and increasing the conductivity of the solutions. No further investigation on the use of this solvent in nonaqueous batteries has been reported since, however.

Pistoia, De Rossi, and Scrosati (2) have recently shown in a preliminary note some of the advantages of using EC solutions in electrochemical cells, for instance the higher specific conductivity with respect to the PC solutions. EC is solid at room temperature (mp 36.2°C) but the high molal lowering of the freezing point (5.5°C) can give liquid solutions at room temperature. Furthermore, the addition of only 9% PC is sufficient to obtain another 5°C decrease in the freezing point.

On the other hand, the use of EC solutions of low salt concentration, which are solid at room temperature, would significantly reduce the solubility shown by many substances used as cathodes (*e.g.*, CuCl, CuF_2, NiF_2, and others) and the resulting self-discharge processes. Batteries containing the above-mentioned solid EC solutions could be thermally activated and should need a very low activation energy because of the small temperature increase necessary to melt the solutions.

Electrolytic solutions in aprotic solvents must possess certain basic properties in order to be used in a battery; they must:

(*a*) be inactive toward the electrodes and, particularly, have low solubility effects toward the cathodic materials
(*b*) have sufficiently high conductivity to minimize the *IR* losses in voltage
(*c*) not appreciably influence the electrode polarization and allow high utilization coefficients, especially of the positive electrode

Key words: lithium, ethylene carbonate, nonaqueous batteries.

This work was carried out to see if these conditions are fulfilled for EC electrolytic solutions and if such solutions are more practical than those of PC.

To this end, viscosity and conductivity measurements of KCNS, KPF_6, and $LiClO_4$ in EC solutions, and solubility measurements of CuF_2 in solutions of $LiClO_4$ in EC at various concentrations, have been performed. Furthermore, polarization curves of Li, CuF_2, and NiS electrodes in $LiClO_4$-EC solutions and constant current discharge curves for cells having lithium anodes and CuF_2 or NiS as cathodes, respectively, have been determined. All results have been compared with those obtained under the same conditions for equivalent PC solutions.

As mentioned above, in addition to CuF_2, which is one of the most frequently used cathode materials (3) in primary organic batteries (the theoretical specific energy for the Li-CuF_2 couple is about 1660 Whr/kg), the NiS cathode was examined (the theoretical specific energy of the Li-NiS couple is 1100 Whr/kg).

The feasibility of using some sulfides such as CuS (4) and NiS (5) in organic batteries has been demonstrated recently. In particular, the nickel sulfide electrodes have been shown to be electrochemically active, capable of high-energy density values, and relatively insoluble in $LiClO_4$-PC. Also, for the sulfides it is possible to develop primary cells only, since Li_2S is apparently insoluble both in $LiClO_4$-PC and $LiClO_4$-EC solutions.

Experimental Section

Materials.—EC (Merck LAB product) was purified by the following vacuum (*ca.* 1 mm Hg) distillation procedures:

(*a*) without additives
(*b*) on Li ribbon
(*c*) on CaO
(*d*) on a molecular sieve (4A) after 2 days' storage.

Usually, 180 cm^3 of solvent were distilled, of which only the middle 60 cm^3 cut was employed. The distillation temperature was about 75°C, that of the pot about 110°C. The commercial product and the four

samples distilled as above were analyzed by gas chromatography. The conductivity measurements were obtained on the same samples (see below). For the preparation of all other solutions and of the cells to be discharged, the middle fractions of EC distilled on CaO were used.

PC (anhydrous Fluka product) was distilled under vacuum without additives.

$LiClO_4$ (anhydrous Fluka product), as received, contained 1.2% of water determined by the Karl Fischer method. Drying under vacuum for 3 days at 150°C reduced the water content to 0.5%. Fusion under vacuum at 260°C was more effective since, after this treatment, the water content was further reduced to 0.1%. Still, this is greater than the amount contained in the solvent after purification (see below).

KCNS (Erba product), KPF_6 (Alfa Inorganics product), and CuF_2 (anhydrous Ozark Mahoning product) were dried by heating under vacuum (10^{-3} mm Hg). NiS was prepared according to the method described by Jasinski (5), by reacting $NiCl_2 \cdot 6\ H_2O$ with $(NH_4)_2S$. The final product was washed with water and dried under vacuum. This salt also contained about 0.1% water.

Graphite (Southwestern 1651) and polyethylene powder were used as received (after drying) for the preparation of the electrodes. The lithium anodes and the molecular sieve (Type 4A, BDH product) for the purification of EC were also used as received.

Apparatus and technique.—Gas chromatography.—Gas chromatograms were obtained on a Perkin Elmer Model 880 instrument with a flame ionization detector, using a 2m stainless steel column, packed with 60-80 mesh chromosorb W coated with 20% Carbowax 1500. Helium was used as the carrier gas (flow rate, 50 cm^3/min). The column, injection block, and detector temperatures were held at 130°, 140°, and 130°C, respectively.

Water content determination.—The water content in the distilled EC samples and in $LiClO_4$ was determined by the Karl Fischer method using a Type TTA1/KF Radiometer apparatus connected to a Type TTT1 Radiometer titrator.

Specific conductivity.—For these measurements, a Type 4896 Tinsley bridge with a Heathkit oscilloscope as null detector and conductivity cells of the type described by Kraus (6) were used. For EC and PC solutions, a cell having a constant of 3.371 cm^{-1} has been employed. For the pure solvent samples, due to their high resistance, a cell having a lower constant, *i.e.* 0.2686 cm^{-1}, was used.

The specific conductivity (χ) *vs.* concentration (c) curves were obtained for the KCNS, KPF_6, and $LiClO_4$-EC solutions at 25.00° ± 0.02°C by the dilution technique. Concentrated solutions for each salt were prepared and the χ of these solutions was determined. Subsequently, weighed amounts of molten EC were progressively added and the resultant χ values were measured after thermal equilibration.

Solubilities.—The CuF_2 solubility at 30.00° ± 0.05°C in $LiClO_4$-EC solutions at various concentrations and in a 0.92M $LiClO_4$-PC solution was determined by adding CuF_2 to about 20 cm^3 of each solution and allowing these to equilibrate for 7 days in a stirred, thermostatted bath. Aliquots of the supernatants from saturated solutions were collected and the Cu^{+2} content determined polarographically with a differential cathode ray polarograph (Southern Davis Analytical, Type A 1660).

Polarization studies.—The lithium anodic polarization and the CuF_2 and NiS cathodic polarization, respectively, in $LiClO_4$-PC and EC solutions were obtained at 30°C by a Type 551 AMEL potentiostat with a Type 494 AMEL cell. A high impedance electrometer (610 C Keithley) was used to measure voltages between working and reference electrodes. In all polarization runs, a lithium sheet counterelectrode and a lithium rod reference electrode, placed near the working electrode, were used. The electrode dimensions were: lithium (working and counter), sheet of 1.8 x 1.0 cm; lithium (reference), rod of 0.8 cm diameter and 1.8 cm height; CuF_2 and NiS (prepared as described below), sheet of 1.5 x 0.7 cm.

The counter and working electrodes were separated about 0.8 cm by a frittered glass plate. The resistance between the working and reference electrodes was about 20 ohms at 30°C. It was found that the *IR* loss between them was not significant for this type of polarization study. In fact, on moving the reference electrode appreciably from the initial position (almost in contact with the working electrode), a maximum voltage change of only 0.05V was detected. This value is of the same dimension as the reproducibility of the polarization measurements. Therefore, no correction was made for this in the voltage data.

Current-voltage curve.—Two platinum electrodes (1.3 cm^2 sheet), separated by 0.1 cm, rigidly mounted in a Plexiglas holder, were dipped in a 1.0M $LiClO_4$-EC solution at 30°C, gently stirred by a water-free nitrogen flux. Variable voltages were supplied to the electrodes by a conventional battery connected to a potentiometer. Keithley electrometers were used to determine both voltages and currents.

Viscosities and densities.—Viscosities at 30.00° ± 0.02°C were determined by a Haake Falling Ball viscosimeter having a precision of about 0.3%. The densities of the solutions at the same temperature were measured with a conventional pycnometer.

Preparation of the solutions.—The handling of the solvents and of the salts for the preparation of the solutions was all done in a dry box under an argon atmosphere. KPF_6 and KCNS in EC and PC solutions showed a certain turbidity, perhaps due to some impurities in the salts. These solutions were filtered before use.

CuF_2 electrodes.—This type of electrode was initially prepared by spreading a paste obtained by dissolving in hot toluene a powder of CuF_2 (85%), graphite (10%), and polyethylene (5%) on a copper net (225 mesh). Before being pressed, the electrode was heated in an oven for 10 min at 90°C. Using this treatment, the adherence of the paste on the metallic support was very satisfactory. However, such electrodes, made with 200 kg/cm^2 pressure, do not have utilization coefficients higher than 15% at 0.5 mA/cm^2. Furthermore, on standing overnight, the performance of these electrodes was adversely affected.

CuF_2 electrodes, obtained by heating the powder in the same proportions under N_2 for 1 hr and pressing at 1000 kg/cm^2 (7), behave much better. Lower compacting pressures resulted in a poor adherence of the powder on the metallic support; higher compacting pressures lowered the utilization coefficient (7).

NiS electrodes.—This type of electrode was prepared according to the method of Jasinski (5). A powder made of NiS (90%) and graphite (10%) was pressed on a copper net electrolytically coated with nickel. This powder shows better adherence properties than that used for the CuF_2 electrode. Therefore, a pressure of 400 kg/cm^2 was sufficient to obtain a good adherence on the support. No attempts to further improve this type of electrode and the CuF_2 electrode were made for this work.

Cell assembly and discharge curves.—The cells were prepared by sandwiching a CuF_2 or NiS cathode (4.3 cm^2 surface each side), surrounded by a glass fiber separator (0.28 mm), between two lithium anodes of the same dimensions as the cathode. This assembly was dipped in an excess of electrolyte (about 15 cm^3 of EC or PC-$LiClO_4$ 1M solutions). External contact to the lithium anodes was made with alligator clips; the cathodes were spot-welded to silver wires.

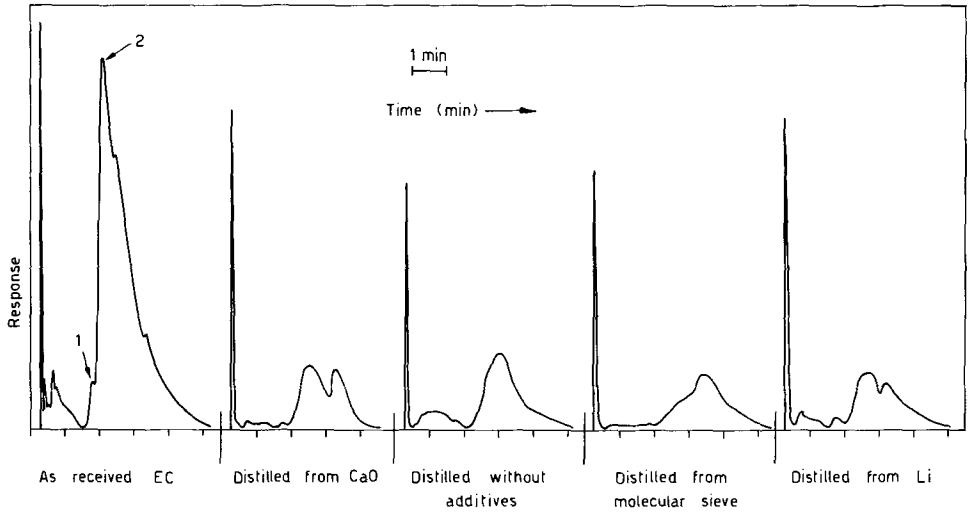

Fig. 1. Gas chromatograms of commercial EC and EC distilled under various conditions.

Approximately 0.6g of cathodic paste was used which corresponded to a nominal capacity of 0.27 A-hr for the CuF_2 electrodes (0.53 A-hr/g) and 0.32 A-hr for the NiS electrodes (0.59 A-hr/g).

The constant current discharges (1.0 or 2.4 mA/cm^2) at 30°C were usually run without interruption. Still, no appreciable changes in performance were detected even when the discharge was interrupted overnight. A Model 370 Keithley recorder connected to a Keithley electrometer was used to record the discharge curves.

Results and Discussion

Purification of the solvent.—In Fig. 1 are shown EC gas chromatograms before and after purification. The results obtained do not differ from each other significantly. Among the organic impurities, propylene glycol (PG, peak 1, 1.8 min retention time) and ethylene glycol (EG, peak 2, 2.2 min retention time) have been identified.

Using gas chromatograms of distilled EC containing 1% each of EG and PG for calibration, the commercial product was found to contain 2500 and 125 ppm, respectively, of these contaminants. In the several distilled materials which were prepared, the EG content is not appreciable and the PG content is 15-20 ppm. Jasinski (8) reports an increase in PG from 30 to 200-500 ppm on distilling PC over CaO. In our preparation of EC from CaO, however, all impurity levels decreased.

The experimental procedure under which the gas chromatograms were obtained is such that it was not possible to determine the water content of the samples. This quantity was measured instead by the Karl Fischer method and varied from 15 to 50 ppm for the several samples examined. Also, the results for a single sample, measured during multiple distillations, fell in this range, indicating the necessity to carefully avoid contamination by moisture.

In Table I are shown the specific conductivity values of various EC samples distilled under vacuum. The conductive impurity level seems to decrease from the sample distilled on a molecular sieve to the one distilled on CaO.

Current-voltage curve.—For a 1M $LiClO_4$-EC solution, the curve at 30°C has the shape shown in Fig. 2. The "decomposition potential" is about 5.7V. Clearly, this value has little significance because of its dependence on the electrode materials used.

Table I. Specific conductivities at 40°C of EC and PC ($ohm^{-1}cm^{-1}$ .10^7)

EC as received	51.7
EC distilled from molecular sieve	5.91
EC distilled without additives	4.19
EC distilled from Li	3.47
PC distilled without additives	2.07
EC distilled from CaO	1.51

Specific conductivity of the solutions.—The conductivity at 25°C of $LiClO_4$, KCNS, and KPF_6, respectively, in EC solutions, is shown in Table II. Solutions close to saturation were progressively diluted to observe the maximum in the χ *vs.* c curves. In the case of the KPF_6-EC solution, only one datum is reported since a decrease in concentration immediately caused the solution to solidify. For the KCNS and particularly the $LiClO_4$ solutions, on the contrary, overcooling experiments across a wide range verified that the solutions, even at low concentration, remain liquid at 25°C. For all salts, the maximum χ values are greater than those of PC solutions (2). In particular, the specific conductivity of a 1.0M $LiClO_4$-EC solution (7.8 x 10^{-3} ohm^{-1} cm^{-1}) is 1.4 times greater than that of a 1.0M $LiClO_4$-PC solution (5.6 x 10^{-3} ohm^{-1} cm^{-1}) (9).

Figure 3 shows the behavior of the conductivity *vs.* temperature for those solutions in which the maximum conductivity is seen. The behavior is linear and the $d\chi/dt$ values for KCNS, KPF_6, and $LiClO_4$ are 0.000307, 0.000263, and 0.000172 ohm^{-1} cm^{-1} $°C^{-1}$, respectively.

Viscosity of the solutions.—The viscosities at 30°C of 1*M* (molal) solutions of KPF_6, KCNS, and $LiClO_4$ in EC and PC were determined. The values obtained are reported in Table III where η_d is the dynamic viscosity and η_c the kinematic viscosity. The ratio η_d $LiClO_4$-PC/η_d $LiClO_4$-EC is 1.05, whereas the ratio of the specific conductivity of 1*M* solutions χ $LiClO_4$-EC/χ $LiClO_4$-PC is 1.5, and that of the equivalent conductances is 1.3 at the same concentration. Therefore, the higher conductivity, observed in $LiClO_4$-EC cannot be related to the lower viscosity only, but it is also due to a lesser amount of associated nonconducting forms

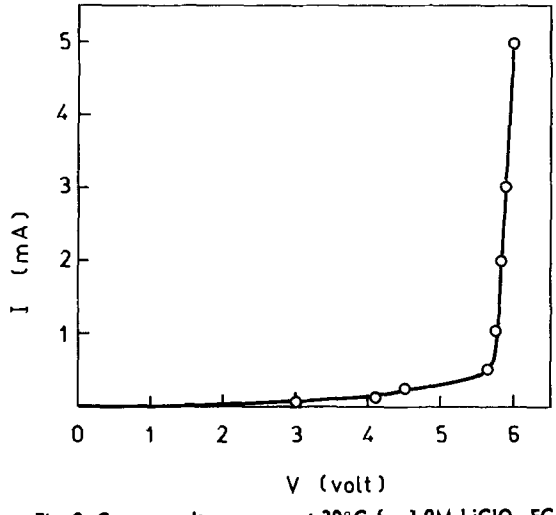

Fig. 2. Current-voltage curve at 30°C for 1.0M $LiClO_4$-EC

Table II. Specific conductivities at 25°C of EC solutions

Salt	c (g/100g solvent)	$\chi \cdot 10^3$ ($ohm^{-1} \cdot cm^{-1}$)
KPF_6	19.0	11.32
KCNS	9.0	11.40
	13.1	11.84
	16.1	11.62
	22.5	10.68
	25.3	10.07
	29.0	9.27
	32.0	8.50
	35.3	7.67
$LiClO_4$	3.5	6.07
	5.2	7.27
	7.7	7.87
	9.8	7.80
	14.5	6.30
	19.8	4.32
	24.9	2.73
	30.0	1.55

Table III. Viscosities at 30°C of EC and PC solutions (1 molal)

	EC		PC	
	η_d (centipoise)	η_c (centistokes)	η_d (centipoise)	η_c (centistokes)
$LiClO_4$	7.91	5.67	8.32	6.58
KCNS	5.09	3.72	4.94	3.99
KPF_6	4.82	3.36	4.87	3.78

Table IV. Solubility of CuF_2 in $LiClO_4$-EC and $LiClO_4$-PC solutions

$LiClO_4$ concentration (M)	Solubility, (moles/kg solution)
0.92 (in PC)	0.0085
0.84 (in EC)	0.0098
1.07 (in EC)	0.0079
1.47 (in EC)	0.0063
1.84 (in EC)	0.0062

(ion pairs and higher associated species), due to the higher dielectric constant of EC.

Solubility of CuF_2 in $LiClO_4$-EC and PC solutions.—The trend of the solubility of CuF_2 as a function of $LiClO_4$ concentration in EC is reported in Table IV. As observed in $LiClO_4$-PC solutions (3), the solubility decreases as the $LiClO_4$ concentration increases. This pattern could be related to an increase in the activity coefficients of the CuF_2 ions with the increase of the ionic strength of the solutions. The solubility of a 0.92M $LiClO_4$-PC solution shows that there is no appreciable difference between the two solvents. It is possible that the solubility of CuF_2 in $LiClO_4$-EC and $LiClO_4$-PC solutions is influenced by the occurrence of the reaction

$$CuF_{2(s)} + 2LiClO_4 \rightleftharpoons 2LiF_{(s)} + Cu(ClO_4)_2$$

One cannot exclude the possibility that the results obtained are affected to a certain extent by the incomplete drying of $LiClO_4$ (0.1% of water).

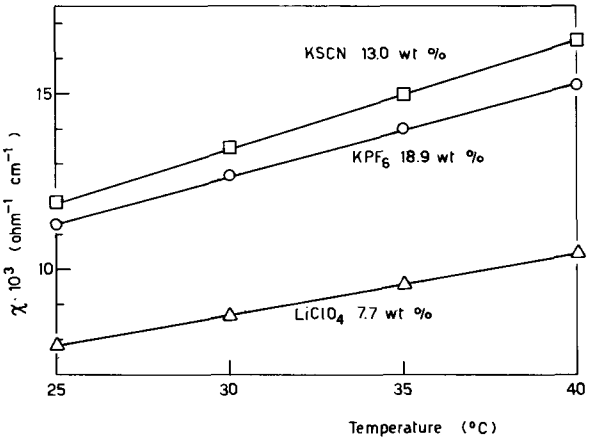

Fig. 3. Specific conductivity as a function of temperature for KPF_6, KCNS, and $LiClO_4$ in EC at the indicated concentrations.

With these values of solubility, it is obviously impossible to maintain Li-CuF_2 cells in activated storage. A test made on a cell Li/1.0M $LiClO_4$-PC/CuF_2, kept 8 days after preparation in a dry box at about 18°C, showed a decrease in the percentage of utilization of the cathode (from 53 to 14%) and in the average potential of discharge to a very low value (*ca.* 1.4V).

Polarization studies.—The behavior of Li, CuF_2, and NiS electrodes was investigated under forced discharge at various current densities (Fig. 4 and 5), using Li rod as a reference electrode; this is considered to be a satisfactory reference electrode in 1.0M $LiClO_4$-PC (10).

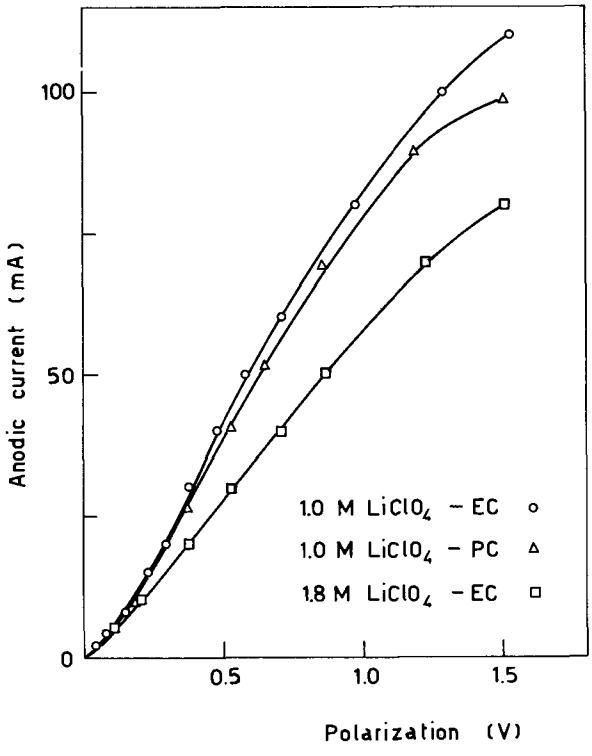

Fig. 4. Lithium anode polarization at 30°C in $LiClO_4$-EC and $LiClO_4$-PC solutions. Electrode surface 1.8 x 1.0 cm.

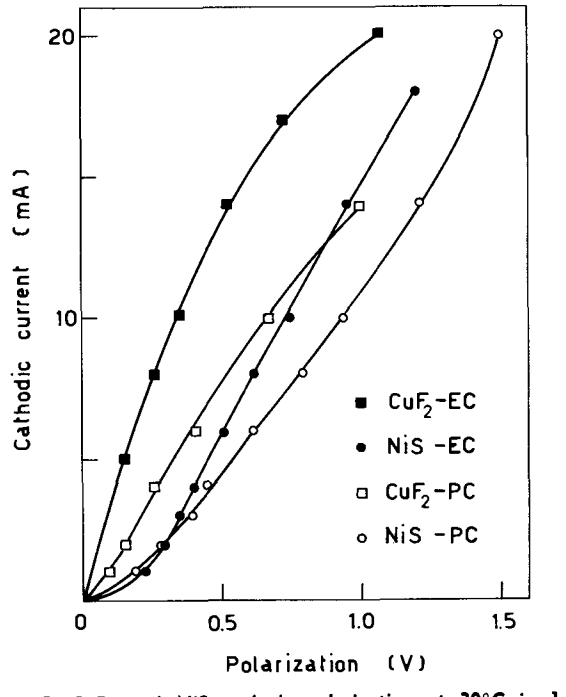

Fig. 5. CuF_2 and NiS cathode polarization at 30°C in 1.0M $LiClO_4$-EC and PC solutions. Electrode surfaces 1.5 x 0.7 cm, OCV 3.45V for CuF_2 and 3.25V for NiS vs. Li/Li^+.

Li seems to show a somewhat better anodic behavior in $LiClO_4$-EC than in the corresponding PC solution. A lower viscosity and a higher conductivity could explain this behavior. A 1.8M $LiClO_4$-EC solution, in fact, shows a more pronounced tendency toward polarization, for the same values of anodic current, with respect to a 1.0M solution having higher χ and lower η.

CuF_2 and NiS electrodes clearly seem to behave better in EC than in PC, probably because they are more sensitive than Li anodes to the effect of viscosity, and conductivity of the solutions. In fact, their reduction reaction involves Li ions

$$CuF_2 + 2\,Li^+ + 2e \rightarrow Cu + 2\,LiF$$

so that the transport of these ions from the bulk of the solution to the cathode could be the rate-determining step.

The polarization seems to be more severe for NiS than for CuF_2, particularly at low current densities. As suggested by Jasinski (5), it is possible that a certain amount of S is present in NiS, this making the OCV *vs.* Li/Li^+ (3.25V) quite high and accounting for the initial rapid decay in voltage. No difference in the polarization behavior was observed between two NiS electrodes prepared at different compacting pressures (400 and 1000 kg/cm^2, respectively).

Cell discharge.—Discharge curves at 1.0 and 2.4 mA/cm^2 for Li-CuF_2 cells are reported in Fig. 6 and those for Li-NiS cells in Fig. 7. The utilization coefficient of CuF_2 in the two solvents at 1 mA/cm^2 (53%) is in agreement with the work of Boden for 1.0M $LiClO_4$-PC (7). At the same discharge current density, the utilization coefficients are practically the same in EC and PC, but the curves in EC have substantially higher V values. The curves for Li-NiS cells show not only higher V values, but also higher utilization coefficients in EC. These results were to a certain extent expected on the basis of the polarization behavior of the positive electrode and of the viscosimetric and conductometric data obtained for $LiClO_4$ solutions in EC and PC. At 30°C the conductivity of 1.0M $LiClO_4$ in EC is 8.68 x 10^{-3} ohm^{-1} cm^{-1}, whereas that of 1.0M $LiClO_4$ in PC is 5.81 x 10^{-3} ohm^{-1} cm^{-1}, the latter value being in agreement with that found by Keller at 25°C (9). This higher specific conductivity in $LiClO_4$-EC is especially beneficial in reducing the concentration polarization resulting from the low electrolyte transport rate. This is also the main cause of the decrease observed in the utilization coefficient of the cathode when discharge current density varies from 1.0 to 2.4 mA/cm^2.

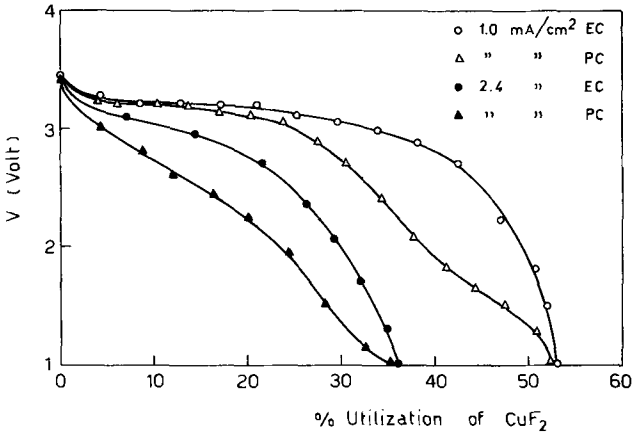

Fig. 6. Discharge curves at 1.0 and 2.4 mA/cm^2 at 30°C for Li-CuF_2 cells in 1.0M $LiClO_4$-EC and PC.

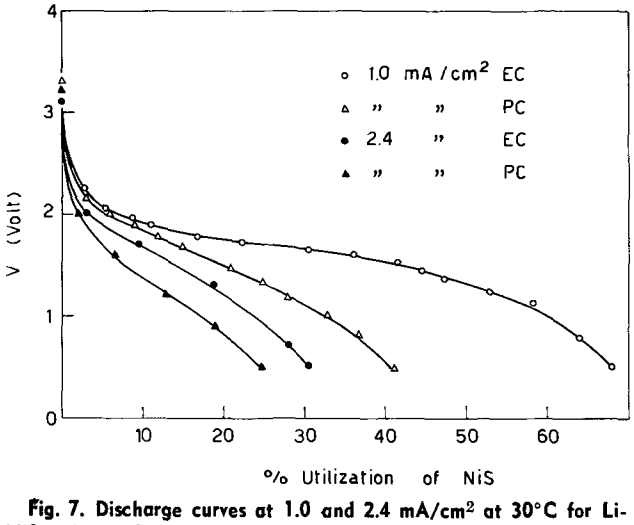

Fig. 7. Discharge curves at 1.0 and 2.4 mA/cm^2 at 30°C for Li-NiS cells in 1.0M $LiClO_4$-EC and PC.

The difference shown by the curves of the Li-NiS cells at 1.0 mA/cm^2 in the two solvents is exaggerated; some unknown factor might have increased the difference in favor of the cell containing $LiClO_4$-EC.

A calculation of the watthours obtained per weight of CuF_2 or NiS in the discharges at 1.0 mA/cm^2 gave the following results: 0.80 Whr/g(CuF_2) and 0.62 Whr/g(NiS). Therefore, the higher average potential of discharge shown by CuF_2 counterbalances the lower utilization coefficient.

Discharge at 1.0 mA/cm^2 was repeated in a cell Li/1.0M $LiClO_4$-EC/CuF_2 in which the weights of the various components (electrodes, electrolyte, and separator) were minimized, except for the outside casing. In particular, a lightweight steel net (4.3 cm^2, 0.16g) was used in place of the copper net as a positive electrode support (0.6g of a cathodic paste); the electrolyte was reduced to the minimum amount (0.8g) required to avoid decrease of the utilization coefficient of CuF_2 (7). Under these conditions, a specific energy of 195 Whr/kg was measured (outside casing excluded). This value could be increased, for example, by increasing the ratio between the weight of the cathodic paste and that of the metallic support or by using a lighter separator. The increase in the total weight due to a lightweight polyethylene case is about 12% (7).

Conclusion

Electrolytes in EC (in particular, $LiClO_4$) and Li, CuF_2, and NiS electrodes in $LiClO_4$-EC solutions seem to behave better than in PC solutions. Discharge curves obtained under the same conditions in the two solvents confirm that EC can be advantageously used in high-energy nonaqueous batteries. At the moment, cells containing an EC solvent obviously have a minimum temperature range limit. This limit can be lowered either by adding PC or by using another salt capable of lowering the EC freezing point still further. On the other hand, solid solutions of electrolytes in EC could solve shelf-life problems in the activated storage of these cells, providing that the cathodes are mechanically stable, *i.e.* not deformable during the solidification. Due to the low temperature gradient necessary for a completely liquid solution, a low activation energy would be required for such thermal batteries.

Acknowledgment

This work was sponsored by the Consiglio Nazionale delle Ricerche (C.N.R.).

Manuscript submitted April 15, 1970; revised manuscript received *ca.* Sept. 8, 1970.

Any discussion of this paper will appear in a Discussion Section to be published in the December 1971 JOURNAL.

REFERENCES

1. W. Elliott *et al.*, Report No. 1, Contract NAS 3-6015 (N 65-11518) (Sept. 1964).
2. G. Pistoia, M. De Rossi, and B. Scrosati, *This Journal*, **117**, 500 (1970).
3. K. Braeuer and J. Harvey, "Organic Electrolyte High Energy Density Batteries," AD 654813 (1967).
4. V. Dechenaux, G. Gerbier, and J. F. Laurent, *Rev. Gen. Elec.*, **76**, 1406 (1967).
5. R. Jasinski and B. Burrows, *This Journal*, **116**, 422 (1969).
6. H. Daggett, E. Bair, and C. Kraus, *J. Am. Chem. Soc.*, **73**, 799 (1951).
7. D. Boden, H. Buhner, and V. Spera, Final Report, Contract DA-28-043-AMC-01394 (E), July 1966.
8. R. Jasinski and S. Kirkland, *Anal. Chem.*, **39**, 1663 (1967).
9. R. Keller, J. Foster, and J. Sullivan, Report NASA CR-72106 (Sept. 1966).
10. B. Burrows and R. Jasinski, *This Journal*, **115**, 365 (1968).

The Mechanism of Adhesion Failure of Plated Plastics in Corrosive Environments

R. R. Wiggle,* V. Hospadaruk,* and D. R. Fitchmun

Ford Motor Company, Dearborn, Michigan 48121

ABSTRACT

The mechanism of adhesion failure of plated ABS and polypropylene (PP) plastics exposed to service conditions was determined. Adhesion failure, through the formation of blisters, proceeds by a corrosion mechanism which involves (*a*) the rapid lateral anodic dissolution of the thin electroless nickel layer at the plastic-metal interface or (*b*) the relatively slower preferential dissolution of an electroless copper layer and the equally reactive adjacent electrodeposited copper layer. The rate of lateral development of blisters is related to the surface topography of the etched plastic substrate. The high-density crack patterns and surface roughness of etched PP provide a greater path length for the anodic dissolution of the thin electroless nickel layer—thereby retarding the lateral undercutting more than with a plastic which has a relatively smooth etched surface (ABS). When the less reactive electroless copper is present in a copper-nickel-chromium system, the plastic substrate surface topography has no effect on the lateral rate of blister development. The weaker tendency toward blister formation is due to preferential corrosion of the relatively thick, two-layered copper deposit.

The use of electroplated plastics has increased dramatically since the commercialization of electroplated ABS plastic. The commercialization was due in large part to the development of molding and process conditions which gave measurable adhesion between the electrodeposit and plastic.

When electroplated plastics became a reality, it was erroneously felt that, since the plastic is a noncorrodible substrate, highly corrosion-resistant electroplating systems were not needed. However, it was soon apparent that the outdoor service performance of plated ABS was frequently not satisfactory and even with good corrosion-resistant systems had a tendency to develop excessive blistering and premature failure. Saubestre and co-workers (1) studied the nature of corrosion of electrodeposits on ABS and found that blistering failure was common. They used the CASS and Corrodkote accelerated corrosion tests in the study and the results showed that sacrificial corrosion in the electrolytic copper layer was the main cause of blistering failure; of secondary importance was the electroless metal. All-nickel decorative coatings tended to blister at or near the plastic-metal interface for reasons not established.

After the advent of electroplated crystalline polypropylene (PP), early service exposure data for some of the specimens showed that it was superior to plated ABS. Adhesion of the electroplate to the plastic was also substantially greater. Innes (2), in comparative study of plated ABS and PP, verified the superior performance of PP. The results were derived from environmental and accelerated tests. Innes did not determine the underlying mechanism of blister failure, but for ABS suggested that moisture absorption, sensitivity to molded-in stresses, and adhesion fluctuations were important factors.

Service exposure results of electroplated plastics showed that a large portion of the blister failures occurred in corrosive environments and seemed to involve the plastic-metal interface. The first consideration was to determine if one of the primary factors was the preferential corrosion of the electroless metal deposits. In agreement with others, it was found that the performance of plated PP was also markedly better than ABS. It was important to understand the reasons for the substantially better service performance and plastic-to-metal adhesion of the PP and the mechanism of failure of both plated ABS and PP. This paper describes the mechanism of blister failure which occurs during exposure of plated ABS and PP to corrosive *service* environments.

Experimental Methods

Service corrosion specimens.—The plated plastic corrosion specimens used in the determination of the failure mechanism were from the Ford Exposure Program. The specimens were exposed to chloride road deicing salts on trucks fitted with special racks. The specimens were flat, 3 x 4 in. panels of ABS and PP, supplied by Marbon Division, Borg-Warner Corporation, and Avisun Corporation, respectively. They were chemically plated with the MacDermid Inc. MACuplex RT process, an alkaline hypophosphite electroless nickel. The electrolytic deposits used were nickel strike (Watts), copper (Udylite UBAC), semibright nickel (Harshaw Perflow), bright nickel (Udylite 66), and chromium (conventional).

* Electrochemical Society Active Member.

Key words: adhesion failure, plated plastics, corrosion.

Reactivity studies.—The relative reactivities of the various deposits were determined by anodic polarization using potentiodynamic techniques. The electrolyte consisted of 1.0 normal sodium chloride (reagent grade in distilled water) at pH 6.0-6.5 which approximates outdoor service electrolytes. The electrolyte was carefully deaerated with prepurified nitrogen for at least 2 hr before the test specimens were immersed. The specimens were immersed at open circuit for a minimum of 1 hr before polarization at a rate of 10 mV/min where the electrode potential was measured relative to a saturated calomel electrode (SCE).

Thermal cycle testing.—Panels were thermal cycled in order to determine if adhesion failure due to thermally induced stresses was significant. All panels used in thermal cycle testing were plated on one side only. This was designed to yield high stresses at the plastic-metal interface resulting from the high differential in the coefficients of expansion for the metal and plastic. The test procedure consisted of the exposure of the panels to the following sequence of temperatures: (*a*) 180°F for 2 hr; (*b*) ambient temperature for 1 hr; (c) −20°F for 2 hr; and (*d*) ambient temperature for 1 hr. This constitutes one cycle.

Results and Discussion

Service performance.—Examination of service exposed panels indicated that good adhesion of decorative plated systems to a plastic substrate does not guarantee good over-all service and corrosion performance. An examination of failed service parts showed the presence of blisters with gradations from fine blisters barely visible to the naked eye to massive detachment of the electrodeposit. The number and size of the blisters were greater on the service parts exposed to the more severe corrosive environments indicating that blistering is related to corrosion attack. Indeed, examination of the exterior of the blisters revealed the presence of a corrosion pit in the center of each blister.

The association of corrosion pits with all of the blisters examined indicates that blister failures solely due to thermally induced stresses normally encountered in service are not significant. This observation was verified by thermal cycle studies of both plated ABS and PP panels. PP panels plated with various composite coatings withstood as many as 20 thermal cycles with no evidence of adhesion loss. Similar results were obtained with plated ABS subjected to 3 thermal cycles. However, the possibility that blister failure, in some instances, may be accelerated by extreme thermal environments is not disregarded.

Some of the metal films on failed service parts were mechanically stripped from the plastic substrate in order to examine the underside or interior of the blisters as shown in Fig. 1. Region A is the underside of the electrodeposit stripped from the surface of an ABS panel and folded back. Region B is the surface of the ABS panel. The periphery of the blisters is indicated by C, and in the centers of the blisters are corrosion pits, D, which extend through the electrodeposit. When the pits are close together, the blisters that develop often coalesce to form larger blisters. The darker rings or bands, E, of corrosion products are probably due to a variable corrosion rate in service. The electron microprobe scanned across these rings or bands, both on the underside of the electrodeposit and the surface of the plastic, revealed the presence of phosphorus-rich residues.

As-plated electroless nickel from hypophosphite baths is not pure nickel but is a nickel-phosphorus alloy (3). Phosphorus is incorporated in the deposit as a result of complicated side reactions which occur during the oxidation of the hypophosphite reducing agent.

Again referring to Fig. 1, a thin layer of plastic, F, adhering to the underside of the electrodeposit is present when deposits with intact plastic-metal interfaces are mechanically stripped. The fracture presumably occurs in a weakened polymer surface layer formed during the etch step. The undersides of the blisters are free of plastic—indicating an essentially electrochemical "detachment" of the metal coating at the plastic-metal interface through anodic dissolution of the electroless deposit.

These results indicate that blister formation is associated primarily with the preferential corrosion of the electroless nickel layer.

To further characterize the exact location of the failures, cross sections of the service blisters were analyzed by optical microscopy and the electron microprobe. Figure 2 is a cross section of a representative service blister showing the center of the corrosion pit, A. The center portion of the blister is shown on the right, and the edge showing the intact plastic-metal interface on the left. The composite system includes ABS plastic, electroless nickel (not

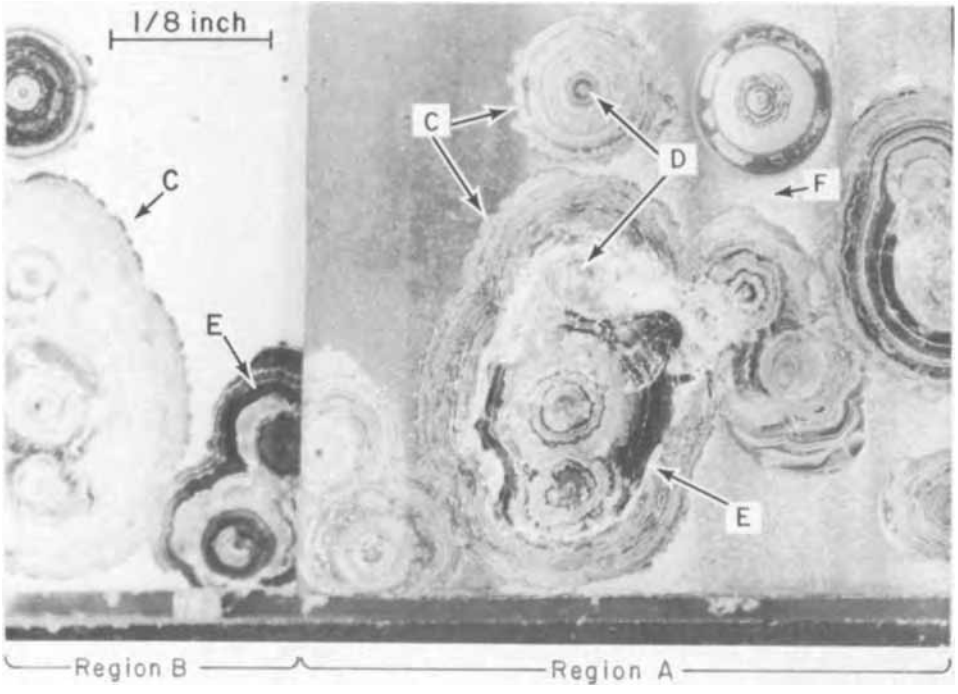

Fig. 1. Underside of blistered electrodeposit mechanically stripped from plastic substrate on failed service part.

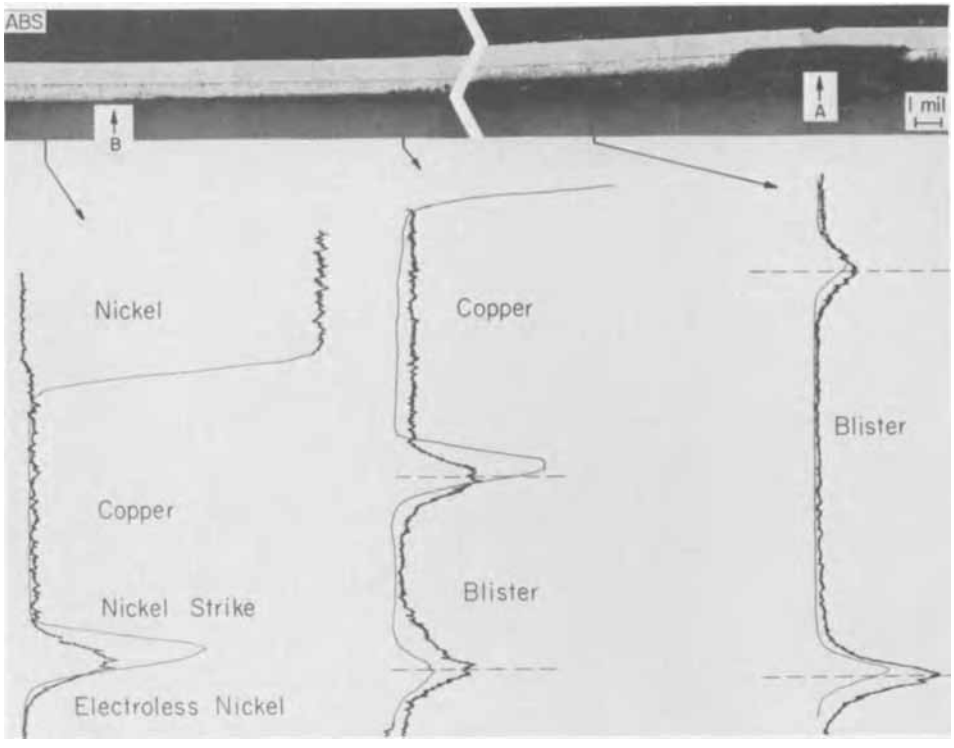

Fig. 2. Cross section of service blister showing location of failure with the aid of electron microprobe traces for phosphorus and nickel.

visible), nickel strike, copper, duplex nickel, and finally chromium. Corrosion has proceeded from the corrosion pit, A, to point B, beyond which the interface is intact. Optical photomicrographs indicated that the corrosion followed a path on the underside of the electrodeposit at or near the plastic-metal interface. The electron microprobe was scanned across the interface and blister void at the points indicated to determine the presence and relative concentrations of two elements, phosphorus and nickel. The phosphorus trace is the complex dark line and the nickel trace is the finer line, with increasing concentration of the elements from left to right along the horizontal axis. The microprobe scanned across the intact interface showed the presence of phosphorus and nickel in the electroless nickel layer, pure nickel in the nickel strike layer, and, of course, no nickel in the copper region and only pure nickel in the duplex nickel region. The middle microprobe traces across a portion of the blister (the separation distance indicated by the region labeled "Blister") showed the presence of phosphorus and nickel residues on the surface of the plastic, and phosphorus and nickel residues plus pure nickel (from the nickel strike) on the underside of the electrodeposit. At another portion of the blister with a wider separation, the microprobe showed the presence of phosphorus and nickel residues both on the plastic surface and underside of the electrodeposit.

Microprobe results of other systems gave similar results and it is concluded that apparent adhesion failure and blisters are related to corrosion in the thin electroless nickel layer. Whether the electrodeposit adjacent to the electroless nickel layer is nickel or copper appears to have little effect on the mode of corrosion after the corrosion pit reaches the electroless nickel deposit. Furthermore, the preferential lateral corrosion of the electroless nickel layer indicates that it is more reactive than the other metals of the composite.

Reactivity studies.—In order to investigate the unusually high anodic reactivity of the electroless nickel, polarization studies were conducted of the various metals deposited. Figure 3 shows the results of anodic polarizations in neutral 1.0M (molar) sodium chloride.

Semibright nickel is the least reactive of the electrodeposited metals followed in order by bright acid copper and the highly reactive bright nickel. The anodic reactivity of electroless copper is identical to that of electrodeposited copper. The polarization curve for electroless nickel shows a definite increase in anodic reactivity, even greater than that of the highly reactive bright nickel. This shows that sacrificial corrosion of the electroless nickel layer can readily occur. After a corrosion pit has penetrated to that layer, it is preferentially dissolved producing blisters by lateral undercutting.

From the data presented so far, it would seem to indicate that the use of a less reactive electroless nickel would be advantageous for service performance. The relative reactivities of other commercial electroless nickel deposits in sodium chloride solution have been determined, two of which are shown in Fig. 4.

Curve A is the reactivity of an electroless nickel deposit containing 4.5 w/o (weight per cent) phosphorus, obtained from the MacDermid 9340 alkaline hypophosphite bath used in most of these corrosion studies. Electroless nickels deposited from commercial acid hypophosphite baths (curves B and C) incorporated a higher weight per cent of phosphorus. Unexpectedly, the relative reactivities are less and the anodic polarization curves approach that for the highly reactive bright nickel shown by the dashed line. Nevertheless, the polarization study has shown that all of the commercial electroless nickels investigated are more reactive than the other metals in neutral and acid chloride media.

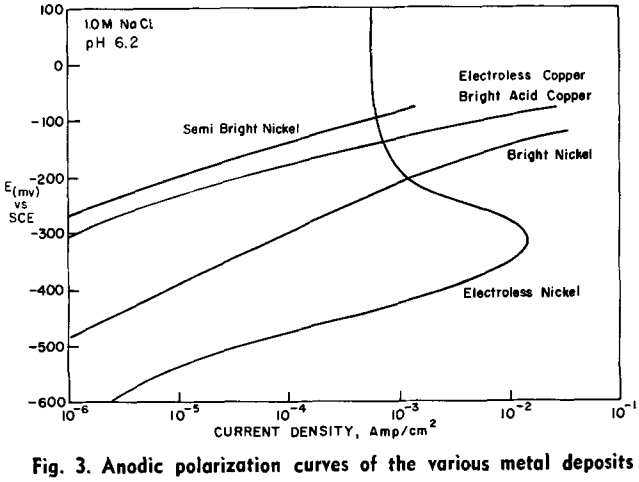

Fig. 3. Anodic polarization curves of the various metal deposits used on the plastics.

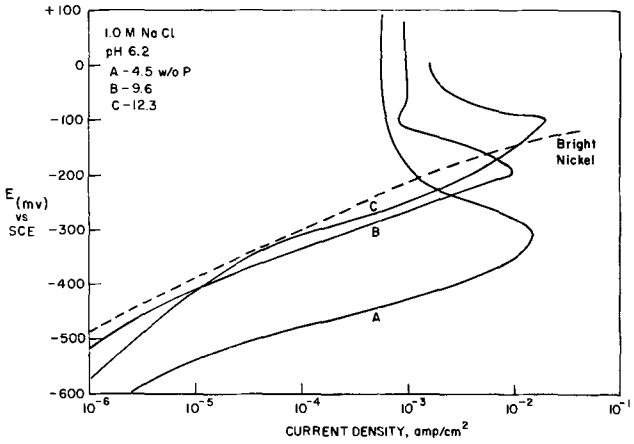

Fig. 4. Anodic polarization curves of some commercial electroless nickel deposits, A, B, and C, containing different amounts of phosphorus. Curve for bright nickel included.

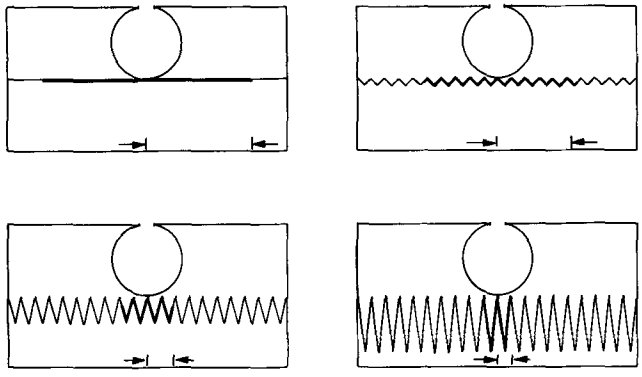

Fig. 6. Schematic showing relationship between surface roughness and degree of lateral undercutting.

It is known that an increase in nickel reactivity can be effected by addition of certain elements to the metal. The effect of the additives on the anodic reactivity of *electrodeposited* nickel was studied by DiBari and Petrocelli (5). Small amounts of the elements sulfur, selenium, tellurium, and phosphorus increased the reactivity of nickel, where the relative reactivities were related to the element electronegativities.

Growth rate of blisters.—Although the investigation had shown that the undercutting and blistering phenomenon is due to the rapid preferential corrosion of the electroless nickel (4.5 w/o P) layer, it was not readily apparent why the blistering tendency for ABS was much greater than for PP with systems using this electroless nickel. To understand the difference, cross sections of plated ABS and PP were studied with a high magnification microscope and electron microprobe.

Figure 5 shows service blisters on ABS and PP substrates polished to the center of the corrosion pit. The electrodeposited systems are the same in both cases and composed of electroless nickel, nickel strike, bright acid copper, duplex nickel, and finally chromium. Blisters on the ABS were 10-100 times larger in diameter than those on the PP. The lower photographs are enlargements of the blister edge and intact plastic-metal interface. Metal filled cracks are clearly visible which extend into the surface of the PP. These characteristic cracks are produced in the surface of the PP, a semicrystalline polymer, by the pretreatment steps (swellant and etchant) of the chemical plating process. The amorphous regions of the PP which are swollen in the hot organic conditioner are oxidized at a greater rate than the crystalline regions in the hot chromic acid producing a cracked surface.

The electron microprobe showed that most of the metal in the cracks is nickel strike. Microprobe studies of both systems showed that the corrosion path is confined essentially to the very thin electroless nickel layer present on the polymer surfaces. For ABS with its relatively smooth interface, corrosion follows a relatively straight lateral path, while, for PP, corrosion has to follow a tortuous path around each of the cracks. Even if the same amount of electroless nickel were anodically dissolved in both cases, the lateral distance of undercutting is less for the PP. This is schematically illustrated in Fig. 6.

Assuming the same amount of electroless nickel anodically dissolved in all cases (darker line), a reasonable conclusion would be that the rougher the surface topography of the plastic substrate, the less would be the distance of lateral undercutting and hence the tendency for blister formation to occur.

This was verified by corroding specially prepared samples of PP in a 1.0M sodium chloride, 0.02M ferric chloride solution. The samples were electroplated with 0.5 mil of bright nickel and 10 μin. of regular

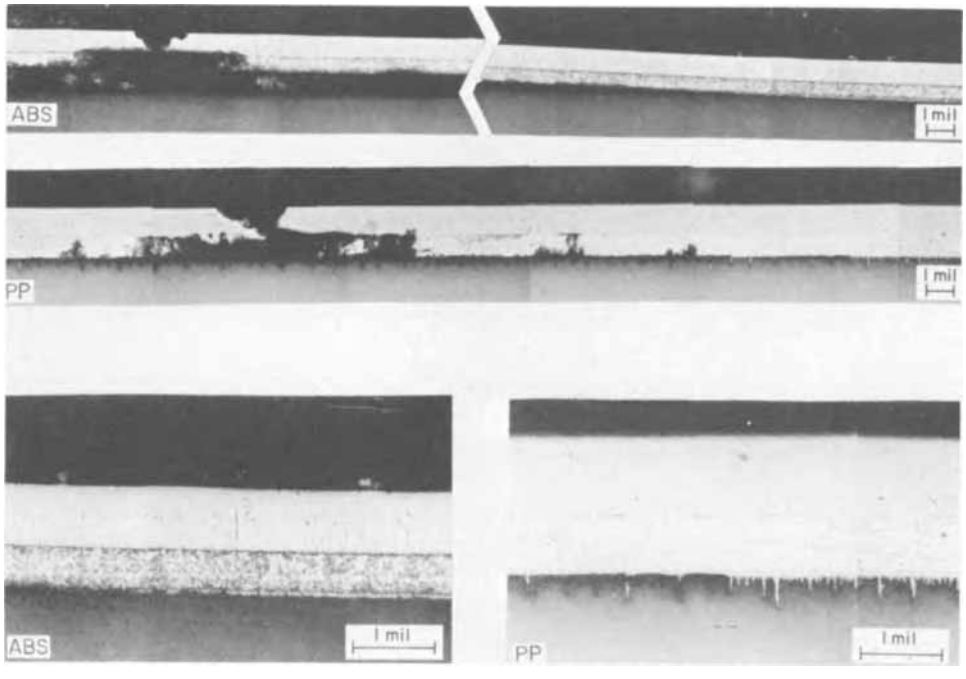

Fig. 5. Cross sections of service blisters on ABS and PP showing relative blistering tendencies.

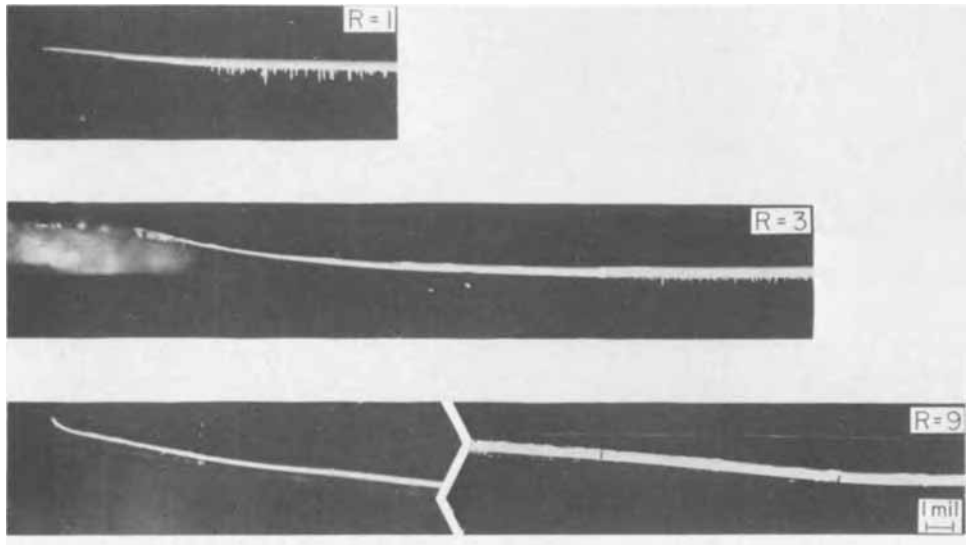

Fig. 7. Cross sections of specially prepared PP samples showing relation of crack pattern and surface roughness to rate of lateral development of blisters. R is the relative blister radius.

chromium. The PP panels were injection molded using conditions determined to produce a surface morphology amenable to uniform crack pattern development (4). The crack depth and density were deliberately varied, by using several combinations of swell and etch times, from 10 to 15μ (top photograph) to essentially a smooth interface (bottom photograph).

Photomicrographs of cross sections of blisters formed on these specimens are shown in Fig. 7. Only half of each blister is shown, the left edge of the photograph corresponding to the center of the corrosion blister. Using the relative radius (R) of the blister in the top photograph as 1, it can be seen that the radius of the blisters increases with decreasing crack depth. In the bottom photograph, with a relatively smooth substrate, the blisters were about 10 times wider than those in the first case.

As with service performance, these results show that there is a direct relation between the surface topography or roughness and service performance. The rate of lateral blister development is related to the crack pattern and type of surface roughness of the etched plastic substrate. Complex crack patterns provide a greater path length for the anodic dissolution of the thin electroless layer—thereby retarding the lateral undercutting more than with an etched plastic which has a relatively smooth surface.

It should be noted that adhesion values for plated plastics as determined by the Jacquet Peel Adhesion Test (6) do not necessarily reflect the blister formation tendency in corrosive environments. As shown above, any increase in crack density and depth yields a corresponding increase in resistance to blister formation. However, adhesion values represent a balance between crack depth and diminished surface strength incurred in the etch step (4). Although adhesion usually increases with crack depth, overetching may actually decrease adhesion even though the crack depth has been increased. For maximum resistance to blister formation, care must be exercised in the control of the molding operation and the pretreatment steps of the plating process to produce plastic surfaces yielding optimum adhesion values without excessive degradation of the plastic substrate.

To complete the picture of the failure mode, it was essential to determine the effect of surface roughness with a less reactive electroless metal. One particular combination of interest involved the use of electroless copper, whose anodic reactivity is identical to the adjacent electrodeposited copper. Unfortunately, no plated PP systems containing electroless copper had been exposed to service for comparison to ABS. However, plated polysulfone (PS) exhibits surface cracking similar in nature to PP, and was used for comparison, shown in Fig. 8.

The metal deposit is composed of electroless copper, bright acid copper, duplex nickel, and chromium. Examination of the blisters of this plating system shows a corrosion mechanism different from that obtained with systems containing electroless nickel. Corrosion is not confined to the electroless metal layer and the blisters are due to preferential corrosion in *both* the electrodeposited and electroless copper layers. No further undercutting has occurred past the points visible in the photograph. The blisters on the plated ABS and PS panels are very small and equal in size.

The data indicate that, as the reactivity of the electroless metal decreases and approaches that of the adjacent electrodeposited layer, the effect of the plastic surface topography on the lateral rate of blister development diminishes. Retardation of the blistering tendency should be evident if less reactive electroless nickels are used and studies with such nickel deposits are in progress.

Conclusions

The adhesion failure mechanism for ABS and PP plated plastic parts involves the formation of blisters by the preferential corrosion of the thin, highly reactive electroless nickel layer. The rate of lateral development of blisters for electroless-nickel-containing systems is related to the surface topography of the etched plastic substrate. Plastic substrates with rougher surface topography (etched PP) retard lateral

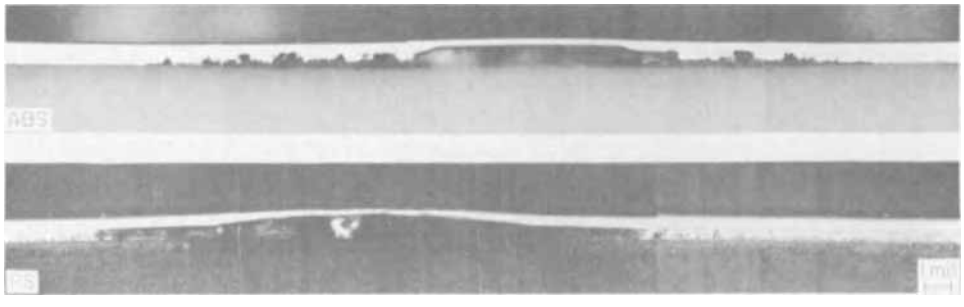

Fig. 8. Cross sections of service blisters showing the combined effects of surface roughness and electroless metal reactivity on the rate of lateral development of blisters.

undercutting more than those with relatively smooth surfaces such as etched ABS.

The lower blister forming tendency for coatings containing electroless copper is due to the essentially equal reactivities of the electroless and adjacent electrodeposited copper layer. The plastic surface topography has no effect on the lateral rate of blister development for coatings which have electrodeposited copper on electroless copper.

Premature failure of plated plastics may be avoided by the use of: (*a*) less reactive metals on the plastic substrate such as electroless copper or less reactive electroless nickel deposited from an acid hypophosphite bath; (*b*) plastics with uniformly cracked surfaces such as properly prepared PP; and (c) suitable composite coatings designed to retard corrosion pit penetration to the electroless metal layer.

Acknowledgment

The authors wish to express their gratitude to W. A. Donakowski for his cooperation and contribution to this work.

Manuscript submitted June 17, 1970; revised manuscript received *ca.* Sept. 9, 1970. This was Paper 138 presented in part at the Detroit Meeting of the Society, Oct. 5-9, 1969.

Any discussion of this paper will appear in a Discussion Section to be published in the December 1971 JOURNAL.

REFERENCES

1. E. B. Saubestre, J. Hajdu, and G. Leibowitz, *Electrochem. Technol.*, **6**, 341 (1968).
2. W. P. Innes, J. J. Grunwald, E. D. D'Ottavio, W. H. Toller, and C. Carmichael, *Plating*, **56**, 51 (1969).
3. G. Gutzeit and E. T. Mapp, *Corrosion Technol.*, **3**, 331 (1956).
4. D. R. Fitchmun, S. Newman, and R. Wiggle, To be published in *J. Applied Polymer Sci.*
5. G. A. DiBari and J. V. Petrocelli, *This Journal*, **112**, 99, (1965).
6. E. B. Saubestre, L. J. Durney, J. Hajdu, and E. Bastenbeck, *Plating*, **52**, 982 (1965).

Chromium Deposition from Dicumene-Chromium to Form Metal-Semiconductor Devices

N. G. Anantha, V. Y. Doo,* and D. K. Seto*

IBM Components Division, East Fishkill Facility, Hopewell Junction, New York 12533

ABSTRACT

Thin chromium films were deposited on silicon openings of oxidized silicon wafers by thermal decomposition of dicumene chromium (DCC) in an argon atmosphere at temperatures between 350°-520°C. The metal-silicon interface thus obtained was characterized by current-voltage and capacitance-voltage measurements. The interface exhibited a rectifying effect and functioned as a Schottky barrier junction. A barrier height of 0.59 ± 0.02 eV with respect to Fermi energy was obtained. The switching speed of the Schottky barrier diodes was found to be less than 0.1 nsec. The electrical properties of the chromium films obtained under various conditions are discussed. This chemical deposition technique, where chromium containing a small amount of carbon can be deposited, gives high quality Schottky barrier diodes.

Fisher and Hafner (1) found that in dicumene chromium (DCC) the chromium atom is attached to two cyclic hydrocarbons by electrons shared with the organic rings. They pointed out that in this unusual type of bonding, the chromium atom is in a metallic or zero-valent state. Consequently, pyrolytic decomposition of DCC occurs readily in the absence of any reducing agent such as hydrogen. Also, because of loose bonding between the chromium atom and the organic rings, the chromium films thus deposited are less contaminated with carbon and oxygen than those from chromium carbonyl (2, 3). Consequently, it appears that the deposition of chromium films by the pyrolytic decomposition of dicumene chromium would be a highly desirable method for making Schottky barrier devices. The purpose of this paper is to demonstrate the feasibility of using just this approach to make excellent Schottky diodes.

Experimental Procedures and Results

The apparatus used for the deposition of chromium by the chemical vapor decomposition of DCC is similar to those horizontal reactors used in depositing epitaxial silicon (4). Briefly, it consisted of a feed system and a quartz reactor (Fig. 1). The feed system consisted of pressure regulators, flow meter, valves, and a DCC vapor generator. To have a realistic deposition rate, the DCC vapor generator was heated to 195°C to obtain a vapor pressure near 12 mm of Hg. The argon carrier gas passed through the vapor generator at a rate of 100 ml/min. The gas lines from the vapor generator to the reactor were heated to minimize the condensation of DCC. The main gas line argon had a flow rate of 2.4 liters/min. The DCC was transferred and kept under argon at all times; this prevents exposure to air and the formation of DCC-hydroxide which does not decompose thermally. A vitreous carbon susceptor was placed in the 50 mm diameter quartz reactor. The susceptor was used as the substrate holder and was inductively heated to deposition temperatures with a megacycle rf generator.

The deposition temperature covered in this work was 350°-520°C, a range desirable for Schottky barrier work. Within the temperature range and gas flow conditions stated above, the deposition rate varied from 45 to 65 Å/min as shown in Fig. 2; note that the peak deposition rate appeared at about 450°C. A deposition rate peak is often observed in chemical vapor deposition systems (4, 5). The deposition rate can be raised to much greater than 60 Å/min by increasing the DCC partial pressure in the reactor. However, our primary objective was to find the most desirable way to

* Electrochemical Society Active Member.
Key words: chromium-silicon rectifiers, hot carrier device, metal-semiconductor contacts, Schottky barrier.

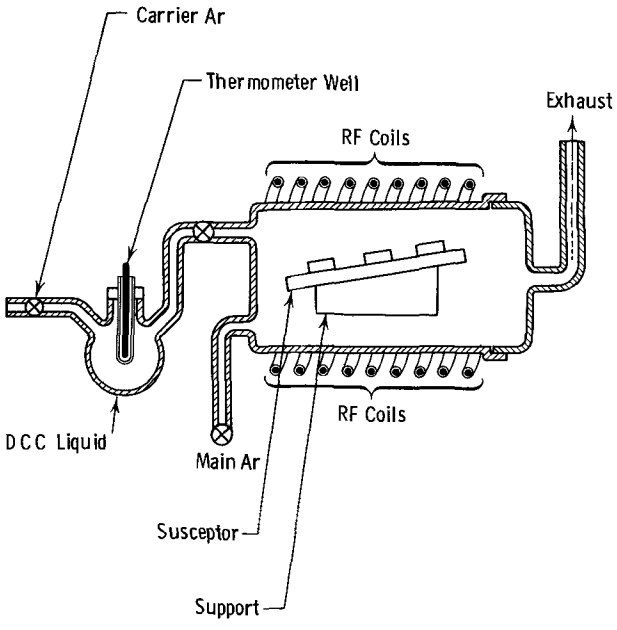

Fig. 1. Chromium reactor schematic

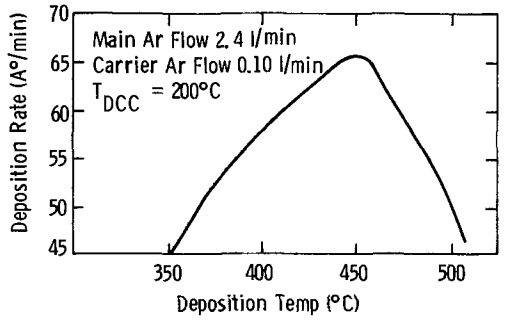

Fig. 2. Deposition rate vs. substrate temperature

fabricate the high-quality Schottky barrier diode's abrupt metal-silicon interface, rather than to investigate the wide range of the chromium deposition kinetics. Because the resistivity of the deposited chromium films was indicative of impurity contamination, the film resistivity was carefully determined. The measured resistivity of the deposited Cr films was plotted as a function of deposition temperature as shown in Fig. 3. The resistivity decreased rapidly with increasing deposition temperature in the 320°-380°C range. The decrease in resistivity due to the increase in deposition temperature above 380°C was at a much slower rate. This latter result is indicative of different contaminating influences; it is surmised that the reaction products within the desired chromium film

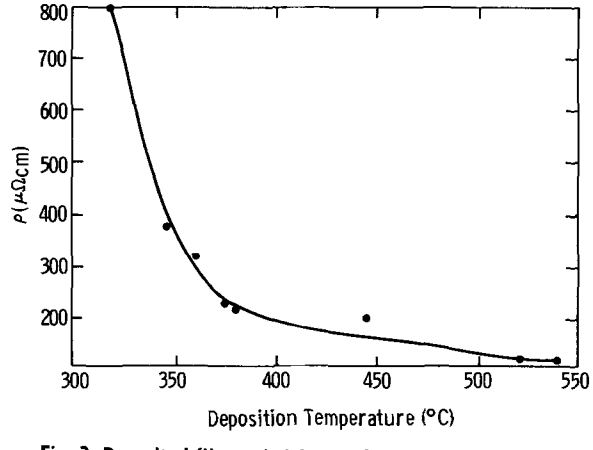

Fig. 3. Deposited film resistivity vs. deposition temperature

below 380°C contain organic contaminants. Above 380°C, the contamination is believed to be only carbon since Knap *et al.* (6) reported only moderate variations of carbon content for large deposition temperature changes. The low change rate of resistivity above 380°C deposition temperature leads to the desired operating temperatures to form Schottky barrier diodes utilizing chromium contaminated with carbon.

For the fabrication of Schottky barrier diodes, epitaxial silicon on heavily doped silicon substrate wafers was used. The substrate wafers had (100) orientation and were "chem-mech" polished using the cupric ion process (7). The epitaxial layer was 4μ thick with a resistivity of 0.25 ohm-cm. The substrate resistivity was 0.002 ohm-cm. After epitaxial deposition, the wafers were oxidized at 970°C using a dry-wet-dry process. Oxide windows were opened using regular photolithographic techniques. The wafers were then placed on the carbon susceptor and a 1200Å layer of chromium was deposited using the above method at 405°C. A high-conductivity metal layer was built on top of the deposited chromium. The oxide windows were 1 mil in diameter; metal patterns 3 mils in diameter were etched using regular photolithographic techniques. The diodes thus formed were diced using an ultrasonic cutter; the chips were mounted on TO-18 headers.

A typical current-voltage measurement of a silicon-chromium diode is shown in Fig. 4. The current-voltage relationship of a Schottky barrier diode can be expressed as

$$J = J_S \{e^{qV/nkT} - 1\} \quad [1]$$

where J is the current density
J_S is the saturation current density, and is given by

$$J_S = A^* T^2 \exp(-q\phi_b/kT) \quad [2]$$

ϕ_b is the barrier height in volts
V is the applied voltage
A^* is the modified Richardson constant
T is the absolute temperature
k is the Boltzmann constant
n is the diode ideality factor. For an ideal Schottky diode, n is numerically equal to one.

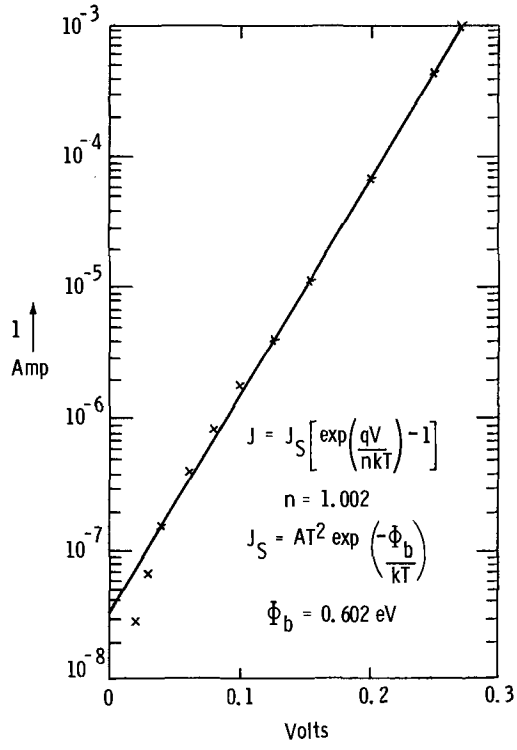

Fig. 4. Current-voltage characteristics of Si-Cr diode

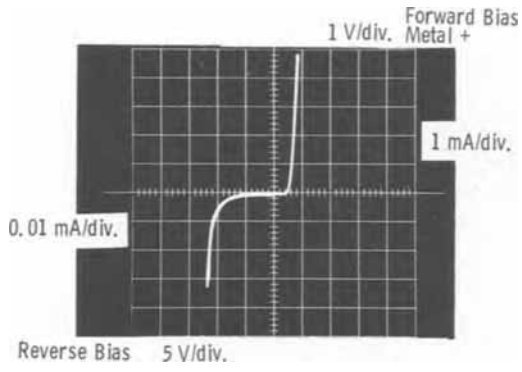

Fig. 5. Typical current-voltage relationships with forward and reverse bias.

Using Eq. [2] and a value of $A^* = 2.05 \times 120$ A/cm²/°K² for the (100) silicon surface (8), we obtain a value of $\phi_b = 0.6$ eV for the silicon-chromium barrier.

The diodes had breakdown voltages of 10-12V at 10 μA and a forward drop of 0.4V at 1 mA. A typical current-voltage relation is shown in Fig. 5. The reverse bias capacitance of the diodes was measured using a Boonton capacitance bridge at a fixed frequency of 1 MHz/sec. Figure 6 shows a plot of $1/c^2$ *vs.* reverse bias voltage, V. From this figure the intercept on voltage axis, V_i, is -0.44V. The barrier height, ϕ_b, is calculated using the relation (8)

$$\phi_b = V_i + \phi_f + \frac{kT}{q} - \Delta\phi \qquad [3]$$

where V_D is the diffusion potential equal to $V_i + kT/q$, ϕ_f is the Fermi potential (Fig. 6) which is calculated using the doping concentration (9), and $\Delta\phi$ is the image force lowering of the barrier height (10). The term kT/q is due to the electric field. Using Eq.

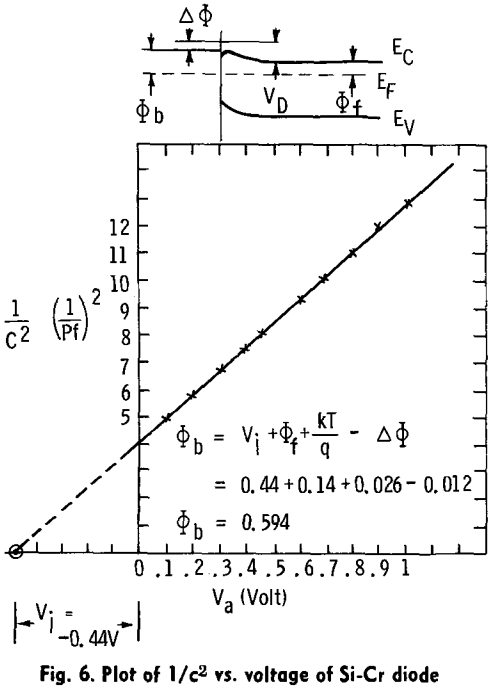

Fig. 6. Plot of $1/c^2$ vs. voltage of Si-Cr diode

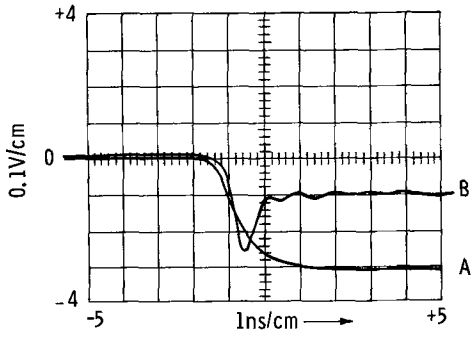

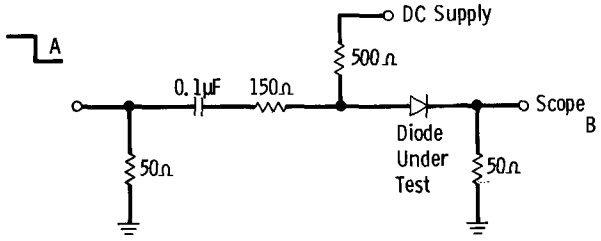

MEASURING CIRCUIT

Fig. 7. Stored-charge measurement of Si-Cr diode

[3] and the values of V_D, ϕ_f, and $\Delta\phi$ shown in Fig. 6, we obtain a value of 0.59 eV for ϕ_b.

The switching speed of the diodes was measured by turning off the forward-biased diode with a fast negative-going pulse as shown in Fig. 7. The total area of the curve below the zero level gives the total stored charge. From this value of stored charge and the forward current, the switching speed was estimated to be about 100 ps.

Conclusion

Chromium-silicon Schottky barrier diodes can be fabricated using chromium deposited by thermal decomposition of dicumene-chromium. This provides an alternative to regular evaporation or sputtering techniques.

Manuscript submitted Nov. 20, 1969; revised manuscript received Sept. 3, 1970.

Any discussion of this paper will appear in a Discussion Section to be published in the December 1971 JOURNAL.

REFERENCES

1. E. O. Fisher and W. Hafner, *Z. Naturforsch.*, **106**, 665 (1955).
2. I. R. Kramer and R. H. Hafner, Am. Inst. Mining Met. Eng. Tech. Publ. 1516 (Oct. 1942).
3. J. J. Lander and L. H. Germer, Am Inst. Mining Met. Eng. Tech. Publ. 2259 (Sept. 1947).
4. V. Y. Doo and E. O. Ernst, *Solid State Technol.*, **10**, 10 (1967).
5. V. Y. Doo, D. W. Boss, R. Valletta, and W. Pliskin, Paper 42 presented at Electrochem. Soc. Meeting, New York, May 4-9, 1969.
6. J. E. Knap, B. Pesetsky, and F. N. Hill, *Plating*, **53**, 778 (1966).
7. E. Mendel and K. H. Yang, *Proc. IEEE*, **57**, 1476 (1969).
8. C. R. Crowell, J. C. Sarace, and S. M. Sze, *Trans. Met. Soc. AIME*, **233**, 478 (1965).
9. S. M. Sze, "Physics of Semiconductor Devices," p. 38, John Wiley & Sons, New York (1969).
10. S. M. Sze, *op cit.*, p. 364.

Studies on the Deposited Asbestos Diaphragm with a Miniature Diaphragm-Type Chlorine Cell[1]

Fumio Hine* and Masaki Yasuda

Nagoya Institute of Technology, Gokiso-cho, Nagoya 466, Japan

ABSTRACT

Mass transfer and voltage drop in the deposited asbestos diaphragm were studied with a miniature chlorine cell. The diaphragm was formed on the steel-mesh cathode with a vacuum, and the voltage drop in the compressed asbestos layer was large. The streaming potential through the diaphragm was very small because of the highly conductive electrolytic solution.

The rate of development of the amalgam-type chlorine cell in the 20 years after World War II is surprising, and many articles have been and are being published on this subject. On the other hand, although the diaphragm-type chlorine cell accounts for a major share of the chlorine produced in the United States, comparatively few papers have been published on the diaphragm cell (1-4).

In the diaphragm cell, the principal anode reaction involves a charge transfer from Cl^- ion to Cl_2 gas, which takes place at the surface of a graphite anode in contact with concentrated NaCl solution.

Other anodic reactions also take place as a consequence of the back migration of OH^- ion through the diaphragm from the catholyte.

The principal cathode reaction involves the formation of hydrogen gas from water in the mixed solution of NaOH and NaCl in contact with a steel cathode. Secondary reactions take place as a consequence of dissolved chlorine in the anolyte which percolates through the diaphragm into the catholyte. The possibility of cathodic reduction of ClO_3^- ion, which also comes from the anode compartment to the cathode, is discussed in a separate paper (5).

Mass transfer and voltage balance in the deposited asbestos diaphragm on the steel-mesh cathode are discussed in this paper.

Mass Transfer and Voltage Drop in the Diaphragm

Since MacMullin (6) was concerned about the possible effects of the zeta potential on the mass transfer through the porous diaphragm, the streaming potential has been determined.

Asbestos fiber for the Hooker Cell, Grade 5D, was deposited on steel-mesh in a glass cylinder cell of 3.6 cm inner diameter at about 70 mm Hg vacuum as shown in Fig. 1. The thickness was 2.5 to 3.0 mm. Calomel electrodes were placed in front of and in the rear of the deposited asbestos diaphragm. The concentration of NaCl was varied from 26 x 10^{-4} to 26 w/o (weight per cent) and the pressure difference was varied between 10 and 60 mm Hg. Temperature was 24°C. The results obtained are shown in Fig. 2.

The streaming potential was proportional to the pressure drop and the slope increased with decreasing NaCl concentration as shown in Fig. 2. Using the Helmholtz-Smoluchowski equation (7), the zeta potential was calculated (Eq. [1]). The results are listed in Table I.

$$\zeta = 4\pi\eta\kappa E_s/DP \qquad [1]$$

where E_s = streaming potential, volt
D = dielectric constant (*ca.* 80), e.s.u.
P = pressure drop, dyne/cm^2
κ = conductivity, mho/cm
η = viscosity, poise
ζ = zeta potential, volt

[1] This study was conducted at Kyoto University at Uji, 1967-1968.
* Electrochemical Society Active Member.
Key words: streaming potential, mass transfer, current efficiency.

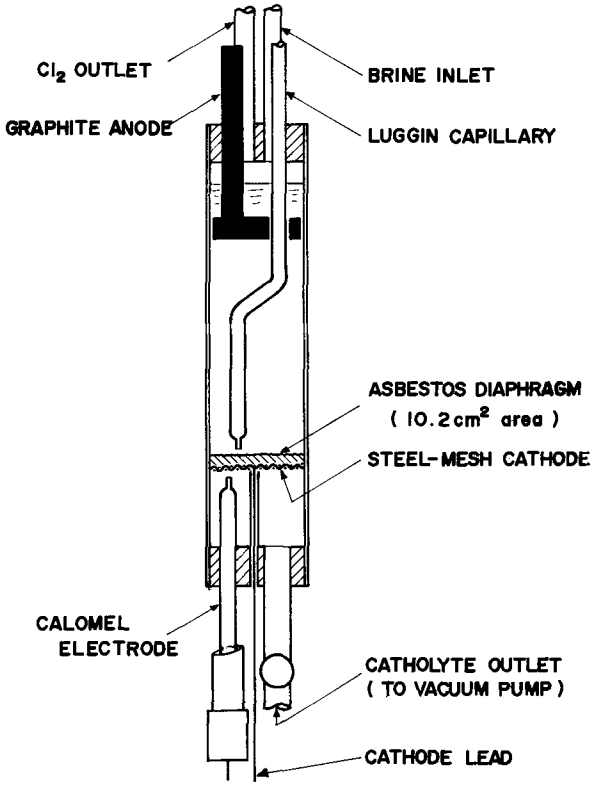

Fig. 1. The miniature diaphragm cell

Because the streaming potential in concentrated solution is very small, no significant effect of the electrokinetic phenomena on a practical diaphragm cell is assured.

The *IR* drop in porous media has been studied by MacMullin *et al.* (8). It was proposed that the resistivity in a diaphragm is uniform, while the porosity may vary in the direction of thickness. Matsuno considered similar assumptions and he estimated a characteristic factor for diaphragms (9). Mukaibo studied the mass transfer phenomena through the diaphragm in a chlorine cell with the assumption of uniform porosity (10).

A graphite anode was placed at the top of the cell shown in Fig. 1. A movable Luggin capillary connecting with a calomel electrode was set in front of the diaphragm and cathode mesh. An example of the *IR*

Table I. The zeta potential at 24°C

Solution NaCl (w/o)	Conductivity (mho/cm)	Zeta potential (mV)
26 × 10^{-4}	0.126_5 × 10^{-2}	−33.2
26 × 10^{-3}	0.824 × 10^{-3}	−33.1
26 × 10^{-2}	2.74_2 × 10^{-3}	−31.9

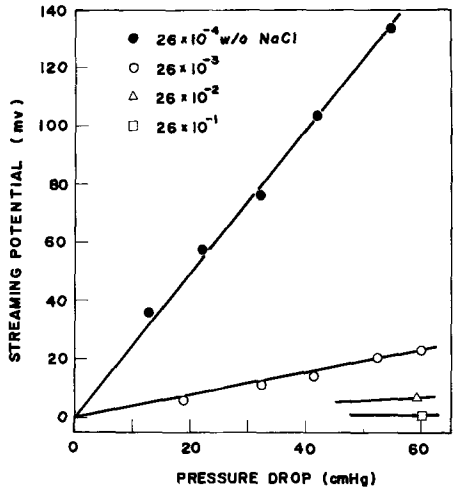

Fig. 2. The streaming potential vs. pressure drop curves in NaCl solutions at 24°C.

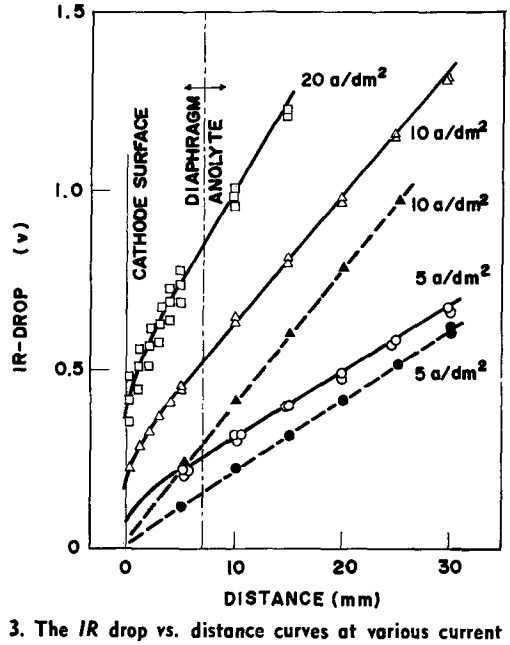

Fig. 3. The IR drop vs. distance curves at various current densities. Pressure drop, 50 cm Hg. Solid line, IR drops with diaphragm; broken line, IR drops without diaphragm.

drop *vs.* distance curve is shown in Fig. 3. As shown in Fig. 1, the tip of the lower calomel electrode is pressed to the back of the steel-cathode screen. The tip of the upper Luggin capillary can be inserted in the deposited asbestos diaphragm until it touches the upper surface of the cathode wire. The potential difference between the two probes would involve the cathode overvoltage and the *IR* drop between them. Our reference point $x = 0$ in Fig. 3 and 4 is the upper surface of the steel cathode and, hence, there is some space between two probes even at $x = 0$. The *IR* drops at $x = 0$ in Fig. 3 are exactly proportional to the current density as shown in Fig. 5, which means a simple *IR* drop between two probes. The relatively low slope of the *IR* drop *vs.* distance curve (Fig. 3) at high current density is probably due to the temperature rise in the vicinity of the cathode caused by electrolysis. The solid lines with open points have curvature in the vicinity of the cathode, but further away they are almost parallel with the corresponding broken lines which show the *IR* drop of the solution at the same current density labeled. The *IR* drop in the diaphragm varies with pressure as shown in Fig. 4.

The compressed layer of the deposited asbestos diaphragm exists near the surface of the steel-mesh cathode, and its thickness is expected to be 2 to 3 mm.

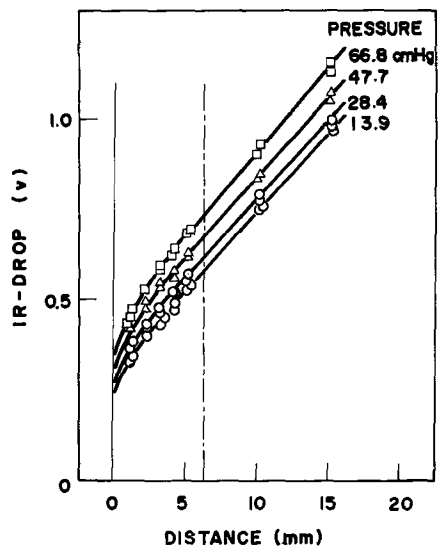

Fig. 4. The *IR* drop vs. distance curves at various pressure drops. Current density, 20 A/dm²; temperature, 55°C.

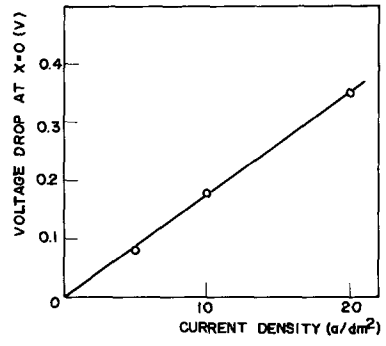

Fig. 5. The voltage drop vs. current density at $x = 0$ calcu from Fig. 3.

Assuming that the resistivity of this compressed layer is linear with distance, the *IR* drop is formulated as follows

$$\rho - \rho_0 = -K(x - L)$$

and

$$V = i\int_0^L \rho\, dx = i\left(\rho_0 L + \frac{K}{2}L^2\right) \qquad [2]$$

where ρ = resistivity at x, ohm-cm
ρ_0 = resistivity beyond L, ohm-cm
K = coefficient, ohm
V = *IR* drop, volt
i = current density, A/dm²
x = distance from the cathode, cm
L = thickness of the compressed layer, cm

The value, K, calculated by this equation with the data in Fig. 3 and 4 is an approximately linear function of the pressure drop as shown in Fig. 6.

MacMullin (11) has offered an alternate explanation from the data plotted in Fig. 3. The slopes of the volt-

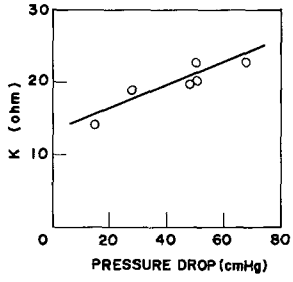

Fig. 6. The resistance vs. pressure curve

Table II. The resistivity of the diaphragm from Fig. 3 (11)

P = 50 cm Hg i (A/cm²)	In anolyte dV/dx	ρ_o	In diaphragm dV/dx	ρ	ρ/ρ_o
0.20	0.52	3.5	0.88	5.9	1.7
0.10	0.36	3.6	0.54	5.4	1.5
0.05	0.18	3.6	0.26	5.2	1.5
Average		3.6		5.5	1.5

Table III. The resistivity of the diaphragm from Fig. 4 (11)

P, cm Hg	i, A/cm²	In anolyte dV/dx, V/cm	ρ_o, ohm-cm	In diaphragm dV/dx, V/cm	ρ, ohm-cm	ρ/ρ_o	ρ_o/ρ, Km	$1-\epsilon$, f
66.8	0.20	0.471	0.235	0.820	0.410	1.74	0.575	0.225
47.7	0.20	0.443	0.222	0.745	0.372	1.68	0.597	0.250
28.4	0.20	0.443	0.222	0.677	0.339	1.53	0.655	0.208
13.9	0.20	0.443	0.222	0.626	0.313	1.41	0.710	0.170

age gradient outside the diaphragm in the anolyte and inside the diaphragm are related to the respective resistivities by the following equation

$$\rho = \frac{dV}{dx}\frac{1}{i} \qquad [3]$$

where x = cm, i = A/cm², and ρ = ohm-cm. The results are given in Table II. Applying this same procedure to Fig. 4, the effect of pressure drop is obtained as shown in Table III. The last two columns are added in order to read the fractional space $f = 1 - \epsilon$ occupied by the fibers from the conductivity ratio $Km = \rho_o/\rho$, using the Meredith plot, Fig. 1 in Ref. (4).

Thus, high flow rates correspond to high pressure drop across the diaphragm, and this compresses the fibers, reduces the voids, and increases the resistivity of the diaphragm, all in the expected way.

The above is not the complete answer. Stender *et al.* have published an excellent article (3) in which the mathematics is correct except for one simplifying assumption—that the conductivity of the electrolyte in the diaphragm is constant. This assumption is inconsistent with his demonstration that the OH^- concentration varies with x, the distance from the cathode inside the diaphragm. That is, when $x = 0$, C_{OH^-} is the same as for the catholyte itself and, when $x = \delta$ (the thickness), C_{OH^-} is practically zero. Realizing that OH^- ion conducts better than Cl^- ion, if OH^- varies, the conductivity must vary. Qualitatively, this appears to be so as shown in Fig. 7. Therefore, the *IR* drop in the diaphragm should be concave upward as shown in Fig. 8. As Stender says, there are no data on the conductivity of mixtures of NaCl and NaOH, as functions of C_{Cl^-}, C_{OH^-}, and temperature.

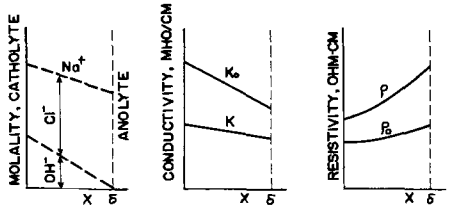

Fig. 7. Model in the diaphragm [by R. B. MacMullin (11)]

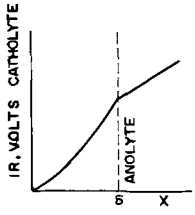

Fig. 8. The *IR* drop in the vicinity of the cathode screen [by R. B. MacMullin (11)].

MacMullin's comments are reasonable if the porosity distribution across the deposited asbestos diaphragm is uniform. But it is obvious that the porosity varies with the normal direction through the cake deposited (12). The curvature of the *IR* drop *vs.* distance diagram in Fig. 3 and 4, then, differs from the estimation shown in Fig. 8. The asbestos in contact with the cathode screen is greatly compressed, while that facing toward the anolyte is rough. Therefore, the voltage gradient at the surface of the diaphragm does not vary significantly.

Operation of a Miniature Cell

A miniature cell shown in Fig. 1 was operated for a few hours, and the flow rate, concentration of NaOH, and cathode potential were measured with time. The temperature stabilized about 60 min after start-up, and other factors reached steady state as shown in Fig. 9. The logarithm of flow rate *vs.* logarithm of pressure drop in Fig. 10 is linear with the slope of about 45°. According to Perry (13), the permeable medium seems to be rigid when the slope of this curve is exactly equal to 45°. However, the diaphragm in this study was somewhat compressible since the *IR* drop between the cathode screen and the upper Luggin capillary, placed 3 mm above the top of the cathode, increases slightly with pressure drop. The concentration of NaOH in the catholyte decreases with increasing pressure drop because of increase in the percolation rate of the brine.

Current efficiency for the formation of NaOH can be calculated with the data of flow rate and concentration. For the particular experimental cell used, it appeared to depend on the current density as shown in Fig. 11 and as independent of other factors such as pressure and temperature. It might be affected by diaphragm material. MacMullin has analyzed the data differently as follows (11).

The current efficiency was calculated from the caustic yield at six different current densities as shown in Fig. 11. However, this does not indicate the current efficiency is dependent solely on current density. The relationship between the current efficiency and the current density has been described by Kircher (14) and Stender (3). Quite simply put, current efficiency depends chiefly on the ratio of current density to percolation rate through the diaphragm. A Hooker cell can achieve a current efficiency of 94-96% over a current density range of 5-15 A/dm² if the conversion

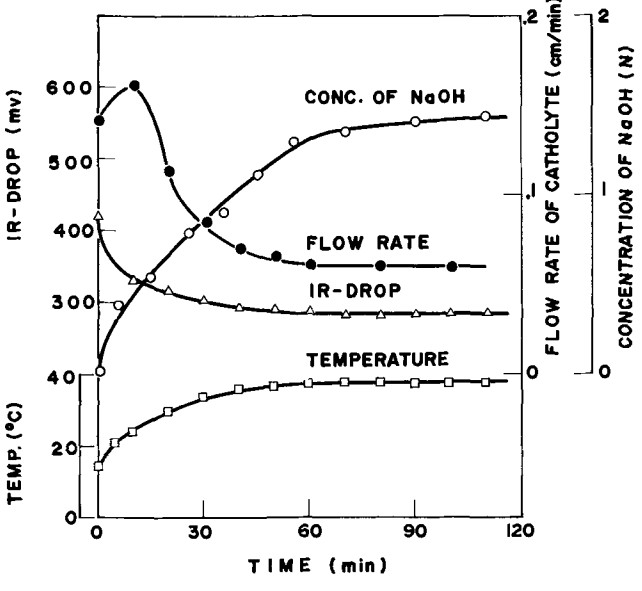

Fig. 9. Operating data of the miniature chlorine cell. Current density, 15 A/dm²; pressure, 13 cm Hg; thickness of diaphragm, 1.5-2.0 mm; distance between cathode and Luggin capillary, 3 mm.

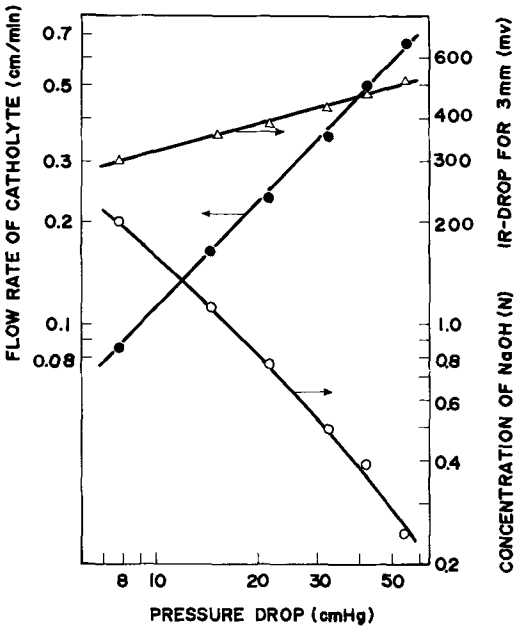

Fig. 10. Flow rate, IR drop, and concentration of NaOH as functions of pressure drop. Current density, 30 A/dm^2; temperature, 53°C.

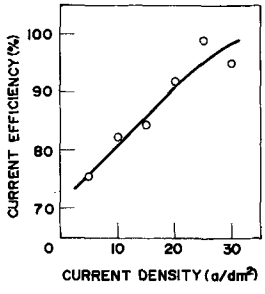

Fig. 11. The current efficiency vs. current density curve

per pass of around 45-55% and a temperature above 95°C are maintained. From Fig. 9, at i = 15 A/dm^2, after 2 hr the current efficiency can be calculated to be 87.5%, which is acceptable for a temperature of 38°C. From Fig. 10, at i = 30 A/dm^2, the average current efficiency for the six runs is 92.8%. The catholyte flow rate varies from 0.085 cm/min up to as high as 0.65 cm/min. The catholyte rate in a typical Hooker cell, at 15 A/dm^2, is about 0.025 cm/min and for the same conversion, at 30 A/dm^2, which is not yet achievable commercially, would be about 0.05 cm/min. The current efficiency is generally about 96%.

Figure 12 shows the current efficiency as a function of the ratio of current density to catholyte flow rate. As shown, the larger the current density and the larger the flow rate at a given current density, the larger is

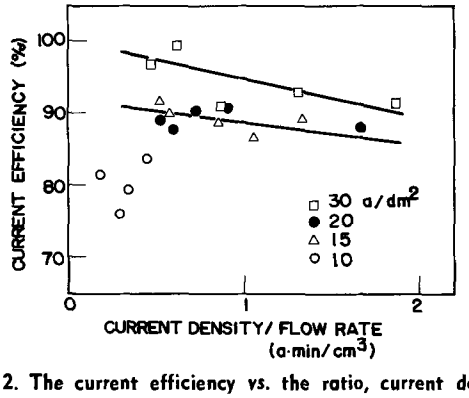

Fig. 12. The current efficiency vs. the ratio, current density to the flow rate of anolyte.

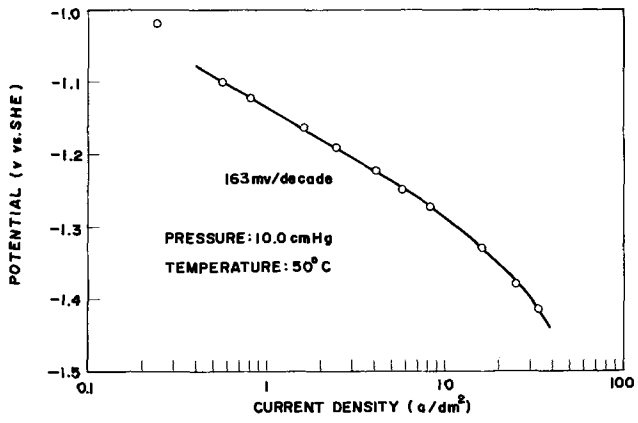

Fig. 13. The potential vs. current density curve of the steel cathode.

the current efficiency. Why the current efficiency decreases with decrease of the flow rate of the catholyte is not clear, but it probably would be due to the back-migration of OH^- through the diaphragm because the concentration of OH^- increases with decreasing flow rate.

Figure 13 shows an example of the polarization curve of the steel-mesh cathode in the same cell. The potential is linear with the logarithm of current density in a range 1-10 A/dm^2 with a slope of 160 mV/decade. The curve deviates from the Tafel line at high current densities. The potential became more noble by a few millivolts with increasing pressure drop at constant current density, the reason for which was not clear. Measurement of the hydrogen overvoltage in concentrated NaOH at elevated temperature is somewhat difficult. The hydrogen overvoltage decreases with increasing temperature. Relative data on the hydrogen overvoltage on the graphite cathode in concentrated NaOH at high temperature ranges have been published by Hine (15).

Complications arise, in that the catholyte of the diaphragm-type chlorine cell is a mixed solution of concentrated NaOH and NaCl, and it contains some amounts of ClO^- and ClO_3^-; thus, the cathode reaction is affected by these contaminations. Details of the cathode reaction are discussed in other papers (5, 16).

Acknowledgments

The authors express many thanks for the useful suggestions of Mr. Robert B. MacMullin, Niagara Falls, New York, and for his financial support of a part of this work. Samples of asbestos were supplied from Nissan Chemical Company, who operate the Hooker S-type chlorine cells at their Oji plant, Tokyo.

Manuscript submitted Aug. 13, 1968; revised manuscript received ca. Sept. 25, 1970.

Any discussion of this paper will appear in a Discussion Section to be published in the December 1971 JOURNAL.

REFERENCES

1. ACS Monograph 154, "Chlorine," Edited by J. S. Sconce, Chap. 5, Reinhold, New York (1962).
2. R. L. Murray and M. S. Kircher, *Trans. Electrochem. Soc.*, **86**, 83 (1944).
3. V. V. Stender, O. S. Ksenzhek, and V. N. Lazarev, "Alkali Migration and Current Yields During the Electrolysis of Chloride Salt Solutions with Membranes," English translation supplied by MacMullin (Language Service Bureau No. 12352). Original reference journal is not clear.
4. R. B. MacMullin, "A Rational Explanation of the Cell Voltage Drop after a Diaphragm Change in the Hooker S-4 Cell" (Unpublished, for R. B. MacMullin Associates only).
5. F. Hine and M. Yasuda, *This Journal*, **118**, 182 (1971).

6. R. B. MacMullin, "Progress and Problems in Electrochemical Engineering," Lecture at Chicago Section of Electrochem. Soc., Jan. 13, 1966.
7. "The Encyclopedia of Electrochemistry," Edited by C. A. Hampel, pp. 537 and 1090, Reinhold, New York (1964).
8. R. B. MacMullin and G. A. Muccini, *A.I.Ch.E. J.*, **2**, 393 (1956).
9. T. Matsuno, *Kogyo Kagaku Zasshi (J. Chem. Soc. Japan, Industrial Chemistry Section)*, **52**, 281 (1949).
10. T. Mukaibo, *Denki Kagaku (J. Electrochem. Soc. Japan)*, **20**, 482 (1952).
11. R. B. MacMullin, Private communication.
12. F. M. Tiller, "Filtration Theory Today," *Chem. Eng.*, p. 151, June 20, 1966.
13. J. H. Perry, "Chemical Engineers' Handbook," 4th Ed., pp. 19-56, McGraw-Hill, New York (1963).
14. M. S. Kircher, Ref. (1), p. 81.
15. See Fig. 2 and 3, F. Hine, *Electrochem. Technol.*, **2**, 79 (1964).
16. F. Hine and M. Yasuda, *This Journal*, **118**, 170 (1971).

Studies on the Cathodic Reaction in the Diaphragm-Type Chlorine Cell[1]

Fumio Hine* and Masaki Yasuda

Nagoya Institute of Technology, Gokiso-cho, Nagoya 466, Japan

ABSTRACT

Polarization of a rotating platinum cathode in mixed solutions of NaCl and NaOH containing dissolved chlorine was measured. At relatively low current densities, cathodic reduction of ClO^- took place as the main reaction. The diffusion-limiting current density was a function of the concentration of ClO^- in solution and the reaction was first order with respect to ClO^-. Therefore, it was concluded that the mechanism

$$ClO^- + H_2O + e = Cl_{ad} + 2\,OH^-$$

$$Cl_{ad} + e = Cl^-$$

was operative at low current densities. At high current densities, hydrogen formation is, of course, the main reaction.

There is no doubt that the hydrogen electrode process is a high light of theoretical electrochemistry. Thus, many papers have been published.

The main reaction on steel-cathode screens in the diaphragm-type chlorine cell under operating conditions—that is, relatively high current densities such as 10-15 A/dm^2—is, of course, hydrogen evolution from H_2O in concentrated caustic soda solution. However, the catholyte of the diaphragm-type chlorine cell is a mixed solution of concentrated NaOH and NaCl and it contains some amounts of ClO^-. Hypochlorite ion, ClO^-, is reduced easily at the cathode and it is one of the factors in the decrease of current efficiency in chlorate cells (1, 2) because of the relatively low current density as compared with chlor-caustic cells.

Frumkin and his co-workers (3) studied the cathodic reaction of chlorine on the rotating platinum cathode in acidic solution and they stated that the over-all reaction was controlled by two consecutive processes, [*A*] and [*B*]

$$Cl_2 + e = Cl_{ad} + Cl^- \qquad [A]$$

$$Cl_{ad} + e = Cl^- \qquad [B]$$

Since the cathodic reduction of chlorine in alkaline solution has not yet been described in detail, mechanisms for the reduction of dissolved chlorine at the rotating platinum cathode in concentrated alkali solution are now discussed.

The rotating steel cathode was examined several times for consideration as a practical chlorine cell, but complicated results were obtained at relatively low current densities due to the anodic dissolution of steel by local cell action. At high current densities, on the other hand, a similar mechanism can be assumed on both platinum and steel cathodes; that is, the hydrogen formation reaction.

Because the equilibrium constant for reaction [C]

$$Cl_2 + 2OH^- = Cl^- + ClO^- + H_2O \qquad [C]$$

is large, 1.33 x 10^{16} at 25°C (4), chlorine passing through the diaphragm toward the cathode compartment may exist as ClO^- on the cathode surface. Hydrogen formation is, of course, taking place at the cathode at high current densities and hence two reactions, [*D*] and [*E*], are proceeding:

$$2H_2O + 2e = 2OH^- + H_2 \qquad [D]$$

$$E_1^\circ = -\,0.828\text{V } vs.\text{ SHE at } 25^\circ\text{C}$$

and

$$ClO^- + H_2O + 2e = Cl^- + 2OH^- \qquad [E]$$

$$E_2^\circ = +\,0.88\text{V } vs.\text{ SHE at } 25^\circ\text{C}$$

where E_1° and E_2° are the standard reversible potentials for [*D*] and [*E*], respectively.

Experimental Procedure

A rotating disk platinum cathode of 5.03 cm^2 area was inserted in a plastic holder and located at the center of the glass electrolytic cell of about 1 liter capacity as shown in Fig. 1. The graphite anode was set in its compartment and was separated from the cathode with a sintered glass diaphragm. Electrolyte was prepared from extra-pure NaOH and NaCl and with deionized water. Chlorine from a cylinder was passed through 2*N* NaOH to prepare NaClO and this solution was added into the cell. The concentration of ClO^- was titrated by iodometry. The solution was deaerated with purified hydrogen for at least 2 hr. Temperature of the cell was controlled at 50° ± 0.5°C.

The mercuric oxide electrode consisting of Hg/HgO/2*N* NaOH was used as the reference elec-

[1] This work was conducted at Kyoto University at Uji, 1967-1968.
* Electrochemical Society Active Member.
Key words: rotating disk electrode, hypochlorite, electrochemical reduction, reaction mechanism.

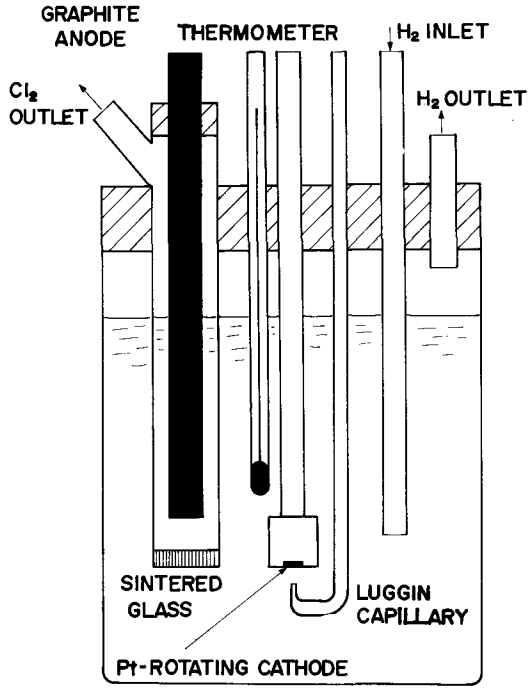

Fig. 1. The cell for polarization measurement

trode and its potential was referred to the hydrogen electrode.

The *IR* drop between the working electrode and the Luggin capillary was calibrated by means of extrapolation of the potential *vs.* distance curve to zero distance.

The working cathode was pre-electrolyzed to stabilize the surface several times before measurement.

Results and Discussion

Because of the large value of the equilibrium constant for reaction [*C*], no change of the concentration of dissolved chlorine due to hydrogen purge can be expected. Contamination of chlorine generated at the anode was also not significant.

Figure 2 shows the potential *vs.* current density curves in 2*N* NaOH + 3*N* NaCl containing various amounts of ClO^- at a constant rotating speed of 1660 rpm. The dotted line is the polarization curve of the rotating platinum cathode in the mixed solution without chlorine. Therefore, hydrogen formation reaction [*D*] may take place in this case. The limiting current density depends on the concentration of ClO^-, but is independent of the concentrations of NaCl and NaOH as shown in Fig. 3 and 4, respectievly. The limiting current density, i_L, at −0.5V *vs.* SHE is proportional to the concentration of ClO^- as shown in Fig. 5.

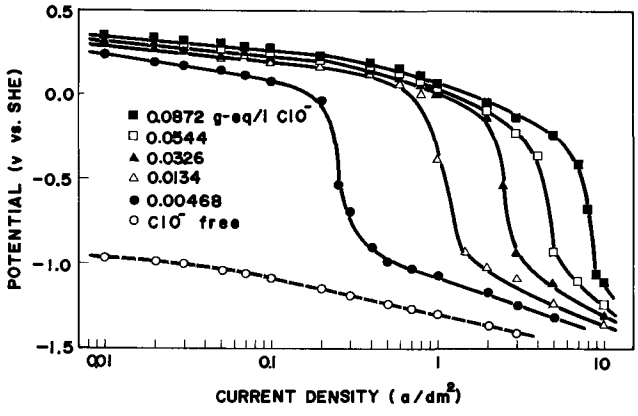

Fig. 2. The potential *vs.* current density curves in 2*N* NaOH + 3*N* NaCl containing various amounts of ClO^-. Rotating speed, 1660 rpm.

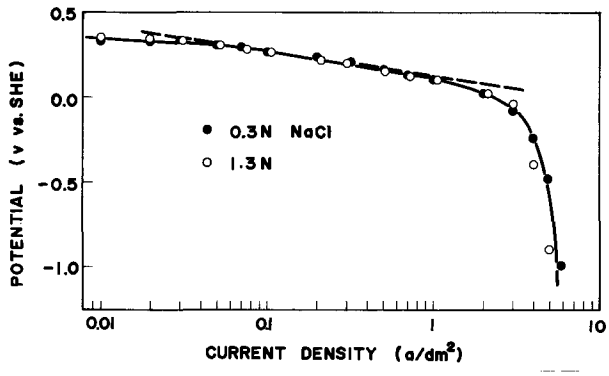

Fig. 3. The potential *vs.* current density curves in 1.45*N* NaOH containing 0.05 g-equiv/liter ClO^-. Rotating speed, 1660 rpm.

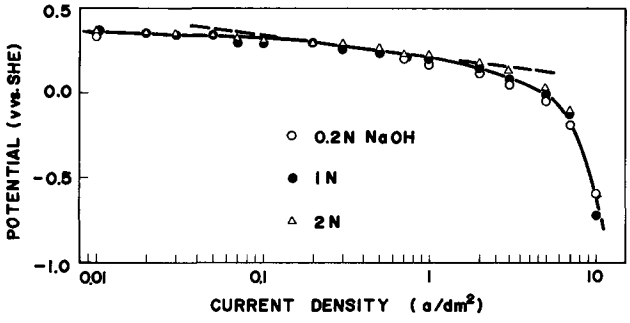

Fig. 4. The potential *vs.* current density curves in 0.2*N* NaCl containing 0.09 g-equiv/liter ClO^-. Rotating speed, 1800 rpm.

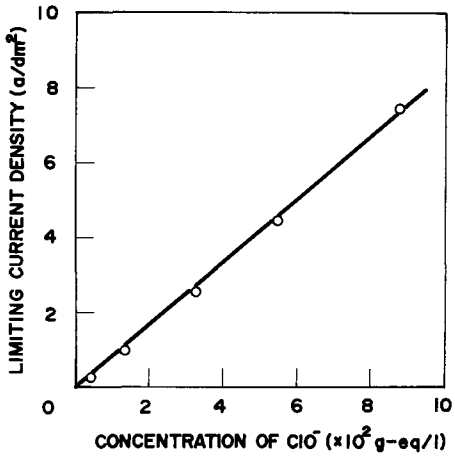

Fig. 5. The diffusion current *vs.* concentration of ClO^- curve at −0.5V. Rotating speed, 1660 rpm.

Lewich described the relationship between the current density, *i*, and the rotating speed, ω, as follows (5)

$$i = A(C - C_0)\omega^{1/2} \qquad [1]$$

where A = constant
C = concentration in the bulk of solution
C_0 = concentration at the electrode surface

At the diffusion-limiting current density

$$i_L = AC\omega^{1/2} \qquad [2]$$

Therefore, the limiting current density is linear to the square root of the rotating speed as shown in Fig. 6.

The current density due to electrochemical reaction is a function of concentration of reactant, *C*, as follows

$$i = kC_0^p \qquad [3]$$

where k is the rate constant and p is the order of reaction. The concentration, C_0, becomes C as the rotating speed approaches infinity, that is

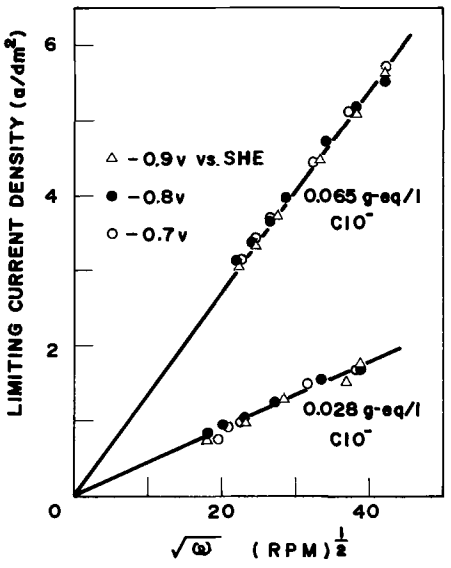

Fig. 6. The limiting current density vs. rotating speed curves in solutions containing various amounts of ClO^-.

$$i = i_r = kC^p \text{ at } \omega = \text{infinity} \quad [4]$$

Because the charge transfer reaction is first order with respect to ClO^- as described below, the next equation is obtained from Eq. [1], [3], and [4]

$$\frac{1}{i} = \frac{1}{i_r} + \frac{1}{AC\omega^{1/2}} \quad [5]$$

The $(1/i)$ *vs.* $(1/\omega^{1/2})$ is shown in Fig. 7. The straight lines project into the origin; therefore, the reaction limiting current density, i_r, is not present in this range.

According to Vetter (6), the reaction rate or the current density for two successive charge transfer reactions, [*F*] and [*G*]

$$S_r = S_m + e \quad [F]$$

$$S_m = S_o + e \quad [G]$$

is represented by Eq. [6]

$$i = -2k'a(1-\theta)\exp\left[-\frac{(1-\alpha)\mathbf{F}}{RT}E\right] \quad [6]$$

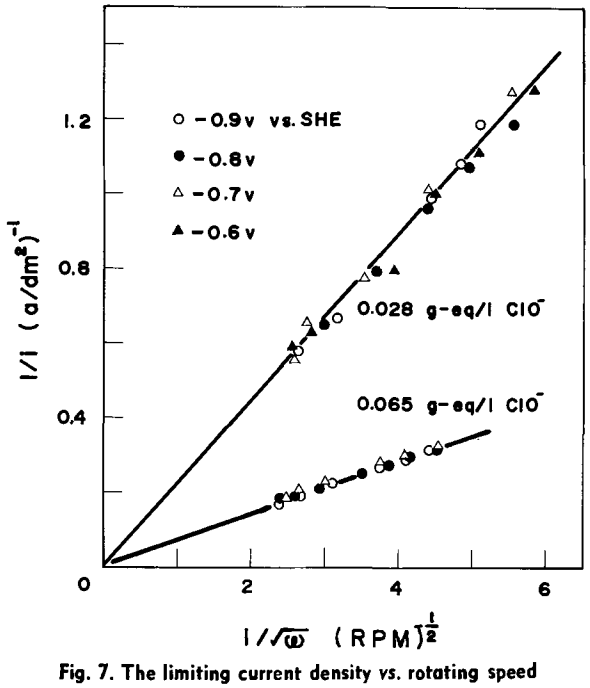

Fig. 7. The limiting current density vs. rotating speed

where k' = rate constant
a = activity of S_o
θ = coverage
α = transfer coefficient

if the overvoltage is much greater than $(RT/\mathbf{F})\ln(i_o'/i_o)$, where i_o and i_o' are the exchange current densities for [*F*] and [*G*], respectively.

Assuming the following relation between the current density and the activity of reactant, a, due to lack of diffusion in the vicinity of the working electrode

$$\frac{a_o}{a} = 1 - \frac{i}{i_L} \quad [7]$$

for reactions [*H*] and [*I*]

$$ClO^- + H_2O + e = Cl_{ad} + 2OH^- \quad [H]$$

$$Cl_{ad} + e = Cl^- \quad [I]$$

$$ClO^- + H_2O + 2e = Cl^- + 2OH^- \text{ (over-all reaction)} \quad [J]$$

we have the next equation from Eq. [6] and [7]

$$\frac{i}{1 - \frac{i}{i_L}} = -2k'a(1-\theta)\exp\left[-\frac{(1-\alpha)\mathbf{F}}{RT}E\right] \quad [8]$$

The dotted lines in Fig. 3 and 4 show the corrected Tafel line by Eq. [8] in a range of diffusion control. The slope of the Tafel line is 120-140 mV/decade and, hence, the transfer coefficient is 0.47-0.54. Here the activity coefficient of the ClO^- ion was assumed to be unity because of the dilute solution.

The current density at a given potential, 250 mV *vs.* SHE, was plotted *vs.* the concentration of ClO^- as shown in Fig. 8. The slope of the curve, $(d \log i/d \log C)$, is unity; therefore, the reaction is first order with respect to ClO^-. Thus, it is concluded that the elementary reaction in this case is reaction [*H*] instead of reaction [*J*], because the latter process is the two-charge transfer reaction for ClO^-. Reaction [*I*] follows reaction [*H*].

MacMullin offers the following comments on the cathodic reduction of ClO^- and ClO_3^- (7):

"The loss of current efficiency due to dissolved Cl_2 in the anolyte seeping into the diaphragm is quite small in a Hooker cell. However, the loss due to ClO^- and ClO_3^- formation in the anolyte is more serious. This loss results from the OH^- back migration through the diaphragm. Most of the chlorate thus formed is reduced to chloride at the cathode, so that only minor amounts of chlorate are left in the cell liquor under normal conditions.

"It would be worthwhile to consider a similar approach to the more important problem of reduction of chlorate at the cathode.

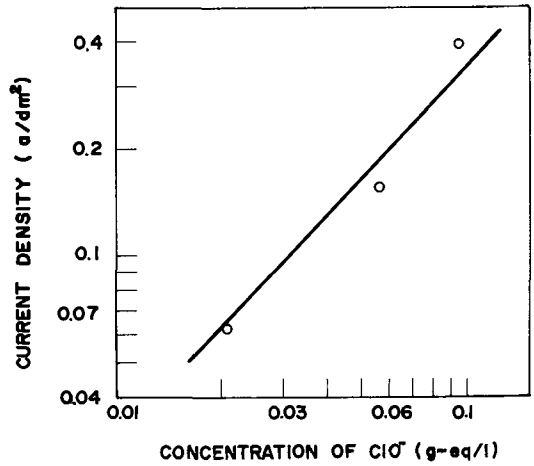

Fig. 8. The current density vs. concentration of ClO^- curve at 250 mV vs. SHE.

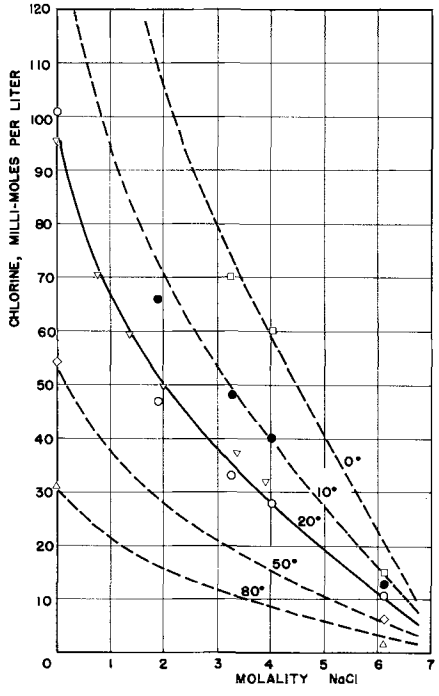

Fig. 9. Effect of NaCl molality on solubility of chlorine in brine (7). Total pressure, 760 mm Hg. 20°C Solid line: ▽, Oliveri-Mandala; ○, Kumpf, Kohn, and O'Brien. 0°, 10°, 50°, 80° Dashed lines: assumes salt effect at 20°C is constant over entire temperature range. Reduced experimental data of Kumpf, Kohn, and O'Brien: □, 0°C; ●, 10°C; ○, 20°C; ◇, 50°C; △, 80°C.

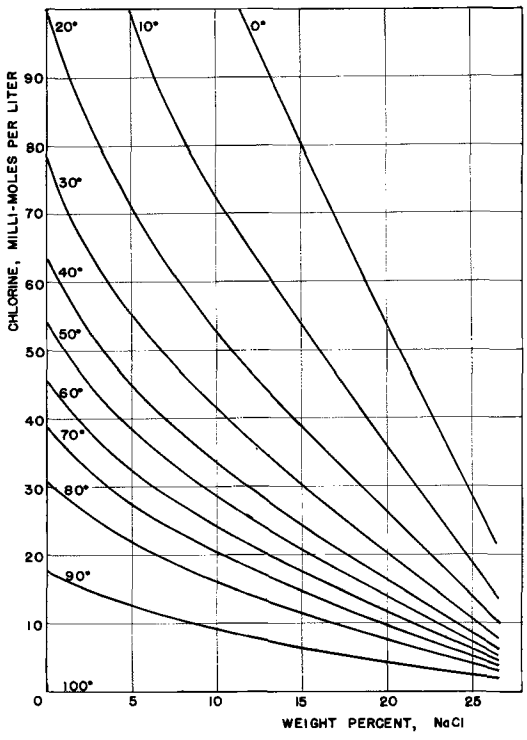

Fig. 10. Estimated solubility of chlorine in NaCl brine, not acidified (7).

"On Fig. 2, assuming the anolyte was 5*N*, or 24.4% NaCl, and the temperature 50°C, the solubility of Cl_2 in the anolyte is about 8 mmoles/L, or the concentration of ClO^- = 8 mmoles/L = 16 mequiv/L, or 0.016 equiv/L. This is in the range of ClO^- concentrations tested in this report. However, in a Hooker cell, where the anolyte is about 22% NaCl, temperature 95°-97°C, the chlorine solubility is only 0.15 mmole/L, corresponding to an ClO^- concentration of 0.0003 equiv/L." [Estimates of Cl_2 solubility made by MacMullin (7) are given in Fig. 9 and 10.]

"On the other hand, the $NaClO_3$ content of the cell liquor leaving the cell is about 0.07 gpl or 0.004 equiv/L of ClO_3^-. The $NaClO_3$ formed at the anode represents a current inefficiency of about 0.5%, if the pH is 4. Assuming 50% decomposition of the salt, this corresponds to a concentration of about

$$(0.005 \times 5N)/2 = 0.0125 \text{ equiv } ClO_3^-$$

or 0.0021 g-mole $NaClO_3$ in the anolyte which seeps through the diaphragm. So, most of the chlorate is reduced to chloride by the cathode, leaving very little ClO_3^- in the cell liquor. There is, of course, no ClO^- left in the cell liquor."

Since receiving MacMullin's comments, the authors have carried out experiments on the cathodic reduction of ClO_3^-. The results obtained with the same procedure as described for ClO^- have been reported in a separate paper (8).

Information on the anodic process would be very useful for discussion of the mechanism of the cathodic reduction of ClO^- and ClO_3^-, but experimental work is difficult because of passivation of platinum electrodes in alkaline solution containing chlorine.

Acknowledgment

The authors express many thanks for the useful suggestions of Mr. R. B. MacMullin of Niagara Falls, New York.

Manuscript submitted Aug. 13, 1968; revised manuscript received *ca.* Sept. 25, 1970.

Any discussion of this paper will appear in a Discussion Section to be published in the December 1971 JOURNAL.

REFERENCES

1. C. Wagner, *This Journal*, **101**, 181 (1954).
2. L. Hammar and G. Wranglen, *Electrochim. Acta*, 9, 1 (1964).
3. A. Frumkin and G. Tedoradse, *Z. Elektrochem.*, **63** 251 (1958).
4. W. M. Latimer, "Oxidation Potentials," 2nd Ed., p. 57, Prentice-Hall (1952).
5. B. Lewich, *Discussions Faraday Soc.*, **1**, 37 (1947).
6. K. J. Vetter, "Elektrochemische Kinetik," p. 129, Springer (1961), also "Electrochemical Kinetics (English translation)," p. 149, Academic Press, New York (1967).
7. R. B. MacMullin, Private communication.
8. F. Hine and M. Yasuda, *This Journal*, **118**, 182 (1971).

Anodic Mechanism of Electrochemical Machining: Study of Current Transient on a Rotating Electrode

Der Tau Chin*

Electrochemistry Department, Research Laboratories, General Motors Corporation, Warren, Michigan 48090

ABSTRACT

Using potentiostatic transients and employing rotating steel anodes, a study has been made of the anodic mechanism occurring during electrochemical machining in sodium chloride and sodium chlorate solutions. For chloride, transient behavior reveals the formation, on the anode surface, of a porous, nonprotective film resulting from the precipitation of the anode product. For chlorate, a less porous film, about 1000Å thick, is formed. Transient behavior reveals that the film is formed by anodic oxidation and that the rate of film growth increases with the increase in the rate of iron dissolution.

During the last decade, electrochemical machining (ECM) has had an impact in machining hard metal alloys. Although the process is still in a state of art, increasing efforts have been devoted to the search of reaction mechanisms. By understanding its electrochemical fundamentals, it is possible to broaden its application as an industrial metal removal method.

ECM generally takes place in a flow cell composed of closely spaced workpiece (anode) and cathode. Metal is removed anodically from the workpiece at a rate on the order of 0.05 in./min, and the dissolution products are removed by flushing electrolyte through the electrode gap space. The most commonly used electrolyte for ECM of steel is the concentrated water solution of sodium chloride. However, sodium chlorate has been found to be a more favorable electrolyte because of its good dimensional control and better surface finish (1, 2). In a series of steady-state polarization (3, 4) and cathodic stripping (5) studies, Hoare and his co-workers relate this excellent property of sodium chlorate to the formation of a protective film on the surface of the workpiece.

Knowledge regarding the formation and property of this film would, therefore, be useful in the development of the ECM process. For this purpose the potentiostatic transient of a steel anode in NaCl and $NaClO_3$ solutions has been investigated. Since the ECM process requires a high flow rate of electrolyte, the study was carried out under hydrodynamic conditions of a rotating disk electrode. Polarization studies of ECM using rotating electrodes have been reported by Hoare, LaBoda, McMillan, and Wallace (3) and by Davydov, Kashcheev, and Kabanov (6). This paper describes transient behavior of a rotating steel anode in the ECM electrolyte. The results are presented in terms of the nature of passivation and the mechanism of film growth on the anode surface.

Experimental

The cell arrangement (Fig. 1) was the same as reported in Ref. (3). The anode was an epoxy rotating disk, 1 in. OD, with an active central portion, 1/8 in. diameter, made of SAE 5160H steel. The cathode was a 1/2 in. copper disk cemented on a Lucite rod, which was inserted through a hole of a Lucite block on the bottom of the cell container, and was fixed in position with a nylon set screw. An electrode spacing of 1 in. was used throughout the study. Aqueous solutions of sodium chloride or sodium chlorate were used as electrolytes. The electrolyte temperature was maintained at 23° ± 1°C, and the concentration varied from 0.1 to 4 moles/liter. A saturated calomel electrode placed in a capillary tube was used to measure the anode potential. The tube was immersed in the electrolyte, and its tip was brought up to the downstream side of the steel anode. Unless otherwise noted, all the anode potentials given in the report are with respect to this reference.

The anode potential was controlled by a GMR-built potentiostat. A Weston d-c milliammeter (Model 911) was used to measure the steady-state current. The current transient was determined by passing the current through a standard resistor and subsequently recording the voltage drop across the resistor on a Sanborn recorder (Model 296).

For each series of runs the surface of the rotating anode was first ground until the steel center and the electrically inert epoxy surface became flush. The surface was then rubbed with a Carbimet 320-grit wet grinding paper, and treated with 6*N* HCl for 1 min followed by rinsing in water. The clean anode was then quickly transferred to the electrolyte, and installed on the spindle of the rotating assembly. To insure reproducibility, the anode was cathodically

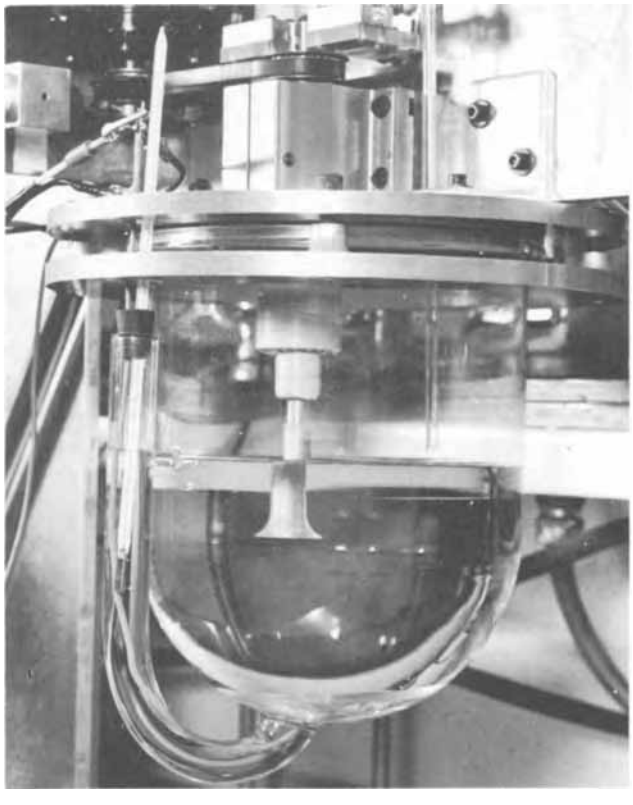

Fig. 1. Cell and rotating disk electrode

* Electrochemical Society Active Member.

Key words: passivity of steel electrode, passive films, anodic dissolution of steel in chloride and chlorate.

treated in the electrolyte for 1 min. A separate electrical circuit having a steel counterelectrode and powered with three Burgess 1.5V batteries was used for the cathodic treatment. After the cathodic treatment, several minutes were required for the anode potential to return to its equilibrium position. The cell circuit was then switched on for a preset anode potential, and the current was recorded on the recorder.

Results

Steady-state measurement.—Before the transient measurement, a run was made for determining the steady-state polarization curves at various electrolyte concentrations and rotational speeds of the disk electrode. Typical results from the NaCl electrolyte are given in Fig. 2 as data points connected by solid lines (curves 1, 2, and 4). The dashed lines (curves 3 and 5) are the plateau current density; its meaning will be explained in the next section. The steady-state current density in 1.0M NaCl is given for two different anode revolution rates. It is seen that the speed of rotation does not have a significant effect on the rate of iron dissolution. The sudden drop on curves 2 and 4 demonstrates that the anode becomes passive beyond the active potential, which increases with decreasing electrolyte concentration. For 0.2M NaCl no passivation occurred with the potential range investigated.

Polarization curves of $NaClO_3$ are given in Fig. 3. The curves were obtained at an electrode speed of 1000 rpm; repeated measurements at different speeds of rotation gave essentially the same results. It is seen that the passive region is approximately from 0.5 to 1.4V *vs.* SCE, beyond which the transpassive region begins and the anodic gas evolution was observed. The active potential also increases with decreasing concentration; at 0.1M, no active-passive transition took place within the potential range investigated.

Current transient in NaCl electrolytes.—Typical transient curves in NaCl electrolytes are given in Fig. 4, where the curves drawn in wide striped bands represent oscillation of the current. The width of the band is the peak-to-peak amplitude of the oscillation.

Curves 4a and 4b were obtained in 1M NaCl at the potentials corresponding to the active region of steady-state polarization curves. These two curves are characterized by an initial current, a rapid drop to a minimum and recovery to a steady-state value having the same order of magnitude as the initial

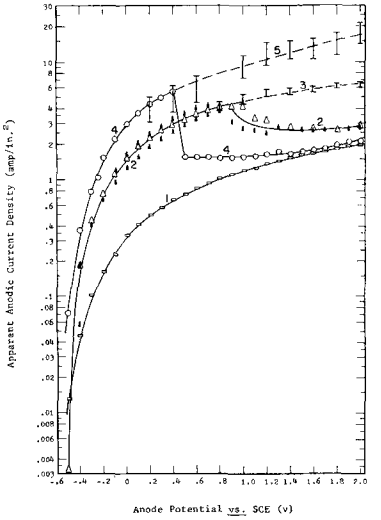

NaCl Conc. (M)	Curve No. and Symbol	Disk Speed (rpm)	Type of Current
0.2	1 □	1000	Steady state
1.0	2 ▲	1000	Steady state
	3 △	2000	Steady state
	3 I	1000	Plateau
3.7	4 ○	1000	Steady state
	5 I	1000	Plateau

Fig. 2. Plateau current and steady-state polarization curves in the sodium chloride electrolyte.

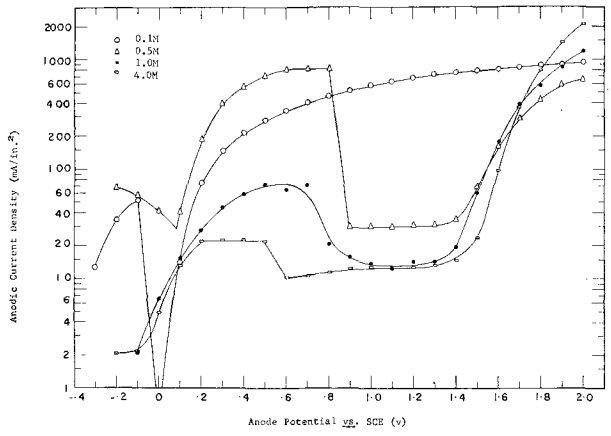

Fig. 3. Steady-state polarization curves in the sodium chlorate electrolyte.

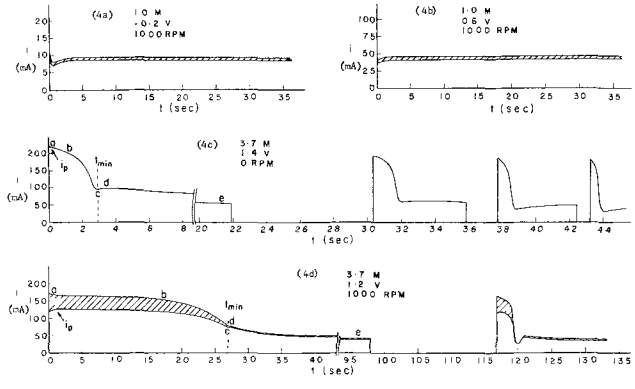

Fig. 4. Recorder traces of current transients in NaCl electrolytes

current. Repeated measurements at higher concentrations showed the same characteristics; the phenomenon of initial current and overshoot to the minimum, however, diminished with increasing electrolyte concentration. In a 3.7M NaCl electrolyte, for instance, a steady-state current was recorded immediately after switching on the cell circuit. If an overshoot did occur, its time constant was too short to be seen on the recorder used presently.

Curves 4c and 4d are typical current transients at the passive potentials for 3.7M NaCl electrolyte. Similar results were also obtained at lower concentrations. These two curves differ from those obtained at lower potentials by having a flat initial current and showing longer recovery time to the steady state. Besides, their steady-state current is considerably smaller than their initial current. The main features of these curves are:

(*a*) An initial plateau, a-b, where the current is large and oscillates about the average value with a frequency equal to the rotational speed of the anode. Curve 4c was obtained at zero revolutions per minute; thus no oscillation occurred in that particular run.

(*b*) A decrease to a minimum, b-c, while the oscillation is also decreasing as the current drops.

(*c*) A fast rise to a second maximum, c-d, and then decreasing asymptotically to a second steady-state value, d-e. In this stage the current oscillates again; its peak-to-peak amplitude, however, is much smaller than stage a.

In these two particular runs, the cell was switched off for varying lengths of time and then switched on again. It is seen that, for every switch-on, the current jumps to the initial value and repeats steps *a* to c as described above. The initial period, however, is much shorter, and the overshoot to the minimum becomes more prominent. The time required to attain the minimum of the subsequent on-period depends on the length of the previous off-period: the longer the off-

period, the longer will be the initial period and the slower the drop to the minimum value. This phenomenon is the same as the anodic transient of iron in sulfuric acid, for which evidence has shown that anodic products precipitate on the anode surface as an adsorbed layer, which in turn hinders the dissolution of iron into the electrolyte (7-9).

In the present study, a layer of dark blue film was observed on the anode surface. The film was so porous that it could be washed away easily with a jet of water. On several occasions, the film fell from the anode as a dark blue platelet at high rotational speeds, and the current jumped up immediately from the steady-state value to that of the higher initial current.

Figure 4 indicates that the current oscillated about its average when the electrode was rotating. For curves 4a and 4b, the peak-to-peak amplitude (for convenience this will be referred to as amplitude henceforth) was about 10% of the average current; for curve 4d, the amplitude was about 30% in the plateau period, a-b, and diminished to 5% in the third period, d-e. The frequency of the oscillation was equal to the frequency of the rotating anode. When the anode was stationary, no oscillation was observed as shown in curve 4c. At this point one might think that this oscillation was an artifact caused by the experimental device, such as the slip-ring contact of the rotating anode. However, with the same experimental setup there was virtually no current oscillation when sodium chlorate was used as electrolyte.

With regard to the film, the time required to reach the minimum current may be designated as a measure of the period of film formation. This time is denoted at t_{min} as shown in curves 4c and 4d. The amount of electricity per unit anode surface area required to pass through the cell before such a film has been formed can be approximated as

$$Q = \frac{1}{S}\int_0^{t_{min}} i\,dt \qquad [1]$$

where i is the total current, and S the apparent surface area of the anode. Figure 5 is a plot of Q and t_{min} at 1000 rpm as a function of anode potential for two different concentrations of NaCl. It is seen that both Q and t_{min} decrease substantially with increasing potential and electrolyte concentrations. The quantity, Q, was calculated graphically from the recorder trace. Since the current was oscillating, the integration was carried out separately according to the upper and the lower limits of the curve. Thus, for each transient measurement, two integrals were obtained; the difference of these two values was then represented by the length of I bars and rectangles as shown in Fig. 5a.

Figure 4 indicates that t_{min} of curve 4c is an order smaller than that of curve 4d. In Fig. 6, Q and the plateau current, i_p, measured at an anode potential of 1.4V are plotted against the rotational speed of the anode (the plateau current is the current of the initial flat portion of the transient as shown in curves 4c and 4d). Again, I bars are used to indicate the upper and the lower limits of the current output, if the current was fluctuating. The data for the plateau current are fairly scattered, and no dependence of the current on the anode speed could be drawn from the data points. The flat line in Fig. 6a is the average of these points. The quantity, Q, and thus the time required to reach the current minimum t_{min}, on the other hand, increases substantially with increasing speed beyond 300 rpm (Fig. 6b). It seems that the rotational speed has a great effect on the current transient in the NaCl electrolyte.

In Fig. 2 variations of the plateau current density with changes in anode potentials are shown as I bars connected by dashed lines (curves 3 and 5). It is seen that the logarithm of the plateau current density increases in direct proportion to the anode potential. In addition, curves 3 and 5 appear to be a smooth extension on the prepassivation, steady-state anodic current density. It seems evident that if no passivity occurred, the plateau current should represent the dissolution rate of iron beyond the activation potentials.

Current transient in $NaClO_3$ electrolytes.—For a given potential setting, the current transient in $NaClO_3$ electrolytes was independent of the speed of electrode rotation. The reproducibility, however, became better at higher speeds. For this reason, all the transients in $NaClO_3$ are reported at 1000 rpm.

Figure 7 represents typical transient curves at various passive and transpassive potentials. The current jumps to a large value as soon as an anode potential is applied; it then drops rapidly to a steady-state value. It has been found that the current can be described by an empirical relation

$$i = \alpha e^{-t/\tau} + i_s \qquad [2]$$

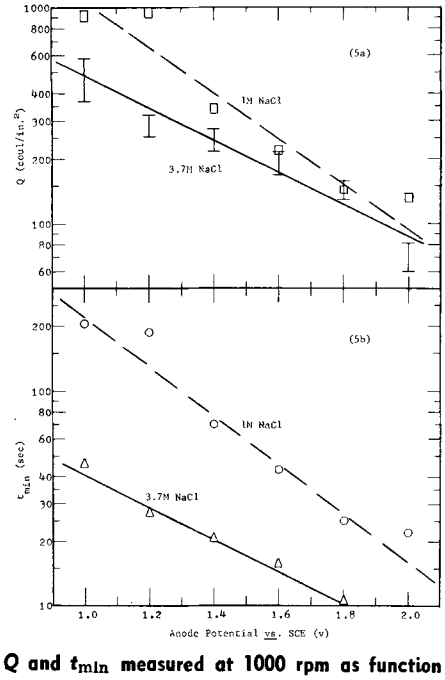

Fig. 5. Q and t_{min} measured at 1000 rpm as function of anode potentials.

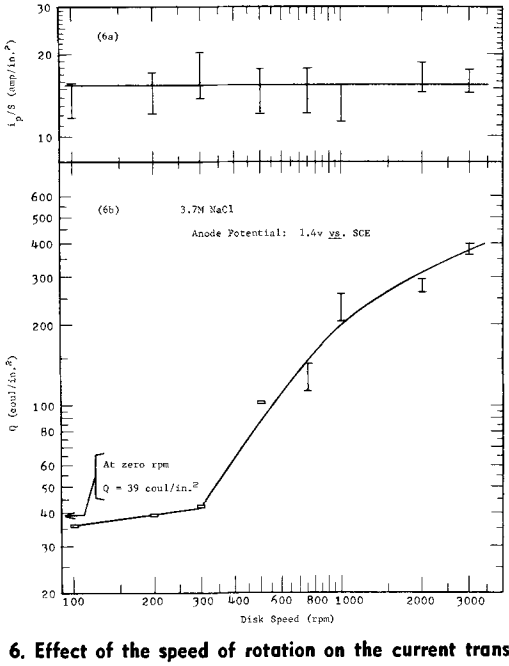

Fig. 6. Effect of the speed of rotation on the current transient

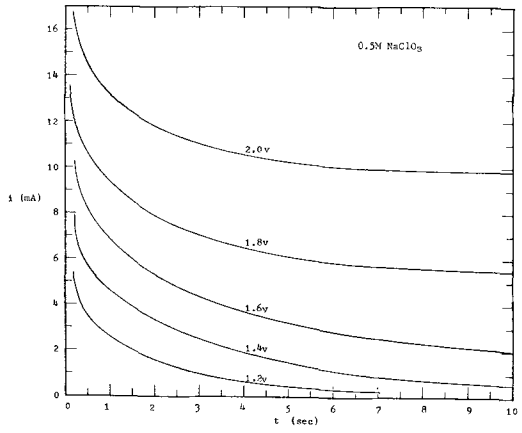

Fig. 7. Current transient in the $NaClO_3$ electrolyte

where α and τ are constants, and i_s is the steady-state current. Figures 8 and 9 are the plots of log $(i-i_s)$ *vs.* t for 0.5M and 4M $NaClO_3$ electrolytes. For $t > 1$ sec, Eq. [2] fits perfectly the experimental data obtained at different passivity potentials. In the transpassive region, the data points plotted this way are slightly curved (see Fig. 8), indicating that the equation is not valid in this region. The cell current measured with 4.0M electrolyte at different passivity potentials falls closely about a straight line. It seems that the potential dependence of the current transient decreases with increasing electrolyte concentration.

Discussion

Nature of passivation in NaCl electrolytes.—Both the transient behavior and the steady-state polarization curves have clearly shown that the steel anode becomes passive in NaCl electrolytes when the anode potential is beyond the active potential. Experimental observation has revealed that the dark blue film formed on the anode surface is quite thick and porous. Parallel examples of this kind are the passivity of iron in sulfuric acid (7-9) and of copper in hydrochloric acid (10). At the passivity potentials, these two systems have the same transient behavior as shown in curves 4c and 4d. Their passivity has been attributed to the formation of an adsorbed layer of anodic product; in the copper-hydrochloric acid system, this layer was identified by Cooper (10) as CuCl.

Apparently, the passivity of steel in the NaCl solution can also be attributed to the formation of an adsorbed layer of anodic products on the electrode surface. The exact composition of this layer is not known. It has been found that during ECM of steel in NaCl, iron dissolves into the electrolyte to form a final product of $Fe(OH)_2$ (11). At sufficiently high potentials, the anodic current density is very large, and the electrolyte in the neighborhood of the anode becomes supersaturated with ferrous compounds. Some of the ferrous compounds, such as $Fe(OH)_2$, thus precipitate on the anode surface as a porous layer of ferrous salts.

This hypothesis may be confirmed by comparing the transient data with Muller's theory of the film formation due to precipitation of reaction products on the electrode surface. The behavior of curves 4c and 4d indicates that the current at the initial period is not affected by the precipitation of the anode product. Only when the electrode becomes nearly covered with the precipitates does the resistance of the film control the flow of current. The current flowing through the cell, therefore, remains constant until the anode is nearly covered with the film, and then drops rapidly. For the film growth of this kind, Muller (12) has derived an equation for the behavior of current when the film nuclei are spreading from random sites to form a platelet over the electrode surface. The current-time relation during this stage of film growth is given as

$$t = C_1 + C_2\left(-\frac{1}{i_p - i} + \frac{1}{i_p}\ln\frac{i_p - i}{i}\right) = C_1 + C_2 f(i) \qquad [3]$$

where i_p is the plateau current, and C_1 and C_2 are constants for a given transient. The constant, C_1, is a measure of the duration of the current plateau, and C_2 is inversely related to the rate of current decrease. To test the validity of the Muller theory to this particular problem, the function, $f(i)$, (calculated for the transient curve, Fig. 4c, obtained at zero revolutions per minute) is plotted against the time, t, in Fig. 10. It is

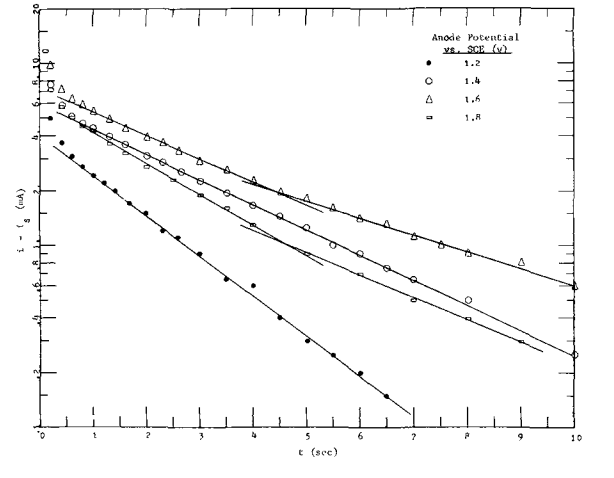

Fig. 8. Semilogarithmic plot of anode transients for 0.5M $NaClO_3$.

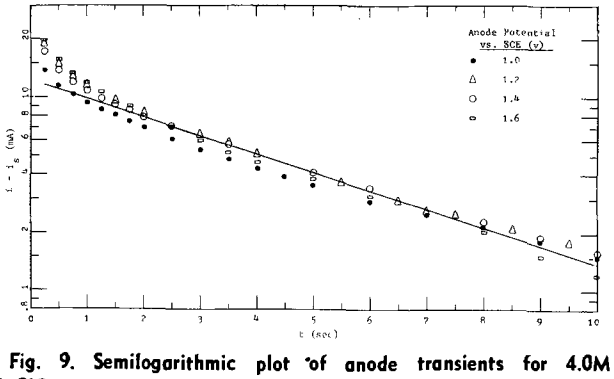

Fig. 9. Semilogarithmic plot of anode transients for 4.0M $NaClO_3$.

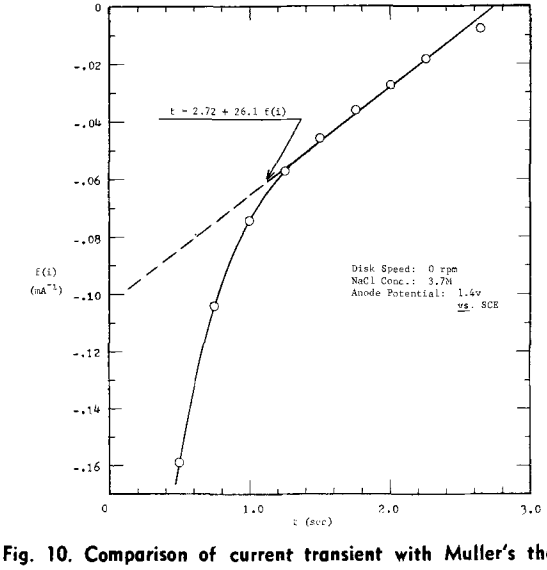

Fig. 10. Comparison of current transient with Muller's theory

seen that for t larger than 1.2 sec, the decrease of current is indeed described by the Muller equation. The time constant C_1 calculated this way is 2.72 sec; interestingly, this value is very close to t_{min} = 2.8 sec as shown in curve 4c.

Since the Muller theory only describes the behavior of current drop, one may assume that the initial period of the current transient represents the period of film nucleation and growth of film nuclei to the critical sizes before spreading over the anode as platelets. Two factors could influence the duration of this period. The first factor is the rate of iron dissolution: the higher the dissolution rate, the higher will be the supersaturation of the anodic product near the anode surface, and consequently the faster will be the rate of nucleation and growth of the nuclei. Figure 2 indicates that the plateau current density represents the dissolution rate before the anode is covered by the film. Therefore, the higher the plateau current, the shorter will be the initial period. This tendency is clearly seen in Fig. 5, where t_{min} and Q are plotted against the anode potential. Recall that t_{min} is the length of time required for the current to reach the minimum; it is nevertheless also a good measure of the duration of the nucleation period because the period of current drop is very small. Since the plateau current, as shown in Fig. 2, increases with potential and electrolyte concentration, it is not surprising that t_{min} decreases considerably with increasing potential and concentration. Furthermore, the amount of charge, Q, required to pass through the cell before a complete layer of film has formed, also decreases with the dissolution rate. This can be seen with a closer look at Fig. 2 and 6a: Take 3.7M NaCl, for instance. The value of Q decreases from 500 coulombs/in.^{2} to about 90 coulombs/in.^{2} when the anode potential increases from 1.0 to 2.0V *vs.* SCE, whereas the corresponding plateau current densities at these two potentials are 9 and 17 A/in.^{2}.

The second factor that affects the period of film nucleation is the convection of the electrolyte in the neighborhood of the anode. In a flowing NaCl electrolyte, apparently only a fraction of the anodic product formed precipitates on the anode surface as a solid film; the rest is washed away by the electrolyte. Figure 6 demonstrates the effect of convection to the length of the nucleation period. In that particular run the plateau current is nearly the same for all the speeds investigated; the duration of nucleation as denoted by Q, however, increases sharply with increasing speeds of rotation beyond 300 rpm. Assuming that there is a boundary layer over the electrode surface within which the electrolyte is saturated with the anode product, the increase in the rate of electrolyte flow would reduce the thickness of this layer and, consequently, more anode product is carried away by the electrolyte before it precipitates on the surface. Therefore, the length of the nucleation period increases with increasing flow rate.

The phenomena of current oscillation and the overshoot to the minimum as shown in Fig. 2 are rather puzzling. At present there are no satisfactory explanations; further investigations are necessary before a definite conclusion can be reached.

Anodic film in $NaClO_3$ electrolytes.—Figure 3 indicates that a protective film is formed on the anode surface when the applied potential is between 0.5 and 1.4V *vs.* SCE. Hoare and his co-workers (3-5) have attributed the property of good shape control of sodium chlorate to the formation of this film on the surface of workpieces. They point out that the extent of shape control increases with increasing slope of transition from the passive to the transpassive region on the steady-state polarization curve. It seems that, among the curves shown in Fig. 3, the best shape control will be obtained at 4.0M. This result agrees with the experience that good cutting can be achieved only in highly concentrated $NaClO_3$.

The composition of the film, according to x-ray diffraction studies (3), is a layer of γ-Fe_2O_3. Nagayama and Cohen (13), who have studied the passivity of iron in borate-boric acid, suggest that the inner layer of the oxide film is composed of Fe_3O_4. In a later paper, Sato and Cohen (14) give an empirical equation

$$i = A \exp\left(-\frac{Q_t}{B}\right) \qquad [4]$$

to describe the growth of an oxide film on iron in the borate-boric acid electrolyte. Here A and B are constant for a given potential and electrode surface area; the quantity, Q_t, is the amount of charge accumulated in the film at the time, t. Accordingly, if the current transient curve is replotted in the form of log i *vs.* Q_t, one should obtain a straight line. The transient data of 4.0M $NaClO_3$ plotted this way are shown in Fig. 11, where Q_t is calculated graphically from the data as $\int_0^t (i - i_s)dt$, for the steady-state current does not contribute to the formation of the film. It is seen that the data are not described by Eq. [4]. Therefore, the mechanism of the film growth in $NaClO_3$ is different from that in the borate-boric acid electrolyte.

At the passivity potentials, Fig. 3 indicates that the anodic current density is on the order of 60 mA/cm^2, while the corresponding current density of an iron anode in borate-boric acid is at least 1000 times smaller. This suggests that the oxide film formed in the chlorate electrolyte is porous in nature, although it serves as a protective layer to prevent the wild cutting in ECM operations. The porosity may be confirmed by comparing Eq. [2] with Vermilyea's theory of film growth. For the situation where the growth is controlled by the rate of metal dissolution, he has derived the following relation describing the decay of current due to spreading of a nonconductive film from random nuclei (15)

$$i = \alpha e^{-t/\tau} \qquad [5]$$

and

$$\tau = \frac{SnF\rho\delta}{\alpha M}$$

Here α is the initial current, and M, ρ, and δ are the molecular weight, density, and thickness of the film. The constant, n, is the number of electrons transferred in the film-formation reaction, and S is the surface area of the electrode. Since there are numerous nuclei spreading laterally during the growth process, the anode surface is soon covered with a film having a great number of pores. One of the major assumptions in Eq. [5] is that the pores are closed entirely; thus, no current will be permitted to flow through the cell after the anode has been covered with the film. Comparing Eq. [2] and [5], it is seen that the two equations have exactly the same form, except that Eq. [2] has an

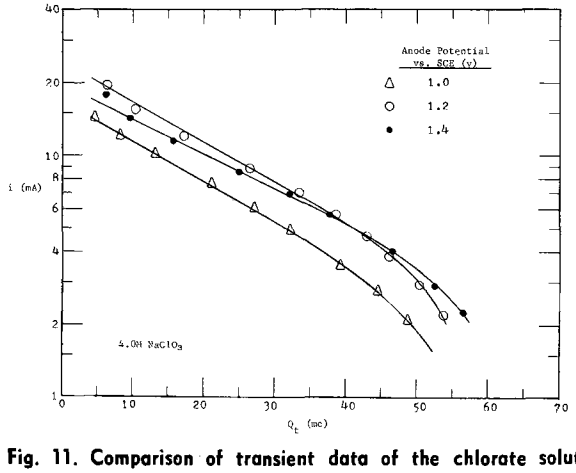

Fig. 11. Comparison of transient data of the chlorate solution with Sato and Cohen's empirical equation.

additional term, i_s. It appears that, after reaching an equilibrium condition, the pore area of the film in the chlorate electrolyte will not diminish to zero. Apparently, there are two processes taking place simultaneously during the anodic treatment of steel in $NaClO_3$. The first one is the dissolution of iron into the electrolyte, and the second one is the formation of an anodic film. The dissolution is inhibited by the film formation process, for the spreading of the film would reduce the area of active sites where the dissolution is taking place. After the steady state has been reached, the normal dissolution reaction can occur only within the pores of the film, and the steady-state current, i_s, may be regarded as the rate of dissolution within the pores. With the assumption that the pores are not closed entirely, Eq. [2] could be derived in a manner similar to that for Eq. [5]. In this case, the time constant, τ, should be modified to

$$\tau = \frac{SnF\rho\delta}{(\alpha - i_s)M} \qquad [6]$$

Figures 8 and 9 show that Eq. [2] fits perfectly with the transient data obtained at the passivity potentials. Probably a surface reaction that controls the rate of iron dissolution is the slowest step in the film-formation process. The rate of film formation would increase with increasing the dissolution rate.

Assuming that the film is γ-Fe_2O_3, one may estimate the film thickness from Eq. [6] with values of α and t evaluated graphically from Fig. 8 and 9. For approximation, the density of the film is assumed to be 5 g/cm^3 (16), and the apparent surface area of the anode is used for all the calculations. The results are listed in Table I. Also given in the table is the thickness calculated from coulometry. The two sets of computation agree with each other very well. The estimated film thickness is on the order of 1000Å. This result agrees with the fact observed from the ECM operation that a visible coating is always obtained on the workpiece after machining, for a film with a thickness of 1000Å is visible to the naked eye.

Table I. Estimated thickness* of oxide film in the chlorate electrolyte

Concentration $NaClO_3$ (M)	Anode potential *vs.* SCE (V)	Coulometry Q_∞,*** mc/cm^2	Coulometry $\delta \times 10^5$** (cm)	Equations 2 and 6 τ, sec	Equations 2 and 6 α, mA	Equations 2 and 6 $\delta \times 10^5$** (cm)
0.5	1.2	144	0.79	1.97	4.0	0.55
	1.4	250	1.40	3.14	6.0	1.32
4.0	1.0	700	3.8			
	1.2	710	3.9	4.79	12.2	4.1
	1.4	780	4.3	4.79	12.2	4.1

* The film is assumed to be γ-Fe_2O_3 having density of 5 g/cm^3 (16).
** Apparent surface area of the anode is used for the calculations.
*** Q_∞ is the amount of charge density required to produce a complete layer of the oxide film on the anode surface.

In summary, the transient measurement reveals formation of an anode film during the ECM of steel in sodium chloride and sodium chlorate solutions. For chloride, the film is very porous and nonprotective; its formation results from precipitation of the anodic product. For chlorate, the film is formed by anodic oxidation; electrode transient reveals that the film is about 1000Å thick and the rate of film growth increases with the increase in the rate of iron dissolution.

Manuscript submitted June 1, 1970; revised manuscript received *ca.* Oct. 1, 1970. This was Paper 218 presented at the Atlantic City Meeting of the Society, Oct. 4-8, 1970.

Any discussion of this paper will appear in a Discussion Section to be published in the December 1971 JOURNAL.

REFERENCES

1. M. A. LaBoda and M. L. McMillan, *Electrochem. Technol.*, **5**, 341 (1967).
2. M. L. McMillan and M. A. LaBoda, *ibid.*, **5**, 346 (1967).
3. J. P. Hoare, M. A. LaBoda, M. L. McMillan, and A. J. Wallace, Jr., *This Journal*, **116**, 199 (1969).
4. J. P. Hoare, *Nature*, **219**, 1034 (1968).
5. J. P. Hoare, *This Journal*, **117** 142 (1970).
6. A. D. Davydov, V. D. Kashcheev, and B. N. Kabanov, *Elektrokhimiya*, **5**, 221 (1969).
7. J. H. Bartlett, *Trans. Electrochem. Soc.*, **87**, 521 (1945).
8. J. H. Bartlett and L. Stephenson, *This Journal*, **99**, 504 (1952).
9. A. Pigeaud and H. B. Kirkpatrick, *Corrosion*, **25**, 209 (1969).
10. R. S. Cooper, *This Journal*, **103**, 307 (1956).
11. R. R. Cole, *J. Eng. Ind., Trans. ASME*, **83b**, 194 (1961).
12. W. J. Muller, *Trans. Faraday Soc.*, **27**, 737 (1931).
13. M. Nagayama and M. Cohen, *This Journal*, **109**, 781 (1962).
14. N. Sato and M. Cohen, *ibid.*, **111**, 512 (1964).
15. D. A. Vermilyea, "Anode Films," in "Advances in Electrochemistry and Electrochemical Engineering," P. Delahay and C. W. Tobias, Editors, Vol. 3, p. 211, Interscience Publishers, Inc., New York (1963).
16. M. Nagayama and S. Kawamura, *Electrochim. Acta*, **12**, 1109 (1967).

Technical Notes

Chemical Polish for Rare Earth Orthoferrites

L. K. Shick

Bell Telephone Laboratories, Incorporated, Murray Hill, New Jersey 07974

Proposed magnetic domain devices require large numbers of strain-free slices of suitable magnetic materials. Presently, after slicing, bulk grown single crystals of rare earth orthoferrites are polished to approximate required thickness using conventional diamond abrasives. The required final finish is obtained by an additional polish utilizing Syton. Syton, a trade name of Monsanto, consists largely of SiO_2 abrasive in

Key words: ferrites, phosphoric acid, polishing, rare earth ferrites, chemical polishing.

a basic colloidal suspension (1). Such polishing produces a smooth surface but has a tendency to round the edges of slices and produce taper in the material. The chemical mechanical action of this process is not understood.

The Syton process produces excellent, usable specimens, but the removal rate is very slow. Estimates of this rate range from 0.125 mil/hr to 0.25 mil/hr and it depends upon a variety of conditions including pad age and wear, total area of slices to a lap, applied pressure, and lap speeds.

A search has been conducted for a suitable chemical polish that would effect a more rapid removal rate and also produce strain-free surfaces. A review of the literature revealed a wide variety of etchants based on common laboratory chemicals. Many have been used successfully on refractory oxide materials (2-4). A survey was made to determine the effect of a number of these etchants on several of the general class $RFeO_3$ (R = rare earth) compounds. The conditions and results are presented in Table I. Ratios are in parts by volume.

As can be seen from the table, few of these etches have any effect. The HF containing formulations seemingly react, but do not polish. The rare earth fluorides are generally only slightly soluble and it is likely that an insoluble fluoride is produced at the surface precluding further reaction.

Phosphoric acid has been used to chemically polish several garnets including YIG (4). The phosphoric acid containing etches all produce pits in orthoferrites at lower temperatures. At temperatures above 160°-180°C only H_3PO_4 remains (commercial H_3PO_4 is 85% acid and evolves H_2O as steam at 160°-180°C and thereby concentrates). Other common diluents will evaporate at elevated temperatures. Above 300°C, H_3PO_4 polishes rare earth orthoferrites. The results reported here have been obtained at 380°-425°C. At 500°C, rapid attack of the crystal is evident and results in a poor surface.

Procedure

Phosphoric acid is heated in a platinum crucible to about 170°C and held there until the vigorous evolution of steam ceases. The temperature is then raised to the polishing range. There are no experimental difficulties encountered in using phosphoric acid at 500°C when only a slight white vapor evolves. However continued heating results in polymerization and increased viscosity necessitating frequent changes of the acid.

The sample to be polished is mounted in a suitable holder at the end of a fused silica rod. Some samples have been tied to the rod with 0.010 in. Pt wire but due to the fragility of the samples a holder similar to that shown in Fig. 1 is preferred. Boron nitride does not react with H_3PO_4 during the short polishing times required and has been used successfully to fabricate the holder. Such a holder could easily be built to accommodate a large number of slices of uniform dimensions. This assembly is rotated at about 40 rpm and immersed in the acid for the desired polishing time. After removal the chips are allowed to cool and then washed in distilled water to remove any remaining acid.

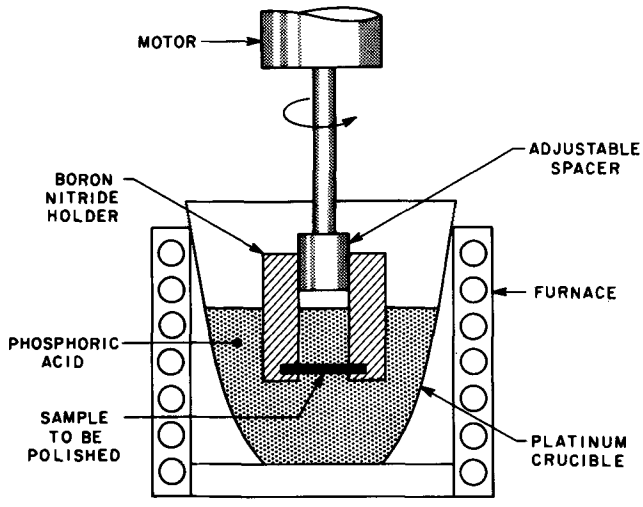

Fig. 1. Apparatus for chemically polishing rare earth orthoferrites

Results and Discussion

The material removal rate at 400°C has been determined by observing the weight loss of a sample during polishing. This rate for polishing times of 1-5 min is about 0.4 mil/min/side.

The surface of slices polished is smoothed to the extent that few features remain upon which an optical microscope can be focused. The Tally Surf trace shown in Fig. 2(a) is of a randomly selected slice of $Sm_{0.55}$ $Tb_{0.45}$ FeO_3 after Syton polishing. The trace in Fig. 2(b) is of a similar slice after a one minute chemical polish. The surface variation is of the order of $\pm 0.25\mu$ for the chemically polished piece while the single peak on the Syton slice is $>0.5\mu$ above the average surface.

Smoothing action of the polish is enhanced by slow rotation of the sample. Static polishing produces surfaces with greater ripple than that evident in Fig. 2. Very fast rotations, *i.e.*, >1000 rpm, result in spiral patterns of ripple on the surface due to vortex effects in the liquid. Results reported here are from samples rotated at about 40 rpm.

Residual surface strain induced in diamond polished rare earth orthoferrites renders them useless for device utilization unless the strain is relieved by annealing (5) or Syton polishing. The domain pattern may be observed by the Faraday rotation of polarized light. A white edge on a normally black domain indicates that the wall passes through the slice at some

Table I. The effects of various etchants on rare earth orthoferrites

Etchant	Temp, °C	Time	Results
1 Cr_2O_3 (Sat H_2O): 3H_3PO_4	80-100	30 min	pits
1 Sat $K_2Cr_2O_7$: 0.1 H_2SO_4: 0.02 Sat NaCl	*room temp*	*several hours*	no effect
1 Sat $K_2Cr_2O_7$, 0.1 H_2SO_4: 0.02 Sat NaCl	180	4 hr	no effect
Sat $K_2Cr_2O_7$ in H_2O	80-100	1.25 hr	no effect
Sodium Potassium Tartrate	molten	1 min	no effect
1 H_3PO_4: 1 HCl: 1 MeOH	80-100	25 min-1.5 hr	pits
1 NaOH: 1 30% H_2O_2	90	15 min	no effect
1 NH_4OH: 1 30% H_2O_2	90	15 min	no effect
1 HF: 2HNO_3: 3H_2O	80-100	5-30 min	attacks surface slowly—leaves it rough
1 HF: 1 H_2SO_4: 1 H_2O	boiling	10 min	opaque film on surface
1 HF: 1 H_2O_2: 1 MeOH	75	5 min	no effect
1 H_3PO_4:1H_2O	rapid "boiling"	5-6 min	smooths damage but tends to pit
1 H_3PO_4: 3 H_2O	rapid "boiling"	5 min	no effect
H_3PO_4	300	1 min	pits
H_3PO_4	400-425	1 min	polishes
H_3PO_4	500	1 min	rapid attack of crystal

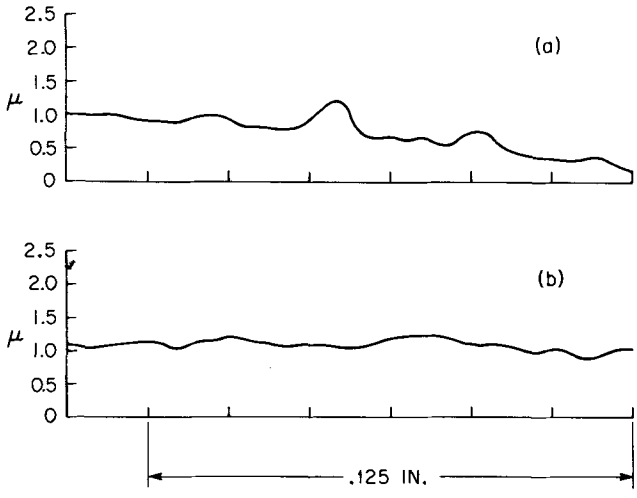

Fig. 2. (a) Tally Surf trace of Syton polished $Sm_{0.55}Tb_{0.45}FeO_3$. (b) Tally Surf trace of chemically polished $Sm_{0.55}Tb_{0.45}FeO_3$.

angle other than 90° thereby changing the Faraday rotation angle. The effect of surface strain on the domains is illustrated in Fig. 3(a) which is a portion of the domain pattern of a 0.004 in. thick slice of $Sm_{0.55}$ $Tb_{0.45}$ FeO_3 that had been polished with 0.1μ diamond abrasive paste. The irregular domain widths and ragged walls are indicative of locally high coercivity induced by surface strain. That the surface is highly strained is further evidenced by the alternate white and black edges of the domain pattern.

Low surface strain is characterized by domains of uniform width and parallel walls. The domains tend to stretch into smooth walled strips with only large radius curves to minimize wall energy. The effect of the chemical polish in removing surface strain is shown in Fig. 3(b) which is a portion of the domain pattern of the same slice shown in Fig. 3(a) after chemically polishing for 10 sec. Much of the strain evident in Fig. 3(a) has been removed. The smooth domain walls, the near uniformity of the domain widths, and absence of the changing Faraday rotation suggest that the strain has been significantly reduced resulting in lowered coercivity. Figure. 3(c) illustrates the domain pattern in a portion of a Syton polished slice of $Sm_{0.55}$ $Tb_{0.45}$ FeO_3. The patterns in Syton polished and chemically polished slices are comparable in that surface strain effects such as seen in Fig. 3(a) are eliminated in each. However the Syton operation required several hours to achieve this degree of strain removal whereas the chemical polish effected a similar result in only 10 sec.

In order to determine sample perfection and suitability for device use, Shumate (6) has developed a device that enables a single cylindrical domain to be systematically scanned through the chip. When the

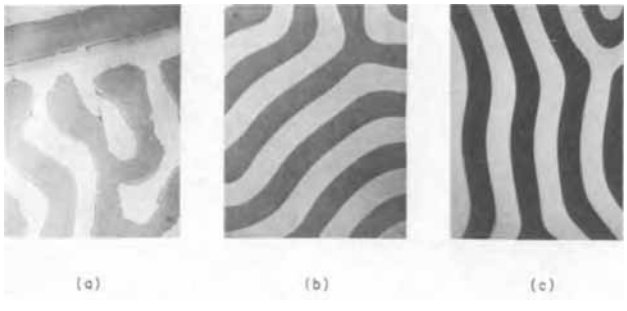

Fig. 3. (a) A portion of the domain pattern in a 0.004 in. thick slice of $Sm_{0.55}Tb_{0.45}FeO_3$ which was polished with 0.1μ diamond abrasive paste. Magnification 200X. (b) Typical domain pattern in the same slice after chemical polishing. Magnification 200X. (c) Domain pattern of a portion of a Syton polished slice of $Sm_{0.55}Tb_{0.45}FeO_3$ 0.002 in. thick. Magnification 200X.

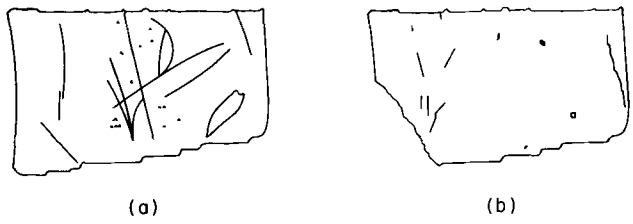

Fig. 4. (a) Defect map of a Syton polished slice of $TmFeO_3$ Magnification 20X. (b) Defect map of the slice shown in a after a 10 second chemical polish. Magnification 20X.

domain encounters a defective area in the crystal, it is indicated by a deflection in a chart trace. At the completion of scanning, a map of the defects in the crystal results. A map of a slice of $TmFeO_3$ that had been Syton polished is shown in Fig. 4(a). The deflections have been joined to emphasize linear defects such as cracks, twins, or scratches. Several scratches are evident through the center of the slice as well as other unidentified domain pinning points. The line formation in lower left is a crack and the nearly vertical line at left is due to a difference in thickness of the slice. The device is sensitive to distortions of the domain and since the domain diameter is a function of chip thickness (7), variations in thickness will appear on the map. A serious defect appears at lower right.

The slice was chemically polished for 10 sec and remapped. The resulting trace is shown in Fig. 4(b). The slice broke along the crack at the left during handling so the shape is different from Fig. 4(a). The central scratches and most of the pinning points in that region have been eliminated. The thickness effect at left remains and two smaller line defects have developed in the upper left. The serious defect at right has been reduced to a single large pinning point. The long line at right is associated with the point of contact of the slice with the holder.

Due to the high sensitivity of the mapping technique and the severe surface strain in crystals that have been diamond polished, it is not possible to obtain a meaningful map of an orthoferrite slice prepared in this manner for direct comparison.

Conclusions

Phosphoric acid at 380°-425°C has been shown to polish thin slices of rare earth orthoferrites rapidly and to remove residual surface strain induced by conventional mechanical polishing. Certain types of defects remaining after Syton polishing are also removed while maintaining comparable smoothness.

It is evident the chemical polish removes many of the defects left behind by mechanical or chemical mechanical polishing methods. Crystallographic defects of course can be eliminated by neither method, but may be exposed by chemical polishing.

Acknowledgments

My sincere thanks are due to P. W. Shumate for mapping the $TmFeO_3$ sample and to R. F. Fischer and S. L. Blank for valuable discussions during the course of this work.

Manuscript submitted July 17, 1970; revised manuscript received Sept. 21, 1970.

Any discussion of this paper will appear in a Discussion Section to be published in the December 1971 JOURNAL.

REFERENCES

1. D. R. Oswald, Private communication.
2. R. R. Soden and F. R. Monforte, *J. Am. Ceram. Soc.*, **48**, 548 (1965).
3. B. Cockayne and D. S. Robertson, *Brit. J. Appl. Phys.*, **15**, 643 (1964).
4. J. Basterfield, *Brit. J. Appl. Phys. (J. Phys. D.) Ser. 2*, **2**, 1159 (1969).
5. E. Heinlein and R. Pierce, *IEEE Trans. Mag.*, **6**, (1970) In press.
6. P. W. Shumate, To be published.
7. A. A. Thiele, *Bell System Tech. J.*, **48**, 3287 (1969).

On the Cathode Reaction in Solutions Containing ClO_3^-

Fumio Hine[*,1] **and Masaki Yasuda**[1]

Kyoto University at Uji, Uji, Japan

The cathodic reduction of ClO^- in the diaphragm-type chlorine cell has been described in a previous paper (1). Since the effects of ClO_3^-, which may form at the graphite anode, on the cathode reaction should be considered (2), some experiments have been carried out.

Hydrogen evolution from H_2O

$$2H_2O + 2e = H_2 + 2\,OH^- \qquad [A]$$

is well known to be the main reaction at the steel cathode of the diaphragm cell, but two processes

$$ClO^- + H_2O + 2e = Cl^- + 2\,OH^- \qquad [B]$$

and

$$ClO_3^- + 3H_2O + 6e = Cl^- + 6\,OH^- \qquad [C]$$

are also considered to be the side reaction according to Kircher *et al.* (3). Of these, reaction [*B*] is fast, but is limited by diffusion of ClO^- to the electrode surface at high current densities.

The anodic formation of ClO_3^- has been studied by many authors and the mechanism is summarized according to Ibl *et al.* (4) as follows

$$6ClO^- + 3H_2O = 2ClO_3^- + 4Cl^- + 6H^+ + \frac{3}{2}O_2 + 6e$$

(by anodic oxidation) [*D*]

$$Cl_2 + H_2O = HClO + Cl^- + H^+ \qquad [E]$$

$$HClO = ClO^- + H^+ \qquad [F]$$

and

$$2HClO + ClO^- = ClO_3^- + 2Cl^- + 2H^+ \qquad [G]$$

(by chemical reaction)

On the other hand, papers on the cathodic reduction of ClO_3^- have not yet been published. Whether reactions [C] and [*D*] take place at the cathode in alkaline solution of NaCl is discussed here.

Experimental Procedure

The electrolytic cell used for polarization measurements was the same as that of previous work (1). A platinum rotating disk of 0.95 cm^2 area was used as the working electrode. The cathode of the diaphragm cell consists of a steel screen. Thus, a steel disk electrode was first examined. Unfortunately, satisfactory results were not obtained due to the disturbance caused by the local anodic dissolution of iron at low current densities. The mechanism of the cathode reaction on both steel and platinum electrodes is the same, while the exchange current density is, of course, related to the cathode material. Therefore, the data obtained with the noble metal cathode are considered feasible for discussion, particularly at high current densities.

The solution was prepared with analytical grade NaCl, NaOH, and $NaClO_3$ with deionized and distilled water. The concentration of ClO_3^- was varied from 0 to 0.4 g-equiv/liter. Chlorate ions were titrated with standard solutions of Mohr salt and cerium sulfate (5).

The electrolytic solution was deaerated with purified hydrogen for 2-3 hr, and pre-electrolyzed with a platinum cathode of about 5 cm^2 area at 10-20 mA for about 12 hr before use.

The potential of the working electrode was measured against the reference electrode consisting of Hg/HgO/2*N* NaOH, then it was converted into the normal hydrogen electrode scale.

Since the *IR* drop between the working electrode and the Luggin probe was considerable at high current densities, it was corrected by extrapolation of the potential *vs.* distance curve to zero distance at a given current (6).

The current efficiency of the hydrogen evolution from the cathode having 1.26 cm^2 area was determined by means of gas analysis.

Results and Discussion

An example of the potential *vs.* current density curve is shown in Fig. 1. The potentials observed in

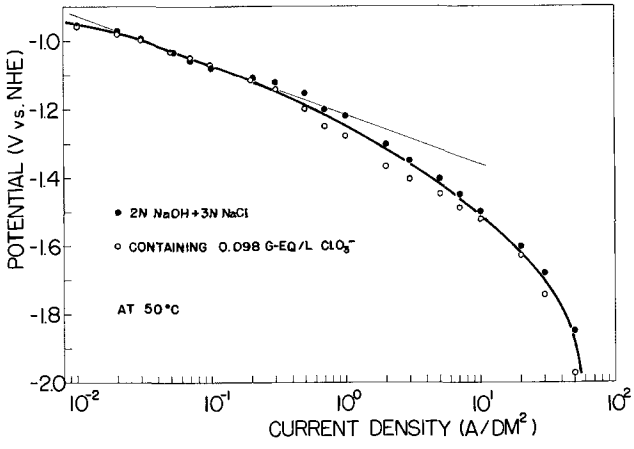

Fig. 1. The potential *vs.* current density curves of a Pt cathode in alkaline solutions of NaCl with and without ClO_3^-.

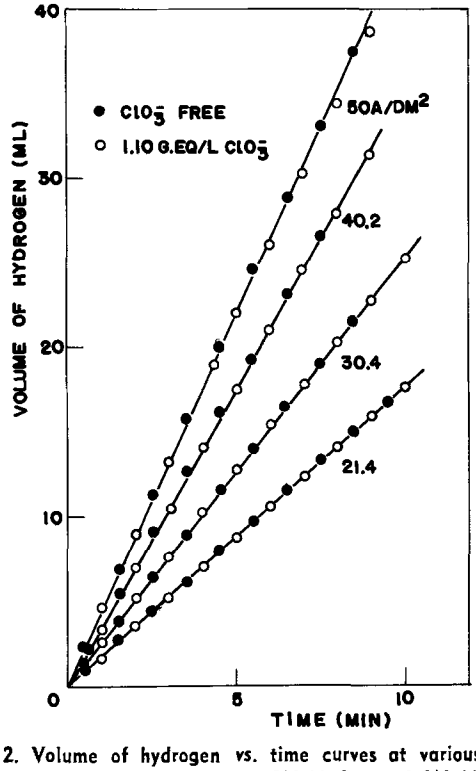

Fig. 2. Volume of hydrogen *vs.* time curves at various current densities in solutions consisting of 2*N* NaOH and 3*N* NaCl with and without ClO_3^- at 20°C (cathode area: 1.26 cm^2).

* Electrochemical Society Active Member.

[1] Present address: Nagoya Institute of Technology, Nagoya, Japan.

Key words: diaphragm cell, electrochemical reduction, hypochlorite, reaction mechanism.

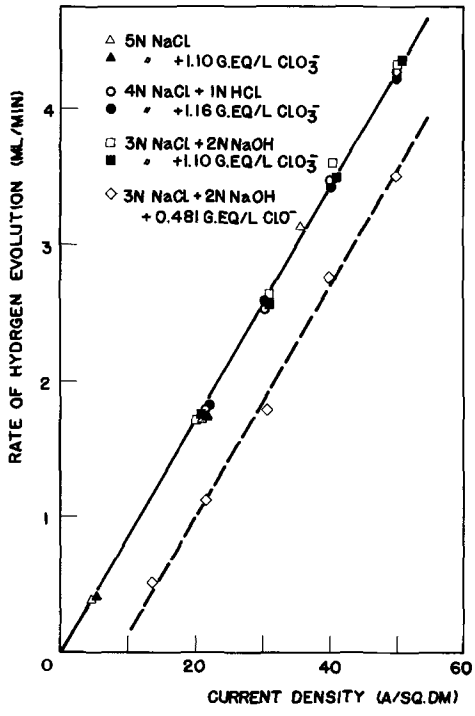

Fig. 3. Rate of hydrogen evolution *vs.* current density curves with various solutions at 20°C.

a solution consisting of 2*N* NaOH and 3*N* NaCl free from ClO_3^- are shown by the closed points and the open points illustrate the data in a solution containing 0.098 g-equiv/liter ClO_3^-. At low current densities, less than 1 A/dm^2, the slope of the potential *vs.* logarithm of current density curve is about 140 mV/decade, if α in the Tafel coefficient, $RT/\alpha\mathbf{F}$, is assumed to be 0.5, as shown by the straight line in Fig. 1. The potential deviates from the Tafel plot at high current densities and the potential tends to be extremely less noble at current densities more than 50 A/dm^2, probably due to the lack of the active sites on the electrode surface. Because the potential *vs.* current density curve is not affected by ClO_3^-, it was assumed that the cathode reaction in a solution containing ClO_3^- is similar to one in a solution free from chlorate ions.

An example of the volume of hydrogen evolved *vs.* time curve is shown in Fig. 2. The closed points show the data obtained in a solution consisting of 2*N* NaOH and 3*N* NaCl without ClO_3^- at 20°C. The current efficiency was almost 100% for various current densities. The open points are the data in a solution containing 1.10 g-equiv/liter ClO_3^- under the same conditions. It also shows that the current efficiency of the hydrogen evolution reaction is independent of ClO_3^-. The same results were found with a variety of solutions as shown by the solid line in Fig. 3. It is interesting that the broken line, which shows the data obtained in a solution containing ClO^-, is lower than and parallel to the solid line. The cathodic reduction of ClO^-, at a limited rate due to the slow step of diffusion, takes place in advance of the charge transfer of H_2O to convert into H_2 and OH^- as described elsewhere in detail (1).

In conclusion, the charge transfer of ClO^- at the cathode is fast, but the cathodic reduction of ClO_3^- may not take place under operating conditions of the diaphragm-type chlorine cell in practice.

Acknowledgment

The authors wish to express their grateful appreciation to Mr. R. B. MacMullin, Niagara Falls, New York, for his suggestions.

Manuscript submitted Feb. 26, 1969; revised manuscript received *ca.* July 7, 1969.

Any discussion of this paper will appear in a Discussion Section to be published in the December 1971 JOURNAL.

REFERENCES

1. F. Hine and M. Yasuda, *This Journal*, **118**, 170 (1971).
2. R. B. MacMullin, Discussion of Ref. (1).
3. R. L. Murray and M. S. Kircher, *Trans. Electrochem. Soc.*, **86**, 83 (1944). Also see, R. B. MacMullin, "Electrolysis of Brines in Mercury Cells," p. 141, "Chlorine," ACS Monograph 154, J. S. Sconce, Editor, (1962).
4. N. Ibl and D. Landolt, *This Journal*, **115**, 713 (1968).
5. M. Ishibashi and Y. Harada, *J. Chem. Soc. Japan*, **62**, 38 (1940).
6. F. Hine, *Denki Kagaku (J. Electrochem. Soc. Japan)*, **26**, 139 (1958).

JOURNAL OF THE ELECTROCHEMICAL SOCIETY

ELECTROCHEMICAL SCIENCE

FEBRUARY 1971

ES

Platinum Electrodes and Calcia-Stabilized Zirconia

The Relation between Electrode Processes and Electrode Structure

R. J. Brook,[1] W. L. Pelzmann,[2] and F. A. Kröger*

University of Southern California, Los Angeles, California 90007

ABSTRACT

Measurements of the direct current-voltage characteristics of calcia-stabilized zirconia using platinum electrodes of various types have been made to investigate possible electrode processes. Depending on the form of the electrode, the rate-limiting step in the electrical conduction sequence can be (*a*) ionic conduction by $O^=$ in the zirconia, (*b*) electronic conduction in the zirconia, (*c*) oxygen atom diffusion through the platinum cathode, (*d*) the transfer of oxygen from the gas phase into the zirconia at the zirconia-gas interface on the cathode side. The conditions, under which each of these situations exists, are explained in terms of the structure of the electrode.

Earlier studies on cells Pt, $O_2|0.85\ ZrO_2 \cdot 0.15\ CaO|Pt$, O_2 with platinum point electrodes (1), or porous platinum electrodes (2), showed the I-V characteristic to be markedly nonohmic. The rate-controlling step responsible for this behavior was found to be confined to the cathode. Two mechanisms of electrode operation appeared to be important (2). At low voltages (*e.g.*, <2.5V), the voltage dependence and oxygen pressure dependence of the I-V characteristic can be explained by a model in which diffusion of oxygen atoms through the platinum grains from the gas phase to the platinum-zirconia interface is the rate-limiting step in the over-all conduction process. However, as discussed in greater detail further on, other processes involving the diffusion of atomic oxygen cannot be excluded. At higher voltages, extreme polarization occurs within the zirconia in the neighborhood of the platinum cathode, and as a result the surface of the zirconia becomes sufficiently nonstoichiometric that it supports electronic conduction. Then, again from consideration of the form of the I-V characteristics and its independence of oxygen pressure at high voltages, it was found that oxygen can move directly from the gas phase into the zirconia and that the rate-controlling step consists of the reaction

$$O\ (\text{adsorbed}) + V_O^x \rightarrow O_O^x \qquad [1]$$

Here O_O^x represents a normal oxygen ion in the zirconia, and V_O^x represents an oxygen ion vacancy with two trapped electrons. Another high voltage mechanism, electronic conduction, requires comparatively long times to build up and was almost completely eliminated by using short observation times. It might be questioned whether the use of this technique does not forbid the application of stationary state considerations as used to arrive at the mechanism characterized by Eq. [1]. We believe, however, that the slow process setting up electronic conduction represents only a small perturbation and that, therefore, the results arrived at are essentially correct. We shall use the same approach in the present paper.

The aim of the present study has been to consider two questions arising from the earlier work, namely: (*i*) if diffusion of oxygen through platinum is rate controlling, then the value of the conductance should be inversely proportional to the diffusion path length. Examination of foil electrodes should reveal this relation specifically; also, the conductance of the paste electrode should depend on the temperature at which it was sintered, *i.e.*, on the grain size of the resulting electrode. (*ii*) If the second mechanism depends on the existence of free zirconia-oxygen interface, then it should be possible to suppress it by examining configurations where such an interface is absent, *i.e.*, cells having large area foil electrodes. Under these conditions, and by allowing sufficient time for a stationary state to be reached, the electronic conduction which is relatively unimportant with the porous electrodes should become the dominant mechanism.

Possible Electrode Mechanisms

The discussion given here is valid in principle for any system in which current flow through an essentially ionic conductor requires reaction at a metal electrode of one of the components of the conductor in gas form. For convenience, the discussion is concentrated on the system ZrO_2*-Pt-O_2. Here and further on, ZrO_2* indicates stabilized zirconia of the composition $0.85\ ZrO_2 \cdot 0.15\ CaO$.

The parameter of interest in the study of electrode mechanisms in this type of system is the extent to which the electrode is blocking for the species present in the gas phase, *i.e.*, is effective in preventing access of ionic carriers to the electrolyte. Where the electrode is partially blocking, it is possible to investigate the path taken by those ionic carriers that are allowed through to the electrolyte by observing the d-c current-voltage characteristics. The presence of electrode effects is then revealed by the nonohmic response of

* Electrochemical Society Active Member.
[1] Currently with the Atomic Energy Research Establishment, Materials Development Division, Harwell, Didcot, Berkshire, England.
[2] Junior Research Assistant under the National Science Foundation Secondary Science Training Program. Currently with El Segundo High School, El Segundo, California.
Key words: electrode structure, platinum electrodes, stabilized zirconia, electrode processes.

the system as a whole, and the nature of these effects can be determined by a study of the partial pressure dependence of the current.

A major division among electrodes can be made on the basis of their porosity. If the electrode is nonporous, for instance a dense foil pressed onto the electrolyte surface, then, as discussed by Tedmon *et al.* (3), ionic carriers are prevented from direct access to the electrolyte surface and must diffuse through the electrode material itself. Under these conditions the rate-limiting step in the ionic conductance may be diffusion of an atomic species from the gas to the conductor through the metal foil or of molecules of the conducting species through a boundary layer in the gas phase to the surface of the electrode. With $ZrO_2^*|O_2$ the diffusing species in the former process should be atomic oxygen, O, and it would have a rate dependent on the root of the gas phase oxygen pressure, $pO_2^{1/2}(g)$. For the case of rate limitation by gas diffusion, the diffusion species would be molecular oxygen, O_2, and would have a rate linearly dependent on $pO_2(g)$. The relative importance of these mechanisms will depend on such factors as foil thickness, gas phase composition, gas phase boundary layer thickness, and magnitude of the attainable ionic current.

When the electrode, by one or other of the mechanisms, is partially effective in blocking the passage of the ionic species, polarization of the electrolyte occurs, and a gradient in the chemical potential of oxygen is established across the electrolyte, which gives rise to electronic conduction. For systems such as stabilized zirconia in which the ionic conduction is practically independent of pO_2, the electronic conductivity of the electrolyte at any point x in the stationary state is given by (4, 5)

$$(\sigma_e)_x = \sigma_e^{\circ} \exp \frac{-[\mu O_{2,x} - \mu O_{2,a}]}{4kT} \qquad [2]$$

Here $\mu O_{2,x}$ and $\mu O_{2,a}$ are the chemical potentials of O_2 inside the zirconia at x, and at the anode, respectively, and σ_e° is the electronic conductivity under zero polarization as it is determined at the anode by the prevalent oxygen pressure. This formula is valid only if σ_e° is independent of the current, *i.e.*, if no overvoltage effects for oxygen discharge and evolution occur. Formula [2] indicates that under extreme polarization large values of σ_e can be attained.

To determine the interaction between the ionic and electronic conductances, the electrode reaction may be written as

$$\tfrac{1}{2}O_2 \rightarrow O_O^x - V_O^{\cdot\cdot} - 2e';$$
$$\tfrac{1}{2}\mu O_2 = \mu(O_O^x) - \eta(V_O^{\cdot\cdot}) - 2\eta(e') \qquad [3]$$

where $V_O^{\cdot\cdot}$ represents a vacant oxygen ion site in the zirconia and e' an electron; the η's are electrochemical potentials. Assuming local equilibrium, and neglecting $d\mu(O_O^x)/dx$ which is practically zero, the gradients should satisfy

$$\frac{1}{4}\frac{d\mu(O_2)}{dx} = \frac{d\eta(e)}{dx} + \frac{1}{2}\frac{d\eta(V_O^{\cdot\cdot})}{dx} \qquad [4]$$

If the electrode is fully transmitting (nonblocking) to ions and electrons

$$\frac{1}{4}\frac{d\mu(O_2)}{dx} = q\frac{J_e}{\sigma_e} - q\frac{J_i}{\sigma_i} = q\frac{dE}{dx} - q\frac{dE}{dx} = 0 \qquad [5]$$

and from [2]

$$\sigma_e = \sigma_e^{\circ} \qquad [6]$$

Here J_e and J_i are current densities of electrons and ions, σ_e and σ_i are the respective conductivities, q is the magnitude of the electronic charge, and E is the electrical potential.

For an electrode totally blocking to ionic carriers, $J_i = O$, and

$$\frac{1}{4}\frac{d\mu(O_2)}{dx} = q\frac{J_e}{\sigma_e} = q\frac{dE}{dx} \qquad [7]$$

Integrating [7] from the anode to the cathode, using [2], assuming the area and J_e to be independent of x, gives

$$\sigma_e = \sigma_e^{\circ}\left[\exp\left\{\frac{qE}{kT}\right\} - 1\right] \qquad [8]$$

This is under the assumption that hole conduction is negligible under all circumstances. If not, then an appropriate hole term has to be added (6, 7). For the intermediate case of a partially blocking electrode, the actual ionic current density, J_a, will be less than the ionic current that would occur in the absence of polarization, J_i, but will be more than zero. Then

$$\frac{1}{4}\frac{d\mu(O_2)}{dx} = q\frac{J_e}{\sigma_e} - q\frac{J_a}{\sigma_i} = q\frac{J_e}{\sigma_e} - q\frac{J_i}{\sigma_i}\frac{J_a}{J_i}$$
$$= q\frac{dE}{dx} - q\frac{dE}{dx}\frac{J_a}{J_i} \qquad [9]$$

Under conditions where blocking is incomplete but nevertheless large, $(1 - J_a/J_i)$ is a slowly varying function of E and the electronic current density is given by

$$J_e = \frac{kT}{ql}\sigma_e^{\circ}\left[\exp\left\{\frac{qE}{kT}\left(1 - \frac{J_a}{J_i}\right)\right\} - 1\right]$$
$$\approx \frac{kT}{ql}\sigma_e^{\circ}\exp\left\{\frac{qE}{kT}\left(1 - \frac{J_a}{J_i}\right)\right\} \qquad [10]$$

with l the specimen thickness. The approximation holds for large E.

In summary, nonohmic behavior in the conductance of a system with a dense, nonporous electrode may arise from the control of ion motion by diffusion through the gas phase or the electrode, or from electron motion, the extent of electronic conductivity being determined by the blocking efficiency of the electrode. A convenient measure of the blocking efficiency is the parameter J_a/J_i which is zero for a totally blocking electrode and unity for a totally transmitting electrode. A schematic picture of the relation between J_a/J_i and σ_e is shown in Fig. 1, where the two contributions to the electron flux, *i.e.*, from the electron concentration gradient (diffusive) and from the electric potential gradient (electrical field) are distinguished. The considerations given so far are limited to the relatively mobile charged species. In the actual system, nonmobile or less mobile species $V_O^{\cdot}$ and V_O^x are formed by the trapping at $V_O^{\cdot\cdot}$ of electrons formed by the polarization process. The centers are visible as color centers (8, 9). The trapping tends to reduce the electronic current until a stationary state has been reached in which just as many electrons are trapped at $V_O^{\cdot\cdot}$ as

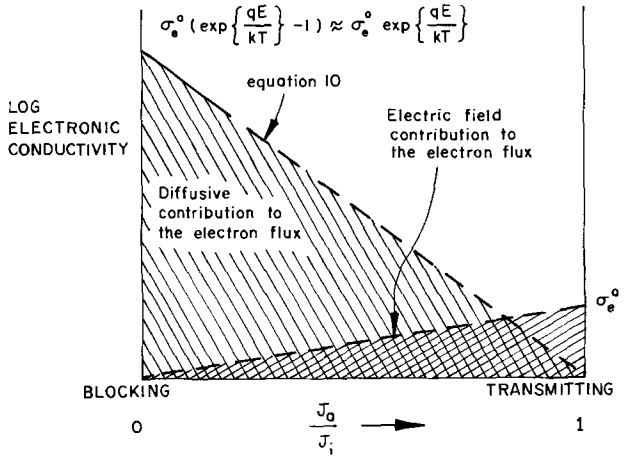

Fig. 1. Effect of the electrode blocking efficiency on the nature of the driving force for electronic conduction. The blocking electrode is the cathode and the anode is the reversible electrode.

are released from $V_O^{\cdot}$ and V_O^x. The time involved in reaching this stationary state was found to be considerable, *i.e.*, $\approx$ 4 hr at 600°C.

For porous electrodes, the situation is more complicated. Tedmon *et al.* (3) have again discussed some of the possibilities. If, for example, the porous electrode consists of a partially sintered platinum paste, then there are so-called triple points where the gas phase (O_2), the platinum (supplying electrons) and the electrolyte all come together. Ionic access then occurs over a limited area in the region of this triple junction which has led to the concept of a "constriction" resistance, where ionic flux through the triple junction is seen as the rate-limiting step.

Convincing evidence for the importance of the triple point has been provided by Karapachev (10), who found that the current provided by a platinum coating is increased at a given voltage by scratching lines in the coating and thus increasing the length of the triple junction. However, the importance of the junction does not in itself explain the detailed mechanism of oxygen access to the electrolyte. An effective junction must have some finite area at which O atoms are transformed into $O^=$ ions, and across which these ions enter the electrolyte.

If this area is at the platinum-zirconia interface, diffusion of oxygen through either the Pt or the zirconia (or along the $Pt|ZrO_2$ interface) must be involved and may be rate controlling. The rates of all three are proportional to $pO_2^{1/2}$ if the diffusion occurs in neutral atomic form as O_i^x. Diffusion of oxygen through Pt was proposed as the rate-limiting step in the low-voltage mechanism for ZrO_2* cells with porous Pt electrodes by Yanagida *et al.* (2). Solution of oxygen in the zirconia at the gas-zirconia interface, followed by diffusion of oxygen through the zirconia to the Pt-zirconia interface was proposed as the main low-voltage mechanism by Tannenberger *et al.* (11). The latter type of mechanism is believed to be the dominant one for gas electrodes in liquid electrolytes (12). Since bulk diffusion in neutral form does not, as a rule, take place to an appreciable extent in inorganic solid compounds (*vide* the Wagner theory of oxidation) we do not consider this a likely mechanism. However, diffusion along the $Pt|ZrO_2$ interface may presumably occur in neutral form, so this possibility remains open.

In principle, transport of O_2 by diffusion through the gas phase may also be rate controlling: mass transport polarization in the terms of Tedmon (3). This would lead to a rate $\propto pO_2$, but this type of limitation is to be expected only at large current densities.

If the transfer area lies at the gas-zirconia interface, electrons from the Pt have to reach the oxygen atoms by diffusion over the surface or through the subsurface of the zirconia. This requires that the zirconia surface be electronic conductive. This is normally not the case for ZrO_2* in contact with an oxidizing atmosphere, but it may become so as a result of polarization. Actually, Kleitz (1) observed that polarization of a Pt point on zirconia made the area of the zirconia around the point electronic conductive. Yanagida proposed this mechanism as the high voltage mechanism for diodes with porous Pt electrodes (2). The limiting step now is either the diffusion of O_2 in the gas phase, or one of the reactions involved in the take-up of oxygen in the zirconia. The latter was found to be the case.

Kleitz (1) suggested that surface diffusion of oxygen toward the triple junction and electrons from this junction along the ZrO_2*-gas interface limited the reaction rate at low voltages. However, as we saw above, electronic surface conduction is not to be expected for zirconia in contact with oxygen in the absence of considerable polarization. Therefore this mechanism may be rejected.

Summarizing the possible mechanisms for a porous electrode or for an electrode with an adjoining free zirconia oxygen interface, ionic conduction may be limited by gas phase diffusion, by diffusion through either the platinum or the zirconia or over the zirconia surface to the platinum-zirconia surface, or (at higher voltages and lower oxygen pressures) by one of the reactions involved in direct incorporation of oxygen into the zirconia at the free zirconia-oxygen interface. In addition, at sufficiently high voltages and after sufficiently long times, bulk polarization and therewith electronic conduction may occur. As noted earlier, it has been shown (2) that for partially sintered platinum pastes the steps limiting the ionic current are diffusion of oxygen through the platinum at low voltages and reaction [1] at high voltages.

Tests on other forms of electrode are the subject of the present work.

Experimental

The electrolyte in all the experiments consisted of specimens of 7.5% by weight calcia stabilized zirconia (0.85 ZrO_2·0.15 CaO), cut from disks, 2.5 cm in diameter and 0.75 mm thick obtained from the Zirconium Corporation of America. The samples, square plates with an area of 20 mm^2 were polished with 1μ diamond powder to a final thickness of $\approx$0.7 mm before application of the electrodes. The grain size of the zirconia was about 30μ in diameter.

The electrodes were prepared in a number of ways. Early in the study it was found that thinly sputtered platinum electrodes gave an ohmic I-V characteristic with a resistance equal to the bulk ionic resistance of the zirconia, a feature already noted by Heyne (13). Accordingly, in all subsequent tests, the electrode to be studied as a cathode was placed on one side of the specimen, and a standard thinly sputtered electrode (1500V, 5 x 10^{-2} Torr argon, 2 min, 2½ cm anode-cathode distance) entirely covered the other side. In this way, it was certain that deviations from an ohmic I-V characteristic could be attributed to the test electrode, and it also guarantees that the value of μO_2 at the anode remains at the equilibrium value; overvoltage of oxygen discharge and O_2 evolution would reveal itself by nonohmic behavior of the $Pt|ZrO_2|Pt$ cell with both electrodes consisting of sputtered Pt.

The test electrodes comprised

(*a*) Nonporous foil platinum electrodes prepared by attaching layers of 30μ thick foil to the zirconia. The foil was attached by pressing it against the zirconia under a 600g load (with powdered Al_2O_3 between the load and the foil to prevent adhesion) and heating to 1350°C for 1 hr.

(*b*) Nonporous foil platinum alloy (40% by weight rhodium) electrodes, attached in a similar way. These electrodes, referred to below as platinum 40-rhodium, behaved as did platinum except for their smaller oxygen diffusion coefficient.

(*c*) Nonporous sputtered electrodes prepared as for the standard electrode but with sputtering times up to 20 min.

(*d*) Porous paste electrodes prepared from nonfluxed platinum "inks" consisting of submicron platinum powder suspended in an organic vehicle. These were painted on the zirconia and fired to different temperatures to vary the degree of porosity and the value of the grain size.

(*e*) A nonporous paste electrode prepared as for (*d*) except that 10 w/o of lead borosilicate glass was added to the ink. This provides a nonporous "fluxed" electrode.

Measurements of the I-V characteristics were made in the circuit shown in Fig. 2. For the studies of ionic processes in all the electrodes, the I-V plot was made by applying an increasing voltage in 1-min steps of 0.6V and measuring the current at the end of the minute. This technique, by limiting the formation and diffusion of F-centers (2), gave the clearest information about the ionic conduction mechanisms. For electrodes (*a*) and (*b*), when in particular the electronic processes were being studied, values were taken after 1 hr when the system had come close to equilibrium;

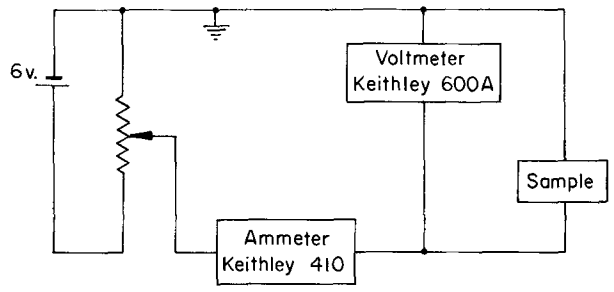

Fig. 2. Scheme of the test circuit

deviations from the true equilibrium value were negligible to two figures.

Measurements were made at temperatures between 500° and 700°C, and in oxygen pressures between 1 and 10^{-4} atm, established by mixing oxygen and technical nitrogen (containing 10^{-5} atm O_2). Buffer systems (H_2O/H_2) were used to achieve lower pressures (10^{-20} atm) but are not satisfactory for the observation of low pO_2 effects due to the decomposition of H_2O at the electrode, as will be discussed.

All the measurements were carried out for $E < 3V$. At this voltage, electrolysis sets in, as indicated by currents increasing continuously with time; the same was reported earlier by Yuan *et al.* (14).

Results

Nonporous foil electrodes.—Low voltage mechanism: the effect of foil thickness.—Thickness effects were tested by using foil electrodes composed of several sheets of the 30μ thick Pt foil. The electrodes were 4 mm^2 in area covering 1/5 of zirconia plates 20 mm^2 in area. The data are shown in Fig. 3.

When the foils were connected as the anode, the I-V curves were ohmic and similar to the I-V curves for cells with thin sputtered electrodes on both sides represented by the dotted line in Fig. 3. The solid lines are all for the foils as cathodes, *i.e.*, where they act as barriers to oxygen access to the electrolyte.

Yanagida *et al.* (2) analyzed the I-V characteristic for the situation where diffusion through a platinum layer is rate controlling in terms of the equation

$$V = IR_b + \frac{RT}{4F}\left[\ln pO_2(g) - 2\ln\left\{pO_2^{1/2}(g) - \frac{I}{B}\right\}\right] \qquad [11]$$

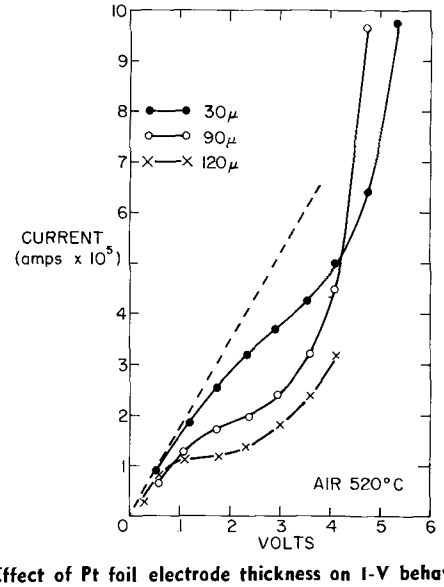

Fig. 3. Effect of Pt foil electrode thickness on I-V behavior. The dotted line is for a thin sputtered electrode. All electrodes are Pt and are observed as cathodes. S (cathode area) = 4 mm^2. The electrode thickness is indicated on the figure.

where R_b is the bulk ionic resistance (in the absence of polarization) and B is a term descriptive of the electrode. For justification of the use of this stationary state equation to describe an essentially nonstationary state, see the introductory paragraphs.

$$B = 2FS\frac{D}{\delta}K_1 \qquad [12]$$

Here S is the area of the electrode, D the diffusion coefficient of oxygen atoms in the Pt electrode, δ the electrode thickness, and K_1 the equilibrium constant for the reaction

$$\tfrac{1}{2}O_2 \rightarrow O(Pt) \qquad [13]$$

$R_b = 6 \times 10^4$ ohms and $pO_2(g) = 0.2$ atm (air). From [11], it may be seen that the current saturates ($V \rightarrow \infty$) when $I = pO_2^{1/2}(g)B$. From Fig. 3 it is seen that a saturation plateau for the thickest foil electrode (120μ) exists at 1.15×10^{-5}A; this means that B has the value 2.57×10^{-5}.

In Fig. 4, the data for the thickest electrode are compared with Eq. [11] plotted with the above values for R_b, $pO_2(g)$, and B. The data match the equation below and at saturation; above saturation another mechanism of conduction appears which is discussed in the next section.

Since B for the 120μ electrode is known, use of Eq. [12] allows calculation of B for the other electrodes since δ is the only variable. Then, from [11], the saturation currents for the other electrodes may be found; these are 1.5×10^{-5}A and 4.6×10^{-5}A for the 90 and 30μ electrodes, respectively. Figure 3 shows substantial agreement with these values, although the saturation levels are less clearly defined than for the 120μ electrode. The evidence is strong, however, that diffusion through the foil is the rate-controlling process at low voltage. This rules out the process in which neutral oxygen diffusion through the zirconia to the Pt-ZrO_2* interface is rate limiting, which is not surprising since a well-made foil electrode does not leave a free ZrO_2*-gas interface. This process, although unlikely for reasons mentioned earlier, still remains a possibility for porous electrodes. However, in view of the similarity in the low voltage behavior of porous and nonporous electrodes, it seems likely that both are limited by the same process, O-diffusion through Pt. Use of the experimental values of Fig. 4 in Eq. [12] indicates that at 520°C DK_1 is 4×10^{-11} g at. cm^{-2} sec^{-1} atm$^{-1/2}$ (D in cm^2/sec. and K_1 in g at. cm^{-3} atm$^{-1/2}$).

High voltage mechanism: electronic conduction.—In the data of Fig. 3, the I-V characteristic was plotted in the 0.6 V-min mode as described earlier. If, however, the sample is allowed to equilibrate under the applied voltage and if measurements are made at lower oxygen pressures, the rapid increase in current at voltages >2V becomes very pronounced as shown in Fig. 5. From the discussion earlier, it is anticipated that this is

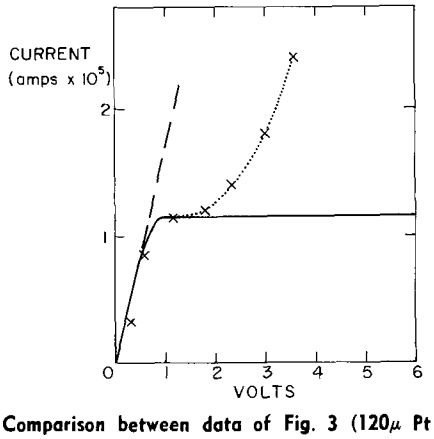

Fig. 4. Comparison between data of Fig. 3 (120μ Pt electrode) and Eq. [11] (ionic current limited by oxygen diffusion through the electrode). T = 520°C; pO_2 = 0.2 atm.; S = 4 mm^2.

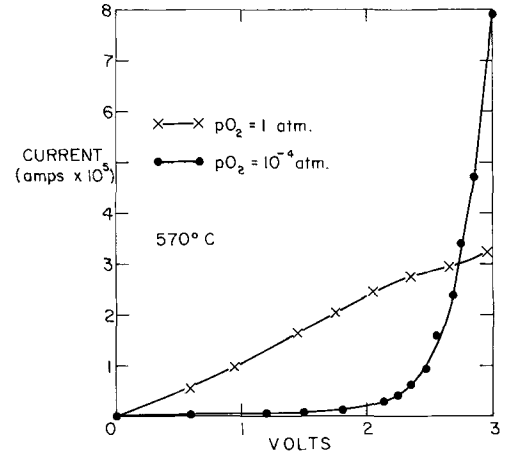

Fig. 5. Equilibrated I-V curves for 30μ foil electrodes under different oxygen pressures; T = 570°C; S = 4 mm^2; δ = 120μ.

caused by electronic conduction and that Eq. [10] should apply when $J_e > J_i$. Taking logarithms (4)

$$\log I = \log \frac{kT}{ql}\sigma_e^0 + \frac{qE}{2.3\,kT}\left(1 - \frac{J_a}{J_i}\right) \quad [14]$$

and

$$\frac{d\log I}{dE} \approx \frac{q}{2.3\,kT} \quad [15]$$

Comparison of the data with the theoretical gradient is shown in Fig. 6 where it can be seen that when the electrode area is smaller than the zirconia area, but, with a completely covering anode, agreement is unsatisfactory. The assumption that $J_a << J_i$ is indicated to be invalid. However, if the electrode area is made equal to the zirconia area, *i.e.* the interface zirconia-oxygen is removed, then agreement between the theoretical line and the data is excellent at high voltages.

The explanation for this effect is analogous to that for the behavior of porous electrodes at high voltages. Under strong polarization the zirconia in the vicinity of the electrode becomes electronically conducting, and direct access of oxygen to the zirconia can occur by [1]. An electronically conducting ring then forms around the foil electrode across which oxygen can move directly into the zirconia; the ionic current, J_a, remains high and so the behavior of [15] is not found. When the foil covers the whole surface, the growth of an electronically conducting region out into the free zirconia surface is restricted to the edges of the sample, J_a remains small, and the high voltage data match Eq. [15].

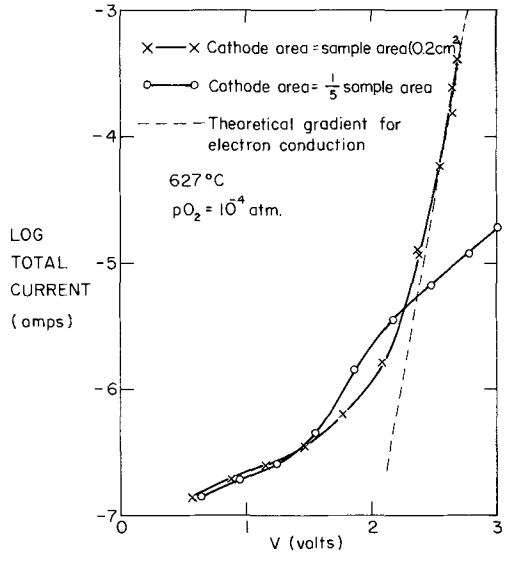

Fig. 6. Comparison between the I-V curves for foil electrodes and the theoretical expression for electronic conductivity in polarized electrolytes for cells in which the electrode area is equal to or 1/5 of the sample area. The large electrodes (S = 0.2 cm^2) are Pt:40 Rh and 200μ thick; the small electrodes (S = 4 mm^2) are Pt and 120μ thick.

Data for several temperatures, taken with the large area Pt:40 Rh electrodes, are compared with the theoretical gradients in Fig. 7. By extrapolating back to zero voltage the data in the region where Eq. [15] is obeyed, the value of σ_e^0 can be calculated from Eq. [14]. This is the electronic conductivity of ZrO_2* under conditions of zero polarization; as seen in Fig. 8, it has an activation energy of 4.62 eV, larger than the value ≈4.15 eV that may be deduced from data reported by Patterson *et al.* (5) (*see*, however, Fig. 10).

The electronic conductivity σ_e^0 should be $\propto pO_2^{-1/4}$ (5, 15). Although Fig. 9 indicates a decrease of σ_e^0 with increasing pO_2, it has not been possible to demonstrate this dependence quantitatively. If we assume a $pO_2^{-1/4}$ dependence, then the σ_e^0 data of Fig. 7 and 8 can be represented by

$$\sigma_e^0 = 1.5 \times 10^7\, pO_2^{-1/4} \exp(-4.62\ \text{eV}/kT) \quad [16]$$

Combination with $\sigma_i = 1.5 \times 10^3 \exp(-1.26\ \text{eV}/kT)$

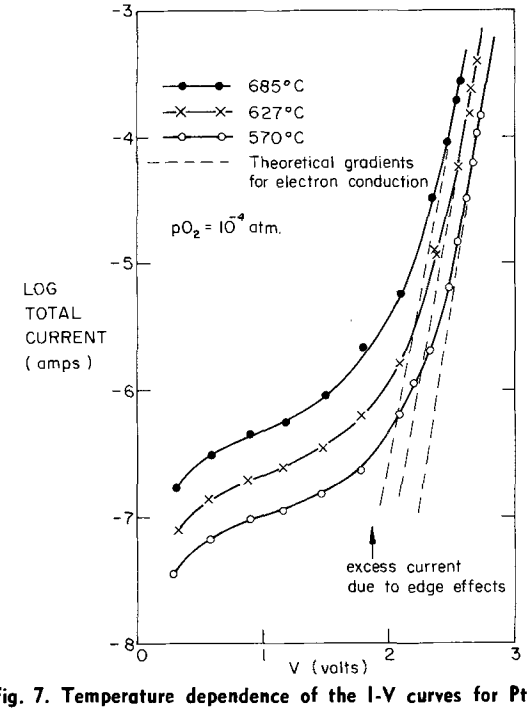

Fig. 7. Temperature dependence of the I-V curves for Pt:40 Rh foil electrodes where the cathode area equals the sample area. S = 0.2 cm^2; δ = 200μ.

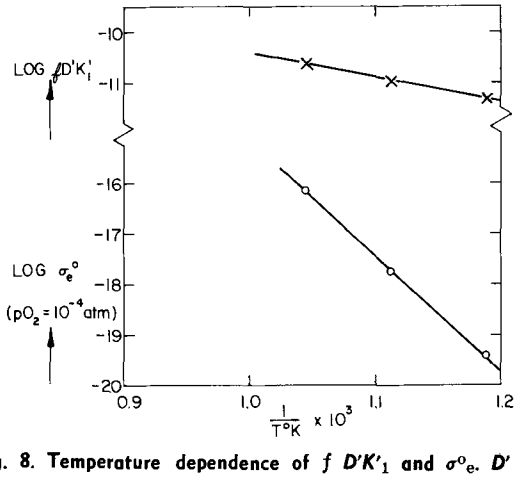

Fig. 8. Temperature dependence of f $D'K'_1$ and σ^0_e. D' is the diffusion coefficient for oxygen atoms in the Pt:40 Rh electrode, and K'_1 the equilibrium constant for the reaction $\frac{1}{2}O_2(g) \rightarrow O$(Pt/40 Rh).

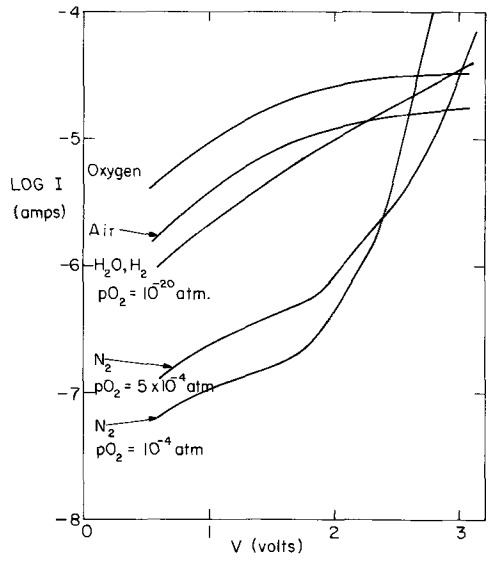

Fig. 9. Oxygen pressure dependence of I-V curves for (Pt:40 Rh) foil electrodes. Cathode area = sample area. T = 570°C; S = 0.2 cm²; δ = 200μ.

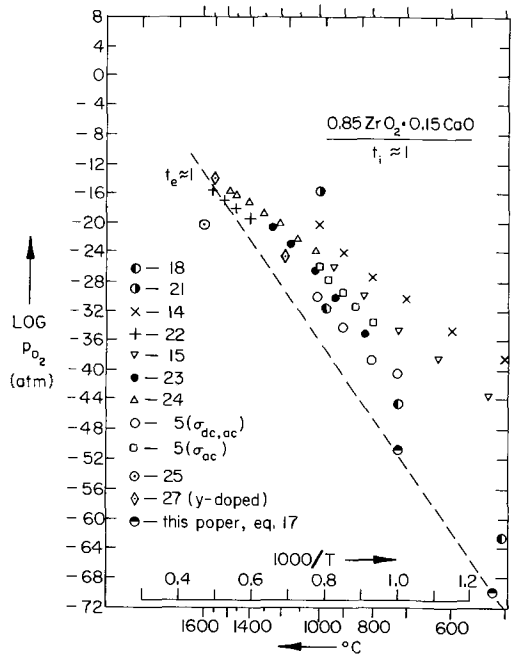

Fig. 10. Values of $p_{\ominus}$, the low-pressure boundary of the ionic conductivity range in ZrO_2* where $\sigma_i = \sigma_e$, according to various authors.

as given by Kingery *et al.* (16) leads to the following expression for $p_{\ominus}$, the oxygen pressure at which

$\sigma_e = \sigma_i$ and where $t_e = t_i = \frac{1}{2}$ (17)

$$p_{\ominus} = 10^{16} \exp(-13.44 \text{ eV}/kT) \qquad [17]$$

As shown in Fig. 10 the values represented by this expression are considerably lower than those found in most other investigations. Only Tretyakov (18) reports data close to ours.[3] Tretyakov's results have been shown to be obtained on the basis of fallacious argument (20).

In the conductivity at low voltages where the oxygen diffusion mechanism applies, the rate $\propto pO_2^{1/2}$, as observed by Kleitz (1) and Yanagida *et al.* (2) is again seen for oxygen pressure $\geq 10^{-4}$ established by gas mixing. The use of buffer systems is not satisfactory since, as shown, the electrode is capable of taking up oxygen from the water vapor by decomposition of the H_2O, and this results in an appreciable current. This also was noted earlier (2, 14), and a similar behavior was found for CO_2 (1). The curves for $N_2 + 10^{-4}$ and 5×10^{-4} O_2 shown in Fig. 9 demonstrate the opposite direction of the oxygen pressure dependencies in the high and low voltage regions by the presence of the cross-over of curves for different oxygen pressures at medium voltages, but J_a in the less pure nitrogen experiment is sufficiently large that correspondence to Eq. [15] and a reliable value for σ_e are not demonstrated.

Figure 7 can be used to find the activation energy for oxygen diffusion in Pt:40 Rh. Subtraction of the electronic currents from the total currents should give the ionic current. Yet the curves obtained do not show clear saturation as required by [11]. An excess of current in the range 1.5-2V, although ionic in nature, is probably due to edge effects by the free surface mechanism. Qualitative examination suggests saturation of the current due to the low voltage mechanism at ≈1V. Both the similarity in the form of the three different curves and the theoretical expression for the low voltage mechanism [11] indicate that a reliable activation energy can be found from current values below saturation.

Using primes to distinguish parameters for Pt:40 Rh from those for Pt, Fig. 8 shows the values of $fD'K'_1$ at 0.9V, f being the ratio of the ionic current to its saturation value; the "activation" energy is 0.94 eV. Assuming the points to represent 80% saturation, *i.e.*, $f = 0.8$, $D'K'_1$ may be represented by

$$D'K'_1 = 2.2 \times 10^{-6} \exp(-0.94 \text{ eV}/kT) \qquad [18]$$

This leads to $(D'K'_1)_{520°C} = 2.2 \times 10^{-12}$ and $(D'K'_1)_{25°C} = 3 \times 10^{-22}$ g at. cm^{-1} sec^{-1} atm$^{-1/2}$. Comparison of the 520°C value of $D'K'_1$ for Pt:40 Rh with the corresponding value for Pt as found earlier, $DK_1 = 4 \times 10^{-11}$, it is seen that the permeability for oxygen is slightly less for Pt:40 Rh than for pure Pt. The room temperature value may be compared with results on pure Pt by Hoare (21), who reports $D = (1.8 - 4.4) \times 10^{-11}$ cm² sec^{-1}. He assumes an oxygen solubility of 1 at. O per atom Pt, *i.e.*, for $pO_2 = 1$ atm, K_1 = density of Pt/atomic weight Pt ≈ 0.1 g at. cm^{-3} atm$^{-1/2}$; therefore $(DK_1)_{25°C} \approx 3 \times 10^{-12}$ g at. (cm sec atm$^{1/2}$)$^{-1}$, much larger than the extrapolated value for $D'K'_1$ found above. Although we found a small difference between the oxygen permeability for Pt:40 Rh and Pt at 520°C, it is unlikely that this will result in a 10^{10} discrepancy at 25°C. This large discrepancy must probably be explained by the predominance of grain boundary diffusion at low temperatures.

Nonporous sputtered electrodes.—All the sputtered electrodes tested were found to have an ohmic I-V characteristic with $R = R_b$. Since even the thickest sputtered film has a thickness <1μ, the value of B is >120 x 2.57 x $10^{-5} \approx 3 \times 10^{-3}$ at 520°C. In air, with $pO_2^{1/2}(g) = 0.447$, this implies a saturation current $I_s \approx 1$ mA, and some 60V would have to be applied before nonohmic effects would appear. Since electrolysis limits the voltage to 3V, such effects cannot be observed.

Porous paste electrodes: the effect of firing temperature.—In the case of paste electrodes, the parameter δ is less clearly defined than in the case of foil electrodes, but it is expected to bear some relation to the grain size of the platinum in the electrode, *i.e.*, the maximum diffusion path length from the gas phase to the electrolyte should be through a single grain of the platinum for a porous electrode. If the paste is fired at 800°C, the organic suspending medium is removed, but the platinum grain size is not markedly increased above that in the original ink (<1μ). Ac-

[3] Tretyakov (18) and Patterson (19) give an expression for pO_2 at the point where $t_e = 0.01$; for $\sigma_e \propto pO_2^{-1/4}$, $p_{\ominus}$ is 10^8 × smaller.

cordingly, in such a sample, δ is itself $<1\mu$ and, as described in the preceding section, nonohmic behavior from diffusion limited currents is not expected below 60V. Results for such a paste are shown in Fig. 11, and they are indeed seen to be ohmic with $R = R_b$.

An additional point is that the over-all thickness of the electrode does not affect this result (Fig. 11). This indicates that gas phase polarization is unimportant in the paste electrodes even at a thickness of 40μ. Actually considerations given in ref. (3) indicate that gas phase polarization is to be expected at ionic current densities of $\approx$10 A/cm^2, *i.e.*, approximately four orders of magnitude higher than the currents of 2 x 10^{-3} A/cm^2 at which the nonlinear effects observed by us occurred.

In pastes fired at 1350°C, sintering and grain growth occur in the platinum until the final structure resembles a slightly porous foil. As seen in Fig. 11, these samples have non-ohmic I-V characteristics and show a thickness dependence similar to that of the foils. The initial current values are less than for the foils since the area of the platinum contact regions is less than the total foil area. The high voltage mechanism in these pastes is as identified by Yanagida *et al.* (2) (Eq. [1]); it occurs because areas of free zirconia surface are directly accessible to the gas phase.

Nonporous paste electrode; the effect of a fluxing agent.—The I-V characteristic with the fluxed paste as cathode is shown in Fig. 12. If the value of I_{sat} is taken from the graph as 5 x 10^{-5}A, B is then 1.1 x 10^{-5} and δ is 280μ, assuming the same value for DK_I as in the case of the foil (Fig. 3). This is close to the total thickness of the electrode which was found by metallographic examination to be around 300μ. Apparently the glass acts to seal the pore phase in the electrode, δ takes on the value of the total electrode thickness, and, as seen in Fig. 12, the high voltage mechanism appears to be electronic. The latter is expected, since the zirconia is protected from the gas phase by the glass and no free, accessible surface is available.

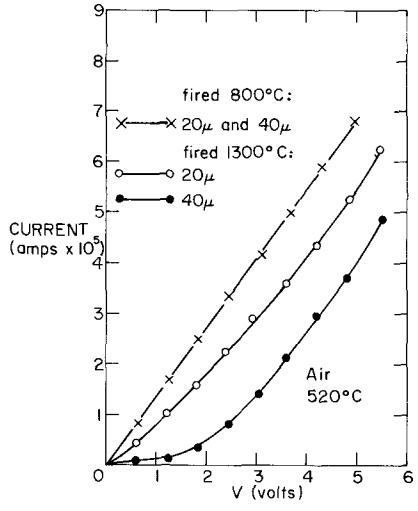

Fig. 11. I-V curves for porous, nonfluxed, paste electrodes fired at different temperatures: $S \approx 4$ mm^2.

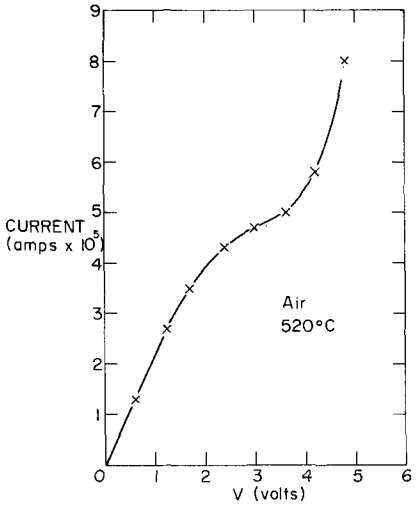

Fig. 12. I-V curve for fluxed (nonporous) platinum paste electrode. $S \approx 4$ mm^2; total electrode thickness $\approx 300\mu$.

Discussion and Summary

The combination of the data in the present paper with those obtained in the earlier work (2) allows a complete description of the electrode effects found in the Pt-ZrO_2* system. These are summarized in Table I. The equations describing the I-V characteristics for the various processes are

$$(\sigma_i)_{ZrO_2}^*: \quad V = IR_b \qquad [18]$$

$$(\sigma_e)_{ZrO_2}^*: \quad I = \frac{kTA}{ql}\sigma_e^{\circ}\exp\left\{\frac{qE}{kT}\left(1-\frac{J_a}{J_i}\right)\right\} \qquad [19]$$

$$D_{O,Pt}: \quad V = IR_b + \frac{RT}{4F}\left[\ln pO_2(g) - 2\ln\left\{pO_2^{1/2}(g) - \frac{I}{B}\right\}\right] \qquad [20]$$

$$(1): \quad V = IR_b + \frac{RT}{2F}\ln\frac{I}{C} \qquad [21]$$

where A is the electrode area and C a constant. Equations [19] and [21] only apply at relatively high voltage (>2V) where substantial polarization has already occurred. The common combinations (v. Table I) are [20] followed by [19], an example of which is shown in Fig. 4, and [20] followed by [21], an example of which is shown in Fig. 11 for the high fired pastes.

There are a number of features in this scheme that may be mentioned. In the first place, for tests designed to measure the bulk ionic conductivity of the electrolyte, the thinnest possible electrodes should be used; from the data here, sputtered electrodes are well suited for this purpose. Low fired pastes also appear to be satisfactory.

Second, in tests designed to observe polarization effects, it is important to use electrodes covering the entire faces of the specimen as emphasized in Fig. 6. Also, unless very thick foils are used (or equally thick fluxed pastes), the value of $I_{sat.}$ provided by oxygen diffusion through the foil can be considerable. Thus, for instance, in the experiments of Danforth and Bodine (22), where the dynamic resistance of ThO_2 was measured as a function of the polarization voltage, it is probable that the dynamic resistance was ionic in nature, and their finding that the two parameters were independent is expected.

Vest *et al.* (23), who carried out polarization experiments with fluxed Pt paste electrodes, cited the above experiment to justify assuming that the electronic resistance is independent of polarization. From the present measurements (Fig. 7) and from Eq. [19], this seems to be invalid.

A final feature in polarization measurements is that the applied voltage should remain below the decom-

Table I. Rate-limiting mechanisms for various types of electrodes

$(\sigma_i)_{ZrO_2}$:	ionic conduction through the zirconia
$(\sigma_e)_{ZrO_2}$:	electronic conduction through the zirconia; $\propto pO_2^{-1/4}(g)$
$D_{O,Pt}$:	diffusion of oxygen through the platinum; $\propto pO_2^{+1/2}(g)$
[1]	the reaction O (ads) + $V_O^x \rightarrow O_O^x$; $\propto pO_2^{\circ}(g)$

Electrolyte type	Low	Applied field	High
Foil	<--------$D_{O,Pt}$---->	<-----$(\sigma_e)_{ZrO_2}$---------->	
Sputtered film	<--$(\sigma_i)_{ZrO_2}$---------->	<$D_{O,Pt}$>	<-$(\sigma_e)_{ZrO_2}$-->
Unfluxed paste	<--------$D_{O,Pt}$----->	<---------[1]---------->	
Fluxed paste	<--------$D_{O,Pt}$----->	<----$(\sigma_e)_{ZrO_2}$---------->	

position voltage for the electrolyte; otherwise electrolysis occurs.

Acknowledgment

The work on this paper was supported by the Directorate of Chemical Sciences, Air Force Office of Scientific Research, under Grant No. AF-AFOSR-68-1405.

Manuscript submitted Aug. 3, 1970; revised manuscript received Oct. 5, 1970.

Any discussion of this paper will appear in a Discussion Section to be published in the December 1971 JOURNAL.

REFERENCES

1. M. Kleitz, "Electrode Reactions in Solid Oxide Electrolytes," Thesis, University of Grenoble, 1968.
2. Hiroaki Yanagida, R. J. Brook, and F. A. Kröger, *This Journal*, **117**, 593 (1970).
3. C. S. Tedmon, Jr., H. S. Spacil, and S. P. Mitoff, *ibid.*, **116**, 1170 (1969).
4. F. A. Kröger, "The Chemistry of Imperfect Crystals," p. 894, North Holland Publishing Co., New York (1964).
5. J. W. Patterson, E. C. Bogren, and R. A. Rapp, *This Journal*, **114**, 752 (1967).
6. D. O. Raleigh, *J. Phys. Chem. Solids*, **25**, 329 (1965).
7. Y. J. Van der Meulen and F. A. Kröger, *This Journal*, **117**, 69 (1970).
8. M. Guillou, J. Millet, M. Asquiedge, N. Busson, M. Jacquin, and S. Palous, *Compt. rend. Ac. S. Paris*, **262**, 616 (1966).
9. J. Millet, C. Deportes, and M. Guillou, *Rev. Gen. Elec.*, **76**, 45 (1967).
10. S. V. Karapachev and A. T. Filyaev, *Elektrokhim.*, **2**, 1330 (1966).
11. H. Tannenberger and H. Siegert, "The Behavior of Silver Cathodes In High Temperature Zirconia Electrolyte Fuel Cells," Paper presented at the Chicago Meeting of the American Chemical Society, 1967.
12. S. Srinivan, H. D. Hurwitz, and J. O'M Bockris, *J. Chem. Phys.*, **46**, 3108 (1967); S. Srinivan and H. D. Hurwitz, *Electrochim. Acta*, **12**, 495 (1967); F. G. Will, *This Journal*, **110**, 145, 152 (1953).
13. L. Heyne, "Mass Transport in Oxides," J. B. Wachtman, Editor, p. 149-164, N. B. S. Special Publication 296 (1968).
14. D. Yuan and F. A. Kröger, *This Journal*, **116**, 594 (1969).
15. H. Schmalzried, *Z. Electrochem.*, **66**, 572 (1962).
16. W. D. Kingery, J. Pappis, J. E. Doty, and D. C. Hill, *J. Am. Ceram. Soc.*, **42**, 393 (1959).
17. H. Schmalzried, *Z. Physik. Chem. (Frankfurt)*, **38**, 87 (1963).
18. Ju. D. Tretyakov, Vesn. Mosk. Univ. Ser. II Khim., cited in Ju. D. Tretyakov and A. Muan, *This Journal*, **116**, 331 (1969).
19. J. W. Patterson in "The Physics of Electronic Ceramics," L. L. Hench and D. B. Dove, Editors, Marcel Dekker Inc., New York (1970).
20. D. A. Shores and R. A. Rapp, Being considered for publication.
21. J. P. Hoare, *ibid.*, **116**, 612, 1390 (1969).
22. W. E. Danforth and J. H. Bodine, *J. Franklin Inst.*, **260**, 467 (1955).
23. R. W. Vest and N. M. Tallan, *J. Appl. Phys.*, **36**, 543 (1965).
24. W. A. Fischer and D. Janke, *Arch. Eisenhüttenw.*, **39**, 89 (1968).
25. R. J. Fruehan, L. J. Martonik, and E. T. Turkdogan, *Trans. Met. Soc. AIME*, **245**, 1501 (1969).
26. R. Baker and J. M. West, *J. Iron and Steel Inst.*, (1966) 212.
27. D. A. J. Swinkels, *This Journal*, **117**, 1267 (1970).

Intergranular Corrosion of Austenitic Stainless Steel

C. S. Tedmon, Jr.,* D. A. Vermilyea,* and J. H. Rosolowski

General Electric Research and Development Center, Schenectady, New York 12301

ABSTRACT

The well-known susceptibility of austenitic stainless steels to intergranular corrosion after heat-treatment in the temperature range of 550°-800°C (*i.e.*, "sensitization") has long been attributed to depletion of Cr from regions of the alloy matrix adjacent to grain boundaries in which $Cr_{23}C_6$ had precipitated. Those regions of the steel in which the local Cr composition falls below about 12% have a diminished ability to form a passive film and hence corrode preferentially.

We have made thermodynamic calculations of the Cr-C-$Cr_{23}C_6$ equilibria in and near grain boundaries in order to determine the chromium content in the vicinity of carbide particles. The calculations show that the equilibrium chromium content is a strong function of the temperature and of the carbon and alloy content of the steel. It is inferred from the analysis that variations in the susceptibility to intergranular attack are determined primarily by changes in the equilibrium chromium content near the carbides and not by changes in the number and distribution of particles. For instance, above 800°C the chromium content near the carbides is high enough to produce passivity, and the alloy is immune not because of the absence of carbides but because chromium depletion is not severe. Experimental studies of rates of grain boundary attack as functions of temperature and composition have confirmed the predictions of the analysis.

A further factor of less importance is the distribution of carbides in the grain boundary. Calculations were made to determine the Cr concentration gradient within the boundary between carbide particles as a function of temperature and composition as well as the Cr gradient normal to the boundary. These calculations predict a strong interdependence between susceptibility to intergranular corrosion, carbide particle spacing, and sensitizing temperature. Experimental results on thinned samples of sensitized material corroded in a Strauss solution and examined by electron microscopy are in good agreement with predicted effects.

In their classic paper (1), Bain, Aborn, and Rutherford developed a model for the intergranular corrosion of sensitized stainless steel which has had general and widespread acceptance for nearly forty years. Their model attributes sensitization to the precipitation of chromium carbide at grain boundaries with concomitant depletion of chromium in regions adjacent to the boundary to levels below that required for passivity. Although other models have been proposed

* Electrochemical Society Active Member.

Key words: intergranular corrosion, stainless steels, carbide precipitation, sensitization, thermodynamics, localized attacks.

position voltage for the electrolyte; otherwise electrolysis occurs.

Acknowledgment

The work on this paper was supported by the Directorate of Chemical Sciences, Air Force Office of Scientific Research, under Grant No. AF-AFOSR-68-1405.

Manuscript submitted Aug. 3, 1970; revised manuscript received Oct. 5, 1970.

Any discussion of this paper will appear in a Discussion Section to be published in the December 1971 JOURNAL.

REFERENCES

1. M. Kleitz, "Electrode Reactions in Solid Oxide Electrolytes," Thesis, University of Grenoble, 1968.
2. Hiroaki Yanagida, R. J. Brook, and F. A. Kröger, *This Journal*, **117**, 593 (1970).
3. C. S. Tedmon, Jr., H. S. Spacil, and S. P. Mitoff, *ibid.*, **116**, 1170 (1969).
4. F. A. Kröger, "The Chemistry of Imperfect Crystals," p. 894, North Holland Publishing Co., New York (1964).
5. J. W. Patterson, E. C. Bogren, and R. A. Rapp, *This Journal*, **114**, 752 (1967).
6. D. O. Raleigh, *J. Phys. Chem. Solids*, **25**, 329 (1965).
7. Y. J. Van der Meulen and F. A. Kröger, *This Journal*, **117**, 69 (1970).
8. M. Guillou, J. Millet, M. Asquiedge, N. Busson, M. Jacquin, and S. Palous, *Compt. rend. Ac. S. Paris*, **262**, 616 (1966).
9. J. Millet, C. Deportes, and M. Guillou, *Rev. Gen. Elec.*, **76**, 45 (1967).
10. S. V. Karapachev and A. T. Filyaev, *Elektrokhim.*, **2**, 1330 (1966).
11. H. Tannenberger and H. Siegert, "The Behavior of Silver Cathodes In High Temperature Zirconia Electrolyte Fuel Cells," Paper presented at the Chicago Meeting of the American Chemical Society, 1967.
12. S. Srinivan, H. D. Hurwitz, and J. O'M Bockris, *J. Chem. Phys.*, **46**, 3108 (1967); S. Srinivan and H. D. Hurwitz, *Electrochim. Acta*, **12**, 495 (1967); F. G. Will, *This Journal*, **110**, 145, 152 (1953).
13. L. Heyne, "Mass Transport in Oxides," J. B. Wachtman, Editor, p. 149-164, N. B. S. Special Publication 296 (1968).
14. D. Yuan and F. A. Kröger, *This Journal*, **116**, 594 (1969).
15. H. Schmalzried, *Z. Electrochem.*, **66**, 572 (1962).
16. W. D. Kingery, J. Pappis, J. E. Doty, and D. C. Hill, *J. Am. Ceram. Soc.*, **42**, 393 (1959).
17. H. Schmalzried, *Z. Physik. Chem. (Frankfurt)*, **38**, 87 (1963).
18. Ju. D. Tretyakov, Vesn. Mosk. Univ. Ser. II Khim., cited in Ju. D. Tretyakov and A. Muan, *This Journal*, **116**, 331 (1969).
19. J. W. Patterson in "The Physics of Electronic Ceramics," L. L. Hench and D. B. Dove, Editors, Marcel Dekker Inc., New York (1970).
20. D. A. Shores and R. A. Rapp, Being considered for publication.
21. J. P. Hoare, *ibid.*, **116**, 612, 1390 (1969).
22. W. E. Danforth and J. H. Bodine, *J. Franklin Inst.*, **260**, 467 (1955).
23. R. W. Vest and N. M. Tallan, *J. Appl. Phys.*, **36**, 543 (1965).
24. W. A. Fischer and D. Janke, *Arch. Eisenhüttenw.*, **39**, 89 (1968).
25. R. J. Fruehan, L. J. Martonik, and E. T. Turkdogan, *Trans. Met. Soc. AIME*, **245**, 1501 (1969).
26. R. Baker and J. M. West, *J. Iron and Steel Inst.*, (1966) 212.
27. D. A. J. Swinkels, *This Journal*, **117**, 1267 (1970).

Intergranular Corrosion of Austenitic Stainless Steel

C. S. Tedmon, Jr.,* D. A. Vermilyea,* and J. H. Rosolowski

General Electric Research and Development Center, Schenectady, New York 12301

ABSTRACT

The well-known susceptibility of austenitic stainless steels to intergranular corrosion after heat-treatment in the temperature range of 550°-800°C (*i.e.*, "sensitization") has long been attributed to depletion of Cr from regions of the alloy matrix adjacent to grain boundaries in which $Cr_{23}C_6$ had precipitated. Those regions of the steel in which the local Cr composition falls below about 12% have a diminished ability to form a passive film and hence corrode preferentially.

We have made thermodynamic calculations of the Cr-C-$Cr_{23}C_6$ equilibria in and near grain boundaries in order to determine the chromium content in the vicinity of carbide particles. The calculations show that the equilibrium chromium content is a strong function of the temperature and of the carbon and alloy content of the steel. It is inferred from the analysis that variations in the susceptibility to intergranular attack are determined primarily by changes in the equilibrium chromium content near the carbides and not by changes in the number and distribution of particles. For instance, above 800°C the chromium content near the carbides is high enough to produce passivity, and the alloy is immune not because of the absence of carbides but because chromium depletion is not severe. Experimental studies of rates of grain boundary attack as functions of temperature and composition have confirmed the predictions of the analysis.

A further factor of less importance is the distribution of carbides in the grain boundary. Calculations were made to determine the Cr concentration gradient within the boundary between carbide particles as a function of temperature and composition as well as the Cr gradient normal to the boundary. These calculations predict a strong interdependence between susceptibility to intergranular corrosion, carbide particle spacing, and sensitizing temperature. Experimental results on thinned samples of sensitized material corroded in a Strauss solution and examined by electron microscopy are in good agreement with predicted effects.

In their classic paper (1), Bain, Aborn, and Rutherford developed a model for the intergranular corrosion of sensitized stainless steel which has had general and widespread acceptance for nearly forty years. Their model attributes sensitization to the precipitation of chromium carbide at grain boundaries with concomitant depletion of chromium in regions adjacent to the boundary to levels below that required for passivity. Although other models have been proposed

* Electrochemical Society Active Member.

Key words: intergranular corrosion, stainless steels, carbide precipitation, sensitization, thermodynamics, localized attacks.

(2-5), it seems clear that the model of Bain *et al.*, is qualitatively valid in most instances. One of the very few cases for which their model is inadequate is that of intergranular corrosion of solution-treated austenitic stainless steels in highly oxidizing environments such as HNO_3-Cr^{+6} solutions (5-6). This rather special case will be considered in a subsequent section of this paper. A critical summary of the various theories of intergranular corrosion of stainless steel has recently been presented by Gellings and deJongh (7).

The theory of Bain *et al.* is based on the fact that a certain minimum chromium content of about 13-15% (8-9) (all compositions are expressed in weight per cent), is required in the steel to render it corrosion resistant. The alloy matrix immediately adjacent to a carbide particle will have a chromium content X_{Cr} which for the case of sensitized steel will be less than the value of 13-15%. Attempts to measure this value, or the gradient adjacent to sensitized grain boundaries have generally been unsuccessful (10-11), probably because of the very limited width of the depleted zone.

It is obviously important to know quantitatively the variation of X_{Cr} with temperature, heat-treatment, and steel chemistry. Further, it has been shown (3, 12) that the carbides which form at grain boundaries may not necessarily be present as a continuous film, but rather, as discrete particles. Therefore, if values of X_{Cr} were known, it would be possible to calculate the chromium gradient within the boundary between carbide particles and determine whether or not the chromium content in and near the boundary between carbide particles exceeds the critical level of 13-15%. If it does not, then the entire boundary would be effectively sensitized even though the carbide was not continuous in the boundary. Alternatively, if the chromium level in the boundary at some point between carbide particles exceeded the critical concentration, then a "patchy" type of intergranular corrosion would be expected.

Values of X_{Cr} and of the chromium concentration gradient in a boundary between carbide particles are usually not experimentally accessible, so it is necessary to resort to analytical techniques for their evaluation. In a recent paper (13), Stawström and Hillert have presented a theory for intergranular corrosion of 18-8 austenitic stainless steel which describes a method for calculating the chromium concentration in the steel adjacent to a grain boundary carbide. An important feature of their model is the assumption that this chromium content is thermodynamically determined by the alloy-carbon-$M_{23}C_6$ local equilibrium. This is in contrast to the more usual assumption that the chromium content in the vicinity of the carbide particles is negligible, and that variation in the degree of sensitivity results from changes in the morphology or distribution of particles along the boundary and not from variation in chromium composition. Stawström and Hillert evaluated the equilibrium using some unpublished thermodynamic expressions which had been developed by Nishizawa for the iron-chromium-carbon system (14). They assumed throughout their analysis that grain boundary diffusion was sufficiently fast at typical sensitizing temperatures that there would be no variation in chromium composition within the boundary between carbide particles. In addition they considered in detail the kinetics of the desensitizing process.

In this paper we present a model for the intergranular corrosion of stainless steel that is conceptually similar to that of Stawström and Hillert, but differs considerably in detail and result. Like Stawström and Hillert, we also make the basic assumption that the grain boundary chromium concentration determines the degree of sensitization, and that this quantity is thermodynamically fixed. However, our method of calculating the grain boundary chromium concentration is much different from theirs, and we believe it to be a more general approach, which can be applied to a variety of alloy compositions. Further, instead of assuming a uniform chromium composition throughout the grain boundary, we will describe a theoretical method for calculating the chromium concentration profile both within the grain boundary between carbide particles, and also normal to the boundary. Both analytical and experimental evidence will be presented to show that for many cases the chromium concentration in a grain boundary is by no means uniform, but in fact, very large gradients exist between carbide particles, which have a significant effect on the corrosion behavior. We do not consider the desensitizing process.

Thermodynamic Analysis

The basic problem is to calculate the minimum chromium content at the grain boundary. For the reaction

$$23Cr + 6C \leftrightharpoons Cr_{23}C_6 \qquad [1]$$

The equilibrium constant is given by

$$K = \frac{1}{(\gamma_{Cr}X_{Cr})^{23}(\gamma_C X_C)^6} \qquad [2]$$

where unit activity has been assumed for the carbide, and compositions are expressed as mole fractions. Iron solubility in the carbide is neglected. Data for the free energy of formation of $Cr_{23}C_6$ are available in the literature (15), and hence K may be determined. In order to calculate X_{Cr} it is then only necessary to determine the activity coefficients for carbon and chromium. Values for these quantities are not available in the literature, but there are several methods by which they may be estimated. It was decided to use the Wagner analysis (16) for calculation of the carbon activity coefficient. Advantages of this approach are that it incorporates available experimental data and permits a physical interpretation to be made of the effect of various alloying elements. Details on the calculation are presented in the Appendix. Figure 1 shows the dependence of γ_C on chromium composition for several temperatures for a nickel composition of 10%. Chromium strongly lowers the carbon activity coefficient, which is expected in view of the pronounced tendency of chromium and carbon to form compounds. The influence of temperature is relatively small. It is noted that the thermodynamic factors

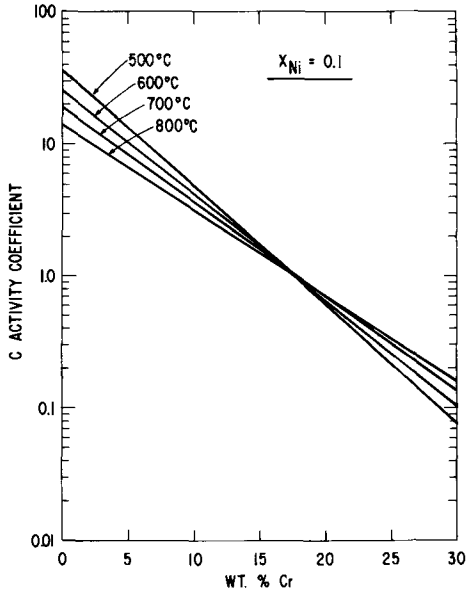

Fig. 1. Carbon activity coefficient vs. chromium content for an austenitic alloy containing 10% Ni, for various temperatures.

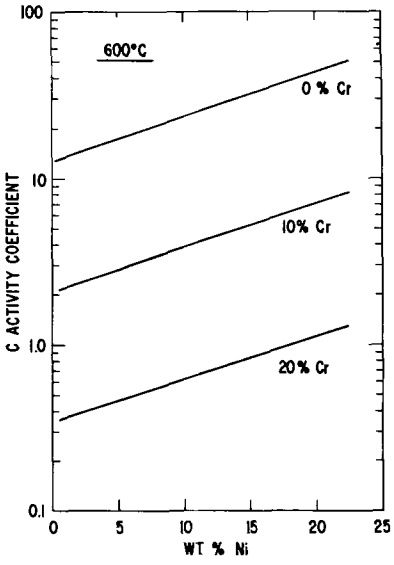

Fig. 2. Carbon activity coefficient in austenitic steel vs. nickel content at 600°C for various chromium levels.

balance in such a way as to result in an ideal solution at about 17.5% chromium. At that point, the activity coefficient is unity and temperature independent.

Nickel acts to increase γ_C as shown in Fig. 2 at 600°C for three chromium levels. This effect is not unexpected in view of the low solubility of carbon in nickel and the absence of stable carbides of nickel.

The dependence of γ_C on carbon content is small, because X_C is small, usually less than 5 x 10^{-3} mole fraction, and for all practical purposes one can assume $\gamma_C \neq f(X_C)$.

The activity coefficient for chromium dissolved in stainless steel can, in principle, be calculated using the Wagner analysis. However, examination of available thermodynamic data for the iron-chromium binary system shows that the higher order terms pertaining to these two elements cannot be neglected (17). The influence of nickel additions on γ_{Cr} in stainless steel is not known. Also, data are lacking for the influence of carbon on γ_{Cr}, although the term $X_C \cdot (\partial \ln \gamma_{Cr}/\partial X_C)$ will probably be small because X_C is usually small. In the absence of these data one approach would be to use the data for the Fe-Cr binary system (17) for γ_{Cr} in stainless steel. However, values of X_{Cr} calculated using this data are somewhat in disagreement with the corrosion results. Treating γ_{Cr} as a semi-adjustable parameter and forcing a fit to corrosion data (see Experimental section for detail) for Type 304 stainless steel that was sensitized at 600°C gives the results shown in Fig. 3. The temperature dependence was estimated by assuming a regular solution, as described in the Appendix for carbon. One means of checking the

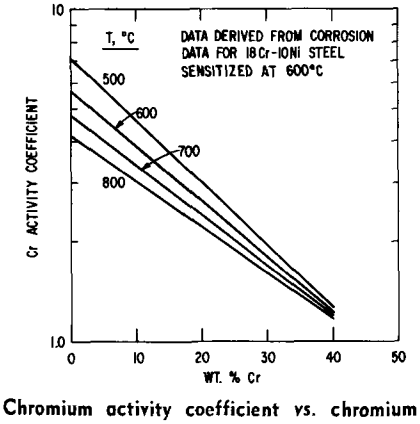

Fig. 3. Chromium activity coefficient vs. chromium content in austenitic stainless steel at various temperatures.

validity of this method is to compare corrosion data for steels sensitized at temperatures other than 600°C with predictions based on values of γ_{Cr} taken from Fig. 3. This point will be discussed subsequently.

Having obtained values for γ_C and γ_{Cr}, the chromium composition at the grain boundary in equilibrium with the carbide may be calculated from Eq. [2], if the assumption is made that the carbon activity is fixed by the bulk chromium composition. This assumption seems reasonable, and at typical sensitizing conditions carbon atoms are much more mobile than chromium atoms.

Grain Boundary Diffusion and Chromium Concentration Profiles

Brailsford and Aaron (18) determined the concentration of diffusant in a grain boundary during the growth of a grain boundary particle using the method described by Shewmon (19) in his solution of the mathematically analogous problem of surface diffusion from an infinite circular source. Leakage of diffusant out of the grain boundaries into the adjacent material was taken into account. This closed form solution gives the concentration of diffusant in the grain boundary after a long diffusion time and is a good approximation to that for the usual times of interest. Shewmon's solution, however, does not give accurate values for the concentration of diffusant in the material adjacent to the grain boundary, especially at large distances from the source. This is because the calculated grain boundary concentration, which is the source of the leakage flux, is much higher than actually is the case during the early stage of the diffusion. This results in overestimating the amount of diffusant that will be found adjacent to a grain boundary.

In calculating the chromium concentration around a carbide particle in a grain boundary we have made many of the same assumptions as Brailsford and Aaron, but have used a different analytical approach to the problem. The method has been described in detail elsewhere (20) so only a few comments on some of the assumptions are made here. Specifically, we have assumed that direct volume diffusion of chromium to the carbide particle can be ignored compared to that which diffuses to it along the grain boundary. Also, we have ignored the complication introduced by the fact that the boundary of the carbide particle is moving. Both of these assumptions have been discussed by Brailsford and Aaron who concluded that no significant error is introduced by invoking them provided the precipitate particles are greater than a few hundred angstroms in size and that reasonable values of the bulk and boundary diffusion coefficients were used.

Figure 4 presents calculated values for the chromium concentration in a grain boundary as a function of distance in the boundary from the carbide particle after 24 hr at 600°C. In the calculation, the following quantities were used: grain boundary width = 10Å; bulk diffusion coefficient, $D_V = 10^{-16}$ cm²/sec (21); D_{GB}/D_V (ratio of grain boundary to bulk diffusion coefficient) = 10^6; carbide radius = 1000Å; bulk Cr content = 18%; Cr content in equilibrium with carbide = 10%. The last value is derived from the thermodynamic analysis of the preceding section and is typical for these conditions. If it is assumed that in order to form a passive film a minimum of 14% chromium is required, then this calculation predicts that the grain boundary will be depleted below this level to a distance of nearly 1μ. This calculation also predicts that it is not necessary to have continuous carbide in the grain boundary for the boundary to be sensitized everywhere. For example, as a first approximation, this calculation indicates that discrete particles separated from each other in the boundary by about 2μ or so ought to lead to a continuously depleted boundary. Data supporting this prediction are presented in the next section.

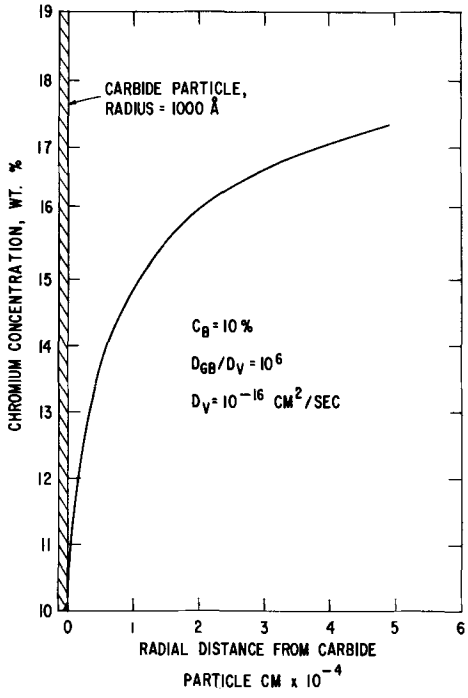

Fig. 4. Chromium concentration in grain boundary vs. radial distance from carbide particle having a radius of 1000Å. Data appropriate to 600°C were used (see text).

In addition to the chromium concentration in the grain boundary between carbide particles, it is also of interest to consider the chromium concentration gradients normal to a grain containing a carbide particle as a function of distance from the carbide. Figure 5 presents results of this calculation for the previous conditions. Note the very rapid change of concentration with distance from the grain boundary compared with the much more gradual change within the boundary (Fig. 4). These calculations indicate that, at least for these particular conditions, direct experimental determination of the chromium concentration gradient normal to a grain boundary, as with a microprobe for example, would be impossible with available instrumentation.

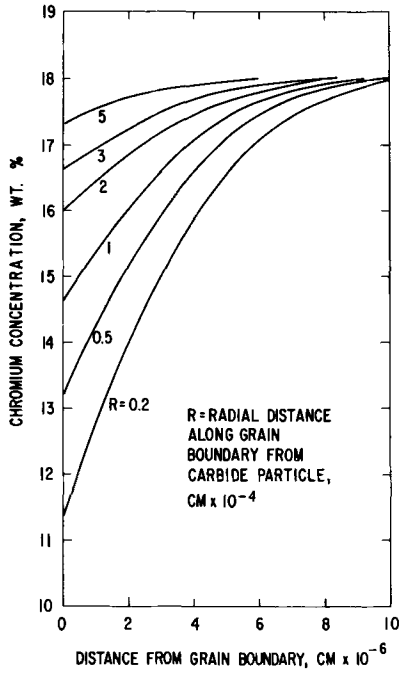

Fig. 5. Chromium concentration as a function of distance perpendicular to the grain boundary for varying distances from the carbide particle. Data appropriate to 600°C were used.

The volume of a chromium carbide particle growing in grain boundary must be consistent with the depletion of chromium and carbon integrated over the volume around the nucleation site. The shape of the particle is determined by the relative rates at which material is brought to it by diffusion along the grain boundary and that at which it is redistributed over the surface of the particle by interfacial diffusion. In the calculations referred to above, a thickness for the carbide particle was not specified, but the volume has been implicitly fixed although its shape has not.

It is evident, by reference to Fig. 4 and 5 that conditions may arise in which the grain boundary is not uniformly sensitized. This will happen when the carbide is present as discrete particles, separated by distances large enough to allow the chromium concentration in the boundary between the particles to exceed 13-15%. Experimental evidence of such nonuniform sensitization will be presented subsequently, and it will be seen that this behavior occurs in samples heat-treated in the upper end of the sensitizing range, because of the lower ratio of grain boundary to bulk diffusion coefficient.

Experimental

Two types of experiments were conducted in order to verify predictions of the theoretical considerations. The first was designed to determine the uniformity of the chromium depletion and consisted of scanning electron microscopy, transmission electron metallography, and surface replica electron metallography of thin specimens which had been sensitized and exposed to corrosive solutions. Specimens of Type 304 annealed stainless steel sheet containing 0.045% carbon were sensitized by heating in a vacuum for 24 hr at 600°C, 1 hr at 650°C, 1 hr at 700°C, 1 hr at 750°C, or 10 min at 800°C. The sensitized specimens were electropolished in an ethanol-perchloric acid-butyl cellosolve solution, exposed to a suitable corrosive solution, and examined. The two solutions used were boiling Strauss solution (10% H_2SO_4 plus 10% $CuSO_4 \cdot 5H_2O$ by weight) and 65% HNO_3 at 25°C.

The second type of experiment was designed to obtain an estimate of the grain boundary chromium content as a function of both heat-treatment and steel composition. Several commercial and experimental alloys were used in these experiments; compositions are given in Table I. The general plan was to obtain data for the rate of corrosion in boiling Strauss solution of Fe + 10 Ni + Cr alloys as a function of chromium content and then to compare the rates of grain boundary penetration in sensitized alloys with the rate *vs.* chromium content data to estimate the grain boundary chromium content. Corrosion rates of induction-melted, rolled, and annealed Fe + 10 Ni + Cr alloys were determined by measurements of weight change. Grain boundary penetration rates of sensitized specimens were determined by breaking corroded specimens in tension and measuring both the fracture stress and the depth of penetration as observed with a microscope. The specimens were in the form of wires or small rods sheared from sheet; dimensions were about 0.030 to 0.060 in. Plots of penetration *vs.* time and strength *vs.* time permitted a determination of penetration rate. Disagreement between these two rates was taken as evidence of patchy behavior, and in such cases the greater rate (always the optically determined rate) was taken.

Prior to corrosion the specimens were abraded to remove shear marks or drawing marks, and were solutionized by heating to 1100°C for 15 min, followed by water quenching. The specimens were again abraded to remove the scale, then sensitized by heating followed by water quenching or cooling at a variety of rates. After a final abrasion they were exposed to the boiling Strauss solution.

Table I. Steel compositions

Steel	Weight Percent of C	Cr	Ni	Mn	Si	P	S	N	Cu	Other
4584[1]	0.018	18.6*	9.60*	1.4*	0.47*	0.022*	0.016*	0.026*	0.05*	0.022 Mo*
4559[1]	0.037	18.8	9.75*	1.25*	0.52*	0.023*	0.018*	0.036*	0.08*	0.25 Mo*
302 AL[2]	0.05	18.7	8.10	0.44	0.32	0.019	0.026	0.06	0.15	
1213[1]	0.056	18.4	9.60	1.50	0.43	0.020	0.015	0.039	0.22	
3025[1]	0.075	17.9*	8.90*	1.53*	0.50*	0.009*	0.026*	0.045*	0.18*	0.25 Mo*
3722[3]	0.008	17.3	9.6	1.88	0.98	0.003				
3723[3]	0.028	16.8	9.3	1.85	0.97	0.003				
3724[3]	0.11	17.5	9.5	1.85	0.99	0.003				
3725[3]	0.15	16.9	9.7	1.86	0.99	0.004				
3726[3]	0.48	17.6	9.6	1.86	0.98	0.003				
3727[3]	0.97	17.0	9.6	1.88	0.98	0.004				
3696[3]	0.003	8.1	10.3	1.85	0.99	0.005	0.005			
3698[3]	0.005	10.4	10.0	2.06	1.00	0.004	0.004			
3699[3]	0.003	12.5	9.4	2.05	1.01	0.004	0.004			
3697[3]	0.003	14.3	9.7	1.99	0.99	0.004	0.005			
308[6]	0.06	20.1	10.6							
308L[5]	0.03	20.4	10.7							
309S[7]	0.06	21.7	12.9	1.50	0.48	0.014	0.015			
3734[3]	0.07	20.0	7.6	0.36		0.004				0.17 Ti
3735[3]	0.06	24.2	9.5	0.38		0.004				0.18 Ti
IN 744[4]	0.06	26.5*	6.6*	0.4*						0.2 Ti*

* Supplier's analysis.
Blanks designate not analyzed.
[1] U.S. Steel.
[2] Allegheny Ludlum Steel Company.
[3] Experimental alloy, arc-melted at R&DC.
[4] International Nickel Company.
[5] Arcos.
[6] Unknown.
[7] Rolled Alloys, Inc.

Experimental Results

Electron microscopy.—Figures 6, 7, and 8 show micrographs made from direct carbon surface replicas of the surfaces of samples sensitized at 600°, 700°, and 800°C, respectively, which were subsequently exposed to boiling Strauss solution for 10 min. Figure 6 shows that, at 600°C, the grain boundary is uniformly and severely attacked by the Strauss solution, even though the carbide is present as discrete particles and not as a continuous film. This is in agreement with the thermodynamic prediction and supports the diffusion calculation. At 700°C (Fig. 7) the boundary is still susceptible to corrosion, whereas a sensitization treatment at 800°C (Fig. 8) caused carbides to form, but no grain boundary attack occurred. According to the thermodynamic analysis, this is because the chromium content in equilibrium with the carbide exceeds the critical quantity required for passivation. It should be noted that samples sensitized at 600°C and then electropolished as described above showed the grain boundary carbides, but were otherwise generally featureless, thus demonstrating that it was the Strauss solution that produced the grain boundary attack.

Electron transmission micrographs of sensitized and corroded foil reinforce the observations made with surface replicas. Figure 9 is from a sample of this

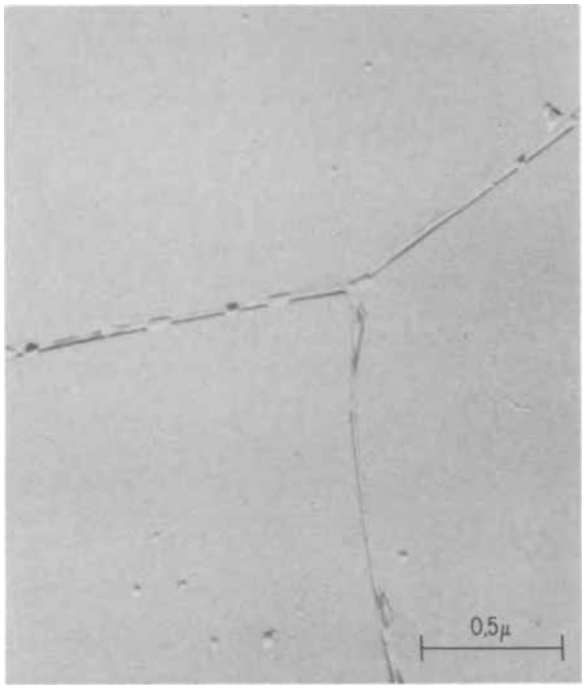

Fig. 6. Electron micrograph of surface replica from sample of Type 304 stainless steel that was sensitized at 600°C for 24 hr, then polished and exposed to a boiling Strauss solution. Note that the grain boundary attack is relatively uniform although the carbide particles do not form a continuous film. Magnification approximately 36,500X.

Fig. 7. Electron micrograph of surface replica from sample of Type 304 stainless steel that was sensitized at 700°C for 1 hr, then polished and exposed to a boiling Strauss solution. Magnification approximately 36,500X.

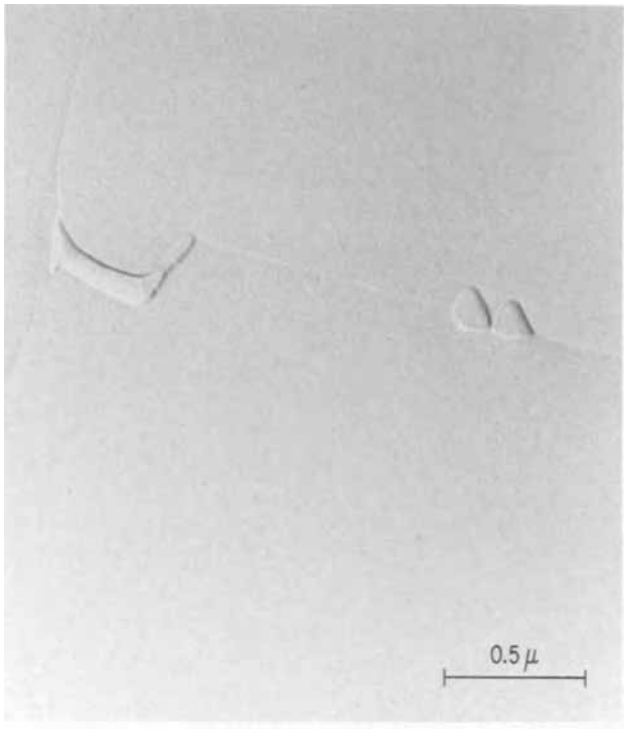

Fig. 8. Electron micrograph of surface replica from sample of Type 304 stainless steel sensitized at 800°C for 1 hr, polished, and exposed to a boiling Strauss solution. Essentially no grain boundary attack has taken place although carbides are present. Magnification approximately 37,500X.

Fig. 9. Transmission electron micrograph of Type 304 stainless steel sensitized at 700°C for 1 hr, then corroded for 10 min in boiling Strauss solution, showing "patchy" type of attack, which arises because grain boundary is not uniformly depleted in chromium. Magnification approximately 6360X.

steel that had been rolled to foil, thinned, sensitized at 700°C for 1 hr, and then exposed to a Strauss solution. In this case, the sample is too thick for significant transmission through the grains, but the corroded

Fig. 10. Transmission electron micrograph of Type 304 stainless steel sensitized at 700°C for 1 hr and then corroded for 10 min in boiling Strauss solution. Note patchy attack in boundary, and lack of attack on carbide particles. Magnification approximately 13,000X.

Fig. 11. Transmission electron micrograph of Type 304 stainless steel sensitized at 800°C for 1 hr and then corroded for 10 min in boiling Strauss solution. Note absence of attack at grain boundaries although grain boundary carbides are clearly present. Magnification approximately 7150X.

grain boundaries are evident, and it is clear that the attack is nonuniform, or "patchy." Figure 10 taken from a thinner region of the same sample provides further evidence of the "patchy" behavior, and further shows that the carbides themselves are inert. Figure 11 is from a sample sensitized at 800°C. Very little if any attack has occurred at or near the carbide particles. An attempt to make such photographs with a specimen sensitized at 600°C resulted in complete uni-

form penetration of the boundaries, and the detached grains fell off the specimen so that no thin section was left for transmission microscopy.

Summarizing the electron microscopic observations, it is evident that sensitization at 600°C produces a depleted zone which is very susceptible to attack and continuous or nearly so. A 700°C treatment produces a less susceptible, patchy boundary, while after heating at 800°C the boundary is fairly resistant.

Further evidence that the 700°C boundaries are patchy was obtained using the scanning electron microscope. A Type 304 stainless steel specimen having a carbon content of 0.076% and dimensions about 0.034 x 0.068 x 3 in. was sensitized at 700°C, corroded is boiling Strauss solution for 4238 min and pulled in tension. Although the fracture surface clearly showed that grain boundaries had been corroded even in the center of the section the specimen still had 35% of the strength of an uncorroded specimen. Figure 12 shows a photograph taken of the fracture surface with the scanning electron microscope. The fracture surface comprises flat areas of intergranular fracture and rough areas of ductile rupture. The fact that some boundaries have been attacked in the center of the specimen while some areas near the periphery were still uncorroded is convincing evidence for the patchy character of sensitization at 700°C.

Grain boundary penetration rates.—Figure 13 shows the corrosion rates of experimental alloys having a composition typical of Type 304 stainless steel, but with varying amounts of chromium. The corrosion rate increases very rapidly when the chromium content is less than 12%. Data from Osozawa and Engell (9), who measured currents in the passive region for 1M H_2SO_4 at 90°C are shown for comparison. It is probable that steels with less than 12% Cr are not fully passive in the Strauss solution.

Table II lists grain boundary corrosion rates for various steels and heat-treatments; from the experimental scatter we believe that the rates are only reproducible to about a factor or two. Several characteristics of sensitization are apparent from these data.

1. For a particular heat-treatment the corrosion rate increases rapidly with carbon content, as predicted by the theory.
2. For a given carbon content the corrosion rate decreases greatly with increasing sensitizing temperature, in agreement with the theory.
3. Slow cooling following heating at 600°-800°C results in far more severe sensitization than water quenching. The effect is very pronounced at higher sensitizing temperatures. We interpret this result to mean that carbides nucleate at the high temperatures, and that on cooling the chromium content adjacent to the carbides approaches a value characteristic of equilibrium at some lower temperature.
4. Reheating to 800°C a specimen sensitized at 600°C and water quenching renders it nonsusceptible to attack. We believe this means that the chromium content near the carbides is that appropriate to the equilibrium at 800°C.
5. Of the duplex (austenite plus ferrite) alloys (308, 308L, 309S, 3734, 3735, IN 744), only Types 308, 308L, and 309S became slightly sensitized. The interpretation for the resistance of this group of alloys is that the carbon activity is low because of the relatively high chromium to nickel ratio, and hence the equilibrium chromium content is high. The high chromium and low nickel contents also result in the duplex structure, and hence there is a correlation between the presence of ferrite and resistance to sensitization.

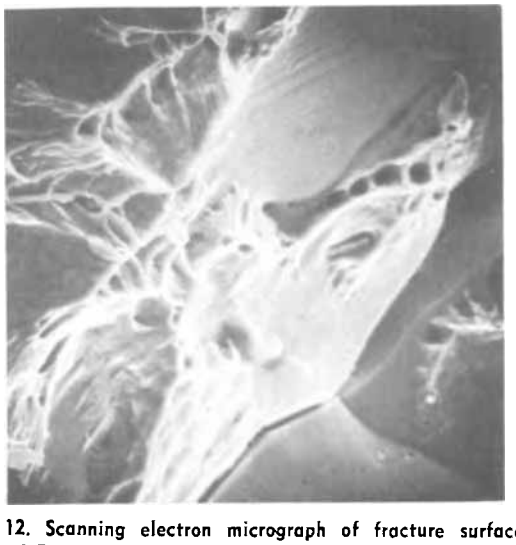

Fig. 12. Scanning electron micrograph of fracture surface of sample of Type 304 stainless steel that was sensitized at 700°C for 1 hr, exposed to boiling Strauss solution, then pulled in tension. Intergranular attack occurred throughout sample, but was "patchy" because the grain boundaries were not uniformly depleted in chromium. Flat facets show areas of intergranular attack; characteristic regions of ductile rupture indicate areas where chromium depletion did not occur. Magnification approximately 1000X.

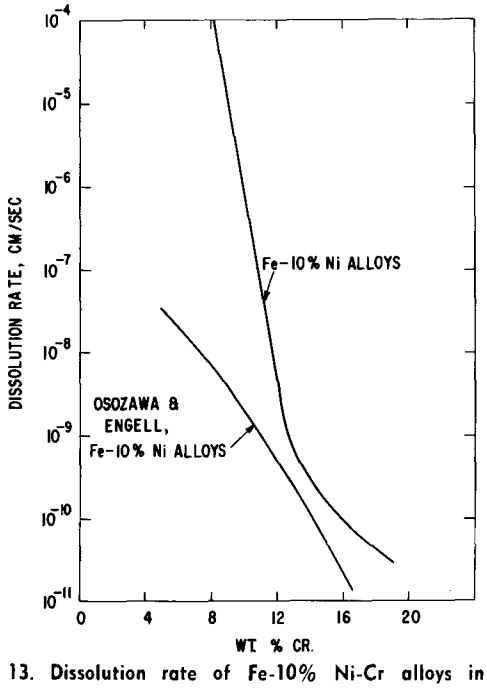

Fig. 13. Dissolution rate of Fe-10% Ni-Cr alloys in boiling Strauss solution as a function of Cr content.

From the data in Table II it is possible to make a quantitative comparison of the experimental results with the thermodynamic theory. The grain boundary penetration rates from Table II are first compared with the data in Fig. 13 to estimate the chromium content in the depleted zone along the boundary. Figure 14 compares data so obtained with the predictions of the thermodynamic theory. While the experimental points for a given temperature suggest a less pronounced variation of equilibrium chromium concentration with carbon content than predicted by the theory the general agreement is very satisfactory. The method is limited to chromium contents between about 9 and 12% because at higher chromium contents the rate is too slow to measure conveniently while at lower chromium contents the rate is limited by diffusion through the grain boundary crevice. Also included in this plot for comparison are results from Stawström and Hillert (adapted from Fig. 9 of their paper). Their curves are derived for a steel containing 8% nickel, so minor variation might be expected from this composition difference. It is evident that at 600°C, both calculated curves are in good agreement with the experimental

Table II. Grain boundary corrosion rates in Strauss solution

Steel	Weight % carbon	Sensitization treatment Temp, °C	Time	Cooling rate	Grain boundary corrosion rate, cm/sec
4584	0.018	600	24 h	slow[1]	$<10^{-9}$
		700	1 h	slow	$<10^{-8}$
		800	10 m	slow	$<10^{-9}$
		800	10 m	W.Q.[2]	$<10^{-9}$
3723	0.028	600	24 h	W.Q.	1×10^{-8}
		650	1 h	W.Q.	4×10^{-9}
		750	1 h	W.Q.	4×10^{-9}
4559	0.037	600	24 h	slow	9×10^{-8}
		600	24 h	slow	$>8 \times 10^{-8}$
		600	24 h	W.Q.	8×10^{-7}
		700	1 h	slow	9×10^{-8}
		800	10 m	slow	$<10^{-10}$
302 AL	0.05	600	24 h	slow	2×10^{-7}
		600	24 h	W.Q.	8.3×10^{-7}
		700	1 h	slow	2×10^{-8}
		700	1 h	W.Q.	$<2 \times 10^{-9}$
1213	0.056	600	24 h	slow	9×10^{-7}
		600	24 h	slow	8×10^{-8}
		700	1 h	slow	1.3×10^{-7}
		700	1 h	W.Q.	1.7×10^{-8}
		800	10 m	W.Q.	$<10^{-10}$
3025	0.075	600	24 h	slow	3×10^{-6}
	Followed by	600	24 h	slow	$<10^{-8}$
		800	10 m	W.Q.	
		600	24 h	slow	8×10^{-7}
		600	24 h	W.Q.	2.4×10^{-6}
3025	0.075	700	1 h	slow	1×10^{-8}
		700	1 h	W.Q.	5×10^{-8}
		800	10 m	slow	1×10^{-8}
		800	10 m	W.Q.	$<10^{-9}$
3724	0.08	600	24 h	W.Q.	5×10^{-6}
		650	1 h	W.Q.	7×10^{-7}
		700	1 h	W.Q.	5×10^{-8}
3725	0.15	600	24 h	W.Q.	3×10^{-5}
		650	1 h	W.Q.	3×10^{-6}
		700	1 h	W.Q.	1×10^{-6}
		750	1 h	W.Q.	7×10^{-8}
		800	10 m	W.Q.	$<2 \times 10^{-8}$
3726	0.48	800	10 m	W.Q.	3×10^{-7}
3727	0.97	800	10 m	W.Q.	4.5×10^{-6}
308	0.06	600	24 h	W.Q.	2×10^{-7}
308L	0.03	600	24 h	W.Q.	1.2×10^{-8}
309S	0.06	600	24 h	W.Q.	3.6×10^{-8}
3734	0.07	600	24 h	W.Q.	$<10^{-9}$
		700	1 h	W.Q.	$<10^{-9}$
3735	0.06	600	24 h	W.Q.	$<10^{-7}$
		700	1 h	W.Q.	$<10^{-9}$
IN 744	0.06	475	24 h	slow	$<10^{-9}$
		600	24 h	slow	$<10^{-9}$
		700	1 h	slow	$<10^{-9}$
		800	10 m	slow	$<10^{-9}$
		800	10 m	W.Q.	$<10^{-10}$

[1] "Slow" means cooled in a furnace. Cooling rate about 0.05°C/sec to 0.2°/sec.
[2] "W.Q." means water-quenched.

data. At 700°C, the agreement is fair. At 800°C, there is considerable difference between the two calculated curves; the experimental data appears to be more in agreement with our result. At 500°C, there is again a significant difference between our result and that of Stawström and Hillert; however, we have no experimental data to support either calculation.

It should be noted that our method of experimentally estimating grain boundary compositions may overestimate the chromium content of the boundaries for two reasons. First, if the grain boundary depletion is patchy the measured penetration rate may be slower than that corresponding to the average depletion. Second, the coupling of the grain boundary region to the matrix may result in passivation of a lower chromium alloy than can be passivated when not coupled, so that the observed corrosion rate would again be too low. It is difficult to estimate the magnitude of the possible errors.

In an effort to obtain more information about the effect of cooling rate from the sensitizing temperature, several solutionized specimens of 3025 alloy were annealed at 700°C and water-quenched, followed by reheating at 500°, 550°, and 600°C. The rates of grain

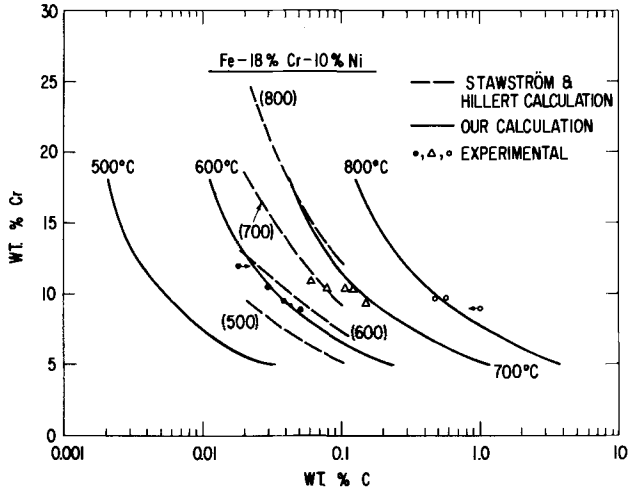

Fig. 14. Comparison of Cr-C-$Cr_{23}C_6$ equilibrium data for Type 304 stainless steel with experimentally obtained corrosion data, for several temperatures.

boundary penetration for these specimens were 4×10^{7}, 1.1×10^{-6}, and 1.1×10^{-6} cm/sec, respectively. A control specimen annealed for only 1 hr at 600°C did not corrode noticeably in 360 min, so the rate was $<10^{-7}$ cm/sec.

It is known from Fig. 6, 8, and 9 that carbides are formed at 700°C. These experiments show that it is possible to form carbides at 700°C, but that the chromium depletion is not severe enough even in an alloy with 0.075% to result in sensitization. Reheating to 500°-600°C allows the attainment of a lower chromium content in the grain boundary and susceptibility to attack.

Discussion

With the thermodynamic analysis presented earlier, it is possible to make quantitative chromium-carbon equilibria predictions for other alloys in addition to Type 304 steels. Figure 15 presents calculated carbon-chromium equilibrium values for various sensitizing temperatures for a nominal Fe-25% Cr-20% Ni alloy. This composition is characteristic of Type 310 austenitic stainless steel. In alloys of this type, the chromium level is increased to provide increased oxidation resistance, and the nickel is also increased in order to keep the alloy austenitic. From the point of view of increased resistance to intergranular attack, however, there is relatively little improvement over Type 304 because the effect of the increased chromium content on lowering the activity coefficient of carbon is largely offset by the effect of nickel on raising γ_C.

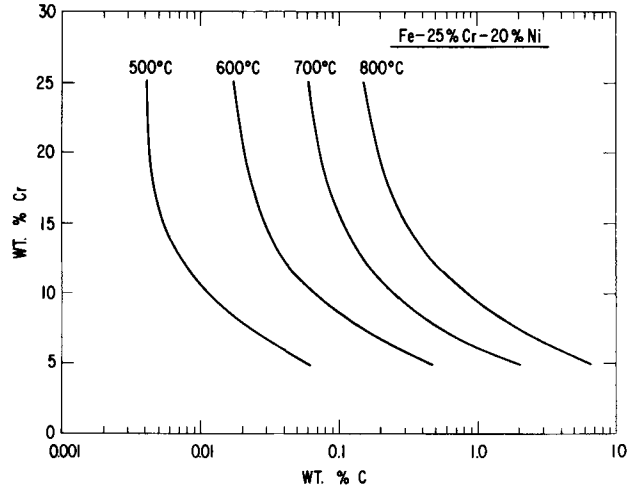

Fig. 15. Calculated Cr-C-$Cr_{23}C_6$ equilibria for Type 310 stainless steels (Fe-25% Cr-20% Ni) for several temperatures.

The data presented in Table II showed that duplex stainless steels were very resistant to intergranular attack. There are also data from the literature (22, 23) that agree with this. We interpret this as follows. In order to make the steel duplex, that is, have both austenitic and ferritic phases present, either the nickel content (austenite stabilizer) is decreased or the chromium content (ferrite stabilizer) is increased, or both. The effect of either is to lower γ_C and for a given carbon content, the carbon activity is therefore lowered. From Eq. [2] it is therefore expected that the equilibrium chromium content X_{Cr} will be higher.

A quantitative discussion is difficult because the compositions of the two phases are generally not known, especially with respect to the carbon distribution. One approach is to ignore the fact of two phases and simply to calculate the chromium content as if the alloy were homogeneous. Results from this calculation are presented in Fig. 16. It may be seen by comparison with austenitic steels (Fig. 14 and 15) that the duplex steels can tolerate much more carbon without becoming susceptible to sensitization.

The effect of the existence of two phases on the behavior of duplex alloys can be rationalized as follows. It is known that the ferrite phase of such alloys is enriched in chromium and depleted in nickel (24). Because of the dependences of γ_C on nickel and chromium contents we therefore expect the ferrite phase to be enriched in carbon. We may therefore expect that during annealing at 500°-850°C carbides will precipitate at the ferrite grain boundaries, but because of the generally low carbon activity X_{Cr} will still be high enough to prevent sensitization. In the austenite grains the chromium will be relatively low and the nickel high, but again the carbon activity will be low in the entire alloy, and hence the austenite grain boundaries will not be susceptible to sensitization either. We expect that the austenite grains of a 26% Cr-6% Ni steel with 0.08% C might have a composition approximating Type 304L (18% Cr-10% Ni-0.02% C).

Another fact made clear by these considerations is the mechanism of weld sensitization of Type 304 stainless. Our isothermal studies show that for 304 with about 0.05% carbon a temperature of 600°C is required to cause sensitization, and that at least several hours at 600°C are needed. The area near the weld is not heated long enough at 600°C to allow carbide precipitation. However, nearer to the weld the steel is heated to the range 700°-750°C, where carbide nucleates within minutes. Then on cooling through the range 500°-650°C the chromium content near the carbide is decreased toward values appropriate for the lower temperature and the steel becomes susceptible.

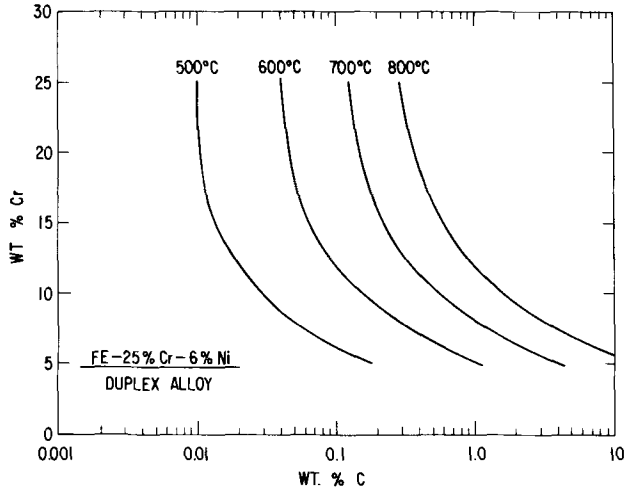

Fig. 16. Calculated Cr-C-$Cr_{23}C_6$ equilibria for Fe-25% Cr-6% Ni duplex stainless steel, for several temperatures.

Reheating to 700°-800°C and water quenching would restore immunity.

Although the thermodynamic analysis has been concerned primarily with the effects of carbon, chromium, and nickel on γ_C, it is of interest to consider the effect of other elements commonly found in stainless steels. Impurities such as phosphorous, sulfur, and nitrogen will probably have relatively little effect on γ_C, because although the derivative terms $\partial \ln \gamma_C/\partial X_i$ may be large, the mole fractions X_i will be small and consequently the product $X_i \cdot (\partial \ln \gamma_C/\partial X_i)$ will be small. An interesting case to consider, however, is that of manganese, which has been used as an austenite stabilizer when nickel was in short supply. It is generally recognized that these steels are less susceptible to intergranular corrosion than their nickel-containing counterparts. The interpretation in terms of thermodynamic behavior of these elements is that whereas nickel acts to increase γ_C the effect of manganese is just the opposite (25), so that in manganese-stabilized steels the carbon activity is lower and the chromium content in equilibrium with the carbide is higher than in the corresponding nickel-stabilized steels.

It is known that solutionized and quenched austenitic stainless steels can be made to corrode intergranularly in highly oxidizing solutions such as HNO_3-Cr^{+6}(5,6), or by potentiostatic corrosion at very high potentials in H_2SO_4 (26). It must be emphasized that corrosion in these environments is fundamentally different for several reasons from that which occurs when sensitized steel is exposed to less oxidizing solutions such as in a Strauss or Huey test. Both uniform surface corrosion as well as intergranular attack take place in these highly oxidizing environments, presumably because they can oxidize Cr^{+3} in the passive film to Cr^{+6} which is soluble. Such oxidation may require the transport of electrons through the oxide film to the metal. Impurities segregated at grain boundaries (5) could locally increase the electronic conductivity of the passive film, thereby facilitating the oxidation and corrosion at grain boundaries (27).

Comment should be made concerning some of the assumptions used in the thermodynamic analysis. First, the principal justification for the basic assumption that these stainless steels are "dilute" alloys (see Appendix) is the success of the model in quantitatively predicting the compositional and temperature dependence of intergranular corrosion of sensitized steel, of weld sensitization, and of the immunity of duplex alloys for intergranular corrosion. It was pointed out earlier that the activity coefficient of chromium was treated as a semiadjustable parameter; that is, using calculated data for γ_C and experimental corrosion data, γ_{Cr} at 600°C was derived. Although it must be admitted that obtaining activity coefficients from corrosion data is not a standard method, we feel it provides reasonable values. Further, the values thus obtained are in very good agreement with Goodell, who from chromium-nitrogen-nitride solubility data for austenitic stainless steel obtained $\gamma_{Cr} \approx 3.1 - 3.5$ at 650°C (28).

Although the approach used here is similar in principle to that of Stawström and Hillert, it differs considerably in detail and yields somewhat different results and predictions. First, it was demonstrated experimentally that their assumption of uniform grain boundary composition is inadequate in certain cases, and, in fact, patchy grain boundary corrosion may result as a consequence of large variations in the chromium content in the boundary. Second, the Wagner analysis permits predictions to be made of the effect of various alloying elements for which interaction coefficient ($\partial \ln \gamma_C/\partial X_i$) data are available. The Stawström-Hillert method leads to the prediction that the carbon solubility in stainless steels increases beyond about 20% chromium. To account for this, they suggest

that the chromium-carbon interaction parameter may be composition dependent, but there are no experimental data to support their prediction, and it seems more likely that it is a result of the method of calculation.

In summary, the theoretical predictions are well supported by the experimental study, and we believe that they are plausible. It is therefore our contention that the chromium content in equilibrium with the carbide particles is a strong function of the steel composition and of the sensitizing temperature and can be predicted by the thermodynamic theory. Furthermore, because of rapid grain boundary diffusion, the chromium depletion may be reasonably uniform despite a considerable separation of carbide particles. When "patchy" behavior is encountered it will generally be more pronounced at higher heat-treatment temperatures, because of the lower ratio of grain boundary to bulk diffusion coefficient. Our results demonstrate that the degree of sensitivity is controlled primarily by the thermodynamically controlled minimum chromium content, with morphological features of carbide particles playing a secondary role.

Acknowledgments

The authors are greatly indebted to D. E. Broecker and Mrs. C. F. Kirk who carried out much of the experimental work, to E. F. Koch for the electron microscopy, and to Dr. E. Lifshin and R. Bolon for the scanning electron microscopy. The Metals Processing Unit provided many of our test alloys, and their assistance is appreciated. The kindness of the International Nickel Company for providing samples of their experimental alloy IN 744 is gratefully acknowledged. We are also indebted to the United States Steel Company for samples of Type 304 steel with varying carbon contents. Stimulating discussions with Dr. H. S. Spacil and Professor J. F. Elliott of the Massachusetts Institute of Technology were very helpful in developing the thermodynamic analysis.

APPENDIX

Calculation of Carbon Activity Coefficients by the Wagner Analysis

Wagner derived an expression for the logarithm of the activity coefficient of a particular alloying component by a Taylor series expansion of the excess partial molar free energy. Thus, for carbon in iron with mole fractions X_i of the various other solute element, one obtains

$$\ln \gamma_C = \ln \gamma^\circ_C + \left[x_c \frac{\partial \ln \gamma_C}{\partial x_C} + x_{Ni} \frac{\partial \ln \gamma_C}{\partial x_{Ni}} + x_{Cr} \frac{\partial \ln \gamma_C}{\partial x_{Cr}} \right] + \left[\tfrac{1}{2} x^2_c \frac{\partial^2 \ln \gamma_C}{\partial x_C^2} + x_C x_{Ni} \frac{\partial^2 \ln \gamma_C}{\partial x_C \, \partial x_{Ni}} + \dots \right] \quad [1A]$$

The higher order terms which appear within the second set of brackets can usually be neglected; they are generally small because the product $x_i x_j$ is small. Also, values for the cross-term derivatives are usually lacking. In principle, the expansion may be made around any composition of interest, but data for evaluation of the derivative terms $\partial \ln \gamma_C / \partial x_i$ are available only for the constituent binary systems. Consequently in practice the expansion is really made around the compositional origin, *i.e.*, at $x_{Fe} \rightarrow 1$, and the derivatives are evaluated for the limiting case of zero concentration of all solutes. Hence, calculations based on this procedure are implicity applicable to dilute solutions only and extension to evaluation of γ_C for stainless steels is based on the assumption that the alloy is a "dilute" solution. With these assumptions, and considering stainless steel to be a solution only of carbon, nickel, and chromium in iron, Eq. [1A] is simplified to

$$\ln \gamma_C = \ln \gamma^\circ_C + x_C \frac{\partial \ln \gamma_C}{\partial x_C} + x_{Ni} \frac{\partial \ln \gamma_C}{x_{Ni}} + x_{Cr} \frac{\partial \ln \gamma_C}{\partial x_{Cr}} \quad [2A]$$

Data for the derivative terms in Eq. [2A] can be obtained from the literature (25, 29). In general the data are not available for the temperature range of interest (500°-800°C). Therefore, the activity coefficient is calculated for the temperature at which the data are available, and the temperature dependence is then estimated by assuming a regular (Hildebrand-type) solution, yielding the following expression

$$\ln \gamma_C = \frac{H^m}{RT} \quad [3A]$$

It is reasonable to assume that the enthalpy of mixing, H^m, is not significantly a function of temperature at least over a relatively small range of temperature. Therefore, if γ_C is known at one temperature, it can be estimated at other temperatures using Eq. [3A].

Equation [2A] was evaluated using the data of Heckler and Winchell (29) and Chipman and Brush (25). Conversion was made to a graphite standard state. It is readily apparent that an advantage of this approach is that the effects of the various alloying elements on the carbon activity coefficient are made explicit in Eq. [2A].

Manuscript submitted March 26, 1970; revised manuscript received *ca.* Sept. 18, 1970.

Any discussion of this paper will appear in a Discussion Section to be published in the December 1971 JOURNAL.

REFERENCES

1. E. C. Bain, R. H. Aborn, and J. J. B. Rutherford, *Trans. Amer. Soc. Steel Treating*, **21**, 481 (1933).
2. A. Baumel, H. E. Bühler, H. J. Schüller, P. Schwaab, W. Schwenk, H. Ternes, and H. Zittner, *Corr. Sci.*, **4**, 89 (1964).
3. R. Stickler and A. Vinckier, *Trans. ASM*, **54**, 362 (1961).
4. K. T. Aust, J. S. Armijo, E. F. Koch, and J. H. Westbrook, *ibid.*, **61**, 271 (1968).
5. K. T. Aust, *Trans. TMS-AIME*, **245**, 2117 (1969).
6. J. S. Armijo, *Corrosion*, **24**, 24 (1968).
7. P. J. Gellings and M. A. deJongh, *Corr. Sci.*, **17**, 413 (1967).
8. K. Shiobura, Y. Sawada, and S. Marioka, *Trans. Jap. Inst. Metals*, **6**, 58 (1969).
9. K. Osozawa and H. J. Engell, *Corr. Sci.*, **6**, 389 (1966).
10. B. E. Hopkinson and K. G. Carrol, *Nature*, **184**, 1479 (1959).
11. S. Alm and R. Kiessling, *J. Inst. Metals*, **91**, 190 (1962-63).
12. R. J. Bendure, L. C. Ikenberry, and J. H. Waxweiler, *Trans. TMS-AIME*, **221**, 1032 (1961).
13. C. Stawström and M. Hillert, *J. Iron Steel Inst.*, **207**, 77 (1969).
14. Ref. (18) of paper by Stawström and Hillert.
15. F. D. Richardson, *J. Iron Steel Inst.*, **167**, 33 (1953).
16. C. Wagner, "Thermodynamics of Alloys," p. 51, Addison-Wesley, Reading, Mass. (1952).
17. A concise summary of thermodynamic data for the Fe-Cr system is given in Hultgren *et al*, "Selected Values of Thermodynamic Properties of Metals and Alloys," John Wiley & Sons, Inc., New York (1963).
18. A. D. Brailsford and H. B. Aaron, *J. Appl. Phys.*, **90**, 1702 (1969).
19. P. G. Shewmon, *ibid.*, **34**, 755 (1963).
20. J. H. Rosolowski, "Surface Diffusion From a Point Source Including Effect of Volume Diffusion Into the Bulk," presented at the 1969 ASM Materials Engineering Congress, Philadelphia, October 13-16, to be published.
21. C. J. Smithells, "Metals Reference Book," Vol. II, 4th ed., Plenum Press, New York (1967).
22. R. C. Gibson, H. W. Hayden, and J. H. Brophy, *ASM Trans. Quart*, **61**, 85 (1968).
23. L. Colombier and J. Hochmann, "Stainless and Heat-resisting Steels," St. Martin's Press, New York (1965).

24. S. Floreen and H. W. Hayden, *Trans. Quart, ASM*, **61**, 489 (1968).
25. J. Chipman and E. F. Brush, *Trans. TMS-AIME*, **242**, 35 (1968).
26. J. S. Armijo, Private communication.
27. D. A. Vermilyea and C. S. Tedmon, Jr., *Metallurgical Trans.*, **1**, 1076 (1970).
28. P. G. Goodell, Private communication.
29. A. J. Heckler and P. C. Winchell, *Trans. TMS-AIME*, **227**, 732 (1963).

The Kinetics of Hydrogen Absorption into Iron during Cathodic Hydrogen Evolution

C. D. Kim and B. E. Wilde*

Applied Research Laboratory, United States Steel Corporation, Monroeville, Pennsylvania 15146

ABSTRACT

An electrochemical technique has been developed with which the steady-state concentration of adsorbed hydrogen on an iron surface, θ, can be determined. By using values of θ determined by electrochemical techniques, a method of evaluating the specific rate constant for hydrogen absorption into iron, k_{abs}, has been developed. Values of θ determined on a cathodically polarized iron surface in 0.0001*N* sodium hydroxide + 0.1*M* sodium sulfate were between 5 and 12% of the total monolayer coverage, over the current-density range 10-300 μA/cm^2. This current-density range represents a hydrogen generation rate equivalent to a corrosion rate of 5-150 mils penetration per year. The variation of θ with cathodic overpotential was in close agreement with theory; values of $\delta\eta/\delta \log_{10} \theta$ were 3.5 V/decade measured experimentally and 4.2 V/decade theoretically. Experimental values of θ permit, for the first time, determination of the specific rate constant for the absorption reaction.

The application of high-strength steels in aqueous corrosive environments is often limited by their susceptibility to hydrogen embrittlement. In general, the higher the yield strength of the alloy, the more susceptible to cracking it becomes. Many workers have studied this problem in attempts to correlate cracking propensity with chemical composition and microstructure (1-5). Most of the approaches to date, however, have been empirical and have not led to a successful solution to the problem. Consequently, steels with yield strengths in excess of 80 ksi are susceptible to hydrogen embrittlement in environments capable of promoting hydrogen entry into the steel.

Because the source of the problem is the absorption of hydrogen into the steel as a result of either (*a*) corrosion, (*b*) electroplating, or (*c*) cathodic protection, we have chosen a new approach in which the kinetics of the hydrogen absorption process are determined. This approach is new in that it studies the aqueous side of the steel/environment interface as opposed to metallurgical studies which are concerned with the solid solution side of the interface. Such a study may indicate some way to hinder the absorption process and thereby preserve or extend the life of the steel without loss of mechanical properties.

Theoretical Background

Almost all the hydrogen embrittlement encountered in practice results from one or more of the above-mentioned processes occurring in aqueous environments. During such reaction, hydrogen is generated on the steel surface by the mechanisms described elsewhere (8). From the viewpoint of the present investigation, the rate of the reaction in Eq. [1] is the critical factor, and depends simply on the specific rate constant k_{abs} and the steady-state concentration of hydrogen atoms on the surface, θ. The present work is concerned with the evaluation of θ and the effect of environmental and metallurgical variables on k_{abs}.

$$H_{adsorbed} \underset{k_{des}}{\overset{k_{abs}}{\rightleftharpoons}} H_{absorbed} \qquad [1]$$

To date no successful evaluation of k_{abs} for hydrogen absorption in steel from aqueous solutions has been made. The reason for this is the extreme difficulty in measuring θ on iron and steel surfaces. The work of the Bockris school is noteworthy in pioneering the development of techniques for measuring θ, but has largely been confined to face-centered-cubic materials such as nickel, silver, etc. (6-11). There have, however, been a few attempts (12, 13) to apply these techniques to body-centered-cubic materials, but problems have been encountered because of the enhanced hydrogen diffusivity in bcc metal and increased metal dissolution rates.

As a starting point, we selected the galvanostatic pulse technique (10) and applied an analysis to correct for both the above problems and make this technique applicable to ferrous materials. Briefly, the principle of this technique is the rapid electrochemical oxidation of adsorbed hydrogen on the metal surface by an anodic pulse. For simplicity, a steady-state θ was maintained by the use of a constant cathodic current applied to the iron in dilute alkaline solution, rather than by direct corrosion of the iron in more acidic environments. Upon application of a relatively large anodic current, i_a, the potential transient varies in shape depending on the steady-state value of θ. Under these conditions, the change in electrode potential with time can be described as

$$\left(\frac{dV}{dt}\right)_i = \frac{1}{C_V}\left[i_a - i_H - i_{ox}(1-\theta)\right] \qquad [2]$$

where i_H is the partial current used to oxidize the adsorbed hydrogen on the surface, $i_{ox}(1-\theta)$ is the partial current used to oxidize the iron, and C_V is the capacity of the electrical double layer at potential V. If the iron surface is oxidized as above, without the presence of adsorbed hydrogen, the transient (dV/dt)

* Electrochemical Society Active Member.

Key words: hydrogen absorption, surface coverage, hydrogen diffusion, electrochemical oxidation, electrode kinetics.

becomes

$$\left(\frac{dV}{dt}\right)_2 = \frac{1}{C_v}[i_a - i_{ox}] \quad [3]$$

From Eq. [2] and [3], it can be seen that the term $(i_H - i_{ox}\theta)$ is given by

$$(i_H - i_{ox}\theta) = C_v\left[\left(\frac{dV}{dt}\right)_2 - \left(\frac{dV}{dt}\right)_1\right] \quad [4]$$

To evaluate Eq. [4], we must determine C_v from Eq. [3] at potentials close to the reversible H_2 potential and assume that i_{ox} is negligibly small. This latter assumption is made on the basis of data to be presented in the discussion and is at present being verified by experiments designed to determine C_v by methods independent of those used in Eq. [3] (14). The area under the curve obtained by plotting $(i_H - i_{ox}\theta)$ against time is equivalent to the amount of adsorbed hydrogen on the iron surface.

Values of θ determined in the above manner can be used in conjunction with hydrogen permeation measurements to evaluate k_{abs}. The principles of the permeation techniques used are as follows. Consider the permeation of hydrogen through an iron membrane, where one side of the membrane is maintained at a constant cathodic overpotential to produce a steady-state value of θ. Let hydrogen be oxidized electrochemically at the opposite side at a rate fast enough to maintain a zero concentration at all times. Under these conditions, the transfer of hydrogen through the membrane may be considered in the following stages.

(*i*) Transference of the adsorbed hydrogen from the surface into the metal matrix. At steady state, the net input flux J_∞ is given by

$$J_\infty = k_{abs}\theta - k_{des}C_o \quad [5]$$

where k_{des} is the rate constant for the desorption process at the entry surface, and C_o is the concentration of metallic hydrogen at the entry surface.

(*ii*) Diffusion of hydrogen within the membrane. At steady state

$$J_\infty = \frac{D}{L}(C_o - C_e) \quad [6]$$

where C_e is the concentration of hydrogen at the exit side (*i.e.*, zero) and L is the thickness of the membrane.

(*iii*) Oxidation of the diffusing hydrogen at the exit surface, which is palladium-plated (13), to avoid problems associated with metal dissolution and hydrogen bubble formation. From Eq. [5] and [6], it can be seen that

$$\frac{1}{J_\infty} = \frac{L}{D\theta}\cdot\frac{k_{des}}{k_{abs}} + \frac{1}{k_{abs}\theta} \quad [7]$$

This equation is similar to that derived previously (13) but had been modified to eliminate an error arising from an incorrect assessment of the boundary conditions prevalent at the input and exit surfaces. By plotting $1/J_\infty$ against L for various membrane thicknesses, $1/(k_{abs}\theta)$ can be evaluated, and because θ is known from previous experiments, k_{abs} can be determined.

Materials and Experimental Work

The apparatus used for the determination of θ is shown schematically in Fig. 1. One compartment contained a platinized platinum electrode which served as a reference. Another compartment contained a bright platinum auxiliary electrode and the central compartment contained the working electrode (iron). The iron electrode, of the composition shown in Table I, was machined to 5 mm diameter by 10 mm long and was prepared by abrasion with silicon carbide paper down to a 600 grit finish. The electrode was mounted on a Stern-Makrides (15) holder and placed in the cell. All three compartments were continuously washed

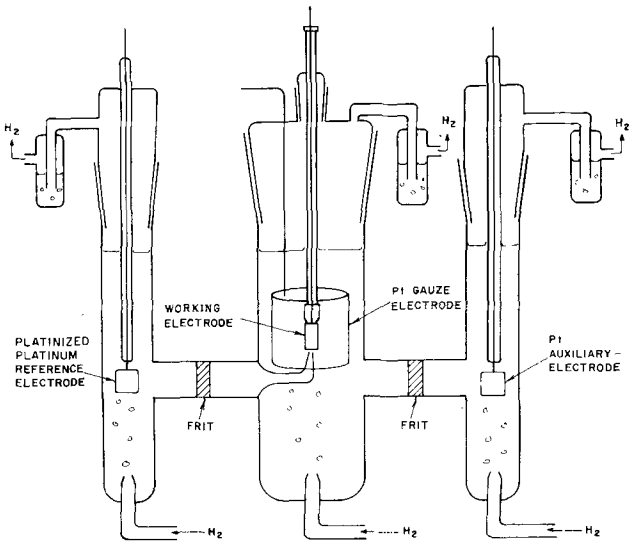

Fig. 1. Schematic representation of polarization assembly

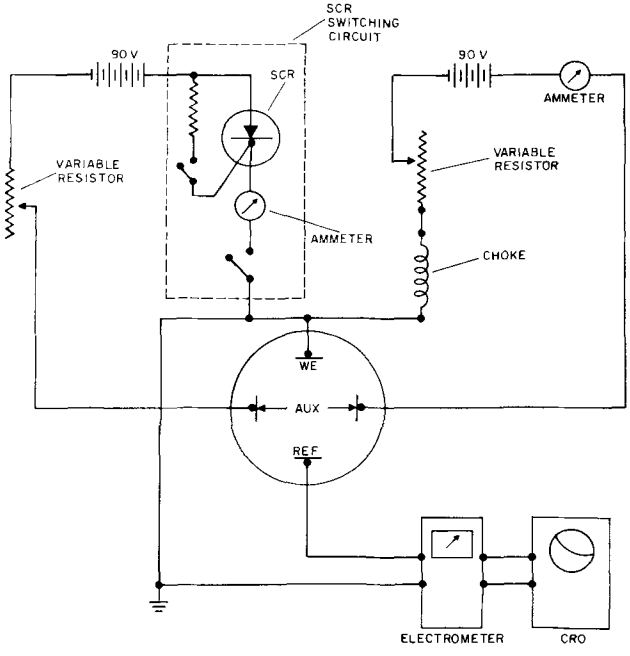

Fig. 2. Schematic representation of electrical circuit

with palladium-purified electrolytic hydrogen.[1] An additional platinum gauze electrode was placed circumferentially around the iron electrode to serve as a cathode during the anode pulsing.

The electrolyte was 0.0001*N* NaOH + 0.1*M* Na_2SO_4 made from reagent-grade chemicals and distilled water (7.6 megohm cm) to give a final *p*H of 9.5 at 25°C. To enhance experimental reproducibility, the electrolyte was pre-electrolyzed on a bright platinum cathode at 30 mA for 12 hr prior to experimental use.

The electrical circuit used is shown in Fig. 2. Two separate polarization circuits were superimposed on the test electrode as previously described (10): one to maintain a constant value of θ on the iron surface by a constant cathodic current, and the other to apply the anodic pulse used to oxidize the adsorbed hydrogen. A high-capacity choke was used to isolate the two

[1] Matheson Generator, Model ER-150.

Table I. Chemical composition of Ferrovac E iron, per cent

C	Mn	P	S	Si	Ni	Cr	H	Mo
0.002	0.001	0.002	0.005	0.007	0.02	0.001	0.0001	0.003

circuits. Electrode potentials were measured with a Keithley electrometer (Model 610 B), which was also used as an amplifier to drive the Y axis of an oscilloscope (Tektronix Model 564). To achieve almost instantaneous turn-on of the anodic pulse, a silicon rectified switching system (SRC) was employed, as shown in Fig. 2. Two 90V dry cells were used as current sources.

To establish the potential transient for $i_H = 0$, the iron electrode was immersed in the electrolyte and was polarized to 20 mV more positive than the reversible hydrogen potential. When a steady-state overpotential was established, an anodic galvanostatic pulse was applied to the iron (35 mA/cm^2), and the potential transient was recorded on the oscilloscope with a Polaroid camera attachment. A fresh iron electrode was then cathodized at a constant current for several hours to establish a steady-state θ and a uniform absorbed hydrogen concentration in the electrode. This electrode was then subjected to a 35 mA/cm^2 anodic pulse, and the transient recorded. Data at various values of θ were determined as above by using different cathodic polarizing currents. We have chosen in this study to express θ in coulomb/cm^2 or grams hydrogen/cm^2 as in Fig. 6. However, previous workers have expressed θ in terms of the fraction of the surface covered with a monolayer of hydrogen. This latter method assumes a 1:1 iron to hydrogen ratio on a (100) plane of the body-centered-cubic cell, having a total of 192 μcoulomb/cm^2 for full coverage. Our data is also presented this way in Fig. 7, although the rate constant k_{abs} is calculated on θ in grams H/cm^2.

Permeation studies were conducted in the manner previously described (16), except that the oxidation side of the membrane was maintained at +100 mV_{SCE} in 1*N* NaOH solution at 25°C and was palladium-plated to prevent loss of sensitivity due to other reactions taking place in preference to hydrogen oxidation.

Results and Discussion

Anodic and cathodic polarization curves were determined potentiostatically (Wenking Model 66 TS-3), from which Tafel constants of +0.041 and −0.127V were obtained. It is important to note that the above constants were not influenced over two decades of applied current by the saturation of the iron electrode with hydrogen in solid solution.

Potential transients were determined over various values of θ; typical results are shown in Fig. 3 for a cathodic current density of 100 μA/cm^2. Values of $(dV/dt)_1$ and $(dV/dt)_2$ were evaluated at various potentials for Fig. 3 and were used to determine $(i_H - i_{ox}\theta)$ from application of Eq. [4]. Values of $(i_H - i_{ox}\theta)$ plotted against pulse time are shown in Fig. 4 and represent the amount of hydrogen adsorbed on the iron surface at a given cathodic current, along with an error term resulting from the oxidation of hydrogen dissolved in solid solution over the time period of the pulse.

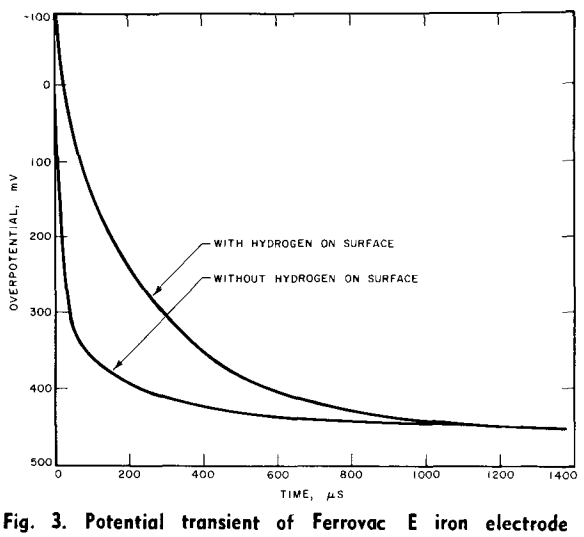

Fig. 3. Potential transient of Ferrovac E iron electrode in 0.0001*N* NaOH + 0.1*M* Na_2SO_4 solution (i_{ca} = 100 μA/cm^2; i_a = 35 mA/cm^2).

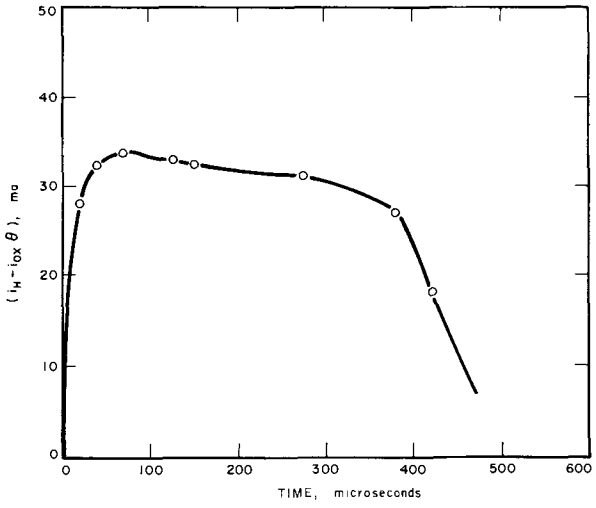

Fig. 4. (i_H-i_{ox}) calculation at various times

To correct θ for this error term, the following analysis was applied. Assume that the dissolved hydrogen was uniformly distributed in the iron and that the concentration at the electrode surface remains zero at all times during the anodic pulse. Under these conditions, a solution to the diffusion equation can be derived for a cylindrical specimen geometry, in terms of Q, the quantity of hydrogen remaining in the iron at time, t

$$Q = \frac{32\, C_0 \rho^2 L}{\pi} \left[\sum_{n=0}^{\infty} \frac{\exp\left[-(2n+1)^2 \pi D t/L^2\right]}{(2n+1)^2} \right] \times \left[\sum_{n=1}^{\infty} \frac{\exp\left[-D \cdot \beta_n^2 \cdot t/L^2\right]}{\beta_n^2} \right] \quad [8]$$

where D is the diffusivity of hydrogen, L and ρ are the length and diameter of the iron electrode, β_n is the root of the zero order Bessel function of the first kind, and C_0 is the initial concentration of metallic hydrogen in the iron. This latter term was obtained by permeation techniques (16) on an iron membrane cathodized in the same manner as that used in the pulse studies.

Values of Q were determined at various times by using a computer. The rate of removal of dissolved hydrogen, R, is simply $-dQ/dt$, and the results are shown in Fig. 5 for the general case of C_0 = 10 mc/cm^3. The portion of the curve relevant to the data in Fig. 4 is shown in the inset, where the hatched area represents the error fraction in θ resulting from the oxidation of dissolved hydrogen. In several experiments R was found to be independent of D over the range 10^{-4} to 10^{-6} cm^2/sec for the first second. The corrected value of θ (determined by subtracting the data in Fig. 5 from that in Fig. 4) varied slightly with applied cathodic current (or input fugacity), as shown in Fig. 6. Previous theoretical studies (17) have shown that θ should vary with overpotential according to

$$\theta = k_{exp}\left(-\frac{\eta F}{4RT}\right) \quad [9]$$

where K is a constant, η is the overpotential, and **F** R, and T have their usual meaning. The data shown in Fig. 6, when plotted in terms of log θ *vs.* η, did produce the straight line required by Eq. [9], as shown in Fig.

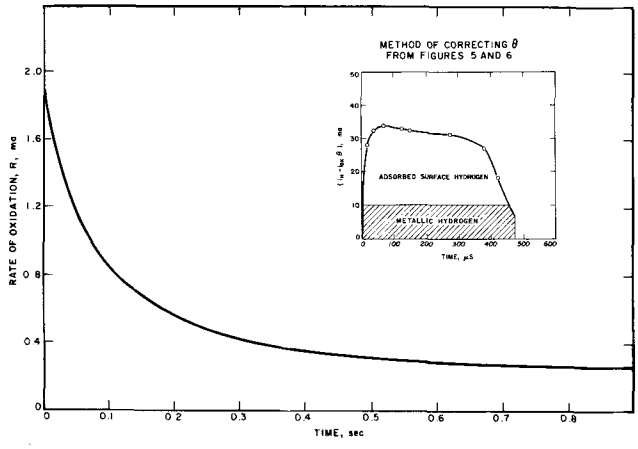

Fig. 5. Computed rate of oxidation of metallic hydrogen during the anodic pulse for an initial hydrogen concentration of 10 mcoulomb/cm³.

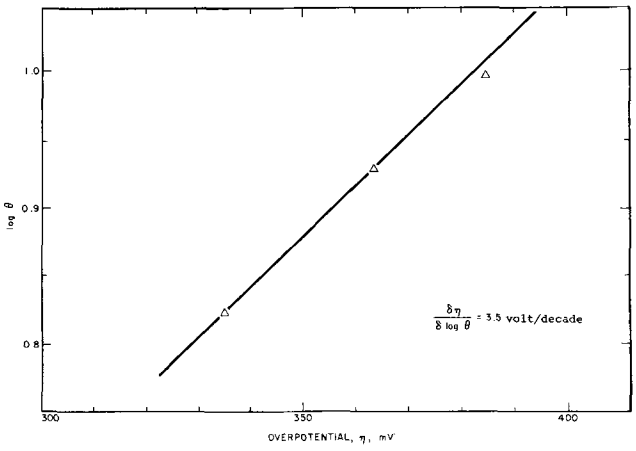

Fig. 7. Relationship between degree of coverage, θ, and the applied cathodic overpotential on iron in 0.0001N NaOH + 0.1M Na_2SO_4 at 25°C.

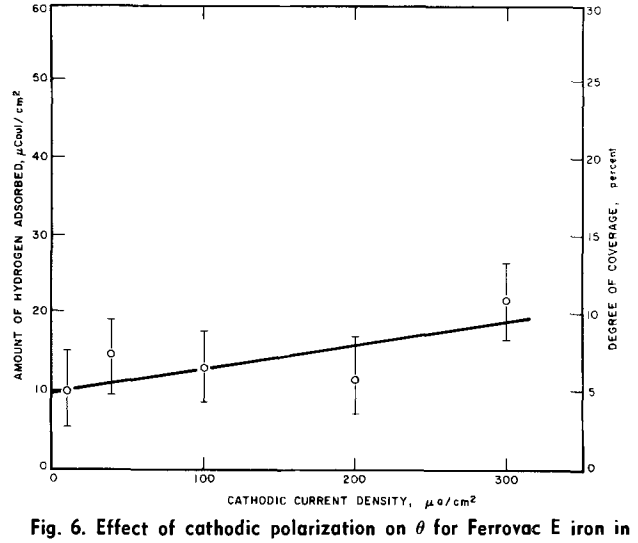

Fig. 6. Effect of cathodic polarization on θ for Ferrovac E iron in pH 9.5 solution.

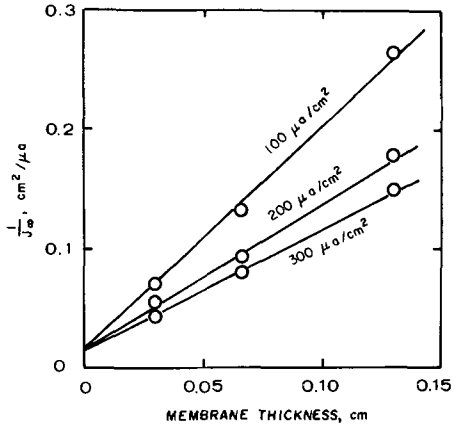

Fig. 8. Variation in the reciprocal of the permeation flux with membrane thickness for several cathodic current densities.

7. According to theory, the slope in Fig. 7 should be equal to $-\mathbf{F}/4RT$ at a maximum, or 4.2 V/decade. The actual slope obtained from Fig. 7 was 3.5 V/decade indicating quite close agreement with theory. On the basis of this close agreement, we feel that the term $i_{ox}\theta$ in Eq. [4] must of necessity be small with respect to i_H, as assumed in the analysis presented earlier.

The permeation flux, J_∞, was determined at three cathodic current densities on iron membranes over the thickness range 0.025-0.13 cm. The data obtained are shown in Fig. 8. It is clear that the relationships for each cathodic current converge to distinct points on the ordinate at $L = 0$, which when analyzed with θ give a value of k_{abs} which is independent of θ, as required by kinetic theory for a first order reaction. The intercept $1/(k_{abs} \cdot \theta)$ was evaluated and solved for k_{abs} by using the corrected values of θ obtained from the pulse measurements. These data are summarized in Table II, where θ has been expressed as grams hydrogen/cm² and k_{abs} has the dimensions of sec^{-1}. The measured values of k_{abs} appeared not to change significantly over the potential range investigated.

Summary

The galvanostatic pulse technique for measuring θ, the adsorbed hydrogen concentration on metal surfaces during cathodic hydrogen evolution, has been successfully applied to ferrous base materials. With this technique, the concentration of adsorbed hydrogen on a cathodically polarized iron surface in 0.0001N NaOH + 0.1M Na_2SO_4 solution has been shown to vary with overpotential in the manner predicted by theory.

Values of θ at three cathodic current densities have been used, along with permeation studies, to evaluate the fundamental adsorption rate constant for hydrogen into iron.

Manuscript submitted April 7, 1970; revised manuscript received ca. Sept. 16, 1970.

Any discussion of this paper will appear in a Discussion Section to be published in the December 1971 JOURNAL.

REFERENCES

1. E. Herzog, *Ind. Eng. Chem.*, **53**, 64A (1961).
2. J. P. Fraser, G. G. Eldredge, and R. S. Treseder,

Table II. Data for the evaluation of the rate constant for hydrogen absorption into iron cathodized in pH 9.5 NaOH

Cathodic current, μA/cm²	Overpotential, mV	$\left[\frac{1}{J_\infty}\right]_{L=0}$ cm²/μA	$\left[\frac{1}{J_\infty}\right]_{L=0}$ cm² · sec/g hydrogen	Degree of coverage, g hydrogen/cm²	Degree of coverage, %	k_{abs}, sec^{-1}
100	−335	1.5 × 10⁻²	1.44 × 10⁹	1.36 × 10⁻¹⁰	6.65	5.1
200	−363	1.5 × 10⁻²	1.44 × 10⁹	1.67 × 10⁻¹⁰	8.24	4.2
300	−385	1.5 × 10⁻²	1.44 × 10⁹	1.98 × 10⁻¹⁰	9.95	3.5

Corrosion, **14**, 517t (1958).
3. J. P. Fraser and R. S. Treseder, *ibid.*, **8**, 342 (1952).
4. C. M. Hudgins, R. L. McGlasson, P. Mehdizadeh, and W. M. Rosborough, *ibid.*, **22** (1966).
5. E. Snape, *ibid.*, **24**, 261 (1968).
6. M. A. V. Devanathan, J. O'M. Bockris, and W. Mehl, *J. Electronanal. Chem.*, **1**, 143 (1960).
7. E. Gileadi, M. A. Fullenwider, and J. O'M. Bockris, *This Journal*, **113**, 926 (1966).
8. J. O'M. Bockris, J. McBreen, and L. Nanis, *ibid.*, **112**, 1025 (1965).
9. M. A. V. Devanathan and Z. Stachurski, *Proc. Roy. Soc.*, **A270**, 90 (1963).
10. M. A. V. Devanathan and M. Selvaratnam, *Trans. Faraday Soc.*, **56**, 1820 (1960).
11. J. O'M. Bockris and F. Colum, Tech. Rep. No. 2, ONR, Contract Nonr 551 (22), (1958).
12. J. O'M. Bockris and H. Kita, *This Journal*, **108**, 676 (1961).
13. J. O'M. Bockris and M. A. V. Devanathan, Tech. Rep. No. 4, ONR, Contract Nonr 551 (22) NR 036-028 (1961).
14. C. D. Kim and B. E. Wilde, To be submitted to *Corrosion Science*.
15. M. Stern and A. C. Makrides, *This Journal*, **107**, 782 (1960).
16. C. D. Kim and A. W. Loginow, *Corrosion*, **24**, 313 (1968).
17. J. McBreen and M. A. Genshaw, Proceedings of the Conference on the Fundamental Aspects of Stress-Corrosion Cracking, p. 51, NACE (1967).

An Ellipsometric Study of the Anodic Deposition of Iron Oxide Films

J. L. Ord*

Department of Physics, University of Waterloo, Waterloo, Ontario, Canada

and D. J. De Smet*

Department of Physics, University of Alabama, University, Alabama 35486

ABSTRACT

Films of iron oxide were deposited on iron, platinum, and gold substrates by the anodic oxidation of ferrous ions contained in neutral electrolytes. The film growth was followed optically to thicknesses of several thousand angstroms with a following ellipsometer. The films deposited from borate electrolyte onto iron and platinum substrates were found to have a real refractive index equal to 1.7 at a wavelength of 6328Å. The films deposited onto a gold substrate from borate electrolyte were found to have a refractive index with a real component of 1.7 and a small but nonzero absorption coefficient. The films deposited onto a platinum substrate from perchlorate electrolyte were found to have a real refractive index equal to 1.93. We conclude that films with index 1.7 have an amorphous structure, films with index 1.93 are crystalline, and films deposited on gold substrates have trace amounts of gold incorporated in the film.

In an earlier paper (1) we presented ellipsometric measurements on the anodic oxidation of an iron substrate in a neutral borate electrolyte. In the course of these measurements, we found that ferrous ions, resulting from the anodic dissolution of iron in the active state, were oxidized in the passive state to a ferric oxide which deposited on the electrode. In that study we excluded ferrous ions from the electrolyte in order to study films formed by direct anodic oxidation of the iron substrate. In this paper we present ellipsometric measurements on the oxide film formed by the anodic oxidation of ferrous ions contained in neutral electrolytes. Iron, platinum, and gold are used as substrates for the deposition. This process has been studied extensively by Cohen and co-workers (2-5) who concluded that the films could be deposited onto any reasonably inert substrate, but that amorphous films were deposited from borate electrolyte whereas crystalline films were deposited from sulfate and perchlorate electrolytes. In the work we present here, we have used *in situ* optical measurements during the deposition of films from borate, sulfate, and perchlorate electrolytes onto iron, platinum, and gold substrates to test these conclusions.

Experimental

The electrodes used as substrates for the deposition were prepared from single crystals of iron, platinum, and gold. In each case the sample was prepared in the form of a cylinder 0.3 in. long by 0.2 in. in diameter. A small hole was drilled down the axis of the cylinder for the mounting assembly (1, 6) and a flat surface for the optical measurements was ground on one side of the cylinder. The samples were then given electrolytic surface treatments. For iron, a mixture of water, oxalic acid (100 g/liter), and hydrogen peroxide in a ratio of 20:7:1 at a temperature of 35°C was used as a chemical polish (7). The film left on the surface after the polishing was removed by cathodic reduction. The platinum sample was cleaned by immersion in concentrated nitric acid then in concentrated hydrochloric acid. The gold was anodized in sulfuric acid (8), then immersed in concentrated hydrochloric acid. The softness of the gold sample made it necessary to remove considerable material in this manner before a clean single-crystal surface was produced.

The cell used was an equilateral hollow prism of 75 ml capacity in which were mounted a platinum cathode, a mercurous sulfate reference electrode, a gas dispersion tube, and the electrode assembly. The surface of the sample under study was vertical. All experiments were performed at room temperature. The electrical equipment and circuitry are similar to those used in earlier work (9).

The electrolytes used were similar to those used by Cohen and co-workers (2-5). The borate electrolyte was the pH 8.4 buffered electrolyte used in our earlier work (1). The sulfate and perchlorate electrolytes were of the same approximate pH but were not buf-

* Electrochemical Society Active Member.
Key words: ellipsometry, anodic deposition, iron oxide.

fered. All electrolytes were bubbled with argon for at least 12 hr prior to the beginning of an experiment in order to remove any traces of dissolved oxygen. The bubbling was continued throughout the course of an experiment, stirring the electrolyte mildly. Ferrous ions were introduced into the electrolyte either by anodic dissolution of iron or by addition of a small amount of ferrous ammonium sulfate. The anodic dissolution introduced only ferrous ions, but low current densities (and hence long dissolution times) were required to avoid passivation of the iron. The experimental results were not sensitive to the method used to introduce the ferrous ions. The ferrous ions can only be maintained in the electrolyte provided it is free of dissolved oxygen.

The following ellipsometer used in this study is described in detail elsewhere (10). It is capable of making a measurement in one second with a resolution of 0.01°. This following speed was more than adequate for the deposition rates used in this work. A helium-neon gas laser (wavelength 6328Å) was used as a light source, and the angle of incidence was 60° for all of the data reported here. Several digital computer programs, including the original program by McCrackin and Colson (11), were used to generate theoretical curves in both tabular and graphical form for fitting the optical data.

Results and Discussion

The first deposition experiment was carried out using an iron electrode as a substrate in neutral borate buffer. The ellipsometer was nulled initially on a cathodically reduced iron surface, then it was set for automatic nulling to follow the film growth. The electrode was passivated at a constant current density of 100 μA/cm^2 to a potential of 0.3V (with respect to the mercurous sulfate reference electrode) and then was held at this potential. The current density was allowed to decrease to 1 μA/cm^2 before ferrous ions were added to the electrolyte. The growth of the deposited film was then followed through several thousand angstroms.

The results of this experiment are shown in Fig. 1 and Fig. 2. In these figures an optical measurement at a particular thickness appears as a point, and as a film grows, the points generally trace out a smooth curve. The actual experimental data consist of over 2000 points, and only representative points are plotted in the figures. The solid lines in the figures are theoretical calculations of the polarizer and analyzer null positions which would result from the growth of layers of constant refractive index. In Fig. 1 the bare surface measurement is plotted at point A, and data obtained during the anodic oxidation of the iron substrate are plotted

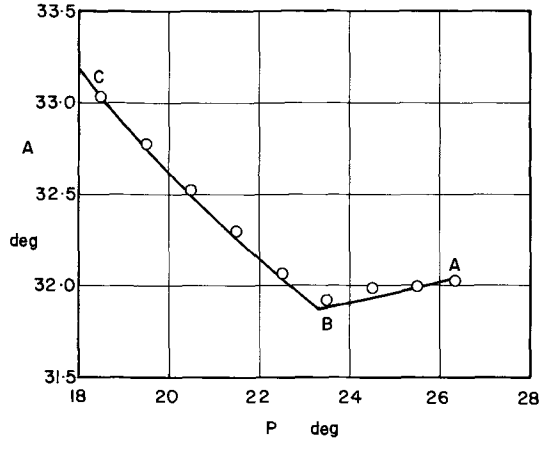

Fig. 1. Optical data on the anodic oxidation of iron in a neutral borate electrolyte (A to B) followed by deposition of an iron oxide (B to C) by anodic oxidation of ferrous ions added to the electrolyte. The curve from A to B is calculated for the growth of a layer of index 2.4-0.3*i* to a thickness of 40Å, and from B to C for an additional layer of index 1.7 to 150Å.

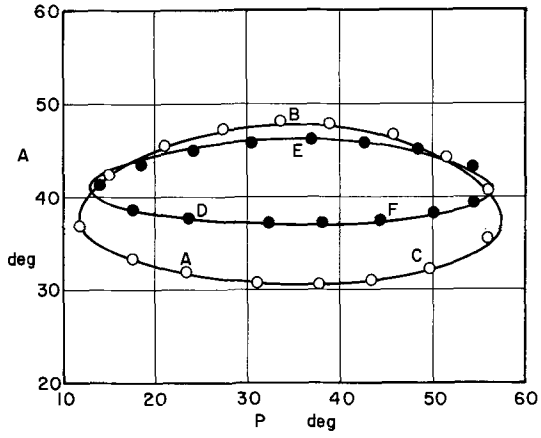

Fig. 2. Optical data on an anodic deposition of iron oxide layers from neutral borate electrolyte containing ferrous ions onto iron (ABC) and platinum (DEF) substrates. The curves in the figure are calculated for the growth of layers with a real refractive index equal to 1.7.

from A to B. The line between A and B is a theoretical curve for the growth of a layer of index 2.4-0.3*i* to a thickness of 40Å on a substrate of index 3.16-3.72*i*. (Other values for the index of the anodic oxide layer are possible, but the choice of an index for this thin layer has virtually no effect on the calculation of the index of the deposited layer.) The data plotted from B to C were obtained after ferrous ions were added to the electrolyte. The curve from B to C represents the growth of a layer of real index 1.7 to a thickness of 150Å. The curve traced out during deposition is plotted in Fig. 2 on a less expanded scale. (The figure also shows the results of the deposition experiment on platinum described below.) The experimental data trace out the loop ABC in the figure as the deposited layer grows. The closure of the loop at A is characteristic of the growth of a layer with a real refractive index. The curve fitted to the data in the figure represents the growth of a film of index 1.7 to a thickness of 2500Å when the curve closes on itself. The fit to the experimental data is good for a layer whose thickness is expected to be somewhat nonuniform due to the diffusion-limited nature of the deposition process. The considerable difference between the index of the layer formed by oxidation of the iron substrate and the index of the deposited layer shows that the layers must differ in composition and structure.

The second deposition experiment was carried out using a platinum single-crystal substrate in borate electrolyte. The ellipsometer was nulled initially on the platinum surface which was under cathodic reduction in an electrolyte containing ferrous ions. The ellipsometer was then switched to the following mode, and the electrode was driven galvanostatically at 20 μA/cm^2 to a potential of 0.4V with respect to the reference electrode, where it was held for the balance of the experiment. The current density was about 10 μA/cm^2 during the deposition. The results of this experiment are plotted in Fig. 2 also. The experimental data trace out the clockwise loop DEF as the layer grows, and the loop closes at D. The theoretical curve through these data represents the growth of a layer of the same index, 1.7, as was used in fitting the iron substrate data. The fit to the data is reasonable, but there is more evidence of layer nonuniformity than previously. From the two sets of data in Fig. 2 we conclude that layers with the same composition and structure are deposited on platinum and iron in borate buffer. The difference between the two sets of data is due solely to the difference between the refractive indices of the iron and platinum substrates.

In an attempt to determine if this film could be deposited on any reasonably inert substrate we next tried a similar experiment using a gold single crystal.

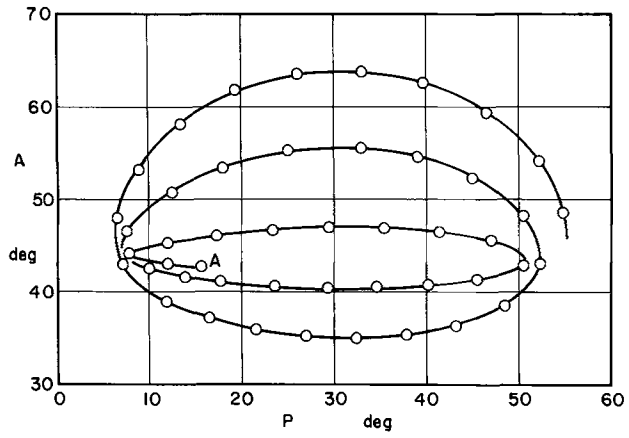

Fig. 3. Optical data on the anodic deposition of an iron oxide layer onto a gold substrate in borate buffer. The data points start at A and trace out an outward clockwise spiral as the layer grows.

The results of this experiment are plotted in Fig. 3. The data points start at A and trace out a clockwise outward spiral as the layer increases in thickness. The first few hundred angstroms of layer growth can be fitted to the growth of a layer of real index 1.7, but an index of $1.7-0.01i$ is required to fit the first complete loop. The final loop of the spiral can only be fitted by assuming that the imaginary part of the index has increased by a factor of three by the time the final thickness is reached. (The layer definitely has a small absorption coefficient, but the apparent increase in the absorption coefficient with thickness actually may be due to nonuniformity of the layer.)

We did not expect that the layer deposited on gold would differ from the layer deposited on the other two metals, but in retrospect the result cannot be considered surprising. Of the three metals, only gold can be anodized, and hence it is not as inert a substrate for oxygen evolution as is either iron or platinum. If gold is not an inert substrate for oxygen evolution, there is no reason to expect it to be inert for oxidation of ferrous ions. Data on the galvanostatic anodic oxidation of gold in a borate electrolyte free of ferrous ions are presented in Fig. 4. The data obtained on the growth of an anodic oxide film below the oxygen evolution potential are plotted from A to B, and the data on continued film growth at low current efficiency during oxygen evolution are plotted from B to C. The inflection in the data at point B shows that the anodized film differs in index from the anodic oxide film formed at lower potentials. Neither iron nor platinum grow a secondary oxide film during oxygen evolution, presumably because the anodic oxide acts as a barrier between the metal and the electrolyte. Once the oxygen evolution potential is reached with these metals, electrons can tunnel through the film, but ions require a field across the film to assist their motion. The film will thicken somewhat after oxygen evolution begins, but since the potential no longer rises, the increase in thickness lowers the field in the film, and a point is soon reached at which ionic conduction and hence further growth effectively ceases. Gold appears to behave quite differently. Conduction of electrons from either the oxygen evolution or ferrous ion oxidation reactions appears to enable ionic transport to continue. The film formed in this manner has a different structure from the anodic oxide film as is indicated by the difference in its refractive index. The results plotted in Fig. 3 cannot be accounted for by assuming that, as the deposited film grows, an anodized film grows under it. The symmetric outward spiral can only be accounted for by the growth of a single layer, and hence we conclude that a trace of gold is incorporated in the deposited film and causes it to be slightly absorbing.

We next devoted considerable effort to studying films deposited onto platinum in neutral sulfate electrolyte. We could not obtain reproducible optical data for this process, and our single positive result was obtained from an x-ray powder pattern of material from a thick deposited film. We identified the material as γ-$Fe_2O_3 \cdot H_2O$ (lepidocrocite) with the aid of the ASTM index of powder patterns. Leibenguth and Cohen (4) made the same identification using electron diffraction techniques.

Hashimoto and Cohen, in reporting their measurements on deposition from perchlorate electrolytes (5), stated that they obtained better electron diffraction patterns than were obtained in sulfate electrolyte. This comment led us to suspect that the films we had been depositing from sulfate electrolyte were not single-phase crystalline films, and hence our optical data on their growth could not be expected to fit theoretical curves for the growth of uniform films. We then tried depositing onto platinum in neutral perchlorate electrolyte, and obtained the data plotted in Fig. 5. Two theoretical curves are plotted in the figure, ABC for a layer of real index 1.7, and ADC for a layer of real index 1.93. The data clearly fall on the latter curve, and we conclude that the iron oxide layer has an index of 1.93 when it is deposited in the crystalline phase as opposed to 1.7 when it is deposited as an amorphous film.

Conclusions

Our measurements confirm the conclusions of Cohen and co-workers that iron oxide films can be deposited anodically onto both iron and platinum, and that the films deposited from perchlorate electrolyte differ in

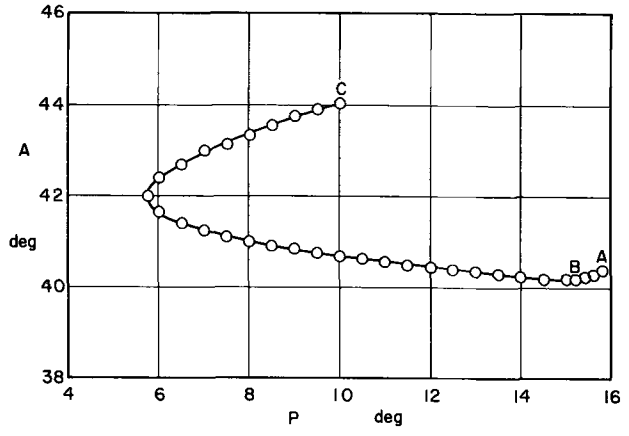

Fig. 4. Optical data on the anodic oxidation of gold in a neutral borate electrolyte. The data from A to B were obtained during the growth of an anodic oxide below the oxygen evolution potential; the data from B to C were obtained as an oxide film grew during oxygen evolution.

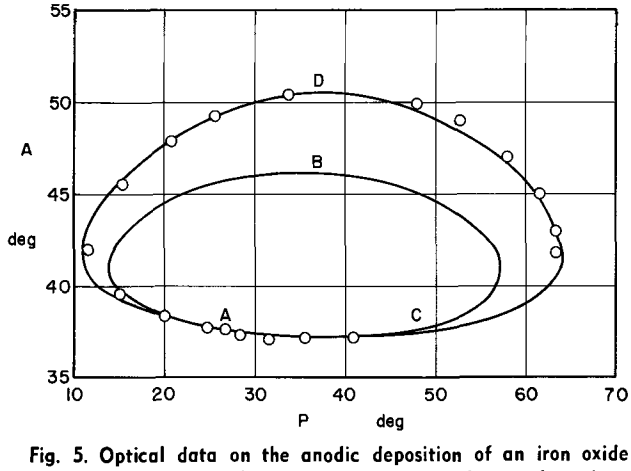

Fig. 5. Optical data on the anodic deposition of an iron oxide layer onto a platinum substrate in neutral perchlorate electrolyte. The curve ABC is calculated for the growth of a layer of real index 1.7; the curve ADC for a real index 1.93.

structure from those deposited from borate electrolyte. We conclude in addition that trace amounts of gold are incorporated in films deposited on gold substrates, rendering the films slightly absorbing. We were unable to deposit uniform single-phase films in sulfate electrolyte.

Acknowledgment

The financial assistance of the National Research Council of Canada is gratefully acknowledged.

Manuscript submitted June 20, 1969; revised manuscript received Sept. 19, 1970. This was Paper 70 presented at the Chicago Meeting of the Society, Oct. 15-19, 1967.

Any discussion of this paper will appear in a Discussion Section to be published in the December 1971 JOURNAL.

REFERENCES

1. J. L. Ord and D. J. DeSmet, *This Journal*, **113**, 1258 (1966).
2. V. Markovac and M. Cohen, *ibid.*, **114**, 674 (1967).
3. V. Markovac and M. Cohen, *ibid.*, **114**, 678 (1967).
4. J. L. Leibenguth and M. Cohen, *ibid.*, **114**, 200C, Abstract No. 71 (1967).
5. K. Hashimoto and M. Cohen, *ibid.*, **115**, 230C, Abstract No. 386 (1968).
6. H. G. Feller and J. Osterwald, *ibid.*, **111**, 119 (1964).
7. W. J. McG. Tegart, "The Electrolytic and Chemical Polishing of Metals," Pergamon Press, London (1956).
8. J. L. Whitton and J. A. Davies, *This Journal*, **111**, 1347 (1964).
9. J. L. Ord, *ibid.*, **113**, 213 (1966).
10. J. L. Ord and B. L. Wills, *Appl. Opt.*, **6**, 1673 (1967).
11. F. L. McCrackin and J. P. Colson, N.B.S. Technical Note 242 (1964).

On Preferential Anodic Dissolution of Alloys in the Low-Current Region and the Nature of the Critical Potential

H. W. Pickering* and P. J. Byrne

Edgar C. Bain Laboratory For Fundamental Research, United States Steel Corporation, Research Center, Monroeville, Pennsylvania 15146

ABSTRACT

Previous investigations on Cu-Au and Cu-Zn alloys have shown that the polarization curves for anodic dissolution of the less noble metal are complex, that the mechanism of preferential anodic dissolution involves the interdiffusion of the components in an alloy layer next to the surface, and that appreciable surface roughening occurs. In the present paper the mechanism of preferential anodic dissolution at lower overpotentials and the nature of the transition (current increases sharply) which occurs at a certain (more noble or oxidizing) potential, E_c, are examined. Results of electrochemical investigations on polycrystalline Cu-Au alloys at $E < E_c$ indicate that Cu atoms in direct contact with the electrolyte readily dissolve, and that a Cu-depleted layer forms both above and below E_c. At potentials more noble than E_c appreciable transport of Cu through the Cu-depleted layer occurs as a result of the onset at E_c of gross surface roughening which provides for a relatively short and time-independent, interdiffusion distance. The change in diffusion conditions which leads to a surface instability at E_c is reasoned to be related to a potential-dependent concentration of excess (di)vacancies in the interdiffusion layer.

Gerischer and Rickert (1) have observed that a stationary current is reached only after a rather long time during anodic dissolution of Cu from Cu-Au alloy at constant potential. It is, however, by no means obvious that a stationary current should be reached since with increasing time an increasing amount of the more noble component is accumulated at the alloy surface and, therefore, anodic dissolution of the less noble component, Cu, is impeded. Pickering and Wagner (2) have shown that the current is maintained by the interdiffusion of the components in the alloy; x-ray and electron diffraction data indicate that Cu diffuses to the surface and Au diffuses backward into the alloy. As a limiting case suppose that only one-dimensional diffusion (normal) to a plane surface occurs. Then the current density would be inversely proportional to the square root of time (2). Actually, however, the situation is far more involved since roughening of the surface also occurs (3-5). Although surface roughening makes the observance of a quasi-stationary current qualitatively understandable, it is difficult to analyze such observations since the increase in the length of effective diffusion path in the alloy with time, and surface roughening both affect (in opposite directions) the current.

Further insight may be obtained from the observation of certain transient phenomena. One may conduct experiments in which the alloy initially is kept at a fairly low potential E'. Subsequently, one may jump the potential to a hgher value E'' at which normally (in the absence of a pretreatment at E') a rather high current (1) and roughening of the surface (4, 5) are observed immediately. During the initial stage (E') Cu atoms are presumably removed from the uppermost lattice plane of the alloy, and subsequently copper depletion may extend to a depth of several lattice planes via counterdiffusion of Cu and Au. Accordingly, the current falls off as the supply of Cu atoms in direct contact with the electrolyte decreases with time (2). When after this pretreatment a higher potential E'' is applied, one may expect first a high current in view of the charging of the double layer of

* Electrochemical Society Active Member.

Key words: anodic-reactions, corrosion, diffusion, surfaces, copper-alloy, dezincification, gold.

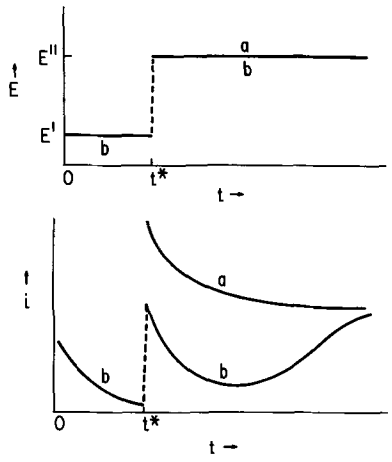

Fig. 1. Schematic diagram of expected current-time behavior for Cu dissolution from Cu-Au alloy. Curves a, specimen held at E'' from $t = t^*$ without pretreatment at E'. Curves b, specimen held at E'' after holding at E' for $t = t^*$.

the electrode; subsequently a rather low current is expected as transport conditions within the Cu-depleted layer adjust in order to attain the higher current characteristic of a sample held solely at E''. This is shown schematically in Fig. 1.

Appropriate potentials for potential-jump investigations may be chosen with the aid of current density-potential curves for dissolution of Cu from Cu-Au alloys. According to data of this kind already available [Gerischer and Rickert (1)], a typical polarization curve contains a region where Cu dissolves at a low, potential-independent rate and another region at higher potentials where the rate of Cu dissolution increases sharply with potential. It is for the increasing current region that Pickering and Wagner found that preferential dissolution of Cu from Cu-Au alloys occurs via interdiffusion of the components in the alloys. Potential-jump investigations then may be made most advantageously, for a range of E' potentials corresponding to the potential-independent, low-current region of the polarization curve, with potentials in the increasing-current region usually chosen for E''. Accordingly, information is obtained on the mechanism of dissolution in the low-current region, and on the nature of the potential E_c (referred to as the critical potential) at which transition to potential-dependent and high currents occurs.

Experimental Procedure

Investigations at 23°C were carried out mainly on Cu-13 a/o (atomic per cent) Au alloy (Cu13Au) in 1N Na_2SO_4-0.01N H_2SO_4 or in 1N Na_2SO_4-0.1N $CuSO_4$-0.01N H_2SO_4. Data are also reported for Cu-18 a/o Au (Cu18Au) and Cu-25 a/o Au (Cu25Au) alloys. High-purity alloys were made from 99.999% Cu and 99.99% Au. After homogenization at 700°C for 48 hr in evacuated silica capsules, cylindrical specimens were prepared by swaging, drawing to final diameter (0.216 cm), machining to length = 1.42 cm (area = 1 cm^2), and mechanical polishing, except with Cu25Au where sheet specimens were prepared by cold rolling. Unless otherwise stated the electrodes were annealed in evacuated silica capsules for 2 hr at 700°C and air cooled, and just prior to a run were polished on fine emery and rinsed in distilled water and methanol.

The cell of Pyrex and Teflon construction is shown in Fig. 2. A stream of prepurified He was passed through the cell prior to and during the run in order to remove oxygen. The reference cell was a mercury-mercurous sulfate electrode in contact with 1N H_2SO_4. The potentials are all reported relative to the standard hydrogen electrode (SHE). Switching of the potential was accomplished with a mechanical switch and two independent power supplies connected to a Wenking potentiostat. Doubly distilled water and reagent-grade chemicals were used to prepare the electrolyte.

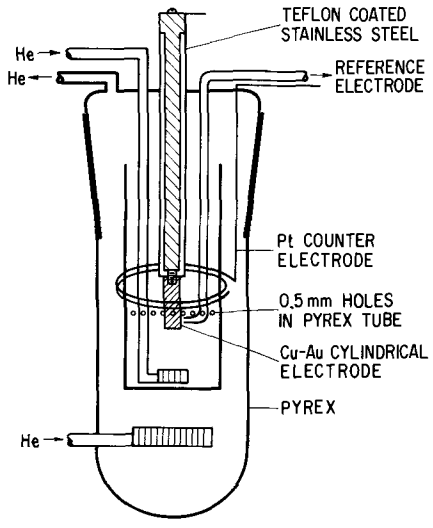

Fig. 2. Cell used for current-time transient experiments

As a check that the directly measured (meter) current was due mainly to Cu dissolution, quantitative chemical analysis of the electrolyte was made after several runs with 1N Na_2SO_4-0.01N H_2SO_4. A cell similar to that in Fig. 2 was used, but which provided for quick draining of the electrolyte (generally 60 ml) from the inner compartment. The minimum Cu content which could be detected was $\sim$ 0.15 μg/ml, whereas the actual amounts in solution after anodic dissolution were more than an order of magnitude higher. Chemical analysis data for a specimen were obtained in two or more dissolution periods. After a 1-hr initial dissolution period the electrolyte was drained for analysis. This was followed by the introduction of fresh electrolyte for further dissolution of the specimen at the same potential, and this procedure was repeated in successive dissolution periods. An average current density for each period was calculated from the amount of Cu in the electrolyte on the basis of the projected area of the specimen. Currents obtained by chemical analysis are specifically indicated in the text or in figure captions; otherwise currents given are the directly measured (meter) values.

Results

Log i_{Cu}-E curve.—In order to arrive at a polarization curve for Cu dissolution from Cu13Au the current-time behavior was determined at various constant potentials. For all potentials of Cu dissolution the current initially is high but falls at a rapid, although ever-decreasing rate; after 1 hr there is little further decrease (quasi-stationary current). Typical current-time transients are shown in Fig. 3 and 4. The curve in Fig. 4 was constructed from data obtained by chemical analysis of the electrolyte as well as from the directly measured current. Excellent agreement was obtained between the current on the microammeter and the current calculated from the amount of copper in the electrolyte.[1] No gold was found in the electrolyte, in agreement with thermodynamic considerations and the results of others (6).

It is clear from the current-time behavior at constant potential shown in Fig. 3 and 4 that in order to arrive at an easily interpretable log i_{Cu}-E curve the time of dissolution must be held constant, although this condition may be relaxed at longer times. Accordingly, the (meter) currents at 2 hr were used to construct the log i_{Cu}-E curves for dissolution of Cu from Cu13Au and Cu18Au (Fig. 5). The curves exhibit

[1] The average current density calculated for the first period, however, is not very meaningful since the current changes by several orders of magnitude; roughly half the charge for this period was estimated to pass in the first few minutes, and accordingly the first period point was plotted at 4 min.

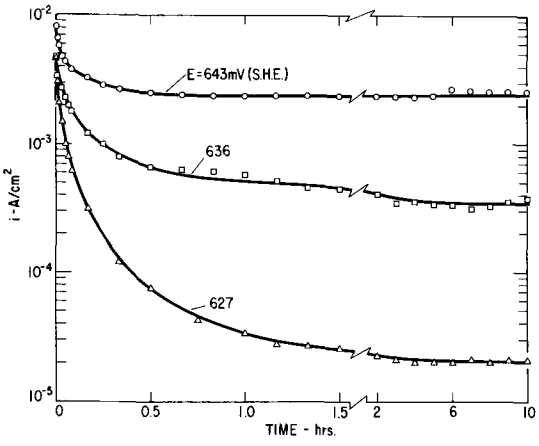

Fig. 3. Log i_{Cu}-t curves based on the projected area for Cu13Au in 1*N* Na_2SO_4-0.1*N* $CuSO_4$-0.01*N* H_2SO_4 with $E_c \cong 630$ mV. Surface roughening occurs at $E \gtrsim E_c$.

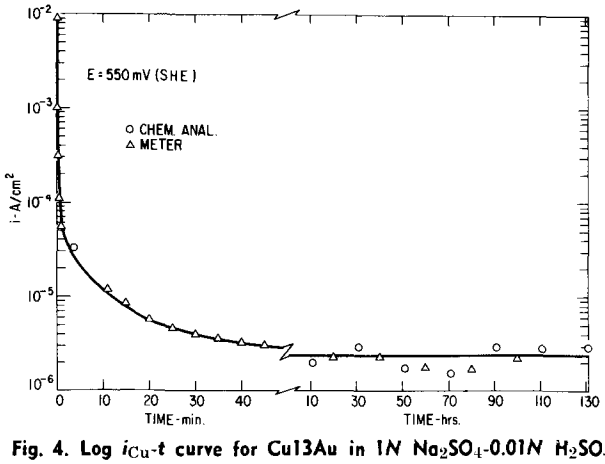

Fig. 4. Log i_{Cu}-t curve for Cu13Au in 1*N* Na_2SO_4-0.01*N* H_2SO_4 at $E = 550$ mV (SHE) with $E_c \cong 630$ mV.

a potential-independent, low-current region, a strongly potential-dependent, increasing-current region, and a critical potential, E_c, which increases with increasing Au content of the alloy. The solid curves in Fig. 5 were obtained with 1*N* Na_2SO_4-0.01*N* H_2SO_4 and the dashed curve with 1*N* Na_2SO_4-0.1*N* $CuSO_4$-0.01*N* H_2SO_4. With the former electrolyte containing no $CuSO_4$, the directly measured current was determined to be entirely due to dissolution of Cu by quantitative chemical analysis of the electrolyte from a 20-hr dissolution period following an initial 1-hr period. With the latter electrolyte containing $CuSO_4$, a higher current of $\sim 10^{-5}$ A/cm² was recorded (meter) at $E < E_c$ (dashed line); at $E > E_c$ the currents were the same for both electrolytes. IR voltages between the specimen and Luggin capillary were negligible, except possibly at the higher current densities and surface roughnesses, and may account in part or total for the "bending over" of the polarization curves at $i \gtrsim 1$ mA/cm².

The critical potentials for Cu13Au and Cu18Au in Fig. 5, defined as the intersection of the tangents drawn to the plateau and the inflection point of the increasing-current regions of the log i-E curve, are $E_c \cong 590$ mV (SHE) and $E_c \cong 810$ mV, respectively. E_c for Cu25Au is ~ 1000 mV, and the current at $E < E_c$ for Cu25Au decreases to less than 0.5 μA/cm² in 1 hr. The critical potentials were quite reproducible for specimens given the prescribed thermal and mechanical treatment as a group; but E_c varied for different groups of specimens. E_c for three groups of Cu13Au specimens was 590, 630, and 660 mV.

The log i_{Cu}-E curve was also obtained for Cu13Au specimens in the "as swaged and drawn" condition (cold worked). The results were qualitatively the same as for annealed alloy (Fig. 5), with E_c generally somewhat lower and varying even among specimens of the same group.

These data may be compared to similar current-time and current-potential data recently obtained for preferential dissolution of Zn from Cu-Zn alloys (dezincification) (7). Sole dissolution of Cu from Cu-Au alloy over the potential range investigated is analogous to the sole dissolution of Zn from Cu-Zn alloys below about +50 mV (SHE). E_C shifts to higher potentials with increasing content of the more noble metal in both systems. The increase of E_c with content of the more noble metal is such in both systems that E_c may be expected to be in the range of dissolution of the more noble metal for alloys rich in the more noble metal, as has actually been observed with α-brass (7). Also preferential dissolution of Zn from Cu-Zn alloys has been found to occur at $E > E_c$ via interdiffusion of the components in the alloy (8), just as was found for preferential dissolution of Cu from Cu-Au alloys (2).

Potential-jump investigations.—When the potential is jumped to $E'' > E_c$ after a pretreatment at $E' < E_c$, there is a period of up to 10^2 sec at E'' when the rate of Cu dissolution is considerably lower than in the absence of the pretreatment. One observes, on jumping the potential to E'', a decreasing current and then a minimum followed by a gradual increase and eventual joining with the current characteristic of a specimen without pretreatment. Thereafter, the curves superimpose and a normal decay of the current occurs in the approach to a quasi-stationary value. A typical current transient for Cu13Au is shown in Fig. 6 where $E' = 627$ mV and $E'' = 640$ mV with $E_c = 630$ mV. In-

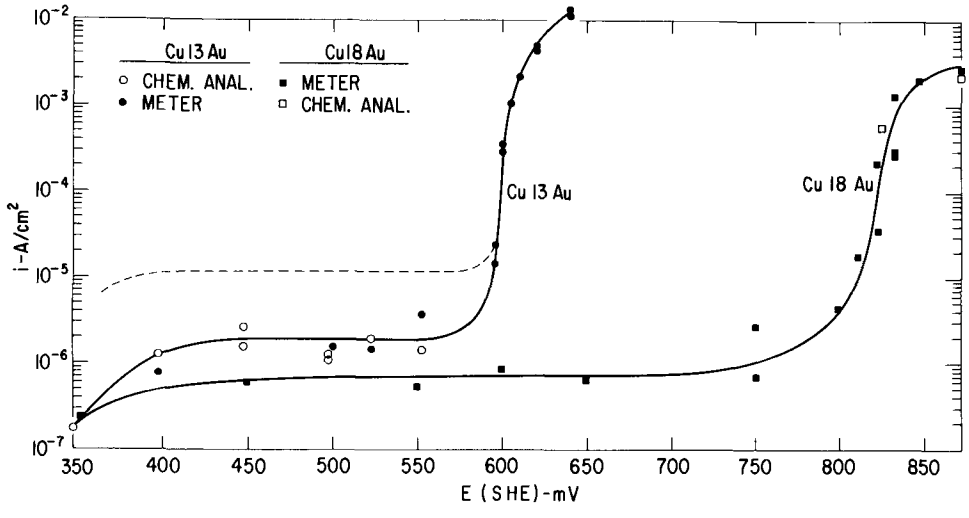

Fig. 5. Quasi-stationary log i_{Cu}-E curves based on the projected area for anodic dissolution of Cu from Cu13Au and Cu18Au in 1*N* Na_2SO_4-0.01*N* H_2SO_4. Higher currents in the plateau region for dissolution in 1*N* Na_2SO_4-0.1*N* $CuSO_4$-0.01N H_2SO_4 are indicated by the dashed line. Open symbols are from chemical analyses data; closed symbols are microammeter readings.

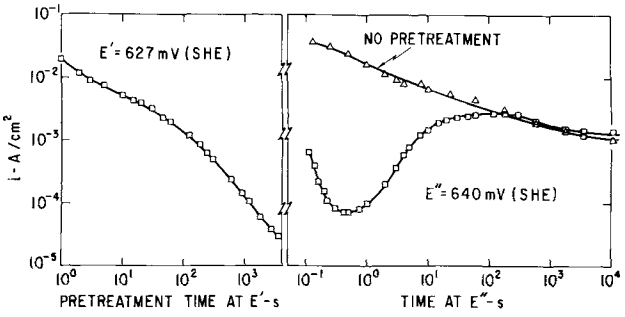

Fig. 6. Current-time transients for dissolution of Cu from two Cu13Au specimens held at E'' = 640 mV ($E_c \cong$ 630 mV) in 1N Na_2SO_4-0.01N H_2SO_4, of which one had been pretreated for 1 hr at E' = 627 mV.

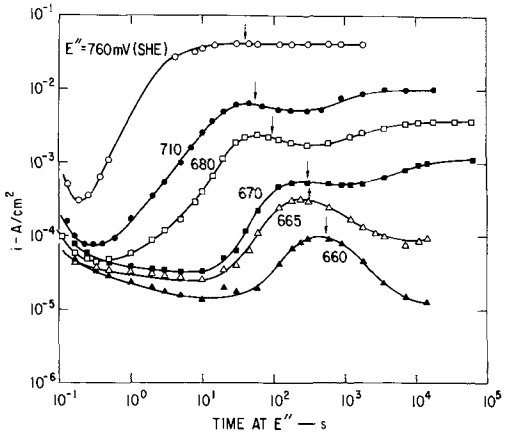

Fig. 7. Current-time transients at various E'' potentials for Cu dissolution from Cu13Au specimens which had received identical pretreatments of 1 hr at 635 mV. 1N Na_2SO_4-0.1N $CuSO_4$-0.01N H_2SO_4. $E_c \cong$ 660 mV. Arrows indicate the approximate time that the current-time behavior becomes identical to that for a nonpretreated specimen held at the same E''.

tegrating the current over the time of pretreatment at E' in Fig. 6 gives 0.8 C/cm², equivalent to 4 x 10^{-6} mole/cm² or ~ 1900 atom layers of dissolved Cu. The reduction in Cu current from the time the E'' potential is impressed until normal dissolution behavior characteristic of E'' is attained, amounts to the equivalent of roughly 800 atom layers of Cu as given by the difference in areas under the E'' curves.

In Fig. 7 current-time data at E'' are shown for 6 Cu13Au specimens jumped to different E'' values after identical pretreatments of 1 hr at E' = 635 mV which provided for the dissolution of ~ 500 atom layers of Cu. At each of the E'' potentials, the rate of Cu dissolution is much lower than that which is obtained for a nonpretreated specimen; the current-time curves for the nonpretreated specimens are not shown but are qualitatively the same as in Fig. 6.

The amount of Cu dissolution during the transient period at E' depends strongly on the E' potential. Table I gives the amounts of dissolved Cu for Cu13Au specimens held 1 hr at different E' potentials ranging from 400 to 635 mV. Also given are the corresponding amounts of Au excess. The response of these specimens when jumped to the same E'' varied greatly as seen in Fig. 8. The specimen held at the highest pretreatment potential, E' = 635 mV, shows the most severe depression in the rate of Cu dissolution when the potential is jumped to E'' (bottom curve). As E' is decreased, the current recovery at E'' is faster. For E' = 400 mV corresponding to the dissolution of less than 10^2 atom layers of Cu, the current at E'' is only slightly depressed compared to a specimen with no pretreatment (top curve).

Table I. Amounts of dissolved Cu from Cu13Au and Au excess on the basis of the projected area in 1 hr at various E' potentials. E_c = 660 mV

	Cu dissolved			Au excess
E', mV	C/cm²	Mole/cm²	Atom layers	Atom layers
400	0.025	1 x 10^{-7}	64	10
500	0.077	4 x 10^{-7}	200	30
600	0.106	6 x 10^{-7}	280	42
635	0.224	11 x 10^{-7}	580	87

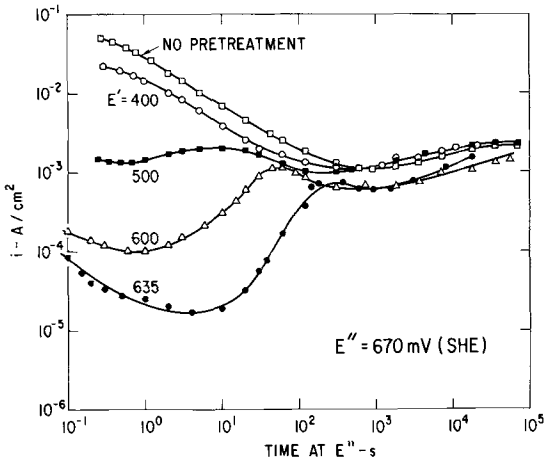

Fig. 8. Current-time transients for Cu dissolution from Cu13Au specimens which were held at different E' potentials for 1 hr prior to jumping the potential to E'' = 670 mV. 1N Na_2SO_4-0.01N H_2SO_4. $E_c \cong$ 660 mV. The curve at E'' for a specimen without pretreatment is also shown.

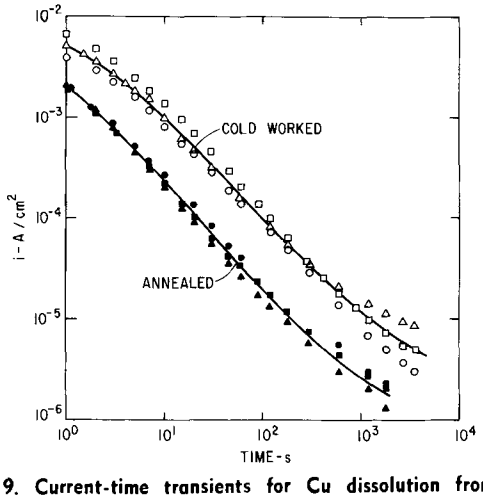

Fig. 9. Current-time transients for Cu dissolution from three cold-worked (open symbols) and from three annealed Cu13Au specimens at 500 mV. 1N Na_2SO_4-0.01N H_2SO_4.

Results of potential-jump investigations with the "as swaged and drawn" (cold worked) Cu13Au specimens, although qualitatively the same as for annealed specimens, always showed higher currents. The amount of dissolved Cu during the transient period at $E < E_c$ is much greater for cold-worked than for annealed specimens. This is illustrated in Fig. 9 where i_{Cu}-time data are shown for cold-worked (open symbols) and annealed Cu13Au specimens held at 500 mV. Approximately five times as much Cu (0.85 *vs.* 0.18 C/cm²) is dissolved in the approach to the quasi-stationary current (~ 10^{-6} A/cm²) from the cold-worked than from the annealed specimens. The cold-worked specimens were prepared as previously described. Other cold-worked specimens from this group were given an

anneal at 500°C in vacuum prior to dissolution.[2] When these specimens were jumped to a higher potential (E''), the currents were higher than for annealed specimens treated similarly. The fact that E_c differs from the cold-worked and annealed conditions, however, precludes the possibility of a detailed comparison at E'' for the two conditions.

A comparison of the amounts of charge passed in the approach to a quasi-stationary current was also made for ordered and disordered Cu25Au specimens. Disordered specimens were obtained by quenching from 700°C. Highly ordered specimens were prepared by cooling from 700° to 400°C in a few hours and from 400° to 100°C at 2.3°C/hr (9). The kinetics of Cu dissolution is different for the two conditions as noted by two rather large deviations from linear behavior (in opposite directions) in a log i_{Cu}-log t plot for the ordered specimens compared to approximately linear behavior for the disordered specimens, although averaged over the total time the charges passed were the same within the experimental error, 0.015 and 0.017 C/cm² for ordered and disordered specimens, respectively.

Metallographic examination.—Metallographic examination of the cross sections of specimens held at $E > E_c$ shows a dark layer next to the surface. In prior investigations this layer was shown to be porous by a-c impedance measurements (4, 5) in agreement with other investigations by Graf (10) and others (1, 6, 11) and was found to be Au-rich by x-ray and electron diffraction (2). The low currents which flow at $E < E_c$ preclude the recognition of Cu dissolution by metallographic examination. Specimens held at E'' after a pretreatment at E' appear much the same as specimens held at E'' without a pretreatment; the thickness of the porous layer varies greatly over the surface, and usually at least one area of the surface is essentially free of attack as seen in Fig. 10a. A much more uniform layer has been observed with specimens made from cold-rolled and annealed stock (2). Some grain boundary penetration is occasionally observed as in Fig. 10b.

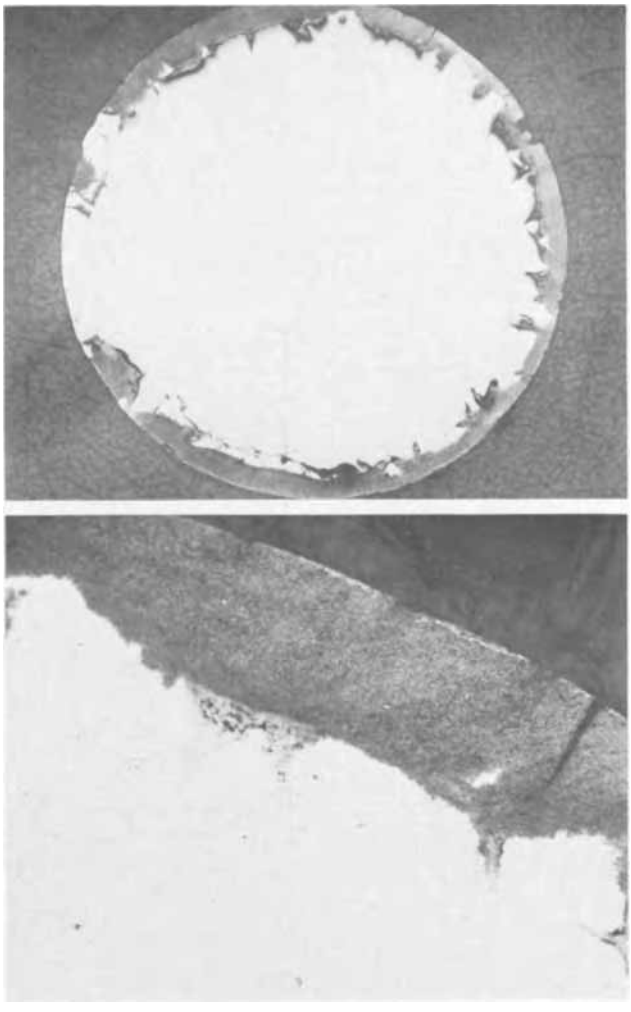

Fig. 10. Cross-section of a Cu13Au specimen which was maintained at $E' = 627$ mV for 1 hr and then jumped to $E'' = 636$ mV for 72 hr. $E_c \cong 630$ mV. a (top) Magnification X30; b (bottom) Magnification X195.

Discussion

The reported current-time and current-potential data for dissolution of Cu from Cu-Au alloy are essentially in agreement with earlier results of this kind obtained by Gerischer and Rickert (1). For the $CuSO_4$-free electrolyte there is at $E < E_c$ a quasi-stationary Cu current of $\sim 10^{-6}$ A/cm² (solid line in Fig. 5) according to quantitative chemical analysis data. The higher quasi-stationary current of $\sim 10^{-5}$ A/cm², which is obtained at $E < E_c$ when 0.1N $CuSO_4$ is added to the electrolyte (dashed line) and which was obtained also by Gerischer and Rickert who used only the $CuSO_4$-containing electrolyte, is probably mainly due to the electrode reaction $Cu^+ = Cu^{2+} + e^-$. The source of the cuprous ion may be impurity in the salt or that formed by equilibration of cupric ion with Cu in particles which have become detached from the electrode. A rough calculation shows that at high overpotentials a current of this magnitude may be expected for the oxidation of cuprous to cupric ion in 0.1N $CuSO_4$ equilibrated with metallic copper. Also, it was found that the current increased by a factor of 2 or 3 with increased stirring, in agreement with this hypothesis.

The high Cu currents recorded at all potentials ($400 < E < 900$ mV) on first contact of the specimen with the electrolyte indicate that Cu atoms in direct contact with the electrolyte are readily ionized, in accord with the existing large overpotential for Cu dissolution ($E°_{Cu/Cu2+} = 337$ mV). At $E < E_c$ the current falls quickly to a very low value as access of Cu atoms to the electrolyte is (effectively) stifled. The possible sources of this stifling process are considered next, followed by a discussion of the nature of E_c.

On the basis of earlier data obtained at $E > E_c$ preferential anodic dissolution is currently best understood as follows (2, 7): Initially, dissolution occurs by the usual (as with a pure metal) lateral motion of steps (12) [kink-step-terrace model of a surface (13, 14)]. Gradual blocking of steps soon begins as a result of the accumulation of the more noble metal (Au in the case of Cu-Au alloy) on the surface eventually causing cessation of step motion. Dissolution of the less noble metal (Cu) continues, however, from sites (2, 8) which result in the formation of surface vacancies, in the interdiffusion of the components in an alloy layer next to the surface and in surface roughening.

When appreciable surface roughening occurs, as is known to be the case at $E > E_c$, (4, 5) a rather high diffusion-controlled, quasi-stationary current is possible (2, 3); but in the absence of surface roughening the interdiffusion distance must on theoretical grounds increase and the current decrease indefinitely (2). The data in the present paper give support to the idea that at $E < E_c$ dissolution occurs by the aforementioned mechanism but that the process is effectively stifled because of an insufficient amount of surface roughening (per unit amount of dissolved copper),

[2] A fine emery treatment was given to some of these specimens to make the surface condition more comparable to that of the cold-worked specimens which also received a (final) fine emery treatment. The amount of dissolved Cu (0.040 C/cm²) for the annealed and emeried specimens was about twice that of the annealed specimens without the emery treatment and probably reflects the cold work introduced by the emery treatment.

i.e., a Cu-depleted layer forms but the average interdiffusion distance, δ, increases with time. Yet the current does not decrease indefinitely but approaches a low value of $\sim 10^{-6}$ A/cm^2, indicating that other factors enter, which may include deformation and cracking of the Cu-depleted layer, diffusion along special paths (*e.g.*, subboundaries and dislocations) or incipient surface roughening. Deformation and cracking of the Cu-depleted layer may occur because of stress arising out of the difference in atom sizes and inhomogeneous accumulation and annihilation of vacancies. Both of these processes tend to decrease the interdiffusion distance and increase the rate of dissolution (15). The greater amount of Cu dissolution and, hence, greater depth of Cu depletion, prior to the attainment of the quasi-stationary value with the cold-worked specimens is in agreement with a defect-enhanced diffusion process.

By the formation of such a Cu-depleted layer at $E < E_c$, one understands the appreciable lag time ($\sim$ 200 sec) at E'' after pretreatment at E' (see Fig. 6) as a period of readjustment of parameters, such as the excess vacancy concentration and the surface roughness, associated with diffusion of Cu through the layer to the surface. Since the number of geometrically different sites (itself a high value for random surfaces) from which Cu atoms may be dissolved may be expected to increase with increasing overvoltage for Cu dissolution (12, 16), it is reasonable to assume that the excess vacancy concentration in the Cu-depleted layer increases with potential through the operation of many of these sites (2, 8). It follows then (*a*) that Cu diffusion to the surface occurs more rapidly as E'' is made more noble (Fig. 7), and (*b*) that the depth of the Cu-depleted layer at $E < E_c$ increases with increasing potential as indicated in Table I and Fig. 8.

Incipient surface roughening is indicated at $E \lesssim E_c$ by the relatively large amounts of Cu dissolution at potentials approaching E_c, *e.g.*, $\sim$ 540 atom layers of dissolved Cu in 1 hr at $E' = 635$ mV with $E_c = 660$ mV (Table I) and $\sim$ 1900 atom layers of dissolved Cu for E' virtually equal to E_c (Fig. 6). In the absence of surface roughening, a diffusion length, δ, of 10^3 Å is required to explain these data on a diffusion basis and this is an order of magnitude longer than that calculated assuming a large excess concentration of vacancies (2). That dissolution of Cu does not occur at $E < E_c$ solely via diffusion of Cu to a planar surface is also indicated by the fact that the current is inversely proportional to the square root of time only for an initial period of a few tens of seconds; thereafter higher currents are observed. Finally, there is a relatively large initial surge of current on jumping the specimens from E' to E'', which in addition to charging the double layer may be the dissolution of Cu atoms in certain "near-surface" sites which are not active dissolution sites at E' but are active at the higher driving force, E''.

The aforementioned data suggest that the change in kinetics at E_c involves the establishment of certain diffusion-surface roughening conditions rather than a change in the basic nature or mechanism of the preferential dissolution process. E_c may coincide with the attainment of a certain diffusion-controlled rate of surface roughening such that the rate of recession of the alloy surface at the base of a penetration becomes equal to the rate of migration of the diffusion front, *i.e.*, the average interdiffusion length, δ, becomes constant as illustrated in Fig. 11, thereby providing the necessary condition to maintain a quasi-stationary, diffusion-controlled current. The increase in the quasi-stationary current with potential at $E > E_c$ follows if the (excess) (di)vacancy concentration increases with potential as has already been assumed.

Data in Fig. 5 show that E_c is a strong function of the Au content of the alloy. This may be explained in

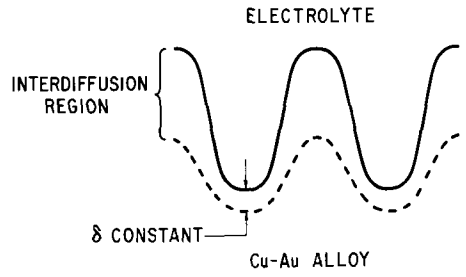

Fig. 11. Schematic diagram illustrating possible situation during preferential anodic dissolution of Cu at $E > E_c$.

the following way. As the Au content of the alloy increases the amount of excess Au per unit amount of dissolved Cu increases. This means, as shown in calculations for diffusion to a plane surface (2), that at a given potential and time the rate of dissolution of Cu will be less and the interdiffusion distance greater for alloys of increasing Au content; also the rate of vacancy production may be expected to be lower with increasing Au content as a result of a correspondingly lower number (at any given time) of Cu-occupied surface sites. This expectation is supported by the data, *e.g.*, 0.017 C/cm^2 of Cu dissolve in the attainment of the quasi-stationary value at 750 mV for annealed Cu25Au compared to roughly the same amount at only 500 mV for annealed Cu13Au. Hence, if a certain diffusion condition, *e.g.*, the concentration of excess vacancies, is important for the establishment of the continuing diffusion-surface roughening process (constant δ), a higher potential must be applied the higher the Au content.

This hypothesis of the nature of E_c clearly is tentative since no formulation can be given which relates quantitatively the value of E_c to the composition of the alloy and other parameters which can at least in principle be determined by independent measurement. Nevertheless, it seems worthwhile to follow the consequences which result from the model indicated in Fig. 11. The model contains the important assumption that the concentration of vacancies in the Cu-depleted layer is much greater than the equilibrium value and that this excess concentration increases with increase in the single-electrode potential. To the extent that there is indirect evidence that excess vacancies are present in Cu-depleted layers, in the demonstration of the occurrence of appreciable volume diffusion during preferential dissolution at $E > E_c$ (2, 8), this assumption is justified; clearly, however, additional experimental support is needed particularly with regard to the potential dependency aspect of the vacancy concentration. Also, coalescence of vacancies will occur to form voids and may contribute to surface roughening, as will deformation and cracking of the Cu-depleted layer. The rates of these processes may increase with potential and content of the less noble metal in the alloy. Finally, the proposed mechanism implies that surface energy (and other forces tending to reduce surface roughness) does not play a dominant role in establishing conditions for a continuing diffusion-surface roughening dissolution process. Surface energy may be expected to be relatively unimportant when the free energy decrease per unit volume accompanying dissolution is large compared to the surface energy; *i.e.*, at high overpotentials for Cu dissolution. That surface energy is of only secondary importance in determining E_c is indicated in the fact that although E_c is a strong function of alloy composition, the surface energy at a given potential may be expected to vary little with (bulk) alloy composition, since the surface composition during dissolution must be roughly the same (nearly pure Au) for all of the alloys.

It is interesting that the factors which are important for preferential anodic dissolution at 23°C are basically

the same as those that are important in preferential dissolution and oxidation at elevated temperatures, as outlined by Wagner (3, 17). Although these processes must differ in detail in view of the different conditions, there are marked similiarities which can go even beyond the main factors of diffusion in the alloy as the rate-determining step and the occurrence of gross surface roughening. Lichter and Wagner (18) found that during sulfidization of Cu-Au alloys at 500°C the Cu-rich alloys form an outer homogeneous sulfide layer and an inner two-phase layer consisting of sulfide and metal. The metal was found to be a sponge-like network of (nearly) pure Au in accord with preferential sulfidization of Cu with interdiffusion of the components in the alloy as rate determining. It was further noted that the tendency for surface roughening and the extent of sulfidization decreased with increasing Au content of the alloy. The decrease in sulfidization rate was more drastic with the Au-rich alloys in agreement with the virtual absence of surface roughening. Similarly as mentioned already, the tendency for surface roughening during preferential anodic dissolution of Cu from Cu-Au alloys decreases with increasing Au content, and preferential anodic dissolution is essentially restricted to the Cu-rich Cu-Au alloys (E_c for the Au-rich alloys appears to be more noble than the potential of Au dissolution).

Conclusions

Log i_{Cu}-t and log i_{Cu}-E relations are presented for the preferential electrolytic dissolution at 23°C of Cu from Cu-rich, Cu-Au alloys. The log i_{Cu}-t data show that at all potentials the current is initially high but falls rapidly at an ever decreasing rate. The log i_{Cu}-E curve (for a given time of dissolution) exhibits a potential-independent current region and a composition-dependent critical potential, E_c, at which potential the rate of Cu dissolution becomes strongly potential dependent, in agreement with the data of Gerischer and Rickert (1).

The results of potential-jump investigations indicate that at $E < E_c$ a Cu-depleted layer forms over the surface which limits the rate of Cu dissolution to that of Cu diffusion through the layer; the latter process becomes very slow since the interdiffusion distance necessarily increases with time in the absence of appreciable surface roughening. The amount of Cu dissolution and hence, the depth of the Cu-depleted layer, required to effectively stifle dissolution at $E < E_c$ is found (*a*) to increase in the direction of more positive potentials, in agreement with an expected increase in the kinetics of vacancy generation with increasing driving force for dissolution of the less noble component, and (*b*) to be larger for cold-worked specimens with their higher defect density than for annealed specimens, also in agreement with a defect enhanced bulk diffusion process at $E < E_c$, and not unlike that found previously by x-ray and electron diffraction investigations at $E > E_c$.

The factor which accounts for the drastic change in kinetics at E_c appears to be the extent of surface roughening. At $E < E_c$ only incipient surface roughening occurs, whereas at $E > E_c$ the surface area continuously and very rapidly increases with time, *i.e.*, a surface instability occurs at E_c and provides for a constant (average) interdiffusion distance in the alloy at the advancing alloy-electrolyte interface, as illustrated in Fig. 11. It is proposed that the change in diffusion conditions which leads to a surface instability is related to a potential-dependent concentration of excess (di) vacancies in the interdiffusion layer.

Acknowledgments

The authors are especially grateful to Professor Dr. Carl Wagner of the Max Planck Institut für Physikalische Chemie for suggesting the potential-jump studies and to him and Drs. R. A. Oriani and R. P. Frankenthal for helpful comments on reading of the manuscript, and to Dr. C. A. Johnson for helpful discussions. The skillful assistance of Mr. H. A. Hughes with the metallographic examination and of Messrs. G. W. Momeyer, W. L. Doyle, and C. C. Sharp with the chemical analysis is gratefully acknowledged. All except Professor Wagner are (or were) members of the E. C. Bain Laboratory for Fundamental Research of the United States Steel Corporation.

Manuscript submitted June 7, 1970; revised manuscript received *ca.* Oct. 15, 1970. This was Paper 414 presented at the Montreal Meeting of the Society, Oct. 6-11, 1968.

Any discussion of this paper will appear in a Discussion Section to be published in the December 1971 JOURNAL.

REFERENCES

1. H. Gerischer and H. Rickert, *Z. Metallk.*, **46**, 681 (1955).
2. H. W. Pickering and C. Wagner, *This Journal*, **114**, 698 (1967); **115**, 143 (1968).
3. J. D. Harrison and C. Wagner, *Acta Met.*, **7**, 722 (1959).
4. H. W. Pickering, *This Journal*, **115**, 690 (1968).
5. C. Wagner, *ibid.*, **116**, 343 (1969).
6. R. Bakish and W. D. Robertson, *Trans. AIME*, **206**, 1278 (1956).
7. H. W. Pickering and P. J. Byrne, *This Journal*, **116**, 1492 (1969).
8. H. W. Pickering, *ibid.*, **117**, 8 (1970).
9. R. M. Fisher and M. J. Marcinkowski, *Phil. Mag.*, **6**, 1385 (1961).
10. L. Graf, *Metallforschung*, **2**, 193, 207 (1947); *Z. Metallk.*, **40**, 275 (1949).
11. H. W. Pickering and P. R. Swann, *Corrosion*, **19**, 369t (1963).
12. W. K. Burton, N. Cabrera, and F. C. Frank, *Phil. Trans. Roy. Soc.*, **243A**, 299 (1959).
13. W. Kossel, Nachr. Ges. Wiss. Göttingen, Math. Physik. Kl., p. 135 (1927).
14. I. N. Stranski, *Z. Physik. Chem.*, **136**, 259 (1928).
15. H. W. Pickering, Conference on the Fundamental Aspects of Stress Corrosion Cracking, Columbus, Ohio (1967), NACE, p. 159, R. W. Staehle, Editor (1969).
16. D. A. Vermilyea, *J. Chem. Phys.*, **25**, 1254 (1956).
17. C. Wagner, *This Journal*, **103**, 571 (1956); **99**, 369 (1952).
18. B. D. Lichter and C. Wagner, *ibid.*, **107**, 168 (1960).

Cathode Overpotential and Electrosorption Effects of Normal Monocarboxylic Acids during Electrodeposition of Copper

R. O. Loutfy and A. J. Sukava*

Department of Chemistry, University of Western Ontario, London, Ontario, Canada

ABSTRACT

The cathode overpotential and electrosorption effects of some normal monocarboxylic acids during electrodeposition of copper were studied galvanostatically at current densities up to 20 mA-cm^{-2}. Equations were derived by means of which overpotential increments caused by the blocking action of adsorbed additive can be used to calculate the separate adsorption free-energy contributions of the carboxyl and methylene groups in the additive molecule, and also a coverage-dependent lateral interaction free energy arising primarily from dipole-dipole interaction between adjacent carboxyl groups in the adsorbed phase. The carboxyl group contribution was found to be −1570 cal mole^{-1} at zero coverage, while the methylene group contribution was −704 cal mole^{-1} and independent of coverage.

A previous paper from this laboratory (1) dealt with the cathode overpotential and electrosorption effects of normal monocarboxylic acids in the electrodeposition of copper from acid sulfate electrolyte. The overpotential data, interpreted in terms of the simple blocking theory, indicated that the adsorption of such compounds on a copper cathode can be represented at low surface coverages by a Langmuir-type isotherm from which the net free energy of adsorption can be calculated. By application of Traube's rule, the adsorption free energy could then be interpreted in terms of the separate contributions of the functional and methylene groups in the additive molecule.

Further work with monocarboxylic acids has shown that a more careful and detailed study is needed, particularly in view of the emerging doubt about the general applicability of the basic Langmuir isotherm to these systems due to the importance of lateral interaction in the adsorbed phase. More complete data are presented and analyzed in this report.

Experimental

Cathode overpotentials were measured with a Luggin probe in a simple glass cell shown in Fig. 1. A cylindrical copper-wire cathode, about 2 mm in diameter, was immersed in about 100 ml of solution. The cathode was fitted with a tight Teflon sleeve so placed that a geometrical 1 cm^2 of its surface was in contact with the solution.

The tip of the Luggin capillary was placed about 1 mm from the cathode, a distance greater than its outside diameter, to avoid possible shielding of the cathode surface from access of polarizing current (2, 3). This causes an error in total overpotential values due to *IR* drop between Luggin tip and cathode surface, but such error cancels out because only the increments in overpotential caused by organic additives were of interest and because such additives can be assumed to have no significant effect on the solution resistance since only highly conducting solutions were employed (1.0M H_2SO_4). Measurement of the *IR* drop from transient overpotential build-up, using a cathode-ray oscilloscope, gave a value of 3 ± 1 mV for all solutions at an apparent current density of 20 mA-cm^{-2}, whether or not additives were present.

It was found that this cell design, with the cathode-to-anode distance much greater than the cathode radius, resulted in a cylindrically symmetrical field in the vicinity of the cathode at all experimental current densities. Overpotential values were the same for a given current density and solution composition, within experimental error, regardless of the location of the Luggin probe in any horizontal plane around the cathode and regardless of vertical displacement along the cathode length, provided only that the distance between cathode surface and probe tip was the same.

Steady-state overpotentials were measured at constant temperature, 25° ± 0.1°C, and at constant apparent current densities controlled and maintained by means of a Harrison Laboratories Type 6201 d-c power supply. Measurements were made with a Sargent SR recorder and in some cases with a L&N Type K potentiometer. Current adjustment was made to give the desired apparent current density for overpotential measurement, taking into account the cathode radius at steady state. The wire cathodes were etched with nitric acid and then thoroughly washed prior to use to ensure removal of possible surface contaminants.

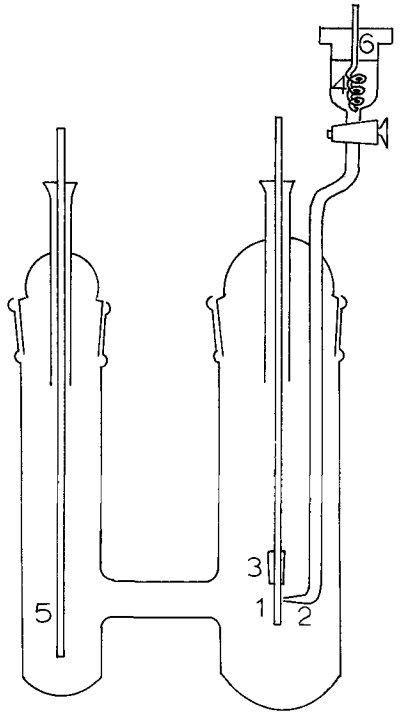

Fig. 1. Electrolytic cell: 1, cathode; 2, Luggin probe; 3, Teflon sleeve; 4, reference electrode; 5, anode; 6, Teflon cap.

* Electrochemical Society Active Member.

Key words: homologous, additives, interaction, free energy, theory.

The preparation of the standard solution (0.5M $CuSO_4$ and 1.0M H_2SO_4) was in all respects the same as described previously (1). High-purity monocarboxylic acids were used as additives and only the normal straight-chain isomers were chosen for study.

Results

The overpotential data in this report are the increments in total steady-state cathode overpotential caused by the additives employed. In these experiments, the overpotential attributable to the standard electrolyte alone with no additive present was 105 ± 5 mV at an apparent current density of 20 mA-cm^{-2}. The overpotential increments were obtained by subtracting this value from the total overpotential in the presence of additive. The total values were reproducible to within ±5%. Steady states were usually obtained after about 45 min of electrolysis.

Data for different concentrations of normal monocarboxylic acids from propanoic to octanoic inclusive are given in Table I. The cathode overpotential increases in each case with increased concentration of additive.

When the overpotential increment is plotted against the concentration of a given additive, it is found that the curve approaches linearity as the concentration approaches zero. Typical behavior is shown in Fig. 2. The initial slopes for all the additives, given in Table II, show that the logarithm of the initial slope increases linearly with the number of methylene groups in the additive molecule, counting the terminal methyl, as shown in Fig. 3. Advantage was taken of this linearity to obtain graphically smoothed overpotential data for the low concentrations of the additives used. For this purpose, smoothed values of the initial slopes as obtained from Fig. 3 are given in the last column in Table II.

Table I. Concentration of additive and cathode overpotential increment

Current density = 20 mA-cm^{-2}; temperature = 25° ± 0.1°C

Additive	C, m/l^{-1}	Δη, mV
Propanoic acid	1.0×10^{-1}	36
	2.5×10^{-1}	62
	5.0×10^{-1}	102
	7.5×10^{-1}	140
	1.0	164
Butanoic acid	2.5×10^{-2}	24
	5.0×10^{-2}	38
	1.0×10^{-1}	88
	2.5×10^{-1}	140
	3.5×10^{-1}	168
Pentanoic acid	7.5×10^{-3}	20
	2.5×10^{-2}	68
	5.0×10^{-2}	110
	7.2×10^{-2}	140
	1.0×10^{-1}	168
Hexanoic acid	2.5×10^{-3}	22
	5.0×10^{-3}	43
	1.0×10^{-2}	84
	1.5×10^{-2}	120
	2.5×10^{-2}	150
Heptanoic acid	1.0×10^{-3}	32
	2.5×10^{-3}	72
	5.0×10^{-3}	110
	7.5×10^{-3}	150
	1.0×10^{-2}	160
	1.6×10^{-2}	170
Octanoic acid	5.0×10^{-4}	37
	8.5×10^{-4}	82
	1.5×10^{-3}	110
	2.3×10^{-3}	146
	4.9×10^{-3}	184

Table II. Slope of Δη vs. C curve as C → 0

Additive	$(\Delta\eta/C)_{C \to 0}$	$(\eta\Delta/C)_{C \to 0}$ (smoothed)
Propanoic acid	2.83×10^{2}	2.86×10^{2}
Butanoic acid	9.10×10^{2}	9.40×10^{2}
Pentanoic acid	3.00×10^{3}	3.08×10^{3}
Hexanoic acid	9.75×10^{3}	1.01×10^{4}
Heptanoic acid	3.55×10^{4}	3.32×10^{4}
Octanoic acid	1.17×10^{5}	1.09×10^{5}

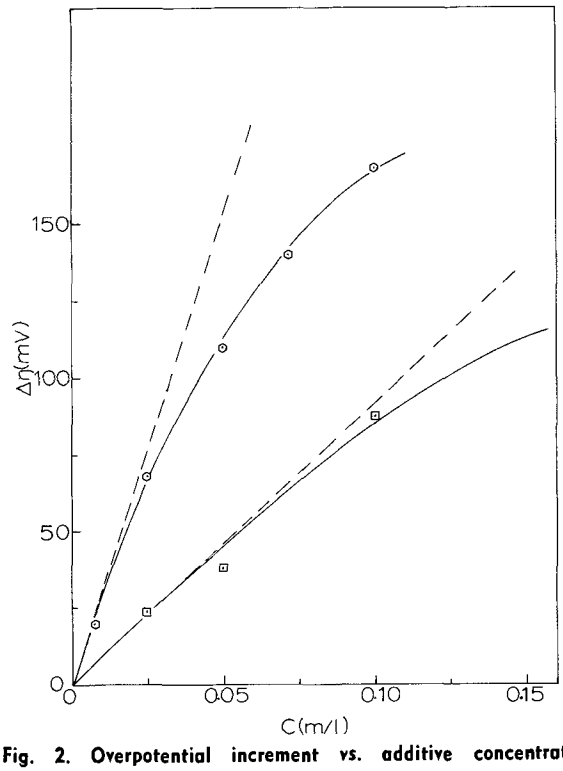

Fig. 2. Overpotential increment vs. additive concentration: □ butanoic acid; ○ pentanoic acid.

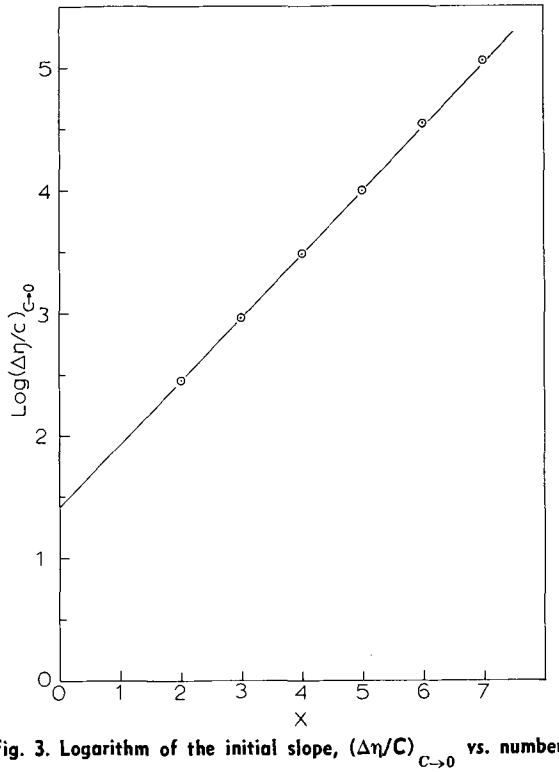

Fig. 3. Logarithm of the initial slope, $(\Delta\eta/C)_{C \to 0}$ vs. number of methylene groups in the monocarboxylic acid molecule.

Overpotentials obtained in this study differ to a degree from those obtained previously with the Haring cell (1). However, just as before (1), and within the accuracy of the measurements, it was found that the Δη *vs.* log C relations for all the homologous monocarboxylic acids can be represented by a family of parallel curves equally spaced along the log C axis as shown in Fig. 4. Advantage was taken of this behavior to obtain graphically smoothed overpotential values for the higher additive concentrations, thus minimizing the effect of error in individual overpotental measurement. The curves in Fig. 4 are the smoothed results

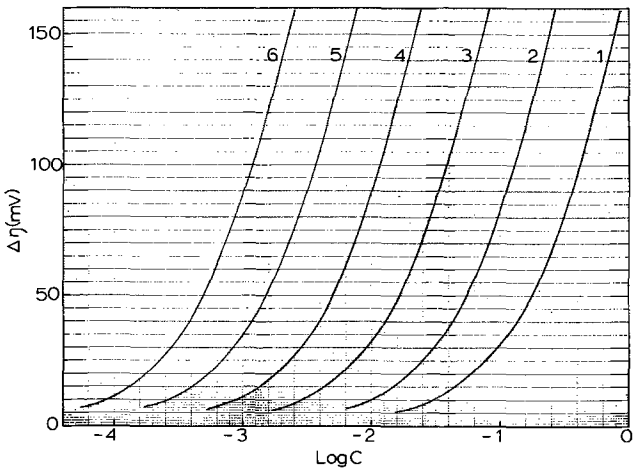

Fig. 4. Overpotential increment vs. logarithm of concentration, monocarboxylic acids: 1, propanoic; 2, butanoic; 3, pentanoic; 4, hexanoic; 5, heptanoic; 6, octanoic.

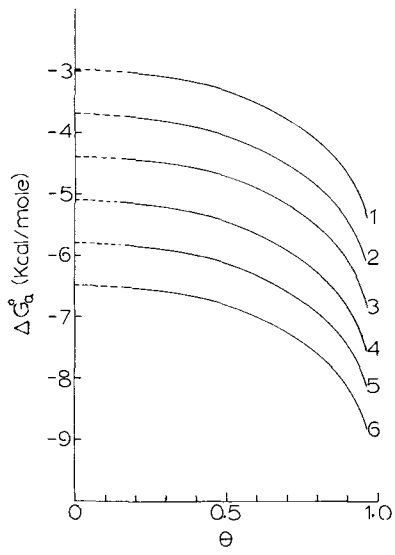

Fig. 5. Free energy of adsorption vs. coverage, monocarboxylic acids: 1, propanoic; 2, butanoic; 3, pentanoic; 4, hexanoic; 5, heptanoic; 6, octanoic.

arising from the data in Table I and the smoothed initial slopes in Table II.

Measurement of steady-state overpotentials at different apparent current densities ranging from about 2 to 20 mA-cm^{-2} gave the same Tafel slope, 52 ± 1 mV, with all the monocarboxylic acids. This indicates that these compounds do not affect the charge-transfer kinetics of copper deposition, their only effect being to increase the true current density in accordance with the simple blocking theory (1, 4, 5).

Discussion

The cathode overpotential effects of normal monocarboxylic acids shown in Fig. 4 can be interpreted and understood in terms of the blocking theory as expressed in the equation (1, 6)

$$\theta = 1 - \exp(-\Delta\eta/b) \qquad [1]$$

where θ is the fraction of the surface covered by adsorbed additive and b is the Tafel slope. Appropriate adsorption theory can be used to derive quantitative relations between the overpotential increment $\Delta\eta$ and additive concentration C.

Calculation of θ from Eq. [1] for the overpotential increments in Fig. 4, with the Tafel slope taken as the experimental 52 mV, and calculation of the standard free energy of adsorption from the Langmuir-type isotherm (1, 7)

$$\frac{\theta}{(1-\theta)^n}\,\frac{\{\theta + n(1-\theta)\}^{n-1}}{n^n} = \frac{C}{55.5}\exp(-\Delta G^\circ_a/RT) \qquad [2]$$

where n, the number of water molecules displaced by a molecule of adsorbed additive, is taken as 2 (1, 8), results in the family of parallel ΔG°_a *vs.* θ curves shown in Fig. 5. It is immediately obvious that the free energy of adsorption of monocarboxylic acids on a copper cathode is markedly dependent on the coverage, becoming increasingly negative with increasing θ. This coverage dependence, which is much the same as that observed by Bockris and Swinkels (7) for the adsorption of n-decylamine on copper, can presumably be attributed to spontaneous lateral interaction in the adsorbed phase (7, 9).

Lateral interaction free energy.—Equation [2], which is a general modification of the Langmuir isotherm for adsorption from solution involving solvent displacement, depends for its basic derivation on the assumption that no lateral interaction occurs in the adsorbed phase (7, 10, 11). In this equation, the adsorption free energy ΔG°_a should therefore be regarded, strictly, as independent of coverage. However, the use of Eq. [2] in calculating ΔG°_a for Fig. 5 assumes the applicability of a modified isotherm similar to that discussed by Conway and Barradas (10) in which ΔG°_a is recognized as coverage dependent.

The curves in Fig. 5 show that the addition of each methylene group to a monocarboxylic acid molecule results in the same increase in the adsorption free energy regardless of coverage. Accordingly, assuming the validity of all procedures leading to Fig. 5, the hydrocarbon part of a monocarboxylic acid makes no significant net contribution to the lateral interaction in the adsorbed phase. This behavior, which is consistent with the applicability of Traube's rule to the adsorption of compounds belonging to a homologous series (1, 12), means that the standard free energy of adsorption of a given monocarboxylic acid on copper can be written as

$$\Delta G^\circ_a = x\,\Delta G^\circ_{CH_2} + \Delta G^\circ_p + g(\theta) \qquad [3]$$

where x is the number of methylene groups present, $\Delta G^\circ_{CH_2}$ is the free energy contribution of each methylene group, ΔG°_p is the contribution of the polar carboxyl group at coverages approaching zero, obviously the same for all the monocarboxylic acids, and $g(\theta)$ is the coverage-dependent lateral interaction free energy, also the same for all the monocarboxylic acids at the same coverage.

An appropriate isotherm for the adsorption from solution of a normal monocarboxylic acid on copper can be written by substituting Eq. [3] for ΔG°_a in [2] and rearranging to give

$$f(\theta)\exp(g(\theta)/RT) = \frac{C}{55.5}\exp\left(\frac{-x\Delta G^\circ_{CH_2} - \Delta G^\circ_P}{RT}\right) \qquad [4]$$

where $f(\theta)$ is the left-hand side of [2]. It will be noted that the θ-dependent exponential factor on the left of [4] is a Frumkin-like correction for lateral interaction (13) except that $g(\theta)$ does not vary linearly with θ at other than very low coverages.

While values of $\Delta G^\circ_{CH_2}$ and ΔG°_P can be estimated by extrapolating the curves in Fig. 5 to zero coverage, it will be useful to consider methods by which these quantities can be obtained more accurately by calculation from the cathode overpotential and additive concentration data.

Calculation of the components of adsorption free energy.—The ΔG°_a *vs.* θ curves in Fig. 5, which are in fact the same $g(\theta)$ *vs.* θ curve, can be shown to correspond very closely to the power series

$$g(\theta) = A\theta + B\theta^2 + C\theta^3 + D\theta^4 + E\theta^5$$

where the coefficients A, B, C, D, and E are −0.56, 2.25,

−12.65, 20.48, and −12.04 kcal, respectively. A more useful quantitative relation is easily derived, however, by rearranging Eq. [4] to give the straight-line equation

$$g(\theta) = RT \ln C - RT \ln f(\theta) - x\Delta G^{\circ}_{CH_2} - (\Delta G^{\circ}_{p} + RT \ln 55.5)$$

where the combination of terms

$$RT \ln C - RT \ln f(\theta) - x\Delta G^{\circ}_{CH_2} = f(C,\theta,x) \quad [5]$$

is the same for all the monocarboxylic acids since the same $g(\theta)$ *vs.* θ relation applies to all. $\Delta G^{\circ}_{CH_2}$ can be calculated directly from the concentration data in Fig. 4 by subtracting Eq. [5] for any two of the additives at a given overpotential increment, since the term $RT \ln f(\theta)$ cancels out in the subtraction. The value found is −704 cal/mole.

To calculate ΔG°_{p}, the free energy contribution of the carboxyl group at zero coverage, it will be necessary to consider the overpotential *vs.* concentration behavior shown in Fig. 3.

Electrosorption effects of monocarboxylic acids at concentrations approaching zero.—The linearity observed in Fig. 3, where the logarithm of the initial slope $(\Delta\eta/C)_{C\to 0}$ is plotted against the number of methylene groups in the monocarboxylic acid molecule, follows as a consequence of the applicability of Traube's rule to this homologous system, and corresponds in essence to the known behavior of these compounds in affecting the surface tension of aqueous solutions as described by Ward (12). A useful equation directly pertinent and applicable to Fig. 3 can be derived from Eq. [4].

According to Fig. 5, $g(\theta)$ becomes zero as θ approaches zero. Application of Eq. [4] to the zero-coverage condition then gives for the homologous monocarboxylic acids

$$f(\theta) = C\left[\frac{e^{-\Delta G^{\circ}_{p}/RT}}{55.5}\right][e^{-\Delta G^{\circ}_{CH_2}/RT}]^{x} = C\alpha\beta^{x} \quad [6]$$

where α and β are constants at constant temperature as shown. On substituting for θ from Eq. [1], and taking n as 2 (1, 8), it is easily shown that $f(\theta)$, the left-hand side of [2], can be written as

$$\tfrac{1}{4}(e^{2\Delta\eta/b} - 1)$$

With these substitutions Eq. [4] becomes

$$e^{2\Delta\eta/b} - 1 = 4C\alpha\beta^{x}$$

which, on substituting the series expansion for $e^{2\Delta\eta/b}$ and dividing through by C, gives

$$\frac{2}{b}\frac{\Delta\eta}{C} + \left(\frac{2}{b}\cdot\frac{\Delta\eta}{C}\right)^{2}\cdot\frac{C}{2!} + \left(\frac{2}{b}\cdot\frac{\Delta\eta}{C}\right)^{3}\cdot\frac{C^{2}}{3!} + \cdots = 4\alpha\beta^{x}$$

In the limit, as C approaches zero for zero coverage, this becomes

$$(\Delta\eta/C)_{C\to 0} = 2b\alpha\beta^{x}$$

The logarithmic form gives the straight-line equation for Fig. 3 as

$$\log (\Delta\eta/C)_{C\to 0} = \log (2b\alpha) + x \log \beta \quad [7]$$

Clearly, according to Eq. [6] and [7], $\Delta G^{\circ}_{CH_2}$ and ΔG°_{p} might be calculated from the experimental slope and intercept, respectively, in Fig. 3. In the present study, because of some uncertainty in the values of $(\Delta\eta/C)_{C\to 0}$ in Table II, the slope for Fig. 3 was first calculated from the value of $\Delta G^{\circ}_{CH_2}$ (−704 cal mole^{-1}) found from Fig. 4 and Eq. [5], and this was then used with the experimental points as shown to find the intercept, as 1.42. Using the experimental 52 mV for the Tafel slope, we then find $\Delta G^{\circ}_{p} = -1570$ cal mole^{-1}.

Certain relevant observations can be made. Since the −704 cal mole^{-1} found for $\Delta G^{\circ}_{CH_2}$ in this study is not very different from the −760 cal mole^{-1} obtained by Ward (12) for the methylene-group contribution to the free energy of adsorption of monocarboxylic acids at the air-solution interface, then, apparently, there is no strong specific interaction between the hydrocarbon chain and the copper surface. In contrast, the −1570 cal mole^{-1} found for ΔG°_{p}, the free energy of adsorption of the bare carboxyl group at zero coverage, is appreciably greater than the adsorption energy at the air-solution interface of methanoic acid, with which the carboxyl group may be theoretically compared. This value for methanoic acid can be estimated roughly as −900 cal mole^{-1} by extrapolating from the results of surface tension measurements made by Ward and Tordai (14) on solutions of the normal monocarboxylic acids, butanoic to decanoic inclusive. The indication here is that significant specific interaction probably does occur between the carboxyl group and the copper surface, and, although the interaction energy appears to be less than 700 cal mole^{-1}, it might be speculatively taken to indicate possible orientation of the carboxyl group toward the metal. This would be contrary to expectation for the adsorption of aliphatic compounds on metals (15), and further study and clarification are required. In any case, if perpendicular orientation actually occurs, then the same value of n in Eq. [2] must apply to the adsorption of all normal monocarboxylic acids regardless of length of the hydrocarbon chain, as appears to be the case.

The quantity β in the above equations is the Traube coefficient for the homologous monocarboxylic acids (12). It is the factor by which the initial slope in Fig. 2 and Table II is multiplied on the addition of each successive methylene group to the additive molecule. Its value as obtained from our data is 3.28.

Theoretical Calculation of $g(\theta)$.—Since $g(\theta)$, the lateral interaction free energy, is not significantly affected by the hydrocarbon part of a monocarboxylic acid molecule (Fig. 5), then it seems reasonable that this free-energy component should be calculable to a first approximation for any coverage θ from only the dipole-dipole interaction expected between adjacent carboxyl groups in the adsorbed phase. Dispersion interaction can be ignored as negligibly small since this effect would in any event arise mainly from the hydrocarbon chain (7).

The interaction between two like dipoles is given by (7)

$$U_{dip.} = -(\mu^{2}_{D}/\epsilon r^{3})$$

where μ_D is the dipole moment, ϵ the dielectric constant of the medium, and r the distance between the dipoles. None of these quantities is accurately known for an adsorbed additive in the primary cathode layer, but reasonable values can be assumed for monocarboxylic acids on the basis of which a calculation of $g(\theta)$ gives approximate agreement with experiment.

The dipole moments of monocarboxylic acids vary with the state and with the solvent, but for a given state the values are nearly the same for all the additives used in this study (16). The pure-liquid value of about 1.3 Debye units will be taken as appropriate in the present calculation since the adsorbed state can be assumed to approximate the liquid state of a particular adsorbate, especially at full coverage. The dielectric constant of the primary layer has been considered to vary linearly with coverage (7, 17). It is assumed to vary in our system from the zero-coverage value of 6 suggested by Bockris, Devanathan, and Müller (15) to the pure-liquid monocarboxylic-acid value of about 2.5 (18) at full coverage, giving $\epsilon = 6 - 3.5\theta$. Finally, an average distance of closest approach between adsorbed dipoles can be estimated from the dimensions of the carboxyl group as about 4Å.

With these values of μ_D, ϵ, and r, and with the added assumption that monocarboxylic acids adsorb on copper in hexagonal array and in parallel orientation (7), it is then possible, using equations given by Bockris and Swinkels (7), to calculate the lateral interaction free energy as the chemical potential due to dipole-dipole interaction, either for localized adsorption from

$$g(\theta) = 9.24\,\theta U_{\text{dip.}}$$

or for nonlocalized adsorption, using

$$g(\theta) = 11.55\,\theta^{3/2} U_{\text{dip.}}$$

The results, converted to kcal mole^{-1}, are shown and compared with the experimental data in Fig. 6.

While it seems that the nonlocalized-adsorption model gives the better agreement with experimental results, no clear distinction can be made between the two models, especially at low coverage, because of the rough approximations used in the calculations. Accordingly, no definite conclusion can be drawn except that dipole-dipole interaction is the most likely cause of the lateral interaction free energy. Adjustment of the parameters can be made to improve agreement with experiment, but the data are not sufficiently reliable to justify this procedure. It should be noted, in addition, that the dipole moment has been treated in this calculation as a constant, while it might in all probability vary with coverage.

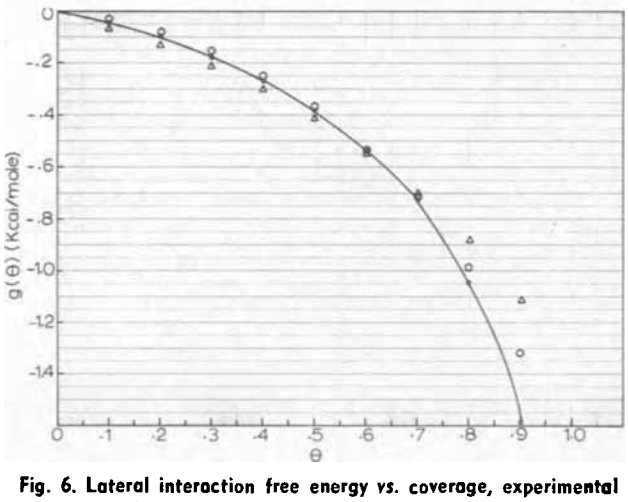

Fig. 6. Lateral interaction free energy vs. coverage, experimental curve compared with calculated values for localized, △, and nonlocalized, ○, adsorption.

Acknowledgments

Many helpful discussions with Dr. R. K. Chan, Chemistry Department, University of Western Ontario, and the financial support of the National Research Council, Ottawa, are gratefully acknowledged.

Manuscript received July 20, 1970.

Any discussion of this paper will appear in a Discussion Section to be published in the December 1971 JOURNAL.

REFERENCES

1. A. K. P. Chu and A. J. Sukava, *This Journal*, **116**, 1188 (1969).
2. K. J. Vetter, "Electrochemical Kinetics," pp. 392-394, Academic Press, New York (1967).
3. R. Piontelli *et al.*, *Z. Elektrochem.*, **58**, 54 (1954).
4. E. Mattson and J. O'M. Bockris, *Trans. Faraday Soc.*, **55**, 1586 (1959).
5. J. O'M. Bockris and M. Enyo, *ibid.*, **58**, 1187 (1962).
6. R. S. Hansen and B. H. Clampitt, *J. Phys. Chem.*, **58**, 908 (1954).
7. J. O'M. Bockris and D. A. L. Swinkels, *This Journal*, **111**, 736 (1964).
8. M. A. V. Devanathan, *Proc. Roy. Soc. London*, **267**, 257 (1962).
9. H. Dahms and M. Green, *This Journal*, **110**, 1075 (1963).
10. B. E. Conway and R. G. Barradas, *Electrochim. Acta*, **5**, 319 (1961).
11. E. Blomgren and J. O'M. Bockris, *J. Phys. Chem.*, **63**, 1475 (1959).
12. A. F. H. Ward, *Trans. Faraday Soc.*, **42**, 399 (1946).
13. E. Gileadi, "Electrosorption," p. 13, Plenum Press, New York (1967).
14. A. F. H. Ward and L. Tordai, *Trans. Faraday Soc.*, **42**, 418 (1946).
15. J. O'M. Bockris, M. A. V. Devanathan, and K. Müller, *Proc. Roy. Soc. London*, **274A**, 55 (1963).
16. A. L. McClellan, "Tables of Experimental Dipole Moments," W. H. Freeman and Co., London (1963).
17. L. Pospisil and J. Kuta, *Coll. Czechoslov. Chem. Commun.*, **34**, 3047 (1969).
18. A. A. Maryatt and E. R. Smith, "Tables of Dielectric Constants of Pure liquids," National Bureau of Standards Circular *514* (1951).

Electrodeposition of Coherent Coatings of Refractory Metals

VII. Zirconium Diboride

G. W. Mellors and S. Senderoff*

Union Carbide Corporation, Parma Research Laboratory, Parma, Ohio 44101

ABSTRACT

The electrodeposition of coherent coatings of zirconium diboride from a solution of ZrF_4 and B_2O_3 in the molten eutectic mixture of NaF-KF-LiF is described. A constant composition is maintained by using a ZrB_2 anode and composition such that no volatile BF_3 is formed. The function of B_2O_3 as an oxide ion getter in the solution is demonstrated.

Zirconium diboride is a hard intermetallic compound, with a melting point in excess of 3000°C, that has, according to recent reports, excellent oxidation resistance at high temperatures, and good stability in contact with many molten metals, *e.g.*, Al and liquid steel. It has been stated (1) that methods for producing ZrB_2 crucibles, boats, tubing, heaters, etc., by pressing in molds are unsatisfactory. A slip casting technique was described as superior, but shrinkage on sintering was excessive, and the final porosity of the articles exceeded 12%. Such articles could probably ideally be made by electroforming with excellent conformation to the dimensions of the substrate and without any porosity.

* Electrochemical Society Active Member.

Key words: zirconium diboride, electrodeposition, refractory metal coatings, fused salts.

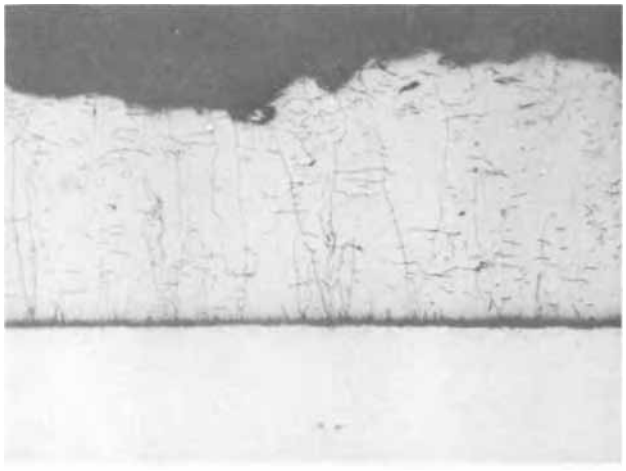

Fig. 1. Cross section of ZrB_2 deposited from pure fluoride melt at 800°C (approximately 150X).

Although there are a number of reports of the electrodeposition of ZrB_2 in particulate form from molten mixed oxide-fluoride systems (2-4) from a mixed fluoride-chloride system (5), and of coherent coatings of TiB_2 from a borate-titanate system (6), the only previous description of the electrodeposition of coherent coatings of ZrB_2 is in a paper (7) and patent (8) by the present authors in which a pure fluoride electrolyte, LiF-KF-K_2ZrF_6-KBF_4, was used for this purpose. Deposits were obtained on stainless steel cathodes by electrolysis of the molten system Flinak[1] containing 9 w/o (weight per cent) ZrF_4 and 10 w/o KBF_4 at 800°C and 250 mA/cm^2 cathode current density. A photomicrograph of this deposit is shown in Fig. 1 and demonstrates the soundness and coherence of this material. The optimum conditions for deposition of ZrB_2 coatings were similar to those for zirconium, but the allowable ranges of current density and temperature were greater and the concentration of boron uncritical above a minimum amount.

Anthony and Welch (3) in discussing this process comment that "this method (7, 8) can be controlled for only a limited period due to the continuous change in melt compositions." The present authors recognized at that time that the use of zirconium metal as anode and the excessive volatility of BF_3 led to composition changes in the bath. In order to obtain a more satisfactory process the following problems had to be overcome: (*a*) at the anode, 4**F** dissolve 1 mole of zirconium while 10**F** are required to deposit 1 mole of ZrB_2 at the cathode and there is thus a net increase of zirconium in the bath; (*b*) while only a relatively low boron content (approx. 1 ~ 3 w/o) is required, the addition has been made as KBF_4 which increases the quantity of KF in the solution; and (c) from this solution boron trifluoride will volatilize, and therefore on prolonged standing the concentration will be reduced to essentially zero. If a ZrB_2 anode could be used in this system, and if BF_3 could be added continuously to the melt to replace the volatilized BF_3, these problems could be solved. Alternatively, a source of boron other than KBF_4 may be sought. Experiments carried out with Flinak-ZrF_4 melts through which BF_3 was bubbled with an argon carrier showed that ZrB_2 could be deposited using a Zr anode. However, the agitation caused by the passage of these gases produced deposits rougher than normal. It became obvious that the bubbler system must be baffled in some manner since the high vapor pressure and low solubility of BF_3 in this bath suggest that to obtain a workable boron concentration the additions of BF_3 must be continuous and not batch-wise. Literature figures (9)

[1] "Flinak" is the acronym for the eutectic composition of KF-LiF-NaF which melts at 454°C. Its composition in mole per cent is 46.5 LiF, 11.5 NaF, 42.0 KF.

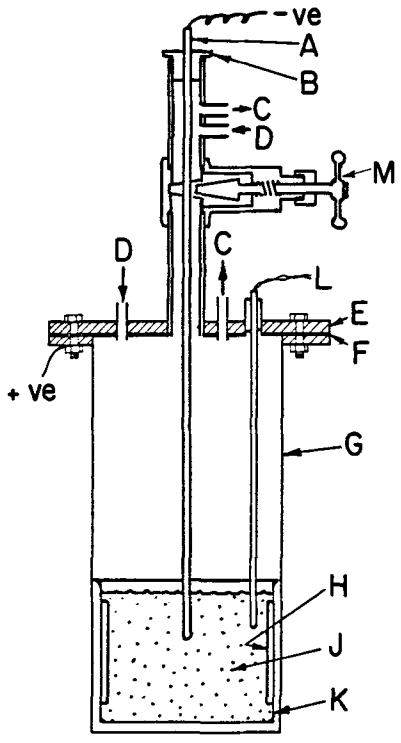

Fig. 2. Apparatus used in electrolysis of fluoride and fluoride-oxide melts: A, stainless steel cathode; B, "Teflon" stopper; C, argon outlets; D, argon inlets; E, stainless steel lid; F, "Teflon" or Sauereisen gasket; G, "Hastelloy, alloy X" can; H, zirconium or ZrB_2 anode; J, fluoride melt; K, nickel or stainless steel crucible; L, thermocouple and well; M, gate valve (1 in.).

indicate that, at 700°C at the saturating pressure of 1.90 atm, the solubility of BF_3 is 6.30 x 10^{-5} moles/cc of melt in the LiF-BeF_2-ZrF_4-ThF_4-UF_4 (65-28-5-1-1) melt. Assuming these figures apply to the Flinak-ZrF_4 melts under discussion here, then at 700°C under about 2 atm pressure a concentration of 0.43 w/o BF_3 could be maintained. This would probably be sufficient for continuous ZrB_2 plating.

The present paper describes further work using pure fluoride melts and some extensions using B_2O_3 additions rather than KBF_4 or BF_3 to overcome this problem.

Experimental

ZrF_4 and K_2ZrF_6 were obtained from General Chemical Division, Allied Chemical and Dye Corporation.

Zirconium in sheet form was obtained from Reactive Metals Inc.

Alkali fluorides (ACS specifications) were obtained from Fisher Scientific Company.

Boron trioxide was obtained from either Matheson, Coleman and Bell or from American Potash and Chemical Corporation.

Zirconium diboride was obtained from the Carborundum Company.

Boron trifluoride was obtained from Harshaw Chemical Company.

Electrolytic cells.—The melts were contained in either a nickel or ATJ graphite[2] crucible. The electrolytic operations were carried out in the apparatus of Fig. 2 which has been described in an earlier publication (10).

Results

Experiments were carried out in the low melting system KF (32.4 w/o)-ZrF_4 (67.6 w/o), mp 390°C. This system will not yield coherent zirconium metal on electrolysis and on the addition of KBF_4 produces mixtures of Zr and ZrB_2 powders. Thus the advantage

[2] Carbon Products Division, Union Carbide Corporation.

of lower BF_3 volatility at 400°-425°C is completely negated by the failure to yield coherent ZrB_2.

The problems of volatility made it necessary to seek other sources of boron for these melts. During work on the electrodeposition of zirconium (11) 0.6 w/o B_2O_3 was added to a working bath in an effort to make ZrB_2 or perhaps to observe an "addition agent" effect. However, the cathodic product obtained between 625° and 750°C was a compacted powder, and little was done further in that direction at that time.

Present work indicates that additions of about 10 w/o B_2O_3 to systems of the type Flinak-(or KF-LiF) ZrF_4 yield far more interesting results. Electrolysis of the melt containing Flinak (80 w/o)-ZrF_4 (8 w/o)-B_2O_3 (12 w/o) in a graphite crucible at 750°C produces a smooth, dark colored deposit at 100% cathode current efficiency, based on the assumption of 10 F/mole of ZrB_2. The anode was zirconium and the cathode a nickel strip. X-ray investigation of the deposit shows it to be ZrB_2, but a photomicrograph (Fig. 3) reveals a poor structure having many voids and inclusions of salts. On raising the temperature to 800°C, a bright, coherent plate was obtained (at 100% cathode current efficiency) that again was identified as ZrB_2. However, the photomicrograph now showed a sound, void free, columnar structure (Fig. 4a). It will be noticed that there exists a considerable diffusion layer between the ZrB_2 and the nickel substrate. This layer is a nickel boride, from which zirconium is absent. By the same token nickel is absent from the ZrB_2 deposit. This indicates that some boron diffuses into the nickel from the initially deposited ZrB_2, resulting in a deposit at the interface having a B:Zr ratio slightly less than two. Electron probe analysis indicates that the intermediate layer is, in all probability, Ni_3B, and it is thought that the presence of this material contributes to the adherence of ZrB_2 to the substrate.

Fig. 3. Plate and cross section of ZrB_2 deposited from fluoride-B_2O_3 melt on nickel at 750°C (approximately 200X).

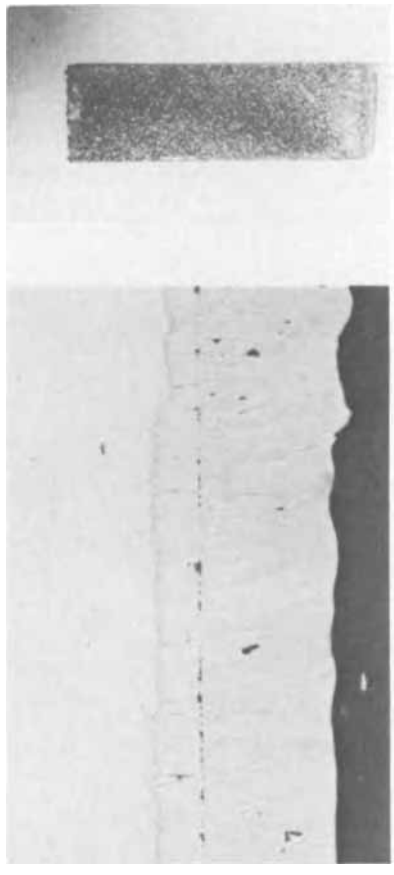

Fig. 4a. Plate and cross section of ZrB_2 deposited from fluoride-B_2O_3 melt on nickel at 800°C (approximately 200X).

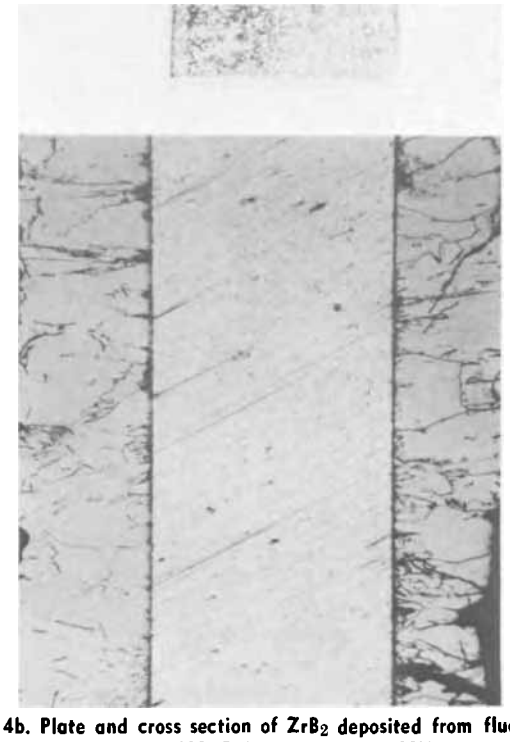

Fig. 4b. Plate and cross section of ZrB_2 deposited from fluoride-B_2O_3 melt on copper at 800°C (approximately 200X).

On copper substrates, adhesion is again excellent, but a photomicrograph (Fig. 4b) shows the almost complete absence of a diffusion layer. Figure 4c is a cross section of a deposit on an ATJ graphite substrate.

Fig. 4c. Plate and cross section of ZrB_2 deposited from fluoride-B_2O_3 melt on ATJ graphite at 800°C (approximately 500X).

Analysis of the bath after the run producing the deposit of Fig. 4a showed 5.81 w/o Zr, 1.77 w/o B, and 6.11 w/o oxygen.

The effect of temperature was shown to be completely reproducible and reversible. If the temperature were lowered from 800°C to 750°C, a poor plate of the type shown in Fig. 3 was obtained. On raising the temperature again to the region of 800°-810°C, the good quality, bright coherent material having the microstructure of Fig. 4a was again deposited. Although excellent plates may be obtained at temperatures in excess of 900°C, it is preferable to operate at 800°C in view of the increased durability of apparatus at the lower temperature.

The cathode current density may range from 5 to 100 mA/cm², but the plates become significantly rougher with increasing current density.

Continued running of Zr anodes through melts of the Flinak-ZrF_4-B_2O_3 type and extraction of ZrB_2 ultimately leads, as previously mentioned, to significant composition changes. However, considerably before the boron content was exhausted, the apparent cathode efficiency increased suddenly to 250-300% (based on the assumption of 10 F/mole of ZrB_2 deposited). The deposits, although superficially satisfactory, were proved to be compacted powders on closer examination. These powders were analyzed and found to be mixtures of ZrB_2 and a glassy phase consisting of ZrO_2 and alkali zirconates. It was this occluded material which caused the apparently high values of current efficiency.

It was found that if B_2O_3 were added to the system, then good deposits of ZrB_2 might again be obtained for a limited time. After the passage of 28 A-hr, through the approximately 1300g of melt, compacted powder deposits of ZrB_2/ZrO_2/zirconate were again produced. Four separate additions each of 100g B_2O_3 were made, but when this procedure was attempted a fifth time the bath could not be resuscitated. Analyses indicated that the bath now contained approximately 32 w/o B_2O_3 and 30 w/o K_2ZrF_6. This, of course, does not imply that boron, oxygen, and zirconium are present as these entities, but serves to indicate the large changes in the concentrations of these materials from the initial values. Experiments were performed with baths containing 35 w/o B_2O_3 initially and between 10 and 30 w/o K_2ZrF_6. These compositions would not plate coherent ZrB_2 under any set of conditions. Also, when melts consisting initially of Flinak-K_2ZrF_6 (or ZrF_4) and $Na_2B_4O_7$ were electrolyzed, nothing but compacted ZrB_2/ZrO_2/zirconate powders were obtained. The implications of these results will be considered later in the Discussion section.

It was thought that possibly a reaction of B_2O_3 with molten alkali fluorides might be involved in this process, especially as compounds with B-O-F linkages are known. For example, in the preparation of BF_3, the following reaction occurs

$$KBF_4 + 2B_2O_3 \rightarrow K[B_4O_6F] + BF_3\uparrow$$

B_2O_3 (119g) was reacted with KF (95.2g) at 800°C. A little gas was evolved that turned out to be dissolved water vapor from the B_2O_3, not BF_3 as might be expected from the above equation. Analysis of the product after holding overnight at temperature gave the following results:

%	Nominal Initial Composition	Analyzed Final Composition
B	17.46	17.42
O	38.10	31.00
K	29.91	29.70
F	14.53	13.70
Totals	100.00	91.82

It may be concluded that BF_3 is not formed from these components and, in view of the near constancy of three of the four elements, it is likely that the difficulties of oxygen analysis may account for the discrepancy in the fourth. The very small loss of fluoride, if real, may have been as HF resulting from hydrolysis with the water vapor impurity.

It was now evident that the mixed oxide-fluoride system had overcome one of the major difficulties experienced with the pure fluoride melt, *i.e.*, that of volatility of BF_3. However, owing to the use of zirconium anodes, the zirconium concentration in the melt was increasing while on the other hand, that of the boron was decreasing. To determine whether ZrB_2 could be used as an anode, a new bath containing Flinak (80 w/o)-ZrF_4 (10 w/o)-B_2O_3 (10 w/o) was electrolyzed with a centrally mounted zirconium anode in a graphite crucible which also acted as a cathode. A layer of ZrB_2 was thus built up on the walls of the crucible. On making the ZrB_2-plated crucible the anode and inserting a centrally located nickel cathode, good quality ZrB_2 was deposited on the cathode. This experiment demonstrated that electroformed ZrB_2 is a satisfactory anode.

To prove the point beyond all reasonable doubt, it would be more desirable to electroform a ZrB_2 anode in one cell followed by the electrorefining of this material through a second cell.

A deposit of ZrB_2 about 0.2 in. total thickness on a copper cathode was prepared by electrolysis of a Flinak-ZrF_4-B_2O_3 melt in a nickel crucible using a zirconium anode. This cathode was then made the anode in an identical second cell. An excellent deposit was obtained and is shown together with a photomicrograph in Fig. 5.

A commercially obtained compacted slug of ZrB_2 [3] (1 in. diameter, 4 in. long) proved to be a very satisfactory anode, dissolving smoothly at 100% anode current efficiency and depositing clean coherent ZrB_2

[3] Carborundum Company.

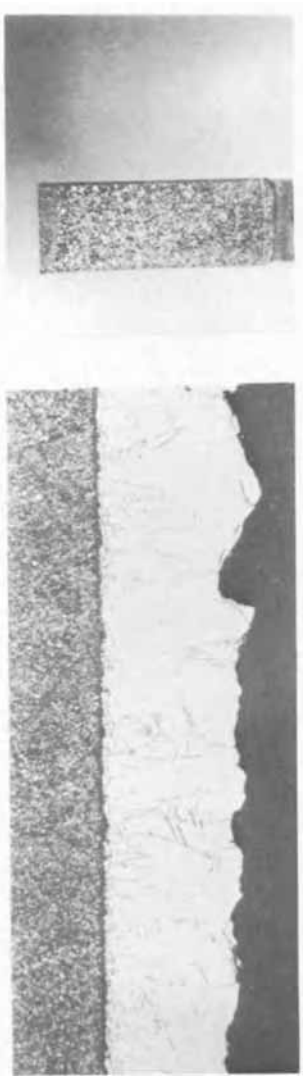

Fig. 5. Plate and cross section of ZrB_2 electrodeposit from fluoride-B_2O_3 melt on copper at 800°C (approximately 200X). Anode: electroformed ZrB_2 made by authors.

Fig. 6. Plate and cross section of ZrB_2 plated from fluoride-B_2O_3 melt on copper at 800°C (approximately 200X). Anode: pressed ZrB_2 (Carborundum Company).

at 100% cathode current efficiency. A typical sample prepared at 810°C is shown together with a photomicrograph of the same material in Fig. 6. The substrate material is copper.

A life test was performed on the above bath and continued until 90.35 A-hr had been passed through the cell which would correspond to the dissolution and deposition of 38.4g ZrB_2 (1 A-hr deposits 0.425g ZrB_2). The initial composition of the cell contained 32.18g Zr and 22.0g B, so it may be seen that while almost complete turnover of the zirconium has been achieved (38.4g ZrB_2 contains 31.03g Zr and 7.37g B) some time remains before the same can be said for the boron. The reason for the relatively slow rate of turnover is that it is necessary that the anode current density be of the order of 5 mA/cm^2 to obtain satisfactory dissolution. Given the present anode together with the geometry of the small laboratory cells, it has been necessary to operate at a slower rate than would be possible with larger equipment. In the latter case one would arrange for a large anode area and obtain consequent low anode current density while a reasonable plating rate would be obtained with a cathode current density of 50 mA/cm^2, *i.e.*, anode:cathode area ratio of 10:1.

Chemical analysis of a typical ZrB_2 deposit showed 79.85% Zr and 19.80% boron compared with the theoretical values of 80.82 and 19.18%, respectively. X-rays of many samples showed excellent matches for both "d" spacings and intensities with the ASTM card. There were no extraneous lines in the patterns.

Discussion

The uniqueness of the present method is that under the experimental conditions and compositions described, it produces only coherent ZrB_2 deposits. The authors have confirmed that the mixed chloride-powders and the oxide-chloride or oxide-chloride-fluoride mixtures are no better. Fullam (5) noted the fluoride bath of Fullam (5) produces only compacted adverse effect of oxide on the purity and yield of ZrB_2. The deposits of Anthony and Welch (3) were also compacted powders containing considerable amounts of occluded electrolyte as can be seen in Fig. 3 of ref. (3).

Although in practice the fluoride-oxide baths described in this paper would be operated using ZrB_2 anodes, the experiments described above in which zirconium anodes were used are valuable in throwing light on the mechanism of the process.

When zirconium anodes are used the zirconium content increases while that of boron decreases. It was found that additions of B_2O_3 would restore the bath to operating condition, but that this process could not be continued *ad infinitum*. At a certain level of B_2O_3 ($\approx$ 32 w/o), the bath failed, and baths made up initially containing this amount of B_2O_3 would not yield coherent deposits under any circumstances.

Analyses showed that, although in all cases sufficient boron and zirconium were present in the bath, when the O/B mole ratio exceed 1.75, the bath failed, *i.e.*, it produced compacted powder deposits of ZrB_2 and ZrO_2. Therefore it is believed that the mechanism of bath revival may be as follows: as the system is electrolyzed boron is extracted, the O/B mole ratio increases above 1.5 (that of B_2O_3) and the reaction occurs.

$$2B_2O_3 + O^{2-} \rightarrow B_4O_7^{2-}$$

When the O/B ratio exceeds that in $B_4O_7^{2-}$, *i.e.*, 1.75, compounds containing oxygen-zirconium bonds are formed, perhaps of the zirconyl type $[ZrO]^{2+}$, and these may not be reducible at a cathode to form coherent ZrB_2. When fresh B_2O_3 is added to the system the reaction

$$[ZrO]^{2+} + 2B_2O_3 \rightarrow B_4O_7^{2-} + Zr^{4+}$$

then takes place. As evidence for this hypothesis the fact is offered that if melts of Flinak-K_2ZrF_6 and $Na_2B_4O_7$ are electrolyzed only compacted powders are obtained. However, on adding B_2O_3 to the melt, despite the presence of $Na_2B_4O_7$, coherent ZrB_2 is then deposited at 100% cathode current efficiency.

It is not implied firmly that $B_4O_7^{2-}$ is the limiting composition; since boron-oxygen structures are numerous, it could well be that a more complex entity is involved. What is fairly certain is that B_2O_3 acts as a getter for excess O^{2-} ions, thus preserving the Zr^{4+} in fluoride complexes for reduction at a cathode.

A perusal of Andrieux's (2) work shows that the O/B ratio of his melts was always well in excess of 7.75 and, if the above hypothesis has validity, not unsurprisingly, powder deposits were always obtained by this author.

Applying this postulate to the work of Anthony and Welch the oxygen:boron ratio of the added oxide components was 2.5:1 whereas the total oxygen:boron ratio was 0.455, including the boron originally associated with KBF_4. It may be that the former ratio is more important, and this would imply that there was insufficient B_2O_3 at the outset to getter all the oxide ions present. Thus, coherent deposits were not obtained.

It is perhaps valuable to contrast and compare the bulk compositions used in the present work, ref. (2) by the same authors and Anthony and Welch (3), as shown in Table I.

Reference has already been made in the preceding text to the deleterious effects of small amounts of B_2O_3 to working fluoride-zirconium baths (11), and it may be that the failure to produce coherent deposits from the solution of ref. (3) may be in part explained by the low B_2O_3 concentration.

Table I. Solutions for electrodepositing ZrB_2

Present work		Ref. (2)		Ref. (3)	
Material	w/o	Material	w/o	Material	w/o
NaF	9.36	—	—	—	—
KF	47.20	KF	60.29	KF	40.41
LiF	23.44	LiF	24.45	—	—
ZrF_4	8.00	ZrF_4	8.80	ZrF_4	38.79
B_2O_3	12.00	—	—	B_2O_3	1.81
—	—	BF_3	6.46	BF_3	15.80
—	—	—	—	ZrO_2	3.19

Summary

Zirconium boride has been anodically dissolved and cathodically deposited as a coherent coating in both Flinak-ZrF_4-KBF_4 and Flinak-ZrF_4-B_2O_3 solutions. The latter solution has been found to be a superior medium for this purpose mainly because of the negligible volatility of the boron compounds in this solution. Coherent deposits of ZrB_2 have been obtained at 100% cathode current efficiency. Ranges of composition, current density, and temperature for satisfactory operation have been established. The preferred composition is shown in the first column of Table I. The preferred cathode current density and temperature are approximately 50 mA/cm^2 and 800°C, and ZrB_2, operated at 5 mA/cm^2, is the preferred anode material. Consideration of the composition changes when using Zr anodes and when resuscitating the bath with B_2O_3 additions has led to useful concepts regarding the nature of the interaction between zirconium fluoride complexes and B_2O_3. The use of ZrB_2 anodes has been shown to be feasible, and that when such anodes are used, the bath composition remains constant indefinitely, with no replenishment of salts required.

Photomicrographs of deposits show sound columnar material and the adherence to thin sheets and tubes of copper, nickel, graphite, and other substrates is excellent. A thicker than usual diffusion layer, shown in all probability to be Ni_3B, is present when ZrB_2 is deposited on nickel.

Acknowledgment

The authors gratefully acknowledge the experimental work of G. W. Sheffield and R. L. Zupancic.

Manuscript submitted June 16, 1970; revised manuscript received Aug. 20, 1970.

Any discussion of this paper will appear in a Discussion Section to be published in the December 1971 JOURNAL.

REFERENCES

1. A. G. and G. G. Dobroval'skii, T. A. Lyudvinskaya, and E. Ya. Popichenki, *Inorg. Materials*, **2**, 735 (1966).
2. J. L. Andrieux, *Ann. Chim.*, **12**, 423 (1929).
3. K. E. Anthony and B. J. Welch, *Austr. J. Chem.*, **22**, 1593 (1969).
4. F. W. Glaser, *Powder Met. Bull.*, **6**, 51 (1951).
5. H. T. Fullam, "Metallic Borides and Silicides by Fused Salt Electrolysis," Ph.D. Thesis, University Washington (1956).
6. D. Schlain, F. X. McCawley, and C. Wyche, *This Journal*, **116**, 1227 (1969).
7. G. W. Mellors and S. Senderoff, *ibid.*, **113**, 60 (1966).
8. G. W. Mellors and S. Senderoff, Can. Pat. 688,546 (1964); U.S. Pat. 3,444,058 (1969).
9. ORNL 3122 (MSR Progress Report, Feb. 28, 1961) p. 113, Oak Ridge National Laboratory, Oak Ridge, Tenn.
10. G. W. Mellors and S. Senderoff, *This Journal*, **112**, 266 (1965).
11. G. W. Mellors and S. Senderoff, Unpublished data (1961).

Metal/Metal Ion Electrodes with Two Charge-Transfer Steps: Me_x-Alloy/Me^{z+} and $Me^{z+}/Me^{(z+1)+}$ Potentiostatic Transients under Charge-Transfer and Diffusion Control

K. J. Bachmann

Bell Telephone Laboratories, Incorporated, Murray Hill, New Jersey 07974

ABSTRACT

A theoretical treatment of the transients obtained in potentiostatic single pulse experiments on metal alloy/metal ion electrodes coupled to a redox reaction is presented. Formulas have been derived for the concentration of the electrochemically active component in the alloy and of the corresponding metal ions of different valent state which form the redox couple in the electrolyte, respectively, as a function of the distance from the interface and the duration of the voltage pulse. Expressions for the partial current densities carried by the two consecutive charge-transfer reactions, $Me = Me^{z+} + ze^-$ and $Me^{z+} = Me^{(z+1)+} + e^-$, and for the total current density flowing through the cell have been worked out. Analysis of the current density transients on the basis of these expressions allows interpretation of experimental curves in terms of the characteristic kinetic parameters of the electrochemical system.

In electrochemical systems containing polyvalent ions, the over-all electrode reaction frequently involves a series of consecutive charge-transfer steps. Although the theory for interpreting experiments under steady-state conditions is well established (1, 2), very little is known on the behavior of such systems under nonsteady-state conditions.

In a preceding paper (3) potentiostatic transients on a pure metal/metal ion electrode with two charge-transfer steps were considered assuming that the surface of the metal remains in equilibrium with the bulk of the metal. It is the aim of this paper to extend the treatment to alloy electrodes where changes in the concentration of the electrochemically active component (Me) at the interface, *i.e.*, diffusion of Me in the alloy, has to be taken into account. Examples of this would be the well-known amalgam electrodes and other types of liquid metal alloy electrodes. At the elevated temperatures of molten salt systems also a sizable mass flow occurs in solid alloy electrodes which are included in this treatment. It should be pointed out, however, that surface alloying ("metalliding") of a pure metal which inherently starts from nonequilibrium conditions requires an independent consideration.

The first charge-transfer step which is considered here is the metal/metal ion charge-transfer reaction

$$Me = Me^{z+} + ze^- \qquad [1]$$

in which the electrochemically active component of the alloy is anodically removed or cathodically deposited on the interface. This charge transfer reaction is coupled to a redox reaction

$$Me^{z+} = Me^{(z+1)+} + e^- \qquad [2]$$

in which the metal ion changes its valency by 1.

Derivation of Concentration of Me in the Alloy and of Me^{z+} and $Me^{(z+1)+}$ in the Electrolyte, Respectively, as a Function of Distance from Interface and of Duration of Voltage Pulse

In the formulation of the diffusion problem, the following assumptions are made:

1. The only irreversible processes are charge-transfer and diffusion in the alloy and in the electrolyte, respectively. In molten salt systems certain metals are soluble in the electrolyte melt as uncharged particles. It is assumed that this does not apply to the metal electrodes treated here.

2. A perfectly rectangular voltage pulse is applied to the electrode.

3. Prior to the voltage pulse the electrode is in equilibrium in respect to both reaction [1] and [2].

4. Changes in the activity coefficients of Me, Me^{z+} and $Me^{(z+1)+}$ can be neglected, *i.e.*, only small signals are considered.

5. The electrode surface is an infinite plane, so that diffusion takes place in a direction x perpendicular to the interface. Although the metal diffuses in a different half volume than the ions Me^{z+} and $Me^{(z+1)+}$, x will be always taken ≥ 0, *i.e.*, x will be defined as distance from the interface. This convention considerably facilitates economical formulation of the diffusion equations and their solutions.

6. Neither stirring nor convection limits the diffusion layer thickness.

7. The disproportionation reaction

$$(z + 1)\ Me^{z+} = zMe^{(z+1)+} + Me$$

does not occur.

If these conditions are fulfilled, the diffusion of Me, Me^{z+} and $Me^{(z+1)+}$ is described by

$$\frac{\partial c_r}{\partial t} = D_r \frac{\partial^2 c_r}{\partial x^2} \qquad [3]$$

$$\frac{\partial c_m}{\partial t} = D_m \frac{\partial^2 c_m}{\partial x^2} \qquad [4]$$

$$\frac{\partial c_o}{\partial t} = D_o \frac{\partial^2 c_o}{\partial x^2} \qquad [5]$$

where $c_r = c_r(x,t)$ is the concentration of Me (most reduced substance of the electrochemical system) in the alloy, $c_m = c_m(x,t)$ is the concentration of Me^{z+} (intermediate substance) and $c_o = c_o(x,t)$ is the concentration of $Me^{(z+1)+}$ (most oxidized substance) in the electrolyte. D_r, D_m, and D_o are the diffusion constants of Me, Me^{z+}, and $Me^{(z+1)+}$, respectively.

The initial conditions are

$$c_r = c_{r,0};\ c_m = c_{m,0};\ c_o = c_{o,0} \text{ for } 0 \leq x \leq \infty \text{ and } t = 0 \qquad [6]$$

The boundary conditions are

$$c_r = c_{r,0};\ c_m = c_{m,0};\ c_o = c_{o,0} \text{ for } x = \infty \text{ and } t \geq 0 \qquad [7]$$

• Key words: potentiostatic single pulse method, electrochemical kinetics.

$$\frac{\partial c_r}{\partial x} = \frac{i_r}{zFD_r} \text{ for } x = 0 \text{ and } t \geqq 0 \quad [8]$$

$$\frac{\partial c_m}{\partial x} = \frac{zi_o - i_r}{zFD_m} \text{ for } x = 0 \text{ and } t \geqq 0 \quad [9]$$

$$\frac{\partial c_o}{\partial x} = -\frac{i_o}{FD_o} \text{ for } x = 0 \text{ and } t \geqq 0 \quad [10]$$

$i_r = i_r(t)$ and $i_o = i_o(t)$ are the current densities carried by reaction [1] and reaction [2], respectively. The total current density is

$$i(t) = i_r(t) + i_o(t) \quad [11]$$

Since the partial current densities $i_r(t)$ and $i_o(t)$ are related to the concentrations $c_r(0,t)$, $c_m(0,t)$ and $c_o(0,t)$ by the equations

$$i_r(t) = i_{r,0} \cdot \frac{c_r(0,t)}{c_{r,0}} \cdot \exp\left(\frac{\alpha_r zF}{RT}\eta\right) - i_{r,0} \cdot \frac{c_m(0,t)}{c_{m,0}} \cdot \exp\left(-\frac{[1-\alpha_r]zF}{RT}\eta\right) = \frac{c_r(0,t)}{c_{r,0}} \cdot i_{r,+} - \frac{c_m(0,t)}{c_{m,0}} \cdot i_{r,-} \quad [12]$$

and

$$i_o(t) = i_{o,0} \cdot \frac{c_m(0,t)}{c_{m,0}} \exp\left(\frac{\alpha_o F}{RT}\eta\right) - i_{o,0} \cdot \frac{c_o(0,t)}{c_{o,0}} \exp\left(-\frac{[1-\alpha_o]F}{RT}\eta\right) = \frac{c_m(0,t)}{c_{m,0}} \cdot i_{o,+} - \frac{c_o(0,t)}{c_{o,0}} \cdot i_{o,-} \quad [13]$$

the differential Eq. [3], [4], and [5] are coupled by the boundary conditions [8], [9], and [10]. Both anodic currents and overvoltages (η) are taken positive. The terms $i_{r,0}$ and $i_{o,0}$ represent the exchange current densities for the two charge transfer reactions [1] and [2], respectively. The terms α_r and α_o are the corresponding charge transfer coefficients. $i_{r,+}$; $i_{o,+}$ and $i_{r,-}$; $i_{o,-}$ are the partial anodic and cathodic current densities (all taken positive), as determined by charge-transfer only. The differences

$$i_{r,D} = i_{r,+} - i_{r,-} \text{ and } i_{o,D} = i_{o,+} - i_{o,-} \quad [14]$$

represent the current densities carried by reaction [1] and [2] under pure charge-transfer control, *i.e.*, when no changes in the concentrations c_r, c_m, and c_o have yet occurred at the interface. Since under potentiostatic conditions the exponentials in Eq. [12] and [13] are constants, boundary conditions [8], [9], and [10] can be rewritten as

$$\left(\frac{\partial c_r}{\partial x}\right)_{x=0} = K_1 c_r(0,t) - K_2 c_m(0,t) \quad [15]$$

$$\left(\frac{\partial c_m}{\partial x}\right)_{x=0} = -K_3 c_r(0,t) + K_4 c_m(0,t) - K_5 c_o(0,t) \quad [16]$$

$$\left(\frac{\partial c_o}{\partial x}\right)_{x=0} = -K_6 \cdot c_m(0,t) + K_7 c_o(0,t) \quad [17]$$

where K_1, K_2 - - -, K_7 are constants. With the initial conditions [6] and the boundary conditions [7], [15], [16], and [17] the differential Eq. [3], [4], and [5] have the following solutions

$$\frac{c_r(x,t)}{c_{r,0}} = 1 - \frac{i_{r,D}}{zF\sqrt{D_r}c_{r,0}} \cdot \frac{\sqrt{\tau_1\tau_2}}{\sqrt{\tau_1}-\sqrt{\tau_2}} \cdot F_r(x,t) - \frac{i_{r,D}i_{o,-}\sqrt{D_m}c_{m,0} + (i_{r,D}i_{o,+} + i_{o,D}i_{r,-})\sqrt{D_o}c_{o,0}}{i_{r,-}i_{o,-}\sqrt{D_r}c_{r,0} + i_{r,+}i_{o,-}\sqrt{D_m}c_{m,0} + i_{r,+}i_{o,+}\sqrt{D_o}c_{o,0}} \cdot G_r(x,t) \quad [18]$$

$$\frac{c_m(x,t)}{c_{m,0}} = 1 + \frac{i_{r,D} - zi_{o,D}}{zF\sqrt{D_m}c_{m,0}} \cdot \frac{\sqrt{\tau_1\tau_2}}{\sqrt{\tau_1}-\sqrt{\tau_2}} \cdot F_m(x,t) + \frac{i_{r,D}i_{o,-}\sqrt{D_r}c_{r,0} - i_{o,D}i_{r,+}\sqrt{D_o}c_{o,0}}{i_{r,-}i_{o,-}\sqrt{D_r}c_{r,0} + i_{r,+}i_{o,-}\sqrt{D_m}c_{m,0} + i_{r,+}i_{o,+}\sqrt{D_o}c_{o,0}} \cdot G_m(x,t) \quad [19]$$

$$\frac{c_o(x,t)}{c_{o,0}} = 1 + \frac{i_{o,D}}{F\sqrt{D_o}c_{o,0}} \cdot \frac{\sqrt{\tau_1\tau_2}}{\sqrt{\tau_1}-\sqrt{\tau_2}} \cdot F_o(x,t) + \frac{(i_{r,+}i_{o,+} - i_{r,-}i_{o,-})\sqrt{D_r}c_{r,0} + i_{o,D}i_{r,+}\sqrt{D_m}c_{m,0}}{i_{r,-}i_{o,-}\sqrt{D_r}c_{r,0} + i_{r,+}i_{o,-}\sqrt{D_m}c_{m,0} + i_{r,+}i_{o,+}\sqrt{D_o}c_{o,0}} \cdot G_o(x,t) \quad [20]$$

The functions $F_j(x,t)$ and $G_j(x,t)$ are defined by

$$F_j(x,t) \equiv \exp\left(\frac{x}{\sqrt{D_j\tau_1}} + \frac{t}{\tau_1}\right)\operatorname{erfc}\left(\frac{x}{2\sqrt{D_jt}} + \sqrt{\frac{t}{\tau_j}}\right) - \exp\left(\frac{x}{\sqrt{D_j\tau_2}} + \frac{t}{\tau_2}\right)\operatorname{erfc}\left(\frac{x}{2\sqrt{D_jt}} + \sqrt{\frac{t}{\tau_2}}\right) \quad [21]$$

and

$$G_j(x,t) \equiv \operatorname{erfc}\left(\frac{x}{2\sqrt{D_jt}}\right) - \frac{\sqrt{\tau_1}}{\sqrt{\tau_1}-\sqrt{\tau_2}} \cdot \exp\left(\frac{x}{\sqrt{D_j\tau_1}} + \frac{t}{\tau_1}\right)\operatorname{erfc}\left(\frac{x}{2\sqrt{D_jt}} + \sqrt{\frac{t}{\tau_1}}\right) + \frac{\sqrt{\tau_2}}{\sqrt{\tau_1}-\sqrt{\tau_2}} \cdot \exp\left(\frac{x}{\sqrt{D_j\tau_2}} + \frac{t}{\tau_2}\right) \operatorname{erfc}\left(\frac{x}{2\sqrt{D_jt}} + \sqrt{\frac{t}{\tau_2}}\right) \quad [22]$$

(j = r, m, o).

The time constants τ_1 and τ_2 are given by

$$\tau_{1,2} = \left(\frac{\alpha}{2\beta}\left[1 \pm \sqrt{1 - \frac{4\beta}{\alpha^2}}\right]\right)^2 \quad [23]$$

where

$$\alpha = \left(\frac{i_{r,+}}{zF\sqrt{D_r}c_{r,0}} + \frac{i_{r,-}}{zF\sqrt{D_m}c_{m,0}} + \frac{i_{o,+}}{F\sqrt{D_m}c_{m,0}} + \frac{i_{o,-}}{F\sqrt{D_o}c_{o,0}}\right) \quad [24]$$

and

$$\beta = \frac{i_{r,-}i_{o,-}\sqrt{D_r}c_{r,0} + i_{r,+}i_{o,-}\sqrt{D_m}c_{m,0} + i_{r,+}i_{o,+}\sqrt{D_o}c_{o,0}}{zF^2\sqrt{D_rD_mD_o}c_{r,0}c_{m,0}c_{o,0}} \quad [25]$$

It can be shown that without exception $\alpha^2 > 4\beta$, *i.e.*, the time constants are always real and positive, τ_1 being greater than τ_2.

By setting $x = 0$ and defining

$$\theta_k(t) \equiv \exp\left(\frac{t}{\tau_k}\right) \cdot \operatorname{erfc}\left(\sqrt{\frac{t}{\tau_k}}\right), \ (k = 1,2) \quad [26]$$

the following expressions for the concentrations of Me, Me^{z+}, and $Me^{(z+1)+}$ at the interface are obtained from Eq. [18], [19], and [20]

$$\frac{c_r(0,t)}{c_{r,0}} = 1 - \frac{i_{r,D}}{zF\sqrt{D_r}c_{r,0}} \cdot \frac{\sqrt{\tau_1\tau_2}}{\sqrt{\tau_1}-\sqrt{\tau_2}} \cdot (\theta_1 - \theta_2) - \frac{i_{r,D}i_{o,-}\sqrt{D_m}c_{m,0} + (i_{r,D}i_{o,+} + i_{o,D}i_{r,-})\sqrt{D_o}c_{o,0}}{i_{r,-}i_{o,-}\sqrt{D_r}c_{r,0} + i_{r,+}i_{o,-}\sqrt{D_m}c_{m,0} + i_{r,+}i_{o,+}\sqrt{D_o}c_{o,0}} \cdot \left[1 - \frac{\sqrt{\tau_1}}{\sqrt{\tau_1}-\sqrt{\tau_2}}\theta_1 + \frac{\sqrt{\tau_2}}{\sqrt{\tau_1}-\sqrt{\tau_2}}\theta_2\right] \quad [27]$$

$$\frac{c_m(0,t)}{c_{m,0}} = 1 + \frac{i_{r,D} - zi_{o,D}}{zF\sqrt{D_m c_{m,0}}} \cdot \frac{\sqrt{\tau_1\tau_2}}{\sqrt{\tau_1} - \sqrt{\tau_2}} \cdot (\theta_1 - \theta_2)$$
$$+ \frac{i_{r,D}i_{o,-}\sqrt{D_r c_{r,0}} - i_{o,D} \cdot i_{r,+}\sqrt{D_o c_{o,0}}}{i_{r,-}i_{o,-}\sqrt{D_r c_{r,0}} + i_{r,+}i_{o,-}\sqrt{D_m c_{m,0}} + i_{r,+}i_{o,+}\sqrt{D_o c_{o,0}}}$$
$$\cdot \left[1 - \frac{\sqrt{\tau_1}}{\sqrt{\tau_1} - \sqrt{\tau_2}}\theta_1 + \frac{\sqrt{\tau_2}}{\sqrt{\tau_1} - \sqrt{\tau_2}}\theta_2\right] \quad [28]$$

$$\frac{c_o(0,t)}{c_{o,0}} = 1 + \frac{i_{o,D}}{F\sqrt{D_o c_{o,0}}} \cdot \frac{\sqrt{\tau_1\tau_2}}{\sqrt{\tau_1} - \sqrt{\tau_2}} (\theta_1 - \theta_2)$$
$$+ \frac{(i_{r,+}i_{o,+} - i_{r,-}i_{o,-})\sqrt{D_r c_{r,0}} + i_{o,D}i_{r,+}\sqrt{D_m c_{m,0}}}{i_{r,-}i_{o,-}\sqrt{D_r c_{r,0}} + i_{r,+}i_{o,-}\sqrt{D_m c_{m,0}} + i_{r,+}i_{o,+}\sqrt{D_o c_{o,0}}}$$
$$\cdot \left[1 - \frac{\sqrt{\tau_1}}{\sqrt{\tau_1} - \sqrt{\tau_2}}\theta_1 + \frac{\sqrt{\tau_2}}{\sqrt{\tau_1} - \sqrt{\tau_2}}\theta_2\right] \quad [29]$$

Current Density as a Function of Time

The current densities $i_r(t)$ and $i_o(t)$ carried by charge-transfer reaction [1] and [2], respectively, can be calculated by introducing [27], [28], and [29], in [12] and [13].

$$i_r(t) = i_{r,D} \cdot \left[\frac{\sqrt{\tau_1}}{\sqrt{\tau_1} - \sqrt{\tau_2}}\theta_1 - \frac{\sqrt{\tau_2}}{\sqrt{\tau_1} - \sqrt{\tau_2}}\theta_2\right]$$
$$- \left[\frac{i_{r,D} \cdot i_{r,+}}{zF\sqrt{D_r c_{r,0}}} + \frac{i_{r,D}i_{r,-}}{zF\sqrt{D_m c_{m,0}}} - \frac{i_{o,D}i_{r,-}}{F\sqrt{D_m c_{m,0}}}\right]$$
$$\frac{\sqrt{\tau_1\tau_2}}{\sqrt{\tau_1} - \sqrt{\tau_2}} (\theta_1 - \theta_2) \quad [30]$$

$$i_o(t) = i_{o,D} \cdot \left[\frac{\sqrt{\tau_1}}{\sqrt{\tau_1} - \sqrt{\tau_2}}\theta_1 - \frac{\sqrt{\tau_2}}{\sqrt{\tau_1} - \sqrt{\tau_2}}\theta_2\right]$$
$$- \left[\frac{i_{o,D}i_{o,+}}{F\sqrt{D_m c_{m,0}}} + \frac{i_{o,D}i_{o,-}}{F\sqrt{D_o c_{o,0}}} - \frac{i_{r,D}i_{o,+}}{zF\sqrt{D_m c_{m,0}}}\right]$$
$$\frac{\sqrt{\tau_1\tau_2}}{\sqrt{\tau_1} - \sqrt{\tau_2}} (\theta_1 - \theta_2) \quad [31]$$

An expression for the variation of the total current density flowing through the working electrode with time is obtained by summing [30] and [31]

$$i(t) = (i_{r,D} + i_{o,D}) \cdot \left[\frac{\sqrt{\tau_1}}{\sqrt{\tau_1} - \sqrt{\tau_2}}\theta_1 - \frac{\sqrt{\tau_2}}{\sqrt{\tau_1} - \sqrt{\tau_2}}\theta_2\right]$$
$$- \left[\frac{i_{r,D}i_{r,+}}{zF\sqrt{D_r c_{r,0}}} + \frac{(i_{r,D} - zi_{o,D})(i_{r,-} - i_{o,+})}{zF\sqrt{D_m c_{m,0}}}\right.$$
$$\left. + \frac{i_{o,D}i_{o,-}}{F\sqrt{D_o c_{o,0}}}\right] \cdot \frac{\sqrt{\tau_1\tau_2}}{\sqrt{\tau_1} - \sqrt{\tau_2}} \cdot (\theta_1 - \theta_2)$$
$$= A \cdot f(t) + B \cdot \frac{\sqrt{\tau_1\tau_2}}{\sqrt{\tau_1} - \sqrt{\tau_2}} \cdot g(t) \quad [32]$$

where A and B are time independent parameters.

Discussion

The measured quantity in potentiostatic single pulse experiments $i(t)$ depends according to Eq. [32] in a rather complicated form on the kinetic parameters of the electrochemical system. Therefore, in the following discussion some characteristic features of the $i(t)$ curves will be worked out which may be used as a guide in the interpretation of experimental current density transients.

As long as a change in electrode potential starting from equilibrium is considered the initial current density is always

$$i(t = 0) = \sum_{m=1}^{n} i_{m,D} \quad [33]$$

where $i_{m,D}$ is the current density carried by the mth charge-transfer step under pure charge-transfer control. This applies for any electrode reaction with an arbitrary number of n consecutive charge-transfer steps, since at the begining of the pulse no changes in the concentrations c_j have yet occurred (initial conditions) and the applied overvoltage in this moment is pure charge-transfer overvoltage. If unlimited diffusion layer thickness is assumed, the $i(t)$ curve approaches zero at infinite time also independently from the special system under consideration, since the concentration gradient becomes zero (boundary conditions).

In practice, however, the overvoltage pulse has a finite rise time and after some time ($t \gtrsim 1$ sec) convection limits the diffusion layer thickness. Therefore, in previous papers (3, 6) on the potentiostatic single pulse method, extrapolation techniques have been proposed for the determination of $i(0)$ and for the consideration of $i(t)$ at large t where the reaction is diffusion controlled. In these treatments, approximations were used for $t << \tau$ and $t >> \tau$, respectively, which facilitate interpretation of the $i(t)$ transients. For small arguments $t/\tau_k << 1$ the approximation

$$\exp\left(\frac{t}{\tau_k}\right) \cdot \operatorname{erfc}\left(\sqrt{t/\tau_k}\right) \approx 1 - 2\sqrt{t/\pi\tau_k} \quad [34]$$

may be applied. Introducing Eq. [34] in Eq. [32] one obtains

$$i(t) = A + B \cdot \frac{2}{\sqrt{\pi}} \cdot \sqrt{t} \quad \text{for } t << \tau_2 \quad [35]$$

On the basis of Eq. [35] the value of A can be derived by an extrapolation to $t = 0$ of the linear part of a plot $i(t)$ *vs.* $\sqrt{t}$. However, such a linearization requires a judgment on the range of useful data points which may be misleading, and the determination of A from an $i(t)$ *vs.* $\sqrt{t}$ plot can only be considered as a first orienting step in the analysis of the $i(t)$ curves. For $t/\tau >> 1$ where

$$\exp(t/\tau_k) \cdot \operatorname{erfc}\left(\sqrt{t/\tau_k}\right) \approx \frac{1}{\sqrt{\pi}} \cdot \sqrt{\tau_k/t} \quad [36]$$

Eq. [32] can be written in the approximate form

$$i(t) \approx \text{const.} \frac{1}{\sqrt{t}} \quad \text{for } t >> \tau_1 \quad [37]$$

Since at large t the current density *vs.* time curves are very likely to be influenced by convective limitation of the diffusion layer thickness, this approximation may not always be applicable and an analysis of the $i(t)$ curve at intermediate time, where both diffusion and charge-transfer determine its shape, appears to be preferable.

The general properties of the $i(t)$ curves in this intermediate time range can be worked out by a consideration of the functions $f(t)$ and $g(t)$. Since

$$\lim_{t \to 0} \theta_k = 1 \text{ and } \lim_{t \to \infty} \theta_k = 0 \quad [38]$$

$f(t)$ monotonically decreases from $f(0) = 1$ to $f(\infty) = 0$ whereas $g(t)$ is 0 at the beginning of the pulse and 0 at infinite time but positive in between. Consistent with the above mentioned conclusions from the initial and boundary conditions, this leads to $i(0) = A = i_{r,D} + i_{o,D}$ and $i(\infty) = 0$. In a previous paper (3) on pure metal/metal ion electrodes with two consecutive charge-transfer steps it was shown that a delayed extreme value $|i_{max}| > |i_{r,D} + i_{o,D}|$ in the c.d. curve may occur. This appearance, which is characteristic for a system with consecutive charge-transfer steps can be

expected for alloy electrodes, too, although additional terms containing $i_{r,+}/\sqrt{D_r}c_{r,0}$ show up in both B and the time constants, thus making the discussion of the alloy case more complex.

The conditions for delayed extreme value in the c.d. curves may be understood best by a consideration of the derivatives

$$f'(t) = \frac{1}{\sqrt{\tau_1} - \sqrt{\tau_2}} \left(\frac{\theta_1}{\sqrt{\tau_1}} - \frac{\theta_2}{\sqrt{\tau_2}} \right) \quad [39]$$

and

$$g'(t) = \frac{\theta_1}{\tau_1} - \frac{\theta_2}{\tau_2} + \frac{\sqrt{\tau_1} - \sqrt{\tau_2}}{\sqrt{\tau_1 \cdot \tau_2}} \cdot \frac{1}{\sqrt{\pi t}} \quad [40]$$

Since $f(t)$ is a monotonically decreasing function, $f'(t)$ is always negative starting from $f'(0) = -1/\sqrt{\tau_1\tau_2}$ and approaching 0 at infinite time. The derivative of $g(t)$ starts with an infinitely large positive value and becomes 0 both at $t = t_{gm}$, where $g(t)$ has its maximum, and at $t \to \infty$ being negative for $t_{gm} < t < \infty$. The slope of the c.d. curve is given by

$$i'(t) = A \cdot f'(t) + B \cdot \frac{\sqrt{\tau_1\tau_2}}{\sqrt{\tau_1} - \sqrt{\tau_2}} \cdot g'(t) = a'(t) + b'(t) \quad [41]$$

Figures 1 and 2 show curves $i'(t)$ *vs.* t and the scaled functions $a'(t)$ and $b'(t)$ corresponding to $f'(t)$ and $g'(t)$, respectively, for same η but slightly different parameter combinations. The conditions for Fig. 1 are such that A and B have same sign. Since $f'(t)$ and $g'(t)$ are opposite in sign for $t < t_{gm}$ there exists always a $t_{im} < t_{gm}$ where $i'(t_{im}) = 0$, *i.e.*, in case sign(A) = sign(B) the function $|i(t)|$ has always a maximum. In Fig. 2 the kinetic parameters were chosen that A and B are opposite in sign. Under these circumstances $i'(t)$ could become 0 only for $t > t_{gm}$. However, in this time range $|a'(t)| > |b'(t)|$ and no minimum appears in the corresponding $i(t)$ curve (compare Fig. 2 and 4).

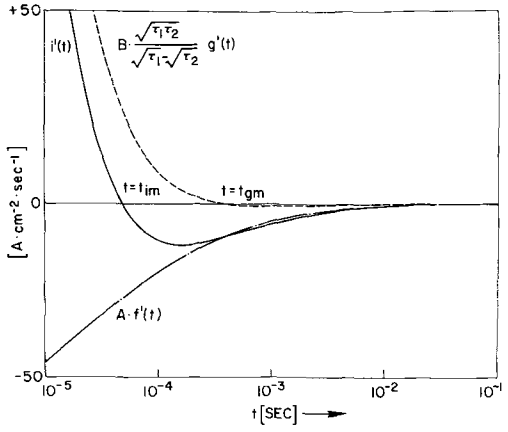

Fig. 1. Slope $i'(t)$ of the c.d. curve as a function of time t. $\eta = +80$ mV, $i_{r,0} = 10$ mA/cm², $i_{o,0} = 1$ mA/cm², $\alpha = 0.5$, $z = 1$, $D_r = D_m = D_o = 1.5 \times 10^{-5}$ cm²/sec, $c_{r,0} = 10^{-2}$M, $c_{m,0} = 10^{-4}$M, $c_{o,0} = 10^{-1}$M.

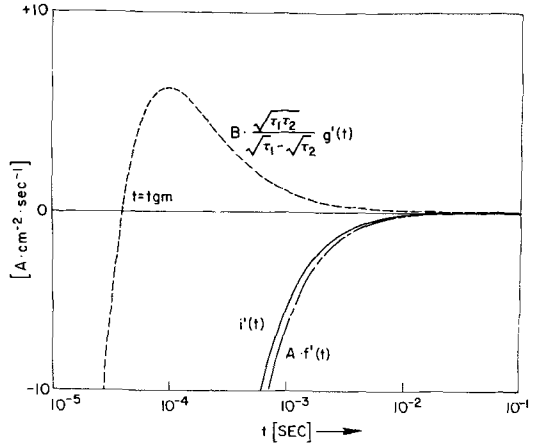

Fig. 2. Slope $i'(t)$ of the c.d. curve as a function of time t. All parameters as Fig. 1 except $c_{r,0} = 10^{-3}$M.

From Eq. [32] it follows that B is the sum of 3 terms $B = -(T_1 + T_2 + T_3)$. Since A and $T_1 + T_3$ have same sign, sign(B) = sign(A) requires sign$(T_2) \neq$ sign$(T_1 + T_3)$. If $\eta > 0$ this condition can only be satisfied for $i_{r,0} > i_{o,0}$ and $i_{r,-} < i_{o,+}$, *i.e.*, $\eta > \eta_{min}$. If $\eta < 0$, sign(B) = sign(A) requires $i_{r,0} < i_{o,0}$ and $i_{r,-} > i_{o,+}$, *i.e.*, $|\eta| > |\eta_{min}|$. Since the relative values of T_1, T_2, T_3 depend on the relative values of the terms $\sqrt{D_j} \cdot c_{j,0}$ in the denominators, the conditions given above are necessary but not sufficient. The behavior of B as a function of overvoltage is demonstrated in Fig. 3a and 3b which show families of curves B *vs.* η with $i_{o,0}$ as parameter and $i_{r,0}$ fixed. In Fig. 3a the intermediate substance is assumed to exist in a much lower concentration than both the reduced and the oxidized substance. In Fig. 3b the initial concentrations of S_r and S_m were assumed both equal and small compared with $c_{o,0}$. Note that in the cathodic branch large variations in $c_{r,0}$ (or D_r) have very little effect on the limit of $|\eta_{min}|$, where sign(B) becomes equal to sign(A), whereas a drastic change occurs in the anodic branch. Varying the initial composition of the electrochemical system and observing the effect on the occurrence of delayed maxima in the $|i(t)|$ curve, provides, therefore, a valuable means for confirming a proposed model of the electrode reaction under investigation.

Figures 4, 5, and 6 show families of digitally simulated $i(t)$ *vs.* t curves (t-axis logarithmic) with $c_{r,0}$ as parameter and $c_{m,0}$ and $c_{o,0}$ fixed. Figure 4 represents an anodic case with $i_{r,0} > i_{o,0}$ and $i_{r,-} < i_{o,+}$. For $c_{r,0} \geq 10^{-5}$ mole/cm³, delayed maxima occur in the $i(t)$ curve (compare the dashed curve in Fig. 3a and the full curve in Fig. 1). However, if $c_{r,0} \leq 10^{-6}$ mole/cm³ the term T_1 in B overrides the influence of T_2, *i.e.*, B has opposite sign of A and the delayed maximum in $i(t)$ disappears (compare Fig. 2 and 3b). Figure 6 represents a cathodic case with $i_{r,0} < i_{o,0}$ and $i_{r,-} > i_{o,+}$. Since at large cathodic overvoltage the term T_1 in B is of minor influence, all curves have maxima. However, with decreasing $c_{r,0}$ the values $i(t_{im})/i(0)$ become smaller and t_{im} is shifted to shorter times. Therefore, the delayed maximum is not observable in curves with $c_{r,0} \leq 10^{-8}$ mole/cm³ assuming that the best attainable rise time of a potentiostatic system at present is of the order of 10^{-6} sec. In Fig. 5 the parameters are chosen in such a way that $i_{r,0} > i_{o,0}$ but $i_{r,-} > i_{o,+}$, *i.e.*,

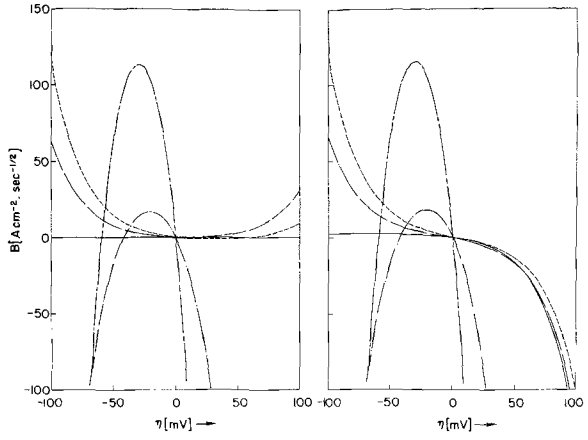

Fig. 3. Coefficient B *vs.* overvoltage η for various $i_{o,0}$. $i_{r,0} = 10$ mA/cm², $\alpha = 0.5$, $z = 1$; $i_{o,0} = 1$ mA/cm² — — — —; $i_{o,0} = 5$ mA/cm² — · — · —; $i_{o,0} = 10$ mA/cm² ————; $i_{o,0} = 50$ mA/cm² — ·· — ·· —; $i_{o,0} = 100$ mA/cm² — — — —; $D_r = D_m = D_o = 1.5 \times 10^{-5}$ cm²/sec. Fig. 3a (left). $c_{r,0} = c_{o,0} = 10^{-1}$M, $c_{m,0} = 10^{-4}$M. Fig. 3b (right). $c_{r,0} = c_{m,0} = 10^{-4}$M, $c_{o,0} = 10^{-1}$M.

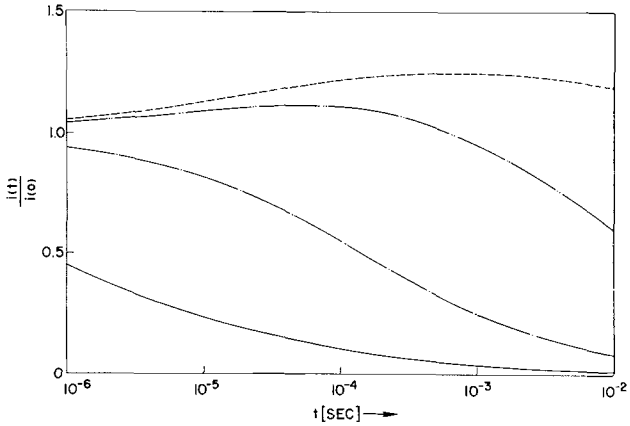

Fig. 4. Current densities $i(t)$, expressed as fractions of the initial current density $i(0) = i_{r,D} + i_{o,D}$, as a function of time t; varied parameter $c_{r,0}$. $\eta = +80$ mV, $i_{r,0} = 10$ mA/cm², $i_{o,0} = 1$ mA/cm²; $\alpha = 0.5$, $z = 1$, $D_r = D_m = D_o = 1.5 \times 10^{-5}$ cm²/sec; $c_{m,0} = 10^{-4}$M, $c_{o,0} = 10^{-1}$M; $c_{r,0} = 10^{-1}$M — — — —; $c_{r,0} = 10^{-2}$M — · · — · · —; $c_{r,0} = 10^{-3}$M — · — · —; $c_{r,0} = 10^{-4}$M ———.

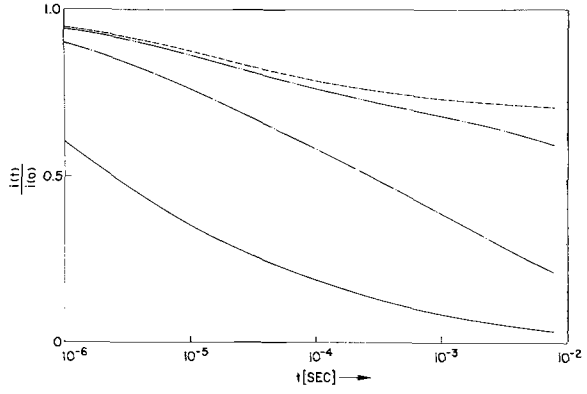

Fig. 5. Current densities $i(t)$, expressed as fractions of the initial current density $i(0) = i_{r,D} + i_{o,D}$, as a function of time t; varied parameter $c_{r,0}$. All parameters as in Fig. 4 except $\eta = +40$ mV.

sign$(B) \neq$ sign(A) for all $i(t)$ curves which exhibit no delayed maxima.

Conclusions

From a consideration of the general properties of $i(t)$ *vs.* t curves in potentiostatic single pulse experiments on systems involving two consecutive charge-transfer reactions, the following steps are suggested to be taken in the analysis of experimentally obtained $i(t)$ transients:

1. Approximate values for A are determined for a set of overvoltages from plots $i(t)$ *vs.* $\sqrt{t}$ and an approximate value for $1/i_{r,0} + 1/i_{o,0}$ is evaluated by a conventional analysis of the charge-transfer resistance.
2. By varying η and, if necessary, by changing initial composition the system is checked for the conditions under which delayed maxima are established in the $i(t)$ curve. If such maxima exist at anodic overvoltages, $i_{r,0} > z \cdot i_{o,0}$; if they exist at cathodic overvoltages, $i_{r,0} < z i_{o,0}$.
3. The limit $|\eta_{min}|$ for which maxima are observable and the way the maxima are affected by changes in composition are investigated. A model of the electrode kinetics is made up on the basis of these observations, *i.e.*, a reasonable range of values is coordinated to the different kinetic parameters.
4. The model has to be confirmed by fitting these parameters to experimental $i(t)$ curves covering the full time range where both diffusion and charge-transfer control the electrochemical reaction. Final adjustments are made in the parameters to obtain best fit for a variety of η and $c_{j,0}$.

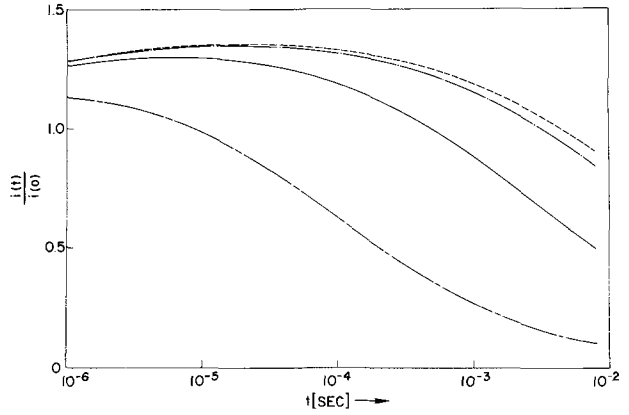

Fig. 6. Current densities $i(t)$, expressed as fractions of the initial current density $i(0) = i_{r,D} + i_{o,D}$, as a function of time t; varied parameter $c_{r,0}$. $\eta = -80$ mV, $i_{r,0} = 10$ mA/cm², $i_{o,0} = 50$ mA/cm², $\alpha = 0.5$, $z = 1$, $D_r = D_m = D_o = 1.5 \times 10^{-5}$ cm²/sec, $c_{m,0} = 10^{-4}$M, $c_{o,0} = 10^{-1}$M; $c_{r,0} = 10^{-1}$M — — — —; $c_{r,0} = 10^{-3}$M — · — · —; $c_{r,0} = 10^{-4}$M ———; $c_{r,0} = 10^{-5}$M — — — —.

Considering the relatively poor accuracy in recording of $i(t)$ data at high speed and the possible systematic errors in potentiostatic single pulse experiments, a quantitative analysis of $i(t)$ curves for electrochemical systems, which do not allow the observation of delayed maxima, appears to be unrealistic at the present state of experimental technique.

Summary

A theoretical treatment of the transients obtained in potentiostatic single pulse experiments on metal alloy/metal ion electrodes coupled to a redox reaction is presented. Formulas have been derived for the concentration of the electrochemically active component in the alloy and of the corresponding metal ions of different valent state which form the redox couple in the electrolyte, respectively, as a function of the distance from the interface and the duration of the voltage pulse. Expressions for the partial current densities carried by the two consecutive charge-transfer reactions, $Me = Me^{z+} + ze^-$ and $Me^{z+} = Me^{(z+1)+} + e^-$, and for the total current density flowing through the cell have been worked out. Analysis of the current density transients on the basis of these expressions allows interpretation of experimental curves in terms of the characteristic kinetic parameters of the electrochemical system.

Acknowledgment

The author would like to express his appreciation to A. R. Storm, Jr., for assistance in the simulation of the c.d. curves.

Manuscript submitted June 25, 1970; revised manuscript received *ca.* Oct. 12, 1970.

Any discussion of this paper will appear in a Discussion Section to be published in the December 1971 JOURNAL.

REFERENCES

1. K. J. Vetter, *Z. Naturforsch.*, **7a**, 328 (1952); **8a**, 832 (1953).
2. R. M. Hurd, *This Journal*, **109**, 327 (1962).
3. K. J. Bachmann and U. Bertocci, *Electrochim. Acta* (1970).
4. T. Kambara and I. Tachi, *Bull. Chem. Soc. (Japan)*, **25**, 135 (1952).
5. P. Delahay, *J. Am. Chem. Soc.*, **75**, 1430 (1953).
6. H. Gerischer and W. Vielstich, *Z. Physik, Chem. N. F.*, **3**, 16 (1955).

Free Energies of Formation of Hydrous Oxides of Technetium in Its Lower Valencies[1]

G. H. Cartledge

Chemistry Division, Oak Ridge National Laboratory, Oak Ridge, Tennessee 37830

ABSTRACT

It has been found possible to measure reversible electrode potentials for couples containing technetium and one or more of its hydrous oxides. The procedure disclosed the existence, in films, of technetium in 1+, 2+, and 3+ valence states, besides oxides Tc_3O_4 and Tc_4O_7, and provided direct means for evaluating their free energies of formation from the metal. The previous calorimetrically based free energy of formation of $Tc(OH)_4$ was confirmed to within 1%. It was found that the radioactivity of technetium is involved in certain processes on the electrode.

The oxides of technetium previously known were TcO_2, TcO_3, and Tc_2O_7. Electroanalytical procedures have been used to study the reduction of the pertechnetate ion, and Tc(III), Tc(V), and Tc(VI) were shown to be formed as intermediate products under certain conditions, besides Tc(IV) (1, 2). The 3+ state was found also as a chlorocomplex by Busey (3), and both the 2+ and 3+ states were isolated as ditert-arsine complex compounds by Fergusson and Nyholm (4). There is no known report, however, of oxides or hydroxides from a valence state lower than 4+.

The initiation of a study of the electrochemical behavior of iron alloyed with a small amount of technetium immediately showed the necessity for determining the anodic behavior of elemental technetium. These experiments led to the result that several lower oxides (hydrous or "precipitated") could be identified and their free energies of formation determined electrochemically. Confidence in the validity of the observation of several reproducible couple potentials was immediately established by the fact that the potential of a technetium electrode coated cathodically with $Tc(OH)_4$ gave a free energy of formation for this hydroxide which closely matched a value previously derived. This earlier value was calculated by combining the measured heat of combustion of technetium to pertechnic acid (5) with the author's determination of the reversible potential of the Tc(IV-VII) electrode (6).

The present study consisted of the measurement of the potential of metallic technetium in sulfate or other electrolytes after various polarizations, with or without prior coating of the electrode with a film formed cathodically from TcO_4^-. Other measurements were made on gold or platinum electrodes after they were coated with a film and subjected to various polarization procedures. It was somewhat surprising to discover that all these types of electrodes gave characteristic halts, or plateaus, in potential-time charts, and that, so far as was investigated, the potentials had the 59 mV/*p*H dependence that would be expected. Although certain of the couples were metastable in that the electromotively active components of the film slowly changed chemically and produced a different couple, even these were found to be sufficiently stable for identification and use in calculating free energies of formation. The results furnish a direct and independent means of referring the free energies of technetium compounds to the metal. In addition, couples were identified which indicate the existence, on the electrode, of new compounds derived from technetium in the 1+, 2+, and 3+ valence states, besides the hybrid oxides, Tc_3O_4 and Tc_4O_7. The results are particularly striking in that hard metals coated with oxides do not usually give reversible potentials.

[1] Research sponsored by the U.S. Atomic Energy Commission under contract with Union Carbide Corporation.

Key words: technetium, technetium oxides, electrode potential, free energy, ionic potential, polarization.

Experimental

For preparation of certain electrodes, the chosen substrate was coated with a film of black, hydrous oxide by cathodic deposition from alkaline TcO_4^-. If the current density is in the range of 0.5 mA/cm^2, electrolysis for a few minutes at room temperature produces a brownish-black film which, after being dried at 110°C in air, has the same electron diffraction pattern as the product from hydrolysis of $K_2Tc(IV)Cl_6$. This product is $TcO_2 \cdot 2H_2O$ or $Tc(OH)_4$. [The author is indebted to Dr. R. H. Busey for the hydrolytic product and to Mr. T. E. Wilmarth, of the Analytical Chemistry Division, for comparison of the diffraction patterns. As is seen subsequently, vigorous cathodic deposition may give a film containing lower oxides in addition to, or rather than, $Tc(OH)_4$.] Elementary technetium, gold, platinum, and gold-plated platinum were used as substrates for the preparation of coated electrodes. The use of gold facilitated observation of colors.

Other electrodes consisted initially of technetium from which any oxide film had been removed either by treatment with ammoniacal hydrogen peroxide, by fusion just above the melting point in KOH containing a little KNO_3, or by reduction in hydrogen at around 425°C, with cooling in helium. In numerous experiments, a 0.72g pellet of rf-melted technetium was used. (The pellet was prepared by Mr. W. J. Martin from powder produced in the Isotopes Division by reduction of fission-product NH_4TcO_4 by hydrogen.) The results obtained with the pellet were confirmed and extended by use of an electrode consisting of a gold coil sealed into soft glass and plated with metallic technetium from 2*N* H_2SO_4 containing $7 \times 10^{-3}f$ $KTcO_4$ (7). The plating covered the golden color completely and gave a bright deposit resembling platinum after reduction in hydrogen. As a variant, a gold coil was first coated with $Tc(OH)_4$, and the black film was then rinsed, dried, and reduced in hydrogen. Two such treatments gave a bright platinum-like surface. For work in the more noble regions of potential, platinum or gold electrodes were coated with technetium tetrahydroxide and subjected to cathodic polarization to produce couples having oxides which correspond to valence states below 4+. The different kinds of electrodes may be identified in the subsequent paragraphs by reference to Table I. Electrolytes were 1*N* and 0.01*N* H_2SO_4, 0.05*f* phthalate buffers, or a mixture 0.9*N* in sulfate and 0.1*f* in phthalate. The acidities for certain couples covered the range of *p*H from 0.35 (1*N*

Table I. Types of electrodes

A.	Pellet of elementary technetium, uncoated
B.	Coated pellet
C.	Technetium plated over gold and reduced in hydrogen
D.	Technetium on gold by reduction of film
E.	Type C or D coated with $Tc(OH)_4$
F.	Platinum or gold carrying cathodically formed film

H_2SO_4) to 6.76. Solutions were prepared from triply distilled water, and concentrated C.P. H_2SO_4 was heated to fuming to remove SO_2 before dilution.

Polarization of electrodes was accomplished by both galvanostatic and potentiostatic procedures (FairPort Instruments, Inc., Model 610). Potentials or currents were measured through a vibrating reed electrometer (APL Model 30) and a Hewlett-Packard Recorder (Model 7100B), stable potentials being checked directly with a Rubicon Potentiometer. Measurements were made at thermostatically controlled room temperature, 24°C, and air was displaced from a large H-cell by helium which had passed over copper turnings at 425°C. Potentials are expressed in accordance with the Gibbs-Stockholm convention (8). Measurements in terms of SCE are converted to SHE by addition of +245 mV. Energies are expressed in thermochemical calories, 1 cal = 4.184J.

Most of the study of the Tc-$Tc(OH)_4$ couple was done with the pellet of technetium, Type B, the result of many such measurements being completely confirmed by use of electrodes of Type E. The pellet was suspended in the electrolyte by a platinum stirrup. When it was found that stable or metastable potentials other than that of the Tc-$Tc(OH)_4$ couple were being observed, electrodes of elementary technetium were used to explore the less noble range of potentials. For this purpose, electrodes of Type A, C, or D were anodically polarized, chiefly in 1*N* H_2SO_4, to form films possibly capable of existence in lower valence states. Alternate anodic and cathodic polarizations (sometimes by chance!) led to recognition of several well-defined potentials in the lower range.

When it developed that the Tc-$Tc(OH)_4$ couple is electrochemically metastable with respect to couples of more noble potential, other measurements were made with electrodes of Type F. These were subjected to a variety of polarizations, from which results were obtained which confirmed certain of the couple potentials observed when electrodes of Type A, B, or E were merely allowed to "age" in the cell. Other details for locating and identifying specific potentials are given under "Results."

Results

The Tc-$Tc(OH)_4$ couple.—The potential of this couple was obtained many times when freshly filmed and rinsed electrodes were inserted into the electrolyte with a rapid stream of helium passing. The potential initially observed depended somewhat on the method of forming the film. Thus it could be varied by changing the current density, by brief reversal of the coating current, or by allowing the electrode to remain in the coating cell briefly after shutting off the current. In any event, the potential soon shifted to a more or less steady value before beginning to drift to a more noble potential. This shift required a few hours or, sometimes, overnight before a second stable potential was attained. Measurements at several *p*H values served to show that both potentials had approximately the 59 mV/*p*H dependency required for couples of the types possibly existing between the metal and one of its insoluble hydroxides, or between two such hydroxides as discrete phases on a conducting, electrochemically inert substrate. The results of 19 determinations of the lower potential and 10 of the more noble one are shown in Fig. 1. When the results are corrected to *p*H = 0 and SHE, one finds V^o_H = 0.296 ± 0.006 and 0.516 ± 0.007V, respectively.

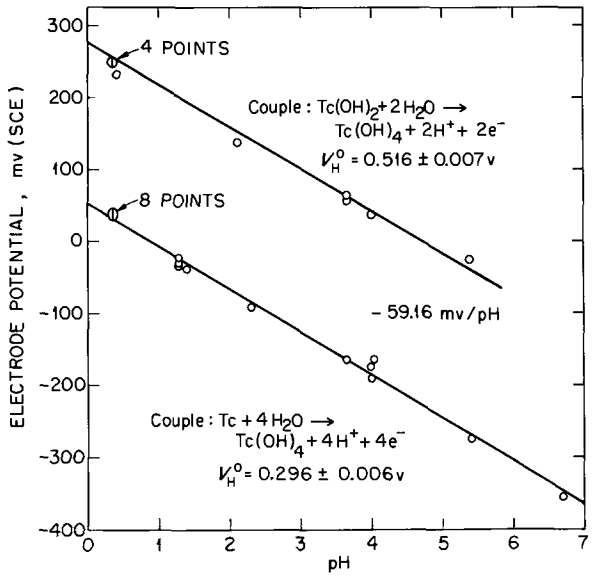

Fig. 1. Electrode potentials (ref. to SCE) as a function of *p*H. The lines are drawn with the theoretical slope.

If V^o_H = 0.296V is taken to be the reversible potential of the couple, $Tc + 4H_2O \rightleftarrows Tc(OH)_4 + 4H^+ + 4e^-$, ΔF^o = +27.3 kcal, from which ΔF^o_f for formation of $Tc(OH)_{4(pptd)}$ is −199.5 ± 0.7 kcal. This is seen to be very close to the value −202 kcal derived from the earlier calorimetric and electrochemical data. The agreement not only approximately confirms the indirectly obtained free-energy value, but shows the surprising speed with which technetium establishes electrochemical equilibrium with this film. (The value −199.5 kcal is adjusted to −199.7 kcal subsequently, for better internal consistency of the several stationary potentials discovered.)

Other couple potentials.—The noble potential V^o_H = 0.516V cannot be ascribed to effects associated with a mere "aging" of the film, such as a change in crystal form or degree of hydration, since the observed potentials show that such processes would have a positive free-energy change. It is therefore necessary to assume that the potential shifts because of slow formation of a couple having at least one new component. Calculations which are explained subsequently show that either $Tc(OH)_2$ or $Tc(OH)_3$ in association with $Tc(OH)_4$ would result in a reasonable free energy for the lower hydroxide, but the data obtained in later experiments are necessary for discrimination between the two possibilities. The existence of such a stable potential, however, is clear evidence of the formation of a couple containing a lower oxide and having an exchange current sufficiently great to escape serious polarization by reaction of metallic technetium. Should there actually be such a polarization, the true couple potential would be even more noble. The fact that the potential of 0.516V was repeatedly observed and had a proper *p*H dependence indicates also that chemically discrete phases are present in the mixed film, rather than a composite phase of continuously variable composition, which may sometimes be formed.

Further measurements were therefore made with both coated and initially uncoated electrodes in order to detect other characteristic potentials. In certain cases, the procedure was to build films by anodic polarization of technetium electrodes (Types A, C, and D). This procedure was used to explore the less noble region of potentials. For the more noble region, Type F electrodes were used. In all these cases, various mild anodic and cathodic polarizations were applied, as necessary, to insure the integrity of observed stationary potentials. By these devices a total of 15

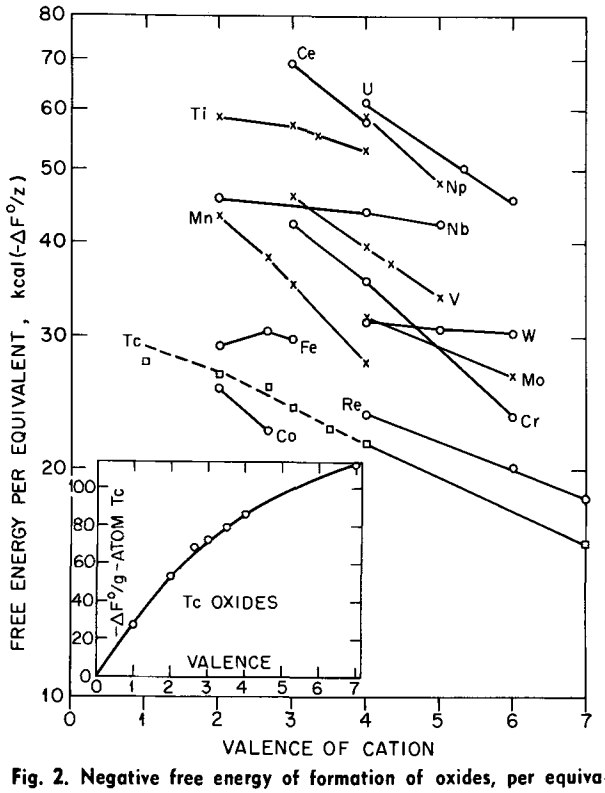

Fig. 2. Negative free energy of formation of oxides, per equivalent, as a function of the valence of the cation. Insert: Negative free energy per gram-atom of Tc, vs. valence of cation.

significant potentials was established, including the two shown in Fig. 1. The values are given in Table III, following a description of the procedure by which the couples responsible for the different potentials were identified.

Identification of the couples.—In earlier publications (9), it was shown that many properties of inorganic compounds may be interpreted or correlated in terms of the ratio of the charge to the radius of their ions. This function, z/r, was designated the ionic potential. Thus, it was shown (10) that, in a series of compounds with a common anion, such as oxides, there is a quite general semilogarithmic relation between the heats or free energies of formation per equivalent and the ionic potentials of the cations based on their univalent crystal radii. The present problem involves the hydroxides or oxides of a single element in various valence states, however, and here the regularities are less obvious. Nevertheless, certain fair approximations become apparent from an inspection of a graph of the free energies of oxides, per equivalent, plotted logarithmically against the valence of the cation. Figure 2 is such a graph. The data were taken chiefly from Brewer (11) and the revisions of Circular 500 of the Bureau of Standards (12). A few are from Latimer (13), and recent redeterminations for rhenium are from King, Richardson, and Mrazek (14). The value for Tc_2O_7 is from Ref. (5). It is to be noted that, in the absence of specific information on the structure of hydrous oxides, Latimer considers them preferably as hydroxides. For the present approximations, the free energies of the oxides and the hydrous, or "precipitated," oxides may be considered to differ by half the free energy of liquid water for each equivalent. Thus, from $\Delta F°_f$ for $Tc(OH)_4$ = −199.5 kcal/mole, we find $\Delta F°_f$ for ¼ TcO_2 to be (¼) [−199.5−(−2 x 56.7)] = −21.5 kcal/equiv.

Table II. Estimated and experimental free energies of formation*

	$\Delta F°_f$(est)	$\Delta F°_f$(exp)
TcOH	−57.35	−56.0
$Tc(OH)_2$	−110.7	−110.1
Tc_3O_4	—	−206.1
$Tc(OH)_3$	−157.35	−157.3
Tc_4O_7	—	−316.6?
$Tc(OH)_4$	(−199.5)	−199.7

* kcal/mole; $\Delta F°_f$(est), estimated from Fig. 2; $\Delta F°_f$(exp), adjusted for maximum consistency of observed potentials.

Figure 2 shows that, for a given metal, the negative free energy decreases numerically as the valence increases, and the slight deviations from straight lines follow similar patterns. It may be assumed, therefore, that the free energies of perhaps hypothetical lower oxides of technetium will not differ greatly from those indicated by the dashed curve in Fig. 2, which was based on a comparison of the experimental values for Re_2O_7, ReO_3, and ReO_2 with the established values for Tc_2O_7 and TcO_2. From this curve, free energies of formation were calculated for TcOH, $Tc(OH)_2$, and $Tc(OH)_3$, with the results shown in Table II in the column $\Delta F°$(est). These estimated free energies were then used for calculation of reversible electrode potentials for the ten couples conceivably obtainable by combining the metal with one of its hydroxides, or two hydroxides as discrete phases on an electrochemically inert substrate. So long as only insoluble components are involved, the potentials of all such couples will have a −59 mV/pH dependence. The initially approximated potentials are shown in Table III under $V°_H$(est). The column headed $V°_H$(obs) gives the potentials of the observed halts in potential-time

Table III. Standard electrode potentials $V°_H$, volts vs. SHE, 24°C

	Couple	$V°_H$(est)	$V°_H$(obs)	$V°_H$ (normalized)	pH (for measurements)
a.	$Tc + H_2O \rightleftarrows TcOH + H^+ + e^-$	−0.029	0.034 ± 0.005(7)*	0.031	0.35, 2.05
b.	$Tc + 2H_2O \rightleftarrows Tc(OH)_2 + 2H^+ + 2e^-$	+0.059	0.073 ± 0.002(7)	0.072	0.35, 3.65
c.	$3Tc + 4H_2O \rightleftarrows Tc_3O_4 + 8H^+ + 8e^-$	—	—	0.112	—
d.	$TcOH + H_2O \rightleftarrows Tc(OH)_2 + H^+ + e^-$	0.147	0.114(2)	0.113	3.65
e.	$3TcOH + H_2O \rightleftarrows Tc_3O_4 + 5H^+ + 5e^-$	—	0.167(2)	0.161	0.35
f.	$Tc + 3H_2O \rightleftarrows Tc(OH)_3 + 3H^+ + 3e^-$	0.185	0.190 ± 0.006(11)	0.185	0.35
g.	$3Tc(OH)_2 \rightleftarrows Tc_3O_4 + 2H_2O + 2H^+ + 2e^-$	—	0.234 ± 0.004(4)	0.234	0.35
h.	$TcOH + 2H_2O \rightleftarrows Tc(OH)_3 + 2H^+ + 2e^-$	0.290	0.264 ± 0.005(7)	0.262	0.35, 3.10, 4.03, 5.00, 5.40
i.	$Tc + 4H_2O \rightleftarrows Tc(OH)_4 + 4H^+ + 4e^-$	0.296	0.296 ± 0.006(19)	0.294	**
j.	$4TcOH + 3H_2O \rightleftarrows Tc_4O_7 + 10H^+ + 10e^-$	—	0.338 ± 0.003(7)	0.338	0.35, 2.05
k.	$TcOH + 3H_2O \rightleftarrows Tc(OH)_4 + 3H^+ + 3e^-$	0.397	0.382 ± 0.002(7)	0.382	0.35, 3.65
l.	$Tc(OH)_2 + H_2O \rightleftarrows Tc(OH)_3 + H^+ + e^-$	0.436	0.411(2)	0.412	0.35
m.	$Tc(OH)_2 + 2H_2O \rightleftarrows Tc(OH)_4 + 2H^+ + 2e^-$	0.522	0.516 ± 0.007(10)	0.518	**
n.	$Tc(OH)_3 + H_2O \rightleftarrows Tc(OH)_4 + H^+ + e^-$	0.608	0.619 ± 0.005(8)	0.620	0.35, 3.65
o.	$Tc_3O_4 + 8H_2O \rightleftarrows 3Tc(OH)_4 + 4H^+ + 4e^-$	—	0.661 ± 0.004(5)	0.657	0.35, 3.65
p.	$Tc_3O_4 + 5H_2O \rightleftarrows 3Tc(OH)_3 + H^+ + e^-$	—	0.765(1)	0.768	3.65

* Numbers in parentheses denote the number of observations.
** See Fig. 1.
$V°_H$(est), potentials derived from initially approximated $\Delta F°$'s given in Table II.
$V°_H$(obs), observed steady potentials, corrected to SHE scale and pH = 0.
$V°_H$(normalized), potentials derived from adjusted $\Delta F°$'s given in Table II.
pH, pH values at which measurements were made.

curves, corrected to pH = 0 and SHE, the number of observations of each couple being shown in parentheses. The last column shows the pH values at which the couple was found. Although most of the work was done in 1*N* H_2SO_4, the table shows that each valence state was confirmed in at least one other electrolyte.

It is seen that most of the estimated potentials are within a few millivolts of one of the observed halts. For couples containing TcOH as one component, there was a significant discrepancy between an estimated potential and one of the experimental potentials. All these discrepancies were removed by taking ΔF°_f for TcOH to be −56.0 kcal/mole, rather than the postulated −57.35. A smaller correction in the free energy for $Tc(OH)_2$ was also indicated. From couples *b*, *f*, and *l*, we may infer the presence of $Tc(OH)_2$ and $Tc(OH)_3$ in the films, with free energies essentially equal to those based on Fig. 2. A completely self-consistent set of values for the ten estimated potentials was found to be achieved by use of the slightly adjusted values of the molar free energies given in Table II under ΔF°(exp). The corresponding standard electrode potentials are shown in Table III under V°_H(normalized) and, without exception, are within the limits of error of the measurements.

In Fig. 2, the points denoted by □ are the free energies of the respective oxides (per equivalent) derived from the ΔF°_f(exp) values of the hydroxides in Table II. In a discussion of the method used to identify the couples, Dr. R. H. Busey suggested that a check on the semilogarithmic curves of Fig. 2 may be obtained from a linear graph so as to include the metal as origin. The insert in Fig. 2 shows the free energy per gram-atom of metal plotted against the valence state. The points represent the experimentally derived values, and the curve is seen to extrapolate neatly to zero.

In certain experiments, definitely stationary potentials were repeatedly observed which did not correspond to any of the ten previously postulated couples. By considering the possible formation of a discrete phase analogous to Fe_3O_4, it was found that certain of these potentials could, indeed, be accounted for by assuming a technetium oxide with a free energy corresponding to the point at an average valence 2.67 in Fig. 2. Figure 3, curve B, which is discussed later, shows one example of the formation of a couple containing this compound. In like manner, other potentials occasionally obtained corresponded almost certainly to formation of a component of average valency 3.5, which might be $Tc_2O_3 \cdot 2TcO_2$, or Tc_4O_7. Curve A in Fig. 3 illustrates this case. The uncertainty in the identification of the lower hydroxide in this couple arises from the fact that almost the same agreement

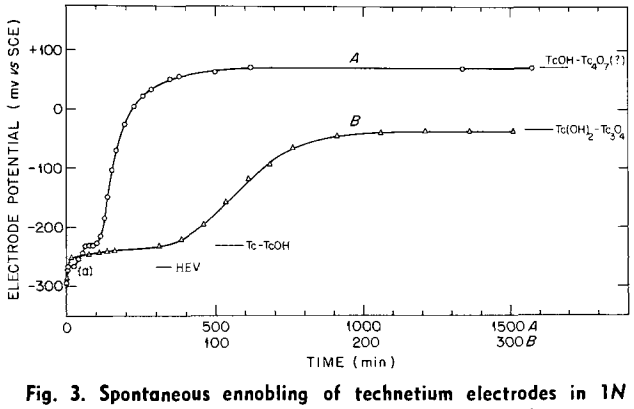

Fig. 3. Spontaneous ennobling of technetium electrodes in 1*N* H_2SO_4 in absence of air (continuous recordings). Curve A, in large H cell, with H_2 passing 25 min (to point *a*), followed by He. Curve B, in miniature cell with He passing. HEV is the reversible potential of the hydrogen electrode at pH = 0.35. The line for Tc-TcOH represents the potential of this couple in 1*N* H_2SO_4, and similarly for the other potentials indicated.

with the observed potential would result if the lower hydroxide were $Tc(OH)_3$, instead of TcOH. The latter seems more probable, however, in view of the demonstrated stability of the TcOH component when the experiment is begun at a low potential and, also, the closer agreement with Fig. 2.

To illustrate the consistency of the observed potentials among themselves, it may be noted that Tc_3O_4 appeared in couples with TcOH, $Tc(OH)_2$, $Tc(OH)_3$, and $Tc(OH)_4$, respectively, in 12 independent observations. By using the ΔF°_f(exp) values for these hydroxides as shown in Table II, one calculates ΔF°_f for Tc_3O_4 to be −206.1 ± 0.4 kcal/mole. [The hybrid compounds, Tc_3O_4 and Tc_4O_7, are written in the anhydrous form, partly for simplicity and also because Feitknecht showed clearly that Fe_3O_4 is formed as magnetite in the incomplete oxidation of $Fe(OH)_2$ in aqueous media (15).]

The metastability of the Tc-$Tc(OH)_4$ couple accords with the potentials of the other couples given, in that several spontaneous reactions are possible. Experiments in which elementary technetium was polarized anodically in H_2SO_4 showed that it first forms a film of TcOH and becomes essentially passive when this film is complete. It is this low reactivity of the passivated metal which permits couples containing two hydroxides to be established reversibly. The potential V°_H = 0.516V spontaneously reached slowly in numerous experiments is seen to be very close to the value calculated for the Tc(II-IV) couple, but 100 mV lower than that for the Tc(III-IV) couple. The assignment of this value to the Tc(II-IV) couple is therefore unambiguous and entirely consistent with the free energy of $Tc(OH)_2$ derived from the Tc(0-II) couple. The free energies of $Tc(OH)_2$, $Tc(OH)_3$, and Tc_3O_4 are such that the hybrid oxide is stable, but apears to be formed only slowly.

The standard potentials of Table III indicate the possible disproportionation only of $Tc(OH)_3$, under the conditions of the experiments. Values for couples (n) and (p) show that its conversion to Tc_3O_4 and $Tc(OH)_4$ would have a free-energy change of only −0.9 kcal/mole, however, and the fact that electrode potentials involving this component were obtained in 29 instances suggests that such a kinetically complex reaction does not occur readily. For TcOH, the situation is just the reverse. Disproportionation to Tc and $Tc(OH)_2$ is disfavored by the small free-energy change of +0.9 kcal/mole. It is to be emphasized, however, that all the measured potentials for TcOH relate to the surface film. It is entirely conceivable that loss of stabilization by surface forces could result in a change in the sign of the free-energy change and instability for material in bulk. The data show that $Tc(OH)_2$ is moderately stable with respect to disproportionation. $Tc(OH)_4$, of course, is a very stable compound (5).

The sluggishness of the solid-state reactions in the film accounts for the observation of a potential for the $Tc(OH)_3$-$Tc(OH)_4$ couple, although it is indicated that Tc_4O_7 may result as a stable phase. The Tc(III-IV) couple was definitely established in several experiments in which the stable potential was approached from both higher and lower potentials.

Spontaneous ennobling of electrodes.—The spontaneous ennobling of the potential of a technetium electrode coated with $Tc(OH)_4$ turned out to be a special case of a quite general behavior. This was further investigated by starting with technetium electrodes which were so treated as to be free of oxide film or else reduced below the potential of the Tc-TcOH couple and then left in the cell with helium passing. In 1*N* H_2SO_4 with H_2 passing initially, such an electrode indicated the reversible hydrogen couple potential (HEV) identically with a platinum electrode. This is shown at point *a* in curve A Fig. 3,

where hydrogen was passed for 25 min before being replaced by helium. Completion of the TcOH film in helium was indicated by a 30 min halt at the potential of the Tc-TcOH couple at *p*H 0.35, after which the potential rose slowly until it stabilized at the value provisionally assigned to the TcOH-Tc_4O_7 couple.

Results of this kind necessitate some oxidation process. Although the H cell in which the experiments were conducted was believed to be adequately protected from access of air, further experiments were carried out to eliminate this possibility more certainly. For this purpose, a miniature cell (25 ml) was constructed to contain the experimental electrode, a platinized platinum electrode, a silver-silver chloride reference electrode, and inlet and outlet tubes for gas. This cell was then mounted in a jar through which helium passed. In starting an experiment, the electrolyte (1*N* H_2SO_4 containing 10^{-3} *N* HCl) was boiled and cooled in helium to expel air just prior to its introduction into the cell. Hydrogen was passed briefly to insure that the electrode was at an active potential. In numerous experiments with this cell, the spontaneous ennobling still proceeded, an example being given by curve B in Fig. 3. In this case, the electrode came quickly to the corrosion potential in 1*N* H_2SO_4 in helium (average value −246 mV SCE) and ennobled slowly as the film of TcOH formed. It is seen that much more rapid ennobling followed passage through the potential of the Tc(0-I) couple, until a stable potential corresponding to the $Tc(OH)_2$—Tc_3O_4 couple was reached. It can only be concluded that the behavior does not depend on access of air into the cell.

Discussion

The number and reproducibility of the more or less stable potentials observed and the close agreement of one of these with the value derived from the calorimetric result for the Tc-$Tc(OH)_4$ couple are sufficient evidence of the reliability of the electrochemical measurements. It is also clear that the approximations from Fig. 2 are a valid basis for identification of the various couples in terms of components of a film in which technetium has valencies less than 4+. The possibility of changing the components in the film by both cathodic and anodic polarization was repeatedly demonstrated, and in only a few instances did the potential fail to come ultimately to one of the numerous calculated couple potentials.

The fact that the potential of the Tc-$Tc(OH)_4$ couple is measurable does not imply a four-electron process. Depending on the conditions under which a film is formed cathodically from a pertechnetate, the film may contain the lower hydroxides as well as $Tc(OH)_4$. Since potentials were observed for couples containing each valence state coupled by a one-electron change with another, these kinetically preferred couples may be regarded as forming cells in series, so that the measured potential will be that of the strongest reducing agent (Tc) coupled with the strongest oxidizing agent (Tc-IV).

Furthermore, the spontaneous shifts of the potential in the noble direction may be accounted for by reactions among the different hydroxides, in view of the demonstrated low reactivity of the metal. The unknown and undoubtedly very complex kinetics of these processes precludes any detailed analysis, but one example may be chosen as a possible illustration. Thus, a technetium electrode (plated on platinum) was subjected to a variety of polarizations in the noble region, after which it was reduced cathodically until it established the Tc-$Tc(OH)_2$ potential. Ennobling set in up to the potential of the $Tc(OH)_2$—$Tc(OH)_3$ potential. This halt was confirmed by brief cathodic and anodic displacements of the potential. Following this halt, a further slow drift to more noble potentials set in. The standard potentials in Table III show that an electrode containing $Tc(OH)_2$ together with either $Tc(OH)_3$ or $Tc(OH)_4$ is only metastable. Thus, if the free energies are expressed as volt-Faradays

$$3Tc(OH)_2 \rightarrow Tc_3O_4 + 2H_2O + 2H^+ + 2e^-; \quad \Delta F^\circ = 0.468 \text{ VF}$$

$$2Tc_3O_4 + 10H_2O \rightarrow 6Tc(OH)_3 + 2H^+ + 2e^-; \quad \Delta F^\circ = 1.536 \text{ VF}$$

$$Tc(OH)_2 + 2Tc(OH)_3 \rightarrow Tc_3O_4 + 4H_2O; \quad \Delta F^\circ = -0.356 \text{ VF} = -8.2 \text{ kcal}$$

If $Tc(OH)_3$ were in excess, the potential could rise from that of the $Tc(OH)_2$—$Tc(OH)_3$ couple (V°_H = 0.412V) to that of the Tc_3O_4—$Tc(OH)_3$ couple (V°_H = 0.768V).

Such solid-state reactions cannot be the sole reason for the spontaneous ennobling, however, for the initial presence of a film containing technetium in a valence higher than 1+ is requisite. Similar ennobling was demonstrated in experiments like that illustrated in curve B of Fig. 3. Here the electrode was drastically reduced prior to the experiment, and yet the rise of potential ensued. It seems necessary to consider the possible effects of the radioactivity of technetium. This is a beta activity of 0.3 MeV maximum energy with a specific activity of 16 μC/mg. It is reasonable to assume a radiolytic *g* factor of 2 for production of hydrogen and hydroxyl radicals in 1*N* H_2SO_4. The reaction is reversible, but the formation of OH at the surface of the metal or one of the hydroxides, while the accumulation of hydrogen is minimized by the gas stream, creates conditions favorable for consumption of hydroxyl by oxidation of the surface. From the data given above, it may be calculated that a single layer of close-packed technetium atoms ($\sim$1.4 x 10^{15}/cm^2) will produce 8 x 10^5 OH radicals per sec per cm^2. The range of the beta particles in the metal is of the order of 10^6Å, or something like 4 x 10^5 atomic layers. Self-absorption, back scattering, recombination of radicals, *etc.*, make a close calculation impossible, but if even a small fraction of the total disintegrations within range of the surface is radiolytically active it follows that self-oxidation of the interface is definitely possible as a slow process.

Possible confirmation of this interpretation may be seen in the observation that the platinum electrode responded fully to replacement of helium by hydrogen in some experiments like those of Fig. 3 only after renewal of the electrolyte in the cell. The oxidant, presumably H_2O_2, would be expected to polarize the technetium potentials also, but this was avoided by replacing the electrolyte in case a long exposure had been necessary to establish the potential.

It is possible that the somewhat surprising formation of discrete solid phases in the film is also a consequence of the radioactivity, which may act to aid the nucleation of stoichiometric components from a film of mixed composition.

Summary

It has been shown that elementary technetium gives reversible electrode potentials when it is electrolytically coated with a film of hydrous oxide. By utilizing an empirical correlation between the valence of the cation and the free energy of formation of the oxides of a given metal in different valence states, it was possible to assign the numerous stationary or metastable potentials observed to definite couples containing technetium in valence states less than 4+. In this way, free energies of formation of TcOH, $Tc(OH)_2$, $Tc(OH)_3$, $Tc(OH)_4$, Tc_3O_4, and Tc_4O_7 in films were established directly. It is suggested that the radioactivity of technetium plays a role in the observations.

Acknowledgments

It is a pleasure to acknowledge fruitful discussions with Drs. R. H. Busey, F. A. Posey, and J. A. Ghormley.

Manuscript submitted June 26, 1970; revised manuscript received Sept. 28, 1970.

Any discussion of this paper will appear in a Discussion Section to be published in the December 1971 JOURNAL.

REFERENCES

1. H. H. Miller, M. T. Kelley, and P. F. Thomason, "Advances in Polarography," Proc. 2nd International Congress, Vol. 2, p. 716, Pergamon Press, New York (1960).
2. (a) Rudolph Münze, *Z. Physik. Chem. (Leipzig)*, **238**, 364 (1968); **239**, 31 (1968).
   (b) George Kissel and Stephen W. Feldberg, *J. Phys. Chem.*, **73**, 3082 (1969).
3. R. H. Busey, *Chem. Div. Ann. Prog. Rept.*, Oak Ridge National Lab., ORNL-2983, p. 10, (1960).
4. J. E. Fergusson and R. S. Nyholm, *Nature*, **183**, 1039 (1959).
5. J. W. Cobble, Wm. T. Smith, Jr., and G. E. Boyd, *J. Am. Chem. Soc.*, **75**, 5777 (1953).
6. G. H. Cartledge and Wm. T. Smith, Jr., *J. Phys. Chem.*, **59**, 1111 (1955).
7. J. D. Eakins and G. D. Humphries, *J. Inorg. Nucl. Chem.*, **25**, 737 (1963).
8. A. J. de Bethune and N. A. Swendeman Loud, "Encyclopedia of Electrochemistry," C. A. Hampel, Editor, pp. 414-426, Reinhold, New York, (1964).
9. G. H. Cartledge, *J. Am. Chem. Soc.*, **50**, 2855, 2863 (1928).
10. G. H. Cartledge, *J. Phys. Colloid Chem.*, **55**, 248 (1951).
11. L. Brewer, *Chem. Rev.*, **52**, 1 (1953).
12. Bur. Standards, Tech. Note 270, parts 1-4, last in 1969.
13. W. M. Latimer, "Oxidation Potentials," 2nd Ed., Prentice-Hall, Inc., New York (1952).
14. E. G. King, D. W. Richardson, and R. V. Mrazek, *U. S. Bur. Mines, Rept. of Investigations*, 7323, Nov. 1969.
15. W. Feitknecht, *Z. Elektrochem.*, **63**, 34 (1959).

Electrochemical Hydrogenation of Ethylene, Acetylene, and Ethylene-Acetylene Mixtures

H. James Davitt[1] and Lyle F. Albright

School of Chemical Engineering, Purdue University, Lafayette, Indiana 47906

ABSTRACT

The electrochemical hydrogenations of ethylene, acetylene, and ethylene-acetylene mixtures were investigated on a platinum cathode as a function of applied potential (0.23V to −0.05V NHE), temperature (25°, 40°, and 55°C), and reactant partial pressures (0.01 to 1 atm) using 2*N* H_2SO_4 as the electrolyte. The principal products of the reactions were ethane and ethylene (from acetylene). Methane formation sometimes occurred at 40° and 55°C. The selective production of ethylene from acetylene or from an ethylene-acetylene mixture generally increased with temperature, acetylene partial pressure, and potential. The hydrogenation of acetylene or ethylene-acetylene is often controlled by the amount of electrically discharged hydrogen atoms at the cathode surface. The rate determining step in the hydrogenation of ethylene may be either mass transport of ethylene or surface kinetics.

Electrochemical hydrogenation of ethylene or acetylene has been investigated to only a limited extent (1-5), and the mechanisms of the reaction are not well understood. Catalytic hydrogenations of these compounds although investigated more thoroughly also involve a complicated mechanism which is not completely understood (6-15).

Langer and Landi (1, 2) reduced electrochemically several unsaturated hydrocarbons in a continuous flow reactor. Reactants in their system were minimally soluble in the electrolyte to avoid diffusion between the anode and the cathode chambers. This restriction resulted in a slow rate of reduction, which is undesirable for a commercial reactor that needs a high rate of mass transport of reactants to the electrodes.

Burke *et al.* (3, 4) report that the rate of ethylene hydrogenation in HCl and NaOH solutions at 25° and 50°C on platinum or palladium electrodes is limited by the supply of electrically discharged hydrogen ions at potentials which are more positive than about 0.08V (NHE) and by the diffusion of ethylene at potentials less than about 0.08V. Their results for the hydrogenation of acetylene were rather preliminary however. Ethylene and acetylene were reduced in a batch system by Beloslyudova and Sokol'skii (5) using platinum electrodes immersed in sulfuric acid. Possible accumulation of reaction products affected their kinetic data.

[1] Present address: Sun Oil Company, Marcus Hook, Pennsylvania 19061.

Key words: fuel cells, platinum, kinetics, catalyst poisoning.

Hydrogenations of ethylene, acetylene, and ethylene-acetylene mixtures were examined in the present investigation as a function of applied potential, temperature, and reactant partial pressure. The rate data indicate the most likely reaction mechanism and the probable reactive surface species.

Equipment and Operating Procedure

The electrochemical reactor used is shown in Fig. 1. The Plexiglas cell consisted of three parts sealed by silicone rubber gaskets: an electrolyte reservoir, a support for the electrodes and filter paper, and a gas cap. The bottom section (H_2SO_4 reservoir) consisted of three subsections which were connected hydrodynamically. A liquid bridge connected the reactor to a reference saturated calomel electrode in a separate constant temperature bath at 30°C. The electrodes employed were American Cyanamid Type AA-1 matrix fuel cell electrodes which were Teflon-bonded tantalum screens impregnated with platinum (16). The electrodes were supported by a Plexiglas sheet and were wetted from the bottom by filter paper dipped into the electrolyte of each subsection. The top of each electrode was exposed to the flowing gas stream. A platinum wire was spot welded to each electrode and extended outside the reactor. The gas cap contained three compartments each of which covered an electrode and corresponded to a subsection in the electrolyte reservoir. The middle electrode (1 x 2 in.)

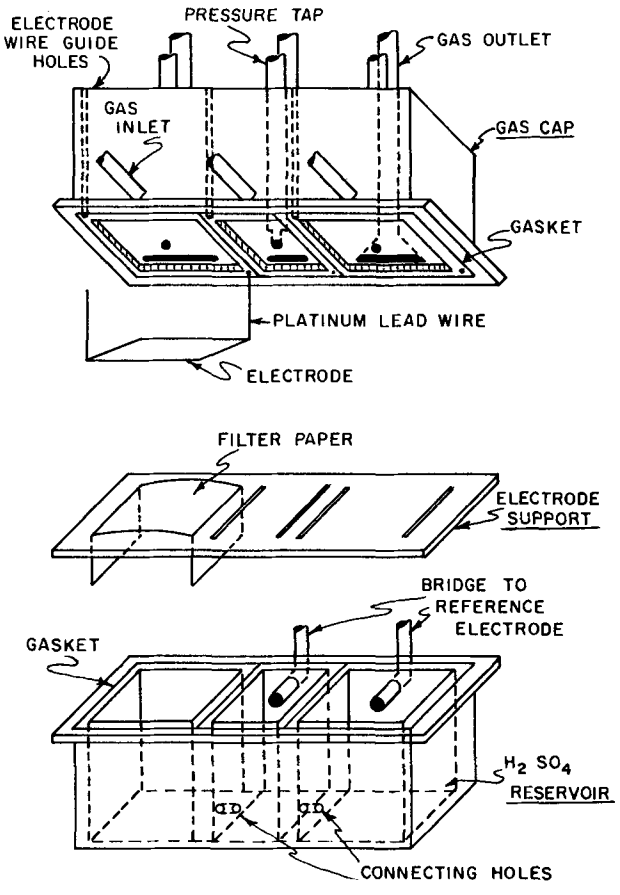

Fig. 1. Reactor design

was used as the anode and the two outside electrodes (each 2 x 2 in.) as the cathodes. The reactor was positioned in a constant temperature bath which was maintained at ±0.01°C of the desired temperature.

The electrolyte was 2*N* H_2SO_4 prepared from reagent grade sulfuric acid. The reactant gases obtained from Matheson Company were electrolytic grade hydrogen, c.p. grade ethylene, and purified acetylene. The hydrogen was purified with a catalytic converter to remove traces of oxygen. The acetylene was contacted with activated alumina and silica gel to remove traces of acetone. Ethylene, acetylene, and helium were each bubbled through pyrogallol solution to remove traces of oxygen, dried in a Drierite column, and then passed through a H_2SO_4 solution at reactor temperature.

Gas flow rates to the reactor were maintained at approximately 20 cc/min. Purified helium was used as a diluent in the feed gas stream for many runs, and the total gas pressure in most runs was about 760 mm Hg.

The potential of the cathode was controlled using a potentiostat to within 0.002V, and the current was continuously recorded. A saturated calomel electrode was used as reference electrode and all potentials were measured with respect to this electrode and were then adjusted to the open-circuit potential of the hydrogen electrode at the operating temperature. Potentials reported here are referenced to this normal hydrogen electrode at the operating temperature. A Perkin-Elmer Gas Fractometer with a silica-gel and activated alumina column was used to analyze the organic streams.

The following procedure was found necessary to obtain reproducible current results in each run. After approximately 4 hr of helium purging at electrical open circuit, the potential of the cathode was adjusted to 1.5V for 10 min followed by 5 min of 0.0V. This cycle of potential adjustments was repeated two additional times for runs with ethylene, and three times for runs with acetylene (since the acetylene was more strongly adsorbed on the cathode). The potential was then adjusted to 0.4V and maintained there for approximately 10 hr. The potential was once again cycled to 1.5V for 5 min and returned to 0.4V (twice in the case of acetylene) until the start of the next run (75 min).

At the start of each run after the reactant gas flows had been established, the polarization of the cathode at 0.4V was stopped, and the change in open-circuit potential with time was recorded for 1 hr. At the end of 1 hr, a potential was applied to the cathode (usually 0.23V) and the change in current with time was recorded for 1 hr. The potential was then adjusted in steps each hour to 0.20, 0.15, 0.00, 0.05, 0.00, and −0.05V. Gas chromatographic samples of the exit organic stream were taken during the 1 hr period at open circuit and at the end of each succeeding hour just before the potential change. After 1 hr at the last potential studied (−0.05V), the circuit was again opened and the change in open-circuit potential with time was recorded for 1 hr.

Open-Circuit Potential Behavior

Rest potentials at start-up.—Upon contact of the cathode with the unsaturated hydrocarbon, the open-circuit potential decreased rapidly during the first 5 min from 0.4V (where it had been maintained potentiostatically), sometimes passed through a minimum, and generally rose after several additional minutes to within 0.010V of the rest potential which was obtained after 1 hr, as reported in Table I. The rate of change of the open-circuit potential was usually less than 0.005 V/hr at the end of the 1-hr period. Exceptions were runs either with low partial pressures of ethylene (the remainder helium) at 25°C or with low partial pressures of acetylene (the remainder helium) at 25° and 40°C. In these cases, the open-circuit potential was changing as much as 0.070 V/hr after 1 hr.

Gas chromatographic analyses of the exit organic gas stream showed that dehydrogenation-hydrogenation reactions and cracking of the reactants were occurring during the open-circuit runs as indicated below:

1. Ethylene equilibrations. Ethane and methane were produced at rates which decreased with time in the 1-hr runs. Higher concentrations of methane and ethane were generally found in runs at low ethylene partial pressure (P_E) than at high pressures, at 55°C than at 40° or 25°C, and with a new cathode than an old one.

2. Acetylene equilibrations. Generally, ethylene concentrations increased with decreased acetylene partial pressures (P_A) and with increased temperature. Ethylene concentrations decreased during the 1-hr period. Only trace quantities of ethane were found at 40° or 55°C; whereas, at 25°C the concentra-

Table I. Rest potentials for ethylene, acetylene, and ethylene-acetylene mixtures

Temperature, °C	P_E (ethylene partial pressure	P_A (acetylene partial presure)	Rest potential, volts
25	760 mm Hg	—	0.254 ± 0.003
	38	—	0.35 ± 0.02
	—	760 mm Hg	0.292 ± 0.002
	—	44	0.34 ± 0.01
	720	40	0.288 ± 0.005
40	760	—	0.264 ± 0.005
	34	—	0.270 ± 0.003
	—	760	0.281 ± 0.005
	—	28	0.31 ± 0.02
	727	39	0.286 ± 0.006
55	695	—	0.270 ± 0.003
	29	—	0.270 ± 0.002
	—	670	0.272 ± 0.002
	—	29	0.291 ± 0.005
	730	31	0.280 ± 0.005

tion of ethane increased with decreased acetylene partial pressure. Methane was never detected.

3. Equilibrations for ethylene-acetylene mixtures. No significant production of ethane or methane was detected under any conditions.

Open-circuit potential after obtaining rate data.— After the rate data were obtained, generally ending at —0.05V, the circuit was opened. The potential usually increased asymptotically to within about 0.04V of the rest potential after 15 min, as indicated by curve 1 of Fig. 2.

An inflection point sometimes occurred in the curve of potential *vs.* time at a potential near 0.0V and less than 12 sec after cessation of polarization (curves 2 and 3, Fig. 2). Immediately after the inflection point, the potential increased asymptotically toward its rest potential. The phenomena occurred in the following runs:

1. All ethylene runs at 55°C except those in which an unusual rapid current increase occurred prior to the cessation of polarization (to be discussed later), and for the first few runs at 40°C immediately following a run at 55°C.

2. Acetylene runs at 55°C for low acetylene partial pressures and the second consecutive run at 40°C for low acetylene partial pressures. Exceptions to the above also occurred when an unusual rapid increase in current occurred prior to the cessation of polarization.

3. Runs at 55°C using ethylene-acetylene mixtures having an acetylene partial pressure of approximately 17 mm Hg (ethylene partial pressure of 761 mm Hg).

Discussion of Open-Circuit Results

The ethylene and acetylene rest potentials reported in Table I are generally consistent with comparable results reported by Wroblowa *et al.* (17) and Johnson *et al.* (18). The suggestion has been made (19-22) that the rest potentials obtained by organic compounds in contact with platinum electrodes are caused by dissociative adsorption (dehydrogenation) followed by equilibration of the adsorbed hydrogen with the solution. The slow increase of the open-circuit potential with time ($\sim$ 0.005 V/hr) probably indicates a decrease of the surface concentration of hydrogen. Dissociative adsorption likely occurred only at sites with a high energy for adsorption or at sites which had adjacent empty sites. As these sites became covered or poisoned with residual hydrocarbon or carbon species, dissociative adsorption was slowly displaced by associative adsorption. The decreasing rates of dehydrogenation and cracking with time during these equilibrations tends to support this postulate.

As discussed above the establishment of the organic rest potential is a dynamic equilibrium between hydrogenation and dehydrogenation. The rate of obtaining this equilibrium is retarded by low temperatures and low organic partial pressure because in these cases stable rest potentials were not established even after 1 hr.

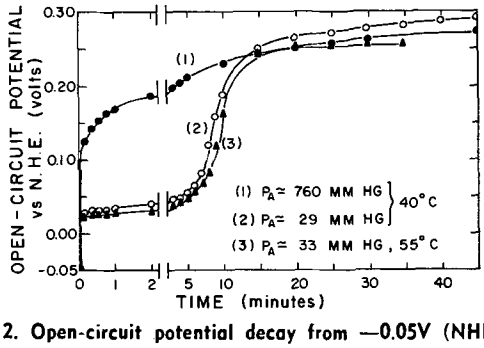

Fig. 2. Open-circuit potential decay from —0.05V (NHE), after obtaining acetylene rate data, *vs.* time.

It is reasonable to expect as a rule more ethylene dehydrogenation than acetylene dehydrogenation; consequently the ethylene rest potential should be the less positive one because of higher hydrogen concentrations. The ethylene rest potential changed little with temperature, indicating that the activation energies for dehydrogenation and hydrogenation were approximately the same. For acetylene, however, the activation energy for dehydrogenation may be higher than hydrogenation since its rest potential decreased with increased temperature.

Current-Time Behavior

The current-time behavior was extensively investigated for the hydrogenations of ethylene, acetylene, and mixtures of them. Immediately after the potential was decreased, a current surge occurred and then the current began to drop. Generally the rate of decay was small after 1 hr, and higher currents occurred at lower potentials. Such results which were noted in most runs are shown in the following figures for the indicated reactants:

1. Ethylene: Fig. 3; curves 1 and 2.
2. Acetylene and ethylene-acetylene mixtures: Fig. 4; curves 1, 2, and 3.

Different types of current-time behavior were found at these conditions:

1. Ethylene (see Fig. 3): At 55°C and at potentials between 0.10 and —0.05V. The very rapid initial current decrease, such as shown by curve 4, always followed a behavior as shown by either curves 3 or 5. The inflection point in the decay of open-circuit potential (see Fig. 2) only followed a series of runs in which curve 3 appeared but not curve 5.

2. Acetylene (see Fig. 4): At 55°C or the second consecutive run at 40°C all at low partial pressures and at potentials between 0.10 and —0.05V. Two maximums were observed in the decay curve at 0.10V (curve 4) for the second consecutive run at 40°C instead of only one maximum for the first such run (curve 2). Subsequent potential changes produced curve 5 which shows a very rapid current decrease from the initial current peak.

3. Ethylene-acetylene mixtures: similar to acetylene runs.

Methane was noted at the end of the hour period in which the unusual current decay phenomena described above occurred (curve 5 of Fig. 3 and curve 4 of Fig. 4). Subsequent gas samples usually also contained some methane. Figure 5 illustrates the changing exit gas composition with potential during Run No. 3-6 shown in Fig. 4. No methane was detected during this run, but in the next run, Run No. 3-7 which was made at duplicate operating conditions and which was made immediately after Run No. 3-6, methane first appeared at a potential of 0.10V, increased by fivefold at 0.05V

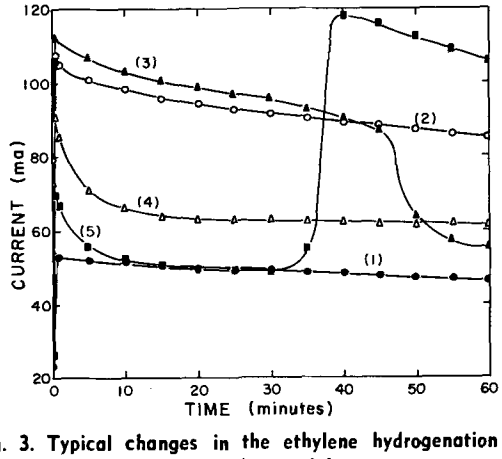

Fig. 3. Typical changes in the ethylene hydrogenation current *vs.* time as a function of applied potential.

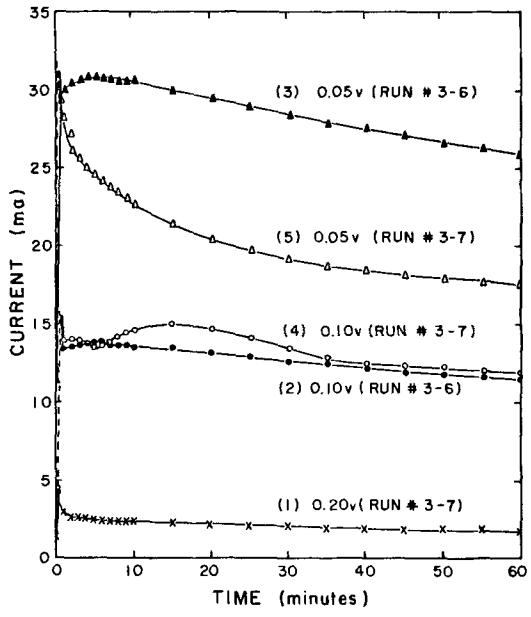

Fig. 4. Typical changes in the current produced during acetylene hydrogenation vs. time as a function of applied potential.

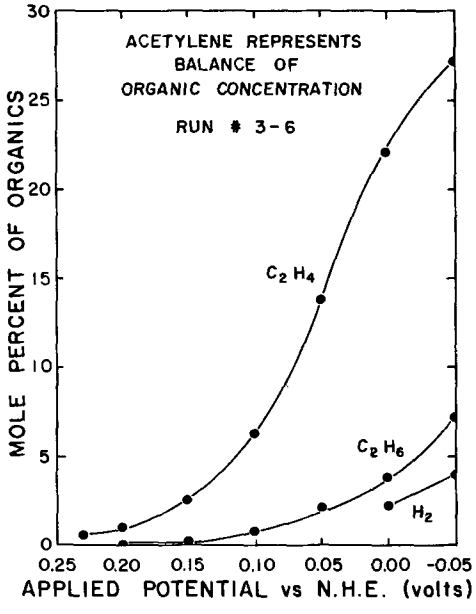

Fig. 5. Exit organic gas composition of acetylene hydrogenation vs. applied potential at 40°C and an acetylene partial pressure of 29 mm Hg.

to about 0.2% concentration, and then decreased to about the same level at 0.00V as at 0.10V. Only a trace of methane was found at −0.05V. Somewhat greater amounts of ethane were produced in the range from 0.05 to 0.10V in Run No. 3-6 as compared to Run No. 3-7, and considerably more hydrogen was obtained in Run No. 3-7. Hydrogen concentrations varied from 5 to 14% as the voltage varied from 0.00 to −0.05V for the latter run. Ethylene concentrations in Run No. 3-7 were in general significantly lower, reaching only 14% at −0.05V. Hydrogen was generally produced at 0.00V and/or −0.05V during runs in which acetylene was a reactant but never in runs in which ethylene alone was a reactant.

Rates of Hydrogenation

Ethylene runs.—Average rate data (currents) for the hydrogenation of ethylene at two partial pressures and 25°, 40°, and 55°C are shown in Fig. 6 as curves 4 through 7. These data, obtained at the end of 1 hr at a given potential, were generally reproducible

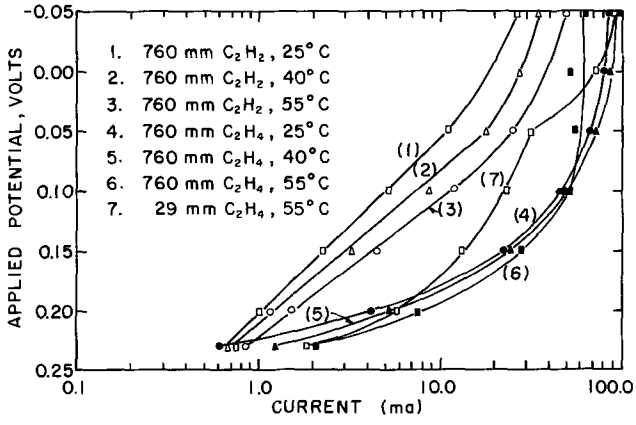

Fig. 6. Current produced during acetylene and ethylene hydrogenation vs. applied potential as a function of reactant partial pressure and temperature.

to within 10% of the average value of 3 to 5 replicate runs. Calculations indicated that the current noted was caused by the simple reduction of ethylene to ethane. The results of these runs are summarized as follows:

1. The logarithm of the current increased for all runs at 25° and 40°C at a decreasing rate with respect to the applied potential. At 55°C and P_E of about 29 mm Hg, however, the current passed through an inflection point as a result of the wide variance in currents as discussed earlier; no significant portions of these curves were found to be linear.

2. Ethylene partial pressure was found to have no significant effect on the rate of hydrogenation at either 25° or 40°C. Currents did increase with increased ethylene partial pressure at 55°C between 0.23V and 0.05V. At 0.00V and −0.05V, the results were inconclusive because of the wide variation in currents as previously noted.

3. At high ethylene partial pressures, the rate of reaction increased with increased temperatures between 0.23V and 0.10V, but between 0.05V and −0.05V, the order of increasing rates was 55°, 25°, and 40°C. At low ethylene partial pressures, the order of increasing rates was also 55°, 25°, and 40°C except at 0.23V and 0.20V. The apparent activation energy for the high partial pressure runs at 0.23V was approximately 8 kcal/mole, but it decreased to about 0.6 kcal/mole at 0.10V.

Acetylene runs.—The results of acetylene hydrogenations at potentials between 0.23V and −0.05V, temperatures of 25°, 40°, and 55°C, and high acetylene partial pressures are shown in Fig. 6 as curves 1 through 3. Reproducibility of these data was generally within 10% of the average value at each experimental condition. Calculations indicated that the current generated was accounted for within 10% by the reduction of acetylene to ethylene and ethane and by the evolution of hydrogen.

A linear relationship existed between the potential and the logarithm of the current between 0.23V and 0.05V for most acetylene runs. Exceptions were the second consecutive run at 40°C and all 55°C runs at low acetylene partial pressures where the linear region was between 0.23V and 0.10V. The data (100 data points) in the linear region were correlated using regression analysis. Only variables with a probability level greater than 97% were retained, and the following equation correlates the data with a correlation coefficient of 0.995 corrected for the mean

$$\ln i = 89.7 + 0.78\,(\ln P_A) - 48.4(E) - 1408.8/(T) - 276.5(\ln P_A)/(T) + 9609.7\,(E)/(T) \quad [1]$$

or

$$i = (\text{antiln } 89.7)\,(P_A)^{(0.78\,-\,276.5/T)} \exp\,[\,-48.4(E) - 1408.8/(T) + 9609.7(E)/(T)\,] \quad [2]$$

Table II. Acetylene hydrogenation kinetic constants

Temperature, °C	b′	γ	βn
25	142 mV ± 4*	−0.15 ± 0.03*	0.42 ± 0.02*
40	130 ± 4	−0.10 ± 0.03	0.48 ± 0.02
55	120 ± 4	−0.06 ± 0.03	0.54 ± 0.02

* 2σ limits.

where P_A = average partial pressure of acetylene (mm Hg), E = potential *vs.* NHE (volts), and T = temperature, °K.

"Tafel" slopes (b′), listed in Table II, were calculated at each temperature from

$$\frac{1}{b'} = \frac{\partial \log i \times 10^{-3}}{\partial E} = \frac{1}{2.3}\left[-48.4 + \frac{9609.7}{T}\right] \times 10^{-3} \quad [3]$$

Acetylene partial pressure had no significant effect on the value of b′.

The current increased with decreased acetylene partial pressures at potentials between 0.23V and 0.05V (or 0.10V) at all temperatures. Equation [4] was used to calculate the effect of acetylene partial pressure on the reaction rate

$$\frac{\partial \ln i}{\partial \ln P_A} = \gamma = 0.78 - 276.5/T \quad [4]$$

Values of γ (see Table II) indicate that the acetylene partial pressure had less effect on the rate at higher temperatures. An extrapolation of Eq. [4] indicates that γ is zero at about 80°C.

Apparent activation energies were calculated for the hydrogenation of acetylene using all the terms involving temperature in Eq. [1]. The standard Arrhenius form for calculating activation energies is as follows

$$i = K\,[\exp(\Delta H^*/RT)] \text{ or } \ln i = \ln K + \Delta H^*/RT \quad [5]$$

Therefore, equating terms with $(T)^{-1}$

$$\Delta H^*/R = -1408.8 - 276.5(\ln P_A) + 9609.7(E) \quad [6]$$

The resulting ΔH^* are listed in Table III as a function of potential and at P_A = 760 mm Hg. Equation [6] shows that at a constant potential ΔH^* decreases with a decreased partial pressure of acetylene.

The first attempt at correlating the acetylene data of the linear regions of curves 1 through 3 of Fig. 6 using a model more consistent with traditional "Tafel" models was unsuccessful. The model tested was the following

$$i = B_1 \times (P_A)^{B_2} \times \exp(B_3 E/T) \quad [7]$$

where $B_3 = \beta n\mathbf{F}/R$ and β is the transfer coefficient, $\mathbf{F}$ is the Faraday constant, and R is the gas constant. This model was unsuccessful because the "constant" βn, was not constant but varied linearly from 0.42 to 0.54 with increased temperature as shown in Table II.

Selectivity (S) for acetylene reductions is defined as the ratio of ethylene production to the total ethylene plus ethane production. The change in S with acetylene partial pressure, temperature, and applied potential is illustrated in Fig. 7. Calculated values of S were within ± 0.04 and often within ± 0.01 of the average value for a constant potential. In general, S increased with increased acetylene partial pressure and temperature; a similar finding for normal catalytic hydrogenations of acetylene has been previously reported (8). S also increased with increased potential. The pronounced minimums shown in curves 5 and 7 are related to the unusual current phenomenon discussed in connection with Fig. 4 and 5, *i.e.*, the history effect of the second consecutive run at 40°C and 55°C runs at low acetylene partial pressures.

Table III. Apparent activation energies (ΔH^*) for acetylene reduction at P_A = 760 mm Hg

Potential *vs.* NHE, V	ΔH^*, kcal/mole
0.05	5.5
0.10	4.5
0.15	3.6
0.20	2.6

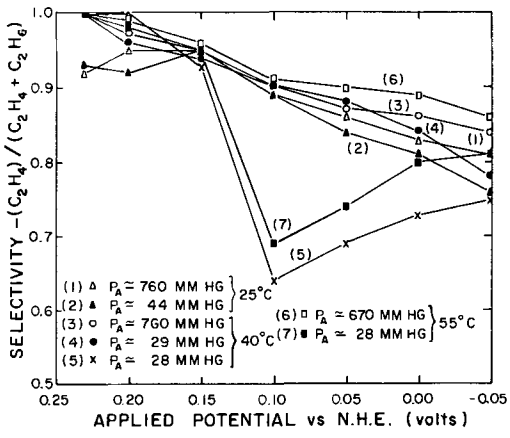

Fig. 7. Selectivity of acetylene hydrogenation to ethylene *vs.* applied potential as a function of temperature and acetylene partial pressure (P_A).

Essentially no ethane was formed during any run at either 40° or 55°C and a potential of 0.23V. Some ethane was formed at 25°C but its concentration varied widely; therefore, the very small increase in S between 0.23V and 0.15V may not be significant.

Runs with ethylene-acetylene mixtures.—The effects of potential and temperature on the rate of hydrogenation of ethylene-acetylene mixtures of high and low partial pressures respectively are shown in Fig. 8. The reproducibility of these data (three runs at each condition) was generally within 10%. One preliminary run was also made at very low acetylene partial pressures ($P_A \simeq$ 5-17 mm Hg) at each temperature to determine the general effect of very low acetylene partial pressures on the rate of hydrogenation.

Plots of the potential *vs.* the logarithm of current had a linear region between 0.23V and 0.10V at all temperatures. The logarithm of the current below 0.10V increased at an increasing rate.

The following empirical equation correlated the data of the linear region (48 data points) with a correlation coefficient of 0.996 corrected for the mean

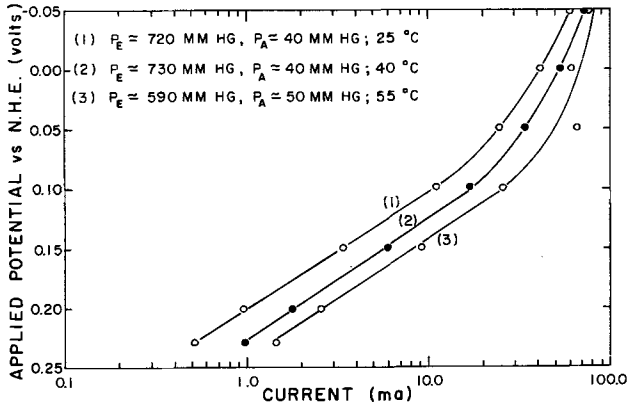

Fig. 8. Current produced during ethylene-acetylene hydrogenation *vs.* applied potential as a function of temperature.

$$\ln i = 15.85 - 0.06\ (\ln P_A) - 23.05(E) - 3261.8/(T) \quad [8]$$

or

$$i = \text{antiln}(15.85) \times (P_A)^{-0.06} \times \exp[-23.05(E) - 3261.8/(T)] \quad [9]$$

Interactions between these variables and also ethylene partial pressure were eliminated with probability levels less than 97%.

The "Tafel" slope (b') calculated from Eq. [8] was independent of temperature and organic partial pressure and was equal to 100 mV ± 3 (2σ limits).

Increased acetylene partial pressure decreased the reaction rate as shown by Eq. [9]. The exponent of P_A varied with 2σ limits of ± 0.03. A single apparent activation energy of 6.5 kcal/mole ± 0.5 (2σ limits) was calculated by equating the temperature term of Eq. [8] to the temperature term in the Arrhenius equation (Eq. [5]).

The actual conversion of acetylene to ethylene and ethylene to ethane could not be calculated because of the large error involved in subtracting two numbers of essentially equal size (acetylene or ethylene concentrations). Therefore, the actual selectivity (S) could not be calculated. The maximum S, S_{max}, and the minimum S, S_{min}, could be calculated however. S_{max} was calculated by assuming that all the ethane produced was from the ethylene feed. S_{min} was calculated by assuming that all the ethane was produced from the acetylene feed. S_{max} values were usually reproducible to within 0.05 of the average for three repeat runs, and decreased from about 0.97 to 0.71 as the potential decreased from 0.25 to −0.05V. S_{min} values decreased over the same potential range from about 0.93 to 0.43. In general selectivity increased slightly from 25° to 40°C. The selectivity at 55°C was lower than that at 40°C and at potentials less than 0.15V.

Discussion of Mechanisms and Rates of Hydrogenation

Ethylene hydrogenation was not apparently limited solely by either kinetics or mass transport of reactants. Kinetics controlled at low reaction rates because the rate increased more than two orders of magnitude and was generally unaffected by ethylene partial pressure. The reaction rate approached a constant value at high rates indicating a mass transport limit.

The results of this study support the following electrolytic reduction mechanism for acetylene between 0.23V and −0.05V

$$C_2H_{2soln} + (*) \rightleftharpoons \underset{*}{C_2H_2}$$

$$(*) + H^+ + e^- \rightleftharpoons \underset{*}{H}$$

$$\underset{*}{C_2H_2} + \underset{*}{H} \rightleftharpoons \underset{*}{C_2H_3} + (*)$$

$$\underset{*}{C_2H_3} + \underset{*}{H} \rightleftharpoons \underset{*}{C_2H_4} + (*)$$

The symbol (*) represents an active site and the second of the above reactions is the rate determining step (R.D.S.). This conclusion is drawn from the following data:

1. The negative effect of acetylene partial pressure on the rate and the zero pressure effect for ethylene hydrogenation indicate that neither acetylene nor any intermediate derived from it could be involved in the rate determining step.
2. Adsorbed hydrogen atoms are known to exist on platinum surfaces in contact with sulfuric acid electrolyte at potentials less than 0.4V which is within the potential range studied (23).
3. The predicted and observed "Tafel" slopes are in the same general range (100-140 mV).
4. The same reaction products resulted from open-circuit studies as from rate studies indicating that although the source of the hydrogen was different, the reactions were probably the same.

At potentials less positive than about 0.05V (high rates of reaction), the rate controlling step appears to be changing from kinetic control to mass transport control (see Fig. 6 and 8).

Associative adsorption of acetylene (and ethylene) is assumed to be the predominate mode of adsorption for the following reasons:

1. Associative adsorption is more energetically favorable than dissociative adsorption (17).
2. The correspondence (usually within 5% for ethylene hydrogenations and 10% for acetylene hydrogenations) between the rates of reaction calculated from gas chromatography and recorded currents which account for all the hydrogen used.
3. The decreasing rates of dehydrogenation and cracking during ethylene or acetylene equilibrations discussed earlier indicated a shift from dissociative to associative adsorption prior to each rate study run.

Apparent activation energies for the hydrogenation of acetylene of 5.5 to 2.6 kcal/mole at 0.05V and 0.20V respectively, although low, are similar to the values reported by Beloslyudova and Sokol'skii (5) of 6.6 kcal/mole in an electrochemical system and by Bond (8) of 9 kcal/mole for the usual gas phase chemical hydrogenation of acetylene on alumina-supported platinum between 40° and 96°C.

The driving force (ethylene partial pressure) for maintaining ethylene on the electrode surface was much greater in the hydrogenations of the mixtures than in pure acetylene alone. The rate of reaction, therefore, should change more, for a given potential change, in the hydrogenation of ethylene-acetylene mixtures than in the hydrogenation of acetylene alone: this was found experimentally [the acetylene "Tafel" slopes were larger than those of ethylene-acetylene (120-140 mV *vs.* 100 mV)].

Figure 9 emphasizes that acetylene in ethylene-acetylene mixtures, even in as low a concentration as 1.0% dominates the surface and controls the rate of reaction. The dominating effect of acetylene on the rate diminishes however as the potential decreases. Increased amounts of adsorbed hydrogen available at lower potentials and the slower rate of acetylene hydrogenation enables ethylene to compete more favorably with acetylene for the available hydrogen as indicated by lower selectivity for ethylene produc-

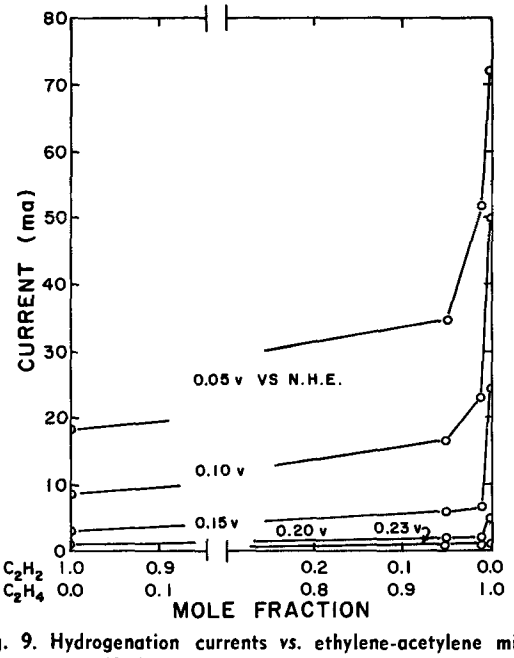

Fig. 9. Hydrogenation currents *vs.* ethylene-acetylene mixtures composition at 40°C and a total organic partial pressure of 760 mm Hg.

tion with decreasing potential (see Fig. 7 as one example).

Increased selectivity with increased temperature may be due to a higher activation energy for the desorption of ethylene relative to its hydrogenation (9) or to decreased hydrogen atom coverage because of increased acetylene coverage. Increased acetylene coverage with temperature is inferred from the findings of Gilman (24), which indicate that ethylene coverage increased with temperature. Since acetylene is more strongly adsorbed than ethylene, its coverage may also increase with temperature. Bond and Wells (8) reported similar selectivity findings for the chemical heterogeneous hydrogenation of acetylene.

Surface Species

The dominate reactive surface species during electrolytic hydrogenation, as mentioned earlier, are believed to be associatively adsorbed ethylene and acetylene and monatomic hydrogen. The "unusual" current-time behavior (Fig. 3 and 4) and open-circuit potential-time behavior (Fig. 2) are complex functions of potential, temperature, organic partial pressure and electrode previous history. These "unusual" behaviors are probably related to changes in the normal distribution of reactive surface species. For example, this redistribution of reactive surface species was in some way connected to the methane production observed during the rate studies. In addition the inflection point in the open-circuit potential curve (Fig. 2), which may be associated with the transient presence of hydrogen, occurred in runs similar to that of curve 7 of Fig. 6. Interestingly, the inflection point was not observed in at least one case each when it was expected for runs with ethylene, acetylene, or mixtures of the two. In each instance, however, a sudden current increase had occurred (curve 5, Fig. 3) at 0.00V or −0.05V prior to the end of the run. Apparently the reactive specie or species, which were responsible for the inflection point, were eliminated from the surface.

Redistributions of surface species at low acetylene partial pressures at 40° and 55° for acetylene-helium mixtures and ethylene-acetylene mixtures aided the rate of ethylene hydrogenation at the expense of acetylene hydrogenation. Sharp decreases in selectivity, therefore resulted at a potential of 0.10V where methane production first started.

Conclusions

The rates of hydrogenation of acetylene and ethylene-acetylene mixtures on platinum in sulfuric acid are limited by the supply of electrically discharged hydrogen ions between 0.23V and about 0.05V. At lower potentials the rate is limited by diffusion of reactants.

The controlling step in the reduction of ethylene in this investigation cannot be unambiguously defined as either mass transport of ethylene or an electrochemical kinetic step.

Ethylene and acetylene first adsorb dissociately on platinum in contact with an acid solution, but later adsorb associatively as the surface becomes "poisoned" with residual hydrocarbon species from the dehydrogenation and cracking reactions.

Selectivity for the production of ethylene from acetylene or ethylene-acetylene mixtures in general increases with increased temperature, increased acetylene partial pressure, and increased potential. Major redistributions of reactive surface species sometimes occurred under conditions of high temperatures and low acetylene partial pressures and potentials, which produced methane as a product and caused a sharp decrease in selectivity.

Acknowledgment

The financial support of the Dow Chemical Company and of The Procter and Gamble Company is gratefully acknowledged.

Manuscript submitted February 11, 1969; revised manuscript received ca. May 6, 1970.

Any discussion of this paper will appear in a Discussion Section to be published in the December 1971 JOURNAL.

REFERENCES

1. S. H. Langer and H. P. Landi, *J. Am. Chem. Soc.*, **85**, 3043 (1963).
2. S. H. Langer and H. P. Landi, *ibid.*, **86**, 4694 (1964). **86**, 4694 (1964).
3. L. D. Burke, C. Kemball, and F. A. Lewis, *Trans. Faraday Soc.*, **60**, 913 (1965).
4. L. D. Burke, F. A. Lewis, and C. Kemball, *ibid.*, **60**, 919 (1964).
5. T. M. Beloslyudova and D. V. Sokol'skii, *Elektrokhimiya (English Translation)*, **1** (10), 1056 (1965).
6. G. C. Bond, D. A. Bowden, and N. Mackenzie, *Trans. Faraday Soc.*, **54**, 1537 (1958).
7. G. C. Bond, J. V. Philipson, P. B. Wells, and J. M. Winterbottom, *ibid.*, **62**, 443 (1966).
8. G. C. Bond and P. B. Wells, *J. Cat.*, **4** (2), 211 (1965).
9. G. C. Bond and P. B. Wells, *Advan. Catalysis*, **15**, 92 (1965).
10. D. Cormack, S. J. Thomson, and G. Webb, *J. Cat.*, **5**, 224 (1966).
11. G. I. Jenkins and E. Rideal, *J. Chem. Soc.*, **1955**, 2469.
12. S. J. Stephens, *Phys. Chem.*, **62**, 714 (1958).
13. T. Takeuchi, *Bull. Chem. Soc. Japan*, **38** (2), 322 (1965).
14. L. A. Wannenger and J. M. Smith, *Chem. Weekblad*, **56**, 273 (1960).
15. P. B. Wells, *Chem. Ind. (London)*, 1742 (1964).
16. R. G. Haldeman, "Thin Fuel Cell Electrodes," in *Fuel Cell Systems, Advan. Chem. Ser.*, **31** (1965).
17. H. Wroblowa, B. J. Piersma, and J. O'M. Bockris, *J. Electroanal. Chem.*, **6**, 401 (1963).
18. J. W. Johnson, H. Wroblowa, and J. O'M. Bockris, *This Journal*, **111**, 386 (1964).
19. S. S. Beskorovainaya, Yu. B. Vasil'ev, and V. S. Bogotskii, *Elektrokhimiya (English Translation)*, **2** (1), 37 (1966).
20. A. N. Frumkin and B. I. Podlovchenko, *Dokl. Akad. Nauk SSSR*, **150**, 349 (1963).
21. L. W. Niedrach, *This Journal*, **111**, 1309 (1964).
22. M. J. Schlatter, *Fuel Cell Systems, Advan. Chem. Ser.*, **31** (1965).
23. F. G. Will and C. A. Knorr, *Z. Elektrochem.*, **64**, 258 (1960).
24. S. Gilman, *Trans. Faraday. Soc.*, **62**, 481 (1966).

Anodic Dissolution of Beryllium in Anhydrous Media

H. Aida, I. Epelboin,* and M. Garreau

Physique des Liquides et Electrochimie, Groupe de Recherches du C.N.R.S. associé à la Faculté des Sciences de Paris, Faculté des Sciences, Paris V, France

ABSTRACT

When the residual water content of currently used ClO_4^- electropolishing solution is reduced to less than 0.1 g/l, the anodic dissolution of beryllium follows Faraday's law with a valence of one over an extended range of anodic potentials. This result is interpreted in terms of a dissolution mechanism occurring in a succession of two individual steps, each involving a simple electron, thus

$Be \rightarrow Be^+ + e^-$ (electrochemical step)
$Be^+ +$ oxidant $\rightarrow Be^{++}$ (chemical step occurring away from the electrode)

Support for the transitory existence of the monovalent ions is derived from thermodynamic considerations allied with the structure of the anodic layer. Microscopic examination of the state of the anode surface during and after the dissolution shows clearly that a mechanical disintegration of the metal lattice by the action of the current cannot be the origin of the anomalous valence observed. On the contrary, it is shown that disintegration of this type contributes only at low anodic potentials. This phenomenon, known as the "chunk effect," is clearly observable by scanning electron microscopy and accounts for faradaic "efficiencies" of greater than 200% in certain electrolytic conditions.

Since 1955 it has been known that the application of Faraday's law to the anodic dissolution of beryllium could lead to calculated anode weight losses which were lower than measured values (1-7).

Although, for more than a century now, a number of investigations has been devoted to the study of analogous effects on other metals, the origin of these anomalous dissolution valences remains very controversial. For some investigators, it consists of nothing more than a more or less incidental intervention of a side effect (difference effect, chunk effect[1]) (7-12). On the other hand, there are those who consider these discrepancies to be evidence, on a macroscopic scale, of a fundamental reaction process. This process, potentially applicable to all dissolution processes leading to multivalent ions, concerns the mechanism of the charge transfer at the metal/electrolyte interface and is proposed as a series of individual single electron steps (13-21). With this latter view, the systematic study of these "deviations" from Faraday's law provides an approach to a better understanding of the electrolytic dissolution of a metal, and thus, as pointed out specifically by Uhlig (22), also to the essential processes in metallic corrosion.

A metal such as beryllium has favorable characteristics for studying anodic dissolution in terms of these two different concepts of the anomalous valences. First, one can use it in the form of the usual industrial polycrystalline material, a form in which it ought to be more sensitive to the occurrence of difference, or chunk, effects, than a single crystal, since these effects are initiated by structure defects. Second, there are conditions, well known, in which Faraday's law will be rigorously followed if one uses a valence of one, a result conforming to that which would be expected, in the limit, if transitory Be^+ ions only are formed in the first step of the dissolution process.

The primary purpose of this paper is to establish the fundamental role played by solvation in the solution of a metal, which we propose should be an essential part of the theoretical study of this phenomenon. In particular, we shall show how these anomalous valences of dissolution may perhaps be due to an insufficiency of solvation molecules in the anodic layer, and to an insufficiency which leads to a local inversion of the relative thermodynamic stability of the ions Be^+ and Be^{++}. Following this we shall show, using results from studies of anodic dissolution in an anhydrous environment, and the complete range of faradaic efficiencies as established by observation of the anodic surface by the scanning electron microscope, that the two concepts of anomalous dissolution (intervention or not of transitory species of unusual valence) are in fact not irreconcilable, but may simply be alternately applicable in different experimental domains.

Theoretical

The concept that anomalous anodic dissolution valences must be a manifestation on a macroscopic scale of a reaction mechanism which must include the formation of monovalent ions as a first step has grown in acceptance at a rate proportional to the increase in examples of "abnormal" dissolutions. There has as yet, however, been no theoretical basis from quantum mechanical considerations to support this hypothesis. Since a quantum treatment of electron transfer at the metal/electrolyte interface in the presence of adsorption is not possible at the present time, we have looked toward using thermodynamic considerations, linked to the structure of the anodic layer, as a means of placing the participation of these transitory ions in the dissolution process on a sounder theoretical basis (19-23).

* Electrochemical Society Active Member.

Key words: dissolution anomalous valences, cation solvation, anodic dissolution efficiency, electrolytic polishing, microscope scanning electron.

[1] The "chunk effect" consists of the disintegration of the metallic lattice under the action of the electrolysis current; a heterogeneous dissolution on an atomic scale provokes a sort of "detachment" of little crystalline unities which are then carried into the solution. The particles thus detached from the metal are sometimes observed in the appearance of a dark coloration in the region of the anode. X-ray studies of these anode layers have shown the presence of particles of significant dimensions, i.e., several microns.

By "difference effect" is meant a modification, under the influence of the current, of the rate of self-dissolution of a metal in an electrolyte. This phenomenon originally was studied only for metals which were attacked by the solution at open-circuit potentials. However, the term "difference effect" has been used recently even in cases where the rate of chemical attack is zero in the absence of an external current. This effect is attributed to a loss of cohesion of the protective layer which isolates the metal from the environment, and which originates at certain defects in the structure of the metal (heterogeneous dissolution).

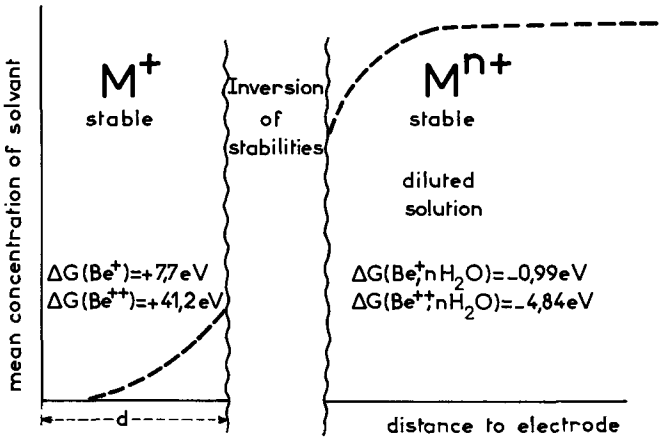

Fig. 1. Pictorial description of the relative stabilities of ions M^+ and M^{n+} in relation to distance to electrode.

These considerations may be summarized briefly using the pictorial description of the anodic layer as given by Fig. 1.

Starting from a concept first given by Epelboin and Darmois (14) in 1953, there exists at the anode a zone of low concentration of solvent molecules, created by the joint action of the electric field and the specific adsorption of anions from the solution. The solvent content then increases regularly with distance from the surface (dashed curve).

A calculation based on the Born-Haber cycle shows that, in the absence of solvation, it is the monovalent ion M^+ which, among all the possible ions which the metal can form, forms with the least energy. It is thus this ion which exhibits maximum stability in the immediate vicinity of the anode where the normal solvation is sharply restricted.

Figure 1 gives the values, for beryllium, of the free energies of formation,[2] ΔG, of the ions Be^{++} and Be^+ in the metal, in dilute aqueous solution [ΔG ($Be^{z+} \cdot n\ H_2O$)] and in absence of solvent [ΔG (Be^{z+})] (limiting case).

The monovalent ion is not stable thermodynamically except in the immediate vicinity of the electrode. As it migrates from the electrode it very rapidly reaches a zone sufficiently rich in solvent molecules that the electrochemical oxidation

$$Be^+ \cdot n\ H_2O \rightarrow Be^{++} \cdot n'\ H_2O + (n' - n)\ H_2O + e^- \quad \text{(from the metal)} \quad [1]$$

will proceed with a decrease in free energy.

There is thus an inversion of the thermodynamic stability in favor of the divalent ion. The distance d between the electrode surface and the zone of stability inversion depends on the electrolyte conditions. The electron involved in the electrochemical oxidation [1] must traverse the distance d to reach the electrode. Now, as the distance across which the charge transfer must take place increases, the rate of the transfer reaction will decrease very rapidly (24). In practice beyond a certain distance the ion M^+ can no longer be oxidized electrochemically. Thus, on arriving in the solvent rich zone, it will be oxidized chemically by reaction with some solution component

$$Be^+ \cdot x\ H_2O + \text{oxidant} \rightarrow Be^{++} \cdot x'\ H_2O + (x' - x)\ H_2O + \text{reduction products} \quad [2]$$

In the presence of perchlorate, for example, analyses have shown that a part of the ClO_4^- has been reduced to Cl^-.

The total number of electrons Ne (initial valence of dissolution) released into the exterior circuit per atom of metal leaving the anode thus depends on the relative magnitudes of reactions [1] and [2]. When the distance at which reaction [2] can proceed easily is clearly greater than the distance at which the rate of reaction [1] goes to zero, Ne attains the limiting value of one.

In some respects one can predict the way in which the profile of the curve of Fig. 1 will be altered as a result of a modification of experimental conditions, and consequently the way in which the faradaic efficiency ρ (or Ne) of the dissolution will be affected. In particular it is noted that lower values of Ne are favored by increasing temperature (23) and by a reduction in residual water content of the (anhydrous) electrolyte. Finally, there should exist an optimum region of anodic potential for values $Ne \rightarrow 1$.

These theoretical predictions have been found to be in good agreement with our results obtained for the anodic dissolution of aluminum in the ternary mixture: ethanol-water-$LiClO_4$ (23). In the case of beryllium, as we have mentioned, the limiting value $Ne = 1$ can be obtained without unusual experimental precautions. Nevertheless, this value $Ne = 1$ does not occur except in a narrow potential range. It is these results which have led us to undertake a study of this anodic dissolution at elevated temperatures and in solutions of very low water content in an attempt to extend the potential range where Ne is rigorously equal to 1, while still maintaining conditions such that any "chunk" or "difference effect" may be excluded.

Before describing the experimental work, it should be noted that several attempts have been made by other workers to detect directly the existence of ions M^+ of unusual valence at some distance from the electrode [ring disk electrodes (6), detection of reducing products in an indicated anode compartment (27-29)].

For ions like Be^+ and Al^+ which are very unstable in dilute aqueous solutions, these tests have resulted either in failures to detect the species or have given evidence which is not particularly convincing. For the same conditions, more stable ions like Cu^+, In^+, . . . , have been detected in a manner which is hardly disputable (30, 31). These results tend to indicate a very narrow depth to the zone near the electrode in which the ions Be^+ and Al^+ are stable.

On the other hand we have verified that in the case of aluminum the rotation of the anode did not lead to a change in the mechanism of dissolution. For rotation speeds up to 1500 rpm, we observed no measurable change in Ne, a result one would expect if the anodic layer consists of a zone of low water content, the thickness of which is small in relation to the total thickness of the diffusion layer. In these conditions it appears unlikely that, as proposed by Kabanov (15), the value of Ne is related to the velocity of diffusion into the solution of the unstable M^+ ions formed at the anode.

Experimental

Electrolyte.—The electrolyte is a ternary mixture of ethanol, water, and lithium perchlorate (reagent grade from G. Frederick Smith Chemical Company, Columbus, Ohio).

In order to reduce the residual water content to very low values, we have used molecular sieves with their selective properties of fixation (27). Possible con-

[2] The Born-Haber relation, for the case of the solution of a metal in water to form an ion M^{n+}, is given as

$$\Delta G = S + I - \Delta G_h - n\psi$$

where S, I, ΔG_h represent, respectively, the energies of sublimation, ionization, and hydration, and $n\psi$ the work to return to the metal the n electrons formed by the ionization. For the case of ions which are not stable in dilute aqueous solutions (Be^+, Al^+, Mg^+, etc.) ΔG_h must be evaluated by an indirect method. To obtain the value in Fig. 1 we have used the Born-Webb relation which is based on the mutual potential energy of ions and solvent molecules

$$\Delta G_h = \frac{Ne^2 z^2}{2}\left(1 - \frac{1}{\epsilon} - \frac{1}{r}\right)$$

where z = charge on the ion, ϵ = dielectric constant of the solvent, and r the effective radius of the ion (23, 25, 26).

tamination of the electrolyte by the sieves is avoided by operating in the gaseous phase, and heating effects are minimized by distilling under reduced pressure. The alcohol (with water) vapor from the boiling solution traverses a sieve column where it is dehydrated, then is returned by reflux condenser to the boiling solution. For safety purposes, one thus avoids the heating of these concentrated perchlorate solutions. This method makes it possible to prepare solutions which, by titration, contain less than 0.1g water per liter.

Electrolysis cell.—In order to work with solutions as anhydrous as possible, the anodic dissolutions have been carried out directly in the boiling flask of the dehydration apparatus.

The counterelectrode is a platinum plate (16 cm^2) and the anode a beryllium plate (1 cm^2).

The principal impurity in the beryllium is the oxide (0.2%); the total impurities are of the order of 0.3%. Dissolutions were carried out in an argon atmosphere. Water contents were determined by Karl Fischer titration.

Measurement of dissolution efficiency.—For the quantitative characterization of the dissolution anomaly, one normally uses either the value of faradaic efficiency of dissolution (rates of weight loss predicted by Faraday's law with valence equal to that of the ion actually found in solution to weight loss actually measured) or the initial valence of dissolution Ne (the average number of electrons flowing in the external circuit per atom of metal dissolved).

Thus

$$\rho = \frac{W_{exp}}{W_{th}};\quad Ne = \frac{AQ}{\mathbf{F}W_{exp}};\quad \rho = \frac{n}{Ne}$$

W_{exp} = weight loss measured
W_{th} = weight loss predicted by Faraday's law
A = atomic weight of metal
Q = quantity of electricity through the cell
$\mathbf{F}$ = Faraday's constant
n = valence of ion found in solution.

The quantity of electricity passing the cell was measured with an electronic integrator, with an accuracy of less than 0.5%. The precision in the determinations of weight losses depends primarily on the treatment of the anode before and after electrolysis. Before dissolution, the anodes are electrolytically polished. During both the electropolishing and the dissolution, there is formed on the metal a viscous layer which can be removed by the vigorous action of an ultrasonic ethanol bath. After repeated cleaning and drying, the weight of the electrode can be obtained within an absolute uncertainty of less than 0.05 mg. Since the quantities of metal dissolved anodically are at least 20 mg, the relative uncertainty in the value of ρ does not exceed 0.5%. It follows that the relative uncertainty in Ne is

$$\frac{\Delta Ne}{Ne} = \frac{\Delta Q}{Q} + \frac{\Delta W}{W} \cong 1\%$$

Observation of the surface state of the metal.—An examination of the anodic layer alone is not sufficient to make definitive conclusions as to the existence of the "chunk" effect in the anodic dissolution. Even the appearance of a gray coloration or the actual identification of the presence of metallic particles in the anode region, although they constitute a strong presumption in favor of this effect, cannot be taken as indisputable proof, since the formation of these metallic particles may always be attributed to the dismutation reaction

$$2Be^{+} \rightarrow Be^{++} + Be\downarrow$$

Only the direct observation of the microprofile of the dissolving metal surface can furnish the necessary complementary information to make a definitive statement as to the existence of the chunk effect.

For beryllium, these very interesting observations, *i.e.*, the anode in microrelief, were made with a scanning electron microscope (Cambridge Stereoscan) in collaboration with Mr. Froment.

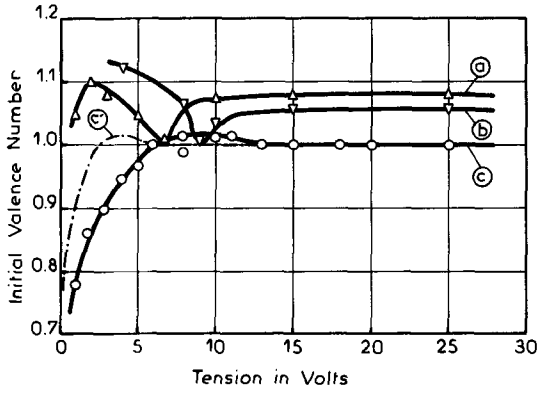

Fig. 2. Anodic dissolution of beryllium in a ternary mixture of ethanol, water, and lithium perchlorate (50g). a, $[H_2O]$ = 25 g/l, t = 25°C; b, $[H_2O]$ = 25 g/l, t = 50°C; c, $[H_2O]$ = 0.1 g/l, t = 60°C; c', curve c after correction of the potential V for the ohmic potential drop.

Results

Measurement of Ne.—Curves a and b of Fig. 2 show Ne as a function of applied potential for anodic dissolutions carried out in solutions containing 25g H_2O and 50g $LiClO_4$ per liter, maintained, respectively, at 25° and 50°C. These curves show, as previously discussed, the critical value $Ne = 1$ at the minima in a very narrow potential range ($\Delta V \simeq 0.5$V). The higher temperature shifts this minimum to higher potentials, but no decrease in the value of Ne at the minimum is observed. This furnishes a first evidence of the limiting nature of the value $Ne = 1$. Curve c of Fig. 2 was taken under conditions most favorable to the observance of low values of initial dissolution valence (high temperature, 60°C, and low water content, < 0.1 g/l).

With these solutions of very low water content, we have attempted to evaluate the magnitude of the potential drop, of ohmic origin, which exists in the anodic layer.

For this evaluation we have studied the response of the cell to the action of an exterior perturbation, using a method developed for another purpose (32). The behavior of the anodic layer is found to be very complex. We first evaluated the impedance of the cell over the frequency range 10^3 to 10^5 Hz.[3] From the values obtained we have obtained curve c' of Fig. 2 from curve c by correcting the potential V for the ohmic potential drop $\Delta V_\Omega = I R$. The curve c' is only a fair approximation, since the system is not sufficiently stable to allow a precise determination of ΔV_Ω. On the other hand the current interruption method (23, 32) does not yield, on returning to the equilibrium potential, a curve $V = f(t)$ with the expected two relaxation time constants. Only the simple exponential trace is observed, with a time constant of the order of 10 μsec, a value which is both too large for an ohmic decay and too small for the analogous anode potential decays observed in aqueous solutions.

Thus important facts are obtained from a comparison of the curves a and b with c': (*i*) the elimination of water leads to the formation of an extended potential range for the value $Ne = 1$, replacing the sharp minima previously observed; (*ii*) at potentials less than 2.5V (curve c'), values of Ne less than 1 are observed, to our knowledge for the first time, in noncorrosive solutions on open circuit.

[3] A perturbation ΔV is imposed on the potentiostatically applied working potential, and the current response ΔI of the cell is followed. On the region of linear response, the ratio $\Delta V/\Delta I$ is the impedance Z of the electrode.

Observation of the state of the surface.—Anhydrous solution.—Samples dissolved at high applied potentials with values of $Ne = 1$ present very smooth surfaces. No appreciable step forming effects can be noticed between the grains of the sample. This aspect of the surface confirms the remarkably homogeneous character (electrolytic polishing) of the dissolution which had been foreseen from previous *in situ* observations by optical interference microscopy, with an objective immersed in the electrolyte (4).

The beginning of the increase in *Ne*, near 5V, is accompanied by the appearance of some relatively rare zones of a granular aspect, separated from a surface still very smooth, Fig. 3.

As soon as *Ne* takes on values less than 1, the grain surfaces lose their parallelism. Near 2V, where *Ne* begins to decrease rapidly, the surface (in relief) becomes very rugged. On the other hand, it no longer presents any of the granular aspect which is observed in the potential range where *Ne* is greater than 1.

For potentials leading to values of *Ne* less than 0.9, clifflike structures can be clearly seen on the surface, overhanging the rest of the surface at their edges, Fig. 4.

For the lowest potential studied, the surface presents an aspect of deep ravines cut through the original surface left intact (summits, plateaus, at the same level), Fig. 5. The dissolution does not take place except along certain valleys with very steep walls. At the interior of the ravines can be seen zones of some several microns in diameter, retained by attachment bridges ready to be broken, thus liberating into the solution bulk metal particles, Fig. 6. It is also easy to distinguish regions in which particles of somewhat larger size (tens of microns) seem to be displaced a small distance from the zone from which they were detached, leaving a corresponding cavity which can itself be clearly distinguished, Fig. 7.

Water containing solutions.—The regular dissolution extending over the entire surface, as obtained with the anhydrous solutions, is not observed in water-containing solutions even at high anodic potentials. Zones appear in which the dissolution occurs in a very heterogeneous fashion. At low potentials, this heterogeneous dissolution extends over the entire surface. There is yet another essential difference between the aspects observed with and without residual water in the electrolyte: in the presence of water the dissolution remains sensitive to crystalline orientation of the grains at all potentials (formation of needles of different orientations following the grains, Fig. 8), an aspect similar to that described by Straumanis for dissolution carried out in aqueous HCl (7), while in the absence of water the orientation effect is no longer visible at potentials for which *Ne* is significantly less than 1.

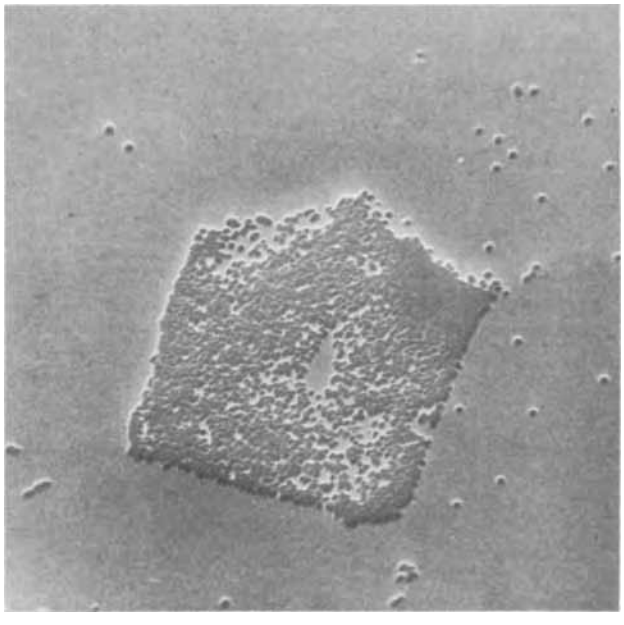

Fig. 3. Scanning electron micrograph (Fig. 3 through 8). Anodic dissolution of beryllium. $[H_2O] < 0.1$ g/l, $V = 5V$, $Ne = 1.02$. Magnification 1400X.

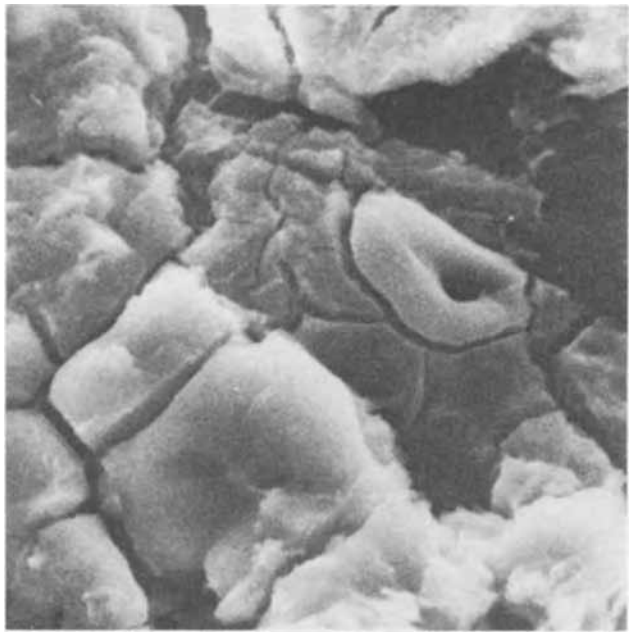

Fig. 4. $[H_2O] < 0.1$ g/l, $V = 1V$, $Ne = 0.86$. Magnification 2000X.

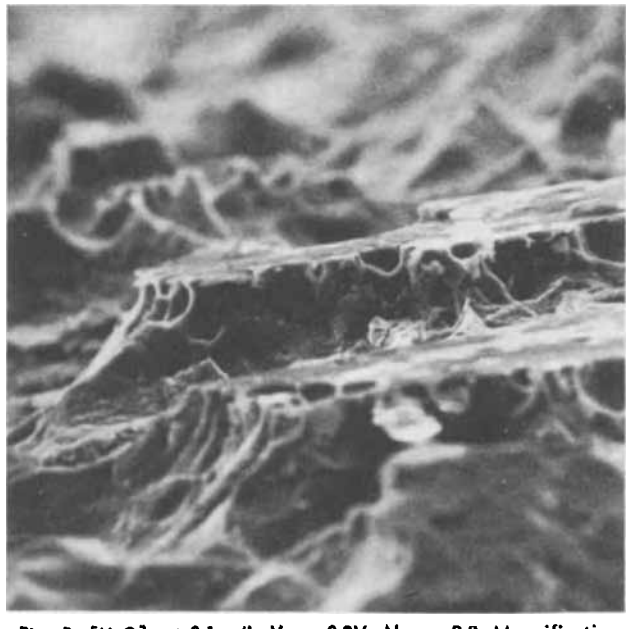

Fig. 5. $[H_2O] < 0.1$ g/l, $V = 0.2V$, $Ne = 0.8$. Magnification 255X.

Discussion

The observation, in practically anhydrous solutions, of the value $Ne = 1$ over an extended anodic potential range constitutes a decisive argument in favor of the number of mechanisms which postulate the exclusive formation of the ion Be^+ as the initial step of the dissolution, whatever the ultimate reactions envisaged for these ions by the different mechanisms. The particular experimental conditions for which this critical

Fig. 6. [H_2O] < 0.1 g/l, V = 0.2V, Ne = 0.8. Magnification 1300X.

Fig. 8. [H_2O] = 25 g/l, V = 1V, Ne = 1.04. Magnification 1200X.

Fig. 7. [H_2O] < 0.1 g/l, V = 0.2V, Ne = 0.8. Magnification 1200X.

limiting value is observed (high anodic potentials and temperature, practically anhydrous solutions) support the previously advanced ideas according to which an obligatory formation of the monovalent ion species as the first step in the dissolution does not lead to a modification of the remainder of the over-all reaction except when conditions give rise to a locally restricted supply of solvent molecules in the anodic layer.

Moreover, under experimental conditions which lead to values Ne = 1, the dissolution occurs in a remarkably uniform and homogeneous fashion over the entire surface. The microprofile observed is absolutely incompatible with any appearance of a chunk effect or with a chemical attack which is concentrated at the grain boundaries. The anodic layer which constrains the metal to dissolve in the form of Be^+ ions constitutes also a protective film which imposes a uniform dissolution on the surface (condition of electrolytic polishing), and excludes the secondary phenomena (parasitic processes) which might lead to values of Ne less than 1.

At potentials less than 2V (curve c', Fig. 2) or in the presence of water, deviations from unity of the value of Ne indicate a more complex mechanism. The dissolution does not occur according to the simple: $Be \rightarrow Be^+ + e^-$ (electrochemical step I) followed by: Be^+ + oxidant $\rightarrow Be^{++}$ + reduced species (chemical step II), but calls into play other steps which are clearly indicated by the different aspects of microrelief revealed in the photomicrographs, (Fig. 2-8).

Thus, the increase of Ne to values greater than 1 (curve c') is accompanied by the appearance (2) of the zones of granular appearance allied with the formation of an oxide (33). The observed modification might be attributed to a diminution of the solvent-poor layer covering the surface, due to a decrease in the strength of the electric field at the metal/electrolyte interface. The previously mentioned difficulties encountered in the application of perturbation methods have, however, prevented us from obtaining the precise character of this layer at low potentials.

For experimental conditions which lead to values of Ne less than 1, it appears to be well established from the observed structural features of the anode surface that the metallic particles which color the solution are due to the "chunk" effect. This physical disintegration of the surface will not appear except when the anodic potential becomes too small to insure the maintenance of the solvent-poor layer which protects the metal.

Manuscript received Oct. 19, 1970.

Any discussion of this paper will appear in a Discussion Section to be published in the December 1971 JOURNAL.

REFERENCES

1. I. Epelboin, *Z. Electrochem.*, **59**, 689 (1955).
2. M. D. Rausch, W. E. McEwen, and J. Kleinberg, *J. Am. Chem. Soc.*, **77**, 2093 (1955).
3. B. D. Laughlin, J. Kleinberg, and A. W. Davidson, *ibid.*, **78**, 559 (1956).
4. M. Froment, *Corrosion-Anticorrosion*, **7**, 98 (1959).
5. M. W. Smirnov, Tschukkrejev, *J. Chem. Phys. (URSS)*, **22**, 2165 (1958).
6. K. E. Heusler, *Z. Electrochem.*, **65**, 192 (1961).
7. M. E. Straumanis and D. L. Mathis, *This Journal*, **109**, 434 (1962).
8. M. E. Straumanis and P. C. Chen, *ibid.*, **98**, 151 (1951).

9. M. E. Straumanis and Y. N. Yang, *ibid.*, **102**, 304 (1955).
10. G. A. Marsh and E. Schaslhl, *ibid.*, **107**, 960 (1960).
11. M. E. Straumanis, *ibid.*, **108**, 1087 (1961).
12. W. J. James, M. E. Straumanis, B. K. Bhatia, and J. W. Johnson, *ibid.*, **110**, 1117 (1963).
13. A. W. Davidson and F. J. Jiric, *J. Am. Chem. Soc.*, **72**, 1700 (1950).
14. E. Darmois and I. Epelboin, *C. R. Acad. Sci.*, **237**, 501 (1953).
15. B. N. Kabanov and D. W. Kakoulina, *Doklady Akad. Nauk. (URSS)*, **120**, 559 (1958).
16. I. Epelboin and M. Froment, *J. Chim. Phys.*, **65**, 192 (1961).
17. R. E. Visco, *This Journal*, **112**, 933 (1965).
18. V. V. Lossev and A. P. Ptchelnikov, *Protection des métaux (URSS)*, **1**, 5, 482 (1965).
19. M. Garreau and I. Epelboin, *J. Chim., Phys.*, **11-12**, 1515 (1966).
20. Yu. K. Delimarsky, W. F. Makogan, and A. Ya Zhigailo, *Electrochim. (URSS)*, **1**, 108 (1969).
21. V. V. Gorodetsky, V. V. Lossev, and L. I. Fedostov, *ibid.*, **11**, 1271 (1969).
22. H. H. Uhlig, *This Journal*, **109**, 9C (1962).
23. M. Garreau, *Métaux*, 1970, In press.
24. E. Sacher and K. J. Laidler, *Trans Faraday Soc.*, **59**, 396 (1963).
25. W. Latimer, J. Pitzer, and M. Slansky, *J. Chem. Phys.*, **7**, 108 (1939).
26. N. S. Hush, *Austr. J. Sci. Res.*, **69**, 480 (1948).
27. R. L. Petty, A. W. Davidson, and J. Klein, *ibid.*, **76**, 363 (1954).
28. E. Raijola and A. W. Davidson, *ibid.*, **78**, 556 (1956).
29. D. T. Sorensen, A. W. Davidson, and J. Kleinberg, *J. Inorg. Nucléar. Chem.*, **13**, 64 (1960).
30. L. N. Nekrasov and N. P. Berezina, *Doklady Akad. Nauk., (URSS)*, **142**, 855 (1962).
31. L. Kiss, J. Farkas, and A. Korosi, *Magy Kem Foly*, **73**, 551 (1967).
32. M. L. Boyer, I. Epelboin, and M. Keddam, *Electrochim. Acta*, **11**, 221 (1966).
33. M. Garreau, *C. R. Acad. Sc., Paris*, **270**, 16 (1970).
34. I. Epelboin, M. Froment, and M. Garreau, *Corrosion*, (1970), In press.

Determination of the Diffusion Layer Thickness at a Cathode in $CuSO_4$ Solutions

Aladar Tvarusko* and Laurence S. Watkins[1]

Engineering Research Center, Western Electric Company, Princeton, New Jersey 08540

ABSTRACT

The diffusion layer thickness, δ, was measured as a function of time by a Mach-Zehnder interferometer on a vertical cathode in $CuSO_4$ solution with and without an excess of H_2SO_4 at current densities, i, up to 100 mA/cm^2. The thickness δ increased linearly with $t^{1/2}$ up to the start of hydrogen gas evolution in $CuSO_4$ solutions with and without H_2SO_4; in the presence of tenfold excess of H_2SO_4, δ rapidly increased just before the gas evolution. At a constant cathodic charge, log δ decreased linearly with increasing log i in both solutions and δ is larger in pure $CuSO_4$ solution than in the presence of excess of H_2SO_4.

A new beam deflecting technique, based on the Lloyd mirror interferometer, has been described for the determination of the refractive index gradient and the concentration change in the cathodic diffusion layer normal to the electrode (1). Either this refractive index gradient, d_n, or the thickness of the diffusion layer, δ, can be calculated from the measurement of the path length change of the deflected beam in the diffusion layer (1,2). Since δ, the subject of this paper, can be independently obtained by the Mach-Zehnder interferometer, d_n was calculated from the path length change (1-3).

The knowledge of the diffusion layer thickness is important from both theoretical and practical viewpoints independently of the aforementioned need. This thickness can be measured directly [see, *e.g.*, ref. (4)] or calculated [see, *e.g.*, ref. (5)]. In this investigation the diffusion layer thickness was measured by a Mach-Zehnder interferometer as a function of time at high current densities up to 100 mA/cm^2 during the electrodeposition of copper.

Experimental

The entire experimental setup based on the Mach-Zehnder interferometer was described earlier in detail (4). The camera was focused onto the end of the vertical cathode nearest the camera. All the sides of the cathode (11.5 mm wide, 0.47 mm thick, 17 mm immersion length) were plastic coated, except the working side. The electrodes were placed in a Plexiglas cell of 23 x 66 x 31 mm dimension and the anode-cathode distance was 6 cm. The cathode was aligned by observing its image and rotating the cell for a minimum cathode image; this could be done to an accuracy of 0.05 mm or better. The diffusion layer thickness values were taken only at one height, about 8 mm below the solution surface (4). $CuSO_4$ solutions were used with and without H_2SO_4 for the galvanostatic experiments.

The interferograms were evaluated on a microphotometer (Jarrel-Ash, Model 23-100). The film was placed between two clear spectrographic plates which were separated by two feeler gauge strips of proper thickness on both sides of the film and held together by pressure sensitive tape. This arrangement ensured the flatness of the film and the movement of the film during the evaluation of an interferogram was prevented by immobilizing the film on both sides of the spectrographic plate. The hair-line on the projection screen was superimposed on the very distinct edge of the horizontal fringe and the position of the reference scale was read to μm. The carriage was moved until the hair-line was superimposed on the edge of the horizontal fringe on the other side of the electrode. The edge of the diffusion layer was taken where the fringes turned down from the horizontal indicating the reduction in refractive index gradient. For the high current density, only the very beginning of this could be seen. The thickness of the diffusion layer was obtained from the difference of these readings from which the electrode

* Electrochemical Society Active Member.
[1] Present address: Department of Electrical Engineering Science, University of Essex, Colchester, Essex, England.
Key words: laser interferometry, mass transfer, galvanostatic transients, supporting electrolyte, hydrogen evolution.

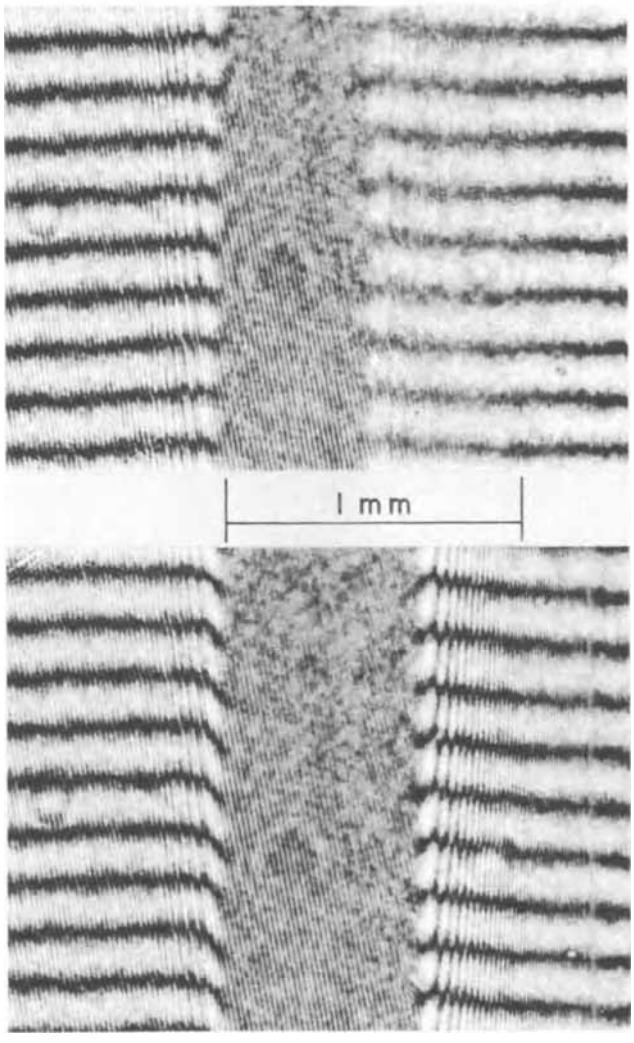

Fig. 1. Mach-Zehnder interferogram of a cathode in 0.24M $CuSO_4$ solution before and after the addition of 62.5 mA/cm². a (top), 0 sec; b (bottom), 4.6 sec.

width, measured from the same film before the addition of the current, was deducted.

Results and Discussion

Figure 1 shows two typical interferograms in 0.24M $CuSO_4$ solution taken before and 4.6 sec after the beginning of electrolysis at a current density of 62.5 mA/cm². The primary horizontal interference fringes are perpendicular to the vertical cathode the right side of which is the working surface. It can be clearly seen that (*a*) the cathode/solution interface is seemingly displaced in the presence of the large refractive index gradient and (*b*) the interference fringes are absent in this extended region, *i.e.*, diffusion layer [compare with Fig. 2 of ref. (4)].

It is well known that a beam of light (r_1,r_2) passing through a layer of varying index of refraction and thickness δ, is deflected into the region of high refractive index as shown in Fig. 2 [for references see ref. (1)]. Because of this beam deflection, the interference fringes and thus the concentration change cannot be determined accurately or at all in the presence of large refractive gradients, *i.e.*, at high current densities on cathodes of a few millimeter widths. This has been described in several studies (4, 6-9). The primary horizontal interference fringes do show the diffusion layer/bulk solution interface (Fig. 1) because the rays outside of the diffusion layer (r_3) travel without deflection (Fig 2), but the position of the working surface of the cathode is not visible. Thus, δ must be

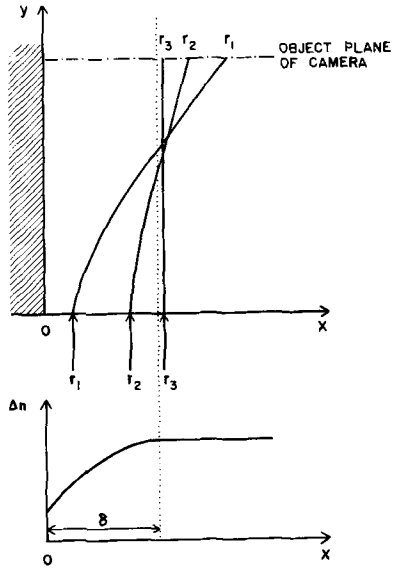

Fig. 2. Deflection of light rays (r_1, r_2) in the diffusion layer caused by the refractive index gradient. Ray r_3 travels without deflection outside of the diffusion layer of thickness δ.

determined indirectly from a nonworking surface (4, 7, 10, 11) or properly placed marking outside the diffusion layer.

Let us return to Fig. 1 and discuss the interferograms in detail in view of the multiplicity of fringes present therein (an inherent problem when using a laser). The slightly diagonal fringes (sloping down to the right) extend over the whole picture and are due to reflections from the beam splitter back surface. These are of no significance to the experiment; nor are the vertical fringes extending from the left, coated side of the cathode since they do not change throughout the experiment. These vertical fringes were a function of cathode alignment and are presumably diffraction effects from the front edge of the cathode or its plastic coating. Since they rarely occurred on the working side of the cathode, the latter explanation seems more likely.

The horizontal fringes are the ones of interest and indicate the constant refractive index outside the diffusion layer. In Fig. 1a they are horizontal right up to the cathode edge. In Fig. 1b they terminate before the cathode edge and begin to turn down indicating the decrease of refractive index at the edge of the diffusion layer. They do not continue toward the cathode, however, because of the deflection produced by the large refractive index gradient. This results in the fringes occurring outside the diffusion layer. The large number of fringes is an indication (not accurate for a Mach-Zehnder interpretation) of the large refractive index change. It is interesting to note that the distance between these fringes decreases with increasing distance from the cathode. This is because the ray undergoes a large optical path length change near the cathode due to the larger refractive index gradient and is deflected more than the ray near the diffusion layer/bulk solution interface. The fringes of minimum separation come from nearest the cathode where the refractive index gradient is largest.

The small circular fringes are caused by pits or depressions in the cell surface which was not specially finished. Finally, there is a small change in the interference fringes of the nonworking side of the cathode (Fig. 1b). This is quite small, amounting to about ½ fringe, and may be due to refractive index gradient changes extending round the front and back edges of the cathode.

Figure 3 shows two interferograms taken just before and after the start of hydrogen gas evolution in 0.24M $CuSO_4$-2.36M H_2SO_4 solution. It can be clearly seen that the gas evolution disrupts the interferogram.

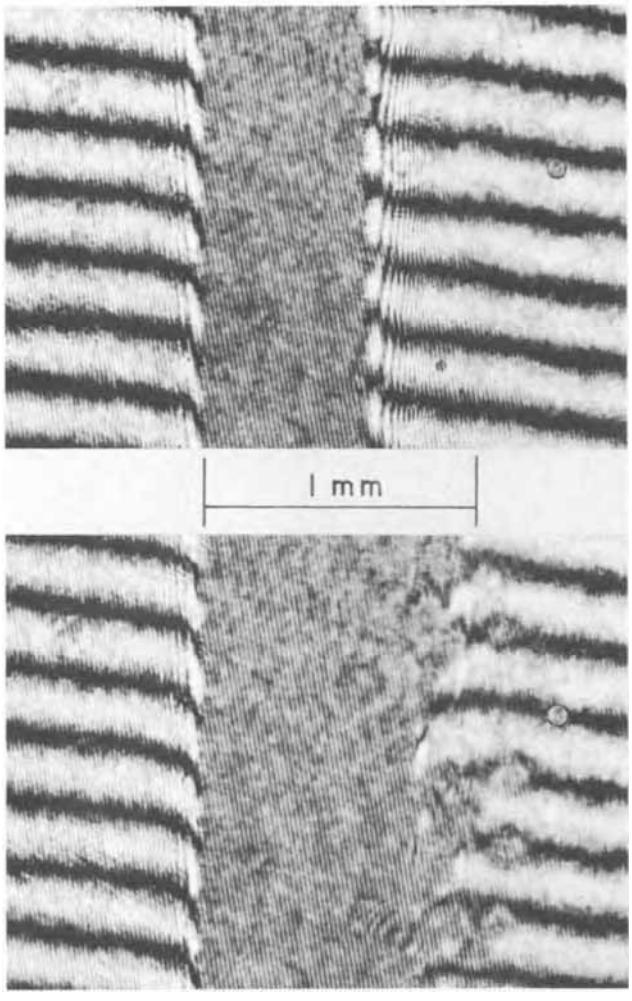

Fig. 3. Mach-Zehnder interferogram of a cathode in 0.24M $CuSO_4$-2.36M H_2SO_4 solution before and after the start of H_2 evolution at 69.1 mA/cm^2. a (top), 2.75 sec; b (bottom), 3.38 sec.

Therefore, meaningful diffusion layer thickness values can be obtained only below and at the limiting current density for metal deposition, i_L. Since the gas evolution does not start instantaneously after the application of current densities higher than i_L, the initial stages of the increase of the diffusion layer can be also investigated. The thickness of the diffusion layer at a gas evolving electrode is nonuniform in time and space. The secondary interference fringes are superimposed on the primary fringes also in the presence of H_2SO_4 but their extent is smaller than in the pure $CuSO_4$ solution. The circular interference fringes are caused by individual gas bubbles.

Figure 4 shows the diffusion layer thickness determined from the nonworking side of the cathode as a function of square root of time in 0.24M $CuSO_4$. The thickness δ increases linearly at all current densities up to the start of the transition to steady state or start of hydrogen gas evolution, respectively. The difference at the three highest current densities investigated is small and the current density seems to have little influence above the limiting current density. This indicates that the conditions in the diffusion layer remain nearly the same above the limiting current density before the start of the hydrogen gas evolution. All the regression lines were fitted by the least squares method and the regression line constants are shown in Fig. 4 (A-intercept, B-slope, R-coefficient of correlation). The linear regression analysis of all data reported here is statistically significant at greater than 95%.

It is to be noted that the displacement of the cathode/solution interface due to the electrodeposited copper

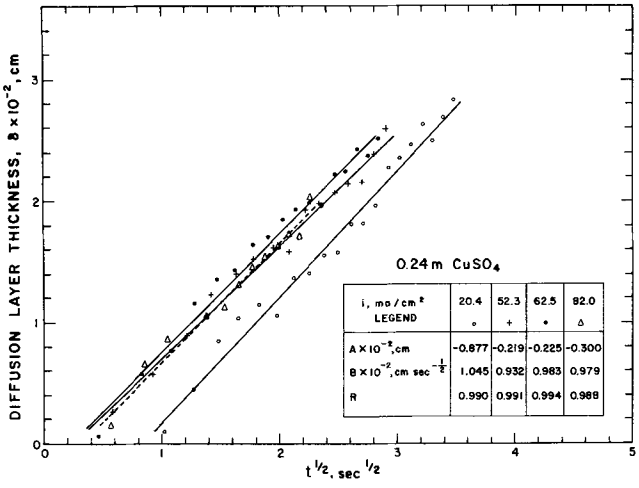

Fig. 4. Diffusion layer thickness as a function of $t^{1/2}$ in 0.24M $CuSO_4$ at various current densities. The regression line constants are given in the inserted table.

layer is negligible in comparison to the diffusion layer thickness because the electrodeposited copper layer is at least three orders of magnitude smaller than δ.

A comparison of Fig. 4 and 5 reveals that the behavior of δ is different in these two solutions. In the presence of tenfold excess of H_2SO_4 it was found that: (*a*) the $\delta - t^{1/2}$ relation is linear only below the limiting current density and in the very beginning of the galvanostatic experiments above i_L; (*b*) the rate of increase of δ with $t^{1/2}$ (slope B) is approximately one third smaller than in pure $CuSO_4$; (c) δ rapidly increases just before the start of the hydrogen gas evolution; the position and to a certain degree, the rate of this increase depends on the current density; and (*d*) the linear $\delta - t^{1/2}$ relation is practically independent of the current density over a larger range than in pure $CuSO_4$ or in the presence of small amount of H_2SO_4 (3). In the presence of 0.11M H_2SO_4 the slope of the $\delta - t^{1/2}$ linear relation (4) falls between the two extreme values (Fig. 4 and 5).

The influence of H_2SO_4 is obvious from these results. In the presence of a large excess of H_2SO_4 the increase of δ is slower than in pure $CuSO_4$ solution. The hydrogen evolution, however, starts at shorter times in the presence of H_2SO_4 than in its absence. The decrease of the elapsed time before H_2 evolution in the presence of H_2SO_4 is supported by the reported results during powder formation at the limiting current density (12). The addition of indifferent electrolytes shortens the time to powder formation (12), *i.e.*, the time required for the metal ion concentration to decrease very closely to zero at the cathode/solution interface. In view of

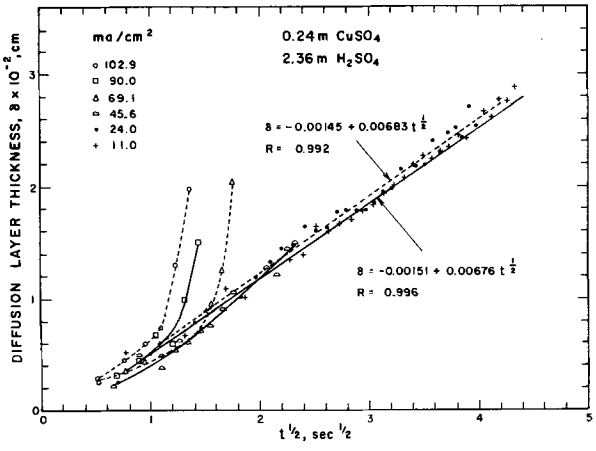

Fig. 5. Diffusion layer thickness as a function of $t^{1/2}$ in 0.24M $CuSO_4$-2.36M H_2SO_4 solution at various current densities.

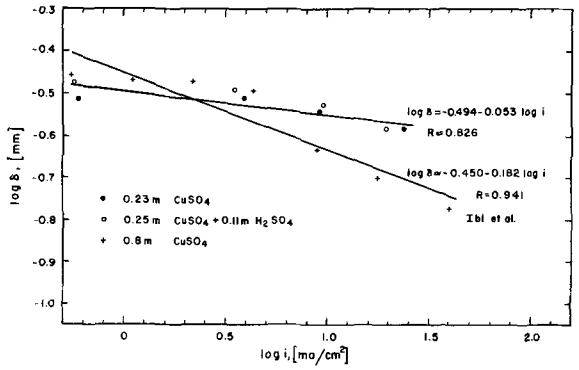

Fig. 6. Steady-state diffusion layer thickness as a function of current density in various $CuSO_4$ solutions.

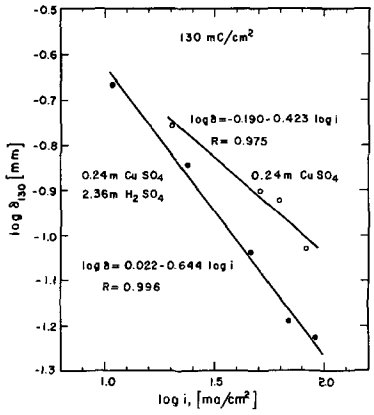

Fig. 7. Diffusion layer thickness as a function of current density at a constant quantity of electricity of 130 mC/cm² in $CuSO_4$ solutions with and without an excess of H_2SO_4.

these facts, the rapid increase of δ before the hydrogen evolution seems to be inevitable.

Figure 6 shows the logarithm of steady-state diffusion layer thickness as a function of the logarithm of current density in three $CuSO_4$ solutions. The steady-state δ decreases with increasing current density. The slope of the linear regression line is −0.053 for our data and the coefficient of correlation, R, is very low. The experimental slope is markedly lower than the theoretically predicted value of −0.20 (10). The δ values of Ibl *et al.* [Table 3, ref. (10)] in 0.8M $CuSO_4$ yield −0.18 for the slope (Fig. 6) which is in closer agreement with the theoretical value. The other data of Ibl *et al.* (10) show smaller slopes and larger scatter of data. Ibl *et al.* (13) found that the experimental determination of $\delta_{0.1}$, *i.e.*, the distance at which the concentration decreased to 10% of the total change, is more reliable than that of δ (the true thickness of the diffusion layer). However, the slope of the experimental line in 0.6M $CuSO_4$ is only −0.16. Our δ values at low current densities (<5 mA/cm²) are comparable to those of Ibl *et al.* (10) but deviate considerably at the higher current densities. In view of our interest in the nonsteady-state behavior of δ at high current densities, the reason for this deviation has not been pursued further.

The steady-state δ values are meaningless at very high current densities ($i > i_L$) because δ varies in time and space due to the evolving H_2. Figure 7 shows the diffusion layer thickness for a constant quantity of electricity of 130 mC/cm², δ_{130} as a function of current density. This value was chosen because it is just below the quantity of electricity at which δ rapidly increased before the H_2 evolution in the 0.24M $CuSO_4$ −2.36M H_2SO_4 solution. Log δ_{130} decreases linearly with increasing log i in both solutions. The slope of the regression line in the $CuSO_4$ solution is approximately a third lower than in the presence of tenfold excess of H_2SO_4. The magnitude of δ_{130} is affected also by the nature of solution and δ_{130} is larger in $CuSO_4$ solution than in the presence of tenfold excess of H_2SO_4. The aforementioned results seem to be caused by the concomitant change of mainly the cation transference number, and to a lesser degree of diffusion coefficient, viscosity and density of the solution near the cathode surface.

Manuscript submitted April 9, 1970; revised manuscript received *ca.* Sept. 16, 1970. This was Paper 288 presented at the Los Angeles Meeting of the Society, May 10-15, 1970.

Any discussion of this paper will appear in a Discussion Section to be published in the December 1971 JOURNAL.

REFERENCES

1. L. S. Watkins and A. Tvarusko, *Rev. Sci. Instr.*, **41**, 1860 (1970).
2. L. S. Watkins and A. Tvarusko, To be published.
3. A. Tvarusko and L. S. Watkins, *This Journal*, To be published.
4. A. Tvarusko and L. S. Watkins, *Electrochim. Acta*, **14**, 1109 (1969).
5. L. J. J. Janssen and J. G. Hoogland, *ibid.*, **15**, 1013 (1970).
6. R. H. Müller, "Optical Techniques for the Study of Phase Boundaries," UCRL-11997, April 1965.
7. K. W. Beach, "A Laser Interferometer for Mass Transfer Studies," M.S. Thesis, UCRL-18037, February 1968.
8. R. H. Müller, K. W. Beach, and C. W. Tobias, Paper presented at the 20th Meeting of CITCE, Strasbourg, 1969.
9. R. N. O'Brien and K. Kinoshita, *This Journal*, **112**, 951 (1965).
10. N. Ibl, Y. Barrada, and G. Trümpler, *Helv. Chim. Acta*, **37**, 583 (1954).
11. N. Ibl, Proc. 7th Meeting of CITCE, Lindau, 1955, pp. 112-33, Butterworths Scientific Publications, London (1957).
12. N. Ibl, in "Advances in Electrochemistry and Electrochemical Engineering," Vol. 2, p. 117, P. Delahay and C. W. Tobias, Editors, Interscience Publishers, New York (1966).
13. N. Ibl, R. Müller, and A. Frei, 8th Meeting of CITCE, Madrid, 1956, pp. 179-182, Butterworths Scientific Publications, London (1958).

Modification of the Cottrell Equation to Account for Electrode Growth; Application to Diffusion Data in the Ag-Au System

K. B. Oldham[1,*] and D. O. Raleigh[**]

Science Center, North American Rockwell Corporation, Thousand Oaks, California 91360

ABSTRACT

The Cottrell equation is invalid if the electrode reaction causes motion of the electrolyte/electrode boundary. The equation has been modified to take account of this effect and the modification applied to previously published data on the interdiffusion of silver and gold. The recalculated interdiffusion coefficients show excellent agreement with values obtained from literature sources. The applicability of the modified equation is discussed and a new method for the measurement of diffusion coefficients is advanced.

A previous publication from this laboratory (1) described a solid-state electrochemical method for determining diffusion coefficients in selected binary metal systems at elevated temperatures. Data were reported for the chemical diffusion coefficient of silver in silver-gold alloys at 394°C. In the composition range 10-50 atomic per cent (a/o) Ag, reasonable agreement was obtained with extrapolation of diffusion data (2) measured conventionally at 650°-1000°C. At higher concentrations, increasing discrepancies were observed, which were attributed to extrapolation errors. It was noted (3), however, that the diffusion treatment should properly include a correction factor to take account of electrode boundary movement during diffusion, but that the complexity of the treatment required its postponement to a future publication. We here report the development of this correction factor, note that it brings the electrochemical data into good agreement with the previous work throughout the composition range, and discuss its range of general applicability.

The diffusion measurement technique which was employed (1) was to measure the faradaic current $i(t)$ which flows following the application of a constant potential E across the cell

$$(-)\,\mathrm{Ag}|\mathrm{AgBr}|(\mathrm{Au\text{-}Ag})\,(+) \qquad [1]$$

The current, crossing the AgBr|(Au-Ag) interface by virtue of the reaction

$$\mathrm{Ag}^+ + e^- = \mathrm{Ag(Au\text{-}Ag)} \qquad [2]$$

flows to maintain the silver activity in the surface layer of the alloy electrode at a value

$$a_s = \exp\{-\mathbf{F}E/RT\} \qquad [3]$$

demanded by the thermodynamic Nernst equation, despite the diffusion of silver into or out of the bulk of the alloy. Equation [3], in which **F**, R, and T have their usual significance, is valid if activation, crystallization, and ohmic polarizations may be ignored, which was the case in these experiments.

The chemical diffusion coefficient of silver was calculated from the current-time dependence by use of the Cottrell equation (6)

$$i(t) = A\mathbf{F}(C_s - C_o)\sqrt{\frac{D_{Ag}}{\pi t}} \qquad [4]$$

where A is the electrode area, C_s is the concentration of silver in the surface layer of the electrode, and C_o is the initial concentration of silver in the electrode, *i.e.* the bulk concentration. Well-established thermodynamic data (4, 5) were used to calculate C_s from the silver activity a_s which was in turn calculated using Eq. [3].

The derivation of the Cottrell equation treats the electrode surface as fixed in space. In the above experiments, however, the electrode surface moves because of the continuous electrodeposition of silver. Indeed, this is the case for any electrolytic metal deposition, although, as we shall see, the effect in most electrodepositions, such as from aqueous solution, is negligible. In what follows, we examine the moving-boundary diffusion problem with a fixed surface concentration and reassess the previous experimental results in the light of the new theoretical result.

Mathematical Analysis

Perpendicular to the planar electrode we erect a distance coordinate, y, choosing $y = 0$ to correspond to the initial position of the silver bromide/electrode interface, and positive y toward the metallic phase. We let $Y(t)$ denote the thickness of the electrodeposit, so that $y = -Y(t)$ is the position of the electrolyte/electrode interface. At $t = 0$, when the previously open-circuited cell is subjected to the constant potential E, $Y(0) = 0$. For $t > 0$, $Y(t)$ is an increasingly positive quantity corresponding to the advance of the interface into the electrolyte phase. By $C(y,t)$ we denote the local concentration of silver in the alloy phase at time $t \geqq 0$ and at positions $y \geqq -Y(t)$.

In the previous study (1), conventionally and electrochemically obtained diffusion data were compared on the basis of the chemical diffusion coefficient of Ag in Ag-Au alloys, as assumed to be given by Eq. [4]. It is more convenient, however, to carry out the present derivation and subsequent literature comparison in terms of the interdiffusion coefficient $\tilde{D}$ (7), which characterizes diffusion in a binary system in terms of a single quantity. We seek a solution to Fick's second law of diffusion

$$\tilde{D}\frac{\partial^2}{\partial y^2}C(y,t) = \frac{\partial}{\partial t}C(y,t) \qquad [5]$$

The initial condition is

$$C(y,0) = C_o,\ y > 0 \qquad [6]$$

and the two boundary conditions are

$$C(L,t) = C(\infty,t) = C_o \qquad [7]$$

and

$$C(-Y(t),t) = C_s,\ t > 0 \qquad [8]$$

The first boundary condition is appropriate because, as

[1] Present address: Trent University, Peterborough, Ontario, Canada.

[*] Electrochemical Society Active Member of a Sustaining Member Company.

[**] Electrochemical Society Active Member.

Key words: Diffusion, alloys, solid solution, solid electrolyte, AgBr, silver-gold, electrochemical theory, potentiostatic experiments.

is generally the case in electrochemical experiments, the thickness, L, of the electrode used by Raleigh and Crowe (1) was very large compared with diffusant penetration depth. The second boundary condition reflects the potentiostatic constraint (Eq. [3]).

The total number of moles of silver present at any time, t, in the electrode is equal to the number present initially plus those added by electrodeposition, *i.e.*

$$A\int_{-Y(t)}^{L} C(y,t)\,dy = ALC_o + \int_o^t \frac{i(t)}{\mathbf{F}}\,dt \qquad [9]$$

On differentiation of this equation wtih respect to time, we obtain

$$\int_{-Y(t)}^{L} \frac{\partial}{\partial t} C(y,t)\,dy + \frac{dY(t)}{dt} C(-Y(t),t) = \frac{i(t)}{A\mathbf{F}} \qquad [10]$$

an equation we will eventually use to formulate $i(t)$.

An equation similar to [9] expressing the conservation of gold throughout the experiment

$$A\int_{-Y(t)}^{L} C'(y,t)\,dy = ALC'_o \qquad [11]$$

where $C'(y,t)$ is the concentration of gold in plane y at time t and C'_o is the bulk gold concentration, serves to completely specify the system. The concentrations of the two components of the binary alloy obey the relationship

$$C(y,t)V_m = x(y,t) = 1 - C'(y,t)V_m \qquad [12]$$

where x denotes the atomic fraction of the silver in the alloy and V_m is the molar volume of the alloy. V_m might be expected to be itself a function of x. Fortunately, however, the lattice dimensions of silver-gold alloys are virtually independent of composition (8), so we may treat V_m as a constant in the present application. With this simplification, Eq. [11] can be recast as

$$\int_{-Y(t)}^{L} \left[\frac{1}{V_m} - C(y,t)\right] dy = L\left[\frac{1}{V_m} - C_o\right] \qquad [13]$$

and time-differentiated to give

$$\int_{-Y(t)}^{\infty} \frac{\partial}{\partial t} C(y,t)\,dy = \frac{dY(t)}{dt}\left[\frac{1}{V_m} - C(-Y(t),t)\right] \qquad [14]$$

wherein we have substituted ∞ for the upper limit, L.

The moving-boundary problem represented by Eq. [5], [6], [7], [8], and [14] was solved by use of a dimensional analysis approach. The solution is

$$C(y,t) = C_o + \frac{(C_s - C_o)\ \mathrm{erfc}\left((y/2\sqrt{\tilde{D}t}\right)}{\mathrm{erfc}\ (-\sigma)} \qquad [15]$$

where erfc ( ) denotes the error function complement operator and σ is a constant for a given experiment. This constant satisfies the functional equation

$$\sqrt{\pi}\,\sigma \exp(\sigma^2)\ \mathrm{erfc}\ (-\sigma) = \frac{C_sV_m - C_oV_m}{1 - C_sV_m} = \frac{x_s - x_o}{1 - x_s} \qquad [16]$$

where x_s and x_o are, respectively, the atomic fractions of silver in the surface layer and bulk of the electrode. Figure 1 shows the values acquired by σ for various values of the $(x_s - x_o)/(1 - x_s)$ ratio.

Comparison of Eq. [8] and [15] shows that

$$Y(t) = 2\sigma\sqrt{\tilde{D}t} \qquad [17]$$

and if this expression is substituted into [10], together with result [15], we find

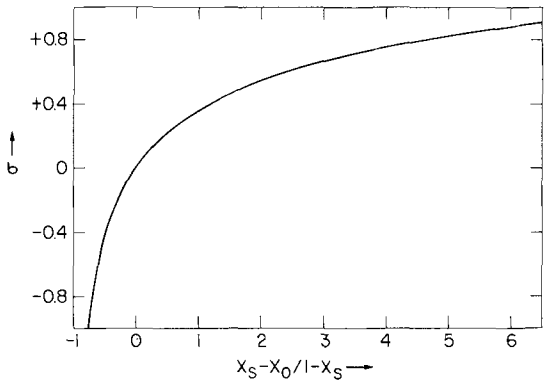

Fig. 1. Graph of σ as a function of $\sqrt{\pi}\,\sigma \exp(\sigma^2)$ erfc $(-\sigma)$

$$i(t) = \frac{\sigma A\mathbf{F}}{V_m}\sqrt{\frac{\tilde{D}}{t}} \qquad [18]$$

This is the result which replaces the Cottrell equation.

Notice that if $x_s < x_o$, σ is negative according to Fig. 1 and that $i(t)$ is negative (anodic) as expected. An experiment under these conditions was termed "out-diffusion" by Raleigh and Crowe (1).

It is pertinent to investigate the limiting form of Eq. [18] when $(x_s - x_o)$ is small. Then, as Fig. 1 shows, σ is also small. In this circumstance, a power expansion of the left hand side of Eq. [16] gives

$$\frac{x_s - x_o}{1 - x_s} = \sqrt{\pi}\,\sigma + 2\sigma^2 + \sqrt{\pi}\,\sigma^3 + \ldots \qquad [19]$$

which results in

$$\sigma = \frac{x_s - x_o}{\sqrt{\pi}(1 - x_s)}\left[1 - \frac{2}{\pi}\left(\frac{x_s - x_o}{1 - x_s}\right) + \frac{8 - \pi}{\pi^2}\left(\frac{x_s - x_o}{1 - x_s}\right)^2 - \ldots\right] \qquad [20]$$

on reversion. Insertion into Eq. [18] leads to

$$i(t) = \frac{A\mathbf{F}(C_s - C_o)}{(1 - x_s)}\sqrt{\frac{\tilde{D}}{\pi t}}\left[1 - \frac{2}{\pi}\left(\frac{x_s - x_o}{1 - x_s}\right) + \ldots\right] \qquad [21]$$

which should be compared with the Cottrell Eq. [4], where we note $\tilde{D} \to D_{Ag}$ in the limit of dilute Ag concentration. We see that the classical result is valid only if both x_o and x_s are small, not only when their difference is small. If D_{cot} is the apparent diffusion coefficient according to the Cottrell equation, then this value is seen to differ from the true interdiffusion coefficient by the factor

$$\frac{\tilde{D}}{D_{cot}} = \frac{(x_s - x_o)^2}{\pi\sigma^2} \qquad [22]$$

Comparison with Previous Work

The previous experimental work (1) reported D_{cot} values for eight $(x_s - x_o)$ compositional jumps of 10 a/o Ag in the range 10-90 a/o Ag, for both "in-diffusion" $(x_s > x_o)$ and "out-diffusion" $(x_s < x_o)$. In this work, the measured diffusion coefficients, which varied with composition, were assigned to the mean compositional values $\frac{1}{2}(x_s + x_o)$. In Table I, we show D_{cot}, the calculated conversion factor (Eq. [22]), and $\tilde{D}$ for those experimental results that were compared with the previous work of Slifkin *et al.* (2). The latter work reported values for D^*_{Ag} and D^*_{Au}, the radiochemical diffusion coefficients of Ag and Au in Ag-Au. These were reported in terms of best values for D^*_o

Table I. Calculation of true interdiffusion coefficient from previous data (1)

Run	x_o	x_s	$\frac{1}{2}(x_o + x_s)$	$\frac{x_s - x_o}{1 - x_s}$		$\frac{(x_s - x_o)^2}{\pi\sigma^2}$	$10^{14} \times D_{cot}$ cm² sec⁻¹	$10^{14} \times \tilde{D}$ cm² sec⁻¹
8	0.1	0.2	0.15	0.125	0.065	0.755	1.34	1.012
8	0.2	0.3	0.25	0.143	0.074	0.580	1.05	0.609
8	0.3	0.4	0.35	0.167	0.085	0.443	0.80	0.354
8	0.4	0.5	0.45	0.200	0.101	0.312	0.71	0.222
8	0.5	0.6	0.55	0.250	0.121	0.217	0.81	0.176
8	0.6	0.7	0.65	0.333	0.156	0.131	1.05	0.138
8	0.7	0.8	0.75	0.500	0.217	0.068	1.53	0.104
8	0.8	0.9	0.85	1.000	0.357	0.024	1.91	0.046
7, 9	0.9	0.8	0.85	−0.500	−0.426	0.0175	3.23	0.057
7, 9	0.8	0.7	0.75	−0.333	−0.244	0.053	2.00	0.106
7, 9	0.7	0.6	0.65	−0.250	−0.164	0.118	1.74	0.205
7, 9	0.6	0.5	0.55	−0.200	−0.127	0.198	1.37	0.271
6	0.5	0.4	0.45	−0.167	−0.103	0.300	0.93	0.279
6	0.4	0.3	0.35	−0.143	−0.087	0.420	1.32	0.554
6	0.3	0.2	0.25	−0.125	−0.074	0.581	1.55	0.901
6	0.2	0.1	0.15	−0.111	−0.065	0.753	2.00	1.506

and Q, the parameters of the conventional temperature depedence expression $D^* = D^*_o \exp(-Q/RT)$ for the various compositions investigated.

In the previous article (1), comparison was made between D_{cot} and the chemical diffusion coefficient D_{Ag}. The relationship

$$D_{Ag} = D^*_{Ag}\left(1 + \frac{d \ln \gamma_{Ag}}{d \ln x_{Ag}}\right) \quad [23]$$

applies (7), where γ_{Ag} is the activity coefficient of silver in the alloy. Values of D^*_{Ag} were taken from the best smooth curve through values of $D^*_o \exp(-Q/RT)$ calculated from Slifkin's data (2) at 394° and $d \ln \gamma_{Ag}/d \ln x_{Ag}$ was evaluated from existing thermodynamic data (4, 5). For comparison with present results, we now calculate $\tilde{D}$ from the Slifkin data by use of the expression (7)

$$\tilde{D} = (x_{Au}D^*_{Ag} + x_{Ag}D^*_{Au})\left(1 + \frac{d \ln \gamma_{Ag}}{d \ln x_{Ag}}\right) \quad [24]$$

where D^*_{Ag} and D^*_{Au} are calculated directly for the specific compositions used in these data and $d \ln \gamma_{Ag}/d \ln x_{Ag}$ is evaluated as before.[2] In addition, a further value of $\tilde{D}$ is available from the work of Cook and Hilliard (9), who employed a novel evaporated-film technique to obtain values for the 50 a/o composition in the range 200°-245°C. These authors presented a graph combining their values with those of Johnson (10) at higher temperatures, from which an intermediate value at 394° may be extracted.

In Fig. 2, the values of $\tilde{D}$ calculated from experimental in-diffusion data in Table I are shown together with the Slifkin and Cook-Hilliard values. Agreement is seen to be respectable throughout the entire composition range. The in-diffusion values were used for this comparison, since they correspond to the phenomenological situation obtaining in conventional diffusion coefficient determinations.

The values of the ratio $\tilde{D}_{out}/\tilde{D}_{in}$ are of special interest because of the possibility of nonunity ratios being due to effects such as boundary motion. Actually, we see from Table I that values of $\tilde{D}/D_{cot}$ for in-diffusion and out-diffusion at a given mean composition differ by less than 10% for all but the two most silver-rich compositions. Figure 3 shows the $\tilde{D}_{out}/\tilde{D}_{in}$ ratio as a function of composition. For this plot, the original D_{cot} values were taken from smoothed curves [Ref. (1), Fig. 5] rather than individual data points, in order to avoid the large scatter previously obtained in out-diffusion data and attributed to the basic nature of the out-diffusion process. We see that significantly nonunity out:in ratios are still obtained. A best smooth curve through the individual ratio points indicates a fairly constant ratio in gold-rich compositions and a possible fall off to unity at the limit of pure silver. The enhancement of out-diffusion was previously attributed to a vacancy injection process resulting from creation of a large expected surface vacancy concentration on selective anodization of the alloy. Such a process might indeed be expected to be most effective when the nonanodized alloy component is present in substantial amount.

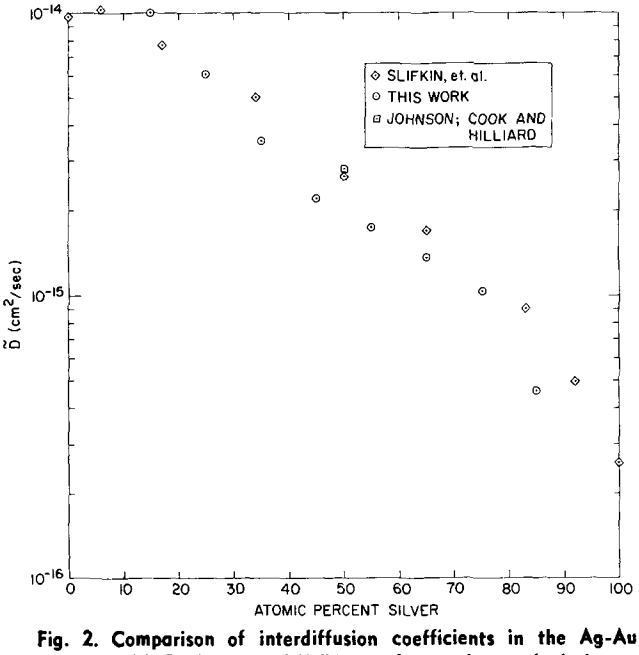

Fig. 2. Comparison of interdiffusion coefficients in the Ag-Au system at 394°C: ◇, data of Slifkin et al.; ⊙, these calculations; □, datum from the work of Johnson, Cook, and Hilliard (see text).

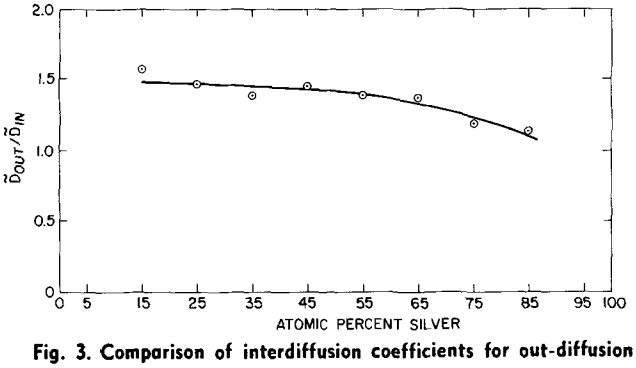

Fig. 3. Comparison of interdiffusion coefficients for out-diffusion and in-diffusion.

[2] Evaluation of $d \ln \gamma_{Ag}/d \ln x_{Ag}$ was aided by use of the fact that it equals unity at both extremes of the phase diagram because of Raoult's law and the Gibbs-Duhem relationship.

Generality of the Modification

In principle, modification to the Cottrell equation is required whenever the electrode reaction leads to the incorporation of material into the electrode or removal of material from the electrode. Many reactions used in electroanalytical chemistry, for example

$$Cd^{2+} + 2e^- \rightarrow Cd(Hg) \qquad [25]$$

fall into this category. A corresponding modification is required for other voltammetric relationships (the Sand equation, Ilkovic equation, *etc.*).

In practice, however, the vast majority of electrochemical experiments employ electroactive species in mole fractions which are very small. In such circumstances the Cottrell equation is always an excellent approximation as Eq. [21] demonstrates.

One circumstance in which the Cottrell equation is not an acceptable approximation is the electrodissolution of a metal from an electrode containing a small amount of an electroinactive impurity in solid solution. Then x_o is close to unity, but, on account of the accumulation of the impurity at the electrode surface, x_s becomes significantly smaller than x_o. The ratio $(x_s - x_o)/(1 - x_s)$ approaches -1, σ has a large negative value as Fig. 1 illustrates, and the asymptotic expansion

$$\sqrt{\pi}\,\sigma \exp(\sigma^2)\,\mathrm{erfc}(-\sigma) = -1 + \frac{1}{2\sigma^2} - \frac{3}{4\sigma^4} + \ldots \qquad [26]$$

may be curtailed after two terms. This permits a simplified definition of σ, namely

$$\sigma = -\sqrt{\frac{1 - x_s}{2(1 - x_o)}} \qquad [27]$$

and leads to a replacement for the Cottrell equation in the form

$$i(t) = \frac{-A\mathbf{F}}{V_m}\sqrt{\frac{\tilde{D}(1 - x_s)}{2(1 - x_o)t}} \qquad [28]$$

In the circumstances of almost pure metal initially, Raoult's law may be used to relate x_o directly to the open-circuit potential, E_o, prior to the experiment; thus

$$1 - x_o \approx 1 - a_o = 1 - \exp\left(\frac{-\mathbf{F}E_o}{RT}\right) \approx \frac{\mathbf{F}E_o}{RT} \qquad [29]$$

If the applied potential E is not too different from E_o, the approximation

$$1 - x_s \approx \frac{\mathbf{F}E}{RT} \qquad [30]$$

similarly holds. The Cottrell replacement then assumes the very simple form

$$i(t) = \frac{-A\mathbf{F}}{V_m}\sqrt{\frac{\tilde{D}E}{2E_o t}} \qquad [31]$$

where we recall from our discussion of Eq. [21] that $\tilde{D}$ becomes the chemical diffusion coefficient of the impurity species in the dilute limit. Thus, a new and simple method is suggested for measuring the diffusion coefficient of a dilute solute in a more electroactive solvent metal. The method has the advantage of requiring no knowledge of the activity-composition relationship. Such determinations, however, are necessarily limited to temperatures high enough for $\tilde{D}$ to be characterizable as an intrinsic property. Thus, for instance, anodization of Fe from carbon steel in aqueous solutions would give highly sample-specific results reflecting extrinsic diffusion processes (11).

Manuscript received July 31, 1970.

Any discussion of this paper will appear in a Discussion Section to be published in the December 1971 JOURNAL.

REFERENCES

1. D. O. Raleigh and H. R. Crowe, *This Journal*, **116**, 40 (1969).
2. W. C. Mallard, A. B. Gardner, R. F. Bass, and L. M. Slifkin, *Phys. Rev.*, **129**, 617 (1963).
3. C. Wagner, Private communication.
4. A. Wachter, *J. Am. Chem. Soc.*, **54**, 4609 (1932).
5. O. Kabaschewski and O. Huchler, *Z. Elektrochem.*, **52**, 170 (1948).
6. P. Delahay, "New Instrumental Methods in Electrochemistry," Chap. 3, Interscience, New York (1954).
7. For an excellent discussion of the various types of diffusion coefficients in solid systems, see P. G. Shewmon, "Diffusion in Solids," Chap. 4, McGraw-Hill, New York (1963).
8. M. Hansen, "Constitution of Binary Alloys," pp. 5-7, McGraw-Hill, New York (1958).
9. H. E. Cook and J. E. Hilliard, *Appl. Phys. Letters*, **8**, 24 (1966).
10. W. A. Johnson, *Trans. AIME*, **147**, 331 (1942).
11. See, for instance, Ref. (7), Chap. 6.

Technical Notes

Investigation of the Direct Reduction of Zinc Oxide in Alkaline Electrolytes

D. Drazic[1] and Z. Nagy*

Electrochemistry Laboratory, University of Pennsylvania, Philadelphia, Pennsylvania 19104

In a Zn/ZnO alkaline battery electrode, the reaction, in principle, can proceed by two considerably different mechanisms: through a soluble intermediate by a dissolution-precipitation mechanism, or through a direct, solid-state, reaction. The solution route has been generally favored (1, 2), but no direct proof has appeared in the literature for the exclusion of the solid-state process. On the contrary, recently the solid-state reaction was proposed as the predominant mechanism (3). The direct electrochemical reduction of zinc oxide, in aqueous electrolytes, to zinc and water has been reported (4, 5) but no kinetic data

* Electrochemical Society Student Associate.
[1] On leave of absence from the Faculty of Technology, University of Belgrade, Belgrade, Yugoslavia.
Key words: alkaline batteries, Zn/ZnO electrode, solid state reduction, dissolution-precipitation.

were given. The possibility of direct reduction in absolute alcohol has also been suggested (6). The aim of this paper is to present some direct evidence which allows the proper selection of the mechanism.

Experimental

Two experimental methods were used. In the first one a ZnO single crystal was polarized cathodically in zincate containing potassium hydroxide solutions at constant current, and the potential-time behavior was recorded. In the second one, the ZnO was cathodically polarized at constant current in either potassium hydroxide or potassium sulfate solutions, and the resulting zinc deposit was determined by anodic stripping in the same solutions. The test electrode was a ZnO single crystal needle (about 3 mm wide and 20 mm long) mounted in epoxy resin and mechanically polished approximately perpendicular to the "c" axis; ohmic contact to the crystal was made through indium amalgam. The crystal was obtained from Semielements, Inc. (Saxonburg, Pennsylvania). Purity was 99.995%; no doping agent was added. Specific resistance of the crystal was approximately 1 ohm-cm. The source of donors causing this high conductivity is not known. Undoped ZnO is usually considered to have interstitial zinc (7) causing the n-type conductivity, although it also has been suggested that the conductivity is due to oxygen vacancies or chemical impurities (8). The cell (9), and the galvanostat (10) are described elsewhere. During the chronopotentiometric experiments, a still solution and a zinc wire reference electrode were used. For the second set of experiments a saturated calomel reference was used and the solution was streamed over the surface of the ZnO electrode at an estimated velocity of 10 cm/sec. All tests were carried out at room temperature.

In the first tests the electrolyte was 0.3M KOH, supersaturated with zincate. The chronopotentiograms exhibited two plateaus; hydrogen gas evolution was observed during the second plateau. One example is shown in Fig. 1. The transition times of the first plateau for different current densities and zincate concentrations are given in Table I. [A diffusion coefficient of 0.7 x 10^{-5} cm^2/sec was used in the calculations (11).]

During the second set of experiments, the ZnO was cathodically polarized at different current densities, for different time durations, in flowing 1M KOH or 0.1M K_2SO_4 solutions. The galvanostat was connected to the electrodes before the solution entered the cell to avoid chemical dissolution of the crystal prior to the application of the cathodic current. After the cathodic treatment, the cell was totally flushed, to remove hydrogen bubbles, and the crystal anodically polarized at 4.5 mA/cm^2 current density. The change of electrode potential with time was recorded, and the sudden shift in positive direction was taken as the indication of the end of zinc removal. The electrode was repolished with 400 and 600 grit silicon carbide papers before each experiment. The amount of charge needed to dissolve the zinc from the surface is plotted against cathodic current density, and length of cathodic treatment in Fig. 2 and 3.

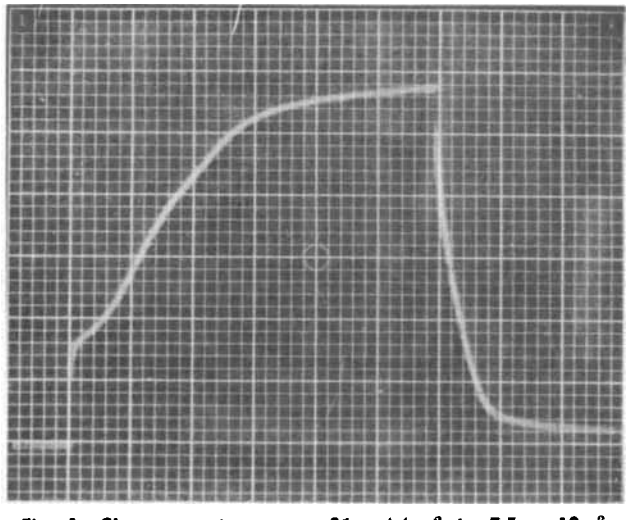

Fig. 1. Chronopotentiogram at 86 mA/cm^2 in 7.5 x 10^{-3}m zincate solution. 100 mV/div, 5 msec/div.

Table I. Transition times

Zincate concentration, mmole/l	Current density, mA/cm^2	Transition time measured, msec	Transition time calculated, msec
7.5	8.6	200	166
7.5	86	2	1.7
3	8.6	20	27
3	3.2	200	195

Discussion

In the chronopotentiometric experiments three cathodic processes are possible: reduction of zincate, reduction of zinc oxide, and hydrogen evolution. Be-

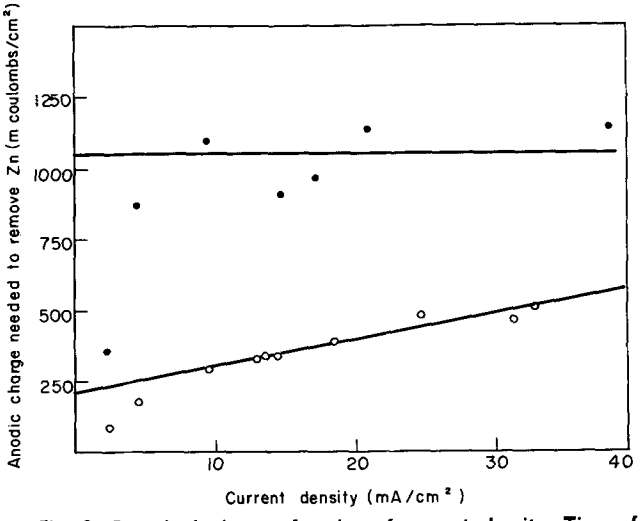

Fig. 2. Deposited zinc as function of current density. Time of cathodic treatment: 360 sec; ●, 1M KOH; ○, 0.1M K_2SO_4.

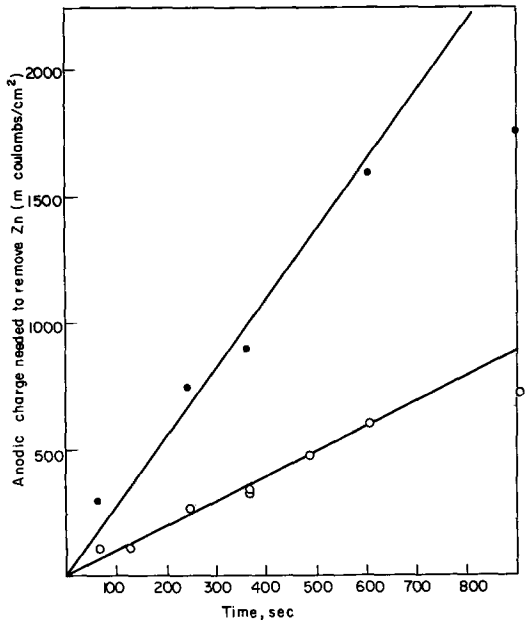

Fig. 3. Deposited zinc as function of time. Cathodic current density: 14 mA/cm^2. ●, 1M KOH; ○: 0.1M K_2SO_4.

cause of the low zincate concentration its reduction should deplete the solution fast; transition times were calculated for this process, using the Sand equation, and are compared to the measured ones in Table I. The agreement is satisfactory. It was concluded therefore that the first plateau represents zincate reduction from the solution and the second plateau represents hydrogen evolution. These data alone indicate that direct reduction in the battery cannot have an important role. At the low overvoltage plateau the current efficiency for direct reduction must be small, if not zero, in view of the good agreement of the measured and calculated transition times for zincate reduction. At the higher overvoltage the current efficiency of direct ZnO reduction cannot be determined from these experiments, but the fact that it proceeds with vigorous hydrogen evolution at 300-400 mV more cathodic overvoltage than that of the zincate reduction, excludes it as a battery process, since these overvoltages are usually not reached in practice.

The second set of experiments gives a possibility to estimate the current efficiency of the direct reduction of zinc oxide, during the hydrogen evolution. For this evaluation, the following simple model is suggested as a first approximation. The zinc coating formed on the surface results from two mechanisms, the crystal can chemically dissolve in the electrolyte and the resulting ions are cathodically deposited, or the crystal can be reduced directly in a solid state reaction. It is further assumed that the resulting coating is porous in nature and does not hinder the further dissolution of the crystal, and the "active area" of the crystal is constant during the experiments except at long times. The current efficiency of direct reduction is assumed to be independent of the current density, within the explored range. Then

$$Q = at + ibt$$

where Q(mcoulomb/cm^2), is the charge needed to remove anodically the zinc coating.
a (mA/cm^2), the chemical dissolution rate of the crystal expressed in equivalent current density.
t(sec), time of cathodic treatment
b, current efficiency of direct ZnO reduction
i (mA/cm^2), applied cathodic current density.

From a Q *vs.* i plot, at constant time, both a and b can be determined; the slope of the Q *vs.* t plot, at constant current density, can then be calculated as $(a + bi)$ and compared to the measured value. These are shown in Table II.

These data indicate that the current efficiency of direct zinc oxide reduction is practically zero even during the hydrogen evolution period in potassium hydroxide solution. Indication of direct reduction in potassium sulfate solution was found with an efficiency of 2.7%. It should be noted that because of the much higher chemical dissolution rate in KOH, and because of the scatter of the points, a small (1-2%) direct reduction efficiency in KOH would be undetectable.

Table II. Chemical dissolution rates and current efficiencies of direct reduction

	1M KOH	0.1M K_2SO_4
a (mA/cm^2)		
Chemical dissolution rate	2.9	0.57
b		
Current efficiency of direct reduction	0	0.027
$(a + bi)$	2.9	0.95
Slope of the Q *vs.* t plot	2.8	1.0

The chemical dissolution rate of ZnO in 1M KOH has been measured before and is reported to be equivalent to 4 mA/cm^2 (12) for sintered ZnO pellet, and 8 mA/cm^2 (13) for a passive layer on a zinc electrode. Considering that the roughness factor in these two cases could be higher than that for the present single crystal, and realizing that the "active area" of the crystal was smaller than the geometric area, the agreement is satisfactory. The deviation from linearity in the plots at low cathodic current densities is probably due to the loss of zincate in the effluent, and that at long times to the change of the active area.

It can be concluded therefore that while the direct reduction of the zinc oxide to zinc in a solid-state process is possible, the contribution of this reaction to the battery electrode process is not likely to be more than a few per cent, if any. The battery electrolyte is more concentrated than the one used in this work, but the conclusions are expected to hold also under actual battery conditions. The chemical dissolution process will be much faster at the higher *p*H (12), and there is no reason to suspect that the direct, solid-state process would be *p*H dependent.

The results of Hladik and Schwabe (3), who suggest the solid-state reaction as the predominant one, could also be explained by the solution mechanism. Their strongest argument in favor of the solid-state reaction is that in 1M and 11M KOH solutions the behavior of their electrode is similar. However, with their "paste electrode" it is quite possible that a large part of the overvoltage is resistance polarization, controlled by the conductivity of the electrolyte. The conductivity goes through a maximum with increased KOH concentration (14), which could explain their data.

Acknowledgments

Our thanks are due to Professor J. O'M. Bockris for helpful discussions. Financial assistance for this work was provided by the National Science Foundation under grant No. NSF-GK-16550, and the A.R.P.A. Program in Materials Science (University of Pennsylvania).

Manuscript submitted July 20, 1970; revised manuscript received *ca.* Sept. 8, 1970.

Any discussion of this paper will appear in a Discussion Section to be published in the December 1971 JOURNAL.

REFERENCES

1. T. P. Dirkse, *This Journal*, **102**, 497 (1955).
2. R. W. Powers and M. W. Breiter, *ibid.*, **116**, 719 (1969).
3. O. Hladik and K. Schwabe, *Electrochim. Acta*, **15**, 635 (1970).
4. H. Gerischer and W. Mindt, *ibid.*, **13**, 1329 (1968).
5. H. Gerischer, *Surface Sci.*, **13**, 265 (1969).
6. A. I. Oshe and V. S. Bagotskii, *Russian J. Phys. Chem.*, **35**, 806 (1961).
7. T. J. Gray, *J. Am. Ceram. Soc.*, **37**, 534 (1954).
8. D. G. Thomas, *J. Phys. Chem. Solids*, **3**, 229 (1957).
9. B. D. Cahan, Z. Nagy, and M. A. Genshaw, To be published.
10. J. O'M. Bockris, H. Wroblowa, E. Gileadi, and B. J. Piersma, *Trans. Faraday Soc.*, **61**, 2531 (1965).
11. J. McBreen, Study to Investigate and Improve the Zinc Electrode for Spacecraft Electrochemical Cells, Yardney Electric Corp., Contract NAS 5-10231 (June 1967).
12. R. Landsberg, H. Fürtig, and L. Müller, *Z. physik Chem.*, **216**, 199 (1961).
13. A. I. Oshe and B. N. Kabanov, *Zashchita Metallov*, **4**, 260 (1968).
14. T. P. Dirkse, *This Journal*, **106**, 154 (1959).

A Study of HCl in the LiCl-KCl Eutectic

John D. Van Norman*,[1] and Richard J. Tivers

Brookhaven National Laboratory, Upton, New York 11973

Many investigations have been made in recent years into the behavior of gases dissolved in molten salts. With the increased interest in high-temperature batteries, fuel cells, and metallurgical processes, the need for knowledge of chemical, electrochemical, and transport properties of gases in solution in molten salts is great.

Since the LiCl-KCl eutectic has become a fairly standard chloride solvent and the generally accepted manner of drying the mixture involves prolonged treatment of the eutectic, both in the solid and liquid state, with HCl gas, it was decided that a study of the behavior of HCl dissolved in the eutectic would be valuable. This paper is a report on the solubility of HCl in the LiCl-KCl eutectic as a function of temperature and on its electrochemical behavior; apparent diffusion coefficients are also presented.

Experimental Section

All chemicals used were of reagent grade. The lithium chloride-potassium chloride eutectic was prepared in a manner described by Laitinen, Ferguson, and Osteryoung (1). The apparatus for the measurement of the solubility of gases in molten salts has been described earlier (2). The method simply stated is to isolate a known volume of eutectic saturated with HCl, then to sparge the HCl from the eutectic with argon and to collect the HCl in water. The HCl is then titrated with standard NaOH solution.

The chronopotentiometric measurements were made in a cell previously described (2). The indicator electrode was a vitreous carbon electrode sealed into Pyrex glass. The vitreous carbon (made by the Beckwith Carbon Corporation) is impermeable to gases and has a coefficient of thermal expansion matched by some Pyrex glass so that the glass to carbon seal was leak tight. A silver foil immersed in an AgCl solution in a separate fritted compartment served as the reference electrode; a porous graphite rod was the counterelectrode. Chronopotentiograms were obtained by passing a constant current between the carbon and graphite electrodes while recording the potential between the carbon and the silver electrodes as a function of time. The constant current regulator was built by the Instrumentation Division of Brookhaven National Laboratory and the chronopotentiograms were recorded on an L&N High Speed Speedomax 6 recorder that had a pen speed of 0.25 sec full scale and a chart speed of 2.0 or 4.0 ips.

The eutectic was saturated with HCl at atmospheric pressure by bubbling HCl through the melt for at least 4 hr, a time found to be more than sufficient to saturate the melt, and an atmosphere of HCl was maintained above the melt at all times for both the solubility and chronopotentiometric studies.

Results

The solubility of HCl was measured at three temperatures, 490°, 570°, and 675°C. Each value reported is an average of eight or more determinations with the average deviation being quoted. The solubility of HCl in the LiCl-KCl eutectic at 490°C is 1.20 ± 0.14 x 10^{-6} moles/cc which corresponds to a mole fraction of 4.11 x 10^{-5}; at 570°C the solubility is 1.44 ± 0.10 x 10^{-6} moles/cc or a mole fraction of 5.05 x 10^{-5} while at 675°C the solubility is 1.74 ± 0.11 x 10^{-6} moles/cc or a mole fraction of 6.31 x 10^{-5}.

The solubility of HCl increases somewhat with temperature. A plot of log X_{HCl} *vs.* $1/T$ should be linear with a slope equal to $\Delta H°/2.303R$, where $\Delta H°$ is the heat of solution of HCl in the LiCl-KCl eutectic. Figure 1 shows this plot. The $\Delta H°_{HCl}$ so calculated is +3.5 kcal/mole with an estimated error of ±10%.

The solubilities found in this investigation are of the same order of magnitude as those found by Ukshe and Devyatkin (3, 4) at higher temperatures for single salts and NaCl-KCl mixtures. They also found that with the exception of the 1:1 mixture of NaCl and KCl the solubility of HCl increases with temperature.

Cathodic chronopotentiograms were obtained for the reduction of HCl in the LiCl-KCl eutectic at various temperatures. As mentioned, the cathode was a vitreous carbon surface and, as was found previously for chlorine systems (2), extreme care had to be taken to make sure there was no bubble formation on the electrode surface. Electrodes were inspected visually for any bubbles which might interfere with proper diffusion conditions at the electrode surface.

Figure 2 shows a typical cathodic chronopotentiogram of hydrogen chloride dissolved in LiCl-KCl eutectic. The transition time, τ, is taken at that point at which the potential rise becomes linear. The basic equation of chronopotentiometry is

$$i_0\tau^{1/2} = \frac{nF\pi^{1/2}D^{1/2}C}{2} \qquad [1]$$

The product $i_0\tau^{1/2}$ should be a constant at any given concentration and temperature, a fact which was verified experimentally for each run, within ±5%, the experimental error.

Many chronopotentiograms were obtained at 490° and 570°C, but attempts to secure meaningful results above 570°C failed because of softening of the Pyrex glass seal around the vitreous carbon electrode. Chronopotentiograms obtained in the absence of HCl showed no holdup of potential indicating no residual H^+ or any diffusion of Cl_2 generated at the anode to the

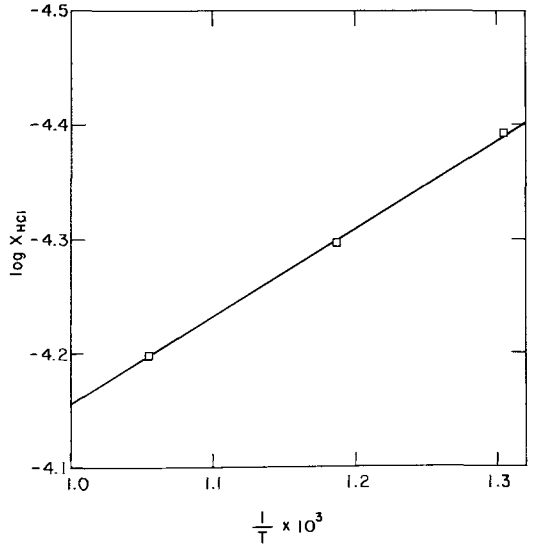

Fig. 1. Temperature dependence of HCl solubility in LiCl-KCl eutectic.

* Electrochemical Society Active Member.

[1] Present address: Department of Chemistry, Youngstown State University, Youngstown, Ohio 44503.

Key words: fused salt gases, chronopotentiometry fused salts, diffusion HCl, hydrogen chloride fused salts, solubility gases.

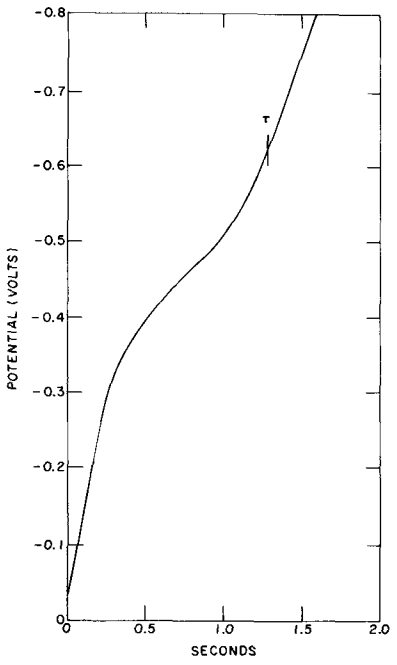

Fig. 2. Cathodic chronopotentiogram of HCl dissolved in molten LiCl-KCl eutectic at 570°C, current density 3.25 mA/cm^2.

cathode. Diffusion coefficients were calculated for the diffusion of HCl in molten LiCl-KCl eutectic. Each diffusion coefficient obtained is the average of ten or more determinations in each of two or more separate batches of salt. The experimental error can only be estimated but, because of variations between batches of salt, the difficulty of getting exact electrode areas and the possibility of undetected bubbles the error is placed at ±20%. The diffusion coefficient of the HCl species in the eutectic, D_{HCl}, is 2.4 ± 0.5 x 10^{-4} cm^2/sec at 490°C and 2.3 ± 0.5 x 10^{-4} cm^2/sec at 570°C.

This value is an order of magnitude greater than usually found for metal ions in the eutectic, 10^{-5} cm^2/sec. A similarly large value was found previously for the diffusion coefficient of Cl_2 in molten chlorides (2, 5). It is also interesting to note that the diffusion coefficient remains constant within experimental error as a function of temperature, again similar to that for Cl_2 in the eutectic (2). However, whereas the high diffusion coefficient results for Cl_2 were rationalized in terms of the trichloride ion Cl_3^- and a chain conduction mechanism, it is difficult to visualize a similar explanation for the D_{HCl} results. It is more likely that the small size of the H^+ ion formed from the dissociation of HCl permits more rapid diffusion through the ionic liquid.

It was impossible to determine from the chronopotentiometric measurements whether the reduction of HCl, or H^+, proceeds in a reversible manner in the eutectic. Further work is needed to ascertain this fact.

Acknowledgments

This work was performed under the auspices of the United States Atomic Energy Commission. The authors would like to acknowledge helpful discussions with Dr. J. J. Egan and Dr. R. H. Wiswall, Jr.

Manuscript submitted Jan. 1, 1970; revised manuscript received Sept. 22, 1970.

Any discussion of this paper will appear in a Discussion Section to be published in the December 1971 JOURNAL.

REFERENCES

1. H. A. Laitinen, W. S. Ferguson and R. A. Osteryoung, *This Journal*, **104**, 516 (1957).
2. J. D. Van Norman and R. J. Tivers, "Halogen Solutions in Molten Halides," in "Molten Salts, Characterization and Analysis," G. Mamantov, Editor, Marcel Dekker, New York (1969).
3. E. A. Ukshe and V. N. Devyatkin, *Russ. J. Phys. Chem.*, **39**, 1222 (1965) (English translation).
4. E. A. Ukshe and V. N. Devyatkin, *ibid.*, 1641.
5. L. S. Leonova, Yu. M. Tyabukhin, and E. A. Ukshe, *Elektrokhim.*, **5**, 210 (1969).

Electrocapillary Measurements in the Presence and Absence of Superimposed A-C Potential

John Lawrence and David M. Mohilner*

Department of Chemistry, Colorado State University, Fort Collins, Colorado 80521

During the last five years there has been some controversy (1-4), in studies of the mercury-solution interface, concerning the origin of the discrepancies between thermodynamic data derived from measurements of differential capacitance by the a-c bridge method and corresponding data derived from measurements of interfacial tension with a Lippmann capillary electrometer. The thermodynamic relationship (5) between interfacial tension and differential capacitance is

$$\left(\frac{\partial^2\gamma}{\partial E^2}\right)_{T,p,\mu} = -C \qquad [1]$$

Here γ is the interfacial tension, C the differential capacitance, E the electrode potential, and the subscripts T, p, and μ imply that measurements are made at constant temperature, pressure, and composition. It follows that double integration of a differential capacitance-potential (C-E) curve should yield the electrocapillary curve if the relevant integration constants are available. Numerous comparisons of this type have been made (1-4, 6) and it has been noted that, for dilute solutions of weakly adsorbed electrolytes, the Lippmann capillary electrometer gives results which are consistently lower on the anodic branch than those calculated from differential capacitance.

Three explanations have been suggested for these discrepancies: (i) inaccuracies in the methods of calculation before a comparison can be made (4), *i.e.*, during double integration of the capacitance data or, as has occasionally been attempted, during double differentiation of electrocapillary data; (ii) a potential-dependent finite contact angle at the three phase boundary mercury-solution-glass inside the electrometer capillary (4, 7); or (iii) the presence of the small a.c. across the interphase giving rise to a nonequilibrium double layer during differential capacitance measurements (1).

Recent evidence (4, 6, 8) indicates that (ii) is the most likely explanation since electrocapillary curves obtained by other methods which do not rely on contact

* Electrochemical Society Active Member.
Key words: double layer, differential capacitance, birth detector, maximum bubble pressure.

angle, *e.g.* drop time measurements and the "maximum bubble pressure" method, agree well with data derived from capacitance measurements. With modern computational procedures (i) has been shown to be incorrect (4, 9-11) but (iii) has never been subjected to a rigorous experimental test. The present investigation of (iii) was undertaken primarily in order to assess the feasibility of constructing a digital-computer-controlled capillary electrometer based on the "maximum bubble pressure" method described recently by Schiffrin (6). In addition, in view of the fundamental importance of the thermodynamic relationship between differential capacitance and interfacial tension (Eq. [1]) to the interpretation of double layer properties, it seemed worthwhile to attempt to settle experimentally the question whether the superimposition of a small a-c potential on the d-c potential of an ideal polarized electrode in dilute solution seriously disturbs the double layer equilibrium and thereby invalidates the conclusions drawn from analysis of *C-E* curves as was suggested previously (1).

Experimental

Following the basic principles described recently by Schiffrin (6), the classical method of "maximum bubble pressure" (MBP) has been successfully applied to the determination of electrocapillary curves. The gas pressure system had a nitrogen inlet and outlet bleed arrangement for coarse adjustment of the pressure and a screw copper bellows for fine adjustment. A 2 liter ballast volume facilitated fine pressure changes. The pressure was measured on a U-tube mercury manometer. The capillary was drawn from regular 1 mm Pyrex tubing to an internal radius of 15μ and then bent into a U-shape so that the tip was inverted. It was then "dewetted" by drawing the vapor of dichlorodimethyl silane (12) through the capillary for a few minutes, and the tip was then recut. The potential of the working electrode was controlled with an operational amplifier potentiostat circuit employing a Philbrick P85AU as control amplifier and a P25AU as voltage follower. The solutions were deaerated with prepurified nitrogen.

The gas pressure above the mercury reservoir was slowly increased during a measurement until the first droplet or "bubble" began to form at the tip of the capillary. This maximum pressure, which is directly proportional to the mercury-solution interfacial tension, was obtained by reading the manometer with a cathetometer and adding to this measurement the height of mercury in the reservoir above the capillary tip. The latter quantity did not change appreciably during the several hours that were required to obtain a complete electrocapillary curve. At the end of each measurement it was necessary to reduce the pressure to near atmospheric in order to stop the flow of mercury through the capillary. The proportionality constant used to convert the maximum "bubble" pressures to interfacial tensions was easily determined by a series of measurements with a solution for which the interfacial tension was known, as is done in the case of the conventional Lippmann electrometer. The absolute precision of the method, using a microscope to determine the instant of droplet formation at the tip, was usually better than ± 0.1 dyne cm^{-1}.

With the eventual aim of running the entire experiment on-line with a PDP-8/I digital computer, an electronic detector was designed which would give an output pulse of several volts at the instant when the first droplet of mercury begins to grow at the tip of the capillary. A controlled 5 mV, 10 KHz a-c potential was superimposed on the d-c potential of the working electrode using the control amplifier in a standard adder configuration (13).

Figure 1 shows the complete "birth" detector circuit which was constructed from Philbrick operational amplifiers. The a-c current flowing across the interphase was monitored by passing it through a current-to-voltage converter, the output of which is shown in Fig. 2(a). This trace shows a very small current until the mercury surface begins to expand at the tip, at which time it increases with a finite slope until the first droplet falls off. Half-wave rectification and smoothing of this a-c signal result in a d-c potential trace of similar shape, shown in Fig. 2(b). Differentiation of this signal then leads to a sharp voltage pulse (of about 40 msec rise time and 3-5V amplitude) at the instant when the mercury surface first begins to expand. This is illustrated in Fig. 2(c) where a dual beam oscilloscope was used to record simultaneously the smoothed d-c signal and the pulse output from the differentiator. The final operational amplifier shown in Fig. 1 is a simple 1/1 inverter to give a positive pulse suitable as an input to a voltage level converter[1] on the interface of the computer. Even in the absence of a computer for on-line experiments, it is much less tedious to determine the "birth" of the droplet by displaying the pulse on an oscilloscope than to observe the capillary tip visually through a microscope.

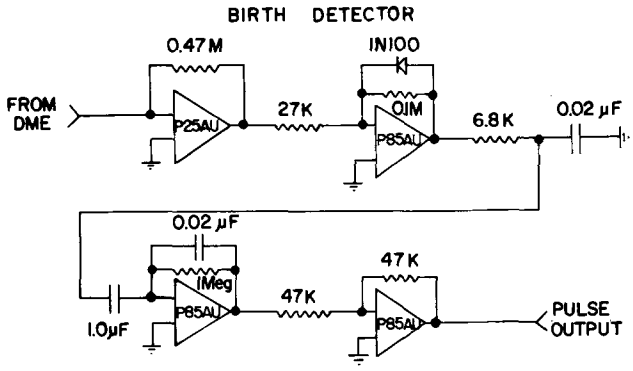

Fig. 1. Birth detector circuit

Results and Discussion

Figure 3 shows a comparison of an electrocapillary curve obtained by the MBP method with the second integral of the corresponding capacitance data for 0.01M NaF. The latter was derived from Grahame's charge density-potential data (17) which he obtained by integrating his own differential capacitance measurements from a potential of zero charge determined from the streaming electrode. We then integrated Grahame's charge density-potential data from five different potentials on the cathodic branch of the electrocapillary curve, taking as the integration constant the value of the interfacial tension determined by the MBP method. The smooth curve in Fig. 3 is the average of these five double integrations. Unlike Fig. 4 of Ref. (4) where an electrocapillary curve obtained with a Lippmann electrometer is compared with capacitance data, it can be seen that there is no systematic deviation between the two curves. It should also be noted in Fig. 4 of Ref. (4) that the size of the deviations (as large as 20 dynes cm^{1-}) depends strongly on the potential, and the deviations disappear on the cathodic branch of the curve.

The necessary requirement for the Lippmann electrometer is that the contact angle at the three phase boundary, mercury-solution-glass inside the capillary must be the same both for the solution used to calibrate the apparatus and for any test solution. Otherwise the radius of mean curvature (15) of the meniscus electrode calculated from the calibration data will not be the same as the radius of mean curvature prevailing in the case of the test solution. {It is usually assumed that the contact angle is not only equal in the presence of calibration and test solutions, but is actually zero. This is equivalent to assuming that the apparatus will behave satisfactorily only when the wall

[1] A DEC W-510 positive level converter and an R-302 one shot delay produce a pulse which can be used to trigger the A/D converter of the computer (14).

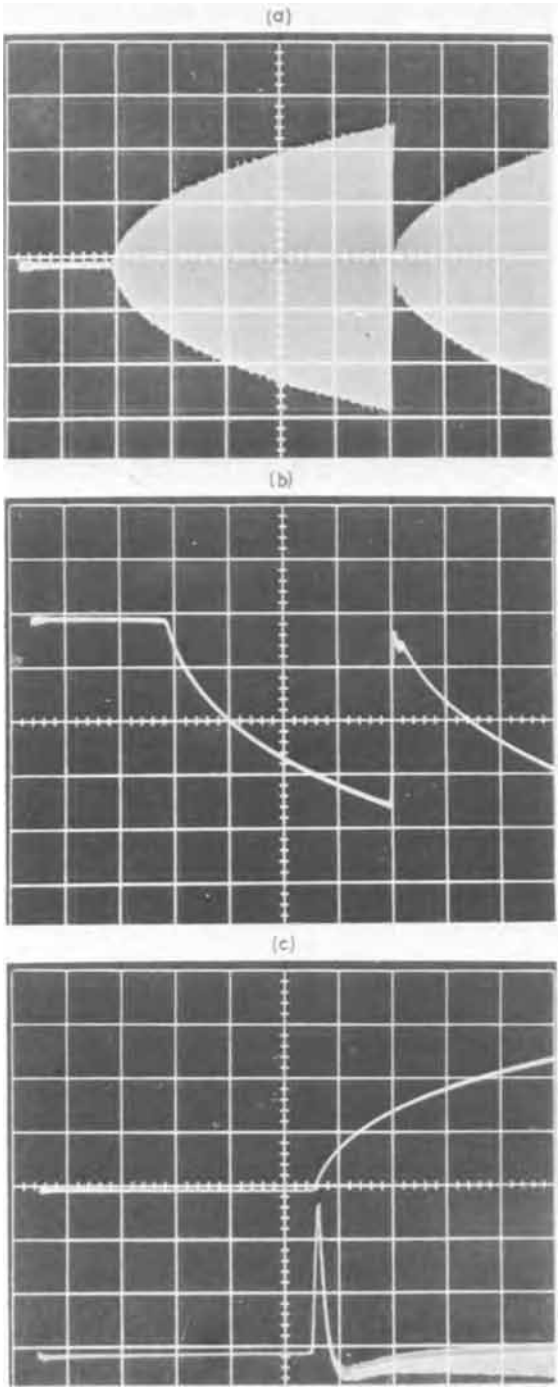

Fig. 2. The three stages of birth detection: (a) a-c current trace (0.5 sec/division, 0.2 V/division); (b) d-c potential trace (0.5 sec/division); (c) d-c potential trace and pulse output (0.5 sec/division, 1.0 V/division).

of the glass capillary is perfectly wet by the solution [*cf.* Gouy (16)].} The condition for mechanical equilibrium of the meniscus electrode is given by the Laplace equation which relates the pressure difference, Δp, across the curved interface to the interfacial tension, γ, and the radius, r, of mean curvature

$$\Delta p = 2\gamma/r \qquad [2]$$

In the calibration procedure, one measures Δp and then, knowing γ from independent (*eg.*, sessile drop) measurements, calculates the radius of mean curvature, r. When one uses a test solution one measures Δp and calculates γ using the same value of r determined in the calibration. If the contact angle is zero in the calibration experiment but finite in the presence of the test solution, the actual radius of mean curvature

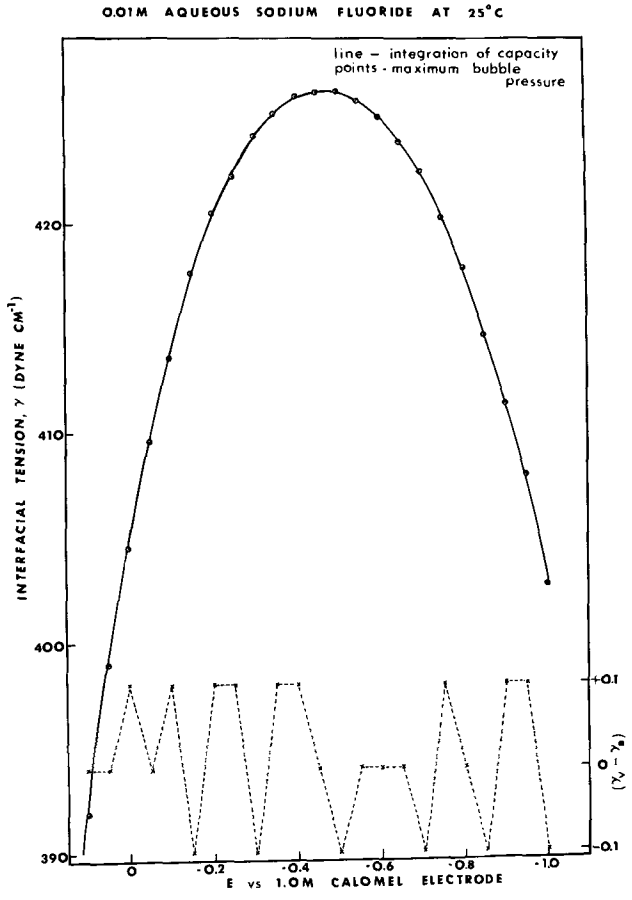

Fig. 3. Electrocapillary curve for 0.01M aqueous NaF at 25°C. Solid curve is doubly integrated differential capacitance. Points are determined by MBP method both visually and by electronic birth detection. Lower points connected by dotted lines indicate difference (γ_V-γ_E) between visual and electronic detection. Scale for these differences is on lower right of figure.

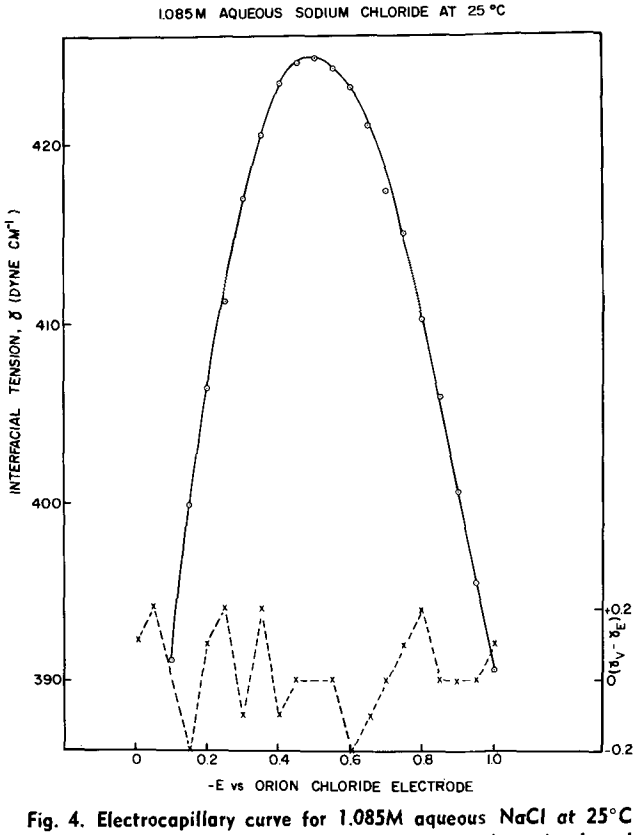

Fig. 4. Electrocapillary curve for 1.085M aqueous NaCl at 25°C and difference (γ_V-γ_E) between measurements using visual and electronic detection.

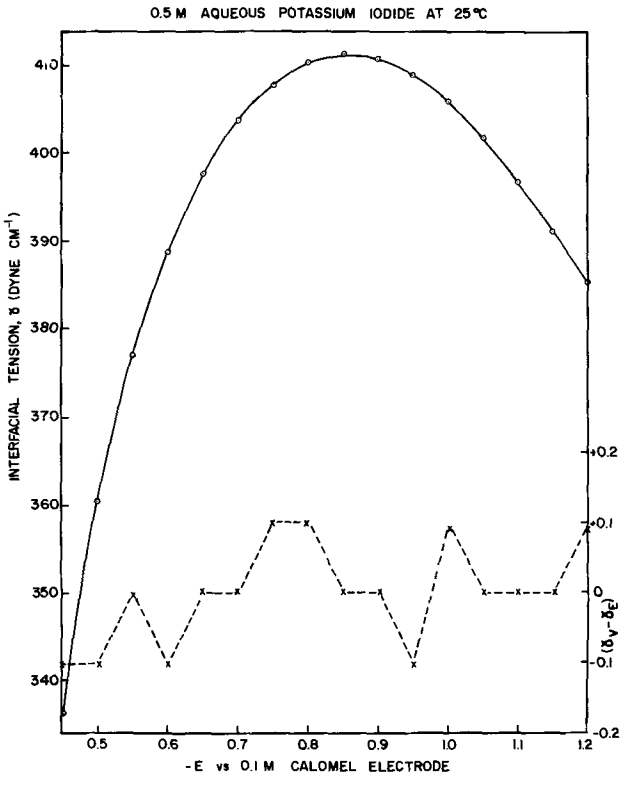

Fig. 5. Electrocapillary curve for 0.5 aqueous KI at 25°C and difference (γ_V-γ_E) between measurements using visual and electronic detection.

of the meniscus electrode in the presence of the test solution will have a different value $r' > r$. Therefore, the value of γ calculated from a Δp measurement with the test solution will be too small because one will necessarily substitute the value r determined by calibration rather than the (unknown) value r' into the Laplace equation. The negative deviations of γ measured with a Lippmann electrometer from those calculated by double integration of differential capacitance curves which were reported in Ref. (4) for the case of NaF solutions can therefore be explained by a finite contact angle at the three phase boundary inside the capillary in the presence of the NaF. Evidently [*cf.* Fig. 4, Ref. (4)] this contact angle becomes larger as the potential becomes more positive and as the solution becomes more dilute. In contrast, measurements of interfacial tension made by the maximum bubble pressure method are not subject to this source of error (6).

The data in Fig. 3-5 were obtained using both visual and electronic methods of "birth" detection in order to investigate precisely the effect of the a.c. on the equilibrium properties of the double layer. During measurements employing visual detection, the detector circuit and the a-c source were disconnected from the cell. The dotted lines show that the measurements obtained by the two methods agreed, within experimental error, for both dilute solutions of weakly adsorbed electrolytes (0.01M NaF in Fig. 3) and concentrated solutions of moderately or strongly adsorbed electrolytes (1.085M NaCl in Fig. 4 and 0.500M KI in Fig. 5). It must be concluded, therefore, that the effect of a low-amplitude a-c potential applied across the interphase is too small to be detected with present experimental techniques. Certainly the large discrepancies observed previously (1-4) cannot be attributed to the presence of the a-c potential.

The above discussion suggests that the controversial differences between electrocapillary measurements and differential capacitance measurements are due to systematic errors in the capillary electrometer and not to the effect of the a-c potential applied during capacitance measurements. Consequently it is suggested that, in all future studies of the electrical double layer involving dilute solutions of weakly adsorbed electrolytes, the conventional Lippmann capillary electrometer should not be used. If electrocapillary curves are required, it is recommended that they be obtained by MBP measurements.

Acknowledgment

This work was supported by the Office of Naval Research under Contract No. N0014-67-0299-0007-AA, Project NR 359-493.

Manuscript submitted July 24, 1970; revised manuscript received *ca.* Sept. 30, 1970.

Any discussion of this paper will appear in a Discussion Section to be published in the December 1971 JOURNAL.

REFERENCES

1. J. O'M. Bockris, K. Muller, H. Wroblowa, and Z. Kovac, *J. Electroanal. Chem.*, **10**, 416 (1965).
2. R. Payne, *ibid.*, **15**, 95 (1967).
3. J. O'M. Bockris, K. Muller, H. Wroblowa, and Z. Kovac, *ibid.*, **15**, 101 (1967).
4. J. Lawrence, R. Parsons, and R. Payne, *ibid.*, **16**, 193 (1968).
5. This was first derived by G. Lippmann, *Ann. Chim. Phys.* [5], **5**, 494 (1875). For a review see: D. M. Mohilner in "Electroanalytical Chemistry," Vol. 1, A. J. Bard, Editor, pp. 241-404, Marcel Dekker, Inc., New York (1966).
6. D. J. Schiffrin, *J. Electroanal. Chem.*, **23**, 168 (1969).
7. G. Gouy, *Ann. Chim. Phys.*, **29**, 145 (1903).
8. J. Lawrence and D. M. Mohilner, Paper 303 presented at Electrochem. Soc. Meeting, Los Angeles, May 10-15, 1970.
9. D. M. Mohilner and P. R. Mohilner, *This Journal*, **115**, 261 (1968).
10. R. G. Barradas and F. M. Kimmerle, *Can. J. Chem.*, **45**, 109 (1967).
11. W. R. Fawcett and J. E. Kent, *ibid.*, **48**, 47 (1970).
12. R. Payne, *J. Electroanal. Chem.*, **7**, 343 (1964).
13. D. E. Smith in "Electroanalytical Chemistry," Vol. 1, A. J. Bard, Editor, p. 109, Marcel Dekker, Inc., New York (1966).
14. D. M. Mohilner and P. R. Mohilner, ONR Tech. Report No. 1, 1969, Project NR 359-493.
15. [*Cf.*] N. K. Adam, "The Physics and Chemistry of Surfaces," p. 9, Dover, New York (1968), or R. Defay and I. Prigogine, "Tension Superficielle et Adsorption," pp. 5-9, Editions Desoer, Liege (1951).
16. G. Gouy, *Ann. Chim. Phys.* [7], **29**, 145 (1903).
17. D. C. Grahame, ONR Tech. Report No. 14, Feb. 18, 1954, Project NR 051-150.

Crystal Structures of the Elements of the Periodic Table and the Mechanisms of Electrolytic Hydrogen Evolution

Ashok K. Vijh*[,1]

Hydro-Quebec Institute de Recherche, Varennes, Quebec, Canada

In previous discussions (1-3) of the mechanisms of hydrogen evolution reaction (h.e.r.) on various metals, exchange current densities (i_o) for h.e.r. have been related to various fundamental properties of the metal, *e.g.*, work function, atomic number, compressibility, heat of sublimation, etc. It was shown (3) that these correlations arise primarily because of the relationship of i_o to the M-H bond strengths which in turn are partly determined by M-M bond energies through the Pauling's well-known equation (4). The M-M energies are usually (1-3) estimated from heats of sublimation by assuming a coordination number of 12 so that

$$D_{(M\text{-}M)} = \frac{1}{6}\Delta H_{Sub}$$

In this type of calculation, it is implicitly assumed that the crystal structure, and hence the coordination number, of the metal has little relationship to the mechanisms of h.e.r. As far as arguments involving M-H bond strength are concerned, this assumption is quite correct since small corrections to the estimated values of M-H bond strength would arise if the crystal structure and the coordination number of every metal were taken separately into account. This has been discussed by Conway and Bockris (1). However, such an implicit assumption of lack of influence of crystal structure of the metal on the mechanisms of h.e.r. contradicts some empirical observations which have been outlined in the following paragraphs.

As regards mechanisms of h.e.r., all metals of the Periodic Table may be divided into two main classes:

Class I: h.e.r. proceeds without significant steady-state chemisorption of hydrogen. The metals are: Zn, Cd, Hg, Al, In, Tl, Pb, Ga, Sn, Sb, As, Bi, Te, Se, Mn, etc.

Class II: h.e.r. proceeds with significant steady-state adsorption of hydrogen. All metals not mentioned in class I belong to this class: *e.g.*, Cu, Ag, Au, Ni, Fe, Pt, Rd, Ir, Mo, Ta, Nb, Ti, Re, etc.

It has been observed that all the metals of class II (*i.e.*, involving chemisorbed hydrogen and hence proceeding with radical-ion or atomic recombination as the r.d.s.), are typical metals in the strictest sense because:

(*A*) They crystallize into one of the three metallic structures, namely, face-centered cubic (fcc), body-centered cubic (bcc) or close packed hexagonal (cph).

(*B*) Their crystals may be regarded to be composed of approximately spherical units packed as closely together as possible.

(C) The crystallographic coordination numbers for these metals are obviously high, *i.e.*, 8 or 12.

However, metals of class I (*i.e.*, which proceed with initial discharge as the r.d.s.) are atypical in the sense that they do not meet one or more of the above three characteristics of typical metals. Even though some of the elements in class I have one of the three (fcc, bcc, cph) metallic structures they are noticeably modified. For example, even though cadmium and zinc are cph, the distance between atoms along one axis is greater than that obtained by packing spheres as closely as possible. Despite the fact that aluminum and lead are cubic, the distance between their atoms is greater than expected on the basis of closely packed spheres. The crystal arrangement in arsenic, antimony, and bismuth is rhombohedral hexagonal type with the atoms arranged as double layers so that each atom has three close neighbors in three directions; the neighbors are farthest away in this structure. This arrangement gives rise to a lattice structure in which the coordination number within a single layer is three. In Se and Te, the atoms are arranged in long spiral chains, with each atom having two close neighbors (5).

According to Slater (6) crystal structures of Mn, Hg, Ga, In, Sn, As, Sb, Bi, Se, and Te are not typically metallic (fcc, bcc, cph), which is consistent with their position in the class I elements here. Again in the classification of Slater (6) based on crystal structures of elements, many of the elements contained in class I here (*e.g.*, Ga, As, Se, In, Sn, Sb, Te, Tl, Bi) are not ordinary metals, but are peculiar in the sense that these elements verge on the nonmetals. One evidence of this approach to nonmetallic behavior in these elements is the fact that their bonds are very similar to nonpolar bonds. Ordinary metals (*viz.* class II here) do not, of course, form homopolar bonds in the accepted sense; this has profound consequences which distinguish them from the typical metals of class I here. Lack of homopolar bonding and the related directional property of the bonds gives rise in ordinary metals (*viz.* class II) to a behavior in which atoms act like spheres without preferred direction, thence the crystal structures with characteristic close packed spheres. From the foregoing the following conclusions may be made:

1. On the basis of crystal structure and related consideration, it has been shown that typically metallic elements (class II) are associated with mechanisms (*i.e.*, radical-ion and atomic recombination) in which h.e.r. proceeds with appreciable amounts of chemisorbed hydrogen in the steady-state. Conversely, on atypical metals (class I), h.e.r. proceeds through a mechanism (initial discharge) involving negligible steady-state concentration of chemisorbed hydrogen on the electrode surface.

2. Previous discussions of the mechanisms of h.e.r. on various metals which were based on the implicit assumption of the same crystal structure and same coordination number for all metals even though resulting in essentially correct arguments, are inaccurate in detail.

Why h.e.r. Involves Chemisorbed Hydrogen Only on Typical Metals?

Any attempt to provide a satisfactory and quantitative answer to this question would be somewhat presumptuous. However, a few lines of speculative thinking may be mentioned. It may be easily shown that, on the whole, the metals in class II here have high heats of sublimation and consequently high M-H (metal-hydrogen) interaction energies. This would tend to favor mechanisms involving strongly chemisorbed hydrogen. This approach has been successfully

[1] Currently, also Visiting Professor in the Energy Center of the National Institute of Scientific Research, University of Quebec, at Varennes, P.Q., Canada.

* Electrochemical Society Active Member.

Key words: hydrogen evolution reaction on metals, dondenergies, crystal structures of metals.

quantified by Conway and Bockris (1) and recently reviewed by Matthews (3). This type of analysis does not, however, yield satisfactory explanation of the qualitative relationship between crystal structure and the mechanisms of h.e.r. on various metals, as outlined here.

It is known that mechanical properties of the metals are closely related to their crystal structures. The close packing arrangement of typical metals (class II) provides the largest number of "planes of flow" when the crystal is stressed. A typical metal, under stress, would not cleave or fracture, but instead form a glide plane in which layers of atom slip over each other with insignificant loss of energy and with the re-establishment of the original structure. In the case of an ideal typical metal (class II) of an absolute purity, it is possible that, it would glide without loss of energy at all, under application of infinitely small stress. In other words, activation energy for the formation of dislocations would aproach zero for an ideal metal (5). In a real typical metal, one may assume that the activation energy for the formation of dislocations, even though not zero, would tend to be small. Since dislocations and other crystal defects are usually regarded as the sites favoring facile chemisorption, it follows that typical metals (class II) would tend to involve reaction mechanisms involving chemisorbed hydrogen as contrasted to atypical metals of class I.

It may be emphasized that the foregoing speculation does not provide a satisfactory causative explanation for the fact that typical (class II) metals sustain h.e.r. with significant steady-state coverage by chemisorbed hydrogen whereas on atypical (class I) metals, h.e.r. proceeds through initial discharge as the rate-determining step.

A generally held view (1-3) that facile chemisorption of hydrogen on class II metals, most of which are transition metals, arises because of presence of unfilled d-bands merits some comment here. These conclusions regarding the high chemisorption activity of transition metals in relation to unfilled d-bands have been derived on the basis of gas-phase adsorption of molecular gases, including hydrogen. Even though the hypothesis of relationship between unfilled d-bands and pronounced tendency to undergo chemisorption appears an attractive one, it does not stand up under closer examination, for the present case where the chemisorption does not involve dissociation of gaseous hydrogen molecules. According to analysis of Ehrlich (7), on chemisorption from gas-phase, the gases lose their molecular constitution and are bound as atoms. The chemisorption, therefore, is dictated by the considerations of thermodynamics: the chemical potential of hydrogen atoms bound together in the hydrogen molecule must exceed that of hydrogen atoms held by the solid in order for chemisorption to take place. Ignoring the entropic factor as a first approximation, the chemisorption would occur if the M-H bond strength of the hydrogen atom to the metal M exceeds half the dissociation energy of the hydrogen molecule in the gas phase. The experimental evidence only shows that among the transition metals this requirement is met, undoubtedly owing to their high heats of sublimation. For the present case of electrolytic hydrogen evolution, the chemisorption results from an initial discharge step which, for acidic solution, is

$$M + H_3O^+ + e^- \rightarrow M - H + H_2O$$

In this case, in order to demonstrate a unique dependence of chemisorption on the electronic structure of the metal, it is necessary to consider the gas-phase adsorption of atomic hydrogen and not molecular hydrogen. It has been found that there is no correlation between d-band configuration of the solid and its chemisorption behavior toward gas-phase atomic hydrogen (7). In fact, it has been observed that chemisorption of hydrogen atoms from gas-phase can occur on such nontransition metals as mercury, aluminum and potassium. It may hence be concluded that the mechanisms for h.e.r. involving significant chemisorption, on class II metal, probably do not arise because of the presence of unfilled d-bands in the transition metals. Other factors, the origin of which is not clear at present, must be involved. The ultimate explanation of the matters outlined in this note must lie in the satisfactory resolution of the rather fundamental questions such as: why do different metals have different crystal structures? In what causative manner are the magnitudes of heats of sublimation and coordination numbers, and thence the M-M bond energies, related to the crystal structure of metals? What are the basic factors which determine the magnitude of M-H bond strength for the chemisorption of electrolytically produced atomic hydrogen? And, finally, how can these and other factors be interrelated to yield a coherent picture which would predict high steady-state chemisorption of hydrogen, and thence the radical-ion and atomic recombination mechanisms, on metals of class II? Lack of significant steady-state chemisorption by atomic hydrogen during h.e.r. on metals of class I will also have to be explained in the foregoing terms. A detailed quantitative study of some of the foregoing matters is in preparation (8).

Manuscript submitted June 15, 1970; revised manuscript received Oct. 28, 1970.

Any discussion of this paper will appear in a Discussion Section to be published in the December 1971 JOURNAL.

REFERENCES

1. B. E. Conway and J. O'M. Bockris, *J. Chem. Phys.*, 26, 532 (1956).
2. H. Kita, *This Journal*, **113**, 1095 (1966).
3. D. B. Matthews, Ph.D. Thesis, Univ. of Pennsylvania, Philadelphia (1965).
4. L. Pauling "The Nature of the Chemical Bond," Cornell Press, Ithaca, N. Y. (1960).
5. W. C. Fernelius and R. F. Robey in "Supplementary Readings for Chemical Bond Approach," R. Fitzgeral and W. Kieffer, Editors, J. Chem. Ed. Publishers (1960).
6. J. C. Slater, "Introduction to Chemical Physics," McGraw-Hill Book Co., New York (1939).
7. G. Ehrlich in "Proceedings of the Third International Congress on Catalysis," W. M. Sachtler, G. C. A. Schuit, and P. Zwietering, Editors, North-Holland Publishing Co., Amsterdam (1965).
8. A. K. Vijh and A. Belanger, In preparation.

Brief Communication

The Exchange of Zn^{65} Between ZnO(s) and Potassium Zincate

L. A. Vander Lugt* and T. P. Dirkse**

Calvin College, Grand Rapids, Michigan 49506

Studies of the system Zn/Zn(II), KOH, especially in concentrations ordinarily used in battery systems, have revealed certain anomalies. Among these may be mentioned the ease of production and stability of supersaturated zincate solutions (1), and the appearance of maximums and minimums in correlations of certain kinetic constants with KOH concentration [exchange currents (2), conductance (3), and passivation time constants (4)]. These anomalies appear to be connected with the electrolyte phase. A fuller understanding of the chemical characteristics of the electrolyte is needed in order to more fully understand the electrochemical behavior of the system.

We have attempted to get more information by investigating the rate of attainment of equilibrium between the electrolyte and the various solid phases using radioactive zinc isotopes. In this note we present some results of our study of the equilibrium between solid ZnO and the potassium zincate electrolyte.

The exchange of Zn^{65} between the complex zincate ion and solid ZnO was studied by following the decrease in activity of the solution phase due to the uptake of Zn^{65} by the ZnO. The results are shown in Fig. 1. Curves 1 and 2 record exchange between powdered ZnO (0.3μ) and the zincate ion. For curve 1 the isotope was added after the solution was saturated with ZnO, while for curve 2 the isotope was added before the solution was saturated with ZnO. Curve 3 shows the exchange between solid crystalline zinc acetate and a saturated solution of zinc acetate at pH = 4.8. Curve 4 shows the same exchange at pH = 5.5.

These results show that exchange of Zn between ZnO and the zincate ion is extremely slow. In fact, no significant exchange occurs over a period of 500 hr. The solid ZnO showed no radioactivity after the exchange study was terminated. Curve 2 suggests that during the saturation period, a small amount of exchange may occur. However, once saturation is achieved (~24 hr) no further exchange is evident.

For zinc acetate the exchange process is normal (curves 3 and 4). The effect of decreasing pH is as predicted, increasing the exchange rate by suppressing hydrolysis. It is interesting to note that the extent of this is somewhat larger than expected.

It has been shown by Gerischer (5) that the following reaction is fast

$$Zn(OH)_4^{=} \rightarrow Zn(OH)_2 + 2\,OH^- \qquad [1]$$

Consequently, it may be concluded from our results that the reaction

$$ZnO + H_2O \rightarrow Zn(OH)_2 \qquad [2]$$

is slow. The apparent low rate of reaction [2] may be of fundamental significance in interpreting the processes occurring in zinc-alkaline batteries where supersaturated zincate electrolytes and solid ZnO are common products of discharge.

This exchange of Zn between ZnO and zincate ion is being studied in a range of electrolyte compositions in an effort to achieve a better understanding of the chemistry of this system. At present we can suggest no mechanism to explain this low rate of exchange.

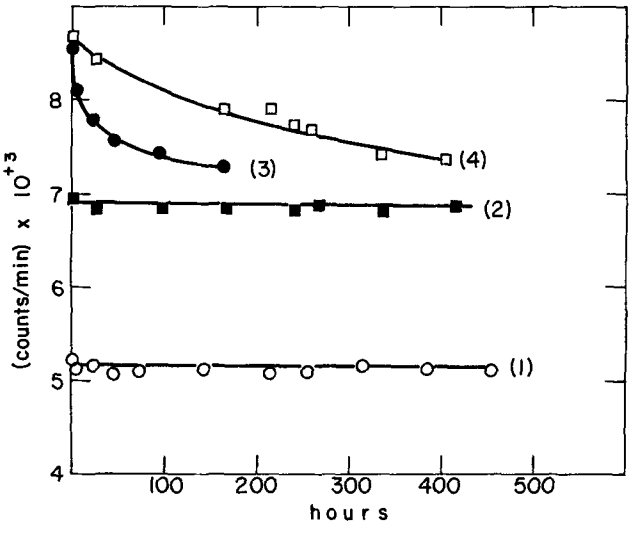

Fig. 1. Radioactivity of solution vs. time curves at 25° for the following systems: (1) solid ZnO, 35% KOH saturated with ZnO; (2) solid ZnO, 30% KOH saturated with ZnO; (3) solid zinc acetate, water saturated with zinc acetate, pH = 4.8; (4) solid zinc acetate, water saturated with zinc acetate, pH = 5.5. Each system had approximately the same amount of dissolved and undissolved zinc compound.

Acknowledgment

We wish to thank Dr. N. A. Hampson for his helpful discussions in connection with this work.

Manuscript submitted July 27, 1970; revised manuscript received *ca.* Oct. 26, 1970.

Any discussion of this paper will appear in a Discussion Section to be published in the December 1971 JOURNAL.

REFERENCES

1. T. P. Dirkse, *This Journal*, **102**, 497 (1955).
2. T. P. Dirkse and N. A. Hampson, To be published.
3. L. S. Darken and H. F. Meier, *J. Am. Chem. Soc.*, **64**, 621 (1942).
4. N. A. Hampson and M. J. Tarbox, *This Journal*, **110**, 95 (1963).
5. H. Gerischer, *Z. Physik. Chem.*, **202**, 302 (1953).

* Electrochemical Society Active Member.
** Electrochemical Society Life Member.
Key words: zincate solution, zinc oxide, Zn exchange, Zn^{65}.

JOURNAL OF THE ELECTROCHEMICAL SOCIETY

SOLID STATE SCIENCE

FEBRUARY 1971

Sulfur Hexafluoride as an Etchant for Silicon

P. Rai-Choudhury*

Westinghouse Research Laboratories, Pittsburgh, Pennsylvania 15235

ABSTRACT

Sulfur hexafluoride (SF_6) gas in hydrogen ambient is used to *in-situ* etch silicon wafers producing very smooth surfaces. The subsequently grown epitaxial silicon layers are of high quality (stacking fault density ≤ 4 per cm^2), and the impurity profiles as measured by the spreading resistance technique are indicative of layers not doped with sulfur. The entire process of etching and epitaxial growth are carried out at temperatures ($\leq 1100°C$) sufficiently low so that no dislocations are generated due to high thermal stresses. Some of the basic limitations introduced by such a highly reactive etchant are discussed.

The importance of substrate surface preparation and cleanliness in the epitaxial growth of silicon is well known to investigators of electronics materials. The defects in the epitaxial films could be caused by several factors; the primary causes are: (*a*) surface impurities derived from the substrate material, (*b*) surface impurities derived from chemical or mechanical polishing treatments, and (*c*) thermal stresses set up due to excessive temperature gradients from rf heating.

In-situ etching in the epitaxial reactors may be effective in removing certain surface oxides and films, mechanical damage, and other impurities which do not homogenize during the initial heating-up period because of their slow diffusion rates. Unfortunately, most of the harmful impurities, such as heavy metals, are fast diffusants and must be removed either at room temperature by some chemical treatment or at higher temperatures by gettering (1). Thermally induced dislocations (2) also suggest the use of low-temperature etchants. Even if one succeeds in developing a low-temperature etch, then the problems of subsequently growing an epitaxial silicon at low temperature still remain. The quality of the epitaxial material may be expected to be poor with decreasing deposition temperature when compared with the currently available good-quality Czochralski or float zone bulk crystals. This is a rather complicated subject under current investigation and therefore only a passing mention is made here. However, many desirable features, such as etching through oxide masks and in the presence of buried layers, make a search for a low-temperature etch worthwhile.

In a recent communication (3), etching characteristics of hydrogen sulfide were examined and compared with those of water vapor and hydrogen chloride. H_2S was found to etch Si at a lower temperature and at a very rapid rate, leaving a smooth surface. However, some of the undesirable features of this etch are high toxicity, extreme poisonousness in small quantities, and low purity. H_2S etching occasionally leaves deposits of sulfur compounds in the downstream of the reaction chamber, although no detrimental effect of sulfur could be detected on the subsequently grown layers. Sulfur hexafluoride (SF_6), on the other hand, is a nontoxic, noncorrosive, less poisonous, and odorless gas available in fairly high purity. Among the major reaction products from SF_6 etching are fluorides and sulfides of Si. If the fraction of SiS_2 formed increases significantly, then the system becomes very similar to the H_2S system, and the etching should be accompanied by some deposits of sulfur compounds near the exhaust of the reaction tubes along with the characteristic odor of sulfur. If the fluorides of silicon are the primary reaction products, then, of course, the reaction tube should be essentially free of deposits and odor of sulfur. The importance of hydrogen carrier gas may also be tested by carrying the reaction in an inert ambient which makes the formation of certain products, such as HF, impossible.

The purpose of this study is to explore the feasibility of SF_6 as a low-temperature etchant for Si so that the *in-situ* etching, as well as the subsequent epitaxial growth, of Si may be carried out below the "critical temperature" without introducing too many dislocations (2). The possibility of low-temperature vapor etching of substrates with mechanical damage resulting from lapping and sawing operations is also examined such that the rate of propagation of the damage-induced dislocations may be less than the rate of etching. Etching of holes in Si through oxide masking is also briefly examined.

Experimental Procedure

The apparatus used was a horizontal quartz reaction chamber in which substrates were placed on a graphite susceptor and heated by an external rf coil. The graphite susceptor was coated with silicon (at about 1500°C) in runs where *in-situ* etching was followed by epitaxial growth. SF_6 used was 10% by volume in ultrapure hydrogen. Desired concentrations of SF_6 were obtained by mixing controlled amounts with palladium-purified hydrogen. The initial surfaces of the silicon (111) wafers used for SF_6 etching were chemically polished, chem-mechanically polished, as well as lapped. In order to explore the possibility of etching holes in the silicon through an SiO_2 mask, oxidized wafers with etched widows were also used. An extensive cleaning and degreasing procedure was

* Electrochemical Society Active Member.
Key words: epitaxial, dislocation, hydrogen, ambient, impurities.

followed to minimize any wafer surface contaminants. Temperatures were measured by a disappearing filament pyrometer corrected for emissivity and absorption errors (4). The etch rates were determined from weight loss and wafer thickness measurements. Scanning electron microscopy (SEM) was used to characterize these surfaces.

Epitaxial layers were grown on etched substrates from the $SiCl_4$-H_2 process, and provisions for doping with B_2H_6 and AsH_3 were made. These layers were subjected to optical examination for stacking faults and other defects. The concentration profiles and any resistivity inhomogeneities were measured by the spreading resistance technique (5).

Results

In order to gain some understanding of the reactions taking place, experiments were carried out in H_2 carrier gas as well as in Ar carrier gas at 1100°C. In both cases comparable etch rates were obtained (~2.0 μ/min). Based on these results, assuming that HF is not formed in any significant amounts, the overall reaction may be tentatively written as

$$4Si(s) + 2SF_6(g) = SiS_2(s \text{ or } l) + 3SiF_4(g)$$

The standard free energy of this reaction is −706.81 kcal at 1400°K, and the equilibrium constant is a very large number indicating that the reaction is spontaneous and irreversible under most experimental conditions. A similar conclusion is reached if SiS instead of SiS_2 is considered as a reaction product. The choice of SiS_2 rather than SiS as one of the reaction products was justified elsewhere (3). Among the reaction products only SiS_2 will condense near the outlet of the tube and emit the characteristic sulfur odor during unloading of the tube. The etched surface in H_2 carrier gas was mirrorlike, whereas in Ar ambient the etching was relatively nonuniform. It is quite possible that the trace amounts of HF that may be formed in H_2 ambient are effective in removing any surface oxides during etching. Unlike H_2S etching, in all these runs the deposits on the tube walls were negligible (provided an uncoated susceptor was used), and only a faint odor of sulfur was detectable during unloading of the reactor tube.

Figure 1 shows the temperature dependence of the etch rate at an SF_6 partial pressure of 1 x 10^{-3} atm and a total H_2 flow rate of 100 liters/min (linear velocity ~25 cm/sec). Although the etch rates are based on the change in total thickness, the back of the wafers remained practically unetched. The shape and the slope of the curve are indicative of the increasing importance of the mass transfer rates, through a boundary layer, to or from the wafer surface, with increasing temperature. The dependence of the etch rate on SF_6 partial pressure at a temperature of 1050°C is shown in Fig. 2. The slope of the curve is only

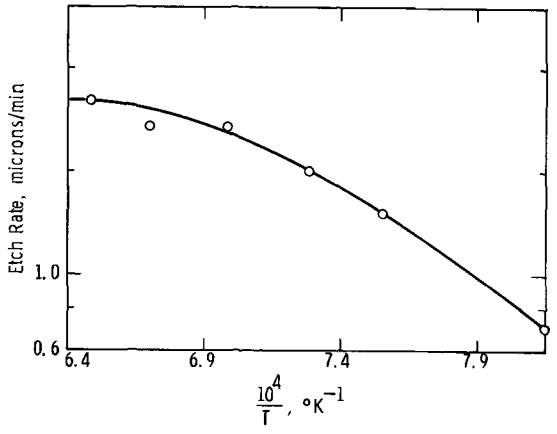

Fig. 1. Effect of temperature on etch rate of silicon: p_{SF_6} = 1 x 10^{-3} atm; total flow rate 100 liters/min.

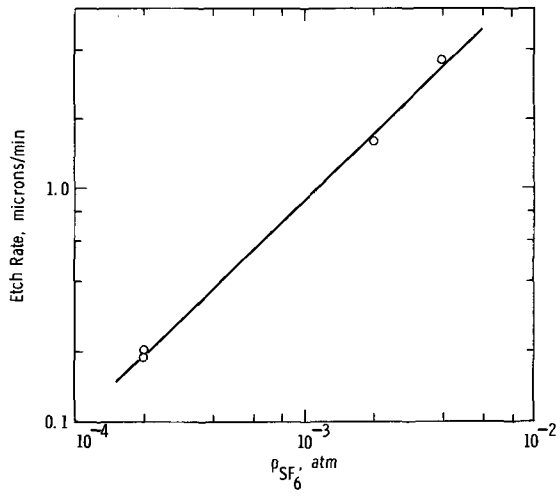

Fig. 2. Effect of sulfur hexafluoride partial pressure on etch rate of silicon at a temperature of 1050°C.

slightly less than unity and indicates that the etch rate is approximately directly proportional to the SF_6 partial pressure. Thus, the rate of diffusion or transport of SF_6 to the Si surface is playing a significant role in the etching process.

The quality of the surface resulting from etching an initially (chemically as well as chem-mechanically) polished surface is described first. The results of SF_6 etching of lapped surfaces are described subsequently. At low temperatures (~850°C), etching is preferential and dislocation etch pits become visible. Smooth nonpreferential etching results from about 1050°C and above. Figure 3 shows scanning electron micrographs of etched surfaces at 1100°C and SF_6 partial pressure of 2 x 10^{-4} atm. The results in general indicate that the temperature is much more critical than the SF_6 partial pressure in determining the surface quality.

Direct etching of a lapped surface is, of course, not desirable, because during heating the mechanical damages from sawing and lapping will anneal out into dislocations which may then propagate into the bulk of the wafer. However, this provides a reasonable indication of the nonpreferential nature of the SF_6 etch. Figure 4 shows how an initially lapped surface changes with the etching temperature. The initial lapped surface (Fig. 4a) has abrasion-induced triangular as well as some hexagonal pits and is relatively free from deep craters or pits. At 950°C the triangular pits almost disappear, and the surface is characterized by deep hexagonal craters as well as some remnants of thin silicon flakes protruding out of the surface. These flakes appear bright in the micrograph because they are thin enough for the primary electron beam to penetrate and produce secondary electrons on both sides of the flakes. It appears that at 950°C the hexagonal pits are etched faster than the rest of the surface, probably because of deeper mechanical damage. At 1050°C relatively larger and shallow etched morphology begins to appear (Fig. 4c) and becomes smoother with increasing temperature (Fig. 4d). X-ray topographs of an initially lapped wafer from which about 136μ were removed at 1100°C (etch rate ~1.7 μ/min) indicate the absence of significant propagation of damage-induced dislocations. It seems surprising that the etching time (~80 min) was not sufficient to propagate damage-induced dislocations through the entire thickness of the wafer (~300μ). The results indicate that, although it may be possible to thin a lapped wafer by vapor etching without inducing dislocations, the etched surface is not suitable for epitaxial growth and subsequent device fabrication.

In the absence of any pinholes, SiO_2 films grown thermally on silicon substrates can be effectively used as a mask against SF_6 etch. However, in the presence of pinholes or etched windows (by standard photo-

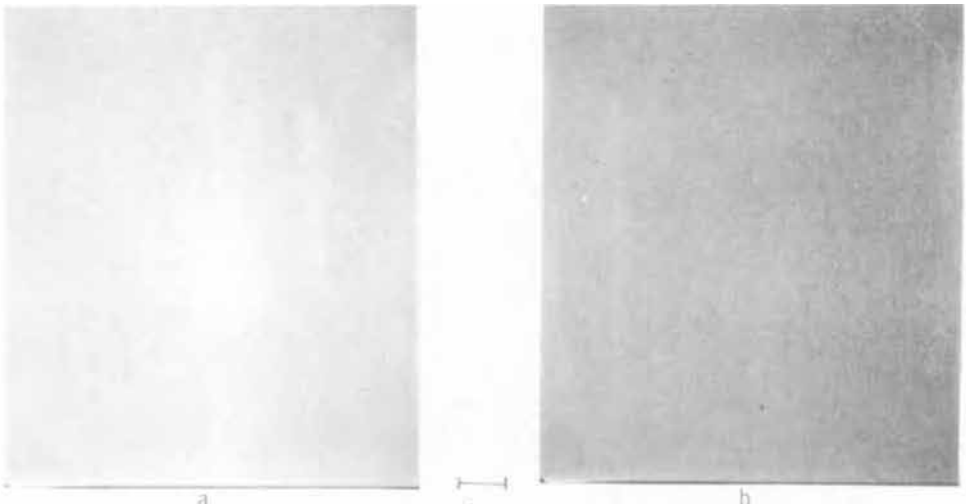

Fig. 3. Scanning electron micrographs at 45° incidence showing smooth surface of silicon etched with SF_6 at 1100°C: (a) surface initially chem-mechanically polished, (b) surface initially chemically etched in $HF\text{-}HNO_3$ mixture.

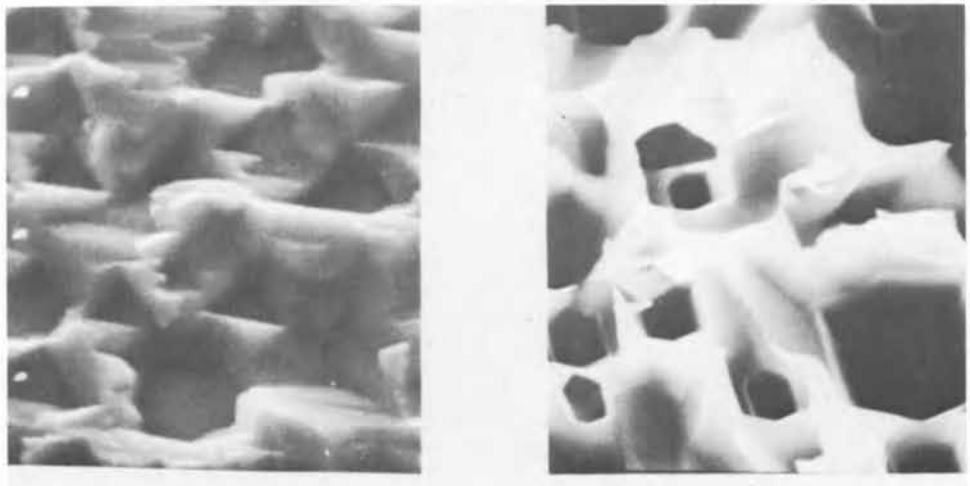

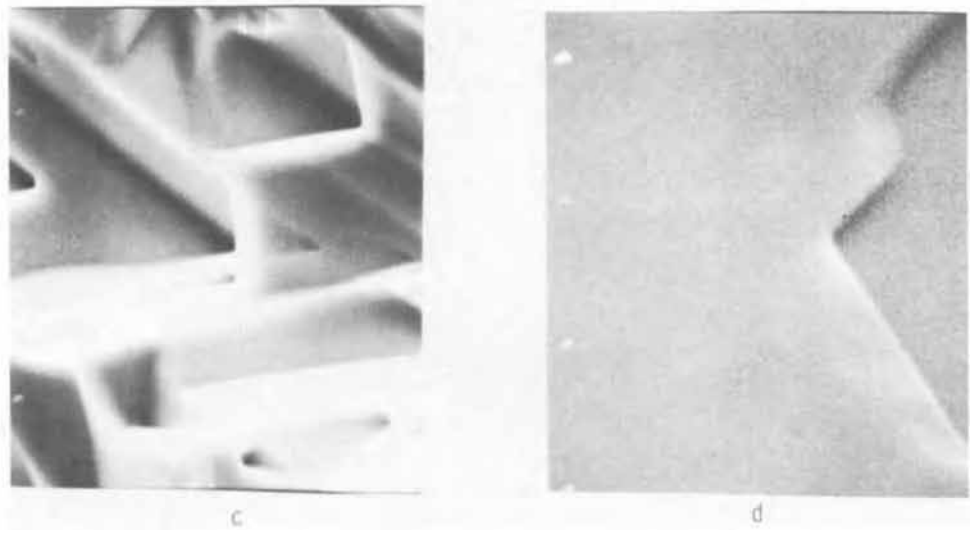

Fig. 4. Scanning electron micrographs at 45°C incidence of surfaces etched at different temperatures starting with a lapped initial surface: (a) initial lapped surface, (b) etched at 950°C, (c) etched at 1050°C, and (d) etched at 1160°C.

lithographic techniques), considerable undercutting of the mask was observed. The SF_6 etching was performed on circular patterns, 9μ in diameter, with center to center separation of 18μ, and about 4μ of Si were removed. Figure 5 is a scanning electron micrograph of an etched silicon surface through an SiO_2 mask showing considerable undercutting.

One of the problems with the SF_6 etch is its extremely high reactivity which imposes severe limitations on selection of materials such as susceptor, reactor tube, *etc.* Although a bare graphite or a SiC-coated susceptor apparently produces good results in the etching cycle of the operation, they are undesirable susceptor materials for the subsequent epitaxial growth operation. Graphite or SiC or any particle that etches relatively slowly in SF_6 gets embedded in the epitaxial layer and often causes stacking faults. A silicon-coated susceptor is preferred only in the sense

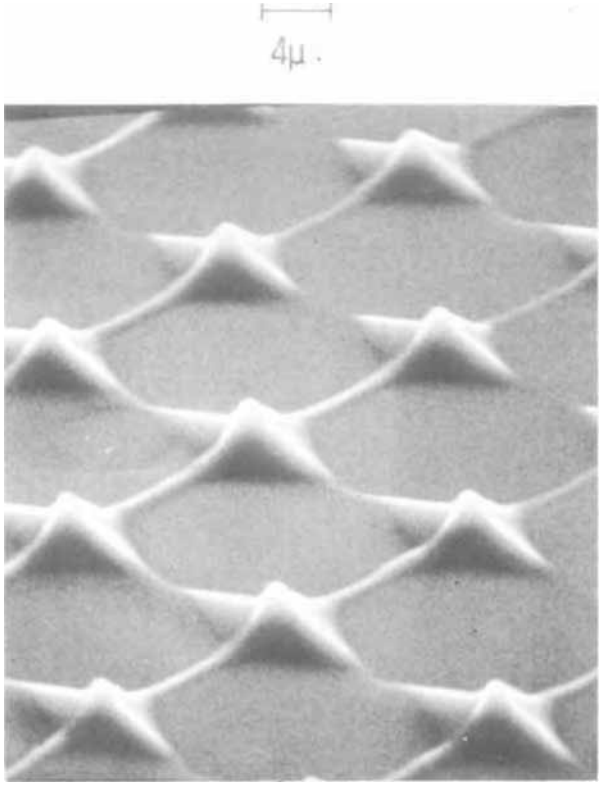

Fig. 5. Scanning electron micrograph at 60° incidence showing the results of etching silicon through an SiO_2 mask.

that the reaction products from such a susceptor are volatile. The undesirable feature of a silicon-coated susceptor is that the susceptor is stripped of silicon during etching, exposing bare graphite surfaces. This problem may be avoided by restricting the etching time. Another limitation of this etch is that it adsorbs strongly on the gas lines and becomes a potential source of contamination and defect nucleation during epitaxial growth. Using the best available susceptor, namely a silicon-coated (at about 1500°C) graphite susceptor, the stacking fault densities in the grown layers were minimized by restricting the *in-situ* etching to about 5μ and introducing SF_6 gas through a separate line. Following these precautions epitaxial layers were consistently grown having a stacking fault density of 2-4 faults/cm^2. The SF_6 etching as well as the epitaxial growth were carried out at 1050°-1100°C, a temperature range at which a significant number of dislocations are not introduced (2).

Several runs were made following SF_6 etching, and the layers were doped with AsH_3 giving net impurity concentrations in the range of 10^{14} to 10^{16} atm/cm^3. The impurity profiles as a function of depth measured by a high-resolution spreading resistance technique (5) indicate normal good-quality epitaxial silicon with *no* detectable effects of sulfur contamination. The substrates used for these runs were 20 ohm-cm, p-type. The doping level of the substrates did not change from the possible introduction of donor levels due to sulfur contamination. However, due to its high diffusivity in silicon, the effects of sulfur at low levels in reducing the carrier lifetime in silicon cannot be ruled out.

In conclusion it should be emphasized that the limitations of the SF_6 gas mentioned should be common among most low-temperature etchants. Besides formation of volatile reaction products a prerequisite for a low-temperature etchant is its high reactivity, and the consequences of its high reactivity are the problems of selection of susceptor material and purging out and/or desorption of the residual etchant from the system.

Summary

Sulfur hexafluoride, unlike hydrogen chloride, etches silicon irreversibly and spontaneously, producing volatile sulfides and fluorides of silicon. The etching results in a very smooth surface on chemically as well as chem-mechanically polished starting substrates, and the process is suitable for wafer thinning. Although lapped wafers may be etched at low temperatures and rapid rates so that significant numbers of damage-induced dislocations are not generated, the resultant surface is relatively rough and is therefore unsuitable for device quality epitaxial growth. SiO_2 does not provide effective masking for etching holes in selective areas of the substrate because of severe undercutting. The entire process of etching and growth on chemically and chem-mechanically polished substrates is carried out at low enough temperatures ($\leq$1100°C) so that no significant dislocations are generated from the thermal stresses induced in the epitaxial reactor. However, because of the high reactivity of SF_6 the silicon coating of the susceptor is attacked rapidly, and the subsequent epitaxial layers are not entirely free from stacking faults.

Acknowledgments

The author wishes to thank W. Cifone for assistance with the experimental work, and F. Berish and Dr. M. C. Driver for taking the scanning electron micrographs.

Manuscript submitted July 14, 1970; revised manuscript received *ca.* Sept. 28, 1970.

Any discussion of this paper will appear in a Discussion Section to be published in the December 1971 JOURNAL.

REFERENCES

1. J. L. Lambert and M. Reese, *Solid State Electron.*, **11**, 1055 (1968).
2. P. Rai-Choudhury and W. J. Takei, *J. Appl. Phys.*, **40**, 4980 (1969).
3. P. Rai-Choudhury and A. J. Noreika, *This Journal*, **116**, 539 (1969).
4. E. Sirtl and K. Reuschel, *Z. Anorg. Allegem. Chem.*, **332**, 113 (1964).
5. R. G. Mazur and D. H. Dickey, *This Journal*, **113**, 255 (1966).

Factors Affecting the Growth Rate of Plasma Anodized Al_2O_3

John F. O'Hanlon*

IBM Thomas J. Watson Research Center, Yorktown Heights, New York 10598

ABSTRACT

This paper discusses the affects of anodization parameters on the growth rate of plasma anodized Al_2O_3. Variations in growth rate were inferred by observing the variations in the anodic current decay while anodizing at a constant bias potential. The following effects have been observed: (*a*) Sputtered cathode oxide was found to contribute significantly to the total film thickness unless adequate shielding was employed. (*b*) Heating the substrate from 30°C to 100°C caused the current to decay tenfold faster. (*c*) A maximum growth rate (quickest current decay) was observed at an O_2 pressure of approx. 50m Torr. Probe measurements taken at the location of the sample showed a maximum electron density at this pressure. The maximum electron density and quickest decay rate shifted to higher pressures (approx. 100m Torr) as the discharge current was increased. (*d*) The presence of small amounts of water vapor in the discharge slightly increased the anodic current decay rate.

The kinetics of oxide growth in a plasma anodizing system are affected by several system parameters. The most important of these are the cathode sputtering rate, oxide temperature, oxygen partial pressure, and water vapor partial pressure. Different investigators (1-3) have studied the effects of a different one or two of these variables while exercising little or no control over the remaining parameters. In addition no two investigators have pursued these studies with identical experimental systems, thus making comparisons of plasma characteristics, sputtering rates, and water vapor content impossible. The purpose of this paper is to systematically study the effects of each of the above parameters on the growth rate of thin (200Å) Al_2O_3 films in a low pressure oxygen d-c glow discharge.

Oxide growth is accomplished by positively biasing an aluminum sample which is immersed in the negative glow of a d-c oxygen glow discharge. The growth of an aluminum oxide film is shown schematically in Fig. 1. It is seen that the oxide growth rate and sample current become diminishingly small with time until the film assumes a limiting thickness. For the purposes of this investigation, the time required for the current to decay to 10% of its initial value shall arbitrarily be taken as a measure of the time required to grow the film.

Experimental System

The vacuum system in which the data were taken is shown schematically in Fig. 2(A). The aluminum cathode ring is mounted between two stainless steel plates which are the anodes; the sample is mounted on a support below the level of the cathode ring to avoid direct exposure to reactively sputtered cathode oxide. Figure 2(B) shows a detailed view of the sample holder. This design, used by Jennings and McNeill (4), was suitably modified so that it could be heated or cooled by N_2 gas. Care was taken to thermally isolate the sample face and the Pyrex walls of the sample holder tube; this was necessary when it was desired to cool the sample to near liquid nitrogen temperature without the complication of the walls acting as a source or sink of water vapor. An independent liquid nitrogen trap was provided for that purpose.

The system pressure was held in dynamic equilibrium by controlling the rate of oxygen input and sorption pump exhaust. Mass analysis of the gas discharge was accomplished by sampling a small amount of the gas in the discharge through a controlled leak.

Prior to anodizing, the sample was rf sputter cleaned in 10m Torr of argon for 25 min to remove any oxide present. Ten minutes after initiating the oxygen glow discharge, a fixed bias voltage ($V_b \simeq 5V$) was applied

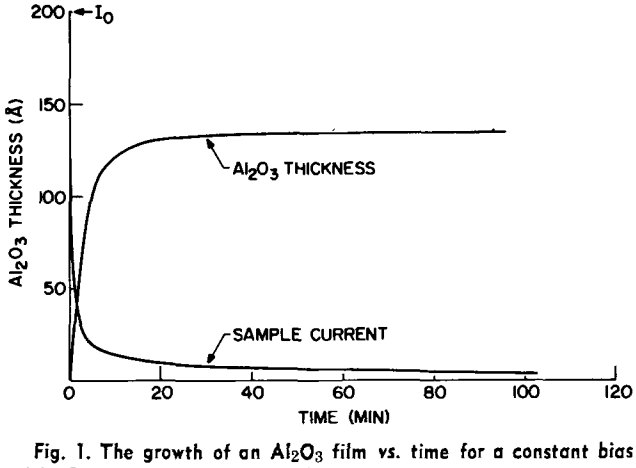

Fig. 1. The growth of an Al_2O_3 film vs. time for a constant bias of 6V [after Miles and Smith (1)].

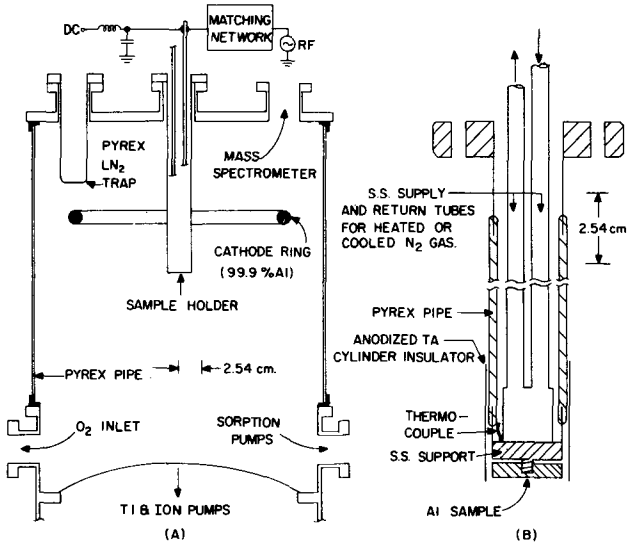

Fig. 2. (*A*) Experimental system used for plasma anodization; (B) Sample holder detail.

* Electrochemical Society Active Member.

Key words: Al_2O_3 growth rate, plasma anodization, oxygen glow discharge.

and the time dependence of the current decay was recorded. The thickness, T, of the Al_2O_3 film grown should be no greater than

$$T \leq (V_b - V_w)K$$

where V_w is the floating potential (−4.5V) and K is the anodization constant (22 Å/V) obtained by Miles and Smith (1) and Tibol and Hull (5) while anodizing to completion at constant voltage in a similar discharge. Thus, these films should be approximately 200Å thick. By successively sputter cleaning and anodizing, all of the data were taken on one sample without breaking the vacuum seal. RF sputter cleaning continually left a mirror smooth surface; however, d-c sputter cleaning was found to leave a rough surface with macroscopic patches of oxide. This is in agreement with Jona (6), who found that rf sputtering was necessary to obtain good LEED patterns on single crystal aluminum surfaces.

The electron density measurements were made with a spherical gold Langmuir probe (r_p = 2 mm). For each probe measurement the electron temperature and saturation electron current at the "knee" of the curve were obtained (see inset, Fig. 6); from these data the electron density of the plasma was obtained. For a weakly electronegative O_2 plasma of this density, the error in estimating the electron density is unlikely to be greater than 40% (7).

Results

Cathode sputtering.—Contamination of the growing oxide by reactively sputtered cathode material (Al_2O_3 in this instance) previously has been shown to increase the thickness of the oxide (8). Two of those observations bear repeating here: First, with the sample a few cm from, and facing the cathode, sputter deposition rates of 2.5 Å/min and higher were recorded. Second, with a sample shielded from the cathode, as in Fig. 1, considerably lower sputter deposition rates were recorded. For the electrode spacings used in this study, the rates were 0.45 to 0.55 Å/min (Al_2O_3) respectively for the 50 mA and 80 mA discharges. Were the sample to be mounted 20 cm below the cathode plane, these deposition rates could be reduced to approx. 0.02 Å/min.

Temperature effects.—In Fig. 3 the effect of substrate temperature at constant pressure on the rate of current decay is illustrated for the range 32°C to 105°C; one observes that the 105°C film formed in one-tenth the time of the 32°C film. The current decay data can be approximately fitted to the sum of two exponentials; an unexplained rapid decay lasting less than 25 sec, followed by a slower temperature dependent decay. An activation energy of 1.8 ± 0.1 eV was obtained for the slower decay which agrees with Charlesby's work on solution anodized aluminum (9), but is higher than the value of 1.3 ± 0.15 eV obtained by Harkness and Young (10) by solution anodization. Since the film thicknesses were not measured, and the anodization constant is temperature dependent, the temperature dependence of the current efficiency could not be obtained.

Some elementary characteristics of the constant current d-c oxygen discharge operating in the range 10m Torr $< P \lesssim$ 150m Torr will be described here. At a suitably low pressure, say 10m Torr, the negative glow is weak and diffuses out from the cathode to fill the volume; good thermal contact exists between the glow and the sample, and the sample temperature, T_s, is high (100°C for the 50 mA discharge). As the pressure is increased toward 150m Torr, less power is required to maintain the discharge current and the negative glow contracts around the cathode, isolating the sample from the source of heat. For these reasons the uncontrolled substrate temperature was found to decrease to 60°C at a pressure of 50m Torr, and 30°C at 150m Torr The strong observed temperature dependence of the growth rate points out the necessity of adequate substrate temperature control while studying the effects of pressure variations on the growth rate.

Pressure effects.—Miles and Smith (1) and Fopiano (3) have observed a pressure dependence in the time required for film growth; both observed a minimum in the time required to form the oxide at pressures of 50 to 60m Torr. These data were taken in systems with a geometry rather like the one used here, that is, a geometry with a large anode to cathode area ratio. These measurements were repeated in this study with similar results. In Fig. 4, the time dependence of the current decay is plotted for three pressures with all other variables held constant. The initial current was maximum, and the current decay time was minimum at a pressure of approx. 110m Torr. From data of this type, one can obtain the relation between the formation time and pressure shown in Fig. 5; the data from this study taken at two discharge currents are shown along with the data of Fopiano (3). For each discharge current studied, a minimum formation time was observed. The minimum for the 50 mA discharge occurred at approximately 50 to 60m Torr, while the minimum for the 80 mA discharge occurred at about 110m Torr.

The effective bias across the oxide is the potential difference between the applied bias voltage and the surface potential of the oxide-plasma interface. In all

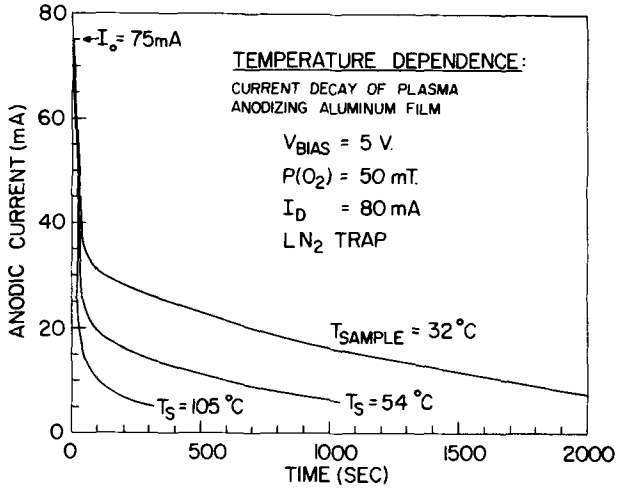

Fig. 3. The temperature dependence of the current decay of a plasma anodizing aluminum film. V_B = 5V, P = 50 mTorr, I_D = 80 mA.

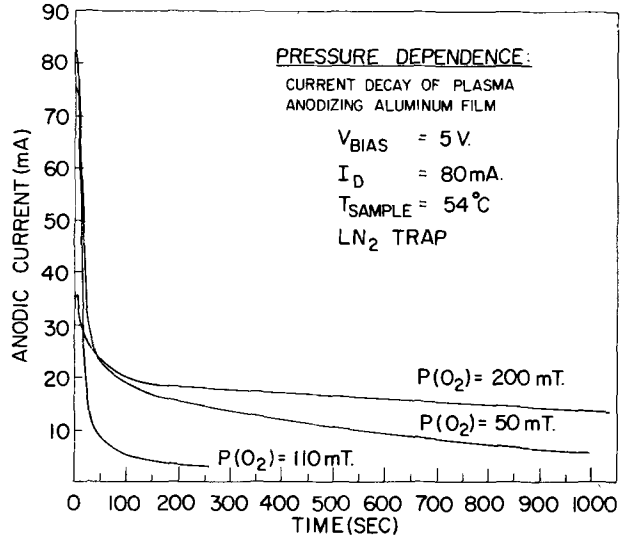

Fig. 4. The pressure dependence of the current decay of a plasma anodizing aluminum film. V_B = 5V, I_D = 80 mA, T_{sample} = 54°C.

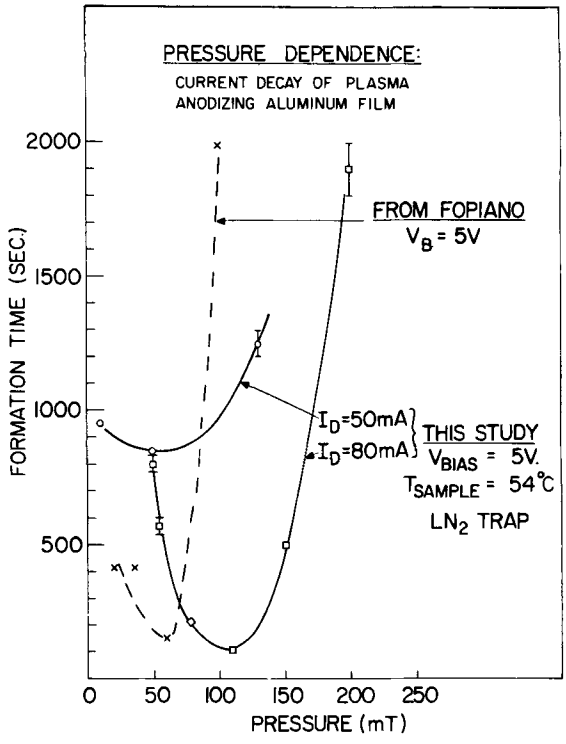

Fig. 5. The pressure dependence of the time of current decay to 10% of initial current. (A) After Fopiano (3). This study for V_B = 5V, T_{sample} = 54°C with (B) I_D = 50 mA, and (C) I_D = 80 mA.

cases the bias voltage was held at +5V, and probe measurements showed the plasma floating potential to be −4.5 ± 0.5V for 10m Torr < $P \lesssim$ 150m Torr. For pressures greater than 150m Torr, the floating potential became very large (−15V at P = 220m Torr) as the negative glow concentrated around the cathode. In this high pressure range the effective bias across the sample is larger and the film is growing to a greater limiting thickness than at pressures less than 150m Torr where the effective bias remained nearly constant; analysis is therefore limited to the pressure range 10 to 150m Torr.

To aid in interpreting the data in Fig. 5, the electron density was measured at the location of the sample with a spherical gold Langmuir probe for the same values of oxygen pressure and discharge current shown is Fig. 5. In Fig. 6 the electron density is seen to have a maximum roughly corresponding to the minimum in anodization time. The variation in electron density may be explained by recalling the discharge characteristics. For low pressures the electron density increases with pressure, but for high pressures where the range of the negative glow becomes less than the cathode-sample distance, the electron density decreases, and the electron temperature increases at the location of the probe. In the abnormal glow, increasing the discharge current causes the negative glow to expand, slightly shifting the peak density to a higher pressure.

The explanation for the minimum anodization time is not obvious. Although the minimum anodization time corresponds to the maximum electron density, the variation in anodization rate with pressure is much greater than the corresponding change in electron density. It was also found that the pressure dependence of the initial value of anodizing current (see Fig. 4) was exactly like the pressure dependence of the saturation electron current (not electron density) of the gold probe, while the total charge passed in forming the film (the area under the I-t curve in Fig. 4) was less for the pressure of most rapid growth, indicating that the current efficiency was greatest for this

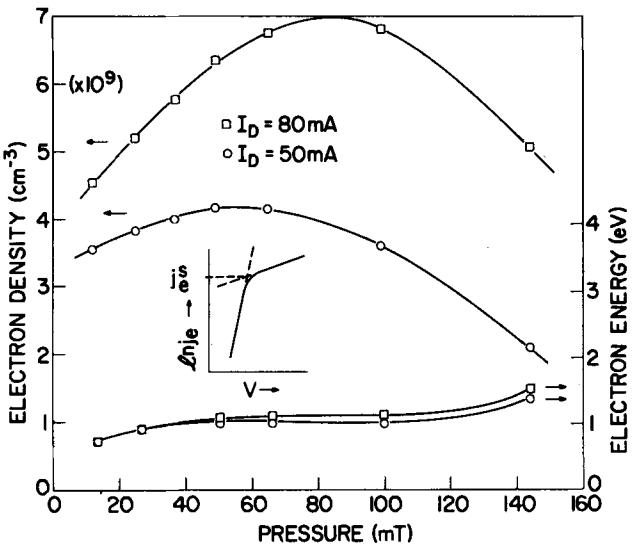

Fig. 6. Electron density vs. pressure and discharge current as measured by a spherical gold Langmuir probe (r_p = 2 mm). The electron density was calculated from the saturation electron current density at the "knee" of the log J_e vs. V curve shown in the inset.

case. These observations imply a large pressure dependence of the negative ion density.

From a practical viewpoint, it is important to know that there exists an optimum pressure for each system of this type which is dependent on the ratio of the negative glow length to the cathode-sample distance; this observation is not valid for cylindrical-confined discharges of equal cathode-anode area.

Water vapor effects.—The effect of water vapor in the glow on the rate of anodization has been observed. In Fig. 7 the current decay for two oxide formation runs at 54°C is illustrated. In one run a liquid nitrogen trap was used, in the second run no liquid nitrogen trap was used, but all other parameters were

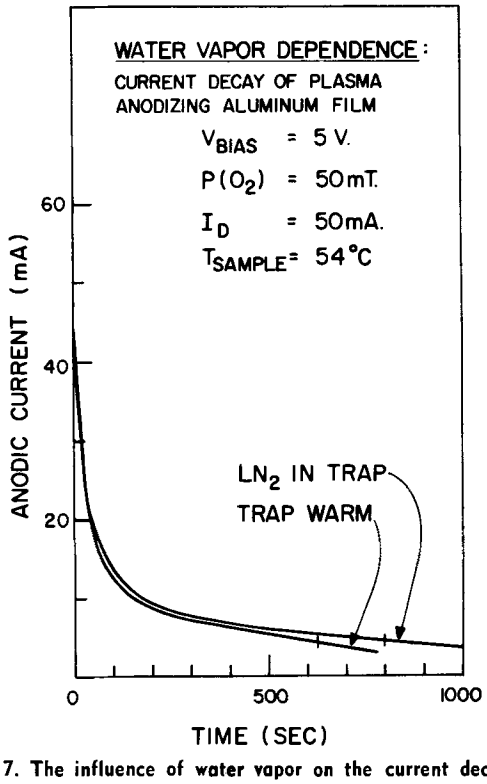

Fig. 7. The influence of water vapor on the current decay of a plasma anodizing aluminum film. V_B = 5V, P = 50 mTorr, I_D = 50 mA, T_s = 54°C.

identical. This second sample anodized about 20% faster.

Mass analysis of the discharge revealed the water vapor pressure to be 10^{-6} Torr, when the auxiliary trap was warm. With the trap cooled to 77°K and locally pumping water vapor, mass analysis in a differentially pumped system is no longer valid. The following experiment demonstrates the effectiveness of the trap in removing water vapor near the sample. When an aluminum sample was cooled to 140°K, the presence of water vapor caused anomalous film growth. To observe this effect, the aluminum sample was anodized at a constant current density of 0.2 mA/cm^2, and a temperature of 140°K; the voltage increased linearly to 5V in 3000 sec. Upon repeating the experiment without use of the auxiliary cold trap, the voltage was observed to rapidly increase to 25V in 2000 sec, implying formation of a very thick film; temperature cycling this second sample to 300°K caused the voltage to drop sharply to 5V, showing that this film was most likely ice. This demonstrates that the cold trap is capable of reducing the water vapor pressure to a lower, unknown value.

Miles and Smith (1) observed that the resistance of tunnel junctions was increased by the presence of water vapor in the discharge and suggested that the aluminum was reacting directly with the water vapor. Such a reaction for very low water vapor concentrations would be in agreement with the more rapid current decay observed here in the formation of thin Al_2O_3 films.

Conclusion

For a given electrode geometry, discharge intensity and sample location, it has been determined that there is an optimum pressure for most rapid anodization. For the parameters used in this study, the optimum pressure occurred between 50 and 100m Torr. It should be emphasized that the particular values of optimum pressure obtained are valid only for this geometry; each similar system will have its own characteristic optimum pressure dependence. Increasing the substrate temperature was also found to increase the current decay rate and probably the oxide thickness for the pressure range studied. Unless the substrate temperature is independently controlled, the substrate will obtain a higher temperature at low pressures where the sample is immersed in the glow. A small increase in the H_2O content of the discharge was found to slightly increase the anodization rate for samples with normal anodization temperatures.

Manuscript submitted May 26, 1970; revised manuscript received *ca.* Oct. 20, 1970.

Any discussion of this paper will appear in a Discussion Section to be published in the December 1971 JOURNAL.

REFERENCES

1. J. L. Miles and P. H. Smith, *This Journal,* **110**, 1240 (1963).
2. T. A. Jennings and W. McNeill, Abstract 23, p. 53, Electrochem. Soc. Extended Abstracts, Spring Meeting, New York, May 4-9, 1969.
3. P. J. Fopiano, *IEEE Trans. Parts, Materials and Packaging,* **PMP-1**, S-217 (1965).
4. T. A. Jennings and W. McNeill, *Appl. Phys. Letters,* **12**, 25 (1968).
5. G. L. Tibol and R. H. Hull, *This Journal,* **111**, 1368 (1964).
6. F. Jona, *J. Phys. Chem. Solids,* **28**, 2155 (1967).
7. R. Boyd and J. B. Thompson, *Proc. Roy. Soc. (London),* **252A**, 102 (1959).
8. J. F. O'Hanlon, *J. Vacuum Sci. Technol.,* **7**, 330 (1970).
9. A. Charlesby, *Proc. Phys. Soc. (London),* **66B**, 317 (1953).
10. A. C. Harkness and L. Young, *Can. J. Chem.,* **94**, 2409 (1966).

Energy Loss and Energy Storage from the Eu^{+3} Charge-Transfer States in Y and La Oxysulfides

W. H. Fonger and C. W. Struck

RCA Laboratories, Princeton, New Jersey 08540

ABSTRACT

In Y_2O_2S:Eu and La_2O_2S:Eu, concentration- and temperature-dependent loss and storage effects are observed for excitation into the Eu^{+3} charge-transfer states (CTS) and into certain Eu^{+3} ^5D states. It is shown that the losses and storage both occur from the CTS. They occur for ^5D excitations only as a consequence of the ^5D excitation having reached the CTS through thermally promoted $^5D \rightarrow$ CTS crossovers. The losses and storage are both attributed to the Eu^{+3} CTS dissociating thermally into Eu^{+2} plus a free hole. The freed holes are stored in hole traps. If the holes are thermally or IR stimulated back to the Eu^{+2} centers and re-form the Eu^{+3} CTS, the stored energy is retrieved as Eu^{+3} line emissions. If the extra electrons at the Eu^{+2} centers migrate through the Eu activators and recombine nonradiatively at the hole centers, the stored energy is lost.

We have recently described transitions that take place between the ^5D and charge-transfer states (CTS) of Eu^{+3} in oxysulfide and oxychloride hosts (1, 2). A configurational-coordinate diagram accounting for these transitions through crossovers was also provided. We now report on energy-loss and energy-storage events that occur from the CTS in oxysulfides. The interplay between these events and $^5D \leftrightarrow$CTS crossovers leads to some interesting luminescence phenomena.

Key words: luminescence, phosphors, rare-earth spectra, concentration quenching, energy transfer.

Configurational-coordinate models with crossover losses to the ground state have been proposed for broad-band luminescence centers by several authors (3). See, for example, their recounting in Blasse and Bril's recent discussion of niobate phosphors (4). However, oxysulfide CTS crossovers to the ground ^7F

multiplet appear to be too high (1, 2) to be significant for losses. Moreover, the oxysulfide losses increase with Eu concentration, whereas the models cited are single-center models and predict losses insensitive to the activator concentration.

For concentration-dependent losses, Dexter and Schulman (5) proposed an ion-ion energy-transfer model. The excitation migrates undegraded through the activator ions until lost at special quenching centers. Many workers in the rare-earth field have emphasized a second energy-transfer model with no special quenching centers. The excitation is degraded in a single transfer of part of the energy to a second activator ion. For example, Van Uitert and Johnson (6) have so interpreted concentration quenching observed from the Sm^{+3} $^4G_{5/2}$, Eu^{+3} $^5D_0$, Tb^{+3} $^5D_3$, Er^{+3} $^4S_{3/2}$, and Nd^{+3} $^4F_{3/2}$ levels.

Van Uitert and Johnson's explanations were directed toward rare-earth losses that occur from emitting 4f levels because they used excitations that efficiently populated these levels. However, if very energetic excitation is used, losses can occur from higher levels. For example, Bril, Blasse, and Bertens (7) have found that most Eu^{+3} phosphors with losses under Hg 254 mμ excitation are very efficient for excitation into the emitting ^5D levels. Riedel (8) similarly found that the dominant losses in Y_2O_3:Eu occur above the ^5D levels.

The work here will show that the oxysulfide losses[1] are of the "higher" variety and, in particular, occur from the short-lived CTS. Although the losses do occur for excitation into certain ^5D states, the work here will show that such losses occur only as a consequence of the ^5D excitation having reached the CTS through thermally promoted $^5D \rightarrow$ CTS crossovers.

With the losses tied to the CTS, the challenge is then to understand their concentration dependence from the short-lived CTS. Insight for this understanding is provided by the more readily interpreted energy-storage effect.

The novel aspect of the oxysulfide storage effect, first discovered by Forest, Cocco, and Hersh (9) in La_2O_2S:Eu, is that it can be induced by excitation into certain ^5D states. One can, under proper conditions, excite into ^5D states with lifetimes less than a millisecond and still induce energy storage for days or weeks. The stored energy is released by thermal or IR stimulation and reappears as normal Eu^{+3} $^5D \rightarrow {}^7F$ line emissions.

The $^5D_2$ state played a special role in the work of Forest *et al.* because they induced storage for $^5D_2$ and higher excitations but not for $^5D_1$ or $^5D_0$ excitation. However, the $^5D_2$ state is incidental to the effect. The work here will show that the storage, like the losses, occurs from the CTS and occurs for ^5D excitations only as a consequence of the ^5D excitation having reached the CTS through thermally promoted $^5D \rightarrow$ CTS crossovers.

The long storage times argue for some spatial separation of electrons and holes. With the losses and storage both tied to the CTS which can be regarded as a hole bound to Eu^{+2}, we believe that both effects commence with thermal dissociation of the CTS into Eu^{+2} plus a free hole. The freed holes become stored in hole traps. The question as to whether the stored energy can be retrieved or is lost then becomes the question as to whether or not the trapped holes can be returned to the Eu^{+2} centers.

Measurements that tie the losses and the storage to the CTS are described in the sections Energy Losses and Energy Storage, and our interpretation of both effects is given in the Discussion section.

[1] In oxysulfides, the Eu^{+3} emissions shift from mixed ^5D emissions at low Eu concentration to mainly $^5D_0$ emissions at high Eu concentration. See J. W. Haynes and J. J. Brown, *J. Electrochem. Soc.*, 115, 1060 (1968). Such shifts are due to excitations in upper ^5D states concentration quenching to $^5D_0$ via Eu-Eu energy transfers of the Van Uitert-Johnson variety. However, since these transfers only redistribute the populations within the ^5D states and do not decrease the total number of $^5D \rightarrow {}^7F$ emissions, they will not be counted as losses here.

Summary of Oxysulfide $^5D \leftrightarrow$ CTS Crossovers

Direct CTS $\rightarrow$ ^5D feeding transitions and inverse $^5D \rightarrow$ CTS quenching transitions were established in ref. (1) and (2). The main results of these references will now be summarized.

Figure 1 of either reference gives the configurational-coordinate diagram showing the ^5D-CTS crossovers. In the feeding direction, the CTS feed all the emitting ^5D states but especially $^5D_2$ and $^5D_1$.

In the quenching direction, excitation in ^5D_j is promoted thermally to the CTS according to the rate constant $A \exp(-E_j/kT)$, where A is $\sim 10^{11}$ sec^{-1} and E_j is the activation energy to the crossover. These upward $^5D_j \rightarrow$ CTS transitions compete with all downward processes from ^5D_j, namely, emission to lower ^5D and ^7F states and relaxation to lower ^5D states via multiphonon emissions and Eu-Eu energy transfers. The rate constant summed over all downward processes is $\sim 10^4$ sec^{-1}. This rate and the rate of upward $^5D_j \rightarrow$ CTS transitions become equal at a temperature T_j approximated by $E_j/kT_j = 17$. Above T_j, $^5D_j \rightarrow$ CTS transitions dominate, and all downward processes fall off sharply. The rate of fall off, determined by the variation of $\exp(E_j/kT)$ near T_j, is about one order per 15% increase in T. Below T_j, downward processes dominate, and $^5D_j \rightarrow$ CTS transitions fall off sharply (about one order per 15% decrease in T).

Table I summarizes, for Y_2O_2S and La_2O_2S, observed and estimated $^5D \rightarrow$ CTS activation energies and the corresponding T_j's. The systematic differences between the two hosts arise because the CTS lie at somewhat higher energy in Y_2O_2S ($\approx$1100 cm^{-1} higher).

Temperature dependences of ^5D emissions described in ref. (2) and temperature dependences of ^5D excitations of storage described in the present paper have mirror-image relationships about the T_j's. Emission from ^5D_j is relatively constant below T_j but falls off sharply above T_j where all downward processes fall off sharply. On the other hand, ^5D_j excitation of storage is relatively constant above T_j but falls off sharply below T_j where $^5D_j \rightarrow$ CTS transitions fall off sharply. These mirror-image relationships will be demonstrated in four figures below.

Experimental

The oxysulfide phosphors were powdered materials prepared under the direction of Dr. P. N. Yocom by the sulfur-carbonate flux method (10). The train for the optical measurements has been described previously (2). ^5D temperature dependences were monitored through prominent lines of each ^5D series. In Fig. 3-6, these dependences were normalized to give the percentages of emitted photons in each ^5D series at 295°K. All slow buildups and decays of luminescence were measured on a recorder with a response time of a few seconds.

The energy stored in a phosphor depends on sample history. For the excitations of storage described in Fig. 8 through 12, traps were emptied prior to each excitation either thermally or optically.[2]

[2] Light from a tungsten lamp through a Corning 3-70 filter, that is, tungsten light above 500 mμ.

Table I. Activation energies E_j from the Eu^{+3} ^5D states to the CTS in oxysulfides. Temperatures T_j at which E_j/kT_j is 17 are also given

State	E_j, cm^{-1}		T_j, °K	
	Y_2O_2S	La_2O_2S	Y_2O_2S	La_2O_2S
$^5D_3$	2100	1100	180	90
$^5D_2$	4400	3000	370	250
$^5D_1$	$\approx$6600	5100	$\approx$560	430
$^5D_0$	>8000	$\approx$6500	>640[a]	$\approx$520[a]

[a] Used $E_0/kT_0 = 18$ because of the longer $^5D_0$ lifetime for downward processes.

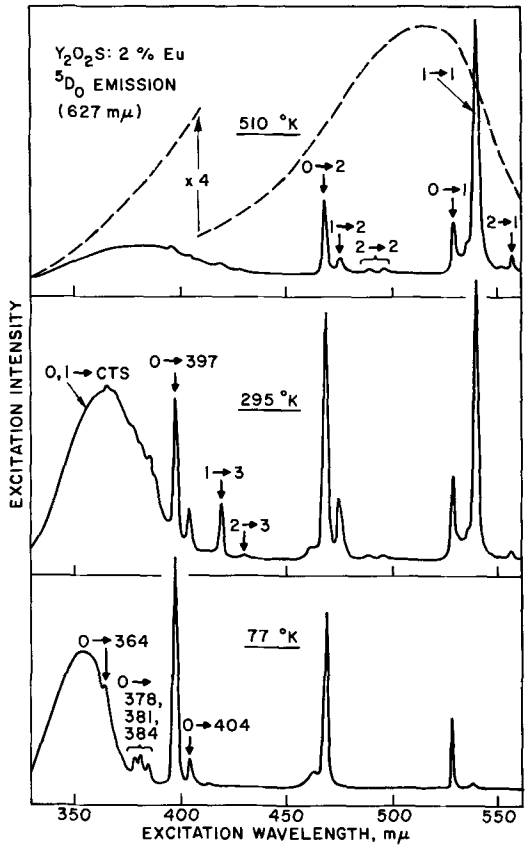

Fig. 1. Excitation spectra (uncorrected) of the $^5D_0$ emissions of Y_2O_2S:2% Eu. The dotted curve gives the distribution of the excitation source (tungsten lamp plus $CuSO_4$ solution plus monochromator) as determined with the quantum counter liumogen. Excitation $^7F_i \rightarrow {}^5D_j$ is labeled i → j. The 4f states above $^5D_3$ are indexed by their absorption wavelengths (mμ) from $^7F_0$. The broad excitation band is $^7F_{0,1}$ → CTS excitation. The shift of the long-wavelength end of this excitation band from 380 mμ at 77°K to 430 mμ at 510°K is temperature broadening due to the large Franck-Condon shift between the CTS and ^7F states. See Appendix of ref. (1).

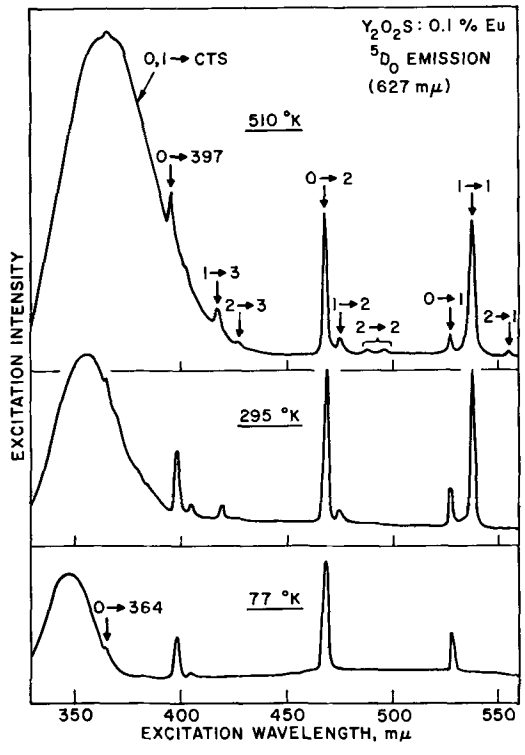

Fig. 2. Excitation spectra of Y_2O_2S:0.1% Eu. See caption of Fig. 1 for conditions and notation. Detector gain was higher than in Fig. 1 but was fixed for all three spectra in each figure.

Energy Losses

It was shown in ref. (2) that Y_2O_2S:0.1% Eu was efficient up to 520°K but that Y_2O_2S:2% Eu developed losses under CTS excitation above ~350°K. The main differences between 0.1 and 2% materials are shown by the excitation spectra in Fig. 1 and 2. The 0.1% material is efficient at all temperatures shown.[3] However, the 2% material shows, at 510°K, inefficient excitation into the CTS [4] and into all 4f states above $^5D_1$.

Figure 3 shows, for the 2% material, detailed temperature dependences of the $^5D_1$ and $^5D_0$ emissions for both CTS and $^5D_1$ excitation. The losses shown above ~350°K for CTS excitation do not occur for $^5D_1$ excitation up to at least 520°K. Thus, the losses do not occur from $^5D_1$ or $^5D_0$. Their absence for $^5D_1$ excitation is consistent with the losses occurring from the CTS because $^5D_1$ excitation is not thermally promoted to the CTS below the 560°K T_1 temperature cited for Y_2O_2S in Table I.

The intermediate case of $^5D_2$ excitation is shown in Fig. 4. The strong decrease in the $^5D_2$ emission above 370°K is due not to losses but to $^5D_2$ emptying thermally to the CTS; see the Y_2O_2S T_2 temperature cited in Table I. [The thermal quenching of these $^5D_2$ emissions and of the La_2O_2S $^5D_0$ and $^5D_1$ emissions shown in Fig. 5 and 6, respectively, complement the ^5D thermal quenching data shown in ref. (2) and (11). These quenchings have been analyzed in the manner of ref. (2). The three dotted projections in Fig. 4-6 show these three ^5D emissions as estimated for no ^5D emptying to the CTS, and the corresponding crosses (×) show, as in ref. (2), the good fit of thermal quenching theory to the observed quenchings. The empirical ^5D-to-CTS activation energies used to fit

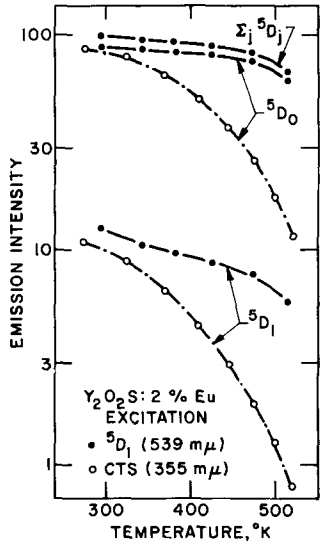

Fig. 3. Temperature dependences of the $^5D_1$ and $^5D_0$ emissions of Y_2O_2S:2% Eu for $^5D_1$ and CTS excitation. These dependences are given for constant excitation intensity. For $^5D_1$ excitation, the excitation was assumed proportional to the temperature-dependent population of $^7F_1$, the initial state for 539 mμ excitation. For CTS excitation, no correction was necessary: the excitation wavelength was selected such that $^7F_{0,1}$ → CTS excitation was insensitive to temperature, as was evidenced by the temperature-insensitive total $^5D \rightarrow {}^7F$ emission observed for low Eu concentrations where losses were small.

[3] In the 0.1% material, excitations to 4f states above $^5D_2$ appear to be weak at 77°K. This is due not to losses but to the monitored $^5D_0$ emissions being smaller relative to total ^5D emissions for these 77°K excitations. See ref. (1).

[4] The broad F → CTS excitation bands in Fig. 1 and 2 were distorted by the excitation source used (spectral distribution given by dotted curve in Fig. 1). This distortion plus temperature broadening of the CTS absorption caused the observed CTS bands to shift progressively with temperature to greater wavelength and amplitude. The corrected CTS excitations peak near 330 mμ.

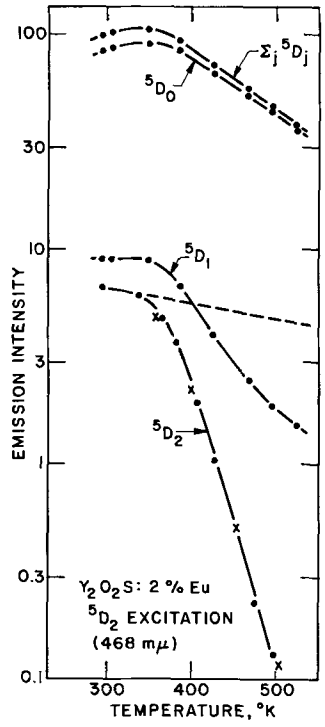

Fig. 4. Temperature dependences of the ^5D emissions of Y_2O_2S: 2% Eu for $^7F_0 \rightarrow {}^5D_2$ excitation. Correction was made for the thermal population of $^7F_0$.

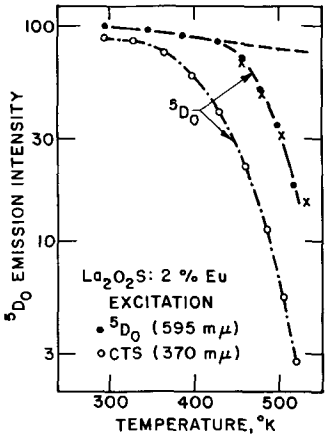

Fig. 5. Temperature dependences of the $^5D_0$ emissions of La_2O_2S: 2% Eu for $^5D_0$ and CTS excitation. For $^5D_0$ excitation, correction was made for the thermal population of the initial $^7F_1$ state.

these data were 4400 cm^{-1} for Y_2O_2S $^5D_2$ and 6300 and 5000 cm^{-1} for La_2O_2S $^5D_0$ and $^5D_1$, respectively. These values have already been quoted in Table II of ref. (2).] The decreases in the $^5D_1$ and $^5D_0$ emissions above 370°K are due to losses. When $^5D_2$ empties to the CTS, feeding of $^5D_1$ and $^5D_0$ is revised from $^5D_2 \rightarrow {}^5D_1$, $^5D_0$ to the chain $^5D_2 \rightarrow$ CTS $\rightarrow {}^5D_1$, $^5D_0$. Since the losses are known not to occur from $^5D_1$ or $^5D_0$, they occur from either $^5D_2$ or the CTS. However, since their 370°K onset coincides with $^5D_2$ emptying to the CTS, it is reasonable to conclude that they occur from the CTS.

With respect to excitation into 4f states above $^5D_2$, it was noted in connection with Fig. 1 and 2 that such excitations, while efficient at 295°K, are, in 2% material, inefficient at 510°K. Above 180°K, all of these excitations reach the CTS via thermally promoted $^5D_2 \rightarrow$ CTS crossovers. Thus, these observations too are consistent with losses developing from the CTS in 2% material above 350°K.

For Eu in La_2O_2S host, Wickersheim, Buchanan, and Yates (11) showed that 0.1% material was efficient

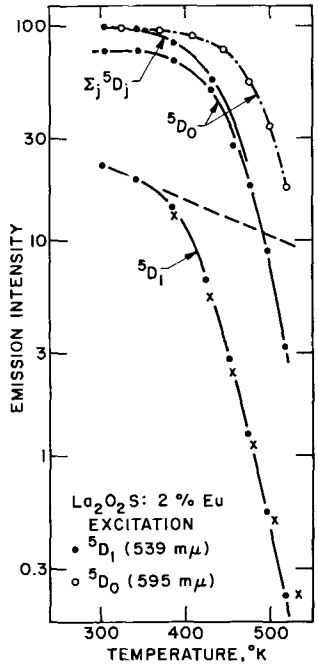

Fig. 6. Temperature dependences of the ^5D emissions of La_2O_2S: 2% Eu for $^7F_1 \rightarrow {}^5D_1$ and $^7F_1 \rightarrow {}^5D_0$ excitation. Correction was made for the thermal population of $^7F_1$.

under CTS excitation up to 530°K, but we (2) showed that 2% material developed losses above ~350°K. Temperature dependences of the dominant $^5D_0$ emissions of the 2% material are shown in Fig. 5 for both CTS and $^5D_0$ excitation. The losses shown above ~350°K for CTS excitation are deferred to ~500°K for $^5D_0$ excitation. Thus, these losses do not occur from $^5D_0$. As cited in Table I, La_2O_2S $^5D_0$ excitation tries to empty thermally to the CTS near 520°K. If the CTS is free of losses (0.1% material), the excitation is returned to $^5D_0$ by reverse CTS $\rightarrow {}^5D_0$ crossovers, and the $^5D_0$ emissions do not decrease. If losses do occur from the CTS (2% material), the excitation is not returned to $^5D_0$, and the $^5D_0$ emissions do decrease.

The intermediate case of $^5D_1$ excitation is shown in Fig. 6 together with a repeat of $^5D_0$ excitation. The strong decrease of the $^5D_1$ emissions above 430°K is due to $^5D_1$ emptying thermally to the CTS; note the La_2O_2S T_1 temperature cited in Table I. The decrease in the $^5D_0$ emissions above 430°K is due to losses. When $^5D_1$ empties to the CTS, $^5D_1 \rightarrow {}^5D_0$ feeding is revised to the chain $^5D_1 \rightarrow$ CTS $\rightarrow {}^5D_0$. Since for $^5D_1$ excitation the onset of the losses is advanced to 430°K and there coincides with the onset of $^5D_1$ emptying to the CTS, one again infers that the losses occur from the CTS.

For $^5D_2$ excitation of 2% material (not shown), the onset of losses is further advanced to ~350°K and there coincides with the onset of losses for CTS excitation. This is to be expected if the losses occur from the CTS since, as noted in Table I, La_2O_2S $^5D_2$ empties thermally to the CTS below the ~350°K temperature at which losses develop.

In summary, losses are small at low Eu concentration in both Y_2O_2S and La_2O_2S. However, at 2% Eu concentration, losses develop above ~350°K for CTS excitation and also for ^5D excitations that empty thermally to the CTS by 350°K. For Y_2O_2S, the onset of losses is deferred to 370°K for $^5D_2$ excitation and to above 520°K for $^5D_1$ or $^5D_0$ excitation. For La_2O_2S, the onset is deferred to 430°K for $^5D_1$ excitation and to 520°K for $^5D_0$ excitation. These deferred onsets are just those required for the excitations in question to empty thermally to the CTS. We conclude that the losses occur from the CTS and occur for ^5D excitations only as a consequence of the excitation having reached the CTS through thermally promoted $^5D \rightarrow$ CTS crossovers.

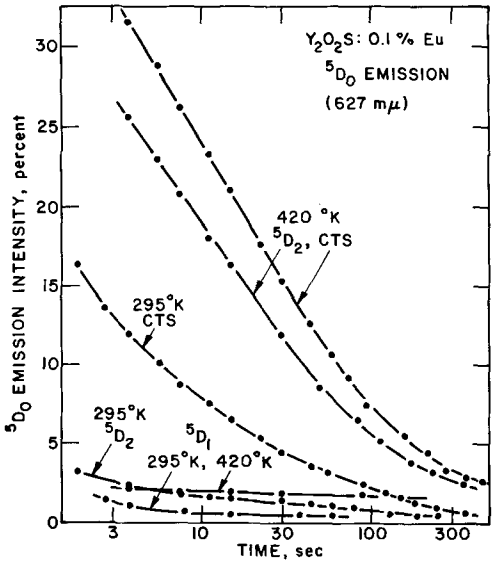

Fig. 7. $^5D_0$ phosphorescence of Y_2O_2S:0.1% Eu after CTS (355 mμ), $^5D_2$ (468 mμ), and $^5D_1$ (539 mμ) excitations at 295° and 420°K. The phosphorescence is given as a per cent of the steady-state $^5D_0$ emission during excitation.

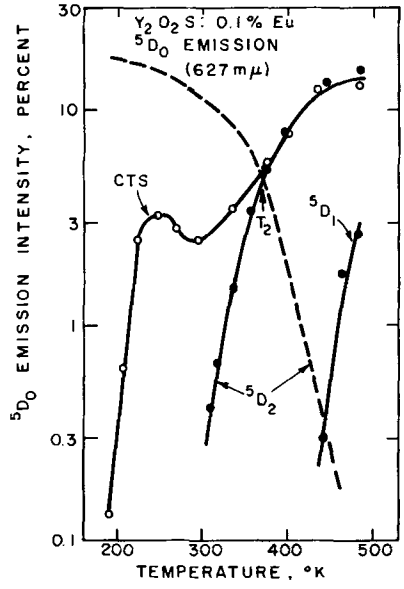

Fig. 8. $^5D_0$ phosphorescence (as per cent of steady-state emission) of Y_2O_2S:0.1% Eu 15 sec after CTS, $^5D_2$, and $^5D_1$ excitations. The dotted curve shows the mirror-image steady-state $^5D_2$ emissions as traced from Fig. 3 of ref. (2). Corresponding phosphorescence per cents are smaller here than in Fig. 7 for two reasons: first, higher excitation intensity was used in Fig. 8, and the ratio of phosphorescence to steady-state emission decreased slightly with increasing excitation intensity; second, the phosphor was annealed at 500°K before each excitation in Fig. 8 but was not annealed in Fig. 7.

Energy Storage

The oxysulfide energy-storage effect was first discovered by Forest, Cocco, and Hersh (9) in La_2O_2S. They excited into $^5D_2$ at a low-temperature T_E and, on heating the phosphor, found that stored energy was released as a glow peak near 270°K. The glow was normal Eu^{+3} $^5D \rightarrow {}^7F$ line emissions. Although small for T_E below 200°K, the glow increased strongly as T_E was raised from 200° to 250°K. At 250°K, excitation into any state above $^5D_2$ (*e.g.*, $^5D_3$, the 4f state at 397 mμ, the CTS) also induced the storage, but excitation into $^5D_1$ below $^5D_2$ did not.

We describe experiments here which show that the storage is induced from the CTS and occurs for ^5D excitations only as a consequence of thermally promoted $^5D \rightarrow$ CTS crossovers. The experiments of Forest *et al.* can be explained this way. As noted in Table I, T_2 for La_2O_2S is 250°K. Below 250°K, $^5D_2 \rightarrow$ CTS crossovers fall off sharply, and $^5D_2$ excitation cannot reach the CTS. Moreover, at 250°K, excitation into any 4f state above $^5D_2$ empties thermally to the CTS, but excitation into $^5D_1$ below $^5D_2$ does not.

The energy-storage effect manifests itself through the slow buildup and decay of luminescence and through thermally or IR stimulated glow peaks. We discovered the effect independently in the course of establishing oxysulfide $^5D \leftrightarrow$ CTS transitions (1, 2). It was found that the resolution of the Y_2O_2S:0.1% Eu $^7F_0 \rightarrow {}^5D_2$ excitation line (468 mμ) was lost above 370°K. This was determined to be due to the slow buildup and decay of Eu^{+3} luminescence during the excitation sweep through this line.[5] Since we knew that Y_2O_2S $^5D_2$ empties to the CTS above 370°K, we suspected from the start that the storage occurs from the CTS.

Slow decays of Y_2O_2S:Eu luminescence at 295° and 420°K are shown in Fig. 7. For CTS excitation, the phosphorescence is strong at both temperatures. However, for $^5D_2$ excitation, it is strong only at the higher temperature, and, for $^5D_1$ excitation, it is weak at both temperatures.

Detailed temperature dependences of the 15-sec phosphorescence (emission 15 sec after termination of the excitation) are shown in Fig. 8. For CTS excitation, the phosphorescence is strong at every temperature above 220°K. However, for $^5D_2$ excitation, strong phosphorescence is deferred to above 370°K, and, for $^5D_1$ excitation, it is further deferred to the highest temperatures studied. The dotted curve shows the temperature dependence of the steady-state $^5D_2$ emissions as traced from Fig. 3 of ref. (2). This curve was normalized to intersect the $^5D_2$-excitation-of-phosphorescence curve at 370°K, the Y_2O_2S T_2 temperature cited in Table I. These two intersecting curves are, for $^5D_2$, the mirror-image emission and excitation-of-storage curves discussed in the section on Summary of Oxysulfide $^5D \leftrightarrow$ CTS Crossovers. The corresponding intersection of mirror-image $^5D_1$ curves is estimated to lie beyond the temperature range studied near $T_1 = 560$°K.

Analogous temperature dependences of La_2O_2S:Eu 30-sec phosphorescence are shown in Fig. 9. Again, for CTS excitation, the phosphorescence is strong at every temperature above 220°K. However, in agreement with the lower T_j temperatures for La_2O_2S, the onset of strong phosphorescence is deferred to only 250°K for $^5D_2$ excitation and to only 430°K for $^5D_1$ excitation. The two dotted curves show the temperature dependences of the steady-state $^5D_2$ and $^5D_1$ emissions. These curves were traced from Fig. 8 of ref. (2) and were independently normalized to intersect their corresponding excitation-of-phosphorescence curves at the La_2O_2S T_2 and T_1 temperatures cited in Table I. These two pairs of intersecting curves are, for $^5D_2$ and $^5D_1$, the mirror-image emission and excitation-of-storage curves discussed in the section on Summary of Oxysulfide $^5D \leftrightarrow$ CTS Crossovers.

In summary, in both Y_2O_2S and La_2O_2S, ^5D excitations of phosphorescence are consistently deferred to the T_j temperatures at which the ^5D excitations empty strongly to the CTS. We conclude that the phosphorescence is induced from the CTS and occurs for ^5D excitations only as a consequence of thermally promoted $^5D \rightarrow$ CTS crossovers.

Our Y_2O_2S:0.1% Eu material had strong glow peaks near 240° and 470°K. Indeed, the existence of these strong peaks was already indicated by the 240° and 470°K maxima in the CTS-excitation-of-phosphores-

[5] Indeed, the 510°K excitation spectrum shown in Fig. 2 was taken at the slow scan rate of 100 mμ/hr so that the excitation would approximate steady-state intensity.

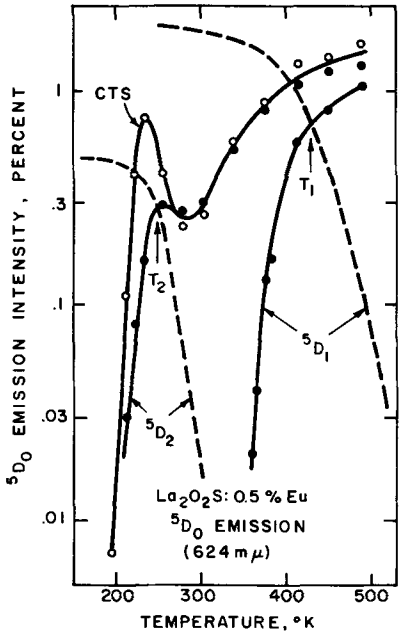

Fig. 9. $^5D_0$ phosphorescence of La_2O_2S:0.5% Eu 30 sec after CTS, $^5D_2$, and $^5D_1$ excitations. The dotted curves show mirror-image steady-state $^5D_2$ and $^5D_1$ emissions as traced from Fig. 8 of ref. (2).

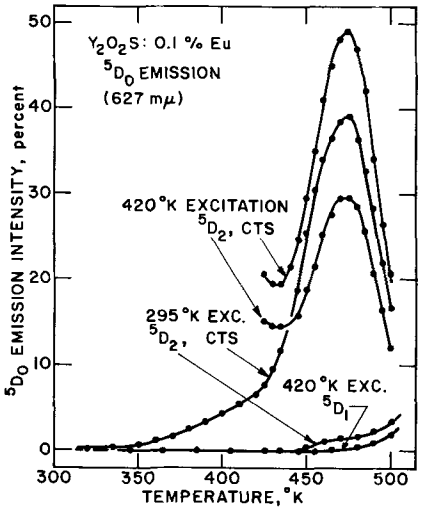

Fig. 10. Thermally stimulated $^5D_0$ glow of Y_2O_2S:0.1% Eu following 10-min CTS, $^5D_2$, and $^5D_1$ excitations at 295° and 420°K. The glow is given as a per cent of the steady-state $^5D_0$ emission during excitation. The heating rate was 6°C/min.

cence curve in Fig. 8. The 470°K glow peak is shown in Fig. 10 for excitations at 295° and 420°K. For CTS excitation, the glow peak is strong for both excitation temperatures. However, for $^5D_2$ excitation, it is strong only for the higher temperature excitation, and, for $^5D_1$ excitation, it is weak for both excitation temperatures.

Detailed temperature dependences of excitations of both glow peaks are shown in Fig. 11. The curves below 300°K give the area under the 240°K glow peak as a function of excitation temperature. This area was integrated from the excitation temperature to 315°K. The integration included whatever phosphorescence followed excitation but did not include phosphorescence during excitation. The curves above 300°K give the analogous area under the 470°K glow peak integrated to 495°K.

For CTS excitation, the glow areas are large for every excitation temperature above ~150°K. However, $^5D_2$ excitation of the 240°K glow peak is always weak, and strong $^5D_2$ excitation of the 470°K glow peak is deferred to above 370°K. The dotted curve shows the

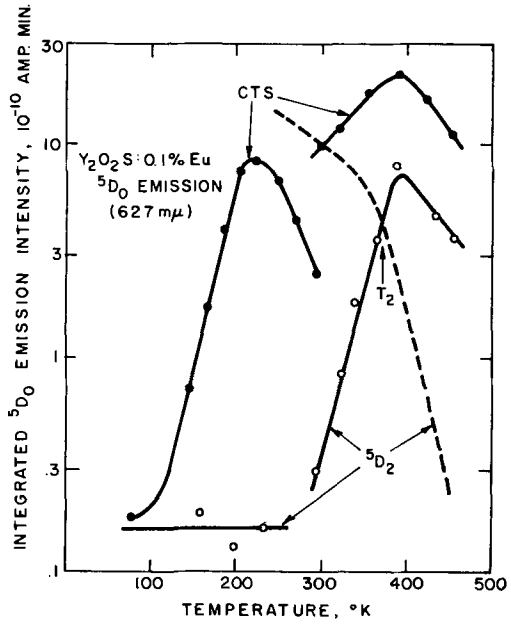

Fig. 11. $^5D_0$ glow areas for the Y_2O_2S:0.1% Eu glow peaks near 250°K (curves below 300°K) and near 470°K (curves above 300°K). The glows followed 5-min CTS and $^5D_2$ excitations at abscissa temperature. The areas are given in arbitrary units (photomultiplier output current × time). The dotted curve shows the mirror-image steady-state $^5D_2$ emissions as in Fig. 8.

mirror-image steady-state $^5D_2$ emissions as traced from Fig. 3 of ref. (2) and normalized to intersect the $^5D_2$-excitation-of-glow curve at Y_2O_2S T_2.

Detailed temperature dependences of $^5D_1$ excitations of glow were not measured. However, it was shown in Fig. 10 that $^5D_1$ does not excite the 470°K glow peak up to at least 420°K. This is consistent with the high Y_2O_2S T_1 temperature.

Our La_2O_2S:0.5% Eu material had strong glow peaks near 250° and 380°K. Excitations of the 250°K glow peak are shown in Fig. 12. In this case, the stored energy was retrieved by IR stimulation rather than heating.

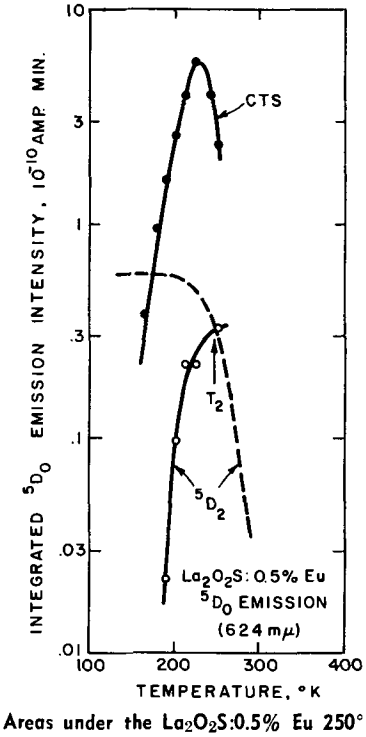

Fig. 12. Areas under the La_2O_2S:0.5% Eu 250°K glow peak following 10-min CTS and $^5D_2$ excitations at abscissa temperature. The dotted curve shows the mirror-image steady-state $^5D_2$ emissions as in Fig. 9.

Following excitation and a brief period of phosphorescence, the IR intensity[6] was increased slowly to give an IR-stimulated glow peak of convenient shape. The curves give the area under the IR-stimulated glow plus the phosphorescence as a function of the excitation temperature.

For CTS excitation, the glow area is, as for Y_2O_2S host, large for every excitation temperature above ~150°K. However, in agreement with the lower La_2O_2S T_2 temperature, the onset of strong $^5D_2$ excitation of the glow is deferred only slightly to ~200°K. The rapid increase of glow for $^5D_2$ excitations above 200°K is analogous to that reported by Forest *et al.* (9) for their La_2O_2S 270°K glow peak. The dotted curve shows the mirror-image steady-state $^5D_2$ emissions as traced from Fig. 8 of ref. (2) and normalized to intersect the $^5D_2$-excitation-of-glow curve at La_2O_2S T_2.

The 380°K glow peak of our La_2O_2S:0.5% Eu material was, at 295°K, strongly excited by CTS and $^5D_2$ excitation but not by $^5D_1$ excitation.

In summary, in both Y_2O_2S and La_2O_2S, ^5D excitations of glow peaks are consistently deferred to the T_j temperatures at which the ^5D excitations empty strongly to the CTS. We conclude that the glow peaks are induced from the CTS and occur for ^5D excitations only as a consequence of thermally promoted $^5D \rightarrow$ CTS crossovers.

Discussion

^5D excitations of energy loss and storage have been successfully explained as consequences of the excitation having reached the CTS through thermally promoted $^5D \rightarrow$ CTS crossovers. This simple explanation of complex loss and storage data gives additional support to oxysulfide $^5D \leftrightarrow$ CTS crossovers. However, we regard these crossovers as already well established (1, 2). Moreover, this particular support was already cited (2) in the work establishing $^5D \leftrightarrow$ CTS crossovers. We turn now to a newer topic, namely, explanation of the losses and storage from the CTS.

The long storage times of the storage effect argue for some spatial separation of electrons and holes. Now the CTS can be regarded as a hole bound to Eu^{+2}. We believe that storage commences with thermal dissociation of the CTS into Eu^{+2} plus a free hole. This CTS dissociation competes with CTS feeding of the ^5D states (CTS $\rightarrow$ ^5D crossovers) which would lead to $^5D \rightarrow {}^7F$ line emissions. The freed holes are trapped in hole traps. After a storage time, thermal or IR stimulation refrees the holes and enables them to return to Eu^{+2} sites. The CTS is re-formed, and CTS $\rightarrow$ ^5D feeding can ensue.

Once the holes are trapped, the effect has analogies to a CaF_2 storage effect studied by Merz and Pershan (12). Their storage was induced by irradiating CaF_2:Re^{+3} with x-rays. The stored energy was released by heating and appeared as glow peaks of Re^{+3} line emissions. The temperatures of the glow peaks were independent of the particular Re activator. The x-ray irradiation induced optical absorption bands that were attributed to Re^{+2}, and these bands disappeared as the glow peaks were annealed out. The following interpretation was given: the x-rays generate free electrons and holes; the electrons are trapped at Re^{+3} centers and reduce them to Re^{+2}; the holes are trapped at hole centers characteristic of the host; heating makes the hole centers mobile; Re^{+2} and a mobile hole center combine to form an excited Re^{+3} center; and relaxation of the excited Re^{+3} leads to the observed Re^{+3} glow. The effect was also observed for SrF_2 and BaF_2 host, and details of the hole centers were elucidated through EPR (13).

In our oxysulfide case, the Re is Eu, and the excited Re^{+3} center is, initially, the Eu^{+3} CTS and, after a crossover, a Eu^{+3} ^5D state. The identities of the hole traps are not known. The multiple glow peaks show that more than one type of hole trap is present.

Forest, Cocco, and Hersh (9) have also considered explanations of the storage effect in La_2O_2S. Although their experiments did not show that the storage occurred from the CTS, one of their explanations is equivalent to the model just given. The first written descriptions of this model, both by Forest and by ourselves, may be found in the discussions at the end of ref. (1).

We turn now to the concentration-dependent losses from the CTS. It is known from studies of ^5D thermal quenching that the lifetime of the CTS against crossovers to the ^5D states is about 10^{-11} sec (2). Thus, it is hard to suggest a Eu-Eu effect that would be fast enough to account for concentration-dependent losses from the CTS. However, this difficulty is overcome if the separation of charges argued in the storage effect also occurs for the loss effect. We believe that the losses similarly commence with thermal dissociation of the CTS into Eu^{+2} plus a free hole. The extra electron bound at the Eu^{+2} center has, at room temperature, a lifetime against thermal detrapping of weeks or greater. More time is thus available for concentration-dependent Eu-Eu effects.

The freed holes are again stored in hole traps as in the storage effect. At low Eu concentrations, the extra electrons remain immobilized at the originating Eu^{+2} centers, and the stored energy can be retrieved by stimulating the holes back to these Eu^{+2} centers (storage effect). At high Eu concentrations and temperatures, the extra electrons can migrate through the Eu ions to the hole centers and recombine there nonradiatively (loss effect). This explanation is offered with no definite picture of the terminating loss process. However, it must differ chemically from free-hole capture at Eu^{+2} which leads to Eu^{+3} line emission.

Thus, storage and loss are viewed as complementary effects which are emphasized at low and high Eu concentrations, respectively. This picture for concentration-dependent losses differs from conventional energy-transfer models in that charges as well as energy are transported.

According to the model given, dissociations of the CTS, in themselves, reduce the Eu emissions. On the other hand, re-formations of the CTS (driven by Eu^{+2} and free-hole concentrations) increase the Eu emissions. Thus, when excitation is applied, steady-state Eu emission can be realized only after these opposing CTS dissociations and re-formations come to equilibrium. Emission transients observed prior to steady state and their interpretation will be described elsewhere (14). However, the emissions described in the section on Energy Losses are steady-state emissions, and any reductions in these emissions must be ascribed to losses, not storage.

The activation energy for dissociation of the CTS is near 1100 cm^{-1} in both Y_2O_2S and La_2O_2S. Detailed measurements showing this value will be reported elsewhere (14). This activation energy prevents dissociation of the CTS at 77°K and leads to the temperature onset for CTS excitation of glow near 150°K cited for both Y_2O_2S (Fig. 11) and La_2O_2S (Fig. 12). CTS excitation of phosphorescence was deferred to $\approx$ 200°K for both hosts (Fig. 8 and 9). These deferred onsets for phosphorescence are attributed to low concentrations of hole traps that empty between 150° and 200°K.

Our La_2O_2S:0.5% Eu had a weak background absorption that also induced storage retrievable as Eu^{+3} line emissions. This absorption extended from 300 to 500 mμ (that is, overlapped the CTS absorption band) and induced storage across a broad temperature range down to at least 77°K. Effects due to this background absorption were subtracted out of the La_2O_2S excitation-of-glow data shown in Fig. 12. With this subtraction, there was no CTS excitation of storage at 77°K. In all other figures, effects due to such background

[6] The IR stimulation was light from a tungsten lamp through a Wratten 87C filter, that is, tungsten light above 850 mμ.

absorptions were negligible compared to the larger effects due to CTS and ^5D excitations.

Although the Forest, Cocco, and Hersh paper (9) is somewhat unclear on this point, they agree (15) that there is no CTS excitation of storage in La_2O_2S at 77°K.

Conclusions

Energy losses and energy storage occur from the Eu^{+3} CTS in Y_2O_2S and La_2O_2S. Both effects also occur for excitation into certain ^5D states but only as a consequence of the excitation having reached the CTS through thermally promoted $^5D \rightarrow$ CTS crossovers. Both effects begin with thermal dissociation of the Eu^{+3} CTS into Eu^{+2} plus a free hole. The holes are stored in hole traps. The stored energy is retrieved as Eu^{+3} $^5D \rightarrow {}^7F$ glow peaks if the holes are stimulated back to the Eu^{+2} centers by thermal or IR stimulation. At high Eu concentrations and temperatures, the extra electrons at the Eu^{+2} centers can migrate through the Eu ions and recombine nonradiatively at the hole centers.

Acknowledgments

We thank Dr. P. N. Yocom for synthesis of the phosphors and Dr. H. Forest for a preprint of the Forest, Cocco, and Hersh paper (9) on storage in La_2O_2S:Eu.

Manuscript submitted May 25, 1970; revised manuscript received *ca.* Sept. 21, 1970. This was Paper 39 presented at the Los Angeles Meeting of the Society, May 10-15, 1970.

Any discussion of this paper will appear in a Discussion Section to be published in the December 1971 JOURNAL.

REFERENCES

1. C. W. Struck and W. H. Fonger, *Bull. Am. Phys. Soc.*, **14**, 868 (1969); *J. Luminescence*, **1, 2**, 456 (1970).
2. W. H. Fonger and C. W. Struck, *J. Chem. Phys.*, **52**, 6364 (1970).
3. R. W. Gurney and N. F. Mott, *Trans. Faraday Soc.*, **35**, 69 (1939); F. Seitz, *ibid.*, **35**, 79 (1939); D. L. Dexter, C. C. Klick, and G. A. Russell, *Phys. Rev.*, **100**, 603 (1955).
4. G. Blasse and A. Bril, *This Journal*, **115**, 1067 (1968).
5. D. L. Dexter and J. H. Schulman, *J. Chem. Phys.*, **22**, 1063 (1954).
6. L. G. Van Uitert and L. F. Johnson, *ibid.*, **44**, 3514 (1966).
7. A. Bril, G. Blasse, and J. A. A. Bertens, *This Journal*, **115**, 395 (1968).
8. E. P. Riedel, *J. Luminescence*, **1, 2**, 176 (1969).
9. H. Forest, A. Cocco, and H. Hersh, Paper RNP 300 presented at the Boston Meeting of the Society, May 5-9, 1968; *J. Luminescence*, **3**, 25 (1970).
10. M. R. Royce, A. L. Smith, S. M. Thomsen, and P. N. Yocom, in "Extended Abstracts of Electronics Division, The Electrochemical Society, Inc., Spring Meeting, New York, 1969," p. 201, The Electrochemical Society, New York (1969).
11. K. A. Wickersheim, R. A. Buchanan, and E. C. Yates, in "Proceedings of the Seventh Rare Earth Research Conference, Coronado, Calif., 1968," p. 835.
12. J. L. Merz and P. S. Pershan, in "Optical Properties of Ions in Crystals," p. 117, H. M. Crosswhite and H. W. Moos, Editors, John Wiley & Sons, New York (1967); *Phys. Rev.*, **162**, 217 (1967); *Phys. Rev.*, **162**, 235 (1967).
13. A. Tzalmona and P. S. Pershan, *Phys. Rev.*, **182**, 906 (1969).
14. C. W. Struck and W. H. Fonger, To be published.
15. H. Forest, Private communication (1970).

Low-Temperature Reduction of Fast Surface States Associated with Thermally Oxidized Silicon

P. L. Castro* and B. E. Deal*

Research and Development Laboratory, Fairchild Camera and Instrument Corporation, Palo Alto, California 94304

ABSTRACT

The effects on fast surface states associated with SiO_2-Si structures due to anneals in nitrogen and hydrogen-nitrogen ambients in the temperature range 300°-550°C are compared with similar anneals of Al-SiO_2-Si structures. Results are reported in terms of capacitance-voltage characteristics and surface recombination velocity values. Although the hydrogen-nitrogen ambients are found effective in the 400°-450°C range for reduction of states in the nonmetallized structures ($s_o \approx 5$ cm/sec for (111) p-type silicon), the final densities are not as low as those found for the structures involving aluminum field plates ($s_o \approx 2$ cm/sec). The role of hydrogen in the reduction of fast surface states is discussed.

During the past two decades much work has been directed toward understanding the behavior of the various surface charges associated with the silicon-silicon dioxide interface (1-3). The use of silicon dioxide for passivation and also as part of circuit components in the bipolar and MOS technologies has resulted in the necessity of understanding the relationship between these surface charges and the processing of the units. Only with this knowledge can the processing be designed to result in optimum device and integrated circuit performance.

The effects of oxidation and high-temperature anneals on the fixed surface state charge, Q_{ss}, have been well documented (4-6). In addition, the effects due to mobile charge, Q_o (positive ion contamination), in the oxide (7-10) and the effects of radiation-induced surface charge, N_{ot}, (11-14), have been thoroughly investigated and are reasonably well understood. It is the fast surface states, N_{st}, that have been investigated most extensively, however, and it is these states which remain the least understood of all the charges associated with the Si-SiO_2 interface (1, 2, 6, 15). Because the fast surface states are located in the silicon band gap near the Si-SiO_2 interface, the total charge in the surface states depends on their distribution in energy through the band gap, the surface potential and their resulting position relative to the Fermi level, and their electrical character, *i.e.*, whether they are acceptor or

* Electrochemical Society Active Member.
Keywords: semiconductors, silicon, silicon dioxide, passivation.

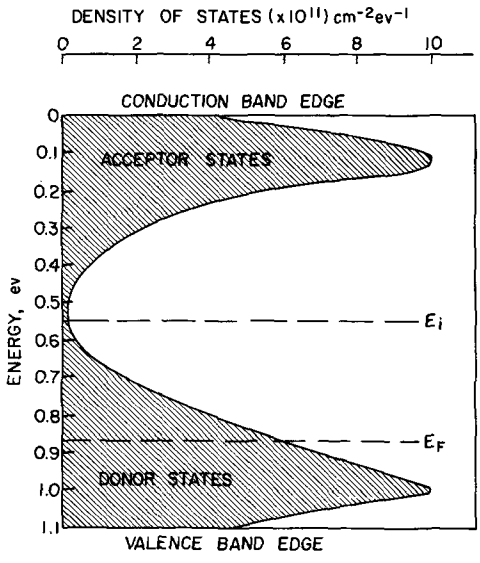

Fig. 1. Approximate distribution of fast states associated with the silicon-silicon dioxide interface following a rapid quench into the room ambient from a 1200°C dry O_2 oxidation.

donor states. These states respond rapidly to fluctuations in the surface potential by charging and discharging according to their position relative to the Fermi level. The data of Nicollian and Goetzberger (15) and Gray and Brown (16, 17), as well as work at this laboratory (18), indicate the distribution of the fast surface states through the silicon band gap has peaks near both band edges with a fairly continuous distribution through the center of the band gap. This is shown in Fig. 1 for a typical 1200°C dry O_2 oxide structure.

Suggestions as to the nature or origin of the fast states generally involve some uncompensated bond defect usually near the Si-SiO_2 interface, which is attributed to the disruption of the periodicity of the silicon lattice (19). Whatever their origin, it has been shown that the density of the fast states can be reduced to a relatively low level by annealing in an inert ambient, such as nitrogen, at low temperatures if an active metal, *e.g.*, aluminum, is present over the thermal oxide (20). Speculating that some hydrogen species is produced by the reaction of water adsorbed on the oxide and the aluminum during this treatment, and is therefore responsible for the reduction of the states, a number of investigators have examined the effects of hydrogen anneals on fast surface states (21-27). The conclusions that can be drawn from these experiments are almost as numerous as the number of investigations. This is probably because very few, if any, systematic studies have been made of the low-temperature reduction of fast states. In addition, other effects such as the presence of competing charges and nonreproducible processing have tended to confuse the results that have been obtained. Therefore a program was carried out to study the reduction of fast surface states in which the processing conditions were closely controlled and the contamination and other competing reactions minimized. The results of these experiments, in which the ability of hydrogen gas to reduce fast states is compared to the effectiveness of the aluminum-water reaction in the temperature range 300°-550°C, are summarized in this paper.

Experimental

Materials.—Single-crystal, Czochralski-grown silicon was obtained in the form of sawed, circular slices approximately 575μ thick. Dislocation densities ranged from 5 x 10^3 to 5 x 10^4 cm^{-2}. All silicon used as starting material for this work was p-type (boron-doped) with concentration in the range 0.5-1.0 x 10^{16} cm^{-3}. Crystal orientation was (111).

The aluminum used for contacts and field plates was specified as 99.999% pure.[1] Filament evaporation of the aluminum was employed to avoid radiation-induced traps in the oxide, which are characteristic of electron beam evaporation. Contamination charge density resulting from the evaporation averaged 3 x 10^{11} cm^{-2}. Gases used for oxidation and annealing (O_2, N_2, and H_2) were obtained in a liquid form.[2] Molecular traps were used in all gas lines to remove any excess water or hydrocarbons. Analyses of these gases had previously shown H_2O content to be less than 1 ppm.

Processing.—For this study, silicon n^+-p gate-controlled diodes were processed which had circular geometry with a junction area of 2.5 x 10^{-4} cm^2. An aluminum field plate (gate), with an area of 1.3 x 10^{-3} cm^2, extended over the metallurgical junction. In addition, an outer gate was used to accumulate the surface adjacent to the gate area and therefore prevent channels from being formed due to Q_{ss}, the fixed positive surface charge associated with the Si-SiO_2 interface.

To ensure that the silicon surface was free of mechanical damage, a careful surface preparation procedure was devised. Initially, the slices were cleaned in both organic and inorganic solvents, and then etched in an iodine-containing HF-HNO_3-acetic acid etchant to remove 125μ from each slice. One side, to be used for device fabrication, was further finished by mechanically lapping to remove 100μ. The slices were cleaned once more and then chemically etched to remove 200μ. The final thickness of each slice was approximately 150μ. A standard processing schedule was followed for the formation of n^+-p diodes in which phosphorus was diffused into oxide cutouts formed by photoresist techniques. The devices were subsequently gettered for low leakage currents. At this stage of processing, the slices were stripped of all oxide in hydrofluoric acid and reoxidized[3] in 1200°C dry O_2 to an oxide thickness of 2000Å in a contaminant-free oxidation furnace. Following reoxidation, the slices were immediately removed from the furnace and allowed to cool quickly in the room ambient. Oxide cutouts for contacts to the diodes were made using photoresist techniques. Throughout the processing history of the diodes, great care was taken to ensure contaminant-free structures. This included the use of organic and inorganic solvent cleaning procedures whenever possible between processing steps. In addition, care was taken to ensure that all slices processed for this study received identical processing, except for the final low-temperature annealing treatment. A control slice was included with each run of diodes to characterize the initial fast surface-state densities of the various runs.

The final low-temperature treatments were carried out in a resistance-heated furnace at temperatures ranging from 300° to 550°C, in 50°C intervals. Ambients employed at each temperature included 100% N_2, 10% H_2-90% N_2, and 50% H_2-50% N_2. Anneal times were 5 or 25 min, with each anneal including an additional 5 min pre-purge of the system prior to introduction of hydrogen, and a 5 min post-purge after the hydrogen was turned off. To ensure that the purging time did not influence the results, 10 min were added to the 100% N_2 anneals. A 7-min total time control anneal in 100% N_2 was also included at each temperature to approximate the effects of the N_2 purging. Slices of diodes in each of three states of processing were included for each anneal: (*a*) slices following oxide cuts, after reoxidation but before aluminum evaporation, referred to as bare oxide anneals for purposes of this paper; (*b*) slices following the aluminum evaporation, but before aluminum gate and contact etch, referred to as pre-alneals (*aluminum anneals* prior to pattern definition); and (*c*) slices following

[1] Cominco Products, Inc., Spokane, Washington.
[2] Air Reduction Company, Richmond, California.
[3] Reoxidation to a lesser oxide thickness was necessary for the type of measurement used. Special tests, however, indicated very little differences in the device characteristics between the original and the reoxidized samples.

the aluminum gate and contact etch, referred to as post-alneals (*al*uminum an*neals* after pattern definition). Following the anneals, processing was continued for the bare oxide annealed and pre-alnealed slices.

Evaluation.—Fast surface states have been investigated using a number of different measurement techniques. Among these, the MOS capacitor is probably the most widely used because of the relative ease in processing the device. Measurements with the MOS capacitor include capacitance-voltage characteristics in which the shift in the flatband voltage, V_{FB}, at liquid nitrogen temperature from the room-temperature curve can be related to the density of fast surface states near the edge of the band gap (16, 19). Other distortions in the C-V curve have been noted with particular processing of the capacitors and have been related to fast surface states elsewhere in the silicon band gap, as well as to effects on device operation. The distortion characteristics of the C-V curves related to fast surface states have been labeled by Deal *et al.* as the Ⓐ-, Ⓑ-, and Ⓒ-state voltages (18, 28), as shown in Fig. 2. A discussion of these states as to their probable location in the silicon band gap and their effects on device operation has been given in ref. (18). The same terminology for the various characteristics will be used in this paper. Instead of MOS capacitors, however, the MOS structure employed in this work was the large gate area of the gate-controlled diode. For the C-V measurements the diode junction and outer gate were grounded to the substrate while the inner gate voltage, V_G, was varied. Although the C-V curves were made at a frequency of 100 kHz, the diffused n^+ region, thus connected, supplied enough minority carriers during the surface inversion to provide the low frequency-type C-V curve. This permitted measurement of all the labeled states, if present. Specifically, the Ⓐ- and Ⓒ-state voltages, related to the peaks of states near the band edges, were obtained.[4]

The gate-controlled diode is also ideally suited for examination of the density of the states in the center of the band gap through the measurement of the surface recombination velocity, s_o. This measurement technique is illustrated in Fig. 2b. It is seen that when the gate is biased to accumulate the surface, the reverse bias current, I_R, of the diode is restricted to the metallurgical junction current, $I_{gen,MJ}$. When the surface is inverted, the current is increased by the field-induced junction current, $I_{gen,FIJ}$. As the gate voltage varies from accumulation to inversion, the surface becomes depleted, but not inverted, at some particular voltage. For the MOS structure employed in this work the depletion voltage is near $V_G = 0$V. During surface depletion, the fast surface states, which are generation-recombination centers, are in the space-charge region of the reverse-biased diode, and will contribute to the reverse current until the surface becomes inverted. This additional current, $I_{gen,s}$, is directly proportional to s_o through the relationship (30)

$$I_{gen,s} = qn_i s_o A_s \quad [1]$$

where q is the electronic charge, n_i is the intrinsic carrier concentration of silicon, and A_s is the area of the depleted surface under the aluminum gate. Using the definition of s_o

$$s_o = \sigma_s v_{th} N_{st} \quad [2]$$

[4] The Ⓒ-state voltages obtained from the C-V curves, as shown in Fig. 2, were subsequently corrected by subtracting the theoretical Ⓒ-state voltage (2.0V for the structure used) from the measured values. It has been pointed out by Nicollian (29) that the channel cutoff effect at higher frequencies can cause an increase in the Ⓒ-state voltage as defined in this paper. Experiments performed by Nicollian on alnealed control devices from this work indicate that the cutoff effect is appreciable above approximately 10 kHz. The Ⓒ-state voltage reported for these devices at 100 kHz, 0.5V, is found to be due entirely to the channel cutoff effect. When measured at 100 Hz, the Ⓒ-state voltage is approximately 0V, or theoretical. Although this effect is present to some extent in all Ⓒ-state voltage values reported in this paper, the relative values of Ⓒ-state voltages for the various anneal conditions are still an indication of the relative density of fast surface states. The authors are grateful to Nicollian for his help in demonstrating and explaining the effect.

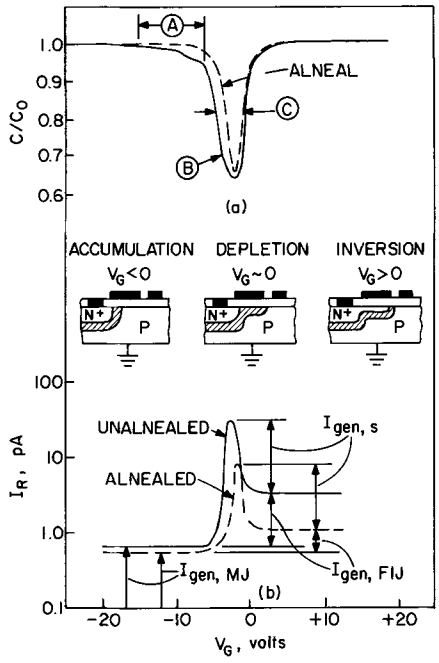

Fig. 2. Typical C-V and I_R-V_G experimental data obtained with the gate-controlled diodes. Both initial (solid lines) and alnealed (dashed lines) data are shown.

where σ_s is the effective capture cross section, v_{th} is the thermal velocity, and N_{st} is the density of fast surface states contributing to surface recombination, we can relate $I_{gen,s}$ to a density of fast states if values are assumed for capture cross section and thermal velocity. The theory of this device, both for C-V and s_o measurements, has been explored extensively by Grove and Fitzgerald (30).

Another technique for investigation of fast surface states is the conductance method of Nicollian and Goetzberger, which employs the frequency dependence of the equivalent parallel conductance of MOS capacitors in determining the distribution and density of fast surface states through the center portion of the silicon band gap (15). Comparison of s_o values obtained on the same devices by the two different techniques has indicated that both methods give the same results. Because the measurement techniques and data analysis are less complicated using the gate-controlled diode, this method was selected for the present work.

The gate-controlled diodes were measured both as MOS capacitors and as reverse-biased diodes. The C-V curves were taken using procedures described earlier (4) which allowed continuous X-Y recorder plots to be made. The gate-controlled diodes were examined for I_R-V_G characteristics at a reverse bias, V_R, of 300 mV. Metallurgical junction currents ranged from 0.5 to 1.0 pA and were measured with a Hewlett-Packard 425AR picoammeter with a sensitivity of 0.1 pA. A Moseley 60B log converter was used to provide a logarithmic current scale for the X-Y recorder. These plots were stepped manually rather than continuously plotted to prevent charging currents which were present with the continuous plots. In both types of measurements, V_G was varied from −20 to +20V. All measurements on the slice were taken at room temperature, using tungsten probes for contacts to the devices. During the measurements, the devices were shielded from exposure to light to prevent spurious generation of carriers. Measurements were taken in a shielded room to eliminate noise interference with the low currents being examined.

The Ⓐ- and Ⓒ-state voltage distortions are the results of the peaks in the distribution of fast states near the silicon band edges. Attempts have been made to convert the Ⓐ-state voltage to a density of fast surface states, N_{st}, (19), but the relationship is only

approximate because the states are not completely at discrete levels. Results of measurements on numerous gate-controlled diodes, following various processing procedures, indicate that the Ⓐ-state voltage is approximately twice the Ⓒ-state voltage for the particular structure, measurement frequency, and techniques employed in this work (18). Although the Ⓒ-state voltage can be measured with reasonable accuracy at room temperature, the Ⓐ-state voltage can only be measured accurately if it is about 5V or greater. The Ⓐ-state voltage values involved in this work are on the order of 5V. Therefore, the results of this experiment will be discussed in terms of the Ⓒ-state voltage, with the understanding that the same discussion applies for the Ⓐ-state voltage. Because the *C-V* curve has a theoretical width of 2.0V, characteristic of the MOS structure involved (31), the experimental Ⓒ-state voltages were corrected by subtracting this amount from the measured data. The variation in the corrected Ⓒ-state voltage and s_o with anneal conditions gives a relative indication of the variation in the density of fast states, and no attempt was made to convert these data to actual N_{st} values.

Results—Effects of Low-Temperature Anneals on Fast Surface States

Initial values of fast surface states.—All of the diodes processed for this experiment had the same history prior to the final low-temperature anneal. Control slices, from each run of ten slices processed together, were examined for fast surface-state densities prior to any low-temperature anneal. These initial values were therefore characteristic of the last high-temperature treatment, the 1200°C, dry O_2 reoxidation with a rapid quench into the room ambient. Initial experimental Ⓒ-state voltage values for these control devices of the ten runs processed ranged from 2 to 3V, after correction for the theoretical Ⓒ-state voltage for this particular MOS structure (2.0V). The initial s_o values ranged from 8 to 12 cm/sec. Based on the reproducibility in values of the initial Ⓒ-state voltage and s_o among the control devices, it was assumed that the initial values of all the devices processed were approximately the same.[5]

Additionally, half of each control slice was given a standard low-temperature post-alneal treatment at 550°C for 2 min in N_2, for comparison of the response of the control devices to an alneal treatment. Following this alneal, the corrected Ⓒ-state voltage values ranged from 0.6 to 1.0V and s_o ranged from 2 to 4 cm/sec. Low-temperature (liquid nitrogen) Ⓐ-state voltages were found to be approximately 0.5V for these units. Again, the reproducibility of the control data indicated that all devices initially were equivalent.

Temperature effects.—Representative data illustrating the variation of s_o and the Ⓒ-state voltage with anneal temperature are given in Fig. 3-5. Each data point represents at least five values with a standard deviation of 10% or less. Minimum values of fast surface-state densities are found in the 400°-450°C range in general. The density of fast states in some cases tends to increase with higher temperatures. In particular, the bare oxide anneals show this increase with temperature, with 550°C anneals resulting in densities actually greater than the initial values. When aluminum is present over the oxide during the alneals, a reduction in the densities of fast states is observed at temperatures as low as 350°C. Additionally, the increase with increasing temperatures does not occur. In most instances, the Ⓒ-state voltage is found to vary with temperature in a manner similar to the s_o data.

Time effects.—The variation with time of the Ⓒ-state voltage and s_o for bare oxide anneals and pre-alneals in ambients of 100% N_2 and of 50% H_2-50% N_2 are shown in Fig. 6 and 7. Results for post-alneals were very similar to the pre-alneal results. The time selected for the anneals included 5 and 25 min anneals. The additional pre- and post-purge times of 5 min each were accounted for by a 7-min total time anneal in N_2 for each set of anneal conditions. The purging time had little or no effect on the bare oxide conditions except at above 500°C, where it significantly increased both the Ⓒ-state voltage and s_o. For the pre- and post-alneals, the purging time was sufficient to reduce, appreciably, the fast surface states at 350°C and above.

The effects of the 5 and 25 min nitrogen anneals in addition to the effects of the purging time in nitrogen were mainly to increase the fast surface states with increasing time for bare oxide anneals. The presence of hydrogen in the ambient tended to suppress this increase somewhat. The increase was more evident in s_o measurements than in Ⓒ-state voltage data. For

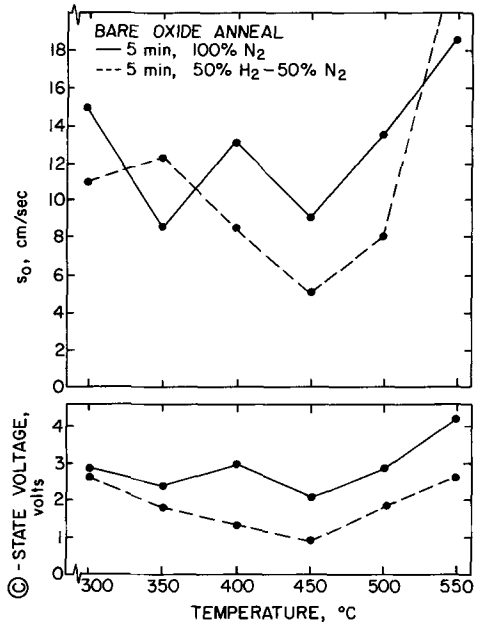

Fig. 3. Temperature dependence of surface recombination velocity and Ⓒ-state voltage for bare oxide anneals in 100% N_2 and in 50% H_2-50% N_2 ambients.

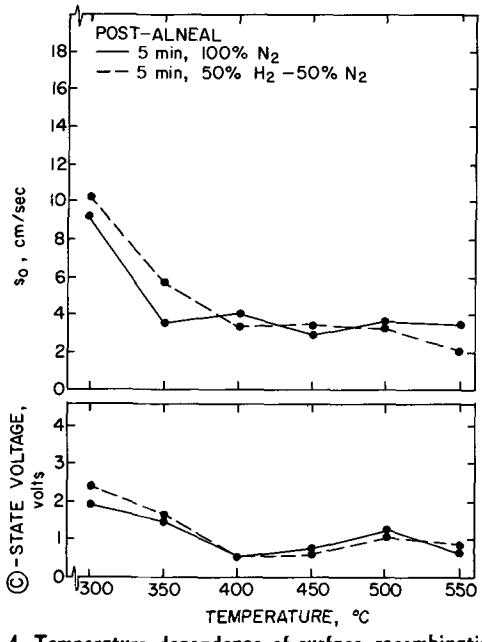

Fig. 4. Temperature dependence of surface recombination velocity and Ⓒ-state voltage for post alneals in 100% N_2 and in 50% H_2-50% N_2 ambients.

[5] It had previously been found that the relatively low value of fast states was due to the moisture content of the room ambient. On the other hand, cooling in a dry ambient (N_2 or O_2) results in a very high fast state density.

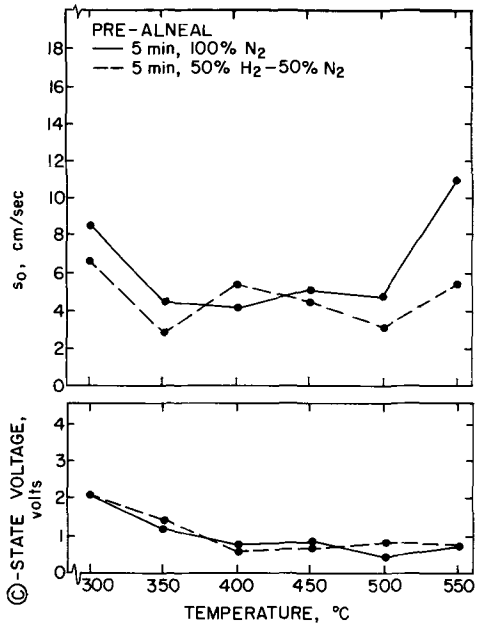

Fig. 5. Temperature dependence of surface recombination velocity and Ⓒ-state voltage for pre-alneals in 100% N_2 and in 50% H_2-50% N_2 ambients.

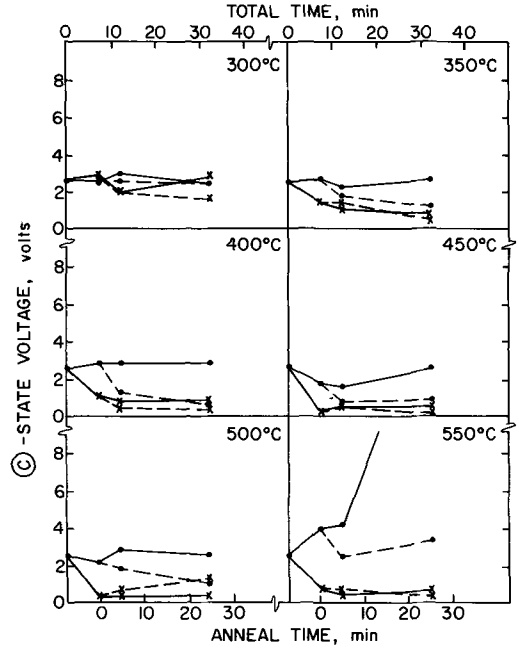

Fig. 6. Dependence of Ⓒ-state voltage on time of anneal treatment at various temperatures for 100% N_2 and 50% H_2-50% N_2 ambients. Anneal time has been offset by 7 min to account for the purging time of the system in 100% N_2. (● Bare oxide, × pre-alneal, — 100% N_2 -- 50% H_2-50% N_2.)

the alneal conditions, the increase with time was not as pronounced. In a few cases the tendency was to decrease with time. In particular, the pre-alneals at 550°C showed an increase in s_0 at shorter times, which then decreased for the longer alneals.

Ambient effects.—The effect of the presence of hydrogen in the annealing ambient was most pronounced for the bare oxide conditions investigated. Generally the greater concentration of hydrogen, 50% H_2, resulted in the lowest values of s_0 and the Ⓒ-state voltage for the bare oxide anneals. However, 10% H_2 was found to be effective in reducing the states to below the values attained with 100% N_2. The optimum temperature for the effectiveness of hydrogen for the bare oxide anneals was found to be in the 400°-450°C range. In general, the shorter anneal times gave lower

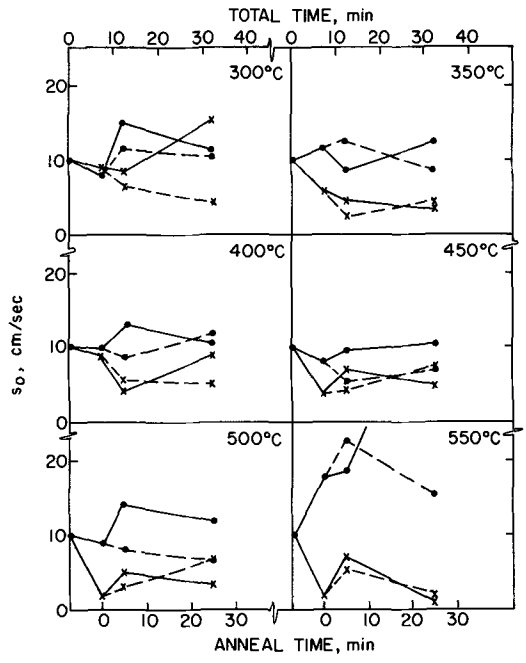

Fig. 7. Dependence of surface recombination velocity on time of anneal treatment at various temperatures for 100% N_2 and 50% H_2-50% N_2 ambients. Anneal time has been offset by 7 min to account for the purging time of the system in 100% N_2. (● Bare oxide, × pre-alneal, — 100% N_2 -- 50% H_2-50% N_2.)

values than the longer times. Under the optimum conditions, the values of s_0 and the Ⓒ-state voltage approached the low values obtained with aluminum present over the oxide-passivated junction.

For the post- and pre-alneals, the presence of hydrogen in the annealing ambient did not appreciably influence the values of s_0 or the Ⓒ-state voltage, as compared with results of similar alneals in 100% N_2.

Because the 7 min N_2 control of purging conditions indicated a large increase in fast surface states at 550°C for bare oxide anneals, it was desirable to separate the effects of the hydrogen anneal and the post-purge in N_2 at this temperature. With the resistance-heated furnace, the only feasible experiment was to process a bare oxide anneal in 50% H_2-50% N_2 at 550°C for 5 min and then to turn the furnace power off, allowing the furnace to cool to room temperature with the hydrogen in the ambient. The cooling time was approximately 3 hr. The values of s_0 and the corrected Ⓒ-state voltage resulting from this treatment were 3.2 cm/sec and 0.6V, respectively. In contrast, the bare oxide hydrogen anneal at 550°C with the standard post-purge in N_2 for 5 min and rapid cool to room temperatures resulted in an s_0 value of about 20 cm/sec and a corrected Ⓒ-state voltage of 3V. A further post-alneal of the specially treated devices did not appreciably change the fast surface-state densities from their low values. It would appear that at least at the higher temperatures, the N_2 post-purge required of the resistance-heated furnace operation was possibly responsible for the introduction of new fast surface states. However, the furnace did cool through the 400° 450°C temperature range, found optimum for reduction of the states of the bare oxide, and this may have been responsible for the extremely low density of the fast surface states resulting from this treatment.

Structure effects.—For any given anneal condition in this work (time, temperature, and ambient), the presence of aluminum over the oxide-passivated junction resulted in lower values of s_0 and the Ⓒ-state voltage than for the same bare oxide anneal conditions. A comparison between the effectiveness of the post- and pre-alneals indicates that the pre-alneal was more effective at the lower and higher temperatures, but that the post-alneals gave the lower values in the

400°-450°C range. The most effective alneals found in this experiment were for the 5 min post-alneals at 400°C and the 5 and 25 min pre-alneals at 550°C, all in a 10% H_2-90% N_2 ambient.

For bipolar devices, the aluminum pattern is usually limited to contact areas within the diffused regions. Therefore no aluminum is present over the oxide-passivated metallurgical junction. For these units, the results of post-alneals will be similar to the bare oxide anneals reported in this paper. If a reduction of the fast surface states is desired and a post-alneal is required, hydrogen anneals in the 400°-450°C range would give the best results.

Discussion

It has been proposed by Balk (20) that when aluminum is present over the SiO_2-Si interface, the annealing of fast surface states is due to the action of a hydrogen species produced by the reaction of the aluminum with water on the oxide surface. The purpose of this study was to attempt to simulate this annealing effect using molecular hydrogen in place of the aluminum-water reaction. To some extent this was successful in that the fast surface states of the bare oxide were reduced from their initial values when hydrogen was present in the annealing ambient in the temperature range 400°-450°C. The reduction, however, was not as complete as in the aluminum-water reaction. This would indicate that either (*i*) the post-anneal purge for 5 min in N_2 is introducing new fast surface states, or (*ii*) the hydrogen species produced by the aluminum-water reaction is some active form of hydrogen and not entirely molecular hydrogen, H_2.

Actually, both situations probably exist to some extent. The first, however, is largely discounted for temperatures below 500°C. This reasoning is based on the effects of the 7 min N_2 purge control anneals of the bare oxides, which showed little or no effects compared to initial values of the devices at the lower temperatures. At 550°C the 7 min N_2 anneal greatly increased the density of these states. It was also found that if the devices were cooled from 550°C to room temperature in a hydrogen ambient, the fast surface-state density was low. This again suggests that at 550°C the N_2 anneal of bare oxides introduces large densities of fast surface states. In addition, the longer anneal times in N_2 at 550°C resulted in greatly increased densities of states.

It would seem reasonable, therefore, to assume that the aluminum-water reaction does produce some active species of hydrogen which is the primary agent in the reduction of fast surface states. Hydrogen is known to exist naturally in three states: molecular hydrogen (H_2), atomic hydrogen ($H\cdot$), and ionic hydrogen (H^+). In chemical equilibrium, any volume of hydrogen contains a very small percentage of both atomic and ionic hydrogen. This percentage depends on temperature, increasing with increasing temperature. This correlates with the greater reduction of the fast states at higher temperatures for the bare oxide anneals in hydrogen. At even higher temperatures, the reduction due to active hydrogen is probably obscured by the effect of the post-anneal in N_2. Therefore, the reduction of the fast states which did occur during the hydrogen anneals of the bare oxides could be attributed to the small amount of the active hydrogen species present in the hydrogen gas.

Another factor that points to active hydrogen being the actual species responsible for the reduction of the states is the absence of any additional reduction of the states due to the presence of molecular hydrogen during the post- and pre-alneals. In these cases, the amount of active hydrogen present in the ambient hydrogen is probably insignificant compared to the amount being produced at the Al-SiO_2 interface. It is also significant to note that the rapid increase in fast states seen at 550°C for the bare oxide anneals, particularly in 100% N_2, is suppressed when aluminum is present. This suggests a close relationship between the two processes.

Earlier work which employed palladium field plates to dissociate molecular hydrogen into atomic hydrogen at 800°C showed that, while molecular hydrogen was unable to diffuse through a silicon nitride layer of an MNOS structure, the active hydrogen species not only diffused through the silicon nitride layer, it also reduced the large density of states at the SiO_2-Si interface (18). Additionally these MNOS devices exhibited positive ion polarization following the palladium-hydrogen dissociation reaction. These experimental data, combined with the present work, strongly support the theory that the aluminum-water product which is responsible for the reduction of fast surface states is some active hydrogen species and not molecular hydrogen.

For all the anneal and alneal conditions examined, the relationship between the s_0 values and the Ⓒ-state voltage values tends to be approximately constant, *i.e.*, any significant increase or decrease in one is seen in the other to some extent. This leads to the assumption that the fast surface-state distribution, as initially produced during the reoxidation and rapid quench to room ambient, has some fixed relationship between the states in the peaks near the band-gap edges and the generation-recombination centers near the middle of the band gap. The reduction of these states by the anneals reported in this work is such that the relationship is maintained. The density of fast states in the peaks at the band edges appears to be about two orders of magnitude greater than in the center of the gap. Because of the similarities between the states contributing to the Ⓐ-state voltage distortion and those contributing to the Ⓒ-state voltage distortion in the *C-V* curve, it might be proposed that the defects which are responsible for these states have an amphoteric nature and can contribute donor and acceptor levels in pairs. The donor levels are found below the intrinsic Fermi level, E_i, and the acceptor levels are found above E_i. If this is the case, the peak distributions would be similar to discrete levels, the difference being that their distribution with energy through the band gap tends to have a tail both toward the center of the gap and toward the band edges.

Because the initial density and distribution of the fast states are consistently reproducible for a given process treatment, the nature of the fast states is most likely related to the fabrication of the structure. This suggests that the states are related to uncompensated bonds at the interface, as has been suggested in the literature (19). Active hydrogen appears to complex with these bonds and to eliminate their active electrical character.

Summary

In an effort to test Balk's earlier proposal (20) that hydrogen is responsible for the reduction of fast surface states associated with the Al-SiO_2-Si structure during low-temperature treatments in dry nitrogen, a comparison was made of the effects of this reaction and of hydrogen-nitrogen anneals of SiO_2-Si structures. In general, the hydrogen ambient was found to be effective in reducing the density of fast states of the SiO_2-Si structure, with the reduction approaching, but not equaling, that of the Al-SiO_2-Si structure in the 400°-450°C range. At higher temperatures an increase in fast surface states was found for the SiO_2-Si structures which was attributed to the post-purge in nitrogen following the hydrogen-nitrogen anneal.

Summarizing, the results indicate that:

1. Hydrogen anneals of SiO_2-Si structures are most effective in the 400°-450°C range for reducing or annihilating fast surface states.

2. Heat treatments in dry nitrogen of Al-SiO_2-Si structures are effective at temperatures as low as 350°C for reduction of the fast surface states.

3. Shorter anneal times at a given temperature tend to give lower densities of fast states.

4. Hydrogen anneals of SiO_2-Si structures do not result in as low a density of fast states as nitrogen anneals of the Al-SiO_2-Si structures.

5. The hydrogen which is the more effective in the reduction of fast surface states is some active species of hydrogen and is not believed to be primarily molecular hydrogen. This agrees with earlier results of an experiment involving the palladium dissociation of hydrogen in which active or atomic hydrogen was found to diffuse through silicon nitride and annihilate fast surface states (18).

Acknowledgments

The authors wish to thank L. Pazdel, P. Fleming, M. Sklar, and P. Kodama for assistance in device processing and electrical measurements during this investigation. They also appreciate the helpful discussions and suggestions concerning this work which were provided by T. Klein, M. Barry, M. Lenzlinger, and E. MacKenna.

Manuscript submitted July 9, 1970; revised manuscript received *ca.* Sept. 17, 1970. This was Paper 108 presented at the Los Angeles Meeting of the Society, May 10-15, 1970.

Any discussion of this paper will appear in a Discussion Section to be published in the December 1971 JOURNAL.

REFERENCES

1. A. Many, Y. Goldstein, and N. B. Grover, "Semiconductor Surfaces," John Wiley & Sons, Inc., New York (1965).
2. A. S. Grove, "Physics and Technology of Semiconductor Devices," John Wiley & Sons, Inc., New York (1967).
3. S. M. Sze, "Physics of Semiconductor Devices," John Wiley & Sons, Inc., New York (1969).
4. B. E. Deal, M. Sklar, A. S. Grove, and E. H. Snow, *This Journal*, **114**, 266 (1967).
5. E. Arnold, J. Ladell, and G. Abowitz, *Appl. Phys. Letters*, **13**, 413 (1968).
6. E. Kooi, "The Surface Properties of Oxidized Silicon," N. V. Philips Gloeilampenfabrieken, Eindhoven, The Netherlands (1967).
7. E. H. Snow, A. S. Grove, B. E. Deal, and C. T. Sah, *J. Appl. Phys.*, **36**, 1664 (1965).
8. S. R. Hofstein, *Appl. Phys. Letters*, **11**, 95 (1967).
9. E. Yon, W. H. Ko, and A. B. Kuper, *IEEE Trans. Electron Devices*, **ED-13**, 276 (1966).
10. W. A. Pliskin, D. R. Kerr, and J. A. Perri, in "Physics of Thin Films," Vol. 4, p. 307, G. Hass, Editor, Academic Press, Inc., New York (1967).
11. E. Kooi, *Philips Res. Repts.*, **20**, 595 (1965).
12. E. H. Snow, A. S. Grove, and D. J. Fitzgerald, *Proc. IEEE*, **55**, 1168 (1967).
13. J. P. Mitchell and D. K. Wilson, *Bell System Tech. J.*, **46**, 1 (1967).
14. K. H. Zaininger, *RCA Rev.*, **28**, 208 (1967).
15. E. H. Nicollian and A. Goetzberger, *ibid.*, **46**, 1055 (1967).
16. P. V. Gray and D. M. Brown, *Appl. Phys. Letters*, **8**, 31 (1966).
17. D. M. Brown and P. V. Gray, *This Journal*, **115**, 760 (1968).
18. B. E. Deal, E. L. MacKenna, and P. L. Castro, *ibid.*, **116**, 997 (1969).
19. For a review of the silicon-silicon dioxide system, see P. V. Gray, *Proc. IEEE*, **57**, 1543 (1969).
20. P. Balk, Paper 111 presented at the Buffalo Meeting of the Society, Oct. 10-14, 1965.
21. P. Balk, Paper 109 presented at the San Francisco Meeting of the Society, May 9-13, 1965.
22. E. Kooi, *IEEE Trans. Electron Devices*, **ED-13**, 238 (1966).
23. A. G. Revesz, K. H. Zaininger, and R. J. Evans, *J. Phys. Chem. Solids*, **28**, 197 (1967).
24. K. H. Zaininger and G. Warfield, *Proc. IEEE*, **52**, 972 (1964).
25. T. M. Buck and F. S. McKim, *This Journal*, **105**, 709 (1958).
26. J. Olmstead, *IEEE Trans. Electron Devices*, **ED-12**, 104 (1965).
27. A. A. Bergh and C. Y. Bartholomew, *This Journal*, **115**, 1282 (1968).
28. B. E. Deal, P. J. Fleming, and P. L. Castro, *ibid.*, **115**, 300 (1968).
29. E. H. Nicollian, Private communication.
30. A. S. Grove and D. J. Fitzgerald, *IEEE Trans. Electron Devices*, **ED-13**, 260 (1966).
31. A. Goetzberger, *Bell System Tech. J.*, **45**, 1097 (1966).

Properties of Gold Films Formed from Organometallic Solution

A. A. Milgram[1]

E. I. Du Pont de Nemours & Company, Electrochemicals Department, Experimental Station, Wilmington, Delaware 19800

ABSTRACT

An experimental study was made of the properties of gold films, nominally 1000Å thick, formed by the thermal decomposition of an organometallic solution. The influence of the firing temperature and of the gaseous atmosphere on the structural, optical, and electrical properties was determined. A model for the film growth during the firing temperature cycle was developed which is consistent with the experimental observations. Film properties were affected by minor additions of soluble compounds of rhodium and chromium to the basic solution. The chromium addition dealkalized the substrate surface. This was accompanied by a significant effect upon the nature of the gold colloids at the substrate-gold interface. Specifically, the fractional volume occupied by the gold colloids at the substrate surface is directly related to the alkali content of the surface. The rhodium addition inhibited grain growth of the gold particles during the film-forming process and produced films which were specularly reflecting and electrically continuous. Gold films not containing the rhodium additive were diffuse reflectors of light and were electrically discontinuous. The residual electrical resistivity was less than 0.2×10^{-6} ohm-cm for gold films containing the Rh addition. This magnitude for the residual resistivity compares with the values obtained for thin gold films formed by vacuum deposition.

Extensive research has been done on gold films prepared by vacuum deposition and by sputtering (1-8). With these methods, great care has been taken to minimize contaminants. However, the optical and electrical properties of sputtered and vacuum-deposited gold films usually differ from those of the bulk material. It has been shown by most of these investigators that the discrepancies are related to the film structure. Deposition parameters such as deposition rate, substrate temperature, and gas environment, have a profound effect on the grain size, orientation, and agglomeration of the deposited film.

The ceramic industry has been using thin gold films to decorate china and glassware for more than a century. In their case, they coat a substrate by the method of thermal decomposition of organometallic compounds applied in solution. Chemical solutions of this nature are described by Langley (9) and by Boetcher (10). A gold film is easily formed simply by firing the solution in air. A proprietary art has developed whereby additives are put into the solution to achieve specific physical (nonelectrical) properties. Although these additives are a relatively small part of the solution, they have a profound effect on the electrical properties of the fired gold film. For example, it was demonstrated from the work to be described that the residual resistivity of a gold film can be as low as 0.2×10^{-6} ohm-cm when the gold film is prepared using rhodium as an impurity additive.

It is the purpose of this paper to discuss the structural and electrical properties of gold films formed from an organometallic compound. The influence of the gaseous atmosphere, the firing temperature, and of additives such as Rh and Cr used in the organometallic solution have been determined. These studies have produced a model of film growth starting from the organometallic solution coated on a substrate and ending in a film of metallic gold.

Experimental

Gold metal decorating solutions (9-13) were used in this work. The organometallic solution (referred to as "liquid gold solution") consisted of pinene mercaptan gold (gold chloride reacted with pinene mercaptan to produce monovalent gold bonded to an organic complex) mixed with B-terpineol and organic resins. Soluble organometallic derivatives of chromium and rhodium were added to the solution. There was approximately 15 w/o gold in the solution, with 0.05 w/o Cr and 0.02 w/o Rh. A du Pont differential thermal analyzer/thermogravimetric analyzer (DTA-TGA) was used to examine the thermal properties of the ingredients of the organometallic solution. The solution was applied to 96% alumina (American Lava Alsimag No. 614) and to glass substrates (New York Laboratory Supply No. 63000 Microscope slides) by brushing on and by screen printing. The substrates were first cleaned in an ultrasonic cleaner using soap and water. After coating, the films were dried in air at 150°C for 15 min and then heated to a higher temperature. The maximum firing temperature was 625°C for the microscope glass slides and 1000°C for the Al_2O_3 substrate.

An investigation was made of the nature of the gold film at the glass-gold interface using optical and electron microscopy. A piece of cellophane tape was placed on top of the gold film and then stripped from the glass surface. In many cases a portion of the gold film would be removed with the tape, and a faint purple color would be observed on the glass slide. The material causing this color at the interface between the glass slide and the solid gold film was examined using optical microscopy. A two-stage carbon replication technique was used to make replicas of this material on the glass surface for study using electron microscopy.

An experiment was performed which demonstrated the effect of the chromium additive. Three glass slides were cleaned and an oxygen-gas torch was played over the surfaces in such a manner that a figure "X" was formed on each surface by fire polishing. One of the glass slides was rinsed with distilled water, dried, then coated with a liquid gold solution containing chromium resinate. This slide was fired in air at 625°C and the gold-glass interface was examined optically. The surface of the second glass slide was examined for sodium using an electron microprobe analyzer. The third glass slide was partially coated with a chromium resinate solution. This last slide was dried and heated in air at 500°C for 30 min. After the glass cooled, it was cleaned,

[1] No longer at E. I. Du Pont de Nemours & Co.

Key words: thin films, gold, electrical properties.

coated with a thin coat of liquid gold solution (not containing chromium resinate), dried, and fired in air at 625°C. The gold-glass interface was examined optically.

The effect of rhodium additive on the gold film was determined both optically and by x-ray diffraction. Two identical liquid gold solutions were prepared except that one contained the Rh additive while the other did not. The slides, after being coated and dried, were heated to progressively higher temperatures. A representative slide was removed from the furnace at 20°C intervals. An x-ray diffraction pattern was also taken of the partially formed gold film using Cu $K\alpha$ radiation.

Rhodium powder (100.00% Rh, J. Bishop and Company) was examined by x-ray diffraction using Cu $K\alpha$ radiation. This powder was then heated to 600°C in air and re-examined by x-ray diffraction. This same powder was then heated to 600°C in a 90% N_2-10% H_2 reducing atmosphere for 1 hr. Other samples of rhodium powder which had been similarly heat treated were examined in a du Pont DTA-TGA analyzer by heating from 20° to 1000°C. These samples were heated in both air and in dry nitrogen.

The electrical resistance of the fired gold films was measured at temperatures between 20° and 100°C by a digital ohmmeter. The lead resistance was measured and subtracted from the total resistance. The electrical resistance at temperatures less than 20°C was measured using a four-point probe method with a Keithley Model 503 milliohmmeter. To effect this type of measurement, an indium solder[2] with a melting point of 138°C was used to make solder connections of 0.003 in. copper strip to the gold film. Two copper strips were used as current electrodes. Another two narrow copper strips were soldered at the edge of the gold film between the current electrodes to act as voltage probes. Measurements were made at 293°, 195° (by immersion in powdered dry ice), and 78°K (by immersion in liquid nitrogen).

The effect of reducing gas atmosphere on the structure of the fired Au films was studied. Gold films were formed by firing glass pieces coated with liquid gold solution containing a rhodium resinate in air at 620°C for 10 min. Opaque gold films were produced. The glass pieces were put in a tube furnace containing a mixture of 90% nitrogen with 10% hydrogen gas. The films were heat-soaked for 15 min at 400°C, and then examined optically for structural changes. This heat-soaking procedure was repeated at 425°C and at higher temperatures in 25°C temperature steps. The optical transmission of a film heated at 600°C in this reducing atmosphere was measured with a Cary spectrophotometer using a dual beam technique. The optical transmission was compared to that of an air-fired gold film.

Results and Discussion

Effect of temperature on the liquid gold composition.—Pinene mercaptan gold compound.—As shown by the TGA in Fig. 1, the pinene mercaptan gold was observed to dissociate rapidly, beginning at approximately 185°C. By 240°C the reaction was essentially complete. The behavior was the same in both air and nitrogen. An endothermic reaction beginning at approximately 185°C can be seen on a typical sample DTA run in Fig. 1B. This agrees with the TGA result. A well-defined exothermic peak believed to be due to the formation of crystalline gold colloids is observed at 230°C.

Rhodium resinate.—Self-heating of the samples was observed by TGA in the vicinity of 300°-335°C due to oxidation of the rhodium. Between the temperatures of 325° and 375°C, the decomposition and oxidation of the rhodium was complete.

Chromium resinate.—A TGA performed on a sample indicated decomposition of the resinate and oxidation of the Cr. The Cr begins to oxidize at 300°C and continues until the resinate completely decomposes at 400°C.

[2] 25 In, 37.5 Sn, 37.5 Pb in weight per cent.

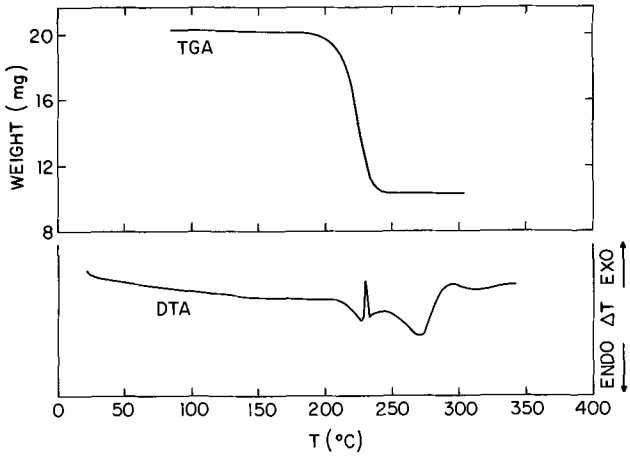

Fig. 1. DTA and TGA of pinene mercaptan gold using a heating rate of 10°C/min. The behavior was the same in both air and nitrogen atmosphere.

Glass-gold interface.—Nature of Gold Structure.—Representative electron micrographs of the surface are shown in Fig. 2A and 2B. Well-formed submicron-size gold crystals showing an octahedral configuration were found. Clusters of larger gold particles surrounded by spaces devoid of gold are seen in both Fig. 2A and 2B. This suggests that particles of 100Å size migrated over the surface to form larger gold particles.

Effect of chromium additive.—The region of the first glass slide (coated with a gold film) that had been fire polished with the X shape had no pronounced color at the gold-glass interface. However, in the vicinity surrounding this fire-polished area, there was a pronounced reddish color. Electron microprobe measurements on slide No. 2 determined that the surface area immediately adjacent to the fire-polished region had excess sodium. The third glass slide, which had been pretreated with chromium resinate solution before firing on the gold film, was examined for coloration at the glass-gold interface. For those areas adjacent to the fire-polished region which had received the pretreatment, there was no pronounced coloration.

The action of the flame, according to Weyl and Marboe (14), is to cause the alkali to migrate over the surface of the glass to a cooler region. Evidently, the presence of excess alkali on the surface influences the nucleation mechanism. The excess alkali causes the gold to form highly dense colloidal deposits on the surface during the firing process. The surface is believed to be dealkalized through the formation of Cr_2O_3, which reacts with the alkali to form Na_2CrO_4 (14).

Effect of firing temperature.—On gold particle size.—The x-ray diffraction patterns all exhibited line-broadening due to particle size effects. In Fig. 3, the gold particle size (computed using the Scherrer formula and the measured width of the diffraction curve) is given as a function of the maximum firing temperature to which the film has been exposed. The particle size for the gold film made from a solution containing the rhodium additive remains constant at approximately 350Å for firing temperatures of greater than 400°C. However, without rhodium, the gold particle size increases with firing temperature. The absence of line broadening indicated a particle size greater than 1000Å for a 400°C firing temperature. For this latter case, the gold particle size increases continuously due to agglomeration at the higher firing temperature. The optical micrograph in Fig. 4 of a gold film (with no Rh additive) fired at 600°C indicated a particle diameter of approximately 6μ.

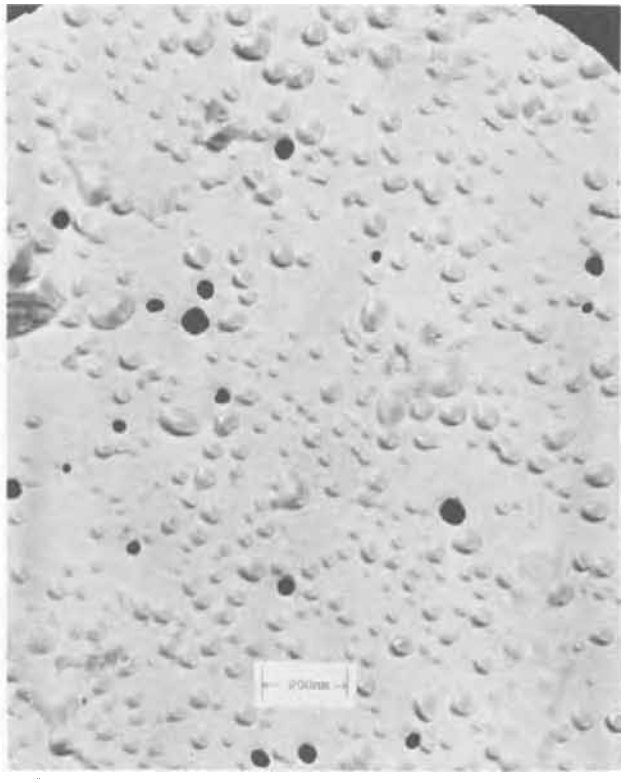

Fig. 2A (left) Fig. 2B (right). Electron micrographs of the glass-gold interface. The light colored particles represent gold. The black particles are due to actual gold particles removed from the glass surface with the carbon replica during the stripping operation. (The black particles were found to be gold by direct electron diffraction of the material on the carbon replica.)

Optical micrographs were made of gold films formed on Al_2O_3 to demonstrate the effect of high firing temperature on the film structure. The gold films containing Rh which were formed at temperatures below 800°C were continuous. Figures 5A and 5B show gold films fired at 900° and 1000°C, respectively. The black portions are the gold. At higher temperatures the gold breaks up into chains and isolated particles, and the agglomeration increases. For a gold film fired at 1000°C, less than 50% of the surface is covered with gold particles.

For firing temperatures of less than 350°C the gold film is a colloidal structure with completely random orientation. As the firing temperature is increased, the degree of (111) orientation increases.

On rhodium powder.—The x-ray diffraction results are tabulated in Table I.

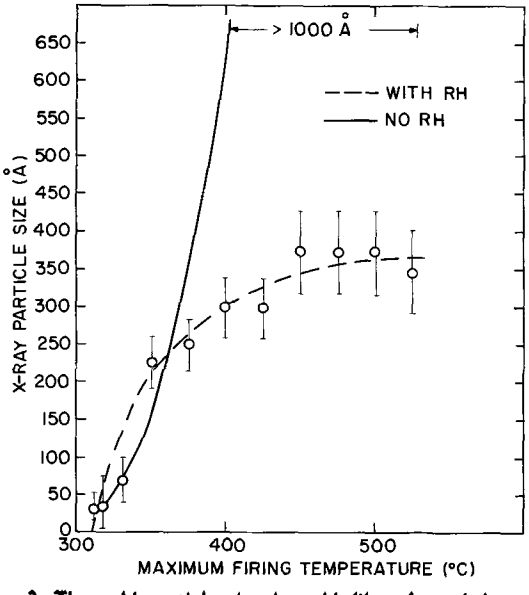

Fig. 3. The gold particle size in gold films formed from liquid gold solution with Rh and without Rh. The gold particle size was calculated using the Scherrer formula and the measured width of the x-ray diffraction curve. The particle size is plotted vs. the maximum firing temperature to which the film has been exposed.

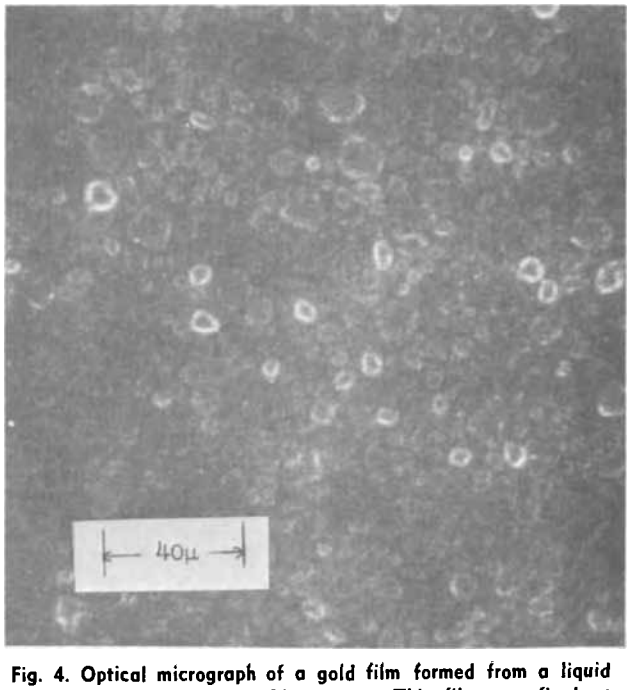

Fig. 4. Optical micrograph of a gold film formed from a liquid gold solution not containing Rh resinate. This film was fired at 600°C.

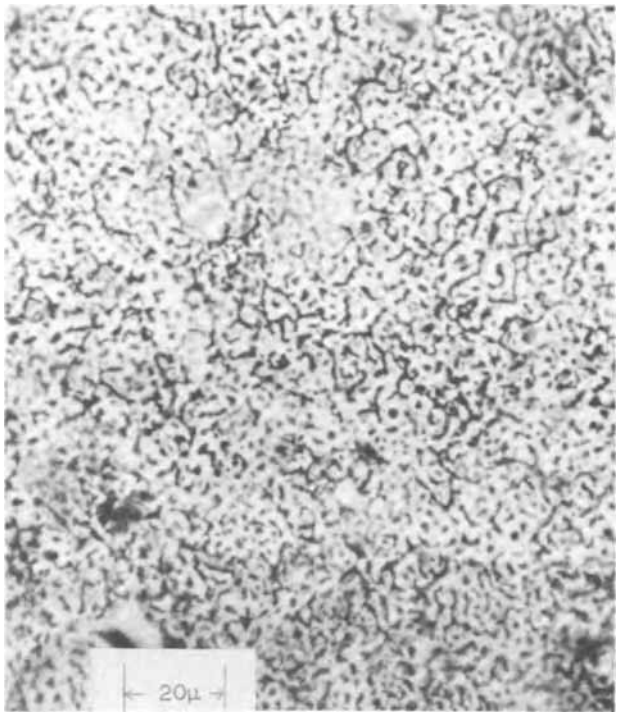

Fig. 5A. Optical micrograph of a gold film formed from a liquid gold solution containing Rh resinate. The gold film was fired in air onto 96% Al_2O_3 at a maximum firing temperature of 900°C. The micrograph was taken using transmitted light through the Al_2O_3 substrate, so that the gold appears as black regions.

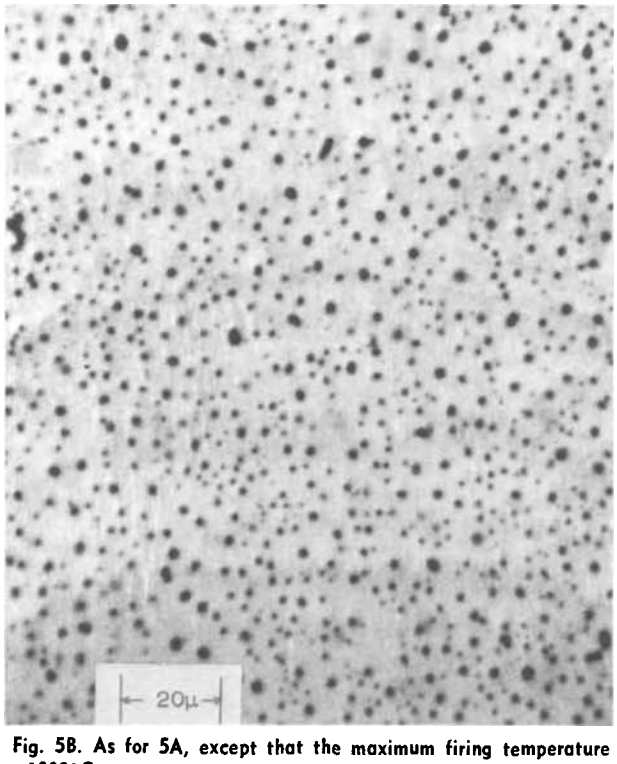

Fig. 5B. As for 5A, except that the maximum firing temperature was 1000°C.

From Table I, it is known that Rh powder heated at 600°C for 1 hr will have been transformed to Rh_2O_3. The TGA results on the oxide sample are shown in Fig. 6. The Rh_2O_3 rapidly decomposes in nitrogen at temperatures greater than 750°C. The decomposition is complete at 900°C. The calculated weight loss (19%) agreed with the observed weight loss (19 ± 1%). No decomposition is observable in air at temperatures up to 1000°C.

Table I. X-ray determination of phases present after heating Rh powder

Sample No.	Sample condition	Phases present
1	Normal	Rh
2	Sample No. 1 heated at 600°C in air	Rh_2O_3
3	Sample No. 2 heated at 600°C in a reducing atmosphere	Rh

Table II. Electrical properties of gold films containing rhodium

Max. firing temp, °C	R(22°C),[a] ohms	Temp. coeff. resistance, α,[b] ppm/°C
300	500×10^6	−10,800
310	600×10^6	−11,000
325	2×10^6	−7,000
335	7.0	+500
350	3.0	+900
375	2.6	+1,000
400	2.2	+1,100
450	1.0	+1,300
500	0.85	+2,000
550	0.42	+2,800
600	0.40	+3,200
625	0.40	+3,300

[a] R(22°C) is the sheet resistance of the film at 22°C. In this case, the distance between measuring electrodes is the same as the width of the film.
[b] The temperature coefficient of resistance at 22°C was calculated from the measured resistance *vs.* temperature relationship over the temperature interval 20°-100°C.

Thus far, results have shown that addition of rhodium resinate to the basic solution produces a gold film that is continuous and fine-grained. The Rh is known to oxidize at 300°-325°C and thus exists as an oxide before the gold particles make physical contact. (It will be shown in the section below on Electrical properties that gold particle contact begins for firing temperatures in excess of 325°C.) The gold film readily decomposes to an agglomerated structure for firing temperatures of greater than 800°C. Rh_2O_3 was also observed to rapidly decompose at temperatures greater than 750°C. These results suggest that Rh_2O_3 precipitates on the grain boundaries of the gold particles during the firing process. The Rh_2O_3 would then prevent the ready diffusion of gold from one gold particle to the next when the particles make physical contact. The results displayed in Fig. 3 show that the gold particle size is constant for firing temperatures beyond that at which the gold particles make physical contact. This result agrees with the concept that the Rh_2O_3 inhibits grain growth of the gold.

Electrical properties.—Gold films not containing Rh additive were electrically discontinuous. Measurements of electrical properties were made on gold films containing the Rh additive. Results for the resistance and temperature coefficient of resistance as a function of the firing temperature are given in Table II. The film resistance was greater than 10^9 ohm/square for firing temperatures less than 300°C. (These gold films had

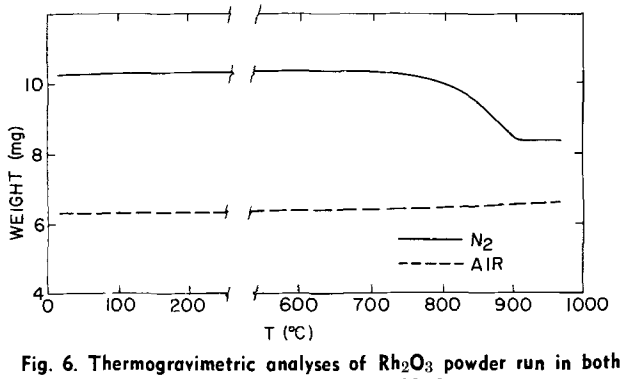

Fig. 6. Thermogravimetric analyses of Rh_2O_3 powder run in both nitrogen and in air. The heating rate was 10°C/min.

dimensions of one resistance square.) The film thickness was measured by a Clevite Brush Surfanalyzer Model No. 150 recording profilometer. The thickness varied between 700 and 1000Å over the surface; thus, no attempt was made to measure the resistivity of the film.

It is noted from Table II that the sheet resistance of the films at 22°C decreased with increase of firing temperature. This type of behavior would not be characteristic of gold films produced by vacuum evaporation. In this latter case, gold is deposited onto a heated substrate in a high vacuum chamber. The ratio of experimentally determined resistivity of vacuum-deposited films to the bulk resistivity reaches a minimum for a substrate temperature during deposition of 360°C (5, 7). When this substrate temperature is employed, the residual resistivity is approximately 0.2×10^{-6} ohm-cm (5, 7). For depositions on substrates at temperatures less than 360°C the resistance ratio is large, presumably due to defects; above 360°C, the resistivity increases with temperature, presumably due to agglomeration. Increasing agglomeration was shown to be characteristic of gold films formed from liquid gold solutions not containing rhodium.

The gold films were electrically discontinuous when fired at temperatures below 300°C. At a slightly higher firing temperature, the films became conducting ($\rho \sim 10^{-4}$ ohm-cm) with a negative temperature coefficient of resistance, as evident in Table II. This behavior is typical of electron tunneling between noncontacting colloids of gold (15). At approximately 340°C the gold colloids form partially continuous chains throughout the film. The resistance decreased by a factor of 10^6 and the temperature coefficient of resistance increased from −10,000 ppm/°C to nearly +0 ppm/°C. At a higher firing temperature, the film resistance continuously decreased, presumably due to annealing of defects. Similarly, the temperature coefficient of resistance (at 20°C) increased from +0 ppm/°C for a 340°C firing temperature to +3300 ppm/°C at a 625°C firing temperature.

The gold films which provided the results in Table II were used in the calculation of the residual resistivity associated with the gold films. The residual resistivity was calculated as follows using data from sheet resistance measurements made at 293°, 195°, and 78°K.

$$\rho(T) = \rho_o(T) + \rho_i \qquad [1]$$

Assuming Matthiesson's rule, and assuming that the resistivity of these films is independent of film thickness,

where $\rho_o(T)$ = resistivity behavior of pure, well-annealed gold at temperature, T
$\rho(T)$ = observed resistivity (sheet resistance) behavior of gold film at temperature, T, °K
ρ_i = residual resistivity.

Using algebra

$$\rho_i = \left\{ \frac{\dfrac{\rho_o(T)}{\rho_o(78)} - \dfrac{\rho(T)}{\rho(78)}}{\left[\dfrac{\rho(T)}{\rho(78)} - 1\right]} \right\} \rho_o(78) \qquad [2]$$

For pure, well-annealed gold (16)

$$\frac{\rho_o(195)}{\rho_o(78)} = 2.50 \qquad [3a]$$

$$\frac{\rho_o(293)}{\rho_o(78)} = 3.87 \qquad [3b]$$

and $\rho_o(293) = 2.4 \times 10^{-6}$ ohm-cm.

There exists another independent method of calculating ρ_i using the temperature coefficient of resistance. Empirically, this method yields more accurate results than does the first method. Equation [1] can be restated as follows

$$\rho_o\alpha_o = \rho\alpha \qquad [4]$$

where α = the experimentally determined temperature coefficient of resistance and α_o refers to the temperature coefficient for the ideal metal. Using the appropriate values for ρ_o and α_o and the empirical value for α at $T = 293$°K, the value of ρ and the residual resistivity can be calculated. Results are tabulated in Table III. The residual resistivity for a gold film containing rhodium formed at 625°C was calculated from Eq. [4] to be 0.2×10^{-6} ohm-cm.

Table III. Residual resistivity of gold films containing rhodium

Max firing temp, °C	Calculated from Eq. 2: T = 293°K, ×10⁻⁶ ohm-cm	Calculated from Eq. 2: T = 195°K, ×10⁻⁶ ohm-cm	Calculated from Eq. [4], ×10⁻⁶ ohm-cm
625	0.4	0.4	0.2
600	0.4	0.4	0.2
550	1.0	1.0	0.5
475	4.2	—	2.1
460	4.5	—	2.1

For gold films containing rhodium, the oxide coating at the interface between the gold particles produces an additional resistance. It was shown by Milgram and Lu (17) that an oxide as thin as 20Å can produce a resistance of 10^{10} ohms/ square for the gold films used in this work. The additional resistance decreases rapidly as the oxide thickness decreases. Experimentally, it was shown that the additional resistance was less than 10^{-1} ohms. Thus, the oxide must be of monolayer thickness to avoid the additional oxide resistance. It is shown in the Appendix that the oxide of rhodium would just coat the surface of a gold particle if it were to exist as a monolayer coating.

Effect of reducing atmosphere.—Film structure.—The first evidence of partial transformation of the continuous film to a discontinuous film was found at a firing temperature of 475°C when the film was soaked for 15 min in a 90% N_2-10% H_2 atmosphere (1 bar). The transformed region consisted of 1μ diameter particles in the form of flat platelets of irregular size. At progressively higher firing temperatures in the reducing atmosphere, the film completely converted to a discontinuous film consisting of irregularly shaped gold platelets of 1-5μ diameter. At approximately 600°C, there was complete conversion to a discontinuous film when the film was exposed for 15 min. In this last case, the gold was in the form of regularly shaped, 1μ diameter gold hemispheres. The film has the particle distribution as shown in Fig. 5B; however, the particles are more uniform than those shown in Fig. 5B.

The effect of heating a fired gold film in a reducing atmosphere was irreversible. A glass piece coated with gold, which had been treated in a reducing atmosphere to bring out an agglomerated structure, was subsequently heated in air again to 600°C. The gold film was found to maintain an agglomerated structure.

The above results are in accordance with the hypothesis that the Rh_2O_3 inhibits the growth of the gold particles. When the Rh_2O_3 is reduced to Rh by heating in a reducing atmosphere, the gold particles can agglomerate. The agglomeration proceeds rapidly with higher temperature due to the increased mobility of the gold. Once the gold particles agglomerate into a discontinuous structure, a postfiring treatment in air will be ineffectual.

Optical transmission.—Gold films were formed from solutions not containing the Rh additive. All of the films were diffuse reflectors of light. However, the addition of Rh to the basic solution yielded fired films with specular reflectivity. The transmission color of gold films containing a rhodium additive was found to be related to the maximum firing temperature.

The observed colors of transmitted light as a function of firing temperature are tabulated in Table IV.

Table IV. Weight per cent of gold in the film and the film transmission color as a function of firing temperature

Maximum firing temperature, °C	Weight per cent gold,[a] %	Transmission color
300	43	Ruby-red
325	46	Dark blue
350	53	Dark blue
375	77	Dark blue
388	94	Light blue
400	96	Light blue-green
425	97	Light blue-green
450	98	Light blue-green
475	99 +	Light green-blue
625	100	Light green

[a] The weight per cent gold in the film was determined by performing a TGA on a liquid gold solution. Between 500° and 650°C there was no observable change of weight. It was assumed that no organic remained in the film at 625°C firing temperature. The weight per cent gold in the film was then calculated directly from the TGA curve.

The ruby red color observed at 300°C is due to the highly dense noncontacting gold colloids embedded in the organic matrix. At a higher firing temperature, the gold particles made contact and produced a green transmission color characteristic of bulk gold. At intermediate temperatures, the transmission color had a blue component due to the influence of the organic remaining in the film.

The optical density of a gold film containing Rh was measured; it had been fired in air at 625°C. The gold film reflected light specularly. It was then heated at 600°C in a reducing atmosphere and the optical density remeasured. Results are given in Fig. 7. The gold film fired in air had a minimum in optical density at 495 nm, which is similar to the behavior of vacuum deposited gold films (6). However, the gold film after being exposed to the reducing atmosphere underwent a major structural change which affected the optical transmission. The optical transmission was flat *vs.* wavelength except between 480 and 700 nm where there was a broad absorption band centered at 540 nm. This transmission minimum is due to the optical properties of submicron size colloidal gold, as shown by the work on vacuum evaporated and sputtered gold films (6, 10). (The reflectivity also peaked in the neighborhood of 540 nm, because the gold film appeared green by reflection from a white light source.)

Summary and Conclusions

The observed electrical and optical behavior can be explained by assuming that film growth proceeds by the following steps during the firing temperature cycle:

1. Dissociation of the organometallic compound and formation of gold colloids. Nucleation is observed throughout the volume of the liquid solution as the organic burns out. Nucleation also takes place at the glass-gold interface.

2. Increase in size of the gold colloids. The particulate size and density at the glass-gold interface will be determined by the same nucleation mechanisms as for vacuum deposited thin films. Gold films formed by vacuum deposition are known to form an agglomerated structure similar to that shown in Fig. 2A and 2B (1, 2). Due to this unique structure at the glass-gold interface, the optical constants vary significantly as a function of the wavelength and will give rise to selective reflectivity (3). The observed color from the back-side of a glass substrate containing a gold film formed from the liquid gold solution will be dependent on the colloidal nature of the gold at the interface. Various colors can be produced depending upon the fractional volume occupied by the colloidal layer (3).

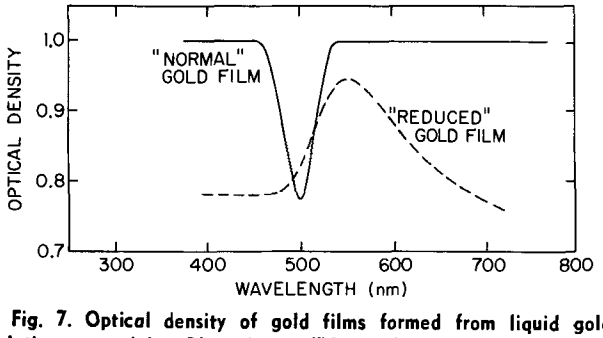

Fig. 7. Optical density of gold films formed from liquid gold solutions containing Rh resinate. "Normal" represents the optical density for an air-fired film. "Reduced" represents the optical density for an air-fired film which has undergone a postfiring in a reducing atmosphere.

It has been determined from this work that the alkali content of the glass surface will affect the particle size and density at the interface during the growth process. The presence of Cr_2O_3 in the gold solution will change the alkali content on the glass surface during firing; thus, the size and density of gold particles at the glass-gold interface will be affected. Because the nucleation mechanisms are the same as for vacuum deposited films, it is suggested that the alkali content of the glass surface affects the nucleation of vacuum deposited gold films.

3. Inhibition of diffusion of gold by the presence of rhodium oxide. Without the rhodium oxide, the gold particles continually increase in size with increase of firing temperature.

4. Loss of the organic material until the gold colloids make contact and form partially continuous networks. If rhodium oxide is present in the film, the gold particle size will not increase after the gold particles make contact. The rhodium oxide is believed to be present at the grain boundaries between gold particles and prevents grain boundary diffusion of the gold. Reducing the oxide by either heating to the decomposition temperature or by heating in a reducing atmosphere causes the gold particle size to increase as if the rhodium were not present.

5. Loss of the rest of the volatile matter from the gold film in addition to annealing of the gold particles in the film. With respect to the specific property of residual resistivity, the gold film containing rhodium compares to that of well-annealed vacuum deposited or sputtered gold films prepared using ultraclean procedures (5, 7). The optical absorption of the former film also compares to that of the latter (6).

The gold films not containing rhodium were electrically discontinuous. Gold films containing rhodium became electrically discontinuous after being exposed to reducing conditions. In this latter case, the film consisted of gold particles of one micron diameter, uniformly spaced on the substrate.

Acknowledgments

The encouragement and thoughtful comments of D. G. Kelemen of the Du Pont Company are appreciated.

APPENDIX

Thickness of Rh_2O_3 Layer on a Gold Particle

If the rhodium were to be present only at the surface of the gold particle, then for a gold particle diameter (considered to be spherical) of 350Å, and a rhodium content of 0.2%

$$\frac{V_{Rh}}{V_{Au}} = \frac{M_{Rh}}{M_{Au}} \times \frac{\rho_{Au}}{\rho_{Rh}} \qquad [1A]$$

where V = volume, M = mass, ρ = density, Rh = rhodium, and Au = gold.

$$\frac{V_{Rh}}{V_{Au}} = 0.2\% \times \frac{19}{12} = 3 \times 10^{-3} \qquad [2A]$$

$$V_{Au} = \frac{4}{3}\pi R^3 \qquad [3A]$$

where R = radius of gold particle.

$$V_{Rh} = 3 \times 10^{-3} \times \frac{4}{3}\pi R^3 \qquad [4A]$$

$$\frac{\text{Rh atoms}}{\text{cm}^3} = \frac{N_o \rho_{Rh}}{N_{Rh}} \qquad [5A]$$

where N_o = Avogadro's number = 6×10^{23} molecules per gram-molecular weight, N_{Rh} = molecular weight of Rh = 103, and ρ_{Rh} = 12.4.

Define $\gamma \equiv$ Number of Rh atoms (in gold particle volume)

$$\gamma \equiv \frac{N_o \times 12}{100} \times 10^{-3} \times 4\pi R^3 \qquad [6A]$$

The surface area per gold particle, S, is given by

$$S = 4\pi R^2 \qquad [7A]$$

$$\frac{\gamma}{S} = 1.3 \times 10^{14} \frac{\text{Rh atoms}}{\text{cm}^2 \text{ Au surface}} \qquad [8A]$$

Using Eq. [5A] with the appropriate values for Au, $N_{Au} = 197$ and $\rho_{Au} = 19.3$

$$\frac{\text{Au atoms}}{\text{cm}^2 \text{ Au surface}} = 2 \times 10^{15} \qquad [9A]$$

Thus, there is approximately one Rh atom for every lattice cell of 5 gold atoms at the surface of the gold particle. After oxidation, the oxide of rhodium (presumably Rh_2O_3) occupies an area less than or equal to the complete surface area of the gold particle. This assumes uniform distribution of the rhodium, uniformly spherical gold particles, and monolayer coverage of the gold.

Manuscript submitted Feb. 19, 1970; revised manuscript received Sept. 16, 1970.

Any discussion of this paper will appear in a Discussion Section to be published in the December 1971 JOURNAL.

REFERENCES

1. G. A. Bassett *et al.*, "Structure and Properties of Thin Films," C. A. Neugebauer *et al.*, Editors, John Wiley & Sons, Inc., New York (1959).
2. R. S. Sennett and G. D. Scott, *J. Opt. Soc. Amer.*, **40**, 203 (1950).
3. O. S. Heavens, "Optical Properties of Thin Solid Films," Chap. 4, Academic Press, New York (1955).
4. K. L. Chopra, L. C. Bobb, and M. H. Francombe, *J. Appl. Phys.*, **34**, 1699 (1963).
5. J. E. Davey and R. H. Deiter, *ibid.*, **36**, 284 (1965).
6. J. E. Davey and T. Pankey, *ibid.*, **36**, 2571 (1965).
7. P. A. B. Toombs and P. Bennet, *ibid.*, **39**, 2949 (1968).
8. C. A. O. Henning and J. S. Vermaak, *Appl. Phys. Letters*, **15**, 3 (1969).
9. R. C. Langley, Engelhard Industries Technical Bulletin, **8**, 49 (1967).
10. H. Boetcher, *Trans. Indian Cer. Soc.*, **13**, 79 (1954).
11. K. H. Ballard. U.S. Pat. 2,490,399, Dec. 6, 1949.
12. H. M. Fitch, U.S. Pat. 2,984,575, May 16, 1961.
13. J. M. Morgan and C. W. Wagner, U.S. Pat. 2,842,-457, July 8, 1958.
14. W. A. Weyl and E. C. Marboe, "The Constitution of Glasses," Vol. 2, Part 2, John Wiley & Sons, Inc., New York (1967).
15. C. A. Neugebauer and M. B. Webb, *J. Appl. Phys.*, **35**, 1983 (1964).
16. *Handbook of Chemistry and Physics*, C. D. Hodgeman, Editor, Chemical Rubber Publishing Co., Cleveland, Ohio (1967).
17. A. A. Milgram and C. S. Lu, *J. Appl. Phys.*, **37**, 4773 (1966).

Glass Source B Diffusion in Si and SiO_2

D. M. Brown* and P. R. Kennicott

General Electric Research and Development Center, Schenectady, New York 12301

ABSTRACT

The general characteristics of B_2O_3-SiO_2 film diffusion sources formed by the oxidation of SiH_4 and B_2H_6 by O_2 were examined, and the diffusion of B from these glass sources into Si and through SiO_2 films was studied at 1000°-1100°C. B diffusion in (100) Si in the solid solubility region exhibits strong concentration variations as junction depths are observed first to increase and then suddenly to decrease with increasing concentrations. B diffusion through SiO_2 films was examined in two distinct regions (*i*) the "solid" state region and (*ii*) the "melt through" region where the doped glass layer dissolves the SiO_2 barrier layer at the diffusion temperatures. Understanding of these glass film diffusion sources as "glasses" aids in the interpretation of these phenomena.

It has been previously ascertained that the use of glass film diffusion sources for the formation of Si planar junctions has several advantages (1). Some of the advantages offered by these glass film diffusion sources formed by the oxidation of gaseous silanes and hydrides are: (*i*) diffused Si surface concentrations can be controlled over a wide range by variation of the dopant concentration in the glass; (*ii*) for shallow diffusions the oxide acts as a source of constant dopant concentration which helps in the reproducibility and predictability of surface concentrations and junction depths; (*iii*) surface concentrations can be held just below solid solubility which results in a minimum number of dislocations being introduced during diffusion. For instance, Fisher *et al.* have eliminated the "emitter dip" phenomenon in diffused planar n·p·n transistors (1). In addition, the dielectric qualities of these glass diffusion sources offer special advantages for the formation of self-registered MOSFET integrated circuits since the glass layer not only acts as a "well-defined" diffusion source, but in addition can also be utilized to isolate dielectrically the first and second level metallization patterns (2).

The use of doped oxide diffusion sources formed by reactive sputtering of doped Si cathodes in O_2 has been reported by Shortes and Wurst[1]; and Benjamini *et al.* have mentioned the formation of doped oxide diffusion sources by the anionic oxidation of Si[2]. Olmstead and Scott (3) have described doped oxides deposited by the pyrolysis of organosilanes. In their method, solutions of organosilanes and trimethyl borate or trimethyl phosphate were utilized as the glass forming sources. A variation of this method was utilized to form the glass sources over thin films of

* Electrochemical Society Active Member.
Key words: diffusion, borosilicate glass, MOSFETs.

[1] S. R. Shortes and E. C. Wurst, *This Journal*, **110**, 187C (1963).
[2] E. A. Benjamini, E. F. Duffek, C. A. Mylroie, and F. Schulenberg, *ibid.*, **110**, 266C (1963).

patterned refractory metal diffusion masks for the formation of self-aligned refractory metal gate MOSFETs (4).

Borosilicate Glass from SiH_4, B_2H_6, and O_2

The use of glass diffusion sources made from the low-temperature oxidation of hydrides has been reported by Mecs (5), Barry and Olofsen (6), and Fisher *et al.* (1, 7). The diffusion data in these previous works are almost exclusively those obtained from Si samples with (111) surfaces coated with the doped glass. Our interest, however, was primarily directed to the investigation of the diffusion of the boron dopant from the glass through undoped barrier oxides. A motivation for this was that, in the fabrication of self-registered MOSFETs, the diffusion of the dopant from the glass through the gate oxide is more direct since it eliminates an etching process. This in turn avoids a possible gate to substrate shorting problem which could occur if any undercutting of the gate oxide beneath the gate electrode is produced during gate oxide removal in the source and drain apertures. The (100) Si surface orientation was used because it is the preferred surface for low threshold p-channel MOSFETs.

Within this context, a number of goals are definable: (*i*) to understand these B_2O_3-SiO_2 glass film diffusion sources as glasses; (*ii*) to obtain high B concentrations within the Si after diffusion in order to minimize contact resistance; (*iii*) to diffuse for reasonable times at temperatures low enough to obtain good control of junction depth; and (*iv*) to fabricate glasses with etch rates suitable for standard photoresist patterning. As a result, these investigations using diffusion temperatures of 1000°-1100°C have (*i*) been limited primarily to the attainment of surface concentrations at or near the solid solubility limit of B in Si, and (*ii*) examined the diffusion of the boron dopant from the glass films through underlying undoped thermal oxides in two distinct regions (*a*) the region of solid-state diffusion in which the glass remains solid, and (*b*) the "melt through region" where the glass layer rapidly converts the undoped oxide into a doped glass.

Chemistry.—The primary reactions taking place in the formation of SiO_2-B_2O_3 glass from the oxidation of SiH_4 and B_2H_6 are shown in Fig. 1. Oxygen was used as the oxidant in this case (reactions A and B); however, other oxidants such as NO also appear to be favorable (A' + B').[3] The reaction kinetics taking place during the deposition of the doped glass are quite complicated, and one must guard against premature reactions in the gas stream before the gases reach the heated substrate. Other factors to consider are the relative instability of B_2H_6 and SiH_4 (C and D) and the oxidation of refractory metal films whenever one wishes to cover a refractory metal FET pattern with these glass diffusion sources (4). These problems were minimized by dilution of the O_2 and the SiH_4/B_2H_6 mixture with an argon buffer gas before introducing these mixtures into the reactor and by using a low deposition temperature (300°C). In addition, the wafers were heated to the deposition temperature in argon before introducing the reactants into the argon gas streams.

The reduction of B_2O_3 by Si (reaction E) at the glass-Si interface is usually assumed to be the mechanism that releases free B from the glass, whereupon it diffuses as an atomic impurity into the Si. The attainment of solid solubility implies the existence of a silicon-boron phase which is produced at the interface whenever the diffusion conditions are such that more B is supplied to the interface than can be dissolved in the Si. The observable existence of this phase, which may be SiB_6 (8), has been utilized by many workers to insure maximum B surface concentrations during Si diffusion processing.[4] However, this phase, usually indicated by a slight brownish stain on the wafer, is not soluble in HF acid, and its presence at the Si surface will probably be reflected in an increase in contact resistance when the diffused region is provided with a metallic electrical contact. In addition, Busen *et al.* (9) have pointed out that complete removal of this phase is required for optimal diffusion results; this requires additional processing steps. No additional steps are required when glasses of proper composition are utilized as the dopant sources during diffusion, because the formation of the B-rich Si phase can be prevented.

[3] The oxidation of SiH_4 and B_2H_6 could form H_2O rather than H_2; both reactions are favorable [see ref. (1), p. 534].

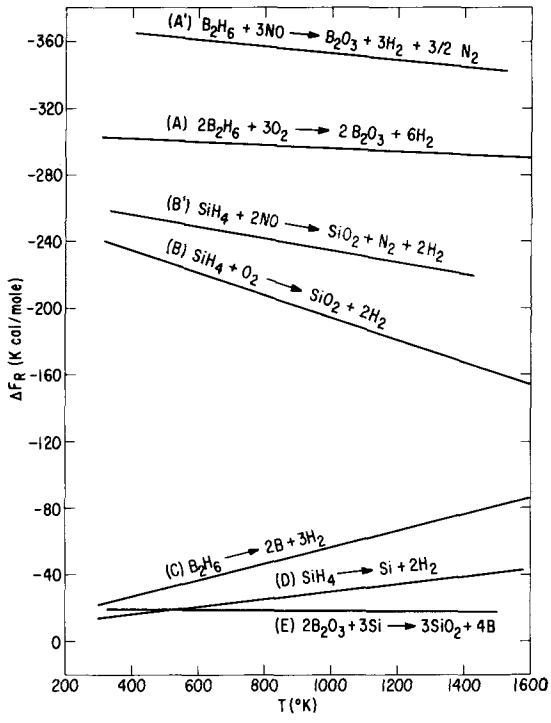

Fig. 1. Free energy of reaction vs. temperature plot for the possible reactions taking place during the pyrolysis of mixtures of SiH_4, B_2H_6, and O_2 or NO. Reaction E is generally assumed to be the reaction at the Si-glass interface which releases B from the B_2O_3 glass during diffusion. From JANAF thermochemical tables (Dow Corning).

Experimental—Sample Preparation

1 ohm-cm n-type (100) Si wafers, 2.5 cm in diameter, obtained from pulled crystal ingots, were purchased with lapped surfaces. These samples were heavily etched in $3HNO_3$:1HF and rinsed in distilled water. Thermal oxidations were carried out in dry oxygen in an apparatus previously described (10). Oxide thickness on adjacent batch control wafers was measured using both ellipsometry and MOS capacitance-voltage curves. In most instances, the thermal oxide was removed from half of the wafer's surface by photoresist and etching techniques before glass deposition. This was done in order to compare accurately the junction depths and surface concentrations for bare Si and for Si covered by undoped thermal oxides whose thickness ranged from 100 to 1500Å.

The glass depositions were done in a quartz vertical reactor 6 cm in diameter. A resistance heated platform 3 cm in diameter provided the heat required for the formation of the glass from SiH_4 diluted to 1% in A, B_2H_6 diluted to 1% in A, and pure O_2. Argon was used as the buffer gas at a total flow rate of 3800 cc/min; the flow rate of the 1% SiH_4 was fixed at 140

[4] The existence of this phase has also been indicated by studies of the ternary system Si-B-O by P. J. Gielisse, T. J. Rockett, and W. R. Foster, "Fundamentals of Silicon Integrated Device Technology," Vol. 1, p. 15, R. M. Burger and R. P. Donovan, Editors, Prentice-Hall, Inc., Englewood Cliffs, N. J.

Table I. Relationship between gas flow rates and composition

B_2H_6,* cc/min	m/o B_2H_6*	m/o B_2O_3 flame spec.	IR ratio**
1	0.7	1.6	0.07
5	3.4	4	0.20
10	6.7	8	0.35
25	15	14	0.60
50	26	18	0.77
75	35	30	1.37
96	41	33	1.55

* By metered gas flow of 1% SiH_4 and 1% B_2H_6 in A. Molar per cent B_2H_6 = $[(B_2H_6)/(B_2H_6 + SiH_4)] \times 100$. Flow meters calibrated for air; A flow = setting × 0.86.
** E. A. Taft and P. R. Kennicott, To be published.

cc/min and the O_2 at 20 cc/min.[5] The 1% B_2H_6 gas flow was varied from 1 to 100 cc/min which results in a $B_2H_6/(B_2H_6 + SiH_4)$ ratio of from 0.7% to 42%.[6] The SiH_4 and B_2H_6 flows were mixed and added simultaneously to half of the A buffer gas, the other half being added to the O_2 flow. These two flow mixtures were brought together at the reactor. During deposition, the substrate's heater platform was held at 300°C.[7] Diffusions were carried out in a very dry A atmosphere at temperatures of 1000°, 1050°, and 1100°C.

Experimental—Glass Properties

Glass composition.—The glass compositions were determined by a flame emission technique before diffusion. After etching in $3HNO_3$:1HF, wafers were rinsed, dried, and weighed on a microbalance.[8] Oxides were deposited using various flow rates of 1% B_2H_6, as described above. After deposition, the wafers were again weighed and etched in 10% HF to remove the glass. The resultant solution was diluted and measured on a flame emission spectrometer[9] to determine the concentration of boron. After etching, wafers were given a final weighing. Film weights obtained by difference between weights before and after deposition agreed with those obtained by weights after deposition and after glass removal to within ±4%. Typical film weights were of the order of 1 mg.

The flame emission spectrometer was calibrated with a series of standards prepared from a stock primary standard solution of boric acid by diluting with 10% HF.

By means of the wafers used for composition studies, a working relationship could be established between gas flow rates used to prepare the glasses and their compositions. This relationship is shown in Table I. Also included in Table I are the ratios of the 7μ B-O and 9μ Si-O infrared absorbance peaks that can be used for nondestructive quantitative control. Another means of determining glass composition is to correlate B surface concentrations in the Si after diffusion with the data of Barry and Olofsen. This comparison is described later.

Glass whose composition exceeded about 40% B_2O_3 were not intensively investigated because of their increasing tendency to absorb water.

Glass growth and etch rates.—The growth rates of the films were found to increase whenever additional amounts of the hydride reactants were added to the gas stream. This effect is shown in Fig. 2 where the growth rate is plotted *vs.* the mole per cent in the reactants and in glass. What is remarkable about this is that the growth rate increase is more than that which can be accounted for by a simple linear combination of SiO_2 and B_2O_3 deposition rates. Index of refraction and preliminary density measurements indicate that the density of these films is not abnormally

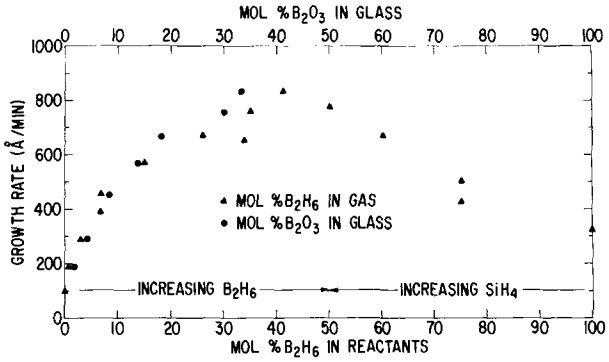

Fig. 2. Doped glass growth rates at 300°C *vs.* molar per cent B_2H_6 in gaseous reactants and molar per cent B_2O_3 in glass. From 0-50 molar per cent, SiH_4 flow kept constant at 140 cc/min; from 100-50 molar per cent, B_2H_6 flow kept constant at 140 cc/min.

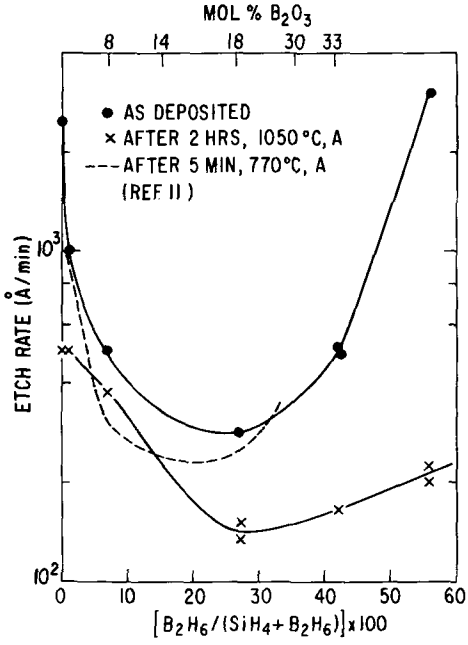

Fig. 3. Buffered HF etch rates of B_2O_3-SiO_2 glass *vs.* $B_2H_6/(SiH_4 + B_2H_6)$ flow rate ratio and glass composition. Rates given are for films after deposition and after 1050°C heating in A. The samples at highest flow ratio were made by reducing the SiH_4 flow to 80 cc/min, and using a B_2H_6 flow of 100 cm/min. Rates from ref. (11) for films heated to 770°C are included.

low. This implies that the presence of another glass forming reactant increases the over-all reaction efficiency and enhances the deposition rate.

The etch rates[10] of these glasses in buffered HF are shown in Fig. 3. The etch rates of the B_2O_3-SiO_2 glasses before being subjected to high temperatures vary between 3000 and 300 Å/min depending on composition. The lightly doped glasses etch much faster than the 750 Å/min rate obtained for dry thermal oxides. This is also true for the heavily doped glasses before heating. As shown in Fig. 3, there is a distinct minimum in the etch rate curve at a $B_2H_6/(SiH_4 + B_2H_6)$ flow rate ratio of about 0.3 (~20% B_2O_3).

A qualitative explanation for this minimum etch rate might be as follows. SiO_2 is dissolved rapidly by HF acid. As B_2O_3 is added to the glass, the etching effectiveness of the buffered HF is initially reduced. B_2O_3, on the other hand, is hygroscopic and very soluble in water, whereas SiO_2 is not, and with increasing amounts of B_2O_3, the glass begins to get hygroscopic and the dissolution rate increases rapidly again.[11] Heat-

[5] Using flowmeters calibrated for air. Flow of A = setting × 0.86.
[6] An exception to this is found in Fig. 2 where in order to investigate the growth rate *vs.* gas ratios above 40% the B_2H_6 flow was fixed at 140 cc/min and the SiH_4 flow increased.
[7] W. Kern and R. C. Heim, [*This Journal*, 117, 562 (1970)] have carried out extensive investigations on deposition techniques.
[8] Cahn Electrobalance.
[9] Instrumentation Laboratory Inc. Model 153.

[10] 10NH_4F (40%):1HF. In a 6:1 solution the etch rates are about 2X faster than those shown in Fig. 2 (J. Sprague, Private communications).
[11] Kern and Heim (11) have shown that dilute HF [1HF (49%): $2H_2O$] produces rapid dissolution of B_2O_3-SiO_2 glass and that the dissolution rate increases markedly with increases in B_2O_3 content. Their observations are consistent with this model.

Table II. Representative diffusion data (100) 1 ohm-cm Si

Diffusion	1% B_2H_6, cc/min*	Bare Si			Under oxide, X_o thick			
		ohm/□	X_j, μ	C_s/cc	X_o, Å	ohm/□	X_j, μ	C_s/cc
5.4 hr	1	131	1.3	2.5×10^{19}	1350	—	0	
1050°C	5	81.5	1.7	4.0×10^{19}	1350	—	0	
5000Å glass	10	36.2	2.3	6.0×10^{19}	1350	—	0	
	25	11.3	3.3	1.5×10^{20}	1350	—	0	
	50	11.8	3.3	4.3×10^{20}	1350	v. high	v. shallow	
	75	5.9	2.6	3.8×10^{20}	1350	6.8	2.5	3.5×10^{20}
	96	5.9	2.6	3.8×10^{20}	1350	6.1	2.6	3.8×10^{20}
1 hr	50	5.5	2.6	4.3×10^{20}	600	v. high	0.2	—
1100°C	96	5.1	2.5	4.8×10^{20}	600	5.0	2.3	5×10^{20}
2000Å glass								
8 hr 1000°C	96	9.1	2.2	3.0×10^{20}	600	8.6	2.5	2.7×10^{20}
15 hr 1000°C	50	7.5	3.0	2.4×10^{20}	600	—	0	—
2000Å glass								

* For corresponding glass compositions see Table I. ohm/□ = diffused sheet resistance of depth X_j and surface concentration C_s.

ing these B_2O_3-SiO_2 glasses to 1050°C causes the etch rates to decrease markedly. Presumably this is because these films originally formed at 300°C are not formed at full density and heating to elevated temperatures causes them to densify. For instance, for B_2H_6 flows <1 cc/min, the etch rate drops from about 2000 to 500 Å/min. This etch rate is lower than the 750 Å/min rate for thermal oxides. This is presumably caused by the presence of small amounts of B_2O_3 produced by reactor or reactor gas B contamination. The buffered HF etch rate data obtained by Kern and Heim (11) on films heated for only 5 min at 770°C are also included in Fig. 3. Comparisons of the data indicate that higher temperature heating results in a more marked decrease in buffered HF etch rates the higher the B_2O_3 concentration.

Experimental—Diffusion Studies

A large number of preliminary runs were made at 1050°C with different combinations of glasses, barrier oxide thicknesses, and diffusion times. Raw data obtained after each diffusion experiment consists of sheet conductivity in ohms per square from 4-point probe measurements and junction depth, x_j, obtained from angle lapping and staining. A conservative estimate of the accuracy of the junction depth determination is ±1000Å. Some of these data which generally summarize the findings are presented in Table II. Surface concentrations, C_s, can be obtained from these data by assuming a complementary error function distribution of electrically active diffused dopant within the Si and the use of Irvin's curves (12).[12]

Diffusion of B in Si

The surface concentration at the Si-glass interface depended on the glass composition. Within the limits of the experimental conditions, however, it was found that the surface concentration was essentially independent of doped glass thickness, diffusion time, or whether or not the B-doped glass is covered with a thin undoped capping oxide. These qualitative findings are in agreement with those reported by Fisher and Amick for diffusions at 1200°C (7).

A plot of C_s *vs.* molar per cent B_2O_3 in the glass is given in Fig. 4. Note that C_s increases with B_2O_3 concentration up to about 20%. Above 20%, C_s saturates indicating that the solid solubility of B in Si at 1050°C is about 3.8×10^{20}/cc. This number is in good agreement with the predictions of Trumbore (13) yet higher than the 2×10^{20}/cc recently given by Vick and Whittle (14).[13]

[12] This is an operational point of view. Barry and Olofsen (6) examined this point and found a satisfactory fit to the complementary-error-function distribution; however, most of their data were taken for high diffusion temperatures and lower concentrations where variations in diffusion constant with concentration are smaller.

[13] In ref. (14), Vick and Whittle assume that solid solubility is maintained by the B rich phase described in the text. These authors have apparently been very careful about taking into consideration the variations in the diffusion coefficient with concentration; however, the diffusion constants for low concentrations, where D_2 is independent of concentration, are considerably larger than any of those previously reported, *e.g.*, compare Fig. 5 and 8 of ref. (14) and (6).

After diffusion, the doping glasses were removed using buffered HF. The brownish stain and hydrophilic nature of the Si surface characteristic of the B rich Si phase (SiB_6) was observed for cases when the doping glasses contained >20% B_2O_3. As is indicated by Fig. 4 and the experimental observations described above, B concentrations approaching solid solubility in the Si can be attained by using glasses containing ≈18% B_2O_3 while at the same time eliminating the undesirable features associated with the formation of SiB_6.

Glass compositions can also be checked using the diffusion data in Fig. 4. Barry and Olofsen using flame photometric analysis showed that the B concentration in their glasses ranged from 2×10^{20} to 4×10^{21}/cc for Si surface concentrations after diffusion of from 4×10^{18} to 10^{20}/cc (6). This implies that our glasses contain about 10^{22} B/cc or about 20 molar weight per cent B_2O_3 when solid solubility in the Si is attained. Using Fig. 7 of ref. (6) with Fig. 4 enables us to check glass compositions for the range of concentrations covered by Barry and Olofsen; this correlation gives good agreement if it is assumed that all the B and Si in the films is in the form of B_2O_3 and SiO_2.

The 1050°C data and the 1000° and 1100°C data given in Table III show that for any particular diffusion time, the junction depth increases with increases in B surface concentration until solid solubility is reached whereupon there is a sudden decrease in junction depth. The raw data is summarized in Fig. 5 where

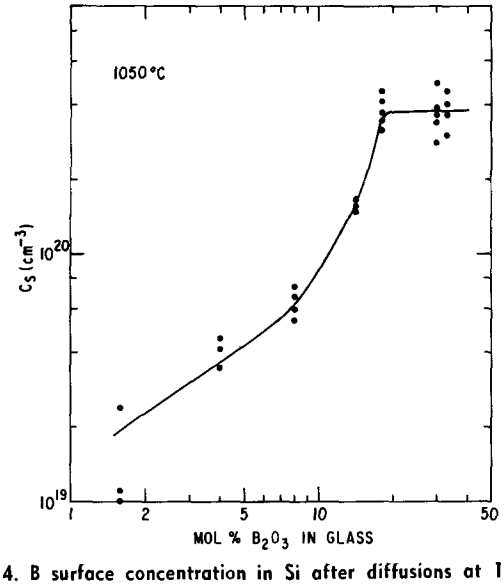

Fig. 4. B surface concentration in Si after diffusions at 1050°C *vs.* molar per cent B_2O_3 in glass sources. Assumes complementary error-function-distribution (see *e.g.*, W. R. Runyan, "Silicon Semiconductor Technology," p. 118, McGraw-Hill Book Co., New York (1965).

Table III. B/Si diffusion 1000° and 1100°C, 1 ohm-cm (100)

	Flow (1%) B_2H_6 (cc/min)	1	5	10	25	50	75	100
	Molar per cent B_2O_3 in glass	1.6	4	8	14	18	30	33
1000°C	X_j, μ	1.0	1.3	1.8	2.9	2.7	2.4	2.4
11.8 hr	ρ_s, ohm/□	200	80	30	9.1	7.7	7.7	7.7
	$C_s/10^{20}$ cc	0.22	0.48	1.1	2.3	2.8	3.2	3.2
	$D_2/10^{-14}$ cm²/sec	0.9	1.4	2.8	5.9	5.0	3.9	3.9
1100°C	X_j, μ	1.6	1.9	2.2	2.6	4.0	3.5	3.5
2 hr	ρ_s, ohm/□	180	52	33	10	3.6	3.7	3.7
	$C_s/10^{20}$ cc	0.14	0.48	0.7	2.3	4.2	4.7	4.7
	$D_2/10^{-14}$ cm²/sec	14	17	21	26	58	45	45

$(x_j/t^{1/2})$ *vs.* $(\rho_s x_j/t^{1/2})^{-1}$ is plotted,[14] x_j being the junction depth and t being the diffusion time.

The increasing part of the plot indicates that the diffusion constant of B in Si is increasing with B concentrations. This increase could be attributed to field aided diffusion (15) and/or by diffusion induced lattice defects. These variations in the diffusion constant with B concentration belie a strict adherence to the complementary error function distribution; however, in order to compare these data easily with others an error function distribution has been assumed

$$1 - \text{erf}\frac{X_j}{2\sqrt{D_2 t}} = \frac{C_B}{C_s} \qquad [1]$$

where C_B and C_s are the bulk concentration of n-type dopant and B surface concentration, respectively. This reduction of the data shown in Fig. 5 is given in Table III and Fig. 6 where the diffusion constant of B in Si, D_2, is plotted *vs.* the surface concentration obtained from Irvin's curves. These data agree well with the data of Barry and Olofsen for surface concentrations between 10^{19} and 10^{20}/cc. However, the data of Barry and Olofsen do not go beyond surface concentrations of 10^{20}/cc.

As pointed out previously, observed junction depths drop just as the solid solubility limit is reached.[15] This phenomenon is observed in the data presented in Tables II and III and Fig. 5. This in turn can be translated into a noticeable decrease in the diffusion constant as shown in Fig. 6. This decrease has not been observed previously by other workers. However, the data presented here extended to higher surface concentrations, and the experiments were done with the (100) Si surface orientation, in most cases on Si surfaces that had been stressed by thermal oxide growth previous to the deposition of the doped glass.[16]

It is not clear what this sudden decrease in the apparent diffusivity of B in Si at these very high concentrations indicates. It would be instructive to study the variation in the B diffusion profile on both sides of the peak to see if there is any noticeable change in the diffusion mechanism. For instance, the attainment of solid solubility might inhibit the substitutional/interstitial double-stream mechanism suggested by Rupprecht and Schwuttke (16). Another related speculation has to do with the character of these glass diffusion sources. During diffusion the deposited glasses could place considerable stress on the Si due to differences in thermal expansion. This stress could produce dislocations within the Si. In this regard, it is interesting to note that these glass sources begin to soften and show signs of liquification just as the solid solubility limit is reached. This point will be examined further when we examine B diffusion through SiO_2 films.

B Penetration of SiO_2 Layers

Covering undoped oxides with layers of B glass of known composition enables one to study carefully the B diffusion mechanisms through SiO_2 films. The diffusion data on the right side of Table II for these situations indicate that thin layers of SiO_2 mask the diffusion of B for the diffusion conditions stated if the glass composition does not exceed 18% B_2O_3. At higher B_2O_3 concentrations the masking ability of the SiO_2 is suddenly destroyed, and for these conditions it makes very little difference whether or not the oxide layer is there, since the junction depths and surface concentrations are nearly identical for diffusions with and without this layer. The reason for this is very likely that

[14] $\rho_s x_j$ is the parameter normally used to get surface concentrations, i.e., from Irvin's curves (12).

[15] The accuracy of the junction depth determinations at the 1-4μ level are $\leq \pm$ 10% using the $\pm$ 1000Å estimated accuracy of the angle lapping and staining technique. It is more difficult to estimate the over-all accuracy of the whole diffusion system. However, some estimate of this is found in the reproducibility of the phenomenon shown in Fig. 5 which summarizes all the data taken for different runs for various lengths of times.

[16] G. N. Willis, (*Solid State Electronics*, 12, 133), has reported a strong increase in the diffusivity of B for (100) oriented Si when diffusing in oxidizing conditions. Furthermore, dislocation generation occurs when Si wafers are thermally oxidized; see *e.g.* G. Onodera and P. Walker, *Physics of Failure in Electronics*, 5, 444 (1967).

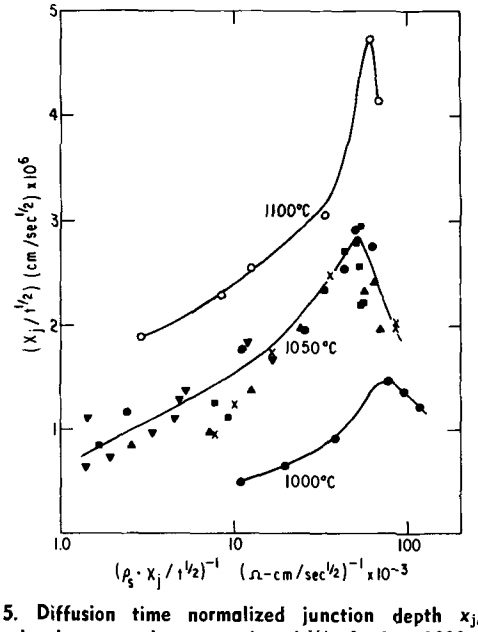

Fig. 5. Diffusion time normalized junction depth $x_j/t^{1/2}$ *vs.* normalized sheet conductance $(\rho_s x_j/t^{1/2})^{-1}$ for 1000°-1100°C diffusions.

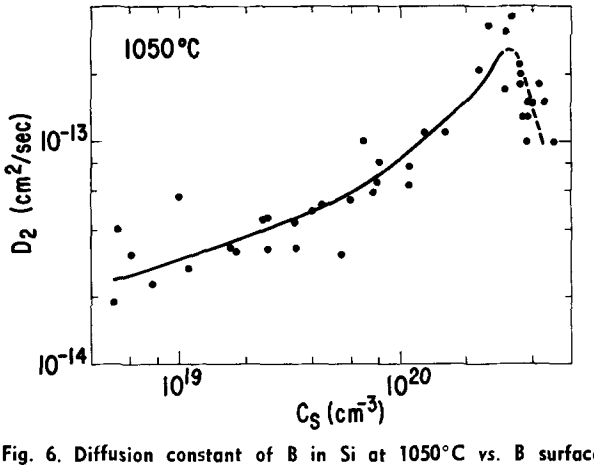

Fig. 6. Diffusion constant of B in Si at 1050°C *vs.* B surface concentration assuming complementary error function distributions.

at the higher concentrations of boron the doped glass rapidly dissolves or "melts through" the underlying oxide at high temperatures and brings B through to the Si surface with very little time delay. Similar observations were made by Horiuchi and Yamaguchi (17) who used a B_2O_3 vapor diffusion source, and found that for low B_2O_3 vapor pressures the migration of the B carrying species through the oxide can be characterized as a solid-state diffusion process but at higher pressures the underlying barrier oxide was transformed into a glassy compound by "glassy liquification."

It should be emphasized that the phase diagram for this system (18) shown in Fig. 7 is a phase equilibrium diagram in which the liquidus phase boundary divides the stable glass region (liquid) from the crystalline forms of quartz plus glasses. However, in our experiments, the substances are formed in the glassy amorphous state at low temperatures from gases, heated to diffusion temperatures and cooled. The samples, therefore, never experience the extended heating (days, weeks, months) required to attain the equilibrium state dictated by the phase diagram below the liquidus (18, 19). Above the liquidus these glasses are of course in full equilibrium. The viscosity of the glasses should have a curve similar to that exhibited by the phase equilibrium liquidus since additions of B_2O_3 lower the melting point as well as lowering the viscosity. Riebling's data at 1300°C show a very rapid decrease is viscosity with increasing B_2O_3 content for glasses containing between 0 and 55% SiO_2 (23). Decreases in viscosity reflect an increase in glass dissolution rates. A meaningful parameter for the description of interdiffusion of glasses would therefore be the viscosity; however, since the viscosity to our knowledge has not been explored for glasses containing 0-30% B_2O_3 and for lack of better words, we distinguish the two distinct regions of slow and rapid diffusion as "solid-state" or "high viscosity" diffusions and as "melt through" diffusions respectively.

In order to delineate these two distinct regions (solid-state diffusion and glassy liquification) two distinct sets of experiments were carried out: (*i*)

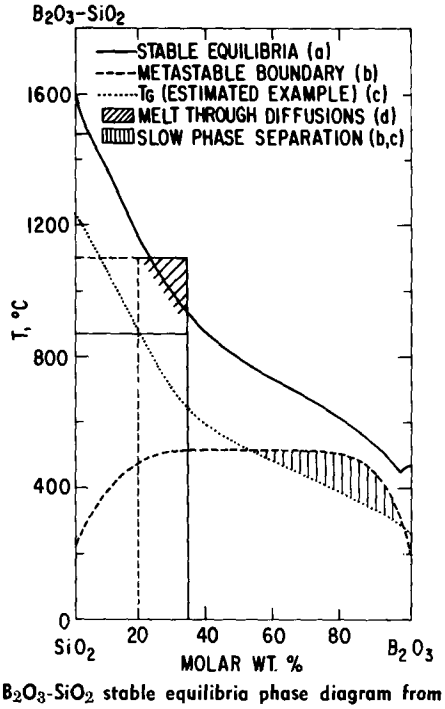

Fig. 7. B_2O_3-SiO_2 stable equilibria phase diagram from ref. (18), (a). Superimposed on this is the subliquidus miscibility gap discussed in ref. (19), (b). Included is an estimated example of the glass transition temperature curve, (c), using the information from ref. (20-22). The "melt through oxide" diffusions examined in this work (d), and the predicted region for phase separation as dictated by (b) and (c) are also shown.

Table IV. B_2O_3/SiO_2 diffusion at 1050° and 1100°C using 18% mol. % B_2O_3 glass

T, °C	t, hr	$D_2/10^{-13}$ cm²/sec	x_{of}, Å	$r^2/10^{-4}$	$D_1/10^{-17}$, cm²/sec
1050	15	1.4 ± 0.6	770	0.76	1.1
1100	8	4.0 ± 1	950	0.8	3.4

solid-state diffusions with glass sources made using a 50 cc/min B_2H_6 flow rate (~18% B_2O_3) and "melt through" diffusions using a glass source formed by using a 75 cc/min B_2H_6 flow rate (~30% B_2O_3).

Solid or high viscosity state diffusion through SiO_2 *films.*—The two boundary diffusion mode of Sah *et al.* (24) which results in a series expansion of erf terms, gives for the concentration of dopant in the Si, C_2

$$C_2(x,t) = m(1-\alpha)\, C_0 \sum_{n=0}^{\infty} \alpha^n \operatorname{erfc} \frac{(2n+1)x_o + rx}{2\sqrt{D_1 t}} \quad [2]$$

where C_0 is the concentration of dopant in the diffusion source layer; m is the segregation constant of diffusant at the Si-SiO_2 interface; $r = \sqrt{D_1/D_2}$ in which D_1 and D_2 are the diffusion constants of the dopant within the oxide and Si, respectively, and $\alpha = (m-r)/(m+r)$. This equation can be approximated by the first term of the series in the nearly masking condition for which x_o, the oxide thickness, is greater than rx_j and $x_o/2\sqrt{D_1 t} > 0.7$. The relation between the oxide thickness and the junction depth x_j then becomes

$$\frac{x_o + rx_j}{2\sqrt{D_1 t}} = \arg\left[\operatorname{erfc} \frac{C_3}{m(1-\alpha)C_0}\right] \quad [3]$$

where $C_3 = C_2(x_j,t)$. Since for a given diffusion condition the right-hand side of Eq. [3] is constant, one can plot x_j for a range of x_o for a constant diffusion time and temperature to obtain r. The extrapolation of this plot to $x_j = 0$ gives the mask failure condition, $x_o(x_j = 0) = x_{of}$ and by Eq. [3], $x_o + rx_j = x_{of}$.

The results of these experiments, Fig. 8, and the determination of D_1 at 1050° and 1100°C using the D_2 values of Fig. 6 and Table III are presented in Fig. 9 and Table IV. Figure 9 compares these points with the higher temperature extension of the D_1 *vs.* (T^{-1}) line of Horiuchi and Yamaguchi (17).

Melt through B *permeation of* SiO_2 *films.*—As pointed out previously there is a sudden appearance of B in the Si covered with thermal oxides if the doped glass layer contains about 30% B_2O_3. This implies a liquification and dissolution of the oxide layer by the doped glass. This phenomena was studied in more detail by covering a series of oxide layers with 3000Å of 30%

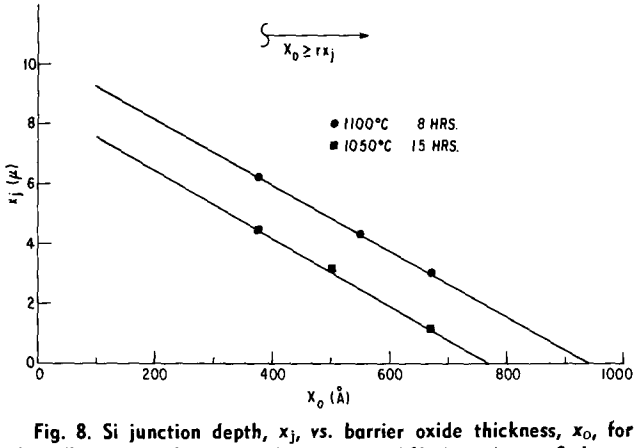

Fig. 8. Si junction depth, x_j, *vs.* barrier oxide thickness, x_o, for "solid" state diffusions with constant diffusion times; 8 hr at 1100°C and 15 hr at 1050°C. Doped glass source is 18% B_2O_3.

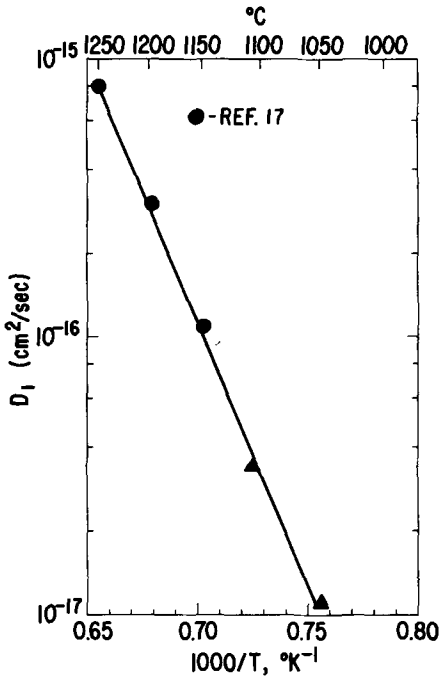

Fig. 9. "Solid" state diffusion coefficient of the B carrying species in amorphous thermal SiO_2 vs. 1000/T, °K^{-1}.

B_2O_3 glass and diffusing these series at 1000°, 1050°, and 1100°C. The junction depth and surface concentration data are summarized in Fig. 10. It can be contrasted to the data of Fig. 8. Several aspects of Fig. 10 are worth noting. For instance, this method greatly decreases the times required to obtain any given junction depth. In fact, for thin oxides this method of diffusion results in very little diminution of the junction depths and surface concentrations obtained for these same temperatures and times compared to those cases when the doped glass is placed directly on Si. The surface concentration obtained after heating is maintained close to the solubility limits by the glass source for a considerable range of underlying oxide thicknesses. For example, at 1100°C, the surface concentration is 3 x 10^{20}/cc for x_o = 1250Å even though the junction depth has been diminished to 1.8μ as compared to 4μ for the very thin oxide layers. This is because the 3000Å 30% B_2O_3 glass dopant source contains enough B_2O_3 to convert the underlying oxide as well as provide enough B to heavily dope the Si. The surface concentrations decrease rapidly by many orders of magnitude as the masking condition is approached. Masking oxides are indicated by the intercept of the curves with the abscissa for the conditions stated.

The mode in which the masking condition is approached is interesting to consider. The "liquid glass" as it "melts through" the underlying SiO_2 is being diluted by additions of SiO_2 and becomes more viscous.

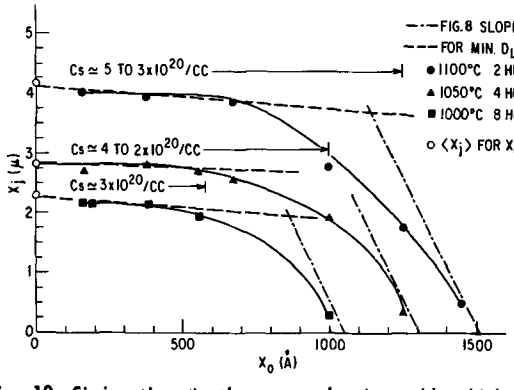

Fig. 10. Si junction depth, x_j, vs. barrier oxide thickness, x_o, for "melt through" diffusions. Doped glass is 3000Å of 30% B_2O_3.

When the concentration drops below that required to maintain a liquid or low viscosity condition, the front comes to a stop, and the diffusion of B impurities is governed by the "solid" state diffusivities of Fig 9. Thus the curves in Fig. 10 are seen to approach asymptotically the slopes given by Fig. 8, as shown. This self-limiting feature can be used to advantage. For instance, lateral diffusion of the dopant in the SiO_2 under the edges of a self-registered MOSFET gate electrode will be automatically inhibited by these glass characteristics.

A lower limit for the liquid or low viscosity diffusion constants of B_2O_3 in SiO_2 can be estimated using the dashed lines in Fig. 10 and Eq. [3]. These estimates for temperatures of 1000°C $\leq T \leq$ 1100°C give diffusion constants of 2 x 10^{-15} cm²/sec $\leq D_1(L) \geq$ 2 x 10^{-14} cm²/sec which are many orders of magnitude higher than the corresponding solid state diffusion constants of Fig. 9 ($\leq$4 x 10^{-17} cm²/sec).

Figure 10 shows that for temperatures $\geq$1050°C, rapid "melt through" diffusion of thin oxides ($\leq$1000Å) can be attained with a 30% B_2O_3 doped glass diffusion source. In turn the resultant glass at the glass-Si interface can supply enough B atoms to the Si to approach B solid solubility. Yet it is interesting to note that the resultant dilution of the 30% glass appears to prevent any noticeable formation of the B-rich Si phase. Visual observations on surfaces of samples with high surface concentrations showed that the side of the wafer that was covered by the thermal oxide was characteristically hydrophobic while the other side was hydrophillic and showed a brownish stain characteristic of the B-rich silicon phase. However, both sides of the wafer had nearly identical sheet conductivities characteristic of surface concentrations close to B solid solubility.

Summary

Glass film diffusion sources were examined from a broad perspective. Their properties as glasses were found to conform with observed diffusion phenomena in Si and SiO_2. An operational point of view was also maintained, because these films are thought to offer methods of fabricating self-registered MOSFETs and integrated circuits in general.

The growth and etch rates and diffusion properties of B_2O_3-SiO_2 glass films formed by the low-temperature oxidation of SiH_4 and B_2H_6, with O_2 were determined. The growth rates, for the conditions stated, ranged between 200 and 800 Å/min and yielded diffusion source glass films which made it possible to obtain B concentrations up to and including solid solubility in the Si surface at diffusion temperatures between 1000° and 1100°C. These films have good physical characteristics in this "solid solubility region." They show no evidence of being hygroscopic and measurement of the glass composition indicates that solid solubility is attained when the glass contains about 20 molar weight per cent B_2O_3. In addition, the B_2O_3-SiO_2 phase diagram indicates that no phase separation should occur for glasses containing less than 40% B_2O_3. "Melt through SiO_2 diffusions" were observed to occur at 30% B_2O_3, and this agrees at least qualitatively with expected decreases in glass viscosity. Unfortunately, the etch rates of the glasses in this region are rather low when buffered HF is used and this will limit the film thicknesses to about 3000Å for ordinary photoresist patterning. However, etches which etch B_2O_3-SiO_2 glasses at rates which increase with the molar per cent B_2O_3 have been developed by others (11, 25, 26) and might be used to advantage.

The diffusivity of B in Si and thermal SiO_2 films was carefully examined. The diffusion of high concentrations of B in Si at 1000°-1100°C exhibits a diffusivity that increases with concentration until the solid solubility limit is reached, whereupon it drops to a smaller level. This sudden decrease was found to correspond with the glass melt through condition, and possible mechanisms for this were discussed.

The diffusion of the boron carrying species in SiO_2 was examined in the region of "solid" state diffusion at 1050° and 1100°C and the diffusion constants, 1.1 and 3.4 x 10^{-17} cm^2/sec, respectively, were found to agree well with the previous higher temperature data of Horinchi and Yamaguchi (17).

The melt through condition for the dissolution of the underlying undoped SiO_2 film was established and examined for a range of temperatures and SiO_2 thicknesses.

The importance of using the melt through condition for diffusions appears to be that: (*i*) the time required to diffuse through thin undoped oxides is greatly reduced, which in turn makes the diffusion properties of B in Si the controlling factor in determining junction depth; and (*ii*) it is expected that the strain on the underlying Si and diffusion barrier films is greatly reduced. For instance, borosilicate glasses containing about 30 molar per cent B_2O_3 have linear thermal expansion coefficients close to that of Si and Mo (27).

The general applicability of these glass film diffusion sources for the fabrication of self-registered refractory metal MOSFETs will be examined in a subsequent article.

Acknowledgments

All the experimental work including the construction of the reactor, glass depositions, diffusions and experimental work was done by G. J. Charney. Oxide thicknesses were measured ellipsometrically by J. R. M. Viertl and by MOS capacitance methods by G. R. Zempel. The flame spectrometer was operated by R. F. Reihl. The authors gratefully acknowledge the discussions with R. J. Charles and J. Wong on B_2O_3-SiO_2 glass phase diagrams. The infrared absorbance information is due to E. A. Taft. Comments by W. E. Engeler, E. A. Taft, and R. N. Hall were extremely helpful.

Manuscript submitted May 21, 1970; revised manuscript received *ca.* Sept. 4, 1970.

Any discussion of this paper will appear in a Discussion Section to be published in the December 1971 JOURNAL.

REFERENCES

1. A. W. Fisher, J. A. Amick, H. Hyman, and J. H. Scott, *RCA Rev.*, **29**, 533 (1968).
2. W. E. Engeler, D. M. Brown, J. Sprague, W. Thompson, and V. Bluhm, RNP 360, presented at the New York Meeting of the Society, May 4-9, 1969; also Paper 191 presented at the Detroit Meeting of the Society, Oct. 5-9, 1969.
3. J. Scott and J. Olmstead, *RCA Rev.*, **26**, 357 (1965).
4. D. M. Brown, W. E. Engeler, M. Garfinkel, and P. V. Gray, *Solid State Electronics*, **11**, 1105 (1968); *This Journal*, **115**, 874 (1968); **114**, 274C (1967).
5. B. M. Mecs, Paper 93 presented at the Boston Meeting of the Society, May 5-9, 1968.
6. M. L. Barry and P. Olofsen, *This Journal*, **116**, 854 (1969).
7. A. W. Fisher and J. A. Amick, *RCA Rev.*, **29**, 549 (1968).
8. C. F. Cline, *Nature*, **181**, 476 (1958).
9. K. M. Busen, W. A. Fitzgibbons, and T. Kloffenstein, *Electrochem. Tech.*, **6**, 256 (1968); K. M. Busen, W. A. Fitzgibbons, and W. K. Tsang, *This Journal*, **115**, 291 (1968).
10. D. M. Brown and P. V. Gray, *This Journal*, **115**, 760 (1968).
11. W. Kern and R. C. Heim, *ibid.*, **117**, 568 (1970).
12. J. C. Irvin, *Bell System Tech. J.*, **41**, 387 (1962).
13. F. A. Trumbore, *ibid.*, **39**, 205 (1960).
14. G. L. Vick and K. M. Whittle, *This Journal*, **116**, 1142 (1969).
15. A. D. Kurtz and R. Yee, *J. Appl. Phys.*, **31**, 303 (1960).
16. H. Rupprecht and G. H. Schwuttke, *ibid.*, **37**, 2862 (1966).
17. S. Horiuchi and J. Yamaguchi, *Jap. J. Appl. Phys.*, **1**, 314 (1962).
18. T. J. Rockett and W. R. Foster, *J. Am. Ceram. Soc.*, **48**, 75 (1965).
19. R. J. Charles and F. E. Wagstaff, *ibid.*, **51**, 16 (1968).
20. P. B. Macedo, W. Capps, and T. A. Litovitz, *J. Chem. Phys.*, **44**, 3357 (1966); C. A. Angell, *J. Amer. Ceramic Soc.*, **51**, 117 (1968).
21. H. Rawson, "Inorganic Glass Forming Systems," p. 67, Academic Press, New York (1967).
22. A. J. Easteal, D. Chin, J. Wong, I. M. Hodge, and C. A. Angell, To be published.
23. E. F. Riebling, *J. Amer. Ceram. Soc.*, **47**, 478 (1964).
24. C. T. Sah, H. Sello, and D. A. Tremere, *J. Phys. Chem. Solids*, **11**, 288 (1959).
25. W. A. Pliskin and H. S. Lehman, *This Journal*, **112**, 1013 (1965).
26. A. H. El-Hoshy, *ibid.*, **117**, 1583 (1970).
27. R. F. Geller, E. N. Bunting, and A. S. Creamer, *J. Research Natl. Bur. Standards*, **20**, 57 (1938).

Liquid Encapsulated Czochralski Growth of GaAs

M. E. Weiner,* D. T. Lassota, and B. Schwartz*

Bell Telephone Laboratories, Incorporated, Murray Hill, New Jersey 07974

ABSTRACT

Melt growth of gallium arsenide single crystals by the Czochralski technique has required rather complex equipment because of the high vapor pressure of arsenic. A recently developed technique known as liquid encapsulated growth overcomes a number of the problems involved and allows gallium arsenide to be grown in a commercial silicon crystal puller. Crystals about 1 in. in diameter weighing 80g have been grown nearly routinely. One crystal with a maximum diameter of 2¼ in. weighing 370g was grown, but it appears to be highly strained. Undoped crystals grown in quartz or alumina crucibles have as-grown resistivities greater than 10^5 ohm-cm. On heat treatment at 800°C for 24 hr, the crystals grown in quartz convert to n-type with carrier concentrations in the range 10^{15} cm^{-3} to 10^{16} cm^{-3} and room temperature mobilities from 5400 cm^2/V-sec to 6300 cm^2/V-sec. The crystals grown in alumina retain high resistivity after heat treatment. The heat treatment behavior is explained by a model based on the incorporation of SiO molecules in the crystals grown in quartz and the breakup of these molecules into silicon atoms and SiO_2 molecules on heat-treatment.

The major problems in the melt growth of the III-V compounds GaP, GaAs, InP, and InAs are associated with the high vapor pressures of phosphorus and arsenic at their respective melting points. In order to keep the melt near stoichiometry, one must either control the vapor pressure of the volatile element or somehow prevent it from leaving the melt. In order to control the vapor pressure, one must have an excess of elemental phosphorus or arsenic at the coldest point in the system. For these compounds, this temperature is in the range 550°-700°C. Clearly, Czochralski growth of these compounds, with its requirement for high temperature gas-tight seals, presents severe technological problems if one must control the vapor pressure of the volatile element. A variety of techniques has been developed for Czochralski growth with vapor pressure control (1). These have been used successfully for GaAs and InAs, where the arsenic vapor pressures are 0.9 and 0.3 atm, respectively (1). However, the vapor pressures of phosphorus over GaP and InP are much higher, making melt growth by these techniques nearly impossible. In order to avoid the problems related to vapor pressure control, the liquid encapsulation technique was developed (2-4). This technique involves covering the melt with a suitable liquid and filling the remaining volume of the system with an inert gas above the vapor pressure of the volatile element. The volatile element is then trapped below the liquid (except for diffusion through it). The term "liquid encapsulation" arises from the idea that the ideal liquid would tend to "encapsulate" both the melt and the growing crystal, thus protecting both from loss of the volatile element and from reaction with the crucible. Since an inert gas is used to balance the vapor pressure of the volatile element, the walls of the crystal puller can be at room temperature. This clearly makes the problem of the gas-tight seals much simpler to overcome. In the case of InAs and GaAs, the pressures are low enough to allow the use of the same type of crystal puller designed for nonvolatile materials. Because the melting point of GaAs is not too far from the melting point of silicon [1238° *vs.* 1415°C (5)], it was decided to try to grow GaAs in a commercial silicon crystal puller. Although this article deals specifically with the problems of liquid encapsulated growths of GaAs, much of it is relevant to the growth of the other compounds mentioned above.

The Encapsulating Liquid

The ideal encapsulating liquid should have the following properties:

1. It should be less dense than the melt.
2. It should not react with the melt.
3. It should wet but not react with both the crucible and the growing crystal.
4. It should be immiscible with the melt.
5. It should be transparent.
6. It should melt well below and have a low vapor pressure at the melting point of gallium arsenide.
7. It should be available in a high-purity grade.

The encapsulant that has been most widely used in the liquid encapsulated growth of gallium arsenide is boric oxide (2-4); it is the only encapsulant used in the experiments described in this article. Boric oxide meets condition 1 very well ($\rho_{B_2O_3}$ = 1.8 g/cm^3 *vs.* ρ_{GaAs} = 5.3 g/cm^3). Condition 2 is met for undoped melts in that there is no reaction severe enough to prevent growth of a single crystal. However, the presence of a significant amount of gallium in the boric oxide after growth (see Table I) does indicate that a reaction of some kind has taken place. Because boric oxide is known to be very hygroscopic, and also because there is a very low concentration of boron in the gallium arsenide after growth (see Table II), it is believed that the presence of the gallium in the boric oxide is related to the presence of water of hydration rather than to a direct reaction with the boric oxide itself (see section on Analysis of Data). However, one

Table I. Quantitative analysis (in w/o) for gallium and silicon in boric oxide after growth

	Undoped crystals grown in quartz		
	C8	C9	C10
Silicon	0.09	0.07	0.20
Gallium	0.18	0.12	0.22
	Undoped crystal grown in alumina		
Silicon		<0.01	
Gallium		0.13	

Table II. Spark source mass spectrographic analysis (ppm atomic) of liquid encapsulated GaAs grown in quartz

	Sample		
Impurity	C8	C9	C10
B	0.01	0.01	0.01
C	3.2	4	2.4
N	0.4	0.6	0.4
O	2.5	5.2	0.7
Si	≦10	≦6	≦6
Cu	<0.01	<0.01	<0.2
P	0.5	0.2	≦0.2

* Electrochemical Society Active Member.

Key words: semiconductor crystal growth, heat-treatment of GaAs, boric acid, silicon contamination of GaAs.

Table III. Emission spectrographic analysis (in w/o) for all metallic impurities in B_2O_3 after growth

Impurity	Sample (quartz crucible) C8	C9	C10	Sample (alumina crucible) C19
Si*	0.X low	0.0X	0.X	0.0X low
Ga	0.X low	0.0X high	0.X	0.0X high
Al	0.000X	None	None	0.X low
Ca*	0.000X low	0.000X low	0.000X	0.000X
Mg	None	None	0.000X	0.000X

* Emission analysis prior to growth of a typical sample of B_2O_3 showed the presence of these elements at the level 0.000X low. No other impurities were found by emission analysis.

would expect the boric oxide to react with melts doped with strong reducing agents, such as silicon (4). Condition 3 is only partly met for quartz or alumina crucibles in that silicon or aluminum is detected in the boric oxide in significant amounts after growth (see Table III). This presents no obvious problems during the actual growth operation, but clearly the electrical properties of the grown crystals are affected (see section on Electrical Properties of Undoped Crystals). The quartz crucibles are wetted very well by the liquid boric oxide, whereas the alumina crucibles are wetted only slightly. There appears to be no reaction between the boric oxide and the growing crystal, and the crystal will be wetted by the boric oxide if the surface is cool enough. Condition 4 is met very well in that the interface between the boric oxide and the gallium arsenide melt is sharply defined. Condition 5 is met well for undoped melts unless the top surface of the boric oxide becomes too cool; then some very fine particles may appear. This visibility problem is eliminated as soon as the surface temperature is raised. Other visibility problems are associated with the high index of refraction (about 1.5) of the boric oxide and the inherent difficulty in seeing an interface between two radiating materials at the same temperature. Condition 6 is met well, since boric oxide melts at about 450°C (nearly 800°C below the melting point of gallium arsenide) and has a vapor pressure of about 0.1 mm at the melting point of gallium arsenide [calculated from thermochemical data (6)]. Actually, boric oxide should not be used below 800°C (2) because it becomes too viscous, but this presents no problems in the growth of gallium arsenide. There is some evidence of evaporation of boric oxide during growth, but not nearly enough to cause a problem. Condition 7 appears to be met satisfactorily, although it is very difficult to determine the source of trace impurities. The boric oxide used in all these experiments was Optran Grade Fused Lumps of 99.995+% purity supplied by the Atomergic Chemetals Corporation. Boric oxide of a lower grade has been used successfully by others (3). The major undesirable component in boric oxide is water (the level of water is not included in the quoted total impurity content). Large amounts of water will lead to severe bubbling when the boric oxide is heated and can cause a loss of up to 50% of the boric oxide by bubbling over the side of the crucible. The effect of a small amount of water seems to be similar to the effect of a small amount of oxygen or Ga_2O on Bridgman crystals (7) (see section on Analysis of Data). Approximately 50g of boric oxide were used for each run.

In order to remove most of the water from the boric oxide, a high temperature bakeout under vacuum conditions was used. The platinum crucibles used for this operation showed no evidence of reaction with the boric oxide and were used repeatedly. Because a determination of the absolute amount of water in the boric oxide is difficult, it was decided to use a standard bakeout procedure to minimize differences caused by variations in the amount of water. The bakeout was done at 1000°C (see Fig. 1) under a starting pressure

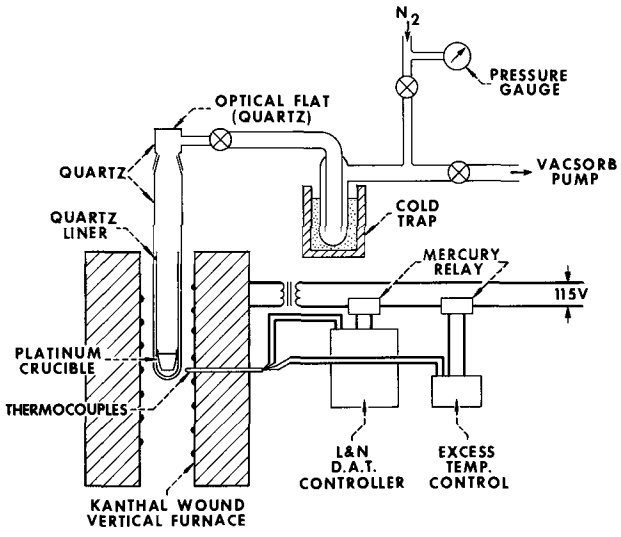

Fig. 1. System for vacuum drying of B_2O_3

of about 200 Torr of nitrogen, with a liquid nitrogen cold trap in the system. The pressure was gradually lowered while the degree of bubbling was observed through the optical flat. When the bakeout proceeded overnight, a dry ice-isopropyl alcohol trap was substituted for the liquid nitrogen trap in order to maintain the equilibrium vapor pressure of water at about 0.5μ. The entire procedure took approximately 24 hr, including 1-2 hr under a vacuum of about 10μ.

No simple way was found to remove the solid boric oxide from the platinum crucible after the bakeout procedure in order to transfer it to the crystal puller. It was decided, therefore, to position the platinum crucible containing the B_2O_3 upside down in the crystal puller and use the heat from the crystal puller to melt the boric oxide (see Fig. 2). Once the boric oxide melts, it pours over the gallium arsenide charge. This melting and pouring takes place with the gallium arsenide at about 700°C and the pressure in the crystal puller at 3-5 psig.

The Crystal Puller

The crystal puller used for all liquid encapsulated growths of gallium arsenide has been the NRC Equipment Corporation Model 2805 Czochralski furnace shown in Fig. 3. The glass rod passing through the viewing port on the right is used to manipulate the boric oxide container (see Fig. 2). The heater assembly used is that designed for NRC's smaller Model 2804 furnace. The only modifications necessary for growing

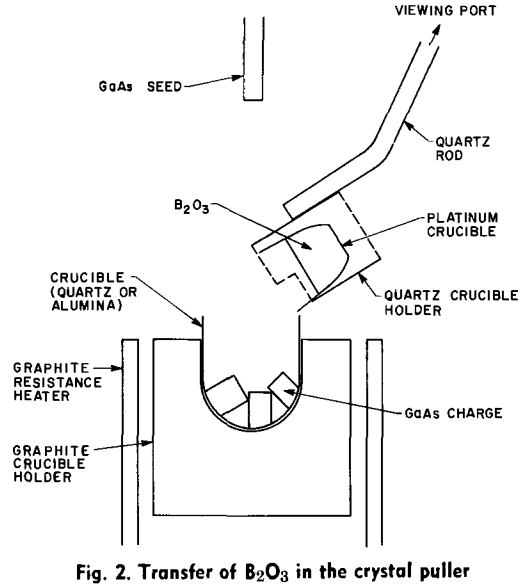

Fig. 2. Transfer of B_2O_3 in the crystal puller

Fig. 3. NRC Model 2805 crystal puller used for liquid encapsulated growth of GaAs.

gallium arsenide were the fabrication of a holder for the platinum crucible containing the boric oxide, and the use of a specially designed seed chuck. The furnace is heated by a graphite resistance heater which is powered by a saturable core reactor. The temperature sensing element is a L & N Rayotube, which is aimed at the bottom of the graphite crucible holder. The temperature may be controlled and programmed automatically via a L & N CAT controller, and the crucible and seed shaft may be rotated and translated at variable rates.

The graphite crucible holder was fabricated by the Ultra Carbon Corporation from grade UF-4S high purity graphite. It has close-fitting spacers available so that the crucible may be positioned at various heights in the holder. The quartz crucibles used in these experiments were fabricated by the Thermal American Fused Quartz Company from Vitreosil fused quartz. The alumina crucibles were supplied by the Coors Porcelain Company. They were grade AD-999 with a nominal purity of 99.98%. The holder for the platinum crucible containing the boric oxide (see Fig. 2) consists of a 9 mm quartz rod attached to a holder so designed that it supports the platinum crucible in an inverted position without itself coming into contact with the boric oxide during the pouring process. A coupling allows the rod to be moved so that the platinum crucible may be properly positioned for pouring the boric oxide and may be pulled out of the way during growth. The seed chuck consists of a molybdenum rod with a ⅛ in. hole drilled in it at its lower end. There is a stainless steel set screw positioned in the side of the rod about ½ in. above the bottom. The seed is supported by several strands of molybdenum wire which are wrapped around the seed and twisted above it. The twisted wire is inserted into a partly split molybdenum rod and held in place by the set screw. This method of supporting the seed is believed to have two main advantages over a more rigid technique. First, less vibration is transferred from the seed chuck to the seed, making it possible to take full advantage of damping by the highly viscous layer of boric oxide. Second, the seed is protected from breaking in case the melt suddenly freezes out to the crucible.

The Crystal Growth Operation

The crucible (quartz or alumina) is degreased, cleaned with aqua regia, rinsed with methanol and a 10% KCN solution, and positioned in the graphite crucible holder. Approximately 100g of polycrystalline gallium arsenide are degreased, etched with aqua regia, rinsed with methanol, and placed in the crucible. The graphite crucible holder is positioned with its top about ½ in. below the top of the heater. The seed is oriented in the <111> direction with the (111)A(Ga) face toward the melt. This arrangement has been shown to give a lower twinning probability than the (111)B(As) face (8). The platinum crucible containing the baked-out boric oxide is removed from the quartz vacuum chamber and positioned in the quartz holder just above the gallium arsenide source material (see Fig. 2). The crystal puller is then evacuated overnight. Before the heater is turned on, the crystal puller is flushed with argon or helium and pressurized to about 1 psig. Heating is started manually at a power level of about 3 kW. At this power level, the boric oxide starts to flow in 30-45 min. The gallium arsenide charge is at about 700°C by this time. After the boric oxide has finished flowing, the quartz holder is moved out of the way, the puller is pressurized to about 5½ psig, and the gallium arsenide is heated to its melting point. When the gallium arsenide starts to melt, one must proceed slowly and carefully, for once all the gallium arsenide is melted the temperature may rise rapidly, causing severe loss of arsenic as the arsenic vapor pressure rises above the inert gas pressure. Some arsenic is always lost during melting, as indicated by a coating on the viewing port. After the melt is stabilized at the growth temperature, very little arsenic is lost. Just prior to seeding, the graphite crucible holder is raised so that its top is level with the top of the heater. This allows a temperature gradient across the 1-1½ cm thick layer of boric oxide sufficient to minimize loss of arsenic from the grown crystal. Some difficulty is encountered in determining the point of contact between the seed and the melt and knowing when growth begins. With experience, however, these problems have gradually been solved. During growth, the seed is rotated at 23 rpm, the crucible is rotated at 7 rpm in the same direction, and the seed is pulled at 0.007 in./min. (Actually, pulling is started at a lower value and increased to this value after about ½ in. of growth.) The surface of the melt is always very clean during growth.

Control of the shape of the crystal is accomplished by varying either the crucible temperature or the rate of temperature change. The crucible is approximately 2 in. in diameter and 2 in. high, and the usual charge of gallium arsenide is 100g. The crystals grown are

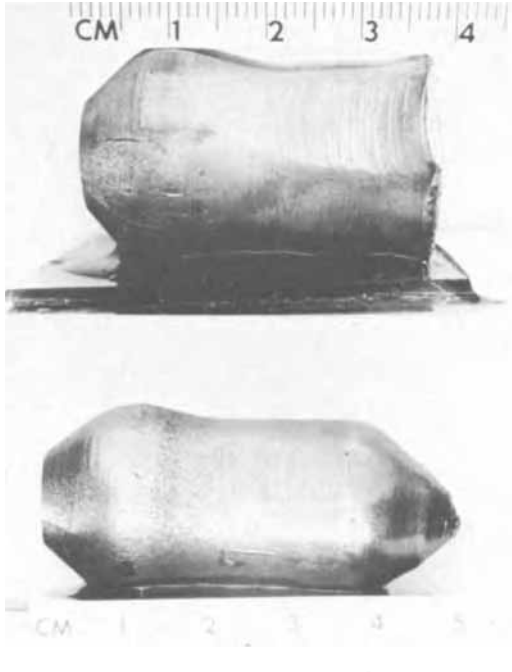

Fig. 4. Two typical liquid encapsulated GaAs crystals

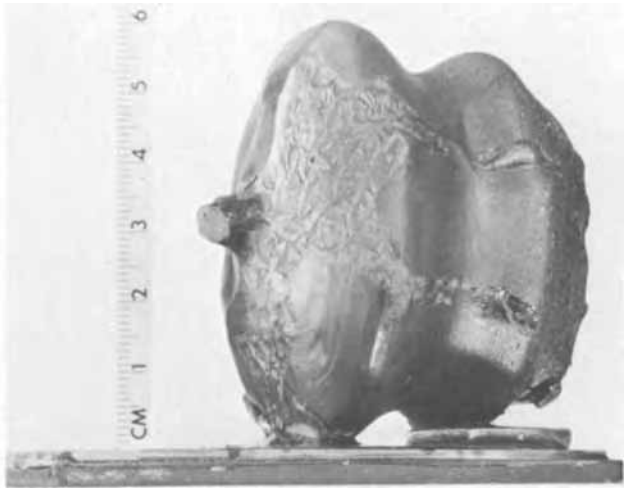

Fig. 5. Photograph of 2¼ in. diameter liquid encapsulated GaAs crystal.

generally ¾-1 in. in diameter and weigh about 80g. Photographs of two crystals of this size are shown in Fig. 4. One attempt was made to grow a crystal of larger diameter by using a larger crucible (3 in. in diameter) and a larger charge (460g). This crystal is shown in Fig. 5; it has a maximum diameter of 2¼ in. and weighs 370g. It is single, as indicated by symmetrical facets except near the end, where the charge was depleted and the crystal touched the crucible. From Fig. 5 it may be seen that the main problem in growing this crystal was temperature control. It appears that as the crystal diameter increased, diameter control became much more sensitive to temperature variations. The main growth problem was in "shouldering" the crystal. The problem of controlling the diameter of a crystal of this size can probably be solved by accumulating experience on temperature control and crucible configuration. A crack may be noticed in Fig. 6. Presumably it is due to strain resulting from too rapid cooling during growth; this problem could be overcome by the use of afterheaters. The "chipped" appearance of the surface was caused by B_2O_3 sticking to the crystal. This problem could be eliminated by varying thermal conditions to lower the viscosity of the B_2O_3. The surfaces of the crystals are usually shiny near the top and slightly etched near the bottom. This indicates that protection against loss of arsenic from the surface decreases as the level of the boric oxide drops. After the crystal is pulled out of the boric oxide and the furnace is cooled, the quartz crucibles generally shatter while the alumina crucibles either remain intact or show only one or two cracks. When a quartz crucible is used, the boric oxide is gray and opaque in appearance after growth, when an alumina crucible is used, the boric oxide is brownish and translucent. In either case, the boric oxide is full of bubbles generated during cooling. The platinum crucible which held the boric oxide is also slightly discolored, presumably because of the reaction of arsenic with the exposed platinum (9). The discoloration of the platinum disappears rapidly when the crucible is heated in air.

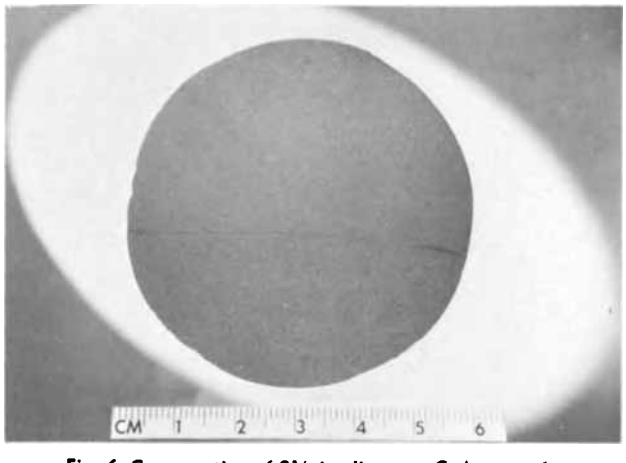

Fig. 6. Cross-section of 2¼ in. diameter GaAs crystal

Electrical Properties of Undoped Crystals

The properties of seven undoped crsytals are described in this article; four of these were grown in quartz and three in alumina. The source material for the four growths in quartz and for one of the growths in alumina was obtained from Bell and Howell Research Laboratories, and the source material for the other growths in alumina was obtained from the Monsanto Company. All seven crystals had resistivities greater than 10^5 ohm-cm as grown. A good value for the resistivities of the samples grown in quartz could not be obtained, apparently because of inhomogeneities in the material. Resistivity measurements on the samples grown in alumina were quite straightforward, with values from 2 x 10^7 to 6 x 10^7 ohm-cm. Slices cut from each of the seven crystals were heat treated in vacuum at 800°C for 24 hr. In order to avoid contamination of the gallium arsenide during heat treatment, Spectrosil fused quartz ampoules rinsed in a 10% KCN solution were used. The ampoules were evacuated with an ion pump to 10^{-6} Torr prior to sealing. After heat treatment, the slices from the crystals grown in quartz converted to n-type. The electron concentrations of the slices from the four crystals grown in quartz are shown in Fig. 7 and their Hall mobilities, in Fig. 8. The slices from the crystals grown in alumina showed no apparent change on heat treatment.

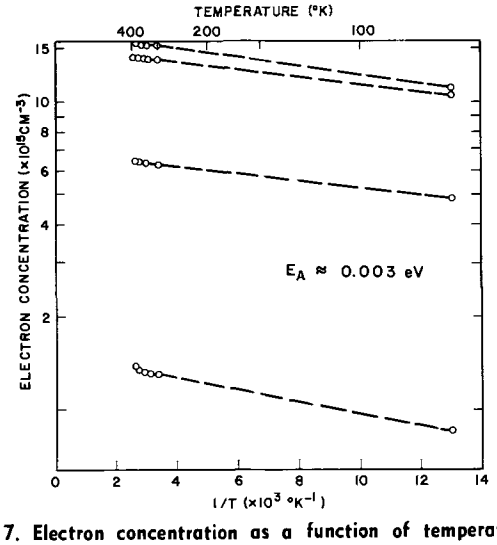

Fig. 7. Electron concentration as a function of temperature of undoped GaAs after heat treatment at 800°C for 24 hr.

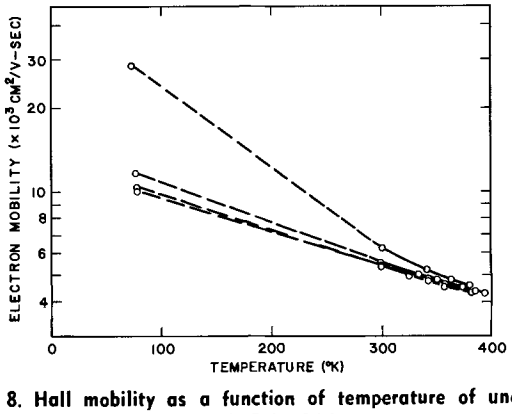

Fig. 8. Hall mobility as a function of temperature of undoped GaAs after heat treatment at 800°C for 24 hr.

Analysis of Data

The conversion of semi-insulating gallium arsenide to n-type on heat treatment has been seen before by Woodall in Bridgman crystals grown in quartz with a small amount of Ga_2O_3 added to the melt (7). (He assumed that the Ga_2O_3 converts completely to Ga_2O by reacting with the melt.) It has been shown thermodynamically (10) that SiO vapor may be expected to form from the reaction of GaAs with quartz. Therefore, the major constituents of the environment above such Bridgman crystals are, in addition to arsenic vapor, Ga_2O and SiO. Since the effect of heat treatment on liquid encapsulated crystals of gallium arsenide grown in quartz is similar to that on these Bridgman crystals, some experiments and analyses were carried out to determine whether these same molecular species were present in the boric oxide. The boric oxide is assumed to be inert except for its role in determining the activities of the various molecular species. Comparisons between liquid encapsulated growth in quartz and the Bridgman growth described above will be qualitative in nature, since the heats of solution and the activities of the various molecular species in the boric oxide are not known.

The first analysis carried out was a quantitative analysis for gallium and silicon in the boric oxide. The results are shown in Table I. Note that there is a significant amount of gallium present in every case and a significant amount of silicon in every case except when an alumina crucible is used. Gallium and silicon are presumably dissolved in the boric oxide as oxides,[1] since one would not expect elemental gallium and silicon to be highly soluble. Although the temperature profile of the boric oxide during growth is not known, clearly the amounts of silicon observed must come from the gradual dissolution of the quartz crucible by the boric oxide. The lack of a large amount of boron in the gallium arsenide (Table II) and the fact that the amount of gallium in the boric oxide is independent of the crucible used (Table I) imply that residual water is responsible for the presence of gallium in the boric oxide. It has been shown by infrared measurements that it is difficult to reduce the water content of boric oxide below 0.05 w/o (weight per cent) by vacuum baking above 1000°C (12). Assuming the presence of 0.05 w/o water before growth and the complete conversion to an oxide after growth, the following possible amounts of gallium in the boric oxide are obtained

$$2Ga + H_2O \rightarrow Ga_2O + H_2 - 0.4 \text{ w/o Ga in } B_2O_3$$

$$2Ga + 3H_2O \rightarrow Ga_2O_3 + 3H_2 - 0.13 \text{ w/o Ga in } B_2O_3$$

The amounts observed (Table I) range from 0.12 to 0.22 w/o. Quantitative calculations of the amounts of each oxide cannot be made without determining the exact amount of H_2O before growth and the amount of any Ga_2O lost during growth. However, the values observed strongly imply that the gallium results from oxidation of the melt by water in the boric oxide.

In order to determine which oxides of silicon and gallium are present during growth, some further observations and experiments were necessary. First, as mentioned in the section on Crystal Growth Operation, the boric oxide is gray and opaque after growth in quartz and brown and translucent after growth in alumina. The gray, opaque color seems to be caused by a very fine metallic powder which forms in the boric oxide after growth during cooling. In either case, the boric oxide is full of bubbles which were generated on cooling. In order to explain both the gray color and the bubbling, the simple experiments shown in Table IV were performed. All the experiments were carried out in porcelain crucibles. The heat cycle consisted of 30 min at about 900°C in addition to the heating and cooling time. It should be noted that the presence of bubbles is correlated with the presence of gallium.

[1] It has been shown (11) that 70 w/o SiO_2 is soluble in B_2O_3 at 1000°C.

Table IV. Experiments to explain gray color and bubbling of boric oxide

	Sample	B_2O_3 after heat cycle
1.	5g Ga + 10g B_2O_3	Clear, full of bubbles generated on cooling.
2.	5g Ga + 10g B_2O_3 + 0.05g SiO_2	Gray, opaque near Ga, full of bubbles generated on cooling.
3.	5g Ga + 10g B_2O_3 + 0.5g SiO_2	Slight gray tint, full of bubbles generated on cooling.
4.	0.5g SiO_2 + 10g B_2O_3	Clear, no bubbles.

Since Ga_2O is the only vapor species associated with gallium, the bubbles must result from Ga_2O coming out of solution on cooling. The gray color is correlated with SiO_2. Furthermore, it is not proportional to the amount of SiO_2 and therefore it cannot be due to a complex silicate. The only other possibilities are

$$Ga_2O + SiO \rightarrow 2Ga + SiO_2$$

$$2SiO \rightarrow Si + SiO_2$$

with the gray color resulting from a very fine precipitate of gallium or silicon. In either case, the presence of SiO is indicated. Therefore, the boric oxide contains both Ga_2O and SiO, just as in the atmosphere over the melt in the Bridgman growth described above. A survey emission spectrographic analysis for all metallic impurities (Table III) shows (in addition to gallium and silicon) only the presence of several parts per million of calcium, magnesium, and aluminum except for the growth in alumina, in which case several tenths of a weight per cent of aluminum are present.

Since Ga_2O is always present in the boric oxide, it is expected that there will be oxygen incorporated in the grown gallium arsenide. Oxygen is known to cause deep level compensation and, therefore, high resistivity in gallium arsenide (7, 13, 14). In order to convert such compensated material to n-type with carrier concentrations in the range observed (see Fig. 7), one must either remove acceptors (shallow or deep) or add shallow donors such that the number of shallow donors exceeds the sum of all acceptors. Woodall (7) interpreted his results on the heat treatment of Bridgman crystals on the basis of a reduction in the number of acceptors as a result of the precipitation of an unidentified acceptor species. Since liquid encapsulated crystals grown in alumina do not show any conversion on heat treatment, the heat treatment behavior appears to be correlated with some form of silicon. Therefore, a model is proposed whereby N_D may be increased on heat treatment by means of a change in the oxygen coordination of silicon atoms. It should be noted that similar donor creation on heat treatment has been seen in silicon crystals containing oxygen (15).

The presence of SiO in the boric oxide must lead to the incorporation of some SiO in the grown crystal of gallium arsenide. Since melt-grown, silicon-doped gallium arsenide is always n-type, it is assumed that an SiO molecule is incorporated with the silicon atom on a gallium site and the oxygen atom on either an interstitial site or an arsenic site. It is known that SiO molecules in the vapor phase become less stable with respect to SiO_2 molecules as the temperature is lowered. Unfortunately, quantitative calculations of the concentrations of SiO and SiO_2 in gallium arsenide cannot be made without knowledge of their heats of solution. However, if one assumes that SiO molecules are quenched in during the rapid cooling of Czochralski crystals and broken up into SiO_2 molecules and silicon atoms on heat treatment by means of a short-range diffusion of oxygen atoms, then shallow donors are created. The gallium arsenide will be n-type if sufficient shallow donors are created such that the number of shallow donors exceeds the sum of all acceptors. The donor level observed (see Fig. 7) is about 0.003 eV or approximately the level expected for a shallow donor in gallium arsenide. This model may also explain the inhomogeneities in the electrical prop-

erties of the gallium arsenide grown in quartz (see section on Electrical Properties of Undoped Crystals). Since there is a strong radial variation in the thermal history of Czochralski crystals, one may expect partial heat-treatment effects in various regions of the crystal. The crystals grown in alumina remain semi-insulating on heat treatment because no shallow donors are created and the deep level compensation is not overcome. Since the crystals are not affected by heat treatment, no inhomogeneities in electrical properties result because of variations in thermal history. Resistivities can therefore be measured more accurately.

Conclusions

The liquid encapsulation process is capable of producing undoped gallium arsenide with electrical properties comparable to those of gallium arsenide prepared by other bulk-growth methods. Equipment problems are thereby greatly reduced and commercially available silicon crystal pullers can now be used. With more study of thermal conditions, growth of crystals over 2 in. in diameter is apparently possible. As suggested by Woodall (7) for his Bridgman crystals, heat treatment of undoped liquid encapsulated crystals grown in quartz may be a good way to obtain bulk gallium arsenide with electron concentrations in the 10^{15} cm^{-3} to 10^{16} cm^{-3} range, should such a need arise. In addition, oxygen-doped semi-insulating gallium arsenide may be grown routinely by using alumina crucibles.

It is evident that the liquid encapsulation process does not isolate gallium arsenide from quartz crucibles. The latter should not be used if silicon contamination is undesirable.

The residual water in the boric oxide after ordinary vacuum baking clearly affects the electrical properties of liquid encapsulated gallium arsenide because it leads to the incorporation of oxygen. In order to reduce the amount of water in the boric oxide, a drying technique more effective than vacuum baking must be developed.

Acknowledgments

The authors would like to thank F. Ermanis for measurements on high resistivity material and helpful discussions, C. J. Hwang for help in the heat treatments, D. Malm for the spark source mass spectrographic analysis of GaAs, D. Nash for the analysis of the B_2O_3 after growth, and A. S. Jordan for helpful discussions.

Manuscript submitted June 3, 1970; revised manuscript received *ca.* Sept. 9, 1970.

Any discussion of this paper will appear in a Discussion Section to be published in the December 1971 JOURNAL.

REFERENCES

1. R. K. Willardson and H. L. Goering, "Compound Semiconductors," Vol. 1, "Preparation of III-V Compounds," Reinhold Publishing Corp., New York.
2. E. P. A. Metz, R. C. Miller, and R. Mazelsky, *J. Appl. Phys.*, **33**, 2016 (1962).
3. J. B. Mullin, B. W. Stranghan, and W. S. Brickell, *J. Phys. Chem. Solids*, **26**, 782 (1965).
4. S. J. Bass and P. E. Oliver, "Gallium Arsenide, Proceedings of the International Symposium," p. 41, Institute of Physics and the Physics Society (1966).
5. A. S. Grove, "Physics and Technology of Semiconductor Devices," p. 103, John Wiley & Sons, Inc., New York (1967).
6. JANAF Thermochemical Tables (1965).
7. J. M. Woodall and J. F. Woods, *Solid State Commun.*, **4**, 33 (1966).
8. A. Steinemann and U. Zummerli, *Solid-State Electron.*, **6**, 597 (1963).
9. M. Hansen and K. Anderko, "Constitution of Binary Alloys," p. 175, McGraw-Hill Book Co., New York (1958).
10. C. N. Cochran and L. M. Foster, *This Journal*, **109**, 149 (1962).
11. T. J. Rockett and W. R. Foster, *J. Am. Ceram. Soc.*, **48**, 75 (1965).
12. E. F. Riebling, *ibid.*, **49**, 19 (1966).
13. C. H. Gooch, C. Hilsum, and B. R. Holeman, *J. Appl. Phys. Suppl.*, **32**, 2069 (1961).
14. J. Blanc and L. R. Weisberg, *Nature*, **192**, 155 (1961).
15. H. Reiss and W. Kaiser, "Properties of Elemental and Compound Semiconductors," Vol. 5, p. 103, "Metallurgical Society Conferences (1959).

Properties of GaP Single Crystals Grown by Liquid Encapsulated Pulling

S. F. Nygren, C. M. Ringel, and H. W. Verleur

Bell Telephone Laboratories, Inc., Reading, Pennsylvania 19604

ABSTRACT

Because it allows the production of substantial quantities of large area, uniformly shaped substrates of GaP, the Liquid Encapsulated Czochralski technique is a major advance in GaP technology. Successful growth of single-crystal ingots requires maintenance of visibility of the growth interface. This is accomplished by baking out the B_2O_3 encapsulant before use, tightly packing the polycrystalline GaP charge into the bottom of the crucible before growth, locating the center of heat at the bottom of the crucible, and keeping the B_2O_3 relatively hot during growth. The resulting ingots have uniformly high Hall mobilities, generally being at least as high as those reported for GaP grown by other techniques. The central regions of the ingots have dislocation densities $\leq 1 \times 10^5$ cm^{-2}. Effective distribution coefficients for S, Se, Te, and Zn have been found to be 0.23 ± 0.08, 0.16 ± 0.05, 0.012 ± 0.003, and 0.096 ± 0.05, respectively.

The liquid encapsulation of a volatile melt to allow Czochralski-type crystal growth was first introduced by Metz *et al.* (1). This method was applied to the growth of GaAs and InAs single crystals by Mullin *et al.* (2); and Bass and Oliver (3) were the first to grow GaP by this technique. Gallium phosphide has a dissociation pressure of approximately 32 atm of phosphorus at its melting point, 1470°C. Without the presence of a liquid encapsulant, a phosphorus pressure in excess of 32 atm would have to be maintained

Key words: gallium phosphide, crystal growth, crystal defects, distribution coefficients.

over the melt to prevent the GaP from boiling. This would require that the walls of the crystal growth chamber be held at approximately 700°C. With a liquid encapsulant that has little interaction with the GaP, an inert gas may be used to maintain a pressure over the encapsulant which is high enough to prevent formation of phosphorus bubbles in the GaP melt. The chamber walls then no longer need to be held at a high temperature, and equipment design is considerably simplified.

Since 1969, crystal pullers suitable for high-pressure Liquid Encapsulated Czochralski (LEC) crystal growth have become commercially available. Their advent allowed, for the first time, the convenient preparation of single-crystal ingots of GaP. From such ingots many large area, uniformly shaped substrates could be prepared, all in a time short compared to the preparation of equivalent substrates by solution growth or vapor transport. As a result, the production of GaP electroluminescent devices has become economically attractive. Gallium phosphide red-emitting diodes have been fabricated on n-type LEC crystal substrates both by single liquid phase epitaxial growth of a p-type layer and by double epitaxial growth of an n-type layer and then a p-type layer. Quantum efficiencies of 1 and 4.5%, respectively, for these two types of structures have been obtained (4, 5). While these efficiencies are below those obtainable using solution-grown substrates (6 and 7%) (4), they establish the potential utility of LEC crystals in the fabrication of efficient electroluminescent diodes.

In the following section of this paper are discussed some of the growth conditions which have been found helpful in establishing a routine, high yield program of growing LEC GaP ingots. The techniques described were evolved during the growth of approximately 100 single-crystal ingots in a high-pressure puller similar to the one described by Mullin *et al.* (2).

The lower efficiencies of GaP electroluminescent diodes thus far obtained by using LEC crystal substrates instead of solution-grown substrates suggests the possibility of basic differences between LEC and solution-grown GaP crystals. The remaining portions of this paper discuss various properties of LEC GaP ingots, relating them to crystal growth parameters and comparing them to the properties of GaP grown by other techniques. In the section on Defect Structure of LEC GaP Ingots, the strain and the dislocation densities which are found in LEC GaP ingots are examined. The section on Controlled Incorporation of Impurities discusses the controlled incorporation of impurities into LEC crystals and presents the distribution coefficients of S, Se, Te, and Zn in GaP at its melting point. Some electrical properties of LEC GaP ingots are the subject of the section on Electrical Properties.

Crystal Growth

A schematic diagram of the LEC crystal growing apparatus is shown in Fig. 1. The GaP charge is totally encapsulated by a layer of B_2O_3,[1] and the encapsulated charge is supported by a vitreous silica crucible. The crucible, in turn, is supported by a carbon susceptor which is surrounded by a silica convection shroud. Heating is by rf coupling into the carbon susceptor. An overpressure of an inert gas (N_2) is contained by a stainless steel jacket.

The primary problem encountered during the growth of a single-crystal ingot from a liquid encapsulated volatile melt arises when some of the melt material mixes with or interacts with the encapsulant. This, in the case of GaP and B_2O_3, results in clouding of the encapsulant, causing loss of visibility of the growth interface and resulting in loss of control over the shape of the ingot. In addition, melt particles

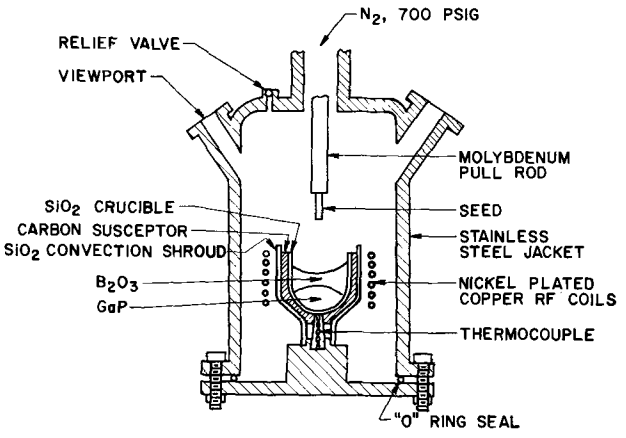

Fig. 1. Schematic diagram of the high pressure crystal puller

suspended in the encapsulant can affect the crystal perfection and even cause polycrystalline growth. To minimize these problems, the gas pressure above the encapsulant and the temperature gradient across the melt and encapsulant must be properly maintained. Also, the GaP charge and B_2O_3 encapsulant must be properly prepared.

Pressure.—The inert gas pressure which is maintained over the encapsulant must exceed the dissociation pressure of GaP at its melting point. An upper limit to this pressure may be obtained by lowering the ambient pressure inside the crystal puller during crystal growth until the melt begins to bubble. Such bubbling was observed at 32.3 atm. This pressure is not necessarily the true phosphorus pressure of GaP at its melting point since the temperature at the crucible walls may be higher than the temperature at the center of the crucible where growth is taking place. In order to protect against accidental overheating and subsequent volatilization during the melt-down period, crystal growth is routinely carried out at a pressure of about 48 atm.

Temperature gradient.—The temperature drop across the B_2O_3 must be chosen carefully. On one hand, a sharp temperature drop is desirable to insure at least initial visibility by minimizing decomposition of the seed when it enters the encapsulant. Since B_2O_3 is an insulator, a steep temperature gradient can easily be created by spacing the rf coils so that the center of heat is near the bottom of the crucible. Nielson and Von Neida (6) have measured the temperature drop across a 1 cm thick layer of B_2O_3 above a GaP melt to be about 240°C under growth conditions.

On the other hand, during the course of crystal growth, gallium and phosphorus from the melt and from the growing ingot contaminate the B_2O_3 and cause an eventual decrease in transparency. This problem can be reduced if the B_2O_3 is kept warm enough so that at least some contaminants can diffuse through the B_2O_3 and vaporize from it. The temperature gradient finally chosen is a compromise between these two desired conditions.

GaP *charge.*—The most desirable form for the starting material would be a solid chunk of polycrystalline GaP which is shaped to fit the lower portion of the crucible. However, this is not essential. In this study the starting material was polycrystalline GaP which had been prepared by dissolving phosphorus obtained from PH_3 into gallium which is held at an elevated temperature.[2] This material has very high purity, but it is porous and irregularly shaped. It is dried and crushed before use. The resulting small chunks and powder can be tightly packed into the crucible, leaving a minimum of voids and presenting a flat in-

[1] Johnson Matthey, High Purity.

[2] Monsanto, Polycrystalline Porous Chunk GaP.

terface to the B_2O_3. This will minimize penetration of the B_2O_3 into voids in the unmelted charge, preventing the GaP particles from being brought up into the encapsulant during melt down.

When the melt is to be doped, the particles of dopant are embedded in the GaP charge. The heating schedule is begun after the system is pressurized; and by the time the temperature reaches 800° or 900°C, the B_2O_3 has melted and has encapsulated the charge. It is hoped that this procedure prevents the loss of significant quantities of dopant from the charge by evaporation.

Encapsulant.—The presence of water in the B_2O_3 will cause bubbling when it is heated. These bubbles bring up particles from the GaP charge, clouding the B_2O_3 and causing loss of visibility. However, all that is necessary to remove most of the water from the B_2O_3 and thus prevent initial clouding of the encapsulant is to bake it out for 24 hr at about 900°C under partial vacuum (<0.1 atm).

To establish the proper temperature drop across the B_2O_3 layer, its thickness should be at least 1 cm when the rf coil geometry described above is used with a crucible that is 4.6 cm in diameter. If the layer is thinner, the B_2O_3 will be too hot to prevent decomposition of the seed and ingot during growth, and the decomposition products will cloud the B_2O_3 layer. A layer thicker than 2 cm inhibits crystal growth. This is probably due to the insulating property of B_2O_3 which prevents adequate heat dissipation to sustain crystal growth. When the proper B_2O_3 thickness is used, care must still be taken during crystal growth. As the large diameter portion of the ingot emerges from the B_2O_3, additional convection and radiation from the ingot will occur. At this time either the pull rate or the rf power must be increased in order to prevent a sudden increase in ingot diameter.

While the precautions discussed in this section will prevent initial and drastic clouding of the encapsulant, a gradual decrease in transparency of the B_2O_3 will take place during a run. This appears to be due to transport into the B_2O_3 of material produced by decomposition of the melt and by reaction of the GaP with H_2O, SiO_2, and B_2O_3. At the end of a run, the B_2O_3 has become colored. There is a greenish layer near the bottom and walls of the crucible, and a yellow layer near the top surface of the B_2O_3. The greenish region contains more gallium and phosphorus than the yellow region. The total amount of phosphorus in the B_2O_3 is considerably less than the total amount of gallium, indicating the loss of phosphorus from the B_2O_3. Weiner (7) has suggested a water vapor and SiO_2 reaction to account for the clouding of B_2O_3 in LEC growth of GaAs. For the growth of GaP, the dissociation process must also be considered.

Defect Structure of LEC GaP Ingots

Defects in grown crystals may arise in two ways. They may be propagated into the crystal from the seed, or they may be generated by forces exerted on the crystal as it solidifies and cools. Conventional techniques for minimizing defect densities in Czochralski-grown crystals include starting with a clean, dislocation-free seed (or, equivalently, growing a long, thin neck which becomes dislocation free before the main part of the ingot is begun), keeping the melt scrupulously clean in order to minimize spurious nucleation, and using a thermal geometry which minimizes the radial temperature gradient in the grown portion of the ingot. In Liquid Encapsulated Czochralski growth of GaP the same techniques are used, but problems in two areas are more severe than with conventional Czochralski growth. First, as has been mentioned, the encapsulant becomes increasingly cloudy as growth progresses, so that the probability of spurious nucleation by suspended matter becomes increasingly greater. This seems unavoidable. Second, the high pressure inside the crystal puller greatly increases the removal of heat from the periphery of the grown ingot by convection, thereby increasing the difficulty of reducing the radial temperature gradient in the growing crystal above the encapsulant.

To study the effects of various growth parameters on crystal perfection, approximately 50 <111> oriented single crystal LEC GaP ingots were chosen for examination. All of these ingots were grown from 60g charges of GaP, and generally all of each melt was used. The median value for the length of these ingots was 6.9 cm, with two-thirds of the ingots being between 5.4 and 8.7 cm. Visual examination of these crystals revealed them to be free from inclusions or polycrystallinity, with the following exception. Due to the accumulation of free gallium at the bottom of the crucible at the end of a run, the few millimeters closest to the tail end of an ingot often contained gross defects. These defects did not alter the quality of the rest of the ingot. Thus, ingots will henceforth be referred to as if they were completely free of gross defects, and it will be understood that such statements are meant to exclude the extreme tail ends of the ingots.

Each ingot was characterized by examining three polished slices which were taken from locations roughly 1.5, 3.0, and 5.0 cm from the seed end of the ingot. The slices were cut normal to the growth axis of the ingot and were about 425 μm thick.

Gallium phosphide crystallizes in the zinc-blende structure, and thus perfect GaP is expected to be optically homogeneous. This means that the principles of photoelasticity can be used to analyze the strain patterns in GaP (8). Figure 2 shows slices from two ingots which are viewed between crossed polarizers using parallel light. The sample on the left is a typical example, showing isoclinic fringes in the shape of a dark cross. It is found that the cross remains fixed with respect to the polarizers when the sample is rotated. Since an isoclinic fringe shows the locations where the directions of principle strain are parallel to the polarizers, it is concluded that the strain is predominantly radial. This is confirmed by the fringes on a slice cut out of the center of an ingot parallel to the growth axis.

The slice on the right in Fig. 2 shows another commonly observed pattern. In this case the slice is triangular with the apexes of the triangle pointing in <211> directions. Two arms of the isoclinic fringe are swept back slightly. These arms move slightly as the slice is rotated, always indicating that the directions of principle strain are parallel to and perpendicular to the surface of the ingot at the periphery of the slice. This is the strain pattern which is expected in a Czochralski ingot where the surface is cooled at a different rate from the core.

Defect densities were measured on the slices described above. They were etched at room temperature for 10 min in a rotating beaker in the ferricyanide etch (8g $K_3Fe(CN)_6$: 12g KOH : 100g H_2O). This etchant

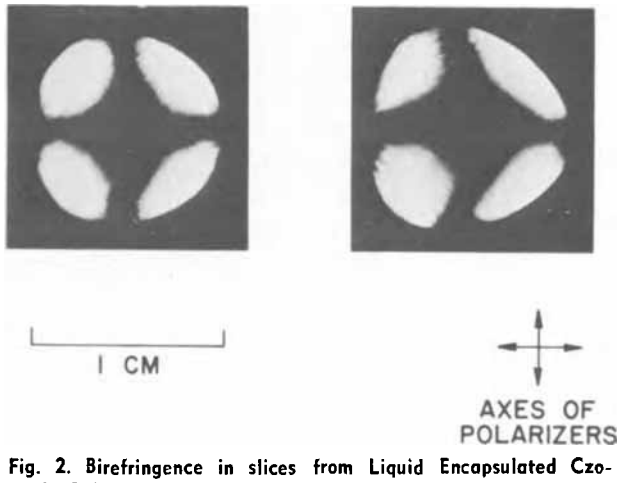

Fig. 2. Birefringence in slices from Liquid Encapsulated Czochralski GaP ingots.

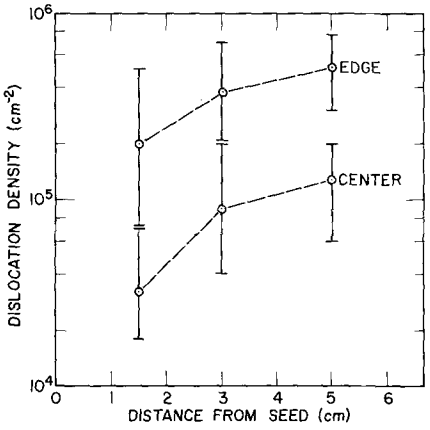

Fig. 3. Dislocation density at the center and at the edge of an LEC GaP ingot vs. distance from the seed end of the ingot. The points are median values, and the error bars show the ranges which include 2/3 of the samples.

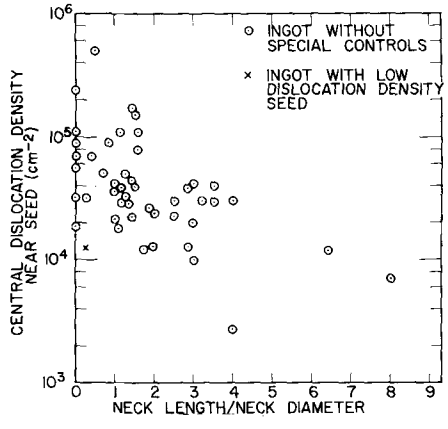

Fig. 5. Central dislocation densities near the seed ends of LEC GaP ingots vs. neck length/neck diameter. ⊙ indicates ingots with seeds whose dislocation densities were not specifically controlled. X indicates an ingot with a low dislocation density seed.

reveals dislocation etch pits on the (111)Ga faces of GaP (9). It will also reveal the traces of twins and stacking faults.

In these ingots only dislocation pits were found; all ingots were free of twins and stacking faults. The data concerning dislocation density are summarized in Fig. 3. Each point represents the median value of a set of measurements, and the error bars show the range which includes two thirds of the samples for each measurement. The value for the dislocation density in the central portion of a slice is determined by measuring the average value over the area contained within one half of a slice radius. The value for the edge of a slice is the average value found 0.5 mm from the edge of the slice.

The distribution of dislocation densities on typical slices is shown in Fig. 4. The dislocation density is highest at the edge of a slice and then decreases until the center of the slice is reached. Occasionally, there is a slight increase at the very center of a slice.

As expected, the dislocation density is highest near the outside of an ingot, both because new dislocations are nucleated there and because that is the region which receives the greatest amount of stress. Slip traces are occasionally seen near the periphery of ingots. It is also no surprise that the dislocation density increases with the distance from the seed since the dislocations are expected to propagate downward and toward the center of the ingot as the ingot grows.

The influence of crystal growth parameters on crystal perfection follows the expected pattern. Among the parameters having no noticeable effect are the nature of the doping species, the doping level (1×10^{14}-1×10^{19} cm^{-3}), the pull rate (0.7-2.5 cm/hr), the rotation rate (3-60 rpm), the encapsulant thickness (0.7-2 cm), and the growth polarity [(111)Ga or (111)P]. On the other

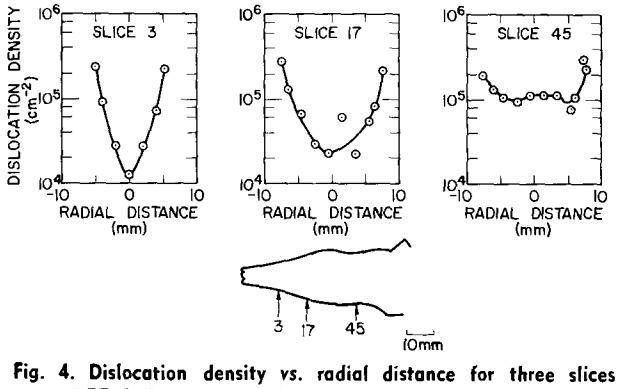

Fig. 4. Dislocation density vs. radial distance for three slices from an LEC GaP ingot. Slice No. 3 is closest to the seed end of the ingot.

hand, the condition of the seed and the geometry of the ingot neck were found to be important. Figure 5 shows the relationship between the neck dimensions (length/diameter) and the dislocation density in the central region of each ingot about 1.5 cm from the seed. Many ingot necks were not grown continuously; that is, some neck was grown, contact between the neck and the melt was broken, and then more neck was grown. Even so, it would be expected that either a long neck or a thin neck would allow dislocations to grow out, leading to ingots which have low defect densities when the neck dimensions are optimal. It is seen from Fig. 5 that this is indeed the case. However, good neck quality is not absolutely necessary for low dislocation density. In particular, one ingot is identified in Fig. 5 as having a low dislocation density but almost no neck; it did, however, have a low dislocation seed. Hence, low dislocation ingots may be prepared if the effective seed (either the seed itself or the region at the end of the neck) has a low dislocation density.

The use of afterheaters and radiation reflectors has been explored, but their effectiveness is severely limited by the relatively high dislocation density of a typical ingot. Afterheaters are most effective when they are used to reduce the radial temperature gradient in a perfect ingot. This reduces the strain in the ingot and minimizes the possibility of creating dislocations by slip. For ingots which have dislocation densities in the mid 10^4 cm^{-2} region, however, the use of afterheaters and reflectors offers no advantage since afterheaters will not remove existing dislocations nor will they prevent dislocations from propagating and interacting.

Growing low dislocation density LEC GaP ingots, then, is an evolutionary process. Using the principles above, a low dislocation density ingot can be used to make seeds with which ingots with still lower dislocation densities can be grown. Using this process, the best ingot obtained to date has a dislocation-free core which is 3 mm in diameter at a point 1.5 cm from the seed (total ingot diameter was 8 mm at this point).

The LEC GaP ingots described here generally compare favorably to GaP which is grown by vapor transport onto GaAs seeds. Such crystals are typically strained and have dislocation densities of 2×10^5-2×10^6 cm^{-2}. On the other hand, solution-grown GaP platelets have substantial areas which are strain and dislocation free (10). This difference between LEC and solution-grown GaP may be part of the explanation for the earlier mentioned difference in electroluminescent efficiencies of diodes grown on these two types of substrates.

Controlled Incorporation of Impurities

Control of the doping level of a semiconductor by the purposeful introduction of impurities requires that

Table I. Residual impurities in GaP

Element	Starting material (atomic ppm)		LEC single-crystal (atomic ppm)	
	Mass spec.	Other methods	Mass spec.	Other methods
B	0.7		0.6	
C	0.9		0.2	
N	0.4	1.3[a]	0.3	0.9[a]
O	1.0		5.0	8.4[b]
Si	2.0		2.3	
S	1.0		1.3	
As	20		2.6	

[a] Optical absorption.
[b] ^{3}He activation analysis.

the undoped semiconductor have residual impurity concentrations which are far below the intended doping level. Thus it is an important result that LEC GaP ingots are quite pure by contemporary standards for GaP. A summary of the chemical analyses which have been performed is given in Table I, where each value is the average of several samples. The samples taken from LEC crystals were representative of the middles of the ingots. The bulk of the data is from mass spectroscopy. In addition, ^{3}He activation analysis (11) was used to provide a supplementary measurement of the oxygen concentration. Also, optical absorption was used to detect substitutional nitrogen and give a lower limit to total nitrogen concentration. In all cases, except for arsenic, the typical impurity concentrations in the LEC ingots are seen to be the same order of magnitude as those in the polycrystalline starting material.

Few electrically or optically active impurities are found in undoped ingots. Such crystals are typically n-type, with electron concentrations below 1×10^{15} cm^{-3}, mobilities above 175 cm^2/V · sec, and optical absorption coefficients less than 0.2 cm^{-1} in the range from 1.2-1.95 eV.

Since undoped ingots have carrier concentrations less than 1×10^{15} cm^{-3}, ingots can be purposely doped in a controllable fashion at concentrations greater than about 1×10^{16} cm^{-3}. The donors S, Se, Te, and the acceptor Zn have been studied in <111> oriented ingots to determine the relationship between the amount of dopant added to the melt and the carrier concentration in the resulting ingot. This is not quite the same as determining the distribution coefficients of these impurities in GaP for several reasons. First, there is no convenient way to measure the concentration of the impurity in the melt at the growth interface, and there is always the suspicion that part of the dopant evaporated from the melt before the melt was encapsulated. Second, since crystal growth is not done under equilibrium conditions, a true distribution coefficient cannot be obtained. Third, the impurity concentration in the ingot is not measured directly. Still, the measurement that is performed provides data which is quite useful in a practical sense, and it will be shown that the values obtained are expected to be very close to the values of the distribution coefficients.

Doping with sulfur was accomplished by adding Ga_2S_2 [3] to the melt. It has been shown that in solution-grown GaP, the concentration of sulfur is equal to the concentration of electrons as determined by surface barrier capacitance measurements up to an electron concentration of about 4×10^{18} cm^{-3}, after which the electron concentration saturates (13). In the present work it was assumed that this relationship also holds for LEC GaP, and sulfur concentrations were determined by measuring electron concentrations as given by surface barrier capacitance. In this fashion the sulfur concentration was measured at several locations along an ingot and then was extrapolated back to the seed end of the ingot using the normal freezing equation

$$C(g) = A(1 - g)^B$$

where g is the weight fraction of the ingot that was grown before the point which is being measured, C is the impurity concentration, and A and B are constants (14). The ratio of the impurity concentration at the seed end of the ingot, C_i, to the initial impurity concentration in the melt, C_o, is the effective distribution coefficient, k. Ideally, the constants A and B in the normal freezing equation should be $A = kC_o$, $B = k - 1$, and hence these two constants may be used to check the experiment for self-consistency.

The scatter in the carrier concentration data and the doping nonuniformity (which will be discussed in the next section) occasionally preclude the use of the constants A and B to determine k and C_o. When such a determination can be made, however, the value of k thus obtained corresponds within ±5% to the value of k determined from $k = C_i/C_o$. Moreover, the value of C_o obtained from the constants A and B corresponds within ±10% to the amount of dopant that was added to the melt, suggesting that very little of it volatilized. The sulfur-doped ingots that were measured had seed-end electron concentrations in the range 5×10^{16} to 5×10^{18} cm^{-3}, pull rates of 0.8-2.5 cm/hr, and rotation rates of 3-30 rpm. Over this range the effective distribution coefficient appears to be constant. The mean value of the distribution coefficient measured is $k = 0.23$, with a standard deviation of 0.08. The value is essentially independent of growth polarity. Since it is also independent of growth and rotation rates, it is likely to be near the equilibrium value of the distribution coefficient.

Selenium doping was investigated by adding Ga_2Se_3[4] to the melt. The doping experiments were interpreted by using the same analysis as for sulfur, assuming that the selenium concentration is equal to the electron concentration up to an electron concentration of 4×10^{18} cm^{-3} (13). Again the normal freezing equation provided self-consistent values for k and C_o. Over the range of doping from 6×10^{16} to 1×10^{18} cm^{-3}, of pull rates from 1.2 to 2.5 cm/hr, and of rotation rates from 6 to 60 rpm, the effective distribution coefficient appears constant at $k = 0.16 \pm 0.05$, suggesting that k is near its equilibrium value. It also appears independent of growth polarity.

The most data have been accumulated for the donor tellurium, for which the doping source was Ga_2Te_3.[5] In this case the electron concentration is expected to equal the donor concentration for $n < 2 \times 10^{18}$ cm^{-3} (13). The effective distribution coefficient appears to be quite independent of growth polarity and is found to be $k = 0.012 \pm 0.003$ over a range of doping from 8×10^{16} to 2×10^{18} cm^{-3}, of pull rate from 1.2 to 2.5 cm/hr, and of rotation rate from 3 to 16 rpm. In this case the normal freezing equation generally cannot be used to verify k and C_o since B usually cannot be found to an accuracy of better than ±5%. However, there was one case where k and C_o were verified, and the agreement for both k and C_o was within 30%.

The acceptor zinc has also been studied by the same technique, using pure Zn[6] as a dopant. Some severe difficulties arise, however. First, zinc is expected to be the most volatile of the four doping sources studied. Second, there is considerable difficulty relating the carrier concentration to the zinc concentration. It has been shown that surface barrier capacitance measurements on zinc-doped solution-grown GaP generally give hole concentrations which are smaller than the zinc concentrations, even at concentrations as low as 5×10^{17} cm^{-3} (13). On the other hand, room temperature Hall effect measurements give hole concentrations which may be greater or less than the zinc concentration, depending on the concentration level (15). In the present work, hole concentrations were ob-

[3] Alusuisse, 6 9's+ pure.

[4] Gallard-Schlesinger, 5 9's pure.
[5] Atomergic, 5 9's+ pure.
[6] Cominco, 5 9's pure.

tained by room temperature Hall effect measurements and were related to zinc concentrations by using the data presented in ref. (15). The interpretation then proceeds as for the donors. Although the scatter in the data is worse than for the donors, the effective zinc distribution coefficient is assigned the value $k = 0.096 \pm 0.05$ for zinc concentrations from 1×10^{17} to 2×10^{19} cm^{-3}, growth rates from 1.2 to 2.5 cm/hr, and rotation rates from 6 to 16 rpm. The constants A and B can be used to provide values of k and C_o which are self-consistent to ± 20%, suggesting that the volatilization of the zinc was not serious.

Electrical Properties

In addition to the defect structure of LEC GaP ingots, the electrical properties of this material ultimately determine its usefulness. Room temperature electrical properties of the GaP ingots were measured using conventional d.c. Hall effect techniques employing the Van der Pauw method. Following common practice, n-type samples were characterized by the relationships $n = (R_H e)^{-1}$, $\mu_H = R_H/\rho$, where n is the electron concentration, R_H is the Hall coefficient, e is the electronic charge, μ_H is the Hall mobility, and ρ is the resistivity. Equivalent relationships are used for p-type samples. Figures 6 through 8 show how electron and hole mobilities vary with carrier concentration.

Two things are apparent from Fig. 6 and 7. First, electron mobilities are consistently high. Very little scatter is seen, and the mobilities are generally at least as high as those reported for good quality GaP grown by other techniques (16, 17). Only GaP grown by vapor transport onto GaP seeds has higher mobilities; *e.g.*, $n = 3.0 \times 10^{16}$ cm^{-3}, $\mu_H = 187$ $cm^2/V \cdot sec$; $n = 1.3 \times 10^{17}$ cm^{-3}, $\mu_H = 170$ $cm^2/V \cdot sec$. Second, it is seen from Fig. 7 that the mobilities of Te-doped samples are somewhat lower than those of other n-type samples in the range of 5×10^{16}-5×10^{17} cm^{-3}. The difference is small, reaching a maximum of 4% at $n = 1 \times 10^{17}$ cm^{-3}, but it is consistent. A similar dependence of mobility on the specific dopant used has been seen in Ge and Si, the differences being as much as 30% at carrier concentrations near 1×10^{19} cm^{-3} (18, 19). These differences in Ge and Si have been attributed to differences in ionized impurity scattering among different ions (20).

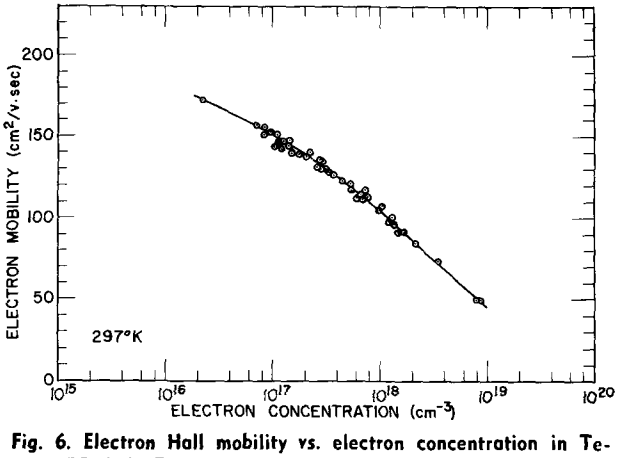

Fig. 6. Electron Hall mobility vs. electron concentration in Te-doped LEC GaP. The solid line has no theoretical significance.

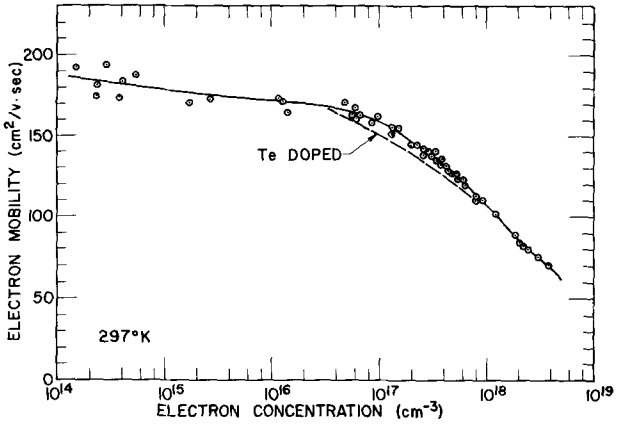

Fig. 7. Electron Hall mobility vs. electron concentration in n-type LEC GaP that is not doped with tellurium. The solid line has no theoretical significance. The broken line shows the mobilities of Te-doped ingots for comparison.

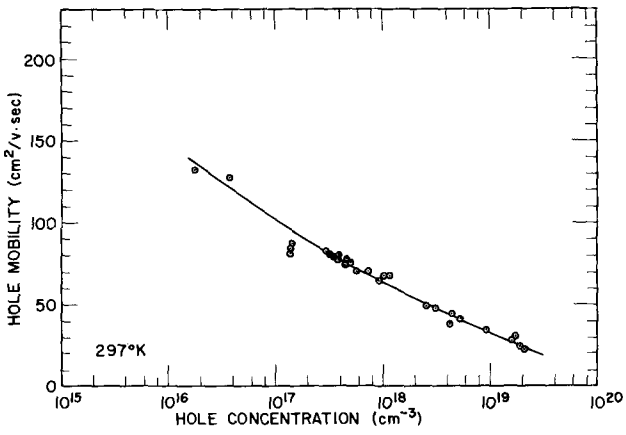

Fig. 8. Hole Hall mobility vs. hole concentration in p-type LEC GaP. The solid line has no theoretical significance.

In Fig. 8, all of the points correspond to zinc-doped samples except for the two at the lowest hole concentrations which correspond to carbon-doped samples. Again the mobilities shown are generally as high as those reported elsewhere, with only GaP grown by vapor transport on GaP seeds showing slightly higher mobilities (21, 22). In contrast, it is found that ingots doped with Zn and large amounts of Ga_2O_3 (1-2g) have mobilities as much as 25% higher than those shown in Fig. 8 at hole concentrations of 1×10^{17}-1×10^{18} cm^{-3}. This is not well understood.

The doping homogeneity of slices cut from <111> oriented LEC GaP ingots has been examined by using Schottky barrier diodes. Gold dots, 0.010 in. in diameter on 0.020 in. centers, were evaporated onto polished GaP surfaces. Doping levels at various points were then evaluated by surface barrier capacitance measurements. The results indicate that the doping level in a typical slice is constant to within ± 20%. The deviation from constancy shows a weak dependence on rotation rate (Fig. 9), but appears indepen-

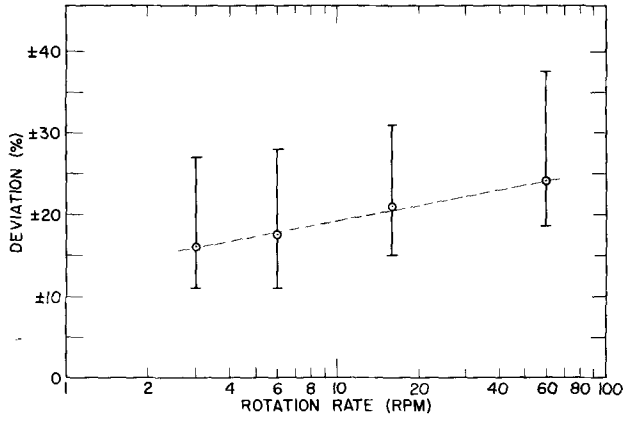

Fig. 9. Deviation in doping level along the diameter of an LEC GaP ingot vs. the rotation rate of the ingot. The points are median values, and the error bars show the ranges that include 2/3 of the samples.

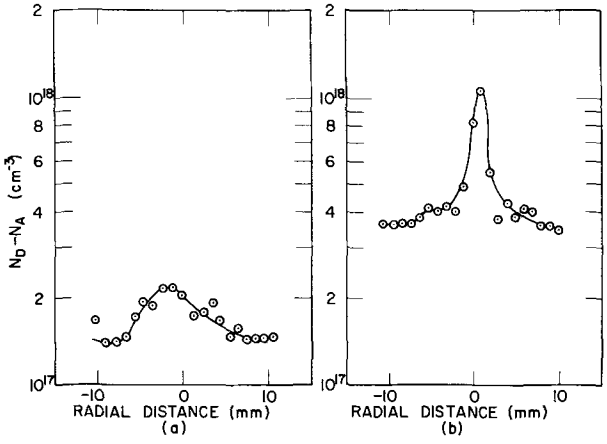

Fig. 10. Electron concentration (N_D-N_A) vs. radial distance in slices of LEC GaP. (a) Typical slice, (b) slice with preferential incorporation of impurities at core of ingot.

dent of slice diameter (0.75-2.5 cm), carrier concentration (6 x 10^{16}-5 x 10^{18} cm^{-3}), and fraction of the melt solidified.

It is found that a majority of <111> ingots have a broad maximum in doping level at their centers, an example being in Fig. 10a. In most cases, there is no evidence for preferential incorporation of impurities at facets; that is, no region of an ingot is found where the doping level is abruptly higher than in the surrounding regions. Occasionally, however, the core of an ingot does have a sharply higher doping level than the rest of the ingot. An example of such an effect is shown in Fig. 10b. If the carrier concentration at such a peak is on the order of 2 x 10^{18} cm^{-3} or higher, the region of increased carrier concentration is obvious under visual inspection as a dark spot in a polished slice.

Conclusion

It is thus seen that the growth of single-crystal gallium phosphide by the Liquid Encapsulated Czochralski technique is a major advance in GaP technology. The LEC process allows, for the first time, the convenient and relatively economical production of substantial quantities of large area, uniformly shaped GaP substrates of good crystal quality.

The main feature of the LEC growth process is the encapsulation of the GaP melt by a layer of B_2O_3. The presence of this layer eliminates the need for a high overpressure of phosphorus to keep the melt from volatilizing and allows the use of an inert gas instead. The major portion of the growth effort is then directed toward maintaining the transparency of the B_2O_3 so that the growth interface remains visible. It was found that the clouding could be made negligible by baking out the B_2O_3 to remove water, by locating the center of heat at the bottom of the crucible, by keeping the B_2O_3 relatively hot during growth, and by packing the GaP charge tightly into the crucible so that the B_2O_3 would not mix with it on melting.

Undoped ingots grown by this process are n-type. They are quite pure, having carrier concentrations less than 1 x 10^{15} cm^{-3} and Hall mobilities greater than 175 cm^2/V·sec. Doping experiments were carried out with S, Se, Te, and Zn, and effective distribution coefficients were obtained for carrier concentrations from 5 x 10^{16} to 5 x 10^{18} cm^{-3}. The values are, respectively, 0.23 ± 0.08, 0.16 ± 0.05, 0.012 ± 0.003, and 0.096 ± 0.05. Slices from ingots generally have carrier concentrations which are constant to ± 20%, independent of rotation rate.

Metallurgically, GaP ingots are superior to vapor-grown GaP. However, they are inferior to solution-grown GaP, and this may be one of the reasons why electroluminescent diodes fabricated on LEC GaP substrates are less efficient than those fabricated on solution-grown substrates. The LEC GaP crystals are strained in the radial direction and have dislocation densities which are typically 1 x 10^5 cm^{-2} in the greater portion of the ingot. However, one ingot was obtained which had a 9 mm^2 core near the seed end which was dislocation free. The GaP ingots have uniformly high mobilities, with the mobilities for both n-and p-type samples being generally as high as those from the best GaP produced by other methods. It is found that Te-doped samples have slightly lower mobilities than other n-type samples.

Acknowledgments

The authors express their thanks to D. L. Malm for providing mass spectroscopy data, C. K. Kim for the ^{3}He activation analysis, P. J. Dean for the measurement of nitrogen concentrations by optical absorption, and M. DiDomenico, Jr., for other optical absorption measurements. The technical assistance of Miss S. L. Davis is also gratefully acknowledged.

Manuscript submitted June 26, 1970; revised manuscript received *ca.* Sept. 27, 1970.

Any discussion of this paper will appear in a Discussion Section to be published in the December 1971 JOURNAL.

REFERENCES

1. E. P. A. Metz, R. C. Miller, and R. Mazelsky, *J. Appl. Phys.*, **33**, 2016 (1962).
2. J. B. Mullin, B. W. Straughan, and W. S. Brickell, *J. Phys. Chem. Solids*, **26**, 782 (1965).
3. S. J. Bass and P. E. Oliver, *Crystal Growth*, **3**, 286 (1968).
4. W. H. Hackett, Jr., and R. H. Saul, *This Journal*, **117**, 94C (1970).
5. W. H. Hackett, Jr., and R. H. Saul, Private communication.
6. J. W. Nielsen and A. R. Von Neida, Private communication.
7. M. E. Weiner, Private communication.
8. See, for example, H. T. Jessop and F. C. Harris, "Photoelasticity Principles and Methods," Dover Publications, Inc., New York (1960).
9. M. I. Valkovskaya and Yu. S. Boyarskaya, *Soviet Phys.-Solid State* (English Transl.), **8**, 1976 (1967).
10. Robert H. Saul, *This Journal*, **115**, 1184 (1968).
11. C. K. Kim, *Radiochem. Radioanal. Letters*, **2**, 53 (1969).
12. D. G. Thomas, J. J. Hopfield, and C. J. Frosch, *Phys. Rev. Letters*, **15**, 857 (1965).
13. F. A. Trumbore, H. G. White, M. Kowalchik, R. A. Logan, and C. L. Luke, *This Journal*, **112**, 782 (1965).
14. William G. Pfann, "Zone Melting," John Wiley & Sons, Inc., New York (1958).
15. L. M. Foster, J. F. Woods, and J. E. Lewis, *Appl. Phys. Letters*, **14**, 25 (1969).
16. Tohru Hara and Isamu Akasaki, *J. Appl. Phys.*, **39**, 285 (1968).
17. R. C. Taylor, J. F. Woods, and M. R. Lorenz, *ibid.*, **39**, 5404 (1968).
18. W. G. Spitzer, F. A. Trumbore, and R. A. Logan, *ibid.*, **32**, 1822 (1961).
19. R. A. Logan, J. F. Gilbert, and F. A. Trumbore, *ibid.*, **32**, 131 (1961).
20. P. Csavinsky, *J. Phys. Soc. Japan*, **16**, 1865 (1961).
21. H. C. Casey, Jr., F. Ermanis, and K. B. Wolfstirn, *J. Appl. Phys.*, **40**, 2945 (1969).
22. R. C. Taylor, *This Journal*, **116**, 383 (1969).

Etch Rate Characterization of Borosilicate Glasses as Diffusion Sources

R. O. Schwenker

IBM Components Division, East Fishkill Facility, Hopewell Junction, New York 12533

ABSTRACT

For diffusion of boron into silicon from a doped oxide diffusion source, the surface concentration of boron in silicon and B_2O_3 in the glass at the glass-silicon interface are independent of diffusion time. In the temperature range studied, the surface concentrations are also independent of temperature and depend only on the dopant concentration in the deposited glass. This dependence is observed as long as the glass thickness is large enough so that the impurity source approximates a semi-infinite source. The concentration dependence of the diffusion coefficients of the B_2O_3 in the glass and the boron in silicon are determined, the diffusion coefficient for boron in silicon being about 100 times that of the diffusion in the oxide. Heating under an oxidizing ambient oxidizes the silicon at the silicon-glass interface with the thickness growth rate of the undoped SiO_2 layer being nearly independent of the original glass thickness. No such interface barrier to the boron diffusion process occurs when argon is used as an ambient.

Although a number of authors have studied doped oxides as diffusion sources for device fabrication (1-7), not all of the basic assumptions concerning the diffusion processes involved in such systems have been checked. In this report, boron diffusion into silicon from doped oxide has been studied as a function of glass composition, glass thickness, diffusion time and temperature, and type of ambient used.

In order to determine if there is equilibrium at the doped oxide-silicon interface during diffusion, it is necessary to know the concentration of B_2O_3 in the glass as well as the boron in the silicon near the silicon-glass interface. By knowing both concentrations, one can then determine the dependence of the segregation coefficient on the concentration of the B_2O_3 in the deposited glass.

The diffusion coefficient of the boron in the silicon has been shown to be concentration dependent (7). The concentration dependence of the diffusion coefficient for the dopant in the oxide is not so well known. Even the inaccurate radiochemical profiling techniques which have been used for phosphorus-doped oxides (8) cannot be used with borosilicates. However, this question and the others can be studied by the use of etch rate characterization of the oxide and electrical measurements of the diffused silicon. Another problem which can be studied by the technique of etch rate profiling is the different effects of oxidizing ambients on the diffusion processes.

Experimental Procedure

The system which was used for deposition of the doped oxide was the low-temperature oxidation of organosilicon and organoboron compounds (4). Silicon wafers were placed on a silicon carbide susceptor coated with silicon in a small round horizontal glass reactor. RF heating was used while an infrascope was used to monitor the 475°C temperature of the wafers during the deposition. Oxygen was bubbled through tetraethyl orthosilicate (TEOS) at room temperature while argon was used as the carrier gas for tri-n-propyl borate (TPB). Additional oxygen and argon were used as dilution gases during the deposition.

During the predeposition heat up cycle of the wafer, only argon was used as an ambient in order to avoid the formation of any silicon dioxide on the substrate. All work was done using 1.0 ohm-cm(100) n-type wafers. Prior to use, all wafers were oxidized under steam, then cleaned with concentrated HF, and finally rinsed with de-ionized water. The diffusions were done in furnaces with argon ambients.

Etch rate techniques (9) for determining characteristics such as densifications and impurity concentration profiles have been commonly used in the past for glasses or doped oxides. For a study of this type, it is necessary to have an etchant which has an etch rate with a strong dependence on the variable which is of interest in the study. We used an etchant of 500 ml nitric acid, 1 ml hydrofluoric acid, and 7 mg $Hg(NO_3)_2$. This etchant was found to etch the glass at a rate with a strong dependence on impurity concentration in the range of 5-15 m/o (mole per cent) B_2O_3 on the glass, as is shown in Fig. 1. This range was the principal range of interest for this study.

The B_2O_3 concentrations in the deposited glasses were determined by measuring the band intensity of the infrared absorption band at 1390 cm^{-1} for the B-O bond relative to the band intensity at 1090 cm^{-1} for the Si-O bond (10). These intensities are best determined by integrating the optical density, O. D., over the band width. The optical density is given by O.D. $= \log_{10} (To_\nu/T_\nu)$ where T_ν is the transmittance at frequency ν and To_ν is the background level at the same frequency. The background level is determined by the

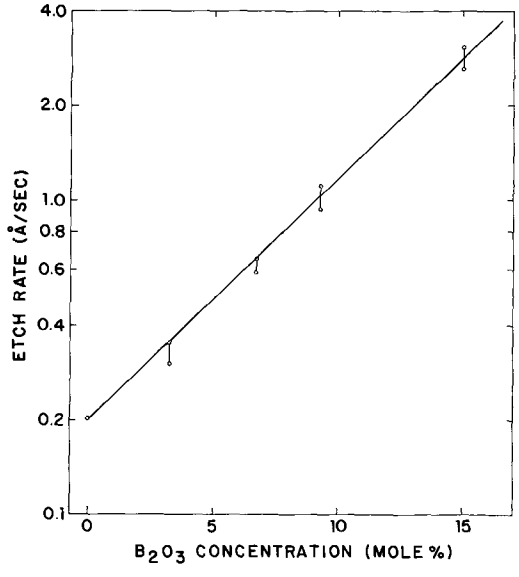

Fig. 1. Etch rate of densified doped oxide as a function of composition of B_2O_3 in the glass.

Key words: deposition, oxide, tetraethyl orthosilicate, tri-n-propyl borate.

line drawn tangent to the edges of the absorption band. Although the integrated intensity is a more accurate quantitative representation, a reasonably good approximation is obtained by using the optical density at the band maximum as was shown for SiO_2 (11). We have assumed that Beer's law is accurate for our range of concentrations so that the absorbance is proportional to the concentration of bonds. The relationship which we used to relate the optical densities to the concentration of the components is

$$\frac{1\text{-}Co}{Co} = 1.5\,\frac{\text{O.D. Si-O}}{\text{O.D. B-O}} \qquad [1]$$

where Co is the weight fraction of B_2O_3 in the glass. The proportionality constant is that determined by Pliskin for GE GSC-1 glass and several other borosilicate glasses (12). It has been shown that the addition of metal oxides in borosilicate glass causes a decrease in the specific intensity of the B-O band (10). However, the 4.5 w/o (weight per cent) Al_2O_3 in the GE GSC-1 glass should cause a reduction of less than 20% in the specific absorption intensity of the B-O bands (12). Ignoring the effect of the Al_2O_3 in the calibrating glass and using Eq. [1] for our two-component glass can result in the calculation of B_2O_3 concentrations which could be greater than the actual values by no more than 20%. Regardless of the absolute error involved, the relative error remains the same for all concentration levels and can be ignored for comparison purposes. The absorption due to oxygen dissolved in the silicon substrate was eliminated by using Lopex material for the infrared measurements instead of the pulled crystals used for diffusion studies.

The same wafers were then used to determine the etch rates for each dopant concentration. Both infrared and etch rate measurements were made after densification of the wafers at 800°C for two or more hours. Other heat treatments for longer times at 800°C and also at higher temperatures were found to produce densified glasses with insignificantly different etch rates from those of Fig. 1. The etchant etched densified glass slowly enough so that etching times of the order of minutes could be used to remove layers of oxide which were a few hundred angstroms thick. Agitation of the etchant was used in order to insure uniformity of the etching.

The thicknesses of the doped oxides on the silicon substrates were measured in all cases with an ellipsometer. This method permitted an accuracy to within a few angstroms in the thickness measurement of the layer removed by etching. In addition to the glass thickness measurement, the index of refraction of the boron-doped oxides in our range of investigation was determined to be $n = 1.460$. The closeness of this value to the index of refraction of SiO_2, $n = 1.463$ (13), allowed thickness measurements of composite layers of SiO_2 and boron-doped oxide to be readily made with the ellipsometric techniques.

Preliminary Studies

Measurements were first made in order to determine the uniformity of the doping of the deposited borosilicate glass. The etch rate profile on as-deposited glass showed a lower etch rate near the silicon-glass interface than the etch rate further from the interface. Since this could result from partial densification of the glass as it was being deposited, and not from an actual change in dopant concentration, a profile was made on deposited borosilicate glass after a 2-hr densification at 800°C in an argon atmosphere. This etch rate profile showed a uniform doping of 14.6 ± 0.3 m/o throughout the glass layer. Comparable uniformity was measured on glasses with lower B_2O_3 content.

The concentration profiles as determined by etch rates were observed to depend significantly on the type of ambient which was used during the densification heat treatment. Four silicon wafers with approximately 5000Å of 9.2 m/o borosilicate glass deposited on them were densified at 800°C for 3 hr under ambients of argon, nitrogen, oxygen, and steam, respectively. From the etch rate profiles of these densified oxides, it was obvious that both steam and oxygen formed SiO_2 at the glass-silicon interface with the steam-grown oxide having a thickness (~1000Å) about ten times thicker than that grown from the oxygen. A 25Å thick layer was present at the interface in the case where nitrogen was used as an ambient. Although temperatures higher than 800°C are generally thought to be necessary in order to produce silicon nitride by direct reaction (14), this layer, which could not be removed with our oxide etchant, was thought to be a nitride. The layer was not thick enough for characterization by a measurement of its index of refraction with the ellipsometer.

Various glass thicknesses were used to determine the growth rates for steam-grown silicon dioxide under the doped oxide layers. Silicon wafers with glass thicknesses of 0, 1100, 2100, 3000, and 4200Å of approximately 15 m/o B_2O_3 in SiO_2 were densified in a steam ambient at 800°C for 3 hr. The wafer with no glass originally present grew 1800Å of SiO_2 under these conditions while the wafers with doped oxide deposited on them grew 760-880Å of SiO_2. We conclude that the presence of the glass layer appreciably affects the growth of SiO_2 at the interface, but that the thickness of SiO_2 which is grown under a layer of borosilicate glass has almost no dependence on the thickness of the glass originally deposited on the wafer.

When we repeated this work with glass which was first densified at 800°C in argon, we got SiO_2 layers grown with thicknesses as given in Fig. 2. The oxide thicknesses were measured on the various wafers after 15 min, 30 min, and 1 hr at 800°C with a steam ambient. These results show that even densified borosilicate glass does not stop the diffusion of oxidizing ambients to the silicon substrate. This attribute could, of course, be used to remove the diffusion source from the silicon wafer without physically removing the wafer from the oven. By switching from an inert ambient to steam, the diffusion would be blocked by a rapidly formed layer of thermally grown SiO_2.

SiO_2 can also be used as a barrier to stop out-diffusion of the dopant from the doped oxide into the ambient. A layer of undoped SiO_2 1000Å thick deposited over the doped oxide layer will eliminate depletion of the dopant by this out-diffusion. An etch rate profile of a wafer with such a composite deposition of undoped SiO_2 over a layer of borosilicate glass is shown in Fig. 3. The wafer had been held at a temperature of 1050°C

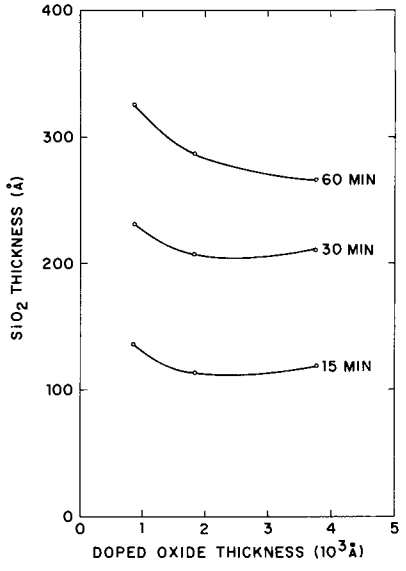

Fig. 2. Thickness of thermal SiO_2 grown from a steam ambient under a borosilicate layer as a function of the deposited glass thickness.

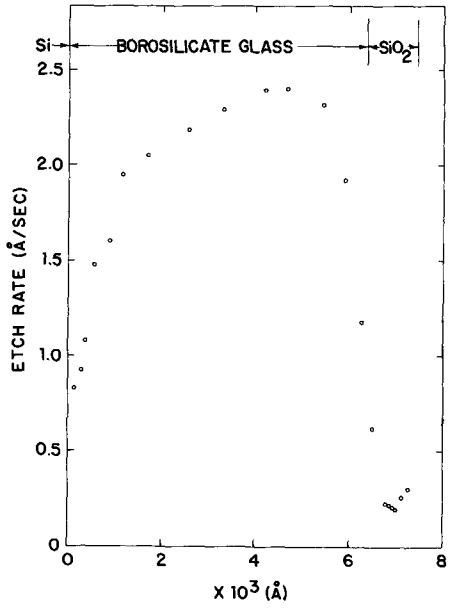

Fig. 3. Etch rate profile of ~15 (m/o) borosilicate glass with an SiO_2 cover after 17-hr-1050°C diffusion.

for 17 hr with an argon ambient. It is seen in the figure that diffusion of the B_2O_3 from the doped oxide into the SiO_2 is negligible since the etch rate drops sharply from a maximum value to the etch rate for undoped SiO_2, 0.2Å/sec. At the same time, appreciable diffusion of dopant into the silicon had occurred as evidenced by the etch rate profile of the doped oxide near the silicon-glass interface.

Diffusion Process

In order to be able to answer the remaining questions about the diffusion process, it was necessary to obtain profiles of the dopant concentrations in borosilicate glasses of various B_2O_3 deposition concentrations after diffusions at different temperatures and with various diffusion times.

According to calculations presented by Crank (15) and recently extended by Hu (16), the surface concentrations of an impurity at the interface between a semi-infinite source (here, the doped oxide) and a semi-infinite sink (the silicon) are time invariant. Crank considers only the simple case where the region $X < 0$ is of one substance with a constant diffusion coefficient D_1, and, in the region $X > 0$, the constant diffusion coefficient is D_2 for the other substance. As in our case, the initial conditions are that the region $X < 0$ is at uniform impurity concentration, Co, and in $X > 0$, the concentration is zero. By taking as his boundary conditions at the interface, a segregation coefficient and constant flux

$$C_2/C_1 = k, \; X = 0 \qquad [2]$$

$$D_1 \frac{\partial C_1}{\partial x} = D_2 \frac{\partial C_2}{\partial x}, \; X = 0 \qquad [3]$$

and by assuming error function solutions in the two regions, he shows that the concentrations at the interface, $X = 0$, are constant in time with the relationships

$$\frac{C_o}{kC_1} = \frac{C_o}{C_2} = \frac{1}{k} + \sqrt{\frac{D_2}{D_1}} \qquad [4]$$

The assumptions which were used to derive Eq. [4] are not completely consistent with our experimental conditions since it is known that the diffusion coefficient in the silicon, D_2, is not independent of the boron concentration (7). The erfc solutions assumed by Crank for his problem cannot be correct in our case. However Hu's work shows that even if the diffusivities in the two regions are concentration dependent and if the more general relationship, $C_2 = f(C_1)$, replaces the segregation coefficient of Eq. [2] at the interface where $f(C_1)$ is any arbitrary function, the impurity concentrations at the interface are still time invariant. Except for the special case of Eq. [2] and constant diffusivities, the simple form of Eq. [4] is not correct, and the interface concentrations would have to be calculated by a complex iteration calculation as given by Hu.

Etch rate profiles of the borosilicate glass on wafers which were diffused under various conditions of diffusion time and temperature were made for approximate Co values of 15, 9.2, and 6.8 m/o of B_2O_3 as the dopant in the glass. Although the concentration dependence of the etch rate method of profiling was not sensitive enough for use with the lowest concentration (see Fig. 1), the profiles of the 15 and 9.2 m/o glasses showed, for each dopant level, that the B_2O_3 concentration at the interface, $C_1(0)$, was independent of the length of time of the diffusion. This is seen for the 15 m/o glass in Fig. 4, where the concentration profiles are given as a function of the distance from the silicon-glass interface. Using complementary error function curves, the extrapolations of the etch rate profiles for all three diffusions give roughly the same intercept at the interface. This shows that the B_2O_3 concentration at the interfaces remained constant at about 8.8 m/o during the time of the diffusion and also are the same for the 1000° and 1100°C diffusions to within the limits of accuracy of the etch rate profiling technique. The time invariance is consistent with the theoretical calculations while the temperature invariance indicates that the reaction at the interface

$$2B_2O_3 + 3Si \rightarrow 4B + 3SiO_2 \qquad [5]$$

is not strongly dependent on the temperature.

A similar result was obtained for the 9.2 m/o glass with the extrapolated interface B_2O_3 concentration being approximately 5.5%. These results are listed in Table I.

We have shown that the constant concentration of B_2O_3 in the glass at the silicon-glass interface, $C_1(0)$, is a function only of the B_2O_3 concentration in the deposited glass, Co. This result can only be expected so long as the oxide can be regarded as a semi-infinite source layer. Since we are working with finite glass thicknesses, we made diffusion profiles on glasses of several thicknesses in order to determine the minimum thickness allowable for maintaining a constant surface concentration. In Fig. 5, diffusion profiles for four different thicknesses of glasses are given. The deposited

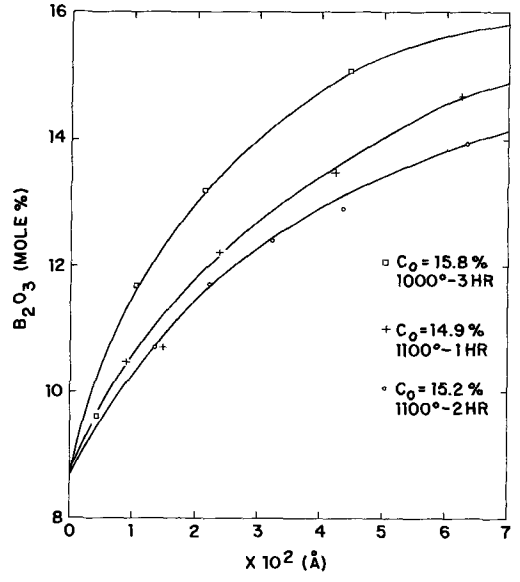

Fig. 4. Concentration profiles of ~15 (m/o) borosilicate glass near the silicon-glass interface after various diffusion conditions.

Table I

Co (m/o)	Diff. temp/time	$C_1(X = 0)$ (m/o)	$Cs = C_2(X = 0)$ (a/o)	$k = \frac{Cs}{C_1}$	$\sqrt{D_1}$ (μ/hr½)	$\sqrt{D_2}$ (μ/hr½)	$\frac{\sqrt{D_2}}{\sqrt{D_1}}$
15.8	1000°/3 hr	8.8	0.35	0.045	0.0092	0.11	12.0
14.9	1100°/1 hr	8.8	0.46	0.059	0.0288	0.32	9.0
15.2	1100°/2 hr	8.7	0.46	0.060	0.0312	0.32	9.8
9.1	1000°/3 hr	5.5	0.12	0.025	0.0063	0.060	9.5
9.4	1100°/1 hr	5.0	0.14	0.032	0.0167	0.20	12.0
9.4	1100°/2 hr	6.3	0.14	0.025	0.0154	0.20	13.0

B_2O_3 concentration was 15 m/o and a 1-hr, 1050°C diffusion was used. Obviously, the combined effects of boron diffusion into the wafer and out-diffusion of the dopant into the ambient caused no appreciable reduction in the maximum B_2O_3 concentration for the three thickest layers in this case. There was a considerable reduction in the maximum B_2O_3 concentration for the 880Å layer, however. From this, it can be concluded that 2000Å of doped oxide is sufficient to assure that the interface B_2O_3 concentration, $C_1(0)$, would remain constant for a 1050°C-1-hr diffusion. For all of the other diffusions in this study, doped oxide thicknesses of at least 4000Å were used to assure no reduction in interface concentrations of B_2O_3.

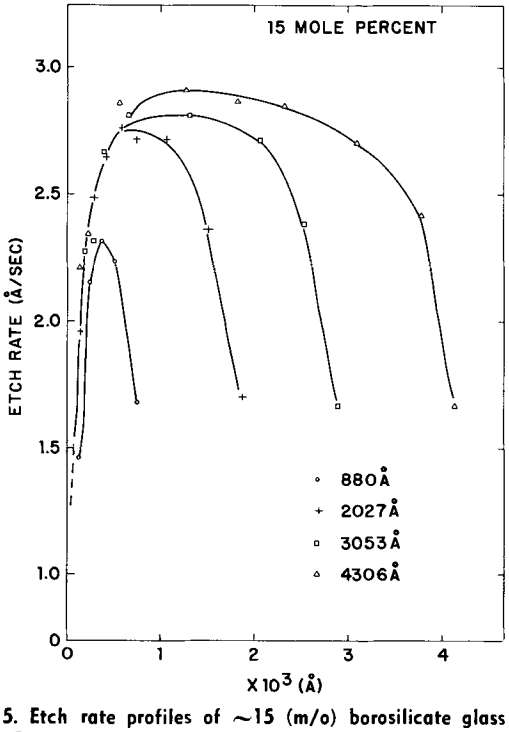

Fig. 5. Etch rate profiles of ~15 (m/o) borosilicate glass after a 1050°C-1-hr diffusion for different glass thicknesses.

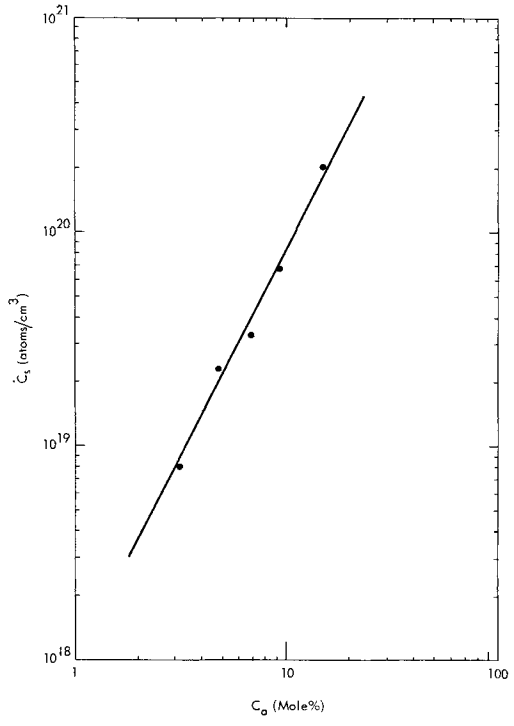

Fig. 6. Surface concentration of boron diffused into silicon as a function of B_2O_3 content in source glass.

The surface concentrations of boron in the diffused silicon wafers, Cs, were calculated from four-point probe sheet resistance and bevel and stain junction depth measurements of many diffused wafers. By assuming a complementary error function distribution and using Irvin's curves (17) these surface concentrations on the silicon side of the interface were also found to be independent of diffusion time and temperature. The values for Cs which were calculated in this way are plotted in Fig. 6 against the dopant concentrations of the B_2O_3 in the oxide. The segregation coefficients, k, as calculated according to Eq. [2], with $C_2(0) = Cs$, are given in Table I for the two highest B_2O_3 concentration sources.

If a complementary error function distribution is assumed for the boron in the silicon

$$C_2(X) = Cs \operatorname{erfc} (X/2\sqrt{D_2 t}) \qquad [6]$$

then, by substituting the junction depth, Xj, for X, and solving for $\sqrt{D_2}$ in the above equation, the diffusion into silicon can be calculated. $C_2(Xj)$ is the background dopant concentration in the silicon. Our values for $\sqrt{D_2}$, calculated in this way, are given in Tables I and II. It should be noted that, since the diffusion coefficient of boron in silicon is concentration dependent, the actual profiles should be flatter near the interface than the complementary error functions. The use of the error function could result in an over estimation of the surface concentration at the high doping levels in this study. In order to check this point, profiles of the electrically active boron were made on the silicon wafers which had been boron diffused at 1100°C for 2 hr. The sectioning was done by anodic oxidation while the sheet resistance measurements were made with a four point probe, as before. The surface concentrations which were obtained by using this measurement technique and Irvin's curves (17) were one half the surface concentration values which had been calculated by assuming a complementary error function distribution. Obviously, the values for k, as obtained from the erfc calculations of Cs and given in Table I, are also higher by a factor of two than the values obtained from the electrically active boron profiles.

Another possible source of error is that the sheet resistance measurement measures only the boron that

Table II. Diffusion coefficient for boron into silicon

$\sqrt{D_2}$(μ/hr½)	Surface concentration 20	6.8	3.3	Cs(10^{19} at./cm³) 2.3	0.8
Temp (°C)					
1000	0.11	0.060	—	—	—
1050	0.18	0.12	0.091	—	—
1100	0.32	0.20	0.18	0.23	0.22
1150	—	—	0.33	0.31	0.33

is in solid solution which is not equivalent to measuring the total boron in the silicon if precipitation or clustering of boron is present. Error due to this effect would cause the measured concentration of boron in the silicon to be lower than the actual concentration. These errors would be opposite in effect to the previously mentioned problem of calculating too large a concentration by means of the assumed complementary error function. Unfortunately, no sufficiently sensitive chemical or radiological method for directly determining the total boron concentration profile is available.

Although we expected the diffusivity of the dopant in the oxide also to be concentration dependent, we considered the profiles of the B_2O_3 concentrations after diffusion to fit a complementary error function of the form

$$Co - C_1(X) = (Co - C_1(0))\ \text{erfc}\ (X/2\sqrt{D_1 t}),\ X > 0 \quad [7]$$

If we rewrite Eq. [7] as

$$\sqrt{D_1} = X/2\sqrt{t}\ \text{arg erfc}\left(\frac{Co - C_1(X)}{Co - C_1(0)}\right) \quad [8]$$

it is easy to see that an average diffusion coefficient, D_1, can be calculated from the concentration profiles which were derived from the etch rate profiles. The diffusion coefficients which were calculated in this way are given in Table I along with the values of $\sqrt{D_2}$ for the boron in the silicon for corresponding temperatures. The large difference between the diffusion coefficients for the two dopant concentrations is inconsistent with the use of a complementary error function profile. This function was used only as a means for estimating an average diffusion coefficient in the oxide. From the table, it is easily seen that the ratio, $\sqrt{D_2}/\sqrt{D_1}$, is approximately 10. One can then roughly estimate that the partially depleted region of the doped oxide should extend a distance from the silicon-glass interface which is roughly equal to one-tenth of the junction depth in the silicon. This is consistent with the earlier result on diffusions from various thicknesses of glass since the 1050°-1-hr 15 m/o diffusion gave a junction depth in the silicon of 1.65μ and a depletion layer of thickness between 880 and 2000Å. Additional thickness over the $Xj/10$ amount should be allowed for the deposited glass layer unless a protective SiO_2 layer is deposited over the source layer to prevent out-diffusion.

Conclusions

The surface concentrations of boron in silicon and B_2O_3 in the glass at the glass-silicon interface have been shown to be independent of diffusion time. This agrees with theoretical calculations for a diffusion system where a doped oxide layer is the impurity source for diffusion into silicon. It was also seen that these surface concentrations are the same for 1000° and 1100°C diffusion temperatures and depend only on the dopant concentration in the deposited glass so long as the glass thickness is larger than the depleted layer thickness. From the ratio of the diffusion coefficients for boron in silicon to the diffusion coefficient for B_2O_3 in the oxide, $D_2/D_1 \sim 100$, it was determined that an interface oxide layer with a thickness equal to one-tenth of the junction depth in the silicon would be partially depleted during a diffusion. It would be possible to also compensate for out-diffusion from the oxide either by depositing a thicker oxide layer, say $Xj/5$ in thickness, or by depositing a diffusion barrier layer of SiO_2 over the doped oxide.

The segregation coefficient at the interface is apparently concentration dependent but the lack of an accurate measurement technique for boron limits the accuracy of our determination of this dependence. The diffusion coefficient of the B_2O_3 in the glass is concentration dependent at least in the 5-15 m/o range of doping, while the diffusion coefficient for boron in silicon is concentration dependent for the highest concentrations of this study.

The study has also shown that an oxidizing ambient will produce an SiO_2 barrier for diffusion at the silicon-glass interface with the oxide growth rate being nearly independent of the glass thickness. A similar, but always very thin, nitride layer might form when a nitrogen atmosphere is used during the diffusion heat treatment. No barrier was observed when argon was used as the ambient.

Acknowledgments

The author is indebted to Dr. J. Basi and Mr. C. Stalowski for providing the deposited oxide wafers and for assistance in making the electrical measurements. He would also like to thank Dr. J. Sandhu for his help and Mr. R. F. Lever for his valuable contributions during the evaluation of the data.

Manuscript submitted March 13, 1970; revised manuscript received *ca.* Sept. 11, 1970.

Any discussion of this paper will appear in a Discussion Section to be published in the December 1971 JOURNAL.

REFERENCES

1. P. F. Schmidt and A. E. Owen, *This Journal*, **111**, 682 (1964).
2. J. Scott and J. Olmstead, *RCA Rev.*, **26**, 357 (1965).
3. W. VonMuench, *Solid-State Electron.*, **9**, 619 (1966); *IBM J. Res. Dev.*, **10**, 438 (1966).
4. D. B. Lee, *Solid-State Electron.*, **10**, 623 (1967).
5. M. L. Barry and P. Olofsen, *Solid-State Technol.*, **11**, 39 (1968).
6. A. Cuccia, G. Shrank, and G. Queirolo, "Semiconductor Silicon," p. 506, R. R. Haberacht and E. L. Kern, Editors, The Electrochemical Society, New York (1969).
7. M. L. Barry and P. Olofsen, *This Journal*, **116**, 645 (1969).
8. A. E. Owen and P. F. Schmidt, *ibid.*, **115**, 548 (1968).
9. W. A. Pliskin, *ibid.*, **114**, 620 (1967).
10. W. A. Pliskin, "Measurement Techniques for Thin Films," p. 280, B. Schwartz and N. Schwartz, Editors, The Electrochemical Society, New York (1967).
11. W. A. Pliskin and R. P. Esch, *Appl. Phys. Letters*, **11**, 257 (1967).
12. W. A. Pliskin, Private communication.
13. W. A. Pliskin and H. S. Lehman, *This Journal*, **112**, 1013 (1965).
14. R. G. Frieser, *ibid.*, **115**, 1092 (1968).
15. J. Crank, "The Mathematics of Diffusion," p. 37, Oxford University Press, London (1956).
16. S. M. Hu, To be published.
17. J. C. Irvin, *Bell System Tech. J.*, **41**, 387 (1962).

The Growth of Epitaxial Gallium Phosphide from the Vapor Phase by Halogen Transport

A. Mottram, A. R. Peaker, and P. D. Sudlow

Ferranti Ltd., Chadderton, Oldham, England

ABSTRACT

Gallium phosphide has been grown epitaxially by open tube vapor transport using the $H_2/PCl_3/Ga$ system. Although GaAs substrates have been used for the majority of the work, the more recent use of Czochralski grown GaP has enabled a reduction in both strain and stacking fault density of the epitaxial layer to be achieved. Sulfur, tellurium, and zinc have been used as dopants in the preparation of both n- and p-type layers, and relationships have been established between the dopant level in the vapor stream and the carrier concentration in the grown crystal. A Schottky diode technique has been used to detect variations in doping level throughout the depth of a slice and, after modifications to the growth process, uniform doping levels have been established. Measurements of the dependence of mobility on carrier concentration over the range 10^{14}-10^{19} cm^{-3} have been made on this substantially homogeneous material and consistent results obtained. The levels of compensation in n-type material have been shown to be between 1 and 2% over the range of carrier concentration 8 x 10^{16}-2 x 10^{18} cm^{-3}. The previously reported dependence of doping level on substrate orientation has been confirmed for (111) surfaces and extended to the (100) and (110) surfaces for homoepitaxy.

The growth of GaP from the vapor phase by halogen transport is a convenient method for the preparation of single-crystal slices, the $Ga/PCl_3/H_2$ system being used to deposit GaP epitaxially on single-crystal substrates of GaAs and GaP.

Previously published work describing this growth technique (1-3) has used various methods to incorporate dopants into the GaP but investigations into the homogeneity of the resultant GaP have not been made in any great detail, although some tentative conclusions have been reached by Taylor *et al.* (2). It is shown in this paper that unless adequate precautions are taken, very significant doping gradients are present in the grown gallium phosphide and it is thought that the use of modified growth techniques to avoid these gradients has enabled a considerable reduction in the scatter of the data relating to the GaP to be achieved.

In addition, a thorough examination of both the growth parameters and the doping processes involved has enabled a consistency of result to be established with the growth system. The material obtained, after removal of the GaAs substrate, has been in the form of self-supporting single-crystal slices and these have been used subsequently both as substrates in liquid epitaxy experiments and for planar array technology development.

Experimental Procedure

The apparatus, which is similar to that used by other workers for open tube vapor transport systems (4, 5), is shown schematically in Fig. 1. Close attention was paid to the elimination of all gas leaks and the complete apparatus was tested to be leak free at 10^{-2} Torr. As oxygen contamination of the gas stream during the growth process caused rapid nucleation and whisker growth of the GaP both on the substrate and in the surrounding deposition zone, a further precaution taken was to maintain the complete system at a pressure of 2-3 mm of mercury above atmospheric, thus keeping oxygen ingress to an absolute minimum. A three zone furnace was used in which the low-temperature region was only utilized for certain doping procedures, the center flat zone being used for the gallium source and the temperature gradient region for deposition purposes on the appropriate substrates. A liner tube was used to collect all dump products, thus enabling the same reaction tube to be used for a number of consecutive runs. Adhesion between the heavy deposit of GaP and the silica substrate holder in the deposition region, besides making removal of the slice from the silica plate difficult, often led to cracking of the grown slice before its removal from the apparatus. A hard carbon film, produced by the thermal cracking of acetone, deposited on the silica plate before insertion in the apparatus, overcame these problems by preventing adhesion, and a film similarly deposited on the liner tube prevented the severe cracking and erosion that normally takes place when the quartz apparatus cools down after deposition. As the presence of carbon in the reaction tube did not have any influence on the electrical properties of the grown material, carbon coating of the liner tube and substrate holder was used as normal procedure in the vapor epitaxy system. The liner tube was restricted to a maximum inner diameter of 19 mm; when larger tubes than this were used, streaming of the vapor resulted in incomplete reaction at the gallium source and inconsistent deposits of gallium phosphide in the growth zone.

A supply of 99.99% pure H_2, further purified by diffusion through a Pd/Ag tube, is passed through 99.999+% PCl_3 at 23°C and diluted using a by-pass supply of the purified hydrogen, thus enabling a wide range of PCl_3 partial pressures to be obtained in the system. The vapor stream is passed over the heated

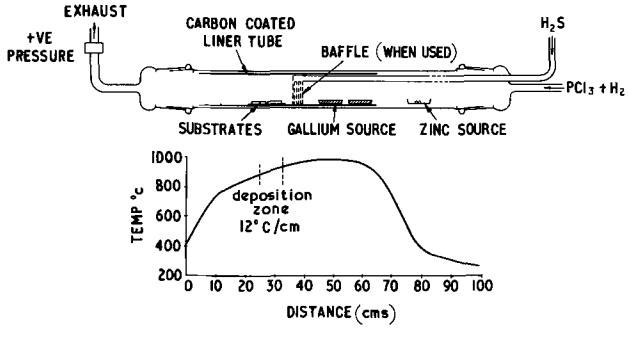

Fig. 1. Schematic diagram of the growth system and temperature conditions for the deposition of epitaxial gallium phosphide.

Key words: gallium phosphide, epitaxial, vapor phase, halogen transport, doping gradients.

gallium source and then down the temperature gradient in which a GaAs or GaP seed is situated. Epitaxial deposition of the GaP takes place on the substrate. For the normal growth system the following conditions have been established for a typical process: 35-40 ml min^{-1} of H_2 is passed through the PCl_3 and diluted to 100 ml min^{-1} with H_2, passed over the gallium source held at 970°C and then down a temperature gradient of 12°C cm^{-1} in which the substrate is situated at a temperature between 850°-910°C. A growth rate of 50-80 μm hr^{-1} has been obtained on (111)A orientated GaAs seeds with these conditions, which together with a growth period of 3-5 hr gave reproducible single-crystal GaP layers up to 400 μm thick. Both 25 and 50g gallium sources have been used, the PCl_3 figure quoted being that for the 50g source, while a correspondingly lower flow rate has been used for the 25g source. It was found that the optimum deposition temperature and the growth rate of the GaP layer were both dependent on the flow rate of the PCl_3, this single item being the principal factor governing the reproducibility of the growth. Complete quantitative examination of a small number of runs and a more comprehensive analysis of the relative Ga and PCl_3 consumption rates over a large number of runs have given experimental evidence for the proposed over-all reactions involved.

Examination of furnace profiles throughout the investigation has shown that the growth rate of the epitaxial layer is partly dependent on the temperature gradient of the growth zone. Under identical flow conditions a gradient of 6°C cm^{-1} gave smooth layers at growth rates up to 40 μm hr^{-1}, 12°C cm^{-1} increased the growth rate to 80 μm hr^{-1} while still maintaining smooth layers, but any further increase in the gradient resulted in hillocky growth.

The conditions outlined above were established for growth on the (111)A face of substrates of undoped n-type GaAs orientated within $\pm\frac{1}{2}°$, with dislocation densities $< 5 \times 10^3$ cm^{-2}. This orientation was chosen for the majority of our experiments because it was the fastest growing face and our prime concern, when growing on GaAs substrates, was for the preparation of self-supporting single-crystal slices. Prior to growth, the substrates were lapped, polished with diamond paste of particle size no greater than 1 μm, etched for 2 min in 3 : 1 : 1 $H_2SO_4/H_2O_2/H_2O$ at 60°C to remove any work damage, and finally etched in 1 : 9 : 10 $HF/HNO_3/H_2O$ at 50°C for 1 min immediately prior to insertion in the apparatus. The substrate was positioned (111)A face uppermost on the flat, carbon-coated, quartz spade. The furnace was heated with the substrate situated in the growth position and the reaction started without any deliberate back-etching procedure. Measurements taken on six consecutive runs have shown automatic back etching to take place, between 100-120 μm being removed in each instance. During the growth process, the GaP would normally be deposited on all faces of the substrate. A SiO_2 mask deposited on the (111)B face of the GaAs substrate, by pyrolytic decomposition of tetraethoxysilane, prevented deposition of GaP on this face and simplified removal of the GaAs after growth. This was done by first etching away the SiO_2 layer with HF and then dissolving the GaAs in hot 50% HNO_3. The (111)B face of the grown GaP layer was then lapped and polished to remove any $GaAs_xP_{(1-x)}$ deposit formed at the interface. The majority of slices of GaP obtained by this technique were self-supporting and single crystal. Growths have also been made on the (111)B, (100), and (110) faces of similar GaAs substrates as well as on all four principal orientations of GaP substrates grown by a liquid encapsulated Czochralski technique (6).

Undoped, sulfur, tellurium- and zinc-doped material have been grown using the standard procedure. Sulfur was introduced into the growth system as hydrogen sulfide, either directly from a bottled supply of 99.5% H_2S or by hydrogenation of 99.999% sulfur vapor in a small tube furnace held in excess of 800°C. Tellurium doping was obtained by adding Te metal to the gallium and continuing the growth technique in the usual manner. Zinc vapor was introduced into the growth ambient by passing the H_2/PCl_3 gas stream over a pellet of zinc situated in the low-temperature zone of the furnace prior to the gallium source.

Hall and resistivity measurements have been used to determine the carrier concentration and mobility of all the vapor epitaxial layers after removal of the GaAs substrate. The van der Pauw technique (7) with either clover leaf or trapezoidal samples has been employed and the measurements taken in a field of 1 kGs at a temperature of 20°C. A number of samples were also measured over a range of temperatures. Alloyed contacts were made in all cases in an atmosphere of 90% N_2/10% H_2, using either pure Sn or Au/2% Sn alloy for n-type material and Au/2% Zn alloy for p-type material. All undoped material grown on GaAs substrates proved to be high-resistivity n-type and the Au/2% Sn alloy was successfully used for contacting.

Doping gradients were investigated by evaporating a square mesh pattern of circular gold Schottky barriers over an angle lapped region of the grown slice and measuring the differential capacitance-voltage characteristics of the individual barriers. This type of construction provided discrete measurements of impurity concentration at equal intervals below the semiconductor surface, the impurity concentration being derived by the use of well-known theoretical relations from the *C-V* data obtained. This technique is described in detail elsewhere (8).

Results and Discussion

Over-all reaction.—A study of the amounts of gallium and phosphorous trichloride used in over two hundred standard runs showed the Ga/PCl_3 consumption ratio to be independent of the PCl_3 flow rate for the range of flow rates investigated, and a plot of the results (Fig. 2) gave an average mole ratio of 2.56. The amount of Ga used during each run and the weight of PCl_3 consumed over a number of consecutive runs were measured for each separate batch of PCl_3. This means that each point on the curve is in effect an average of not less than seven consecutive growths. The results were obtained from runs in which slow PCl_3 flow rates used a 25g Ga source and faster rates a 50g source. The mole ratio of 2.56 $\pm$ 0.1 is in agreement with the value of 2.64 predicted from thermodynamic data and supports the result of 2.5 $\pm$ 0.2 obtained with the halide transport system by Luther and Roccasecca (3). The weight of the GaP skin formed on the unused part of the 25g gallium source during

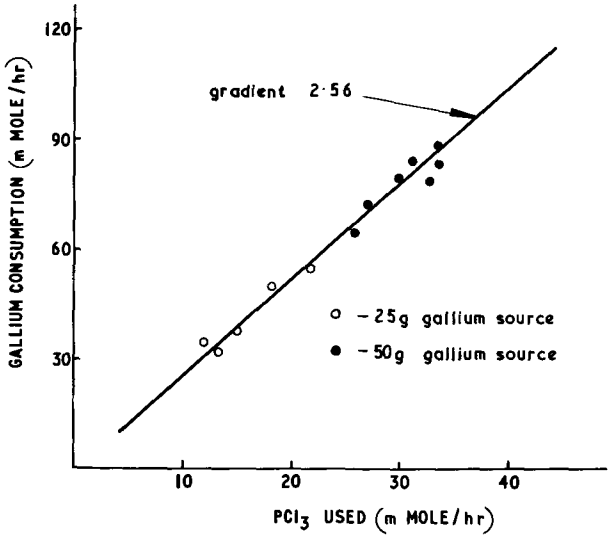

Fig. 2. Gallium:phosphorous trichloride consumption ratio

cooling was approximately 0.25g in each instance. This corresponds to the complete saturation of the gallium with phosphorus at 970°C (9) and indicates that the phosphorus-saturated gallium is very close to being in equilibrium with solid GaP during the growth process.

Observation of the early stages of the growth process showed that during the initial saturation of the source, gallium metal was transported to the dump end of the reaction tube and the GaAs substrate was back-etched to the extent of 100-120 μm by the excess halides present. If the PCl_3 was in excess at this stage, then the formation of white, needle crystals of $GaCl_3$ was apparent at the cold end of the tube, whereas the formation of the grayish $GaCl_2$ deposit indicated that the correct flow rates were being used. It has been assumed in previous publications that both the di- and trichloride are only present in negligible amounts at 970°C, and indeed the agreement between the practical Ga/PCl_3 consumption ratio and the theoretical value, in which $GaCl_2$ has been neglected, indicates that only GaCl and HCl are present in the reaction zone at 970°C. A further reaction must, therefore, take place in the deposition zone in which the incoming fraction of HCl which does not react with the gallium converts the monohalide to the dihalide. The $GaCl_2$ invariably shows some dissociation into Ga and $GaCl_3$, but this process is not included in the over-all scheme of the reaction. The above points indicate that the reaction may be described as follows

$$4PCl_3 + 6H_2 \rightarrow 12HCl + P_4 \quad \text{— } H_2 \text{ through the } PCl_3 \quad [I]$$

$$P_4 \rightarrow 2P_2 \quad \text{— Dissociation} \quad [II]$$

$$2Ga + 2HCl \rightarrow 2GaCl + H_2 \quad \text{— At 970°C} \quad [III]$$

$$4GaCl + 2HCl \rightarrow 3GaCl_2 + H_2 + Ga \quad [IV]$$

$$2Ga + P_2 \rightarrow 2GaP \quad \text{— At the deposition zone} \quad [V]$$

If at any stage the gallium source is reduced to a low level, then the excess HCl present in the growth zone can act as a transporting medium for the GaP previously deposited and a situation can arise whereby not only the GaP but also the GaAs seed can be completely removed by the HCl.

A quantitative examination of a number of experiments was made by measuring the weights of pure Ga and PCl_3 used during the run, weighing the total products obtained from the reaction, dissolving away the dump products, and finally reweighing the pure GaP formed. The results showed that the over-all equation most acceptable for the reaction was

$$5Ga + 2PCl_3 \rightarrow 2GaP + 3GaCl_2$$

This agrees with the above scheme of reaction and also supports the result observed by Kamath and Bowman (5).

Physical properties of the grown GaP.—Although layers were grown on the (111)A, (111)B, (100), and (110) orientations of both GaAs and GaP, very smooth surfaces were obtained only on the (111)A face, and as this was also the fastest growing surface it was used for the majority of growths where removal of the GaAs substrates was required. After removal of the GaAs substrate the GaP layers were shown to be self-supporting, and x-ray diffraction studies confirmed that they were single-crystal growths.

A comparison of the layers grown on both substrate materials showed those grown on GaAs to have much higher stacking fault and dislocation densities, as well as a great deal of residual strain in the crystal. Stacking faults and dislocations were revealed as line and point defects, respectively, by etching the (111)A face in boiling $K_3Fe(CN)_6/KOH/H_2O$ 2/3/25 for 60 sec (10).

Layers grown on GaAs always had densities $> 2 \times 10^5$, this being the case even when the GaAs was dislocation free. On the other hand the dislocation densities of those layers grown on GaP were more dependent on the substrate and were never greater than 2×10^5 even on substrates with a dislocation density (D) $> 10^6$. On good quality substrates ($D \leq 10^4$) the epitaxial layer was uniformly dislocated in the low 10^4 region.

It can be seen from Fig. 3a and b, which show representative areas of epitaxial layers grown under similar conditions on GaAs and GaP, respectively, that an order of magnitude increase in dislocation density caused by the use of GaAs substrates is represented by the predominance of dislocations aligned along slip planes; this is compared to a fairly uniform distribution of dislocations when GaP substrates were used. It is fairly obvious that the aligned dislocations are a result of the heteroepitaxy nature of the GaAs/GaP system in which the 4% lattice and 15% thermal mismatch between GaAs and GaP (11) causes severe strain in the epitaxial layer during cooling. The uniform distribution of dislocations observed when GaP substrates were used ($\sim 2 \times 10^4$ cm^{-2}) can be attributed to the growth conditions (deposition rate, thermal gradient, etc.). Progressive polishing and etching of layers throughout their total thickness (up to 500 μm) showed this level of dislocation to remain constant throughout the layer. A number of layers exhibited severe pitting which occurred during the latter part of the growth process, an example is shown in Fig. 4a. These appear to occur under conditions when excess HCl would be expected to be present in the vapor stream and are probably at the sites of impurity segregation caused by the dislocations formed at the growth temperature. The only other major surface

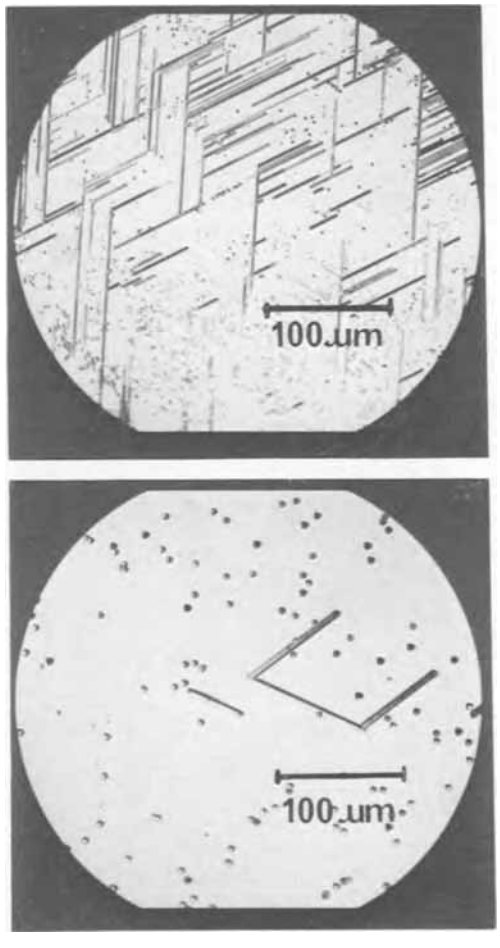

Fig. 3. Comparison between GaP layers grown on GaAs and GaP substrates, (a, top) shows the case in which a GaAs substrate was used and (b, bottom) the improvement obtained by using a GaP substrate.

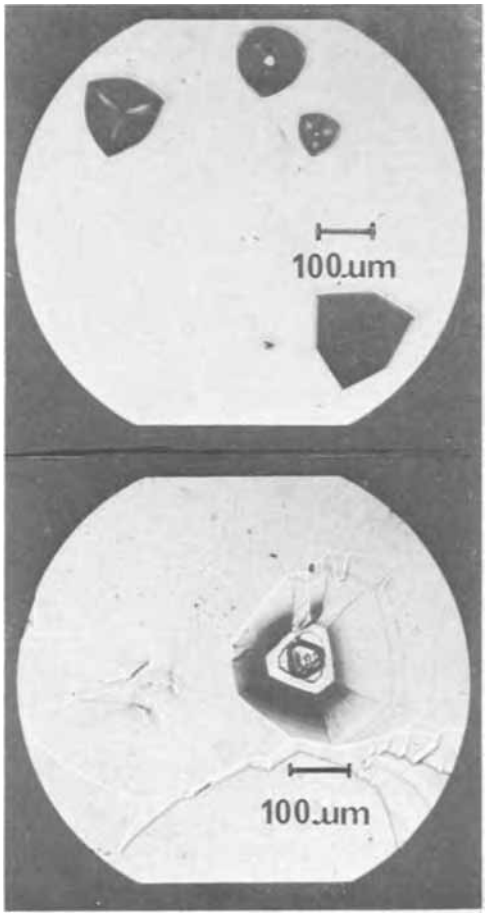

Fig. 4. Major surface defects on the GaP formed during growth, (a, top) pitting, (b, bottom) hillocks.

defect has been the formation of growth hillocks as shown in Fig. 4b. These are similar to those reported in GaAs epitaxy and have been attributed to dust particles or gallium droplet formation on the surface of the substrate immediately prior to GaP nucleation (12).

The difference in thermal expansion coefficients between the GaAs substrate and the GaP causes a pronounced curvature in the structure after cooling, and during the last stages of removal of the GaAs, microcracking at the interface is often observed. This extends a small distance into the GaP and together with the obvious inhomogeneity at the interface means that the (111)B face of the grown slice had to be lapped and polished before any further use could be made of it. Small inclusions, darker in color, found on the (111)B face, were determined by electron microprobe analysis as being regions of $GaAs_xP_{(1-x)}$ and mass spectrometric analysis of the GaP showed arsenic to be present in most layers between 0.01 and 0.1%. These results were obtained from layers where the GaAs substrates had no SiO_2 film on the (111)B face and it can be assumed that in all cases where the protective film has been used the arsenic contamination will have been somewhat reduced.

Doping gradients.—The gaseous doping technique initially used for sulfur, which involved passing a diluted supply of bottled H_2S into the vapor stream prior to the gallium source, was found to produce severe doping gradients throughout the entire thickness of the grown layer. Variations in doping level were found by angle lapping the crystal and using Schottky barrier measurements at fixed points throughout its thickness as described previously. The large variations of impurity with depth in earlier layers as seen in Fig. 5 are caused by the absorption of the sulfur by the gallium during the early stages of

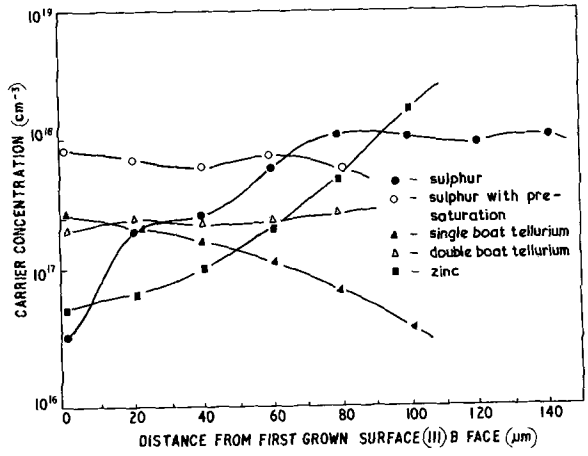

Fig. 5. Variation of carrier concentration with depth in epitaxial layers of GaP.

growth, followed by random fluctuations in the flow rate of the H_2S vapor during the remainder of growth. Elimination of the absorption effect was effected by either pre-quasi-saturation of the source or by the use of a baffle so that the dopant stream bypassed the gallium, this latter system caused nucleation prior to the deposition zone and was therefore later dispensed with. As minor fluctuations in flow conditions were found difficult to eliminate, very fine valve control being required over periods of 3-4 hr, the alternative means of sulfur doping by hydrogenation of sulfur vapor was used. This proved to be a much simpler system to control, as the doping level could be regulated by adjusting the temperature of the solid sulfur source and keeping the hydrogen flow over the dopant constant at 10 ml/min. A similar system of presaturation was again used and a typical doping profile through a grown layer (Fig. 5) indicated that a stable carrier concentration was established and maintained from the onset of growth.

Doping gradients were also present in tellurium- and zinc-doped layers, although in neither case were they as severe as sulfur. The tellurium-doped layers have since been grown free from severe doping gradients by using a double-boat gallium source. Both boats of gallium are identically doped with pure Te metal and held in the flat temperature zone in the reaction tube. One of the sources remains virtually unchanged throughout the entire growth period and thus provides a constant Te vapor pressure. A similar single-boat system yielded layers which were Te depleted toward the last grown surface, and Fig. 5 shows a comparison in doping profile of two layers grown by the separate systems.

Profiles of the zinc-doped layers indicated that although a constant doping level was maintained over their surface, a rapid rise in carrier concentration occurred toward the last grown face (Fig. 5). Although the absorption of zinc by the gallium source has been previously calculated by Luther and Roccasecca as being 3% of the total amount of dopant transported during the run (3), the evidence presented here suggests a much greater loss to the source and an effect similar to that seen in the sulfur-doped layers occurs in which zinc is absorbed into the gallium source during the earlier stages of growth.

Investigations of doping gradients in material with a mean carrier concentration of approximately 10^{18} cm^{-3} grown on gallium phosphide substrates and on orientations other than (111) have shown that the gradients observed in the material other than at the actual GaAs/GaP interface are functions of the growth conditions and not of the orientation or nature of the substrate. This is in contrast to the results of Taylor *et al.* (2) for selenium-doped material which indicated from Hall measurements and progressive lapping that the carrier concentration increased in the growth di-

rection on samples grown on GaAs but not on GaP substrates.

Electrical measurements made on early samples which were shown to have doping gradients or striations of varying carrier concentration throughout their depth indicated that the Hall value as measured by the van der Pauw technique gave a value weighted toward the more highly doped strata. For the almost uniform profiles now observed in slices grown by the modified techniques, the Hall measured values are in agreement with the free carrier concentration calculated from the Schottky diode measurements, and it is layers of this type that have been used in the investigations described in the remainder of this paper.

Although the variation in carrier concentration along the length of any individual crystal was found to be minimal, a check was made on the variation along the entire deposition zone. A factor of two change was observed over the temperature range 910°-850°C, the higher values being obtained at the higher temperature. Layers grown at lower temperatures as well as having low carrier concentration were also of poor surface nature. The growth zone, covering a range of 60°C, had a length of 5 cm and was therefore suitable for multiple crystal growths.

Added impurity and carrier concentration.—All carrier concentration values in this section were determined from GaP layers grown on (111)A orientated GaAs substrates. Undoped layers were always n-type with resistivities of the order 10^3 ohm-cm and carrier concentrations in the 10^{14} cm^{-3} range. Reproducible values for sulfur, tellurium, and zinc doping were obtained over the range of doping levels investigated.

For each of the dopants used a relationship was established between the impurity present in the vapor stream and its incorporation into the grown crystal in an electrically active form. In Fig. 6 a plot of the room temperature carrier concentration against the sulfur vapor pressure shows an almost linear relationship to about 2 x 10^{18} cm^{-3}. Above this value the carrier concentration tends to level off with further increases in the sulfur vapor and the crystal takes on a metallic appearance as the carrier concentration approaches 5 x 10^{18} cm^{-3}. At this point the solid solubility of sulfur in gallium phosphide is limiting the electrically active impurity concentration and an increasing proportion of the sulfur is present in the form of precipitates or neutral complexes at room temperature. A similar situation can be seen to occur in the case of tellurium, although the relationship is sublinear at a somewhat lower level. It is thought that complexes such as $GaTe_3$ are present in an electrically inactive form at the higher concentrations. A similar effect has been noted by Taylor in selenium-doped GaP, saturation occurring at a carrier concentration of 2 x 10^{18} (13).

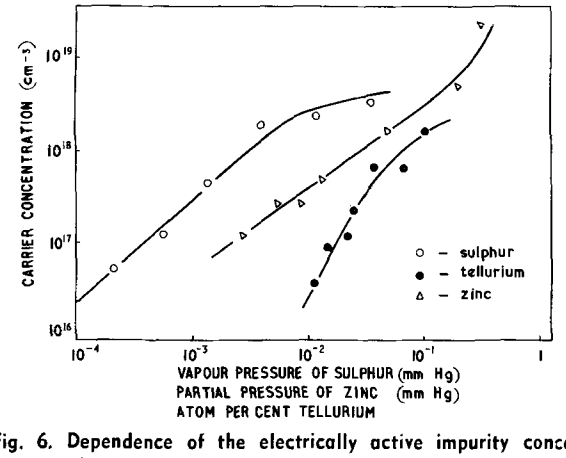

Fig. 6. Dependence of the electrically active impurity concentration in the grown crystal on the impurity level present in the vapor stream.

The case of zinc-doped material is somewhat different as the solid solubility of Zn in GaP at the growth temperature is known to be considerably higher than the impurity levels used (14) and there is no evidence for the formation of precipitates on cooling over the range of carrier concentrations investigated. In the region 10^{17}-10^{19} cm^{-3} the carrier concentration-partial pressure relationship is slightly sublinear, above this region the carrier concentration increases considerably faster than the partial pressure. This could be explained by the observations of Foster *et al.* (15) and Casey *et al.* (16) who measured hole densities greater than the zinc concentration in solution-grown and diffused gallium phosphide, respectively.

For the three separate dopants, over a limited range, a linear dependence of impurity concentration on the partial pressure of the dopant has been established when growth takes place on the (111)A face. For an extrinsic semiconductor, grown under equilibrium conditions, a square root dependence is normally expected and has in fact been observed both in solution (17) and vapor growth (18). The deviation observed here has been reported elsewhere (3) and can be attributed to the incorporation of the impurity being a nonequilibrium process in the halogen transport system. At the comparatively low temperatures used for deposition the diffusion of the dopants is slow, and fast growth rates have been used for the growth of all crystals measured. This means that a nonequilibrium situation is established between the absorption of the dopant atom on the growth face and their incorporation into the bulk crystal and creates the linear dependence observed.

Effect of substrate.—Unlike GaAs epitaxy in which the smoothest surfaces have always been obtained using substrates misorientated from the low index planes by a few degrees (19), misorientation of (111)A GaAs substrates by 1°, 2°, 3°, and 6°, produced increasingly severe pitting in the grown layer and a requisite of reproducibly smooth growths on this face was for the orientation to be within ±1° after polishing. The effect of misorientation on the other planes was not investigated and therefore a strict comparison with GaAs is not possible at this stage.

Although a high percentage of the runs carried out have used (111)A orientated GaAs substrates and consequently the information on doping levels, *etc.*, is particularly relevant to this orientation, a number of runs have been made on the other three principal orientations (111)B, (110), (100) of both GaAs and GaP.

Under similar flow conditions the growth rates could be placed in the order (111)A > (110) > (111)B > (100). This order appeared to be independent of the substrate material (GaAs or GaP) and under the flow conditions previously stated the growth rates were approximately 80 μm hr^{-1}, 50 μm hr^{-1}, 40 μm hr^{-1}, and 10 μm hr^{-1}, respectively. Layers grown on the (111)A orientation of either GaAs or GaP had mirror-like surfaces and were of uniform thickness, while the other orientations were generally faceted and of uneven thickness. Figure 7 shows a polished (111)A orientated GaAs substrate, an epitaxial GaP layer with the GaAs still intact and an unsupported single-crystal wafer of GaP.

The dependence of carrier concentration on growth orientation as observed on the (111)A and (111)B faces for both n- and p-type dopants as previously reported by Taylor *et al.* (2) is supported by the results obtained here for both GaAs and GaP substrates (Table I). Undoped layers grown on the (111)B face of both GaAs and GaP are strongly n-type with carrier concentration of the order 10^{17} cm^{-3}, whereas similar layers grown on the (111)A face prove to be high resistivity (10^3 ohm-cm), n-type for cases in which GaAs substrates were used and high resistivity p-type for GaP substrates. Previously reported values for undoped layers grown in the (111)A face have been p-type, and the result observed here can probably be accounted

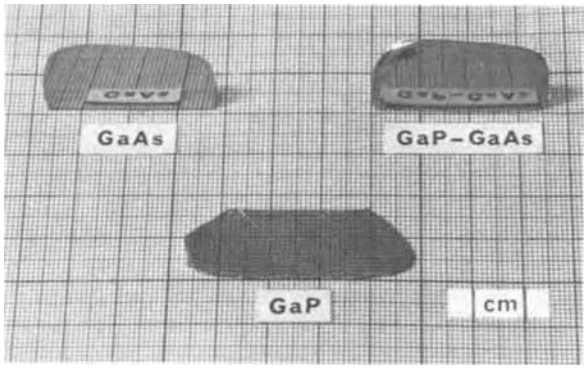

Fig. 7. Example of a GaAs slice; an epitaxial layer of GaP with the GaAs substrate still intact; and a polished self-supporting slice of epitaxial GaP.

for by autodoping from an n-type impurity present in the GaAs substrate.

A number of layers grown simultaneously on both the (111) faces of GaAs substrates showed that donor impurities (S, Te) were incorporated more readily into the (111)B face by a factor of between 10 and 30, while the acceptor zinc showed a similar marked preference for the (111)A face.

The use of GaP substrates, which removed the necessity of producing thick growths, meant that the orientations dependence could be investigated on all four principal orientations. A combination of the reduced layer thickness and the use of n-type (high 10^{17} cm^{-3}) substrates meant that the Schottky diode technique previously described was more suitable for carrier concentration determinations for growths on GaP substrates, and this method was used for all such values reported in Table I. It can be seen, that although the donor atom preference for the (111)B face is similar to that previously observed, the doping levels for both the (100) and (110) orientation are approximately midway between the two extremes and differ from the values observed by Taylor (13), where the doping levels tended to be biased toward the preferred orientation (111)B in each instance. The undoped values are similar to those reported and show both the (110) and (100) to be n-type at a level of 6×10^{16} and 8×10^{15}, respectively.

The orientation effect can be explained by the difference in bonding behavior of the orientated surfaces. A Group VI donor atom will substitute for a P atom in the lattice, this means that on the (111)A (Ga) face the donor atom will be loosely held by only one bond while on the (111)B (P) face three Ga atoms are available for bonding. The more loosely held donor atoms on the (111)A face will have a greater tendency to be lost to the vapor stream and thus establish a lower doping level in the crystal for similar growth conditions. A similar argument can be put forward for both the (100) and (110) values obtained. In the former case each P atom is bonded downward into the crystal to two Ga atoms, and normally would bond upward to another two Ga atoms. The donor atom, replacing the P atom and subsequently having two surface bonds, would therefore have a bonding force somewhere between the values obtained for the (111) faces. For the (110) surface, where each P atom makes two bonds to Ga atoms on the surface and only one bond to a Ga atom in the underlying layer, an arrangement similar to the (111)A face can be seen. The donor atom is only loosely held by one bond in the underlying layer, but this is immediately supported by two surface bonds, which again would lead to a bonding force somewhere between the opposite face (111) values.

Table II. Donor and acceptor concentrations

Sample	Dopant	N_D, cm^{-3}	N_A, cm^{-3}	E_D, meV
319	S	$(2.05 \pm 0.1) \times 10^{18}$	$(5.3 \pm 0.1) \times 10^{16}$	80 ± 5
371	S	$(8.0 \pm 0.3) \times 10^{16}$	$(1.2 \pm 0.3) \times 10^{15}$	107 ± 10
383	S	$(8.8 \pm 0.2) \times 10^{17}$	$(8.6 \pm 0.2) \times 10^{15}$	97 ± 10
2/213	Te	$(7.5 \pm 0.2) \times 10^{17}$	$(1.1 \pm 0.2) \times 10^{16}$	81 ± 10

Donor and acceptor concentrations.—The donor and acceptor concentrations and the donor binding energy of sulfur and tellurium-doped material have been determined by Hall measurements. The analysis (20, 21) assumes that only one donor level is present and that $N_D > 10\ N_A$, it also equates Hall and drift mobility. The experimental results obtained over the temperature range 80°-350°K were fitted to the relationship

$$\frac{n(n + N_A)}{N_D - n - N_A} = N_c \left\{ \frac{m^*}{m_o} \right\}^{3/2} g^{-1} \exp - \frac{E_D}{kT}$$

putting

$$N_c = 2(2\pi m_o\, kT/h^2)^{3/2}$$

Where n is the concentration of conduction electrons per cubic centimeter, N_D and N_A the donor and acceptor concentrations, N_c the effective density of states in the conduction band at temperature T, g the degeneracy factor associated with the donors, m^* the effective mass of the electrons, and E_D the donor binding energy. The results obtained on four typical samples are shown in Table II. It can be seen that the acceptor concentration increases with the donor concentration representing between 1 and 2% of total impurity content. It seems unlikely that this could be attributed to impurities in the hydrogen sulfide used for doping as the level is so high and is probably due to autocompensation effects associated with vacancies.

The values deduced for donor binding energy are in agreement with the results of Montgomery and Feldman (22) obtained on crystals produced by the floating zone technique. They show a linear relationship between E_D and $N_D^{1/3}$ which implies that the variation is due to interaction between donors.

Hall mobility.—The highest mobilities, measured at 20°C, were those of undoped samples with background carrier concentrations of 10^{14} cm^{-3}, the values obtained being in the range 140-150 $cm^2\ V^{-1}\ sec^{-1}$. As

Table I. Variation of carrier concentration with orientation

Sample	Substrate	Dopant	Type and carrier concentration (111)A	(111)B	(110)	(100)
VP492	GaAs	Undoped	n— 6×10^{14}	n— 2×10^{17}		
VP3/48	GaAs	Sulfur	n— 2×10^{17}	n—2.7×10^{18}		
VP534	GaAs	Sulfur	n—3.3×10^{17}	n— 4×10^{18}		
VP561	GaAs	Zinc	p— 5×10^{16}	n— 1×10^{17}		
VP560	GaAs	Zinc	p— 5×10^{17}	n— 9×10^{16}		
VP559	GaAs	Zinc	p— 1×10^{19}	p— 1×10^{18}		
VP510	GaP	Undoped	p-type	n— 3×10^{17}		
VP573	GaP	Undoped	p-type	n— 2×10^{17}	n— 6×10^{16}	n— 8×10^{15}
VP576	GaP	Tellurium	n— 7×10^{15}	n—1.5×10^{18}	n—1.3×10^{17}	n— 2×10^{17}
VP577	GaP	Tellurium	n—1.5×10^{16}	n— 4×10^{18}	n—3.6×10^{17}	n—3.2×10^{17}
VP495	GaP	Tellurium	n—3.4×10^{17}	n—2.5×10^{18}	—	—
VP3/33	GaP	Sulfur	n— 1×10^{16}	n—3.8×10^{17}	—	—
VP580	GaP	Sulfur	n— 5×10^{16}	n—3.0×10^{17}	n—7.5×10^{16}	n—1.5×10^{17}
VP582	GaP	Sulfur	n— 1×10^{17}	n—3.4×10^{18}	n—4.0×10^{17}	n—6.1×10^{17}
VP578	GaP	Sulfur	n— 7×10^{17}	n—3.8×10^{18}	n— 8×10^{17}	—

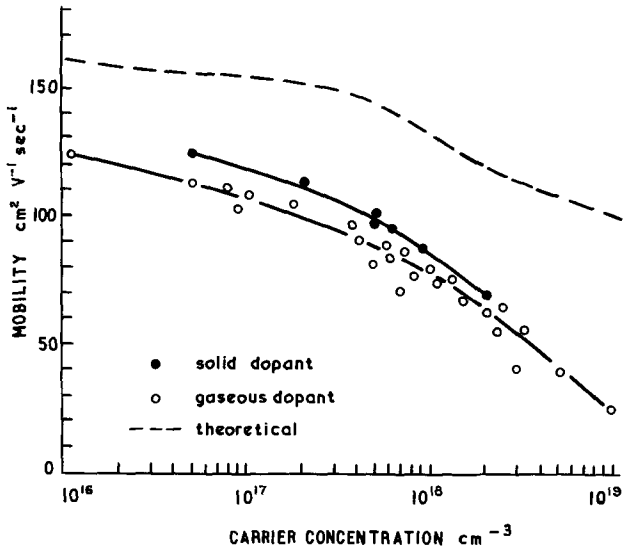

Fig. 8. Relationship between mobility and carrier concentration for sulfur-doped gallium phosphide at 20°C.

dopants are added the mobility falls, the values for sulfur-doped material being shown in Fig. 8. The mobility of layers doped using the solid sulfur source are approximately 10% higher than those prepared with the gaseous doping source. It is unlikely that this can be accounted for by the reduction in compensation due to the improved purity of the system and can almost certainly be attributed to the somewhat larger doping gradients in those layers doped via the bottled H_2S source and the improved homogeneity of the material prepared in the solid sulfur system as discussed previously.

The theoretical mobility relationship is derived from the work of Hara and Akasaki (23) and considers only the contribution of polar mode and ionized impurity scattering and assumes that the energy dependence of these relaxation times to be equal. The values calculated are much higher than those observed and as such discrepancies (30%) cannot be accounted for on the basis of the measured levels of compensation, it can only be assumed that other scattering mechanisms play a significant part.

The mobility of the tellurium-doped material (Fig. 9) is comparable with that of the sulfur-doped although the mobility decreases slightly more rapidly at the higher carrier concentrations. The results shown in Fig. 8 and 9 indicate that the hole mobility in zinc-doped GaP is considerably lower than the electron mobility in sulfur- and tellurium-doped material over the range 10^{16}-10^{18} cm^{-3}. At very high doping levels however, the hole mobility does not appear to fall rapidly as is the case with the electron mobility. This is probably a result of the much higher solid solubility of zinc and the consequent freedom from the additional contributions to scattering which will occur in the presence of sulfur and tellurium microprecipitates.

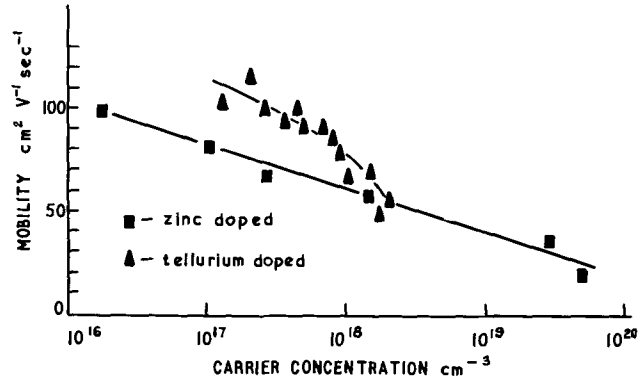

Fig. 9. Relationship between mobility and carrier concentration for zinc- and tellurium-doped gallium phosphide at 20°C.

Acknowledgments

We would like to thank Mr. M. Rowland of S.E.R.L. and Mr. R. Nicklin of the Plessey Company for helpful discussions, Dr. B. Smith and Mr. R. Grover of U.M.I.S.T. for their help with the electrical measurements and our colleagues at Ferranti for their assistance and advice. This work was done under a C.V.D. contract and is published by permission of the U.K. Ministry of Defence (Navy Department).

Manuscript submitted May 4, 1970; revised manuscript received *ca.* Sept. 16, 1970.

Any discussion of this paper will appear in a Discussion Section to be published in the December 1971 JOURNAL.

REFERENCES

1. W. O. Groves, *J. Phys. Chem. Solids, Suppl. 1,* 669 (1967).
2. R. C. Taylor, J. F. Woods, and M. R. Lorenz, *J. Appl. Phys.*, **39**, 5404 (1968).
3. L. C. Luther and D. D. Roccasecca, *This Journal,* **115**, 850 (1968).
4. W. G. Oldham, *J. Appl. Phys.*, **36**, 2887 (1965).
5. G. S. Kamath and D. Bowman, *This Journal,* **114**, 192 (1967).
6. S. J. Bass, P. E. Oliver, and F. E. Birbeck, *J. Cryst. Growth,* **2**, 169 (1968).
7. L. J. van der Pauw, *Philips Res. Repts.*, **13**, 1 (1958).
8. A. R. Peaker and B. L. Smith, *Solid State Electron.*, **13**, 1407 (1970).
9. R. N. Hall, *This Journal,* **110**, 385 (1963).
10. M. I. Val'kovskaya and Yu. S. Bayanskaya, *Soviet Phys.-Solid State (English Transl.),* **8**, 1976 (1967).
11. E. D. Pierron, D. L. Parker, and J. B. McNeeley, *J. Appl. Phys.*, **38**, 4669 (1967).
12. B. D. Joyce and J. B. Mullin, *Solid State Commun.*, **4**, 463 (1966).
13. R. C. Taylor, *This Journal,* **116**, 383 (1969).
14. L. L. Chang and G. L. Pearson, *J. Appl. Phys.*, **35**, 374 (1964).
15. L. M. Foster, J. F. Woods, and J. E. Lewis, *Appl. Phys. Letters,* **14**, 25 (1969).
16. H. C. Casey, F. Ermanis, and K. B. Wolfstim, *J. Appl. Phys.*, **40**, 2945 (1969).
17. F. A. Trumbore, H. G. White, M. Kowalchik, R. A. Logan, and C. A. Luke, *This Journal,* **112**, 782 (1965).
18. L. C. Luther, *ibid.*, **116**, 374 (1969).
19. M. C. Rowland in "Gallium Arsenide Lasers," p. 162, C. H. Gooch, Editor, John Wiley & Sons Ltd., London (1969).
20. A. R. Hudson, *Phys. Rev.*, **108**, 222 (1957).
21. B. L. Crowder and W. N. Hammer, *ibid.*, **150**, 541 (1966).
22. H. C. Montgomery and W. L. Feldman, *J. Appl. Phys.*, **36**, 3228 (1965).
23. T. Hara and I. Akasaki, *ibid.*, **39**, 285 (1968).

Tracer Investigation of Hydroxyls in SiO_2 Films on Silicon

P. F. Schmidt* and J. D. Ashner

Bell Telephone Laboratories, Inc., Allentown, Pennsylvania 18103

ABSTRACT

The introduction of hydroxyls into steam-grown SiO_2 films on Si by application of an anodic bias about 20% below the forming voltage in a tritiated electrolyte has been measured; the concentration profile of the injected hydroxyls is exponential with distance. On contact with the electrolyte, there is an induction period during which the oxide surface is hydrated by reaction with the electrolyte; the electric field is able to aid the injection of hydroxyls only after hydration has taken place. At high field strengths the growth of anodic oxide films on Si occurs almost exclusively by cation drift; at low field strengths hydroxyls, if present in ample supply, are the mobile species and cause hydration of the growing or pre-existing SiO_2 film. Large concentrations of hydroxyls in the SiO_2 film enable penetration of protons from the electrolyte into a hydrogen-bonded network at low cathodic field strengths, whereas relatively "dry" SiO_2 films block the current also under cathodic bias.

It has been observed that lack of wettability by dilute HF solution is not necessarily an indication of a bare Si surface. Oxide-films 140-150Å were repeatedly seen to become hydrophobic. Beginning crystallinity of the SiO_2 film at the Si/SiO_2 interface has been observed rather regularly, both on (111) and (100) oriented surfaces. The detection efficiency when counting tritium from a thin solid film (about 88.4% for betas actually emerging from the front surface of the samples) in the Beckmann Low Beta II is excellent. We estimate that 2×10^{10} atoms H/cm^2 of a thin surface film can be conveniently detected by *in situ* counting.

This research was undertaken to gain a better understanding of the behavior of hydroxyl groups in thermal SiO_2 films, and also in order to clarify some questions left open by earlier work by one of the authors (1).

The tool chosen for this investigation was tritium tagging of the hydroxyl group of tetrahydrofurfuryl alcohol (THFA). It is not certain that incorporation of hydroxyl groups into growing SiO_2 films can proceed directly from the hydroxyl group of the alcohol; more likely the hydroxyl group is oxidized to water in a first step, and it is this water which then enters into the anodization reaction with the silicon (2). But regardless of the detailed mechanism, the method enables the incorporation and subsequent determination of the hydroxyl groups in the SiO_2 films. Aqueous solutions, as is well known, are not suitable anodization media for silicon because of the relatively high solubility of SiO_2 in water, which leads to the formation of porous films.

It is known that heavily tritiated organic compounds undergo autoradiolysis, with water being one of the reaction products, and that the rate of this radiolysis is accelerated by the presence of oxidizing species. Since water is detrimental for anodization of Si, it was not expected that the anodizing solution chosen for this work, 0.078M KNO_2 in THFA of a specific activity of 90 ± 10% curies/mole, would remain useful for anodization very long; the rate, however, at which deterioration would occur was unknown. This rate turned out to be too fast for many of the finer details which we had hoped to examine. But after the tracer solution had deteriorated to the extent that good quality anodic oxide films could no longer be grown in it, it still remained useful for the injection of hydroxyls into thermally grown SiO_2 films by subjecting these to an anodic bias. It was this latter type of investigation which yielded the more interesting results.

* Electrochemical Society Active Member.

Key words: anodization, growth mechanism, tritium counting, electrolytic rectification, mechanical stress.

We were specifically interested in the following questions: (*i*) role of hydroxyls in the anodic oxidation mechanism; (*ii*) concentration profile of anodically injected hydroxyls in thermal SiO_2 films; (*iii*) suitability of the Beckmann Low Beta II for determination of tritium in thin solid films; and (*iv*) effect of hydroxyl concentration in the SiO_2 film on electrolytic rectification by the film.

A comment is in order on the third of these points. Some of the literature on determination of tritium refers to *in situ* counting as the least attractive choice, because of low detection efficiencies and contamination of the counting chamber by volatile tritium compounds (3). These comments apply only to organic compounds. Thin inorganic films, composed of low atomic weight atoms, and with a thickness not much in excess of about 1000Å, should be ideal for *in situ* counting; at this thickness self-absorption of the low energy tritium betas is still negligible, and any tritium lost to the ambient as hydrogen gas or water vapor does not constitute a serious contamination problem; water absorbed on the walls of the counting chamber will readily exchange with moisture from the air.

The volatility of hydroxyls in (anodic) films was not known beforehand, but turned out to be sufficiently low not to interfere with the measurements. As expected, the counting efficiency for tritium in thin SiO_2 films turned out to be very high.

Experimental

The THFA was obtained from the Amersham (England) Radiochemical Centre through Nuclear Chicago Corporation. The activity upon receipt was 117 ± 10% curies/mole, but was reduced to 90 curies/mole by the addition of a solution of KNO_2 in normal THFA to arrive at a final concentration of 0.078 mole/liter of KNO_2. The water content of the tagged THFA, prior to the addition of KNO_2, was 0.7%, as established by infrared measurements. One week after addition of the KNO_2 the formation of anodic oxide films on bare Si surfaces became unsatisfactory, indicating that the water content had risen above 2%,

the highest water concentration tolerable for anodization of bare silicon; the solution, however, still was useful for anodization of thermally oxidized Si wafers. At the end of the investigation, about two months later, the water content seems to have risen above 5%.

Anodizations were carried out in a special anodization cell in which the cathode consisted of a mercury pool, and the reference electrode of an abraded tantalum wire. No hydrogen evolution could be detected at a Hg cathode in THFA, even at 100 mA/cm^2; thus the Hg cathode suppressed evolution of volatile tritium gas. Tantalum instead of platinum was used for the reference electrode in order not to catalytically accelerate the exchange of tritium in the hydroxyl group for hydrogen from the carbons atoms of the THFA molecule, thus reducing the effective activity during anodization. The anodization cell was cooled to 0°C before opening the vessel to further depress the vapor pressure of the THFA, already quite low at room temperature.

After anodization, wafers were carefully rinsed and swabbed to eliminate adhering solution, blown dry, and then counted *in situ* underneath the windowless detector of the Beckmann Low Beta II counting system. Highly active wafers had to be reduced in activity for the counting, in order not to jam the detector, by placing a metal mask over them, a small hole in the mask constituting a measured fraction of the total active wafer area.

Oxide thicknesses were determined by ellipsometry, and by means of a monochromatic light reflection technique (4), which enables film thickness measurements with good accuracy down to about 25Å. For determination of the concentration profile, the oxides were etched in 100-200Å steps in very dilute HF, the etching solutions saved, and later counted by means of liquid scintillation technique, while the wafers after each etching step were counted *in situ* with the Low Beta II.

In order to convert the counting rates to hydrogen concentrations, a standard is needed. Tritium standards are commercially available, however, only for liquid scintillation or for gas phase counting. The Low Beta II counts were therefore evaluated in two different ways.

1. A measured quantity of the tracer solution was diluted in a ratio 1:10^7, and the resulting solution counted by means of the liquid scintillation system,[1] for which the counting efficiency was known. Differences in counting rate between two etching steps obtained on the Low Beta II were then compared to the counting rates obtained by liquid scintillation on the etching solution stemming from the etching step in question.

2. A polymethylmethacrylate disk, supplied as a standard for gas phase[2] counting by New England Nuclear Corporation was counted in the Low Beta II, and the counting rate evaluated according to an approximation method indicated by Libby (5).

Comparison of the Low Beta II results with those from liquid scintillation lead to a detection efficiency of 88% for the Low Beta II (assuming that 50% of the betas were emitted in a direction which enables their detection); evaluation of the polymethylmethacrylate standard by Libby's approximation formula leads to a detection efficiency of the Low Beta II for tritium betas of 60%. We believe that the higher of the two figures (88%) is more nearly correct, but in any case it is obvious that the detection efficiency for tritium betas is indeed very high.

These counting efficiencies make sense when comparing various radioactive sources as to the average energy of the emitted beta particles, the number of ions formed per centimeter of path in air at atmospheric pressure (6), and the detection efficiency of the Low Beta II counting system as measured by us or stated by Beckmann Instruments (Table I).

[1] ANS—Picker Nuclear.
[2] After complete combustion of the plastic.

Table I. Comparison of radioactive sources

	Average energy of β's	Ion pairs/cm/particle	Detection efficiency, %
Tritium	0.0057 MeV	1520	88.4 (our determination, windowless)
Carbon^{14}	0.052 MeV	250	35 (Beckmann, ultra-thin window)
Phosphorus^{32}	0.675 MeV	46	15.25 (our determination, windowless)

The geometrical distances of the detection chamber are such that it appears reasonable that a large fraction of the ion pairs produced by the tritium primary beta will be able to reach the collector under the applied bias (1825V in the beta proportional region), whereas the primary beta from P-32 will be absorbed by the chamber housing after having traversed a distance of less than 1 cm, *i.e.*, before having had an opportunity to generate many ion pairs.

When comparing the advantages or disadvantages of using liquid scintillation or *in situ* counting in the Low Beta II for determination of tritium, it should be borne in mind that the efficiency of liquid scintillation detection is lower, and that the background of liquid scintillation is typically 15 counts/min, whereas the background of the Low Beta II is as low as 0.5 counts/min.

Results and Discussion

Anodic oxide films.—Mechanism of anodic oxide growth.—It has been shown by implantation of radioactive inert gas ions that both cations and anions move during anodization to higher voltages of anodic films on Al, Ta and W, whereas only oxygen ion movement was observed in ZrO_2 and HfO_2 (7). Silicon seemed to occupy a position by itself, in that experiments using P-32 as the marker indicated the motion of cations only; for instance, it is possible to encapsulate a phosphorous-doped anodic SiO_2 film in a layer of pure SiO_2 by anodization to a higher voltage (8) without loss of phosphorus to the solution or to the new-grown oxide layer, even at quite low phosphorous concentrations in the P-tagged film. It was, however, noticed that the constant current anodization of silicon must be done at a current density of not less than 3 mA/cm^{-2}, otherwise oxide films of inferior quality were obtained. The deterioration shows up as a slightly larger thickness/voltage increment, a slower decay of the current at constant voltage, and a larger final leakage current. The amount of water in the anodizing solution controls the current density at which deterioration of the anodic SiO_2 film becomes noticeable. The current density of 3 mA/cm^2 refers to a reasonably "dry" solution of KNO_2/THFA. This observation indicated that the mechanism of oxide growth on Si may be changing at lower field strengths. This expectation was fully confirmed by the tritium tracer experiment.

Anodization of silicon in dry electrolytes requires a field strength of about 2 x 10^7 V/cm; oxide growth rate falls to essentially zero if the field strength is lowered by 10% from the above value. Steam grown oxide films 1200-1500Å thick biased anodically in a dry electrolyte at a field strength of 1.5 x 10^7 V/cm do not increase in thickness beyond about 10-15Å, but the electronic leakage current through the film decreases with time to very small values (9). Initially the anodic leakage current of such a thermal SiO_2 film is much higher than that of an anodic SiO_2 film of the same thickness, but eventually decreases to values many orders of magnitude lower than characteristic of the anodic SiO_2 film.

This behavior changes with increasing water content of the anodizing solution. Substantial additional film growth occurred in the tracer solution on steam grown SiO_2 films at an initial field strength of 1.5 x 10^7 V/cm, but the leakage current, while decreasing with time, never reached the low levels characteristic of keeping the same films under anodic bias in a dry electrolyte. It also seemed that oxide growth did not stop at constant voltage (F = 1.5 x 10^7 V/cm, initially) at least not within reasonable lengths of time.

In the section on the concentration profile of injected hydroxyls it will be seen that the hydroxyls indeed penetrate all the way through the steam-grown oxide film. In other words, oxide growth at low field strength occurs by the inward motion of hydroxyl ions, thus leading to the formation of a hydrated, poor quality oxide film. Since even the driest electrolytes used for the anodization of silicon always contain some water during the actual anodization—it even appears possible that oxide growth may not occur in the complete absence of water—it can now be understood why anodization at current densities below 3 mA/cm^2 leads to oxide films of inferior quality. Silicon thus follows the pattern of aluminum with respect to the current density dependence of the cationic transport fraction during anodization, except that on silicon significant anionic transport commences at a rather sharply defined current density, whereas on aluminum the transition is rather gradual (7). It should, however, be noted that the current efficiency on Si is quite low, about 2.5% in the KNO_2/THFA solution, whereas on aluminum the current efficiency, while dependent on the particular anodizing solution, rarely drops below 60%. Thus when comparing total current densities, it must be remembered that the ionic current on Si constitutes only 2-3% of that on Al at the same total current density (*i.e.*, ionic + electronic current).

It is also worth noting that the theory of anodic oxidation is usually presented in a form which suggests that oxygen ions are the moving anionic species. We believe that hydroxyl ions may be carrying most of the anionic current during the anodization of some other metals as well, and that the oxide ions themselves are much less mobile than the hydroxyl ions. This is essentially the picture used by Hoar and Mott (10) to explain the formation of porous Al_2O_3 films, but it applies in all probability also to nonporous films.

In subjecting steam-grown SiO_2 films to an anodic bias in the tracer solution, an induction period, ranging from between 5 to 15 min could be clearly observed, during which time the leakage current of the film did not decrease. This incubation period is apparently related to a hydration of the oxide surface by reaction with water in the electrolyte. Dreiner (11) has observed a similar incubation period when following the increase of capacitance of anodic SiO_2 films in contact with electrolytes of different water content. The rate of capacitance change was independent of the *pH* of the solution, but depended on the water content of the solution. It could be accelerated, except for the incubation period, by application of a low anodic bias (insufficient to cause additional oxide growth). This result was interpreted to mean that the primary step involves reaction of the oxide surface with water in the electrolyte to produce OH groups: Si-O-Si + $H_2O \rightarrow$ 2 Si — (OH). The OH groups can then be acted upon by the electric field. An interesting aspect of Dreiner's work is the observation that the rate of change in capacitance with and without applied bias obeys a square-root-of-time law, though of different slope. This would tend to indicate that the field does not dominate the drift, but rather enhances the diffusion of the hydroxyl groups.

Hofstein (12), in a study of thermal SiO_2 films contaminated with ethanol, tritium tagged in the hydroxyl group, has shown that application of an anodic bias enhances tritium injection into the oxide film. In these experiments the SiO_2 surface was first contaminated by heating in ethanol for 15 min at 75°C, followed by evaporation of Al contacts and BT-stress at 250°C and 1 x 10^6 V/cm for 10 min. After removal of the bias, it was found, however, that the surface potential has not changed, indicating that the injected tritiated species is electrically neutral. Application of a cathodic instead of an anodic bias in the above experiment still permits injection of a tritiated hydroxyl, but at a reduced concentration compared to the anodic bias case. Hofstein suggested that the injected species is charged negatively only during some transition state at the metal/oxide interface at which point its injection into the oxide can be field aided. From Dreiner's work, and from the incubation period observed in this work, it appears, however, that the species is already inside the oxide at the time when its diffusion into the oxide can be accelerated by an electric field.

Two mechanisms appear plausible by which a strong electric field (about 4 x 10^6 V/cm at room temperature, as in Dreiner's experiments, or 1.0 x 10^6 V/cm at 250°C, as in Hofstein's work) might enhance the diffusivity of hydroxyls in SiO_2 films without dominating the drift: (*i*) distortion of the partially ionic SiO_2 lattice to facilitate the passage of the hydroxyl through constrictions along its path, and (*ii*) hydroxyl groups are known to be deep electron traps in SiO_2 (13). Since the anodic injection of hydroxyls is accompanied by a (relatively very large) electronic leakage current, many of the hydroxyls will become negatively charged by trapping of electrons. This should weaken the strength of the Si-OH bond, so that this bond will be broken more frequently than it would be in the absence of the field. The hydroxyl breaking away from a Si atom will probably not remain charged very long. It may become a free radical and re-attach itself at another lattice defect.

At the much larger fields used in our work (1.5 x 10^7 V/cm at room temperature) it might well be that drift will dominate over diffusion. Since we have made no rate studies, this question remains open.

Injection of tagged hydroxyl groups into steam-grown SiO_2 films also produced the answer to another question: Is it the degree of hydration or the change in structure, or both, which is responsible for the faster etch rate of anodic as compared to steam-grown SiO_2 films? Even though only the very slightest shift in the IR Si-O stretch frequency was noticeable after hydration of the steam-grown oxides in the tracer solution at 1.5 x 10^7 V/cm, the dissolution velocity of the hydroxyl-rich part of the film corresponded to that of anodic oxide films; the rate dropped back to that typical of thermal oxide when the hydroxyl concentration in the film dropped to low values. Thus it is mostly, or possibly exclusively, the degree of hydration which determines the etch rate.

It was pointed out before that the anodic resistance of the thermal oxide film increased as hydroxyls were being injected into it; this increase in resistance occurred without a significant change in structure of the film, since the IR spectrum showed almost no change. It would thus appear that the different structure of the anodic oxide film has relatively little to do with its electrical properties or its rate of etching. However, the oxide films hydrated in these experiments did not develop the very high electrical resistance typical of steam-grown oxide films anodized in a dry electrolyte, and it is quite possible that the very highest insulation resistance requires not only hydration of the oxide, but also a change in structure to that of the purely anodic film, this change in struc-

ture affecting the number and energy distribution of trapping sites. Elimination of crystalline nuclei by anodization (14) will, of course, also improve the resistivity of the film.

Mechanical stresses in anodic oxide films on Si.—In a separate study (15) it had been noticed that the mechanical stress in anodic oxide films is compressive at low forming voltages; goes through zero at about 1200Å, and becomes tensive at high forming voltages. Details depend on the forming solution. Prolonged exposure of a high-voltage film to moist air leads to a decrease in the tensive stress and can eventually reverse the sign of the stress. It was, therefore, thought that the transition from compressive to tensive stress with increasing film thickness is indicative of progressive dehydration of the growing film. This hypothesis can be checked by monitoring the tritium content of an anodic SiO_2 at successive anodization voltages, and by etchback from a given thickness.

The experiment was performed in a solution of 0.55g KNO_2 in 100 cc THFA with the addition of 0.5 v/o (volume per cent) H_2O, the water being tritium tagged to an activity of 50 mcuries cm^{-3}. This solution gave reproducible results.[3] It is still sufficiently dry that growth of anodic SiO_2 occurs only or almost only by cation migration, and keeping the film under constant voltage in this solution for 10 min (see below) does not falsify the hydroxyl profile of the as-grown film due to additional injection from the solution. The highest forming voltage that could be reached in this solution without deterioration of the silicon surface (a hazy appearance in reflected light) was only 210V. The maximum forming voltage in THFA for good quality SiO_2 films is apparently a sensitive function of the water content of the THFA (22).

A low resistivity P-type Si wafer was anodized at 10 mA/cm² in three 70V steps to 70, 140, and 210V. At each voltage the current was permitted to decay for 10 min at full forming voltage; the wafer was rinsed and swabbed to remove adhering radioactive liquid, and then counted in the Low Beta II system. The activity at the three different film thicknesses was little different, indicating that most of the activity in each case must be confined to the surface layer of the oxide. Actually, the activity of the film decreased in the ratio 1.00:0.93:0.90 with increasing film thickness. In the next experiment another wafer was anodized in one step to only 185V (10 min current decay) in order to avoid any possible surface deterioration, its activity measured, and the oxide then removed in small steps. The remaining activity was determined after each etch-back step. The result is shown in Fig. 1, where it can be seen that the activity, and therefore the hydroxyl content of the anodic oxide, does indeed decrease quite rapidly with increasing distance into the oxide.[4]

Only the general shape of the profile is important; not too much significance should be attributed to the individual points shown. Because of the required low activity of the tracer solution, long counting times were required to obtain sufficient number of counts. These long times in turn led to a loss of activity to the ambient, evident from a slight drop in counting rate during the course of an individual measurement. The error bars shown in Fig. 1 refer only to the counting statistics, they do not reflect the losses in activity to the ambient during counting. Also, the profile may differ from that obtained in a drier electrolyte.

Rectification behavior.—The tagged THFA solution, as received, did not permit the formation of cathodically blocking films, and the hydroxyl content of anodic SiO_2 films formed in this solution was very high already in the first anodizations tried (approximately 1×10^{20} cm^{-3}). The nonblocking property of the oxide was uniform across the whole surface of the (epitaxial) silicon disk. It was thus not possible to observe the gradual reduction of cathodic breakdown voltage with increasing hydroxyl content. The result, however, is what would be expected on the basis of the model postulated in (1), namely the easy penetration of protons into a hydrogen bonded network of hydroxyls.

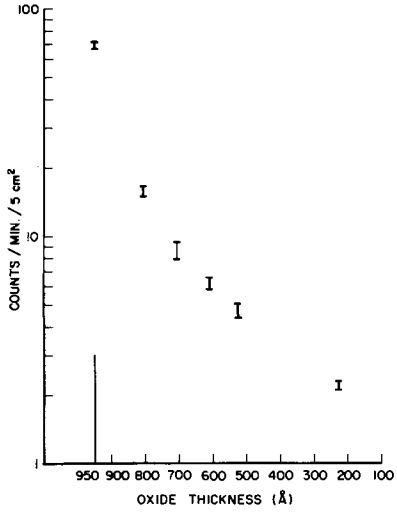

Fig. 1. Tritium activity profile in anodic oxide film grown to a thickness of 950Å in weakly radioactive KNO_2/THFA solution at a current density of 10 mA/cm². Current was permitted to decay to 1 mA/cm² during 10.0 min at the forming voltage of 185V.

Steam-grown oxide films.—Concentration profile of hydroxyl ions injected into steam-grown, SiO_2 *film.*—Figure 2 shows a typical concentration profile in a steam-grown SiO_2 film as obtained from *in situ* counting and from liquid scintillation counting. There is a small systematic shift between the two sets of data, which may stem from the assumption that 50% of the betas generated by radioactive decay are emitted under an angle leading to their detection. This assumption neglects the possibility of back-reflection, probably not a good assumption at the film

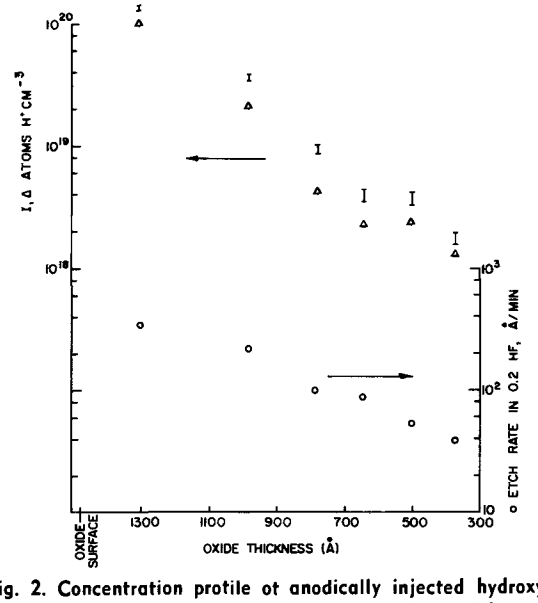

Fig. 2. Concentration profile of anodically injected hydroxyls in steam-grown SiO_2. Data from *in situ* counting (I) and from liquid scintillation counting (Δ), taken on the same sample. Bottom curve (O) shows etch rate of film *vs.* oxide thickness. The etch rate of a steam-grown (1050°C) SiO_2 film in 0.2*N* HF is approximately 20Å/min.

[3] Whereas the high activity THFA solution was not suitable for this experiment because of its high and rapidly varying water content.

[4] Dehydration of the oxide probably occurs by reaction of hydroxyls in the oxide with Si ions in transit through the oxide.

thickness employed. Also shown is the etch rate of the film in 0.2*N* HF.

It can be seen that the two sets of counting data are in good agreement with each other, and that the profile is exponential except for a deviation at about 800Å. A deviation in the etch rate is observed at the same film thickness. While the cause for these deviations is not known, it is believed that they are real and related to each other, as they were observed on a number of films. Error bars are shown for the Low Beta II data. The accuracy of the oxide thickness determination is about ±10Å in the oxide thickness range shown.

The fact that the diffusion profile shown in Fig. 2 is exponential rather than Gaussian suggests that initial penetration of the hydroxyls occurred along narrow channels rather than uniformly through the bulk. Lateral diffusion from the channel then results in an over-all diffusion profile that is exponential with distance, provided that the diffusion coefficient in the channel or grain boundary is much higher than in the bulk, as shown by Fisher (16) and by Smoluchovski (17). Channels of diameters "near atomic dimensions" have been postulated to exist in thermally grown SiO_2 films by Ing *et al.* (18) on the basis of permeation of gases through SiO_2 films. The channel area was found to occupy about a fraction of 10^{-8} of the total area. At first glance this degree of porosity looks too low to result in the uniform hydration of the anodized thermal SiO_2 films, as must be postulated on the basis of the very strong increase in electrical resistivity (9). In the gas permeation tests, however, a channel must be essentially open along the entire thickness of the film in order to enable fast diffusion of gases through the film. In the case of field-aided diffusion of hydroxyls this requirement may be relaxed considerably. This concept is also not in contradiction to the sodium drift results by Hofstein (12) since it is found there that only a small fraction of the total sodium is a fast diffusant. The same model of fast diffusion along "an inter-connected network of small disturbed regions" has also been used by Holmberg *et al.* in a very recent publication (23).

We are thus led to speculate on the existence of channel or grain boundaries in so-called amorphous films. It has been shown by Drobek (19) that steam-grown SiO_2 films crystallize quite readily even at room temperature. The eventual crystallization product is tridymite, with the open channels along the C-axis preferentially oriented perpendicular to the Si surface. Formation of tridymite, however, occurs via formation of beta-cristobalite, the latter having a close-packed, face-centered-cubic structure without any open canals in which enhanced diffusion could occur. Thus the grain boundary picture (rather than diffusion in open canals of a beta tridymite structure) appears more applicable. It was shown by Snow and Gibbs (20) that the open canals in natural quartz extend for an average length of 1000Å before being blocked by crystal defects. In the very poorly crystallized SiO_2 films (so poorly indeed that they have been regarded as amorphous until very recently) it is probably reasonable to assume that the length of grain boundaries will on the average be much less than 1000Å before the grain boundary terminates in a way that suppresses easy diffusion.

The extrapolated surface concentration of hydroxyls in the thermally grown SiO_2 film did not change from run to run, but the slope of the profile became progressively more shallow as the age of the anodizing solution; *i.e.*, its water content, increased. This change in slope is probably an indication that the diffusivity of hydroxyls in SiO_2 is concentration dependent, as indeed one would expect it to be.

Figure 3 shows the tagged, *i.e.*, newly introduced, hydroxyl concentration in a steam-grown SiO_2 film which was left in contact with the anodizing solution at room temperature for 28 hr without any bias applied. The profile shows the swing-up at the Si/SiO_2 interface also noted by Hofstein (12) for oxidized wafers heated in tritiated water at 100°C. The tritium is definitely present as hydroxyl groups and not as absorbed water. Even when the oxide films were etched down to thicknesses as small as 50Å, the remaining counting rate was quite stable during repeated measurements, indicating that the species present did not exchange rapidly with moisture from the air. It may also be noted in Fig. 3 that the hydroxyl content of the oxide after 28 hr in contact with the solution but without bias is considerably lower than after application of an anodic bias for 3-4 hr (Fig. 2). These two runs were taken a few days apart toward the end of the investigation, when the water content of the solution was no longer a rapidly varying function of time. The larger hydroxyl content in Fig. 2 shows directly the effect of the electric field on hydroxyl penetration. It should be pointed out that the applied field in Fig. 2 was considerably larger than in the corresponding experiments of Dreiner (11).

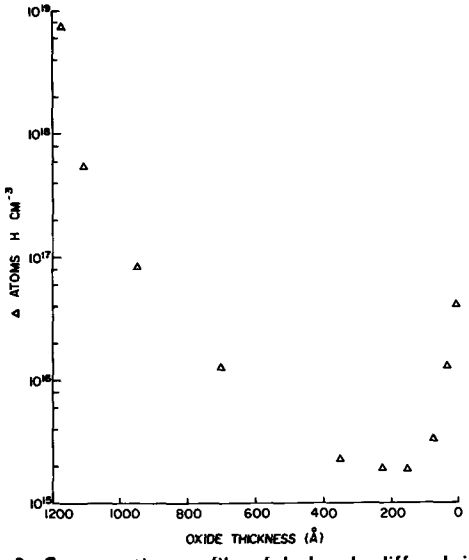

Fig. 3. Concentration profile of hydroxyls diffused into steam-grown SiO_2 at room temperature without application of a bias.

Wettability of oxide films.—A very interesting phenomenon was observed when etching down to very small oxide thicknesses. It was noted that the 0.2*N* HF ceased to adhere to the oxide surface at an oxide thickness of approximately 140Å, and water ceased adhering when the oxide thickness was approximately 25Å. There was still activity on the surface which could not be removed by further etching in 0.2*N* HF, and electron diffraction showed presence of a very thin film. Etching in buffered HF then would remove the last traces of activity.

Crystallographic effects on the adsorbtivity of HF and, consequently, on the dissolution rate of different crystal faces (and modifications) of quartz have been discussed by Ernsberger (21). The etching and wettability behavior appears reasonable if the oxide in the vicinity of the Si/SiO_2 interface is crystalline. Crystallinity of the nonwetted very thin oxide films was indeed detected rather regularly on our samples by means of electron diffraction. On <111> oriented wafers the crystallinity occurred in uniform fashion, whereas it was patchy on <100> oriented wafers.

Conclusions

The induction period observed in the decay of the anodic leakage current when first applying an anodic bias to thermally grown SiO_2 films strongly suggests that the primary step for injection of hydroxyls (and therefore probably also for protons) is the hydration of the oxide surface. In practice this means that SiO_2 films should not be exposed for any length of time to liquid water before metallization for MOS purposes.

The beginning crystallinity observed at the Si/SiO_2 interface raises the question whether the electrical sur-

face properties for the amorphous and for the crystalline SiO_2 in contact with the Si interface may be different. If this should be the case, then the interface will not be stable if nucleation and/or growth of the crystalline phase may proceed at room temperature. That crystallization of the steam-grown SiO_2 film does indeed happen quite regularly at room temperature was shown some time ago by Drobek by means of electron diffraction (19).

The cause for the hydrophobicity of oxide-covered Si surfaces at small oxide film thicknesses has not been established, but since it is at these oxide thicknesses that beginning crystallization of the SiO_2 was noted, there exists at least a suspicion that the structure of the oxide may be a contributing factor.

The excellent detection efficiency of counting tritium from a thin solid film by means of the Beckmann Low Beta II may well make this method attractive for determination of hydrogen content of thin solid films on conductive substrates. If one extra count per minute is accepted as a reasonable detection limit in view of the low background count of the Low Beta II, then at the specific activity employed in our experiments, ~100 curies/mole, a hydrogen concentration of 2×10^{10} atoms/cm^2 in a thin (10^{-5} cm) surface film is conveniently detectable. Since tritium is a very low energy pure beta emitter, a specific activity of 100 curies/mole does not constitute much of a health hazard and can be handled with ease.

Acknowledgments

We wish to acknowledge the extensive help by M. J. Rand in measuring the thickness of very thin SiO_2 films, the assistance of F. H. Doleiden with the liquid scintillation measurements, and of D. R. Wonsidler with examining surfaces by electron diffraction. As yet unpublished studies by J. Drobek on crystallization at the Si/SiO_2 interface were helpful in interpreting our results. Helpful discussions with A. L. Tyler, J. W. Colby, and C. Y. Bartholomew are gratefully acknowledged. Measurements of the water content of THFA solutions by infrared spectroscopy were carried out in the WE analytical laboratory under the supervision of T. H. Briggs. We are also indebted to E. H. Nicollian for bringing ref. (15) to our attention.

Notes Added in Proof

Limitation of breakdown strength of the oxide by the percentage of water in the anodizing solution has also been noted by C. R. Fritsche (21).

Movement of zirconium ions during anodization of Zr has now been shown to occur at very large field intensities, see P. A. Brook *et al.* Abstract 94, Corrosion Division, Electrochem. Soc. Extended Abstracts, Fall Meeting, Atlantic City, N. J., Oct. 4-8, 1970.

In a very recent publication (23), Holmberg, Kuper, and Miraldi use the same concept of fast diffusion in an "interconnected network of small disturbed regions" as proposed in this paper.

Manuscript submitted March 30, 1970; revised manuscript received *ca.* Sept. 11, 1970.

Any discussion of this paper will appear in a Discussion Section to be published in the December 1971 JOURNAL.

REFERENCES

1. P. F. Schmidt, *This Journal*, **115**, 167 (1968).
2. E. F. Duffek, C. Mylroie, and E. A. Benjamini, *ibid.*, **111**, 1042 (1964).
3. E. A. Evans, "Tritium and its Compounds," Chap. 5, Butterworth & Co., Ltd. (1966).
4. M. J. Rand, Paper 49 presented at the New York Meeting of the Society, May 4-9, 1969; To be published in *J. Appl. Phys.*
5. W. F. Libby, *Anal. Chem.*, **19**, 2 (1947).
6. J. B. Hoag and S. Korff, "Electron and Nuclear Physics," pp. 484 ff, D. Van Nostrand Co. (1948); G. J. Hine and G. L. Brownell, "Radiation Dosimetry," p. 87, Academic Press (1956).
7. J. A. Davis, B. Domeij, J. P. S. Pringle, and F. Brown, *This Journal*, **112**, 675 (1965).
8. P. F. Schmidt, T. W. O'Keefe, J. Oroshnik, and A. E. Owen, *ibid.*, **112**, 800 (1965).
9. P. F. Schmidt and M. J. Rand, *Solid State Commun.*, **4**, 169 (1966).
10. T. P. Hoar and N. F. Mott, *J. Phys. Chem. Solids*, **9**, 97 (1959).
11. R. Dreiner, *This Journal*, **113**, 1210 (1966).
12. S. R. Hofstein, *Trans. IEEE*, **ED-14**, 749 (1967).
13. W. Ehrenberg, V. B. Gutan, and L. K. Vodopyanov, *Brit. J. Appl. Phys.*, **17**, 63 (1966).
14. C. Fritsche, *Z. Angew. Phys.*, **24**, 48 (1967).
15. C. M. Drum, J. D. Ashner, and P. F. Schmidt, To be published.
16. C. J. Fisher, *J. Appl. Phys.*, **22**, 74 (1951).
17. R. Smoluchovski, *Phys. Rev.*, **87**, 482 (1952).
18. S. W. Ing, Jr., R. E. Morrison, and J. E. Sandor, *This Journal*, **109**, 221 (1962).
19. J. Drobek, Private communication, To be published.
20. E. H. Snow and P. Gibbs, *J. Appl. Phys.*, **35**, 2368 (1964).
21. F. M. Ernsberger, *J. Phys. Chem. Solids*, **13**, 347 (1959).
22. C. R. Fritsche, *ibid.*, **30**, 1885 (1969).
23. G. L. Holmberg, A. B. Kuper, and F. O. Miraldi, *This Journal*, **117**, 677 (1970).

Properties of Polycrystalline Silicon Deposited on Silicon Nitride Layers

C. C. Mai,*[1] T. S. Whitehouse,[2] R. C. Thomas,*[3] and D. R. Goldstein[4]

Sylvania Electric Products Inc., Woburn, Massachusetts 01801

ABSTRACT

The properties of polycrystalline silicon deposited on silicon nitride by the thermal decomposition of silane were investigated. It was found that the deposition temperature of the silicon and the thickness of the layer had a marked effect on the diffusion characteristics. The diffusion profile of boron in the silicon layer was determined and the diffusion constant of boron into silicon at 1050°C was found to be 1.85-2.5 x 10^{-13} cm^2/sec. This compares with 3.3 x 10^{-14} cm^2/sec for (111) oriented single-crystal silicon under the same conditions. The ratio of Hall mobility of holes in polycrystalline silicon to the mobility in single-crystal silicon was found to be 0.57. No significant difference was found between the oxidation rate of polycrystalline-single and (111) oriented single-crystal silicon.

Recently there has been increased interest in the properties of silicon deposited on dielectrics because of the use of these layers in making silicon-gate field effect transistors (1, 2). Several processes are available for depositing silicon. These include sputtering, evaporation, and the vapor-phase reaction between hydrogen and silicon tetrachloride, or other silicon halides such as $SiHCl_3$, $SiBr_4$, or SiI_4.

It has been reported by Bhola and Mayer (3) that, at the relatively high concentrations required for the deposition reaction, halide ions can transport and deposit unwanted impurities at the growth face; they also report that silicon layers of excellent electrical properties can be deposited on silicon by the thermal decomposition of silane (SiH_4). Polycrystalline silicon has also been deposited by the decomposition of silane in a glow discharge at substrate temperature between 25° and 650°C (4).

Usually when silicon is deposited on a dielectric such as silicon dioxide or silicon nitride a polycrystalline silicon layer is formed. DeLuca reported the effect of deposition parameters on the structure of silicon film deposited by low-pressure silane pyrolysis (5). Very little has been reported on the diffusion and oxidation of polycrystalline silicon deposited on dielectrics. We have investigated layers deposited on silicon nitride by the thermal decomposition of silane. Reported here are:

1. The effect of deposition temperature on the properties of the deposited layers.
2. The characteristics of boron diffusion into the silicon layer.
3. The Hall mobility of holes in polycrystalline silicon.
4. The oxidation of polycrystalline silicon.

Deposition Apparatus

A schematic of the apparatus used is shown on Fig. 1. A 50 kW rf generator was employed. The source used was 10% silane in N_2. The carrier gases were N_2 and H_2. The susceptor was silicon carbide coated graphite ⅝ in. x 5 in. x 22 in. The tube had a rectangular cross section, 2 in. x 6 in. The susceptor was tilted to improve uniformity of deposition. The flow rates of gases were N_2, 43 liters/min; H_2, 15 liters/min: and SiH_4 mixture, 270 cc/min The gases were mixed before entering the reaction chamber.

Samples and Preparation

Silicon slices of (111) orientation, polished on one side, were used as substrates. Approximately 500Å of silicon nitride were deposited on each slice at 900°C, by the reaction of ammonia and silane. Polycrystalline silicon was then deposited on top of this nitride layer. Different thicknesses of silicon were deposited at various temperatures. All of the silicon layers obtained this way were intrinsic as determined by no deflection when using a thermal probe.

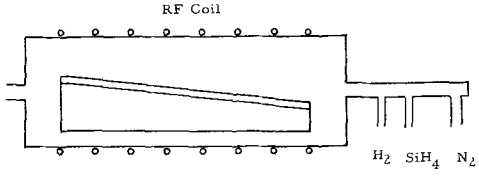

Fig. 1. Schematic of deposition apparatus

Effect of Deposition Temperature

It was found that the deposition temperature played a very important role in the characteristics of the polycrystalline silicon. The temperature range in this study was from 800° to 1000°C. The deposition was very slow for temperatures below 750°C.

Typical deposition rates for the standard condition used are shown in Table I. The samples of silicon deposited on silicon nitride at 800°, 900°, and 1000°C were examined by replica electron microscopy and reflection electron diffraction.

The 800°C sample shown in Fig. 2a, had a smooth, highly reflecting surface. The electron micrograph revealed a finely grained texture with an approximate grain size of 0.3μ. Both the 900°C (Fig. 2b) and the 1000°C (Fig. 2c) samples had extremely rough surfaces with a high density of small, deep pits, the latter being the worse of the two. The grain sizes on the 900°C and the 1000°C samples were very nonuniform. At growth rates up to approximately 2000Å/min at 800°C and in excess of 1μ in thickness, the 800°C sample still had a smooth, highly reflecting surface of silicon.

Reflection diffraction patterns revealed random orientation in the 800°C sample. Both the 900° and the 1000°C samples displayed some degree of preferred orientation as evidenced by the variation in the intensity of the (111) and (220) rings. At higher temperatures the silicon molecules possess higher energy al-

Table I. Typical deposition rates

Deposition temp.	Deposition rate
800	410 Å/min
900	1200 Å/min
1000	1850 Å/min

* Electrochemical Society Active Member.
[1] Present address: Mostek Corp., Worcester, Massachusetts.
[2] Present address: 120 Westgate, Wellesley, Massachusetts.
[3] Present address: Systonics, Winchester, Massachusetts.
[4] Present address: Transitron, Wakefield, Massachusetts.
Key words: silicon gate, diffusion profile, resistivity.

Fig. 2. Micrographs of polycrystalline silicon layers (11,900X). (a) (top) 800°C sample; (b) (center) 900°C sample; (c) (bottom) 1000°C sample.

Table II. Average sheet resistances

Polycrystalline Si deposition temp, °C	Average sheet resistance, ohms/square
800	52
900	550
1000	1320

lowing them to attempt to rearrange themselves according to preferred growth directions. The lack of orientation below 800°C agreed with DeLuca's finding (5). To compare the effects of deposition temperature on the diffusion characteristics of polycrystalline silicon, layers of approximately 0.8μ were deposited at 800°, 900°, and 1000°C. These slices were then inserted into a boron diffusion furnace for a half hour at 1050°C with a BBr_3 source held at 20°C. The sheet resistance of the initial polycrystalline silicon layer was above 4500 ohms/square which is the upper limit of the available equipment.

The average sheet resistances obtained from a four-point probe are listed in Table II. A single crystal silicon slice of 6 ohm-cm N type has a sheet resistance of 21 ohms/square after the same treatment. As can be seen from the table, the sheet resistance goes up rapidly with deposition temperature.

The uniformity of four-point probe readings was much better in the layer deposited at 800°C than at higher temperatures. The variation on 800°C polycrystalline silicon was less than 20% from slice to slice and within different areas of the slices, while the 900°C deposited layer shows a variation of more than 40% and the 1000°C sample had a 100% variation. It was concluded that polycrystalline silicon deposited at 800°C has the most reproducible boron diffusion. Also a lower sheet resistance can be obtained.

The comparatively good uniformity of boron diffusion into the 800°C samples can be explained by the fact that this layer has a very fine and uniform grain size and is free of pits in the surface. As mentioned previously, the roughness of the surface and the preferred orientation of the polycrystalline silicon increases with deposition temperature, such that the 1000°C samples had a much higher density of pits than the 900°C samples. The uniformity of boron diffusion in the 1000°C sample was much worse than the 900°C samples.

The 800°C deposited polycrystalline silicon layer was used to study diffusion in further detail since diffusion uniformity is better and lower sheet resistance can be achieved.

Diffusion of Boron Polycrystalline Silicon

Effect of polycrystalline silicon layer thickness on sheet resistance after diffusion.—Different thicknesses of silicon were deposited on the top of silicon nitride. The range of thickness was from 2250 to 13,500Å. These slices were inserted into a boron deposition furnace for 30 min at 1050°C and then driven in steam for 40 min at 950°C. The sheet resistances of these slices were measured before and after drive. Another set of samples was driven for 45 min in argon at 1000°C after the same boron deposition. The data are shown in Fig. 3. It was found that the thickness of the polycrystalline layer did affect the sheet resistance. As the thickness went down, the sheet resistance went up. However, when the layer was thicker than 7000Å, the curve approached a saturation point and the sheet resistance changed very little with increasing layer thickness.

This change in resistance is due to the presence of silicon nitride. The flux of boron across the silicon surface is the same for thick or thin polycrystalline layers. In thin layers terminated by silicon nitride which acts as a diffusion barrier, the concentration of boron at the barrier builds up. This slows down the in-diffusion of boron due to the reduced gradient and results in a greater percentage of the boron being beyond the electrical solid solubility. This, combined with the

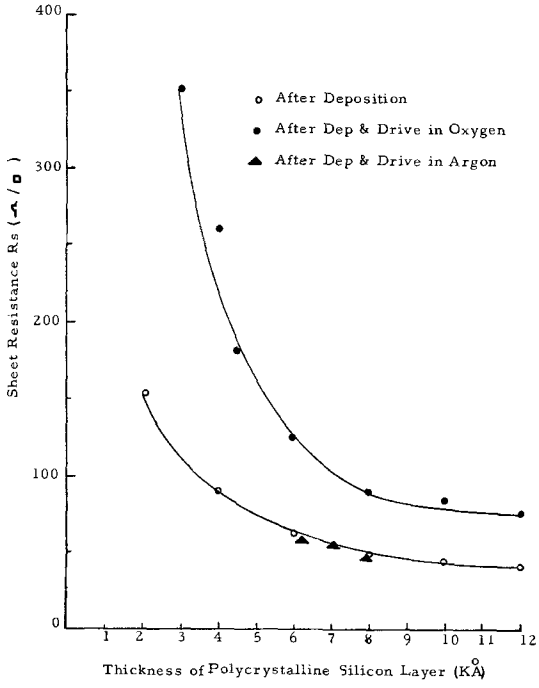

Fig. 3. Sheet resistance as a function of thickness of polycrystalline silicon layer after boron deposition and drive.

lower mobility of active carriers at high concentrations, results in higher sheet resistivities. The sheet resistance of the layer went up after a drive in an oxygen ambient primarily due to the redistribution of boron in the oxide formed during this drive. During this oxidation approximately 1200Å of silicon was consumed in forming the oxide. Thus in the thinner layers there is an additional increase in sheet resistivity beyond that due to the mechanism mentioned previously. The sheet resistance did not change significantly from the original value of boron deposition after 45 min drive in argon. This was due to the fact that no oxide was formed in the drive, so that no boron out-diffusion occurred.

It was concluded that a 7000Å layer of polycrystalline silicon is sufficient to produce either a low or a high sheet resistance after diffusion as desired.

Diffusion profile by anodic oxidation method.—A polycrystalline silicon layer 1.5μ thick was deposited on a nitride layer at 800°C. Then 15 min of boron diffusion was performed on these crystals at 1050°C with a BBr_3 source held at 20°C. Single-crystal silicon slices of 6 ohm-cm n-type were used as controls. Sheet resistance was measured after diffusion. They were 104-135 ohms/square for polycrystalline silicon and 22.6-31.6 ohms/square for the n-type control slices.

After boron diffusion, thin layers of the polycrystalline silicon were removed by the anodic oxidation and etch method (6). A sheet resistance was measured after each subsequent step. The sheet conductance was derived from the above data and plotted against the distance from the surface in Fig. 4. It was found that the slope of the curve dropped sharply after a distance of about 0.6μ from the surface.

The concentration profile of the diffusion was calculated from

$$Nx = \frac{1}{\mu q}\frac{d\sigma s}{dx}$$

Where σs is the sheet conductance, x the distance from the surface, $d\sigma s/dx$ the slope at point x in Fig. 4, μ the mobility, q the electron charge, and Nx the concentration of the active carrier at point x.

The profile calculated by the above equation is plotted in Fig. 5. The effective mobilities used in the calculation were 0.57 times the value for single-crystal silicon mobilities obtained from published data (7). This was done because the Hall mobility of the polycrystalline silicon was found to be 0.57 of the mobility for single-crystal silicon as will be discussed in a later section of this report.

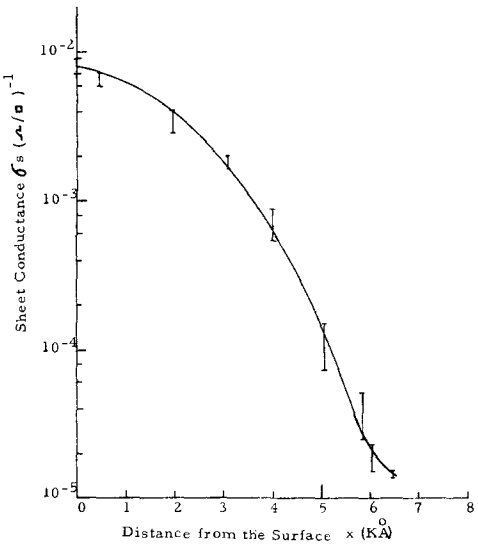

Fig. 4. Sheet conductance of the polycrystalline silicon layer as a function of depth after boron diffusion.

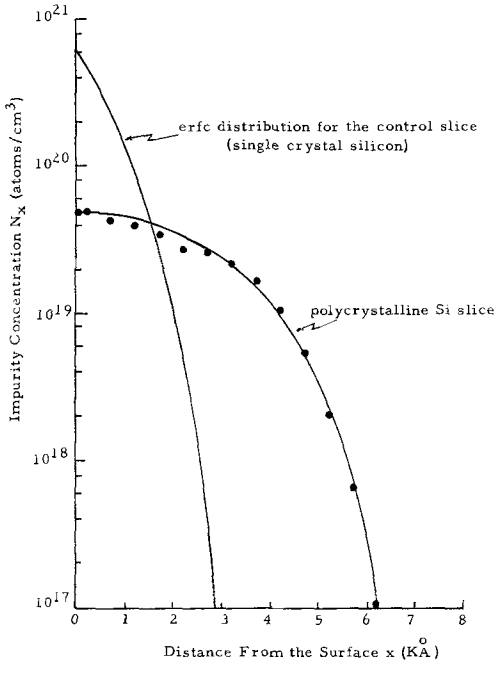

Fig. 5. Impurity concentration profile of the boron diffused layers

The concentration profile was neither a complementary error function nor a Gaussian distribution.

The profile of the control single crystal is also plotted in Fig. 5 for comparison purposes by assuming an erfc distribution. It is interesting to note that for the same diffusion condition, the junction depth was larger and the surface concentration was smaller for the polycrystalline silicon than the single-crystal silicon. It can be explained that the diffusion constant for polycrystalline silicon is higher as explained in the next section, hence a deeper junction. The lower surface concentration is probably due to more precipitation of species in the polycrystalline silicon so that these species were electrically inactive, and the four-point probe only measures the electrically active species.

The diffusion constant.—The diffusion constant was calculated by the equation (6, 8)

$$D\ (N = Nx) = \frac{1}{2t}\left(\frac{dx}{dN}\right) Nx \int_0^{Nx} x\, d\, N$$

where D is the diffusion constant, t is the time of diffusion, x is the distance from surface, and Nx is the boron concentration at point x. The integral was solved by graphical integration. The diffusion constant calculated from this method for polycrystalline silicon is 1.85-2.5 x 10^{-13} cm²/sec. The diffusion constant for the control single-crystal silicon was found to be 3.3 x 10^{-14} cm²/sec by assuming an erfc distribution and using Irvin's curves (9). This value is in agreement with published data (10). It is found that the diffusion constant for boron in a polycrystalline silicon layer is several times higher than in single crystalline silicon under identical diffusion conditions.

The higher diffusion constant in polycrystalline silicon is in agreement with the finding of other investigators (11). The reason for the higher diffusion constant can be explained as due to the presence of grain boundaries. The grain boundary diffusion is favored over bulk diffusion.

Hall Mobility of Holes in Polycrystalline Silicon

The Hall mobility of holes was measured by the method outlined by Van der Pauw (12). The samples were prepared in the same way as in the experiment on concentration profile. Namely, 1.5μ of polycrystalline silicon was deposited on a nitride layer at 800°C followed by a 15 min boron diffusion at 1050°C. The control single-crystal silicon slices went through the same diffusion. The Hall mobility of the polycrystalline silicon was 137 cm²/V-sec and for the single-crystal silicon it was 240 cm²/V-sec. It is well known that the Hall mobility is a function of impurity concentration. Most of the reported Hall mobility was measured on homogeneous silicon layers. But the above polycrystalline silicon and control slices both had a diffused graded profile. Therefore, the mobility we obtained was only an average mobility of the layers, not a value for any particular concentration. Hence the absolute value of this measurement has less significance than the ratio of the two values, namely

$$\frac{\text{Hall mobility of polycrystalline silicon}}{\text{Hall mobility of single crystal silicon}} = 0.57$$

The Hall mobility of holes in polycrystalline silicon was found to be about half of that in single-crystal silicon. This phenomenon is one of the reasons that the sheet conductance in polycrystalline silicon is lower than the single-crystal silicon under identical diffusion condition.

Oxidation of the Polycrystalline Silicon

Slices with polycrystalline silicon layers deposited on silicon nitride layers were oxidized in steam at 950°C for 1, 2, 3, 4, and 16 hr. Single-crystal silicon slices of (111) orientation were used as controls. The oxidation thickness *vs.* time is plotted in Fig. 6. It was found that no significant difference existed between the oxidation rate of polycrystalline silicon layers and single-crystal silicon of (111) orientation. The etch rate of the above two kinds of oxides was investigated. It was found that both have approximately the same etch rate in a buffered HF solution.

Conclusion

The properties of polycrystalline silicon deposited on a silicon nitride layer are very much process dependent, and significantly depart from single-crystal silicon. The grain boundaries have the effects of enhancing the diffusion of boron atoms, reducing active carrier concentration, and lowering hole mobility. Layers formed at lower temperatures have a more uniformly small grain size contributing to more reproducible diffusion characteristics as evidenced by sheet resistivity measurements.

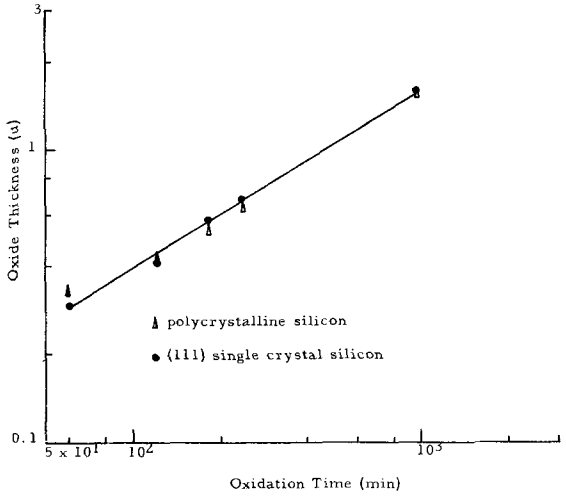

Fig. 6. Oxide thickness as a function of oxidation time at 950°C in steam.

It was found from this study that polycrystalline silicon layers thicker than 7000Å and deposited at 800°C can be made to approach the conductivity of diffused single-crystal silicon especially when non-oxidizing drives are used.

No significant differences between the oxidation properties of polycrystalline and single-crystal silicon were found.

Acknowledgment

The authors wish to acknowledge Mr. V. Lyn for his work on making the electron micrographs and reflection diffraction analysis on the samples, and also thanks to Mr. W. Heath who accomplished the experimental work on depositing the polycrystalline silicon layer.

Manuscript submitted July 20, 1970; revised manuscript received ca. Sept. 11, 1970.

Any discussion of this paper will appear in a Discussion Section to be published in the December 1971 JOURNAL.

REFERENCES

1. J. C. Sarace, R. E. Kerwin, D. L. Klein, and R. Edwards, *Solid State Electron.*, **11**, 553 (1958).
2. L. L. Vadaz, A. S. Grove, T. A. Rowe, and G. E. Moore, *IEEE Spectrum*, **6**, 28 (1969).
3. S. R. Bhola and A. Mayer, *RCA Rev.*, pp. 511-522, Dec. 1963.
4. R. C. Chitlick, J. H. Alexander, and H. F. Sterling, *This Journal*, **116**, 77 (1969).
5. R. D. DeLuca, "Semiconductor Silicon," pp. 299-315, Electrochemical Society, Inc., New York (1969).
6. E. Tannenbaum, *Solid State Electron.*, **2**, 123 (1961).
7. A. Philips, "Transistor Engineering," McGraw-Hill Book Co., New York (1962).
8. J. Crank, "The Mathematics of Diffusion," Clarendon Press, Oxford (1956).
9. J. C. Irvin, *Bell System Tech. J.*, **41**, 387 (1962).
10. A. S. Grove, "Physics and Technology of Semiconductor Devices," John Wiley & Sons, Inc., New York (1967).
11. M. L. Barry and J. Manolin, *This Journal*, **117**, 258 (1970).
12. L. J. Van Der Pauw, *Philips Res. Repts.*, **13**, 1 (1958).

Growth Characteristics of Alpha-Silicon Carbide

I. Chemical Vapor Deposition

J. M. Harris[1]

IBM Components Division, East Fishkill Facility, Hopewell Junction, New York 12533

and H. C. Gatos* and A. F. Witt*

Center for Materials Science and Engineering, Massachusetts Institute of Technology, Cambridge, Massachusetts 02139

ABSTRACT

Single-crystal layers of α-(hexagonal) silicon carbide (SiC) were successfully deposited on the [0001] and [000$\bar{1}$] surfaces of α-SiC substrates from silane and propane in a hydrogen atmosphere and in the 1500°-1650°C temperature range. Above 1650°C the amount of SiC deposited was found to be significantly decreased because of increased hydrogen etch rates and diffusion-limited reactant transfer to the substrate. The growth characteristics are best described by a model in which the surface of the sample is in equilibrium with the reactants diffusing through a boundary layer. Undoped n-type deposits (grown on p-type substrates) exhibited a resistivity of 0.40 ohm-cm and a Hall mobility of approximately 200 cm^2/V-sec at 77°C.

The use of SiC in electronic devices continues to be limited by problems of purity control and crystalline perfection; these problems are strongly related to the high temperatures (about 2500°C) at which α-SiC is grown by the standard Acheson and Lely techniques. Growing α-SiC from the vapor phase has the distinct advantage (regarding purity control) that it takes place at appreciably lower temperatures (about 1600°C). Growth of SiC from the vapor phase using SiH_4 and C_3H_8 (and other reagents) has been reported (1). This and subsequent studies (2) have considered the dependence of growth rate on temperature and the effects of varying the Si/C ratio. In all instances SiC was grown on SiC. It has been found, here and previously (1), that changes in temperature and in gas composition may lead to either α- or β- (cubic) SiC layers.

An important aspect of growing SiC from the vapor phase is that, at the temperature of growth, thermal etching of SiC takes place concurrently. Thus, it has been reported (1) that above 1775°C the growth was much reduced; by 1900°C the substrate was etched. The authors have found (3) that above 1550°C the etching rate of α-SiC in hydrogen varies with the susceptor material on which the inductively heated SiC rests. The highest etching rate was observed when molybdenum was used. The present study attempts to elucidate the growth by vapor deposition on the basis of the processes (chemical and physical) taking place between the vapor phase reactants and the substrate.

Experimental Procedure

The vapor growth experiments were performed in a 1.5 in. ID, horizontal, water-cooled, quartz reaction tube using a silane-propane mixture and hydrogen as carrier gas. Details of the experimental arrangement and procedure have been described elsewhere (3). The substrates, (0001) platelets of α-SiC, were polished with 3μ diamond paste, chemically etched in an alkaline ferricyanide solution (4), and thermally etched in hydrogen at 1650°C. This procedure yielded the extremely smooth surfaces desired for chemical vapor deposition. In all experiments a tantalum susceptor measuring ¼ x ⅞ x 2 in. was employed. All temperatures reported here are those of the susceptor, determined with an optical pyrometer (uncorrected readings).

The "thickness" of the grown layers was determined from the weight change of the samples; the substrate surface areas were measured from enlarged photomicrographs of the platelets or were computed from thickness and weight measurements. Since epitaxial deposition and "thermal etching" took place concurrently over the whole temperature range investigated, the growth rates are reported here not in microns per minute but in microns per Standard Time Interval (μ/STI). The STI was 22 min: a 2 min heat-up period in argon, a 2 min hold at deposition temperature in argon, a 2 min hold in pure hydrogen, a 10 min deposition period, and a 6 min hold in argon at deposition temperature.

Results and Discussion

Figure 1 shows the dependence of the growth rate on reactant input concentration (with a fixed Si/C ratio of 0.88) and temperature (a constant hydrogen flow of 6.0 liters/min was employed). Over the temperature range investigated, the growth characteristics of SiC varied markedly with increasing reactant input concentration. Up to about 1.5 x 10^{-4} moles/min of Si input, the system exhibited an "effective" negative growth rate. Since polycrystalline SiC deposits were observed occasionally under these conditions, it appears that the weight loss due to hydrogen etching on the bottom face of the substrate exceeded the weight increase due to SiC deposition on the upper face. Thus, in this range of reactant concentration the deposition rate is greater than the etching rate of the

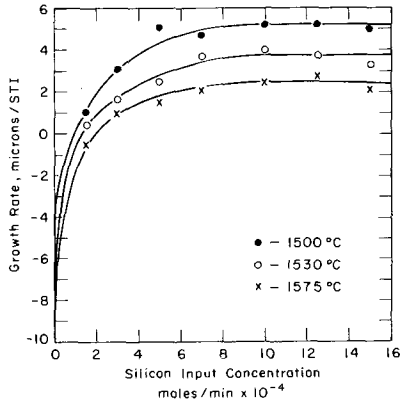

Fig. 1. Growth rate vs. Si concentration for α-SiC on α-SiC substrate.

[1] Present address: Monolithic Memories, Incorporated, 1165 Arques Avenue, Sunnyvale, California 94086.

* Electrochemical Society Active Member.

Key words: silicon carbide, vapor deposition.

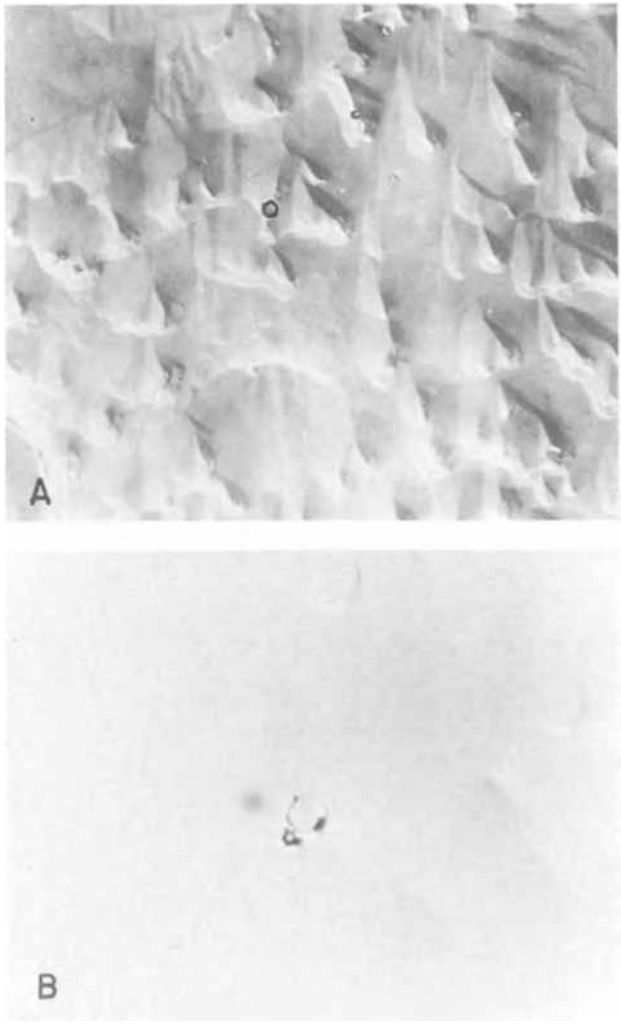

Fig. 2. Single-crystal SiC overgrowth on [0001] substrate: (A) 30X, (B) 150X.

surface available for deposition but less than the overall etching rate of the sample. Upon increasing the Si input concentration beyond 1.5×10^{-4} moles (to about 3.5×10^{-4} moles/min), the SiC deposit was single crystalline and the samples exhibited a net weight increase. Figure 2 shows typical epitaxial growth under these conditions. The hexagonal stacking faults on the deposit constitute a convenient identification of α-SiC. At Si input concentrations above 3.5×10^{-4} moles/min, the epitaxial deposits were invariably polycrystalline. The effective growth rate under such conditions is virtually independent of reactant input concentration and is apparently controlled by mass transport. The observed temperature dependence of the growth rate in this region, however, is not in good agreement with that expected for a process under diffusion control.

This result is not surprising because the etching rate of SiC increases as does the rate of homogeneous nucleation and heterogeneous nucleation of silicon on the reactor wall (5) with increasing temperature; furthermore, the efficiency of SiH_4 and C_3H_8 in forming SiC decreases with increasing temperature (2). It should be pointed out that the values of reactant concentrations at which either single crystal or polycrystalline growth takes place (Fig. 1) must not be considered absolute or specific to the silane-propane-hydrogen system. These values do depend, for example, on the geometry of the system and the interaction of the reactants with the susceptor material.

The growth experiments were primarily carried out on the Si (0001) surfaces of the SiC substrate platelets. However, deposits of the same nature were also obtained on the carbon (0001) surfaces except that the growth rate was about half of that for the silicon surfaces. This difference in growth rates has been observed in many other crystallographically polar materials (6), but the details of the growth mechanisms involved are still not clear.

Fig. 3. Polycrystalline β-SiC deposit in a stacking fault on α-SiC substrate (33X).

As in previous studies, hexagonal as well as cubic SiC was obtained, depending on the experimental conditions. The β-SiC form shown in Fig. 3 was obtained above 1640°C, and in relatively high reactant concentrations (Si $> 5 \times 10^{-4}$ moles, Si/C = 0.88, and H_2 = 0.27 moles). The polycrystalline cubic modification apparently nucleated on substrate irregularities and could be readily identified from its bright yellow color and its cubic morphology (not apparent in the photomicrographs).

Resistivity and Hall coefficient measurements [employing the van der Pauw (7) technique] were carried out at room temperature and 77°K on undoped n-type SiC layers deposited on p-type substrates. A few deposits became p-type at 77°K. Electron Hall mobility at 77°K was about 200 cm²/V-sec; resistivity was approximately 0.40 ohm-cm. No differences in electrical properties were observed between deposits grown on (0001) and on $(000\bar{1})$ substrates. The van der Pauw resistivity ratio, R_1/R_2, varied only 5% from room temperature to 77°K, whereas a variation of about 20% was measured for the substrate. It is believed that the less the variation of R_1/R_2 with temperature, the more homogeneous the sample (8).

There have been extensive theoretical treatments of epitaxial growth in open-tube systems. The results of the present study summarized in Table I are quite consistent with the model developed by Bradshaw (9) which is based on "boundary layer" considerations. Bradshaw's relationship is

$$G(Y) = 100S \left[\frac{VP}{\overline{M}Y} \right]^{1/2} \qquad [1]$$

where G is the growth rate in microns per minute, Y is the distance in centimeters from the leading edge of the boundary layer, V is the mainstream gas velocity in centimeters per second, P is the pressure in atmospheres, $\overline{M}$ is the average molecular weight of the boundary layer, and S is a term related to thermodynamic efficiency. The growth rate of α-SiC plotted in Fig. 4 and 5 as a function of $1/\sqrt{Y}$ is in reasonable agreement with Bradshaw's model. In the experiment the leading edge of the boundary layer was taken to be the front edge of the susceptor. The slope of the curves is indicative of the thermodynamic efficiency, S.

Based on "boundary layer" considerations but assuming somewhat different boundary conditions, Rundle (10) has arrived at the following relationship

$$G(Y) = \frac{120\,\overline{m}DC_{(o)}}{\overline{M}\,\rho\,b} \exp\left[-\frac{D\pi^2 Y}{4Vb^2} \right] \qquad [2]$$

Table I. Growth rate under various experimental conditions

Exp. No.	H_2, liters/min	Si, moles/min (10^{-4})	Si/C Ratio	Temp, °C	S (Eq. [1])	Growth rate, μ/STI	$1/\sqrt{Y}$ ($cm^{-1/2}$)
D-2	6.0	3.0	0.88	1530	2.66	1.36	0.466
						2.26	0.572
						3.26	0.697
						10.8	1.68
D-3	6.0	3.0	0.88	1560	2.33	−2.04	0.468
						2.27	0.848
						5.41	1.51
D-4	10.0	5.0	0.88	1590	4.36	−1.54	0.468
						2.27	0.667
						9.02	1.12
D-5	3.0	1.5	0.88	1620	0.14	0.945	0.458
						1.15	0.48
						1.4	0.86
						1.4	1.67
D-6	3.0	1.5	0.88	1560	1.43	0.945	0.464
						1.147	0.71
						4.07	1.51
O-1	6.0	3.0	0.6	1590	1.21	0.0	0.462
						0.0	0.518
						1.14	0.596
						3.6	1.59
O-2	6.0	3.0	0.43	1560	2.31	0.0	0.63
						2.5	1.025
						6.9	1.67
O-3	6.0	3.0	0.33	1560	9.87		
O-5	6.0	9.0	0.6	1560	0.96	2.4	0.464
						2.28	0.584
						5.5	1.59
O-6	6.0	15.0	1.5	1560	2.91		
O-7	6.0	15.0	0.75	1560	3.57	3.19	0.462
						4.56	0.59
						5.7	0.65
						9.3	0.984
						11.0	1.39
O-8	6.0	15.0	0.45	1560	4.69		

where $\overline{M}$ is the average molecular weight of the boundary layer, $\overline{m}$ is the average molecular weight of the deposit, D is the diffusion coefficient of the reactant species in square centimeters per second at the mean temperature of the boundary layer (all reactants are assumed to have the same D), $C_{(o)}$ is the input concentration of reactants in grams per cubic centimeter, and b is the vertical distance from the substrate surface to the wall of the tube ($b = 1$ cm).

The difference between the two models is that Rundle assumes a concentration gradient in the vertical direction (perpendicular to the flow direction), whereas Bradshaw neglects it. Furthermore, Rundle assumes that the reaction at the substrate-gas interface goes to completion, *i.e.*, the reactant concentration is zero, whereas Bradshaw calculates a concentration for the reactant species at the interface. In Fig. 6, ln G of two runs at approximately 1550°C is plotted against Y. The diffusion coefficient for the transport process is obtained directly from the slope of the curves. The average of the two curves in Fig. 6 gives a value for $D = 2.41$ cm²/sec. This value is in good agreement with the value of 2.27 cm²/sec reported (3) for the diffusion coefficient of silicon in hydrogen at 1600°C. This present result implies a minimum value of about 2.41 cm²/sec for the diffusion of carbon in hydrogen at 1550°C.

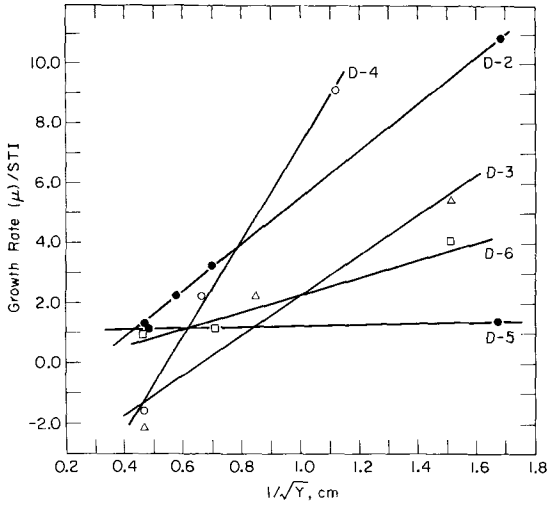

Fig. 4. Growth rate of α-SiC vs. $1/\sqrt{Y}$ for experiments D-2 to D-6 in Table I.

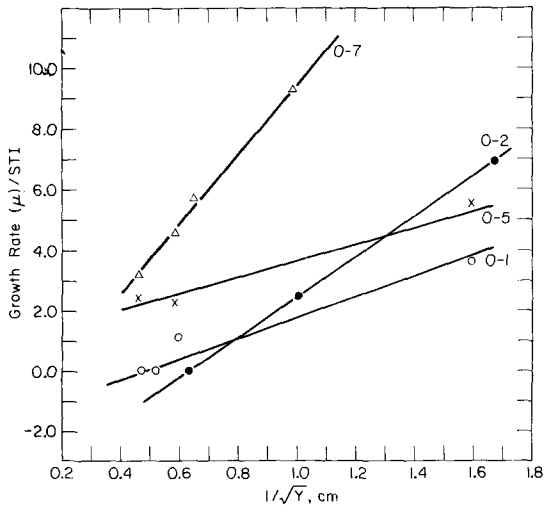

Fig. 5. Growth rate of α-SiC vs. $1/\sqrt{Y}$ for experiments O-1, O-2, O-5, and O-7 in Table I.

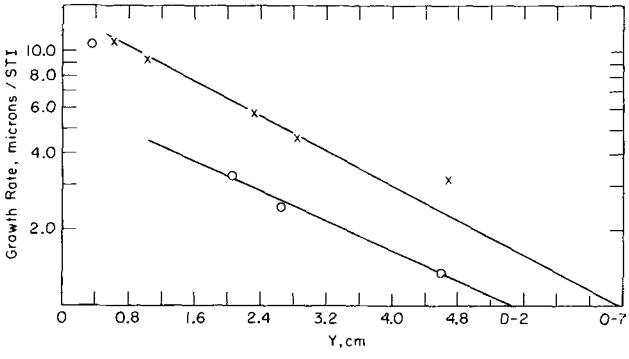

Fig. 6. Growth rate vs. Y for deposition of α-SiC on α-SiC substrates.

Summary

Epitaxial single-crystal layers of α-SiC were successfully deposited from SiH_4 and C_3H_8 on [0001] and [000$\bar{1}$] surfaces of α-SiC. The growth characteristics were found to be consistent with a model in which the growth is controlled by the diffusion of the reactants through a "boundary layer" adjacent to the substrate surface. Above 1600°C, growth was significantly inhibited by thermal etching in the presence of hydrogen. The epitaxial layers exhibited higher crystalline perfection and better electrical characteristics than the α-SiC obtained by the standard direct crystal growth methods.

Acknowledgments

The work was supported by the Advanced Research Projects Agency under contract SD-90. J. M. Harris wishes to acknowledge IBM for an IBM Resident Study Fellowship.

Manuscript submitted May 9, 1970; revised manuscript received *ca.* Sept. 23, 1970. This was Paper 198 presented at the Los Angeles Meeting of the Society, May 10-15, 1970.

Any discussion of this paper will appear in a Discussion Section to be published in the December 1971 JOURNAL.

REFERENCES

1. H. C. Chang, Final Report, Cont. AF 19 (604)-8499, AFCRL-63-1, AD. No. 402193 (1962).
W. K. Spielmann and K. Brack, *Z. Angew. Phys.*, **18**, 321 (1965).
R. B. Campbell and T. C. Chu, *This Journal*, **113**, 826 (1966).

2. J. M. Harris, H. C. Gatos, and A. F. Witt, *This Journal*, **118**, 338 (1971).
3. J. M. Harris, H. C. Gatos, and A. F. Witt, *This Journal*, **116**, 380 (1969).
4. J. M. Harris, H. C. Gatos, and A. F. Witt, *ibid.*, **116**, 672 (1969).
M. Kumagawa *et al.*, *Japan. J. Appl. Phys.*, **8**, 421 (1969).
5. B. A. Joyce and R. R. Bradley, *This Journal*, **110**, 1235 (1963).
S. E. Mayer and D. E. Shea, *ibid.*, **111**, 550 (1964).
6. H. C. Gatos, P. L. Moody, and M. C. Levine, *J. Appl. Phys.*, **31**, 212 (1960).
7. L. J. van der Pauw, *Philips Res. Rept.*, **13**, 1 (1958).
8. H. J. van Daal, *Philips Res. Rept. Suppl.*, **3** (1965)
H. J. van Daal *et al.*, *Phys. Chem. Solids*, **24**, 109 (1963).
9. S. E. Bradshaw, *Intern. J. Electronics*, **21**, 205 (1966) and **23**, 381 (1967).
10. P. C. Rundle, *ibid.*, **24**, 405 (1968).

Growth Characteristics of Alpha-Silicon Carbide

II. Equilibrium Considerations

J. M. Harris[1]

IBM Components Division, East Fishkill Facility, Hopewell Junction, New York 12533

and H. C. Gatos* and A. F. Witt*

Center for Materials Science and Engineering, Massachusetts Institute of Technology, Cambridge, Massachusetts 02139

ABSTRACT

The equilibrium partial pressures of various vapor species in the system silicon-carbon-hydrogen were computed for conditions under which epitaxial SiC deposition has been achieved. It was found that in the temperature range 1300°-1700°C the tendency to form solid silicon carbide decreases with increasing temperature and with increasing silicon to carbon atom ratio. The limiting conditions under which single crystalline deposits of α-SiC could be experimentally obtained were those within which SiC was computed to be the only thermodynamically stable solid phase. At 1650°C single-phase silicon carbide condenses at Si/C ratios ranging from 0.2 to 0.89. The computed results were in good agreement with experiments.

The experimental conditions for single crystalline deposition of epitaxial α-SiC were examined in an earlier study (1). At present, the results of theoretical computations of equilibrium vapor pressures in the system silicon-carbon-hydrogen are reported and correlated with experimental findings. Under the conditions investigated it was found that up to 27 different vapor species can coexist with the three possible condensed phase species, *i.e.*, carbon, silicon and silicon carbide. Obviously this type of computation gives no information as to how the condensed phases physically coexist, which polytypes are formed, and whether or not α-SiC appears in single-crystal or polycrystalline form.

Results and Discussion

The computation of the equilibrium concentrations of the thermodynamically stable species (gaseous and solid) in the present system was carried out with a program (2) based on minimizing the total Gibbs free energy with the constraint of conservation of mass (3). The accuracy of the program was tested by applying it to similar systems for which experimental results were available (4). The agreement was found to be excellent. The thermochemical data in the temperature range from 1300° to 2000°C were computed for varying silicon and carbon input concentrations at a fixed pressure of 1 atm and a constant hydrogen concentration of 0.27 moles. The partial pressures of thermodynamically stable species for input concentrations of 3.0 x 10^{-3} moles silicon and 3.2 x 10^{-3} moles carbon in the temperature range from 1573° to 2173°K are listed in Table I, together with the concentration of stable condensed phases.

The computed compositions of the condensed phases as a function of silicon and carbon input concentrations at 1650°C are presented in Fig. 1. The solid lines delineate three regions of varying input concentrations (silicon and carbon) in which the vapor phase coexists

Table I. Thermodynamically stable compounds in the system Si-C-H_2 and their equilibrium concentrations in the temperature range from 1650° to 1800°C

H = 0.54 moles
Si = 3.0 x 10^{-3} moles
C = 3.2 x 10^{-3} moles
Si/C = 0.9375
Total pressure = 1 atm

Vapor species / T°K / P_i (atm)	1923	1973	2023	2073
CH_2	$0.1592 \cdot 10^{-5}$	$0.2203 \cdot 10^{-5}$	$0.295 \cdot 10^{-5}$	$0.3864 \cdot 10^{-5}$
CH_3	$0.1336 \cdot 10^{-4}$	$0.1473 \cdot 10^{-4}$	$0.159 \cdot 10^{-4}$	$0.1696 \cdot 10^{-4}$
CH_4	$0.3138 \cdot 10^{-3}$	$0.2459 \cdot 10^{-3}$	$0.1917 \cdot 10^{-3}$	$0.1501 \cdot 10^{-3}$
C_2H_2	$0.2043 \cdot 10^{-3}$	$0.2386 \cdot 10^{-3}$	$0.2676 \cdot 10^{-3}$	$0.2939 \cdot 10^{-3}$
C_2H_4	$0.2277 \cdot 10^{-5}$	$0.1984 \cdot 10^{-5}$	$0.1685 \cdot 10^{-5}$	$0.142 \cdot 10^{-5}$
H	$0.9387 \cdot 10^{-3}$	$0.1344 \cdot 10^{-2}$	$0.1892 \cdot 10^{-2}$	$0.2619 \cdot 10^{-2}$
SiH	$0.4951 \cdot 10^{-8}$	$0.1242 \cdot 10^{-7}$	$0.3022 \cdot 10^{-7}$	$0.7093 \cdot 10^{-7}$
H_2	0.9985	0.9981	0.9976	0.9969
SiH_4	$0.2081 \cdot 10^{-6}$	$0.2595 \cdot 10^{-6}$	$0.3252 \cdot 10^{-6}$	$0.406 \cdot 10^{-6}$
Si	$0.1628 \cdot 10^{-5}$	$0.4005 \cdot 10^{-5}$	$0.9572 \cdot 10^{-5}$	$0.2209 \cdot 10^{-4}$
Si_2	$0.132 \cdot 10^{-7}$	$0.4599 \cdot 10^{-7}$	$0.1554 \cdot 10^{-6}$	$0.5018 \cdot 10^{-6}$
Si_3	$0.1747 \cdot 10^{-9}$	$0.7618 \cdot 10^{-9}$	$0.3235 \cdot 10^{-8}$	$0.1307 \cdot 10^{-7}$
C_3H_4	$0.7897 \cdot 10^{-8}$	$0.7734 \cdot 10^{-8}$	$0.7219 \cdot 10^{-8}$	$0.6606 \cdot 10^{-8}$
C_3H_5	$0.2932 \cdot 10^{-7}$	$0.2662 \cdot 10^{-7}$	$0.2312 \cdot 10^{-7}$	$0.1977 \cdot 10^{-7}$
Condensed species / Moles				
C	0	0	0	0
SiC	$0.2999 \cdot 10^{-2}$	$0.2999 \cdot 10^{-2}$	$0.2997 \cdot 10^{-2}$	$0.2994 \cdot 10^{-2}$
Si	0	0	0	0

[1] Present address: Monolithic Memories, Incorporated, 1165 Arques Avenue, Sunnyvale, California 94086.
* Electrochemical Society Active Member.
Key words: silicon carbide, vapor deposition, thermochemical equilibrium.

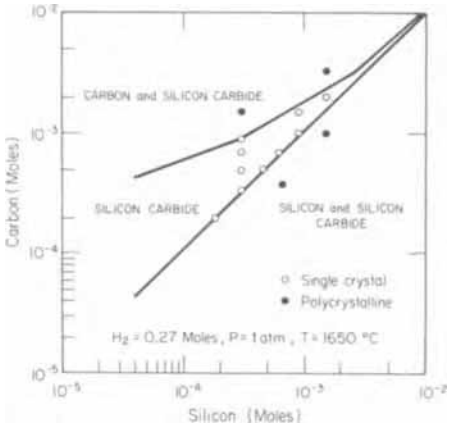

Fig. 1. Formation of silicon carbide as a function of carbon and silicon input concentration. Solid lines were theoretically computed; the circles represent individual experiments (see text). (Units for experimental points are moles per min.)

in equilibrium with one of the following condensed phases: SiC + C, SiC, or SiC + Si. The circles in the figure represent actual deposition experiments. The experimental procedure has been outlined elsewhere (1). It is of interest to note that single-crystalline deposits of α-SiC were consistently obtained over the whole input concentration range for which SiC is the only thermodynamically stable condensed phase. Polycrystalline layers of varying morphology were invariably obtained under conditions corresponding to the two-phase regions. Figures 2 and 3 are typical examples of deposits corresponding to the regions with excess carbon and silicon, respectively. These findings are in agreement with the observations by Lely (5) according to which monocrystalline SiC can exist only stoichiometrically [with a maximum deviation of 10^{-5} atomic per cent (a/o) from stoichiometry]. Figure 4 shows the upper and lower limits of partial pressures of two critical vapor species within which single-phase silicon carbide condensation can occur. If the concentration limits of either species are exceeded, two-phase condensation is observed. This figure reflects further the temperature dependence of the width of the single-phase silicon carbide region shown in Fig. 1 (for 1650°C).

Figure 5 presents the computed variation of the equilibrium partial pressure of acetylene as a function of reactant concentration and Si/C atom ratio. It is seen that $P_{C_2H_2}$ decreases with increasing Si/C ratio and increases with increasing input concentration. Furthermore, as shown in Fig. 6, the vapor pressure of C_2H_2 is directly related to the excess input carbon concentration; carbon excess is defined as input carbon

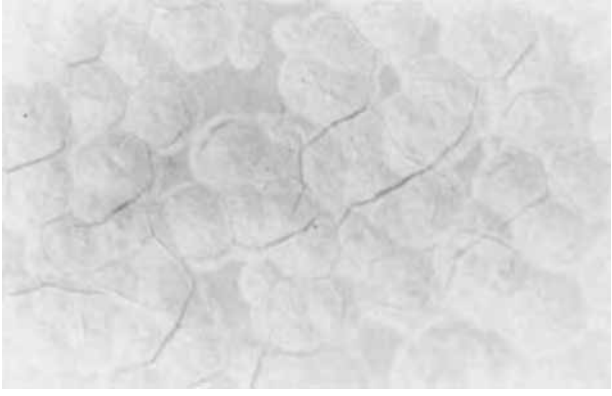

Fig. 2. SiC deposit on (0001) surface of SiC under conditions corresponding to the carbon and silicon carbide region of Fig. 1 (50X).

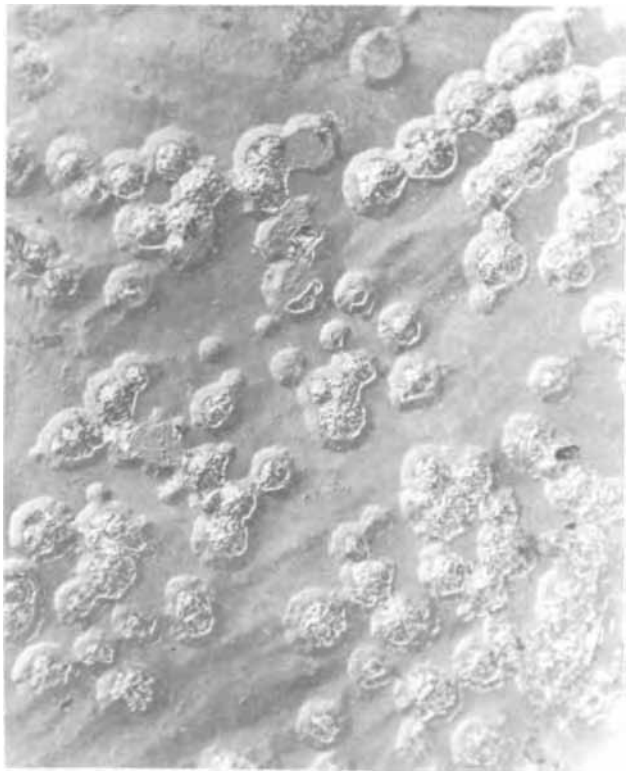

Fig. 3. SiC deposit on (0001) surface of SiC under conditions corresponding to the silicon and silicon carbide region of Fig. 1 (45X).

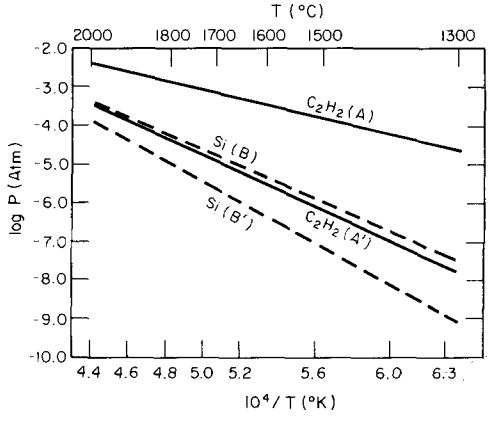

Fig. 4. Maximum and minimum partial pressure of C_2H_2 and Si as a function of temperature for single-phase silicon carbide condensation. The two partial pressure regions are confined between lines A-A' and B-B'.

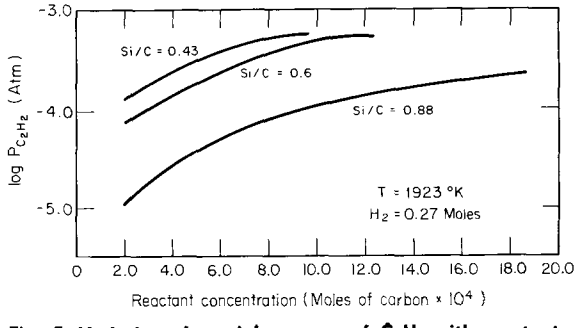

Fig. 5. Variation of partial pressure of C_2H_2 with reactant concentration and silicon to carbon atom ratio.

concentration (X_c) minus input silicon concentration (X_{si}).

The data presented in Fig. 5 and 6 explain why single-phase (stoichiometric) silicon carbide can be

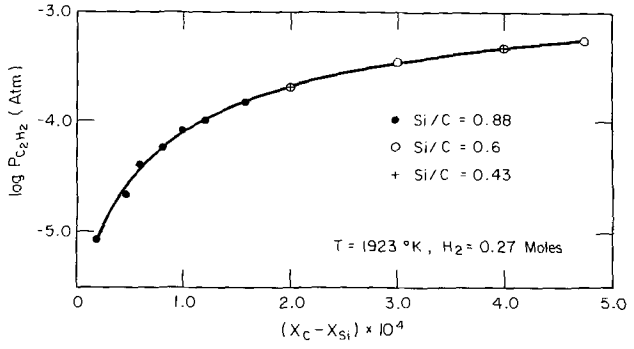

Fig. 6. Variation of partial pressure of C_2H_2 as a function of excess carbon concentration.

obtained over a considerable range of silicon to carbon input concentration ratios; when thermodynamically stable vapor-phase species of the constituent in excess (Si or C) are present and if these species can increase in concentration and, thus, "take up" the excess of that constituent, then stoichiometric condensation of SiC will take place. The finding that the boundary between the SiC single-phase region and the SiC + Si region has a slope of approximately one and an intercept of virtually zero (Fig. 1) is consistent with the fact that there are only five stable silicon vapor species of which four can achieve but negligible concentrations. On the other hand, there are more than 20 carbon vapor species of which at least five exhibit significant stability (see Table I); thus, significant amounts of carbon can be retained in the vapor phase, whereas very little excess silicon can be accommodated if single-phase SiC is to be achieved. The presence of carbon species such as C_2H_2 have essentially a "buffering" effect on the concentration of the carbon constituent. Thus, the position and shape of the boundaries of the single-phase SiC region in Fig. 1 obviously reflect the ability of the carbon and silicon vapor-phase species to accommodate any excess of either constituent.

The relative efficiency of silicon carbide formation as computed for equilibrium conditions at varying temperatures and Si/C atom ratios is summarized in Fig. 7 and 8. It can be seen that the efficiency decreases with increasing temperature and with increasing Si/C

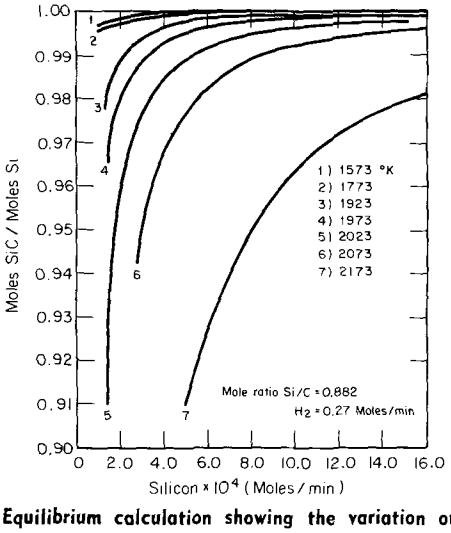

Fig. 7. Equilibrium calculation showing the variation of silicon carbide formation as a function of temperature and reactant concentration.

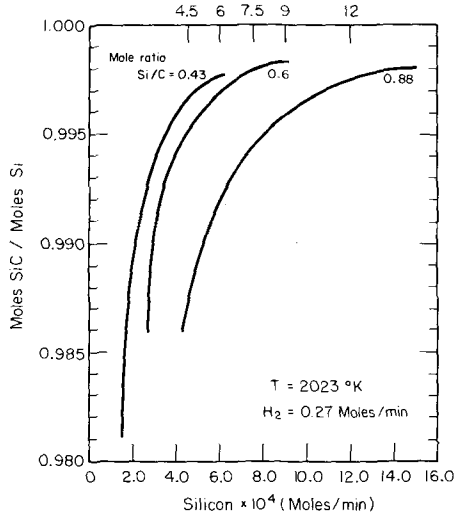

Fig. 8. Equilibrium calculation showing the variation of silicon carbide formation as a function of silicon to carbon atom ratio.

ratios. Since these results are computed for equilibrium conditions they are not expected to apply quantitatively (or in an absolute way) to the open-tube growth system. They are generally consistent, however, with the results reported in an earlier paper (1) and with the variation of the thermodynamic parameter, S [Table I, Ref. (1)], introduced by Bradshaw (4) in his boundary-layer model of epitaxial growth in an open-tube system.

Summary

The general variation of the growth characteristics of SiC from the vapor phase with temperature, reactant concentration, and Si/C atom ratios was computed through equilibrium calculations on the hydrogen-carbon-silicon system. The computed results were found to be in reasonable agreement with experimental data. It was theoretically explained why there is no unique Si/C atom ratio at which single-phase stoichiometric SiC deposition can be achieved: under actual SiC growth conditions, there are many more carbon-containing vapor species with significant vapor pressure than silicon-containing species allowing for stoichiometric SiC formation at Si/C input concentration ratios varying from 0.21 to 0.89.

Acknowledgments

The work was supported by the Advanced Research Projects Agency under contract SD-90. J. M. Harris wishes to acknowledge IBM for an IBM Resident Study Fellowship.

Manuscript submitted May 4, 1970; revised manuscript received *ca.* Sept. 23, 1970. This was Paper 199 presented at the Los Angeles Meeting of the Society, May 10-15, 1970.

Any discussion of this paper will appear in a Discussion Section to be published in the December 1971 JOURNAL.

REFERENCES

1. J. M. Harris, H. C. Gatos, and A. F. Witt, Paper submitted to *This Journal.*
2. "Input and Output Computations and Procedures for Thermochemical Equilibrium Programs 1291 and 1313," Avco Computer Services, 201 Lowell St., Wilmington, Mass. 01887.
3. J. Warga, *J. Soc. Indust. Appl. Math.*, **11**, 588 (1963).
4. T. J. Lewis, *Mater. Res. Bull.*, **4**, 321 (1969).
5. J. A. Lely, *Ber. Deut. Keram. Ges.*, **32**, 229 (1955).
6. S. E. Bradshaw, *Intern. J. Electronics*, **21**, 205 (1966).

Materials for Use in a Durable Selectively Semitransparent Photomask

W. Robert Sinclair,* Miles V. Sullivan, and R. A. Fastnacht

Bell Telephone Laboratories, Incorporated, Murray Hill, New Jersey 07974

ABSTRACT

The object of this study was to screen a group of metal oxides as possible candidates for use as semitransparent mask materials. For this study, all masks were prepared by d-c reactive sputtering onto glass. The uv-visible spectra for the entire group of oxide films were recorded. The spectral characteristics desired for a photomask are (*i*) transmission of less than 1% in the region below 404 nm (for masking), and (*ii*) transmission of greater than 30% at 589 nm (for the see-through characteristic). Because of inferior spectral absorption properties, the following systems were eliminated from further consideration: lead oxide-silicon oxide, lead oxide-germanium oxide, copper oxide, copper oxide-vanadium oxide, molybdenum oxide, chromium oxide, uranium oxide, mercury oxide, and zinc oxide. Those systems which satisfied the spectral requirements were: iron oxide, vanadium oxide, nickel oxide, iron oxide-nickel oxide, and iron oxide-vanadium oxide. These materials were then further evaluated to assure etchability in solvents compatible with photoresist processsing and resistance to abrasion. These latter two properties will be discussed in greater detail in a forthcoming article. Considering only sputtered films, the 10 m/o (mole per cent) iron oxide-90 m/o vanadium oxide is the most promising material based on these additional requirements.

Two main types of masks are used at present for defining images on photoresist materials in the manufacture of semiconductor devices and integrated circuits. One is the photographic emulsion-on-glass mask; the other is the chromium film-on-glass (1) mask. The silver emulsion mask acts by absorbing most of the incident light in desired areas and transmitting it in other areas to interact with the photoresist material thus making the photoresist either more soluble (positive resist) or less soluble (negative resist) (2) in these exposed areas. The chrome-on-glass mask performs the same function by a combination of reflection and absorption.

Both types of masks have liabilities. The emulsion mask is easily scratched and is difficult to clean. Its dimensions are affected by moisture absorption. The chrome-on-glass mask eliminates these difficulties, but unfortunately other problems arise. Registration of a chrome mask with prior patterns may be difficult when the substrate is also mirror-bright. The high reflectivity of the metal mask tends to increase the probability of halation effects and may result in loss of resolution in the exposed resists. Also, preparation of films free of pinholes is difficult.

The work to be described here was aimed at the fabrication of a durable, selectively semitransparent ("see through") mask which would be strongly absorbent to the light used in the exposure process but reasonably transparent to yellow or red light to allow observation for alignment purposes. At present, the radiation used in exposing photoresist is usually a mercury lamp with a strong line at 365 nm and a weak line at 404.6 nm. Microscope observation for alignment purposes usually employs the sodium D line at 589 nm. Our problem then was to prepare a hard film, etchable in solvents appropriate to the steps involved in processing photoresist, strongly absorbing in the spectral region of 360-404 nm, and reasonably (at least 30%) transparent near 589 nm.

For our study, oxide films, which are often hard, were chosen and the technique of reactive sputtering used because such a wide variety of materials can be deposited in this manner and because the equipment was available. Since use of this technique can easily lead to glassy films or films of very small crystal size, it was appropriate to consider the compositions of colored oxide glasses as a starting point for our investigation. From the literature of colored glasses, certain ions can be chosen as having absorption spectra in the region of interest (cf. Table I) (3). In addition, other ions which can give yellowish oxide compounds are Hg^{+2} and Mo^{+6}.

In this paper we present results of studies of oxide films of the various ions in Table I and of those mentioned above. In the text we discuss oxide films of the iron-vanadium system and of the iron-nickel system. In our studies these films came closest to meeting the properties desired in the proposed mask. Results obtained on other systems are presented in the Appendix.

Experiment and Discussion

The apparatus used is diagrammed in Fig. 1. Sputtering was upwards to minimize pinholes caused by dust. The clamped sample could be heated if desired. At a later date a water-cooled holder was used which led to valuable results. Typical and often optimal sputtering conditions were 100 mA at 2500V, and a total pressure of 60 mTorr. It will be noted that most of the ions in Table I are in their highest valence state and, therefore, usually a highly oxidizing atmosphere was used (10-100% O_2). Commercial grade oxygen and argon-oxygen were used without further purification. The sputtering electrodes were 6 ½ in. disks. The films were deposited onto 2 x 2 in. glass slides (Kodak HRP plates with emulsion stripped off).

Table I. Approximate wavelength of maximum absorption for various metal ions in oxide glasses, according to Weyl (3)

Ion	Wavelength, nm
Cr^{+6}	375
V^{+5}	425
Cu^{+2}	400
Ni^{+2}	425
U^{+6}	420
Mn^{+3}	430
Fe^{+3}	370
Pb^{+2}-Pb^{+4} mixture	400-500

* Electrochemical Society Active Member.

Key words: semitransparent photomask, thin films, sputtering.

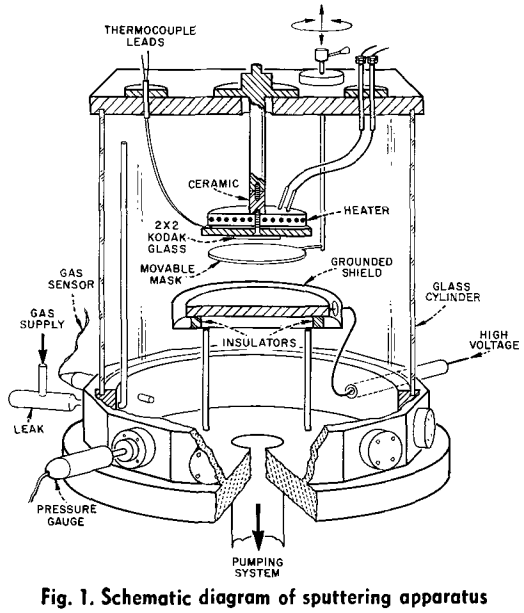

Fig. 1. Schematic diagram of sputtering apparatus

Exploratory work with iron electrodes (cold-rolled steel), vanadium foil electrodes (99.9% pure) and nickel (99% pure) showed some promising spectra as indicated in Fig. 2. Most of the systems studied deviated from Beer's law somewhat when prepared in different thicknesses, possibly because of temperature changes during a run, so that nonnormalized spectra are presented in the figures. The temperature of the substrate was not controlled, and the thermocouple attached to the metallic substrate holder indicated a temperature of about 160°C at the end of the run. The spectrum of the nickel oxide film showed too much absorption at 589 nm to be useful. Unfortunately, the iron oxide film, which exhibits a promising spectrum, is extremely insoluble in even concentrated HCl. The vanadium oxide film also possesses an encouraging spectrum and is etchable. Well-defined patterns could be produced as shown in Fig. 3, wherein windows 1.25 μm wide separated by 1.25 μm lines have been etched using standard photoresist procedures and a 1% HCl etch. However, the etch rate was so fast, even in water, that this film would not be practical for common use.

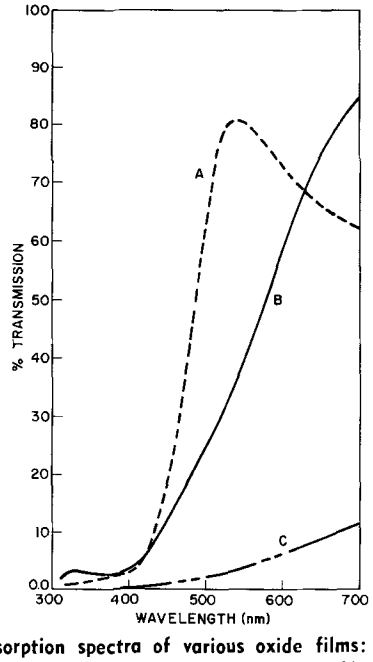

Fig. 2. Absorption spectra of various oxide films: A, vanadium oxide (800 nm thick); B, iron oxide (1800 nm thick); C, nickel oxide (4700 nm thick).

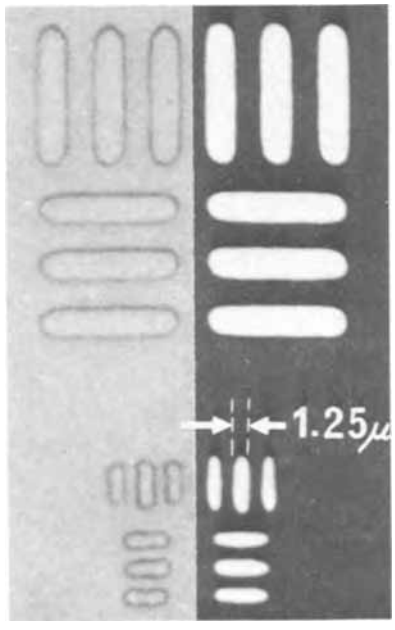

Fig. 3. Semitransparent vanadium oxide mask (left) compared with silver-gelatin master mask used in its preparation illustrating the fidelity and definition achievable using an inorganic oxide semitransparent photomask.

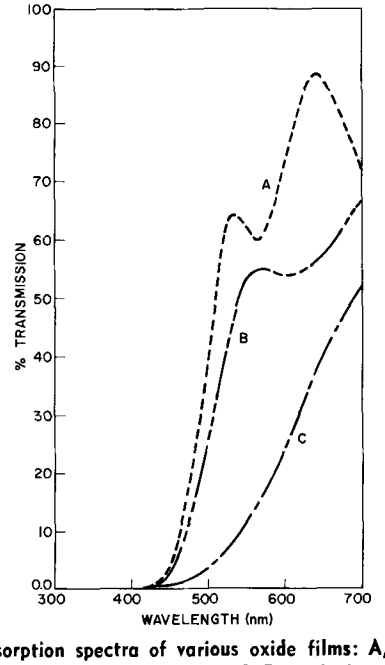

Fig. 4. Absorption spectra of various oxide films: A, iron oxide-vanadium oxide (3860 nm thick) from 25Fe-75V electrode; B, iron oxide-vanadium oxide (3150 nm thick) from 10Fe-90V electrode; C, iron oxide-nickel oxide (3700 nm thick) from 65Fe-35Ni electrode.

In addition, these films are too soft and thus easily scratched. It was felt that mixed films of vanadium oxide and iron oxide would have acceptable spectra and probably be intermediate in solubility and hardness between the two end members.

For exploratory measurements in the system iron oxide-vanadium oxide, varying numbers of ¼ x ¼ x 0.1 in. parallelepipeds of cold-rolled steel were spot-welded to a vanadium sputtering disk. From spectral transmission and etching results on films of several compositions, two, 10Fe-90V and 25Fe-75V,[1] were chosen for further study. Typical spectra are shown in Fig. 4 which also includes the spectrum for an oxide

[1] All materials compositions are expressed as mole fractions in per cent.

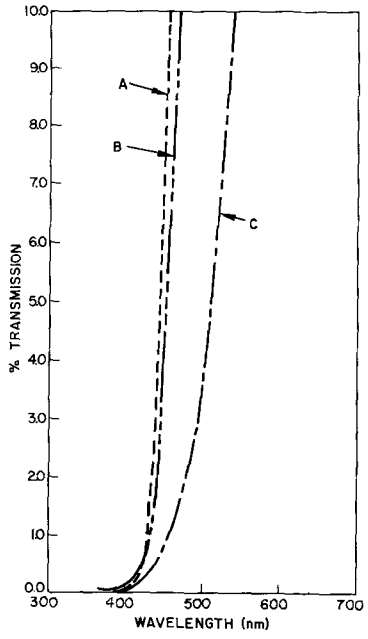

Fig. 5. Absorption spectra on an expanded scale near 400 nm for the same films as in Fig. 4.

film prepared from Nilvar (4), a 65Fe-35Ni alloy. Figure 5 shows on an expanded scale the spectra (near 400 nm, where strong absorption is required) for these same films.

These spectra (Fig. 4 and 5) are in general agreement with predictions from Table I. Thus, one notes that, as the Fe/V ratio increases, the absorption at wavelengths above 400 nm decreases presumably because the vanadium ion, which is being decreased in concentration, has an absorption maximum at about 425 nm. Such reasoning is highly suspect in general, however, because of the complex situation with respect to valence states possible in the system and the possibilities for charge transfer effects on the absorption spectrum.

The films in the iron-vanadium oxide system with a high vanadium oxide concentration show a strong tendency to become mottled when prepared on uncooled substrates. This has been shown to be due to plasma heating. In this regard, we note that the Fe_2O_3-V_2O_5 phase diagram (5) has a 635°C eutectic at about 12% Fe_2O_3 so that films with the highest percentage of vanadium oxide have a tendency to become fluid under our sputtering conditions. As the V_2O_5 concentration decreases, the fluidity should decrease with consequent decrease in mottling, as is observed.

Etching studies on these various film systems show that both the iron oxide and the iron oxide-nickel oxide films are extremely insoluble in both acids and bases when prepared either on uncooled substrates, where plasma heating raised the temperature of the substrate holder to about 160°C, or on substrates raised to 250°C with supplementary heaters. Etching studies on films prepared from the iron-vanadium alloy electrodes and deposited on either uncooled or heated substrates show a wide variety of solubilities from preparation to preparation even under ostensibly identical conditions. The tendencies were for the films with higher iron oxide concentration and those deposited at higher substrate temperatures (250°C was the highest studied) to be less soluble.

Concurrent with this investigation, MacChesney *et al.* (6) have been studying the preparation of iron oxide films by chemical vapor deposition. They noted a startling increase in solubility on lowering the substrate temperature from 185° to 160°C. It was found that the solubility of sputtered films containing iron oxide increased markedly if the temperature of the substrate holder was lowered to between 25° to 50°C by water cooling. Both the iron oxide and iron-nickel oxide lose patches of material during etching and the curvature of these patches suggests that there is strain in the films. These films are, therefore, not considered acceptable. The oxide film derived from the 10Fe-90V electrode could be heat treated at 300°C to decrease its solubility to values appropriate for use in preparing masks. Undoubtedly, this crystallite growth process would proceed considerably faster at 350°C but this has not been studied. The film dissolves nicely without the detached patches mentioned above for the iron oxide and iron-nickel oxide films. Long term heating of the film from the 25 Fe-75V electrode at 350°C apparently did not lead to sufficient crystal growth to decrease the solubility enough to be useful. It is possible that higher temperature heat treatment would be efficacious here but deformation of the glass substrate becomes increasingly a factor to consider. The etching rates of these and other films will be considered in greater detail in a forthcoming article.

In general, with these systems there is greater transmission above 500 nm if the films are prepared in 100% O_2 rather than 90% Ar-10% O_2. Somewhat surprisingly, the sputtering rates of the Fe-V alloys are higher in the pure oxygen than in argon-oxygen mixtures. This is perhaps due to the formation of a conducting ferric vanadate glass on the surface of the cathode (7). In general, d-c reactive sputtering deposition rates, of the order of 5-10 A/min, are undesirably low for practical use. However, Sosniak (8) has shown that deposition rates of about 100 A/min can be obtained by rf reactive sputtering. There is also the possibility of rf sputtering from an oxide cathode in argon.

Summary

Films of iron oxide, vanadium oxide, nickel oxide, iron oxide-vanadium oxide, and iron oxide-nickel oxide have been prepared by d-c reactive sputtering. All of these compositions show strong absorption of light near 400 nm and sufficient transmission at the sodium D line to be considered for use in a durable, selectively semitransparent mask. Of the various compositions studied, the films from the 10Fe-90V electrode show the most promising etching properties in acids and alkalis.

Acknowledgments

The authors are pleased to acknowledge help from a variety of sources. J. Sosniak performed some rf reactive sputtering studies which verified that practicable deposition rates can be obtained in the iron-vanadium oxide system. C. R. Kurkjian furnished advice on the selection of systems for study. Miss S. M. Vincent and J. E. Kessler performed the necessary chemical analyses.

Manuscript submitted March 13, 1970; revised manuscript received *ca.* Sept. 10, 1970. This was Paper 125 presented at the Los Angeles Meeting, May 10-15, 1970.

Any discussion of this paper will appear in a Discussion Section to be published in the December 1971 JOURNAL.

APPENDIX

In addition to the systems discussed in the body of this paper, some other systems suggested by the list in Table I were investigated which proved to be less encouraging. These are grouped here for reference purposes with some remarks.

Lead silicate systems.—Lead silicate glasses are known (9) to absorb strongly in the spectral region near 400 nm. The electrodes used in preparing lead silicate films were made by wrapping lead foil around a silicon disk allowing both lead and silicon to be exposed. The ratio of lead to silicon was varied by varying the ratio of exposed areas. The composition of the gas phase (*i.e.*, the Ar/O_2 ratio) was quite important and may indicate that both valence states of

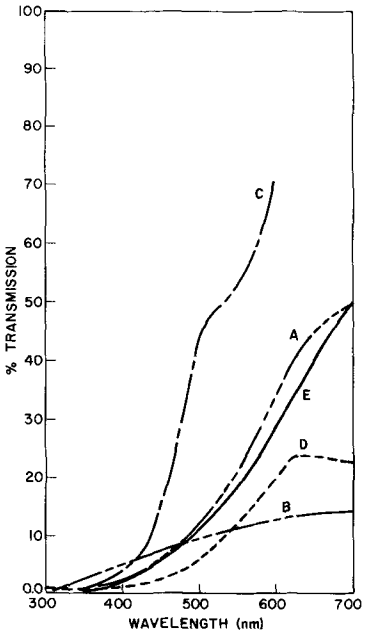

Fig. 6. Absorption spectra of various oxide films: A, lead silicate (2800 nm thick), Pb/Si ≈ 3 in. film; B, lead germanate (700 nm thick), Pb/Ge ≈ 3 in. film; C, molybdenum oxide (2800 nm thick); D, copper oxide (900 nm thick); E, vanadium oxide-copper oxide (2900 nm thick) from 50V-50Cu electrode.

lead should be present in approximately equal concentrations as suggested by Weyl (10). An example of one of the more encouraging spectra is shown in Fig. 6. Comparison with spectra in Fig. 4 for the films containing iron oxide indicates that the lead silicate films do not absorb as strongly at 400 nm as the iron oxide containing films. Etching of the lead oxide from the film was accomplished with hot (just below boiling) 30% H_2O_2. The resulting silica skeleton was removed by gently rubbing with a cotton swab. Fairly good test patterns were delineated as shown in Fig. 7.

Copper oxide.—This oxide film was formed by sputtering copper in 100% O_2. No etching studies were made (*cf.* Fig. 6).

Copper oxide-vanadium oxide.—This mixture was prepared from a 6½ in. disk electrode of copper on which ½ x ½ in. squares of vanadium foil were laid. The exposed areas were about 50Cu-50V. The etching properties of this combination were not studied because the Fe-V combination has a superior spectrum for our purposes. The Cu-V combination sputtered in O_2 about 4 times faster than Fe-V (*cf.* Fig. 6).

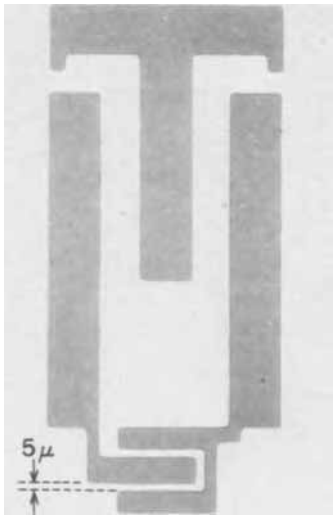

Fig. 7. A lead silicate photomask used to make an experimental transistor.

Molybdenum oxide.—Molybdenum oxide films were prepared by sputtering in 100% O_2. No etching studies were performed (*cf.* Fig. 6).

Other systems.—We have attempted to prepare CrO_3 and a high oxide of uranium with no success. Probably rf sputtering techniques should be used here. Also mercury oxide and zinc oxide films were prepared but proved uninteresting.

REFERENCES

1. A. Rogel, *Rev. Sci. Instr.*, **37**, 1416 (1966).
2. "Thin Film Technology," Chap. 10, pp. 419-466, R. W. Berry, P. M. Hall, M. T. Harris, Editors, D. Van Nostrand Company, Inc., New York (1969).
3. W. A. Weyl, "Coloured Glasses," The Society of Glass Technology, Sheffield, England (1957).
4. Nilvar, a product of Driver-Harris Co., Newark, N. J.
5. A. Burdese, *Ann. Chim. (Rome)*, **47**, 804 (1957).
6. J. B. MacChesney, P. B. O'Connor, and M. V. Sullivan, Paper 126 presented at the Los Angeles Meeting of the Society, May 10-15, 1970.
7. E. P. Denton, H. Rawson, and J. E. Stanworth, *Nature*, **173**, 1030 (1954).
8. J. Sosniak, Private communication.
9. E. Kordes and E. Worster, *Glastechn. Ber.*, **32**, 36 (1959).
10. W. A. Weyl, *loc. cit.*, p. 95.

Observation of Mixed Thermoelectric Power in ThO_2 [1]

N. M. Tallan

Aerospace Research Laboratories, Wright-Patterson Air Force Base, Ohio 45433

and I. Bransky[2]

Ohio State University Research Foundation

ABSTRACT

Electrical conductivity measurements were made on high purity ThO_2 at temperatures between 1000° and 1600°C and oxygen partial pressures of 10^{-1} to 10^{-22} atm. These measurements showed the presence of an oxygen pressure independent region of ionic conductivity at intermediate oxygen pressures and temperatures below about 1400°C, as well as a transition to predominant electron hole conductivity at high oxygen pressures. The Seebeck coefficient was measured over a wide range of oxygen partial pressures in several different gas mixtures at 1000° and 1200°C. The Seebeck coefficient in the region of pure ionic conduction is shown to be a function of the entropy of oxygen in the gas phase, rather than the oxygen partial pressure, as expected for the ionic Seebeck coefficient in the case of a constant ionic defect concentration. The behavior of the Seebeck coefficient in the mixed conduction region is also discussed.

It has been shown by Howard and Lidiard (1, 2) that valuable thermodynamic data for the enthalpies of formation of point defects and their heats of transport can be obtained by studies of the Seebeck coefficient in pure and doped ionic conductors. A number of such studies in the alkali and silver halides have appeared (3-6). Although some metal oxides are known to be ionic conductors over extensive temperature and oxygen partial pressure ranges, their ionic Seebeck coefficients have, until recently, received little attention. Recently, Ruka *et al.* (7), Fischer (8), and Goto *et al.* (9) have studied the ionic Seebeck coefficient of heavily doped metal oxide electrolytes containing very large charge carrier concentrations.

Previously reported studies (10-13) of nominally pure ThO_2 have shown that it is a mixed ionic-electronic conductor, the extent of the region of predominant ionic conduction being a function of temperature, oxygen partial pressure, and probably impurity content. The present study reports results of conductivity and thermal emf measurements on high purity ThO_2. The form of the Seebeck coefficient of a metal oxide mixed conductor in equilibrium with an oxygen electrode will be developed, and the experimental thermal emf results will be shown to be in accord with this analysis. Several of the contributions to the magnitude and temperature dependence of the ionic Seebeck coefficient will be discussed.

Experimental Techniques

Electrical Space Products (ESPI) 99.999% pure ThO_2 powder was pressed in a nylon die into bar-shaped, 3 x 3 x 15 mm specimens. The pressed samples, contained in ThO_2 crucibles and covered with loose pure ThO_2 powder, were sintered in air at 1800°C for about 4 hr. The resultant samples were typically about 96% of theoretical density. Mass spectroscopic analysis of the sintered specimens, given in Table I, showed less than 75 ppm of total metallic impurities and less than 15 ppm of nonmetallic impurities.

Thermoelectric power and total electrical conductivity measurements were made simultaneously on two specimens at temperatures between 1000° and 1600°C in oxygen partial pressures of 1 to 10^{-22} atm. These oxygen pressures were established by mixtures of oxygen-argon, CO_2-CO, or H_2O-H_2. The construction of the sample holder is shown in Fig. 1.

Table I. Spark-source mass and optical emission spectrographic analyses of *thoria*

Element	Concentration in ppm	Element	Concentration in ppm
B	20.0	Cl	1.0
C	<300.0	K	1.0
N	<30.0	Ca	10.0
F	3.0	Ti	6.0
Na	10.0	Cr	1.0
Mg	3.0	Fe	3.0
Al	5.0	Y	2.0
Si	10.0	La	1.0
P	0.2	Ce	1.0
S	10.0	Nd	<3.0

The sample for thermoelectric power measurements was suspended from two Pt/Pt-10% Rh thermocouples,

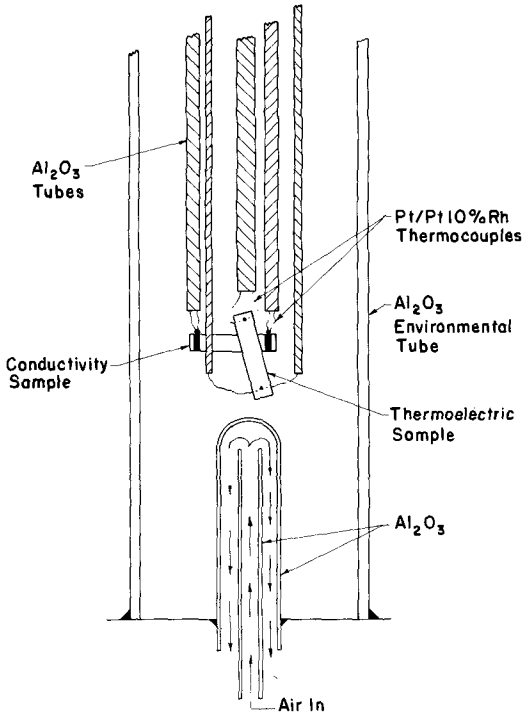

Fig. 1. Sample holder for thermal emf and electrical conductivity measurements.

[1] This study was conducted at Aerospace Research Laboratories, Wright-Patterson Air Force Base, Ohio 45433.
[2] Currently Visiting Scientist at Aerospace Research Laboratories, Wright-Patterson Air Force Base, Ohio 45433.
Key words: Seebeck coefficient, electrical conductivity, defect structure.

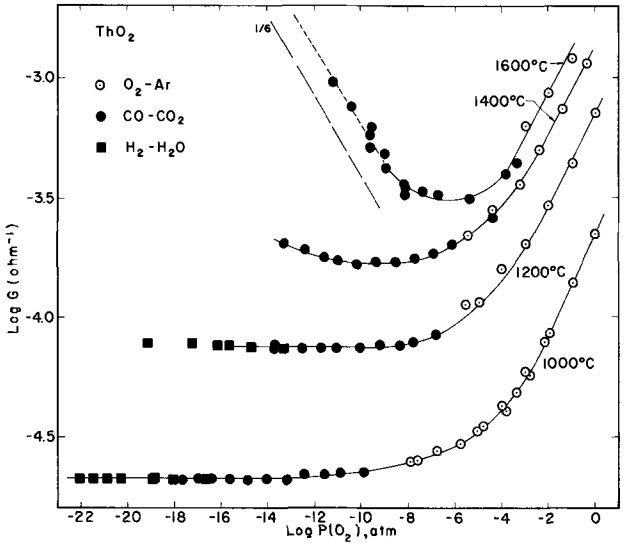

Fig. 2. Total conductance of ThO_2 as a function of oxygen partial pressure.

whose junctions were either embedded in small conical holes drilled through the ends of the bar-shaped sample or simply wrapped around the specimen ends. A cold finger immediately below the sample was used to impose various temperature gradients on the specimen. The gradients used did not exceed 10°C. Using a Fluke differential voltmeter and the platinum leads of the thermocouples, the thermal emfs at constant oxygen pressure and furnace temperature were measured as a function of the temperature gradient imposed. The Seebeck coefficient, $\alpha = |dE/dT|$, was calculated by a least squares analysis of about fifteen measured values of the thermal emf at various temperature gradients. The sign of the Seebeck coefficient was determined from the polarity of the cold end of the specimen, *i.e.*, from the relation $\alpha = (V_c - V_h)/(T_h - T_c)$ where the subscripts h and c denote the hot and cold ends respectively. Using this definition, the sign of α is consistent with the sign of the charge carrier.[3] The absolute Seebeck coefficient of ThO_2 was obtained by correcting the measured coefficient relative to platinum for the platinum contribution (14).

Platinum contacts were applied to the ends of the electrical conductivity sample with Engelhard platinum paste (No. 6082). At low oxygen pressures (in CO_2-CO and H_2O-H_2 mixtures) and high temperatures, particularly above 1400°C, the platinum wires supporting the relatively heavy ThO_2 specimens failed rapidly, apparently because of grain growth and boundary sliding. Two-terminal electrical conductivity measurements were made with a Wayne Kerr Type B601 radio frequency bridge. All of these measurements were made at 100 kHz after initial measurements showed no frequency dependence from 0.1 to 100 kHz and good agreement between a-c and d-c values.

Results

The results of the measurements of total electrical conductivity as a function of oxygen partial pressure at several fixed temperatures between 1000° and 1600°C are shown in Fig. 2. Three regions, characteristic of three different conduction mechanisms or charge carriers, are observed.

A region of pressure independent electrical conductivity is found at intermediate oxygen partial pressures at temperatures below about 1200°C. The galvanic cell measurements of Lasker and Rapp (10) showed that the ionic transference number in this region is essentially unity. It is clear in Fig. 2 that the decrease in width of this ionic conduction region with increasing temperature is caused by the rapid increase in n-type electronic conduction with increasing temperature

At high oxygen partial pressures, above about 10^{-3} atm, the conductivity appears to have a simple pressure dependence, of the form $\sigma \propto P(O_2)^{1/5}$. Simultaneous thermoelectric power measurements in this high oxygen partial pressure region showed that the electronic charge carriers involved are electron holes.

At high temperatures and low oxygen partial pressures ($T \geq 1400$°C and $P(O_2) \leq 10^{-10}$ atm), an n-type electronic conduction region was observed with $\sigma \propto P(O_2)^{-1/x}$ where x appears, from the very limited data available, to be about 6. The rapid increase in n-type electronic conduction with temperature would correspond to an activation energy of at least 3 eV for the defect formation process giving rise to the electrons.

The results of the measurements of the Seebeck coefficient of thoria in argon-oxygen, CO_2-CO, and H_2O-H_2 mixtures at 1000° and 1200°C are shown as a function of oxygen pressure in Fig. 3 and 4 respectively.

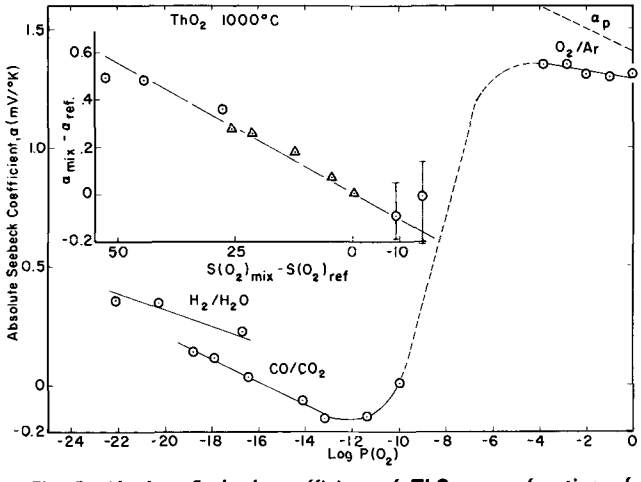

Fig. 3. Absolute Seebeck coefficient of ThO_2 as a function of oxygen partial pressure in several different gas mixtures at 1000°C. The inset is a plot of change in Seebeck coefficient with change in partial molar entropy of oxygen in the gas phase, relative to an arbitrary reference value. The dashed line, α_p, is the calculated electron hole Seebeck coefficient.

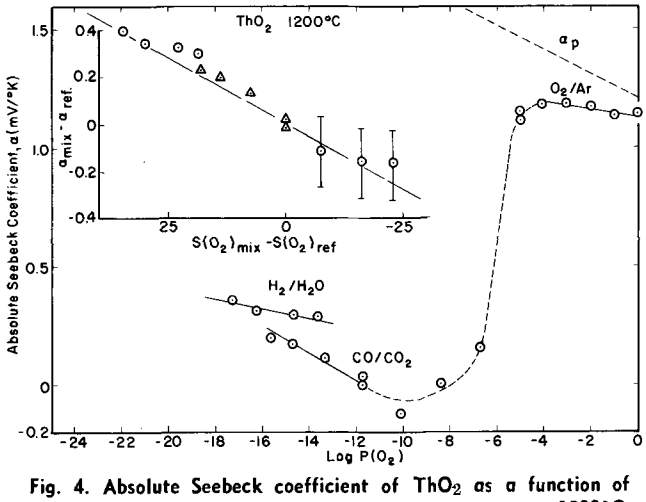

Fig. 4. Absolute Seebeck coefficient of ThO_2 as a function of oxygen partial pressure in several different gas mixtures at 1200°C. The inset is a plot of change in Seebeck coefficient with change in partial molar entropy of oxygen in the gas phase, relative to an arbitrary reference value. The dashed line, α_p, is the calculated electron hole Seebeck coefficient.

[3] This is always true for a pure electronic conductor. For a pure ionic conductor, only the homogeneous part of the Seebeck coefficient has a sign characteristic of the sign of the charge carrier. The homogenous and heterogeneous parts of the ionic Seebeck coefficient will be developed in a later section of the paper.

Discussion

The increased conduction at high oxygen partial pressures, shown in Fig. 2, is due to a transition from the purely ionic conduction observed at intermediate pressures to a predominance of p-type electronic conduction at 1 atm[10]. The apparent 1/5 dependence of the total conductivity on oxygen pressure is within the expected transition between the pressure independence of the purely ionic conduction region and a 1/4 dependence which would be expected for purely electronic conduction if the electron holes arise by either

$$O_2 \rightleftharpoons V_M'''' + 4h^\bullet \quad [1]$$

or

$$\tfrac{1}{2}O_2 \rightleftharpoons O_i'' + 2h^\bullet \quad [2]$$

with the ionic defect concentrations fixed (either intrinsically or by the presence of an impurity). The notation used and the development of the pressure dependence through the use of mass action and electroneutrality equations are described by Kröger and Vink (15). The symbol describes the defect, the subscript gives its position, the superscript gives its effective charge state (a prime representing a negative charge and a dot a positive one), and $h^\bullet$ represents an electron hole. This defect model involving a transition from ion to electron hole conduction within a region of constant ionic defect concentration was proposed by Lasker and Rapp (10). A detailed quantitative treatment of the conductivity behavior expected for this defect model and a fit of their experimental data to it has been given by Bransky and Tallan (16).

The 1/5 and 1/6 pressure dependences characteristic of Reactions [1] and [2], when the ionic defect concentrations involved are not constant, would be observed only at oxygen pressures much higher than those experimentally accessible. The nature of the predominant ionic defect in the ionic conduction region cannot, therefore, be stated with any certainty. However, based on geometrical considerations, it has frequently been suggested (10) that oxygen interstitials are the predominant ionic defect. For convenience, this assumption will be used throughout the remainder of this paper, since the essential features to be discussed do not depend on the nature of the ionic charge carrier assumed to be present.

The total Seebeck coefficient of a mixed ionic-electric conductor is given by the expression

$$\alpha_T = t_p \alpha_p + t_i \alpha_i \quad [3]$$

where α_T is the measured total Seebeck coefficient, α_p and α_i are the electron hole and ionic Seebeck coefficients, t_p is the electron hole transference number given by $\sigma(\text{hole})/\sigma(\text{total})$, and t_i is the ionic transference number given by $\sigma(\text{ionic})/\sigma(\text{total})$. Equation [3] and the specific forms of α_p and α_i for a given defect model can be derived for the cell

$$O_2(\text{gas}), \text{Pt} \;\overset{T}{||}\; ThO_2 \;\overset{T+\Delta T}{||}\; \text{Pt}, O_2(\text{gas}) \quad [4]$$

in a number of ways. The procedure that will be followed here is that used by Kröger (17) for a number of other materials and defect models. Three individual thermal potentials contribute to the over-all thermal potential measured; a homogeneous potential difference $\Delta\phi_{hom}$ due to the temperature gradient across the specimen, a heterogeneous potential $\Delta\phi_{het}$ due to the difference in contact potentials at the two electrode-specimen interfaces (which are at different temperatures because of the imposed temperature gradient), and the homogeneous potential differences $\Delta\phi_M$ due to the temperature gradients in the metal lead wires. When platinum is used for the leads, the potentials $\Delta\phi_M$ are very small (14) and will be neglected in the following discussion (the measured Seebeck coefficients reported here, however, have been corrected for the contribution of α_{Pt}). The over-all Seebeck coefficient of the cell is, therefore

$$\alpha_T = -\frac{\Delta\phi}{\Delta T} = -\frac{\Delta\phi_{hom}}{\Delta T} - \frac{\Delta\phi_{het}}{\Delta T} = \alpha_{hom} + \alpha_{het} \quad [5]$$

The specific case which will be treated here is that of an oxide with composition MO_2 having a defect structure dominated by a constant concentration of ionized defects introduced by impurities. Since as discussed earlier we do not know the true identity of the ionic charge carriers, we will assume here that they are fully ionized oxygen interstitials. The effect of alternate selections of the defect on the expression to be derived will be discussed later. We derive first the short-time homogeneous part of the ionic Seebeck coefficient, which is obtained from the potential across the oxide at times such that there is still no impurity concentration gradient, but the steady-state condition

$$2j(O_i'') = j(h^\bullet) \quad [6]$$

is fulfilled. The oxygen interstitial current, $j(O_i'')$, and the hole current, $j(h^\bullet)$, are given by

$$j(O_i'') = D(O_i'')\left\{ -\frac{\partial[O_i'']}{\partial x} + \frac{2q}{kT}[O_i'']\frac{\partial\phi}{\partial x} - \frac{Q(O_i'')}{kT^2}[O_i'']\frac{\partial T}{\partial x}\right\} \quad [7]$$

and

$$j(h^\bullet) = D(h^\bullet)\left\{ -\frac{\partial p}{\partial x} - \frac{q}{kT}p\frac{\partial\phi}{\partial x} - \frac{Q(h^\bullet)}{kT^2}p\frac{\partial T}{\partial x}\right\} \quad [8]$$

where $D(i)$ and $Q(i)$ are the diffusion coefficient and heat of transport of the *i'th* species. Since, in the present case, the total concentration of oxygen interstitials is assumed to be constant, fixed by the impurities, the concentration gradient of free oxygen interstitials appearing in the first term of Eq. [7] is obtained from the temperature dependence of the degree of association of interstitials and impurities given by

$$[(F_MO_i')] = \text{const}\,[O_i'']^2 \exp\left(\frac{\Delta H_p}{kT}\right) = [F_M]_T - 2[O_i''] \quad [9]$$

where $[F_M]_T$ is the total impurity content and ΔH_p is the enthalpy change for the association reaction

$$F_M^\bullet + O_i'' \rightleftharpoons (F_MO_i') \quad [10]$$

Accordingly

$$\frac{\partial[O_i'']}{\partial x} = \frac{\beta}{1+\beta}[O_i'']\frac{\Delta H_p}{kT^2}\frac{\partial T}{\partial x} \quad [11]$$

where β, the degree of association, is defined by

$$\beta \equiv \frac{[(F_MO_i')]}{[F_M]_T} \quad [12]$$

The hole gradient, appearing in the first term of Eq. [8], is obtained by applying the law of mass action to the defect formation reaction

$$\tfrac{1}{2}O_2 \rightleftharpoons O_i'' + 2h^\bullet \quad [13]$$

so that

$$p = \text{const}\,[O_i'']^{-1/2} P(O_2)^{1/4} \exp\left(-\frac{\Delta H_{ox}}{2kT}\right) \quad [14]$$

and

$$\frac{\partial p}{\partial x} = \frac{p}{2kT^2}\left\{\Delta H_{ox} - \frac{\beta}{1+\beta}\Delta H_p\right\}\frac{\partial T}{\partial x} \quad [15]$$

where $P(O_2)$ is the oxygen partial pressure and ΔH_{ox} is the enthalpy change for Reaction [13]. Combining Eq. [6-8], [11] and [15] and solving for $\partial\phi/\partial T$, we obtain for the homogeneous part of the Seebeck coefficient of the impurity controlled mixed conductor

$$\alpha_{hom} = -\frac{\partial\phi}{\partial T} = \frac{1}{qT}\left[t_p \left\{ \frac{\Delta H_{ox}}{2} + Q(h^{\cdot}) - \tfrac{1}{2}\frac{\beta}{1+\beta}\Delta H_p \right\} - t_i \left\{ \tfrac{1}{2}Q(O_i'') + \tfrac{1}{2}\frac{\beta}{1+\beta}\Delta H_p \right\} \right] \quad [16]$$

To obtain the heterogeneous part of the Seebeck coefficient applicable to this case, we consider the transfer reactions for oxygen between the gaseous oxygen electrode and the ThO_2

$$\tfrac{1}{2}O_2(g) + 2e^- \text{ (Pt)} \rightleftharpoons O^=\text{(elect)}$$
$$O^=\text{(elect)} \rightleftharpoons O_i'' \text{ (ThO}_2\text{)} \quad [17]$$

Equating the electrochemical potentials of the species involved in the over-all transfer reaction, the contact potential can be written

$$2q\,\Delta\phi_{Pt,\,ThO_2} = \tfrac{1}{2}\mu(O_2)_g + 2\mu(e^-)_{Pt} - \mu(O_i'')_{ThO_2} \quad [18]$$

where $\mu(i)$ is the chemical potential of the *i'th* species. The heterogeneous part of the Seebeck coefficient is given by

$$\alpha_{het} = -\frac{\Delta\phi_{het}}{\Delta T} = -\frac{1}{q}\left[\tfrac{1}{2}S(O_i'')_{ThO_2} - \tfrac{1}{4}S(O_2)_g - S(e^-)_{Pt}\right] \quad [19]$$

Since $Q(i)/T = S^*(i) - S(i)$, where $S^*(i)$ and $S(i)$ represent the transport and partial molar entropies respectively of the *i'th* species, Eq. [16] and [19] can be combined to obtain the total Seebeck coefficient. In the region of pure ionic conduction, where $t_i = 1$, the Seebeck coefficient for this defect model would be given by

$$\alpha_i = -\frac{1}{q}\left[\tfrac{1}{2}S^*(O_i'') - \tfrac{1}{4}S(O_2)_g - S(e^-)_{Pt} + \tfrac{1}{2}\frac{\beta}{1+\beta}\frac{\Delta H_p}{T}\right] \quad [20]$$

If α_i had been derived on the basis of a fully ionized metal vacancy model, it would have essentially the same form as Eq. [20], but would be given by

$$\alpha_i = -\frac{1}{q}\left[\tfrac{1}{4}S^*(V_M'''') - \tfrac{1}{4}S(O_2)_g - S(e^-)_{Pt} + S(O_o^x) + \tfrac{1}{4}\frac{\beta}{1+\beta}\frac{\Delta H_p}{T}\right] \quad [21]$$

where the partial molar entropy of oxygen on oxygen lattice sites is introduced because of the over-all transfer reaction

$$\tfrac{1}{2}O_2(g) + 2e^- \text{ (Pt)} \rightleftharpoons O_o^x + \tfrac{1}{2}V_M'''' \quad [22]$$

The form of α_p can be obtained easily by expressing the heterogeneous part of the Seebeck coefficient in somewhat different terms. If we consider the transfer of electrons between the electrode and the ThO_2 and make use of Eq. [15] for $\partial p/\partial T$, it can be shown that

$$\alpha_{het} \simeq \frac{1}{qT}\left[kT\ln\frac{N_v}{p} - \frac{\Delta H_{ox}}{2} + \tfrac{1}{2}\frac{\beta}{1+\beta}\Delta H_p\right] \quad [23]$$

where N_v is the density of states for electron holes. In the region of pure electronic conduction, where $t_p = 1$, the Seebeck coefficient for this defect model would be found by combining Eq. [16] and [23], to obtain

$$\alpha_p = \frac{k}{q}\left[\ln\frac{N_v}{p} + \frac{Q(h^{\cdot})}{kT}\right] \quad [24]$$

Although thermodynamic data are available for the calculation of $S(O_2)$ in the gas phase, the absolute Seebeck coefficient in the ionic region cannot be calculated from Eq. [20] or [21] without calculated or experimental values of the transport and partial molar entropies of the defects in the metal oxide and ΔH_p. However, as indicated by Ruka *et al.* (7), the Seebeck coefficient difference for two different gas mixtures can be calculated for a range of oxygen pressures over which all terms on the right of Eq. [20] or [21], except $S(O_2)$ in the gas phase, are either essentially constant or negligible. Under these conditions, Eq. [20] and [21] simplify to

$$(\alpha_i)_{gas\ 1} - (\alpha_i)_{gas\ 2} = \frac{1}{4\mathbf{F}}\left[S(O_2)_{gas\ 1} - S(O_2)_{gas\ 2}\right] \quad [25]$$

where **F** is the Faraday constant. Experimentally, it is convenient to choose the Seebeck coefficient at some gas mixture within the purely ionic conduction region as a reference value so that

$$(\alpha_i)_{gas\ 1} - (\alpha_i)_{ref} = \frac{1}{4\mathbf{F}}\left[S(O_2)_{gas\ 1} - S(O_2)_{ref}\right] \quad [26]$$

The calculation of molar entropies of oxygen in the gas phase is reviewed in the Appendix.

It may be noted from Eq. [26] that the change in ionic Seebeck coefficient is a unique function of the change in entropy of oxygen in the gas phase, not the change in oxygen partial pressure. Precisely this behavior was observed for ThO_2 in oxygen-argon, CO_2-CO, and H_2O-H_2 mixtures at 1000° and 1200°C, as shown in Fig. 3 and 4. The discontinuities in magnitude and slope between segments of the α_i *vs.* $P(O_2)$ plots obtained in different gas mixtures are absent in the α_i *vs.* $\Delta S(O_2)$ plots, which are linear with the anticipated $1/(4\mathbf{F})$ slope

Calculated values of α_i in the mixed conduction region, where $0 < t_p < 1$, are also included in the $\Delta\alpha$ *vs.* $\Delta S(O_2)$ plots of Fig. 3 and 4, along with their probable error limits. These values were satisfactorily calculated from Eq. [3] using values of the transference numbers calculated from Fig. 2, the measured values of α_T, and extrapolated values of α_p. The agreement of the $\Delta\alpha_i$ *vs.* $\Delta S(O_2)$ plot with Eq. [26] over a wide range of oxygen partial pressures indicates the validity of the assumptions made in the derivation of that equation for this case of nominally pure ThO_2.

Using the measured values for the magnitude of α_i, shown in Fig. 3, reported values of $S(O_2)_g$ (19) and $S(e^-)_{Pt}$ (14), and assuming $\beta\Delta H_p/T$ very small in Eq. [20], values for the transport entropy of oxygen interstitials can be calculated. The value found, $S^*(O_i'') = 14.5 \pm 0.5$ eu, at 1000°C over the whole range of oxygen pressures from 10^{-13} to 10^{-23} atm may be compared to the value of 10.3 to 10.9 eu found for $S^*(V_o'')$ in stabilized zirconia by Ruka *et al.* (7). Because of the small magnitude of α_i, evident in Fig. 3 and 4, it was not possible to obtain a good measured value for its temperature dependence and, therefore, it was not possible to obtain the temperature dependence of $S^*(O_i'')$ from the derivative of Eq. [20].

Thus, the Seebeck coefficient of the ThO_2 used in this study displays the behavior anticipated for a mixed ionic-electronic conductor with a fixed concentration of ionic defects. However, to extract thermodynamic values for the enthalpies of formation and heats of motion of the defects, one would have to have a ThO_2 specimen of sufficient purity that the intrinsic defect behavior can be observed.

APPENDIX

The molar entropy of oxygen in the gas mixture, $S(O_2)_g$, is calculated thermodynamically. Assuming the reaction

$$X + \tfrac{1}{2}O_2 \rightleftharpoons XO$$

where X can be CO or H_2 and XO would then be CO_2 or H_2O, then summing chemical potentials at equilibrium

$$\mu(XO) - \mu(X) - \tfrac{1}{2}\mu(O_2) = O$$

Over a range of gas mixtures where

$$\mu(a) - \mu^\circ(a) - RT \ln P(a)$$

where $P(a)$ is the partial pressure of gas "a" in the mixture

$$S(O_2)_g = -\frac{\partial \mu(O_2)}{\partial T}$$

$$= 2\left[S^\circ(XO) - S^\circ(X) - R \ln \frac{P(XO)}{P(X)}\right]$$

For a mechanical mixture of oxygen in an inert gas, one has simply

$$S(O_2)_g = S^\circ(O_2) - R \ln P(O_2)$$

Acknowledgment

The authors are indebted to Mr. William Leisler for his assistance in the experimental measurements involved in this study.

Manuscript submitted March 2, 1970; revised manuscript received *ca.* Sept. 15, 1970.

Any discussion of this paper will appear in a Discussion Section to be published in the December 1971 JOURNAL.

REFERENCES

1. R. E. Howard and A. B. Lidiard, *Discussions Faraday Soc.*, **23**, 113 (1957).
2. R. W. Howard and A. B. Lidiard, *Rept. Progr. Phys.*, **27**, 161 (1964).
3. R. W. Christy, Y. W. Hsueh, and R. C. Mueller, *J. Chem. Phys.*, **38**, 1647 (1963).
4. A. R. Allnatt and P. W. M. Jacobs, *Proc. Royal Soc. (London)*, **A267**, 31 (1962).
5. P. W. M. Jacobs and J. N. Maycock, *Trans. AIME*, **236**, 165 (1966).
6. H. Hoshino and M. Shimoji, *J. Phys. Chem. Solids*, **28**, 1169 (1967).
7. R. J. Ruka, J. W. Bauerle, and L. Dykstra, *This Journal*, **115**, 497 (1968).
8. W. Fischer, *Z. Naturforschg*, **22a**, 1575 (1967).
9. K. Goto, T. Ito, and M. Someno, *Trans. AIME*, **245**, 1662 (1969).
10. M. K. Lasker and R. A. Rapp, *Z. Physik. Chem. (Frankfurt)*, **49**, 198 (1966).
11. J. E. Bauerle, *J. Chem. Phys.*, **45**, 4162 (1966).
12. J. W. Patterson, E. C. Bogren, and R. A. Rapp, *This Journal*, **114**, 752 (1967).
13. J. W. Patterson, Special Report, *Electronic Conductivity of Undoped Thoria*, Contract F 33615-68-C-1034, Eng. Res. Inst., Iowa State University.
14. R. R. Heikes and R. W. Ure, "Thermoelectricity," Interscience Publishers, New York (1961).
15. F. A. Kröger and H. J. Vink, in *Solid State Physics*, F. Seitz and D. Turnbull, Editors, Vol. 3, pp. 307-435, Academic Press, New York (1956).
16. I. Bransky and N. M. Tallan, *J. Am. Ceram. Soc.*, **53**, 625 (1970).
17. F. A. Kröger, "The Chemistry of Imperfect Crystals," pp. 938-940, John Wiley & Sons, Inc., New York (1964).
18. A. R. Allnatt and P. W. M. Jacobs, *Proc. Royal Soc. (London)*, **A260**, 350 (1961).
19. C. E. Wicks and F. E. Block, "Thermodynamic Properties of 65 Elements-Their Oxides, Halides, Carbides and Nitrides," Bulletin 605, Bureau of Mines, Washington, D. C. (1963).

Technical Notes

The Effect of Water on the Dielectric Constant of Vapor Deposited Silica Films

T. O. Sedgwick* and S. Krongelb

IBM Thomas J. Watson Research Center, Yorktown Heights, New York 10598

While making capacitance *vs.* voltage measurements below room temperature on MOS structures fabricated with chemically vapor deposited SiO_2 on Ge, we found a marked decrease in the capacitance with decreasing temperature for some of the SiO_2 films. The temperature sensitivity of the dielectric constant was found to be dependent on the oxide deposition conditions and subsequent annealing treatments, and was shown to be related to the water content of the film. The temperature dependence of the capacitance proved to be a conveniently measured, nondestructive indicator of the water content in SiO_2 films on completed devices, and was used to demonstrate the reaction between water in the film and Al metallization.

Experimental

The oxide films were vapor deposited by the pyrolysis of tetraethylorthosilicate in oxygen at 432°C (1) (designated LT SiO_2) or in forming gas at 735°C (2) (designated HT SiO_2). Films 1500-2000Å thick were deposited on Ge wafers for electrical measurements or on doubly polished Si wafers for IR measurements. Where densification (DENS) is indicated, the samples were subjected to 800°C in forming gas for 17 min;[1] where temperature-humidity stressing (T&H) is cited, the films were exposed to 85% relative humidity at 85°C for 4 days. The MOS structures were completed by the evaporation of approximately 30 mils diam, 5000Å thick Au or Al dots through metal masks. Samples were stored in dessicators with "Drierite" between fabrication steps and measurements.

The capacitance of the devices was measured at 150 kHz under a d-c bias sufficient to accumulate strongly the Ge surface (4). Where it was desired to know the actual dielectric constant, the oxide thickness was measured by interferometry, and the dot size was measured with a Nikon shadowgraph. The IR optical density of the films was measured at 3400 cm^{-1} for H_2O and 3650 cm^{-1} for the SiOH absorptions (3).

Results and Discussion

Figure 1 shows the temperature dependence of the capacitance by plotting the ratio $C_{T°K}/C_{300°K}$ *vs.* tem-

* Electrochemical Society Active Member.

Key words: temperature dependence, anneal, MOS devices.

[1] Pliskin (3) has shown that densification in steam is more effective than treatment in a dry atmosphere; however, the high reactivity of Ge with water at elevated temperatures precluded the use of a wet densification process.

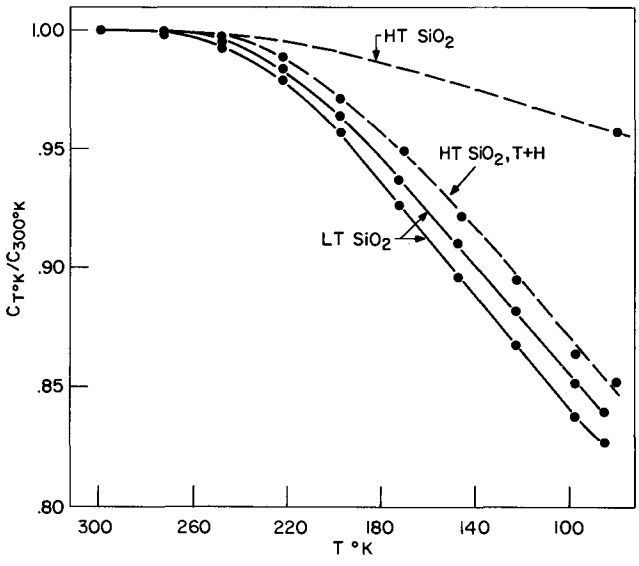

Fig. 1. Capacitance ratio, $C_{T°K}/C_{300°K}$ as a function of temperature for several SiO_2 films.

perature. We note that the capacitance of HT SiO_2 which was subject to T&H and the capacitance of LT SiO_2 exhibit a similar dependence on temperature, and that both of these films are much more sensitive to temperature than HT SiO_2 which was not subject to T&H. This behavior suggests that water or some polar reaction product of H_2O and SiO_2 whose dielectric relaxation motion is frozen out at low temperatures accounts for the low value of $C_{T°K}/C_{300°K}$. It would appear that H_2O is not present in the free state in the oxide films, since the capacitance did not exhibit a discontinuity at 0°C which could be associated with the freezing of an aqueous phase.

The above picture is supported by the data in Fig. 2 which show that the decrease in $C_{77°K}/C_{300°K}$ for various films correlates with an increase in the H_2O and OH content of corresponding films as measured by IR absorption. (The ratio of the capacitance at 77°K to that at 300°K is a convenient over-all indication of the temperature sensitivity of the dielectric constant and is the parameter used in subsequent discussion). The optical density per micron measured at 3400 cm^{-1} is used as an indicator of the H_2O content; a similar measurement at 3650 cm^{-1} represents the OH content.

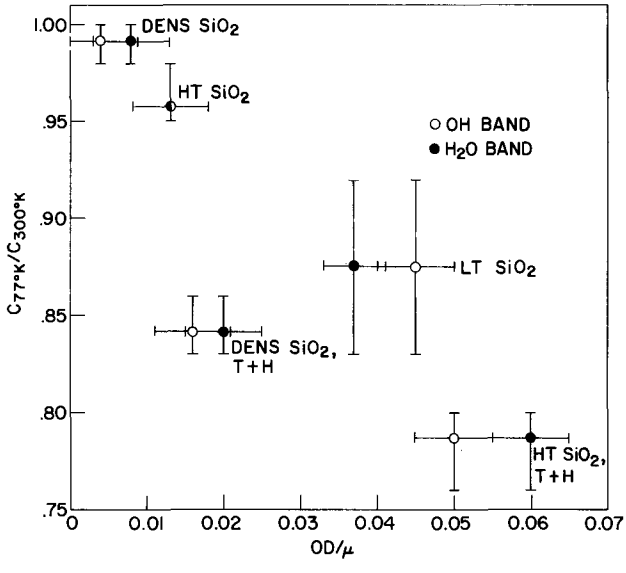

Fig. 2. Capacitance ratio, $C_{77°K}/C_{300°K}$, as a function of optical density per micron, O.D./μ, of H_2O (●) and SiOH (○) absorption maxima for various SiO_2 films.

Actually, there is some overlap of these bands, especially at the higher H_2O and OH levels, so there is considerable uncertainty in these measurements. Nevertheless, the general correlation between $C_{77°K}/C_{300°K}$ and the IR measurements is visually apparent for all but the DENS SiO_2, T&H samples. We can suggest no explanation for this one exception.

Figure 3 shows that the measured dielectric constant at room temperature for films, prepared in a variety of ways, approaches the value of 3.8-3.9 expected for pure SiO_2 as $C_{77°K}/C_{300°K}$ approaches 1.00. This finding is consistent with the hypothesis that water in the film is responsible for the decrease of $C_{77°K}/C_{300°K}$ from unity, since the addition of water to SiO_2 can increase the dielectric constant (5).

Several interesting features become apparent when we observe how the temperature sensitivity of the dielectric constant is affected by various annealing treatments as shown in Fig. 4. If we densify either LT SiO_2 or HT SiO_2, the capacitance ratio is increased to about 0.99 for both films. Previous work (3, 6) has shown that a densified film contains less water and is generally superior to ordinary HT SiO_2 which in turn is drier and superior to LT SiO_2. This grading of films is reflected in the ratio of $C_{77°K}/C_{300°K}$. Exposure of either the densified or undensified films to T&H (dotted lines) causes a marked decrease in $C_{77°K}/C_{300°K}$ indicating the pickup of water as discussed above.

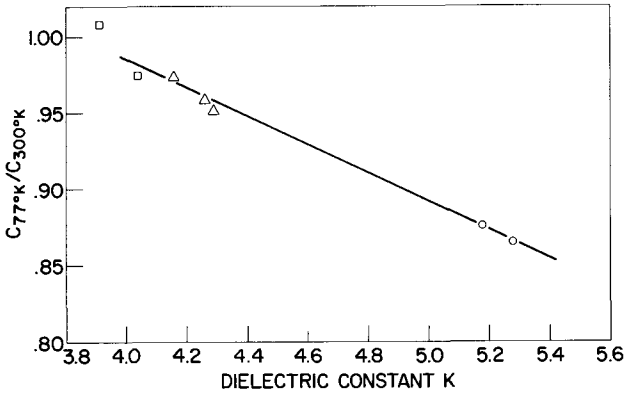

Fig. 3. Capacitance ratio, $C_{77°K}/C_{300°K}$ vs. dielectric constant for various SiO_2 films; □ DENS, △ HT, ○ LT SiO_2.

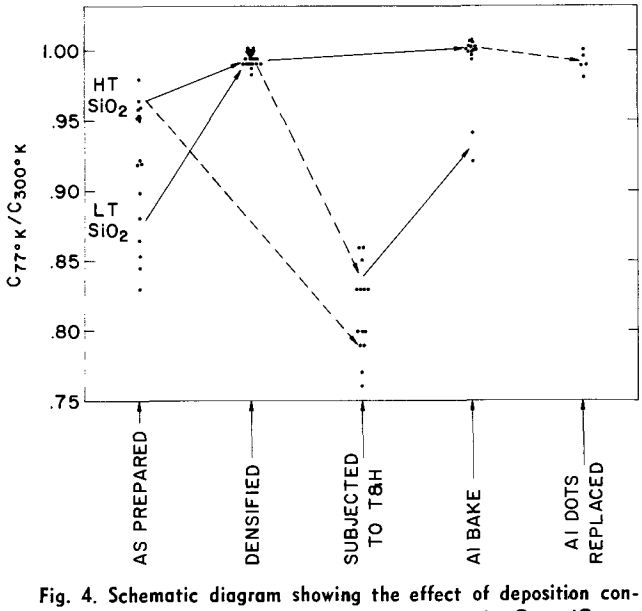

Fig. 4. Schematic diagram showing the effect of deposition conditions and annealing processes on capacitance ratio, $C_{77°K}/C_{300°K}$ for SiO_2 films (the terms LT SiO_2, T&H, Al BAKE, etc., are defined in text).

A particularly interesting point is the effect of annealing the completed devices, *i.e.*, with Al metallization in place, at 230°C in air for from 2 to 60 hr (referred to as Al BAKE). This treatment brings the $C_{77°K}/C_{300°K}$ ratio to 1.000 ± 0.003, which is as close to unity as we can measure. The reduction of the temperature sensitivity is attributed to the removal of water or of the water-SiO_2 reaction product and is demonstrated even more clearly in the case where the oxide has previously been exposed to T&H. The Al presumably reacts with the water or water-SiO_2 reaction product to form Al_2O_3 and some form of hydrogen. This picture is supported by the fact that in a similar experiment (not shown in Fig. 4) on HT SiO_2 in which gold, a nonreactive metal, was used in place of Al, there was no change in $C_{77°K}/C_{300°K}$. Since previously Hu and Young (7) and Burkhardt (8) have found no reaction between Al and thermal SiO_2 below 400°C we believe that the present results associated with Al BAKE are totally attributable to an Al-H_2O reaction.

If the Al is removed by wet chemical etching after the Al bake and a fresh Al metallization is applied, the $C_{77°K}/C_{300°K}$ ratio reverts to the pre-Al BAKE value of 0.99 (see Al REMOVE in Fig. 4). It is, therefore, thought that the last 1% difference is due directly or indirectly to H_2O retained in just the surface layers of the SiO_2.

It is interesting to note that Balk (9), Deal *et al.* (10), and Sedgwick and Krongelb (11) have all postulated that Al reacts with residual H_2O in SiO_2 to produce atomic hydrogen. The atomic hydrogen is thought to be responsible for the removal of surface states on Si surfaces or for the induced effective negative charge on Ge surfaces. The present work supports this hypothesis by showing that under certain conditions Al does interact with SiO_2 films resulting in a decrease in temperature sensitivity of the capacitance. This fact is most readily accounted for postulating that the Al reacts to remove some form of H_2O in the SiO_2 films.

The capacitance change with temperature effect reported on above would seem to be a relatively easy nondestructive technique for the determination of H_2O or water produced reaction products in SiO_2 films on completed devices.

Acknowledgments

The authors wish to acknowledge the assistance of Miss B. J. Agule and B. J. Stoeber in obtaining the data on which this work is based.

Manuscript submitted June 19, 1970; revised manuscript received *ca.* Oct. 13, 1970.

Any discussion of this paper will appear in a Discussion Section to be published in the December 1971 JOURNAL.

REFERENCES

1. S. Krongelb, *Electrochem. Technol.*, **6**, 251 (1968).
2. E. L. Jordan, *This Journal*, **108**, 487 (1961).
3. W. A. Pliskin and H. S. Lehman, *ibid.*, **112**, 1013 (1965).
4. T. O. Sedgwick, *J. Appl. Phys.*, **39**, 5066 (1968).
5. A. E. Owen and R. W. Douglas, *J. Soc. Glass Technol.*, **43**, 159T (1959).
6. T. O. Sedgwick, J. A. Aboaf, and S. Krongelb, *IBM J. Res. Develop.*, **14**, 2 (1970).
7. S-M Hu and D. R. Young, Private communication. In this study the resistivity of thin Al films was measured as a function of annealing temperature of Al-SiO_2 structures. No measurable resistivity change attributable to Al reaction was found below 400°C.
8. P. J. Burkhardt, IEEE Trans. of Electron Devices, **ED-13**, 268 (1966).
9. P. Balk, Paper 111 presented at Electrochem. Soc. Meeting, Buffalo, Oct. 10-14, 1965.
10. B. E. Deal, E. L. MacKenna, and P. L. Castro, *This Journal*, **116**, 997 (1969).
11. T. O. Sedgwick and S. Krongelb, *ibid.*, **117**, 1199 (1970).

Magnesium Germanate and Fluorogermanate

E. Kostiner* and P. W. Bless

Baker Laboratory of Chemistry, Cornell University, Ithaca, New York 14850

Manganese-activated magnesium germanate and magnesium fluorogermanate have found wide use as red-emitting phosphors. Since their original discovery (1) and further development (2-5), the activator center has been identified as quadrivalent manganese in an approximately octahedral crystal field (6, 7). Little or no mention has been made in the literature as to the effect of the addition of magnesium fluoride (to form the fluorogermanate) on the fluorescence properties of the manganese activator except for the increase in fluorescence efficiency (5).

The compound "Mg_4GeO_6" (magnesium germanate) has been reported to occur in the magnesium oxide-germanium oxide system as a stable phase up to a temperature of 1495° ± 10°C where it dissociates to form Mg_2GeO_4 (forsterite form) and MgO (8). The powder pattern of magnesium germanate has previously been indexed on the basis of an hexagonal unit cell (a_o = 11.773, c_o = 14.445Å) with several unassignable peaks (9).

We have been successful in growing small single crystals of both the germanate and the fluorogermanate by standard flux growth techniques. This note reports the crystal growth and powder x-ray crystallographic data for these two compounds.

Experimental

The phosphors were prepared using conventional ceramic techniques. Magnesium oxide (Mallinckrodt Analytical Reagent) and germanium oxide (Electronic Grade, Kawecki Chemical Company) in a 4:1 mole ratio with one mole per cent (m/o) manganese carbonate (Fisher Certified Reagent) added as an activator were mixed and ground under acetone to form the germanate. The formulation of the fluorogermanate involves the substitution of one-eighth of the MgO by magnesium fluoride (Crystal Grade, Sylvania Electric Products Company). After removal of the acetone at 110°C the mixtures were fired in platinum crucibles at 1000°C in air for one hour, reground and fired for 16 hr at 1200°C.

A suitable high temperature flux for the growth of the fluoride-free germanate was lead oxide (Fume Litharge, Evans Lead Company). Lead fluoride (Extra Pure Grade, BDH Chemicals Company, Ltd.) was used for the fluorogermanate. Typical crystal growth runs were : 67.5g PbF_2, 6.75g fluorogermanate; 75g PbO, 27g germanate; each in a 50 cc platinum crucible. The charges were held at 1300°C for 4 hr in a silicon car-

* Electrochemical Society Active Member.

Key words: crystal growth, magnesium germanate, magnesium fluorogermanate.

bide resistance-heated furnace, cooled at ~4°/hr to 900°C and then removed from the furnace. To protect the platinum crucibles dry oxygen was passed through the furnace.

The germanate crystals were removed from the flux by leaching with hot dilute hydrochloric acid. Since the fluorogermanate crystals are soluble in acid they had to be separated mechanically or by repeated extraction with water. In all cases, crystals of magnesium oxide were found as a secondary product.

Results

Crystals of both the germanate and the fluorogermanate are lathe-shaped with typical dimensions 1 x 2 x 0.2 mm. Occasionally, needle crystals grew out of the flux. Macroscopic twinning was quite common with a twin angle of 59-60°. The experimental densities (pycnometric) are both 3.98(4) g/cc.

The compounds are isostructural. Single crystal precession and Weissenberg photographs indicate *mmm* (orthorhombic) symmetry. The complete three-dimensional crystal structure of the unsubstituted germanate has been completed (10). This x-ray diffraction study, along with careful analytical results, establish the true stoichiometry to be $Mg_{3.5}Ge_{1.25}O_6$ rather than Mg_4GeO_6. Indeed, careful powder x-ray diffraction photographs (focusing Guinier camera) of a fully sintered ceramic mixture of composition $4MgO \cdot GeO_2$ show additional lines assignable to MgO.

The indexed powder patterns of ground single crystals (x-ray diffractometry and Guinier photographs, Cu Kα radiation) are given in Table I. Indexing was only carried out to a d-spacing of 1.56 since by that point an orthorhombic cell of this size gives a continuum of possible index assignments. Powder line assignments were made with the aid of the single crystal photographs.

Table I.

Magnesium germanate

a_o = 14.515(4) A
b_o = 10.214(4)
c_o = 5.939(6)

d	I	hkl	$\sin^2\theta$ (×10⁴) obs.	calc.
5.933	13	001	168.6	168.2
		210		169.4
5.139	11	020	224.6	227.5
4.829	15	120	255.6	255.5
4.604	15	201	279.8	280.8
4.371	30	310	310.6	310.3
4.187	6	220	338.4	340.1
		211		337.7
3.868	67	021	396.5	395.7
3.748	11	121	422.4	423.8
3.525	8	311	477.4	478.5
3.420	4	410	507.2	507.4
		221		508.3
3.092	17	401	620.6	618.8
2.974	36	002	670.7	672.8
2.897	11	131	707.7	708.2
2.802	19	112	755.6	757.8
2.740	13	231	790.1	792.7
2.656	15	212	840.7	842.3
2.572	13	022	896.7	900.3
2.554	2	040	909.3	909.9
2.523	100	331	932.0	933.5
2.458	45	312	981.8	983.1
2.423	4	222	1010.5	1012.9
2.350	11	041	1074.5	1078.1
2.317	2	141	1105.5	1105.3
2.269	21	322	1152.4	1153.7
2.2435	4	412	1178.8	1180.2
2.2092	11	530	1215.6	1215.8
2.1877	1	611	1239.7	1238.8
2.1119	17	341	1330.2	1331.6
2.0970	28	422	1349.2	1350.9
1.9709	2	441	1527.3	1528.7
1.9216	11	720	1606.6	1607.3
1.8797	4	350	1679.1	1675.2
1.8457	1	023	1741.5	1741.3
1.8283	1	721	1774.7	1775.5
1.7723	6	532	1888.8	1888.6
1.7564	1	640	1923.1	1923.7
1.7357	2	801	1969.4	1970.5
1.7086	4	442	2032.2	2033.3
1.6819	1	641	2097.2	2091.9
1.6439	2	423	2195.4	2191.9
1.6260	2	161	2244.0	2243.7
1.6129	13	333	2280.5	2279.1
		722		2280.1
1.5632	1	043	2427.8	2423.7

Magnesium fluorogermanate

a_o = 14.335(4) A
b_o = 10.203(4)
c_o = 5.929(6)

d	I	hkl	$\sin^2\theta$ (×10⁴) obs.	calc.
7.195	7	200	114.6	115.5
5.976	10	001	166.1	168.8
5.110	28	020	227.2	227.9
4.815	20	120	255.9	256.8
4.560	20	201	285.3	284.2
4.127	32	310	316.9	316.8
3.981	10	220	341.9	343.4
3.865	67	021	397.1	396.7
3.739	17	121	424.5	425.6
3.487	13	320	487.7	487.8
3.39	7	221	514.1	512.2
3.063	23	401	632.4	630.7
2.966	17	002	674.2	675.0
2.936	17	420	688.3	689.9
		411		687.7
2.890	13	131	710.6	710.5
2.792	23	112	761.1	760.9
2.761	3	510	778.4	778.8
2.628	20	421	859.2	858.7
2.563	23	022	903.2	902.9
2.505	100	331	945.7	941.5
		511		947.6
2.4680	3	430	974.0	974.8
2.4460	50	312	991.6	991.8
2.4142	10	222	1017.9	1018.4
2.4037	1	240	1026.9	1027.3
2.3439	13	041	1079.9	1080.5
2.2855	13	402	1135.8	1137.0
2.2596	27	322	1161.9	1162.8
2.2291	7	412	1194.0	1194.0
2.1933	17	530	1233.3	1234.7
2.1367	17	232	1299.5	1303.4
2.0841	37	422	1365.9	1364.9
2.0553	1	531	1404.5	1403.5
2.0238	3	332	1448.5	1447.7
1.9632	7	441	1539.3	1542.5
1.9348	1	042	1584.9	1586.8
1.9083	20	522	1629.1	1624.8
		540		1633.6
1.8941	1	432	1653.7	1649.8
1.8768	10	350	1684.3	1684.5
1.8634	1	251	1708.5	1708.9
1.8444	3	023	1744.1	1746.7
1.7977	1	313	1835.8	1835.6
1.7872	1	223	1857.5	1862.2
		351		1852.2
1.7618	10	532	1911.4	1909.7
1.7461	1	640	1945.8	1951.2
1.7296	3	403	1983.3	1980.7
1.7131	1	801	2021.7	2016.6
1.6992	13	451	2054.7	2055.4
1.6879	1	160	2082.3	2080.4
1.6732	1	641	2119.3	2120.0
1.6620	1	233	2147.9	2147.1
1.6350	3	061	2219.2	2220.3
1.6226	3	161	2253.4	2249.1
1.6083	23	333	2293.7	2291.5
1.6009	1	722	2315.0	2317.7
1.5623	1	043	2430.8	2430.5

A least squares refinement of the powder data gave the orthorhombic lattice parameters listed in the table. The relationship between the orthorhombic cell and the previously reported pseudo-hexagonal cell can be seen as follows: Each of the 100 planes of the orthorhombic cell describes a network of C face-centered hexagonal cells. Inspection of these networks indicates the presence of the orthorhombic b and c axes whose vector sum makes a 60° angle with the orthorhombic c axis and represents the pseudo-hexagonal a axis. This c axis in turn becomes one-half of the pseudo-hexagonal a axis. The a axis of the orthorhombic cell and the c axis of the pseudo-hexagonal cell are identical.

We are proceeding with the structure refinement of magnesium fluorogermanate. Analytical data indicates that approximately 8 w/o (weight per cent) fluorine is substituted into the structure and that charge compensation is attained by a deficiency of germanium. A detailed discussion of the stoichiometry will appear with the publication of the complete structure.

In summary, we have prepared single crystals of magnesium germanate and fluorogermanate and reported their indexed powder patterns. Analytical results indicate that fluorine is incorporated into magnesium fluorogermanate. Since crystal x-ray diffraction shows the two compounds to be isostructural and that the compound magnesium germanate does not have the stoichiometry Mg_4GeO_6 but $Mg_{3.5}Ge_{1.25}O_6$.

Work is in progress on the complete three-dimensional structure of the fluorogermanate and will be published shortly.

Acknowledgment

This work was supported in part by The Advanced Research Projects Agency through the Materials Science Center, Cornell University, Ithaca, New York 14850.

Manuscript received Sept. 23, 1970.

Any discussion of this paper will appear in a Discussion Section to be published in the December 1971 JOURNAL.

REFERENCES

1. H. W. Leverenz, U.S. Pat. 2, 066,044 (1936).
2. F. E. Williams, U.S. Pat. 2,447,448 (1948).
3. F. E. Williams, *J. Opt. Soc. Am.*, **37**, 302 (1947).
4. S. H. Patten and F. E. Williams, *ibid.*, **39**, 702 (1949).
5. L. Thorington, *ibid.*, **40**, 579 (1950).
6. F. A. Kroeger and J. van den Boomgaard, *This Journal*, **97**, 377 (1950).
7. G. Kemeny and C. H. Haake, *J. Chem. Phys.*, **33**, 783 (1960).
8. C. R. Robbins and E. M. Levin, *Am. J. Sci.*, **257**, 63 (1959).
9. M. Rubenstein, quoted in Ref. 8.
10. R. B. VonDreele, P. W. Bless, E. Kostiner, and R. E. Hughes, *J. Solid State Chem.*, **2**, 612 (1970).

Reaction of Water Vapor with Anodic Aluminum Oxide

Studied by Wide-Line NMR Spectroscopy

Bernard R. Baker and Robert M. Pearson

Kaiser Aluminum and Chemical Corporation, Center for Technology, Pleasanton, California 94566

Porous anodic oxide films on aluminum are conventionally sealed by immersion in boiling water. Current theories state that conversion of essentially anhydrous oxide occurs, predominantly at the pore mouth, to form a less dense hydrated oxide which partially plugs the pores. The literature on sealing and on anodizing in general was reviewed by Diggle, Downie, and Goulding (1).

A different view of sealing, presented by Murphy, regards sealing as an ion exchange replacement of surface anions by hydroxyl ions (2). Murphy considers the coating produced in sulfuric acid electrolyte to consist of an array of alumina crystallites similar to a rock pile in which the pores are regions of lesser density packing of crystallites.

We have begun a study of the sealing process using wide-line proton NMR spectroscopy and present here the results of the first phase of our work, namely, the interaction of porous anodic oxides with water vapor.

A typical NMR spectrum of an anodic coating is shown in Fig. 1. This spectrum consists of a narrow line due to physically adsorbed water, $\Delta H \sim 0.2G$, superimposed on a broad line, $\Delta H \sim 7G$, due to hydroxyl groups, *i.e.*, chemisorbed water. The narrow line in Fig. 1 is artificially broadened here by instrument conditions.

The broad hydroxyl band can be suppressed by using a narrow modulation. Under these conditions a single narrow line is obtained which can be used as a quantitative measure of the adsorbed water present. The physically adsorbed water, and therefore the narrow band of the spectrum, can be removed under vacuum at room temperature allowing study of the broad band.

Experimental

Eight 6 x 4.05 in. pieces of 0.003 in. thick 1199 foil were partially slit into nine 0.45 in. strips leaving the ends intact. The eight pieces were bolt racked to a 2024 alloy frame as one rack load and were anodized for 1 hr at 15V in 15% sulfuric acid at 25°C. The work was thoroughly rinsed in deionized water and blown dry in a stream of nitrogen. The strips were hung as banks of nine from a glass frame in a covered battery jar containing a small amount of water. No direct contact of the work with liquid water was permitted. The jar was kept at ambient laboratory temperature (21° ± 2°C). At intervals a bank of nine strips was withdrawn. One strip was used for a coating weight determination; the remaining eight strips were cut into 1 in. pieces and placed in a 15 mm sample tube fitted with a ground glass joint and stopcock, allowing attachment to a vacuum line.

The NMR measurements were made at 16 MHz using a Varian spectrometer Model DA-100-15 equipped with a 4210 variable frequency oscillator. We found that the orientation of the sample strips relative to the receiver coil was critical, care being necessary to achieve a minimum reading on the detector level meter before introduction of the leakage to obtain an absorption mode spectrum. The magnetic field was modulated at 40 Hz with an amplitude depending on the width of the line. The amplitude varied between 0.125 and 2.0G, the wider modulation being used to study the broad hydroxyl band.

The area under the absorption curve can be obtained by double integration of a derivative curve such as shown in Fig. 1.

The concentration of physically adsorbed water on the anodic coating was measured by comparing the double integral of the NMR spectrum obtained using a modulation of 0.125G with the double integral of a

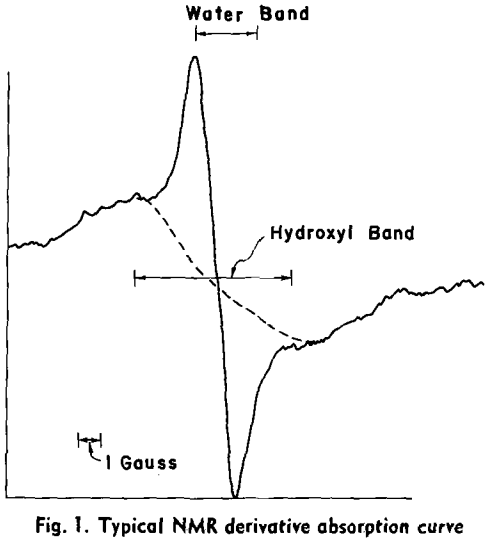

Fig. 1. Typical NMR derivative absorption curve

Key words: anodizing, sealing, adsorption.

spectrum from a transition alumina containing a known concentration of adsorbed water.

The anodic coating was then placed on a vacuum rack and the physically adsorbed water pumped off. The NMR spectrum was measured using a modulation of 2G. Double integration and comparison to a gibbsite spectrum gave the concentration of hydroxyl groups in the anodic coating.

Nitrogen adsorption and desorption isotherms were measured on an Aminco Adsorptomat using portions of each anodized sample reserved for that purpose. Pore radius distribution curves were calculated from these data along with surface area calculations by the BET procedure and cumulative area procedure assuming cylindrical pores.

Discussion

The rate of uptake of hydroxyl and physically adsorbed water is shown in Fig. 2 along with the weight gain expressed as a percentage of total oxide weight. The weight gain was about 14% after a two-week exposure to 100% relative humidity. The increase in hydroxyl content was something less than twice this value. This is consistent with the following mechanism for water adsorption. We assume the initial surface to be largely anhydrous. It must consist of oxide ions and a considerable concentration of aluminum ions having an incomplete coordination sphere similar to the picture developed by Peri for an active alumina surface (3). This is shown in Fig. 3. Every water molecule chemisorbed to fill an aluminum ion coordination site creates 2 hydroxyl groups on the surface. A concentration of 19% hydroxyl observed in Fig. 2 must therefore represent a 9.5% weight gain. The additional 4.5% weight gain shown in Fig. 2 is accounted for by the physically adsorbed water, presumably bound to the surface hydroxyls by hydrogen bonding.

The BET surface area of the sample before exposure to water vapor was 62 m^2/g. The mean pore diameter was 120Å. This is consistent with the known pore densities and diameters obtained by electron microscopy (4). After two weeks exposure to water vapor the specific surface area dropped to 5 m^2/g and the pore diameter fell to 40Å. Surface areas can also be estimated from the line width of the broad hydroxyl NMR band (5). This estimate is based on a linear relationship observed between line width and BET surface areas of a series of transition aluminas. The relationship was rationalized by the assumption that a surface hydroxyl proton is more mobile than that of an interior hydroxyl. Surface hydroxyls therefore give rise to a narrower band than do interior hydroxyls. Using this relationship we estimated the NMR surface area to be 329 m^2/g. The apparent discrepancy is resolved, however, if we consider the oxide structure to be a "rock-pile" of crystallites similar to the picture suggested by Murphy (2) and Michelson (6). We suggest that nitrogen adsorption occurs only on pore walls but that the internal surface in the crystallite interstices is accessible to hydrogen ions and oxide or hydroxyl ions by surface migration on the crystallite faces.

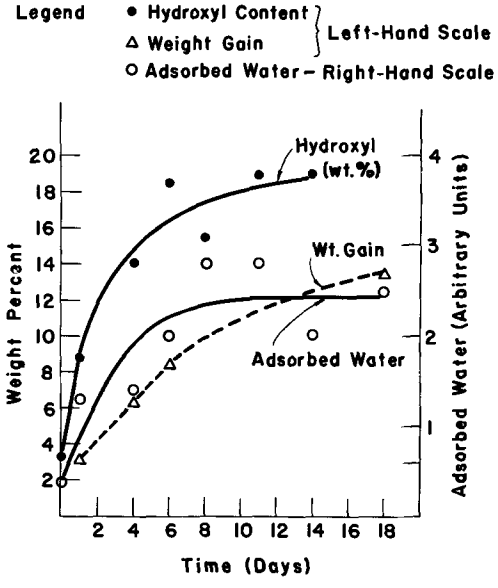

Fig. 2. Increase of hydroxyl and adsorbed water with time at 100% relative humidity.

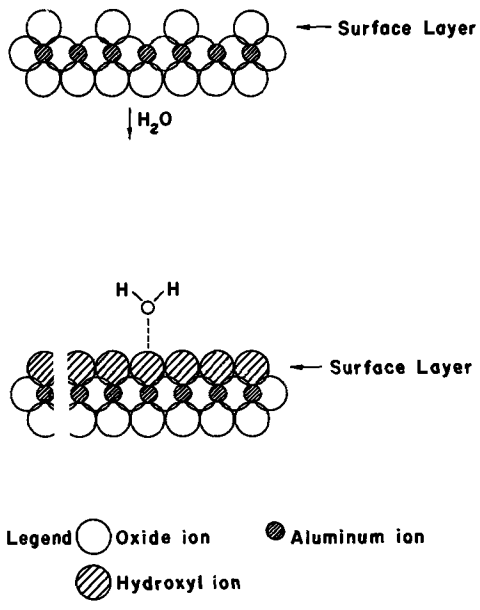

Fig. 3. Model for water adsorption

Acknowledgments

We thank Kaiser Aluminum and Chemical Corporation for permission to publish this work and Dennis Przybycien for the nitrogen adsorption experiments.

Manuscript submitted July 6, 1970; revised manuscript received *ca.* Sept. 23, 1970.

Any discussion of this paper will appear in a Discussion Section to be published in the December 1971 JOURNAL.

REFERENCES

1. J. W. Diggle, T. C. Downie, and C. W. Goulding, *Chem. Rev.*, **69**, 365 (1969).
2. J. F. Murphy, Anodizing Symposium, Birmingham, April 1967.
3. J. B. Peri, *J. Phys. Chem.*, **69**, 220 (1965).
4. F. Keller, M. S. Hunter, and D. L. Robinson, *This Journal*, **100**, 411 (1953).
5. R. M. Pearson, Presented at Pacific Conference on Chemistry and Spectroscopy, San Francisco, October 6-9, 1970.
6. C. E. Michelson, *This Journal*, **115**, 213 (1968).

GaAs-GaAsP Heterostructure Injection Lasers

M. G. Craford, W. O. Groves,* and M. J. Fox*

Monsanto Company, St. Louis, Missouri 63166

GaAs-GaAlAs heterostructure injection lasers with performance far superior to previous GaAs lasers have been reported (1-5). These devices consist of a layer of p-type GaAs with a thickness, W, sandwiched between n-type GaAs and p-type GaAlAs. In this paper we report results obtained using a GaAs-GaAsP heterostructure.

The GaAs-GaAsP structure which can be grown using vapor phase epitaxy allows better control of the impurity profile and degree of compensation than can be obtained using the GaAlAs structure which must be grown by means of liquid phase epitaxy. On the negative side the lattice mismatch in the GaAsP system is much greater than in the GaAlAs system, the lattice parameters of GaP, GaAs, and AlAs being 5.4506, 5.6533, and 5.6606, respectively (2). The resulting lattice mismatch gives rise to dislocations at the GaAs-GaAsP interface (6) which can act as nonradiative recombination centers for the injected electrons.

In the laser heterostructure the high band gap alloy layer provides a barrier which serves both to confine the injected electrons in the narrow p-type GaAs region and as a waveguide to confine the modes of electromagnetic radiation. If the dominant effect of the barrier is to confine injected electrons, and if the misfit dislocations at the GaAsP-GaAs interface lead to a high surface recombination velocity, then no improvement in laser performance would be expected with this system. However, if the minority carrier diffusion length is short compared to the width of the confinement region and if the barrier is effective with regard to confining electromagnetic radiation, then improved laser performance should be possible because the dislocations would not be expected to provide effective photon scattering centers. As will be seen below, improved laser performance was not observed, and there was no evidence that electromagnetic mode confinement contributed to the performance of these devices. The reason that electromagnetic mode confinement apparently has a major effect in GaAlAs heterostructures and not in the GaAsP structures studied here is not understood.

Crystal Growth and Fabrication

The device structures which are shown schematically in Fig. 1 were grown using standard vapor epitaxial techniques on GaAs substrates. Initially a 100-200μ thick n-type layer of GaAs was grown with a Te impurity concentration of $n \sim 3 \times 10^{18}/cm^3$. This was followed by the growth of a compensated p-type GaAs layer of the desired thickness, W, which formed the recombination region of the device. In this layer the n-type carrier concentration remained unchanged, but Zn was added to give a net carrier concentration of $p \sim 1 \times 10^{19}$. Finally an uncompensated GaAsP alloy layer ($p \sim 1 \times 10^{19}$) was grown. For one series of runs the alloy layer was grown so that an abrupt alloy composition step from $x = 0.0$ to $x \sim 0.1$ m/o (mole per cent) GaP occurred at the GaAs-GaAsP interface, see Fig. 1(a). This composition change corresponds to change in band gap energy or barrier height of $\Delta E \sim 0.1$ eV. Previous work indicated that a barrier of this height would confine the majority of injected electrons (7) as well as provide an effective waveguide for electromagnetic mode confinement (4). It was hoped that interfacial dislocations could be reduced to a satisfactory extent by keeping Δx as small as possible.

In a second series of runs the alloy composition was graded to a final composition of $x \sim 0.10$ at the rate of $\sim 4\%/\mu$, Fig. 1(b). In all cases the total thickness of the alloy layer was $15 \pm 5\mu$.

In the case of the abrupt heterostructures the thickness of the recombination region was measured on the finished devices to within $\pm 0.2\mu$ using a scanning electron microscope. There was no clear boundary in the case of the graded structures so W was calculated from the growth rate with an estimated accuracy of $\pm 1\mu$.

After growth the heterostructure received a 10-min 875°C $ZnAs_2$ diffusion which lowered the diode resistance and eliminated contacting difficulties. Diode fabrication was standard and consisted of lapping the structure to a thickness of $\sim 100\mu$, metallizing the p- and n-type surfaces, and sawing and cleaving the wafer into 100 x 250μ chips. The Fabry-Perot surfaces were not metallized, and generally the structures were not heat-treated after growth. In a few cases the structures were heat-treated, but no significant improvement in performance was observed.

Experimental Results

The threshold current densities *vs.* W are shown in Fig. 2. Each data point in Fig. 2 as well as Fig. 3, 4, and 5 represents the average of a batch of ≥ 10 diodes. Diodes which exhibited markedly inferior performance were considered unrepresentative and were not included in the average. Values of W investigated range from $W = 0$, in which case the $GaAs_{0.9}P_{0.1}$ layer was grown immediately on the n-type epitaxial layer, to $W > 10\mu$ where the devices were simply grown junction GaAs lasers with no alloy layer.

It can be seen that at 300°K the threshold current density, J_{th} increases monotonically with decreasing W and for $W = 0$ lasing was not observed. The performance of devices with graded alloy layers was generally similar to that obtained with abrupt structures with the exception of the devices with $W = 5.6\mu$ which were somewhat better. The improved performance

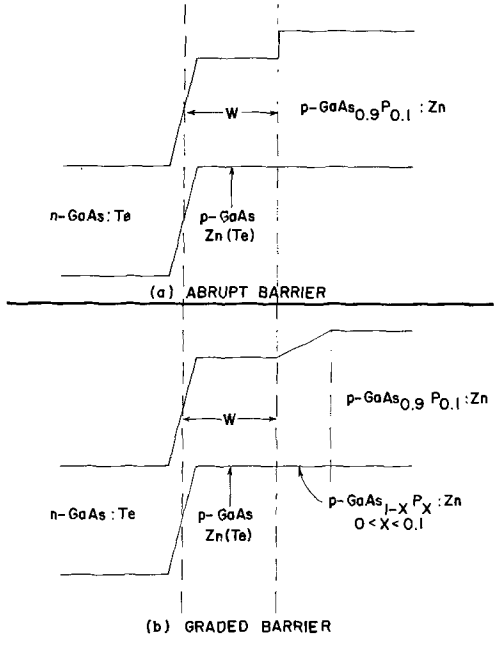

Fig. 1. Schematic GaAs-GaAsP heterostructure: (a) abrupt interface between p-GaAs and p-$GaAs_{0.9}P_{0.1}$; (b) graded interface.

* Electrochemical Society Active Member.

Key words: GaAsP, injection lasers, electroluminescence, heterojunctions.

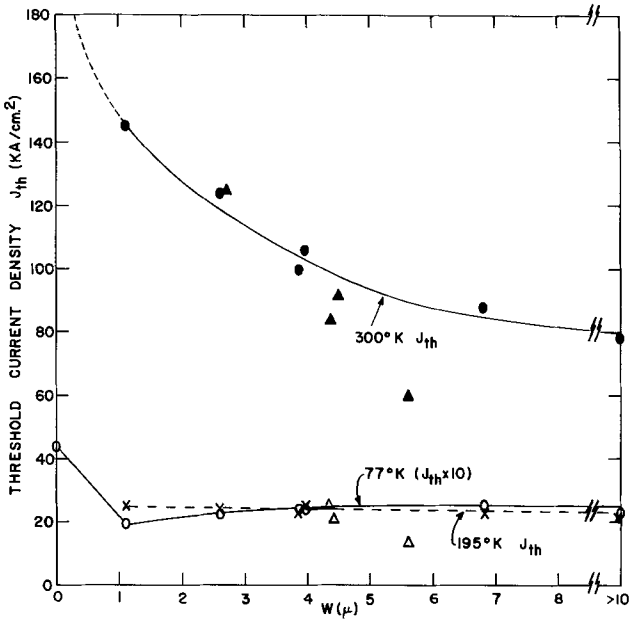

Fig. 2. Threshold current density vs. the p-type GaAs thickness. The abrupt heterostructure data are represented by closed (open) circles at 300°K (77°K) and crosses at 195°K. The graded heterostructure data is represented by closed (open) triangles at 300°K (77°K).

of this batch of devices is not understood but, due to the comparably large W and the fact that the alloy layer was graded, it appears unlikely that the heterojunction had an appreciable effect.

At 77° and 195°K the threshold current density is independent of W for $W \geq 1\mu$. For $W = 0$ the performance is degraded, but lasing was observed at 77°K. The threshold current densities are approximately ten times as high at 195° as at 77°K.

The data suggest that at 77° and 195°K the radiative lifetime is reduced and for $W > 1\mu$ few electrons penetrate to the GaAs-GaAsP interface. It is surprising that at these temperatures electromagnetic mode confinement, which apparently has a strong effect in GaAs-GaAlAs devices, has no observable effect in the GaAs-GaAsP devices studied here.

The external differential quantum efficiency of the abrupt laser structures is shown in Fig. 3. This efficiency was measured from one end of an uncoated de-

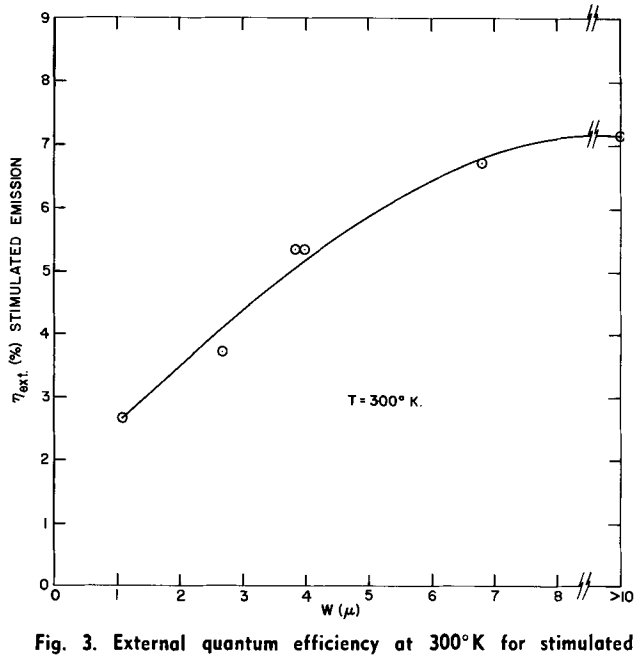

Fig. 3. External quantum efficiency at 300°K for stimulated emission vs. the p-type GaAs thickness for the abrupt heterostructure.

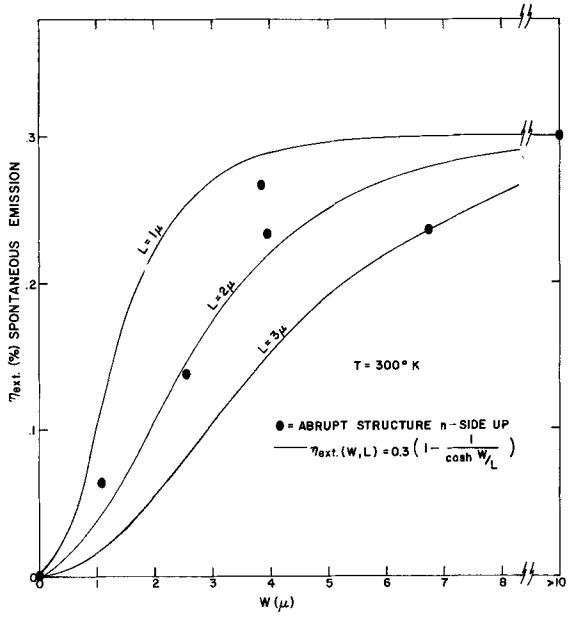

Fig. 4. External quantum efficiency at 300°K for spontaneous emission vs. the p-type GaAs thickness for the abrupt heterostructure. Also shown is the calculated efficiency for several different diffusion lengths.

vice so the total efficiencies are approximately twice the values shown. The spontaneous external quantum efficiencies for the abrupt heterostructures are shown in Fig. 4. The devices used to obtain the spontaneous data were square 375 x 375μ chips. The chips were planar and uncoated and were mounted n side up with the radiation being emitted through a 100μ thick GaAs layer. A 10 mA drive current was used.

Both the spontaneous and stimulated external efficiency increase with increasing W, correlating well with the decrease in threshold current density shown in Fig. 2. It is apparent from the data that interfacial dislocations are highly effective nonradiative dislocation centers and that a GaAs-GaAsP heterostructure cannot be used within the active region of a high performance light emitting device. The spontaneous efficiencies obtained with a graded alloy "window" are somewhat higher than that obtained with the abrupt structures. This may be due to the fact that by grading the alloy composition the window can be closer to the peak recombination region without introducing strain and dislocations which degrade the internal efficiency of the device. Efficiencies of ~0.5% have been obtained by reducing the thickness of the n-type GaAs layer. These spontaneous results are similar to those obtained earlier by Neuse *et al.* (8).

Also shown in Fig. 4 are calculated curves for the efficiency as a function of confinement distance for minority carrier diffusion lengths of 1, 2, and 3μ. These curves were calculated following the work of Burnham *et al.* (7) using the low-level injection formulation for a p/n junction. It can be shown that, as the surface recombination velocity at the GaAs-GaAsP interface approaches infinity, the ratio of the radiative current density, J_R, to the total injected current density, J_O, can be written as

$$J_R/J_O = K\left(1 - \frac{1}{\cosh W/L}\right)$$

where L is the injected minority carrier diffusion length and K is a constant of proportionality. This equation assumes that the radiative recombination current density is proportional to the total bulk recombination current density, J_B, and the total injected current density $J_O = J_B + J_I$ where J_I is the interfacial recombination current density and is assumed to be entirely nonradiative. Since the external efficiency is proportional to J_R/J_O the external quantum effi-

ciency as a function of W can be written as

$$\eta_{ext(W/L)} = 0.3\left[1 - \left(\frac{1}{\cosh W/L}\right)\right]$$

where the constant of proportionality was determined from the structure where $W > 10\mu$ ($W >> L$).

The data shown in Fig. 4 are scattered, but they do suggest an injected minority carrier diffusion length of $\sim 2\mu$ at 300°K.

If we assume $L \sim 2\mu$ at 300°K and that the electron mobility $\mu \simeq 2000$ cm^2/V sec, which is typical for GaAs with 3 x 10^{18} carriers/cm^3, we can approximate the lifetime for the injected electrons

$$\tau = \frac{eL^2}{kT\mu} \sim 10^{-9} \text{ sec}$$

At 77°K and 195°K the data indicate that $L < 1\mu$. It follows that $\tau \leq 3 \times 10^{-10}$ sec below 195°K assuming τ decreases monotonically with temperature. Both the lifetimes and diffusion lengths determined here are in reasonable agreement with those found by Vilms and Spicer (9).

Since at 300°K a significant number of the injected electrons penetrate $\geq 4\mu$ into the p-type region of the GaAs lasers studied here it is probable that they penetrate a similar distance in other types of GaAs lasers. In the case of GaAlAs heterojunction devices the optimum recombination region width W has been found to be $\sim 2\mu$ so many of the electrons would be expected to reach the GaAs-GaAlAs heterojunction. This implies that there is a very low dislocation density at the interface in the GaAs-GaAlAs system.

The change in diffusion length from $\leq 1\mu$ at 195°K to $\sim 2\mu$ at 300°K may also be related to the performance of GaAs lasers which do not have a confining GaAlAs barrier. Stripe geometry lasers with 2.5μ thick p-type regions have been operated continuously at temperatures up to ~200°K (10). The narrow p region was used to facilitate heat sinking of the devices. The ~200°K limit may be due predominantly to the increasing diffusion length in this temperature range which allows many of the electrons to traverse the p-type region and be lost at the metal contact thereby increasing the threshold of the device. The Q-switching which is observed in these devices between 100° and 300°K may also be related to electrons reaching the defects which undoubtedly are present at the GaAs metal interface.

The delay time at 300°K between the beginning of the current pulse and the onset of stimulated emission is shown in Fig. 5. The delay time has generally been measured immediately above threshold for stimulated emission, $I \simeq I_{th}$, but some workers have considered the delay at 50% above threshold, $I = 1.5\, I_{th}$ (11), to be a more reliable parameter because it is not so dependent on the exact shape of the current pulse. In Fig. 5 the delay time *vs.* W is plotted at both current levels as well as the delay at a constant current of 45A. As in Fig. 2 and 3 the data points represent average values for a batch of devices. For the delay time measurements there was approximately 20% scatter within a batch of diodes. The delay was measured from the time at which the rectangular (20 nsec rise time) current pulse reached its maximum value to the time at which the light output pulse reached 50% of its peak height. It can be seen that at both $I = I_{th}$ and $I = 1.5\, I_{th}$ the delay time decreases with decreasing W, and at a constant current the delay is nearly independent of W. For a given W the delay time decreased with current as has been previously observed. At 77°K no measurable delay time was observed in any of the devices.

The data indicate that the 300°K delay time in these devices is a function of the current density. This behavior is consistent with the idea that a certain density of traps, where the density is independent of W, must be filled before stimulated emission can occur (12). The presence of the misfit dislocations which strongly affects I_{th} and η_{ext} affect the delay time only through the dependence of I_{th} on W.

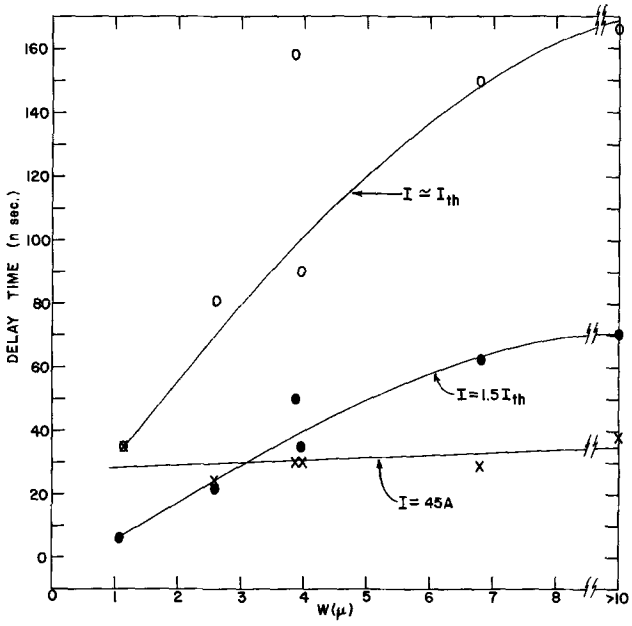

Fig. 5. Delay time at 300°K *vs.* the p-type GaAs thickness. The open and closed circles represent data taken at $I \simeq I_{th}$ and 1.5 I_{th}, respectively. The crosses represent data taken at a constant current of 45A.

The peak intensity of the emitted radiation of 77° and 300°K was investigated for stimulated emission at $I \sim I_{th}$ and for spontaneous emission at $I << I_{th}$. The spectral distribution of the emitted radiation is characteristic of heavily doped GaAs [λp(300°K) $\simeq$ 1.37 eV, λp(77°K) $\simeq$ 1.46 eV] and is relatively independent of W although there is a slight tendency for the energy to decrease with decreasing W. No detectable recombination takes place in the alloy layer. The fact that no radiation characteristic of the alloy layers is emitted indicates once again how effective the misfit dislocations are as nonradiative recombination centers. For $W = 0$ at 77°K the peak emission energy was somewhat higher [λp(77°K) $\simeq$ 1.47 eV] which may be due to hole injection and recombination in the n-type region of the device. The stimulated emission generally occurs at a slightly higher energy than the spontaneous peak due to band filling.

The emission spectra of the devices were also investigated in the region from 1.0 to 1.8μ using a PbS detector. Although some devices exhibited a broad band of radiation centered at ~1.2μ, the peak intensity of the band was 2-3 orders of magnitude lower than the band edge radiation and did not depend on W. This indicates that the misfit dislocations act as true nonradiative centers or, at least, very long wavelength centers and not as "normal" deep levels producing long wavelength radiation in the 1.0-1.5μ range.

Acknowledgments

The authors would like to thank L. A. Fergason who performed the scanning electron microscope measurements used in this work, and A. H. Herzog and N. Holonyak for helpful discussions.

Manuscript received Aug. 21, 1970. This was Paper 71 presented at the Los Angeles Meeting of the Society, May 10-15, 1970.

Any discussion of this paper will appear in a Discussion Section to be published in the December 1971 JOURNAL.

REFERENCES

1. I. Hayashi, M. B. Panish, and P. W. Foy, *IEEE J. Quantum Electron*, **QE-5**, 211 (1969).
2. H. Kressel and H. Nelson, *RCA Rev.*, **30**, 106 (1969).
3. Zh. I. Alferov, V. M. Andreev, V. I. Korolkov, E. L. Portnoi, and D. N. Tretyakov, *Fiz. Tekh. Polup-*

rov., 2, 1545 (1968), [Soviet Phys.—Semicond. 2, 1289 (1969)].
4. H. Kressel, H. Nelson, and F. Z. Hawrylo, *J. Appl. Phys.*, **41**, 2019 (1970).
5. I. Hayashi and M. B. Panish, *ibid.*, **41**, 150 (1970).
6. D. A. Grenning and A. H. Herzog, *ibid.*, **39**, 2783 (1968).
7. R. D. Burnham, P. D. Dapkus, N. Holonyak, Jr., D. L. Keune, and H. R. Zwicker, *Solid-State Electron.*, **13**, 199 (1970).
8. C. J. Nuese, J. J. Tietjen, J. J. Gannon, and H. F. Gossenberger, *Trans. TMS-AIME*, **242**, 400 (1968).
9. J. Vilms and W. E. Spicer, *J. Appl. Phys.*, **36**, 2815 (1965).
10. J. C. Dyment and L. A. D'Asaro, *Appl. Phys. Letters*, **11**, 292 (1967).
11. J. C. Dyment and J. E. Ripper, *IEEE J. Quantum Electron*, **QE-4**, 155 (1968).
12. G. E. Fenner, *Solid-State Electron.*, **10**, 753 (1967).

A New Manganese-Activated Phosphor: $Li_2ZnGe_3O_8$

David A. Grisafe[1]

Chemical and Metallurgical Division, Sylvania Electric Products, Towanda, Pennsylvania 18848

In certain host lattices, it is well known that divalent manganese in tetrahedral coordination gives rise to a green luminescence. Well-known examples include the phenacite structure such as Zn_2SiO_4:Mn in which all the cations are in tetrahedral coordination or the spinel structure such as $ZnAl_2O_4$:Mn in which one-third of the cations—zinc in this example—possess tetrahedral coordination.

During the search for new manganese-activated green phosphors containing zinc as one of the host ions, the compound $Li_2ZnGe_3O_8$, discovered by Durif (1), was found to be activated by manganese. The present work contains the results of the investigation of this compound.

The desired amounts of reagent grade Li_2CO_3, $ZnCO_3$ or ZnO, $MnCO_3$ and GeO_2 were weighed to the nearest 0.0001g, mixed dry or mortared in an acetone slurry and fired in crucibles from 700° to 1000°C, usually for several hours. To insure complete reaction the materials were remixed and refired in the same temperature range. After pulverizing, the samples were heated in a mildly reducing atmosphere from 15 min to several hours, and the resulting powder was passed through a 325 mesh sieve.

Accurate x-ray diffraction data for the host lattice was obtained by back-packing powder into a sample holder and scanning at one-quarter degree 2θ per min using a curved crystal monochromator and CuKα radiation. Silicon was used as an internal standard. After indexing, the lattice parameter and standard deviation were obtained from a least squares computer program.

Using −325 mesh material, emission spectra under cathode ray excitation were obtained with a Jarrell Ash Spectrometer (Model No. 78-496) while spectra under ultraviolet radiation were obtained from a Perkin Elmer Spectrophotofluorimeter (Model No. 195).

X-ray powder data for $Li_2ZnGe_3O_8$ prepared in our laboratory are presented in Table I. The compound possesses a primitive cubic cell with a lattice parameter of $a_0 = 8.191 \pm 0.001$Å. The $00l$ reflections are only present when $l = 4n$ which indicates the space group is $P4_332$ or $P4_132$. In general, the strongest reflections are those whose Miller indices are all odd or all even thus suggesting a relation to the spinel structure. The data show strong similarity to those reported by Datta (2) for the low temperature form of $LiAl_5O_8$.

Unactivated $Li_2ZnGe_3O_8$ is a white material with a melting point of 1000°C ± 10°C. Assuming a spinel structure ($Z = 4$) the material possesses an x-ray density of 5.13 g/cm^3 compared with a picnometric density of 5.0 g/cm^3. These values compare relatively well with those of Durif (1) who reported $a_0 = 8.190 \pm 0.002$Å, a melting point of 995° ± 5°C, and a density of 5.11 g/cm^3.

When fired in air, $Li_2ZnGe_3O_8$:Mn samples showed a dull green luminescence and a tan body color typical of incompletely reduced manganese (to the divalent state). A variety of reducing conditions were explored

Table I. X-Ray powder data for $Li_2ZnGe_3O_8$

hkl	$I_{vis.}$	$d_{obs.}$	$d_{calc.}$
110	22	5.784	5.792
111	45	4.720	4.729
210	34	3.660	3.663
211	16	3.341	3.344
220	19	2.893	2.896
310	4	2.589	2.590
311	100	2.468	2.470
222	11	2.361	2.365
320	4	2.270	2.272
321	4	2.188	2.189
400	39	2.047	2.048
411 330	3	1.930	1.931
331	2	1.878	1.879
421	6	1.786	1.787
422	5	1.672	1.672
510 431	4	1.606	1.606
511 333	34	1.579	1.576
520 432	5	1.521	1.521
521	3	1.496	1.496
440	44	1.447	1.448
530 433	1	1.405	1.405
531	6	1.3846	1.3845
610	1	1.3463	1.3466
611 532	2	1.3289	1.3288
620	2	1.2952	1.2951
541	1	1.2640	1.2639
533	8	1.2492	1.2491
622	7	1.2348	1.2348
630 542	3	1.2209	1.2210
631	<1	1.2076	1.2077
444	5	1.1824	1.1823
710 550 543	1	1.1586	1.1584
711 551	3	1.1471	1.1470
720 641	2	1.1252	1.1251
721 633 552	<1	1.1148	1.1146
642	2	1.0947	1.0946
731 553	12	1.0665	1.0664
650 643	1	1.0488	1.0487
732 651	<1	1.0402	1.0402
800	4	1.0239	1.0239
811 741 554	<1	1.0082	1.0082
821 742	<1	0.9860	0.9861
653	<1	0.9789	0.9790
822 660	<1	0.9654	0.9653
831 750 743	<1	0.9522	0.9522
751 555	7	0.9459	0.9458
662	3	0.9397	0.9396
832 654	1	0.9335	0.9334
840	5	0.9157	0.9158
910 833	<1	0.9043	0.9045
911 753	1	0.8991	0.8991
920 760	<1	0.8884	0.8884
921 761 655	<1	0.8833	0.8832
930 851 754	<1	0.8635	0.8634
931	5	0.8587	0.8586
852	<1	0.8495	0.8494
844	10	0.8361	0.8360
941 853 770	<1	0.8275	0.8274
933 771 755	1	0.8234	0.8232
10,10 942 861 764	1	0.8151	0.8150
10,20 862	<1	0.8033	0.8032

[1] Present address: State Geological Survey, University of Kansas, Lawrence, Kans. 66044.

Key words: green photoluminescence, green cathodoluminescence, pseudospinel phosphor.

in an attempt to eliminate the body color of the phosphor and improve its brightness. The phosphor is extremely sensitive to reducing conditions and turns a grayish color when exposed to only 1 or 2% hydrogen in nitrogen, the atmosphere often used for divalent manganese-activated spinel phosphors. The same discoloration was observed when the phosphor was fired in NH_3, CO and some NH_3-N_2 and CO-N_2 mixtures. An analysis of residue collected at the exhaust end of a tube furnace during one of these "over-reductions" showed a high germanium content. Firing in atmospheres such as CO_2, N_2, or N_2-H_2O did not sufficiently reduce the manganese.

The brightest phosphors were prepared by a stepwise reduction consisting of firing in short periods of nitrogen containing traces of hydrogen alternating with longer periods of nitrogen. Phosphors prepared in this manner possessed brightnesses of up to 60% of Zn_2SiO_4:Mn under cathode ray excitation and an $x = 0.245$ and $y = 0.718$.

Reflectance spectra in the ultraviolet region for the unactivated and manganese-activated $Li_2ZnGe_3O_8$ are shown in Fig. 1. Although the host lattice absorbs under 2537Å excitation, its emission is a very dull blue at best. The large increase in absorption due to the addition of manganese indicates the phosphor is largely activator-sensitized.

Typical emission spectra for $Li_2ZnGe_3O_8$:Mn and Zn_2SiO_4:Mn under 2537Å excitation are shown in Fig. 2. The germanate phosphor is brighter under 2537Å compared with cathode-ray excitation. The presence of only a green emission band and the similarity of the emission curve to such phosphors as β-$LiAl_5O_8$:Mn reported by Jaffe (3), Zn_2SiO_4:Mn, and $ZnAl_2O_4$:Mn are strong evidence that $Li_2ZnGe_3O_8$:Mn is activated by divalent manganese in tetrahedral coordination.

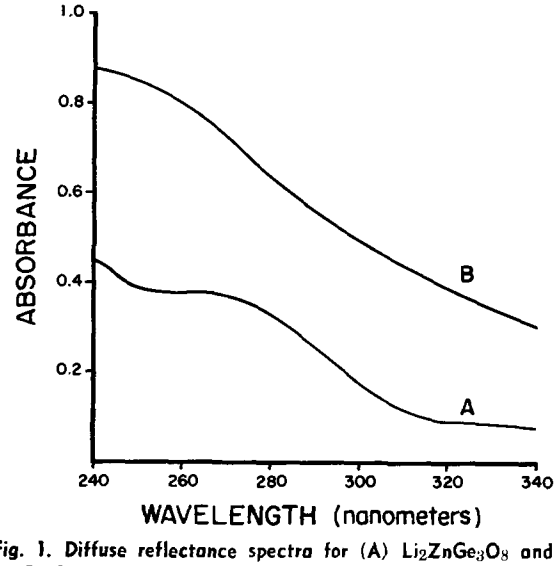

Fig. 1. Diffuse reflectance spectra for (A) $Li_2ZnGe_3O_8$ and (B) $Li_2ZnGe_3O_8$:Mn.

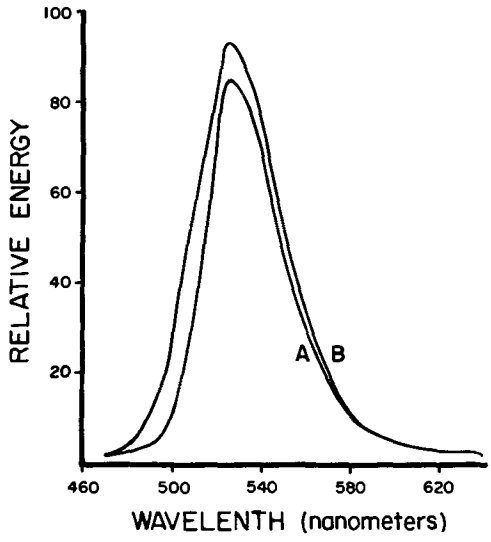

Fig. 2. Emission spectra for (A) $Li_2ZnGe_3O_8$:Mn and (B) Zn_2SiO_4:Mn under 2537Å excitation.

In summary, $Li_2ZnGe_3O_8$ possesses a primitive cubic lattice related to the spinel crystal structure and represents a new host lattice for manganese-activated green phosphors. The phosphor is extremely sensitive to reducing conditions, but when properly prepared, it yields an emission curve similar to green-luminescing spinels and phenacites.

Acknowledgments

The author is indebted to Olney Bullock for some of the sample preparation and to D. T. Palumbo for the corrected ulfraviolet spectra.

Manuscript submitted July 28, 1970; revised manuscript received *ca.* Sept. 29, 1970.

Any discussion of this paper will appear in a Discussion Section to be published in the December 1971 JOURNAL.

REFERENCES

1. A. Durif and J. C. Joubert, *Compt. Rend.*, **255**, 2471 (1962).
2. R. Datta, *J. Am. Ceram. Soc.*, **46**, 388 (1963).
3. P. M. Jaffe, *This Journal*, **115**, 1203 (1968).

Depolarization Current Characteristics of Naphthalene Photoelectrets

P. K. C. Pillai and Malti Goel

Department of Physics, Indian Institute of Technology, New Delhi-29, India

Electret science is becoming an important branch of pure and applied physics. An electret is simply a dielectric material with remanent polarization. Thermoelectrets and photoelectrets are formed by simultaneous application of electric field and heat or light, respectively. Properties of naphthalene thermoelectrets were first discussed by Baldus (1) and then by Mascarenhas (2). Later Belyaev, Belikova, Fridkin, and Zheludev (3) reported on the thermo- and photoelectret effects in naphthalene and showed that these states are inseparable. Campos *et al.* (4) used the thermal depolarization technique to investigate trapped polarization in naphthalene thermoelectrets. The higher values of charge storage in naphthalene (3) led to further investigation. Depolarization current characteristics and contact electrification processes of naph-

Key words: organic semiconductor, naphthalene, photoelectret, dark depolarization current.

in an attempt to eliminate the body color of the phosphor and improve its brightness. The phosphor is extremely sensitive to reducing conditions and turns a grayish color when exposed to only 1 or 2% hydrogen in nitrogen, the atmosphere often used for divalent manganese-activated spinel phosphors. The same discoloration was observed when the phosphor was fired in NH_3, CO and some NH_3-N_2 and CO-N_2 mixtures. An analysis of residue collected at the exhaust end of a tube furnace during one of these "over-reductions" showed a high germanium content. Firing in atmospheres such as CO_2, N_2, or N_2-H_2O did not sufficiently reduce the manganese.

The brightest phosphors were prepared by a stepwise reduction consisting of firing in short periods of nitrogen containing traces of hydrogen alternating with longer periods of nitrogen. Phosphors prepared in this manner possessed brightnesses of up to 60% of Zn_2SiO_4:Mn under cathode ray excitation and an $x = 0.245$ and $y = 0.718$.

Reflectance spectra in the ultraviolet region for the unactivated and manganese-activated $Li_2ZnGe_3O_8$ are shown in Fig. 1. Although the host lattice absorbs under 2537Å excitation, its emission is a very dull blue at best. The large increase in absorption due to the addition of manganese indicates the phosphor is largely activator-sensitized.

Typical emission spectra for $Li_2ZnGe_3O_8$:Mn and Zn_2SiO_4:Mn under 2537Å excitation are shown in Fig. 2. The germanate phosphor is brighter under 2537Å compared with cathode-ray excitation. The presence of only a green emission band and the similarity of the emission curve to such phosphors as β-$LiAl_5O_8$:Mn reported by Jaffe (3), Zn_2SiO_4:Mn, and $ZnAl_2O_4$:Mn are strong evidence that $Li_2ZnGe_3O_8$:Mn is activated by divalent manganese in tetrahedral coordination.

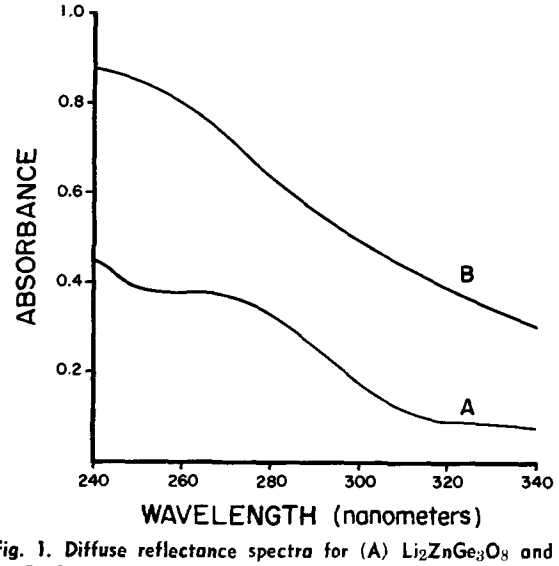

Fig. 1. Diffuse reflectance spectra for (A) $Li_2ZnGe_3O_8$ and (B) $Li_2ZnGe_3O_8$:Mn.

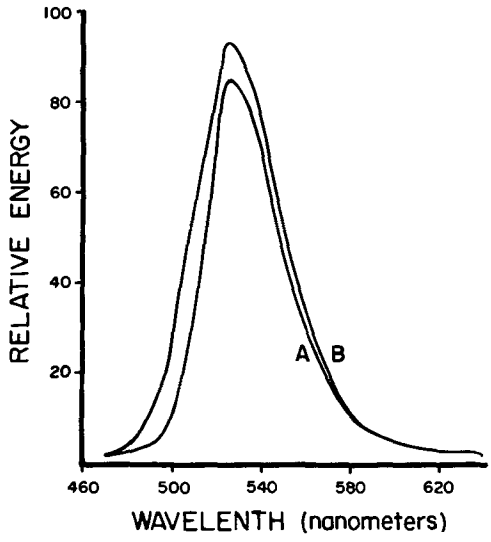

Fig. 2. Emission spectra for (A) $Li_2ZnGe_3O_8$:Mn and (B) Zn_2SiO_4:Mn under 2537Å excitation.

In summary, $Li_2ZnGe_3O_8$ possesses a primitive cubic lattice related to the spinel crystal structure and represents a new host lattice for manganese-activated green phosphors. The phosphor is extremely sensitive to reducing conditions, but when properly prepared, it yields an emission curve similar to green-luminescing spinels and phenacites.

Acknowledgments

The author is indebted to Olney Bullock for some of the sample preparation and to D. T. Palumbo for the corrected ulfraviolet spectra.

Manuscript submitted July 28, 1970; revised manuscript received *ca.* Sept. 29, 1970.

Any discussion of this paper will appear in a Discussion Section to be published in the December 1971 JOURNAL.

REFERENCES

1. A. Durif and J. C. Joubert, *Compt. Rend.*, **255**, 2471 (1962).
2. R. Datta, *J. Am. Ceram. Soc.*, **46**, 388 (1963).
3. P. M. Jaffe, *This Journal*, **115**, 1203 (1968).

Depolarization Current Characteristics of Naphthalene Photoelectrets

P. K. C. Pillai and Malti Goel

Department of Physics, Indian Institute of Technology, New Delhi-29, India

Electret science is becoming an important branch of pure and applied physics. An electret is simply a dielectric material with remanent polarization. Thermoelectrets and photoelectrets are formed by simultaneous application of electric field and heat or light, respectively. Properties of naphthalene thermoelectrets were first discussed by Baldus (1) and then by Mascarenhas (2). Later Belyaev, Belikova, Fridkin, and Zheludev (3) reported on the thermo- and photoelectret effects in naphthalene and showed that these states are inseparable. Campos *et al.* (4) used the thermal depolarization technique to investigate trapped polarization in naphthalene thermoelectrets. The higher values of charge storage in naphthalene (3) led to further investigation. Depolarization current characteristics and contact electrification processes of naph-

Key words: organic semiconductor, naphthalene, photoelectret, dark depolarization current.

thalene photoelectrets, formed under different experimental conditions, have been studied in detail in this investigation.

Naphthalene is a photoconducting dielectric material with a permittivity of 2.7 and a band gap of 3.7 eV (5). This band gap value gives an optical absorption edge in solid naphthalene at 3400Å.

The naphthalene used in this investigation was obtained from British Drug Houses Ltd. (BDH) Laboratory Chemicals Division, Poole, England, and had a molecular weight of 128.17.

Experimental Conditions

About 25 naphthalene samples were prepared by solidifying melted naphthalene (mp 79.5°C) in mica cavities, 1 cm^2 in area and 1 mm thick, between two aluminum electrodes. Sample surfaces were made uniform by means of a remelting and resolidification technique; keeping a heated aluminum electrode over the surface and applying pressure to remove extra material. This special technique also helped to maintain a uniform thickness for all samples. To avoid the initial molding charge, the samples after preparations were kept in a desiccator under dry conditions for about 12 days. The samples were then placed inside a photoelectret jig specially designed for the application of forming field and polarizing light simultaneously.

Details of the photoelectret jig are shown in Fig. 1. It consists of a brass cylinder, 1, 3 in. in diameter, closed on both ends except for an aperture, 2, for light illumination. Another small cylinder, 3, 1 in. in diameter, is screwed into the aperture to obtain perfect darkness surrounding the sample. The sample, 4, is held tightly by means of a spring, 7, and a movable electrode, 11, between two aluminum electrodes, 5 and 6, and is placed inside the guard ring of mica, 8.

To illuminate the sample, one of the aluminum foil electrodes, 5, was made into a grid with 1 mm^2 holes spaced 1 mm apart. The other aluminum electrode, 6, was solid. A brass rod, 9, was attached to the spring through insulation, 10. A circular brass disk, 11, connected to this rod was used to apply uniform pressure to the sample. An insulated knob, 12, to adjust the pressure on the sample, is held by the cover. A door, 13, is provided for handling the sample. The casing and the shielding of all connecting wires are grounded.

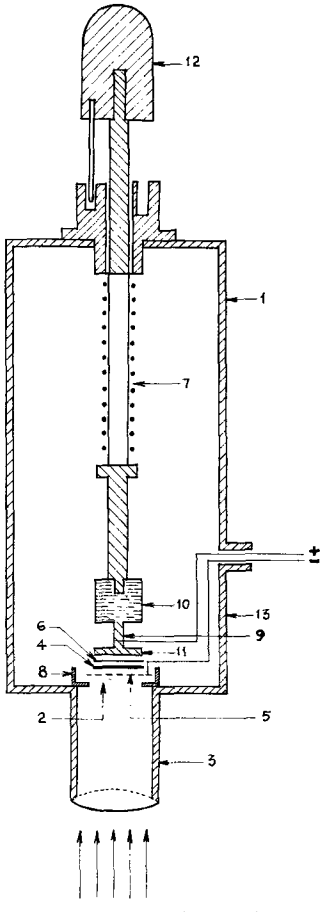

Fig. 1. Photoelectret jig

Aluminum electrodes make blocking contact with naphthalene monocrystal (6), but with polycrystalline material, the nature of contact is effectively ohmic due to the presence of surface states. Deviations from Ohm's law can occur at higher fields due to space charge effects.

To measure dark depolarization current, the sample was illuminated for 10 min with white light from a 100W, 220V, tungsten filament lamp, and a high polarizing field was applied simultaneously, keeping the perforated electrode negative. The field and illumination were then switched off, and the jig containing the sample was covered with a black cloth. Discharge current was measured by means of a microammeter E A 810A, supplied by Electronic Corporation of India; that can read current down to 10^{-12}A.

In another series of measurements the photoelectrets formed as above were kept short-circuited in complete darkness for half a minute, then re-illuminated with the same light intensity as used during polarization process. Photodepolarization current measurements were carried out simultaneously.

In the third series, photoelectrets were formed by the application of field and light for 10 min, then the field was continued for another 5 min after the illumination was switched off, *i.e.*, the sample was dark polarized for 5 min. After these polarization processes the samples were kept short-circuited in the dark for half a minute. The photodepolarization current measurement was taken while re-illuminating the photoelectrets. Measurements were carried out at room temperature, *i.e.*, 32° ± 2°C.

Experimental Results

Dark depolarization current measurements were carried out on ten different samples. A separate sample was used a each value of the field strength varying in steps of 0.9 kV/cm from 0.9 to 9 kV/cm. Results are shown in Fig. 2. The decay of dark depolarizing current with time is similar in each case. Illumination was kept constant in each of these measurements.

The results of experimental investigation of the second series of measurements are shown in Fig. 3. Initial values of currents in this case are much less than those of the photoelectrets processed without storing. Final values of the currents are slightly higher than the values without storing, indicating that the storing process stabilizes the traps. In Fig. 4 the results of the third series of measurement are plotted. Here the initial current is more than its corresponding value in the second series shown in Fig. 3. This suggest that the process of dark polarization for an extra 5 min after photopolarization for 10 min gives better results.

It can be seen from Fig. 2 and 3 that the initial value of depolarization current increases with increasing field strength. But the depolarization current curves cross at certain points due to different decay rates, which depend on the variation of temperature and humidity conditions during measurement, and also on the slight variation of thickness and structure from sample to sample. It has been observed that decay curve do not cross if a single sample is used at all field strengths under controlled conditions. Uncharged samples are used in this case at each field strength to preclude any effect of retention of previous charge on the measured value of current.

Five different samples were polarized by light and field at different field strength. Depolarization currents measured after re-illumination are shown in Fig. 5. Under similar experimental conditions, a single naphthalene sample was also polarized at each field

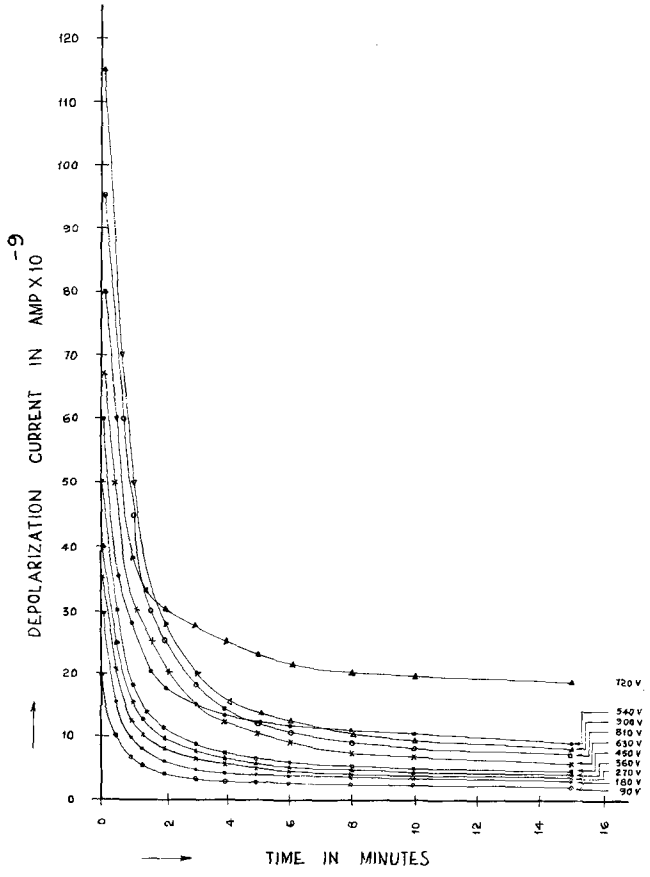

Fig. 2. Dark depolarization currents, for naphthalene photoelectrets formed in 10 min time at different field strengths varying from 0.9 to 9 kV/cm.

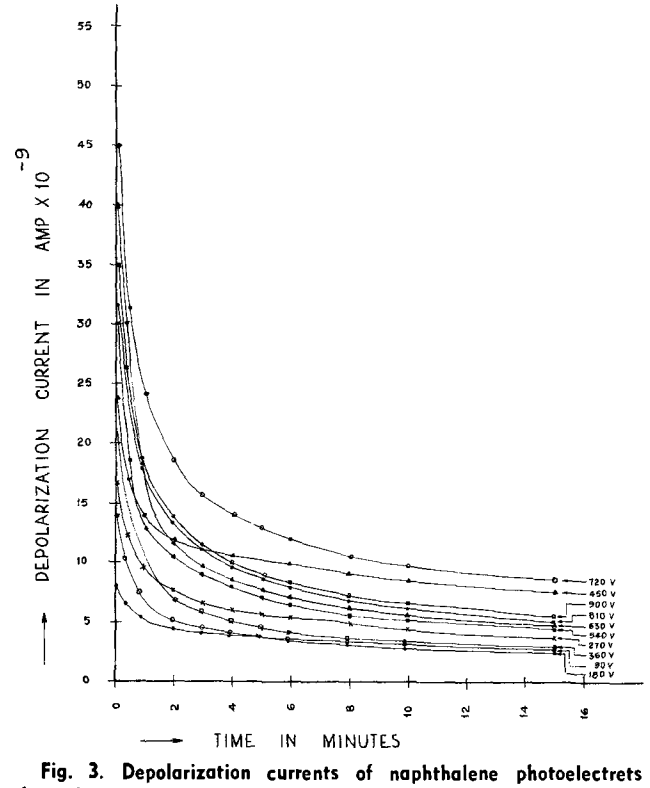

Fig. 3. Depolarization currents of naphthalene photoelectrets formed as in Fig. 2, but stored in dark for half a minute longer and then illuminated during measurements.

strength and depolarization current while re-illuminating was observed. Results are plotted in Fig. 6. The curves in Fig. 6 tend to converge while those in Fig. 5 are approximately equally spaced. This interesting

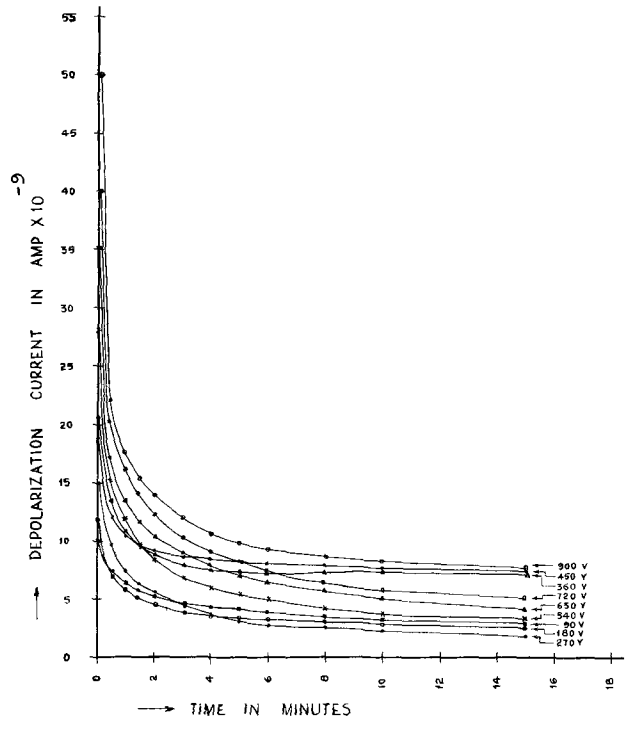

Fig. 4. Depolarization currents of naphthalene photoelectrets formed as in Fig. 2 and also dark polarized for another 5 min. The current measurements have been taken by re-illuminating the samples which were stored in dark for half a minute more.

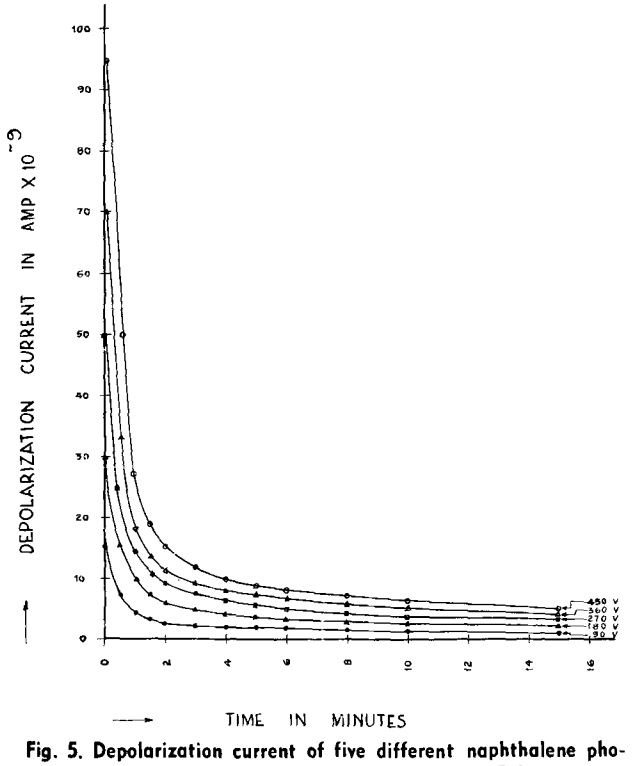

Fig. 5. Depolarization current of five different naphthalene photoelectrets for field strengths varying from 0.9 to 4.5 kV/cm.

phenomenon of convergence can be called the heat quenching effect (7).

In Fig. 7, current measurements on different fresh, unpolarized samples, *i.e.*, dummy samples, prepared under identical conditions without any application of field and illumination are shown. These stripping charges are introduced at the metal insulator contact during the molding of samples. It can be seen that currents on one side of the sample are always higher than those on the other side. High discharge currents are obtained on the side which solidifies on the alumi-

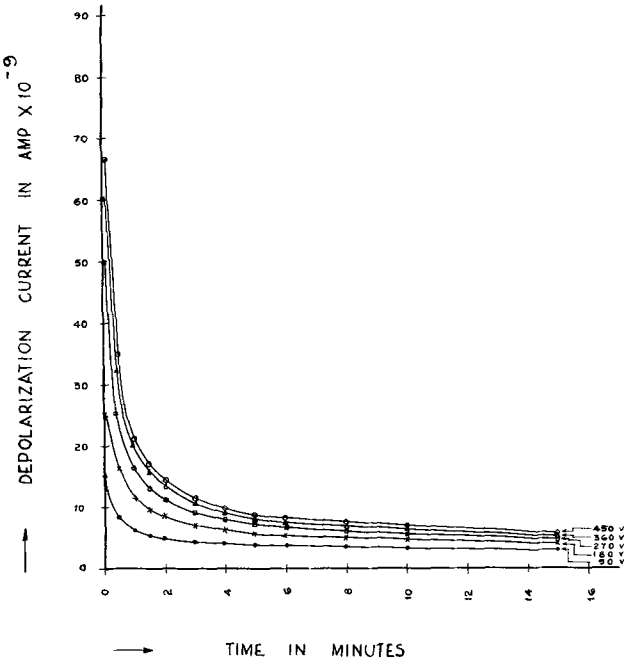

Fig. 6. Depolarization current of naphthalene photoelectrets prepared from the same sample at field strength varying from 0.9 to 4.5 kV/cm.

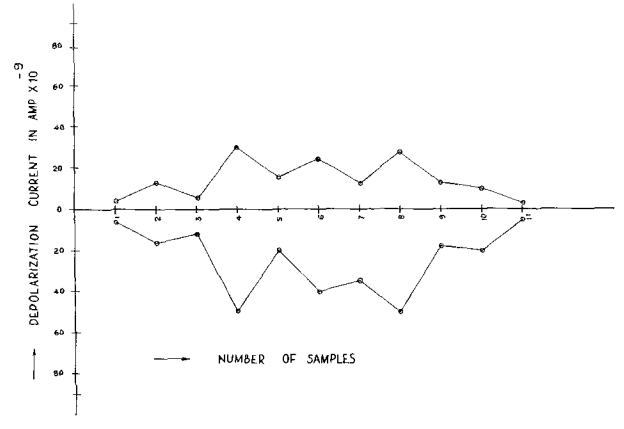

Fig. 7. Discharge current of different fresh samples formed without the application of field or light.

num electrode. The other side of the sample was treated by the remelting and resolidification process; reheating each time destroys the charge produced the previous time, and ultimately less current is observed on that surface. Such currents in samples left in open air, decay quickly in humid surroundings; however, in samples kept short-circuited by metallic foils in a desiccator, the currents retain their values for a longer time.

Depolarization current of a dummy sample and a polarized sample, prepared at 4.5 kV/cm, are compared in Fig. 8. For the dummy sample, depolarization current increases to a maximum value in 24 hr and then decays to a constant value in 3 days time (curve a). After 6 days it again starts decaying and ultimately becomes zero. Another sample was kept short-circuited for 24 hr (curve b) and then polarized. Current in this case increases from 50 x 10^{-9} to 130 x 10^{-9}A on the side subjected to illumination and from 110 x 10^{-9} to 150 x 10^{-9}A on the other side; it then falls sharply to a much lower value in the next 24 hr. Afterwards it decays slowly to zero in approximately 12 days. After measurements, samples were kept short-circuited in a desiccator for further studies. The high value of depolarization current in the dummy sample have been found to be associated with high humid environment.

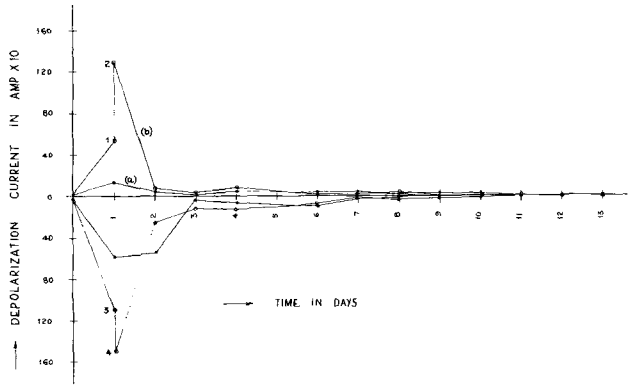

Fig. 8. Depolarization currents of a dummy sample (a) and a polarized photoelectret (b) formed at 4.5 kV/cm in 10 min.

Discussion

Kepler and Le Blanc (8, 9) have suggested that band structure model can be effectively applied to explain photoelectret phenomena in organic semiconductors. Incident light excites electrons and holes in the valence band of naphthalene, and when the condition of absorption is satisfied for any particular wavelength, electrons are excited either to the conduction band or to traps. Depolarization current is a maximum initially and then decays asymptotically due to the fact that the supply of trapped electrons is maximum in the initial stage and only a small number of electrons are available after some time. Excited electrons travel toward the positive electrode and holes toward the negative electrode, and the sample becomes polarized as shown in Fig. 9(a) (top) and (b) (bottom). If the number of electrons per unit volume in the trapping levels at the initial polarization state is N_0 and the number of electrons per unit volume contributing to depolarization current at any time t is n, then we can write

$$n = N_0 \exp(-t/\alpha) \quad \ldots \quad \ldots \quad \ldots \quad [1]$$

where α is the lifetime of electrons in electron traps. Similarly for holes

$$p = P_0 \exp(-t/\beta) \quad \ldots \quad \ldots \quad \ldots \quad [2]$$

where β is the lifetime of holes in hole traps. Values of α and β are of the order of several seconds for naphthalene crystal.

Total depolarization current density J at any time t is the current due to electrons as well as holes, which can be written as

$$J = ne\,\mu_e E + pe\,\mu_h E = J_{No} \exp(-t/\alpha) + J_{Po} \exp(-t/\beta) \quad \ldots \quad [3]$$

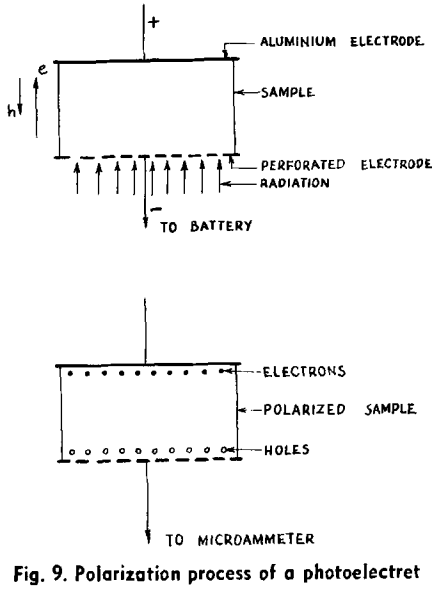

Fig. 9. Polarization process of a photoelectret

where E is the electric field and e the charge of the carrier; μ_e and μ_h are mobilities of electrons and holes, respectively,

$J_{No} = N_o\, e\, \mu_e\, E$, *i.e.*, initial electron current density
$J_{Po} = P_o\, e\, \mu_h\, E$, *i.e.*, initial hole current density

The decay of depolarization current, as shown in Fig. 2 to 6 can be explained by Eq. [3]. It is assumed that mobilities μ_e and μ_h do not change appreciably during illumination. The expression for depolarization current is valid for all values of electric fields except for one or two discrepancies. Since we do not know the exact contributions of electrons and hole, we cannot make exact calculations.

Dark depolarization current is the current due to thermal release of electrons; its decay is faster in the beginning and slow afterwards tending to become constant (Fig. 2). Dark depolarization current as a function of applied field is shown in Fig. 10, immediately after the formation of the electret. This initial depolarization current shows an almost linear increase from 20 x 10^{-9}A to 115 x 10^{-9}A with the applied field increasing from 0.9 to 9 kV/cm under constant illuminance (curve a). No saturation is observed in this case. Due to the application of field, electrons and holes are liberated from traps replacing conduction electrons which are already displaced by the applied field. The stronger the field the greater is the number of electrons displaced; this explains the rise of depolarization current with applied field. The fact that there is no saturation suggests that during formation of the photoelectret there is only partial filling of trapping levels by electrons. When short-circuited samples are stored in the dark for half a minute before photodepolarization current measurements, and then re-illuminated, charge carriers are excited from traps due to light induced transitions as well as due to thermally induced transitions. The initial depolarization current increases from 8 x 10^{-9} to 45 x 10^{-9}A for the same field values as above (curve b). The smaller value of initial discharge current in this case suggests that the phenomenon of recombination between electrons and holes is taking place during short-circuiting, thereby reducing the number of electrons in trapping levels and thus the density of conduction electrons. Discharge current increases with field from 10 x 10^{-9} to 50 x 10^{-9}A when the external field is applied for 5 min more after the illumination is switched off (curve c). Here an increase in the duration of the applied field has increased the initial depolarization current, indicating that more and more charge carriers are carried along by the field, depending on the duration of applied field.

Final depolarization current after 15 min, Fig. 11, curve a, shows a much shallower slope as compared to the slope of initial current as shown in Fig. 10. The dark depolarization current increases from 2 x 10^{-9} to 7.8 x 10^{-9}A for the field values from 0.9 to 9 kV/cm, except for a peak around 7.2 kV/cm where the current is 20.5 x 10^{-9}A. Depolarization current after storing (curve b) increases from 2.6 x 10^{-9} to 5.3 x 10^{-9}A and that after application of external field (curve c), from 2.9 x 10^{-9} to 7.5 x 10^{-9}A for the same field range. The small variation in final depolarizing current in these cases suggests that release of trapped electrons can take place at almost the same rate in all these cases. The data for Fig. 10 and 11 are taken from Fig. 2, 3, and 4.

The heat quenching effect, Fig. 6, occurs due to prolonged illumination of the sample with white light. The infrared component quenches electrons present in shallow traps without producing any further excitation. If separate samples are used at different field strengths, no such quenching effects occur, as shown in Fig. 5.

A dummy sample molded between two electrodes without any application of field and illumination also gives a depolarization current comparable to that of a polarized photoelectret (Fig. 8, curve a and b). This is associated mainly with the contact electrification of the sample.

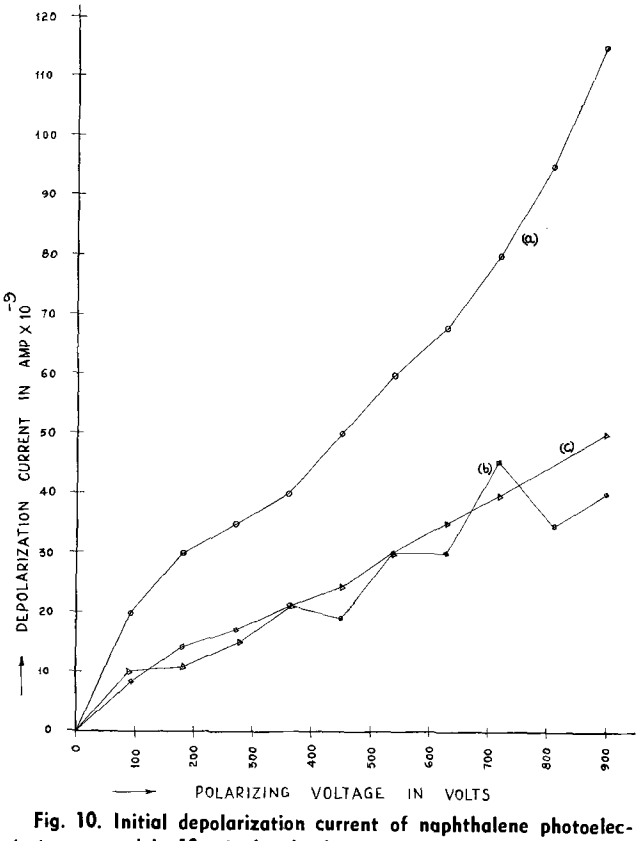

Fig. 10. Initial depolarization current of naphthalene photoelectrets prepared in 10 min by simultaneous application of field and illumination as a function of applied field strength: (a) immediately after formation of electret; (b) after dark storage, sample short-circuited; (c) external field maintained for 5 min after removal of illumination.

Summary and Conclusions

1. Naphthalene photoelectrets can be prepared in 10 min time with simultaneous application of an electric field and light.

2. Initial dark depolarization current increases almost linearly with increasing field; the final current after 15 min does not increase in the same proportion,

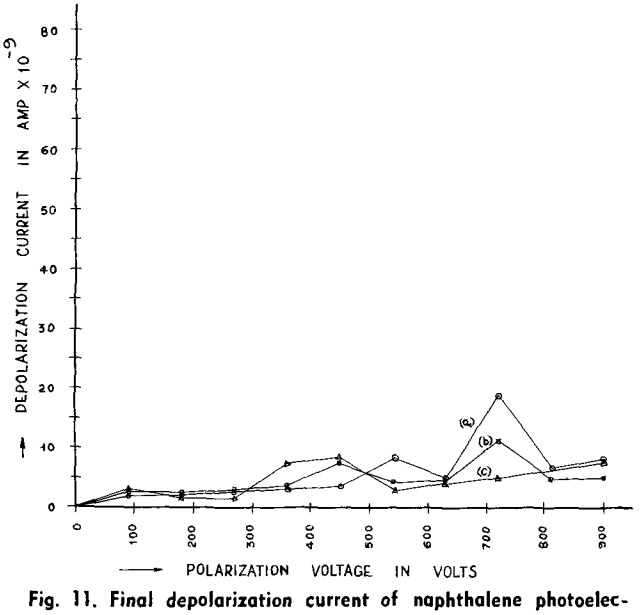

Fig. 11. Final depolarization current of naphthalene photoelectrets, prepared as in Fig. 10, after 15 min, as a function of applied field: (a) immediately after formation of electret; (b) after dark storage, sample short-circuited; (c) external field maintained for 5 min after removal of illumination.

indicating that decay is faster at higher voltages than at lower voltages.

3. When photoelectrets are stored in dark for 0.5 min, the depolarization current shows much more stability than it does in photoelectrets not stored.

4. The application of an external field after switching off the illumination increases the initial value of depolarization current; therefore this technique is advantageous for getting larger currents. The final current after 15 min is, however, not much affected by an extra field.

5. Prolonged illumination with the tungsten filament source produces a heat quenching effect and, therefore, the use of infrared filters is suggested for future work.

6. Contact electrification plays an important role in the behavior of a naphthalene photoelectret, especially under humid surroundings.

Acknowledgments

The authors are grateful to Professor M. S. Sodha, Head of the Department of Physics, Indian Institute of Technology, Delhi, for the encouragement given to them during the course of this investigation. Special thanks are also due to Mr. V. K. Jain for the useful suggestions and discussions at all stages of this experimental investigation. The authors are thankful to the Council of Scientific and Industrial Research, Government of India, for the research grant for carrying out this work.

Manuscript submitted Oct. 27, 1969; revised manuscript received *ca.* Oct. 22, 1970.

Any discussion of this paper will appear in a Discussion Section to be published in the December 1971 JOURNAL.

REFERENCES

1. W. Baldus, *Z. Tech. Phys.*, **6**, 481 (1954).
2. S. Mascarenhas, *Ann. Acad. Brazil*, **31**, 395 (1959).
3. L. M. Belyaev, G. S. Belikova, V. M. Fridkin, I. S. Zheludev, *Soviet Physics, Crystallography*, **3**, 772 (1960).
4. M. Campos, G. Leal Ferreria, and S. Mascarenhas, *This Journal*, **115**, 388 (1968).
5. H. Pick and G. Wiseman, *Z. Physik*, **138**, 436 (1954).
6. H. Boroffka in "Electrical Conductivity of Solids," H. Kallman and M. Silver, Editors, p. 395, Interscience Publishers, New York (1961).
7. "Photoelectret and the Electro-photographic Process," by V. M. Fridkin and I. S. Zheludev, Consultants' Bureau, New York (1961).
8. R. G. Kepler in "Organic Semiconductors," J. J. Brophy and J. W. Buttrey, Editors, p. 1, Macmillan, New York (1962).
9. O. H. LeBlanc, Jr. ,in "Organic Semiconductors," J. J. Brophy and J. W. Buttrey, Editors, p. 21, Macmillan, New York (1962).

Behavior of Te in Vapor-Grown GaP

R. C. Taylor*

IBM Research Division, Yorktown Heights, New York 10598

During the course of recent photoluminescence studies of tellurium donors in vapor-grown GaP (1) it was found that dark, trigonally shaped patterns appeared in crystals grown in the (111)A direction at high tellurium concentrations. These dark areas were clearly visible at low magnification when the crystals were viewed with transmitted light. Similar findings were also made by Luther (2). Because of the importance of tellurium doping in GaP light-emitting diodes we attempted to gain a more quantitative picture of the nature of these dark areas and of the general behavior of Te in vapor-grown GaP, including the solubility of the electrically active species. To accomplish this a series of crystals was grown using radioactive Te as the dopant. The desired information was obtained from a correlation of the radiotracer data with the electrical measurements. Use was also made of transmission photomicrographs, autoradiographs, and electron microprobe analysis.

Experimental

The vapor-grown GaP crystals were prepared by a previously described Ga-PCl_3 transport method (3). The gallium source temperature was 900°C, the substrate temperature 800°C, and the PCl_3 bubbler temperature −30°C. The PCl_3 flux was maintained constant at 1×10^{-3} moles/hr for all runs by passage of 50 cm^3/min of hydrogen through the cooled bubbler. Radioactive Te was introduced into the system in the form of a Te pellet in the doping line. The Te vapor flux required to give the desired doping level was controlled by the pellet temperature and hydrogen flow over the pellet. The Te flux was determined by pellet weight loss. Total hydrogen flow in the system was 100 cm^3/min.

For the most part the substrates used were GaAs wafers oriented 5° off (111)A. This orientation was chosen because it had been found that high donor concentrations could be employed without significantly affecting growth rates and surface morphology of GaP growths as opposed to the case with growths on (111)B substrates (4, 5). Also the (111)A growths tend to reject the residual sulfur impurity that is present in PCl_3 (3) so that the electrical measurements should reflect only Te donor concentrations. A few (100) and 5° off (111)B substrates were used to determine whether the solubility of electrically active Te and the appearance of the discolored defect areas might be orientation dependent and to determine the $Te_{(111)B}/Te_{(111)A}$ orientation effect [the ratio of Te incorporated into (111)B growths to Te incorporated into (111)A growths under identical conditions].

The substrates were chemically polished with an H_2SO_4/H_2O_2 etch before use. After growth the GaAs was removed by a $3HNO_3/HCl$ etch. The radioactive Te was produced by neutron irradiation of six nines purity Te, and its concentration was determined in the GaP by gamma scintillation counting. Since the radiochemistry of Te is quite complex and several isotopes emit gamma radiation, the notation Te* will be used throughout this paper to indicate total Te concentration as determined by gamma counting of all radioactive Te species. A possible complication in determining Te in a sample by radiotracer methods is the decay of Te^{131} resulting in the growth of gamma activity in the daughter product I^{131}. The iodine being retained in the standard would not be incorporated into the growing GaP crystal and as a result erroneous radiotracer data would be obtained. Therefore the neutron-irradiated Te was not used until the I^{131} had decayed below the limit of detectability as determined by gamma ray spectrometry. In this way we were certain that all gamma activity from both sample and

* Electrochemical Society Active Member.

Key words: tellurium segregation, donor solubility, substrate orientation effect.

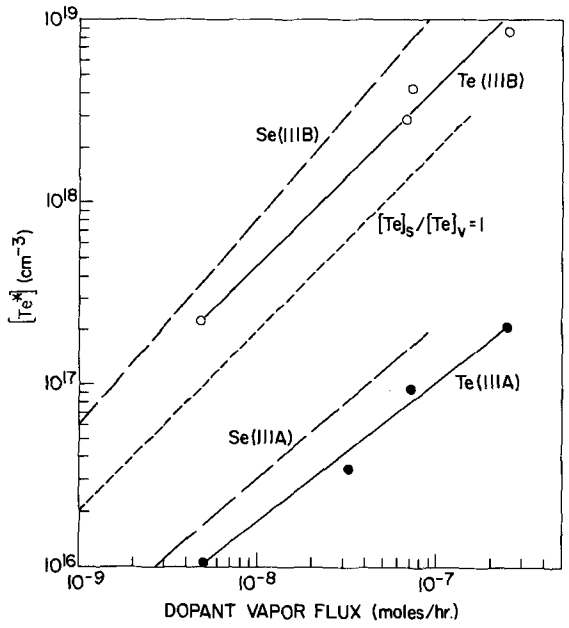

Fig. 1. The dependence of Te* concentration in (111)A and (111)B GaP crystals on dopant vapor flux.

standard was due exclusively to radioactive Te species. As a further check, the doped GaP samples were remeasured after a few weeks and were found to have the same Te concentration as compared with the standard. Electrical measurements were made by the Van der Pauw method. The GaP crystals were polished for the transmission photomicrographs, autoradiographs, and electron microprobe analysis. The autoradiographs were taken with Kodak R-X-ray film using 16-hr exposures.

Results and Discussion

Dependence of Te concentration on dopant vapor flux.*—The concentration of Te* in the GaP crystals as a function of dopant vapor flux is shown in Fig. 1. Previously obtained results for Se^{75} doping (4) are also shown for purposes of comparison. The Te concentration in the crystal shows an approximately linear dependence on dopant vapor concentration for both (111)A and (111)B growths. This was also found for Se doping and indicates that doping occurs under nonequilibrium conditions since under equilibrium conditions at an 800°C growth temperature the doping should reflect extrinsic behavior and the donor concentration should be proportional to the square root of the vapor phase concentration. A linear dependence has also been found by van der Does de Bye and Peters in an open tube GaP-HCl transport system (6). However Dyakonov (5) observed the expected extrinsic behavior in a closed-tube system, which lends itself more to equilibrium conditions than does an open system.

The orientation effect doping ratio, $Te_{(111)B}/Te_{(111A)}$, increases from about 20 at a dopant flux of 5×10^{-9} moles/hr to about 45 at a flux of 1×10^{-7} moles/hr. The same ratio is exhibited by Se-doped crystals, so it is apparently independent of donor species. We have explained this ratio previously for Se doping based on the fact that Se going onto a P site as a donor will form two surface bonds on a (111)B surface and only one on a (111)A surface and will therefore be more strongly held on the (111)B surface (4). Although the orientation effect ratio is independent of donor species, the distribution coefficient of the donor between solid and vapor is not. The distribution coefficient for Te is about one-half of that for Se. The difference decreases somewhat as lower dopant concentrations are approached. The distribution coefficient for Te is about 2 on (111)B face growths and about 0.05 to 0.1 on (111)A face growths.

Correlation of radiotracer and electrical data.—The results of radiotracer and electrical measurements on the Te-doped samples are given in Tables I and II and in Fig. 2. Table I shows the Te* concentration and the room temperature and 77°K electrical properties for (111)A growths. Table II gives similar results for (100) and (111)B growths. It should be noted that the Te* concentration at high concentrations is an average value due to segregation of the dopant.

In Table I all samples except A1 are n-type. The two principal effects illustrated by this table are those due to compensation and to impurity conduction. Compensation is indicated at Te* values below 10^{17} cm^{-3} by the discrepancy between the Te* concentration and the room temperature carrier concentration. This discrepancy becomes as large as 6 to 1 for sample A2 and decreases until a concentration 2×10^{17} cm^{-3} is reached (samples A5 and A6). Compensation is also reflected in room temperature and

Table I. Radiotracer and electrical data for Te-doped GaP (111)A

Sample	[Te*], cm^{-3}	n(RT), cm^{-3}	μ(RT), cm^2/V-sec	ρ(RT), ohm-cm	n(77°), cm^{-3}	μ(77°), cm^2/V-sec	ρ(77°), ohm-cm
A1	1.0×10^{16}			$>10^4$			
A2	3.4×10^{16}	5.2×10^{15}	82	15.0	2.7×10^{12}	62	3.7×10^4
A3	7.3×10^{16}	3.0×10^{16}	125	1.70	3.6×10^{13}	323	540
A4	9.8×10^{16}	4.7×10^{16}	143	0.94	9.0×10^{13}	731	96.0
A5	2.0×10^{17}	1.5×10^{17}	130	0.31	2.2×10^{14}	606	47.0
A6	2.0×10^{17}	1.9×10^{17}	113	0.29	3.9×10^{14}	382	42.0
A7	5.0×10^{17}	3.7×10^{17}	107	0.16	1.1×10^{15}	382	15.0
A8	7.7×10^{17}	7.5×10^{17}	91	0.091	2.2×10^{16}	277	10.0
A9	2.7×10^{18}	1.2×10^{18}	83	0.062	7.3×10^{15}	222	3.9
A10	6.0×10^{18}	2.4×10^{18}	85	0.031	7.3×10^{16}	89	0.95
A11	1.1×10^{19}	3.7×10^{18}	61	0.028	7.5×10^{17}	22	0.38
A12[a]		3.1×10^{18}	64	0.031	6.8×10^{16}	94	0.98

[a] Doped with nonradioactive Te.

Table II. Radiotracer and electrical data for Te-doped GaP (100) and (111)B

Sample	[Te*], cm^{-3}	n(RT), cm^{-3}	μ(RT), cm^2/V-sec	ρ(RT), ohm-cm	n(77°), cm^{-3}	μ(77°), cm^2/V-sec	ρ(77°), ohm-cm
(100)							
O1	3.5×10^{18}	1.8×10^{16}	82	0.043	9.4×10^{15}	166	4.6
O2	1.4×10^{19}	3.4×10^{18}	56	0.033	3.8×10^{17}	21	0.80
(111)B							
B1	2.3×10^{17}	2.8×10^{17}	115	0.19	8.0×10^{14}	747	10.0
B2	2.9×10^{18}	1.6×10^{18}	60	0.066	9.9×10^{15}	175	3.6
B3	4.6×10^{18}	2.4×10^{18}	65	0.039	4.8×10^{16}	77	1.7
B4	8.8×10^{18}	2.6×10^{18}	25	0.097	9.3×10^{16}	21	3.2

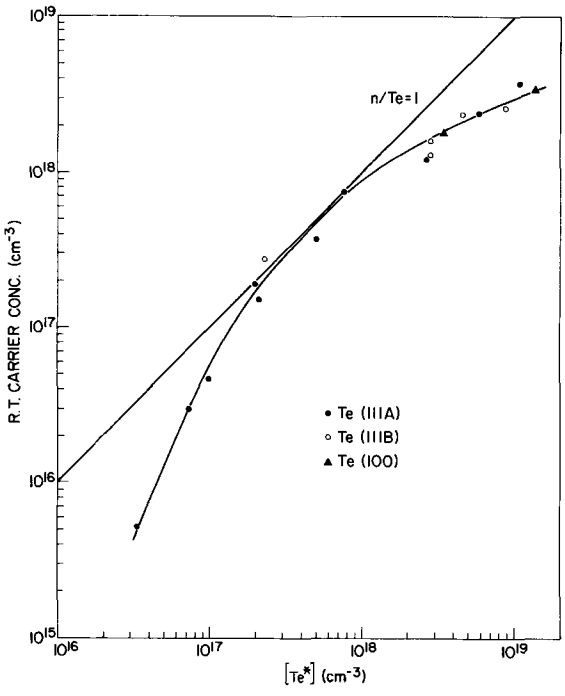

Fig. 2. The dependence of room temperature carrier concentration on Te* concentration in GaP crystals grown on (111)A-, (111)B-, and (100)-oriented substrates.

77°K mobility values, which peak at a Te concentration of 1 x 10^{17} cm^{-3} and fall off at lower concentrations. We have previously speculated (7) that this compensation is due to a Ga vacancy deep acceptor (triply ionized) at a concentration of about 1 x 10^{16} cm^{-3} which is introduced into (111)A growths to alleviate surface strain. Other investigators (6, 8) have calculated that a deep acceptor is present in (111)A growths at a level of 0.85 eV above the valence band, but they have failed to identify it.

The indication of impurity conduction is seen in the heavily doped samples (A10 and A11) where Te* is above the mid 10^{18} cm^{-3} range. Carrier freezout drops from three orders of magnitude for donor concentrations in the low 10^{16} cm^{-3} range to less than one order of magnitude at 10^{19} cm^{-3} (sample A11). Also at 10^{19} cm^{-3}, the mobility at 77°K is less than at room temperature. Table II shows the same tendency toward impurity conduction for (100) and (111)B growths as does Table I for (111)A growths and at the same donor concentration.

Figure 2 shows the experimental and n/Te = 1 curves for room temperature carrier concentration as a function of Te* concentration for three different substrate orientations. The previously mentioned compensation in (111)A growths is reflected on the divergence of the two curves at low Te concentrations. In the 10^{17} cm^{-3} range the two curves closely parallel each other. The fact that the (111)B point is above the n/Te = 1 line is perhaps due to the contribution of the sulfur impurity. At high concentrations the carrier concentration falls increasingly below the Te concentration due to increased donor ionization and the approach to saturation solubility of Te as an electrically active species. The points for high doping levels show the solubility limit to be independent of substrate orientation. Using the data if Montgomery (9) for Te binding energy *vs.* Te concentration and calculating the per cent ionization, it has been determined that for a sample with a Te concentration of 1 x 10^{19} cm^{-3} and a room temperature carrier concentration of 3-4 x 10^{18} cm^{-3} (upper limit of curve, Fig. 2) the donor concentration at exhaustion is about 6-7 x 10^{18} cm^{-3}, or about 60% of the Te concentration. This is probably the solubility limit for electrically active Te. This substantially agrees with the results of Trumbore (10), but is about three times the solubility determined by Dyakonov (5).

Tellurium segregation.—Figures 3-5 show transmission photomicrographs of the Te segregation which occurs at high concentrations. Figure 3 shows the most heavily doped (111)A and (100) growths. In (a) and (b) the view is along the (111) growth direction. The Te concentration in the sample of Fig. 3a (A10) is 6 x 10^{18} cm^{-3}, or about half that of the sample of Fig. 3b (A11) which is 1.1 x 10^{19} cm^{-3}. Both photomicrographs show the remnant of an as-grown surface pit not completely removed by polishing. The trigonally shaped dark areas appear to have their origin at the apex of these pits and display the three-fold symmetry of the (111) growth direction. The first signs of these defect areas appear at a Te concentration of about 2 x 10^{18} cm^{-3}. The number of trigonally shaped areas is considerably greater than the number of obvious pits in the as-grown surface, which suggests that the pits coalesce or fill in during growth. The filling in process has been observed by Luther (2). It is possible that the apex of each trigon is at a dislocation site either present in the substrate or generated to relieve heterojunction strain, the number generated increasing with increasing Te concentration. The reason for the shape of the trigon is probably that the pit walls are of an orientation which allows nucleation and retention of Te more readily than does the (111)A growth surface. Figure 3c is an autoradiograph of the sample in Fig. 3b. The clearly visible trigon in the center of the figure shows that the three blades of the trigon are truly Te rich. In Fig. 3d and 3e the view is along the (100) growth direction. The Te concentration in the sample of Fig. 3e(02) is 1.4 x 10^{19} cm^{-3}, or four times that in

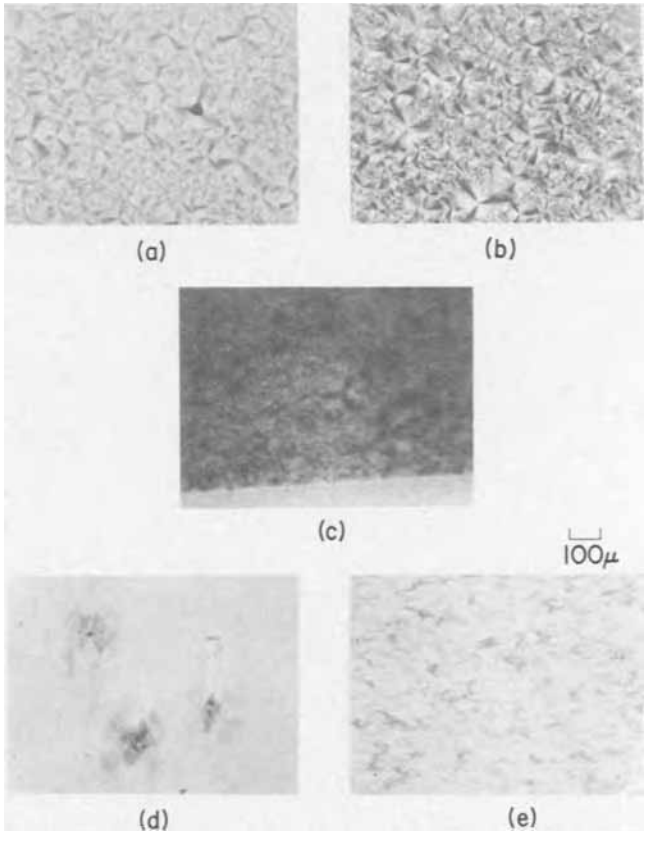

Fig. 3. (a) Transmission photomicrograph of sample A10 (t = 7 mils) viewed along (111)A growth direction. (b) Transmission photomicrograph of sample A11 (t = 7 mils) viewed along (111)A growth direction. (c) Autoradiograph of (111) surface of sample A11. (d) Transmission photomicrograph of sample 01 viewed along (100) growth direction (t = 4 mils). (e) Transmission photomicrograph of sample 02 viewed along (100) growth direction (t = 4 mils).

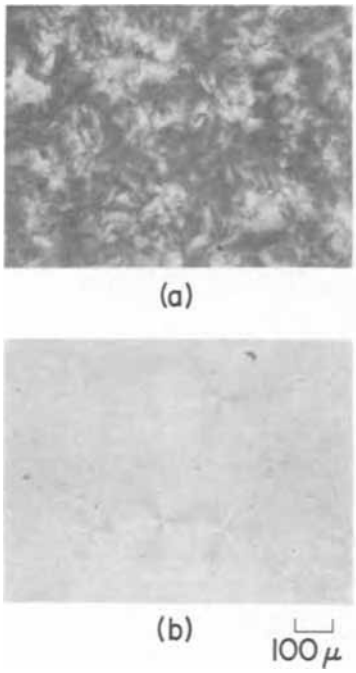

Fig. 4. (a) Transmission photomicrograph of Se-doped sample viewed along (111)B growth direction. (Se^{75}) = 1.3 x 10^{19}, n(RT) = 2.1 x 10^{18} cm^{-3}. (b) Transmission photomicrograph of Se-doped sample viewed along (111)A growth direction. (Se^{75}) = 3.2 x 10^{18}.

Fig. 5. Transmission photomicrograph of sample A12 (t = 8 mils) substrate and film viewed perpendicular to (110) cleavage plane and (111)A growth direction.

Fig. 3d(01) which is 3.5 x 10^{18} cm^{-3}. The typical "maltese cross" fourfold symmetry of the (100) plane is apparent in some of the areas. Precipitates are also evident.

Figure 4a is a transmission photomicrograph of a sample grown on a (111)B substrate, the view being along the (111) growth direction. The dopant here is Se^{75} at a concentration of 1.3 x 10^{19} cm^{-3}, but high Te doped samples look exactly the same. Figure 4b is a (111)A growth with an Se concentration of 3.2 x 10^{18} cm^{-3}. In contrast to (111)A growths the dark areas in (111)B growths show no distinguishable form. This is further evidence that the trigonally shaped areas are associated with pits since, while both (111)A and (111)B growth planes have the same threefold symmetry, there is never any pit formation observed in (111)B face growths. It may also be that the reason for the more drastic effect of high doping levels on growth rate and surface morphology of (111)B growths is the nonlocalized nature of the defect areas leading to a more highly strained surface.

In order to get a more quantitative idea of the Te distribution in heavily doped samples the electron microprobe was used on a cross section of one sample. Figure 5 is a transmission photomicrograph of a sample doped with nonradioactive Te (A12). The view is through a cross section of the film and the substrate (111A GaP) and is perpendicular to the (111)A growth direction and the (110) cleavage plane. The grown crystal is 1.5 mm in thickness. The room temperature carrier concentration in this sample is 3.1 x 10^{18} cm^{-3}. The complete set of electrical data for this sample (Table I) is almost identical to that of sample A10; thus it may be assumed that the average Te concentration is about 6-7 x 10^{18} cm^{-3}, as in A10. Electron microprobe analysis of this sample showed a Te concentration of 3 x 10^{19} cm^{-3} in the dark areas. It was below the limit of detectability (1 x 10^{19} cm^{-3}) in the light areas. From the electrical and microprobe data, the ionization energy data of Montgomery, and the previously calculated electrical solubility limit, it can be calculated that for a sample with an average Te concentration of 6-7 x 10^{18} cm^{-3} the Te is distributed at about 5 x 10^{18} cm^{-3} in the light areas (90% by volume) and 3 x 10^{19} cm^{-3} in the dark areas (10% by volume). Both light and dark areas would be expected to have a room temperature carrier concentration of 3 x 10^{18} cm^{-3} and an exhaustion region carrier concentration of about 5-6 x 10^{18} cm^{-3}. All of the Te in the light areas would be electrically active and only 1/6 or 1/5 of that in the dark areas. This is probably a fairly typical Te distribution for heavily doped samples.

Conclusions

It has been demonstrated that compensation occurs in lightly Te-doped GaP grown on (111)A substrates and that impurity conduction takes place at high Te concentrations. The effect of orientation on donor incorporation is the same for both Se and Te doping and in both cases doping occurs under nonequilibrium conditions. Visible segregation begins at an average Te concentration of 2 x 10^{18} cm^{-3}.

None of the studies made were capable of positively identifying the Te species in the dark areas in the Te-doped GaP crystals. However, in the light of previous work on Se- and Te-doped GaAs by other investigators (11-13) where precipitates appeared at high donor concentrations it is most probable that the dark areas observed in this study are either Ga_2Te_3-GaP solid solutions (with less than 1% Ga_2Te_3), or Ga_2Te_3 precipitates. In the Ga_2Te_3 structure, one-third of the Ga sites are unoccupied ($Ga_2V_{Ga}Te_3$). Thus when precipitation or solid solution formation begins there is one vacancy introduced for each three Te atoms. Since the Ga vacancy is a triply charged acceptor it compensates the three Te donors and the Te becomes electrically inactive (14, 15) above a concentration of 6 x 10^{18} cm^{-3}.

According to Saul (16), the number of dislocations generated at the substrate film interface is considerably greater in vapor phase epitaxy than in liquid phase epitaxy. It appears from this study that the dislocations lead to a growth morphology which promotes donor segregation due to the effect of orientation on donor incorporation. Thus on (111)A growths, for instance, the pit walls take on Te far more readily than the (111)A face, which leads to localized high Te concentrations and Ga_2Te_3 formation. This segregation is enhanced by the low growth temperature which prevents bulk diffusion of the Te to lower concentration regions. One possible consequence of this is the lower efficiency of vapor-grown GaP electroluminescent diodes as compared with that of diodes grown by liquid phase epitaxy. Precipitates such as Ga_2Te_3 can introduce strain and can also function as nonradiative recombination centers (12).

Acknowledgments

The author wishes to thank W. Haag, J. Keller, J. Kuptsis, and R. Robinson for their technical assistance and Dr. D. F. Woods for calculations with regard to the electrical results.

Manuscript submitted June 12, 1970; revised manuscript received *ca.* Sept. 23, 1970. This was Paper 147 presented at the Los Angeles Meeting of the Society, May 10-15, 1970.

Any discussion of this paper will appear in a Discussion Section to be published in the December 1971 JOURNAL.

REFERENCES

1. A. Onton and R. C. Taylor, *Phys. Rev.*, **B1**, 2587 (1970).
2. L. C. Luther, *Met. Trans.*, **1**, 593 (1970).
3. R. C. Taylor, J. F. Woods, and M. R. Lorenz, *J. Appl. Phys.*, **39**, 5404 (1968).
4. R. C. Taylor, *This Journal*, **116**, 383 (1969).
5. L. I. Dyakonov, E. S. Kopeliovich, V. N. Maslov, and R. L. Petrusevich, *Inorg. Mat.* (USSR), **4**, 437 (1968).
6. J. A. W. van der Does de Bye and R. C. Peters, *Philips Res. Rept.*, **24**, 210 (1969).
7. R. C. Taylor and R. S. Title, *Appl. Phys. Letters*, **11**, 355 (1967).
8. G. S. Kamath and D. Bowman, *This Journal*, **114**, 192 (1967).
9. H. C. Montgomery, *J. Appl. Phys.*, **39**, 2002 (1968).
10. F. A. Trumbore, H. G. White, M. Kowalchik, R. A. Logan, and C. L. Luke, *This Journal*, **112**, 782 (1965).
11. M. S. Abrahams, C. J. Buiocchi, and J. J. Tietjen, *J. Appl. Phys.*, **38**, 760 (1967).
12. H. Kressel, F. Z. Hawrylo, M. S. Abrahams, and C. J. Buiocchi, *ibid.*, **39**, 5139 (1968).
13. H. Kressel, N. E. Byer, H. Lockwood, F. Z. Hawrylo, H. Nelson, M. S. Abrahams, and S. H. McFarlane, *Met. Trans.*, **1**, 635 (1970).
14. L. J. Vieland and I. Kudman, *J. Phys. Chem. Solids*, **24**, 437 (1963).
15. G. Schottky, *ibid.*, **27**, 1721 (1966).
16. R. H. Saul, *This Journal*, **115**, 1184 (1968).

Polarity Dependence of Contact Angles between Liquid Gallium and {111} Surfaces of GaAs

B. E. Liebert and Z. A. Munir

Department of Materials Science, School of Engineering, San Jose State College, San Jose, California 95114

Although results of numerous sessile-drop measurements have been reported in the literature, apparently no attempt has been made to correlate these measurements with the crystalline orientation of the substrate materials. Aside from purely theoretical reasons, such information is of considerable practical interest since it relates directly to ohmic-contact phenomena and thus offers possible solutions to related problems in numerous device-oriented technologies. Because of these considerations, a study was initiated in order to investigate some of the parameters influencing contact angles between liquid metals and oriented surfaces of III-V and II-VI compounds. This note reports some initial observations of the dependence of contact angles made between liquid gallium and GaAs, on the polarity of the {111} planes of this compound.

Gallium arsenide, which crystallizes in the zinc-blende structure, has its (111) or A faces entirely populated by Ga atoms while the $(\bar{1}\bar{1}\bar{1})$ or B planes are occupied exclusively by As atoms. This polar nature of the {111} planes has been given as the reason for the anisotropic behavior of these planes with respect to chemical etch (1, 2), thermal stability and oxidation resistance (3), and the energetics of incorporation of impurity atoms (4).

Experimental

Contact angles between liquid gallium and GaAs were determined by the sessile-drop technique, which has been described in the literature (5) and is schematically represented in Fig. 1, in which γ is the surface energy vector between two adjacent phases (solid, liquid, or vapor).

The apparatus employed in the present study, schematically shown in Fig. 2, consisted of a horizontally positioned cylindrical tantalum heating element situated in the middle portion of an evacuated bell jar. Contained in this heating element is a graphite "dee" which served as a platform for the substrate wafers. To establish conditions approximating black-body radiation, the heating element was shielded around its major axis as well as at both ends. A small hole in the center of each end-shield provided openings for sighting on the liquid drop through one side, and for back-lighting the drop through the opposite side. The latter provision gave greater contrast between the sessile drop and its background. Power was introduced to the heating element by means of heavy-wall water-cooled copper tubing attached to the ends of the element. Measurements of contact angles between gallium drops and GaAs substrates were accomplished by

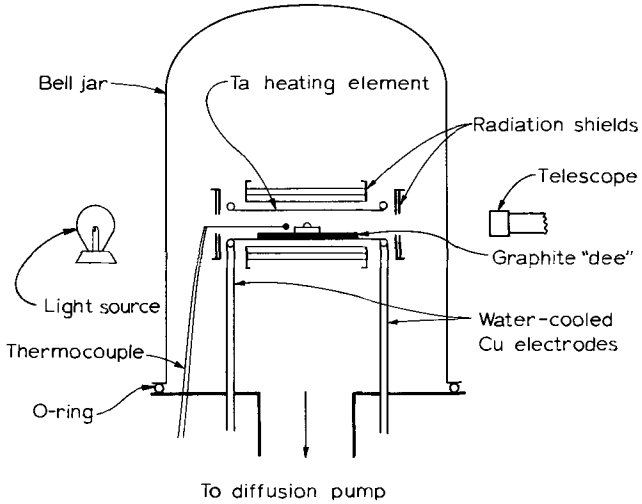

Fig. 1. Schematic of contact angle between liquid Ga and GaAs

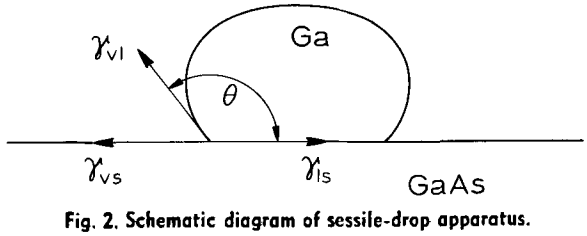

Fig. 2. Schematic diagram of sessile-drop apparatus.

Key words: sessile drop, interfacial interactions.

means of a telescope equipped with movable cross hairs and an especially designed goniometer capable of measuring angles to the nearest 0.25 degrees. All angular measurements were made under a vacuum of about 10^{-6} Torr, maintained by a liquid nitrogen-equipped diffusion pump.

To establish confidence in the angles measured by the telescope and to ascertain the absence of any significant contribution arising from optical distortion due to the wall of the bell jar, calibrations were made utilizing contact angle standards. The standards were stainless steel ball bearings with grounded facets representing mathematically calculated angles of contact from 33° to 180°. Telescopic determinations of these angles were made with and without the bell jar in position. The measured angles corresponded to the actual values to within ± 1° when the bell jar was removed and to within ± 2° when the jar was in place.

Crystals of semiconductor grade GaAs were cut along (111), (100), and (110) planes by means of a high-speed diamond saw. Laue patterns of the resulting 2 mm thick wafers indicated that deviations from the desired orientations were within about ± 1°. The surfaces of these wafers were then cleaned, chemically etched, and mechanically polished. Cleaning, whose purpose was to rid the samples of oil contaminants introduced during cutting and handling, was accomplished by successive washes with trichloroethylene, acetone, and deionized water. After drying with nitrogen gas, the wafers were chemically etched to remove surface layers believed damaged in the cutting process. The etchant used consisted of a hot mixture of 1:1 concentrated H_2SO_4 and 30% H_2O_2. Mechanical polishing was achieved by using 1μ diamond grit. Final treatment of the surface, which was performed just before their use in the contact angle measurements, included a wash with dilute HCl followed by water and acetone. Six-nine pure gallium pellets of approximately 2 mm diam were treated immediately before use in the sessile-drop experiments. This treatment, designed to eliminate any surface oxide layer, consisted of washing with dilute HCl followed by water and acetone. These pellets were then placed on the GaAs wafers which had already been placed on the graphite "dee" in the vacuum system. Using procedures suggested by Mariano and Wolff (2), chemical etch techniques were employed in order to identify the Ga and As faces of the {111} oriented wafers.

Temperatures were measured by means of a calibrated Chromel-Alumel thermocouple placed in contact with the substrate in the middle portion of the heating element. Calibration of this thermocouple was achieved *in situ* by observing the melting points of gallium and indium metals.

Results and Discussion

Table I gives the experimentally determined contact angles between drops of liquid gallium and substrates of GaAs, as a function of temperature and crystalline orientation. These measurements, which were made under identical experimental conditions, show a strong dependence of the contact angles on crystalline orientation and an apparent lack of dependence on temperature in the range investigated. The dependence on orientation is especially marked in the case of the {111} planes. A difference of about 30 degrees exists between contact angles measured on the A(111) side and those determined on the B($\bar{1}\bar{1}\bar{1}$) side, or about 25% of the former values. Apparently, therefore, a stronger interfacial interaction exists between liquid gallium and the Ga or A($\bar{1}\bar{1}\bar{1}$) surfaces than with the As or B($\bar{1}\bar{1}\bar{1}$) faces. Preliminary measurements using (110) oriented substrates of GaAs, which are composed of both Ga and As atoms, gave contact angle values of about 135° at 80°C. These values lie between those obtained for the surfaces populated exclusively by either of the two atomic species. Furthermore, contact angles on (100) oriented substrates were found to be about 150° at ~ 80°C.

Table I. Contact angles between liquid gallium and oriented surfaces of GaAs

T, °C	θ, deg	T, °C	θ, deg
a.	(111) surfaces	b.	($\bar{1}\bar{1}\bar{1}$) surfaces
35	114	46	144
35	113	65	143
45	113	77	144
57	113	479	142
82	113		
131	112		
203	113		
271	112		
331	112		

Seemingly, the observations reported here indicate that the charge transfer model of Gatos and Lavine (6, 7) is not significant in contact angle considerations. However, results of this study cannot be exclusively interpreted in terms of differences of wetting of GaAs by gallium as related to the atomic nature of the surface atoms. The role of absorbed impurities, as influenced by the nature of the surface composition, cannot be overemphasized. Studies now in progress at our laboratories are aimed at determining the influence of such parameters as surface finish and orientation as well as the role of inert and semi-inert gaseous atmospheres on the wetting behavior between liquid metals and oriented substrates of several III-V and II-VI compounds.

Acknowledgment

We are grateful to Professor Joseph A. Pask for making available to us some of his laboratory facilities.

Manuscript submitted July 13, 1970; revised manuscript received *ca.* Nov. 4, 1970.

Any discussion of this paper will appear in a Discussion Section to be published in the December 1971 JOURNAL.

REFERENCES

1. J. G. White and W. C. Roth, *J. Appl. Phys.*, **30**, 946 (1959).
2. A. N. Mariano and G. A. Wolff, Investigation of Evaporation and Condensation Mechanism, Technical Report AFML-TR-13, p. 116 (1969).
3. D. P. Miller, J. G. Harper, and T. R. Perry, *This Journal*, **108**, 1123 (1961).
4. R. C. Taylor, *ibid.*, **116**, 383 (1969).
5. J. J. Brennan and J. A. Pask, *J. Am. Ceram. Soc.*, **51**, 569 (1968).
6. H. C. Gatos and M. C. Lavine, *J. Appl. Phys.*, **31**, 743 (1961).
7. H. C. Gatos and M. C. Lavine, *This Journal*, **107**, 427 (1960).

Nonequilibrium Effects in Quasi-Static MOS Measurements

M. Kuhn and E. H. Nicollian*

Bell Telephone Laboratories, Incorporated, Murray Hill, New Jersey 07974

The low frequency MOS capacitance method first described by Berglund (1) has several advantages which make it useful for the study of the electrical properties of oxide-semiconductor interfaces. The two major advantages are: (*i*) it provides a method for measurement of the silicon surface potential over most of the bias range, and (*ii*) it is possible to extract the interface state density over most of the silicon energy bandgap. The major requirement which must be met to exploit these advantages is that the MOS capacitor must remain in thermal equilibrium over the entire bias range. This can be most easily satisfied by measuring the displacement current flowing through the MOS capacitor in response to a slow, linear voltage ramp (2-5). When the sweep rate (typically 5 to 100 mV/sec) is sufficiently slow so that both minority carriers and surface states can follow and the MOS capacitor remains essentially in thermal equilibrium, the response is directly proportional to the low frequency incremental capacitance. However, under certain conditions, the lowest practical sweep rates of about 5 to 10 mV/sec are not sufficiently slow to maintain thermal equilibrium over the entire bias range, and the resulting response is distorted. These conditions can occur at a room temperature for long lifetime silicon ($\tau > 100$ μsec), at low temperatures and also under illumination. The dominant effects observed are a peak in the response near weak inversion, and also a small voltage shift in strong inversion, when sweeping out of inversion. When deviation from thermal equilibrium is large, as for example at reduced temperatures, large distortions occur in the inversion region, as a result of the formation of a partial deep depletion condition when sweeping out of accumulation.

The purpose of this paper is to describe these effects and to show that they can be adequately explained in terms of well known minority carrier generation and injection effects (6, 7) in the field induced junction below the MOS field plate. They must be recognized and minimized in order to fully exploit the low frequency MOS capacitance technique.

Experimental Procedure

MOS capacitors were fabricated on 0.1 ohm-cm p-type epitaxial silicon and 5 ohm-cm n-type silicon by growing approximately 600 to 800Å of SiO_2 in steam under bias (8), and evaporating CrAu contact dots. The displacement current response, $i = C(V)\ dV/dt$, to a slow linear voltage ramp was measured. Under thermal equilibrium conditions, this ramp response is proportional to the low frequency differential capacitance (2). MOS ramp response measurements were performed using Keithley 602 electrometer, and an operational amplifier integrator was used to provide a low noise, slow, linear voltage ramp as described in Ref. (2). Measurements were made over the temperature range of 200° to 300°K with sweep rates varying from 0.01 to 1 V/sec with the sample in an atmosphere of dry nitrogen. The response for both sweep directions, from accumulation into inversion and the return sweep out of inversion toward accumulation was obtained and recorded on an x-y recorder.

Experimental Observation

A typical set of response characteristics are shown in Fig. 1, for both thermal equilibrium and nonequilibrium conditions and both sweep directions.[1] Curve 1 is the thermal equilibrium response when sweeping from inversion toward accumulation while curve 1′ is the thermal equilibrium response for the opposite sweep direction, from accumulation toward inversion. The ideal thermal equilibrium response would be symmetrical in sweep direction; the difference in scales of measured curve 1 and 1′ is due to a small difference in the magnitude of the sweep rate caused by the instrumentation. For comparison, curves 2 and 2′ show the typical nonequilibrium response measured at 270°K. The nonequilibrium characteristic, when sweeping from inversion toward accumulation shows a small shift in strong inversion and a peak near weak inversion. The nonequilibrium characteristics obtained when sweeping from accumulation to inversion (curve 2′) is similar.

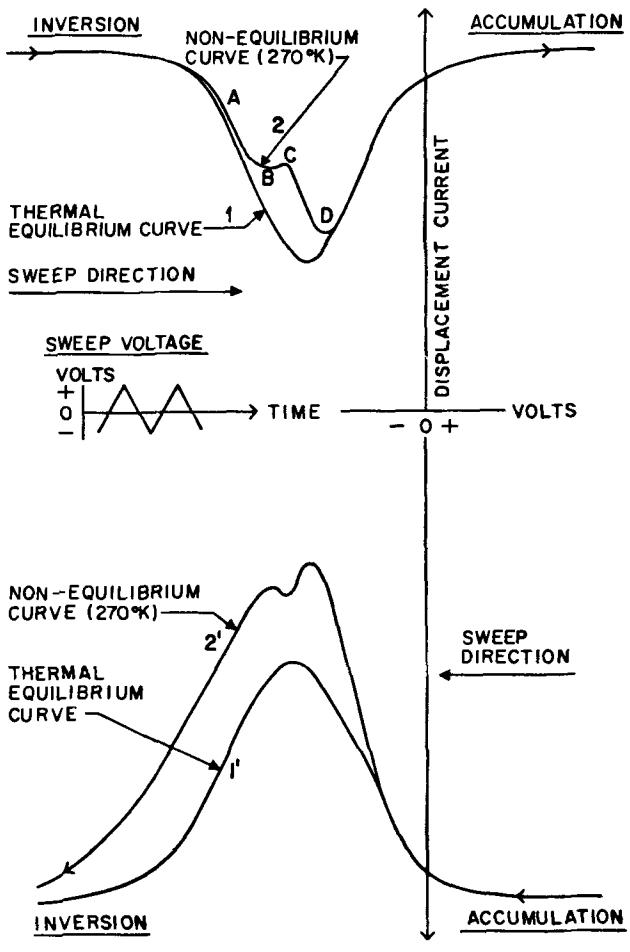

Fig. 1. Equilibrium and nonequilibrium response of an MOS capacitor to a triangular voltage sweep. The MOS capacitor was formed with 5 ohm-cm n-type Si, 800Å bias steam grown 7 oxide and Au-Cr contacts. The sweep rate was ±100 mV/sec.

Deviation from thermal equilibrium is due to those physical processes characterized by large time constants, *i.e.*, the inversion layer and the surface state response. The inversion layer response time constant (9, 10) and also the surface state time constants (10)

* Electrochemical Society Active Member.

Key words: surface states, silicon surfaces, inversion layers.

[1] Edge effects can be ruled out in these measurements because displacement currents scale linearly with gate area and the response characteristics are similar on both n and p type samples.

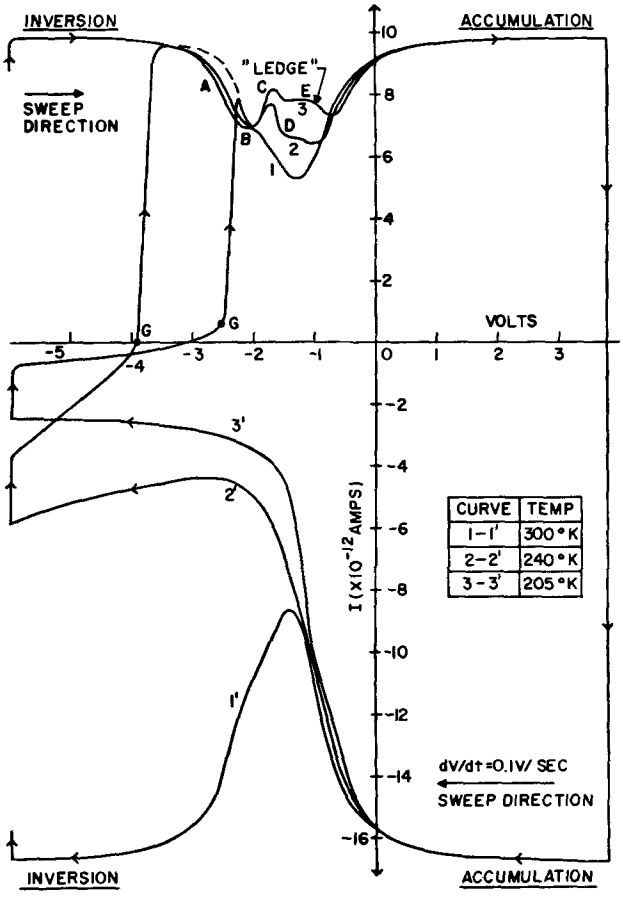

Fig. 2. Temperature dependence of the response of an MOS capacitor to a triangular voltage sweep. The MOS capacitor was 5 ohm-cm n-type Si, 800Å bias steam grown 7 oxide and Au-Cr contacts.

increase exponentially with decreasing temperature; therefore effects on the ramp response become dominant at low temperatures. A more detailed family of curves showing the temperature dependence of the ramp response of an MOS capacitor is shown in Fig. 2. The family of curves 1′ to 3′ show the temperature dependence of the response sweeping from accumulation toward inversion, and the family of curves 1 to 3 show the temperature dependence for the return sweep from inversion toward accumulation; a pair of curves such as 3 and 3′ is the ramp response to a triangular sweep at a fixed temperature.

We consider first the sweep direction from accumulation toward inversion (curves 1′ to 3′) in Fig. 1 and 2. Because the inversion layer formation is governed by generation of minority carriers, the system can remain in thermal equilibrium only if the maximum displacement current required by the sweep rate is much smaller than the generation current; that is $C_{ox}\, dV/dt << q\, n_i/\tau\, W$, where W is the depletion layer width, τ the minority carrier lifetime and n_i the intrinsic carrier concentration. At low temperatures, n_i and therefore the generation rate becomes small so that the above inequality can no longer be satisfied at normal sweep rates. Consequently, an equilibrium inversion layer cannot form, and the depletion layer expands more deeply into the bulk. The increasing space charge width results in a reduced displacement current and an increased generation current. Both of these effects tend toward restoring thermal equilibrium.[2] The peak in curve 2′ of Fig. 1 is due to surface state generation as the quasi-Fermi level passes through midgap at the surface. At lower temperatures, as in curves 2′ and 3′ of Fig. 2, surface state generation is so small that no peak is observed when sweeping toward accumulation.

When the sample is deeply depleted such as in curves 2′ and 3′ a net generation current flows, and minority carriers are stored at the semiconductor insulator interface. When the sweep direction is reversed, the generation current continues to flow, building up minority carrier charge at the interface while the depletion layer is being reduced by the sweep voltage. At the points G in Fig. 2 the silicon surface potential approaches that value required to hold the total minority carrier charge stored at the interface, in thermal equilibrium. At this point, the generation current abruptly ceases, and a field induced junction, in thermal equilibrium, is established below the field plate of the MOS capacitor. At lower temperatures, the equilibrium point G occurs at successively lower values of bias because the total minority carrier charge accumulating by generation at the interface becomes smaller at lower temperatures. Application of light increases the generation rate and will therefore move the equilibrium point G as if temperature were increased.

Sweeping through this equilibrium point towards accumulation a small forward bias V_F develops on the field induced junction. Initially this results in net recombination, in the depletion region, of minority carriers from the inversion layer with majority carriers from the bulk and occurs in region A of Fig. 1. This forward bias is necessary to sustain the displacement current and leads to a voltage shift between curves 1 and 2 in Fig. 1 and 2, given by $\Delta V = V_F + \Delta Q_s/C_{ox}$ where ΔQ_s is the excess minority carrier surface charge in the inversion layer and in the surface states. At room temperature and for typical sweep rates, ΔV is usually negligibly small (2). However, at lower temperatures a larger forward bias is required for a given recombination current density, ΔV can become appreciable, of the order of several tenths of a volt, as shown in region A of Fig. 2. In this region, the minority carrier surface charge and the surface potential are being reduced while V_F and ΔQ_s remain nearly constant as the ramp voltage decreases.

At point B in Fig. 1 and 2 the surface potential has been reduced sufficiently to make diffusion current dominant. The inversion layer charge is rapidly injected into the bulk, dissipating the excess minority carrier charge at the surface. The discharging of excess minority carrier surface charge ΔQ_s by injection produces the observed current peaks in region BCD of Fig. 1 and 2. The peaks at lower temperature are larger because ΔV and hence ΔQ_s is larger at lower temperature. At the lower temperatures, however, the reduced diffusion current density cannot restore equilibrium as rapidly, thus producing the ledge at E (15). The forward bias at which diffusion current becomes dominant is less in a field induced junction then in a metallurgical junction because in a field induced junction, inversion layer charge density is a function of V_F.

This observed peak is clearly a nonequilibrium effect and cannot be attributed to any particular surface state distribution. This peak would be observable in an ideal MOS capacitor without surface states. The magnitude of the peak however depends on the surface state density only through the excess minority carrier charge that may be stored in surface states.

The peak in weak inversion and the shift in strong inversion can be observed under illumination in both n and p-type MOS structures. An example of the effect of illumination on a p-type MOS capacitor is given in Fig. 3, showing C-V curves at room temperature in the dark and under room light. The response under illumination is essentially independent of the sweep direction.

[2] The response in this regime is determined by a complex dynamic equilibrium between the increasing voltage tending to increase the depletion layer width and minority carrier generation tending to reduce the depletion layer width and restore equilibrium. At temperatures as low as 77°K when the generation rate becomes negligible compared to the displacement current, the response is determined by the oxide capacitance, and yields the well known depletion characteristics (12, 13). These can of course be obtained at room temperature but a considerably faster sweep rate is required (14).

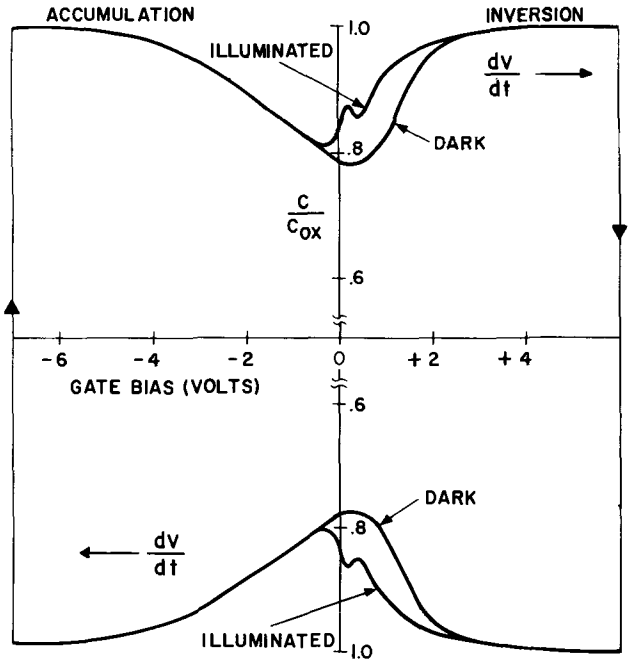

Fig. 3. Response at room temperature with and without illumination of an MOS capacitor to a triangular voltage sweep. The MOS capacitor was formed with 0.1 ohm-cm p-type, 600Å bias steam grown SiO_2 and Cr-Au contacts.

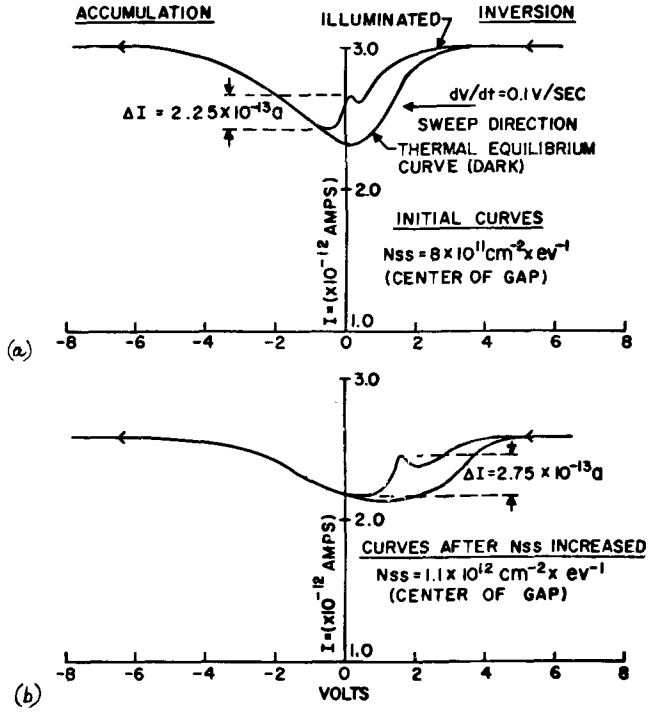

Fig. 4. Response at room temperature of an MOS capacitor to a linear voltage ramp with and without illumination before and after avalanche injection of minority carriers into the oxide. Sweep rate for upper curves was slightly greater than for lower curves. The MOS capacitor was 0.1 ohm-cm p-type, Si, 600Å bias steam grown SiO_2, and Cr-Au contacts.

Under illumination, the minority carrier concentration near the surface and beyond the field plate is increased and an excess minority carrier distribution is established below the field plate. This excess minority carrier concentration results in the shift of the *C-V* characteristics in strong inversion and also in the displacement current peak in the same fashion as described in the previous section.

Because the current peak observed under illumination is also produced by relaxation of the excess minority carrier surface charge, the magnitude of this peak is also expected to increase with an increase in surface state density. An experiment was devised to verify this dependence, and will be described below.

The quasi-static *C-V* characteristics with and without illumination shown in Fig. 4a, were obtained. Avalanche injection (16) of electrons was then carried out on this same sample in order to increase the surface state density, and the ramp response was measured with and without illumination. An example of the results is shown in Fig. 4b. From the shape of the *C-V* curves without illumination it is clearly evident that the surface state density after avalanche injection has increased, and that the peak under illumination has also increased. Additional measurements of the minority carrier lifetime and the surface recombination velocity using the Zerbst technique (17) also show that after avalanche injection the surface recombination velocity has increased.

An analysis of the quasi-static response was performed to determine the surface state distribution before and after avalanche injection. This showed that avalanche injection introduces surface states uniformly over a large part of the energy gap. The increase in the peak under illumination is also approximately proportional to the increase in surface state density.

Conclusions

Under some conditions, nonequilibrium effects can be encountered in low frequency capacitance-voltage measurements which can cause distortion of the response, even at the lowest practical sweep rates of 5 to 10 mV/sec. These conditions can occur even at room temperature for long lifetime silicon ($\tau > 100$ μsec), at low temperature, and under illumination. These nonequilibrium effects result in a small voltage shift of the inversion response and a peak near weak inversion when sweeping from inversion to accumulation and a partial deep depletion condition when sweeping from accumulation toward inversion. These effects have been explained in terms of field induced junction phenomena; they would still be observed in the absence of interface states. At most, interface states play a secondary role.

These nonequilibrium effects must be minimized in order to obtain meaningful results for surface potential and surface state density. They can be minimized and made negligible by using short lifetime silicon ($\tau \leq 1$ μsec), making measurements in the dark, and using sweep rates smaller than 100 mV/sec. Measurements on longer lifetime silicon can be performed by using elevated temperatures, normally not more than 100°C to avoid ionic drift.

Manuscript submitted June 4, 1970; revised manuscript received *ca.* October 27, 1970.

Any discussion of this paper will appear in a Discussion Section to be published in the Dec. 1971 JOURNAL.

REFERENCES

1. C. N. Berglund, *IEEE Trans. Electron Devices*, **ED-13**, 701 (1966).
2. M. Kuhn, *Solid-State Electron.*, **13**, 863 (1970).
3. D. R. Kerr, Conf. on Prop. and Uses of MIS Structures, Grenoble, France, June 17-21, 1969.
4. R. Castagne, *C. R. Acad, Sci., Paris*, **B267**, 866 (1968).
5. R. Castagne and A. Vapaille, *ibid.*, **B270**, 552 (1970).
6. C. N. Berglund, *Appl. Phys. Lett.*, **9**, 441 (1966).
7. V. G. K. Reddi, *IEEE Trans. Electron Devices*, **ED-13**, 381 (1966).
8. A. Goetzberger, *This Journal*, **113**, 138 (1966).
9. S. R. Hofstein and G. Warfield, *Solid-State Electron.*, **8**, 321 (1965).
10. A. Goetzberger and E. H. Nicollian, *Bell System Tech. J.*, **46**, 513 (1967).
11. E. H. Nicollian and A. Goetzberger, *ibid.*, **46**, 1055 (1967).
12. J. L. Moll, *IRE Wescon Conv. Record*, **3**, pt. 3, 32 (1959).
13. A. S. Grove, B. E. Deal, E. H. Snow, and C. T.

Sah, *Solid-State Electron*, **8**, 145 (1964).
14. M. Kuhn, IEEE Int. Electron Devices Conf., Oct. 29-31, 1969.
15. A. Goetzberger and J. C. Irvin, *IEEE Trans. Electron Devices*, **ED-15**, 1009 (1968).
16. E. H. Nicollian and C. N. Berglund, *Appl. Phys. Lett.*, **15**, 174 (1969).
17. M. Zerbst, Z. *Angew. Phys.*, 22:2, 30-33 (1966).

Note on the Preparation of Rhenium Oxychlorides

Abner Brenner* and Harvey J. Anderson

National Bureau of Standards, Washington, D.C. 20234

Perrhenyl chloride, ReO_3Cl, is of potential interest for the chemical vapor deposition (CVD) of rhenium, as we have shown (1) that it readily reduces to the metal when passed with hydrogen over a substrate heated above 300°C. We found the methods given in the literature for the preparation of perrhenyl chloride unsatisfactory because of low yields and the inconvenience in the manipulations. We wish to report briefly on a simple procedure that yielded material of sufficient purity for use in experiments in chemical vapor deposition.

Brukl and Ziegler (2) first reported the preparation of the two oxychlorides, ReO_3Cl and $ReOCl_4$, which they obtained as a mixture by heating rhenium heptaoxide with rhenium chlorides (probably a mixture of $ReCl_3$ and $ReCl_5$). The product of the reaction was difficult to fractionate into its pure components. Briscoe, Robinson, and Rudge (3) heated rhenium with oxygen and chlorine or the mixed rhenium chlorides with oxygen. Geilmann, Wrigge, and Blitz (4) heated rhenium trichloride or rhenium pentachloride with oxygen and obtained a vigorous reaction which yielded a mixture of oxychlorides. No further work was published on the preparation until about 25 years later, when Wolf, Clifford, and Johnston (5) described a method consisting of the passage of chlorine over rhenium trioxide at 160°-190°C. The yield was 70%. The trioxide was prepared by thermally decomposing the adduct of rhenium heptaoxide and dioxane.

We did not have success with the earlier methods and only partial success with the method of Clifford *et al.* In four trials with the latter method we obtained one yield of 60%, which is in line with the stated yield, but in the other three trials the yields ranged from 0 to 20%. Apparently the method of preparing the trioxide affects its activity. The preparation of the trioxide is a drawback to the method since it adds a time-consuming step.

We prepared perrhenyl chloride by the direct passage of dry hydrogen chloride over rhenium heptaoxide. The reaction occurred even at room temperature but was facilitated by gentle warming, for example to 75°C.

$$Re_2O_7 + 2HCl \rightarrow 2ReO_3Cl + H_2O$$

The yields of the crude product were about 50%. Along with the formation of the perrhenyl chloride a more volatile compound of rhenium was formed, probably an adduct of ReO_3Cl and HCl.[1]

The simplest arrangement for conducting the reaction was to place the rhenium heptaoxide in a tap-funnel, which was in a horizontal position, and pass HCl through. The rhenium heptaoxide soon became transformed into a viscous blue liquid with a pale yellow fluid (perrhenyl chloride) above it. By chilling the side of the tap funnel with ice, the viscous blue layer was immobilized and the perrhenyl chloride was readily drained from the tap-funnel. This operation was repeated a number of times until the rate of formation of the oxychloride became too low for further operation of the process to be profitable. The reaction can also be carried out in an ordinary flask and the perrhenyl chloride distilled over in a current of hydrogen chloride.

We believe that the viscous blue liquid remaining in the reaction vessel consisted mainly of a solution of the heptaoxide dissolved in the water which was formed in the reaction along with some blue reduction products. The blue liquid can be treated with nitric acid and heated to about 200°C to regenerate the anhydrous heptaoxide which is used again. The yield of perrhenyl chloride (about 50%) together with the recovery of rhenium heptaoxide brings the utilization of the rhenium up to about 90%.

We attempted to improve the yield of perrhenyl chloride by using dehydrating agents to remove the water. In one procedure, the rhenium heptaoxide was dissolved in sulfuric acid heated to 200°-225°C and a rapid stream of HCl passed through. The yield was not improved over the simpler procedure already described and the lost rhenium was not readily recoverable. Other disadvantages were that the method was slow, requiring several hours to process 30g of the oxide, and the product collected was not pure enough to use for CVD. It contained sulfuric acid and had to be redistilled.

In another experiment, phosphoric acid was tried as a dehydrating agent, but apparently it formed too stable a complex with the rhenium. A partially successful method consisted in the suspension of rhenium heptaoxide in carbon tetrachloride. The passage of HCl through the system caused the oxide to turn quickly into a viscous blue liquid which settled out and the perrhenyl chloride formed went into solution. The perrhenyl chloride could be separated from the carbon tetrachloride by distillation.

Rhenium oxytetrachloride is also serviceable for CVD, although it has a higher boiling point (225°C) than perrhenyl chloride (130°C). Recently it has been prepared by Edwards and Woolf (6), who heated rhenium powder in a sealed tube with sulfuryl chloride, and by Bagnall, Brown, and Colton (7), who treated the heptaoxide with thionyl chloride. They reacted the materials at room temperature, then poured off the supernatant liquid from an adduct which had formed. They evaporated the supernatant liquid at 50°C in vacuo to obtain the oxytetrachloride. We found that simply refluxing the heptaoxide with thionyl chloride for an hour or two, followed by distilling off all volatile materials until the temperature reached the boiling point of the oxytetrachloride, sufficed to give a product usable for CVD without further purification. The yield was about 95%.

* Electrochemical Society Active Member.

Key words: chemical vapor deposition, perrhenyl chloride, rhenium heptaoxide, rhenium oxytetrachloride.

[1] The evidence of the formation of an adduct of ReO_3Cl and HCl is as follows. At the start of the experiment, at room temperature, the reaction vessel filled with a yellow vapor which was too deep in color to be chlorine. Perrhenyl chloride (bp 130°C) is not sufficiently volatile at room temperature to produce vapor of this intensity of color. In the experiments the product of the reaction was first collected in a receiver cooled with ice. This receiver was backed up by a trap cooled with solid carbon dioxide, and this trap communicated with a mercury trap. All of the perrhenyl chloride should have condensed in the ice-cooled receiver. However, (as an example) at the conclusion of an experiment in which about 25g of perrhenyl chloride was prepared, a few grams of a yellow solid (chlorine would be a liquid at this temperature) were found in the carbon dioxide-cooled trap. As the yellow solid warmed up to room temperature it swelled, effervesced, and melted, giving off HCl. After the effervescence had ceased, the yellow liquid remaining was identified as perrhenyl chloride by its boiling point. The adduct must be slightly volatile even at the solid carbon dioxide temperature, since the mercury in the trap was discolored by the presence of rhenium compounds.

Manuscript submitted June 23, 1970; revised manuscript received Oct. 21, 1970.

Any discussion of this paper will appear in a Discussion Section to be published in the December 1971 JOURNAL.

REFERENCES

1. H. J. Anderson and A. Brenner, "Chemical Vapor Deposition of Rhenium," in "Chemical Vapor Deposition, Second International Conference," J. M. Blocher, Jr., and J. C. Withers, Editors, pp. 355-366, Electrochem. Soc., New York (1970).
2. A. Bruckl and K. Ziegler, *Chem. Ber.*, **65B,** 916 (1932).
3. H. V. A. Briscoe, P. L. Robinson, and A. J. Rudge, *J. Chem. Soc.*, **1932,** 1104.
4. W. Geilmann, R. W. Wrigge, and W. Biltz, *Z. Anorg. Allgem. Chem.*, **214,** 248 (1933).
5. C. J. Wolf, A. F. Clifford, and W. H. Johnson, *J. Am. Chem. Soc.*, **79,** 4257 (1957).
6. D. A. Edwards and A. A. Woolf, *J. Chem. Soc., A, (No. 1),* **1966,** 91.
7. K. W. Bagnall, D. Brown, and R. Colton, *J. Chem. Soc.*, **1964** 3017.

JOURNAL OF THE ELECTROCHEMICAL SOCIETY

ELECTROCHEMICAL TECHNOLOGY

FEBRUARY 1971

Testing Batteries for Vehicular Applications

III. Selection and Characterization of a Power Battery

Bernard Agruss*

Electrochemistry Department, Research Laboratories, General Motors Corporation, Warren, Michigan 48090

ABSTRACT

The problem was to find an acceptable "power" battery (*i.e.*, a high power density battery to deliver short time acceleration pulses) for an electric commuter vehicle concept powered by a dual battery system. A number of batteries were tested, both Pb-acid and Ni-Cd. The best battery was a Ni-Cd aircraft starting battery. It could deliver 14 consecutive 1900W, 10 sec acceleration power pulses. It was calculated that about 180 lb of battery would be required for the particular power plant design envisioned. The high cost and scarcity of Cd militated against the use of a Ni-Cd battery. The next best candidate was a Pb-acid aircraft starting battery designed for high current drains for short time periods. It, too, delivered 14 consecutive 1900W, 10 sec pulses. In addition, it had sufficient energy capacity to provide some low speed range in the event of failure of the "base-load" energy battery. It had a power density of 70 W/lb at an energy density of 2 Whr/lb. About 270 lb of this battery would be required for the "power" battery pack. A Delco-Remy 2HN-11A military battery was tested to yield design data for the power plant. From these data, a battery was designed which would fit into an available lightweight container. Prior to this, a 2HN-11A modified battery was tested to confirm the design. Test results confirmed the designed capacities.

Several of the design batteries were built. Each consisted of seven cells containing 11 plates per cell. One of the batteries was tested. It delivered 15 consecutive 2500W acceleration power pulses to 10.5V. It weighed 32 lb; hence, the entire power pack would weigh 256 lb. Since the 11-plate cell performed so well, it was hoped that a 9-plate cell might just deliver adequate power. A 27 lb weight reduction would be realized. However, it could not deliver adequate power when tested. Nothing could be obtained at 2500W. The voltage fell immediately below 10.5. In fact, only 1.8 min were obtained at 1900W.

In a prior paper (1), a versatile test facility was described for testing batteries under actual operating conditions. In a following paper (2), a number of S.L.I. batteries were characterized. They could be called the energy batteries for a dual battery system since they were designed for energy capacity rather than power density. The system was a new, experimental, all G.M., electric car test bed, code named XEP, powered by two different kinds of batteries. To complete the dual battery system, a power battery had to be found. This paper presents the capacity data obtained on a number of commercially available Pb-acid and Ni-Cd batteries. It is shown how a battery was designed from the Pb-acid data for a power battery pack.

Experimental

All of the battery tests were carried out at ambient temperature. The test facility (1) described in a prior report was used for all of the tests. The tests performed were capacity at varying constant current discharges, constant power discharges at varying power levels, consecutive 10 sec acceleration power pulses to cutoff voltage, and charge discharge voltage *vs.* current at varying capacity levels.

* Electrochemical Society Active Member.

Key words: battery tests, storage batteries, lead-acid batteries, vehicular application tests, constant power capacity, acceleration power pulses.

Pb-acid aircraft starting battery results.—The first battery tested was an aircraft starting battery designed for lightweight and high current drains. Its nominal characteristics are given in Table I.

Figure 1 shows the results of the constant current capacity tests. These tests were for battery No. 2 and showed a nominal 5 hr capacity of about 29 A-hr. Typically lower capacities were obtained at higher current drains.

Figure 2 shows the constant power profiles for battery No. 1. Here the voltage is plotted against ampere-hours. As was shown in a prior report (2), it is better to plot voltage against time as in Fig. 3. The advantage comes in directly ascertaining by inspection range at any road load (power level) or number of acceleration power pulses. The most significant curve for the power battery for the XEP is the 1900W discharge. This is the power required from one battery for a 10 sec accelera-

Table I. Aircraft starting battery characteristics

	Pb-acid	Ni-Cd
A-hr capacity (5 hr)	29	8
Nominal volts	12	24
Cells/battery	6	20
Plates/cell	11	—
Battery weight (lb)	27	10

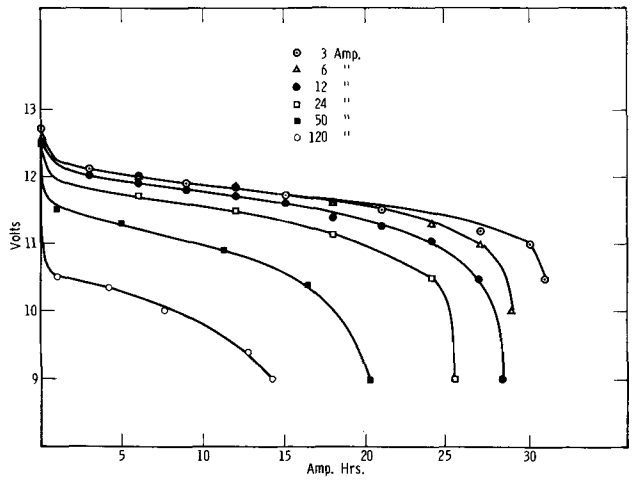

Fig. 1. Pb-acid aircraft starting battery No. 2, constant current discharge (A-hr).

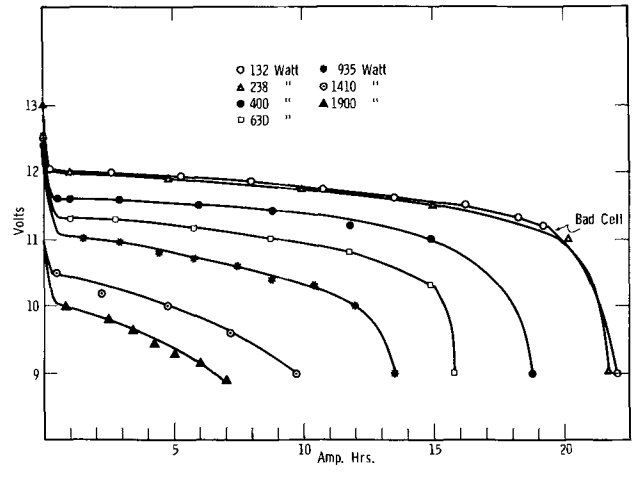

Fig. 2. Pb-acid aircraft starting battery No. 1, constant power discharge (A-hr).

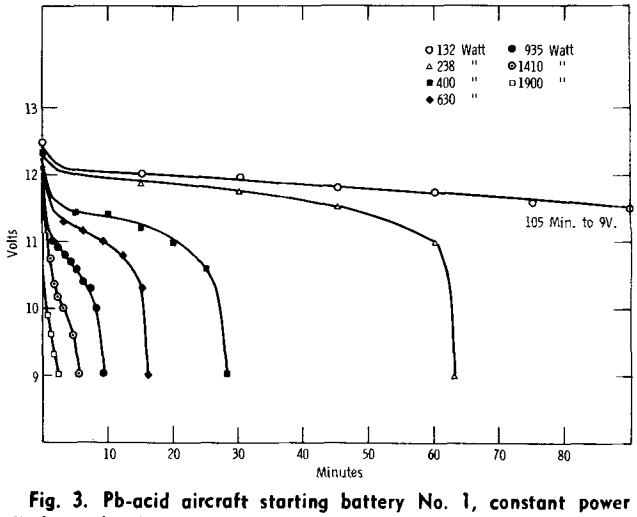

Fig. 3. Pb-acid aircraft starting battery No. 1, constant power discharge (min).

tion to 1.5 V/cell cutoff. It shows a capacity of 2.5 min to 9V. This is equivalent to fifteen 10 sec discharges.

It was noticed that one cell lost voltage rapidly and made the total battery voltage drop faster. It was felt that this might limit the capacity of the battery; hence, another battery was tested.

Figure 4 shows the power profiles for battery No. 2. This one discharged 3 min at 1900W equivalent to eighteen 10 sec discharges. All the capacities were just slightly better than battery No. 1. The difference, however, was not significant.

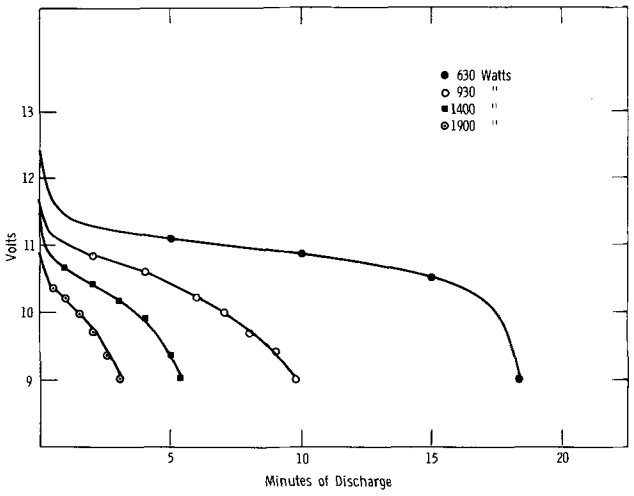

Fig. 4. Pb-acid aircraft starting battery No. 2, constant power discharge (min).

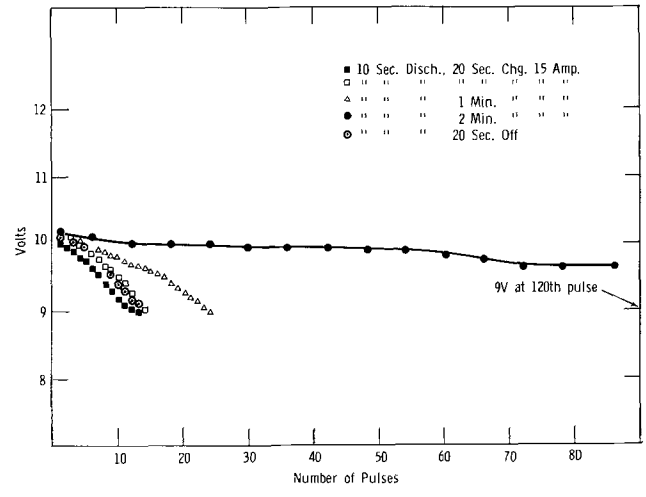

Fig. 5. Pb-acid aircraft starting battery No. 2, 1900W power pulses.

The number of consecutive 1900W, 10 sec pulses to 9V are shown in Fig. 5. Here, both batteries, No. 1 and 2, delivered 14 pulses. The constant power discharge predicted 15 and 18, respectively. Note that there was no change in the number of pulses whether the battery was charged at 15A or not charged during the 20 sec rest period. One minute and 2 min charge periods increase the number of pulses appreciably to 24 and 120, respectively.

For the voltage requirements, 10 of these batteries in series are needed. Each battery weighed 27 lb; hence, the total power pack would weigh 270 lb.

Useful range data may be derived from Fig. 4 by replotting as in Fig. 6. Using the principle of additivity (2), the range at any power level or a variety of power levels may be easily calculated. These curves may be of special interest to a systems analysis group.

Also for the benefit of systems and power plant design analyses are the charge-discharge, voltage *vs.* current plots at varying charge capacities shown in Fig. 7. These are useful in calculating charge-discharge efficiencies. They also give some indication as to what capacity the battery can be charged rapidly before the voltage efficiency deteriorates badly. Using a 15V upper limit, the battery can be charged at 100A to 50% capacity and to 75% capacity at 50A.

The discharge curves at all capacity levels have the same voltage-current characteristics. The slope is much less than the charge curves, except for the 50% capacity. Up to 50% capacity, the charge curve will be nearly a reflection of the discharge curve. Above 50% capacity, the charge curves have a much greater slope than the discharge curves. Apparently there is an increase

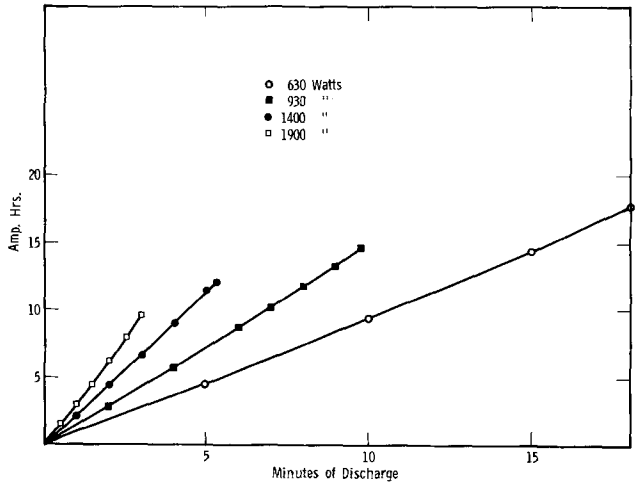

Fig. 6. Pb-acid aircraft starting battery No. 2, constant power discharge capacity vs. discharge time.

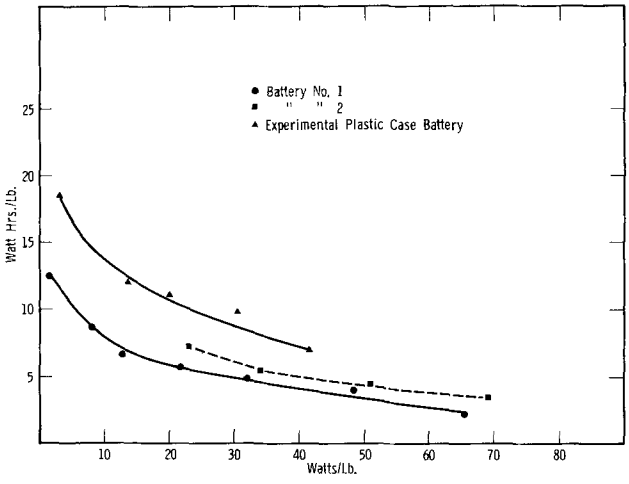

Fig. 9. Pb-acid aircraft starting battery, energy density vs. power density.

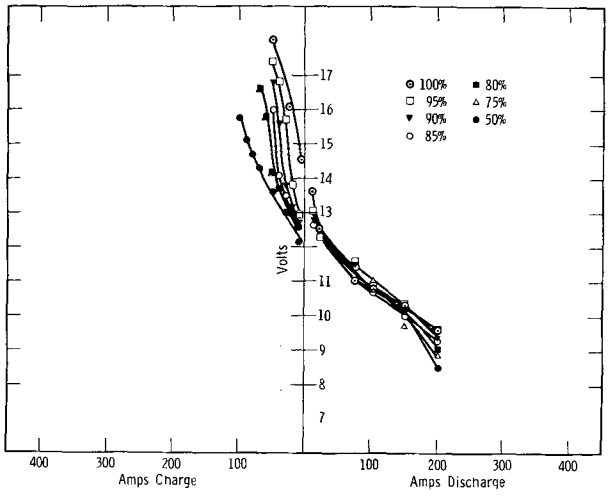

Fig. 7. Pb-acid aircraft starting battery, voltage vs. current

in polarization during charge after 75% capacity is reached. Usually, this is associated with the high hydrogen overvoltage on the Pb plate and the increased acid specific gravity in the pores of the plate.

The data in Fig. 8, taken from the power profiles, are given as an aid to systems analysis and power plant design. This shows the voltages under which the power plant will have to operate at any power level.

For purposes of analysis, also, the energy density *vs.* power density relation is important. This curve is shown in Fig. 9 and was derived from the power profiles. The bad cell in battery No. 1 depressed its energy density. It is interesting to note that this battery had a power density of 70 W/lb at an energy density of 3 Whr/lb.

Ni-Cd aircraft starting battery.—Table I lists the nominal characteristics of this Ni-Cd battery; Fig. 10 shows the constant power discharges. Since this battery was only a power battery, only high power discharges were made. At 2350W, only about two consecutive accelerations could be predicted. However, at the usual 1900W, about 12 consecutive accelerations would be predicted from the 1850W discharge to a 14V cutoff.

Figure 11 shows that 14 actually were obtained. A 2 min rest period between pulses increased the number to 18.

What is noteworthy, though, is that each battery weighed only 18 lb. It was calculated that 10 Ni-Cd batteries would be needed for the power package. This pack will weigh 180 lb, compared to the 270 lb of the Pb-acid pack. Also, the energy storage in the Ni-Cd battery is only 8 A-hr. But this amount of active material supplies the same acceleration pulses as 30 A-hr in the Pb-acid battery.

Figure 12 shows the charge-discharge voltage *vs.* current characteristics of the Ni-Cd battery. It is interesting that, between 50 and 95% capacity, the charge and discharge curves are very nearly continuations of one another. The rapid decrease in voltage during discharge for both 50 and 10% capacity at 50A is probably due to the increased polarization and resistance for the large amounts of $Cd(OH)_2$ and $Ni(OH)_2$ in the plates. The increase in resistance of the reacted forms of the active material may explain

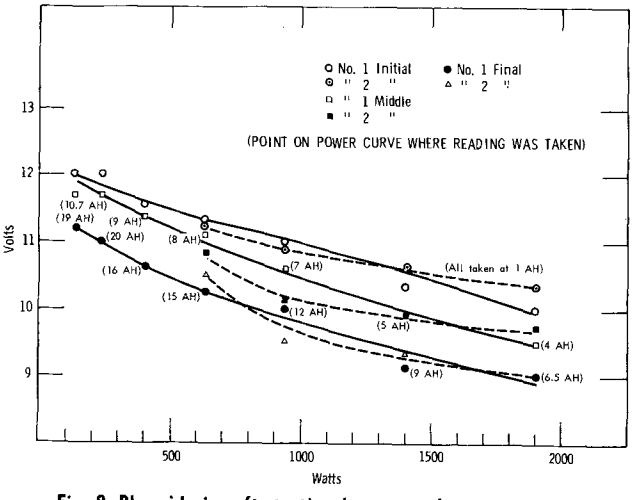

Fig. 8. Pb-acid aircraft starting battery, voltage vs. power

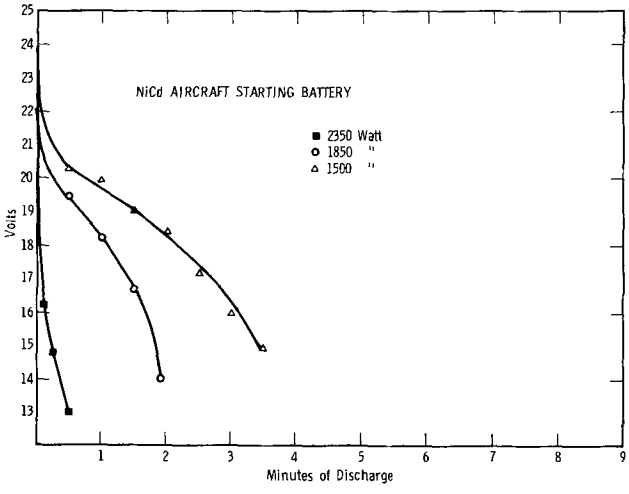

Fig. 10. Ni-Cd aircraft battery, constant power discharge

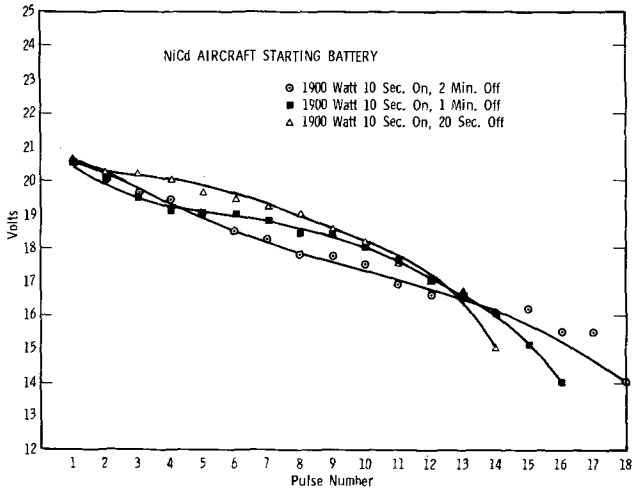

Fig. 11. Ni-Cd aircraft starting battery, consecutive acceleration power pulse discharge.

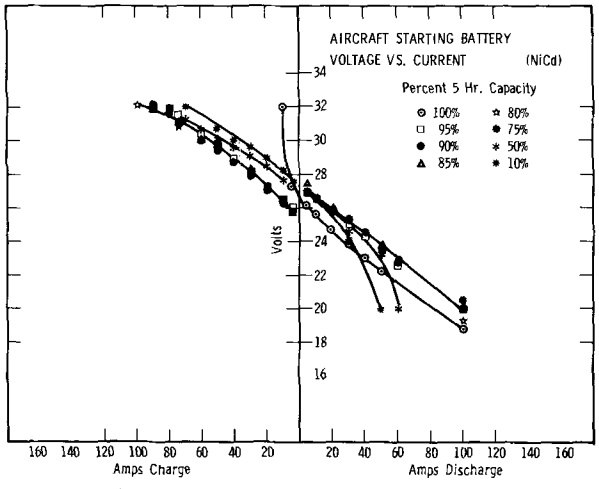

Fig. 12. Ni-Cd aircraft starting battery, voltage *vs.* current

the slightly higher charge voltage seen for the 10% capacity level. In contrast to the Pb-acid battery, the Ni-Cd battery may be charged to 95% capacity before the voltage rises precipitously. At 100A charge, the voltage is only 32V which is about maximum starting voltage for a Ni-Cd battery. This rate can be used until the battery is 95% charged before a reduction in charge rate is necessary. Thus, the Ni-Cd takes less power to charge.

Although range is not important for a power battery, range calculations can be made from Fig. 13 where capacity *vs.* discharge times are plotted.

The energy density-power density relationship is given in Fig. 14. For this battery, the relationship appears to be a linear one. At 2 Whr/lb, the power density is 130 W/lb, a significant improvement over the lead acid battery.

2HN-11A Pb-acid military battery.—The 2HN-11A battery is made by Delco-Remy for military use. Although of higher capacity than required, it could serve as a "power" battery. Discharge data were obtained from which an appropriate battery could be designed.

Figure 15 shows that this battery had more than sufficient capacity for a power battery. In fact, the capacity is nearly as good as some of the energy batteries previously tested (2). Based on the 1900W discharge, which is the power required for acceleration, this battery should deliver about 30 consecutive 10 sec acceleration pulses.

As shown in Fig. 16, 29 pulses were obtained. For this battery, resting between pulses for 1 or 2 min increased the number of pulses slightly. The battery for the 1 min test started at a higher voltage and came right off charge. For the others, they rested awhile before being tested. This could explain the reversed order of the two tests.

It is interesting to note from Fig. 9 and 17 that the energy density-power density curve for the 2HN-11A battery is about the same as the Pb-acid aircraft battery. Both showed about 70 W/lb at 2 Whr/lb. It was this similarity that brought to mind the use of 2HN plates for the power battery.

2HN-Thin plate (2HN-T.P.) Pb-acid battery.—Design considerations.—Table II shows the design data from which the final design was made for the DRX 47965-7 Pb-acid battery. The element weight divided

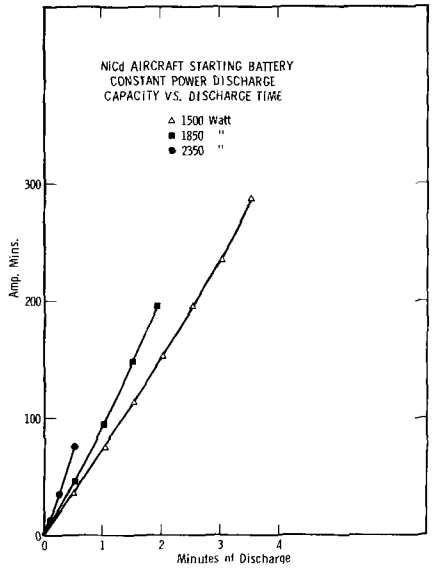

Fig. 13. Ni-Cd aircraft starting battery, constant power discharge capacity *vs.* discharge time.

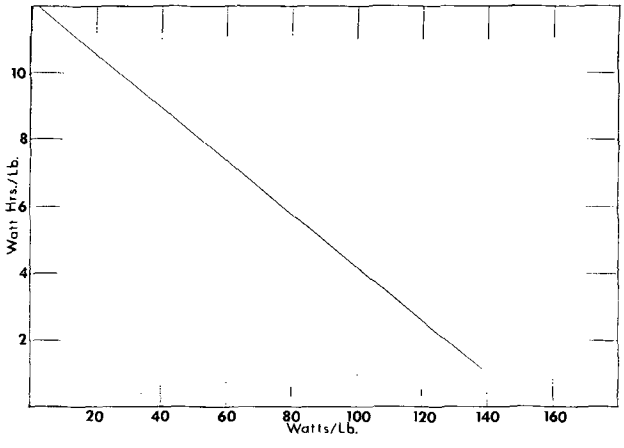

Fig. 14. Ni-Cd aircraft starting battery, energy density *vs.* power density.

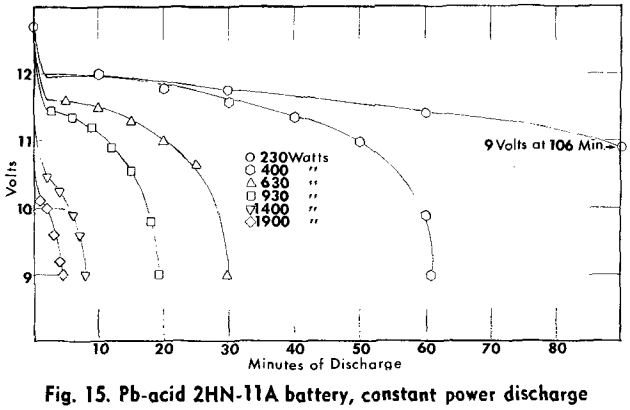

Fig. 15. Pb-acid 2HN-11A battery, constant power discharge

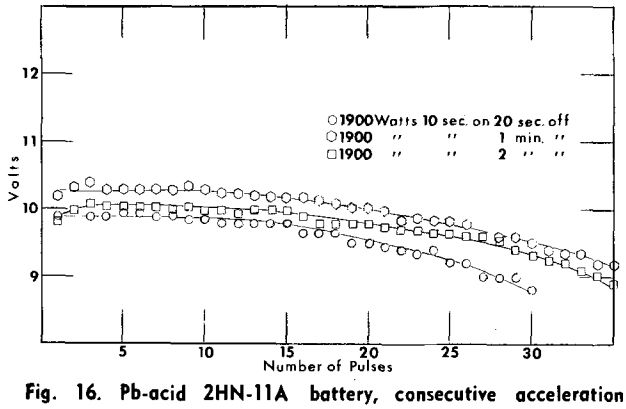

Fig. 16. Pb-acid 2HN-11A battery, consecutive acceleration power pulse discharge.

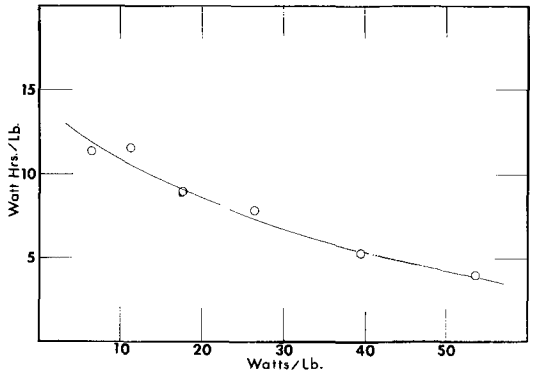

Fig. 17. Pb-acid 2HN-11A battery, energy density *vs.* power density.

by the volume of the plates gave the apparent density. The ampere-hour capacity divided by the element weight gave the specific capacity. From experience with other batteries, an apparent density of 0.2 lb./in.^{3} was assumed, from which the element weights and specific capacity were calculated.

A basic parameter was the amperes per square inch of positive plate surface. At the 1930W discharge, the maximum current was 215A. This is equivalent to about 1 A/in.^{2} for the 2HN-11A battery. Hence, a current density around 1 A/in.^{2} was fixed for the design.

It was also desired to use an available thin-walled, lightweight, hard rubber container. However, only seven plates of the 2HN-11A size could fit into a cell of this container. This design gave a positive plate current density of 1.5 A/in.^{2}. This increase in current density plus the large reduction in active material ruled out this design.

An alternative, proposed by Delco-Remy, was to press down the 2HN grids to 0.060 and 0.050 in. before pasting for the respective positive and negative plate thicknesses. Then, using standard 0.040 in. separators, 11 plates could be fitted into the thin-walled cell. The current density would be slightly less than 1 A/in.^{2}, and there would be a minimal reduction in the amount of active material.

The final design is given in the last column of Table II.

Table II. Battery design data

	2HN-11A	2HN-T.P.	DRX 47965-7
A-hr capacity	45	34	34
No. of plates/cell	11	11	11
Plate size (w) × (h) (in.)	4.19 × 5.25	4.19 × 5.25	4.19 × 5.25
Pos. plate area (in.^{2})	220.0	220.0	220.0
Pos. thickness (in.)	0.070	0.060	0.060
Neg. thickness (in.)	0.062	0.050	0.050
Sep. thickness (in.)	0.059	0.040	0.040
Volume of plates (in.^{3})	15.88	13.2	13.2
Element wt (lb)	3.18	2.64	2.64
Apparent density (lb/in.^{3})	0.2	0.2	0.2
Specific capacity (A-hr/lb)	14.15	12.88	12.88
Battery dimensions, L	10-1/8	10-1/8	8-1/4
W	5-3/16	5-3/16	5-1/2
H	9-1/8	9-1/8	9-3/4
Battery weight (lb)	36.0	33.5	32.0
Weight battery pack (lb)	360.0	335.0	256.0*

* For eight 7-cell batteries.

Evaluation tests.—Before proceeding to make any thin-plate batteries, it was decided to evaluate the thin-plate design in a standard 2HN-11A container. This was considered the fastest and easiest way to confirm the design.

Figure 18 shows the constant power discharge curves for this battery. It delivered 2 min at 1900W to 9V. This is equivalent to 12 consecutive 10 sec acceleration pulses to 9V.

Figure 19 shows that actually 13 consecutive 10 sec, 1900W pulses were obtained to 9V.

The voltage *vs.* current curves in Fig. 20 have the same general shape as the aircraft battery except possibly for a slightly better charge acceptance for the 2HN-TP. However, this might be an artifact caused by the large container.

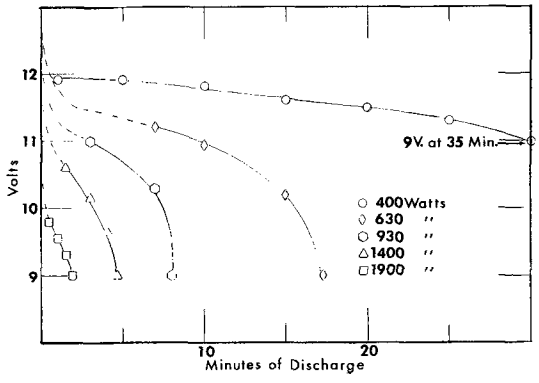

Fig. 18. Pb-acid 2HN-T.P. battery, constant power discharge

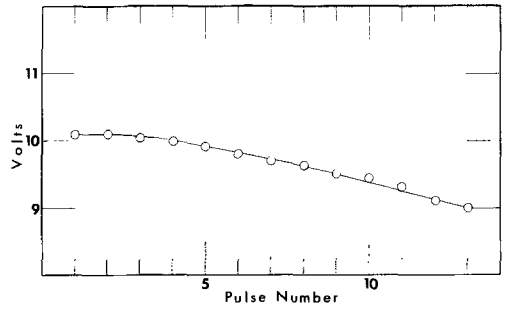

Fig. 19. Pb-acid 2HN-T.P. battery, consecutive acceleration power pulse discharge.

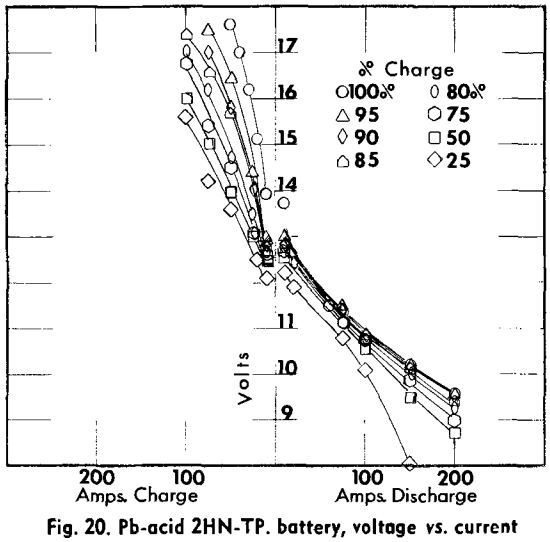

Fig. 20. Pb-acid 2HN-TP. battery, voltage *vs.* current

These evaluation tests confirmed the thin-plate design.

DRX 47965-7 Pb-acid battery.—The above designation was used for the battery made by Delco-Remy using thin 2HN-11A plates in the lightweight container. This battery contains seven cells instead of the usual six; hence, the nominal battery voltage is 14V instead of 12V. This increase in voltage meant that 2200W (1900 x 7/6) could be drawn from this battery and be equivalent to 1900W from a 12V battery. To provide acceleration power on this basis, 8.6 or 9 batteries would be required for the power pack. However, because of the good discharge characteristics of the 2HN plates, it was decided to use eight batteries instead of nine. This meant a current density slightly above 1 A/in.^{2}, which was tolerable. To provide some additional margin (*e.g.*, added accessories), the battery-proof test requirement was increased to 2500W.

Figure 21 shows how well the DRX 47965-7 battery performed. The design was seen to be conservative since 2 min were obtained at 2500W to 10.5V (1.5 V/cell). This is equivalent to 12 consecutive accelerations. By actual test, 15 were obtained. This means that eight batteries are sufficient for the power pack at 2500W per battery per 10 sec acceleration.

Figure 22 confirms the good charge acceptance of this battery. Large currents can be applied to this battery without a large voltage rise, up to 85% capacity. All the discharge curves have about the same slope. The same slope is shown by the Pb-acid aircraft and 2 HN batteries. The voltage starts to drop off more rapidly at high current drains, especially at the lower capacities.

The data in Fig. 21 are replotted in Fig. 23 so that the additivity principle can be applied to any projected duty cycle. This family of curves makes it easy to add up the discharge time at several different power levels.

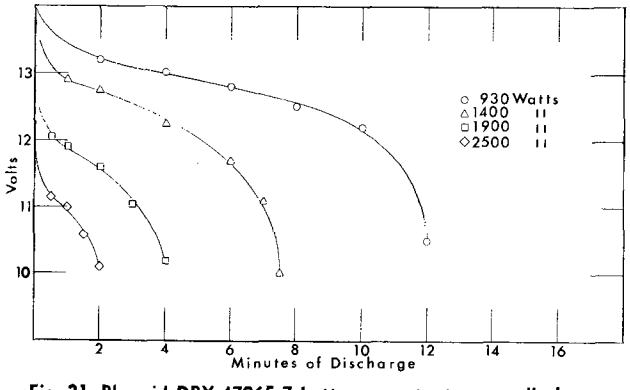

Fig. 21. Pb-acid DRX 47965-7 battery, constant power discharge

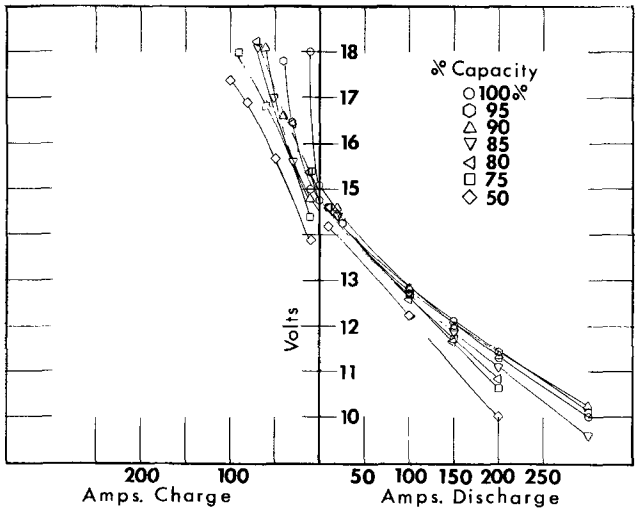

Fig. 22. Pb-acid DRX 47965-7 battery, voltage vs. current

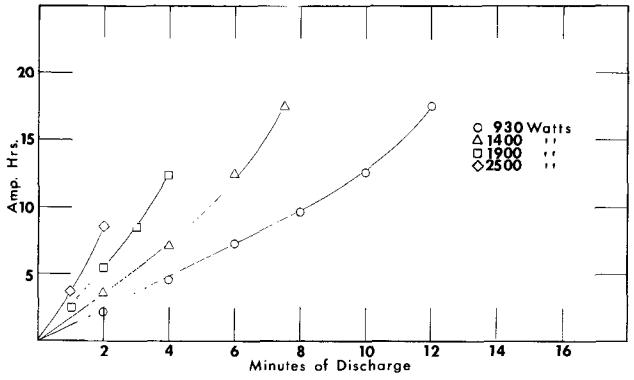

Fig. 23. Pb-acid DRX 47965-7 battery, constant power discharge capacity vs. discharge time.

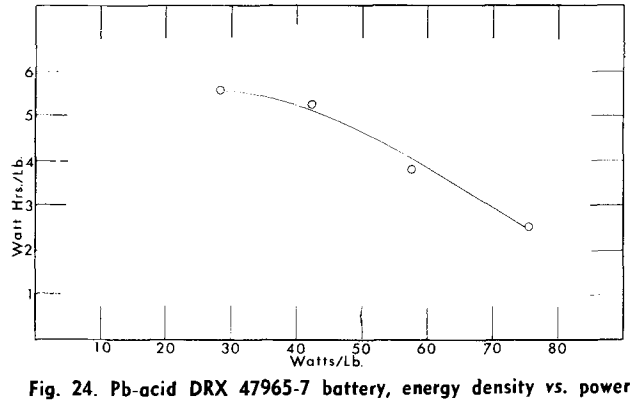

Fig. 24. Pb-acid DRX 47965-7 battery, energy density vs. power density.

Figure 24 shows the energy density-power density relationship for this power battery. It is definitely not an energy battery. It does show a relatively good power density for a lead acid battery, *viz.* 75 W/lb at 2.5 Whr/lb.

DRX 47965-26 Pb-acid battery.—In an effort to save weight and to take advantage of the excellent discharge characteristics of the 2HN plates, one battery was made using only nine plates per cell. Its constant power discharge curves are shown in Fig. 25. This battery was entirely inadequate. It does not even yield 2 min at 1900W, when at least 2 min are necessary at 2500W. No further tests were made on this battery.

Conclusions

A lead-acid power battery was designed by Delco-Remy and General Motors Research Laboratories, based on data obtained on commercially available batteries for the XEP electric car.

Eight batteries made up the pack which weighed 256 lb. Each battery had seven cells with 11 plates per cell.

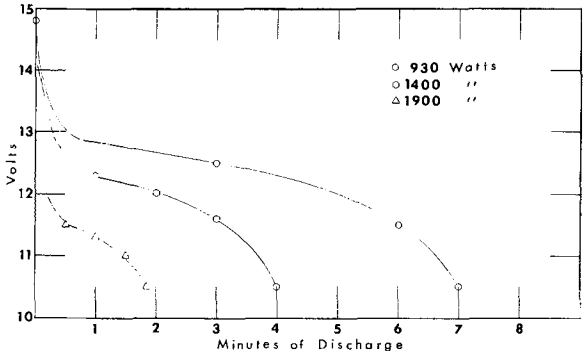

Fig. 25. Pb-acid DRX 47965-26 battery, constant power discharge

It was capable of 15 consecutive, 20 kW, 10 sec acceleration pulses before reaching 84V. It showed a power density of 75 W/lb at 2.5 Whr/lb.

Two alternatives are available. One is a lead-acid aircraft starting battery which gives the same characteristics as the Delco-Remy power pack and weighs 270 lb for ten batteries.

The second is a nickel-cadmium battery which has the same characteristics also but weighs only 180 lb for ten batteries. If volume and weight are at a premium, then this pack can be used. Otherwise, the scarcity and cost of cadmium rule out this battery.

Since the XEP was to be an all G.M. car, it was decided to use in it the specially designed Pb-acid power battery pack rather than use commercially available batteries.

Manuscript submitted June 26, 1970; revised manuscript received *ca.* Oct. 5, 1970.

Any discussion of this paper will appear in a Discussion Section to be published in the December 1971 JOURNAL.

REFERENCES

1. B. Agruss, *This Journal*, **117**, 1204 (1970).
2. B. Agruss, *ibid.*, **117**, 1207 (1970).

A Scanning Electron Microscope Study of Etched Aluminum Foil for Electrolytic Capacitors

C. G. Dunn* and R. B. Bolon

General Electric Company, Research and Development Center, Schenectady, New York 12301

and A. S. Alwan[1],* and A. W. Stirling**

General Electric Company, Electronic Capacitor & Battery Department, Irmo, South Carolina 29063

ABSTRACT

A scanning electron microscope study of oxide replicas of aluminum electrolytic capacitor foils has provided information on tunneling produced by a given etch. Tunnel morphology depends on microstructure of the aluminum and on etching conditions. With increasing current density in an electrochemical etch, the number of etching tunnels per unit area increases and tunnel diameter decreases. A simplified model predicts the number of tunnels per unit area and the tunnel diameter needed for maximum capacitance for a given anodic Al_2O_3 film thickness.

Two of the present authors previously described a scanning electron microscope (SEM) method for revealing the complex morphologies produced during the etching of aluminum foils for electrolytic capacitors (1). A number of variables affect the etch morphology, and those of principal concern in the present paper are: (*a*) electroetching current density, (*b*) microstructure of the aluminum foil, (*c*) the substitution of a hot nitric acid etch for the last part of an electroetch, and (*d*) some additives to a 20% NaCl electrolyte. The effect of extent or degree of an etch and the effects produced by varying the composition of the aluminum are treated briefly. Use is made industrially of such etching variables to produce various kinds of electrolytic capacitors.

Regarding effects of current density and microstructure, Hunter (2) pointed out that the morphological detail became finer with increasing current density and this resulted in lower capacitance gains at high formation voltages. Hunter stated that microstructure was a variable. Bakish *et al.* (3) similarly reported that the morphological detail became finer with increasing current density and that this led to higher capacitance gains at low formation voltages. Later Bakish *et al.* (4) reported still finer morphologies and higher capacitance gains with the use of suitable hard aluminum foil [presumably the microstructure of such foil consists of subgrains of about 1μ size, *i.e.* the limiting subgrain size reported by Ball (5) for polycrystalline aluminum deformed at about room temperature; this is quite different from the microstructure of annealed aluminum foil]. Such results clearly indicated that current density and microstructure are important variables to be considered according to final use of the etched foil. Nothing specific was mentioned about a tunnel type etch morphology.

On the other hand, Burger *et al.* (6) had reported the tunneling character of suitable electrolytic etching methods and the production of tunnels ranging from 0.1 to 1μ in diameter. Edeleanu (7) discussed the nature of tunneling and showed that tunneling occurred in <100> directions in the aluminum. Altenpohl (8, 9) briefly discussed the tunnel morphology revealed optically in cross sections of etched foil. Additional detail about tunnel morphology, however, was revealed in SEM micrographs of oxide replicas of etched foil (1).

Two of the present authors (CGD and RBB) have developed a simple model of a tunnel morphology which leads to quantitative predictions of theoretical capacitance gains. The model is therefore useful in the discussion of morphologies of the kind obtained experimentally.

A Tunnel Model

Consider the specific model with N tunnels of radius ρ and length λ arranged in an hexagonal array normal to a flat surface of unit area (cm^2). This morphology implies a specific weight loss, w; a tunnel area or dimensionless area factor, f_A; and a tunnel capaci-

[1] Present address: General Instruments, Tazewell, Virginia 24651.
* Electrochemical Society Active Member.
** Electrochemical Society Active Member of a Patron Member Company.
Key words: electroetch, etch-morphology, tunnel-etch-model, replica-oxides.

tance, C_t (μF/cm^2), after anodic film formation. Thus, in grams per square centimeter

$$w = 2.70\, N\pi\rho^2\lambda \qquad [1]$$

where 2.70 is the density of aluminum (g/cm^3). The factor $N\pi\rho^2$ in [1] is the fraction of surface area etched and the product $N\lambda$ is the total tunnel length (cm/cm^2). (The geometry places an upper limit on N for a given value of ρ, namely $N < \sqrt{3}/6\rho^2$). And, for the area factor

$$f_A = 2N\pi\rho\lambda \qquad [2]$$

Film formation to a thickness X may be expressed by

$$X = \alpha V \qquad [3]$$

where V is the formation voltage and α is a constant which depends on electrolyte temperature and holding time at the final voltage.

With this relationship one can then express a volt μF/cm^2 product in terms of X. Thus, for flat unetched aluminum with dielectric constant ϵ

$$V\, C_{flat} = 8.84\ (\epsilon/\alpha) \times 10^{-8} \qquad [4]$$

which is independent of X or formation voltage.

The corresponding product for the tunnel capacitance, C_t, is

$$VC_t = 5.55\, N\ (\lambda - X)\ X\ (\epsilon/\alpha)\ [\ln R/r]^{-1} \times 10^{-7} \qquad [5]$$

where R is the outer radius and r is the inner radius of the cylindrical oxide of thickness X, *i.e.* $R - r = X$. (The upper limit of N for a given value of R is $\sqrt{3}/6R^2$ and a number $N\pi R^2$ gives the fraction of original surface occupied by holes and cylindrical oxide). Equation [5] does depend on X.

If we neglect the contributions of flat areas, we obtain as a first approximation a dimensionless capacitance gain factor, $f_C = C_t/C_{flat}$, on combining [4] and [5]. Thus,

$$f_C = 2\,\pi N\ (\lambda - X)\ X\ [\ln R/r]^{-1} \qquad [6]^2$$

Since (ϵ/α) is a constant in [5], one notes that [6] differs from [5] only by a constant multiplying factor; therefore, [5] gives the functional form of [6]. However, for a given value of ρ it is necessary to express R/r in [5] in terms of ρ and X. The relationship is given in the Appendix.

For illustrative purposes we consider first two morphologies given by N, λ, ρ values of 6 x 10^8/cm^2, 35μ, 0.1μ and 6 x 10^6/cm^2, 35μ, 1.0μ, respectively. According to Eq. [1] the weight losses are the same (1.78 mg/cm^2). The area fractions, $N\pi\rho^2$, are also the same (about 0.19). According to Eq. [2] the morphologies represent tunnel area factors of 132 and 13.2, respectively. The total tunnel lengths are 21 and 0.21 km/cm^2, respectively. Taking the value of ϵ as 8.4 (10) and α as 13.7 Å/V and using [4] and [5], we obtained the curves shown in Fig. 1. Some minimum volt-microfarad products presently accepted for commercial foils, which are designated "M" in Fig. 1, were added for comparison purposes. At low voltages the 0.2μ diameter morphology (curve A) corresponds to excellent capacities approximately double those of the best foils currently available, but the 2.0μ diameter morphology (curve B) corresponds to capacities that are unacceptably low. At high voltages the situation is reversed; *i.e.*, curve B actually corresponds to acceptable capacities in the range above 200V since it lies above the M points, but the 0.2μ diameter morphology (curve A) is useless above 120V.

The model not only leads to simple predictions of possible capacity gains, as in these illustrated examples, but also predicts upper limits as shown in curves D and E in Fig. 2. Curves D and E are described more fully in the Appendix.

[2] f_C and f_A are compared in the Appendix (see footnote to Table AI).

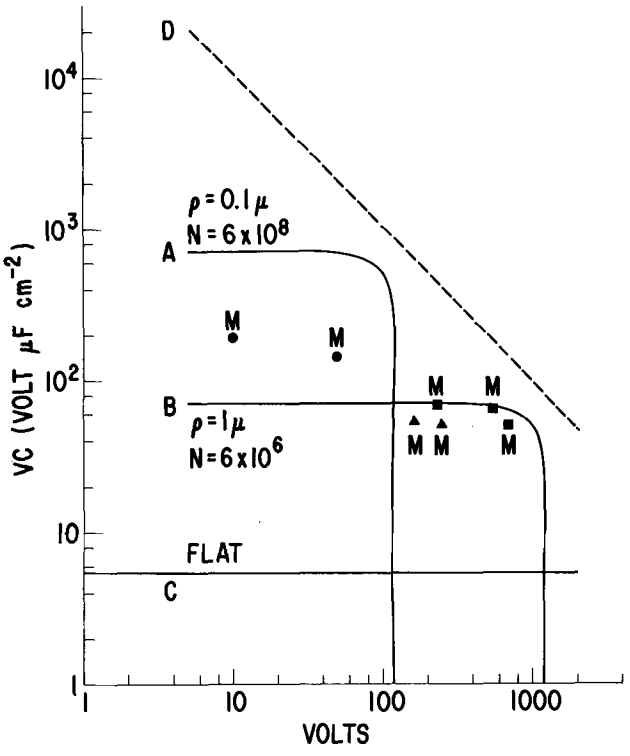

Fig. 1. Calculated volt microfarad products vs. formation voltage for *(a)* two etch-model morphologies with 35μ tunnel lengths (curves A and B) and *(b)* flat unetched sheet (curve C). Also, some acceptable minimum $V\cdot\mu$F values for various foils—circles: 99.99 (H19); squares: 99.99 (0); triangles: 99.88 (H19 and 0).

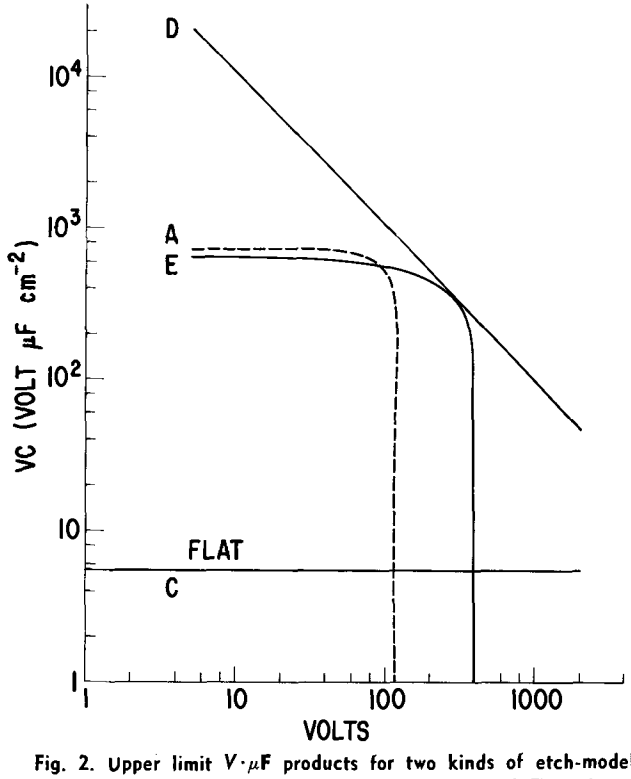

Fig. 2. Upper limit $V\cdot\mu$F products for two kinds of etch-model morphologies with 35μ tunnel lengths (curves D and E) and unetched sheet (curve C of Fig. 1). Curve *E*: $N = 10^8$/cm^2, ρ variable. Curve D: both N and ρ variable.

Experimental

Current density and microstructure.—Specimens of commercial grade 99.99% aluminum foils, 84-90μ thick, from two lots—one annealed (0 temper) and the other hard (H19 temper)—were etched at either 77.5 mA/cm^2 or 775 mA/cm^2 (etching times, measured weight losses,

and calculated weight losses are listed in Table I). In certain instances one surface was masked to restrict etching to one surface and provide easy release of the oxide replicas for the transverse views of SEM samples. The electrolyte was a 20% NaCl solution at 90°C. Specimens which were etched completely in the NaCl bath were washed in deionized water, dried, immersed in a 25°C nitric acid solution (2 parts HNO_3 to 1 part H_2O) for 2 min, and washed again.

Current density and hot nitric acid.—Specimens of 0 temper foil were etched at either 77.5 mA/cm² for 210 sec or 775 mA/cm² for 21 sec, thus for the same coulombs per square centimeter. Specimens were washed, dried, and then chemically etched in an 8% nitric acid solution at 93°C until the weight loss was about 1.6 mg/cm² (see Table I).

Additives to 20% NaCl electrolyte.—Other specimens of the hard foil were etched in special baths as indicated in Table II.

Annealed 99.88% Al foil.—A specimen of 99.88% Al foil, 75μ thick, was etched at 77.5 mA/cm² for 300 sec in the 20% NaCl electrolyte, washed, and dried. The specimen was then chemically etched in the hot nitric acid bath for a weight loss of about 0.96 mg/cm².

Preparation of SEM samples.—The thickness of a reaction replica film should be kept as small as possible for best replication of the etch morphology, but the replica also needs to be relatively strong after separation from the aluminum matrix. Anodic oxide films meet these conditions better than boehmite films produced by hydration and were therefore used. The oxide replicas for the present paper were produced by formation to 50V generally in a 0.1% aqueous solution of $NH_4H_2PO_4$ at 90°C. Transverse views of the oxide replicas were obtained in the manner described previously (1). In order to obtain cross-section views showing the extent of tunneling into the foils, only partial removal of the aluminum matrix was required. This was accomplished by an electropolishing treatment that brought the oxide into relief (1). The surface view of the 50V oxide replica was obtained without removal of the aluminum matrix. All replicas were given a gold coating of about 500Å in the normal direction.

Preparation for capacitance measurements.—A cell containing 10% boric acid solution, adjusted to a pH of 4.3 and a resistivity of 560 ohm-cm at 90°C, was used in the formation of the dielectric film. Formation was accomplished in two steps, *i.e.*, constant current at 7.75 mA/cm² (projected area of one surface) and constant voltage with decreasing current until a density of 0.77 mA/cm² was reached. Another cell was used to measure a "65°C formation voltage" or the voltage, *V* appearing in the *VC vs. V* plot of data. Capacitance measurements were made at 120 Hz using a General Radio Capacitance bridge with the test specimen as one electrode in a low-resistance cell (37 ohm-cm ammonium tartrate).

Table I. Measured and calculated weight losses for 0 temper and H19 temper 99.99 foils: (a) electroetching at two current densities in 20% NaCl solution and (b) chemical etching in a hot nitric acid solution

Temper	Electroetch mA/cm²	Electroetch time (sec)	Weight loss (mg/cm²) Meas.	Weight loss (mg/cm²) Cal.	Acid etch Meas.	Complete etch Meas.
0	77.5	432	3.47	3.12	none	3.47
0	77.5	210	1.66	1.52	none	—
0	77.5	210	1.71	1.52	1.63	3.34
0	775	54	4.65	3.89	none	4.65
0	775	21	1.73	1.52	none	—
0	775	21	1.69	1.52	1.60	3.29
H-19	77.5	432	3.43	3.12	none	3.43
H-19	775	54	4.58	3.89	none	4.58

Table II. Measured and calculated weight losses for H19 temper 99.99 foil etched at 775 mA/cm² for 54 sec in 20% NaCl solutions with various additives

Additive	Weight loss (mg/cm²) Meas.	Weight loss (mg/cm²) Cal.
None	4.46	3.89
1% Na_2SO_4	4.53	3.89
0.5% CrO_3	4.65	3.89
HCl until pH dropped to 0.6	4.52	3.89

Results and Discussion

Effects of current density and of hot nitric acid etch.—SEM micrographs of cross-section, transverse, and surface views of the oxide replicas of etched annealed 99.99 foils are shown in Fig. 3-8. Portions of Fig. 4 appear in Fig. 8 at higher magnifications. Transverse views corresponding to Fig. 3 and 4 appear in Fig. 5 and 6, respectively, but at a higher magnification. The surface views in Fig. 7 represent the same specimens as the transverse views in Fig. 5 (bottom) and Fig. 6 (bottom); clearly transverse views provide more information on etch morphology than do surface views.

Progress of the etches is displayed in Fig. 3-6 as follows: the center micrographs, the incomplete etches; the top micrographs, the complete electroetches; and the bottom micrographs, the etches completed with the hot nitric acid treatment. These micrographs show that more tunnels and smaller diameter tunnels occur for the high current density etch, but the distinction is not strong due to the wide variations in tunnel diameters. Observations made on the oxide replicas for the same number of coulombs (center micrographs in Fig. 3-6) revealed that low current density produced slightly greater penetrations into the specimens, while high current density produced more lateral tunneling. Rate of penetration (and tunneling) appeared to decrease with time (center and top micrographs in Fig. 3-6). The average penetration rate for the 21 sec electroetch at 775 mA/cm² was about

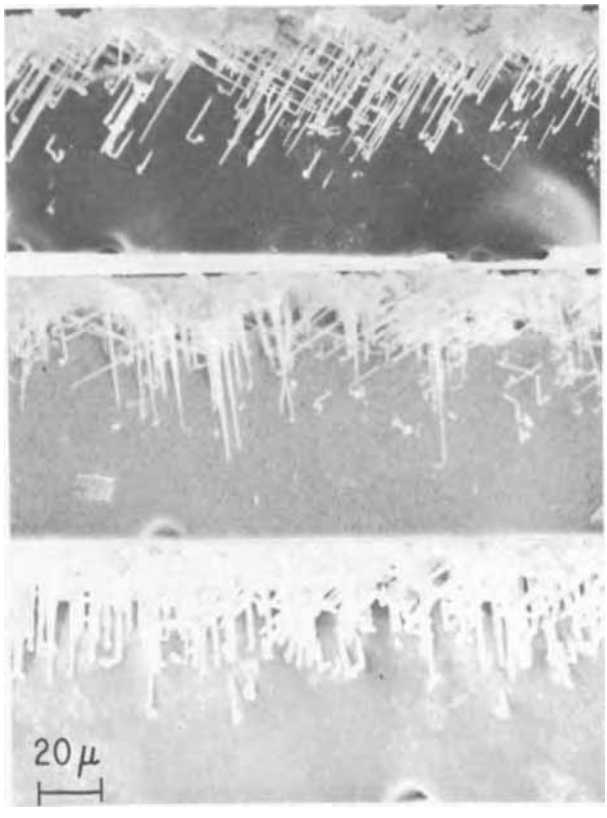

Fig. 3. SEM micrographs of annealed 99.99 foil after a one-surface etch at 77.5 mA/cm² as indicated. Cross sections showing 50V oxide replicas in relief. X400. Top, 432 sec; center, 210 sec; bottom, 210 sec plus 1.6 mg/cm² weight loss in hot nitric acid.

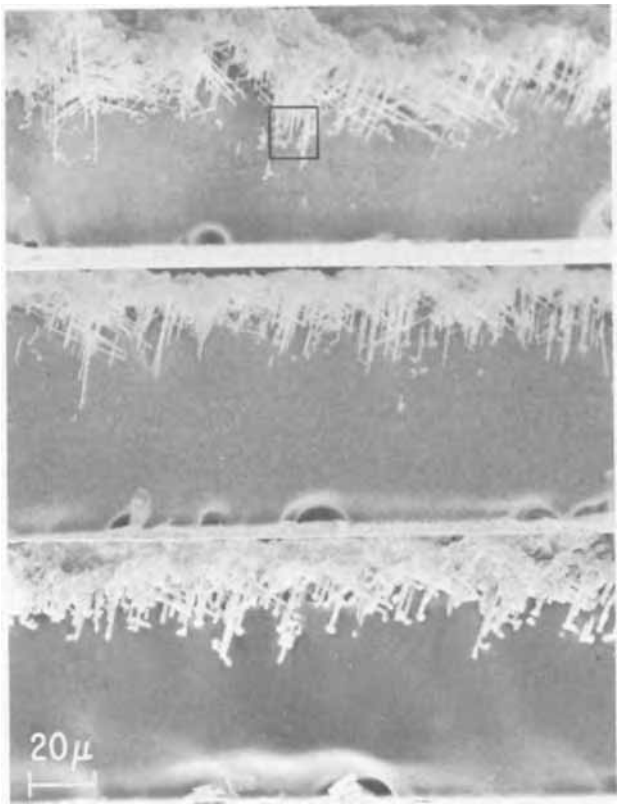

Fig. 4. SEM micrographs of annealed 99.99 foil after an etch at 775 mA/cm^2 as indicated. Cross section. X400. *Top*, 54 sec; *center*, 21 sec; *bottom*, 21 sec plus 1.6 mg/cm^2 weight loss in hot nitric acid.

2 μ/sec; the rate was below 1.5 μ/sec for the full 54 sec etch. Moreover, rates approaching 5 μ/sec were found for times below 10 sec. The estimated rates are in agreement with those reported by Edeleanu (6). The average penetration rates for etching at 77.5 mA/cm^2 were roughly a factor of ten lower than those for 775 mA/cm^2. Both low and high current density etches involved tunnel multiplication along with lateral tunneling and this resulted in oxide replica morphologies of the "jungle gym" type described previously (1).

It seems likely that some of the decrease in penetration rate with electroetching time is due to a relatively slow but uniform type of dissolution at tunnel walls, which may be characterized by definite rates of increase of tunnel diameters. Evidence of this appears in Fig. 5 since tunnel diameters for the complete etch (top micrograph) are larger than the tunnel diameters for the incomplete etch (center micrograph).

On the other hand, tunnel diameter growth may be obtained separately from tunneling; this aspect of etching is illustrated by the bottom micrographs in Fig. 3-6 for specimens partly electroetched then chemically etched in hot nitric acid. Larger diameter tunnels were obtained with the nitric acid etch (Fig. 6 bottom *vs.* Fig. 6 top) and this feature is needed for better high-voltage capacitance. For example, most tunnels are now sufficiently above 1μ diameter to make good contributions up to 700V, whereas parts of many tunnels in the complete electroetch are below 1μ diameter and contribute nothing above 600V. It is also interesting to note that the weight loss in nitric acid was less than the weight loss in the final 222 sec of the electroetch (Table I).

Although an increase in tunnel diameter may be needed for high-voltage applications, an increase in diameter after an initial high current etch (Fig. 7 bottom *vs.* Fig. 7 top) is less likely to be beneficial for low-voltage applications. First, the needed tunnel length $N\lambda$ may not develop in the electroetch step (compare appearances of Fig. 4 center with Fig. 4 top). Second, acid etching may reduce N (and $N\lambda$) as

Fig. 5. SEM micrographs of 50V oxide replicas of annealed 99.99 foil after a one-surface etch at 77.5 mA/cm^2 (same as Fig. 3). Transverse views. X1000. *Top*, 432 sec; *center*, 210 sec; *bottom*, 210 sec plus 1.6 mg/cm^2 weight loss in hot nitric acid.

Fig. 6. SEM micrographs of 50V oxide replicas of annealed 99.99 foil after a one-surface etch at 775 mA/cm^2 (same as Fig. 4). Transverse views. X1000. *Top*, 54 sec; *center*, 21 sec; *bottom*, 21 sec plus 1.6 mg/cm^2 weight loss in hot nitric acid.

neighboring tunnels merge together. Third, tunnels of tapered shape are usually produced, thus severely reducing the separation space and contributing to a

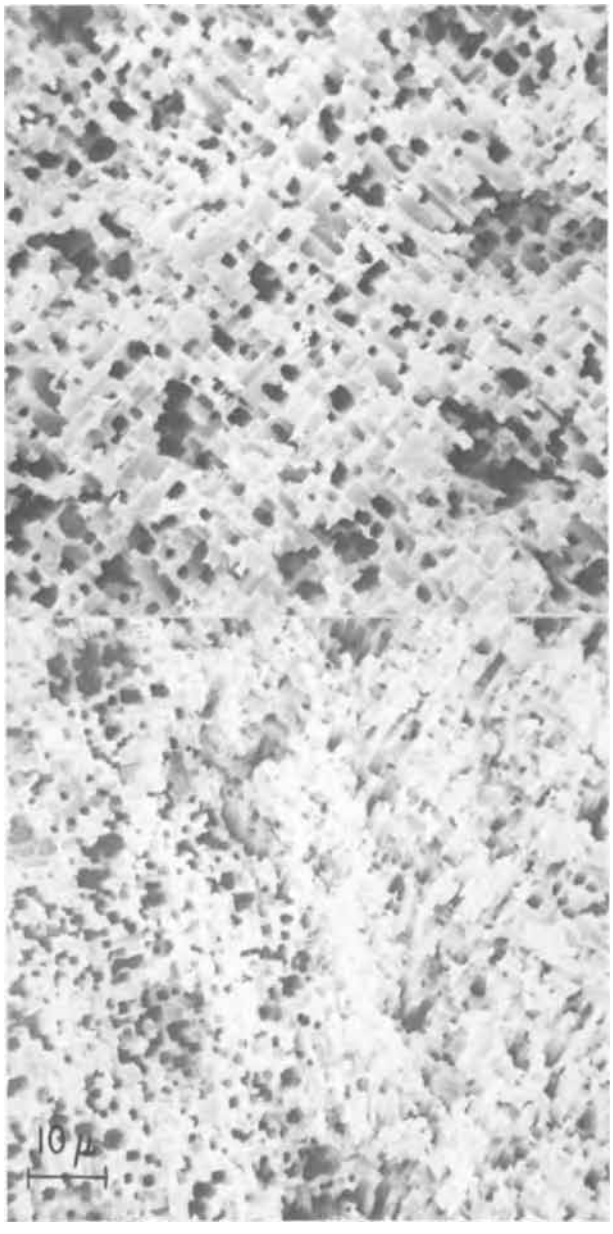

Fig. 7. SEM micrographs of the surfaces of annealed 99.99 foil after etches as indicated (also after formation to 50V). X1000. *Top*, 210 sec at 77.5 mA/cm^2 plus 1.6 mg/cm^2 weight loss in hot nitric acid; *bottom*, 21 sec at 775 mA/cm^2 plus 1.6 mg/cm^2 weight loss in hot nitric acid.

further reduction in $N\lambda$ with acid etching. In fact, capacitance data show that the complete electroetch generally produces higher gains at low voltages than the sequence of electroetch and acid etch. Theoretically, of course, with ideal geometry there could be significant gains with an increase in tunnel diameter (curve E of Fig. 2, described in the Appendix, gives upper limits for $N = 10^8$/cm^2; and f_A increases according to Eq. [2]).

Effect of microstructure and current density.—SEM micrographs of cross-section and transverse views of hard 99.99 foils are given in Fig. 9-11 and Fig. 12 (top). Views at different magnifications are given to show coarse and fine detail. It is clear that tunneling occurred in the heavily cold rolled foil. In Fig. 11 (center) there are many reasonably parallel tunnels for tunnel lengths $\sim 10\mu$, thus indicating a definite crystallographic feature to tunneling in this material. Bakish *et al.* (4), on the other hand, using optical methods found no clear evidence of crystallographic etching. The present morphology, however, appears to

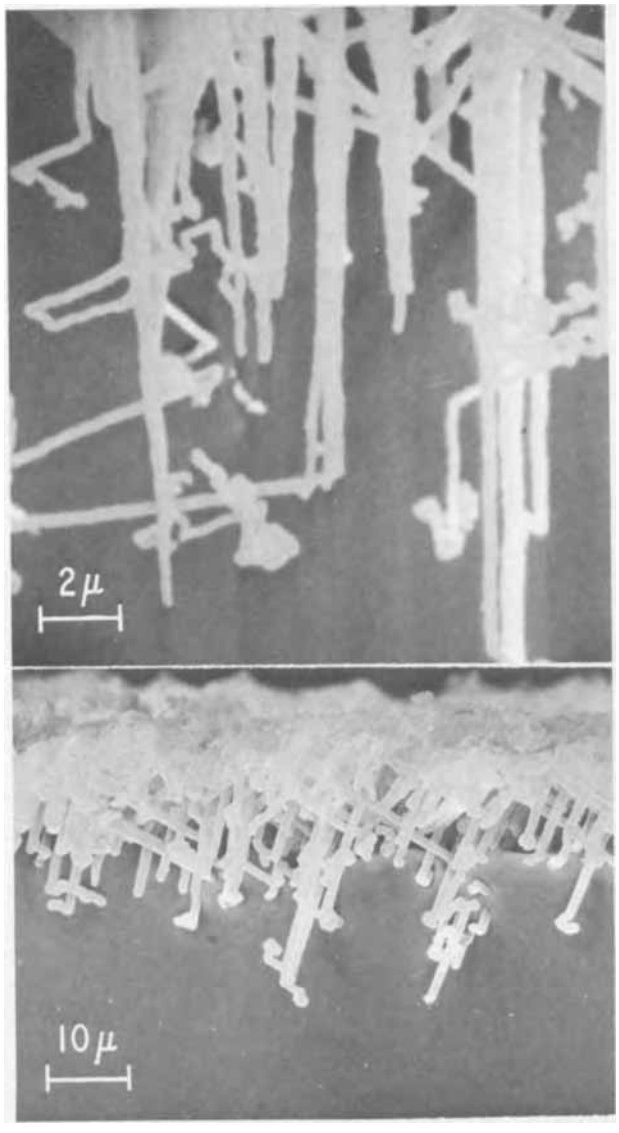

Fig. 8. SEM micrographs. *Top*, enlarged part of Fig. 4 top. X5000. *Bottom*, enlarged part of Fig. 4 bottom. X1000.

be consistent with <100> tunneling in a matrix with a strong (1$\bar{2}$3) [$\bar{5}$23] texture, the texture of heavily cold-rolled aluminum (11). The presence of tunnels that remain relatively straight over distances of about 10μ in a structure of subgrains of about 1μ size (5, 8) may be explained in terms of the very small disorientations of neighboring subgrains and the occurrence of mixed kinds of rotations, which tend to cancel out and keep the net amount of deviation small over a region of several subgrains' size.

Tunnel diameters were smaller for the hard foils than for annealed foils and were slightly smaller after etching at 775 mA/cm^2 than at 77.5 mA/cm^2. According to Eq. [1] and [2] the smaller tunnel diameters should produce larger area factors, f_A, if other factors are the same [in fact, capacitance measurements confirmed the effect of current density reported by Bakish *et al.* (4) because hard foil etched at 77.5 mA/cm^2 failed to meet the minimum acceptance levels, whereas the same material etched at 775 mA/cm^2 had acceptable qualities for low-voltage applications]. On the other hand, tunnel diameter differences may represent only part of the morphology difference. A comparison of micrographs in Fig. 11 (top) and Fig. 12 (top) indicates that the coarse features are far more uniform for the high current density etch. This difference in etch structure may favor greater etching efficiency and larger total tunnel lengths ($N\lambda$) in a layer of

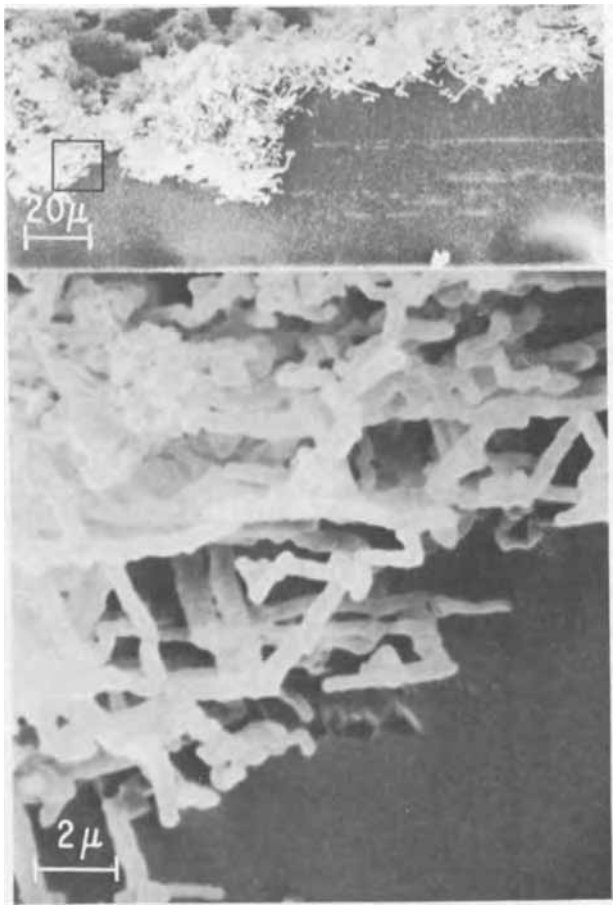

Fig. 9. SEM micrographs of hard 99.99 foil etched at 77.5 mA/cm^2 for 432 sec. Cross sections. *Top*, X400; *bottom*, enlarged area X5000.

depth λ; this point will be treated further in connection with effects of additives to the electrolyte.

Effects of additives to the NaCl electrolyte.—Etched structures.—Although both optical and SEM views of the etched surfaces at low magnification revealed large variations among the specimens etched in different electrolytes, the SEM micrographs of the transverse views of oxide replicas were rather similar in appearance (Fig. 12). Moreover, SEM observations at high magnifications revealed a fine tunnel structure which was also similar for specimens representing all four electrolytes. Qualitatively, there was little difference in tunnel diameters and only a small indication that all three additives decreased the tunnel diameters a very small amount. Rather extensive measurements and perhaps other etching conditions would be required for a more precise evaluation of the effect of these additives on tunnel diameters.

Capacitance results.—The volt μF products of one lot of 99.99 (H19) foil etched in the 20% NaCl electrolyte with various additives (Table II) are plotted in Fig. 13 as a function of formation voltage. (All samples were etched the same amount, *i.e.*, to 41.85 coulombs with measured weight losses 15-20% above the calculated values). At low voltages there is a higher etch gain with each additive; at 25V the etch ratio increases from about 44 to 65. For the particular amounts of additive used, the etch gain increases in the following order: HCl, CrO_3, and Na_2SO_4. There is a substantial increase in etch gain for the sulfate additive, and this confirms the claims of Martin (12). Present results also confirm those of N. V. Philips' Gloeilampenfabrieken (13) on CrO_3 additive.

Since the weight losses are approximately the same (Table II), the electrolyte additives apparently improve the efficiency of tunnel structure production.

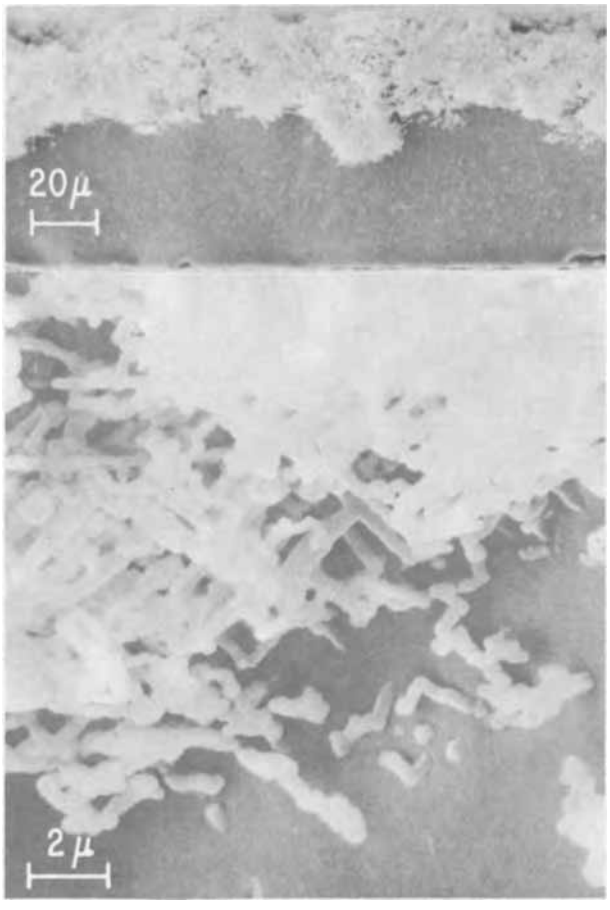

Fig. 10. SEM micrographs of hard 99.99 foil etched at 775 mA/cm² for 54 sec. Cross sections. *Top*, X400; *bottom*, X5000.

The weight losses are near 50% of the total mass in a layer 35μ deep. Such a fraction is higher than that for the points of curve D, which is constant at 38.6%. The higher fraction is within the 34.2-90.7% range for curve E (see Appendix and Fig. 2) where $N = 10^8/cm^2$ and the high values apply only to low formation voltages. A maximum fraction of about 30% would be the limit for a hexagonal array of conical tunnels which taper to zero diameter in a distance λ. A morphology involving truncated conical tunnels, however, would allow somewhat higher fractional weight losses before reaching the point of diminishing etch gains, but not as high as those for the cylindrical tunnel model.

All three morphologies have an area factor, f_A, given by Eq. [2], *i.e.*, $2\pi\rho N\lambda$ if ρ is replaced by the average radius $\bar{\rho}$. Values of $N\lambda$ obtained by the etches may be calculated if $\bar{\rho}$ and f_A are known. Actually, we may substitute the low-voltage etch gains, *i.e.*, 44-65, for f_A and take 0.30μ as a rough estimate of $2\bar{\rho}$ (see Fig. 10 bottom). These numbers yield tunnel lengths of 5×10^5 to 7×10^5 cm/cm². Such lengths divided into segments 35μ in length correspond to 1.3×10^8 to 2.0×10^8 tunnels/cm² (*i.e.*, values of N).

N may also be expressed as tunnel length per cubic centimeter; call this N^*. Since the above tunnel lengths average about 6×10^5 cm/cm² and are confined to volumes of 1 cm² $\times$ y, where $y \leq$ half the specimen thickness, N^* or its lower limit may be calculated. From Fig. 4(top) it is clear that $y \leq 45\mu$. Therefore, $N^* \geq 1.3 \times 10^8$ cm/cm³.

A uniform array of cylindrical tunnels with $N \geq 10^8$/cm² cannot contribute to the $V \cdot \mu F$ product above 400V (Fig. 2). However, the actual behavior of tunnels of varying size is clearly different from the behavior of one particular size (namely, $2\bar{\rho}$); without going into a detailed analysis, departures from uniformity should lead to decreasing $V \cdot \mu F$ products with increasing voltage, which is the case in Fig. 13, and the precipitous decline certainly is consistent with too many tunnels (N), and therefore unsatisfactory morphology, for high-voltage applications (compare with curves A and

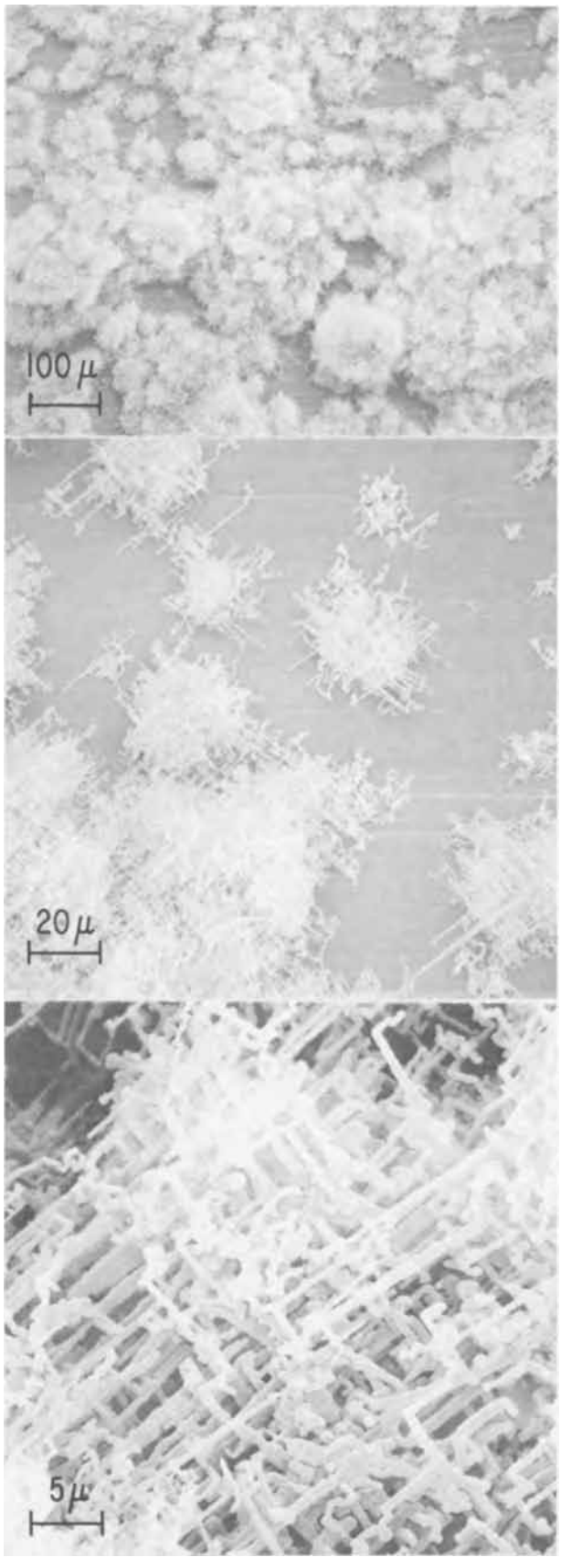

Fig. 11. SEM micrographs of 50V oxide replicas of hard 99.99 foil after a one-surface etch at 77.5 mA/cm² for 432 sec. Transverse views. *Top*, X100; *center*, X500; *bottom*, X2000.

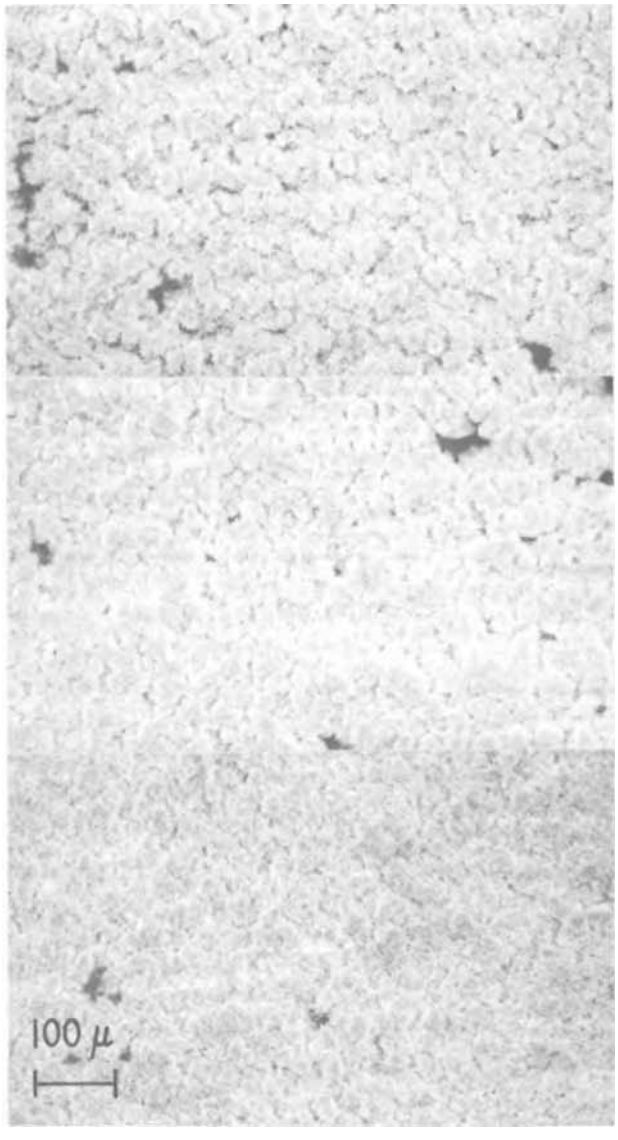

Fig. 12. SEM micrographs of 50V oxide replicas of hard 99.99 foil after a one-surface etch at 775 mA/cm² for 54 sec in various electrolytes. Transverse views. X100. *Top*, NaCl; *center*, NaCl + Na_2SO_4; *bottom*, NaCl + CrO_3.

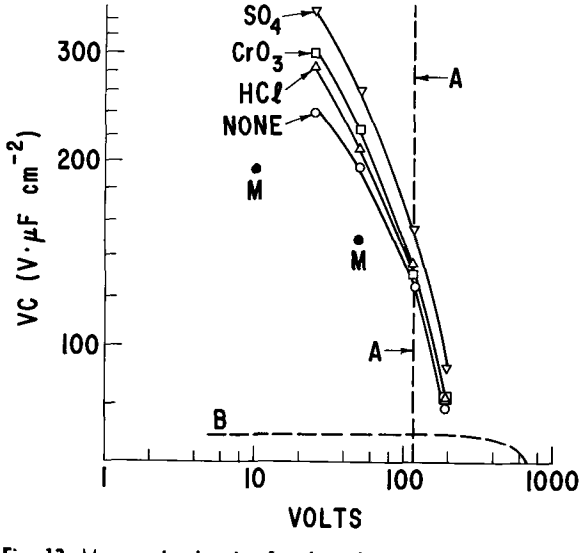

Fig. 13. Measured volt microfarad products vs. formation voltage showing effects of electrolyte additions (see Table II). Also shown are portions of curves A and B of Fig. 1 and two minima points for 99.99 (H19) foil.

E with $N \geq 10^8/cm^2$). The morphology needed for high-voltage applications involves larger diameter tunnels and greater separation distances, *i.e.*, features which are more easily obtained with annealed foil than with hard foil.

Effect of composition of the aluminum.—The etch gains of annealed 99.88% Al foil are similar, but generally somewhat lower, than those of annealed 99.99% Al foil (see Fig. 1 for some listed M points). The morphology produced by etching is also similar (compare Fig. 14 with Fig. 5 bottom). The SEM stereomicrographs in Fig. 14 show a typical "jungle-gym" structure of the oxide replica of the etch tunnels within a single-crystal grain of aluminum. Such three-dimensional structures are viewed best stereoscopically.

Summary and Conclusions

On the basis that tunnel diameter is a measure of "fineness of the etch morphology," present results confirm the earlier observations that increased current density produces a finer etch morphology (2, 3) and that hard foil etches to a finer morphology than soft foil (4).

More importantly, however, the observed morphologies not only confirm the presence of tunnel etching (6, 7, 1) but indicate that tunnel configurations are the principal features responsible for large etch gains. Therefore, in addition to tunnel diameters 2ρ, the description of a given morphology requires information on either the tunnel density, N (number per square centimeter), and average tunnel length, λ, or the tunnel density, N^* (total tunnel length per cubic centimeter), and the thickness, y, of the layer etched, where $y \cong \lambda$. The morphology parameters, ρ, N, and λ, in fact, are those needed for a "simple tunnel model." The model gives properties as functions of N, λ, ρ and X, where X is the thickness of the dielectric film. Only to a limited degree are N and ρ independent; also $\lambda \leq$ half the foil thickness.

The following conclusions were reached based on a "simple tunnel model" and experimental results.

1. Etched hard foil has a tunnel morphology, which is somewhat similar to that of etched soft foil; *i.e.*, there is a crystallographic feature which we believe arises from <100> tunneling.

2. Tunnel diameters of etched hard foil are smaller than those of etched soft foil, other factors being the same.

3. Slightly smaller tunnel diameters result from an etch at 775 mA/cm² than one at 77.5 mA/cm²; the more important morphology parameter is the product $N\lambda$ (tunnel length per square centimeter) according to the simple tunnel model.

4. Both SEM information on tunnel diameters and the simple tunnel model indicate that the maximum voltages for useful tunnel contributions to capacitance gains increases with tunnel diameter. The interdependence of tunnel diameter and tunnel density, however, places limits on tunnel diameter, especially if large etch gains are to be attained.

5. When electroetching produces a suitable tunnel density, but tunnel diameters of insufficient size for the formation voltage planned, chemical etching in a hot 8% nitric acid solution may be used to increase the tunnel diameters to the desired value.

6. Tunnel electroetching may be described in terms of increase in tunnel length and increase in tunnel diameter with time. The former has a high rate initially and decreases to almost zero toward the end of a long etch. The rate of tunnel diameter increase, or radial growth, on the other hand, is relatively low; the fraction of the current taken by radial growth appears to increase with time, perhaps approaching 100% in long etches.

7. Additives to the 20% NaCl electrolyte, such as Na_2SO_4, or CrO_3 or HCl in suitable amounts, increase the etch gains of hard foil for low-voltage capacitors (*e.g.*, etch gains of 44-65 after formation to 25V). SEM

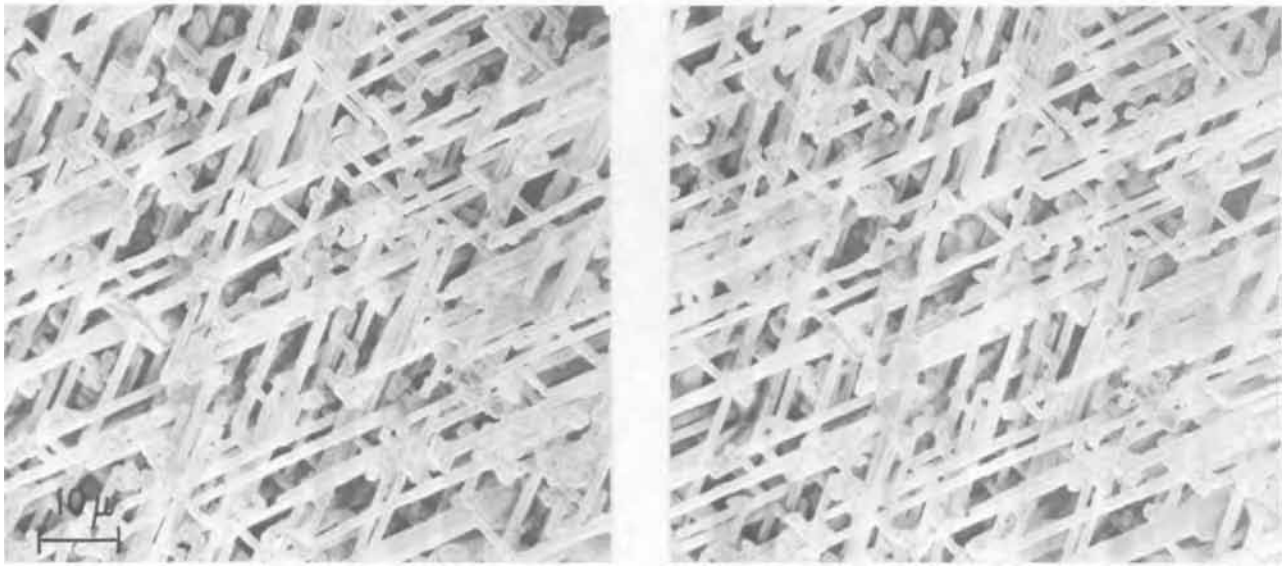

Fig. 14. SEM stereomicrographs of a 50V oxide replica of 99.88 soft foil. Transverse view. X1000.

data and calculations based on the simple tunnel model indicate that these additives increase the tunnel density, N^*, in a layer, y, where $y \leq$ half the foil thickness.

8. According to the tunnel model, etch gains of 44-65 and an observed tunnel diameter near 0.3μ indicate the production of tunnel lengths ($N\lambda$) of 5 x 10^5 to 7 x 10^5 cm/cm^2 (or 6 x 10^5 cm/cm^2 as an average) and tunnel densities, N, of 1.3 x 10^8 to 2.0 x 10^8 tunnels/cm^2. Alternatively, since half the specimens thickness (45μ) is the maximum depth of the etch a calculation of the tunnel density N^* for $N\lambda = 6 \times 10^5$ gives $N^* \geq 1.3 \times 10^8$ cm/cm^3.

9. The morphologies that gave etch gains of 44-65 at 25V (*i.e.*, $N\lambda$ values of 5 x 10^5 to 7 x 10^5 cm/cm^2) are unsuitable for use at high voltages according to the simple tunnel model. The tunnel densities for high voltages should be high, but not too high. N or N^* equal to 10^8 cm^{-2} is too high even for 400V; the properties of hard foil etched at 775 mA/cm^2 and formed to high voltages confirm this prediction.

Acknowledgments

The use of hot nitric acid and the experiments involving the HCl additive to the NaCl electrolyte were based on earlier investigations of R. A. Ruscetta. Mrs. Mary L. Mann carried out the etching and oxide-forming operations and made the capacitance tests.

Manuscript received Sept. 10, 1970. This was Paper 16 presented at the Los Angeles Meeting of the Society, May 10-15, 1970.

Any discussion of this paper will appear in a Discussion Section to be published in the December 1971 JOURNAL.

REFERENCES

1. C. G. Dunn and R. B. Bolon, *This Journal*, **116**, 1050 (1969).
2. M. S. Hunter, *Electrochem. Technol.*, **1**, 151 (1963).
3. R. Bakish, E. Z. Borders, and R. Kornhaas, *This Journal*, **109**, 791 (1962).
4. R. Bakish and R. J. Kornhaas, *Electrochem. Technol.*, **6**, 192 (1968).
5. C. J. Ball, in "Dislocations and Mechanical Properties of Crystals," p. 353, John Wiley & Sons, Inc., New York (1956).
6. F. J. Burger, V. F. G. Tull, and L. P. Harris, *Bull. J. Inst. Metals*, **3**, 6 (1955-1957).
7. C. Edeleanu, *J. Inst. Metals*, **89**, 90 (1960-1961).
8. Dietrich Altenpohl, *Z. Metallk.*, **49**, 331 (1958).
9. D. Altenpohl, *in* "Aluminium und Aluminiumlegierungen," p. 84, Springer, Berlin (1965).
10. W. J. Bernard and J. W. Cook, *This Journal*, **106**, 643 (1959).
11. Hsun Hu, P. R. Sperry, and Paul A. Beck, *Trans. AIME*, **194**, 76 (1952). See also C. G. Dunn, *Acta Met.*, **2**, 386 (1954) on description of textures.
12. H. A. Martin, U.S. Pat. 3,284,326 (Nov. 18, 1966); also Canadian Pat. No. 728,628 (Feb. 22, 1966).
13. N. V. Philips' Gloeilampenfabrieken, French Pat. 1,379,538 (Jan. 20, 1964).

APPENDIX

Assuming 100% coulomb efficiency in the formation of the Al_2O_3 film on the tunnel walls, an Al_2O_3 density of 3.17 g/cm^3 (10), and $\lambda >> X$, it follows that

$$(R^2 - r^2)/(R^2 - \rho^2) = 1.6 \qquad [A1]$$

Also, since $R - r = X$, both R and r can be expressed as functions of X and ρ. Dividing R by r gives

$$R/r = \frac{X + \sqrt{2.56\rho^2 - 0.6X^2}}{-0.6X + \sqrt{2.56\rho^2 - 0.6X^2}} \qquad [A2]$$

Combining [A2] and [5] with $\epsilon = 8.4$ and $\alpha = 13.7 \times 10^{-8}$ cm/V gives an expression for VC_t in terms of X, which may be evaluated for given values of N, λ, and ρ.

N, λ, and ρ given.—Some calculated values of VC_t for curves A and B of Fig. 1 are listed in Table AI. Values of C_t/C_{flat} or f_C are also listed.

N and λ given but ρ variable to give the upper limit of VC_t.—Consider the case of curve E in Fig. 2 with $N = 10^8$/cm^2, $\lambda = 35\mu$, and ρ made just large enough that R approaches its upper limit of $\sqrt{\sqrt{3}/6N}$ or 0.537μ. For a given value of X in microns, r is equal to 0.537 − X, and the value of ρ needed is then determined by [A1]. Substituting $0.537/(0.537 - X)$ for R/r in [5] determines VC_t. The range of X is zero to 0.537μ (or zero to about 393V). The corresponding range of ρ is 0.537 down to 0.330μ with $N\pi\rho^2$ varying from 90.7

Table AI. Illustrative calculations of VC_t for curves A, B, and D in Fig. 1 and 2; also calculated values of f_C*

Voltage	A ($N = 6 \times 10^8$, $\rho = 0.1\mu$)		B ($N = 6 \times 10^6$, $\rho = 1\mu$)		D (N & ρ variable)	
	VC_t	f_C	VC_t	f_C	VC_t	f_C
5	720.4	133−	71.55	13.2	20,460	3770
10	724.3	133+	71.60	13.2+	10,230	1890
25	728.3	134	71.72	13.2+	4089	754
50	706.4	130	71.91	13.3−	2042	378
100	507.5	93.6	72.18	13.3	1019	188
300	0	0	71.91	13.3−	337	62.2
550	0	0	68.38	12.6	182	33.6
700			64.24	11.9−	142	26.2
900			55.52	10.2		
1000			49.0	9.0	98	18.1
1100			39.4	7.3		
2000			0	0	47	8.7

* Note that f_C approaches f_A, i.e., 132 for curve A and 13.2 for curve B according to Eq. [2] at low voltages and is equal to or greater than f_A over relatively wide voltage ranges.

to 34.2%. The fraction of aluminum remaining in the layer of thickness, λ, after anodic film formation is constant, i.e., $1 - N\pi R^2 = 9.3\%$.

Curve D: $\lambda = 35\mu$, both N and ρ variable for maximum VC_t.—Starting with Eq. [5] one replaces N with the upper limit value $\sqrt{3}/6R^2$ and r with $R - X$. One then finds the value of R that makes VC_t a maximum for any value of X (or V). The solution is given by $R/r = 3.51$. Therefore, $r = X/2.51$, $R = X\ 3.51/2.51$, and $\rho = 0.91X$. Table AI lists values of VC_t for curve D in Fig. 2. It is interesting to note that for each point of curve D the fraction $N\pi\rho^2$ is 38.6% and the fraction $N\pi R^2$ is 90.7%. Also, an increase of N from 6 x 10^8 to 1.23 x $10^9/cm^2$ with $\rho = 0.1\mu$ and $\lambda = 35\mu$ gives a VC_t curve similar to curve A, but above it with one, and only one, point common with curve D. For $\rho = 1\mu$ (like curve B), the value of N needed is 1.23 x $10^7/cm^2$. The unique combination needed for 700V to produce the upper limit, which is only a factor 2.2 above curve B, is $N = 6$ x $10^7/cm^2$, $\rho = 0.875\mu$, with $\lambda = 35\mu$. There is no hexagonal array of tunnels of constant radius and 35μ length that will produce a VC_t product above curve D. Corrections due to neglect of flat area contributions, or an increase in λ, or an increase in ϵ above 8.4, or a decrease in α in Eq. [5] from 13.7 Å/V could, of course, produce $V \cdot \mu F$ products above the limit set by the present model.

The Two-Level Effect in Sheet Resistance Measurements Made with a Four-Point Probe

Alvin H. Tong* and Andrew Dupnock

IBM Components Division, East Fishkill Facility, Hopewell Junction, New York 12533

ABSTRACT

Sheet resistance measurements by the four-point probe technique have been investigated on diffusions into opposite-type backgrounds with junction depths from 0.25 to 3.0 μm. Sheet resistances, measured with a probe each of whose four points was weighted with 30-60g and whose tips were five mils in radius, were independent of this loading between 34 and 1570 ohms/sq. As the voltage is varied, sheet resistances show a two-level effect, followed by a breakdown at 5.5V. The transition takes place, independent of the sheet resistance, at a constant voltage of 100 mV. This transition is explained by the correction factors for a four-point probe derived from the multilayer potential distribution theory.

Characterization of a diffused layer in silicon involves the following parameters: *Co*, the surface concentration; ρ_s, the sheet resistance; *xj*, the junction depth; *Cb*, the background concentration and the type of diffusion profile. A knowledge of these parameters is essential to the design, development, and manufacture of integrated circuits.

A complete profile of the diffused layer which contains all the above parameters can be obtained by the spreading resistance technique (1-3) with correction factors (4). Another widely used method is to measure ρ_s by the four-point probe technique, *xj* by the bevel and strain technique; and, assuming the profile to be either Gaussian or a complementary error function profile, *Co* can be obtained with a knowledge of *Cb* (5, 6).

Because of the need for fast devices, diffusion layers are being made shallower and shallower and the demand for accurate and reproducible sheet resistance measurement becomes more urgent. What follows is our investigation of the following important parameters in the four-point probe measurement of sheet resistance: probe loading, configuration and tip radius, and current levels.

It has been reported (7) that a different current level should be used for different resistivities to give the correct value in bulk materials. It was also noticed (8) that the resistivity measurement in silicon epitaxial layers is a function of the current level. For thin diffused layers, the current level is even more critical, and was therefore closely investigated.

Four-point probes that are commonly used in the semiconductor industry have two different configurations: in-line array and square array. Probe tip radii of 1.5 and 5.0 mils are most popular. Probe loadings are adjusted by the spring tension in the probe head. Because of the shallow diffusion layer involved in the sheet resistance measurement, a bad combination of probe loading, tip radius, and the velocity of impact of the probe can produce erratic readings caused by the penetration of the probe points through the diffused layer.

The diffused layer thicknesses investigated ranged from 0.25 to 3.0 μm. Sheet resistances range from 34 to 1570 ohms/sq. The substrate wafers are all 1 ohm-cm p<111> silicon. The diffusant is As, with *Co* ranging from 10^{18} cm^{-3} to 10^{20} cm^{-3}. The diffusion profiles are of the complementary error function type determined by the spreading resistance technique with correction factors.

Experimental and Results

The in-line array and square array configurations are shown in Fig. 1. A current, *I*, is sent through probe points 1 and 4, and the voltage difference, *V*, is measured between points 2 and 3. From the sample geometry and the measured resistance, the resistivity for bulk material and the sheet resistance (ρ_s) for diffused layers can be calculated (9).

Probe loading, configuration, and tip radius.—Table I lists sheet resistance values derived from different probe configurations and loadings. All measurements were made below 100 mV.[1] For the range of 30 to 60 g/point, sheet resistances measured by probe No. 1 are independent of the probe loading. A scatter is seen for probe No. 2 on sample No. 2 which has the highest sheet resistance of 1570 ohms/sq and a shallow junction of 0.5 μm. Probe No. 3 had a square-array probe which had a constant loading of 50 g/point and was not varied

* Electrochemical Society Active Member.
Key words: silicon, diffusion, semiconductor.

[1] This 100 mV limit is discussed later.

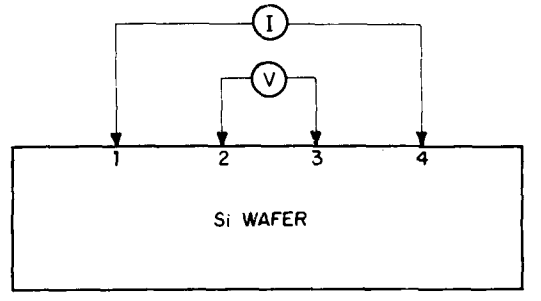

IN-LINE ARRAY

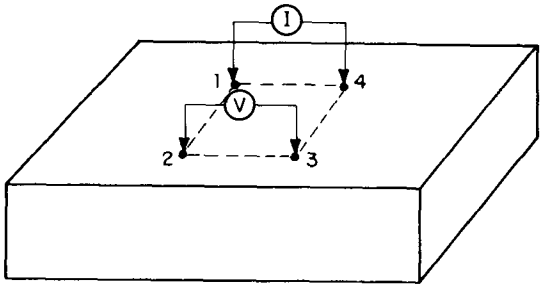

SQUARE ARRAY

Fig. 1. In-line and square array configurations of the four-point probe.

because of the design of the probe. Sheet resistances measured by this probe were lower than those measured by probes No. 1 and 2, especially on sample No. 2.

The reproducibility of probe No. 1 as a function of the probe loading is attributed to the broad point (the tip radius is 5.0 mils) as well as to the careful lowering of the probe points onto the wafer surface. (Since it is the "pressure," not the "velocity," that causes the probe points to make good contact, the probe points were lowered as slowly as possible.)

The scatter observed in the data from probe No. 2 could be caused by the combination of sharp probe point (tip radius of 1.5 mils), high sheet resistance, and shallow junction. Greater probe wander error reported for the square array technique (10) is a possible explanation for the deviation of sheet resistances measured by probe No. 3.

Probe No. 1 was used for the rest of the experiments; for convenience it was given a middle-of-the-range probe loading of 40 g/point.

Table I. Sheet resistance values* from different probe configurations and loadings

Sample No.	Probe No. 1 50-Mil in-line 5-Mil tip radius Load, g/point	ρ_s, ohms/sq	Probe No 2 25-Mil in-line 1.5-Mil tip radius Load, g/point	ρ_s, ohms/sq	Probe No. 3 25-Mil square 1.5-Mil tip radius Load, g/point	ρ_s, ohms/sq
1	60	128.3	60	126	—	
2		1578		1600		
3		146		140		
4		169.8		163		
5		260		256		
6		34		33		
	50		50		50	
1		128		126		117
2		1575		1189		890
3		146		140		135
4		166		161		156
5		263		255		254
6		34		34.5		32.8
	40		40		—	
1		129		124		
2		1570		1320		
3		146		145		
4		165		163.7		
5		264		259.3		
6		34		34		
	30		35		—	
1		127		120		
2		1568		1530		
3		146		143		
4		165		164		
5		263		260		
6		34		34		

* Each of these sheet resistance measurements represents an average of five readings.

I-V Characteristics

Room temperature.—Figure 2 shows a family of I-V characteristics taken at room temperature for different sheet resistance samples. There are three distinctive features: (*a*) all I-V curves are linear below 100 mV; (*b*) all I-V curves go through a transition region starting from 100 mV and then reach a different level where they are linear again; (c) finally, the voltage difference between the two inner probe points stays constant, independent of the current through the two outer probe points. (We refer to this effect as the "breakdown.")

At elevated temperatures.—To assure that heating is not the cause of the two-level phenomenon in the I-V characteristics mentioned above, we measured sample No. 5 at 125° and 175°C (Fig. 3). The heating introduces a shift in the I-V curve while maintaining the two-level effect. Also shown in this figure is the I-V curve measured at room temperature with a large heat sink underneath the silicon wafer. This curve is identical to the one measured without a heat sink. It is worth pointing out that the heating did change the voltage at the "breakdown." The "breakdown" voltage is lower for higher temperatures as reported by others (11).

Theoretical Model of the Two-Level Effect

A theoretical model may explain both the two-level and the "breakdown" mechanism.

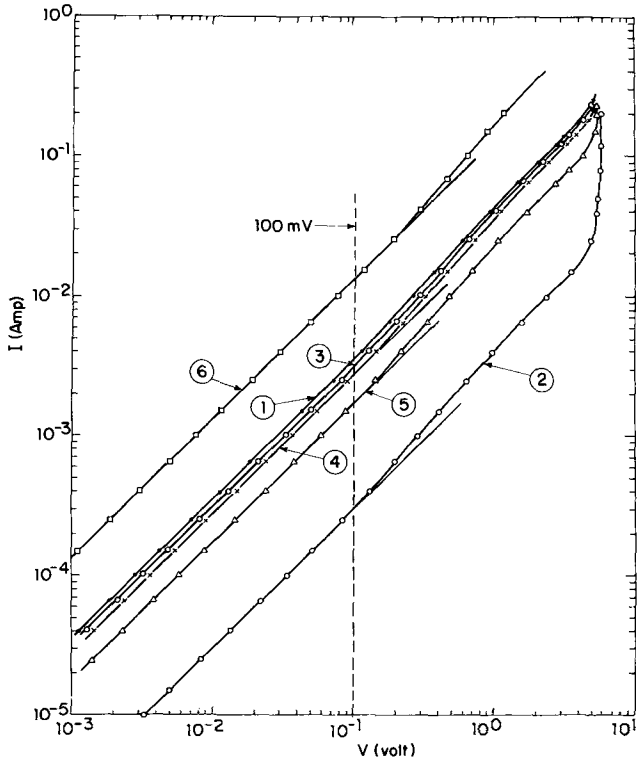

Fig. 2. I-V characteristics at room temperature for samples having different sheet resistances.

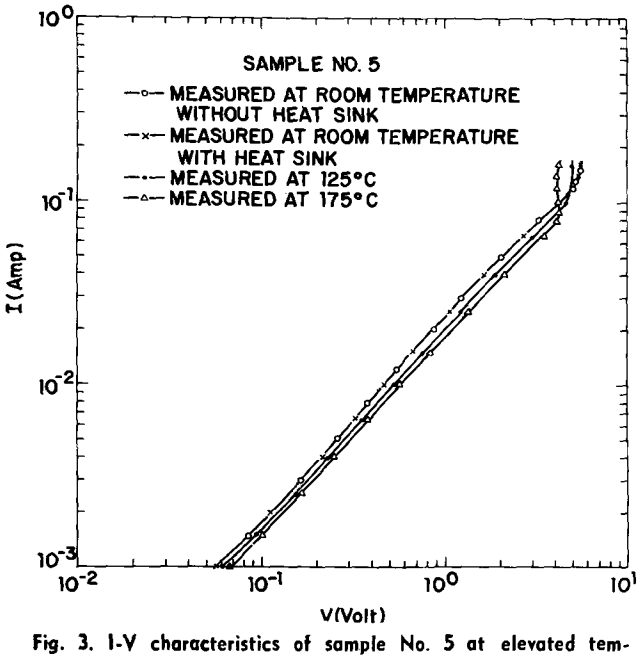

Fig. 3. I-V characteristics of sample No. 5 at elevated temperatures.

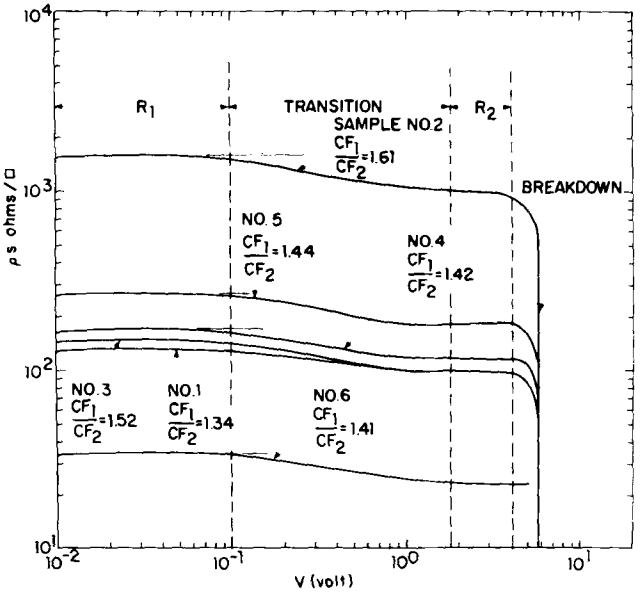

Fig. 4. Sheet resistance "breakdown" caused by varying the voltage. The two-level effect is reflected in the relationship between CF_1 (the correction factor at low voltage) and CF_2 (the correction factor at high voltage).

If we take the data of Fig. 2 and plot the sheet resistance *vs.* V, the results are shown in Fig. 4. The four sections of the curve are labeled R_1, transition, R_2, and "breakdown." Similar to the correction factors for spreading resistance reported by Schumann and Gardner (12), correction factors can also be derived for a four-point probe on a two-layer structure with uniform resistivity in both layers, as shown in Fig. 5. The relationship between V and I can be shown to be

$$V = \frac{I\rho_1}{2\pi S} \times \left[\frac{S}{a} \int_0^\infty \frac{[1 + 2\theta_1] \text{ Sin } (\lambda a)\ Jo\ (\lambda r)}{\lambda}\, d\lambda \right] \quad [1]$$

$$\theta_1 = \frac{K_1 e^{-2\lambda h_1}}{1 - K_1 e^{-2\lambda h_1}} \quad [2]$$

$$K_1 = \frac{\rho_2 - \rho_1}{\rho_2 + \rho_1} \quad [3]$$

where a is the radius of the probe

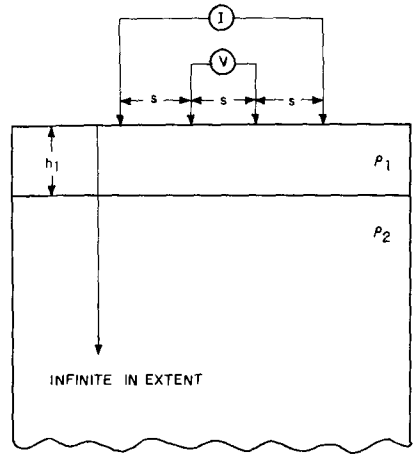

Fig. 5. Four-point probe correction factors for a two-layer structure.

$Jo(\lambda r)$ is the Bessel function of zero order
ρ_1 is the resistivity of the top layer
ρ_2 is the resistivity of the substrate
S is the probe spacing
h_1 is the thickness of the top layer

This equation can be written as

$$V = \frac{I\rho_1}{2\pi S} \times CF \quad [4]$$

where CF signifies the "correction factors" representing the expression in the bracket. When these correction factors are plotted against S/h_1 for various K_1 values, they are as shown in Fig. 6.

If the two layers have opposite conductivities (the result of an isolating junction), ρ_2 appears to be much greater than ρ_1, and therefore $K_1 = 1$. When $\rho_2 = \rho_1$, $K_1 = 0$ for the case of a bulk sample with infinite thickness. When the two layers are of the same conductivity but $\rho_2 > \rho_1$, K_1 has a positive value between "zero" and "one."

Suppose we have a structure of N+/N with $\rho_1 = 0.001$ ohm-cm (N $\simeq 10^{20}$ cm^{-3}) and $\rho_2 = 1$ ohm-cm. Then $K_1 = (\rho_2 - \rho_1)/(\rho_2 + \rho_1) = 0.999$, which corresponds to a correction factor of 1150, as indicated in Fig. 6. The probe spacing, S, is 1270 μm ($\simeq$ 50 mils) and the thickness, h_1, is 1 μm. If an isolating junction structure N+/P with the same ρ_1, ρ_2, S, and h_1 is used, then $K_1 = 1$, and the corresponding correction factor is 1800. The ratio of these two correction factors indicates the ratio of the two sheet resistances, which is

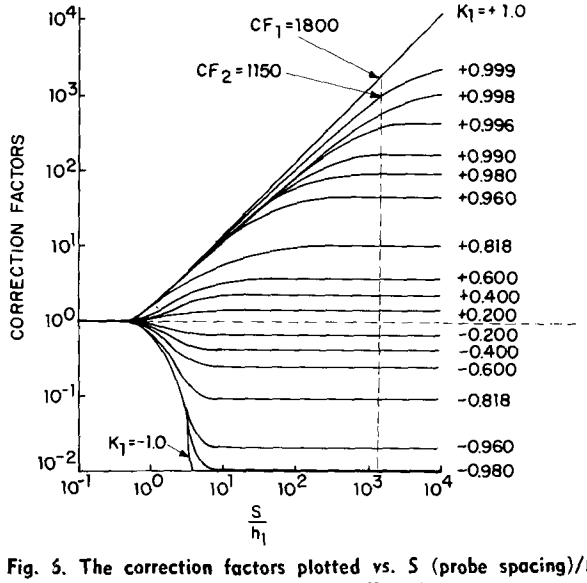

Fig. 6. The correction factors plotted vs. S (probe spacing)/h_1 (thickness of the top layer) for various K_1 values.

$$\frac{CF_1}{CF_2} = \frac{\rho_{S1}}{\rho_{S2}} = 1.56 \qquad [5]$$

So the sheet resistance, ρ_{S1}, of N+/P structure is 1.56 times higher than the sheet resistance, ρ_{S2}, of N+/N structure.

Our case is N+/P structure. Although the diffused layer does not have a uniform resistivity, ρ_1, the two-level sheet resistance effect can be explained by the difference in correction factors for an isolated and a "leaky" junction. When the current level, I (or voltage difference, V), is low, the relationship between V and I is

$$V = \frac{I\rho_1}{2\pi S} \times CF_1 \qquad [6]$$

because of the isolating junction. This is region R_1 in Fig. 4.

As I increases (or V increases), the isolating junctions underneath the two current probes start "leaking." This leakage current causes our N+/P structure to behave similar to that of a N+/N structure. Although the substrate resistivity, ρ_2, is still three orders of magnitude higher than ρ_1, K_1 is no longer "1" but "0.999." Therefore

$$V = \frac{I\rho_1}{2\pi S} \times CF_2 \qquad [7]$$

This is region R_2 in Fig. 4.

Since $CF_1 > CF_2$, sheet resistance values in R_1 are higher than those of R_2 (Fig. 4).

At this point, it is important to understand the voltage distribution under the current probe. When a current, I, is passed into the semiconductor, which has a two-layer structure as shown in Fig. 7, the voltage at a point (y, z) can be shown to be

$$V(y,z) = \frac{I\rho_1}{2\pi a} \times {}_2Q_1 \qquad [8]$$

where

$${}_2Q_1 = \int_0^\infty \frac{e^{-\lambda z} \sin(\lambda a)\, Jo(\lambda y)}{\lambda}\, d\lambda + \int_0^\infty \frac{\theta_1 (e^{\lambda z} + e^{-\lambda z}) \sin(\lambda a)\, Jo(\lambda y)}{\lambda}\, d\lambda$$

and θ_1 is the same as in Eq. [2].

In Fig. 7, ${}_2Q_1$ is plotted as a function of Y (or y/a) for the case of $h_1/a = 2$. The running parameter is Z or z/a. The curve indicated by $Z = 0$ is the voltage distribution on the surface of the semiconductor. The curve indicated by $Z = 2.0$ is the voltage distribution at the interface of this two-layer structure. For a distance of $Y \geq 5$ (or $y \geq 5a$), the voltage distribution

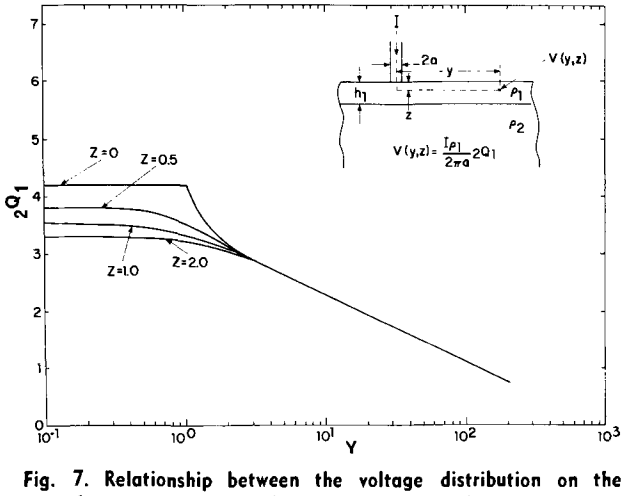

Fig. 7. Relationship between the voltage distribution on the semiconductor surface, Z = 0, and that at the P/N junction interface, Z = 2.0.

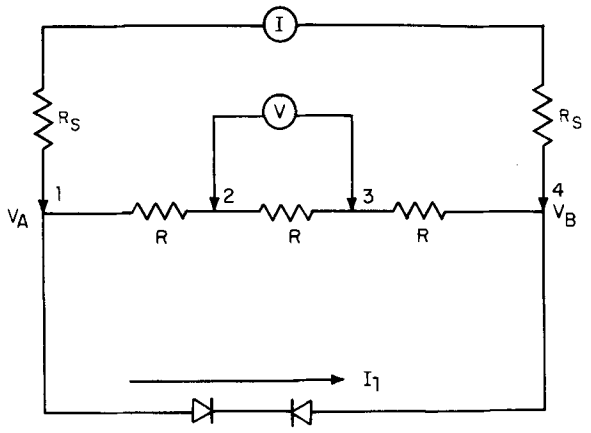

Fig. 8. A simplified equivalent circuit

on Z = 0 (the surface) and Z = 2.0 (the interface) are practically the same. In other words, the voltage difference measured on the surface of the wafer is no different than the voltage difference at the interface of the two layers.

To check that the condition $y \geq 5a$ is met, we calculated from the spreading resistance (12) measurement using this same current probe and obtained $a = 1.5$ μm.[2] The probe spacing, y, in our case is 1270 μm (50 mils) so the condition of $y \geq 5a$ is certainly satisfied. Therefore, the voltage difference measured on the surface can be thought of as the voltage difference at the P/N junction interface.

When I is increased further, the N-P junction underneath the two current probes breaks down and most of the current now flows through the substrate. A simplified equivalent circuit is shown in Fig. 8. The back-to-back diodes simulate the two N-P junctions underneath the two current probes. R represents the resistance of the thin layer. R_s is for the spreading resistance of the current probe. When the diodes break down, an increase in I from the constant current supply will increase I_1 through the diodes while maintaining a constant $\Delta V = (V_A - V_B)$ across the diode. A constant ΔV will in turn keep V between the two inner probes a constant. This "breakdown" situation is what we observed in Fig. 4.

Summary and Recommendations

The two-level effect is explained qualitatively by the correction factors for the four-point probe. The sample calculation shows $(CF_1)/(CF_2) = 1.56$. Calculated ratios of the two levels of the samples range from 1.34 to 1.61. This difference is due to the actual structure, which consists of diffused layers of different thicknesses.

The transition region starts at 100 mV, and the "breakdown" is around 5.5V. Both are independent of the sheet resistances, suggesting that this is an effect due to the nature of the N-P junction.

For reproducible sheet resistance measurements on thin diffusions, we recommend the following:

1. Use of a broad probe tip, since small tip radius might pierce through the diffusion and cause erratic readings.
2. Probe points should be loaded with between 30 and 60g and lowered as slowly as possible.
3. The current levels should be so adjusted that the voltage difference between the two inner probes is less than 100 mV.

Acknowledgments

The authors would like to thank Paul A. Schumann, Jr., for his many helpful discussions on the subject matter of this paper, and for the use of the correction factors curve constructed by him and E. E. Gardner.

[2] $R = \rho/4a$ is the relationship that exists between the spreading resistance (R), the resistivity of the sample (ρ), and the radius of contact (a) of the probe. For a sample with $\rho = 1.0$ ohm-cm, R was measured to be 1.68 kohm, which resulted in $a = 1.5$ μm.

Manuscript submitted May 26, 1970; revised manuscript received ca. Nov. 3, 1970. This was Paper 185 presented at the Detroit Meeting of the Society, Oct. 5-9, 1969.

Any discussion of this paper will appear in a Discussion Section to be published in the December 1971 JOURNAL.

REFERENCES

1. R. G. Mazur and D. H. Dickey, *This Journal*, **113**, 255 (1966).
2. E. E. Gardner, "Symposium on Manufacturing In-Process Control and Measuring Techniques for Semiconductors," Vol. II, p. 19, Manufacturing Technology Division, Air Force Materials Lab., Wright-Patterson Air Force Base (1966).
3. E. E. Gardner, P. A. Schumann, and E. F. Gorey, in "Measurement Techniques for Thin Films," B. Schwartz and N. Schwartz, Editors, p. 258, The Electrochemical Society (1967).
4. T. H. Yeh and K. H. Khokhani, *This Journal*, **116**, 1461 (1969).
5. G. Backenstoss, *Bell System Tech. J.*, **37**, 699 (1958).
6. J. C. Irvin, *ibid.*, **41**, 387 (1962).
7. L. H. Garrison, "SCP and Solid State Technology," p. 47, May 1966.
8. W. J. Patrick, *Solid-State Electron.*, **9**, 203 (1966).
9. F. M. Smits, *Bell System Tech. J.*, **37**, 711 (1958).
10. Shou-Chien Ting, Chinese J. Phys., **22**, 606 (1967).
11. P. A. Schumann, *This Journal*, **115**, 1197 (1968).
12. P. A. Schumann and E. E. Gardner, *Solid-State Electron.*, **12**, 1 (1969).

Technical Notes

The Control of Insoluble Magnesium Compounds Formed during Seawater Battery Discharge

Carl E. Mueller* and Frederic M. Bowers*

U. S. Naval Ordnance Laboratory, White Oak, Silver Spring, Maryland 20910

The capacity of seawater activated batteries containing magnesium anodes is often limited by clogging. During discharge the space between the electrodes of the cells nearest to the negative terminal gradually fill with an insoluble precipitate that replaces the seawater electrolyte and reduces battery capacity.

The problem of clogging has been encountered in both high and low discharge rate batteries. In batteries designed for high rate (15 min) applications, the electrolyte is forced through each cell. In these applications, the flow of electrolyte is usually sufficient to flush the insoluble precipitate from the cells. However, Faletti and Nelson (1) found that the use of AZ61 magnesium anodes which had not been properly heat treated resulted in the formation of an adherent precipitate during high rate discharge. This precipitate could not be flushed from the affected cells and caused a reduction in battery capacity.

Clogging is usually more severe in batteries designed for low rate applications. In these batteries the electrolyte is not forced through the cells and there is a greater tendency for the precipitate to build up and reduce capacity. This problem was encountered during the development of a low rate (6 hr, 150 mA constant current discharge) 10 cell, 15V, AgCl/Mg seawater battery at the Naval Ordnance Laboratory, White Oak, Maryland. When prototype batteries were discharged in seawater, a flocculent adherent precipitate formed that gradually filled the space between electrodes in those cells nearest to the negative terminal of the battery. The precipitate also formed outside these cells and blocked the bottom water-entry holes. This condition limited the capacity to less than half of that theoretically available. However, when similar batteries were discharged in aqueous sodium chloride of equal salinity, a granular nonclogging precipitate was formed. This fine precipitate together with hydrogen gas escaped through the top port hole of each negative cell. As a result, the capacity of these batteries was two to four times greater than those discharged in seawater.

* Electrochemical Society Active Member.

Key words: silver chloride/magnesium battery, seawater battery filter, control of $Mg(OH)_2$ formation.

This paper describes the experiments that were conducted to determine the cause for the formation of the flocculent clogging precipitate in seawater. The results of these experiments are discussed. Methods for controlling the formation of this precipitate are presented.

Experimental

The experimental battery model used in this study is shown in Fig. 1 and 2. It consisted of a clear Lucite

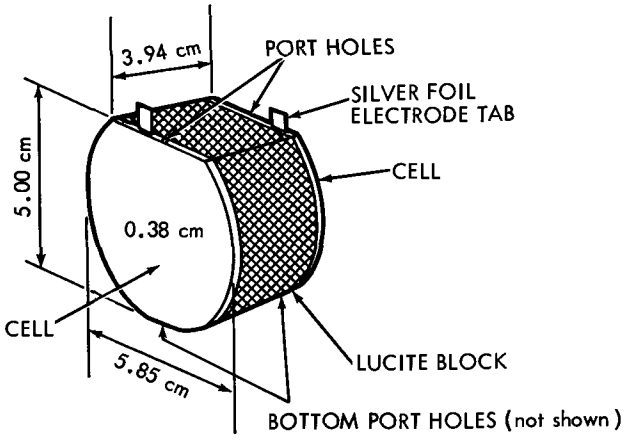

Fig. 1. Experimental battery model

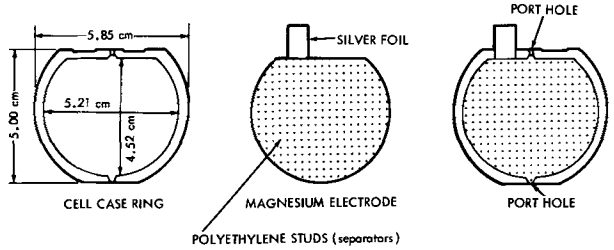

Fig. 2. Cell and electrode configuration of experimental battery model.

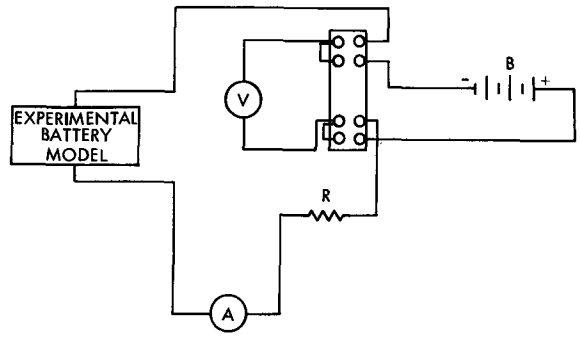

Fig. 3. Experimental apparatus and circuitry

block with a cell containing an AZ61 magnesium electrode attached to each end. The clear Lucite permitted *in situ* observations during the experiments. The configuration of the model was similar to the low rate, 10 cell, 15V battery that was being developed. When the model was immersed in an aqueous salt solution with a d-c voltage of 15.1 ± 0.1V impressed across the electrodes, the parasitic drain condition (2) similar to that occurring during the discharge of the 10 cell battery was simulated. A variable resistor was used to maintain the voltage between the desired limits. A Sensitive Research voltmeter (10,000 ohms/V) was used to monitor the voltage, and the current which represented the parasitic drain (2) was measured with a Weston milliammeter, Model No. 622. The circuitry is shown schematically in Fig. 3.

The experiments were conducted in various electrolytes: (a) in seawater obtained from the Gulf Stream near Ft. Lauderdale, Florida, which was representative of typical seawater, and (b) in other aqueous salt solutions of equal salinity (3.5%). The aqueous salt solutions were made up from ACS reagent grade salts and distilled water. These solutions contained varying proportions of NaCl, $MgCl_2$, Na_2SO_4, and $MgSO_4$. The ions contained in these aqueous salt solutions represented the four major ions found in seawater which are Na^+, Mg^{++}, Cl^-, and $SO_4^=$ (3-6). The composition of each electrolyte is given in Table I. The specific resistivity of the prepared salt solutions was similar to that of the Gulf Stream seawater which was 20.3 ohm-cm at 20°C (3-6). Before the start of each experiment, the *p*H of the electrolyte was measured and adjusted, if necessary, to 8.25 ± 0.05 with 0.1*N* Na_2CO_3. Upon the completion of each experiment, the *p*H was again determined. The volume of electrolyte used for each experiment was 1800 ml; the temperature was maintained at 23° ± 2°C. Experimental runs were usually of 3 hr duration, but some exploratory experiments ran for as long as 7 hr. The precipitate from each experiment was qualitatively analyzed using x-ray diffraction spectra.

Table I. Identification of electrolyte solutions

Electrolyte solution	Electrolyte composition 3.5% by weight:	Major ions present	Bulk *p*H initial	Bulk *p*H final
A	NaCl	Na^+,Cl^-	8.30	11.00
B	Na_2SO_4	Na^+,$SO_4^=$	8.25	10.90
C	32/39 NaCl & 7/39 Na_2SO_4	Na^+,Cl^-,$SO_4^=$	8.25	11.00
D	$MgCl_2$	Mg^{++},Cl^-	8.25	9.05
E	$MgSO_4$	Mg^{++},$SO_4^=$	8.25	8.50
F	32/39 NaCl & 7/39 $MgSO_4$	Na^+,Mg^{++},Cl^-,$SO_4^=$	8.25	9.90
G	32/39 NaCl & 7/39 $MgCl_2$	Na^+,Mg^{++},Cl^-	8.25	9.80
H	Gulf Stream seawater (salinity ~35‰)	Na^+ ~10.56 g/kg Mg^{++} ~1.27 g/kg Ca^{++} ~0.40 g/kg Cl^- ~18.98 g/kg $SO_4^=$ ~2.65 g/kg	8.30	9.65

Results

The data in Table II show that large flocculent agglomerates were formed only when magnesium salts were initially present in the electrolyte (solutions D, E, F, G, and H of Table I). This flocculent precipitate formed inside of the negative cell and also in the bulk electrolyte around the bottom inlet port of this cell. This condition was similar to that observed during the seawater discharge of the prototype batteries. However, in electrolyte solutions initially free of Mg^{++} ions (solutions A, B, and C of Table I) a granular precipitate was formed. This precipitate did not clog the negative cell and was flushed out into the surrounding body of electrolyte. These results indicate that the type of precipitate formed depends on whether Mg^{++} ions are initially present in the electrolyte.

The precipitates obtained from these experiments were analyzed by x-ray diffraction spectra. The spectrum of precipitates collected from solutions A, C, D, E, F, and G had only one readily identifiable component, $Mg(OH)_2$. In addition, there were two unidentified constituents found in these samples. One of these materials was probably free magnesium, for spalling of the anode was observed and metal was visible in the corrosion products. The precipitate from solution B was identified as being only magnesium metal. However, the concentration of this material may have been high enough to mask out any other constituents present, including $Mg(OH)_2$. The precipitate obtained from solution H (seawater) had only one identifiable component, $CaCO_3$. There were other materials present, but they were not identified. Although the results obtained from the x-ray diffraction analyses are somewhat limited, they seem to indicate that in most every case $Mg(OH)_2$ is formed as the principal corrosion product.

Table II also shows that the maximum simulated parasitic current value obtained for each experiment varied only slightly with the chemical composition of the electrolyte indicating that the conductivity of the different solutions was essentially the same. The values ranged from 47 to 65 mA. The lower values occurred when hydrogen gas bubbles were partially blocking the top port holes in each cell, and the higher values occurred when the holes were essentially free of gas.

Table I lists the *p*H values of each electrolyte at the end of a run. Electrolysis in those solutions initially free of Mg^{++} ions resulted in *p*H values of 11.0 ± 0.1 and granular precipitates. Is solutions to which mag-

Table II. Summary of electrolytic corrosion data

Electrolyte solution	Time of electrolysis (hr)	Maximum simulated parasitic current (mA)	Characteristics of insoluble precipitate
A	2.70	55	white, granular type
B	3.05	50	white, granular type
C	3.00	52	white, granular type
D	2.50	47	white, large flocculent agglomerates
E	2.35	47	white, large flocculent agglomerates
F	3.00	65	white, large flocculent agglomerates
G	3.00	50	white, large flocculent agglomerates
H	3.00	65	white, large flocculent agglomerates

nesium salts were added the resulting pH values were 9.4 ± 0.5 and the precipitates were flocculent. The pH values of these electrolytes agree with the results obtained by J. L. Robinson and P. F. King (7) and H. A. Robinson (8) who studied the electrochemical behavior of magnesium anodes in aqueous environments. They found that the pH of aqueous salt electrolytes decreases as the Mg^{++} ion concentration increases. However, they did not report the type of $Mg(OH)_2$ formed in these electrolytes.

Control of $Mg(OH)_2$ Formation

The first approach that was investigated was the use of a chemical filter that would remove the Mg^{++} ions from the electrolyte entering the battery by precipitation in a nonflocculent form. Thallous fluoride (TlF), a white powdery compound that exhibits appreciable aqueous solubility (9), was used as the filter material. In aqueous solution, Mg^{++} ions may react with TlF according to the following reaction

$$Mg^{++} + 2TlF \rightarrow MgF_2 + 2Tl^{+} \quad [1]$$

and form MgF_2, a granular precipitate. Experiments were conducted in which a TlF filter was used during the low rate discharge of the 10 cell AgCl/Mg batteries in seawater. The filters used in these experiments were large enough to encompass the bottom inlet ports of the five cells nearest the negative terminal of the battery which was where the flocculent precipitate had previously formed. The filter was fabricated by compressing the TlF powder into the configuration shown in Fig. 4, and gluing the formed block into a four-sided Lucite case. Hence, the seawater electrolyte came in direct contact with the TlF before entering the five most negative cells. When batteries containing the TlF filter were discharged in Gulf Stream seawater, the capacity was about 15 per cent more than the controls which had no filter, and the amount of flocculent $Mg(OH)_2$ formed during discharge was reduced. Figure 5 shows typical voltage-time curves of AgCl/Mg seawater batteries discharged with and without the TlF filter.

A second approach was the use of a chemical filter that would remove the Mg^{++} ions from the electrolyte entering the battery by the formation of a soluble magnesium complex. Disodium ethylenediaminetetraacetate (disodium EDTA), a white crystalline compound that is moderately soluble in water, was used as the filter material. Disodium EDTA occurs with two molecules of water of hydration and is represented by the formula $Na_2H_2Y \cdot 2H_2O$. In aqueous

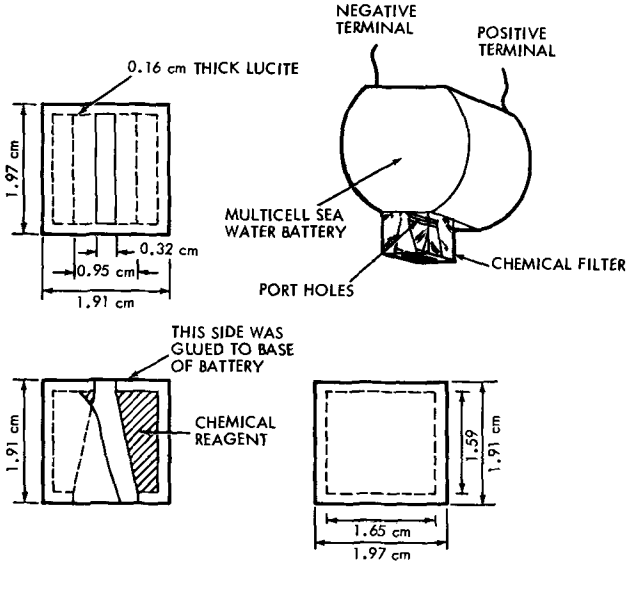

NOTE: SCALE 1:2

Fig. 4. Configuration of chemical filter

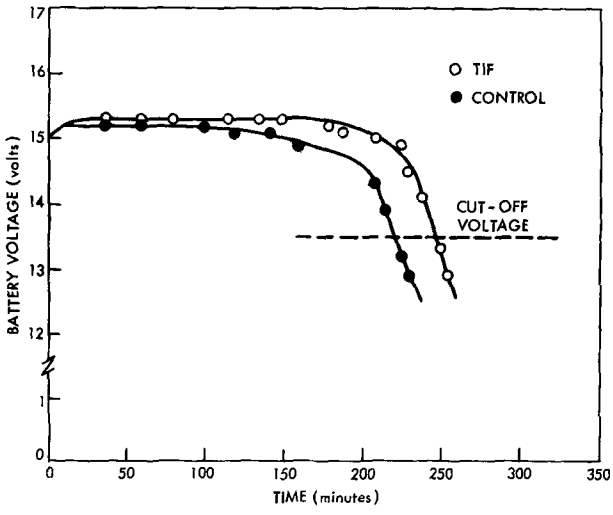

Fig. 5. The effect of a TlF filter on the capacity of a 10 cell AgCl/Mg seawater battery when discharged at a constant current of 150 mA.

solution $H_2Y^{=}$ is the complex forming ion and reacts with cations according to the following equation

$$Me^{+n} + H_2Y^{=} \rightleftharpoons MeY^{(n-4)} + 2H^{+} \quad [2]$$

where n ranges from 2 to 4 (10). One gram-ion of the complex forming ion reacts with one gram-ion of the metal without regard to its valence. The resulting complexes have the same composition but differ from one another in the charge they carry (10).

The complexes of the divalent metal ions (Me^{++}) occur as complex anions and are represented by the formula $MeY^{=}$. The stability of the complex is characterized by its formation constant (K). The larger the value of K, the greater the stability of the metal complex (11). In seawater there are two metal ions, calcium (Ca^{++}) and magnesium (Mg^{++}), that may form the $MeY^{=}$ complex. The formation constant of either complex, $CaY^{=}$ or $MgY^{=}$, is approximately of the same magnitude so that both complexes can occur (11).

Experiments were conducted in which disodium EDTA filters were used during the low rate discharge of 10 cell AgCl/Mg batteries in seawater. The filters used in these experiments were similar in design to the TlF filter shown in Fig. 4. However, since disodium EDTA is not compressible, the loose salt was placed within a Lucite case and sealed in with a Dynel-Webril paper of 0.00254 cm thickness. In aqueuos solution the resulting complex forming ions, $H_2Y^{=}$, were free to migrate through the thin paper and react with the Mg^{++} ions in the electrolyte prior to entering the five most negative cells. When batteries containing the disodium EDTA filter were discharged in Gulf Stream

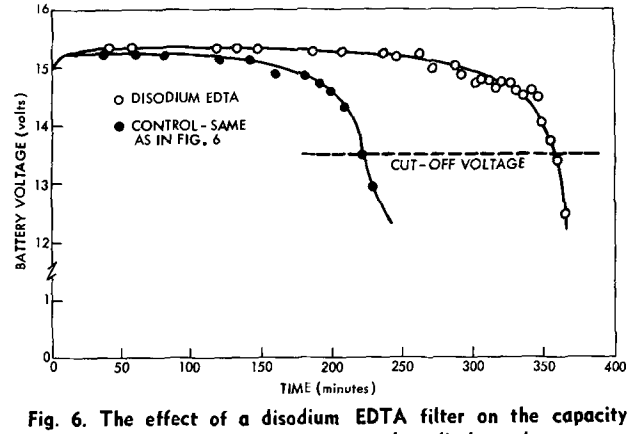

Fig. 6. The effect of a disodium EDTA filter on the capacity of a 10 cell AgCl/Mg seawater battery when discharged at a constant current of 150 mA.

seawater, the capacity was about 50% more than the controls which had no filter and the amount of flocculent $Mg(OH)_2$ formed during discharge was negligible. Figure 6 shows typical voltage-time curves of AgCl/Mg seawater batteries discharged with and without the disodium EDTA filter.

The results of these experiments demonstrate that the formation of flocculent $Mg(OH)_2$ during discharge of low rate AgCl/Mg seawater batteries can be controlled by using a filter. When disodium EDTA is used as the filter medium, the capacity of these batteries is significantly increased.

Acknowledgments

The authors wish to express their gratitude to Dr. G. Atkinson for his helpful suggestions and discussions throughout this study.

Manuscript submitted May 25, 1970; revised manuscript received *ca.* Oct. 11, 1970.

Any discussion of this paper will appear in a Discussion Section to be published in the December 1971 JOURNAL.

REFERENCES

1. D. W. Faletti and L. F. Nelson, *Electrochem. Tech.*, **3**, 98 (1965).
2. National Defense Research Committee, "Final Report on Seawater Batteries," App. B, Bell Telephone Laboratories, Inc., New York (1945).
3. Sverdrop, Johnson, and Fleming, "The Oceans," Prentice-Hall, Inc., New York (1946).
4. K. Park, *J. Deep Sea Res.*, **2**, 729 (1964).
5. C. Adler, *Undersea Technol.*, **3**, 28 (1962).
6. D. W. Faletti and N. A. Gackstetter, *This Journal*, **114**, 299 (1967).
7. J. L. Robinson and P. F. King, *ibid.*, **108**, 36 (1961).
8. H. A. Robinson, *Trans. Electrochem. Soc.*, **90**, 485 (1946).
9. Kleinberg, Argersinger, and Griswals, "Inorganic Chemistry," D. C. Heath and Co., Boston, Mass. (1960).
10. F. J. Welcher, "The Analytical Uses of Ethylenediamine Tetraacetic Acid," D. Van Nostrand Co., Inc., New York (1958).
11. L. G. Sillen and A. E. Martell, "Stability Constants of Metal-Ion Complexes," Chemical Society of London, London, England (1964).

Oxide Films on Beta-Silicon Carbide

R. W. Bartlett*

Stanford Research Institute, Menlo Park, California 94025

Motzfeldt (1) has correlated the rate data of four investigators for oxidation of hexagonal α-silicon carbide (2-5) in dry oxygen and compared the results with Norton's data (6) for oxygen permeation of silica. He also correlated parabolic rate data for the dry oxidation of silicon (7-12). With one exception the results of these investigators are remarkably consistent. The absolute values of the parabolic rate constant for oxidation of silicon and α-silicon carbide agree within 1% at 1200°C and the activation energies agree within experimental error. It should be noted that the oxidation rate for both silicon and α-silicon carbide are for the formation of an amorphous silicon dioxide film. Jorgensen *et al.* (4) found that in the range of 1100° to 1300°C, there was a transition in the parabolic oxidation rate constant for α-silicon carbide after an initial oxidation period. This increase in oxidation rate was associated with a transition from an amorphous silica film to cristobalite and suggests that it is preferable to oxidize silicon carbide below 1100°C to avoid formation of a devitrified oxide film. They also found that water vapor promoted devitrification and accelerated the oxidation rate (13), as it does for silicon.

Growth of Insulating Oxide Films

The present note is concerned with oxide films on solution grown single crystals of cubic β-silicon carbide (14). The crystals used, which were platelets with a dominant {111} face, were cleaned in hydrofluoric acid, and rinsed in alcohol just prior to oxidation.

Several β-silicon carbide crystals were oxidized in dry oxygen or steam, both at 1 atm, to provide specimens for evaluation of the oxide films. Oxidation temperatures near 1000°C were used in conjunction with variable oxidation periods to obtain specimens with oxide film thicknesses from 500Å to over 3000Å. A polished silicon wafer was oxidized with each run and its oxide film thickness was determined to confirm the oxidation conditions.

The thicknesses of oxide films on transparent β-silicon carbide crystals were determined in two ways. The step height formed by etching part of the oxide film was measured with an interferometric microscope. This procedure required evaporating a thin reflecting film since silicon carbide is transparent. Interpretation was complicated by growth steps in the silicon carbide substrate surface, and the method was limited to thick oxide films. The oxide film thickness determinations for silicon carbide (dry oxidation) also agreed with the results of interferometric oxide film thickness measurements on the corresponding silicon monitor wafers. This was expected because of the identical oxidation rates for silicon and α-silicon carbide. In the most convenient technique, the oxide film thickness on silicon carbide was determined from a measurement of the oxide capacitance using the dielectric constant for silica, $k_o = 3.9$. This method was verified by comparing results with similar results obtained by the interferometric method on identical samples. Application was limited to insulating oxide films.

A few thermogravimetric oxidation rate experiments were made on β-silicon carbide platelets in dry oxygen at 0.2 atm and temperatures from 990° to 1220°C. Oxide film thickness is proportional to weight gain. During the first hour of oxidation weight increases were usually greater than predicted from the parabolic rate data (quasi steady state diffusion limited) for oxidation of silicon while the subsequent weight gain conformed with the parabolic oxidation rate of silicon. Evidently variable amounts of oxide are produced in the initial stages before a protective oxide (diffusion limiting) film is formed.

Several isolated aluminum field plates with dimensions of 10 mils by 10 mils were evaporated on each oxidized crystal. A 90% Au-10% Ta alloy fused on one end of each crystal made an ohmic contact with the silicon carbide crystal. The oxide films were tested for dielectric breakdown up to 50V using a point probe on the alloy contacts and a 4-mil-diameter gold spherical probe on the field plates. A Boonton 75C capacitance/conduction bridge with 0.001 μohm resolution was used.

The oxide films grown in dry oxygen were either sufficiently insulating to prevent measurable current flow or they exhibited negligible resistances. None of the oxide films resulting from the steam oxidation

* Electrochemical Society Active Member.
Key words: β-silicon carbide, oxidation, MOS structures.

Table I. Insulating properties of oxide films grown on β-silicon carbide crystals in dry oxygen at 1 atm

Oxidizing temperature (°C)	Oxidizing time (min)	Oxide thickness (Å)	Field plates shorted at 50 V
985	2790	7000	None
985	1030	3400	None
1000	795	3100	5%
980	275	1400	15%

were insulating. Some of the steam grown films were quite thick, equivalent to 24,000Å on a silicon monitor. Over 90% of the oxide films produced by the dry oxidation experiments and summarized in Table I were insulating if the thickness was 1400Å or greater. The measured oxide film thickness agreed with the thicknesses predicted from the parabolic oxidation kinetics. The yield of insulating 10 mil square films decreased for thinner oxide films and with a 500Å equivalent parabolic oxidation treatment, none of the oxide films tested were insulating.

Typical replica electron micrographs of the {111} surface of a crystal before and after dry oxidation are shown in Fig. 1. Growth steps in the crystal are replicated in the oxide surface. Although the texture of the oxidized surface is very similar to the unoxidized surface, there are more small pits, typically 500Å and all less than 1000Å in diameter, on the oxidized surface. It appears from these and other micrographs that lack of adequate oxide growth may cause dielectric breakdown of the oxide film at these depressions and at growth steps; however, it was not possible to differentiate between inadequate oxide growth and stronger adhesion of the replica film at growth steps.

Capacitance-Voltage Measurements

The metal-oxide-semiconductor structures (MOS) made of oxidized β-silicon carbide with evaporated 10 mil platinum field plates were tested by measuring the a-c capacitance at 100 kHz with a superimposed d-c bias voltage on the field plate, V_G, which was varied from +50V to −50V. The β-silicon carbide crystals were n-type. The reproducibility in capacitance change with d-c bias for three different field plates on the same crystal with an oxide film thickness of 1400Å is shown in Fig. 2. The variation in capacitance expressed as the ratio of measured capacitance under bias over the measured oxide film capacitance is plotted against the d-c bias.

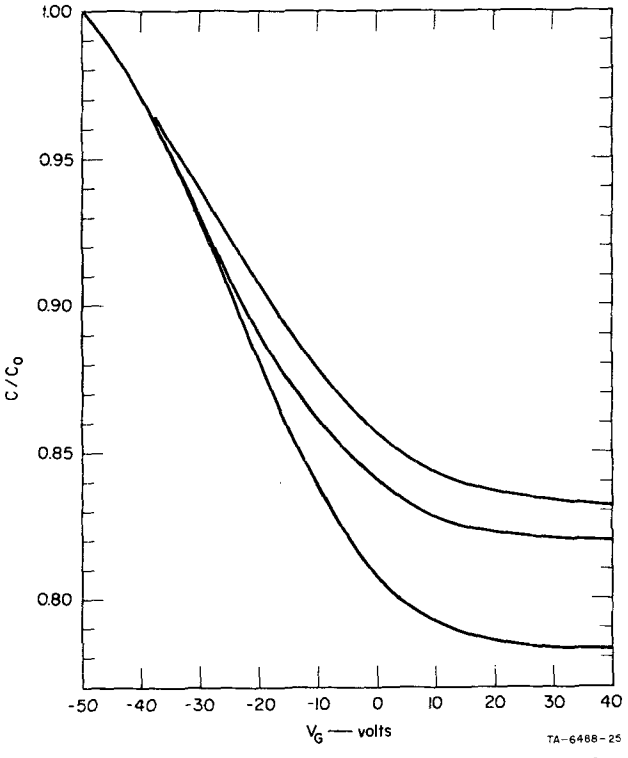

Fig. 2. Capacitance vs. gate voltage for MOS structure with n-type β-silicon carbide, $X_0 = 1400$Å.

The amount of variation in capacitance increases with decreasing carrier concentration in the underlying semiconductor and decreasing thickness of the oxide film. For the 1400Å oxide film shown in Fig. 2, the change in capacitance was greater than 20%. At a film thickness of 3000Å the change in capacitance was only 5%.

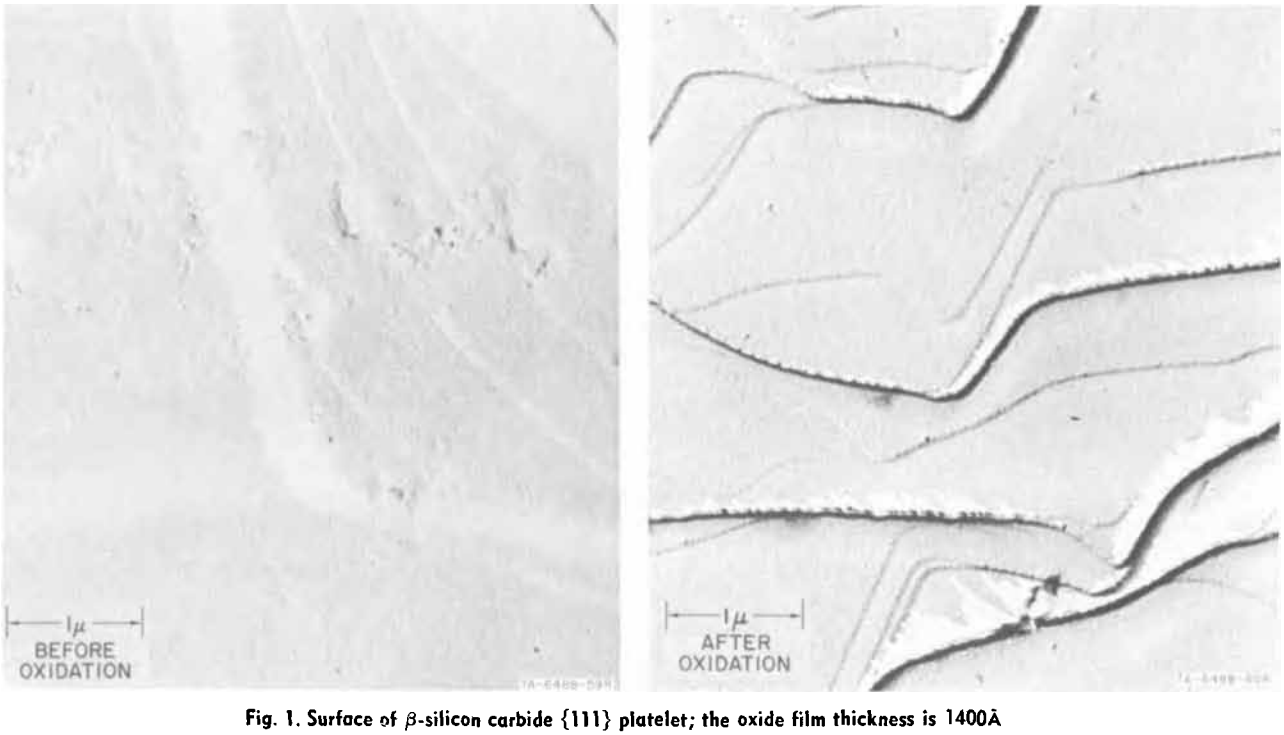

Fig. 1. Surface of β-silicon carbide {111} platelet; the oxide film thickness is 1400Å

The change in capacitance with applied d-c bias for an MOS structure has been discussed in several papers on thermally oxidized silicon surfaces. The paper by Grove *et al.* (15) gives a detailed description of the theory of an MOS structure. The variation in unit area capacitance, C, depends on the space charge within the semiconductor, since the total capacitance of both the oxide film and the underlying semiconductor space charge capacitance are being measured

$$C = \frac{1}{1/C_o + 1/(C_s + C_{ss})} \qquad [1]$$

where C_o is the oxide capacitance per unit area, C_s is the semiconductor capacitance per unit area, and C_{ss} denotes the capacitance per unit area of the surface states. Assuming that the surface state charge is constant, the surface state capacitance is zero and the capacitance of the MOS structure is

$$C = \frac{1}{1/C_o + 1/C_s} \qquad [2]$$

Calculating the space charge in the semiconductor is an involved process. For an MOS structure, the variation in energy bands and charge distribution in the semiconductor with distance in a direction normal to the semiconductor-oxide interface will depend on the d-c gate voltages, electric charge in the surface states, and the work function difference between the metal gate and semiconductor. However, for a given MOS specimen, only the gate voltage can be varied.

Biasing the gate voltage to deplete majority carriers in the semiconductor from near the oxide/semiconductor interface, without a sufficient field to accumulate minority carriers, will leave a space charge region of uncompensated acceptor or donor ions in the depletion region.

The effective width of the depletion region, X_d, can be defined from the charge distribution under a unit area of the semiconductor

$$Q_s = Q_p + q(N_D - N_A)X_d \qquad \text{(n-type)} \qquad [3]$$

where $(N_D - N_A)$ is the net donor concentration, Q_s is the total charge induced within the semiconductor, and Q_p is the charge associated with electron holes.

Plots of Q_s *vs.* Q_p for various $(N_D - N_A)$ have been calculated for silicon by integrating Poisson's equation with an appropriate Boltzmann relation for charge carrier concentration (15). Equation [3] can then be used to determine X_d as a function of Q_s and $(N_D - N_A)$. Similar curves have not been calculated for silicon carbide. Nevertheless, it was of interest to calculate the depletion mode semiconductor capacitance for undoped n-type solution grown β-silicon carbide crystals, using the maximum values of X_d as a function of $(N_D - N_A)$ determined for silicon

$$C_s = k_s\epsilon_o/X_d \qquad [4]$$

The following equation results when Eq. [4] and a similar equation for the oxide capacitance are substituted in Eq. [2]

$$C/C_o = [1 + (k_o/k_s)(X_d/X_o)]^{-1} \qquad [5]$$

where k_o is the oxide dielectric constant, X_o is the oxide thickness, and k_s is the silicon carbide dielectric constant. The dielectric constants are $k_o = 3.9$ and $k_s = 10.0$. The resulting values of $(N_D - N_A)$ *vs.* C/C_o for various oxide film thicknesses, X_o, on β-silicon carbide are plotted in Fig. 3.

These curves can be used to estimate net donor concentrations in the crystal. For example, the minimum capacitance values in Fig. 2, $C/C_o = 0.78$-0.82, measured with a 1400Å oxide film, indicate a net donor concentration of 1 x 10^{17} to 2 x 10^{17} cm^{-3}. The minimum C/C_o data measured for several β-silicon carbide MOS structures with oxide film thicknesses from 1400Å to 3400Å were analyzed using Fig. 3 to determine the net donor concentrations. In all cases the results indicated that $(N_D - N_A)$ was in the range 10^{17} to 10^{18} cm^{-3}.

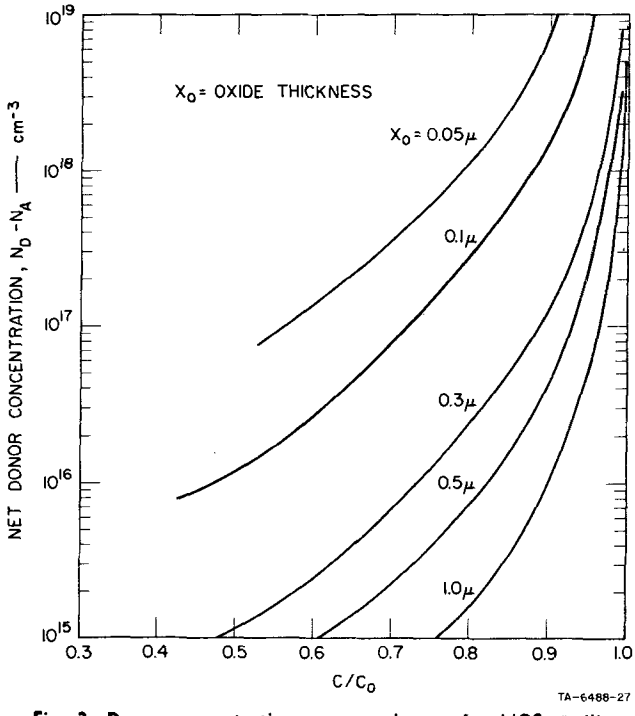

Fig. 3. Donor concentration vs. capacitance for MOS β-silicon carbide structures.

These results are in good agreement with net donor determinations from Hall measurements made on β-silicon carbide crystals grown in the same apparatus under identical conditions (14).

Although charge depletion near the surface of β-silicon carbide in MOS structures has been demonstrated, thinner insulating films than those grown by thermal oxidation, without leading to dielectric breakdown, are required before MOS devices can be developed using β-silicon carbide.

Acknowledgments

The author is indebted to Frank A. Halden, Arne Rosengreen, and Paul J. Jorgensen for discussions. This work was sponsored by Air Force Cambridge Research Laboratories, Office of Aerospace Research, under Contract F19628-67-C0243.

Manuscript submitted July 18, 1970; revised manuscript received *ca.* Oct. 7, 1970. This was Paper 90 presented at the Detroit Meeting of the Society, Oct. 5-9, 1969.

Any discussion of this paper will appear in a Discussion Section to be published in the December 1971 JOURNAL.

REFERENCES

1. K. Motzfeldt, *Acta Chem. Scand.*, **18**, 1596 (1964).
2. T. J. Nakatogawa, *Chem. Soc. Japan, Ind. Chem. Sec.*, **57**, 348 (1954).
3. R. F. Adamsky, *J. Phys. Chem.*, **63**, 305 (1959).
4. P. J. Jorgensen, M. E. Wadsworth, and I. B. Cutler, *J. Am. Ceram. Soc.*, **42**, 613 (1959).
5. G. Wiebke, *Ber. Deut. Keram. Ges.*, **37**, 219 (1960).
6. F. J. Norton, *Nature*, **171**, 701 (1961).
7. M. M. Atalla, "Properties of Elemental and Compound Semiconductors," H. C. Gatos, Editor, p. 163, Interscience (1960).
8. J. R. Ligenza and W. G. Spitzer, *J. Phys. Chem. Solids*, **14**, 131 (1960).
9. P. J. Jorgensen, *J. Chem. Phys.*, **37**, 874 (1962).
10. B. E. Deal, *This Journal*, **110**, 527, 1292 (1963).
11. B. E. Deal, Private communication to K. Motzfeldt, December 1963.
12. B. H. Claussen and M. J. Flower, *This Journal*, **110**, 983 (1963).
13. P. J. Jorgensen, M. E. Wadsworth, and I. B. Cutler, *J. Am. Ceram. Soc.*, **44**, 258 (1961).
14. W. E. Nelson, F. A. Halden, and A. Rosengreen, *J. Appl. Phys.*, **37**, 333 (1966).
15. A. S. Grove, B. E. Deal, E. H. Snow, and C. T. Sah, *Solid-State Electron.*, **8**, 145 (1965).

Electrodeposition of Boron

A. J. G. Maroto and J. Merlo Flores

Gerencia de Energia, Comisión Nacional de Energia Atómica, Buenos Aires, Argentina

A procedure has been developed to produce B^{10} deposits on aluminum disks used in ionization chambers. The method works equally well on Cu, brass, and stainless steel substrates.

The B^{10} is deposited from a colloidal suspension in anhydrous isopropyl alcohol which contains approximately 0.3 mg/ml of boron (1 μm particles) and 23 ppm of $MgCl_2$. A relatively high electric field of 900 V/cm is used (in our case the electrode spacing was 2 mm). The deposit should be well dried before handling.

The value of the electric field required was obtained by applying the model of E. J. Verwey and J. T. Oberbeek (1).

Figure 1 shows the percentage of deposited boron on an aluminum disk as a function of the deposition time.

Compared with the method described by Lange *et al.* (2), this method has the following advantages: (*a*) anhydrous conditions are not required, (*b*) the suspension is easier to prepare and is more stable, (c) no stirring is needed during deposition, (*d*) there is no need to cool the suspension.

In our case the deposit is cathodic in fluorine; in the Lange method it is anodic.

Procedure

1. Finely grind the boron in an agate mortar and mix with a small amount of anhydrous isopropyl alcohol.
2. Add $MgCl_2$, preferably in an anhydrous methanol solution.

Key words: electrodeposition, boron.

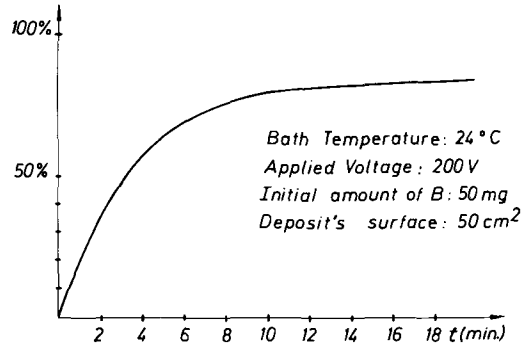

Fig. 1. Percentage of deposited boron on an aluminum disk as a function of deposition time.

3. Transfer the mixture to the electrodeposition cell containing the rest of the needed amount of isopropyl alcohol.
4. Stir thoroughly before commencing electrodeposition.

Manuscript received Sept. 8, 1970.

Any discussion of this paper will appear in a Discussion Section to be published in the December 1971 JOURNAL.

REFERENCES

1. A. J. G. Maroto, *Com. Cientif.* (*Argentina*), **17**, 1 (1969).
2. F. M. Lange, P. Magnier, and C. J. Finck, *J. Nucl. Energy*, **3**, 301 (1956).

Brief Communications

Formation of Electrolytic Rutile Film Containing Barium

M. Yamazaki and H. Nozaki

Institute of Industrial Science, University of Tokyo, Tokyo, Japan

Thin insulating films of controlled thickness may be formed on a number of metals including aluminium, titanium, tantalum, zirconium, *etc.*, by anodization of the metal in a suitable electrolyte (1, 2), and anodic oxide films formed in this way have been widely used in electrolytic capacitors. It would be of interest in connection with electrolytic capacitors if the high dielectric constant material $BaTiO_3$ could be produced on titanium by anodization. In the present work we formed oxide films on titanium by applying either d-c or a-c current to a titanium electrode in an aqueous solution of barium hydroxide. It was found that the oxide film contained barium only when alternating current was used.

Key words: electrolytic capacitors, dielectrics, thin films.

The electrodes (1 x 20 x 40 mm) were prepared from Kobe Seiko Company KS-50 titanium (H_2, <0.01%; O_2, <0.20%; N_2, <0.05%; Fe, <0.20%). The surface of the electrodes was first treated in 16 weight per cent H_2SO_4 solution at 25°C, using alternating current (50 Hz) at 50 mA/cm² for 2 hr. Then, the oxide films were formed on the surface of the electrodes in two methods as follows.

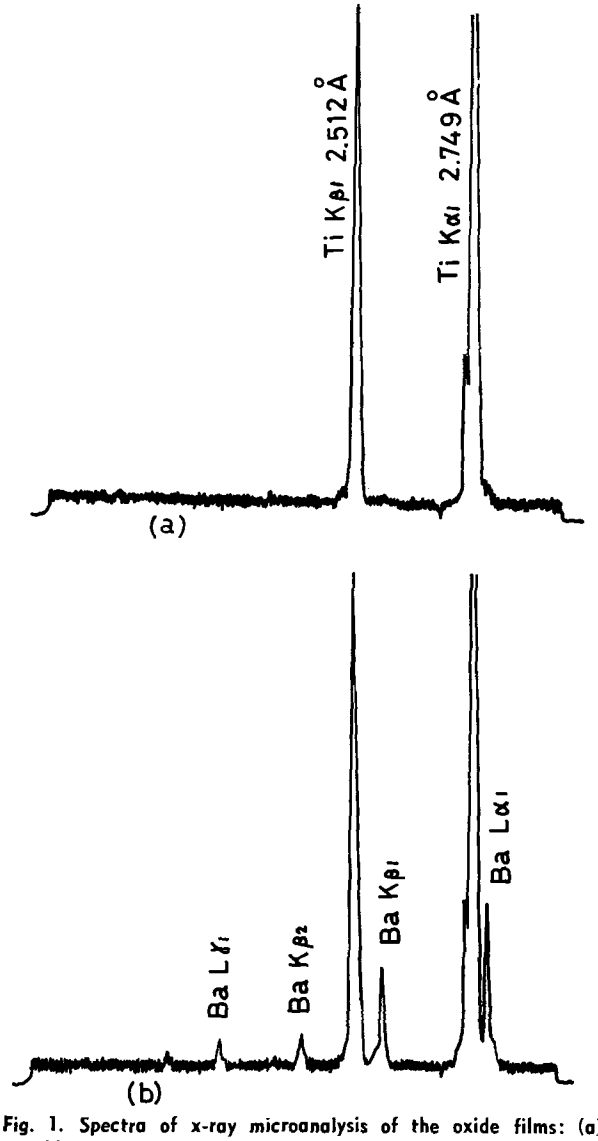

Fig. 1. Spectra of x-ray microanalysis of the oxide films: (a) oxide film formed by anodic current; (b) oxide film formed by alternating current.

(*A*) The electrode was anodized with direct current in a saturated solution of barium hydroxide for 1 hr at 25°C, at 5 mA/cm^2.

(*B*) The electrode was electrolyzed by applying alternating current (50 Hz) with the same solution first for 1 hr at 40 mA/cm^2 and next for ½ hr at 70 mA/cm^2. The procedure of electrolyzing with two levels of current density was useful in increasing the film thickness.

The films obtained were examined by x-ray microanalysis and by electron diffraction analysis. The surface of the oxide films was observed with an electron microscope.

X-ray microanalysis (Fig. 1) showed barium to be present only in the a-c film. Electron diffraction indicated that the d-c film contained anatase, while the a-c film contained rutile. According to the electron microscope both films were polycrystalline.

Capacitor-like Ti-oxide-Au samples were fabricated by the vacuum evaporation of gold onto the oxide films through a mask with slits of 5 x 5 mm^2. Then the capacitance of the samples was measured at room temperature with a bridge (Yokokawa Electric Work Company Model 4255 A). Film thicknesses were estimated from the capacitance of the samples as 0.5 ~ 1.0μ for the d-c film and 1.5 ~ 2.5μ for the a-c film. In these estimations, a value of 40 was used for the dielectric constant of the d-c film (3) and a value of 100 was used for the a-c film. It is reasonable to use 100 for the value of dielectric constant of the a-c film, since a small amount of barium in rutile hardly affects its dielectric constant (4).

Manuscript submitted Aug. 3, 1970; revised manuscript received Oct. 26, 1970.

Any discussion of this paper will appear in a Discussion Section to be published in the December 1971 JOURNAL.

REFERENCES

1. L. Young, "Anodic Oxide Films," Academic Press Inc., London and New York (1961).
2. D. A. Vermilyea, "Advances in Electrochemistry," Vol. 3. P. Delahav. Editor, Interscience Publishers Inc., New York (1963).
3. F. Huber and J. Bloxsom, *Trans. IRE*, **CP-8**, 80 (1961).
4. E. N. Bunting, G. R. Shelton, and A. S. Creamer, *J. Res. Nat. Bur. Std.*, **38**, 337 (1947).

Ethylene Diamine-Pyrocatechol-Water Mixture Shows Etching Anomaly in Boron-Doped Silicon

A. Bohg

IBM Laboratories, Boeblingen, Germany

Recently Greenwood (1) reported that the ethylene diamine-pyrocatechol-water etch described by Finne and Klein (2) etches only n-type silicon in samples containing p-n junctions. We found no preferential etching of p-n junctions, but an abrupt change in the etch rate with concentration for boron-doped silicon.

Finne and Klein had already studied the influence of boron doping on the etch rates for <100> silicon and found a constant etch rate of 50 μm/hr for the resistivity range between 10^{-1} and 10^2 ohm-cm, corresponding to boron concentrations from $2 \cdot 10^{14}$ cm^{-3} to $5 \cdot 10^{17}$ cm^3.

To study the influence of boron concentration above $5 \cdot 10^{17}$ cm^{-3}, a 1° bevel of a <100> sample was etched for 10 min. A glass refluxing system was used, with N_2 bubbling through the boiling solution (110°C). No drying tubes were used, as the etch times never extended over 10 min. The etch solution consisted of 17 ml ethylene diamine, 8 ml water, and 3g pyrocatechol. The boron concentration in the sample decreased with depth, the surface concentration being $5 \cdot 10^{20}$ cm^{-3}. The sample contained a background As doping of about 10^{17} cm^{-3}. The p-n junction was 7.7 μm under the surface.

The 10 min etch resulted in a sharp step on the bevel, as shown in Fig. 1. From the known concentration profile and the distance of the step on the bevel from the unattacked silicon surface, the critical concentration of electrically active boron atoms in silicon was estimated

Key words: semiconductor technology, preferential etching, boron doping.

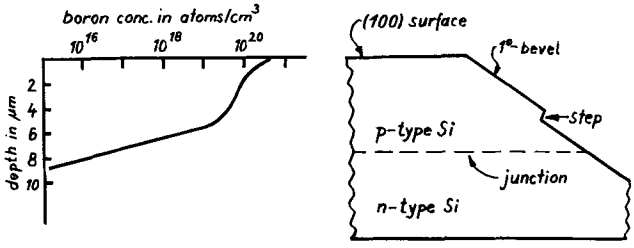

Fig. 1. Cross section of etched sample with correspondng boron concentration profile.

to about $7 \cdot 10^{19}$ cm^{-3}, corresponding to a resistivity of $1.7 \cdot 10^{-3}$ ohm-cm.

Silicon with a higher boron concentration remained completely unattacked. On the other hand, we could not find any influence of the junction itself on the etch rate. In the above example, the etching stopped at a depth of 4.8 μm, almost 3 μm above the junction.

With this result, Greenwood's observations can be easily explained. In his sample, the maximum boron concentration was above the critical value of $7 \cdot 10^{19}$ cm^{-3}. The etching occurred from the n-type side of the sample, etched away the junction region, and stopped within the p-type layer at the critical concentration level.

Manuscript received Sept. 28, 1970.

Any discussion of this paper will appear in a Discussion Section to be published in the December 1971 JOURNAL.

REFERENCES

1. J. C. Greenwood, *This Journal*, **116**, 1325 (1969).
2. R. M. Finne and D. L. Klein, *ibid.*, **114**, 965 (1967).

Electrochemical Preparation of Stannous Sulfate Using Periodically Reversed Direct Current

Chung-Chiun Liu* and Richard E. Horn

Chemical and Petroleum Engineering Department, University of Pittsburgh, Pittsburgh, Pennsylvania 15213

Stannous sulfate can be prepared by direct dissolution of metallic tin in sulfuric acid. However, tin dissolves only slowly in sulfuric acid, and the use of either excess acid or heat is not effective. The use of a periodically reversed direct current (1) has been employed in an electrolytic process to prevent or greatly retard the cathodic reaction. This method might be used to promote the rapid dissolution of a metal in the suitable electrolyte (2). This communication reports the experimental studies of the electrochemical preparation of stannous sulfate using periodically reversed direct current.

Solid-state circuitry was developed in this laboratory to operate a reversing relay which permitted applying alternate polarities to the cell over a frequency range from 0.5 to 120 sec/cycle. The circuitry to accomplish this is shown in block diagram form in Fig. 1.

The experimental assembly is conventional. The experimental cell used was a 600 ml Pyrex beaker, and 500 ml of electrolyte were used each time. Two strengths of sulfuric acid were used as electrolyte, namely 1*N* and 3*N* in concentration. The tin electrodes were made of grade A straits tin (Thisarco Brand) of 99.98+% purity. Tin was first melted and cast into bars which had a width of 0.635 cm, a length of 12.7 cm, and a thickness of 0.635 cm. The cast tin bars were then used as the electrodes and were submerged in the electrolyte to a depth of 7.62 cm, and the electrodes were placed approximately 7 cm apart in each run.

The operation temperature was set at 333° ± 1°K and remained at that value throughout the experiment. Constant stirring of the electrolyte was provided. The tin concentration in the electrolyte was analyzed using an atomic absorption spectrometer (Perkin-Elmer Corporation Model 290). Throughout this study, the current supplied was maintained at 3A. Thus, the current density employed was 0.155 A/cm^2. It should be noted that the potential supplied to the cell was not measured.

The dissolution rate was considered insignificant during the period of placing the electrodes in the electrolyte when no current was passed. The tin concentration in the electrolyte was considered zero initially. As time proceeded, samples were removed periodically from the electrolyte and analyzed for tin by the atomic absorption spectrophotometer.

The first set of experimental runs utilized 1*N* sulfuric acid. However, in 1*N* sulfuric acid, the reprecipitation of undesirable SnO_2 indicated that sulfuric acid of higher concentration should be used to inhibit the hydrolysis of stannous sulfate.

For the 3*N* sulfuric acid electrolyte, seven different intervals of time for the periodically reversed current were employed in this study, varying from 0.5 to 120 sec/cycle. At each cyclic time, the current was supplied for a period up to 60 min or more. Within this period of time, it was found that the dissolution of tin in the electrolyte became saturated throughout our experimental conditions. The experimental results are presented in Fig. 2 which is self-explanatory. Under the experimental conditions investigated, the best yield of stannous sulfate occurs at 11 sec/cycle. It was estimated that approximately a 3% saturated solution was achieved and was considerably better than a direct dissolution of tin in sulfuric acid.

Experimental results show the formation of stannous sulfate increases as the interval of time of the periodically reversed current changes from 0.5 to 11 sec/cycle and decreases as the interval of time changes from 11 to 120 sec/cycle. Qualitatively, it can be explained as follows.

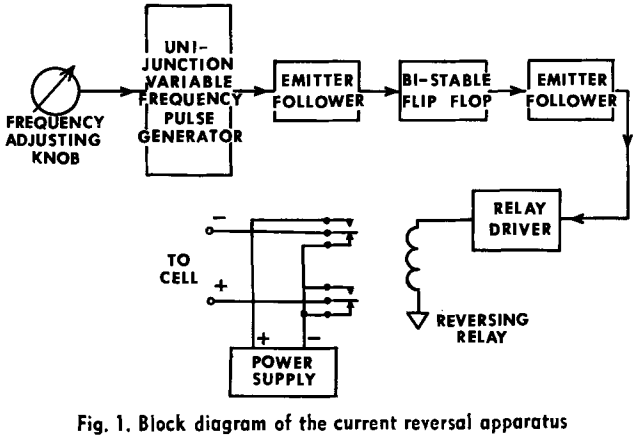

Fig. 1. Block diagram of the current reversal apparatus

* Electrochemical Society Active Member.

Key words: tin, a-c electrolysis, mass transport.

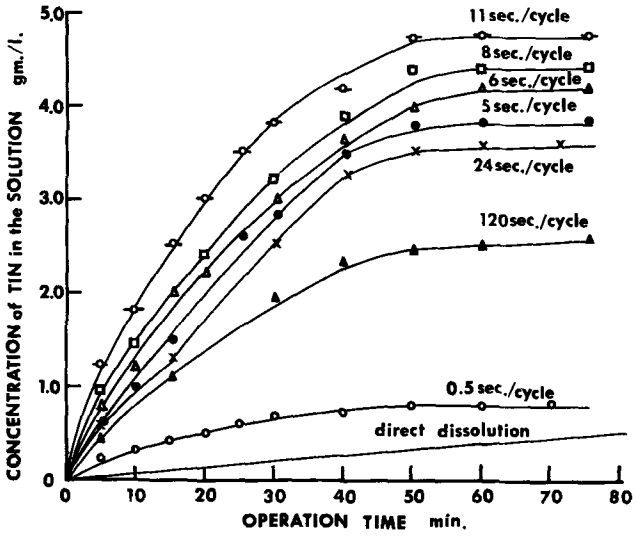

Fig. 2. Experimental results of preparation of $SnSO_4$ using periodically reversed direct current at 333°K.

At a value of 0.5 sec/cycle, the short time interval between cycles does not permit sufficient stannous ions to migrate from the tin electrode and dissolve in the electrolyte. On the other hand, at a longer interval of time of 24 or 120 sec/cycle, stannous ions plate on the cathode over this time interval similar to a d-c electroplating process. Thus, the optimum value of the time interval for the periodically reversed current would be the one which is long enough to permit sufficient stannous ions to migrate into the electrolyte but not long enough to allow the ions to be plated out. However, quantitative interpretation has not been made here.

Acknowledgment

The authors would like to thank Dr. Peter Danna of Olin Corporation for his valuable criticism in preparing this manuscript.

Manuscript submitted March 13, 1970; revised manuscript received *ca.* Nov. 3, 1970.

Any discussion of this paper will appear in a Discussion Section to be published in the December 1970 JOURNAL.

REFERENCES

1. C. L. Mantell, "Electrochemical Engineering," 4th Ed., pp. 63-65, McGraw-Hill Book Co., Inc., New York (1960).
2. N. F. Murphy and B. C. Doumas, *Bull Va. Polytech. Inst. Eng. Exp. Sta. Ser.*, **104**, (Oct. 1955)

JOURNAL OF THE ELECTROCHEMICAL SOCIETY

ELECTROCHEMICAL SCIENCE

MARCH 1971

ES

Electrochemical Behavior of the Aluminum Electrode in Molten Salt Electrolytes

Betty S. Del Duca

Lewis Research Center, National Aeronautics and Space Administration, Cleveland, Ohio 44135

ABSTRACT

The kinetics for dissolution and deposition of solid aluminum in molten $AlCl_3$·NaCl and $AlCl_3$-$(LiCl\text{-}KCl)_{eut}$ electrolytes were studied by means of galvanostatic and potentiostatic techniques over a temperature range of 175°-313°C. The apparent exchange current densities varied from 1 to 56 mA/cm². Surface diffusion was found to be the rate-determining step at low overpotentials, and charge transfer the rate-determining step at high overpotentials. The most probable anodic rate-determining step was found to be $Al \rightarrow Al^+ + e^-$; the most probable cathodic rate-determining step was $Al^{+++} + e^- \rightarrow Al^{++}$ in $AlCl_3$-$(LiCl\text{-}KCl)_{eut}$ electrolyte and $Al^{++} + e^- \rightarrow Al^+$ in $AlCl_3$·NaCl electrolyte. Current efficiencies for dissolution were close to 100%.

For high-energy-density, rechargeable anodes, aluminum appears to be a promising choice for several reasons. It has low equivalent weight, is readily available and inexpensive, and exhibits a high potential. Its use in aqueous systems is hampered by passivity in most electrolytes or by corrosion in nonpassivating electrolytes. Zaromb (1) has discussed its application in aqueous primary and chemically rechargeable cells. Aluminum can be electrodeposited from nonaqueous organic solutions (2) and from molten salts (3). Molten-salt systems appear promising for three main reasons: (*i*) aluminum can be deposited from the electrolyte, (*ii*) the alkali halide-aluminum chloride mixtures have relatively low melting temperatures, and (*iii*) these melts have electrical conductivities in the range of 0.1-0.2 ohm^{-1} cm^{-1} (4), which is one to two orders of magnitude higher than those of the typical organic electrolytes.

The aluminum-cryolite system has been studied extensively (3, 5, 6), but the melting point of this electrolyte is greater than 725°C, which is unattractive for battery applications. Laitinen and Liu (7) have measured the potential of aluminum electrodes in the lithium chloride-potassium chloride (LiCl-KCl) eutectic relative to the Pt/Pt^{++} reference electrode. Piontelli and Sternheim (8) studied the current-potential behavior of aluminum electrodes in $AlCl_3$-NaCl at 200°C and found the charge transfer polarization to be negligible for both the anodic and cathodic reactions. More recently, King, Brown, and Frayer (9) found no measurable charge transfer or diffusion polarization at current densities as high as 1-2 A/cm² in 40 m/o (mole per cent) NaCl-60 m/o $AlCl_3$. Giner and Holleck (10) studied the electrochemical behavior of aluminum anodes in 67% $AlCl_3$-13.6% KCl-19.4% NaCl and 59% $AlCl_3$-17% KCl-24% NaCl at 157° and 105°C. "Passivation" was observed and was attributed to the partial freezing of the electrolyte at the electrode surface.

Key words: aluminum anode, molten chloride electrolytes.

In the present work, current-potential curves, current efficiencies, and the nature of the cathodic deposit were examined. The polarization measurements were carried out on solid aluminum electrodes using transient and steady-state galvanostatic and potentiostatic techniques. Tafel plots were constructed and interpreted in terms of the rate-determining steps for the anodic dissolution and cathodic deposition reaction. The electrolytes studied were mixtures of aluminum chloride with alkali halides melting between 110° and 160°C.

Experimental Procedure

Instrumentation.—Galvanostatic measurements.— Galvanostatic techniques were used to determine the ohmic (IR) drop of the solution and electrodes in the conventional manner (Fig. 1) and to obtain transient overpotential time data (Fig. 2). A potentiostat with a rise time specification of 1-3 μsec (±60V ±300 mA) was used to apply steady anodic and cathodic currents to the electrode. (Rise times of less than 10 μsec were

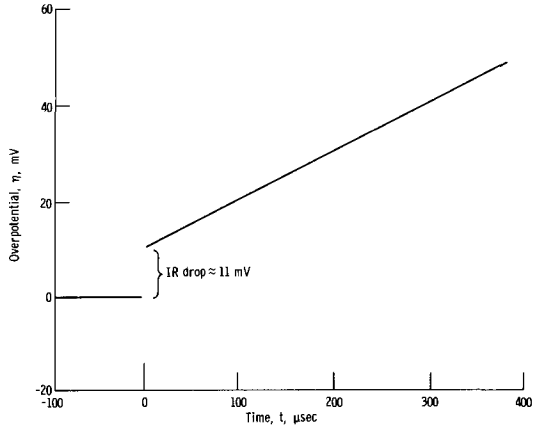

Fig. 1. Overpotential-time transient. Aluminum anode in 50 m/o $AlCl_3$-50 m/o NaCl; current density, 40 mA/cm².

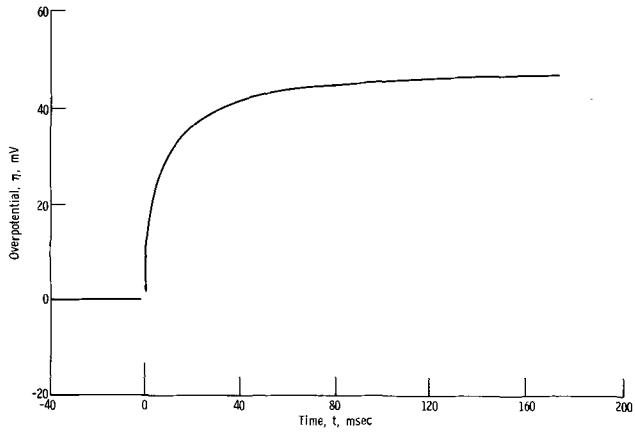

Fig. 2. Transient overpotential-time data. Aluminum anode in 50 m/o $AlCl_3$-50 m/o NaCl; current density, 9.1 mA/cm^2.

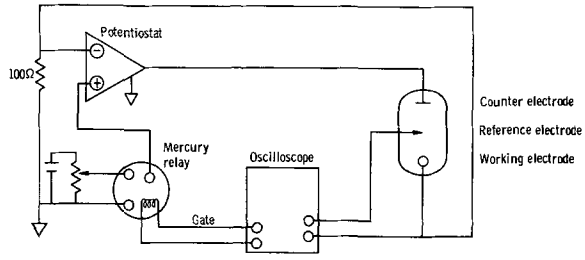

Fig. 3. Block diagram of circuit for galvanostatic measurements

obtained with this circuit applied to aqueous Cu/Cu^{++} system, indicating that the performance of the instrumentation is acceptable.) The block diagram is shown in Fig. 3. The control amplifier inputs (+, −) and output should be identified with the potentiostat terminals: "control potential," "reference electrode," and "counterelectrode," respectively. A mercury-relay pulse generator of conventional design supplied a potential pulse of selected length and magnitude to the control circuit of the potentiostat. This, in turn, controlled the potential across a precision resistor of 100 ohms, thereby establishing a constant current through the cell. The pulse was triggered by the gate output of a Tektronix 535A oscilloscope. The potential transients were displayed on the oscilloscope with a Type D differential amplifier and photographed (see Fig. 1 and 2 for typical traces).

Potentiostatic measurements.—Steady-state current-potential relations were determined by potentiostatically controlling the overpotential and observing the current on the potentiostat milliammeter after a time of approximately 30 sec. This time was chosen for two reasons: (*i*) at all potentials applied, the current density had reached a steady value within this time period; and (*ii*) it was relatively short so that very little electrolysis took place, thus minimizing electrode surface changes. It should be noted that the current density was not affected by concentration gradients since vigorous stirring (> 100 rpm) had no effect on the magnitude of the current density, and that the 30-sec, or steady, current density was only slightly higher than that observed in oscillographic traces recorded over a 10-sec time interval. All potentials were corrected for the IR drop determined from the galvanostatic transient. This correction for uncompensated resistance never exceeded 5% of the potential.

Electrochemical cell.—The cell used to obtain the electrochemical data is shown in Fig. 4. Forty-mil wires of 99.99% aluminum were washed with reagent-grade acetone to remove grease and were then mechanically connected to tungsten rods to form working, counter, and reference electrodes. Aluminum wire was used as a reference for the galvanostatic and potentiostatic measurements. This gives an open-circuit voltage of zero, and the applied or resultant voltage is thus the overpotential on the working electrode.

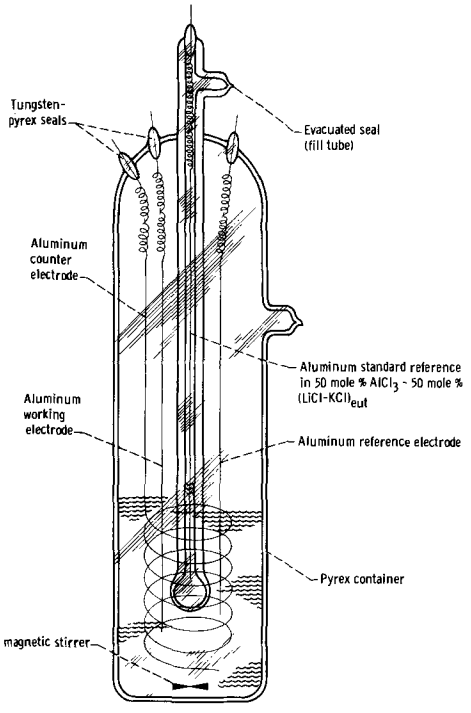

Fig. 4. Electrochemical cell

Equilibrium potentials of the aluminum anode in the various electrolytes were measured relative to a "standard" reference electrode of aluminum wire in $AlCl_3 \cdot (LiCl\text{-}KCl)_{eut}$. The reference electrode was made by sealing a piece of 8-mm Pyrex tubing so as to leave a micro-opening at the bottom.

The cell temperature was controlled within ±5°C by means of a thermostated oil bath. A magnetic stirrer was used to agitate the electrolyte when this was desired.

At the conclusion of the electrochemical experiments, all the melts were analyzed for metals by emission spectrographic methods. In all cases, compositions were within ±5% of the values listed in Table I.

Preparation of melts.—The lithium chloride-potassium chloride eutectic (41 m/o LiCl-59 m/o KCl), hereinafter referred to as $(LiCl\text{-}KCl)_{eut}$, and mixtures of $AlCl_3$ in the eutectic were obtained from Anderson Physics Laboratories in evacuated sealed vials. The former was certified as having a residual current not larger than 1.6 μA at 2V and 410°C. The $AlCl_3$-NaCl mixtures were prepared at this laboratory from reagent-grade chemicals which were dried at 110°C.

All samples containing $AlCl_3$ even though specified as "high purity" were found to be contaminated with organic materials which pyrolyzed on heating. The techniques used for purification varied depending on the concentration of aluminum chloride in the melt.

Equimolar mixtures [$AlCl_3 \cdot NaCl$, $AlCl_3 \cdot (LiCl\text{-}KCl)_{eut}$].—Melts in which $AlCl_3$ and alkali chloride were present in equal amounts had low vapor pressures (<1 Torr at 500°C). The organic impurities were removed by thermal decomposition. The mixture was heated in Pyrex tubes under flowing nitrogen. Vigorous bubbling began at 520°C and continued for one to several hours. When bubbling ceased, a clear straw-colored melt was obtained with a black carbon residue. The yellow coloration was attributed to the presence of small amounts of an oxychloride (private communication from Anderson Physics Laboratories, Inc.) and was removed by introducing an aluminum wire into the melt. A black precipitate formed on the wire and the melt became water-white. Presumably the oxychloride reacts with metallic aluminum to form

soluble aluminum chloride and insoluble aluminum oxide. The yellow coloration could be recreated by bubbling (undried) oxygen into the purified melt and could be removed again by the aluminum treatment. Other investigators have reported a yellow coloration due to iron impurities which were removed by sublimation (11) or by treatment with metallic aluminum (12). No iron was detected by spectrographic analysis (sensitivity, 0.03 ppm) of the melts used in the present work.

After purification, the clear melt was transferred under inert conditions to a dry, heated electrochemical cell, which was evacuated to 1 Torr and sealed off.

Mixtures containing more than 50 m/o $AlCl_3$.—It was not possible to thermally decompose organic material present in these solutions because of the high partial vapor pressure of aluminum chloride over the melts. The organic material and oxychloride were removed by heating at 250°C in the presence of metallic aluminum for several days. The organics slowly distilled into cold traps in an adjacent sidearm. A second sidearm was kept heated and used to transfer the purified melt into the attached electrochemical cell by tipping the apparatus. The melt was allowed to freeze, and the cell was sealed under reduced pressure.

Mixtures containing less than 50 m/o $AlCl_3$.—Three methods were used in an attempt to prepare melts of less than 50 m/o $AlCl_3$ in LiCl-KCl eutectic (13). All resulted in the formation of a multiphase system which was unaffected by heating to 550°C.

Preliminary experiments.—Experimental conditions considered initially included (*i*) the influence of the atmosphere within the cell (inert gas or vacuum) and (*ii*) the magnitude of changes in the measured polarization curves with time. With respect to the former, vacuum-sealed cells and cells open to an excess pressure of dry nitrogen gas gave identical results. With respect to the latter, marked effects were observed. This is shown in Fig. 5, where the log of current density i against overpotential η is plotted for an electrode held at constant temperature and tested at various times up to 48 hr. The observed changes, no doubt, partly reflect roughening of the electrode surface. Since it is difficult to evaluate and correct for this kind of change, only freshly prepared cells were used for each series of runs reported, and the time period over which data were recorded never exceeded 3 hr from the time of filling the cell.

Experimental variables considered.—Table I lists the compositions of the electrolytes used and the temperatures and current density ranges over which measurements were made. All current densities are based on the apparent geometrical area of the electrode.

Results and Discussion

Transient results.—In this work, rise times to the steady state were observed which were in excess of 10 sec at low current densities. This is much longer

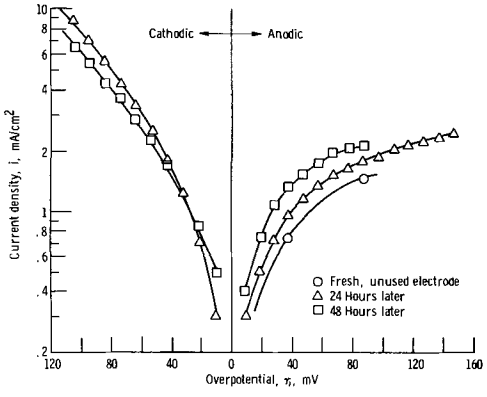

Fig. 5. Tafel plot for aluminum electrode in 50 m/o $AlCl_3$-50 m/o NaCl; time dependence. Temperature, 316°C.

Table I. Range of experimental variables

Electrolyte composition, m/o	Temperature, °C	Current density, mA/cm²
50 $AlCl_3$-50 $(LiCl\text{-}KCl)_{eut}$	202	0 to 25 anodic
	213	0 to 100 cathodic
67 $AlCl_3$-33 $(LiCl\text{-}KCl)_{eut}$	187	0 to 30 anodic
		0 to 100 cathodic
75 $AlCl_3$-25 $(LiCl\text{-}KCl)_{eut}$	235	0 to 300 anodic
	265	0 to 300 cathodic
50 $AlCl_3$-50 NaCl	175	0 to 200 anodic
	197	0 to 300 cathodic
	253	
	260	
	304	
	313	

than the 150 μsec rise-time calculated by the equation of Mehl and Bockris (14). The rise time was observed to decrease with increasing current densities. Figure 2 illustrates the potential rise for the first 180 msec at a current density of 9.1 mA/cm² in $AlCl_3$·NaCl electrolyte. The potential-time data are shown in Fig. 1 for times up to 375 μsec at a current density of 40 mA/cm². A linear relation is obtained for times which are longer than normally expected. A capacitance C calculated from the slope $\partial\eta/\partial t$ and current i in the equation

$$C = \frac{i}{\left(\frac{\partial\eta}{\partial t}\right)_{t\to 0}} = \frac{0.040 \times 10^{-3}}{0.104} = 385\ \mu\text{F/cm}^2 \quad [1a]$$

is too large to be a double-layer capacitance and is therefore apparently an adsorption capacitance. The surface diffusion model described by Bockris and Damjanovic (15) allows the concentration of adsorbed species C_o to be estimated, using this potential-time data at low potentials, by means of the equations

$$C_o = \frac{RT}{n^2\mathbf{F}^2} \frac{i}{\left(\frac{\partial\eta}{\partial t}\right)_{t\to 0}} \quad [1b]$$

$$C_o = \frac{RT}{n^2\mathbf{F}^2} C \quad [1c]$$

Equations [1b] and [1c] are derived by assuming (*i*) a small coverage of the surface by adions and (*ii*) a potential smaller than $RT/\alpha n\mathbf{F}$. Table II lists the concentration of adions calculated for the aluminum anode in 50 m/o $AlCl_3$-50 m/o NaCl at 220°C at various current densities. The average value is $(0.17 \pm 0.03) \times 10^{-10}$ moles/cm², which is the same order of magnitude as that reported for gallium in aqueous solution (16). Mehl and Bockris (17) report C_o values of 4×10^{-10} moles/cm² for silver in aqueous solution, and Reddy (18) reports $C_o = 9 \times 10^{-10}$ mole/cm² for silver in molten $(LiCl\text{-}KCl)_{eut}$.

An adion concentration of 0.18×10^{-10} moles/cm² corresponds to a surface coverage of only 0.001 if the radius of the adion is assumed to be the crystal radius of trivalent aluminum [0.5×10^{-8} cm (19)].

Table II. Concentration of adions, surface diffusion rate, and exchange current density as calculated from surface diffusion rate for aluminum anode in $AlCl_3$·NaCl at 220°C

Current density, i, mA/cm²	Concentration of adions, C_o, moles/cm²	Surface diffusion rate, $n\mathbf{F}v_o$, mA/cm²	Calculated exchange current, $i_{o,calc}$, mA/cm²
6.5	0.15×10^{-10}	3.7	1.52
8.5	0.16	3.2	1.48
12.0	0.15	3.7	1.72
25.5	0.20	5.5	2.46
40.0	0.19	5.7	2.66
Average	$0.17 \pm 0.03 \times 10^{-10}$	4.3 ± 1.4	1.97 ± 0.47

The diffusion rate of adions on the surface $n\mathbf{F}v_o$ may be obtained provided the time dependence of overpotential as it approaches the steady state is measured experimentally. The appropriate equation (15) is

$$n\mathbf{F}v_o = -\frac{d\ln(\eta_\infty - \eta)}{dt} n\mathbf{F}C_o \qquad [2]$$

Values of η_∞ were obtained potentiostatically and are discussed further under Steady-state results. Table II summarizes values of the surface diffusion rates obtained for aluminum anodes in $AlCl_3$·NaCl at 220°C. As expected from the long rise times observed, the diffusion rates which average 0.0043 A/cm² are slower than those reported for silver either in aqueous solution [0.015 A/cm², (16)] or molten salts [3.3 A/cm², (18)]. They are, however, larger than the value reported for the dissolution of gallium in aqueous solution at the same current density [0.0003 A/cm², (16)].

In their monograph, Bockris and Razumney (20) indicate that the surface diffusion rate and the steady-state overpotential may be used to calculate an exchange current $i_{o,calc}$ which generally agrees with experimental exchange currents obtained from Tafel plots to within ±30%. Values of $i_{o,calc}$ obtained from the equation

$$\eta_\infty = -\left(\frac{RT}{n\mathbf{F}}\frac{i}{i_{o,calc}} + \frac{RT}{n^2\mathbf{F}^2}\frac{i}{v_o}\right) \qquad [3]$$

at various current densities i are also summarized in Table II. The average value is 1.97 mA/cm², which agrees well with the experimental value of 1.88 mA/cm² obtained from a Tafel plot.

All transient data discussed so far were taken in the 0 to 250-μsec time period. Similar analyses of data in the 0 to 20-msec range gave smaller values for $i_{o,calc}$.

It appears then that the nonsteady-state data for aluminum at low current densities (so that $\eta < RT/\alpha n\mathbf{F}$) fit reasonably well into the surface diffusion model described by Bockris and co-workers. Aluminum in $AlCl_3$·NaCl melts appears to be quite similar to solid gallium in alkaline aqueous solutions as far as the surface diffusion parameters are concerned.

Bockris and Razumney (20) conclude that probably all metals undergo deposition and dissolution at planar sites on the surface with subsequent diffusion along the surface to other sites. This is based on calculations of the heats of activation for transfer of silver ions to different kinds of sites on the surface: that is, planar surface, edge, kink, vacancy in an edge, and vacancy in a surface. The rate constant for transfer to a planar site is 10^6 times greater than to any other type of site. The rate-controlling process then becomes the diffusion on the surface either to or from this planar site. These same authors point out that there is a transition from surface diffusion control to another rate-controlling mechanism, such as charge transfer at higher current densities or overpotentials, and that a limiting current due to the surface diffusion occurs at still higher overpotentials.

Steady-state results.—Figure 6 is typical of the Tafel plots constructed from steady-state measurements. This particular plot is for aluminum in a 75 m/o $AlCl_3$-25 m/o $(LiCl\text{-}KCl)_{eut}$ mixture at 235°C. A region of linearity is observed for both the anodic and cathodic branch extending from 80 mV on the anodic side and 170 mV on the cathodic side.

The deviations from linearity are attributed partly to normal deviations from Tafel behavior caused by the increased importance of the back reaction at low overpotentials and partly by the surface diffusion effects already discussed. Since deviations from straight-line behavior resulting from the back reaction usually occur around 60 mV, the existence of surface diffusion effects might well not be evident from inspection at a Tafel plot such as Fig. 6.

No evidence of a limiting current density is found at potentials as high as ±350 mV. In one experiment,

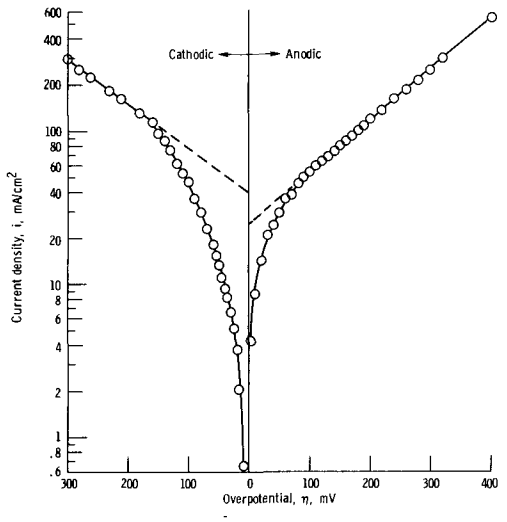

Fig. 6. Tafel plot for aluminum in 75 m/o $AlCl_3$-25 m/o $(LiCl\cdot KCl)_{eut}$. Temperature, 235°C (508°K).

however, the potential was increased to several volts in the anodic direction. An apparent limiting current density of about 1 A/cm² was observed, the value of which did not oscillate with time or vary with the rate of stirring. This suggests a limiting current density not caused by mass transport in the molten salt (23) but perhaps caused by chemical reaction or surface diffusion phenomena (22). This result is not conclusive, however, as the surface undergoes rapid changes at these high current densities.

The Tafel slopes in Fig. 6 are $b_a = 2.3\ RT/0.29\mathbf{F}$ and $-b_c = 2.3\ RT/0.29\mathbf{F}$, for the anodic and cathodic reactions, respectively. The respective exchange current densities are 26 and 39 mA/cm².

Results for the other temperatures and electrolytes studied are summarized in Table III. The standard deviations obtained for the exchange current densities and

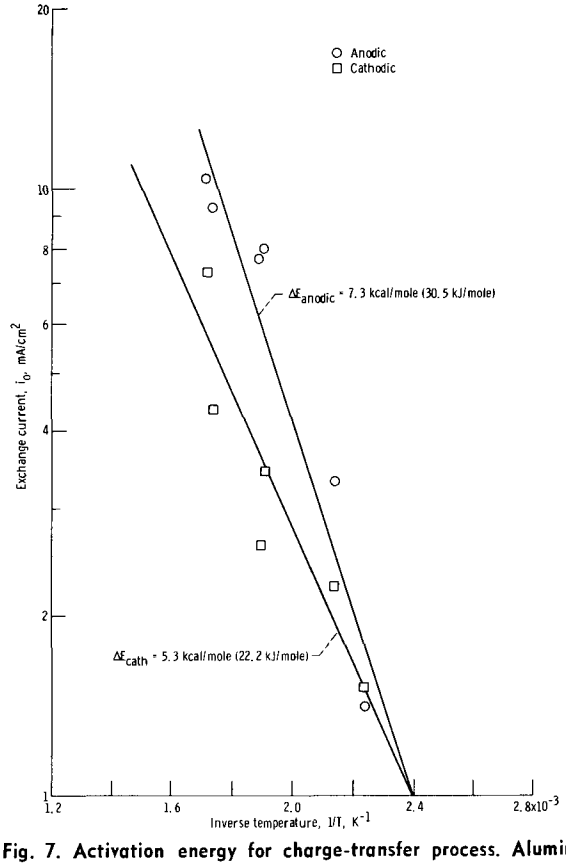

Fig. 7. Activation energy for charge-transfer process. Aluminum electrode in $AlCl_3$·NaCl.

Table III. Summary of Tafel data

Electrolyte, m/o	Temperature, °C	Exchange current density, mA/cm²		Tafel slope		$E - E_{ref}$, mV
		Anodic	Cathodic	Anodic, b_a	Cathodic, b_c	
50 $AlCl_3$-50 (LiCl-KCl)$_{eut}$	202	1.95 ± 0.03	—	$\frac{2.303\,RT}{(0.304 \pm 0.005)F}$	—	<1
	213	2.93 ± 0.05	—	$\frac{2.303\,RT}{(0.244 \pm 0.006)F}$	—	<1
67 $AlCl_3$-33 (LiCl-KCl)$_{eut}$	187	1.92 ± 0.02	9.6 ± 0.5	$\frac{2.303\,RT}{(0.48 \pm 0.02)F}$	$\frac{2.303\,RT}{(0.40 \pm 0.01)F}$	275
75 $AlCl_3$-25 (LiCl-KCl)$_{eut}$	235	31 ± 2	39 ± 3	$\frac{2.303\,RT}{(0.29 \pm 0.01)F}$	$\frac{2.303\,RT}{(0.29 \pm 0.2)F}$	400
	265	56 ± 2	—	$\frac{2.303\,RT}{(0.27 \pm 0.03)F}$	—	—
50 $AlCl_3$-50 NaCl	175	1.3 ± 0.1	0.9 ± 0.4	$\frac{2.303\,RT}{(0.28 \pm 0.02)F}$	$\frac{2.303\,RT}{(1.0 \pm 0.3)F}$	—
	197	3.2 ± 0.2	1.7 ± 1.0	$\frac{2.303\,RT}{(0.20 \pm 0.02)F}$	$\frac{2.303\,RT}{(1.2 \pm 0.3)F}$	—
	253	7.9 ± 0.4	3.4 ± 0.1	$\frac{2.303\,RT}{(0.21 \pm 0.03)F}$	$\frac{2.303\,RT}{(1.23 \pm 0.03)F}$	—
	260	7.7 ± 0.1	2.6 ± 0.3	$\frac{2.303\,RT}{(0.18 \pm 0.1)F}$	$\frac{2.303\,RT}{(1.29 \pm 0.04)F}$	—
	304	9.3 ± 0.4	4.3 ± 0.4	$\frac{2.303\,RT}{(0.27 \pm 0.02)F}$	$\frac{2.303\,RT}{(1.39 \pm 0.06)F}$	—
	313	10.5 ± 0.2	7.4 ± 0.6	$\frac{2.303\,RT}{(0.24 \pm 0.01)F}$	$\frac{2.303\,RT}{(1.20 \pm 0.05)F}$	—

Table IV. Calculated Tafel slopes

Mechanism	Rate determining step (RDS)	Tafel slope	
		Anodic, b_a	Cathodic, $-b_c$
I, II	$Al^0 \rightarrow Al^+ + e^-$	$\frac{2.3\,RT}{\beta F}$	$\frac{2.3\,RT}{(3-\beta)F}$
I	$Al^+ \rightarrow Al^{+2} + e^-$	$\frac{2.3\,RT}{(\beta+1)F}$	$\frac{2.3\,RT}{(2-\beta)F}$
I, III	$Al^{+2} \rightarrow Al^{+3} + e^-$	$\frac{2.3\,RT}{(\beta+2)F}$	$\frac{2.3\,RT}{(1-\beta)F}$
III	$Al^0 \rightarrow Al^{+2} + 2e^-$	$\frac{2.3\,RT}{2\beta F}$	$\frac{2.3\,RT}{(3-2\beta)F}$
IV	$Al^0 \rightarrow Al^{+3} + 3e^-$	$\frac{2.3\,RT}{3\beta F}$	$\frac{2.3\,RT}{3(1-\beta)F}$
II	$Al^+ \rightarrow Al^{+3} + 2e^-$	$\frac{2.3\,RT}{(2\beta+1)F}$	$\frac{2.3\,RT}{2(1-\beta)F}$

Tafel slopes were less than ±10% in most cases. While the uncertainty within one set of data was usually ±2 to ±3%, the reproducibility of one fresh cell to another varied as much as ±10%.

Note that the anodic exchange current densities in Table III range from a value of 1.3 mA/cm² for the 50 m/o $AlCl_3$-50 m/o NaCl electrolyte at 175°C to a value of 56 mA/cm² for the 75 m/o $AlCl_3$-25 m/o (LiCl-KCl)$_{eut}$ electrolyte at 265°C. For all $AlCl_3$-(LiCl-KCl)$_{eut}$ mixtures, the anodic and cathodic Tafel slopes are similar and vary with composition from about 2.3 $RT/0.25F$ to 2.3 $RT/0.5F$. In contrast, for the $AlCl_3$·NaCl electrolyte, the anodic slope is comparable to the others, but the cathodic slope is about a factor of 5 smaller.

The activation energies from a plot of log i_o against $1/T$ (Fig. 7) for both the anodic and cathodic processes in the $AlCl_3$·NaCl electrolyte are 7.3 ± 1.0 and 5.3 ± 0.6 kcal/mole, respectively. These lie a little below the values of about 10 kcal/mole usually encountered (18).

In order to determine which processes are rate determining at high overpotentials (*i.e.*, Tafel region), it is necessary to calculate Tafel slopes for various postulated sets of reactions and compare them with experiment. Fraser and Barradas (24) have described a simple method for carrying out these calculations.

The mechanism chosen for analysis consisted of consecutive steps and did not consider the possibility of parallel processes. They are as follows, written for the anodic process

$$\text{I} \quad Al^0 \rightarrow Al^+ + 1e^- \rightarrow Al^{+2} + 1e^- \rightarrow Al^{+3} + 1e^- \quad [5]$$

$$\text{II} \quad Al^0 \rightarrow Al^+ + 1e^- \rightarrow Al^{+3} + 2e^- \quad [6]$$

$$\text{III} \quad Al^0 \rightarrow Al^{+2} + 2e^- \rightarrow Al^{+3} + 1e^- \quad [7]$$

$$\text{IV} \quad Al^0 \rightarrow Al^{+3} + 3e^- \quad [8]$$

For the cathodic process the reactions are reversed. The use of simple bare-ion symbolism does not imply the absence of ligand coordination with Cl^- for example.

The calculated Tafel slopes for various rate-determining steps are presented in Table IV. By comparing these expressions for the Tafel slopes with the experimental values in Table III, it is possible to select the most probable rate-determining steps consistent with the data (Table V).

Table V. Most probable rate-determining steps for charge-transfer reaction

Electrolyte, m/o	Anodic rate-determining step	Anodic true transfer coefficient, β	Cathodic rate-determining step	Cathodic true transfer coefficient, β
50 $AlCl_3$-50 LiCl · KCl	$Al^0 \rightarrow Al^+ + e^-$	0.31	[a]	[a]
67 $AlCl_3$-33 LiCl · KCl	$Al^0 \rightarrow Al^+ + e^-$	0.59	$Al^{+++} + e^- \rightarrow Al^{++}$	0.60
75 $AlCl_3$-25 LiCl · KCl	$Al^0 \rightarrow Al^+ + e^-$	0.29	$Al^{+++} + e^- \rightarrow Al^{++}$	0.71
50 $AlCl_3$-50 NaCl	$Al^0 \rightarrow Al^+ + e^-$	0.20	$Al^{++} + e^- \rightarrow Al^+$	0.75

[a] No analysis performed.

For the anodic reaction in all electrolytes, the most probable rate-determining step is the one-electron transfer constituting the first step in mechanisms I or II

$$Al \rightarrow Al^{+} + 1e^{-}$$

For this step, reasonable values of the true transfer coefficient β from 0.20 to 0.59 (Table V) are obtained. The variation of β with composition should be noted. This implies structural changes, possibly, as the concentration of $AlCl_3$ is changed relative to the concentration and nature of the cations. Similar effects have been noted by Morrey (25, 26) in spectroscopic studies in these media.

For the cathodic reaction in the $AlCl_3$-$(LiCl\text{-}KCl)_{eut}$ mixtures, the most probable rate-determining step is

$$Al^{+++} + 1e^{-} \rightarrow Al^{++}$$

with true transfer coefficients β of 0.60 and 0.71. All other possibilities give values for β which are very close to 1 or larger. The cathodic reaction in the $AlCl_3$·NaCl electrolyte clearly has a different rate-determining step than for the other solutions. Four possible rate-determining steps which give reasonable values for β are

$$Al^{++} + 1e^{-} \rightarrow Al^{+} \qquad \beta = 0.75$$

$$Al^{++} + 2e^{-} \rightarrow Al^{0} \qquad \beta = 0.90$$

$$Al^{+++} + 2e^{-} \rightarrow Al^{+} \qquad \beta = 0.375$$

$$Al^{+++} + 3e^{-} \rightarrow Al^{0} \qquad \beta = 0.583$$

The first of these reactions is proposed as the most probable rate-determining step since the activation energy for a multi-electron transfer is very high (> 100 kcal/mole) and therefore improbable (20). It should be noted, though, that above 650°C in fluoride melts, a three-electron transfer has been observed (27). The most probable rate-determining steps and the corresponding values for β are presented in Table V.

That the rate-determining step for the cathodic reaction in the $AlCl_3$-$(LiCl\text{-}KCl)_{eut}$ melts is different from that in the AlCl·NaCl melt is not surprising in view of recent Raman results on the structure of the $AlCl_4^-$ complex ion in $AlCl_3$·KCl and $AlCl_3$·NaCl melts (28). A regular tetrahedral symmetry T_d is found in the Na^+-containing melts, while a distorted tetrahedral (C_{2v}) symmetry is found in the K^+-containing melts. These structural differences could influence the relative rates of the steps in the reduction reaction.

In closing this discussion of the most probable rate-determining steps, it should be mentioned that a recent paper by Rangarajan (29) has criticized the analysis of Bockris and co-workers used in the present work. Very briefly, Rangarajan concludes that in cases where surface diffusion is rate limiting at low overpotentials, the Tafel slope at higher overpotentials is equal to twice the "true" slope (for charge transfer) and the observed exchange current is larger than the true exchange current. The present results are not adequate to settle this theoretical dispute. In the present work, the Bockris treatment of surface diffusion has been employed since there is some evidence in the literature which experimentally supports it. Rangarajan's approach would lead to

$$Al^{+} + e^{-} \rightarrow Al^{0}$$

as the most probable rate-determining step for the cathodic reaction in $AlCl_3$·NaCl electrolyte. Both anodic and cathodic reactions in $AlCl_3$ $(LiCl\cdot KCl)_{eut}$ and the anodic reaction in $AlCl_3$·NaCl electrolyte remain the same as predicted by the Bockris treatment.

In addition, Rangarajan's treatment does not predict a limiting anodic current which was observed in at least one electrolyte in this study and has been observed by others for gallium (16). The Bockris approach predicts such a limiting current.

Table VI. Anodic and cathodic efficiencies of Al in LiCl·NaCl

Anodic		Cathodic	
Current density, mA/cm²	Efficiency, %	Current density, mA/cm²	Efficiency, %
0.3	100 ± 1	0.1	>83
0.5	98 ± 2	0.5	>62

Current efficiencies.—Current efficiencies determined for aluminum anodes and cathodes in the AlCl·NaCl melt by passing a known number of coulombs and measuring the weight loss of the anode and the weight gain of the cathode are summarized in Table VI. The cathode efficiency could not be determined accurately because of the loss of some material during the repeated washings which were necessary to remove all traces of electrolyte from the electrode. While the apparent inefficiency of the cathode is not considered to be real, it should be noted that these are preliminary results and further study is indicated.

Photographs at an enlargement of X14 were taken of both an anode and a cathode after electrolysis. The smooth surface of the anode with visible grain boundaries may be seen in Fig. 8a. The crystallites of aluminum deposited on the cathode are seen in Fig. 8b. These crystallites greatly increase the surface area. While some crystallites were mechanically removed during vigorous washing procedures, the deposit appears to adhere well enough to the surface that it would not create a problem in secondary cell applications. Very high current densities (10 A/cm²) do produce a dendritic deposit and would not be suitable for use in a cell unless measures were taken to prevent such growth.

Conclusions

Aluminum appears to show promise of being a suitable negative electrode for a secondary battery when charged and discharged in alkali chloride-aluminum chloride molten salts at temperatures less than 250°C. The apparent exchange current densities for discharge (dissolution) vary from about 2 to over 20 mA/cm² as the concentration of $AlCl_3$ in the KCl-LiCl eutectic is increased from 50 to 75 m/o. The apparent exchange current densities for charging (deposition) vary from about 10 to 40 mA/cm² over the same range of composition.

On the basis of an analysis of steady-state and transient overpotential data using the theoretical framework of Bockris *et al.*, the following rate-determining steps for the anodic and cathodic reactions in the various electrolytes can be proposed:

1. At low overpotentials, less than 70 mV anodic and 170 mV cathodic, the rate-determining step is the diffusion of adions on the metal surface. The concentration of adions was found to be 0.2 x 10^{-10} moles/

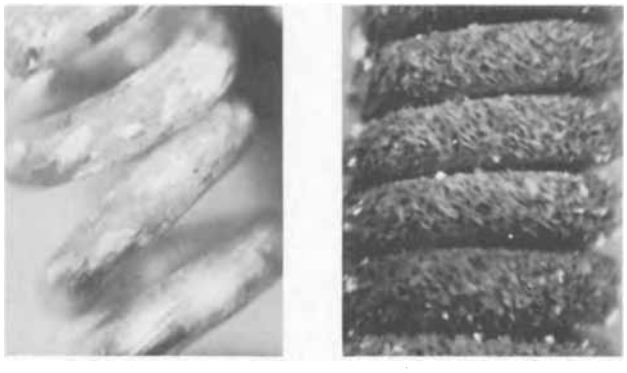

Fig. 8. Nature of electrode surface. X14. a (left) Anode, electrolyzed at 0.3 mA/cm². b (left) Cathode, electrolyzed at 0.1 mA/cm².

cm^2 and the surface diffusion velocity 0.0043 A/cm^2 in $AlCl_3$·NaCl melts.

2. At higher overpotentials the rate-determining steps are charge transfer. In the anodic reaction, for all electrolytes, the most probable rate-determining step is $Al \rightarrow Al^+ + e^-$. For the cathodic reaction, the most probable rate-determining step is $Al^{+++} + e^- \rightarrow Al^{++}$ in the $AlCl_3$-(KCl-LiCl) eutectic mixtures and $Al^{++} + e^- \rightarrow Al^+$ in the $AlCl_3$·NaCl melts. These conclusions about the charge-transfer steps cannot be considered unambiguous as they are deduced from a consideration of Tafel data and are based on the assumption that the true transfer coefficient should be between 0.20 and 0.80 and that one-electron transfers are most probable.

Current efficiencies for dissolution were close to 100% at current densities up to 0.5 mA/cm^2. The measurements were inaccurate for deposition, but a strong adherent deposit was obtained at low current density. Dendrites were observed at current densities larger than 10 A/cm^2.

Acknowledgment

The author gratefully acknowledges the assistance of Dr. Jacob Greenberg who constructed the electrochemical cells and carried out the purification of all materials used in these experiments.

LIST OF SYMBOLS

a	Tafel slope, mV
C	double-layer capacitance, μF/cm^2
C_o	concentration of adions, moles/cm^2
F	faraday, 96,500 coulombs
i	current density (anodic+, cathodic−), mA/cm^2
i_o	apparent exchange current, mA/cm^2
n	number of electrons transferred in over-all reaction
$n\mathbf{F}v_o$	surface diffusion velocity, mA/cm^2
R	gas constant, 8.314 Vc/mole deg
T	temperature, °K
t	time, sec
v_o	surface diffusion flux, mole/(cm^2) (sec)
Z	number of electrons transferred in charge-exchange rate-determining step
α	anodic, cathodic apparent transfer coefficient
β	true transfer coefficient
η	overpotential (anodic +, cathodic −), mV
η_1	steady-state overpotential

Subscripts:

a	anodic
c	cathodic
calc	calculated

Manuscript submitted Feb. 16, 1970; revised manuscript received Oct. 28, 1970. This was Paper 200 presented at the Detroit Meeting of the Society, Oct. 5-9, 1969.

Any discussion of this paper will appear in a Discussion Section to be published in the December 1971 JOURNAL.

REFERENCES

1. S. Zaromb, Paper presented at the Power Systems for Electric Vehicles Symposium, U.S. Dept. Health, Education, and Welfare, April 6-8, 1967, Public Health Service Publication No. 999-AP-37.
2. A. Brenner, *This Journal*, **106**, 148 (1959).
3. J. D. Edwards, C. S. Taylor, L. A. Cosgrove, and A. S. Russell, *ibid.*, **100**, 508 (1953).
4. Y. Yamaguti and S. Sisido, *J. Chem. Soc. Japan*, **62**, 304 (1941).
5. W. B. Frank and L. M. Foster, *J. Phys. Chem.*, **61**, 1531 (1957).
6. W. E. Haupin, *This Journal*, **107**, 232 (1960).
7. H. A. Laitinen and C. H. Liu, *J. Am. Chem. Soc.*, **80**, 1015 (1958).
8. R. Piontelli, Politecnico di Milano, Laboratoris di Elettrochimica, Italy Tech. Note 7, OSR TN 56-546 (1956).
9. L. A. King, A. D. Brown, Jr., and F. H. Frayer, in "Proceedings of the 1968 OAR Research Applications Conference," Vol. 1, Institute for Defense Analyses Rep. OAR-68-001, AD-666800 (1968).
10. J. Giner and G. L. Holleck, NASA CR-1541 (1970).
11. T. C. F. Munday and J. D. Corbett, *Inorg. Chem.*, **5**, 1263 (1966).
12. J. Giner and B. Burrows, NASA CR-100763 (1968).
13. B. S. Del Duca, NASA TN D-5503 (1969).
14. W. Mehl and J. O'M. Bockris, *Can. J. Chem.*, **37**, 190 (1959).
15. J. O'M. Bockris and A. Damjanovic, in "Modern Aspects of Electrochemistry," p. 224, Butterworth Publishing Co. (1964).
16. J. O'M. Bockris and M. Enyo, *This Journal*, **109**, 48 (1962).
17. W. Mehl and J. O'M. Bockris, *J. Chem. Phys.*, **27**, 818 (1957).
18. T. B. Reddy, *This Journal*, **113**, 117 (1966).
19. L. C. Pauling, "The Nature of the Chemical Bond and the Structure of Molecules and Crystals," 2nd ed., p. 346, Cornell Univ. Press (1940).
20. J. O'M. Bockris and G. A. Razumney, "Fundamental Aspects of Electrocrystallization," Plenum Press (1967).
21. P. Delahay, "Double Layer and Electrode Kinetics," p. 163, Interscience Publishing Co. (1965).
22. A. Damjanovic and J. O'M. Bockris, *This Journal*, **110**, 1035 (1963).
23. K. J. Vetter, "Electrochemical Kinetics: Theoretical and Experimental Aspects," p. 400 Academic Press (1967).
24. G. H. Fraser and R. G. Barradas, *This Journal*, **112**, 462 (1965).
25. J. R. Morrey, *Inorg. Chem.*, **2**, 163 (1963).
26. J. R. Morrey and E. E. Voiland, *Spectrochim. Acta*, **18**, 1175 (1962).
27. S. Senderoff and G. W. Mellors, *This Journal*, **113**, 66 (1966).
28. K. Balasubrahmanyam and L. Nanis, *J. Chem. Phys.*, **42**, 676 (1965).
29. S. K. Rangarajan, *J. Electroanal. Chem.*, **16**, 485 (1968).

Potential Measurements on a Si,SiO_2 Electrode Using a ThO_2-Y_2O_3 Electrolyte

F. J. Salzano,* H. S. Isaacs,* and B. Minushkin

Brookhaven National Laboratory, Upton, New York 11973

ABSTRACT

A series of emf *vs.* temperature measurements were made on the cell

$$Si,SiO_2|ThO_2\text{-}15\ w/o\ Y_2O_3|Pt|ThO_2\text{-}15\ w/o\ Y_2O_3|Ni,NiO$$

in order to establish the ionic range of ThO_2-15 w/o Y_2O_3 (ThO_2-17 m/o $YO_{1.5}$) at very low oxygen activities. The use of platinum between the ThO_2-15 w/o Y_2O_3 disks extended the useful life of the cell. In the temperature range 600°-1000°C the emf falls progressively below the expected thermodynamic value with increasing temperature. These data were found to be reproducible in several different cell configurations. The apparent ionic transference number, t_i, at the Si,SiO_2 electrode is given by

$$t_i = \{1 + 6.64 \times 10^{13} P^{-1/4} \exp[-99{,}800/RT]\}^{-1}$$

where P is the partial pressure of oxygen, T is the absolute temperature, and R is the gas constant. The fall off in emf from the thermodynamic value is not predictable from measurements of the ionic range of ThO_2-Y_2O_3 reported by other workers. Some possible factors responsible for the fall off in emf from the thermodynamic value are discussed.

Solid anionic conducting oxide electrolytes have been used extensively to measure the thermodynamic properties of oxides and metal alloy systems (1-3). The properties of these electrolytes have been studied, but the results differ due to the presence of impurities in these ceramics, variations in experimental techniques, and the possibility of complicating electrode electrolyte interactions (4-7).

At present, high-temperature oxygen activity monitoring devices are being applied to industrial processes (8-10). In liquid sodium coolant systems it is necessary to monitor and control the chemical activity of oxygen in order to avoid excessive corrosion. A device has been developed to monitor continuously the chemical activity of oxygen in sodium coolant systems (8, 9). This device is based on the cell

$$Na(O)|ThO_2\text{-}15\ w/o\ Y_2O_3|^{oxygen}_{reference} \qquad (I)$$

where Na(O) represents sodium containing dissolved oxygen. The ThO_2-15 w/o Y_2O_3 (w/o, weight per cent) electrolyte in these cells is in the form of a closed end tube (test tube). The sensitivity and accuracy of the device depends on the value of the ionic transference number at the sodium electrode. The oxygen activity in these systems is as low as 10^{-50} atm at 400°C with respect to oxygen gas at 1 atm pressure and limits the usefulness of some solid electrolyte compositions. The present work was initiated to establish if the ionic transference number of ThO_2-15 w/o Y_2O_3 is unity at oxygen activities corresponding to those in liquid sodium.

The cell chosen for study was

$$Ni,NiO|ThO_2\text{-}15\ w/o\ Y_2O_3|Si,SiO_2 \qquad (II)$$

since the ionic transference number at the Ni, NiO electrode has been established to be unity (2, 4-6) and the oxygen activity of the Si, SiO_2 electrode is close to and slightly below the values found in practical sodium-oxygen systems (11). Furthermore, the thermodynamic properties of NiO and SiO_2 are known and ThO_2-15 w/o Y_2O_3 was found to be inert to the metal species of the electrodes even at 1100°C.

In preliminary experiments it was noted that the Ni, NiO electrode lost weight while the cell was operating. This is very likely due to transport of oxygen through the cell as a result of the electronic conductivity of the electrolyte (12). We believe that this transport process was affecting the stability and reproducibility of the cell as a result of the inability of Si, SiO_2 to consume or Ni, NiO to supply oxygen and maintain their respective equilibrium oxygen activities. Several techniques were tried which could partially block or otherwise alter the oxygen flux through the cell. The most successful technique utilized cells of the type

$$Ni,NiO|ThO_2\text{-}15\ w/o\ Y_2O_3|\chi|ThO_2\text{-}15\ w/o\ Y_2O_3|Si,SiO_2 \qquad (III)$$

where χ is a barrier placed between two ThO_2-15 w/o Y_2O_3 disks to reduce the oxygen flux through the cell. This cell had an additional advantage in that the ThO_2-15 w/o Y_2O_3 disk on the Si, SiO_2 side could be changed without changing the disk at the Ni, NiO reference electrode.

Theory

The useful range of a solid oxide electrolyte is determined by the onset of electron or positive hole conduction due to changes in stoichiometry.

At very low oxygen activities electronic conductivity may appear in a solid oxide electrolyte according to the reaction

$$O_l \rightarrow 1/2\ O_2(g) + V_{O=} + 2e' \qquad (a)$$

where O_l is an oxygen ion at a normal oxygen lattice site, $V_{O=}$ is a doubly ionized oxygen vacancy, and e' is an excess electron (6). These excess electrons lead to enhanced electronic conductivity in the electrolyte which decreases the ionic transference number, t_i, defined as the ratio of ionic conductivity to the sum of the total ionic and electronic conductivities.

If the electrolyte in an electrochemical cell exhibits significant electronic conductivity at either one or both electrodes, the ionic transference number is less than unity and is dependent on the chemical potential of oxygen at the electrode-electrolyte interface. The emf of the cell is lower than the thermodynamic value and is given by (4, 6)

$$E = -\frac{1}{4F}\int_{\mu_1}^{\mu_2} t_i(\mu)\, d\mu \qquad [1]$$

* Electrochemical Society Active Member.
Key words: Si, SiO_2 electrode; ThO_2-Y_2O_3 electrolyte; ionic domain of ThO_2-Y_2O_3; anionic conducting oxides.

where E is the emf, $t_i(\mu)$ is a function which expresses the ionic transference number at any value of μ; μ_1 and μ_2 are the chemical potentials of diatomic oxygen at the respective electrodes, and **F** is the Faraday constant. If the ionic transference number is unity, Eq. [1] reduces to the familiar expression

$$E_O = \frac{\mu_1 - \mu_2}{4F} \quad [2]$$

where E_O is the theoretical emf.

Based on a model described by Lasker and Rapp (6)

$$t_i(\mu) = (1 + KP^{-1/4})^{-1} \quad [3]$$

where P is the partial pressure of oxygen and is related to μ by the expression

$$P = \exp[(\mu - \mu^\circ)/RT] \quad [4]$$

where the reference state is oxygen at 1 atm pressure. K is given by

$$K = K_O \exp[E_a/RT] \quad [5]$$

where K_O and E_a are constants. K^4 is the oxygen partial pressure where the excess electronic and ionic conductivities are equal. It is equivalent to the parameter P_θ given by Schmalzried (13). Substituting Eq. [3] into [1], integrating, and assuming that t_i at μ_1 is unity, we obtain

$$E = E_O + \frac{RT}{F} \ln(1 + KP_2^{-1/4}) \quad [6]$$

where P_2 is the partial pressure of oxygen at the electrode (Si, SiO_2) where t_i is less than unity. Thus, from measurements of the emf *vs.* temperature behavior of a cell and the known thermodynamic properties of the electrodes we can calculate K_O and E_a and determine $t_i(\mu)$.

Experimental

Materials.—The ThO_2-15 w/o Y_2O_3 (ThO_2-17 mole per cent Y_2O_3) was in the form of ¾ in. OD by ⅛ in. disks and was purchased from the Zircoa Corporation, Solon, Ohio.

The Ni and NiO were standard reagent-grade material obtained from the J. T. Baker Chemical Co., Phillipsburg, New Jersey. The silicon metal powder was obtained from Alfa Inorganics, Beverly, Massachusetts. The SiO_2 was prepared by firing reagent-grade silicic acid ($SiO_2 \cdot xH_2O$) in air at 850°C.

Procedure.—In order to establish that the ionic transference number at the Ni, NiO electrode is unity as reported (6) and to test the apparatus, a series of emf *vs.* temperature measurements were made using ThO_2-15 w/o Y_2O_3 electrolyte and Ni, NiO and Cu, Cu_2O electrodes in the same apparatus. The results of these measurements were in agreement with the data reported for these electrodes using ZrO_2-CaO electrolytes in the temperature range 350°-850°C (1). This indicates that the ionic transference numbers of ThO_2-15 w/o Y_2O_3 for both Ni, NiO and Cu, Cu_2O electrodes is unity since ZrO_2-CaO is known to have a unity transference number at these oxygen partial pressures. This result is in agreement with data reported previously for various ThO_2-Y_2O_3 compositions at oxygen activities up to 1 atm (2, 4-6).

All of the cell configurations studied were in the form of stacks of disks having the general form

SS|Pt|Ni,NiO|ThO_2-15 w/o Y_2O_3|χ|ThO_2-15 w/o Y_2O_3|Si,SiO_2|SS (III)

where χ was either empty (disks in direct contact), 1 mil platinum foil or Al_2O_3, and SS represents the 304 stainless steel parts of the cell assembly.

The Ni, NiO electrodes were pressed disks ⅜ in. OD x ⅜ in. thick and contained 25 v/o nickel. These electrode disks were pressed in a 304 SS die at ≈5000 psig and sintered in vacuum (10^{-6} mm Hg) at 850°C for 4 hr. Before loading into a cell the surface of each disk was ground on medium fine emery paper using a figure-eight motion to assure a flat surface, and the loose powder was removed with a clean, coarse brush.

The Si, SiO_2 electrodes were prepared from two compositions: (*i*) a 50 v/o mixture of Si and SiO_2 powders and (*ii*) pure Si powder plus its normal surface oxide film. These electrode disks were ⅜ in. OD x ⅜ in. thick and were pressed in a 304 SS die at ≈1000 psig. Disks prepared from both compositions were fragile and had to be carefully handled until vacuum sintered at 950°C for a minimum of 4 hr. The ThO_2-15 w/o Y_2O_3 disks were also ground flat on medium fine emery paper and vacuum fired before assembly into a cell.

The cells studied were assembled on a 304 SS block which contained a ⅜ in. OD depression on top for the Ni, NiO reference electrode and a ⅛ in. OD 304 SS thermocouple sheath which was inserted in the bottom and which served to support the block. The stack of disks was held together with a 200g 304 SS weight which rested on top of the stack and contained a ⅜ in. OD depression for the Si, SiO_2 electrode. Each cell was enclosed in a quartz envelope, further enclosed by a 304 SS sheet metal electrical shield which was electrically connected to ground and to the Ni, NiO electrode. The voltage developed by the cell was measured with a high impedance electrometer (Cary Model-30CV) and a precision reference voltage source (General Resistance Model-DA45D), and the signal was continuously recorded.

Each cell was operated with a continuous purge of helium obtained from the boil off from a 50-liter liquid helium Dewar. No effort was made to isolate the electrodes from their common helium purge. The flow rate was controlled by means of a heat leak into the Dewar to give a flow rate ≈100 cm^3/min. The emf was independent of gas flow at rates from approximately 50 to 200 cm^3/min.

These cells were run for various periods ranging from several days to three weeks. The time to reach equilibrium varied from several hours at the high temperatures to one or two days at the lower temperatures.

Results

Emf *vs.* temperature data were obtained for the following cells

SS|Si,SiO_2|ThO_2-15 w/o Y_2O_3|Pt|ThO_2-15 w/o Y_2O_3|Ni,NiO|Pt|SS (IV)

SS|Si,SiO_2|ThO_2-15 w/o Y_2O_3|Al_2O_3|ThO_2-15 w/o Y_2O_3|Ni,NiO|Pt|SS (V)

SS|Pt|Si,SiO_2|ThO_2-15 w/o Y_2O_3|ThO_2-15 w/o Y_2O_3|Ni,NiO|Pt|SS (VI)

SS|Si,SiO_2|ThO_2-15 w/o Y_2O_3|Pt|ThO_2-15 w/o Y_2O_3|Ni,NiO|Pt|SS[1] (VII)

The data obtained from cell (IV) in the temperature range 600°-1000°C are shown in Fig. 1. The upper line is the thermodynamic value, *i.e.*, $t_i = 1$, and to a good approximation is independent of temperature (11). It is evident from Fig. 1 that at low temperatures the emf approaches the thermodynamic value and at temperatures above 700°C shows large deviations which are approximately linear to 900°C. The data from these cells did not show hysteresis, were reproducible at temperatures above 750°C, and showed little scatter. The data for temperatures below 750°C were difficult to reproduce and showed greater scatter, especially as the cells aged.

The emf *vs.* temperature data from cells (V), (VI), and (VII) are shown in Fig. 2. The data from cell IV are also shown in Fig. 2 for comparison.[1] All of the emf data from the cells studied, *i.e.*, (IV), (V), (VI), and (VII), show the same behavior with temperature

[1] All the Si, SiO_2 electrodes, with the exception of cell (VII), were prepared from mixture (*ii*), i.e., with pure silicon powder and its normal impurity oxygen without addition of SiO_2.

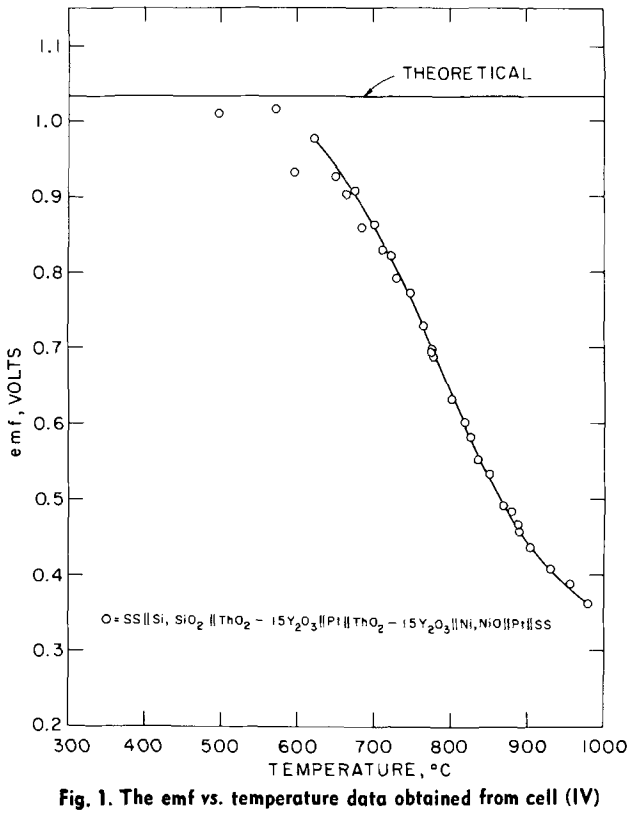

Fig. 1. The emf vs. temperature data obtained from cell (IV)

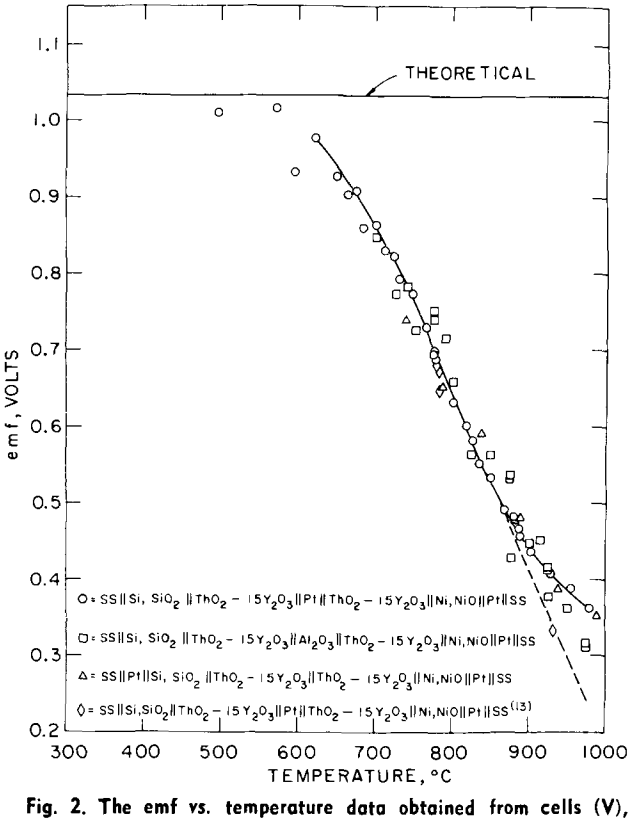

Fig. 2. The emf vs. temperature data obtained from cells (V), (VI), and (VIII).

and are in good agreement. The data from cells (V), (VI), and (VII) show more scatter than the data from cell (IV), but all the data fall uniformly around the average line drawn through the data from cell (IV).

Using Eq. [6] and the available data on the thermodynamic properties of NiO and SiO_2 (11), the values of K were calculated from the line of best fit through the emf *vs.* temperature data. The values of K obtained in the temperature range 650°-1000°C are plotted as log K *vs.* the reciprocal temperature in Fig. 3.

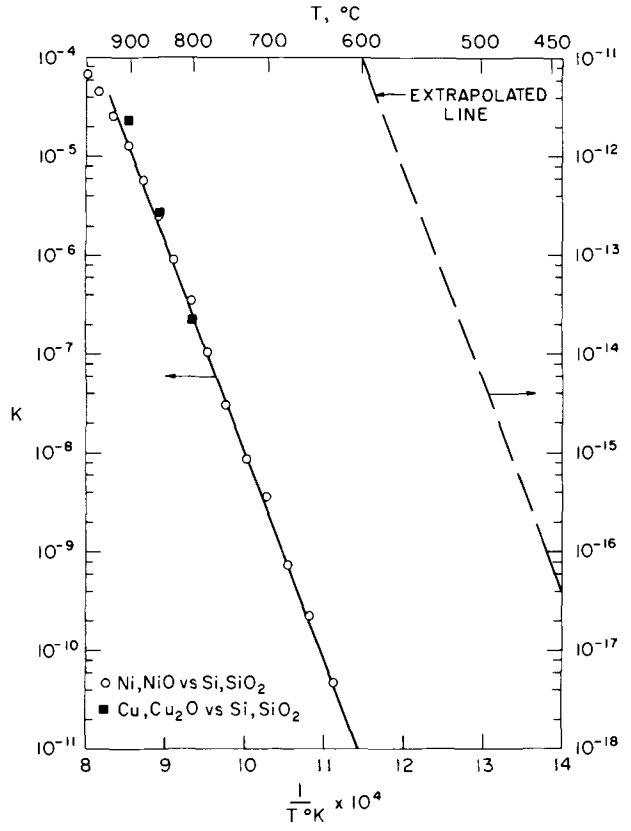

Fig. 3. Plot of log K vs. the reciprocal absolute temperature from which the values of E_a and K_O were derived.

Plotted in this form the data are linear and show a slight tailing off above 900°C.

A limited amount of data from the cell

$$SS|Si,SiO_2|ThO_2\text{-}15 \text{ w/o } Y_2O_3|ThO_2\text{-}15 \text{ w/o } Y_2O_3|Cu,Cu_2O|Pt|SS \quad \text{(VIII)}$$

are also shown in Fig. 3. These data are in good agreement with the data obtained from the cells which used Ni, NiO reference electrodes.[2]

The expression

$$K = 6.64 \times 10^{13} \exp [-99{,}800/RT] \quad [7]$$

where T is the absolute temperature and R is the gas constant, was calculated from the data shown in Fig. 3. Assuming the observed emf fall off is due to electronic conduction effects, the t_i value at any temperature and at oxygen activities up to Cu, Cu_2O can be calculated using Eq. [7] and [3]. However, other effects may be responsible for the fall off as explained below. If this is the case, Eq. [7] and [3] cannot be used to calculate t_i.

Discussion

Preliminary measurements using cell (II) demonstrated that spontaneous loss of oxygen was occurring from the Ni, NiO reference electrodes, causing this cell to give poorly reproducible data. Similar behavior was observed in cells with Cu, Cu_2O reference electrodes. This spontaneous loss of oxygen could not be accounted for by transport into the gas phase since electrochemical measurement of the oxygen activity in the helium indicated it was in the range of 10^{-6} to 10^{-7}. Thus, the hydrogen content was also low and was estimated from vapor pressure data to be ~4 x 10^{-7} mm Hg. The transport of oxygen could only be between the Ni, NiO and Si, SiO_2 electrodes through the electrolyte. It results from the finite electronic conductivity present in this electrolyte at the low oxygen partial pressures corresponding to Si, SiO_2 (12).

[2] We were reluctant to use Cu, Cu_2O as the reference electrode since this mixture readily fuses to the ThO_2-15 w/o Y_2O_3 disk and could only be removed by grinding the surface of the disk, but some data were obtained with Cu, Cu_2O (see Fig. 3).

The arrangement of cell (III) with a metal or Al_2O_3 barrier between the electrolyte tablets was devised to minimize the oxygen flux. It is obvious that in all of the cells studied a flux is still present since the oxygen activity in the helium purge gas is higher than at either of the two electrodes. However, the transport of oxygen is expected to be from the gas phase (helium) directly to each of the electrodes and is believed to be slight since we obtain theoretical emfs in Cu, Cu_2O *vs.* Ni, NiO cells. However, the direct oxidation of the Si, SiO_2 electrode may not be as slight. In any case the use of the barrier resulted in cells which were reproducible and remained so for a longer period of time than cells without the barrier.

In principle, the junction between the two electrolyte tablets will have no effect on the emf of the cell provided $t_i(\mu)$ is unity and that μ is the same in both electrolyte barrier interfaces.[3] We believe that both these conditions were satisfied, (*a*) since the composition of the two disks was the same and (*b*) measurements of t_i at high oxygen activities, *i.e.*, corresponding to the oxygen activity in the helium indicate that t_i is close to unity at an oxygen activity of 10^{-6}, *i.e.*, at both platinum electrolyte interfaces (13). In order to evaluate the possible importance of the transport of oxygen or that the nature of the electrolyte-electrolyte junction was not seriously affecting the results, a series of emf *vs.* temperature measurements were made on cells with different internal resistances, resulting from the use of different barrier materials, which would be expected to transport oxygen at different rates, *i.e.*, cells (IV), (V), (VI), and (VII). Agreement between the data from all the cells suggests that transport through the cells and the nature of the junction did not have a significant effect on the measurements.

Comparison with other data.—The model described by Lasker and Rapp (6) has been used to calculate the value of $t_i(\mu)$ from the experimental data. Equation [7], which is derived from the experimental data, has the same form as Eq. [5]. The experimental emf *vs.* temperature data is, as predicted from Eq. [6], approximately a linear function of temperature at high temperatures, *i.e.*, where $KP^{-1/4} > 1$. Thus, the empirical form of the data is predicted by the model. These results are also qualitatively in accord with reported measurements of the ionic range of ThO_2-Y_2O_3 at low oxygen activities which indicate that the electronic conductivity increases at a faster rate than the ionic conductivity with increasing temperature (14, 15). However, the magnitude of the relative increase is substantially in disagreement with results reported by previous investigators (14-16).

Based on results obtained in this study with Si, SiO_2 electrodes (cell III) cell (I) should give theoretical emfs at 550°C and oxygen concentrations in sodium as low as 1 ppm. However, we observe t_i for cell (I) at the Na(O) electrode to be less than unity at 550°C, at oxygen concentrations in sodium in the range of 1 to 10 ppm oxygen. Tretyakov and Muan (14) and Hardaway *et al.* (15) have measured values of K by means of a technique which does not depend on knowledge of the exact partial pressure at the low oxygen activity electrode. Their results predict similar behavior for the Na, Na_2O system, *i.e.*, cell (I). Both investigations measured K at oxygen activities where t_i is effectively zero. Their results predict that there should be no readily observable deviation in the emf of cell (III) from the calculated emf until 1000°C. Furthermore, Fruehan (16) claims he does not see the emf fall-off in the cell

$$Si,SiO_2|ThO_2\text{-}Y_2O_3|Cr,Cr_2O_3$$

at 1600°C. This disagrees with the extrapolated values of Tretyakov and Muan (14) and Hardaway *et al.* (15) whose results predict significant falloff in the emf at this temperature. Thus, it appears the deviation in emf from the calculated value of a particular cell system can depend on other factors such as the nature of the physical surface or chemical interactions between the electrode and the electrolyte in addition to the onset of electronic conduction. However, we found that using solid polished or pressed porous silicon did not have a significant effect on the emf *vs.* temperature behavior of cell (III). Furthermore, there were no obvious chemical interactions between Si, SiO_2 and ThO_2-15 w/o Y_2O_3. The effect of gas phase impurities can also be ruled out because they would not give the rapid fall-off of emf with increasing temperature observed. We cannot rule out the possibility of forming SiO_2 or some other oxide layer at the Si, SiO_2-electrolyte interface whose properties could effect the behavior of the cell. Thus, it appears that the behavior of a particular cell combination is not always predictable from measurements of the inherent ionic domain of a solid oxide electrolyte. We suggest that further investigations to define the useful oxygen activity range of ThO_2-Y_2O_3 be made at oxygen activities in the vicinity of the ionic domain boundary predicted by Tretyakov and Muan (14) and Hardaway *et al.* (15) using a variety of metal-metal oxide systems. We believe that the use of the barrier technique described in this paper will facilitate these studies by extending the useful life of the cells.

[3] In calculating the emf of this composite cell, Eq. [1] must be applied to each electrolyte disk with its adjacent contacts and the emfs summed for each disk.

Acknowledgments

This is to acknowledge the contribution of W. Kalinowski who constructed the experimental apparatus and helped solve many of the technical problems which developed during the initial phases of this work. We would like to thank Dr. L. Newman and Dr. D. H. Gurinsky for their encouragement and helpful discussions during the course of this study. This work was performed under the auspices of the United States Atomic Energy Commission.

Manuscript submitted Feb. 24, 1970; revised manuscript received *ca.* Nov. 17, 1970.

Any discussion of this paper will appear in a Discussion Section to be published in the December 1971 JOURNAL.

REFERENCES

1. T. L. Markin, R. J. Bones, and V. J. Wheeler, *Proc. Brit. Ceram. Soc.*, **8**, 51 (1967).
2. B. C. H. Steele and C. B. Alcock, *Trans. Met. Soc. AIME*, **233**, 1359 (1965).
3. B. C. H. Steele, "Mass Transport in Oxides," Proc. of a symposium held at Gaithersburg, Md., Oct. 22-25, 1967, p. 165, J. B. Wachtman, Jr. and A. D. Franklin, Editors, National Bureau of Standards Publication 296, Aug. 1968.
4. R. A. Rapp, "Thermodynamics of Nuclear Materials," Proc. of a symposium held in Vienna, Sept. 4-8, 1967, p. 559, sponsored by the International Atomic Energy Agency.
5. J. W. Patterson, E. C. Bogren, and R. A. Rapp, *This Journal*, **114**, 752 (1967).
6. M. F. Lasker and R. A. Rapp, *Z. Phys. Chem. N.F.*, **49**, 198 (1966).
7. L. Heyne, "Mass Transport in Oxides," Proc. of a symposium held at Gaithersburg, Md., Oct. 22-25, 1967, p. 149, J. B. Wachtman, Jr. and A. D. Franklin, Editors. National Bureau of Standards Publication 296, Aug. 1968; *see* especially p. 160 for a review of available data on oxides.
8. M. Kolodney, B. Minushkin, and H. Steinmetz, *Electrochem. Technol.*, **3**, 244 (1965).
9. B. Minushkin and M. Kolodney, AEC Report UNC-5131 (1967), United Nuclear Corp., Elmsford, N. Y.
10. R. J. Fruehan, L. G. Martonik, and E. T. Turkdogan, *Trans. Met. Soc. AIME*, **245**, 1501 (1969).
11. J. F. Elliott and Molly Gleiser, "Thermochemistry for Steel Making," Vol. I. Addison-Wesley Publishing Co., Inc., Reading, Mass.
12. See ref. (3), p. 167 and ref. (2), p. 1367.

13. Hermann Schmalzried, *Z. Phys. Chem.*, **38**, 87 (1963).
14. Ju. D. Tretyakov and Arnulf Muan, *This Journal*, **116**, 331 (1969).
15. J. B. Hardaway, III, *et al.*, *J. Am. Ceram. Soc.*, **54**, 94 (1971).
16. R. J. Fruehan, L. J. Martonik, and F. T. Turkdogan, *TMS-AIME*, **245**, 1501 (1969).

Ionic Range of ThO_2-15 w/o Y_2O_3 at High Oxygen Activities

F. J. Salzano,* C. Auerbach, H. S. Isaacs,* and B. Minushkin

Brookhaven National Laboratory, Upton, New York 11973

ABSTRACT

The ionic transference numbers (t_i) of ThO_2-15 w/o Y_2O_3 was determined at oxygen activities corresponding to approximately 1 atm by (*a*) emf measurements utilizing air-O_2 and air-Pb/PbO cells and (*b*) four-point resistance measurements, both as a function of temperature. The expression

$$t_i = \left[1 + 8.3 \times 10^{-2} P^{1/4} \exp\left(\frac{3420}{RT}\right)\right]^{-1}$$

was deduced from the emf measurements. The resistance data are in good agreement with these results, but the latter technique is not sensitive enough to discriminate easily between cases where $t_i < 1$ and where ionic and electronic contributions to the resistance are of comparable magnitude.

Yttria doped thoria is being used extensively as a solid oxide electrolyte in oxygen activity monitors for liquid sodium coolant systems (1). These applications require that the ionic transference number of the electrolyte either be unity, *i.e.*, that the electrolyte be a purely ionic conductor, or be readily reproducible. Since air or gaseous oxygen electrodes have shown advantages as reference electrodes over the solid metal-metal oxide system used heretofore, it was necessary to study the electrolyte at high oxygen activities. The behavior of ThO_2-15 w/o Y_2O_3 at low oxygen activities has been studied by some of the present authors to determine the ionic transference number (2). In this paper we report pertinent emf measurements on the following pairs of cells

$$Pb(l),PbO(s)\,|ThO_2\text{-}15\text{ w/o }Y_2O_3|O_2(0.21\text{ atm}),Au \quad (I)$$

$$Pb(l),PbO(s)\,|ZrO_2\text{-}CaO|O_2(0.21\text{ atm}),Au \quad (I')$$

and

$$Au,O_2(0.21\text{ atm})\,|ThO_2\text{-}15\text{ w/o }Y_2O_3|O_2(1\text{ atm}),Au \quad (II)$$

$$Au,O_2(0.21\text{ atm})\,|ZrO_2\text{-}CaO|O_2(1\text{ atm}),Au \quad (II')$$

The ZrO_2-CaO electrolyte is known to be a purely ionic conductor at all oxygen activities considered in this work, and the oxygen activity determined by the Pb-PbO system falls well within the 99% ionic conductivity range of ThO_2-15 w/o Y_2O_3 (3). In addition, four-point conductivity measurements, taken over a wide temperature and oxygen partial pressure range, are reported and discussed in the light of the emf data.

Results

Measurements on cells (I) and (I') were carried out using electrolyte tubes filled with a 9:1 Pb-PbO mixture. The tubes were coated on the outside with a porous gold film and rested inside a furnace on a bed of platinum gauze to which contact was made, air being allowed to circulate through the furnace and over the gold film. A piece of iridium wire served to make contact with the lead mixture. The cells were studied over the 500°-700°C temperature range; below 500°C cell (I) was excessively slow in reaching equilibrium. The results shown in Fig. 1 indicate that cell (I') gave values in close agreement with calorimetric data, in accord with previous work (4), while the values for cell (I) were noticeably lower. If $E_{(I')}$ and $E_{(I)}$ are the respective emf's, it may be shown based on the model described by Lasker and Rapp (5, 2), that

$$E_{(I)} - E_{(I')} = \frac{RT}{F} \ln t_i \qquad [1]$$

In this equation t_i is the value of the ionic transference number of ThO_2-15 w/o Y_2O_3 at the electrolyte-air interface ("point value"). Values of t_i calculated from Eq. [1] ranged from 0.66 at 500°C to 0.76 at 700°C. Similar results were obtained by comparing emf measurements on the cell

$$Cu(s),Cu_2O(s)\,|ThO_2\text{-}15\text{ w/o }Y_2O_3|O_2(0.21\text{ atm}),Au$$

with appropriate thermochemical data.

Cells (II) and (II') were studied in analogous fashion, air and oxygen being allowed to flow over the

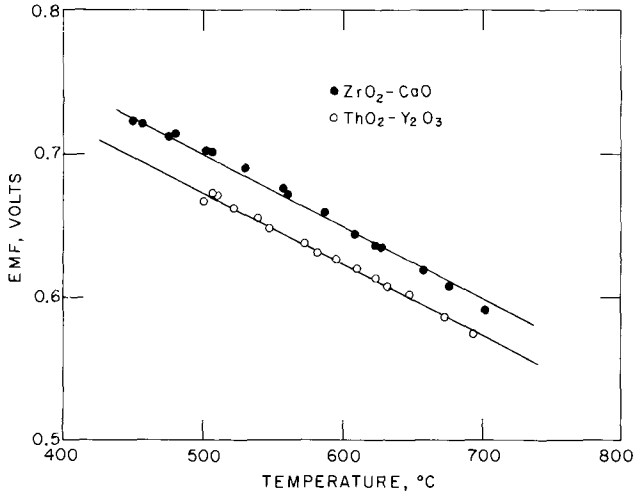

Fig. 1. Emf *vs.* temperature data obtained from cells (I) and (I').

* Electrochemical Society Active Member.

Key words: oxide electrolytes, ThO_2-Y_2O_3 electrolytes, ionic domain of $ThO_2Y_2O_3$, anionic conducting oxides.

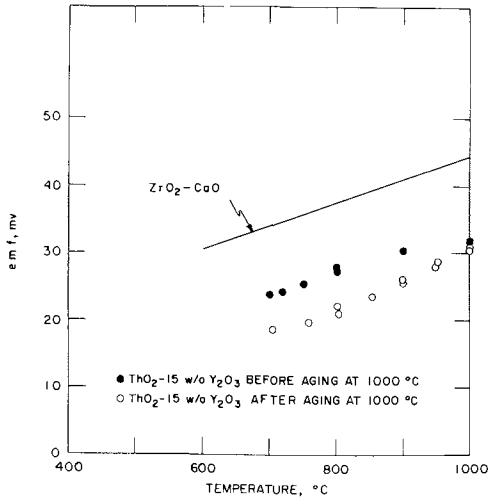

Fig. 2. Emf *vs.* temperature data obtained from cells (II) and (II').

outside and inside, respectively, of both tubes. Results are shown in Fig. 2; it is seen that aging the gold-coated ThO_2-Y_2O_3 tube at 1000°C has a marked effect on $E_{(II)}$. In the case of cells (II) and (II'), the average ionic transference number, $\bar{t}$, given by

$$\bar{t} = \frac{E_{(II)}}{E_{(II')}} \qquad [2]$$

may be considered to represent the point value, t_i, at each electrode, since the oxygen activity difference between the two electrodes is very small. Using Eq. [2], $\bar{t}$ at 700°C was found to be 0.7 for a freshly coated ThO_2-15 w/o Y_2O_3 tube and 0.5 for a tube aged at 1000°C. This constitutes satisfactory agreement with the results obtained from cell (I). The following explanation may account for the decrease of t_i (increase in $E_{(II)}$) on aging. In the above experiments the films consisted of porous gold, as in cells (I) and (I'), and sintering of such films is likely to occur at 1000°C. This would reduce the three-phase contact area (gas-gold-electrolyte) and thereby alter the polarization phenomena which may occur as a result of the partial electronic conductivity present in ThO_2-15 w/o Y_2O_3. Such a hypothesis is supported by the observation, made in prior experiments, that the same tube, equipped with a 1/16 in. solid gold button contact gave even lower emf values than were observed with the aged porous film.[1]

Four-point resistance measurements were made on a ThO_2-15 w/o Y_2O_3 ceramic sample cut from a sodium oxygen meter electrolyte tube (4 cm long by 1.3 cm wide by 0.15 cm thick) (1). The sample was placed in a quartz apparatus which in turn was enclosed in a 304 SS sheet metal electrical shield. Various gases could be passed through the vessel to control the oxygen activity of the sample. Four leads, numbered 1, 2, 3, and 4, were attached equally spaced on the long axis of the sample. The technique employed was that of brazing on four 1/16 in. diameter gold button contacts at 1100°C and subsequently brazing four platinum lead wires to the gold contacts. Contacts 1 and 4, attached to the ends of the sample, served to carry the current into and from the sample. The other two contacts, 2 and 3, served as potential probes. Measurements were made using Keithley Electrometers, Model 602. Each resistance measurement was made over as broad a range of current as allowed by the sensitivity of the electrometers. The resistance was always independent of the current.

Data were obtained in the temperature range 800°-200°C at three typical oxygen activities: dry hydrogen

[1] A ZrO_2-CaO tube equipped with the same solid gold button contacts gave theoretical emfs in a cell of the type (II') at temperatures down to 600°C.

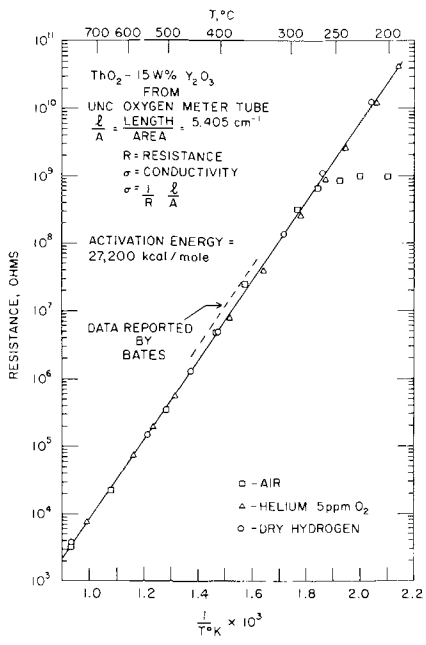

Fig. 3. Temperature dependence of the resistance of ThO_2-15 w/o Y_2O_3 taken from a UNC oxygen meter tube (1).

(<10 ppm H_2O, $\approx 10^{-28}$ atm O_2 at 800°C), 5 ppm O_2 in helium, and air. The data obtained are shown in Fig. 3 as a plot of log resistance *vs.* the reciprocal absolute temperature, and are seen to fall on a single straight line.

From these data the activation energy for the observed conductance was found to be −27,200 cal/mole, in good agreement with the values previously reported (3, 6). Two-point resistance measurements on the cells

$$Na,Na_2O|ThO_2\text{-}15\ w/o\ Y_2O_3|Na(O)$$
$$Cu,Cu_2O|ThO_2\text{-}15\ w/o\ Y_2O_3|Na(O)$$

give similar values for the activation energy.

Discussion

The emf measurements clearly indicate that ThO_2-15 w/o Y_2O_3 does not behave as a purely ionic conductor at the high oxygen activities considered in this work. Based on the work of Lasker and Rapp (5) and others one can define the parameter K by the equation

$$t_i = \left(1 + \frac{p^{1/4}}{K}\right)^{-1} \qquad [3]$$

where p is the oxygen partial pressure corresponding to t_i. Note that K raised to the fourth power represents the oxygen partial pressure corresponding to $t_i = 0.5$.[2] Values of K based on the data from cells (I) and (I') are plotted in Fig. 4 and yield the relationship

$$K = 12 \exp\left(-\frac{3420}{RT}\right) \qquad [4]$$

The fact that all the conductivity data may be represented by the same straight line, independent of pressure and temperature over a wide range, might at first sight indicate a t_i value of unity even at high oxygen activities, in contradiction to the potentiometric findings and the results of Bauerle (7). The measurements of Bauerle were limited to 1000°C, and he observed only a 25% change in conductivity at the highest Y_2O_3 composition he studied (4.5 w/o Y_2O_3) in the pressure range 10^{-6} to 1 atm pressure. His results show that the percentage change in conductivity decreases with increasing Y_2O_3 content. It is evident from these results that in ThO_2 containing more than three times as much Y_2O_3 (15 w/o Y_2O_3), changes in conductivity in this pressure range are expected to be very small

[2] Note the difference between this Eq. [3] and Eq. [3] in ref. (2). This is done so that the units of K will be (pressure)$^{1/4}$ in both cases.

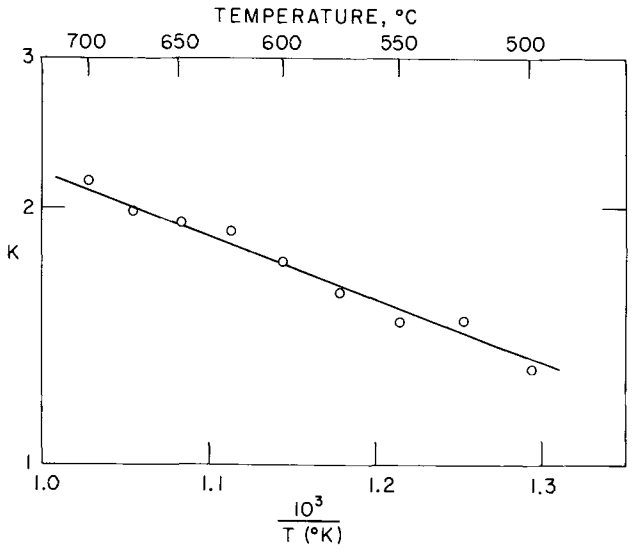

Fig. 4. Temperature dependence of K is obtained from emf measurements on cells (I) and (I').

and thus not easily detectable with techniques used in this study. The following considerations will show that there is no inconsistency between the emf and conductivity results reported in this paper. Since the ionic conductivity (σ_i) and the positive hole conductivity (σ_e) are given by the expressions

$$\sigma_i = \sigma_{io} \exp\left(\frac{-\Delta E_i}{RT}\right)$$

and

$$\sigma_e = \sigma_{eo} p^{1/4} \exp\left(\frac{-\Delta E_e}{RT}\right)$$

respectively, and since

$$t_i = \left(1 + \frac{\sigma_e}{\sigma_i}\right)^{-1}$$

it follows from Eq. [3] that

$$K = K_o \exp\left(\frac{\Delta E_e - \Delta E_i}{RT}\right) \qquad [6]$$

where the ΔE's represent the respective activation energies and

$$K_o = \frac{\sigma_{io}}{\sigma_{eo}}$$

Comparing Eq. [4] and [6] one finds that $\Delta E_e - \Delta E_i = -3420$ cal. If one makes the reasonable assumption that the slope of the plot in Fig. 3, which traverses a very low oxygen pressure range, is a measure of ΔE_i, *i.e.*, that $\Delta E_i = -27{,}200$ cal, one concludes that ΔE_i and ΔE_e differ by less than 15%. It is therefore not surprising that the temperature dependence of the conductivity continues to be constant, reflecting largely ΔE_i, even at appreciable oxygen pressures where σ_e is large enough to make $t_i < 1$. A slight drop in R is observed in air at the low temperature end, as predicted qualitatively from the oxygen partial pressure dependence of σ_e. However, no attempt was made in this work to study the pressure dependence in detail.

The reaction primarily responsible for the onset of hole conductivity at high oxygen activities is

$$\tfrac{1}{2}\, O_2(g) + V_o'' \rightleftarrows O_o + 2\oplus$$

where V_o'' is a doubly ionized oxygen vacancy, O_o is an oxygen ion on an oxygen site, and $\oplus$ represents the concentration of positive holes (5). We can estimate the value of the heat of reaction for the above equilibrium from the temperature dependence of K (2). According to the model

$$K^{-1} \propto \frac{k^{1/2}}{\mu_V}$$

and we expect

$$\Delta E_i - \Delta E_e \cong \frac{E_k}{2} - E_v$$

where k is the equilibrium constant for the above reaction, μ_v is the mobility of vacancies, E_k is the heat of reaction for the above equilibrium, and E_v is the activation energy for vacancy migration. Using the value $+3420$ cal/mole for $E_k/2 - E_v$ and the value E_v, $-27{,}200$ cal/mole obtained from the conductivity measurements, we calculate E_k to be $-47{,}500$ cal/mole. Thus, the heat of reaction for the above equilibrium is of the order of 50,000 cal/mole. The results obtained in this work have shown that t_i is less than unity at oxygen pressures close to 1 atm. In more quantitative terms, the ionic conductivity range corresponding to $t_i \geq 0.99$, may be defined by a limiting oxygen partial pressure, $p_{0.99}$, at which $t_i = 0.99$. Based on Eq. [3] and [4] it may be shown that

$$p_{0.99} = 2.07 \times 10^{-4} \exp\left(-\frac{1.37 \times 10^4}{RT}\right) \qquad [7]$$

Conductivity measurements on ThO_2-15 w/o Y_2O_3 do not contradict this finding but simply cannot easily discriminate between cases where σ_i and σ_e are of comparable magnitude, *i.e.*, $t_i < 1$, and $\Delta E_i \approx \Delta E_e$. Air or oxygen electrodes may nevertheless be used as reference electrodes in oxygen activity meters for sodium provided appropriate allowance is made for deviations of t_i from unity.

Acknowledgments

The authors are indebted to W. Kalinowski and G. Kissel for their substantial aid in construction of the apparatus and solution of other mechanical problems. They would like to thank Dr. L. Newman and Dr. D. H. Gurinsky for their encouragement and helpful discussions during the course of this study. This work was performed under the auspices of the United States Atomic Energy Commission.

Manuscript submitted Feb. 24, 1970; revised manuscript received *ca.* Aug. 27, 1970.

Any discussion of this paper will appear in a Discussion Section to be published in the December 1971 JOURNAL.

REFERENCES

1. M. Kolodney, B. Minushkin, and H. Steinmetz, *Electrochem. Technol.*, **3**, 244 (1965).
2. F. J. Salzano, H. S. Isaacs, and B. Minushkin, *This Journal*, **118**, 412 (1971).
3. C. H. Steele and C. B. Alcock, *Trans. Met. Soc. AIME*, **233**, 1359 (1965).
4. G. G. Charette and S. N. Flengas, *This Journal*, **115**, 796 (1968).
5. M. F. Lasker and R. A. Rapp, *Z. Physik Chem. (N.F.)*, **49**, 198 (1966).
6. J. L. Bates, Private communication.
7. J. E. Bauerle, *J. Chem. Phys.*, **45**, 4162 (1966).

Free Energies of Formation of Silver Sulfide and Lead Sulfide by Electromotive Force Measurements at High Temperature

W. T. Thompson[1] and S. N. Flengas*

Department of Metallurgy and Materials Science, University of Toronto, Toronto 5, Ontario, Canada

ABSTRACT

The Gibbs free energy of formation of Ag_2S and PbS were measured in the temperature range 500°-800°C. The measurements were made with an electrochemical formation cell employing a sulfur vapor electrode and a fused chloride electrolyte saturated with the sparingly soluble sulfide. For the reaction

$$2Ag_{(solid)} + \tfrac{1}{2}S_{2(gas,\ 1\ atm)} \rightarrow Ag_2S_{(solid)}$$

$$\Delta G^\circ = -21{,}000 + 8.85T \text{ cal/g-mole}$$

For the reaction

$$Pb_{(liquid)} + \tfrac{1}{2}S_{2(gas,\ 1\ atm)} \rightarrow PbS_{(solid)}$$

$$\Delta G^\circ = -40{,}000 + 22.5T \text{ cal/g-mole}$$

An accurate knowledge of the Gibbs free energy of formation of sulfides, particularly base metal sulfides at high temperature, is of considerable importance in metallurgical process design. Although it is possible to determine free energies of formation at high temperatures by applying the appropriate heat capacity and enthalpy of transformation data to enthalpies and entropies of formation at 298°K, it is desirable to circumvent the cumulative errors of such calculations by directly measuring the free energies of formation at the temperatures of interest whenever this is feasible. Of the procedures available for such measurements, electrochemical methods are perhaps the most reliable and accurate when suitable electrolytes are available.

For the oxides with low free energies of formation, an electrochemical technique employing a solid ZrO_2-CaO solution as electrolyte has been particularly successful in yielding thermodynamic data at high temperature of high accuracy (1). An analogous procedure for the study of sulfides has not been possible because no similar solid sulfide electrolyte is at present well enough understood to yield emf data of unquestioned thermodynamic significance. The electrochemical procedure described in this paper, therefore, involves a fused salt electrolyte saturated with sulfide. This type of solution is suitable as an electrolyte since sulfide saturation is reached at a sufficiently low level that the salt solution still conducts current exclusively by ionic transference (2-4).

Of equal importance to the present electrochemical procedure has been the development of a reversible sulfur vapor electrode (5). In a previous publication, the reversibility of this electrode was demonstrated by measurements of the cell

$$-Ag \left| \begin{matrix} AgCl \\ Ag_2S \end{matrix} \right| S_{vapor},\ C+$$

When the mole fraction of Ag_2S was less than 0.1, the melt conducted ionically (4) and Nernst behavior was observed with respect to Ag_2S concentration and partial sulfur pressure in the temperature range 490°-860°C.

Experimental

The cell used to measure the free energy of formation of Ag_2S may be represented schematically as follows

$$-Ag \left| \begin{matrix} Ag_2S\ (satd.) \\ AgCl \\ ACl \end{matrix} \right| S_{vapor},\ C+$$

where ACl is molten alkali chloride (KCl or a KCl-NaCl mixture). The PbS formation cell may be similarly represented. The important physical features of these cells are shown in Fig. 1 and 2. The upper Pyrex portions of these cells containing sulfur were connected to a lower quartz portion containing the fused electrolyte. The entire cell was located in a two compartment furnace assembly such that the temperature of the sulfur and the electrolyte could be independently controlled.

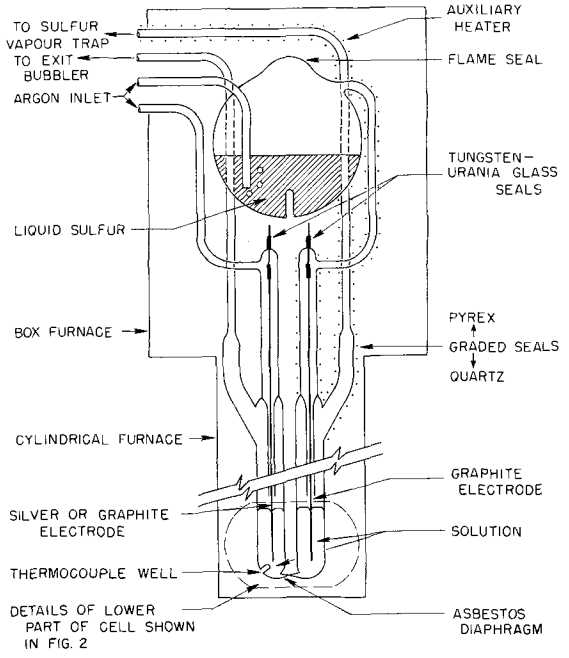

Fig. 1. Upper part of sulfide formation cell

* Electrochemical Society Active Member.

[1] Present address: Department of Metallurgical Engineering, McGill University, Montreal, Quebec, Canada.

Key words: electrode potentials, silver sulfide, lead sulfide.

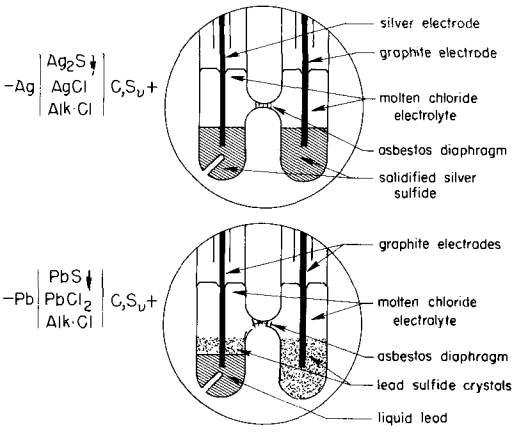

Fig. 2. Details of lower parts of sulfide formation cells

A gas mixture of fixed partial sulfur pressure was created by bubbling dry, oxygen-free preheated argon through the molten sulfur. The bubbling action tended to reduce temperature gradients in the sulfur and assure saturation of the argon. The sulfur for this purpose was laboratory reagent grade; purification by repeated sublimation was not performed since the impurities consist chiefly of insoluble matter known not to affect the sulfur pressure (6). The sulfur-argon mixture was led down and over the sulfide electrolyte and then passed to a sulfur condenser from which sulfur-free argon was expelled to the atmosphere.

In order to be certain that the temperature of the liquid sulfur in the bulb would control the sulfur pressure over the electrolyte, it was necessary to heat all tubing conducting the vapor from the bulb to the condenser. This was accomplished by wrapping the tubing with auxiliary chromel heating elements. Electrode connections were made using tungsten leads sealed in urania glass, the electrodes being threaded or silver soldered to the tungsten. The metal exposed to the sulfur rapidly formed a thin sulfide layer which rendered the connections immune to further vapor attack. The saturation of the argon with sulfur was verified by approximate dew point measurements taken on the tube leading from the bulb; by slowly reducing the power to the heating element on the tube while peering through a small inspection window in the upper furnace, sulfur was observed to condense at temperatures only 4° or 5°C cooler than the sulfur bath temperature. The flow rate of argon is important in this connection. At high flow rates, the argon does not become saturated with sulfur vapor. On the other hand, at very low flow rates thermal diffusion in the gas mixture may occur. This would account for the slight decrease in cell potential when the argon flow was stopped entirely. Preliminary experiments, however, showed that the cell voltage was insensitive to changes in argon flow rate in the range 20-100 ml/min. Accordingly for all subsequent experiments, the flow rate was adjusted to fall approximately in the middle of this range and no further attention was given to this experimental variable.

The two electrode compartments were separated by an asbestos diaphragm but contained melts of the same composition. The diaphragm was made by collapsing quartz tubing around a small prefired strand of asbestos fibers. The capillaries formed between the interstices of the fibers allowed electrolytic contact but prevented significant diffusion of dissolved sulfur to the metal electrode. This is a most important feature of the cell design if the results are to have thermodynamic significance.

The metal electrodes were fine silver rods or graphite rods dipping through the electrolyte into pools of high purity lead. The metal electrodes in each case were slowly flushed with argon during the course of an experiment. The inert electrodes for the sulfur side of the cell were ⅛-in. diameter spectroscopic grade graphite rods. Prior to use, these were heated in vacuum at 1000°C for about 24 hr to remove volatile matter. This did not result in any observable difference in the magnitude or stability of the cell potential. To test its reactivity, a small section of graphite rod was heated in a flowing sulfur-argon mixture for 48 hr at 850°C; an insignificant weight loss indicated that graphite was essentially inert to sulfur at temperatures below 850°C.

The Ag_2S was prepared by precipitation from an aqueous $AgNO_3$ solution using ammonium sulfide solution. The precipitate was thoroughly washed in distilled water then dried in vacuum at 150°C. Lead sulfide was prepared by reacting stoichiometric quantities of high purity lead with doubly distilled sulfur in sealed quartz capsules that were slowly raised to 1000°C (2). The reacted material was then melted and crystallized in a double walled evacuated quartz capsule. The reagent grade chloride salts were all vacuum oven dried but were otherwise untreated.

Considerable glass blowing was involved in preparing cells for an experiment. The entire cell was therefore carefully evacuated and maintained in this state at an elevated temperature for several hours to remove accumulated water vapor. It was only after this procedure that the electrolyte was fused and the argon admitted. In the case of the experiments with Ag_2S, the electrolyte temperature was raised initially above the melting of Ag_2S and then lowered to assure crystallinity of this component.

The temperatures of both the sulfur and sulfide melts were measured with chromel-alumel thermocouples constructed from calibrated wire. The hot junctions of the couples were in good thermal contact with the liquids by locating them in small wells blown directly into the glass cell.

Results

The emf measurements are presented in Tables I and II. Based on temperature fluctuations during the

Table I. EMF measurements of Ag_2S formation cell

X_{NaCl}	X_{KCl}	X_{AgCl}	T_B, °C	T_E, °C	E, mV	log P_{S_2}	$E°$, mV
0.457	0.457	0.085	225	700	191	−1.622	268.9
0.457	0.457	0.085	221	699	188	−1.681	268.7
0.457	0.467	0.085	223	799	160	−1.648	247.6
0.457	0.457	0.085	252	802	180	−1.251	246.6
0.457	0.457	0.085	275	797	194	−0.980	245.7
0.457	0.457	0.085	235	797	168	−1.476	246.3
0.457	0.457	0.085	218	798	155	−1.723	246.5
0.457	0.457	0.085	215	740	169	−1.770	258.1
0.457	0.457	0.085	209	779	152	−1.863	249.0
0.457	0.457	0.085	205	702	167	−1.930	260.0
0.457	0.457	0.085	207	799	145	−1.895	245.8
0.457	0.457	0.085	212	798	149	−1.815	245.5
0.0	0.700	0.300	175	697	151	−2.456	269.0
0.0	0.700	0.300	177	752	139	−2.418	261.4
0.0	0.700	0.300	176	731	143	−2.437	264.6
0.0	0.700	0.300	175	715	146	−2.456	266.4
0.0	0.700	0.300	174	680	156	−2.476	272.6
0.0	0.700	0.300	176	722	149	−2.437	269.4
0.0	0.700	0.300	179	759	140	−2.380	261.5
0.0	0.700	0.300	176	659	164	−2.439	277.0
0.0	0.700	0.300	173	658	161	−2.496	276.5
0.0	0.700	0.300	203	661	186	−1.964	277.2
0.0	0.700	0.300	241	660	214	−1.404	279.0
0.0	0.700	0.300	281	660	233	−0.938	276.2
0.0	0.700	0.300	336	660	253	−0.501	276.6
0.0	0.700	0.300	304	665	245	−0.731	278.2
0.0	0.700	0.300	264	660	227	−1.121	278.7
0.0	0.700	0.300	218	661	198	−1.729	278.2
0.0	0.700	0.300	162	659	150	−2.712	275.7
0.0	0.700	0.300	158	663	144	−2.794	274.1
0.0	0.732	0.268	203	641	190	−1.974	279.4
0.0	0.732	0.268	200	603	200	−2.019	287.2
0.0	0.732	0.268	201	656	182	−1.998	274.2
0.0	0.660	0.340	194	748	155	−2.121	262.7
0.0	0.660	0.340	177	751	140	−2.427	262.8
0.0	0.660	0.340	215	752	172	−1.770	262.4
0.0	0.660	0.340	258	747	205	−1.180	264.7
0.0	0.660	0.340	311	749	229	−0.638	261.1
0.0	0.660	0.340	281	748	216	−0.920	262.5
0.0	0.660	0.340	234	750	189	−1.492	264.9
0.0	0.660	0.340	174	716	149	−2.475	270.4
0.0	0.660	0.340	172	677	158	−2.514	275.9
0.0	0.660	0.340	171	642	165	−2.544	280.5
0.0	0.660	0.340	169	612	171	−2.575	283.7
0.0	0.660	0.340	169	618	168	−2.574	281.5
0.0	0.660	0.340	211	619	200	−1.841	281.1
0.0	0.660	0.340	245	616	223	−1.363	283.5
0.0	0.660	0.340	278	618	236	−0.996	280.2

Table II. EMF measurements of PbS formation cell

X_{NaCl}	X_{KCl}	X_{PbCl_2}	T_B, °C	T_E, °C	E, mV	log P_{S_2}	E°, mV
0.458	0.456	0.086	171	798	216	−2.532	350.5
0.458	0.456	0.086	170	765	229	−2.551	360.4
0.458	0.456	0.086	168	717	252	−2.591	378.8
0.458	0.456	0.086	166	681	273	−2.631	397.5
0.458	0.456	0.086	165	653	289	−2.652	410.3
0.458	0.456	0.086	160	586	332	−2.756	449.4
0.0	0.622	0.378	184	503	393	−2.322	482.4
0.0	0.622	0.378	211	501	415	−1.939	489.4
0.0	0.622	0.378	186	532	238	−2.271	472.7
0.0	0.622	0.378	188	553	373	−2.230	464.4
0.0	0.622	0.378	183	500	405	−2.342	494.8
0.0	0.622	0.378	181	573	363	−2.351	461.7

temperature-controlling cycle, and the accuracy of the thermocouples, the reported sulfur bath temperatures, T_B, and the electrolyte temperatures, T_E, are considered accurate to 1° and 2°C, respectively. The composition of the electrolytes reported in the tables refers to the composition before sulfide saturation. However, sulfide saturation in alkali chloride-rich melts is known to be very small (2, 7), and as a result the concentrations of the chloride components in the electrolyte when actually saturated with sulfide should not differ appreciably from the values reported in Tables I and II. It was observed that several hours were required to reach a stable cell potential (±1 mV for 2 hr) when the electrolyte temperature was altered. This was attributed to the sluggishness in saturating the chloride melt with sulfide. It will be noted that a much more extensive study was undertaken of the Ag_2S formation cell. This was done to check the sulfur pressure dependence of the cell emf. In the light of the measurements on the Ag_2S formation cell, it was considered unnecessary to perform a similar study on the lead sulfide formation cell. In the case of measurements on the Ag_2S cell, a thermoelectric voltage was created by the dissimilar electrode materials. The leads from the potentiometer to the tungsten connectors were both of silver; as a result, the temperature of the cold junction for the +Ag/C− thermocouple effect was nearly that of the liquid sulfur. The true electrochemical voltage, reported in Table I, was computed by adding the thermoelectric voltage to the measured voltage, taking the cold junction temperature to be T_B. The output of the +Ag/C− thermocouple was measured as a function of temperature in an argon atmosphere. The results fitted by the method of least squares gave the equation

$$V = 4.36 - 8.80 \times 10^{-2}T + 1.29 \times 10^{-2}T \ln T \quad [1]$$

where V is the output in mV relative to 25°C and T is the hot junction temperature in °K.

Discussion

Sulfur vapor equilibria.—If sulfur were a simple vapor that could exist only in one molecular form, the sulfur pressure at the electrode would be equal to the vapor pressure of sulfur in equilibrium with the liquid in the bulb. It is known however that sulfur in the vapor phase is a complex mixture of various molecular species ranging essentially from S_2 to S_8, the concentration of each being temperature and pressure dependent. For this reason the relative concentration of the various molecules will be different at the electrode than in the bulb and, if diffusionless flow of sulfur saturated argon is assumed, then the total sulfur pressure will be increased as the gaseous solution is increased in temperature. If the vapor passes through the temperature gradient from the sulfur bulb to the electrode while at all times preserving local equilibrium, it is possible to calculate the composition of the sulfur vapor at the electrode when both bulb and electrode temperatures are known.

The assumption of local equilibrium is reasonable; the number of sulfur collisions per unit time is large in the pressure range of this investigation, and the time constants for dissociation and association processes of sulfur molecules are small (8). Therefore, before a sulfur molecule can move an appreciable distance within the temperature gradient, it will enter the equilibrium required by the temperature and total sulfur pressure in the new position. Furthermore, the partial pressure decrease in argon, as sulfur dissociates, is relatively small. There is thus very little tendency for argon diffusion. The small relative change in the argon pressure is a consequence of the fact that sulfur generally represents only a small fraction of the total volume of the gas phase.

For calculation purposes let a volume element V_B at temperature T_B, the temperature of liquid sulfur in the bulb, contain argon at pressure $(P_A)_B$ and sulfur at pressure $(P_{S\bar{v}-})_B$ where

$$(P_{S\bar{v}-})_B = \sum_{v=2}^{8} (P_{S_v})_B \quad [2]$$

Since the total gas pressure is fixed experimentally at 1 atm by the exit bubbler, the argon pressure in the bulb is

$$(P_A)_B = 1 - \sum_{v=2}^{8} (P_{S_v})_B \quad [3]$$

In passing from the sulfur bulb to the electrode compartment, the volume element V_B gradually expands to V_E as the sulfur vapor dissociates into lighter molecules and the molecules acquire more kinetic energy at the higher temperature. The total sulfur pressure within this element is now

$$(P_{S\bar{v}-})_E = \sum_{v=2}^{8} (P_{S_v})_E \quad [4]$$

However the total gas pressure remains at 1 atm. The argon pressure in element V_E is thus

$$(P_A)_E = 1 - \sum_{v=2}^{8} (P_{S_v})_E \quad [5]$$

Since diffusionless flow is being assumed, no net mass can leave the volume element and so the ratio of argon atoms to sulfur atoms in volume elements V_E and V_B are the same. Therefore

$$\frac{\left[1 - \sum_{v=2}^{8} (P_{S_v})_E\right](V_E/RT_E)}{\left[\sum_{v=2}^{8} (vP_{S_v})_E\right](V_E/RT_E)} = \frac{\left[1 - \sum_{v=2}^{8} (P_{S_v})_B\right](V_B/RT_B)}{\left[\sum_{v=2}^{8} (vP_{S_v})_B\right](V_B/RT_B)} \quad [6]$$

or

$$\frac{1 - \sum_{v=2}^{8} (P_{S_v})_E}{\sum_{v=2}^{8} (vP_{S_v})_E} = \frac{1 - \sum_{v=2}^{8} (P_{S_v})_B}{\sum_{v=2}^{8} (vP_{S_v})_B} \quad [7]$$

Comprehensive thermodynamic data on the equilibrium composition of sulfur vapor has been calculated from mass spectrometric studies (9, 10) assuming the vapor species to be ideal. These investigations showed that only the species S_2 to S_8 were significant contributors to the total sulfur pressure; S, S_9, and S_{10}, though observed, existed only in exceedingly small

quantities. For equilibria of the type

$$S_2 \leftrightharpoons 2/v\ S_v \qquad [8]$$

the equilibrium constants have the form

$$K_v = \frac{P_{S_v}{}^{2/v}}{P_{S_2}} \qquad [9]$$

In these equations v is an integer varying from 3 to 8. The relative populations of vapor molecules at various temperatures and total sulfur pressures, obtained from the existing mass spectrometric data, allow log K_v to be expressed as a linear function of reciprocal temperature. The work of Detry *et al.* (10) gives the following equations

$$\log P_{S_3} = 1.50 \log P_{S_2} + \frac{2.91 \times 10^3}{T} - 4.11 \qquad [10]$$

$$\log P_{S_4} = 2.00 \log P_{S_2} + \frac{6.16 \times 10^3}{T} - 8.00 \qquad [11]$$

$$\log P_{S_8} = 4.00 \log P_{S_2} + \frac{21.2 \times 10^3}{T} - 24.1 \qquad [12]$$

$$\log P_{S_5} = 0.625 \log P_{S_8} - \frac{2.79 \times 10^3}{T} + 2.88 \qquad [13]$$

$$\log P_{S_6} = 0.750 \log P_{S_8} - \frac{1.37 \times 10^3}{T} + 1.66 \qquad [14]$$

$$\log P_{S_7} = 0.875 \log P_{S_8} - \frac{1.26 \times 10^3}{T} + 1.57 \qquad [15]$$

These equations constitute six independent relationships involving partial sulfur pressures. For vapor in equilibrium with liquid sulfur at temperature T_B. The evaluation of the partial pressures in Eq. [10] to [15] is possible because the total vapor pressure [11] provides a seventh independent equation

$$\log \sum_{v=2}^{8} (P_{S_v}) = -\frac{4830}{T_B} - 5.0 \log T_B + 21.00 \qquad [16]$$

The partial pressures of sulfur species over liquid sulfur at temperature T_B determine a value for the right hand side of Eq. [7] and hence a value for

$$\frac{1 - \sum_{v=2}^{8} (P_{S_v})_E}{\sum_{v=2}^{8} (vP_{S_v})_E}$$

This relationship among partial pressures at the electrode is independent of Eq. [10] to [15] that can be written for temperature T_E. It is therefore possible to calculate all the partial pressures over the sulfide melt at the sulfur electrode at temperature T_E for a given liquid sulfur temperature T_B.

The actual solutions to the simultaneous equations for measured experimental conditions of T_B and T_E were accomplished by an iteration method using a digital computer. The forms of the various equations that lead to solution of these simultaneous equations are shown graphically in a previous paper (5). The calculated logarithms of the S_2 partial pressure over the sulfide electrolyte are listed in Tables I and II. The S_2 pressures are estimated to be accurate to about ±5%.

Electrochemistry of sulfur vapor electrode.—In the Ag_2S formation cell, the expected primary cell process is

$$2Ag + 1/vS_v \rightarrow Ag_2S \qquad [17]$$

In this reaction pure silver is solid, S_v is gas (the mean value of v being a function of temperature and total sulfur pressure), and Ag_2S is in a state of unit activity with respect to pure solid. When reaction [17] is the primary cell process two conditions must be observed experimentally: the cell emf must be independent of the electrolyte composition so long as Ag_2S is saturating it, and the cell voltage must vary in the Nernst manner with respect to partial sulfur pressure.

The Nernst expression for the proposed cell reaction is

$$E = E_{S_v}{}^\circ + \frac{RT}{2v\mathbf{F}} \ln P_{S_v} - \frac{RT}{2\mathbf{F}} \ln a_{Ag_2S} \qquad [18]$$

where v may assume any integral value from 2 to 8. The choice of this value affects both the numerical value of the partial sulfur pressure and $E_{S_v}{}^\circ$ in such a way that E is independent of the choice. This is consistent with the assumption of local equilibrium made in the previous section. Since S_2 is the predominant molecule in sulfur vapor at temperatures above 500°C, v will be taken to be 2 in all subsequent calculations making S_2 gas at 1 atm pressure the standard state for sulfur. In accord with Eq. [18], plots of E against log P_{S_2} must be linear with a slope of $4.575T/2n\mathbf{F}$ where n is the number of Faradays of charge associated with the formation of a mole of Ag_2S. These plots are shown in Fig. 3 at four temperatures. The slopes were determined by the least squares method and values of n were calculated; these are shown on each line, the mean value, $\bar{n}$, being 2.01. This is in good agreement with the required value of 2 considering the complexity of the sulfur vapor equilibria.

It should be noted that the same value for n is observed with electrolytes of different composition. This suggests that the process responsible for the cell voltage depends only on the activity of Ag_2S, this being fixed at unity with respect to pure solid, and in no way on the concentrations of the other components of the electrolyte.

The cell potentials for both the Ag_2S and PbS formation cells given with respect to a standard S_2 electrode are listed in Tables I and II. The corrections from the experimental conditions of measurements involved the addition of

$$-\frac{4.575T}{4\mathbf{F}} \log P_{S_2}$$

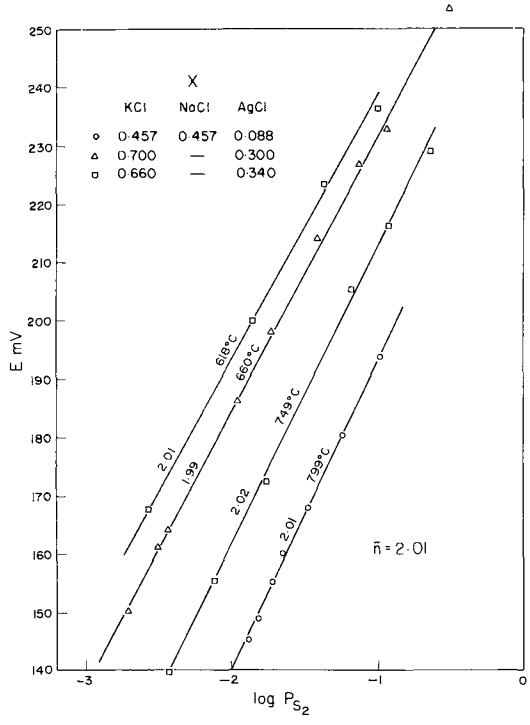

Fig. 3. Variation of emf with respect to calculated partial S_2 pressure for solutions saturated with Ag_2S.

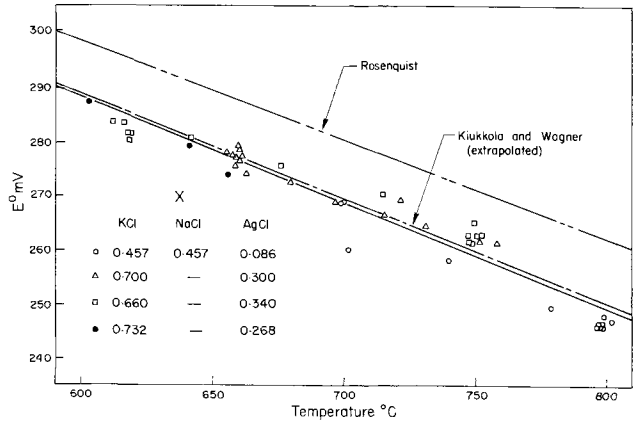

Fig. 4. Variation of standard potential of Ag_2S formation cell with respect to temperature. All solutions are saturated with Ag_2S.

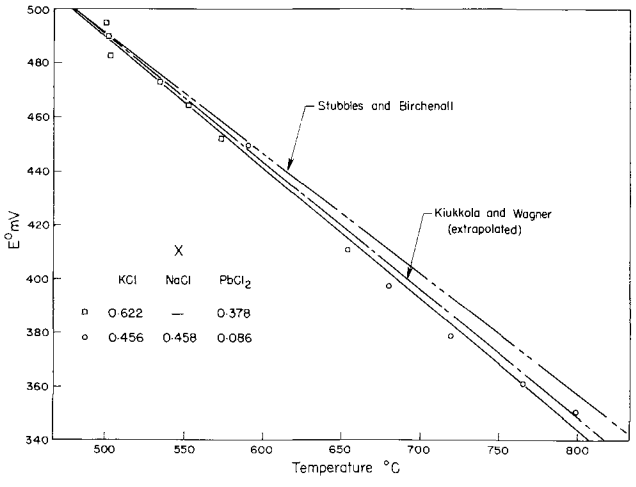

Fig. 5. Variation of standard potential of PbS formation cell with respect to temperature. All solutions are saturated with PbS.

to the measured cell voltages. The corrected voltages are plotted in Fig. 4. Within a few millivolts, it is apparent that the measurements are independent of the composition of the sulfide saturated electrolytes.

It should be noted that all electrolytes contain the chloride salt of the corresponding base metal sulfide. This was found to be essential if cell voltages were to correspond to the free energy of formation of the sulfide and to satisfy the requirements of the Nernst equation. Apparently the solubility of base metal sulfide in alkali chloride is insufficient to yield enough base metal ions to establish a reversible potential at the metal electrode. In addition, the concentration of base metal ion may be limited by incomplete dissociation of the dissolved base metal sulfide in pure alkali chloride.

Thermodynamic calculations.—The least squares equation for the line through the data for the Ag_2S formation reaction shown in Fig. 4 is

$$E^\circ = 455.3 - 0.1919T \quad [19]$$

or equivalently

$$\Delta G^\circ = -21{,}000 + 8.85T \quad [20]$$

where E° is the potential in millivolts relative to a standard S_2 electrode, ΔG° is the standard free energy of formation in cal/mole Ag_2S, and T is temperature in °K. The standard deviation is 3.2 mV or 152 cal/mole. The results of Rosenqvist (12), determined using H_2-H_2S mixtures, are shown for comparison in Fig. 4. His results are given with an error limit corresponding to 10 mV. There is better agreement between the present work and the extrapolated results of Kiukkola and Wagner (13). Their measurements were made at lower temperatures using a solid AgI electrolyte and a liquid sulfur electrode and are reported to be accurate to 1 mV in the temperature range 150°-425°C. The extrapolation involves changing the standard state of sulfur to S_2 gas at 1 atm pressure. This procedure is outlined in the Appendix.

The standard electrode potentials for the PbS formation reaction are shown in Fig. 5. The least squares equation representing the line through the points is

$$E^\circ = 867.4 - 0.4884T \quad [21]$$

or equivalently

$$\Delta G^\circ = -40{,}000 + 22.5T \quad [22]$$

where E° is the potential in millivolts relative to a standard S_2 electrode, and ΔG° is the standard free energy of formation in cal/mole PbS. The standard deviation is 4.5 mV or 207 cal/mole.

The experimental procedure of having a lead sulfide saturated melt in contact with molten lead results in the dissolution of a maximum of 4 m/o (mole per cent) sulfur in the lead (14). The lead electrode therefore is not at unit activity. Assuming ideal solution behavior of sulfur in lead the activity of lead is about 0.96 at 800°C. This effect reduces the cell voltage by about 1.9 mV from the value it would have at 800°C if the lead were pure. This difference is within the uncertainty of the experimental measurements; as a result no corrections for sulfur dissolution in the lead were applied to the measurements.

Stubbles and Birchenall (15) carefully studied the H_2-H_2S equilibrium over lead-lead sulfide mixtures. The line shown in Fig. 5 was calculated from their measurements; the suggested error in their free energy is equivalent to 10 mV. The results of the present study are just below their suggested lower limit of accuracy. The comparison with the extrapolated measurements of Kiukkola and Wagner (13) is better. However, since the accuracy of their measurements was only 4 mV, the extrapolation is less certain than in the case for Ag_2S.

Recently in this laboratory, the enthalpy contents of PbS and Ag_2S were measured using a sapphire calibrated drop calorimeter (16). These make possible comparisons of the present high-temperature electrochemical measurements with data available at 298°K using the Σ function.

When the difference in the molar heat capacity of the reactants and products of a chemical process can be expressed in the form

$$\Delta C_p = \Delta a + \Delta bT + \Delta cT^{-2} \quad [23]$$

the Σ function is

$$\Sigma = \frac{\Delta G^\circ}{T} - \Delta a + \Delta a \ln T + \frac{\Delta b}{2} T + \frac{\Delta c}{2} T^{-2} \quad [24]$$

When written in this form Σ is a simple linear function of temperature given by

$$\Sigma = \frac{\Delta H^\circ_0}{T} - \Delta S^\circ_0 \quad [25]$$

where ΔH°_0 and ΔS°_0 are integration constants.

Figure 6 shows the Σ plot for the Ag_2S and PbS formation reactions. The values for Σ were calculated using the electrochemically determined free energies of formation, the thermal data for the sulfides listed in Table III, and the heat capacities for the elements tabulated by Kelley (17). It is apparent that Σ is a linear function of temperature for both reactions as required by Eq. [25].

In the case of the formation reaction to produce γ-Ag_2S, the integration constants determined by a least squares analysis are

$$\Delta H^\circ_0 = -24.03 \text{ kcal/mole} \quad [26]$$

$$\Delta S^\circ_0 = -40.68 \text{ cal/°K mole} \quad [27]$$

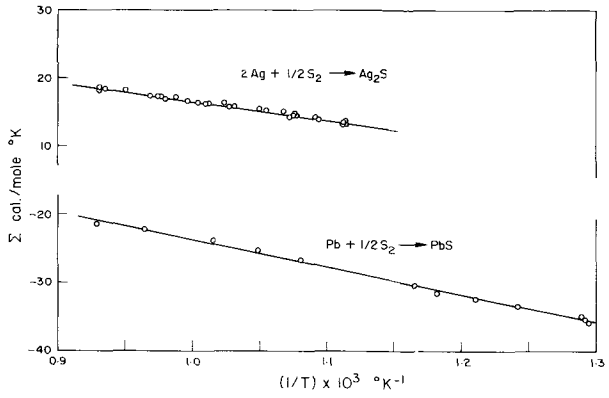

Fig. 6. Sigma plot for silver and lead sulfide formation reactions

Performing the integrations, care was taken to account for the two solid state transformations of Ag_2S

$$\Delta H°_{298} = -23.52 \text{ kcal/mole} \quad [28]$$

$$\Delta S°_{298} = -13.81 \text{ cal/°K mole} \quad [29]$$

$$\Delta G°_{298} = -19.40 \text{ kcal/mole} \quad [30]$$

These properties apply to the formation of α-Ag_2S from pure silver and S_2 gas at 1 atm pressure. At 298°K, however, sulfur is a solid; accordingly, rhombic crystal is used as the standard state for purposes of expressing enthalpies and entropies of sulfide formation reactions. The enthalpy and entropy for the formation of 1 mole of S_2 gas at 1 atm pressure from rhombic crystal at 298°K is calculated in the Appendix. Using these values, the thermal properties for the formation of α-Ag_2S from rhombic sulfur and silver are

$$\Delta H°_{298} = -8.57 \text{ kcal/mole} \quad [31]$$

$$\Delta S°_{298} = +4.73 \text{ cal/°K mole} \quad [32]$$

$$\Delta G°_{298} = -9.98 \text{ kcal/mole} \quad [33]$$

These data compare with N.B.S. values (18) of

$$\Delta H°_{298} = -7.79 \text{ kcal/mole} \quad [34]$$

$$\Delta S°_{298} = 6.48 \text{ cal/°K mole} \quad [35]$$

$$\Delta G°_{298} = -9.72 \text{ kcal/mole} \quad [36]$$

In the case of the reaction to form PbS, the integration constants determined from the Σ plot are

$$\Delta H°_0 = -40.17 \text{ kcal/mole} \quad [37]$$

$$\Delta S°_0 = -16.43 \text{ cal/mole °K} \quad [38]$$

Integrating and taking account of the freezing of lead at 327°C, the thermal properties associated with the formation of solid PbS from solid lead and S_2 gas at 1 atm at 298°K are

$$\Delta H°_{298} = -39.67 \text{ kcal/mole} \quad [39]$$

$$\Delta S°_{298} = -20.08 \text{ cal/mole °K} \quad [40]$$

$$\Delta G°_{298} = -33.68 \text{ kcal/mole} \quad [41]$$

With respect to formation from rhombic sulfur these become

Table III. Thermal data for Ag_2S and PbS

	$C_p = a + bT$ cal/mole °K		
	a	$b \times 10^3$	Temp. range, °K
αAg_2S	14.80	12.1	298-449
βAg_2S	19.44	0.702	449-859
γAg_2S	19.77	—	859-1103
PbS	10.78	2.72	298-1281

$(\Delta H_t)^{440}_{Ag_2S} = 940$ cal/mole
$(\Delta H_t)^{859}_{Ag_2S} = 120$ cal/mole

$$\Delta H°_{298} = -24.72 \text{ kcal/mole} \quad [42]$$

$$\Delta S°_{298} = -1.54 \text{ cal/mole °K} \quad [43]$$

$$\Delta G°_{298} = -24.26 \text{ kcal/mole} \quad [44]$$

These quantities compare with N.B.S. values (19) of

$$\Delta H°_{298} = -24.0 \text{ kcal/mole} \quad [45]$$

$$\Delta S°_{298} = -1.3 \text{ cal/°K mole} \quad [46]$$

$$\Delta G°_{298} = -23.6 \text{ kcal/mole} \quad [47]$$

Only fair agreement exists between the high-temperature measurements reported in this investigation and values reported at 298°K. It must be recognized, however that a large quantity of thermodynamic data was required in order to effect this comparison. The possible errors in the enthalpy and entropy of formation of S_2 gas from rhombic crystal alone, could readily account for most of the discrepancy in the previous comparisons.

Conclusion

A sulfur vapor electrode has been used in sulfide-saturated multicomponent chloride electrolytes to measure the standard Gibbs free energy of formation of silver sulfide and lead sulfide.

In the temperature range 876°-1075°K, for the reaction

$$2Ag_{(solid)} + \tfrac{1}{2}S_{2(gas,\ 1\ atm)} \rightarrow Ag_2S_{(solid)}$$

$$\Delta G° = -21{,}000 + 8.85T$$

The standard deviation of the experimental points from this line is 152 cal/mole.

In the temperature range 773°-1071°K, for the reaction

$$Pb_{(liquid)} + \tfrac{1}{2}S_{2(gas,\ 1\ atm)} \rightarrow PbS_{(solid)}$$

$$\Delta G° = -40{,}000 + 22.5T$$

The standard deviation of the experimental points from this line is 207 cal/mole.

APPENDIX

The free energy of formation of S_2 gas from liquid sulfur, ΔG, may be represented by

$$2S_{(liquid)} \rightarrow S_{2(gas,\ 1\ atm)} \quad [A\text{-}1]$$

At the same temperature, the free energy for the process

$$S_{2(gas,\ P_{eq})} \rightarrow 2S_{(liquid)} \quad [A\text{-}2]$$

is zero, P_{eq} being the partial pressure of S_2 in equilibrium with pure liquid sulfur. The free energy for the process represented by Eq. [A-1] is thus equal to that for the reaction

$$S_{2(gas,\ P_{eq})} \rightarrow S_{2(gas,\ 1\ atm)} \quad [A\text{-}3]$$

that is

$$\Delta G = \int_{P_{eq}}^{1} V\,dP \quad [A\text{-}4]$$

Assuming the S_2 to be ideal

$$\Delta G = RT \ln (P_{S_2})_{eq} \quad [A\text{-}5]$$

The partial pressure of S_2 gas in equilibrium with liquid sulfur may be evaluated at temperatures from 119° to 444°C by solving Eq. [10] to [15] with Eq. [16]. In this way, the free energy of formation of S_2 from liquid sulfur can be calculated at any temperature. This calculation was employed to convert the data of Kiukkola and Wagner (13) to correspond to sulfide formation from S_2 gas.

At 400°K

$$\Delta G^{400} = 15{,}132 \text{ cal/mole } S_2 \quad [A\text{-}6]$$

By calculating the free energy at other temperatures near 400°K. it was possible to evaluate the temperature dependence of this free energy at 400°K. The enthalpy and entropy for process [A-1] were then evaluated at this temperature as follows

$$\Delta H^{400} = \frac{d(\Delta G_1/T)}{d(1/T)} = 28{,}640 \text{ cal/mole } S_2 \quad [A\text{-}7]$$

$$\Delta S^{400} = -\frac{d(\Delta G_1)}{dT} = 33.77 \text{ cal/°K mole } S_2 \quad [A\text{-}8]$$

Using the data of Kelley (17), the enthalpy of formation of S_2 at 298°K from rhombic crystal is

$$\Delta H^{298} = 2\,(H^{400}_{S,\text{liquid}} - H^{298}_{S,\text{rhombic}}) + (\Delta H)^{400} - (H^{400}_{S_2,\text{gas}} - H^{298}_{S_2,\text{gas}}) = 29{,}900 \text{ cal/mole } S_2 \quad [A\text{-}9]$$

Similarly, the entropy of formation is 37.1 cal/°K mole S_2 at 298°K.

Acknowledgment

The authors wish to thank the National Research Council of Canada for financial assistance in the form of equipment grants and a maintenance fellowship for W.T.T.

Manuscript submitted March 30, 1970; revised manuscript received Sept. 22, 1970.

Any discussion of this paper will appear in a Discussion Section to be published in the December 1971 JOURNAL.

REFERENCES

1. G. G. Charette and S. N. Flengas, *This Journal*, **115**, 796 (1968).
2. A. D. Pelton, M.A.Sc. Thesis, University of Toronto, 1968.
3. M. C. Bell and S. N. Flengas, *This Journal*, **113**, 31 (1966).
4. M. C. Bell and S. N. Flengas, *ibid.*, **111**, 576 (1964).
5. W. T. Thompson and S. N. Flengas, *Can. J. Chem.*, **46**, 1611 (1968).
6. W. A. West and A. W. C. Menzies, *J. Phys. Chem.*, **33**, 1880 (1929).
7. M. C. Bell, Ph.D. Thesis, University of Toronto, 1964.
8. S. Peter, *Z. Elektrochem.*, **57**, 289 (1953).
9. J. Berkowitz and J. R. Marquart, *J. Chem. Phys.*, **39**, 275 (1963).
10. D. Detry, J. Drowart, P. Goldfinger, H. Keller, and H. Rickert, *Z. Phys. Chem.*, **55**, 314 (1967).
11. O. Kubaschewski and E. Evans, "Metallurgical Thermochemistry," Pergamon, London (1955).
12. T. Rosenqvist, *J. Metals*, **185**, 451 (1949).
13. K. Kiukkola and C. Wagner, *This Journal*, **104**, 308 (1957).
14. C. J. Smithell, "Metals Reference Book II," Butterworths, London (1957).
15. J. R. Stubbles and C. E. Birchenall, *Trans. AIME*, **215**, 535 (1959).
16. W. T. Thompson and S. N. Flengas, To be published.
17. K. K. Kelley, *Bull. U.S. Bur. Mines No. 584* (1960).
18. National Bureau of Standards, Technical Note 270-3, 1968.
19. National Bureau of Standards, Technical Note 270-4, 1969.

Electrical Conductivities of Molten $AlBr_3$-NaBr Mixtures

C. R. Boston[1]

Atomics International Division of North American Rockwell Corporation, Canoga Park, California 91304

ABSTRACT

The electrical conductivities of $AlBr_3$-NaBr mixtures have been measured from 25 to 98 m/o (mole per cent) $AlBr_3$ at temperatures ranging from 140° to 1000°C. A minimum in the equivalent conductance *vs.* composition diagram was observed near 33 m/o $AlBr_3$ and a maximum near 50 m/o $AlBr_3$. With increasing temperature, conductivities increased linearly at low temperatures and gradually went through a maximum at high temperatures. The maximum was actually reached for only one composition; namely, that corresponding to the compound $NaAlBr_4$ at a temperature of 800°-900°C. Arrhenius coefficients were lower than those observed for the $AlCl_3$-KCl mixtures but showed a similar pattern of behavior with composition.

Conductivity measurements previously reported (1) for the $AlCl_3$-KCl system gave rather interesting results, the most outstanding being the effect of composition. With increasing $AlCl_3$ at constant temperature the equivalent conductance first went through a pronounced minimum near 33 m/o (mole per cent) $AlCl_3$ followed by an equally pronounced maximum at 50 m/o $AlCl_3$.

The choice of $AlBr_3$-NaBr for this study was based primarily on the availability of a reasonably detailed phase diagram (2) since the conductivity behavior for the $AlCl_3$-KCl system appeared to be related in a qualitative way to phase equilibria occurring in the system. The $AlBr_3$-NaBr system had the additional advantage of normal consolute behavior in the two-liquid region. This permitted conductivity measurements in the 80 to 100 m/o AlX_3 region which was not possible for the $AlCl_3$-KCl system.

Experimental

$AlBr_3$ was prepared by two methods. The first method was essentially the same as that described (3) for $AlCl_3$ except that high-purity HBr instead of HCl was reacted with aluminum metal. The HBr was prepared by bubbling H_2 through Br_2 and passing the mixture over a platinum catalyst.

The second method was a purification of commercial $AlBr_3$ (anhydrous, technical grade, Matheson, Coleman and Bell). This was done by digesting the $AlBr_3$ at 230°-250°C with aluminum metal followed by two distillations. The apparatus consisted of a three-chamber Pyrex tube. The chambers were about 13 cm long x 4.1 cm in diameter and separated from each other by sintered glass disks. The first chamber was also separated from the remaining chambers by a break-off tip. Before loading, the entire apparatus was baked out under a vacuum of 10^{-5} mm Hg to remove surface moisture. The second and third chambers were then evacuated and sealed off and the first chamber was loaded with $AlBr_3$ and aluminum metal (99.9999%, Cominco Products, Inc.). This end of the apparatus was then evacuated and sealed off. The entire apparatus was held in a rocking furnace at 230°-250°C for several days. At first the crude $AlBr_3$ had a deep red color, but as digestion proceeded it became colorless and a black precipitate formed. The latter was presumably carbon resulting from the decomposition

[1] Present address: Metals and Ceramics Division, Oak Ridge National Laboratory, Oak Ridge, Tennessee 37830, which is operated by Union Carbide Corporation for the U.S. Atomic Energy Commission.

Key words: conductivity, molten, electrical, aluminum bromide, sodium bromide.

of organic impurities. Distillation was started by breaking the break-off tip and allowing the material to distill into the second chamber. The first chamber was then sealed off and the final product distilled from the second into the third chamber. $AlBr_3$ samples prepared by these two methods gave identical conductivity results.

Anhydrous NaBr was prepared from reagent grade material by a method similar to that used by Boston and Smith (4) for the purification of LiCl-KCl eutectic. The $AlBr_3$-NaBr mixtures were weighed into the conductivity cells in a dry box purged with high-purity argon.

The apparatus and methods for measuring electrical conductivities of volatile molten salts have been described by Grantham and co-workers (5-7). As in the case of $AlCl_3$-KCl mixtures, the tungsten electrodes were found to be inert to corrosive attack by $AlBr_3$-NaBr mixtures at temperatures as high as 1000°C. To prevent cell rupture, external pressures were applied to the conductivity cell for the more volatile mixtures, 80, 92, and 98 m/o $AlBr_3$.

Results

The specific conductivities (κ) against temperature are shown in Table I and Fig. 1 and against composition at 600° and 800°C in Fig. 2. Although measurements were made up to 1000°C, only the 600° and 800° isotherms are shown since they are representative and show quite adequately the trend with temperature. Equivalent conductivities were calculated at 600°C using the density data of Boston and Ewing (8) and are shown plotted against composition in Fig. 3. Again, the effect of temperature was quite similar to that shown for specific conductivities in Fig. 2 so a single isotherm was considered adequate. The 600°C isotherm should be the most reliable since it required the minimum amount of extrapolation of density and specific conductivity data.

The points in Fig. 2 and 3 which are represented by open circles or squares were obtained by extrapolation of the linear portions of the conductivity *vs.* temperature curves and the solid points by direct measurement. At 0 and 25 m/o $AlBr_3$ the open circles represent extrapolations to temperatures below the liquidus. Such low-temperature extrapolations should be reliable since the curves are linear in this region. At higher $AlBr_3$ compositions open points represent extrapolations to temperatures above those where the

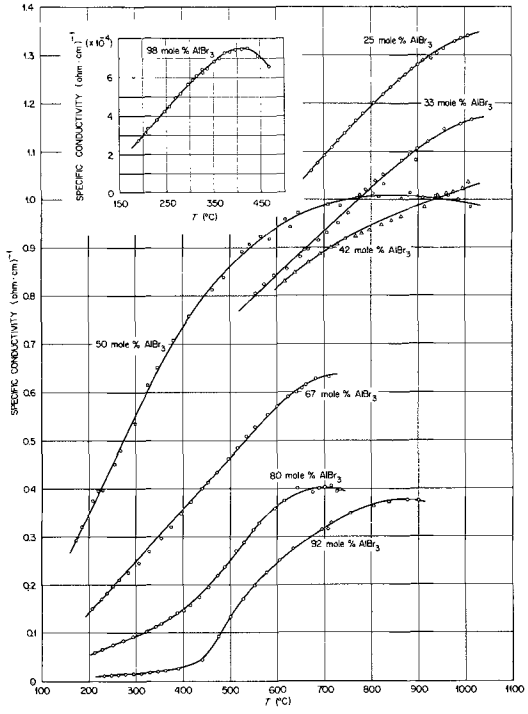

Fig. 1. Specific conductivity *vs.* temperature for the $AlBr_3$-NaBr system.

conductivity *vs.* temperature curves are linear. At 42 and 50 m/o $AlBr_3$ both measured and extrapolated points are shown. The extrapolated points produce more pronounced maxima as shown by the dotted curves but otherwise do not change the general shapes of the curves.

The unusual shapes of the 80 and 92 m/o $AlBr_3$ curves were presumably due to changes in composition of the liquid as significant amounts of $AlBr_3$ moved into the gas phase. The conductivity of the NaBr enriched liquid phase thus increased more rapidly than would be expected for temperature increase alone. To test this possibility the 92 m/o $AlBr_3$ composition was repeated using a larger melt volume which reduced the vapor volume by about one half. This produced about a 50° increase in the temperature at which the conductivity curve began its sharp increase which

Table I. Specific conductivities of molten $AlBr_3$-NaBr mixtures[a]

25% $AlBr_3$		33% $AlBr_3$		42% $AlBr_3$		50% $AlBr_3$		67% $AlBr_3$		80% $AlBr_3$		92% $AlBr_3$		98% $AlBr_3$	
t, °C	κ, ohm-cm^{-1}	t, °C	κ, ohm-cm^{-1}	t, °C	κ, ohm-cm^{-1}	t, °C	κ, ohm-cm^{-1}	t, °C	κ, ohm-cm^{-1}	t, °C	κ, ohm-cm^{-1}	t, °C	κ, ohm-cm^{-1}	t, °C	κ, ohm-cm^{-1}
674	1.060	555	0.805	617	0.829	172	0.294	206	0.151	212	0.0593	233	0.0107	191	2.74
687	1.076	573	0.824	629	0.843	184	0.321	226	0.171	228	0.0659	248	0.0118	205	3.14
702	1.092	594	0.842	639	0.847	208	0.376	237	0.183	251	0.0750	262	0.0127	211	3.36
717	1.109	622	0.855	668	0.869	218	0.396	250	0.198	273	0.0833	278	0.0140	229	3.82
730	1.123	650	0.881	692	0.886	229	0.398	264	0.211	293	0.0921	295	0.0152	246	4.26
744	1.138	659	0.894	715	0.900	254	0.451	284	0.226	322	0.104	311	0.0166	257	4.48
756	1.151	667	0.896	728	0.906	268	0.480	306	0.246	341	0.113	329	0.0182	269	4.94
768	1.164	688	0.915	745	0.918	298	0.536	328	0.270	353	0.119	346	0.0199	281	5.16
783	1.179	706	0.931	767	0.923	324	0.616	353	0.297	372	0.132	362	0.0219	296	5.67
806	1.201	730	0.951	780	0.929	345	0.652	374	0.320	387	0.142	390	0.0261	306	5.88
826	1.219	751	0.972	797	0.936	379	0.708	396	0.348	401	0.147	440	0.0441	314	6.09
842	1.233	776	1.009	822	0.946	414	0.758	417	0.373	415	0.158	475	0.0935	327	6.41
861	1.248	789	1.020	843	0.955	463	0.813	440	0.401	434	0.175	500	0.134	328	6.25
873	1.259	803	1.013	864	0.963	487	0.839	453	0.413	454	0.195	527	0.171	337	6.46
887	1.270	810	1.039	892	0.992	525	0.892	471	0.434	474	0.219	552	0.199	352	6.82
900	1.280	827	1.052	914	0.983	542	0.907	495	0.462	489	0.237	578	0.226	363	6.99
911	1.288	828	1.032	942	1.007	565	0.924	516	0.486	512	0.270	605	0.251	375	7.26
928	1.293	866	1.081	960	1.012	584	0.918	535	0.509	529	0.288	634	0.275	387	7.32
942	1.303	883	1.094	975	1.015	617	0.958	553	0.528	549	0.314	695	0.315	398	7.43
956	1.313	896	1.082	996	1.022	628	0.942	581	0.555	561	0.328	708	0.316	411	7.47
980	1.328	899	1.106	1008	1.035	644	0.972	600	0.572	594	0.359	715	0.329	424	7.51
993	1.337	922	1.120			708	0.989	624	0.591	614	0.375	755	0.348	435	6.94
1009	1.340	956	1.147			734	0.987	641	0.601	641	0.400	804	0.363	445	7.09
		991	1.157			770	1.003	653	0.609	675	0.392	838	0.372		
		1015	1.166			816	1.005	661	0.616	689	0.400	878	0.377		
						864	1.002	683	0.628	701	0.403	901	0.375		
						883	1.013	710	0.632	714	0.405				
						910	1.003			727	0.395				
						937	1.007			733	0.398				
						964	1.007								
						986	0.999								
						1011	0.984								

[a] All compositions in mole percent.

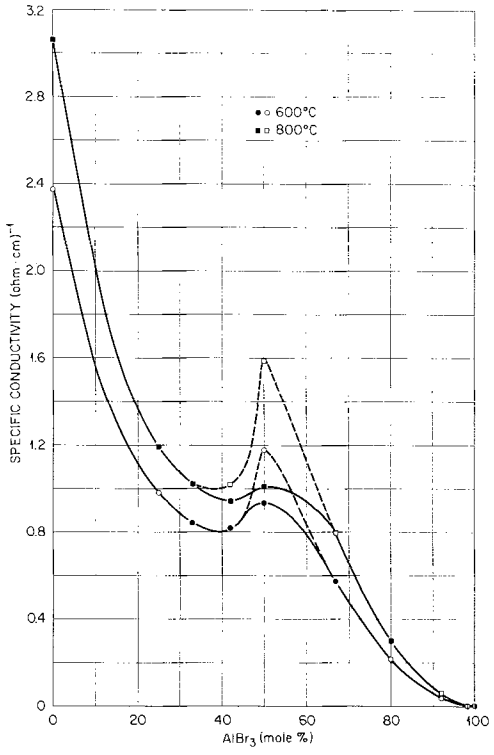

Fig. 2. Specific conductivity *vs.* composition for the $AlBr_3$-NaBr system.

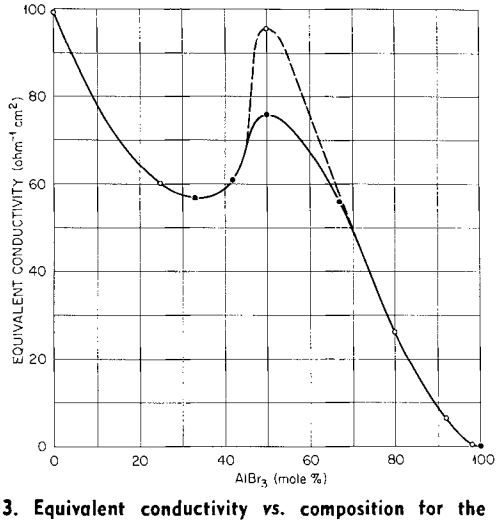

Fig. 3. Equivalent conductivity *vs.* composition for the $AlBr_3$-NaBr system.

supports the presumption that the increase is due to loss of $AlBr_3$ from the liquid phase. The low-temperature, linear portions of these curves were extrapolated to obtain the values shown in Fig. 2 and 3.

Arrhenius coefficients for electrical conductivity were calculated from the slopes of log κ *vs.* $1/T$ (°K) plots and are shown plotted against composition in Fig. 4. The coefficients usually decreased with increasing temperature. The term "Arrhenius coefficient" as used here corresponds to the activation energy for conductance. However, the latter term implies temperature independence which is definitely not the case here so Arrhenius coefficient is used instead. The values shown in Fig. 4 were obtained from the low-temperature region of the log κ *vs.* $1/T$ curves where linearity was usually observed. Arrhenius coefficients for the $AlCl_3$-KCl system are also shown in Fig. 4 for comparison.

Discussion

The effect of temperature on conductivity for the $AlBr_3$-NaBr system is shown in Fig. 1. As in the case

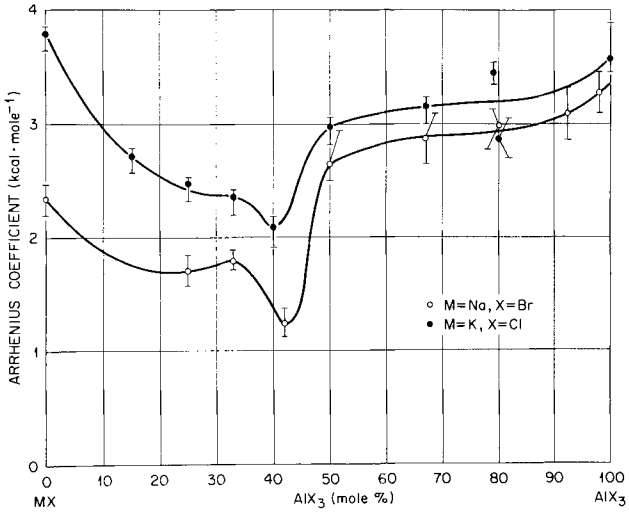

Fig. 4. Arrhenius coefficient *vs.* composition for the $AlBr_3$-NaBr system.

of pure compounds, the conductivity increases linearly at low temperatures and eventually goes through a maximum as the temperature increases. The temperature of maximum conductivity, T_{max}, was reached only for the 50 m/o mixture corresponding to the compound $NaAlBr_4$. The observed value of T_{max} at this composition was about 850°C. The maxima observed for 80 and 92 m/o $AlBr_3$ are due to the compositional changes mentioned earlier. Grantham and Yosim (6) have shown that a rough correlation exists between the heat of vaporization and T_{max}.

The compositional effects on conductivity are shown in Fig. 2 and 3. Minima in specific and equivalent conductivities occurred near 40 and 33 m/o $AlBr_3$, respectively. A pronounced maximum in both specific and equivalent conductivities occurred at 50 m/o $AlBr_3$. This behavior pattern is quite similar to that observed for $AlCl_3$-KCl mixtures (1). The conductivities are generally somewhat higher for the bromide system.

As pointed out in the chloride study (1), the 1:1 compound is so stable that it may be more reasonable to consider the NaBr-$AlBr_3$ system as consisting of the two systems, NaBr-$NaAlBr_4$ and $NaAlBr_4$-Al_2Br_6. When this is done, instead of a conductivity maximum, one finds negative deviations from additivity for NaBr-$NaAlBr_4$ and both negative and positive deviation for $NaAlBr_4$-Al_2Br_6. The latter effect is discussed below and the former effect has been discussed in some detail in the chloride study (1) and will not be repeated here.

In treating compositional effects in binary systems Delimarskii and Markov (9) suggest that qualitative correlations exist between deviations from additivity of conductance and degree of association in the melt as may be indicated by the complexity of the phase diagram. In analyzing several systems he has found that deviations tend to increase both in number and magnitude as one progresses from phase diagrams showing solid solutions to those showing eutectics and finally to those having congruently melting compounds. Both the $AlCl_3$-KCl and the $AlBr_3$-NaBr systems fit into this qualitative picture quite well since they both exhibit extremely stable 1:1 compounds (existing even in the vapor phase) and both have large conductivity deviations.

The most noticeable difference in compositional behavior between the two systems was observed for AlX_3-rich mixtures. A plot of equivalent conductivity *vs.* composition for the $NaAlBr_4$-Al_2Br_6 systems shows a negative deviation from additivity in the region of immiscibility (> 60 m/o Al_2Br_6-$NaAlBr_4$) and a positive deviation at lower Al_2Br_6 compositions. This

in contrast with the $KAlCl_4$-Al_2Cl_6 system where only positive deviations were observed. For example, at 60 m/o Al_2X_6 and 600°C, a positive deviation of 55% was found for the chloride system while for the bromide system a negative deviation of 20% was observed. It was suggested that the large positive deviation in the $KAlCl_4$-Al_2Cl_6 system was due to the drastic changes in melt structure when the nonconducting Al_2Cl_6 molecules reacted with $AlCl_4^-$ ions to form conducting ionic species such as $Al_2Cl_7^-$. [Evidence for the species $Al_2Cl_7^-$ in KCl-$AlCl_3$ (10) and NaCl-$AlCl_3$ (11) melts has recently been obtained by means of Raman spectroscopy.] From this point of view, then, the reversal in behavior for the $NaAlBr_4$-Al_2Br_6 system may indicate a less drastic change in melt structure on addition of $NaAlBr_4$ to Al_2Br_6 and a greater compatibility of Al_2Br_6 with anionic species such as $Al_2Br_7^-$ than is the case for the $KAlCl_4$-Al_2Cl_6 systems. This might be expected from a consideration of relative polarizabilities of chloride and bromide with the bromoaluminates being more molecular in nature than the chloroaluminates and thus more compatible with the corresponding aluminum halide. The phase diagram (2) for the bromide system shows a narrower miscibility gap and lower consolute temperature than does the chloride system as perhaps further indication of less pronounced changes in melt structure in the bromide system.

Compositional effects on Arrhenius coefficients are shown in Fig. 4 for the $AlCl_3$-KCl and $AlBr_3$-NaBr systems. This information was not presented in the previous study (1) on $AlCl_3$-KCl since the behavior pattern did not seem particularly significant in the light of inherent uncertainty limits. However, when the points for $AlBr_3$-NaBr are plotted as shown in Fig. 4 the striking similarity of the two systems adds considerable credibility to the results. The Arrhenius coefficients at first decrease with increasing AlX_3 composition, undergo a sharp drop near 40 m/o AlX_3 and then gradually increase beyond this point. The sharp drop near 40 m/o AlX_3 is close to the conductivity maxima observed for these systems (Fig. 2 and 3) and may reflect the pronounced changes in melt structure occurring in this composition range.

Acknowledgments

This work was supported by the U.S. Atomic Energy Commission and performed while the author was on leave from the Oak Ridge National Laboratory. The author wishes to thank S. J. Yosim and L. F. Grantham for their contribution to this work, E. Harrelson for technical assistance, and J. Brynestad of the Oak Ridge National Laboratory for providing high-purity aluminum bromide.

Manuscript submitted Aug. 28, 1970; revised manuscript received Nov. 9, 1970.

Any discussion of this paper will appear in a Discussion Section to be published in the December 1971 JOURNAL.

REFERENCES

1. C. R. Boston, L. F. Grantham, and S. J. Yosim, *This Journal*, **117**, 28 (1970).
2. J. Kendall, E. D. Crittenden, and H. K. Miller, *J. Am. Chem. Soc.*, **45**, 963 (1923).
3. N. J. Bjerrum, C. R. Boston, and G. P. Smith, *Inorg. Chem.*, **6**, 1162 (1967).
4. C. R. Boston and G. P. Smith, *J. Phys. Chem.*, **62**, 409 (1958).
5. L. F. Grantham and S. J. Yosim, *J. Chem. Phys.*, **38**, 1671 (1963).
6. L. F. Grantham and S. J. Yosim, *ibid.*, **45**, 1192 (1966).
7. L. F. Grantham, E. B. Harrelson, P. H. Shaw, and C. M. Larsen, *Rev. Sci. Instr.*, **39**, 699 (1968).
8. C. R. Boston and W. M. Ewing, To be published.
9. Yu. K. Delimars'kii and B. F. Markov, "Electrochemistry of Fused Salts," The Sigma Press, Publishers, Washington, D. C. (1961).
10. S. J. Cyvin, P. Klæboe, E. Rytter, and H. A. φve, *J. Chem. Phys.*, **52**, 2776 (1970).
11. G. Torsi, G. Mamantov, and G. M. Begun, *Inorg. and Nucl. Chem. Letters*, **6**, 553 (1970).
12. C. A. Angell, *J. Phys. Chem.*, **68**, 1917 (1964).
13. C. A. Angell, *ibid.*, **70**, 2793 (1966).

A Correlation of the Solution Properties and the Electrochemical Behavior of the Nickel Hydroxide Electrode in Binary Aqueous Alkali Hydroxides

E. J. Rubin* and R. Baboian*

Metallurgical Materials Division, Technical Center, Texas Instruments Inc., Attleboro, Massachusetts 02703

ABSTRACT

The electrochemical behavior of the nickel hydroxide electrode in binary aqueous alkali hydroxide solutions was investigated in the temperature range —40°-60°C. Maxima were observed in the electrode capacity *vs.* temperature curve for each electrolyte. The nature of the interaction of the alkali metal ion has a marked effect on the charge acceptance of the electrode. At the higher temperatures, the charge acceptance is greatest with the LiOH-H_2O electrolyte. At the lower temperatures, the charge acceptance is greatest with the RbOH-H_2O and CsOH-H_2O electrolytes. The results correlate with the variation in solution properties at these temperatures.

The role which the electrolyte plays in the nickel-cadmium battery is extremely important and complex. In addition to providing a current-carrying medium, the electrolyte participates in the half-cell reactions and is involved in the transfer of material to and away from the electrodes. The nature of the electrolyte and the factors influencing the properties of the electrolyte have marked effects on the behavior of the nickel-cadmium battery. However, the nature of these effects is not clearly understood because of the complexity of the problem.

In this initial study, we have investigated the behavior of the nickel-hydroxide electrode in binary,

* Electrochemical Society Active Member.

Key words: electrode, nickel hydroxide, alkali hydroxide solutions, electrolytic battery interactions.

aqueous, alkali hydroxide solutions. A correlation of this behavior with the properties of the electrolyte solutions is made in the temperature range −40°-60°C.

Experimental

The LiOH, NaOH, and KOH solutions were prepared using reagent grade chemicals and deionized water. The purity of the RbOH used was 99.9%. Cesium hydroxide solutions (>99% purity) of 50 w/o (weight per cent) were diluted to the appropriate concentration with deionized water. Precautions were taken to prevent the introduction of CO_2 during the preparation and use of these solutions.

All solution property measurements were made using alkali hydroxide resistant polypropylene containers. Sealed systems at atmospheric pressure were used wherever possible. For the conductivity measurements, a Beckman Instruments' Model CEL-K10 conductivity cell and an Industrial Instruments' conductivity bridge were used. The cell constant for the conductivity cell was determined using the method of Jones and Bradshaw (1). Viscosity measurements were made using a Brookfield Model LTV viscometer. The instrument was calibrated with distilled water using the published data of Swindells *et al.* (2). The desired temperature for all measurements was maintained using a Lauda Model TK-30 temperature bath.

The behavior of the nickel hydroxide electrode particularly oxidation potentials and the efficiency of the oxidation (charging) process were studied using the apparatus as shown in Fig. 1. The electrochemical cell was made from alkali hydroxide resistant Lucite with three interconnected compartments. The center compartment contained the test electrode (NiOH/NiOOH deposited into the pores of a porous sintered nickel plaque), with known theoretical capacity. An Hg/HgO and a partially discharged nickel hydroxide electrode served as the reference electrodes. The outer compartments contained conventional sintered plaque cadmium hydroxide plates as counterelectrodes with approximately ten times the capacity of the test electrode.

The experiments were carried out in the flooded condition with the appropriate electrolyte. The temperature was varied from −40° to +60°C and was controlled to ±0.5°C in a Tenney environmental chamber. In each case, the total charge input was 150% of the theoretical capacity of the test electrode. After each charging cycle, the cells were discharged at constant current to determine the charge acceptance of the nickel hydroxide electrode.

To determine the point of incipient gas evolution, the cell shown in Fig. 1 was connected to a manometer and gas buretts. Gas pressures produced in the cell displaced a conducting liquid in the manometer which actuated an electronic sensor, thus indicating the time of pressure rise. Immediately after gas evolution was detected, the manometer was bypassed and the evolved gas was collected in the buretts.

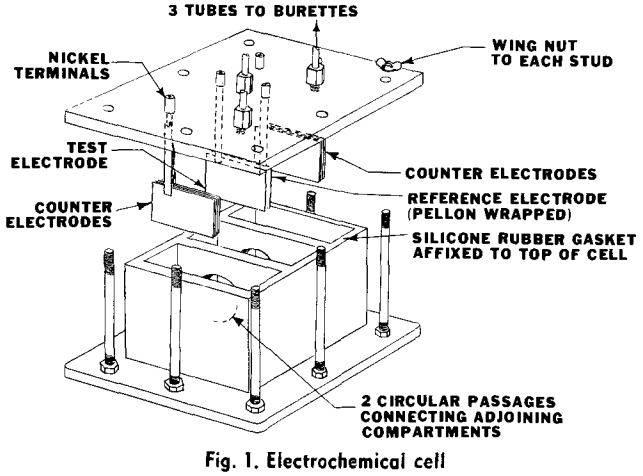

Fig. 1. Electrochemical cell

The accuracy of the apparatus was determined by electrolytically generating gas using an unimpregnated nickel plaque. Gas evolution was detected within 2 A-min after start of the test. The total gas evolved was greater than 95% of the volume (after STP corrections) predicted by Faraday's law. Deviations from the theoretical values were attributed to experimental error, gas adsorption on the plaque, and the quantity of gas necessary to overcome the water leg of the manometer. In actual operation, these effects were minimized by precycling the test electrode in the apparatus thus pressurizing the system and saturating the electrolyte with oxygen.

Results

Solute-solvent interactions.—Ionic solvation has been the subject of numerous articles. Bockris (3) suggested that the term "primary solvation" be used to refer to the number of solvent molecules near to an ion which have lost their translational degrees of freedom and move as one entity with the ion. Secondary solvation was used to refer to solvent molecules which interact with the primary solvated ion.

The magnitude of the hydration numbers for various ions reported in the literature vary widely because the methods used to measure these values include primary and secondary hydration contributions. For example, the values of the hydration number for Na+ reported in the literature vary from 2 to 70 (4).

The data in Table I show that the crystal radius of the alkali metal ions increases in the order of their atomic number.

The small lithium ion has a high charge density and should interact more strongly with surrounding water molecules than does the rubidium ion. This is reflected in the magnitude of the experimental mean primary hydration numbers $h_{meas.}$ in Table I. The values decrease for the alkali metal ions in going from Li+ to Rb+.

Also listed in Table I are the hydration numbers (h_{calc}) derived from activity-coefficient measurements. These values are thought to be the lower limit of hydration numbers because the method used to obtain them tends to emphasize the primary hydration. The calculated ionic radii (r_h) resulting from these measurements show the effect of solvation on the size of the ions in solution. In contrast to the trend of the crystal radii, the solvated ion size decreases in going from Li+ to Cs+.

The model used most frequently to describe the hydrated alkali metal ion is shown in Fig. 2a. The alkali metal ion polarizes the water molecules orienting them so that the oxygen end of the dipole is nearest the ion.

A number of authors have found, in aqueous solutions, that the hydroxide ion is strongly hydrated. This conclusion was based on heat capacity measurements (5), calculations based on activity coefficient data (6), Raman spectra (7), infrared spectra (8), and ionic entropy data (9). The formula $[OH(H_2O)_3]^-$ has been used most frequently to represent the state of the hydroxide ion in solution. The models proposed for such a species are shown in Fig. 2b and c. In Fig. 2b, all three water molecules are bound to the oxygen of

Table I. Ionic properties of alkali metals

Ion	$r_{cryst.}$,* Å	h_{meas}**	h_{calc}*	r_h,* Å
Li+	0.60	5 ± 1	4.25	2.50
Na+	0.95	5 ± 1	2.9	2.17
K+	1.33	4 ± 2	1.2	1.75
Rb+	1.48	3 ± 1	0.5	1.53
Cs+	1.69		0	1.47
OH−	1.4		3.5	2.46

* C. B. Monk, "Electrolytic Dissociation," p. 271, Academic Press, New York (1961).

** B. E. Conway and J. O'M. Bockris, "Modern Aspects of Electrochemistry" (No. 1), p. 71, Butterworths, London (1954).

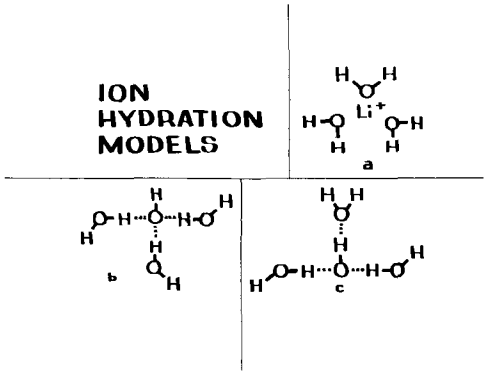

Fig. 2. Ion hydration models

the hydroxide ion. In Fig. 2c, one of the water molecules is bound to the hydrogen of the hydroxide ion. The former model is favored because the high-frequency O-H mode of the Raman spectrum remains unchanged (7) when an alkali hydroxide is dissolved in water. In concentrated alkali hydroxide solutions, the magnitude of the interactions in the trihydrated hydroxide ion depends on the nature of the alkali metal cation.

Solute-solute interactions.—The degree of ion association in solution depends on the nature of the anion, cation, and solvent. Concentration, temperature, and pressure have a marked effect on this parameter. At high concentrations the calculated separation of ions is small. Therefore, depending on the extent of interaction with the solvent, the ion solvation spheres may overlap interacting with one another.

This model for ion association in water is adequate for interpreting the magnitude of the activity coefficient for most alkali metal solutions. The values for most electrolytes of the alkali metal family decrease in the order lithium to cesium (10).

This is consistent with the increasing hydration of the cation from cesium to lithium (Table I). The reverse is true for the alkali metal hydroxides. The activity coefficients decrease in the order cesium to lithium (10).

To account for the low activity coefficient found for lithium hydroxide, Robinson and Harned (10) postulated the existence of water-bridged ion-pairs. The model in Fig. 3a shows that in the hydration shell surrounding the lithium ion, the water molecule is highly polarized with protons directed away from the cation. The proton then interacts with the oxygen of the hydroxide ion. In concentrated solutions, the model in Fig. 3a would best describe ion association in lithium hydroxide solutions because of the high charge density of the lithium ion. Ion association in cesium hydroxide solutions may be more direct as in Fig. 3b because the cesium ion is not bound by a sheath of highly polarized water molecules.

Solution properties.—Aqueous solutions in which the ions are strongly hydrated and/or have strong electrical forces between the ions in adjacent layers, have high viscosities. The viscosities measured at 25°C for LiOH, NaOH, KOH, RbOH, and CsOH solutions are

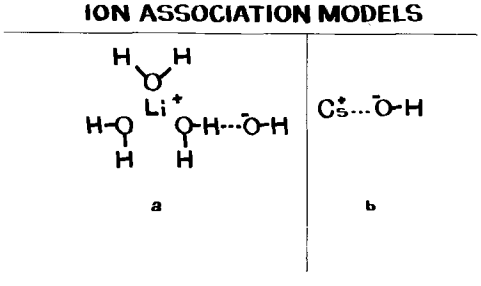

Fig. 3. Ion association models

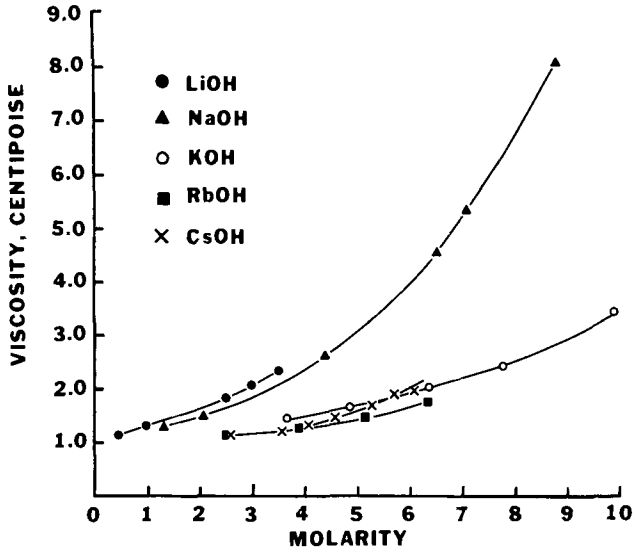

Fig. 4. Viscosity of alkali metal hydroxide solutions at 25°C

plotted *vs.* concentration in Fig. 4. In the concentrated region, the viscosities rise rapidly with concentration due to increased ion association. The highest viscosities are measured for LiOH and NaOH solutions in which ion hydration and water bridge ion pairing is appreciable.

The specific conductivities at 25°C for solutions of the alkali metal hydroxides are plotted *vs.* concentration in Fig. 5. In the dilute region, the increase in conductivity with concentration is due to the increase in the population of ions per unit volume. The decrease in conductivity at high concentrations is due to increased ion association which is characteristic for these 1:1 electrolytes. The lowest conductivities are found for the LiOH and NaOH systems. This is due to the effect of ion hydration and water bridge ion pairing and is in agreement with the viscosity measurements.

The phase diagrams (11) for the binary alkali metal hydroxide-water systems are shown in Fig. 6. Notice that the eutectic temperature decreases in the order LiOH through CsOH and that the compositions of the eutectic and the conductivity maximum at room temperature correspond closely for the KOH-H_2O system whereas marked differences are observed for the other systems. The specific conductivities are strongly temperature dependent because they are sensitive to the types of interactions which prevail. Conductivity

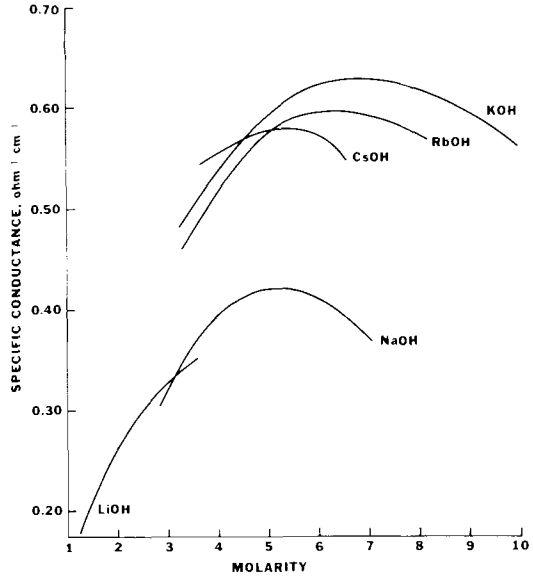

Fig. 5. Specific conductance of alkali metal hydroxide solutions at 25°C.

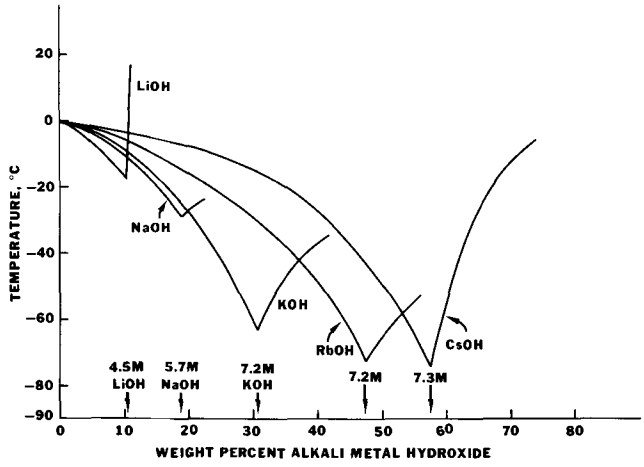

Fig. 6. Alkali metal hydroxide-water phase diagrams

maxima, therefore, shift with temperature. For example, the conductivity maximum in the KOH-H_2O system was found to occur below 4M at −15°C, about 6M at 0°C, and 6.7M at 25°C.

The electrolytes chosen for the comparative investigation were those having the highest specific conductivity at 25°C. In the case of lithium hydroxide, the liquidus is so steep beyond the eutectic composition that this concentration could not be used. A 3.0M LiOH solution was used for this system. In Fig. 7, the specific conductivities of these solutions are plotted *vs.* temperature. Below 0°C, the CsOH solution has the highest conductivity. At −10°C the order is

$$\text{LiOH} < \text{NaOH} < \text{KOH} < \text{RbOH} < \text{CsOH}$$

At 25°C the KOH solution has the highest conductivity and the order is

$$\text{LiOH} < \text{NaOH} < \text{CsOH} < \text{RbOH} < \text{KOH}$$

This data can be compared to the viscosity data and the freezing points listed in Table II. To some extent, the behavior of the electrolytes correlate; however, the lowest viscosity electrolyte is shifted to RbOH at 25°C and the order is

$$\text{NaOH} > \text{KOH} > \text{CsOH} > \text{RbOH}$$

Nickel hydroxide electrode behavior.—The oxygen-free capacities of the nickel hydroxide electrode developed in the various electrolytes are plotted as a function of temperature in Fig. 8 and 9. In Fig. 8 the

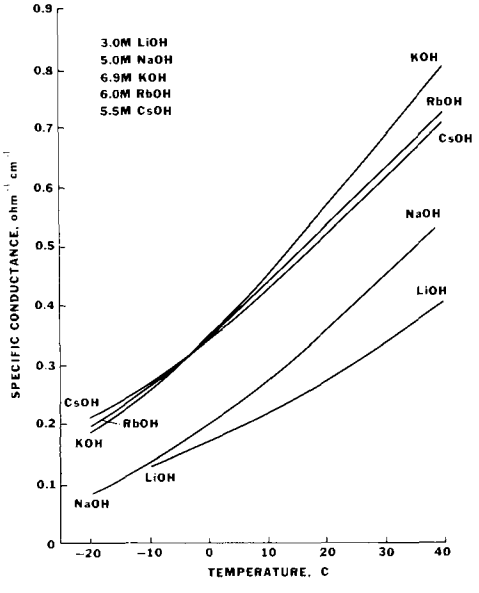

Fig. 7. Temperature dependence of specific conductance of alkali metal hydroxide solutions.

Table II. Solution properties

Solution (conc.)	Freezing point, °C	Specific conductance, ohm^{-1}-cm^{-1}, 25°C	Viscosity, centipoise 25°C	Viscosity, centipoise −10°C
LiOH (3M)	−11	0.33	2.0	—
NaOH (5M)	−23	0.42	3.0	6.9
KOH (6.9M)	−64	0.63	2.1	3.8
RbOH (6M)	−50	0.59	1.6	3.1
CsOH (5.5M)	−43	0.57	1.7	2.9

values were obtained at the c/5 charge rate and the c/2 discharge rate. In Fig. 9 the values were obtained at the c charge and the c/2 discharge rate. The oxygen-free capacities are similar for the two charge rates except at low temperatures where they are higher at low charge rates. In Fig. 10 and 11 the delivered capacities are plotted as a function of temperature for the various electrolytes. Figure 10 shows the results of the low charge rate and Fig. 11 shows the results of the fast charge rate.

Discussion

The dependence of oxygen-free capacity and delivered capacity of the nickel hydroxide electrode on electrolyte type is significant. At temperatures where the oxygen-free capacity is high the delivered capacity is correspondingly high so that the capacity maxima occur at the same temperature. The capacities are high with the sodium and lithium electrolyte at high temperatures, are high with the potassium electrolyte at intermediate temperatures, and are high with the rubidium and cesium electrolytes at low temperatures. Specifically, the delivered capacity is highest with the

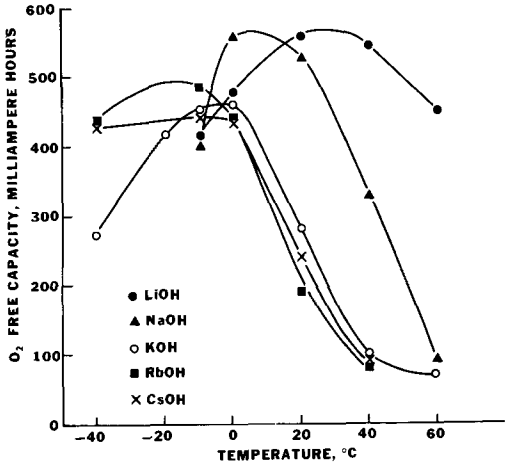

Fig. 8. Nickel hydroxide electrode oxygen-free capacity (112 mA charge rate).

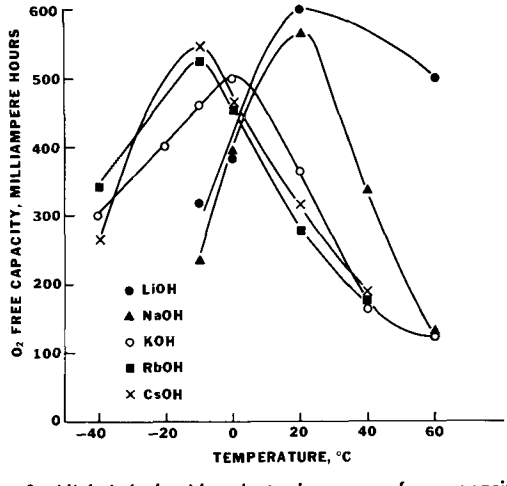

Fig. 9. Nickel hydroxide electrode oxygen-free capacity (500 mA charge rate).

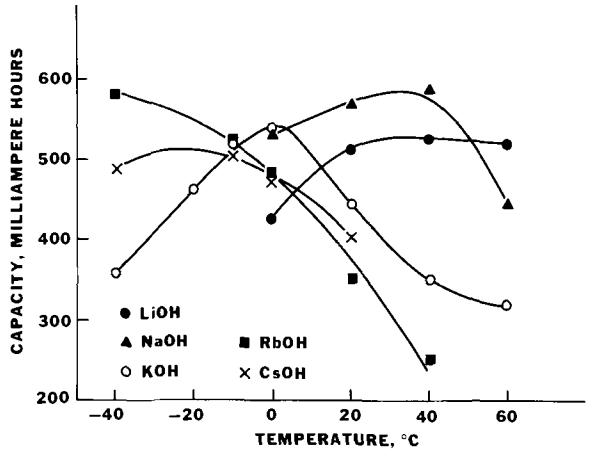

Fig. 10. Nickel hydroxide electrode capacity (112 mA charge rate).

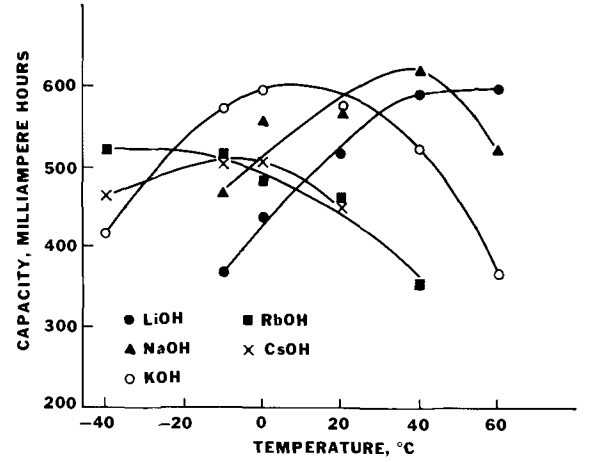

Fig. 11. Nickel hydroxide electrode capacity (500 mA charge rate).

rubidium hydroxide electrolyte at −40°C, with the KOH electrolyte at 0°C, with the sodium hydroxide electrolyte at 40°C, and with the lithium hydroxide electrolyte at 60°C.

In general, this same trend is observed for the specific conductance of these electrolytes with temperature. Since the solution compositions used in this study are the ones with the highest specific conductance (Fig. 5) at 25°C, some degree of correlation is expected. However, the correlation is surprisingly good over a wide temperature range.

The magnitude of the difference in isothermal electrode capacities with the various electrolytes cannot be totally explained by differences in electrolyte properties and suggests that structural changes occur in the electrode. Bode (12) has reported that alkali metal cations present in the nickel hydroxide crystal lattice have an effect on the stability of the higher nickel oxidation states. The stability varies with the alkali metal cation and therefore leads to variations in electrode capacity with electrolyte type. This effect has been studied extensively and has been reported previously (13, 14).

For a given electrolyte over the temperature range investigated the structure of the nickel hydroxide electrode does not change significantly enough to explain the maxima observed in the electrode capacity *vs.* temperature curves (Fig. 8-11). However, the results can be explained by consideration of electrolyte interactions.

In Table III, differences in nickel hydroxide electrode potential during charging and end-of-charge (oxygen evolution) electrode potential are listed at various temperatures. For each electrolyte, this difference in potential decreases rapidly with increasing temperature. This indicates that electrode polarization is reduced as the temperature is increased and follows the trend of increasing conductance (Fig. 7) and decreasing viscosity (Table II) with increasing temperature.

Table III. ΔE plateau oxygen evolution-nickelous hydroxide oxidation (500 mA charge rate)

Temp, °C	LiOH	NaOH	KOH	RbOH	CsOH
−10	268	230	145	130	115
20	195	143	87	65	93
40	155	101	30	33	50
60	105	26	10	—	—

Table IV. ΔE (mV) incipient O_2 evolution-nickelous hydroxide oxidation (500 mA charge rate)

Temp, °C	LiOH	NaOH	KOH	RbOH	CsOH
−10	38	22	10	7	41
20	84	43	27	3	27
40	93	15	13	0	2
60	28	0	10	—	—

The differences in nickel hydroxide electrode potential and the potential at which incipient oxygen evolution occur at the nickel hydroxide electrode are listed in Table IV. These data include not only effects of electrode polarization, but also tendency toward oxygen evolution. The latter effect is dependent on the nature of electrolyte interactions represented diagrammatically in Fig. 2b and c, and 3a and b. The magnitude of these electrolyte interactions decrease with increasing temperature.

In Table IV, the trend (ΔE *vs.* temperature) is the same as that observed for electrode capacity *vs.* temperature. The maxima in Table IV and in Fig. 8-11 appear at approximately the same temperature for each electrolyte. This indicates that the capacity maxima are a result of superimposed effects of variations in electrode polarization and oxygen evolution with temperature.

When ΔE values in Table IV are very low the electrode should become unstable or inefficient. For rubidium hydroxide and cesium hydroxide electrolytes, the ΔE values are zero and two millivolts respectively at 40°C. Spontaneous decomposition of charged nickel hydroxide electrodes in these electrolytes was observed.

The effect of charge rate on the nickel hydroxide electrode oxygen free capacity is significant since the results support the above interpretation of observed capacity maxima. The lower temperatures yield delivered capacities which are higher at slow charge rates. This effect is not observed at the higher temperatures due to reduced electrode polarization.

Acknowledgment

The authors wish to thank D. Whitaker and A. Conti for their technical assistance in this work.

Manuscript submitted July 28, 1970; revised manuscript received Nov. 4, 1970. This was Paper 373 presented at the Montreal Meeting of the Society, Oct. 6-11, 1968.

Any discussion of this paper will appear in a Discussion Section to be published in the December 1971 JOURNAL.

REFERENCES

1. G. Jones and B. C. Bradshaw, *J. Am. Chem. Soc.*, **55**, 1780 (1933).
2. J. F. Swindells, J. R. Coe, and T. B. Godfrey, *J. Res. Nat. Bur. Std.*, **48** (1952).
3. J. O'M. Bockris, *Quart. Rev.*, **3**, 173 (1949).
4. A. J. Rutgers and Y. Hendrik, *Trans. Faraday Soc.*, **58**, 2184 (1962).
5. T. Ackermann, *Discussion Faraday Soc.*, **24**, 180 (1957).

6. E. Glueckauf, *Trans. Faraday Soc.*, **51**, 1235 (1955).
7. W. R. Busing and D. F. Hornig, *J. Phys. Chem.*, **65**, 284 (1961).
8. T. Ackerman, *Z. Physik. Chem.*, **27**, 253 (1961).
9. H. S. Frank, Unpublished work.
10. R. A. Robinson and H. S. Harned, *Chem. Rev.*, **28**, 455 (1941).
11. A. P. Rollet and R. Cohen-Aded, *Rev. Chim. Minerale*, **1**, 451 (1964).
12. H. Bode, K. Dehmelt, and J. Witte, *Z. Anorg. Chem.*, **366**, 1 (1969).
13. P. Bro and D. Cogley, *This Journal*, **113**, 521 (1966).
14. M. A. Aia, *ibid.*, **114**, 418 (1967).

The Anodic Dissolution Reaction of InSb: Etch Patterns, Electron Number, Anodic Disintegration, and Film Formation[1]

M. E. Straumanis* and Lih-da Hu

Department of Metallurgical Engineering and Graduate Center for Materials Research, University of Missouri-Rolla, Rolla, Missouri 65401

ABSTRACT

The etching behavior of the inverse {111} planes of undoped, semiconducting, n-type, InSb single crystals was explored. Depending upon the etchant, including anodic dissolution, various etch patterns were obtained on the inverse planes. In general the etch pits on the In{111} plane were round, and the face was shiny, whereas the face of the inverse plane was dark and rough. The rates of dissolution in the electrolytes used were very low, especially in absence of oxidizers. The components dissolve as In^{3+} and Sb^{3+}. At current densities above 40 or 60 mA cm^{-2} (on Sb{$\bar{1}\bar{1}\bar{1}$} or In{111}), growth of a black, collodial film of $Sb_4O_5Cl_2$ containing very fine metallic Sb particles occurs on both planes. The Sb particles result from the partial disintegration of InSb. Upon heating the film in vacuum, recrystallization occurs and the Sb aggregates to form larger particles. An explanation is offered for the different behaviors of the inverse {111} planes.

The chemical and anodic dissolution reactions occurring on various planes of III-V semiconductors in several electrolytes have been studied by Gatos *et al.* (1, 2), Pleskov (3), Dewald (4), Gerischer (5, 6), Harvey (7), Straumanis *et al.* (8, 9), and others. Dewald attempted to explain why the {111} inverse faces of InSb in an aqueous solution of KOH behave differently. Anodic oxide films of varying composition with the ratio of Sb:In close to one at the surface of the crystal planes were formed during electrolysis.

The aim of the present investigation was, therefore, to check once more the etch patterns formed on the inverse {111} faces of InSb, to determine the valences of the ions (In and Sb) going into solution in acidic electrolytes, to look for disintegration phenomena and film formation, and determine the composition of the films.

Electrodes and Their Treatment

The electrodes were prepared as for GaAs by mounting InSb wafers (~ 2 mm thick and 8 to 12 in diameter) into Teflon holders provided with a screw cap and Cu lead wires (9). The wafers were cut from single InSb crystals obtained from the Monsanto Company (St. Louis, Missouri), grown in the [111] direction by the Czochralski or the gradient-freeze technique. They were n-type with no intentionally added dopants, and the impurity level was less than 1 ppm. The {111}, {110}, and {100} directions were established from Laue x-ray back reflection patterns. Deviations from these faces were adjusted by successive grinding to give the desired orientation on the Laue patterns.

These faces had a mirror-like appearance after mechanical polishing (Fig. 1a). To remove mechanical surface damage, they were subsequently treated with CP-4 (2, 4) (mixture of concentrated acids HNO_3, HF, and CH_3COOH) for 2 sec, washed, and dried. Although still mirror-like, the faces showed a slight undulation in the interference microscope (Fig. 1b).

This etchant and several others, including anodic dissolution, were used to check the previous results and to determine which of the {111} faces was In {111} and which Sb {$\bar{1}\bar{1}\bar{1}$.} The distinction is based on x-ray work and its comparison with the results obtained by etching (1, 10, 11).

Results

Etching.—The two inverse {111} planes of InSb, following etching for 5 or more sec in CP-4, showed the expected results: one side of the wafers was glossy, exhibiting round, flat etch pits—(In{111}), and the other was dark and rough—(Sb{$\bar{1}\bar{1}\bar{1}$}).

The HNO_3-HF etchant (1:1 of the concentrated acids) worked similarly: rounded etch pits appeared on the glossy side, as on the Ga{111} side of GaAs (8) but on the inverse Sb{$\bar{1}\bar{1}\bar{1}$} side, irregular triangular etch pits appeared (Fig. 5).

The HCl-$FeCl_3$ etchant produced a different kind of pattern, especially after prolonged treatment (Fig. 2a and b and Fig. 3).

Anodic etching led to round or rounded, triangular pits on the In{111} face. These pits grew in size with the time of etching and finally merged together as observed by Gatos and Lavine (1). The anodic dissolution in 2*N* HCl lasted 15 to 45 min (10 mA/cm^2) and 60 min in 1*N* HNO_3 containing 1*N* tartaric acid. Figure 4 shows a surface which displays merging, round etch pits.

The Sb{$\bar{1}\bar{1}\bar{1}$} plane becomes rough after etching displaying irregular triangular etch pits (Fig. 5) and frequently pits within pits.

[1] GCMR Contribution No. 91.
* Electrochemical Society Active Member.
Key words: inverse {111} planes, self-dissolution rates, $FeCl_3$ etchant, colloidal Sb, $Sb_4O_5Cl_2$.

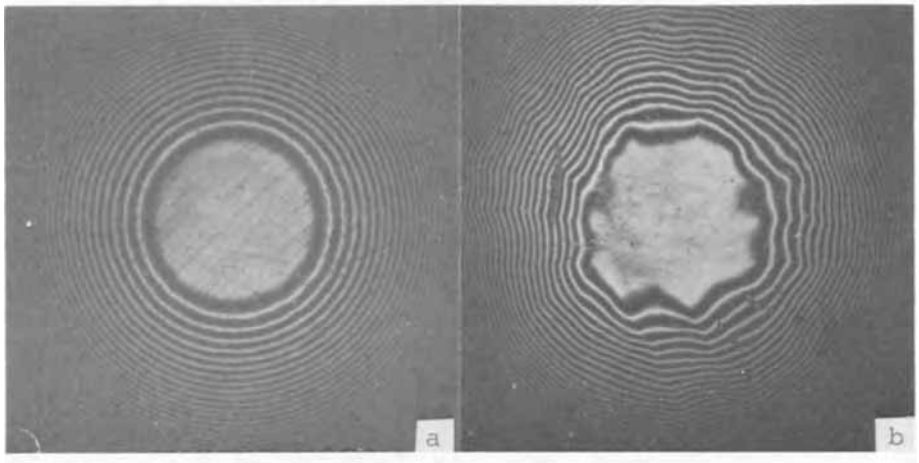

Fig. 1. Interference rings on InSb faces, 165X; a—highly polished; b—etched with CP-4 for 2 sec.

Fig. 2. a—In{111}, etchant: 6*N* HCl-0.2*N* $FeCl_3$; 20 min; 80°C; 970X. b—In{111}, etchant: 2*N* HCl-0.5*N* $FeCl_3$, 24 hr; 25°C; 90X.

Anodic or chemical etching, excepting $FeCl_3$ additions, produced round pits on In{111} faces. The latter were then treated with the HCl-$FeCl_3$ etchant. Dense triangular etch pits, as pictured on Fig. 2a, developed on these faces; even the walls of the deep round pits (Fig. 4) consisted of triangular steps. Thus, submicroscopic steps, which might have been present on the walls of the round pits were developed to microscopic size by the HCl-$FeCl_3$ etchant. No superimposed pattern was observed on the Sb{$1\bar{1}\bar{1}$} face.

The main characteristic in distinguishing the two inverse faces is, therefore, the shiny appearance of In{111} and the dark, rough one of the inverse face. Consideration of etch pits only for recognition may be misleading as the etch pattern changes with the nature of the etchant, its concentration, and time of etching.

Apparent electron number of InSb.—Since some of the anodic dissolution experiments were continued up to 24 hr, it was necessary to know the self-dissolution rate of the InSb used in the various electrolytes. These rates are summarized in Table I, which clearly shows that the self-dissolution rate of InSb in pure 2*N* HCl is nearly zero. It increases considerably in the presence of oxidizers. There is some difference in the dissolution rates of the inverse {111} planes.

The electron number determinations were, therefore, carried out in 2*N* HCl and in tartaric-HNO_3 acid (Table I). The results can be read from Fig. 6, which

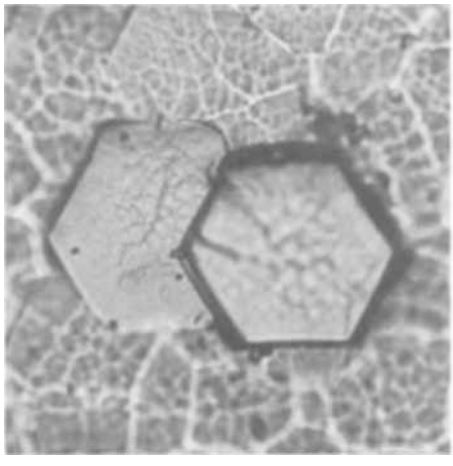

Fig. 3. Sb{111}, etchant: 6*N* HCl-0.2*N* $FeCl_3$; 20 min; 80°C; 970X.

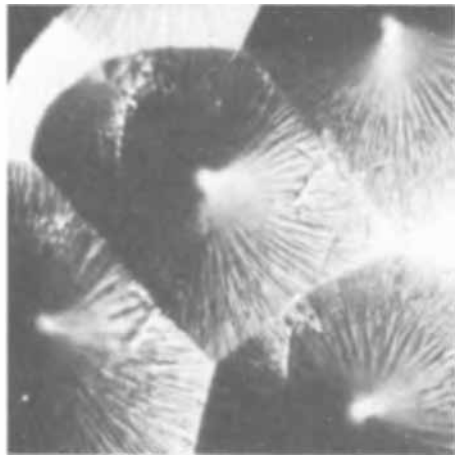

Fig. 4. In{111} etched anodically in 1*N* HNO_3-1*N* $H_2C_4H_4O_6$; 10 mA/cm^2; 60 min; 500X.

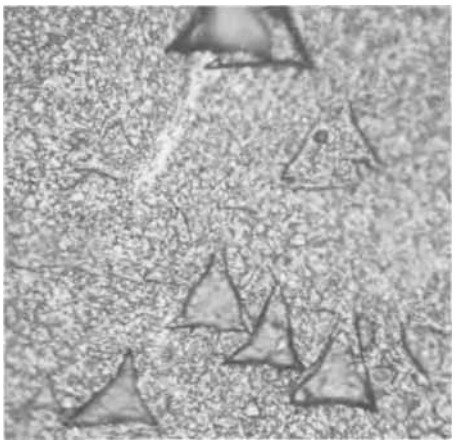

Fig. 5. Sb{$\bar{1}\bar{1}\bar{1}$}; the same etch as in Fig. 4 or simple HNO_3-HF etchant.

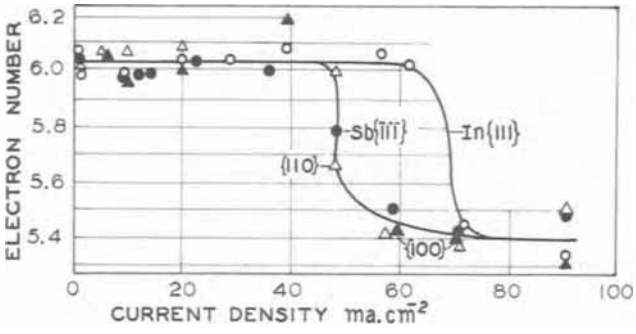

Fig. 6. Apparent electron number of InSb as a function of current density. The faces In{111}, Sb{$\bar{1}\bar{1}\bar{1}$}, {110}, and {100} were dissolved anodically in 2*N* HCl.

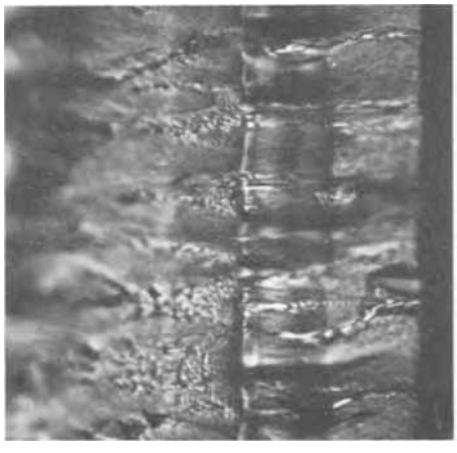

Fig. 7. Cross section of the black film formed on In{111} of the InSb electrode. 2*N* HCl; 70 mA cm^{-2}; 970X.

Table I. Self-dissolution rates of InSb in various electrolytes in air
Estimated accuracy: ±0.02

Face	Electrolyte	Time, hr	Self-dissolution rate, mg cm^{-2} day^{-1}
In{111}	2*N* HCl	24	0.00
Sb{$\bar{1}\bar{1}\bar{1}$}	2*N* HCl	24	0.00
In{111}	1*N* $H_2C_4H_4O_6$ + 1*N* HNO_3	30	0.07
Sb{$\bar{1}\bar{1}\bar{1}$}	the same	30	0.04
In{111}	2*N* HCl + 0.005*N* $FeCl_3$	45	1.06
Sb{$\bar{1}\bar{1}\bar{1}$}	the same	45	1.33
In{111}	2*N* HCl + 0.01*N* $FeCl_3$	37	2.25
Sb{$\bar{1}\bar{1}\bar{1}$}	the same	37	2.60

indicates that up to current densities below 50 mA cm^{-2} the electron number is 6.00 within error limits. Since In goes into solution as In^{3+} (12, 13), Sb must do the same. The In{111} face seems to be more resistive than the inverse and the {110} and {100} planes, as it tolerates current densities up to 60 mA cm^{-2}. At higher current densities, the apparent electron number decreases, that is more In or Sb goes into solution than predicted by Faraday's law. This can be attributed to the formation of ions of lower valency (14), increased local corrosion and/or anodic disintegration (15-18). However, no particles were observed separating from the InSb anode, only the formation of a film at current densities above 40 to 60 mA cm^{-2}.

Anodic film formation and disintegration.—The films formed on the anode at elevated current densities were nearly black, but displayed a mother of pearl luster. They had a stratified structure (Fig. 7) and were colloidal in nature as they did not produce x-ray diffraction lines. The electron diffraction method was not used.

The same kind of film was produced on both inverse {111} planes. The film could usually be removed from the crystal surface by a soft brush. The substrate side of the film appeared more even than the electrolyte side (Fig. 8a and b).

To investigate the composition of the films, fragments were heated in vacuum at 350°C for about 2 hr. As a result of this treatment, an x-ray diffraction pattern consisting of many sharp lines was obtained. The position of these lines coincided with those of a powder resulting from anodic dissolution of pure Sb in 2*N* HCl and with those of a precipitate obtained by (aqueous) hydrolysis of $SbCl_3$. According to Mellor (19) and the ASTM cards, the composition of the white precipitate is $Sb_4O_5Cl_2$. Since the Sb is trivalent in this compound, this is a further confirmation for the trivalency of Sb ions going anodically into solution from InSb.

The above x-ray patterns exhibited some weak, additional lines. To identify them, the black anodic

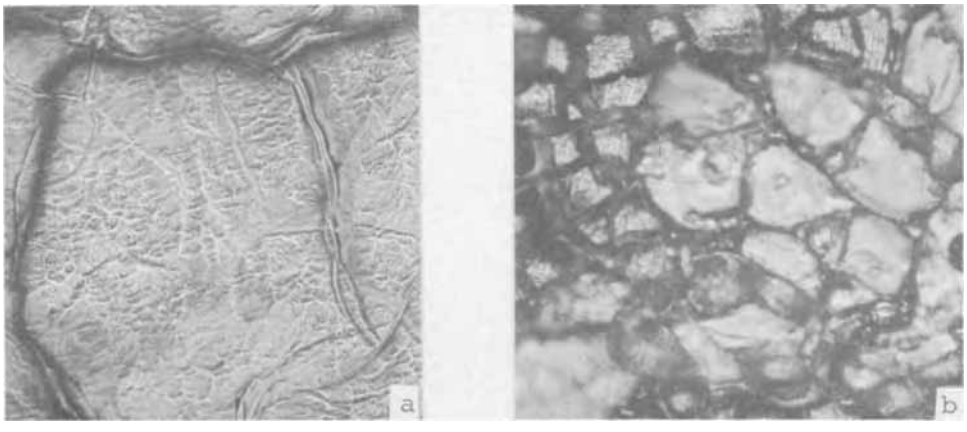

Fig. 8. Black film resulting from anodic dissolution of the In{111} face of InSb in 2*N* HCl at 70 mA cm^{-2}; 970X. a—Substrate side; b—Electrolyte side.

film fragments were heated in vacuum above 650°C (melting point of Sb-630°). At that temperature the black and the white material separated. The latter proved to be $Sb_4O_5Cl_2$, while the former appeared as molten spheres, identified as metallic Sb.

Discussion

Since no reducing species were in the black anodic deposits, metallic Sb must have already been present as very fine particles.

The explanation of the anodic behavior of InSb is then as follows. Both components dissolve anodically as trivalent ions

$$In \rightarrow In^{3+} + 3e \quad [1]$$

$$Sb \rightarrow Sb^{3+} + 3e \quad [2]$$

Although the In^{3+} pass directly into solution, the Sb^{3+} ions hydrolyze, particularly at increased current densities (above 40 to 60 mA cm^{-2}), as a sufficient amount of H^+ cannot penetrate to the surface of the anode

$$Sb^{3+} + H_2O + HCl \rightleftharpoons Sb\begin{matrix}=O\\ \diagdown Cl\end{matrix} + 3H^+ \quad [3]$$

or complete hydrolysis may occur

$$2Sb^{3+} + 3H_2O \rightleftharpoons Sb_2O_3 + 6H^+ \quad [4]$$

The oxychloride as well as the oxide or hydroxide $Sb(OH)_3$ are relatively insoluble and adhere to the anode as layers consisting of crystallites of colloidal dimensions. A further reaction may occur on the surface and after heating

$$Sb_2O_3 + 2SbOCl = Sb_4O_5Cl_2 \quad [5]$$

Simultaneously, during heating, the colloidal product is converted into a crystalline one, detectable by x-ray diffraction.

Since metallic Sb is much more noble than In, the Sb atoms of the InSb have a tendency to retain their valence electrons whereas In is readily oxidized and goes easily into solution. Consequently, especially at increased current densities, the In atoms surrounding the Sb atoms dissolve and some of the latter embed themselves into the oxychloride film (Eq. [5]), which is simultaneously formed according to Eq. [3] and [4] by a part of Sb^{3+}. The oxychloride film prevents the Sb atoms from collecting into particles larger than colloidal (20). As a consequence, the white, possibly transparent film turns dark, and the electron number (or the apparent valency) drops. Thus, partial disintegration of the Sb on the surface of the InSb occurs, and the resulting product does not produce x-ray interference lines. The film formation process may proceed periodically, starting where there is a weakness in the thin film or where a breakdown of the film takes place. A film of stratified structure results (Fig. 7). Upon heating in vacuum, the colloidal particles of the oxychloride and the Sb grow separately to form larger entities which can now produce x-ray diffraction lines.

That the Sb{111} is more susceptible than In{111} to partial Sb disintegration (Fig. 6) depends evidently on the characteristic structure of these inverse planes. According to Galaev and Gorelik (21), the bond strength on the Sb{$\bar{1}\bar{1}\bar{1}$} plane should be weaker than on the In{111} plane. Consequently, the former is easier to destroy; its hardness is less; and the outer Sb atoms are more remote from the In atomic layer than on the inverse side (21). This explains why the partial Sb disintegration on Sb{$\bar{1}\bar{1}\bar{1}$} and on {110} and {100}) planes starts at lower anodic current densities than on In{111}.

Finally the weaker bond strength on Sb{$\bar{1}\bar{1}\bar{1}$} suggests that this plane should be attacked by etchants at a faster rate than the inverse plane. Table I shows the correctness of this conclusion. The difference in the rates of corrosion of the two inverse {111} planes in HNO_3-tartaric acid is, however, within the limits of error.

Acknowledgments

The authors wish to thank Dr. J. W. Johnson, Professor of Chemical Engineering, for advice and Dr. W. J. James, Professor of Chemistry and Director of the Graduate Center for Materials Research, for assistance with this study. The authors are also grateful to the New Enterprise Division of the Monsanto Company in St. Louis, especially to Mr. J. B. McNeely, for donation of the InSb crystals and to the Office of Naval Research for financial support.

Manuscript submitted May 25, 1970; revised manuscript received Nov. 6, 1970. This was Paper 104 presented at the Los Angeles Meeting of the Society, May 10-15, 1970.

Any discussion of this paper will appear in a Discussion Section to be published in the December 1971 JOURNAL.

REFERENCES

1. H. C. Gatos and M. C. Lavine, *This Journal*, **107**, 427 (1960).
2. H. C. Gatos and M. C. Lavine, *J. Phys. Chem. Sol.*, **14**, 169 (1960).
3. Yu. V. Pleskov, *Dokl. Akad. Nauk USSR*, **143**, 1399 (1962).
4. J. F. Dewald, *This Journal*, **104**, 244 (1957).
5. H. Gerischer, *Z. Elektrochem.*, **69**, 578 (1965).
6. H. Gerischer, *Z. Physik. Chem. N. F.*, **49**, 112 (1966).
7. W. W. Harvey, *This Journal*, **114**, 472 (1967).
8. J.-P. Krumme and M. E. Straumanis, *Trans. Met. Soc. AIME*, **239**, 395 (1967).
9. M. E. Straumanis, J.-P. Krumme and W. J. James, *This Journal*, **115**, 1050 (1968).
10. E. P. Warekois and P. H. Metzger, *J. Appl. Phys.*, **30**, 960 (1959).
11. J. G. White and W. C. Roth, *ibid.*, **30**, 946 (1959).
12. M. E. Straumanis and R. L. Martin, *Z. Anorg. Allegem. Chem.*, **334**, 321 (1965).
13. M. E. Straumanis, *This Journal*, **113**, 636 (1966).
14. B. D. Laughlin, J. Kleinberg, and A. W. Davidson, *J. Am. Chem. Soc.*, **78**, 559 (1956).
15. M. E. Straumanis and Y. Wang, *Corrosion*, **22**, 132 (1966).
16. M. E. Straumanis and M. Dutta, *Inorg. Chem.*, **5**, 992 (1966).
17. W. J. James, M. E. Straumanis, and J. W. Johnson, *Corrosion*, **23**, 15 (1967).
18. M. E. Straumanis, *Latvijas PSR Zinatnu Akad. Vestis Kim. Ser.*, 1967, 643.
19. J. W. Mellor, "A Comprehensive Treatise of Inorganic and Theoretical Chemistry," IX, pp. 469-484, Longman, Green & Co., London (1922).
20. B. Jirgensons and M. E. Straumanis, "A Short Textbook of Colloid Chemistry," pp. 1, 4, 9, 14, 469, MacMillan, New York (1962).
21. A. A. Galaev and S. S. Gorelik, *Dokl. Akad. Nauk SSSR*, **184**, 635 (1969).

Anodic Dissolution of N^+ Silicon

Ronald L. Meek

Bell Telephone Laboratories, Incorporated, Murray Hill, New Jersey 07974

ABSTRACT

An experimental study has been made of the anodic dissolution of silicon in aqueous HF solution with emphasis on heavily doped n-type. Current-voltage curves, the effective dissolution valence, and the critical current density have been determined for n, n^+, and p samples. Since n^+ silicon has a resistivity less than 0.05 ohm-cm, it can be electropolished while higher resistivity material exhibits a current saturation effect although breakdown occurs at only a few volts. Minority carrier generation within the space charge region does not account for the magnitude of the saturation current for n-type and extensive attack was evident at the surface of n-type which had received prolonged anodic treatment. The critical current density for n^+ samples was found to be a function of the resistivity.

Numerous applications (1) of electrochemical processes in semiconductor technology have been proposed and utilized since the paper of Brattain and Garrett (2) established the field of semiconductor electrochemistry. Many of these utilize selective etching or staining effects exhibited by the semiconductor electrode dependent on resistivity, type, potential, and the nature of the solution. In particular, it is well known that n^+ and p silicon electrodes are readily anodically dissolved, electropolished, in HF solution, whereas those of n material are not. While the behavior of p-type, and to a lesser extent n-type, has been thoroughly investigated, the behavior of n^+ silicon in aqueous HF has not been widely studied and consequently is poorly understood.

Anodic Dissolution of Silicon

The anodic dissolution and electropolishing of silicon in aqueous hydrofluoric acid solutions was first accomplished by Turner (3) and has recently been studied by Memming and Schwandt (4). The dissolution mechanism for semiconductors in general and silicon in particular has been discussed by numerous authors (3-9), the over-all reaction being most simply written as

$$Si_{(solid)} + 6F^- + (4 - n)h^+ \rightarrow SiF_6^{=}{}_{(soln.)} + ne^- \quad [1]$$

where quadrivalent dissolution has been assumed and n is a number between zero and four. (h^+ represents a hole-valence band charge transfer, and e^- an electron-conduction band charge transfer.) The physical picture behind Eq. [1] is that the primary reaction (perhaps the initial breaking of covalent bonds) requires holes and that these reaction products are unstable allowing electrons to go into the conduction band (2). This leads naturally to current saturation on n-type anodes (2). The importance of valence band charge transfer has been well established by the multitude of experiments which have shown the dissolution current to be increased by any process which increases the supply of holes (2, 5, 8).

As might be expected from its form, Eq. [1] reveals little of the dissolution chemistry. Its vagueness becomes apparent once it is realized that n is not an integer and in general depends on the material resistivity and the current density (2, 5). Part of the difficulty is that effectively divalent dissolution has not been considered and, as will be seen shortly, a significant fraction of the semiconductor atoms always enter solution divalently. Although it is not certain that they are present, if the formation of divalent silicon compounds is allowed, say SiF_2, the disproportionation

$$2SiF_2 + 2F^- \rightarrow Si + SiF_6^{=} \quad [2]$$

or, in general, polymerization

$$(1 + x)SiF_2 \rightarrow Si_xF_{2x+2} + Si \quad [3]$$

reactions must be accounted for.

In principle, analysis of the elementary steps

$$Si^{+m} + h^+ \rightarrow Si^{m+1} \quad [4a]$$

or

$$Si^{+m} \rightarrow Si^{m+1} + e^- \quad [4b]$$

where $m = 0$ to 3, should be undertaken. (In writing [4a] and [4b] it is understood that silicon atom is bonded to and complexed with the crystal lattice and/or appropriate solution species.) Then allowing for any other reactions such as are illustrated by [2] and [3] and for any larger aggregate dissolved species would yield an over-all description of the dissolution if the appropriate concentrations and rate constants (energy barriers and their tunneling probabilities) were known. From the data on n- and p-silicon it can be concluded that reaction [4a] is favored over [4b] for $m = 0$ (the initiating step). Reaction [4b] presumably becomes more competitive as m successively increases to 1, 2, and 3. The numerous possible reaction paths clearly allow n in Eq. [1] to have a noninteger value even if no divalent dissolution occurs.

Any hypothetical mechanism must account for the fact that heavily doped n-type semiconductors can pass large currents and be electropolished quite nicely (10, 11). Gereth and Cowher (12) have concluded from measurements of the corrosion potential, I-V curves in alkaline solution with and without added oxidizing agents, and the temperature dependence, that dissolution of heavily doped n-type germanium does not depend on holes but goes entirely by a conduction band mechanism. The details of what occurs are not at all clear.

It must not be supposed that n^+ material becomes "just like a metal" since the bonds are still covalent, as opposed to the metallic bonding and consequent indistinguishability of charge transfer paths for a metal. A detailed semiconductor dissolution mechanism must deal with the electrons in these localized covalent bonds. Evaluation of possible current flow mechanisms in light of capacitance-voltage measurements of the n^+ silicon-electrolyte interface will be made in a separate paper.

Experimental Method

All current-voltage data reported herein were taken using thick (6 mm) silicon slices about 3 cm in diameter which were held vertically in the Teflon sample holder shown in place in a thermostated electrolyte bath in Fig. 1. The electrolyte was 5 w/o (weight per cent) aqueous HF (2.5N) which is in about the center of the practical range of concentrations for electropolishing silicon (1-5N) (13). The area of the slice exposed to the solution was 1.27 cm^2 and, unless stated

Key words: silicon electrochemistry, anodic dissolution, n-type silicon.

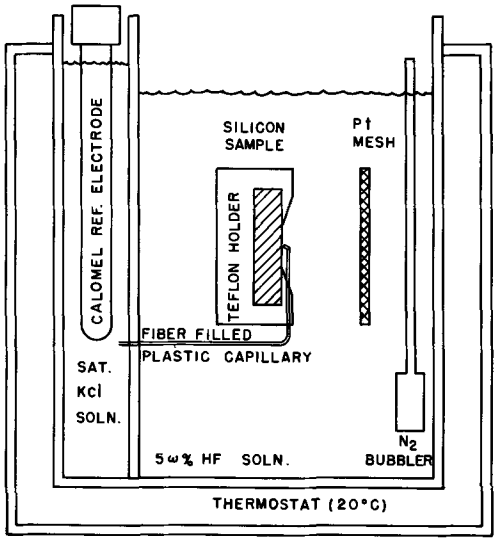

Fig. 1. Experimental arrangement for current-voltage measurements.

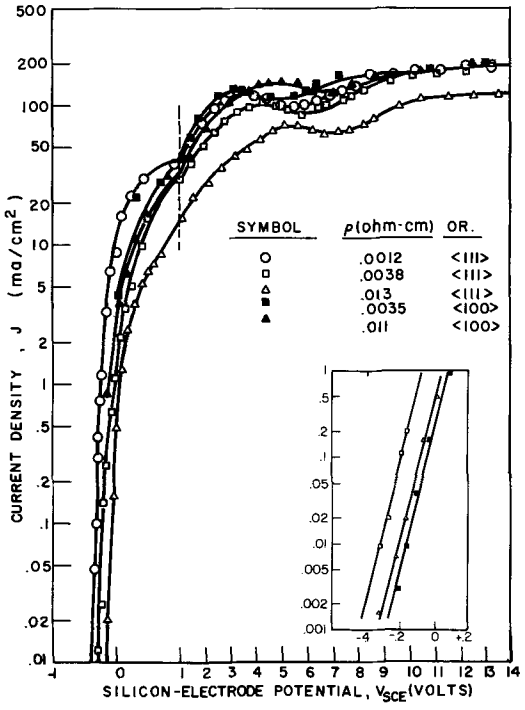

Fig. 2. Current density *vs.* silicon electrode potential for n^+ silicon. (Note change of scale at +1V.)

otherwise, all experiments were performed at 20°C and in the dark. The cell configuration and dimensions were chosen to simulate as closely as possible the conditions used for an electrochemical process of technological interest. The electrolyte was purged with nitrogen before data were taken and during experimentation nitrogen very slowly bubbled through the solution near one wall of the cell which was kept under a nitrogen cover. The silicon samples of <111> and <100> orientation were of n- and p-type doped with As and B, respectively, and were initially chemically etched and silica-sol polished.

The silicon sample was held at a set potential relative to a platinum mesh auxiliary electrode having a projected area of 25 cm². This electrode is placed 2 cm from the exposed silicon surface and the tip of the capillary which connects to the reference electrode chamber is about 1 mm removed (see Fig. 1). The cell potential, the silicon electrode potential *vs.* the saturated calomel reference electrode, and the current are recorded on a point to point basis (as opposed to sweeping through a potential range).

For the case of silicon samples that could be electropolished (n^+ and p), the surface was prepared before each measurement by electropolishing. This was found to give reproducible results whereas simply going from one cell potential value to another yielded a hysteresis effect at intermediate current densities. In the case of n-silicon, which cannot be electropolished, reproducible data could be taken by step-wise increasing of the cell potential. Selected values of potential and current which were taken in this way were checked by repeating the measurement at the same cell potential using a fresh silica-sol polished surface.

Only anodic currents are considered here. Attempts to measure cathodic currents showed that two rather reproducible current values were obtained for a given cell potential depending on whether the surface was electropolished or had received an extended cathodic treatment at relatively large negative potential (several volts). Furthermore, the two values do not approach one another for current densities less than a few milliamperes per square centimeter even after many tens of minutes. [Similar effects have previously been observed for both Ge and Si (5).] Clearly some sort of hydrogen pretreatment of the electrode is involved, but since it was not of direct interest to the present study this phenomenon was not investigated further.

Experimental Results

Current voltage relation for n^+ silicon.—Current density as a function of the silicon potential (relative to the saturated calomel reference electrode) has been measured on samples having resistivities in the range 0.001-0.01 ohm-cm with <111> and <100> surface orientations. The results are summarized in Fig. 2. The open-circuit potential, $V_{SCE}(J = 0)$, is in the range −0.3 to −0.4V for these heavily doped samples as well as for lightly doped n and p specimens to be discussed shortly. The value, however, is not too reproducible (±20 mV) although in general most negative for n^+ and p samples being usually somewhat less negative for n silicon. For current densities below a few tenths of a milliampere per square centimeter a Tafel relation applies, the slope being about 0.1V/decade in agreement with other measurements on silicon anodes (8).

For descriptive purposes attention is focused on one of the curves of Fig. 2, −0.0012 ohm-cm, <111>-orientation. Above a few tenths of a milliampere per square centimeter the experimental curve departs from the Tafel line and below 17 mA/cm² a film forms on the silicon surface. (This "critical" current density will be discussed further in a subsequent section.) Above this current density no film is formed. As the potential is further increased, the current goes through a maximum of about 120 mA/cm² at 3V. Below this potential, dissolution with no film formation occurs but the surface is not electropolished; for greater potentials, a bright electropolished surface is produced.

Figure 3a shows a surface after extensive anodic dissolution at a current density only slightly greater than that at which film formation is observed. Numerous small pits are observed and the surface appears almost as if sand blasted. At a somewhat greater current density, Fig. 3b, the surface exhibits the familiar "orange peel" appearance often observed on chemically etched surfaces. This figure also displays one of the conical pits which are sometimes observed at these intermediate current densities. When such a surface is etched with a dislocation revealing etch, a pit is usually formed at the site of the electroetched pit and it is suggested that they are due to dislocations.

As the potential is further increased beyond the point corresponding to the current maximum, electropolishing of the surface takes place and the current density first goes through a minimum and then steadily increases with applied potential. This maximum/minimum behavior is presumably due to change in

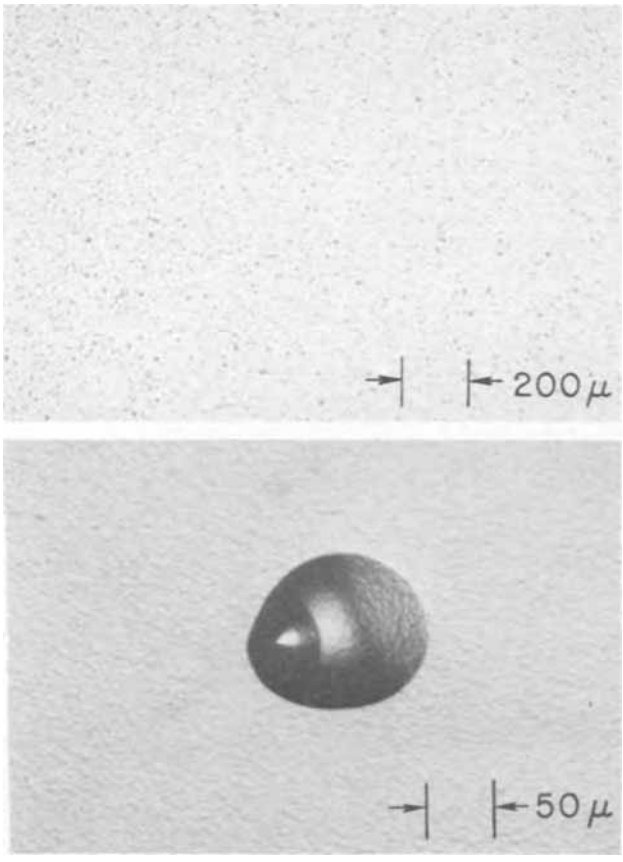

Fig. 3. n^+ Silicon surfaces after anodic dissolution at low current densities. (a) (top) $J \simeq 1.1\ J_c$; (b) (bottom) $J \simeq 50$ mA/cm^2.

structure of the silicon/solution interface; that is, development of the "polishing film."

At a given silicon potential, the current density is seen to be a function of the material resistivity and orientation. <100> surfaces draw a greater current density than <111> surfaces for the same resistivity. That this is to be expected can be argued from the number and accessibility of the surface bonds. Such orientation effects have been well documented (8). Also, for a given potential and surface plane, the current density decreases with increasing resistivity. The curves could be made to coincide only by shifting along both the current and potential axes since the maximum and minimum occur at different potentials for different silicon resistivities. Clearly, this J-V behavior cannot be explained in any detail until the dissolution mechanism can be clarified. Measurements on samples where the dopant was Sb or P rather than As showed the J-V relation to be independent of the dopant atom.

In Fig. 4 J-V data are presented for p silicon in the resistivity range 0.01-1 ohm-cm and of <111> and <100> orientation. The general behavior of the current voltage curve is the same as was observed for n^+ samples, the current density magnitude being comparable to that for the most heavily doped n material. While <100> surfaces may draw slightly more current than <111> surfaces at the same potential, there is no resolvable dependence on the material resistivity. It is tempting to explain this resistivity effect by arguing that for p silicon of any resistivity all the holes that could possibly be consumed are readily available at the surface whereas for n^+ silicon a barrier to current flow exists and that the magnitude of this barrier decreases with decreasing resistivity. The orientation dependence for n^+ would seem to imply that bond accessibility is also important in determining this barrier.

Effective dissolution valence and critical current density.—An effective dissolution valence, ν_e, is defined

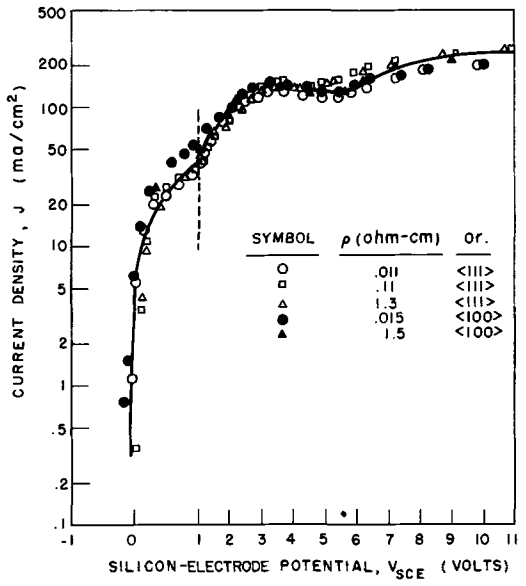

Fig. 4. Current density vs. silicon electrode potential for p silicon. (Note change of scale at +1V.)

as the number of electronic charges passing through the external circuit per atom of silicon entering solution. If both divalent and quadrivalent dissolution are allowed, then the ratio of the number of atoms going into solution as Si^{+2}, N_2, to those as Si^{+4}, N_4, is

$$\frac{N_2}{N_4} = \frac{4 - \nu_e}{\nu_e - 2} \qquad [5]$$

The experimental data for heavily doped n-type silicon are given in Fig. 5 where the effective valence has been plotted *vs.* the silicon-electrode potential. The range of potentials covered is from at or very slightly below the potential at which surface film-formation is observed to well into the electropolishing region. Even for large potentials and current densities (~200 mA/cm^2) a significant fraction ($N_2/N_4 \simeq 0.1$) of the silicon goes into solution in the effectively divalent form. When ν_e drops much below 3 ($N_2/N_4 = 1$) formation of a surface film is observed. Figure 5 may be used with the J-V curves to obtain the electropolishing (or etching) rate.

It has been observed by a number of authors, but in particular by Turner (3), that below some characteristic current density a thick brown film forms on anodically biased silicon electrodes, which film was thought to be amorphous silicon (13). Based on the facts that this characteristic, or critical, current density increased with increasing temperature, with increasing concentration of HF in solution, and with decreasing solution viscosity, Turner (3) concluded that the phenomenon was due to the HF concentration

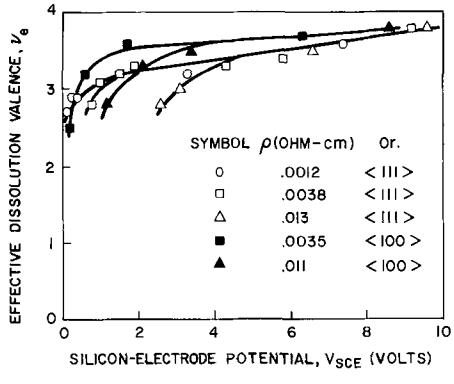

Fig. 5. Effective dissolution valence vs. silicon electrode potential for n^+ silicon.

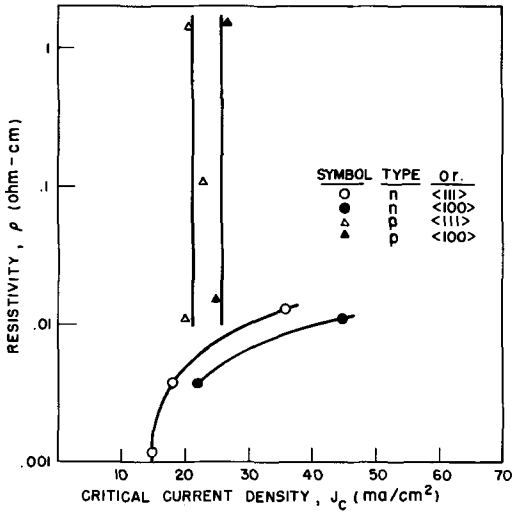

Fig. 6. Critical current density for brown film formation as a function of resistivity, conductivity type, and orientation.

at the silicon-solution interface increasing above some critical value.

The present determinations of this critical current density, J_C, are presented as Fig. 6 for various resistivities and orientations of n^+ and p silicon. The HF concentration, as in all experiments, was 5 w/o. The first rather startling observation to be made is that this current density is definitely a function of resistivity and apparently also of surface orientation for n^+ material. This is not explicable on the basis of a limiting surface concentration of some species transported from the bulk of the solution. For p silicon, the critical current is independent of resistivity and the apparent orientation dependence is hardly greater than the experimental uncertainty.

Turner (3) found for horizontal p-type electrodes facing up and conditions otherwise the same as the present experiments that $J_{c(H)} = 55$ mA/cm² whereas the present determination is $J_{c(V)} = 20$ mA/cm² for a vertical surface. For some species transported from the solution bulk to the interface

$$W_H = k_H(C_s - C_i) \quad [6a]$$

and

$$W_V = k_V(C_s - C_i) \quad [6b]$$

where W is the mass flux to the surface, k is the mass transfer coefficient, and $C_s(C_i)$ is the bulk solution (interface) concentration of the species in question. The subscript H(V) specifies a horizontal (vertical) electrode. At steady state, and if this diffusing species enters the dissolution reaction it is to be expected that

$$J \propto W \quad [7]$$

Thus the conclusion is that

$$J \propto k$$

or

$$\frac{J_V}{J_H} = \frac{k_V}{k_H} \quad [8]$$

The free convection problem for the vertical surface has been solved (14) but not that for the horizontal one. Appeal can be made however, to the well-known similarity between the mass-transfer and heat-transfer problems (14, 15). For free convection heat transfer from plates to fluids (15) it is known that the coefficient is less for the vertical than the horizontal plate. In addition, the present experimental arrangement is not fully equivalent to the vertical surface as the sample is considerably set back in the holder, further reducing the mass transfer coefficient (increasing the boundary layer thickness) relative to a horizontal surface. Thus from Eq. [8] it is expected that the critical current density in the present experiments should be less than that measured by Turner (3), as was in fact found to be the case.

The present results then support the earlier conclusions (3), but for n^+ silicon other factors must also be of importance. This difference appears to be related to the interface barrier which for p silicon is independent of resistivity but on n^+ silicon depends on the doping level.

Some further comments on the nature of the thick surface film are in order. First, the film in no sense passivates the surface. After a few minutes, the film thickness appears to reach a constant value and neither the current density nor the silicon electrode potential change with time even while the film is developing. Second, it is often stated that the films produced react vigorously, even explosively, with strong oxidizers (HNO_3,H_2O_2). Silicon samples, upon which such films were grown, have been placed in nitric acid and hydrogen peroxide solutions for 24 hr and no reaction whatsoever has ever been observed. If, however, the film is removed and placed in the oxidizing solution, it disintegrates immediately. (Dissolves or reacts do not seem to be appropriate descriptions.) Apparently the latter observation is the result of some change induced in the film when it was removed from the silicon (by raising the potential and polishing out the underlying silicon so that the film floated off).

The chemical composition of the films which form on silicon when anodized at low current in HF solution or when etched in HF:HNO_3 mixtures, very dilute in HNO_3, is uncertain. Mass analyses (13, 19) have indicated the films are 90+ w/o silicon and Turner (13) postulated that they were amorphous silicon while Archer (19) proposed that they were silicon hydrides at least in the case of films formed in HF:HNO_3 mixtures. Yoshioka (20) and Beckmann (21) have studied the films formed in HF:NO_2 gas mixtures (20), anodically in HF, and in HF:HNO_3 (21) by infrared spectroscopy (20, 21) and omegatron mass analysis (20) and have found them to be mostly silicon hydrides. It is felt that in the anodic case the film is probably at least partially silicon hydrides and that it is in fact the presence of hydride films which passivates silicon surfaces to direct attack by HF which would be expected thermodynamically. It may be mentioned that hydride films are known to be formed on the surfaces of some metals dissolving in hydrofluoric acid (22).

Current voltage relation for n silicon.—Silicon of n-type resistivity greater than 0.05 ohm-cm shows current saturation as the potential is increased. Figure 7 presents the J-V data measured for n-type samples. Up to a current density of about 50 μA/cm² the current remains at a constant value for at least an hour. Here again, it must be noted that no passivation occurs and some slow dissolution is always taking place. However,

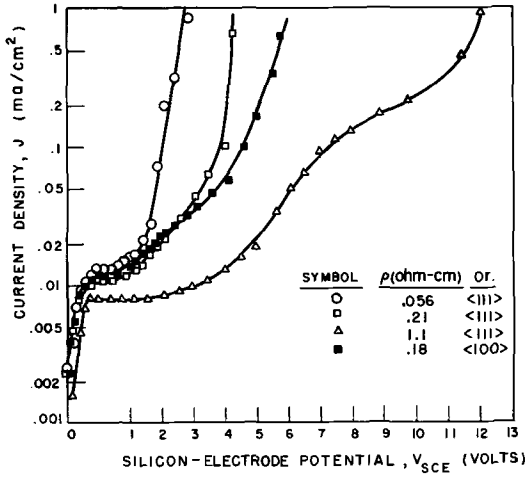

Fig. 7. Current density vs. silicon electrode potential for n silicon.

a measurable uniform etching of n-type has never been observed, rather pitting occurs. For somewhat greater potentials (but current densities less than 1 mA/cm²) the current stabilizes at a constant value for about the first minute after the potential is applied (it is this point that is plotted in Fig. 7) and then slowly increases over a period of about an hour to a second value of the current density (but with larger fluctuations, 10-20%, about the mean) of about 2 to 5 times the initial value. Beyond the range plotted in Fig. 7 (that is, currents greater than 1 mA/cm²) the fluctuations in current are so large and erratic that no meaningful measurement can be made. This may indicate the breakdown of a surface film and the existence of a second current voltage relationship in its absence. The saturation currents observed, about 10 μA/cm², are comparable to those measured by Flynn (16) for silicon. The present data, however, show lower saturation currents for the higher resistivity material, whereas the opposite is observed for Ge (17). This could be due to differences in the concentration of generation centers from sample to sample. For silicon, the saturation current is said to be dominated by the space charge generation current (8), I_g where

$$I_g \propto N_g \sqrt{\rho} \qquad [9]$$

N_g is the density of generation centers and ρ the resistivity. It is not unreasonable to suppose that N_g is greater for the more highly doped material due to incorporation of greater amounts of foreign substances which do not affect the resistivity and due to the expected increase in crystallographic defects.

However, from the observed saturation current, an effective lifetime may be estimated from (8)

$$J_{gen} = \frac{en_i}{2\tau_0} W \qquad [10]$$

where e is the electronic charge, n_i the intrinsic carrier density, W the space charge width, and τ_0 the lifetime. For the 1.1 ohm-cm sample, for which the current density is 8 μA/cm², τ_0 is, from Eq. [10], 7 $(10)^{-9}$ sec; whereas the actual lifetime was determined to be 3 $(10)^{-8}$ sec by use of the MOS deep depletion technique. A low-temperature plasma oxide was used so the lifetime would not be changed by high-temperature processing. Therefore, the currents observed cannot be explained on the basis of space charge generation alone. It would appear that other factors such as surface generation and injection may also be important, and there may be localized areas of high current density at the surface connected with the localized breakdown examined next. As will be discussed later, the silicon is observed to be nonuniformly attacked after extensive anodic dissolution above the saturation current region.

As has been observed also for germanium (17), saturation breakdown occurs at a voltage an order of magnitude less than would be expected from abrupt junction avalanche considerations. Breakdown is not uniform, but occurs at numerous isolated spots on the surface. This results in a heavily pitted surface, to be discussed further in the following section, and would appear to be due to local electrochemical attack. The breakdown has not been studied in detail but it is possible that it occurs at crystal defects or points of impurity segregation (8, 18). The apparent explanation for the initial and final steady currents observed for the initial current values greater than 50 μA/cm² is that the initial value is characteristic of the smooth polished surface and the final value corresponds to the pitted surface. It has been observed (8) that for 1 ohm-cm n silicon in KOH and H_2SO_4 solutions, breakdown does not occur until potentials of 70 or 80V are applied, but it seems likely that a significant portion of this voltage appears across an anodic oxide film.

Figure 8 illustrates the familiar increase in saturation current due to illumination of the surface. When

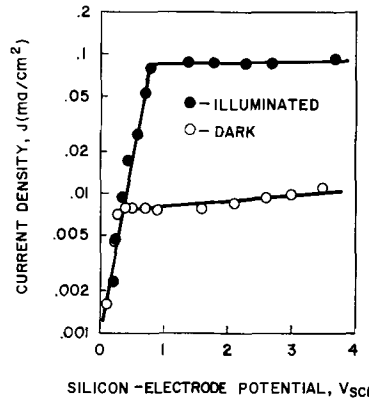

Fig. 8. Current density, potential relation for n silicon (ρ = 1.1 ohm-cm <111>) in the dark and illuminated.

the same light is shined on n+ samples no effect is observed over the entire range of current densities.

Effect on n silicon of prolonged anodic treatment.— Due to the large and erratic currents which n silicon was observed to draw at relatively low potentials and the fact that an electrochemical process of interest allows n material to be exposed to the solution at significant potentials for extensive times, it was deemed necessary to ascertain the effect of prolonged anodic treatment. A total charge of 0.2 coulomb was passed through the samples at various cell potentials, and the surface was microscopically examined. This was followed by a 10-sec etch (white etch-1HF:3HNO_3) examination, a 2 min-etch, and a final observation of the surface. The surfaces subsequently to be described are all of <111> orientation.

Figure 9a shows the surface of a sample for which the (initial) current density was 0.2 mA/cm² (well above the saturation current) after anodization. The surface is very densely and harshly pitted and is somewhat reminiscent of a mechanically damaged one. After the 10-sec etch a curious phenomena is observed as illustrated by Fig. 9b which shows the surface to be covered by a dense brownish-black adherent layer. This cannot be wiped or even scraped off and always covers all of the area which was exposed to the electrolyte. A subsequent 2-min etch removes this film and

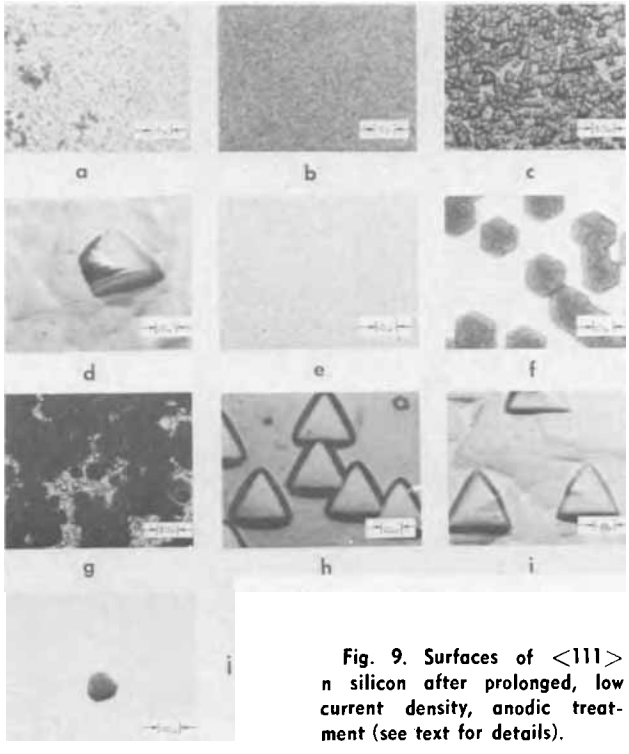

Fig. 9. Surfaces of <111> n silicon after prolonged, low current density, anodic treatment (see text for details).

produces a densely pitted surface, Fig. 9c. Most of these pits are not further resolvable, but in some places pits as shown in Fig. 9d are found. At or slightly above the saturation current, 10 to 20 μA/cm^2, the surface after anodic treatment appears as in Fig. 9e. The small shallow pits produced are of a surprisingly regular size and spacing. A 10-sec etch produces the hexagonal features of Fig. 9f and g and it is at once realized that 9b consisted of a complete coverage of the surface by these features which appear to be shallow pits, the bottoms of which are filled with the brownish-black matter. Figure 9f is for saturation current and Fig. 9g for a current twice the saturation value. When the 2-min etch is performed, the surface is again observed to be covered with pits as shown in Fig. 9h and i. Those of Fig. 9h are much more common than the more structured pits of 9i. (It must be emphasized that no pitting occurs on portions of the sample not exposed to the electrolyte.) When the current is below the saturation value, in particular 2 μA/cm^2, no resolvable features are observed after 0.2 coulomb are passed. However, after a 10-sec etch, of the order of 10 of the hexagonal features as shown in Fig. 9j are observed per square centimeter of surface. For <100> surfaces the same behavior is observed except that the hexagons become squares. It is apparent then that if usable n-type silicon is to be reclaimed after it has been anodically exposed that careful attention must be paid to the process parameters such as silicon potential and exposure time. Clearly, this also introduces limitations on the structures which may be produced by electroetching processes.

Summary

The details of the mechanism of anodic silicon dissolution are at present rather obscure especially for heavily doped n-type samples. More information will be needed before a thoroughly convincing model can be constructed because the properties of the interface region where the relevant electrochemical reactions take place are largely unknown.

Current-voltage curves, the effective dissolution valence, and the critical current density have been measured for silicon of various orientation, type, and doping level. The n$^+$ silicon of resistivity less than 0.05 ohm-cm can be electropolished and the J-V relation, which depends on the resistivity and orientation, may be divided into three regions. Below a critical current density, which itself is a function of orientation and resistivity, a steady current passes at constant cell potential but the well-known thick brown film forms on the electrode surface. It has been found, as a supplement to previous observations, that the film does not react at all with strong oxidizing agents if it is not removed from the silicon. This also applies to films formed on p silicon for which the resistivity has no effect on the critical current density value.

The second portion of the J-V curve extends from the critical current density to a maximum in the J-V curve observed at a silicon electrode potential of a few volts and $J \simeq 100$ mA/cm^2. In this range dissolution occurs without any film formation but the surface is rough and pitted; this is an etching, as opposed to electropolishing, regime. Beyond the maximum, bright electropolishing occurs. Measurements on p samples show the J-V curve to be independent of resistivity, the general features being the same as for n$^+$.

From measurement of the effective dissolution valence it is seen that even at large potentials a significant portion, 10%, of the material enters solution effectively divalently. The thick brown film apparently forms once the effective valence drops much below three, that is when more than half of the dissolution is divalent. It appears that for n$^+$ silicon a factor in addition to the surface HF concentration is involved in the critical current density determination.

The n-type silicon having resistivity greater than 0.05 ohm-cm exhibits current saturation but breakdown occurs at only a few volts even for 1 ohm-cm material. The breakdown is not uniform but occurs at localized points on the surface and causes extensive damage to it at least for <111> and <100> surfaces. Prolonged anodic bias at currents above saturation has been shown to result in extensive attack at the surface.

Acknowledgments

The author would like to thank R. H. Braun for assistance with the measurements and P. J. Boddy and M. P. Lepselter for valuable discussions. G. W. Reutlinger determined the lifetime quoted and J. R. Ligenza grew the low-temperature plasma oxide involved.

Manuscript submitted Aug. 10, 1970; revised manuscript received Nov. 4, 1970. This was Paper 182 presented at the Atlantic City Meeting of the Society, Oct. 4-8, 1970.

Any discussion of this paper will appear in a Discussion Section to be published in the December 1971 JOURNAL.

REFERENCES

1. J. I. Pan-kove, "The Electrochemistry of Semiconductors," p. 290, P. J. Holmes, Editor, Academic Press, London (1962).
2. W. H. Brattain and C. G. B. Garrett, *Bell System Tech. J.*, **34**, 129 (1955).
3. D. R. Turner, *This Journal*, **105**, 402 (1958).
4. R. Memming and G. Schwandt, *Surface Sci.*, **4**, 109 (1966).
5. E. A. Efimov and I. G. Erusalimchik, "Electrochemistry of Germanium and Silicon," Sigma Press, Washington (1963).
6. D. R. Turner, "The Surface Chemistry of Metals and Semiconductors," p. 285, H. C. Gatos, Editor, John Wiley & Sons, Inc., New York (1959).
7. H. Gerischer, *Surface Sci.*, **13**, 265 (1969).
8. V. A. Myamlin and Y. V. Pleskov, "Electrochemistry of Semiconductors," Plenum Press, New York (1967).
9. H. Gerischer and W. Mindt, *Electrochim. Acta*, **13**, 1329 (1968).
10. M. V. Sullivan *et al.*, *This Journal*, **110**, 412 (1963).
11. D. Baker and J. R. Tillman, *Solid-State Electron.*, **6**, 589 (1963).
12. R. Gereth and M. E. Cowher, *This Journal*, **115**, 645 (1968).
13. D. R. Turner, "The Electrochemistry of Semiconductors," p. 176, P. J. Holmes, Editor, Academic Press, London (1962).
14. V. G. Levich, "Physiochemical Hydrodynamics," p. 127, Prentice-Hall, Englewood Cliffs, N. J. (1962).
15. S. T. Hsu, "Engineering Heat Transfer," p. 384, D. Van Nostrand, Princeton (1963).
16. J. B. Flynn, *This Journal*, **105**, 715 (1958).
17. A. Uhlir, *Bell System Tech. J.*, **35**, 333 (1956).
18. P. J. Boddy, *This Journal*, **111**, 1136 (1964).
19. R. J. Archer, *J. Phys. Chem. Solids*, **14**, 104 (1960).
20. S. Yoshioka, *Philips Res. Repts.*, **24**, 299 (1969).
21. K. H. Beckmann, *Surface Sci.*, **3**, 314 (1965).
22. W. J. James and M. E. Straumanis, *This Journal*, **106**, 631 (1959).

Corrosion and Passivation of Thin Molybdenum Films

L. H. Lee* and V. Y. Doo*

IBM Components Division, East Fishkill Facility, Hopewell Junction, New York 12533

ABSTRACT

Corrosion behavior of thin molybdenum films was investigated in the environments of air, fluorochemical liquid coolant ($C_5F_{11}NO$), and deionized (DI) water in the 70°-100°C temperature range. A striking similarity both in kinetics and mechanism was observed for the corrosion of molybdenum film in dry air and dry coolant ($C_5F_{11}NO$), as well as moist air and wet coolant ($C_5F_{11}NO/H_2O$). Molybdenum remains inert in dry environments and corrodes in the wet media. In addition, molybdenum forms a nonprotective, porous corrosion film and dissolves in DI water at 85°C. The simultaneous presence of water and oxygen in these environments is the controlling factor on the corrosion of molybdenum films. An effective passivation of thin molybdenum films can be provided by either a single layer of silicon dioxide or a composite layer of silicon nitride over silicon dioxide on the metal film.

For the past decade, metal and insulating thin films have received increased attention principally for their broad application in microelectronic components. Metal thin films serve as ohmic contacts and interconnections in integrated circuits, and insulating films serve as diffusion masking and surface passivation. To have good performance and reliability, the metal films require low-resistance ohmic contacts, good adhesion to oxide and silicon, and resistance to deterioration at the temperature and conditions of use. Among the limited materials (1) which meet these criteria, molybdenum has been suggested (2) for integrated circuits because of the unique combination of such properties as good thermal stability, reasonably high electrical conductivity, and good adhesion to oxide and silicon. However, limited information on the corrosion of molybdenum is available (3, 4). For a fuller understanding of molybdenum corrosion behavior in the environments of air and several commonly used coolants including water and fluorochemical liquid ($C_5F_{11}NO$), accelerated corrosion tests were conducted in these environments to study the kinetics and mechanism of corrosion. A method of passivating the molybdenum films by pyrolytic silicon dioxide and silicon nitride films was also developed.

Experimental

Materials.—A 6000-7000Å layer of silicon dioxide was thermally oxidized on 1¼ in. diameter silicon wafers. Two 12,800Å thick molybdenum films were deposited on the silicon dioxide, the first by RF sputtering and the second by chemical vapor deposition. Molybdenum blanket films were produced by the RF sputtering process at a rate of 500 Å/min at 500°C. The pyrolytic molybdenum films were deposited by the hydrogen reduction of $MoCl_5$, followed by the formation of a photolithographic pattern. For passivated samples, pyrolytic silicon dioxide of various thickness was deposited at 475°C at a rate of 350 Å/min using an O_2:SiH_4 ratio of 10:1; silicon nitride films were produced by RF glow discharge at 450°C. All samples were degreased in acetone and air dried before testing. Fluorochemical liquid coolant ($C_5F_{11}NO$), air, and DI water were employed as the basic environments for corrosion study.

Exposure details.—Liquid coolant was used with water ($C_5F_{11}NO/H_2O$) and without ($C_5F_{11}NO$) as a second phase. When the tests were performed in aerated condition, specimens were enclosed in a mechanically sealed 50 ml Pyrex tube. Each tube contained one specimen along with 25 ml of $C_5F_{11}NO$ which had been saturated with compressed air by bubbling for 10 min. An additional 5 ml of DI water was added to the tube whenever required. For the tests in deaerated $C_5F_{11}NO$, the liquid was degassed by an alternating freeze/melting vacuum technique (5). Specimens were vacuum sealed in a heavy-walled Pyrex tube which contained one specimen and 5 ml of $C_5F_{11}NO$, plus 1 ml of DI water. By deaeration, the oxygen concentration in $C_5F_{11}NO$ was reduced from 84 to 18 μg/ml. All test tubes were placed in the conventional laboratory ovens in such a position that the specimens were completely immersed in $C_5F_{11}NO$. Unless otherwise stated, aerated $C_5F_{11}NO$ and $C_5F_{11}NO/H_2O$ were employed. During the experiment, specimens were removed alternately for the measurements and carefully handled to eliminate any direct contact with water. When the tests were conducted in DI water, a similar procedure was employed. Test temperature was accurately controlled and maintained constant within ±1°C. For the tests in dry air, a laboratory oven was used; in moist air, a temperature-humidity cabinet[1] was employed. The specimens were handled in glass cradles to permit air circulation.

Methods of evaluation.—The corrosion of molybdenum films was determined by several measuring techniques. The method chosen depended entirely on the characteristics of the corrosion film. The gravimetric method was used when the corrosion film was thick and visible to the naked eye. Ellipsometry was employed when the corrosion films were thin and invisible. Both measurements were made in the atmosphere at room temperature.

The gravimetric method has long been favored for conducting laboratory corrosion experiments. Samples were weighed with a microbalance[2] which gives accurate readings to ±5 μg. The changes in weight per unit area were recorded.

Ellipsometry is the measurement of the changes in the state of polarization of light when reflected from a surface. By determining and comparing the optical properties of a film-free and a film-covered metal surface, the film thickness can be determined with accuracy. The principle and application of the ellipsometer[3] have been detailed elsewhere (6-8). Metallographic examination and statistical evaluation were also employed to study the corrosion and passivation of molybdenum films.

Results

Corrosion of thin molybdenum films.—$C_5F_{11}NO$ was used as an effective coolant for high-power electronic devices (9). Sputtered films exposed to $C_5F_{11}NO$ at

* Electrochemical Society Active Member.

Key words: corrosion kinetics and mechanisms, molybdenum film corrosion behavior, molybdenum film passivation, silicon dioxide passivating layer, composite silicon nitride/silicon dioxide passivating layers.

[1] Blue M. Electric Company, Blue Island, Illinois.
[2] Mettler Instrument Corporation, Hightstown, New Jersey.
[3] Gaertner Scientific Corporation, 1201 Wrightwood Ave., Chicago, Illinois.

temperatures of 70°, 85°, and 100°C remained shining with no measurable weight change after 2000 hr immersion. Electron diffraction showed the presence of oxides, but their exact composition was not identified. Figure 1 shows the increase of oxide film thickness as a function of time. It was observed that all specimens oxidized slowly, reaching a film thickness less than 35Å after 2000 hr immersion. Tests in dry air gave similar results. Note that good agreement both in magnitude and curve shape was obtained in these two environments. The oxide film grew linearly with the logarithm of time. A distinct break was observed on these curves corresponding to a two-stage oxidation. The film thickness increased with increasing temperature and the critical time for the transition of the oxidation rate decreased with increasing temperature. Generally, the logarithmic rate relationship prevails at low temperatures for thin oxide films (10).

During the ellipsometer measurements, it is difficult to determine the optical constants of the clean metal surface without any superficial oxide film. In this investigation, we assume that the clean metal surface gives a minimum value of the measured azimuth φ and a maximum value of the phase difference Δ. The theoretical values of Δ and φ were plotted and compared with those experimental data obtained from various periods of the surface film growth (11, 12). A trial curve fitting gave a refractive index of 2.3.

In $C_5F_{11}NO$, the influence of dissolved water on molybdenum corrosion was studied with the presence of water as a second phase. Molybdenum formed a nonprotective porous corrosion film in aerated $C_5F_{11}NO/H_2O$ from 70° to 100°C. Figure 2 shows that the sputtered molybdenum films reacted at a continuously increasing rate with time and temperature. Further, the corrosion film tended to disintegrate and flake off after reaching a critical thickness or critical time as indicated by the arrows. In this instance, the corrosion film served no protective purpose and did not reduce the corrosion rate. Comparing the results obtained in $C_5F_{11}NO$ with those in $C_5F_{11}NO/H_2O$, the corrosion rates differed by three orders of magnitude. In addition, the character of the film changed from protective to nonprotective. There is no doubt that water exerts a significant effect on the corrosion of molybdenum in $C_5F_{11}NO/H_2O$. Attempts have been made to analyze the dissolved water concentration in $C_5F_{11}NO$ and $C_5F_{11}NO/H_2O$. The results obtained by the Karl Fischer Spectrometric method showed that the water concentration in $C_5F_{11}NO$ was less than 23 μg/ml at 70° and 85°C. However, the water concentration in $C_5F_{11}NO/H_2O$ increased to 133 μg/ml at 70°C and to 261 μg/ml at 85°C.

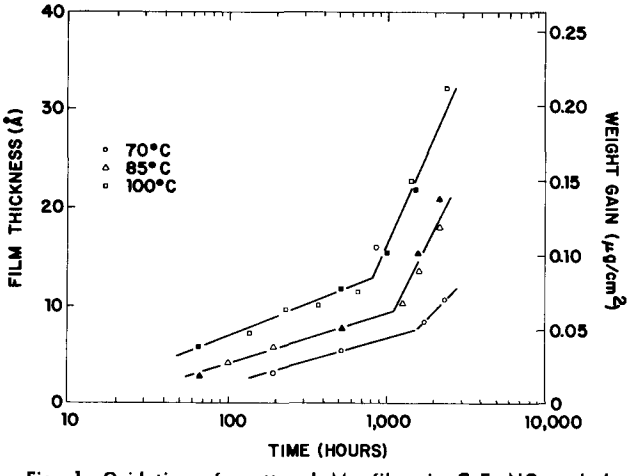

Fig. 1. Oxidation of sputtered Mo films in $C_5F_{11}NO$ and dry air. Weight gain data were calculated from the oxide film thickness, assuming the film is MoO_2 (density = 6.47 g/cc). Solid symbols indicate dry air environment.

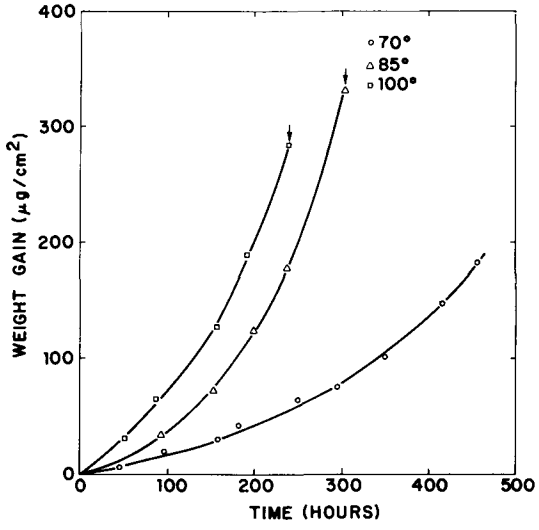

Fig. 2. Corrosion of sputtered Mo films in $C_5F_{11}NO/H_2O$

The pronounced influence of water was further verified by a simple experiment: specimens were partially contaminated by water droplets before exposure to $C_5F_{11}NO$. Rapid destruction was observed locally only at contaminated points, while the rest of the specimen remained unattacked. However, tests in deaerated $C_5F_{11}NO/H_2O$ showed no measurable weight change and no visible discoloration of molybdenum films after 2000 hr exposure at 100°C. Obviously, water is important for the corrosion of molybdenum only when oxygen is present. In other words, both oxygen and water are the major corrosive ingredients in the corrosion of molybdenum in $C_5F_{11}NO$. Neither aerated $C_5F_{11}NO$ nor deaerated $C_5F_{11}NO/H_2O$ corrodes molybdenum to any practical extent. To demonstrate the importance of relative humidity on the atmospheric corrosion of molybdenum, samples were also exposed to moist air at 85°C/85% RH. It was observed that molybdenum oxidized linearly with time and gave a constant rate of 2.3 μg/cm^2 hr. A similar rate relationship in moist air was reported by other investigators (3, 4). In moist air at 85°C, a critical relative humidity exists at 60%, below which the corrosion of molybdenum is nil. In $C_5F_{11}NO/H_2O$, molybdenum produced a water-soluble, porous corrosion film and discolored successively yellow, brown, blue, and black with increasing time exposure. This discoloration is most likely associated with the changing film thickness, oxidation state of the corrosion film, and test temperature. A similar corrosion film was obtained in moist air at 85°C/85% RH. X-ray diffraction analysis of the corrosion film showed no diffraction pattern; the film was practically amorphous in nature.

The destructive action of aerated water and the corrosion of molybdenum has been reported (4). Further tests in DI water at 85°C demonstrated the progressive deterioration of molybdenum film. Pyrolytic molybdenum films on oxidized silicon wafers were employed with subetched patterns. Figure 3 shows the degree of corrosion after various periods of immersion in DI water at 85°C. The samples clearly showed uniform corrosion after 24 hr, cracking after 40 hr, and disintegration along the cracks after 53 hr. Since the corrosion product is water soluble, molybdenum completely dissolved in DI water at 85°C after 65 hr immersion.

Passivation of thin molybdenum films.—Insulating films have become important for the surface passivation of electronic devices. In this investigation, insulating films such as pyrolytic silicon dioxide and silicon nitride were employed over pyrolytic molybdenum film with various thicknesses.

For the tests in moist air (85°C/85% RH), molybdenum-patterned silicon wafers containing 1000 units

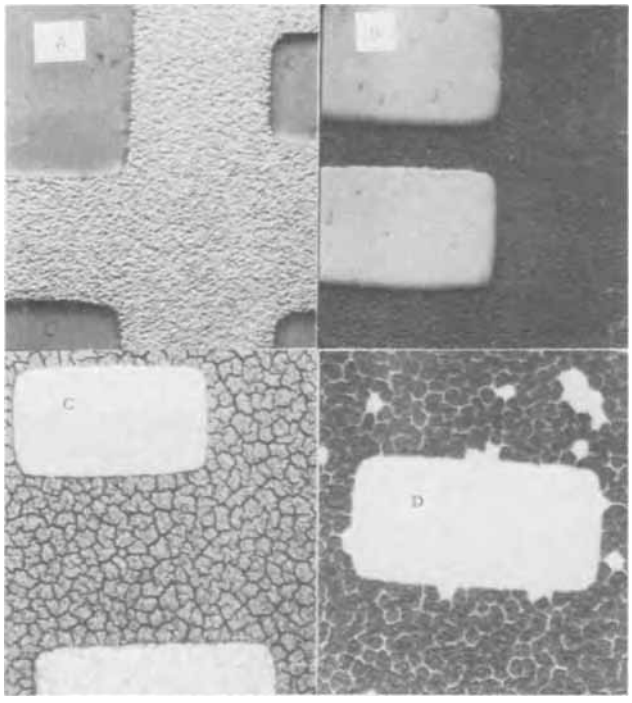

Fig. 3. Corrosion of bare pyrolytic Mo films in DI water at 85°C (525X): A, initial appearance; B, uniform attack after 24 hr; C, cracking after 41 hr; D, disintegration after 53 hr.

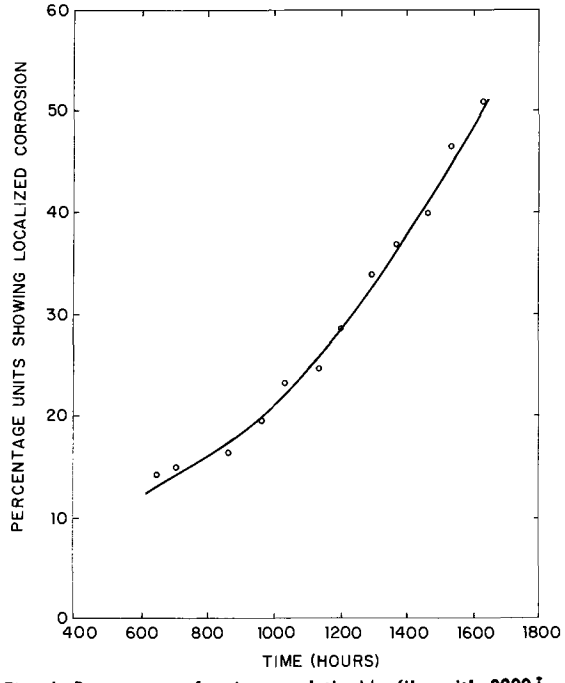

Fig. 4. Percentage of units, pyrolytic Mo film with 8000Å pyrolytic SiO_2 overlay, showing localized corrosion as a function of immersion time in 85°C DI water.

were used to determine the effective thickness for passivation. The percentage of corrosion is defined as the number of units corroded among the total number of units examined. It was observed that all units showed corrosion after 1500 hr with a 350Å silicon dioxide overlay. Corroded units were less than 10% after 2180 hr with 1750Å silicon dioxide overlay. No corrosion was noted on any of the units after 2360 hr exposure with 3500-7000Å silicon dioxide coatings. Samples with a composite layer of 770Å silicon nitride over 400Å silicon dioxide had corrosion on only 5% of the units after 1150 hr exposure.

For the tests in DI water at 85°C, the passivated samples with 400Å silicon dioxide overlay exhibited slight discoloration after 67 hr, localized corrosion at sharp corners after 85 hr, uniform corrosion along all film edges and narrow molybdenum stripes after 120 hr, and disintegration after 165 hr. The corrosion of molybdenum was delayed up to three times longer. A composite layer of 770Å silicon nitride over 400Å silicon dioxide tended to delay corrosion onset six times longer than a single layer of 400Å silicon dioxide, and 20 times longer than the bare molybdenum film. When these units were overlaid with 8000Å silicon dioxide, corrosion was detected after 500 hr immersion in DI water at 85°C; only localized corrosion was noted with increasing immersion time.

Figure 4 illustrates the increase of localized corrosion recorded among a total of 268 units examined. On every corroded site, there was evidence of incomplete protection caused by the presence of 4-8μ dust particles. Comparing the results on bare and passivated molybdenum films in DI water, the lifetime of 12,800Å molybdenum films was increased about 3X by adding 400Å pyrolytic silicon dioxide, approximately 20X by a composite layer of 770Å silicon nitride and 400Å pyrolytic silicon dioxide, and about 60X by 8000Å pyrolytic silicon dioxide overlay.

Discussion

A similar corrosion behavior of molybdenum films was observed in $C_5F_{11}NO$ and dry air, and in $C_5F_{11}NO/H_2O$ and moist air. In $C_5F_{11}NO$ and dry air molybdenum reacts with oxygen, forming molybdenum oxides. However, the reaction rates are so slow molybdenum is essentially inert. Our observations support earlier reports (12, 13) that molybdenum retains its brightness up to 200°C and forms an oxide film of 1-3 atomic layers after 70 days exposure at room temperature. In contrast, molybdenum corrodes in $C_5F_{11}NO/H_2O$ and moist air and dissolves in DI water (85°C) after 65 hr immersion. As described previously, the presence of water in aerated $C_5F_{11}NO/H_2O$ plays an important role in the corrosion of molybdenum. Similarly, relative humidity controls the atmospheric corrosion of metal films. It is believed that in $C_5F_{11}NO/H_2O$ and moist air, the corrosion of molybdenum proceeds electrochemically:

1. Water and oxygen diffuse to the metal-liquid interface where reaction occurs forming a nonprotective porous corrosion film.
2. The spongy corrosion film serves as an electrolyte; oxygen and water migrate freely toward the bare metal film and corrosion continues.

The over-all reaction includes the dissolution of metallic molybdenum to molybdenum ions and the reduction of oxygen to hydroxide ions.

$$\text{Oxidation:} \quad Mo \rightarrow Mo^{+n} + ne$$

$$\text{Reduction:} \quad O_2 + 2H_2O + 4e \rightarrow 4\,OH^-$$

Charge conservation is maintained so each electron released is immediately consumed by oxygen reduction. In DI water free of oxygen, the cathodic reduction is a hydrogen evolution reaction which is very slow in neutral solution. Since the rate of oxidation depends on the rate of reduction, this can be speeded by dissolved oxygen. This explains why the simultaneous presence of oxygen is required to corrode molybdenum in $C_5F_{11}NO$, air, and water. This type of corrosion is characterized by porous corrosion film forming and reacting continuously until the metal is completely consumed. Determination of the exact composition of the corrosion film was extremely difficult. Numerous investigators (3, 4, 15) were not wholly successful for two reasons: (*i*) molybdenum oxides exist in different valence states ranging from 2 to 6; and (*ii*) slight changes in test condition may change the coordination number. From the literature (16), the most stable oxides are MoO_2 and MoO_3; hydroxide exists as $Mo(OH)_3$, or as $MoO(OH)_3$. Moreover, water-soluble molybdenum blue exists as $MoO_{2.5\text{-}3} \cdot XH_2O$, whose

composition is still not exactly defined. It is also reported that molybdenum exists as MoO_2 in air and dissolves in solution with a valence of six (17).

The effectiveness of passivation of molybdenum film is directly related to the pinhole density and moisture permeability of the passivative film (18). A pyrolytic silicon dioxide film less than 1000Å thick has a high pinhole density. For 1000Å films and thicker, the pinhole density decreases linearly with increasing film thickness; it approaches zero for oxide films with 6000 to 7000Å thickness. There is no doubt that the corrosion of passivated molybdenum film is greatly suppressed by increasing the silicon dioxide film thickness, *i.e.*, decreasing the pinhole density of the film. As described elsewhere (19), pyrolytic silicon dioxide has low pinhole density and good edge conformity, although its moisture absorption is relatively high. However, this disadvantage can be overcome by covering with silicon nitride film, which is known for its greater density, low moisture permeability, and excellent chemical inertness (20). It is expected that a composite layer of silicon dioxide and silicon nitride exhibited better performance than a single layer of silicon dioxide. Therefore, we conclude that molybdenum can be protected from corrosion by covering it with passivating films.

Summary

1. In $C_5F_{11}NO$ and dry air, molybdenum forms a thin oxide film that reaches a thickness less than 35Å after 2000 hr exposure at temperatures of 70°, 85°, and 100°C. The oxidation follows a logarithmic rate law.

2. In moist air (85°C/85% RH), molybdenum corrodes at a linear rate. In $C_5F_{11}NO/H_2O$ (70°-100°C), molybdenum reacts at a continuously increasing rate with time and temperature. In both media, molybdenum forms a nonprotective, porous corrosion film. The reaction is electrochemical in nature.

3. In DI water at 85°C, molybdenum films (up to 12,800Å) dissolve completely after 65 hr immersion.

4. Water and oxygen are the major corrosives in these environments.

5. Comparing the results on bare and passivated molybdenum films in DI water, the lifetime of 12,800Å molybdenum films was increased about 3X by adding 400Å of pyrolytic silicon dioxide, approximately 20X by a composite layer of 770Å silicon nitride and 400Å pyrolytic silicon dioxide, and about 60X with an 8000Å pyrolytic silicon dioxide overlay.

Acknowledgments

The authors gratefully thank J. A. Adley, E. F. Gorey, M. Revitz, F. A. Toman, A. Walker, A. A. Arcus, and J. Gardiner for their valuable support and assistance.

Manuscript submitted July 24, 1970; revised manuscript received *ca.* Oct. 30, 1970. This was Paper 199 presented at the Atlantic City Meeting of the Society, Oct. 4-8, 1970.

Any discussion of this paper will appear in a Discussion Section to be published in the December 1971 JOURNAL.

REFERENCES

1. N. Schwartz and R. W. Berry, "Physics of Thin Films," Vol. 2, p. 363, Academic Press Inc., New York (1964).
2. R. Glang, *J. Vacuum Science and Technol.*, **3**, 37 (1966).
3. S. A. Gintsberg and B. Ya. Kazovskaya, *Tsvetnye Metally*, **36(3)**, 84 (1963).
4. A. Hornung and S. J. Zanin to L. H. Lee, Private Communication, Feb. 7, 1969.
5. L. H. Lee, "Corrosion of Copper in Fluorochemical Liquid Coolants," Paper presented at NACE annual conference, Philadelphia, Pa., March 1970.
6. F. L. McCrackin, E. Passaglia, R. R. Stromberg, and H. L. Steinberg, *J. Res. Nat. Bur. Stand.*, **67A**, 363 (1963).
7. R. J. Archer, *J. Opt. Soc. Am.*, **52**, 970 (1962).
8. K. Vedam, R. Rai, F. Lukes, and R. Srinivasan, *ibid.*, **58**, 526 (1968).
9. R. E. Simons and J. H. Seeley, *Electrical Design News*, **14(1)**, 53 (1969).
10. O. Kubaschewski and B. E. Hopkins, "Oxidation of Metals and Alloys," 2nd ed., pp. 35-45, Butterworths, London (1967).
11. *Ibid.*, pp. 190-194.
12. E. Passaglia, R. R. Stromberg, and J. Kruger, "Ellipsometry in the Measurement of Surfaces and Thin Films," National Bureau of Standards Miscellaneous Publication, **256**, 215 (1963).
13. E. Nachtigall, *J. Metall.*, **43**, 23 (1952).
14. K. Friedrich, *J. Less-Common Metals*, **16**, 147 (1968).
15. H. F. Mark, J. J. McKetta, and O. F. Othmer, "Encyclopedia of Chemical Technology," 2nd ed., Vol. 13, pp. 646-649, Interscience Publisher, New York (1967).
16. C. D. Hodgman, R. C. Weast, and S. M. Selby, "Handbook of Chemistry and Physics," 42nd ed., p. 610, The Chemical Rubber Publishing Co., Cleveland (1960).
17. Th. Heumann and G. Hauck, Z. *Metallkunde*, **56**, 75 (1965); *Ber. Bunsengesellschaft*, **71**, 404 (1967).
18. V. Y. Doo and V. M. L. Sun, *Metallurgical Trans.*, **1**, 741 (1970).
19. V. Y. Doo, D. W. Boss, R. M. Valletta, and W. A. Pliskin, *This Journal*, **116**, 119C (1969).
20. V. Y. Doo, *IEEE Trans. Electron Devices*, **ED-13**, 561 (1966).

Electrolytic Reductive Coupling

XIX.[1] Effect of Counterions in Cathodic Reactions of 1,2-Diactivated Olefins

John P. Petrovich and Manuel M. Baizer*

Central Research Department, Monsanto Company, St. Louis, Missouri 63166

ABSTRACT

Certain 1,2-diactivated olefins XCH=CHY (I) in which X and Y are electron-withdrawing groups not themselves reduced under the conditions used were electrolyzed in the presence of counterions (M^+) chosen from the group Li^+, Na^+, K^+, Rb^+, R_4N^+. Cyclic voltammetric techniques permitted the measurement of the change in rate of decomposition of the anion radical as M^+ was varied. Bulk electrolyses yielded reduced coupled products whose identity and distribution varied with changes in M^+.

In a previous paper in this series (2) we reported that reductive coupling of olefins I (in which X and Y are electron-withdrawing groups not themselves reduced under the conditions of the electrolysis) in the presence of quarternary ammonium cations led to the formation of reduced dimers mainly by path [1] rather than by path [2]. That is

$$\underset{\text{I}}{\text{XCH—CHY}} \xrightarrow{e^-} \underset{\text{II}}{(\text{XCHCHY})^{\cdot-}}$$

$$(\text{XCH=CHY}) \longrightarrow (\text{XCHCHY})_2^{=}$$

$$\xrightarrow[2\text{H}_2\text{O}]{e^-} \text{XCH}_2\text{CHYCHXCH}_2\text{Y} + \text{YCH}_2\text{CHXCHXCH}_2\text{Y} \quad [1]$$

$$\underset{\text{I}}{2\text{XCH=CHY}} \xrightarrow{2e^-} \underset{\text{II}}{2(\text{XCHCHY})^{\cdot-}} \rightarrow (\text{XCHCHY})_2^{=}$$

$$\xrightarrow{2\text{H}_2\text{O}} \text{XCH}_2\text{CHYCHYCH}_2\text{X} \quad [2]$$

the intermediate anion radical II led to products more likely by an ECE mechanism than by an EC mechanism. The supporting evidence presented was based on an analysis of the cyclic voltammetry data and on the determination of the structures and distribution of the products obtained in macroelectrolyses.

Now II is always in the presence of a counterion and the ensemble anion-radical-counterion-solvent is present in a medium whose polarity may, within certain limits, be varied. It was of interest to determine whether varying these parameters judiciously would make it possible to direct the reaction of II toward either route [1] or route [2], both of which could be then regarded as limiting cases of anionic and free radical behavior, respectively. It was anticipated that the results would also have a bearing on the question of the mechanism(s) whereby anion radicals enter into other reactions, *e.g.*, the formation of "living" dianions (3) and the condensation with alkyl halides (4). As will become apparent the "directive" influence of the counterion may be offset by steric factors in the monomer which may be more decisive in blocking path [1] or path [2].

Experimental

Materials.—Dimethylformamide (DMF) was purified as described previously (1). Tetramethylammonium, tetraethylammonium tetrapropylammonium, tetrabutylammonium, lithium, sodium, potassium, and rubidium perchlorates, were recrystallized from appropriate solvents and dried immediately before use. Tetraethylammonium *p*-toluenesulfonate was purified as described previously (1). Sodium and lithium *p*-toluenesulfonate were recrystallized from acetic acid and dried before use.

Olefins.—Diethyl fumarate, cinnamonitrile, and α-phenylcinnamonitrile were obtained commercially.

The saturated analogs of these olefins, required as VPC references, were prepared by reduction of the corresponding olefin with hydrogen over palladium on carbon with ethanol as solvent using a Parr shaker at room temperature.

Cyclic voltammetry.—The cyclic voltammograms were obtained as described previously using anhydrous DMF as the solvent (2).

Preparative electrolysis.—The apparatus used for the preparative electrolysis has been described (5). A mercury cathode, area 55 cm^2, was used throughout.

General electrolysis method.—The anolyte consisted of either a saturated aqueous solution of tetraethylammonium *p*-toluenesulfonate, 2*M* aqueous solution of lithium *p*-toluenesulfonate or 2*M* aqueous solution of sodium *p*-toluenesulfonate depending on the electrolyte used in the catholyte. The catholyte consisted of 0.2 mole of the depolarizer, 0.03 mole of the electrolyte and 5 ml of water diluted to 150 ml dimethylformamide. The electrolyses were conducted at a constant current of 2A as described previously. The yields of electrolysis products, the relative yields of dihydro and hydrodimeric products as well as the isomer distribution are given in Table I.

Electrolysis of cinnamonitrile in the presence of lithium ion.—The products were isolated and identified as described previously (2). The only dimeric product isolated was 3,4-diphenyladiponitrile (16.9g). VPC analysis[2] indicated the presence of *ca.* 2% 2-benzyl-3-phenylglutaronitrile. Distillation gave 5.9g of 3-phenylpropionitrile.

Electrolysis of N,N-dimethylcinnamamide (1) *in the presence of lithium ion.*—The main dimeric product was purified by crystallization from benzene-methanol, 16.6g, mp 126°-128° [lit. (7) N,N,N',N'-tetramethyl 3,4-diphenyladipdiamide, 127°-129°]. The yield of N,N-dimethyl-3-phenylpropionamide was estimated by VPC.[2]

Electrolysis of α-phenylcinnamonitrile in the presence of tetraethylammonium ion.—A solid product formed during the electrolysis and was subsequently removed by filtration, 5.6g. VPC analysis[2] indicated

[1] For Part XVIII see (1).
* Electrochemical Society Active Member.
Key words: reductive coupling, anion radicals, free radicals, cyclic voltammetry, ion pairs.

[2] A 6 ft 10% SE-30 Ultraphase on 80-100 mesh Chrom W-HP column programmed from 200°-300° at 15°/min. This column was used throughout.

Table I. Electrolytic reductive coupling of activated olefins with various cations

$$2PhCH=CRX \xrightarrow[2H_2O]{2e^-} [(PHCHCRX)H]_2$$

$$PhCH\text{-}CRX \xrightarrow[2H_2O]{2e^-} PhCH_2CHRX$$

Compd.	R	X	Cation	% Yield[a]	Product dist.[b] Dihydro[c]	Hydrodimer[c]	PhCHCHRX | PhCHCHRX	PhCHCHRX | RXCCH$_2$Ph	RXCHCH$_2$Ph | RXCHCH$_2$Ph
V	H	CN	Et$_4$N	92	20	80	22	67	9
			Li	94	35	65	98	2	—
VI	H	CON(CH$_3$)$_2$	Et$_4$N	94	18	82	—	—	100
			Li	93	55	44	95	—	5
IV	Ph	CN	Et$_4$N	96	—	100	14[e]-86[d]	—	—
			Na	87	21	79	51[e]-49[d]	—	—
			Li	92	17	83	89[e]-11[d]	—	—

[a] % Yield based on current.
[b] Based on VPC analysis without standards.
[c] Dihydro + hydrodimer is 100%.
[d] Compound XI.
[e] Compound X.

that this was a mixture of two dimeric isomers.[3] Recrystallization from dimethylformamide gave a pure isomer A, mp 346°-347°.

Anal.—Calcd. for $C_{30}H_{24}N_2$: C, 87.10; H, 5.86; N, 6.81. Found: C, 87.30; H, 5.86; N, 7.26.

Mass spectra of isomer A showed the parent ion peak at m/e 412 with fragment peaks in decreasing order of intensity at m/e of 180 ($\phi CH=CH\phi$), 116 ($\phi CHCN$), 218 ($\phi CH=C\phi CHCN$), and 296 ($\phi CHC\phi HC\phi CNH$). Of the possible dimeric products only 2,3,4,5-tetraphenyladiponitrile would be expected to have all of these peaks.

Work-up of the electrolysis mixture in the usual manner gave an oily product. VPC analysis[2] of this product showed none of the isomer A but a mixture of a dimer B and the starting olefin. The oily product was chromatographed on activated alumina using benzene as the solvent. The solid dimer (28.1g) obtained was recrystallized from acetone, mp 222°-223°.

Anal.—Calcd. for $C_{30}H_{24}N_2$: C, 87.10; H, 5.86; N, 6.81. Found: C, 87.22; H, 5.74; N, 6.97.

Isomer B is apparently identical with Wawzonek's reported imine.[3]

Electrolysis in the presence of sodium cation.—The electrolysis products were worked up as described above. Isomer A, 13.6g, was isolated by crystallization. Isomer B was obtained by VPC analysis.[2]

Electrolysis in the presence of lithium cation.—The electrolysis products were worked up as described above. The products distribution was found to be 17% saturated monomer and 83% dimer mixture which was 89% Isomer A' and 11% Isomer B. Isomer A' was isolated and recrystallized from DMF (mp 255°-258°). The VPC retention time[2] (4.3 min) and mass spectrum of this material were identical to those obtained for Isomer A in electrolysis described above. The difference in melting points is probably due to different diastereoisomers (four asymmetric carbon atoms)

Anal.—Calcd. for $C_{30}H_{24}N_2$: C, 87.10; H, 5.86, N, 6.81. Found: C, 87.07; H, 6.12; N, 7.00.

Results and Discussion

We have used (8) the relation between the peak current and the scan rate from cyclic voltammetry as a means of distinguishing between an EC and an ECE mechanism (essentially an irreversible charge transfer due to dimerization of II) (9). The expected dependence of $i_p/V^{1/2}$ *vs.* $V^{1/2}$ is shown in Fig. 1, along with the observed behavior of diethyl fumarate (III) and α-phenylcinnamonitrile (IV) using both the alkali metal cations and the tetraethylammonium cation. It is clear that, in the presence of the sodium cation, α-phenylcinnamonitrile behaves as expected for an EC mechanism.[4] However, in the presence of the tetraethylammonium cation, IV shows an intermediate behavior between an EC and an ECE mechanism, indicating that both paths, Eq. [1] and [2], are taken in this case. In the case of diethyl fumarate the $i_p/V^{1/2}$ behavior is not as conclusive. A trend, however, is apparent. On changing from the tetraethylammonium ion to the lithium ion, the curve shifts from the curve expected for an ECE process toward the expected curve for an EC process, indicating that both paths are taken in the decomposition of the anion radical from diethyl fumarate in the presence of the lithium ion. However, there is essentially no change in the rate of decomposition of the anion radical from diethyl fumarate (lithium counterion) in the presence of 1*M* acrylonitrile,[5] indicating that the anion radical dimerization path, Eq. [2], predominates.

In each of these cases olefins III and IV reduce well before the background electrolyte cations discharge.

From the cyclic polarograms, the rate constants, k_{obs}, for the decomposition of the anion radicals electro-

[2] A 6 ft 10% SE-30 Ultraphase on 80-100 mesh Chrom W-HP column programmed from 200°-300° at 15°/min. This column was used throughout.

[3] S. Wawzonek *et al.* (6) reported obtaining a dimeric nitrile and the cyclic imine formed from it by a Ziegler-Thorpe reaction on electrolysis under similar conditions.

[4] Similar experiments using the lithium cation were inconclusive due to a preadsorption wave.

[5] By contrast, in the presence of the tetraethylammonium ion, a substantial rate increase was observed with added acrylonitrile (8).

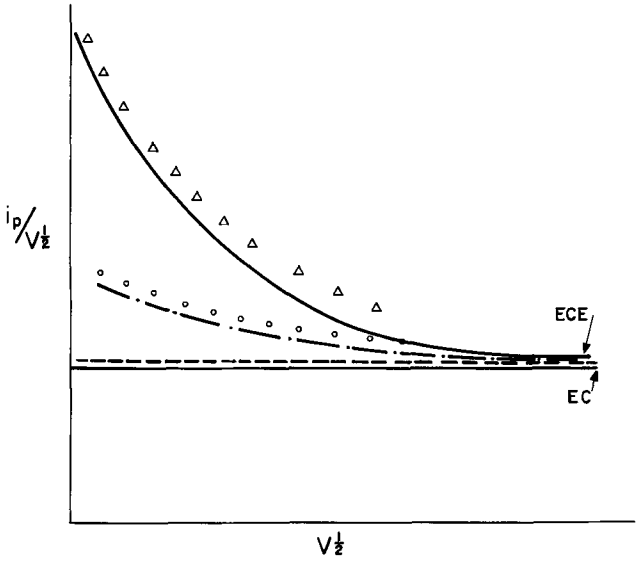

Fig. 1. Plot of $i_p/V^{1/2}$ *vs.* $V^{1/2}$ as indicator of EC or ECE mechanism. ———— Expected curves for EC and ECE mechanisms; — — — observed behavior of α-phenylcinnamonitrile with the sodium ion; —·—· observed behavior of α-phenylcinnamonitrile with the tetraethylammonium ion; o o o observed behavior of diethyl fumarate with the lithium ion; △ △ △ observed behavior of diethyl fumarate with the tetraethylammonium ion.

chemically generated from the diactivated olefins were calculated by the method of Nicholson (10). In each case, the decomposition rate is faster in the presence of the alkali metal cations than in the presence of the tetraethylammonium ion. In typical nucleophilic reactions, where no charge is formed in the transition state, *i.e.*, only a reorganization of charge occurs, the rate of attack of the nucleophile on an aceptor (analogous to Eq. [1]) would be expected to decrease on changing the cation from larger tetraethylammonium to the smaller sodium or lithium due to ion-pairing considerations (11). The anion radical/sodium or lithium ion pair should be less nucleophilic than the essentially free anion radical which is present when the tetraethylammonium ion is the counterion

$$XCH{=}CRY \xrightarrow{e^-} (XCHCRY)^{\cdot-} \xrightarrow[\text{proton source}]{k_1} \xrightarrow{k^2} (XCHCRY)^{\cdot-} \xrightarrow{k^3} XCH{=}CRY$$

$k_{obs} = k_1 + k_2 + k_3$, assuming the concentration of the second reactant is a constant. Therefore, the effect of changing the cation from tetra-alkylammonium to an alkali metal cation should be a decrease in k_{obs} due to a decrease in k_3. The increase in k_{obs} is indicative of an increase in k_2. The final result k_{obs} in any particular case will be a blend of these three reactions.

Furthermore, these same ion-pairing considerations would tend to favor the dimerization of two anion radicals, Eq. [2], because of the neutralization of the negative charge by the relatively small cations. It would be expected that the dimerization of two free anion radicals would be disfavored by charge repulsion. However, in a tight ion pair, the charge is essentially absent and the typical radical reactions can occur.

In these systems, especially for olefins (III) and (IV), both limiting cases were observed as well as the intermediate case. With olefin III, k_3 dominates in the presence of the tetraethylammonium ion, and with olefin IV, k_2 is the main path in the presence of the sodium ion. Both paths (k_2 and k_3) are taken by olefin III with lithium ion and possibly by olefin IV with tetraethylammonium ion.

On macroelectrolysis, the isomer distribution of dimeric products as implied by the rate constants depends on the cation of the electrolyte, Table I. Cinnamonitrile (V) gave a mixture of isomers. The main product, 57%, was 2-benzyl-3-phenyl glutaronitrile VII in the presence of the tetraethylammonium ion (1) and almost exclusively 3,4-diphenyladiponitrile VIII in the presence of the lithium ion.

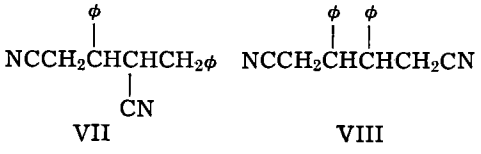

VII VIII

In the ion pair, consisting of the anion radical of cinnamonitrile and the lithium counterion, the lithium ion is probably associated with the electron-rich nitrile group, IX. The most likely pseudo-radical through which coupling can

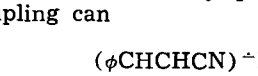

IX

occur is the benzylic-type radical. Coupling $\beta,\beta-$ to the nitrile is indeed what is observed.

Similar dual behavior was observed in the macroelectrolysis of N,N-dimethylcinnamamide VI. Olefin VI gave N,N,N',N'-tetramethyl 2,3-dibenzylsuccinamide in the presence of the tetraethylammonium ion and N,N,N',N'-tetramethyl 3,4-diphenyladipamide in the presence of the lithium ion.

Table II. Rate constants for the decomposition of anion radicals electrochemically generated from diactivated olefins with various electrolytes at 25°C

Compound		Cation[a]	$10^3 M$[b]	K_{obs}[c]
$H_5C_2O_2CCH{=}CHCO_2C_2H_5$	(III)	Et_4N	1.99	0.31
		Li	1.72	6.5
$\phi CH{=}CCN$	(IV)	Et_4N	1.87	10.8
		Na	1.92	12.9
$\phi CH{=}CHCN$	(V)	Et_4N	1.96	2.2
		Li	1.92	13.8
$\phi CH{=}CHCON(CH_3)_2$	(VI)	Et_4N	1.95	0.15
		Li	2.01	too fast

[a] 0.1*M*.
[b] In DMF solvent.
[c] ±10% reproducibility.

For olefins V and VI, the $i_p/V^{1/2}$ behavior was not obtainable because the current peak comes too close to the background electrolyte discharge. The rate constants were estimated but, because of the proximity of the background discharge, are probably not very accurate.

The macroelectrolysis of α-phenylcinnamonitrile (IV) gave 86% of dimer X and 14% of dimer XI in the presence of the

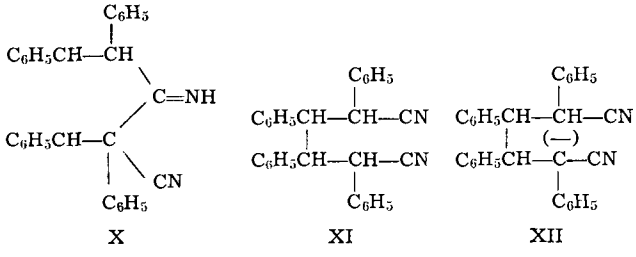

X XI XII

tetraethylammonium ion, while, with sodium as the counterion, about equal amounts of these two isomers were obtained. In the case of the lithium ion 89% of the dimeric product was XI.[6] Since the final intermediate leading to both X and XI must be the anion XII, these results again illustrate (12) the differences in effect of the hydrated alkali metal cations and the unhydrated quaternary ammonium cations: in the former case XII is immediately hydrated to XI; in the latter case XII escapes hydration long enough to be able to engage in the intramolecular reaction leading to X.

We find this hypothesis useful: In the limiting cases a small counterion may form an intimate ion-pair (perhaps a covalent bond when X or Y contains oxygen) with II whereby the ensemble behaves like a free radical; a large counterion well separated from II by a polar solvent favors anionic behavior of II. In most cases, particularly in electrolytic experiments in which solvents of some polarity are required and the choice of counterions is not always free, an admixture of both behaviors is to be expected. This interpretation of counterion effects is applicable to an explanation of the merger of two polarographic waves of benzil into one when Li^+ is the counterion (13); the changes in equilibrium constant between dimer dianion and mono anion radical of benzophenone with counterion (14); and the course of some polymerization reactions depending on the metal initiator used (15). This hypothesis must be tested in additional systems. Controversies concerning the mechanism of anion radical reactions which do not simultaneously take into consideration the counterion and the medium are fruitless.

[6] It is an interesting observation, for which we do not presently have explanation, that different diastereoisomers of XI were formed in the presence of lithium and of sodium cations.

Acknowledgment

The authors wish to express their appreciation to John L. Chruma for excellent technical assistance.

Manuscript submitted July 28, 1969; revised manuscript received *ca.* November 16, 1970.

Any discussion of this paper will appear in a Discussion Section to be published in the December 1971 JOURNAL.

REFERENCES

1. M. M. Baizer and J. P. Petrovich, *This Journal*, **117**, 173 (1970).
2. J. P. Petrovich, M. M. Baizer, and M. R. Ort, *ibid.*, **116**, 749 (1969).
3. G. Spach, H. Monteiro, M. Levy, and M. Szwarc, *Trans. Faraday Soc.*, **58**, 1809 (1962).
4. D. Lipkin, F. R. Galiano, and R. W. Jordan, *Chem. Ind.* (London), 1657 (1963); D. Lipkin, G. J. Divis, and R. W. Jordan, *Preprints, Div. Petrol. Chem.*, **13**(2). D60 (1968); J. F. Garst, J. T. Barbas, and F. E. Barton, II, *J. Am. Chem. Soc.*, **90**, 7159 (1968); G. D. Sargent and G. A. Lux, *J. Am. Chem. Soc.*, **90**, 7161 (1968).
5. M. M. Baizer, *This Journal*, **111**, 215 (1964).
6. S. Wawzonek, R. Zegman, and G. R. Hansen, *ibid.*, **117**, 1351 (1970).
7. I. L. Knunyants and N. P. Gambaryan, *Uspekhi Khim.*, **23**, 781 (1954).
8. J. P. Petrovich, M. M. Baizer, and M. R. Ort, *This Journal*, **116**, 743 (1969).
9. R. S. Nicholson and I. Shain, *Anal. Chem.*, **36**, 706 (1964).
10. R. S. Nicholson, *ibid.*, **38**, 1406 (1966).
11. D. J. Cram, "Fundamentals of Carbanion Chemistry," pp. 32 and 138, Academic Press, New York, N. Y. (1965).
12. M. M. Baizer and J. P. Petrovich, *This Journal*, **114**, 1023 (1967).
13. R. H. Philip, Jr., T. Layloff, and R. N. Adams, *ibid.*, **111**, 1189 (1964).
14. M. Ashworth, *Coll. Czech. Chem. Comm.*, **13**, 229 (1948).
15. K. F. O'Driscoll, R. J. Bondreau, and A. V. Tobolsky, *J. Polymer Sci.*, **31**, 115 (1958); K. F. O'Driscoll and A. V. Tobolsky, *J. Polymer Sci.*, **31**, 123 (1958), **37**, 363 (1959); A. V. Tobolsky, A. Rembaum, and A. J. Eisenberg, *J. Polymer Sci.*, **45**, 347 (1960).

Electrolytic Reductive Coupling

XX.[1] Mixed Reductive Couplings with Acrylonitrile

Reductions at the Cathode Voltage Required for the More Difficultly Reduced Partner

Manuel M. Baizer* and John L. Chruma

Central Research Department, Monsanto Company, St. Louis, Missouri 63166

ABSTRACT

Acrylonitrile has been reductively coupled with acetone, styrene, 1,1-diphenylethylene, benzophenone, and benzaldehyde. When the reduction is carried out at the cathode voltage required for the more difficultly rather than the more easily reduced partner (*a*) current efficiencies for the mixed products are increased, (*b*) couplings which otherwise fail can occur, (*c*) by-product polymer formation may be suppressed, and (*d*) when either of two by-product hydrodimers must be accepted, the more useful one may be chosen.

It has been pointed out before (2) that mixed reductive coupling between two different types of activated olefins A and B (in which A as arbitrarily the most easily reduced species) provides a convenient route to the synthesis of molecules **4** with two different functions. When the cathode

$$\underset{\mathbf{1}}{A} + \underset{\mathbf{2}}{B} \xrightarrow[H_2O]{F} \underset{\mathbf{3}}{HAAH} + \underset{\mathbf{4}}{HABH} + \underset{\mathbf{5}}{HBBH} \qquad [1]$$

voltage can be controlled at a value required for the reduction of A but not of B, only products **3** and **4** are formed (2); the more negative the cathode voltage can be made without reducing B[2] the higher the ratio of **4** to **3** (3). Even under the latter circumstances, however, if the reduction potentials of A and B are more than *ca.* 0.4V apart, **3** is formed along with very little,[3] if any, **4** (4).

The maximization of the yield of **4** at the expense of **3** and **5** is a challenging synthetic goal since the latter two can be made individually by electrolytic hydrodimerization of **1** and **2**, respectively, while the former is usually very difficult to prepare by alternate means.

This paper reports the results obtained in attempting to increase the yield of **4** by carrying out the reductive couplings of Eq. [1] at cathode voltages negative enough to reduce B. Further, in view of Sugino and Nonaka's (6) successful reductive coupling of acetone[4] and acrylonitrile at −1.9V in the presence of tetraalkylammonium salts in neutral or alkaline medium, the carbonyls acetone, benzophenone, and benzaldehyde were also included here as representatives of A or B.[5]

Possibly related work, involving the anodic oxidation of cyclohexane (more positive voltage) in the presence of chloride, has been published (7).

Previous papers in this series have pointed out the difficulties in establishing the mechanism whereby **4** is formed when only A is reduced (Eq. [1]). When the coupling is carried out at the (more negative) voltage for the reduction of B, the elucidation of the routes to **4** becomes formidable. This paper poses, but does not grapple with, these mechanistic problems.

Experimental

Reagents.—The purification and/or quality of tetraethylammonium *p*-toluenesulfonate, diethyl maleate

* Electrochemical Society Active Member.

[1] For Part XIX see (1).

Key words: potentiostatic electrolyses, cross coupling, hydromerization.

[2] It was observed (3) that, when the cathode voltage was negative enough to reduce 2 also, the ratio of 4 to 3 increased even further, but now some 5 was also formed.

[3] In addition to the work cited in (4) it may be mentioned that our attempt several years ago (5) to couple acrylonitrile with styrene at 1.9V *vs.* SCE resulted in only a very small yield of 5-phenylvaleronitrile.

[4] Benzophenone was reported (6) to be unsuitable as a coupling partner.

[5] The carbonyls are electroreducible but obviously are not activated olefins.

(DEM), DMF, and acrylonitrile (AN) have been described before (3). The acetone was Mallinckrodt reagent grade. Styrene (Eastman, practical grade) was distilled *in vacuo* and stored over a trace of *p*-nitrosodimethylaniline. Benzophenone (Fisher, reagent grade) and 1,1-diphenylethylene (Aldrich, technical grade) were used as received.

Equipment.—Except where otherwise specified, the assembly previously described was used (3); the salt bridge was positioned directly under the alundum cup diaphragm which contained the anode. A mercury cathode of 55 cm^2 was used throughout.

Synthesis of reference compounds.—5-Hydroxy-5-methyl-valeronitrile and γ,γ-dimethylbutyrolactone were made according to the literature by the electroreduction of a sulfuric acid solution of acetone in the presence of acrylonitrile (6). The preparation of the 5-phenyl-valeronitrile has been described (5). 4-Phenylvaleronitrile was prepared from 4-phenylvaleric acid (Aldrich) by conventional means *via* the acid chloride and amide, bp 85° (0.2 mm) [reported (8) 125° (13 mm)], chromatographically pure, ir spectrum consistent with structure. 1,1,4,4-Tetraphenylbutane was prepared by the electrohydrodimerization of 1,1-diphenylethylene, mp 120°-121° [reported (9) 122°].[6] 1,3-Diphenylbutane and *meso*- and *dl*-2,3-diphenylbutane were prepared according to (11). 4,4-Diphenylbutyrolactone was prepared by the method of (12). The benzyl 2-cyanoethyl ether was prepared by cyanoethylating benzyl alcohol (13).

Procedures.—Except in the case of experiments done for comparison purposes, the general electrolysis procedure involved dissolving B, the most difficultly reducible component, in a solution of water-DMF-tetraethylammonium *p*-toluenesulfonate, deaerating with purified nitrogen for at least 15 min, presetting the cathode voltage by potentiostat at the desired value, starting the electrolysis and shortly thereafter beginning the addition of component A either neat or dissolved in DMF or B. The pH was kept at *ca.* 7-8 by occasional addition of acetic acid dropwise to the catholyte. At the end of the electrolysis the catholyte, if necessary, was neutralized with acetic acid and poured onto ice. After separation of the mercury, the mixture was filtered, if necessary, and the filtrate extracted several times with methylene chloride. The extracts were washed with water, dried, filtered, and analyzed by the methods described below. Isolation of products involved fractional distillation or crystallization as appropriate. The electrolysis data are gathered in Table I; the products obtained are given in Table II.

Analytical methods.—Gas chromatography employing the F and M Hewlett Packard Model 5750 instrument was used throughout. The preliminary treatment of the sample and the choice of chromatographic column depended on whether it was desired to analyze for both "low" and "high" boiling products. (*A*) When "low boilers" analysis was required the methylene chloride and other relatively volatile products were removed by distillation at $< 100°$ and collected in a chilled receiver. The distillate was analyzed on a 6 ft 10% Carbowax 20M on Chromosorb W (80-100 mesh) column[7] (No. 1) isothermally at 70° or on a 1 ft Par 1 (80-120 mesh) column (No. 2) isothermally at 100°. (*B*) When only "high boiler" analysis was required, the more volatile materials were removed on a hot water bath *in vacuo* and the residue analyzed on column No. 1 programmed from 100° to 210° at 15°/min or on column No. 2 programmed at 200° to 240° at 6°/min or on column No. 3 (10 ft 3% OV-225 on Chromosorb G, 80-100 mesh) programmed 150° to 300° at 15°/min. When pure samples of expected products

[6] Wawzonek and Fan had reported (10a) no reductive coupling under polarographic conditions; Funt and Gray (10b) found no hydrodimerization under cyclic voltammetric conditions using tetrabutylammonium perchlorate.

[7] Occasionally, the crude catholyte was directly analyzed for low boiling components.

Table I. Conditions for reductive coupling of acrylonitrile with electroreducible partners, 15°-25°C

Run	−Cathode, V, SCE	A	A, hr	Catholyte A (1), moles	$-E_{1/2}$,[a] SCE	B (2), moles	$-E_{1/2}$,[a] SCE	H_2O, ml	salt,[b] g	DMF, ml
1[c]	1.90	0.5-0.8	4.00	AN[d] 0.265	1.9	acetone 1.45	2.4	62.5	71	0
2[e]	1.90	0.02-0.16	0.96	AN 0.049	1.9	acetone 1.45	2.4	62.5	71	0
3	2.10	0.3-1.3	4.05	AN 0.113	1.9	acetone 1.18	2.4	62.5	71	0
4	2.25	0.4-0.7	3.13	AN 0.034	1.9	acetone 1.18	2.4	62.5	71	0
5	2.05	0.04-0.20	0.92	AN 0.051	1.9	styrene 0.29	2.4	3	25	115
6	2.30	0.2-0.4	1.94	AN 0.055	1.9	styrene 0.29	2.4	3	25	115
7	2.45	0.7-0.9	4.80	AN 0.074	1.9	styrene 0.29	2.4	3	25	115
8	1.94	0.04-0.10	0.55	AN 0.047	1.9	1,1-diphenylethylene 0.167	2.2	3	25	115
9	2.30	0.4-0.6	3.34	AN 0.115	1.9	1,1-diphenylethylene 0.167	2.2	3	25	115
10	1.73	0.03-0.40	2.03	$\phi CO\phi$ 0.0275	1.63, 2.08[i]	AN 0.47	1.9	5	25	113
11	2.00	0.4-0.7	3.40	$\phi CO\phi$ 0.022	1.63, 2.08[i]	AN 0.47	1.9	7.5	25	113
12[f]	2.20	0.3-1.2	8.55	$\phi CO\phi$ 0.0275	1.63, 2.08[i]	AN 0.47	1.9	5	25	113
13[g]	1.425	0.1-0.4	3.38	DEM 0.075	1.2	AN 0.64	1.9	8	50	72
14	2.01	0.05-0.7	3.80	DEM[h] 0.05	1.2	AN 0.64	1.9	8	50	60
15	1.575	0.01-0.30	4.75	ϕCHO 0.094	1.4	AN 1.6	1.9	8	50	0
16	1.95	0.6-0.8	4.75	ϕCHO 0.094	1.4	AN 1.6	1.9	10	50	0

[a] Approximate reported values in neutral aqueous medium. These are cited to clarify the relationship between the voltage used in the macroelectrolyses and the reduction potentials of A and B, respectively.
[b] Tetraethylammonium *p*-toluenesulfonate.
[c] All AN in catholyte at start.
[d] Acrylonitrile.
[e] AN added dropwise to catholyte.
[f] The entire $\phi CO\phi$ was dissolved in the total AN and the solution added dropwise at the cathode surface.
[g] Taken from Table I, ref. (3).
[h] Diethyl maleate.
[i] Reported (18) polarographic values in *ca.* 95% DMF (transposed to SCE) for reduction to the anion radical and dianion.

Table II. Products obtained under conditions of Table I

Run	Products (mM) Type 3	Type 4	Type 5	Other
1	adiponitrile (38.7)	5-hydroxy-5-methyl-valeronitrile (9.3 and lactone (4.3)	none	propionitrile (51.0)
2	adiponitrile (trace)	5-hydroxy-5-methyl-valeronitrile (6.1) and lactone (trace)	none	propionitrile (0.22) diacetone alcohol (8.6)
3	adiponitrile (6.1)	5-hydroxy-5-methyl-valeronitrile (28.5) and lactone (4.1)	—	propionitrile (69.1)
4	adiponitrile (0.3)	above nitrile (13.4) above lactone (2.8)	isopropyl alcohol (17) pinacol (1.0)	diacetone alcohol (5.0) propionitrile (trace)
5	adiponitrile (23.1)	5-phenylvaleronitrile (trace)	none	ethylbenzene (trace) propionitrile (trace)
6	adiponitrile (11.6)	5-phenylvaleronitrile (5.15) and 4-phenylvaleronitrile (2.24)	1,4-diphenylbutane (trace)	propionitrile (1.28) ethylbenzene (trace)
7	adiponitrile (8.8)	5-phenylvaleronitrile (33.4) and 4-phenylvaleronitrile (2.18)	1,4-diphenylbutane (trace)	ethylbenzene (66.0)
8	adiponitrile (1.0)	none	none	propionitrile (10.0)
9	adiponitrile (1.0	5-5-diphenylvaleronitrile (12.8)[b]	1,1,4,4-tetraphenylbutane (0.5)	propionitrile (2.0)
10	none	none	adiponitrile (16.0)	polyacrylonitrile,[a] 18g AN hydrotrimer (3.75) α-methyleneglutaronitrile (25.0)
11	—	4,4-diphenylbutyrolactone (2.94) and 4,4-diphenyl 4-hydroxybutyronitrile[c] (6.3)	adiponitrile (9.4)	polyacrylonitrile, 20g AN hydrotrimer (trace)
12	—	4,4-diphenylbutyrolactone (2.1) and above nitrile (6.3)	adiponitrile (91.5)	polyacrylonitrile, 0.5g propionitrile (trace)
13	tetraethyl butane-tetracarboxylate (3.88)	diethyl 2-cyanoethyl succinate (4.71)	none	diethyl succinate (43.1)
14	none	diethyl 2-cyanoethyl succinate (12.0)	adiponitrile (12.8)	polyacrylonitrile, 6.5g diethyl succinate (10.0)
15	hydrobenzoin (trace)	4-phenyl, 4-(2-cyanoethoxy) butyronitrile[d] (27.0)	no adiponitrile	benzyl alcohol (1.7) bis-(2-cyanoethyl) ether (10.0) several unidentified minor products
16	hydrobenzoin (trace)	above ether (38.4)	adiponitrile (15.0)	polymer 0.5g benzyl alcohol (4.4) bis-(2-cyanoethyl) ether (26.0) several unidentified minor products

[a] Infrared and elemental analyses indicated that no moiety derived from benzophenone had been incorporated, See ref. (14).
[b] MP 57°-58°. Calcd. for $C_{17}H_{17}N$: C, 86.76; H, 7.28; N, 5.95. Found: C, 86.80; H, 7.11; N, 5.86.
[c] MP 95°-95.5° (2 × from alc.), bp 180°-190° (0.03 mm). Calcd. $C_{16}H_{15}NO$: C, 81.02; H, 6.32; N, 5.90. Found: C, 81.19; H, 6.33; N, 5.81. The infrared spectrum showed OH (2.9μ), CN (≯45μ) C_6H_5 (13.4μ) and no >CO or R-O-R absorption.
[d] BP 155° (0.3 mm). Calcd. for $C_{13}H_{14}N_2O$: C, 73.0; H, 6.52; N, 13.10. Found: C, 72.75; H, 6.76; N, 13.17. The infrared spectrum showed no OH, CN (4.5μ), no >CO, ether (9.1μ), C_6H_5 (13.3 and 14.5μ).

were available, analysis was carried out using dimethyl terephthalate or octadecane (runs 13 and 14) as the internal standard. Otherwise, semiquantitative analyses were obtained using corrected area percentages.

The infrared spectra were obtained on a Beckman Microspec spectrophotometer. The nmr spectra were obtained on Varian A-60 and T-60 instruments.

Discussion of Results

In reductive couplings according to Eq. [1], the parameters that can be controlled are cathode voltage, mode of addition of **1** and **2** to the catholyte, and, within certain limitations (3), concentration of proton donor (water). If the cathode voltage is controlled so as to be close to the value required for the reduction of **1** but not of **2**, it is clear from a comparison of the results of runs 1 and 2 that slow addition of **1** to the catholyte favors the formation of mixed product **4** at the expense of **3**. We have frequently [*e.g.*, (3)] employed this strategy. When the cathode voltage is negative enough to reduce **2** (run 4)[8] the ratio of **4** to **3** + **5** is maximum.

In runs 1-4, involving the acrylonitrile-acetone system, it is significant that, when the acceptor is acetone rather than an activated olefin, cross-reductive coupling occurs [runs 1 and 2 and ref. (6)] even though the separation of cathode voltage between AN and acetone is *ca.* 0.5V; if the acceptor had been an activated olefin which reduces at *ca.* the acetone cathode voltage, cross-reductive coupling would not have been expected to occur (4). This point is, indeed, verified in runs 5 and 8. Comparison with runs 6 and 9, respectively, however, illustrates that electrolysis at the more negative voltage does produce type **4** products.[9]

The data thus far discussed illustrate that electrolyses at the more negative voltage (*a*) increase the ratio of cross-coupled to self-coupled products and (*b*) permit couplings to occur which fail at the more positive voltage.

The experiments (runs 10-12) with the AN-benzophenone system illustrate additional features of the electrolyses at negative voltages. Benzophenone was reported (6) not to couple with AN and we have verified this result [at −1.73V, run 10]. Sugino and Nonaka did not report what did occur in their experiment. We obtained some adiponitrile and, in spite of the presence of a quantity of water ordinarily sufficient to arrest anionic polymerization/oligomerization (15), a large quantity of polyacrylonitrile together with AN hydrotrimer and α-methyleneglutaronitrile. The polymer was carefully examined for the presence of benzophenone-derived end-groups: none were found. The polymer may be free radical-initiated and may have arisen by electron-transfer to acrylonitrile from benzophenone dianion *ex* benzophenone radical anion (14). The possibility (16) that polymerization was initiated by $CH_2{=}\bar{C}CN$, also an intermediate to α-methyleneglutaronitrile, is not consistent with the fact that increasing the quantity of water in the catholyte (run 11 *vs.* run 10) while maintaining a constant concentration of the hydrophobic quaternary ammonium cations did not decrease the yield of polymer, although it did reduce the quantities of AN hydrotrimer and of α-methyleneglutaronitrile.

Cross-coupled products between AN and benzophenone were formed at −2.00V (run 11) and at −2.20V (run 12)[10] together with major amounts of adiponitrile. In this case, then, cross-coupling occurred at a negative voltage which failed at a more positive voltage and, in addition, by-product polymer formation could be avoided by operating at a very negative voltage.

A comparison of runs 13 and 14 shows that again type **4** product is maximized at the more negative

[8] At the beginning of the experiment the background current and the current in the presence of acetone were determined to establish that the latter was, indeed, being reduced.
[9] It is an interesting fact that the 2-cyanoethyl moiety was joined to the α-(→ 4-phenylbutyronitrile) as well as the β-(→ 5-phenylvaleronitrile) carbon atoms of styrene, that the 5-isomer predominated considerably, and that its ratio to the 4-isomer increased even more at the more negative voltage (run 7 *vs.* run 6).
[10] At this voltage very little polymer was formed, presumably because any free radical initiators were immediately reduced and anionic polymerization was aborted by the proton donors. The possibility cannot be ruled out that benzophenone dianion participated in the coupling.

voltage. In addition, since hydrodimer **5** rather than hydrodimer **3** is formed as the major[11] bimolecular by-product, and since one must usually accept **5** or **3** as a by-product in the synthesis of **4**, one can, by choice of cathode voltage, select the more useful by-product.

Benzaldehyde coupled reductively with AN both at −1.575V (run 15) and at −1.95V (run 16). The current efficiency for the formation of coupled product was higher at the more negative voltage but at the expense of forming adiponitrile as a by-product. It is interesting that because of difficulty in preventing the catholyte from becoming too alkaline, as evidenced by the formation of bis-(2-cyanoethyl) ether, both C and O cyanoethylation of benzaldehyde occurred

$$C_6H_5CHO + 2CH_2{=}CHCN \xrightarrow[2H_2O]{2e^-} C_6H_5CH(OCH_2CH_2CN)\text{-}CH_2CH_2CN \quad [3]$$

This result finds a certain analogy in the report (17) that a small quantity of the ethyl ether of ethylphenylcarbinol was formed during the electrolysis of benzaldehyde[12] in the presence of ethyl iodide

$$C_6H_5CHO + 2C_2H_5I \xrightarrow{2e^-} C_6H_5CH(OC_2H_5)C_2H_5 \quad [4]$$

Mechanistic Problems

When only reactant B (together with supporting electrolyte and solvent) is present in the catholyte, electrolysis at a cathode voltage sufficient to reduce B is started and A is added in gradually, the following situation obtains initially. B is reduced to its radical anion or derived anion.[13] The reduced intermediate may anionically attack proton donor to yield dihydro **B**, or **B** to yield eventually its hydrodimer or incoming A to yield eventually the cross-coupled product **4**. However, B anion radical (say from benzophenone) may also disproportionate and the resulting dianion (or even the initial anion radical) may transfer an electron to readily reducible A, so that coupling may be of the radical combination type. If A has acquired one electron from the reduced intermediate formed from B, radical combination of two A radicals would lead to **3**; reduction of A radical *via* the electrode or by relay *via* the B-reduced species would lead to A anion and then to **3** and **4**; if the electron-transfer to A had occurred under circumstances under which A radical could not be reduced, free radical-initiated polymerization could occur.

As B is being reduced and its concentration at the electrode surface diminished, new B and competitively A reach the electrode surface. If A is electroreduced, then the couplings described in our previous papers occur.

To study the mechanistic phenomena in an ideal system would require precise control of pH, proton donor concentration, and rate of addition of A in the vicinity of the electrode surface. Current density adjustment would be required so that the rate of reaction of reduced B with A, in conjunction with all other processes in which reduced B participates, was just sufficient to prevent any direct reduction of A. It appears that there will be some delay before this can be achieved.

Manuscript submitted Aug. 24, 1970; revised manuscript received Nov. 9, 1970.

Any discussion of this paper will appear in a Discussion Section to be published in the December 1971 JOURNAL.

[11] The complete elimination of tetraethyl butanetetracarboxylate in run 14 is a fortuitous result.

[12] On the other hand, benzophenone and ethyl iodide yielded only the C-ethylated product (18).

[13] Following protonation and a second reduction. Depending on the stability of the radical anion (19) and the proton paucity near the electrode these processes may be relatively slow.

REFERENCES

1. J. P. Petrovich and M. M. Baizer, *This Journal*, **118**, 447 (1971).
2. M. M. Baizer, *J. Org. Chem.*, **29**, 1670 (1964).
3. M. M. Baizer, J. P. Petrovich, and D. A. Tyssee, *This Journal*, **117**, 173 (1970).
4. J. P. Petrovich, M. M. Baizer, and M. R. Ort, *ibid.*, **118**, 749 (1969).
5. J. H. Wagenknecht and M. M. Baizer, *J. Org. Chem.*, **31**, 3885 (1966).
6. K. Sugino and T. Nonaka, *Electrochim. Acta*, **13**, 613 (1968).
7. G. Faita, M. Fleischmann, and D. Pletcher, *J. Electroanal. Interfacial Electrochem.*, **25**, 455 (1970).
8. J. v. Braun and A. Stuckenschmidt, *Ber.*, **56**, 1724 (1923).
9. W. Schlenk, J. Appenrodt, A. Michael, and A. Thal, *ibid.*, **47**, 473 (1914).
10. (a) S. Wawzonek and J. W. Fan, *J. Am. Chem. Soc.*, **68**, 2541 (1946); (b) B. L. Funt and D. G. Gray, *This Journal*, **117**, 1020 (1970).
11. K. T. Serijan and P. H. Wise, *J. Am. Chem. Soc.*, **74**, 365 (1952).
12. R. E. Lutz, *ibid.*, **49**, 1111 (1927).
13. W. Untermohlen, *ibid.*, **67**, 1505 (1945).
14. G. Mengoli and G. Vidotto, *Makromol. Chem.*, **129**, 73 (1969).
15. M. M. Baizer and J. D. Anderson, *J. Org. Chem.*, **30**, 1351 (1965).
16. G. Mengoli, G. Farnia, and E. Vianello, *European Polymer J.*, **5**, 61 (1969).
17. J. M. Nelson and A. M. Collins, *J. Am. Chem. Soc.*, **46**, 2256 (1924).
18. S. Wawzonek and A. Gundersen, *This Journal*, **107**, 537 (1960).
19. M. Nicolas and R. Pallaud, *Compt. rend.*, **267C**, 1834 (1968).

Engineering Applications of Current and Potential Distributions in Disk Electrode Systems

Leonard Nanis*

School of Chemical Engineering, University of Pennsylvania, Philadelphia, Pennsylvania 19104

and Wallace Kesselman**

Chemical Engineering Department, Shell Development Company, Emeryville, California 94608

ABSTRACT

Integral transform methods are used to obtain analytic solutions for the current density (J) and potential distributions on a disk in an infinite plane for the four limiting cases of: (i) uniform potential disk-insulating plane; (ii) uniform J disk-insulating plane; (iii) uniform J disk-uniform potential plane and; (iv) uniform potential disk-uniform potential plane. Examples of applications of results are drawn from electrochemical engineering problems related to fuel cell design, corrosion enhancement due to inclusions, and rotating disk systems.

Advances in the mathematical treatment of current density problems have been made recently through the use of machine computation methods (1, 2). Analytic results remain attractive because of their generality, although the mathematical effort for all but the simplest geometries becomes excessive. Methods usually associated with idealized two-dimensional fields become increasingly complex for three-dimensional problems related to practical electrode geometries. However, the cylindrical field geometry may be treated in terms of two space coordinates when angular symmetry prevails, *i.e.*

$$\nabla^2 V = \frac{\partial^2 V}{\partial z^2} + \frac{1}{r}\frac{\partial}{\partial r}\left(r\frac{\partial V}{\partial r}\right) = 0 \qquad [1]$$

The resulting simplification permits solutions to be obtained by integral transform methods which provide insight to practically important situations. For full utilization of analytic solutions to Eq. [1], the result should be processed to yield additional useful information. It is customary to obtain the local gradient of potential in order to evaluate the variation of current density along electrodes. For the constant potential electrode type of boundary condition, the current density so obtained represents the limiting case of primary distribution in the absence of electrode overpotential. This bound on the current density may be useful in estimating worst possible cases. For example, in electroplating, a highly nonuniform, nearly primary current distribution will result in wasting possibly expensive metal in order to obtain a specified plate thickness in the central region of a flat electrode.

A second type of practical information available from the solution to Eq. [1] concerns the ohmic resistance associated with an electrode configuration. The virtual resistance of electrolyte between two electrodes may be found by application of Ohm's law using the total potential difference between electrodes and the total current, obtained by integrating the current density along the surface of the electrode with respect to area. When potential varies at the interface with an electrode, the area average potential may be used. Bounds to the resistance obtained from limiting cases of constant potential and constant current density electrodes are useful in applications such as electrolytic cell design and studies of corrosion enhancement due to impurity inclusions.

Additional useful information may be derived from the variation of the field in a few principal directions. The "range" in which the potential and current distributions become negligibly small permits the application of already obtained results to different electrode configurations. For example, it could be estimated how far away sidewalls must be in order for them not to affect the current distribution through a "shielding" effect.

* Electrochemical Society Active Member.
Key words: current distribution, disk geometry, resistance limits, corrosion, fuel cells, impurity enhanced corrosion, rotating disk resistance.

Background

Nobili (3) in 1827 refers to a laboratory curiosity in which rings of color are produced on metallic sheet anodes facing a wire cathode. This curiosity became known as a "metallochrome" and clearly derived from a combination of nonuniform current distribution and interference effects (Newton's rings) in thin oxide layers. The interest of mathematicians in the "metallochrome" led to many mathematical developments. Thus, Riemann (4) solved the "metallochrome" current distribution problem in 1855, and Weber (5), using some of Riemann's results, derived the solution for the primary current distribution on an isolated disk in an insulating plane as well as the resistance for the disk electrode in 1873, using certain "discontinuous integrals." The equivalent electrostatic problem was worked out by Green (6) in 1832. Later (1887) Schafheitlin (7) generalized the result for these discontinuous functions in a thorough fashion so that these integrals of products of Bessel functions are known as Weber-Schafheitlin integrals. [These integrals are of the form

$$\int_0^\infty \frac{J_\mu(at)\,J_\nu(bt)}{t^\lambda}\,dt$$

and can be evaluated in terms of the hypergeometric function with μ, ν and λ as parameters and a/b as the independent variable (8)].

Fortunately, hypergeometric functions often reduce to well-known elementary functions. The use of these functions, coupled with the Hankel (Fourier-Bessel) transformation of Laplace's equation, facilitates the solution of certain problems of direct application in electrochemical engineering [see, for example, Watson (9) and Sneddon (10) for reviews].

Although there is no *a priori* scheme for the selection of one calculational method over another, recent researchers (1, 11, 12) have favored the use of rotational elliptic coordinates for disk problems. It is, however, satisfying in the present study, to extend and reapply mathematical methods originally inspired by electrochemical problems.

Mathematical

The Hankel transform (as used in this paper) of a function $V(r)$, is defined as follows

$$\mathbf{H}_\nu[V(r)] \equiv \overline{V}_\nu(p) = \int_0^\infty r J_\nu(pr) V(r)\, dr \qquad [2]$$

where J_ν is the Bessel function of the first kind and of order ν, and p is the transformed variable.

Mathematical details regarding Hankel transforms may be found elsewhere (13). It will suffice here to show just two formulas which will be useful in our development. The first is the inversion theorem

$$V(r) = \int_0^\infty p J_\nu(pr) \overline{V}_\nu(p)\, dp \qquad [3]$$

which allows us to get the potential from its transform. The other property is, as can be shown by methods of elementary calculus (14), that

$$\mathbf{H}_\nu \left[\frac{1}{r} \frac{\partial}{\partial r} \left(r \frac{\partial V}{\partial r} \right) - \frac{\nu^2 V}{r} \right] = - p^2 \overline{V}_\nu(p) \qquad [4]$$

Equation [4] is especially important in the case where $\nu = 0$, since it reduces Laplace's equation (Eq. [1]) in cylindrical coordinates to an extremely simple form.

Applying Eq. [4] to Eq. [1] with $\nu = 0$, we obtain

$$\frac{d^2\overline{V}}{d^2 z} - p^2 \overline{V} = 0 \qquad [5]$$

Equation [5] is an ordinary differential equation, with the convenient solution

$$\overline{V} = A_1(p) e^{-pz} + A_2(p) e^{+pz} \qquad [6]$$

For the presently treated class of problems with remote counterelectrode, in order that the transform not become infinite for large z, we must have $A_2(p) = 0$. Applying the inversion formula, Eq. [3], we have finally the direct result for the potential

$$V(r,z) = \int_0^\infty p A_1(p) J_0(pr) e^{-\nu z} dp \qquad [7]$$

with $A_1(p)$ to be determined from the boundary condition at $z = 0$, *i.e.*, the problem is to find $A_1(p)$ in either Eq. [8] or Eq. [9] (or both)

$$V(r) = \int_0^\infty p A_1(p) J_0(pr)\, dp \qquad [8]$$

$$J(r) = \kappa \int_0^\infty p^2 A_1(p) J_0(pr)\, dp \qquad [9]$$

since Eq. [9] is obtained from Eq. [7] by use of Eq. [10]

$$J(r) = -\kappa \left. \frac{\partial V}{\partial z} \right|_{z=0} \qquad [10]$$

For subsequent convenience, we define a p-multiplied coefficient as

$$A(p) = p A_1(p) \qquad [11]$$

so that Eq. [8] and Eq. [9] become

$$V(r) = \int_0^\infty A(p) J_0(pr)\, dp \qquad [12]$$

$$J(r) = \kappa \int_0^\infty p A(p) J_0(pr)\, dp \qquad [13]$$

Depending on the types of boundary conditions given, two types of problems are encountered.

Mixed boundary conditions.—Case 1, Constant potential disk.—For the classic case of the disk at constant potential in an insulating plane, we must solve Eq. [12] and [13] as a set fitting the conditions

$$V(r) = V_0 \; ; \; r < a \qquad [14]$$

$$J(r) = 0 \; ; \; r > a \qquad [15]$$

To solve this set of equations for $A(p)$, it is convenient to use the dual integral equation formulation

$$\int_0^\infty y^\alpha f(y) J_\nu(xy)\, dy = g(x) \qquad 0 < x < 1$$

$$\int_0^\infty f(y) J_\nu(xy)\, dy = 0 \qquad x > 1 \qquad [16]$$

whose solution is known (15) to be

$$f(x) = \frac{2^{-\alpha/2} x^{-\alpha}}{\Gamma(1 + \tfrac{1}{2}\alpha)} \Bigg[x^{1+1/2\alpha} J_{\nu+1/2\alpha}(x) \int_0^1 y^{\nu+1} (1 - y^2)^{1/2\alpha} g(y)\, dy + \int_0^1 u^{\nu+1} (1 - u^2)^{1/2\alpha} du \int_0^1 g(yu) (xy)^{2+1/2\alpha} J_{\nu+1+1/2\alpha}(xy)\, dy \Bigg] \qquad [17]$$

Applying this to the disk problem, described by Eq. [12], [13], [14], and [15], we have

$$A(p) = \frac{2V_0}{\pi} \frac{\sin ap}{p} \qquad [18]$$

Combining Eq. [18] with Eq. [11], [7], [8], and [9] gives us an integral representation of the potential field and current distribution as

$$V(r,z) = \frac{2V_0}{\pi} \int_0^\infty \frac{\sin (ap) J_0(pr)}{p} e^{-pz} dp \qquad [19]$$

$$J(r, z = 0) = \frac{2\kappa V_0}{\pi} \int_0^\infty \sin (ap) J_0(pr)\, dp \qquad [20]$$

The integral in Eq. [19] may be evaluated in terms of elementary functions from tables of Laplace transforms for $r = 0$ [since $J_0(0) = 1$]; for $z = 0$, Eq. [19] and [20] are special cases of the previously mentioned Weber-Schafheitlin discontinuous integral, and may be expressed (8) in terms of the hypergeometric function, which in turn is often expressible in terms of elementary functions. In this case, the integral in Eq. [19] is known for all z (16), and the well-known results for the primary distribution are

$$V(r,z) = \frac{2V_0}{\pi} \sin^{-1} \left\{ \frac{2}{[(r/a-1)^2 + (z/a)^2]^{1/2} + [(r/a+1)^2 + (z/a)^2]^{1/2}} \right\} \qquad [21]$$

$$V(r, z = 0) = V_0 \qquad ; \; r < a \qquad [22a]$$

$$V(r, z = 0) = \frac{2}{\pi} V_0 \sin^{-1} (a/r) \qquad ; \; r > a \qquad [22b]$$

$$V(z, r = 0) = \frac{2}{\pi} V_0 \tan^{-1} (a/z) \qquad [23]$$

From Eq. [20], using the area average current density

$$J_{ave} = \frac{\int_0^a J(r) 2\pi r dr}{\pi a^2} \qquad [24]$$

we get

$$\frac{J(r)}{J_{ave}} = \frac{1}{2} \frac{1}{\sqrt{1 - (r/a)^2}} \qquad [25]$$

where

$$J_{ave} = \frac{4}{\pi} \left(\frac{\kappa V_0}{a} \right) \qquad [26]$$

The primary current distribution Eq. [25] has long been known (6, 5). The ohmic resistance for such a system is easily shown by Ohm's law to be

$$R = \frac{\Delta V}{I} = \frac{V_0}{J_{ave} \pi a^2} = \frac{1}{4\kappa a} \qquad [27]$$

From Eq. [21], [22], and [23], it is possible to calculate the range of the field, *i.e.*, the distance over which the field of the disk will vary significantly. For example, from Eq. [22b] it may be seen that the potential has fallen to 10% of its value on the disk at

$$a/r = \sin \pi/20 = \sin 9° = 0.15643$$

or $r/a = 6.393$ (roughly 3 diameters away). Similarly, along the centerline ($r = 0$) the potential falls to 10% at $a/z = \tan \pi/20 = \tan 9° = 0.15838$ (again, roughly 3 diameters away). This ranging effect has been used in discussions concerning reference probe placement for the rotating disk electrode (12) and occurs frequently in related problems. For example, Ellison (17) has recently found that in electroplating elliptical cylindrical wires, the presence of the wire anodes has very little effect on the field at the substrate when they are located 10 semi-minor-axes away.

Dirichlet and Neumann type boundary conditions.—Case 2, Constant current density disk.—When either the potential or its gradient is given on the entire boundary, a different procedure may be employed to solve for $A(p)$ in Eq. [12] or [13]. This problem is typified by the case of the disk with uniform current distribution embedded in an insulating plane. For this situation, the boundary conditions when substituted in Eq. [13] give

$$\int_0^\infty pA(p)J_0(pr)dp = J_D/\kappa \quad ; r < a$$
$$\int_0^\infty pA(p)J_0(pr)dp = 0 \quad ; r > a \qquad [28]$$

By comparing Eq. [28] with Eq. [2] and [3], it may be seen that the unknown $A(p)$ may be obtained by application of the Hankel transform inversion formula, giving

$$A(p) = \left(\frac{J_D a}{\kappa}\right)\frac{J_1(pa)}{p} \qquad [29]$$

Combining Eq. [29], [7], and [11], gives the integral representation for the potential field, which, for $z = 0$, may be solved from the Weber-Schafheitlin integral formulas. As before, the result is in terms of hypergeometric functions which, in this case, finally reduce to complete elliptic integrals of the first and second kind. The potential near the surface of the disk is as follows

$$V(r,z=0) = \begin{cases} \frac{2}{\pi}\left(\frac{J_D a}{\kappa}\right)\mathbf{E}\left(\frac{r}{a}\right) & ; r < a \quad [30a] \\ \frac{2}{\pi}\left(\frac{J_D a}{\kappa}\right)\frac{r}{a}\left\{\mathbf{E}\left(\frac{a}{r}\right) - \left[1-\left(\frac{a}{r}\right)^2\right]\mathbf{K}\left(\frac{a}{r}\right)\right\} & ; r > a \quad [30b] \end{cases}$$

as previously reported by Nanis (18). Numerical values for the radial field variation which closely match Eq. [30a] have also been computed by Newman for a limiting case which insures uniform current distribution, *i.e.*, large variation of overpotential with current density for mass transport limitation. Along the central axis of the disk, the potential may be found by combining Eq. [29], [7], and [11] and setting $r = 0$

$$V(z,r=0) = \left(\frac{J_D a}{\kappa}\right)\left\{\left[1+\left(\frac{z}{a}\right)^2\right]^{1/2} - \left(\frac{z}{a}\right)\right\} \qquad [31]$$

The range of the field may be found using Eq. [30] and [31]. For simplicity, the truncated series approximation for the elliptic functions (19) may be used to obtain

$$\frac{V(r,z=0)}{(J_D a/\kappa)} = \frac{V}{V_{max}} = \frac{1}{2}\left(\frac{a}{r}\right) + \frac{1}{16}\left(\frac{a}{r}\right)^3 + \ldots \qquad [32]$$

The potential drops off to 10% of its peak value at $a/r \cong 0.2$ or $r/a \cong 5$, *i.e.*, at a distance of only 2.5 diameters from the center of the disk. Similarly, along the axis of the disk, using binomial expansion, Eq. [31] becomes

$$\frac{V}{V_{max}} = \frac{1}{2}\left(\frac{a}{z}\right) - \frac{1}{8}\left(\frac{a}{z}\right)^3 + \ldots \qquad [33]$$

Again, the potential has dropped to 10% of its peak value at $r/a \cong 5$, roughly 2.5 diameters from the center of the disk in the vertical direction.

The resistance associated with the constant current density disk configuration may be calculated by introducing the concept of average potential in the electrolyte at the plane $z = 0$. By stipulating constant current density as a boundary condition, it is implicitly assumed that for a given solution conductivity and disk size, the slope of the overpotential *vs.* current density curve is sufficiently great so as to insure uniform current density on the disk, *i.e.*, good "throwing power." It should be noted that the overpotential conditions thus assumed at the electrode-electrolyte interface are located (in the mathematical sense) at $z = 0$, whereas the solution to Eq. [1] applies to the region $z > 0$ (strictly, $z \to 0^+$). Definition of the resistance associated with the constant current density case requires an analysis equivalent to that given by Jeans (20). Such a treatment in the present notation is given in the Appendix. Integrals of complete elliptic integrals used in potential averaging are known (19, 16). Use of Ohm's law yields

$$R = \frac{\Delta V}{I} = \frac{V_{ave}}{J_D \pi a^2} = \frac{\frac{8}{3\pi}\left(\frac{J_D a}{\kappa}\right)}{J_D \pi a^2} = \frac{8}{3\pi^2 \kappa a} \qquad [34]$$

Thus the ohmic resistance for constant current density on the disk is about 8% greater than the resistance associated with the constant potential (primary distribution) disk (Eq. [27]). (Results for the various cases are summarized in Table I.)

A comparison between radial potential at the plane $z = 0$ for the primary and uniform current distribution is shown in Fig. 1, where Eq. [30a, b] have been normalized by the average potential (*cf.* Eq. [34]).

Case 3, Constant J disk, constant potential plane.—Another boundary condition which proves useful in the treatment of corrosion problems concerns a disk at constant current density in a constant potential plane, *i.e.*

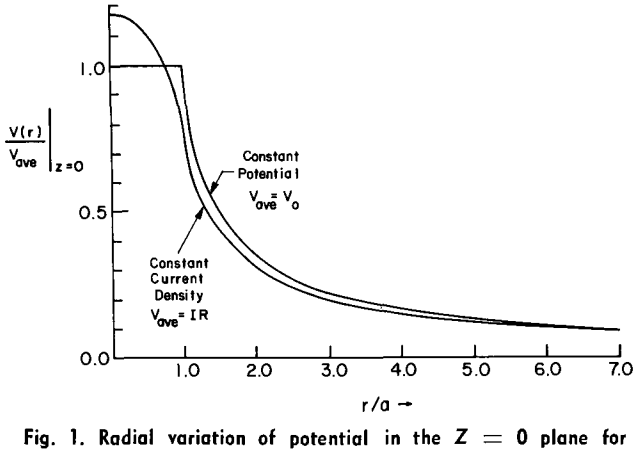

Fig. 1. Radial variation of potential in the Z = 0 plane for limiting cases of constant potential and constant current density on disk.

Table I. Field parameters

Boundary conditions		Case 1	Case 2	Case 3	Case 4
	Disk	Const. $V = V_o$	Const. $J = J_D$	Const. $J = J_D$	Const. $V = V_o$
	Plane	$\frac{\partial V}{\partial Z} = 0$	$\frac{\partial V}{\partial Z} = 0$	$V = 0$	$V = 0$
Range for $\frac{V}{V_o}, \frac{V}{V_{max}} = 0.1$	Plane ($Z = 0$) $r/a =$	6.392	5.025	—	—
	Axis ($r = 0$) $Z/a =$	6.314	4.950	1.660	2.065
Range for $\frac{J}{J_D}, \frac{J}{\kappa V_o/a} = 0.1$	Plane ($Z = 0$) $r/a =$	—	—	1.517	1.923
Equation No. for variation of	Current	[25]	—	[40]	[44]
	Potential	[21], [22], [23]	[30], [31]	[39], [41]	[45]
Resistance, ($\times \kappa a$)	$R_\kappa a$	$\frac{1}{4}$	$\frac{8}{3\pi^2}$	$\frac{4}{3\pi^2}$	0

$$\frac{\partial V}{\partial z} = \frac{J_D}{\kappa} \; ; \; r < a \qquad [35a]$$

$$V = 0 \; ; \; r > a \qquad [35b]$$

The solution of the Laplace equation with boundary conditions given in Eq. [35] is readily obtained by applying the dual integral equation approach (Eq. [16], [17]). Equation [35a] combined with Eq. [13], and Eq. [35b] with Eq. [12] become

$$\int_0^\infty pA(p)J_0(pr)\,dp = J_D/\kappa \quad ; \; r < a \qquad [36a]$$

$$\int_0^\infty A(p)J_0(pr)\,dp = 0 \quad ; \; r > a \qquad [36b]$$

Solution for $A(p)$ using Eq. [17] leads to the result

$$A(p) = \frac{2}{\pi}\frac{J_D}{\kappa}\left[\frac{\sin(ap) - ap\cos(ap)}{p^2}\right] \qquad [37]$$

which may also be written as

$$A(p) = \sqrt{\frac{2a}{\pi}}\frac{J_D a}{\kappa}\left[\frac{J_{3/2}(pa)}{p^{1/2}}\right] \qquad [38]$$

By substitution of Eq. [38] into Eq. [12] and Eq. [13], results are obtained in terms of an integral representation which may be reduced by use of the Weber-Schafheitlin formula to tabulated elementary functions or directly (21). For the plane $z = 0$

$$V(r,z=0) = \begin{cases} \frac{2}{\pi}\frac{J_D a}{\kappa}\sqrt{1 - \left(\frac{r}{a}\right)^2} & ; \; r < a \\ 0 & ; \; r > a \end{cases} \qquad [39]$$

$$J(r,z=0) = \begin{cases} J_D & ; \; r < a \\ \frac{2}{\pi}J_D\left[\sin^{-1}\frac{a}{r} - \frac{1}{\sqrt{(r/a)^2 - 1}}\right] & ; \; r > a \end{cases} \qquad [40]$$

Along the axis ($r = 0$), Eq. [38] together with Eq. [7] and [11] result in

$$V(z,r=0) = V_{max}\left[1 - \frac{z}{a}\tan^{-1}\frac{a}{z}\right] \qquad [41]$$

Levich and Frumkin (11) used elliptical cylindrical coordinates to arrive at Eq. [39] and [40] in terms of Legendre polynomials [a procedure later used by Newman (1, 12)]. Levich and Frumkin treated the resistance as a function of radius. It is difficult to assign a physical meaning to such a radial resistance function. By the methods used previously (cf. Eq. [34]), we can calculate a resistance based on the average potential along the disk (from Eq. [39]) as

$$R = \frac{\Delta V}{I} = \frac{V_{ave}}{J_D \pi a^2} = \frac{\frac{4}{3\pi}\left(\frac{J_D a}{\kappa}\right)}{J_D \pi a^2} = \frac{4}{3\pi^2 \kappa a} \qquad [42]$$

It is interesting to note that Eq. [42] indicates a resistance which is just one-half that for the constant current-density disk in the insulating plane (Case 2). It is also interesting to note that the range for such a situation is much smaller than for Cases 1 and 2. Inspection of Eq. [40] and [41] show that the current density drops to 10% of the value on the disk, J_D, at $r/a = 1.52$ and the potential along the centerline similarly decays to 10% of its peak value at $z/a = 1.66$, both less than a diameter away. This reduced range is because of a variation of potential as the inverse square of distance for large r and z compared with an inverse distance variation for Cases 1 and 2.

Case 4, Constant potential disk, constant potential plane.—For completeness, the limiting case of the constant potential disk in the constant potential plane has been treated. The boundary conditions for this case may be stated as

$$V = \begin{cases} V_o & ; \; r < a \\ 0 & ; \; r > a \end{cases} \qquad [43]$$

This boundary condition is of the Dirichlet type and may be solved following an inversion procedure (Case 2). Two difficulties encountered by this procedure reflect the "short circuit" indicated by Eq. [43]. First, current density is described by an integral of the form

$$\int_0^\infty pJ_1(pa)J_0(pr)\,dp$$

which can be shown to neither diverge nor converge (in the limit, the integrand approaches an undamped sine function). Hence the integral must be evaluated in the limit from the Weber-Schafheitlin formulas (8) as a special case involving the principle of summability of integrals (22). Second, the result so obtained (Eq. [44]) exhibits a "strong" infinity at $r = a$, so that an infinite current is obtained upon applying Eq. [24]. Waber (23) has encountered similar difficulties in considering the analogous case of a strip of fixed potential embedded in a conducting plane at a different potential. Despite difficulties in determining the average current density, the results for the local current density are

$$J(r,z=0) = \begin{cases} \dfrac{2}{\pi}\dfrac{\kappa V_0}{a}\dfrac{\mathbf{E}\left(\dfrac{r}{a}\right)}{1-\left(\dfrac{r}{a}\right)^2} & ; r<a \quad [44a] \\ \dfrac{2}{\kappa}\dfrac{\kappa V_0}{a}\dfrac{a}{r}\left[\mathbf{K}\left(\dfrac{a}{r}\right) - \dfrac{\mathbf{E}(a/r)}{1-(a/r)^2}\right] & ; r>a \quad [44b] \end{cases}$$

For $r/a = 0$, Eq. [17] and [11] yield the simple form

$$\frac{V(z,r=0)}{V_0} = 1 - \frac{z/a}{\sqrt{(z/a)^2+1}} \qquad [45]$$

From Eq. [45], it may be seen that the range for 10% potential remaining is about one diameter ($z/a = 2.06$) and, from Eq. [44b], the dimensionless current $J(r)/(\kappa V_0/a)$ drops to 0.1 at $r/a = 1.92$ (in the $z = 0$ plane).

Results derived from the field solutions for the bounding cases treated above are summarized in Table I.

Applications

Fuel cell technology.—For the application of general field solution characteristics to complex engineering problems, we consider the internal resistance of a fuel cell of the type treated by Gorin and Recht (24) and later discussed by Fick and Eisenberg (25). The system consists of an electrolyte matrix contacted on both sides by wire mesh screen electrodes (Fig. 2a). Their exact mathematical analysis of constant potential screen contact points results in an answer (Eq. [46]) consisting of several slowly converging series

$$\frac{R_{eff}}{R} = 1 - \left[4/\pi^2 r(h/d)\right]\sum_{m=1}^{\infty}\left[\frac{1}{m^2}\sin m\pi(1-r)\cdot\cos m\pi\tanh(m\pi h/d)\right] + \left[4/\pi^3 r^2(h/d)\right]\cdot\sum_{m=1}^{\infty}\sum_{n=1}^{\infty}\left[\sin m\pi(1-r)\sin n\pi(1-r)/mn\sqrt{m^2+n^2}\right]\cdot\cos m\pi\cos n\pi\tanh\left[\sqrt{m^2+n^2}\,\pi\,(h/d)\right] \qquad [46]$$

where $r = \Delta/d$, R_{eff} is the effective ohmic resistance, and R is the resistance of the matrix in contact with continuous sheet electrodes. In view of the present development of "range" and of individual electrode

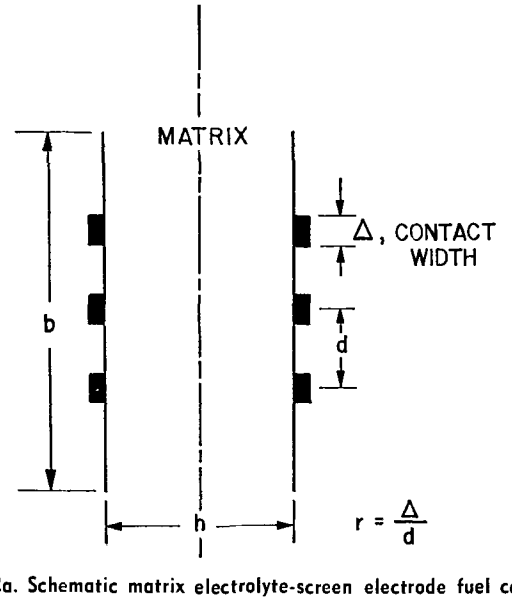

Fig. 2a. Schematic matrix electrolyte-screen electrode fuel cell

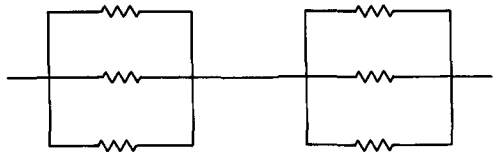

Fig. 2b. Equivalent circuit, individual resistances according to Eq. [47].

resistance, each contact may be considered (as a first approximation) as a disk of radius $\Delta/2$. By considering all of the screen mesh points on one side of the matrix as an array of individual disks in a parallel resistance circuit, the approximate equivalent circuit will be as shown in Fig. (2b), where each contact point is represented by the ohmic resistance for an isolated disk, R_i. From Eq. [27]

$$R_i = \frac{1}{4\kappa(\Delta/2)} = \frac{1}{2\kappa\Delta} \qquad [47]$$

where κ is the conductivity of the matrix (ohm^{-1} cm^{-1}). For the matrix of thickness h, assuming a square of edge b, the true resistance is

$$R = \frac{1}{\kappa}\frac{h}{b^2} \qquad [48]$$

For the equivalent circuit of Fig. 2, the over-all resistance, R_{eff}, is determined by

$$\frac{1}{R_{eff}/2} = \Sigma\frac{1}{R_i} = 2\kappa\Delta\frac{b^2}{d^2} \qquad [49]$$

since the number of contact points is b^2/d^2 in a square array of dimension b, and since each screen contributes to R_{eff}. Thus the resistance of the screen-matrix combination may be simply represented in terms of the two naturally resulting dimension ratios in Eq. [50]. The upper limit for each mesh point (and thus the entire system) may be based on the result for constant current density (Eq. [34]) so that the bounds are given as

$$\frac{d}{\Delta}\frac{d}{h} \leq \frac{R_{eff}}{R} \leq 1.08\frac{d}{\Delta}\frac{d}{h} \qquad [50]$$

From previous discussion of the range of a potential distribution, Eq. [50] will be most accurate when the contacts are spaced so that their fields do not interact, requiring that

$$\frac{d}{\Delta} > 6 \quad \text{and} \quad \frac{h}{\Delta} > 6$$

The tabulated values of Fick and Eisenberg are shown in Fig. 3 together with the lines representing the lower limit of Eq. [50] for comparably selected values of d/h. Note that agreement extends well beyond the limits imposed by range considerations. Clearly, where fields interact, the limit $R_{eff}/R = 1$ is ultimately to be expected, *i.e.*, as mesh spacing decreases and contact points increase in size to resemble a continuous sheet electrode.

Effect of inclusions in corrosion.—The effect of minor inclusions or sites with relatively large exchange current density for cathodic processes is associated with several practical problems. For example, in chlorine production cells, particles detach from the graphite anode and fall on the mercury cathode. The resulting local cell can result in production of unwanted hydrogen. Similarly on a single electrode, an iron impurity site on a zinc surface can provide a location for cathodic action (*i.e.*, hydrogen production), with corresponding enhanced corrosion of the zinc.

We may idealize such corrosion situations by considering the impurity to be a disk at constant current density imbedded in an infinite plane at constant potential (Case 3). This approximation may be made

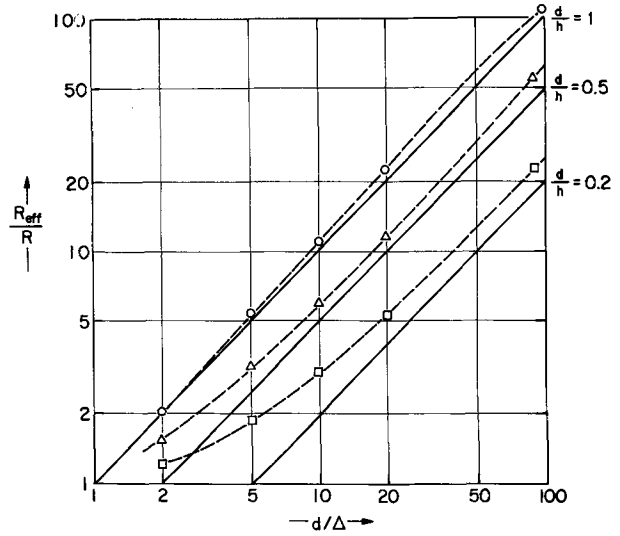

Fig. 3. Comparison of points according to Eq. [46] (ref. 6) and Eq. [50] (approximate model).

since the lateral range of the disk field does not extend much beyond $r/a = 1.5$. The same is true for the vertical range (see Eq. [41]), in general agreement with the computations of Simmons *et al.* (2) for the effect of electrolyte depth in a related problem.

In order to determine the corrosion current for the disk-plane system, it is necessary to locate the point of intersection of the two curves describing the overpotential-current relation for each of the half reactions involved. In addition, although not usually considered in such computations, the ohmic resistance of the system must be included. This tends to decrease the corrosion current, in much the same fashion as the internal resistance of a battery. Thus, the *IR* drop associated with the cathodic process (disk) will determine a lower corrosion current than would be expected if resistance were ignored (see Fig. 4) That is, if the anode and cathode reactions are described by general current-potential function such as

$$I_C = I_1(E_C) \qquad [51a]$$

$$I_A = I_2(E_A) \qquad [51b]$$

then we can rewrite Eq. [51] in terms of inverse functions as

$$E_C = I_1^{-1}(I_C) \qquad [52a]$$

$$E_A = I_2^{-1}(I_A) \qquad [52b]$$

By including the *IR* drop, Eq. [52] leads to

$$\frac{I_2^{-1}(I_A) - I_1^{-1}(I_C)}{I} = -R \qquad [53]$$

which must be solved for I, the corrosion current. Equation [53] is a restatement of the requirement that the sum of the potential drops in a closed circuit must equal zero (Kirchoff's rule).

As an example, consider a 1 cm² spot of iron impurity on a 100 cm² sheet of zinc, which will result in metal corroding to zinc ion and hydrogen evolution on iron as the two half-cell reactions. If we first calculate a corrosion current neglecting ohmic drop, we will have

$$|J_C| = 2 \times 10^{-6}\, e^{-FE/2RT} \qquad [54a]$$

$$J_A = 3 \times 10^{-4}\, e^{F(E+0.763)/RT} \qquad [54b]$$

The value of exchange current density for the hydrogen reaction (Eq. [54a]) is taken from the review of Kita (26) and the value for zinc dissolution from the work of Piontelli and Poli (27). Reversible potentials of −0.763V and 0.000V for zinc and hydrogen, respectively, in a solution of 1*N* H_2SO_4 + 1*N* $ZnSO_4$ are used as a basis. Equation [54a] is multiplied by the cathode area (1 cm²) and Eq. [54b] by the anode area (99 cm²) and are equated to solve for a corrosion current of 0.968A (uppermost intersection, 1000 mA, Fig. 4).

Using Eq. [53], the calculation of corrosion current for the case where the resistive potential drop is included is now considered. For the resistance associated with a single cathode site we may use Eq. [42] with an experimentally determined (28) conductivity of 0.157 ohm^{-1} cm^{-1}, which yields $R = 1.525$ ohms. Equation [53] reduces to

$$\frac{0.002 + 0.1777 \log I}{I} = -1.525 \qquad [55]$$

which must be solved by trial and error to yield a new corrosion current density of 1.10 mA/cm², almost a 90% decrease from the value of 9.7 mA/cm² obtained neglecting resistance. Clearly, the resistance associated with the cathodic sites must be included in such calculations.

We may now consider the important question concerning the physical dispersion of the low hydrogen overpotential sites. That is, would one 1 cm² patch of Fe produce the same corrosion current as one hundred 0.01 cm² patches? The answer may be deduced from Eq. [53] by representing $I_2^{-1}(I_A)$, $I_1^{-1}(I_C)$ and R as functions of area, and treating each site as an isolated spot. Equation [53] then becomes

$$\frac{0.1777 \log I + 0.1206 - 0.05922 \log \frac{A_A}{A_C} - 0.1777 \log A_C}{I} = -\frac{1.525}{\sqrt{A_C}} \qquad [56]$$

where I is the corrosion current, and A_A and A_c are the anodic and cathodic areas, respectively. Equation [56] shows that the corrosion current depends on the size of the corrosion spots (A_c) and also on the fraction of total area occupied (A_A/A_c). If we maintain the 99:1 ratio used previously, then Eq. [56] reduces to

$$\frac{0.1777 \log J_C + 0.0024}{J_C} = -1.525\sqrt{A_C} \qquad [57]$$

Hence, for a finer dispersion, corrosion current density goes up to 4.21 mA/cm². This effect may be rationalized if we recall that the finely dispersed particles, although

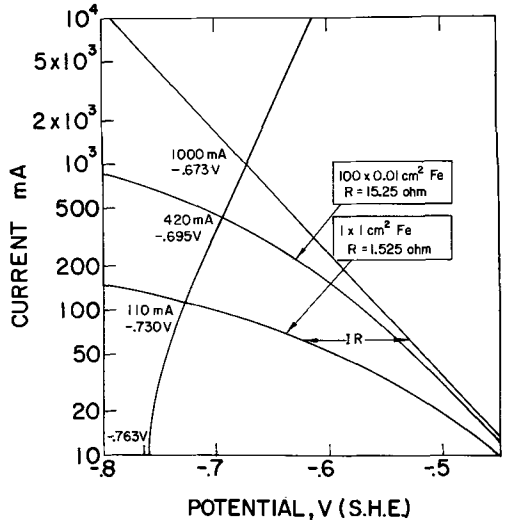

Fig. 4. Effect of impurity dispersion on internal cell resistance and corrosion rate. Zinc area, 99 cm²; iron area, 1 cm². Anode reaction: $Zn \rightarrow Zn^{++} + 2e^-$, $J_0 = 3 \times 10^{-4}$A cm^{-2} (1*N* $ZnSO_4$). Cathode reaction: $2H^+ + 2e^- \rightarrow H_2$, $J_0 = 2 \times 10^{-6}$ A cm^{-2} (1*N* H_2SO_4). Cathode site resistance $R = \frac{4}{3\pi^2\kappa a}$ with $\kappa = 0.157$ ohm^{-1} cm^{-1}.

having higher individual resistances ($R\alpha A_c^{-1/2}$), are in a parallel circuit which lowers the total resistance.

Placement of electrodes.—In the recent literature on rotating disk systems there has been some discussion (29, 12) on the proper placement of probes to measure the potential near rotating disk electrodes. Thus, Newman (12) suggests remote placement of the probe so as not to distort the field near the disk combined with estimation of the ohmic potential drop (unavoidably included in the measurement), based on the resistance of a disk at constant potential in an insulating plane. In a later paper, Hsueh and Newman (30) do indeed locate the reference probe in the plane of the electrode (10 radii away) and estimate the ohmic contribution to the potential from the equivalent of Eq. [22]. However, from present considerations it may be considered that the use of the probe is then rendered superfluous. All that need be measured in such a situation is the potential between the disk and a large remote unpolarized counterelectrode with the ohmic drop being approximated from either Eq. [22b] or [30b] as limits.

In this regard, Newman, in a later paper (1), recognizing that potential varies near the surface of the disk, defines a dimensionless effective resistance based on the group (in our notation)

$$\frac{V(r = z = 0)4\kappa a}{J_{ave}\pi a^2}$$

and uses this as a correction factor for Eq. [27]. In so doing, he finds that, when summing calculated overvoltage and resistive (IR) drops, the current-potential data of Hsueh and Newman (30) on a rotating disk are well fitted. However, use of his effective resistance approach requires that the ohmic resistance associated with a disk change by a factor of as much as 27.3% ($4/\pi = 1.273$; see Eq. [30a]) for the uniform current distribution, whereas we have seen that, in reality, the change of resistance is only on the order of 8% when changing from the uniform potential to uniform current distribution.

APPENDIX

Resistance of Nonisopotential Disk

As indicated by Jeans (20) and also Levich (31), the thermal energy, W, generated due to current flow in a medium of conductivity κ is given by the volume integral (for unit time)

$$W = \int\int\int \vec{J} \cdot \vec{E} d\tau \qquad [58]$$

where

$$\vec{J} = -\kappa \nabla V \qquad [59]$$

$$\vec{E} = -\nabla V \qquad [60]$$

Furthermore, Gauss' theorem for two arbitrary scalar quantities u and w is (32)

$$\int\int\int \nabla u \cdot \nabla w d\tau + \int\int\int u \nabla^2 w d\tau = \int\int u \frac{\partial w}{\partial n} dA \qquad [61]$$

where n indicates component normal to the bounding surface A. If we associate u and w with V, the potential, *i.e.*, let

$$\nabla u = \vec{J} = -\kappa \nabla V \qquad [62]$$

$$\nabla w = \vec{E} = -\nabla V \qquad [63]$$

then, since

$$\nabla^2 V = 0 \qquad [1]$$

combination of Eq. [1] with Eq. [58] to [63] yields

$$W = \kappa \int\int V \frac{\partial V}{\partial n} dA \qquad [64]$$

In the cases treated in the present cylindrical coordinate system

$$\frac{\partial V}{\partial n} \equiv -\left.\frac{\partial V}{\partial z}\right|_{z=0} \quad \text{and} \quad dA = 2\pi r dr$$

and since $W = I^2R$ (*cf.* Eq. [58]), Eq. [64] becomes

$$I^2R = -\kappa \int_0^\infty V(r) \left.\frac{\partial V(r)}{\partial z}\right|_{z=0} 2\pi r dr \qquad [65]$$

Equation [65] describes the system resistance in terms of arbitrary potential and current distributions on the plane $z = 0$. If, for $r > a$, we have an insulation or zero potential condition, and $\partial V/\partial z$ is constant on the disk then

$$I^2R = -\kappa \left.\frac{\partial V}{\partial z}\right|_{z=0} \times \int_0^a V(r) 2\pi r dr \qquad [66]$$

or finally

$$R = V_{ave}/I \qquad [67]$$

(*cf.* Eq. [34], [42]) where V_{ave} is based on area.

Acknowledgment

This work is based in part on a thesis submitted by W. Kesselman to the School of Chemical Engineering, University of Pennsylvania, in partial fulfillment of the requirements for the degree Doctor of Philosophy. The financial assistance of NASA(NSG-316) is gratefully acknowledged.

Manuscript submitted July 30, 1969; revised manuscript received *ca.* Oct. 13, 1970.

Any discussion of this paper will appear in a Discussion Section to be published in the December 1971 JOURNAL.

LIST OF SYMBOLS

A	area, cm^2
a	disk radius, cm
b	fuel cell dimension, cm
d	disk spacing, cm
$\vec{E}$	electric field, V cm^{-1}
E_A	potential of anode, V
E_C	potential of cathode, V
$\mathbf{E}$	complete elliptic integral of second kind
f, g	arbitrary functions
$\mathbf{F}$	Faraday's constant, cal V^{-1} (g-equivalent)$^{-1}$
$\mathbf{H}$	Hankel transform
h	fuel cell dimension, cm
I	current, A
$J, \vec{J}$	current density, A cm^{-2}
J_A	anodic current density, A cm^{-2}
J_{ave}	area average current density, A cm^{-2}
J_C	cathodic current density, A cm^{-2}
J_D	constant current density on disk, A cm^{-2}
J	Bessel function of first kind
$\mathbf{K}$	complete elliptic integral of first kind
m, n	dummy variables
p	transformed variable
r	radial distance from center of disk, cm
R	ohmic resistance, ohm
R_{eff}	effective ohmic resistance, ohm
R_i	resistance of isolated disk, ohm
u, w	arbitrary scalar quantities
V	potential, V
V_{ave}	area average potential, V
$\overline{V}$	transformed potential
V_o	applied potential, V
W	thermal energy per time, watt
z	vertical distance from plane, cm
α	arbitrary power (also indicates proportionality)
Γ	gamma function
Δ	contact point diameter, cm
κ	conductivity, ohm^{-1} cm^{-1}
ν	order of Bessel function
$d\tau$	infinitesimal volume, cm^3

REFERENCES

1. John Newman, *This Journal*, **113**, 1235 (1966).
2. J. A. Simmons, S. R. Coriell, and F. Ogburn, *This Journal*, **114**, 782 (1967).
3. M. Nobili, *Ann. Chim.*, **34**, 288, 419 (1827).
4. G. Riemann, *Ann. Physik*, **XCV**, 130 (1855).
5. H. Weber, *Crelle J. for Mathematics*, **75**, 75 (1873). Also to be found in "A Treatise on Bessel Functions and Their Applications to Physics," A. Gray, V. Mathews, and T. M. MacRobert, Editors, 2nd ed., p. 142, MacMillan and Co., Ltd., London (1952).
6. G. Green, *Trans. Cambridge Phil. Soc.*, **5**, 1 (1832).

7. P. Schafheitlin, *Math. Ann.*, **33**, 161 (1887).
8. M. Abramowitz and I. Stegun, "Handbook of Mathematical Functions," NBS-AMS 55, p. 487, Washington, D. C. (1964).
9. C. N. Watson, "A Treatise on the Theory of Bessel Functions," Cambridge University Press (1966).
10. I. N. Sneddon, "Mixed Boundary Value Problems in Potential Theory," John Wiley & Sons, Inc., New York (1966).
11. B. Levich and A. Frumkin, *Acta Physicochim URSS*, **18**, 325 (1943).
12. John Newman, *This Journal*, **113**, 501 (1966).
13. I. N. Sneddon, "Fourier Transforms," Chap. 2, McGraw Hill Book Co., New York (1951).
14. Ibid., p. 60.
15. Ibid., p. 70.
16. I. S. Gradshteyn and I. M. Ryzhik, "Table of Integrals, Series and Production," Academic Press, New York (1965).
17. G. N. Ellison, *This Journal*, **116**, 616 (1969).
18. L. Nanis, Paper 150 presented at the Dallas Meeting of the Society, May 7-12, 1967.
19. P. R. Byrd and M. D. Friedman, "Elliptic Integrals for Engineers and Physicists," Springer-Verlag, Berlin (1954).
20. J. H. Jeans, "The Mathematical Theory of Electricity and Magnetism," pp. 357, 358, Cambridge University Press (1958).
21. A. Erdelyi *et al.*, "Tables of Integral Transforms," Vol. 2, McGraw Hill Book Co., New York (1954).
22. J. Irving and N. Mullineux, "Mathematics in Physics and Engineering," p. 588, Academic Press, New York (1959).
23. J. T. Waber and M. Rosenbluth, *This Journal*, **102**, 344 (1955).
24. E. Gorin and H. L. Recht, *Chem. Eng. Prog.*, **55**, 51 (1959).
25. L. Fick and M. Eisenberg, *ibid.*, **57**, 74 (1961).
26. H. Kita, *This Journal*, **113**, 1095 (1966).
27. R. Piontelli and G. Poli, *CITCE*, **2**, 136 (1950).
28. W. Kesselman, Ph.D. Thesis, University of Pennsylvania, Philadelphia (1969).
29. D. H. Angell, T. Dickinson, and R. Greef, *Electrochim. Acta*, **13**, 120 (1968).
30. L. Hsueh and J. Newman, *ibid.*, **12**, 429 (1967).
31. B. Levich, "Physicochemical Hydrodynamics," p. 265, Prentice-Hall Book Co., Englewood Cliffs, N. J. (1962).
32. "International Dictionary of Applied Mathematics," p. 418, D. Van Nostrand Co., New York (1960).

Technical Note

Note on an Organic-Electrolyte Cell with a High Voltage

Abner Brenner*

National Bureau of Standards, Washington, D. C. 20234

In the course of some experiments directed toward the electrodeposition of lithium, I chanced on a cell which delivered the unusually high back emf of 5.2V. I believe that this is the highest voltage which has been reported for a single cell. The voltage approaches the theoretical voltage of about 5.9V that can be obtained by the combination of lithium and fluorine. It is approximately equal to the voltage that would be obtainable from lithium and chlorine trifluoride, which combination is about the most active that could be considered feasible for operation as a cell near room temperature and atmospheric pressure (ClF_3 boils at 12°C).

Experimental

The electrolyte consisted of a 10% solution of lithium fluoborate in sulfolane or 3-methyl sulfolane. The latter is easier to use, because it is a liquid at room temperature, whereas the former is a solid. The solution of lithium fluoborate in sulfolane, however, is fluid at room temperature, although somewhat viscous. Smooth, gray coatings of lithium were readily electrodeposited from these electrolytes.

A combination of three materials was required in the cell to obtain the voltage of 5.2. These were: sulfolane or its methyl derivative, a fluorine-containing lithium compound, either the fluoborate or hexafluorophosphate, and a graphite anode. A series of qualitative experiments showed that replacing any one of the three materials led to a lower voltage. For example, a solution of lithium fluoborate in tetrahydrofuran or dimethylsulfoxide when electrolyzed yielded good deposits of lithium, but the back emf ranged between 4.3 and 4.5V. Use of platinum or a few other metals as anode in place of the graphite anode in the sulfolane electrolyte yielded a back emf of only about 3.7V. The electromotively active material was not in solution, as replacement of the polarized graphite rod by a fresh rod did not yield the high voltage. Substitution of lithium fluoborate by lithium bromide, in the sulfolane electrolyte, yielded an electrolyte which did not give a satisfactory deposit of lithium and the back emf (with graphite anode) was only 3.8V. Lithium hexafluorophosphate was a less satisfactory solute than the fluoborate, because it did not yield a satisfactory lithium deposit on electrolysis, and to obtain the back emf of 5.2V it was necessary to start the electrolysis with a lithium cathode (along with the graphite anode).

The back emf of 5.2V was obtained after only several minutes of electrolysis and in repeated experiments was reproducible to about 0.1V. On open circuit the voltage slowly decreased to about 5.0V in the course of a minute or two and then more slowly. A graphite anode, which had been polarized for a longer period of time, stored up some of the electromotively active material, as when the polarized cell was shorted through a milliameter the initial current was more than 10 mA/cm^2 and then slowly decayed. As a basis of comparison, a fresh, unpolarized graphite electrode with a lithium electrode in the sulfolane electrolyte initially had a voltage (open circuit) of 3.4 and yielded only about 1 mA/cm^2. The electromotively active compound was not too evanescent, as a graphite electrode was removed from the cell, rinsed in water, dried with a cloth and replaced and yielded a back emf of 4.3V, as compared with the voltage of an untreated graphite electrode of 3.4.

A matter of secondary interest, but still rather unusual was the electromotive activity of graphite and its deterioration in the solutions when used as an electrode. Graphite was not attacked by simple immersion. As an anode it was rapidly eroded away. With a lithium counterelectrode it behaved as a positive plate

* Electrochemical Society Active Member.
Key words: lithium deposition, high energy density cell, organic electrolyte, graphite electrode.

(cathode) in the sulfolane electrolyte and delivered a small current for a day or two. The initial current was about 1 mA/cm^2 which dropped down to about 0.2 mA/cm^2 after 24 hr. The graphite was somewhat etched.

The electromotive activity and disintegration of graphite was more pronounced in an electrolyte consisting of a 10% solution of lithium chloride in dimethylsulfoxide. Although this cell (with lithium and graphite electrodes) did not produce as high a back emf as the sulfolane-fluoborate cell previously described, it exhibited more reactivity with graphite electrodes, and for that reason is described here in a little more detail. All types of graphite utilized were rapidly disintegrated when made anodic in the DMSO solution. These included ordinary graphite rods, purified graphite obtained from the AEC, and pyrolytic graphite. The latter disintegrated into lamellae about 0.01 in. thick. Even more suprising was the rapid disintegration of graphite rods when used as the positive plate of a current producing cell. A graphite rod ¼ in. in diameter, for example, when used as part of a current delivering cell in DMSO-LiCl with a lithium anode completely disintegrated into a sludge after about 24 hr operation. The currents initially were about 1 mA/cm^2 of graphite surface and slowly dropped down to about 0.5 mA/cm^2.

In these experiments, a divided cell was not used. A test tube sufficed. The sulfolane and dimethylsulfoxide were used as received.

Conclusion

I do not suggest that the cells described herein have any utility in their present form as a high energy density battery. However, if the reactive material, that gives the sulfolane-fluoborate-graphite system the high back emf of 5.2V when the graphite is made anode, can be isolated or identified, perhaps such substances can be synthesized in quantity by other means and made available for the construction of cells. Also, the functioning of graphite in the organic electrolyte as a positive plate in the discharge of the cell is an unusual phenomenon and worthy of further investigation.

Manuscript submitted Sept. 14, 1970; revised manuscript received *ca.* Nov. 18, 1970.

Any discussion of this paper will appear in a Discussion Section to be published in the December 1971 JOURNAL.

Brief Communication

The Low-Temperature Passivation of Cadmium in 8M KOH

Hong Yol Kang*

P. R. Mallory & Co. Inc., Laboratory for Physical Science, Northwest Industrial Park, Burlington, Massachusetts 01803

It has been reported (1) that cadmium anodes have desirable properties for their use in primary alkaline cells at low temperatures. The discharge of cadmium electrodes is normally terminated by the onset of passivation. Although the passivation of cadmium in alkaline solutions has been studied by a number of authors (2-10), little data have been reported for the low-temperature range. In the present work measurements of cadmium passivation at low temperatures were carried out to provide the data necessary for an analysis of the intrinsic rate capabilities of cadmium at low temperatures. The behavior of flat cadmium electrodes was studied in order to avoid the uncertainties associated with the interpretation of passivation data on porous electrodes. Eight molar KOH solution was used as the electrolyte to cover a wider range of temperatures. The position of the cadmium (bottom) and the range of current densities (low) were chosen to minimize the effect of convection. The results fitted a kinetic expression proposed in the literature based on a dissolution-precipitation mechanism.

KOH solutions were prepared from a Fisher polypac 45% solution and stored under CO_2 free conditions. Cadmium sheet with a purity of 99.995% supplied by Alpha Inorganics, Inc., was degreased, treated with dilute acid, and cathodically reduced at 3 mA/cm^2 for 5 sec prior to anodization. The passivation cell consisted of a threaded Lucite block and a plug to form an electrolysis compartment. The Lucite block also had an opening for the reference electrode. The cadmium anode was tightly pressed by the plug in a horizontal position at the bottom of the cell, the area exposed to the electrolyte being exactly 1 cm^2. The conductor in contact with the working electrode was a platinum sheet welded on a nickel disk. The counter-electrode was a platinum wire and the reference electrode was a HgO/Hg electrode in the same KOH solution. The whole cell was covered by a lid to prevent an extensive change of the electrolyte composition by carbonation during the cooling down period. The amount of the KOH electrolyte was 5 ml and the cell was cooled in an Associate Testing Labs SK2101 temperature control chamber. The passivation measurements were made at constant currents supplied by a H/P Harrison 6200B d-c power supply combined with resistance regulators. The passivation time was determined from the time of closing the circuit to the instant at which the anode potential increased rapidly.

The passivation time of the flat cadmium electrode was measured at several current densities in 8M KOH at various temperatures ranging from 25° to −60°C. Results are shown in Table I. The values in the table are the average of 3-6 measurements, the reproducibility of the data in terms of the standard deviation being about 15% throughout the ranges of current and temperature.

There have been two different mechanisms proposed in the literature for the anodic reaction of cadmium

* Electrochemical Society Active Member.

Key words: cadmium, temperature dependence of passivation, vitreous point and passivation.

Table I. Passivation of cadmium in 8M-KOH

Temp, °C	Current density, i, mA/cm²	Passivation time, τ, sec
25	0.05	32,920
	0.1	9,135
	0.2	2,675
	0.3	1,395
	0.5	615.5
	0.75	357.6
	1.0	251.7
0	0.05	14,210
	0.1	4,329
	0.2	1,338
	0.3	739.3
	0.5	352.8
	0.75	231.4
	1.0	170.2
−10	0.05	7,511
	0.1	2,383
	0.2	889.2
	0.3	495.8
	0.5	249.0
	0.75	153.8
	1.0	113.0
−20	0.05	3,779
	0.1	1,350
	0.2	588.1
	0.3	354.4
	0.5	163.2
	0.75	110.2
	1.0	72.9
−30	0.05	2,388
	0.1	907.1
	0.2	390.8
	0.3	253.6
	0.5	105.6
	0.75	69.8
	1.0	49.3
−40	0.05	1,550
	0.1	527.4
	0.2	244.9
	0.3	139.0
	0.5	65.3
	0.75	38.9
	1.0	26.1
−50	0.05	919.7
	0.1	282.3
	0.2	130.0
	0.3	60.4
	0.5	13.8
	1.0	10.2
−60	0.05	219.1
	0.1	72.4
	0.2	24.8
	0.3	19.1
	0.5	9.4
	0.75	4.4
	1.0	3.2

in alkaline solutions: the dissolution-precipitation mechanism (2-4, 8-10) and the film growth mechanism (5, 7). Recent investigations (8-10) appear to favor the former more than the latter. The data obtained in the present work fitted reasonably well the kinetic expression (8, 15) based on a dissolution-precipitation mechanism involving a competing reaction. This mechanism was characterized by the linear dependence of $i\tau^{1/2}$ on i at low current densities, where τ is the passivation time at constant current density i

$$i\tau^{1/2} = a + b\,i \qquad [1]$$

Figure 1 shows the i *vs.* $i\tau^{1/2}$ plot at various temperatures. Although further investigation is required to establish detailed reaction schemes, the data seem to indicate that under the conditions of this work cadmium is indeed anodically passivated through a mechanism satisfying the above kinetic expression.

Table II. Passivation of cadmium in 8M-KOH

Temp, °C	25°C		0°C		−30°C	
i, mA/cm²	$i\tau^{1/2}$ (obs)	$i\tau^{1/2}$ (calc)	$i\tau^{1/2}$ (obs)	$i\tau^{1/2}$ (calc)	$i\tau^{1/2}$ (obs)	$i\tau^{1/2}$ (calc)
0.05	9.07	7.78	5.96	5.88	2.44	3.32
0.1	9.56	8.26	6.58	6.24	3.01	3.51
0.2	10.34	9.20	7.32	6.94	3.95	3.90
0.3	11.20	10.15	8.15	7.65	4.78	4.29
0.5	12.40	12.05	9.39	9.06	5.14	5.06
0.75	14.18	14.41	11.41	10.83	6.26	6.03
1.0	15.86	16.78	13.04	12.59	7.02	7.00

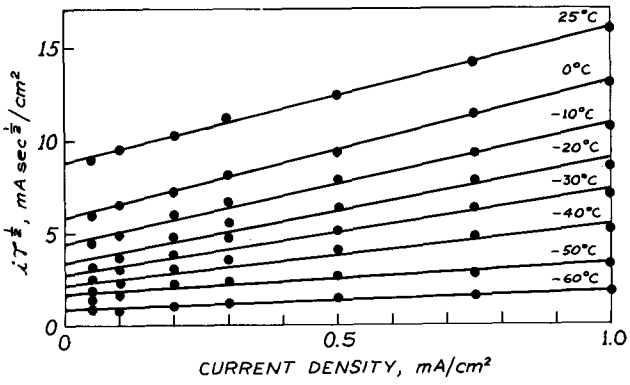

Fig. 1. i *vs.* $i\tau^{1/2}$ plot at various temperatures

If the above mechanism is the case, the passivation time is controlled by the rate of precipitation and/or the rate of mass transfer of the dissolved cadmium species (8, 15). Thus, a temperature dependence of the Arrhenius type is expected of the passivation time τ and thus $i\tau^{1/2}$. In considering the temperature dependence the concept of the vitreous point T_o (12-14) was introduced since the mechanism involves the movement of ions. The vitreous point T_o is the temperature below which mobility of ion in the electrolyte ceases (14). Then Eq. [1] can be expressed by

$$i\tau^{1/2} = \mathrm{A}\exp\left(-\frac{E_a}{T - T_o}\right) + B\,i\exp\left(-\frac{E_b}{T - T_o}\right) \qquad [2]$$

or

$$a = A\exp\left(-\frac{E_a}{T - T_o}\right) \qquad [2a]$$

$$b = B\exp\left(-\frac{E_b}{T - T_o}\right) \qquad [2b]$$

T_o was determined by Laurent and Tarrousseau (14) to be 165°K for 8M KOH. Based on the data in Table I parameters a and b were computed at different temperatures, and the values of A, B, E_a, and E_b were computed by the regression method. The results are: $A = 24.35$, $B = 33.70$, $E_a = 160.0 \pm 10.9$, and $E_b = 168.8 \pm 14.7$. E_a and E_b are equal within the standard error of statistical computation, and Eq. [2] can be expressed as

$$i\tau^{1/2} = (24.35 + 33.70\,i)\exp\left(-\frac{164.4}{T - 165}\right) \qquad [3]$$

The observed values of $i\tau^{1/2}$ were compared with the calculated ones based on Eq. [3] in Table II. The experimental data agree reasonably well with the calculated values. Although the fundamental significance of this equation, if any, depends on further study of the system, the expression may be interesting in suggesting a certain model of the passivation mechanism.

Acknowledgment

The author wishes to extend his appreciation to Dr. P. Bro and Dr. R. Selim for helpful discussions.

Manuscript submitted April 10, 1970; revised manuscript received *ca.* Nov. 2, 1970.

Any discussion of this paper will appear in a Discussion Section to be published in the December 1971 JOURNAL.

REFERENCES

1. W. H. Conson, Jr. and J. R. Wifore, NAS5-11556 Fin. Rep. (Sept. 1968).
2. K. Huber, *This Journal*, **100**, 376 (1953).
3. P. K. Lake and E. J. Casey, *ibid.*, **105**, 52 (1958).
4. I. Sanghi, *ibid.*, **106**, 532 (1959).
5. G. T. Croft, *ibid.*, **106**, 278 (1959).
6. M. Fleischman, K. S. Rajagapslan, and H. R. Thirsk, *Trans. Faraday Soc.*, **59**, 741 (1963).

7. J. P. G. Fan and N. A. Hampson, *Electrochem. Techol.*, **6**, 10 (1968).
8. M. A. V. Devanathan and S. Lakshman, *Electrochim. Acta*, **13**, 667 (1968).
9. M. W. Beiter and J. L. Weininger, *This Journal*, **113**, 651 (1966).
10. Y. Okinaka, *ibid.*, **117**, 289 (1970).
11. P. C. Milner and U. B. Thomas, "Advances in Electrochemistry and Electrochemical Engineering," C. W. Tobias, Editor, Vol. 5, Interscience Publishers, New York (1967).
12. J. H. Gibbs and E. A. Dimarzzio, *J. Chem. Phys.*, **38**, 373 (1958).
13. C. A. Angell, *J. Phys. Chem.*, **70**, 3988 (1966).
14. J. F. Laurent and J. C. Janousseau, Paper 23, Detroit Fall Meeting of the Society, Oct. 6-9, 1969.
15. A. K. N. Reddy, M. A. V. Devanathan, and J. O'M. Bockris, *J. Electroanal. Chem.*, **6**, 61 (1963).

JOURNAL OF THE ELECTROCHEMICAL SOCIETY

SOLID STATE SCIENCE

MARCH 1971

Investigations of the Variations of Dielectric Constant and Surface Charge of Polyvinyl Chloride Electrets with Time

P. K. C. Pillai, V. K. Jain, and Meenakshi Kamdar

Department of Physics, Indian Institute of Technology, New Delhi 29, India

ABSTRACT

This paper deals with the charge formation, decay characteristics, and variation of dielectric constant of thermoelectrets of SR_8 (polyvinyl chloride) and SR_{10} (polyvinyl chloride) prepared at different voltages with different polarizing times. It has been found that polarizing time has a major influence in determining the initial as well as the final surface charge and also the final value of the dielectric constant. The results also show that surface charge formation is due not only to dipolar orientation but also to some other charging mechanism, which in turn affects the dielectric constant of the sample. Studies of variation of dielectric constant prove the pulsatory nature of the charge decay and also show qualitatively the orientation effect obtained by x-ray diffraction studies of electrets.

Electrets have been known for many years but have recently become a subject of considerable interest. Heaviside (1) used the word electret to denote a permanently electrified material having electric charges of opposite sign at its extremities. Eguchi (2) has shown from his experimental investigations that electret effect is a volume effect and not merely a surface effect.

Many other workers (3-7) in this field have studied the characteristics of electrets prepared from different materials by measuring their surface charge, charging and discharging current, and dipole movement. In this investigation, measurements have been made on the variation of the dielectric constant of the polarized samples along with the surface charge studies. Useful information about the variations in the surface charge and dielectric constant have been obtained from these studies.

Experimental Details

The materials used for these investigations were SR_8 (vinyl) and SR_{10} (vinyl) manufactured by the Rajasthan Vinyl and Chemical Industries, Kota, India. These are PVC compounds with different physical properties and are available in powder form with different particle sizes. Although these materials are copolymers and do not show any definite melting point, most of the ingredients of these compounds are molten at about 160°C.

Samples were molded by using these powders in a mica cavity of 1 mm thickness and 1 cm^2 size in between two aluminum electrodes, keeping the device inside an electric oven at 190°C. During formation, the upper electrode was connected to the positive terminal of a d-c source and the lower electrode to the negative of the d-c supply in all cases. The heating and cooling of the sample were done under the influence of the electric field for the required polarizing time. The sample formed in this manner was taken out of the electrode assembly for surface charge and dielectric constant measurements. After the measurements, the electret was wrapped with a metallic foil and kept in a desiccator for further measurements.

Another series of samples were prepared in 15 min polarizing time by the application of low polarizing voltages, keeping the device on a regulated heater. In this case, the temperature gradient between the two surfaces was found to have a significant effect on the characteristics of these types of electrets. The variation of surface charge and dielectric constant with time of these samples was also measured, and the results obtained from these investigations show some useful information about the variation of dielectric polarization with time in such electrified samples.

Method of Measurement

The surface charge of the polarized sample was measured by a Lindemann Electrometer and a specially made measuring device using the induction method. After charge measurement on either side, the electret was short-circuited by a metallic foil and kept in a desiccated condition for further studies.

For the measurement of the variation in the dielectric constant of the polarized sample, another instrument was developed with the help of a spherometer. A metallic circular electrode was screwed into the central leg of a spherometer and the other three legs were fixed on a plane ebonite plate. At the center of the ebonite plate, just below the upper electrode, another circular metallic plate with a guard ring was fixed so that the arrangement would act as a variable guard ring condenser. By this arrangement the capacitance of the air space between the two parallel electrodes or the sample could be measured very accurately, as the least count of the spherometer was

Key words: dielectric properties, PVC electrets.

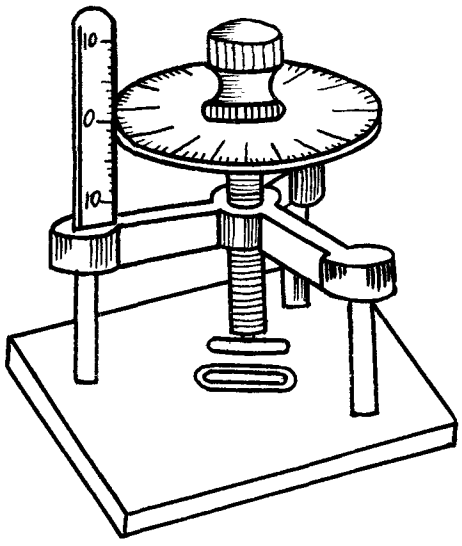

Fig. 1. Variable guard ring condenser used for the measurement of dielectric constant.

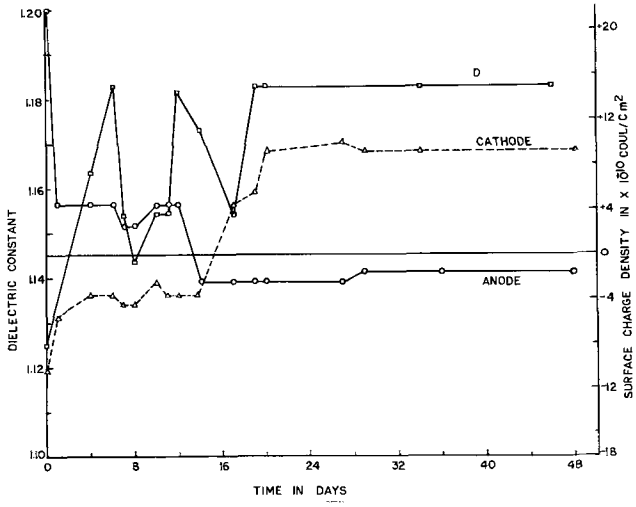

Fig. 2. Variation of dielectric constant and surface charge density vs. time for SR_8 (PVC) electret formed at 10 kV/cm in 4 hr polarizing time.

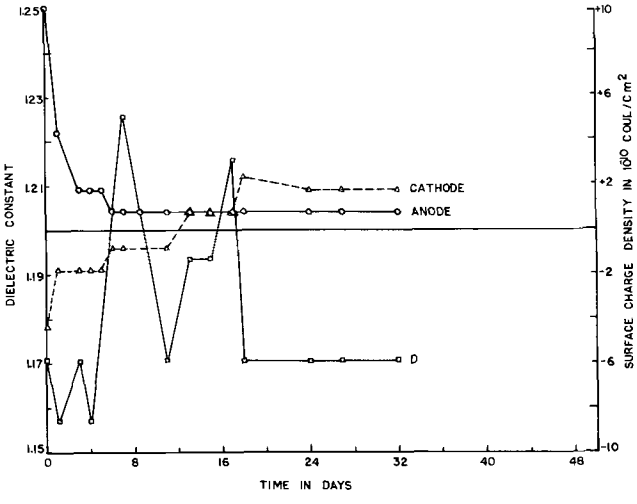

Fig. 3. Variation of dielectric constant and surface charge density vs. time for SR_8 electret formed at 10 kV/cm in 6 hr polarizing time.

0.005 mm. The two electrodes of this device (Fig. 1) were connected to the Picro Farad (PF) meter with the help of two short leads for capacitance measurement. With the help of this PF meter the capacitance can be measured directly in picrofarads, using the bridge method principle. The capacitance of the condenser was measured by keeping the polarized sample between the two electrodes. After removing the sample, the capacitance of the air condenser of the same thickness as that of the electret was also observed to determine the dielectric constant. If C is the capacitance measured with the polarized sample and C_o with the air between the plates, then the dielectric constant, ϵ, of the polarized samples can be written as

$$\epsilon = \frac{C}{C_o}$$

Using this relation and the above-mentioned technique, the variation of the dielectric constant with time of the electrets was measured for more than 30 days.

Results and Discussion (8, 9)

Figures 2-7 show the charge decay characteristics, and change in dielectric constant with time, of the electrets of SR_8 prepared to 10, 12, and 14 kV/cm in 4 and 6 hr of polarizing time. It has been observed from these curves that the cathode side of the samples prepared in 4 and 6 hr of polarizing time initially give homocharge which decays and reverses to a permanent heterocharge. From an analysis of these curves it can be seen that existence of the initial homocharge of samples prepared in 4 hr time decreases with the increase of the polarizing voltages (15 days for the sample prepared at 10 kV/cm; 2 days and 1 day for the samples prepared at 12 and 14 kV/cm, respectively). The same also happens with the anode surface, and the time varies from 13 to 2 days with increase of voltage as shown in Table I.

The charge retention characteristics of the anode and cathode sides of the series of electrets prepared at different polarizing voltages with 6 hr of polarizing time have been shown in Table I and in Fig. 2, 4, and 6. From this it can be seen that the cathode of these samples shows a reversal of charge from homo to hetero in a few days as indicated, whereas the anode side shows only a homocharge without any reversal.

The presence of heterocharge can be explained on the basis of the two-charge theory given by Gross (10), which has been accepted by most of the recent workers in this field. Wiseman and Feaster (11) considered the electret assembly as a three-layer capacitor and explained the experimental results by giving the analytical expressions. Cross and Hart (12) have shown that the current in the medium is $i = GE$, where G is the electrical conductance and E is the electric field in the medium. The current through the surface layers in therefore $i_1 = G_1E_1$. The current

Table I. Material SR_8

Polarizing voltage, kV/cm	Time of polarization in hours	Type of charge on the cathode side		Type of charge on anode side		Existence of homocharge on cathode side in days	Existence of heterocharge on anode side in days
		Initial	Final	Initial	Final		
10	4	Homo	Hetero	Homo	Hetero	15	13
12	4	Homo	Hetero	Homo	Hetero	2	5
14	4	Homo	Hetero	Homo	Hetero	1	2
10	6	Homo	Hetero	Homo	Homo	12	—
12	6	Homo	Hetero	Homo	Homo	7	—
14	6	Homo	Hetero	Homo	Homo	7	—

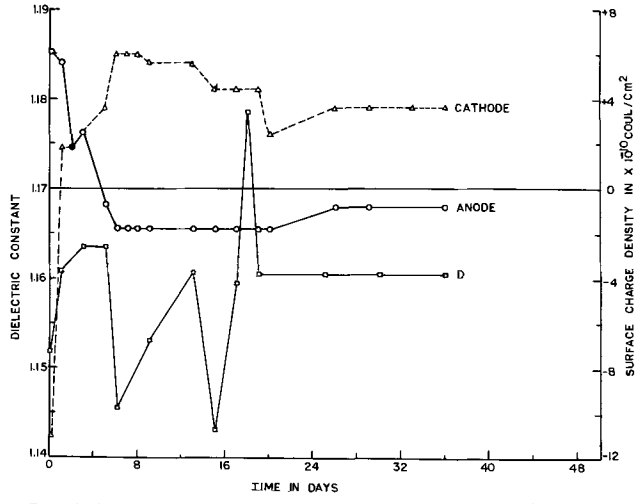

Fig. 4. Variation of dielectric constant and surface charge density vs. time for SR_8 electret formed at 12 kV/cm in 4 hr polarizing time.

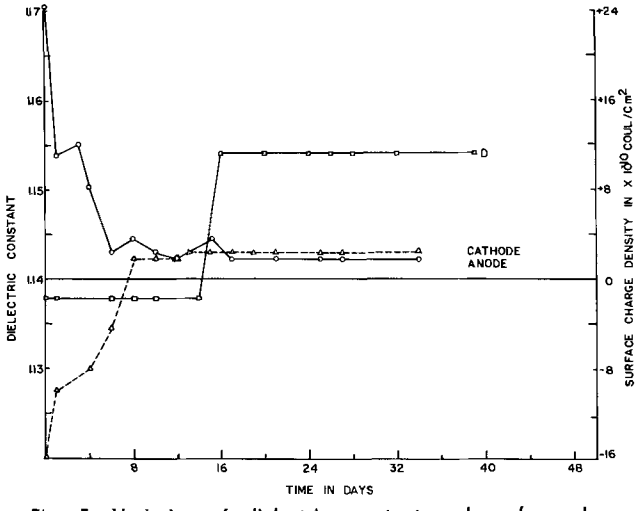

Fig. 5. Variation of dielectric constant and surface charge density vs. time for SR_8 electret formed at 12 kV/cm in 6 hr polarizing time.

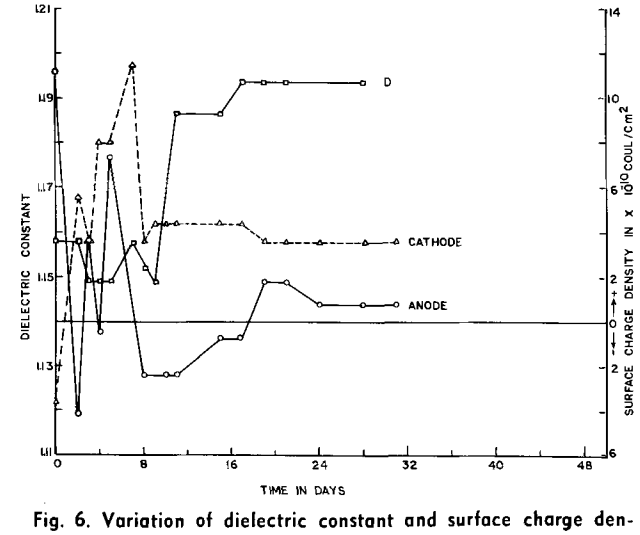

Fig. 6. Variation of dielectric constant and surface charge density vs. time for SR_8 electret formed at 14 kV/cm in 4 hr polarizing time.

through the main body of the sample is given by $i_2 = G_2E_2$. In general

$$G_1E_1 + G_2E_2$$

Here there is an accumulation of charge at the interface between the surface layer and main body and can be given as

$$\sigma_{\text{hom}}{}^{\gamma} = G_1E_1 - G_2E_2 = -\sigma_{\text{het}}{}^{\gamma}$$

This equation shows that the nature of the initial charge depends on the relative magnitude of G_1E_1 and G_2E_2.

Although the above theory explains the nature and magnitude of the initial and final charges appearing on the electret surface, it fails to give a proper explanation for the appearance of initial homocharge and reversal of homo to heterocharge. The presence of initial homocharge on the cathode side of the SR_8(PVC) electret may be due to the existence of excessive negative ions in the bulk of the material, and under high-temperature conditions they may be aligned on the cathode side of the electret. In the study of the thermal degradation of polyvinyl chloride, it was found that the weakest C-Cl bond will be ruptured at temperatures above 165°C (13). This is followed by an abstraction of a hydrogen atom from an adjacent carbon and formation of a double bond in the chain. Therefore, above 165°C negative ions are produced in PVC which in turn will be collected near the cathode side due to the attraction of the dipoles. Similarly, positive ions from the decomposed products collect near the anode side due to the action of the dipolar field.

When a field is applied in the molten state of the material, the dipoles will be oriented in the direction of the field and these oriented dipoles in turn will attract the ions of opposite polarity from the bulk of the material, which will stick to the surface when the sample is solidified. This can be seen also by observing the decay curve of initial homocharge on the cathode, as well as on the anode, side of the samples (Fig. 2-7) (14). As the field increases, decay time of initial homocharge decreases considerably as shown in Table I. When the field increases more, more dipoles are oriented in the direction of the field; consequently, the charge due to dipolar orientation will be much more than what is obtained at lower fields.

It has been observed that polarizing time is a major influence in giving the polarity of charge. Samples prepared in 6 hr give permanent homocharge at the anode side. It shows that the predominance of ionic charge increases with time of preparation.

Figure 8 shows the charge decay characteristics and change in dielectric constant of an electret prepared at 8 kV/cm in 4 hr of polarizing time with SR_{10} (PVC) material. SR_{10} is again a PVC compound with different compositions. It has lower dielectric constant than SR_8 (PVC). This material also shows similar behavior.

In the next part of this paper, characteristics are given of three samples prepared from SR_{10} vinyl at 15,

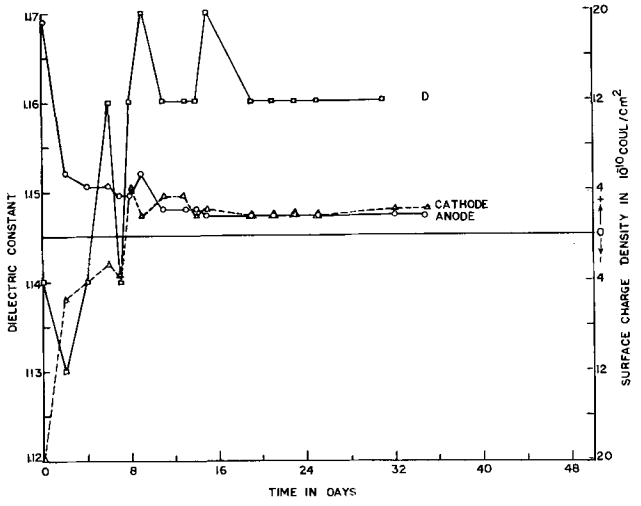

Fig. 7. Variation of dielectric constant and surface charge density vs. time for SR_8 electret formed at 14 kV/cm in 6 hr polarizing time.

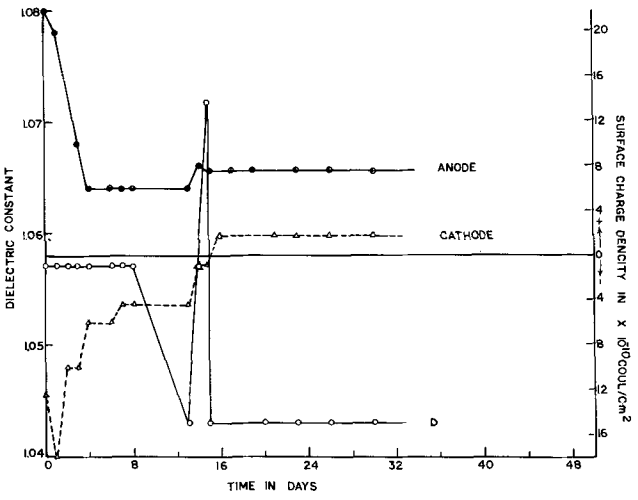

Fig. 8. Variation of dielectric constant and surface charge density vs. time for SR_{10} (PVC) electret formed at 8 kV/cm in 4 hr polarizing time.

360, and 720 V/mm, in 15 min polarizing time, following the method adopted by Jain and Pillai (15).

Here again the cathode side shows behavior similar to that of the high-voltage samples. It shows that, even at 15 V/mm, ions are collected on the negative side to give rise to homocharge, although the lifetime is much less than that of the high-voltage samples. It can be seen again that the lifetime of these initial homocharges is longer at higher voltages up to 720 V/mm.

The decay curves of the low-voltage electrets (Fig. 9-11) show that the charge decay is rather smooth in this case, which indicates that the rapid reorientation of dipoles may not be taking place at these low voltages. The curves (Fig. 9-11) showing the variation of the dielectric constant with time also show that the changes are not as significant as in the case of high-voltage samples.

Therefore, it is apparent that the formation of charge in thermoelectrets is not merely a contribution from the volume polarization taking place in the bulk of the sample, but is also due to the contribution from external polarizations. At high voltage it is possible to have spray charge from the electrode to the surface of the sample. The magnitude of this may depend on the work function of the electrode material, the interspace gap, and the gas in the interspace. In addition to these, another possible contribution is due to the molding and stripping charges which are also dependent on temperature and on the type of surface contact. To account for all these, Pillai, Jain, and Vij (16, 17) have given the following expression for the effective charge of an electret.

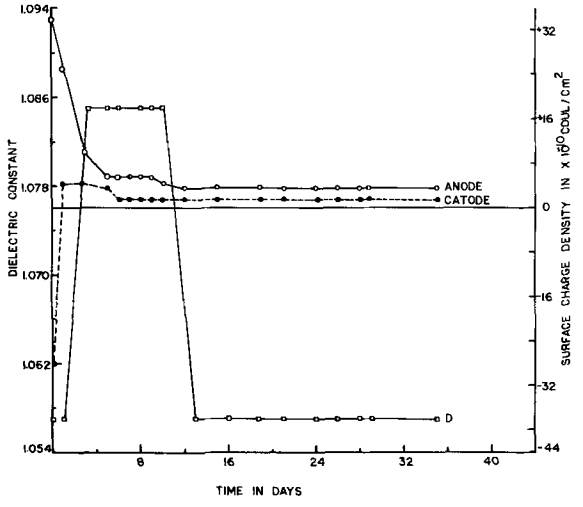

Fig. 9. Variation of dielectric constant and surface charge density vs. time for SR_{10} (PVC) electret formed at 15 V/mm in 15 min polarizing time.

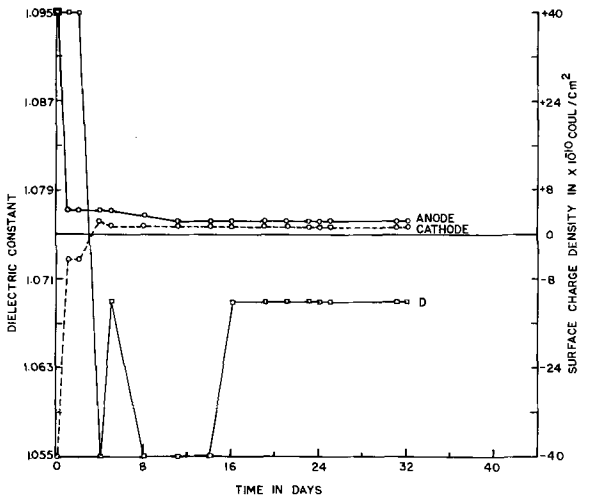

Fig. 10. Variation of dielectric constant and surface charge density vs. time for SR_{10} electret formed at 360 V/mm in 15 min polarizing time.

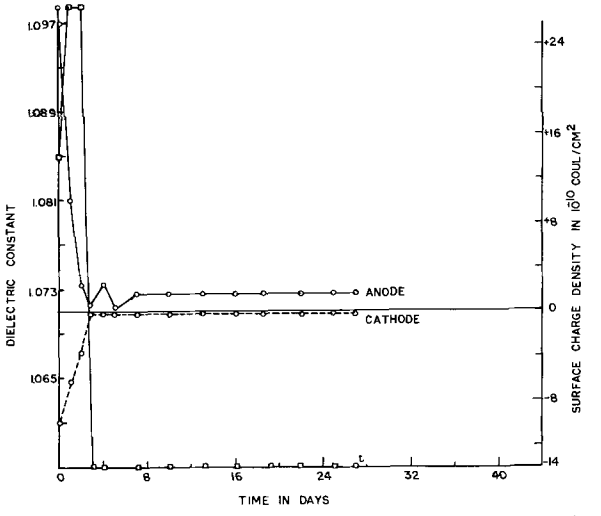

Fig. 11. Variation of dielectric constant and surface charge density vs. time for SR_{10} electret formed at 720 V/mm in 15 min polarizing time.

$$\sigma_E = \sigma_D + \sigma_i + \sigma_{hom} + \sigma_M$$

where σ_E is the effective surface charge of the electret
σ_D is the contribution of charge due to dipolar orientation
σ_i is component due to ionic polarization
σ_{hom} is contribution due to external polarization like spray charge
σ_M is charge due to molding and stripping

In every figure from 2 to 11 the variation of dielectric constant has also been plotted with surface charge to see both the effects simultaneously. Figure 12 shows the variation of dielectric constant with time in SR_{10} (PVC) electrets prepared at different voltages and also in different polarizing times.

From Fig. 2 to 7 and 12 it can be seen that the dielectric constant changes with time and reveals some peaks in the beginning. It shows that the dipoles aligned in the direction of the field slowly start reorienting in other directions. This gives rise to a change in dielectric constant as well as a change in surface charge. It can also be observed from these figures, 2-8, that the variation of dielectric constant takes place only in the initial few days and thereafter

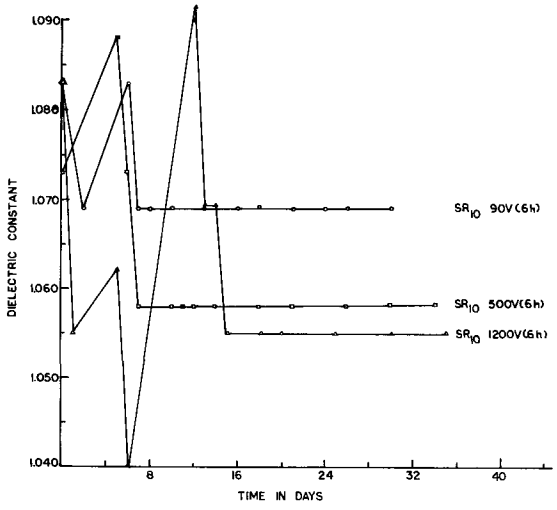

Fig. 12. Variation of dielectric constant vs. time for SR_{10} electrets prepared at 90, 500, and 1200 V/mm in 6 hr polarizing time.

it becomes constant almost simultaneously with the surface charge which also starts showing constancy.

On the application of the field in the molten condition of the material, only a fraction of the dipoles orient in the direction of the field and a larger portion orients randomly in all other possible directions. Alignment of the dipoles in the parallel direction increases the dielectric constant. The orientation of dipoles depends on the polarizing voltage, temperature, and time of the sample. In the initial stage, there are some peaks in the curves of the dielectric constant *vs.* time curve for all the samples prepared at high voltages. It clearly shows that the maximum reorientation of dipoles takes place in the initial stage. Surface charge measurements also show drastic charge density variation in the initial stage. But the phenomena of surface charge and variation of dielectric constant cannot be correlated directly, as the surface charge is not merely a dipolar phenomena; it also includes other mechanisms of charge formation. Other charging mechanisms also affect the dielectric constant variation. The dipoles are also bound by the presence of ions over the surface due to spraying, molding, and stripping. As soon as the surface loses some of these ionic charges, oriented dipoles become disturbed due to an unbalanced force which causes the variation in the dielectric constant.

After a few days time, there is no variation in dielectric constant as well as in surface charge. This clearly shows that there is no reorientation of dipoles at this stage. The permanent value of surface charge of the samples shows that presence of polarization. The dielectric constant of an unpolarized sample of SR_8 prepared under similar conditions is 1.181. But the final value of the dielectric constant of the polarized samples, Fig. 2-7, is not always higher than this value. It may be due to the fact that, on application of the field in the molten condition of the material, some dipoles were aligned in the parallel direction and some in the other directions. Moreover the contribution due to external polarizations varies from sample to sample, which also affects the variations from the normal value observed in the dielectric constant.

From Fig. 9 to 11 it can be seen that the variation observed in the dielectric constant *vs.* time curves for the electrets prepared at low voltages in 15 min time is not appreciable. Figure 12 shows the dielectric constant variation of samples of SR_{10} prepared at different voltages in 6 hr time. It can be seen from these curves that the variation of the dielectric constant in the initial stage is more for higher voltages. But the final value of the dielectric constant decreases with increase of polarizing voltages.

The present investigations show that the value obtained for the apparent dielectric constant is very low (1.1-1.2) in comparison to the value quoted in the literature for this material. The dielectric constant given for PVC is 3-5. The sample used in the present investigations is of much lower density than the standard sheets prepared under high-pressure conditions. In the present studies the microcrystallites cannot be packed closely, as the samples were made just between the two mica sheets without high pressure. The low apparent dielectric constant measured here is attributed to the low density of these specimens, which was measured to be about 0.6 g/cc, whereas the resin has a density of about 1.4.

This investigation thus confirms the pulsatory nature of surface charge decay as observed by Kojima and Kato (18). This also shows that the variation of the surface charge of an electret is intimately related to the variation of the dielectric constant of the polarized sample. In addition, the studies of variation of the dielectric constant of a polarized dielectric provide another important technique for investigating the characteristics of an electret.

Summary and Conclusions

The results obtained from these experimental investigations show that SR_8 (PVC) and SR_{10} (PVC) are good materials for electret preparation.

Polarizing time has a major influence in determining the initial, as well as final, surface charge of an electret and also on the final value of the dielectric constant.

It also shows that surface charge formation in electrets is not merely a dipolar phenomenon but includes other charging factors, which in turn affect the dielectric constant of the polarized samples.

Acknowledgments

The authors are thankful to Professor M. S. Sodha, Head of the Department of Physics, Indian Institute of Technology, Delhi for the encouragement given to them during the course of these investigations; and to Mr. K. G. Balakrishnan and Malti Goel for their helpful discussions. They are also grateful to the Council of Scientific and Industrial Research, Government of India, for financial help.

Manuscript submitted Dec. 30, 1969; revised manuscript received *ca.*, Oct. 8, 1970.

Any discussion of this paper will appear in a Discussion Section to be published in the December 1971 JOURNAL.

REFERENCES

1. O. Heaviside, *Electrical Papers*, **1**, 488 (1892).
2. M. Eguchi, *Phil. Mag.*, **49**, 178 (1925).
3. H. H. Wieder and S. Kaufman, *Elec. Eng.*, **12**, 511 (1953).
4. F. Gutman, *Rev. Mod. Phys.*, **20**, 457 (1948).
5. A. Gemant, *Phil. Mag.*, **20**, 929 (1935).
6. W. M. Good and J. D. Stranathan, *Phys. Rev.*, **56**, 810 (1939).
7. B. Gross, *ibid.*, **66**, 26 (1944).
8. R. Von Hippel, "Dielectric Materials and Applications," Technology Press of M.I.T. and John Wiley & Sons, Inc., New York, London (1961).
9. C. P. Smyth, "Dielectric Behavior and Structure," McGraw-Hill Book Co., Inc., New York (1955).
10. B. Gross, *J. Chem. Phys.*, **17**, 866 (1949).
11. G. G. Wiseman and G. R. Feaster, *ibid.*, **26**, 521 (1957).
12. J. D. Cross and J. Hart, *Brit. J. Appl. Phys.*, **17**, 311 (1966).
13. N. Grassie, *Trans. Faraday Soc.*, **48**, 379 (1952).
14. A. Gemant, *Direct Current*, **1**. No. 6, 145 (1953).
15. V. K. Jain and P. K. C. Pillai, *Phys. Stat. Sol.*, **28**, 415 (1968).
16. P. K. C. Pillai, V. K. Jain, and G. K. Vij, *This Journal*, **116**, 836 (1969).
17. P. K. C. Pillai and V. K. Jain, *J. Appl. Phys.*, **40**, 3487 (1969).
18. S. Kojima and K. Kato, *J. Phys. Soc. Japan*, **6**, 207 (1951).
19. C. J. F. Bottcher, "Theory of Electric Polarisation," Elsevier Publishing Co., Amsterdam (1952).

Phase Equilibria in the $Sr_3(PO_4)_2$-$Cd_3(PO_4)_2$ System and Eu^{2+}-Activated Luminescence of $Sr_3(PO_4)_2$ and Related Phases

James R. Looney[1]

Chemical and Metallurgical Division, Sylvania Electric Products Incorporated, Towanda, Pennsylvania 18848

and Jesse J. Brown, Jr. [1,*]

Department of Metals and Ceramic Engineering, Virginia Polytechnic Institute and State University, Blacksburg, Virginia 24061

ABSTRACT

The phase equilibria relationships in the $Sr_3(PO_4)_2$-$Cd_3(PO_4)_2$ system were established in air using DTA and melting point data obtained from compositions previously equilibrated by solid-state reactions. In addition to the previously reported rapid, reversible $\alpha \rightleftarrows \beta$-$Sr_3(PO_4)_2$ polymorphic inversion at 1305°C (1), a second rapid reversible transition $\beta \rightleftarrows \gamma$-$Sr_3(PO_4)_2$ was found to occur at 1410°C prior to melting at 1620°C. $Cd_3(PO_4)_2$ is soluble in: (*a*) α-$Sr_3(PO_4)_2$ to a maximum of 1 or 2 m/o (mole per cent), (*b*) β-$Sr_3(PO_4)_2$ to a maximum of 21 m/o at 1075°C with 12 m/o sufficient to stabilize the β-phase to room temperature, and (*c*) γ-$Sr_3(PO_4)_2$ to a maximum of 31 m/o at 1125°C. A eutectoid reaction exists at 1075°C where β-$Sr_3(PO_4)_2$ solid solution, γ-$Sr_3(PO_4)_2$ solid solution, and a ternary compound $Cd_2Sr(PO_4)_2$ are in equilibrium. $Sr_3(PO_4)_2$ is soluble in $Cd_3(PO_4)_2$ to a maximum of about 3 m/o at 1050°C. The luminescence of Eu^{2+}-activated $Sr_3(PO_4)_2$ is very dependent on composition and the polymorph present at the reaction temperature. Small additions of $Cd_3(PO_4)_2$ to all $Sr_3(PO_4)_2$ polymorphs rapidly quench the luminescence. Although both high-temperature forms of $Sr_3(PO_4)_2$ revert to the α-modification upon cooling to room temperature, phosphors prepared by solid-state reaction in the temperature stability range of β-$Sr_3(PO_4)_2$ possess superior brightness levels.

In recent years considerable interest has been directed toward the discovery and characterization of Eu^{2+}-activated phosphors (1-9). One of the most efficient phosphors in this class is $Sr_3(PO_4)_2$ (10, 11). Strontium orthophosphate is known to exhibit polymorphism on heating and cooling (12); however, the effect of this phase change on luminescence has not been investigated previously.

In the present investigation the polymorphism of $Sr_3(PO_4)_2$ is re-examined and the effect of polymorphism on luminescence is studied. The scope of the investigation is also expanded to include phase equilibria studies in the $Sr_3(PO_4)_2$-$Cd_3(PO_4)_2$ system. This is especially relevant because of the similarity in ionic sizes between Sr^{2+} (1.27Å), Cd^{2+} (1.06Å), and Eu^{2+} (1.24Å) and the previously reported stabilizing effect of Cd^{2+} for Sr^{2+} substitutions in β-$Sr_3(PO_4)_2$ (13).

Related Literature

The luminescence of Eu^{2+}-activated $Sr_3(PO_4)_2$ has been described by Nazarova (10) and Levshin *et al.* (11). More recently, Shaffer (14) reported that $Sr_3(PO_4)_2$:Eu^{2+} possesses a characteristic peak emission at 408 nm, with a band width of 42 nm at half the peak intensity. The phosphor is approximately equally efficient to ultraviolet and cathode-ray excitation. The emission has saturated blue color coordinates at $X = 0.162$ and $Y = 0.016$ and is relatively fast decaying.

Sarver, Hummel, and Hoffman (12) demonstrated the polymorphic nature of $Sr_3(PO_4)_2$. The low-temperature (α) modification undergoes a rapid, reversible transition to β-$Sr_3(PO_4)_2$ at 1305°C. The high-temperature (β) polymorph crystallizes with the β-$Ca_3(PO_4)_2$ (Whitlockite) structure. Kreidler and Hummel (15) more recently established the melting temperature of $Sr_3(PO_4)_2$ at 1620°C. Powder x-ray diffraction data for $Cd_3(PO_4)_2$ were presented previously by Brown and Hummel (16).

Experimental Procedure

The phase equilibria relationships in the $Cd_3(PO_4)_2$-$Sr_3(PO_4)_2$ system were established using the 17 compositions listed in Table I. The raw materials used were C.P. grade $CdCO_3$, $SrCO_3$, and $NH_4H_2PO_4$. The batch materials were weighed to ±0.1 mg on an analytical balance and mixed to dryness under acetone in a glass mortar and pestle. The preparations were slowly heated to 900°C and reacted at this temperature for 2 days with one intermittent mixing. Weight loss experiments carried out in platinum crucibles in air indicated that no significant loss of CdO, SrO, or P_2O_5 occurred during the preparation process.

All single-phase regions were activated by substituting 0.01 mole of europium for the alkaline earth cation. The europium was added as Eu_2O_3 obtained from Michigan Chemical Corporation. The preparations were slowly heated to the desired reaction temperature in air and allowed to react for 12-24 hr. The reduction of Eu^{3+} to Eu^{2+} *in situ* was carried out by a second heat treatment in a mullite tube furnace under an atmosphere of approximately 95% N_2-5% H_2. All preparations were heat treated in the reducing atmosphere for 1½ hr and allowed to cool in a protective atmosphere of N_2.

X-ray diffraction data were obtained using CuKα ($\lambda = 1.5418$Å) radiation from a Norelco diffractometer operated at 40 kV and 15 mA. Precise lattice spacings were obtained using silicon powder ($a_0 = 5.4305$Å) as

[1] At the time this work was initiated, both authors were employed by Sylvania Electric Products Incorporated, Towanda, Pennsylvania. Mr. Looney at present is a student at Drexel Institute of Technology, Philadelphia, Pennsylvania, and Dr. Brown is Associate Professor of Ceramic Engineering at VPI.

A part of this investigation was supported by the Research Division of the Virginia Polytechnic Institute and State University, Blacksburg, Virginia.

* Electrochemical Society Active Member.

Key words: phase equilibria, luminescence, phosphors, polymorphism, divalent europium, alkaline earth phosphates.

Table I. Compositions and experimental data used to construct $Sr_3(PO_4)_2$-$Cd_3(PO_4)_2$ phase diagram

Sample No.	Composition $Sr_3(PO_4)_2$	(m/o) $Cd_3(PO_4)_2$	Heat treatment (°C/hr)	Phase assemblages	Remarks
1	100	0	1400/48	α-S_3P	
			1300	α-$S_3P \rightleftarrows \alpha$-$S_3P$	DTA
			1410	β-$S_3P \rightleftarrows \alpha$-$S_3P$	DTA
			DTA experiment stopped at 1450°C, sample unmelted		
2	95	5	1050/48	α-S_3P + β-S_3P	
			1281	α-$S_3P \rightleftarrows \beta$-$S_3P$	DTA
			1380	β-$S_3P \rightleftarrows \gamma$-$S_3P$	DTA
			1425	Solidus	DTA
			DTA experiment stopped at 1450°C, sample partly melted		
3	92	8	1050/48	α-S_3P + β-S_3P	
			1277	β-$S_3P \rightleftarrows \gamma$-$S_3P$	DTA
			1400	Solidus	DTA
			DTA experiment stopped at 1450°C, sample partly melted		
4	90	10	1050/48	β-S_3P	Possible trace α-S_3P
			1275	β-$S_3P \rightleftarrows \gamma$-$S_3P$	DTA
			1400	Solidus	DTA
			DTA experiment stopped at 1450°C, sample partly melted		
5	82	18	1050/48	β-S_3P	Possible trace C_2SP
			1044	Eutectoid	DTA
			1180	Solidus	DTA
			DTA experiment stopped at 1450°C, sample partly melted		
6	80	20	1050/48	β-S_3P + C_2SP	
			1044	Eutectoid	DTA
			1150	Solidus	DTA
			DTA experiment stopped at 1450°C, sample partly melted		
7	78	22	1050/48	β-S_3P + C_2SP	
			1044	Eutectoid	DTA
			1140	Solidus	DTA
			1450	Liquidus	DTA—sample melted
8	74	26	1050/48	β-S_3P + C_2SP	
			1040	Eutectoid	DTA
			1110	Solidus	DTA
			1380	Liquidus	DTA—sample melted
9	70	30	1050/48	β-S_3P + C_2SP	
			1068	Eutectoid	DTA
			1120	Solidus	DTA
			1320	Liquidus	DTA—sample melted
10	60	40	1050/48	β-S_3P + C_2SP	
			1075	Eutectoid	DTA
			1125	Solidus	DTA
			1310	Liquidus	DTA—sample melted
11	50	50	1050/48	β-S_3P + C_2SP	
			1080	Eutectoid	DTA
			1130	Solidus	DTA
			1200	Liquidus	DTA—sample melted
12	40	60	1050/48	β-S_3P + C_2SP	
			1078	Eutectoid	DTA
			1130	Solidus	DTA
			1140	Liquidus	DTA—sample melted
13	33.3	66.7	1050/48	C_2SP	
			1080	Eutectoid	DTA
			1145	Melting point	DTA—sample melted
14	30	70	1000/48	C_2SP + C_3P	
			1050	Eutectoid	DTA
			1115	Liquidus	DTA—sample melted
15	20	80	1000/48	C_2SP + C_3P	
			1055	Eutectoid	DTA—sample melted
16	10	90	1000/48	C_2SP + C_3P	
			1050	Eutectoid	DTA
			1100	?	DTA
			1150	?	DTA
			1175	Liquidus	DTA—sample melted
17	0	100	1000/48	C_3P	
			1190	Melting point	DTA—sample melted

Abbreviations:
C_2SP = $Cd_2Sr(PO_4)_2$
C_3P = $Cd_3(PO_4)_2$
S_3P = $Sr_3(PO_4)_2$
DTA = differential thermal analysis.

an internal standard and a diffractometer scanning rate of ¼°-2 θ/min.

Differential thermal analysis (DTA) data were obtained using a Model 12BC2 apparatus manufactured by Robert L. Stone Company, Austin, Texas. A heating rate of approximately 10°C/min was used. Melting point determinations were made using a TemPres platinum strip furnace and a calibrated optical pyrometer.

Luminescence spectra were measured using an Aminco-Bowman Spectrophotofluorimeter. Spectra were compared with a standard $Sr_3(PO_4)_2$:Eu^{2+} phosphor.

Experimental Results

Phase equilibria studies.—The phase relationships for the $Sr_3(PO_4)_2$-$Cd_3(PO_4)_2$ binary system as shown in Fig. 1 were established from the experimental data listed in Table I.

The $Sr_3(PO_4)_2$ rapid reversible $\alpha \rightleftarrows \beta$ polymorphic transition previously reported (12) at 1305°C was confirmed by DTA experiments. Upon heating β-$Sr_3(PO_4)_2$ to still higher temperatures, a second sharp reproducible heat effect at 1410°C was observed (see top curve in Fig. 2). Because this heat effect was observed on both heating and cooling through this temperature range, it was interpreted to indicate a second rapid reversible polymorphic transition for $Sr_3(PO_4)_2$. The high-temperature $Sr_3(PO_4)_2$ polymorph is designated γ in Fig. 1.

The $\beta \rightleftarrows \gamma$-$Sr_3(PO_4)_2$ transition apparently was not observed by previous investigators because they did not carry their DTA experiments to temperatures above 1350°-1400°C. An x-ray diffraction characterization of γ-$Sr_3(PO_4)_2$ was not obtained because of the temperature limitations of the x-ray diffraction furnaces available. Attempts to stabilize γ-$Sr_3(PO_4)_2$ to room temperature by chemical substitutions, as was done with β-$Sr_3(PO_4)_2$, were unsuccessful.

Upon addition of $Cd_3(PO_4)_2$ to $Sr_3(PO_4)_2$, three solid solution regions are developed. A very small amount of $Cd_3(PO_4)_2$ is soluble in α-$Sr_3(PO_4)_2$, apparently less than 2 m/o. Approximately 12 m/o $Cd_3(PO_4)_2$ dissolved in β-$Sr_3(PO_4)_2$ is sufficient to stabilize this polymorph to room temperature. This result is in good agreement with the previously reported results of Koelmans and Cox (13). The β-$Sr_3(PO_4)_2$ solid solution is relatively narrow below 1000°C, with a maximum solubility of 21 m/o $Cd_3(PO_4)_2$ at 1075°C. A

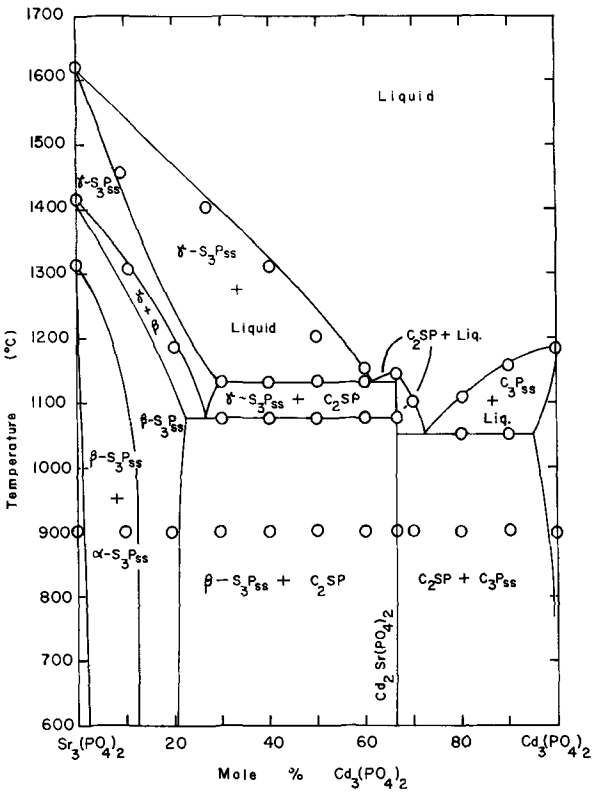

Fig. 1. Phase equilibrium diagram for the system $Sr_3(PO_4)_2$-$Cd_3(PO_4)_2$.

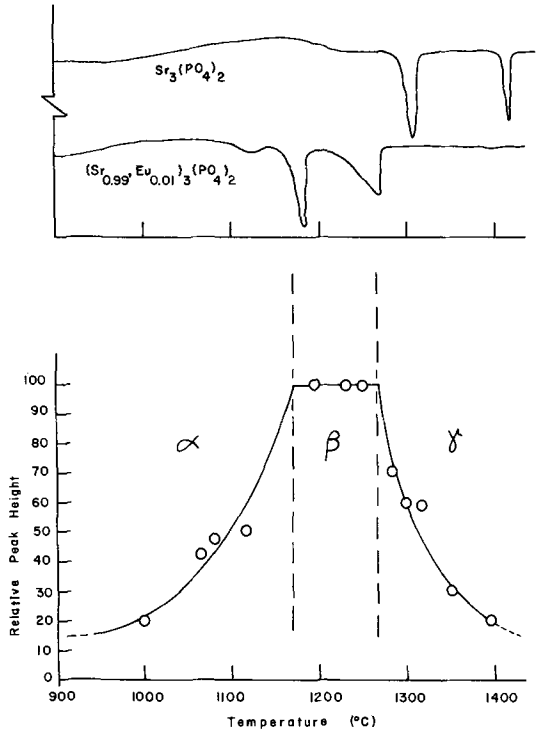

Fig. 2. *(Top)* DTA curves for $Sr_3(PO_4)_2$ and $(Sr_{0.99},Eu_{0.01})_3(PO_4)_2$. *(Bottom)* Variation of phosphor peak intensity with temperature of final (reducing) heat treatment for $Sr_3(PO_4)_2$:Eu^{2+}.

maximum solid solubility of 31 m/o $Cd_3(PO_4)_2$ in γ-$Sr_3(PO_4)_2$ was observed at 1125°C.

A ternary compound, $Cd_2Sr(PO_4)_2$, ($2CdO \cdot SrO \cdot P_2O_5$), was isolated and definitive x-ray diffraction data are listed in Table II. DTA experiments indicated that this compound does not exist in more than one crystalline modification and that congruent melting occurs at 1145°C.

Table II. Powder x-ray diffraction data for $Cd_2Sr(PO_4)_2$

d	I/I_0
8.7	14
7.7	tr
7.5	tr
6.24	35
5.80	tr
5.01	tr
7.45	39
4.40	tr
3.99	35
3.95	49
3.87	8
3.69	tr
3.17	42
3.11	17
3.04	17
2.91	100
2.83	41
2.70	21
2.61	70
2.59	43
Other reflections	

DTA data clearly indicate two reaction isotherms between the $Sr_3(PO_4)_2$ solid solution phases and the ternary compound $Cd_2Sr(PO_4)_2$. At 1075°C a eutectoid reaction isotherm exists where β-$Sr_3(PO_4)_2$ solid solution, γ-$Sr_3(PO_4)_2$ solid solution, and $Cd_2Sr(PO_4)_2$ are in equilibrium. The intensity of the heat effect is very weak for compositions near $Cd_2Sr(PO_4)_2$ and becomes more and more intense as the $Sr_3(PO_4)_2$ content increases. Maximum intensity was observed near the eutectoid point. The existence of this eutectoid reaction substantiates the previous evidence for the existence of a third polymorph of $Sr_3(PO_4)_2$.

A second series of DTA heat effects in this compositional range were observed at 1125°C. These heat effects become more intense as the eutectic point at 60 m/o $Cd_3(PO_4)_2$ is approached. The equilibrium phases on the eutectic isotherm are γ-$Sr_3(PO_4)_2$ solid solution, $Cd_2Sr(PO_4)_2$, and liquid.

On the $Cd_3(PO_4)_2$ side of $Cd_2Sr(PO_4)_2$ a eutectic reaction was observed at 1125°C. A maximum of about 3 m/o $Sr_3(PO_4)_2$ is soluble in $Cd_3(PO_4)_2$ at this temperature. Liquid, $Cd_2Sr(PO_4)_2$, and $Cd_3(PO_4)_2$ solid solution are in equilibrium along this eutectic isotherm. Several weak unidentified heat effects between the solidus and liquidus temperatures were observed for compositions containing 80 and 90 m/o $Cd_3(PO_4)_2$.

Because the $Sr_3(PO_4)_2$-$Cd_3(PO_4)_2$ system is not glass forming, all liquidus temperatures were determined by DTA and visual methods and are accurate to ±10°C. The liquidus temperature decreases rapidly from 1620°C as the $Cd_3(PO_4)_2$ content increases to the eutectic at 1125°C and 60 m/o $Cd_3(PO_4)_2$. The liquidus curve then increases to 1145°C at $Cd_2Sr(PO_4)_2$, then decreases to the second eutectic at 1050°C and 72 m/o $Cd_3(PO_4)_2$. The liquidus curve increases again to 1180°C, the melting point of $Cd_3(PO_4)_2$.

Luminescence studies.—All single-phase regions in the $Sr_3(PO_4)_2$-$Cd_3(PO_4)_2$ system were investigated for Eu^{2+}-activated luminescence. $Cd_2Sr(PO_4)_2$:Eu and $Cd_3(PO_4)_2$:Eu were found to be inert. In addition, substitution of Cd^{2+} for Sr^{2+} in $Sr_3(PO_4)_2$ was observed to quench the Eu^{2+}-activated luminescence. Stabilized β-$(Sr,Cd)_3(PO_4)_2$ was a very weakly emitting blue phosphor.

As pointed out previously, both the $\alpha \rightleftarrows \beta$ and $\beta \rightleftarrows \gamma$ transitions of $Sr_3(PO_4)_2$ are rapidly reversible. Because of this nonquenchable characteristic, α-$Sr_3(PO_4)_2$ is always obtained at room temperature in phosphor preparations. The substitution of 1.0 m/o Eu^{2+} for Sr^{2+} in pure $Sr_3(PO_4)_2$ significantly lowers the inversion temperatures as shown in the DTA curves at the top of Fig. 2 The two sharp peaks for $Sr_3(PO_4)_2$ illustrate the characteristic heat effects of the two polymorphic transitions at 1305° and 1410°C. The corresponding two heat effects for the phosphor, $(Sr_{0.99}, Eu_{0.01})_3(PO_4)_2$, occur at temperatures of 125°-150°C

Table III. Summary of Eu^{2+}-activated luminescent data of phases in the $Sr_3(PO_4)_2$-$Cd_3(PO_4)_2$ system

Composition	Heat treatment*	Phase**	Photoluminescence Brightness	Photoluminescence λ pk nm
$(Sr_{0.985},Eu_{0.01})_3(PO_4)_2$	1000/24 + 1000/1½	α-S_3P	20	410
	1000/24 + 1020/1½	α-S_3P	90	410
	1000/24 + 1075/1½	α-S_3P	47	410
	1000/24 + 1085/1½	α-S_3P	50	410
	1000/24 + 1125/1½	α-S_3P	50	410
	1000/24 + 1200/1½	α-S_3P	100	410
	1000/24 + 1215/1½	α-S_3P	100	410
	1000/24 + 1250/1½	α-S_3P	100	410
	1000/24 + 1280/1½	α-S_3P	70	410
	1000/24 + 1295/1½	α-S_3P	59	410
	1000/24 + 1305/1½	α-S_3P	57	410
	1000/24 + 1350/1½	α-S_3P	30	410
	1000/24 + 1380/1½	α-S_3P	56	410
	1000/24 + 1395/1½	α-S_3P	20	410
$(Sr_{0.835},Cd_{0.15},Eu_{0.01})_3(PO_4)_2$	1000/24 + 1000/1½	β-S_3P	Weak blue	
$(Sr_{0.905},Cd_{2.00},Eu_{0.09})(PO_4)_2$	1000/24 + 1000/1½	C_2SP	Inert	
$(Cd_{0.985},Eu_{0.01})_3(PO_4)_2$	1000/24 + 1000/1½	C_3P	Inert	

* First heat treatment in air, second in 95% N_2-5% H_2.
** Phase present at room temperature.

lower. In addition, the two peaks are not nearly as sharp, indicating the presence of a two-phase region.

Phosphors of composition $(Sr_{0.99},Eu_{0.01})_3(PO_4)_2$ were prepared by reaction in air at 1000°C for 2 days. The preparations were divided into smaller portions and reduced at temperature from 1000° to 1400°C. Extreme care was taken to assure that each phosphor was exposed to identical reducing conditions. In other words, only temperature was changed. Table III summarizes the results of these experiments.

Upon cooling, all samples contained α-$Sr_3(PO_4)_2$ as the major phase. In addition, the photoluminescent spectra for all preparations were identical. The only significant difference in the samples was in the peak emission intensities (brightness). The variations of the brightness values are illustrated in the bottom curve in Fig. 2. There is a very marked difference in the brightness of the phosphors depending on the $Sr_3(PO_4)_2$ polymorph present at the reducing temperature. This can be seen by comparing the brightness *vs.* temperature curve with the DTA curve for the phosphor.

Discussion

Luminescence.—In view of the data presented, it appears that the photoluminescent brightness of Eu^{2+}-activated $Sr_3(PO_4)_2$ is extremely dependent on the polymorph of $Sr_3(PO_4)_2$ present at the reducing temperature. Maximum brightness is obtained only when β-$Sr_3(PO_4)_2$ is present at these high temperatures. Moreover, in Fig. 2 it can be seen from the DTA curves that the stability range of β-$Sr_3(PO_4)_2$ solid solution decreases with increasing europium content.

These results indicate that the Eu^{2+} activator enters different cation lattice sites in the $Sr_3(PO_4)_2$ lattice, depending on the polymorph present at high temperatures. It seems likely that the Eu^{2+} is quenched into these sites upon cooling. The low temperature (α) form of $Sr_3(PO_4)_2$ is known to have two nonequivalent Sr^{2+} sites in the crystal lattice (17). It would seem reasonable to suspect one of these sites to be a more efficient luminescence center than the other. When α-$Sr_3(PO_4)_2$ is the polymorph present at the reducing temperature, Eu^{2+} enters the less efficient cation site. When β-$Sr_3(PO_4)_2$ is the polymorph present, the Eu^{2+} enters a lattice site, which upon cooling corresponds to the more efficient site in the α-$Sr_3(PO_4)_2$ lattice. Cooling quenches Eu^{2+} into this lattice position. Finally, when γ-$Sr_3(PO_4)_2$ is the polymorph present at high temperatures, the Eu^{2+} appears to enter a lattice position which upon cooling corresponds to the less efficient site in α-$Sr_3(PO_4)_2$.

Summary

1. A third polymorph of $Sr_3(PO_4)_2$ has been isolated which is stable only above 1410°C.

2. The $Sr_3(PO_4)_2$-$Cd_3(PO_4)_2$ phase diagram contains four solid solution regions. A very small amount (1 or 2 m/o) of $Cd_3(PO_4)_2$ is soluble in α-$Sr_3(PO_4)_2$. Approximately 12 m/o $Cd_3(PO_4)_2$ stabilizes β-$Sr_3(PO_4)_2$ to room temperature. The β-$Sr_3(PO_4)_2$ solid solution region is very small below 1000°C. A eutectoid reaction isotherm at 1075°C indicates substantial solid solution of $Cd_3(PO_4)_2$ in γ-$Sr_3(PO_4)_2$, probably as much as 30 m/o. Slight solid solubility of $Sr_3(PO_4)_2$ in $Cd_3(PO_4)_2$ exists.

3. A ternary compound, $Cd_3Sr(PO_4)_2$, was discovered which melts congruently at 1145°C.

4. Efficient Eu^{2+}-activated $Sr_3(PO_4)_2$ is obtained only when the reducing heat treatment is carried out in the temperature stability range of β-$Sr_3(PO_4)_2$.

Manuscript submitted Aug. 13, 1970; revised manuscript received Oct. 21, 1970. This was Paper 34 presented at the Los Angeles Meeting of the Society, May 10-15, 1970.

Any discussion of this paper will appear in a Discussion Section to be published in the December 1971 JOURNAL.

REFERENCES

1. T. L. Barry, *This Journal*, **115**, 733 (1968).
2. G. Blasse, W. L. Wanmaker, and J. W. ter Vrugt, *ibid.*, 673 (1968).
3. W. L. Wanmaker and J. W. ter Vrugt, *Philips Res. Repts.*, **22**, 355 (1967).
4. G. Blasse and A. Bril, *ibid.*, **23**, 201 (1968).
5. G. Blasse, W. L. Wanmaker, J. W. ter Vrugt, and A. Bril, *ibid.*, **23**, 189 (1968).
6. A. Bril and W. L. Wanmaker, *This Journal*, **111**, 1363 (1964).
7. F. C. Palilla and B. E. O'Reilly, *ibid.*, **115**, 1076 (1968).
8. F. C. Palilla, A. K. Levine, and M. Tomkus, *ibid.*, **115**, 642 (1968).
9. P. M. Jaffe, *ibid.*, **117**, 918 (1970).
10. V. P. Nazarova, *Bull. Acad. Sci. USSR*, **25**, 322 (1961).
11. V. L. Levshin *et al.*, *Trans. P. N. Lebedev.*, Physics Inst. "Soviet Research on Luminescence," D. V. Skabel'tsyn, Editor, English Transl., Chap. 3, Consultants Bureau, New York (1964).
12. J. F. Sarver, F. A. Hummel, and M. V. Hoffman, *This Journal*, **108**, 1103 (1961).
13. H. Koelmans and A. P. M. Cox., *ibid.*, **104**, 442 (1957).
14. F. N. Shaffer, Personal communication, Sylvania Electric Products Inc., Towanda, Pa. (1967).
15. E. R. Kreidler and F. A. Hummel, *Inorg. Chem.*, **6**, 884 (1967).
16. J. J. Brown, Jr., and F. A. Hummel, *This Journal*, **110**, 1218 (1963).
17. H. W. Zacariasen, *Acta Cryst.*, **1**, 263 (1948).

Luminescence of $xZnO \cdot (1-x)\ MgF_2 \cdot y\ SiO_2 \cdot zGeO_2$:Mn Solid Solutions

W. A. McAllister*

Westinghouse Electric Corporation, Bloomfield, New Jersey 07003

ABSTRACT

Manganese-activated zinc germanate, and solid solutions with zinc silicate, have been synthesized and exposed to high-energy ultraviolet radiation in plaques and lamps. Replacement of germania by silica, and/or zinc oxide by magnesium fluoride, gave improved phosphor maintenance, the best output-maintenance combination being for phosphors having equal germania and silica concentrations. The influence of these substitutions on reaction sequence and product purity, surface characteristics of the phosphor, and the output-temperature behavior were considered and related qualitatively to the bonding properties of the cation species present.

Although zinc orthosilicate:Mn has been investigated in some detail and found useful in lamps and cathode-ray tubes, the corresponding zinc germanate has not been extensively considered since the early work of Schulman *et al.* (1) on the emission and excitation spectra of the ortho-zinc compound and its beryllium derivative. Absorption and emission characteristics of the zinc silicate and germanate are similar, with the latter having better luminosity and being responsive to a wider range of ultraviolet wavelengths (1, 2). Since the maintenance of the silicate in fluorescent lamp application has been a problem, a similar propensity may exist for the germanate also. To explore this possibility, we have made zinc germanates and solid solutions with silica and examined the maintenance characteristics; output-temperature relations were also considered.

Experimental

Solid-state reactions among oxides, carbonates, and halides were used, firing 2 hr at 1200°C in air, then 1 hr in nitrogen at 1100°C with grinding between firings, to effect phosphor formation. Products were identified by powder diffraction patterns and plaque maintenance measured by exposure to the radiation from a 40W Sterilamp having a Suprasil envelope. Both samples and lamp were housed in an outer jacket which was flushed with nitrogen prior to exposure in static nitrogen atmosphere. Plaque output was measured using a Spectra Brightness Spot Meter, which also was used, in conjunction with a hotplate, for the temperature dependence measurements on thick powder samples.

Results

The products from firing the raw mix compositions in Table I were found to have poor plaque maintenance when zinc oxide, germania, and manganese carbonate were the only constituents. Replacement of some zinc oxide by magnesium fluoride was found to give relatively large gains in output and maintenance at 100 hr time. However, even the best of these was still inferior to the commercial zinc silicate:Mn standard used for comparison. Subsequent substitution of silica for germania gave generally improved resistance to degradation until roughly half the germania was replaced. Thenceforth, both the output and maintenance stabilized at values higher than the commercial zinc silicate:Mn phosphor.

Since extraneous phases were detected in compositions with no fluoride (ZnO) or 0.5 mole fluoride ($MgGeO_3$), only the silicate-germanate solid solutions having 0.3 mole MgF_2 were considered in greater detail. In Table II, the variation in output and maintenance with manganese concentration is shown to be generally downward with increasing manganese concentration for each solid solution series. Use of zinc fluoride or magnesium oxide (added as the basic carbonate) as alternates to magnesium fluoride indicates better, and comparable, maintenance for the magnesium compounds (Table III).

* Electrochemical Society Active Member.
Key words: luminescence, solid solutions, germanates, manganese, willemite, hybrid bonds, symmetry.

Table I. Plaque output, maintenance of $(2-x)ZnO \cdot xMgF_2 \cdot (Ge,Si)O_2$:0.03 Mn phosphors

(λ_{exc} = 254 nm)

Base composition (moles)		100 Hr output (maintenance) for			
GeO_2	SiO_2	$x = 0$	0.1	0.3	0.5
1.0	0	0.5 (10)	1.5 (25)	2.9 (57)	2.9 (46)
0.8	0.2	1.0 (19)	1.5 (25)	2.7 (41)	3.2 (60)
0.6	0.4	1.7 (34)	2.4 (38)	4.1 (59)	4.6 (79)
0.4	0.6	2.3 (62)	4.2 (78)	4.1 (80)	5.2 (91)
0.2	0.8	2.8 (70)	4.1 (84)	4.2 (84)	4.1 (84)
0	1.0	2.3 (73)	2.2 (70)	2.6 (75)	3.6 (83)
Commercial Zn_2SiO_4:Mn 3.7 (78)					
Extraneous phases present		ZnO	None	None	$MgGeO_3$

Table II. Plaque output and maintenance of silicogermanate phosphors

(λ_x = 254)

Composition (moles)					Plaque brightness (ft-L)		Per cent maintenance
ZnO	MgF_2	GeO_2	SiO_2	$MnCO_3$	0 hr	100 hr	
1.7	0.3	0.8	0.2	0.01	6.5	3.2	48
				0.03	6.6	2.7	41
				0.09	7.6	2.7	34
		0.6	0.4	0.01	5.9	4.2	71
				0.03	6.0	4.1	69
				0.09	7.8	3.5	44
		0.2	0.8	0.01	5.1	3.5	68
				0.03	5.0	4.2	84
				0.09	6.8	4.3	67
Commercial Zn_2SiO_4:Mn					4.75	3.7	78

Table III. Plaque maintenance of silicogermanate phosphors

(λ_{exc} = 254 nm)

Basic composition (moles)*			Maintenance (%) using		
ZnO	GeO_2	SiO_2	$0.3MgF_2$	$0.3ZnF_2$	0.3MgO
1.7	1.0	0	57	39	58
1.7	0.8	0.2	41	17	62
1.7	0.6	0.4	69	30	73
1.7	0.4	0.6	80	41	72
1.7	0.2	0.8	84	54	76
1.7	0	1.0	75	52	82
Commercial Zn_2SiO_4:Mn = 78%					

* $MnCO_3$ = 0.03.

Table IV. Output of 40W fluorescent silicogermanate lamps

Composition					Output (lumens)		Per cent maintenance
ZnO	MgF_2	GeO_2	SiO_2	$MnCO_3$	0 hr	100 hr	
1.7	0.3	1.0	0	0.03	2317	1276	55
1.7	0.3	1.0	0	0.03	2237	1232	55
1.7	0.3	0.8	0.2	0.03	3728	2484	66.6
1.7	0.3	0.8	0.2	0.03	3801	2526	67.7
1.7	0.3	0.6	0.4	0.03	4478	3597	80.3
1.7	0.3	0.6	0.4	0.03	4493	3613	80.4
1.7	0.3	0.4	0.6	0.03	4578	3901	85.2
1.7	0.3	0.4	0.6	0.03	4672	3988	85.4
1.7	0.3	0.2	0.8	0.03	4218	3604	85.4
1.7	0.3	0.2	0.8	0.03	4263	3594	85.2

Lamps were made using phosphors containing the magnesium fluoride modification, at several Ge/Si levels, with the small additions of lead and arsenic customary for zinc silicate:Mn type phosphors. The readings presented in Table IV follow closely those of the plaque data and again indicate best output and maintenance for solid solutions on the silica-rich side of the midpoint.

The plaque output-temperature relations were examined for each Ge/Si ratio at different fluoride levels and *vice versa*. Representative curves for the former variation are in Fig. 1, the Ge/Si ratio being 0.6/0.4 here. Though the fluoride confers some benefit up to 150°C, the curves converge to a similar quenching temperature thereafter. More pronounced is the change in output with temperature for $MgF_2 = 0.3$ mole (Fig. 2), it being generally true that initial output decreases, quenching temperature increases, as silica replaces germania. A similar statement applies to the influence of manganese concentration, shown for the Ge/Si ratio of 0.8/0.2 in Fig. 3, while curves abstracted from the previous three show best temperature dependence for low germania and manganese, poorest behavior for the high germania-high activator combination (Fig. 4).

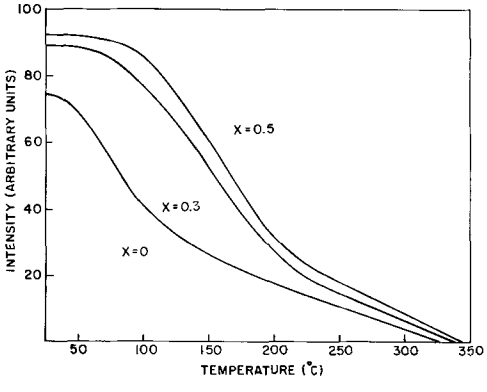

Fig. 1. Temperature dependence of $(2-x)ZnO \cdot xMgF_2(Ge_{0.6}Si_{0.4})O_2$: 0.03Mn phosphors ($\lambda_{exc} = 254$ nm).

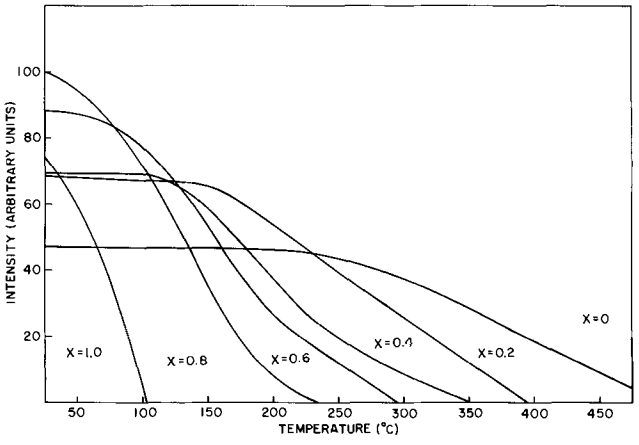

Fig. 2. Temperature dependence of $1.7ZnO \cdot 0.3MgF_2(Ge_xSi_{1-x})O_2$: 0.03Mn phosphors ($\lambda_{exc} = 254$ nm).

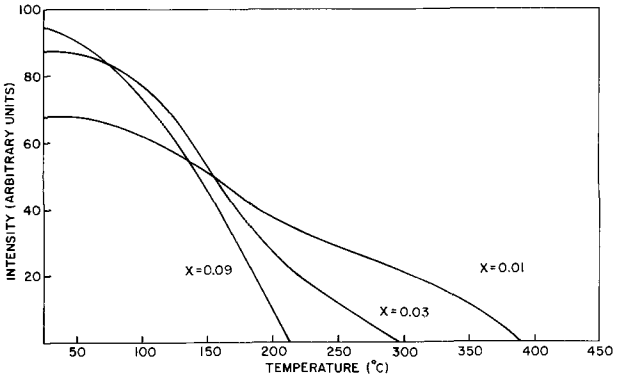

Fig. 3. Temperature dependence of $1.7ZnO \cdot 0.3MgF_2 \cdot (Ge_{0.8}Si_{0.2})O_2$:xMn phosphors ($\lambda_{exc} = 254$ nm).

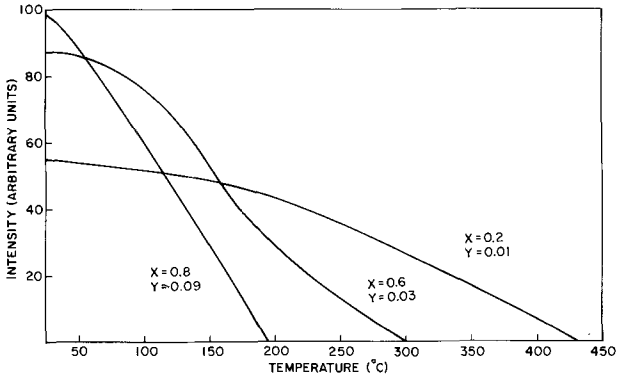

Fig. 4. Temperature dependence of $1.7ZnO \cdot 0.3MgF_2(Ge_xSi_{1-x})O_2$:yMn phosphors ($\lambda_{exc} = 254$ nm).

Discussion

Substitution of magnesium fluoride for zinc oxide gives willemite solid solutions with improved resistance to degradation and, for modest halide concentrations, without extraneous phases. Without halide there is unreacted zinc oxide for all solid solutions, while high fluoride gives $MgGeO_3$ as second phase. Since the latter is the product of a reaction in competition with the desired one giving solid solution, the products of reactions among various combinations of the raw mix constituents were examined by powder diffraction methods, using the 0.3 molar halide composition found to give only solid solution.

The data in Table V show that orthosilicate or germanate form in reactions involving these oxides with zinc oxide and magnesium fluoride; the silica-halide combination alone also gives an orthosilicate, Mg_2SiO_4. However, the companion reaction of fluoride and germania produces the $MgGeO_3$ already noted in the complete firing mix. MgF_2-GeO_2-SiO_2 combinations were fired also and found to have the metagermanate as the sole reaction product until the Ge/Si ratio was ¼. Though the phase diagram of the MgF_2-MgO-GeO_2 (3) shows no fluoride-germania interaction, conversion of the fluoride to MgO in our firing conditions leads to the reaction forming $MgGeO_3$, the stable phase at 1200°C. Its persistent occurrence in mixes containing

Table V. Interactions among silicogermanate raw mix constituents

Composition (moles)				Phases identified
ZnO	MgF_2	GeO_2	SiO_2	
1.7	0.3	1.0	—	Zn_2GeO_4, ZnO
—	0.3	—	1.0	Mg_2SiO_4
—	0.3	1.0	—	MgF_2, $MgGeO_3$
—	0.3	0.8	0.2	$MgGeO_3$, MgF_2
—	0.3	0.5	0.5	$MgGeO_3$, SiO_2
—	0.3	0.2	0.8	Mg_2SiO_4, $MgGeO_3$, $MgSiO_3$, SiO_2

silica, as well as germania, can be explained by noting that the latter melts at 1116°C (4) giving it an advantage over silica in the competition for MgO in mixes having no zinc oxide or low (1.5 moles) concentrations thereof. With zinc oxide present the magnesium metagermanate was not detected, however, and, while this is largely due to the greater tendency for zinc orthogermanate formation, there may be contributions from vapor-phase reactions like those in Table VI. Such would consume both MgF_2 and GeO_2 needed for $MgGeO_3$ formation and, concurrently, effect transport of reactants like silica and germania, not especially noted for mobility in conventional solid-state reactions. It is likely that, as written, the reactions are oversimplified since gaseous oxyhalides of the Group IV elements could also be present and contribute. Indeed, such species as $SiOF_2^+$, $SiOF^+$, and $Si_2OF_5^+$ have been detected by mass spectrometry over reaction mixes of zinc oxide and silica having $NaZnF_3$ as flux (5).

It is a well-known fact that silica, in excess of that amount required for zinc orthosilicate stoichiometry, is used to assure complete reaction of the zinc oxide raw material (6). It is thus not surprising that, in our solid solutions without magnesium fluoride, there is always unreacted zinc oxide. In replacing some zinc by magnesium, one effectively alters the Zn/Si (Ge) ratio, the silica (germania) being in excess now even though the over-all metal ion concentrations are in the orthosilicate ratio.

In addition, the magnesium fluoride (and magnesium oxide) confer improved plaque output and maintenance properties when such substitution is made. Now Harrison (6) has associated the instability of zinc silicate:Mn with a surface phase different from that of the bulk material and has presented electron and x-ray diffraction results suggesting a spinel surface modification. In our phosphors the presence of magnesium, specifically its site preference tendencies, could be an important factor in the surface properties. For example it is known that magnesium, though found in tetrahedral sites in some host lattices (7), is most frequently in sixfold coordination (8). Thus magnesium orthosilicate has the olivine structure with silicon in fourfold, magnesium in sixfold, coordination. Although magnesium silicate is soluble in zinc orthosilicate to some extent without changing the phenacite structure of the major constituent (9), the unique conditions at surfaces could favor existence of a phase having the olivine structure. The relative strengths of octahedral (2.9) and tetrahedral (2.0) bonds (10) should result in lowered mobility of surface oxygens and protect against oxidation of manganese during cooling of the fired phosphor; the tan and white body colors of phosphors without and with magnesium fluoride, respectively, support this. Further, there is no visual evidence of the gray body color, ascribed by others (6, 11) to reduction or photolytic decomposition of zinc, in our plaque tests. This, too, suggests relative scarcity of zinc atoms at the phosphor surface, *i.e.* a magnesium-rich layer.

Improved plaque and lamp maintenance (Tables I, IV) also attended substitution of silica for germania, optimum performance being that for near-equal concentrations of these constituents. The lower luminosity expected for increased silica must be balanced by some beneficial effect. One clue may be the temperature behavior, quenching temperature increasing with silica concentration. Since the rate at which output drops with temperature reflects the influence of lattice

Table VI. Proposed vapor transport reactions

$$2SiO_2 + 2MgF_2 \rightarrow SiF_4\uparrow + Mg_2SiO_4$$
$$GeO_2 + SiF_4 \rightarrow GeF_4\uparrow + SiO_2$$
$$\overline{2SiO_2 + GeO_2 + 2MgF_2 \rightarrow GeF_4\uparrow + SiO_2 + Mg_2SiO_4}$$

$$3GeO_2 + 2MgF_2 \rightarrow GeF_4\uparrow + 2MgGeO_3$$
$$SiO_2 + GeF_4 \rightarrow SiF_4\uparrow + GeO_2$$
$$\overline{3GeO_2 + SiO_2 + 2MgF_2 \rightarrow SiF_4\uparrow + GeO_2 + 2MgGeO_3}$$

Table VII. Size and electron distribution for ionic species

Ion	Electron configuration	Orbital radius (Å)
Zn^{+2}	$3d^{10}$	0.292
Mg^{+2}	$2p^6$	0.246
Ge^{+4}	$3d^{10}$	0.260
Si^{+4}	$2p^6$	0.201
Mn^{+2}	$3d^5$	0.388

vibrations on the luminescence center, this means relatively greater isolation of the latter as silica increases in the solid solution. Since this coupling ultimately resides in chemical bond characteristics, consideration of these is merited.

For this purpose, the orbital radii (12) and electron configurations of the cation species involved in this system are presented in Table VII. It is apparent that simultaneous replacement of Zn^{+2} by Mg^{+2} and Ge^{+4} by Si^{+4} involves substitution of large ions by smaller. [In all phosphors, the activator manganese (Mn^{+2}) is the largest cation.] More important are the electron configurations, $3d^{10}$ for Zn^{+2} and Ge^{+4}, $3d^5$ for Mn^{+2}, and $2p^6$ for Mg^{+2} and Si^{+4}. Although, to a first approximation, all the cation sites in willemite are equivalent (13) and tetrahedral, the hybrid orbitals giving this tetrahedral orientation must meet both symmetry and energy requirements. Combinations of s with either the three p orbitals or three of the d orbitals (T_2) are allowed by symmetry (14) and doubtless a mixture of sp^3 and sd^3 hybrids is used in most situations.

For zinc, germanium, and manganese, the energies of the 3d, 4s, and 4p orbitals are quite similar, favoring the p-d mixing in the hybrids forming the primary (σ) tetrahedral bonds. However, the energies of the lowest d orbitals (3d) available to magnesium and silicon, may still be too high for their effective participation in bonding, *i.e.* the sp^3 set constitutes the hybrid responsible for the tetrahedral bonds between silicon or magnesium and oxygen.

In addition to the primary σ bonds, π bond formation is also possible between metal p,d or p-d hybrid orbitals and oxygen p orbitals. Symmetry considerations again limit the possibilities for bond formation (14), in this case to combinations of the two d orbitals belonging to the E representation with either or both T_2 sets used for the σ orbitals. Thus both σ and π bonds require the use of T_2 orbitals, but if the magnesium and silica use chiefly sp^3 hybrids for the σ bonds, they have only the d orbitals available for π bonding. If, as was suggested above, the d orbitals are too high in energy for effective utilization, then the degree of π bonding is negligible. This is not so for the other host species, zinc and germanium, or the activator manganese, where 3d, 4s, and 4p orbital energies are nearly equal.

A property of π bonds is delocalization of the electrons involved, a factor of some possible importance in the phosphors described here. Consider several adjacent tetrahedra occupied by zinc, germanium, and manganese and sharing a common oxygen ion (see Fig. 5). The three cations are disposed in a plane about the oxygen at the center (15) permitting extensive π bond formation among the positive ions and the 01 oxygen. Extension to the lattice as a whole provides considerable host-activator coupling and poor shielding of activator center from lattice vibrations, *i.e.* low quenching temperature. Progressive replacement of zinc and germanium by magnesium and silicon serves to limit the π bonding and improves the resistance to thermal quenching. This presumed lability of electrons in predominantly zinc germanate members of the solid solution series is also probably responsible for their rapid degradation. Electrons raised to excited states can be lost to the lattice in these members of the solid solution series and subsequently trapped at defects. The existence of traps is qualitatively demonstrated in

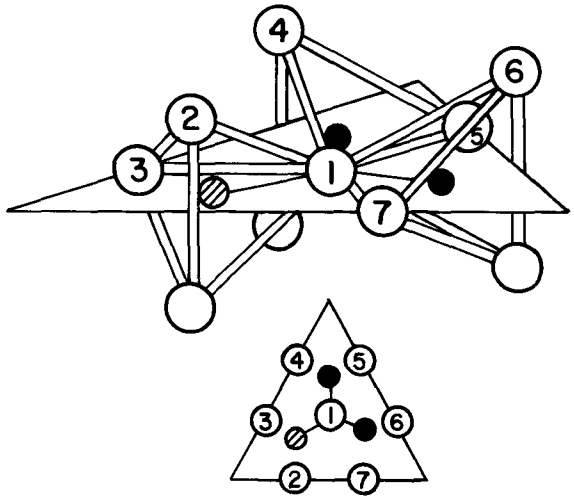

Fig. 5. Perspective and plan views of local structure in willemite (○ is O^{-2}, ⊘ is Ge^{+4} or Si^{+4}, ● is Zn^{+2}, Mg^{+2}, or Mn^{+2}).

the persistent phosphorescence observed in both phosphors and unactivated host materials. Only the zinc orthosilicate materials have no visually detectable afterglow, supporting the suggestion that silica inhibits electron migration and the attendant damage.

Acknowledgment

The writer wishes to thank C. K. Lui Wei for x-ray powder diffraction results and E. S. Panaccione for sample preparations.

Manuscript submitted Aug. 27, 1970; revised manuscript received *ca.* Oct. 26, 1970. This was Paper 58 presented in part at the Los Angeles Meeting of the Society, May 10-15, 1970.

Any discussion of this paper will appear in a Discussion Section to be published in the December 1971 JOURNAL.

REFERENCES

1. J. H. Schulman, R. J. Ginther, and E. W. Claffy, *J. (and Trans.) Electrochem. Soc.*, **96**, 57 (1949).
2. G. F. J. Garlick, "Luminescent Materials," Oxford University Press (1949).
3. G. R. McCormick, *J. Am. Ceram. Soc.*, **49**, 620 (1966).
4. C. R. Robbins and E. M. Levin, *Am. J. Sci.*, **65**, 257 (1959).
5. A. V. Novoselova, *Krist. Tech.*, **2**, 511 (1967).
6. D. E. Harrison, *This Journal*, **107**, 210 (1960) and references cited therein.
7. R. Roy, *J. Am. Chem. Soc.*, **72**, 3307 (1950).
8. A. F. Wells, "Structural Inorganic Chemistry," 3rd Ed., pp. 503-508, Oxford University Press (1962).
9. J. F. Sarver and F. A. Hummel, *J. Am. Ceram. Soc.*, **45**, 304 (1962).
10. L. Pauling, "The Nature of the Chemical Bond," Cornell University Press (1948).
11. G. Kressin, "Tech. Wiss. Abhard Osram Gesell.," p. 235, Springer Verlag (1950).
12. J. T. Waber and D. T. Cromer, *J. Chem. Phys.*, **42**, 4116 (1965).
13. See, however, H. K. Perkins and M. J. Sienko, *ibid.*, **46**, 2398 (1967) and references therein.
14. F. A. Cotton, "Chemical Applications of Group Theory," Interscience (1963).
15. H. Lozykowski, R. G. Wilson, and F. Holuj, *J. Chem. Phys.*, **51**, 2309 (1969).

Cathodoluminescence of $CaS:Ce^{3+}$ and $CaS:Eu^{2+}$ Phosphors

W. Lehmann* and F. M. Ryan

Westinghouse Research Laboratories, Pittsburgh, Pennsylvania 15235

ABSTRACT

Data are presented on green-emitting $CaS:Ce^{3+}$, red-emitting $CaS:Eu^{2+}$, and doubly activated $CaS:Eu^{2+},Ce^{3+}$, including spectra, efficiency, and decay characteristics. Green $CaS:Ce^{3+}$ rivals the best green ZnS-type phosphors in efficiency, color, and brightness at low beam current and is appreciably better at high current. Red $CaS:Eu^{2+},Ce^{3+}$ is better than $YVO_4:Eu^{3+}$ in terms of efficiency but, because of the less favorable emission spectrum, only about equal to it in brightness.

Calcium sulfide has been known for a long time as an excellent and versatile phosphor host material. Nevertheless, calcium sulfide phosphors seem to have suffered some disrepute in recent years; they are almost completely neglected now compared to the vast amount of research done in other phosphor systems. One reason for this decline of interest may be the relatively poor reproducibility, and the uncertain compositions, of so-called "Lenard Phosphors" (1). This prejudice may have been valid in earlier days but we believe it to be invalid now since it has been demonstrated many times that well-defined CaS and related phosphors can be very well and reproducibly prepared (2-6).

Another and more serious objection to alkaline earth sulfide phosphors is their chemical instability against atmospheric carbon dioxide and water, which in most cases requires special precautions during storage and use. This is doubtlessly the case for MgS, BaS, and, to a lesser degree, SrS. CaS phosphors are comparatively stable when consisting of well-grown particles, however, and they can freely be incorporated into various devices with only a minimum of precaution.

Red-emitting $CaS:Eu^{2+}$ phosphors are already described in the literature (5, 7-9) although their cathodoluminescence does not seem to have been investigated before. Luminescence due to trivalent cerium has been reported in MgS (10, 11) and in SrS (12, 13). Also, work on doubly activated CaS:Bi,Ce and CaS:Sm,Ce (mainly glow curves) is reported (14) but, peculiarly, publications on green-emitting CaS:Ce do not seem to exist (15) although this phosphor certainly is one of the most efficient we are aware of.

Experimental

The nominal composition of a good $CaS:Ce^{3+},Cl$ phosphor is CaS(100%):Ce(0.03%),Cl(2%) where the numbers indicate the concentrations on a molar basis added before firing. Starting materials used in our in-

* Electrochemical Society Active Member.

Key words: luminescence, phosphor, calcium sulfide, cerium, europium.

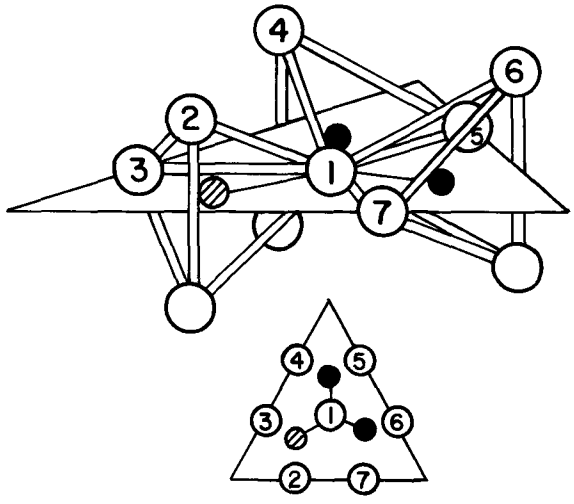

Fig. 5. Perspective and plan views of local structure in willemite (○ is O^{-2}, ⊘ is Ge^{+4} or Si^{+4}, ● is Zn^{+2}, Mg^{+2}, or Mn^{+2}).

the persistent phosphorescence observed in both phosphors and unactivated host materials. Only the zinc orthosilicate materials have no visually detectable afterglow, supporting the suggestion that silica inhibits electron migration and the attendant damage.

Acknowledgment

The writer wishes to thank C. K. Lui Wei for x-ray powder diffraction results and E. S. Panaccione for sample preparations.

Manuscript submitted Aug. 27, 1970; revised manuscript received *ca.* Oct. 26, 1970. This was Paper 58 presented in part at the Los Angeles Meeting of the Society, May 10-15, 1970.

Any discussion of this paper will appear in a Discussion Section to be published in the December 1971 JOURNAL.

REFERENCES

1. J. H. Schulman, R. J. Ginther, and E. W. Claffy, *J. (and Trans.) Electrochem. Soc.*, **96**, 57 (1949).
2. G. F. J. Garlick, "Luminescent Materials," Oxford University Press (1949).
3. G. R. McCormick, *J. Am. Ceram. Soc.*, **49**, 620 (1966).
4. C. R. Robbins and E. M. Levin, *Am. J. Sci.*, **65**, 257 (1959).
5. A. V. Novoselova, *Krist. Tech.*, **2**, 511 (1967).
6. D. E. Harrison, *This Journal*, **107**, 210 (1960) and references cited therein.
7. R. Roy, *J. Am. Chem. Soc.*, **72**, 3307 (1950).
8. A. F. Wells, "Structural Inorganic Chemistry," 3rd Ed., pp. 503-508, Oxford University Press (1962).
9. J. F. Sarver and F. A. Hummel, *J. Am. Ceram. Soc.*, **45**, 304 (1962).
10. L. Pauling, "The Nature of the Chemical Bond," Cornell University Press (1948).
11. G. Kressin, "Tech. Wiss. Abhard Osram Gesell.," p. 235, Springer Verlag (1950).
12. J. T. Waber and D. T. Cromer, *J. Chem. Phys.*, **42**, 4116 (1965).
13. See, however, H. K. Perkins and M. J. Sienko, *ibid.*, **46**, 2398 (1967) and references therein.
14. F. A. Cotton, "Chemical Applications of Group Theory," Interscience (1963).
15. H. Lozykowski, R. G. Wilson, and F. Holuj, *J. Chem. Phys.*, **51**, 2309 (1969).

Cathodoluminescence of $CaS:Ce^{3+}$ and $CaS:Eu^{2+}$ Phosphors

W. Lehmann* and F. M. Ryan

Westinghouse Research Laboratories, Pittsburgh, Pennsylvania 15235

ABSTRACT

Data are presented on green-emitting $CaS:Ce^{3+}$, red-emitting $CaS:Eu^{2+}$, and doubly activated $CaS:Eu^{2+},Ce^{3+}$, including spectra, efficiency, and decay characteristics. Green $CaS:Ce^{3+}$ rivals the best green ZnS-type phosphors in efficiency, color, and brightness at low beam current and is appreciably better at high current. Red $CaS:Eu^{2+},Ce^{3+}$ is better than $YVO_4:Eu^{3+}$ in terms of efficiency but, because of the less favorable emission spectrum, only about equal to it in brightness.

Calcium sulfide has been known for a long time as an excellent and versatile phosphor host material. Nevertheless, calcium sulfide phosphors seem to have suffered some disrepute in recent years; they are almost completely neglected now compared to the vast amount of research done in other phosphor systems. One reason for this decline of interest may be the relatively poor reproducibility, and the uncertain compositions, of so-called "Lenard Phosphors" (1). This prejudice may have been valid in earlier days but we believe it to be invalid now since it has been demonstrated many times that well-defined CaS and related phosphors can be very well and reproducibly prepared (2-6).

Another and more serious objection to alkaline earth sulfide phosphors is their chemical instability against atmospheric carbon dioxide and water, which in most cases requires special precautions during storage and use. This is doubtlessly the case for MgS, BaS, and, to a lesser degree, SrS. CaS phosphors are comparatively stable when consisting of well-grown particles, however, and they can freely be incorporated into various devices with only a minimum of precaution.

Red-emitting $CaS:Eu^{2+}$ phosphors are already described in the literature (5, 7-9) although their cathodoluminescence does not seem to have been investigated before. Luminescence due to trivalent cerium has been reported in MgS (10, 11) and in SrS (12, 13). Also, work on doubly activated CaS:Bi,Ce and CaS:Sm,Ce (mainly glow curves) is reported (14) but, peculiarly, publications on green-emitting CaS:Ce do not seem to exist (15) although this phosphor certainly is one of the most efficient we are aware of.

Experimental

The nominal composition of a good $CaS:Ce^{3+},Cl$ phosphor is CaS(100%):Ce(0.03%),Cl(2%) where the numbers indicate the concentrations on a molar basis added before firing. Starting materials used in our in-

* Electrochemical Society Active Member.

Key words: luminescence, phosphor, calcium sulfide, cerium, europium.

vestigation were pure CaS (16), Ce_2S_3, NH_4Cl, and sulfur. They were intimately mixed (dry) in the desired ratios and fired in capped quartz tubes, surrounded by a flow of argon, at 1200°C for 2 hr.

The addition of a halide (Cl may be replaced by F, Br, or I) to the phosphor is essential as it strongly enhances the otherwise very weak or completely absent Ce^{3+} emission. While it is relatively certain that all added cerium stays in the phosphor during firing, it is equally certain that most of the volatile halides "boil out" so that the halide content after firing is much smaller then the starting amount. The addition of some free sulfur to the raw material is not essential. It only serves to provide a sulfurizing atmosphere surrounding the phosphor during firing and protecting it from oxidation to $CaSO_4$. At the high firing temperature, the sulfur vaporizes and drives all air out of the quartz tube. It is then carried away by the flowing argon gas.

The preparation of red-emitting CaS:Eu^{2+},Cl phosphor is completely analogous to that of green CaS:Ce^{3+},Cl only with Ce_2S_3 replaced by Eu_2S_3. Presence of a halide is also essential here. Europium is unique among the rare earth elements as it appears to enter the CaS lattice only as divalent ion. Thus all attempts to prepare CaS:Eu emitting in the typical orange to red line spectrum of Eu^{3+} were without success (17) in agreement with similar experience reported by Jaffe and Banks (8) and by Brauer (7). The measurement techniques used to determine the phosphor properties are described elsewhere (16).

Properties of CaS:Ce^{3+}

Trivalent cerium produces two partly overlapping emission bands in all alkaline earth sulfides. In CaS their peaks are at about 2.10 and 2.37 eV, respectively (λ = 590 and 523 nm). The spectral energy distribution of these bands is plotted in Fig. 1. The energy difference between these two peaks is almost precisely the same as the difference of 0.28 eV reported for the two lowest states ($2F_{5/2}$ and $2F_{7/2}$) of the single 4f electron of Ce^{3+} (18) so that, with a high degree of certainty, the electronic transition responsible for the luminescence terminates in these two states. The point of origin of the electronic transition is open to speculation. The transition yielding the high-energy peak of the emission is invariably the stronger of the two. The two peak positions vary only very little with the cerium concentration or with temperature, and the intensity ratio of the two bands ($\approx$ 65/100 in terms of quanta) seems to be completely independent of all preparational parameters and of the conditions of excitation. The green color of the emission corresponds closely to that of a (Zn,Cd)S:Ag phosphor containing 30 m/o (mole per cent) of CdS (Fig. 2).

The optical absorption spectrum of CaS:Ce^{3+} is also plotted in Fig. 1. It corresponds closely to its excitation spectrum and is characterized by a fairly well-defined absorption band with a single peak at 2.73 eV (λ = 454 nm) in the blue, giving the material a greenish-yellow body color. The green cerium emission is excited well by blue light and by ultraviolet in the vicinity of the optical absorption edge of CaS ($\approx$ 4.8 eV) but, for lack of absorption, not by near-ultraviolet of a high-pressure mercury discharge lamp ($\approx$ 3.4 eV).

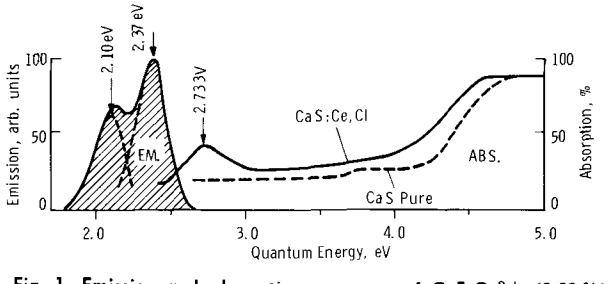

Fig. 1. Emission and absorption spectrum of CaS:Ce^{3+} (0.03%), Cl.

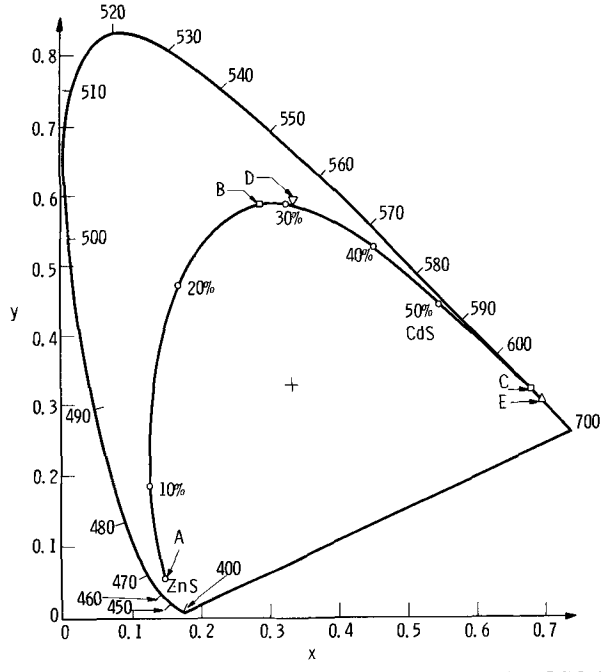

Fig. 2. ICI diagram containing the colors of various (Zn,Cd)S:Ag phosphors (circles), blue ZnS:Ag (point A), green (Zn,Cd)S:Ag (point B), red YVO_4:Eu^{3+} (point C), green CaS:Ce^{3+} (point D), and red CaS:Eu^{2+} (point E).

The influence of the cerium concentration on the intensity of cathodoluminescence of CaS:Ce^{3+},Cl is shown in Fig. 3. Quasi-infinitely thick powder samples of the phosphor were excited in a demountable system by 10 kV electrons of constant low current density ($\sim 10^{-6}$ A/cm^2). The light output was measured from the excited side by a selected silicon photo diode of flat quantum response over the visible range and compared to that of the best available green (Zn,Cd)S:Ag phosphor (P-22) used in color TV picture tubes. Such comparison is accurate and reproducible to about ±5%. Since there are very little differences either in the mean wavelength or in the luminosity factor between the two phosphors, the measured quanta can very approximately be considered to express also the differences in energy efficiency and in visible brightness. Figure 3 shows efficiencies measured in this way to have a flat maximum between about 0.02 and 0.03 m/o of cerium but decreasing only very little up to 0.1% of cerium. The energy efficiency at the optimum cerium concentration is about equal to that of the green P-22

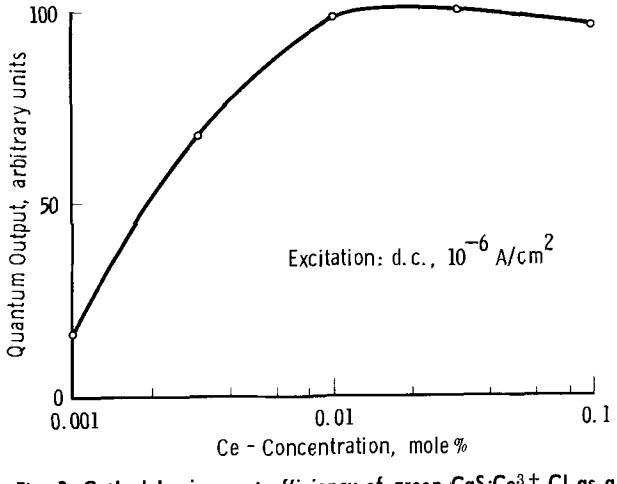

Fig. 3. Cathodoluminescent efficiency of green CaS:Ce^{3+},Cl as a function of the cerium concentration.

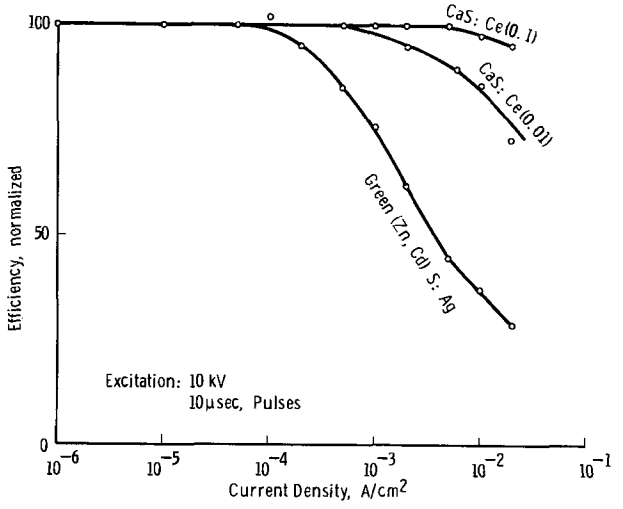

Fig. 4. Current saturation of two samples of CaS:Ce^{3+},Cl excited by 10 kV electron beam pulses of 10 μsec widths, compared to green (Zn,Cd):Ag.

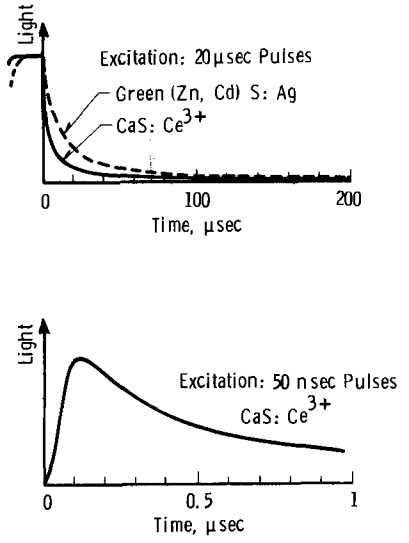

Fig. 5. Decay curves of cathodoluminescence of green CaS:Ce^{3+},Cl and of green (Zn,Cd)S:Ag.

phosphor whose efficiency was estimated to be about 22%.

The influence of the current density on the efficiency was tested on thin phosphor layers spread on glass with little binder and aluminized on top. The phosphors were excited by 10 kV electron beam pulses of 10 μsec length and the emission was observed through the glass. The results in Fig. 4 show the measured efficiencies (actually the ratios quantum output/current density) as functions of the current density during the pulse; all curves in Fig. 4 are normalized to 100 units at low currents. The three phosphors corresponding to the three curves are about equally efficient at low current but they differ considerably at high currents. CaS:Ce^{3+} phosphors saturate much less at high currents then the standard green P-22 phosphor so that the former is superior over the latter, at high currents, by an appreciable margin. It can also be seen that the saturation in CaS:Ce^{3+} is less pronounced for the higher cerium concentrations. This is indicative that the saturation of CaS:Ce^{3+} is caused by exhaustion of available unexcited Ce^{3+} ions in the phosphor (19).

Cerium-activated oxygen-dominated phosphors are well known to be relatively fast, typically with decay times between about 10^{-8} and 10^{-7} sec (example: P-16). We observe the decay of green CaS:Ce^{3+} phosphors, after excitation by an electron beam pulse at room temperature, to be slower and to consist of (at least) three components:

(*a*) The first decay, immediately after cessation of the pulse, is approximately exponential with a τ of $\sim 10^{-7}$ sec.

(*b*) A slower decay follows with a τ of a few 10^{-4} seconds.

(c) A very slow decay finally extends over several seconds.

Typical observed decay curves are shown in Fig. 5. Components (*b*) and (c) are nonexponential. Components (*a*) and (*b*) are observable after electron beam excitation; the slowest component (c) requires photoexcitation to be observed. Time-resolved spectra have shown that all three components of the decay result in the same identical cerium emission spectra. We believe all observed decay components to be due to traps thermally releasing carriers to the cerium ions. One must assume several trapping energies (or a range of trapping energies) to explain all observed decay phases at room temperature. Cooling of the phosphor to 77°K results in a nearly perfectly exponential decay with a τ of about 80 nsec which probably is the intrinsic recombination time within the Ce^{3+}-ion in CaS.

Properties of CaS:Eu^{2+}

Divalent europium is well known to produce a single, relatively narrow, but diffuse emission band in all alkaline earth sulfides. Its peak is near 1.90 eV ($\lambda = 652$ eV) in CaS at room temperature, almost independent of the europium concentration but somewhat dependent on the temperature. The emission shifts slightly to lower energies with decreasing temperature. At room temperature, the emission color is somewhat deeper red than that of YVO_4:Eu^{3+} (Fig. 2). Its spectral energy distribution is plotted in Fig. 6.

The optical absorption spectrum of CaS:Eu^{2+},Cl contains as its main feature a broad absorption band uniformly extending from about 2.1 (yellow) to 3.0 eV (violet) causing the characteristic pink body color of this phosphor. The red Eu^{2+} emission is well excited by optical irradiation within this band and by ultraviolet near the optical absorption edge of CaS but only weakly by the near ultraviolet of 3.4 eV ($\lambda = 365$ nm) of a high-pressure mercury lamp. Its optical absorption spectrum is plotted in Fig. 6.

The efficiency of cathodoluminescence of red CaS:Eu^{2+},Cl as a function of the europium concentration follows about the same concentration dependence as shown in Fig. 3 for CaS:Ce^{3+},Cl with the optimum located at about 0.05% europium. However, this optimum is lower than that of CaS:Ce^{3+},Cl. Even in the best materials it comes only to about 10-12%. This lower value (compared to the $\sim$ 22% observed in CaS:Ce^{3+}) cannot be completely explained by the lower mean quantum energy of the emission of CaS:Eu^{2+} and we have to assume the existence of a nonradiative recombination mechanism in CaS:Eu^{2+} which is not, or to a lesser degree, present in CaS:Ce^{3+}.

We have observed a drastic improvement of the efficiency of cathodoluminescence of red CaS:Eu^{2+} by incorporating small amounts of cerium into the phosphor, too small to let the green Ce^{3+} emission appear noticeably besides the red Eu^{2+} emission. Some re-

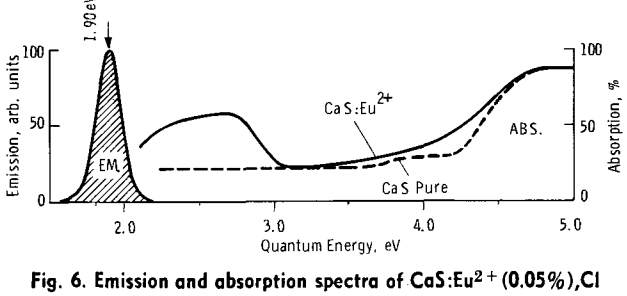

Fig. 6. Emission and absorption spectra of CaS:Eu^{2+}(0.05%),Cl

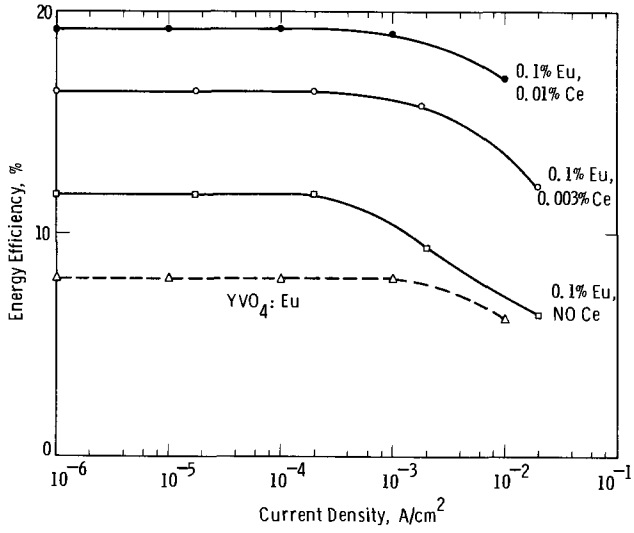

Fig. 7. Energy efficiencies of cathodoluminescence of CaS: Eu^{2+},Cl of CaS:Eu^{2+},Ce^{3+},Cl and of YVO_4:Eu^{3+} as functions of the current density. Excitation by 10 kV electron beam pulses of 10 μsec widths.

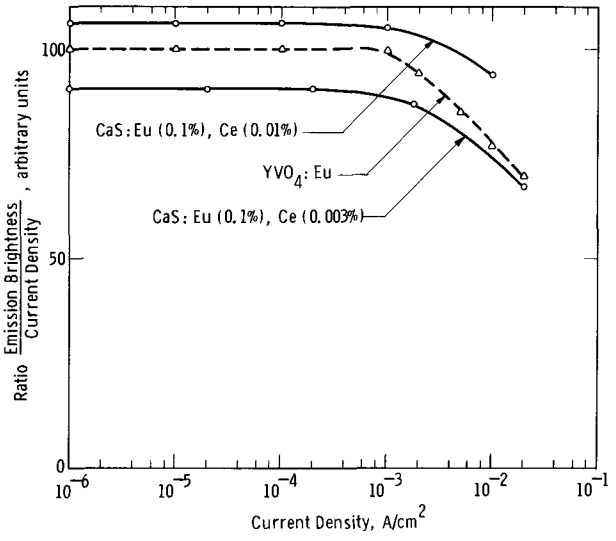

Fig. 9. Visible brightness of cathodoluminescence of CaS: Eu^{2+},Ce^{3+},Cl as a function of current density (compared to YVO_4:Eu^{3+} = 100 at low currents).

sults measured on these phosphors compared to that of commercial YVO_4:Eu^{3+} are shown in Fig. 7-9.

The efficiency of singly activated CaS:Eu^{2+},Cl compares well to that of YVO_4:Eu^{3+} in terms of energy (Fig. 7) but not in terms of brightness because of the less favorable emission spectrum. Increasing amounts of cerium added to CaS:Eu^{2+},Cl improve the low-current efficiency from about 12% (no cerium) to about 18% (0.01% cerium) which we believe to be about the maximum that can be obtained from this phosphor.

The saturation of singly activated CaS:Eu^{2+} at high current density decreases with increasing europium concentration (Fig. 8). We conclude that the saturation probably is caused by exhaustion of available unexcited Eu^{2+} ions in the phosphor (19) similar to the case of green CaS:Ce^{3+},Cl. At a given europium concentration, the saturation is decreased yet further by the addition of small amounts of cerium. It may be stressed here that all CaS:Eu^{2+},Ce^{3+},Cl phosphors of Fig. 7-9 emit only in the red Eu^{2+} band. There is no green Ce^{3+} emission contribution of noticeable intensity.

Figure 9 shows the emission brightness (actually the ratio of brightness/current) of two representative red-emitting CaS:Eu^{2+},Ce^{3+},Cl phosphors compared to that of YVO_4:Eu^{3+}. While the former are much superior to the latter in terms of energy (Fig. 8), the higher luminosity factor of the line emission of YVO_4:Eu^{3+} ($\sim$ 0.33) compared to the band emission of CaS:Eu^{2+} ($\sim$ 0.15) offsets this advantage. Therefore, the luminous efficiencies of the two phosphors are about equal. Cathodoluminescent decay curves of red CaS:Eu^{2+},Cl (no cerium) and YVO_4:Eu^{3+} for comparison are shown in Fig. 10. As to be expected, the allowed 5d→4f electron transition responsible for the emission of Eu^{2+} is much faster then the forbidden 4f→ 4f transition within the Eu^{3+} ion. A closer inspection of the decay curve of CaS:Eu^{2+} at room temperature reveals three components approximately equal to those observed in CaS:Ce^{3+}. All three components are nonexponential and are believed to be due to thermal trap emptying. The most striking difference between the decay characteristics of CaS:Ce^{3+} and CaS:Eu^{2+} is observed when those phosphors are cooled below room temperature. While CaS:Ce^{3+} decays fast and near-exponential already at 77°K, CaS:Eu^{2+} phosphors are nonexponential and very slow, slower than at room temperature, down to about 13°K. Details permitting an understanding of this difference are not yet known.

Discussion

One of the factors determining the efficiency of cathodoluminescence of a phosphor is the width of the forbidden band gap of the host material; the wider the

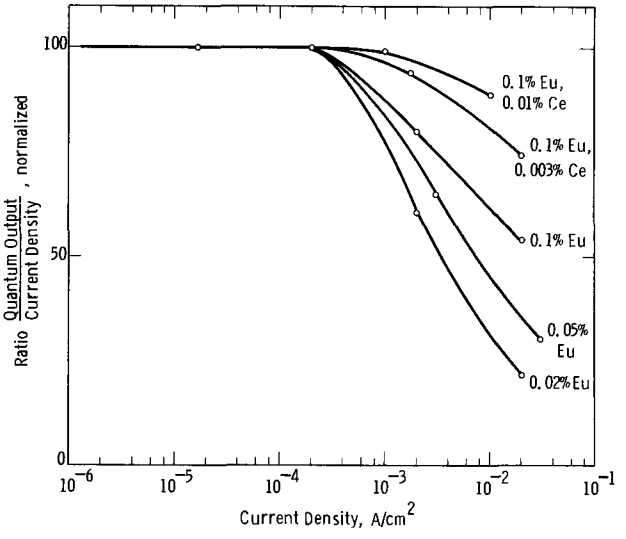

Fig. 8. Current saturation of red CaS:Eu^{2+},Cl and CaS: Eu^{2+},Ce^{3+},Cl (all normalized to 100 at low currents).

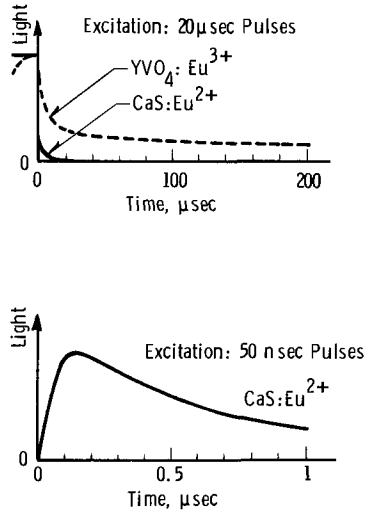

Fig. 10. Decay curves of cathodoluminescence of red CaS: Eu^{2+},Cl and of YVO_4Eu^{3+}.

gap, the lower the efficiency (all other factors kept constant). It came somewhat as a surprise, therefore, to observe the very high efficiency obtainable with CaS which, in the case of CaS:Ce^{3+}, about equals that of the best (Zn,Cd)S-type phosphors despite the much wider band gap of CaS (~4.8 eV) over that of (Zn,Cd)S (~3.0-3.7 eV dependent on the Zn/Cd ratio). This interesting observation may be discussed separately (20).

The action by which the addition of small amounts of cerium to red-emitting CaS:Eu^{2+} cathodoluminescent phosphors increases their efficiency probably involves optical cascading. The green Ce^{3+} emission (Fig. 1) coincides with the broad, strong absorption band of Eu^{2+} (Fig. 6) and any emission emanating from a Ce^{3+} ion will immediately be reabsorbed by a neighboring Eu^{2+} ion and reappear as red Eu^{2+} emission. In this mechanism, the Eu^{2+} ions are partly excited by relatively low-energy (< 2.6 eV) light quanta and it seems that this low-energy excitation of the Eu^{2+} ion is more efficient than excitation by the much higher energies available in the avalanches of free carriers during direct excitation by an electron beam. Whatever the details are, we can consider the enhancement effect as a case of sensitization of cathodoluminescence; the emission intensity by the europium is enhanced by the presence of cerium.

The puzzle least understood at the moment is a chemical one. It is our experience that none of the rare earth elements yields a luminescence worth speaking of if, under rigorously clean conditions, all other impurities are carefully avoided or if coactivation is attempted by addition of an alkali metal (Li, Na, K). The rare earth emission does appear, however, if either a halide (F, Cl, Br, I) or a group-V impurity (P, As) is added to the material before firing. This observation includes, besides the various line emitters (Sm^{3+}, Tb^{3+}, *etc.*), also the activators Ce^{3+} and Eu^{2+}. We have tried to clear up the situation with several experiments which may briefly be described here:

(*a*) A good green-emitting CaS:Ce^{3+} (0.05%), Cl phosphor was refired in an open boat, in flowing H_2S, at 1200°C for several hours. The H_2S gas can be expected to remove some of the volatile chlorine out of the phosphor under these firing conditions and, accordingly, the material was nearly nonluminescent afterwards. Addition of new chlorine (added as NH_4Cl) and refiring this near-dead material in a capped tube at 1200°C for 1 hr completely restored the green Ce^{3+} luminescence in full intensity. This cycle can be repeated several times with always the same results. Also, red-emitting CaS:Eu^{2+} tested in the same way behaves similarly. Hence, the halide does not simply act as a flux promoting particle growth. It is more actively involved in the luminescent process.

(b) A larger batch of CaS:Ce^{3+} (0.05%) was first fired without any second impurity and, afterwards, split into many small samples to which predetermined amounts of NH_4Cl were added. After refiring in tightly capped (but not sealed) tubes at 1200°C for 1 hr, the green Ce^{3+} emission appeared in full intensity in all samples to which 0.2 m/o or more Cl was added. The amount of chlorine actually retained in the phosphor after firing probably is still lower than that. A molar ratio of Ce:Cl = 1/1 in the phosphor is suggestive, although we have no reliable evidence for this yet (21).

(c) X-ray examination of CaS: samples fired in capped tubes at 1200°C for many hours with the addition of 10 m/o of either cerium or europium, and either without or with addition of 10% of $CaCl_2$, gave results which are summarized in Table I (22). The extremely large amounts of added cerium or europium may be the reason why, in these cases, even the samples made without chlorine were luminescent. The concentration of cerium dissolved in the CaS lattice is estimated to be between 1 and 10% if Cl was present but much below 1% if no Cl was present. The corresponding numbers for europium are 10% with Cl and much below 1% without Cl.

Table I. Some properties of CaS:Ce(10%) and CaS:Eu(10%) made without or with addition of 20%Cl

	10% Ce		10% Eu	
	No Cl	20% Cl	No Cl	20% Cl
Body color	Light green	Dark yellow-green	Light pink	Dark brown-red
Luminescence	Green	Yellowish	Red	Deep red
Undissolved Ce_2S_3 or Eu_2S_3	Much	Little	Much	None
Increase of lattice constant	0.007%	0.051%	0.005%	0.204%

The conclusions from these three experiments are that the solubilities of cerium and of europium in CaS are very enhanced by the presence of a halide, and that the ratios of Ce/Cl and Eu/Cl in good luminescent CaS:Ce^{3+},Cl and CaS:Eu^{2+},Cl phosphors are not far from unity. This strange behavior is completely in line with equal oddities observed in CaS phosphors made with many other activators. It cannot readily be understood on the basis of charge compensation which is so well established for ZnS-type phosphors, and a plausible explanation is still missing.

Manuscript received Sept. 23, 1970. This was Paper 49 presented at the Los Angeles Meeting of the Society, May 10-15, 1970.

Any discussion of this paper will appear in a Discussion Section to be published in the December 1971 JOURNAL.

REFERENCES

1. P. Lenard, F. Schmidt, and R. Tomaschek, "Handb. Exp. Phys." Vol. 23, Springer Verlag (1928).
2. F. Urbach, D. Pearlman, and H. Hemmendinger, *J. Opt. Soc. Am.*, **36**, 372 (1946).
3. R. Ward, *This Journal*, **93**, 171 (1948).
4. O. Sorge, "Untersuchungen über die Erdalkalisulfidphosphore," Thesis, Techn. Univ. Berlin (1959).
5. A. Wachtel, *This Journal*, **107**, 199 (1960).
6. M. Avinor, A. Carmi, and Z. Weinberger, *J. Chem. Phys.*, **35**, 1978 (1961).
7. P. Brauer, Z. *Naturforsch.*, **6A**, 561 (1951) and **12A**, 233 (1957).
8. P. M. Jaffe and E. Banks, *This Journal*, **102**, 518 (1955).
9. W. Low, *Ann. N. Y. Acad. Sci.*, **72**, 69 (1958).
10. E. Riede and A. Schleede, *Ann. Phys.*, **67**, 578 (1922).
11. J. W. Gilliland, *J. Appl. Phys.*, **38**, 2427 (1967).
12. E. Banks and R. Ward, *J. (and Trans.) Electrochem. Soc.*, **96**, 297 (1949).
13. S. P. Keller, *J. Chem. Phys.*, **29**, 180 (1958) and **30**, 434 (1959).
14. V. L. Levshin and N. K. Faizi, *Opt. Spectr. (USSR) (English Transl.)*, **8**, 458 (1960).
15. D. R. Vij and V. K. Mathur, *Ind. J. Pure Appl. Phys.*, **6**, 67 (1968), describe a yellow-to-orange-emitting CaS:Ce phosphor apparently containing sodium but no halide; and *ibid.*, **7**, 638 (1969).
16. W. Lehmann, *This Journal*, **117**, 1389 (1970).
17. S. P. Keller, *J. Chem. Phys.*, **30**, 556 (1959), assumes a blue emission band in SrS:Eu prepared in air to be due to Eu^{3+}. We have repeated Keller's experiments with SrS and with CaS. A blue emission band does indeed appear after prolonged firing of SrS:Eu or CaS:Eu in air, but the material is no longer sulfide; it is partly or completely converted to sulfate. Also, the emission of Eu^{3+} in any host material can be expected to consist of lines predominantly in the orange and red rather than of a band in the blue.
18. R. Lang, *Can. J. Res.*, **A13**, 1(1935) and **A14**, 127 (1936).
19. A. Bril, *Physica*, **15**, 361 (1949).
20. W. Lehmann, To be published.
21. Chemical analysis for chlorine actually retained in fired samples of CaS:Ce^{3+},Cl phosphors gave no conclusive results; molar ratios of Cl:Ce from about 2:1 to 10:1 were observed. Part of this

chlorine may be present as separate $CaCl_2$ phase so that the amount of Cl actually dissolved in the CaS lattice is uncertain.

22. This experiment was made jointly with M. Rubenstein of this laboratory. Free Ce_2S_3 or Eu_2S_3 was observed microscopically, clearly distinguishable from the CaS by the dark body colors. The lattice constants were checked by x-ray analysis.

The Effect of Exciting Wavelength on Optimum Activator Concentration

L. Ozawa,* H. Forest, P. M. Jaffe,* and G. Ban

Zenith Radio Corporation, Chicago, Illinois 60639

ABSTRACT

The concentration dependence curves of several Eu^{+3}-, Tb^{+3}-, and Pr^{+3}-activated phosphors for different excitations have been studied. The optimum activator concentration was found to be a function of the number of excited activator ions as well as the exciting wavelength. For exciting radiation having a high absorption coefficient, the optimum activator concentration of a given phosphor shifted to low concentration. The concentration dependence curves of $(Y_{1-x}Eu_x)_2O_3$ and $(Y_{1-x}Pr_x)_2O_2S$ phosphors under cathode-ray excitation are almost identical to the curves obtained with host photoexcitation.

The emission intensity of many phosphors as a function of activator concentration initially increases proportionately with activator concentration and then decreases, going through a maximum at some concentration. The emission intensity decrease at high activator concentration is referred to as concentration quenching. Dexter and Schulman (1) have reported that concentration quenching in nonphotoconductive inorganic phosphors (many commerical phosphors are of this type) is due either to an electrostatic multipolar interaction or to a magnetic dipole interaction (exchange coupling). In a phosphor where concentration quenching is mainly due to exchange coupling between nearest neighbors, the emission intensity as a function of activator concentration depends on the concentration of isolated single activator ions which is given by $C(1 - C)^z$ (2-4) where C [1] is the activator concentration in molar fraction and z is related to the number of nearest neighbor cation sites. For quenching arising from electrostatic multipolar interactions, the emission intensity as a function of activator concentration is proportional to $C\{1 + \beta' (C)^{\theta/3}\}^{-1}$ (5) where $\theta = 6$, 8, or 10 for dipole-dipole, dipole-quadrupole, quadrupole-quadrupole interaction, respectively, and β' is a constant for each interaction for a given host crystal.

However, these expressions apply only when the exciting radiation is weakly absorbed by the activator. For practical phosphors, where the exciting radiation is strongly absorbed by the activator or absorbed by a "sensitizer," the optimum activator concentration is found to be lower than the calculated results. A point commonly overlooked in concentration quenching studies on phosphors is the importance of the absorption coefficient for the exciting radiation as well as the type of excitation. In this paper the optimum activator concentration is found to depend not only on the luminescent activator ions but also on the type of excitation; for example, weakly absorbed, strongly absorbed, sensitized, or cathode-ray.

Experimental

The phosphors studied were Eu^{+3}-activated Y_2O_3, $LiYO_2$, and YVO_4, and Eu^{+3}-, Tb^{+3}-, and Pr^{+3}-activated Y_2O_2S. The yttrium oxide and the rare earth oxides used to prepare the phosphors were 5*N* and 3*N* pure, respectively. The rare earth oxides as host and activator were dissolved in hot nitric acid and precipitated with oxalic acid. The oxide phosphors were prepared by firing the oxalates at 1200°C for 2 hr in oxygen. The vanadate phosphors were prepared by firing the proper mixture of the oxalates and 10% excess ammonium vanadate at 1000°C for 2 hr in air. After firing the samples were washed, first with 6*N* HCl and then with concentrated NH_4OH, rinsed several times with hot deionized water, and finally dried at 110°C. The oxysulfide phosphors were prepared from the oxide by a flux technique: a mixture of the proper rare earth oxide, sulfur, and sodium carbonate in the molar ratio 1:3:1, respectively, which was fired at 1100°C for 2 hr in a nitrogen atmosphere. After firing, the samples were washed with hot deionized water and dried. The lithium yttrium oxide phosphors were prepared as reported earlier (6).

The optical measurements were made on 2 mm thick powder samples, which were packed in planchettes. The emission spectra for various exciting wavelengths were obtained with a monochromatized light source consisting of a 200W d-c xenon lamp and a Bausch and Lomb grating monochromator (1300 lines/mm). Since the luminescence intensity for direct excitation in the visible is very weak, it is necessary to remove all stray uv excitation which can produce a significant emission. By proper choice of filters the emission from the desired excitation can be determined.

Results

In general, the emission of rare earth activated phosphors can be optically excited in three ways: by (*a*) indirect host excitation, (*b*) direct excitation into associated activator-host absorption (charge transfer) bands, and (*c*) direct excitation into the narrow $4f^n$ absorptions. The terms "direct" and "indirect" refer, respectively, to the classes of phosphors in which the absorption of the exciting radiation involves either an activator or a "sensitizer."[2] The dominant excitation for cathodoluminescence falls in the indirect class. Only (*a*) and (*b*) correspond to strongly absorbing excitations and are of practical interest; the $4f^n$ excitations are very weak.

* Electrochemical Society Active Member.

Key words: concentration quenching, concentration dependence, absorption coefficient, excitation, emission, phosphors.

[1] $C = n_a/(n_a + n_h)$ where n_a is the number of activator ions and n_h is the number of host cations.

[2] The host-matrix in many phosphors can act as a sensitizer.

Table I. Exciting wavelengths for the phosphors studied

Phosphor	Exciting wavelengths (nm)		
	Host excitation	Charge transfer	$4f^n$ or 4f-5d excitation*
YVO_4:Eu	320	—	467
$LiYO_2$:Eu	—	254	467 and 365
Y_2O_3:Eu	214	254	467 and 365
Y_2O_2S:Eu	254	320	467
Y_2O_2S:Tb	254	—	290
Y_2O_2S:Pr	254	290	460

* Only Tb^{+3} has a 4f-5d excitation.

The exciting wavelengths used for each of the phosphors studied are listed in Table I by type of excitation. The concentration dependence of selected emission lines was determined from the emission spectra by measuring their intensities as a function of activator concentration. The concentration dependence curves, including the one for cathode-ray (CR) excitation, are shown in Fig. 1-6. The optimum activator concentration for each photoexcitation and for cathode-ray excitation is shown in Table II. The optimum activator concentrations, as shown in Table II, were determined from linear concentration dependence curves (not shown). A linear representation was used because it was easier to determine the optimum activator concentration from this than from the usual log-log dependence curves. The log-log representation, however, is preferable for large concentration ranges and is used in the figures. The reproducibility of the data, which was checked by measuring three series of samples, is within ±5%.

For the weakly absorbing $4f^6$ Eu^{+3} direct excitation, the optimum activator concentration for $^5D_0$ emission of each phosphor exactly coincided with the concentration calculated by the exchange model, as shown in

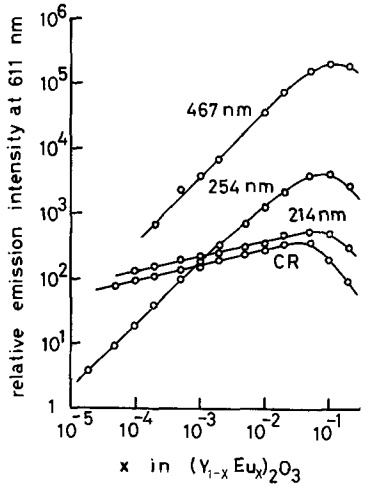

Fig. 1. Concentration dependence curves of $(Y_{1-x}Eu_x)_2O_3$ phosphors excited by 214 nm (host), 254 nm (charge transfer), and 467 nm ($4f^6$) radiation and by cathode rays. The 611 nm emission line was monitored.

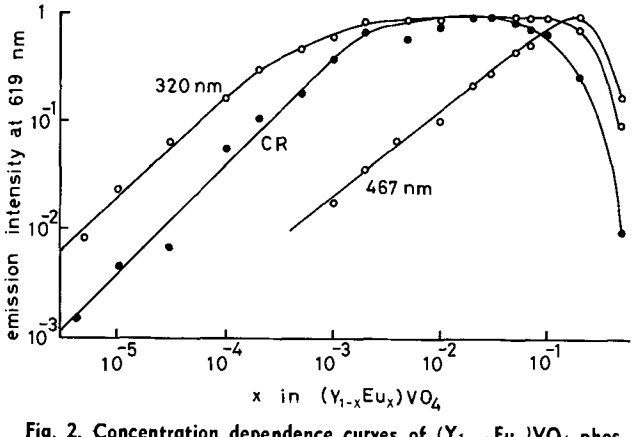

Fig. 2. Concentration dependence curves of $(Y_{1-x}Eu_x)VO_4$ phosphors under excitation by 320 nm (host) and 467 nm ($4f^6$) radiation and by cathode rays. The 619 nm emission line was monitored.

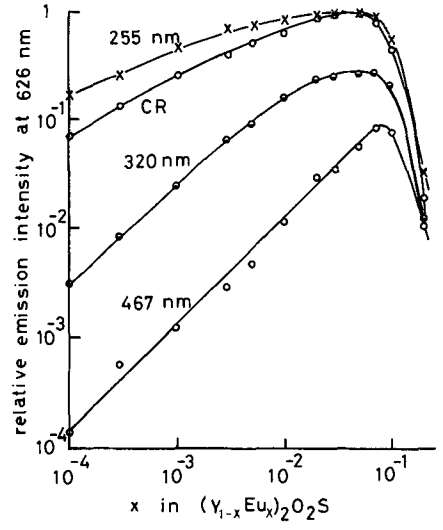

Fig. 3. Concentration dependence curves of $(Y_{1-x}Eu_x)_2O_2S$ phosphors under excitation by 255 nm (host), 320 nm (charge transfer), and 467 nm ($4f^6$) radiation and by cathode rays. The 613 nm emission line was monitored.

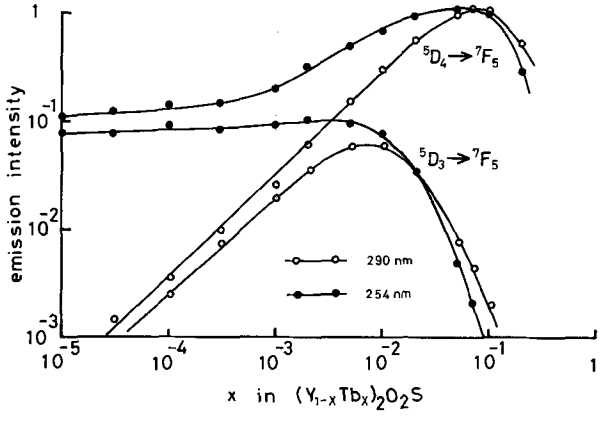

Fig. 4. Concentration dependence curves of $(Y_{1-x}Tb_x)_2O_2S$ phosphors under 254 nm (host) and 290 nm (direct) irradiation. $^5D_4 \rightarrow {}^7F_5$ (542 nm) and $^5D_3 \rightarrow {}^7F_5$ (416 nm) emission lines were monitored.

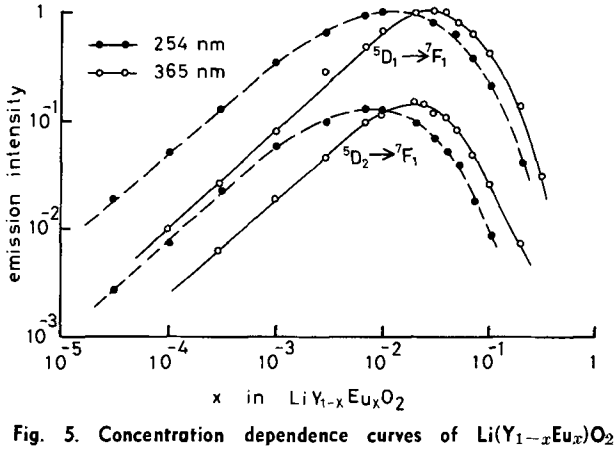

Fig. 5. Concentration dependence curves of $Li(Y_{1-x}Eu_x)O_2$ phosphors under excitation by 254 nm (charge transfer) and 365 nm ($4f^6$) radiation. $^5D_1 \rightarrow {}^7F_1$ (540 nm) and $^5D_2 \rightarrow {}^7F_1$ (476 nm) emission lines were monitored.

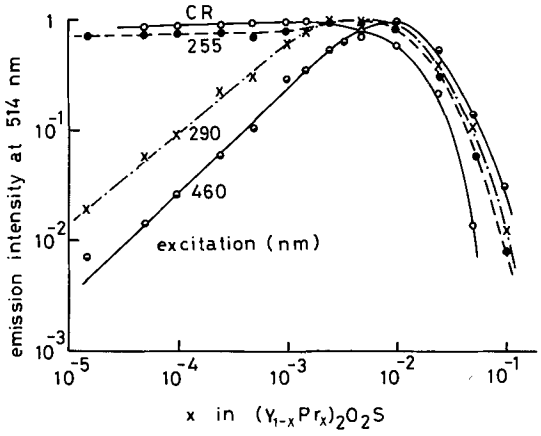

Fig. 6. Concentration dependence curves of $(Y_{1-x}Pr_x)_2O_2S$ phosphors under 255 nm (host), 290 nm (charge transfer), and 460 nm ($4f^2$) radiation and cathode-ray excitation. The 514 nm emission line was monitored.

Table II. However, the emission of $(Y_{1-x}Pr_x)_2O_2S$ and all of the $^5D_1$ and $^5D_2$ Eu^{+3} emissions quenched at considerably lower concentrations, indicating that the quenching is probably due to an electrostatic multipolar interaction (1).

In all cases, whether the quenching is due to exchange coupling or electrostatic multipolar interaction, the optimum activator concentration for a particular emission shifts to lower concentration as the excitation varies in the following sequence: $4f^n$ excitation, charge transfer excitation, host excitation, and finally cathode-ray excitation.

Discussion

In order to discuss the results, it is necessary to consider the dependence of the emission intensity from a packed powder on the absorption of the exciting radiation. Two cases are discussed: (*a*) where the scattering is large compared to the absorption (direct excitation) and (*b*) where the scattering is negligible (indirect excitation). For either case the observed emission intensity, I_{ob}, is given by the rate of formation of excited activator ions (ΔI) multiplied by the probability that an excited activator ion will undergo emission (η). This can be expressed by

$$I_{ob} = \Delta I \eta \qquad [1]$$

For a thin single crystal of a phosphor, ΔI can be obtained from Lambert absorption law as follows

$$\Delta I = I_o - I_t \qquad [2]$$

where I_o is the incident radiation intensity and I_t is the transmitted radiation intensity. But $I_t = I_o e^{-ad}$, where a [3] is the fractional decrease in the intensity per unit length due to absorption and d is the path length in the crystal, so that

$$\Delta I = I_o(1 - e^{-ad}) \qquad [3]$$

Now, Eq. [3] can also apply to a packed powder, but the path length must be modified to take into account the scattering. When an incident radiation beam encounters a packed powder, it is surface scattered through Fresnel reflections and the remainder penetrates the powder undergoing absorption as well as further scattering. The depth of penetration into the powder depends on both the scattering and the absorption. For extremely high absorption the penetration will be small, just as the case for a single crystal and Eq. [3] will apply except for the Fresnel surface losses. As the absorption decreases, the penetration will increase to the scattering limit which depends on the particle size of the powder. For 5μ particles, which includes most phosphors, the scattering limited penetration depth (*i.e.*, no absorption) is less than 1 mm. As a result of the scattering, the actual path length of the incident beam may be greater than the penetration depth. Therefore, Eq. [3] can be used for powders, in general, provided the path length can be properly determined.

In the present paper, the concentration quenching curves under various excitations are compared for a particular phosphor. The thickness of the powder samples was 2 mm to insure that none of the exciting radiation would be transmitted through the sample.

Direct excitation.—In the case of direct excitation, it is assumed that the penetration is limited by the scattering, so that the path length of the exciting radiation is fixed. This is certainly true for the weak $4f^n$ absorptions and is probably true for the charge transfer excitations at low activator concentrations. This means that Eq. [1] can be used to describe the emission intensity of a packed powder for a fixed penetration depth as follows

$$I_{ob} = I_o\,(1 - e^{-ad})\eta \qquad [4]$$

Only the qualitative features of the absorption factor are used in this paper since the path length is difficult to estimate.

For the quenching, there are two kinds of mechanisms to consider: exchange coupling and electrostatic multipolar interactions. For a phosphor in which the concentration quenching mechanism is due only to exchange coupling, the probability for emission η is proportional to the fraction of isolated single activator ions which is given by

$$(I - C)^z \qquad [5]$$

For electrostatic multipolar quenching, the probability for emission is given by

$$\{1 + \beta'\,(C)^{\theta/3}\}^{-1} \qquad [6]$$

Then, the following expressions for I_{ob} under direct excitation as a function of activator concentration (neglecting energy transfer from single ions to paired ions) are obtained:

For exchange interaction

$$I_{ob} = AI_o\{1 - \exp(-kCd)\}\,(1 - C)^z \qquad [7]$$

For multipolar interaction

$$I_{ob} = AI_o\{1 - \exp(-kCd)\}\{1 + \beta'\,(C)^{\theta/3}\}^{-1} \qquad [8]$$

The last factor in Eq. [7] and [8] merely depends on the crystal structure. Equations [7] and [8] both have a common factor which depends on the exciting wavelength. Therefore, the effects of exciting wavelength are qualitatively similar for each expression. For this reason, Eq. [7] is mainly discussed in this paper.

Figure 7 shows the calculated curves of Eq. [7] for three arbitrary values of kd, namely 1, 10, and 100, for Eu^{+3} occupying the C_2 yttrium site in Y_2O_3 where z

[3] $a = kC$, where k is expressed in cm^{-1} and depends only on the oscillator strength of the absorption, and C is the concentration expressed in molar fraction.

Table II. Optimum activator concentration of Eu^{+3}-, Tb^{+3}-, and Pr^{+3}-activated phosphors under various excitation modes

Phosphor	Emission from ^5D_j	Emission from ^3P_j	Excitation modes: Cathode ray	Host	Charge transfer	$4f^n$	Calculated $C^*_{opt} = \frac{1}{1+z}$
YVO_4:Eu	$j = 0$		0.04	0.06	—	0.2	0.2
$LiYO_2$:Eu	0		—	—	0.08	0.2	0.2
	1		—	—	0.01	0.02	—
	2		—	—	0.01	0.02	—
Y_2O_3:Eu	0		0.04	0.05	0.06	0.1	0.1
	1		—	—	0.01	0.03	—
	2		—	—	0.007	0.01	—
Y_2O_2S:Eu	0		0.035	0.04	0.06	0.08	0.08
	1		—	0.003	0.01	0.02	—
	2		—	0.003	0.01	0.02	—
Y_2O_2S:Tb	4		0.03-4	0.05	—	0.08	0.08
	3		—	0.007	—	0.01	—
Y_2O_2S:Pr		$j = 0$	0.0025	0.003	0.005	0.01	—

* From exchange model.

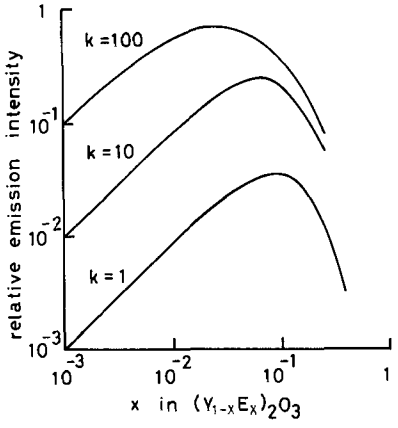

Fig. 7. Calculated concentration dependence curves for $(Y_{1-x}Eu_x)_2O_3$ with three arbitrary absorption coefficients, k, namely 1, 10, and 100.

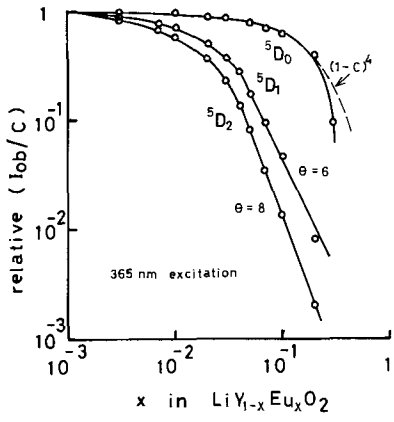

Fig. 8. Concentration dependence curves (I_{ob}/C vs. C) for the $^5D_1$ and $^5D_2$ emissions from $Li(Y_{1-x}Eu_x)O_2$ under 365 nm ($4f^6$) excitation.

is nine. These curves are relative since the constant AI_0 has not been evaluated. It can be seen that, for a fixed value of the penetration depth (d), the optimum activator concentration shifts to lower concentration as k increases. The shift is due to the saturation of the $\{1 - \exp(-kCd)\}$ factor in Eq. [7] which is linear with concentration only for small values of kCd, and as k increases the deviation from linearity occurs at successively lower concentrations.

As shown in Fig. 1-6 and Table II, regardless of the mechanism responsible for the concentration quenching, the optimum activator concentration changed with a change in the exciting wavelength. It was difficult to determine quantitatively the absorption by the phosphor powder; however, the experimental results agreed qualitatively with the results predicted by Eq. [7] and [8].

For a weak absorption, $kC << 1$, Eq. [7] becomes

$$I_{ob} = AI_0\, kCd\, (1 - C)^z$$

or

$$I_{ob} = BC\, (1 - C)^z \qquad [9]$$

where B is a constant for a given exciting intensity and penetration depth (d). Equation [9] has commonly been used as the concentration dependence equation (2-4). Therefore, if the excitation is made with radiation that is weakly absorbed, the data should fit Eq. [9].

The concentration dependence curve for the $^5D_4$ Tb^{+3} emission from $(Y_{1-x}Tb_x)_2O_2S$ for 290 nm excitation (4f-5d) was found to coincide exactly with the calculated curve using Eq. [9] (Fig. 4). Except for $(Y_{1-x}Eu_x)_2O_2S$, all of the $^5D_0$ Eu^{+3} data showed some discrepancies at concentrations greater than the optimum value. In the case of $(Y_{1-x}Eu_x)_2O_2S$, the $^5D_0$ Eu^{+3} emission curve between $x = 0.02$-0.08 showed an additional positive deviation from the calculated curve.

From Eq. [9], the optimum activator concentration C_{opt}, is given by (4)

$$C_{opt} = 1/(1 + z) \qquad [10]$$

Since z is four in YVO_4 and $LiYO_2$, nine in Y_2O_3, and twelve in Y_2O_2S, the optimum activator concentration should be, respectively, at $C = 0.2$, 0.1, and 0.08. As indicated in Table II, the observed optimum activator concentrations for the $^5D_0$ Eu^{+3} and $^5D_4$ Tb^{+3} emissions under direct excitation exactly coincide with the calculated values.

The optimum activator concentrations of the $^5D_3$ Tb^{+3} emission, $^5D_1$ and $^5D_2$ Eu^{+3} emissions, and Pr^{+3} emission, however, are at 0.01, 0.02, and 0.01, respectively; electrostatic multipolar interactions are responsible for the quenching of these emissions.

If kCd is small, Eq. [8] becomes

$$I_{ob} = BC\{1 + \beta'\,(C)^{\theta/3}\}^{-1} \qquad [11]$$

or expressed as emission per activator ion

$$I_{ob}/C = B\{1 + \beta'\,(C)^{\theta/3}\}^{-1} \qquad [12]$$

The value of θ can be estimated from Eq. [12]. Figure 8 shows the concentration dependence curves (I_{ob}/C vs. C) for $^5D_1$ and $^5D_2$ Eu^{+3} emissions from $Li(Y_{1-x}Eu_x)O_2$ under 365 nm excitation. Between 0.04-0.2 molar fraction, the curves are linearly decreasing with a slope of 6/3 and 8/3, respectively. These results indicate that dipole-dipole ($\theta = 6$) and dipole-quadrupole ($\theta = 8$) interactions are involved in the quenching. For the $^5D_3$ Tb^{+3} emission from $(Y_{1-x}Tb_x)_2O_2S$ under 290 nm excitation, it is found that the dipole-quadrupole interaction is responsible for the quenching, which agrees with other Tb^{+3}-activated phosphors (7).

Indirect excitation.—With indirect excitation, the incident energy is absorbed by a sensitizer or donor, for example the host lattice, and transferred to the activator or acceptor. This excitation process is more complicated than the direct case since it involves additional energy transfer steps. Perhaps it is for this reason that there is such a sparsity of theories and data for indirect excitations of so-called oxygen-dominated phosphors, such as oxides and oxysulfides. Even though our knowledge is too limited to describe indirect excitation by an analytical expression, it is possible to present a qualitative picture for the dependence of the emission intensity on activator concentration.

For host photoexcitation, a constant fraction of the incident radiation is absorbed which is independent of the activator concentration. This is unlike the direct excitation case where the absorption increased with activator concentration. Since host absorptions are very intense ($\sim 10^5$ cm^{-1}), the penetration depth is less than the dimensions of a single particle.

In the absence of an activator, the absorbed energy will be degraded by various mechanism (radiative and nonradiative) which can collectively be referred to as the "sink." As the activator concentration increases, the activator competes with the "sink" for the excitation until all of the absorbed energy is ultimately transferred to the activator at some "critical" concentration. Beyond this concentration the activator emission will no longer increase but will remain constant until concentration quenching begins. Therefore, the dependence of the emission intensity on activator concentration for host photoexcitation can be expected to show an initial rise, a flat region, and finally a decrease due to concentration quenching. The concentration dependence curves for host photoexcitation reported in this paper (see Fig. 1-4 and 6) show some similarities to this qualitative description. For the $^5D_3$ and $^5D_4$ Tb^{+3} emissions (Fig. 4) and the Pr^{+3} emission (Fig. 6) in Y_2O_2S, the host-to-activator energy transfer is apparently very efficient since the "critical" concentration is less than 10^{-5} mole fraction.

Under cathode-ray excitation, all of the excitations are involved; however, the dominant one is most likely

host excitation. Then, the concentration dependence curves for cathode-ray excitation and host photoexcitation should be similar. In $(Y_{1-x}Eu_x)_2O_3$ and in $(Y_{1-x}Pr_x)_2O_2S$ phosphors, the concentration dependence curves obtained by cathode-ray excitation (CR) are almost identical to the concentration dependence curves obtained for the host photoexcitation as shown in Fig. 1 and 6. However, the concentration dependence curves for the other Eu^{+3}-activated phosphors under cathode-ray excitation deviate from the host photoexcitation curve at high europium concentrations. This deviation may be due to the direct excitation of Eu^{+3} under cathode-ray excitation, which can occur at high europium concentrations.

Conclusion

Under direct excitation, an expression for the emission intensity as a function of activator concentration can be derived for the case where the exciting radiation is weakly absorbed. For this type of excitation, the optimum activator concentration of a phosphor, in which the quenching is due to an exchange interaction, exactly coincided with the value calculated from the isolated single activator ion concentration. Where the absorption coefficient is not negligible the number of excited activator ions saturates, causing the optimum activator concentration to shift to lower concentrations.

Under cathode-ray excitation and host photoexcitation the concentration dependence curves are similar, indicating common excitation mechanisms.

Acknowledgments

The authors wish to thank Mrs. H. Stanczyk for her assistance in preparation of samples and Mr. L. Flemming for cathodoluminescent data.

Manuscript submitted May 27, 1970; revised manuscript received Oct. 23, 1970. This was Paper 45 presented at the Los Angeles Meeting of the Society, May 10-15, 1970.

Any discussion of this paper will appear in a Discussion Section to be published in the December 1971 JOURNAL.

REFERENCES

1. D. L. Dexter and J. H. Schulman, *J. Chem. Phys.*, **22**, 1063 (1954).
2. L. G. Van Uitert and L. F. Johnson, *ibid.*, **44**, 3514 (1966).
3. P. D. Johnson and F. E. Williams, *ibid.*, **18**, 1477 (1950).
4. L. G. Van Uitert in "Luminescence of Inorganic Solids," P. Goldberg, Editor, p. 489, Academic Press, New York (1966).
5. L. G. Van Uitert, *This Journal*, **114**, 1048 (1967).
6. P. M. Jaffe and J. D. Konitzer, *ibid.*, **116**, 633 (1969).
7. T. Hoshina, *Japan. J. Appl. Phys.*, **6**, 1203 (1967).

Concentration of Zinc in Gallium Arsenide Crystals Grown by Slowly Cooling Gallium-Rich Solutions[1]

S. F. Guo,[2] C. D. Thurmond,[3,*] and G. L. Pearson

Stanford Electronics Laboratories, Stanford University, Stanford, California 94305

ABSTRACT

Gallium arsenide crystals were grown from Ga-rich solutions having initial compositions near the 900°C isotherm of the Ga-As-Zn ternary phase diagram. They were grown over the temperature range from 900° to 700°C. The concentration of Zn in GaAs appears to vary linearly with the Zn atomic fraction in the liquid at lower doping levels and with the square root of the atomic fraction of Zn in the liquid at higher doping levels. In fitting the experimental data to the theoretical expression for the solid solubility, the intrinsic carrier concentration of GaAs was found to be about 8×10^{17} cm^{-3}. The corresponding temperature has been estimated to be 825°-850°C.

The solid solubilities of Zn in GaAs crystals grown from solutions along the 1000°C isotherm of the Ga-As-Zn ternary phase diagram have been obtained by Panish and Casey (1). Chang and Pearson (2) have made several solid solubility measurements at 900°C from diffusion curve extrapolations.

The objective of the experiments reported here is to obtain the dependence of the Zn concentration in GaAs on the liquid phase concentration. Ideally, such experiments should be done at a particular temperature. However, the expected temperature dependence of solubility (1, 2) is small. A crystal grown over a temperature range from 900° to 700°C should have about a factor of 3 variation. This should be true for most of the extrinsic range. The variation in concentration for intrinsic crystals should be smaller. Since the solid concentration will be varied by 4 orders of magnitude in the experiments represented here, the small variation with temperature will not obscure the concentration dependence.

Self-nucleated crystals were grown in sealed and evacuated ampoules by cooling slowly from solutions (3) containing Ga, GaAs, and Zn. The Zn concentration in the GaAs crystals was determined from Hall measurements. In addition, radioactive tracer measurements, electron beam measurements, Schottky barrier, and p-n junction diode capacitance measurements were made on certain samples.

Experiments

The materials used in these experiments were Asarco undoped polycrystalline GaAs containing a donor impurity of 3.5×10^{16} cm^3, Eagle Picher seven 9's Ga, and Cominco five 9's Zn. Radioactive ^{65}Zn was used in one experiment.

The starting composition of solutions was chosen to be near the 900° isotherm of the liquidus surface of the Ga-As-Zn ternary phase diagram presented by Panish (4). The atomic fractions of Ga, As, and Zn used in each run are given in Table I.

[1] This work was supported by USAECOM Night Vision Laboratory, Fort Belvoir, Virginia, through Contract No. DAAK 02-68-C-0355.
[2] Present address: National Chiao Tung University, Hsinchu, Taiwan, China.
[3] Permanent address: Bell Telephone Laboratories, Murray Hill, New Jersey.
* Electrochemical Society Active Member.
Key words: GaAs, Zn, solubility, slow-cooling, intrinsic carriers, Ge-rich proteins.

Table I. Composition of solutions

Run No.	Atomic fraction Ga	As	Zn
1	0.919	0.081	1.2×10^{-4}
2	0.94	0.06	8.7×10^{-4}
3	0.935	0.065	8×10^{-7}
4	0.83	0.07	0.1
5	0.93	0.06	0.01
6	0.94	0.06	9.2×10^{-7}
7	0.94	0.06	2.5×10^{-5}
8	0.50	0.13	0.37
9	0.24	0.24	0.52
10	0.96	0.04	9.3×10^{-6}

The materials were loaded in a clean quartz tube. The tube was evacuated to about 10^{-5} Torr and sealed. The volume of the ampoule was about 3 ml. The ampoule was put into a vertical furnace and heated to a temperature above the liquidus curve of the phase diagram for a few hours. The solution was then cooled slowly at a rate of 27°C/day. Single platelets were recovered.

The hole concentration obtained from Hall measurements at room temperature can be used to determine the Zn concentration in GaAs. The van der Pauw method was used for crystal plates of arbitrary shape (5). From the data of Ermanis and Wolfstirn (6) and this work, a relation between Zn and hole concentrations is established up to 5×10^{18} cm^{-3} as shown in Fig. 1. The zinc concentration is larger than the hole concentration by the factor 1.3. Electron beam microprobe analysis shows that the correction factor is unity at a concentration of 10^{20} cm^{-3}. We have chosen to make the small 1.3 correction to the Hall measurement below 5×10^{18} cm^{-3} and no correction at higher concentrations.

The junction capacitance method was used to measure the hole concentration in lightly doped GaAs; n^+-p junction diodes were formed either by alloying Sn dots directly on the p-type GaAs wafer in a forming gas atmosphere or by evaporating and alloying procedures in a vacuum system. Ohmic contacts to the p-type bulk were made by alloying Au-Zn alloy to the sample.

The resistivity ρ (ohm-cm), mobility μ_p (cm^2/V-sec), and hole concentration p (cm^{-3}) obtained from Hall measurements are given in Table II. The Zn concentrations obtained from the Hall measurements and from measurements used are also included in Table II.

Results and Discussion

The measured concentration of Zn in GaAs, grown from solutions with initial compositions near the 900°C isotherm of the Ga-As-Zn ternary phase diagram, is shown in Fig. 2. The results of Chang and Pearson (2) for 900°C are also shown in the figure. The concentration of Zn in GaAs appears to vary linearly with the atomic fraction of Zn in the liquid at the lower doping levels and with the square root of the atomic fraction of Zn in the liquid at the higher doping levels. This result is in good agreement with the theoretical expression discussed below.

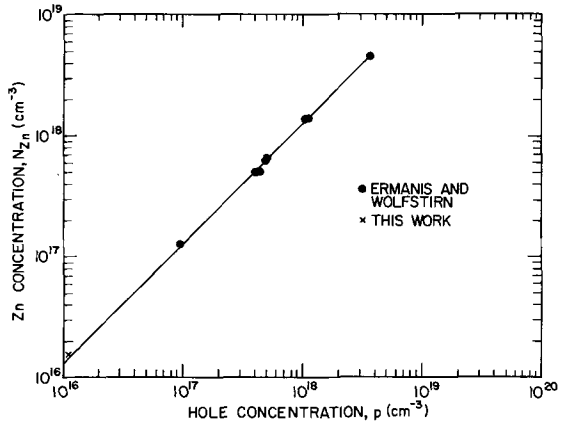

Fig. 1. Zinc concentration vs. hole concentration in Zn-doped GaAs.

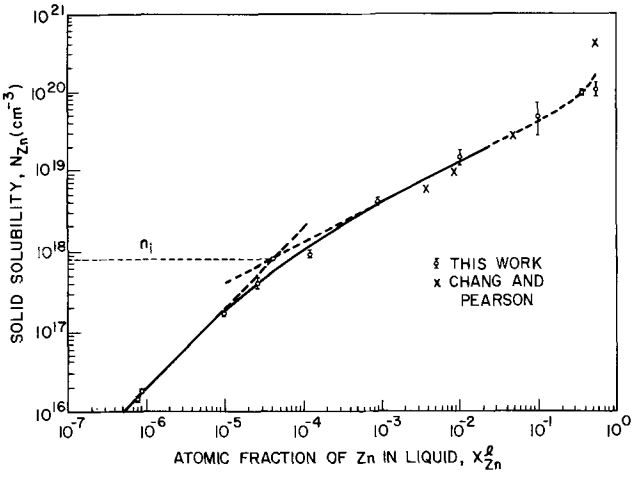

Fig. 2. Zinc concentration in GaAs as a function of the zinc concentration in the liquid at 825°-850°C. Chang and Pearson, 900°C.

Table II. Hall data and zinc concentrations

Sample No.	Hall measurement ρ(ohm-cm)	μ_p (cm^2/V-sec)	p(cm^{-3})	Zn concentration N_{Zn} (cm^{-3}) From Hall data	From other methods
1-1	0.059	155	6.8×10^{17}	8.8×10^{17}	
1-2	0.056	166	6.5×10^{17}	8.5×10^{17}	
1-3	0.054	150	7.8×10^{17}	10.5×10^{17}	
2-1	0.017	110	3.3×10^{18}	4.3×10^{18}	
2-2	0.019	114	2.9×10^{18}	3.8×10^{18}	
2-3	0.018	102	3.4×10^{18}	4.4×10^{18}	
3-1	1.61	347	1.12×10^{16}		1.55×10^{16}[a]
4-1	0.0028	54.5	4.1×10^{19}		7.5×10^{19}[b]
4-2	0.0035	63	2.8×10^{19}	2.8×10^{19}	
5-1	0.0049	66	1.9×10^{19}	1.9×10^{19}	
5-2	0.0052	69	1.7×10^{19}	1.7×10^{19}	
5-3	0.0067	77	1.22×10^{19}	1.22×10^{19}	
6-1	1.37	270	1.7×10^{16}		2×10^{16}[c]
7-1	0.097	231	2.8×10^{17}	3.6×10^{17}	
7-2	0.083	207	3.6×10^{17}		4×10^{17}[c]
8-1	0.0016	38.5	1.01×10^{20}		0.97×10^{20}[b]
9-1	0.0014	41	1.1×10^{20}		1.3×10^{20}[b]
9-2	0.0015	47	0.87×10^{20}	0.87×10^{20}	
10-1	0.168	260	1.4×10^{17}	1.8×10^{17}	

[a] Radioactive tracer data.
[b] Microprobe data.
[c] n^+-p junction data.

From the thermodynamic equilibrium relation for the incorporation reaction of Zn atoms in the liquid with Ga vacancies in the solid to form singly ionized Zn acceptors and free holes in the solid and from the charge neutrality condition and the electron-hole mass action relation, the Zn concentration in GaAs can be expressed as

$$N_{Zn} = KX^{l}_{Zn}/(KX^{l}_{Zn} + n_i^2)^{1/2} \quad [1]$$

Here n_i is the intrinsic carrier concentration, K is proportional to the thermodynamic equilibrium constant for the incorporation reaction, and X^{l}_{Zn} is the atomic fraction of Zn in the liquid. Equation [1] applies to solutions sufficiently dilute to assure that the activity coefficients of Zn in the liquid and solid, the activity of arsenic in the liquid, and the activity coefficient γ holes in the solid are not functions of composition. The proportionality constant is $\gamma^{l}_{Zn}\gamma^{l}_{As}/\gamma_p\gamma^{s}_{Zn}$.

At low doping levels, $X^{l}_{Zn}K << n_i^2$, the Zn concentration is proportional to the atomic fraction of Zn in the liquid

$$N_{Zn} = (K/n_i)X^{l}_{Zn} \quad [2]$$

At high doping levels, $X^{l}_{Zn}K >> n_i^2$, the Zn concentration is proportional to the square root of the Zn fraction in the liquid

$$N_{Zn} = (KX^{l}_{Zn})^{1/2} \quad [3]$$

The experimental results, plotted in Fig. 2, appear to follow these relations quite well. It can readily be shown from Eq. [2] and [3] that the value of N_{Zn} at the point of intersection of the linear and square root lines is n_i and, to fit the data shown, has a value of 8 x 10^{17} cm^{-3}. The theoretical curve shown in Fig. 2 was obtained by plotting Eq. [1] in terms of reduced variables on a log-log scale and finding the best fitting position over the experimental points plotted on the same scale. Only points below 5 x 10^{19} cm^{-3} were used. The uncertainty in n_i from data scatter is about 30%. At concentrations higher than 5 x 10^{19} [4] it is expected that the experimental curve will depart from the square root line in the direction shown in the figure (1).

The above analysis assumes a constant temperature. In fact, the experimental results have been obtained from crystals grown over a 200°C temperature range. However, the variation in concentration of Zn in a grown crystal is expected to be about a factor of 3, as obtained from the temperature dependence of the Zn distribution coefficient (1, 2), about 12 kcal. Since the variation due to concentration dependence is much larger, the concentration dependence of Fig. 1 should be a good approximation to a single isotherm.

A temperature corresponding to the average measured composition can be estimated. At a particular starting composition at 900°C, the Zn concentration in GaAs can be calculated as a function of the fraction of GaAs crystallized between 900° and 700°C. The fraction crystallized is a known function of temperature. The curves obtained for various assumed values of the distribution coefficient, its temperature dependence, and the initial composition of the liquid were found to give an average concentration for the 900°-700°C temperature interval that fell in the range of 825°-850°C.[5] These estimates apply to extrinsic solid solutions. Intrinsic solid solutions are expected to have a temperature coefficient of solubility appreciably smaller than the temperature coefficient for extrinsic solutions. The temperature coefficient of n_i subtracts from that of the extrinsic solutions as can be shown to follow from Eq. [1]. Near cancellation occurs.

The value of n_i obtained from Fig. 2 can be compared to an estimate of n_i from band structure information.

[4] Early work (1) suggested that the hole activity coefficient began to change in the 5 x 10^{18} cm^{-3} range, but more recent work (7) indicates 5 x 10^{19} cm^{-3} or higher is required.

[5] A. S. Jordan (14) has recently evaluated the available solid solubility information for Zn in GaAs and has constructed a thermodynamically concise set of solubility isotherms. His 800° and 900°C isotherms, in the square root region, bracket the isotherm we have found to fit our measurements, shown in Fig. 2.

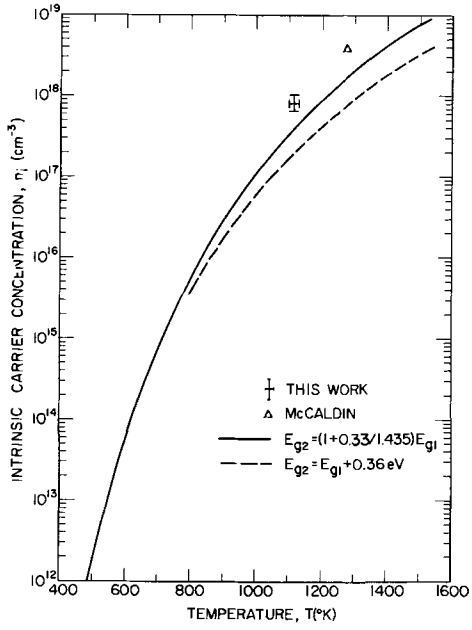

Fig. 3. Intrinsic carrier concentration of GaAs vs. temperature

For a multivalley semiconductor it can be written as

$$n_i = 4.9 \times 10^{15}T^{3/2} \sum_j (m_p m_{nj}/m_o^2)^{3/4} \exp(-E_{gj}/2kT) \quad [4]$$

The density-of-state effective mass of holes in GaAs is

$$m_p = (m_{p1}^{3/2} + m_{p2}^{3/2})^{2/3} = 1.03\, m_o \quad [5]$$

where the theoretical values (8) $m_{p1} = m_o$ and $m_{p2} = 0.1\, m_o$ have been used for the heavy and light hole masses, respectively. The <000> conduction band minimum has an effective electron mass (8) $m_{n1} = 0.084\, m_o$. The energy gap as a function of temperature is (9)

$$E_{g1} = 1.522 - 5.8 \times 10^{-4}T^2/(T + 300) \quad [6]$$

The second lowest minimum <100> has a density-of-state effective electron mass (10) $m_{n2} = 1.2\, m_o$. Hall and Racette (11) have calculated n_i by taking $E_{g2} = E_{g1} + 0.36$ eV. Recently, James and Moll (12) have found that the energy difference between the two minima is 0.33 eV at 300°K and 0.35 eV at 80°K. These data show that the energy difference is a function of temperature in the same manner as Eq. [6]. Thus the second energy gap can be written as

$$E_{g2} = E_{g1}(T)\,[1 + 0.33/E_{g1}(300°K)] \quad [7]$$

The results obtained from the calculation of the two-band model are given in Fig. 3. The experimental value of n_i falls a factor of 2 higher than that given by the theoretical curve. The result of McCaldin (13) at 1000°C is also shown in the figure and it is a factor of 2 above the theoretical curve.

Conclusions

The solid solubility data obtained in this work fit the theoretical expression given in Eq. [1]. The singly ionized substitutional acceptor model of the incorporation reaction seems to be correct. A value of n_i of 8 x 10^{17} cm^{-3} at a temperature in the range of 825°-850°C has been obtained.

Acknowledgments

The authors are indebted to J. L. Moll for helpful discussions. The technical assistance of U. Sorenson for quartz assembly and H. Gabe for electron microprobe measurements is greatly appreciated.

Manuscript submitted June 1, 1970; revised manuscript received Sept. 20, 1970.

Any discussion of this paper will appear in a Discussion Section to be published in the December 1971 JOURNAL.

REFERENCES
1. M. B. Panish and H. C. Casey, *J. Phys. Chem. Solids*, **28**, 1673 (1967).
2. L. L. Chang and G. L. Pearson, *ibid.*, **25**, 23 (1964).
3. G. Wolff, P. H. Keck, and J. D. Broder, *Phys. Rev.*, **94**, 753 (1954).
4. M. B. Panish, *J. Phys. Chem. Solids*, **27**, 291 (1966).
5. L. J. van der Pauw, *Philips Tech. Rev.*, **20**, 220 (1959).
6. F. Ermanis and K. Wolfstirn, *J. Appl. Phys.*, **37**, 1963 (1966).
7. H. C. Casey, M. B. Panish, and L. L. Chang, *Phys. Rev.*, **162**, 660 (1967).
8. M. Cardona, *J. Phys. Chem. Solids*, **24**, 1543 (1963).
9. M. B. Panish and H. C. Casey, *J. Appl. Phys.*, **40**, 163 (1969).
10. H. Ehrenreich, *Phys. Rev.*, **120**, 1951 (1960).
11. R. N. Hall and J. H. Racette, *J. Appl. Phys.*, **25**, 379 (1964).
12. L. W. James and J. L. Moll, *Phys. Rev.*, **183**, 740 (1969).
13. J. O. McCaldin, *J. Appl. Phys.*, **34**, 1748 (1963).
14. A. S. Jordan, Paper submitted to *This Journal*.

New Optical Quenching Bands in CdS Crystals

Mamoru Oshima and Ryoji Takahashi

Engineering Research Institute, Faculty of Engineering, University of Tokyo, Tokyo, Japan

ABSTRACT

The effects of bombardments with pentavalent ions on the photoconductivity and optical quenching of photoconductivity in CdS single crystals have been investigated. A striking effect of bombardment with P, As, Sb, and Bi ion, each with an energy of 5 keV, is a considerable reduction in long wavelength, extrinsic response. As a result, optical quenching starts at very short wavelengths. At the high-energy side of the optical quenching band, in addition to two well-known bands situated at 0.9 and 1.4μ, respectively, we observed a new band with long wavelength cutoff at about 0.8μ (1.55 eV). This band has its maximum at about 0.63μ (1.97 eV), 0.64μ (1.94 eV), 0.66μ (1.88 eV), and 0.68μ (1.82 eV) for P, As, Sb, and Bi, respectively. These bands, as well as the 0.9μ band, are observable at temperatures as low as 77°K. Measurements of the thermally stimulated current show that relatively large numbers of vacancies of both sulfur and cadmium are produced in the bombarded region. It is believed that pentavalent ions in CdS crystals are substituted for sulfur ions forming the new acceptor levels related to the third band phenomena. The third band probably corresponds to excitation of trapped holes from these levels directly to the valence band.

It is well known that the spectral distribution of infrared quenching of photoconductivity in CdS shows two bands with maxima at 0.9μ and 1.5μ, respectively (1-5). A number of investigators have discussed the origin of these two bands, and by many reporters it was regarded as excitation of holes from two different types of hole traps, *i.e.*, "sensitizing centers," and successive recombination of the released holes with free electrons at certain recombination centers (1, 6, 7). The fact that optical quenching is observable in any kind of crystal, except for very insensitive ones, whether crystals were doped or undoped and, moreover, independently of impurity elements, naturally leads to the suggestion that some intrinsic imperfections of the crystals should be connected with the sensitizing centers, for instance Cd vacancies, which can act as acceptors in CdS crystals. Bube and Barton (8) suggested the formation of Cd vacancies for charge compensation in their report on highly photosensitive CdS crystals in which iodine was incorporated. Excitation in those crystals did not extend far beyond the absorption edge, and strong quenching was observed at higher energies than for the common ones with long wavelength response. Thomas and Hopfield (9) proved the presence of a single characteristic acceptor imperfection in CdS crystals by investigating recombination radiation from bound excitations. The presence of intrinsic acceptor-like defects in CdS crystals is also supported by other evidence (10-12). On the other hand, for the last ten years, various particle bombardments on semiconductors have been employed by several workers to investigate the effects of crystal defects on the electrical and photoelectric properties of the materials. Kulp and Kelley (13) showed that the threshold for the production of vacancy-interstitial pairs of sulfur atoms in CdS by electron bombardment is 115 ± 5 keV and that the center for the green edge emission in CdS is the interstitial sulfur atom. They also observed (14) the photoconductive peaks at 0.67, 0.9, and 1.4μ in 150 keV electron bombarded CdS crystals; the first one gave electronic conduction and the latter two gave hole conductivity. Bombardment by 100 keV electrons partially removed the 1.4μ quenching band and also removed the edge emission. Therefore, they concluded that the center for the 1.4μ quenching band is the interstitial sulfur. Im and Bube (15) reported that the ratio of quenching in the 1.4μ band to that in the 0.9μ region decreased continuously with increasing energy of irradiating electrons from 75 to 400 keV.

Various impurities, particularly the pentavalent ones, which are to be treated here, have been studied as dopants in the II-VI compounds by a number of workers (16-24). However, their effect on the electrical or optical properties were often not very pronounced. Originally most of the experiments dealt with thermal equilibrium situations. More recently, however, Anderson and Mitchell (25) and Chernow and co-workers (26), succeeded in forming highly conductive p-type CdS by P and Bi ion bombardment, respectively, and ion implantation, essentially a nonequilibrium process, was established as a new doping technique.

We bombarded CdS single crystals by various kinds of ions to investigate the effects of defects and, at the same time, we studied the effects of those impurity ions on optical quenching. Bombardment by almost all other kinds of ions with an energy of 5 keV had no influence on the optical quenching bands.

Key words: photoconductivity, CdS crystals, ion bombardment (P, As, Sb, Bi), thermally stimulated currents, optical quenching.

Pentavalent ions with this same energy, however, drastically changed the properties of the surfaces of the crystals (about 1μ in depth); namely, it (*a*) made the surface region highly resistive, *i.e.*, almost intrinsic, and (*b*) diminished extensively the long wavelength response, almost exactly the effects reported for CdS:I by Bube and co-workers (8). The cut off of photoconduction occurred at about 0.7μ, and quenching started at about 0.57μ. Especially in Sb ion-bombarded CdS crystals, the optical quenching band clearly showed three peaks with maxima at 0.65, 0.9, and 1.45μ, respectively; in crystals bombarded with other pentavalent ions, the third band at 0.65μ was more or less obscured under the foot of the broad band at 0.9μ. In this paper we deal mostly with the third band through measurements of spectral photoresponse, optical quenching of photoconductivity, temperature dependence of optical quenching, etc., and we come to a significant conclusion with regard to the center related to the third band.

Experimental

The CdS crystals used in this experiment were single crystals which were grown by the vapor phase technique at our laboratory. These crystals showed a bright red emission under uv stimulation at liquid nitrogen temperature, with the center of the band at 6200Å. This band has previously been associated with a silver center (27). Actually, spectrographic analysis showed the presence of 0.1 ppm Ag as an impurity besides Si, Mg, and Ca of the order of 1 ppm. The crystal rod (15 mm in diameter) was cut at right angles to the c-axis into 1 mm thick slices, which were then polished to an optical finish. Etching by dilute hydrochloric acid removed the very thin ($\sim$ 100Å) amorphous layer at the surface of the crystal which was caused by polishing. After preheating at 350°C for 20 min in argon gas of 1/2 atm pressure, the crystals were bombarded by ions at room temperature in a vacuum of 3 x 10^{-5} mm Hg. Various ions were produced and accelerated in an ion bombardment chamber by applying the "exploding wire" technique[1] which has been developed at our laboratory (28). Carbon, Al, P, Cl, Mn, Fe, Ni, Cu, Zn, As, Ag, In, Sb, Au, and Bi ion bombardments, each with an energy of 5 keV, were performed. The cross section of the ion beam incident on the target was limited to 0.03 cm^2 by a baffle with a circular window. The bombardment density was measured (29) at least 10^{12} ions/cm^2 for Cu. Estimated bombardment densities for the various ions are summarized in Table I. The bombarded crystals were heated at 400°C for 1 hr under 200 kg/cm^2 argon gas pressure in an autoclave, thus preventing the vaporization of the implanted ions from the surfaces. Both directly after the bombardment and after heating, the red emission became weaker for the 3.5 keV bombardment and entirely vanished for the 5 keV bombardment, no matter what kind of ions were used.

[1] "Exploding wire" phenomenon is an explosive evaporation of a metallic wire in the air resulting from a big electric current through the wire. We utilized the ionization of the metallic wire and the applied high voltage realized in the phenomenon for the ion bombardment performances.

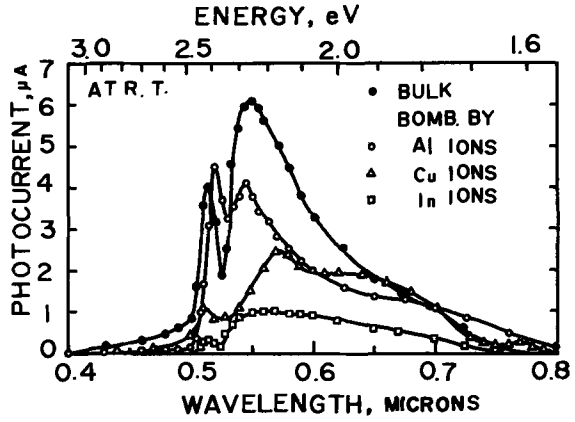

Fig. 1. Spectral response curves for CdS crystals bombarded by various kinds of ions, with an energy of 5 keV, compared with that for the nonbombarded crystal. The dark resistivity of the original crystal is 1 x 10^4 ohm·cm; those of the crystals bombarded by Al, Cu, and In ions are 3 x 10^3, 1.5 x 10^5, and 7 x 10^3 ohm·cm, respectively. (Curves marked "bulk" refer to nonbombarded crystals.)

Photoelectric measurements were carried out in a cryostat, which was kept evacuated at a pressure of 10^{-3} mm Hg during the experiments. The primary excitation was effected by an incandescent lamp with a 5200Å interference filter. The second beam of infrared light used for the measurement of optical quenching was obtained from a Hitachi EPU-2 type monochromator. Measurements were made with indium amalgam surface contacts, which showed ohmic characteristics for both nonbombarded and bombarded surfaces of the crystals through the whole range of voltage used. The dark resistivity of the crystal before bombardment was about 1 x 10^4 ohm·cm. A small change was detected in the resistivities of the specimens bombarded with C, Al, Cl, In, Zn, Cu, Ag, Mn, Fe, and Ni ions; for example for Al the resistivity was reduced to one-third of that before bombardment; for Cu the resistivity increased ten times. Also no marked change was observed in the spectral photoresponse curves, except for a somewhat impurity-dependent unevenness between 0.55μ and 0.80μ. Figure 1 shows this for crystals bombarded with various ions as well as for the nonbombarded crystal. Figure 2 shows the corresponding optical quenching spectra at room temperature. Each quenching band starts at about 0.75μ showing the usual two bands with maxima between 0.9 and 0.95μ, and between 1.35 and 1.50μ, respectively.

The effects of P, As, Sb, and Bi ion bombardments on the photoresponse and optical quenching are given in Fig. 3 and Fig. 4, respectively. There is a relatively larger decrease in response for extrinsic excitation at longer wavelengths than near the absorption edge. For crystals bombarded with Sb and Bi, the dark resistivity increased to 10^7 and 10^5 ohm·cm., respectively. The depth of the high resistivity layer, measured by direct microscopic observation of sections of the specimens, was found to be about 1μ. In Fig. 4 it may be noted that

Table I. Summary of densities of the various ions implanted into CdS crystals

Elements to be implanted	C	Al	Fe	Ni	Cu	Ag
Densities of ions implanted, ions/cm^2	$\sim 10^{13}$	2 x 10^{15}	3 x 10^{15}	2 x 10^{15}	1 x 10^{15}	2 x 10^{15}

Au	P, Cl, Mn, As, In, Sb, or Bi	Sb,Al or Sb,In
5 x 10^{14}	$\sim 10^{14}$	each of $\sim 10^{14}$

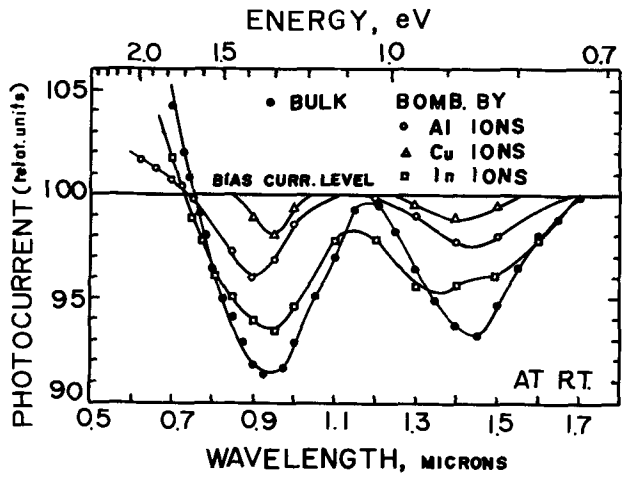

Fig. 2. Optical quenching spectra for the photoconductivity for CdS bulk and the surfaces bombarded by Al, Cu, and In ions, each corresponding to Fig. 1.

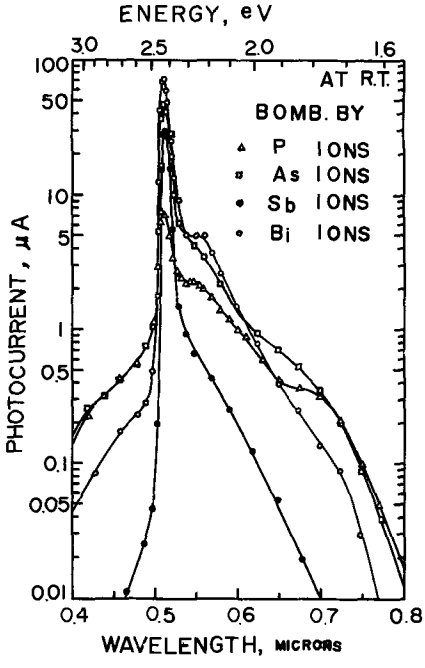

Fig. 3. Spectral response curves for CdS crystals bombarded by various pentavalent ions. An ion energy of 5 keV was used in each case. The dark resistivities of the crystals bombarded with P, As, Sb, and Bi, are 5 x 10^4, 8 x 10^4, 3 x 10^7, and 1 x 10^5 ohm·cm, respectively. An extremely large reduction of response is seen in the extrinsic region at longer wavelengths (compare with Fig. 1).

in addition to the well-known two quenching peaks, a third band appears with maxima at about 0.66 and 0.68μ for Sb and Bi, respectively. In the case of P and As, the total current in the third band region is larger than the bias current because excitation overcomes quenching. To investigate the effects of two kinds of ions on quenching we carried out the bombardment of CdS crystals using a special wire, which was prepared by simultaneous evaporation of a pair of metals onto a quartz tube (1 mm in diameter). Thus, almost equivalent numbers of two sorts of ions. *e.g.*, Sb and Al, or Sb and In, (10^{14} ions/cm^2), were simultaneously implanted in CdS crystals. We use the notation "Sb,Al" or "Sb,In" to represent such an ion bombardment. The spectral response of photoconductivity and the optical quenching spectra at room temperature for samples resulting from those bombardments are shown in Fig. 5 and Fig. 6, respectively. As one notices, the longer wavelength response from 0.6 to 0.8μ is thoroughly removed. More striking, however, are the results of

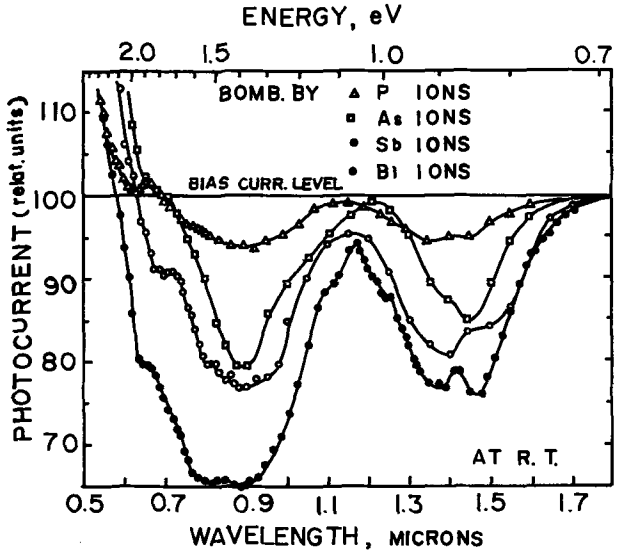

Fig. 4. Spectral distribution of quenching of photoconductivity in CdS crystals bombarded with various pentavalent ions for which Fig. 3 showed the spectral response curves. The third bands appear with maxima at 0.63μ (1.97 eV), 0.64μ (1.94 eV), 0.66μ (1.88 eV), and 0.68μ (1.82 eV) for P, As, Sb, and Bi, respectively. Subbands can be observed at about 0.75μ (1.65 eV) for P and at about 0.80μ (1.55 eV) for Sb and Bi.

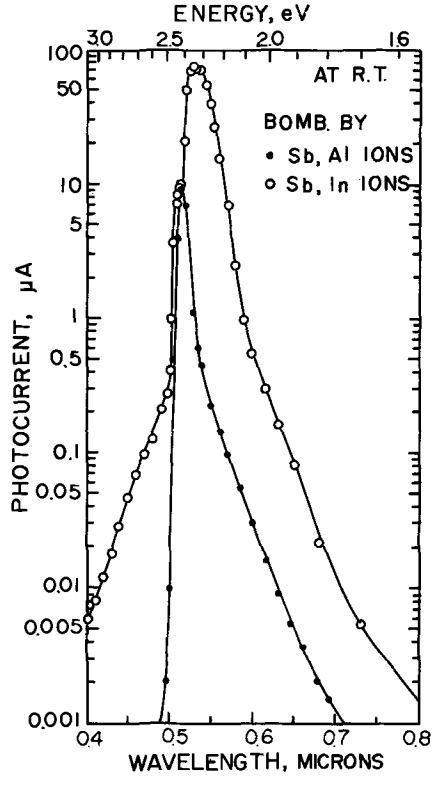

Fig. 5. Effect of simultaneous bombardments with two kinds of ions, Sb and Al, or Sb and In, on the spectral response curves. The dark resistivities of these crystals are $\gtrsim$ 10^8 and 1 x 10^7 ohm·cm for Sb,Al and Sb,In, respectively. A reduction of response similar to those shown in Fig. 3 is seen in the extrinsic region.

measurement of the quenching effects. Over the entire wavelength range from 0.58 to 1.60μ, at least 30% of the primary photocurrent is quenched. The third band asserts its existence showing a new clear peak in the samples bombarded with Sb and Al, with a maximum quenching percentage of 90%. For the nonbombarded crystal the quenching percentage is about 10%; in the crystals bombarded by ions of P, As, Sb, or Bi the quenching effect at the maximum of the 0.9μ band was

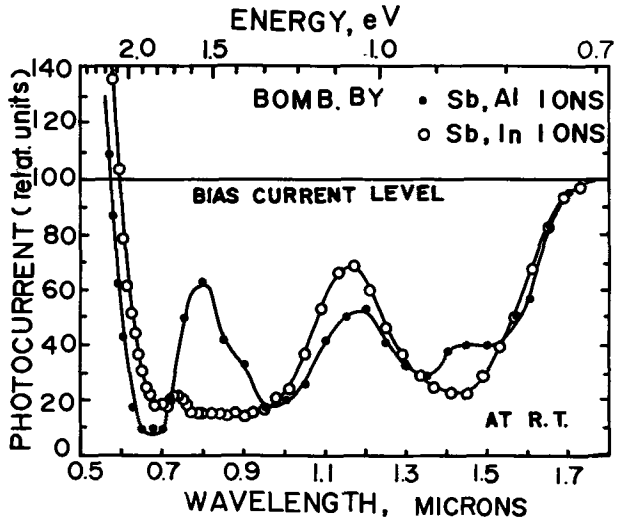

Fig. 6. Optical quenching spectra for CdS crystals bombarded by Sb,Al and Sb,In ions, correspondingly to Fig. 5. For Sb,Al, the third band forms a clear peak with maxima at 0.66μ (1.88 eV) and with longer wavelength cutoff at about 0.80μ (1.55 eV). At about 0.85μ (1.46 eV) for "Sb,Al' a subband can be seen.

a little higher. It may be pointed out that besides the third bands with the maxima at 0.63μ (1.97 eV), 0.64μ (1.94 eV), 0.66μ (1.88 eV), and 0.68μ (1.82 eV) for P, As, Sb, and Bi, respectively, several subbands are observed, *e.g.*, a group of bands at 0.75μ (1.65 eV) for P, 0.80μ (1.55 eV) for Sb and Bi, and 0.85μ (1.46 eV) for Sb,Al and another group of bands at 1.1μ (1.12 eV) and 1.2μ (1.03 eV) for Sb. Generally, in contrast with electron bombardment (14-15), no decrease of the ratio of quenching in the 1.4μ band to that in the 0.9μ one by ion bombardment was observed.

At low temperature, quenching effects in the region of the third band can still be detected, though the effects become considerably weaker. Figure 7 shows the results of experiments at 77°K. Because of the similarity in behavior of this band and the 0.9μ band, we believe that in accordance with the model (4) for the latter, 0.65μ radiation excites trapped holes from the new centers, the third hole traps, directly to the valence band. We notice that not only the 1.4μ band but also the 0.75-0.80μ subbands have vanished at low temperature.

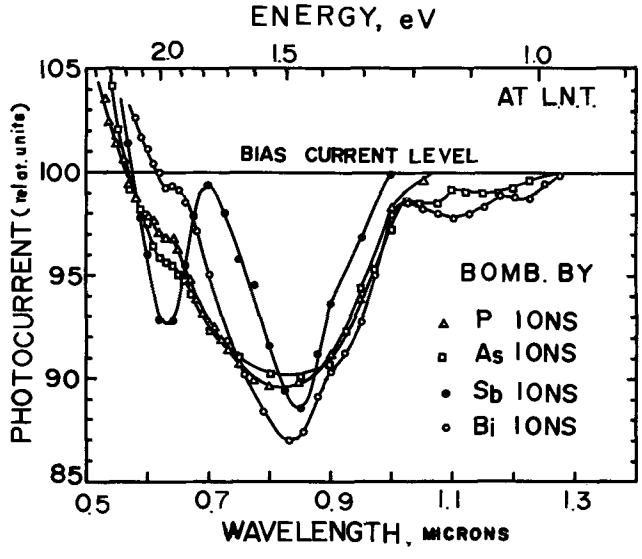

Fig. 7. Optical quenching spectra at liquid nitrogen temperature for CdS crystals bombarded by various kinds of pentavalent ions. In each case the third bands do exist in addition to the 0.9μ one. Subbands at 0.75-0.80μ on the other hand have disappeared together with the 1.4μ band.

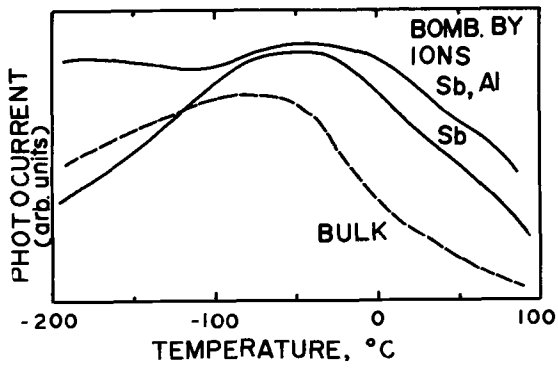

Fig. 8. Temperature dependence of photocurrent, excited by band gap light excitation, for CdS crystals bombarded by Sb and Sb,Al ions, as well as for the nonbombarded crystal. Thermal quenching sets in at higher temperature for the Sb-ion bombarded crystals than for the nonbombarded crystal.

In Fig. 8 we show the temperature dependence of the photocurrent, under band gap light excitation, for Sb and Sb,Al in contrast to that for the nonbombarded crystal. In the surfaces of the ion-bombarded crystals, thermal quenching of photoconductivity sets in at a higher temperature than in the nonbombarded inside. This means that the distribution of hole traps has moved to higher energies, *i.e.*, nearer to the conduction band.

Figure 9 shows the observed thermally stimulated current curves. It may be noted that the shallow traps, the depth of which ranged from 0.18 to 0.30 eV, are enhanced relative to the deeper ones near room temperature. Woods and Nicholas (30-31) have assigned traps at 0.25 and 0.30 eV to sulfur and cadmium vacancies, respectively. The results shown in Fig. 6 therefore suggest that a considerable number of defects are produced near the surface by bombardment and remain after heating.

Discussion

The existence of a third band of optical quenching in CdS crystals was suggested for the first time by Taft and Hebb (1) in 1952; Yoshizawa (32) found this band in phosphorus doped CdS. However, this crystal did not show a well-defined peak, but only a shoulder with the edge at 2.15 eV (0.577μ). Our experimental results show that the new bands have their maxima at 1.97 eV (0.63μ), 1.94 eV (0.64μ), 1.88 eV (0.66μ), and 1.82 eV (0.68μ) for P, As, Sb, and Bi, respectively; perhaps these energies give the position of new levels in the forbidden gap relative to the top of the valence band. More important than the peak is the wavelength cutoff of the band. For Sb,Al, the new band shows a cutoff at about 1.55 eV (0.80μ). These level positions are illustrated in Fig. 10. The greater part of the dif-

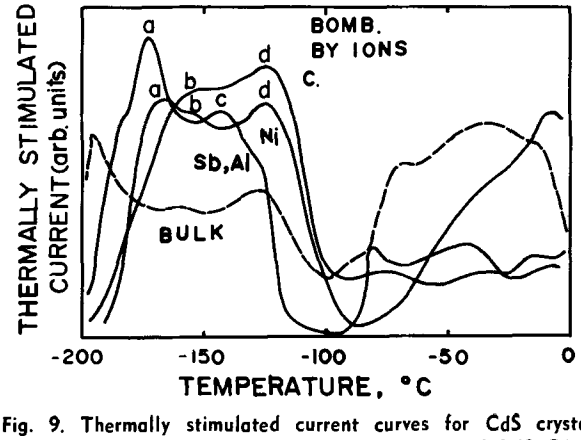

Fig. 9. Thermally stimulated current curves for CdS crystals bombarded by various kinds of ions. Heating rate of 0.43°C/sec. Peaks a, b, c, and d correspond to the depths of traps 0.18, 0.22, 0.25, and 0.30 eV from the conduction band, respectively.

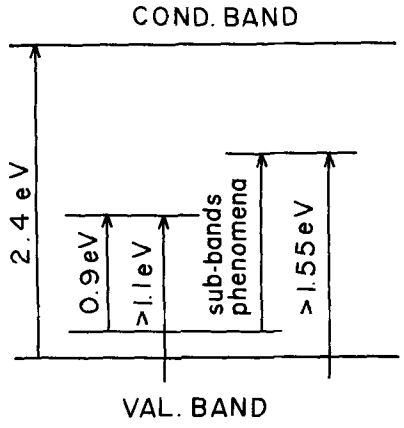

Fig. 10. A possible interpretation for the third band phenomenon in optical quenching. The levels for the two common centers are drawn as proposed by Hemila and Bube (35); for the higher energy center, the energy does not refer to the peak but to the long wavelength cut off of the 0.9μ band. In a similar way, the level of the third quenching band for Sb is based on the long wavelength cutoff of the third quenching band. For P, As, and Bi, the corresponding levels will be slightly different, the difference with the Sb level being perhaps in proportion to the differences of the energies of the third band peak from Sb. The figure shows the subbands as the excitation of trapped holes from the third center level to the lowest level of the common quenching centers.

ference in the maximum energies reported for phosphorus doped CdS by Yoshizawa and by us is thought to be attributable to the difference in quantity and/or properties of imperfections. In Yoshizawa's crystals the defects are essentially native ones; in our experiments we purposely set out to create an excess of defects within the surface layer of the crystal concurrently with the addition of impurities. According to a simple law of impulse and energy conservation (33), the thresholds (13) of 115 and 290 keV for the production of vacancy-interstitial pairs of sulfur and cadmium atoms, respectively, in CdS by electron bombardment, correspond to several tens of electron volts for almost all the ions with which we bombarded our crystals, from carbon to bismuth. The energy of 5 keV used by us will be more than enough to form both sulfur and cadmium vacancies, as is proved by the thermally stimulated current curves shown in Fig. 9. The disappearance of the red emission after 5 keV ion bombardment is probably more complex than a simple annihilation of silver centers.

If the third band phenomenon is caused only by the defects newly produced by the bombardment in the surface layer of the crystal, it ought to be independent of the nature of the bombarding ions. However, in the crystals bombarded by many kinds of ions, other than pentavalent ones, no quenching effect was detected before the wavelength of the second light exceeded 0.75μ. The third band, in consequence, must be due to pentavalent ions.

A possible interpretation of the doping mechanism in the processes of our ion bombardments and successive annealing is as follows: (*i*) a large number of vacancies is produced within the surface layers of the crystals in a depth of about 1μ, and (*ii*) implanted ions stop at interstices or lattice points which are vacant. (*iii*) After heat-treatment, pentavalent ions enter into the active sites, *i.e.*, sulfur vacancies, to form a new sensitizing center, while (*iv*) trivalent ions occupy cadmium vacancies. The last process, we believe, greatly promotes the third band by charge compensation, just as Apple (34) showed in his paper on P-, As-, and Sb-doped ZnS, that in addition to acting as activators, pentavalent atoms could also act as coactivators in the presence of Cu, presumably substituting for Zn as trivalent ions. The new sensitizing centers reported in this paper are possibly not identical with the ones introduced by Sb-doping in ZnS, the levels of which were investigated by Bube and Lind (21) who concluded that they are situated in the forbidden gap, 0.7 and 1.3 eV from the top of the valence band, respectively; levels which, as suggested by the contributors, could be related in part to vacancies rather than the Sb. The reason is that even if the new hole traps at 1.82-1.97 eV correspond to the 1.3 eV level, the subbands observed in the optical quenching at 1.65 eV for P, 1.55 eV for Sb and Bi, and 1.46 eV for Sb,Al are at too large an energy to correspond to the 0.7 eV level. It is more reasonable to interpret the subbands as the excitation of trapped holes from the level of the third center to the lower level of the usual two hole traps; the energies of the subbands region, for instance 1.46 eV for Sb,Al, fit fairly well with the energy difference between those two levels (see Fig. 10). This assignment finds further support in the fact that, as shown in Fig. 7, the quenching in the subbands vanishes at low temperature together with the disappearance of the 1.4μ one. Another group of subbands at 1.03-1.12 eV are at times also observed in undoped CdS; the origins of these are unknown. The slight differences, 0.15 eV at the most, between the energies of the peaks of the third bands from ion to ion are thought to be due to the differences between their ionic radii. The fine structure which can be seen in the 1.4μ band for Sb and Sb,Al, consisting of two peaks with maxima at about 1.35 and 1.45μ, respectively, has been interpreted by Hemila and Bube (35) as the effect of spin-orbit and crystal-field splitting of the levels concerned in the 1.4-μ quenching. perhaps the larger splitting of the level nearer to the valence band.

Acknowledgments

The authors are greatly indebted to Takao Tuno for completion of the ion bombarding system.

Manuscript submitted Sept. 16, 1970; revised manuscript received Nov. 14, 1970.

Any discussion of this paper will appear in a Discussion Section to be published in the December 1971 JOURNAL.

REFERENCES

1. E. H. Taft and M. H. Hebb, *J. Opt. Soc. Am.*, **42**, 249 (1952).
2. R. H. Bube, *Phys. Rev.*, **99**, 1105 (1955).
3. S. H. Liebson, *This Journal*, **102**, 529 (1955).
4. S. Tutihashi, *J. Opt. Am.*, **46**, 443 (1956).
5. J. Auth, E. H. Niekisch, and H. Puff, *Z. Physik Chem. (Leipzig)*, **212**, 175 (1959).
6. A. Rose, *RCA Rev.*, **12**, 362 (1951); *Phys. Rev.*, **97**, 322 (1955).
7. F. A. Kröger, H. Vink, and J. Volger, *Philips Res. Repts.*, **10**, 39 (1955).
8. R. H. Bube and L. A. Barton, *RCA Rev.*, **20**, 564 (1959).
9. D. G. Thomas and J. J. Hopfield, *Phys. Rev.*, **128**, 2135 (1962).
10. P. H. Kasai and Y. Otomo, *Phys. Rev. Letters*, **7**, 17 (1961); *J. Chem. Phys.*, **37**, 1263 (1962).
11. J. Schneider, W. C. Hoiten, T. L. Estle, and A. Rauber, *Phys. Letters*, **5**, 312 (1963).
12. R. S. Title, G. Mandel, and F. F. Morehead, *Phys. Rev.*, **136**, A300 (1964).
13. B. A. Kulp and R. H. Kelley, *J. Appl. Phys.*, **31**, 1057 (1960).
14. B. A. Kulp and R. H. Kelley, *ibid.*, **32**, 1290 (1961).
15. H. B. Im and R. H. Bube, *ibid.*, **39**, 2908 (1968).
16. A. H. McKeag and P. W. Ranby, *This Journal*, **96**, 85 (1949).
17. J. S. Prener, *ibid.*, **98**, 406 (1951).
18. D. A. Jenny and R. H. Bube, *Phys. Rev.*, **96**, 1190 (1954).
19. K. Hauffe and H. G. Flint, *Ann. Physik*, **15**, 141 (1955).
20. K. T. Wilke, *Z. Physik. Chem. (Leipzig)*, **205**, 73 (1955).
21. R. H. Bube and E. L. Lind, *Phys. Rev.*, **110**, 1040 (1958).
22. H. Gobrecht, H. Nelkowski, and P. Albrecht, *Z. Naturforsch.*, **16a**, 857 (1961).
23. H. Tubota, *Japan. J. Appl. Phys.*, **2**, 259 (1963).

24. N. Watanabe and S. Usui, *ibid.*, **4**, 467 (1965).
25. W. W. Anderson and J. T. Mitchell, *Appl. Phys. Letters*, **12**, 334 (1968).
26. F. Chernow, G. Eldridge, G. Ruse, and L. Wahlin, *ibid.*, **12**, 339 (1968).
27. For instance, W. V. Gool, *Philips Res. Repts.*, **13**, 157 (1958).
28. R. Takahashi, T. Tuno, M. Oshima, and A. Kobayashi, *Japan. J. Appl. Phys.*, **8**, 284 (1969).
29. R. Takahashi and M. Oshima, At the press in Annual Rept. of Eng. Res. Inst., Fac. of Eng., Univ. of Tokyo (1970).
30. J. Woods and K. H. Nicholas, *Brit. J. Appl. Phys.*, **15**, 1361 (1964).
31. J. Woods, *J. Elect. Control*, **5**, 417 (1958).
32. M. Yoshizawa, *Japan. J. Appl. Phys.*, **7**, 182 (1968).
33. F. Seitz and J. S. Koehler, *Solid State Phys.*, **2**, 305 (1956).
34. E. F. Apple, *This Journal*, **106**, 271 (1959).
35. S. O. Hemila and R. H. Bube, *J. Appl. Phys.*, **38**, 5258 (1967).

Technical Notes

Surface Properties of Oxidized Germanium-Doped Silicon

P. Balk

IBM Thomas J. Watson Research Center, Yorktown Heights, New York 10598

Oxidized silicon surfaces have a strong tendency toward n-type behavior. This has generally been attributed to the presence of positive charges in the SiO_2 layer and at the SiO_2-silicon interface (1). It is also known that GeO_2 rather readily becomes oxygen deficient, which gives rise to deep electron traps (2). Therefore, one might expect that incorporation of germanium into the SiO_2 film, obtained by thermal oxidation of silicon, could result in negative surface charge, and consequently a p-type space charge layer in the silicon. Such p-type surfaces on oxidized silicon have so far only been obtained by adding elements such as Ga (3) or Au (4, 5), which also appreciably affect the electronic characteristics of the substrate. On the other hand, the only substrate effect to be expected from adding germanium to silicon samples is a gradual decrease of the bandgap with increasing germanium concentration (6). It thus appeared convenient to use germanium-doped silicon alloys as substrate materials for the present investigation.

The samples were prepared from <111> oriented, 5 ohm-cm, n- and p-type Dow-Corning silicon, with a nominal germanium concentration of approximately 0.1, 1, and 2.5 w/o (weight per cent). These wafers were etched and then oxidized in O_2 at various temperatures (from 700° to 1100°C) in a resistance heated furnace. Upon oxidation, they were rapidly removed from the hot zone of the furnace and allowed to cool in the oxidation ambient. The resulting oxide thicknesses were determined either with an ellipsometer (7) or by the VAMFO method (8). The oxidation rates for germanium-doped and undoped samples were identical, within experimental accuracy. Table I shows that the oxide films do indeed contain germanium, and at a level which is only slightly lower than that of the starting material. The films grown on the 0.1 w/o germanium samples were not analyzed because of their low dopant concentration.

The characterization of the electrical surface properties of oxidized specimens was carried out by means of the MOS capacitance-voltage (C-V) technique (11). The shape of the C-V curves and the change of their position with measurement frequency indicated a considerable fast state density over an appreciable part of the forbidden gap, particularly for structures prepared at lower oxidation temperatures. However, the displacement of the C-V curves, measured at room temperature and 1.5 Mc, with respect to the curves for surfaces free of charge and interface states, always indicated the presence of positive surface charge.

Key words: oxidation of Ge doped Si, defects in SiO_2-GeO_2 alloys, C-V measurements, interface states.

Table I. Germanium content of oxide film and substrate of oxidized germanium-doped n-type silicon samples

Substrate				
Ge content (w/o)*	0.8	0.8	0.8	2.2
Oxide				
Oxidation temp. (°C)	1100°	800°	800°	800°
Oxide thickness (Å)	6110	2180	3950	1970
Oxide wt (μg)	1135	450	1015	415
Ge wt (μg)†	2.0	1.5	3.0	2.5
$\frac{\text{Ge wt}}{\text{Si wt}} \times 100$	0.4	0.7	0.6	1.2

* Determined by manitol titration (9); accuracy 0.1 w/o.
† Determined using phenylfluorone method (10); accuracy 10%.

A convenient indicator of the number of interface states was obtained by measuring their density (N_{ss}) between the room and liquid nitrogen temperature Fermi levels, according to (12)

$$N_{ss} = \frac{C_{ox}}{q} [V_{FB}(\text{room temp}) - V_{FB}(\text{liq. } N_2 \text{ temp})]$$

where C_{ox} is the oxide capacitance, and V_{FB} the (apparent) flatband voltage at 1.5 Mc. Data for films approximately 1000Å thick are shown in Fig. 1. All results were obtained after aluminum electrodes had been evaporated onto the surfaces, and the samples had been annealed for 5 min at 500°C in dry N_2. In agreement with earlier observations (13) this procedure was found to reduce the interface state density below 4×10^{10} cm^{-2} for germanium-free samples, oxidized in parallel with the doped substrates. The same result was obtained on samples with 0.1 w/o germanium. The annealing was applied in the present case since the flatband voltage for some of the p-type substrates with higher Ge doping could not be observed without this heat-treatment. Subsequent treatment in H_2 (14) at 500°C did not significantly affect N_{ss}.

Three conclusions stand out upon inspection of the data in Fig. 1: (*i*) The density of fast states (N_{ss}), not removable by Al (N_2) or H_2 annealing at 500°C, as detected by the present method, is strongly dependent on the oxidation temperature. It appears to reach a maximum around 800°C, and becomes quite small at

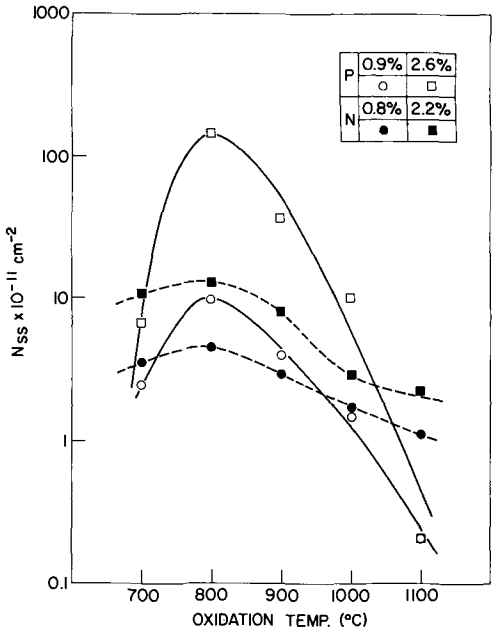

Fig. 1. Interface state densities in n- and p-type germanium doped silicon samples, oxidized at various temperatures. Germanium concentrations, determined by manitol titration (9), are indicated.

1100°C. (*ii*) Larger N_{ss} values are observed near the valence band on p-type samples than near the conduction band on n-type samples for substrates oxidized between 800° and 1000°C. This difference cannot be attributed to the slightly higher germanium concentrations in the p-type substrates (see Fig. 1). (*iii*) The N_{ss} values are strongly dependent on the germanium concentration in the substrate.

The interface states observed on germanium doped silicon are different in nature from those observed on undoped specimens, which are readily removed by low temperature H_2 annealing (14). However, the centers on germanium-doped silicon samples could be completely eliminated by heating in N_2 at temperatures over 900°C, followed by a post-metallization annealing at 500°C.

In view of the different behavior of n- and p-type germanium-doped substrates, it appears that the distribution of interface states is not symmetrical with respect to the middle of the forbidden gap. In drawing this conclusion, the assumption was made that this distribution is not dependent on conductivity type (12). The data show that the centers are related to the presence of the germanium dopant. There is no indication at the present time what the exact nature of these centers is and why the expected surface charge effects are absent. A similar difficulty to introduce negative oxide charge was reported by Sedgwick (15) for SiO_2-passivated germanium surfaces, which most likely contain a thin, residual germanium oxide film. In this case negative surface charge was only observed upon H_2 annealing at 700° or 800°C. However, for bulk GeO_2 the formation of deep electron traps takes place in this ambient already at 400°C (2). The H_2 annealing at 500°C in the present study had not the expected effect. Exposure to H_2 at higher temperatures was not attempted, since such treatments on silicon, according to our experience and that of others (16), lead to large positive surface charge.

Acknowledgment

The author is indebted to B. L. Gilbert and W. Reuter for analytical support, and to D. Dong for carrying out the measurements of the oxidation rates and the electrical characteristics.

Manuscript submitted Sept. 14, 1970; revised manuscript received Nov. 12, 1970.

Any discussion of this paper will appear in a Discussion Section to be published in the December 1971 JOURNAL.

REFERENCES

1. B. E. Deal, M. Sklar, A. S. Grove, and E. H. Snow, *This Journal*, **114**, 266 (1967).
2. V. G. Canina and J. Denoncin, *Compt. rend.*, **250**, 1815 (1960).
3. F. Fang and H. N. Yu, Paper presented at Solid State Device Research Conference, Princeton, N. J., 1965.
4. D. R. Collins, D. K. Schroeder, and C. T. Sah, *Appl. Phys. Letters*, **8**, 323 (1966).
5. N. Chou, F. F. Fang, and P. Balk, Paper 175 presented at the Chicago Meeting of the Society, Oct. 15-19, 1967.
6. R. Brannstein, A. R. Moore, and F. Herman, *Phys. Rev.*, **109**, 695 (1958).
7. R. J. Archer, *J. Opt. Soc. Am.*, **52**, 970 (1962).
8. W. A. Pliskin and E. E. Conrad, *IBM J. Res. Develop.*, **8**, 43 (1967).
9. C. L. Wilson and D. W. Wilson, "Comprehensive Analytical Chemistry," Vol. I^c, p. 167, Elsevier Publishing Co., New York (1963).
10. E. D. Sandell, "Volumetric Metal Analysis," p. 490, Interscience (1959).
11. A. S. Grove, B. E. Deal, E. H. Snow and C. T. Sah, *Solid-State Electron.*, **8**, 145 (1965).
12. D. M. Brown and P. V. Gray, *This Journal*, **115**, 760 (1968).
13. P. Balk, Paper 111 presented at the Buffalo Meeting of the Society, Oct. 10-14, 1965.
14. P. Balk, Paper 109 presented at the San Francisco Meeting of the Society, May 9-13, 1965.
15. T. O. Sedgwick, *J. Appl. Phys.*, **39**, 5066 (1968).
16. M. V. Whelan, *Philips Res. Rept.*, **22**, 289 (1967).

Solidus Boundary in the InAs-AlAs Pseudobinary System

L. M. Foster* and J. E. Scardefield

IBM Research Division, Yorktown Heights, New York 10598

The $In_xAl_{1-x}As$ semiconductor alloy system is of interest for the fabrication of new electronic and electroluminescent devices. By varying the composition of the alloy the forbidden energy gap, which is one of the fundamental parameters that determine semiconductor behavior, can be varied from that of InAs (0.36 eV) to that of AlAs (2.16 eV). Direct radiative transitions ($k = 0$) of high quantum efficiency would be expected in alloys with AlAs content up to about 68 m/o (mole per cent), which is the crossover point of the direct band edges (1). Knowledge of the equilibrium T-x phase diagram is important when devising crystal growth practices for a new alloy system. The determination of the solidus boundary of the InAs-AlAs system is reported here.

The experimental procedure was that described by the authors for the InP-GaP system (2). In brief, a pellet pressed from a finely ground mixture of the two components is held at a constant temperature, T which is chosen so that the composition of the mixture falls within the two-phase region of the diagram between the liquidus and solidus boundaries. This could be assured by making up the starting composition to

* Electrochemical Society Active Member.
Key words: phase diagrams, III-V compounds, electron microprobe.

lie approximately along the straight line between the melting points of the two separate components. After allowing sufficient time for equilibrium to be attained, the sample consists of particles of a solid solution whose composition corresponds to the intersection of the isotherm, T, with the solidus boundary, suspended in a liquid whose composition corresponds to the intersection with the liquidus boundary. After quenching the sample, an electron microprobe analysis of the solid solution phase gives the composition of the point on the solidus corresponding to the equilibration temperature. By equilibrating a sufficient number of different starting compositions at the appropriate temperatures, the entire boundary can be determined.

The preparation and encapsulation of the pellets were described in the earlier paper (2). Departures from that procedure, which was developed for InP-GaP, were the shortening of the time at temperature to 3 days to minimize devitrification of the quartz capsule that occurred at these higher temperatures and the taking of precautions to avoid contact of the reactive AlAs with moisture.

Six experimental points were determined. The data are given in the following table:

Temp. (°C)	AlAs (m/o)
999	0.306
1040	0.547
1110	0.736
1212	0.850
1450	0.956
1513	0.967

The solidus boundary is shown in Fig. 1. The melting point of InAs (937°C) is from Lichter and Sommelet (3). The melting point of AlAs (1770°C) was determined in these laboratories by Chicotka (4). This system is seen to exhibit strong positive deviation from Raoult's law of mixing. Although numerical comparison with other systems cannot be made in the absence of liquidus data, it appears that the deviation is greater than in the InP-GaP system that was reported previously. This probably reflects the greater lattice mismatch between the two separate components of the InAs-AlAs system.

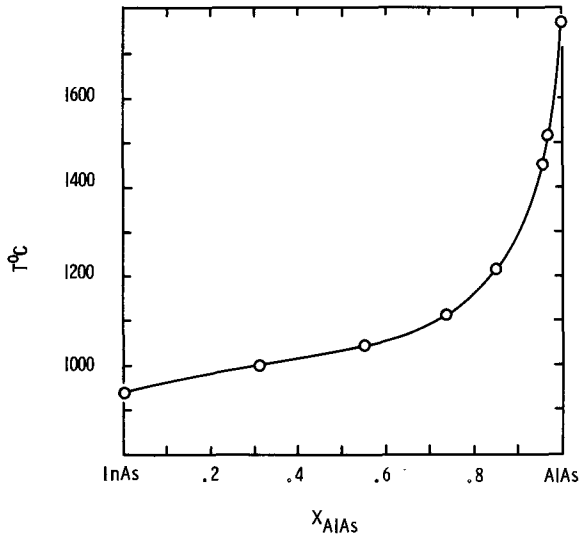

Fig. 1. Solidus boundary of the InAs-AlAs system

Acknowledgment

The authors wish to thank Mr. R. J. Chicotka for supplying the AlAs, and Mr. J. D. Kuptsis for performing the electron microprobe analysis.

This study was supported in part by the National Aeronautics and Space Administration, Contract No. NAS 12-2169, Electronic Research Center, Cambridge, Massachusetts.

Manuscript received Oct. 27, 1970.

Any discussion of this paper will appear in a Discussion Section to be published in the December 1971 JOURNAL.

REFERENCES

1. A. Onton, T. J. Watson Research Center, IBM, Yorktown Heights, N. Y., Private communication, to be published.
2. L. M. Foster and J. E. Scardefield, *This Journal*, **117**, 534 (1970).
3. B. D. Lichter and P. Sommelet, *Trans. Met. Soc. AIME*, **245**, 1021 (1969).
4. R. J. Chicotka, T. J. Watson Research Center, IBM, Yorktown Heights, N. Y., Private communication.

JOURNAL OF THE ELECTROCHEMICAL SOCIETY

ELECTROCHEMICAL TECHNOLOGY

MARCH 1971

Low-Temperature Cathode Performance of Porous Ag/Ag_2O Electrodes

E. G. Gagnon[1,*] and L. G. Austin*

Department of Materials Science, The Pennsylvania State University, University Park, Pennsylvania 16802

ABSTRACT

The performance of porous, silver-silver oxide electrodes decreases rapidly below 0°C, and galvanostatic discharge curves show several different regions. Most of the work reported here was done on thin Ag/Ag_2O electrodes, prepared by electrodeposition or by powder pressing. An attempt is made to explain the regions in the discharge curves, and the apparent Tafel parameters, from a plausible kinetic mechanism. The application of theories of porous electrode behavior is demonstrated by results from thick electrodes made by stacking thin electrodes together. The use of the information in designing electrodes is discussed, as is future work.

It is well known that the performance of Zn|KOH| silver oxide cells decreases considerably at temperatures less than 0°F. Preliminary results on thin, porous electrodes (1), supplied by Harry Diamond Laboratories, Army Materiel Command, indicated that the major loss of performance was caused by increased polarization at the silver oxide electrode. It was decided, therefore, to perform a detailed half-cell study of the behavior of silver oxide electrodes in KOH eutectic [31 w/o (weight per cent)], concentrating at first on $Ag|Ag_2O$ electrodes to avoid the complexity of mixed $Ag_2O|AgO$ compositions during discharge.

Although the formation of Ag_2O and AgO on silver by anodic charging has been studied at room temperature (2, 3) using a variety of electrochemical techniques, cathodic discharge at low temperatures has not been widely investigated. The form of the anodic charge of solid silver at constant current is well known: polarization increases rapidly by double-layer charging until Ag_2O is formed on the surface, then polarization decreases somewhat to a plateau. After some time, polarization increases from this plateau to the AgO formation potential, passes through a peak, and again decreases to a higher plateau corresponding to continued AgO formation from Ag_2O and Ag; polarization eventually increases to oxygen evolution. There is good evidence (4) that thick, continuous films are not formed on anodic charge and that silver is removed from the surface and redeposited in the form of attached crystallites of Ag_2O, followed by disappearance of these crystals and the appearance of discrete AgO crystallites on the surface. Similarly, on discharge, massive rearrangement of the molecules occurs to give new crystal forms. The growth size of the crystallites is a function of rates of charge and discharge, being small at high current densities; lower current densities give fewer, but larger, crystallites.

The effect of porosity of practical battery electrodes can give added complexity to interpreting results. The reactions involve transfer of ions dissolved in the electrolyte contained in the pores of the electrode, and potential gradient is required for this transfer. This has the effect of making polarization greater at the exterior of the electrode (5-7). This effect is more pronounced for thicker electrodes, and it is possible during charge for potential in the interior to correspond to the $Ag|Ag_2O$ reaction, and potential at the exterior to correspond to $Ag_2O|AgO$. These effects are enhanced at low temperatures: for example, the specific resistance of eutectic KOH goes from 1.9 at 60°F to 33 ohm-cm at −60°F.

Experimental Techniques

A 250 ml beaker with a Lucite cover was used as the electrochemical cell (8). The Lucite cover contained five holes: three for the test, counter, and reference electrodes; one for nitrogen gas used to deaerate the electrolyte; and one hole for a glass U-tube which was used to remove trapped gas bubbles that occasionally formed on the surface of the electrode during a run. The electrolyte was a 31 w/o aqueous KOH solution, prepared from a 45% w/w Fischer reagent (Cat. No. SO-P-236) and distilled water that had been obtained from a Barnstead still (Model No. SM-5). The temperature of the cell was controlled by a Tenney Jr. test chamber (Model TJR) capable of controlling temperatures between −100° to 350°F to within ±1°F; electrical contacts were made through a terminal board on one of the walls of the chamber. The temperature within the chamber was measured with chromel-P-alumel thermocouple in conjunction with a Keithley d-c differential voltmeter (Model 660).

The test electrodes had a plane surface area of 0.317 cm^2 and were obtained by using a punch and die, where the die opening was 0.25 in. The electrode disks were press fitted into a Teflon collar where the opening had been machined about 1 mil less than the diameter of the electrode disk. The Teflon collar con-

[1] Present address: Research Laboratories, General Motors Corporation, Warren, Michigan 48090.
* Electrochemical Society Active Member.
Key words: Ag/Ag_2O discharge, low-temperature kinetics, porous electrodes, distributed reactions.

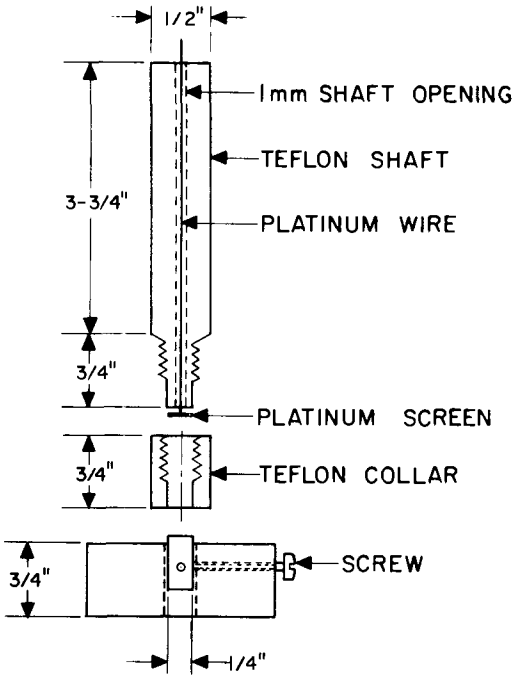

Fig. 1. Electrode holder

taining the electrode was then screwed onto a Teflon shaft as shown in Fig. 1, and the electrode pressed tightly against the current collector using the adjustable ¼ in. rod shown, which was then removed. A platinum screen was used as a current collector, positioned between the electrode and the solid Teflon shaft. An external contact wire was connected to the screen and passed up through the center of the Teflon shaft. The electrode holder thus exposed one face of the electrode to the electrolyte and insured uniform current density through this face. A coil of silver wire was used as counterelectrode, and the surface of the wire was periodically cleaned of reaction products by dipping the wire into an HNO_3-distilled water solution (1:1) for several seconds and then thoroughly rinsing the electrode in distilled water.

A Hg/HgO/31 w/o KOH reference electrode was used and was prepared as described by Hamer and Craig (9). A salt bridge filled with 31 w/o KOH was placed between the test and reference electrodes. One end of the salt bridge ended in a fine capillary (Luggin capillary) which was positioned close to the surface of the test electrode.

The cell was assembled in the test chamber with the test electrode raised above the level of the electrolyte, and the test chamber set to the appropriate temperature. The test electrode was then lowered into the electrolyte. Steady-state, open-circuit voltages *vs.* the Hg/HgO reference electrode were measured before steady-state and unsteady-state galvanostatic measurements, with a Fairchild digital multimeter (Model 7000). Constant current measurements were made using the rapid-switching circuit described by Austin and Almaula (10) in conjunction with a Nesco (Model JY120A-2) chart recorder. The desired current flowing through the cell was determined by the known voltage generated from a Harrison (Model 6206B) d-c power supply and the value of the precision resistor in the control circuit of the galvanostatic circuit. A Potter and Brumfield Hg-wetted contact relay (Type JMY-115-22) was used to eliminate switching transients.

A Tektronix Type RM564 storage oscilloscope (Type 3A3 differential amplifier and Type 2B67 time base) and Polaroid camera (Model C-12) were used to record voltage-time traces up to a few seconds. On initiation of a current, a vertical blanked-out portion of the trace showed the immediate establishment of an ohmic potential change, referred to hereafter as *IR* polarization. This polarization includes the resistance of the ionic current path in electrolyte between the face of the electrode and the Luggin tip, and electronic resistance in the current path through the test electrode, current collector, and wire to the point of attachment of the lead from the oscilloscope. During galvanostatic discharge, currents were interrupted and the decay of polarization *vs.* time measured with the oscilloscope. The blanked-out parts of the trace on break and make of the current were again used to indicate *IR* polarization at that stage of the discharge.

Test Electrodes

One of the electrodes (HDL) shown in Table I was prepared by Whittaker Corporation according to the procedures developed by the Harry Diamond Laboratories. The procedures as supplied by Harry Diamond Laboratories are as follows.

An Ag_2O-deionized water slurry was extruded onto an expanded metal screen (Exmet 5AG5-5/0), sintered, and anodically charged (using both faces of the electrode) in a 9-10% $NaHCO_3$ solution for 60 min at a current density of 0.125 A/in.^{2} The electrode material was then:

1. Discharged in $NaHCO_3$ solution at 0.125 A/in.^{2} for 60 min
2. Rinsed in deionized water for 30 min
3. Allowed to drain for 30 min
4. Dried at 165°F in a recirculating type oven for 30 min
5. Charged in 5% KOH at 2.5 A/in.^{2} for 20 sec
6. Rinsed in deionized water for 30 min
7. Allowed to drain for 30 min
8. Placed in a 160°F dry vacuum chamber for 4 hr
9. Stored in dry nitrogen gas

It will be noted that this procedure may leave some silver carbonate and AgO on the electrode, although at room temperature the electrode rapidly comes to the reversible potential of the Ag/Ag_2O reaction on immersion in electrolyte. The electrode is about 70% porous and contains silver (apart from the screen) and Ag_2O in approximately equal weights.

In order to test whether certain of the results were due to the electrolytic formation of the HDL electrode, and to provide more flexibility in the variation of important electrode properties, a number of the electrodes were prepared in the laboratory as follows: Ag_2O powder (Fischer reagent grade) was well mixed with an equal weight of Ag powder (Fischer reagent grade) in a mechanical shaker. Some of this material was used to fabricate electrodes, while another part was mixed with minus 400 mesh $NaNO_3$ to give a mixture containing 35 w/o of the salt. Electrodes were manufactured using the work of Morrell and Smith (11) as a starting point.

Silver expanded metal screen was etched in concentrated nitric acid for 30 sec and well rinsed in distilled water. This roughened the surface and promoted adhesion between powder and screen. A 0.25 in. diameter die of hardened steel was fitted with a bottom punch also of hardened steel, and a layer of the powder spread evenly on the face of the punch. A 0.25 in.

Table I. Characteristics of 50:50 w/o Ag-Ag_2O electrodes (TD is silver from thermal decomposition of silver oxalate)

Code No.	% Porosity	Silver type	Thickness, mm	Observed discharge capacity, coulombs/cm^2
HDL	70	Electroformed	0.25	15.4
16-TD	16	T. D.	0.312	70.5
65-TD	65	T. D.	0.405	45
63-TD	63	T. D.	0.262	19.5
63-F	63	Fischer	0.51	57
20-F	20	Fischer	0.34	57
81-F	81	Fischer	0.70	27

diameter portion of screen was cut from the roughened screen with a paper punch and placed on the surface of the powder. This was covered with another layer of powder, a top punch placed in the die, and the contents in the die were cold-compressed at 55,700 psi for 2 min. The electrode prepared in this way without $NaNO_3$ filler was about 20% porous and was mechanically strong. When the filler was present, the electrode was placed in 200 ml of distilled water and left for 3 days, with water replacement every day; the filler dissolved and slowly diffused out without mechanical rupture of the electrode structure. The electrode was then washed, and dried in a dessicator. This procedure gave an electrode of about 63-66% porosity. Similarly, an electrode of 80% porosity was prepared using 60% $NaNO_3$ and a pressure of 65,000 psi.

In an attempt to make electrodes containing high internal silver area, electrodes were made from Ag powder prepared by thermal decomposition of silver oxalate, following the procedure of Schroeder *et al.* (12). However, BET measurements on this powder showed it had areas of only 0.45 m^2/g instead of the 5 m^2/g expected.

Results

It was found that the test electrodes reached a stable, open-circuit potential after a few minutes of immersion in the electrolyte at room temperature, but took longer times at lower temperatures; for example, stabilization times were up to 1 hr at −70°F. The open-circuit potential was always within ±10 mV of the expected theoretical value. Figure 2 shows the variation of the effective resistance (times three) obtained from the initial blanked-out portion of the oscilloscope trace as a function of temperature, for an undisturbed position of the Luggin capillary. Also shown is the specific resistance of the electrolyte (solid line). The two sets of results are in reasonable agreement at the various temperatures, indicating that the resistance is due primarily to the mean electrolyte path between the electrode and the tip of the Luggin capillary. This mean path length can be calculated from $r = \rho l/A$, r being measured resistance, ρ specific resistance, l path length, and A the plane area of the electrode; thus, l is approximately 1/9 cm, which appears to be reasonable from the dimensions and position of the Luggin capillary. The data at −52°F show typical spread of results of repositioning the Luggin. There were sometimes differences between the effective resistances determined initially and at some later stage in discharge, but these differences were usually small, except as noted later.

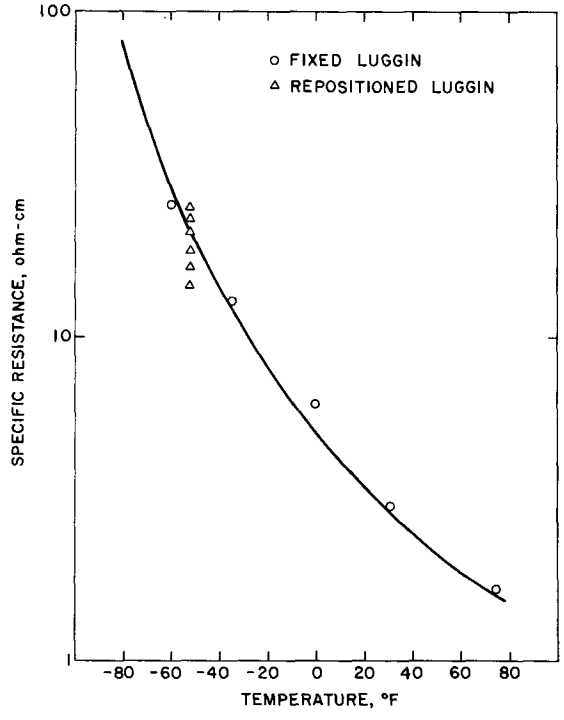

Fig. 2. Specific resistance of 31 w/o KOH (solid line) and effective resistance (times three) between test electrode and the Luggin capillary.

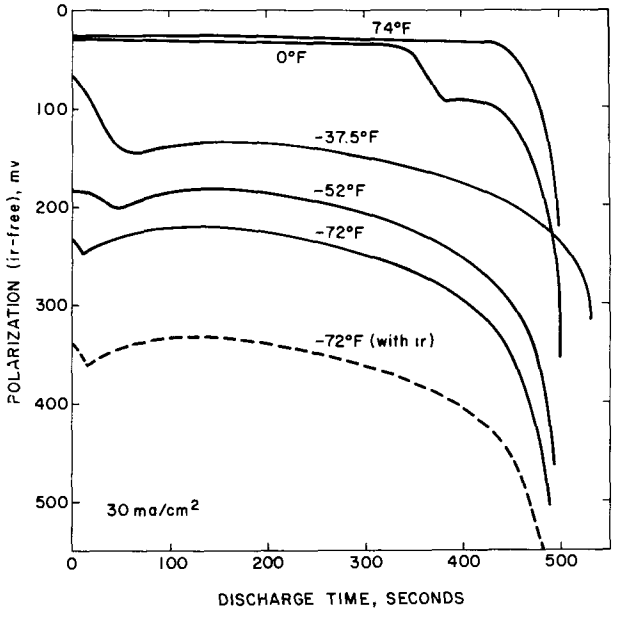

Fig. 3. Galvanostatic discharge at 30 mA/cm^2: HDL electrodes

Figure 3 shows typical results of polarization *vs.* time for HDL electrodes, discharged at 30 mA/cm^2 (27.9 A/ft^2), as a function of temperature. The results were corrected for *IR* polarization determined at 150 sec; the broken curve also shows the uncorrected values at −72°F, where the *IR* correction was maximum for this set of results. At room temperature, there is a small amount of polarization (about 20 mV), which is almost constant until the electrode is almost completely discharged. At 0°F, there is again a small amount of polarization at first, but it increases significantly after the electrode is about two-thirds discharged. The reason for the sudden increase in polarization preceding the final discharge of the electrode is not known. As temperature decreases, the polarization increases, and the shape of the curve becomes more complex. Figure 4 shows the polarization after 150 sec of discharge (about 30% discharged), which corresponds to the almost flat discharge regions; a marked increase in polarization below 0°F is apparent. Since the correction for the *IR* effect was also made at this time, the data are corrected reasonably well for *IR*.

The capacity of the HDL electrodes is somewhat variable, which is to be expected for such small electrodes (1/3 cm^2) stamped out from larger sheet sam-

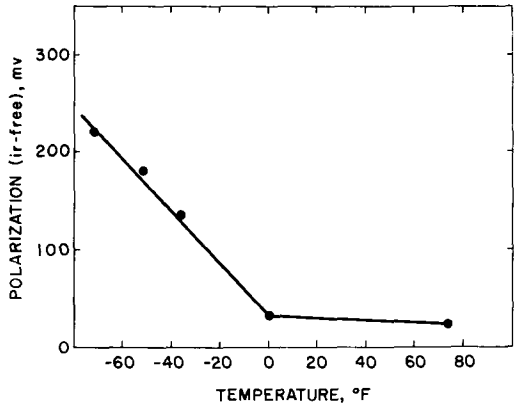

Fig. 4. Polarization (*IR*-free) at 30 mA/cm^2, measured at about 4.5 coulombs/cm^2 of discharge.

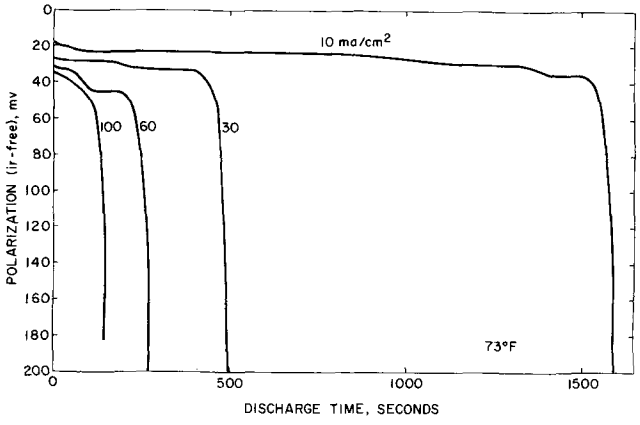

Fig. 5. Galvanostatic discharge at various current densities: HDL electrodes at room temperature.

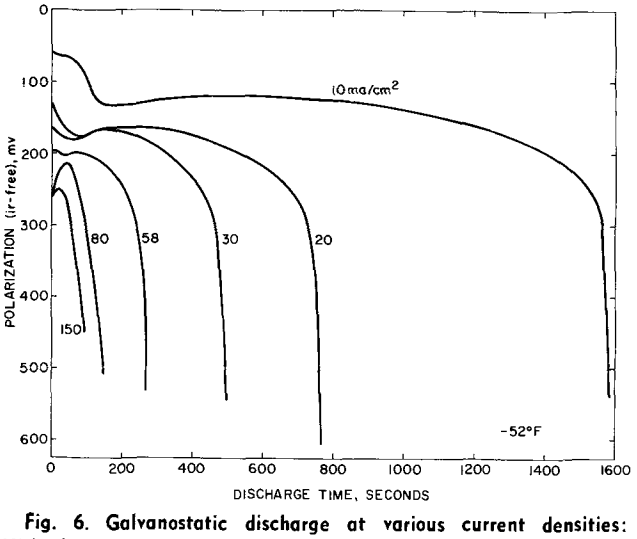

Fig. 6. Galvanostatic discharge at various current densities: HDL electrodes at −52°F.

ples, since the Ag/Ag_2O cannot be perfectly distributed over the Exmet support. The mean value was 4.89 coulombs (for area of 0.316 cm^2), with extremes of about ±5%. The capacity results were random in variability and showed no trend with temperature or with current density.

Figure 5 shows typical galvanostatic discharge curves (HDL electrodes) at 73°F, and Fig. 6 shows curves at −52°F. Values were corrected for *IR* assuming that the value measured at 1.42 coulombs of discharge applied over the whole curve. This point of discharge corresponds to a region between 1/4 to 1/3 of total coulombs, and corresponds to the minimum polarization in the plateau region following the initial peak polarization. Figure 7 shows Tafel plots of polarization *vs.* log current density at this point. The values for lower current densities were obtained by discharging the electrode at 10 mA/cm^2 until it reached the plateau, then changing the current density to low values and measuring steady polarization at the low

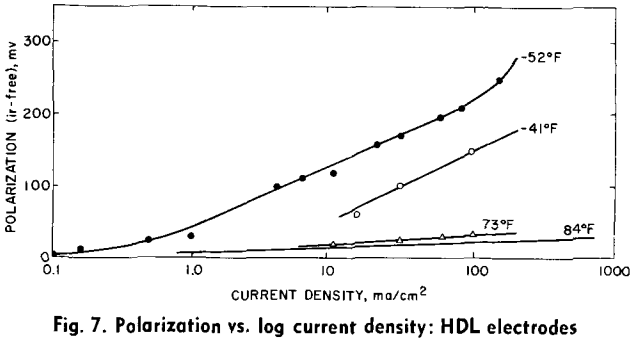

Fig. 7. Polarization vs. log current density: HDL electrodes

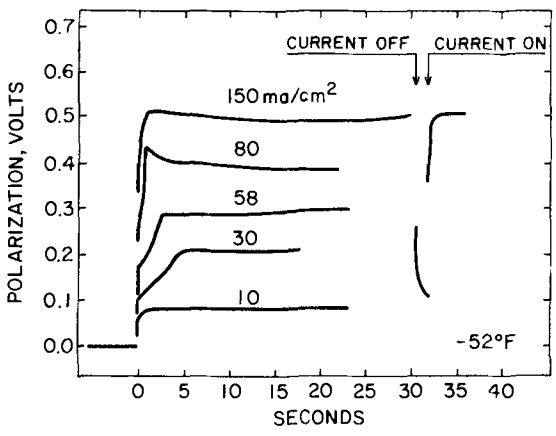

Fig. 8. Oscilloscopic traces showing the initial discharge characteristics of the curves shown on Fig. 6.

currents. A range of current from 0.1 mA/cm^2 to 5 mA/cm^2 was accomplished within the next coulomb of discharge. It was noticed that the initial parts of the curves of Fig. 6 were variable from sample to sample. For example, the 30 and 58 mA/cm^2 curves sometimes looked like the 80 mA/cm^2 curve shown, with a high initial polarization peak.

Recorder plots such as in Fig. 6 do not show fine detail at short times and Fig. 8 shows oscilloscope traces for the first few seconds of discharge. Again, the initial peak was more pronounced in some samples than in others. The 58 mA/cm^2 line in Fig. 6 contains all of the general features; there is evidence for an initial polarization peak occurring within 5 sec. followed by a slowly-developing second peak, followed by rapid increase of polarization as the electrode approaches complete discharge. At higher current densities, the two peaks fuse, while at lower current densities the first peak does not develop.

Since the presence of peaks and plateaus varied between samples the HDL electrodes and since the electrodes were prepared by electrolytic charging, it was decided to charge electrodes with anodic current and then perform discharge tests. Figure 9 illustrates typical results of cathodic discharge immediately after anodic charging; the broken line indicates the "normal" values, as found in Fig. 8, for example. The regions in the curve can be described by: a is the *IR* jump; b is a rapid rise of polarization due to double-layer charging; c is a plateau of discharge followed by a shallow peak at d; e is a plateau of discharge followed by rapidly increasing polarization as the electrode approaches complete discharge in region f. By prior anodic charging, at potentials more anodic than the $Ag_2O|AgO$ equilibrium potential, the plateau at c is lengthened proportionately to the coulombs of charge, to c′ as shown. In addition, a pronounced peak is developed after b′. The polarization level at e and f is virtually unchanged. If such a charged electrode is left standing at open circuit in the electrolyte, the

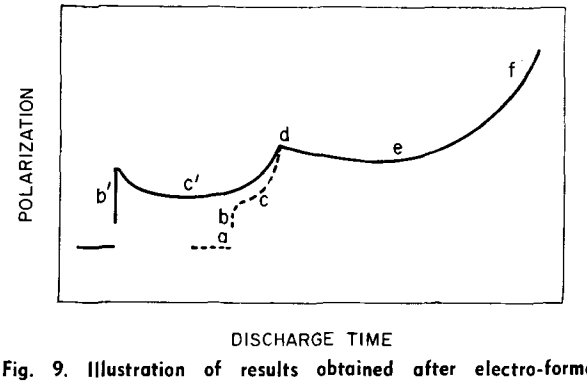

Fig. 9. Illustration of results obtained after electro-formed electrodes were anodically charged prior to discharge.

length of plateau c' decreases with time and comes back to normal values after standing overnight at −54°F. Alternatively, if a normal electrode is discharged to region e just after peak d, allowed to return to open circuit potential, then discharged again at the same current density, the coulombs in region c is shortened. Then if the electrode is left for some time at open circuit, the length of region c increases again to usual values.

Table I shows the characteristics of a group of electrodes prepared from silver and Ag_2O powder, as described previously. The BET area of the constituents were 0.57 m^2/g for Fischer silver, 0.45 m^2/g for T. D. silver, and 0.60 m^2/g for Fischer Ag_2O. These correspond to equivalent spherical diameters of 1.01μ, 1.3μ, and 1.0μ, obtained using the expression $D = 6/Bd$ where D is the equivalent spherical diameter (microns); B is the BET area (m^2/g); d is the density of the powder (g/cc). On galvanostatic discharge at 30 mA/cm^2, −52°F, it was observed that some electrodes gave high initial IR jumps. After some discharge, IR values measured at various points in the discharge were almost constant and usually comparable to previous results, see Table II. (Although electrode 63-TD gave an effective resistance of 11 ohms which is high compared to the usual values of 4 to 8 ohms, its discharge curve after correction for this value was similar to that of 65-TD.) It must be remembered that these values include the resistance of the electrolyte between test electrode and Luggin capillary (see Fig. 2). It can be concluded that high initial IR values decreased to normal values after no more than 2% of discharge. It is also concluded that these normal values of IR polarization did not increase even when electrodes were 95% discharged.

Figure 10 shows polarization *vs.* degree of discharge, corrected for IR. The marked effect of porosity is apparent; for example, comparing 63-F with 20-F, the 20-F electrode contains more Ag_2O and Ag and is thinner, yet operates at 75 to 200 mV more polarization. There was no correlation between high initial IR values and later performance. Figure 11 shows typical initial time results for the electrodes. A significant polarization peak was observed, similar to that found with the electro-formed HDL electrodes, but more pronounced. For some of the electrodes, 81-F for example, part of this peak was due to a high initial IR value which decayed during discharge. Even after

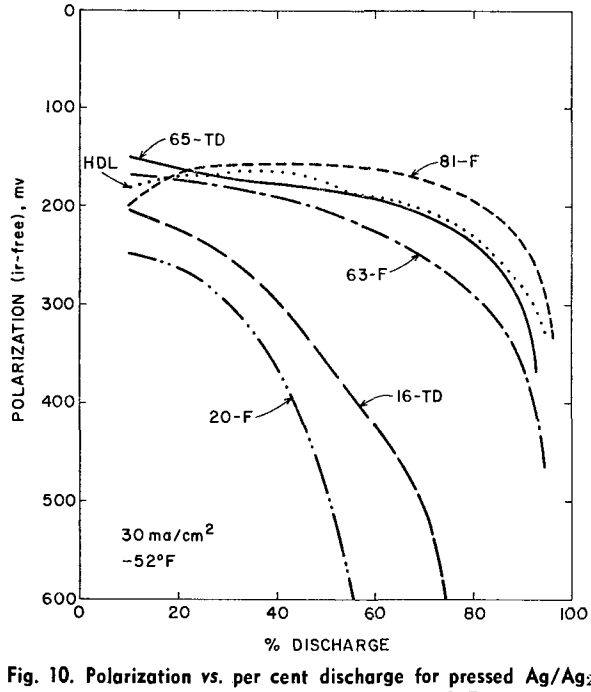

Fig. 10. Polarization *vs.* per cent discharge for pressed Ag/Ag_2O powder electrodes of different porosities at −52°F.

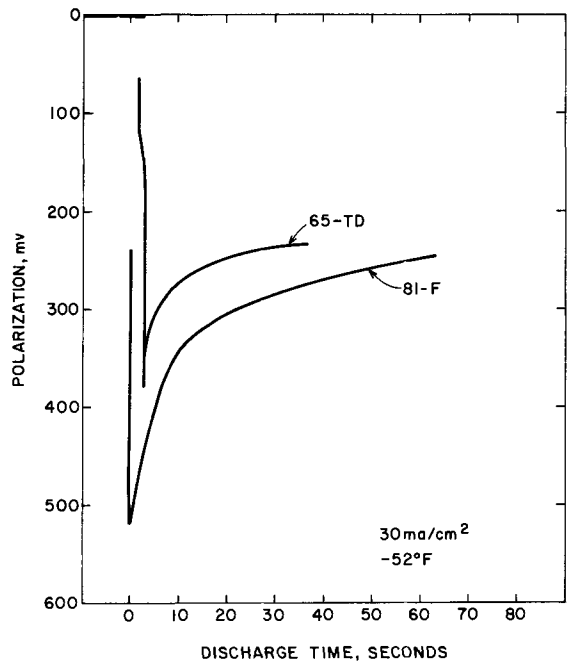

Fig. 11. Oscilloscopic traces showing initial discharge characteristics of electrodes 65-TD and 81-F.

allowing for this, a pronounced peak is still present, and it is also present in cases, 65-TD for example, where the initial and steady IR values were nearly the same. The shape of the initial polarization curve, when it is not obscured by a high initial IR, contains the a, b, c, d, e, regions discussed previously. The reason for the high IR values obtained with some of the pressed powder electrodes as compared to the electroformed electrodes is not known, but it is possible that because of the manner in which the Ag and Ag_2O particles are pressed together, good electrical contact throughout some of the electrodes is not achieved.

The effect of the porous nature of the test electrodes was investigated by making thicker electrodes from 5 of the 10 mil HDL electrodes stacked together. The stack was mounted in the electrode holder in the usual way with only one face exposed. Some preliminary tests, and some theoretical calculations (see Discussion) suggested that 30 mA/cm^2 at −52°F should give a small but significant amount of reaction at the back section and a lot of reaction in the first section. It was also found that there was some evidence for poor electronic contact between the sections, therefore a fine dusting of silver powder was applied between the sections before compressing in the holder. The stack was discharged to about 45% of total capacity,

Table II. IR polarization at 30 mA/cm^2 for 0.316 cm^2 electrodes, −52°F

Electrodes	% Discharge	IR polarization, mV
81-F	0	240
	45	40
20-F	0	90
	2	62
	20	60
20-F	75	75
	96	75
63-F	0	65
	2	50
63-TD	0	145
	12	110
	80	110
65-TD	0	80
	7	70
	40	67
	70	68
16-TD	0	180
	6	80
	32	80
	60	80
	80	80
	96	80

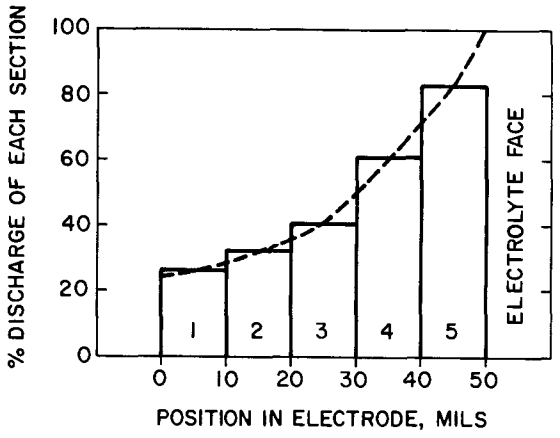

Fig. 12. Distribution of reaction at −52°F through a 50 mil thick electrode.

disassembled and discharge completed on each of the sections. Knowing the average coulombic capacity of the sections, the amount of the coulombs discharged in each section during the first discharge was readily calculated. The results are shown in Fig. 12. Distribution of reaction through the 50 mil thick stack is clearly evident.

Figure 13 shows the polarization of this thick electrode during discharge. If reaction were uniformly distributed through the electrode, a current density of 30 mA/cm^2 would be 6 mA/cm^2 per section. On the other hand, if reaction were concentrated in the outer section, polarization would be similar to that for just one section at 30 mA/cm^2. As expected from Fig. 12, polarization lay between these two extremes. Of interest is the more rapid increase in polarization with amount of discharge for the thick electrode.

Figure 14 shows polarization for the remainder of discharge for each section. It can be seen that partial discharge develops the pronounced peak of polarization seen previously at higher current densities. This peak decays on further discharge so that each curve fuses into a common curve nearer completion of discharge.

Discussion

Considering first the HDL electrodes produced by electro-forming of sintered silver powder, and considering the internal surface of the electrode before

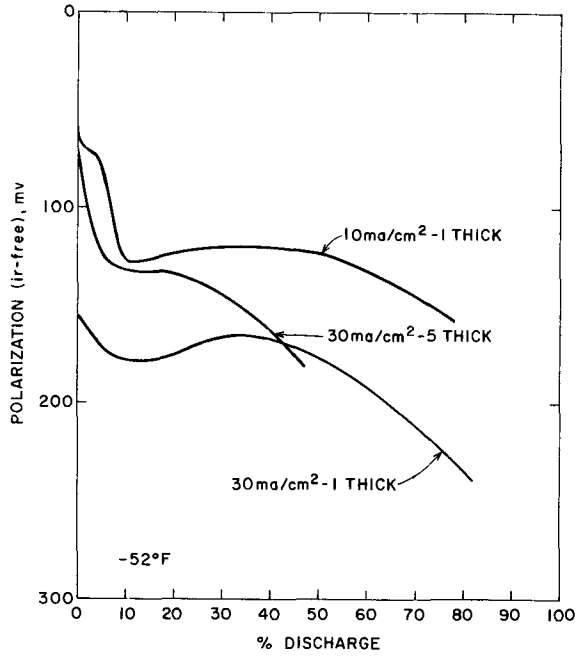

Fig. 13. Galvanostatic discharge for various thicknesses of HDL electrodes; 30 mA/cm^2 and −52°F.

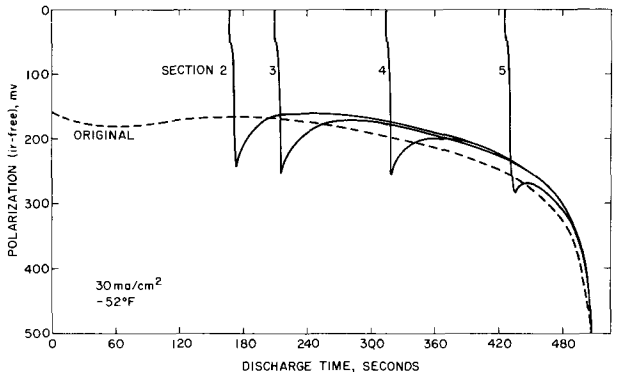

Fig. 14. Galvanostatic discharge of individual electrodes used in the stacked electrode experiment.

charge to be like an extended solid surface of silver, there are two possible forms in which Ag_2O can be produced. First, the entire surface of the silver can be covered with a tight layer of Ag_2O which grows by solid state film growth. BET measurements on these electrodes give an area of 0.4 m^2/g of silver, which is approximately 300 cm^2 of internal area per cm^2 of electrode. Thus at 30 mA/cm^2, the true current density would be about 0.1 mA/cm^2. A continuous film of Ag_2O of 0.1μ thick would give a resistance of 10^3 ohm cm^2 and an *IR* polarization of 100 mV, taking the specific resistance of Ag_2O to be 10^8 ohm cm. This is an order of magnitude higher than the experimental electronic *IR* values for these electrodes and it must be concluded that if a continuous film of Ag_2O covers the silver it must be less than 100Å in thickness. It seems more logical to conclude, from the experiments described by Thirsk (13), that the major part of the Ag_2O formed is in discrete crystallites (which can grow to about 1μ in size on solid silver) attached to the silver surface thus leaving relatively bare silver present to take and supply electrons. It can be argued that whatever is the mechanism of anodic formation or discharge of Ag_2O, it cannot involve charge transfer through thick crystallites or solid layers of Ag_2O, since no large electronic resistance is present.

The plateau of discharge at c in Fig. 9 indicates that there is some material which discharges more readily (at lower polarization) than the major amount of Ag_2O present. In the electro-formed electrodes this might be ascribed to silver carbonate or silver peroxide, but the typical S shape of b, c, d, is also clearly apparent in the other electrodes made from reagent grade Ag_2O. One explanation is that thin, continuous layers of Ag_2O cover the silver in the electrode and that these layers are more active than the bulk crystallites of Ag_2O. Assuming that a monolayer has roughly 0.2 mcoulombs/cm^2 of capacity, 300 cm^2 of internal surface would give 0.06 coulombs/cm^2 of electrode. Estimates of the amount of charge in region c under normal conditions gives about 0.1 coulombs/cm^2, thus the layers might be only a few molecules thick. After anodic charge at low temperature, region c is increased, possibly representing thickening of the layer. However, on soaking in electrolyte at open circuit, the charge in region c returns to about 0.1 coulombs/cm^2, indicating that there is an equilibrium amount of surface film in the Ag/Ag_2O/KOH system of a few angstroms thick. The solubility of Ag_2O is too small for the plateau to be due to discharge of dissolved oxide in the pores of the electrode. Possibly, this S shape, with a plateau of c, has not been observed in room temperature measurements because operation at low temperatures accentuates the polarization peak at d, thus clearly separating it from the plateau region. It is interesting that similar results at low temperature have been obtained with the cathodic discharge of a solid silver sheet anodized to Ag_2O formation (14), although the current density to obtain similar voltage-time curves is re-

duced from 30 mA/cm² for HDL electrodes to 0.3 mA/cm² for the anodized sheet.

Whatever the cause of this initial region of discharge, it caused variability in the first time interval of discharge of HDL electrodes which made it difficult to observe quantitative results on the magnitude of peak d as a function of current density and temperature. A general pattern is evident, however; the peak at d is more pronounced at higher current densities and at lower temperatures. If the electrode is partially discharged, allowed to rest at open circuit, and then further discharged, the peak is clearly evident (see Fig. 14). Alternatively, the peak is clearly present in the pressed powder electrodes (Fig. 11). It is not due to the porous nature of the electrodes because it is observed on discharge of anodized silver sheet (14). On the other hand, fairly rapid break-and-make of the current to perform *IR* measurements show no peak on make (see Fig. 8). It can be concluded that the peak reappears only after some stand time.

Three obvious explanations for peak d come to mind. First, by analogy with anodic charging, the peak could be a nucleation polarization. This would fit in with the dependence on current density and temperature. It is not clear, however, what is being nucleated. It could be dissolved silver deposition on pre-existing silver by

$$Ag_2O(s) + H_2O \rightarrow [Ag_2O \cdot H_2O] \rightarrow 2Ag^+ + 2OH^- \quad [1]$$

$$Ag(s) + Ag^+ + e^- \rightarrow 2Ag(s) \quad [2]$$

Equation [2] would be the nucleated step. Polarization produces growth of nucleation centers which are still present after rapid break-and-make of the circuit. On stand, the growth centers become poisoned by impurity adsorption or decay by molecular rearrangment to a non-nucleating structure.

Second, if the reaction in Eq. [1] were slow at low temperature, then the concentration of Ag^+ would decrease with current, giving concentration polarization in reaction [2]. The rate of dissolution of Ag_2O could be voltage dependent, increasing with cathodic polarization. The polarization overshoot would then be ascribed to the removal of surface impurities which slow down dissolution, or initial removal of stable surface layers leaving more reactive, freshly formed surface underneath. Third, if Reaction [2] had charge transfer polarization, the production of silver during discharge would have an autocatalytic effect. However, the large polarization overshoots would indicate at least a tenfold increase in silver area as the polarization decreases to the plateau at e, whereas there is 50% of unreacted silver present initially in the electrodes. In addition, silver area produced during discharge does not presumably disappear on stand, whereas the peak is reinstated after stand at open circuit. This last fact could be explained by postulating that on stand at open circuit the silver becomes covered with a continuous film of Ag_2O. However, it has already been argued that plateau c before peak d corresponds to the discharge of a surface film. It is planned to test the autocatalytic hypothesis by making double-layer capacity measurements during periods c, and in the regions d to e to f, since the double-layer capacity will be primarily due to metallic silver.

Further information can be deduced from Fig. 4 if it is assumed that electrodes at different temperatures can be compared in the plateau region, with only temperature as the prime variable. Figure 7 indicates that a Tafel-type relation exists and assuming

$$i = I_A \exp(\alpha \mathbf{F}\eta/RT) \quad [3]$$

$$I_A = k \exp(-\Delta H^{\ddagger}/RT) \quad [4]$$

the apparent activation enthalpy can be obtained from

$$\eta = \frac{\Delta H^{\ddagger}}{\alpha \mathbf{F}} + \frac{2.3RT}{\alpha \mathbf{F}} \log (i/k)$$

Applying this relation to the irreversible line in Fig. 4, with i constant, gives $\Delta H^{\ddagger} = \eta \alpha \mathbf{F}$ at absolute zero temperature; assuming $\alpha = 0.5$, $\Delta H^{\ddagger} = 14.5$ kcal/g-mole. The apparent exchange current density at −52°F from Fig. 7 is 0.3 mA/cm². From these data, the values of exchange current density at various temperatures are shown in Table III, with values of $b = 2.3RT/\alpha\mathbf{F}$. It must be clearly understood that the data presented here are not sufficient to prove the existence of a charge transfer-controlled reaction with the determined kinetic parameter. However, since Eq. [3] appears to describe the results fairly well, it can be used as a basis for the discussion of distributed reaction in the next section.

Equation [1] shows that water is the reactant to be transported from the bulk of the electrolyte through the pores of the porous electrodes to the interior. Even at 31 w/o of KOH, water is still present in high molar concentration in the electrolyte, and application of the Austin ϕ criteria (6) shows that distributed reaction will be due principally to ohmic effects. This greatly simplifies analysis of the system because an analytical solution exists for this case when η is large enough for the reaction to be considered irreversible. The basic equation (6) for a plane, porous electrode in which the pores are small compared to the thickness of the electrode is

$$d^2\eta/dx^2 = i_o S\rho\{(R/R_b) \exp(\alpha\eta/b) - (P/P_b) \exp[-(1-\alpha)\eta/b]\} \quad [5]$$

This equation relates the polarization η at a position x (measured from the back face of the electrode) to the distance x, where η is a function of x,η (x); S is the electroactive area per unit volume of electrode, cm²/cm³; ρ is the effective specific resistance of electrolyte in pores, ohm cm; i_o is the true exchange current density A/cm² at a reactant concentration of R_b and R is the concentration at x, g-moles/cm³; P_b, P are the corresponding product concentrations. Since water is present in high concentration, $R/R_b \sim 1$, and for the second term of Eq. [5] negligible

$$d^2\eta/dx^2 = i_o S\rho \exp(\alpha\eta/b) \quad [6]$$

The solution to this equation has been given elsewhere (15) and only the results of significance to the present work will be given. At low values of η (but still large enough for irreversible reaction), the total current density is approximated by

$$i = I_A \exp(\alpha\eta/b) \quad [7]$$

where

$$I_A = i_o SL$$

Thus a normal Tafel region may be seen with an apparent exchange current density, I_A, which represents complete utilization of the interior of the electrode. On the other hand, when reaction is concentrated toward the electrolyte face

$$i = I_0 \exp(\alpha\eta/2b) \quad [8]$$

where

$$I_0 = \sqrt{2i_o Sb/\rho\alpha}$$

Thus a Tafel slope of double the normal value is predicted, and L does not occur in the apparent current density as expected if the deep interior of the elec-

Table III. Exchange currents and Tafel slopes as a function of temperature based upon −52°F data

Temperature °C	°F	°K	Exchange current i_o, mA/cm²	Tafel slope b, volt/decade
21	70	294	540	0.117
16	60	289	340	0.115
4	40	277	118	0.110
−7	20	266	40	0.106
−18	0	256	12.7	0.101
−29	−20	244	3.3	0.097
−40	−40	233	0.74	0.092
−51	−60	222	0.16	0.087
−62	−80	201	0.03	0.083

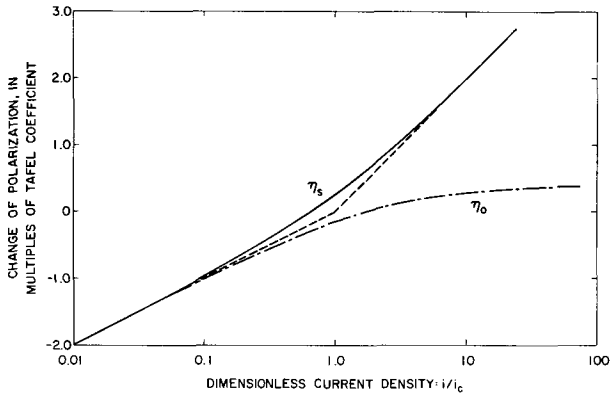

Fig. 15. Dimensionless plot of solution to Eq. [6]

trode is not contributing to the current-producing reaction. The simple relations of Eq. [7] and [8] are quite useful even though they are only approximations. For example, the current at which these two Tafel lines cross can be called the cross-over current, i_c, and

$$i_c = 2b/\alpha L\rho \qquad [9]$$

This is an important relation because it does not contain the kinetic parameters of i_o and S and it can be fairly accurately estimated knowing the porosity of the electrode. If the actual current density is much less than i_c, reaction is uniform through the electrode; if it is much greater than i_c, distributed reaction occurs, and Eq. [8] applies.

Figure 15 shows plots of the complete solution to Eq. [6] compared with the approximate solutions represented by the two Tafel lines. Polarization is plotted in dimensionless form $\eta/2.3b$, where 2.3b is the (log base 10) Tafel coefficient, that is 0.12V at room temperature, $\alpha = \frac{1}{2}$. The zero of the polarization scale is arbitrarily taken at $i/i_c = 1$; in practice this point would correspond to a definite polarization which would be higher for a lower exchange current, and the zero of the scale is shifted accordingly (15). The maximum deviation in polarization of the complete solution from two Tafel lines is about 2.3b/4, that is, 30 mV at room temperature.

It is not claimed that the current-polarization relation is given exactly by two straight Tafel lines or by the curve in Fig. 15, since the equations are derived for an idealized system. However, it seems likely that the equations will apply well enough to aid in deciding what thickness of electrode should be used for a given duty, even if they cannot predict the exact shape of the current-polarization relation.

Table IV shows values of $I(O)/I(L)$, $I(\frac{1}{2})/I(L)$ *vs.* i/i_c, where $I(O)/I(L)$ is the ratio of the specific currents at $x = 0$ and $x = L$, $I(\frac{1}{2})/I(L)$ the ratio of specific currents at $x = L/2$ and $x = L$. These represent the relative rates of reaction at these positions, obtained from the solution of Eq. [6] with the appropriate boundary conditions (15). As expected, as i/i_c increases, reaction is less and less uniform throughout the electrode.

Considering the conditions for the data in Fig. 12, the specific conductivity of electrolyte is 20 ohm-cm, and L is 50 mil = 0.127 cm. The labyrinth factor (q/θ) can be taken as about 2 giving $\rho = 40$ ohm-cm. From the Tafel slope of 85 mV, $b/\alpha = 0.085/2.3 = 0.037$V. Thus $i_c = 14.6$ mA/cm², and Table IV predicts that a current density of 30 mA/cm² would give $I(O) : I(\frac{1}{2}) : I(L) :: 0.22 : 0.3 : 1$. Figure 12 gives the relative rates of reaction as roughly 0.25:0.4:1. This is a remarkable agreement bearing in mind that the reactive surface is undergoing change during the discharge, and that the transfer factor may also be changing during discharge. A more exact way of comparing theoretical with experimental results is as follows. The solution to the equation enables the fraction of the reaction occurring between 0 and x to be calculated, or the fraction between x_1 and x_2, for any value of i/i_c.

In a later and more complete paper, extensive tabulated solutions will be given which will enable the appropriate data to be readily picked out. The specific solution to be used here is that the fraction of reaction, $i(x)/i$, occurring between 0 and x is related to the total current density (i), the cross-over current (i_c), and fractional position in the electrode (x/L), by

$$i/i_c = X \tan X \qquad [10]$$

$$i(x)/i = \tan\left(\frac{x}{L}X\right) \Big/ \tan X \qquad [11]$$

X is an intermediate in the calculation, defined by Eq. [10]. Values of $i(x)/i$ can be compared directly with the experimentally determined fraction of reaction occurring in the various slices making up the electrode. Table V gives results for electrodes made of two sections.

It can be seen that agreement between predicted and experimental is good. The percentage of reaction occurring in each section of the 50 mil stack of Fig. 12 were predicted to be 11.6, 13, 16, 22, 38; the experimental values were 11, 13, 17, 25, 34.

The above results indicate that it is possible to predict the effect of distributed reaction for one electrode thickness. At −52°F, the estimated value of i_c for the 10 mil thick HDL electrode is 73 mA/cm². For 30 mA/cm², i/i_c is 0.41 which corresponds to $I(O)/I(L)$ of about 0.7; the predicted increase of polarization above a uniform reaction condition is about 11 mV. Thus at 30 mA/cm², a distributed reaction effect is present but it is not very great. At higher temperatures or at lower current densities, the distributed reaction effect is negligible for the HDL electrodes. Similar reasoning can be applied to the electro-forming of the 10 mil electrodes, which was carried out at 200 mA/cm² on each side of the electrode; this corresponds to an electrode used with current on one face with thickness 5 mils. At room temperature, the effective specific resistance of electrolyte can be estimated at about 10 ohm-cm, giving an estimate of i_c of about 500 mA/cm². Again the value of i/i_c of 0.4 corresponds to a greater rate of production of Ag_2O at the electrolyte face than in the interior and the ratio of Ag_2O to Ag in the outer face will be somewhat higher than the average of 50:50, while it will be somewhat less in the interior.

The above calculations also go some way in explaining the effect of porosity shown in Fig. 10. The more porous electrodes will avoid distributed reaction

Table IV. Calculated values of $I(O)/I(L)$, $I(\frac{1}{2})/I(L)$ *vs.* i/i_c

i/i_c	$I(O)/I(L)$	$I(\frac{1}{2})/I(L)$
0.010	0.990	0.995
0.169	0.852	0.888
0.273	0.772	0.817
0.410	0.682	0.746
0.588	0.594	0.671
1.005	0.427	0.517
1.83	0.249	0.333
3.09	0.132	0.193
4.62	0.072	0.113
10.10	0.020	0.035

Table V. Predicted *vs.* experimental values of percentage of reaction in each electrode section

Temp, °F	i, mA/cm²	Electrode thickness, cm	i/i_c	Percentage of reaction in electrode section: Back section, Predicted	Back section, Experimental	Front section, Predicted	Front section, Experimental
−35	150	0.050	2.25	29	24	71	76
−35	100	0.050	1.50	35	36	65	64
−35	30	0.050	0.45	42	40	58	60
−35	10	0.050	0.15	49	49	51	51
−52	50	0.050	1.35	35	43	65	57

at these conditions, whereas the 20% porous electrodes will be undoubtedly in the completely distributed reaction condition and will have higher polarization at a given state of discharge because only part of the electrode interior is being utilized. When the reaction is concentrated at the outer face, a layer of fully discharged material will build up over the electrolyte face and this layer will grow thicker into the electrode as discharge proceeds. Figure 13 indicates that at the point where discharge of the 50 mil stack was stopped, polarization was increasing quite rapidly. Figure 12 shows that this corresponded to complete discharge of the outer face of the electrode. It is possible that this fully discharged layer is relatively impermeable, giving an additional *IR* polarization for ionic transport. Because of the double-layer capacity of this porous layer, this type of *IR* polarization will not disappear instantaneously when current is interrupted. (This postulate will be tested in future work by fully discharging a 10 mil electrode, making it the outer face of a 50 mil stack, and discharging the stack.)

Again, the concept of distributed reaction goes part of the way to explaining region f in the discharge. The evidence is that polarization increases more rapidly with the state of discharge when the reaction is concentrated toward the outer face. At lower currents and higher temperatures, a more extended plateau of region e is seen, followed by sudden development of region f at high percentage discharge. As current is increased or temperature decreased, region f starts at a lower per cent of discharge and is more spread out.

There are probably several reasons for the increase of polarization in region f. Certainly, much increased polarization is expected when the state of discharge has progressed to the point where the active area of Ag_2O present in the electrode is too small to support current. However, the Tafel relation indicated in region e suggests that a simple, charge-transfer reaction is rate-controlling. It has already been argued that this cannot involve a reaction occurring on an Ag_2O crystal, since the Ag_2O is nonconductive, would not have a simple double-layer on its surface, and would not give simple Tafel-type rate relations. Thus it appears that the reaction of Eq. [2] is the likely candidate.

$$Ag(s) + Ag^+ + e^- \rightarrow 2Ag(s) \qquad [2]$$

(This will be examined further by varying the area of silver by orders of magnitude keeping other parameters constant, and determine the effect on polarization.) The influence of Ag_2O would occur only via its production of dissolved Ag^+. If the rate of dissolution of Ag_2O from the crystallites (electro-formed electrodes) or powder (pressed electrodes) of Ag_2O is large, the concentration of Ag^+ in electrolyte in the pores of the electrode would be maintained constant until almost all of the Ag_2O had been reacted.

If the above postulate is correct, increased activation polarization can be obtained (at low temperatures where the polarization corresponds to irreversible reaction) by decrease in the concentration of Ag^+. This could arise from a slow rate of dissolution, or from a slow rate of mass transfer to the conductive silver matrix. Examining this last hypothesis, it is difficult to give a mean diffusion path from the surface of an Ag_2O particle to the surface of an adjacent Ag particle (16). In electro-formed material, the crystals of Ag_2O are presumably in contact with Ag, and the mean distance must be of the order of 1 micron or less. In the powder electrodes, if the elementary particles of Ag_2O and Ag are well mixed, the distance will again be of the order of 1 micron. However, if an agglomerate of Ag_2O particles touches an agglomerate of Ag particles, the mean diffusion path might correspond to the agglomerate size rather than the particle size.

Using the solubility-diffusivity results of Miller (17), the room temperature values are about $(3)(10^{-4})$ moles Ag_2O/liter and $(3)(10^{-6})$ cm²/sec. Taking a value of 100 cm² as a conservative estimate of the internal area of 1 cm² plane of the electrode, the steady-state limiting current due to mass transfer of Ag_2O across a diffusion path of 1 micron is

$$i_L \simeq (10^2)(2)(96500)(3)(10^{-7})(3)(10^{-6})/(10^{-4}) \text{ A/cm}^2$$
$$\simeq 180 \text{ mA/cm}^2 \text{ plane}$$

As temperature decreases, the diffusion coefficient will decrease comparably to the increase in electrolyte resistivity and the solubility may also decrease. Thus the order-of-magnitude calculation shows that region f at the higher current densities and lower temperatures might involve mass transfer limitations of dissolved silver between an Ag_2O surface and an adjacent silver surface within the electrode. This mass transfer effect would not be altered by stirring the electrolyte except inasmuch as stirring could move electrolyte within the micropores of the electrode. Presumably this mass transfer effect becomes more important as the electrode discharges because, the smaller particles of Ag_2O are consumed first leading to an increased mean diffusion path.

Conclusions

At low temperatures the galvanostatic discharge curve in general contains five regions of polarization with time; a, b, c, d, e, f. Region a represents an immediate *IR* polarization, due primarily to the electrolyte path between the test and Luggin tip. Region b is double-layer charging, and is followed by a short plateau c which corresponds to discharge of some active material. Region c progresses into a polarization peak at d, and is probably a nucleation overpotential. After the peak, a plateau at region e is obtained which appears to correspond to an activated, charge transfer reaction, possibly $Ag(s) + Ag^+(aq) + e^- \rightarrow 2Ag(s)$. In this region the active area of silver is not changing very much.

Finally, the polarization again increases as the electrode tends to more complete discharge, region f, which again is not due to an increased electronic *IR* effect. If the electrode current density and temperature are such as to cause distributed reaction, the electrode reacts more toward the face, giving increased polarization and a more rapid onset of region f. The increased polarization in region f may be due to layers of discharged material formed at the electrode face and to mass transfer of dissolved Ag_2O from Ag_2O surface to Ag surface.

Although the work in this paper is obviously not a comprehensive picture of how this electrode behaves at low temperature, the plateau region for steady discharge can be fairly quantitatively considered. First, the current density-polarization relation is the Tafel relation

$$\eta = b \log i - b \log I_A \qquad [12]$$

where I_A is given by

$$I_A = i_o SL$$

and the temperature coefficient of i_o is $\exp(-14.5/RT)$. In order to get lower polarization (loss of ideal potential) at a fixed temperature, the apparent exchange current I_A must be increased. This can be done by increasing the thickness L (but see below), or by increasing the specific reactive area S by using very fine Ag and Ag_2O powder. The thickness L should be less than a value L_c defined by

$$i_m < i_c < 2b/\alpha L_c \rho \qquad [13]$$

where $\alpha = \frac{1}{2}$ for the results reported in this paper, and i_m is the maximum current density of operation. Thicker electrodes will give lower polarization when $i << i_m$, but the value of i_c is reduced. When $i_m \geq i_c$, the reaction is concentrated toward the outer face, and polarization increases rapidly with increased i.

It is essential to design electrode thickness and porosity to avoid entering into region f at the outer

face when the electrode is only slightly discharged in the interior, for then the polarization increases rapidly with time during discharge. The effect of porosity is contained within the factor ρ, which is the effective specific resistance of electrolyte within the electrode. This factor appears to increase rapidly as porosity is decreased, thus causing a smaller i_c. To avoid this effect, porosities of 60 to 80% should be used. These high porosities reduce the value of S and the coulombic capacity of the electrodes so, again, a balance must be made between the various factors dependent on the conditions of operation and the duty required.

Acknowledgments

The authors wish to express their appreciation to the Harry Diamond Laboratory, Washington, D. C., and the Office of Vice President for Research of the Pennsylvania State University for their support of this work.

Manuscript submitted June 18, 1970; revised manuscript received *ca.* Nov. 16, 1970. This was Paper 312 presented at the Montreal Meeting of the Society, Oct. 6-11, 1968.

Any discussion of this paper will appear in a Discussion Section to be published in the December 1971 JOURNAL.

REFERENCES

1. L. G. Austin and E. G. Gagnon, Report No. 2, October, 1966, Contract No. DA 49-186-AMC-197 (D), United States Army Materiel Command, Harry Diamond Laboratories, Washington, D. C.
2. M. Fleischman and H. R. Thirsk, in "Advances in Electrochemistry and Electrochemical Engineering," Vol. 3, p. 123, P. Delahay, Editor, Interscience Publishers, Inc., New York (1963).
3. D. A. Vermilyea, in "Advances in Electrochemistry and Electrochemical Engineering," Vol. 3, p. 211, P. Delahay, Editor, Interscience Publishers, Inc., New York (1963).
4. C. P. Wales and J. Burbank, *This Journal*, **112**, 13 (1965).
5. L. G. Austin, *Trans. Faraday Soc.* (London), **60**, 1319 (1964).
6. L. G. Austin, in "Handbook of Fuel Cell Technology," p. 1, C. Berger, Editor, Prentice Hall, Inc., New Jersey, (1968).
7. R. deLevie, Advan. Electrochem. and Electrochem. Eng., **6**, 359 (1967).
8. E. G. Gagnon, Ph.D. Thesis, The Pennsylvania State University, University Park, Pa. (1970).
9. W. J. Hamer and D. N. Craig, *This Journal*, **104**, 206 (1957).
10. L. G. Austin and S. C. Almaula, Report No. 10 Contract No. DA 49-186-AMC-146 (D), United States Army Materiel Command, Harry Diamond Laboratories, Washington, D. C., May (1966).
11. D. H. Morrell and D. W. Smith, "Proceedings of The 5th International Symposium on Power Sources," Pergamon Press, New York (1967).
12. J. E. Schroeder, D. Powli, and H. J. Seim, 154th Meeting A. C. S., Division of Fuel Chem. Preprints, Sept. 10-15, Vol. 11, No. 3, pp. 81-90, (1967).
13. H. R. Thirsk and D. Lax, Paper 287 presented at Electrochem. Soc. Meeting, Montreal, October 6-11, 1968.
14. W. Pauli, Harry Diamond Laboratory, Washington, D. C., Private communication.
15. L. G. Austin and E. G. Gagnon, Paper submitted for publication.
16. L. G Austin, I. and E. C. Fundamentals, **3**, 321 (1965).
17. B. Miller, Paper 291 presented at Electrochem. Soc. Meeting, Montreal, October 6-11, 1968.

Electrochemical Detection of H_2, CO, and Hydrocarbons in Inert or Oxygen Atmospheres

A. B. LaConti and H. J. R. Maget*

General Electric Company, Direct Energy Conversion Business Section, Lynn, Massachusetts 01905

ABSTRACT

A unique electrochemical sensor is described for quantitatively detecting hydrogen in gas mixtures containing electrochemically inert species. Limiting diffusion current measurements in the range of +0.25 to 0.65V *vs.* a platinum electrode in the same acid solution are proportional to the hydrogen content in the bulk phase. When active species, such as oxygen, are present in binary or ternary gas mixtures, the hydrogen content of the gas phase is determined by maintaining a working electrode potential of +1.06V (oxygen or air rest potential on Pt black in acid) at which hydrogen is immediately ionized even in the presence of oxygen on the electrode surface. The feasibility of detecting carbon monoxide and hydrocarbons in oxygen-containing atmospheres using the electrical biasing technique is demonstrated. The limitations and practical applications of the sensing devices are discussed.

The electrochemical oxidation of hydrogen takes place at high rates and low anodic overvoltages in most aqueous electrolytes, even at room temperature. The process is accelerated by noble metal electrocatalysts such as platinum or palladium which display rather large kinetic constants (high exchange current densities). These anodic overvoltages are limited by potentials at which surface oxidation of the metal may take place, followed eventually by oxidation of the water in the electrolyte. Over a large potential region the electrode surface can be considered as clean, *i.e.* the surface concentration of hydrogen is essentially zero (Nernst's equation can be used to predict extremely low equilibrium partial pressures of hydrogen), and simultaneously the surface concentration of metal oxide is nearly zero. If the working electrode is maintained at potentials corresponding to the region of zero-surface coverage, all hydrogen arriving on the electrode will be instantaneously ionized. The rate of hydrogen ionization measured as a Faradaic current is then equal to the rate of hydrogen diffusion to the electrode. Under these conditions the rate of diffusion is proportional to ΔC (hydrogen concentration difference between the bulk gas phase and the electrode surface, $\Delta C = C_b - C_E$). However, since C_E is essentially equal to zero, the measured current is proportional to the hydrogen concentration in the bulk gas phase.

* Electrochemical Society Active Member.

Key words: gas sensor, fuel cell, electrocatalyst, ion exchange, membrane, limiting current.

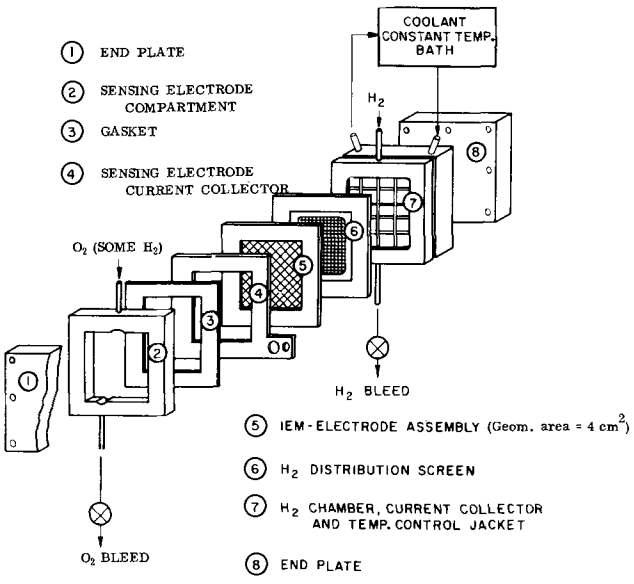

Fig. 1. Electrochemical hydrogen sensor

In the presence of oxygen, the situation is more complex since the electrode will tend to stabilize around the oxygen electrode rest potential. The detection of hydrogen in oxygen-containing atmospheres is accomplished by electrically biasing the platinum black sensing electrode at +1.06V [1] *vs.* a Pt/H_2 electrode in the same solution. The principles underlying the choice of the biasing potential and the unique features of the detector are as follows.

The rest potential of a hydrogen/oxygen acid fuel cell is 1.06V. When a potentiometer or similar device for applying a constant d-c voltage is used to counter the 1.06V, no current will flow in an external circuit. If hydrogen or other oxidizable gas is present in the oxygen stream and the applied potential is maintained at 1.06V, the following reactions will occur assuming hydrogen as the oxidizable gas.

Electrode	Atmosphere	Electrode reactions
Sensing	Some H_2 in O_2 stream	$H_2 = 2H^+ + 2e$
Counter-reference	Pure H_2	$2H^+ + 2e = H_2$

The current flowing in the external circuit is directly proportional to the quantity of hydrogen present in the oxygen stream. The novelty of the concept is that the electrical bias potential is exactly equal to the rest potential of the Pt/O_2 electrode; thus, making the device insensitive to oxygen and the utilization of a stable counter-reference electrode. Pure H_2 is passed over the hydrogen evolution counter-reference electrode to insure a quasi-constant potential of 0.0V. A diagram of the sensor is given in Fig. 1.

Experimental

All work on the development of a hydrogen sensor was conducted using a sulfonic acid cation exchange membrane (AMF-C 311) as the electrolyte. Teflon treated, platinum black electrodes (5 mg/cm^2 of Pt) having gold screen current collectors were attached to the membrane. The geometric area of the electrodes was 4.0 cm^2. A diagram of the device which is essentially an electrically biased cation exchange membrane fuel cell is given in Fig. 1. For complete cells, the hydrogen electrode served as a combination counter-reference electrode. For potentiostatic half-cell measurements, a reference Pt/H_2 electrode which contacted the membrane through a H_2SO_4 solution ($pH = 0$) was used as a third electrode. During the half-cell measurements, air was in contact with the counter-electrode. All cells were run at 25°C unless specified otherwise.

[1] All voltages are referred to a Pt/H_2 electrode in same solution unless otherwise specified. Signs for half-cell reactions are those discussed by Licht and de Bethune (1).

Experimental investigations were conducted on half and complete cells under controlled conditions, to determine the magnitude of the sensing electrode response when exposed to binary H_2-N_2 gas mixtures (limiting diffusion current measurements) and gas mixtures containing an oxidant, *i.e.* H_2-O_2 or H_2-N_2-O_2 (Faradaic hydrogen ionization current at oxygen electrode potentials).

Simultaneously, response times were measured to determine the time necessary before stabilization of the measured variable could be achieved. Half-cell measurements were necessary because of the technique used and also to avoid possible interference of the counterelectrode on the output signal. An oxygen electrode (as a possible counterelectrode in a hydrogen sensor) frequently displays potential fluctuations depending on variables such as electrolyte concentration, oxygen partial pressure, *etc.* These problems were alleviated by using potentiostatic techniques or quasi-reversible counterelectrode such as pure H_2 electrodes.

Relation between voltage and limiting currents.—The electrochemical oxidation of H_2 (pure or in presence of inert gases as nitrogen) takes place at high rates and low anodic overvoltages up to conditions where a rate-controlling process limits oxidation rates or up to a potential where oxygen deposition occurs on the electrode surface. Figure 2 displays this behavior on a 4.0 cm^2 platinum black anode operating with a binary H_2/N_2 mixture. In this instance, a 3 v/o (volume per cent) H_2 in N_2 was used in order to limit the maximum observable current. At anodic potentials between +0.25 and 0.65V, the limiting diffusion current is potential insensitive. Beyond +0.70V, oxygen deposition reduces the current progressively until the oxygen rest potential is observed. For purpose of comparison, a polarization curve for cathodic oxygen reduction is also presented in Fig. 2. From these results, it can be concluded that an anode operating in the range of +0.25 to 0.65V should display limiting diffusion currents (at low hydrogen partial pressures) essentially insensitive to the potential. Based on these observations, experimental investigations were started to determine the electrode current as a function of hydrogen partial pressure and the response time required to observe current stability.

Effect of partial pressure on limiting diffusion currents.—Half-cell measurements were conducted at a fixed potential of +0.45V as a function of hydrogen partial pressure in binary H_2/N_2 mixtures. The results plotted in Fig. 3 show linearity between current and partial pressure

$$i = KC(H_2) \qquad [1]$$

where i = maximum observed current in mA, $C(H_2)$

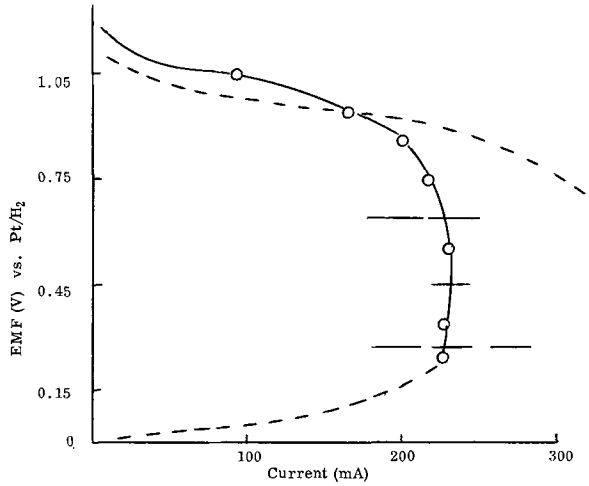

Fig. 2. Voltage-current relationship, ○ for increasing anodic potentials (H_2-N_2 oxidation), - - - for cathodic oxygen reduction.

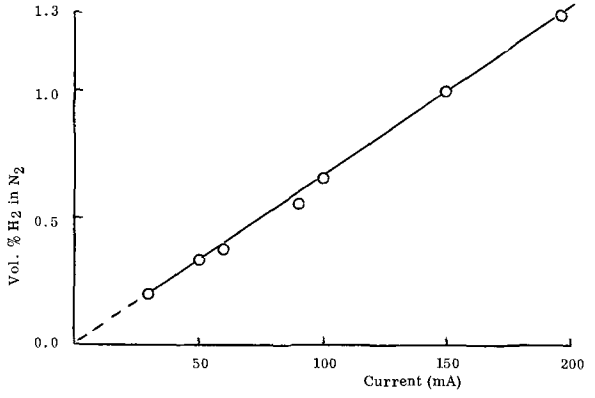

Fig. 3. Effect of hydrogen partial pressure in H_2-N_2 mixtures on limiting currents.

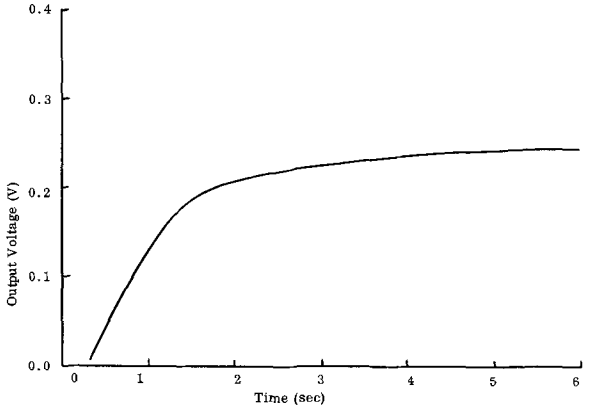

Fig. 4. Voltage (or current)—time response of the hydrogen sensing electrode.

= v/o H_2 in the gas phases, and the proportionality constant $K = 40$ with a maximum variance of ±3%.

Current time response.—Measurements on half cells and complete cells show that current read-out becomes stable within 4.5 to 6 sec. Figure 4 illustrates a representative current time behavior of a binary H_2/N_2 mixture. Response time at any fractional current (or equivalent potential) read-out can be estimated from the relationship

$$(i - I)/i = e^{t/\tau} \qquad [2]$$

where I = current observed at time t, sec
τ = time constant = 1 sec

The time constant will be somewhat sensitive to cell design, size, geometry, etc.

Hydrogen/oxygen (air) gas mixtures.—The rest potential of a Pt/O_2 half cell in acid solution at 25°C is approximately +1.06V, and currents observed in absence of hydrogen at this potential are only of the order of microamperes. Under these potential conditions, any current observed after exposure of the electrode to a hydrogen-containing gas mixture is related to the rate of hydrogen oxidation. This condition is favorable for hydrogen sensing since: (*i*) chemical surface oxidation of hydrogen is essentially avoided, (*ii*) the surface concentration of hydrogen is always maintained at an extremely low value, and (*iii*) hydrogen is electrochemically oxidized as soon as it appears on the surface. Comparative results for hydrogen/oxygen and hydrogen/air mixtures are presented in Fig. 5. Currents at various concentrations of hydrogen in oxygen and air were observed for flow rates of 1 ml/sec at a fixed potential of +1.06V. Flow rates of 3 ml/sec were also studied to show that the observed currents are not influenced by appreciable variations of hydrogen partial pressure along the electrode surface. Results between 1 and 3 ml/sec are identical. Again the currents

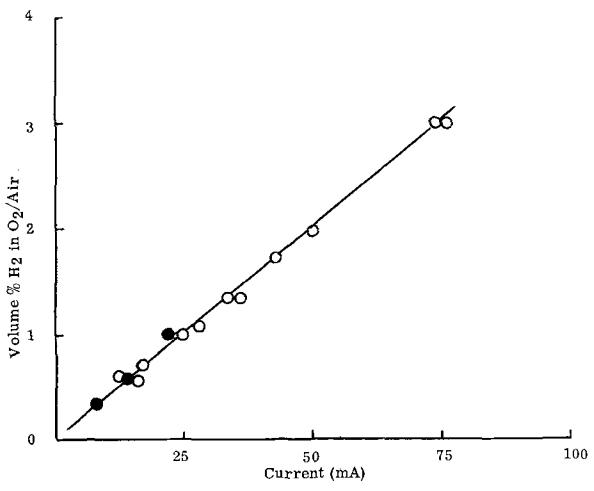

Fig. 5. Effect of hydrogen partial pressure in H_2-O_2 (air) mixtures on currents in: ○ half cells and • complete cells.

are proportional to the hydrogen partial pressure and can be expressed by Eq. [1]. If (*i*) is in mA, the constant $K = 25$ with a maximum variance of ±2%.

Results on complete cells.—To show applicability of the approach to an ion exchange membrane fuel cell, the current read-out was determined for a complete cell. Now it was essential to keep the counterelectrode at a quasi-constant potential (since this approach does not include the presence of a reference electrode), and thus be able to apply a cell and working electrode potential of +1.06V.

This can be accomplished by flowing hydrogen over the counterelectrode and keeping the electrode potential at nearly 0.0V. Applying 1.06V to the cell by means of an external constant voltage device insures a working electrode potential of approximately +1.06V since the hydrogen evolution counterelectrode is nearly reversible. Under these conditions, the fuel cell should behave essentially in a manner comparable to a half cell. All the results obtained on half cell and complete cells for H_2/O_2 and H_2/air mixtures are presented in Fig. 5. Linearity between current and partial pressure was observed in all cases.

Detection of Carbon Monoxide in Oxygen/Air.—The electrical biasing technique was extended to the detection of CO in oxygen-containing atmospheres. An optimization was made of the sensing electrode structure, electrolyte, and electrolyte concentration to obtain reproducible stable currents of less than 1.0 mA. A reversible metallic counter-reference system was substituted for the Pt/H_2 electrode. Studies entailed an investigation of the temperature characteristics of the sensor when detecting carbon monoxide in oxygen.

In the development of the hydrogen sensor, a sulfonic acid ion exchange membrane (IEM) served as the electrolyte. The problem with the (IEM) system is that it is difficult to find a reversible counter-reference electrode other than Pt/H_2, and water management is difficult. A sulfuric acid electrolyte was investigated due to its good conductivity, and also many reversible metal/sulfate couples exist. A 63% by weight sulfuric acid solution was chosen because of its very low vapor pressure at 25°C, 2.4 Torr, making it insensitive to flow of gases, which affects the concentration and temperature changes due to water evaporation.

A constant voltage source kept the carbon monoxide sensing electrode at a fixed potential *vs.* a stable metallic electrode which served both as a counter and reference electrode. An Alford-Niedrach (2) platinum on boron carbide electrode containing 3.4 mg/cm² platinum and a tantalum current collector served as the sensing electrode at a fixed potential *vs.* a stable kept at 0.18 cm² to insure a fast response time and minimal polarization of the counter-reference electrode,

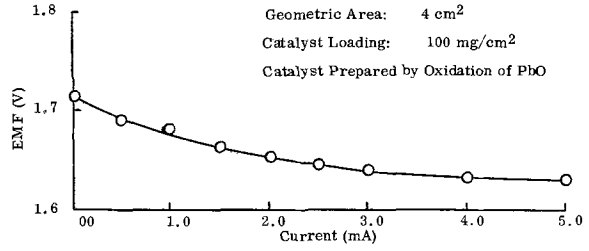

Fig. 6. Polarization of PbO_2 electrode in 63% H_2SO_4

i.e. observed currents were less than 1.0 mA. Of the metallic couples investigated as counter-reference electrodes, the $PbO_2/PbSO_4$, H_2SO_4 was most compatible with the system under investigation exhibiting minimal polarization when undergoing a reduction process in the sensor. The polarization characteristic of the lead peroxide electrode is demonstrated in Fig. 6 where a current-voltage curve is given for the cell

$$Pt/H_2, H_2SO_4\ (63\%), PbSO_4/PbO_2$$

The oxidation of CO on platinum black has been a subject of recent review (3, 4). Carbon monoxide adsorbs strongly on platinum, and appreciable reaction in acid only occurs at voltages greater than +0.70V as can be seen in the current voltage curve given in Fig. 7 for oxidation of CO on platinum black. At +1.06V the electrochemical oxidation of CO to CO_2 on platinum black occurs immediately, thus it can be expected at this voltage faradaic currents proportional to bulk concentration of CO will be observed.

The prototype sensor for detection of CO consisted of a Pt on B_4C electrode (3.4 mg Pt/cm²) with a sensing area of 0.18 cm², H_2SO_4 (63%) and PbO_2 counter-reference electrode containing 100 mg/cm² PbO_2 with geometric area of 4 cm². Tantalum current collectors were employed for both electrodes. When the Pt electrode was exposed to oxygen, the observed $\Delta E(V_r - V_1)$ was 0.71 for the cell

$$Pt/O_2, H_2SO_4\ (63\%), PbSO_4/PbO_2$$

When this voltage was exactly matched with a constant voltage source, no current flowed. When CO was present in O_2/air and the applied potential was maintained at 0.71V, a current proportional to the CO in the bulk phase was observed. The results plotted in Fig. 8 show linearity between current and partial pressure

$$i = KC(CO)$$

where C(CO) = v/o CO in O_2/air, the proportionality constant $K = 0.19$ with a maximum variance of ±6%. The stability and reproducibility of the sensor was examined by introducing three times daily a fixed concentration of CO in O_2. For a CO in O_2 sample, a 0.42 ± 02 mA reading was obtained for over a three-week period.

An investigation was conducted on the temperature characteristics of the sensor when detecting carbon monoxide in oxygen. An Arrhenius plot of log i *vs.* $1/T$ was found to be linear (Fig. 9). The observed current for oxidation of CO in O_2 approximately doubles for each 10°C increase in temperature. The described sensor appears to be a stable, low-cost sensitive instrument for detecting carbon monoxide in air or oxygen from 20° to 80°C.

Detection of hydrocarbons.—The CO sensor operating at room temperature is insensitive to hydrocar-

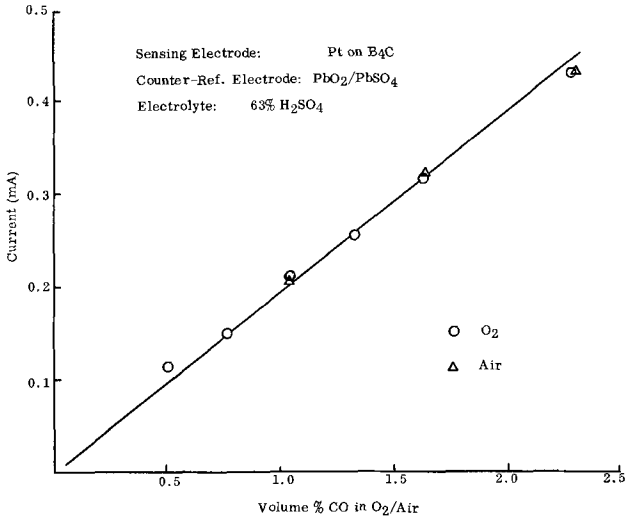

Fig. 8. Effect of CO partial pressure in CO-O_2/air mixtures on currents.

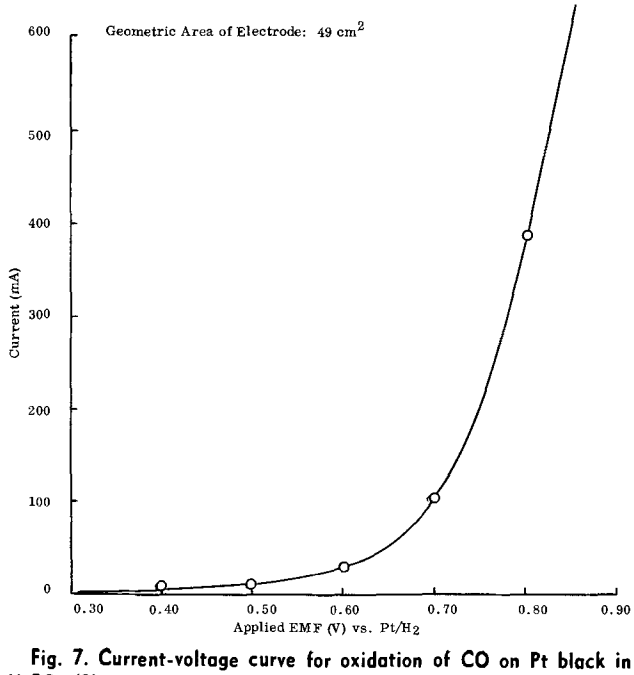

Fig. 7. Current-voltage curve for oxidation of CO on Pt black in H_2SO_4 (3).

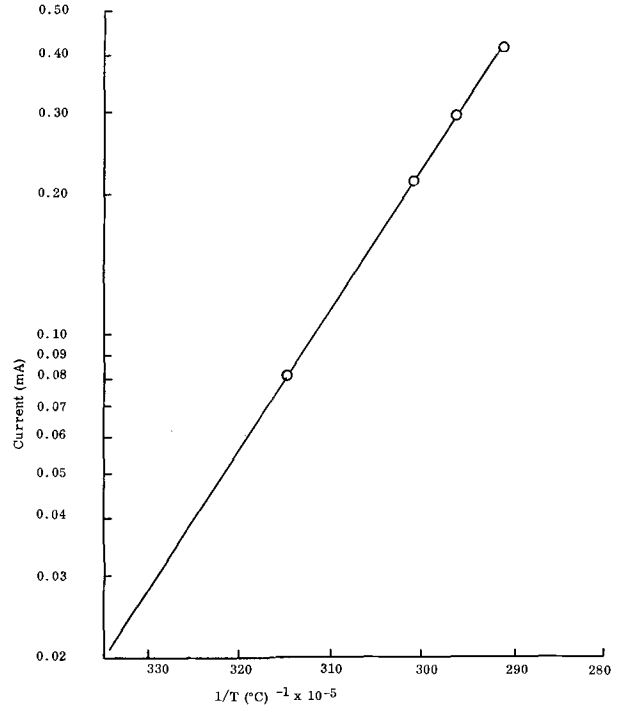

Fig. 9. Effect of temperature when oxidizing a fixed concentration of CO in O_2.

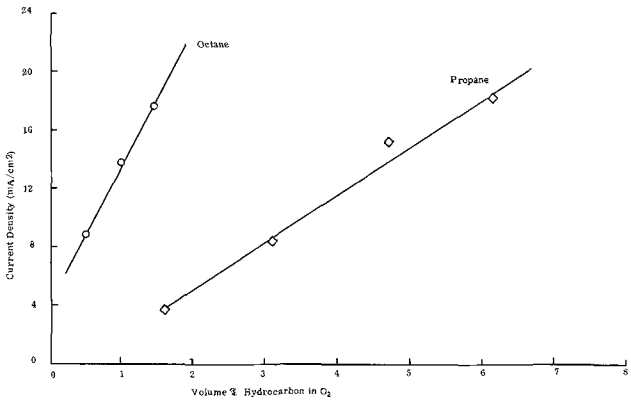

Fig. 10. Hydrocarbon gas detection with phosphoric matrix at 150°C.

bons. At elevated temperatures, however, the sensor will respond to hydrocarbons. The detection of hydrocarbons in O_2 was demonstrated with a fuel cell device consisting of a zirconium phosphate matrix saturated with H_3PO_4, at Pt black sensing electrode and a Pt/H_2 counter-reference electrode. A linear relationship was found between current and partial pressure of propane or octane in oxygen when the device was operated at 150°C as can be seen in Fig. 10. Of particular interest is the characteristic curve obtained for propane and octane. The novelty of the device is the insensitiveness to air or O_2 because of the biasing potential of +1.06V *vs.* Pt/H_2 applied to the sensor electrode.

Characteristics of the sensing devices.—The electrochemical sensors described have a lower limit of detection of approximately 500 ppm based on a volume basis. The prototype sensor described for detection of CO which uses a PbO_2 counter-reference electrode is a practical device for detecting easily oxidizable species such as H_2 and CO in O_2 and air streams. Some practical applications include use of the device as a gas leak detector to avoid the formation of an explosive mixture such as H_2 in air and buildups of toxic levels of CO in air. Novel features of the device are low cost, portability, and simplicity. At the current stage of development, the detector cannot be used directly for trace analysis which is best done by spectroscopic techniques (5). A reasonable goal is to reduce the detection limit to 100 ppm by more accurate control of electronic circuitry and electrode manufacturing process. With an applied biasing potential of +1.06V, the sensing electrode is not readily poisoned by species which normally adsorb strongly on platinum at low anodic potentials such as CO at low temperature ($\leq$80°C) and hydrocarbon intermediates at high temperature ($\geq$100°C). At an anodic potential of +1.06V, these species are readily oxidized to CO_2. This was evidenced by a 3-week life test at 25°C for a CO in O_2 gas mixture and a 2-day run at 150°C for a propane in O_2 mixture.

Manuscript received August 24, 1970.

Any discussion of this paper will appear in a Discussion section to be published in the December 1971 JOURNAL.

REFERENCES

1. T. S. Licht and A. J. de Bethune, *J. Chem. Educ.*, **34**, 433 (1957).
2. L. W. Niedrach and H. R. Alford, *This Journal*, **112**, 117 (1965).
3. A. B. LaConti and M. E. Cranney, Measurement of Electrochemically Active Surface Area of Fuel Cell Electrodes, TIS 66 DE 5, General Electric Company, Lynn, Massachusetts, October 24, 1966.
4. S. Gilman, *J. Phys. Chem.*, **67**, 78 (1963).
5. R. K. Skogerboe, *Anal. Chem.*, **42**, 876 (1970).

Desalting by Means of Porous Carbon Electrodes

A. M. Johnson and John Newman[1]

The Marquardt Company, Van Nuys, California 91409

ABSTRACT

A porous electrode model is developed and analyzed for ionic adsorption on porous carbon. In the absence of concentration variations, the system behaves like a distributed network of resistances and capacitances. Experimental results support the basic model and show a preferential adsorption of divalent ions. Consideration is given to the optimization of operating parameters.

A process for desalting water can be based on periodic sorption and desorption of ions on the extensive surfaces of porous carbon materials. Blair and Murphy (1) have described early work. Electrodialysis, ion exchange, and the present method of ion sorption remove the electrolyte from the solution and should be economically suited to waters of moderate salinity. Processes like evaporation and reverse osmosis, which remove the solvent should be preferable for dealing with high salinities. In addition to the practical aspects of desalting, the present work is relevant to the analysis of the behavior of porous electrodes. Experimental verification obtained here would be a reflection on the basic validity of models commonly used for porous electrodes. The present system should also provide a convenient means to study parametric pumping (2, 3). Porous carbon electrodes can also be used for storage of electrical energy and for ion exchange processes.

[1] Permanent address: Department of Chemical Engineering, University of California, Berkeley, California 94700.
Key words: porous electrode, desalination.

Concepts of Charge Sorption

At any interface between an electrolytic solution and another medium, there is generally present an electric double charge layer, the interface as a whole being electrically neutral. On the solution side of the interface, the double layer consists of an excess of cations or anions from the electrolytic solution itself. It is the adsorption of the electrolyte here which is responsible for the desalting accomplished by this process. Porous carbon materials contain large interfacial areas, on the order of several hundreds of square meters per gram, and consequently it is possible to store a significant amount of salt in these electrical double layers. For our purposes, it is not particularly important to distinguish between ions of the solution which are tightly bound to the surface and those which exist in the diffuse layer adjacent to the surface.

It is presumed here that no charge passes directly from the carbon into the solution, and consequently a flow of current into the carbon is compensated by an

equal and opposite magnitude of charge on the solution side of the interface. In this case, the interface is similar to a simple electrical capacitor. Because of the small distances involved here, the double layer capacity can be quite high, on the order of 30 $\mu f/cm^2$. [The measurements of Evans (4) on porous carbons are of interest is the present application.] Grahame (5) has developed these concepts of the double layer in detail and gives sketches of the distributions of charge and potential near an interface as well as experimental results for double layer capacities and surface concentrations at mercury-solution interfaces.

The surface concentrations of the ions depend on the potential of the electrode, measured with respect to a suitable reference electrode. As the electrode is made more negative, it attracts cations and repels anions, and conversely. The absolute magnitude of ion adsorption is difficult to ascertain at solid electrodes. However, it is the variations in the amounts of adsorbed ions which are important in a process for desalting water. These can be represented by the quantity

$$f = \frac{dq_+}{dq} - \frac{dq_-}{dq} \qquad [1]$$

plotted in Fig. 1 as calculated from the data of Grahame (5) for the interface between mercury and a 0.3*M* NaCl solution. The potential is relative to a calomel electrode in the same solution.

The dashed curve in Fig. 1 is an idealization of the actual behavior and corresponds to a sharp change from sorption and desorption of cations at potentials more negative than V_z to sorption and desorption of anions at potentials more positive than V_z. In contrast, an increase in the net charge in the double layer can actually be accomplished by a combination of adsorption of cations and desorption of anions. The potential V_z indicates the potential at which the electrode changes from anion responsiveness to cation responsiveness. Strictly speaking, it does not represent the point of zero charge, which can be measured only with difficulty on solid electrodes.

We see from Fig. 1 that f can be less than -1 for positive potentials. This is due to specific adsorption of anions with a consequent adsorption of cations in the diffuse layer. The result is that more ions can be adsorbed than would be predicted from simple concepts of the double layer.

Porous Electrode Model

For the present system, the macroscopic model of porous electrodes (6) should be modified to account for the capacitive adsorption of ions. This is the only change which needs to be introduced. Two potentials are used, the potential Φ_1 of the porous matrix and the potential Φ_2 of the solution in the pores. Similarly, two current densities i_1 and i_2 are defined; these current densities are referred to the projected area of the electrode rather than to the areas of the individual phases. The concentrations c_i of species in the solution are referred to the volume of the solution phase; thus the concentration per unit volume of the electrode is pc_i where p is the porosity of the electrode. The fluid velocity v will be referred to the over-all area.

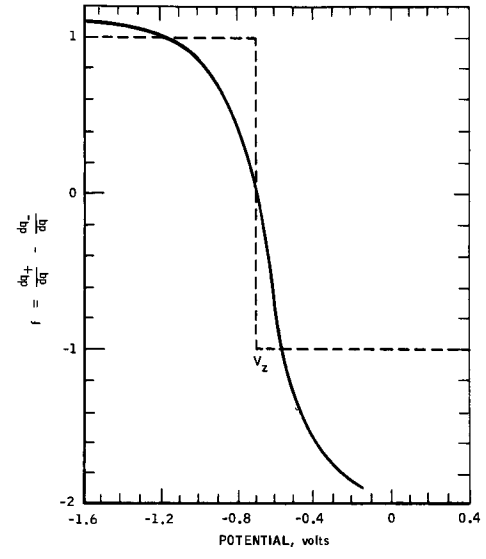

Fig. 1. Change of total ion sorption with potential, for the interface between mercury and a 0.3*M* NaCl solution.

The electrode consists of carbon particles with void spaces in between, but each particle is itself quite porous, with micropores which are much smaller than the particles. This accounts for the large surface area of porous carbons. The fluid flows between the particles but not through them, while the electric current in the fluid phase may or may not flow through the particles. At any rate, the surfaces of the micropores are electrically accessible to the solution phase. Material desorbed inside the particle will have to diffuse to the surface of the particle before it can enter the flowing stream. One could define a microporosity p_μ (corresponding to the void volume within the particles relative to the volume of particles) and a macroporosity p_M (the void volume between the particles divided by the total volume) as well as the over-all porosity p. These are related by

$$1 - p = (1 - p_M)(1 - p_\mu) \qquad [2]$$

At the interface between the matrix and the solution, the rate of change of the double layer charge (per unit volume of electrode) is

$$\nabla \cdot i_1 = -\nabla \cdot i_2 = -aC\frac{\partial(\Phi_1 - \Phi_2)}{\partial t} \qquad [3]$$

where C is the capacity per unit area and a is the interfacial area per unit volume. $\nabla \cdot i$, is the divergence of the current density in the matrix and represents flow of current from the solution to the matrix. This equation represents the major assumption of the model, that ionic adsorption can be approximated as a capacitive process, that the kinetics of adsorption do not limit the rates, and that faradaic reactions are negligible.

Let N_+ and N_- be the fluxes of cations and anions in the solution phase based on the over-all area of matrix and solution. We confine our attention to a solution with two types of ions; the rigorous treatment of complex waters is complicated, but their behavior can be adequately discussed on the basis of simple extensions of the present treatment of a binary electrolyte. A material balance for the ionic species reads

$$p\frac{\partial c_i}{\partial t} = -\nabla \cdot N_i - \frac{dq_i}{dq}\frac{\nabla \cdot i_1}{z_i\mathbf{F}} \qquad [4]$$

In the pore phase, the fluxes of ionic species can be expressed as

$$N_i = -z_i u_i \mathbf{F} p c_i \nabla\Phi_2 - D_i p \nabla c_i + c_i v \qquad [5]$$

Mobilities u_i and diffusion coefficients D_i are approximately equal to their values in a free solution except for tortuosity factors; that is, there is no need for an additional porosity factor. In the matrix, the current density obeys Ohm's law

$$i_1 = -\sigma\nabla\Phi_1 \qquad [6]$$

where σ is the effective conductivity of the matrix phase. The current density in the solution phase is due to the charge carried by ionic species

$$i_2 = \mathbf{F}\sum_i z_i N_i \qquad [7]$$

Finally, we adopt the electroneutrality equation for the solution phase

$$\sum_i z_i c_i = 0 \qquad [8]$$

Combination of Eq. [4], [5], and [8] yields an equation for the solution concentration

$$p\frac{\partial c}{\partial t} + v \cdot \nabla c = D\nabla \cdot (p\nabla c) - \frac{\nabla \cdot i_1}{z_+\nu_+\mathbf{F}}\left(t_- \frac{dq_+}{dq} - t_+ \frac{dq_-}{dq}\right) \quad [9]$$

if the mobilities and diffusion coefficients are taken to be constants and the fluid is incompressible. Here

$$D = \frac{z_+u_+D_- - z_-u_-D_+}{z_+u_+ - z_-u_-} \quad [10]$$

is the effective diffusion coefficient of the electrolyte

$$t_+ = 1 - t_- = \frac{z_+u_+}{z_+u_+ - z_-u_-} \quad [11]$$

is the cation transference number, and the solution concentration is

$$c = c_+/\nu_+ = c_-/\nu_- \quad [12]$$

where ν_+ and ν_- are the numbers of moles of cations and anions per mole of electrolyte.

Substitution of Eq. [5] into Eq. [7] yields an equation relating current and potential drop in the pore phase

$$i_2 = -\kappa\nabla\Phi_2 - z_+\nu_+\mathbf{F}(D_+ - D_-)p\nabla c \quad [13]$$

where

$$\kappa = z_+\nu_+pc\mathbf{F}^2(z_+u_+ - z_-u_-) \quad [14]$$

is the effective conductivity of the solution phase.

Assumptions in the Model

The fundamental Eq. [3] through [8] describe the porous electrode. For a solution of a binary electrolyte, Eq. [4], [5], [7], and [8] can be replaced by Eq. [9] and [13]. Thus, Eq. [3], [6], [9], and [13] represent five equations for the determination of the quantities c, i_1, i_2, Φ_1, and Φ_2.

These equations are typical of those used to analyze the behavior of porous electrodes, and the assumptions inherent in them are discussed in the literature (6, 7). Experimental verification with the present system would help to substantiate these models.

Here the transfer of charge from the solution to the matrix is assumed to occur by means of the capacity of the electric double layer. The effect of concentration changes on the potential relationships has been neglected in writing Eq. [3]. A similar assumption is involved if dq_i/dq in Eq. [4] is supposed to depend only on the potential difference $\Phi_1 - \Phi_2$ and not on the concentration. Thus, the charge and potential are assumed to be the main factors determining ionic adsorption, and the dependence of electrolyte adsorption on concentration is effectively ignored. One consequence of this assumption is that the velocity of a concentration wave through the bed is equal to the velocity of nonadsorbed solvent, whereas in a bed with concentration-dependent adsorption, this wave velocity is different (usually less) than the fluid velocity.

The double layer itself is assumed to be in local equilibrium at the appropriate concentration and potential difference $\Phi_1 - \Phi_2$. One might imagine that highly mobile ions (for example, hydrogen ions) would be preferentially adsorbed on the basis of transport considerations. Actually, equilibration times for the double layer (8) are quite short compared to the time scales involved here. The preferential adsorption of divalent ions from complex waters, mentioned later, is further evidence for equilibration of the double layer since divalent ions have lower mobilities, in general, than monovalent ions.

Faradaic or charge transfer reactions, also ignored here, could manifest themselves in three ways. First, they detract from the current used to charge the double layer. These can safely be ignored except at large applied potentials. Second, they can oxidize or reduce the surface, forming surface compounds or oxidizing the carbon matrix itself, and lead to a gradual change in the character of the electrodes. Finally, they can lead to a gradual change in the net charge on a pair of carbon electrodes used for desalting. This will degrade the performance if operating conditions had previously been optimized for the initial state of the electrodes.

The porous electrode model assumes that the concentration and potential Φ_2 in the solution phase are essentially uniform across a pore cross section (6, 7), which effectively means in the solution inside a porous particle as well as in the space between particles. Actually, as mentioned earlier, the electrolyte must diffuse from within a porous particle to the surface before it can reach the flowing stream. The time required for a particle of radius R to become 90% depleted by diffusion with an effective diffusion coefficient D is (9) 0.43 R^2/D or 3.2 min for R = 0.06 cm and D = 0.8 x 10^{-5} cm^2/sec. Furthermore, with a solution flowing between the particles, the distance in the direction of flow required for the solution concentration to reach 90% of the concentration at the surface of the particles is roughly (10) 0.037 d^2v/p_MD, where d is the equivalent diameter of the passages between the particles. For d = 0.02 cm, v = 1 cm/min, and p_M = 0.25, this gives a distance of 0.124 cm.

Under most conditions, it should be possible to neglect the diffusion terms $D\nabla \cdot (p\nabla c)$ in Eq. [9]. This is in harmony with the concepts that there is little upstream propagation of effects and only the inlet concentration to a bed need be specified, not the outlet concentration. Note that if the transference numbers are equal, the last term in Eq. [9] is simply related to f defined by Eq. [1] and plotted in Fig. 1 for a mercury surface. Even without this assumption, the quantities dq_+/dq are, in principle, measurable for a solid electrode. In the absence of cosorption of anions and cations, dq_+/dq = 1 and dq_-/dq = 0 for a cation responsive electrode, and dq_-/dq = 1 and dq_+/dq = 0 for an anion responsive electrode.

Analysis in the Absence of Concentration Variations

A simple system for desalting water by the process described here might consist of porous carbon electrodes through which the solution flows axially, alternate electrodes being connected together electrically [see also ref. (11)]. To achieve desalting, one set of electrodes should be displaced toward more positive potentials so that they will adsorb anions, and the other set, being displaced toward negative potentials, will adsorb cations. To regenerate the electrodes, the potential relationships would be reversed, so desorbed anions and cations would be put back into the solution and carried out with the waste water. For maximum efficiency, it is essential that one set of electrodes should operate in a potential range where cations are sorbed and desorbed and the other set of electrodes should be operated in a potential range where anions are sorbed and desorbed.

If concentration variations are negligible, then Eq. [9] can be ignored for the present, and Eq. [13] reduces to

$$i_2 = -\kappa\nabla\Phi_2 \quad [15]$$

A pair of electrodes can then be represented by the equivalent circuit in Fig. 2. The double layer capacity is represented here as connecting the electrode matrix and the solution in the pores. R_A represents the distributed resistance to the flow of electrons in the porous carbon matrix of one electrode, and R_C represents the distributed resistance to the flow of ions in the pore solution within the same electrode. These are connected to each other by the distributed double layer capacity. The other electrode is similarly represented by the electrode matrix resistance R_B and the pore solution resistance R_D. The two electrodes are connected to each other through the power source connected between the two electrode matrices and through

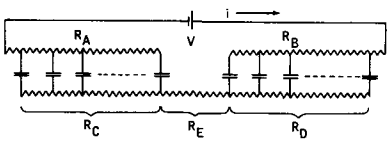

Fig. 2. Equivalent circuit of two porous electrodes and a separator

the solution by means of, for example, a porous cloth separator represented by the resistance R_E.

When the applied potential is changed, a current flows from the power source into the electrode matrices. This current consists of the flow of electrons within the electronically conducting portion of the circuit. The current flows from the matrices through the double layer capacity into the solution in the pores, resulting in a change in the double layer composition and the solution composition. The current is then carried from one electrode to the other by the ions of the electrolytic solution in the separator.

For constant values of σ, κ, and aC, Eq. [3], [6], and [15] can be rewritten as

$$Y = -\nabla\theta \text{ and } \frac{\partial\theta}{\partial t} = -\alpha\nabla \cdot Y \qquad [16]$$

or

$$\frac{\partial\theta}{\partial t} = \alpha\nabla^2\theta \text{ and } \frac{\partial^2 Y}{\partial t} = \alpha\nabla\nabla \cdot Y \qquad [17]$$

where

$$Y = i_1/\sigma - i_2/\kappa, \quad \theta = \Phi_1 - \Phi_2, \quad \alpha = \kappa\sigma/aC(\kappa + \sigma) \qquad [18]$$

Equations [17] are then analogous to the equations for heat conduction or diffusion in solids, and α might be termed the "electrical diffusivity," having the value 5×10^{-6} cm^2/sec for $\kappa = 4.3 \times 10^{-4}$ ohm^{-1}-cm^{-1}, $\sigma = 0.068$ ohm^{-1}-cm^{-1}, and $aC = 83.5$ f/cm^3.

Consider two electrodes having identical values of σ, κ, and aC, each of half thickness L, with a separator of effective thickness L_s and conductivity κ. At present there is no compelling reason to consider electrodes having different values of these parameters. We treat the case where the current is zero and the applied potential is $V = V_0$ for times $t < 0$. The values of Y and θ within the electrodes do not change discontinuously at the instant when the potential is changed.

The analysis is conveniently carried out by means of Laplace transforms. The most interesting result is the relationship between the Laplace transform $\mathcal{V}(s)$ of the applied potential and the Laplace transform $\mathcal{I}(s)$ of the resulting current density

$$\frac{\mathcal{V} - V_0/s}{\mathcal{I}} = R_1\left[1 + \frac{1/\sqrt{s\tau_1}}{e^{2\sqrt{s\tau_2}} - 1}\left(e^{2\sqrt{s\tau_2}} + 1 + \frac{4\kappa\sigma}{\kappa^2 + \sigma^2}e^{\sqrt{s\tau_2}}\right)\right] \qquad [19]$$

where

$$R_1 = \frac{2L}{\sigma + \kappa} + \frac{L_s}{\kappa}, \quad \sqrt{\tau_1} = \frac{R_1}{2\sqrt{\alpha}}\frac{(\kappa + \sigma)\kappa\sigma}{\kappa^2 + \sigma^2}, \quad \tau_2 = \frac{L^2}{\alpha} \qquad [20]$$

The system has associated with it two characteristic times, τ_1 and τ_2. For $L = 0.32$ cm, $L_s = 0.015$ cm, and the values of α, κ, and σ given below Eq. [18], we obtain

$$R_1 = 44.2 \text{ ohm-cm}^2, \quad \tau_1 = 18.4 \text{ sec}, \quad \tau_2 = 5.68 \text{ hr}, \quad \kappa\sigma/(\kappa^2 + \sigma^2) = 6.31 \times 10^{-3} \qquad [21]$$

The two characteristic times have quite different values. We illustrate their significance by considering two special cases.

For short times, the capacity of the electrodes is utilized only near the separator and near the current collector. Thus, when $e^{\sqrt{s\tau_2}}$ is large, Eq. [19] simplifies to

$$\frac{\mathcal{V} - V_0/s}{\mathcal{I}} = R_1\left(1 + \frac{1}{\sqrt{s\tau_1}}\right) \qquad [22]$$

If the applied potential is changed at $t = 0$ from V_0 to $V_0 + \Delta V$ and then maintained at the new value, the resulting current density is

$$i = (\Delta V/R_1)\, e^{t/\tau_1} \operatorname{erfc}(\sqrt{t/\tau_1}) \qquad [23]$$

For large values of t, this expression gives

$$i\sqrt{t} \to \frac{\Delta V}{R_1}\sqrt{\frac{\tau_1}{\pi}} = \frac{\Delta V}{2\sqrt{\pi}}\frac{\kappa + \sigma}{\kappa^2 + \sigma^2}\sqrt{aC(\kappa + \sigma)\kappa\sigma} \qquad [24]$$

Equation [23] is plotted in Fig. 3.

On the other hand, if the applied potential is maintained long enough, the capacity of the electrodes will eventually be used up. To illustrate this, we assume that σ is very large, and we neglect the resistance of the separator. Then Eq. [19] reduces to

$$\frac{\mathcal{V} - V_0/s}{\mathcal{I}} = \frac{R_1}{\sqrt{s\tau_1}}\frac{e^{2\sqrt{s\tau_2}} + 1}{e^{2\sqrt{s\tau_2}} - 1} \qquad [25]$$

The response to a step change in potential is shown in Fig. 4.

When $\tau_1 << \tau_2$, the two curves represented by Fig. 3 and 4 can be superposed to give a complete picture of the current response to a step change in potential. Equation [24] then applies over a considerable portion of the charging period. In this case, the current is independent of the values of L and L_s. At zero time, the current density cannot be infinite; it is limited by the resistance of the electrodes and the separator.

$$i = \Delta V/R_1 \text{ at } t = 0 \qquad [26]$$

Thus, for values of t on the order of τ_1, the values of L and L_s are important, and the current density is less than the value predicted by Eq. [24]. For values of t on the order of τ_2, the value of the electrode half thickness L again becomes important because the electrode capacity depends upon this parameter. As the electrode capacity becomes saturated, the current density again drops below the value predicted by Eq. [24].

The preceding analysis applies to a single step change in potential, whereas a desalting system would be operated with periodic changes alternating between ΔV and $-\Delta V$. Because the current due to a po-

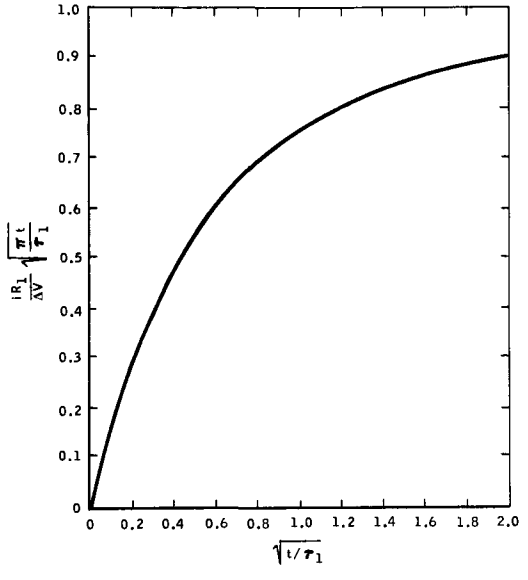

Fig. 3. Current response to a step change in potential, before the penetration layers begin to interact.

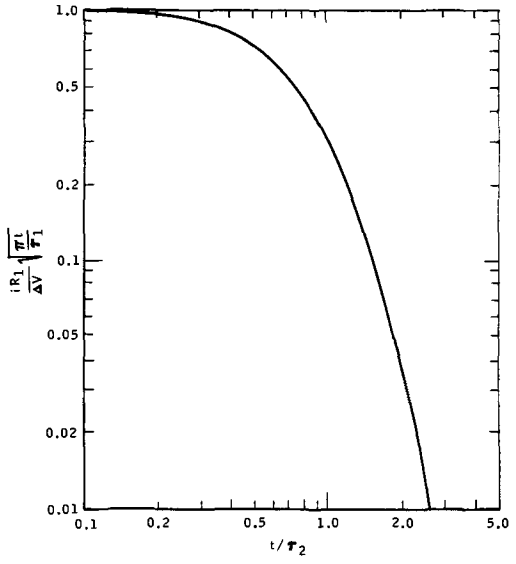

Fig. 4. Current response to a step change in potential, showing the approach to saturation of the capacity of the electrodes.

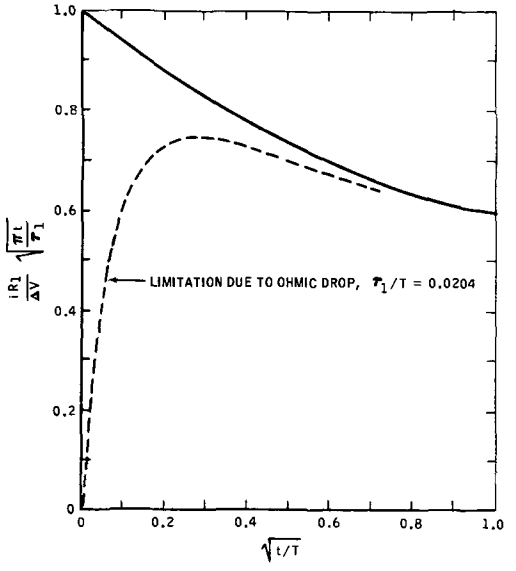

Fig. 5. Current response after extended cycling. The duration of each half cycle is T.

tential step decreases roughly as $1/\sqrt{t}$, the effect of previous changes will persist into a given cycle. Figure 5 indicates the magnitude of this effect. The solid curve was calculated by assuming that Eq. [24] is applicable to each potential change. Thus, for a single potential change, the ordinate value would be unity. The dashed curve represents the expected behavior when one accounts for the fact that the current cannot become infinite at $t = 0$. Here, the current resulting from the most recent potential change was determined according to Fig. 3 with $\tau_1/T = 0.0204$.

Let us now calculate concentration changes, assuming that the current density is given by the preceding considerations. In Eq. [9] we drop the diffusion term and average the last term over two electrodes, with $dq_+/dq = 0$ for one electrode and $dq_-/dq = 0$ for the other electrode. This gives

$$p\frac{\partial c}{\partial t} + v \cdot \nabla c = \frac{i}{2Lz_{+}\nu_{+}\mathbf{F}} \qquad [27]$$

where i is the current density, positive for regeneration and negative for desalting. If $i\sqrt{t}$ can be regarded as constant over a half cycle, the effluent salinity for steady cycling is given by

$$\left.\begin{aligned} c_{out} - c_{in} &= (I_{avg}\sqrt{T}/z_{+}\nu_{+}\mathbf{F}p)\,(\sqrt{t} - \sqrt{T} \\ &\quad + \sqrt{t + T - t_{res}}) \text{ for } t < t_{res}, \\ c_{out} - c_{in} &= (I_{avg}\sqrt{T}/z_{+}\nu_{+}\mathbf{F}p)\,(\sqrt{t} - \sqrt{t - t_{res}}) \\ &\quad \text{for } t > t_{res} \end{aligned}\right\} \qquad [28]$$

where I_{avg} is the average stack current per unit of active volume of the stack

$$I_{avg} = \frac{1}{2nLT}\int_0^T nidt \qquad [29]$$

and the residence time is given by

$$t_{res} = 2nLp/v \qquad [30]$$

Here n is the number of faces between electrodes; for example, $n = 5$ for a stack with six electrodes. The porosity p enters into the expression for the residence time on the assumption that the particles have time to equilibrate with the flowing stream. These calculations are carried out for $t_{res} < T$, the only practical case. The assumption, that $i\sqrt{t}$ is constant corresponds to Eq. [24]. Furthermore, it is good approximation for a half cycle as shown in Fig. 5. The effluent concentration predicted by Eq. [28] is plotted in Fig. 6 for $t_{res}/T = 0.2$.

Finally, one might like to have a more complete idea of the potential distribution within the electrode. We take the case where σ is large, L_s is negligible, there is a step change in the applied potential of ΔV, and t is small enough that the capacity of the electrodes is not used up. Then, in one electrode

$$\theta = \Phi_1 - \Phi_2 = \theta_0 \pm \tfrac{1}{2}\Delta V \operatorname{erfc}(y/2\sqrt{\alpha t}) \qquad [31]$$

where y is the distance from the face of the electrode into its interior. Under these conditions, one half of the applied potential step is applicable to each electrode, and the capacity of the electrodes becomes charged progressively starting at its face and proceeding into the electrode in such a way that the charge distribution is given by the similarity variable $y/2\sqrt{\alpha t}$ according to Eq. [31]. The thickness of the region of charged capacity is thus proportional to $\sqrt{\alpha t}$. This behavior should be representative of the potential distribution in the electrodes under conditions where Eq. [24] is applicable.

Efficiency of the Process

All of the current passed is not used effectively for desalting. This leads one to define the current efficiency

$$\eta = \frac{z_{+}\nu_{+}\mathbf{F}v}{2nLI_{avg}T}\int_{t_{b1}}^{t_{b2}} \Delta c dt \qquad [32]$$

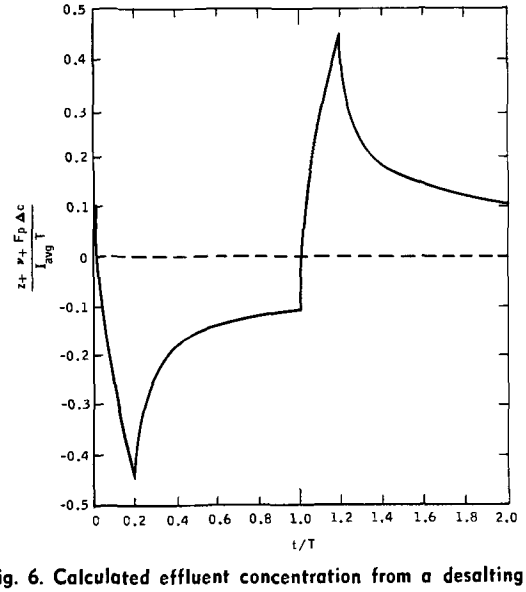

Fig. 6. Calculated effluent concentration from a desalting stack, for $t_{res}/T = 0.2$.

where Δc is the difference between the effluent concentration and the feed concentration and t_{b1} and t_{b2} are successive values of t at which the effluent concentration is equal to the feed concentration, it being presumed that the feed concentration is the point of demarcation between product water and waste water. The effective current density is then the product of the average current density and the current efficiency and is a quantity which should be maximized since it represents the rate of desalting per unit area of the electrodes.

A number of factors can contribute to the inefficiency of the process. For example, if the cycle time is too short compared with the residence time in the stack, water which is partially desalted will then be reconcentrated because it has not had a chance to leave the stack. An efficiency factor for this effect, indicated in Fig. 7, can be obtained by integrating Eq. [28] according to Eq. [32].

If $i\sqrt{t}$ is constant for a half cycle, use of the flow efficiency in Fig. 7 shows that the effective current density is maximized when the half-cycle time is 1.5 times the residence time. Consideration of the limitation of the current at short times (see Fig. 3 or 5) indicates that the optimum is shifted to roughly $T = 1.8t_{res}$. The diffusion within the particles will also favor a larger optimum value for T.

Another source of inefficiency is the cosorption of ions on the same electrode. Two possible charge-potential curves for a set of electrodes are indicated in Fig. 8. The electrode with the larger value of the zero point potential, which might be the result of a suitable chemical treatment, will be denoted as the cation responder, and the other electrode as the anion responder. Positive values of q are assumed to correspond to adsorption of cations, and negative values to anions. Figure 8 indicates a set of potentials which might apply to the desalting and regenerative parts of a cycle. When the two electrodes are shorted together, the potential is V_{sc}, relative to a suitable reference electrode. For desalting, the two electrodes are displaced from the potential V_{sc} in opposite directions, the cation responder increasing its charge and the anion responder decreasing its charge. On regeneration, the cation responder is displaced positively, and the anion responder is displaced negatively on the potential scale. If, on regeneration, the potentials are displaced too

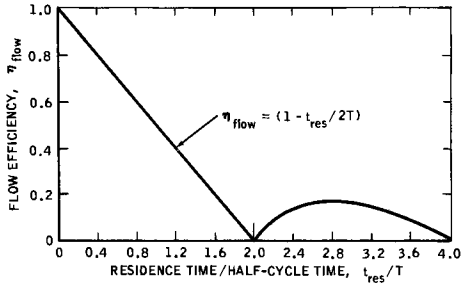

Fig. 7. Dependence of calculated flow efficiency on flow rate for equal durations of desalting and regeneration.

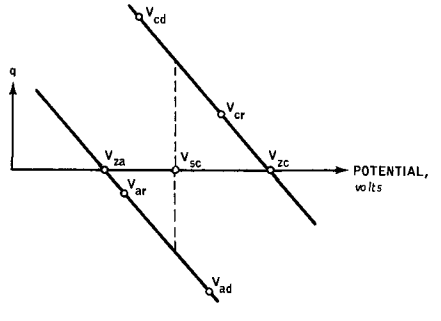

Fig. 8. Idealized charge-potential relationships for a set of electrodes with different zero points.

far, the zero points are exceeded, and, for example, the anion responder will begin to adsorb cations instead of desorbing anions. This represents a loss in efficiency for the desalting process, expressed by the cosorption efficiency η_{co}.

Let the fraction of cation responsiveness of the electrodes denote the charge of cations sorbed or desorbed during a half cycle divided by the total charge transferred during a half cycle. For the linear charge-potential relationships in Fig. 8, this can be represented as

$$\left.\begin{aligned} F_c &= (V_{cd} - V_{zc})/(V_{cd} - V_{cr}) \\ F_a &= (V_{ar} - V_{za})/)\,(V_{ar} - V_{ad}) \end{aligned}\right\} \quad [33]$$

but restrict F_a and F_c to lie between 0 and 1. Then the cosorption efficiency is

$$\eta_{co} = |F_c - F_a| \quad [34]$$

These formulas could be refined by a more detailed consideration of the potential distribution within the electrodes, for example, that given by Eq. [31].

The potentials which can be set are the applied desalting potential

$$V_d = V_{ad} - V_{cd} \quad [35]$$

the applied regeneration potential

$$V_r = V_{ar} - V_{cr} \quad [36]$$

and the short-circuit potential V_{sc}, which can be adjusted by charging both electrodes together by means of an auxiliary electrode. For electrodes symmetric in σ, κ, aC, and L, the potential variations in cyclic operation will be equal and opposite for the two electrodes and F_a and F_c can be re-expressed is terms of the operating variables

$$F_c = \frac{2(V_{zc} - V_{sc}) + V_d}{V_d - V_r} \text{ and } F_a = \frac{2(V_{za} - V_{sc}) - V_r}{V_d - V_r} \quad [37]$$

but where F_a and F_c are still restricted to lie between 0 and 1.

If, for such electrodes, the value of $(V_d - V_r)\eta_{co}$, analogous to the effective current density, is maximized while unnecessary power consumption is avoided, then the short-circuit potential V_{sc} should optimally lie halfway between the zero points of the anion and cation responders, and the minimum value of the regeneration potential should be such that the zero points of the electrodes are not exceeded

$$V_r = -(V_{zc} - V_{za}) \quad [38]$$

Under these conditions, the cosorption efficiency will be unity. Acceptable desalting potentials are not limited in the same way as regeneration potentials. The desalting potential may, in practice, be limited by current losses through faradaic reactions or by a change in the character of the electrodes due to these same reactions. Some faradaic reactions may be tolerable, merely leading to a drift of V_{sc} (faradaic rectification) which can be compensated for by a small charging current by means of an auxiliary electrode.

It may also be possible to change V_{zc} and V_{za} by chemical treatment. Then Eq. [38] suggests that these zero points should be as different as possible in order to maximize the magnitude of the optimum regeneration potential.

This model, relating desalting to the charging of the double layers of the electrode surfaces, leads to a method of analyzing the behavior of porous carbon electrodes and suggests how to achieve efficient operation by utilizing the correct range of potential. In particular, the displacements of potential from the short-circuit potential need not be symmetric on the desalting and regeneration parts of the cycle. For example, two basically identical sets of electrodes can be used. By using unequal times for desalting and regeneration,

and particularly by using unequal potentials, it has been possible to operate such electrodes with an overall efficiency better than 50%.

Other sources of inefficiency include

1. faradaic reactions which produce no desalting but consume current;
2. shorting of the electrodes through the separator;
3. axial dispersion, which tends to mix the product water and the waste water;
4. diffusion of electrolyte from within the porous carbon particles to their surface where it enters the flowing stream.

Experimental Results

For a description of the experimental program, see ref. (11). (This report also contains some cost analysis.) Only results which have a direct bearing on the analysis thus far presented will be cited here. Figure 9 shows the effluent salinity from a stack and can be compared with Fig. 6. The sharp concentration variations in Fig. 6 corresponding to the residence time are, in the experimental results, smoothed out by axial dispersion and the fact that the current is not infinite at the point of switching the potential. Furthermore, the experimental curve is not symmetric with respect to the desalting and regeneration half cycles. This can be attributed to conductivity changes associated with concentration variations. On regeneration, higher concentrations are produced, resulting in initially higher current densities and a sharper regeneration curve. This suggests that the regeneration half cycle can profitably be made shorter than the desalting half cycle. Despite the higher concentrations on regeneration, the amount of charge passed in the two half cycles is generally the same.

Figure 10 shows the product of current and the square root of time plotted against the square root of the ratio of the time to the half-cycle time. This curve compares favorably with Fig. 5. In order to improve the agreement, currents for the desalting and regeneration half cycles are averaged to produce Fig. 10. This eliminates the effect of the asymmetry of the two half

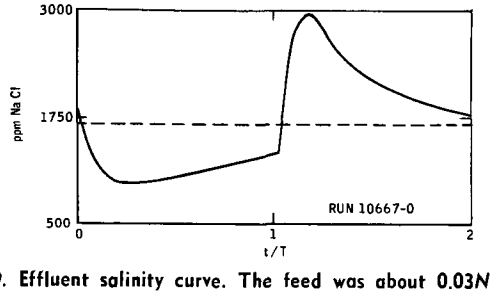

Fig. 9. Effluent salinity curve. The feed was about 0.03*N* NaCl flowing at a rate of about 5.6 g/min. Periods of 15 min each were allowed for desalting and regeneration at potentials of 1.0 and −1.0V, respectively.

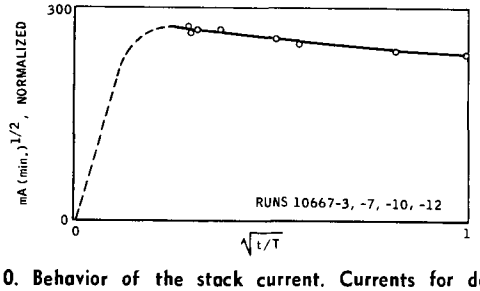

Fig. 10. Behavior of the stack current. Currents for desalting and regeneration were averaged to improve agreement with Fig. 5. The electrodes and conditions were the same as for Fig. 9 except as noted. The composition of the complex feed water is given in Table I. Average potentials were ±0.85V; average flow rate was 4.8 g/min.

Table I. Composition of complex feed water (pH = 5)

	ppm		ppm
Sodium	295	Calcium	150
Potassium	31	Magnesium	44
Chloride	750	Sulfate	178

cycles due to concentration variations, as alluded to in the preceding paragraph.

Experiments with complex water of the composition shown in Table I show preferential adsorption of divalent ions, with a separation factor of about 2.3 relative to univalent ions. This is in harmony with the theory of the diffuse layer and has important implications for the softening of complex waters.

Discussion and Conclusions

Porous carbon materials can be used to desalt water by periodic adsorption of ions. How many ions can be adsorbed depends on the electrical capacity of the double layer, the interfacial area available, and the applied potential. How fast they can be adsorbed depends on the rate of transport of charge to these surfaces and hence on the ohmic potential drop in the solution and the carbon matrix, since the kinetics of ion sorption are generally not rate determining. Equation [24] is useful for estimating these rates. For dilute solutions where $\kappa << \sigma$, this equation shows that the capability of the process should be approximately proportional to the square root of the salinity. It is important that the electrodes be operated in potential ranges where one electrode sorbs and desorbs cations while the other electrode sorbs and desorbs anions. The process shows a preference for adsorption of divalent ions over univalent ions, which is in accord with the double layer model.

Figure 10 shows that $I\sqrt{t}$ has a value of about 250 mA-min$^{1/2}$ for an electrode area of 25.3 cm^2 and a potential change of about 1.7V. With $\kappa = 7.3 \times 10^{-4}$ mho/cm and $\sigma = 0.068$ mho/cm, and with the assumption that this value of $I\sqrt{t}$ is 70% of that corresponding to a step change in applied potential (compare Fig. 5), Eq. [24] yields $aC = 69$ f/cm^3. For a double layer capacity of $C = 30$ μf/cm^2, the effective interfacial area per unit volume would be $a = 230$ m^2/cm^3. This calculation shows that much of the internal surface area of the porous carbon must be available for adsorption.

For processes which do not depend critically on the passage of a faradaic current, the appropriate property of the interface is the electrical capacity of the double layer. A "reversible electrode" has a clearly defined equilibrium potential, and a steady current is passed when the potential is shifted from this value. In contrast, an "ideally polarizable electrode" can be at equilibrium over a range of potentials; after a shift of potential, within this range, the steady current will drop to zero. The double layer capacity is a macroscopic property which describes the charge-potential relationship for such an ideally polarizable electrode and does not depend in its definition upon the detailed mechanism of charge sorption at the interface. The capacitive model is appropriate for analyzing the present process, where faradaic reactions constitute only a small part of the current and the depletion of electrolyte shows a potential dependent saturation of the sorbent. This double layer model can be contrasted with the electrochemically controlled ion exchange model of Evans and others (12-15).

If faradaic reactions were negligible, porous carbon electrodes could store significant amounts of energy. At a potential of 1V with a capacity of 69 f/cm^3, this would amount to about 1 Whr/lb, which, however, is not large enough to be interesting.

The potential dependent adsorption of ions on carbon surfaces should allow these materials to behave as ordinary ion exchangers. A negatively charged carbon in NaCl solution has adsorbed sodium ions. These can

be exchanged, without the flow of current, with calcium ions from a $CaCl_2$ solution. Conversely, a positively charged carbon should be an anion exchanger.

Acknowledgment

This work was supported by the Office of Saline Water of the United States Department of the Interior.

Manuscript submitted Nov. 3, 1969; revised manuscript received *ca.* Nov. 2, 1970.

Any discussion of this paper will appear in a Discussion Section to be published in the December 1971 JOURNAL.

LIST OF SYMBOLS

- a specific interfacial area, cm^{-1}
- c concentration of electrolyte, mole/cm^3
- c_i concentration of species i, per unit volume of the solution phase, mole/cm^3
- C double layer capacity, farad/cm^2
- d equivalent diameter of macropores, cm
- D effective diffusion coefficient of the electrolyte, cm^2/sec
- D_i diffusion coefficient of species i, cm^2/sec
- f ion adsorption characteristic
- $\mathbf{F}$ Faraday's constant, 96,500 coul/equiv.
- F_a, F_c fraction of cation responsiveness of electrodes
- i over-all current density, A/cm^2
- i_1 superficial current density in matrix, A/cm^2
- i_2 superficial current density in the pore solution, A/cm^2
- I total current, A
- I_{avg} average stack current per unit volume, A/cm^3
- $\mathcal{I}$ Laplace transform of the current density, coul/cm^2
- L half thickness of electrode, cm
- L_s effective thickness of separator, cm
- n number of faces between electrodes
- N_i superficial flux of species i, mole/cm^2-sec
- p porosity of the electrode
- p_M macro porosity
- p_μ micro porosity
- q surface density of charge in the double layer, coul/cm^2
- R particle radius, cm
- R_1 resistance (see Eq. [20]), ohm-cm^2
- s Laplace transform variable, sec^{-1}
- t time, sec
- t_i transference number of species i
- $t_{res} = 2nLp/v$, residence time, sec
- T half cycle time, sec
- u_i mobility of species i, cm^2-mole/joule-sec
- v superficial velocity of pore solution, cm/sec
- V applied potential, volt
- $\mathcal{V}$ Laplace transform of applied potential, volt-sec
- $Y = i_1/\sigma - i_2/\kappa$ V/cm
- z_i charge number of species i
- α electrical diffusivity, cm^2/sec
- η efficiency
- $\theta = \Phi_1 - \Phi_2$, V
- κ effective conductivity of solution phase, mho/cm
- ν_+, ν_- numbers of moles of cations and anions per mole of electrolyte
- σ effective conductivity of matrix phase, mho/cm
- τ_1, τ_2 characteristic times (see Eq. [20]), sec
- Φ_1 potential of porous matrix, V
- Φ_2 potential of solution in pores, V

REFERENCES

1. J. W. Blair and G. W. Murphy, "Electrochemical Demineralization of Water with Porous Electrodes of Large Surface Area" in "Saline Water Conversion," pp. 206-223. Advances in Chemistry Series, Number 27. Washington, D. C.: American Chemical Society, 1960.
2. R. H. Wilhelm, A. W. Rice, and A. R. Bendelius, *Ind. Eng. Chem. Fundamentals*, **5**, 141 (1966).
3. R. L. Pigford, Burke Baker III, and D. E. Blum, *Ind. Eng. Chem. Fundamentals*, **8**, 144 (1969).
4. S. Evans, *This Journal*, **113**, 165 (1966).
5. D. C. Graham, *Chem. Rev.*, **41**, 441 (1947).
6. J. S. Newman and C. W. Tobias, *This Journal*, **109**, 1183 (1962).
7. Robert de Levie, "Electrochemical Response of Porous and Rough Electrodes," *Advances in Electrochemistry and Electrochemical Engineering*, **6**, 329-397 (1967).
8. F. C. Anson, R. F. Martin, and Chaim Yarnitzky, *J. Phys. Chem.*, **73**, 1835 (1969).
9. J. Crank, "The Mathematics of Diffusion," p. 90. Oxford: Clarendon Press, 1956.
10. John Newman, "The Graetz Problem" UCRL-18646. Berkeley: Lawrence Radiation Laboratory, University of California, January, 1969.
11. A. M. Johnson, A. W. Venolia, R. G. Wilbourn, and John Newman, *The Electrosorb Process for Desalting Water*. Washington: U.S. Department of the Interior, March, 1970. (R&D Progress Report No. 516.)
12. S. Evans and W. S. Hamilton, *This Journal*, **113**, 1314 (1966).
13. S. Evans, W. S. Hamilton, and J. E. Lewis, *Electrochem. Technol.*, **6**, 153 (1968).
14. S. Evans, M. A. Accomazzo, and J. E. Accomazzo, *This Journal*, **116**, 307 (1969).
15. M. A. Accomazzo and S. Evans, *ibid.*, **116**, 309 (1969).

JOURNAL OF THE ELECTROCHEMICAL SOCIETY

ELECTROCHEMICAL SCIENCE

APRIL 1971

Discharge Profiles in a Porous Cadmium Electrode

P. Bro* and H. Y. Kang*

P. R. Mallory & Company Inc., Laboratory for Physical Science, Northwest Industrial Park, Burlington, Massachusetts 01803

ABSTRACT

Porous cadmium electrodes were discharged galvanostatically at current densities between 2 mA/cm² and 200 mA/cm² in 30% KOH at 25°C, and the discharge profiles were determined by chemical analyses of thin sections sliced from the electrode. The discharge profiles were given by $q/q_0 = A \cosh B(1 - X)/\cosh B$, where A is the state of discharge at the front of the electrode and B is an electrochemical Thiele parameter. The retention of the discharge product in the electrode affected the discharge noticeably. The discharge efficiency was limited by both faradaic processes and mass transfer.

The discharge of battery electrodes is accompanied by structural changes in the electrodes; solid phases are both consumed and generated. The changing morphology poses a formidable mathematical problem which has not yet been solved for any practically useful systems.

Investigations of porous electrodes range from analyses of idealized invariant electrodes (1-3), which are useful as a first approximation, to theoretical and experimental studies of model systems comprising both simple pores, serially coupled electrodes, and actual electrodes (4-7). The work of Alkire, Grens, and Tobias involving a changing geometry is the most advanced, and it is hoped that it will be extended to systems of practical interest. The studies of Euler, Brodd, and Austin are significant in their focus on practical electrode structures, and they have given useful insights into the operation of cathodes used in practical cells.

We have found that data obtained on model configurations cannot be extrapolated to practical systems with any degree of confidence, and that, in fact, detailed experiments on actual battery electrodes are necessary. As part of our studies we have developed and used experimental techniques which introduce a minimal perturbation on the normal functioning of a battery electrode, and we describe our methods here. The work reported in this paper pertains to what must still be considered a model system since an excessive amount of electrolyte and a low specific surface area powder were used. However, the techniques are directly applicable to actual cells without these limitations, and data on such systems will be reported later.

Experimental Techniques

Conventional electrochemical techniques were employed, and we describe only their adaptation to our particular problem. Analytical grade reagents were used throughout the work.

The cadmium powder was obtained from the American Smelting and Refining Company, and it had a stated purity of 99.994% cadmium. Microscopic observations indicated that the powder consisted of nearly spherical particles. The particle size distribution was determined by measuring and counting particle images on photomicrographs, and they were found to have a mean diameter of about 7μ and to be represented by a nearly Gaussian distribution. Calculations from the smoothed distribution curve indicated that the surface area of the powder was 502 cm²/g on the assumption that all the particles were spherical.

The porous cadmium anodes were made by sintering loose powder compacts in 3N HCl (8). This resulted in reasonably strong sintered pellets. The anodes were rinsed in distilled water and stored under distilled water before use to avoid air oxidation. They were 0.20 in. thick and had a diameter of 0.444 in. The porosity of the anodes was calculated from their size and weight to give the values shown in Table I.

The test cell has been described elsewhere (9). It was maintained at 25°C, and the experiments were performed in the presence of a stoichiometric excess of deaerated 30% (wt) KOH. The anode potentials were recorded with respect to a Hg/HgO reference electrode in the same electrolyte, and they were measured with a Keithley Model 610B electrometer and a Moseley Model 680 strip chart recorder. All the dis-

Table I. The accuracy of the analytical methods

Anode	Porosity, %	Total Cd by weight, g	Total Cd by analysis, g	Total Cd^{+2} by discharge, mAh	Total Cd^{+2} by analysis, mAh
RPT 2a	62.7	1.636	1.610	40	40
RPT 2d	65.4	1.520	1.383	90	97
RPT 2b	63.6	1.598	1.418	140	144
RPT 2c	53.4	2.045	1.954	240	255
RPT 2e	55.3	1.965	1.941	340	344
RS 7B	57.3	1.874	1.820	546	552
RS 6B	64.3	1.556	1.460	310	314
RS 8B	62.2	1.661	1.607	268	272
RPT 1a	64.1	1.576	1.412	25	28
RPT 1b	71.7	1.241	1.215	50	48
RPT 1c	67.6	1.422	1.396	75	76
RPT 1d	68.7	1.373	1.228	100	102
RS 14	73.2	1.176	1.068	151	155
RS 12	71.1	1.268	1.100	106	106
RS 10	61.3	1.700	1.610	106	93
RS 11	61.5	1.734	1.671	30.2	30.5

* Electrochemical Society Active Member.

Key words: conductance choking, current distribution, effectiveness factor, electrode efficiency, Thiele parameter.

charges were performed under constant current conditions using a Harrison Model 6200B power supply.

The anode holder fitted into a fixture with a micrometer advancing screw which allowed the slicing of about 0.015 in. thick sections from the anodes with a razor saw blade. The transfer of the anodes from the cells to the microtome, the slicing operation, and the transfer of the slices to the analysis vessels were performed inside an argon filled glove bag to avoid air oxidation of the cadmium.

The analysis of Cd^{+2} and unreacted Cd was carried out as follows: Each anode slice was transferred to a standard 20 ml Cu^{+2} solution in a 1.0*N* HAc-NaAc buffer. The displacement reaction

$$Cd + Cu^{+2} \rightarrow Cd^{+2} + Cu$$

was allowed to proceed to completion (20 hr), and argon was bubbled through the solution to prevent air oxidation of the copper. The copper powder and the supernatant solution were separated by decantation and distilled water washings of the powder were combined with the supernatant solution. The latter was diluted to 250 ml and a 5 ml aliquot was diluted to 100 ml with a 1.0*N* HAc-NaAc buffer and used for the polarographic determination of Cd^{+2} and Cu^{+2}. The total amount of Cd^{+2} found by analysis corresponded to the total amount of Cd and Cd^{+2} in the anode slice, and the consumption of Cu^{+2} corresponded to the amount of unreacted Cd in the slice. Thus, the state of discharge of the various sections of the anodes could be calculated.

The accuracy of the method was checked by the material and charge balances illustrated in Table I. The chemical analyses underestimated the total cadmium content by about 5%, which may be attributed, in part, to cutting losses even though attempts were made to collect all the cuttings with the slices. The depths of discharge calculated from the chemical analyses were about 5% greater than the values determined from the galvanostatic discharge curves. Although these inaccuracies will lead to some uncertainties in the interpretation of the data, it is believed that the data provide a reasonably faithful description of the true behavior of the electrodes.

Experimental Results

The end of the constant current discharges of the porous cadmium electrodes was well defined, Fig. 1. The electrode potentials remained nearly constant or increased slowly until a point was reached where the potentials increased quite sharply. This point was used to define the end of the discharge process; the resulting discharge efficiencies are shown in Fig. 2. It may be seen that the electrodes discharged efficiently at low integral current densities where values of about 70% were obtained. At higher integral current densities the discharge efficiencies decreased markedly and reached a value of about 4% at 200 mA/cm^2. The term

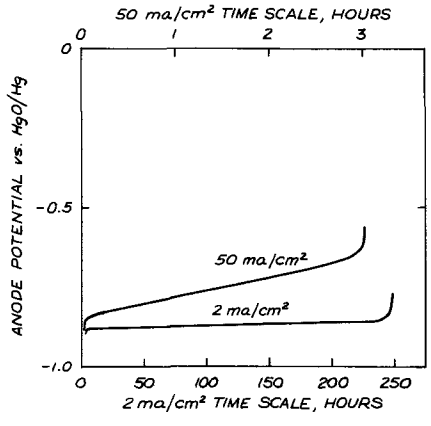

Fig. 1. Galvanostatic polarization curves at 2 and 50 mA/cm^2

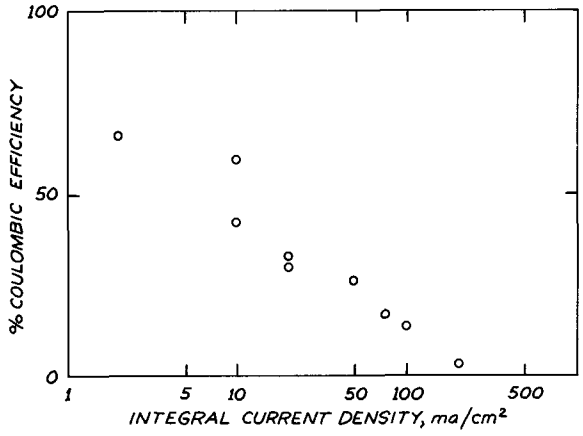

Fig. 2. Coulombic discharge efficiency of the porous cadmium electrode.

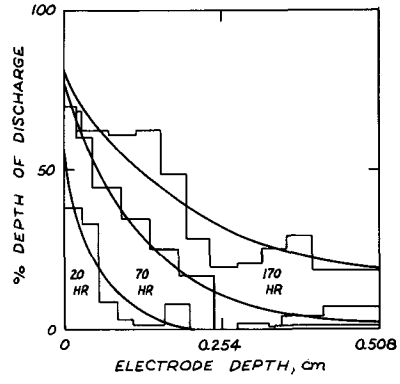

Fig. 3. Typical discharge profile histograms at 2 mA/cm^2

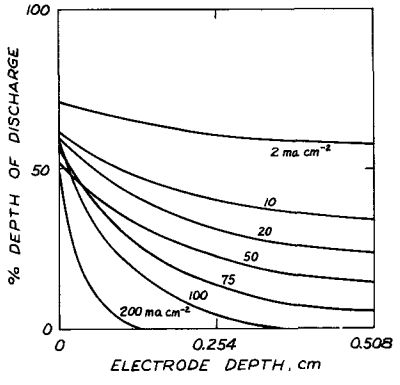

Fig. 4. Discharge profiles at the end of discharge

"integral current density" designates the total current to the electrode per unit front surface area.

The analyses of the anode slices gave rise to discharge profile histograms.[1] Three representative histograms are shown in Fig. 3 and the smooth curves fitted to the histograms to facilitate the comparison of the discharge profiles. The correlations we used are discussed in the next section. It may be seen from Fig. 3 that the chosen correlation represented the data well.

The discharge profiles in the electrodes at the end of discharge are shown in Fig. 4. At low integral current densities the porous electrodes reacted uniformly throughout their thickness. At 2 mA/cm^2 the depth of discharge at the rear of the electrode, 60%, was almost as great as at the front of the electrode, 70%. As the integral current density increased the discharge profiles became increasingly distorted, and the rear of the electrodes gradually ceased to participate in the discharge. However, the front surface of the electrodes

[1] Complete data tables are available from the author on request.

discharged almost as deeply as at the lower integral current densities. For example, at 200 mA/cm² the front surface discharged to about 50%, but the rear three fourths of the electrode did not discharge at all.

Two series of experiments were done to explore the time course of development of the discharge profiles at 2 and 50 mA/cm². Results are shown in Fig. 5 and 6. Although the experimental data gave rise to some crossovers in the profiles, the general reaction patterns are well defined. The initial discharge was confined to the front of the electrodes, and, subsequently, the discharge penetrated into the interior of the electrodes. The differences between the low and the high current density profiles are those expected from the profiles at the end of discharge; the interior and rear sections of the electrodes discharged much less at the higher than at the lower integral current density. The data show that the front surface tended to discharge quite extensively at the onset of the discharge, and the rear sections did not contribute much until the discharge was about half completed.

Discussion

The discharge of the cadmium anodes terminated when the electrode potentials increased abruptly at the end of the discharges. Several factors need to be considered in the analysis of this phenomenon. The most difficult factor to quantify is the changing geometry of the anodes during discharge, and we have not been able to develop any reasonable models which can be solved mathematically. The equations presented by Alkire *et al.* (6) pertain to a dissolving anode and cannot be used for our case where a precipitate is formed. We chose to pursue an heuristic approach in the search for an equation to describe the behavior of the porous anodes.

The behavior of finite networks is generally described in terms of hyperbolic functions, and, it turns out, it is possible to make a particular choice of hyperbolic functions and arrive at an adequate description of the discharge profiles in the porous cadmium anodes. As a guide, we note that the front surface of the electrodes generally reacted to a high and almost constant degree, and the rear of the electrodes participated to varying degrees depending on the current density and the fractional extent of discharge.

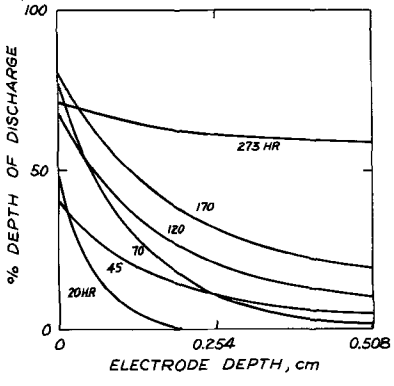

Fig. 5. Evolution of the discharge profiles at 2 mA/cm²

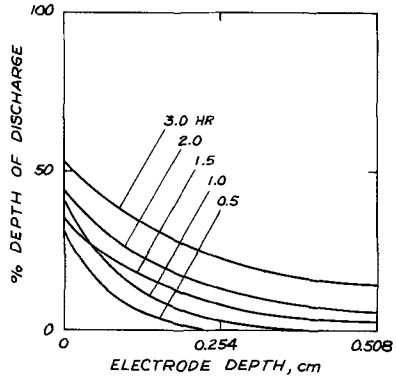

Fig. 6. Evolution of the discharge profiles at 50 mA/cm²

Table II. Parameters for histogram correlations

Anode	Integral current density, mA/cm²	A	B	Standard deviation,* q/q_0, %
RPT 2a	2	0.546	10.3	4.69
RPT 2d	2	0.392	2.76	6.07
RPT 2b	2	0.757	4.03	5.06
RPT 2c	2	0.672	2.53	4.89
RPT 2e	2	0.780	2.04	8.31
RS 7B	2	0.702	0.613	5.31
RS 6B	10	0.600	1.16	4.83
RS 8B	20	0.583	1.56	3.51
RPT 1a	50	0.301	7.70	3.03
RPT 1b	50	0.405	4.86	9.56
RPT 1c	50	0.356	3.07	3.59
RPT 1d	50	0.443	2.53	6.72
RS 14	50	0.511	1.89	7.95
RS 12	75	0.557	3.00	9.48
RS 10	100	0.576	5.05	7.75
RS 11	200	0.525	17.1	2.65

* Obtained by least square fitting of q/q_0 as a function of X to Eq. [1].

The hyperbolic functions should be chosen to reflect these characteristics. The following expression appears to satisfy these requirements

$$q/q_0 = A\ (\cosh B\ (1 - X))/\cosh B \qquad [1]$$

q = discharge density, mAh/cm³
q_0 = stoichiometric charge density of fresh anode, mAh/cm³
A, B = parameters
X = fractional depth in anode from front surface.

We used Eq. [1] to describe the discharge profile histograms with the results shown in Table II. Representative comparisons of some experimental data and Eq. [1] were given in Fig. 3. The data fit the hyperbolic expression with an average standard deviation of about 6% over the entire range of integral current densities and discharge times. Thus, whether or not the expression has any fundamental significance, it represents the data reasonably well, and it may be useful in suggesting the mathematical forms that should be sought in model considerations.

An examination of Eq. [1] indicates that A may be defined most simply as the depth of discharge at the front of the electrode. The effect of the integral current density on A at the end of discharge is shown in Fig. 7. The depth of discharge at the front of the electrode reached a value of about 54%, and it remained constant over the greater part of the integral current density range. It increased at integral current densities below 20 mA/cm², and as the integral current density approached zero the depth of discharge of the front surface approached 70% at the end of discharge. Some of the scatter in the data may be attributed to varia-

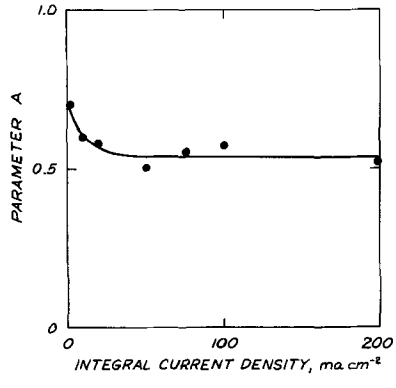

Fig. 7. Effect of the integral current density on parameter A in Eq. [1] at the end of discharge.

tions in the porosity of the anodes. Assuming the applicability of the mean initial porosity of 64% to all the low integral current density anodes, we find that the depths of discharge of 54% and 70% correspond to residual porosities of 38% and 30%, respectively, at the end of discharge. Such changes in the porosities imply a considerable blocking of the pores in the anodes, especially at the lower integral current densities.

The evolution of the state of discharge of the front surface during discharge is given in Fig. 8 for the integral current densities of 2 and 50 mA/cm^2. The best linear fits of the data are given by

$$2\ \text{mA/cm}^2\ \text{data: } A = 0.527 + 0.00103t \quad [2]$$

$$50\ \text{mA/cm}^2\ \text{data: } A = 0.281 + 0.0765t \quad [3]$$

t = time since start of discharge in hours.

At the lower integral current density the front of the electrode reached a high state of discharge at the very beginning of the discharge process, 53%, and it increased gradually to a value of 81% at the end of discharge. The discrepancy of the latter value from the earlier value of 70% obtained from $A(i)$ in Fig. 7 is attributable to their different origins which are those of a current correlation and a time correlation, respectively. The high value merely confirms that the front of the electrode becomes quite dense. At the higher integral current density the front of the electrode appeared to attain a lower initial depth of discharge, 28%, and it increased to only 51% at the end of the discharge. Although the latter value corresponds to some densification of the front of the electrode, it represents a much less blocked pore structure than obtains in the low integral current density anodes at the end of discharge.

There may be some question regarding the validity of the linear A-t equations, especially for the 2 mA/cm^2 data. If a nonlinear representation be employed, as indicated in Fig. 8, the initial depth of discharge at the front of the 2 mA/cm^2 electrode would be about 30% and the final value about 75%. The initial value would be, therefore, the same for the electrodes regardless of the integral current density. This appears to be more reasonable, but more data are needed to settle the question. Deviations from linearity are small for the 50 mA/cm^2 data.

A tentative interpretation of B can be obtained by a consideration of some analogies. Integration of Eq. [1] over the entire thickness of the electrode gives

$$q/q_o = (q/q_o)_{x=0}\ (\tanh B)/B \quad [4]$$

This equation has been used by Selim (10) to correlate the performance of a variety of batteries and electrodes. It was derived from a distributed network model, and in some simple cases the quantity B could be reduced to

$$B^2 = (\text{Ionic impedance})/(\text{Faradaic impedance}) \quad [5]$$

A similar quantity has been used by de Levie (11). Equation [4] is well known in chemical kinetics for the description of first order reactions in catalyst pellets (12) where the factor $(\tanh B)/B$ is referred to as an "effectiveness factor." It is equally to be considered an effectiveness factor for porous electrodes since it measures the extent to which the average discharge of the electrode approaches the discharge of the front surface of the electrode. In chemical kinetics B^2 is the Thiele parameter (13), and it is a measure of the ratio of the rate of the chemical surface reaction and the rate of diffusion into the porous structure. We arrive at a consistent description, therefore, if we identify B^2 as the Thiele parameter for electrochemical systems.

The Thiele parameter contains the effects of the geometry of the electrode, the degradation of the electrode, the operating parameters, as well as the effects of the electrochemical characteristics of the system. We restrict our discussion to the effects of the integral current density on B and the changes in B during the discharge.

The experimental data showed that B decreased noticeably during the evolution of the discharge process. Several correlations were tried to express B as a function of t, the time of discharge, and the exponential expressions

$$B_2\ (2\ \text{mA/cm}^2) = (245/t)^{0.898} \quad [6]$$

$$B_{50}\ (50\ \text{mA/cm}^2) = (6.45/t)^{0.806} \quad [7]$$

appeared to be the most satisfactory. They are shown in Fig. 9. The changes in B during discharge agree with our interpretation of the Thiele parameter, although the simple equality of B^2 and the ratio of the ionic and faradaic impedances is considered an oversimplification. The decrease of B with time at both the high and the low integral current densities reflects the gradual displacement of the reaction to the interior of the electrode. We know that the porosity decreases during discharge and the diffusive conductance should, therefore, decrease as well, making B^2 larger. However, the faradaic conductance decreases even more since the front regions of the electrodes approach passivation. We shall see later that the true current density at the front surface vanished near the end of the low integral current density discharges, but not so at the higher integral current densities. We would expect, therefore, a much greater decrease in B^2 during discharge for the former, and values of B^2 (initial)/B^2 (final) were found to be 282 and 16.7, respectively, for the two sets of data, in agreement with expectations. We conclude that the definition of B^2 as a Thiele parameter leads to a consistent interpretation of the data.

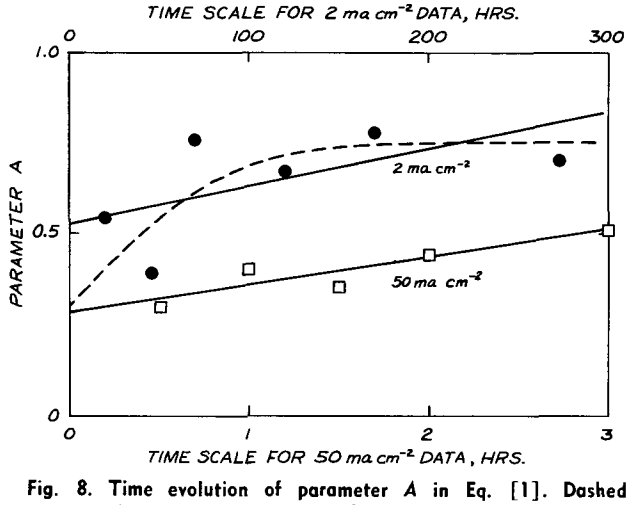

Fig. 8. Time evolution of parameter A in Eq. [1]. Dashed curve: an alternate fit of 2 mA/cm^2 data.

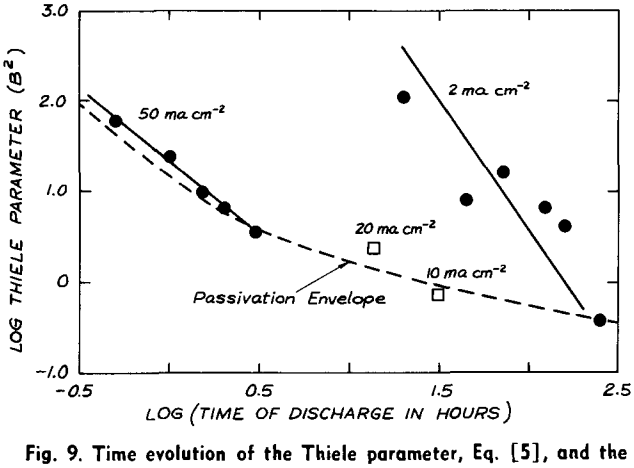

Fig. 9. Time evolution of the Thiele parameter, Eq. [5], and the Thiele parameter at the end of discharge.

The experimental data were used to obtain the $B(t)$ curve at the end of discharge for the entire integral current density range, and it is shown in Fig. 9. The near equality of the slopes of the log B *vs.* t curves at 2 and 50 mA/cm^2 suggests that it may be possible to interpolate and extrapolate from Fig. 9 to obtain the $B(t)$ values for other integral current densities and, thus, to obtain the detailed discharge profiles for electrodes operating over a wide range of integral current densities. The $B(t)$ curve at the end of discharge serves to delimit the interpolations.

The effect of the integral current density on B at the end of discharge may be expressed by

$$B = 0.445 \exp (0.244\, i^{1/2}) \qquad [8]$$

B increased with the integral current density, reflecting the progressive confinement of the reaction zone to the front of the electrode. In terms of the Thiele parameter interpretation, the ionic impedance became more significant relative to the faradaic impedance at the higher integral current densities.

From an operational point of view it is of interest to predict when the end of discharge will occur for any given integral current density. This follows directly from Eq. [4] using the A values from Fig. 7 ($A = (q/q_0)_{x=0}$) and the B values from Eq. [8]. The mean deviation of the efficiencies (in per cent) calculated from these expressions is 2.5% relative to the observed efficiencies (in per cent).

It is instructive to consider the true current distribution in the electrodes during the discharge. The smoothed discharge profile data were differentiated with respect to time to give the current distributions shown in Fig. 10 and 11. The specific surface area of 502 cm^2/g, and the average porosities were used to calculate the current densities. The internal surface areas change during the discharge, and the true current densities would differ somewhat from the values shown as t increases. Although it is possible to use the $q(x,t)$ values to estimate the area changes and to obtain a better estimate of the true current densities this refinement is not considered to be necessary since the given curves in their present form represent the essential features of the process.

The 2 mA/cm^2 data illustrate the advancement of the reaction zone into the electrode. During the early part of the discharge the current is concentrated near the front of the electrode. As the discharge continues the current wave advances into the interior of the electrode and moves gradually to the rear of the electrode. As it does so, the front of the electrode ceases to participate in the discharge altogether. At the higher integral current density of 50 mA/cm^2 there is also a high initial concentration of the current near the front of the electrode, and as the discharge proceeds the current wave moves into the electrode. However, the rearward advancement of the current wave is strongly damped, and the front surface remains active during the entire discharge.

Another effect associated with the discharge process is the accumulation of the reaction product inside the porous structure. Since the amount of Cd^{+2} recovered by analysis agreed reasonably well with the measured electrical charge it may be concluded that the $Cd(OH)_2$ remained inside the electrode where it would obstruct mass transfer and the flow of current. The discharge profiles were used to calculate the choking patterns shown in Fig. 12 and 13. It was assumed that the expansion of the anodes during discharge could be ignored.

The choking patterns are given in terms of a choking factor, F, that can be defined as a first approximation with reference to the Bruggeman-Baron equation (14) for the electrolytic conductivity of a porous body

$$K_p = K_s\,(1 - f)^{3/2} \text{ (Bruggeman-Baron)} \qquad [9]$$

K_p = conductivity of porous body
K_s = conductivity of solution in the pores
f = volume fraction of solids in the body

$$F = (1 - f)^{3/2}{}_{t=0}/(1 - f)^{3/2}{}_{t=t} \text{ (Choking factor)} \qquad [10]$$

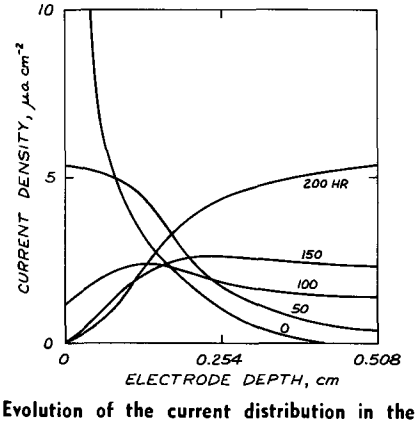

Fig. 10. Evolution of the current distribution in the electrodes at 2 mA/cm^2.

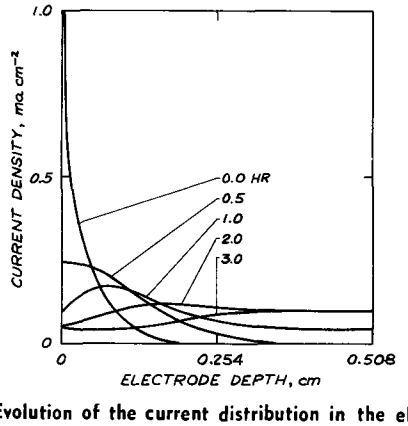

Fig. 11. Evolution of the current distribution in the electrodes at 50 mA/cm^2.

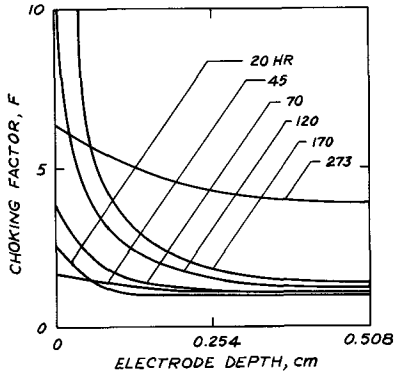

Fig. 12. Development of the choking patterns at 2 mA/cm^2

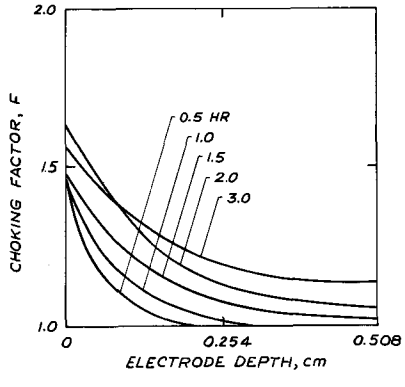

Fig. 13. Development of the choking patterns at 50 mA/cm^2

The choking factor is simply the ratio of the resistance of the porous body at any time, t, and the initial resistance of the porous body.

The curves in Fig. 12 show that the electrodes operating at 2 mA/cm^2 experienced an appreciable choking effect throughout their entire thickness near the end of discharge. The electrolytic resistance near the front of the electrode had increased about sixfold; near the rear it had quadrupled at the end of discharge. The electrodes operating at 50 mA/cm^2, Fig. 13, experienced a smaller choking effect. The electrolytic resistance had increased 55% near the front surface when the electrode ceased discharging, and at the rear it had increased 12%.

The choking factor and the current distribution provided an indication of the processes involved in the polarization of the anode. Since the faradaic current density vanished at the front of the electrode at the low integral current density, the front of the electrode may have reached passivation, and the ionic transfer path to the active region of the anode must have increased correspondingly. The concomitant increase in the choking factor would inevitably lead to an excessive mass transfer impedance and the anode would polarize. At the greater integral current density there was no front surface passivation, but the faradaic current density decreased markedly there, indicating an appreciable increase in the local faradaic impedance, sufficient to displace the current to the interior of the electrode, leading again to an increase in the mean ionic transfer path and an increase in the mass transfer polarization.

Calculations of the resistive polarization due to conductance choking during the discharge, using the faradaic current densities and their time change to obtain the pore current distribution and using the Bruggeman-Baron equation for the effective conductivity, predicted a gradual increase in the overvoltage with time but not the observed, abrupt increase in polarization at the end of discharge. The failure of the calculations to predict the terminal polarization curve may be attributed, in part, to an inadequate analysis of the choking effect. The choking is probably locally inhomogeneous, and complete choking may occur before the residual porosity vanishes. Since no satisfactory theory is available on the topography of conductance choking in electrodes undergoing structural transformations, a rigorous discussion of this phenomenon is not yet possible.

Another consideration is the coarseness of the cuts used to slice the electrodes. The implied averaging may have obscured a much more extensive choking of the front surface of the electrodes than was indicated by the values obtained from the experimental data. If such were the case, the terminal polarization would be explained.

An alternate hypothesis is that local passivation may have occurred in the electrodes to a greater extent than indicated by the current distribution curves. This possibility needs to be examined in more detail, both by obtaining more extensive current distribution curves and by doing passivation studies on flat electrodes using the observed local current-time profiles.

It was assumed in the polarization calculations that the bulk conductivity of the electrolyte remained constant in the anode. However, OH^- ions are consumed during discharge, and at the lower integral current densities the total amount of OH^- consumed exceeds that initially present inside the anode and that provided by electrical transport from the external solution. Some OH^- are also lost by electrolyte expulsion due to the densification of the anode. At the higher integral current densities less OH^- is consumed than is present initially. Local OH^- depletion would occur, therefore, in the anodes with a concomitant decrease in the electrolyte conductivity and an increase in the anode polarization. It is conjectured that the OH^- depletion may have contributed significantly to the terminal polarization of the anodes.

Conclusions

The experimental work shows that it is possible to determine the discharge profiles of porous electrodes by slicing the electrodes into thin sections parallel with their front surfaces and by analyzing the individual sections chemically to obtain histograms of the discharge profiles. Our study was limited to the effect of the integral current density on the discharge profiles of porous cadmium electrodes.

The discharge profiles could be described by a hyperbolic cosine function and the mean electrode efficiency by a hyperbolic tangent function. The latter is equivalent to the effectiveness factor used in chemical kinetics, and it is a function of an electrochemical Thiele parameter that depends on the relative magnitudes of the transport and reaction impedances in the electrode. The effectiveness factor measures the extent to which the discharge zone penetrates into the electrode. The given correlations provide a means for calculating the efficiency and the discharge profiles at any particular integral current density.

The product formed during the discharge of cadmium electrodes remains inside the electrode and causes the eventual choking of the porous structure. A choking factor was introduced to provide a quantitative description of the geometric choking effect. It was most pronounced at the low integral current densities near the end of discharge where a high degree of discharge had occurred. It was less pronounced at the higher integral current densities.

The discharge of the cadmium anodes was affected by both the faradaic and the transport limitations of the electrode. The increase in the faradaic impedance near the front of the electrode forced the current into the interior of the anode, and this extension of the transfer path combined with the increase in the transport impedance due to the choking effect led to the polarization of the anode. Although the exact cause of the terminal increase in the polarization could not be ascertained, it is believed to be due to an excessive choking effect near the front of the electrode and the depletion of OH^- ions inside the anode.

Manuscript submitted Aug. 17, 1970; revised manuscript received *ca.* Dec. 8, 1970. This was Paper 67 presented at the Atlantic City Meeting of the Society, Oct. 5-9, 1970.

Any discussion of this paper will appear in a Discussion Section to be published in the December 1971 JOURNAL.

REFERENCES

1. A. Winsel, *Z. Elektrochem.*, **66**, 287 (1962).
2. J. S. Newman and C. W. Tobias, *This Journal*, **109**, 1183 (1962).
3. E. A. Grens and C. W. Tobias, *Ber. Bunsenges.*, **68**, 236 (1964).
4. J. Euler, *Electrochim. Acta*, **7**, 205 (1962).
5. R. J. Brodd, *ibid.*, **11**, 1107 (1966).
6. R. C. Alkire, E. A. Grens, and C. W. Tobias, *This Journal*, **116**, 1328 (1969).
7. L. G. Austin and E. G. Gagnon, Report No. 3, May 1969. Contract DAAG 39-67-C-0065, U.S. Army Materiel Command, Harry Diamond Labs., Washington, D.C.
8. D. W. Smith, British Pat. 1 091 664 (1967).
9. H. Y. Kang, *This Journal*, **118**, 462 (1971).
10. R. Selim, Personal communication.
11. R. de Levie, *Adv. Electrochem. & Electrochem. Eng.*, **6**, 329 (1967).
12. E. E. Petersen, "Chemical Reaction Analysis," p. 48, Prentice Hall, Inc., Englewood Cliffs, N. J. (1965).
13. *Ibid.*
14. R. E. Meredith and C. W. Tobias, *Adv. Electrochem. & Electrochem. Eng.*, **2**, 15 (1962).

Crystallization of $PbSO_4$ on Anodes of Lead-Antimony Alloy

Jeanne Burbank*

Electrochemistry Branch, Naval Research Laboratory, Washington, D. C. 20390

ABSTRACT

The morphologies of crystals of $PbSO_4$ depositing on 5% antimonial lead alloy in 1.25 sp gr H_2SO_4 were examined by electron microscopy. The crystals formed on open circuit stand and during discharge of PbO_2 coatings, developed by electrochemical cycling, were examined. Well developed prisms, dendrites, and hopper crystals were observed. The discharge of the antimonial coatings appeared to be limited by the crystal growth rate.

Individual particle morphology is directly related to the stability of polycrystalline masses (1, 2). Especially in the case of porous conglomerates, this factor is of supreme technological importance when the body is required to serve usefully in practical applications. Recent studies of the positive active material of the lead-acid cell have emphasized the relation of the crystal morphology to plate function and durability (3, 4).

Antimony is normally present in the cell as an alloying agent to stiffen the grids used to support the active materials. It is further recognized that it contributes significantly to successful cycle operation of the positive plate (5-7) where it appears to act as a nucleating catalyst for the PbO_2, promotes intercrystal bonding, and modifies the crystal size and habit. As a continuation of the investigation of the mechanism of the action of antimony in the positive plate, it was of interest to examine the habit of $PbSO_4$ crystallizing on anodes of lead-antimony alloy.

The modification of the crystal habit of $PbSO_4$ by addition agents in the negative plate of the lead-acid cell has been recognized by Willihnganz (8), and the morphology of $PbSO_4$ crystallizing on pure lead anodes in H_2SO_4 has been examined by electron microscopy (9-12), however crystallization on lead-antimony alloys has not been investigated.

Lead sulfate, occurring natively as the mineral anglesite, crystallizes in the orthorhombic system with unit cell parameters of $a_o = 8.5$, $b_o = 5.4$, and $c_o = 6.99$Å containing four molecules. The space group is Pnma, and the structure, made up of distinct Pb and SO_4 ions, has recently been refined by Sahl (13). It is isostructural with $BaSO_4$ and $SrSO_4$.

Shannon and others (14-23) have described the numerous crystal habits of $PbSO_4$ is many mineral and synthetic specimens. The frequently observed diamond-shaped platelet is the basal pinacoid//(001), prismatic with {210}. It may be modified by other prisms and domes. Older descriptions characterize {210} as {110} because of the axial ratios chosen for the optical measurements prior to the establishment of the crystal structure by x-ray diffraction which, in effect, doubled the a_o axis. The earlier optical designations of the {h01}, {hk0} and {hkl} forms must be corrected accordingly.

Lead sulfate also frequently grows in columnar prisms parallel to a_o, b_o, and c_o terminated with pyramidal and dome faces. The pinacoids (100) and (010) are often small or absent. The habit of synthetic material may be modified by impurities in and composition of the solutions from which it is precipitated (17, 20), and it has been reported that crystal size is increased by the presence of hydronium ion (23). Changes in habit and crystal size are generally attributed to preferential adsorption processes that alter the relative growth rates of the crystallographic directions.

Because of its sparing solubility $PbSO_4$ has been used extensively for studying crystal nucleation and growth rates (17, 19, 23, 24). Owing to the complexities of the processes that take place during a crystal deposition reaction, the fundamental theories presently available are somewhat restricted in application. Recent reviews of the field are found in VanHook, Botsaris *et al.*, and others (25-28). The necessary steps involved in crystallization are often conceived to be: the clustering of a few ions or particles into a unit called a crystal embryo, structural arrangement of the particles into a lattice network accompanied by addition of material to form a critical nucleus, growth of this nucleus into a crystallite, which may then grow into a typical crystal. Any one of these steps may be rate determining, however, in most instances the nucleation processes appear to be retarded, requiring an activation energy manifested by the phenomena of supercooling, supersaturation and, in electrocrystallization, polarization. The activation energy required for heterogeneous nucleation is usually less than in homogeneous cases, and most instances fall into the former category. Growth of the crystallites may also be very slow, and the rate may vary with the crystallographic direction. In general, but not always, a crystal will grow most rapidly in directions perpendicular to the lattice planes having the highest reticular density (29). Because the different crystallographic directions grow at different rates, the fastest growing planes become smaller in area, and, given time, disappear from the crystal surface. The rates of growth of the remaining enclosing faces are slower. For these reasons, the growth rate varies with time. The final shape of the crystal is determined by the various rates of growth in the different crystallographic directions as well as by the influence of factors such as adsorption of foreign material, mechanical restrictions, temperature, time allotted for growth, and degree of perfection of the crystal structure.

In order for a crystal to grow, the solution must be supersaturated, and the surface of the growing crystal must offer sites for the accretion of new structural units (ions or molecules). Present theories postulate deposition at emergent screw dislocations, kinks, and similar flaws in the crystal structure.

Complex as the crystallization process is, electrochemical crystallization adds further parameters that must be taken into consideration (30-36).

The reaction at the positive plate of the lead-acid cell is particularly complicated because it involves dissolution and crystallization of two solid phases, PbO_2 and $PbSO_4$ as well as the two electron exchange reaction. The plate reaction takes place by way of solution in the H_2SO_4 electrolyte (37, 38), and the solubilities of $PbSO_4$ and PbO_2 are limited. Despite these complexities, the electrode performs very well at relatively high current densities. Willihnganz, following the work of Kapitza (39-41), concluded that the charge exchange reaction is not the limiting step in the discharge reaction at current densities as high as 3.5 A/cm^2.

In discharge of a β-PbO_2 electrode in H_2SO_4 at constant current, the potential passes through a minimum

* Electrochemical Society Active Member.

Key words: lead-acid-cell, $PbSO_4$, crystal morphology, lead-antimony alloys, anodic coatings.

(42). This is reflected in the cell voltage and is known as the coup de fouet of spannungssack. It is during this period that supersaturation of Pb^{2+} in the electrolyte is built up, and the critical nuclei of $PbSO_4$ are formed (43, 44). Growth of the $PbSO_4$ crystals then follows at a lower polarization. This behavior is fairly typical of nucleation and growth kinetics in many electrocrystallization reactions (33, 34).

Antimony is coprecipitated with $PbSO_4$ to such a degree that it interferes with the gravimetric analytical procedure (45), and separation from lead is required for accurate results. The chemistry of antimony has been summarized by Maeck (46) and Sidgwick (47). Dawson *et al.* (48, 49) recently suggested that in H_2SO_4 solutions, antimony is present as the anions $Sb(SO_4)_2^-$, $SbOSO_4^-$, and $Sb_3O_9^{3-}$. Strong adsorption on the $PbSO_4$ surface may occur, and result in alteration of habit, growth rates, and lattice substitution in the growing crystals.

Experiments

Aged castings of nominal 5% lead-antimony alloy were used for this study. The specimens measured approximately 6 x 3 x 0.4 cm and fit the sample holder of the x-ray diffractometer so that x-ray patterns could be registered without destruction of the sample. Immediately prior to use, the specimens were washed in saturated ammonium acetate solution and thoroughly rinsed in distilled water. While wet with the final rinse, they were assembled in beaker cells containing two sheet lead cathodes, a Hg, Hg_2SO_4 reference electrode, and 1.2549 sp gr H_2SO_4. The cells were allowed to stand on open circuit for 30 min before the anodic current of 1 mA/cm² of apparent surface was applied. The cell voltages and anode potentials were continuously recorded and frequently checked manually with a potentiometer. Experiments were run in triplicate. The cycled samples were discharged at 1 mA/cm² to a potential of 0.75-0.8V *vs.* the reference electrode, recharged at the same current density, and anodization continued between discharges.

The electrodes were cycled to develop electrochemical capacity of approximately 2 mA-hr/cm². During discharge the interval known as the coup de fouet had a duration of approximately 5 min under these conditions and the minimum was reached at 3.25 min. Discharging electrodes were examined at 0.5, 2, 3.25, 4, and 5 min and at 1 hr (half discharge capacity) and at the knee of the curve. X-ray diffraction patterns were registered using CuKα radiation and the diffractometric method (50) with a scanning speed of 2°/min. Specimens for electron microscopy were removed following the 30-min presoak in H_2SO_4, and at the above indicated intervals during the discharge of the anodic coatings. They were blotted dry, and replicated for electron microscopy.

Two-stage polystyrene-carbon replicas were used (51-54). Dissolution of the particles embedded in the primary plastic replica proved to be tedious because of the tendency of antimony to hydrolize to the very stable hydrous oxides (45-47) which then could not readily be removed from the replica. Cleaning these replicas remains an art. By using oxalic acid to reduce the PbO_2, and tartrates to complex the antimony, the replica may be cleared. It was necessary to use occasional dips in H_2SO_4 to precipitate $PbSO_4$, which could then be removed in saturated ammonium acetate solution. By alternately treating with these reagents, rinsing with distilled water between the various baths, the formation of the curdy antimony oxide could be minimized. When all the PbO_2 had been reduced, HCl containing tartaric acid was used as a final treatment. It is, of course, the very stable insoluble hydrolytic product that gives rise to the chemical replica of lead antimony alloys (55) and interferes with the analytical chemistry of antimony (45).

Results

The $PbSO_4$ coating formed during open circuit stand for 30 min was made up of rhomboidal crystals of $PbSO_4$, Fig. 1. At some intercrystalline boundaries, clusters of radiating acicular crystals appeared. The larger crystals were several microns in diameter and appeared to be implanted in a bed of smaller crystals ranging in size down to approximately 0.1μ. These coatings are very similar to those observed by Feitknecht and Pavlov (9-12) on pure lead surfaces.

At 0.5 and 2 min discharge, no $PbSO_4$ crystals or nuclei could be identified in the electron micrographs, and the coating had the same appearance as the fully charged electrode (54). This is not unexpected because the critical nuclei or $PbSO_4$ are very small, about 11Å diameter (24).

Once the critical nuclei are formed, however, they grow very rapidly. These initial crystals are parallel growths of the basal pinacoid, Fig. 2. The larger crys-

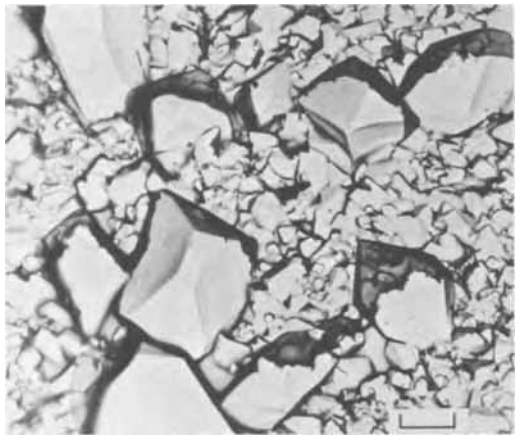

Fig. 1. Lead sulfate coating formed on lead antimony alloy on open circuit for 30 min in 1.2549 sp gr H_2SO_4. Larger prismatic crystals are implanted in a layer of smaller crystals. In the lower right hand corner, the bed of small crystals is seen through the "overhang" of the replica of the larger crystal, and the line of contact between the two types of crystal is visible. Magnification marker on all electronmicrographs = 1μ.

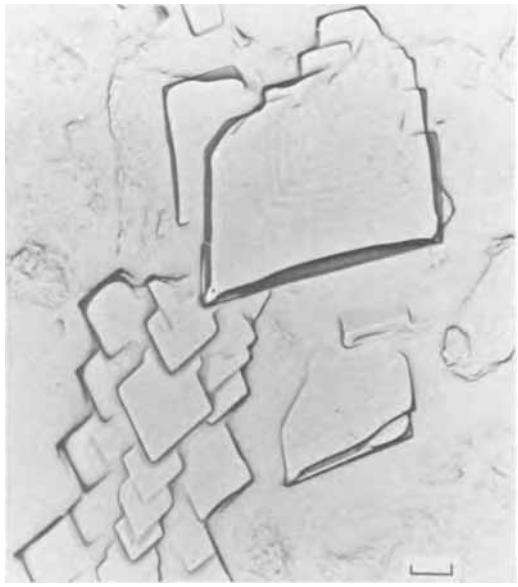

Fig. 2. $PbSO_4$ crystals formed on the discharging electrode at 5 min, immediately following the coup de fouet. The large crystal has a hopper type of face development. In the string of smaller crystals several interplate bridges are visible, and one of the basal pinacoids is modified by the {201} domes. These crystals stand out in relief from the layer of PbO_2 and only the most prominent features of this layer are replicated here.

tal has a hopper type of face development, and the overlapping plates in the string can be seen to be connected by bridges. When viewed from the side, Fig. 3, it is seen that the {210} prism faces are not developed, the platelets are usually less than 0.5μ thick, and the interplate attachments are small bridges that may have resulted from growth in the [201] and [011] directions. It is concluded that growth in the [001] direction is inhibited and may be the result of adsorption of an antimony species on the (001) face. Although domes appear on some of these basal plates, the pinacoids (100) and (010) are absent, indicating that growth in these directions was most rapid. Although an effort was made to observe these crystals at an earlier stage when they could be expected to display these faces, they had grown themselves out of existence by the time the electrodes were examined, *i.e.*, at 3.25 and 4 min.

When discharged to 0.8V *vs.* the reference electrode, corresponding to the cut off voltage of the positive plate of the lead-acid cell, the $PbSO_4$ crystals exhibited a different morphology, Fig. 4. These appear to be typical prisms parallel to the crystallographic axes, described for many mineral specimens, and resemble the crystals forming on self discharge of pure lead anodes (10). These lie implanted in the PbO_2 layer and could not have grown from the original strings of basal plane crystals formed on the electrodes, Fig. 2. It is possible that those platelets lying in the electrode surface on their sides in the manner shown in Fig. 3, grow into the prisms appearing at the end of discharge, Fig 4. On the other hand, some residual basal pinacoids were observed, Fig. 5. The appearance of these crystals suggests that during discharge, this crystal form became energetically unstable, and began to dissolve, hence few remain at the end of discharge. This is further suggested by the appearance of the electrode when half discharged, when the surface appeared to be more completely covered with $PbSO_4$ than at the termination of discharge. It appears possible that some of the anomalies associated with aging of chemically prepared $PbSO_4$ may result from similar transformations (17, 23, 56).

It is seen in the micrographs that the $PbSO_4$ crystals are several orders of magnitude larger than the PbO_2 crystals and $PbSO_4$ does not completely cover the elec-

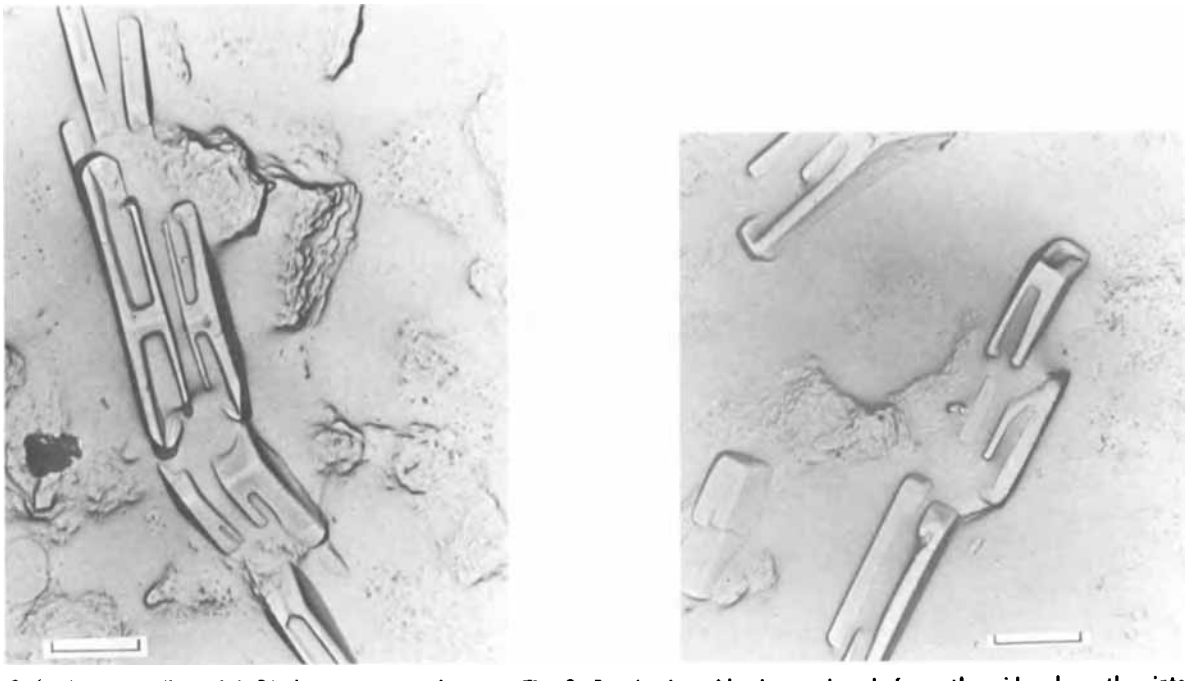

Fig. 3 (a, left) and (b, right) Discharging electrode as in Fig. 2. Basal pinacoid plates viewed from the side show the interplate bridging and the poor development of the {210} prism faces indicating inhibited growth in the c_0 direction. Most of these platelets are less than 0.5μ thick.

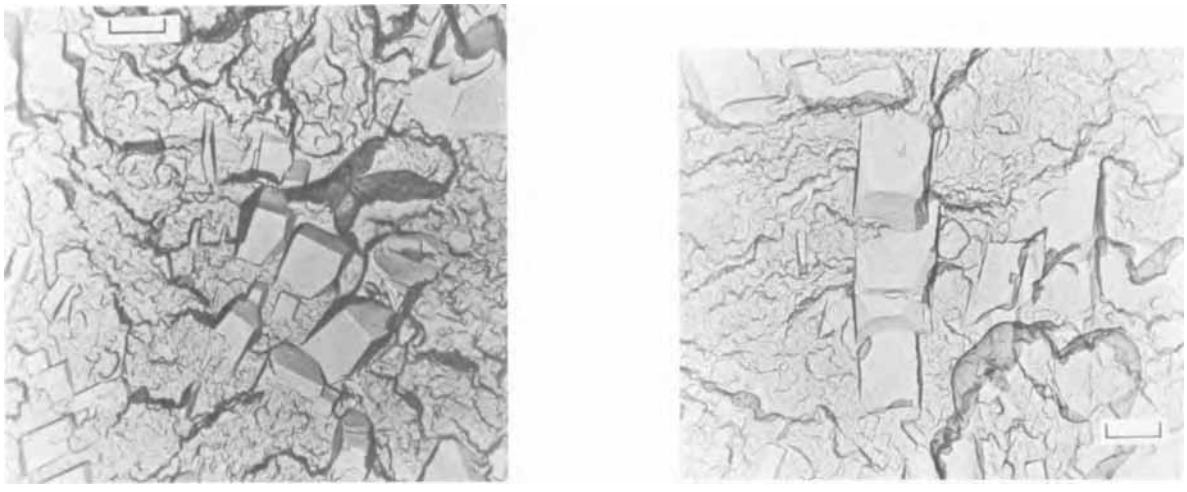

Fig. 4 (a, left) and (b, right). $PbSO_4$ crystals on the surface of electrode discharged to 0.8V *vs.* the Hg, Hg_2SO_4 reference. At the end of discharge the $PbSO_4$ crystals are implanted in the PbO_2 coatings. Much of the PbO_2 surface appears to remain available for discharge.

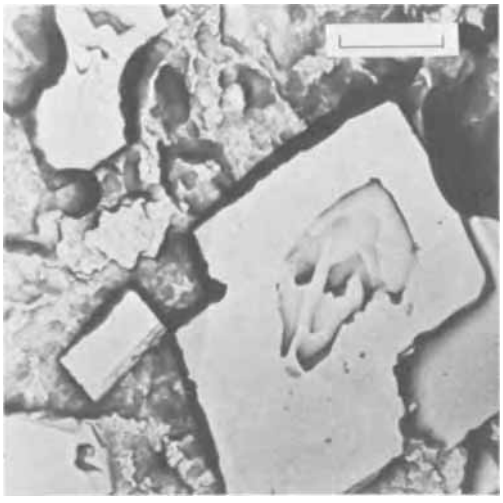

Fig. 5. Basal pinacoids remaining on the surface at the end of discharge. The etched appearance of the edges of these crystals, and the labyrinthine interior suggests that these crystals have been dissolving during the discharge, rather than growing. The PbO_2 is heavily pitted in the immediate vicinity of these $PbSO_4$ crystals. This would be expected if the reaction takes place by way of solution.

trode surface at the end of discharge. The observations of this study support the conclusions of other investigators (37, 38, 57) that the reaction takes place by way of the solution. It has been suggested that the end of discharge of PbO_2 on pure lead anodes is a result of a covering over of the surface by $PbSO_4$ (37). In the case of PbO_2 discharging on lead-antimony alloy, the electron micrographs, Fig. 4, suggest that nucleation and growth of the $PbSO_4$ crystals take place at "active centers" and that termination of discharge might be said to result from an "exhaustion or covering over of the active centers."

Another possible cause of the termination of discharge on the alloy may be the limited growth rate of the $PbSO_4$ crystals themselves. As indicated earlier, it is the slow growing faces that ultimately enclose a crystal. If the growth rate is significantly retarded, it is possible that accretion of additional material cannot keep pace with the electrochemical reaction, supersaturation of Pb ions would increase and the nucleation overvoltage associated with less active centers may require excessive polarization. The discharge would then be terminated in order to avoid secondary electrochemical reactions and homogeneous nucleation of $PbSO_4$ in the solution. The possibility that the crystal growth rate may limit the discharge is further supported by the fact that additional discharge capacity is usually available from the electrode at reduced current densities. A crystal-growth control mechanism has been established for the deposition of $PbSO_4$ on pure lead in $2N$ H_2SO_4 (34, 58). Similar potentiostatic studies of the discharge of the PbO_2 electrode on antimonial lead would be of interest to further clarify the mechanism.

Manuscript submitted Sept. 10, 1970; revised manuscript received Nov. 9, 1970. This was Paper 50 presented at the Atlantic City Meeting of the Society, Oct. 4-9, 1970.

Any discussion of this paper will appear in a Discussion Section to be published in the December 1971 JOURNAL.

REFERENCES

1. C. S. Smith, *Trans. AIME*, **175**, 15 (1948).
2. C. S. Smith, *Met. Rev.*, **9**, No. 33, 1 (1964).
3. A. C. Simon, in "Batteries 2," p. 63, D. H. Collins, Editor, Pergamon Press, New York (1965).
4. J. Burbank, in "Batteries," p. 43, D. H. Collins, Editor, Pergamon Press, New York (1963).
5. D. Kordes, *Chem.-Ing. Tech.*, **38**, 638 (1966).
6. J. Burbank, *This Journal*, **111**, 1112 (1964).
7. E. J. Ritchie and J. Burbank, *ibid.*, **117**, 299 (1970).
8. E. Willihnganz, *Trans. Electrochem. Soc.*, **92**, 281 (1947).
9. W. Feitknecht and A. Gaumann, *J. Chim. Phys.*, **49**, 135 (1952).
10. W. Feitknecht, *Z. Elektrochem.*, **62**, 795 (1958).
11. D. Pavlov, *Ber. Bunsenges.*, **71**, 398 (1967).
12. D. Pavlov, *Electrochim. Acta*, **13**, 2051 (1968).
13. K. Sahl, *Beitr. Mineral. Petrog.*, **9**, 111 (1963).
14. E. V. Shannon, *Proc. U.S. Nat. Museum*, **58**, 437 (1921).
15. C. Anderson, *Records Australian Museum*, **13**, 201 (1922).
16. E. S. Dana and W. E. Ford, "A Textbook of Mineralogy," 4th ed., John Wiley & Sons, New York (1932).
17. I. M. Kolthoff and B. Van't Riet, *J. Phys. Chem.*, **63**, 817 (1959).
18. A. N. Winchell and H. Winchell, "The Microscopical Characters of Artificial Inorganic Solid Substances," p. 131, Academic Press, New York (1964).
19. M. Hahnert and W. Kleber, *Kolloid-Z.*, **162**, 36 (1959).
20. S. Otani and M. Miura, *J. Sci. Hiroshima Univ. Ser. A-II*, **25**, 145 (1963).
21. F. Rinne, *Centr. Mineral Geol.*, 1924, 161.
22. O. C. Farrington and E. W. Tillotson, Jr., *Field Columbian Museum Pub. Geol. Ser.*, **3**, No. 7 (1908).
23. L. B. Nelson, *Dissertation Abstr.*, **16**, 36 (1956). "Crystal Growth and Isotopic Exchange of Lead Sulfate in Aqueous Media," New York University, 1955.
24. A. G. Walton, *Mikrochim. Acta*, **1963**, 422.
25. A. VanHook, "Crystallization: Theory and Practice," Reinhold Publishing Corp., New York (1961).
26. R. F. Strickland-Constable, "Kinetics and Mechanism of Crystallization," Academic Press, New York (1968).
27. A. G. Walton, *Science*, **148**, 601 (1965).
28. G. D. Botsaris, E. G. Denk, G. S. Ersan, D. J. Kirwan, G. Margolis, M. Ohara, R. C. Reid, and J. Tester, *Ind. Eng. Chem.*, **61** (10) 86; (11) 92; (12) 65 (1969).
29. M. Bentivoglio, *Proc. Roy. Soc. (London)*, **115**, 59 (1927).
30. J. O'M. Bockris and G. A. Razumney, "Fundamental Aspects of Electrocrystallization," Plenum Press, New York (1967).
31. M. Fleischmann and H. R. Thirsk, *Electrochim. Acta*, **1**, 146 (1959).
32. G. W. D. Briggs, M. Fleischmann, and H. R. Thirsk, in "Batteries 2," D. A. Collins, Editor, Pergamon Press, New York (1965).
33. M. Fleischmann and H. R. Thirsk, in "Advances in Electrochemistry and Electrochemical Engineering," Vol. 3, Chapt. 3, p. 123, P. Delahay, Editor, Interscience Publishers, New York (1963).
34. D. A. Vermilyea, in "Advances in Electrochemistry and Electrochemical Engineering," Vol. 3, Chapt. 4, p. 211, P. Delahay, Editor, Interscience Publishers, New York (1963).
35. A. Damjanovic, M. Paunovic, T. H. V. Setty, and J. O'M. Bockris, *Acta Met.*, **13**, 1092 (1965).
36. E. Budevski, *Electrochim. Metallorum*, **1**, 131 (1966).
37. B. N. Kabanov, D. I. Leikis, and E. I. Krepakova, *Doklady Akad. Nauk S.S.S.R.*, **98**, 989 (1954).
38. S. Hisano, *Kogyo Kagaku Zasshi*, **62**, 376 (1959).
39. P. L. Kapitza, *Proc. Roy. Soc. (London)*, **105**, 691 (1924).
40. P. Kapitza and H. F. Heath, Brit. Pat. 226,857 Jan. 5, 1925. "Improvements in Electric Storage Apparatus."
41. E. Willihnganz, "The Cold Test Voltage of the Storage Battery," National Lead Co., Research Laboratories, Publication No. 85, 1944.
42. H. B. Mark, Jr., *This Journal*, **109**, 634 (1962).
43. A. C. Simon, *Electrochem. Technol.*, **1**, 82 (1963).
44. D. Berndt and E. Voss, in "Batteries 2," p. 17, D. H. Collins, Editor, Pergamon Press, New York (1965).
45. W. F. Hillebrand, G. E. F. Lundell, H. A. Bright, and J. I. Hoffman, "Applied Inorganic Analysis," 2nd ed., Chapt. 14, John Wiley & Sons, New York (1953).

46. W. J. Maeck, "The Radiochemistry of Antimony," Department of Commerce, Washington, D. C., 1961.
47. N. V. Sidgwick, "The Chemical Elements and Their Compounds," Vol. 1, pp. 758 ff., Clarendon Press, Oxford (1951).
48. J. L. Dawson, J. Wilkinson, and M. I. Gillibrand, *J. Inorg. Nucl. Chem.*, **32**, 501 (1970).
49. J. L. Dawson, M. I. Gillibrand, and J. Wilkinson, "The Chemical Role of Antimony in the Lead-Acid Battery," paper presented at 7th International Power Sources Symposium, Sept. 15-17, 1970, Brighton, England.
50. H. P. Klug and L. E. Alexander, "X-Ray Diffraction Procedures," John Wiley & Sons, New York (1954).
51. G. W. Bailey, *Norelco Reporter*, **13** (4) 111 (1966); **14** (1) 26 (1967).
52. E. P. Dahlberg and C. D. Beachem, "Fractography Part XV. Some Artifacts Possible with Two-Stage Plastic Carbon Replication Technique," Naval Research Lab. Memo Report 1457, Sept. 1963.
53. B. V. Whiteson, A. Phillips, and V. Kerlins, in "Techniques of Metals Research," Vol. II, Part I, p. 460, R. F. Bunshah, Editor, Interscience Publishers, New York (1968).
54. J. Burbank, "Cycling Anodic Coatings on Pure and Antimonial Lead in H_2SO_4," paper presented at 7th International Power Sources Symposium, Sept. 15-17, 1970, Brighton, England.
55. J. Burbank, *Trans. AIME*, 55 (1953).
56. I. M. Kolthoff and C. Rosenblum, *J. Am. Chem. Soc.*, **57**, 597, 607 (1935).
57. A. C. Simon, C. P. Wales, and S. M. Caulder, *This Journal*, **117**, 987 (1970).
58. M. Fleischmann and H. R. Thirsk, *Trans. Faraday Soc.*, **51**, 71 (1955).

Concerning the Critical Pitting Potential

David A. Vermilyea*

Research and Development Center, General Electric Company, Schenectady, New York 12301

ABSTRACT

The critical pitting potential, defined as the least positive potential at which pits can be grown, may be that potential at which the metal salt of the aggressive ion in solution is in equilibrium with the metal oxide. Such an equilibrium may be achieved when the activity of the anion in the pit has been increased by the potential difference between the inside and outside of the pit. The theory successfully predicts the critical pitting potentials for aluminum, magnesium, iron, and nickel, but fails for zirconium, titanium, and tantalum.

Passive metals are susceptible to localized attack by pitting when polarized above some potential in a solution containing aggressive ions, usually halides. The potential E_c above which pitting starts has been referred to as the "critical pitting potential." For a particular alloy the critical pitting potential is known to be a function of temperature and of the nature and concentration of the aggressive ion. The experimental determination of E_c is difficult because of a variety of kinetic effects, and the values are not reliable to less than a few tenths of a volt. In this paper a new theory, based on thermodynamic considerations, is presented for the calculation of E_c. The objective is only to make a rough estimate of E_c; the current understanding of the nature of concentrated aqueous solutions precludes more precise predictions. It is the intent of the theory to predict the *minimum* E_c, which would presumably be observed at an infinitely slow increase of potential. The minimum E_c may be equal to the so-called "protection potential" at which a growing pit would become repassivated on lowering the potential.

Vetter (1) has proposed that pitting occurs when the normally protective oxide is in equilibrium with the salt of the metal and the aggressive anion. In order for such equilibrium to occur it is usually necessary for the free energies of the oxide or of the salt layer or of both layers to deviate widely from the values for the bulk compounds. As an example, the reaction

$$AlCl_3 + 3/2\ H_2O \rightarrow 1/2\ Al_2O_3 + 3HCl_{(aq)} \qquad [1]$$

results in a free energy decrease of 45.4 kcal. In order for the $AlCl_3$ and Al_2O_3 to be at equilibrium the free energy for that reaction would have to be zero, and that could be true if the solid phases were nonstoichiometric or contained aluminum with an unusual valence. Since the standard free energies of $AlCl_3$ and $\frac{1}{2}$ Al_2O_3 are -150.2 and -188.4 kcal/mole, respectively, it is clear that very large changes of some kind are required. In view of the strong preference of aluminum for a valence of $+3$ it is debatable whether such large free energy changes are reasonable.

Other investigators (2, 3) have proposed that the critical pitting potential is that potential at which adsorption of the aggressive anion becomes favored over adsorption of oxygen. At present such theories do not permit a prediction of the critical pitting potential.

The present theory of the critical pitting potential is based on changes in the free energies of substances in the aqueous solution. Consider a pure passive metal corroding at potential E_1 in a solution containing an aggressive anion. Imagine that the passive film becomes ruptured locally so that the metal starts to dissolve rapidly, forming metal ions according to

$$M \rightarrow M^{+z} + ze \qquad [2]$$

where z is the valence of the metal. If E is below E_c, repassivation occurs, while above E_c repassivation fails and the ruptured area continues to corrode according to [2]; consider the latter condition. If reaction [2] were entirely reversible and if no other reaction occurred in the pit, the local potential would fall to E_M, the value of the metal-metal ion potential appropriate to the concentration of metal ions in the pit. Actually some overvoltage is required to drive reaction [2]. If the activation overvoltage, η, is taken as the difference between the local specimen potential and E_M, then

$$\eta + \Delta\phi = E_1 - E_M \qquad [3]$$

where $\Delta\phi$ is the potential difference between the Helmholtz plane in the pit and the bulk solution.

Under the influence of $\Delta\phi$, anions move into the pit until a concentration gradient is established so that their net flux is zero. Under these conditions the electrochemical potentials of the anions inside and outside the pit are equal, so that

* Electrochemical Society Active Member.
Key words: corrosion, passivation, reaction products.

$$\mu_p + z\mathbf{F}\phi_p = \mu_b + z\mathbf{F}\phi_b \quad [4]$$

where the subscripts p and b refer to the pit and bulk solutions, respectively. From [4] it can be seen that the chemical potential of anions inside the pit is greater than that in the bulk solution by $z\mathbf{F}\Delta\phi$.

Now consider the repassivation of the ruptured area. Passivation may occur when the metal potential rises to that required to form an oxide on the surface according to

$$M + z/2\ H_2O \rightarrow MO_{z/2} + zH^+ + ze \quad [5]$$

A possible competing reaction is the formation of a solid salt on the surface according to

$$M + zX^- \rightarrow MX + ze \quad [6]$$

It is proposed that if reaction [6] becomes thermodynamically favored over reaction [5] the ruptured area will not be repassivated but will continue to corrode at a high rate. When the metal is covered with a highly soluble salt the corrosion rate can be very high even if the solution near the surface is nearly saturated with respect to the salt. For instance, if the undersaturation is 10% and the solubility 10M the diffusion-limited corrosion rate based on a stationary layer 10^{-2} cm thick would be 10^{-1} A/cm^2. For simplicity it is assumed that the normal oxide and salt are the compounds of interest. The nonprotective layer could as well be some kind of oxy-salt.

The formation of salt will be favored because of the increased chemical potential of the anion. The formation of oxide will be impeded because of the decreased chemical potential of water in the concentrated solution and possibly because of the increased chemical potential of protons caused by hydrolysis of the cations of the metal. The decreased chemical potential of water results from the fact that, at very high salt concentrations, much of the water in the solution is closely associated with the ions as water of solvation. Hydrolysis of metal ions in concentrated salt solutions can readily produce proton activities which are much higher than expected by extrapolation from dilute solutions.

While it is not possible to calculate the chemical potentials of all the species in reactions [5] and [6], it is possible to measure them and hence to test the underlying principle. While such data are not readily available, some estimates can be made to demonstrate the plausibility of the theory.

As an example, consider aluminum in chloride solutions. The standard potential for forming $AlCl_3$ according to reaction [6] is -0.84V (all potentials are on the standard hydrogen electrode scale). For the oxide the normal potential is -1.5V, and the Al/Al^{+3} standard potential is -1.66V. The pH of a saturated solution of $AlCl_3 \cdot 6\ H_2O$ was measured to be -0.3. The vapor pressure of water over such a solution is not known, but might be lower than that over pure water by a factor of 10. The equilibrium potential for forming Al_2O_3 according to reaction [5] in such a solution would be -1.45V. Because of the change of chemical potential of anions obtained from [4], the corresponding potential for $AlCl_3$ is $-0.84 - \Delta\phi$ and hence, for a bulk solution with unit chloride ion activity, salt and oxide are equally stable when $\Delta\phi = 0.61$V. The activity of aluminum ions cannot be calculated. However, the chloride ion concentration must be very high if $AlCl_3$ is to be formed, and the Al^{+3} concentration must also be high to keep the solution neutral. The activity of Al^{+3} in the pit will probably be of the same order of magnitude as that of Cl^-. With that assumption $E_M = -1.66 + \Delta\phi/3 = -1.46$V. Equation [3] then gives $E_1 = -0.85 + \eta$. The overvoltage cannot be calculated, but for the large current densities associated with pitting it is probably a few tenths of a volt. Thus the theory predicts a pitting potential somewhere in the vicinity of -0.6V; aluminum is actually observed to pit at about -0.5V. The predicted pitting potential is close enough to the observed values to be intriguing and to suggest that there is some validity to the theory.

A similar analysis for magnesium shows that pitting should occur at about -1.5V, again in reasonable agreement with observations. For iron and nickel the chlorides should form at -0.2 and -0.05V, respectively, which are lower than the corresponding potentials for the oxides in acid solutions. Iron and nickel do pit in chloride solutions at potentials just above those at which the chlorides become stable.

The theory fails badly for some metals, however. Zirconium is predicted to pit at $E_1 = 0.9 + \eta$, while pitting is observed at about $+0.4$V. About 10V must be applied to cause titanium to pit, and tantalum can be anodized in chloride solutions to at least 100V without pitting. It is not known why these metals of higher valence do not pit at lower potentials. The answer may lie in the details of the molecular processes which yield the halides and oxides.

Discussion

According to this theory the pitting potential must always be sufficiently positive to the metal-metal ion potential to make equal the free energies of formation of the oxide and the salt. Thus a minimum pitting potential is a clear prediction of the theory. The actual pitting potential may exceed the minimum because of a variety of kinetic factors but, if this theory is valid, may not be less than the predicted minimum.

Experimental determination of the critical pitting potential appears to be very difficult, for values reported by different authors for the same system often differ greatly. Evidently the critical potential is a function of time, film history, and metal surface preparation. The theory predicts a change of the critical pitting potential by about 0.059V per decade of concentration at 25°C. A recent paper by Leckie (4) reports a variation of 0.070V per decade for stainless steel in chloride solutions in reasonable agreement with the theory. Kolotyrkin (5) has quoted results by Gilman which show such a dependence of critical pitting potential of zirconium on chloride concentration, but as pointed out above the theory does not seem to work well for zirconium. Studies on alloys (6, 7) and on nickel show that the critical pitting potential changes by 0.2-0.4V per decade of anion concentration, in conflict with the prediction above. However, the experiments reported often used a supporting electrolyte, which provides a complication not easy to resolve, and the behavior of an alloy may be different from that of a pure metal. Studies using pure metals in solutions containing only one anion are required to test the theory, and care must be taken to minimize contributions from convection and resistive potential drops in the bulk solution (outside the Nernst layer).

Some of the examples above led to the conclusion that potential differences as large as several tenths of a volt might be present in the solution. For reasonably concentrated solutions such potential differences are probably possible only with some kind of restricted geometry. For example, the growing section of the pit may be covered with a perforated layer of the passive film which originally covered the metal. Such films have been reported by many investigators.

Prediction of the ions which will act in an aggressive manner is not straightforward. The theory proposed above predicts the formation of a concentrated solution of any anion and, presumably, the precipitation of the salt of that anion. Whether the ion will be aggressive or not depends on the next step: Will the salt layer simply dissolve at a high rate and prevent passivity or will it be converted in some way to a passive layer? The answer to that question requires a more complete understanding of the mechanism of the active-passive transition. It is worth noting, however, that the most aggressive ions do not contain oxygen. Possibly films containing oxyanions can more easily be

converted to passive layers than can films containing halides, cyanides, sulfides, and other aggressive anions.

Manuscript submitted March 26, 1970; revised manuscript received Nov. 16, 1970.

Any discussion of this paper will appear in a Discussion Section to be published in the December 1971 JOURNAL.

REFERENCES

1. K. J. Vetter, *Ber. Bunsenges.*, **69**, 683 (1965).
2. M. Prazhak, Ya. Toushek, and V. Spanily, *Protection of Metals*, **5**, 329 (1969).
3. H. H. Uhlig, "Corrosion and Corrosion Control," p. 70, John Wiley & Sons, Inc., New York (1965).
4. H. P. Leckie, *This Journal*, **117**, 1152 (1970).
5. Ya. M. Kolotyrkin, *ibid.*, **108**, 209 (1961).
6. Ya. M. Kolotyrkin, G. V. Golovina, and G. M. Florianovich, *Dokl. Phys. Chem.*, **148**, 113 (1963).
7. I. V. Riskin and A. V. Turkovskaya, *Protection of Metals*, **5**, 390 (1969).

The Electrochemical Oxidation and Reduction of Gold

Kotaro Ogura,,[1] Shiro Haruyama, and Kyuya Nagasaki**

Chemistry of Metals Laboratory, Faculty of Engineering, Tokyo Institute of Technology, Tokyo, Japan

ABSTRACT

Anodic film was formed on a gold electrode by the potentiostatic technique and then reduced cathodically. The amounts of charge needed for anodization, Q_a, were evaluated by graphical integration of transient currents, and the amounts of charge, Q_c, needed to reduce the film were obtained from the chronopotentiogram. In weak acidic solutions, log Q_a was proportional to E_a, and the auric hydroxide could grow continuously at noble potentials without the accompanying evolution of oxygen. In strong acidic solutions, however, log Q_a was not proportional to E_a but log $(Q_a - Q'_{a\ 1600\ mV})$ was proportional to E_a at noble potentials. In these strong acidic solutions, oxygen evolved on the auric oxide, and this oxide layer grew only to a fixed thickness. On galvanostatic reduction of the oxide film, an arrest was observed in the chronopotentiogram. It was concluded that the potential determining reaction at this arrest potential varied according to the pH ranges as shown in the following reactions

$$Au_2O_3 + 6H^+ + 6e \rightarrow 2Au + 3H_2O$$

(in strong acidic solutions)

$$Au(OH)_3 + 3H^+ + 3e \rightarrow Au + 3H_2O$$

(in weak acidic solutions).

The electrochemical formation and reduction of oxide films on noble metals, especially platinum, have been actively investigated (1-5). The surface oxide formed on platinum has been reported to have the ability to transfer electric charge from the metal to a reactant in the solution without an appreciable increase in film thickness; that is, the oxide film on platinum is an electronic conductor.

However, in the case of a gold electrode, the anodic film can grow thicker than a monolayer; a charge transfer reaction always accompanies this increase in film thickness. This means that the oxide film on gold is ion conducting rather than electron conducting.

Noble metals have been considered to be inert. However, two different types of oxide may exist on these noble metals and may affect electrochemical reactions in different ways. Also, there may be some differences in polarization behavior among the noble metals. In this sense, the gold electrode was studied in this work.

Some investigators (6-10) have studied an oxide film on gold by means of the galvanostatic technique of oxidation and/or reduction. Recently, some work has been performed using the potentiostatic technique combined with galvanostatic measurements (11, 12). This process is potentiostatic oxidation and galvanostatic reduction; however, the results of these latter studies do not always agree with each other. The investigators who used the potentiostatic technique paid attention not to the amount of charge passed during oxidation, Q_a, at constant potential, but to the amount of charge, Q_c, needed for cathodic reduction after charging the circuit to the galvanostatic technique. There is no experimental evidence that Q_c can be considered to equal Q_a; rather data reported in this paper and supported by Vetter and Berndt (6) show that they do not coincide.

In the present work, the amount of charge needed for potentiostatic oxidation was evaluated by a graphical integration of current-times curves. Also, the kinetics of the oxidation and reduction of a gold electrode were studied by the combination of potentiostatic and galvanostatic techniques. The oxygen evolution reaction on gold and the manner in which it is affected by the oxide formed during anodization are also discussed.

Experimental

Sample.—The electrode used in this study was a 99.99% gold foil 0.1 mm thick and 0.9 cm^2 in apparent area. The specimen was abraded with emery paper. Electropolishing was tried at first to obtain minimum roughness but had to be abandoned because of preferential attack at the edges. The foil was connected through a piece of gold wire to a tungsten wire, which was sealed in a glass tube. Only the foil and the lower part of the gold wire were immersed into the electrolytic solution during experiments.

Electrolytic solution.—The solution was prepared to 0.1 m/l in $HClO_4$ by perchloric acid of analytical grade and water redistilled from a basic permanganate solution. The pH of the solution was adjusted from 0.5 to 7.6 with sodium hydroxide solution. The solution was deaerated with purified nitrogen which was passed through a column of active copper heated at 200°C.

** Electrochemical Society Student Associate.
[1] Present address: Department of Chemistry, Rice University, Houston, Texas 77001.

Key words: oxidation, reduction, gold, amount of charge, rest potential.

The final solution was pre-electrolyzed for 48 hr. This was carried out at a current density of 80 $\mu A/cm^2$ so that the impurities would be eliminated but no H_2O_2 would be formed.

Cell.—Electrochemical measurements were made with a three-electrode system composed of a gold test electrode, a platinum counterelectrode, and a hydrogen reference electrode which was connected to the working electrode through a Luggin capillary. The counterelectrode was a cylindrical platinum foil sealed into a cylinder of 3 cm diameter. The reference electrode was put in a separate compartment which was connected to the test cell through a stopcock. The electrolytic solution in which the reference electrode was immersed was the same as the test solution. Potentials were measured with respect to the reversible hydrogen electrode (RHE) unless otherwise noted.

Method.—The specimen was polished with emery paper and was cathodically reduced to eliminate the oxide film or adsorbed oxygen formed on it in air. The cathodic current density was 22.4 $\mu A/cm^2$. Cathodic reduction was stopped when the potential reached 0 mV (RHE) in order that the effect of hydrogen evolution during cathodic reduction might be minimized. In order to obtain reproducible results, the cleaned specimen was pre-anodized at a constant potential of 600 mV (RHE) for 1 min. The amount of charge needed for the pretreatment was small enough to be neglected.

The specimen was then anodically oxidized by means of a potentiostat (Nichiya NP 250 Type) for a measured length of time. The change of current with time after application of the constant potential was followed by recording the ohmic drop across a standard 100 ohm resistor inserted in the polarization circuit. The amount of charge passed during anodization was evaluated by graphical integration of transient currents. This was performed with a planimeter. The oxidized gold electrode was reduced electrochemically at a constant current density. The change of potential with time was monitored by means of a recorder equipped with a preamplifier having an input impedance of 10^9 ohms.

The experiments were carried out at 16° ± 2°C in an atmosphere of purified nitrogen gas. Solution agitation was accomplished by bubbling nitrogen gas through a capillary tube placed beneath the test electrode.

Results and Discussion

Anodic oxidation.—Oxidation at less noble potentials.—The amount of charge passed, Q_a, at various constant potentials was calculated by graphical integration. Q_a was increased by shifting the potential to more positive values, as shown in Fig. 1 and 2.

From these figures, it can be seen that Q_a also increased by increasing the anodizing time and that Q_a is generally larger in higher *p*H solutions, from a comparison of Fig. 1 and 2. The following process may be envisioned to interpret these figures: a *p*H dependent chemical species adsorbs on the electrode surface

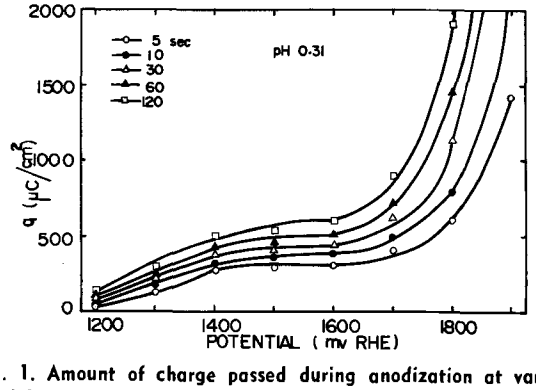

Fig. 1. Amount of charge passed during anodization at various potentials.

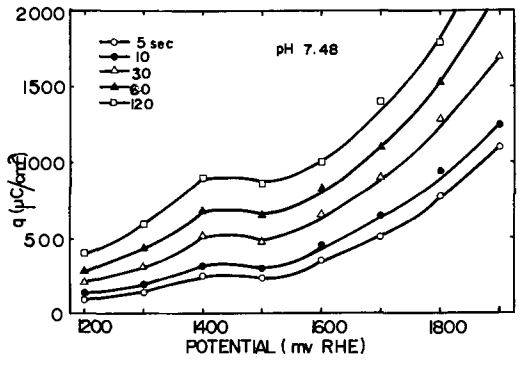

Fig. 2. Amount of charge passed during anodization at various potentials.

at less noble potentials; a stoichiometric compound of this species forms at about 1450 mV. At potentials more positive than about 1600 mV, either this compound continues growing or some other electrochemical reaction like oxygen evolution occurs. In the following sections, these assumptions are discussed in relation to additional experimental results.

In Fig. 3, values of Q_a obtained at various set potentials are plotted against the logarithm of time. Q_a can be seen to increase in proportion to log t_a at potentials less than or equal to 1300 mV. At potentials greater than or equal to 1400 mV, the linear relation between Q_a and log t_a is divided into two parts. It may be considered that a single reaction occurs at constant potentials less than or equal to 1300 mV.

As shown in Fig. 4, Q_a at lower *p*H values is independent of *p*H but does become *p*H dependent at higher values. This means that the single reaction which occurs at less noble potentials is *p*H dependent. The following equation holds for the more negative potential range

$$Q_a = \log t_a{}^n + m \qquad [1]$$

In weak acidic solutions, n and m are constants at fixed values of potential and *p*H. In the initial period

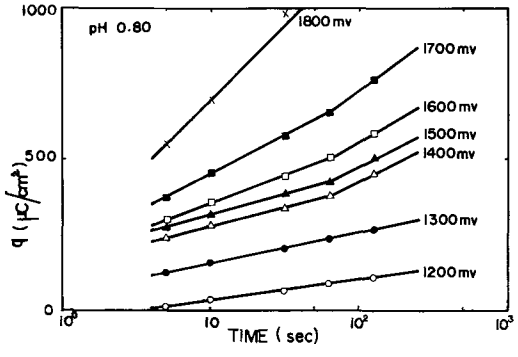

Fig. 3. Amount of charge as a function of time at various potentials.

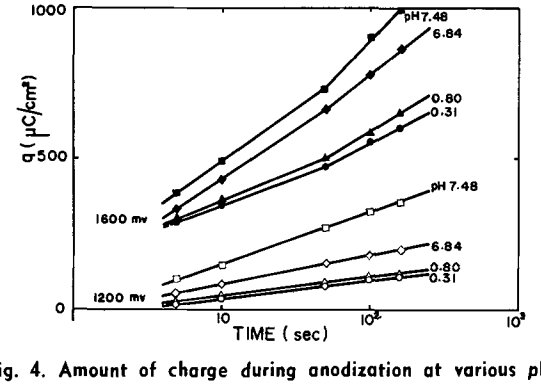

Fig. 4. Amount of charge during anodization at various *p*H's

of time (within a few seconds in this experiment), n of Eq. [1] depends only on potential as shown in Fig. 4. At lower pH, Q_a was essentially independent of solution pH. It is reasonable to assume that oxygen is adsorbed in the potential range in which the linear relationship between Q_a and log t_a holds. As shown in Fig. 1, Q_a increases with potential and has an arrest at about 1450 mV; these effects may be due to the adsorption of oxygen and auric oxide formation. The following process may be considered upon anodization at lower pH: $Au \rightarrow AuO \rightarrow Au_2O_3$. Oxygen evolution follows this process and is discussed in the next section.

As shown in Fig. 4, Q_a is pH dependent in weak acidic solutions. Figure 2 shows an arrest of Q_a at about 1450 mV. These results can be interpreted by considering OH radical adsorption followed by complex hydroxide formation and a stoichiometric layer of $Au(OH)_3$, as illustrated in the following process: $Au \rightarrow AuOH \rightarrow Au(OH)_x \rightarrow Au(OH)_3$. After $Au(OH)_3$ is formed on the surface of gold, Q_a increases again continuously with potential, as shown in Fig. 2. However, oxygen could not be visibly observed even at high anodic potentials (about 1900 mV); therefore, at least within the limits of these experiments, $Au(OH)_3$ could grow without the accompanying evolution of oxygen.

Oxidation at noble potentials.—As shown in Fig. 5, log Q_a increases in proportion to the set potential, E_a, in high pH solutions. Based on the linearity between log Q_a and E_a, it may be assumed that only a single reaction occurs under the experimental conditions used in this section. In the former section, the formation of $Au(OH)_3$ was assumed to occur in high pH solution. This same assumption can be used to interpret the results shown in Fig. 5; that is, $Au(OH)_3$ may grow in the range from 1500 to 1900 mV. By comparing Fig. 2 and Fig. 5, it can be determined that $Au(OH)_3$ which formed at about 1450 mV continues to grow at more noble potentials without the accompanying evolution of oxygen.

A similar plot of log Q_a *vs.* E_a was tried for strong acidic solutions; however, there was no linearity between log Q_a and E_a in this case. This lack of linearity means that the oxide film on gold in low pH solutions does not continue to grow at more noble potentials. However, the logarithm of the amount of charge, $(Q_a - Q'_{a1600\ mV})$, which is the charge that passed at 1600 mV, $Q'_{a1600\ mV}$, subtracted from the total charge passed, Q_a, was proportional to the set anodizing potential, E_a, as shown in Fig. 6 and 7. $Q'_{a1600\ mV}$ can be regarded as the amount of charge used in the formation of a fixed amount of Au_2O_3 film on gold. Thus, $(Q_a - Q'_{a1600\ mV})$ must be considered to be the amount of charge which was used for the other charge transfer reaction. This reaction is oxygen evolution as described earlier. The effect of solution agitation is shown in Fig. 6. The slope, $(Q_a - Q'_{a1600\ mV})/E_a$, did not change, but the magnitude of $(Q_a - Q'_{a1600\ mV})$ increased at each potential. If the Au_2O_3 film was continuing to grow, then the effect of agitation would be negligible, because the growth of this film is the reaction between

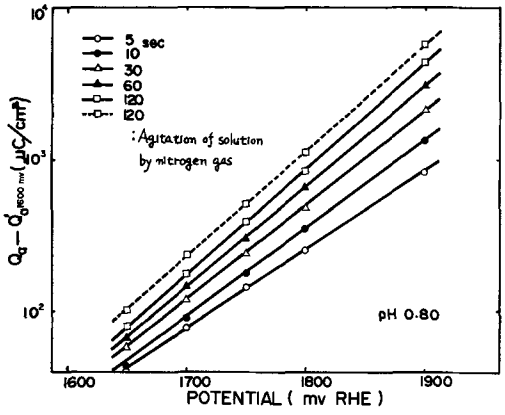

Fig. 6. Logarithmic dependence of charge on potential

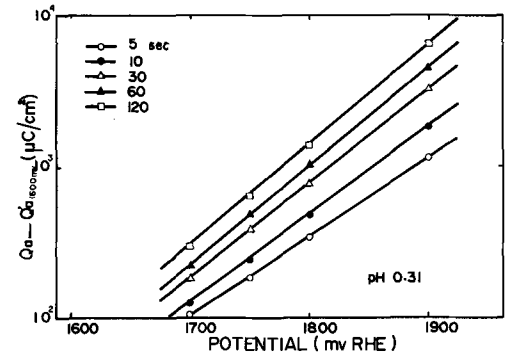

Fig. 7. Logarithmic dependence of charge on potential

two solid phases. However, experimentally, the effect of agitation is not negligible; therefore, the charge transfer reaction is not the growth of the oxide, Au_2O_3, but oxygen evolution at potentials more positive than 1600 mV. It may be concluded that Au_2O_3 is a better electronic conductor than $Au(OH)_3$, and conversely, $Au(OH)_3$ is a better ionic conductor than Au_2O_3. Oxygen evolves on Au_2O_3 without being affected by its presence; however, the oxygen evolution reaction on $Au(OH)_3$ is concealed by the growth of the oxide, $Au(OH)_3$. At pH values intermediate between extreme values used in this study, the growth of oxides occurs simultaneously with the occurrence of oxygen evolution.

Cathodic reduction.—At low pH solutions.—The gold specimen was anodized for an arbitrary length of time at constant potential and then was quickly cathodized by a constant current in order to reduce the oxide film on it. The chronopotentiograms obtained are shown in Fig. 8. These reduction curves have the same arrest potential and, indeed, are very similar in shape. A typical chronopotentiogram has an arrest potential at 1200 mV. This arrest potential was not affected either by the anodizing potential or by agitation of the

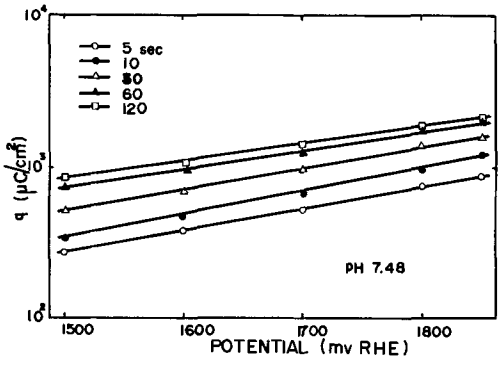

Fig. 5. Logarithmic dependence of charge on potential

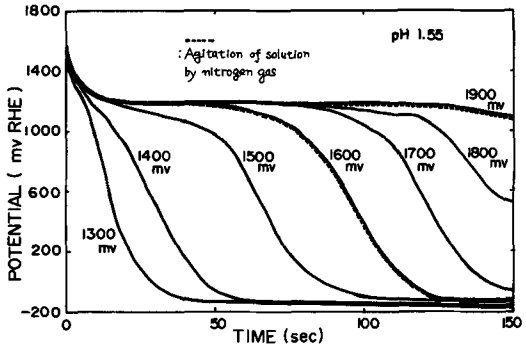

Fig. 8. Cathodic reduction curves

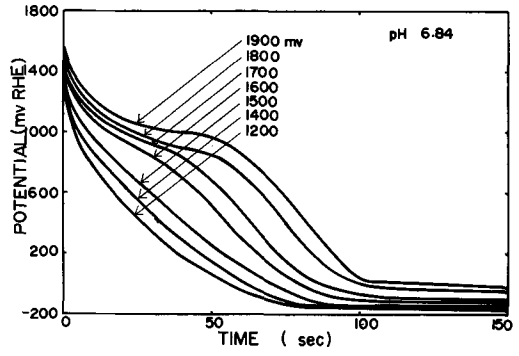

Fig. 9. Cathodic reduction curves

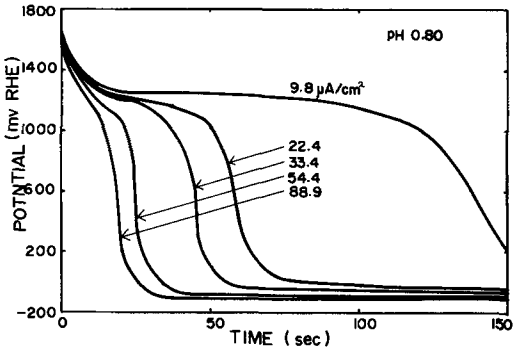

Fig. 10. Cathodic reduction curves

solution; therefore, the compositions of the oxide formed at various potentials in these low pH solutions are all the same. The arrest potential may be due to the reduction of Au_2O_3; this is discussed in a later section.

At high pH solutions.—In weak acidic solutions, the arrest potential shifts in a more cathodic direction as the anodizing potential is decreased, as shown in Fig. 9. This shift of potential may be interpreted as being caused by a change in activity of the $Au(OH)_3$ film; that is, the activity of $Au(OH)_3$ layer may decrease with the shift of the set anodizing potential toward the more cathodic direction. In a strong acidic solution, however, the arrest potential does not depend on the anodizing potential, possibly because the activity of oxide, Au_2O_3, is scarcely changed by the set anodizing potential.

Dependence of the arrest potential[2] *on current density.*—As shown in Fig. 10, the potential arrest shifts in a more cathodic direction as the reduction current density is increased. This dependence can be interpreted as the current dependent shift of overpotential. In Fig. 11, the arrest potential is plotted in the SCE scale *vs.* the logarithm of current density. The resulting plot shows that the potential-current density relationship obeys the Tafel relation

$$E_c = a + b \log i \qquad [2]$$

The value of b was found to be approximately 60 mV. The arrest potential, E_c, depended on the pH; however, the Tafel relation held in all of the experimental conditions.

Dependence of the arrest potential on pH.—From Fig. 12, it can be seen that E_c shows two different pH dependencies, one for weak acidic solutions and one for strong acid solutions. However, in both pH ranges, E_c was proportional to pH; this slope was approximately 60 mV/pH. This result corresponds very closely to the value of 59.2 mV/pH obtained by Vetter and Berndt (6). The reaction occurring at the arrest potential can be inferred from the dependence of E_c on pH in the following manner. Considering only the contribution

[2] This potential was measured at high sensitivity by changing the range of the recorder (±0.5 mV) in the region of the inflection.

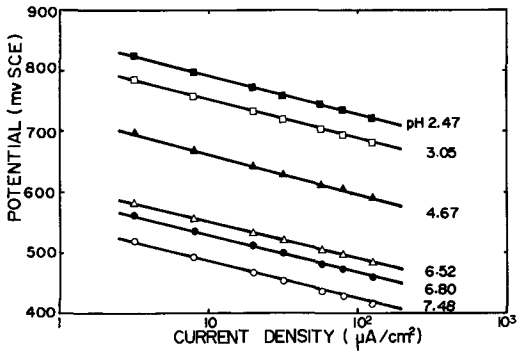

Fig. 11. Dependence of the arrest potential on cathodic current density.

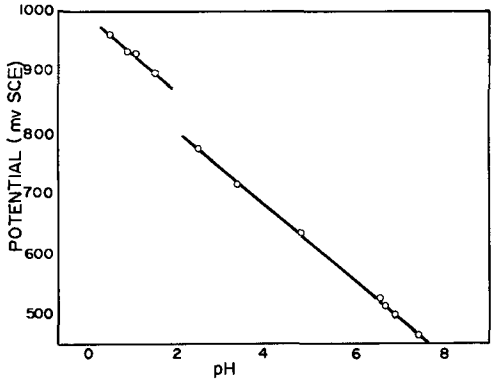

Fig. 12. Dependence of the arrest potential on pH

of H^+, the potential may be expressed by the following equation

$$E_c = E'_c + RT/n\mathbf{F} \log (H^+)^{n'} \qquad [3]$$

where n' is the number of moles of hydrogen ions which participate in the potential determining reaction. Differentiating Eq. [3] by pH

$$\partial E_c/\partial \mathrm{pH} = -2.30\, n'RT/n\mathbf{F} \qquad [4]$$

Since $\partial E_c/\partial$pH was experimentally found to be −60 mV/pH, n' equals n. Therefore, the number of electrons which participated in the reaction must be equal to the number of moles of hydrogen ion.

A metallic ion in solution can be assumed not to participate in this potential determining reaction, because the potential was not affected by the agitation of solution as was shown in Fig. 8. Accordingly, the potential determining reaction must be a solid-solid reaction involving hydrogen ions. It is reasonable to assume the following reactions for the potential arrest in strong and weak acidic solutions

$$Au_2O_3 + 6H^+ + 6e \rightarrow 2Au + 3H_2O \qquad [5]$$

(in strong acidic solutions)

$$Au(OH)_3 + 3H^+ + 3e \rightarrow Au + 3H_2O \qquad [6]$$

(in weak acidic solutions)

The equilibrium potential was calculated to be 1.511V for Eq. [5] and 1.457V for [6] (13).

Q_c and ratio of Q_c/Q_a.—The amounts of charge, Q_c, needed for cathodic reduction were calculated from the chronopotentiograms and were found to depend on the set potentials as shown in Fig. 13. Similar results have been reported by other investigators (11, 12). In strong acidic solutions, there are two discontinuous points, but in weak acidic solutions there is only one continuous point. There seems to be certain relations between these experimental results and the anodizing process; that is, the three linear parts in the Q_c-potential diagram in strong acidic solutions may correspond

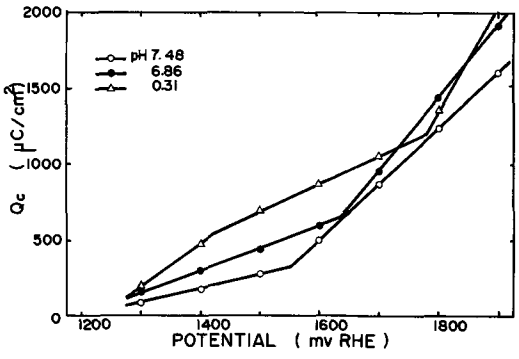

Fig. 13. Relation between the amount of charge needed for cathodic reduction and anodizing potentials.

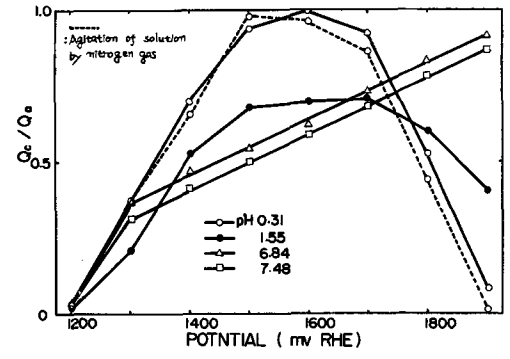

Fig. 14. Relation between Q_c/Q_a and anodizing potentials

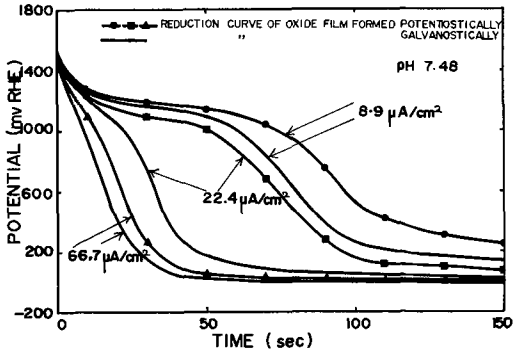

Fig. 15. Cathodic reduction curves

to the formation of a monolayer, the growth of Au_2O_3, and the evolution of oxygen, respectively. The two linear parts in the case of weak acidic solutions can be considered to correspond to the formation of non-stoichiometric $Au(OH)_x$ and the growth of $Au(OH)_3$, respectively.

The ratio of Q_c to Q_a has been reported to have values from unity to 0.5 (6) or to be unity (10). However, in this study, the relation between Q_c/Q_a and potential in several solutions with different pH values is shown in Fig. 14. In strong acidic solutions, Q_c/Q_a increased with increasing potential until about 1600 mV but then decreased on shifting the potential to values more positive than 1600 mV. In weak acidic solutions, Q_c/Q_a always increased with increasing potentials. It is clear that the decrease of Q_c/Q_a in the case of strong acidic solutions is due to the oxygen evolution reaction. In the anodizing process, some excess change may have been used for the formation of molecular oxygen in addition to that used for the oxide film on gold. In the reduction process, it may be difficult for an oxygen molecule which has desorbed from the electrode surface to be reduced, because the oxygen can diffuse away from the electrode surface. This view was also supported by the effect of agitation of solution. At potentials more positive than 1600 mV, Q_c/Q_a on solution agitation was always smaller than for the case in which the solution was not agitated. The desorption of molecular oxygen from the electrode surface became easier as a result of solution agitation; therefore, Q_a increased. In the case of weak acidic solutions, Q_c/Q_a increased continuously with potential as the result of the growth of $Au(OH)_3$ which may occur at all ranges of potential used in this experiment. When the set anodizing potential was shifted to more positive potentials, the amount of charge which participated in the oxidation process seems to approach that which participated in the reduction process.

Galvanostatic oxidation and reduction.—In the above section, the oxide film on gold produced by the potentiostatic technique was discussed; in this section, oxide film produced galvanostatically is discussed. The oxidized gold was reduced at a constant current density, and the change of potential with time was measured as shown in Fig. 15. The cathodic chronopotentiograms were compared with the results obtained for the specimen anodized at constant potential. It is found from Fig. 15 that the arrest potential during reduction was the same regardless of whether the gold electrode was anodized potentiostatically or galvanostatically. The oxide film formed by the two different techniques can be considered to be identical at the same pH. Accordingly, it is reasonable for the present results to be compared with the galvanostatic oxidation results obtained by others (6-10).

Acknowledgment

The authors would like to thank Dr. David Dixon Justice for reading the manuscript and offering suggestions.

Manuscript submitted August 15, 1969; revised manuscript received *ca.* July 6, 1970.

Any discussion of this paper will appear in a Discussion Section to be published in the December 1971 JOURNAL.

REFERENCES

1. S. W. Feldberg, C. E. Enke, and C. E. Bricker, *This Journal*, **110**, 826 (1963).
2. H. A. Laitinen and C. G. Enke, *ibid.*, **107**, 773 (1960).
3. F. C. Anson and J. J. Lingane, *J. Am. Chem. Soc.*, **79**, 4901 (1957).
4. M. Breiter, C. A. Knorr, and W. Volkl, *Z. Elektrochem.*, **59**, 681 (1955)
5. A. Hickling and W. H. Wilson, *This Journal*, **98**, 425 (1951).
6. K. J. Vetter and D. Berndt, *Z. Elektrochem.*, **62**, 378 (1958).
7. D. Clark, T. Dickinson, and W. N. Mair, *Trans. Faraday Soc.*, **55**, 1937 (1959).
8. S. Barnartt, *This Journal*, **106**, 722 (1959).
9. G. Armstrong, F. R. Himsworth, and J. A. V. Butler, *Proc. Roy. Soc.*, **A143**, 89 (1934).
10. A. Hickling, *Trans. Faraday Soc.*, **42**, 518 (1946).
11. S. B. Brummer and A. C. Makrides, *This Journal*, **111**, 1122 (1964).
12. H. A. Laitinen and M. S. Chao, *ibid.*, **108**, 726 (1961).
13. M. Pourbaix, "Atlas of Electrochemical Equilibria," p. 400 (1966).

Kinetics of Anodic Processes on Iron in Alkaline Solutions

S. Asakura* and Ken Nobe*

School of Engineering and Applied Sciences, University of California, Los Angeles, California 90024

ABSTRACT

Anodic transients of iron in 1*N* KOH solution have been investigated. After the electrode was maintained at a potential E_R until steady state was achieved, either an anodic potential step or a potential sweep were imposed. For a potential step, the current transient i_a followed the relations

$$i_a \alpha 1/t, \text{ for } E_R < -1.1\text{V } vs. \text{ SCE}$$

and

$$i_a \alpha 1/\sqrt{t} \exp\left(-\frac{FE_R}{7RT}\right), \text{ for } E_R > -1.0\text{V}$$

where t is the time after the imposition of the potential step. For a potential sweep of sweep rate, λ, a peak current i_p was observed where

$$i_p \alpha \sqrt{\lambda} \exp\left(-\frac{FE_R}{6.5RT}\right), \text{ for } E_R > -1.0\text{V}$$

For $E_R < -1.1$V the current transients for both potential step and potential sweep polarization were interpreted in terms of the logarithmic growth of an oxide. For $E_R > -1.0$V, a duplex structure of the oxide layer, Fe/Fe_3O_4/ mixed oxide/solution, was assumed, where the mixed oxide consisted of Fe(II) and Fe(III) oxy compounds. The current transient behavior was attributed to composition changes in the mixed oxide layer due to diffusion of Fe(II). The experimental results can be satisfactorily interpreted by assuming the existence of the complex ions, $Fe(OH)_6^{4-}$ and $Fe(OH)_6^{3-}$, in the oxide film.

It is known that iron is easily passivated in alkaline solutions. However, Weil (1) did not observe a Flade potential during the decay after anodic polarization of iron in 1*N* NaOH. Kabanov, Burstein, and Frumkin (2) reported that iron in NaOH oxidized to $Fe(OH)_2$ and $Fe(OH)_3$. Initially, Fe oxidized readily to $Fe(OH)_2$ until the formation of a passive oxide layer. Burstein (3) found that small amounts of oxygen activated rather than passivated iron. Hurlen (4) observed that galvanostatic anodic transients of iron in alkaline solutions exhibited potential arrests at about the reversible FeO/Fe_2O_3 or $Fe(OH)_2/Fe(OH)_3$ and Fe_3O_4/Fe_2O_3 potentials. He concluded that active iron dissolution in both acidic and alkaline solutions followed the same mechanism since the same anodic Tafel slopes and the reaction orders were obtained. Foley, Kruger, and Bechtoldt (5) examined anodic surface films on iron by electron diffraction and concluded that the passive film was γ-Fe_2O_3; the non-passive film did not contain γ-Fe_2O_3; in 0.1*N* NaOH solution, the film consisted of Fe_3O_4 or a mixture of γ-Fe_2O_3 and Fe_3O_4 at -1.0V (*vs.* SCE), γ-Fe_2O_3 at $+0.5$V and Fe_3O_4 in the transpassive region at 1.0V.

Shepherd and Schuldiner (6) examined the steady state potentiostatic polarization of iron in NaOH and LiOH solutions. Their experiments were conducted in a highly pure gas tight system. Under these conditions, iron did not corrode significantly and behaved like an inert noble metal. This behavior was not observed for solutions containing small amounts of chloride ions. An examination of the literature indicated that, in general, iron in alkaline solutions exhibited rather unstable steady state behavior. In addition, reproducible surface conditions were very difficult to attain. Although transient studies could provide additional information, few such studies have been reported. In this study, the anodic transient behavior of pure iron in alkaline solution was studied by means of the potential step and potential sweep methods. While the steady state experiments usually yielded irreproducible results, the transient results were reproducible.

* Electrochemical Society Active Member.
Key words: corrosion, oxide, oxidation.

Experimental

1*N* KOH solution deaerated with purified nitrogen was used as an electrolyte. The electrodes which were made of Ferrovac E iron with a purity of 99.91% was sealed in Teflon tubing. The electrode surface was polished with 2/0 emery paper and washed with water, degreased, and rinsed several times with benzene. The potential steps were provided by an electronic step function generator and a potentiostat. A function generator was used for the potential sweep experiments. Potentials were measured with respect to the saturated calomel electrode.

Results

Potentiostatic experiments.—The electrode was oxidized briefly at the potential where oxygen evolution was first observed and then set at a more negative potential, E_R, until a steady state current was attained. Then, an anodic or positive potential step, E_a, having a value more positive than E_R, was imposed. A few examples of current transients are given in Fig. 1 and 2. As can be seen in the log-log plots of Fig. 1 and 2, log

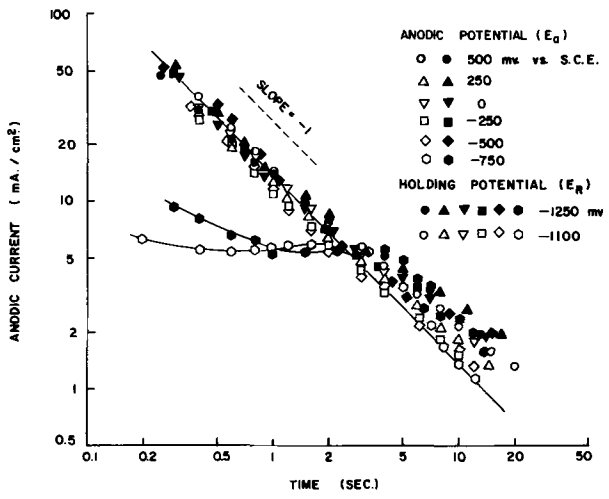

Fig. 1. Current transients of potential steps. $E_R < -1.1$V

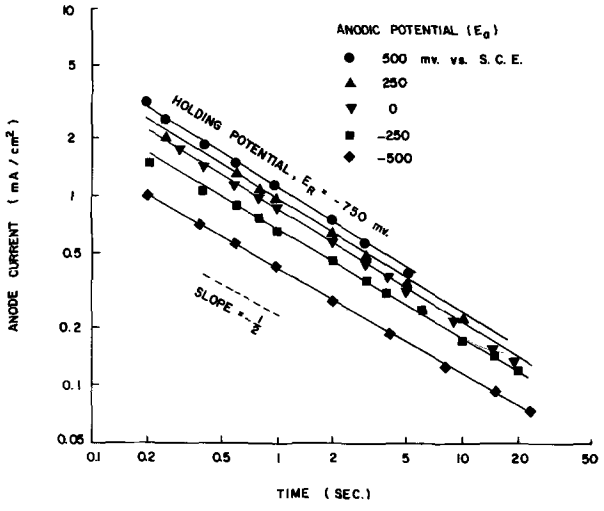

Fig. 2. Current transients of potential steps. $E_R > -1.0V$

current decreased linearly with log time except for a few cases which will be discussed later. The current i is related to time t as follows

$$i = k\,t^p \qquad [1]$$

where k and p are functions of E_a and E_R. The variation of p with respect to E_R and E_a is shown in Fig. 3.

It is found that p is indepedent of the anodic potential and changes from -1 to about -0.5 at approximately -1050 mV.

$$\begin{aligned} p &= -1 \text{ for } E_R < -1100 \text{ mV} \\ p &= -0.5 \text{ for } E_R > -1000 \text{ mV} \end{aligned} \qquad [2]$$

In the region, $E_R < -1100$ mV, the current transient was not affected by the anodic potential as long as E_a was positive enough. However, when E_a is not positive enough relative to E_R, for example, $E_a = -750$ mV as in Fig. 1, the current initially stays at a fairly constant value and then follows the same relation as other curves.

In the region $E_R > -1000$ mV, the current was dependent on the anodic potential, E_a. In Fig. 4, the current at $t = 1$ sec was plotted *vs.* E_a for two different values of E_R. These plots show that the current tends toward limiting values. The current at $t = 1$ sec and $E_a = 500$ mV was plotted *vs.* E_R in Fig. 5. A linear relation was obtained between the log of the above current and E_R with the slope of -425 mV/ decade.

$$\left(\frac{\partial E_R}{\partial \log i}\right)_{t=1,\,E_a} = -425 \text{ mV/decade}; \; E_R > -1000 \text{ mV} \qquad [3]$$

Thus, the current transients can be expressed by

$$i = k_1/t \text{ for } E_R < -1100 \text{ mV} \qquad [4]$$

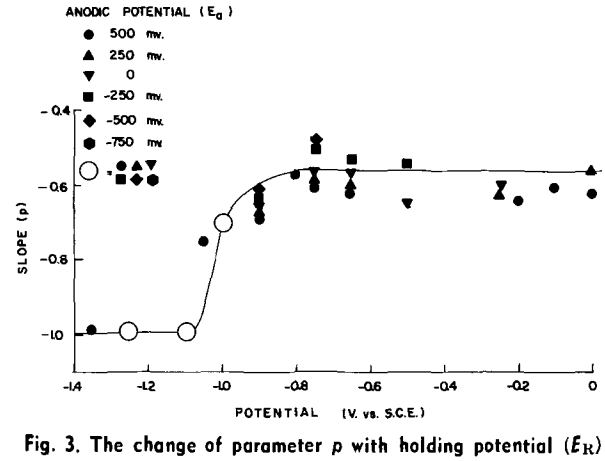

Fig. 3. The change of parameter p with holding potential (E_R)

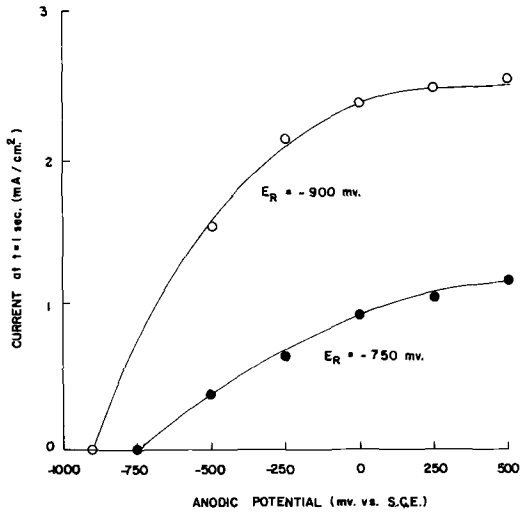

Fig. 4. Dependence of current at $t = 1$ sec on anodic potential (E_a). $E_R > -1.0V$

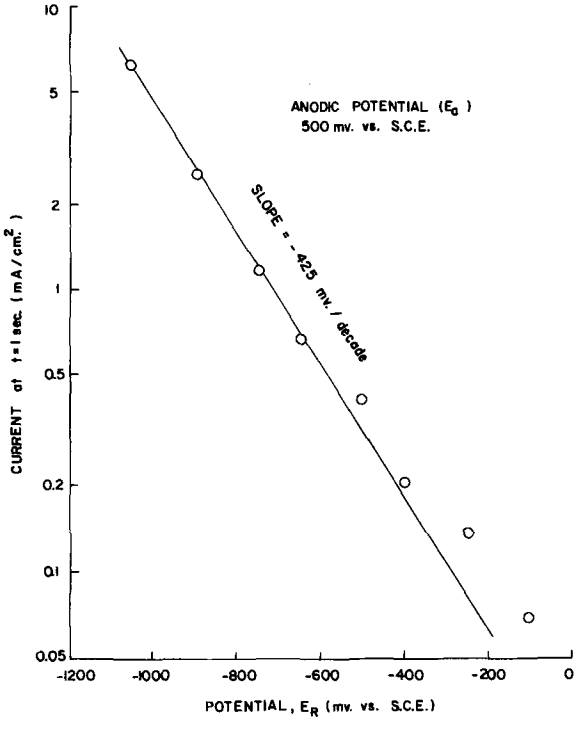

Fig. 5. Dependence of current at $t = 1$ sec on the holding potential (E_R).

$$i = k_2/\sqrt{t}\exp\left(-\frac{mF}{RT}E_R\right) \text{ for } E_R > -1000 \text{ mV} \qquad [5]$$

where k_1 and k_2 are constants and $m \approx 1/7$.

Potential sweep experiments.—After the electrode was maintained at E_R until the steady state was reached, a potential sweep in the positive potential direction was imposed. A few examples of the potential-current behavior are shown in Fig. 6 and 7. As seen in these figures, the potential-current characteristics for the holding potentials above -1000 mV and below -1100 mV are different. The peak potential E_p is defined as the potential at the maximum or peak current i_p, in the potential-current curves shown in Fig. 6 and 7. The peak potentials are plotted against E_R in Fig. 8. While E_p was constant for $E_R < -1100$ mV, it increased linearly with E_R for $E_R > -1000$ mV.

$$\partial E_p/\partial E_R \approx 1 \text{ for } E_R > -1000 \text{ mV} \qquad [6]$$

It should be noted that E_p is a minimum at approximately $E_R = -1050$ mV.

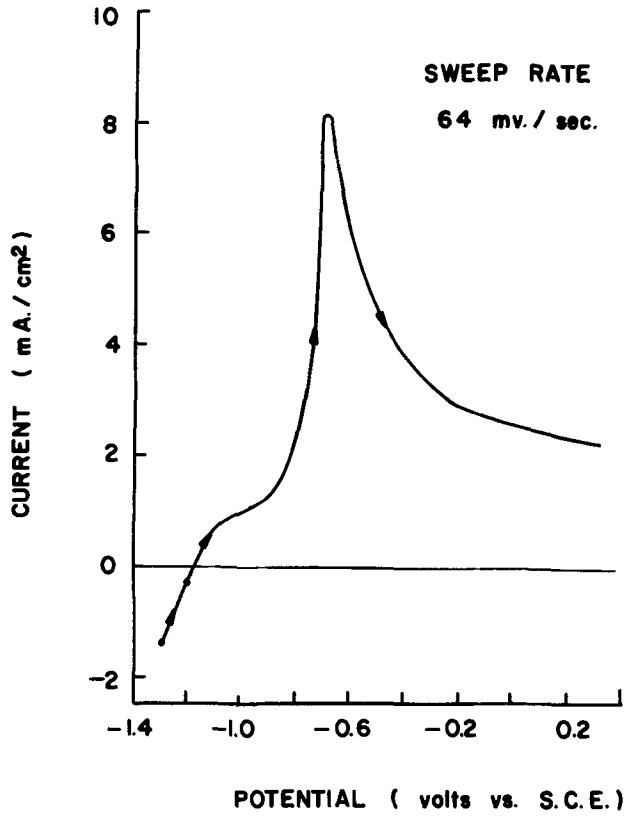

Fig. 6. Potential-current curve for a potential sweep polarization. $E_R < -1.1V$.

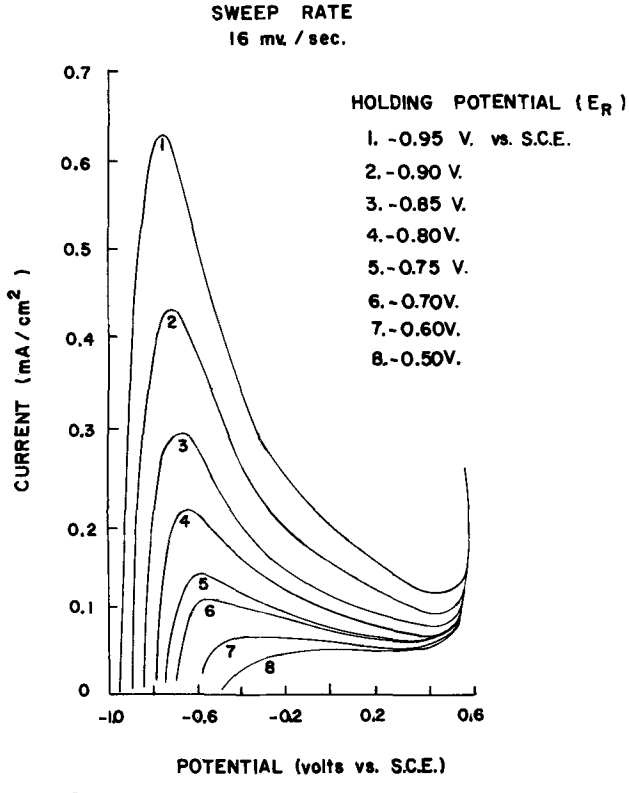

Fig. 7. Potential-current curve for a potential sweep polarization. $E_R > -1.0V$.

A Tafel plot of the ascending part of the $E_a - i_a$ curve in Fig. 6 is shown in Fig. 9. The Tafel slope was approximately 120 mV/decade

$$\frac{\partial E_a}{\partial \log i_a} \approx 120 \text{ mV/decade for } E_R < -1100 \text{ mV} \quad [7]$$

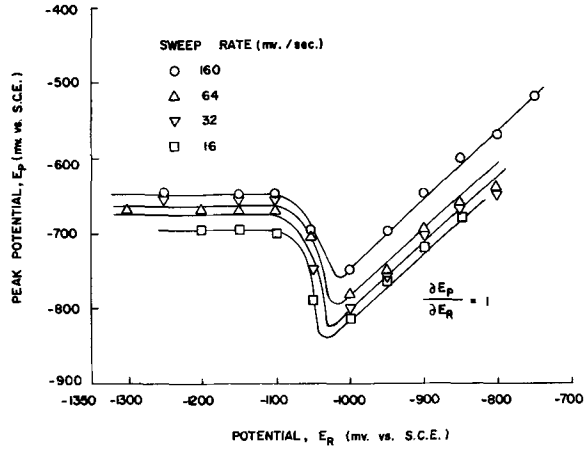

Fig. 8. Dependence of peak potential on holding potential (E_R)

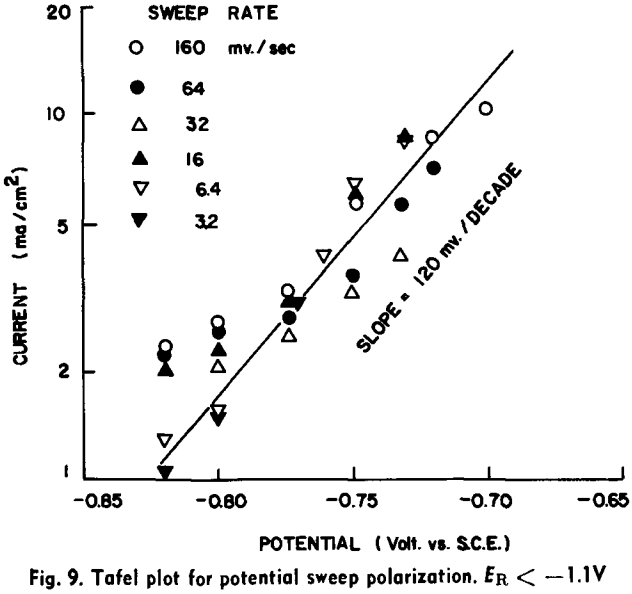

Fig. 9. Tafel plot for potential sweep polarization. $E_R < -1.1V$

The peak current, i_p, was plotted as a function of E_R in Fig. 10. For the potential region, $E_R < -1100$ mV, i_p is independent of E_R and only a function of the sweep rate, λ, as shown in Fig. 11. Therefore

$$i_p = k_3 \lambda^{\alpha} \text{ for } E_R < -1100 \text{ mV} \quad [8]$$

where k_3 and α are constants. On the other hand, for $E_R > -1100$ mV, i_p varied with both E_R and λ. A linear relationship was obtained for the log i_p *vs.* E_R plot as shown in Fig. 10.

$$\frac{\partial \log i_p}{\partial E_R} \approx -390 \text{ mV/decade for } E_R > -1000 \text{ mV} \quad [9]$$

A log-log plot of peak current at $E_R = -800$ mV and λ is shown in Fig. 11. A linear relationship with a slope of ½ was obtained. Thus

$$i_p = k_4 \sqrt{\lambda} \exp\left(-\frac{MF}{RT} E_R\right) \text{ for } E_R > -1000 \text{ mV} \quad [10]$$

where $M \approx 1/6.5$ and k_4 is a constant. In both potentiostatic and potential sweep experiments, stirring the solution did not affect the transient current. Furthermore, no measurable dissolution of iron was observed. The steady state current at E_R was less than 10 μA/cm² in the potential region from −1.2V to +0.55V.

Discussion

Thermodynamic consideration.—The experimental results indicate that anodic characteristics of iron are

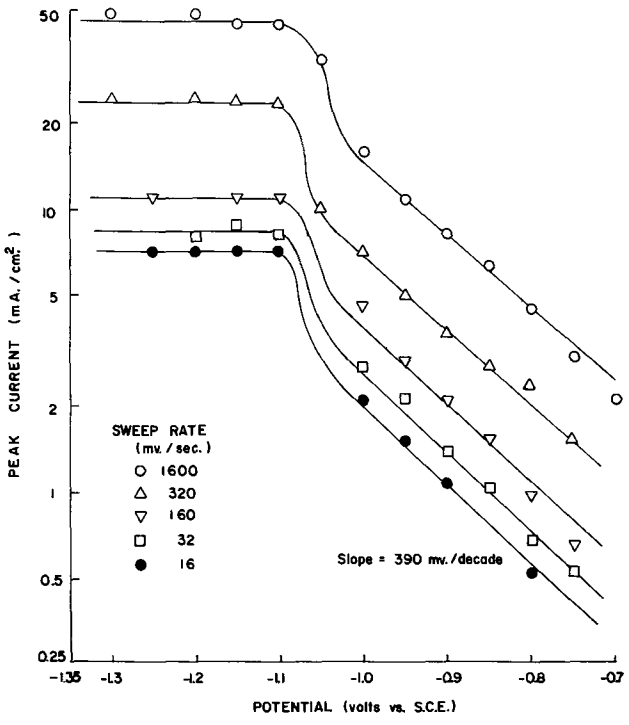

Fig. 10. Peak current *vs.* holding potential (E_R)

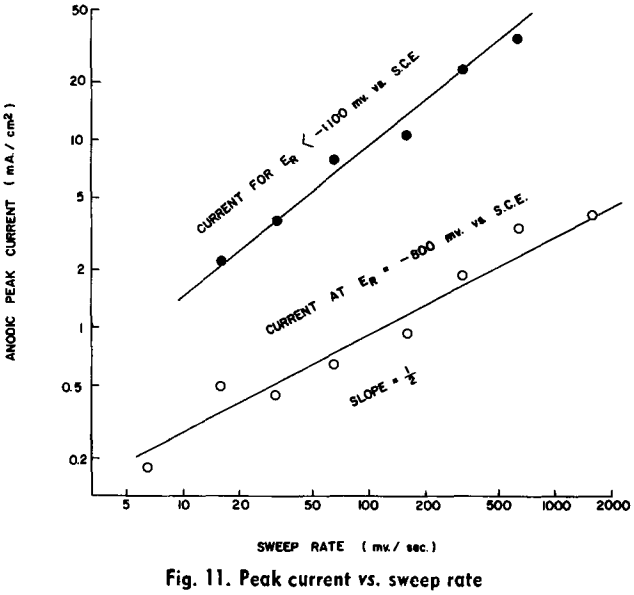

Fig. 11. Peak current *vs.* sweep rate

different for $E_R < -1100$ mV than for $E_R > -1000$ mV. It was observed that the transient behavior for $E_R < -1100$ mV was not affected by E_R, but varied with E_R for $E_R > -1000$ mV. The former case suggests that the iron surface is either unoxidized or covered with an irreducible iron oxide. The equilibrium electrode potential of the Fe/Fe_3O_4, Fe/Fe_2O_3, $Fe/Fe(OH)_3$ reactions at pH = 13.8 are (7)

Fe/Fe_3O_4: $E^e = -1142$ mV *vs.* SCE (anhydrous) [11]

Fe/Fe_2O_3: $E^e = -1110$ mV (anhydrous) [12]

Fe/Fe_2O_3: $E^e = -1000$ mV

(hydrated Fe_2O_3-equivalent to $Fe(OH)_3$ [12a]

For $E_R > -1000$ mV, the surface is covered with a mixture of Fe_3O_4 and Fe_2O_3 or $Fe(OH)_3$, and its composition is a function of E_R.

Oxide growth mechanism on iron reduced at $E_R < -1100$ mV.—In neutral solutions, the rate of growth of a thin oxide on iron has been shown to follow the logarithmic law. This rate equation can also be applied to the growth of a thin oxide on iron in alkaline solutions.

Potentiostatic polarization.—According to Sato and Cohen (8), the current can be expressed by Eq. [13] when the metal surface is anodically oxidized by a logarithmic rate equation.

$$i = k_5 \exp(\beta E_a - Q/B) \quad [13]$$

where E_a is the anodic potential, Q is the charge associated with formation of the oxide on the electrode, and k_5, β, and B are constants.
Since

$$i = dQ/dt \quad [14]$$

Eq. [13] becomes

$$dQ/dt \exp(Q/B) = k_5 \exp(\beta E_a) \quad [15]$$

Under potentiostatic conditions, the solution of Eq. [15] is

$$Q = B \ln\left[\frac{k_5 t \exp(\beta E_a)}{B} + \exp(Q_o/B)\right] \quad [16]$$

where Q_o is the value of Q at $t = 0$. Therefore

$$i = \frac{k_5 \exp(\beta E_a)}{k_5 \exp(\beta E_a)\, t/B + \exp(Q_o/B)} \quad [17]$$

For

$$k_5 \exp(\beta E_a)\, t/B >> \exp(Q_o/B) \quad [18]$$

$$i = B/t \quad [19]$$

Equation [19] is in accord with Eq. [4]. Empirically, $B = 15$ mc/cm² which is two orders of magnitude greater than that obtained in neutral solution (8). The same relation as Eq. [19] or [4] was reported by Nagayama and Cohen (9) for iron in neutral solutions. For comparatively long time duration, the deviations of the plots in Fig. 1 from Eq. [19] may be due to a change in mechanism of oxidation.

When the applied positive potential step E_a, as in the plots of $E_a = -750$ mV, was not large enough, deviations from Eq. [4] or [19] were also observed in Fig. 1. However, these deviations were due to Eq. [18] being invalid. Equation [17] can be transformed to Eq. [20]

$$i = \frac{1}{t/B + (1/i)_{t=0}} \quad [20]$$

As shown in Fig. 12 the plots obtained experimentally are approximated reasonably well by Eq. [20]. Thus, the transient behavior for relatively small values of

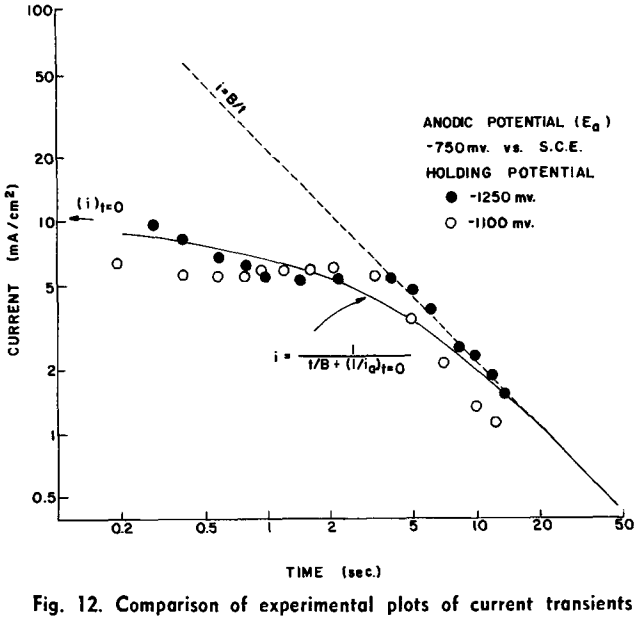

Fig. 12. Comparison of experimental plots of current transients with theory for potential step polarization.

E_a can also be interpreted in terms of logarithmic film growth.

Potential sweep polarization.—The solution of Eq. [15] can be obtained with the condition

$$E_a = \lambda t + E_R \quad [21]$$

where λ is the sweep rate. The solution for Eq. [15] is then

$$Q = B \ln \left[\frac{k_5 \exp(\beta \lambda t) \exp(\beta E_R) + c}{(B\beta\lambda)} \right] \quad [22]$$

where $c = B\beta\lambda \exp(Q_o/B) - k_5 \exp(\beta E_R)$
Therefore

$$i = \frac{B\beta\lambda}{1 + c/[k_5 \exp(\beta E_a)]} \quad [23]$$

It is of interest to determine the two limiting forms of Eq. [23]. First, for E_a sufficiently large such that

$$\exp \beta E_a >> \left[\frac{B\beta\lambda}{k_5} \exp\left(\frac{Q_o}{B}\right) - \exp \beta E_R \right]$$

Eq. [23] simplifies to

$$i = B\beta\lambda \quad [24]$$

On the other hand, for E_a sufficiently small such that

$$\exp \beta E_a << \left[\frac{B\beta\lambda}{k_5} \exp\left(\frac{Q_o}{B}\right) - \exp \beta E_R \right]$$

Eq. [23] becomes

$$i = \frac{k_5 \exp(\beta E_a)}{\exp\left(\frac{Q_o}{B} - k_5 \exp \beta E_R\right)} \quad [25]$$

Since $\exp(\beta E_a) = \exp \beta(E_R + \lambda t) > \exp \beta E_R$, $\exp \beta E_R << B\beta\lambda/k_5 \exp Q_o/B$. Therefore, Eq. [25] simplifies to

$$i = k_5 \exp\left(\beta E_a - \frac{Q_o}{B}\right) \quad [26]$$

Equation [26] shows that i is independent of λ and is the same form as $(i)_{t=0}$ for potentiostatic polarization (see Eq. [17]). Equation [26] gives

$$\frac{\partial E_a}{\partial \log i} = \frac{2.303}{\beta} \quad [27]$$

The parameter β can be determined by comparing Eq. [7] and [27]. Thus

$$\beta \approx 19.2 \text{ volt}^{-1} \quad [28]$$

This value of β is in accord with the one obtained by Sato and Cohen (8).

Transient behavior for $E_R > -1000$ mV. Potentiostatic polarization.—The variation of current with time for an anodic potential step in the region $E_R > -1000$ mV is proportional to $1/\sqrt{t}$ which suggests that the reaction process is diffusion controlled. Since there was no effect by stirring the electrolyte, the diffusion controlling process was considered to occur within the oxide layer. Since the iron oxides Fe_2O_3, $Fe(OH)_3$ are known to react with Fe to form Fe_3O_4 at room temperature (10), the oxide adjacent to Fe should always be Fe_3O_4. The oxide layer is assumed to have a duplex structure as previously proposed for iron in neutral and acidic solutions (9, 11). The following assumptions are made: (*i*) The outer layer is composed of Fe(II) and Fe(III) and is an ionic conductor. (*ii*) Since the magnetite is an electronic conductor, electron transfer for the Fe(II)/Fe(III) reaction occurs at the I/II interface. (*iii*) The charge transfer step is fast. Thus, the composition of layer II at the I/II interface is determined by the applied potential. (*iv*) The change in composition of layer II with E_a, occurs by diffusion of Fe(II) and Fe(III). Since the steady state current at E_R is very low, the concentration gradient in layer II at E_R is small. Thus, prior to the potential step, E_a, layer II has a uniform composition which is a function of only E_R. When the anodic potential step is imposed on the electrode, the concentration of the oxidant, C_{ox}, and of the reduced species, C_{Red}, is increased and decreased, respectively. Since for high anodic potentials, E_a, $C_{Red} \to 0$ at the I/II interface, a limiting current is obtained and should follow the following relation (12)

$$i = k_7 (C_{Red})_{ss}/\sqrt{t} \quad [29]$$

where k_7 is a constant and $(C_{Red})_{ss}$ is the steady state value of C_R at E_R.

By comparing with Eq. [5]

$$(C_{Red})_{ss} = \frac{k_2}{k_7} \exp\left(-\frac{mF}{RT} E_R\right) \quad [30]$$

Potential sweep polarization.—The potential-current curves in Fig. 7 are similar to those obtained for reversible electrode reactions where the potential is a function of C_{ox} and C_{Red} (12). For the anodic reaction

$$E = E^o - \frac{RT}{nF} \ln (C_{Red})_o \quad [31]$$

where $(C_{Red})_o$ is the value of C_{Red} at the I/II interface.

If E_a is related to $(C_{Red})_o$ by Eq. [31] and independent of C_{ox}, the peak current and peak potential, as shown by Delahay (12), can be expressed as

$$i_p = k_8 (C_{Red})_{ss} \sqrt{\lambda} \quad [32]$$

$$E_p = E_p^o - RT/nF \ln (C_{Red})_{ss} \quad [33]$$

where k_8 and E_p^o are constants. Comparison of Eq. [32] with Eq. [10] gives

$$(C_{Red})_{ss} = \frac{k_4}{k_8} \exp\left(-\frac{MF}{RT} E_R\right) \quad [34]$$

Combining Eq. [33] and [34]

$$\frac{\partial E_p}{\partial E_R} = \frac{M}{n} \quad [35]$$

is obtained. Since C_{Red} is uniform throughout layer II under steady state conditions at E_R

$$E_R = E^o_R - \frac{RT}{nF} \ln (C_{Red})_{ss} \quad [36]$$

Equations [34] and [36] give $M = n$. Thus, $\partial E_p/\partial E_R = 1$ is obtained. Equations [30] and [36] show that

$$n = m = M \quad [37]$$

Reacting species in the outer layer.—A comparison of Eq. [37] with Eq. [5] or [10] gives

$$n = \frac{1}{6.5} \text{ or } \frac{1}{7} \quad [38]$$

It may be assumed that the outer layer consists of Fe^{++}, Fe^{+++}, OH^-, $O^=$. Since iron has a tendency to form complex ions with six ligands like $Fe(CN)_6^{4-}$ and $Fe(CN)_6^{3-}$, it seems reasonable that the complex ions, $Fe(OH)_6^{3-}$ and $Fe(OH)_6^{4-}$ are present in the outer layer. It is postulated that the potential difference across the I/II interface is determined by the redox couple

$$Fe(OH)_6^{3-} + e \rightleftharpoons Fe(OH)_6^{4-} \rightleftharpoons Fe^{++} + 6OH^- \quad [39]$$

Thus

$$E = E^o_1 + \frac{RT}{F} \ln \frac{[Fe(OH)_6^{3-}]}{[Fe^{++}][OH^-]^6} \quad [40]$$

Since the dissociation constant of $Fe(CN)_6^{4-}$ is much larger than $Fe(CN)_6^{3-}$, $Fe(OH)_6^{4-}$ should be less stable than $Fe(OH)_6^{3-}$. Therefore, the concentrations

of Fe^{++} and OH^- are related by

$$[OH^-] = 6[Fe^{++}] \quad [41]$$

If the main iron component of the outer layer is Fe(III), the concentration of $Fe(OH)_6^{3-}$ is much higher than the concentrations of Fe^{++}, OH^-, and $Fe(OH)_6^{4-}$ and is not appreciably affected by concentration changes in Fe^{++} or $Fe(OH)_6^{4-}$.

$$E = E^\circ_2 - \frac{7RT}{F} \ln [Fe^{++}] \quad [42]$$

or

$$E = E^\circ_3 - \frac{7RT}{F} \ln [OH^-] \quad [43]$$

Thus, if it can be assumed that either Fe^{++} or OH^- is the reduced species discharged at the I/II interface, $n = 1/7$.

Acknowledgment

This work was supported by a grant from the U. S. Department of Interior, Office of Saline Water.

Manuscript submitted June 18, 1970; revised manuscript received *ca.* Dec. 14, 1970.

Any discussion of this paper will appear in a Discussion Section to be published in the December 1971 JOURNAL.

REFERENCES

1. K. G. Weil, *Z. Electrochem.*, **62**, 638 (1958).
2. B. Kabanov, R. Burstein, and A. Frumkin, *Discussions Faraday Soc.*, **1**, 259 (1947).
3. R. C. Burstein, *Z. Electrochem.*, **62**, 655 (1958).
4. T. Hurlen, *Electrochim. Acta*, **8**, 609 (1963).
5. C. L. Foley, J. Kruger, and C. J. Bechtoldt, *This Journal*, **114**, 994 (1967).
6. C. M. Shepherd and S. Schuldiner, *ibid.*, **115**, 1124 (1968).
7. M. Pourbaix, "Atlas of Electrochemical Equilibrium in Aqueous Solution," Pergamon Press (1966).
8. N. Sato and M. Cohen, *This Journal*, **111**, 512 (1964).
9. M. Nagayama and M. Cohen, *ibid.*, **109**, 781 (1962).
10. N. Sato and M. Cohen, *ibid.*, **111**, 624 (1964).
11. K. J. Vetter, *Z. Electrochem.*, **62**, 642 (1958).
12. P. Delahay, "New Instrumental Methods in Electrochemistry," Interscience Publishers, Inc., New York (1954).

Radiotracer Studies of Metal-Metal Ion Exchange Inhibition Using Organic Corrosion Inhibitors

David S. Newman,* Janet McCarthy, and Michael Heckaman

Department of Chemistry, Bowling Green State University, Bowling Green, Ohio 43403

ABSTRACT

The exchange between cadmium and its ions and between silver and its ions has been studied with radiotracers in solutions containing organic corrosion inhibitors. The inhibitors were butane 1,4 diol, cis-2-butene 1,4 diol, and 2 butyne 1,4 diol. The organic inhibitors reduced the rate of exchange by adsorbing onto the metal surface and this diminution in rate of exchange was correlated with the structure of the metal solution interfacial region. In the cadmium system the diols adsorbed parallel to the surface while in the silver system they seem to be adsorbed perpendicular to the surface. Free energies of adsorption and inhibition efficiencies were calculated.

When a solid metal, M, is placed in a solution containing M^{n+} ions and a comparatively inert anion such as ClO_4^- or Cl^- an exchange between M and M^{n+} ions occurs. This exchange can be followed by making the M^{n+} ions in solution radioactive and measuring the increase in radioactivity of M as a function of time. The rate of exchange, R, is obtained by dividing the total activity of M by the time of immersion and is therefore a measure of the mean flux at the metal surface. Re-exchange is undoubtably occurring but is not observed by this technique. R does however, represent the minimum rate of exchange and can be thought of as a fundamental property of the metal-solution system. As a consequence, this rate may be affected by several factors including changes in the structure of the metal-solution interfacial region, changes in crystal orientation, nature of the negative ion, variation in temperature, and changes in pressure. When all variables, except the structure of the metal-solution interfacial region, are held constant then variations in the exchange rate can be used to help elucidate this structure. Certain organic molecules can reduce the exchange rate by either adsorbing onto the metal surface, forming complexes with the metal ions in solution, or both. By selecting a series of organic compounds in such a way that a particular structural feature varies from molecule to molecule within the series while all other molecular parameters are held relatively constant and noting the decrease in R as a function of this feature, these molecules become sensitive probes of the metal-solution interfacial region. Proper use of molecular models allow further inferences to be drawn concerning the metal-solution interface.

The decrease in R can be measured using radiotracers, by comparing the radioactivity of a metal specimen that had been immersed in an inhibited solution for a period of time with a specimen that was in a similar solution with no inhibitor for the same period of time.

The metal-metal ion systems chosen for this investigation were $Cd\text{-}Cd^{++}$ and $Ag\text{-}Ag^+$. Each of these systems has been studied in the absence of inhibitors (1-3) and many of the important steps in the exchange mechanism are known (4). Furthermore, in the solid state, silver and cadmium differ from each other profoundly considering their close proximity to one another in the periodic table. For example, cadmium exhibits a positive Hall effect while silver, like most metals, has a negative Hall effect (5). This difference,

* Electrochemical Society Active Member.

Key words: inhibition, adsorption, diffusion, metal-metal ion exchange.

while not easily explained in detail, certainly implies a significant difference in the structure, and shape of the Fermi surface which in turn suggests that each metal might interact qualitatively differently with its environment.

The organic molecules selected for this study were butane 1,4 diol, cis-2-butene 1,4 diol, and 2 butyne 1,4 diol. These compounds were shown to inhibit the corrosion of iron in acid solution (6) and it was therefore thought that they would also decrease the rate of exchange in the systems under investigation by adsorbing onto active sites on the surface of the metal.

In all of the studies, the ratio of metal ion to inhibitor was one hundred to one. This ratio insured that a sizable decrease in the exchange rate had to be due to adsorption of the inhibitor onto the metal surface rather than complexing between metal ion and inhibitor in solution. The kinds of inference that can be drawn from these studies are illustrated by the following examples. If the organic molecules adsorb onto the metal parallel to the surface then the inhibition efficiency, given by the equation

$$I = 100\ (R_u - R_i)/R_u \qquad [1]$$

where R_u and R_i are the rates of exchange in the uninhibited and inhibited solution, respectively, should vary in the order —butyne— > —butene— > —butane— > uninhibited. This order of efficiency presumes metal inhibitor interaction is both through the two oxygen atoms and, in the case of —butene— and —butyne—, through the π electrons. If the inhibitors are oriented perpendicular to the metal surface and adsorption is through the oxygen atom then the efficiency should follow the order butane $\approx$ butyne $\approx$ butane > uninhibited.

Experimental Details

General experimental techniques.—The glass cell used for each of the experiments is described elsewhere (4). In each series of metal-metal ion exchange experiments, one solution contained no inhibitor, and each of three others was 0.001M in inhibitor. Reagent grade inhibitors were used and care was taken to see that no measurable decomposition occurred during an experiment.

The radiation was measured with a Beckman liquid scintillation counter (Model LS 133) using the standard PPO-POPOP-toluene scintillation cocktail. Because of the way in which the standards were prepared, and the fact that the instrument is sensitive to light, the γ rays were counted in essentially the same way as were the β rays.

The disks were immersed in methanol immediately upon removal from the reaction vessel and then washed in a stream of water. Two minutes of washing sufficed to remove all adsorbed material from cadmium while 5 min were required to insure that all material was removed from silver. Presumably, the $AgNO_3$ adsorbs more strongly onto the silver surface than the $CdCl_2$ adsorbs onto the cadmium surface.

The edge of each disk was coated with Paraffin wax. The disk was then suspended in the solution by means of a platinum wire which was wrapped around the edge and held in place by the wax. This procedure left two surfaces of each disk free to exchange.

The disks were carefully weighed prior to and after immersion to determine if dissolution or deposition occurred to any great extent. In no experiment for which data was recorded was the change in weight greater than 0.1 mg.

The average molecular area covered by each of the organic inhibitors was obtained with Stuart-Briegleb models by a method similar to that of Aramaki and Hackerman (7).

Cadmium-cadmium ion exchange.—Single-crystal disks of cadmium were immersed in solutions of 0.1M reagent grade $CdCl_2$. The radiotracer was Cd^{115m}, a β emitter, with a half life of 43 days. The solutions were deaerated and stirred with dry nitrogen, and maintained at a temperature of 25°C in a constant temperature bath. The electropolishing technique for the preparation of the disks and the method for preparing the standard for converting counts per minute to gram atoms exchanged so as to account for sample quenching are described elsewhere (1). The crystal of cadmium was oriented so that the surface of each disk was parallel to the 0001 plane of the crystal. Each disk had a diameter of approximately 18.5 mm and a thickness that varied between 3-4 mm. The disks were suspended in solution for periods of not less than 12 hr and not more than 72 hr. The ambient pH of the solutions was approximately 5.6.

Silver-silver ion exchange.—Single-crystal disks of silver were immersed in solutions of 0.1M $AgNO_3$. Ag^{110m}, a γ emitter with a half life of 270 days served as the tracer. The solutions were maintained at 25°C and stirred with nitrogen gas. The silver disks were approximately the same size as the cadmium disks.

The silver disks were mechanically cut from a large single crystal, etched back with dilute HNO_3 until no traces of a polycrystalline or amorphous materials formed by the cutting process remained. Laue diffraction patterns of every third disk were taken and in each case a single crystal was shown to be present. The crystal of Ag was oriented so that the surface of each disk was parallel to the 111 plane. The surfaces were prepared by using 25% HNO_3 as an etching bath and chromic acid-HCl as a polishing solution in a manner similar to that used by Tingley (3). The disks were then annealed for 12 hr at 850°C to insure that strains and other distortions were minimized. The ambient pH of the solutions was between 5.3 and 5.5. Because of the comparatively low rate of penetration of radioactive silver into solid silver the disks were left in solution for periods exceeding 100 hr in order to acquire enough activity to be accurately counted.

The standards for converting cycles per minute to gram atoms exchanged were prepared by depositing an accurately weighed amount of radioactive silver solution of known concentration on the surface of a polycrystalline silver coupon and allowing the coupon to dry. The activity of the coupon was measured and the counts per minute per gram atom silver computed. The single-crystal disks were immersed in similar solutions to those deposited on the coupons. Differences in rate of penetration into single-crystal silver and into polycrystalline silver were not important because measurable sample quenching by the silver does not occur.

Results and Discussion

The results of the cadmium-cadmium ion exchange studies together with the structure of each inhibitor are shown in Table I. The total activity, a_t, acquired by the disk is given by the equation

$$a_t = 2C_o\ (Dt/\pi)^{1/2} \qquad [2]$$

where C_o is the concentration of metal ions at the surface, t is the time, and D is the self-diffusion coefficient of the metal.

Equation [2] is a solution to the "mass transfer" analogue of the linear "heat flow" equation for a semi-infinite solid (8)

Table I. Rate of exchange and inhibition efficiency values for $Cd\text{-}Cd^{++}$ exchange

Compound		R, g-atoms/cm² sec × 10^{11}	I (%)
butane 1,4 diol	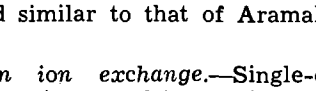	1.91	21.1
cis-2-butene 1,4 diol	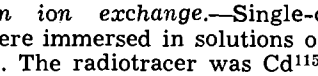	1.15	51.8
2 butyne 1,4 diol	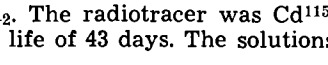	1.07	55.4
uninhibited		2.42	—

$$\frac{D\partial^2 C}{\partial x^2} = \frac{\partial C}{\partial t} \qquad [3]$$

where C is the concentration, D is the diffusion coefficient, x is the distance from the surface, and t is the time.

The equation is solved subject to the boundary conditions at $x = 0$, $C(0,t) = C_o$ = constant and $x = \infty$, $C(\infty,t) = 0$. This model applies because the initial radioactivity of the disk is zero and the distance of penetration into the disk is very small relative to its thickness. The values for R were obtained by dividing a_t in units of gram atoms exchanged/cm², by the total immersion time and averaging the results of a minimum of six different experiments with each solution.

The data in Table I indicate that the three organic compounds are efficient exchange inhibitors and adsorption of the organic molecule onto the metal surface is the primary inhibition mechanism. If complexing did contribute significantly to the inhibition and if each cadmium ion were tying up as many as one inhibitor molecule, a value for I of only 1% would result. The relative values of I imply that the two unsaturated molecules are adsorbed onto the metal surface primarily via their π electrons but that adsorption through the oxygens is a significant contributing factor because the butane 1,4 diol has an I value of 21.1% but no π electrons.

The three inhibitors are therefore assumed to be lying flat on the metal with the oxygens and, in the unsaturated compounds, the π electrons directed toward the metal surface.

The observed I values for the unsaturated alcohols are fairly close, indicating factors other than the number of π electrons play a role. The cis configuration of the butene diol possibly presents a favorable geometry for bidentate-like adsorption which is presumably stronger than the monodentate-like adsorption postulated for the butyne diol. At the same time, the four π electrons of the butyne diol probably repel each other slightly at the metal surface because of crowding so that they would bond slightly less than twice as strongly with the metal surface as would two π electrons.

The percentage of the disk covered by inhibitor may be computed from the equation

$$S_i = 100\,[1 - (C_{oi}/C_{ou})^{2/3}] \qquad [4]$$

where C_{oi} and C_{ou} are the surface concentrations of metal ion in an inhibited and uninhibited solution, respectively. C_{oi} and C_{ou} are calculated from Eq. [2] using a value of 3.6×10^{-15} cm²/sec for D_{Cd} (3).

In the inhibited solution the competition for active sites upon which to adsorb is between Cd^{++} and inhibitor and presumably one wins out at the expense of the other. Therefore, the chemical equation that best describes the adsorption process is

$$Cd^{++}\ (ads) + In\ (sol) = In\ (ads) + Cd^{++}\ (sol) \qquad [5]$$

The standard free energy of adsorption is given by the equation

$$\Delta G^o = -RT \ln \frac{[X_{In}\ (ads)]\,[X_{Cd++}\ (sol)]}{[X_{Cd++}\ (ads)]\,[X_{In}\ (sol)]} \qquad [6]$$

where the X's are the mole fractions of the various species in a two dimensional cross section area and are, in turn, given by the equation

$$X_{In} = \Gamma_i/(\Gamma_i + \Gamma_{Cd++}) \qquad [7]$$

Where the Γ_i's are the surface concentrations in gram atoms/cm².

In order to calculate Γ_i a roughness factor of 1.1 was assumed for the polished cadmium surface. The measured geometric area of the metal disk was multiplied by this roughness factor to give the "correct" area. A monolayer of adsorbed substrate was assumed to cover the fraction of this corrected metal surface area given by Eq. [4]. The total area covered by each inhibitor was then divided by the average area of the inhibitor molecule as computed by the Stuart-Brieglieb models. Γ_{Cd++} was calculated directly from $(C_o)^{2/3}$.

Errors in estimating the roughness factor will tend to cancel because nearly the same "roughness" is seen by both cadmium ions and inhibitors. A further justification for assuming a roughness factor near unity lies in the fact that C_{ou} is very close to the best value for the average bulk density of cadmium. This value for C_{ou} also serves as an internal check on the experimental method since it is the expected value if a single layer of Cd^{++} is adsorbed onto the metal surface or if the surface concentration of metal atoms has equilibrated. Values for S_i, $(C_o)^{2/3}$, ΔG^o, area of molecule, and X_{In} (ads) are listed in Table II.

The results of the Ag-Ag^+ experiments are shown in Table III. The data were obtained in the same way as in the Cd-Cd^{++} system.

The measured rate of exchange, R_u, in the uninhibited system compares very favorably with the value obtained by King, Simmons, and Berlin (9) in their exchange studies. When their results are cast in the same units as ours a value of 4.2×10^{-14} gram atoms/cm² sec obtains. Considering the difference in concentrations, difference in crystal orientation and the fact that they used a G.M. counter rather than a scintillation counter the values are in excellent agreement.

The relative values of I once more indicate that the alcohols are efficient exchange inhibitors and that adsorption is the primary inhibition mechanism. However, the data also implies that there is probably a qualitative as well as a quantitative difference in the mode of adsorption onto the two metal surfaces. In the Ag-Ag^+ system, the alcohols seem to be adsorbing "end on" or perpendicular to the plane of the metal. This interpretation most reasonably accounts for the fact that in this instance, the inhibition efficiencies of the three molecules are nearly the same. A possible reason for cis-2-butene 1,4 diol being slightly better at preventing exchange than the other two diols is because it has a cis configuration which can place two OH groups near the metal surface.

The generally greater efficiency of the three inhibitors in the silver system is difficult to account for in detail. The most obvious reason is that the metal inhibitor bond is stronger in silver than in cadmium. However, many other interesting explanations are possible. Evidence strongly suggests that NO_3^- is adsorbing onto the metal surface, blocking active sites, and thus preventing exchange (10, 11). Therefore a particularly intriguing idea is that a synergistic effect between NO_3^- and inhibitor is occurring similar to that described by Aramaki and Hackerman (12) in the case of medium sized polymethylenimine rings in the pres-

Table II. Surface coverage, free energy of adsorption, and average area of inhibitor in the Cd-Cd^{++} system

	S_i, %	$C_o^{2/3} \times 10^{-14}$ atoms/cm²	ΔG^o, kcal/mole	Average area of molecule, Å²	X_{In}(ads)
—butane—	16.0	10.0	−1.08	55.7	0.06
—butene—	34.0	7.95	−1.96	44.4	0.212
—butyne—	36.8	7.50	−1.58	69.6	0.127
uninhibited		11.9		—	

Table III. Rate of exchange and inhibition efficiency values for Ag-Ag^+ exchange

Compound	R, g-atoms/cm² sec $\times 10^{14}$	I, %
butane 1,4 diol	4.6	68
cis-2-butene 1,4 diol	2.7	74
2 butyne 1,4 diol	3.7	70
uninhibited	21.0	

ence of I^-. That this synergistic effect is likely to be present can be inferred from the fact that NO_3^- like I^- is an exceedingly efficient "structure breaker" in aqueous solution (13) and can be expected to "break up" the water sheath about the inhibitor, thus making it more efficient.

Another strong possibility is that the difference between the mode of penetration of Ag atoms into solid Ag and the mode of penetration of Cd atoms into Cd causes an apparent increase in inhibitor efficiency. At 25°C Ag atoms penetrate single-crystal silver via a grain boundary mechanism. The grain boundary mechanism implies the existence of dislocation pipes, the diameter of which can be shown to be nearly equal to that of a Ag atom (14). If the inhibitors should block dislocation pipes then the only means of penetration into the disk would be volume diffusion. Since the diffusion coefficient for volume diffusion is some twelve orders of magnitude smaller than the "dislocation pipe" diffusion coefficient (14) the inhibitors will appear to be much more efficient even if they do not bond significantly more strongly.

In this discussion it has been assumed that there is a continuous dynamic competition for adsorption sites between metal ion and inhibitor so the efficiency, in a given system, can be thought of as being a function of the strength of the metal-inhibitor interaction despite the method of penetration. As this strength increases the efficiency will increase because the entrances to the dislocation pipes will be covered a greater percentage of the time. The fact that the efficiencies observed in the silver system are similar, therefore, implies that the inhibitor-metal interactions are similar and the most reasonable explanation for this similarity is that the inhibitors are adsorbing perpendicular to the surface. However, it should be noted that if an inhibitor blocks a dislocation pipe and there is virtually no other means for the metal to penetrate it is impossible to tell, without some additional assumptions, whether the "blocking" molecule has adsorbed perpendicular or parallel to the surface. In either case, the efficiencies will be similar. Therefore, without an independent measurement the orientation of the molecules is still open to question.

The uninhibited solution as well as each of the inhibited solutions are 0.1M in NO_3^- so the presence of the NO_3^- is not felt in these experiments unless it manifests itself in the form of a synergistic effect. The "net" reaction seen by the exchange experiments is described by the equation

$$Ag^+ \text{ (ads)} + \text{In (sol)} \rightleftharpoons Ag^+ \text{ (sol)} + \text{In (ads)} \quad [8]$$

and the free energy of adsorption is computed from the equation

$$\Delta G^\circ = -RT \ln \frac{[X_{\text{In}} \text{ (ads)}]\,[X_{Ag+} \text{ (sol)}]}{[X_{Ag+} \text{ (ads)}]\,[X_{\text{In}} \text{ (sol)}]} \quad [9]$$

where the X's are defined as in Eq. [7].

The percentage of the disk's surface covered by the inhibitor, S_i, the "measured" surface concentration, free energy of adsorption, average area of adsorbed molecule, and mole fraction of inhibitor at the surface are given in Table IV. In addition, a quantity C_o', the theoretical surface concentration, is given. A value of 2.1×10^{-21} cm²/sec was used for D in Eq. [2] (3, 9).

The average number of Ag atoms in the 111 crystal plane is 1.4×10^{15}. This number was multiplied by 1.1, the estimated roughness factor, to obtain a theoretical value for the surface concentration, C'_{ou}. This value for C'_{ou} was used as the basis for calculation of the mole fractions appearing in Table IV.

It is easily seen that the values of C_{ou} are too high unless a roughness factor approaching ten is assumed. It is more likely, based on King's data (9), Tingley's data (3), and our own experience that no single diffusion coefficient can accurately describe the penetration of radioactive Ag atoms into single-crystal Ag at room temperature. At least two diffusion coefficients are necessary, one for diffusion through the surface layers, and one for diffusion into the bulk of the crystal. In other words, the rate of diffusion of Ag atoms into the crystal of solid silver is a function of penetration distance. Therefore, while Eq. [2] is satisfactory for the calculation of C_{ou} and C_{oi} to be used to calculate S_i, it is not satisfactory for the calculation of the mole fractions.

Table IV. Surface coverage, free energy of adsorption and average area of inhibitor molecule in the Ag-Ag^+ system

Molecule	S_i, %	$C_o^{2/3}$ × 10^{-15} atoms/cm²	ΔG°, kcal/mole	Average area of inhibitors, Å²	X_{In}(ads)	$C_o^{2/3}$ × 10^{-15} atoms/cm²
—butane—	64	5.4	−5.7	30.4	0.70	0.56
—butene—	75	3.8	−11.2	27.4	0.90	0.38
—butyne—	68	4.6	−6.9	28.6	0.76	0.45
uninhibited		14.9				1.5

The assumption that C_o in Eq. [2] is equal to the bulk metal concentration was made because it generates the known diffusion coefficient for Cd and a reasonable one for Ag. Moreover, using the correct diffusion coefficient for Cd and an acceptable one for silver gives a value of C_o equal to the bulk metal concentration in Cd and a value greater than the bulk metal concentration in Ag. The high value in silver is easy to understand if the diffusion pipe mechanism is working. Using the solution concentration in either system gives absurd results.

Discussion of Errors

The data obtained from experiments with the Cd-Cd^{++} system are estimated to range in absolute accuracy from ±10% for the inhibition efficiencies to ±20% for the quantities that involve average area covered by the organic molecule. This estimate, for the error in I, includes the counting error of approximately 3%. Although our knowledge of the surface roughness contains a minimum of ±10% error, the variation in surface area from one cadmium disk to the next will differ by much less than ±10%. The estimate for the error in X_{In} and ΔG°(ads) assumes a ±10% error in the average surface area covered by the organic inhibitor as well as miscellaneous smaller errors such as not having an exact value for D_{Cd} in the 0001 plane. The errors involved in the silver-silver ion exchange experiments are slightly larger than in the cadmium-cadmium ion experiments primarily because of the uncertainty in D_{Ag}.

Conclusion

Radiotracer studies of exchange inhibition using organic inhibitors have been shown to yield information about the mode of adsorption, free energy of adsorption, and structure of the metal solution interfacial region. The errors involved in the experimental technique are smaller than those encountered by other authors attempting to study the adsorption of organic molecules on metal surfaces. Bockris and Swinkles estimate an absolute error of nearly ±65% for their measurements of the adsorption of n-decylamine on solid metal electrodes (15). These authors tagged their organic molecules with C^{14} which leads to a much larger counting error than occurs in our experiments. It is interesting to note however, that our values for ΔG°(ads) are well within the same order of magnitude as their values for the same quantity.

The hypothesis that a bidentate linkage between the butene diol and the metal surface exerts a significant effect on the efficiency of the butene needs further testing. The simplest way would be to study the inhibition efficiency of the trans compound. Presumably its efficiency should be less than that of the cis compound.

Finally, radiotracer studies of metal-metal ion exchange inhibition offer a potentially powerful tool for obtaining information about the interfacial region of

many heterogeneous systems where exchange occurs at a significant rate.

LIST OF SYMBOLS

I	inhibition efficiency, %
R_u	rate of exchange in uninhibited solution
R_i	rate of exchange in inhibited solution
a_t	total activity acquired by the disk
C_o	surface concentration, atoms/cm^3
D_{Cd+}	self diffuson coefficient of cadmium
D_{Ag+}	self diffusion coefficient of silver
S_i	percentage of surface covered by inhibitor
ΔG^o	standard free energy of adsorption
X_{1n}	mole fraction of species i in a two dimensional cross sectional area
Γ_i	surface concentration of adsorbed species in moles/cm^2
t	time in seconds
T	temperature

Manuscript submitted April 6, 1970; revised manuscript received Nov. 9, 1970. This was Paper 244 presented at the New York Meeting of the Society, May 4-9, 1969.

Any discussion of this paper will appear in a Discussion Section to be published in the December 1971 JOURNAL.

REFERENCES

1. C. V. King and N. E. McKinney, *Can. J. Chem.*, **37**, 205 (1959).
2. C. V. King, D. S. Newman, and E. Suriani, *This Journal*, **108**, 291 (1961).
3. I. I. Tingley, *ibid.*, **112**, 60 (1965).
4. D. S. Newman, *J. Chem. Ed.*, **42**, 424 (1965).
5. J. M. Ziman, "Electrons and Phonons," p. 488, Oxford University Press, London (1963).
6. C. Mayer, W. J. Lorenz, and H. Fisher, *Z. Phys. Chem.*, NF., **52**, 193 (1967).
7. K. Aramaki and N. Hackerman, *This Journal*, **115**, 1007 (1968).
8. H. S. Carslaw and J. C. Jaeger, "Conduction of Heat in Solids," Chap. II, Oxford University Press, London (1959).
9. C. V. King, T. Simmons, and A. Berlin, *This Journal*, **110**, 1261 (1963).
10. C. V. King and R. K. Schochet, *J. Phys. Chem.*, **57**, 895 (1953).
11. B.V.K.S.R.A. Tilak and M.A.V. Devanathan, *J Phys. Chem.*, **73**, 3582 (1969).
12. K. Aramaki and Norman Hackerman, *This Journal*, **116**, 569 (1969).
13. H. S. Frank, "Solvent Models and the Interpretation of Ionization Solvation Phenomena," Chapt. 4 of "Chemical Physics of Ionic Solutions," B. E. Conway and R. G. Barradas, Editors, John Wiley & Sons, Inc., New York (1964).
14. J. C. Fisher, *J. Appl. Phys.*, **22**, 74 (1951).
15. J. O'M. Bockris and D. A. J. Swinkles, *This Journal*, **111**, 736 (1964).

Electrochemical Characteristics of Iron in H_2SO_4 Containing Benzotriazole

Robert J. Chin and Ken Nobe***

School of Engineering and Applied Science, University of California, Los Angeles, California 90024

ABSTRACT

The effect of benzotriazole on the corrosion of iron in H_2SO_4 has been studied. The experimental data are consistent with the slow proton discharge step for the hydrogen evolution reaction on iron. No change in mechanism was observed by the addition of benzotriazole, but a significant decrease in the rate of hydrogen evolution was observed. The inhibitor concentration had a significant influence on the behavior of the open-circuit capacitance. Surface coverages determined from capacitance and corrosion rate data were consistent and found to fit a Langmuir adsorption isotherm.

Benzotriazole is an effective corrosion inhibitor of copper and copper alloys (1). It has also been shown to be a corrosion inhibitor of steel (2). Up to the present time there has not been a systematic study of the effect of benzotriazole on the electrode processes of active iron. This investigation examines the effect of benzotriazole on the hydrogen evolution reaction on iron in acidic solutions.

Experimental

Cylindrical electrodes (0.5 in. in diameter and 0.375 in. in length) were machined from Ferrovac E iron rod. The cross-sectional surface was exposed to the electrolyte. This surface was polished with increasingly fine grades of aluminum oxide paper, followed by degreasing with boiling benzene in a soxhlet column for several hours. After degreasing the electrode was annealed at 700°C for 1 hr in a vacuum. The electrode was then encased in shrinkable Teflon to prevent leakage of electrolyte and mounted in a Teflon holder. The details of the Teflon electrode holder are given elsewhere (3).

A three-electrode cell of Teflon and Pyrex glass was used in the experiment. A saturated calomel electrode and a platinized platinum electrode were used as the reference and auxiliary electrodes, respectively. The auxiliary electrode was separated from the test cell by fritted glass. A Luggin probe was used for the reference electrode.

Solutions of different *p*H (0.3, 1.0, and 1.9) were obtained by adding KOH to 1*N* H_2SO_4 prepared from doubly distilled water and reagent grade acid. The benzotriazole was supplied by the Maumee Chemical Company. Solutions were deaerated with prepurified nitrogen for several hours before introducing the test electrode.

The test electrode was activated in 5*N* H_2SO_4 for 10 min and then rinsed in distilled water before immersion in the electrolyte. The d-c pulse technique was employed for capacitance measurements. Galvanostatic polarization was utilized to study the hydrogen evolution reaction. Capacitance and polarization measurements were made periodically at various electrode immersion times. Each electrode was immersed approximately 72 hr. Capacitance measurements were also made during cathodic polarization of uninhibited iron. For cathodic polarization, one minute current pulses were utilized. Steady-state polarization was achieved in less than one minute.

Results

The cathodic polarization of iron was dependent on inhibitor concentration, solution *p*H, and immersion

* Electrochemical Society Active Member.
** Electrochemical Society Student Associate.
Key words: corrosion inhibition, hydrogen evolution.

time. In all cases constant polarization curves were reached within 40 hr after immersion. Cathodic polarization of iron in 1*N* H_2SO_4 at various concentrations of benzotriazole is shown in Fig. 1. Increasing the concentration of benzotriazole shifted the polarization curves toward more negative potentials. Similar behavior was observed for *p*H 1.0 and 1.9 solutions. This means that the rate of the hydrogen evolution reaction is decreased by the organic compound. An increase in the *p*H shifted the polarization curves of uninhibited iron toward more negative potentials as shown in Fig. 2. This behavior was observed for both uninhibited and inhibited iron. A cathodic Tafel slope of 100 ± 5 mV was obtained regardless of the *p*H or inhibitor concentration.

The corrosion current was determined by the intersection of the corrosion potential and the extrapolation of the cathodic Tafel line. The corrosion current as a function of immersion time of iron in 1*N* H_2SO_4 is shown in Fig. 3 for different inhibitor concentrations. Uninhibited iron reached steady state within 10 hr of immersion. In general, steady-state corrosion currents were obtained within 30 hr of immersion.

It is seen that the addition of 4.16 mM benzotriazole reduced the corrosion current of iron in 1*N* H_2SO_4 from 1.0 to 0.02 mA/cm^2. An additional increase of the inhibitor did not lower the corrosion current further. The effect of benzotriazole on the corrosion current up to this concentration is shown in Fig. 4.

The open-circuit capacitance increased with immersion time for uninhibited iron in H_2SO_4 as observed by others (3, 4). As the inhibitor concentration increased, this capacitance increase with immersion time decreased. The time to reach a steady-state capacitance decreased with increase in inhibitor concentration. The open-circuit capacitance of iron in 1*N* H_2SO_4 at various inhibitor concentrations is shown *vs.* immersion time in Fig 5. The capacitance of uninhibited iron in 1*N* H_2SO_4 did not achieve a steady-state value during the duration of the experiment. After 96 hr of immersion, the capacitance of uninhibited iron in 1*N* H_2SO_4 was 210 μf/cm^2 and still increasing. Table I presents the values of the initial open-circuit capacitance (at 30-min immersion) and the steady-state values for *p*H 0.3, 1.0, and 1.9 at various inhibitor concentrations.

The steady-state capacitance values (C_{ss}) were related to the steady-state corrosion current as shown in Fig. 6, *i.e.*,

$$\frac{\partial \log I_{corr}}{\partial \log C_{ss}} = \text{constant} \qquad [1]$$

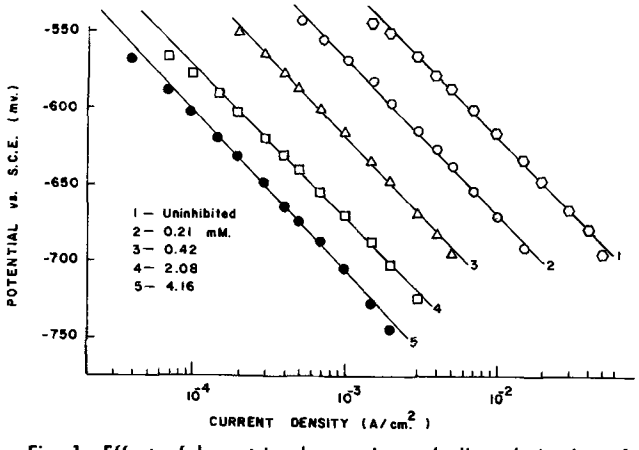

Fig. 1. Effect of benzotriazole on the cathodic polarization of iron in 1*N* H_2SO_4.

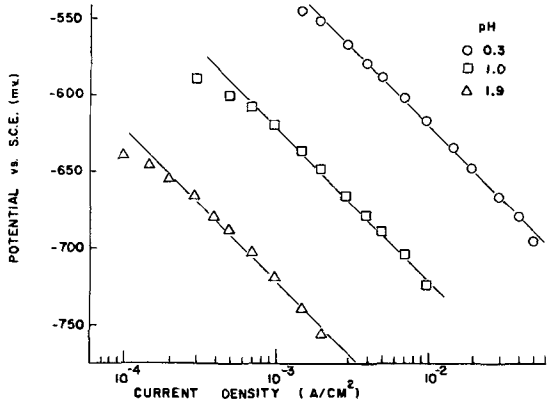

Fig. 2. Effect of *p*H on the cathodic polarization of iron in H_2SO_4.

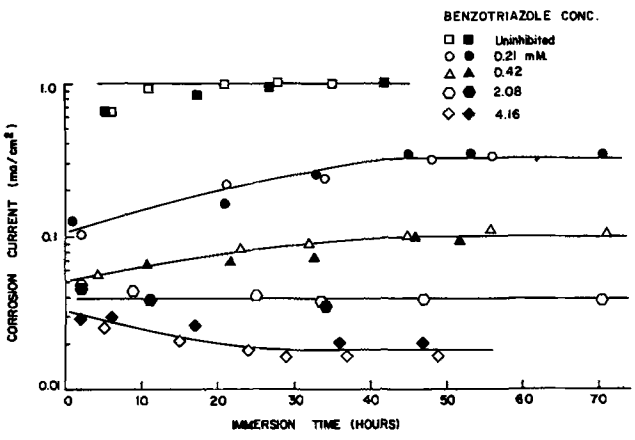

Fig. 3. Corrosion current *vs.* immersion time for iron in 1*N* H_2SO_4 containing benzotriazole.

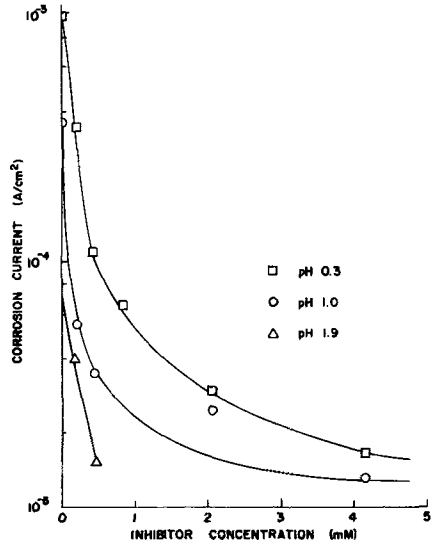

Fig. 4. Effect of benzotriazole on the corrosion current of iron in H_2SO_4.

The steady-state capacitance values (C_{ss}) were related to the steady-state corrosion current as shown in Fig. 6, *i.e.*,

$$\frac{\partial \log I_{corr}}{\partial \log C_{ss}} = \text{constant} \qquad [1]$$

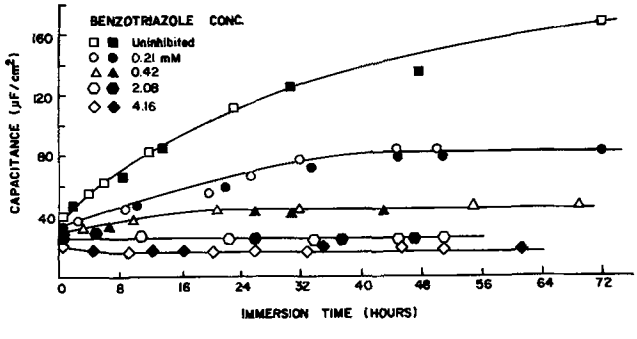

Fig. 5. Open-circuit capacitance of iron in 1*N* H_2SO_4 *vs.* immersion time at different benzotriazole concentration.

Table I. Open-circuit capacitance vs. concentration of benzotriazole

H_2SO_4 pH	Inhibitor conc, mM	Capacitance, $\mu f/cm^2$ Initial	Steady state
0.3	0.00	40	230*
	0.21	31	83
	0.42	30	46
	0.83	28	37
	2.08	26	25
	4.16	20	18
1.0	0.00	38	75
	0.21	33	40
	0.42	30	30
	2.08	25	20
	4.16	23	18
1.9	0.00	40	51
	0.21	33	40
	0.42	30	29

* Estimated.

The reaction order with respect to the hydrogen ions can be determined from a plot of log I_c *vs.* pH at constant potential in the Tafel region as shown in Fig. 7 for inhibited and uninhibited iron in 1*N* H_2SO_4. The results show that

$$\frac{\partial \log I_c}{\partial \text{pH}} = -1 \qquad [2a]$$

regardless of the concentration of inhibitor in the solution. Also for uninhibited iron

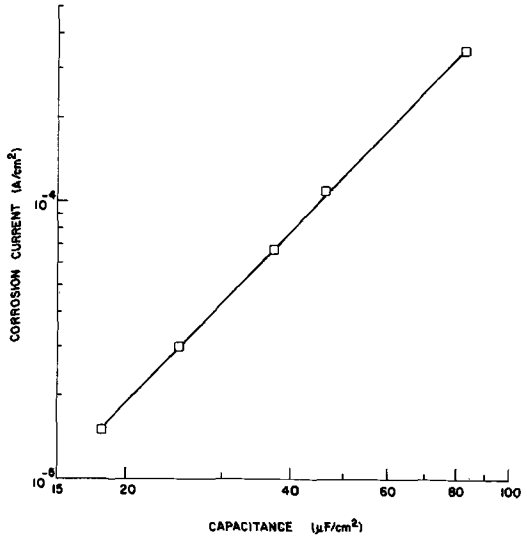

Fig. 6. Log-log plot of steady-state open-circuit capacitance *vs.* corrosion current of iron in 1*N* H_2SO_4.

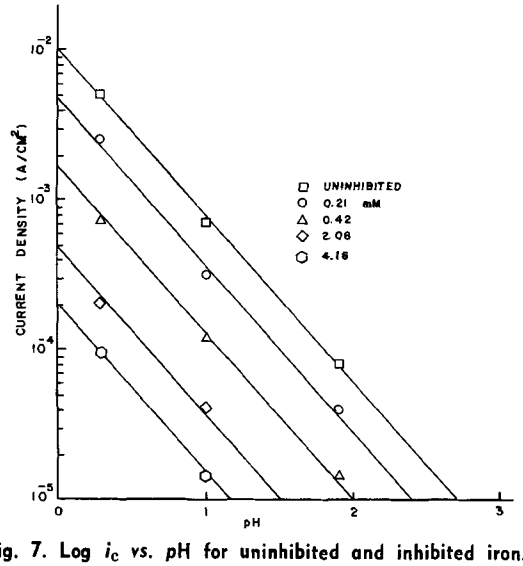

Fig. 7. Log i_c *vs.* pH for uninhibited and inhibited iron. ϕ = 600 mV.

$$\frac{\partial \log I_{corr}}{\partial \text{pH}} = -0.55 \qquad [2b]$$

$$\frac{\partial \phi_{corr}}{\partial \text{pH}} = -0.060\text{V} \qquad [2c]$$

and

$$\left(\frac{\partial \phi}{\partial \text{pH}}\right)_I = -0.11\text{V} \qquad [2d]$$

These results are in accord with those reported by Bockris *et al.* (4) and Kelly (5).

The absence of pseudocapacitance of uninhibited iron throughout the range of cathodic polarization was in accord with the results of Devanathan (6).

Discussion

The mechanism of the hydrogen evolution reaction in acidic solutions is assumed to be as follows

$$H^+ + e^- \rightarrow H \text{ ads} \qquad [3]$$

$$H \text{ ads} + H^+ + e^- \rightarrow H_2 \qquad [4]$$

or

$$H^+ + e^- \rightarrow H \text{ ads} \qquad [3]$$

$$H \text{ ads} + H \text{ ads} \rightarrow H_2 \qquad [5]$$

The experimental data obtained in this study for uninhibited iron are consistent with the results of Bockris (4), Kelly (5), and Devanathan (6) indicating that the discharge step is the rate-determining step. In the presence of benzotriazole, the rate of the h.e.r. is decreased. However, the cathodic Tafel slope and the reaction order with respect to the hydrogen ions is the same for iron in the absence and presence of the organic inhibitor. This result indicates that the inhibition of the h.e.r. by benzotriazole is by the simple adsorption mode and that the mechanism of the h.e.r. on uninhibited and inhibited iron in H_2SO_4 is the same.

If the above is valid, the apparent corrosion rate of inhibited iron is proportional to the surface area not covered by benzotriazole and it follows that

$$\theta_I = \frac{I^o_{corr} - I_{corr}}{I^o_{corr} - I^m_{corr}} \qquad [6]$$

where I^o_{corr} is the corrosion rate of uninhibited iron, I_{corr} is the corrosion rate of inhibited iron and I^m_{corr} is the limiting corrosion rate of inhibited iron, and θ_I is the fraction of the surface covered by adsorbed inhibitor. Furthermore, for the simple adsorption mode of inhibition, the surface coverage of inhibitor may also be determined from the differential capacitance of inhibited and uninhibited iron, since the apparent double layer capacitance is also proportional to the surface area not covered by the organic. Thus

$$\theta_I = \frac{C_o - C}{C_o - C_m} \qquad [7]$$

where C_o, C, and C_m are the steady-state capacitance of uninhibited iron, inhibited iron of surface coverage θ_I and inhibited iron of surface coverage $\theta_I = 1$, respectively. Equation [7] has been previously used by Hackerman (7) for adsorption of organics on solid electrodes. The experimental data indicate that maximum surface coverage is attained at a benzotriazole concentration of 4.16 mM.

Values of θ_I determined by Eq. [6] and [7] are given in Table II. As shown in Table II, good agreement is obtained between θ_I determined by Eq. [6] and [7]. Sufficient experimental data was not obtained for iron in pH 1.9 to determine θ_I.

A correlation between θ_I and C_I, the concentration of inhibitor in the electrolyte can be achieved with the Langmuir adsorption isotherm

$$\theta_I = \frac{KC_I}{1 + KC_I} \qquad [8]$$

Table II. Surface coverage of benzotriazole on iron in H_2SO_4

H_2SO_4 pH	Inhibitor conc, mM	Surface coverage Eq. [6]	Surface coverage Eq. [7]
0.3	0.21	0.66	0.69
	0.92	0.90	0.87
	0.83	0.94	0.91
	2.08	0.98	0.97
	4.16	1.00	1.00
1.0	0.21	0.88	0.69
	0.42	0.94	0.84
	2.08	0.97	0.97
	4.16	1.00	1.00

Rearranging Eq. [8]

$$\frac{C_I}{\theta_I} = \frac{1}{K} + C_I \qquad [9]$$

Several other isotherms correlated the adsorption data reasonably well for the higher surface coverages, but correlations were not obtained for the lower θ values in Table II. Only the Langmuir isotherm correlated all the $\theta - C_I$ data. Figure 8 is a plot of Eq. [9] and shows that the Langmuir adsorption isotherm correlates the experimental data for pH 0.3 and 1.0 well. The constant, $K = 10^4 M^{-1}$, and indicates that benzotriazole is strongly adsorbed on the iron surface.

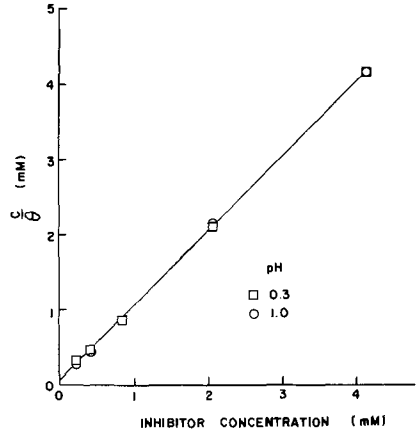

Fig. 8. Langmuir adsorption isotherm for adsorption of benzotriazole on iron in H_2SO_4.

Acknowledgment

This work was supported by a grant from the Office of Saline Water, U.S. Department of Interior.

Manuscript submitted Sept. 30, 1970; revised manuscript received *ca.* Nov. 27, 1970.

Any discussion of this paper will appear in a Discussion Section to be published in the December 1971 JOURNAL.

REFERENCES

1. I. Drysdale and J. B. Cotton, *Corrosion Sci.*, **3**, 69 (1963).
2. S. A. Balezin, E. G. Zak, and F. B. Glikina, *Soviet Electrochem.*, **4**, 111 (1968).
3. R. J. Chin, Thesis, U.C.L.A., March 1969.
4. J. O'M. Bockris, D. Drazic, and A. R. Despic, *Electrochim. Acta*, **4**, 325 (1961).
5. E. J. Kelly, *This Journal*, **112**, 124 (1965).
6. M. A. Devanathan, and Z. Stachurski, *ibid.*, **111**, 619 (1964).
7. N. Hackerman, T. Murakawa, and S. Nagura, *Corrosion Sci.*, **7**, 79 (1967).

Electrodeposition of Manganese Using Amide Solutions

M. A. Qazi[1] and J. Leja

Department of Mineral Engineering, The University of British Columbia, Vancouver, British Columbia, Canada

ABSTRACT

Laboratory study on electrodeposition of manganese was carried out in a diaphragm cell using an amide solution of $MnCl_2$ as catholyte and an aqueous solution of NH_4Cl as anolyte. Metallic manganese of approximately 98% purity was deposited at a current efficiency of 76%. The effects of several variables were investigated, and the optimum conditions were found to be: 10-15 g/liter Mn in formamide at pH 7.5 with 90-100 g/liter NH_4Cl anolyte solution at pH 2.5, cathode current density ~50 mA/cm^2 and temperature about 35°C.

Electrolytic production of manganese from aqueous solutions of manganese sulphate or chloride, containing large quantities of ammonium salts as buffer, in a diaphragm cell, has been investigated for several decades (1-3). The U. S. Bureau of Mines (4) developed a process for the electrowinning of manganese from aqueous solutions.

Very little work appears to have been done on the electrowinning of manganese from nonaqueous media. Dirkse and Brisco (5) reported on work which included deposition of manganese from ethers, acetones, and alcohols. The present paper deals with deposition of Mn from amide solutions; this topic has been investigated by Qazi (6) as a final step in recovering Mn metal from low-grade iron-manganese ore (from New Brunswick, Canada).

Schneider (7) electrolyzed amides and detected the presence of cyanuric acid in the electrolyte. This was confirmed later by Couch (8) who, in addition to cyanuric acid, identified secondary and tertiary amines in the amide solution after electrolysis.

[1] Senior Research Officer, Metallurgy Division, P.C.S.I.R., Lahore, Pakistan.

Key words: metallic Mn deposition, nonaqueous electrodeposition, formamide catholyte.

Experimental

The laboratory cell for the electrodeposition of manganese is illustrated in Fig. 1; it is an H-type, two-compartment cell with a sintered glass separating disk. The volumes of catholyte and anolyte used were ~30 ml each. Direct current was obtained using a Sorensen Model 560 BB rectifier.

The anode was a rod of a spectrograde graphite and the cathode was an 18/8 stainless steel strip of 3 cm^2 area. The current was determined using a copper coulombmeter in series with the cell. Oxygen dissolved in the electrolyte was removed by bubbling nitrogen through the cell.

Manganese ($Mn^{++}/Mn = -1.18V$) readily evolves hydrogen from aqueous solutions unless buffered with large quantities of ammonium salts (~100-150 g/liter). The disadvantages of using aqueous electrolytes in

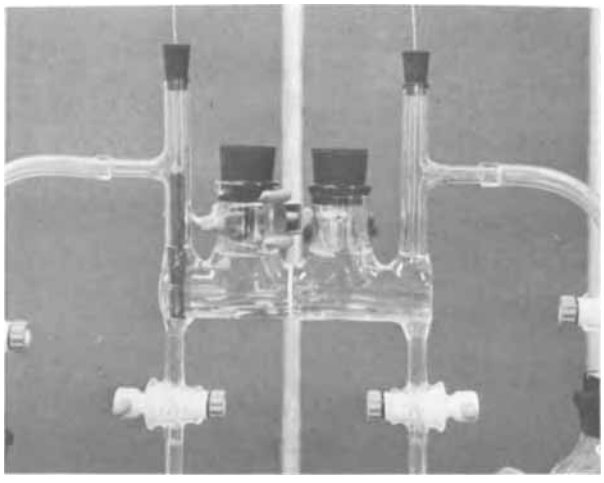

Fig. 1. An H-type two-compartment (separated by a fritted disk) laboratory cell for electrodeposition of manganese.

manganese depositions are: low current efficiency (~65%), low Mn concentration in catholyte, redissolution of some of the deposited manganese due to the lowering of pH (as the electrolysis proceeds).

The organic solvents which were used in the exploratory electrolysis tests for manganese deposition are listed in Table I.

$MnCl_2$ was found to be more soluble than $MnSO_4$ in most of the organic solvents, but even so the solutions of $MnCl_2$ in dimethyl sulfoxide, pyridine, and nitrobenzene were found poorly conducting and yielded brown or black, apparently nonmetallic, deposits (although presence of metallic manganese was detected qualitatively). Only the electrolysis of $MnCl_2$ in amides produced a dark, metallic deposit of manganese.

When the anolyte and catholyte products were allowed to mix, a brown coloration was produced around the anode with the result that the cathode product began to dissolve. The decomposition of amide at the anode meant the loss of valuable electrolyte. This problem was solved by using a diaphragm separating the cell into compartments and replacing amide in the anode compartment with an aqueous ammonium chloride; in this way the pH control of the cell and the quality of the deposited manganese were improved.

Results

The chemical analyses of the electroplated manganese from the catholytes containing 18 g/liter Mn as $MnCl_2$ in formamide, dimethylformamide, and dimethyl acetamide at a pH around 7.2, and using anolyte containing 90 g/liter NH_4Cl and 20 g/liter HCl, at a current density of 40 mA/cm² are given in Table II. The manganese deposited from a formamide bath was smoother and brighter, more metallic in appearance, than that from other organic electrolytes.

The conductivity of formamide (1.12×10^{-5} mho cm^{-1}) increases on dissolving manganous chloride, as plotted in Fig. 2. The abrupt change in the slope at ~3% $MnCl_2$ indicates the formation of some complex of the type $MnCl_2 \cdot n(HCONH_2)$. The solubility of anhydrous $MnCl_2$ in formamide was found to be 82.6 g/liter (~7.3%).

Table I. Physical properties of organic solvents

Solvent	Density, g/ml	Viscosity, C.P.	Spec. cond., mho cm^{-1}	Dielec. const.
Formamide	1.129	0.330	1.12×10^{-5}	109.50
N-N Dimethyl-formamide	0.944	0.080	1.60×10^{-7}	36.71
Dimethyl sulfoxide	1.096	0.196	3.00×10^{-8}	46.60
N-N Dimethyl acetamide	0.937	0.092	1.40×10^{-7}	37.80
Pyridine	0.978	0.088	1.00×10^{-9}	12.30
Nitrobenzene	1.198	0.182	1.00×10^{-10}	34.91

Table II. Chemical analyses of the electroplated manganese from organic solvents

Catholyte with 41 g/liter $MnCl_2$	%Mn	%C*	%O*
Formamide ($H \cdot CO \cdot NH_2$)	98.6	1.07	0.94
N-N Dimethylformamide	81.4	5.7	4.4
N-N Dimethylacetamide	76.9	8.2	6.5

* Analyses by Schwarzkopf Microanalytical Laboratories, New York, N. Y.

The data showing the effects of the variation of anolyte pH on the current efficiency at different NH_4Cl concentrations in anolyte solutions are plotted in Fig. 3. The optimum conditions for maximum current efficiency appear to be ~90 g/liter NH_4Cl and pH ~2.

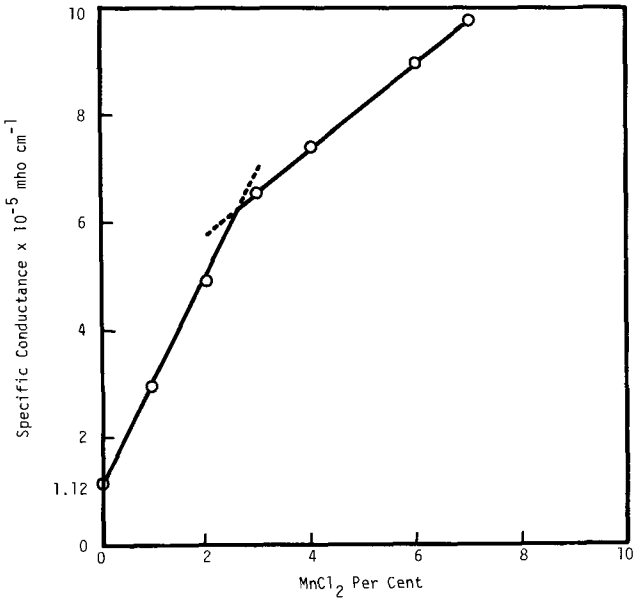

Fig. 2. Specific conductance of $MnCl_2$-formamide solutions at 25°C.

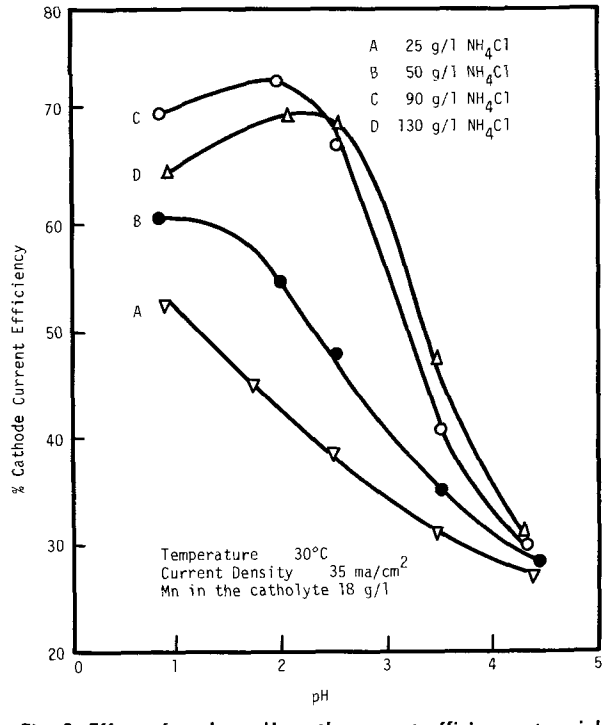

Fig. 3. Effect of anolyte pH on the current efficiency at variable NH_4Cl concentrations.

Manganese deposited at anolyte pH greater than 2.5 was black, flaky and tended to fall off the cathode.

Catholyte composition and pH.—It was found that even 40 g/liter $MnCl_2$ dissolved in formamide was gradually reacting with O_2 dissolved in the liquid giving a brown $Mn(OH)_2$ colloidal suspension in a few hours. When the formamide was made slightly acidic by HCl addition with 1 g/liter NH_4Cl the formation of $Mn(OH)_2$ was prevented for 3-4 days. An addition of a reducing agent, 0.4 g/liter of sodium ethyl xanthate, prevented the formation of $Mn(OH)_2$ indefinitely, *i.e.* after 30 days the solution was still colorless.

The results obtained on varying pH with various $MnCl_2$ concentrations in the catholyte containing 0.4 g/liter sodium ethyl xanthate are plotted in Fig. 4. The anolyte contained 80 g/liter NH_4Cl and its pH was adjusted at 2.5. After 90 min of electrolysis, pH of anolyte dropped to 0.8. It is seen that the critical pH of catholyte for a maximum in current efficiency decreases with the increase in the manganese concentration of the catholyte. Also, the current efficiency increases with the decrease in the manganese concentration. When the pH of catholyte was adjusted to pH 7.2, it changed after 90 min of electrolysis to pH 7.8.

Figure 5 shows the appearance of manganese of approximately 99% purity, (analyzed polarographically) chipped off on flexing the cathode. The maximum overall cathode current efficiency achieved was 76%. When a higher catholyte concentration was used, *e.g.* 20 g/liter Mn, a nodulized deposit was obtained as in Fig. 6, and the current efficiency decreased. Analysis of Mn deposit obtained in several batches of testing indicated a nearly constant C content (~1%) and O_2 content varying from 1-2.5%.

Manganese could be deposited from the formamide baths using a wide range of current densities with only a slight variation in the current efficiency. At higher current densities, however, the cathode current efficiency increased until the formation of nodules or trees occurred (as shown in Fig. 6), then it steadily decreased (see Fig. 7).

Temperature.—Using a current density of 50 mA/cm^2 and catholyte containing 16 g/liter Mn at pH 7.3, with anolyte containing 90 g/liter NH_4Cl at pH 2.4, an optimum cell temperature of 35°C was established, as given by the results in Table III.

Stirring of the electrolyte improved the rate of manganese deposition, presumably due to a more uniform distribution of the electrolyte at the electrode surface. The nature of the deposit was not affected.

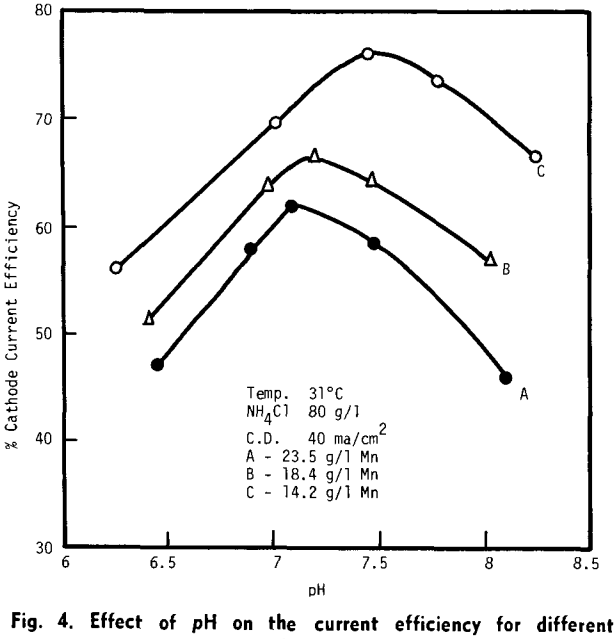

Fig. 4. Effect of pH on the current efficiency for different manganese concentrations in the catholyte.

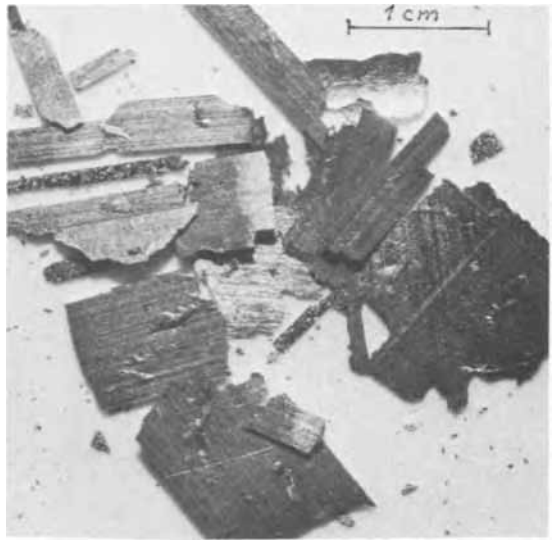

Fig. 5. Approx. 98% Mn flakes chipped off from stainless steel cathode, obtained at 14.2 g/liter Mn in catholyte.

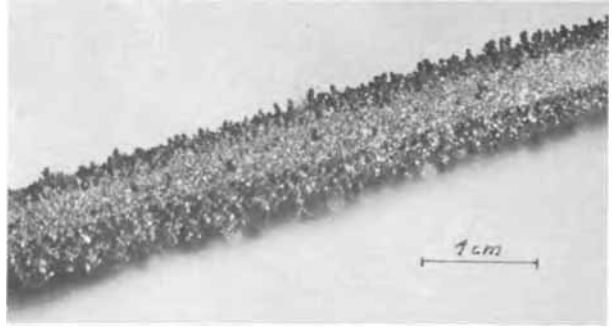

Fig. 6. Mn nodules and trees formed on the cathode when manganese concentration in catholyte was increased to 20 g/liter.

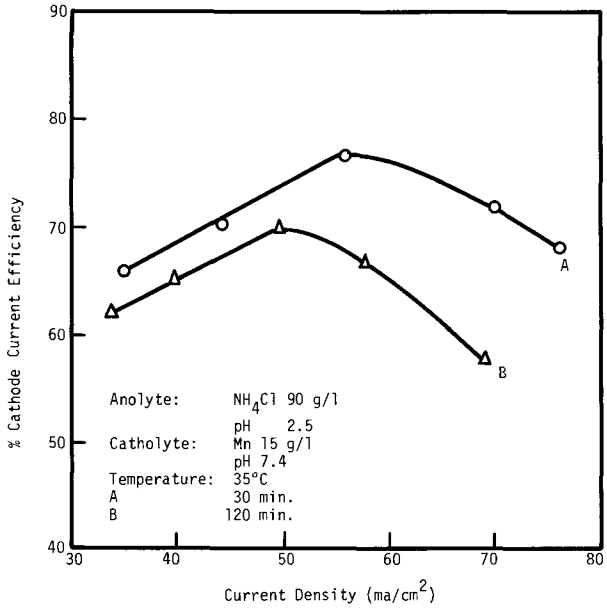

Fig. 7. Effect of current density on current efficiency

Electrode reactions.—Formamide and other alkyl amides coordinate through oxygen with metal ion, as Lewis acid, decreasing the force constant for C=O. The complex can be broken on electrolysis liberating the metal and regenerating the ligand. Cryoscopic

Table III. Effect of temperature on the current efficiency

Cell temperature, °C	Mn plated, mg	Cell, pH	Cell voltage	Cathode current efficiency, %
28.6	81.6	7.30	6.30	74.6
35.5	83.5	7.35	6.20	77.4
40.3	82.3	7.50	6.05	76.2
45.0	78.6	7.75	5.95	71.6
51.4	71.6	7.90	5.80	66.9

determination indicated that on the average 2-4 moles of ($HCONH_2$) are involved in the complex with $MnCl_2$. The solution, therefore, may contain $Mn(HCONH_2)_2Cl_2$ and $Mn(HCONH_2)_4Cl_2$.

On the dissociation and electrolysis, the reaction at the anode should involve liberation of chlorine

$$2Cl^- \rightarrow Cl_2 + 2e^-$$

Anode gas evolved during 90 min of electrolysis of 30 ml of catholyte (containing 40 g/liter $MnCl_2 \equiv 17.5$ g/liter Mn in formamide, with 0.4 g/liter sodium ethyl xanthate and 1 g/liter NH_4Cl, pH 7.2) amounted to 21 ± 1 ml. It was analyzed with a Pye gas chromatograph and showed ~1% Cl_2, ~7% O_2, balance N_2. The reaction of Cl_2 with NH_4Cl (100 g/liter NH_4Cl in water at pH 2.5) would be expected to involve

$$2NH_4Cl + 3Cl_2 \rightarrow N_2 + 8HCl$$

The volume of N_2 generated at 120 mA for 90 min should be ~25 ml. The lowering of anolyte pH from 2.5 to 0.8 did confirm the acidification of anolyte. However, the presence of O_2 must have resulted from the reaction

$$H_2O \rightarrow 2H^+ + \tfrac{1}{2}O_2 + 2e$$

Cathode gas has been collected during several tests; its volume exceeded slightly the volume of the anode gas. Its composition, as determined with a Pye chromatograph, showed ~4% O_2, balance H_2. In addition, qualitative tests and infrared spectroscopy of the catholyte after electrolysis showed presence of primary, secondary, and tertiary amines. Also, catholyte pH became slightly more alkaline (pH 7.2 → 7.8) at the end of the tests instead of becoming acidic, as expected theoretically. The details of the over-all reactions remain to be ascertained.

Conclusions

Electrolysis of 1-1.5% Mn as $MnCl_2$ in formamide resulted in the deposition of ~98% Mn, if the decomposition of the solvent and the undesirable side reactions were eliminated. These conditions were achieved by using a diaphragm cell and an aqueous solution of ammonium chloride (90-100 g/liter NH_4Cl at a pH around 2.5) as anolyte, with a current density of 50 mA/cm², and catholyte pH of about 7.5; a maximum current efficiency of 76% was obtained.

Compared with the electrolytic process using aqueous $MnCl_2$, the formamide solution of $MnCl_2$ results in a higher conductivity and higher current efficiency, enables higher pH of the catholyte to be used (up to about 8.0) without precipitating $Mn(OH)_2$.

Acknowledgment

The support of this work from the National Research Council of Canada grants is gratefully acknowledged. M. Qazi expresses thanks to the External Aid Office for the Assistance of the Colombo Plan Scholarship. The help of Mr. F. Kaempffer, M.Sc., in carrying out duplicate deposition tests and gas analyses is gratefully acknowledged.

Manuscript submitted April 21, 1970; revised manuscript received *ca.* Nov. 16, 1970.

Any discussion of this paper will appear in a Discussion Section to be published in the December 1971 JOURNAL.

REFERENCES

1. A. J. Allmand and A. N. Campbell, *Trans. Faraday Soc.* **20**, 379 (1924).
2. H. H. Oaks and W. E. Bradt, *Trans. Electrochem. Soc.*, **69**, 567 (1936).
3. J. H. Jacobs and D. E. Churchward, *This Journal*, **94**, 108 (1948).
4. J. Koster and S. M. Shelton, *Eng. Mining J.*, **137**, 510 (1936).
5. T. P. Dirkse and H. T. Brisco, *Metal Ind. (London)*, p. 284 (June 1938).
6. M. D. Qazi, Hydrometallurgy of a low-grade iron-manganese ore. Ph.D. thesis, University of Alberta 1967.
7. H. Schneider, *Ber. Deut. Chem. Ges.*, **56**, 2460 (1923).
8. D. E. Couch, *Electrochim. Acta*, **9**, 327 (1964).

Electrodeposition of Gold by Pulsed Current

H. Y. Cheh*[1]

Bell Telephone Laboratories, Incorporated, Murray Hill, New Jersey 07974

ABSTRACT

A diffusion model was developed to calculate the rate of deposition of metals by a periodically pulsed current. The results indicate that although the magnitude of the instantaneous applied current for deposition can be considerably higher than that of direct current plating under suitable conditions, the limiting over-all plating rate was in general lower. Experimental confirmation was established using the phosphate, citrate, and cyanide gold solutions. The diffusion coefficient of the complexed gold cyanide ion ($Au(CN)_2^-$) was measured. The values were 1.63 x 10^{-5} cm²/sec, 1.67 x 10^{-5} cm²/sec, and 1.68 x 10^{-5} cm²/sec at 60°C for the phosphate, citrate, and cyanide solutions, respectively. The pH value, specific conductance, and kinematic viscosity of these solutions were also measured and tabulated. The rate of chemical dissolution of gold in the cyanide solution was also investigated.

Electrodeposition of metals by a periodic variation of the applied current has been practised by a growing number of electroplaters. Jernstedt (1) obtained fine-grained deposits from a copper cyanide solution at high current densities by periodically reversing the polarity of the applied current (p-r plating). Similar observations were also reported by applying pulsed currents (p-c plating) in acid copper solutions by Popkov (2) and by Ozerov *et al.* (3). Hickling and Rothbaum (4) observed a decrease in deposit roughness in copper cyanide solutions by applying p-r plat-

* Electrochemical Society Active Member.
[1] Present address: Department of Chemical Engineering and Applied Chemistry, Columbia University, New York, New York 10027.
Key words: electrodeposition, gold.

ing under suitable conditions. Most recently, Avila and Brown (5) presented a discussion on applying pulsed current to gold plating in the semiconductor industry.

Two advantages were most frequently cited by investigators in this field. First, in contrast to applying a direct current (d-c plating), it is claimed that a higher instantaneous cathodic current density for deposition can be applied to the plating system because of the higher concentration of metal ion in the diffusion layer. Second, more fine-grained deposits can be obtained. Although higher cathodic current density for deposition has been confirmed in the plating literature, confusion exists concerning the over-all plating rate which involves an integration of the current over the total cyclic period. From theoretical considerations, Ozerov *et al.* (3) claimed that the rate of deposition could be increased indefinitely in p-c plating by decreasing the duration of the pulsed current. A closer examination of their derivation revealed that their diffusion model was completely unrealistic for a practical plating system, and, in fact, they presented no experimental confirmation of an increased over-all plating rate. Hickling and Rothbaum (4) presented results of a careful experimental study on the rate of deposition of silver by both p-r and p-c plating. An increase of instantaneous cathodic current density for deposition but a decrease in the over-all plating rate was observed in both cases. A simple model of mass transport of the metal ion was suggested which showed satisfactory agreements with the periodic reversal of current experiments but failed completely to describe the pulsed current experiments.

In this paper, we present a realistic mass transport model to calculate both the limiting instantaneous cathodic current density for deposition and the limiting over-all rate of deposition by pulsed current. Results are then compared with the rate of deposition of three gold plating solutions.

Theoretical Analysis

We assume that a planar cathode is situated in a well-stirred plating solution. The cathode-anode distance is large as compared to the thickness of the diffusion layer so that the anode can be considered to be far away for the present model. The number of coulombs passed during a plating experiment is assumed to be so small that the depletion of the metal ion in the solution can be neglected. In other words, the concentration of the reacting species at the outer edge of the diffusion layer remains unchanged. The deposition process is assumed to be controlled by the mass transport of metal ion and current density is the controlled variable. Both the nonfaradaic component of the applied current and the electrical migration of the metal ion are considered to be negligible due to the relatively high conductivity of most plating solutions. Let the outer edge of the diffusion layer be located at $x = 0$ and the cathode at $x = \delta$. Under these conditions, the concentration of metal ion is governed by Fick's second law of diffusion

$$\frac{\partial c}{\partial t} = D\frac{\partial^2 c}{\partial x^2} \qquad [1]$$

with the following boundary conditions

1. $c = c_o$ for $t = 0$ and all x [2]
2. $c = c_o$ for $t > 0$ and $x = 0$ [3]
3. $D\left(\frac{\partial c}{\partial x}\right) = \frac{i}{n\mathbf{F}}$ for $t > 0$ and $x = \delta$ [4]

where c is the concentration of the metal ion, c_o is its concentration in the bulk of the solution, D is the diffusion coefficient of the metal ion, δ is the thickness of the diffusion layer, n is the number of electrons transferred during the deposition process, $\mathbf{F}$ is Faraday's constant, t is the time, and i is the applied current density which is negative for cathodic deposition.

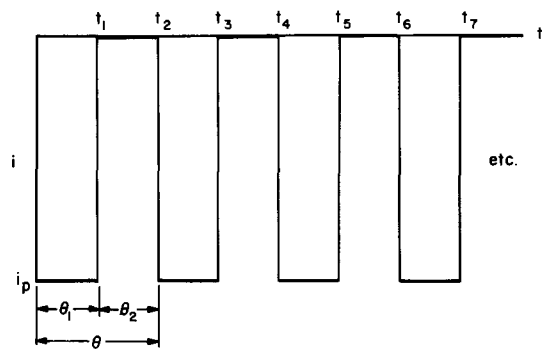

Fig. 1. Schematic diagram of a pulsed current

If we let the cyclic period for the pulsed current be θ, the time when the current is on in a period be θ_1, and the time when the current is off in the same period be θ_2, the form of the pulsed current density can be shown schematically in Fig. 1. Consequently, the pulsed current density in Eq. [4] can be expressed as

1. $i = i_p$ for $0 < t \leq t_1$, $t_2 < t \leq t_3$, etc. [5]
2. $i = 0$ for $t_1 < t \leq t_2$, $t_3 < t \leq t_4$, etc. [6]

and the cyclic period θ is given by

$$\theta = \theta_1 + \theta_2 = t_2 = (t_4 - t_2) = (t_6 - t_4), \text{etc.} \qquad [7]$$

where i_p is the pulsed current density and t_n is defined in Fig. 1.

Equation [1] subject to the boundary conditions, Eq. [2] to Eq. [6] was originally solved by Rosebrugh and Miller (6). The results for the surface concentration of the metal ion are

1. during periods when the current is on

$$\frac{(c_i - c_o)n\mathbf{F}D}{i_p\delta} = 1 - \frac{8}{\pi^2}\sum_{j=1}^{\infty}\frac{\exp[-(2j-1)^2a\tau]}{(2j-1)^2} \cdot \frac{(\exp[(2j-1)^2a\theta] - \exp[(2j-1)^2a\theta_1])}{(\exp[(2j-1)^2a\theta] - 1)} - \frac{8}{\pi^2}\sum_{j=1}^{\infty}\frac{\exp[-(2j-1)^2at]}{(2j-1)^2} \cdot \frac{(\exp[(2j-1)^2a\theta_1] - 1)}{(\exp[(2j-1)^2a\theta] - 1)} \qquad [8]$$

2. during periods when the current is off

$$\frac{(c_i - c_o)n\mathbf{F}D}{i_p\delta} = \frac{8}{\pi^2}\sum_{j=1}^{\infty}\frac{\exp[-(2j-1)^2a\tau]}{(2j-1)^2} \cdot \frac{(\exp[(2j-1)^2a\theta] - \exp[(2j-1)^2a\theta_2])}{(\exp[(2j-1)^2a\theta] - 1)} - \frac{8}{\pi^2}\sum_{j=1}^{\infty}\frac{\exp[-(2j-1)^2at]}{(2j-1)^2} \cdot \frac{(\exp[(2j-1)^2a\theta_1] - 1)}{(\exp[(2j-1)^2a\theta] - 1)} \qquad [9]$$

where

$$a = \frac{\pi^2 D}{4\delta^2} \qquad [10]$$

$$\tau = t - N\theta \qquad [11]$$

c_i is the surface concentration of the metal ion, and N is the number of cycles of current already passed. Equation [8] and Eq. [9] indicate that the surface concentration of the metal ion during p-c plating con-

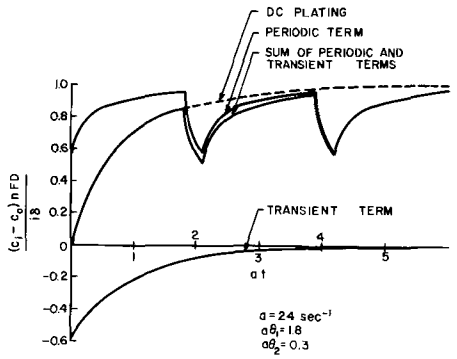

Fig. 2. Surface concentration of metal ion during p-c plating

sists of two periodic terms (first two terms in Eq. [8] and first term in Eq. [9]) and a transient term (third term in Eq. [8] and second term in Eq. [9]).

It is of interest to note that Eq. [8] can also be extended to calculate the surface concentration of the metal ion for d-c plating by letting $a\theta = a\theta_1$. Therefore, for d-c plating

$$\frac{(c_i - c_o)nFD}{i_{d\text{-}c}\delta} = 1 - \frac{8}{\pi^2}\sum_{j=1}^{\infty}\frac{\exp\left[-(2j-1)^2 at\right]}{(2j-1)^2} \qquad [12]$$

where $i_{d\text{-}c}$ is the applied direct current density.

Numerical calculations for the surface concentration of metal ion for both p-c and d-c plating were performed using $i_p = i_{d\text{-}c}$, $a = 24\ sec^{-1}$, $a\theta_1 = 1.8$ and $a\theta_2 = 0.3$. These conditions are often used in practice. The results are shown in Fig. 2. Since i_p is negative for cathodic deposition, a comparison of these results indicates that the surface concentration of the metal ion in p-c plating is always higher than that in d-c plating after the first pulse. Consequently, in order to make the lowest surface concentration in p-c plating which occurs at the end of each pulse after the transient term has completely vanished equal to that from d-c plating at steady state, the instantaneous current density employed in p-c plating must be higher than that in d-c plating. If the instantaneous pulsed current density which causes the lowest surface concentration to reach zero is defined as the limiting current density for p-c plating, the ratio of the limiting current density to that of d-c plating can be calculated by dividing the steady-state term in Eq. [12] by the periodic terms in Eq. [8] and letting $c_i = 0$ and $\tau = \theta_1$

$$\frac{(i_p)_l}{(i_{d\text{-}c})_l} = \frac{1}{1 - \frac{8}{\pi^2}\sum_{j=1}^{\infty}\frac{1}{(2j-1)^2}\cdot\frac{(\exp\left[(2j-1)^2 a\theta_2\right] - 1)}{(\exp\left[(2j-1)^2 a\theta\right] - 1)}} \qquad [13]$$

where $(i_p)_l$ and $(i_{d\text{-}c})_l$ are limiting current densities for p-c and d-c plating, respectively. The asymptotic form for $a\theta << 1$ is, therefore[2]

$$\left[\frac{(i_p)_l}{(i_{d\text{-}c})_l}\right]_{a\theta<<1} = \frac{\theta}{\theta_1} \qquad [14]$$

Numerical results from Eq. [13] and Eq. [14] for various values of $a\theta$ and θ_1/θ are plotted in Fig. 3. The results indicate that high limiting current densities can be obtained by decreasing the value of either $a\theta$ (shorter pulse periods) or θ_1/θ (shorter duration of pulsed currents).

[2] In deriving Eq. [14], the mathematical identity $\sum_{j=1}^{\infty}\frac{1}{(2j-1)^2} = \frac{\pi^2}{8}$, was used.

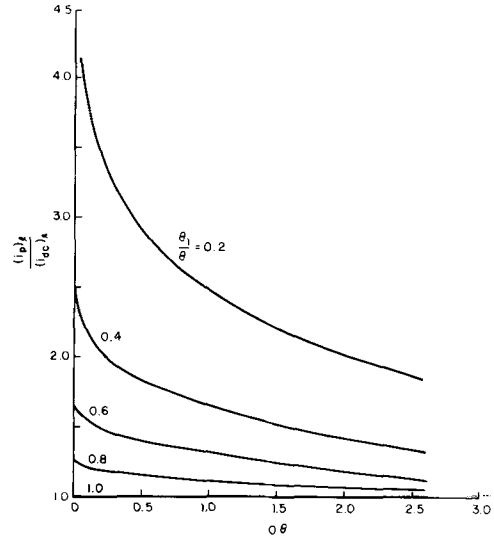

Fig. 3. Limiting current density for p-c plating

In order to calculate the over-all rate of plating, however, the pulsed current must be integrated over the entire cycle. Multiplying both sides of Eq. [13] by θ_1/θ, the following result is obtained,

$$\frac{\text{Max over-all rate of p-c plating}}{\text{Max rate of d-c plating}} = \frac{(i_p)_l\theta_1}{(i_{d\text{-}c})_l\theta} = \frac{\theta_1/\theta}{1 - \frac{8}{\pi^2}\sum_{j=1}^{\infty}\frac{1}{(2j-1)^2}\cdot\frac{(\exp\left[(2j-1)^2 a\theta_2\right] - 1)}{(\exp\left[(2j-1)^2 a\theta\right] - 1)}} \qquad [15]$$

Consequently, the asymptotic form for large values of $a\theta$ is

$$\left[\frac{(i_p)_l\theta_1}{(i_{d\text{-}c})_l\theta}\right]_{a\theta>>1} = \frac{\theta_1}{\theta} \qquad [16]$$

Numerical results of Eq. [15] are given in Fig. 4. It is clearly indicated here that even though the pulsed current can be made considerably higher than that of direct current, the limiting over-all rate of p-c plating simply cannot exceed that of d-c plating.

In order to determine the applicability of this model, experimental investigation was carried out using three different gold plating solutions.

Experimental Results and Discussion

Gold plating solutions were chosen to compare with the theoretical calculations for two reasons. First, gold deposition is of extreme importance in the modern semiconductor industry and little basic information is available for the gold plating processes. Second, the

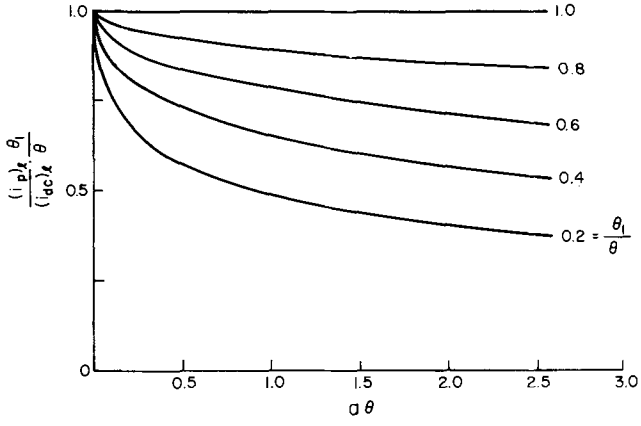

Fig. 4. Limiting over-all rate of deposition during p-c plating

Table I. Properties of gold plating solutions at 60°C

	pH	Specific conductance, κ, ohm^{-1} cm^{-1}	Kinematic viscosity, ν, cm^2/sec	Diffusivity of $Au(CN)_2^-$, D, cm^2/sec	Schmidt number, ν/D
Phosphate gold solution	7.5	0.159	0.00604	1.63×10^{-5}	370
Citrate gold solution	5.0	0.0548	0.00518	1.67×10^{-5}	310
Cyanide gold solution	10.8	0.105	0.00469	1.68×10^{-5}	279

electrochemical behavior of various gold plating solutions is rather different one from the other. For instance, the classical alkaline cyanide gold solution is a relatively reversible system with an exchange current density for the deposition process in the range of 1 mA/cm^2. Both the neutral phosphate gold and acid citrate gold solutions are highly irreversible systems. A detailed discussion on the electrochemical aspects of gold deposition will be published in the near future (7).

The composition of the three gold plating solutions used in the experiments were

1. Phosphate gold solution

$KAu(CN)_2$	1.3 g/l
K_2HPO_4	120 g/l
KH_2PO_4	30 g/l

2. Citrate gold solution

$KAu(CN)_2$	1.3 g/l
$(NH_4)_2HC_6H_5O_7$	50 g/l

3. Cyanide gold solution

$KAu(CN)_2$	1.5 g/l
KCN	35 g/l

Although these relatively dilute gold solutions are not full strength gold plating solutions, they can typically be used as gold strike solutions.[3] The reason for choosing to study these dilute solutions is because of their better defined tranport properties. The pH, specific conductance, and kinematic viscosity of these solutions were measured at 60°C by a Beckman Expanded Scale pH meter, a Type RC Conductivity Bridge by Industrial Instruments, Inc., operating at a bridge current of frequency 1000 Hz and a Cannon-Fenske Viscosimeter of cell constant of 2.194×10^{-5} cm^2/sec^2, respectively. Results are tabulated in Table I.

In order to test the proposed model, the diffusion coefficient of $Au(CN)_2^-$, the diffusion layer thickness at the cathode, the limiting current density of d-c plating and finally, the limiting current density of p-c plating must all be measured. Fortunately, all of this information can be obtained using a rotating disk electrode.

Limiting current density of d-c plating.—A high speed rotator[4] described by Napp and Bruckenstein (8) was used to drive the electrode. A platinum disk of 0.635 cm diameter (0.317 cm^2 area) imbedded in a Teflon sleeve was used as the rotating electrode. A platinum coil was used as the counterelectrode. Plating was performed in all three solutions at constant total current of −5 mA (or a current density of −15.8 mA/cm^2) at 60°C and 1520 rpm for 10 min. Gold stripping was carried out in a 0.1M KCN solution at room temperature, 1520 rpm, and a total current of 2 mA. Current efficiency and consequently the limiting current density were then calculated by a comparison of the number of coulombs passed in plating to that in stripping. The values obtained were −4.95, −5.39, and −6.00 mA/cm^2 for the phosphate, citrate, and cyanide solutions, respectively.

[3] A strike solution in the plating industry refers to a dilute metal solution used in preplating. By applying high current densities for a short duration in a strike solution, the adhesion and possibly other physical properties of subsequent deposits on the substrate surface are generally improved.

[4] Supplied by the Pine Instrument Company, Grove City, Pennsylvania.

Diffusion coefficient of $Au(CN)_2^-$ and thickness of the diffusion layer.—The problem concerning mass transport to a rotating disk was originally solved by Levich (9) for asymptotically large Schmidt number. Gregory and Riddiford (10) empirically improved the Levich derivation to include the effect of finite Schmidt number and presented the following equations

$$(i_{d\text{-}c})_l = \frac{-0.554\, nFD^{2/3}\nu^{-1/6}\omega^{1/2}c_0}{(0.8934 + 0.316\,(D/\nu)^{0.36})} \qquad [17]$$

and

$$\delta = 1.80\left(0.8934 + 0.316\left(\frac{D}{\nu}\right)^{0.36}\right)\left(\frac{D}{\nu}\right)^{1/3}\left(\frac{\nu}{\omega}\right)^{1/2} \qquad [18]$$

where ν is the kinematic viscosity of the solution and ω is the rotational speed.

The limiting current densities for the three gold plating solutions were measured at a number of rotational speeds using the same technique mentioned in the last section. Results were plotted in Fig. 5. The diffusion coefficients were then calculated by Eq. [17] and the results summarized in Table I. Due to experimental uncertainties, the third significant figure of D for the citrate gold solution is probably not meaningful. Knowing D and ν, the thickness of the diffusion layer can easily be calculated by Eq. [18].

Rate of deposition by pulsed current.—Similar experimental procedures for limiting current density measurements by d-c plating were used to study the rate of deposition by p-c plating. The magnitude of the pulsed current was 6 mA (*i.e.*, 18.9 mA/cm^2) and the total duration for a pulsed experiment was 10 min for all solutions. All experiments were carried out at 60°C and 1520 rpm. Five $a\theta$ values (0.5, 1.0, 1.5, 2.0, 2.5) and four θ_1/θ values (0.2, 0.4, 0.6, 0.8) were used. Values of δ and a for the phosphate, citrate, and cyanide solutions at 1520 rpm were calculated from Eq. [18] and Eq. [10] to be 0.00144 cm, 19.5 sec^{-1}, 0.00142 cm, 20.6 sec^{-1}, 0.00140 cm and 21.2 sec^{-1}, respectively. The pulsed current was supplied by feeding the square-wave voltage pulse from a Tacussel GSTP2 function generator to a fast-rise Wenking Model 61 RS potentiostat and converting the final output to the galvanostatic-control mode. The pulse was recorded on a Tektronix Model 564B oscilloscope. The rise time for the pulse was found to be less than 10 μsec for all cases.

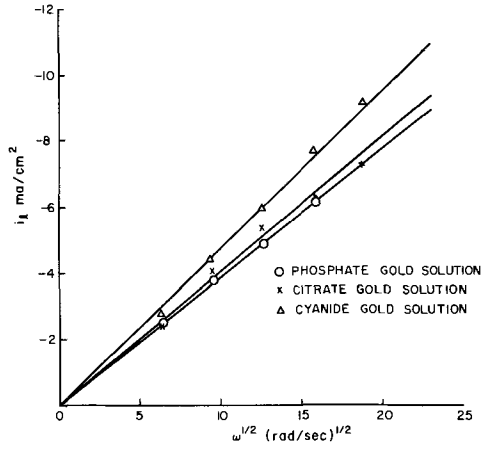

Fig. 5. Limiting current densities in phosphate, citrate, and cyanide gold solutions.

The rate of deposition and consequently the limiting current for p-c plating were then calculated from the same stripping experiments described earlier. The experimental data points for the phosphate and the citrate solutions are given in Fig. 6 to Fig. 9. Good agreement is observed between the proposed model and experimental results for both the phosphate and citrate solutions.

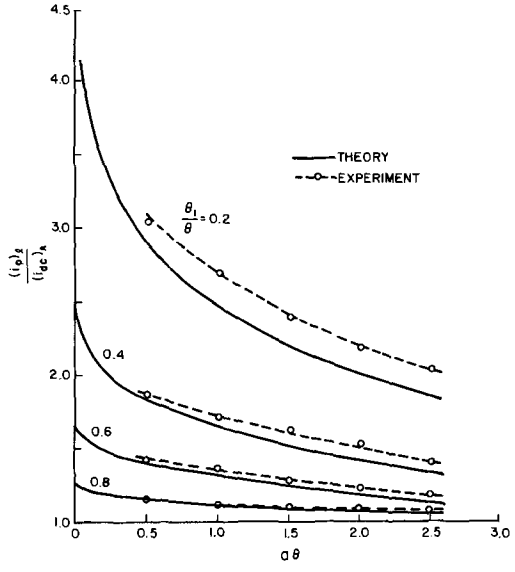

Fig. 6. Limiting current density for p-c plating in a phosphate gold solution.

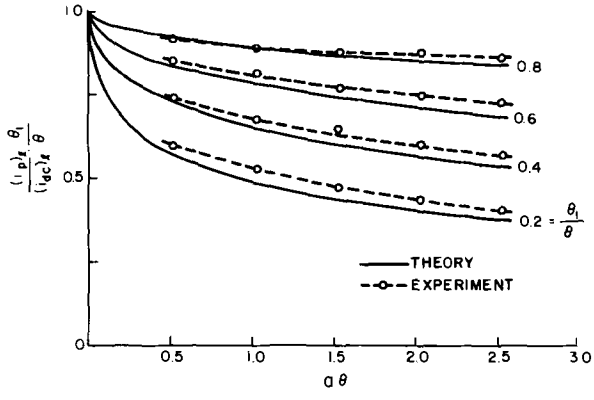

Fig. 7. Limiting over-all rate of deposition for p-c plating in a phosphate gold solution.

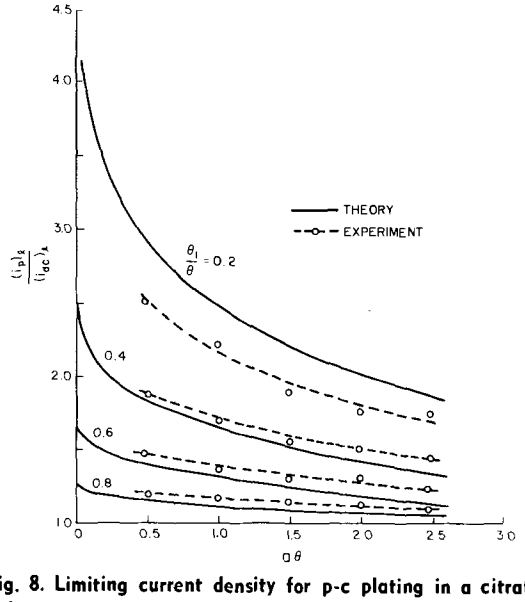

Fig. 8. Limiting current density for p-c plating in a citrate gold solution.

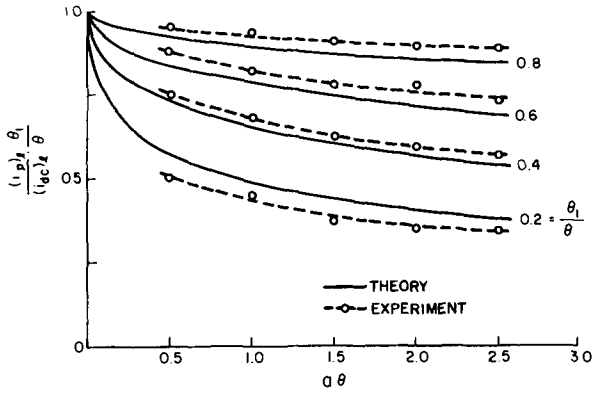

Fig. 9. Limiting over-all rate of deposition for p-c plating in a citrate gold solution.

Initial results from the alkaline cyanide bath indicated that the measured limiting current density and rate of deposition were considerably lower than those predicted from the theory. These are shown in Fig. 10 and Fig. 11. Turner (11) suggested the possibility of chemical dissolution of gold in a solution containing a large amount of cyanide ion and oxygen. This chemical dissolution process was studied using the same rotating disk electrode arrangement. Gold was plated onto the rotating platinum cathode at -15.8 mA/cm^2

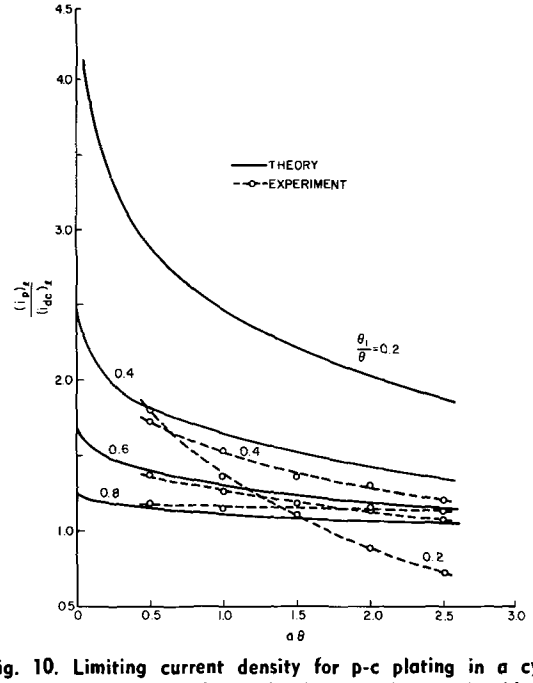

Fig. 10. Limiting current density for p-c plating in a cyanide gold solution; uncorrected for chemical dissolution of gold.

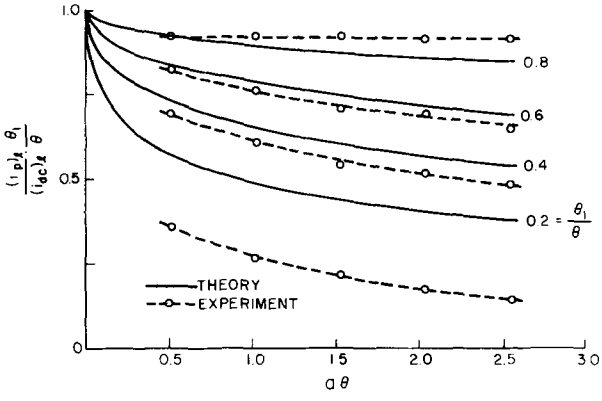

Fig. 11. Limiting over-all rate of deposition for p-c plating in a cyanide gold solution; uncorrected for chemical dissolution of gold.

and 1520 rpm for 10 min. At the end of the plating period, the electrode was disconnected electrically, but rotation was continued for 10 min to provide chemical dissolution. A stripping experiment was then performed to determine the amount of gold left on the electrode. The rate of chemical dissolution was calculated from the difference in amount of gold plated and gold stripped. The experiment was repeated changing only the rotational speed during chemical dissolution. Results are shown in Fig. 12. With this dissolution information, the results for p-c plating in the cyanide solution were corrected and shown in Fig. 13 and 14. In view of the relatively complex nature of the experiments, the agreement can also be considered to be satisfactory for the alkaline cyanide solution.

Chemical dissolution of gold in the cyanide solution is in itself an interesting problem. In an alkaline medium, the dissolution proceeds according to the reaction

$$2Au + 4CN^- + \tfrac{1}{2}O_2 + H_2O \rightarrow 2Au(CN)_2^- + 2OH^- \quad [19]$$

Little is known about the rate of this process. In the present study, the rate of this process was needed only as a correction factor. Consequently, no measurements of the oxygen concentration in the solution were made, and the present study was probably not accurate enough to calculate the reaction order and the rate constant of the dissolution process. Levich (12) discussed the application of the rotating disk electrode to study kinetics of surface reactions. Comparing

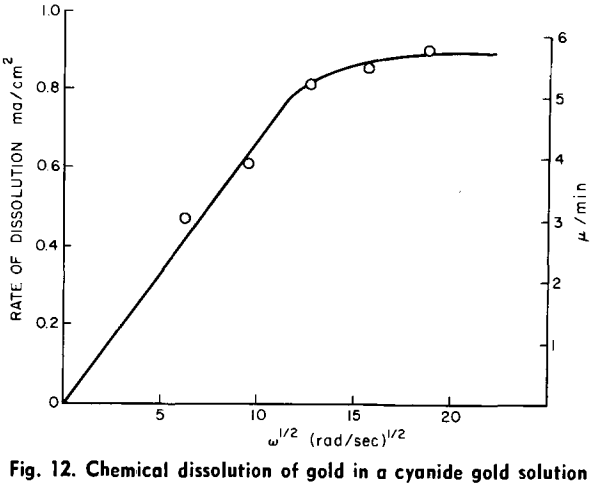

Fig. 12. Chemical dissolution of gold in a cyanide gold solution

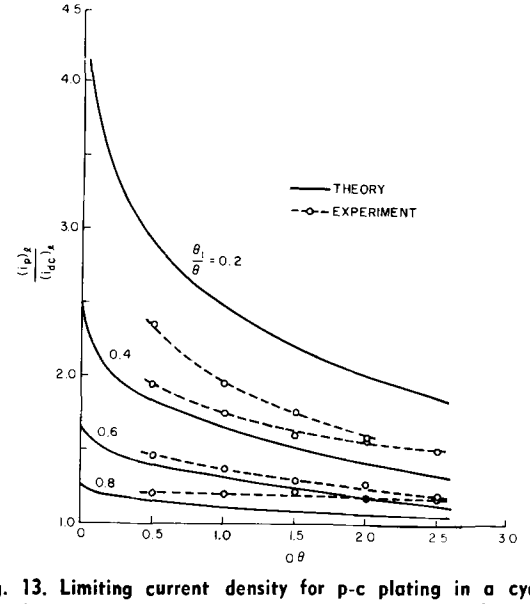

Fig. 13. Limiting current density for p-c plating in a cyanide gold solution; corrected for chemical dissolution of gold.

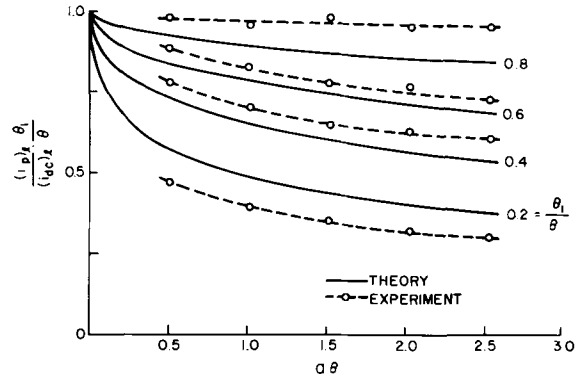

Fig. 14. Limiting over-all rate of deposition for p-c plating in a cyanide gold solution; corrected for chemical dissolution of gold.

Levich's theory and the experimental results, it can be concluded qualitatively that the chemical dissolution of gold is controlled by mass transport of oxygen at low rotational speeds, but is controlled by surface kinetics at high rotational speeds.

The only data on the diffusion coefficient of $Au(CN)_2^-$ were measured by Kakovskii *et al.* (13) in KCN solutions by the method of diffusion through a porous diaphragm. At infinite dilution the value was reported to be 1.60×10^{-5} cm²/sec at 25° C. A direct comparison of this information to the present data is not possible because of the different temperature where these data are presented. However, the difference is probably not significant.

Conclusions

A simple diffusion model was suggested to calculate the rate of deposition by p-c plating. In contrast to several claims made in the literature, the results indicate that although the limiting value of the instantaneous pulsed current for deposition can be considerably higher than that of d-c plating, the limiting over-all plating rate is lower than that of d-c plating.

Experimental investigations were carried out in three gold plating solutions. Results agree satisfactorily with the theoretical model.

The diffusion coefficient of $Au(CN)_2^-$, specific conductance, kinematic viscosity, and *p*H values for all three solutions were measured.

In conclusion, the advantage of applying pulsed current during electrodeposition is not to increase the limiting over-all plating rate but to raise the limiting current density; thereby possibly improving the physical properties through structural modifications of the electrodeposits.

Acknowledgment

The author wishes to thank D. R. Turner and P. J. Boddy for reviewing the manuscript.

Manuscript submitted Aug. 17, 1970; revised manuscript received Nov. 17, 1970.

Any discussion of this paper will appear in a Discussion Section to be published in the December 1971 JOURNAL.

LIST OF SYMBOLS

- a, a diffusion parameter, $a = \pi^2 D/4\delta^2$ (sec^{-1})
- c, concentration of the metal ion, moles/cm³
- c_i, c_o, concentration of the metal ion at the electrode-solution interface and at the bulk, respectively, moles/cm³
- D, diffusion coefficient of the metal ion, cm²/sec
- F, Faraday's constant, coulomb/equiv
- i, current density, A/cm²
- $i_{d\text{-}c}$, i_p, current density for deposition for d-c plating and for p-c plating, respectively, A/cm²
- $(i_{d\text{-}c})_l$, $(i_p)_l$, limiting current density for d-c plating and for p-c plating, respectively, A/cm²
- N, number of cycles passed during p-c plating
- n, number of electrons transferred in an electrochemical reaction
- t, time, sec

t_1, t_2, etc., time periods during p-c plating defined in Fig. 1, sec
x, distance coordinate, cm
δ, thickness of the diffusion layer, cm
θ, period of a pulsed current, sec
θ_1, θ_2, portion of the period when the current is on and portion of the period when the current is off, sec
κ, specific conductance of a solution, $ohm^{-1}\ cm^{-1}$
ν, kinematic viscosity of a solution, cm^2/sec
τ, a time parameter, $\tau = t - N\theta$, sec
ω, rotational speed, rad/sec

REFERENCES

1. G. W. Jernstedt, *Ann. Proc. Amer. Electroplaters' Soc.*, **36**, 63 (1949); **37**, 151 (1950).
2. A. P. Popkov, *J. Appl. Chem. USSR*, **39**, 1632 (1966).
3. A. M. Ozerov, N. P. Litvishko, I. N. Vavilina, P. M. Chetvertnov, and Ya. E. Zhak, *ibid.*, **40**, 1101 (1967).
4. A. Hickling, and H. P. Rothbaum, *Trans. Inst. Met. Finishing*, **34**, 53, 199 (1957).
5. A. J. Avila and M. J. Brown, Paper presented at Montreal Convention, Amer. Electroplaters' Soc., June, 1970.
6. T. R. Rosebrugh and W. L. Miller, *J. Phys. Chem.* **14**, 816 (1910).
7. H. Y. Cheh and R. Sard, To be published.
8. D. T. Napp and S. Bruckenstein, *Anal. Chem.*, **40**, 1036 (1968).
9. V. G. Levich, *Acta Physicochim. USSR*, **17**, 257 (1942).
10. D. P. Gregory and A. C. Riddiford, *J. Chem. Soc. (London)*, **1956**, 3756.
11. D. R. Turner, Private communication.
12. V. G. Levich, "Physicochemical Hydrodynamics," Prentice-Hall, Englewood Cliffs, N. J. (1962).
13. I. A. Kakovskii, A. N. Lebedev, and O. K. Shcherbakov, *Chem. Abstracts*, **69**, Abstr. No. 99994 m (1968).

The Thermodynamics and Electrode Kinetic Behavior of Nickel in Acid Solution in the Temperature Range 25° to 300°C

R. L. Cowan*,[1] and R. W. Staehle*

Department of Metallurgical Engineering, The Ohio State University, Columbus, Ohio 43210

ABSTRACT

The electrode kinetic behavior of nickel was studied by potentiokinetic, potentiostatic, and potential decay techniques in sulfate solutions of *p*H 1.3, 3.4, and 6.3 adjusted to constant 0.1*N* ionic strength by K_2SO_4 additions. The active-passive transition characteristic of the room temperature behavior of nickel was found to be absent at temperatures above 100°C. However, at temperatures above 250°C, indications of oxide formation were found although there was little contribution to passivity therefrom. In addition, the temperature stability of passive films and these oxides seems to be *p*H dependent. Theoretical potential-*p*H diagrams were also constructed for the nickel-water systems for the temperature range used in these experiments.

The vast majority of electrode kinetic data reported in the literature for aqueous solutions have been determined at 25° ± 15°C, and very few data are reported for temperatures above 100°C. In view of this state of affairs, this study was initiated to investigate systematically the effect of temperature on the electrode kinetic behavior of nickel in acid solutions through the temperature range 25° to 300°C.

Nickel was chosen as the test material for three reasons: (*i*) Nickel serves as the base element for many alloy systems used industrially for corrosion resistance at high temperatures. (*ii*) The electrode kinetic behavior of nickel at 25°C is well documented (1-11) and could serve as a useful basis for interpreting higher temperature results. (*iii*) Nickel shows an active to passive transition which is typical of many corrosion resistant industrial alloys.

The experimental work on electrode kinetics involved potentiodynamic determinations of anodic and cathodic behavior, current decay at constant potential, and potential decay. To supplement the understanding of the kinetic results, the effect of temperature on the equilibrium thermodynamic behavior of nickel-water reactions was calculated, and potential-pH diagrams were constructed over the temperature range 25°-300°C. These thermodynamic calculations are discussed first to provide a basis for interpreting the subsequent kinetic behavior.

* Electrochemical Society Active Member.
** Electrochemical Society Student Associate.
[1] Present address: Vallecitos Nuclear Center, General Electric Company, Pleasanton, California.
Key words: autoclave, corrosion, Pourbaix.

Potential—pH Diagrams

In electrochemical thermodynamics the standard hydrogen electrode (SHE) is defined as the zero potential [*i.e.*, $\mu^\circ_{H^+} = 0 \neq f(T)$] at all temperatures. The standard electrode potential, E°, of any other half-cell reaction is then given by the whole cell voltage of the cell shown in Eq. [1].

$$H_2\ (1\ atm)/H^+ || (aq., a = 1)$$
$$[\text{Half-cell in question, } a \text{ (all species)} = 1] \quad [1]$$

The standard electrode potential of such a cell is a thermodynamic quantity that can be measured accurately by experiment (12-15). Unfortunately, the determination of E° values for one reaction over a range of temperature is a long and arduous process, *i.e.*, see Greeley (16). If it is desired to construct potential-*p*H diagrams over a significant temperature range, *i.e.*, 25°-300°C, the experimental data for E°_T are not available at present for any system, and the needed data must be determined theoretically.

By using the relation $\Delta F^\circ = -nFE^\circ$, the standard electrode potential of any half-cell reaction at any temperature T can be referred to its standard value at 25°C by the use of Eq. [2], derived from thermodynamics by

Table I. Comparison of experimentally determined data of Greeley (16) for the Ag/AgCl H^+/H_2 cell to those values calculated by the method of Lewis (22) and Criss and Cobble (23-25)

T°C	$E°$ (SHE) Experimental values of Greeley	$E°$ Calculated by Lewis (assuming C_p (ion) = 0 for Eq. [2])	$E°$ (SHE) Calculated by Criss and Cobble method
25	+0.2222	—	—
50	+0.2047	+0.221	—
60	+0.1967	—	+0.196
100	+0.1600	+0.219	+0.159
150	+0.1032	+0.216	+0.101
200	+0.0348	+0.211	+0.028
250	−0.054	+0.204	−0.053
300	−0.138	+0.195	−0.145

$$\Delta F°_{T_2} = \Delta F°_{T_1} + \int_{T_1}^{T_2} \Delta C_p dT - T_2 \int_{T_1}^{T_2} \frac{\Delta C_p}{T} dT - \Delta T\, \Delta S°_{T_1} \quad [2]$$

Unfortunately, the C_p data required for Eq. [2] are not available for most ionic species (17-21) and attempts by Lewis (22) at solving it by assuming that the C_p value of ionic species are zero do not correspond with experimental data, as is shown in Table I, and the need for ionic C_p data is clear. Recently Criss and Cobble (23-25) have devised a theoretical method for solving Eq. [2]. Their method rests on what they call the "Correspondence Theory of Ionic Entropy," and their procedure (which is the one used herein) is described as follows. The absolute entropy of the hydrogen ion at 25°C, $S°_{H+}$ (25°C), is estimated to be −5.0 eu. Criss and Cobble normalize all of the literature values of the ionic entropy at 25°C to the absolute scale as follows by the relationship

$$S°_{25}\ (i,\text{abs}) = S°_{25}\ (i, \text{conventional}) - 5.0\ Z \quad [3]$$

where $S°_{25}$ (i,abs) = absolute entropy of i at 25°C, Z = ionic charge (with sign) of i, and where the conventional scale is based on $S°(H^+) = 0$ at any temperature. Criss and Cobble show that Eq. [3] is valid for any temperature, T_2.

$$S°_{T_2}\ (i,\text{abs}) = S°_{T_2}\ (i, \text{conventional}) - S°_{T_2}\ (H^+, \text{abs})\ Z \quad [4]$$

The problem then remains to relate $S°_{T_2}$ (i,abs) to $S°_{25}$ (i,abs). Criss and Cobble show that this can be done by the following relationship which they call the Correspondence Principle of Ionic Entropy.

$$S°_{T_2}\ (i,\text{abs}) = a(T_2) + b(T_2)\ S°_{25}\ (\text{abs}) \quad [5]$$

The basis for Eq. [5] rests on Criss and Cobble's analysis of the available experimental data in the literature. For each temperature T_2 they found that only one assigned value of $S°_{T_2}$ (H^+, abs) could be used in Eq. [4] to give a linear relationship between $S°_{T_2}$ (i,abs) and $S°_{25}$ (i,abs) for every ion type. An example of their analysis is shown in Fig. 1 for T_2 equaling 100°C. The Correspondence Principle does have some theoretical justification, and the reader is referred to Criss and Cobble's papers (23-25) for its discussion and justification.

To calculate values of $\Delta F°_{T_2}$ from Eq. [2] using the Correspondence Principle it is convenient, following Criss and Cobble, to use the following definitions

$$\overline{C_P}\Big|_{T_1}^{T_2} = \text{average value of the heat capacity}$$

$$\overline{C_P}\Big|_{T_1}^{T_2} = \frac{\int_{T_1}^{T_2} \overline{C_P} dT}{\int_{T_1}^{T_2} dT} = \frac{\int_{T_1}^{T_2} C_p d \ln T}{\int_{T_1}^{T_2} d \ln T} \quad [6]$$

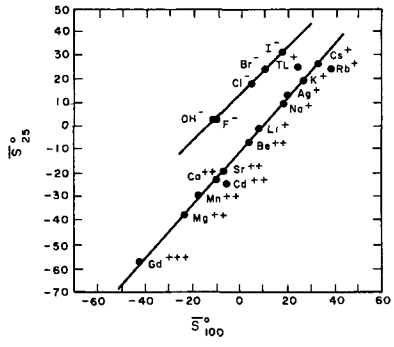

(a)

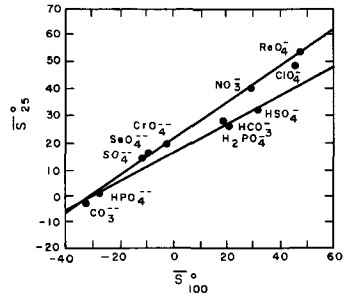

(b)

Fig. 1. Diagram illustrating the linear relationship between the absolute entropies of (a) simple cations and simple anions and (b) oxyanions and acid-oxyanions at 25° and 100°C, from Criss and Cobble (23).

Thus from Eq. [2]

$$\Delta F°_{T_2} = \Delta F°_{T_1} - \Delta T \Delta S°_{T_1} + \overline{\Delta C_p}\Big|_{T_1}^{T_2} \left[\Delta T - T_2 \ln \frac{T_2}{T_1}\right] \quad [7]$$

For nonionic species $S°$ and $C°_p$ values are easily found in handbooks such as Wicks and Block (26). For ionic species, $\overline{C_p}\Big|_{T_1}^{T_2}$ is calculated from the entropy data of Criss and Cobble by the following relation

$$\overline{C_p}\Big|_{T_1}^{T_2} = \frac{S°(T_2) - S°(T_1)}{\ln (T_2/T_1)} \quad [8]$$

To employ Eq. [7] for the calculation of potential-pH diagrams at elevated temperatures, one must write the whole cell reaction in Eq. [2] with the half-cell reaction in question written in the reduction direction. For example, if one were to consider the half-cell reaction $Ni \rightarrow Ni^{++} + 2e^-$ the whole cell reaction corresponding to Eq. [2] for use in Eq. [7] would be

$$Ni^{++} + H_2 = Ni + 2H^+ \quad [9]$$

The $\Delta F°_T$ value calculated from Eq. [7] would then be converted to $E°_T$ by using the usual relationship

$$E°_T = -\frac{1}{n\mathbf{F}} \Delta F°_T$$

If T_2 is greater than 200°C, the right-hand side of Eq. [8] will be in some error if 25°C is taken as the base temperature because of the averaging method used in Eq. [6]. To circumvent this problem the $\Delta F°$ value for 200°C should be calculated and then 200°C should be used as the base temperature T_1, when using Eq. [7] and [8]. A similar procedure should then be employed for each 50°C increment.

The question now is the validity of the method. A comparison of the $E°$ values for the Ag/AgCl half-cell reaction as calculated by the method of Criss and

Cobble and the experimentally determined values reported by Greeley (16) are shown in Table I. The agreement is excellent and suggests that it is reasonable to use for calculating $E°$ values of electrochemical reactions in aqueous solutions at elevated temperatures.

The use of C_p data to calculate $\Delta F°$ for reactions in aqueous solutions over a range of temperatures is not strictly valid since the changing vapor pressure of the solvent in a closed system causes a pressure change. This is especially true as the temperature nears the critical point. Pressure can influence the chemical equilibrium in the following three ways.

1. The activity of water will change, and this introduces an additional free energy change of the type

$$\Delta F = \int_1^P V dp$$

p = vapor pressure of H_2O at temperature T.

2. Changes of the partial molal volumes will introduce a free energy change of the type

$$\Delta F = \int_1^P \overline{\Delta V} dp$$

3. The pressure change will also affect the activity coefficients of dissolved species by

$$\frac{\delta \ln \gamma}{\delta P} = \frac{V_i \quad V_o}{2RT}$$

Criss and Cobble have shown that these effects are important, but can be ignored up to 300°C since the magnitude of the errors introduced are within the limited accuracy of the data used to formulate the Correspondence Principle.

After calculating $E°_T$ values for all of the reactions being considered for a metal-water system, the potential-pH diagram can be constructed as described by Pourbaix (27). Townsend (28) was first to adopt the method of Criss and Cobble and has recently determined the potential-pH diagram for iron at temperatures to 200°C using the method of Criss and Cobble.

The potential-pH diagrams for the nickel-water system are shown for the temperatures 25°, 60°, 100°, 150°, 200°, 250°, and 300°C in Fig. 2-5. These diagrams are based on the half-cell reactions and corresponding potential-pH equations shown in Table II. The thermodynamic data used to calculate the diagrams are shown in Table III. Because values of $S°_{25°C}$ and C_P are not reported in the literature for Ni_3O_4, Ni_2O_3, and NiO_2, values were assigned to oxides of elements nearest nickel in the periodic table with similar crystal structures and free energies of formation as is noted in

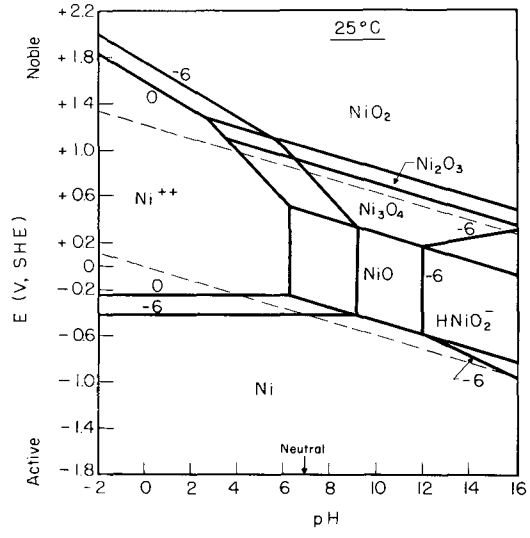

Fig. 2. Potential-pH diagram of nickel-H_2O system at 25°C

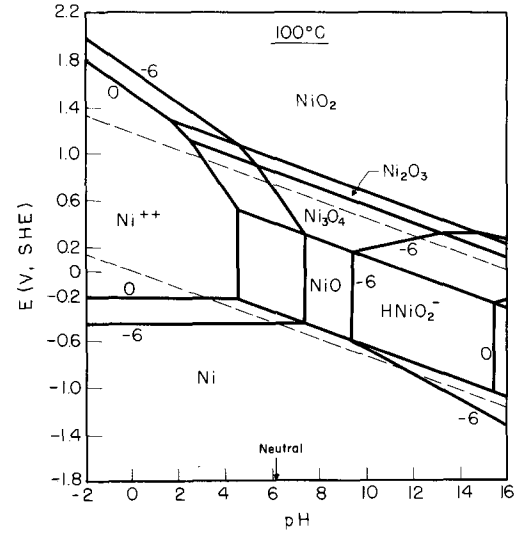

Fig. 3. Potential-pH diagram of nickel-H_2O system at 100°C

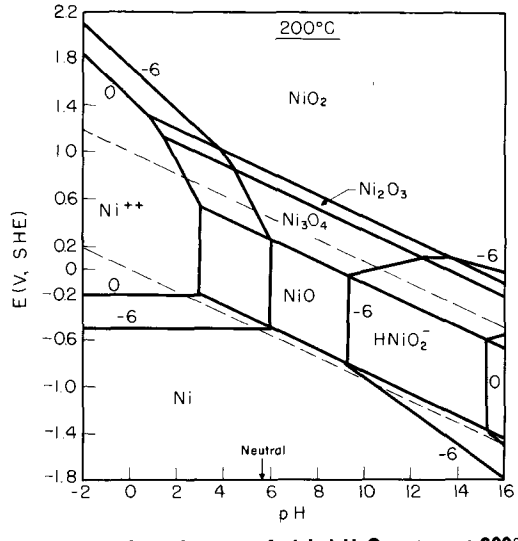

Fig. 4. Potential-pH diagram of nickel-H_2O system at 200°C

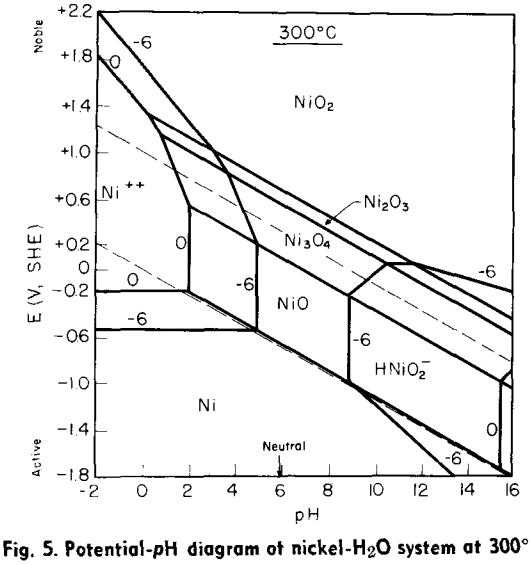

Fig. 5. Potential-pH diagram of nickel-H_2O system at 300°C

Table III. The calculated values of $E°_T$ of the different reactions are listed in Table IV, and it is these values that were used in the equations in Table II to construct the potential-pH diagrams at the different temperatures. The lower dotted line in these diagrams in-

Table II. List of reactions for Ni-H_2O system and corresponding pH dependence of E

(a) $H_2 = 2H^+ + 2e^-$	$E_T = 0 - \frac{2.3RT}{F} pH - \frac{2.3RT}{2F} \log p\ (H_2)$
(b) $2H_2O = O_2 + 4H^+ + 4e^-$	$E_T = E°_T - \frac{2.3RT}{F} pH + \frac{2.3RT}{4F} \log p\ (O_2)$
1. $Ni = Ni^{++} + 2e^-$	$E_T = E°_T + \frac{2.3RT}{2F} \log [Ni^{++}]$
2. $Ni + H_2O = NiO + 2H^+ + 2e^-$	$E_T = E°_T - \frac{2.3RT}{F} pH$
3. $Ni^{++} + H_2O = NiO + 2H^+$	$\log [Ni^{++}] = + \frac{\Delta F°_T}{2.3RT} - 2pH$
4. $Ni + 2H_2O = HNiO_2^- + 3H^+ + 2e^-$	$E_T = E°_T - \frac{3}{2} - \frac{2.3RT}{F} pH + \frac{2.3RT}{2F} \log [HNiO_2^-]$
5. $NiO + H_2O = HNiO_2^- + H^+$	$\log [HNiO_2^-] = - \frac{\Delta F°_T}{2.3RT} + pH$
6. $3NiO + H_2O = Ni_3O_4 + 2H^+ + 2e^-$	$E_T = E°_T - \frac{2.3RT}{F} pH$
7. $2Ni_3O_4 + H_2O = 3Ni_2O_3 + 2H^+ + 2e^-$	$E_T = E°_T - \frac{2.3RT}{F} pH$
8. $Ni_2O_3 + H_2O = 2NiO_2 + 2H^+ + 2e^-$	$E_T = E°_T - \frac{2.3RT}{F} pH$
9. $3Ni^{++} + 4H_2O = Ni_3O_4 + 8H^+ + 2e^-$	$E_T = E°_T - \frac{4(2.3)RT}{F} pH - \frac{3(2.3)RT}{2F} \log [Ni^{++}]$
10. $2Ni^{++} + 3H_2O = Ni_2O_3 + 6H^+ + 2e^-$	$E_T = E°_T - \frac{3(2.3)RT}{F} pH - \frac{2.3RT}{F} \log [Ni^{++}]$
11. $Ni^{++} + 2H_2O = NiO_2 + 4H^+ + 2e^-$	$E_T = E°_T - \frac{2(2.3)RT}{F} pH - \frac{2.3RT}{2F} \log [Ni^{++}]$
12. $3HNiO_2^- + H^+ = Ni_3O_4 + 2H_2O + 2e^-$	$E_T = E°_T + \frac{2.3RT}{2F} pH - \frac{3(2.3)RT}{2F} \log [HNiO_2^-]$

Table III. Thermodynamic data used for calculation of potential-pH diagram. From Wicks and Block (26), Pourbaix (27), and Circular 500 (44)

Species	$°_{298}$, cal/mole	$C_p(T)$, cal/°K	$S°_{25°C}$ (H − 0 scale)	$S°_{25(abs)} = S°_{25-5\,oz}$*
H_2	0	$6.52 + 0.78 \times 10^{-3}T + 0.12 \times 10^5 \times T^{-2}$	31.22	31.22
O_2	0	$7.16 + 1.00 \times 10^{-3}T - 0.40 \times 10^5 \times T^{-2}$	49.01	49.01
H_2O	−56,690	18.04	16.75	16.75
OH^-	0	—	−2.519	−2.481
H^+	0	—	0	−5.0
Ni	0	$4.06 + 7.04 \times 10^{-3}$	7.12	7.12
Ni^{++}	−11,530	—	38.1	−48.1
NiO	−51,300	298°K to 525°K − $4.99 + 37.58 \times 10^{-3}T + 3.89 \times 10^5T^{-2}$ 525°K to 565 13.88 565 to 1,800°K − $12.63 + 30.4 \times 10^{-3}T + 4.09 \times 10^5T^{-2}$	9.08	9.08
$HNiO_2^-$	−83,465	—	*10.0	15.0
Ni_3O_4	−170,150	**$30.84 + 17.08 \times 10^{-3}T - 5.72 \times 10^5T^{-2}$	**35.66	35.66
Ni_2O_3	−112,270	†$23.49 + 18.60 \times 10^{-3}T - 3.55 \times 10^5T^{-2}$	†21.5	21.5
NiO_2	−51,420	‡$16.60 + 2.44 \times 10^{-3}T - 3.88 \times 10^5T^{-2}$	‡12.68	12.68

* From $S°(25) = 43.5 - 46.5\,(Z - 0.28n)$ where: Z = No. of unit charges/ion and n = No. of oxygen ions (exclusive of hydroxyl group). Taken from Connick & Powell (45).

** $S°_{25°C}$ and C_p data for Ni_3O_4 have not been determined experimentally so they were assigned the values of CO_3O_4 which has the same crystal structure and is its nearest neighbor in group VIII of the periodic table: $\mu(Ni_3O_4) \cong \mu(CO_3O_4)$.

† $S°_{25°C}$ and C_p values for Ni_2O_3 have not been determined and they were assigned the values of Fe_2O_3.

‡ $S°_{25°C}$ and C_p values of NiO_2 are not known so the values of MnO_2 were assigned.

Table IV. Calculated values of $E°_T$ for the different reactions

Reaction No.	$E°_{298°K}$	$E°_{323°K}$	$E°_{373°K}$	$E°_{423°K}$	$E°_{473°K}$	$E°_{523°K}$	$E°_{573°K}$
(a)	0	0	0	0	0	0	0
(b)	+1.228	+1.200	+1.167	+1.127	+1.092	+1.056	+1.0175
1	−0.250	−0.239	−0.229	−0.216	−0.212	−0.202	−0.189
2	+0.116	+0.104	+0.091	+0.075	+0.062	+0.048	+0.034
3*	pH = +9.20	pH = +8.21	pH = +7.33	pH = +6.47	pH = +5.93	pH = +5.42	pH = +4.97
4	+0.648	+0.6517	+0.663	+0.690	+0.779	+0.828	+0.889
5*	pH = +11.98	pH = +10.55	pH = +9.43	pH = +8.65	pH = +9.25	pH = +8.94	pH = +8.95
6	+0.876	+0.860	+0.842	+0.822	+0.811	+0.794	+0.779
7	+1.305	+1.298	+1.291	+1.280	+1.266	+1.254	+1.241
8	+1.434	+1.420	+1.405	+1.388	+1.378	+1.363	+1.350
9	+1.977	+1.893	+1.804	+1.697	+1.637	+1.548	+1.465
10	+1.753	+1.695	+1.633	+1.558	+1.513	+1.450	+1.391
11	+1.593	+1.557	+1.519	+1.474	+1.446	+1.407	+1.370
12	−0.718	−0.781	−0.872	−1.023	−1.329	−1.539	−1.778

* pH values for ion concentrations = 10^{-6} moles/liter and coexistence of condensed phase.

dicates the H^+/H_2 equilibrium for $p_{H_2} = 1$ atm and the upper dotted line indicates the $2H_2O = O_2 + 4H^+ + 4e^-$ equilibrium for $P_{O_2} = 1$ atm. The solid lines indicate the coexistence between the nickel species. The activities of condensed phases were chosen as unity. Lines shown for coexistence between solid and ionic species are given for ionic activities of both unity and 10^{-6}M.

The most significant feature of these diagrams is the increasing stability of the nickel oxides in the acid range with increasing temperature. The range of pH over which the oxides are stable reaches a minimum at about 100°C and then increases with increasing temperature. At the high pH end of the diagram, the range of stability of the nickel oxy-anion, $HNiO_2^-$, increases greatly with increasing temperature. The absolute value of the slope, dE/dpH, of all lines increases with increasing temperature by the term $2.3RT/n\mathbf{F}$ from the Nernst equation. On each diagram, the neutral pH of pure water for the given temperature is indicated.

From a corrosion point of view, the range of stability of NiO as a potentially protective oxide film has shifted from a pH range of 9-12 to a pH range of 5-9. Thus, with increasing temperature, a basic pH that could have been quite protective at low temperatures might give rise to larger corrosion rate at high temperatures, especially if excess oxygen were present to raise the potential substantially above the hydrogen equilibrium potential. The diagrams also show that if the predominant reduction reaction is hydrogen ion discharge, the corrosion potential at 300°C will be such that corrosion of nickel will be impossible between the pH values of 5 and 10. The driving force for corrosion in this case will also be very small for the pH ranges 2-5 and 10-13, and lower rates should be expected. This observation probably explains the excellent corrosion performance of nickel base alloys (*e.g.*, Inconel 600) in pressurized water nuclear reactors that are overpressured with hydrogen gas and operated in the pH range 7-10. At 300°C in high pH solutions (>10) the $HNiO_2^-$ ion is the only species stable over the range of potential of water stability. This fact might in part explain the susceptibility to stress corrosion cracking of high nickel alloys in caustic solutions. Protective films formed at lower temperatures, when ruptured by stress, offer sites for rapid dissolution.

The detailed application and significance of potential-pH diagrams such as the one calculated here should be applied with some caution. The limitations therein are well known. For example, it is well known (1-11) that the region of thermodynamic stability of Ni^{++} at 25°C on a potential-pH diagram actually exhibits a wide range of effective passivity. The kinetic data reported in this study for the room temperature range are in agreement with these findings. However, the fundamental basis for passivity which produces this "anomalous" passivity is far from clear at present.

Experimental

The experimental system for obtaining kinetic data consisted of a high-temperature electrochemical cell and the supporting instrumentation necessary for electrode kinetic measurements. A schematic diagram of the experimental system is shown in Fig. 6. Electrochemical kinetic measurements in aqueous solutions at elevated temperatures are difficult for two reasons. First, the high pressure (over 1000 psi at 300°C) requires special seals and a high strength vessel. This is usually solved by some type of autoclave arrangement (29-34). The second problem is finding a suitable reference electrode arrangement that will give a half-cell potential that is thermodynamically meaningful (32-38).

Cell design.—A standard one liter double ended autoclave supplied by Autoclave Engineers (Erie, Pennsylvania) served as the electrochemical cell. The cell was constructed of Hastelloy B and employed a high-purity alumina liner to insure that corrosion from

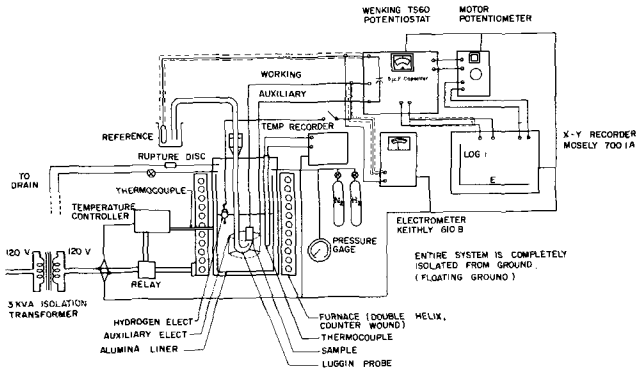

Fig. 6. Schematic diagram of experimental system used for high-temperature electrochemical measurements.

the hot solutions would neither harm the structural integrity of cell nor contaminate the test solution. Conax fittings were installed in the top head of the autoclave to seal the electrodes and thermocouple. Fittings were also provided on the body for the pressure gauge, rupture disk assembly, and gas inlet and outlet. The cell was heated by a 3 kW anti-induction wound resistance heater. A temperature controller regulated the outside temperature of the autoclave using a thermocouple held firmly against the autoclave wall by a spring. The temperature within the autoclave was controlled constant to within ±1°C. However, temperatures were only reproducible to ±5°C. The solution temperature was measured with a tantalum sheathed iron-constantan thermocouple. At temperatures below 100°C, the heat transfer characteristics of the cell were such that the temperature of the solution could not be controlled effectively, and all data below 100°C were obtained using a glass cell.

Electrode design.—The hydrogen electrode was a 1 in. piece of platinized platinum, replatinized for each run, suspended from a silica float as described by Greeley (36). The electrode could then "see" both the solution phase and the gas phase. The working electrode design was similar to that described by Wilde (32-33). The nickel specimen is the only metallic part of the electrode assembly that "sees" the solution. The nickel sample was a ¼ x ½ in. cylinder. The sample was screwed snugly to a rod and then was pulled tightly against a Teflon washer and alumina support tube. The Luggin probe solution bridge assembly was similar in design to those described by others (31-34). The probe was made of clear quartz capillary tubing. An external reference electrode of saturated calomel was used. Thus, it was possible to compare the behavior of an internal and external reference. To establish ionic conduction to the reference electrode during the low temperature experiments, a 200 psi overpressure of nitrogen was admitted to the cell to force solution through the cellulose plug. A thread was used in the Luggin probe to act as a wick to maintain electrolytic conductor through bubbles that sometimes formed in the lower temperature (but high-pressure) part of the bridge. A piece of 45 mesh platinum gauze 1 in. in width and 2¾ in. diameter served as the auxilliary electrode.

Electronic apparatus.—A Wenking potentiostat (Model 66TS10) was used for all potentiostatic work. For potentiokinetic scans, a Wenking motor potentiometer was employed to drive the potentiostat. Polarization curves were recorded directly on a Mosley 7601A recorder. Although shielded twisted cable was used in all electrical leads as well as the other usual precautions, a-c pickup on all electrodes was a major difficulty and caused instability in the potentiostat. A combination of an isolation transformer and 10 μF capacitive shunt between the reference and auxiliary electrode terminal solved the problem. A Keithley

610B electrometer and L&N potentiometer were used for potential measurements. The thermocouple output voltage from inside the cell was monitored throughout each test by a recorder.

Test materials.—Nickel 270 (99.97% Ni) supplied by the International Nickel Company was used in all experiments. The nickel stock material was solution annealed at 1090°C for 1 hr to assure homogeneity. Tests solutions were prepared from distilled water, analytical grade sulfuric acid and analytical grade potassium sulfate. The composition of these solutions was as follows:

pH 1.3	$0.050N$ H_2SO_4 + $0.05N$ K_4SO_4
pH 3.4	$0.001N$ H_2SO_4 + $0.099N$ K_4SO_4
pH 6.3	0.100 K_4SO_4

The hydrogen used to saturate the solution and the atmosphere over the solution was ultra high purity and contained less than 1 ppm O_2. The nitrogen used to provide overpressure contained less than 1 ppm O_2.

Experimental procedure.—The nickel specimens were degreased in acetone, rinsed copiously in distilled water, and polished successively with 280, 400, and 600 grit paper. The specimen was then screwed to the working electrode. The Luggin probe was adjusted until the tip was 1 mm away from the sample. A piece of filter paper was ground and wet with the test solution and then used as packing for the solution bridge assembly. The head and all fittings were tightened into place, and the system was pressure tested with nitrogen. Hydrogen was then bubbled through the test solution for twelve hours by means of a Hastelloy-B capillary inserted in the thermocouple fitting. The thermocouple was replaced and the plenum was flushed with hydrogen to remove the last tracers of oxygen. If the run was to be at a temperature below 175°C, a 200 psi of nitrogen was introduced to provide sufficient pressure across the cellulose plug to assure proper operation of the solution bridge. A glass solution bridge connected the solution bridge assembly to the calomel reference electrode which was maintained at 25°C and room pressure.

Results and Discussion

Measurement of potential.—To insure that the results determined in the high-temperature electrochemical cell were the same as those obtained by the conventional glass cell, the anodic polarization curve of Ni 270 was determined in each system at 25°C in $1N$ H_2SO_4. The two curves were practically identical, especially in the passive region, except that the curve determined in the autoclave was displaced in the noble direction by about 70 mV on the potential axis. This behavior was expected since the potential of the sample in the autoclave was measured through the high-pressure salt bridge by a standard calomel electrode at ambient pressure. This increment in potential is produced by the streaming potential and junction potential resulting from the 200 psi internal pressure acting across the cellulose plug.

Since it is desirable to avoid gross inaccuracies in the measurement of potentials over the range of experimental conditions, a standard procedure was developed for adjusting experimentally measured potentials. This procedure involves using a calculated correction obtained as follows. Since the hydrogen activity of the solution was known by the pH of the solution ($pH = -\log a_H$) and the partial pressure of hydrogen in the cell was set at 1 atm, the redox potential of the hydrogen electrode could be calculated by the Nernst equation.

$$E(H^+/H_2, \text{calc.}) = 0 - \frac{2.3RT}{nF} \log \frac{(pH_2)^{1/2}}{a_{H^+}} \quad [10]$$

Thus, the measured corrosion potential of the nickel electrode could be changed to the standard hydrogen scale by

$$E_{corr} = E(\text{corr, meas.}) - E(H^+/H_2, \text{meas.}) + E(H^+/H_2, \text{calc.}) \quad [11]$$

where:

E_{corr} = true corrosion potential on the SHE scale

E(corr, meas.) = corrosion potential of the nickel sample in the autoclave as measured through the solution bridge

$E(H^+/H_2, \text{meas.})$ = hydrogen redox potential of the floating hydrogen electrode as measured through the solution bridge

$E(H^+/H_2, \text{calc.})$ = calculated hydrogen redox potential from Eq. [1].

When the corrosion potential determined for nickel in the autoclave was adjusted by this calculation it agreed within 5 mV [E_{corr} (autoclave) = −0.045V, (SHE) of the value as determined in the glass cell (E_{corr} (glass cell) = −0.040V, SHE)] in which there was neither a streaming potential nor significant junction potential in the salt bridge.

This same technique was used to determine the corrosion potential on the standard hydrogen scale in the tests at elevated temperatures. Equation [10] was calculated for the temperature and pH of the test. Then $E(H^+/H_2, \text{calc})$, E_{corr} (measured) and $E(H^+/H_2, \text{measured})$ were substituted into Eq. [11] to determine the actual value of E_{corr} on the SHE scale at the test temperature. Using this technique, the corrosion potential, and thus the potentials of the polarization curves were on the same thermodynamically meaningful scale, SHE at T, as the calculated potential-pH diagrams. This technique for correcting measured potentials assumes that a_{H^+} and pH_2 do not change with temperature, *i.e.*, in this calculation we assume that a_{H^+} calculated at 25°C pH and $pH_2 = 1$ do not change with temperature. Greeley (36) has shown that indeed there are some small changes in a_{H^+} and pH_2 with temperature for a closed hydrogen saturated acid solution. However, since these two quantities are in the log term of Eq. [10], small changes should not affect $E(H^+/H_2, \text{calc.})$ appreciably.

Values of E_{corr} (measured), $E(H^+/H_2, \text{measured})$, $E(H^+/H_2$ calculated) and E_{corr} for the different test pH's and temperatures are given in Table V. These

Table V. Calculation of the corrosion potential on the SHE scale at the test temperature from Eq. [11]

Temp, °C	$E(H^+/H_2$, meas) SHE at 25°C	$E(H^+/H_2$, calc) SHE at temp	E_{corr} (meas) SHE at 25°C	E_{corr} SHE at temp
		pH 1.3		
25	−0.082	−0.0766	−0.040	−0.040
50	−0.082	−0.0829	−0.070	−0.071
75	−0.079	−0.0894	−0.100	−0.100
97	−0.049	−0.0951	−0.087	−0.133
128	−0.109	−0.1030	−0.158	−0.152
150	−0.063	−0.109	−0.100	−0.146
197	−0.118	−0.121	−0.183	−0.188
250	−0.088	−0.134	−0.173	−0.219
298	−0.098	−0.147	−0.178	−0.227
		pH 3.4		
25	−0.222	−0.200	−0.219	−0.197
50	−0.229	−0.217	−0.223	−0.211
75	−0.223	−0.234	−0.224	−0.235
106	−0.321	−0.255	−0.321	−0.255
124	−0.247	−0.267	−0.244	−0.264
150	−0.200	−0.284	−0.196	−0.288
180	−0.257	−0.304	−0.255	−0.302
208	−0.204	−0.323	−0.231	−0.350
255	−0.223	−0.355	−0.224	−0.356
300	−0.128	−0.385	−0.123	−0.382
		pH 6.3		
25	−0.363	−0.371	−0.346	−0.354
50	−0.402	−0.402	−0.411	−0.411
75	−0.427	−0.433	−0.423	−0.430
102	−0.270	−0.367	−0.271	−0.468
129	−0.385	−0.501	−0.391	−0.495
155	−0.228	−0.532	−0.227	−0.531
203	−0.118	−0.593	−0.116	−0.591
257	−0.106	−0.660	−0.104	−0.658
288	−0.034	−0.698	−0.032	−0.697
301	−0.207	−0.715	−0.205	−0.713

are the initial values measured after 1 hr at the test temperature. One noticeable feature in Table V is that there is very little difference between $E(H^+/H_2$, measured) and E_{corr} (measured) at every pH and temperature. This is surprising since nickel has a relatively active standard potential of $E^\circ = -0.250$; E_{corr} should lie somewhere between $E(H^+/H_2)$ and $E(Ni^{++}/Ni)$. However, the Ni/Ni^{++} half-cell reaction is quite irreversible, having a relatively low i_o value and thus behaves approximately as a hydrogen redox electrode in acid solutions (27). With increasing pH, the difference between $E(H^+/H_2)$ and $E(Ni/Ni^{++})$ also decreases owing to the pH dependence of the former. In addition, as the temperature increases, the E° values of nickel changes in the positive direction with respect to the SHE, and thus one would expect the corrosion potential to remain near the hydrogen redox potential. Both of these effects are shown in the potential-pH diagrams.

Polarization behavior.—The polarization behavior of nickel 270 was determined in dilute H_2SO_4-K_2SO_4 solutions of pH 1.3, 3.4, and 6.3 over the temperature range 25°-300°C. The polarization curves were determined by the potentiokinetic technique at a scan rate of 2000 mV/hr. Anodic curves were determined in both the active to noble and noble to active directions while the cathodic curves were determined only in the noble to active direction. Figures 7 to 11 show the data obtained at pH 1.3. Both active-noble and noble-active anodic scans are shown at pH 1.3 since substantial differences between the two were observed. Figures 12 to 15 show the active-noble anodic scans determined at pH 3.4 and 6.3. The noble to active anodic curves

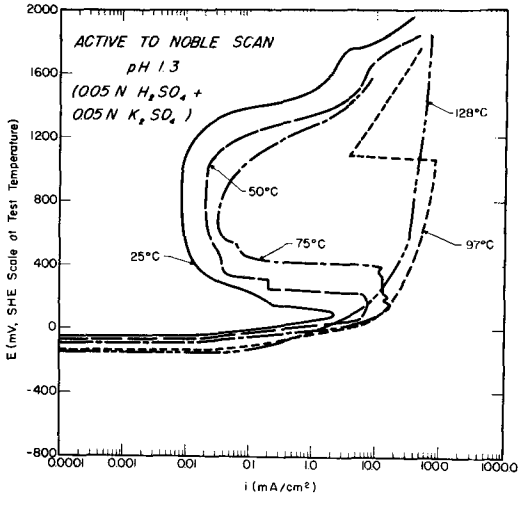

Fig. 7. Anodic polarization behavior of nickel 270 in the active to noble scan mode at 25°, 50°, 75°, 97°, and 128°C at a scan rate of 2000 mV/hr in pH 1.3 solution.

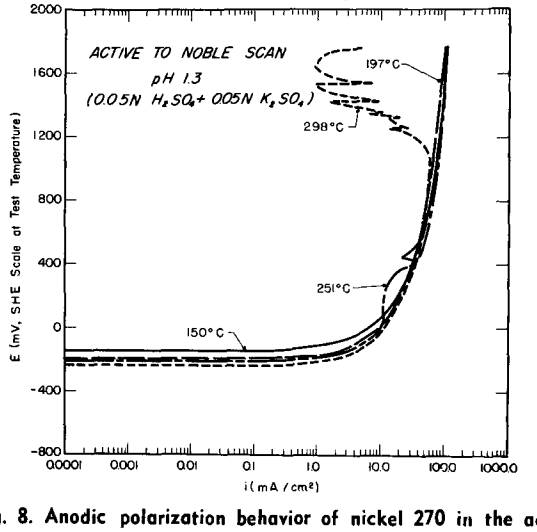

Fig. 8. Anodic polarization behavior of nickel 270 in the active to noble scan mode at 150°, 197°, 271°, and 298°C at a scan rate of 2000 mV/hr in pH 1.3 solution.

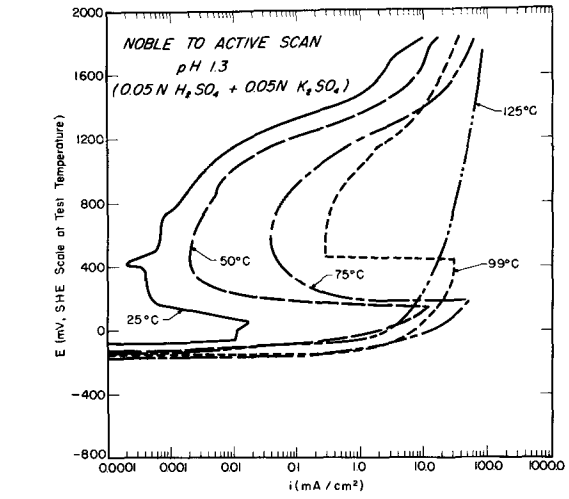

Fig. 9. Anodic polarization behavior of nickel 270 in the noble to active scan mode at 25°, 50°, 75°, 99°, and 125°C at a scan rate of 2000 mV/hr in pH 1.3 solution.

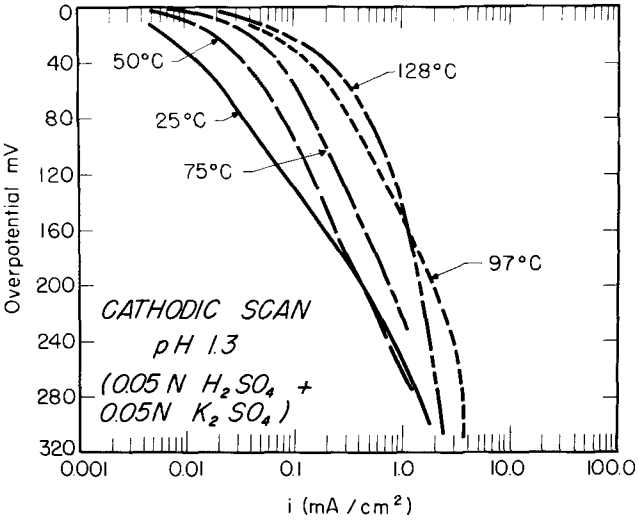

Fig. 10. Cathodic polarization behavior of nickel 270 in the noble to active scan mode at 25°, 50°, 75°, 97°, and 128°C at a scan rate of 2000 mV/hr in pH 1.3 solution.

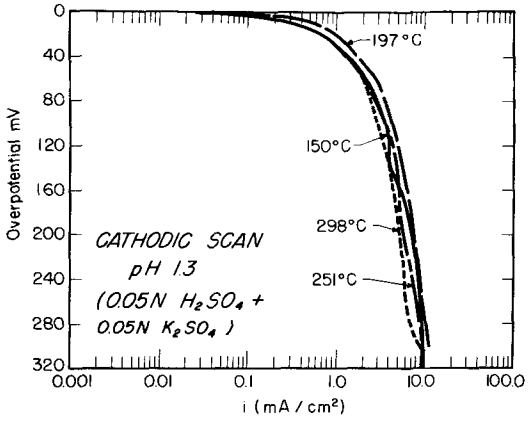

Fig. 11. Cathodic polarization behavior of nickel 270 in the noble to active scan mode at 150°, 197°, 251°, and 298°C at a scan rate of 2000 mV/hr in pH 1.3 solution.

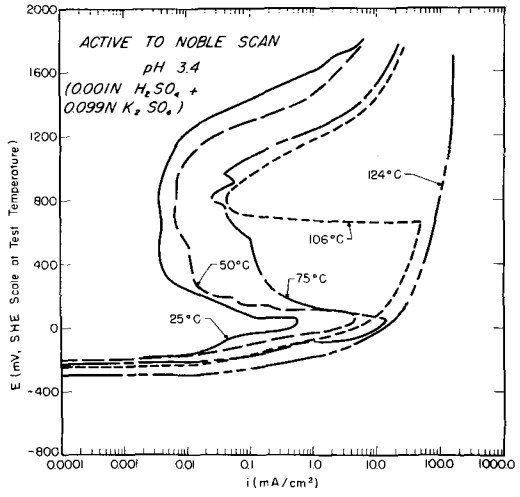

Fig. 12. Anodic polarization behavior of nickel 270 in the active to noble scan mode at 25°, 50°, 75°, 106°, and 124°C at a scan rate of 2000 mV/hr in pH 3.4 solution.

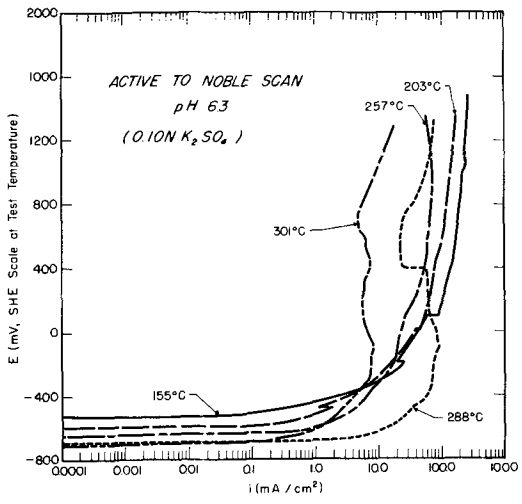

Fig. 15. Anodic polarization behavior of nickel 270 in the active to noble scan mode at 155°, 203°, 257°, 288°, and 301°C at a scan rate of 2000 mV/hr in pH 6.3 solution.

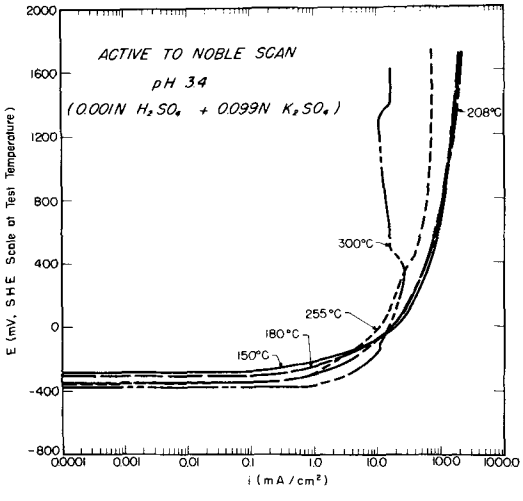

Fig. 13. Anodic polarization behavior of nickel 270 in the active to noble scan mode at 150°, 180°, 208°, 255°, and 300°C at a scan rate of 2000 mV/hr in pH 3.4 solution.

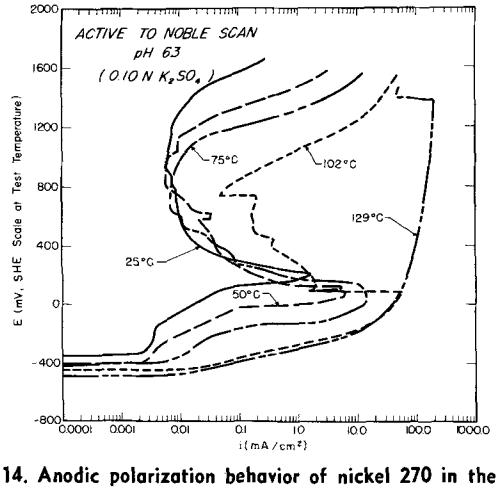

Fig. 14. Anodic polarization behavior of nickel 270 in the active noble scan mode at 25°, 50°, 75°, 102°, and 129°C at a scan rate of 2000 mV/hr in pH 6.3 solution.

were quite similar and are therefore omitted. The reduction kinetics are included for the pH 1.3 case, Fig. 10 and 11, but for brevity are omitted for the other two solutions.

The most significant feature of the anodic polarization curves is the abrupt loss of an active to passive transition at temperatures in the range of 100°-150°C. The exact temperature at which passivity is no longer apparent is a function of both the scan direction and the solution pH. For a given pH the noble to active scan shows remnants of passivity at slightly higher temperatures than the active to noble scan, as shown in Fig. 7 and 9. The temperature at which passivity breaks down increases with increasing pH, although the effect is not a strong one. There is a noticeable hysteresis effect between the active-to-noble and the noble-to-active scans in the passive region at the lower temperatures. The passive current density is about an order of magnitude smaller for the noble-to-active scan at the same pH and temperature. Osterwald and Uhlig (8) found this same effect for nickel in 1*N* H_2SO_4 at 40°C. At the temperatures where passivity is no longer present, the potentiostatic curves obtained in both scanning directions are virtually the same.

As the temperature is increased above that at which passivity is no longer present, the anodic curves have the shape expected for a diffusion-controlled process. However, as temperatures approach 300°C the current density in this region begins to decrease. This latter behavior can be explained by the potential-pH plots in Fig. 2 to 5. With increasing temperature at a given pH, the range of stability of the bulk oxides increases with increasing temperature. Thus, the slight but significant reduction of limiting current density above a certain critical temperature can be attributed to the formation of bulk oxide on the surface. The temperature at which the current reaches a maximum decreases in going from pH 3.4 to pH 6.3 as would be expected from the potential-pH diagrams. For the experiments at pH 1.3 the bulk oxides are not stable over the temperature range except for the 300°C case at high potentials where we see the expected drop in current as an oxide is formed. Note that the potential-pH diagrams tell only whether an oxide phase is stable and provide no information as to the reduction of anodic current density. The exact conditions for the onset of passivity will depend on the local Ni^{++} concentration close to the surface. Since the concentrations are generally high at high potentials, precipitation of an insoluble product would be expected somewhat earlier than predicted from bulk concentration. Qualitatively, the diagrams do agree well with the experimental results.

The temperatures above which passivity was no longer observed is shown below as a function of pH and scan direction

pH	Active to noble, °C	Noble to active, °C
1.3	100	125
3.4	125	150
6.3	130	155

Since the results from potentiokinetic experiments are not exact relative to potentiostatic measurements, the above values should be taken as approximate. It is clear however that a critical temperature for loss of passivity does exist and is in the range of 75°-150°C. Myers *et al.* (11) have reported an inflection point in the Arrhenius plot of log minimum passive current density. This inflection point is a function of *p*H and is characterized by the equation $1/T \times 10^3 = -0.11$ pH + 3.04. The inflection point calculated for the *p*H values of the experiments reported herein would be T(pH 1.3) = 72°C, T(pH 3.4) = 102°C, and T(pH 6.3) = 153°C, which is the range of temperature at which passivity is no longer observed.

An Arrhenius plot of the current density at a constant potential of +0.800V SHE for the active to noble anodic scans is shown in Fig. 16. This potential is well into the passive region for all three solutions at 25°C. Above the critical temperature, the current density required to maintain the potential of +0.800V SHE increases two orders of magnitude. Obviously, there are separate processes operating over the experimental temperature range at the lower temperatures where passivity is present the kinetics seem to be activation controlled (although the data have too much scatter for the determination of a significant value for the activation energy). At the higher temperatures, the anodic current is insensitive to temperature over a broad range and may be indicative of a diffusion-controlled process. At the highest temperatures the current decreases with increasing temperature. A possible explanation for this latter behavior will be presented in conjunction with the potential decay measurements.

The corrosion current, i_{corr}, was determined by extrapolation of the cathodic Tafel region to the corrosion potential. These corrosion currents are plotted *vs.* $1/T$ in Fig. 17 and an activation energy of $\Delta G^* = +3.30 \times 10^{+3}$ cal/mole is obtained. The process to which the ΔG^* refers may be deduced by recalling that the corrosion potential was very close to the hydrogen equilibrium potential as shown in Table V. Thus the corrosion current density is approximately equal to the exchange current density for the reaction $H_2 = 2e^- + 2H^+$ on the nickel surface. The exchange current density is as follows

$$i_o = z\mathbf{F}fC_sV_L \exp(-\Delta G^*/RT) \qquad [12]$$

Assuming that f, C_s, and V_L are not a function of temperature

$$\frac{\log i_o}{1/T} = -\frac{\Delta G^*}{R} \qquad [13]$$

Thus, a plot of log i_{corr} *vs.* $1/T$ for the case of nickel should give a straight line of slope $= -\Delta G^*/R$ where ΔG^* will be the activation energy for the hydrogen redox reaction on nickel. The best straight lines through the points of each *p*H give the same slope, each line displaced from the other slightly with the *p*H 1.3 line being uppermost and the *p*H 6.4 line being lowest. This behavior agrees with Eq. [12] in that C_s, the hydrogen ion concentration in the double layer, will be less at the higher *p*H values and thus the curve should be displaced down for higher pH values. The activation energy calculated by the slope of the lines is $\Delta G^* = +3.30 \times 10^{+3}$ cal/mole. This compares fairly well with the value $\Delta G^* = 5.7 \times 10^{+3}$ cal/mole for the hydrogen reaction on nickel in 0.12*N* NaOH as determined by Bockris and Potter (39).

The reproducibility of polarization results was excellent. The anodic active-to-noble curves determined at 25°C agree within the scatter of the data of previous investigations (1-11). The curves determined at 25°C were the object of a rather intense study of the reproducibility of the polarization behavior. If the same sample was used for repeated curves at the same *p*H, the curves were identical. If different samples were used, the passive region was still identical, but the active region showed some variation. This type of behavior has been found by others in nickel (7) as well as in iron (40) and stainless steel (41). Since the object of this research was to characterize the effect of temperature on the polarization response of nickel at different temperatures, only selected checks of reproducibility were made. One of these checks involved determining the anodic polarization behavior of one sample in the same solution from 25° to 300°C. The anodic polarization curve was determined at one temperature; the temperature was then increased and

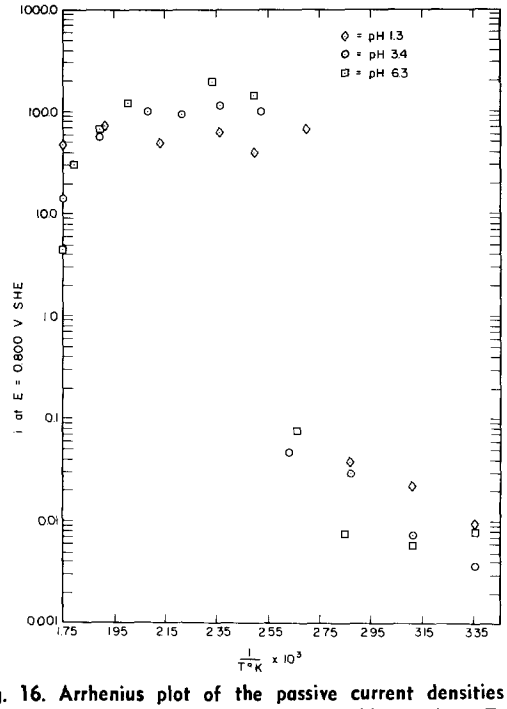

Fig. 16. Arrhenius plot of the passive current densities in the active to noble anodic scans at $E = 0.800$V SHE at T for the three different solutions.

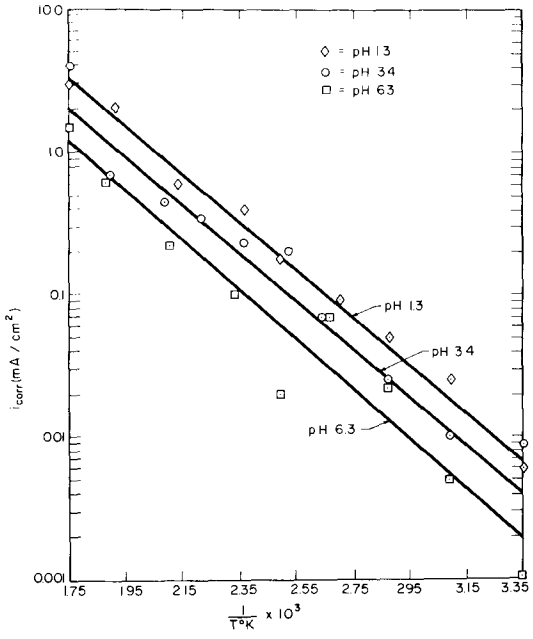

Fig. 17. Arrhenius plot of the corrosion current densities for the three different solutions as determined from the cathodic polarization curves.

Table VI. Summary of constant potential and potential decay experiments

Temp, °C	E_{corr}, V, SHE at T	$E_{polarization}$, V, SHE at T	$i(t =$ 30 sec), mA/cm²	$i(t =$ 30 min), mA/cm²	i_p(potentiokinetic minimum, mA/cm²
			pH 1.3		
22	−0.040	+0.760	+0.047	+0.007	+0.008
54	−0.072	+0.698	+0.082	+0.028	+0.023
75	−0.100	+0.678	+0.820	+0.160	+0.035
100	−0.135	+0.630	+62.0	+64.0	+4.0
200	−0.190	+0.530	+63.0	+63.0	+100.0
301	−0.230	+0.430	+40.5	+45.0	+100.0
			pH 3.4		
22	−0.195	+0.508	+0.031	+0.0031	+0.035
55	−0.215	+0.493	+0.037	+0.0058	+0.007
79	−0.240	+0.510	+0.073	+0.026	+0.025
97	−0.250	+0.520	+0.530	+0.130	+0.045
120	−0.261	+0.524	+65.0	+65.0	+160.0
298	−0.380	+0.120	+12.0	+2.2	+10.0
			pH 6.3		
22	−0.350	+0.506	+0.016	+0.004	+0.006
54	−0.415	+0.489	+0.049	+0.0087	+0.006
81	−0.435	+0.415	+0.070	+0.0095	+0.007
108	−0.465	+0.385	+0.083	+0.014	+0.05
130	−0.495	+0.525	+105.0	+105.0	+180.0
301	−0.710	+0.110	+10.3	+2.06	+8.0

another curve was determined, etc. This procedure was followed for a test at each pH. The curves obtained in this manner agreed well with the data reported herein. In every case, the temperature at which passivity became absent was in exact agreement.

Decay of potential and decay of current at constant potential.—The presence of a passive film can usually be detected by appropriate decay experiments. When the potential is held constant and the current measured, a constant high current indicates that no film exists. A steady decay in current indicates that a film exists and is improving its protective quality. When the potential is first brought to a high value and allowed to decay, an immediate return to the corrosion potential indicates the absence of a protective film. When there is an intermediate arrest(s) before returning to the corrosion potential the presence of a protective film is indicated. In the constant potential experiments and for temperatures and pH combinations at which passivity was expected, the overpotential selected was such that the potential was well into the passive region. For temperatures and pH values at which passivity was not expected, the potential was selected to be in the diffusion controlled region. A summary of the experimental results from the measurements of current decay at constant potential is shown in Table VI.

For those cases in which passivity was expected, the current fell exponentially to values corresponding closely to the minimum passive current density found by the potentiokinetic scans. The steady-state ($t = 30$ min) passive current densities are summarized in Table VI and are compared with the values obtained potentiokinetically. The agreement is excellent. For those intermediate temperatures in which passivity was absent in the potentiokinetic curves, the agreement was good within an order of magnitude. In this latter case, the current did not change with time as can be seen by comparing $i(t = 30$ sec) and $i(t = 30$ min) in Table VI. At 300°C, where the potentiokinetic data and the potential-pH diagrams indicate that an oxide(s) of nickel is present for the pH 3.4 and 6.3 solutions, the current did decay somewhat with time, indicating that some diffusion barrier, probably an oxide, was inhibiting nickel dissolution. For the pH 1.3 case at 300°C, this behavior was not observed, as was expected from the 300°C potential-pH diagram.

In the case of the potential decay experiments the specimen was held for 30 min at constant potential, the potentiostat was turned off and the open-circuit potential of the sample was recorded as a function of time. The potentials were those used for the current decay studies. For the temperatures and pH values at which the potentiokinetic polarization curves indicated passivity, there was an abrupt arrest in the decay curve. The arrest should occur near but slightly below the equilibrium redox potential of nickel and the oxide composing the passive film, Ni/NiO_n, or at some redox potential of two oxides, NiO_n/NiO_m.

A listing of the experimentally observed arrest potentials is given in Table VII. At the lower temperatures at which passivity was present in the potentiokinetic curves, a potential arrest was observed. At the intermediate temperatures no arrests were found, but at 300°C arrests were observed for the pH 3.4 and 6.3 cases. Two exceptions in the above general behavior were the 75°C cases at pH 1.3 and 3.4. Although the decay curves for these cases were markedly different from the higher temperature cases, no clear arrest potential could be determined. At those temperatures for which neither passivity nor an oxide was present, the time for decay to the corrosion potential was practically instantaneous. In Table VII, an attempt is made to compare the observed arrest potentials with all the possible Ni/NiO_n and NiO_n/NiO_m redox potentials of the bulk oxides. These redox potentials were calculated in the same manner as the coexistence lines of the potential-pH diagrams described earlier. For those temperatures at which passivity was observed, the arrest potentials were close to the Ni/Ni_3O_4 equilibrium in the pH 1.3 and 3.4 cases. This behavior would be in good agreement with the Bockris, Reddy, and Rao (1) result that the passive film is composed of $NiO_{1.5\text{-}1.8}$. For the pH 6.3 case, at the temperatures where passivity was observed, the arrest potentials were very close to the Ni/NiO equilibrium. This latter

Table VII. Comparison of experimentally observed potential arrest values with calculated Ni/NiO_x and NiO_x/NiO_y redox potentials

Temp, °C	E_{arrest}	Ni/NiO	Ni/Ni_3O_4	Ni/Ni_2O_3	Ni/NiO_2	NiO/Ni_3O_4	Ni_3O_4/Ni_2O_3	Ni_2O_3/MO_2
				pH 1.3				
22	+0.240	+0.050	+0.230	+0.340	+0.595	+0.810	+1.230	+1.360
54	+0.213	+0.020	+0.205	+0.320	+0.570	+0.760	+1.205	+1.340
75	none	+0.010	+0.195	+0.310	+0.560	+0.755	+1.200	+1.325
100	none	+0.000	+0.180	+0.298	+0.555	+0.750	+1.200	+1.310
200	none	−0.060	+0.130	+0.240	+0.520	+0.690	+1.140	+1.260
301	none	−0.110	+0.075	+0.190	+0.440	+0.620	+1.080	+1.200
				pH 3.4				
33	+0.078	−0.075	+0.100	+0.210	+0.465	+0.680	+1.105	+1.230
55	+0.048	−0.120	+0.065	+0.180	+0.430	+0.620	+1.075	+1.200
79	none	−0.135	+0.040	+0.160	+0.415	+0.610	+1.065	+1.080
97	−0.075	−0.150	+0.030	+0.140	+0.400	+0.600	+1.060	+1.160
120	none	−0.175	+0.020	+0.115	+0.380	+0.570	+1.020	+1.130
298	−0.205	−0.340	−0.140	−0.055	+0.200	+0.390	+0.850	+0.970
				pH 6.3				
22	−0.204	−0.254	−0.080	+0.030	+0.290	+0.510	+0.930	+1.060
54	−0.261	−0.310	−0.120	−0.005	+0.240	+0.430	+0.880	+1.000
81	−0.335	−0.345	−0.160	−0.050	+0.210	+0.405	+0.850	+0.965
108	−0.350	−0.380	−0.200	−0.090	+0.180	+0.380	+0.820	+0.930
130	none	−0.420	−0.240	−0.130	+0.140	+0.330	+0.780	+0.890
301	−0.500	−0.700	−0.505	−0.390	−0.140	+0.050	+0.510	+0.630

result was expected since the potential-pH diagram, Fig. 2, shows that NiO should be stable at the overpotentials in question. This result does not necessarily imply that NiO causes passivity at this pH, for the bulk NiO present probably obscures the redox arrest potential of the passive agent.

The arrest potentials at 300°C for the pH 3.4 and 6.3 agree best with the Ni/Ni_3O_4 equilibrium potentials. This behavior is not easily explained, since in both cases the applied overpotential should have produced NiO according to the potential-pH diagram of Fig. 5. In any event, the presence of an arrest potential did imply that an oxide was on the surface, in agreement with the potentiokinetic curves.

In summary, both the constant potential and potential decay experiments agreed well with the behavior expected from consideration of the potentiokinetic curves. The possibility of the presence of a stable oxide at the higher temperatures in the pH 3.4 and 6.4 solutions was also strengthened.

The question not answered by the present work is why the active-to-passive transition in nickel seems to disappear abruptly above a critical temperature that is only slightly pH dependent. One possible explanation is that the dissolution kinetics of the passive film are such that at the critical temperature the dissolution rate of the film is equal to the rate of film growth. Another possibility is that the precursor film described by Bockris, Reddy, and Rao (1) is not stable above the critical temperature. Since they conclude that this film is necessary, but not sufficient, for the formation of passivity, its absence would preclude any chance for the formation of the passive state. Whatever the cause, the observed phenomenon is not predicted by any current theory of nickel passivity.

Conclusions

Significant conclusions and observations from this study are:

1. The active-to-passive transition in nickel is absent at temperatures above the 90°-125°C range for the solutions studied.
2. Potential-pH diagrams for $Ni-H_2O$ were calculated over a range of potentials and indicate that the range of stability (with respect to pH) of the oxide phases of nickel in the acid region increases with increasing temperature.
3. At temperatures above the presence of an active to passive transition, the anodic polarization curves have the appearance of a film free diffusion-controlled process. At 300° in the pH 3.4 and 6.3 solutions, bulk oxide forms during anodic polarization as predicted by the potential-pH diagrams.
4. A hydrogen electrode within the autoclave can be used effectively to determine potentials on the standard hydrogen scale at test temperature.
5. Potential decay experiments suggest the presence of Ni_3O_4 (pH 1.3 and 3.4) and NiO (pH 6.3) during decay from the passive region at temperatures where "anomalous" passivity is present. At temperatures and pH where bulk oxide formation is present, potential decay experiments indicate the presence of Ni_3O_4.
6. The corrosion potential of nickel is always near the hydrogen redox potential at all temperatures and pH, indicating that nickel is acting as a hydrogen electrode. An Arrhenius plot of i_{corr} gives an activation energy of 3.3×10^3 cal/mole which is close to the activation energy for the hydrogen redox reaction on nickel.

Acknowledgments

The authors would like to acknowledge the United States Air Force's support of this research through Contract AF 33 (615)-5108. The encouragement of Dr. C. T. Lynch and Dr. H. Kirkpatrick of the Air Force Materials Laboratory is especially appreciated. R. L. Cowan would also like to acknowledge the Atomic Energy Commission for a fellowship throughout most of this work. This paper is based in part on work done by one of the authors (R.L.C.) in partial fulfillment of the Ph.D. requirement at The Ohio State University.

Manuscript submitted April 24, 1970; revised manuscript received Nov. 20, 1970.

Any discussion of this paper will appear in a Discussion Section to be published in the December 1971 JOURNAL.

REFERENCES

1. J.O'M. Bockris, A. K. N. Reddy, and B. Rao, *This Journal*, **113**, 1133 (1966).
2. J. R. Myers, Ph.D. dissertation, The Ohio State University (1964).
3. Y. M. Kolotyrkin, *Z. Elektrochem.*, **62**, 664 (1958).
4. G. Okamato and N. Sato, *Nippon Kinzoku Gakkai*, **23**, 662 (1959).
5. K. J. Vetter and L. Arnold, *Z. Elektrochem.*, **64**, 407 (1960).
6. K. Arnold and K. J. Vetter, *ibid.*, **64**, 407 (1960).
7. G. Economy, R. Speiser, F. H. Beck, and M. G. Fontana, *This Journal*, **108**, 337 (1961).
8. J. Osterwald and H. H. Uhlig, *ibid.*, **108**, 515 (1961).
9. D. O. Condit, M.S. thesis, The Ohio State University, 1964.
10. Okamato *et al.*, *Z. Elektrochem.*, **62**, 775 (1958).
11. J. R. Myers, W. B. Crow, F. H. Beck, and R. K. Saxer, *Corrosion*, **21**, 32 (1966).
12. H. S. Harned and B. B. Owen, "The Physical Chemistry of Electrolytic Solutions," American Chemical Society Monograph Series, Reinhold Publishing Co., New York (1958).
13. W. M. Latimer, "Oxidation Potentials," Prentice Hall, New York (1952).
14. S. H. Maron and C. F. Prutton, "Principles of Physical Chemistry," Macmillan Co., New York (1958).
15. D. Ives and G. Janz, "Reference Electrodes," Academic Press, New York (1961).
16. R. S. Greeley, R. W. Staughton, and M. H. Lietzke, *J. Phys. Chem.*, **64**, 652 (1960).
17. A. J. de Bethune, *This Journal*, **107**, 829 (1960).
18. A. J. de Bethune, T. S. Licht, and N. Swendeman, *ibid.*, **106**, 617 (1959).
19. A. J. de Bethune and G. R. Salvi, *ibid.*, **108**, 672 (1961).
20. A. J. de Bethune and N. A. S. Laud, "Standard Aqueous Electrode Potentials and Temperature Coefficients at 25°C," C. A. Hanpel, Skokie, Ill. (1967).
21. A. J. de Bethune, H. O. Dalley, N. S. Laud, and R. G. Salvi, *This Journal*, **114**, 578 (1967).
22. D. Lewis, First Annual Report: The Thermodynamics of Corrosion Processes, AB Atomenergi, Stockholm, 1966.
23. C. M. Criss and J. W. Cobble, *J. Am. Chem. Soc.*, **86**, 5390 (1964).
24. *Ibid.*, 5387.
25. J. W. Cobble, *J. Am. Chem. Soc.*, **86**, 5394 (1964).
26. C. E. Wicks and F. E. Block, *Bulletin 605*, Bureau of Mines, U.S. Gov't Printing Office, Washington.
27. M. Pourbaix, "Atlas of Electrochemical Equilibria in Aqueous Solutions," Pergamon Press, Oxford (1966).
28. H. E. Townsend, *Corrosion Sci.*, To be published.
29. deG. Jones and H. G. Masterson, "Techniques for the Measurement of Electrode Processes above 100°C," Vol. I, "Advances in Corrosion Science and Technology," R. W. Staehle and M. G. Fontana, Editors, Plenum Press, New York (1970).
30. A. L. Bacarella, *This Journal*, **108**, 331 (1961).
31. V. V. Gerasimov, A. I. Gromova, A. A. Sabinin, and E. T. Shapovolv, Corrosion of Reactor Materials Translation, A.E.C.—TR 5219.
32. B. E. Wilde, *Corrosion*, **23**, 331 (1967).
33. B. E. Wilde, *ibid.*, **23**, 379 (1967).
34. B. E. Wilde, *ibid.*, **24**, 338 (1968).
35. J. Postlethwaite, *Electrochim. Acta*, **12**, 333 (1967).
36. R. S. Greeley, Ph.D. dissertation, University of Tennessee, 1959.
37. M. H. Lietzke and R. W. Stoughton, *J. Am. Chem. Soc.*, **75**, 5226 (1953).
38. *Ibid.*, **39**, 230 (1962).

39. J. O'M. Bockris and E. C. Potter, *J. Chem. Phys.*, **20**, 614 (1952).
40. J. R. Reinoehl, Ph.D. dissertation, The Ohio State University, Columbus, Ohio, 1967.
41. R. Frankenthal, *This Journal*, **114**, 542 (1967).
42. J. Osterwald and H. H. Uhlig, *ibid.*, **108**, 515 (1961).
43. J. R. Myers, Ph.D. dissertation, The Ohio State University, 1964.
44. Circular 500, National Bureau of Standards, U.S. Government Printing Office, 1951.
45. R. E. Connick and R. E. Powell, *J. Chem. Phys.*, **21**, 2206 (1953).

The Anodic Oxidation of Hydrogen in Aqueous Acids by Conducting Compounds of the Transition Elements

R. D. Armstrong

The Electrochemistry Research Laboratory, Newcastle University, Newcastle-upon-Tyne, England

and A. F. Douglas and D. E. Keene

The Gas Council, London Research Station, Fulham, London, England

ABSTRACT

A number of compounds of the transition elements with B, C, H, N, P, S, and Si have been screened for corrosion resistance and catalytic activity for anodic hydrogen oxidation in M H_2SO_4. Only WC and alloys of WC with TaC were found to be active. A plot of apparent activation energy against overpotential was linear in the range 200-500 mV The activity of WC is discussed in the context of (*a*) surface defects acting as active centers and (*b*) the formation of hydrogen tungsten bronzes.

Several articles have been published recently on the use of tungsten carbide as an alternative electrocatalyst to noble metals for the anodic oxidation of hydrogen in aqueous acid fuel cells (1-3). Tungsten carbide is, however, only one of a large range of similar interstitial compounds which can be prepared from reaction of the transition metals with boron, carbon, phosphorus, and silicon. A number of these compounds exhibit metallic conduction and have excellent corrosion resistance, even in the presence of strong acids. There seemed to be no known reason why the electrocatalytic activity for anodic hydrogen oxidation should be confined to tungsten carbide, and therefore a study was made of a range of similar compounds. This study was made in two parts: (*a*) a screening program to examine the compounds for bulk corrosion and catalytic activity for anodic hydrogen oxidation in M H_2SO_4, and (*b*) analysis of selected compounds to attempt to relate catalytic activity with measured physical-chemical parameters.

Experimental

Test samples were obtained from various suppliers as outlined in Table I. Hydrophobic gas diffusion test electrodes were prepared from these samples as follows: 60 mesh nickel wire gauze was cut into 1 cm squares, degreased in hot trichlorethylene, and a gold wire spot welded to one edge. The nickel gauze was then electroplated with gold (Johnson, Matthey and Company Ltd., G.88 plating solution) at 5 mA for 4 hr to produce electrodes which did not corrode in M H_2SO_4 over the potential range used. The catalyst sample was mixed with a polytetrafluoroethylene (PTFE) emulsion (Fluon G.P.1., I.C.I. Ltd.), to give a final PTFE: catalyst ratio of 1:3 (w/w); the slurry so formed was applied onto the electrodes which were then subsequently dried at 100°C before sintering in air at 300°C (±5°C) for 30 min.

Electrodes were tested in a typical half-cell arrangement. Each electrode was floated on the surface of the electrolyte and a Luggin capillary placed directly beneath it. A dynamic hydrogen electrode (4) in the same solution was used as reference electrode. The counterelectrode was a large piece of platinum gauze separated from the test electrode by a glass frit. Gas sparge tubes were fitted to each cell compartment.

All glassware was thoroughly degreased and cleaned with (*i*) alcoholic potash and (*ii*) a 1:1 mixture of concentrated nitric and sulfuric acids, and was finally washed in triply distilled water immediately before use. The electrolyte was prepared from AnalaR sulfuric acid and triply distilled water. All measurements were made at ambient temperature (22°-25°C), unless otherwise stated.

Steady-state measurements were made with the solution and atmosphere in the cell saturated with either nitrogen or hydrogen. Current readings were taken at 50 mV steps, allowing at least 10 min at each step for equilibrium to occur.

A selected number of samples were analyzed for the following information: phase composition, crystallinity of the various phases, impurity elements, and particle size distribution and average particle size.

Phase composition and crystallinity were determined by x-ray diffraction. Impurity elements were identified by x-ray fluorescence, and the average particle size and particle size distribution were estimated by optical and electron microscopy.

Results

Table I lists the compounds screened and shows the corrosion current and hydrogen oxidation current at 200 mV. Where measured, the average particle size is shown; in other cases the average particle size was larger than 3μ. Table IIa is a summary of the analytical results, set out to facilitate the correlation of the measured parameters with the hydrogen oxidation current. A number of ternary compounds and tungsten carbide samples, on which a full analysis was not made but which show catalytic activity or are otherwise especially interesting, are listed in Table IIb.

Figure 1 shows I-V plots at a number of temperatures for the most catalytically active sample tested. This was tungsten carbide (WC) which had an average particle size of 0.45μ (see Table IIb, sample 10).

Key words: hydrogen electrode, electrocatalysis, transition elements.

Table I. Performance of PTFE bonded hydrophobic electrodes for the oxidation of hydrogen in M H_2SO_4

Catalyst	Source*	Description	Performance (I, mA cm^{-2}) at 200 mV N_2	H_2	Comments
		Catalyst materials from compounds of the first row transition metals			
TiB_2	B		—	—	Dissolves in hot M H_2SO_4
TiC	C	Submicron	0.00	−0.02	See Table II
TiH_2	H		−0.1	−0.05	
$TiO_{1.9}$	F	Reduced titania	−0.018	−0.02	
$TiSi_2$	C		0.00	0.00	
TiC/WC	G		0.00	0.00	
VC	C		+0.3	+0.4	Reacts with electrolyte
VSi_2	C		+0.02	+0.002	
CrB_2	C		—	—	Dissolves in hot M H_2SO_4
Cr_3C_2	G	2.5μ	0.00	0.00	
MnP	E		—	—	Dissolves in hot M H_2SO_4
$FeSi_2$	E		−0.1	−0.1	
NiP	A		−0.02	−0.05	
		Catalyst materials from compounds of the second row transition metals			
ZrB_2	E		−0.18	−0.18	Dissolves in hot M H_2SO_4
ZrC	G	Vacuum grade 3.0μ	−0.005	−0.005	
ZrH_2	H		−0.17	−0.15	Corrodes at anodic potentials
$ZrSi_2$	C		−0.001	−0.001	
NbB_2	C		−0.06	−0.07	Some corrosion
NbC	G	1.0μ	−0.40	−0.10	Corrodes at anodic potentials
$NbSi_2$	C		0.00	0.00	
MoS_2	G	Grade A.1	+0.01	−0.016	
$MoSi_2$	E	1.5μ	−0.004	−0.006	
$MoSi_2$	A	1.0μ	0.00	+0.01	
		Catalyst materials from compounds of the third row transition elements			
LaB_6	B	Solid sample	—	—	Dissolves in hot M H_2SO_4
TaB_2	C		−0.1	−0.1	Some corrosion
TaC	G	2.0μ	−0.018	−0.065	No corrosion; some activity, see Table II.
TaC	E	Submicron	−0.004	−0.19	
TaC	D	Submicron	−0.001	−0.007	
TaC/NbC	D		0.00	0.00	
TaN	A		−0.012	−0.03	
$TaSi_2$	C		0.00	0.00	
WB	E		−0.2	−0.2	Some corrosion
WC			−0.02	−3.4	See Table II
W_2C	G	4.2μ	−0.007	−0.012	See Table II
WS_2	E		−0.17	−0.06	Some corrosion
WSi_2	E	2.0μ	−0.03	−0.06	

* Key to suppliers:

A	Alfa Inorganics, Inc.	USA
B	Borax Consolidated	UK
C	Cavendish Laboratory, Cambridge	UK
D	CIBA	UK
E	Koch Light Laboratories Ltd.	UK
F	Morganite	UK
G	Murex Ltd.	UK
H	New Metals and Chemicals Ltd.	UK

Apparent activation energies, calculated from Fig. 1 and similar plots, showed a characteristic linear variation with potential from 19.8 kJ $mole^{-1}$ at 500 mV to 27 kJ $mole^{-1}$ at 200 mV.

Discussion

In this comparison of the performance of hydrophobic gas electrodes prepared from various compounds, for the anodic oxidation of hydrogen, a number of reservations must be made. The performance of these electrodes is known to be dependent on their microstructure and method of preparation (5); Tantrum and Tseung (6) have shown that for oxygen reduction on PTFE bonded carbon electrodes, the performance of an electrode is related to the size of the particle aggregates rather than their surface area (measured by BET method). Clearly, when using submicron and ultrafine materials one may expect that there is an optimum particle size for maximum activity. But, as a result of differences in the surface energies of the catalyst materials, this optimum particle size may vary from compound to compound.

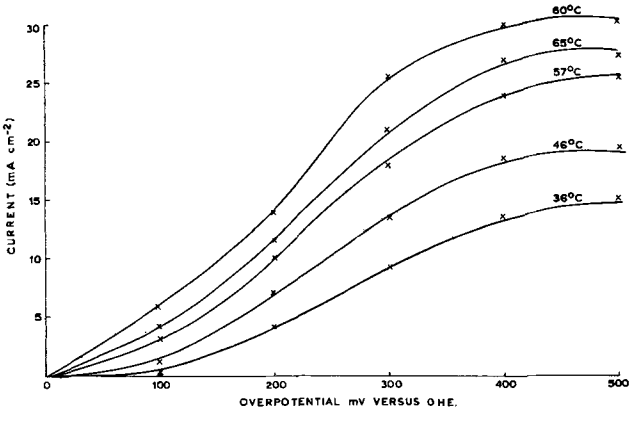

Figure 1. Current voltage curves at a series of temperatures for WC, particle size 0.45μ (sample 10, Table IIb).

The ratio of PTFE to catalyst for optimum activity may also be dependent on the particle size of the catalyst and its composition and cannot be ignored when comparing results. Tests in these laboratories with WC of particle size 0.45μ showed that 25% w/w PTFE gave the best results for this material, and this value was used in the fabrication of all the electrodes.

From the initial screening program two points immediately became apparent:

1. The borides of all the elements tested dissolve or corrode badly at anodic potentials in M H_2SO_4 and are therefore unsuitable for use in acid fuel cells.
2. Useful levels of catalytic activity are unlikely unless the average particle size of the catalyst is less than 1μ.

Results from Tables IIa and IIb show that the particle size is the most significant parameter for correlation with catalytic activity. Best results were obtained with WC with an average particle size of 0.45μ. This is very close to the figure of 0.3μ which Bohm (2) claims for optimum activity. The lower level of activity observed with the WC sample of smaller particle size is thought to be associated with the higher surface energy of these fine powders. Because of this surface

Table IIa. Summary of analytical measurements and correlation with electrochemical activity for the oxidation of hydrogen in *N* H_2SO_4

Sample No.	Compound (obtained from various sources)	Phases detected	Impurity elements	Avg particle size and range, μ	Crystallite size, A	Catalytic activity (mA cm^{-2}) at 200 mV N_2	H_2
1	WC—submicron	WC major, W_2C trace 1%, W trace 1%, WO_3 2%	Fe 0.03%; W. trace Cu, Mo, Nb, Ca, Cr, Ti	0.1-2μ. Small noncrystalline agglomerates. High surface area	001 312 ± 10 100 322 ± 10	0.095	1.1
2	WC	WC only	Trace 0.02% Fe; Cu; W. trace Ca, Cr, Mo, K	1.1; range 0.5-3	001 680-780 100 690-790	0.20	1.1
3	WC 0.9μ	WC only	Trace Fe, Cu; W. trace Ca, Ni, Cr, Pb	0.9; range 0.3-3	100 700-800	0.01	0.3
4	WC 0.3μ	WC only	Trace 0.05% Fe, Cu; W. trace Ca, Cr	0.8; range 0.3-3	001 580-680 100 600-700	0.03	0.24
5	WC; prepared by fused salt electrolysis	WC (40-50%), W_2C (10-20%), W (2-3%); C, Si in traces	Fe (0.6%), Ni (0.28%), trace Ca, Cu, Co, Mn, Pb; W. trace Ti, Si	1.0; range 0.2-4	WC—100-310 ± 10	0.005	0.18
6	WC 4.0μ	WC only	As for sample 3	4.0; range 1.0-10	"Infinite"	0.04	0.07
7	TiC Cavendish Lab.	TiC, $TiC_{0.4}$	Co, 1%; Fe, 0.5%; Cr, 0.6%; Ni, 0.1%; trace Cu, Zn, Ca, K	Clusters of cubic particles of side 100-3000A	200-350	0.00	0.00
8	As above; increase in C deficiency	TiC, $TiC_{0.4}$, Ti_2O	As above		200-350	0.00	0.00
9	W_2C—fused	WC (30-40%), W_2C (60-70%), trace W (1-2%)	Fe (0.24%), trace Cu, W. trace Ca, Ni (0.04%), Co, Cr, Mo, Mn, Ti	4.2; range 0.5-8	600-700	0.007	0.012

Table IIb. Electrochemical activity for oxidation of hydrogen by samples on which analyses were not carried out

10	WC Murex 1311 5/9/21		0.45		0.02	3.4
11	WC Murex 13129		0.50		0.02	0.62
12	TaC (2%)/WC Murex		1.1		0.05	0.40
13	TaC (2%)/WC Murex		2.0		0.001	0.091
14	TaC Koch Light submicron		Agglomerates of ultrafine particles 100-1000A		0.005	0.18
15	TiC/WC Murex Vacgrade T_2		3.0		No activity or corrosion detected	
16	TiC/WC Murex Vacgrade T_8		3.0		No activity or corrosion detected	
17	WSi_2, Koch Light		2.0; range 0.5-3		0.03	0.06

energy the particles show a strong tendency to cluster when in suspension, resulting in large aggregates.

The highly catalytic WC electrodes produced elsewhere (2) were prepared by carburizing tungsten particles in either CH_4 or CO gas streams with the lowest temperatures and shortest reaction times possible. Since the results both here and elsewhere do not appear markedly dependent on the stoichiometry, the increased activity may be due to an increase in the concentration of surface defects which are more probable with low-temperature short-duration preparations. Surface defects have been proposed as creating active centers and are therefore an important parameter effecting catalytic activity (7).

In an attempt to strain the host WC lattice, thus introducing surface defects, we tested a number of specially prepared ternary compounds based on WC. Of the ternary compounds tested the solid solution of TaC in WC (2% TaC/WC) might be expected to introduce surface defects, resulting from the difference in lattice parameters between TaC and WC. Catalytic activity of this solid solution was at least as good as that of the WC samples of similar particle size (1.1μ). Unfortunately, it was not possible to reduce the particle size of this compound further by grinding.

Binder *et al.* (3) have proposed that the catalytic activity of WC is due to the formation of hydrogen tungsten bronzes on the surface of the WC, as a result of oxidation of surface tungsten atoms in a hydrogen environment. Recently, we have shown (9) that the analogous sodium tungsten bronzes are completely inactive for anodic hydrogen oxidation. Also the plot of apparent activation energy against overpotential for WC (calculated from Fig. 1) showed a linear variation between 200 and 500 mV, while the value at 200 mV (27 kJ $mole^{-1}$) was consistent with those found elsewhere (2, 3). This linear variation is not indicative of the formation of a different surface on the electrode. It seems therefore unlikely that the reason for catalytic activity of WC is due to the formation of surface bronzes.

Manuscript received Oct. 19, 1970.

Any discussion of this paper will appear in a Discussion Section to be published in the December 1971 JOURNAL.

REFERENCES

1. W. T. Grubb and L. H. King, Report AD 649 895, Sect. 2-44, Dec. 31, 1966.
2. H. Bohm and F. A. Pohl, Third Int. Symp. Fuel Cells, Brussels, 1969, p. 183.
3. H. Binder, A. Kohling, and G. Sandstede, *Sixth Biennial Fuel Cell Symp., Div. Fuel Chem.*, **13**, [3], 99 (Sept. 1969).
4. J. Giner, *This Journal*, **111**, 377 (1964).
5. J. Giner, J. Parry, L. Swette, and R. Cattabriga, Tyco Laboratories, Inc. Contract No. NASW 1233, Q-12 Final Report covering July 1, 1965-June 30, 1968, p. 86.
6. A. D. Tantrum and A. C. Tseung, *Nature*, **221**, 167, (1969).
7. U. R. Evans, *Electrochim. Acta*, **14**, 197 (1969).
8. H. Bohm, *Nature*, **227**, 483 (1970).
9. R. D. Armstrong, A. F. Douglas, and D. E. Williams, To be published.

Ion Selective Electrochemical Sensors—Fe^{+3}, Cu^{+2}

Charles T. Baker* and Isaac Trachtenberg*

Texas Instruments Incorporated, Dallas, Texas 75222

ABSTRACT

Ion selective electrochemical sensors which respond to Fe^{+3} and Cu^{+2} have been developed. The sensor material consists of a chalcogenide glass (60% Se, 28% Ge, and 12% Sb) doped with Fe^0, Co^0, or Ni^0. Response has been observed at concentrations as low as 10^{-6} moles/liter (0.056 ppm Fe) in both membrane and electrode configurations. Nernstian behavior is observed in the 10^{-5} to 10^{-1} moles/liter concentration range. Interference tests demonstrate good selectivity for Fe^{+3} in the presence of most cations, particularly Fe^{+2}. Potential response behavior supports a redox potential mechanism rather than the ion exchange mechanism.

Within the past five years, research and development in analytical potentiometry has increased. The impetus for this effort is due mainly to the simplicity of analysis offered by ion selective electrochemical sensors. The application of such sensors can result in the control required to insure water quality, attain optimum yields in chemical processes, maintain the critical K^+ balance of patients undergoing surgery, and, in general, obtain rapid analysis at low cost.

A general survey of the field of ion-selective electrodes was given by Rechnitz (1), who categorized the sensors into three major classes: glass electrodes, solid-state electrodes, and liquid-liquid membrane electrodes. In a review article by Toren and Buck (2), electrodes in each class were presented and pertinent references regarding electrode characterization, applications, and theory of operation were given. Lakshminarayanaiah (3) discussed the transport phenomena in membranes, and the excellent format of this work offers the physical and biological scientists a well-organized presentation of background material regarding theoretical treatments and experimental results of membrane phenomena. The history, theory, applications, limitations, compositions, and construction of ion selective glass electrodes have been presented in a book edited by Eisenman (4). The fixed anionic site ion exchange model has also been used by Buck (5) to study the transient electrical behavior of glass membranes. Solid-state membranes viewed in light of the fixed site ion exchange model have been treated by Buck (6). Eisenman (7) compared the similarities and differences between liquid and solid ion exchanges. In a book edited by Durst (8) the views and specialties of a number of scientists in the ion selective electrode field have been presented.

This investigation discusses the preparation, characterization, and tests of a doped chalcogenide glass as the active material in ion-selective electrochemical sensors for Fe^{+3} and Cu^{+2}.

Experimental

The composition in gram-atomic weight per cents of the chalcogenide glass host material used in this ex-

* Electrochemical Society Active Member.

Key words: ion selective sensors, ferric sensors, cupric sensor, chalcogenide glasses, potentiometry.

perimental work (hereafter referred to as 1173 glass) was 60% selenium, 28% germanium, and 12% antimony. Undoped 1173 has a resistivity of 2 x 10^{14} ohm-cm and is not usable as a sensor. Doping 1173 glass with elemental iron, cobalt, or nickel lowers the resistivity and yields a material suitable for use in a sensor.

A standard compounding procedure was used in the preparation of the sensor materials. High-purity elements (five nine's or better Se, Ge, and Sb; and three nine's Fe, Co, or Ni) were weighed and sealed in an evacuated quartz ampoule. The ampoule was placed in a rocking furnace and heated slowly to 900°-1000°C. The melt was allowed to mix and/or react for 16 to 24 hr, then air-quenched to solid and annealed for 2 to 3 hr at 275°C to remove strain.

The success of the doping process was determined by visual examination and by the d-c resistivity of the material. Information about the vitreous nature of the sample, its ruggedness, and rejection of dopant was obtained by visual examination and optical microscopy. Additional information regarding the glassy nature of the material or the dispersion of crystallites in the glass was obtained from the infrared transmission of the sample. More detailed work on the infrared transmission characteristics of 1173 glass and Fe^0-doped 1173 has been reported by Johnson, Haisty, and Brown (9).

One of the more important physical properties of the material for sensor use is resistivity. Resistivity measurements indicate the effectiveness of the doping process and can be used to determine the homogeneity of the material as well as the reproducibility of preparation. Resistivity measurements were employed as a screening procedure to eliminate certain samples from further consideration as sensor elements.

Material samples (glass disks 1.1-1.2 cm in diameter, 0.04-0.06 cm thick) were prepared for resistance measurement by polishing each surface to a mat finish. The disk was rinsed thoroughly in deionized water and left to dry in air. Gold was evaporated onto each side of the disk, and the edges were ground to remove any traces of gold, which could short the sample.

Each prepared disk was placed in a shielded can, pressure contacts were made to the gold on each side of the disk, and the shielded can was evacuated. A voltage was applied to the sample by a Harrison Laboratories 6264A d-c Power Supply, and the current was monitored by a Keithley 610B Electrometer used as an ammeter. The resistance of the sample was calculated from current-voltage data. The current-time behavior was recorded on a Texas Instruments Model 341 function/riter®, which was connected to the output of the Keithley 610B Electrometer.

Two configurations (Fig. 1) have been used in testing the response of the sensors to specific ions. In the first, the glass is used as a membrane or solid electrolyte like the glass in a conventional *p*H electrode. The sensor element is sealed in the end of a Plexiglas tube with one surface of the disk exposed to the test solution and the other to the internal reference solution. The internal reference solution is composed of a concentration of the ion being measured (usually 10^{-3} *M*) in 0.1*M* KNO_3. A saturated calomel reference electrode (SCE) or a Ag/AgCl reference electrode makes contact with the internal reference solution and completes the assembly for the membrane configuration. The second configuration is an electrode in which gold is evaporated on one side of the glass disk, and a Pt-wire lead makes contact with the gold by Silver Micropaint. The lead side of the glass electrode is isolated from test solutions by sealing the glass disk in a Plexiglas tube.

The responses of each sensor were investigated by measuring the potential *vs.* a SCE or a Ag/AgCl reference electrode with a Keithley 610B or C electrometer. The unity-gain output of the Keithley electrometer was fed into a Hewlett-Packard 3440A digital voltmeter

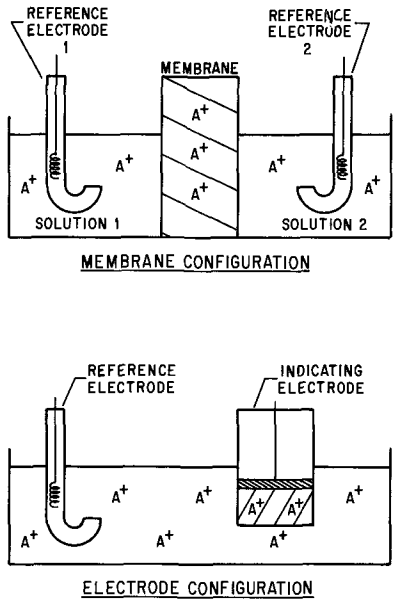

Fig. 1. Sensor configuration

equipped with a Hewlett-Packard 3443A high gain/auto range unit for digital display of potentials. During continuous run experiments, the unity-gain output of the electrometer was fed into a Sargent Model SR recorder.

All test solutions were prepared from reagent grade chemicals using deionized water. Varying concentrations of a given ion were prepared by volumetric dilution of the stock solution.

Results and Discussion

In the preparation of doped 1173 glass, there was no observable difference in the properties of samples prepared by compounding from prereacted 1173 glass and those of the same doped glass prepared from the elements. All materials discussed in this investigation were made by doping prereacted 1173 glass.

For the Fe-doped 1173 glasses, samples of 0.8, 1.6, 2.0, and 2.4 at. w/o Fe^0 were studied. The materials were uniformly vitreous, at the 0.8 and 1.6% Fe^0 level, with the Fe^0 remaining in solution when the glass was quenched. At 2.0% Fe^0 some totally glassy samples were prepared, but inhibiting the formation of a second phase was quite difficult. The presence of a second phase dispersed in a glassy matrix was always observed at doping levels above 2.0% Fe^0. The number and size of the second phase clusters were dependent on dopant concentration. If crystallites were present in the cluster phase, they were not detectable with x-ray diffraction or the scanning electron microscope, but analyses with the electron microprobe showed that the cluster phase and the glassy phase have the same elemental composition.

Electron spin resonance (ESR) spectra of undoped 1173, 0.05% Fe^0-1173, and 0.8% Fe^0-1173 confirmed that Fe^{+3} was present in the Fe-doped 1173 glasses. Qualitative analyses for the oxidation states of Fe in 1173 were made on a 1.6% Fe^0-1173 glass sample. The sample was dissolved in 10% KOH, acidified with H_2SO_4, and filtered. The filtrate was tested for the presence of Fe^{+3} and Fe^{+2}. Spot tests with $K_4Fe(CN)_6$ and KSCN indicated that Fe^{+3} was present, and the presence of Fe^{+2} was confirmed by a positive spot test with ferroin. From the results of cyclic voltammetry and controlled potential electrolysis experiments with a 2.4% Fe^0-1173 glass electrode, it was concluded that probably all the oxidation states of Fe (Fe^0, Fe^{+2}, and Fe^{+3}) were present in the Fe-doped samples which had clusters. These electrochemical techniques were applicable to the 2.4% Fe^0-1173 glass electrode because of the low resistivity of the cluster phase. These quali-

tative results indicated that Fe^{+2} and Fe^{+3} were present in doped 1173 glass samples when the doping level was less than 2% Fe^0; and Fe^0, Fe^{+2}, and Fe^{+3} were present when the doping level was greater than 2%. The relative concentration of each oxidation state of Fe in the Fe^0-doped 1173 glasses could not be stated conclusively.

Samples of 1173 glass doped with 1.5% Ni^0 and 1.5% Co^0 were studied. Physically, the materials consisted of a glassy matrix in which crystals were uniformly dispersed. The resistivities of these materials were of the order of 150 ohm-cm.

The effect of dopant concentration on the resistivity of Fe^0-doped 1173 glass is shown in Fig. 2. As the concentration of Fe in the glass is increased, the resistivity decreases significantly. The large drop in resistivity between 2.0 and 2.4% Fe^0-1173 is related to the cluster phases, which increase in size as the doping level of Fe^0 increases above the 2.0% Fe^0 value. When the diameter of individual clusters approaches the thickness of the sensor disk, or when the density of clusters increases so that clusters touch each other, the glass matrix is essentially shorted by the more conductive cluster phase. The Fe^0-1173 glasses exhibited ohmic behavior at all doping levels. At a given applied voltage, the current flow through the glasses was independent of time, indicating that the major conduction mechanism is electronic rather than ionic.

The case for an electronic conduction mechanism was further substantiated by an electrolysis experiment with a 2.0% Fe^0-1173 glass sensor in the membrane configuration. With 0.1*M* KNO_3 on each side of the membrane and large-area laboratory saturated calomel electrodes making contact with the KNO_3 solutions by means of 4% agar-saturated KNO_3 salt bridges, current was passed through the membrane. Gas bubbles formed at one membrane-electrolyte interface, and at the other membrane-electrolyte interface a brown product diffused away from the membrane into the bulk of the solution. Reversing the current caused the same reactions to occur at the opposite interfaces. The direction of the current in each case suggests that H_2 was the gas evolved, and the brown product was formed by the dissolution of the membrane. This electron transfer at the membrane-electrolyte interfaces is consistent with an electronic conduction mechanism.

Both the membrane and the electrode configuration were evaluated for potential responses to various ions. In the membrane configuration, the potential would ideally be related to

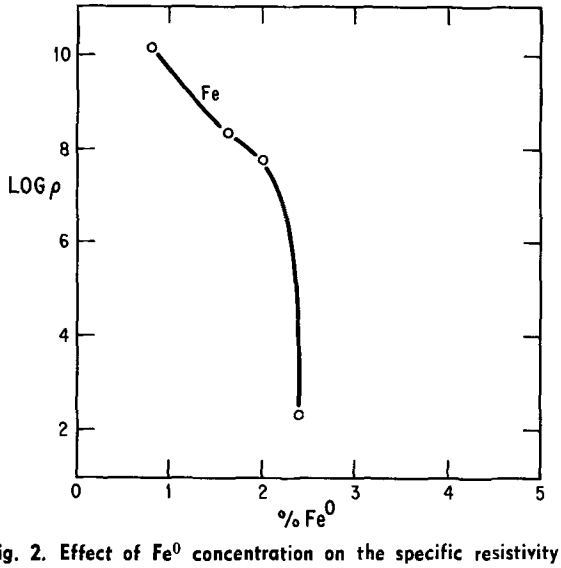

Fig. 2. Effect of Fe^0 concentration on the specific resistivity of doped 1173 glass.

$$E = E_a + \frac{2.3RT}{n\mathbf{F}} \log \frac{[M_1]}{[M_2]} \quad [1a]$$

or

$$E = E_a + \frac{2.3RT}{Z\mathbf{F}} \log \frac{[M_1]}{[M_2]} \quad [1b]$$

where E_a in [1a] is related to the asymmetry of the redox processes occurring on each side of the membrane. In [1b], E_a is the asymmetry potential for the ion exchange processes occurring at the two interfaces. For the ion exchange case, [1b] assumes that the diffusion potential contributions on each side of the membrane cancel out and the potential changes observed are related to changes in the phase boundary potential. The n in [1a] is the number of electrons transferred in the redox process, and Z in [1b] is the charge of the ion involved in the exchange process. $[M_1]$ and $[M_2]$ are the activities of ion M in solution on each side of the membrane.

For the electrode configuration, the potential equations take the form of

$$E = E_R + \frac{2.3RT}{n\mathbf{F}} \log \frac{[M^{+n}]}{[M]} \quad [2a]$$

and

$$E = E_1 + \frac{2.3RT}{Z\mathbf{F}} \log \frac{[M^{+Z}]\text{sol.}}{[M^{+Z}]\text{glass}} \quad [2b]$$

for redox and ion exchange processes, respectively. In the redox equation, [2a], E_R is a constant containing the standard potential for reduction of ion M^{+n} to M, the potential for any redox process occurring in the glass itself, and the metal-glass junction potential on the backside of the glass sensor element. For the ion exchange equation, [2b], E_1 is an analogous type constant which includes a diffusion potential, redox potential in the glass associated with the conduction mode changing from ionic to electronic, and the metal-glass junction potential mentioned above. $[M^{+Z}]$sol. and $[M^{+Z}]$ glass represent the activities of ion M^{+Z} in the solution and the glass, respectively.

Samples of 1173 glass doped with 0.8, 1.6, 2.0, and 2.4% Fe^0 were tested in the membrane and electrode configurations for potential response to changing Fe^{+3} concentration. All Fe^0-1173 sensors were responsive to Fe^{+3}, and the potential behavior was linear and reproducible in the concentration range from 10^{-5}-10^{-4} to $10^{-1}M$. The Fe^{+3} test solutions were prepared by diluting the 0.1*M* $Fe(NO_3)_3$ stock with 0.1*M* KNO_3 and adjusting the pH to ~1.7 (pH of the 0.1*M* Fe^{+3} stock solution). In this way wide variations in ionic strength were avoided so that the relationship between the potential and the concentration of Fe^{+3} could be used. Figure 3 shows the potential response of an electrode and a membrane of 2.0% Fe^0-1173 to Fe^{+3} concentration. For both configurations, a linear response is observed from $10^{-5}M$ to $10^{-1}M$ Fe^{+3}, and the slope in each case is approximately 60 mV. In view of Eq. [1a] and [2a], the slope of 60 mV per order of magnitude change implies that a redox potential involving the Fe^{+3}/Fe^{+2} couple is potential determining. If this is the case, then the Fe^{+2} must either be in the glass or generated at its surface. Ion exchange involving Fe^{+3} at the solution-glass interface is ruled out, since a slope of 20 mV is predicted from Eq. [1b] and [2b].

In Fig. 4, the potential response of an 0.8% Fe^0-1173 glass in the electrode configuration to Fe^{+3} and Fe^{+2} is shown. The slope of the E-log$[Fe^{+3}]$ is 53 mV from $<10^{-4}$ to $10^{-1}M$ Fe^{+3} and is consistent with the Nernst expression for a redox process. The response to Fe^{+2}, however, was suspicious because the potential shift is in the wrong direction when considered with respect to Eq. [2b]. Spot tests with $K_4Fe(CN)_6$ and KSCN confirmed the presence of Fe^{+3} in our Fe^{+2} test solutions. Therefore, the response in the Fe^{+2} solution was actually a response to the contaminant, Fe^{+3}. Our E-log $[Fe^{+3}]$ curve indicated Fe^{+3} was present at

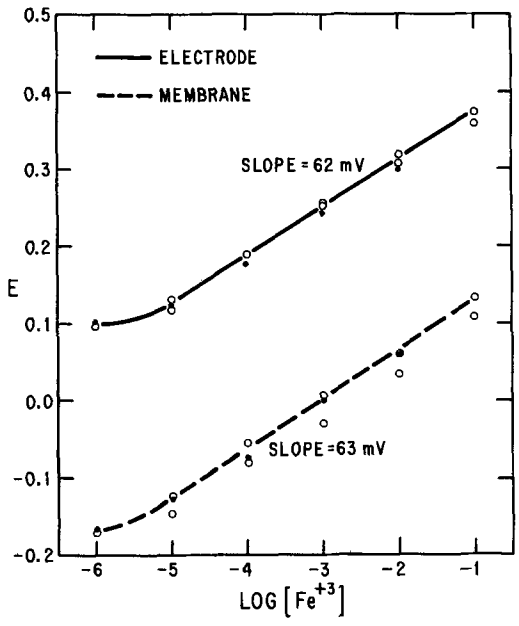

Fig. 3. Potential response of electrode and membrane of 2.0% Fe^0-1173 glass to Fe^{+3} concentration. All solutions are 0.1M in KNO_3 and pH = 1.8

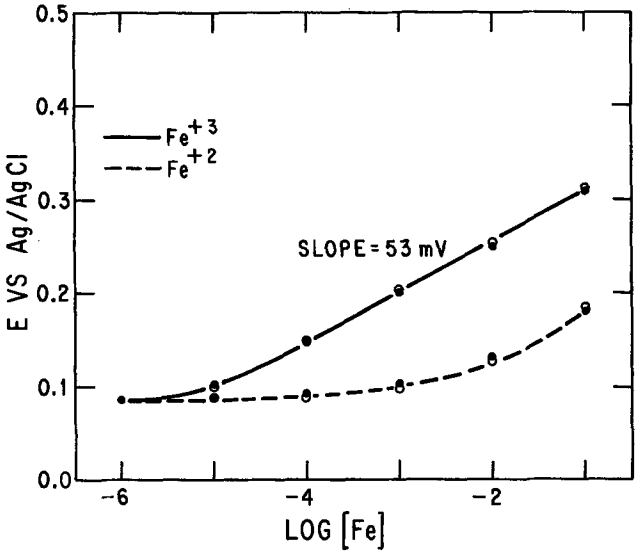

Fig. 4. Effect of Fe^{+3} and Fe^{+2} concentrations on the potential of a 0.8% Fe^0-1173 glass electrode. All solutions are 0.1M in KNO_3 and pH = 1.67.

a level that was less than 1% of the given Fe^{+2} concentration.

Additional support for the sensor response being independent of the Fe^{+2} concentration in the bulk of solution was gained from experiments in which the ratio of $[Fe^{+2}]/[Fe^{+3}]$ was varied from 0.1 to 100. The potential did not vary linearly with the log $[Fe^{+3}]/[Fe^{+2}]$, but was linearly related to log$[Fe^{+3}]$. When the ratio of $[Fe^{+3}]/[Fe^{+2}]$ was held constant, but the total iron concentration varied by dilution, the potential decreased as the concentration of Fe^{+3} decreased. These results indicated that the Fe^0-doped 1173 sensor was insensitive to Fe^{+2} in the bulk of solution.

Although Nernstian behavior has been observed for all the Fe^0-1173 glasses tested, the optimum doping level for potential stability, response time characteristics, and Nernst response is approximately 2.0% Fe^0-1173. At the lower doping levels, the high resistivity of the sensors is undesireable. With the heavily doped samples, more deviations from Nernstian behavior are recorded.

The potential response of the Fe^0-doped 1173 glasses to changing Fe^{+3} concentration is fairly rapid. A limited investigation of the potential-time characteristics suggested that establishment of equilibrium (stable potential) is mass transport controlled.

Several interference tests were made with the Fe^0-1173 glass sensors. As mentioned earlier, the sensors do not respond to Fe^{+2}. In addition, the sensor potential was independent of concentrations of Na^+, K^+, NH_4^+, Ca^{+2}, Ba^{+2}, Mg^{+2}, Mn^{+2}, Zn^{+2}, Cr^{+3}, and NO_3^-. Figure 5 shows results of some of the interference tests in which the contaminant concentration varied and the test solution remained 0.1M in KNO_3, 0.001M in Fe^{+3}, and at pH 1.6. As noted, Ag^+ represents a major interference. A decrease in potential is observed as the concentration of Cl^- and $SO_4^=$ is increased. In the absence of Fe^{+3}, however, the potential response is independent of these anion concentrations. Complexing of the Fe^{+3} by the anions is responsible for the potential shift noted in Fig. 5. These Fe^0-1173 glass sensors are sensitive to free Fe^{+3} concentration, and this coordination shifts the electrode potential negatively, as would be predicted by the Nernst expression. In the presence of excess Cl^- (Fig. 6), a 2.0% Fe^0-1173 glass electrode still exhibits close to Nernstian behavior to Fe^{+3} in the 10^{-4} to 10^{-1}M range. The apparent electrode sensitivity has decreased by an order of magnitude. In actuality, the free Fe^{+3} concentration is approximately an order of magnitude less than the total Fe^{+3} concentration.

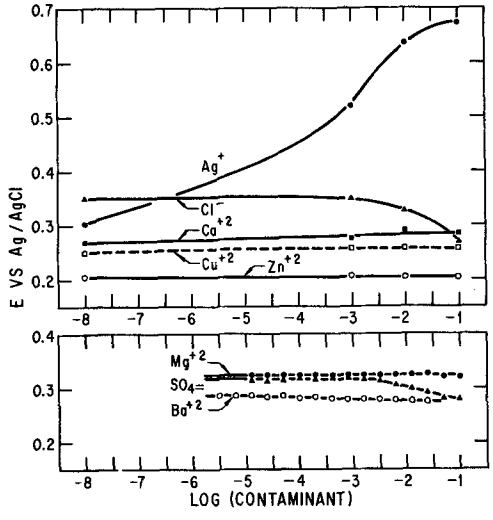

Fig. 5. Effect of contaminant concentration on the potential of a 2.0% Fe^0-1173 glass electrode. All solutions are 0.1M in KNO_3, 0.001M in Fe^{+3}, and pH = 1.6.

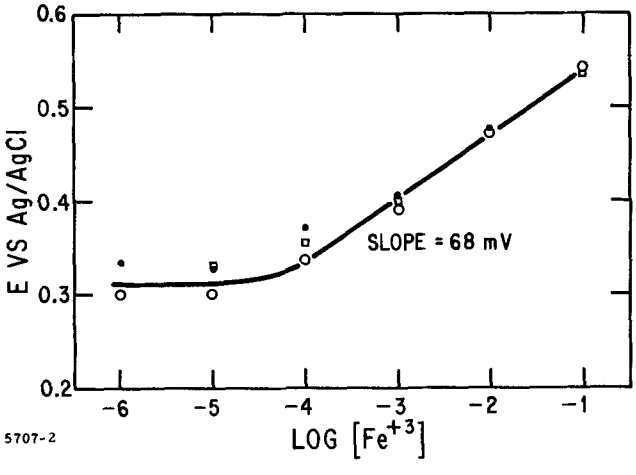

Fig. 6. Response of 2.0% Fe^0-1173 glass electrode to Fe^{+3} concentration in an excess Cl^- medium. All solutions are 1.0M in KCl and pH = 1.7.

One further comment with regard to Fig. 5 is necessary. When Fe^{+3} is present in the test solution, no potential response to Cu^{+2} is observed, even when the Cu^{+2} concentration is 100 times greater. Figure 7 is a plot of the potential behavior of 1.6% Fe^0-1173 and 2.0% Fe^0-1173 glass electrodes to Cu^{+2} in nitrate and chloride media in the absence of Fe^{+3}. The E-log $[Cu^{+2}]$ curves for Cu^{+2} in 0.1M KNO_3 (27 mV) have the slopes that would be expected for a $2e^-$ redox process or an ion exchange reaction involving a cation with a +2 charge. In the chloride medium, slopes of 53 and 62 mV for the 1.6% Fe^0-1173 and 2.0% Fe-1173, respectively, are indicative of a $1e^-$ redox process, especially since Cu^{+1} is known to be relatively stable in an excess Cl^- medium (10). These results suggest that the Cu^{+2} response in the nitrate medium was due to a $2e^-$ redox process. This redox type behavior for Cu^{+2} further supports the $1e^-$ redox potential mechanism for Fe^{+3}.

The redox potential mechanism for the response to Cu^{+2} raises some interesting questions. Since Cu is not present in the Fe^0-1173 glasses, how is the other half of the redox couple generated? In addition, must Fe be incorporated in 1173 to obtain a response to Fe^{+3}?

With these questions in mind, sensors of 1.5% Co^0-1173 and 1.5% Ni^0-1173 in the electrode configuration were prepared and evaluated. No response to Co^{+2} or Ni^{+2} was measured. The sensors exhibited a potential response to Fe^{+3} (Fig. 8) over the entire concentration range tested, with Nernstian behavior displayed from 10^{-5} to $10^{-1}M$ Fe^{+3}. The presence of Fe in the 1173 glass appears not to be a prerequisite for potential responses to Fe^{+3}. Figures 9a and 9b show the response of the 1.5% Co^0-1173 and 1.5% Ni^0-1173 electrodes to Cu^{+2} in nitrate and chloride media. In the NO_3^- medium the response to Cu^{+2} is linear in the 10^{-5} to $10^{-1}M$ range with a slope of ~30 mV. The slope increased to 54 mV in a Cl^- medium. These results, like those for the Fe^0-doped 1173 electrodes, indicate that the potential determining process shifts from a $2e^-$ mechanism to a $1e^-$ mechanism in going from a NO_3^- medium to a Cl^- medium.

The responses to Fe^{+3} and Cu^{+2} indicate the redox processes involved are

$$Fe^{+3} + e^- \leftrightharpoons Fe^{+2} \quad [3]$$

$$Cu^{+2} + 2e^- \leftrightharpoons Cu^0 \quad [4]$$

$$Cu^{+2} + e^- + 3Cl^- \leftrightharpoons CuCl_3^{-2} \quad [5]$$

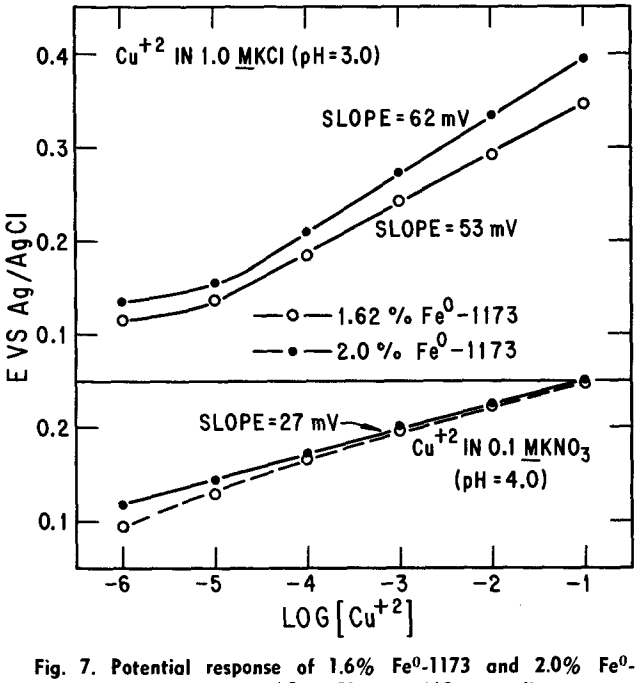

Fig. 7. Potential response of 1.6% Fe^0-1173 and 2.0% Fe^0-1173 glass electrodes to Cu^{+2} in Cl^- and NO_3^- media.

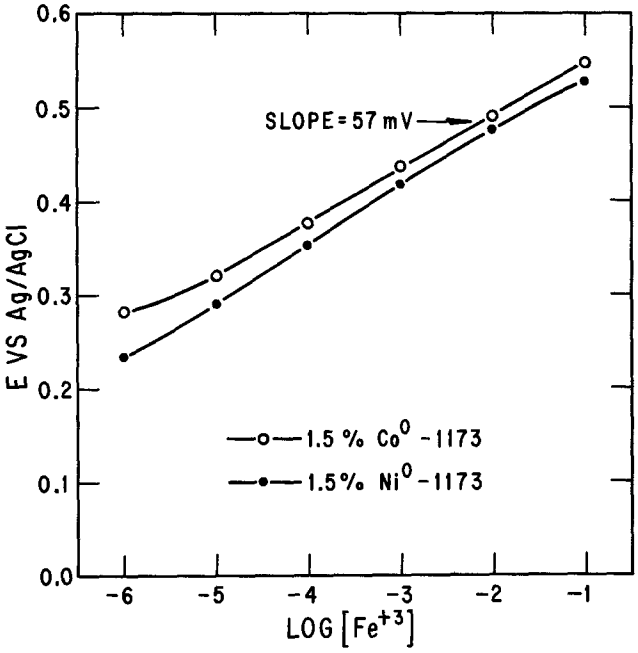

Fig. 8. Potential response of 1.5% Co^0-1173 and 1.5% Ni^0-1173 glass electrodes to Fe^{+3}.

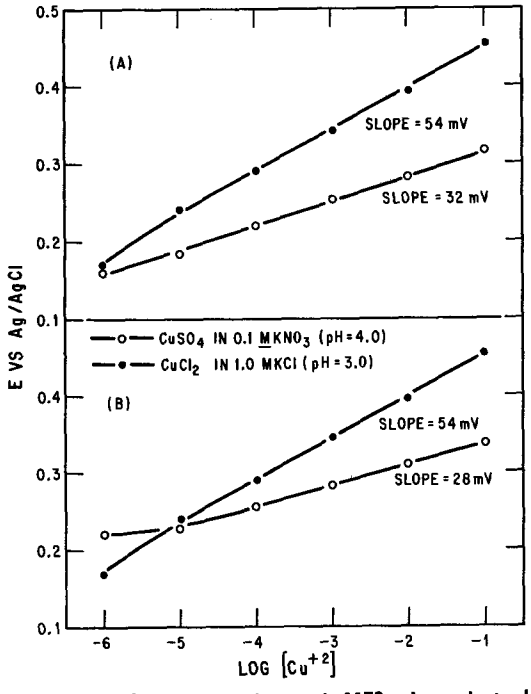

Fig. 9. Potential response of doped 1173 glass electrodes to Cu^{+2} in NO_3^- and Cl^- media. A, 1.5% Co^0-1173. B, 1.5% Ni^0-1173.

and the lower oxidation state of each redox couple is generated at the electrode surface. Furthermore, the activity of the lower oxidation state of the particular redox couple must remain constant at the sensor surface for the linear E-log[Ox] curve to be displayed.

With the redox mechanism established, it appeared that there should be other ions associated with a reversible redox couple that could be measured with the Fe^0-, Ni^0, or Co^0-doped 1173 glass sensors. These sensors were found to be insensitive to Cd^{+2}, Co^{+2}, Ni^{+2}, and Pb^{+2}, but responsive to Cu^{+2} (excess Cl^-), Cu^{+2}, Fe^{+3}, Ag^+, Hg^{+2}, Mn^{+3}, and Ce^{+4}. The potential response is related not only to reversible redox couples, but also to the position of the redox couple in the emf series. In the emf series, the single electrode potential

for the reducing agent in the doped 1173 glass is between −0.12 and +0.18V.

Generation of the lower oxidation state for an ion which can be measured with the doped 1173 sensors, therefore, involves a redox reaction between the higher oxidation state of the reversible redox couple and the reducing component of the glass. Possibly due to limited reduction sites of the glass, the activity of the lower oxidation state is held constant while the higher oxidation state of the redox couple varies from 10^{-5} to $10^{-1}M$ in the bulk of solution.

Summary

Ion selective electrochemical sensors were prepared containing Fe^0-, Co^0-, and Ni^0-doped chalcogenide glasses (28% Ge, 60% Se, 12% Sb) as the active material. The potential responses of these sensors support a redox potential mechanism rather than the ion exchange mechanism. The sensors respond only to the higher oxidation state of reversible redox couples, and the response is dependent on the standard electrode potentials of the redox couples. The sensing element of doped 1173 glass does not appear to be inert, but acts as a reducing agent which generates the lower oxidation state of the redox couple and maintains it at a constant activity.

While the redox response characteristics greatly limit the applicability of the sensors to certain ions, they also eliminate many of the interferences. Interferences may be expected only from the higher oxidation state of redox couples other than the specific ion of interest or from ions (usually anions) which complex the specific ion to be determined.

Acknowledgment

Financial support of this work by the Office of Saline Water, U.S. Department of Interior, is gratefully acknowledged. The authors also wish to thank Dr. R. M. Brown and Dr. R. W. Haisty for helpful discussions concerning material preparation procedures.

Manuscript submitted July 17, 1970; revised manuscript received Oct. 26, 1970. This was Paper 301 presented at the Los Angeles Meeting of the Society, May 11-15, 1970.

Any discussion of this paper will appear in a Discussion Section to be published in the December 1971 JOURNAL.

REFERENCES

1. G. A. Rechnitz, *Chem. Eng. News*, **45**, (25), 146 (1967).
2. E. C. Toren and R. P. Buck, *Anal. Chem.*, **42**, 398R (1970).
3. N. Lakshminarayanaiah, "Transport Phenomena in Membranes," Academic Press, New York & London (1969).
4. "Glass Electrodes for Hydrogen and Other Cations," G. Eisenman, Editor, Marcel Dekker, New York (1967).
5. R. P. Buck, *J. Electroanal. Chem. Interfacial Electrochem.*, **18**, 363 (1968).
6. R. P. Buck, *Anal. Chem.*, **40**, (10), 1432 (1968).
7. G. Eisenman, *ibid,*. **40**, (2), 310 (1968).
8. "Ion-Selective Electrodes, Proceedings of a Symposium," R. A. Durst, Editor, Gaithersburg, Maryland, Jan. 30-31, 1969. NBS Special Pubn. No. 314. U.S. Government Printing Office, Washington, D.C. (1969).
9. R. E. Johnson, R. W. Haisty, and R. M. Brown, Paper 37 presented at the New York Meeting of the Society, May 4-9, 1969.
10. H. Diehl and R. Brouns, *Iowa State Coll. J. Sci.*, **20**, 155 (1945).

Concentration Reversion in Potentiostatic Electrode Kinetics

C. A. Johnson,[1] S. Barnartt,* and F. D. Glasser[2]

Edgar C. Bain Laboratory for Fundamental Research, United States Steel Corporation, Monroeville, Pennsylvania 15146

ABSTRACT

Coupled diffusion of two substances taking part in a potentiostatic electrode reaction can lead to a maximum concentration change at finite time for one of the substances. It is shown that this phenomenon can occur at spherical and cylindrical electrodes, with first-order and with higher-order reactions, but not at planar electrodes.

In heterogeneous chemical kinetics it is known (1-4) that the coupled migration of two substances to or from an interface can result in one substance (A) exhibiting a maximum change in concentration. Thus the concentration c_A can change from its initial value c_A^0 to a maximum or minimum value, and then revert back (in the direction of c_A^0) to attain an intermediate steady-state value as $t \to \infty$. We shall refer to such concentration-time behavior as "concentration reversion." [3]

This phenomenon has been observed in the sulfurization of iron by a calcium aluminosilicate slag containing sulfur (1). In that system, which involved the coupled diffusion of sulfur and silicon, the sulfur concentration at the slag side of the interface passed through a minimum. Good evidence has been given for carbon concentration reversion during diffusion across welds of an Fe-Si-C alloy to Fe-C or to Fe-Mn-C alloys (2, 3). Another example is the sulfur-concentration maximum produced near the surface of a ferrous silicate melt during simultaneous sulfurization and oxidation of the melt by a CO-CO_2-SO_2 atmosphere (4). In the latter study it was possible to correlate a portion of the concentration-time curve quantitatively with the equilibrium oxidation state of the melt.

The present paper deals with concentration reversion in electrochemical kinetics, specifically in electrode reactions carried out at constant potential. The concentration changes which can occur in a potentiostatic reaction are limited, and a knowledge of the maximum possible concentration changes is very useful. Such knowledge helps the experimenter to design

* Electrochemical Society Active Member.

[1] Present address: Division of Materials Science, Argonne National Laboratory, Argonne, Illinois, 60439.

[2] Present address: Department of Chemistry, Ohio State University, Columbus, Ohio, 43210.

Key words: concentration polarization, coupled diffusion, concentration-time curves.

[3] This term was suggested by L. S. Darken. The term implies only that concentration changes reverse direction. It should not be inferred that the direction of diffusion changes; diffusion always proceeds in the direction of decreasing chemical potential.

experiments which permit only moderate concentration changes: (*a*) to avoid side reactions which contribute to the observed current or passivate the electrode, and (*b*) to permit accurate analysis of current-time curves (5-7). We can often calculate maximum concentration changes as those for the condition $t \to \infty$, provided concentration reversion does not occur. The aim of this study, therefore, was to determine under what potentiostatic conditions and with what electrode geometries concentration reversion is possible.

We demonstrate below that concentration reversion can indeed occur in the case of first-order reactions at spherical electrodes. In this case the reaction conditions that give rise to concentration reversion can be specified, and the entire concentration-time curve can be described by an exact closed-form equation. The possibility that concentration reversion can occur with higher-order reactions at spherical electrodes, or with electrode reactions of any order at planar and cylindrical electrodes, is also examined.

The generalized higher-order electrode reaction to be treated is fomulated as

$$\mathrm{bB}^{z+} + \mathrm{xX} + ne^- = \mathrm{yY}^{[(bz-n)/y]+} + \mathrm{wW} \qquad [1]$$

The charge-transfer mechanisms are restricted to those in which the electrical work involved all occurs during the rate-determining step. The solution is assumed to contain an excess of supporting electrolyte and high concentrations of substances X and W, so that only one reactant and one reaction product exhibit significant changes in concentration. For these conditions the rate of reaction [1] in the anodic direction (right to left), as a function of the concentrations at the electrode surface, may be expressed as current density at time t by (8)

$$i(t) = i_o \left(\frac{c_Y}{c_Y{}^o}\right)^{y/\nu} \exp\left[(1-\beta)\frac{n}{\nu}\epsilon\eta\right] - i_o \left(\frac{c_B}{c_B{}^o}\right)^{b/\nu} \exp\left[-\beta\frac{n}{\nu}\epsilon\eta\right] \qquad [2]$$

Here i_o is the exchange current density, β the transfer coefficient, and ν the stoichiometric number of the charge-transfer mechanism. Also η is the overpotential and $\epsilon \equiv \mathbf{F}/RT$, where $\mathbf{F}$ is the Faraday, R the gas constant and T absolute temperature. The concentrations of Y and B in the solution at the electrode surface are the bulk values $c_Y{}^o$, $c_B{}^o$ at time $t = 0$, and are written c_Y, c_B (without added notation) for time t. The reaction order (defined at constant potential) is y/ν with respect to Y and b/ν with respect to B.

It is assumed that the electrode is initially at the reversible potential, so that the potential step applied to begin the reaction is equal to η. At first sight we might expect the concentration ratio of the anodic reactant, $c_Y/c_Y{}^o$ in Eq. [2], to decrease continuously with time and the product ratio $(c_B/c_B{}^o)$ to increase continuously with time, each of these effects causing the current to decrease continuously with time. Although the current is a measure of the over-all reaction and decreases monotonically, the coupling of c_Y and c_B at the electrode surface through Eq. [2] means that one of c_Y, c_B is required to change monotonically, but not necessarily both. Coupled migration of this type makes concentration reversion possible but does not assure its occurrence, as is demonstrated later.

Mass transfer of Y or B to the electrode surface is restricted to diffusion only. The fundamental problem is then a boundary-value diffusion problem. The flux at the electrode boundary is given by Fick's first law as

$$i(t) = (n/y)\mathbf{F}D_Y(\partial c_Y/\partial x) = -(n/b)\mathbf{F}D_B(\partial c_B/\partial x) \qquad [3]$$

where $i(t)$ is the current in Eq. [2]. This boundary-value problem varies in detail for planar, spherical, and cylindrical electrodes, but the mathematical details need not be discussed here.

Planar Electrodes

The general diffusion problem for planar electrodes has been examined in a previous paper (5). By application of a powerful theorem of Mann and Wolf (9), rigorous proof was given that the concentration of anodic reactant Y at the electrode surface (c_Y) must decrease monotonically for all $t > 0$, and that c_B must increase monotonically. This proof encompasses higher-order as well as first-order electrode reactions. Therefore, concentration reversion will not occur at planar electrodes.

Spherical Electrodes

First-order reactions.—In the case of spherical electrodes, it is expedient to consider first-order reactions separately, because there exists an exact analytical solution of the general boundary-value problem only for reactions of first-order. The concentration-time curves for first-order reactions are given by (10)

$$c_Y(r=a,t) = c_Y{}^o - \frac{i_{t=0}}{n\mathbf{F}\sqrt{D_Y}(\xi-\mu)}\left\{\frac{\sqrt{D_B}}{a}\left(\frac{1}{\mu}-\frac{1}{\xi}\right)+\left(1-\frac{\sqrt{D_B}}{a\mu}\right)C[\mu\sqrt{t}] - \left(1-\frac{\sqrt{D_B}}{a\xi}\right)C[\xi\sqrt{t}]\right\} \qquad [4]$$

$$c_B(r=a,t) = c_B{}^o + \frac{i_{t=0}}{n\mathbf{F}\sqrt{D_B}(\xi-\mu)}\left\{\frac{\sqrt{D_Y}}{a}\left(\frac{1}{\mu}-\frac{1}{\xi}\right)+\left(1-\frac{\sqrt{D_Y}}{a\mu}\right)C[\mu\sqrt{t}] - \left(1-\frac{\sqrt{D_Y}}{a\xi}\right)C[\xi\sqrt{t}]\right\} \qquad [5]$$

Here D_Y and D_B are the diffusivities of Y and B, respectively: $i_{t=0}$ is the charge-transfer controlled current density, which is given by Eq. [2] with $c_Y = c_Y{}^o$ and $c_B = c_B{}^o$; also a = electrode radius, and

$$C[x] \equiv \exp(x^2)\,\mathrm{erfc}(x) \qquad [6]$$

$$\xi \equiv \frac{1}{2}\{\lambda + (\sqrt{D_Y}+\sqrt{D_B})/a + \sqrt{\psi}\} \qquad [7]$$

$$\mu \equiv \frac{1}{2}\{\lambda + (\sqrt{D_Y}+\sqrt{D_B})/a - \sqrt{\psi}\} \qquad [8]$$

$$\psi \equiv \lambda^2 + (\sqrt{D_Y}-\sqrt{D_B})^2/a^2 + (2/a)(\lambda_Y\sqrt{D_Y}-\lambda_B\sqrt{D_B})(\sqrt{D_Y}-\sqrt{D_B}) \qquad [9]$$

$$\lambda \equiv \lambda_Y\sqrt{D_Y} + \lambda_B\sqrt{D_B} \qquad [10]$$

$$\lambda_Y \equiv \frac{i_o \exp[(1-\beta)n\epsilon\eta]}{n\mathbf{F}\,c_Y{}^o D_Y}, \lambda_B \equiv \frac{i_o \exp(-\beta n\epsilon\eta)}{n\mathbf{F}\,c_B{}^o D_B} \qquad [11]$$

The corresponding current-time relation is

$$\frac{i(t)}{i_{t=0}} = \frac{1}{1+a\lambda_Y+a\lambda_B} + \frac{1}{\xi-\mu}\left\{\frac{(\sqrt{D_Y}-a\xi)(\sqrt{D_B}-a\xi)}{a^2\xi}C[\xi\sqrt{t}] - \frac{(\sqrt{D_Y}-a\mu)(\sqrt{D_B}-a\mu)}{a^2\mu}C[\mu\sqrt{t}]\right\} \qquad [12]$$

In examining Eq. [4] for possible concentration reversion, we note first that normal behavior requires the derivative $\partial c_Y/\partial t$ at $r = a$ to be negative and to decrease in absolute magnitude with time. A sufficient condition for reversion is that this derivative be posi-

Table I. Potentiostatic reactions exhibiting concentration reversion. Spherical electrodes

Test No.	D_Y cm² sec⁻¹ × 10⁵	D_B	c_Y^0 mol cm⁻³ × 10⁵	c_B^0	η, mV	a, mm	$\frac{1}{a\lambda_B}$ *	$\frac{1}{a\lambda_Y}$ **	$-u_{Y,\infty}$	$-u_{B,\infty}$	t_m, sec	At t_m $-u_Y$	u_B	$i/i_{t=0}$
Group I: First-order reactions ($y=n=b=\nu$), i_0 = 0.1 mA cm⁻², β = 0.5, 25°C														
1	5	0.5	1	1	50	4.505	0.283		0.3026	3.026	5680.	0.364	1.92	0.256
2	5	0.5	1	1	10	3.064	0.191		0.0355	0.355	1550.	0.0501	0.244	0.332
3	0.5	5	1	1	10	2.232		0.178	0.259	0.0259	784.	0.184	0.0380	0.350
4	0.5	5	1	1	50	1.079		0.169	0.724	0.0724	173.	0.527	0.1100	0.367
Group II: Reactions second order in Y ($y=n=2$, $b=\nu=1$), i_0 = 0.1 mA cm⁻², β = 0.5, 25°C														
5	5	0.5	2	1	10	2.976	0.478		0.0620	0.620	5110.	0.0714	0.419	0.390
6	5	0.5	4	0.2	35	1.732	0.435		0.0825	8.25	1570.	0.0976	5.64	0.405
7	0.5	5	2	1	60	0.04165		1.121	0.265	0.0265	8.24	0.208	0.0273	0.624
8	0.5	5	40	0.1	60	2.561		0.365	0.392	7.85	3970.	0.268	9.07	0.446

* Compare $\sqrt{D_Y/D_B} - 1 = 2.16$.

** Compare $\sqrt{D_B/D_Y} - 1 = 2.16$.

tive and approach zero (steady-state condition) as $t \to \infty$. The general form of the derivative, as obtained from Eq. [4] for $r = a$, is

$$\frac{\partial c_Y}{\partial t} = -\frac{i_{t=0}}{n\mathbf{F}\sqrt{D_Y}(\xi-\mu)}\left[\left(1-\frac{\sqrt{D_B}}{a\mu}\right)\left\{\mu^2 C[\mu\sqrt{t}] - \frac{\mu}{\sqrt{\pi t}}\right\} - \left(1-\frac{\sqrt{D_B}}{a\xi}\right)\left\{\xi^2 C[\xi\sqrt{t}] - \frac{\xi}{\sqrt{\pi t}}\right\}\right] \quad [13]$$

For large values of t this may be simplified by use of the asymptotic expansion

$$C[x] = (1/\sqrt{\pi})x^{-1} - (1/2\sqrt{\pi})x^{-3} + 0(x^{-5}) \quad [14]$$

to yield

$$\frac{\partial c_Y}{\partial t} = \frac{i_{t=0}}{2\,n\mathbf{F}(\pi D_Y)^{1/2}t^{3/2}(\xi\mu)}\left[1 - \frac{(a\lambda_Y\sqrt{D_Y}+\sqrt{D_Y})+a\lambda_B\sqrt{D_B}+\sqrt{D_B}}{(a\lambda_Y\sqrt{D_Y}+\sqrt{D_Y})+a\lambda_B\sqrt{D_Y}}\right] \quad [15]$$

Noting that $(\xi\mu)$ must always be positive, we see from the term in square brackets that the derivative at long times is always negative when $D_Y = D_B$ or when $D_Y < D_B$. If $D_Y > D_B$, however, the derivative becomes positive for the condition

$$\sqrt{D_Y/D_B} - 1 > 1/a\lambda_B \quad [16]$$

Thus the concentration-time curve for reactant Y exhibits reversion when simultaneously $D_Y > D_B$ and $a\lambda_B$ is sufficiently large. The latter condition requires a moderately rapid electrode reaction and is favored by low bulk concentration of product B; also, the electrode radius must not be too small.[4]

Similar differentiation of Eq. [5] reveals that only normal $c_B - t$ curves can occur when $D_Y = D_B$ or when $D_Y > D_B$. This result tells us formally that the $c_B - t$ and $c_Y - t$ curves can never both exhibit concentration reversion in a single experiment. A sufficient requirement for obtaining reversion of a $c_B - t$ curve is found, as above, to be

$$\sqrt{D_B/D_Y} - 1 > 1/a\lambda_Y \quad [17]$$

Examples of first-order reactions which satisfy condition [16] are tests 1 and 2 of Table I. In each case the concentration of reactant Y at the electrode passes through a minimum at a finite time, t_m. Relative concentration changes

$$u_Y \equiv (c_Y - c_Y^0)/c_Y^0, \quad u_B \equiv (c_B - c_B^0)/c_B^0 \quad [18]$$

are tabulated for comparison purposes. The time t_m corresponding to the maximum concentration change was determined to better than ±1% accuracy from listings of u_Y and u_B as functions of time, obtained by computer from Eq. [4], [5]. Table I lists the minimum in u_Y (shown underlined), as well as the values of u_B and $i/i_{t=0}$ corresponding to it. Also tabulated are the ultimate values $u_{Y,\infty}$ and $u_{B,\infty}$ corresponding to $t \to \infty$. Examples of first-order reactions satisfying condition [17] are tests 3 and 4 of Table I; here the maximum value of u_B was determined and is shown underlined.

By way of illustration, curves of u_Y, u_B, and $i(t)/i_{t=0}$ as functions of time, calculated from Eq. [4], [5], [12], are plotted for test 1 of Table I in Fig. 1. The existence of a minimum in the $u_Y - t$ curve has no effect on the monotonic decrease of current or on the monotonic increase of u_B. This curve exhibits the characteristically slow rate of recovery of concentration after the maximum concentration change is passed. In this case the maximum concentration change exceeds the ultimate change ($t \to \infty$) by 21%. Many other reaction conditions gave relatively larger percentage changes, *e.g.*, 41% for test 2 and 52% for test 6 of Table I.

Higher-order reactions.—No exact analytical solution of the general diffusion problem for higher-order reactions at spherical electrodes has appeared as yet.

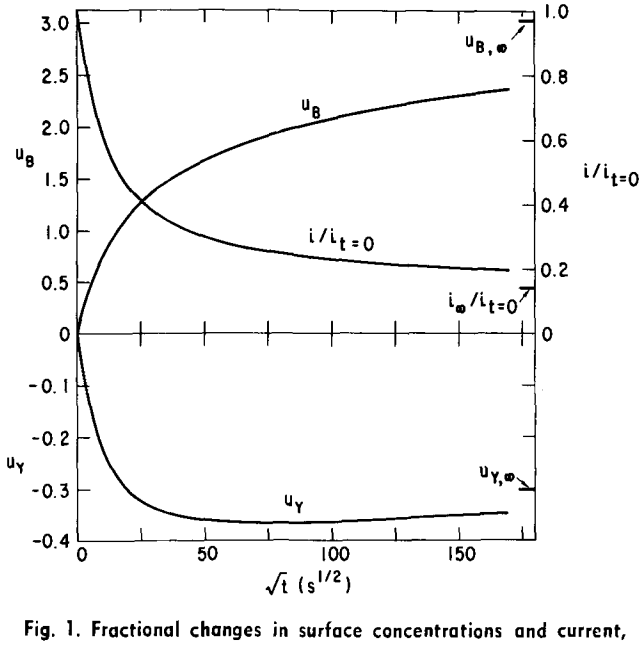

Fig. 1. Fractional changes in surface concentrations and current, first-order reaction at spherical electrode, test 1 of Table I.

[4] We are indebted to a referee for bringing to our attention the work of R. W. Lyczkowski, D. Gidaspow, and C. W. Solbrig, *Chem. Eng. Progress Symp. Series No. 77, 63*, 1 (1967). These authors showed that concentration reversion can occur with chemical reactions taking place on a catalytic surface. The surface constraints on their reacting system are essentially similar to those in the present paper. The criteria which we find, for the occurrence of concentration reversion in potentiostatic reactions, are similar to those which they found for catalytic chemical reactions.

Table II. Potentiostatic reactions exhibiting concentration reversion. Cylindrical electrodes

Test No.	D_Y cm² sec⁻¹ × 10⁵	D_B	c_Y^0 mol cm⁻³ × 10⁵	c_B^0	i_0, mA cm⁻²	β	η, mV	a, mm	$\frac{1}{a\lambda_B}$ *	$\frac{1}{a\lambda_Y}$ **	t_m, sec	At t_m: $-u_Y$	u_B	$i/i_{t=0}$
Group I: First-order reactions (y=n=b=ν)														
1	4	0.4	5	1	1	0.5	10	0.1356	0.346	35.6		0.01327	0.324	0.278
2	4	0.4	5	1	1	0.5	40	0.2045	0.411	114.		0.0914	2.31	0.268
3	0.4	4	0.5	1	0.1	0.5	10	0.2		790.	0.794	0.210	0.01729	0.313
4	0.4	4	1	1	1	0.5	10	0.0827		16.	0.384	0.206	0.0415	0.273
Group II: Reactions second order in Y (y=n=2, b=ν=1)														
5	5	0.5	10	1	1	0.5	30	1.0	0.310	1200.		0.1791	4.27	0.182
6	5	0.5	10	1	3	0.25	20	0.1	0.475	29.6		0.0797	2.08	0.252
7	0.5	5	10	1	0.4	0.5	20	1.0		2070.	0.277	0.317	0.316	0.239
8	0.5	5	5	0.5	3	0.75	30	0.1		18.3	0.224	0.414	0.416	0.229

* Compare $\sqrt{D_Y/D_B} - 1 = 2.16$.

** Compare $\sqrt{D_B/D_Y} - 1 = 2.16$.

A first approximation has been obtained by solving the general problem after linearizing Eq. [2] with respect to concentrations (11). The resulting $c_Y - t$, $c_B - t$ and $i - t$ relations are the same as Eq. [4], [5], [12], provided λ_Y and λ_B are redefined to include the reaction orders

$$\lambda_Y \equiv \frac{(y/\nu)^2 i_0 \exp[(1-\beta)(n/\nu)\epsilon\eta]}{(n/\nu)\mathbf{F}\, c_Y^0\, D_Y},$$

$$\lambda_B \equiv \frac{(b/\nu)^2 i_0 \exp[-\beta(n/\nu)\epsilon\eta]}{(n/\nu)\mathbf{F}\, c_B^0\, D_B} \quad [19]$$

This result indicated to us that Eq. [16] and [17], which are conditions for concentration reversion with first-order reactions, might lead us to higher-order reactions which show this phenomenon, if reversion is indeed possible in higher-order systems. Accordingly we selected several particular reactions which were second order in anodic reactant Y and first order in B; some of these obeyed Eq. [16] and the others Eq. [17]. For each case, the true $c_Y - t$, $c_B - t$, and $i - t$ curves were determined numerically on a computer following the Schmidt method (12). The solution was carried out sufficiently far in time to include the maximum concentration change. In each of the particular cases examined concentration reversion was found; a small sampling of these results is included in Table I. Tests 5 and 6 represent reaction conditions obeying criterion [16], and each exhibits a minimum in c_Y. Tests 7 and 8 obey criterion [17] and exhibit maximum c_B. The values of $u_{Y,x}$ and $u_{B,x}$ tabulated for these higher-order cases were calculated from equations previously developed (11).

Cylindrical Electrodes

In a potentiostatic experiment, the electrode reaction rate decreases monotonically with time whether the electrode is planar, spherical, or cylindrical. At planar electrodes the two coupled concentration changes, u_Y and u_B, stand in constant ratio at all times (5). At spherical electrodes the ratio of these concentration changes is initially ($t \to 0$) the same as at planar electrodes, because the diffusion layer thickness is small with respect to electrode radius, but as the reaction proceeds this ratio changes (10, 11). Cylindrical electrodes also behave initially like planar electrodes but, as with spherical electrodes, the ratio u_Y/u_B varies with time. Such time variation is a necessary condition for concentration reversion to occur. Although this is not a sufficient condition, it motivated us to look for concentration reversion at cylindrical electrodes. In addition, the success of Eq. [16], [17] as criteria for revealing concentration reversion in higher-order reactions at spherical electrodes encouraged us to apply these criteria to cylindrical electrodes, for both first-order and higher-order reactions. The admittedly tenuous rationale behind such application to cylinders is the fact (6, 13) that, for an appreciable time starting at $t = 0$, a constant-potential reaction exhibits almost the same kinetics at a cylinder of radius a as it does at a sphere of radius $(8/3)a$.

Several particular cases of first-order reactions at cylindrical electrodes were selected initially, on the basis of Eq. [16], [17], and the true curves of $c_Y - t$, $c_B - t$, and $i - t$ were obtained by solving the boundary value problem numerically on a computer. Again the Schmidt procedure (12) was followed, the boundary conditions on the concentration gradients being handled by a method also ascribed to Schmidt [ref. (14), designated Method II]. Concentration reversion was found to occur, as is shown by the group I tests in Table II (maximum relative concentration changes are underlined). Equation [16] was successful as a criterion for revealing c_Y reversion; tests 1 and 2 are typical examples. Equation [17] led to c_B reversion, *e.g.*, tests 3 and 4.

Next the two criteria were applied to particular reactions second-order in reactant Y and first-order in B as examples of higher-order reactions. In each case true concentration-time and current-time curves were generated numerically as above. Again Eq. [16] led us to c_Y reversion, *e.g.*, tests 5 and 6 of Table II; and Eq. [17] led to c_B reversion, *e.g.*, tests 7 and 8.

Conclusions

In electrode reactions at constant potential, the coupled concentration changes of two substances involved in the reaction can lead to concentration reversion, *i.e.*, the absolute value of the concentration change of one substance passes through a maximum at some finite reaction time. This phenomenon occurs at spherical and cylindrical electrodes, both with first-order and higher-order reactions, but it cannot occur at planar electrodes. In the case of first-order reactions at spherical electrodes, the known closed-form solutions for the concentration-time behavior permit one to predict experimental conditions that give rise to the reversion phenomenon.

Acknowledgments

We are very grateful to Dr. N. P. Louat and Dr. L. S. Darken for their helpful suggestions and discussions.

Manuscript submitted April 27, 1970; revised manuscript received *ca.* Nov. 26, 1970.

Any discussion of this paper will appear in a Discussion Section to be published in the December 1971 JOURNAL.

REFERENCES

1. L. D. Kirkbride and G. Derge, *Trans. AIME*, **218**, 87 (1960).
2. L. S. Darken and R. W. Gurry, "Physical Chemistry of Metals," p. 462, McGraw-Hill Book Co. Inc., New York (1953).
3. L. S. Darken, *Trans. AIME*, **221**, 654 (1961).
4. E. T. Turkdogan and M. L. Pearce, *ibid.*, **227**, 940 (1963).
5. S. Barnartt and C. A. Johnson, *J. Phys. Chem.*, **71**, 4430 (1967).

6. C. A. Johnson and S. Barnartt, *ibid.*, **73**, 3374 (1969).
7. S. Barnartt and C. A. Johnson, *Trans. Faraday Soc.*, **65**, 1091 (1969).
8. S. Barnartt, *Electrochim. Acta*, **11**, 1531 (1966).
9. W. R. Mann and F. Wolf, *Quart. Appl. Math.*, **9**, 163 (1951).
10. C. A. Johnson and S. Barnartt, *J. Phys. Chem.*, **71**, 1637 (1967).
11. C. A. Johnson, S. Barnartt, and F. D. Glasser, *J. Electroanal. Chem.*, **28**, 1 (1970).
12. H. S. Carslaw and J. C. Jaeger, "The Conduction of Heat in Solids," 2nd ed., Section 18.3, Clarendon Press, Oxford (1959).
13. S. Barnartt and C. A. Johnson, *Anal. Chem.*, **43**, 2 (1971).
14. P. H. Price and M. R. Slack, *Brit. J. Appl. Phys.*, **3**, 379 (1952).

Interferometric Study of the Concentration Change at High Cathodic Current Densities

Aladar Tvarusko* and Laurence S. Watkins[1]

Engineering Research Center, Western Electric Company, Princeton, New Jersey 08540

ABSTRACT

The refractive index change, Δn, *i.e.*, the concentration of the solution at a vertical cathode was studied by a Lloyd mirror laser interferometer during the electrodeposition of copper from $CuSO_4$ solutions with and without tenfold excess of H_2SO_4. The initial galvanostatic transients were studied below the limiting current density and above to the start of H_2 bubble formation. It was found that the concentration decreased linearly with $it^{1/2}$ for both solutions. The effect of an assumed linear refractive index gradient on the measured value of Δn is discussed in addition to the influence of the H_2SO_4 supporting electrolyte.

The change of the refractive index, *i.e.*, concentration of the solution in the diffusion layer during electrochemical processes, has been extensively studied by interferometry, mainly at low current densities (1). At high current densities, the refractive index change of the solution cannot usually be obtained from the various interferograms because the beam of light is deflected due to the presence of large refractive index gradient in the diffusion layer (2, 3). Similar observations were made also in interferometric heat transfer studies (4). The complex light deflection errors were treated by several workers (2, 4-6).

We have described separately (2) a Lloyd mirror laser interferometer for the determination of the refractive index gradient. The optical path length change of the reflected ray was measured as a function of time, incidence angle, and electrode displacement (2). The refractive index gradient is calculated from the measured optical path length change (2) by an iterative solution of the derived equation (7) on a digital computer. The change of refractive index is obtained by multiplying the refractive index gradient with the diffusion layer thickness (2, 3).

The electrodeposition of copper from 0.24M $CuSO_4$ solutions without and with tenfold excess of H_2SO_4 was studied by a Lloyd mirror laser interferometer at high constant current densities ($\leq$90 mA/cm^2). We shall describe the interference fringe behavior especially above the limiting current density, the optical path length change as a function of time at various current densities, and the refractive index change as a function of $it^{1/2}$.

Experimental

The experimental setup was described separately in detail (2). Figure 1 shows schematically the electrolysis cell and the Lloyd mirror laser interferometer. A diverging laser beam is partially reflected off the electrode producing an interference pattern between the reflected and unreflected part of the beam. In the experiment, fixed photo devices are used to monitor the movement of the interference fringes and their outputs are recorded on oscillographs. The interference fringes move past the detectors after the current addition because the optical path length of the reflected beam changes in the developing diffusion layer (2, 7). The distance between neighboring maxima or minima of the sinusoidal signal (Fig. 2) correspond to the movement of one fringe and the optical path length change of the deflected beam equals the wavelength of the laser light (632.8 nm).

Results and Discussion

The sinusoidal oscillograph traces are basically the same in the beginning of the galvanostatic experiments regardless of the current density but not the number of cycles, *i.e.*, fringes and the frequency of the waveform, *i.e.*, number of fringes per second (compare Fig. 3). Below the limiting current density the sinusoidal waveform becomes smooth when the steady state is reached, whereas it abruptly ends after a certain time above the limiting current density. Figure 2 shows the latter for a 0.24M $CuSO_4$-2.36M H_2SO_4 solution and the signal undergoes a large rapid change which is followed by a slow recovery. The traces eventually become randomly rough due to the evolving hydrogen gas bubbles.

The aforementioned large change of the signal occurs first at large θ angles (θ is the complementary angle of incidence) and proceeds toward shallower angles with time (in less than 1 sec, depending to a

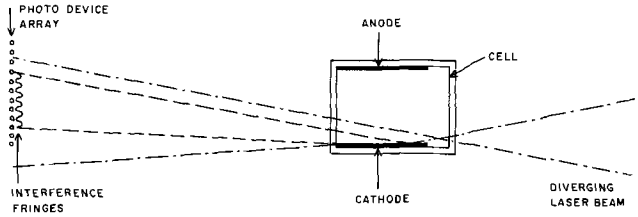

Fig. 1. Schematic of the electrolysis cell and Lloyd mirror laser interferometer (not drawn to scale).

* Electrochemical Society Active Member.
[1] Present address: Department of Electrical Engineering Science, University of Essex, Colchester, Essex, England.
Key words: Lloyd mirror laser interferometry, electrodeposition of copper, hydrogen evolution, galvanostatic transients, supporting electrolyte.

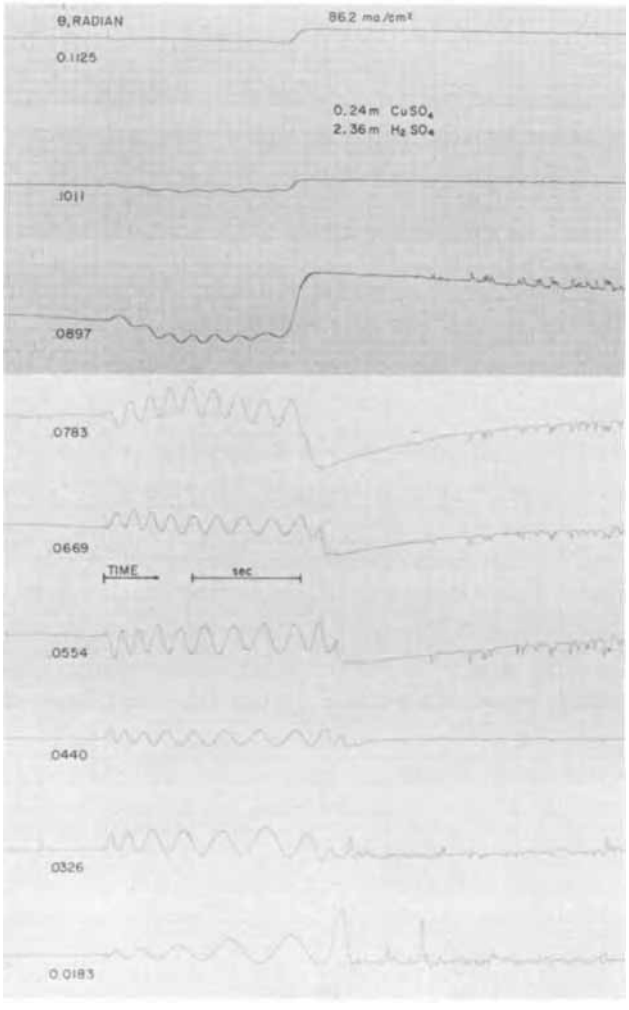

Fig. 2. Oscillograph record of the photodevice array output at various complementary angles of incidence (θ) before and after the addition of 86.2 mA/cm^2 which is well above the limiting current density. The solution is 0.24M $CuSO_4$-2.36M H_2SO_4.

certain degree on the current density). This large change of the trace coincides with the movement of a brighter spot of the interfering laser beam across the photodevice array from larger to smaller θ values. The random signal excursions, on the other hand, begin at the lowest θ value after the aforementioned large rapid change of the signal has already occurred at higher θ values.

The time dependence of the transition of the large change could be explained by the deflection of the ray on various segments of the diffusion layer normal to the cathode, if the diffusion layer is assumed to be uniform along the cathode. It is clear from initial appearance of the large signal change at large θ angles that the phenomenon responsible for it occurs first in a segment of the diffusion layer adjacent to the cathode. This phenomenon extends with progressing electrolysis time toward the diffusion layer/bulk solution interface. High-speed color motion pictures of the laser beam in the diffusion layer and on the cathode showed no visible change until the H_2 bubble formation. The H_2 bubbles were very clearly visible in the path of the ray and the ray was randomly bounced off the bubbles.

The aforementioned large change and its time dependent propagation through the diffusion layer are caused by the processes occuring in the immediate vicinity of the cathode. Let us see what happens at the cathode and in the diffusion layer during galvanostatic transient above the limiting current density. Cu^{++} are discharged in the beginning at the cathode until its concentration at the cathode/solution interface decreases to zero when the H^+ present in the solution will start to be neutralized at the cathode simultaneously with the Cu^{++}. The electrodeposited copper will be very rough and the H_2 will dissolve in the solution adjacent to the cathode. According to the unsteady-state model of electrolytic bubble growth (8), first developed by Hsu (9) for a boiling liquid at a heated wall, there is a waiting time before a gas bubble forms. During this waiting time the continuously generated hydrogen gas diffuses away from the cathode due to the concentration gradient and the gas concentration increases in the solution adjacent to the cathode until it reaches a critical value at a specific distance from the cathode. Then, a gas bubble will start to grow from the supersaturated solution at a nucleation site.

Glas and Westwater (8) found that the waiting times for hydrogen bubble formation from pure H_2SO_4 solutions were usually much less than 1 sec but were up to 30 sec on nickel at 40 mA/cm^2. The elapsed time in Fig. 2 for the large change between the largest and smallest θ angles is 0.42 sec and elapsed times of 0.4 to 0.7 sec were found for Cu cathodes during the electrodeposition of copper from both $CuSO_4$ solutions. The delayed appearance of gas bubbles, *i.e.*, randomly rough signal trace after the large change of the signal and its time dependent propagation toward the bulk solution could be assigned to the H_2 dissolution and supersaturation phase during the waiting time. Unfortunately, there are no experimental data available on the refractive index of electrolytes supersaturated with gases under comparable conditions and the aforementioned possible correlation cannot be ascertained on the basis of Lloyd mirror interferometric experiments. It is interesting to note that the diffusion layer thickness (determined from Mach-Zehnder interferograms) increased rapidly during the corresponding time before the visible H_2 bubble evolution in the presence of tenfold excess of H_2SO_4 (3). Another possible explanation for the time dependent large change would be the formation of submicroscopic hydrogen gas bubbles which are slowly growing from the solution rapidly becoming supersaturated.

The large change of the signal in 0.24M $CuSO_4$, *i.e.*, in the absence of tenfold excess of H_2SO_4, is present also but at approximately twice the previous current densities (due to the influence of migration). In the absence of H_2SO_4 the random signal excursions start practically immediately after the disappearance of the sinusoidal signal at all angles in contrast to the absence of these random traces at large θ angles with the tenfold excess of H_2SO_4. If they are present, they cannot be detected because of the aforedescribed large change of the signal.

It is hoped that a future interferometric study of the initial galvanostatic transients of gas evolution in aqueous acid and alkaline solutions will answer whether or not these large signal changes are present in absence of simultaneously occurring metal deposition and are caused by the supersaturation of the solution or by others.

Figure 3 shows the optical path length change of the deflected beam in terms of fringes at a recommended (2) higher θ angle ($\theta = 0.0807$ radian) as a function of time for various current densities. It can be clearly seen that (*a*) the optical path length change develops faster at higher current densities; and (*b*) the number of fringes increases with current density, but starts to decrease approximately above the limiting current density. The same is true for the change of the optical path length at low θ angle ($\theta = 0.0193$ radian, not reproduced here) but the number of fringes is not sensitive to current density ($\gtrsim$5 mA/cm^2). The reason for this current independence of the optical path length change at low θ angles is as follows: At shallow angles the beam penetration is quite small and so a change in the refractive index does not alter much the optical path of the beam through the diffusion layer; the beam will be very close to the edge of the diffusion layer.

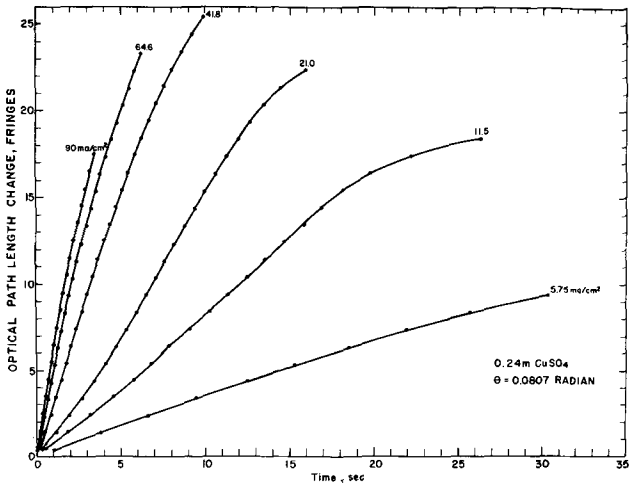

Fig. 3. The optical path length change of the deflected beam at higher complementary angle of incidence as a function of time at various current densities in 0.24M $CuSO_4$.

A change in the diffusion layer thickness, however, will alter the optical path length significantly since the diffusion layer edge has moved.

The refractive index gradient is calculated from the measured optical path length change (2) by an iterative solution of the derived equations (7) on a digital computer. The change of the refractive index at the cathode/solution interface, Δn during the current flow is obtained by multiplying the refractive index gradient with the diffusion layer thickness (2, 3). The refractive index change in our case is practically linearly dependent on the concentration change of the solution, Δc (refractive index change of 1.10^{-4} equals 3.68×10^{-6} mole $CuSO_4/cm^3$). Thus, a linear relationship should be obtained between Δn (Δc) and $it^{1/2}$ in $CuSO_4$ solutions with and without tenfold excess of H_2SO_4 (10).

Figure 4 shows Δn as a function of $it^{1/2}$ at various current densities in 0.24M $CuSO_4$. It can be seen in the left half that the linear regression fits the data well (the coefficient of correlation, R, is high) but the regression line (fitted by the least squares method) does not go through zero. The highest Δn value is 40×10^{-4} which is significantly below the expected value of 69×10^{-4} if the concentration of $CuSO_4$ at the cathode surface is zero at and above the limiting current density.

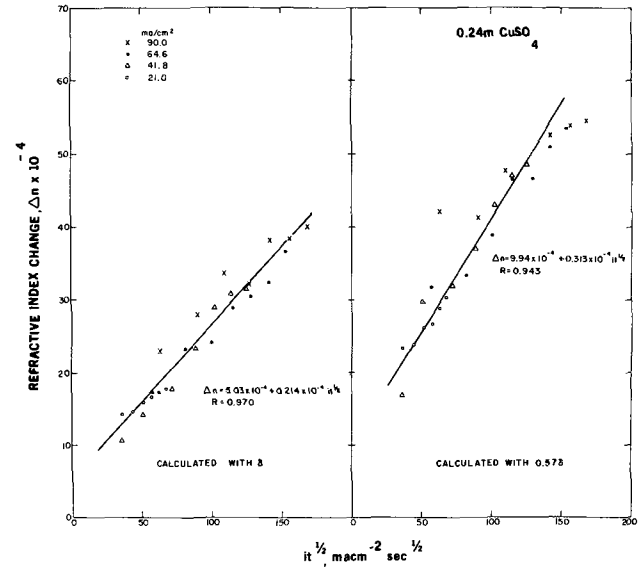

Fig. 4. The refractive index change as a function of $it^{1/2}$ at various current densities in 0.24M $CuSO_4$. Δn is calculated with the actual diffusion layer thickness, δ, and the idealized Nernst diffusion layer thickness (0.57 x δ), respectively.

The derived correlations (7) assume, as a first approximation, that the refractive index gradient is linear over the entire diffusion layer (idealized Nernst case). Interferometric measurements have shown that the gradient is linear over a substantial part of the diffusion layer (11) and the change of refractive index is exponential near the edge of the diffusion layer. The diffusion layer thickness, δ used for the calculation of Δn in Fig. 4, was obtained from Mach-Zehnder interferograms (1, 3) and is a measure of the diffusion layer thickness to its outside edge. If this δ is used to calculate the refractive index gradient, a much lower value of Δn results because the average linear value of the gradient over the entire diffusion layer is smaller (7). To obtain a more accurate value of Δn, a value of 0.57δ, derived by Ibl (11), should be used instead of the full δ values since the average gradient for this shorter distance more closely approximates the actual gradient at the cathode (7). We have recalculated Δn with 0.57δ and the result is shown in the right half of Fig. 4. The linear correlation is slightly lower and the highest Δn is within approximately 15% of the expected value. Thus, a better agreement is obtained with the expected value through this simple correction.

As mentioned, δ was obtained from Mach-Zehnder interferograms (1, 3). This requires another experimental setup and a time consuming interpretation of the interferograms. An empirical diffusion layer thickness, δ_θ was described separately (2, 7) and is obtained from the computer printout of the refractive index gradient calculation (7). Δn calculated with δ_θ was found to increase linearly with $it^{1/2}$ (similarly to Fig. 4) and the value of Δn is about half of the expected one. Since δ_θ corresponds to a point near the edge of the actual diffusion layer, we can use again $0.57\delta_\theta$ and Δn was found to increase markedly but it is still slightly lower than the expected value. The advantage of using δ_θ is that it yields an approximate value of Δn without an additional experimental setup.

During the electrodeposition of copper from $CuSO_4$ solution, the sulfate ions remain in the diffusion layer and must react with water to preserve the electroneutrality and HSO_4^- and/or H_2SO_4 forms. The presence of H_2SO_4 in the vicinity of the cathode would likely falsify the calculated Δn value and lower Δn values would be obtained. In view of this, we have measured the optical path length change in 0.24M $CuSO_4$ with a tenfold excess of H_2SO_4. Figure 5 shows

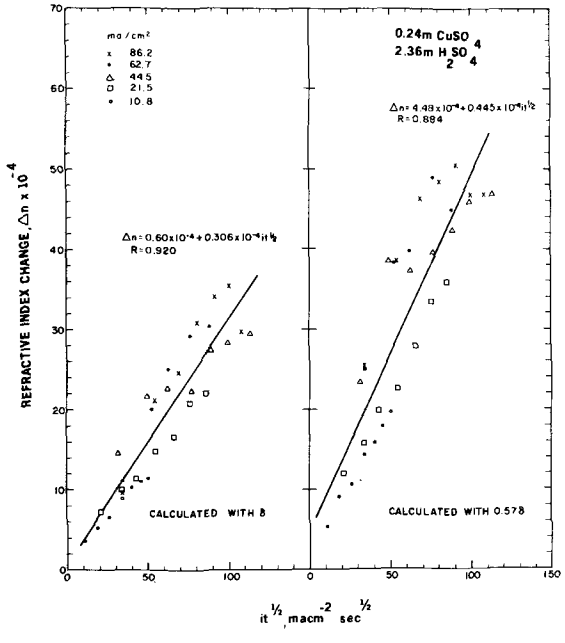

Fig. 5. The refractive index change as a function of $it^{1/2}$ at various current densities in 0.24M $CuSO_4$-2.36M H_2SO_4 solution. Δn is calculated as in Fig. 4.

that the calculated Δn values are approximately the same as in the absence of H_2SO_4 (Fig. 3) and the coefficients of correlation are smaller in the presence of the tenfold excess of H_2SO_4 then in its absence. The Δn values calculated with the empirical diffusion layer thickness values are similar to those obtained in the absence of H_2SO_4.

The slope of Δn-$it^{1/2}$ regression line is markedly larger, *i.e.*, Δn develops faster in the presence of tenfold excess of H_2SO_4 than in pure $CuSO_4$ (Fig. 4, 5). The ratio of the slope in pure 0.24M $CuSO_4$ solution, s_m, to that in the presence of tenfold excess of H_2SO_4, s_d, equals to 0.70. In view of the practically linear relationship between Δn and Δc, the s_m/s_d ratio can be calculated for the $CuSO_4$ solutions from

$$\Delta c = \frac{2(1 - n_c)}{z\mathbf{F}\,(\pi D)^{1/2}}\, it^{1/2} \qquad [1]$$

where n_c is the cation transference number, and the others have their usual significance (10). Using $D_{salt} = 5.6 \times 10^{-6}$ cm^2/sec (12), $n_c = 0.34$ (12) for the $CuSO_4$ binary electrolyte and $D_{Cu++} = 7.2 \times 10^{-6}$ cm^2/sec (13), $n_c \approx 0$ (14) for the $CuSO_4$ with large excess H_2SO_4, we obtain 0.748 for the s_m/s_d ratio which compares favorably with the aforementioned experimentally obtained s_m/s_d ratio of 0.70. These results clearly demonstrate that the change of the slope is due to the effects of migration.

Earlier (1) we have determined Δc by Mach-Zehnder interferometer as a function of $it^{1/2}$ in the presence of small amount of supporting electrolyte at low current densities and practically the same $CuSO_4$ concentration (0.25M). For these experiments $s_m/s_d^* = 0.77$ (s_d^* is the slope of Δc-$it^{1/2}$ regression line in the presence of 0.11M H_2SO_4) which is higher than the experimentally determined ratio for the presence of large excess of H_2SO_4. Unfortunately, independently determined values of D and n_c are not available for this solution and the slopes cannot be calculated.

Newman (15) studied the effect of H_2SO_4 addition on the limiting current for copper deposition from $CuSO_4$ solutions. If we assume that Newman's results are applicable also below the limiting current densities then we can compare them with our results. The $s_m/s_d^*/s_m/s_d$ ratio is preferred because thus any possible influence of the different interferometric techniques is eliminated and it equals 0.77/0.70 = 1.10. Newman's concentration ratio, r, for the 0.25M $CuSO_4$-0.11M H_2SO_4 solution is 0.3055 ($r^{1/2} = 0.553$) and we obtain 1.27 from his Fig. 3 and Table II for the I_L/I_D, *i.e.*, the ratio of limiting currents in the presence and absence of migration, respectively. Since Newman's results are valid for a disk electrode, we have to convert 1.27 for a plane electrode (our case) by dividing it by 1.1198 (Newman's Eq. [36]) and the result is 1.13. This value compares very favorably with our interferometrically determined ratio of 1.10. Unfortunately, we have no additional data at the present for further verification at other H_2SO_4 concentrations.

It should be noted that the Δn values obtained from Mach-Zehnder and Lloyd mirror interferometer measurements at low current densities (~10 mA/cm^2) agreed well.

Manuscript submitted Sept. 14, 1970; revised manuscript received *ca.* Nov. 15, 1970. This was Paper 289 presented at the Los Angeles Meeting of the Society, May 10-15, 1970.

Any discussion of this paper will appear in a Discussion Section to be published in the December 1971 JOURNAL.

REFERENCES

1. A. Tvarusko and L. S. Watkins, *Electrochim. Acta*, **14**, 1109 (1969).
2. L. S. Watkins and A. Tvarusko, *Rev. Sci. Instr.*, **41**, 1860 (1970).
3. A. Tvarusko and L. S. Watkins, *This Journal*, **118**, 248 (1971).
4. F. W. Schmidt and M. E. Newell, *Rev. Sci. Instr.*, **39**, 592 (1968).
5. K. W. Beach, UCRL-18037, February 1968.
6. R. H. Müller, K. W. Beach, and C. W. Tobias, Paper presented at the 20th Meeting of CITCE, Strasbourg (1969).
7. L. S. Watkins and A. Tvarusko, To be published.
8. J. P. Glas and J. W. Westwater, *Intern. J. Heat Mass Transfer*, **7**, 1427 (1964).
9. Y. Y. Hsu, *Trans. ASME, J. Heat Transfer*, **84**, 207 (1962).
10. N. Ibl, in "Advances in Electrochemistry and Electrochemical Engineering," Vol. 2, pp. 82-85, P. Delahay and C. W. Tobias, Editors, Interscience, New York (1962).
11. Ref. 10, p. 80.
12. Ref. 10, p. 105.
13. R. Parsons, "Handbook of Electrochemical Constants," p. 79, Butterworths Scientific Publications, London (1959).
14. E. J. Fenech and C. W. Tobias, *Electrochim. Acta*, **2**, 311 (1960).
15. J. Newman, *Ind. Eng. Chem., Fundamentals*, **5**, 525 (1966).

Technical Note

An Automated Procedure for Obtaining Steady-State Current-Potential Relationship

G. Belanger*

Hydro-Quebec Institute of Research, Varennes, Province of Quebec, Canada

In the experimental investigations on the mechanism of activation-controlled electrode reaction, the relevant data are partly gathered by measurement of steady-state current-potential relationships (1-3). The current-potential curves thus obtained provide quantitative values of Tafel slopes, exchange current densities, reaction orders, apparent heats of activation, and, under favorable conditions, stoichiometric numbers. In addition to these parameters, a great deal of

* Electrochemical Society Active Member.
Key words: automation, measurement of current-potential curves.

other useful information may also be obtained in some cases from these curves, *e.g.*, inhibition inflections and associated negative Tafel slopes, mechanism change as a function of potential as deduced from abrupt changes in the Tafel slopes caused by parallel or consecutive reactions, and, some other general features of the over-all current-potential plots. In short, a variety of useful details, which are indispensable to the elucidation of the reaction mechanism, are obtained from these curves.

The usual procedure of obtaining these curves, is the point-by-point measurement (either potentiostatic or galvanostatic) which is quite tedious and time-consuming. A recent alternative has been proposed to measure a slow potentiodynamic curve, which in most cases, yields current-potential relationships very similar to those obtained by the steady-state procedure. The potentiodynamic method, even at slowest speed, is still open to the objection that the true steady state is never achieved since the potential is being continuously varied.

Here, an attempt has been made to describe a procedure which may be used to obtain true steady-state relationship in a fully automated manner. In most cases, the present method would yield results very similar to those obtained by a slow potentiodynamic sweep. However, in several cases in which a knowledge of the true steady-state current-potential relations is necessary for a precise mathematical analysis of the kinetic data (2), the present procedure may be used to acquire the data in an automated manner.

Experimental

Measurements were made in a conventional three-compartment Pyrex cell (Fig. 1A). The hydrogen reference electrode in the same solution was used, and the test electrode was studied under helium atmosphere. The gases used were purified by the usual techniques (4).

The electronic equipment used is commercially available; only a slight modification to one of the component, as described below, was required to put the system into operation.

Figure 1 gives the block diagram of the experimental arrangement. The potentiostat (B), Tacussel Model PRT 20-10, controlling the electrochemical reaction was regulated by a motor driven potentiometer (C): the potentiometer of the potentiostat was by-passed. The potential between the working and reference electrode was controlled by this mechanical device (Tacussel's Servovit pilot scanner Model 9B): the advantage of this particular instrument is that it can be controlled remotely by an appropriate switching program. To achieve this programming, a series of microswitches activated by cams (D), Industrial timer, series MC was used in our experiment. The potential span is regulated by the time the scanner is on and by the speed at which resistance of the potentiometer is made to vary. The current is measured by a logarithmic amplifier (E) whose voltage output is proportional to the logarithm of the input current (Tacussel's logalex, Model 100B). The lower limit of current measurement is 0.1 μA. The log i is fed to the X axis of X-Y recorder (F). The potential between the working and reference electrode is recorded on the Y axis. The pen of the recorder is activated by a switch closure provided by the cam system (D).

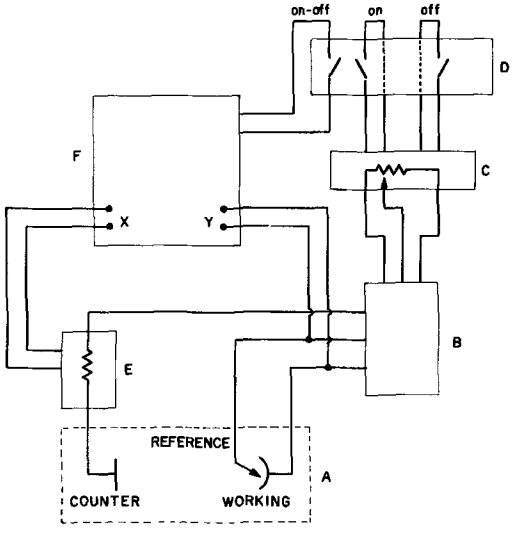

Fig. 1. Block diagram of the experimental set up: A, three-compartments cell; B, potentiostat; C, motor-driven potentiometer; D, microswitches and cam assembly; E, logarithmic current amplifier; F, X-Y recorder.

In Fig. 2 we present the schematic potential-time sequence to which the working electrode was subjected. In this figure, τ_1 represents the time the scanner is on: this time gives us the voltage span, ΔV. For a given time τ_2, the potential is kept constant: τ_2 is chosen long enough for the electrochemical steady-state to be established. Just before a new increment of potential is applied to the working electrode, one cam closes the switch, thus activating the pen of the X-Y recorder. This is illustrated as τ_3 in Fig. 2.

As mentioned above, slight modifications to the relay circuits of the Servovit scanner were made so that potentiostatic cycles could be performed (*i.e.* starting at 2V anodic going to zero and back at 2V or any other program). The modified circuit of the Servovit scanner is given in Fig. 3. The nomenclature and arrangement in Fig. 3 refer to the blue print of the instruction manual. Two double-pole double-throw relays (A and R) of this original instrument were replaced by two quadrupole double-throw relays. The relay (RT) originally used as a marker, is now used in conjunction with the new circuit. The remote control wiring diagram is also given in Fig. 3.

Other types of scanner could be used for the same purpose. The Wenking scanning potentiometer, Model S M P 69 would be equally suited for this experimental procedure.

Results

Figure 4 shows an example of the use of this procedure for the case of anodic oxidation of 5M methanol in 1*N* H_2SO_4 on bright platinum electrodes. This curve was plotted over a 24-hr period. The potential span is 10 mV, and the fixed potential was retained for 3.75 min at every point in order for the steady state to be achieved.

Detailed interpretation of this curve will be presented elsewhere, but some features can be compared with previous results (5, 6). The maxima on the ascending curve at 0.95 and at 0.7V on the descending

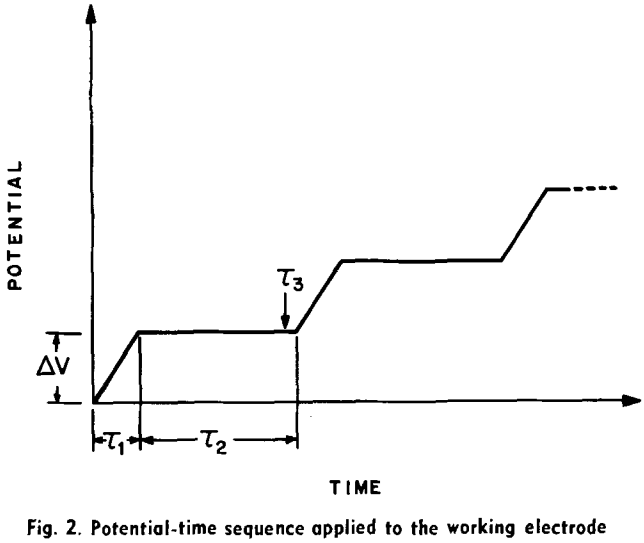

Fig. 2. Potential-time sequence applied to the working electrode

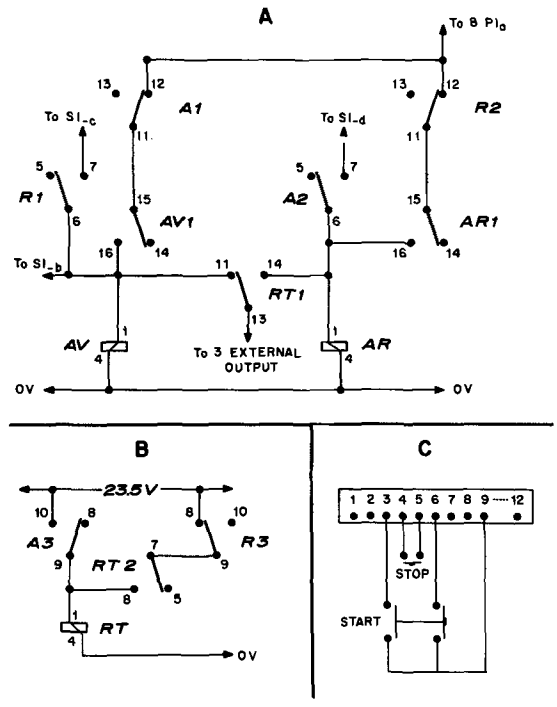

Fig. 3. Modification of the Relay circuits of Tacussel's Pilot Servovit, Model 9B (A and B); remote control circuit diagram (C).

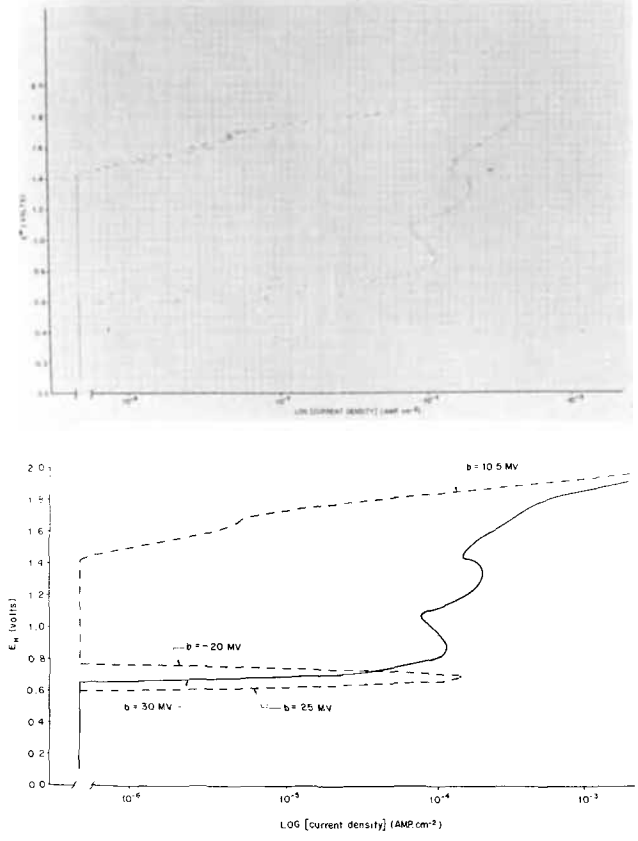

Fig. 4. Steady-state potentiostatic plot of 5M methanol in InH_2SO_4. (A) (top) Raw data from the recorder; (B) (bottom) final forms: – – – descending and ——— ascending directions of potential.

curve agree roughly with those obtained potentiodynamically by Gilman and Breiter (6). However, our rates are lower than those reported by them (6), since a steady state was not achieved in their work.

It may be mentioned that the same procedure was also used (7) for the investigation of hydrogen evolution reaction and found to be quite satisfactory.

After 2 min at a given potential, the current variations with time were very small at most potentials so that the 3.75-min interval was sufficient for the steady-state conditions to be achieved. However, in the low current region (10^{-6}A) it appears that some irregular oscillation of the currents occurred, due mainly to the oxidation, it is believed, of some residual impurities. These oscillations produced straight dashes (Fig. 4A) instead of points in the log current-potential relationship. By the addition of cams to the microswitch system (Fig. 1) several points could be recorded during the constant potential time interval (τ_2 in Fig. 2). This could give us an idea on the log current-time variations at a given potential.

The direct recording of the current-time variations could not be achieved directly with the instruments used in the experiment. The difficulty of matching the impedances between the different instruments produced meaningless results specially at low current values (10^{-7} to 10^{-6}A). This limitation does not appear to be intrinsic, however.

Conclusion

The advantage of this automated procedure is evident when a great number of such curves have to be obtained. Studies of certain variables in a given experimental condition can be made on a continuous basis, *e.g.*, variation of concentration to determine reaction orders, addition of certain poisons or accelerators in a given solution, etc.

Further extension in the automation of this simple system can be easily forseen: instead of recording the data on a X-Y recorder, they could be fed directly into a computer (with the appropriate interfaces). The format of the results could then be either digital or/and graphical. In this case the logarithmic amplifier could be replaced by a resistance, and the voltage drop across it would thus be the measure of the current.

Among further developments of this automated procedure, our attention will be focused on the means of defining and reaching the "true steady-state" conditions. This goal could be achieved by measuring the change of the current with time at a given potential and recording the value of the current only when this variation becomes less than a preset value (*i.e.*, less than 1%). This procedure implies comparison of data sampled at a given time interval and, to achieve this goal efficiently, the use of an automatic data acquisition and treatment system will be essenital.

By minor modifications of our scanner, other forms of potential time program can also be achieved.

Acknowledgment

The author wishes to thank Dr. A. K. Vijh for his help in the preparation of the manuscript and Dr. P. Lenfant for his interest in this work. The help of Mr. G. Trudel in the physical realization of the work is acknowledged.

Manuscript submitted Nov. 6, 1970; revised manuscript received *ca.* Dec. 15, 1970.

Any discussion of this paper will appear in a Discussion Section to be published in the December 1971 JOURNAL.

REFERENCES

1. E. Gileadi and B. Piersma, "Modern Aspects of Electrochemistry," Vol. 4, Chap. 2, J. O'M. Bockris, Editor, Plenum Press, New York (1966).
2. B. E. Conway, "Theory and Principles of Electrode Processes," The Ronald Press, New York (1965).
3. A. K. Vijh, and B. E. Conway, *Chem Rev.*, **67**, 623 (1967).
4. B. E. Conway and M. D. Dzieciuch, *Can. J. Chem.*, **41**, 21, 38, 55 (1963).
5. V. S. Bagotzky and Yu. B. Vasilyev, *Electrochim. Acta*, **9**, 869 (1964).
6. S. Gilman and M. W. Breiter, *This Journal*, **109**, 1099 (1962).
7. A. K. Vijh and A. Bélanger, To be published.

JOURNAL OF THE ELECTROCHEMICAL SOCIETY

SOLID STATE SCIENCE

APRIL 1971

Dielectric and Optical Properties of Stoichiometric Magnesium Aluminate Spinel Single Crystals

C. C. Wang* and P. J. Zanzucchi

RCA Laboratories, Princeton, New Jersey 08540

ABSTRACT

Stoichiometric magnesium aluminate spinel ($MgAl_2O_4$) single crystals grown by the flux, Czochralski, and Verneuil methods have been characterized for their dielectric and optical properties. Dielectric properties were determined from capacitance measurements in the frequency range 10^2-10^5 Hz. The dielectric constant and loss tangent of $MgAl_2O_4$ spinel crystals grown by the various methods are comparable. At 1 kc the $MgAl_2O_4$ spinel has a dielectric constant of 8.4 and a loss tangent of 10^{-4}. Optical transmission and reflection measurements were made in the wavelength range uv to IR (0.2-40 μm). Optical characteristics of the $MgAl_2O_4$ crystals are highly dependent on the method of growth. Chromium-doped $MgAl_2O_4$ spinel single crystals have also been grown by a flux technique. Optical emission and absorption characteristics of Cr^{+3} in flux-grown $MgAl_2O_4$ spinel have been studied. The results are compared with those of Cr^{+3} in natural spinel and synthetic spinel crystals prepared by the Czochralski and Verneuil methods.

The use of single crystal magnesium aluminate spinel as an insulating substrate material for epitaxial semiconductor devices has recently been reported (1-4). It is also reported to be of potential use in passive ultrasonic delay line application (5, 6). This has stimulated considerable interest in obtaining high quality, single crystalline spinel which is difficult to grow because of its high melting point, wide solid solubility range, and its tendency toward heterogeneous composition through a complicated precipitation phenomena (7, 8). In the past few years significant progress was made on the growth of stoichiometric spinel of large sizes (>½ in. diameter) by the Czochralski (9-12), Verneuil (1), and flux (13, 14) methods. Many important physical properties of single crystal spinel remain to be characterized. In this paper research results are presented on the dielectric and optical properties of single crystal stoichiometric spinels ($MgAl_2O_4$) grown by the various methods. Chromium doped $MgAl_2O_4$ crystals were also grown by a flux technique. Emission and absorption characteristics were studied, and these results are compared with those obtained from crystals grown by other methods.

Experimental

Crystal growth.—Crystal growth of stoichiometric spinel by a flux technique, both undoped and chromium doped, was carried out using a PbF_2 flux-solvent and B_2O_3 as a liquid encapsulant. Vaporization of the flux at constant temperature was used for the generation of supersaturation to promote the crystal growth. A schematic drawing of the growth apparatus is presented in Fig. 1. The furnace was constructed from insulating brick and SiC globar heating elements. Feed nutrients were prepared from mixtures of MgO (reagent grade from Fischer Scientific Company and Optran grade from B.D.H. Labs.) and Al_2O_3 (type A alumina from Linde Company and Optran grade from B.D.H. Labs.). Doping was achieved by using feed prepared by calcining at 1050°C coprecipitated mixtures of ammonium alum and chrome alum (both Baker analytical reagent grade) so that 0.5% by weight of Cr_2O_3 is added to the $MgAl_2O_4$ spinel. The nutrients were mixed with the PbF_2 flux (extra pure and Optran grades from B.D.H. Labs.). A degree of filling of 70-90% by volume was attained by premelting the initial charge in a platinum crucible at about 900°C followed by refilling with more of the mixture. A thin layer (1-2% by weight of flux) of B_2O_3 (reagent grade from

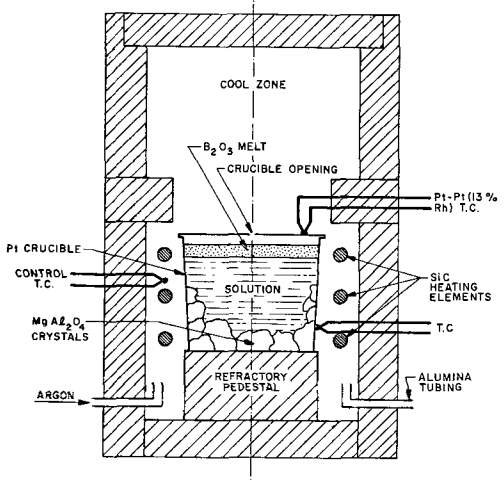

Fig. 1. Apparatus for flux growth of $MgAl_2O_4$ spinel single crystals.

* Electrochemical Society Active Member.

Key words: crystal growth, stoichiometric spinel, spinel optical properties, spinel dielectric properties.

Fischer Scientific Company) was generally added on top of the mass as a liquid encapsulant to control the vaporization of the flux. The crucible was sealed with a platinum cover having a circularly shaped opening and heated at the growth temperature (~1250°C) for the desired period of time. The furnace temperature was regulated by a West temperature controller. To prevent the reaction between the flux vapor and the globar heating elements, argon gas was used during the growth to carry the flux into the cool zone of the furnace. After the desired period of growth, the spinel crystals were recovered, after cooling, by leaching the flux in the crucible with hot nitric acid. The growth process is controlled by three factors: (*i*) the growth temperature, which governs the vapor pressure of the PbF_2 flux-solvent and the solubility of the nutrient, (*ii*) the size of the crucible opening and the thickness of the B_2O_3 liquid encapsulant layer, which limit the vaporization rate of the flux, and (*iii*) the initial composition of the melt. Typical growth conditions are (*a*) composition of melt: 2350g PbF_2 flux, 81g MgO and 204g Al_2O_3 feed nutrient, 40g B_2O_3 liquid encapsulant; (*b*) growth temperature: 1250°C; (*c*) growth time: 500 hr; and (*d*) crucible dimension: volume of 1000 cc and opening of ¼ in.

In addition to the flux grown crystals, stoichiometric spinel single crystals were grown from melt using the Verneuil and Czochralski techniques. Details on the growth processes and techniques were reported (1, 9-12, 15). The Verneuil crystals were grown by flame fusion using a three-tube, post-mix Verneuil burner (16) with critical dimensions to avoid sharp turbulent mixing zones. This burner produces a wide flame pattern which minimizes turbulence and allows larger diameter crystals to be grown. Feed materials were prepared by calcining coprecipitated mixtures of ammonium alum and magnesium sulfate (both Baker analytical reagent grade). Crystals were grown at a rate of ¼ in./hr. The Czochralski growth of $MgAl_2O_4$ spinel crystals were carried out[1] by pulling from melts contained in rf inductively heated iridium crucibles. The spinel melts were prepared from mixtures of the oxides. Crystals were grown on (110) or (111) seeds at pull and rotation rates within the ranges 0.1-0.3 in./hr and 0 to 20 rpm respectively.

Characterization.—The spinel single crystals were analyzed by wet chemical, emission spectroscopic, and x-ray diffraction methods for the gross composition, impurity contents, dislocation densities, and lattice parameters. Chemical analyses[2] were performed by alkali fusion of the spinel crystals followed by volumetric techniques. A mixture of sodium borate and sodium carbonate (ratio of 3 to 1 by weight) was used for the decomposition of the spinel. After decomposition the melt was treated with HCl, after which an excess of EDTA (ethylene-diaminetetraacetic acid) is added and heated to boiling to complex the Al. The Al content was determined by back titrating with a standard lead solution at *p*H 5.5-6.0 using Xylenol Orange as indicator. By adding 2,2′,2″-nitrilotriethanol as a masking agent for Al, Mg was directly titrated with EDTA at *p*H 10.0 using Eriochrome Black T as indicator. The dislocation density of the crystals was determined by the Lang x-ray topographic technique (17). The accurate lattice parameters were determined using x-ray diffraction (Cu/Ni radiation) Debye-Scherrer powder patterns.

The bulk crystals were oriented, cut, and polished in the form of wafers (surface area of ½ to 1 cm^2) of about 20 mil thick for measurements. Orientation for cutting was determined by the x-ray Laue back reflection method, and wafers were prepared by cutting the oriented crystals using a standard type diamond wheel. An accuracy of better than ±¼° was maintained through the operation. Most wafers used in this study were (111) oriented, although (100) and (110) oriented wafers were also measured. No dependence of dielectric and optical properties on orientation has been observed. The spinel wafers were mechanically lapped and polished to produce a flat, smooth surface. Lapping was carried out with about 30-μm boron carbide abrasives to obtain a flat coplanar surface. The lapped suface was further polished using successively finer grades of alumina, generally ending with the 0.3-μm grade.

The dielectric properties of stoichiometric spinel crystals grown by the three methods were determined using polished single-crystal wafers with evaporated gold electrodes (0.4 μm thick). The dielectric constant and dissipation factor were derived from capacitance measurements after edge corrections (18). The measurements were made using a General Radio Model 1615 capacitance bridge in the frequency range 10^2-10^5 Hz. Optical properties of spinel crystals grown by the three methods were measured in the range uv to IR. Transmission measurements were made in the wavelength range 0.2-7 μm using a Cary Model 14 spectrometer and a Perkin Elmer Model 457 spectrometer. Reflection measurements were made in the range 7-40 μm using the Perkin Elmer Model 457 spectrometer and a Wilks Model 9 reflection attachment.

Emission and absorption characteristics of Cr^{+3} in flux grown $MgAl_2O_4$ crystals were determined in the visible range. The fluorescence spectra were measured using a Spex Model 1700-1 spectrometer under ultraviolet stimulation using a Bausch and Lomb Model 33-86-40-01 monochromator and a 500W Hg arc lamp as the light source.

Results and Discussions

Crystal growth and crystallinity.—Flux grown $MgAl_2O_4$ single crystals up to 1 in. on an edge were obtained under the conditions cited above. The as-grown crystals are octahedral in shape with well-developed (111) facets (Fig 2). The crystals are transparent and free from macroscopic flux inclusions. They resemble closely their natural counterparts in habit and appearance. It was found that there is a limited crystallization temperature range for the $MgAl_2O_4$-PbF_2 system. Below about 1100°C, MgO reacts with the flux, and MgF_2 needles and α-Al_2O_3 platelets precipitate from the solution. Above 1293°C, the boiling point of PbF_2, the evaporation rate of PbF_2 is excessive, and the quality of the crystals is poor. Because of the restricted temperature range for crystallization, the technique of slow cooling, which is most commonly used in flux growth, is not feasible for the growth of spinel crystals from PbF_2 solvent. Beside the evaporation technique, growth of $MgAl_2O_4$ single crystals was reported (19) by a flux hydrolysis method.

Several Verneuil $MgAl_2O_4$ crystals (up to ⅝ in. diameter) were successfully grown under closely controlled growth conditions with no cracking[3] occurring during and/or after growth. The size of the crystals is appreciably larger than those (~¼ in. diameter) of flame fusion $MgAl_2O_4$ crystals reported previously (15). The crystals were grown in the <100> directions and have well-developed facets. They are clear, transparent, and free of macroscopic bubbles. Czochralski spinel crystals (about ½ in. diameter) of good optical and crystallographic qualities were grown using an iridium crucible (1.8 in. diameter x 2.3 in. height). Details on the growth of $MgAl_2O_4$ spinel by the Verneuil and Czochralski methods were reported (1, 9-12, 15). The gross composition impurity content, dislocation density, and lattice parameter of spinel crystals grown by the three methods were determined. Typical results are presented in Table I.

[1] The Czochralski $MgAl_2O_4$ single crystals employed in this study were prepared in-house by A. D. Morrison of RCA Laboratories.

[2] The analyses were made by B. L. Goydish and K. L. Cheng of RCA Laboratories. Details will be reported separately.

[3] The ease of growing spinel crystals (1) by the Verneuil method increases with increasing Al content in the material. Commercial spinel has an approximate composition of $MgO{:}3.3Al_2O_3$ and can be most easily prepared by the Verneuil method. Various investigators have reported (15, 20-22) the difficulty (cracking) involved in growing Verneuil stoichiometric spinel.

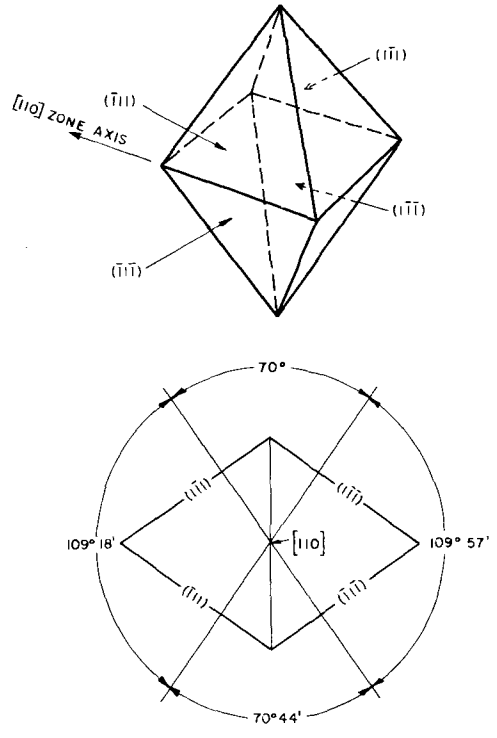

Fig. 2 a and b. Growth shape and habit of flux $MgAl_2O_4$ single crystals. Fig. 2a (top). As-grown $MgAl_2O_4$ octahedron. Fig. 2b (bottom). Growth habit.

It is seen from Table I that the experimentally determined Mg and Al contents are, within the range of experimental error, in agreement with the theoretical values for stoichiometric $MgAl_2O_4$ spinel. The melt grown (Verneuil and Czochralski) crystals may have slight Mg deficiencies due to the incongruent vaporization (20) of $MgAl_2O_4$ with preferential loss of Mg constituent at high temperatures. The flux grown spinel crystals seem to have a slightly lower lattice parameter than the melt grown crystals. The difference may be ascribed to the difference of the two kinds of crystals in ion distribution, impurity content, and gross composition.

The flux grown spinel crystals exhibit much less dislocations than the melt grown spinels because of the low growth rates and temperatures (~1200°C). The low temperatures are thermodynamically favorable for the growth of stoichiometric spinel from the phase behavior of the MgO-Al_2O_3 system (23). An interesting aspect of the flux spinel crystals is that they resemble

Table I. Composition, impurity content, dislocation density, and lattice parameter of single crystal $MgAl_2O_4$ spinel

	Flux spinel	Czochralski spinel	Verneuil spinel
Gross composition			
Mg, w/o	17.0	16.8	16.7
Al, w/o	37.9	37.8	37.9
Metallic impurity, ppm wt			
Cu	6-60	6-6	3-3
Ag	3-30	—	—
Fe	100-1000	3-30	6-60
Ga	15-150	6-60	1-10
Si	3-300	3-30	1-10
Pb	300-3000	—	—
Dislocation density, line/cm²	0-200	10^3-10^4	$>10^4$
Lattice parameter, Å	8.080-8.085	8.085-8.087	8.082-8.085

the natural stoichiometric spinel in growth habit and shape. It is likely that the natural spinel was also grown by a flux solution process at temperatures much lower than the melting point (2105°C) of spinel.

Dielectric properties.—The dielectric properties of $MgAl_2O_4$ spinel crystals grown by the three methods were determined in the frequency range 10^2-10^5 Hz. Typical results on the dielectric constant and dissipation factor (tan δ) are presented in Fig. 3 and 4. It is seen that in the frequency range measured the dielectric constant of $MgAl_2O_4$ spinel crystals grown by the three methods is comparable. The values are virtually the same. The dielectric constant falls slightly with frequency, and exhibits a change of about 0.1% per frequency decade over the measured frequency range. The dissipation factor also depends on frequency. The initial drop at lower frequencies is due to dissipation in the parallel leakage resistance, and the rise at higher frequencies is caused by loss in the series electrode resistance. The internal loss in the spinel dielectric is low and has values on the order

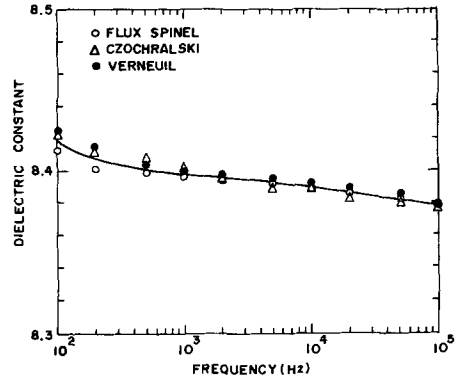

Fig. 3. Dielectric constant of flux, Czochralski, and Verneuil grown single crystal spinel.

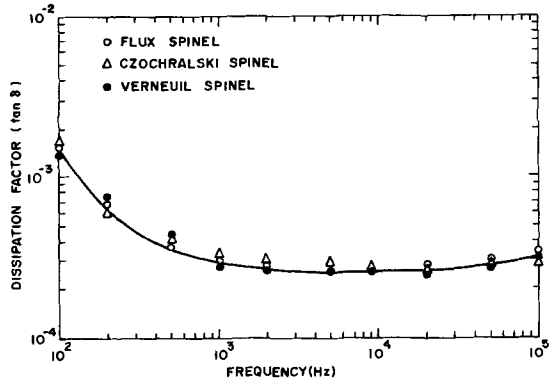

Fig. 4. Dissipation factor of flux, Czochralski, and Verneuil grown single crystal spinel.

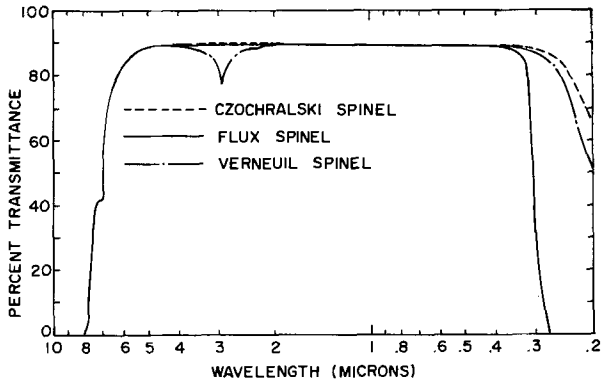

Fig. 5. Transmittance of flux, Czochralski, and Verneuil grown single crystal $MgAl_2O_4$ spinel.

of 10^{-4} in the measured frequency range. The minimal permittivity dependence on frequency and the low dielectric loss properties in a wide frequency range are characteristic generally of refractory insulating oxides.

Optical properties.—Transmission characteristics of stoichiometric spinel.—Transmission spectra of stoichiometric spinel single crystals (cut to an average thickness of 0.020 in.) grown by the flux, Czochralski, and Verneuil methods are shown in Fig. 5. It is seen that the spinel crystals are generally transparent from about 0.3 to 7.0 μm. In this region, the small apparent absorption of the variously grown crystals is largely due to Fresnel reflection losses (24) consistent with a refractive index of 1.70-1.72 for spinel (21). In the uv region, between 0.200 and 0.300 μm, the transmission of Czochralski and Verneuil grown crystals begins to decrease slightly, while the transmission of the flux grown crystals decreases sharply around 0.280 μm (as shown in Fig. 5). The strong uv absorption in the flux grown crystal may be due to impurities, most probably Fe, incorporated into the spinel lattice during the crystal growth. In the infrared region near 3 μm, an absorption band is present for the Verneuil $MgAl_2O_4$ spinel. This band has not been observed for the flux and Czochralski grown spinel crsytals. It is therefore not an intrinsic property of spinel. This absorption band occurs at 3360 cm^{-1} suggesting the presence of hydroxyl groups or water in the spinel lattice (21, 25). Since an oxyhydrogen flame is used in the Verneuil method, hydroxyl ions or water molecules are present in the flame, and these ions or molecules can be incorporated into the spinel lattice during the crystal growth (1, 21). Verneuil grown rutile has been reported to contain hydroxyl groups (26).

The O-H absorption characteristics at 3360 cm^{-1} of stoichiometric ($MgAl_2O_4$) and aluminum-rich ($MgO:1.5Al_2O_3$) spinels are compared in Fig. 6. It is seen that the band in the stoichiometric Verneuil spinel but not in the aluminum-rich spinel is somewhat broadened on the long wavelength side of the band. The band broadening suggests that some hydrogen bonding is occurring (27-28) among the hydroxyl groups in the Verneuil grown $MgAl_2O_4$ spinel. A significant structural difference (23) between the stoichiometric and the aluminum-rich spinels is that in the aluminum-rich phases the aluminum excess in the lattice is accompanied by cation vacancies. Because of the presence of vacancies, the hydrogen ions in the aluminum-rich spinels may be accommodated differently from those in the stoichiometric spinel. Extensive studies (29) reveal that the absorption characteristics of Verneuil grown spinel crystals are highly dependent on the aluminum content in the lattice. Details will be reported (29) separately.

Spinel grown by either of the three growth methods absorbs infrared radiation at approximately 6.6-7.0 μm, just before the transmission cutoff shown in Fig. 5. This absorption band is probably due to the presence of

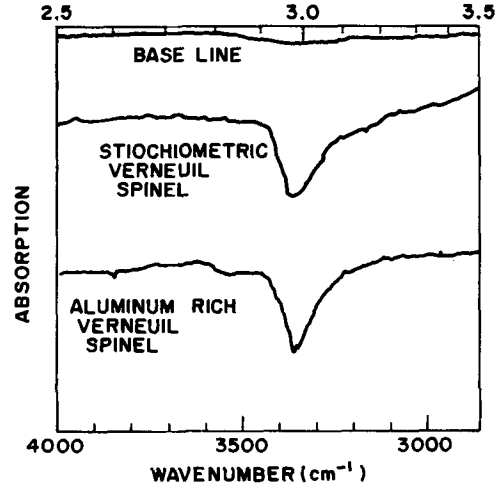

Fig. 6. Comparison of absorption band at 3360 cm^{-1} in Verneuil grown stoichiometric and aluminum-rich single crystal spinel.

carbonate groups in the spinel lattice originated from carbon dioxide or carbonate impurities.

Reflection characteristics of stoichiometric spinel.—Beyond 10 μm spinel lattice vibrations strongly absorb radiation. Transmission measurements were reported (30, 31) using Verneuil $MgAl_2O_4$ powder samples in wavelength to 30 μm. In the present work, reflection and transmission measurements were made in wavelength to 40 μm using, respectively, single crystal wafers and powder disks (KBr binder). Reflection spectro of flux, Czochralski, and Verneuil grown stoichiometric spinel and of Verneuil grown aluminum-rich spinel ($MgO:1.5Al_2O_3$) are shown in Fig. 7. The wavelengths of single crystal reflection bands and powder transmission bands are summarized in Table II.

It is seen that the Czochralski, Verneuil, and flux grown stoichiometric crystals have very similar reflection spectra. The observed lattice bands correlate with vibrations (30, 31, 34-37) occurring at the tetrahedral and octahedral sites for the spinel lattice with symmetry properties of the O^7_h space group (33). The absolute reflectivity of the flux grown spinel is somewhat

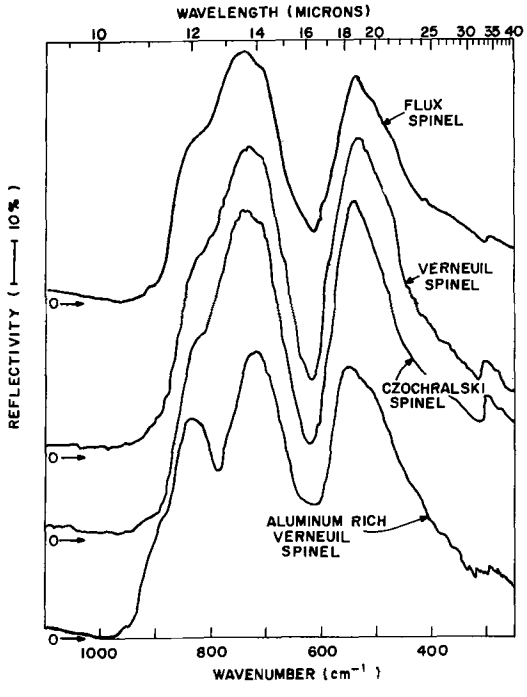

Fig. 7. Reflection spectra of flux, Czochralski, and Verneuil grown single crystal stoichiometric spinel and of Verneuil grown single crystal aluminum-rich spinel.

Table II. Comparison of the wavelengths of reflection and transmission bands for stoichiometric and aluminum-rich spinels

Spinel composition	Reflection bands, μm	Transmission[a] bands, μm	Transmission[b] bands, μm
Stoichiometric ($MgAl_2O_4$)	12.2(sh)[c]	13.3-13.4(sh)	12.5(sh)
	13.5-13.6	14.5	14.5
	18.5-18.6	18.7	18.6
	33-34	33-34	—[d]
Aluminum-rich ($MgO:1.5Al_2O_3$)	12.1-12.2		
	13.6-13.7		
	18.0		

[a] Present work, powder disk method using KBr binder.
[b] Ref. (30) and (31).
[c] (sh) Shoulder.
[d] Reported data did not extend beyond 30 μm.

lower than that of the Czochralski or Verneuil grown spinel. This may be due to the impurities in the flux grown spinel, e.g., the lattice band for PbO occurs between 18 and 40 μm. Reflection losses have also been associated with surface damages (32, 33). Since a unique surface preparation of spinel wafers was made, this effect is not likely to be an important one. The reflection spectrum changes somewhat with changes in the composition of spinel. As shown in Fig. 7 and Table II, three sharp reflection bands appear in the spectrum of aluminum-rich spinel. The differences between the reflection spectra can be used to readily distinguish stoichiometric spinel from aluminum-rich spinel.

Absorption and emission characteristics of Cr-doped stoichiometric spinel.—Absorption spectra of chromium-doped flux grown spinel crystals were obtained in the visible region. A plot of optical density *vs.* wavelength is shown in Fig. 8. The spectra are very similar to those of ruby (38) and hence arise from the transition of Cr^{+3} in octahedral symmetry (39). There are two broad absorption bands observed with peaks at 5480 and 3910Å, corresponding to transition from the ground state to the $^4T_2$ and $^4T_1$ excited states, respectively. The absorption peaks of the spectra, as shown in Table III, are in general agreement (with slight differences in peak positions) with those reported for Cr^{+3} in natural (40) stoichiometric spinel and in stoichiometric spinel grown by Verneuil (41) and Czochralski (11) methods. A sample was annealed at 1000°C for ½ hr. After annealing, no change in position and intensity of the $^4T_2$ band, as reported for natural spinel (40), was observed.

Emission spectra of the chromium-doped spinel crystals were also measured in the visible region. A spectrum is shown in Fig. 9. The emission has vibrational fine structure with peaks at 6750, 6875, 6980, 7075,

Table III. Absorption characteristics of $MgAl_2O_4$:Cr crystals grown by various methods

Growth method	Transition energy, cm^{-1} (Ground state—$^4T_1$ state)		Transition energy, cm^{-1} (Ground state—$^4T_2$ state)
Natural[a]	25,640	24,200	18,520
Natural[a] (annealed, 1000°C ½ hr)	25,640	24,200	18,350
Flux[b]	25,575	23,529	18,300
Czochralski[c]	25.640	—	18,350
Verneuil[d]	25,634	23,413	18,343

[a] Ref. (40).
[b] Present work.
[c] Ref. (11).
[d] Ref. (41).

Table IV. Emission characteristics of $MgAl_2O_4$:Cr crystals grown by various methods

Growth method	Maxima in spectrum, Å					Half width (principal component) Å
Natural[a]	6755	6855	6979	7072	7177	<10
Flux[b]	6750	6875	6980	7075	7165	~50
Czochralski[c]	6758	6876	6983	7079	7178	~50
Verneuil[d]	6763	6885	6995	7095	7185	~50

[a] Ref. (42) and (43).
[b] Present work.
[c] Ref. (11).
[d] Ref. (41).

and 7165Å. The principal component at 6875Å is the sharpest. The width of this component is considerably wider than that of natural spinel (42, 43), but is similar to those reported on Verneuil (41) and Czochralski (11) grown stoichiometric spinel crystals. The sharp line components of Cr^{+3} in Czochralski spinel was not observed. The emission characteristics of $MgAl_2O_4$:Cr crystals grown by various methods are compared in Table IV.

Conclusions

The growth of single crystal stoichiometric magnesium aluminate spinel has been successfully achieved in recent years by the flux, Czochralski, and Verneuil methods. Some physical properties of this material are not critically sensitive to the method of growth. These include the lattice parameter, dielectric properties, lattice vibration characteristics, emission and absorption properties of Cr^{+3} in $MgAl_2O_4$, and thermal properties (44). On the other hand, the crystalline perfection and the optical transmission properties are highly dependent on the growth methods. A pronounced difference is seen between the synthetic and natural $MgAl_2O_4$ spinel crystals. The Cr^{+3}:$MgAl_2O_4$ emission band widths of the synthetic spinels are con-

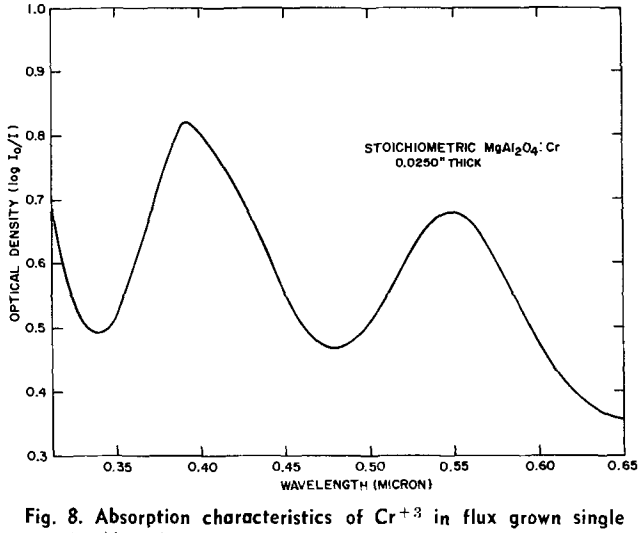

Fig. 8. Absorption characteristics of Cr^{+3} in flux grown single crystal $MgAl_2O_4$ host.

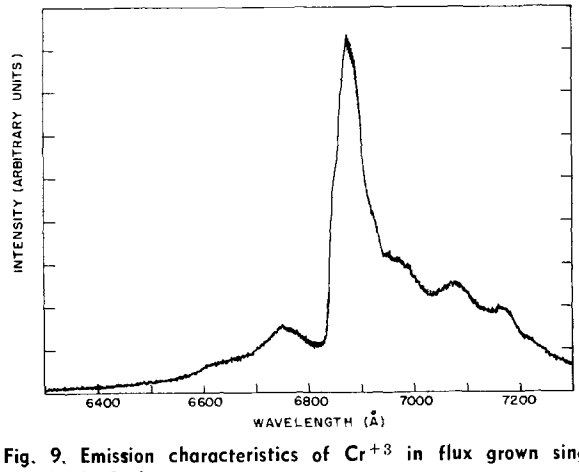

Fig. 9. Emission characteristics of Cr^{+3} in flux grown single crystal $MgAl_2O_4$ host.

siderably wider than that of the natural material. This fact rules out the potential of using the synthetic spinel as a laser host material.

Acknowledgments

The Czochralski spinel crystals were provided for this work through the generosity of A. D. Morrison. The authors wish to express their indebtedness to R. Bates for the Verneuil and flux crystal growth experiments. They also wish to thank B. L. Goydish and H. H. Whitaker for wet chemical and emission spectroscopic analyses. Thanks are also due to R. J. Paff for the x-ray work and to J. Gerber for optical measurements. Research reported in this paper was sponsored jointly by the Air Force Materials Laboratory, Wright-Patterson Air Force Base, under Contract No. F33615-68-C-1025 and RCA Laboratories, Princeton, New Jersey.

Manuscript submitted Sept. 10, 1970; revised manuscript received Dec. 3, 1970.

Any discussion of this paper will appear in a Discussion Section to be published in the December 1971 JOURNAL.

REFERENCES

1. C. C. Wang, *J. Appl. Phys.*, **40**, 3435 (1969).
2. G. W. Cullen, G. E. Gottlieb, C. C. Wang, and K. H. Zaininger, *This Journal*, **116**, 1444 (1969).
3. C. C. Wang. G. E. Gottlieb, G. W. Cullen, S. H. McFarlane, III, and K. H. Zaininger, *Trans. Met. Soc. AIME*, **245**, 441 (1969).
4. W. Heywang, *Mat. Res. Bull.*, **3**, 315 (1968).
5. M. F. Lewis and E. Patterson, *J. Appl. Phys.*, **39**, 3420 (1968).
6. D. W. Oliver, Contract Report AFML-TR-68-260 (1968).
7. H. Saalfeld and H. Jagodzinski, *Z. Krist.*, **109**, 87 (1957).
8. A. M. Alper, R. N. McNally, P. H. Ribbe, and R. C. Doman, *J. Am. Ceram. Soc.*, **45**, 263 (1962).
9. B. Cockayne and M. Chesswas, *J. Mats. Sci.*, **2**, 498 (1967).
10. J. G. Grabmaier and B. C. Watson, *J. Am. Ceram. Soc.*, **51**, 355 (1968).
11. H. M. Dess, S. R. Bolin, and O. H. Nestor, Contract Report NONR-4793(00) (1967).
12. M. L. Hammond, RNP 221 presented at the Detroit Meeting of the Society, October 5-9, 1969.
13. C. C. Wang and S. H. McFarlane III, *J. Crystal Growth*, **3-4**, 485 (1968).
14. J. D. C. Wood and E. A. D. White, *ibid.*, **3-4**, 482 (1968).
15. R. H. Arlett and M. Robbins, *J. Am. Ceram. Soc.*, **50**, 273 (1967).
16. J. A. Adamski, *J. Appl. Phys.*, **36**, 1784 (1965).
17. A. R. Lang, *ibid.* **30**, 1748 (1959).
18. A. H. Scott and H. L. Curtis, *J. Res. Natl. Bur. Std.*, **22**, 747 (1939).
19. C. O. Dugger, *This Journal*, **113**, 306 (1966).
20. H. Palmour, III, R. D. McBrayer, D. E. Witter, and W. W. Kriegel, Contract Report AF33(616)-7820 (1964).
21. K. A. Wickersheim and R. A. Lefever, *J. Opt. Soc. Am.*, **50**, 831 (1960).
22. R. C. Linares, Contract Reports AF19(628)-4057 and AF19(628)-2954 (1964).
23. A. D. Wadsley, "Non-Stoichiometric Compounds," L. Mandelcorn, Editor, Academic Press, New York (1964).
24. T. S. Moss, "Optical Properties of Semiconductors," Butterworth's Scientific Publications, London (1959).
25. K. Nakamoto, "Infrared Spectra of Inorganic and Coordination Compounds," John Wiley & Sons, Inc., New York (1963).
26. B. Soffer, *J. Chem. Phys.*, **35**, 940 (1961).
27. C. B. Baddiel and E. E. Berry, *Spectrochim. Acta*, **22**, 1407 (1966).
28. K. A. Wickersheim and G. K. Korpi, *J. Chem. Phys.*, **42**, 579 (1965).
29. P. J. Zanzucchi and C. C. Wang, To be published.
30. R. S. Halford, *J. Chem. Phys.*, **14**, 8 (1946).
31. S. Hafner, *Z Kristallogr.*, **115**, 331 (1961).
32. A. S. Barker, Jr., *Phys. Rev.*, **132**, 1474 (1963).
33. H. E. Bennett and J. O. Porteus, *J. Opt. Soc. Am.*, **51**, 123 (1961).
34. S. Hafner and F. Laves, *Z. Kristallogr.*, **115**, 321 (1961).
35. H. Jagodzinski and H. Saalfeld, *ibid.*, **110**, 197 (1958).
36. P. Tarte, *Spectrochim. Acta*, **23A**, 2127 (1967).
37. R. D. Waldron, *Phys. Rev.*, **99**, 1727 (1955).
38. D. S. McClure, *J. Chem. Phys.*, **36**, 2757 (1962).
39. S. Sugano and Y. Tanabe, *J. Phys. Soc. Japan*, **13**, 880 (1958).
40. E. F. Farrell, A. Linz, and M. Redman, Contract Report AF19(628)-3884 (1965).
41. R. H. Arlett, *J. Am. Ceram. Soc.*, **45**, 523 (1962).
42. N. A. Tolstoy and S. F. Liu, *Optics and Spectroscopy*, **14**, 202 (1963).
43. O. Deutschbein, *Ann. Physic*, **14**, 729 (1932).
44. C. C. Wang, To be published.

Some Charge Phenomena in D-C Reactively Sputtered Alumina Films on Silicon

Mao-Chieh Chen*

Research Laboratories, General Motors Corporation, Warren, Michigan 48090

ABSTRACT

The charge behavior of d-c reactively sputtered Al_2O_3 films has been studied with MOS techniques. Both positive and negative oxide surface charges were observed in the Al_2O_3-Si structure in separate cases. This may be due to positive and negative oxygen ions which were created during the sputtering process and were then adsorbed by the silicon surface and by the deposited Al_2O_3 layer. Bias temperature stress revealed that both ion migration and carrier injection-trapping polarization participate in the charging phenomenon. The injection process appears to dominate the migration process at high applied electric fields. The trapping time constant is very large at low temperatures, but becomes smaller at higher temperatures. Change in the shape of the capacitance-voltage curves during a series of bias temperature stress tests was observed, notably whenever the carrier injection-trapping becomes the dominant instability mechanism.

The study of aluminum oxide (Al_2O_3) and its various properties, as well as its applications such as surface passivation of semiconductor devices, has been gradually drawing greater attention. These Al_2O_3 films are considered amorphous. There have been a variety of methods reported for the preparation of aluminum oxide films: by anodization (1-3), by evaporated deposition (4-10), by d-c reactive sputtering (11), and by rf sputtering (12).

* Electrochemical Society Active Member.
Key words: charges in alumina MOS.

The metal-oxide-semiconductor (MOS) technique of studying the passivating properties of oxide films has proved to be a convenient and effective method. There have been reports concerned with the MOS study of aluminum oxide (10, 13), as well as the alumina/silicon dioxide (MAOS) system (13). A carrier injection phenomenon has been observed (10, 13). Both positive and negative flat-band voltages were observed in one case (10), while in the other case only positive flat-band voltages were detected (13). Prolonged annealing treatment reduced the positive flat-band voltage, and it eventually became negative after 15 hr of treatment at 200°C in air (13).

In this paper, along with the experimental procedure, we report the observed oxide surface charges and the results of various bias and temperature stresses on Al_2O_3 films. This is followed with a brief discussion on the introduction of oxygen ions from the sputtering plasma into the oxide.

Experimental Technique

Epitaxial n-type silicon wafers of 10 and 40 ohm-cm, both (111) orientated, were used as substrates in the fabrication of the test samples. Prior to oxide deposition, the silicon wafers were cleaned in trichloroethylene and acetone, and rinsed in ultrasonically agitated, flowing, deionized water for at least 10 min. The aluminum oxide (Al_2O_3) films were then deposited by d-c reactive sputtering in a pure oxygen atmosphere.

The deposition of aluminum oxide was performed under two different sputtering conditions using two separate d-c reactive sputtering systems. Sputtering conditions "A" were: cathode potential 1200V, cathode current density 2.4 mA/cm^2, and (pure) oxygen gas pressure 300 mTorr (300μ). An aluminum disk target 2.8 in. in diameter was used as a cathode, and a cathode current of 120 mA was recorded during the sputtering process. The substrate was a 10 ohm-cm silicon wafer. This substrate was set on a substrate holder which was electrically floating and placed underneath the cathode for downward sputtering. The spacing between the cathode and the substrate was approximately 2 cm, and the spacing between the cathode and the anode was approximately 10 cm. Another d-c sputtering system was used for the deposition of Al_2O_3 under conditions "B," which were: cathode potential 700V, cathode current density 1.6 mA/cm^2, and oxygen gas pressure 150 mTorr. An aluminum disk target 5.5 in. in diameter was used and a cathode current of 250 mA was maintained during the sputtering process. Silicon wafers of 40 ohm-cm were used as substrates. In this apparatus, upward sputtering was used, and the substrate was clamped to the plate and was electrically grounded to the system. The spacing between the cathode and the substrate was 2 cm. The oxide films deposited under condition "A" for 30 min were 1250Å and those deposited under condition "B" for the same period of time were about 400Å. For convenience hereafter, the oxide deposited under condition "A" will be referred to as "sample A," and that deposited under condition "B" as "sample B."

For annealing treatments, the Al_2O_3 deposited wafers were quartered, and each was subjected to a different annealing schedule, except that one of the quarter wafers was reserved for use as a "control" sample. The annealing was carried out in a helium atmosphere. The wafers were set in a furnace through which helium gas was flowing. The helium gas passed through a liquid nitrogen "trap" before it was admitted to the furnace. The trap eliminated oxygen and water vapor contamination.

Aluminum gate electrodes were applied to the control and to the annealed oxide films, using evaporated deposition and photomasking. Gate areas were 3.44 x 10^{-3} cm^2 (26 mils diameter aluminum dot). Individual devices were diced out, die bonded, and lead bonded to TO-5 headers.

MOS Device Characteristics

MOS capacitance and effective surface charges.— Samples A and B demonstrated different behavior in their MOS capacitance-voltage characteristics. The MOS capacitance was measured at 1 MHz and all the measurements were made at room temperature unless otherwise specified. Figure 1 shows the experimentally observed typical C-V characteristics of sample A for the control and the 500°C annealed specimen, along with the corresponding theoretical curve. In this experiment, four sets of samples were prepared: control samples and three annealed samples each subjected to annealing treatments in a He atmosphere for 1 hr at 300°, 500°, and 750°C, respectively. The resultant C-V characteristics show no obvious change for the 300°C annealed sample from that of the control sample, although the various C-V curves from the randomly selected 300°C annealed samples disperse a little bit more. The C-V curves also show no obvious change between those of the 500° and 750°C annealed samples, although the variation of the C-V curves of the randomly selected samples is a little bit larger for the 750°C annealed samples. The flat-band voltage of the control sample is −4.1V and that of the 500°C He gas annealed sample is −1.5V. The negative flat-band voltages indicate that positive surface charges were in the oxide.

Figure 2 shows the typical C-V curves of sample B as well as the corresponding theoretical characteristic. In this experiment, a 40 ohm-cm n-type silicon wafer was coated with Al_2O_3. Since annealing at 300°C showed no obvious effect and 500° and 750°C annealed samples make no obvious difference, the annealing treatments here were chosen at 500°C for 1, 2, and 3 hr, respectively. Several devices from each of the treatments were randomly picked and their C-V characteristics measured. It is seen that all four curves show a positive flat-band voltage indicating that negative, effective oxide surface charges are present. The flat-band voltages for each case are: 0.42V for control sample, 0.68V for the 1 hr annealed sample, 0.60V for the 2 hr annealed sample, and 0.55V for the 3 hr annealed sample.

The effective oxide surface charge density for the various oxide specimens was evaluated from the flat-band voltage. The results are tabulated in Table I. It is clear that the positive oxide surface charge of sample A is greatly reduced upon annealing. In the other case, however, the negative oxide surface charge of sample B increased upon annealing and then decreased somewhat during a prolonged annealing period. It has been observed (13) that a prolonged annealing treatment (at 200°C in air) reduces the positive flat-band voltage and eventually changes it to negative. In our

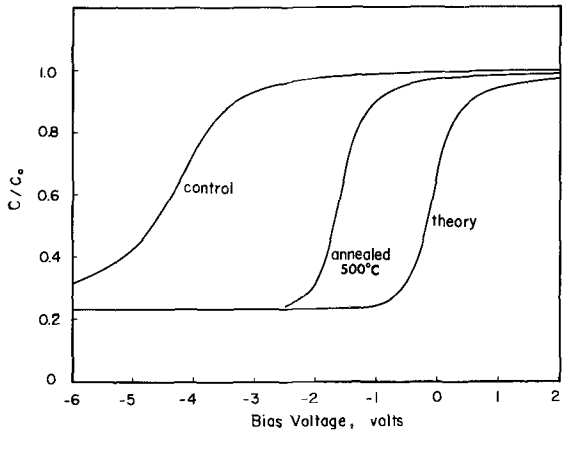

Fig. 1. Theoretical and experimental MOS C-V characteristics of sample A measured at 300°K and 1 MHz. The substrate wafer is 10 ohm-cm n-type silicon. The oxide thickness is 1250Å. The sample was annealed at 500°C in He atmosphere for 1 hr.

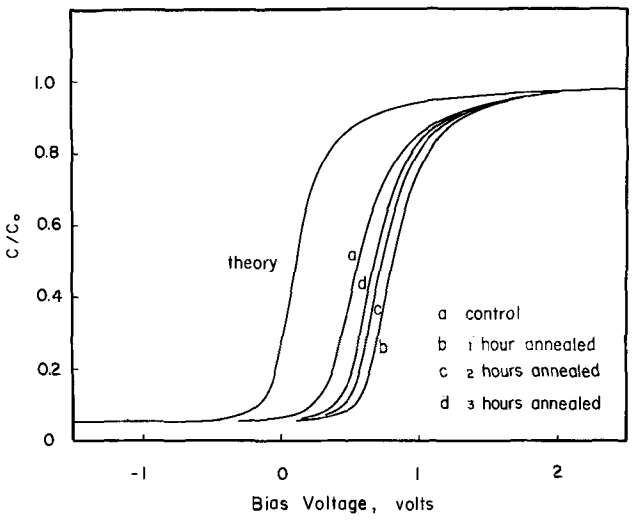

Fig. 2. Theoretical and experimental MOS C-V characteristics of sample B measured at 300°K and 1 MHz. The substrate wafer is 40 ohm-cm n-type silicon. The oxide thickness is 400Å. Annealing was performed at 500°C in He atmosphere.

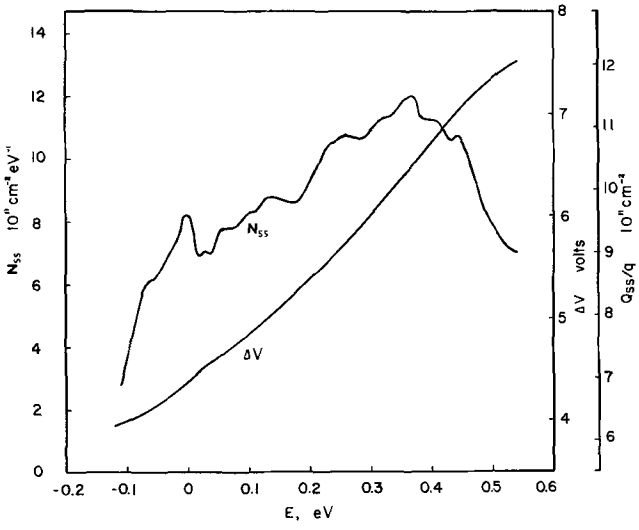

Fig. 3. Density of states of the interface states and the effective surface charge density vs. energy of sputtered oxide (sample A) on n-type silicon substrate. Reference for energy, E, is chosen at the intrinsic Fermi level in the bulk silicon.

case, the increase in the positive flat-band voltage upon annealing during the first hour might be due to a faster and greater elimination of the positive oxide surface charges, causing an effective increase in the effective negative oxide surface charges. The subsequent prolonged annealing further reduced negative oxide surface charges and shifted the C-V curve in the negative voltage direction. However, the exact mechanism is not yet understood.

Interface state density.—Comparison of the three C-V characteristics in Fig. 1 reveals that the C-V curve of the annealed sample, within the resolution of our measurement, is essentially parallel to the theoretical curve over the entire range of the variation in the capacitance. On the other hand, the C-V curve of the control sample is not just a parallel shift of the theoretical curve along the voltage axis. The curve exhibits a broader shape. This reveals, therefore, that the annealing effect has not only reduced the positive oxide surface charge but also the fast interface states as well. The parallel shift in the C-V curve of the annealed sample indicates that the charge in the oxide film is independent of the surface potential in the range of measurement at room temperature.

Figure 3 depicts the results of the investigation of Fig. 1 for sample A. This figure shows ΔV (the difference in voltage between the measured and the ideal C-V curve), effective oxide surface charge density, and the numerically calculated density of interface states *vs.* energy. The reference for energy, E, is chosen at the intrinsic Fermi level in the bulk silicon. The oxide surface charges are positive. The curve near the valence band edge is not shown because of limitations of MOS techniques on n-type silicon substrates (14). The interface state density shows a continuous distribution and seems to be increasing from near the middle of the silicon energy gap toward the conduction band, but drops near the conduction band edge. No clear high density peak was observed.

Table I. Effective surface charge density for various oxide specimens. Samples A are 1250Å and samples B are 400Å in thickness. Annealing is done in He atmosphere at 500°C

Unit	Effective surface charge density (No./cm²)	Sample	Remarks
1126-25-2	6.94×10^{11}	Control	Samples A
1126-33-2	2.47×10^{11}	1 hr anneal	Positive charges
1158-50-1	1.31×10^{11}	Control	
1158-55-1	2.68×10^{11}	1 hr anneal	Samples B
1158-59-2	2.26×10^{11}	2 hr anneal	Negative charges
1158-61-2	1.97×10^{11}	3 hr anneal	

Examination of the C-V curves in Fig. 2 shows that the four curves, a, b, c, and d, are almost parallel to one another. These experimental curves also show a slight broadened shape as compared to the theoretical curve, indicating the existence of a small amount of interface state charge. However, for the densities less than 10^{11} cm^{-2} eV^{-1}, the resolution of the present technique limits the meaningful derivation from these curves.

The technique of cooling samples to 77°K and measuring the resultant shift in flat-band voltage has been shown to be an excellent method of detecting and measuring the approximate total number of fast interface states between the 300° and 77°K Fermi levels (15-17). The results of this measurement show that the number of interface states is around 2×10^{11} cm^{-2} for all samples whether annealed or not. The 300°K bulk Fermi level (E_F) for 40 ohm-cm silicon is 0.225 eV below the conduction band edge. At 77°K, E_F is very close to the band edge. Investigations on the density of SiO_2-Si interface states have shown that fast interface states acting like acceptors and donors in nearly equal numbers exist near the conduction band and valence band, respectively (15, 18, 19). These are states perturbed from the nearby intrinsic silicon bands as was suggested by Gray and Brown (19) . We would, therefore, also expect a high density of states near both band edges in the case of the Al_2O_3-Si interface, and the above measured number of interface states would approximately represent the total number of interface states in the upper half of silicon's forbidden band. Unfortunately, at these low values of interface states, the distribution of the interface state density near the conduction band edge could not be measured by MOS techniques on samples B.

Bias and temperature stresses.—The devices were stressed at a given bias and temperature (BT) for 12 min. They were then cooled to room temperature with the bias still applied for about 1 hr. Subsequently, the C-V curves were taken, and the flat-band voltages were measured.

Devices from sample A.—Figure 4 shows the flat-band voltage *vs.* the gate voltage under repetitive bias cycling for both the control and the annealed samples. The annealing condition was 500°C in a He atmosphere for 1 hr. Both samples show essentially the same pattern of flat-band voltage variation, except the pattern of the annealed sample shifts to a less negative

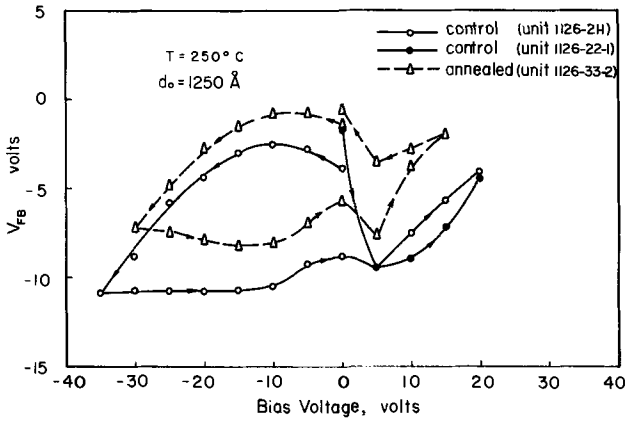

Fig. 4. Flat-band voltage *vs.* gate voltage at 250°C for sample A under repetitive bias cycling.

voltage position indicating a smaller effective, positive oxide surface charge. The devices were first subjected to negative bias, increasing in 5V steps up to −35V (or −30V for the annealed sample), then returned to zero volts in 5V steps. The procedure was repeated for positive bias. Under negative bias at about −10V, the flat-band voltage showed a little shift toward the positive direction and then shifted back to a more negative value when a negative bias of more than −10V was applied. When the stress direction was reversed, the flat-band voltage first shifted to a more negative value at low positive biases up to about +5V and then shifted back in a positive direction when a positive bias larger than +5V was applied. This phenomenon is more clearly depicted by a sample (unit 1126-22-1) which was subjected to positive bias from an initially unstressed condition. The flat-band voltage *vs.* temperature with gate voltage as a parameter during the BT stress is illustrated in Fig. 5.

The shift in the flatband voltage, for low-voltage stresses, is believed to be caused by a migration of charged ions in the Al_2O_3 films under the applied electric field (20). This is shown in Fig. 4 wherein the flat-band voltage shifts toward more negative values for small positive bias stresses (<5V), and toward more positive values for small negative bias stresses (<−10V). The much larger negative shift with positive bias as compared to the small positive shift with

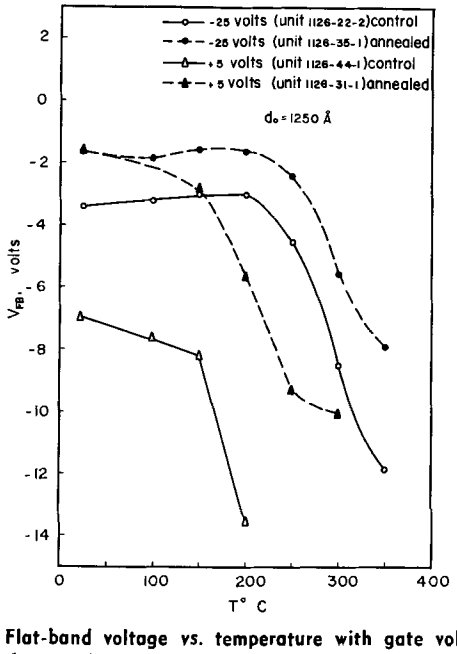

Fig. 5. Flat-band voltage *vs.* temperature with gate voltage as parameter for samples A.

negative bias is most probably because most of the positive ions released at elevated temperature (250°C) do not come from the region close to the Al_2O_3-Si interface. In Fig. 5, the flat-band voltage under +5V BT stress became more negative at higher temperatures and clearly indicates the ion migration. At higher temperatures, more positive ions can be released in the oxide and drift to the Al_2O_3-Si interface under the positive field.

At higher bias stress, however, the instability is characterized by positive shifts in flat-band voltage during applied positive bias greater than 5V and negative shifts in flat-band voltage during applied negative bias greater than 10V as shown in Fig. 4 and 5. This is the phenomenon that carrier injection-extraction would explain. The carrier injection-extraction phenomenon has been observed in Si_3N_4 films (21, 22), thermally grown SiO_2 films (23, 24), d-c reactively sputtered SiO_2 films (25), and reactively evaporated Al_2O_3 films (10, 13). Under applied high electric field, electron injection or extraction would occur across the barrier at the oxide-silicon interface. This mechanism was found to be thermally activated (23). This shifts the flat-band voltage in the direction opposite to what would be expected from ion migration and constitutes the slow trapping instability. In Fig. 5, with −25V bias, the flat-band voltage remains almost unchanged or shifts in a positive direction very slightly up to the temperature of 200°C during the BT stress. This slight positive shifting probably results from the competing effects of ion migration and carrier injection-extraction polarization. For temperatures above 200°C, however, the flat-band voltage starts to shift substantially in a negative direction. This would be expected since the slow trapping time constant is very large at low temperature and becomes smaller at higher temperatures (23). The involvement of the trapping time constant was tested in that, with −25V bias at a given temperature, prolonged BT stress did shift the C-V curve toward a more negative position. With +15V bias, however, it shifted more and more in a positive direction as the period of BT stress increased. In addition, a trapping (or injection) type hysteresis (10, 17, 26) was also observed in the C-V curve.

The shifting of the flat-band voltage under BT stress indicates that the effect of ion migration under negative applied bias is small, where under positive applied bias the effect is quite large. The shifting with −25V and 350°C BT stress is therefore presumed to be essentially due to the slow trapping instability. At room temperature, the device subjected to this stress condition remains stable; *e.g.*, the flat-band voltage measured two weeks after BT stress did not show any obvious change. On the other hand, ion migration is believed to be dominant under +5V BT stress. After a device was subjected to this positive bias BT stress and cooled back to room temperature, it was observed that the device was very unstable. For a device from the control sample, under +5V and 250°C BT stress for 12 min, the flat-band voltage was measured to be −24V. The device was open-circuited at room temperature for 22 hr. The flat-band voltage shifted to −10V. This is due to some sort of recovery ion migration. After being released at an elevated temperature, the ions were driven toward oxide-silicon interface under positive field. Some ions were trapped when the device was cooled to room temperature, and others remained relatively free. After removal of the positive bias, the positive ions repelled each other and moved away from oxide-silicon interface. Some of those ions staying near the interface may combine with injected electrons and become neutralized.

Devices from sample B.—Illustrated in Fig. 6 and 7 are the measured results for devices from sample B. Figure 6 shows the flat-band voltage *vs.* the gate voltage under repetitive bias cycling for both the control and the annealed (2 hr in He atmosphere at 500°C) samples.

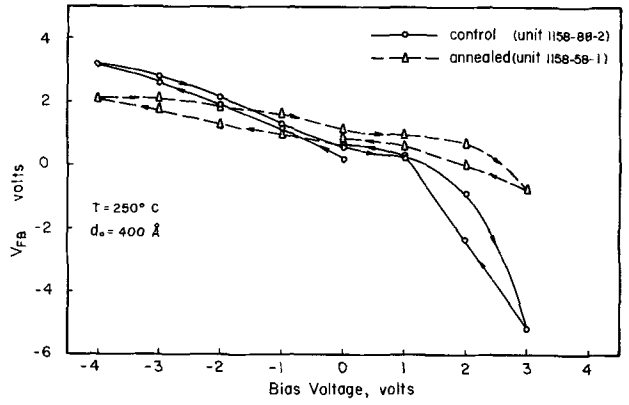

Fig. 6. Flat-band voltage vs. gate voltage at 250°C for sample B under repetitive bias cycling.

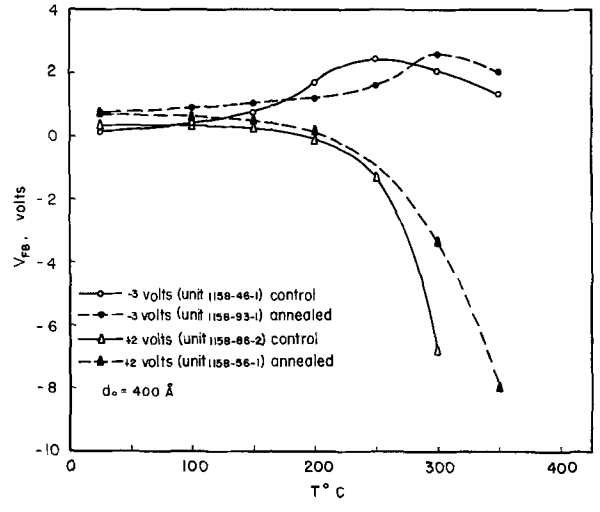

Fig. 7. Flat-band voltage vs. temperature with gate voltage as parameter for samples B.

The flat-band voltages of the original devices are positive, indicating a net negative oxide surface charge. The devices were stressed in the same way as in the previous experiment. Both the control and annealed samples exhibit essentially the same characteristics; however, the annealed sample shows a smaller shift in its flat-band voltage under the BT stress. The positive shift for negative bias and the negative shift for positive bias clearly indicates that the shifting of the flat-band voltage is due to ion migration. Figure 7 shows the flat-band voltage *vs.* temperature with the gate voltage as parameter for both the control and annealed samples. Under positive bias stress, the flat-band voltage decreased and became negative at temperatures beyond 200°C. The change of sign indicates that, in addition to ion migration which originates from the initial ion distribution, a lot of additional positive ions were released in the oxide at the higher temperatures and they migrated to the Al_2O_3-Si interface. The original ion distribution, *i.e.* before BT stress, is believed to consist of both the positive and negative ions. However, their number and distribution are such that the oxide charge is effectively negative. The negative ions are probably due to negative oxygen ions trapped in the oxide during sputtering which was performed in a pure oxygen glow discharge. The existence of negative oxygen ions has also been reported in reactively sputtered SiO_2 (25).

Under negative bias (−3V in the present case), the shifting of the flat-band voltage shows the increasing effect of ion migration as the temperature increased. However, when the temperature is increased beyond 250°C for the control sample and 300°C for the annealed sample, the flat-band voltage reverses shifting direction and shifts toward the negative direction. This indicates that the effect of slow trapping instability has dominated the effect of ion migration. This is also similar to the previous observation and would involve the temperature dependence of the trapping time constant.

Discussion

Oxygen ions in the sputtered oxide.—The different charge polarities of ionic species in the reactively sputtered Al_2O_3 as observed from the sign of the measured flat-band voltages can be attributed to the formation of positive and negative oxygen ions in the sputtered Al_2O_3. It is considered that the location of the substrate in the glow discharge chamber during the sputtering process is the most sensitive factor in determining the oxide charge contamination, with the effects of the sputtering parameters such as cathode voltage, gas pressure, *etc.*, having secondary importance (27). It would be better if in the experiment the only difference between conditions A and B were the substrate location. However, the configuration of our sputtering systems limited this effort. The substrate for sample A was sitting in the cathode dark space which is a region of high positive ion density. These positive oxygen ions can be adsorbed on the substrate upon collision with the surface or be accelerated to the cathode and subsequently reflected and adsorbed by the substrate (25, 28, 29). Of course, we should also admit to the very likely possibility that some positive oxide charges, most probably from alkali ions, will also be present.

On the other hand, we observed negative oxide charges in sample B, from the positive flat-band voltage of measured C-V curves. In this case, the substrate was sitting right on the anode which is 2 cm away from the cathode. Under this sputtering condition, the substrate was quite likely sitting in plasma where a large population of slow electrons exists (30). The low-energy, slow electrons in the plasma would likely favor the electron attachment process when they collide with oxygen molecules. The process in which O^- ions are formed through $O_2 + e \rightarrow O^- + O$ has been studied by Lozier (31), Hagstrum (32), Craggs *et al.* (33), and Chanin *et al.* (34). The negative oxygen ions may diffuse through the plasma and be adsorbed on the substrate.

Interface state instability.—Under certain bias temperature stresses, a third instability characterized by a change in shape of the C-V curve was observed. The characteristic of this instability is broadening or "smear-out" of the C-V curve. Under positive BT stress, the C-V curves became more broad as the positive bias increased. The phenomenon is quite prominent and was observed in the devices made from sample A. For the devices made from sample B, the broadening of the C-V curves is not obvious, probably because the change is below the sensitivity of our measurement. Under negative BT stress, similar phenomena were also observed, although to a smaller degree. Refer to Fig. 4. Under the repetitive bias cycling at 250°C, the observed change of C-V curve was as follows. At first, the curve had little change at low negative bias BT stress. As the negative bias was increased to the point where the flat-band voltage starts to shift toward the negative voltage direction, *i.e.*, when the slow trapping instability becomes dominant as was discussed in the previous section, the C-V curve began to show a clear change in its shape. The curves became broadened. This shape then remained in the subsequent repetitive cycling stress until the stress condition was brought back to the point where the flat-band voltages started to shift toward the positive direction again, *i.e.*, around −10V in our case. The broadened C-V curves then became sharp again.

The only obvious change in the shape of the C-V curves observed in the devices made from sample B occurred on the two following occasions. These are, referring to Fig. 7, at −3V and 300° and 350°C BT

stress for the control and annealed sample, respectively. As the stressing process proceeded from low temperature step by step, the shape of the C-V curve remained roughly unchanged until the above indicated temperatures were reached or exceeded. Above these temperatures, the curves showed an obvious broadening.

The observed broadening of the C-V curves described above was shown to coincide with the observation of the slow trapping instability. However, for a clear understanding of the reported phenomena, further effort should be pursued.

Conclusion

In d-c reactively sputtered aluminum oxide, oxide surface charges of both polarities were observed in the Al_2O_3-Si structure. The effective oxide surface charge densities are in the order of 10^{11} cm^{-2}. For the sample containing positive oxide surface charges, an annealing treatment in a He atmosphere at 500°C for 1 hr reduced the charge density, both in the oxide and in the interface states. However, this effect was not observed in the sample containing negative oxide charges. The density of the interface states in the semiconductor forbidden gap was evaluated in one case, but was limited by the MOS technique in the other.

Different polarities of the observed oxide surface charges can be attributed to the positive and negative oxygen ions which are created during the sputtering process and are then adsorbed in the silicon surface and in the deposited Al_2O_3 layer. Contamination of positive or negative ions in the oxide seems to be greatly determined by the location of the substrate in the glow discharge during the oxide deposition process. Bias temperature stress revealed that both ion migration and carrier injection-trapping polarization effects are present. The latter process dominates the former process at higher applied electric fields. The trapping time constant is quite large at low temperatures, but becomes smaller at high temperatures. During the series of BT stress, broadening of the C-V curves was observed, notably whenever the carrier injection-trapping becomes the dominant instability mechanism.

Acknowledgments

The author wishes to express his sincere gratitude to Dr. S. Y. Wu of the Westinghouse Research Laboratories for helpful suggestions and discussions. Thanks are also due to A. Fritz and J. W. Miller for their technical assistance, and to J. W. Hile for various suggestions and encouragement.

Manuscript submitted June 22, 1970; revised manuscript received Oct. 30, 1970.

Any discussion of this paper will appear in a Discussion Section to be published in the December 1971 JOURNAL.

REFERENCES

1. L. Harries, *J. Opt. Soc. Am.*, **45**, 27 (1955).
2. J. L. Miles and P. H. Smith, *This Journal*, **110**, 1240 (1963).
3. A. Waxman and K. H. Zaininger, *Appl. Phys. Letters*, **12**, 109 (1968).
4. E. M. DaSilva and P. White, *This Journal*, **109**, 12 (1962).
5. S. R. Pollack, W. O. Freitag, and C. E. Morris, *Electrochem. Technol.*, **1**, 96 (1963).
6. L. H. Kaplan, *ibid.*, **3**, 335 (1965).
7. B. Lewis, *Microelectronics and Reliability*, **3**, 109 (1964).
8. J. A. Aboaf, *This Journal*, **114**, 948 (1967).
9. S. K. Tung and R. E. Caffrey, *ibid.*, **114**, 275C (1967).
10. E. Ferrieu and B. Pruniaux, *ibid.*, **116**, 1008 (1969).
11. R. G. Frieser, *ibid.*, **113**, 357 (1966).
12. I. H. Pratt, *Thin Solid Films*, **3**, R23 (1969).
13. S. Nishimatsu, T. Tokuyama, and M. Matsushita, "Thin Film Dielectrics," F. Vratny, Editor, p. 338, Electrochem. Soc., New York (1969).
14. K. H. Zaininger and G. Warfield, *IEEE Trans.*, **ED-12**, 179 (1965).
15. D. M. Brown and P. V. Gray, *This Journal*, **115**, 760 (1968).
16. B. E. Deal, E. L. Mackenna, and P. L. Castro, *ibid.*, **116**, 997 (1969).
17. P. V. Gray, *Proc. IEEE*, **57**, 1543 (1969).
18. P. V. Gray and D. M. Brown, *Appl. Phys. Letters*, **8**, 31 (1966).
19. E. H. Nicollian and A. Goetzberger, *Bell Syst. Tech. J.*, **46**, 1055 (1967).
20. E. H. Snow, A. G. Grove, B. A. Deal, and C. T. Sah, *J. Appl. Phys.*, **36**, 1664 (1965).
21. T. L. Chu, J. R. Szedon, and C. H. Lee, *Solid-State Electron.*, **10**, 897 (1967).
22. S. M. Hu, D. R. Kerr, and L. V. Gregor, *Appl. Phys. Letters*, **10**, 97 (1967).
23. S. R. Hofstein, *Solid-State Electron.*, **10**, 657 (1967).
24. Y. Miura and Y. Matukura, *Japan. J. Appl. Phys.*, **5**, 180 (1966); *ibid.*, **6**, 582 (1967).
25. S. Y. Wu and N. P. Formigoni, *J. Appl. Phys.*, **39**, 5613 (1968).
26. E. H. Snow and B. E. Deal, *Trans. Met. Soc. AIME*, **242**, 512 (1968).
27. S. Y. Wu, Private communication.
28. W. A. Grant and G. Carter, *Vacuum*, **15**, 477 (1965).
29. H. F. Winters and E. Kay, *J. Appl. Phys.*, **38**, 3928 (1967).
30. J. D. Cobine, "Gaseous Conductors," McGraw-Hill Book Co., New York (1941).
31. W. W. Lozier, *Phys. Rev.*, **46**, 268 (1934).
32. H. D. Hagstrum, *Rev. Mod. Phys.*, **23**, 185 (1951).
33. J. D. Craggs, R. Thorburn, and B. A. Tozer, *Proc. Roy. Soc. (London)*, **A240**, 473 (1957).
34. L. M. Chanin, A. V. Phelps, and M. A. Biondi, *Phys. Rev.*, **128**, 219 (1962).

Low-Energy Electron Irradiation of Thin Paraffin Hydrocarbon Films[1]

W. B. Berry*

Department of Electrical Engineering and the Radiation Laboratory, University of Notre Dame, Notre Dame, Indiana 46556

ABSTRACT

Low-energy photoelectrons are excited through thin paraffin hydrocarbon films at 77°K. The photocurrent is measured as a function of film thickness which is increased in steps of 20-80Å. The attenuation length or range for electrons of approximately 1 eV initial energy is 65Å for 3-methylpentane, 59Å for hexane, and 55Å for nonane. The mean free paths determined from Baraff Theory are of the order of 12Å.

Interest in stopping power and range theory has been revived in recent years with the advent and promise of ion implantation in electron device technology (1). While the fundamental question addressed here is the stopping power, that is, the particle range, the particle under consideration is the electron, not an atom, ion, or molecule. This particular subject has been of interest to radiation chemists for at least the past decade. The basic questions evolve around the lifetime and range of electrons once they have been freed from their parent atoms or electron states. Ionizing radiation may impart energies from several electron volts to several mega electron volts and, therefore, the study can be divided into three parts involving high-, intermediate-, and low-energy exchange. In this study, electrons of low initial energy, *e.g.* 1 eV above the substrate free energy, are photoexcited into amorphous thin films of organic materials, alkanes, which have been condensed onto the substrate (cathode) surface. While the energies of these electrons are not subexcitational in an absolute sense, the cross sections for subexcitational exchange are considered to be dominant. Therefore, the problem reduces to consideration of the hot electron.

The excited electrons have an initial energy equivalent to that of the absorbed photon, if the assumption is made that only Fermi electrons are excited. To be emitted into the film, the electrons must overcome the effective work function of the cathode, which, for the source employed, results in electrons of 2 eV maximum, if the film-emitter interface is assumed to have a negligible effect on the cathode work function, no barrier potential exists, and film charging can be neglected. The energy diagram is given in Fig. 1. The magnitude of this extra energy is such that the electron is subexcitational. The equivalent total energy is considerably greater if one assumes that the amorphous film has an equivalent Fermi energy, work function, and band structure, but still subexcitational. The vibrations which can be excited are intramolecular, rotational, and intermolecular excitations. Each of these has a finite probability of occurring, but the cross section for intermolecular excitation is expected to dominate (2). In general, the one dimensional photoelectron flux is measured to attenuate exponentially with increasing film thickness. This compares well with Crowell's hot electron theory (3) which is typical of that found in most solids (4).

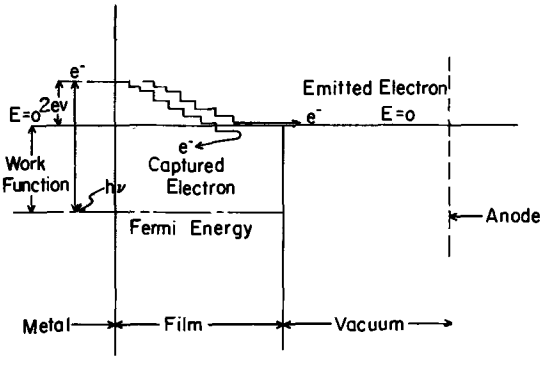

Fig. 1. Emission energy diagram

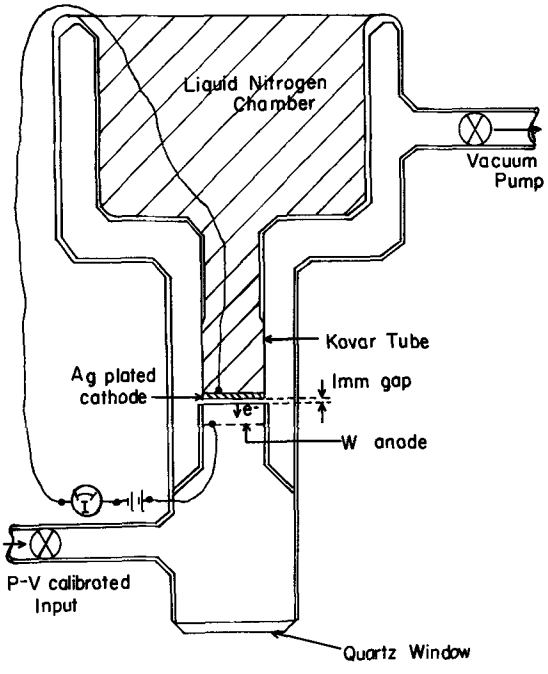

Fig. 2. Test cell for photoemission measurements

Experimental

As outlined above, the objective of this study was to determine whether or not a thin hydrocarbon film would significantly resist penetration by low-energy electrons. In the initial phase, the study has been restricted to paraffin hydrocarbons, such as 3-methylpentane, nonane, and hexane, to avoid significant charging of the film itself. To assist in this determination, the data chamber of Fig. 2 was designed. The controlled inputs required for the chamber design are vacuum, radiant energy, vaporized sample inlet, temperature control, and electrical sensing.

[1] The Radiation Laboratory is operated by the University of Notre Dame, under contract with the Atomic Energy Commission. This is AEC Document No. COO-38-749.

* Electrochemical Society Active Member.

Key words: range theory, low-energy electron irradiation, attenuation length, mean scattering length, stopping power.

A mercury vapor diffusion pump was used to establish the vacuum. Two liquid nitrogen traps were inserted between the diffusion pump and the data chamber. The vacuum of the manifold to which the data chamber was connected was monitored with either a McLeod gauge or a CVC discharge gauge. The vacuum was maintained at approximately 2 x 10^{-5} Torr.

The sample was admitted to the data chamber in vapor phase, in calibrated units at established pressure and volume, through the valve shown at the lower left of Fig. 2. The volume of the controlled sample was 11 cc and the pressure was in the range of 10-100μ. Upon opening the valve, the vapor passed into the lower chamber, along the guide tube, through the tungsten mesh, and into contact with the silver-plated, liquid nitrogen cooled cathode onto which it condensed. By admitting controlled samples of the hydrocarbon, the thickness of the condensed film could be increased in steps and the transmission of electrons through the film could be measured as a function of the film thickness. The separation between the end of the guide tube and the cathode was about 1 mm. This separation was kept reasonably small to insure that the hydrocarbon condensed on the cathode bottom surface. A Consolidated Engineering Micromanometer was employed to monitor the pressure of the vapor in a storage chamber from which the calibrated sample was drawn.

The source of photons for the generation of photoelectrons was a mercury vapor lamp positioned below the window at the bottom of the data chamber. The window was Suprasil-2 quartz which admitted both 2537 and 1849Å quanta into the chamber. The radiant energy passed through the tungsten mesh anode, through the condensed film, and into the cathode. The tungsten mesh had a transmission coefficient of 0.85.

The photoemitted electrons which penetrated through the condensed film were collected by the positively biased anode. The bias voltage was approximately 100V and the electrode separation about 1 cm. The photocurrent of the collected electrons was recorded with the aid of a Cary vibrating reed electrometer and Varian Graphic Recorder. Bare cathode currents were of the order of 10^{-9} to 10^{-10} A. The noise level was normally three or four orders of magnitude below the bare cathode response.

Samples of 3-methylpentane, hexane, and nonane were dried by passing the liquids through an 8 ft column of silica gel. The material was then stored in a glass container until used. After these samples were inserted into the system, they were outgassed by a repetitive freeze-pump-thaw procedure. Prior to cooling the cathode for condensation of the film, the data chamber and preceding stages were flushed out with vapors from the outgassed sample.

Results

Typical photoresponse data are presented in Fig. 3 which shows the dependence of the photocurrent on the number of film layers for 3-methylpentane films. In the figure, δ represents the layer thickness which was varied in successive experiments by controlling the pressure of the vapor in the calibrated inlet chamber. The film thickness was increased in increments of 20-80Å and the photocurrent recorded following each incremental increase. The response saturated at a level approximately two orders of magnitude below the bare cathode response. A reasonably good fit to the data curves is obtained by assuming simple exponential attenuation as a function of film thickness. This attenuation continues until a residual signal level is reached which is independent of film thickness. The relative magnitude of this residual response is represented on the figure by the "A" value. The initial layer attenuation was always significantly greater than that for subsequent film layers. A brief discussion of the probable reason for this is given below.

As mentioned above, the functional form of the photoresponse can be represented by the equation:

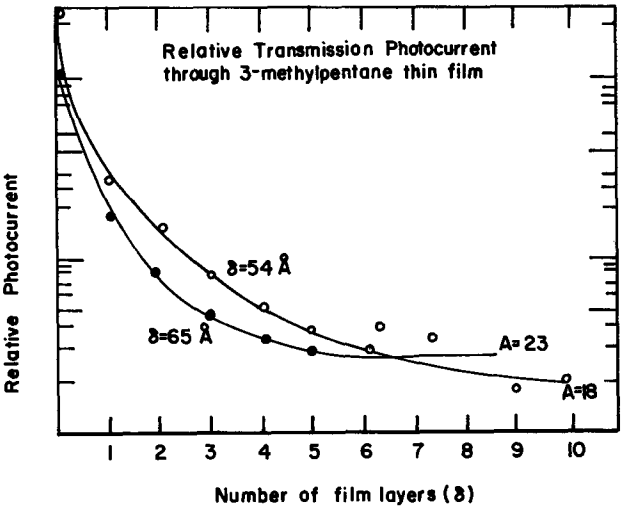

Fig. 3. Raw photoemission data for 3MP films

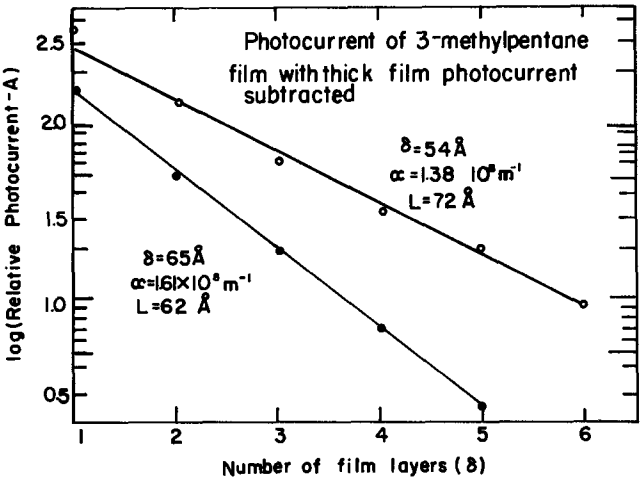

Fig. 4. Replotted 3MP photoemission data to obtain attenuation length.

$I = A + I_0 \exp(-n\delta/L)$, where A is the final value of the response as n becomes reasonably large, $(I_0 + A)$ is the initial value of the photoresponse, $\alpha = 1/L$ is the extinction coefficient, L is the mean attenuation length, δ is the layer thickness, and n is the number of layers. By plotting $\log[(I - A)/I_0]$ against n, as in Fig. 4, the magnitude of α and L can be determined. The figure presents data for different layer thickness, *i.e.*, inlet pressure, for 3-methylpentane. The determined value for L was, on the average, 64Å. The data, which are presented for contrast, represent the extremes in data obtained. Calculated values of mean attenuation length for hexane and nonane are also presented in Table I and are discussed below.

The data presented in Fig. 3 and 4 represent response to 1849Å radiation, since 2537Å radiation from the mercury lamp resulted in negligible collectable emission from the cathode. The principal reason for this stems from the fact that the work function of silver is approximately 4.7 eV and 2537Å photons have approximately 4.8 eV. While the 2537Å emission could be detected from the bare cathode, a film of 20Å or less reduced the photocurrent below the noise level.

Table I. Comparison of attenuation lengths and mean free scattering lengths for three materials

Material	Attenuation length	Mean free length
Hexane	59	12.5
3-Methylpentane	65	14
Nonane	55	12

The 1847Å radiation, which is significantly weaker for the lamp employed, resulted in very strong emission despite the fact that the photon intensity was an order of magnitude lower. To insure that this emission was due to 1849Å photons, a Corning 7910 filter was inserted between the source and the sample chamber at each film thickness. When this was done, the photocurrent dropped below the detection level. These emitted electrons have an average energy of approximately 1 eV above the work function of the cathode and an anticipated spectrum of approximately uniform density from 0 to 2 eV. The actual electron energy distribution was not determined. The fact that a very thin film eliminated the photoemission due to the 2537Å line and that the attenuation for the initial layer was, in all cases, greater than that which would have been anticipated from the data for subsequent layers indicated that the thin hydrocarbon film affected the work function of the metal surface, a not too surprising result. The effective increase was not measured, but the 2537Å data suggest that it was at least 0.1 eV. The fact that this initial attenuation took place for initial layers of 20Å or less supports the assumption of uniform thickness.

The potential applied between the electrodes is assumed to have negligible effect on the emission. The electric field, 100 V/m, is too small to significantly alter the image force potential out to a film thickness of 1000Å, which is beyond the maximum thickness of the films on which these data were taken. The boundary conditions for the film, *i.e.*, at the metal-film and film-vacuum interfaces, are essentially unchanged for each incremental thickness increase. Therefore, the measured change in photoresponse is a measure of internal losses alone.

Discussion

The elementary technique employed in the evaluation of the data in the previous section leads one to postulate a rather simple range model for the electrons. To minimize obvious complications, the model to be discussed assumes near-charge neutrality throughout the film. The elementary model simply implies that an electron which is scattered returns immediately to the cathode or else induces another electron to do so. Since the film is constantly in the flux of the complete radiation spectrum of the lamp, there are photons of lesser energy which are sufficiently energetic to excite electrons from traps which can migrate through the film and thereby readily return to the cathode, maintaining a near-neutral film.

There are two emission phenomena which must be considered. The first of these is emission from the cathode and subsequent transmission through the film. Second, some electrons will be assumed to be excited from the film itself, either from low-lying traps or by two-photon processes.

The form of the first emission phenomenon simply assumes that N_0 electrons are emitted per second per unit area from the cathode and collide with molecules, losing energy in increments along the path. Those electrons which lose sufficient energy to fall below the work function of the film are captured and returned to the cathode. Those which retain a portion of their initial energy over and above the work function are transmitted and collected by the cathode. Then the decrease in N is proportional to the stopping probability, *i.e.*, $dN/dx = -pN$, where N represents the number of electrons transmitted to the position x per unit area per second and p is the stopping probability. From this equation, $N = N_0 \exp(-px)$, where $p = \alpha = 1/L$ and $x = n\delta$ when comparison is made with the previous section. The photocurrent due to cathode-emitted electrons becomes $I_c = eN = eN_0 \exp(-n\delta/L)$.

Electrons which are excited from the film itself are transmitted from the point of excitation with the same probability as electrons emitted from the cathode through a film of that thickness. This emission is dependent on the absorption coefficient of the film for whichever process, single or double absorption, dominates. Even if this absorption coefficient is $10^6\ m^{-1}$, the film would have to be at least 1000Å in thickness for the absorption not to be considered as uniform throughout. The films considered here seldom exceed 500Å and, therefore, uniform excitation is a reasonable approximation. The exact emission for electrons excited from the film is formulated as

$$I_f = \frac{eP}{2} \int_0^{n\delta} \alpha \exp(-\alpha x) \exp(-x/L)\, dx$$

where $P\alpha\exp(-\alpha x)$ represents the number of electrons, per unit area per second, excited at x, and $\exp(-x/L)$ represents the probability that these electrons will be transmitted. The factor 1/2 is included since the excited electrons will have velocities both toward and away from the cathode in equal numbers. Integration of this equation yields

$$I_f = \frac{e}{2} [P\alpha L/(1 + \alpha L)]\, [1 - \exp(-[1 + \alpha L]n\delta/L)]$$

Since $L \sim 100$Å, and $\alpha \sim 10^{-4}$ Å^{-1}, then

$$I_f = \frac{e}{2} P\alpha L\, (1 - \exp[-n\delta/L])$$

which is the uniform excitation response. The total photocurrent is obtained by combining these two results. That is,

$$I = I_{f_x} + (I_{co} - I_{f_x}) \exp(-n\delta/L)$$

where $I_{f_x} = e/2\, P\alpha L$ represents the excitation from the film alone, that is, a very thick film, and $I_{co} = eN_0$ represents the bare cathode emission. A comment should be added here on the completeness of this relation because of the obvious strong reflection at the metal film interface. The reflected photons will indeed increase the excitation from the film. However, only the magnitude of I_f will be changed. The functional form will be essentially unchanged as long as wavelengths with sufficiently small absorption coefficients are used. I_{co} must be the bare cathode current adjusted to account for the metal-film interface potential.

The data fit this model which lends itself to a satisfactory explanation thereof. However, further examination and interpretation are necessary to gain some knowledge of the physical phenomena surrounding the determination of L. There are several items which one must consider such as the effects of trapping and therefore charging of the film, the scattering mechanism, which for subexcitational electrons is elastic or inelastic, and the adequacy of this model. The inelastic scattering results in the generation and annihilation of intermolecular vibrations or phonons.

The last item will be discussed first. Let the primed currents, I'_x, represent the three-dimensional model currents. If one were to consider a three-dimensional isotropic emission model for electrons emitted by both the cathode and the film, then the following photocurrents would be observed. These currents are determined by counting all electrons which would penetrate the film to the region to the right of the film in Fig. 1.

$$I'_c = I_{co}\, g_f\, (1 + x/L) \exp(-x/L)$$

$$I'_f = I_{f_x}\, g_f\, [(1 - \exp(-x/L)) - (x/L) \exp(-x/L)]$$

The geometrical factor, g_f, is actually an effective area factor which implies that the emitting area is proportional to L^2 rather than a unit area. The total current has the form

$$I' = g_f I + g_f (I_{co} - I_{f_x})\, (x/L) \exp(-x/L)$$

where the unprimed currents represent those for the one-dimensional model.

The additional current term would not be sufficiently significant for films of the thicknesses observed. The

dependence of the exponential coefficient varies much more slowly than the exponential term itself, especially when the data are plotted on a semilog scale. A comparison of the two shows that the maximum error in estimating the slope would be about 15%.

The question does arise as to whether this scattering model is appropriate since the electron would be expected to experience many elastic scattering events and therefore proceed by diffusion or random walk. The elastic scattering model which describes the electron's path must include the constraints of capture at the cathode surface and emission at the film surface. In one dimension, such a model leads to a reciprocal film-thickness dependence which does not fit the data.

If the film were charged, then that charge would inhibit the transmission of electrons. This possibility was investigated by observing the response for various radiation intensities. The emission from the cathode is proportional to the incident radiation, and transmission through the film was observed to be proportional to the incident radiation also. Incident intensity was varied by inserting neutral density filters between the lamp and the quartz window.

The spectral output of the lamp is quite broad. Since the electron traps in 3-methylpentane are known to be both deep and shallow, that is, capable of being emptied by infrared and uv radiation, it is expected that the lifetime of electrons in these traps is very short. Attempts were made to determine whether or not post emission occurred after the source was interrupted. However, the signal level was too small to be certain that such emission was actually present.

The scattering mechanism proposed above limits scattering to intermolecular vibrations since the electron energies are subexcitational. At least it is certain that intramolecular excitation would be accomplished in the first 20Å of travel or in the first layer of the film (2). The data support this analysis through the initial decrease in photocurrent which exceeds that for further increases in film thickness. Rotational excitations are ruled out for these nonpolar materials. The remaining, at least dominant, scattering mechanism is the intermolecular vibration or phonon. Raman spectra for the materials in question, in the liquid phase, indicate a vibrational range of 30-80 cm^{-1} or 0.004-0.01 eV. In the analysis and results of the calculations presented in Table I, the latter is used.

The analytical model proposed in the previous section assumes that a good fit to the data is obtained by exponential attenuation of the photoemitted carriers, or that the probability for a sufficient number of energy loss collisions to occur in a given distance is constant. This assumption is in good agreement with the range theory for hot electrons in metals (5) and electrons excited into materials where the dominant scattering is by optical phonons (6). In the latter reference, Baraff's attenuation length (range) is related to the initial average electron energy, 3 $kT_e/2$, the energy of the scattering phonon, E_r, and the mean scattering length, l, by the relation

$$l = L(3E_r/kT_e)^{1/2}$$

This relation leads to the values of l shown in Table I for the hydrocarbons mentioned above. On the average, an electron travels about three molecular diameters between scatters, if one assumes an energy loss of 0.01 eV for each occurrence. An electron will travel a distance of 1500Å in losing 1 eV. This agrees reasonably well with random walk theories (7) for total distance of travel. An additional advantage of the Baraff model is its independence of electron source energy distribution.

In the former reference, Sze *et al.* (5) treat metal films and electrons of energy above the Fermi energy but below the work function. The functional dependence of the response in this reference agrees with those of this effort, but the range is found to be energy dependent for electrons of energy near the top of the barrier over which they are collected. While the energy dependence of this theory is in general agreement with the Baraff theory, it lacks the incremental energy loss as an integral part of the range determination.

Acknowledgment

The author wishes to thank Dr. W. H. Hamill of the Radiation Laboratory for his suggestions, advice, and discussions.

Manuscript submitted July 6, 1970; revised manuscript received Nov. 13, 1970. This was Paper 52 presented at the New York Meeting of the Society, May 4-9, 1969.

Any discussion of this paper will appear in a Discussion Section to be published in the December 1971 JOURNAL.

REFERENCES

1. J. F. Gibbons, *Proc. IEEE*, **56**, 295 (1968).
2. A. Mozumber and J. L. Magee, *J. Chem. Phys.*, **47**, 939 (1967).
3. C. R. Crowell, W. G. Spitzer, L. E. Howarth, and E. E. Labate, *Phys. Rev.*, **127**, 2006 (1962).
4. William Pong, *J. Appl. Phys.*, **38**, 4103 (1967).
5. S. M. Sze, J. L. Moll, and T. Sugano, *Solid-State Electron.*, **7**, 509 (1964).
6. G. A. Baraff, *Phys. Rev.*, **135**, A528 (1964).
7. R. N. Stuart, F. Wooten, and W. E. Spicer, *ibid.*, **135**, A495 (1964).

NOMENCLATURE

Å,	Angstrom units
A,	Const-final photocurrent, amperes
eV,	Electron volts
ϵ,	Exponential symbol
E_r,	Phonon energy
g_f,	Geometry factor
I_{co},	Bare cathode photocurrent
I_c,	Photocurrent from cathode
I'_c,	Three-dimensional cathode photocurrent
I,	Total photocurrent, amperes
I',	Three-dimensional total photocurrent
I_o,	Exponential component of photocurrent, amperes
I_f,	Photocurrent from film
$I_{f\infty}$,	Film photocurrent for infinitely thick film
I'_f,	Three-dimensional film photocurrent
k,	Boltzmann's constant
l,	Mean free scattering length
L,	Mean attenuation length or range, Angstroms or meters
mm,	Millimeters
N,	Electron flux, per unit area per second
N_0,	Initial electron flux, per unit area per second
n,	Film thickness layer index
p,	Stopping probability, classical scattering probability
P,	Probability factor
T_e,	Electron temperature
x,	Distance parameter, indexing subscript
α,	Attenuation or extinction coefficient, m^{-1} or $Å^{-1}$
δ,	Film layer thickness, Angstroms
3MP,	Three-methylpentane
∞,	Infinite distance

Application of Triangular Voltage Sweep Method to Mobile Charge Studies in MOS Structures

N. J. Chou

IBM Thomas J. Watson Research Center, Yorktown Heights, New York 10598

ABSTRACT

The present paper examines the theoretical aspects of the triangular voltage sweep (TVS) technique and describes the development of a unified quasi-equilibrium approach wherein various polarization processes in an MOS capacitor structure subjected to the changing applied field are evaluated in terms of their contributions to the externally observed current. It is shown that a self-consistent experimental and analytical approach must be used when the TVS technique is applied to mobile charge studies in MOS structures.

The triangular voltage sweep (TVS) technique has been widely used by electrochemists to investigate anodic reactions in fuel cells (1). It is basically a voltammetric method where the voltage applied to a system $[V(t)]$ is made to follow a triangular waveform. Application of this technique to mobile charge studies in metal-oxide-silicon structures was first proposed by Yamin (2). More recently, Kerr (3) has reported that the method can be used to detect mobile Na^+ concentrations as low as 10^9 ion-cm^{-2} in SiO_2 films. So far, however, the capabilities and limitations of the TVS technique for analyzing various polarization processes in MOS structures at elevated temperatures have not been fully explored.

In the present paper a unified quasi-equilibrium analysis is developed wherein various electrical and electrochemical effects in an MOS capacitor are evaluated in terms of their contributions to the total current flow in the external circuit. It is shown that, under certain conditions, a faradaic polarization process may take place whose contribution will be superimposed on the polarization current normally attributed to the displacement of mobile charge in the insulator. A self-consistent analytical and experimental approach must therefore be used when the TVS technique is applied to mobile charge studies in insulating films. Extensive current-voltage measurements have been conducted in an electrochemically symmetrical Si-SiO_2-Si structure, and the results demonstrate that such an approach is indeed necessary. Experimental data in this simple structure indicate, for example, that the quasi-equilibrium analysis of mobile charge polarization in thermally grown SiO_2 films is applicable only in a limited range of temperature and voltage sweep rate. Indiscriminate use of the TVS technique may thus lead to erroneous interpretation of experimental data.

Quasi-Equilibrium Analysis of Polarization Currents

For a thin film sandwiched between two large electrodes, the current flow may be regarded as unidirectional and it is generally dependent in a complex way on $V(t)$ at elevated temperatures. The externally observed current density, j_{ex}, will be composed of various bulk and interfacial components and their interactive terms. In practice, where the interactions are negligible, the remaining components can be treated additively. Since the MOS structure constitutes a solid electrolyte cell at elevated temperatures (4), j_{ex} measured during the voltage sweep may contain: (*a*) a steady-state electronic component, j_e, due to the bulk conduction of the insulator; (*b*) a faradaic component, j_f, associated with the ions of reacting species; (*c*) a capacitive component, j_c, resulting from the charging and discharging of the MOS capacitor structure; (*d*) a polarization current, j_p, associated with slow-moving ionic defects in the insulator; and (*e*) a faradaic polarization current, j_{fi}, which may arise from the electrochemical reactions at the interfaces even when the faradaic current is negligibly small ($j_f \cong 0$). For convenience, these components are summarized in Table I. A typical current-voltage or I(V) characteristic obtained by the TVS method is also shown in Fig. 1, which demonstrates how various components of j_{ex} are superimposed.

Key words: insulator, solid electrolyte, MOS structure, ionic transport, triangular voltage sweep technique.

Table I. Various bulk and interfacial components of the externally observed current density: $j_{ex} = j_e + j_c + j_p + j_{fi} + j_f$

Component	Nature	Origin	Parameters affecting its magnitude
j_e	Steady-state, particle current	Electronic	Applied field, conduction mechanism
j_f	Steady-state or non-steady-state particle current	Electrochemical, ionic	Overpotential and rate of electrolysis
j_c	Displacement current	MOS capacitor charging; interface state polarization	Sweep rate, oxide capacitance, interface state concentration
j_p	Displacement current	Mobile charge polarization	Sweep rate, mobile charge concentration
j_{fi}	Displacement current	Faradaic polarization	Sweep rate, characteristics of transfer layer at the interface

For a given applied voltage, the magnitude of j_c depends on the specific conduction mechanism brought

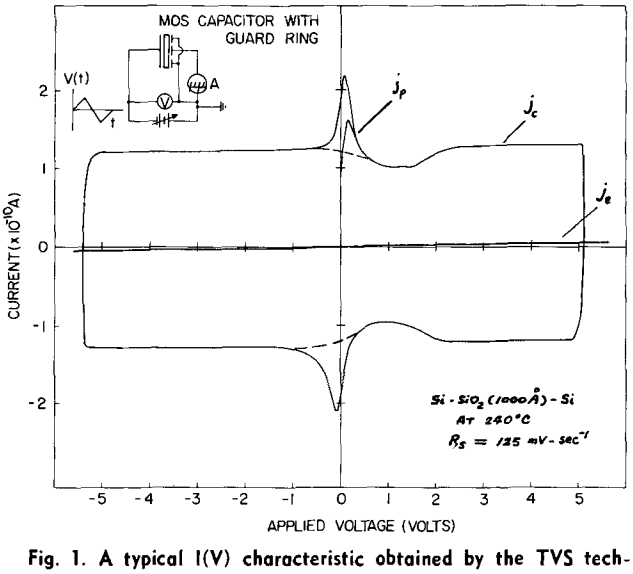

Fig. 1. A typical I(V) characteristic obtained by the TVS technique. Note that in the absence of faradaic polarization, j_{ex} is composed of j_e, the steady-state electronic component; j_c, the MOS capacitor charging component; and j_p, the mobile charge polarization component. Since j_e is independent of sweep rate, R_s, it constitutes the bisecting line for the j_c loop.

about by the applied field. The faradaic component, j_f, on the other hand, is determined by the rate-limiting step in the over-all reaction of the solid electrolytic cell. When the cell reaction becomes eventually diffusion controlled at sufficiently high temperatures, interactive effect of j_f on various polarization processes cannot be ignored. At these temperatures, ions of reacting species will be injected at one electrode and/or removed at the other in appreciable quantities. As a result, the polarization processes in the SiO_2 layer may become very complicated. For mobile charge studies, which are aimed at obtaining quantitative information about the extrinsic and intrinsic ionic defects in the the insulating film (*i.e.*, impurity ions and/or thermally generated vacancies and interstitials of constituent ions), the TVS measurements should be made in the temperature range where the electrodes are completely blocking ($j_f = 0$).

In the following analysis, the j_c, j_p, and j_l components will be estimated separately by postulating a state of quasi-equilibrium for each of their associated polarization processes. Provided that j_f is negligibly small and j_{ex} is not predominantly composed of j_c during the entire potential sweep, this quasi-equilibrium condition can be realized experimentally by varying two common external parameters (*i.e.*, potential sweep rate and temperature) either jointly or independently in the appropriate temperature range. It will be seen that the onset of electrode reactions in the MOS systems, usually undetectable by ordinary experimental techniques, sometimes manifests itself in the occurrence of a component, j_l, on the TVS plot. This component j_l, with its distinctive features, can often be used to define a suitable temperature range for mobile charge polarization studies.

Interface state polarization.—Component j_c is associated with the charging or discharging of the MOS capacitor which takes place concurrently with the formation of space charge in the semiconductor and also the capture or emission of charge carriers by the surface states or oxide traps[1] near the SiO_2-Si interface. When an external voltage is applied across the MOS structure, the surface charge of the metal electrode (σ_1) is balanced by the charges in the surface states (Q_{ss}) and in the space charge region (Q_{sc}): $\sigma_I = Q_{sc} - Q_{ss}$. Furthermore, the applied voltage is taken up by the surface potential of the semiconductor, ψ_s (*i.e.*, the potential rise or drop from the semiconductor bulk to its surface) plus the potential difference (V_{ox}) across the insulating layer and the work function difference (ψ_{ms}) between the metal and silicon electrodes (5)

$$V = \psi_s + V_{ox} + \psi_{ms} = \psi_s + (Q_{ss} - Q_{sc})/C_{ox} + \psi_{ms} \quad [1]$$

where C_{ox} is the oxide capacitance. Consequently, the capacitive current contribution is

$$j_c = d\sigma_I/dt = \left(\frac{\partial Q_{sc}}{\partial V} - \frac{\partial Q_{ss}}{\partial V}\right)\frac{dV}{dt} + \frac{\partial Q_{sc}}{\partial t} - \frac{\partial Q_{ss}}{\partial t} \quad [2]$$

or, by virtue of the relationship in Eq. [1]

$$j_c = C_{ox} R_s (1 - \partial\psi_s/\partial V) + (\partial Q_{sc}/\partial t - \partial Q_{ss}/\partial t) \quad [2a]$$

where dV/dt has been replaced by the constant sweep rate, R_s. When the system is stable and in a state of quasi-equilibrium such that the space charge and surface state population can readily follow the changing applied field, $\partial Q_{sc}/\partial t$ and $\partial Q_{ss}/\partial t$ vanish, and j_c reduces to

$$j_c = C_{ox} R_s (1 - \partial\psi_s/\partial V) \quad [3]$$

In the absence of other polarization processes, therefore, j_{ex} can be equated to j_c, and the $j_{ex} - V$ curve obtained by the TVS technique can be identified with the low-frequency capacitance *vs.* voltage characteristic of the MOS structure, as has been shown by previous investigators (6).

When the system is in a state of quasi-equilibrium, the following relationship holds (7)

$$\partial\psi_s/\partial V = \left[1 - \frac{1}{C_{ox}} \cdot \left(\frac{dQ_{sc}}{d\psi_s} - \frac{dQ_{ss}}{d\psi_s}\right)\right]^{-1} \quad [4]$$

At voltages corresponding to the accumulation and inversion regions for the semiconductor, the space charge term predominates and $\partial\psi_s/\partial V \approx 0$; in the depletion region, the value of $\partial\psi_s/\partial V$ depends on the relative magnitude of both the space charge and surface state terms. If a high surface state density is present such that $\partial\psi_s/\partial V$ will vanish when the Si surface is depleted, component j_c will describe a rectangular loop on a TVS plot as if the MOS structure consisted of an insulating film between two metal electrodes. In case the surface state density is not very high, $\partial\psi_s/\partial V$ will be less than unity in the depletion region. Then a surface state contribution will be superimposed on the ideal low-frequency $C(V)$ characteristics (*i.e.*, interface-state free). It is important to note that, at elevated temperatures, this contribution is usually negligible in comparison with others discussed in this paper.

On the other hand, if the potential sweep is so fast that the system is no longer in a state of quasi-equilibrium, the non-steady-state term in Eq. [2] often produces one or more current peaks of substantial magnitude on the I(V) plot at voltage values determined by the time constant and the energetic spectrum of the surface states (8). Appearance of such peaks obviously complicates the interpretation of the TVS plots.

In MOS specimens usually encountered in practice, a large interface state concentration often manifests itself in a small asymmetry in the $j_c - V$ curve with respect to the voltage axis. These states cannot be quantitatively evaluated without concurrent high-frequency $C(V)$ measurements (6).

Mobile charge polarization.—Redistribution of mobile charge centers in an insulator induces a change of surface charge (σ_I) on the metal electrode while contributing a component, j_p, to the externally measured current flow. Since σ_I depends implicitly on V and t during the potential sweep

$$j_p = d\sigma_I/dt = \frac{\partial\sigma_I}{\partial V} \cdot \frac{dV}{dt} + \frac{\partial\sigma_I}{\partial t} \quad [5]$$

For an arbitrary space charge distribution, $\rho = \rho(V, x, t)$, in an insulating film of thickness l, the instantaneous surface charge $\sigma_I(V, t)$ induced on the electrode (at $x = 0$) can be concisely expressed by (9)

$$\sigma_I(V, t) = Q(V, t)\,[1 - \overline{X}(V, t)/l] \quad [6]$$

where $Q(V, t) = \int_0^l \rho(V, t, x)dx$ is the area of the space charge profile (or the total space charge) between the two electrodes; and $\overline{X}(V, t) = \int_0^l \rho x dx / \int_0^l \rho dx$ is the coordinate of centroid for the space charge profile with respect to the axis at $x = 0$.

The polarization current is therefore

$$j_p = \left\{\frac{\partial Q}{\partial V}\left(1 - \frac{\overline{X}}{l}\right) - \frac{Q}{l}\left(\frac{\partial\overline{X}}{\partial V}\right)\right\}\frac{dV}{dt} + \left(1 - \frac{\overline{X}}{l}\right)\frac{\partial Q}{\partial t} - \frac{Q}{l} \cdot \frac{\partial\overline{X}}{\partial t} \quad [7]$$

When the system is in a state of quasi-equilibrium (*i.e.*, when the charge redistribution can readily follow the changing voltage), both $\partial Q/\partial t$ and $\partial\overline{X}/\partial t$ will vanish if the electrodes are blocking with respect to the moving ionic species. The polarization component, j_p,

[1] Oxide traps are regarded as effective surface states (5).

thus reduces to

$$j_p = R_s \left[dQ/dV \left(1 - \overline{X}/l\right) - (Q/l)\, d\overline{X}/dV \right] \quad [8]$$

where dV/dt has been replaced by R_s. When the total charge is independent of the applied voltage (*i.e.*, there is no field generation of mobile charge), $dQ/dV = 0$ and Eq. [8] simplifies to a more manageable form

$$j_p = -R_s\, (Q/l)\, d\overline{X}/dV \quad [9]$$

Analysis of the polarization current can now be treated as an electrostatic problem which essentially involves solving for static charge profiles in an insulating layer subjected to an applied field and determining the centroid of charge mass and its voltage derivative as a function of the applied potential. In addition, such solutions can be readily found by numerical calculations since Eq. [9] usually cannot be evaluated in a closed form (see Appendix I).

Component j_p obviously has a maximum at a voltage, V_m, for which $d^2\overline{X}/dV^2 = 0$. In an electrochemically symmetrical cell such as Si-SiO_2-Si, the polarization current peak will appear at zero applied voltage. In an asymmetrical cell, j_p will still peak when the mobile charge becomes uniformly or, more correctly, symmetrically distributed in the insulator. However, it should be noted that this distribution does not necessarily prevail when V is equal in magnitude and opposite in sign to the open-cell potential E^o (or equivalently, the work function difference, ψ_{ms}) of the MOS structure.[2] In Pt-SiO_2-Si structures, for example, V_m has been found to vary with the oxide thickness while other parameters were held constant (10).

Faradaic polarization.—When the electrode reactions occur but the faradaic component remains negligibly small ($j_f \cong 0$) during the whole potential sweep, the MOS structure can be treated as an electrolytic cell at virtual equilibrium. That is to say that, provided that the applied potential sweep rate is sufficiently slow, the concentration change in the transfer layers immediately adjacent to the electrode-insulator interfaces may be considered to be realized in an infinite number of perfectly reversible steps for which $j_f = 0$. Under appropriate conditions, a polarization component, j_l, associated with this concentration change may appear in the external circuit if, during the sweep, ionization-discharge is the rate-determining step of the electrode reactions.

Depending on the relative magnitudes of various parameters in the system under investigation (see Appendix II), j_l may exhibit any one of the following characteristics.

(*a*) When one of the interface reactions predominates, j_l has a maximum at

$$V_m = \frac{1}{\epsilon}\left(E^o - \frac{RT}{zF} \ln K_i\right) \quad [17]$$

where E^o is the equilibrium cell potential, ϵ the correction factor, K_i the equilibrium constant for the prevailing electrode reaction, and other symbols have their usual significance. In this case, j_l cannot be separated from j_p since ϵ and K_i are usually unknown.

(*b*) When the extent of both interfacial reactions is comparable, j_l appears double peaked with well-defined maxima at

$$V_1 = \frac{1}{\epsilon}\left(E^o - \frac{RT}{\delta_{1z}F} \ln K_I\right)$$

and

$$V_2 = \frac{1}{\epsilon}\left(E^o - \frac{RT}{\delta_{11z}F} \ln K_{II}\right) \quad [18]$$

where δ's are overpotential distribution factors.

[2] If the initial distribution of uncompensated mobile charge centers has the shape of a delta function at one of the interfaces, as postulated by Snow *et al.* (11), then quasi-equilibrium condition cannot be achieved throughout the course of the potential sweep. As the mobile charge leaves the boundary layer at low applied voltages, the diffusion and drift terms in the transport equation will be of the same sign, and the quasi-equilibrium condition does not hold until a concentration gradient is built up in the bulk of the insulator.

(*c*) For more intermediate cases, j_l exhibits a primary and a secondary peak, which are often difficult to resolve on a TVS plot. Nevertheless, double-peaked faradaic polarization current has been observed in both Cr-SiO_2-Si (12) and Pt-SiO_2-Si (10) structures.

The magnitude of the current peaks for j_l, normalized with respect to sweep rate R_s, is proportional to the equilibrium constant and the number of activated sites in the corresponding transfer layers (Appendix II). If a single peaked j_l is mistaken for j_p in the mobile charge studies, the error involved can therefore be several orders of magnitude. On the other hand, the appearance of a double-peaked component on a TVS plot can be taken as indicative of the onset of electrode reactions, and consequently sets an approximate temperature limit for ideally blocking electrodes.

For example, the j_l component observed in Pt-SiO_2-Si systems at 390°C indicates that the silicon electrode is no longer ion-discharge blocking above this temperature ($j_l \neq 0$) (see Fig. 2).

Mobile Charge Studies by TVS Technique

It is evident from the preceding discussion that meaningful data for mobile charge analysis can be obtained only when one has experimentally established that: (*a*) the system is in a state of quasi-equilibrium during the TVS measurement, and (*b*) the observed polarization component is solely attributable to the mobile charge excursion (*i.e.*, $j_l = 0$). Intuitively, either an increase in ambient temperature or a decrease in voltage sweep rate should eventually bring about the desired equilibrium. However, a continued decrease in sweep rate will lower the external current below the level of detectability, whereas an excessive temperature increase introduces complicating effects (*e.g.*, the electrodes become nonblocking and $j_l \neq 0$). A plausible experimental approach is therefore to determine the temperature limit by monitoring the occurrence of j_l on the TVS plot. After establishment of this temperature regime, the following three quantities associated with the mobile charge polarization current can then be used as self-consistent criteria to test the onset of quasi-equilibrium, as well as the validity of the various assumptions in the quasi-equilibrium analysis.

1. *Normalized area:* For voltages exceeding some value, $\pm|V_o|$, where mobile charge profile can be ap-

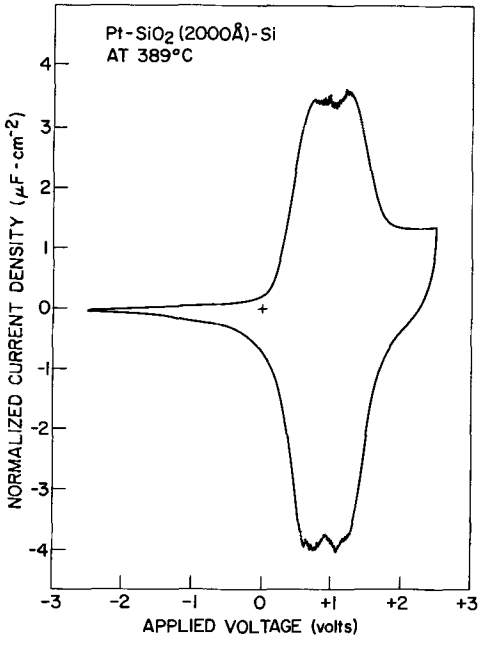

Fig. 2. Experimental evidence showing the occurrence of a double-peaked faradaic polarization current, j_l, in a Pt-SiO_2-Si cell. The TVS plot was taken at a sweep rate of 41.7 mV-sec^{-1}.

proximated by a delta function at each electrode (*i.e.*, $\bar{X}_2 - \bar{X}_1 \approx l$) the area under j_p on the TVS plot can be normalized with respect to R_s to yield

$$\frac{1}{R_s}\int_{\leq -|V_o|}^{\geq +|V_o|} j_p dV = -(Q/l)\int_{\bar{X}_1}^{\bar{X}_2} d\bar{X} \approx Q = \text{const} \quad [19]$$

Upon the onset of quasi-equilibrium, therefore, the normalized area should be independent of the sweep rate and the number of sweeps and should remain virtually constant for voltage sweeps exceeding $\pm|V_o|$.

2. *Normalized peak current*: Transposing Eq. [9] gives

$$(j_p)_{max}/R_s = -(Q/l)\,(d\bar{X}/dV)_{j_p=(j_p)_{max}} \quad [20]$$

Consequently, the normalized current peak should also be rate- and field-independent in the quasi-equilibrium regime.

3. *Voltage corresponding to current peak*: The equilibrium position of the current peak, V_m, is defined by the condition $d^2\bar{X}/dV^2 = 0$. Upon the onset of quasi-equilibrium, V_m should become rate independent and assume the value determined by static charge profile calculations.

In order to properly apply the quasi-equilibrium analysis of mobile charge polarization, it is therefore mandatory to determine the above-mentioned quantities at a given temperature over a wide range of R_s values. If the rate dependence of these quantities indicates that quasi-equilibrium has been achieved, the subsequent detailed analysis follows directly. The procedure consists of determining the charge profile (ρ) as a function of V, extracting therefrom the centroid of charge mass $\bar{X}(V)$ and its voltage derivative $d\bar{X}/dV$, and constructing a theoretical I(V) plot for j_p according to Eq. [9]. Since the charge profile can be determined under a variety of assumed conditions (13), a particular set of conditions which yields the best agreement between the calculated and observed polarization current will not only define the concentration of mobile charge centers but also supply insight into some of their physical properties. Furthermore, by repeating this type of experiment over a suitable temperature range, an activation energy for thermal generation of mobile ions can be quantitatively determined.

Experimental results and discussion.—Virtually symmetrical Si-SiO_2-Si guard-ringed capacitor structures were fabricated. Polycrystalline silicon counterelectrodes (with matched resistivities)[3] were deposited from an E-gun heated source, through 0.041 cm^2 mask holes onto SiO_2 films of various thicknesses, which were previously grown in dry O_2 on (100)-oriented, p-type, 1000 ohm-cm substrates. The specimens were annealed for 30 min at 1100°C in dry N_2 in order to crystallize the amorphous Si counterelectrodes while improving the electrochemical symmetry of the insulating layer at the interfaces. The final symmetry was verified both by $C(V)$ measurement and by a steady-state I(V) measurement after the electrical breakdown of oxide layer has occurred.

Since silicon electrodes have been found to be no longer ion-discharge blocking at 390°C, mobile charge polarization in these structures was investigated in the temperature range from 145° to 365°C. The TVS measurements were taken with sweep rates ranging from 1 mV/sec to 1 V/sec in a vacuum of 10^{-3} Torr. The field dependence of mobile charge concentration was checked by repeating the potential sweep to increasingly higher voltages at each temperature (see, for example, Fig. 3). The rate dependencies of the normalized area, the normalized peak current and the peak voltage, extracted from I(V) plots for various

[3] Polycrystalline silicon, obtained by E-gun deposition, usually has a high resistivity (10^4-10^6 ohm-cm). In our experiment, resistivity matching was achieved by using high-resistivity substrates and a highly B-doped evaporation source.

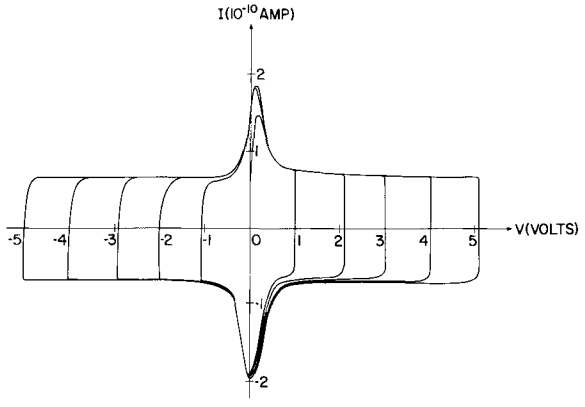

Fig. 3. Experimental evidence of the field independence of mobile charge concentration in a Si (poly)-SiO_2 (2000Å)-Si(100) capacitor structure. This I(V) plot was obtained at 247°C at a sweep rate of 41.7 mV-sec^{-1}.

sweep rates and temperatures, are shown in Fig. 4, 5, and 6, respectively. Below 145°C, the onset of quasi-equilibrium cannot be discerned experimentally by further lowering of the sweep rate since the currents cannot be accurately differentiated from the background noise (compare 145° curves in Fig. 4, 5, and 6). Somewhat above approximately 307°C, the total charge and peak current were found to increase with increasing voltage and decreasing sweep rate, suggesting thermal and field generation of new mobile charge species ($dQ/dV \neq 0$ in Eq. [9]) (see, for example, 307° and 365° curves in Fig. 5 and 6). Clearly, our quasi-equilibrium model of mobile charge polarization is self-consistent only in a limited temperature range below 300°C, where the normalized area and current cease to be rate dependent when the current peak assumes the theoretically predicted position of $V_m = 0$ (compare 192° and 247° curves in Fig. 4, 5, and 6). In this range the total mobile charge appears to be independent of temperature.

A computer program has been developed to determine mobile charge profiles under various boundary conditions which are considered appropriate for a symmetrical Si-SO_2-Si structure (see Appendix I).[4] Based on the assumption of blocking electrodes and

[4] The program was written by H. P. Crowder.

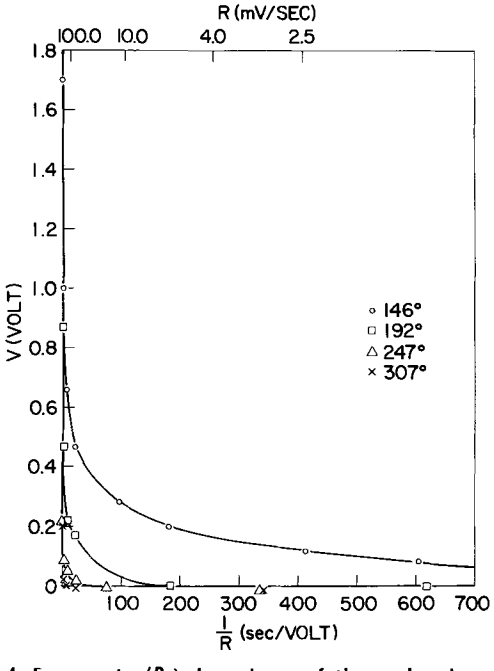

Fig. 4. Sweep rate (R_s) dependence of the peak voltage (V) of the polarization component measured at various temperatures.

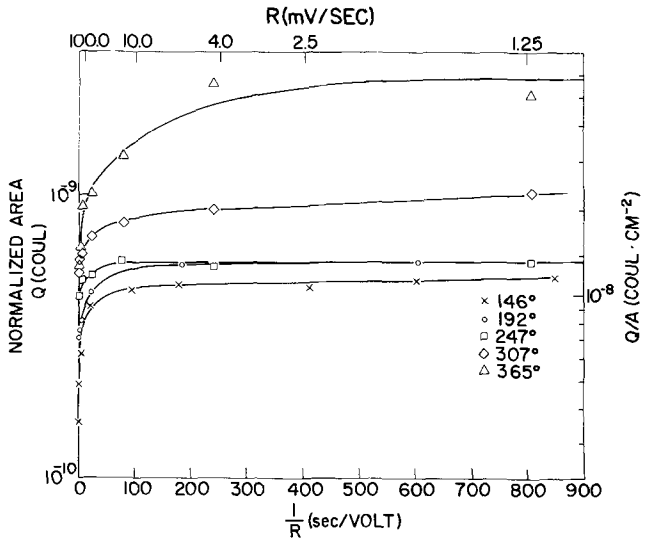

Fig. 5. Rate dependence of normalized area, Q (or charge density Q/A), for various measurement temperatures.

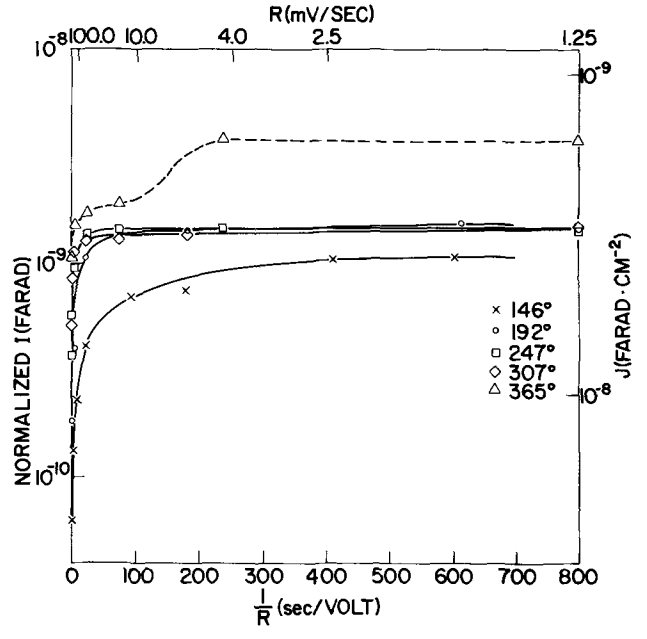

Fig. 6. Rate dependence of normalized peak current, I (or normalized peak current density, J), for various measurement temperatures.

one-carrier polarization, this program permits the polarization current to be calculated for any given temperature and oxide thickness, using the initial mobile charge concentration ($N_0 = Q/l$) as a disposable parameter. A detailed comparison was made between the calculated and observed polarization current based on the data obtained at 247°C for a 2000Å oxide specimen. At this temperature, the normalized area gives an initial concentration of $N_0 = 4.4 \times 10^{15}$ q-cm^{-3}. This value of N_0 was used as a starting point for the static charge computation. After a few trials, the best agreement between the calculated and the observed polarization was obtained for $N_0 = 5 \times 10^{15}$ q-cm^{-3}. The final results of this computation are shown graphically in Fig. 7, where $\bar{X}$ and its derivative $d\bar{X}/dV$ are plotted as a function of V. The theoretical polarization current was constructed in accordance with Eq. [9] and shown as a dotted line superimposed on the observed polarization component in Fig. 8. Since, in the absence of faradaic polarization, the normalized area should tally with the normalized current peak (compare Eq. [19] and [20]), the agreement between the

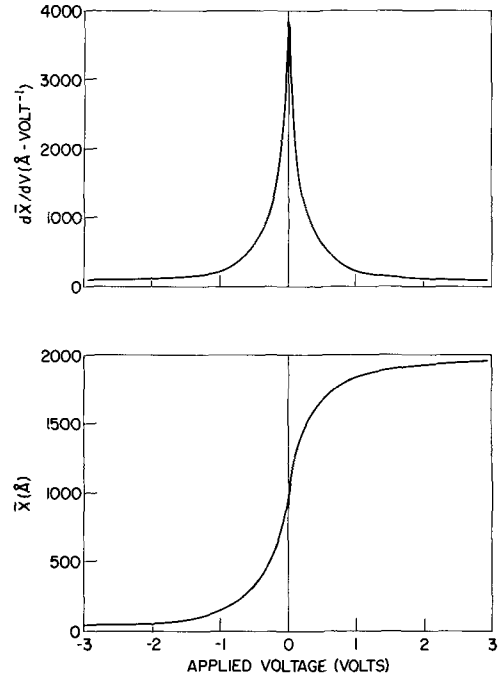

Fig. 7. Voltage dependence of $\bar{X}$, the center of mass, and its derivative $d\bar{X}/dV$, extracted from the space charge profiles which have been calculated with the following parameters: $T = 247$°C; $l = 2000$Å. $N = 5 \times 10^{15}$ q/cm^3. It should be noted that the $\bar{X}$ vs. V curve exhibits a kink near 0.1-0.2V, which has been deliberately smoothed out.

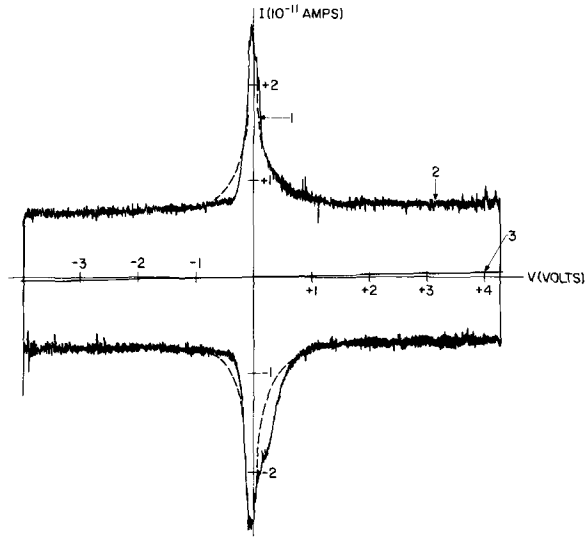

Fig. 8. Calculated and observed j_{ex} for the same capacitor structure as in Fig. 2. The TVS plot was obtained at 247°C at $R_S = 12.5$ mV·sec^{-1}. j_{ex} can be resolved into: (a) polarization component, 1; (b) capacitive component, 2; and (c) steady-state component, 3. Note the dotted line, which represents the polarization current calculated on the basis of a quasi-static model. The difference between the dotted line and the actual curve in the lower half of the plot is attributed to interface effects (see text). Note also the difference between the two polarization components in Fig. 2 and 8. This is due to the fact that quasi-static equilibrium was not quite achieved at the sweep rate of 41.7 mV-sec^{-1}.

calculated and observed currents is probably the most convincing evidence attesting the validity of the quasi-static model of mobile charge polarization.[5]

The asymmetry of the observed polarization current with respect to the voltage axis suggests the

[5] Yamin, for example, has found that at 500°C the charging peak was much higher than that calculated from the expected impurity concentration of 10^{18} ions-cm^{-3}. He attributed the discrepancy to the electrochemical effect, which is quantitatively analyzed in this paper.

presence of interface states at one of the interfaces [see the lower portion of the I(V) plot, Fig. 8]. In the light of the discussion on interface state polarization, it seems likely that these states reside near the interface between the oxide and the counterelectrode since, on the return sweep, the semiconductor surface of the counterelectrode goes from the accumulation to inversion regime.

When the total mobile charge was determined under quasi-equilibrium conditions for oxide specimens of various thicknesses, it exhibited no thickness dependence (Fig. 9). Since these specimens have been prepared under virtually identical conditions, the absence of thickness dependence strongly suggests that the mobile ionic species were introduced into the oxide layers not during the film growth, but either by surface contamination or by some process wherein the ionic species in the surface layer were rendered mobile (14). In view of the fact that stable Si-SiO_2-Si devices have been fabricated, it may be concluded that the observed mobile charge is due to external contamination.

Summary

Various bulk and interface effects in an insulator sandwiched between two electrodes have been shown to contribute to the anomalous charging current observed during a potential sweep at elevated temperatures. A unified quasi-equilibrium analysis indicates that a careful separation of these effects is necessary when the voltage sweep technique is used in either mobile charge or electrochemical studies in a solid electrolytic cell.

Observation of the double-peaked charging component, j_i, in the Pt-SiO_2-Si structure has established the temperature ranges ($T \leq 390°$) where the silicon electrode is blocking. The TVS measurements made in Si-SiO_2-Si structures in this temperature regime indicate that our quasi-equilibrium model for mobile charge analysis is applicable only up to 250°C. Above this temperature both field and thermal generation of new mobile charge species seem to have occurred, which is not accounted for in our model. However, in the range where the model is valid, excellent agreement has been obtained between the calculated and observed polarization currents. In this regime, the mobile charge concentration in the thermally grown oxide appears to be independent of temperature and applied field. This implies that the mobile charge in question is most likely associated extrinsic defects such as impurity ions in the SiO_2 film, which requires little or no activation energy for thermal generation. Such contention is further supported by the thickness data, which suggest that the mobile ionic species do not originate from thermal oxidation, but from surface contamination.

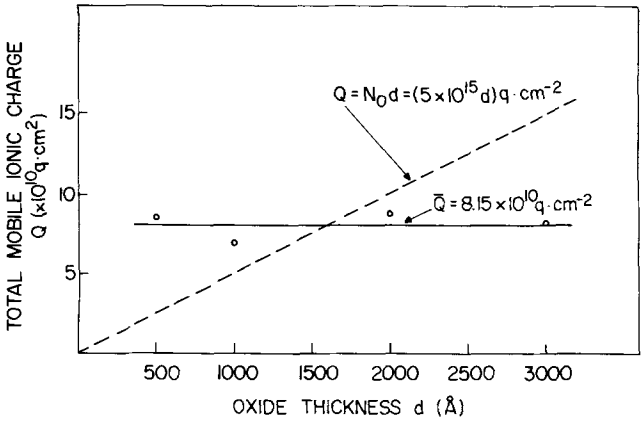

Fig. 9. Total mobile ion concentration in thermal SiO_2 films of various thicknesses, which have been prepared under virtually identical conditions. The dotted line indicates the thickness dependence which would have been observed if the mobile charge was not due to surface contamination or surface layer effect (see text).

Acknowledgments

The author is indebted to R. Hammer for his valuable assistance in the experimental work; to H. P. Crowder for developing the computer program used in the mobile charge analysis; to J. M. Eldridge, T. Sedgwick, and Y. van der Meulen for their critical reading of the manuscript; and to T. Hickmott for furnishing his prepublication data on low-frequency $C(V)$ measurements.

Manuscript submitted June 8, 1970; revised manuscript received Oct. 11, 1970. This was Paper 25 presented at the Los Angeles Meeting of the Society, May 10-15, 1970.

Any discussion of this paper will appear in a Discussion Section to be published in the December 1971 JOURNAL.

REFERENCES

1. A. Sevcik, *Collection Czech. Chem. Consm. Engl. Sdn.*, **13**, 349 (1948).
2. M. Yamin, *IEEE Trans. Electron Devices*, **ED-13**, 79 (1966).
3. D. R. Kerr, Conference on Properties and Use of MIS Structures, Grenoble, June 1969.
4. P. J. Jorgensen, *J. Chem. Phys.*, **49**, 1594 (1968).
5. F. P. Heiman and G. Warfield, *Trans. IEEE*, **ED-12**, 165 (1965).
6. R. Castagne, Academie des Science, Paris, 267 series B, 866 (1968). See also, M. Kuhn, *Solid-State Electron.*, **13**, 873 (1970).
7. K. H. Zainiger and G. Warfield, *Trans. IEEE*, **ED-12**, 179 (1965).
8. T. W. Hickmott, Private communication.
9. See, for example, E. H. Snow and M. E. Dumesnil, *J. Appl. Phys.*, **37**, 2123 (1966).
10. N. J. Chou, Paper 25 presented at Electrochem. Soc. Meeting, Atlantic City, Oct. 4-8, 1970.
11. E. H. Snow, A. S. Grove, B. E. Deal, and C. T. Sah, *J. Appl. Phys.*, **36**, 1664 (1965).
12. J. S. Logan, IBM Internal Communication (Aug. 1965).
13. T. M. Proctor and P. M. Sutton, *J. Chem. Phys.*, **30**, 212 (1959).
14. G. Hetherington, K. H. Jack, and M. W. Ramsay, *Phys. and Chem. Glasses*, **6**, 6 (1965).
15. E. Mattsson and R. Lindstrom, *Proc. Sixth Meeting, C.I.T.C.E.*, 263 (1955).
16. P. van Rysselberghe, "Modern Aspects of Electrochemistry," Vol. 4, p. 1 (1966).
17. See, for example, Laidler, "Chemical Kinetics," Chapt. 3, McGraw-Hill Co., New York (1950).
18. J. A. V. Butler, *Trans. Faraday Soc.*, **20**, 659 (1924).
19. S. Srinivasan and E. Gileadi, *Electrochim. Acta*, **11**, 321 (1966).

APPENDIX I

For an electrochemically symmetrical cell, which has neither emf nor work function difference, we shall assume that:

(*a*) The insulator thickness, *l*, is sufficiently small as compared to the electrode diameter so that the problem may be formulated one-dimensionally.

(b) At a given temperature, the concentration of dissociable charge pairs in the insulator is a fixed value.

(c) Application of external field can dissociate the charge pairs but creates no new pairs.

(d) Only one of the dissociated charge species is mobile under the influence of the applied field. Furthermore, it will not be compensated (recombined) because of the lack of oppositely charged centers in the new location it has moved into.

(*e*) The electrodes are ideally blocking: *i.e.*, no charge transfer or ionic charge injection takes place at the metal-insulator interfaces.

The electric field, E, in the specimen is related to the net space charge by Poisson's equation

$$\frac{\partial E}{\partial x} = \frac{4\pi q}{\epsilon}(\rho_p - N_o) \qquad [A\text{-}1]$$

where q is the electronic charge, ϵ the permittivity, ρ_p the mobile charge density, x the spatial coordinate of the insulator, and N_o the number of initial dissociable charge pairs per unit volume.

Since the electrodes are blocking, there is no mobile charge flow across the boundary

$$D\left(\frac{\partial \rho_p}{\partial x}\right) - \mu E \rho_p = 0 \text{ for } x = 0, l \quad [A\text{-}2]$$

where D and μ are the diffusivity and drift mobility of the mobile charge.

For a given applied voltage, V_a, a static equilibrium is established when

$$\frac{\partial \rho_p}{\partial t} = D\frac{\partial^2 \rho_p}{\partial x^2} - \mu\frac{\partial (E\rho_p)}{\partial x} = 0 \text{ for all } x\text{'s} \quad [A\text{-}3]$$

Integrating Eq. [A-3] between 0 and x gives

$$D\left(\frac{d\rho_p}{dx}\right)_{x=x} - D\left(\frac{d\rho_p}{dx}\right)_{x=0} = \mu(E\rho_p)_{x=x} - \mu(E\rho_p)_{x=0} \quad [A\text{-}4]$$

Application of the boundary conditions yields the important relationship

$$D\left(\frac{d\rho_p}{dx}\right) - \mu(E\rho_p) = 0 \text{ for all } x\text{'s} \quad [A\text{-}5]$$

Standard substitution of $y = \ln \rho_p$ (13) gives

$$D\frac{dy}{dx} = \mu E \quad [A\text{-}6]$$

and

$$D\frac{d^2y}{dx^2} = \mu\frac{dE}{dx} \quad [A\text{-}7]$$

By virtue of Eq. [A-1]

$$D\frac{d^2y}{dx^2} = \frac{4\pi q}{\epsilon}\cdot\mu(\rho_p - N_o)$$

or

$$2\frac{d^2y}{dx^2} = \frac{1}{L_D^2}(P - 1) \quad [A\text{-}8]$$

where

$$P = \frac{\rho_p}{N_o}$$

and

$$L_D^2 = \left(\frac{8\pi q}{\epsilon_{ox}}\frac{\mu}{D}N_o\right)^{-1}$$

have been substituted.

Setting $dy/dx = v$, [A-18] may be reduced to

$$L_D^2\, d(v^2) = (e^y - 1)\,dy \quad [A\text{-}9]$$

when the frequently used relation

$$2\frac{d^2y}{dx^2} = \frac{d}{dy}\left[\left(\frac{dy}{dx}\right)^2\right]$$

is applied.

Consequently

$$\int_{v_o}^{v} L_D^2\, d(v^2) = \int_{y_o}^{y} (e^y - 1)\,dy$$

or

$$L_D^2 v^2 = L_D^2 v_o^2 + e^y - e^{y_o} - (y - y_o) \quad [A\text{-}9a]$$

or

$$L_D\frac{dy}{dx} = [L_D^2 v_o^2 + e^y - e^{y_o} - (y - y_o)]^{1/2} \quad [A\text{-}9b]$$

Integration of [A-9b] results in

$$\int_{y_o}^{y} [L_D^2 v_o^2 + e^y - e^{y_o} - (y - y_o)]^{-1/2}\,dy = \frac{x}{L_D} \quad [A\text{-}10]$$

giving y or $\ln \rho_p$ in terms of x.

In addition, since

$$\int_o^l P\,dx = \int_o^l \frac{\rho_p}{N_o}\,dx = \frac{1}{N}\int_o^l \rho_p\,dx = \frac{N_o l}{N_o} = l$$

[A-8] can be integrated to give

$$\frac{dy}{dx_{x=l}} - \frac{dy}{dx_{x=0}} = \frac{1}{2L_D^2}\int_o^l (P - 1)\,dx = 0$$

or

$$v_l = v_o \quad [A\text{-}11]$$

From the relationship in [A-6]

$$\int_{y_o}^{y_l} dy = \int_o^l \frac{\mu}{D} E\,dx = \frac{\mu}{D}\int_{V_o}^{V_l} dV$$

or

$$y_l - y_o = \frac{\mu}{D}V_a \quad [A\text{-}12]$$

where $V_a = V_l - V_o$ is the applied voltage.

[A-19a] now gives

$$e^{y_o} = \left(\frac{\mu}{D}V_a\right)\Big/\left[\exp\left(\frac{\mu}{D}V_a\right) - 1\right] \quad [A\text{-}13]$$

and [A-9b] may be integrated between y_o and y_l to give

$$\int_{y_o}^{\left(y_o + \frac{\mu}{D}V_a\right)} [L_D^2 v_o^2 + e^y - e^{y_o} - (y - y_o)]^{-1/2}\,dy = l/L_D \quad [A\text{-}10a]$$

Equations [A-10], [A-10a], and [A-13] constitute the solution to our problem of space charge distribution.

Equation [A-10] cannot be integrated in a closed form. A computer program has been developed by H. P. Crowder to integrate [A-10] numerically by a trial-and-error scheme. y_o, l/L_D, and μ/D are determined from the initial charge concentration, temperature, applied voltage, and insulator thickness; v_o is chosen as a variable parameter subject to

$$[L_D^2 v_o^2 + e^y - e^{y_o} - (y - y_o)]_{\min} \geq \zeta$$

where ζ is a prefixed small value such that the integrand in [A-17] will not become infinite or imaginary. Integration of [A-10a] is carried out with v_o altered recursively until

$$\int_{y_o}^{y_o + \frac{\mu}{D}V_a} [L_D^2 v_o^2 + e^y - e^{y_o} - (y - y_o)]^{-1/2}\,dy = \frac{l}{L_D} < \epsilon$$

where ϵ is another predetermined tolerance.

When v_o and y_o are thus established, the space charge profile for a given voltage is obtained by integrating [A-10] with their established values.

APPENDIX II

Consider the SiO_2 film in an MOS capacitor as a solid electrolyte containing the metal ions of electrodes I and II. At equilibrium ($j_f = 0$), the over-all cell reaction may be written as

$$M^{z+}(\text{I}) + \gamma\text{M}(\text{II}) = \text{M}(\text{I}) + \gamma M^{z'+}(\text{II}) \quad [A\text{-}14]$$

where $\gamma = z/z'$ is the stoichiometric factor, and I and II refer to the electrodes. The open-cell potential, E^o, can be determined from the condition that the chemical potential changes associated with the reactants transversing the transfer layers is balanced by the electrical potential changes

$$E^o = E^o{}_{1-3} - \gamma E^o{}_{2-3} = -\frac{\Delta G_I}{z\mathbf{F}} + \gamma\frac{\Delta G_{II}}{z'\mathbf{F}} \quad [A\text{-}15]$$

where ΔG's are free energy changes, and $E^o{}_{1-3}$ and $E^o{}_{2-3}$ are equilibrium electrode potentials at I and II, respectively (see Fig. 10a). When an external voltage ($|V| > E^o$) is applied to the cell, potential drops (V_i) different from those of equilibrium values may appear in three regions of the electrolytic cell, i.e.

$$V = V_I + V_{III} - V_{II} \quad [A\text{-}16]$$

or

$$V = \zeta_I V + \zeta_{III} V - \zeta_{II} V$$

where ζ's denote the potential distribution factors. A detailed examination of the potential distribution in

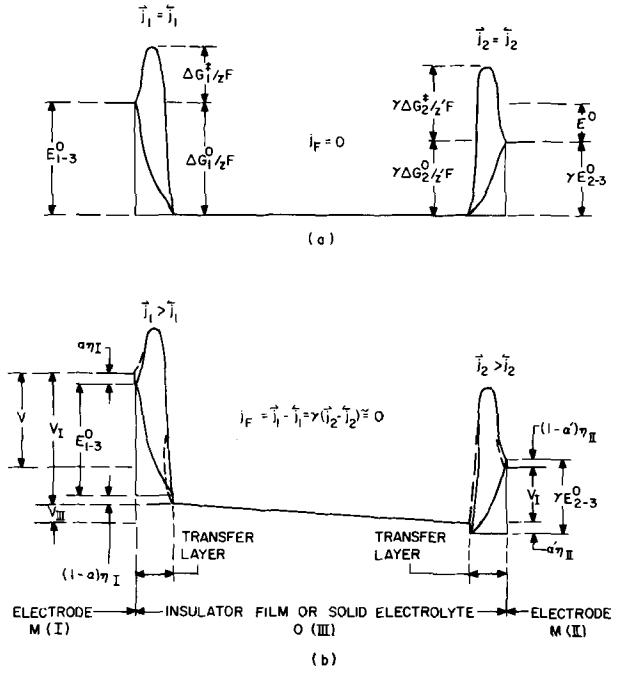

Fig. 10. Schematic representation of electrical activation in a solid electrolytic cell: *(a)* at equilibrium ($j_f = 0$)—there is no electrical activation, and the cell potential is $E^\circ = E^\circ_{1-3} - \gamma E^\circ_{2-3} = -(\Delta G^\circ_I - \gamma \Delta G^\circ_{II})/zF$; *(b)* potential distribution in the case of electrical activation—at electrode I $\eta = \delta_I V - E^\circ_{1-3}$; at electrode II $\eta_{II} = \delta_{II} V - \gamma E^\circ_{2-3}$. Note that the activation energy is represented by $\Delta G^{\neq}/zF$, which, according to the absolute rate theory, is associated with the free energy change between the reactants and the activated complex.

the electrolytic cell (Fig. 10b) shows that

$$V = [\alpha\eta_I + E^\circ_{1-3} + (1-\alpha)\eta_I] + V_{III} + [\alpha'\eta_{II} - \gamma E^\circ_{2-3} + (1-\alpha')\eta_{II}] \quad [A\text{-}17]$$

where α and α' denote the transfer coefficients, and, η_I and η_{II} the effective overpotentials for the two electrodes. Comparison of Eq. [A-16] and [A-17] yields the following relationship

$$\eta_I = \delta_I \eta = \zeta_I V - E^\circ_{1-3}$$

$$\eta_{II} = \delta_{II}\eta = \gamma E^\circ_{2-3} - \zeta_{II} V$$

and

$$\eta = (1 - \zeta_{III})\, V - E^\circ = \epsilon V - E^\circ \quad [A\text{-}18]$$

where η denotes the effective overpotential for the electrolytic cell, δ_I and δ_{II} are overpotential distribution factors, and ϵ may be regarded as the correction factor for the potential drop in the oxide bulk.

If the faradaic current, j_f, remains negligibly small during the voltage sweep, the concentrations of metal ions in the electrolyte adjacent to the transfer layers do not change and the total numbers of ions and atoms in the transfer layers which participate in the reaction (*i.e.*, total number of "activated sites" n_o and n_o') may be considered to be constant in spite of the passage of j_f. Consequently, the concentrations of the atoms $[C_{M(I)}, C_{M(II)}]$ and ions $[C_{Mz+}$ and $C_{Mz'+}]$ in the transfer layers can be related by

$$C_{Mz+} = \tilde{n} - C_{M(I)};\ C_{Mz'+} = \tilde{n}, - C_{M(II)} \quad [A\text{-}19]$$

where $\tilde{n} = n_o/\bar{N}_o$ and $\tilde{n}' = n'_o/\bar{N}_o$ are the ratios of n_o and n'_o to Avogadro's number, $\bar{N}_o$, respectively.

When ionization and discharge are the rate-limiting step of the electrode reactions, a pseudocapacitive component, j_l, appears in the external circuit during the voltage sweep even though j_f may be negligibly small. This component, j_l, can be evaluated by invoking a state of quasi-equilibrium for the rate-determining step. The quasi-equilibrium in this case is taken to mean that, while C_{Mz+} and $C_{Mz'+}$ are realized in an infinite number of reversible steps in which $j_f = 0$. Application of the theory of overpotential (17) and the absolute rate theory (18) yields

$$\frac{C_{Mz+}}{\tilde{n} - C_{Mz+}} = \frac{\vec{k}}{\overleftarrow{k}} \exp\left(\frac{zF\eta_I}{RT}\right) = K_I \exp\left(\frac{zF\eta_I}{RT} \exp\frac{zF\eta_I}{RT}\right) \quad [A\text{-}20]$$

and

$$\frac{C_{Mz'+}}{\tilde{n}' - C_{Mz'+}} = \frac{\vec{k}'}{\overleftarrow{k}'} \exp\left(\frac{z'F\eta_{II}}{\gamma RT}\right) = K_{II} \exp\left(\frac{z'F\eta_{II}}{\gamma RT}\right)$$

where k's and k''s are forward and reverse rate constants, and K's are the equilibrium constants for the rate-determining step of the electrode reactions. The change in C_{Mz+} ($C_{Mz'+}$) is accompanied by a corresponding change in the surface charge, σ_I (σ_{II}), on electrode I(II). In a mathematical approach analogous to that given by Srinivasan and Gileadi (19), one finds that the resultant polarization current is

$$j_l = R_s \left(\frac{zF}{RT}\right) \left\{ \exp\left(-\frac{zF\delta_I\eta}{RT}\right) \cdot \frac{k_I K_I}{\left\{\exp\left(-\frac{zF\delta_I\eta}{RT}\right) + K_I\right\}^2} + \exp\left(-\frac{zF\delta_{II}\eta}{RT}\right) \cdot \frac{k_{II}K_{II}}{\left\{\exp\left(-\frac{zF\delta_{II}\eta}{RT}\right) + K_{II}\right\}^2} \right\} \quad [A\text{-}21]$$

where $k_I = zqn_o$ and $k_{II} = zqn'_o$ convert the concentration changes into the changes in surface charge on the advancing or receding electrode-electrolyte interfaces. The exponential nature of the two terms in Eq. [A-21] suggests that the faradaic polarization component, j_l may exhibit two peaks at voltage values for which $K_I = \exp(-zF\delta_I\eta/RT)$ and $K_{II} = \exp(-zF\delta_{II}\eta/\gamma RT)$, respectively.

The magnitude of these two peaks can be evaluated by substituting the preceding expressions into Eq. [A-21]. Thus

$$(j_l)_{max} \cong \frac{z^2F}{RT} n_o\, qK_I \cdot R_s$$

and

$$(j_l)'_{max} \cong \frac{z'^2F}{\gamma RT} \cdot n'_o\, qK_{II} \cdot R_s$$

NOTATIONS

j_{ex},	Measured current density, A-cm^{-2}
j_s,	Steady-state component, A-cm^{-2}
j_c,	Capacitive component, A-cm^{-2}
j_p,	Mobile charge polarization component, A-cm^{-2}
j_l,	Faradaic polarization component, A-cm^{-2}
j_e,	Steady-state electronic current, A-cm^{-2}
j_f,	Steady-state faradaic current, A-cm^{-2}
σ_I,	Surface charge on metal electrode I, q-cm^{-2} or coulomb-cm^{-2}
ψ_s,	Surface potential of silicon substrate, V
V_{ox},	Potential difference across the oxide layer, V
C_{ox},	Oxide capacitance per unit area, F-cm^{-2}
R_s,	Voltage sweep rate, V-sec^{-1}
ρ,	Space charge distribution, q-cm^{-3} or coulombs-cm^{-3}
Q,	Total space charge in the insulating layer, q-cm^{-2} or coulombs-cm^{-2}
l,	Thickness of the insulating film, Å
$\bar{X}$,	Center of mass with respect to the axis at $x = 0$, Å
E°,	Open-cell potential, V
k,	$k = zn_oq$, the conversion factor, coulombs-cm^{-2}
n_o,	Total number of atoms and ions in the transfer layer, which participate in the ionization-discharge step
z,	Valency of metal ions
γ,	Stoichiometric factor

K, Equilibrium constant for the ionization-discharge step
η, Over-all effective overpotential, V
η_i, Effective overpotential at electrode i, V
$\mathbf{F}$, Faraday's constant, $\mathbf{F} = 96{,}500$ coulombs (g-equiv.)$^{-1}$
R, Gas constant, $R = 8.31$ joule-deg^{-1}-mole^{-1}
T, Absolute temperature, °K
$z\mathbf{F}/\gamma RT = \mathbf{F}/nRT = 11{,}600/nT$ volt^{-1}, where n is the number of Faradays involved in the reaction
ζ_i, Potential distribution factors: $\zeta_I + \zeta_{III} - \zeta_{II} = 1$
ϵ, Correction factor for potential drop in the oxide layer
$(j_p)_{max}$, Peak polarization current density, A-cm^{-2}
J_m, Normalized peak current density, F-cm^{-2}
A_p, Area under the polarization current, watt·cm^{-2}
Q, $Q = A_p/R_s$, normalized area or total mobile charge, coulombs·cm^{-2}
$M^{\neq}$, Activated complex
$\vec{v}, \overleftarrow{v}$, Rate of reaction in the forward and reverse directions, cm^{-2}·sec^{-1}
h, Planck's constant
$\vec{k}, \overleftarrow{k}$, Forward and reverse rate constants, cm-sec^{-1}
k, Boltzmann's constant
$f^{\neq}$, Partition function for the activated complex $M^{\neq}$
f_M, f_{Mz+}, Partition functions for the atoms and ions participating in the ionization-discharge step
$C_{M(T)}, C_{Mz+(T)}$, Concentration of atoms and ions in the transfer layer, which participate in the ionization-discharge step, g-atom-cm^{-3}
$\Delta G^{\neq}$, Activation energy, kcal·(g-atom)$^{-1}$
ΔG^{o}, Gibb's free energy change, kcal·(g-atom)$^{-1}$
j_o, Exchange current, A-cm^{-2}
$\tilde{n} = n_o/N_o$, with n_o = total number of ions and atoms in the transfer layer, which participate in the discharge-ionization reaction; N_o = Avogadro's number

Synthesis of Gallium Phosphide

C. M. Ringel

Bell Telephone Laboratories, Incorporated, Reading, Pennsylvania 19604

ABSTRACT

An open-flow synthesis system for the production of polycrystalline GaP, using PH_3 flowing over Ga in a temperature gradient, has been investigated with regard to purity of the product and yield of GaP in terms of the elements Ga and P. This material is suitable as starting material for single-crystal growth by the liquid-encapsulated Czochralski technique. Optimization of the synthesis time, flow rate, and temperature gradient resulted in a P reaction efficiency of 50-55% and a GaP yield of 35-38g per 50g of Ga. A mechanism involving the formation of a reaction barrier over the Ga was used to explain the increase in P reaction efficiency and GaP yield with decreasing PH_3 flow rate. Both an increased reaction efficiency and GaP yield were observed with increasing temperature gradients, indicating a diffusion-controlled reaction. It was found that 1.5×10^{19} Si atoms cm^{-3} were incorporated in the GaP when pyrolytic boron nitride boats and silica liners were used. When He was substituted for H_2 as the carrier gas, the Si contamination dropped to about 5×10^{18} cm^{-3}. Silicon contamination of about 1×10^{19} atoms cm^{-3} was observed using an all silica system. When water vapor was introduced in small amounts to He in the pyrolytic boron nitride-SiO_2 system, the GaP yield was reduced by about 10% but the material produced was found to have an optically active Si content of about 10^{16} cm^{-3}. These results indicate the dominance of the vapor transport mechanism for Si contamination of GaP. Material grown in an all-pyrolytic boron nitride system, where the boats were physically separated from hot silica, had a Si contamination of less than 5×10^{16} cm^{-3}.

Considerable interest in polycrystalline gallium phosphide has been stimulated by the introduction of liquid-encapsulated Czochralski (LEC) crystal growth as a means to mass produce large-area gallium phosphide single crystals (1). If GaP electroluminescent devices are to be competitive relative to incandescent lamps, manufacturing expenses including the cost of polycrystalline starting material need to be minimized.

One method for preparing polycrystalline GaP was initially suggested by Grimmeiss *et al.* (2) and Frosch and Rao (3). In this method, polycrystalline GaP is prepared in an open-tube system in which Ga-containing boats, positioned in a liner, are placed in a temperature gradient. Gallium phosphide is formed by the reaction of phosphorus, obtained from the decomposition of PH_3, with Ga. The GaP dissolves in the excess Ga and, because of the temperature gradient, precipitates at the cooler ends of the boats. This high-purity GaP, precipitated in the form of porous polycrystalline ingots, has been used to produce LEC substrates (4). The present study is concerned with optimizing yields while maintaining or improving the purity of the GaP produced by this open-tube synthesis technique.

In the Experimental section of this paper, the experimental work is discussed. The effects of PH_3 flow rate and temperature gradient on the GaP yield, P and Ga reaction efficiencies, and length of run using pyrolytic boron nitride (PBN) system are the subjects of the following section.

The remaining part of the paper is concerned with the purity of the GaP and the effects of liner and boat materials and gaseous ambients. The possible mechanisms which can contaminate the GaP with Si and the results obtained using PBN and vitreous silica (SiO_2) liners and boats are discussed first. The interest in SiO_2 liners and boats stems from the considerable cost reduction that would result if these could be used rather than the quite expensive PBN liners and boats. Finally, the results obtained when He, with and without water, is substituted for H_2 as the PH_3 carrier gas in a SiO_2 liner-PBN boat system are presented.

Experimental

Raw materials.—The Ga used is commercially available 99.9999% pure delivered in sealed ampoules.[1] The

Key words: gallium phosphide, synthesis, growth.

[1] Supplier: Alusuisse.

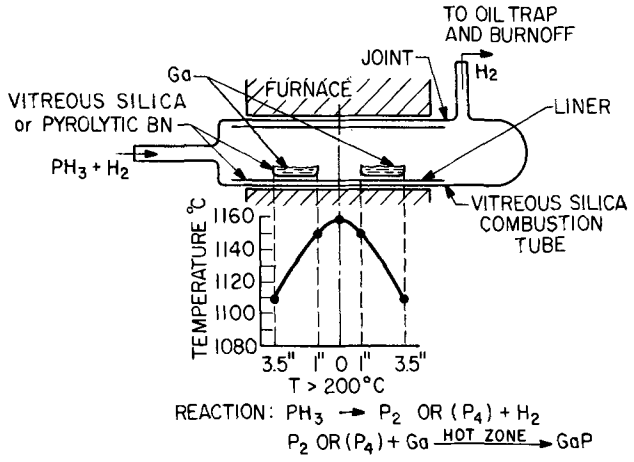

Fig. 1. Diagram of synthesis system with components and typical temperature gradient.

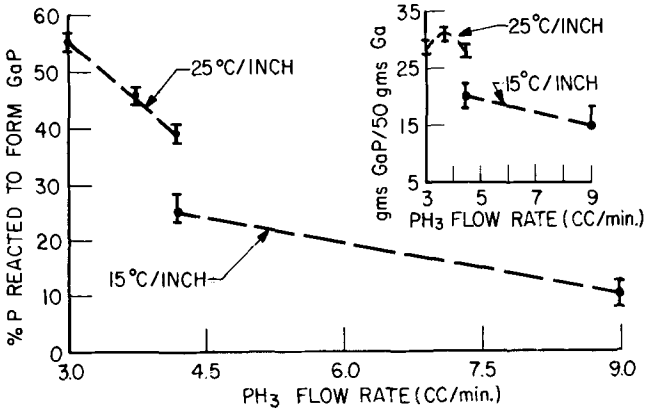

Fig. 2. Effect of PH_3 flow rate on average P reaction efficiency and GaP yield using temperature gradients of 15° and 25°C/in.

PH_3 used has been either a 3 or 5% PH_3 mixture in H_2 and has a total impurity content of less than 10 ppm.[2] For some experiments, He was substituted for H_2 as the carrier gas.

Furnace.—Figure 1 shows a diagram of the furnace, boats, and flow system, as well as a typical temperature gradient. The synthesis is carried out in a 1½ in. ID, three-zone resistance heated furnace with each zone controlled independently. The maximum temperature is controlled by a Pt-Pt 10% Rh thermocouple in the center zone. This furnace is capable of producing temperature gradients from 0° to a maximum of 40°-50°C/in. across the Ga-containing boats. Maximum temperatures of 1150°-1200°C were attainable with this furnace.

Boat and liner materials.—SiO_2 was always used as a combustion tube. One system used an SiO_2 liner and SiO_2 boats, the second system used an SiO_2 liner and PBN boats, and the third system used a PBN liner and PBN boats. The PBN liner used in this system was extended into the cooler ends of the furnace (600°-800°C) to minimize the formation of SiO in the vicinity of the reaction vessels.

Synthesis.—After cleaning the PBN and SiO_2 components in *aqua regia*, rinsing in D. I. water and alcohol, and drying, the SiO_2 combustion tube is placed into the furnace. The boats are loaded with 25g of Ga each and positioned in the liner. The liner is placed in the furnace in a position such that each boat extends from 1 to 3½ in. on either side of the center of the furnace. Helium, followed by hydrogen, is introduced to purge and clean the system. The PH_3 reaction mixture is then introduced. At the completion of the run, the PH_3 flow is stopped and He purge gas is introduced. The liner and boats are then removed from the system, while under He flow, and the Ga-GaP products are taken out of the boats and etched in hot HNO_3. After removal of the excess Ga by this acid treatment, the GaP is washed in D.I. water until no trace of acid is left. The GaP is dried and then baked out at 1-10 μm of vacuum at 300°-400°C to remove water.

Optimization of GaP Yield and P and Ga Reaction Efficiencies

Flow rates and length of run using an all-PBN system.—The reaction efficiency of P[3] to form GaP and the yield of GaP were examined as a function of flow rate. The reaction efficiencies are averaged over the total length of the run. The range of PH_3 flow rates examined was between 3 and 9 cc/min. The data are shown in Fig. 2. A nearly linear increase in P reaction efficiency as a function of decreasing PH_3 flow rate is observed for two different temperature gradients. At the same time, the GaP yield[4] is shown to reach a maximum of 29-32g at about 3.75 cc of PH_3/min with a 25°C/in. temperature gradient. Since a constant time interval is used with different flow rates, an increased P reaction efficiency does not necessarily mean an increased GaP yield. When either a 3 or 5% PH_3 mixture in H_2 was used to produce an equivalent PH_3 flow rate, the P reaction efficiency to form GaP and the GaP yield was found to be quite similar and relatively independent of the total H_2 flow rate used. The following explanation may be offered for the increased P reaction efficiency with decreasing flow rate.

When material was examined during the early stages of growth, it was found that upon cooling a crust of GaP had formed over the Ga. The crust formation is due to the lower density of GaP compared to Ga. Additional P can efficiently react with the Ga only when solution and diffusion of the reaction barrier from the hot end toward the cooler end of the boat are no longer rate controlling. Hence, increasing the PH_3 flow rate over that necessary to form the reaction barrier and maintaining a positive P pressure above the GaP will result in decreased over-all P reaction efficiency during a run.

An optimum time of about 72 hr was used for the synthesis. We found that this time resulted in a proper balance between total GaP yield, which does not increase significantly after this running time, and efficient conversion of P and Ga for a given flow rate and temperature gradient.

Temperature gradients using an all-PBN system.—In order to examine the relative importance of the solution and diffusion steps, yields were determined as a function of temperature gradient using the optimum flow rate for this system, 3.75 ± 0.3 cc of PH_3/min, and a 72 hr synthesis time. The concentration gradient is the driving force for the diffusion of the more soluble GaP at high temperature and its precipitation at lower temperatures. Increased diffusion of the dissolved GaP and its subsequent precipitation at the low-temperature end of the boat will consequently increase the reaction rate of P with Ga at the higher temperature to form more GaP. Symmetrical temperature gradients were examined over a 2½-3 in. length, the approximate length of the boats, on either side of a 2 in. center zone held at 1160° ± 10°C. Gradients of 15°-40°C/in. were investigated. Figures 3, 4, and 5 show the effect of temperature gradients on P and Ga reaction efficiency[5] and GaP yield.

For a flow rate of 3.75 ± 0.3 cc of PH_3/min, the GaP yield increased from 15 to 17.5g at a gradient of 15°C/in. to 35-38g with a 40°C/in. gradient. The corresponding increase in P and Ga reaction efficiencies were from 20-25 to 50-55%. Since only the temperature gradient was changed, not the maximum temperature

[2] Supplier: Precision Gas Products, Incorporated.
[3] Expressed as weight of P in GaP per total weight of P used.
[4] Weight of GaP formed per weight of Ga used.
[5] Weight of Ga in GaP/50g of Ga.

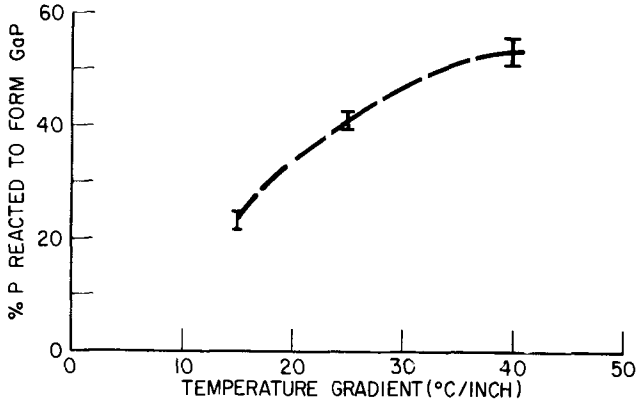

Fig. 3. Effect of temperature gradient on average P reaction efficiency.

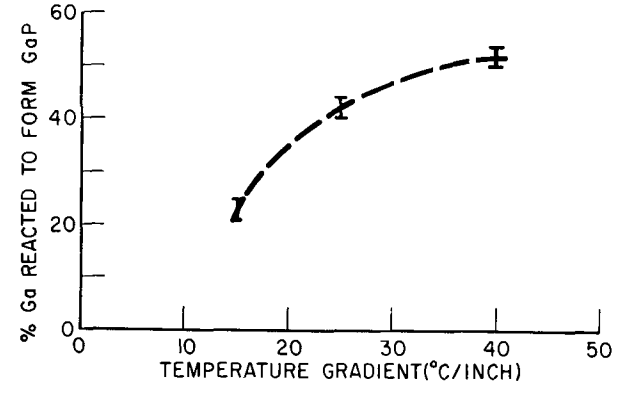

Fig. 4. Effect of temperature gradient on average Ga reaction efficiency.

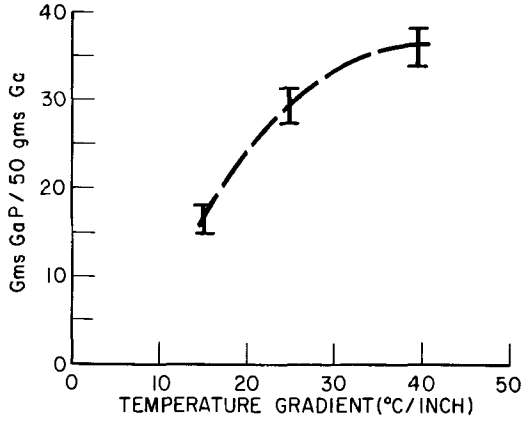

Fig. 5. Effect of temperature gradient on GaP yield

at the hot end of each boat (1150°C), the increased yield and conversions would suggest a diffusion-controlled reaction.

As seen from Fig. 3, 4, and 5, the increases in yields and reaction efficiencies tend to level off at the higher gradients. The deposition requires the diffusion of GaP from the hot end of the boat to the cooler end. By increasing the temperature gradient, and thereby the concentration gradient at the hot end of the boat, the diffusion rate should be proportionately increased. The data shown in Fig. 3-5 would then suggest the increased importance of the vapor-liquid interface reaction and/or the solution steps in the control of the reaction kinetics.

Due to furnace limitations, temperatures higher than 1200°C were not investigated. At these higher temperatures, higher PH_3 concentrations would be needed because of the higher dissociation pressure of GaP. If too high a temperature is used, an open-flow system becomes impractical because the P dissociation pressure could exceed atmospheric pressure and any yields would be drastically reduced.

Purity of GaP

Effect of liner and boat materials on purity.—All-PBN system.—The impurity content of the GaP using H_2 as a carrier gas in an all-PBN system was examined by: near band gap low-temperature optical absorption (5), a special analytical technique for Si (6), spark source mass spectroscopy (7), and inert gas fusion (8). Optically (5), the only substitutional impurity of the group N, S, Se, and Te found was nitrogen in concentrations of 3-6 x 10^{16} cm^{-3}. By HCl transport of a fixed quantity of GaP and weighing the SiO_2 residue, the total Si content was found to be less than 5 x 10^{16} cm^{-3} which is the detectability limit of this method (see Table I) (6). Mass spectroscopy (7), which is most sensitive for elements other than oxygen, nitrogen, and carbon, indicates that As and S probably derived from the PH_3 [6] are the only substantial impurities (see Table II). Inert gas fusion shows a concentration of total nitrogen and oxygen of about 10^{18} atoms/cm^{-3}.

Single crystals pulled from this material were usually n-type with carrier concentrations $\leq 10^{15}$ cm^{-3}, and electron mobilities in excess of 170 cm^2/V-sec, as determined by Hall measurements.

Silicon contamination.—If the PBN liner and boats are replaced by SiO_2 components, increased contamination by silicon is to be expected. In view of the potential cost reduction that is possible if SiO_2 material is used, the effects of such components on the purity of the GaP were examined.

Thermodynamics.—Some of the interactions to form Si, Si-SiO_2(SiO_x) in the GaP synthesis system are shown below (9).

The direct interaction of SiO_2 with Ga is given by:

$$SiO_2 + 2Ga \rightleftarrows SiO + Ga_2O \qquad [1a]$$

The equilibrium constant, K, for this reaction is defined as

$$K_{[1a]} = \frac{A_{SiO}\, A_{Ga_2O}}{A_{SiO_2}\, A_{Ga}}$$

where A = activity.

The activities of SiO_2 and Ga are unity. The reaction of SiO and Ga is

$$SiO + 2Ga \rightleftarrows Ga_2O + Si \qquad [1b]$$

The Si or the SiO (SiO_x solid) formed by reactions [1a] and [1b] or the sum of reactions [1a] and [1b] could then be incorporated into the Ga and GaP.

[6] As and S are not major contaminators of PBN, SiO_2, or Ga.

Table I. Si contamination in GaP(6)

System	Carrier gas	Si concentration
All-PBN system	95% H_2	$<5 \times 10^{16}$*
SiO_2 liner PBN boats	95% H_2	1.5×10^{19}
All SiO_2 system	95% H_2	1.1×10^{19}
SiO_2 liner PBN boats	95% He	5×10^{18}

* Detectability limit.

Table II. Impurity content of GaP produced in the all-PBN system as determined by mass spectrograph (7)

Impurity	ppm
C	0.2
O	0.4
S	0.7
As	2.0
N	<0.1
Si	<0.1
B	<0.1

Table III. Free energies (ΔF) and equilibrium constants (K)

ΔF of formation (kcal/mole)				ΔF of reaction (kcal/mole) Equation							
$SiO_{2(s)}$*	$SiO_{(v)}$*	$H_2O_{(v)}$*	$Ga_2O_{(v)}$**	[1a]	[1b]	[1a] + [1b]	[2a]	[1b]	[2a] + [1b]	[3a]	Temp, °K
−173	−46.4	−45.1	−40.7	85.9	5.7	91.6	81.5	5.7	87.2	14.4	1073
−158.5	−52.2	−41	−43.3	63	8.9	71.9	65.3	8.9	74.2	−2.3	1373
				59.2			62.5			−5.1	1423***

K (Equilibrium constant)

Equation [1a]	[2a]	[3a]	Temp, °K
3×10^{-18}	2×10^{-17}	1.6×10^{-7}	1073
1×10^{-10}	4×10^{-11}	7	1373
7.5×10^{-10}	2×10^{-10}	67	1423***

* Janaf Thermochemical Tables.
** C. D. Thurmond and C. J. Frosch, *This Journal*, 111, 184-191 (1964).
*** Linear extrapolation of above data.

Another set of reactions involving a vapor-transport mechanism is also possible. In this set of reactions, direct contact of SiO_2 with Ga is not needed and we have instead

$$SiO_2 + H_2 \rightleftarrows SiO + H_2O \qquad [2a]$$

The equilibrium constant for this reaction is

$$K_{[2a]} = A_{SiO} A_{H_2O}/A_{H_2} \qquad [2a_1]$$

since $A_{SiO_2} = 1$.

The reaction of SiO from Eq. [2a] with Ga would then be the same as Eq. [1b] and Si or SiO could subsequently be incorporated in the Ga and GaP.

The water vapor formed by reaction [2a] can also interact with Ga and GaP as follows

$$H_2O + 2Ga \rightleftarrows Ga_2O + H_2 \qquad [3a]$$

$$H_2O + 2GaP \rightleftarrows Ga_2O + P_2 + H_2 \qquad [3b]$$

Free energy (ΔF) compilations for Eq. [1a], [1b], [1a] + [1b], [2a], [2a] + [1b], and [3a] are presented in Table III at different temperatures. The approximate equilibrium constants at 1073°, 1373°, and 1423°K for reactions [1a], [2a], and [3a] are also shown in Table III. Equilibrium constants for both the direct reaction of SiO_2 with Ga (Eq. [1a]) or the reduction of SiO_2 by H_2 (Eq. [2a]) are about 10^{-9} to 10^{-10} at 1150°-1100°C for both reactions. SiO mole fractions of approximately 10^{-5} can then be expected and some Si or SiO_x contamination of the GaP in measurable quantities seems reasonable. Due to the open-flow system and volatility of the reaction products, the kinetics of these reactions should be relatively high.

All-SiO_2 system.—In this system, both reactions [1] and [2] are applicable. The direct interaction of SiO_2 with Ga, the reaction of H_2 with SiO_2, and the possible solution of SiO in Ga or reduction of SiO by Ga can occur. Therefore, one would expect that synthesis in this system would result in the highest level of silicon contamination. As seen from Table I, the level of Si contamination is quite similar to the PBN boats-SiO_2 liner system. Thurmond and Kowalchik (10) found that Si in concentrations of 10^{20} cm^{-3} can be incorporated into GaP at 1050°C.

Since the solubility of Si in GaP has not been exceeded, it seems that reaction [2], the hydrogen reduction of SiO_2, may be of equal or greater importance than the direct reaction of SiO_2 with Ga in the incorporation of Si or SiO_x in GaP using this synthesis system.

SiO_2 liner—PBN boats.—In this system, the only mechanism for incorporation of Si into GaP is *via* reaction [2a]. The level of Si contamination was found to be 1.5×10^{19} atoms cm^{-3}. Since Luther and Verleur give an accuracy of ±30% for their analytical results (6), the Si contamination is about the same for this system as was obtained for the all-SiO_2 system. Therefore, no reduction in the level of Si contamination can be expected using boats other than SiO_2 when using an SiO_2 liner.

Effect of carrier gas on purity of GaP using a SiO_2-PBN system.—A distinct cost advantage can be realized using SiO_2 liners. Since high levels of Si contamination were observed using H_2 as a carrier gas in the SiO_2 liner-PBN boat system, an examination of the effect of the gaseous environment of that system to reduce the equilibrium SiO concentration was made. The equilibrium constant for reaction [2a], the vapor transport mechanism for Si contamination, is given by Eq. [2a$_1$]. If the H_2O pressure is increased using a constant H_2 pressure, the concentration of SiO will decrease. One can thus reduce the Si contamination by increasing the H_2O pressure (9), *i.e.*, by adding water vapor to the carrier gas. But from Eq. [3b], it follows that the addition of H_2O will increase the loss of GaP by the water-vapor transport reaction. Another method for reducing the Si contamination is to change the carrier gas from H_2 to He. By substituting He for H_2 according to Eq. [2a], the concentration of SiO should be reduced. However, some H_2 will be present because the reacting gas is PH_3. If the hydrogen pressure is 0.98 atm for the 95% H_2 gas mixture, by substitution of He for H_2 the H_2 gas pressure will be reduced to about 0.07 atm.

If X is the initial mole fraction of H_2 (0.98 or 0.07) and Y is the mole fraction of SiO or H_2O formed by reaction [2a], then $X - Y$ is the final mole fraction of H_2. Let the total pressure be P. If it is then assumed that the thermodynamic equilibrium constant, K, is equal to the one based on partial pressure, Eq. [2a$_1$] becomes

$$K_{[2a]} = \frac{Y^2 P^2}{(X - Y)P} = \frac{Y^2}{X - Y} \text{ since } P = 1 \qquad [4]$$

Since $K_{[2a]}$ is quite small (see Table III), Y is much less than X and therefore $X - Y \simeq X = 0.98$ or 0.07 depending on whether H_2 or He is used as the carrier gas. Equation [4] can then be simplified to

$$K_{[2a]} \simeq \frac{Y^2}{X} \text{ and } Y = (KX)^{1/2} \qquad [5]$$

If we then substitute the two values of the initial mole fractions of H_2, we obtain

$$\frac{Y_1}{Y_2} = \left(\frac{0.98}{0.07}\right)^{1/2} = 3.75 \qquad [6]$$

This value is quite similar to the threefold increase observed experimentally (see Table I) when 95% He is replaced by 95% hydrogen using the PBN boats-SiO_2 liner system. This result also substantiates the mechanism of reaction [2] and indicates that the kine-

tics of this reaction are reasonably rapid. The use of He as a carrier gas, rather than H_2, thus reduces the SiO concentration to about 1/3 and the Si content in GaP by a similar value. However, since the reactant gas contains PH_3, the H_2 mole fraction can be reduced only by about two orders of magnitude when using He. Therefore, the reduction of the SiO concentration by a factor of 10 is the maximum obtainable, which still leaves the Si content of the GaP at too high a value.

With water vapor, much greater reductions in SiO concentration can be realized although some oxygen doping of GaP may occur.[7] The use of He and water vapor should be more efficient in keeping the SiO concentration low than the H_2 and water vapor system, since less water vapor would be needed in the He system.

The addition of water vapor to the He carrier gas changes Eq. [4] to

$$K_{[2a]} = 2 \times 10^{-10} = \frac{YZ}{X - Y} \qquad [7]$$

where $X = 0.07$ is the mole fraction of H_2, Y is the SiO mole fraction, and Z is the H_2O mole fraction, equal to Y plus the water vapor added to the carrier gas. An H_2O mole fraction of 2×10^{-3} was added to the carrier gas. Hence, the resultant SiO mole fraction will be $Y \simeq 7 \times 10^{-9}$ under these conditions.

When the same calculation is made using hydrogen as the carrier gas, Y becomes 1×10^{-7}. Thus, using the same amount of water in the He system will reduce the SiO mole fraction by a factor of about 15.

GaP was prepared in an SiO_2 liner using PBN boats with a 95% He-5% PH_3 gas mixture containing about a 2×10^{-3} mole fraction of H_2O vapor. The material produced looked quite similar to that produced in an all-PBN system. The material was examined by optical fluorescence (11) and was found to have an optically active Si concentration of about 10^{16} cm^{-3}. The GaP yield obtained in these experiments was about 10% lower than comparable runs made without water.

Summary

Polycrystalline GaP was prepared in an open-flow system using the reaction of PH_3 with Ga to form GaP in pyrolytic boron nitride boats and liners in a temperature gradient. The spectrographic analysis of the material is shown in Table II. Optimization of synthesis time, PH_3 flow rate, and temperature gradient increased the P reaction efficiency from 10 to 50-55%, the Ga reaction efficiency from 20 to 50-55%, and the GaP yield from 15g/50g of Ga to 35-38g/50g of Ga. The increased P reaction efficiency and GaP yield with decreasing PH_3 flow rate was explained by the formation of a reaction barrier layer over the Ga. The increased yield and reaction efficiency with increased temperature gradient were suggested to be due to the solution of the reaction barrier layer and an increased driving force for the rate-controlling diffusion of GaP in Ga.

Pyrolytic boron nitride and water-free vitreous silica were used alone and in combination as liners and reaction vessels for the synthesis. It was found that the hydrogen reduction of SiO_2 produced as much, if not more, silicon contamination of the GaP as did the direct interaction of SiO_2 with Ga.

Since this hydrogen reduction reaction is so prevalent, experiments were performed to lower the Si contamination by examining this reaction. There are two ways to lower the SiO concentration: (*a*) increase the H_2O content of the gas and/or (*b*) decrease the H_2 content of the gas. The first method would decrease the GaP yield because of the water-vapor transport reaction with GaP. Therefore, the second method was investigated first by substituting He instead of H_2 as the carrier gas in the PBN boat-SiO_2 liner system. The use of He resulted in a threefold reduction of the Si contamination and produced material with a Si concentration of 5×10^{18} cm^{-3}. This reduction in Si is quite close to that theoretically calculated.

Since the H_2 content of the reactant gas cannot be lowered more than one to two orders of magnitude, the addition of water vapor to the carrier gas was examined in the SiO_2-PBN system. It was found that the optically active Si concentration in the GaP was reduced to about 10^{16} cm^{-3} when a 2×10^{-3} mole fraction of H_2O was introduced to the He-PH_3 gas mixture. Under the above conditions, the GaP yield was reduced by about 10% when water was added to the reactant gas. Thus, GaP of low Si content can be prepared in the presence of SiO_2.

[7] Water vapor may react with the PBN boats increasing the amount of nitrogen in the GaP. Analysis of crystals pulled from materials grown using water vapor in the SiO_2-PBN system indicated an optical nitrogen content similar to that obtained using an all-PBN system without water.

Acknowledgments

The author gratefully acknowledges the mass spectrometric analysis work, the analytical work on Si in GaP, the optical and fluorescence examinations, and the inert gas fusion analysis by D. L. Malm, L. C. Luther, W. G. Guldner, P. J. Dean, and G. Kaminsky, as well as the use of their unpublished data.

The author wishes to express his appreciation to R. B. Zetterstrom for illuminating discussions and would like to thank H. W. Verleur for his critical reading of the manuscript and valuable comments.

Manuscript submitted July 29, 1970; revised manuscript received Dec. 5, 1970.

Any discussion of this paper will appear in a Discussion Section to be published in the December 1971 JOURNAL.

REFERENCES

1. S. J. Bass and P. E. Oliver, *Crystal Growth*, **3**, 286 (1968).
2. H. G. Grimmeiss, N. Kischio, and H. Scholz, *Philips Tech. Rev.*, **26**, 136 (1956).
3. C. J. Frosch and G. S. Rao, Unpublished work; B. J. Dean, C. H. Henry, and C. J. Frosch, *J. Appl. Phys.*, **39**, 5631 (1968); T. S. Plaskett, *This Journal*, **116**, 1723 (1969).
4. S. F. Nygren, C. M. Ringel, and H. W. Verleur, To be published.
5. P. J. Dean and G. Kaminsky, Unpublished data.
6. L. C. Luther and H. W. Verleur, To be published.
7. D. L. Malm, Unpublished data.
8. W. G. Guldner, Unpublished data; W. G. Guldner, "Standard Methods of Chemical Analysis," Vol. 2, Part B, 1563, 6th Ed., D. Van Nostrand Co., Inc., Princeton, N. J. (1963).
9. C. J. Frosch, C. D. Thurmond, H. G. White, and J. A. May, *Trans. Met Soc. AIME*, **239**, 365 (1967); J. F. Woods and N. G. Ainslie, *J. Appl. Phys.*, **34**, 1469 (1963); C. N. Cochran and L. M. Foster, *This Journal*, **109**, 149 (1962).
10. C. D. Thurmond and M. Kowalchik, *Bell System Tech. J.*, **39**, 169 (1960).
11. P. J. Dean, Unpublished data.

Hydrides and Hydroxyls in Thin Silicon Dioxide Films

K. H. Beckmann

Philips Forschungslaboratorium Hamburg GmbH, 2 Hamburg 54, Germany

and N. J. Harrick[1]

Philips Laboratories, Briarcliff Manor, New York 10510

ABSTRACT

Determinations of the hydroxyl content of anodically and thermally grown silicon dioxide films by internal reflection spectroscopy in the infrared show that hydroxyl and silicon hydride are already incorporated into these films during their formation. The concentration, as well as the distribution, of these compounds within freshly formed anodic and thermal films is given.

In the investigation of silicon dioxide films which act as diffusion masks and protective coatings on semiconductor devices, the importance of the chemical purity of these films with respect to such applications has been shown [for review see (1)]. The chemical and electrical properties of thermally produced films, which have found wide applications in semiconductor device technology, have been investigated as well as those of anodically grown silicon dioxide films. The formation of relatively dense silicon dioxide films by anodization had been described by Schmidt and Michel (2). The electrical properties and the etching behavior, as well as other properties, were investigated by Schmidt and Rand (3) and by Pliskin and Lehman (4). These authors concluded that the insulating properties of such films depended highly on their hydrogen content. Dreiner (5) observed changes in the capacitance of the system silicon/anodic oxide/electrolyte, which depended on the time of exposure of the system to aqueous or water-containing electrolytes. From this he concluded that water or some hydrogen compound diffused into the anodic film at room temperature. Nannoni (6) reported changes of the electrical properties and also of the capacitance of the system silicon/anodic oxide/metal upon exposure to room air, which he also ascribed to the migration of hydrogen or hydrogen compounds into the oxide.

Studies of the influence of heat treatments in different ambients on the electrical properties of the silicon/silicon dioxide interface led several authors to the conclusion that hydrogen or hydrogen compounds might diffuse into the oxide (mostly thermal oxides) at elevated temperatures there forming hydrides or hydroxides [see (1, 7, 8)]. Radiotracer measurements of the distribution of hydrogen within silicon dioxide films thermally grown in tritium-tagged steam revealed high concentrations of hydrogen within these layers (9). By the same technique it was also shown that protons from ethanol adsorbed at the surface of thermal silicon dioxide films could be forced to migrate into the film at elevated temperatures by applying a bias between the silicon substrate and a metal electrode on top of the oxide (10). These methods could only reveal the presence of hydrogen within the oxide films, while no direct determination of the compound into which it was incorporated could be performed. Schmidt and Rand (3) and Pliskin and Lehman (4) reported an OH absorption band in the infrared absorption spectrum of anodically grown silicon dioxide, and Villemant and Kover (11) detected by the same method the presence of OH groups in films grown in wet oxygen and in those produced by hydrolysis of $SiCl_4$. These infrared spectroscopic investigations, however, were not sensitive enough to allow quantitative determinations of the concentration of these compounds.

For the above reason we performed quantitative measurements of the content of hydrogen compounds of anodic and thermal silicon dioxide films produced in different ways and after various postoxidation treatments. We used ellipsometry for the determination of film thickness and measured the infrared absorption by internal reflection spectroscopy (IRS) which offers a much higher sensitivity for measurements of the absorption by thin films than a simple transmission technique.

Experimental

The anodic films were grown on wafers of p-type silicon (15 ohm-cm) with optically polished faces (unoriented) in a 0.25*N* solution of KNO_2 in tetrahydrofurfuryl alcohol (THFA). In order to remove the polished layer and to achieve a well-defined crystalline state of the faces, all polished wafers were first covered with an oxide film several microns in thickness by thermal oxidation. This film was then removed by etching prior to the formation of the first anodic film to be measured. The growth of the anodic films was performed at constant current (10 mA cm^{-2} in most cases). The constant current generator used allowed a certain voltage to be preset, at which it automatically switched over to constant voltage operation (crossover). This voltage was set according to the film thickness wanted. After crossover the current was in most cases allowed to decrease to one tenth of its original value, which took approximately 10 min for a film thickness of 300Å and 25 min for 1000Å. During this period of constant voltage operation the film continued to grow, however, with a growth rate decreasing with time. After this time the wafer was removed from the electrolytic cell, rinsed in methanol, and dried in a stream of warm air. The thermal films were formed in an oxygen atmosphere or in oxygen saturated (at 85°C) with water vapor, at temperatures between 1050° and 1200°C.

The thicknesses of these films and the indexes of refraction were determined ellipsometrically with a Rudolph 43603-200 E thin film ellipsometer. The calculation of the film thickness and refractive index from the ellipsometer data was performed on a computer by using Fresnel's equations and the exact expression for the amplitude reflection coefficients of a thin film.

The infrared absorption by these thin films had to be measured by using the technique of internal reflection spectroscopy (IRS) as developed by Harrick (12), because of the small film thickness and the low number of absorbing bonds. We used a differential setup as shown in Fig. 1. A beam of monochromatic infrared radiation is split into two by a beam splitter (BS) (silicon plate). The transmitted portion is focused on the entrance face of the oxdized wafer which

[1] Present address: Harrick Scientific Corporation, Ossining, New York, 10562.

Key words: infrared spectroscopy, internal reflection spectroscopy, thermal silicon dioxide films, anodic silicon dioxide films, quantitative determination of hydroxyl content.

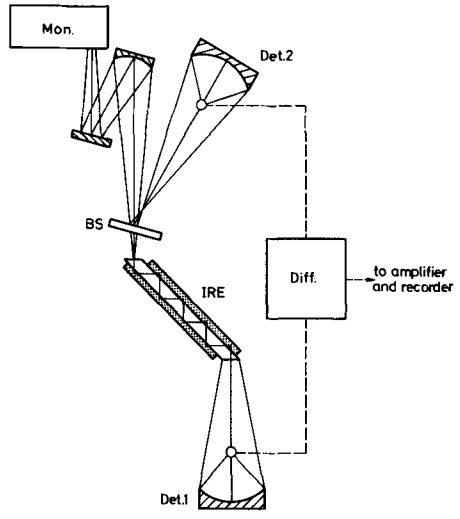

Fig. 1. Setup for the differential measurement of the infrared absorption spectrum of a thin film on a substrate (internal reflection element, IRE) by internal reflection spectroscopy (IRS). (Mon: monochromator; BS: beam splitter; Det: ellipsoidal mirror-detector unit; Diff: unit for the attenuation of the electrical signals and for the formation of the differential signal.)

is shaped in a trapezoid form so that it acts as an internal reflection element (IRE) [see (12)]. At the totally reflecting silicon/silicon dioxide interface, absorption of radiation occurs at those wavelengths at which absorption bands of the molecules incorporated into the oxide film exist. Since the beam suffers a great number of total reflections before leaving the wafer, the attenuation of the light intensity by absorption processes within the thin oxide film is amplified. This can be seen by comparing the two ordinate scales of Fig. 2. In the investigation of anodic films we used 60 reflections, and with thermal films 180 reflections were employed. Thus, absorption signals much larger in strength than those which could be obtained by one normal transmission through the films on both sides were obtained. After leaving the wafer the light of intensity, I, is focused on a thermocouple (Det. 1). That part of the incident beam (I_0) which is reflected at the beam splitter (BS) (reference beam) is focused on a second thermocouple (Det. 2). By this differential technique the relatively high level

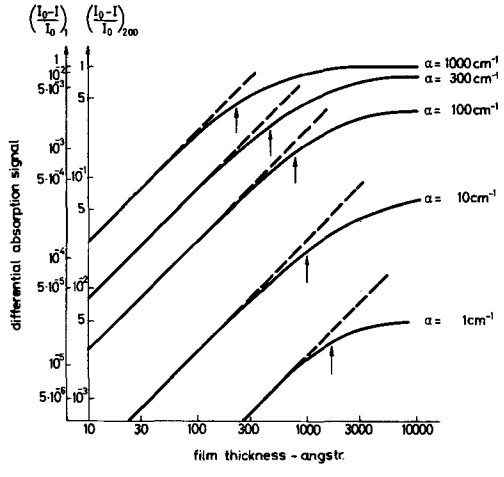

Fig. 2. Calculated dependence of the differential absorption signal for 1 (left vertical scale) and 200 (right vertical scale) reflections on film thickness for different magnitudes of the thin film's absorption coefficient. The other optical parameters needed for the calculation are those of the system silicon/silicon dioxide film ($\lambda = 3$ μm). The dashed lines give the slope of the same curves for the case of normal transmission through the films.

of the signal corresponding to the light intensity incident on the detectors can be suppressed. Thus, it is possible to choose the highest possible electronic amplification for the differential absorption signal. If absorption peaks due to the oxide film appear in the spectrum, this differential signal is thus proportional to the change in transmittance ($I_0 - I$) of the film-covered IRE. Since the magnitude of the intensity of the light in the wafer beam at the wavelength of absorption, I_0, is also determined by measuring the single beam spectrum at much lower electronic amplification, the expression $(I_0 - I)/I_0$ can be calculated.

Quantitative Evaluation

For a quantitative determination of the absorption constant from the transmission spectrum, the path length of the radiation within the absorbing medium has to be known. Since the spatial distribution of the energy flow within the rarer medium during total reflection follows a complicated pattern (13), no path length of the radiation within the absorbing medium can be defined in this case. On the other hand the validity of the concept of effective thickness (14) is limited to small values of the absorption coefficient. We therefore used for the evaluation of the absorption signals Fresnel's equations and the exact expressions for the reflectivity of a thin film on top of a substrate [see, *e.g.*, (15)]. By these relations the energy distribution within the rarer medium as well as the boundary conditions, *etc.*, are being properly taken into account. Since these relations cannot be solved for the absorption coefficient, this quantity was determined by a trial-and-error procedure on a computer.

To calculate from a measured absorption peak the number of absorbing bonds, the effective charge of the oscillating group has to be known. From this magnitude the strength of absorption per concentration unit of the oscillating group (absorption cross section, molar absorbance or molar extinction) may then be calculated. These values have been determined experimentally for the case of hydroxyl in fused quartz (16-18), but these data show only a poor agreement. In this publication we use the relation between the integrated absorption and the number of absorbing groups as given by Kats (16).

This relation, however, refers to the case of free oscillating OH groups. It is known that in the case of hydrogen bonding the integrated absorption at the fundamental frequency may be increased by a factor of up to 10 (19). One can see that the OH vibration within anodic oxide films at 3375 cm^{-1} (2.98μ) has a half-width of 435 cm^{-1}, whereas that within thermal oxide at 3600 cm^{-1} (2.78μ) has a half-width of 130 cm^{-1} (see Fig. 3). As we have proved by measuring the deuteration shift, both vibrations are due to the

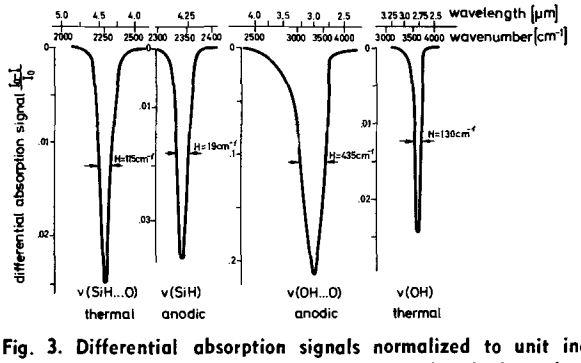

Fig. 3. Differential absorption signals normalized to unit incident intensity for four absorption peaks obtained with thermal and anodic silicon dioxide films. ν(OH), Fundamental O-H stretching vibration in thermal films; ν(OH. . .O), fundamental O-H stretching vibration in anodic films (hydrogen bridging); ν(SiH), fundamental Si-H stretching vibration in anodic silicon dioxide films and ν(SiH. . .O) of hydrogen-bonded silicon hydride as found in thermal films.

fundamental OH stretching vibrations. Therefore the difference between the two wave numbers measured with differently produced films as well as the increase in half-width demonstrates that the anodic film contains hydrogen bonding OH groups, whereas the OH vibration in thermal oxides occurs relatively free.

It has been found that in the presence of hydrogen bonding the integrated absorption by the fundamental vibration increases with the frequency shift, due to the same effect (20). Since quantitative results concerning these relations in the case of hydroxyl groups within an oxide lattice do not exist, we can only assume that this increase in the integrated absorption is a function of the frequency shift. In the system phenol/diethyl ether, a frequency shift of 270 cm^{-1} and an increase in the integrated absorption by a factor of 6.9 has been observed (21). Since we found a shift of 225 cm^{-1} due to hydrogen bridging, we assume an increase in the integrated absorption by a factor of 5. This relation looks reasonable also in view of the fact that the half-width of the stretching vibration band of hydrogen-bridged OH is 3.35 times greater than that of the "free" OH (see Fig. 3). Therefore we corrected the expressions given by Kats (16) for this influence of hydrogen bonding on the strength of absorption. The equation for estimation of the concentration of OH groups per cubic centimeter in the presence of hydrogen bonding reads

$$N_{OH\ldots O} = 0.4 \cdot 10^{16} H \alpha_{max} \quad [1]$$

where H, the half-width and α_{max}, the absorption coefficient at the fundamental frequency, are given in cm^{-1}. In the absence of hydrogen bonding, this equation becomes

$$N_{OH} = 2 \cdot 10^{16} H \alpha_{max} \quad [2]$$

There are, however, no literature data available concerning the absorption cross sections of the silicon-hydrogen valence vibration ν(SiH). We therefore calculated the partial charge resident on the hydrogen atom of SiH incorporated into a SiO_2 lattice using data given in the literature (22), and with this value the calculation of the specific absorption (23) could be performed. In this calculation the index of refraction of the thin film was taken as 1.4. This leads to the relation for unbonded SiH

$$N_{SiH} \approx 7.5 \cdot 10^{17} H \alpha_{max} \quad [3]$$

where H and α_{max} have the same meaning as is Eq. [2], now referring only to the SiH absorption band.

Comparing the SiH absorption bands shown in Fig. 3 one has also to conclude that SiH may be subjected to hydrogen bonding, since with thermal oxide we observe a band shifted to greater wavelengths and increased in half-width with respect to that obtained with anodic oxide. Referring to the arguments used in the calculation of the OH vibrations, we take the increase in half-width as a measure for the increase in the specific absorption. Thus, we may use for the estimation of the SiH concentration

$$N_{SiH\ldots O} \approx 10^{17} H \alpha_{max} \quad [4]$$

Since the magnitudes inserted into the relations [1-4] contain several uncertainties, these determinations can with respect to the absolute value of the SiH concentration be regarded only as an estimation of the order of magnitude. For the relative values, however, a greater accuracy can be claimed (±50%).

When determining the absorption coefficient by using Fresnel's equations for a boundary between different media, it is implied that these media and the thin film which are involved in this process of total reflection are homogeneous, especially that the absorption coefficient is constant throughout the film. Since the concentration of the absorbing groups will be calculated from the absorption coefficient thus determined, a constant distribution of the oscillators within the thin film is also assumed. As is seen from the results, this is not always the case. This is the reason the concentration thus determined is called the average concentration.

The question remains, what information can be obtained regarding the distribution of these oscillators within the film from measurements of the *IR* absorption. If we assume that the concentration, c, of the groups to be studied varies with the distance, x, from the silicon/silicon dioxide interface, $c = c(x)$, and that—as in a transmission experiment—the whole radiation passes through the whole film, then we could define the average concentration measured by one such experiment

$$c_{av}(t) = \frac{1}{t} \int_0^t c(x)\, dx \quad [5]$$

where x indicates the distance from the Si/SiO_2 interface and t the film thickness. If we reduce the film thickness stepwise by successive etching of the film and if we measure the *IR* absorption after each etching process, we may determine $c_{av}(t)$ as a function of the remaining film thickness, t. To calculate from this plot the dependence of the (local) concentration, $c(x)$, on the distance from the Si/SiO_2 interface for the original film, we derive from [5]

$$c(x) = \frac{d}{dt}(t\, c_{av}(t)) = c_{av}(t) + t \frac{dc_{av}(t)}{dt} \quad [6]$$

or, in a difference expression, if $c(t_1)$ and $c(t_2)$ are the concentrations found with thicknesses t_1 and t_2, for $x = (t_1 + t_2)/2$

$$c(x) = \frac{t_1 c_{av}(t_1) - t_2 c_{av}(t_2)}{t_1 - t_2} \quad [7]$$

(local concentration)

However, these relations apply only when the radiation penetrates practically through the entire film. Since in the case of total reflection—which is applied in IRS—the intensity of the light within the rarer medium shows an exponential attenuation with distance from the silicon/silicon dioxide interface even in the absence of absorption, the applicability of Eq. [6] and [7] has to be checked.

This has been done in Fig. 2. This figure shows a plot of the change in the intensity transmitted by the IRE normalized to unit incident intensity, $(I_o - I)/I_o$ (as defined in Experimental), calculated on a computer by using the exact equations, as a function of film thickness for different values of the absorption constant, α, for 200 total reflections, $(I_o - I/I_o)_{200}$, and (left scale) for one reflection, $(I_o - I/I_o)_1$. The dashed line gives the slope of the same expression *vs.* film thickness for one normal transmission of the film; that means for the case where the whole film contributes fully to the absorption signal. The absolute values—to which the left scale refers—are slightly smaller in this case because of the smaller path length. As long as there is no appreciable difference between the corresponding dashed and full drawn curves, we may assume that also in the case of total reflection practically the entire film contributes fully to the absorption signal so that relations [5-7] remain applicable. The arrows indicate the film thicknesses at which the contribution to the absorption of the region more distant from the Si/SiO_2 interface is 25% smaller than the contribution of that part adjacent to that interface. We wish to emphasize that this is taken into account exactly in the calculation of α for the case of a constant α throughout the film. If in the case of thicker films the outer region has a greater absorption constant than the inner, the average concentration of absorbing groups thus determined will be smaller, and in case of smaller absorption constant in the more distant part it will be larger than the concentration determined from a transmission measurement.

Finally, the total number of absorbing groups is defined as the number of absorbing groups within the whole film per square centimeter area.

Since all the measurements had to be performed in room air, some difficulty arose due to the adsorption of water and hydrocarbons at the surface of the IRE during the measurements which led to absorption bands at 3355 cm^{-1} (2.98μ) for the OH- and at 2857 cm^{-1} (3.50μ) for the CH-stretching vibration (24). Since the bands of adsorbed and of OH-groups built into the film occur at the same wavelength, a correction was required, especially with very thin anodic films ($t < 50$Å).

Since we found with, *e.g.*, very thin thermal films into which no hydroxyl groups had been built in that the ratio of the amount of hydrocarbons to that of water adsorbed at the surface was practically constant, we took the strength of the CH-absorption band as a measure of the degree of adsorption. The contribution of the adsorbed species to the optical absorption could thus be subtracted from the measured signal.

Results

Figure 3 shows the absorption bands which were recorded with anodic and thermal silicon dioxide films. As already pointed out in the preceding paragraph, the anodic films contain hydrogen bonding hydroxyl, whereas these groups are relatively "free" in thermal oxide. This assignment could be proved by deuteration of these groups which led to absorption peaks at approximately 1.4 times the original wavelength. The assignment of the peaks near 4.25 and 4.5 μm to the SiH stretching vibrations could not be checked directly by this method since the deuteration of these compounds would shift the absorption peaks to 6.0 or 6.3 μm, respectively. In this wavelength region certain combination vibrations of the oxide lattice occur so that the transmission of the internal reflection element is very low. We could perform only an indirect deuteration check, since these peaks decreased in strength upon heat treatment in deuterium gas, and they increased again upon subsequent heat treatment in hydrogen. Furthermore, it has been shown (23) that the SiH stretching vibrations in an oxidic lattice are positioned near $\lambda = 4.4\mu$.

The dependence of the initial average OH concentration of anodic films on several parameters of the film formation is shown in Table I. The given average concentrations are the mean values obtained with several films. We wish to point out that the error in these determinations is about ±50%.

We see from lines *a*, *b*, and *d* of Table I that the OH content of the anodic oxide films is reduced by keeping the film at the crossover voltage for some time. For an estimation of the relative concentration of these groups in the oxide lattice, one should bear in mind that, *e.g.*, fused silica contains 2.3 x 10^{22} SiO_2 groups/cm^3. By forming the anodic films in a solution the water content of which had been reduced from 300 ppm to 60 ppm with the aid of molecular sieves, a lower OH concentration may be achieved. Thus the water present in this electrolyte has to be regarded at least as one of the sources for the OH groups incorporated into the film. Line *e* of Table I indicates that during anodization [see (3)] the number of hydroxyl groups does not increase, as can be seen from line *f* of this table where are given the data of the thermally produced film prior to anodization.

Thermal films produced in wet oxygen at 1050°C contain 10^{19} OH groups/cm^3. No OH groups could be found with films produced in "dry" oxygen (which contained 60 ppm H_2O). For this reason the smallest amount detectable with our apparatus is inserted in lines *i*, *k*, *l* as the upper limit of a possible OH content. By a heat treatment at 530°C in wet nitrogen (this gas was saturated with H_2O at 85°C), the concentration can be increased with both oxides to approximately 2 x 10^{19}. This seems to be the saturation concentration for heat treatment at this temperature, since a prolonged annealing did not result in a further increase of the concentration.

Table II gives the concentrations of the silicon hydride groups found in different oxides. The most surprising result is that, after formation of the oxide film in a "dry" oxygen atmosphere, such a high concentration of silicon hydride groups has been found. Determinations of the water content of this oxygen gas, however, demonstrated that the humidity amounted to 60 ppm. We see from Table II that the silicon hydride concentration may be increased by subsequent heat treatment in hydrogen, whereas this process has practically no influence on the concentration of the hydroxyl groups. Silicon hydride groups in anodic films can be made to disappear by heat treatment at 300°C. Such a treatment only results in a small reduction (by 30%, approximately) of the hydroxyl content. Annealing the anodic films at 500°C in dry N_2 leads to a shift of the OH absorption band to $\lambda \approx 2.78$ μm. This indicates that the hydrogen bonds are being broken at this temperature.

Figure 4 shows the dependence of the average concentration of OH within anodically grown films on the remaining film thickness during step etching. One of these films had been kept at the crossover voltage in the forming solution for about 10 min, until the current had decreased to one tenth its original value. The other film was kept at this voltage for 24 hr. The local concentrations have been calculated by using Eq. [7]. The fact that the local concentration is smaller than the average concentration at greater distances from the interface indicates that there must be a very high

Table I. Initial average concentrations, c_{av}, of OH-groups determined immediately after formation

	Type of film	Kind of formation + treatment given after formation	Thickness, A	c_{av}, cm^{-3}
a	Anodic	Pulled out at crossover[1]	130	$8 \cdot 10^{20}$
b	Anodic	Normal[2]	330	$2 \cdot 10^{20}$
c	Anodic, in dry THFA[3]	Normal[2]	330	10^{20}
d	Anodic	24 hr kept at crossover[4]	327	$3 \cdot 10^{19}$
e	Anodized thermal[5]	1050°C in wet O_2[6]	1,000	10^{19}
f	Thermal	1050°C in wet O_2[6]	1,000	10^{19}
g	Thermal	1050°C + 3 hr 530°C in H_2O vapor	1,000	$2 \cdot 10^{19}$
h	Thermal	1050°C + 7 hr 350°C in H_2	1,000	10^{18}
i	Thermal	1100°C in "dry" O_2	10,000	$<5 \cdot 10^{18}$
k	Thermal	1100°C + 3 hr 350°C in H_2	10,000	$<5 \cdot 10^{18}$
l	Thermal	1100°C + 10 min 500°C in H_2	10,000	$<5 \cdot 10^{18}$
m	Thermal	1100°C + 3 hr 350°C in H_2O	10,000	$2 \cdot 10^{19}$

[1] The wafer had been removed from the electrolytic cell in which the film had been formed immediately after the preset voltage had been reached (crossover).
[2] After reaching the crossover voltage, the current had been allowed to drop to one tenth its original value before removing the wafer from the electrolyte.
[3] The water content of the solution (originally 300 ppm) had been reduced to 60 ppm by molecular sieves.
[4] After having reached the crossover voltage, this voltage was applied to the sample for 24 hr.
[5] A thermally produced film, the data of which are given in line *f* of this table, had been kept in the THFA solution for 24 hr at a voltage just below that at which further film growth would happen.
[6] Oxygen saturated with water vapor at 85°C.

Table II. Initial average concentrations, c_{av}, of SiH-groups determined immediately after formation

	Type of film	Kind of formation + treatment given after formation	Thickness, A	c_{av}, cm^{-3}
(*a*)	Anodic, in dry THFA[3]	Normal[2]	300	$2 \cdot 10^{21}$
		Normal + 30 min 300°C in N_2	300	$<3 \cdot 10^{19}$
(*b*)	Thermal	1050°C in wet O_2	10,000	$5 \cdot 10^{19}$
	Thermal	1050°C + 30 min 350°C in H_2	10,000	$5 \cdot 10^{19}$
	Thermal	1100°C in dry O_2	10,000	$7 \cdot 10^{19}$
	Thermal	1100°C + 30 min 450°C in H_2O	10,000	$8 \cdot 10^{19}$
	Thermal	1100°C + 30 min 350°C in H_2	10,000	10^{20}
	Thermal	1100°C + 10 min 500°C in H_2	10,000	$2 \cdot 10^{20}$

For explanations see Table I.

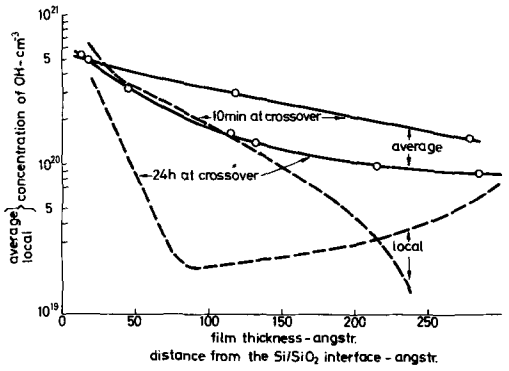

Fig. 4. Variation of the average concentration, c_{av} (vs. film thickness), and local concentration, c_{loc} (vs. distance), of hydroxyl determined from the absorption peak at 2.98 μm within anodic oxide films produced in a 0.25*N* solution of KNO_2 in tetrahydrofurfuryl alcohol. The solution was dehydrated by molecular sieves. Film formation at 10 mA cm^{-2}.

concentration of absorbing groups near this interface. One observes that an appreciable reduction of the local concentration happens almost throughout the film upon keeping it for 24 hr at crossover voltage, whereas a steep increase of this density can be seen near the Si/SiO_2 interface.

As has been stated in Table I, there are practically no OH groups present in thermal oxide films formed in "dry" oxygen, but they contain a great number of silicon hydride groups. Their distribution within the film is shown in Fig. 5. Since this film was 10,000Å thick, the outer regions are only weakly coupled to the evanescent wave. For this reason there is an increasing uncertainty in the concentration thus determined above 1000Å as has been described in the paragraph "Quantitative Evaluation."

Figure 6 shows the distribution of hydroxyl groups in an oxide film thermally produced in an oxygen

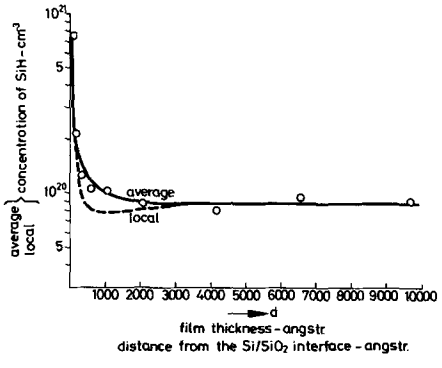

Fig. 5. Average concentration of SiH vs. film thickness and local concentration vs. distance from the Si/SiO_2 interface for an oxide film thermally produced in an oxygen atmosphere.

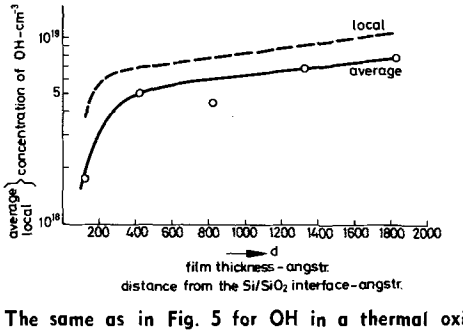

Fig. 6. The same as in Fig. 5 for OH in a thermal oxide film produced in wet oxygen atmosphere. After formation the film had been given a heat treatment at 350°C for 30 min in H_2 atmosphere.

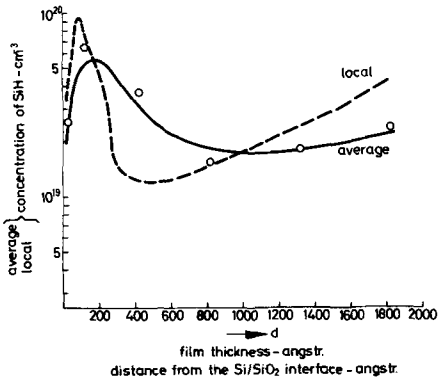

Fig. 7. Hydride content of the film whose hydroxide concentrations are shown in Fig. 6.

atmosphere which has been saturated with water vapor at 85°C. The distribution of the silicon hydride groups within the same film is shown in Fig. 7.

Conclusions

As has been found earlier, there exist structural differences between thermal and anodic silicon dioxide films (3). Nevertheless it is surprising that in anodic films hydroxyl groups show hydrogen bonding and silicon hydride does not, whereas with thermal films one observes hydrogen bonding SiH and nonbonded hydroxyl. This at least indicates that hydroxyl, as well as hydride groups occupy well-defined sites in both oxides.

From the results reported here, nothing can be said concerning the kind of compound into which the OH groups detected are incorporated; *i.e.*, whether they belong to SiOH or H_2O. The characteristic combination vibrations by which this question could be answered could not be detected by us.

The mean values of our results are summarized in Tables I and II and indicate that one of the sources for hydroxyl groups found with anodic films might be water present in the electrolyte, since we obtained a smaller average concentration of OH with an electrolyte dehydrated by molecular sieve. The fact that the OH concentration (see Fig. 4) within anodically grown films is markedly reduced throughout the film by keeping it for 24 hr at the crossover voltage (Fig. 4) indicates a consumption of hydroxyl at this anodic polarization. The increase of the concentrations toward the silicon-silicon dioxide interface points out that there must be a migration of the OH groups to the Si/SiO_2 interface under the action of the applied field which finally results in the further oxidation of silicon at the interface. In this reaction the oxidation process must be the rate-determining step thus leading to a higher concentration near the interface with respect to the interior of the film. In addition, however, one has to state that the supply with OH from the electrolyte is also reduced at the crossover voltage, since otherwise the over-all decrease of the hydroxyl concentration could not be explained.

The results obtained with thermally produced films are in good agreement with the data published after radiotracer measurements of the hydrogen content of such films (9, 10). A comparison of our findings with the concentrations published in these papers allows the conclusion to be drawn that at least an appreciable fraction of the hydrogen atoms present in such films is incorporated as hydroxyl or as silicon hydride.

A consumption of hydroxyl groups during the thermal oxidation process, too, is indicated by Fig. 5, 6, and 7. The decrease of the OH and the increase of the SiH groups near the interface may be explained by a reaction of silicon atoms with hydroxyl leading to silicon oxide and to some extent also to silicon hydride bonds. The same refers to the "dry" oxide since we have already mentioned that the oxygen used for oxidation contained some water.

Further experiments which may yield some insight into the diffusion mechanism of hydrogen or hydrogen compounds in anodic films, as well as such which may give additional information regarding the influence of hydrogen and its compounds on the electrical properties of the Si/SiO_2 interface [see, *e.g.*, (1) and (7)] are being undertaken.

Acknowledgments

The authors gratefully appreciate the assistance of Ing. Th. Tempelmann and Ing. C. Wiech in the performance and evaluation of the measurements. Thanks are due to Dr. E. Kooi and Ir. J. J. H. Schatorjé from Philips Research Laboratories, Eindhoven, for the growth of the thermal films. They also express their gratitude to Dr. R. Memming for valuable discussions.

Manuscript submitted April 20, 1970; revised manuscript received Aug. 24, 1970.

Any discussion of this paper will appear in a Discussion Section to be published in the December 1971 JOURNAL.

REFERENCES

1. A. G. Revesz and K. H. Zaininger, *RCA Rev.*, **29**, 22 (1968).
2. P. F. Schmidt and W. Michel, *This Journal*, **104**, 230 (1957).
3. P. F. Schmidt and M. J. Rand, *Solid State Commun.*, **4**, 169 (1966). P. F. Schmidt, *This Journal*, **115**, 167 (1968).
4. W. A. Pliskin and H. S. Lehman, *ibid.*, **112**, 1013 (1965).
5. R. Dreiner, *ibid.*, **113**, 1210 (1966).
6. R. Nannoni, *Rev. Phys. Appl.*, **3**, 265 (1968).
7. E. Kooi, *Philips Res. Repts.*, **20**, 578 (1965). E. Kooi, *ibid.*, **21**, 477 (1966).
8. B. E. Deal, E. L. MacKenna, and P. L. Castro, *This Journal*, **116**, 997 (1969).
9. P. J. Burkhardt, *ibid.*, **114**, 196 (1967).
10. S R. Hofstein, *Appl. Phys. Letters*, **11**, 95 (1967).
11. C. Villemant and F. Kover, *Rev. Phys. Appl.*, **1**, 90 (1966).
12. N. J. Harrick, "Internal Reflection Spectroscopy," Interscience Publishers (1967).
13. A. Eichenwald, quoted in C. Schaefer and G. Gross, *Ann. Phys.*, **32**, 648 (1910).
14. Cit. (12), p. 41.
15. W. N. Hansen, *J. Opt. Soc. Am.*, **58**, 380 (1968).
16. A. Kats, *Philips Res. Repts.*, **17**, 223 (1962).
17. G. Hetherington and K. H. Jack, *Phys. and Chem. Glass.*, **3**, 129 (1962).
18. G. O. Brunner, H. Wondratschek, and F. Laves, *Z. Elektrochem.*, **65**, 735 (1961).
19. G. C. Pimentel and A. L. McClellan, "The Hydrogen Bond," p. 101, W. H. Freeman and Co., (1960).
20. H. Tsubomura, *J. Chem. Phys.*, **24**, 927 (1956).
21. Cit. (19), pp. 86 and 102.
22. R. T. Sanderson, "Chemical Periodicity," p. 39, Reinhold Publishing Co., New York (1962).
23. K. H. Beckmann, *Surface Sci.*, **3**, 314 (1965).
24. Cit. (12), p. 262.

Video Display of X-Ray Images

I. X-Ray Topographs

Eugene S. Meieran

Research and Development Laboratory, Fairchild Camera and Instrument Corporation, Palo Alto, California 94304

ABSTRACT

This paper discusses in detail the direct viewing of x-ray topographs via a secondary electron conduction (SEC) vidicon system. The various geometries used to record large area topographs, the theoretical and experimentally obtainable resolutions, and the applications of the different geometries for obtaining information about the defects within crystals are illustrated. Finally, some qualitative comparisons of a practical nature are made with other video systems used for recording x-ray topographs.

Approximately thirteen years have passed since Lang first described the transmission x-ray topographic technique for studying nearly perfect crystals, the technique that now bears his name (1, 2). Subsequently, several hundred papers concerned with both theoretical and experimental aspects of Lang topography have been reported. However, although there have been numerous modifications to the technique for particular applications (3-5), Lang topography in most common use today remains essentially the same as when first introduced.

In Lang topography, a crystal oriented for diffraction from a set of crystal planes is translated or scanned through a narrow characteristic incident x-ray beam; an x-ray sensitive film fixed to the (moving) crystal and normal to the diffracted beam records the diffracted beam intensity as a function of translation position, and is the Lang topograph of the crystal. In the topograph, defects appear as dark images on a gray background, since the defective areas of the otherwise perfect crystal diffract more integrated x-ray intensity than do the surrounding perfect areas, during the scan of the crystal through the incident beam. The film used to record the topograph is generally a high-resolution nuclear tracking plate with a thick emulsion (for example, Ilford nuclear plates, emulsion L-4, 50 μm thick). However, in spite of this thick emulsion, the recording of a topograph requires a long exposure as well as film processing time; in general, several hours pass before a topograph of even a small crystal can be viewed. Faster films can be used with a significant reduction in exposure time; this results in lower resolution topographs that still require some exposure time as well as film processing time. Furthermore, the films must be enlarged photographically for viewing, since the Lang topograph is recorded at unit magnification.

X-ray topography has provided much valuable information about the defects within semiconductor crystals. This information is useful for showing the possible effect of defects on devices made from the crystals. However, due to the time delay before an x-ray topograph can be viewed, Lang's method has found its way into production or quality control use only on a limited basis, since for these purposes large numbers of topographs need to be taken and viewed within a short period of time. Often a permanent record of the topograph is not required; all that is

Key words: x-ray topography, Laue patterns, television systems, semiconductor crystals, crystal defects.

necessary is a go, no-go analysis of the topograph. Consequently, there have been several attempts by semiconductor manufacturers to develop rapid methods for imaging topographs via video display techniques. While the reports of these efforts are rather superficial, they have shown that there are several ways of converting an x-ray signal into an instantly viewable television image, with reasonable resolution. Although this resolution must be improved by at least an order of magnitude before it can compete (in resolution) with film recording, the results to date are nonetheless encouraging. A topograph that may require several hours to record and process on film may now be viewed instantly, with reasonable magnification. So far as contrast is concerned, the video display does not compare to film recording, since the dynamic range of the video system is limited compared to the best x-ray films. However, the contrast does compare favorably to some of the faster, lower resolution films.

Four different systems for displaying x-ray topographs on a television monitor have been described within the past year. These are the PbO plumbicon, used in conjunction with an extremely high intensity x-ray source (6), the silicon diode array (7, 8), the cascaded image intensifier (9), and the combination image intensifier-SEC vidicon camera (10). The latter three systems use conventional x-ray sources. Other x-ray vidicon systems used for converting x-rays to a television picture, used primarily for radiography or medical fluoroscopy, are not suitable for x-ray topography due to a lack of sensitivity to the low intensity diffracted x-ray beams, or to low resolution.

This paper discusses in more detail the SEC (secondary electron conduction) vidicon system reported earlier (10). Special attention is paid to details of the optical system and geometrical arrangements used, and to factors affecting image quality. Finally, examples of the application of the television system to the study of defects in silicon crystals are shown. In the following paper (Part II), use of the television system for the orienting of silicon wafers or crystals via transmission or back reflection Laue patterns is illustrated.

Imaging System

The imaging system described here consists of four major components: a standard x-ray tube supplying characteristic x-rays, a diffracting crystal mounted on an x-ray camera, an x-ray sensitive phosphor screen that converts the diffracted x-rays into a visible light image, and an L^3-TV (low light level television) system that transforms the optical image into a television picture displayed on a monitor. Each portion of this over-all system will have some effect on the quality of the final image, and will be discussed separately.

X-ray source.—Geometry.—There are three general geometrical arrangements for taking large area x-ray topographs, and each arrangement has different advantages, disadvantages, and geometrical resolutions.

First, a topograph may be taken in transmission or reflection geometry by using a small point focus x-ray source and a set of collimating slits, and scanning the crystal through the narrow beam in a direction parallel to the surface of the crystal. The collimating slits limit the diffracted beam to a single component of the $K\alpha_1$-$K\alpha_2$ doublet. In transmission geometry (the normal Lang technique), a second set of slits must be placed between crystal and film, which is scanned synchronously with the crystal, in order to prevent the transmitted direct beam from exposing the film. The scanning method has high resolution, since the x-ray focal spot is small, and the imaging phosphor or film can be placed reasonably close to the sample (11). The only inconveniences of this geometry are the necessity of scanning the crystal and film continuously during exposure, and the long exposure times. Virtually every crystal orientation can be imaged by this

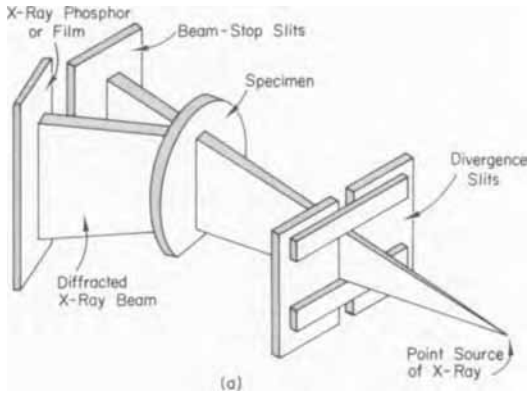

Fig. 1a. Schematic illustration showing geometry of x-ray topographic arrangement: scanning method using a point source of x-rays, transmission geometry.

arrangement, which is schematically shown in transmission geometry in Fig. 1a. This method may be slightly modified by holding the film stationary and scanning only the crystal at an angle ϕ with respect to the normal scan direction, *i.e.*, at an angle to the surface of the crystal. By choosing the appropriate angle ϕ, a width W on the crystal will expose a width W on the stationary film, giving an angularly undistorted large area picture (12). While the vertical resolution is not constant over the scan, since the crystal-to-film distance varies during the exposure, the fact that the film or other x-ray sensitive screen is stationary makes the technique valuable for high resolution direct viewing topography.

A point source of x-rays and set of collimating slits to limit the diffracted beam to the $K\alpha_1$ component are also used in the second arrangement. However, the sample geometry is selected such that the narrow beam of incoming x-rays impinges on the sample at a very shallow angle to the surface, and the diffracting planes and x-ray radiation wavelength are chosen to give diffraction angles 2θ of about 90°. Due to the shallow incidence angle, even the narrow beam illuminates a large area of the sample, which consequently need not be scanned through the incident beam (13). Since the diffracted beam is almost at right angles to the incident beam, the beam-stop slits are not necessary, and as an added advantage, the image of the surface is almost undistorted angularly, as shown in Fig. 1b. This geometry has high resolution and provides large area undistorted topographs of stationary crystals, and with relatively short exposure times. The major inconvenience of this method is that only particular x-ray wavelengths and crystal planes are usable; most common wafer orientations do not satisfy the geometrical conditions.

The third arrangement is to use a horizontal line source of x-rays, along with the geometry of Fig. 1a. Since an area of a wafer as wide as the line focus of

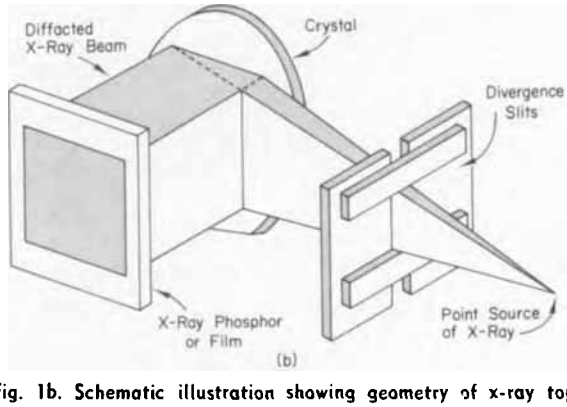

Fig. 1b. Schematic illustration showing geometry of x-ray topographic arrangement: stationary method using a point source of x-rays and a specially oriented crystal, reflection geometry.

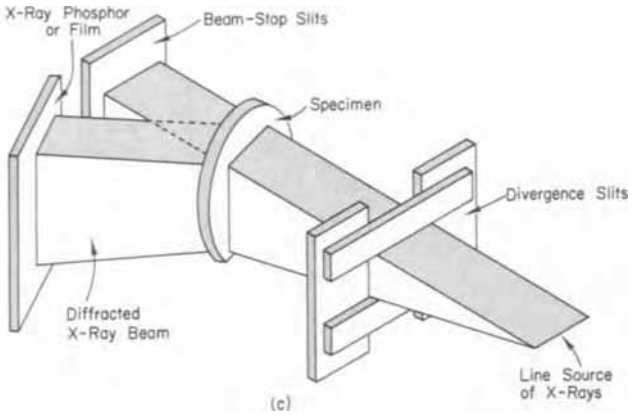

Fig. 1c. Schematic illustration showing geometry of x-ray topographic arrangement: stationary method using a line source of x-rays, transmission geometry.

x-rays is long can diffract at any instant, the sample does not have to be continuously scanned (14, 15); however, in order to examine a larger crystal, a simple mechanism for sample translation must be provided. This geometry can be used for transmission or reflection topographs of most common wafer orientations. The resolution of this method is poor compared to the previous methods, since, in general, the $K\alpha_1$ as well as the $K\alpha_2$ image appears and the x-ray detector must be placed far from the crystal in order to spatially separate direct and diffracted beams. The geometry of method 3 is shown in Fig. 1c.

These three geometrical arrangements are not completely distinct from one another; for example, methods 1 and 2 merge if the Bragg angle θ approaches 45° and the area of the crystal irradiated at any instant becomes large enough to display all the information desired. Similarly, methods 3 and 2 overlap if the Bragg angle is such as to give separate $K\alpha_1$ and $K\alpha_2$ images, irrespective of focal spot size.

For all work reported here, General Electric CA-7 Cu or Mo target x-ray tubes with a 1 mm spot or 1 mm x 10 mm line, were employed. The tubes were operated at 45 kV, 15 mA, with suitable $K\beta$ filters. The filters helped prevent stray ghost images which would strike the x-ray sensitive screen and contribute to background noise.

Resolution.—The geometrical resolution of x-ray topographs, arising from the finite size of the x-ray focal spot and divergence of the incident beam, can be separated into vertical and horizontal components (11). For a first approximation, the horizontal resolution is considered to be dependent only on the separation of the $K\alpha_1$-$K\alpha_2$ doublet and on the distance of the x-ray film from the crystal. If the $K\alpha_2$ component is suppressed, a geometrical horizontal resolution of about 2 μm results. However, if the $K\alpha_2$ component contributes to the image, double images of separation $D\Delta\theta_{1\text{-}2}$ are observed, where D is the distance of the imaging screen or film from the crystal, and $\Delta\theta_{1\text{-}2}$ is the angular separation of the $K\alpha_1$ and $K\alpha_2$ components. This gives an apparent resolution on the order of 40 μm, for most applications. (The true spatial resolution in a topograph containing double images due to the $K\alpha_1$ and $K\alpha_2$ components is still a few microns; however, for the purposes described here, the apparent resolution given by $D\Delta\theta_{1\text{-}2}$ will be used, since the double images appear as if a single smeared image.) The vertical resolution depends on the height h of the x-ray focal spot, the distance L of the crystal from the focal spot, and on D, and is given by $R = Dh/L$. For all geometries described above, h is generally small and L is large, and the vertical resolutions are on the order of a few microns.

For the first and second geometries above, the horizontal resolution is also on the order of a few microns, since the $K\alpha_2$ image is suppressed, the x-ray focal spot is small and is distant from the crystal, and the imaging screen or film can be placed close to the crystal. The third arrangement has low horizontal resolution due to the large D (on the order of 5 cm) and the wide beam divergence leading to the appearance of both $K\alpha_1$ and $K\alpha_2$ images; this point will be discussed later.

Table I. Resolutions of various x-ray geometries

	L, cm	Focal spot, mm × mm h	l	D, cm	Resolution, μm Vertical	Horizontal	2θ
Method 1							
(220) Si, Mo $K\alpha$, transmission	100	1	1	1	10	3	21°
	50	0.1	0.1	1	2	3	
(440) Si, Cu $K\alpha$, reflection	100	1	1	0.5	5	5	105°
	50	0.1	0.1	0.5	1	3	
Method 2							
(440) GaAs, Cu $K\alpha$, reflection	100	1	1	0.5	5	5	95°
	50	0.1	0.1	0.5	1	3	
Method 3							
(220) Si, Mo $K\alpha$, transmission	50	0.1	0.1	5	10	40	21°
(440) Si, Cu $K\alpha$, reflection	50	0.1	10	1	2	40	105°

Values of D, h, L, and approximate geometrical vertical and horizontal resolutions for the three geometries discussed are given in Table I, for some useful x-ray radiations and crystal reflections.

Crystal and camera.—The diffracting crystal and x-ray camera used have little effect on the resolution of the final image. The only requirement for the camera is that it have the movements necessary to allow the entire crystal to be aligned and imaged. For method 1, the camera must be a normal Lang camera, complete with precision scan system, precision incoming and direct beam-stop slits, and accurate specimen goniometer. For the second method, the beam-stop slits can be eliminated, and an accurate scan system is usually not necessary. For the third method, the precision incoming beam slits can be replaced by a simple slit, and only a rudimentary specimen holder is required. A sample scanner may be included in the latter two methods to allow large crystals to be imaged in their entirety; for example, most x-ray focal spots are only about 1 cm long and hence allow only a 1 cm topograph of perhaps a 7 cm wide crystal to be taken by arrangement 3. The sample scanner need not be very accurate; any simple slide mechanism will suffice, since a large portion of the crystal is visible at any one time.

Virtually all crystal reflections are suitable for methods 1 and 3, in both transmission and reflection geometries. Most commonly, {220} transmission topographs of (111) Si wafers are taken, using either Ag or Mo $K\alpha$ radiation. In reflection geometry, the {333}, {400}, {311}, and {440} reflections from (111) and (100) wafers are taken using Cu $K\alpha$, Fe $K\alpha$, or Cr $K\alpha$ radiation. For reflection geometry, the thickness of the crystal is immaterial, since only the first few microns near the surface contribute to the image. In transmission geometry, the crystal thickness t_o and x-ray radiation must be chosen to give $\mu_o t_o \sim 1$, where μ_o is the linear absorption coefficient of the crystal.

For method 2, only special reflecting planes can be used for (111) or (100) crystals, since both 2θ and the crystal position are restricted. Otherwise, the crystals must be cut to order, a somewhat inconvenient procedure that cannot be applied to production quantities of wafers.

X-ray sensitive phosphor.—In the system described here, the x-ray phosphor is the single most important component affecting final image quality. This phosphor must satisfy two conflicting requirements: it must transform x-rays into light with high efficiency, and

Table II. X-ray properties of experimental phosphors

Phosphor	Backing thickness, μm	Phosphor thickness, μm	I/I_0 Mo	I/I_0 Cu	I/I_0 Fe	Effective absorption, μ Mo	Effective absorption, μ Cu	Effective absorption, μ Fe	Resolution, μm	Light efficiency*
High resolution	250	230	0.3	0.1	<0.003	50	100	>260	20	1
Radelin FGC	375	330	0.2	<0.002	<0.002	50	>190	>190	50	9
PTG-2-9057	125	125	0.6	0.3	0.02	40	100	310	20	7
FGP-8X-007	125	75	0.65	0.2	0.01	60	210	600	50	10
FG-3M05-005	150	400	0.1	<0.001	<0.001	60	>170	>170	20	7
PTB-4-155-17	75	65	0.7	0.6	0.1	55	80	350	15	5
ZnS(Ag)	250	200	0.5	0.2	0.02	35	80	200	20	8

* 1 = bad, 10 = good.

it must have good resolution. For the former, thick phosphors are desired in order to absorb sufficient x-rays; for the latter, thin phosphors with small grain sizes are required. In all cases, the phosphor must be uniform in coating thickness.

In the present study, several types of phosphors have been examined. The one found most satisfactory was selected solely on the basis of experimentally observed resolution; the light output was boosted artificially if necessary by the SEC vidicon, by using long integration times. The resolution of all phosphors was determined by examining video displays of x-radiographs of fine wire meshes used as electron microscope grids; the best result obtained is from the U.S. Radium Corporation Radelin PTB-4-155-17, a blue-light emitting phosphor which actually showed a resolution of about 15 μm. This particular phosphor screen is about 65 μm thick, with a 10 μm grain size; it was coated on a 75 μm plastic backing. As will be seen, the phosphor resolution limits the final image resolution. All phosphors used were coated on the back with a flash of Al in order to reflect light back through the phosphor to the front side, light that would otherwise be lost. The phosphor side of the screen was placed facing the television camera, so that the x-rays entered on the screen through the aluminized back side.

A comparison of some of the experimentally available physical characteristics of several phosphors along with their measured resolutions and relative light emitting efficiencies are given in Table II.

Some comments are in order here concerning the properties of the fluorescent screens used in the present work. The properties listed in Table II were all experimentally determined; other properties that can be of interest, primarily phosphor grain size, were generally unavailable. The screens used were all commercially available, and while some attempt was made to obtain high resolution combined with good light output, no effort was devoted to improving screen quality experimentally. Consequently, the results discussed here are typical of the screens used, but probably could have been improved somewhat had special attention been paid to optimizing screens. None the less, the resolutions shown in Table II, which in many cases are surprisingly small fractions of the screen thicknesses, were observed experimentally. These resolutions were obtained using the x-ray tubes and operating conditions mentioned earlier. Unfortunately, the incident x-ray energies, which are known to affect screen resolution (16) were not determined.

L^3-TV system.—The television camera used here is a commercially available image intensifier-SEC vidicon combination L^3-TV.[1] The final image is displayed on a Sony 9-in. low persistence screen monitor for normal viewing, or a Conrac 15-in. long persistence screen monitor for recording via Polaroid film. The video system is unmodified from normal television operation except for the choice of optical lenses. The camera is equipped with automatic gain control in order to prevent burning of the SEC target or video screen.

[1] Quantex Corporation, a subsidiary of Commercial Electronics, Inc., Mountain View, California.

The video system takes the light image formed in the phosphor and transmits it via a system of optical lenses and fiber optic bundles onto the photocathode of an image intensifier. The electrons formed by the photocathode are accelerated by an electric field and are reconverted into a brightened light image as the output of the image intensifier; this intensified light image is transferred by a fiber optic faceplate to the input photocathode of an SEC vidicon tube. The electrons formed by this photocathode are accelerated, and impinge on an SEC target, which emits large numbers of secondary electrons for each incident high energy electron. Since the target is of high resistivity, it retains its resulting charge as a function of position, until it is neutralized by a scanning electron beam. The variation of stored charge as a function of position is sensed by the scanning beam and is electronically processed and transferred to a video monitor. The gain of the over-all camera is on the order of 10^5. A schematic diagram illustrating the operation of the SEC camera is shown in Fig. 2. Details of the operation of SEC tubes may be found elsewhere (17, 18).

The optical resolution of the televison camera portion of the over-all system is determined by the number of television lines per inch of displayed field. The input to the photocathode of the image intensifier is 0.6-in. high and is read out of the SEC vidicon using 525 lines. For a one-to-one image transferred from the phosphor to the input photocathode, a television line resolution of 0.6 in./525 ~ 30 μm results. If a different set of lenses is used to transfer a 0.3-in., twice magnified image to the input photocathode, the television line resolution becomes ~ 15 μm, and if a four-times magnified 0.15-in. image is transferred, the television line resolution is about 7 μm.[2] Consequently, a phosphor whose resolution is 15 μm can be read out on the television monitor by the proper choice of magnification lenses to give better than 15 μm television line resolution.

The light level of the phosphor is, of course, important, but for the purposes discussed here, with a high signal-to-noise ratio even for low intensity x-rays, does not appreciably affect resolution. The L^3-TV system is not noise-limited by the electronics, but by the x-ray statistics. For the low power x-ray tubes used in these experiments, x-ray quanta fluctuations are occasionally observed on the screen, but

[2] These calculated resolutions must be divided by the Kell factor (19) of about 0.7, in order to give measurable resolution. Hence the calculated resolutions above become about 43, 21, and 10 μm, respectively.

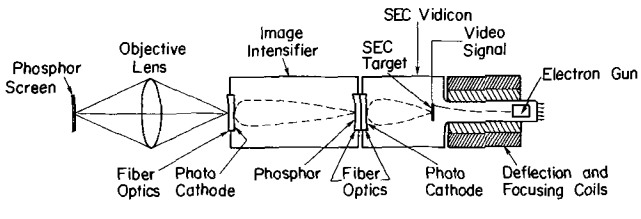

OPTICS AND ELECTRON OPTICS

Fig. 2. Schematic diagram showing operation of SEC camera

reasonable quality images can then be obtained by integrating the image, via a time exposure on the Polaroid film, or by allowing the SEC target to store information for longer times before readout. In general, for the photographs shown, total integration times of up to 1 min were required for Polaroid Type 55, ASA 50 speed film. The television image can be integrated and stored on a disk recorder and then played back

Fig. 3 a-d. Transmission topographs showing a microcrack in a Si wafer [$(2\bar{2}0)$ reflections from a (111) wafer]

Fig. 3a. Method 3, video display. Magnification 10X

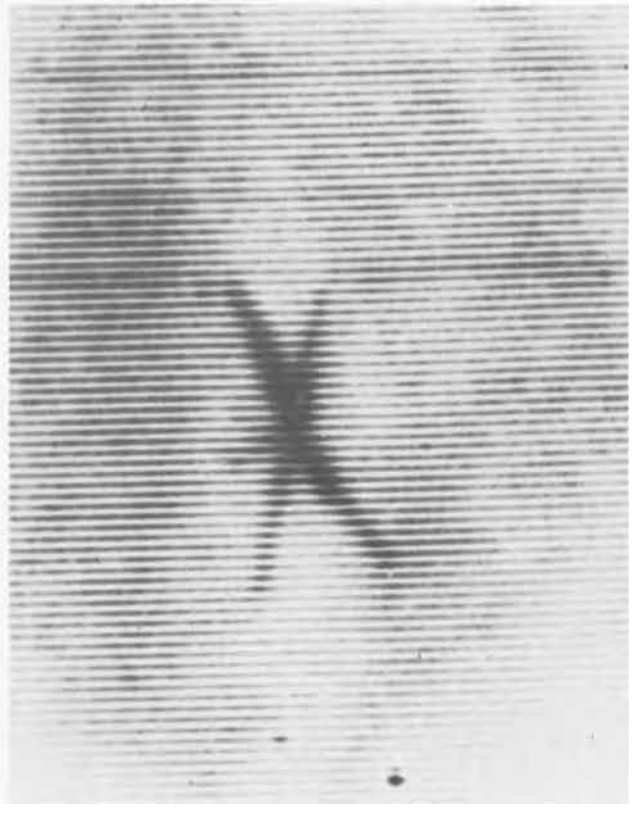

Fig. 3b. Method 1, video display. Magnification 25X

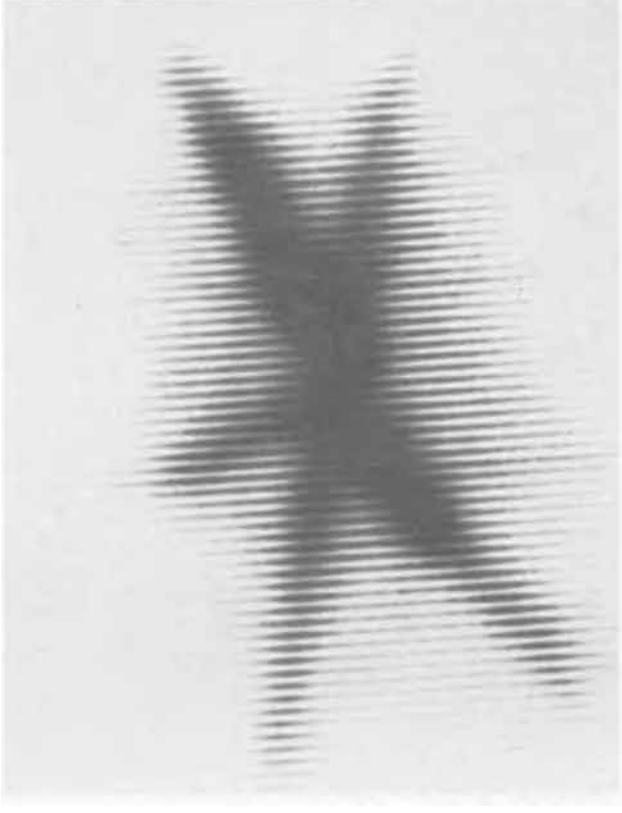

Fig. 3c. Method 1, video display. Magnification 50X

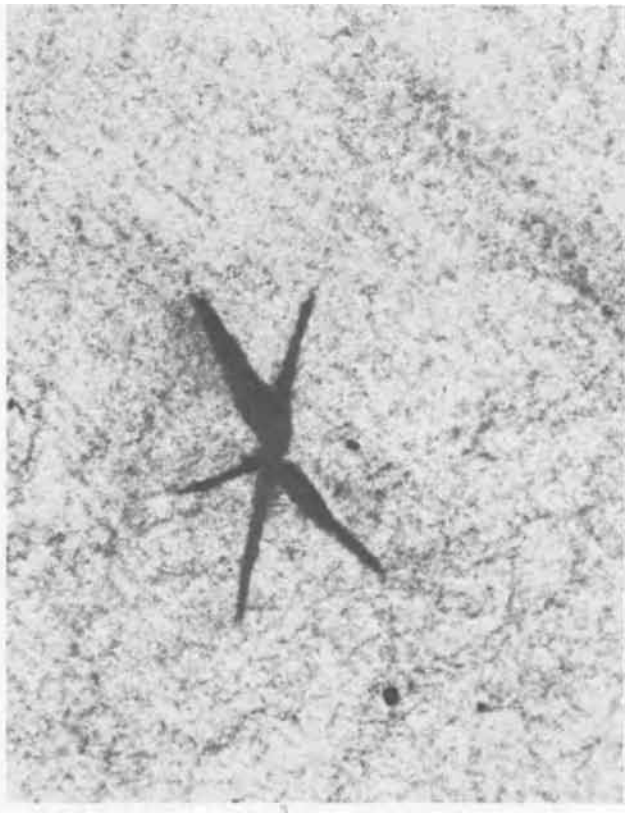

Fig. 3d. Method 1, dental film. Magnification 25X

Fig. 4. ($22\bar{0}$) video display transmission topograph, showing slip bands in a Si wafer, method 3. Magnification 12X.

continuously, eliminating the periodic flashes that would otherwise occur.

In order to gather sufficient light from the phosphor, high aperture lenses are used to transfer the phosphor image to the photocathode of the L^3-TV. For the one-to-one image, two back-to-back 50 mm f/0.95 lenses were used. For the two-to-one magnified image, either a 50 mm f/0.95-100 mm f/2 combination or a 25 mm f/1.4-50 mm f/0.95 combination was used. For the four-to-one magnification, a 25 mm f/1.4-100 mm f/2 combination was used. Better lenses are available; a 25 mm f/0.75 would provide considerably more light than the 25 mm f/1.4 lens actually used. In order to take topographs of large crystals, the various lenses can be reversed, giving two-to-one or four-to-one reduced images, covering larger fields of view with lower televison line resolution. More recently, fiber optic coupling of the phosphor screen to the input photocathode has been used, with a large gain in light collection. However, results quoted in the following sections were mainly obtained using the lenses rather than fiber optics, due to the restricted fields of view and magnifications available with presently available fiber optic bundles.

Results

Resolution, magnification, and field of view.—As discussed earlier, resolution and field of view are related, as is final image magnification. In order to observe a large 3-in. diameter wafer at one time, the 3-in. image height must be reduced to the 0.6-in. size of the first photocathode window; this is read off with 525 lines and displayed on any size monitor, with a television line resolution of ~60 μm. Hence, for this application, both the $K\alpha_1$ and $K\alpha_2$ components can be used to form the image, without affecting the resolution, and method 3 provides the best results. However, the image width viewable at any one time is restricted to about 1 cm, the length of the line focus of the x-ray tube, and the crystal is slowly scanned through the incident beam in order to observe the entire wafer.

With a resolution of ~60 μm, only gross defects such as microcracks or large dislocation arrays can be seen. Examples of both of these are given in Fig. 3a and 4, topographs taken by method 3. This type of topograph can only be used in production areas such as crystal growing, in order to sort out grossly imperfect wafers; the resolution is not satisfactory to be used for experimental Lang topography or to examine fine details. However, the resolution is sufficient to observe contrast asymmetries due to strain fields on opposite sides of oxide stripes on Si wafers (20, 21). Figure 5 shows a (220) video display topograph of a Si wafer containing several oxide stripes, with oxide thicknesses ranging from 0.1 to 1 μm. The contrast asymmetries of an oxide stripe as thin as 0.3 μm can

Fig. 5 a and b. Transmission x-ray topographs of a Si wafer strained by thin stripes of thermal oxide. Magnification 15X

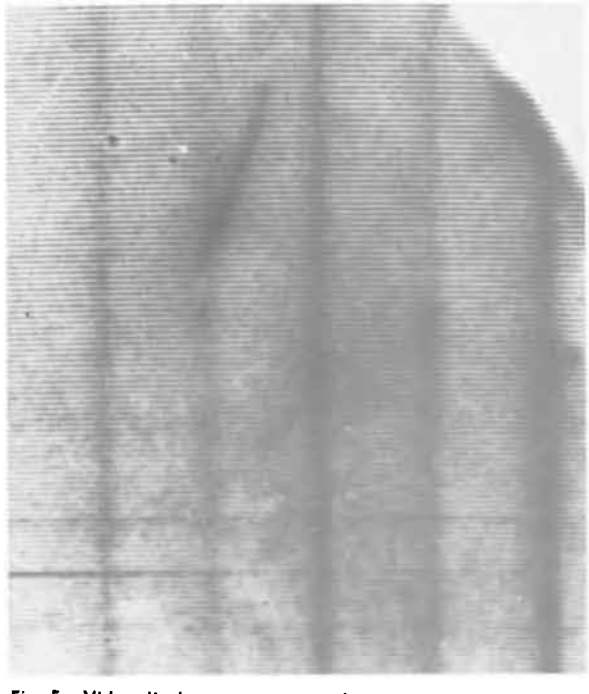

Fig. 5a. Video display x-ray topograph, method 3, nonscanning

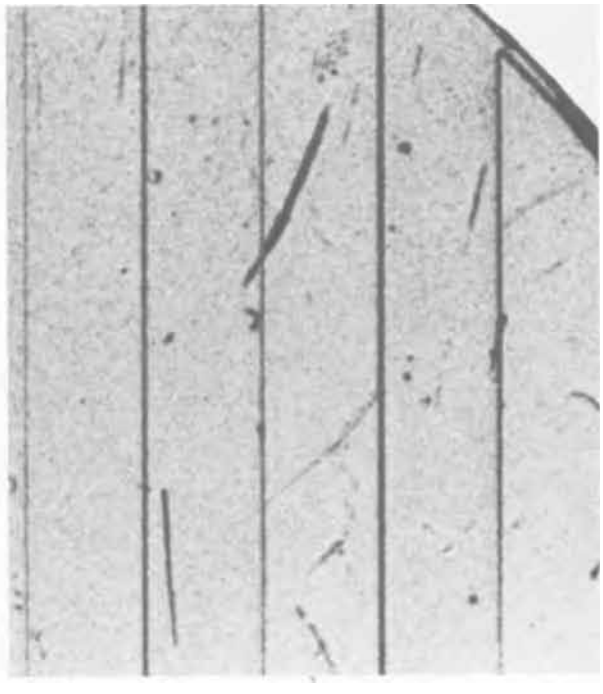

Fig. 5b. Dental film x-ray topograph, method 1, scanning

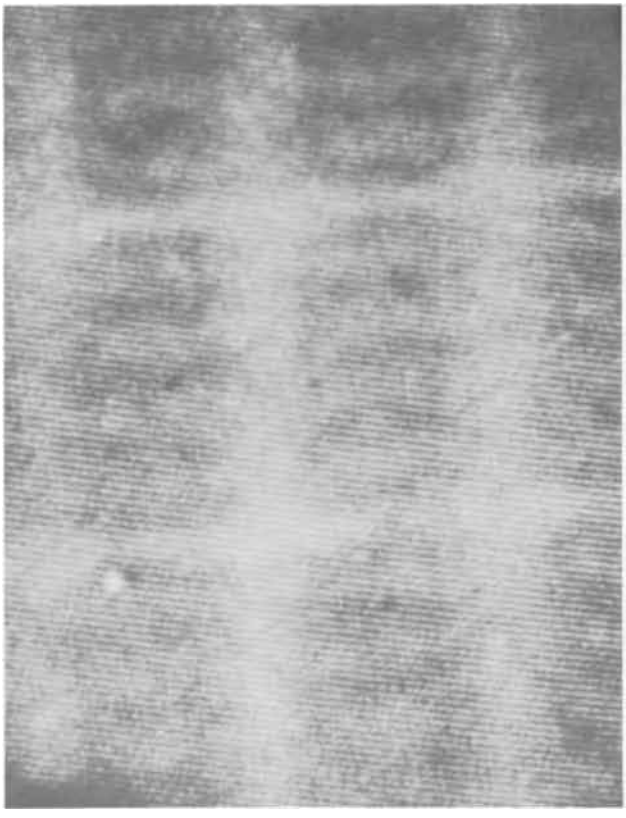

Fig. 6 a-c. Device pattern shown by video display reflection x-ray topograph [(440) reflections from a (111) wafer]. Fig. 6a. Method 3 (nonscanning) reflection geometry. Magnification 15X.

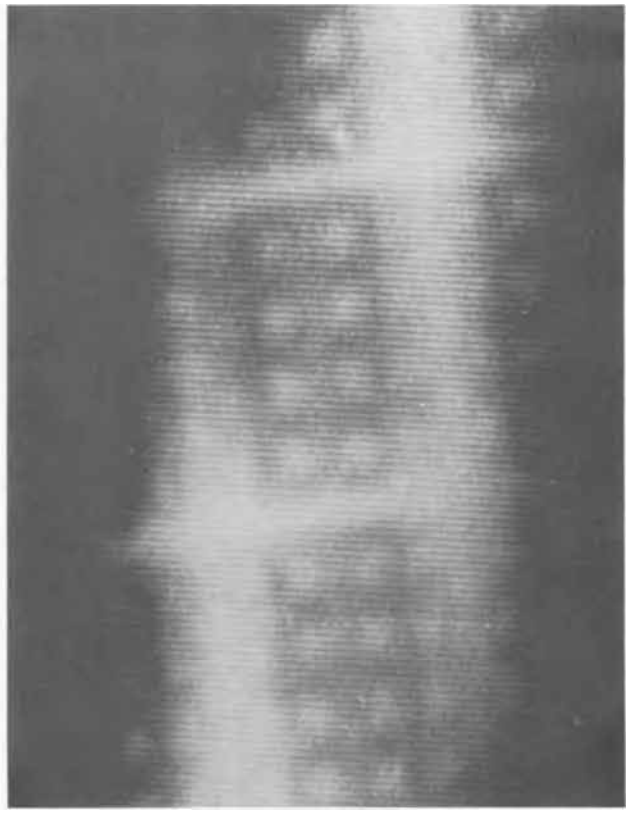

Fig. 6b. Method 1, nonscanning, reflection geometry. Magnification 15X.

be seen, even though the resolution is about 40 μm due to the combination of $K\alpha_1$ and $K\alpha_2$ images.

If the field of view can be restricted, *i.e.*, entire wafers need not be viewed, better resolution is obtainable. This is clearly shown in Fig. 3; the microcrack seen in Fig. 3a is shown at different magnifications and fields of view in Fig. 3b and 3c. Also included for comparison is a dental x-ray film topograph of the same area, taken by method 1, Fig. 3d.

When resolution better than that obtainable with the $K\alpha_1$-$K\alpha_2$ doublet is required, the $K\alpha_2$ component must be suppressed. Hence, method 3 becomes unusable, unless $K\beta$ radiation rather than $K\alpha$ radiation is used (22); this is sometimes impractical because strong $K\alpha$ images may overlap the weaker $K\beta$ image. On the other hand, if method 1 is used, as it was to take Fig. 3b and 3c, the image recorded at any instant is narrow due to the narrow incoming beam. The television camera itself can be scanned along with the crystal and integrated over the entire image (9), or the crystal only can be scanned at an angle to the diffraction vector (12), in order to obtain large area topographs. Also, narrow images themselves can be used, if they include the desirable information, Fig. 3d. A possible application of this type is in the imaging of section topographs (23); here, large fields of view are not required, but higher resolution is desirable.

As the magnification increases from Fig. 3a to Fig. 3c, the same amount of light is being spread over larger areas, and hence the x-ray intensity available becomes a critical factor. Figure 3a required about 1/10 the exposure on the Polaroid film that Fig. 3c required.

Another example of resolution *vs.* field of view is shown in Fig. 6. In Fig. 6a, a large area of a Si wafer with a device pattern is shown in reflection geometry. For the (111) Si wafer, Cu $K\alpha$ radiation, the {440} peak is at $2\theta = 107°$, so the diffracted x-ray beam is not quite perpendicular to the wafer surface. This angle is too great to obtain a large image via method 2, so method 3 was used. However, the $K\alpha_2$ component is then included and the image shown in Fig. 6a therefore has low resolution. If the $K\alpha_2$ component is suppressed by using a point source of x-rays, colli-

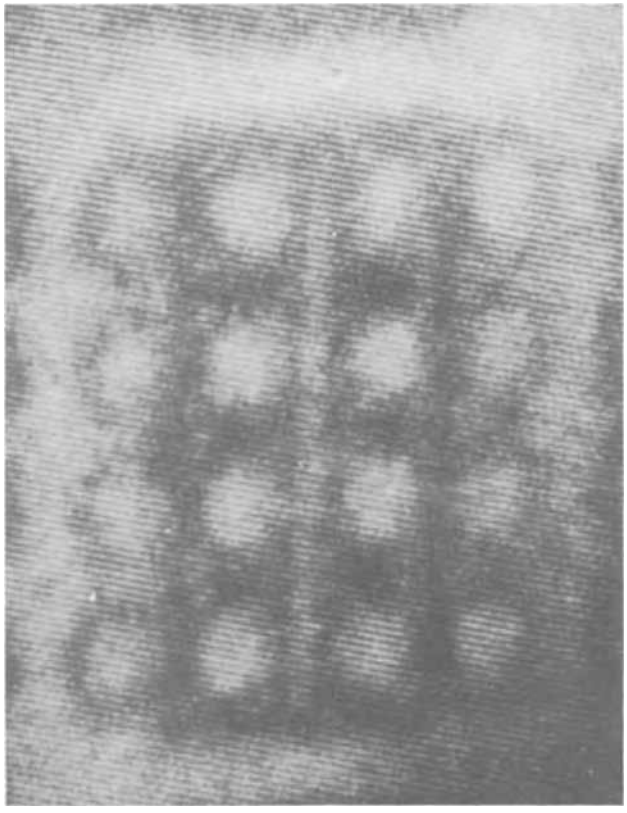

Fig. 6c. Method 1 (nonscanning) reflection geometry. Magnification 30X.

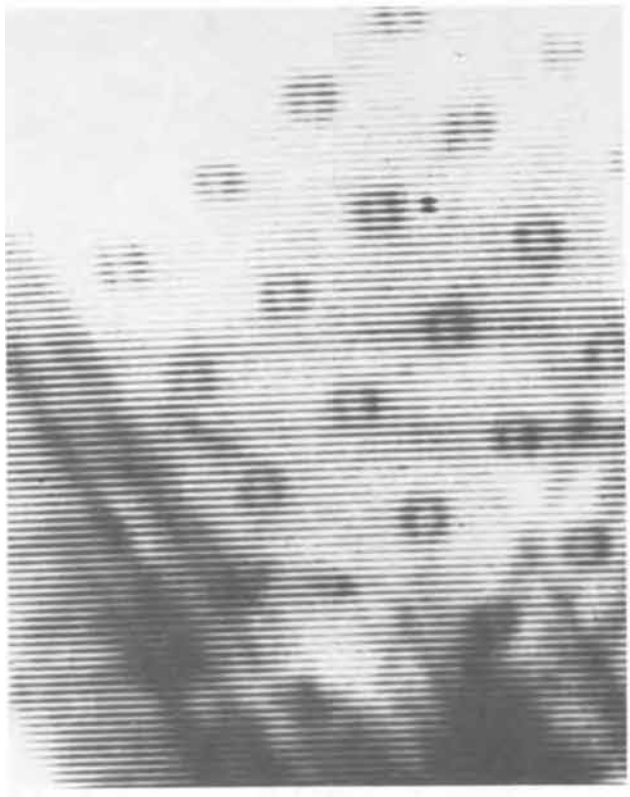

Fig. 7a-c. (111) Si wafer with diffused diode array [(440) reflection topographs]. Fig. 7a. Video display, nonscanning. Magnification 15X.

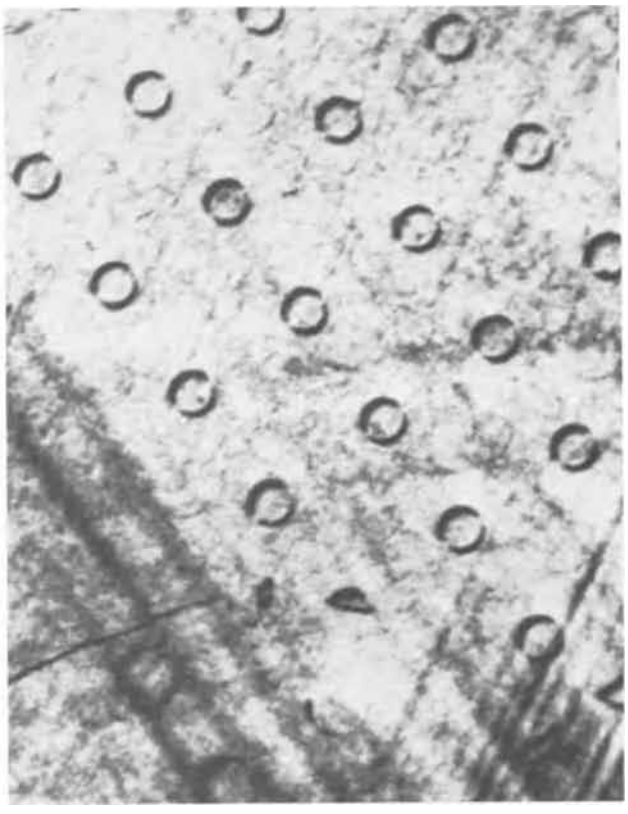

Fig. 7b. Dental film, scanning. Magnification 15X

mated by a divergence slit (method 2), the image appears sharper, Fig. 6b, but is much smaller in area. This image can then be magnified more on the television screen by selecting a different lens system, giving an enlarged view of a small part of the wafer, Fig. 6c.

A similar series of reflection topographs of a Si wafer is shown in Fig. 7; the contrast asymmetries arising from strain fields surrounding the boron diffused diodes are clearly visible (20).

The best examples of x-ray topographs are taken using method 2; these are the most convenient topographs to take since a stationary crystal is used and the television camera can be placed very close to the diffracting crystal. In addition, the diffracted beam can be limited to the $K\alpha_1$ component. However, as pointed out previously, only selected crystal reflections are usable. For example, {311} reflections from (100) Si or GaP are usable with Cr $K\alpha$ radiation, but there are no other very good reflections. With GaAs {400} Cu $K\alpha_1$ reflections from (111) or (100) crystals are obtainable, the intensities are high, the angles are ideal to give large area undistorted topographs without scanning, and the distance from the crystal to the television camera face can be less than 1 cm. For all the reasons given above, video display experimental x-ray topographs are most applicable to method 2; all conditions are favorable. Useful images of Si and GaP can be made with method 2 using reflections other than {311} (*i.e.*, nonscanning method 1) if the restriction of a narrow image and some angular distortion can be accepted.

Fig. 7c. Video display, nonscanning. Magnification 30X

Comparison with Other Video Systems

In comparison with other television systems for displaying x-ray topographs, the SEC vidicon has certain practical advantages, but also some disadvantages. For all practical purposes, the SEC vidicon is similar in operation and performance to Lang's cascaded image intensifier L^3-TV (9), so all comparisons made with the PbO plumbicon (6) and diode display (7, 8) apply equally well to his method. Some qualitative comparisons between the optical performances of SEC *vs.* a cascaded intensifier have been made by Emberson (24) and by Whitmell and Southon (25).

Field of view.—L^3-TV offers the only method whereby crystals larger in diameter than the x-ray window of the television camera can be imaged in

their entirety. Since optical lenses are used to transfer the image formed on the phosphor to the L³-TV window, virtually any size crystal can be displayed. Both the plumbicon and diode array camera read the information directly off the x-ray target, so the final image is restricted in size to that of the target window. The L³-TV can easily record a topograph of a 3-in. diameter crystal, while the other two methods are restricted to less than 1-in. diameter crystals.

Resolution, contrast, and magnification control.—The resolution of the L³-TV is at present limited by the x-ray sensitive phosphor. Since the optical image can be magnified (or demagnified) by the lenses to any desired size before it is focused on the input photocathode, the television line resolution can always be made better than the phosphor resolution, presently about 15 μm.

In the diode array, the ultimate resolution depends on the diode spacing, also about 15 μm. As new arrays are made, this resolution will be improved, to probably better than 10 μm. At high magnification, the image quality of the diode array is visibly better than that of the L³-TV, mainly due to better contrast. Comparison of resolution or contrast with the PbO plumbicon is difficult, since entirely different crystals, x-ray sources, geometries, etc., were used (6).

In the L³-TV, magnification is controlled by the choice of optical lenses. This system works well, so long as high aperture lenses are used. If interchangeable lenses are used for magnification control, provision must be made for focusing the lenses mechanically.

Magnification is easier to control in the diode array and plumbicon, since the magnification is determined electronically by varying the area of the target scanned by an electron beam. Since the image is displayed on a uniform-size screen monitor, the magnification is simply the ratio of the monitor screen size to the area of the target scanned. This also relates to resolution; the television line resolution in these two systems is determined by the number of scans per centimeter that are made by the electron beam on the target. Both the diode array and plumbicon can be zoomed electronically; zoom lenses can also be employed in the L³-TV system.

In the L³-TV, a 0.6-in. field is read off with 525 lines, as mentioned previously. This number of lines can be increased by perhaps a factor of 2 before other factors starting limiting resolution; for example, the fiber optics or SEC target (17). Hence, a one-to-one image can be read in the L³-TV with a maximum of $0.6/1050 \sim 15$ μm resolution. Therefore, direct imaging of x-ray topographs on the fiber optic input to the photocathode is impractical from a field of view viewpoint; the image cannot be magnified before it reaches the photocathode, and the resolution would be limited to about 15 μm, with a maximum field of view of 0.6-in. However, image intensifier-SEC vidicon systems with large input photocathodes can be used for imaging low resolution Laue patterns or fluoroscope displays directly on the input photocathode (26, 27). Also, use of fiber optic coupling from a phosphor to the input photocathode leads to significant advantages in light collection compared to lens coupling.

Sensitivity to x-rays.—In all television systems, the x-rays fall on some target, which transforms the x-rays into a signal which is electronically sensed and displayed as a television picture. The efficiency of the target depends on how much of the x-ray beam is absorbed by the target, and on how well the absorbed x-rays are converted into the proper signal.

In the L³-TV, x-rays are converted into visible light. As shown in Table II, the various x-ray wavelengths are absorbed differently by the assorted screens, and have different light output efficiencies. However, all screens emit sufficient light to be intensified and displayed, for the objective lens magnifications attempted.

For the diode array camera, soft x-rays are required, since the thin Si crystal into which the diodes are diffused is almost transparent to hard x-rays. The softer x-rays are absorbed reasonably well, the hard x-rays hardly at all.

This dependence on x-ray wavelength is reflected in the potential use of the various kinds of cameras. Soft x-rays are generally used for reflection topography, while hard x-rays are used for transmission topography. Hence, the diode array camera is best suited to reflection geometry, where it can provide instantaneous, good quality topographs of small areas of semiconductor crystal surfaces. The L³-TV is better suited to larger area transmission as well as reflection topographs, but can be used for higher resolution, smaller area topography as well.

Consequently, it appears that the L³-TV and diode array systems are complementary with some area of overlap, rather than directly competitive. L³-TV has certain advantages in some situations, while the diode array has advantages in other situations.

While it is difficult to directly compare the PbO plumbicon to the diode array or L³-TV, for reasons previously stated, it would appear that both systems would be useful for reflection or transmission geometry, since the PbO would absorb both hard and soft x-ray. However, the PbO system is limited due to its sensitivity; only extremely high intensity x-ray sources have been used (6).

Conclusions

On the basis of the foregoing, it is clear that instantaneous video display of x-ray topographs is possible, but that considerable room for improvement remains before the method becomes truly competitive with film techniques. It appears that perhaps two different types of television systems will be required in order to achieve the two ends of the topography spectrum: the high-resolution small field of view, and the low-resolution large field of view. The high resolution end seems to be covered at present by the diode array camera; however, this system is not sensitive to high energy Mo or Ag Kα x-rays. Consequently, the L³-TV system with its slightly lower resolution appears to be more versatile. On the large field of view end, the L³-TV has little competition from the diode array or PbO plumbicon systems discussed above, since any image size can be accommodated by proper choice of optical lenses. Most effort should be directed toward improving the phosphor for L³-TV, since this element has the largest effect on image quality. Lang (28) discusses this subject in some detail, and suggests that single crystal phosphors may provide better resolution than polycrystalline phosphors.

There are several obvious immediate applications for L³-TV. First, and most important from the point of view of experimental x-ray topography, the system can be used as an x-ray detector, replacing the scintillation or geiger counter, for aligning crystals in the Lang camera for subsequent film recording. Since the topograph can be viewed instantly unwanted ghost reflections and image inhomogeneities can easily be eliminated. Second, the system can be used in production for quality control to separate grossly imperfect wafers from reasonably good ones; high resolution is not necessary for this application. Similarly, the system can be used for low resolution topographical application, for example, observation of Moiré fringes (28) or double crystal "zebra" patterns (29). Third, the system can be used for Laue orientations of Si crystals; this subject is discussed in the paper that follows (Part II). With suitable improvement in the systems, however, video display of x-ray topographs may replace film techniques for many applications.

Acknowledgments

The author wishes to thank John Landre and Paul Mengers, of Commercial Electronics Corp., Mountain View, California, for providing the SEC camera used in this work, and for giving generously of their time and effort in endless discussions. He also wishes to thank Frank Masi, of the United States Radium Corporation, and Professor Andrew Lang, of the University of Bristol, for supplying the various x-ray sensitive phosphors. Finally my appreciation to Mike Callahan for his valuable laboratory assistance.

Manuscript submitted June 9, 1970; revised manuscript received Nov. 9, 1970. This was Paper 91 presented at the Los Angeles Meeting of the Society, May 10-15, 1970.

Any discussion of this paper will appear in a Discussion Section to be published in the December 1971 JOURNAL.

REFERENCES

1. A. R. Lang, *Acta Met.*, **5**, 358 (1957).
2. A. R. Lang, *J. Appl. Phys.*, **29**, 597 (1958); **30**, 1748 (1959).
3. G. H. Schwuttke, *ibid.*, **36**, 2712 (1965).
4. A. E. Jenkinson, *Philips Tech. Rev.*, **23**, 82 (1962).
5. K. Kohra and Y. Takano, *Japan. J. Appl. Phys.*, **7**, 982 (1968).
6. J. Chikawa and I. Fujimoto, *Appl. Phys. Letters*, **13**, 387 (1968).
7. A. N. Chester and F. B. Koch, *Adv. in X-ray Anal.*, **12**, 165 (1969).
8. G. A. Rozgonyi, S. E. Haszko, and P. L. Statile, *Appl. Phys. Letters*, **16**, 443 (1970).
9. A. R. Lang and K. Reifsnider, *ibid.*, **15**, 258 (1969).
10. E. S. Meieran, J. K. Landre, and S. O'Hara, *ibid.*, **14**, 368 (1969).
11. M. Hart, "Dynamic X-ray Diffraction in the Strain Fields of Individual Dislocations," Thesis, Bristol University (1963).
12. S. Kishino, Y. Sugita, and K. Kohra, *Japan. J. Appl. Phys.*, **6**, 1393 (1967).
13. J. K. Howard and R. D. Dobrott, *This Journal*, **113**, 567 (1966).
14. H. A. Carlson and H. A. Richard Wegener, *J. Appl. Phys.*, **32**, 125 (1961).
15. P. Skalicky, *J. Appl. Phys.*, **38**, 5426 (1967).
16. H. Kollmann and J. Dresner, *Phys. Rev.*, **114**, 71 (1959).
17. G. W. Goetze, in *Advan. in Electronics and Electron Physics*, **22A**, 219 (1966).
18. A. H. Boerio, R. R. Beyer, and G. W. Goetze, in *ibid.*, **22A**, 229 (1966).
19. "Television Engineering Handbook," p. 8-22, D. G. Fink, Editor, McGraw-Hill Book Co., New York (1957).
20. E. S. Meieran and I. A. Blech, *Phys. Stat. Solidi*, **29**, 653 (1968).
21. I. A. Blech and E. S. Meieran, *J. Appl. Phys.*, **38**, 2913 (1967).
22. G. Dionne, *ibid.*, **38**, 4094 (1967).
23. A. R. Lang, *Brit. J. Appl. Phys.*, **14**, 904 (1963).
24. D. L. Emberson, in *Advan. in Electronics and Electron Phys.*, **22A** 129 (1966).
25. D. S. Whitmell and M. J. Southon, *ibid.*, **22A**, 903 (1966).
26. G. W. Goetze and A. Taylor, *ibid.*, **16**, 557 (1962).
27. J. Adams, *ibid.*, **22A**, 139 (1966).
28. A. R. Lang, To be published.
29. M. Renninger, *Z. Naturforsch.*, **19a**, 783 (1964).

Video Display of X-Ray Images

II. Laue Patterns

Eugene S. Meieran

Research and Development Laboratory, Fairchild Camera and Instrument Corporation, Palo Alto, California 94304

ABSTRACT

The SEC vidicon system described in Part I has been adapted to display Laue orientation patterns. In this paper, the geometries of both transmission and symmetrical back reflection video display Laue patterns are illustrated.

Although Laue patterns have been used for many years for orienting single crystals via film techniques, only recently has it been possible to view them directly with image intensifiers or video system displays (1-4). These recent results have been due mainly to the development and improvement of low light level image intensification systems, generally for night vision applications.

The first Laue patterns so displayed were imaged directly from the fluorescent screen onto the intensifier photocathode and were then brightened sufficiently to be observed directly. Consequently, the patterns were generated in transmission geometry, since the x-ray tube itself would be in the way of the intensifier for back reflection geometry. Symmetric back reflection Laue patterns can be displayed only if high gain intensifiers are used, and if the Laue pattern can be transferred optically to the intensifier photocathode to provide room for the x-ray tube.

In Part I of this paper, an SEC (secondary electron conduction) video system capable of imaging low-intensity x-ray topographs was described. This same system is directly applicable to the display of both transmission and back reflection Laue patterns, since a large enough field of view to cover an entire pattern is optically transferred to an extremely high sensitivity television camera. To observe Laue patterns, the television camera is unmodified compared to normal television viewing or to topographic imaging, except for minor changes to the optical lens system. The camera is basically an L^3-TV (low light level television) camera which displays the image of a phosphor screen that has converted the x-ray signal into a visible light pattern (5). A schematic drawing of the system is given in Fig. 2 of Part I.

There are a number of reasons why direct display of Laue patterns is desirable (1, 2):

1. Detection of rapid phase changes or transient phenomena.
2. Identification of low-symmetry crystal Laue patterns, where large numbers of patterns must be taken to obtain correct orientations.
3. Remote display of x-ray patterns.
4. Low-cost display and storage via video tapes of very large numbers of patterns, where the cost of Polaroid film eventually becomes greater than the capital expenditure for the television camera.
5. Display of extremely large numbers of patterns, where the time required to take a film exposure becomes prohibitive.

Key words: x-ray topography, Laue patterns, television systems, semiconductor crystals, crystal defects.

As stated, Laue patterns are recorded on film in transmission geometry, or more commonly for semiconductor crystal growing industries, in back reflection geometry (6). For transmission geometry, the television camera needs no modification from topographic imaging, except for the proper choice of optical lenses to give the desired field of view. For back reflection geometry, the front end of the camera must be adapted to provide access for the x-ray tube. An asymmetrical back reflection Laue pattern can be taken without this adaptation (5); however, the resulting pattern is considerably distorted angularly, as seen in Fig. 1, and is difficult to interpret. The remainder of this paper is devoted to a qualitative description of transmission or symmetrical back reflection Laue display, since these geometries are used most often and are most convenient to interpret. Details of the theory and measurement of Laue patterns are not included, since they are adequately covered by textbooks such as ref. (6).

Geometry

Back reflection patterns.—A mirror is used in conjunction with the normal television camera optics in order to display an undistorted symmetrical back reflection Laue pattern. The geometry of this arrangement is shown schematically in Fig. 2a. The Laue pattern is first imaged on a phosphor screen which has been placed at right angles to the television camera axis and normal to the primary x-ray beam. A mirror with a small hole cut in it to allow passage of the primary beam is placed at 45° to the camera axis; this mirror reflects the Laue pattern through a demagnifying lens onto the television camera input photocathode. The collimator from a normal film Laue camera is used to define the x-ray beam; this collimator is about 8-cm long, in order to pass through the SEC camera front end, and has a pinhole diameter of 0.8 mm. The collimator passes through the mirror and also through the phosphor screen in order to cut down background fluorescence due to scattering from the air in the immediate vicinity of the screen.

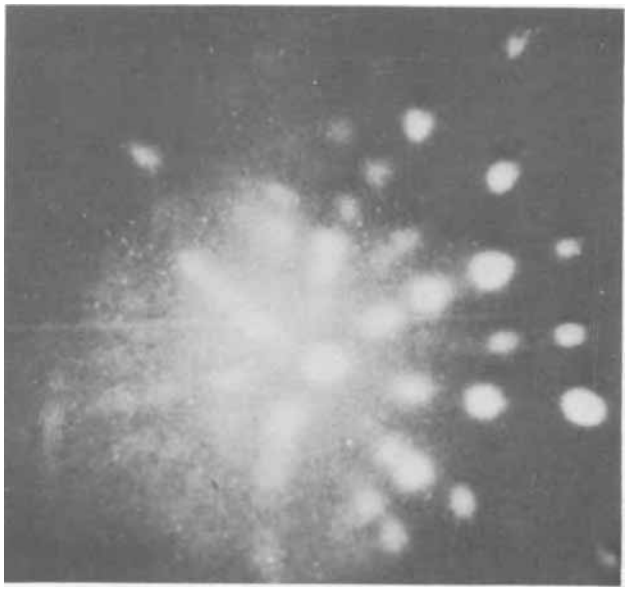

Fig. 1. Asymmetric back reflection Laue pattern

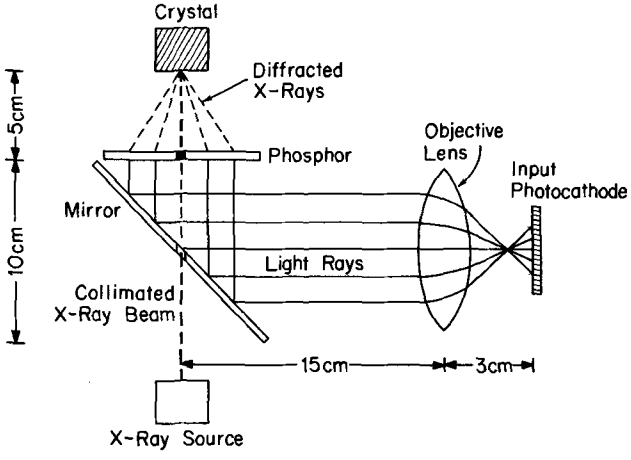

Fig. 2 a and b. Schematic diagrams showing geometry of direct display of Laue patterns. Fig. 2a. Symmetric back reflection geometry.

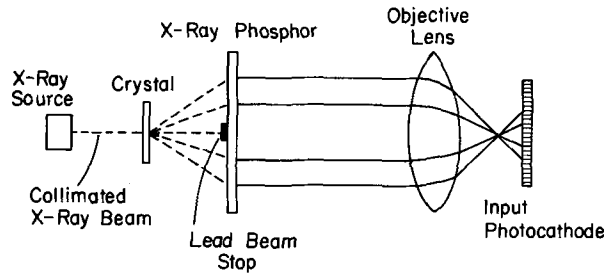

Fig. 2b. Symmetric transmission geometry

A normal Laue pattern is recorded at a distance of 3 or 5 cm from the diffracting crystal (6), and for general purposes, the same dimensions can be used for the video system display. The diffracted x-ray beams cover a total angular spread of about 50°, giving rise to a 6- or 10-cm wide Laue pattern, respectively. This width must be reduced to the 0.6-in. width (1.5 cm) of the input photocathode of the SEC camera; for the purposes described here, a single 50 mm f/0.95 lens was used. The approximate dimensions of the optical system are given in Fig. 2a.

A back reflection Laue pattern of a (111) Si crystal, recorded from a Sony 9-in. monitor, is shown in Fig. 3a. This pattern was integrated by the SEC camera for 10 sec before display; the image was stored on a disk recorder and then played back. Figure 3b shows a normal film Laue pattern for comparison, taken with the Polaroid XR-7 holder; it required 10 min of exposure. Both patterns were taken using a CA-7 W target x-ray tube, operating at 25 kV and 30 mA. Back reflection Laue patterns are useful for all crystal orientations, but are especially useful for crystals that are too thick to orient by transmission techniques.

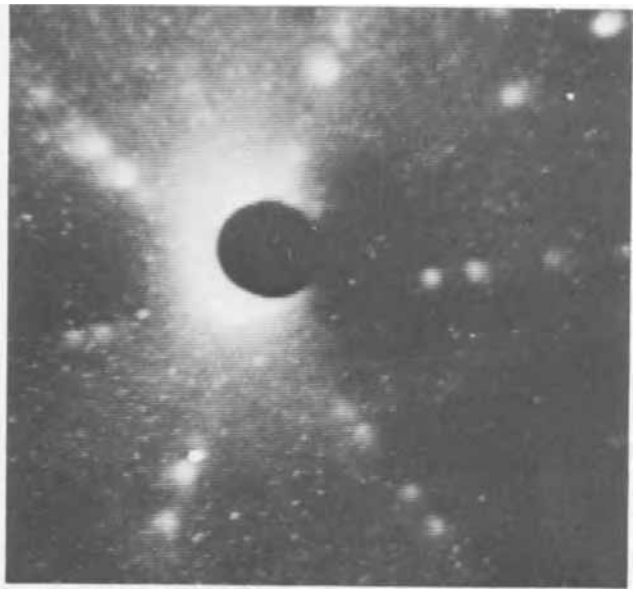

Fig. 3 a and b. Back reflection Laue patterns. Fig. 3a. Video display, 10-sec exposure.

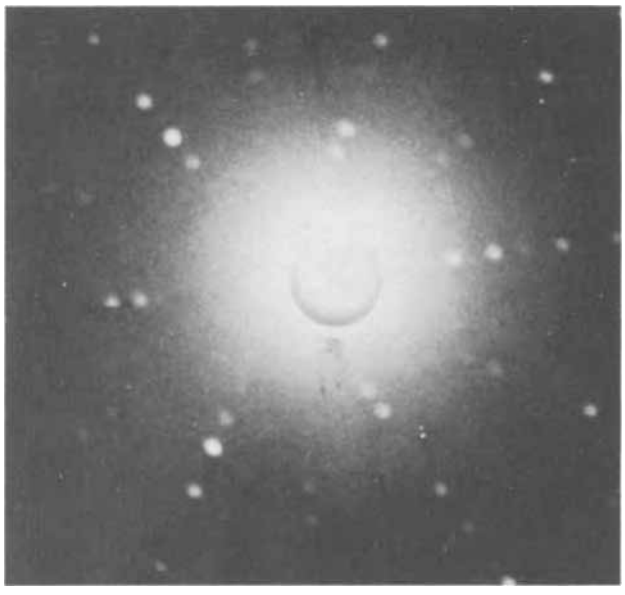

Fig. 3b. Film display, 10-min exposure

Transmission Laue patterns.—Transmission Laue patterns are taken using the geometry schematically shown in Fig. 2b. Since the direct x-ray beam transmitted through the crystal is so intense compared to the diffracted beams that it could burn the SEC target or television screen if the gain is set to allow viewing of the diffracted beams, it must be stopped from striking the x-ray phosphor. This is accomplished by using either a small lead beam stop, or by cutting a hole in the phosphor and trapping the beam behind it.

The transmission Laue patterns are useful for orienting single wafers, for example, to check out a wafer-sawing operation for accuracy. The dimensions of the system are similar to that of the back reflection technique; approximately 6-10 cm field of view is necessary, with a crystal placed 3-5 cm from the phosphor. A video display of a transmission Laue pattern of a Si wafer is shown in Fig. 4a, compared to the Polaroid pattern, Fig. 4b. The times of exposure for transmission geometry are about half that required for back reflection patterns.

X-Ray Sensitive Phosphor

The requirements for the x-ray sensitive phosphor used to image Laue patterns are substantially different from those needed for topography, described in the previous paper. Resolution is not as critical, since the original incident beam and Laue spot sizes are on the order of millimeters in diameter. Considerable light output by the phosphor is desirable and is obtained by using thicker screens. The most efficient screen of those tested that combines reasonable resolution with efficient light output is FG-3M05-005,[1] with the properties listed in Table II of Part I, although other screens are comparable. Much effort has been devoted to determining optimum phosphors for film and direct recording of Laue patterns (7-9); the results shown in this paper could probably have been improved if other phosphors had been used.

Measurement of Patterns

A 9-in. Sony monitor has an intrinsic magnification factor compared to the 0.6 in. diameter of the input photocathode window of $9/0.6 \sim 15$. Since the initial image formed on the phosphor is demagnified by about a factor of 5 by the optics, the final image on this monitor is about three times as large as a Polaroid film pattern recorded under the same conditions. Thus each Laue spot is about 3 mm in diameter.

[1] Supplied by the United States Radium Corporation, Morristown, New Jersey.

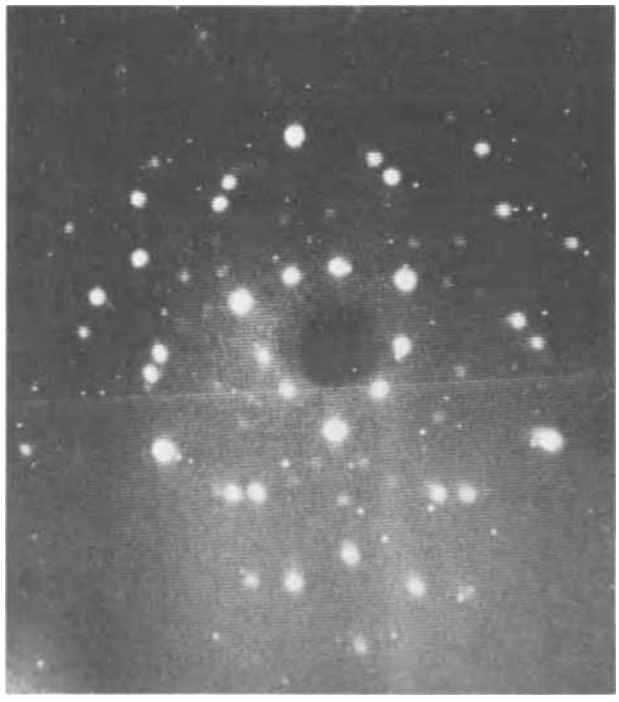

Fig. 4 a and b. Transmission Laue patterns. Fig. 4a. Video display, 2-sec exposure.

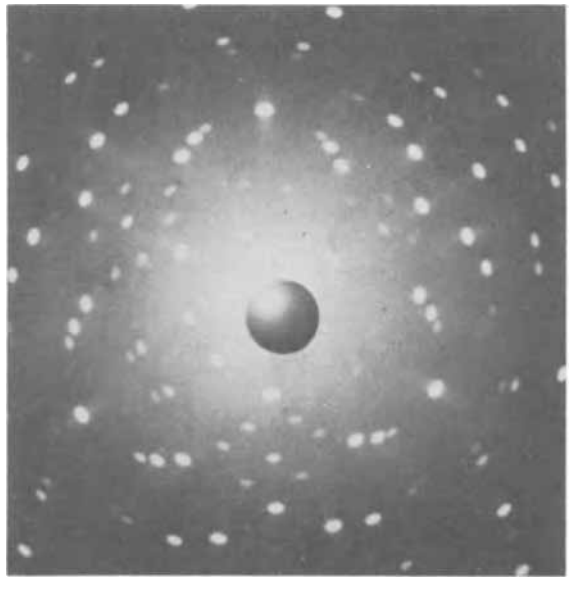

Fig. 4b. Film display, 4-min exposure

Measurement of the pattern to within 0.5° becomes measurement of the position of a Laue spot located at the edge of the pattern to within about 1 mm, one-third of the spot diameter. Often the Laue pattern is viewed in direct time, and corrections to the crystal orientation can be made visually. For less intense patterns, the image can be integrated for a short period of time and stored on a disk or tape; this pattern can then be displayed at will and measured.

Conclusions

L^3-TV is suited to the display of Laue patterns because of the use of optical transfer of the pattern to the input photocathode, the large field of view that can be obtained, the high light-sensitivity of the camera, and the capability of integrating the image for long periods of time before readout, if necessary. Since a significant capital expenditure for equipment is necessary, the system pays for itself in terms of the cost of Polaroid film and time savings only if large

numbers of patterns need to be taken. Although the quality of directly displayed Laue patterns does not yet compare to film recording, the speed of video display makes the method valuable for many applications.

Manuscript submitted June 9, 1970; revised manuscript received Nov. 9, 1970. This was Paper 91 presented at the Los Angeles Meeting of the Society, May 10-15, 1970.

Any discussion of this paper will appear in a Discussion Section to be published in the December 1971 JOURNAL.

REFERENCES

1. G. W. Goetze and A. Taylor, *Advan. in X-Ray Anal.*, **5**, 86 (1961).
2. G. W. Goetze and A. Taylor, *Adv. in Electronics and Electron Phys.*, **16**, 557 (1962).
3. S. W. Kennedy, *Nature*, **210**, 936 (1966).
4. K. Reifsnider and R. Green, Jr., *Rev. Sci. Instr.*, **39**, 1651 (1968).
5. E. S. Meieran, J. K. Landre, and S. O'Hara, *Appl. Phys. Letters*, **14**, 368 (1969).
6. B. D. Cullity, "Elements of X-Ray Diffraction," Addison-Wesley, Reading, Mass. (1956).
7. H. Herglotz, *Rev. Sci. Instr.*, **39**, 1658 (1968).
8. J. Beesley and D. J. Norman, *Advan. in Electronics and Electron Phys.*, **22A**, 565 (1966).
9. H. D. Stone, *Advan. in Electronics and Electron Phys.*, **22A**, 551 (1966).

Solid-Liquid Phase Equilibria for the Ternary Systems Li(F,Cl,I) and Na(F,Cl,I)[1]

Carl E. Johnson and Ellen J. Hathaway

Argonne National Laboratory, Argonne, Illinois 60439

ABSTRACT

The solid-liquid phase equilibria for the ternary systems Li(F,Cl,I) and Na(F,Cl,I) have been determined using thermal analysis techniques. The binary mixtures which make up the ternary system are all eutectic in nature. The diagram of the crystallization surface for each ternary consists of three areas, one for each of the pure components in the system. At the intersection of these three fields lies the minimum in the system; for the Li(F,Cl,I) system, a ternary eutectic of 11.7 m/o (mole per cent) LiF-29.1 m/o LiCl-59.2 m/o LiI melting at 340.9°C, and, for the Na(F,Cl,I) system, a ternary eutectic of 15.2 m/o NaF-31.6 m/o NaCl-53.2 m/o NaI melting at 529.4°C.

In searching for electrolytes suitable for use in energy conversion devices, criteria such as high conductivity, stability with respect to the anode metal, and low melting point have been applied. When using alkali metals as the anode, fused alkali halides generally meet these requirements. Experimental efforts have focused on the determination of the solid-liquid equilibria for ternary alkali halide systems suitable for use in cells employing either a lithium or sodium anode. The systems studied, Li(F,Cl,I) and Na(F,Cl,I), are simple eutectics with no apparent solid solution formation.

Experimental

Thermal analysis has been used to define the temperature-composition solid-liquid equilibrium characteristics in the binary and ternary mixtures. The thermal analysis apparatus used in this work has been described in detail elsewhere (1). Reagent grade lithium chloride and lithium iodide were purified by modification of the procedure described by Laitinen *et al.* (2) in which the anhydrous hydrogen halide was used to remove the last traces of water from the molten salt. The halide melting points were: lithium chloride, 606.8°C, and lithium iodide, 469.2°C. Single-crystal lithium fluoride, having a melting point of 848°C, was used without further purification. Reagent grade sodium fluoride, sodium chloride, and sodium iodide were heated to 130°C to drive off any moisture before use. The melting points of the pure reagents were: sodium fluoride, 990.0°C; sodium chloride, 801.0°C; and sodium iodide 659.3°C.

[1] Work performed under the auspices of the U.S. Atomic Energy Commission.

Key words: fused salts, eutectics, lithium halides, sodium halides, fused halide systems.

Temperatures were sensed with a Pt/Pt-10% Rh thermocouple, which was calibrated against NBS pure Zn (mp 419.5°C) and NBS pure Al (mp 660.0°C). The accuracy of the absolute value of the temperature was estimated to be ±0.3°C.

The amounts of the pure crystalline salts required for a given composition were weighed into a SS-347 sample capsule; all operations were carried out in a high purity helium atmosphere box. After being placed in the thermal analysis apparatus, the sample was heated to a temperature high enough to insure complete melting, and was held in the liquid state for about 1 hr. Preliminary cooling and heating cycles were then executed until reproducible first breaks in the cooling curves were obtained. Only then were complete cooling and heating curves recorded. Cooling rates were set in the range of 0.5-1 centigrade deg/min, thereby maintaining close control of the heat flow into and out of the sample. The sample composition was calculated from the weights of the pure materials; however, periodic checks were made by chemical analysis on selected samples. The above experimental melting points are in excellent agreement with the most reliable experimental data which is found in JANAF tables (3).

Except for the direct measurement of the melting point of pure sodium fluoride at 990.0°C, the upper experimentally measured temperature in the sodium systems was restricted to 850°C. This restriction was imposed primarily to conserve time, because it took about as long to heat the apparatus from 850° to 1000°C as it did to heat it from room temperature to 850°C. In all the systems studied, both binary and ternary, solid solutions were not observed for the mixtures in either thermal analysis or in x-ray diffraction analysis of selected solid samples.

Table I. Crystallization temperatures for the LiF-LiI system

Composition mole fraction LiI	Temperature, °C Liquidus	Solidus
0.000	848.0	—
0.100	822.2	411.3
0.200	798.7	410.2
0.275	779.9	411.5
0.350	755.3	411.7
0.450	709.8	411.3
0.550	652.0	411.2
0.650	583.9	410.8
0.700	547.5	411.0
0.800	448.1	411.1
0.835	410.9	—
0.849	416.2	411.5
0.900	436.6	410.4
0.950	455.2	409.4
1.000	469.2	—

Discussion

Temperature-composition data for the LiF-LiI binary system were obtained over the composition range of 10-95 m/o LiI. These data are given in Table I and in Fig. 1 where the other binary systems of interest here (LiCl-LiI and LiF-LiCl) are given for completeness. A eutectic composition of 83.5 m/o LiI in LiF melting at 410.9°C was observed.

The LiCl-LiI binary system was investigated by Johnson and Hathaway (4) and has a eutectic composition of 34.6 m/o LiCl in LiI melting at 368.2°C. The LiF-LiCl binary system was investigated by Haendler, Sennett, and Wheeler (5) who reported a eutectic composition containing 30.5 m/o LiF in LiCl melting at 501°C. These data have been confirmed by studies carried out in this laboratory.

Temperature-composition data for the NaF-NaCl, NaCl-NaI, and NaI-NaF binary systems are given in Table II and Fig. 2. In the NaF-NaCl binary system, a eutectic composition of 33.0 m/o NaF was observed melting at 680.4°C. Many investigators have studied this system, obtaining results which varied over an 8 centigrade deg range for the eutectic temperature and a 1.6 m/o range in composition. Plato (6) reported a eutectic temperature of 679.8°C at 34.6 m/o NaF; Rassonskaya and Bergman (7) obtained 674°C as the eutectic temperature at 33 m/o NaF; at a eutectic composition of 33.2 m/o NaF, Kuvakin and Kusakin (8) found the temperature to be 682°C.

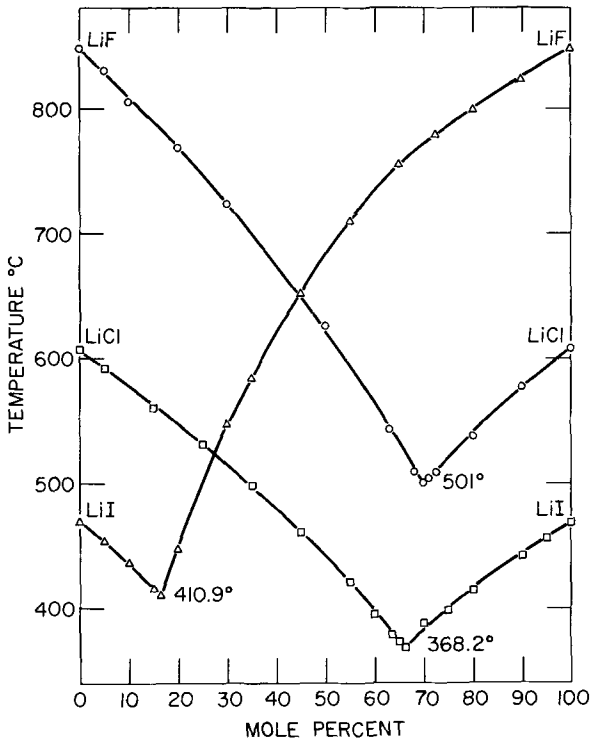

Fig. 1. Binary systems LiF-LiCl, LiF-LiI, and LiCl-LiI

For the NaCl-NaI binary system, we found a eutectic composition of 38.5 m/o NaCl melting at 572.9°C. Amadori (9) reported the eutectic temperature as 578°C at 37 m/o NaCl, and Ilyasov and Bostandzhiyan (10) published data giving the eutectic temperature as 585°C and the composition as 37.5 m/o NaCl.

Table II. Crystallization temperatures for the systems NaF-NaCl, NaCl-NaI, and NaI-NaF

NaF-NaCl Mole fraction NaCl	Temperature, °C Liquidus	Solidus	NaCl-NaI Mole fraction NaI	Temperature, °C Liquidus	Solidus	NaI-NaF Mole fraction NaF	Temperature, °C Liquidus	Solidus
0.000	990.0	—	0.000	801.0	—	0.000	659.3	—
0.350	858.5	679.1	0.150	755.1	572.4	0.050	643.4	596.6
0.450	804.0	681.5	0.300	706.6	573.2	0.150	609.5	597.3
0.600	720.0	680.5	0.400	671.1	573.2	0.185	597.1	—
0.650	683.2	680.6	0.500	634.0	574.4	0.250	661.1	597.0
0.658	693.4	680.7	0.525	615.1	572.5	0.350	742.8	597.3
0.667	680.4	—	0.550	602.2	573.1	0.450	808.6	597.4
0.670	680.5	681.4	0.575	592.1	573.0	0.550	855.8	597.4
0.682	685.7	681.1	0.575	589.0	572.9	1.000	990.0	—
0.750	712.3	680.2	0.600	576.2	574.0			
0.850	751.6	680.1	0.614	572.9	—			
1.000	801.0	—	0.631	576.6	573.0			
			0.650	581.1	572.9			
			0.699	594.7	573.1			
			0.750	605.1	572.5			
			0.800	519.0	572.6			
			0.900	638.3	572.3			
			1.000	659.3	—			

Table III. Crystallization temperatures for the system LiF-LiCl-LiI

Series I mole ratio LiCl:LiI 9:1 LiF mole fraction	Temp, °C	Series II mole ratio LiCl:LiI 7:3 LiF mole fraction	Temp, °C	Series III mole ratio LiCl:LiI 1:1 LiF mole fraction	Temp, °C	Series IV mole ratio LiCl:LiI 3:7 LiF mole fraction	Temp, °C	Series V mole ratio LiCl:LiI 1:9 LiF mole fraction	Temp, °C
0.000	577.3	0.000	513.3	0.000	439.8	0.000	388.2	0.000	442.3
0.100	543.2	0.100	482.5	0.050	428.1	0.050	370.9	0.100	411.0
0.200	508.3	0.150	466.7	0.100	417.8	0.100	380.2	0.200	444.1
0.250	489.1	0.200	453.8	0.150	398.8	0.150	383.2	0.300	542.1
0.300	501.1	0.250	471.6	0.225	459.6	0.200	439.0	0.482	667.9
0.350	544.3	0.300	513.8	0.300	531.2	0.300	533.1	0.500	678.4
0.400	579.6	0.400	589.3	0.400	598.0	0.400	606.4	0.600	737.6
0.500	638.9	0.500	650.8	0.500	666.3	0.500	668.7	0.700	766.3
0.600	691.8	0.600	700.3	0.600	719.8	0.600	720.5	0.800	796.4
0.700	737.3	0.700	745.0	0.700	753.5	0.700	761.2	0.900	821.9
0.800	775.3	0.800	782.5	0.800	786.5	0.800	791.4	1.000	848.0
0.900	811.8	0.900	814.2	0.900	816.5	0.900	818.2		
1.000	848.0	1.000	848.0	1.000	848.0	1.000	848.0		

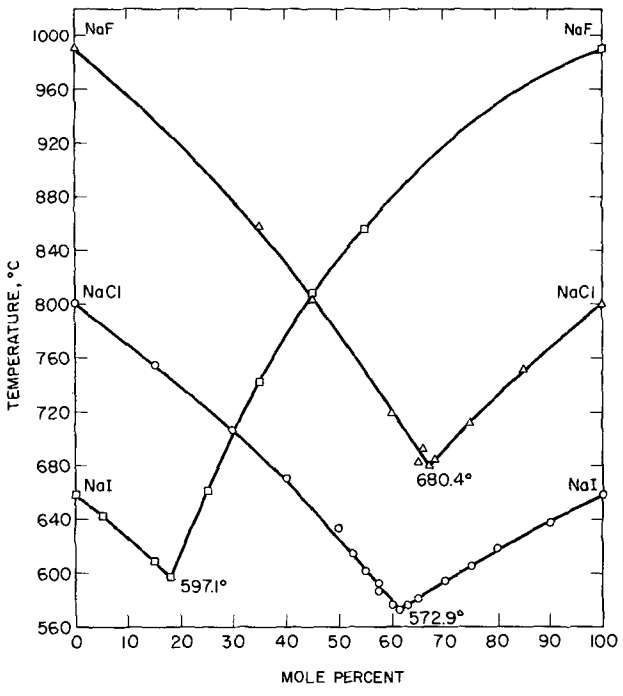

Fig. 2. Binary systems NaF-NaCl, NaCl-NaI, NaI-NaF

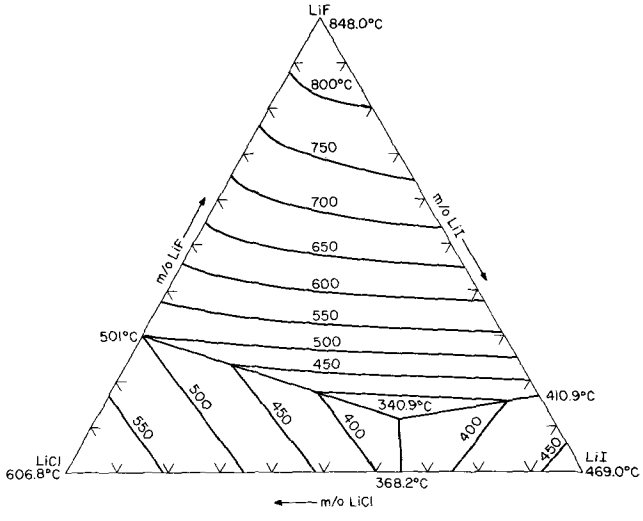

Fig. 3. LiF-LiCl-LiI ternary system

For the NaI-NaF binary system, we found a eutectic composition of 18.0 m/o NaF melting at 597.1°C. Ruff and Plato (11) reported a eutectic temperature of 620°C at a composition of 20 m/o NaF. Dombrovskaya (12) reported the eutectic at 603°C and 18 m/o NaF.

In characterizing the liquidus surface for the two ternary systems, Li(F,Cl,I) and Na(F,Cl,I), tempera-

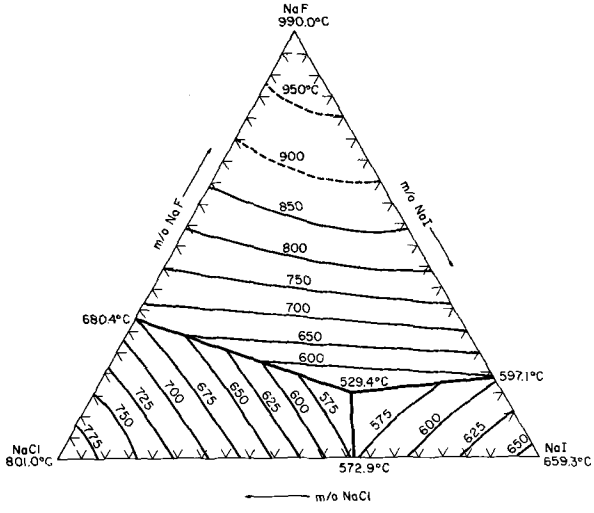

Fig. 4. NaCl-NaF-NaI ternary system

ture-composition data were obtained for various quasi-binary systems within each ternary system. For the Li(F,Cl,I) system, data were obtained for various LiCl:LiI mole ratios radiating from the LiF corner of the ternary field. The experimental compositions investigated and the equilibrium temperatures at which inflections and halts were observed are given as Series I to V of Table III. A contour diagram of the liquidus isotherms for the ternary system, given in Fig. 3, was constructed using the quasi-binary systems described in Series I-V. Similarly, for the Na(F,Cl,I) system, liquidus-solidus temperature data were obtained for various NaCl:NaI mole ratios radiating from the NaF corner of the ternary field and are given as Series VI-X in Table IV. An additional quasi-binary cross section, the 8.5:1.5 mole ratio of NaI-NaF, radiating from the NaCl corner was studied in order to describe more completely the area of the minimum temperature in this system. These data appear as Series XI in Table IV. A contour diagram of the liquidus isotherms for the ternary system, given in Fig. 4, was constructed from the quasi-binary systems described in Series VI-XI. The solid line isotherms are based on experimental data, while the dotted line isotherms result from extrapolations of the experimental data.

Inspection of the liquidus surface for both systems indicates that each is a simple eutectic with three fields of crystallization, one for each of the pure components in the system. The Li(F,Cl,I) system has a ternary eutectic with a composition of 11.7 m/o LiF-29.1 m/o LiCl-59.2 m/o LiI melting at 340.9°C, and, for the Na(F,Cl,I) systems, a ternary eutectic composed of 15.2 m/o NaF-31.6 m/o NaCl-53.2 m/o NaI melting at 529.4°C was found.

Acknowledgments

The authors wish to acknowledge the assistance of Myron Homa for x-ray diffraction analyses and the

Table IV. Crystallization temperatures for the system NaF-NaCl-NaI

Series VI mole ratio NaCl:NaI 1:4		Series VII mole ratio NaCl:NaI 2:3		Series VIII mole ratio NaCl:NaI 3:2		Series IX mole ratio NaCl:NaI 7:3		Series X mole ratio NaCl:NaI 4:1		Series XI mole ratio NaI:NaF 8.5:1.5	
NaF mole fraction	Temp, °C	NaF mole fraction	Temp, °C	NaF mole fraction	Temp, °C	NaF mole fraction	Temp, °C	NaF mole fraction	Temp, °C	NaCl mole fraction	Temp, °C
0.000	607.3	0.000	579.5	0.000	668.7	0.000	706.0	0.000	739.2	0.000	609.5
0.050	603.0	0.050	569.3	0.050	652.6	0.050	693.3	0.050	721.5	0.151	586.7
0.100	585.9	0.102	556.2	0.100	637.1	0.100	688.4	0.100	706.8	0.250	567.6
0.150	571.1	0.150	539.5	0.150	623.8	0.149	661.6	0.150	690.2	0.350	562.8
0.200	597.8	0.200	567.5	0.200	608.4	0.200	645.2	0.199	673.4	0.450	604.0
0.250	655.5	0.250	634.2	0.250	633.0	0.249	626.7	0.250	656.7	0.550	646.9
0.300	707.9	0.300	688.0	0.301	669.6	0.300	663.7	0.300	665.4	0.650	683.2
0.350	735.4	0.350	725.7	0.349	710.3	0.350	711.0	0.350	697.0	0.750	720.1
0.400	767.5	0.400	761.5	0.400	751.7	0.400	738.5	0.400	724.5	1.000	801.0
0.450	803.4	0.450	793.5	0.450	778.5	0.450	771.7	0.450	763.2		
0.500	835.5	0.500	821.5	0.500	805.8	0.500	803.6	0.500	803.2		
0.550	848.4	0.550	843.8	0.550	835.5	0.550	828.3	0.550	820.0		
1.000	990.0	1.000	990.0	0.600	855.2	0.600	852.3	0.600	844.3		
				1.000	990.0	1.000	990.0	1.000	990.0		

encouragement of A. D. Tevebaugh and E. J. Cairns throughout this work.

Manuscript submitted Aug. 6, 1970; revised manuscript received Nov. 18, 1970.

Any discussion of this paper will appear in a Discussion Section to be published in the December 1971 JOURNAL.

REFERENCES

1. C. E. Johnson, S. E. Wood, and C. E. Crouthamel, *Inorganic Chemistry*, **3**, 1487 (1964).
2. H. A. Laitinen, W. S. Ferguson, and R. A. Osteryoung, *This Journal*, **104**, 516 (1957).
3. JANAF Thermochemical Tables, Dow Chemical Co., Midland, Mich. (1962).
4. C. E. Johnson and E. J. Hathaway, *J. Chem. Eng. Data*, **14**, 174 (1969).
5. H. M. Haendler, P. S. Sennet, and C. M. Wheeler, *This Journal*, **106**, 264 (1959).
6. W. Plato, *Z. Physikalische Chem.*, **58**, 350 (1907).
7. N. S. Rassonskaya and A. G. Bergman, *J. Gen. Chem. USSR (English Transl.)*, **33**, 11 (1953).
8. M. A. Kuvakin and P. S. Kusakin, *Russ. J. Inorg. Chem. (English Transl.)*, **4**, 1188 (1959).
9. M. Amadori, *Atti della reale accademia nazionale deu Lincei*, **21I**, 467 (1912).
10. I. I. Ilysov and A. K. Bostandzhiyan, *J. Gen. Chem. USSR (English Transl.)*, **26**, 2673 (1956).
11. O. Ruff and W. Plato, *Berichte*, **36**, 2357 (1903).
12. N. S. Dombrovskaya, *Izvest. Sektora Fiz.-Khim. Anal. Inst. Obshchei Neorg. Khim. Akad. Nauk. SSSR*, **20**, 127 (1950).

Technical Notes

Gas-Phase Etching of Silicon With Chlorine

J. P. Dismukes*,[1] and R. Ulmer

RCA Laboratories, Princeton, New Jersey 08540

Clean, smooth silicon substrates are of prime importance in achieving high quality epitaxial growth of silicon on silicon. For this purpose, *in situ*, gas-phase etching of silicon substrates at high temperatures with hydrogen halides has been extensively investigated (1-7). In contrast, very little work has been reported on etching of silicon with halogens, and the meager information available (1, 8) suggested that these reagents give only rough or preferentially etched surfaces. In this work, etching of silicon surfaces with dilute concentrations of chlorine in helium has been investigated over the temperature range 900°-1100°C, and the surfaces have been studied by scanning electron microscopy. The results showed that chlorine is a more efficient etch than HCl and gives smooth surfaces above 1000°C.

Experimental

Silicon wafers supported on a SiC-coated graphite susceptor were etched with chlorine in 10 l/min He carrier gas using the quartz chamber of 4 cm^2 cross section shown schematically in Fig. 1. The susceptor was heated by a 5 kW, 450 kHz, Lepel RF generator, and temperature was monitored by an optical pyrometer calibrated at the melting point of germanium, 937°C. In most cases the silicon wafers were <111> orientation, 8 mils thick, low resistivity p-type, and Lustrox polished.

To convert traces of oxygen in the Ultrapurity helium to water, the helium together with 0.1 vol % palladium-diffused hydrogen was passed through a Deoxo purifier containing platinum catalyst. The water and other trace impurities in the helium stream were removed in a series of two traps containing Linde 5A and Linde 13X molecular sieves cooled to liquid nitrogen temperature. Prior to etching, the thin oxide layer on the silicon was removed by heating in palladium-diffused hydrogen for 30 min at 1100°C. After switching to helium, etching was conducted for about 30 min at temperatures in the range 900°-1100°C, and

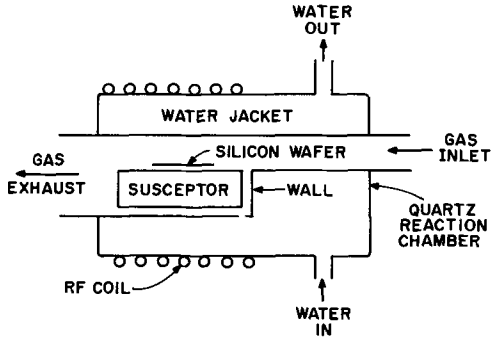

Fig. 1. Water-cooled quartz reaction chamber used for gaseous *in situ* etching of silicon.

etch rates were determined from weight loss using a balance sensitive to 0.01 mg.

The etched surfaces were first examined visually and by optical microscopy for gross features. To resolve features of surface morphology less than a few microns, the surfaces were studied using a scanning electron microscope operated in the emissive mode (9).

Results

Table I gives representative data for etching of silicon with chlorine in helium over the temperature range 900°-1100°C and as a function of concentration. These data show that the etch rate varies approximately as the first power of chlorine concentration over the range of conditions studied. The efficiency of the most probable etching reaction

Table I. Etching of silicon with Cl_2 in helium

Temp, °C	Concentration of Cl_2, %	Etch rate, μ/min	Surface appearance
1100	0.2	1.0	Smooth
1100	0.6	2.5	Rough, large steps
1040	0.2	0.87	Smooth
1000	0.2	0.73	Smooth
975	0.2	0.69	Smooth, small steps
900	0.1	0.25	Rough, large steps, pits
900	0.2	0.53	Rough, large steps, pits
900	0.4	1.3	Rough, large steps, pits

* Electrochemical Society Active Member.
[1] Present address: Laboratories RCA, Inc., 569 Badenerstrasse, 8048 Zurich, Switzerland.
Key words: silicon epitaxial technology, chemical kinetics, surface structure.

$$Si + Cl_2 \rightarrow SiCl_2 \quad [1]$$

is 2% at 900°C and 4% at 1100°C. A plot of the etch rate for 0.2% Cl_2 as a function of reciprocal temperature yields an apparent activation energy of +10 kcal/mole.

For 0.2% Cl_2 concentration, smooth, reflecting surfaces were obtained in the temperature range 1000°-1100°C. For higher concentrations of Cl_2 and at temperatures below 1000°C rough surfaces were obtained. As indicated in Table I, the roughness is due to steps and pits, examples of which are shown in Fig. 2 and Fig. 3, respectively, for a sample etched at 900°C with 0.2% Cl_2. The pits (Fig. 2) are about 5μ on an edge, while the steps (Fig. 3) are about 0.3-0.5μ in height and 3μ in width. In most experiments no other surface features were observed. However, in several experiments in which leaks occurred, the silicon surface was severely roughened and was covered with small particles of carbon, apparently due to the attack of the SiC susceptor by Cl_2 gas in the presence of oxygen (10).

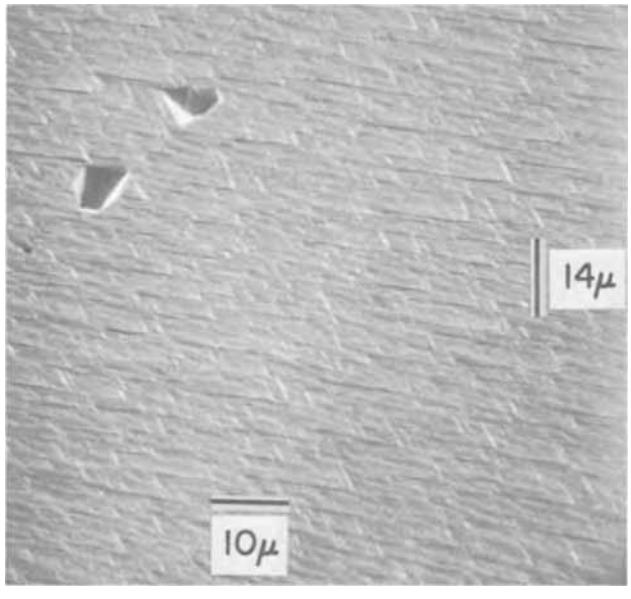

Fig. 2. Scanning electron micrographs at 45° incidence showing etch pits on a silicon surface etched with 0.2% Cl_2 at 900°C.

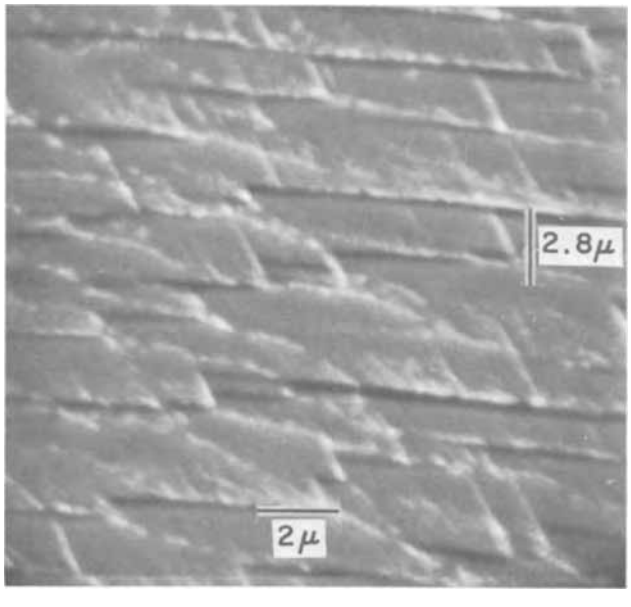

Fig. 3. Scanning electron micrograph at 45° incidence showing step pattern on a silicon surface etched with 0.2% Cl_2 at 900°C.

Discussion

The over-all kinetics in a gas phase reactor such as that shown in Fig. 1 can be quite complex, since the gas stream is not heated uniformly and since the residence time in the reactor depends on the gas flow velocity. Nevertheless, from experimental data it is often possible to distinguish one of the following three processes (11) as the rate-limiting step: (*i*) transport of the reactants to the reaction zone; (*ii*) diffusion of reactants and products to and from the reaction surface; and (*iii*) chemical reaction, which includes the separate steps of adsorption of reactants on the surface, reaction on the surface, and desorption of products from the surface. For large flow velocities such as employed here, case I can be neglected, so that the problem reduces to distinguishing between diffusion (case II) and chemical reaction (case III) as the rate-limiting processes.

The rate of gaseous diffusion (12) increases with temperature as T^n, where n is between 1.5 and 2, whereas the rate of etching increases with temperature approximately as T^4 in the temperature range 900°-1100°C. Therefore diffusion appears not to be rate limiting.

The calculated free energy change (13, 14) for the reaction in Eq. [1] at 900°C is −49 kcal/mole, in contrast to the observed activation energy of +10 kcal/mole determined from the data in Table I. This result indicates that Eq. [1] does not represent the rate-limiting step in the attack of silicon by chlorine gas, although it may well represent the over-all chemical reaction. But one of the elemental detailed steps (case III) of the total reaction could be rate limiting.

Conclusions

Chlorine is a more rapid and efficient etch for silicon than hydrogen chloride (7) between 900° and 1100°C, and gives smooth surfaces above 1000°C for concentrations $\leq$1% Cl_2. Preferential etching, characterized by pits and steps, occurs at temperatures below 1000°C. The rate-limiting process in the attack of silicon by chlorine appears not to be diffusion, but instead chemical reaction.

Acknowledgments

The authors are grateful to Dr. E. R. Levin for scanning electron micrographs.

The research reported herein was supported in part by the Air Force Materials Laboratory, Wright-Patterson Air Force Base, Dayton, Ohio 45433 under Contract No. F33615-68-C-1331.

Manuscript submitted July 13, 1970; revised manuscript received Dec. 16, 1970.

Any discussion of this paper will appear in a Discussion Section to be published in the December 1971 JOURNAL.

REFERENCES

1. G. A. Lang and T. Stavish, *RCA Rev.*, **24,** 488 (1963).
2. K. Beam and P. Gleim, *This Journal,* **110,** 2656 (1963).
3. T. L. Chu, G. A. Gruber, and R. Stickler, *ibid.*, **113,** 156 (1966).
4. L. V. Gregor, P. Balk, and F. J. Campagna, *IBM J. Res. Dev.*, **9,** 327 (1965).
5. W. H. Shepherd, *This Journal,* **112,** 988 (1965).
6. A. Reisman and M. Berkenblit, *ibid.*, **112,** 812 (1965).
7. J. P. Dismukes and E. R. Levin, Paper presented at the Atlanta Meeting of the American Institute of Chemical Engineers, Feb. 15-18, 1970.
8. J. G. Gualtieri, M. J. Katz, and G. A. Wolff, *Z. Krist.*, **114,** 9 (1960).
9. K. C. A. Smith and C. W. Oatley, *Brit. J. Appl. Phys.*, **6,** 391 (1955).
10. L. J. Haga and T. N. Tucker, Method of Etching Silicon Carbide, U.S. 3,398,033, Aug. 20, 1968.
11. S. Glasstone, K. J. Laidler, and H. Eyring, "The Theory of Rate Processes," pp. 369-370, McGraw-Hill Book Co., Inc., New York (1941).

12. W. Jost, "Diffusion in Solids, Liquids, Gases," p. 425, Academic Press, Inc., New York (1952).
13. C. E. Wicks and F. E. Block, "Thermodynamic Properties of 65 Elements-Their Oxides, Halides, Carbides, and Nitrides," Bureau of Mines Bull. 605, U.S. Government Printing Office, Washington, D. C. (1963).
14. H. Schäfer, H. Bruderreck, and B. Morcher, Z. Anorg. u. Allgem. Chem., 352, 122 (1967).

Mechanism of Cu_2O Tarnish Formation on Cu/30Zn: A $_{29}Cu^{64}$ Tracer Study

Stuart S. Birley and Desmond Tromans

Metallurgy Department, University of British Columbia, Vancouver 8, British Columbia, Canada

The mechanism of black tarnish film formation on the surface of alpha-phase copper-based zinc alloys immersed in either aqueous ammoniacal solutions of copper sulfate (pH ~ 7) or concentrated ammoniacal solutions containing dissolved copper is uncertain. It is generally agreed that the tarnish is composed primarily of Cu_2O (1-6). However, it is debatable whether or not the formation of Cu_2O proceeds by preferential dissolution of zinc accompanied by solid-state diffusion processes to produce Cu_2O (7), or whether both copper and zinc atoms are simultaneously dissolved with subsequent deposition of Cu_2O from solution (8). Recent kinetic studies on Cu_2O tarnish formation suggest that the mechanism involves dissolution of copper and zinc atoms followed by deposition of Cu_2O (5). The present work reports a more direct study involving the use of a radioactive copper tracer, $_{29}Cu^{64}$.

Experimental Procedures

The essence of the present technique involved the formation of Cu_2O on alpha Cu-Zn in the presence of an ammoniacal solution of copper sulfate containing $_{29}Cu^{64}$. Consequently, if Cu_2O formation entails dissolution of copper atoms from the alloy, and their subsequent deposition as Cu_2O, once these atoms enter solution they become chemically indistinguishable from the radioactive $_{29}Cu^{64}$ already in solution. Hence, Cu_2O formed by deposition should contain a mixture of both the normal copper isotopes ($_{29}Cu^{63}$ and $_{29}Cu^{65}$) and the tracer $_{29}Cu^{64}$, and should be measurably radioactive.

The tarnishing solution consisted of 0.04M $CuSO_4$ and 1.57M $(NH_4)_2SO_4$ with a pH of 7. This was of similar composition to that used in previous studies (4, 6). Two solutions were prepared, one containing the radioactive isotope $_{29}Cu^{64}$, and the second a control solution containing normal unirradiated copper. The radioactive solution was prepared by irradiating 1.27g of coiled copper strip (99.99% purity) for 1 min in a flux of 4.4×10^{13} thermal neutrons $\cdot$ cm^{-2} $\cdot$ sec^{-1} in the WR-1 Pneumatic Capsule Facility of Atomic Energy of Canada Ltd. The irradiated copper was subsequently dissolved in 63 cc of boiling 12.8M H_2SO_4 solution, the solution cooled, and neutralized with 104 cc of 15M NH_4OH. The volume of the resulting solution was raised to 500 cc by addition of distilled water and the pH adjusted to 7.0 by addition of 2M NH_4OH. All individual solutions were oxygenated prior to final mixing to prevent the aging and precipitation phenomena sometimes encountered in ammoniacal copper sulfate solutions (4, 9). The control solution was prepared in an identical manner except that the copper was unirradiated.

The alpha-brass employed for the studies consisted of Cu-29.38 w/o (weight per cent) Zn, and was of identical composition to that used previously (6). The actual specimens were in the form of squares of annealed strip 0.75 mm in thickness and 12 mm square. Prior to tarnishing the squares were degreased in trichlorethylene, cleaned in 45 v/o (volume per cent) HNO_3, washed in distilled water, and allowed to dry.

Tarnishing was conducted at room temperature in both the radioactive and control solution by placing 5 squares in a 150 cc aliquot of the active solution and 5 squares in a 150 cc aliquot of the control solution. Immersion time was 15 hr during which the solutions were stirred continuously. This procedure yielded tarnish films of 8μ thickness (as revealed by subsequent optical microscopy on sectioned specimens). After immersion, the tarnished squares were removed singly from the radioactive solution, agitated vigorously for 5 min in fresh distilled water to remove residues of solution, and allowed to dry. In the case of the nonradioactive control solution, 2 tarnished brass squares were removed, washed, and dried as before, and 3 brass squares were removed and further immersed for 5 sec in a 150 cc aliquot of fresh radioactive solution and again washed and dried in a similar manner. The further-immersion treatment allowed radioactive solution to penetrate any pores (1, 5) present in the Cu_2O tarnish and facilitated assessment of the residual radiation arising from entrapment of residues of radioactive solution within such pores. The 5 sec further-immersion treatment was of insufficient duration to produce appreciable growth of tarnish in the presence of the radioactive solution, as confirmed by subsequent comparison of the tarnish thickness with the 2 control specimens which did not undergo a further-immersion treatment.

All tarnished squares exposed to the radioactive solution were sealed in polythene bags and the intensity of the γ-radiation spectrum of $_{29}Cu^{64}$ determined for each specimen. The radiation was measured with a NaI scintillation detector, recorded autographically, and tabulated. The area beneath the low energy intensity peak of the γ-spectrum (*i.e.*, the integrated activity), corresponding to the 511 keV positron annihilation, was taken as a relative measure of the amount of $_{29}Cu^{64}$ present in the Cu_2O tarnish film. The 511 keV was chosen as this is the highest intensity peak in the spectrum and is more sensitive to measurement. The count corresponding to the area of the peak was corrected to a reference time as contingency for the different degree of radioactive decay in the tarnish films during the counting period.

Observations and Discussion

An example of the low-energy γ-spectrum peak for a specimen tarnished for 15 hr in the radioactive solution and an example of the same peak for a specimen immersed 15 hr in the nonradioactive control solution followed by 5 sec further immersion in radioactive solution are shown in Fig. 1. The γ-radiation intensity

Key words: ammoniacal, dissolution, deposition, irradiation, stress corrosion.

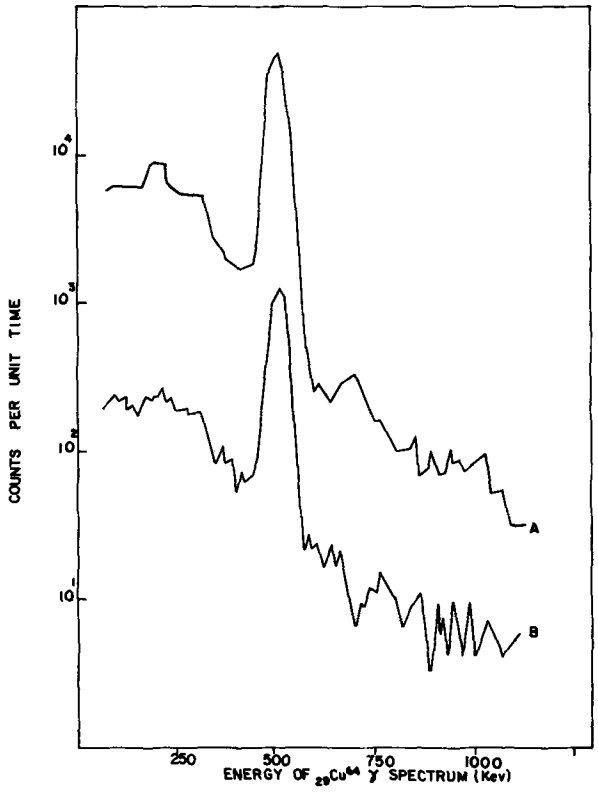

Fig. 1. An example (A) of the low energy γ-spectrum peak for a specimen tarnished for 15 hr in the radioactive solution, and an example (B) of the same peak for a specimen immersed 15 hr in the unirradiated control solution followed by 5 sec further immersion in radioactive solution.

(counts per unit time) is plotted on a log scale and it is readily seen that the area (integrated activity) beneath the γ-peak of the control specimen is considerably smaller than the area beneath the peak of the specimen exposed to the radioactive solution for 15 hr. This suggests that the activity of the latter arises principally from the presence of $_{29}Cu^{64}$ chemically combined in the actual Cu_2O tarnish and not from residues of $_{29}Cu^{64}$ solution entrapped in pores within the tarnish. The corrected areas beneath the γ-peak for all specimens are shown in Table I. It is seen that the integrated activity (counts per minute, c.p.m.) of the γ-peak for specimens tarnished 15 hr in the radioactive $_{29}Cu^{64}$ solution is ~40 times larger than the integrated activity of the γ-peak of the control specimens. Thus, the results suggest that the mechanism of Cu_2O tarnish formation on alpha-brass in the presence of aqueous-ammoniacal copper sulfate solutions involves the deposition of Cu_2O from solution. This has far-reaching implications in the field of ammoniacal stress-corrosion cracking of alpha-brass where Cu_2O tarnish films are believed to play a role (1, 2, 5-7, 10), because the kinetics of stress-corrosion cracking may now be considered in terms of the kinetics of the Cu_2O deposition process.

Table I. Activity of tarnished specimens

Tarnished specimens	Integrated activity of γ-peak (c.p.m.)
15 hr immersion in radioactive $_{29}Cu^{64}$ solution	
Spec. 1	2.4×10^6
Spec. 2	3.2×10^6
Spec. 3	2.5×10^6
Spec. 4	1.7×10^6
Spec. 5	2.5×10^6
	Average, 2.5×10^6
Control specimens	
Spec. 1	3×10^4
Spec. 2	7×10^4
Spec. 3	8×10^4
	Average, 6×10^4

c.p.m. = counts per minute.
Control specimen immersed for 15 hr in unirradiated tarnishing solution, followed by further immersion for 5 sec in radioactive $_{29}Cu^{64}$ solution.

Acknowledgments

The authors wish to thank the Canadian Defence Research Board for financial assistance under D.R.B. Grant No. 9535-50. Also, the authors wish to thank Dr. P. J. Dyne, Head of the Material Science Branch, Atomic Energy of Canada Ltd., Pinawa, Manitoba, for providing research facilities; Dr. T. T. Vandergraaf, of A.E.C.L. Pinawa, for his valuable assistance with the experimental work; and Dr. E. Peters, of the University of British Columbia, for suggesting a radioactive tracer study.

Manuscript submitted Oct. 19, 1970; revised manuscript received ca. Dec. 11, 1970.

Any discussion of this paper will appear in a Discussion Section to be published in the December 1971 JOURNAL.

REFERENCES

1. A. J. Forty and P. Humble, *Phil. Mag.*, **8**, 247 (1963).
2. A. J. Forty and P. Humble, "Environment Sensitive Mechanical Behaviour," A. R. C. Westwood and N. S. Stoloff, Editors, p. 403, Gordon and Breach, New York (1966).
3. T. P. Hoar and C. J. L. Booker, *Corrosion Sci.*, **5**, 821 (1965).
4. H. E. Johnson and J. Leja, *Corrosion*, **22**, 178 (1966).
5. J. A. S. Green, H. D. Mengelberg, and H. T. Yolken, *This Journal*, **117**, 433 (1970).
6. S. S. Birley and D. Tromans, Submitted to *Corrosion*.
7. E. N. Pugh, J. V. Craig, and A. J. Sedriks, "Proceedings of Conference on Fundamental Aspects of Stress Corrosion Cracking," R. W. Staehle, A. J. Forty, and D. van Rooyen, Editors, p. 118, N.A.C.E. (1969).
8. D. A. Vermilyea, *ibid.*, p. 152.
9. E. Mattsson, *Electrochim. Acta*, **3**, 279 (1961).
10. A. J. McEvily, Jr., and A. P. Bond, *This Journal*, **112**, 113 (1965).

Silicate Oxyapatites: New High-Energy Storage Laser Hosts for Nd^{+3}

R. H. Hopkins, G. W. Roland, K. B. Steinbruegge, and W. D. Partlow

Westinghouse Research Laboratories, Pittsburgh, Pennsylvania 15235

Materials with the apatite structure, space group $P6_3/m$, are widely used as fluorescent-ion hosts (1, 2). One of these materials, fluorapatite (FAP), $Ca_5(PO_4)_3F$, has the highest long-pulse efficiency and lowest threshold of any known Nd^{+3}-doped crystalline laser material (3), properties which are attributed to the broad absorption spectrum and unique site

Key words: optics, fluorescence, oscillator, rare earth, infrared.

symmetry of Nd^{+3} in the structure. The high gain of the FAP:Nd^{+3} laser, although beneficial in long-pulse and CW applications, severely limits its use in Q-switched operation, and for this reason we sought other apatite varieties in which the local ionic environment of the fluorescing ion (*e.g.*, Nd^{+3}) could be altered to enhance the energy storage capabilities while still retaining the high-efficiency characteristic of FAP.

We developed a series of new hosts, the silicate oxyapatites (4, 5). A general chemical formula for these compounds can be written $MeLn_4(SiO_4)_3O$, where Me is a divalent alkaline earth ion, Mg^{+2}, Ca^{+2}, Sr^{+2}, etc., and Ln is a trivalent rare earth ion, Y^{+3}, La^{+3}, Gd^{+3}, etc. Since a large fraction of the ions in silicate oxyapatites are trivalent, doping of these hosts with trivalent fluorescing ions should be appreciably easier than in the case of FAP where charge compensation must accompany rare earth substitution for calcium (6). We synthesized polycrystalline samples of various silicate oxyapatites doped with Nd^{+3} and other activators and grew single crystals of the more promising hosts by Czochralski pulling.

This paper describes the crystal growth, characterizes the quality of the early crystals, and presents typical physical, optical, and laser properties for the crystals. For the sake of brevity, we have chosen to discuss only the compounds $SrLa_4(SiO_4)_3O$ and $CaLa_4(SiO_4)_3O$ as representative members of the material class.

Reactant material was prepared from 99.99% purity rare earth oxides (American Potash and Chemical Co.) and standard Luminescent Grade alkaline earth carbonates (Mallinckrodt) weighed according to the stoichiometric formulas. The doping ion, *e.g.* Nd^{+3}, was substituted in oxide form for the rare earth host constituent, La^{+3}. Charges were melted by induction heating in an iridium crucible protected from oxidation by a flowing argon atmosphere. Silicate oxyapatites melt congruently and are therefore amenable to growth by the Czochralski method; the pulling apparatus we used is essentially that described by Mazelsky *et al.* (6, 7). It was suitably modified with zirconia refractories to support the high temperatures required for growth of $SrLa_4(SiO_4)_3O$ and $CaLa_4(SiO_4)_3O$ (melting points about 2180°C by uncorrected pyrometer reading). Crystals were pulled at rates between 1 and 5 mm/hr with crystal rotation in the range of 70-90 rpm. Crystals as large as 12.5 cm long x 0.64 cm diameter have been grown with Nd^{+3} doping levels as high as 3% of the total (Ca^{+2} + La^{+3}) sites in the structure.

Typical crystals grown in the *a* or c direction have poorly developed facets, and the crystal surfaces are somewhat wrinkled. This may be due to selective volatility of one of the components (8), and apparently does not seriously impair crystal quality. By comparing decay times for Nd^{+3} measured in polycrystalline samples of known composition with those measured for single crystals, as well as by chemical analysis, we place the value of effective distribution coefficient of Nd^{+3} in $CaLa_4(SiO_4)_3O$, K'_{Nd}, in the range 0.8-1.0.

Single crystals of $CaLa_4(SiO_4)_3O$ were studied by means of a Buerger precession x-ray camera using both MoKα and CuKα radiation. The only systematic absences are reflections of the type $000\underline{l}$ with $\underline{l}$ odd. The Laue class is $6/m$ and diffraction aspect $P6_3/*$ so that either $P6_3$ or $P6_3/m$ are possible space groups. $P6_3/m$ is chosen on the basis of etch pits (see below) which clearly show the presence of a mirror plane normal to *c* in the structure. The relative intensities of spots from single-crystal x-ray patterns confirm that this silicate oxyapatite is essentially isostructural with FAP, although it is unclear whether La^{+3} substitutes randomly or preferentially on either the CaI and CaII sites in the fluorapatite structure. Debye-Scherrer x-ray powder photographs from polycrystalline samples were indexed on the basis of a hexagonal cell with dimensions slightly larger than those of FAP. The lattice dimensions for $SrLa_4(SiO_4)_3O$ and $CaLa_4(SiO_4)_3O$ are $a = 9.645 \pm 0.003$Å, $c = 7.215 \pm 0.004$Å, and $a = 9.631 \pm 0.004$Å, $c = 7.133 \pm 0.004$Å, respectively.

We qualitatively evaluated the perfection of $CaLa_4(SiO_4)_3O$ crystals by studying etch pit arrays on chemically polished surfaces and by Twyman-Green interferometry with a He-Ne laser. Immersing crystals of $CaLa_4(SiO_4)_3O$ in a fused eutectic mixture of NaF and KF at 350°C produced smooth polished surfaces on both *a* and c faces, though the quality of polish was better on *a* faces. Etching crystals with *aqua regia* for 1-3 min revealed well-defined etch pits displaying the symmetry characteristic of the etched face. The etch pit density on the *a* face of crystals pulled in the c direction was about 6 x $10^4/cm^2$. Etch pits in FAP correspond to dislocation sites (9, 10) and, although we did not verify this for silicate oxyapatites, we assume the etch pit density is representative of the dislocation content. A Twyman-Green interferogram (Fig. 1) taken through 4.6 cm of a $CaLa_4(SiO_4)_3O$ crystal containing 3% Nd^{+3} (pulled at 5 mm/hr) shows approximately seven fringes across a 0.64 cm diameter. We consider that the crystal quality is quite good considering that the rapid growth rate promoted the formation of second-phase inclusions along the rod center. The circular nature of the fringes is not indicative of a "core" or facet defect, from which the crystals are apparently free, but is related to variations of dopant distribution about the centrally located inclusions. When viewing crystals in the optical microscope, we occasionally observed 3-5 μm sized particles having color and shape similar to iridium oxide flakes (11) which are often present in high-melting Czochralski-grown crystals.

We measured the spectroscopic properties of Nd^{+3} in polycrystalline and single-crystal silicate oxyapatite samples. Typically, the primary transition at 1.06 μm is 50-60Å broad, Fig. 2, and only slightly polarized with a π to σ ratio of about 1.3. The net radiative branching of $^4F_{3/2}$ into this transition is similar to that for FAP:Nd^{+3} which has a 6Å line width and $\pi/\sigma = 2.6$ (3). The lifetime of the $^4F_{3/2}$ state of Nd^{+3} in the silicate oxyapatites is 200-250 μsec at low dopant concentrations. Thus the peak gain per excited Nd^{+3} ion in $CaLa_4(SiO_4)_3O$:Nd^{+3} and $SrLa_4(SiO_4)_3O$:Nd^{+3} should be down by nearly an order of magnitude, and energy storage capabilities increased by the same factor, relative to FAP. Energy storage for Nd^{+3}-doped

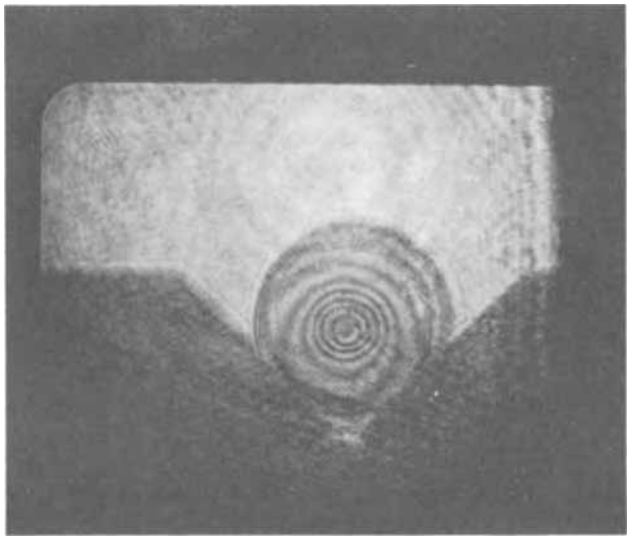

Fig. 1. Twyman-Green interference pattern observed with He-Ne laser traversing a 4.6 cm length of 3%Nd-doped $CaLa_4(SiO_4)_3O$. Crystal is 0.64 cm in diameter.

Table I. Comparison of long-pulse laser test data (298°K) for various Nd laser hosts

Laser material	Fluorescence peak (Å)	Fluorescence line width (Å)	Rod size (cm)	Distributed loss coefficient (cm^{-1})	Maximum slope efficiency, %	Threshold 99-99% Refl* (joules)
$CaLa_4(SiO_4)_3O$:3% Nd	10,613	~53	0.64 × 4.6	0.010	1.9	5.5
$SrLa_4(SiO_4)_3O$:2% Nd	~10,580	~53	0.43 × 7.5	0.016	2.1	3.2
FAP:2% Nd	10,629	6.6	0.64 × 3.8	0.045	1.53	2
YAG:1.5% Nd	10,637	7.1	0.64 × 3.8	0.017	1.05	3.3

* Both external mirrors had 99% reflectivity, peaked at 1.06 μm.

Table II. Physical and optical properties of Nd laser hosts

Property	$CaLa_4(SiO_4)_3O$:Nd	$SrLa_4(SiO_4)_3O$:Nd	FAP:Nd	YAG:Nd
Hardness				
Knoop (100g load)	857	—	540	1300
Moh	7	7	5.5	8
Melting point (°C)	~2180	2180	1644	1970
Refractive index				
(6328Å) n_o	1.8567	1.7915	1.634	1.83
n_e	1.8227	1.7637	1.631	—

silicate oxyapatite will also exceed that of YAG:Nd^{+3} but by a smaller amount than it exceeds FAP:Nd^{+3}.

Concentration quenching of Nd^{+3} fluorescence is relatively weak in the silicate oxyapatite specimens we have examined. For example, when 2% Nd^{+3} is added to a crystal, the $^4F_{3/2}$ lifetime in $CaLa_4(SiO_4)_3O$:Nd^{+3} is reduced by only 15% from the low concentration value. This fact, combined with the large value of $K'_{Nd^{+3}}$ in silicate oxyapatite, indicates that it is practical to obtain high laser slope efficiency in these materials by using high Nd^{+3} concentrations.

Our first laser tests of $CaLa_4(SiO_4)_3O$ and $SrLa_4(SiO_4)_3O$ have verified for the most part the behavior predicted from our spectroscopic data. The test setup and methods used here were the same as described in ref. (3), although it was not necessary to use an aqueous sodium nitrite solution to prevent the coloring of the silicate oxyapatite rods during testing. The results of long pulse tests on the first crystals grown and tested are summarized in Table I. No attempt was made to optimize the growth conditions or laser test setup to obtain these data. While it is difficult to draw direct comparisons due to the variation in laser rod diameter, doping level, and quality among the hosts, the high efficiency, relatively low threshold, and low loss coefficient for these early silicate oxyapatite crystals are evident. Preliminary tests indicate that the slope efficiency of these lasers is essentially the same in the long-pulse and Q-switched modes of operation.

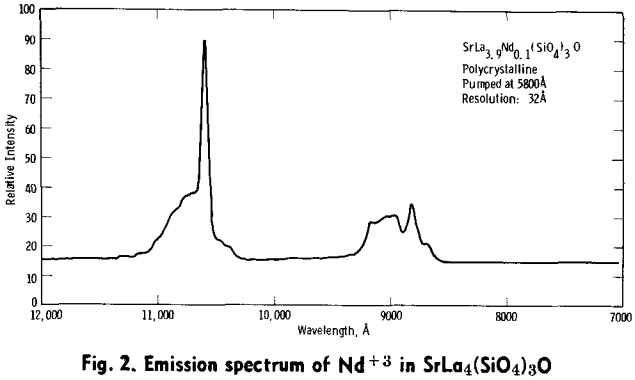

Fig. 2. Emission spectrum of Nd^{+3} in $SrLa_4(SiO_4)_3O$

Table II summarizes some of the other properties of the silicate oxyapatites, pertinent to laser performance, which we have measured to date. The indexes of refraction were determined by the normal incidence method on single-crystal wedges of the various materials. We find that the hardness of silicate oxyapatites lies between those of FAP and YAG, though closer to YAG. Silicate oxyapatites should, therefore, be much more resistant to distortion and fracture at high pump power levels than is FAP.

Acknowledgments

We would like to thank Mr. R. L. Remski, Air Force Avionics Laboratory, for performing the Twyman-Green analysis of our crystals; Dr. J. D. Feichtner for measuring the indexes of refraction; Mr. A. M. Stewart who contributed to all phases of the crystal-growth studies; and Mr. R. Perevuznik who carried out some spectroscopic measurements.

Manuscript submitted Oct. 29, 1970; revised manuscript received *ca.* Dec. 31, 1970.

Any discussion of this paper will appear in a Discussion Section to be published in the December 1971 JOURNAL.

REFERENCES

1. H. G. Jenkins, A. H. McKeage, and P. W. Ranby, *J. (and Trans.) Electrochem. Soc.*, **96**, 1 (1949).
2. P. D. Johnston, *This Journal*, **108**, 159 (1961).
3. R. C. Ohlmann, K. B. Steinbruegge, and R. Mazelsky, *Applied Optics*, **7**, 905 (1968).
4. J. Ito, *Amer. Mineralogist*, **53**, 890 (1968).
5. A. G. Cockbain and G. V. Smith, *Min. Mag.*, **36**, 411 (1968).
6. R. Mazelsky, R. C. Ohlmann, and K. B. Steinbruegge, *This Journal*, **115**, 68 (1968).
7. R. Mazelsky, R. H. Hopkins, and W. E. Kramer, *J. Crystal Growth*, **3, 4**, 360 (1968).
8. B. Cockayne and M. Chesswas, *J. Mat. Sci.*, **2**, 498 (1967).
9. R. H. Hopkins, *J. Crystal Growth*, **6**, 91 (1969).
10. G. M. McManus, R. H. Hopkins, and W. J. Takei, *J. Appl. Phys.*, **40**, 180 (1969).
11. B. Cockayne, M. Chesswas, and D. B. Gasson, *J. Mat. Sci.*, **2**, 7 (1967).

A Comparison of the Hole Mobility and Early Growth of Epitaxial Silicon on Flame Fusion, Flux, and Czochralski Spinel

G. W. Cullen* and C. C. Wang*
RCA Laboratories, David Sarnoff Research Center, Princeton, New Jersey 08540

Sapphire has been investigated more extensively than magnesium aluminate spinel as an insulating substrate material for the heteroepitaxial growth of silicon (1). This has been due more to the commercial availability of high quality flame fusion sapphire (2) than to the inherent properties of the two materials. The lattice match between the cubic spinel and cubic silicon is closer than the match between rhombohedral sapphire and cubic silicon (3-5), and the silicon epitaxially deposited on flame fusion spinel has proved to be less contaminated by substrate constituents than silicon deposited on sapphire (6).

The heteroepitaxial growth of silicon on spinel was initially demonstrated (5) on commercially available flame fusion spinel with a composition of $MgO \cdot 3.0\text{-}3.5Al_2O_3$. Material of this composition, however, is unstable at temperatures commonly employed during integrated circuit processing (7), and therefore the development of epitaxial silicon on the commercial flame fusion spinel was not pursued. The thermal stability of the flame fusion spinel has proved to be inversely proportional to the alumina content within the composition range $MgO \cdot Al_2O_3$ to $MgO \cdot 3.5Al_2O_3$ (7). Unfortunately, the ease of growth has proved to be directly proportional to the alumina content (7). A workable compromise between ease of growth and thermal stability has been established within the composition range $MgO \cdot 1.5Al_2O_3$ to $MgO \cdot 2.5Al_2O_3$ (7, 8), and relatively high hole mobilities have been realized in silicon deposited on this material (9-11). Flame fusion spinel within this composition range is not at present commercially available.

The stoichiometric ($MgO \cdot Al_2O_3$) flux grown spinel (12, 13) has also been investigated as a substrate material (14). A disadvantage to the use of the flux spinel is that it commonly contains constituents of the flux from which it was grown. Although methods have been developed for the removal of the impurities (14), the flux spinel has not been emphasized for silicon substrate use because of the inconvenience of using these procedures. Interest has recently been renewed in the flux spinel because the microwave attenuation in this material is lower than in other materials measured to date (15, 16). For a number of device applications, it would be advantageous to have epitaxial silicon on a microwave delay line material.

A number of investigators have reported on the Czochralski growth of stoichiometric spinel (17-19), and this material has recently been made commercially available (2). There is little information to be found in the literature, however, on the electrical properties of silicon on Czochralski spinel.

In this communication the magnitude of the hole mobilities before and after thermal oxidation and the nature of the film growth prior to complete coverage of the substrate are compared in silicon on flame fusion, flux, and Czochralski spinel. The characteristics of silicon on spinel are also compared with those of silicon on flame fusion sapphire.

Hole Mobilities in Silicon on Spinel

The hole mobility, which is highly dependent on both the crystallographic structure and the impurity content of the silicon films, has been used both as a means to compare the quality of the films epitaxially deposited on the various substrates and to anticipate the applicability of the films in device structures. The hole mobility is also a strong function of thermal treatment and film thickness. Therefore the mobility was measured in the as-deposited film and also after exposure to dry oxygen for 1 hr at 1100°C. This treatment is approximately equivalent to the total oxidation employed during the processing of an MOS transistor.

[While it is convenient and rapid to use the Hall mobility to monitor the film quality, this results in a pessimistic evaluation of the silicon films for use in MOS transistor structures. The field effect mobility of a completed MOS device is measured only in ~500Å of the silicon most remote from the silicon-substrate interface. In 1.5μ thick silicon on sapphire with hole mobilities ~30% of bulk, MOS field effect mobilities have been measured which are ~70% of the values measured in devices fabricated in bulk silicon (20)].

The thickness of all the silicon on spinel films discussed in this communication is $1.5 \pm 0.1\mu$. Diborane diluted with hydrogen was used as the dopant source. As-deposited hole concentrations of the films are between 1 and 5×10^{16} cm^{-3}. Within this range, for comparative purposes, the differences in the hole concentrations may be normalized by reference to a curve (21) of experimentally determined bulk silicon hole mobility *vs.* hole concentration (*i.e.*, per cent of bulk mobility values are compared). The silicon was deposited by the pyrolysis of silane in a hydrogen ambient, the substrate was heated by contact with an inductively heated pyrolytic carbon coated carbon susceptor, and the growth ampoule was water cooled. The film thickness was measured both during growth (22) and after deposition by interferometry. Details of the apparatus and procedures have been previously reported (9).

The hole mobilities realized on flame fusion, flux, and Czochralski spinel are compared in Table I. The hole mobility of 330 cm^2/V-sec ($n_a = 1.8 \times 10^{16}$ cm^{-3}) is typical of many 1.5μ thick samples prepared on (111) flame fusion spinel (9). This film was deposited at a temperature of 1100°C and a growth rate of 0.8 μ/min. The substrate was hydrogen prefired for 20 min at 1150°C to remove the work damage introduced by mechanical polishing. Single crystal low angle electron diffraction patterns are obtained on hydrogen etched flame fusion spinel surfaces. In this carrier

Table I. Hole mobilities in silicon epitaxially deposited on flame fusion, flux, and Czochralski spinel

Substrate	Thermal treatment	Hole concentration, cm^{-3}	Hole mobility, cm^2/V-sec	Per cent of bulk mobility
Flame fusion	As-deposited	1.8×10^{16}	330	100
$MgO \cdot 2.2Al_2O_3$	Oxidized	1.1×10^{16}	320	92
Flux	As-deposited	1.3×10^{16}	200	58
$MgO \cdot Al_2O_3$	Oxidized	2.8×10^{16}	200	60
Czochralski	As-deposited	4.2×10^{16}	250	80
$MgO \cdot Al_2O_3$	Oxidized	4.2×10^{16}	220	70

Deposit thickness: $1.5 \pm 0.1\mu$.
Oxidation: Dry oxygen, 1 hr; flame fusion—1200°C, flux and Czochralski—1100°C.
Substrate and film orientation: (111).

* Electrochemical Society Active Member.
Key words: silicon thin films, semiconductor thin films, insulating substrates, silicon on insulating substrates, chemical vapor deposition.

concentration range the hole mobilities are degraded by less than 5%, and the magnitude of the degradation is relatively insensitive to the growth rate (9). The after-oxidation hole mobility of 320 cm^2/V-sec (n_a = 1.1 x 10^{16} cm^{-3}) is ~92% of the bulk reference value.

Using hydrogen etching and deposition conditions identical to those used with flame fusion spinel, a hole mobility of 200 cm^2/V-sec (n_a = 1.3 x 10^{16} cm^{-3}) was obtained in a 1.5μ thick silicon film on (111) flux spinel. Flux impurities were gettered by deposition of silicon, removal, and redeposition of the silicon. The hole mobilities increased with each deposition to the value reported, which is a typical value after the third deposition. The substrate impurity content may also be reduced by vacuum firing of the substrate wafers (14). The mobilities in silicon on flux spinel, within this carrier concentration range, are also not significantly degraded during thermal oxidation. The after-oxidation mobility of 200 cm^2/V-sec (n_a = 2.8 x 10^{16} cm^{-3}) represents 60% of the bulk reference value. A mobility of 300 cm^2/V-sec in a 2μ thick film has been previously reported (14). The relatively low hole mobility in the 1.5μ thick silicon on flux spinel is attributed to contamination of the silicon films by flux impurities (lead compounds) from the substrate.

If the hydrogen prefiring and deposition conditions used with flux and flame fusion spinel are employed for epitaxial growth on Czochralski spinel, high resistivity films are obtained. The resistivities are relatively insensitive to the amount of added dopant (diborane), and doping levels must be used which are more than an order of magnitude greater than are required to obtain the same hole concentration in silicon on flame fusion spinel. The hole mobilities of these films are less than 100 cm^2/V-sec (n_a ~ 5 x 10^{16} cm^{-3}), and therefore it appears that the added dopant is compensated by, and the mobility degraded by, impurities introduced as the result of interaction with the substrate. Similar properties were obtained using substrate wafers cut from in-house and commercially available (2) Czochralski spinel crystals.

Silicon gettering procedures employed with the flux spinel were not effective in improving the properties of silicon on Czochralski grown material. After testing a variety of conditions for the growth of silicon on Czochralski spinel in a hydrogen ambient, it was found that the highest mobilities were obtained on substrates which had been exposed to a minimum of thermal treatment. The highest as-deposited hole mobility achieved to date in 1.5μ thick films was 250 cm^2/V-sec (n_a = 4.2 x 10^{16} cm^{-3}). This value decreased to 220 cm^2/V-sec (n_a unchanged) during thermal oxidation. The after-oxidation value represents ~70% of the reference bulk value. It has been found that under conditions where thermal pregrowth treatment in hydrogen of the substrate must be minimized, the electrical properties of the epitaxial silicon are highly sensitive to small variations in the surface polishing and cleaning procedures.

Higher hole mobilities have been observed in (111) silicon on (111) spinel than in (100) silicon on (100) spinel (9). But the mobilities of thin (100) silicon on the $(1\bar{1}02)$ sapphire have been higher than in (111) silicon on (0001) sapphire (23). After-oxidation hole mobilities of 150 cm^2/V-sec (n_a = 1 x 10^{16} cm^{-3}) have been typically observed in 1.7μ thick (100) silicon on sapphire (24, 25).

Nature of Silicon Growth Prior to Complete Coverage of Substrate Surface

Silicon was simultaneously deposited on (111) flame fusion and Czochralski spinel and on $(1\bar{1}02)$ flame fusion sapphire in a single growth run, and on (111) flux spinel in a separate run. The samples were all hydrogen prefired, and the silicon was deposited for 5 sec under conditions which give an over-all growth rate of 0.8 μ/min. Scanning electron micrographs of the surfaces are shown in Fig. 1.

The geometry of the incomplete films and the per cent of the surface coverage are similar on the flame fusion (Fig. 1a) and Czochralski spinel (Fig. 1b). The most obvious difference between the deposits on these two materials is that substrate reaction products are seen on the exposed areas of the Czochralski spinel. It also appears, from the nature of the silicon surface,

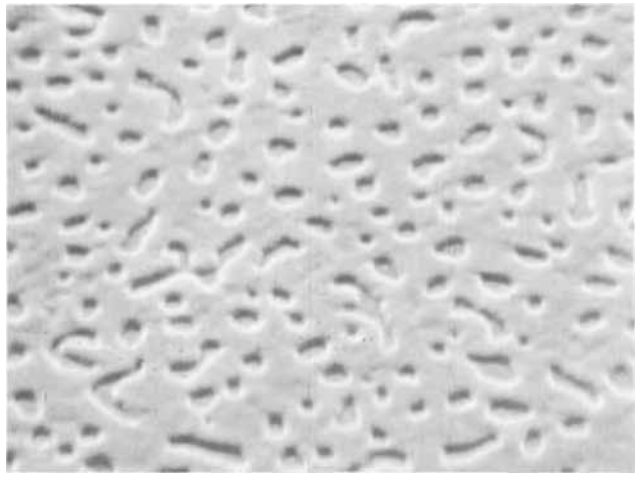

Fig. 1a-d. Scanning electron micrographs of silicon after deposition for 5 sec at 0.8 μ/min. Magnification 10,000X, beam sample angle 45°. Fig. 1a. On flame fusion spinel.

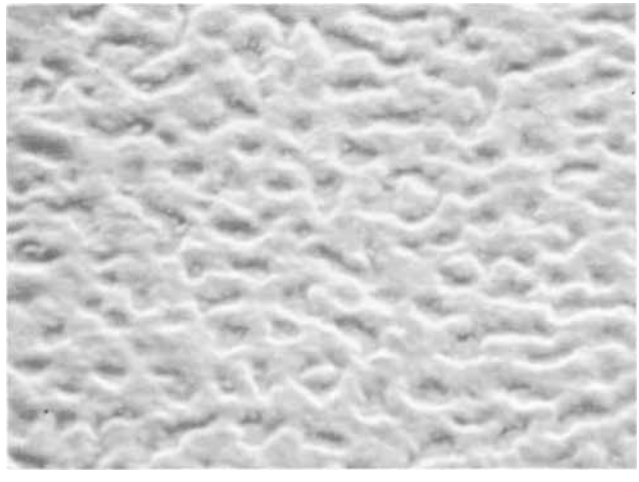

Fig. 1b. On Czochralski spinel

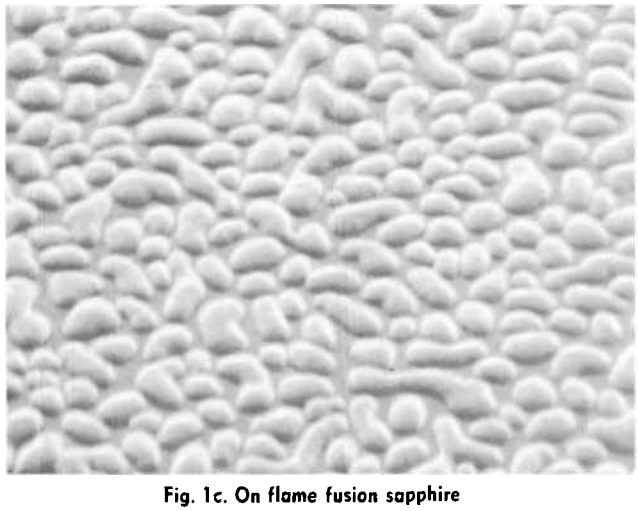

Fig. 1c. On flame fusion sapphire

Fig. 1d. On flux sample

that the reaction products have been incorporated into the growing film. The difference between the deposits on the flame fusion and Czochralski spinel may be seen in more detail at double the magnification and at a sample-beam angle more nearly normal to the surface (Fig. 2a and b). The geometry and per cent of surface coverage of silicon on flame fusion sapphire (Fig. 1c) are considerably different. The nature of the incomplete growth on the flux spinel (Fig. 1d) is more similar to that on sapphire than to the growth on the other two spinel samples. The appearance of the growth on flux spinel and sapphire is similar to that observed on flame fusion spinel during an earlier stage of growth prior to coalescence of the individual silicon islands. The lack of coalescence on the flux spinel can be attributed to a slight difference in growth duration, but the silicon on flame fusion sapphire was deposited in the same run as on the flame fusion and Czochralski spinel. Thus it appears that, under the same growth conditions, the surface coverage is more rapid on spinel than on sapphire.

Scanning electron micrographs are shown of the flame fusion (Fig. 3a), and Czochralski spinel (Fig. 3b), and the flame fusion sapphire (Fig. 3c) after removal of the silicon with an aqueous HNO_3-HF etch.

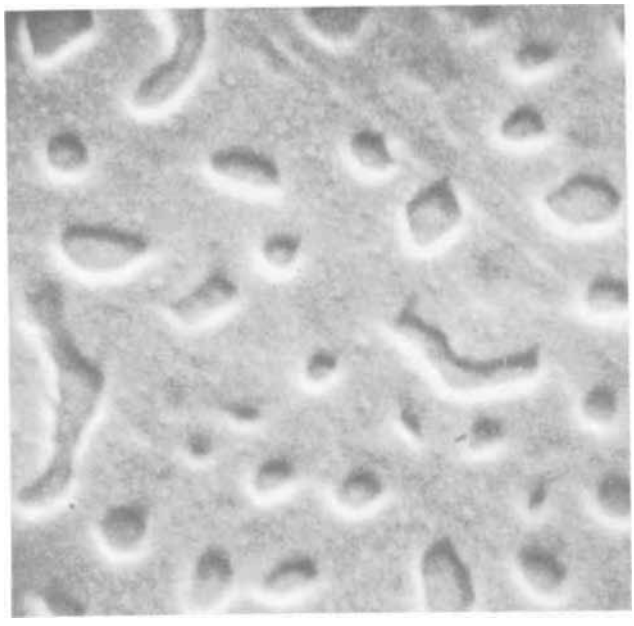

Fig. 2a and b. Scanning electron micrographs of silicon after deposition for 5 sec at 0.8μ/min. Magnification 20,000X, beam sample angle 70°. Fig. 2a. On flame fusion spinel.

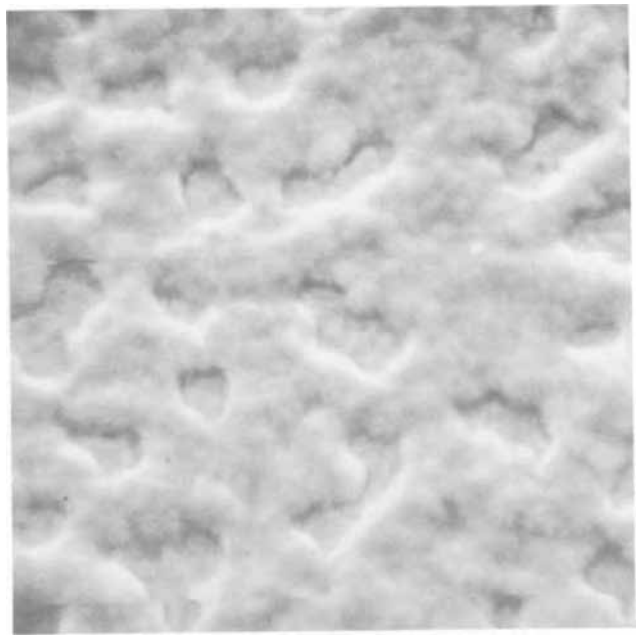

Fig. 2b. On Czochralski spinel

Fig. 3 a, b, c. Scanning electron micrographs of the substrate surfaces after the chemical dissolution of the silicon deposit. Magnification 10,000X, beam sample angle 45°. Fig. 3a. Flame fusion spinel.

Fig. 3b. Czochralski spinel

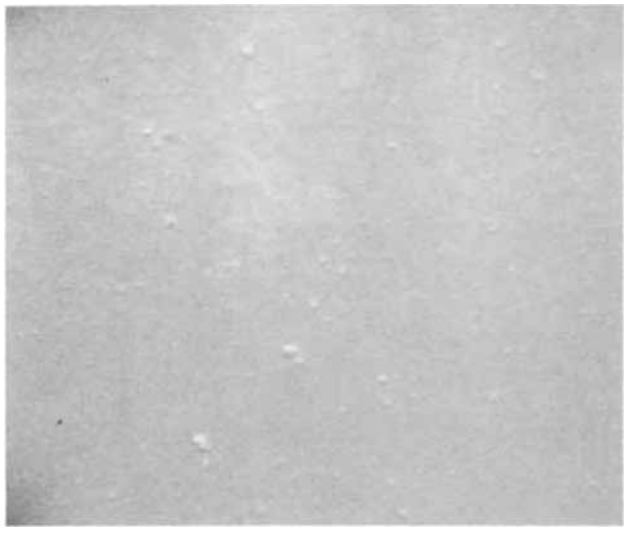

Fig. 3c. Flame fusion sapphire

The flame fusion substrate has been eroded at work damaged areas. This surface is characteristic of a hydrogen etched spinel which was not sufficiently polished to remove work damage introduced during the lapping step. Electron microscopic examination of hydrogen fired substrates has been adopted as a means to evaluate the mechanical finishing procedures.

The surface of the Czochralski spinel from which the silicon has been removed is uniformly and relatively deeply eroded. The surface of this spinel had been polished using the same procedures employed for polishing the flame fusion spinel, but the erosion appears to have extended deeper than the work damage. The surface of the sapphire is free of work damage erosion. Some residues remain on the surface which were not removed by the HNO_3-HF etch. These residues have been identified as highly nonreactive aluminum silicates.

Discussion

The defect density decreases, but the impurity content increases, in spinel crystals grown by the three methods in the following order: flame fusion — Czochralski — flux. This is due to the relative steepness of the thermal gradient and the chemical ambient in which the crystals are grown. It is interesting to note that no difference has been observed in the electrical properties of silicon deposited on flame fusion and Czochralski sapphire (26). The nature of silicon on sapphire appears to be dominated more by the lattice mismatch than by the defect density of the substrate.

It has been demonstrated in this communication that the properties of silicon on spinel are a strong function of the method by which the substrate crystals are grown, even for crystals of nominally the same composition. The lattices of the silicon and spinel are more closely matched than those of silicon and sapphire, but as with silicon on sapphire, the differences observed in the electrical properties of silicon deposited on spinel prepared by the three methods cannot be related to differences in the defect densities of the substrates. The highest hole mobilities have been realized on the relatively imperfect flame fusion spinel. The relatively low mobility of silicon on the flux spinel can be attributed to the incomplete removal of constituents of the flux from the substrate, but the impurity content of the flame fusion and Czochralski spinels is similar.

The most obvious difference between the Czochralski and flame fusion spinel is that the flame fusion crystals used in this study contain alumina considerably in excess of the stoichiometric composition. It is difficult, however, to associate the observed mobility-substrate effect with the presence of excess alumina. Both on the basis of lattice match and autodoping effects it is anticipated that the electrical properties of epitaxial silicon would be degraded with increasing alumina content. The lattice constant decreases, and the mismatch between the spinel and silicon lattice increases, with increasing alumina content. Since it has been demonstrated that silicon deposited on flame fusion spinel is less autodoped than silicon on sapphire (6), decreasing the alumina content should, if anything, lead to a decrease in the autodoping. Further evidence for the lack of involvement of the excess alumina *per se* is the observation that different deposition conditions are required for epitaxial growth on the two stoichiometric materials (flux and Czochralski), while the same conditions may be used to deposit on the low-alumina-rich flame fusion and the stoichiometric flux spinels. It is evident from examination of scanning electron micrographs of partially covered substrate surfaces that a difference in surface chemical reactivity is the source of the differences in electrical properties observed in silicon on flame fusion and Czochralski spinel. The surface reactivity is strongly influenced by the thermal treatment immediately prior to epitaxial growth. The highest mobilities have been obtained in silicon on Czochralski spinel which has been exposed to a minimum of annealing, while optimum properties are obtained in silicon on flame fusion spinel and flame fusion or Czochralski sapphire which has been annealed in hydrogen at or above the growth temperature. The surface conditioning-ambient-growth characteristic relationship of silicon on the Czochralski spinel is not well understood and requires further study.

The origin of the difference in the surface reactivity of the two substrate materials is not obvious. Two possible sources are proposed. While excess alumina does not degrade the use of spinel as a substrate, it is possible that excess magnesia influences the surface reactivity (27). The alumina:magnesia ratio is difficult to determine accurately by wet chemical procedures, and the lattice constant is insensitive to small deviations from stoichiometry on the magnesium rich side (28). The difference in surface reactivities may also be the result of the differences in the chemical ambient during crystal growth. The flame fusion crystals are grown in a highly oxidizing ambient in the presence of water (the reaction product in a hydrogen-oxygen flame), while the Czochralski crystals are grown in a dry neutral, or slightly oxidizing, ambient. These conditions affect the hydroxyl content and the arrangement of the magnesium and aluminum on the crystal lattice sites (7). Both of these factors may have a significant influence on the surface reactivity. The relatively high surface reactivity of the nominally stoichiometric Czochralski spinel has been observed specifically under conditions commonly employed for the epitaxial growth of silicon on Czochralski sapphire and flame fusion spinel. Crystal growth, surface conditioning, and epitaxial growth conditions are currently being sought to suppress the surface reactivity and optimize the electrical properties of silicon on Czochralski spinel.

Acknowledgment

The silicon growth and electrical measurements were carried out by F. C. Dougherty, and the scanning electron micrographs were taken by B. J. Seabury. The flame fusion spinel was grown by H. Temple and A. J. Wasielewski, the flux spinel was grown by R. F. Bates, and the "in-house" Czochralski spinel was grown by A. D. Morrison.

The research reported in this communication was supported in part by the Naval Electronic Systems Command, Contract No. N00039-69-C-0549 and in part by the Air Force Materials Laboratory, Contract No. F33615-69-C-1073.

Manuscript submitted Sept. 1, 1970; revised manuscript received Dec. 2, 1970.

Any discussion of this paper will appear in a Discussion Section to be published in the December 1971 JOURNAL.

REFERENCES

1. J. D. Filby and S. Nielson, *Brit. J. Appl. Phys.*, **18**, 1357 (1967).
2. The Union Carbide Corporation, Crystal Products Division, San Diego, California.
3. A. Miller and H. Manasevit, *J. Vac. Sci. and Tech.*, **3**, 68 (1966).
4. T. S. La Chapelle, A. Miller, and F. L. Morritz in "Progress in Solid State Chemistry," Vol. 3, H. Reiss, Editor, Pergamon Press, London (1967).
5. H. M. Manasevit and D. H. Forbes, *J. Appl. Phys.*, **37**, 734 (1966).
6. P. H. Robinson and D. J. Dumin, *This Journal*, **115**, 75 (1968).
7. C. C. Wang, *J. Appl. Phys.*, **40**, 3433 (1969).
8. J. G. Grabmaier and B. C. Watson, *Z. Angew. Physik*, **24**, 108 (1968).
9. G. W. Cullen, G. E. Gottlieb, C. C. Wang, and K. H. Zaininger, *This Journal*, **116**, 1444 (1969).
10. H. Seiter and C. Zaminer, *Z. Angew. Physik.*, **20**, 158 (1965).
11. H. Schlötterer, *Solid State Electronics*, **11**, 947 (1968).
12. C. C. Wang and S. H. McFarlane, III, *J. Crystal Growth*, **3-4**, 485 (1968).
13. J. D. C. Wood and E. A. D. White, *ibid.*, **3-4**, 480 (1968).
14. C. C. Wang, G. E. Gottlieb, G. W. Cullen, S. H. McFarlane, III, and K. H. Zaininger, *Trans. Met. Soc. AIME*, **245**, 441 (1969).
15. D. W. Oliver and J. D. Young, Private communication.
16. M. F. Lewis and E. Patterson, *J. Appl. Phys.*, **39**, 3420 (1968).
17. B. Cockayne and M. Chesswas, *J. Mat. Sci.*, **2**, 498 (1967).
18. J. G. Grabmaier and B. C. Watson, *J. Am. Ceram. Soc.*, **51**, 355 (1968).
19. B. Cockayne, M. Chesswas, P. J. Born, and J. D. Filby, *J. Mat. Sci.*, **4**, 236 (1969).
20. E. Boleky, *RCA Rev.*, **31**, 372 (1970).
21. W. R. Runyan, "Silicon Semiconductor Technology," p. 179, McGraw Hill Book Co., New York (1965).
22. D. J. Dumin, *Rev. Sci. Instr.*, **38**, 1107 (1967).
23. D. J. Dumin and P. H. Robinson, *This Journal*, **113**, 469 (1966).
24. D. J. Dumin and P. H. Robinson, *J. Appl. Phys.*, **39**, 2759 (1968).
25. G. W. Cullen, G. E. Gottlieb, and C. C. Wang, *RCA Rev.*, **31**, 355 (1970).
26. P. B. Hart, P. J. Etter, B. W. Jervis, and J. M. Flanders, *Brit. J. Appl. Phys.*, **18**, 1389 (1967).
27. S. R. Bolin, To be published.
28. A. M. Alper, R. N. McNally, P. H. Ribbe, and R. C. Doman, *J. Am. Ceram. Soc.*, **45**, 263 (1962).

The Use of Metal-Organics in the Preparation of Semiconductor Materials

II. II-VI Compounds

H. M. Manasevit and W. I. Simpson*

Autonetics Division of North American Rockwell Corporation, Anaheim, California 92803

Based on a continuing program to examine the use of metal-organics in the preparation of films of semiconductor materials, this paper describes the formation of II-VI compounds on insulating substrates using this approach. The effort on II-VI compounds was first undertaken and successfully demonstrated several years ago in our laboratories and has recently been expanded to include several additional II-VI compound materials. The advantages of the metal-organic approach to semiconductor formation over other CVD processes have been demonstrated in prior studies involving the formation and properties of several epitaxial gallium-group V compounds (1-4) and aluminum-group V compounds (5). For example, the process requires only one hot temperature for the formation and growth of the semiconductor directly on the heated substrate, it simplifies the growth procedure for II-VI's considerably, it is halide-free, and it makes compound semiconductor film growth compatible with the equipment used for the growth of elemental semiconductors.

The studies with II-VI compounds to date have been limited to feasibility studies of the growth process and require further investigation for the optimization of the process; but with the increasing interest being shown in the area of photoconductors, phosphors, and electroluminescent devices, it seems appropriate at this time to report the successful use of the metal-organic technique for the preparation of the selenides, sulfides, and tellurides of zinc and cadmium.

The II-VI films described here were produced by reacting diethylzinc (DEZ) or dimethylcadmium (DMCd) with hydrogen selenide, hydrogen sulfide, or dimethyltellurium (DMT), using essentially the same apparatus previously described (2, 6) for the formation of GaAs and other III-V compounds (Fig. 1). It consists principally of a vertical 60-mm OD quartz reactor containing a side arm and a center tube extending to about 1-2 in. from a rotatable SiC-covered carbon pedestal which can be heated inductively; stainless-steel bubblers containing the liquid metal-organic compounds; appropriate flowmeters for monitoring the carrier gas and the H_2Se and H_2S flows; a burn-off area for hydrogen; and a manifold made from ¼-in. stainless steel tubing. Provisions are made for evacuation of the apparatus and reactor and for bypassing the reactor and keeping the reactants separate until they are to be mixed within the reactor. The hydrides and DMT in a carrier gas are usually intro-

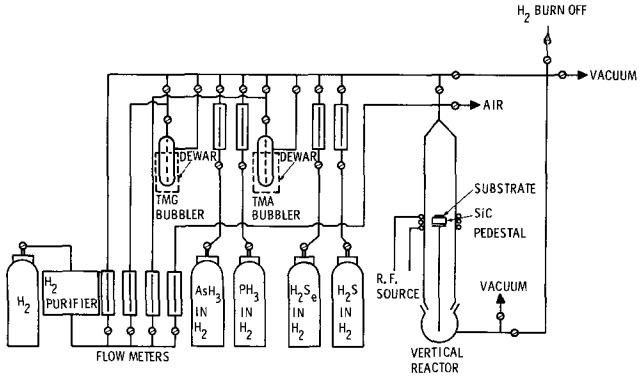

Fig. 1. Schematic of CVD apparatus used in growth studies

* Electrochemical Society Active Member.

Key words: heteroepitaxy, chemical vapor deposition, single crystal insulating substrate.

duced into the reactor through the side arm prior to admitting the group II-metal-organic in its carrier gas via the center tube. The product of their mixing is then decomposed at the heated pedestal to produce the II-VI compound. Total gas flow rates in the range of 2-3 l/min were used in these experiments.

By handling the metal-organics in steel tanks and using adequate ventilation, the reactivity and toxicity problems which are reported for the metal-organics and hydrides are minimized. Only during the studies of telluride formation were extra precautions in ventilation considered necessary to remove the obnoxious odors.

Mechanically polished wafers of Verneuil Al_2O_3 and Czochralski $MgAl_2O_4$ and the naturally occurring facets of flux-grown BeO were used as substrates after a thorough degreasing in trichloroethylene and cleaning in water and methanol. Although this cleaning process is not considered optimum, it was sufficient for providing the films indicated and to establish the feasibility of the process.

Growth temperatures at the SiC-covered pedestal were estimated by comparing the readings of an infrared thermometer with those of an optical pyrometer at pedestal temperatures greater than 750°C (uncorr), establishing an average emissivity value for the system, and then extrapolating the infrared thermometer signal readings to still lower temperatures. The readings are made just prior to the actual deposition. Deposition temperatures in these studies were varied to accommodate the stability of the particular II-VI compound in H_2 or to be consistent with ordered growth and epitaxy. The temperatures reported should not be considered optimum without further experimentation.

Table I. ZnSe epitaxial relationships

Substrate surface plane	Parallel plane in ZnSe film
$(0001)Al_2O_3$	(111)ZnSe
$(11\bar{2}3)Al_2O_3$	(111)ZnSe
$(10\bar{1}4)Al_2O_3$	(111)ZnSe
$(01\bar{1}2)Al_2O_3$	(111)ZnSe
$(10\bar{1}1)$BeO	(111)ZnSe
$(10\bar{1}0)$BeO	(100)ZnSe
(0001)BeO	(111)ZnSe
$(111)MgAl_2O_4$	(111)ZnSe

The structural nature of the deposits, which were several microns thick, was examined first by viewing them in an optical microscope and then by x-ray diffraction and/or electron diffraction analysis. Because of the preliminary nature of these experiments, no measurements of the electrical properties of the films were made.

Single crystal films of ZnSe were grown on single crystal α-Al_2O_3, $MgAl_2O_4$, and BeO at 725°-750°C by decomposing on the heated substrate the product formed by mixing DEZ with H_2Se. Typical ZnSe surface structures are shown in Fig. 2. Growth on a number of orientations of these substrate materials supplied the heteroepitaxial relationships given in Table I. These results are consistent with the growth orientations of GaAs on these substrate planes (6) and, therefore, suggest a similar growth mechanism. Goodman (7) also obtained (111)ZnSe growth on $(01\bar{1}2)$ Al_2O_3 but by using an evaporation technique.

The nature of the surface of ZnS growth on Al_2O_3, $MgAl_2O_4$, and BeO is recorded in Fig. 3. Some crazing can be observed in the films grown on $(0001)Al_2O_3$

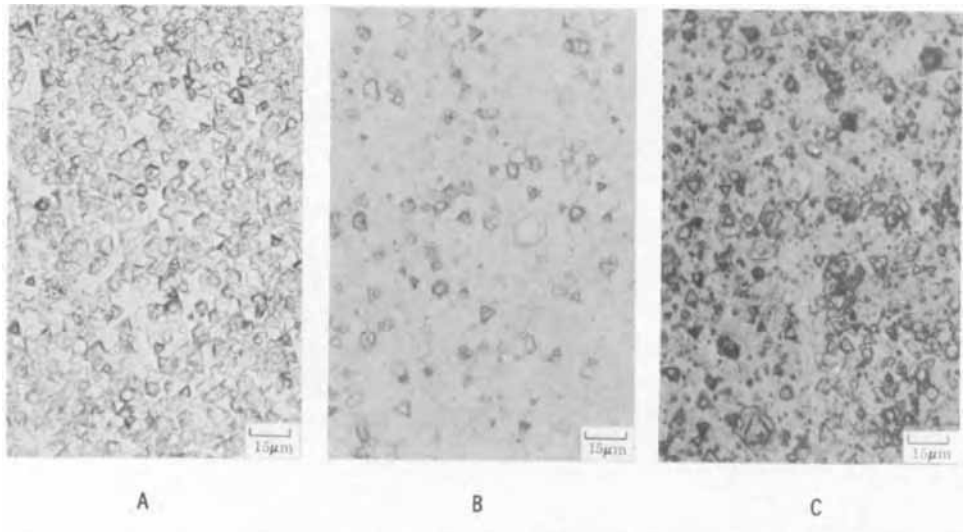

Fig. 2. ZnSe growth on: (a) (left) $(0001)Al_2O_3$; (b) (center) $(111)MgAl_2O_4$; (c) (right) $(10\bar{1}1)$BeO.

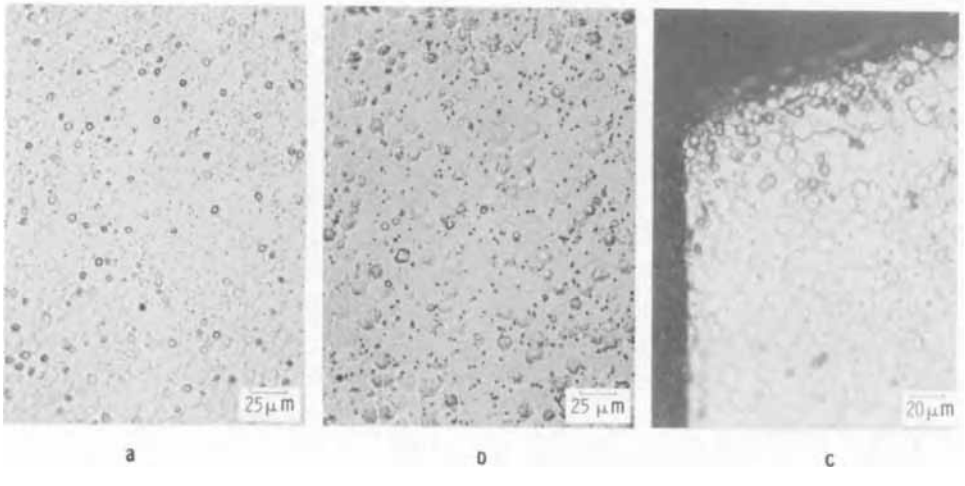

Fig. 3. ZnS growth on (a) (left) $(0001)Al_2O_3$; (b) (center) $(111)MgAl_2O_4$; (c) (right) $(10\bar{1}1)$BeO.

and (111) spinel. The films were grown at about 750°C from DEZ and H_2S.

Single crystal films of ZnTe were produced on Al_2O_3 by reacting DEZ with DMT at about 500°C. The nature of the surface and a Laue pattern of the composite is shown in Fig. 4. The growth shown is (111)ZnTe on (0001)Al_2O_3.

Replacing the DEZ with DMCd led to the formation of the corresponding Cd-group VI semiconducting compounds. The overgrowth of the yellow film of CdS obtained on (0001)Al_2O_3 by reacting DMCd with H_2S at 475°C is shown in Fig. 5. The order seen in the hexagonal structure found on regions of the substrate suggests that heteroepitaxial growth was achieved in those areas.

The growth of CdSe on (0001)Al_2O_3 also displayed a high degree of hexagonal order (Fig. 6). This dark, almost black, film was grown from DMCd and H_2Se at a pedestal temperature of about 600°C.

Specular single crystal films of CdTe were produced at about 500°C from DMCd and DMT on several orientations of Al_2O_3, $MgAl_2O_4$, and BeO. Evidence for the growth of (111)CdTe on $(11\bar{2}6)Al_2O_3$ is shown in Fig. 7, in which a hexagonal and symmetrical array of spots due to the CdTe are distinguishable from those due to the Al_2O_3 substrate, which does not possess this predominant Laue spot configuration.

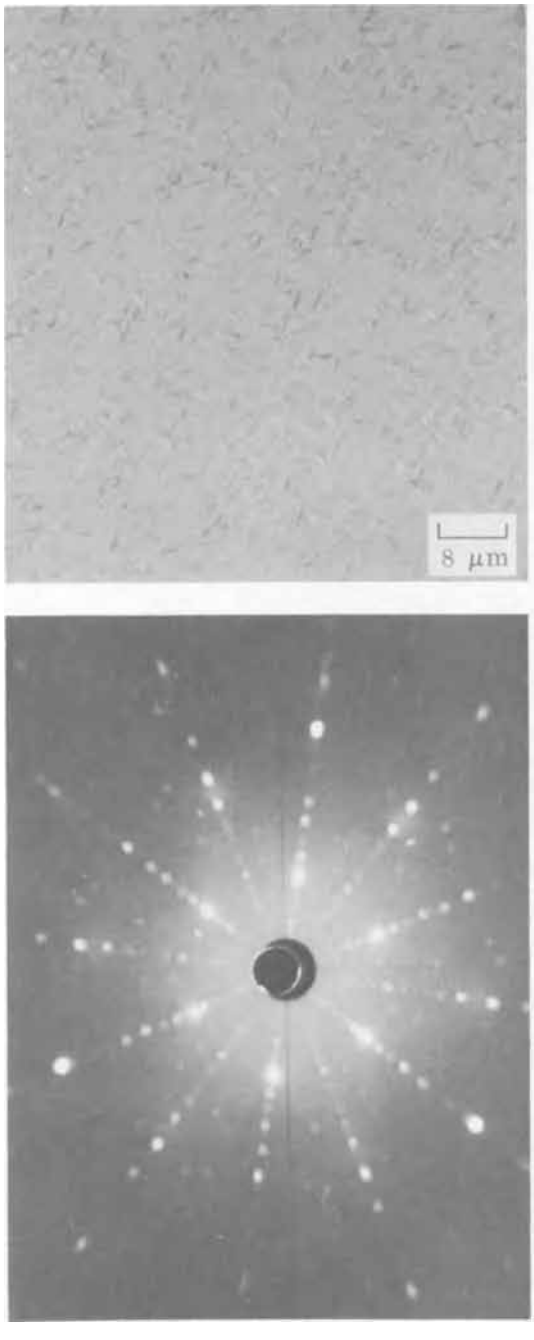

Fig. 4. (111)ZnTe growth on (0001) Al_2O_3; (a) (top) surface structure; (b) (bottom) Laue of composite.

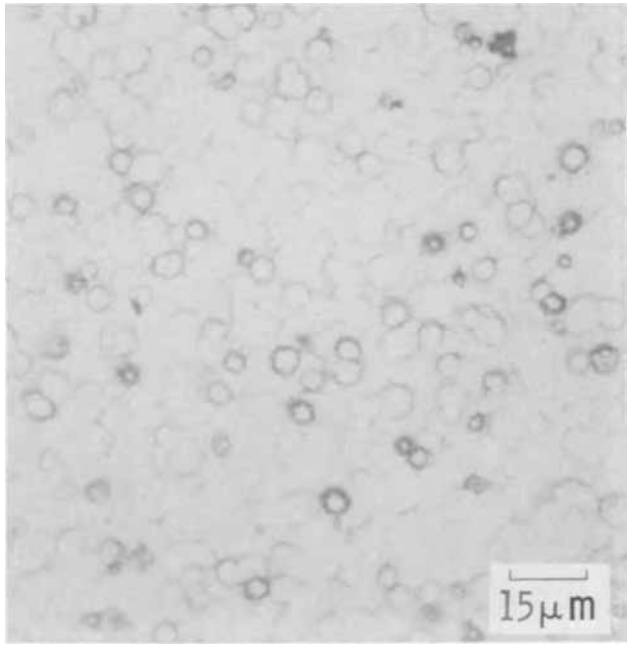

Fig. 5. Growth features of CdS on (0001) Al_2O_3

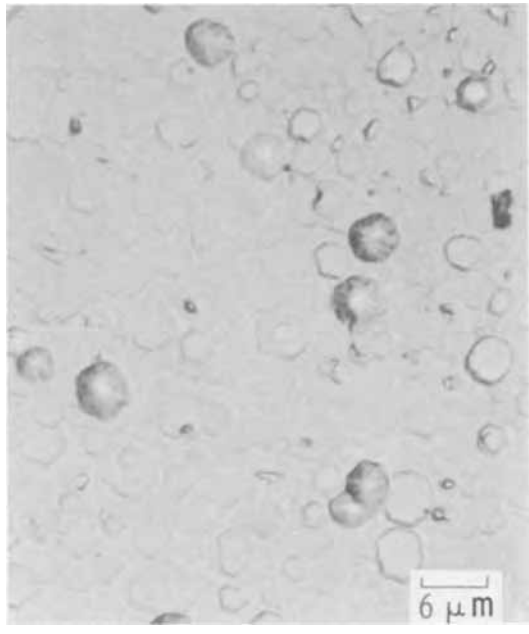

Fig. 6. Growth features of CdSe on (0001)Al_2O_3

Growth studies of the group II tellurides had not been undertaken until quite recently mainly because H_2Te, which might have been the preferred source of tellurium, was essentially unavailable commercially, probably because of instability and handling difficulties. Therefore, an alternate to H_2Te for producing group II Te compounds, *i.e.*, a low molecular weight alkyl telluride, specifically DMT, was obtained and used in these studies. Further studies will be required to determine whether the alkyl selenium and sulfur compounds are to be preferred over H_2Se and H_2S, respectively, in preparing the II-VI compounds.

In summary, the use of metal-organics for the formation of a number of II-VI semiconductor com-

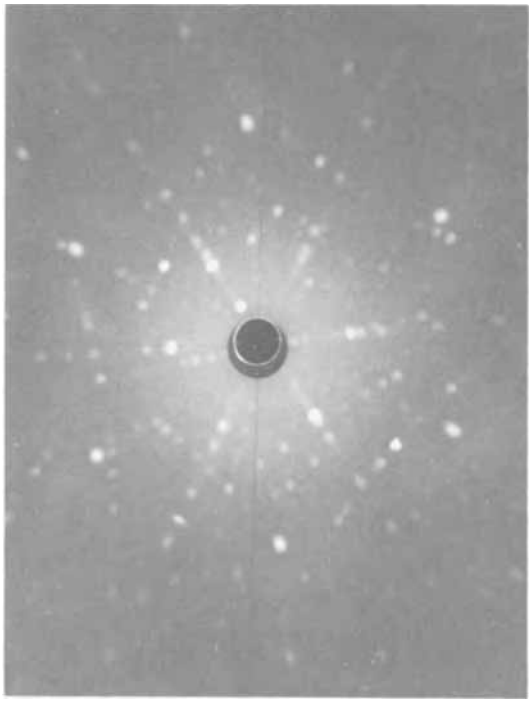

Fig. 7. Laue pattern for (111)CdTe growth on $(11\bar{2}6)Al_2O_3$

pounds on insulating substrates has been demonstrated. The advantages and ease of this approach for the formation of these compounds, either singly or in multilayer structures on insulators or semiconductors, suggest that the method should be exploited vigorously.

Acknowledgment

The authors wish to thank G. W. Johnson for the photomicrographs, Dr. R. P. Ruth for his most helpful discussions and review of this paper, and Frank M. Erdmann for assisting in the growth studies.

Manuscript submitted Aug. 27, 1970; revised manuscript received Nov. 20, 1970. This was Paper RNP 369 presented at the Los Angeles Meeting of the Society, May 10-15, 1970.

Any discussion of this paper will appear in a Discussion Section to be published in the December 1971 JOURNAL.

REFERENCES

1. H. M. Manasevit, *Appl. Phys. Letters*, **12**, 156 (1968).
2. H. M. Manasevit and W. I. Simpson, *This Journal*, **116**, 1725 (1969).
3. H. M. Manasevit and A. C. Thorsen, *Met. Trans.*, **1**, 623 (1970).
4. R. W. Thomas, *This Journal*, **116**, 1449 (1969).
5. H. M. Manasevit, *ibid.*, **116**, 250C (1969); **118**, 647 (1971).
6. H. M. Manasevit and A. C. Thorsen, "Heteroepitaxy of III-V Compound Semiconductors on Insulating Substrates," Final Report, prepared by Autonetics Division of North American Rockwell Corporation for NASA-ERC under Contract No. NAS 12-2010, January 1970.
7. A. M. Goodman, *This Journal*, **116**, 364 (1969).

The Use of Metal-Organics in the Preparation of Semiconductor Materials

III. Studies of Epitaxial III-V Aluminum Compound Formation Using Trimethylaluminum

H. M. Manasevit

Autonetics Division of North American Rockwell Corporation, Anaheim, California 92803

In 1968 it was first demonstrated that metal-organics and hydrides can be used successfully in chemical vapor deposition (CVD) processes for the production of single-crystal layers of III-V semiconductor compounds (1, 2). GaAs was formed on GaAs, Ge, and a variety of single-crystal insulators such as sapphire (Al_2O_3), spinel, and BeO by reacting triethylgallium (TEG) or trimethylgallium (TMG) and arsine (AsH_3) in H_2 at an rf heated pedestal. The addition of various amounts of phosphine (PH_3) to TMG-AsH_3 mixtures led to the formation of single-crystal films of mixed $GaAs_{1-x}P_x$ alloys. GaP was produced by decomposing TMG-PH_3 mixtures. $GaAs_{1-x}Sb_x$ was produced from TMG, AsH_3, and SbH_3 mixtures.

This new approach to epitaxial film formation eliminated many of the drawbacks of the usual two- or three-temperature-zone methods and is also compatible with CVD processes used for the formation of elemental semiconductors.

Rai-Choudhury (3) has since also used this process to produce films of GaAs on GaAs, and Thomas (4) produced single-crystal GaP on Si by the thermal decomposition of a gas-phase mixture of TEG and triethylphosphine.

Key words: heteroepitaxy, chemical vapor deposition, insulating substrates, gallium aluminum arsenide, aluminum arsenide.

This note reports the successful use of trimethylaluminum (TMA) in the production of single-crystal films of AlAs and mixed III-V aluminum compounds, materials of interest for optoelectronic devices. The studies represent a series of feasibility experiments and are, therefore, far from complete; but the results again demonstrate the simplicity and flexibility of this process for thin-film epitaxial growth. A schematic of the apparatus is shown in Fig. 1.

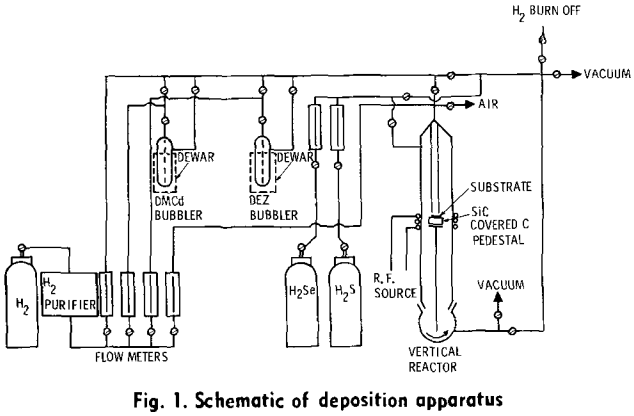

Fig. 1. Schematic of deposition apparatus

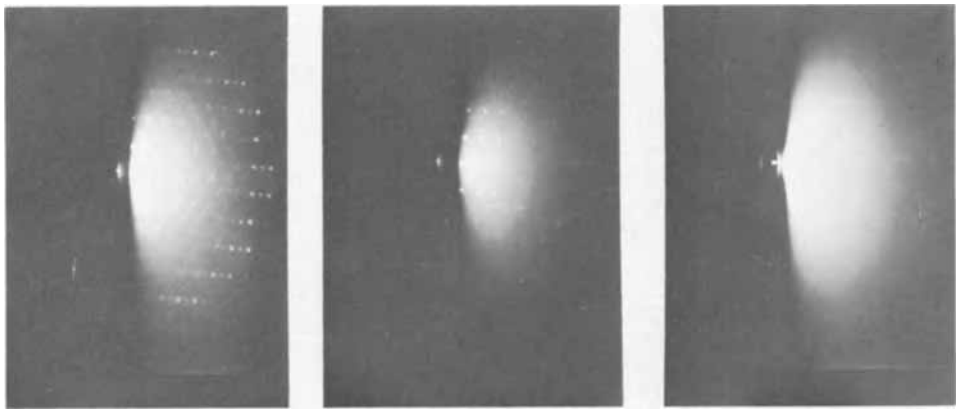

Fig. 2. The instability of (111) AlAs on (0001) Al_2O_3 in moist air, as followed by reflection electron diffraction patterns: (left) after 1 min; (center) after 3 min; (right) after 6 min.

The experimental deposition techniques are essentially those previously described (2). The TMA was kept at ambient room temperature, the bubbler being immersed in a dewar containing distilled water. For these experiments, total carrier gas flows of about 1500 ccpm were used.

Aluminum Arsenide

By pyrolyzing TMA and AsH_3 in a H_2 atmosphere at about 700°C, single-crystal films of AlAs have been formed on GaAs and on single-crystal insulating substrates. But the surface of the AlAs, yellow in thin-film form, was found to be unstable in the laboratory atmosphere. The instability of this film (<1 μm thick) was followed by reflection electron diffraction techniques. The results are recorded in Fig. 2. The pattern shown in Fig. 2 (left) was obtained within 1 min after the composite was removed from the CVD reaction chamber. Single-crystal spots and fairly strong Kikuchi lines are evident for this (111) deposit on (0001) Al_2O_3. This surface appeared stable under the vacuum of the electron microscope. However, after 3 min of its exposure to the laboratory air, the Kikuchi lines had faded [Fig. 2 (center)], the diffraction pattern spots became weaker, and indications of some twinning were observed. Only very faint spots were discernible after 6 min [Fig. 2 (right)], and the single-crystal diffraction patterns completely disappeared within about 10 min of exposure to the laboratory atmosphere. A back-reflection Laue x-ray pattern for an AlAs film on (0001) Al_2O_3 obtained during a half-hour exposure is shown in Fig. 3. Two hexagonally arranged sets of broad and diffuse spots are found, symmetrical to the center of the Laue pattern. They seem to suggest a high degree of strain in the AlAs film, which was decomposing at the surface during the x-ray exposure.

Other means were used for examining the epitaxial nature of the film. This was accomplished by growing multilayer heteroepitaxial films on Al_2O_3 and GaAs, *i.e.*, first growing a film of AlAs on the substrate and then switching from TMA to TMG and encapsulating the AlAs film with GaAs. The surface of a ~10.5 μm thick film of GaAs/AlAs on (0001) Al_2O_3 is shown in Fig. 4 (top); its back-reflection Laue pattern, Fig. 4 (bottom). The surface displays considerable order; and, from the parallel and triangular structure, one might infer essentially a (111)-oriented overgrowth. The Laue pattern displays strong spots typical of a single-crystal composite with heavy twinning present.

AlAs was then grown sandwiched between GaAs grown on Al_2O_3 and a final GaAs surface layer. Since the surface of a GaAs/AlAs/GaAs/(0001)Al_2O_3 composite grown under essentially the same deposition parameters appeared almost identical to Fig. 4(a), it is probable that the AlAs surface is the (111)"A" face with bonding through As atoms to Al_2O_3 and to Ga in GaAs, as was suggested by the (111) GaAs/(0001)-Al_2O_3 studies (2).

The quality of multilayer growth on bulk GaAs was found to be very surface- and orientation-sensitive, the GaAs/AlAs appearing to grow better on (100) and (110) than on the (111)"A" face of GaAs. The positions of sandwiched 0.8 and 1.5 μm layers of AlAs were revealed by angle-lapping the (110)-oriented III-V composites with a glycerin-Al_2O_3 slurry (Fig. 5).

Aluminum Phosphide

An attempt was made to produce AlP by the pyrolysis of TMA in H_2 at 700°C in an atmosphere containing excess P formed by decomposing phosphine (PH_3). The resulting film (~1 μm thick) was not stable in the laboratory atmosphere, even during the minute it took to transfer the wafer to the electron microscope chamber. Reid *et al.* also observed reaction at the AlP surface on exposure to moist air (5) for films formed at 900°C. Some of the unexpected optical effects observed by Richman for AlP films (6) may be related to this instability. No attempt has yet been made to encapsulate the AlP with GaAs or GaAs/AlAs multilayers. This will await future experimentation.

One experiment was performed with the intention of forming a GaAs/AlAs$_{1-x}$P$_x$/AlAs/(0001)Al_2O_3 composite. Based on the time of deposition, it is estimated that the approximate thicknesses of the layers are 15 μm GaAs, 3 μm AlAs$_{1-x}$P$_x$, and 0.5 μm AlAs. The surface characteristics of this composite film,

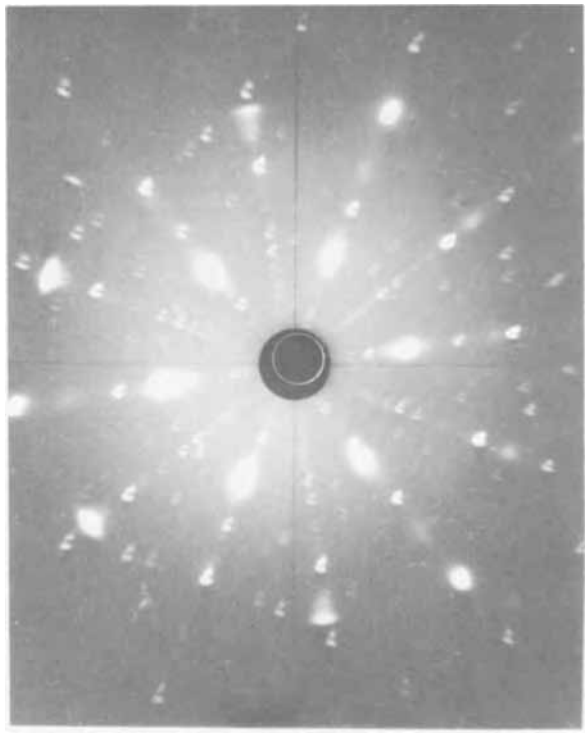

Fig. 3. Back-reflection Laue x-ray pattern for AlAs on (0001) Al_2O_3.

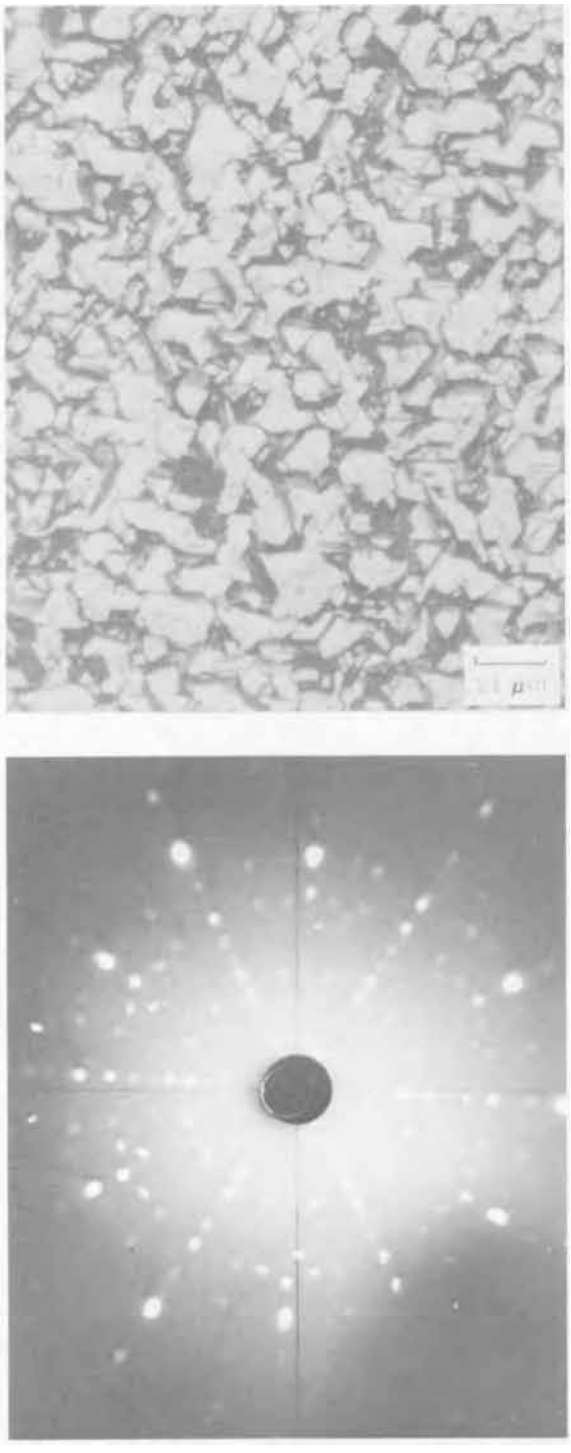

Fig. 4. (Top) Surface structure of 10 μm GaAs film grown on 0.3 μm layer of AlAs on (0001) Al_2O_3; (bottom) back-reflection Laue pattern for composite.

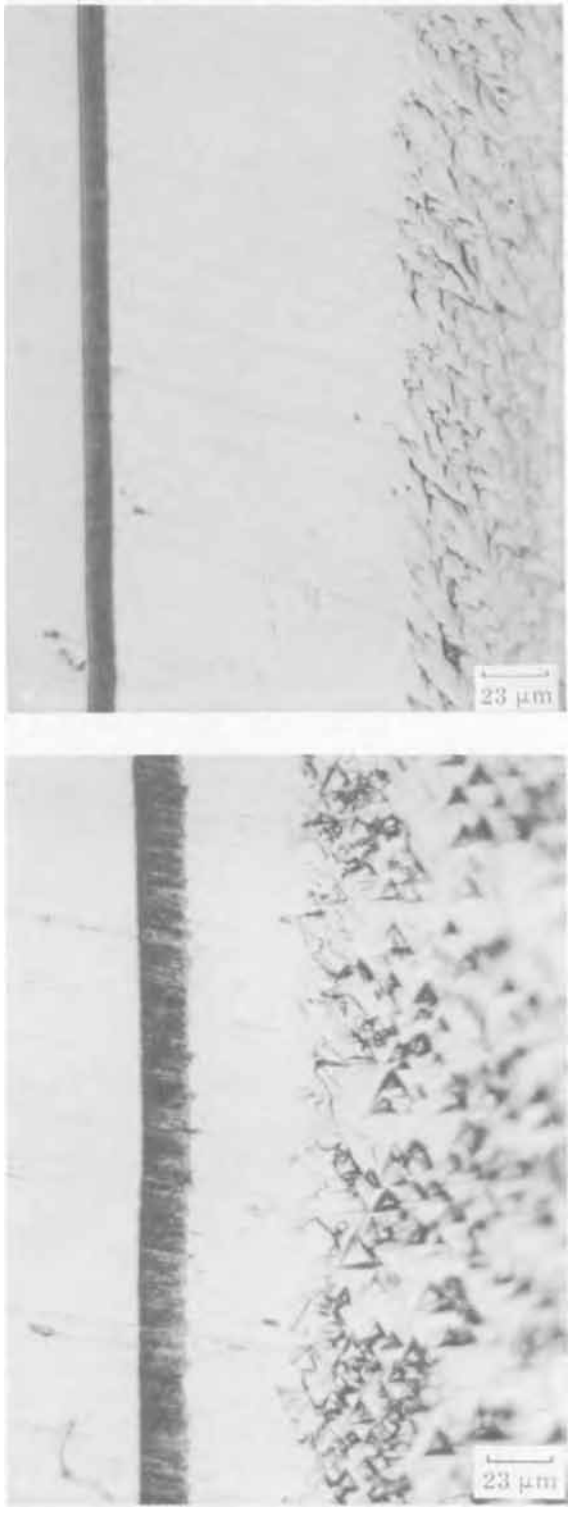

Fig. 5. The position of GaAs/AlAs/GaAs interfaces as revealed by angle lapping: (top) 0.8 μm AlAs, 7.7 μm GaAs; (bottom) 1.5 μm AlAs, 4.4 μm GaAs.

shown in Fig. 6, suggest a high degree of order exists throughout the multilayer structure.

$Ga_xAl_{1-x}As$

Alloys of $Ga_xAl_{1-x}As$ were relatively easily prepared by mixing different quantities of TMA and TMG and reacting these with AsH_3 at the heated pedestal. Alloys in the composition range $Ga_{0.1}Al_{0.9}As$ to $Ga_{0.8}Al_{0.2}As$, as analyzed with the electron microprobe, have been prepared on Al_2O_3 and GaAs substrates at 700°C.

The effect of arbitrarily changing the flowmeter settings of the H_2 carrier gas bubbled through the liquid TMG and TMA on film composition is reported in Table I.

Figure 7 is the back-reflection Laue pattern obtained for a 4.4 μm thick layer of $Ga_{0.8}Al_{0.2}As$ on (0001) Al_2O_3. Many of the spots shown can be identified as characteristic of the alloy film and not of the substrate.

Summary

The use of metal-organics for semiconductor compound formation has again been demonstrated, this time in the formation of III-V Al compounds and their alloys. Trimethylaluminum was the source of the Al. The feasibility of producing alloys of the III-V compounds was shown by reacting AsH_3 with various

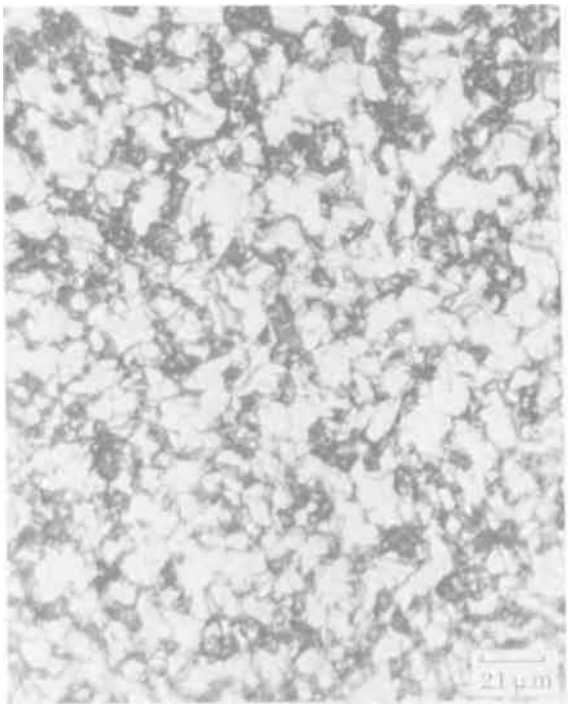

Fig. 6. Surface structure of a GaAs/AlAs$_{1-x}$P$_x$/AlAs/(0001)Al$_2$O$_3$ composite.

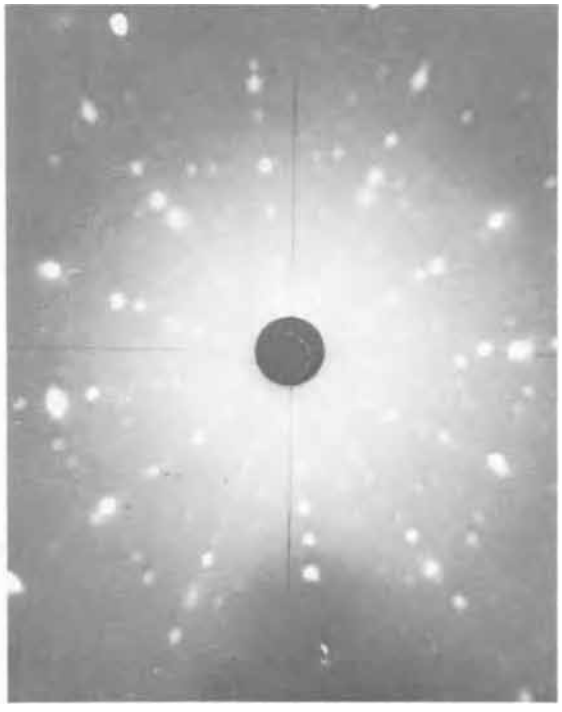

Fig. 7. Back-reflection Laue pattern for 4.4 μm layer of Ga$_{0.8}$Al$_{0.2}$As on (0001) Al$_2$O$_3$.

mixtures of TMA and TMG, forming Ga$_x$Al$_{1-x}$As, with x varying from 0.1 to 0.8. Both Al$_2$O$_3$ and GaAs substrates were used as hosts for the epitaxial growth of these alloys and AlAs. The process is compatible with the growth of elemental semiconductors and can be applied to the formation of various combinations of III-V compounds.

Table I. Effect of flowmeter changes on film composition of Ga$_x$Al$_{1-x}$As films grown on Al$_2$O$_3$

Flowmeter settings (arbitrary units) AsH$_3$*	TMG**	TMA	Film Composition	Color of transmitted white light
180	1.5	40	Ga$_{0.1}$Al$_{0.9}$As	Orange
180	3	22	Ga$_{0.2}$Al$_{0.8}$As	Red-orange
150	6	10	Ga$_{0.6}$Al$_{0.4}$As	Red
90	10	10	Ga$_{0.7}$Al$_{0.3}$As	Reddish black
90	10	3	Ga$_{0.8}$Al$_{0.2}$As	Black

* 10% AsH$_3$ in H$_2$.
** TMG stored at 0°C.

Acknowledgments

The author wishes to thank W. I. Simpson for assisting in the growth of the layers; R. F. Cunningham for the electron microprobe analyses and electron diffraction work; J. L. Healy and G. W. Johnson for the angle lapping and some of the photomicrographs; and Dr. R. P. Ruth for his most helpful discussions and review of the manuscript.

Manuscript submitted Sept. 14, 1970; revised manuscript received ca. Jan. 4, 1971. This was Paper RNP352 presented at the New York Meeting of the Society, May 4-9, 1969.

Any discussion of this paper will appear in a Discussion Section to be published in the December 1971 JOURNAL.

REFERENCES

1. H. M. Manasevit, *Appl. Phys. Letters*, **12**, 156 (1968).
2. H. M. Manasevit and W. I. Simpson, *This Journal*, **116**, 1725 (1969).
3. P. Rai-Choudhury, *ibid.*, **116**, 1745 (1969).
4. R. W. Thomas, *ibid.*, **116**, 1450 (1969).
5. R. J. Reid, S. E. Miller, and H. L. Goering, *ibid.*, **113**, 467 (1966).
6. D. Richman, *ibid.*, **115**, 945 (1968).

Effect of Nitrogen Purity on the Nitriding of Metals Using Purity Controlled Nitrogen

J. Aubry and R. Streiff*,[1]

Laboratoire de Metallurgie et Chimie du Solide associé au CNRS, Faculté des Sciences, Nancy, France

Many studies in the oxidation of metals have shown that the impurity concentration, as low as a few ppm, can have considerable influence on the oxidation behavior (1). However, the effect of small amounts of impurities in the gas phase has been usually neglected. Usually, former investigators only considered very high ratios of foreign species in the oxidizing atmosphere, *e.g.*, steam in oxygen with a partial pressure close to the water vapor pressure at room temperature. The concentrations have to be regarded as gas mixtures rather than impurities. If the effect at these percentages can be important, the effect of smaller

* Electrochemical Society Active Member.
[1] Present address: Laboratoire de Chimie des Matériaux, U.E.R. de Chimie, Université d'Aix-Marseille, Place Victor Hugo, Marseille, France.
Key words: nitrogen purity influence, nitriding kinetics.

amounts of impurities in the gas phase (in the ppm region) cannot be neglected, especially for very reactive metals. Thus, a former study of calcium nitriding (2) has shown that the usual method of removing oxygen or water from nitrogen is ineffective and that the kinetics of the reaction can be considerably altered by residual traces of those impurities. This led us to perfect a means of preparing pure nitrogen by decomposition of sodium azide. This pure nitrogen was used for nitriding studies, and the results were compared with those of nitriding studies which used nitrogen purified in the usual manner, *i.e.*, passage of commercial grade N_2 through dryers and cold traps. Thus we were able to study the effect of impurities on the nitriding kinetics of calcium and magnesium.

Preparation of Nitrogen

The nitrogen is obtained by decomposition of sodium azide under vacuum as follow

$$2N_3Na \rightarrow 2Na + 3/2N_2$$

This reaction as nitrogen supply is well known (3), but no indications are available up to now on the purity of the nitrogen from that source.

The generator is very simple (Fig. 1). The azide is contained in a glass tube connected to a storage volume through a trap filled with glass wool. The latter traps the sodium vapors generated by the decomposition reaction. A manometer located near the storage flasks gives the pressure of nitrogen. Finally, the assembly is connected to a vacuum system and to the nitriding reaction chamber. The whole device must be constructed of glass or metal.

The sodium azide is carefully dried in a dry box and then is outgassed by heating under high vacuum inside the decomposition chamber at a temperature slightly less than the decomposition temperature. The decomposition is initiated by local heating with a Bunsen burner. It starts at about 275°C. Any later purification is unnecessary since the last traces of oxygen or water are removed by the sodium which behaves as a getter.

The oxygen partial pressures were measured with a calibrated calcia stabilized zirconia galvanic cell. They were equal to 10^{-6} to $10^{-5.6}$ atm, corresponding to an oxygen concentration in the range 1-3 ppm. After three decomposition runs, the concentration of residual oxidizing impurities decreased to an average value of 0.1-0.2 ppm. No traces of CO_2, CO, or NH_3 have been revealed by mass spectrometry analysis.

In comparison, the nitrogen purified in the conventional manner (passed first over copper at 480°C, then over magnesium perchlorate and phosphoric acid, and finally through a trap cooled by a mixture of dry ice and acetone) contained 100-200 ppm of oxygen. These latter values are higher than those determined by other studies which used the same procedure (4, 5). This lack of reproducibility can be ascribed to the joint tubes of plastic or rubber present in assemblies used for purification of N_2 in the conventional manner (4).

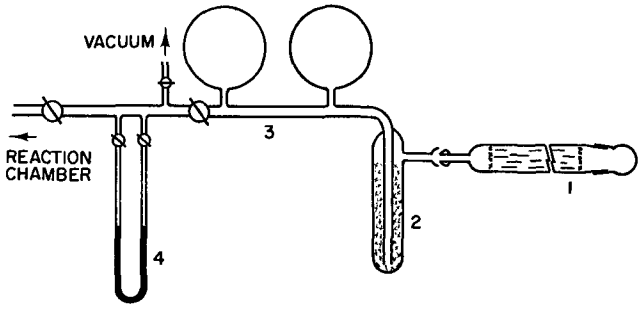

Fig. 1. Apparatus: 1, decomposition tube; 2, trap filled with glass wool; 3, storage flasks; 4, manometer.

Effect of Nitrogen Purity on the Nitriding of Metals

The most successful application of this nitrogen preparation has been the study of the effect of nitrogen purity on the nitriding kinetics of calcium and magnesium.

These studies have been carried out by thermogravimetric measurements. The reactions were followed by recording the weight gains with an automatic MacBain microbalance of cylindrical specimens with approximate dimensions 0.5 cm diameter by 2.5 cm. The surfaces of specimens were prepared by mechanical polishing. In the case of calcium, this polishing was followed by a high-temperature vacuum treatment with sublimation of a fixed amount of metal. This sublimation treatment involves a controlled break of the pre-existing oxide film on the surface metal. The sublimation of the metal is permitted by high vapor pressure of calcium at high temperatures (2).

The effect of the impurities in the nitrogen was determined by comparison of data from the nitriding with conventionally purified nitrogen and from nitriding with pure nitrogen prepared as detailed above. Three kinetic parameters are affected by the presence of impurities in the gas phase: the reaction threshold, the rate, and the type of reaction kinetics.

The nitriding of calcium begins at about 200°C in pure nitrogen whereas it commences at room temperature in undried commercial nitrogen. After a few days, such a specimen is covered by a dark scale of nitride exhibiting white spots of hydroxide. The same behavior can be observed by exposing the sample to the atmosphere of the laboratory. It would appear that traces of water vapor behave as an initiator of the reaction probably by transformation of the compact preoxidation film to a porous hydroxide. In pure nitrogen, calcium remains bright indefinitely at room temperature. Identical observations have been made by Fromont (6) for the nitriding of lithium.

In dry nitrogen the residual oxygen produces an important reduction in the nitriding rate and even a change in the type of kinetics. The results of nitriding by dried commercial nitrogen and pure nitrogen are shown for calcium at 600° and 675°C and magnesium at 510°C (Fig. 2, 3, and 4, respectively). The nitriding of calcium at 600°C corresponds to the formation of the tetragonal form of the nitride. At this temperature the kinetics of nitriding by pure nitrogen followed a parabolic law. Traces of residual oxygen in commercial nitrogen lower the reaction rate considerably (Fig. 2). Nitriding at 675°C corresponds to the formation of the cubic form of the nitride. In this case,

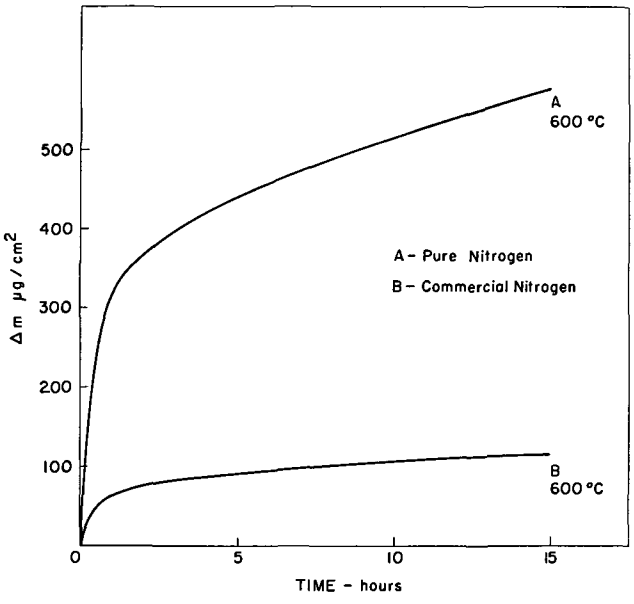

Fig. 2. Nitriding of calcium at 600°C

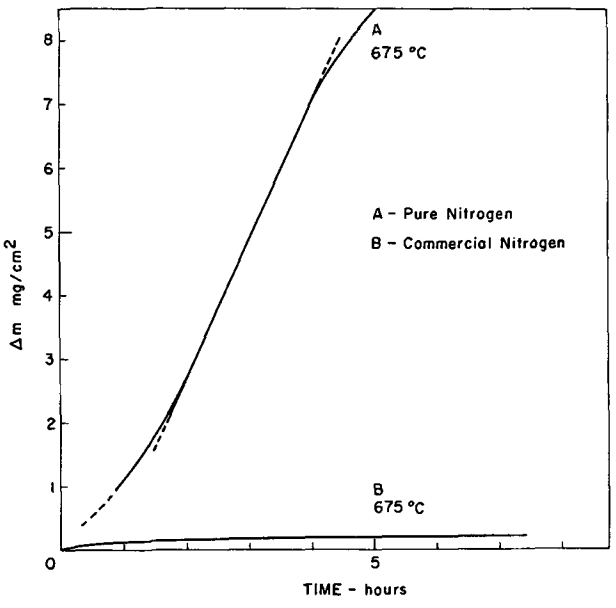

Fig. 3. Nitriding of calcium at 675°C

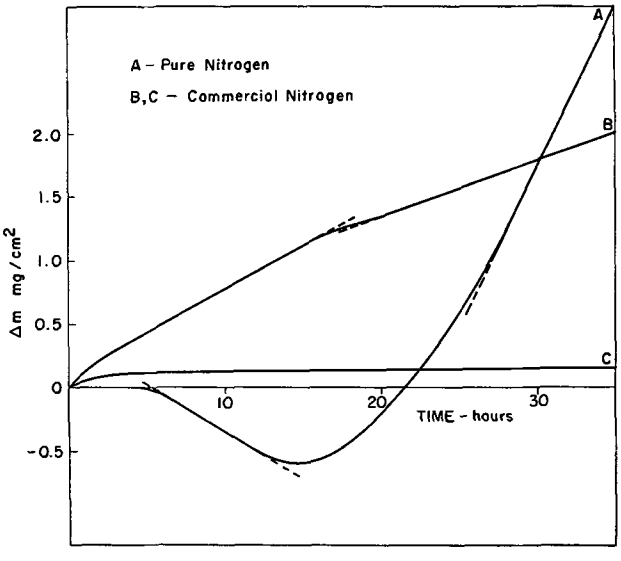

Fig. 4. Nitriding of magnesium at 510°C; curve A, by pure nitrogen; curve B, by flowing commercial nitrogen; curve C, by static commercial nitrogen in a closed system.

the reaction rate is lower in the presence of impurities, and the kinetics are also modified. The kinetics pass from a linear regime in pure nitrogen to a parabolic regime in commercial nitrogen (Fig. 3). It is significant that the formation of the two crystallographic forms of calcium nitride correspond to two types of kinetics (2). In both former experiments with commercial nitrogen, the specimens exhibit an inner dark compact scale covered by an external white porous scale. The compact scale has been found to be identical to the oxynitride scale formed during reaction of calcium with air (7). The white scale is pure CaO. On the other hand, in pure nitrogen the product of the reaction is only nitride without any traces of oxide. It therefore appears that the calcium reacts preferentially with the residual oxygen in the nitrogen to form a compact scale, resulting in an important decrease in the reaction rate.

This feature is identical in the case of nitriding of magnesium. In Fig. 4, two kinds of experiment for nitriding of magnesium by commercial nitrogen are shown. The first one (curve B) was done by reaction in flowing nitrogen, the second one (curve C) in a closed system. Both involve a significant decrease of the reaction rate compared with the nitriding by pure nitrogen (curve A). After reaction, the specimens exposed to commercial nitrogen are covered by a double scale of an inner compact layer, mainly of black non-stoichiometric oxide, and an outer porous layer of white MgO (8). Thus, as in nitriding of calcium, the residual oxygen in the nitrogen reacts preferentially with the metal forming a protective layer which decreases the reaction rate. This is particularly evident in a closed-system experiment where the reaction stops when all the initial impurities have been absorbed by the metal (curve C). Finally, the kinetics of nitriding of magnesium by pure nitrogen (curve A) show that sublimation of metal occurs simultaneously with the surface reaction. These kinetics are very different from those observed in previous investigations (9). These latter results are always more or less similar to the kinetics observed here for reaction of magnesium with commercial nitrogen.

Summary

The preparation of pure nitrogen by decomposition of sodium azide allowed a study of the effect of impurities in the gas phase on the nitriding of calcium and magnesium. It has been found that the residual oxygen in nitrogen reacts preferentially with both metals, and that in pure nitrogen the kinetics of nitriding of these metals are very different from those formerly ascribed to these reactions. A wide range of applications for this supply of high-purity nitrogen has also been found in nitrides syntheses (10-12) or would be possible in any reactions involving nitrogen atmosphere, such as the study of nitrogen diffusion in nitrides by solid-gas exchange method.

Safety Recommendations

Drying and decomposition of sodium azide are the two most dangerous steps in this nitrogen preparation technique. A too-rapid decomposition may involve the explosion of the decomposition tube and projection of hot sodium. In order to prevent nitrogen over-pressure, this tube is closed at one end by an ejectable glass joint. Also, the heating of the decomposition tube has to be slow and localized and directly controlled by the operator.

Manuscript submitted April 20, 1970; revised manuscript received Dec. 17, 1970.

Any discussion of this paper will appear in a Discussion Section to be published in the December 1971 JOURNAL.

REFERENCES

1. J. Bénard, "L'oxydation des métaux," p. 18, Gauthier-Villars, Paris, (1962).
2. R. Streiff, *Rev. Chim. Miné.*, **4**, 707 (1967).
3. G. Brauer, "Handbuch der Prëparative Anorganishem Chemie," Vol. 1, p. 411, Enke Stuggart (1960).
4. F. Marion, A. Duquesnoy, and P. Dherbonnez, *Bull. Soc. chim. France*, 1290 (1964).
5. A. Kotlar and P. Gerdanian, *ibid.*, 629 (1965).
6. M. Fromont, *Rev. Chim. Miné*, **4**, 447 (1967).
7. R. Streiff, *C. R. Acad. Sc.*, **265**, 587 (1967).
8. J. Aubry, B. Dupré, and R. Streiff, *ibid.*, **266**, 1223 (1968).
9. L. G. Murgulescu and D. Cismaru, *Rev. Chim. Acad. Rep. Pop. Roumaine*, **5**, 251 (1960).
10. J. Aubry, M. Fromont, and R. Streiff, *C. R. Acad. Sc.*, **262**, 1785 (1966).
11. J. F. Brice, J. P. Motte, and R. Streiff, *ibid.*, **269**, 910 (1969).
12. J. P. Motte, Thesis, University of Nancy (1970).

Chemical Polish and Etch for Lithium, Sodium and Potassium

R. N. Castellano and P. H. Schmidt

Bell Telephone Laboratories, Incorporated, Murray Hill, New Jersey 07974

A survey of various alcohols has been made to determine the surface conditions that occur on immersion of lithium, sodium, and potassium. Alcohols are often used in the laboratory to polish and etch these alkali metals. Bowers *et al.* (1) report that a bath of 98% xylene and 2% isopropyl alcohol is a simple method of etching sodium. Grimes (2) notes that potassium is etched in a bath of 99% xylene and 1% isopropyl alcohol. Both solutions require critical surface conditions and timing prior to and during etching before grain boundary delineation is observed. A bath of 2-6% secondary butyl alcohol in xylene has been reported to be an effective etch for potassium metal (3-4).

Other polishes and etches of alkali metals employ the use of chemicals other than alcohols. Methyl ethyl ketone is a satisfactory polish for potassium (5), and (1) has reported using diethyl ether as an etch for lithium after first polishing the metal in methanol.

The surfaces of lithium and potassium are polished to a high luster with certain nondiluted alcohols used in the survey. Excellent grain boundary delineation on the surfaces of lithium and sodium is observed after only 30 sec.

The results of this survey indicate that these alcohols are superior to other chemicals in producing a strain free etch and/or polish of the alkali metals investigated. The surfaces of these metals exhibit a brilliant metallic luster and are smooth and free of pits (minute indentations of the surface). These alcohols are now commonly used in the preparation of bulk samples of lithium, sodium, and potassium for the investigation of certain phenomena such as conduction electron spin resonance (CESR) and cyclotron resonance.

Key words: alkali metals, alcohols.

Method

Lithium, sodium, and potassium were cut under mineral oil with a razor blade and were then placed in heptane to dissolve the oil and prevent oxidation of the metal by moist air. After immersion in the alcohol, the metal was taken directly to a beaker of tetrahydrofuran in order to stop the reaction and to dissolve the alkali metal alcoholate (alkoxide) which formed. The following reaction occurred

$$\underset{\text{alcohol}}{ROH} + \underset{\text{metal}}{M} \rightarrow \underset{\text{alcoholate}}{RO^{-}{}^{+}M} + 1/2\,H_2 \qquad [1]$$

The reaction of the alkali metals with alcohols decreased with increasing molecular weight of the alcohol due to the decreasing solubility of the alcoholate in the alcohol.

The metal was placed in a petri dish containing tetrahydrofuran and observed visually and then optically with a microscope.

The surface conditions of lithium, sodium, and potassium observed after immersion in the alcohols used in this investigation are explained in Table I.

Results

The best polish (the removal of material due to the nonpreferential cutting of the various {hkl} planes) for lithium is obtained using methanol. 2-Propanol is as effective as ethanol to produce a brilliantly polished surface on potassium. The reaction is less rapid with 2-propanol, however, and there is less risk of an explosive reaction.

Table I. Surface conditions observed after immersion in alcohols

Alcohol used	Lithium*	Sodium	Potassium
Methanol CH_3OH MW 32.04	Surface had a high luster and was smooth after 30 sec	Grain boundary delineation was observed. Some {hkl} planes brilliant, some dull, but all are pitted	Violent reaction
Ethanol CH_3CH_2OH MW 46.05	Grain boundary delineation was observed after 30 sec. Some {hkl} planes brilliant and smooth	Grain boundary delineation was observed. Some {hkl} planes brilliant, some dull, but all are pitted	Surface brilliant and smooth after 3 sec
2-Propanol $CH_3CHOHCH_3$ MW 60.10	Grain boundary delineation was observed after 30 sec. Most {hkl} planes dull	Grain boundary delineation was observed. Some {hkl} planes brilliant, some dull	Surface brilliant and smooth after 10 sec
3-Pentanol $CH_3CH_2CHOHCH_2CH_3$ MW 88.15	Surface became black after 30 sec even after preliminary methanol polish	Grain boundary delineation was observed after 30 sec. All {hkl} planes brilliant, but razor marks still observed	Surface became dull after 30 sec
1-Heptanol $CH_3(CH_2)_5CH_2OH$ MW 116.20	Surface became dull after 30 sec even after preliminary methanol polish	Grain boundary delineation was observed after 30 sec. Most {hkl} planes brilliant, but all are pitted	Surface became dull after 30 sec
1-Octanol $CH_3(CH_2)_6CH_2OH$ MW 130.23	Surface became dull after 30 sec even after preliminary methanol polish	Grain boundary delineation was observed after 30 sec. All {hkl} planes were dull and pitted	Surface became dull and pitted after 30 sec
2-Octanol $CH_3CHOH(CH_2)_5CH_3$ MW 130.23	Surface became dull after 30 sec even after preliminary methanol polish	Grain boundary delineation was observed after 30 sec. All {hkl} planes were dull and pitted	Surface became dull and pitted after 30 sec
2,4-Dimethylphenol $(CH_3)_2C_6H_3OH$ MW 122.17	Surface became dark after 15 sec even after preliminary methanol polish	Surface became dull and pitted after 30 sec	Surface became dull and pitted after 30 sec
Nonyl $CH_3(CH_2)_7CH_2OH$ MW 144.26	Surface became dark after 15 sec even after preliminary methanol polish	Grain boundary delineation was observed after 30 sec. Most {hkl} planes brilliant and smooth	Surface became dull and pitted after 30 sec
α-Propylbenzyl $C_6H_5CHOH(CH_2)_2CH_3$ MW 150.22	Surface became dark after 15 sec even after preliminary methanol polish	Grain boundary delineation was observed after 30 sec. Some {hkl} planes brilliant	Surface became dull and pitted after 30 sec
p-iso-propylbenzyl $(CH_3)_2CHC_6H_4CH_2OH$ MW 150.22	Surface became dark after 15 sec even after preliminary methanol polish	Grain boundary delineation was observed after 30 sec. Some {hkl} planes brilliant	Surface became dull and pitted after 30 sec
α,α-Dimethylphenethyl $(CH_3)_2COHCH_2C_6H_5$ MW 150.22	Surface remained brilliant for several min after preliminary methanol polish	Surface became dark after 30 sec	Surface turned purple after 30 sec

* Immersion of lithium metal in methanol was required to remove the oxide layer prior to immersion in the higher molecular weight alcohols.

Bowers *et al.* (1) reports that the reaction rate for the chemical etch (the removal of material due to the preferential cutting of the various {hkl} planes) for sodium requires several minutes. Superior results are obtained using nonyl alcohol, and excellent grain boundary delineation is observed after 30 sec. Ethanol is a very effective etch for lithium.

Conclusion

A survey of various alcohols has been made to determine the surface conditions that occur on immersion of lithium, sodium, and potassium. Only a few seconds are required to polish the surfaces of lithium and potassium to a high luster using methanol and 2-propanol respectively. Excellent grain boundary delineation on the surfaces of lithium and sodium is observed after immersion of the metals in ethanol and nonyl alcohol respectively for 30 sec. The results of this survey indicate that these alcohols are superior to other chemicals in producing a brilliant polish and/or etch of the alkali metals investigated.

Manuscript submitted Sept. 25, 1970; revised manuscript received Dec. 9, 1970.

Any discussion of this paper will appear in a Discussion Section to be published in the December 1971 JOURNAL.

REFERENCES

1. R. Bowers, D. Pinnow, and S. Tallman, "Single Crystals of Sodium and Lithium Metals," Materials Science Center Report #3, Cornell University, Ithaca, N. Y. (1961).
2. C. C. Grimes, Doctoral Dissertation, University of California (1962).
3. A. F. Hoyte and E. V. Mielczarek, *Appl. Mater. Res.*, **4**, 121 (1965).
4. H. J. Foster and P. H. E. Meijer, *J. Res. Nat. Bur. Stand.*, **71A**, 127 (1967).
5. P. H. Schmidt and L. W. Rupp, Jr., Unpublished.

The Role of Homogeneous Reactions in Chemical Vapor Deposition

Karl J. Sladek

Department of Chemical Engineering and Electronics Research Center, The University of Texas, Austin, Texas 78712

Chemical vapor deposition (CVD) finds increasing use in the fabrication of thin films for solid-state devices, as well as films for optical and protective coatings. For all of these applications, control of stoichiometry and structure is essential. A knowledge of the detailed mechanism of CVD would be very helpful in devising means to control these critical properties.

Most previous investigators of CVD processes have assumed that deposition reactions are heterogeneous; that is, they occur as catalytic reactions in an adsorbed layer on the surface of the growing film. Interpretations of CVD have accordingly been based on heterogeneous models. For example, Joyce and Bradley (1) discuss their measurements on epitaxial Si growth from SiH_4 in terms of a catalytic mechanism.

There is, however, a large body of evidence which suggests that homogeneous reactions play an important role in CVD. The purpose of the present work was to evaluate the possible importance of homogeneous reactions in CVD. Some qualitative evidence for homogeneous reactions is described next.

Evidence for Homogeneous Reactions

It is helpful to consider first the effect of temperature on homogeneous and heterogeneous reactions. One useful rule, which appears to be rather generally true, is that a catalyst serves to lower the activation energy, E, of a reaction. This suggests that heterogeneous reactions are favored at lower temperatures, while homogeneous reactions are favored at higher temperatures. For the many CVD reactions that take place in the neighborhood of 1000°C, one might expect *a priori* that homogeneous reactions would be favored.

The nonspecificity of substrates for CVD reactions should also be mentioned. By analogy with most catalytic reactions, one would expect that very few materials would serve as effective catalysts for a particular reaction under a given set of conditions. However, it is found in a variety of CVD experiments that solid product is deposited not only on the substrate but also on all hot surfaces which are exposed to the reactant stream. This observation is significant only for the very early stages of growth, since, after a coherent film has appeared, the reactants are exposed only to the surface of the deposited material. However, if no homogeneous formation of product occurred, then growth could not be initiated on noncatalytic substrates.

Key words: chemical vapor deposition, homogeneous reaction model, Si_3N_4, thin films.

Regarding experimental evidence, many investigators have observed formation of a solid precipitate in the gas phase above a heated substrate. For example, Joyce and Bradley (1) observed that precipitation of Si particles was favored by high SiH_4 pressures. Schaffer (2) reports that the use of lower operating pressures prevented formation of Al_2O_3 particles during CVD of that material from $AlCl_3$-H_2O mixtures. Grieco, Worthing, and Schwartz (3) observed the precipitation of NH_4Cl on the cold wall of a reactor during a study of the growth of Si_3N_4 from $SiCl_4$-NH_3 mixtures on a hot Si substrate. Evidently, the NH_4Cl was formed as an intermediate or byproduct in a homogeneous reaction. A similar effect was noted by Joyce and Bradley (1), who observed very thin films of product on the cold walls of their reactor.

All of these observations can be explained by assuming that the reaction occurs in the gas phase and that the product then diffuses to the substrate and forms a film, or instead condenses in the gas phase to form powder.

Homogeneous Reaction Model

The features of a homogeneous CVD reaction can best be considered by treating the limiting case wherein the substrate is completely noncatalytic and serves only as a site for condensation of the solid product, S. For this case, single molecules of S, denoted as S_1, will be formed by the gas phase reaction. If a hot substrate is exposed to a cold reactant stream, as is usually done, then the reaction zone in which S_1 is formed will be localized in a thin region very near the hot substrate; most of the S_1 will then diffuse to the substrate and undergo condensation to form a film. There is, however, a competing process which can

cause powder formation in the gas phase. If the gas phase concentration of S_1, which will be called C_1, becomes too large, then the rate of S_1-S_1 collisions will become appreciable. This will lead to the formation of polymers, S_2, S_3, . . . S_n, in the gas phase, or, in other words, to powder formation.

For the case of a single gaseous reactant, A, these two processes are summarized as follows

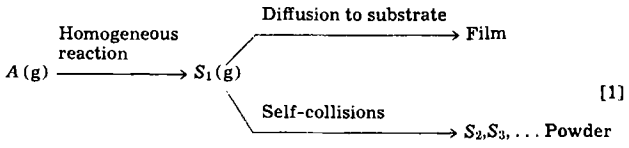

[1]

To quantify this model, a parallel flow geometry is chosen as shown in Fig. 1. Gas at velocity, v, and entrance temperature, T_∞, flows along the substrate, which is maintained at temperature, T_0. Heat transfer occurs, producing a temperature field, $T(x,y)$. Product molecules, S_1, are produced in the gas phase at a local rate depending on $T(x,y)$. Once formed, S_1 can diffuse in the $-x$ direction toward the substrate, or can accumulate along the y direction, or, if C_1 becomes large enough, S_1 dimerizes to S_2 (concentration C_2), and addition of further molecules eventually produces powder particles in the gas phase. A material balance on S_1 follows.

Production = Diffusional Transport + Accumulation + Condensation to Powder

$$k'e^{-E/RT(x,y)} = -D\frac{\partial^2 C_1}{\partial x^2} + v\frac{\partial C_1}{\partial y} + k_{11}C_1^2 + k_{12}C_1C_2 + \ldots \quad [2]$$

The production term consists of a reactant concentration dependent function, k', and an Arrhenius function with activation energy, E. The diffusional transport term represents the rate of change of the flux of S_1 with x. The powder condensation terms represent collisions of S_1 with S_1, with S_2, and so on. As this equation is rather complicated in its original form, some simplifications are in order.

The function k' depends on reactant concentration C_A. To simplify the equation, only situations in which C_A is constant for all x and y are considered here. This applies to cases in which the fractional conversion of A is small and the mass transfer coefficient of A is large. To evaluate the accumulation term, $v\,\partial C_1/\partial y$, an approximate boundary layer analysis was carried out, and this term was found to be negligible. Neglect of this term amounts to a steady-state approximation. The concentration of S_1 is always very small; the S_1 that is formed at a point either diffuses away or undergoes condensation to powder.

The powder condensation terms involve polymers S_n with $n = 1, 2, \ldots$. Material balances can be written for diffusion and growth of every S_n, but this leads to a very complicated set of equations. A considerable simplification is achieved by including only the term for formation of dimers, S_2. Qualitatively, when dimers have been formed, they will diffuse more slowly than S_1, since they are larger, but they will grow more rapidly than S_1, again because they are larger. For this reason, it is suggested that if the dimerization rate becomes significant, not only dimers but also solid particles will be found.

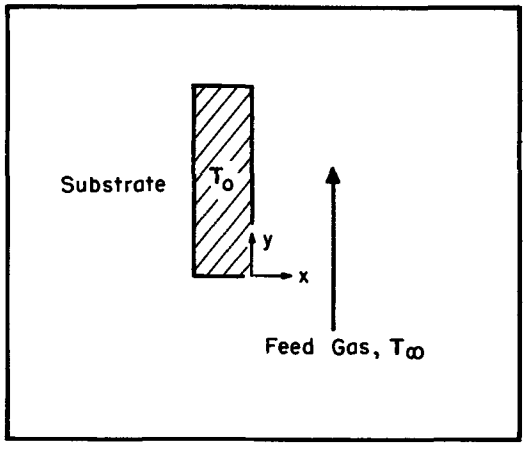

Fig. 1. Coordinate system

With these simplifications, Eq. [2] becomes

$$k'e^{-E/RT(x)} = -D\frac{d^2C_1}{dx^2} + k_{11}C_1^2 \quad [3]$$

The boundary condition at the substrate is $C_1 = 0$ at $x = 0$. This condition assumes that the growing film is sufficiently refractory that it exerts a negligible vapor pressure; that is, every molecule of S_1 that arrives at the film sticks to it. A similar assumption allows the calculation of k_{11} from a hard sphere kinetic theory model; it is assumed that S_1-S_1 bonds are sufficiently strong that S_2 has no tendency to dissociate. The "critical nucleus" is then just one molecule and every S_1-S_1 collision results in dimerization. The rate of removal of S_1 is then twice the S_1-S_1 collision rate

$$k_{11} = 2\left(\frac{4\pi kT}{m}\right)^{1/2}\sigma^2 \quad [4]$$

where σ is the collision diameter of S_1

The parameter of most interest is the film growth rate, which is equal to the flux of S_1 at the wall, J_0

$$J_0 = D\left(\frac{dC_1}{dx}\right)_{x=0} \quad [5]$$

As is shown presently, J_0 depends on the temperature gradient at the substrate, T_0'

$$T_0' = \left|\frac{dT}{dx}\right|_{x=0} \quad [6]$$

This quantity depends on the fluid mechanical and thermal properties of the flow and can be calculated by well-known methods; an example is given later.

Equation [3] now applies to each point, y, along the substrate. Normal to each point there is a gas phase temperature distribution, $T(x)$. However, as pointed out earlier, the reaction rate is localized very near the substrate because the Arrhenius term varies so steeply with temperature. This allows linearization of $T(x)$ and $1/T(x)$ near $x = 0$, with little loss of accuracy.

$$\frac{E}{RT(x)} = \frac{E}{RT_0}\left(1 + \frac{T_0'}{T_0}x\right) \quad [7]$$

The relative importance of film condensation and powder formation can be shown by incorporating Eq. [7] and converting Eq. [3] to dimensionless form using the following definitions

$$X \equiv \left(\frac{E}{RT_0}\right)\left(\frac{T_0'}{T_0}\right)x \quad [8]$$

$$Y \equiv \frac{D\left(\frac{E}{RT_0}\right)^2\left(\frac{T_0'}{T_0}\right)^2}{k_0}C_1 \quad [9]$$

$$k_0 \equiv k'e^{-E/RT_0} \quad [10]$$

The resulting equation is

$$e^{-X} = -\frac{d^2Y}{dX^2} + MY^2 \quad [11]$$

$$M \equiv \frac{k_0k_{11}}{D^2\left(\frac{E}{RT_0}\right)^4\left(\frac{T_0'}{T_0}\right)^4} \quad [12]$$

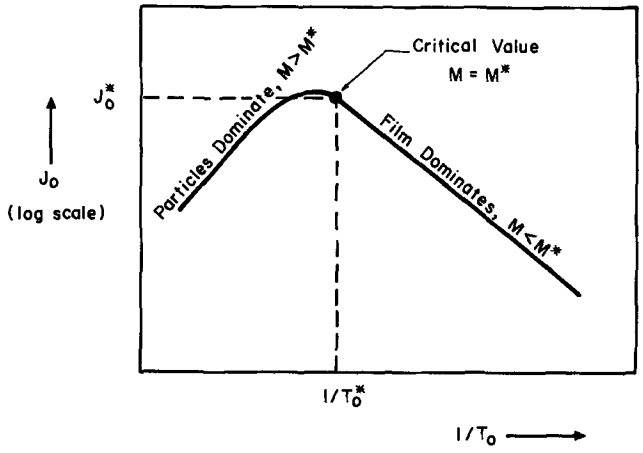

Fig. 2. Interpretation of growth rate curves

All the physical parameters now appear in the single dimensionless group, M. The size of M determines the importance of powder formation.

A typical growth rate-temperature curve is sketched in Fig. 2, along with the interpretation of the present model. At low temperatures, M is small and powder formation is negligible. For this condition, solution of Eq. [11] without the last term gives

$$J_o = \frac{k_o}{\left(\frac{E}{RT_o}\right)\left(\frac{T_o'}{T_o}\right)} \qquad [13]$$

As T_o increases, M increases rapidly until the rate of dimerization becomes comparable with the rate of film formation. Dimers are followed by larger clusters, and at higher M most of the reaction product is in the form of particles rather than film. The transition from film to particle formation occurs rather suddenly at a critical value, M^* (with associated values, J_o^* and T_o^*), which is taken to be the point at which the curve begins to deviate from a constant slope. The exact value of M^* has not been determined, but approximate solutions to Eq. [11] indicate that M^* is of order unity.

Substituting Eq. [13] into Eq. [12] gives the limiting film growth rate J_o^* above which particle formation becomes important

$$J_o^* = M^* \frac{D^2 \left(\frac{E}{R}\right)^3 (T_o')^3}{k_{11}(T_o^*)^6} \qquad [14]$$

Since the purpose of a CVD process is to grow a film, the value of J_o^* represents an approximate upper limit on the useful growth rate. From the form of Eq. [14] one can predict, for example, that J_o^* can be increased by increasing the diffusivity of S_1 through the gas mixture; D would be increased, for example, by lowering the total pressure.

In order to test Eq. [14], several sets of Si_3N_4 growth rate data were interpreted as shown in Fig. 2. An example calculation is described in the Appendix. Calculated results are given in Table I.

Comparison of J_o^* with the last quantity in Table I shows agreement with Eq. [14] to about an order of magnitude, if M^* is taken to be unity. However, the values of J_o^* cover less than an order of magnitude and, consequently, this is not a very strong test of the equation. Considering the uncertainties required in all the estimates, the agreement is at least encouraging.

Discussion

It has been suggested that homogeneous reactions often play an important role in CVD processes. A quantitative model was developed for the limiting case in which reaction occurs only in the gas phase. After some simplifications and approximations, it was shown that the relative importance of film *vs.* powder formation is controlled by a dimensionless group containing all the physical parameters of the system. Literature values of maximum film growth rates of Si_3N_4 showed order of magnitude agreement with the predicted behavior.

CVD processes can be expected to cover a broad range, including completely homogeneous, completely heterogeneous catalytic, and intermediate or mixed mechanisms. It is likely that many of the CVD processes which have previously been assumed to arise from heterogeneous catalytic reactions are, in fact, the result of homogeneous reactions. The present work provides one means of evaluating this possibility.

APPENDIX

As a sample calculation, use of the data of Chu, Lee, and Gruber (5) is described. Curve A in Fig. 2 of that reference gives a value of J_o^* of 250 Å/min at $10^3/T_o^*$ of 0.85. Converting the units using the observed product density of 2.8 g/cm^3 gives 830 x 10^{-12} moles/cm^2-sec. To estimate k_{11}, Eq. [4] was used, with a collision diameter for Si_3N_4 of 5.06Å, which was estimated from the density (3.44 g/cm^3) of the crystalline solid. The same type of estimate of σ is incorporated into the Gilliland Equation (7), which was used to find D, the diffusivity of Si_3N_4 in NH_3. Since D and k_{11} are both relatively insensitive to temperature, a fixed value of 1000°C was used in these calculations.

The temperature gradient at the surface, T_o', was estimated using known results for heat transfer in laminar boundary layers (8). Using the reported reactor size and gas flow rate (5) and estimates of properties of NH_3 at 1000°C (7), the Reynolds Number was estimated to be 10.2, and the Nusselt Number, averaged between $y = 0$ and $y = 1$ cm, was found to be 2.0. Using $T_o = 1180$°K and $T_\infty = 298$°K gave a T_o' of 1770°K/cm.

The other sets of data (4, 6) were treated in the same way. In these studies, H_2 was the carrier and consequently D was larger. For the data of Yoshioka and Takayanagi (6) flow was transverse instead of parallel to the substrate. For this case, T_o' was estimated from equations for heat transfer to a sphere (8).

It should be clear from all the estimates required that the test of the model shown in Table I is only a rough approximation.

Acknowledgment

This work was supported by the Joint Services Electronics Program under Research Grant AFOSR 69-1792.

Manuscript submitted May 28, 1970; revised manuscript received *ca.* Dec. 7, 1970. This was Paper 153

Table I. Si_3N_4 deposition parameters

Reference	Reactants/carrier	J_o^* (mole/cm^2-sec)	$1000/T_o^*$ (°K^{-1})	E (kcal/mole)	T_o' (°K/cm)	k_{11}/D^2 (sec/mole-cm)	$D^2\left(\frac{E}{R}\right)^3 (T_o')^3/k_{11}(T_o^*)^6$ (mole/cm^2-sec)
(4) Fig. 3, Upper curve	$SiH_4 + NH_3/H_2$	6000 x 10^{-12}	0.85	52	730	1.86 x 10^{12}	1410 x 10^{-12}
(5) Fig. 2, Curve A	$SiH_4 + NH_3/NH_3$	830 x 10^{-12}	0.85	17	1770	17.9 x 10^{12}	73 x 10^{-12}
(6) Fig. 2, Lower N_2H_4 curve	$SiH_4 + N_2H_4/H_2$	1300 x 10^{-12}	1.05	54	440	1.86 x 10^{12}	1420 x 10^{-12}

presented at the Los Angeles Meeting of the Society, May 10-15, 1970.

Any discussion of this paper will appear in a Discussion Section to be published in the December 1971 JOURNAL.

REFERENCES

1. B. A. Joyce and R. R. Bradley, *This Journal*, **110**, 1235 (1963).
2. P. S. Schaffer, "Evaluation of Vapor Deposition Growth of Oxide Single Crystals from Metal Halides," AD-616914 (1965).
3. M. J. Grieco, F. H. Worthing, and B. Schwartz, *This Journal*, **115**, 525 (1968).
4. K. E. Bean, P. S. Gleim, and R. L. Yeakley, *ibid.*, **114**, 733 (1967).
5. T. L. Chu, C. H. Lee, and G. A. Gruber, *ibid.*, **114**, 717 (1967).
6. S. Yoshioka and S. Takayanagi, *ibid.*, **114**, 962 (1967).
7. J. H. Perry, Editor, "Chemical Engineers' Handbook," Third Ed., pp. 370-371, 538-539, McGraw-Hill, New York (1950).
8. H. Grober, S. Erk, and U. Grigull, "Fundamentals of Heat Transfer," Chap. 10 and 12, McGraw-Hill, New York (1961).

Brief Communication

Preliminary Results on the Oxidation of GaAs and GaP during Chemical Etching

B. Schwartz*

Bell Telephone Laboratories, Incorporated, Murray Hill, New Jersey 07974

Most of the studies on chemical etching of semiconductors have concentrated on systems used for silicon and germanium (1), while relatively little effort has been expended in studying etchants used on compound semiconductors (2). As part of a program to study chemical etching of GaAs and GaP, it was decided to examine first the oxidation step of the etching process. This communication describes results obtained on exposing clean GaAs and GaP surfaces to a number of different oxidizing reagents. All samples were prepared using a bromine-methanol (3) solution (2 ml to 4 l, respectively for GaAs and 1½ ml to 4 l when GaP was being polished) on a rotating assembly containing a Pellon-W face cloth. Both (100)- and ($\bar{1}\bar{1}\bar{1}$)-oriented, irregularly shaped samples of heavily doped ($\sim 10^{18}$) n-type and high-resistivity semi-insulating material were used for this study. After being polished and cleaned, the samples were placed in a test tube containing 25 to 50 ml of the desired concentrated reagent; the test tube was lightly corked and then allowed to stand for the desired time. For the high-temperature exposures, the samples were immersed in a heated Pyrex beaker containing the reagent. Just before measurement (in some instances the day before) the samples were carefully removed from the test tube, blot dried with the edge of a piece of filter paper, and then allowed to air dry further at room temperature in a laminar flow hood. In only one case, the H_2SO_4-treated samples, was heat used for drying the samples; the maximum temperature reached was about 250°C.

After drying, the samples were examined by powder pattern x-ray diffraction and by electron diffraction to determine the structure and composition of the surface films. Those samples which were still highly reflecting were then evaluated by ellipsometry.[1] The refractive index of a deposited film was determined and one sample of oxidized GaAs was analyzed further with an electron beam microprobe.

The results of these experiments are shown in Tables I and II for GaAs and GaP, respectively. The following is a brief summary of some of the more important aspects of these results.

1. $Ga_2O_3 \cdot H_2O$ is a major intermediate in the etching of GaAs and GaP in aqueous systems.

2. H_2O is an important oxidant for GaAs, and H_2O_2 is an important oxidant for GaP.

3. H_2O also serves as the solvent for As_2O_3 or P_2O_5 in the formation of $Ga_2O_3 \cdot H_2O$ as the principal component of the as-grown native oxide film (4).

4. The solubility of As_2O_3 in H_2O depends strongly on the pH of the system.

5. Residual oxide layers of 25 to 50Å are always present on GaAs and GaP after being etched in bromine-methanol.

6. Oxide layers of less than a few hundred angstroms grown on both GaAs and GaP appear to be amorphous when examined by x-ray or electron diffraction.

Table I. Effect of oxidants on GaAs

Orientation	Dopant	Oxidant	Time (days)	Surface product
(100)	Te $\sim 10^{18}$	—	—	25Å[a]
(100)	Te $\sim 10^{18}$	CH_3OH	6	35Å[a]
(100)	Te $\sim 10^{18}$	H_2O (Room T)	6	850Å[a] (R.I. $\sim$ 1.7)[a]
(100)	Si $\sim 10^{18}$	H_2O (Warm 60°C)	6	$Ga_2O_3 \cdot H_2O$[b] (Ga:O::1:2)[c]
(100)	Te $\sim 10^{18}$	H_2O_2	6	115Å[a]
(100)	Te $\sim 10^{18}$	H_2SO_4[d]	6	$Ga_2(SO_4)_3$[b]
($\bar{1}\bar{1}\bar{1}$)	S.I.	HNO_3	5	As_2O_3[b] powder[e]
(100)	Te $\sim 10^{18}$	HCl	5	55Å[a]
($\bar{1}\bar{1}\bar{1}$)	S.I.	NaOH	5	Na_2CO_3[b]
(100)	Te $\sim 10^{18}$	NaOCl	6	dull strained surface

R.I.—Refractive Index.
S.I.—Semi-insulating.
[a] From ellipsometric analysis.
[b] From x-ray analysis.
[c] From electron microprobe analysis.
[d] Sample dried at 250°C.
[e] The GaAs was completely converted to a white powder.

* Electrochemical Society Active Member.

Key words: oxidation, gallium arsenide, gallium phosphide, gallium oxide monohydrate.

[1] The film thicknesses reported are to be considered as relative, since the absolute references have not been specifically defined for these materials as yet.

Table II. Effect of oxidants on GaP

Orientation	Dopant	Oxidant	Time (days)	Surface product
$(\bar{1}\bar{1}\bar{1})$	Te $\sim 10^{18}$	—	—	35Å[a]
$(\bar{1}\bar{1}\bar{1})$	Te $\sim 10^{18}$	CH_3OH	7	45Å[a]
$(\bar{1}\bar{1}\bar{1})$	Te $\sim 10^{18}$	H_2O (Room T)	7	60Å[a]
$(\bar{1}\bar{1}\bar{1})$	Te $\sim 10^{18}$	H_2O (100°C)	1/3	100Å[a]
$(\bar{1}\bar{1}\bar{1})$	Te $\sim 10^{18}$	H_2O_2	7	250Å[a]
$(\bar{1}\bar{1}\bar{1})$	Te $\sim 10^{18}$	H_2SO_4[c]	28	$Ga_2O_3 \cdot H_2O$[b,d]
$(\bar{1}\bar{1}\bar{1})$	Te $\sim 10^{18}$	HNO_3	7	90Å[a]
$(\bar{1}\bar{1}\bar{1})$	Te $\sim 10^{18}$	HCl	7	matte finish
$(\bar{1}\bar{1}\bar{1})$	Te $\sim 10^{18}$	H_3PO_4	7	dull stained surface
$(\bar{1}\bar{1}\bar{1})$	Te $\sim 10^{18}$	NaOCl	5	NaCl[b]

[a] From ellipsometric analysis.
[b] From x-ray analysis.
[c] Sample dried at 250°C.
[d] Only found on one part of sample.

7. Thicker oxides can be grown at room temperature on heavily doped GaAs than on GaP equivalently doped.

The potential device applications of these "native oxide" films are presently being investigated (5).

Acknowledgments

I would like to thank A. C. Adams and R. H. Kaiser for their ellipsometry measurements, G. W. Kammlott for his electron diffraction evaluations, D. R. Wonsidler for his electron microprobe analysis, J. Colby for his ion microprobe mass analysis, Mrs. M. H. Read and S. E. Haszko for their x-ray analyses of the films, and A. J. Sayko for the help he has given me throughout this study.

Manuscript submitted Jan. 4, 1971.

Any discussion of this paper will appear in a Discussion Section to be published in the December 1971 JOURNAL.

REFERENCES

1. P. J. Holmes, "The Electrochemistry of Semiconductors," Academic Press, New York (1962).
2. H. Gerischer and I. Wallem-Mattes, *Z. Physik. Chem.*, **64**, 187 (1969).
3. M. V. Sullivan and G. A. Kolb, *This Journal*, **110**, 585 (1963).
4. J. Colby, Private communication.
5. R. L. Hartman, B. Schwartz, and M. Kuhn, Submitted to *Appl. Phys. Letters*.

JOURNAL OF THE ELECTROCHEMICAL SOCIETY

ELECTROCHEMICAL TECHNOLOGY

APRIL 1971

The Crystallography of Formed and Cycled PbO_2 Electrodes

A. C. Simon*

Naval Research Laboratory, Electrochemistry Branch, Washington, D. C. 20390

and S. M. Caulder*

International Lead-Zinc Research Organization Research Associate at the Naval Research Laboratory

ABSTRACT

The discharge-recharge cycle process of the lead dioxide electrode was followed by means of optical microscopy. The lead dioxide microstructure obtained from the original formation, using cured electrode materials consisting of a mixture of PbO and basic lead sulfates, was different from that obtained by recharge from an electrode reduced to normal lead sulfate. The lead dioxide electrodes, obtained from various sources and with various microstructures in the original as-formed condition, all converted to practically the same microstructure after receiving only a few cycles. Although the microstructure underwent further change with increasing cycling, the plates from different manufacturers continued to resemble one another after any given number of cycles.

The purpose of this investigation was to explore the possible relationship between the microstructure produced by electrolytic forming and that developed during cycling of the PbO_2 electrode, in particular as to whether such a relationship increased battery longevity. Microscopic examination, made in this laboratory, of large numbers of samples had revealed that there was considerable variation in microstructure among cured or formed plates obtained from different manufacturers. In addition, the microstructure of the formed PbO_2 electrode was also found to be determined by the prior structure of the cured plate of the same manufacture.

Factors which were found to influence the structure of the cured plate were: the type of oxide used in the preparation of the paste, the method by which the acid was added to the paste, how the paste was dried (cured), the temperature and humidity used in curing, and the amount of free lead remaining after curing. Battery manufacturers have found by experience that variations in these factors have a strong effect both on the service life and the available capacity.

It seemed logical to assume that the type of microstructure produced in the formed PbO_2 electrode was the actual end product of these various controlling factors and was therefore important in determining performance. Although random examination had been made of cycled $PbO_2/PbSO_4$ electrodes, no information was available as to whether the microstructure underwent systematic change during cycling. The following experiment was set up to obtain this information and to test the correctness of the above assumptions concerning the relationship between formed and cycled plate structures.

* Electrochemical Society Active Member.

Key words: storage batteries; PbO_2 electrode; lead-acid battery; microstructure, PbO_2 electrode; microscopy of PbO_2 electrodes.

Source and Preparation of the Examined Material

For this examination to be significant, it was necessary that commercial plates of different initial microstructures be examined at intervals during cycle testing. Since NRL is not a manufacturer of batteries, it would obviously not be significant to test and cycle batteries of our own inexpert construction, nor would the microstructure produced necessarily be representative of any commercial battery.

With the cooperation of several manufacturers, four different series of cycled plates were obtained. Two of these series were obtained from manufacturers in the U.S.A., the other two were obtained outside of this country. Two of the series, while consisting of proprietary plates, were cycled in the laboratory of the company of manufacture. The other two series were taken from the assembly line and cycled routinely for life testing.

The only unfortunate result of obtaining plates in this fashion is that, because of the proprietary nature of the product, one is not at liberty to divulge details of preparation, formulation, and curing. Also, in routine plant cycling, significant factors are not always recorded.

After cycling the cells were disassembled in the charged state and the plates were washed and dried according to our specifications and shipped. When the plates were received at NRL, samples were cut from them which were then impregnated with a polyester resin. After this had hardened, the samples were sectioned and the sections polished for microscopic examination.

Observations

The most important observations are stated below.

1. Although the as-formed electrodes obtained from different manufacturers differed in microstructure,

with similar cycling treatment all of the electrodes were found to develop the same type of microstructure. This similarity in structure was observed in the first comparison at 50 cycles, although it probably represented a gradual development from earlier cycles.

2. The microstructure continued to change with additional cycling but remained comparable for each series of cycled plates at an equal number of cycles.

3. Between the 1st and 50th cycle, there was a large change in the electrode structure that transformed the active material to a more or less continuous and interconnected network, which was surrounded by void spaces that were large and of nearly equal size.

4. The large, featureless, and irregularly shaped particles of the electrode structure originally present were gradually replaced by much smaller, more uniformly shaped particles which had the actual appearance of crystals and which were formed along the surfaces of the network as the larger particles were replaced.

5. Electrode failure was accompanied by a breakup of the network structure and a dispersion of the small crystals composing it.

Structure of the formed, dry charged electrodes.— The plates of series A were made from a non-leady oxide, containing a mixture of basic sulfates and which was presumably a furnace product. Series B plates were made from a ball mill oxide containing approximately 25% of free lead. In addition, this oxide had been blended with 25% of Pb_3O_4. The plates of series C were made from a Barton pot oxide which contained 15% of free lead and had also been blended with 5% of Pb_3O_4. Series D was also a Barton pot oxide containing 15% of free lead but had not been blended with another oxide.

There was considerable difference in the way the paste was prepared by the four manufacturers, in the relative amounts of water and sulfuric acid used, and in the method by which these ingredients were added. There was very little difference in the curing of B, C, and D. These three series were stack cured for 72 hr at 90-100% humidity and at uncontrolled room temperature. The method of cure used with series A was not given. Because of the lack of free lead, it was probably an oven-cured product. This material, as cured, also contained large quantities of well-formed tetrabasic crystals, so was probably cured at high temperature and humidity. The grids of the plates were in all cases of an Pb-Sb alloy.

Despite these considerable differences in manufacture, series B, C, and D had a greater similarity in structure after formation than was expected. However, the structures were only superficially the same. Very noticeable in B was the different structure surrounding the sites where filaments of free lead had been present in the uncured plate. In series C and D this was much less noticeable because the free lead particles had been much smaller and spherical, as well as being present in a smaller amount. Two types of particles were evident in B and C, one which was formed from the Pb_3O_4 and the other representing the usual type of PbO_2. A difference in reflectivity, as well as in shape, indicated that the two types of particles were not the same material. A portion of the Pb_3O_4 thus appeared to have gone through the formation unchanged. Other differences were noted when polarized light was used in the examination. Series A was, of course, considerably different from the others and even after formation contained considerable quantities of basic oxides. The types of structures found in the four series of plates after electrolytic formation are shown in Fig. 1-4.

With the exception of series A, the formed but uncycled electrodes were found to have a surface layer with a microstructure that was quite different from that found in the interior of the electrode. This is illustrated by Fig. 5 and, at higher magnification, by Fig. 6. The blurred nature of some portions of Fig. 6 is produced by a combination of the very limited depth of focus at this magnification and by the small curvature of the specimen surface at the intersection of the hard PbO_2 and the soft supporting plastic. Here the PbO_2 forms the elevated portion, while the more depressed areas consist of the plastic impregnant.

The exact cause of this surface layer of different microstructure has not been definitely determined but

Fig. 1. Microstructure of plate A, as formed. Black areas represent voids between the particles. Magnification 600X.

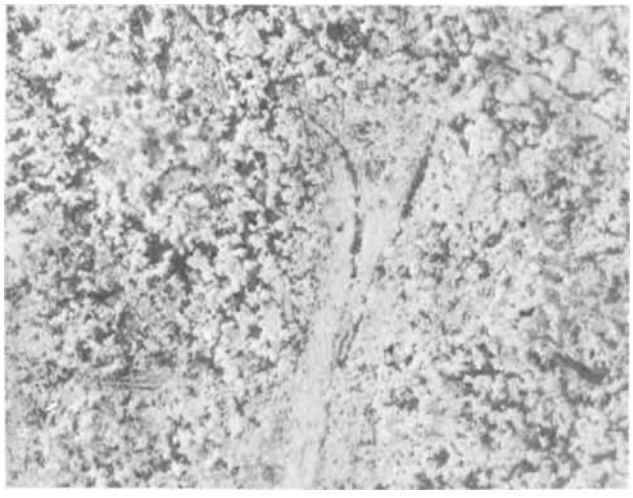

Fig. 2. Microstructure of plate B, as formed. Compare with Fig. 1. Magnification 600X.

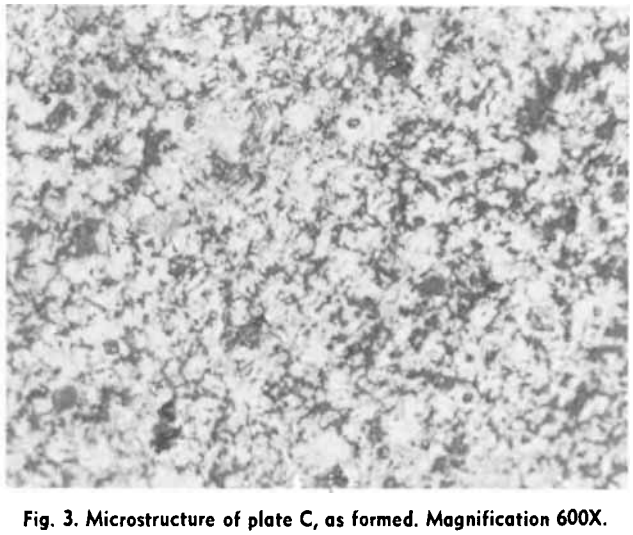

Fig. 3. Microstructure of plate C, as formed. Magnification 600X.

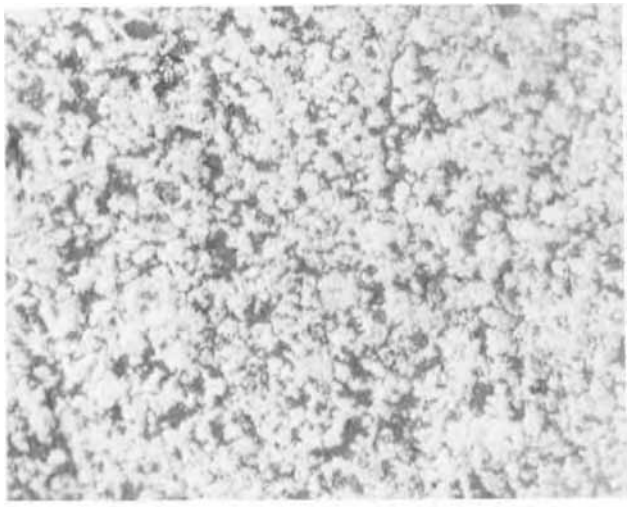

Fig. 4. Microstructure of plate D, as formed. Note similarity to Fig. 3. Magnification 600X.

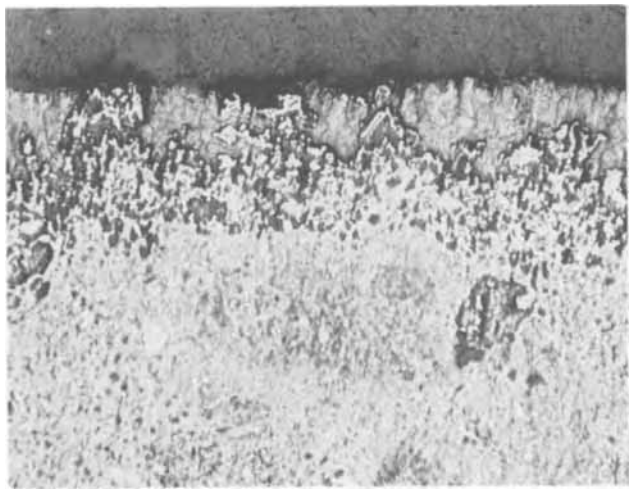

Fig. 5. Microstructure of plate D, near edge, showing the quite different microstructure found at the edge (surface) of the section. Magnification 115X.

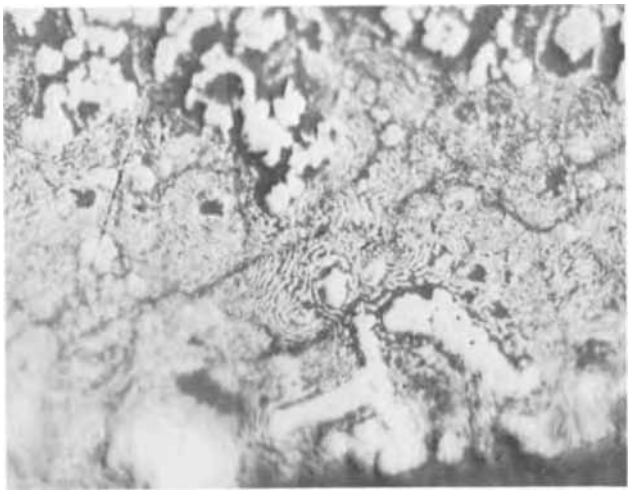

Fig. 6. Edge of plate D at higher magnification showing its odd and relatively fine structure. Magnification 600X.

it is suspected that the cause lies in the chemical change that occurs during the period of time that the cured electrodes are immersed in acid electrolyte before the electrical circuit can be completed for the purpose of electrolytic formation. In this case the surface layers would be converted from basic to normal lead sulfate and this and the surrounding acid environment may be responsible for the changed microstructure.

Changes following a single discharge and recharge.—A series D sample was available that had been given a single discharge and recharge after the original forming. The microstructure of this recharged electrode (Fig. 7) had changed considerably from that of the formed, but uncycled, electrode (Fig. 4). In this recharged plate the microstructure had a finer and more uniform texture, with smaller particles of PbO_2 and with the particles in closer contact with one another than was the case in the formed, uncycled plate. The over-all effect of a single discharge-recharge cycle was to produce a plate with a much more uniform structure and one in which most of the characteristics of the as-formed plate had been removed. It was evident that reformation of PbO_2 from $PbSO_4$ produced a different structure than when formed from the basic sulfate paste of the original manufacture.

Changes during the first 50 cycles of charge-discharge.—Series B, C, and D were compared in the charged state after approximately 50 cycles of operation. Areas were present in each series which contained large residual $PbSO_4$ crystals. However, most areas of the plate contained only PbO_2. The most notable feature of each electrode was the increase in the size of voids within the plate. From structures such as shown in Fig. 1-4, where the voids were relatively small and the PbO_2 particles uniformly distributed, there had been a change to a structure like that shown in Fig. 8. After 50 cycles the void spaces were found to be much larger and somewhat elongated. The PbO_2 had separated into clumps or agglomerates that seemed to be interconnected at one or more points yet mostly surrounded by void.

At 50 cycles there was also a gradient in the electrode structure. The elongated void spaces and chain-like agglomerates of PbO_2 were most evident near the surface of the plate and less evident near the center, so that at the center there was still a uniform structure like that shown in Fig. 7. The three series examined near 50 cycles all showed this opening up of the structure and agglomeration of the PbO_2 particles. Plates of all three series showed the same increase in void size and agglomeration of particles into clumps, as well as an unchanged central portion. When examined in areas where change had occurred, however, all three showed remarkedly similar structure. Compare, for example, Fig. 8 (series D) and 9 (series C).

In addition to the opening up of the structure in the manner just described, there was also a change in the

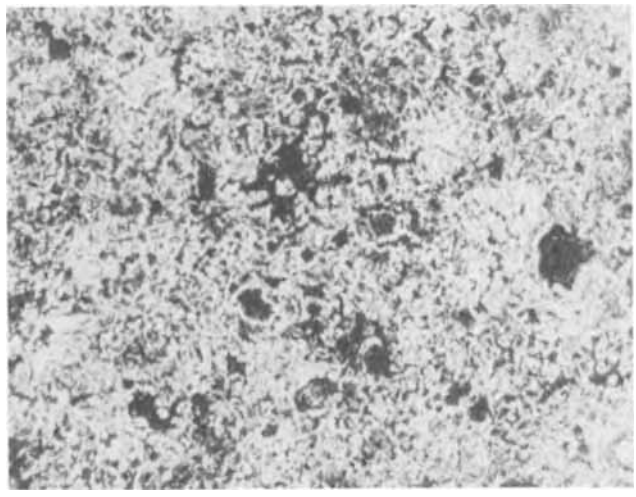

Fig. 7. Structure of plate D after a single discharge-recharge cycle. Compare with Fig. 4. Magnification 600X.

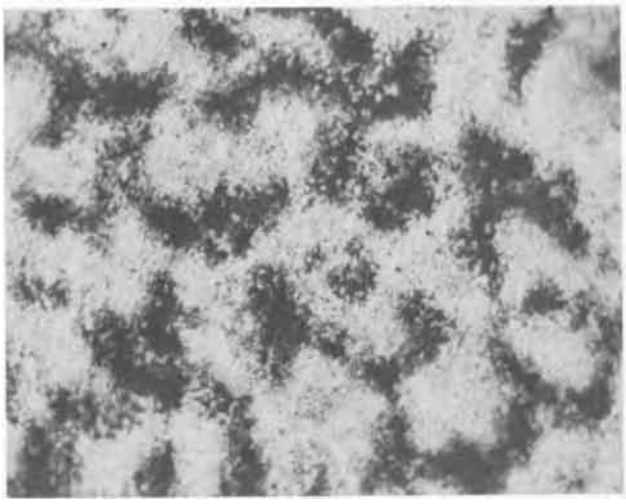

Fig. 8. Structure of plate D after 53 discharge-recharge cycles. Magnification 600X.

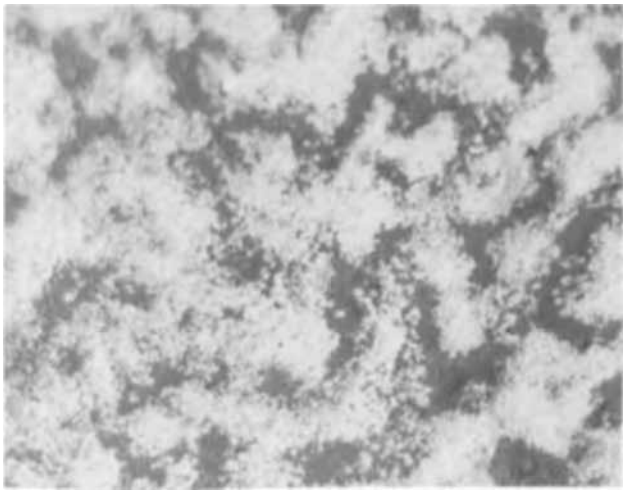

Fig. 9. Structure of plate C after 50 discharge-recharge cycles. Magnification 600X.

appearance of the PbO_2 particles in the reacted portions of the structure. Instead of the small, cell-like structure of PbO_2 formed after one discharge-charge cycle as in Fig. 10 (series D) or the rather nondescript particles found in the formed plate of series C (Fig. 11), for example, all of the plates now showed a structure similar to Fig. 12, in which the agglomerated particles of PbO_2 seemed to be very much smaller and more densely packed.

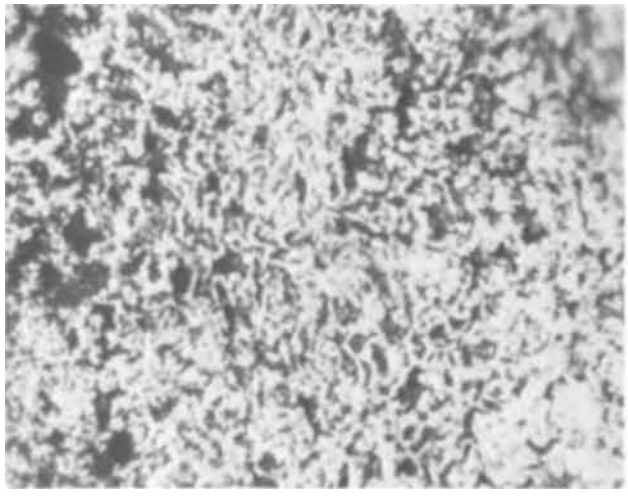

Fig. 10. Structure of plate D after a single discharge-recharge cycle and at a magnification of 1520X.

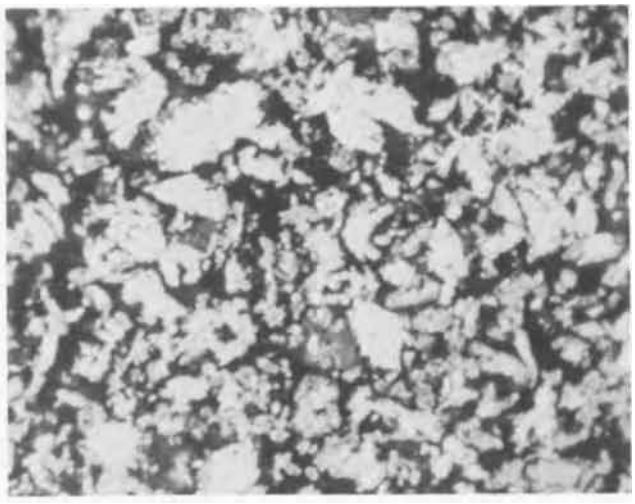

Fig. 11. As-formed structure of plate C at a magnification of 1520X.

Changes occurring between 50 and 100 cycles.—With continued cycling the voids became larger and the amount of material in the agglomerates smaller. The average diameter of the agglomerates decreased and there were less points of apparent contact. The average density of packing of the small particles of PbO_2 in the agglomerates appeared to be about the same as in plates with 50 cycles (Fig. 12).

This was true of series B, C, and D which all looked much as did Fig. 13, but series A was slightly different. A sample of this plate was not available with 50 cycles but at 100 cycles it was found to resemble Fig. 14 in most areas. It will be noted that, while the tendency to form large voids is about the same as in other plates, the agglomerates of the PbO_2 particles have a greater diameter, principally because the particles are less densely packed. The particles making up the agglomerates, however, were only slightly larger than those found in the other series. The size and general shape of the PbO_2 particles in all of the series remained the same in appearance as had been the case at 50 cycles (Fig. 12). A few areas of the series A plate had not yet opened up into the voids like those shown in Fig. 14, but these areas nevertheless had the same structure as that shown in the agglomerates of Fig. 14.

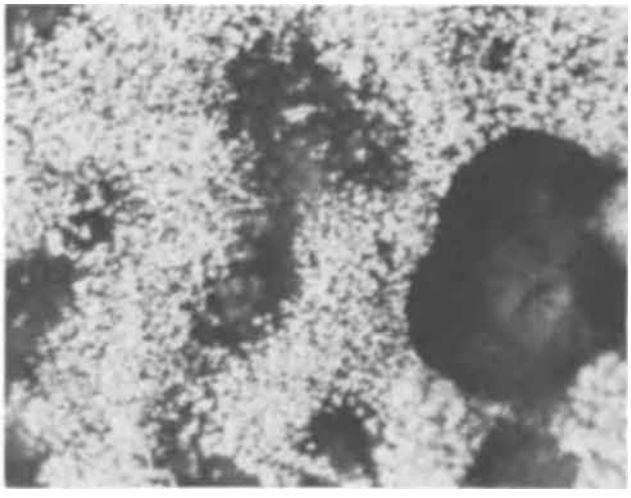

Fig. 12. Appearance of positive active material of plate D after 53 cycles and at a magnification of 1520X.

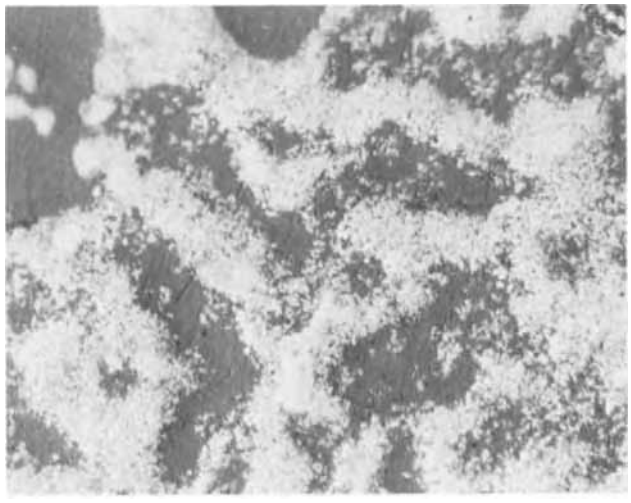

Fig. 13. Microstructure of plate D after 115 cycles and at a magnification of 600X.

Fig. 14. Appearance of plate A after 100 cycles and at a magnification of 600X.

Another distinguishing characteristic of this series A plate was a fairly uniform distribution of small sulfate crystals, absent in the other series. It is true that occasional large sulfate crystals were found in the other plates but they were much less numerous, larger, and very randomly distributed. Since all plates examined had been removed at the end of a charge cycle, these residual sulfate crystals must have represented material no longer in electrical contact, or else material that had reacted too slowly to have been converted in the time available.

It has also been mentioned that the as-formed plate had a different structure at its surface than in the interior (Fig. 6). This type of structure was still found at 50 cycles but had completely disappeared at 100 cycles. It was not clear whether this material near the surface had been converted to the same structure as the remainder of the plate or whether it had simply been removed by the gradual shedding of the active material.

The gradient in structure noted at 50 cycles, where the interior had no large voids, had also disappeared at 100 cycles and the structure throughout the plates was similar to Fig. 12 in plates B, C, and D.

Changes beyond 100 cycles.—Beyond 100 cycles, in the plates of all the series, an increasing number of particles appeared in the former void space surrounding each agglomerate. These particles appeared to be unattached but it is believed that they were really in the electrical circuit and attached to the main aggregate for the following reasons: (*a*) they had survived the washing to remove acid, which was necessary before the plastic impregnation could be made; (*b*) they were not swept away or compacted by the entrance of the fairly viscous imbedding resin; and (*c*) they disappeared from the voids on the discharge cycle and reappeared with the following recharge. With an increasing number of cycles, the number of such PbO_2 particles in the voids correspondingly increased. The former voids were gradually filled with a low-density distribution of such particles. Meanwhile the agglomerate particles formed less densely packed structures with each cycle. These simultaneous processes eventually filled the whole area with uniform but scattered particles (Fig. 15).

Although it would seem from Fig. 15 that no contact existed between particles, examination by polarized light revealed loosely piled crystals, roughly spherical. Only a portion of these were intersected by the plane of cutting, so that the crystals appeared smaller and further apart than was the actual case. The fact that these crystals had survived washing, drying, and impregnation indicated a more coherent structure than appears to be the case in Fig. 15.

After prolonged cycling the amount of lead sulfate remaining in the charged electrode also increased. This sulfate was found in fairly large areas as an almost continuous impregnant and it had encapsulated much of the PbO_2 remaining in these areas. It seemed unlikely that such encapsulated PbO_2 was continuing to take part in further reaction.

Discussion

There are several points brought out by this investigation that require further discussion.

Change in as-formed microstructure following a single discharge-recharge cycle.—It is not surprising to find that the mechanisms of formation and recharge are essentially different in the positive plate. During formation the plate structure is initially much more dense than when beginning recharge. In addition, the plate composition at the beginning of formation is nonuniform and contains many areas of mixed sulfates, residual PbO and Pb. After the first discharge, microscopic examination shows that only $PbSO_4$ and residual PbO_2 remain and the plate is found to have become much more porous than at the start of the forming process. PbO_2 is also present to nucleate the recharge process, which is not true at the beginning of formation (unless red lead, Pb_3O_4, has been used in the original mixing).

It is also quite usual to employ an electrolyte of considerably lower specific gravity during the formation than is used in actual service. Metzler and

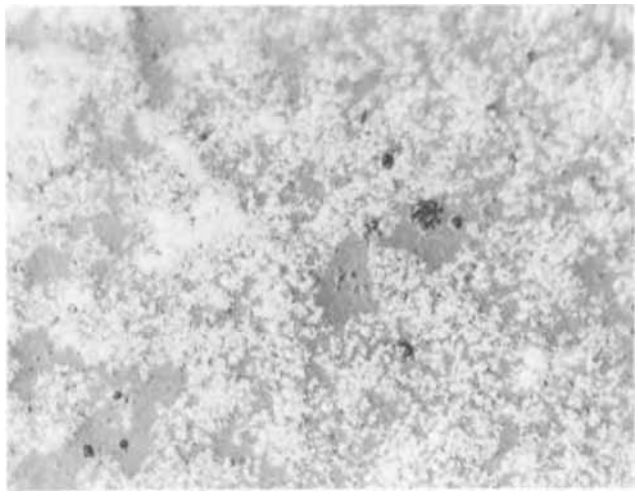

Fig. 15. Type of structure developed in positive plate after several hundred cycles. Magnification 600X.

Schwarz (1) have shown that the $PbSO_4$ crystals formed on soft lead in sulfuric acid of 1.12 sp gr were three times larger than those formed in 1.28 sp gr acid. While we are unaware of a similar study having been made for the $PbSO_4$ in active material, it is probable that a similar relationship exists. The different solubility of $PbSO_4$ in varied concentrations of H_2SO_4 may also be a factor.

It has also been shown by Simon and Jones (2) and Pierson (3) that many features of the unformed positive plate were reproduced in the formed plate, despite a change in chemical composition. In particular, it was observed that certain acicular or needlelike crystals which were found in the cured but unformed plate were preferentially converted to PbO_2. The normal $PbSO_4$ formed on discharge has a considerably different form, which also may be a factor in the difference in the recharged and as-formed plates.

It is assumed that, had samples of the other three manufacturers' plates with one discharge-recharge cycle been available for study, they would have also shown the same difference between as-formed and recharged microstructure.

Change in plate structure within the first 50 cycles.—The plates underwent further change in microstructure somewhere between the 1st and 50th cycle. Not only did the microstructure change from that developed after one cycle but the active material developed large internal voids, separated by nearly continuous walls of PbO_2, which formed a cell-like structure. Since no samples were available for study between the 1st and the 50th cycle, it is not known how many cycles were actually required to obtain the observed structure and whether the change occurred abruptly or gradually. From the fact that a gradual continuation of the process was observed beyond 50 cycles, it is assumed that the process was gradual in the initial stage as well. It was not possible, with the samples on hand, to determine the source of the change in structure. The rearrangement of the microstructure seemed to be brought about by a combination of the repeated change in chemical composition during cycling and the strictly physical effect of gas generation within the structure during the charge cycle. Although the structure found suggested the formation of cells, it is more likely that channels were being formed through which gas was able to escape to the surface of the plate. The escape of this gas would be accompanied by the removal of a certain portion of the more loosely held PbO_2 particles from the channel walls.

Some may object to the idea that gas could act as a pore former in the positive plate, preferring to believe that the pores are due only to the rearrangement and repeated change that occurs during cycling. At the beginning of the investigation we also supported this idea. It is obvious that growth of large sulfate crystals would be at the expense of the surrounding PbO_2 structure, and observation has also shown that upon recharge the PbO_2 structure appears more compact. The growth of large $PbSO_4$ crystals and their dissolution followed by the regeneration of PbO_2 must therefore be a contributing factor in opening up the structure. However, if this were the only or major cause, then one would expect the amount of $PbSO_4$ found in these pores to increase markedly as the pores become larger. This was not the case, for neither the size nor number of the $PbSO_4$ crystals within the pores changed with increasing cycling time.

Gas is generated and released, not only at the surface of the plate, but also on the inside of the electrode. When direct observation was made of the electrode surface while in a microcell, it was observed that gas bubbles repeatedly issued from the same pores in the electrode surface, even after several cycles. Such bubbles of gas increased to a diameter many times that of the original pore before leaving the surface so that they seemed to originate at the surface. However, microscopic observation revealed that, immediately after departure of the large bubbles, new ones were already forming within the original pores.

Hauel (4) reported an increase in negative plate permeability during repeated cycling, presumably because of an increase in number or size of pores or voids. This work was based on repeated measurement of the flow rate of electrolyte under constant pressure through the plate structure and extended over a considerable period of cycling. Unfortunately, no similar study appears to have been done on the positive plate.

Dittman and Sams (5) have shown that the apparent density of the active material decreased during service and have published a curve which indicates that the apparent density of the positive plate continued to decrease over a period of 16 weeks of SAE cycling. The work of Dittman and Sams, however, describes a phenomenon other than porosity. Dittman and Sams measured the apparent plate density in the following manner. The dried plate was weighed and then the amount of water displaced by the weighed plate was measured. Approximately 2/3 of the active material was then removed from the plate and, after again drying, the plate was reweighed. The volume of water displaced by this residual plate was again measured. From the results the apparent density was calculated.

It is obvious that the results would not be affected by a change in pore size or volume, provided that all the pores were open to the surface. The ease with which the samples used in our investigation were impregnated by a fairly viscous polyester, and the absence of unfilled pores, indicates that all pores were open. Only the development of pores into which water could not penetrate or an actual change in chemical composition would account for the decreased density noted by Dittman and Sams. Since their measurements were always made with the batteries in the same apparent state of charge, the only chemical change would seem to be in that portion of the $PbSO_4$ crystals that were unconverted by the charge process and no longer able to take part in the cell reaction. The statements that storage of the charged plate in sulfuric acid, overcharging, and cycling all decreased the apparent density, and that deep cycling caused more decrease in density than shallow cycling, all indicate that what Dittman and Sams actually measured was the increase in residual $PbSO_4$ left at the end of charge. Microscopic studies made in this laboratory confirm that residual $PbSO_4$, in the form of unreactive crystals, increases under the same conditions for which Dittman and Sams reported a specific gravity decrease.

Consideration of volume change as a cause of active material disintegration.—Because the specific volume of $PbSO_4$ is greater than that of PbO_2, it has frequently been suggested that the formation of $PbSO_4$ during discharge produces stresses not only within the active material but also against the grid bars. This explanation sounds attractive and reasonable until an actual microscopic examination is made of the changes that occur during charge and discharge. It has been shown that even the initial formation of the plate produces a PbO_2 microstructure that is full of voids and in which the PbO_2 uses only a portion of the available space.

In a previous paper (6) it was shown that the growth of $PbSO_4$ crystals during discharge occurs within some of the voids of the plate and that this growth of the $PbSO_4$ crystals takes place with a simultaneous disappearance of the PbO_2. During the entire process of discharge, the $PbSO_4$ crystals seemed to be surrounded by a considerable amount of void space and were not in close contact with surrounding PbO_2. Because the $PbSO_4$ grew as compact, regular crystals and because the original PbO_2 active material was very porous and therefore less dense than expected, it was decided that the increase of specific volume caused by the growing $PbSO_4$ crystals was more than compensated for by the original high porosity of the mass of PbO_2 active material. Therefore, no pressure

could have been exerted on the mass by the growing $PbSO_4$ crystals.

Possible factors contributing to the loss of capacity.—As the number of cycles increased, the positive active material developed a network of large voids and the PbO_2 structure itself became made up of very small crystals. There was some evidence that the formation of the large voids by gas evolution had also caused compacting of the surrounding PbO_2 particles into a denser agglomerate than might otherwise have been the case. It seems likely that gas evolution, with accompanying movement of electrolyte in the channels, would be sufficient to dislodge many of the more loosely attached PbO_2 particles along the channel walls and carry them to the surface.

This view is supported by the fact that the diameters of the agglomerates of PbO_2 particles decreased with increasing number of cycles. If this deduction is correct it presents a somewhat different picture than commonly accepted. The usual view is that softening takes place at the plate surface and that particles are loosened and carried away by the "washing" action of the gas bubbles rising along its face.

In the later stages of the cycling, it is evident that the plate has become so porous that channels are no longer necessary for the escape of the gas and that therefore the gas can escape without so much erosion of the plate's internal structure. At the same time contacts between particles have become much more limited and internal resistance must be higher.

A second consideration is the agglomeration of the PbO_2 particles and the formation of very small particles that takes place after a few cycles. While these agglomerates appear to be porous, the pores are very much smaller than those that were present in the as-formed plate or one with only a single discharge-recharge cycle. The pores formed after considerable cycling are very small. It would seem that penetration of the reaction into such small, relatively deep, pores would be limited to very short distances at the usual rates of discharge.

The increasing number of large-size $PbSO_4$ crystals that encapsulated many areas of remaining PbO_2 particles were at least a partial factor in capacity loss. It was not evident why these unreactive crystals should form and grow to large size, but it was suspected that in such areas there was no electrical contact with the rest of the electrode.

Development of a cycled structure independent of the original as-formed structure.—The most definite information obtained from this investigation was that plate structures from all sources investigated were quite similar after cycling and seemingly independent of the structures that had been developed during either curing or cycling. While this does not seem to agree with the known fact that different paste formulations produce plates with different performance characteristics and service lives, it is nevertheless significant. It indicates that the structure developed in the plate is evidently a function of the mode of operation and of such factors as gas formation, current density, and rate and habit of crystal growth. More subtle changes such as variations of the Pb/O ratios in the PbO_2 lattice, α- and β-PbO_2 ratios, introduction of crystal growth modifying additives from the separators or the expander of the negative, or destruction of nucleation sites, are very likely factors that not only determine the life of the plate but that would also be strongly influenced by paste formulation. Such factors as the above cannot readily be proven by microscopy, although their presence may be indicated by changes in color, hardness, or reflectivity. In such cases other methods of investigation are necessary.

Other evidence for increasing similarity in active material, in plates of different manufacture, with increasing cycle time.—A differential thermal analysis of the active material of the plates used in this investigation has confirmed some of the conclusions arrived at here. This differential analysis is the subject of a following paper.

Acknowledgments

The various battery companies that have contributed samples for this and other of our investigations prefer anonymity but we gratefully acknowledge their assistance. We also wish to thank the Naval Research Laboratory for its support of this joint investigation and for permission for publication of this work. Appreciation is also expressed to the International Lead-Zinc Research Organization, Inc., which has assisted in this and other investigations by maintaining the position of Research Associate for one of the authors at the Naval Research Laboratory.

Manuscript submitted June 18, 1970; revised manuscript received *ca.* Nov. 13, 1970. This was Paper 51 presented at the Atlantic City Meeting of the Society, Oct. 4-8, 1970.

Any discussion of this paper will appear in a Discussion Section to be published in the December 1971 JOURNAL.

REFERENCES

1. H. Metzler and W. Schwarz, *Electrochim. Acta*, **11**, 111 (1966).
2. A. C. Simon and E. L. Jones, *This Journal*, **109**, 760 (1962).
3. J. R. Pierson, *Electrochem. Technol.*, **5**, 323 (1967).
4. A. P. Hauel, *This Journal*, **78**, 231 (1940).
5. J. F. Dittman and J. F. Sams, *ibid.*, **105**, 553 (1958).
6. A. C. Simon, C. P. Wales, and S. M. Caulder, *ibid.*, **117**, 987 (1970)

Electrical Conductivity Measurements in Anhydrous Hydrogen Fluoride[1]

Robert P. Clark

Sandia Laboratories, Albuquerque, New Mexico 87115

and James R. Moser*

Catalyst Research Corporation, Baltimore, Maryland 21209

ABSTRACT

The specific conductivities of LiF, NaF, $KF \cdot 2H_2O$, SrF_2, and KNO_3 in distilled anhydrous hydrogen fluoride were measured over the temperature range −75° to 0°C. Standardization of the Teflon conductivity cells was made with a 0.100*N* solution of NaI in CH_3OH. Conductivities are presented for five concentrations of each solute ranging from saturation at −75°C to 1/10 of this concentration. An empirical equation has been developed which relates the specific conductivity to concentration and temperature. A table of constants is given which applies the equation to a particular solute.

Until recently, anhydrous hydrogen fluoride (HF) as a battery electrolyte has essentially been overlooked. In many ways, this seems reasonable because of its toxic and chemically corrosive properties. On closer examination, one finds that anhydrous HF passivates many metals in much the same way that oxygen passivates aluminum. Metals such as copper, nickel, and magnesium are passivated readily, as would be expected from the solubilities of their respective fluoride salts (1-3). Suitable materials are available for containers, and the problem of toxicity can be minimized by using sealed battery cases.

Previous use of anhydrous hydrogen fluoride as an electrolyte solvent has been limited. Koerber and DeVries (4) determined emf values and free energies of formation using cells of the type M, $MF_2(s)$/ $HF(NaF)/Hg_2F_2(s)/Hg$. Krefft (5) measured the potential of the cell Pt, $H_2/HF(KF)/F_2$, Pt and evaluated the free energy of formation of HF. Clifford and co-workers (6, 7) conducted potentiometric studies of several systems in liquid HF. More recently, Jasinski (8) has reported on studies of Cu/CuF_2 reference electrodes in anhydrous HF.

To the authors' knowledge, only one other group has undertaken any research aiming toward the development of a practical primary cell with anhydrous hydrogen fluoride as a main component of the electrolyte (9, 10).

Narrow ranges of specific conductivities have been measured by various workers. Simons (1) reports data at low concentrations for KF and KNO_3 and Fredenhagen (3) also studied the same solutes. Quarterman *et al.* (11) have published the specific conductivity of many organic solutes in anhydrous HF over an extensive concentration range but over a restricted temperature range, 0°-25°C. It appears that no comprehensive conductivity literature exists over a wide range of temperature and concentration for inorganic fluorides dissolved in anhydrous hydrogen fluoride.

In an over-all plan of battery development, the availability of an electrolyte with sufficient conductivity to minimize undesired *IR* losses must be ascertained. This study was designed to provide some of the necessary information for such an evaluation.

Experimental

The chemicals used were: $KF \cdot 2H_2O$, Fisher certified reagent; NaI, Fisher certified reagent; NaF, Fisher reagent; KNO_3, Fisher certified reagent; KCl, Fisher certified reagent; SrF_2, Mallinckrodt analytical reagent; CH_3OH, Fisher 99.5% min; "anhydrous" HF, Allied Chemical 99.7% min. Water used in the preparation of KCl solution was distilled. All operations were conducted in a glove box within a "dry room" at less than 1% relative humidity (300 ppm H_2O at 25°C). Water concentrations inside the glove box were not monitored. Any increase in conductivity resulting from moisture absorption is insignificant, as discussed in a later section.

The HF was purified by a single distillation with all-Teflon apparatus to rid it of traces of water and iron, the latter impurity originating from the shipping container. HF, which boils at 19.6°C (12), was vaporized at room temperature (~24°C), passed through Teflon cooling coils, and collected in a Teflon receiver at −25°C. The as-received tank of HF had a specific conductivity of 1.7×10^{-2} ohm^{-1} cm^{-1} at 0°C. After a single distillation, the specific conductivity had decreased to 5.0×10^{-4} ohm^{-1} cm^{-1} at 0°C. A second distillation resulted in no further decrease in specific conductivity. Further purification by electrolysis, using the method of Evans *et al.* (13), resulted in an increase in conductivity due to the dissolution of nickel fluoride which was formed at the nickel anode. Singly distilled HF was used in all further experiments.

The latter conductivity value is identical to that obtained by Fredenhagen (14) at −15°C. Efforts to duplicate the results of Schmidt and Schmidt (15) (7.5×10^{-6} ohm^{-1} cm^{-1} at −15°C) or Runner, Balog. and Kilpatrick (16) (5.7×10^{-6} ohm^{-1} cm^{-1} at 0°C) were not considered practical or necessary since the conductivities of the solutions being investigated were approximately 2-3 orders of magnitude higher than that of the HF solvent. Runner *et al.* (16) have demonstrated the impracticality of maintaining a specific conductivity less than 10^{-4} ohm^{-1} cm^{-1}.

Measurements were made at 1 kHz using a General Radio Type 1650-A impedance bridge. The conductivity cell constructed of Teflon is shown in Fig. 1. Platinum wire electrical connections to the electrodes were made through small pinholes in the end plugs. The platinum wire leads were spot welded to circular platinum electrodes.

The Pt electrodes were platinized using a 5% solution of chloroplatinic acid containing 0.02% lead acetate. A current density of 84 mA/cm^2 was employed for 3 min with current reversals each 30 sec. The electrodes were platinized *in situ* and rinsed clean of the plating solution with five washings of distilled HF. The test solutions were introduced through two 1.27 cm diameter holes. A calibrated chromel-alumel

[1] This work was supported by the U.S. Atomic Energy Commission.

* Electrochemical Society Active Member.

Key words: electrical conductivity, hydrogen fluoride, specific conductivity.

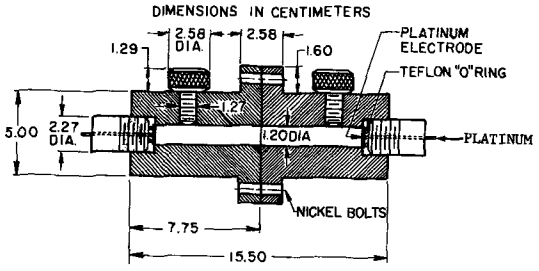

Fig. 1. Conductivity cell

thermocouple encased in a Teflon sleeve was used to monitor the temperature of the solution but was always removed immediately prior to making a conductivity measurement.

The Teflon cells were standardized with a 0.100*N* NaI solution in methanol. The conductivity of this solution was itself determined using a Pyrex "U" tube conductivity cell which was previously standardized with a 0.100*N* KCl solution at 25°C. Since Pyrex has a low coefficient of thermal expansion, 3.6 x 10^{-6} deg^{-1} (17), the Pyrex cell constant (13.07 cm^{-1}) determined at 25°C was assumed to apply over the temperature range of −75° to 25°C.

A Revco ULT-903 cold box was used to maintain temperature for these experiments. Temperatures were controlled to ±0.2°C. Conductivity data for electrolyte systems over the temperature range of −75° to 0°C are nonexistent; consequently, the conductivity of a solution of 0.100*N* NaI in CH_3OH was determined over this range. The conductivity measured for this solution between −75° and 0°C is given in Table I.

Since Teflon has a relatively high coefficient of linear thermal expansion, 10.0 x 10^{-5} deg^{-1} (18), the conductivity cell was standardized throughout the range −75° to 0°C. The cell constant (k) varied linearly according to the equation

$$k = 0.00437\,t + 12.69$$

where t is temperature in degrees centigrade and k is the cell constant in cm^{-1}.

Solution preparation.—The minimum solubility for each of the five salts studied occurs at the lowest temperature studied, *i.e.* −75°C. These data are shown in Table II. Salt concentrations were chosen such that solubility at −75°C was not exceeded.

The solubility of the salts at −75°C was determined as follows. One hundred grams of HF were placed in a Teflon beaker and solute was added from a previously weighed quantity until no more would dissolve with stirring. The solution was filtered through a Teflon filter, and the excess salt in the filter was dried and weighed. The quantity of salt dissolved was determined by difference.

Because the density of HF varies by approximately 20% over this temperature range (19), it is appropriate to express the solute concentrations in molality units.

The precision of these conductivity measurements is ±1.5%. The irreproducibility resulted from temperature variations (±0.2%), solubility measurement reproducibility (±0.1%), cell constant error (±0.2%), and bridge precision (±1.0%).

Table I. Specific conductivity (κ) vs. temperature for 0.100*N* NaI in CH_3OH

Temperature (°C)	(Pyrex cell constant = 13.07 cm^{-1}) Specific conductivity (ohm^{-1} cm^{-1})
10	0.00512
0	0.00436
−10	0.00374
−20	0.00320
−30	0.00288
−40	0.00222
−50	0.00179
−60	0.00136
−70	0.00094
−80	0.00054

Table II. Solubility of salts in anhydrous HF at −75°C

Salt	Solubility moles/1000g HF
LiF	3.70
NaF	5.83
$KF \cdot 2H_2O$	2.00
SrF_2	1.09
KNO_3	1.87

Results and Discussion

Figures 2 through 6 show specific conductivity as a function of concentration and temperature for LiF, NaF, $KF \cdot 2H_2O$, SrF_2, and KNO_3, respectively. Curves represent conductivity values calculated from the empirical equations which are discussed later in this article. Experimental data points are also shown in the figures.

It will be observed in Fig. 3 that specific conductivity values for NaF decrease at higher concentrations. Values for 5.83*M* (molal) NaF are: less than those for 4.31*M* NaF at all temperatures measured, less than those for 2.92*M* NaF at −20°C and below, and less than those for 1.46*M* NaF at −50°C and below. Although viscosity has not been determined for these solutions, this effect is probably the result of increased viscosity at the higher concentration in accordance with the Walden Rule.

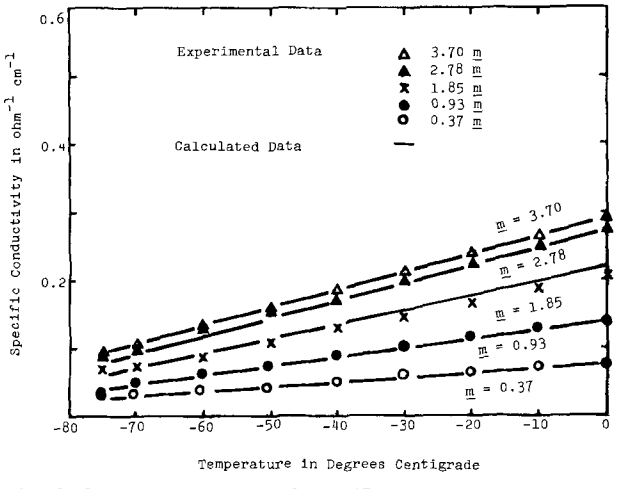

Fig. 2. Specific conductivity of LiF/HF solutions vs. temperature. Molality range, 0.37-3.70*M*.

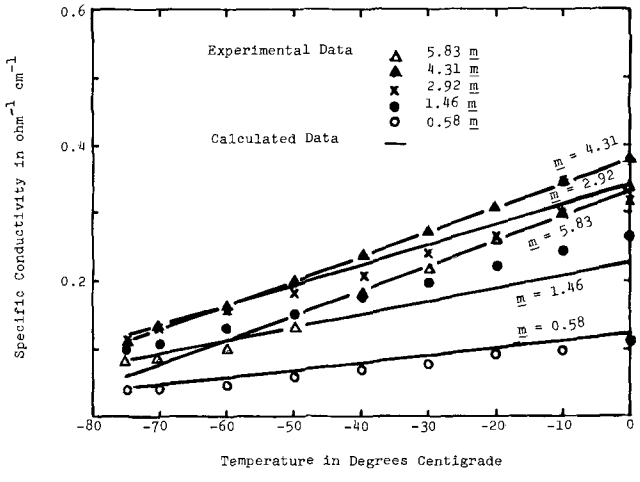

Fig. 3. Specific conductivity of NaF/HF solutions vs. temperature. Molality range, 0.58-5.83*M*.

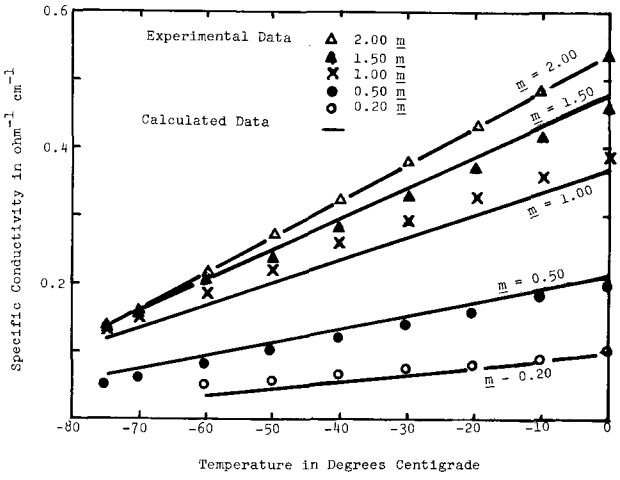

Fig. 4. Specific conductivity of $KF \cdot 2H_2O/HF$ solutions vs. temperature. Molality range, 0.20-2.00M.

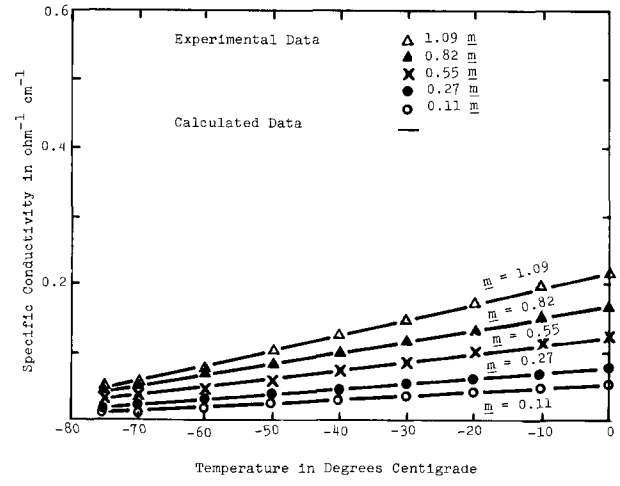

Fig. 5. Specific conductivity of SrF_2/HF solutions vs. temperature. Molality range, 0.11-1.09M.

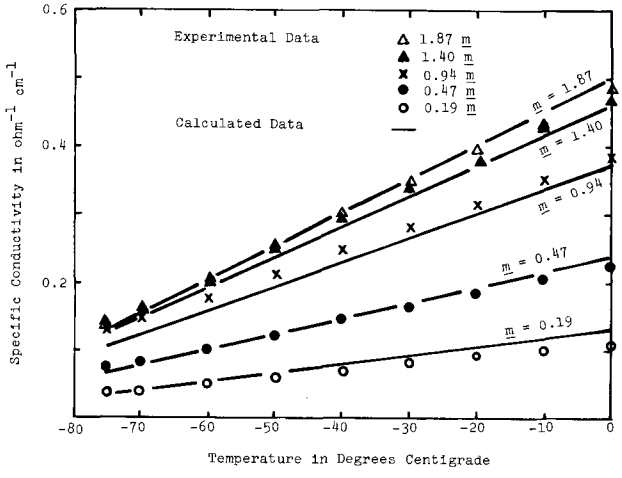

Fig. 6. Specific conductivity of KNO_3/HF solutions vs. temperature. Molality range, 0.19-1.87M.

The use of $KF \cdot 2H_2O$ (Fig. 4) produced conductivities twice as high as those reported by Simons (1) and Fredenhagen (3) for anhydrous KF. These values are included to show the effect of water of hydration.

Figure 7 shows the conductivity *vs.* temperature for singly distilled HF used in the preparation of the electrolyte solutions. These data were reproducible after several weeks' storage in the glove box indicating that no significant amounts of water were absorbed by the HF. Since the salt solutions exhibited conductivities several orders of magnitude greater than the values measured for HF itself, it is even less likely that water impurities have affected the conductivity data for the solutions.

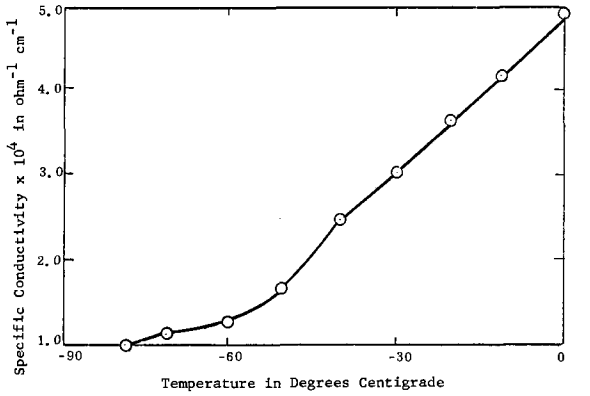

Fig. 7. Specific conductivity of singly distilled HF vs. temperature.

Conductivity *vs.* temperature curves for the solutions are straight lines and can be represented by the general linear equation

$$\kappa = at + b \qquad [1]$$

where κ is specific conductivity in ohm^{-1} cm^{-1}, a is the slope of the curve, t is temperature in degrees centigrade, and b represents the y-intercept at 0°C. Both the slope, a, and the intercept, b, are dependent on the concentration of the solution. Plotting a and b *vs.* concentration results in parabolic curves opening downward. The general equation representing these curves is

$$(m - c)^2 = -d\,(y - e) \qquad [2]$$

where m is the solution concentration in molality; y is either a or b from the previous linear equation; and c, d, and e are constants. Solving the general parabolic equation successively for a and b and substituting these results into the general linear equation give an equation relating specific conductivity to the solution temperature and concentration of the form

$$\kappa = (Am^2 + Bm + C)t + Dm^2 + Em + F \qquad [3]$$

where A, B, C, D, E, and F are constants. The constants were determined for each of the five salts using a least-squares analysis.

The results are shown in Table III.

Manuscript submitted Aug. 13, 1970; revised manuscript received Dec. 7, 1970.

Any discussion of this paper will appear in a Discussion Section to be published in the December 1971 JOURNAL.

Table III. Coefficients for κ-t-m equation x 10^3
$\kappa = (Am^2 + Bm + C)t + Dm^2 + Em + F$

Salts ⟶ Coefficients	LiF	NaF	$KF \cdot 2H_2O$	SrF_2	KNO_3
A	−0.226	−0.113	−0.493	0.545	−0.91
B	1.51	1.21	3.46	1.07	4.05
C	0.153	0.443	0.365	0.440	0.59
D	−18.0	−18.8	−96.1	21.0	−109.0
E	138.	160.	454.	142.	443.
F	28.5	37.3	9.94	35.3	53.5

REFERENCES
1. J. H. Simons, *Chem. Rev.*, **8**, 213 (1931).
2. A. W. Jacke and C. H. Cady, *J. Phys. Chem.*, **56**, 1106 (1952).
3. K. Fredenhagen, Z. *Phys. Chem.*, **164A**, 174 (1933).
4. G. G. Koerber and T. DeVries, *J. Am. Chem. Soc.*, **74**, 5008 (1952).
5. C. T. Krefft, "Inaug. Diss.," Griefswald Institute for Physikalische Chemie, Griefswald, Germany (1939).
6. A. F. Clifford, W. D. Pardieck, and M. W. Wadley, *J. Phys. Chem.*, **70**, 3241 (1966).
7. A. F. Clifford and E. R. Zamora, *Trans. Faraday Soc.*, **57**, 1963 (1961).
8. B. Burrows and R. Jasinski, *This Journal*, **115**, 348 (1968).
9. S. Evans, H. H. Rogers, and J. H. Johnson, *ibid.*, **111**, 704 (1964).
10. R. Keller and S. Evans, *ibid.*, **114**, 655 (1967).
11. L. Quarterman, H. H. Hyman, and J. J. Katz, *J. Phys. Chem.*, **65**, 90 (1961).
12. J. H. Simons, *J. Am. Chem. Soc.*, **46**, 2179 (1924).
13. S. Evans, H. H. Rogers, and J. H. Johnson, *This Journal*, **111**, 701 (1964).
14. K. Fredenhagen and G. Cadenbach, Z. *Phys. Chem.*, **146**, 245 (1930).
15. H. Schmidt and H. D. Schmidt, Z. *Anorg. Chem.*, **279**, 278 (1955).
16. M. E. Runner, G. Balog, and M. Kilpatrick, *J. Am. Chem. Soc.*, **78**, 5183 (1956).
17. "Handbook of Chemistry and Physics," 44th Ed., p. 2332, Chem. Rubber Company, Cleveland (1963).
18. "Modern Plastics Encyclopedia," Vol. 46, p. 974, McGraw-Hill, Inc., New York (1970).
19. J. H. Simons and J. W. Bouknight, *J. Am. Chem. Soc.*, **54**, 129 (1932).

Epoxide-Containing Polymers as Highly Sensitive Electron-Beam Resists

Takako Hirai, Yoshio Hatano, and Saburo Nonogaki

Central Research Laboratory, Hitachi Limited, Kokubunji, Tokyo, Japan

ABSTRACT

High sensitivities to electron beams have been found in epoxide-containing polymers such as epoxidized polybutadiene, epoxidized polyisoprene, and poly(glycidyl methacrylate). The sensitivities of these polymers to electron beams are 50-300 times higher than those of the commercial photoresist KTFR. Epoxidized polybutadiene, with the highest sensitivity, becomes insoluble upon an electron beam exposure of 2 x 10^{-8} coulombs/cm^2 at an accelerating voltage of 15 kV; the *G* value for crosslinking was calculated to be about 200. These polymers can be used as resists for the etching of chromium and aluminum, as well as of oxide layers formed on silicon wafers.

In recent years, several investigations have been made on the application of electron beams to the fabrication of semiconductor devices. Using electron-beam scanning equipment, Hatzakis (1) made transistors with a 1μ wide emitter which is difficult to make by ordinary photoetching techniques. Where the electron-beam process is applied to the fabrication of semiconductor devices, electron-beam resists are usually used. Electron-beam resists are generally organic polymers which become insoluble (negative working resists) or soluble (positive working resists) in particular solvents. Polymers examined up to now as electron-beam resists include polymethacrylates (2, 3), commercial photoresists (4, 5), silicone resins (6), *etc.* As far as the authors know, the highest sensitivity reported to date is that of silicone resins, an exposure of charge density of about 3 x 10^{-6} coulombs/cm^2 being sufficient to insolubilize the resins. This sensitivity, however, still seems to be insufficient for rapid scanning by electron beams. Use of electron-beam resists with higher sensitivity will shorten the exposure time.

In the present investigation, electron-beam resists with high sensitivity have been sought in connection with the development of an electron-beam drafting machine (7) for IC photomask making. A preliminary study was made with the purpose of finding groups to make polymers sensitive to electron beams. The results indicated that epoxy groups 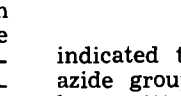 and the azide group ($-N_3$) are highly sensitive to electron beams (8).

Key words: electron beam resists, epoxide-containing polymers.

On the basis of this result, we synthesized epoxide-containing resists. The epoxy group was preferred to the azide because of its insensitivity to light.

Experimental

Material.—Epoxidized polybutadiene.—Polybutadiene (JSR BRO1, obtained from Japan Synthetic Rubber Co., cis content 97%, intrinsic viscosity [η] 2.8 in toluene) was epoxidized as follows. Polybutadiene (6g) was dissolved in 160 ml of toluene and epoxidized for 30 min at 45°C with 160g peracetic acid solution (0.9M) which was prepared from 30% hydrogen peroxide and acetic anhydride by the method of Findley (9). After 150 ml of cyclohexanone were added, the reaction mixture was washed repeatedly with water and aqueous sodium bicarbonate. The epoxidized polymer was precipitated from the solution by adding methanol; it was then dissolved in cyclohexanone. The epoxide content of the polymer, as determined by the hydrochloric acid procedure, was 6.0 mmoles/g. The intrinsic viscosity [η] was 3.0 in toluene at 25°C.

Epoxidized polyisoprene.—Polyisoprene (Cariflex IR 309, Shell Chemical Corp.) was masticated at 30°C for 60 min. Then 3g of the masticated polyisoprene ([η]

1.86 at 25°C in toluene) were dissolved in 60 ml of toluene and epoxidized with 40g of peracetic acid solution at 35°-38°C for 20 min. The epoxidized polymer was washed acid free and stored as a cyclohexanone solution. Epoxide content of the polymer was 6.2 mmoles/g.

Poly(glycidyl methacrylate).—The monomer, freed from inhibitor by distillation under reduced pressure in nitrogen, was polymerized in a sealed tube at 65°C for 20-35 min with 0.2% of α,α'-azobisisobutyronitrile as a catalyst. The polymer was purified by repeated precipitation from methyl ethyl ketone by addition of methanol and stored as a methyl ethyl ketone solution. The epoxide content was 7.2 mmoles/g.

Infrared spectra.—*IR* absorption spectra of polymers were obtained using a Hitachi Infrared Spectrophotometer EPI-2. Polymers coated on silicon wafers were exposed to an electron beam at an accelerating voltage of 35 kV. Their *IR* spectra were taken before and after exposure to the electron beam.

Insolubility characteristics.—Thin layers (0.3-1.0μ) of the polymers were laid on silicon wafers by spin-coating from 3 to 5% solutions and exposed to an electron beam at an accelerating voltage of 15 kV. After the exposure, the polymer layers were developed with cyclohexanone and the thicknesses of the layers remaining on the exposed areas were determined with an interferometer.

Resistance to etching solution.—Substrates (*e.g.*, oxidized silicon wafer) were coated with the polymer, exposed to electron beams through a mechanical mask (fine copper mesh), developed with cyclohexanone, baked, and etched. The substrates were then inspected with an optical microscope to check whether the etching had proceeded correctly or not.

Application to IC-mask making.—Chromium-evaporated glass plates were coated with the polymers and exposed in an electron-beam drafting machine (7) specially designed for the purpose of drafting the patterns of IC photomasks. The exposed plates were developed with cyclohaxanone, heated at 180°C for 10 min and then etched with NaOH-$K_3Fe(CN)_6$ etchant (Kodak Etch Bath EB-5) for 2-3 min.

Results

Electron-beam exposure characteristics of the epoxidized polymers are compared with those of unepoxidized polymers in Fig. 1. As is readily seen, the epoxidization increases sensitivities of the polymers by factors of 10-30. The sensitivity of a polymer depends on both its type and its molecular weight. It is known that the crosslinking sensitivity is proportional to molecular weight (10, 3). However, no significant change in the degree of polymerization by the epoxidization was observed; for example, [η]'s of epoxidized and unepoxidized polybutadiene are 3.0 and 2.8, respectively. Therefore, the high sensitivity in the epoxidized polymers is attributed to the existence of the epoxy groups in the polymers. The sensitizing effect of the epoxy group was also observed in poly (glycidyl methacrylate) PGMA. As shown in Fig. 2, PGMA is much more sensitive than Lucite 45, whose epoxy-free structure resembles that of PGMA.

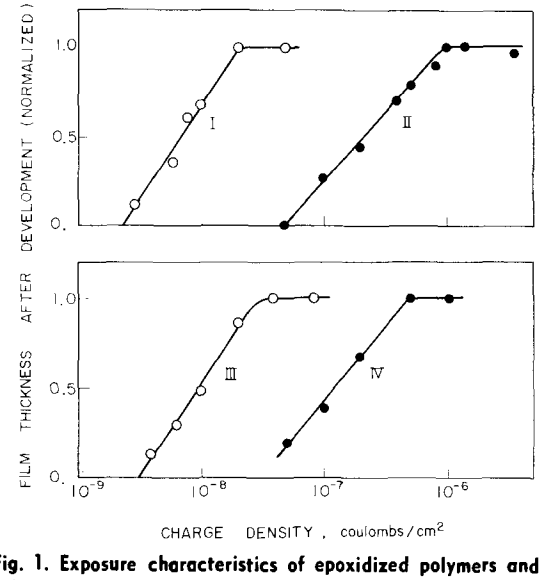

Fig. 1. Exposure characteristics of epoxidized polymers and their starting polymers: I, epoxidized polybutadiene; II, polybutadiene; III, epoxidized polyisoprene; IV, polyisoprene.

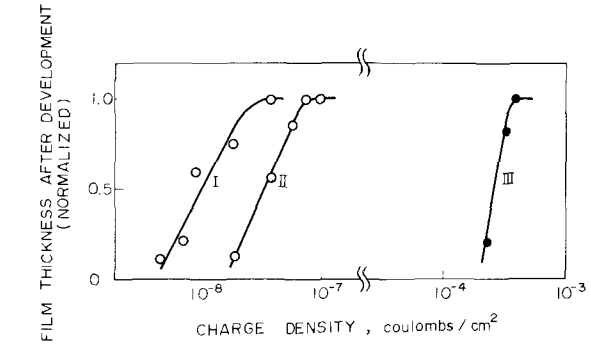

Fig. 2. Exposure characteristics of poly(glycidyl methacrylate) and Lucite 45: I, poly(glycidyl methacrylate) [η] = 1.94; II, poly(glycidyl methacrylate) [η] = 1.28; III, Lucite 45 (polyisobutyl methacrylate) [η] = 1.02.

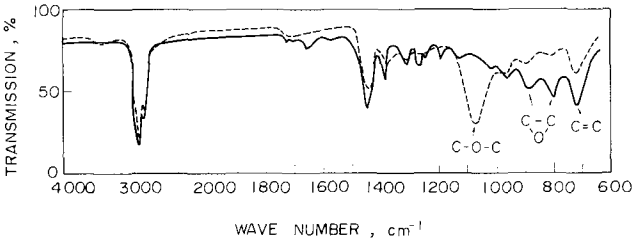

Fig. 3. Infrared spectra of epoxidized polybutadiene before and after exposure: ——, before exposure; - - -, after exposure (3 x 10^{-5} coulombs/cm².)

Figure 3 shows the infrared spectra of epoxidized polybutadiene before and after an exposure of 3 x 10^{-5} coulombs/cm². In the case of exposure, the absorption peaks at 810 and 900 cm^{-1}, corresponding to the epoxy group CH$\overset{O}{\diagup\!\!\diagdown}$CH, almost disappeared, a new peak at 1075 cm^{-1} assignable to the ether linkage C—O—C appeared, and no other significant changes were observed. This indicates that, through an electron-beam irradiation process, the epoxy ring opens only to give crosslinks.

In Fig. 4 is plotted the change in epoxy and ether contents of epoxidized polybutadiene in *IR* spectra as a function of irradiation dose. As the figure shows, the rates of ring opening of the epoxy groups and of formation of the ether bonds almost coincide.

The resistance of the epoxide-containing polymers to chemical etch was examined. It was found that thin layers of the polymers insolubilized on substrates are, after being improved in adhesion and chemical resistance by baking at 180°C for 10 min, capable of protecting the substrates from etch solutions. Thus, oxide layers on silicon wafers and evaporated chromium layers can be etched lithographically using these polymers as electron-beam resists.

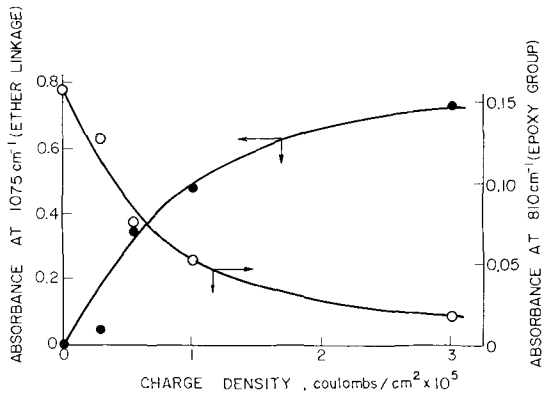

Fig. 4. Change in absorbance for ether linkage (●) and epoxy group (○) in epoxidized polybutadiene as a function of exposure.

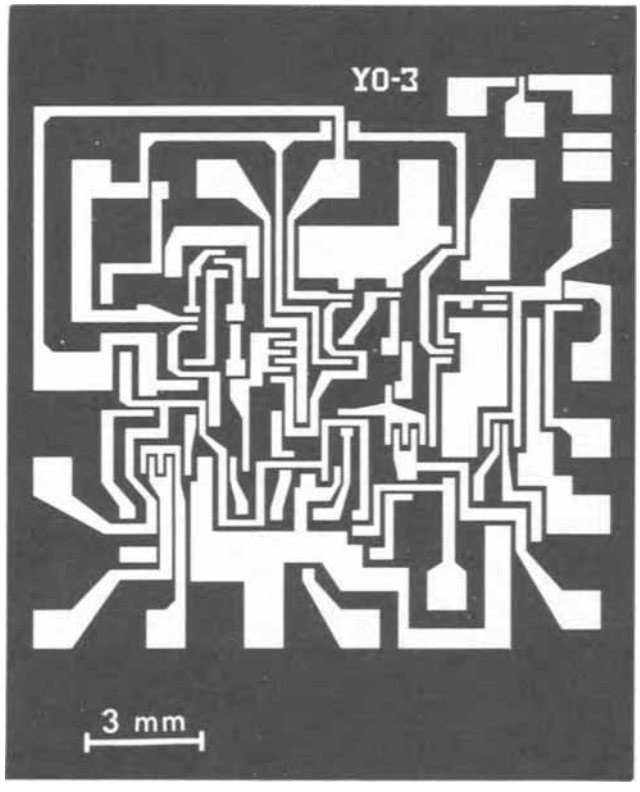

Fig. 5. Chromium mask for IC

Chromium patterns are made with an electron-beam drafting machine and with the electron-beam resists prepared in the present study. An example of the patterns of these masks is shown in Fig. 5. This pattern (14.8 x 15.0 mm) was drafted directly by computer-controlled, electron-beam scanning. The electron-beam diameter used in this drafting machine is not small enough to determine the resolution capability of these resists. To examine the line definition of the resists, further experiments using a scanning electron microscope are now being carried out.

Discussion

As described above, we found that epoxide-containing polymers are highly sensitive to an electron beam. For example, epoxidized polybutadiene starts insolubilizing at a charge density of 2×10^{-9} coulombs/cm^2, whereas a charge density of 7×10^{-7} coulombs/cm^2 is necessary for the commercial photoresist KTFR (8).

The structures of epoxidized polybutadiene or polyisoprene and PGMA are shown below.

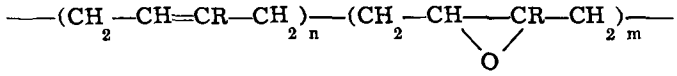

[1]

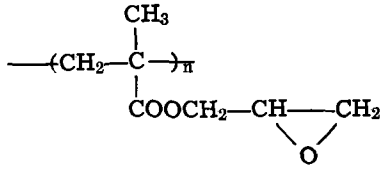

[2]

where R is H or CH_3.

The radiation sensitivity of a system is expressed in terms of the G value, which is defined as the number of chemical changes of a given kind produced per 100 eV absorbed. The G values for crosslinking of the epoxidized polymers can be calculated in two ways.

In the first, G is derived from the insolubilization data. According to Charlesby (10), three-dimensional network formation first starts occurring at the crosslinking density of one crosslinked unit per weight average molecule. This point, usually called gel point, corresponds to the threshold of charge density for insolubilization with exposure characteristics shown in Fig. 1. The number of crosslinks produced in the polymer per unit area at the gel point is equal to $0.5\ d\rho N/M$, where d, ρ, N, and M are the thickness, the density of the polymer, Avogadro's number, and the weight average molecular weight of the polymer, respectively. The energy absorbed in this case, at the accelerating voltage of V volts, is expressed as $Q_g V \alpha d$, where Q_g and α are the charge density at the gel point in coulombs/cm^2, and the energy absorption coefficient, respectively.

G is then expressed as follows

$$G = \frac{\rho N q}{Q_g \alpha V M} \times 50$$

where q is the electronic charge.

M's of polybutadiene and polyisoprene are calculated using Eq. [3] and [4], respectively (11).

$$[\eta] = 11.0 \times 10^{-4} M^{0.62} \quad [3]$$

$$[\eta] = 4.9 \times 10^{-4} M^{0.64} \quad [4]$$

The M's of the epoxidized polymers are corrected for the weight increase caused by the epoxidization. As the value of α is difficult to obtain by direct measurement, it is roughly estimated from the data obtained by Ehrenberg and King (12) to be 0.28 per μ at $V = 15{,}000$ for all the polymers considered here.

The G values calculated by use of Q_g and M thus obtained are shown in the second column of Table I.

In another way, G is calculated from the IR-spectrum data. By plotting the IR absorbance against the radiation dose, as shown in Fig. 4, we obtain the charge density required to decrease the epoxide content by a definite percentage, say 1%. It has been ascertained, as described previously, that the ring opening of the epoxy group leads to the formation of ether linkages almost exclusively. So we can assume that one crosslink is formed by one opened epoxy ring. And G then becomes

$$G = \frac{\rho N q}{Q_{0.01} \alpha V E}$$

where E and $Q_{0.01}$ are the epoxide equivalent (*i.e.*, the weight of the polymer containing 1 mole of epoxide)

Table I. G values for the crosslinking of the epoxidized polymers

Materials	G values: From insolubility data	G values: From IR data
Epoxidized polybutadiene	190	200
Epoxidized polyisoprene	160	70

and the charge density necessary to decrease the epoxide content by 1%, respectively. E is calculated from the epoxide content determined analytically. α is again estimated to be 0.070 per μ at $V = 35{,}000$. The G values obtained from $Q_{0.01}$ and E are shown in the third column of Table I.

It is seen from Table I that the G values of the epoxidized polymers are extraordinarily large compared with those of ordinary polymers. For example, G values for KPR and KTFR are reported by Broyde (5) to be 0.65 and 1.20, respectively. If a chain reaction is assumed to take place by an electron-beam exposure to produce three-dimensional structures, high G values of crosslinking can be explained. However, it is uncertain that such a chain reaction occurs smoothly in relatively rigid polymer layers. It may also be worthwhile considering that the highly exothermic character of crosslinking reactions contributes to the large G values. Bond-energy data show that heat of about 35 kcal/mole evolves in the crosslinking process with one epoxide-ring opening. Although we do not have data for further discussions, it may be possible to regard this exothermic character as one of the reasons for the high sensitivities of the epoxidized polymers to electron beams.

Conclusion

Selected polymers having large molecular weights and containing epoxy groups in high concentration are more sensitive to electron beams than any known negative resist. These polymers are: epoxidized polybutadiene, epoxidized polyisoprene, and poly (glycidyl methacrylate). They become insoluble by an exposure of 15 keV electron beams with charge density between 10^{-8} to 10^{-7} coulombs/cm^2. G values for crosslinking of the epoxidized polymers are calculated to be about 200. These high sensitivities and high G values are attributed to the presence of epoxide structures in the polymers. By use of these polymers as electron-beam resists, we can etch selected areas of chromium-coated plates and oxidized silicon wafers. Owing to their high sensitivities, these polymers shorten the exposure time when used in electron-beam techniques.

Acknowledgments

The authors are grateful to H. Morishita for his assistance with the etching tests and in making the chromium masks, and to A. Maekawa for his help with an electron-beam drafting machine.

Manuscript submitted Aug. 3, 1970; revised manuscript received Nov. 19, 1970.

Any discussion of this paper will appear in a Discussion Section to be published in the December 1971 JOURNAL.

REFERENCES

1. M. Hatzakis, *This Journal*, **116**, 1033 (1969).
2. I. Haller, M. Hatzakis, and R. Srinivasan, *IBM J. Res. Develop.*, **12**, 251 (1968).
3. H. Y. Ku and L. C. Scala, *This Journal*, **116**, 980 (1969).
4. R. F. M. Thornley and T. Sun, *ibid.*, **112**, 1151 (1965).
5. B. Broyde, *ibid.*, **116**, 1241 (1969).
6. Y. Yatsui, T. Nakata, and K. Umehara, *ibid.*, **116**, 94 (1969).
7. A. Maekawa, C. Munakata, C. Hirano, O. Morita, T. Kozawa, K. Isoda, and S. Nonogaki, Paper 254 presented at 4th Intern. Conf. on Electron and Ion Beam Science and Technology, Electrochem. Soc. Meeting, Los Angeles, May 10-15, 1970.
8. T. Hirai, Y. Hatano, S. Nonogaki, and T. Kobayashi, Paper presented at 17th Annual Meeting of the Japan Society of Applied Physics, Tokyo, March 1970.
9. T. W. Findley, D. Swern, and J. T. Scanlan, *J. Am. Chem. Soc.*, **67**, 412 (1945).
10. A. Charlesby, "Atomic Radiation and Polymers," Pergamon Press Ltd., England (1960).
11. W. Ehrenberg and D. E. N. King, *Proc. Phys. Soc.*, **81**, 751 (1963).
12. R. Scott, W. Carter, and M. Magat, *J. Am. Chem. Soc.*, **71**, 220 (1949).

A Continuous Manufacturing Process for Solid Tantalum Capacitors Based on the Powder-on-Foil Concept

Gerhart P. Klein*

P. R. Mallory & Company Incorporated, Laboratory for Physical Science, Northwest Industrial Park, Burlington, Massachusetts 01803

ABSTRACT

A manufacturing process for solid tantalum capacitors in the lower CV range based on the use of a continuous tape approach eliminates the handling of individual parts through the most critical stages of the process and thereby eliminates mechanical damage, operator error, and reduces the labor requirements drastically. The process extends from the initial phase of anode fabrication by sintering to lead attachment and encapsulation. High process yields and very uniform device parameters can be achieved through the mechanization of all process operations. The process lends itself to complete automation and operation by means of a process control computer.

Problems in solid tantalum capacitor (STC) manufacturing that result from contamination and physical damage due to the use of organic binders, mechanical pressing, and individual parts handling are eliminated in the new powder-on-foil (POF) process (1). In it, tantalum foil in the form of a continuous tape serves both as the substrate which supports the powder compact and as an interconnecting means between a multitude of sintered anodes. The foil substrate contains depressions which serve as receptacles for Ta powder which is deposited dropwise in the form of a slurry of powder in water. After drying, the powder is fused to itself and the foil in a single sintering operation in inert atmosphere.

Tantalum tape with integral sintered anodes can be processed into solid tantalum capacitors with high processing yields, consistently low leakage currents, and superior reliability (2). The POF process is par-

* Electrochemical Society Active Member.
Key words: solid tantalum capacitors, continuous tape manufacturing process, binderless anodes, powder dispensing and measuring apparatus, continuous tape sintering furnace, continuous anodizing apparatus.

ticularly well suited to smaller types of STC's with radial leads in the range to about 200 $\mu f \cdot V$.

STC's in the conventional process are manufactured by batch processing techniques. Anodes are pressed individually, presintered in bulk, provided with leads individually, sintered in bulk, and are then fixtured and arranged in processing heads. The heads are taken through the process either manually or at various degrees of mechanization.

Various schemes for single-file continuous processing have been proposed (2, 3) for parts of the STC process. Obviously, the initial phase of the process is the most difficult to translate into a continuous process. Pressing of anodes with binder and sintering in vacuum are serious obstacles to any such attempt. Sintering must be done in vacuum because the binder cannot be removed reliably in inert gas sintering. A linear vacuum sintering process is expensive both from the point of view of initial equipment cost and its operation because of low loading density.

Other problems such as how to press and attach individual anodes to a common carrier before sintering and, after sintering, process them into good capacitors and separate them from the carrier at the end of the process without damaging them are equally far from a solution.

The advantages of a continuous process are as obvious as are the difficulties of achieving this goal by way of the conventional STC process.

A linear continuous process is defined as one in which the parts to be manufactured move through subsequent stages of the process in single (or multiple) file. Materials continuously enter the process line, pass through all stages without holdup, and finished devices come off the line continuously. This mode of operation provides for identical processing conditions for all parts. Manual labor is eliminated as are handling of individual parts and the chance of physical damage. The process variables can be controlled tightly and human error is largely eliminated. This can be the basis for full automation and computer control.

The POF process, in addition to providing an alternative to the pressing of anodes with binders which by itself leads to a significant improvement in product quality, provides at the same time an ideal basis for a continuous manufacturing process for STC's. The purpose of this paper is to report some of the work that was done toward this latter goal. A flow diagram of a continuous POF process (5) is shown in Fig. 1.

Description of Manufacturing Process

Tape preparation.—Any continuous process requires that individual parts be interconnected in some way such that they are aligned in single or multiple file. In the POF process, this is accomplished by means of tantalum foil which serves both as a substrate for a porous pellet and as an interconnecting carrier tape.

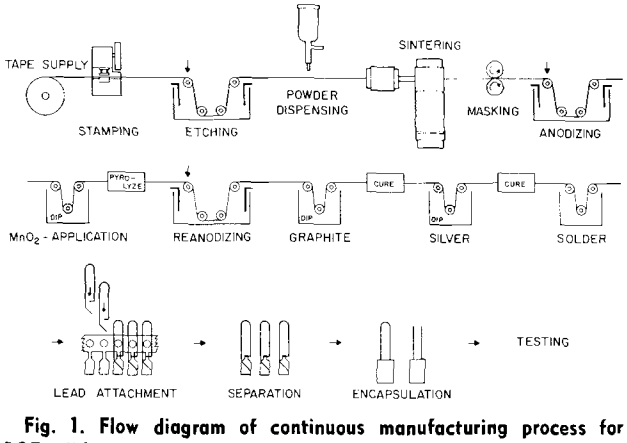

Fig. 1. Flow diagram of continuous manufacturing process for POF solid tantalum capacitors.

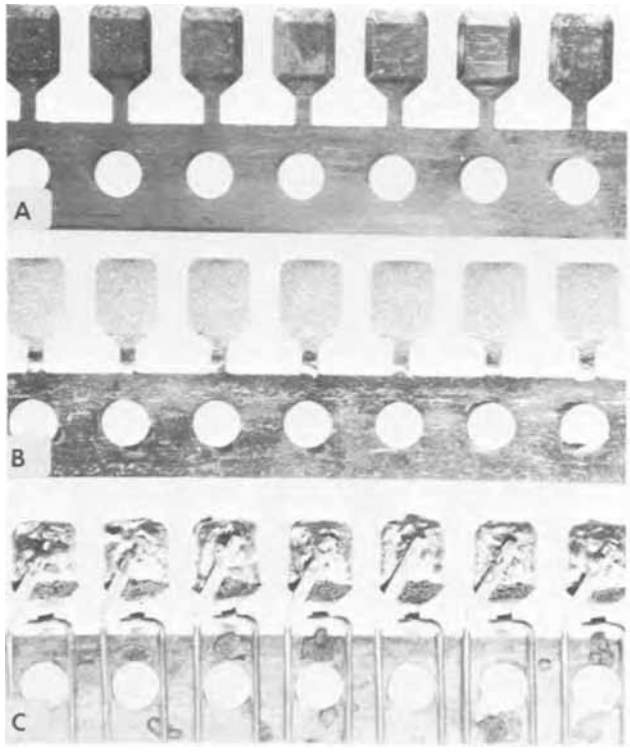

Fig. 2. POF tantalum tape. A, stamped; B, sintered after masking; C, finished capacitors with leads before separation and encapsulation.

The tape can have any number of configurations, one of which is shown in Fig. 2A. In the stamping operation (Fig. 1), a configuration with rectangular projections to one side and a continuous carrier strip with circular indexing holes are produced. The rectangular appendages are connected to the carrier by means of an integral narrow neck which serves as the contact to the substrate metal after the completion of the device. The appendage is made with a slight depression to provide a receptacle for the tantalum powder to be deposited in a subsequent operation. The use of tape with individual substrates projecting to one side greatly facilitates the design of process equipment and facilitates the cutting of the finished device from the tape at the end of the process. The indexing holes are provided to allow tape transport through the process by means of a sprocket drive

A cleaning operation is used to remove any surface contamination from the tantalum substrate and to remove impurities introduced during the stamping operation. After washing with deionized water followed by drying, the tape is fed to the next operation.

Powder dispensing.—In the powder dispensing operation, a measured amount of wet Ta powder is deposited in the appendages projecting from the tape. This dispensing technique is based on the discovery that Ta powder in a liquid carrier can be dispensed dropwise in measured amounts. The amount of powder dispensed per drop is determined by the geometry of the tip and the surface tension which holds a drop at the tip from which the slurry is being released. The principle underlying this dispensing technique has been described previously (2).

A dispensing apparatus on the basis of this principle which is suitable for controlled continuous operation (6) is shown schematically in Fig. 3. It consists of a reservoir (a) which is filled with firmly packed wet powder and water and is closed at the top with an airtight cover plate (b). The reservoir extends into a dispenser tube (c) which terminates in a tip (d) of special design. A closely metered stream of water enters the dispenser tube at (e). The flow is deter-

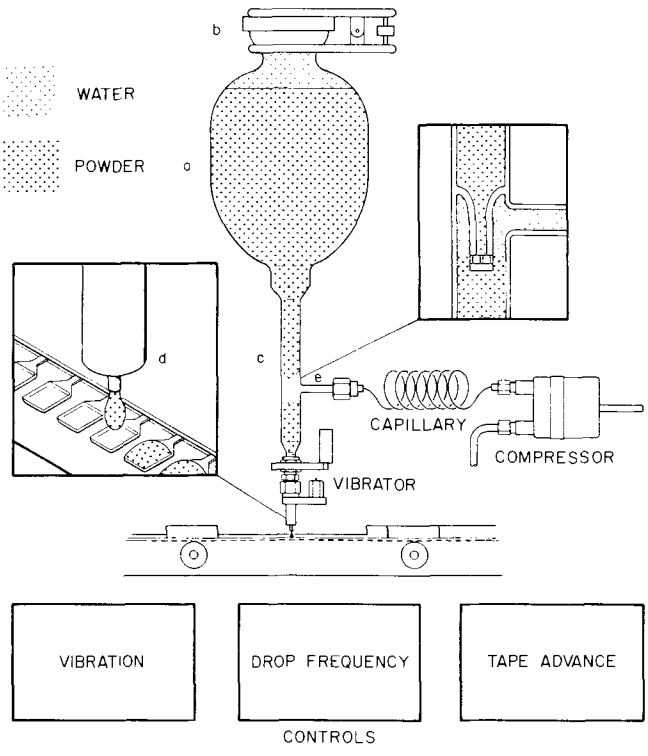

Fig. 3. Powder dispensing apparatus

mined by a water compressor in conjunction with a stainless steel capillary. Vibration is applied at the tip of the dispenser tube in order to provide for the smooth flow of powder in this part of the apparatus.

The size of the powder droplets is determined by the geometry of the tip. The ratio of diameter to length determines the ratio of water to powder. The droplets must contain a sufficient amount of water to spread out on the substrate. The amount of powder that can be dispensed dropwise is of the order of a fraction of a gram. Several drops have to be dispensed on the same substrate area if larger amounts of Ta powder are required.

The dropping frequency is determined by the rate of flow of water into the dispenser tube. Controls have been provided to insure continuous operation within narrow tolerances of dropping frequency and drop weight. The falling drop, sensed by a photocell, actuates the tape drive to advance the tape to the next position.

Both the short- and long-term stability of the dispensing apparatus have been found to be satisfactory. Drop weights fall well within the $\pm 10\%$ bracket of the average drop weight. This is within the specifications for STC's which normally require the capacitance to be within $\pm 20\%$ of the nominal capacitance.

Sintering.—Tantalum anodes for use in solid tantalum capacitors are commonly sintered in vacuum at temperatures between 1900° and 2200°C. However, vacuum sintering on a continuous basis with the material to be sintered moving in and out of the furnace continuously presents problems which can be overcome only at high cost.

We found sintering in inert atmosphere to be equally effective and selected this method because it could be adapted more readily to the sintering of tantalum tape.

The sintering equipment is shown in schematic form in Fig. 4. It consists of a furnace in two sections: A short horizontal presinter furnace is used to fuse the powder to itself and to the substrate, thereby removing the restraint from the tape orientation that required the tape to remain in horizontal position in order to avoid disturbing the loose and dry powder. After presintering, the tape can be wound through a

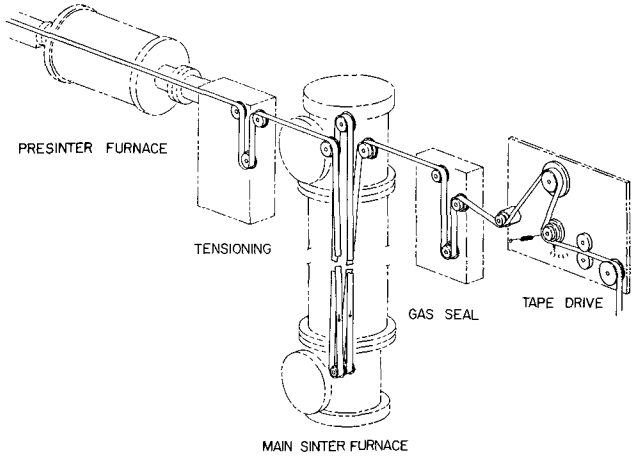

Fig. 4. Furnace for sintering POF tantalum tape

vertical sinter furnace of special design. The tape passes through the main furnace in two full loops for better utilization of the heat zone.

The furnace system is continuously being flushed with inert gas. The tape enters the furnace through a long tube in order to minimize the back-diffusion of the ambient atmosphere. A mercury-filled gas seal is used at the exit to block the flow of gas and force it out through the entrance tube.

The movement of the tape through the sinter furnace is paced by the dispensing apparatus.

Masking.—In the operations following sintering, it is important to limit the build-up of materials to areas where no ill effects will be found to occur in later process operations. In particular, the deposition of manganese dioxide and other cathode materials must be limited to those areas that have been covered with anodic oxide and that will not be subject to physical strain during lead attachment and encapsulation. For this reason, a narrow band of silicone adhesive is applied across the neck of each appendage (Fig. 2B), effectively suppressing creepage of solution over this part and limiting the build-up of cathode materials to the appendage proper. The neck area remains sufficiently clean for the positive lead to be welded to the riser at a later stage in the process.

The major operations after sintering and masking are: anodic oxidation, application of manganese dioxide, application of additional cathode materials, lead attaching, and encapsulation.

The discussion of the process steps is limited to those aspects that cannot be considered trivial adaptations from batch processes to an endless tantalum tape with anodes projecting at right angles from a continuous carrier tape.

Anodic oxidation.—In this operation, an insulating oxide film which is to serve as the dielectric of the finished capacitor is generated on the substrate metal by anodic oxidation. The tape is immersed in a suitable electrolyte, *e.g.* dilute phosphoric acid, and a potential is applied between the tape (positive) and a counterelectrode (negative). Anodic oxidation is carried out preferably at elevated temperature and with controlled current density. The voltage to be reached during anodization depends on the operating voltage of the finished capacitor and does not normally exceed 300V in the case of tantalum.

Anodizations are conventionally done in tank systems. Ta anodes are formed in batches, a mode which poses few problems with regard to controlling the critical parameters. The rate of voltage increase, in particular, can be programmed readily. Continuous tape anodization is widely practiced with aluminum foil and suggests itself for use with tantalum strip as well. However, problems arise with tantalum which require special solutions. In continuous tank forma-

tions, the current to the whole strip undergoing anodization has to be supplied at the entrance to the tank. The current required depends, among other factors, on the desired rate of formation, the loading of the tape (amount of powder per inch), and the tape speed (production rate). In the case of POF tantalum tape, the cross section of the carrier strip is far too small to supply the required current without overheating and intolerably high voltage drop along the tape under formation. The cross section of the tape cannot be increased at will because of the cost of tantalum. In addition, the anodization of porous anodes requires controlled current density which cannot be achieved readily in a tank formation system.

The shortcomings of the conventional tank anodization techniques have been overcome in the cascade formation which is illustrated in Fig. 5. The tape is suspended with its plane vertical between pairs of idlers and sprockets which guide the tape and serve as contacts for grounding the tape at the same time. Between contact wheels, the tape passes through electrolyte cascades which emerge from two rows of metallic nozzles alongside the tape path. The cascades have been subdivided into sections with electrolyte discontinuity between adjacent sections. Electrolyte is fed to each nozzle from a reservoir by means of insulating spaghetti tubing. The nozzles of each section have been interconnected electrically and serve as counterelectrode within a given section. Sections between the entrance and exit points of the tape are connected to power sources so that each one is more negative in potential than the preceding one by a fixed amount. The positive terminal of the power supply as well as the contact wheels are grounded. The tape is thus exposed during its travel through the formation system to a series of electrolyte cascades which are consecutively polarized at stepwise decreasing potentials by means of the counterelectrode nozzles. The magnitude of the potential step between adjacent sections as well as their length are determined such that optimal formation of a given type of anode is obtained. In the limit of small potential steps, formation will approach constant current formation. Large steps correspond to constant voltage formation.

The electrolyte is heated and thermostatically controlled in a tank and circulated through the formation system by means of pumps. Electrical isolation between electrolyte flowing to different nozzle sections is a requirement that is best met by long electrolyte paths. Grounded auxiliary electrodes have been placed in the electrolyte reservoirs to suppress cross currents which might otherwise flow between sections by way of the tank and the connecting tubing and cause corrosion in anodically polarized sections.

The continuous carrier strip is not being anodized to permit electrical contact to be made to the tape during anodization. Contact rollers are spaced such as to keep the current flow per contact within acceptable limits. The electrolyte is prevented from creeping up the neck by the silicone adhesive barrier applied earlier.

The rate of formation can be controlled by proper selection of the magnitude of the voltage steps, of the electrolyte conductivity, the cascade configuration, and the speed of the moving tape.

The anodization process can be programmed externally by selecting the number of sections at the same voltage and the magnitude of the voltage step according to the requirements of the rating being processed. The programmability facilitates the change-over between different ratings and minimizes the loss of tape between changes.

High formation rates become possible because of improved heat transfer between the electrolyte and the anodes in a flow system.

The same kind of equipment can be used for formation to voltage, stabilization at voltage, and reformation after the deposition of manganese dioxide.

Deposition of manganese dioxide.—After the generation of an insulating oxide film on the tantalum substrate which serves as the dielectric of the finished capacitor, a counterelectrode of manganese dioxide is deposited on the inner and outer surfaces of the porous tantalum slug. Conventionally, this is done by impregnating the porous slug with a concentrated solution of manganese nitrate in water and converting the manganese nitrate by heating it in air at temperatures between 200°-400°C. The operation is repeated several times in order to provide a dense, highly conducting layer of manganese dioxide.

The whole operation consists of a sequence of dipping and heating steps which pose no particular problems when applied to a continuous tape, and includes one or more reanodizations between MnO_2 applications. Obviously, the depth of immersion of the tantalum slugs must be controlled carefully in order to limit the build-up of manganese dioxide to those parts that have been coated with anodic oxide. The earlier masking step is an essential precondition for control of the build-up in the neck area.

A device which was found to permit dipping with the tape in the horizontal position is illustrated in Fig. 6. A metallic or plastic rod was provided with a hori-

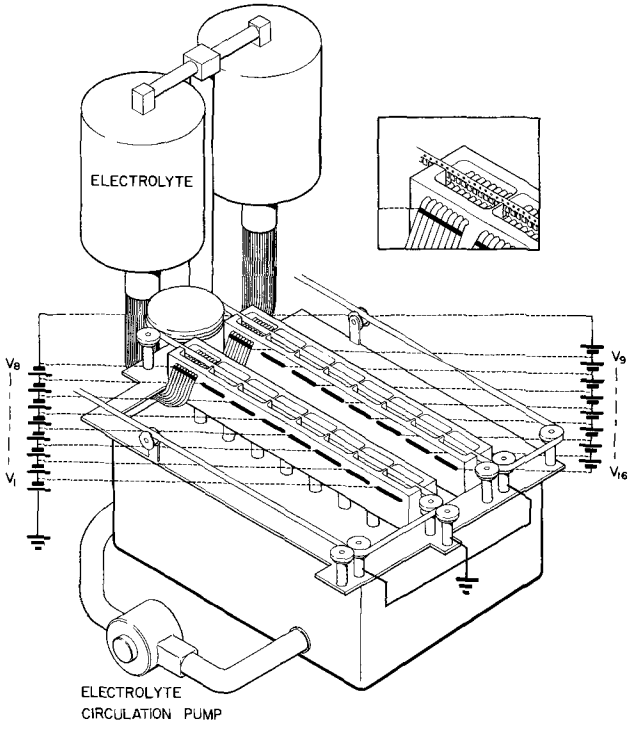

Fig. 5. Cascade anodization system

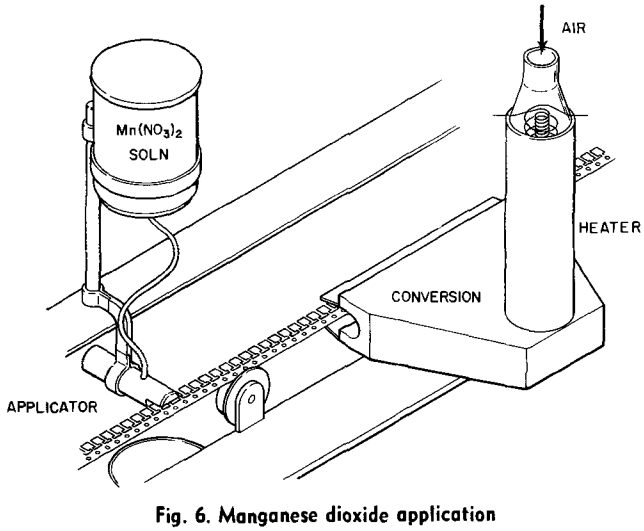

Fig. 6. Manganese dioxide application

zontal slot and a passage to permit feeding manganese nitrate solution to this slot. The solution is held in the slot by surface tension. A reservoir is thus provided from which the tantalum slugs can pick up the solution. The solution is pumped into the slot from a reservoir to which excess solution is returned.

Following dipping, the tape passes through hot gas which converts the manganese nitrate to oxide. The gas is heated by means of a cartridge heater with proportional control.

The preceding operations are repeated until an optimal coating with manganese oxide has been obtained. Reanodizations are carried out in an anodization system as described in the previous section.

Additional cathode contact layers.—Following manganese dioxide application, additional coatings of colloidal graphite and silver paint are applied in order to provide ohmic contact to the manganese dioxide semiconductor and to provide solderability. Both materials are applied by dipping, followed by drying and heat curing. The dipping is most conveniently done using the same applicators as used for manganese nitrate. Their use is particularly advantageous in the case of fast-drying materials, such as silver paint, because of the minimal surface area exposed to the atmosphere and the continuous replenishment of the small volume of solution which exists in the slot of the applicator. It has been found desirable to coat the silver layer with a layer of solder prior to lead attachment. Dipping of the whole strip in a pool of solder such as is generated in wave solder equipment is suitable for this operation.

Lead attachment.—The application of solder prior to lead attaching makes it feasible to attach the anode by welding and the cathode lead by reflow soldering. The anode lead is attached to the neck portion of the appendage using capacitor discharge or resistance welding. The negative lead is attached to the cathode contact by heating a section of the negative lead extending across the capacitor part and fusing it with the solder coating (Fig. 2C).

Separation from continuous tape and encapsulation.—Following lead attachment, the capacitor is severed from the tape by cutting the neck between the positive lead and the continuous tape. The capacitors are then transferred to fixtures for encapsulation which may be by means of transfer molding, dip coating, or hermetic sealing in metal cans, or other means depending on the use of the device.

Conclusions

In the POF process, a combination of novel techniques makes it possible to overcome the limitations inherent in the conventional process. The usual pressing of powder with binder has been replaced by the deposition of a powder slurry in water on a substrate of the same material which is sintered continuously in inert atmosphere. The special configuration of the substrate eliminates the requirement of attaching individual anodes to processing fixtures after sintering. The anodes thus made are of high purity and uniformity.

Truly continuous processing of tantalum capacitors with continuous flow of material through the line without any direct handling of individual capacitors has been achieved. The POF process can be mechanized and lends itself to automation and computer control.

Contamination and physical damage which could affect the final product quality through the presence of imperfections in the anodic oxide film have been minimized. Every device encounters processing conditions as nearly the same as possible. Operator influence on product quality and uncontrolled holdups during processing have been eliminated. As a result, uniformity of device parameters, near optimal electrical characteristics, and high yields can be expected.

Manuscript submitted Sept. 28, 1970; revised manuscript received ca. Dec. 1, 1970.

Any discussion of this paper will appear in a Discussion Section to be published in the December 1971 JOURNAL.

REFERENCES

1. G. P. Klein, U.S. Pat. No. 3,458,916 (1969) and 3,403,303 (1968).
2. G. P. Klein, M. Kallianidis, and W. F. Vierow, *Proc. 20th Electron Components Conf.*, **1970**, 311.
3. M. Wagner, German Pat. No. 1,038,193 (1958).
4. C. Havoshi *et al.*, U.S. Pat. No. 3,469,294 (1958).
5. G. P. Klein, U.S. Pat. No. 3,412,444 (1968).
6. G. P. Klein, U.S. Pat. No. 3,456,694 (1969)

Potentiostatic Anodic Pickling of Stainless Steels

G. Bombara,* A. Tamba, and N. Azzerri

Centro Sperimentale Metallurgico S.p.A., 00129 Rome, Italy

ABSTRACT

Surface Cr-depletion beneath the oxide scale in heat-treated stainless steels plays a determining role in both functions of acid pickling which are: (*i*) scale detachment or descaling proper and (*ii*) restoration at the metal surface of the base Cr content, *i.e.* of the highest passivity properties. As the anodic behavior of the impoverished alloy is quite different from that of the base alloy, definite advantages may be obtained by potentiostatically polarizing the steel during pickling in a potential range where the anodic dissolution of the Cr-depleted alloy is kinetically favored over that of the base alloy. Experimental evidence is given for AISI Type 304 steel in both HNO_3-HF and simple H_2SO_4 baths, showing the attractiveness of potentiostatic pickling in allowing the replacement of the usual nitric-hydrofluoric acid pickles with less toxic and cheaper sulfuric baths.

Rolling of stainless steels requires the quick and complete removal of oxide scales formed in hot rolling, for which temperatures below 900°C are unadvisable as well as during solubilizing heat-treatments carried out at 1050°-1100°C. Oxide scales of high-alloy steels are much more impervious and adherent than those of nonalloyed or low-alloy steels. Scales formed on Cr and Cr-Ni steels have a complex structure owing to the oxidation mechanism of these oxidation-resistant alloys. In fact, because of the higher oxidizability of chromium, the main step consists in the formation of

* Electrochemical Society Active Member.

Key words: acid pickling, Cr-depletion, descaling, fluoronitric pickle, passivity evaluation, potentiostatic treatments, sulfuric pickle, stainless steels.

a highly protective Cr-rich oxide layer which inhibits outward diffusion of iron. However, on growing, the oxide layer undergoes mechanical ruptures allowing the rapid oxidation of the underlying alloy which is less oxidation resistant because of the Cr impoverishment. The succession of low-rate (parabolic) oxidation stages under a continuous Cr-rich oxide layer and high-rate (linear) oxidation stages under a ruptured oxide layer results in the formation of stratified scales with alternate layers of Cr-rich and Fe-rich oxides (1, 2). The final situation of an oxidized surface (Fig. 1) will show the prevalence of a Cr-depleted alloy under an adherent and compact layer of Cr-rich oxides together with the presence, to a much lower extent, of surface areas of less Cr-impoverished alloy under a much more porous and strongly adherent layer of Fe-rich oxides. The resulting subsurface alloy is Cr depleted up to a depth of a few microns (3). Such a depletion is of the utmost importance in the acid pickling of rolled sheets and strips. A previous electrochemical investigation (3) showed indeed that the main descaling mechanism does not consist in disintegrating the scale by direct dissolution, but rather in detaching and exfoliating the scale *via* dissolution of the Cr-depleted surface alloy supporting the most adherent scale. Such an alloy has an electrochemical behavior much different from that of the base alloy. This led to the idea, preliminarily experimented and patented (4, 5), of increasing the rate and efficiency of stainless steel acid pickling through the electrochemical control of the anodic dissolution of the subscale layer in such a way as to accelerate the rate of attack on the Cr-depleted alloy over that of the undepleted material. So far as final cold-rolled products are concerned, the restoration at the steel surface of the base Cr content (giving the maximum "passivability," *i.e.* resistance, to the general and localized corrosion) depends on the complete removal of the depleted alloy. Indeed, the reduction in chromium, which is less noble thermodynamically than iron and nickel but highly contributing to the "kinetic nobility" (*i.e.*, passivity), produces, accordingly, a substantial enlargement of the activity range in the anodic polarization curve of the alloy together with a definite shift of the anodic peak potential in the noble direction and a marked increase of passive current densities. Besides, dechromization makes the active-passive transition less sharp, enlarging the region of incomplete passivity. All these effects are shown schematically in Fig. 2.

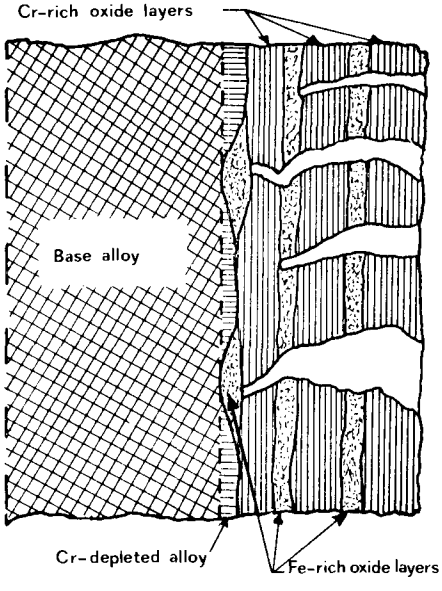

Fig. 1. Schematic picture of an oxide-scaled, high-Cr steel

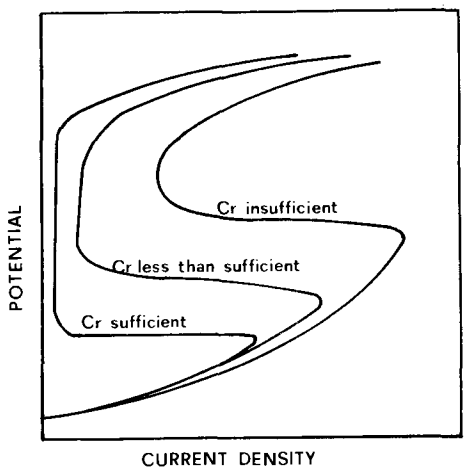

Fig. 2. Influence of Cr content on anodic polarization curve of Cr steels.

From such considerations it can be easily shown that the anodic polarization curve of an oxidized stainless steel, *i.e.* of a broadly dechromized steel surface, will give both the primary peak of the base alloy and a dissolution peak of the Cr-depleted alloy at more positive potentials (Fig. 3). A marked broadening of the active dissolution range will result, as well as an increase in passive current density. The mechanism of ordinary acid pickling of stainless steels may now be explained. If the pickle contained nitric acid only, owing to the oxidizing power of this acid, the working potential of the steel would shift quickly to the passivity range where the dissolution rate would be negligible on nondechromized areas and minimal on Cr-depleted areas. When hydrofluoric acid is present with the nitric acid, the strong activating power of F^- ions confers on the medium a definite depassivating character which affects the polarization behavior in the same way as lowering the Cr content in the alloy to insufficient levels. As indicated in Fig. 4, active dissolution rates increase remarkably, and the working potential of the steel keeps close to the zero current value.

The principle of potentiostatic anodic pickling lies in maintaining the steel potential polarized by a potentiostat within the range (shown in Fig. 4) where the anodic dissolution rate of the Cr-depleted alloy is at its maximum.

Experimental and Results

Specimens.—All tests were carried out on strip specimens, 8 x 3 cm, of AISI Type 304 steel from commercial sheet, 1 mm thick, with a standard finish No. 2B. A necessary prerequisite was the production of a

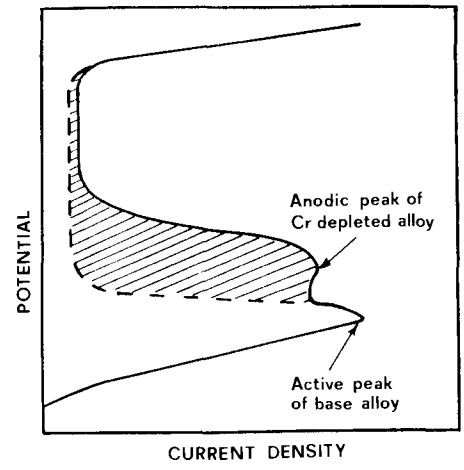

Fig. 3. Typical potentiodynamic anodic polarization curve for an oxidized Cr steel in acid solution.

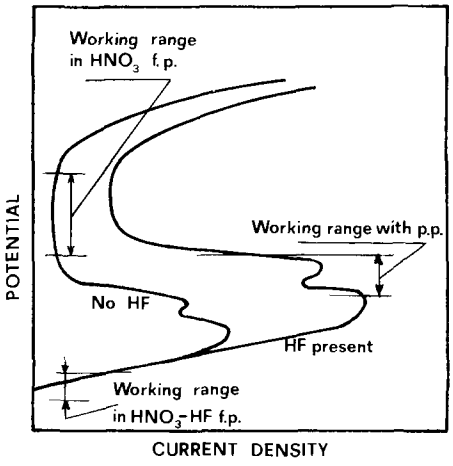

Fig. 4. Influence of HF on anodic polarization curve in HNO_3; working position for potentiostatic pickling.

uniform oxide scale sufficiently reproducible from one specimen to another. Satisfactory results were obtained by accurately controlling in each experiment both the surface preparation and the final oxidation treatment. The following succession of operations to be carried out on one specimen at a time was adopted: (*i*) prolonged pickling in (HNO_3 (d 1.4) vol. 20% + HF (d 1.15) vol. 2%) at 60°C for 20 min, aiming at leveling the metal surface microgeometrically and chemically; (*ii*) accurate rinsing in running water and dipping in a passivating HNO_3 (d 1.4) vol. 46% solution at room temperature for 30 min; (*iii*) drying in a current of air at 80°C (*iv*) oxidizing at 1050°C for 20 min in air flowing at 60 liters/ hr in a vertical tubular furnace (6 cm diameter); (*v*) final rapid cooling in air at room temperature.

For the oxidizing treatment each specimen was placed in a definite position within the furnace by means of a special supporting device, to prevent the specimen from any contact or impact with the furnace wall (especially during the final air quenching) which could possibly lead to scale scratching or detaching. Specimens so treated presented uniform, adherent oxide layers and gave reproducible results with regard to the electrochemical behavior. Scales, however, were much thicker and more uniform than those produced in practice, where heat treatment is much shorter.

Evaluation of pickling.—It was necessary to set up suitable technique for assessing the efficiency of any pickling treatment tested from the standpoint of descaling proper and passivability restoration.

Descaling was evaluated by measuring with a special photodiode device the average reflectivity of the pickled surface, assuming a conventional linear scale ranging from 0 to 100. The figure 100 was assigned to a blank consisting of a deeply pickled surface (20 min in nitric-hydrofluoric acid mixture at 60°C), whereas the figure "zero" was given to a surface oxide scaled by treating in the furnace as described above. Such values were determined as the average of measures on 20 specimens for each extreme condition.

The second criterion of evaluation, aimed at assessing the stainless quality of pickled surface, was strictly electrochemical and was based on the determination, in a deaerated 20% H_2SO_4 solution at 30°C, of the tensiodynamic anodic polarization curve of the pickled specimens. The area of the passivation peak, being inversely proportional to the passivability, gave a measure of residual Cr depletion at the surface, *i.e.*, of the extent at which pickling succeeded in restoring the proper base composition at the surface.

In order to minimize the effect of minor variations in scale properties from one specimen to another, the comparison between the efficiency of each experimental potentiostatic pickling (p.p.) and that of a free pickling (f.p.) was made on each specimen. Namely, while a half specimen was pickled freely, the other half was pickled under potentiostatic control, at the same bath temperature and for an equal time, and a direct reflectometric and electrochemical comparison was made of the two halves.

Potentiostatic pickling in HNO_3-HF.—On the basis of preliminary tests, a mixture [HNO_3 (d 1.4) vol. 10% + HF d 1.15 vol. 1%] was adopted as the pickling solution to be operated at 30°C. Such a low temperature gave descaling kinetics slowly enough to allow an easy comparative evaluation; *i.e.*, a definite differentiation could be made between the time dependence of p.p. and f.p.

Figure 5 shows the trend of successive polarization curves obtained by scanning the same oxidized area in the pickle chosen. Potentials are referred to a Hg/Hg_2SO_4 electrode in K_2SO_4 saturated solution (SMSE). The progressive decrease in current densities and the clear tendency of the active dissolution peak to split on repeating the scanning can be seen.

Descaling.—The results obtained are presented as reflectivity-pickling time curves at different polarization potentials (Fig. 6) and as plots of the per cent advantage of p.p over f.p. *vs.* pickling time at various constant potentials (Fig. 7) and *vs.* potential at various constant pickling times (Fig. 8). Each experimental point was obtained as the average for four different

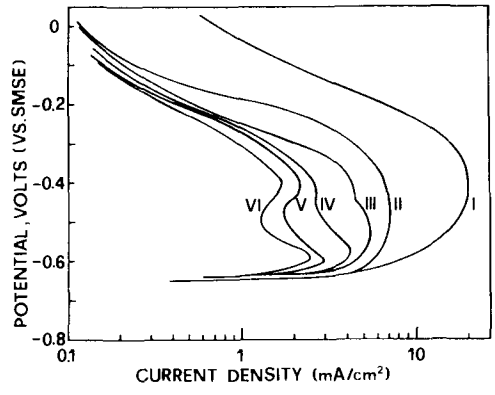

Fig. 5. Anodic polarization curves from successive scans on oxidized AISI Type 304 steel in HNO_4-HF (10:1) at 30°C.

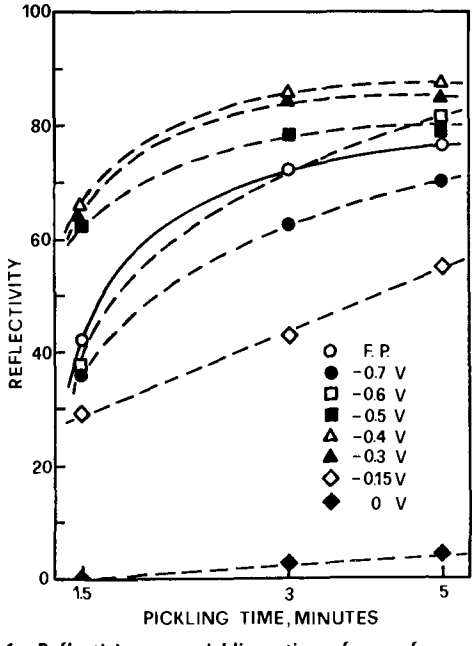

Fig. 6. Reflectivity *vs.* pickling time for surfaces potentiostatically pickled in HNO_3-HF (10:1) at 30°C at different potentials.

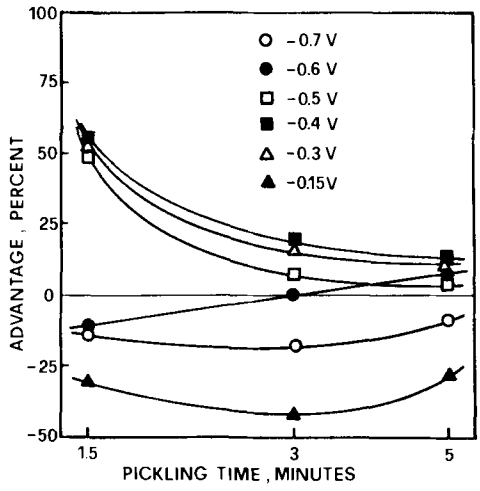

Fig. 7. Time dependence of descaling improvement by p.p. over f.p. in HNO_3-HF.

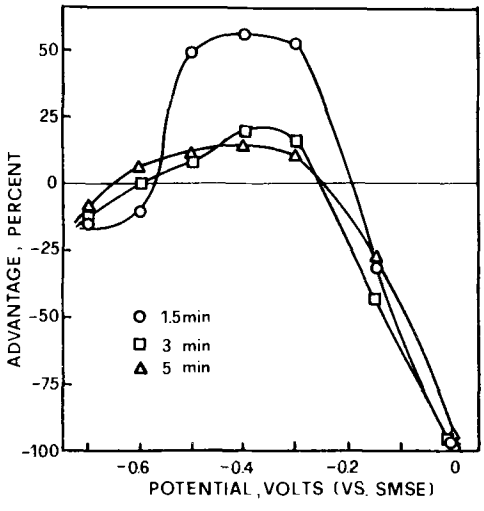

Fig. 8. Potential dependence of descaling improvement by p.p. over f.p. in HNO_3-HF.

specimens. Figure 6 shows that, by polarizing at −300 to −500 mV (SMSE), the descaling rate was faster with p.p. than with f.p. At −600 mV, only for relatively long pickling times was the descaling efficiency of f.p. surpassed, while at the other potentials tested a marked inferiority of p.p resulted.

The superiority of p.p. was particularly marked in the potential range corresponding to the active dissolution peak of the Cr-depleted alloy (Fig. 5). The equivalence between f.p. and p.p. at −600 mV may be explained by considering that free corrosion potentials of oxidized specimens ranged between −590 and −625 mV. At −150 and at 0 mV only an incomplete descaling was obtained since the steel worked in the passivity region (Fig. 5). Also, at potentials (−700 mV) more negative than the free corrosion potential, descaling was inferior to that with f.p.

The beneficial effects of p.p. are seen in Fig. 7 in terms of gain in reflectivity as a function of pickling time. The highest advantages (over 50%) were obtained for short pickling times at potentials ranging from −500 to −300 mV. For longer times, obviously, the difference reduced since f.p. is also completely efficacious. Figure 8 represents the gain in descaling rate as a function of working potential at different constant times, showing again that the optimum working range was −300 to −500 mV.

The practical profit of the potentiostatic control can be simply expressed as the shortening of the time required to reach the maximum reflectivity obtainable with f.p. Since in this way descaling could be considered accomplished in 3 min while an equal reflectivity was reached in about 1.5 min with p.p. (at −300 to −400 mV), the practical time profit in terms of descaling rate was about 100%.

Cr restoration.—The results obtained are presented as: (*i*) passivation charge-pickling time curves at different constant potentials and (*ii*) plots of the per cent advantage of p.p over f.p. Figure 9 shows the curves in (*i*) drawn from polarization curves obtained by anodic scans in 20% H_2SO_4 at 30°C as mentioned above. For short pickling times a definite differentiation appears, depending on the potential. F. p. always gave passivation charges higher than those for p.p. at proper potentials. This demonstrates the superiority of p.p. in Cr restoration at the steel surface.

The advantages obtained with p.p. over f.p. are reported in Fig. 10 in terms of lowering the electric charge for passivating. For short pickling times (0.5 min), the gain was about 65% at −300 mV, while somewhat lower figures resulted at −400 and −500 mV. For longer times the gain reduced gradually as f.p. also worked and in 3-5 min almost completely restored the base Cr content at the surface..

Figure 11 presents the plot of the per cent advantage *vs.* polarized potential at three different constant pickling times. It appears that there is a broad potential range (about 400 mV large) in which p.p. is bene-

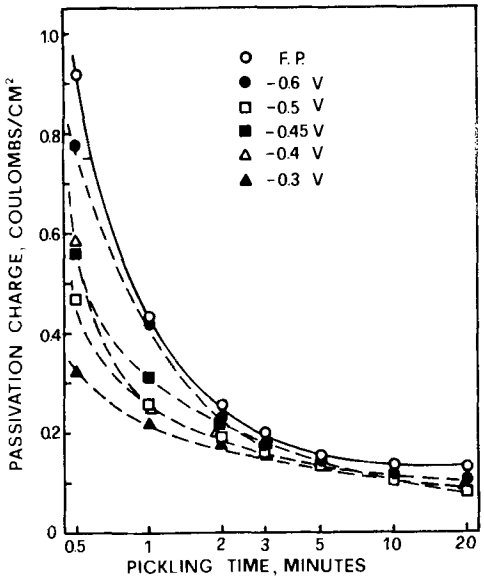

Fig. 9. Time dependence of electrical charge for passivation of specimens potentiostatically pickled and free pickled in HNO_3-HF.

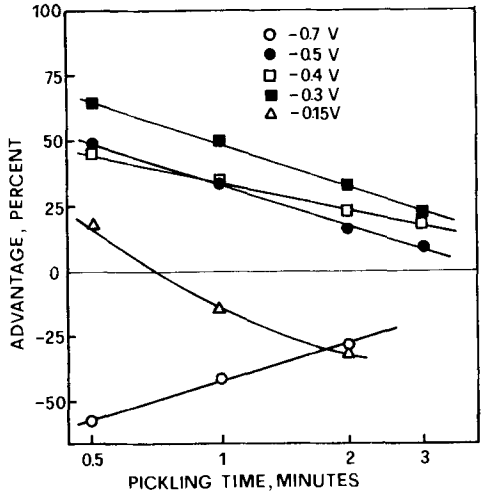

Fig. 10. Time dependence of Cr-restoration improvement by p.p. over f.p. in HNO_3-HF.

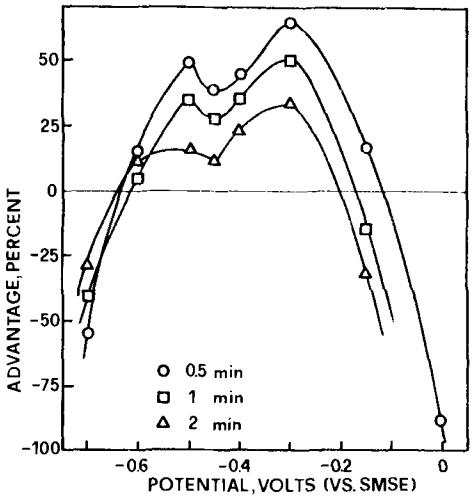

Fig. 11. Potential dependence of Cr-restoration improvement by p.p. over f.p. in HNO_3-HF.

ficial. The optimum conditions appear to coincide with those for the descaling proper. A practical profit figure can also be drawn for the Cr restoration rate. In accordance with the above criterion, assuming 3 min to be the time required with f.p. to reach the maximum passivability, this same result could be obtained in about 1 min by p.p. at −300 to −400 mV. This leads to an over-all time profit of about 200%.

Potentiostatic pickling in H_2SO_4.—An attractive possibility offered by the introduction of potentiostatic techniques in stainless steel pickling lies in substituting simple sulfuric acid solutions for ordinary nitric-hydrofluoric acid baths. This would allow substantial lowering of direct costs such as those of chemicals used in the bath, as well as indirect ones such as those connected with the abatement of nitrous vapors from the bath and the neutralization of exhausted pickles prior to discharging. Further, owing to the stability of sulfuric acid, lower evaporation losses would result, and many problems could be avoided connected with handling such a toxic chemical as hydrofluoric acid. The essential function of the potentiostatic control in sulfuric pickling would be in substituting the depassivating action of hydrofluoric acid allowing the steel to work constantly in a range of active dissolution. In this connection, in order to outline the right potential range, an anodic potentiodynamic scan was carried out in 20% H_2SO_4 on an oxidized specimen (Fig. 12). The

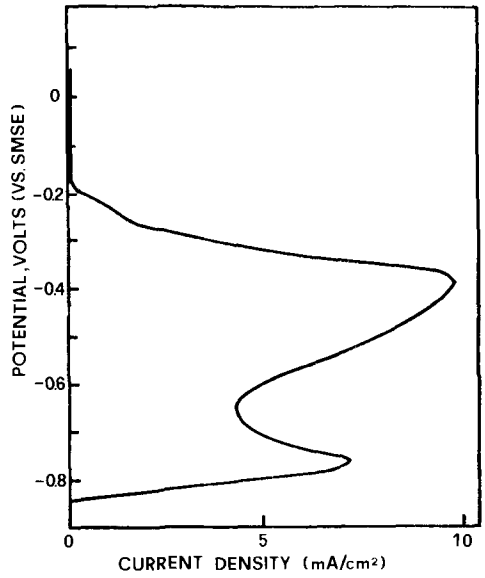

Fig. 12. Potentiodynamic anodic curve of oxidized AISI Type 304 steel in 20% H_2SO_4 at 30°C.

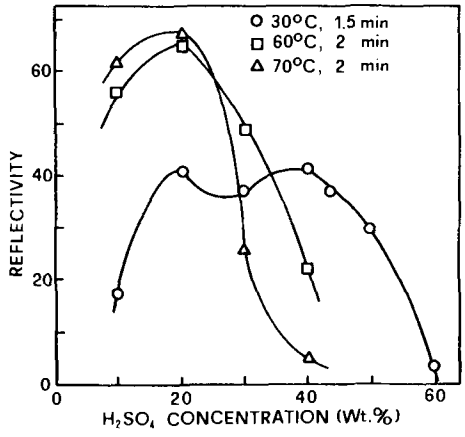

Fig. 13. H_2SO_4 concentration dependence of reflectivity for specimens potentiostatically pickled at −600 mV (SMSE).

curve obtained clearly displays the two dissolution peaks of the base alloy and the Cr-depleted alloy.

Prior to experimenting in sulfuric acid baths, exploratory potentiostatic pickling tests at −600 mV (SMSE) were carried out, aimed at determining the most suitable temperature and acid concentration. Figure 13 shows a plot of descaling efficiency (measured through reflectivity) *vs.* H_2SO_4 concentration, at three constant temperatures. It appears that the highest efficiencies were obtained with 20% H_2SO_4 at 60° and 70°C and, because of the essential equivalence of the two temperatures, the lower one was adopted for all p.p. tests.

Owing to the insufficiency of descaling by f.p. in H_2SO_4, the f.p. in HNO_3 (d 1.4) vol. 20% + HF (d 1.15) vol. 2% mixture at the same temperature of 60°C was chosen as the reference. As for p.p. experiments in nitric-hydrofluoric bath, each experimental p.p in H_2SO_4 was carried out on one-half of an oxidized specimen, while on the other half f.p. in the above HNO_3-HF reference pickle was carried out, time and temperature being equal.

Descaling.—The experimental results were plotted as a function of pickling time at various constant potentials, each point being the average for four specimens (Fig. 14). It appears that the efficiency of ordinary HNO_3-HF f.p. can be approached under certain con-

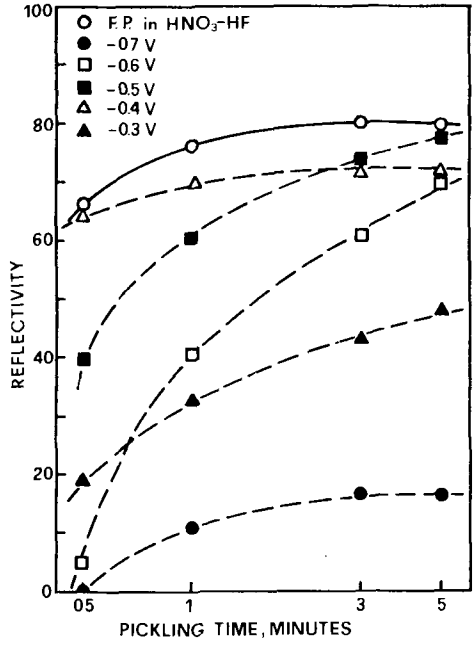

Fig. 14. Reflectivity *vs.* pickling time for surfaces potentiostatically pickled in 20% H_2SO_4 at 60°C.

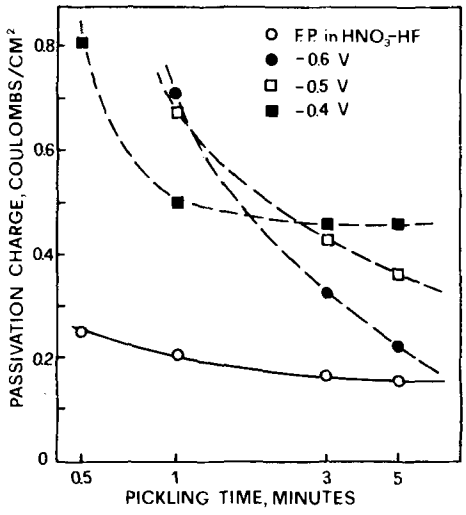

Fig. 15. Time dependence of passivation charge for specimens potentiostatically pickled in 20% H_2SO_4 at 60°C.

ditions by that of p.p. in H_2SO_4. In fact, p.p. at −400 mV (SMSE) in short times (0.5-1 min) or at −500 to 600 mV in longer times (3 and 5 min, respectively) gave descaling degrees almost equivalent to those with HNO_3-HF f.p.

Cr restoration.—The efficiency of p.p. in H_2SO_4 in removing the Cr-depleted alloy from the steel surface was evaluated by the coulometry of the residual passivation peak (in 20% H_2SO_4) in comparison with that obtained with f.p. in the reference HNO_3-HF mixture, time and temperature being equal. The results obtained are plotted in Fig. 15 showing that in this respect p.p. in the simple sulfuric solution tested was inferior to the ordinary pickling in nitric-hydrofluoric acid bath. Comparable results between the two, however, were obtained with p.p. at −600 mV prolonged for 5 min at least. This indicates that, under particular operating conditions and of course at lower speed, p.p. in H_2SO_4 could give about the same final surface quality of ordinary pickling baths.

Conclusions

With necessary reservations about the particular conditions of laboratory treatment and the special techniques for evaluating descaling and Cr restoration, the experimental results presented in this paper have definitely shown the potentiality of the potentiostatic control of nitric-hydrofluoric pickling in terms of both descaling acceleration and surface quality improvement, as well as of possible replacement of nitric and hydrofluoric acids with cheaper and less toxic sulfuric acid. In this latter respect, however, H_2SO_4 p.p. appeared to compete with ordinary HNO_3-HF pickling in descaling efficiency while being somewhat inferior as to the stainless quality of the pickled surface. However, this point seems to be easily surmountable by means of suitable additions to the bath, or by raising the operation temperature, or, perhaps, by a final "flash" dipping in HNO_3-HF pickle.

Other aspects of practical interest such as those regarding the other stainless grades, the metal losses, and the life of baths, require further systematic investigations in order to draw out useful information on the over-all economy of the potentiostatic treatment.

Acknowledgments

The authors are strongly indebted to Dr. L. Gilberti, FIAT Ferriere Laboratories, Turin, for stimulating this study.

Manuscript submitted Aug. 5, 1970; revised manuscript received Nov. 10, 1970.

Any discussion of this paper will appear in a Discussion Section to be published in the December 1971 JOURNAL.

REFERENCES

1. D. P. Whittle and G. C. Wood, *This Journal*, **114**, 986 (1967).
2. T. Ericsson, *Oxidation of Metals*, **2**, 173 (1970).
3. B. Vicentini and G. Bombara, *Electrochim. Metall.*, **3**, 313 (1968).
4. A. Tamba, N. Azzerri and G. Bombara, Paper P. 106 presented at the International Conf. on the Science and Technology of Iron and Steel, Tokyo, Sept. 7, 1970.
5. Italian Pat. No. 829.174 (1969).

Technical Note

Gold Plating on Copper Substrates from Gel Electrolytes

H. Y. Cheh[1,*]

Bell Telephone Laboratories, Incorporated, Murray Hill, New Jersey 07974

Thin deposits of gold are often applied on substrate surfaces of electronic parts to protect the parts from corrosion and to provide a conducting path between devices. Additionally, the concept of gold plating on selected areas is interesting, often mandatory and economically most attractive because of the high intrinsic values of the yellow metal.

In this paper, preliminary investigations on one means of selective plating, namely, gold plating from gel electrolytes, are described. In principle, a gel electrolyte can be shaped to any desirable geometry for selective plating. However, many practical questions must be answered in order to demonstrate the feasibility of plating through a gel electrolyte. For instance, no convection exists in a gel electrolyte. The transport of ions must be accomplished by diffusion and electrical migration alone. Little is known about the diffusion of ions in a gel. Consequently, a study on the rate of deposition in a gel is crucial. When the current efficiency for gold deposition is low, hydrogen bubbles generated at the substrate surface tend to adhere to the surface and shield off, to a large extent, further deposition. The contact, or wettability, between the gel electrolyte and the substrate surface is another important parameter to consider. Nonuniform contact be-

[1] Present address: Department of Chemical Engineering and Applied Chemistry, Columbia University, New York, New York 10027.
* Electrochemical Society Active Member.
Key words: plating, gel electrolyte, gold.

tween the two phases yields a nonuniform deposition which also affects the porosity of the electrodeposit. Experiments designed to study both the current efficiency of the plating process and the porosity of the gold deposits are reported here.

Experimental

An acid citrate gold bath (1) which contained 21.3 g/liter potassium gold cyanide and 50 g/liter ammonium citrate (dibasic) and a neutral phosphate gold bath (2) which contained 20 g/liter potassium gold cyanide, 30.5 g/liter potassium phosphate (dibasic), and 10 g/liter potassium phosphate (monobasic) were chosen for these experiments. A number of gelling agents were considered, but only two proved satisfactory for this application. These were the high viscosity sodium carboxymethyl cellulose and hydroxyethyl cellulose.

A circular OFHC copper disk and gold disks with diameters of 0.78 cm were used as cathode and anode, respectively. The cell container was a glass tube (ID 0.8 cm) 4 cm long.

In order to find the optimum composition of gel electrolytes, several solutions containing various amounts of gelling agents were prepared. It was subsequently found that electrolytes containing 5 to 10 w/o (weight per cent) gelling agents were most suitable for performing the deposition experiments. When the concentration of the gelling agent was less than 5 w/o, the resulting solution did not solidify. At concentrations above 10 w/o, gelling occurred spontaneously, and uniform mixing became a difficult task. It was also found that hydroxyethyl cellulose dissolved much more readily in the gold solution than the sodium carboxymethyl cellulose.

Prior to plating, the copper cathode was cleaned and degreased using acetone and trichloroethylene, respectively. It was then bright-dipped for approximately 10 sec in a solution containing 250 ml H_2SO_4, 125 ml HNO_3, 4 ml HCl and 250 ml water, then rinsed with distilled water and dried. The gel electrolyte was injected into the plating cell by a plastic syringe. To ensure uniform current distrbution, the cathode and anode were placed at two ends of the cell facing each other. Plating was then carried out under constant current density condition. The rate of deposition was then calculated by comparing the weight increase of the cathode after the deposition process. Depending on the applied current density, the duration of plating was varied between 10 min to 3 hr for optimum weighing. The porosity of the electrodeposit was measured by an electrographic porosity tester.[2] Deposits 0.5μ thick were used in the test. A voltage of 5V and a pressure of 800 lb/in.^{2} were applied for pore printing. The results were then compared with a standard deposit which was also 0.5μ thick and was plated from the aqueous acid citrate gold bath at 60°C and a current density of 4 mA/cm^2.

Results and Discussion

The results from measurements of current efficiency are summarized in Table I-IV. The product of the applied current density and current efficiency for gold deposition ($i \cdot E$) represents the current density for gold plating. This quantity is directly proportional to the rate of deposition. The current density for gold deposition observed in these experiments varies between 0.15 mA/cm^2 to 0.50 mA/cm^2, and this corresponds to a deposition rate of 0.6 μ/hr to 2 μ/hr. This relatively fast rate of deposition in a convection-free medium can be explained by a consideration of electrical migration and diffusion of ions in a gel. It is known that the electrical conductivity of a gel electrolyte does not change appreciably from its aqueous solution with no gelling agents in it (3). In other words, the mobility of an ion is not hampered during a gel formation. The theory that a gel contains a network of capillary spaces filled with unchanged solvent and the "micro-viscosity" of the system remains unchanged is often suggested in the literature (3). The mean free path of a cation in a gel electrolyte is in the order of 1Å. This is often much smaller than the size of the structure introduced into the system during a gel formation. Consequently, the diffusion coefficient of a cation in a gel is of the same order of magnitude as that in an aqueous solution. The transport of ions due to electrical migration can be ignored because of the relatively high electrical conductivity of the system. Assuming diffusion as the only means of transporting ions and using a semi-infinite model, the concentration of the reacting species has the following form (4)

$$c = c_0 - \frac{iE}{n\mathbf{F}} \sqrt{\frac{4t}{D}}\, i\,\mathrm{erfc}\,\frac{x}{2\sqrt{Dt}} \qquad [1]$$

where c is the concentration of the cation in the system, c_0 is the initial concentration of the cation, n is the number of electrons transferred for the deposition reaction, $\mathbf{F}$ is Faraday's constant, t is the time, D is the diffusion coefficient of the cation and x is the distance from the electrode surface. The concentration of the cation at the electrode-solution is therefore

$$c_{x=0} = c_0 - \frac{iE}{n\mathbf{F}} \sqrt{\frac{4t}{\pi D}} \qquad [2]$$

The transition time τ is defined as the time when $c_{x=0}$ becomes zero. From Eq. [2]

Table I. Current efficiency for gelled acid citrate gold bath (High viscosity sodium carboxymethyl cellulose)

Gel concentration, w/o	Applied current density, i, mA/cm^2	Efficiency, E, %	iE, mA/cm^2
5.0	0.28	77	0.22
	0.56	62	0.35
	1.11	37	0.41
	1.85	23	0.43
7.5	0.46	58	0.27
	0.93	30	0.28
	1.85	20	0.37

Table II. Current efficiency for gelled neutral phosphate gold bath (High viscosity sodium carboxymethyl cellulose)

Gel concentration, w/o	Applied current density, i, mA/cm^2	Efficiency, E, %	iE, mA/cm^2
5.0	0.46	59	0.27
	0.93	38	0.35
	1.85	27	0.50
7.5	0.46	54	0.25
	0.93	34	0.32
	1.85	22	0.41

Table III. Current efficiency for gelled acid citrate gold bath (Hydroxyethyl cellulose)

Gel concentration, w/o	Applied current density, i, mA/cm^2	Efficiency, E, %	iE, mA/cm^2
7.5	0.28	58	0.16
	0.46	64	0.29
10	0.28	52	0.15
	0.46	61	0.28

Table IV. Current efficiency for gelled neutral phosphate gold bath (Hydroxyethyl cellulose)

Gel concentration, w/o	Applied current density, i, mA/cm^2	Efficiency, E, %	iE, mA/cm^2
7.5	0.28	71	0.20
	0.46	65	0.30
10	0.28	61	0.17
	0.46	58	0.27

[2] Supplied by Sel-Rex Corporation, Nutley, New Jersey.

$$\tau = \frac{\pi c_o^2 n^2 F^2 D}{4i^2 E^2} \quad [3]$$

c_o for the plating system is 7×10^{-5} moles/cm^3. iE, as shown in Tables I-IV, varies between 0.15 mA/cm^2 to 0.50 mA/cm^2. Assuming a diffusion coefficient of 5×10^{-6} cm^2/sec, τ is 8×10^3 sec for an iE of 0.15 mA/cm^2 and 720 sec for an iE of 0.50 mA/cm^2. Comparing τ with the duration of the deposition experiment, it is confirmed that the concentration of the cation at the electrode-solution interface was never depleted completely for all the experiments. This explains both the fast rate of deposition and the increase of deposition rate at higher applied current density.

The electrographic porosity test provides a qualitative rather than a quantitative measurement. The preliminary results indicate that pore formation is due largely to hydrogen bubbles which are generated during the deposition and trapped at the interface. The porosity of the bulk of the deposit is similar to that plated from an aqueous solution.

Conclusions

Preliminary investigations on gold plating from gel electrolytes are presented. The rate of deposition is found to be sufficiently rapid to render the deposition process worth considering. The feasibility of such a process will depend largely on future efforts in either eliminating or separating hydrogen gas bubbles from the electrode-solution interface thereby reducing porosity of the deposit.

Acknowledgment

The author wishes to thank D. R. Turner who suggested the possibility of plating through a gel medium.

Manuscript submitted June 1, 1970; revised manuscript received *ca.* Dec. 18, 1970.

Any discussion of this paper will appear in a Discussion Section to be published in the December 1971 JOURNAL.

REFERENCES

1. R. A. Ehrhardt, *Proc. Am. Electroplaters' Soc.*, **47**, 78 (1960).
2. M. J. Elkind, Private communication.
3. P. H. Hermans, "Gels," Colloid Science **2**, 483 (1949).
4. H. S. Carslaw and J. C. Jaeger, "Conduction of Heat in Solids," 2nd Ed., Oxford University Press (1959).

JOURNAL OF THE ELECTROCHEMICAL SOCIETY

ELECTROCHEMICAL SCIENCE

MAY 1971

Film Formation and Hydrogen Evolution on the Alkaline Zinc Electrode

R. W. Powers*

General Electric Research and Development Center, Schenectady, New York 12301

ABSTRACT

The duplex structure of anodic films formed in concentrated KOH solutions with convection nearly absent—a hydrodynamic condition present near a battery plate in proximity to a separator—has been confirmed on high-purity polycrystalline zinc and to a more limited extent on some polycrystalline zinc alloys as well. Previously, the use of a very slow potential scan with simultaneous microscopic observation of single-crystal zinc electrodes showed that a precipitated coating of ZnO particles (type I film) overlies a more coherent film also of ZnO (type II). The experimental conditions required for following stages in the formation of the precipitated film, the one most difficult to observe, are defined more explicitly in this paper. Evidence is presented that the type II film serves as a catalyst for hydrogen evolution at potentials anodic to the zinc/zinc oxide equilibrium value. Hydrogen bubbles, whose formation is so catalyzed, can mechanically dislodge overlying passivating film to cause reactivation of the electrode. The presence of complex tin or lead anions at concentrations about 10^{-3}M (molar) in KOH solutions gives rise to very smooth, almost imperceptible, films of metallic tin or lead over the zinc electrode surface. Such films are made visible, though, during zinc dissolution as they rumple and eventually gather into a wad after being undercut. These foreign metal films inhibit the dissolution of zinc to an extent that depends on the particular complex anion, its concentration, and exposure time to the zinc surface. Lead films can be made sufficiently inhibitive that zinc dissolution is reduced to such a rate that very little precipitation of ZnO occurs.

Studies of the anodic films that form on pure zinc electrodes in concentrated alkaline electrolyte under different hydrodynamic conditions—their composition, the mechanism of their formation, their effects on the current density-electrode potential curve, and some aspects of their relationship to the problem of passivation and to the problem of dendrite formation during subsequent cathodic deposition—have been reported previously (1-3). In particular, when convection is nearly absent, a hydrodynamic situation present near a battery plate in proximity to a separator, the anodic film is shown to be duplex. A precipitated film of zinc oxide covers a more coherent skinlike film, also of zinc oxide. Recently, the notion of anodic film formation by precipitation from a layer of electrolyte supersaturated with electrode dissolution product has been questioned (4). It is perhaps a little surprising that the formation of the outer film, the one that forms by precipitation according to this author, is the more difficult one to document. Its observation does, however, require considerable attention to some experimental problems.

In this paper, the special experimental conditions required for viewing successive stages in the formation of this film are defined more explicitly. They are illustrated in part by presenting evidence for the formation of the duplex film structure on polycrystalline zinc. Such photomicrographic documentation both confirms and complements that presented previously for single-crystal zinc electrodes. Finally, this concept of the duplex film is shown to be useful in relating the phenomenon of electrode reactivation to hydrogen evolution and in explaining some effects associated with the presence of small concentrations of lead and tin anions in the KOH electrolyte.

A rather lengthy discussion of past anodic studies on the alkaline zinc electrode has been presented previously (1). Consequently, only a very brief recounting of past work on this topic and on others relevant to this study is given below.

Anodic Film Formation

In 1965, the Russian chemists, Vozdvizhenski and Kochman, reported two peaks in the current potential curve for zinc between the rest potential and that potential at which the electrode remains passive, using solutions 2M and 5M in KOH. They speculated that the different peaks might be associated with the formation of various oxides with different degrees of hydration, structure, and solubility (5). The results of Vozdvizhenski and Kochman differed markedly from those reported by other workers (6, 7). These differences were resolved by Powers and Breiter, who found that the course of passivation, as reflected in the current-potential curve, as well as the structure of the

* Electrochemical Society Active Member.

Key words: anodic films, hydrogen evolution, zinc oxide films, zinc passivation.

passivating films depend strongly on the hydrodynamic conditions in the electrolyte near the zinc electrode. Two peaks can be observed in the anodic current if convection is nearly absent and if the potential scan rate from the rest value is very small, typically 0.05 mV/sec (1).

The first peak, near −1.27V *vs.* a mercury-mercuric oxide reference electrode, is associated with the formation of a white, particulate film by precipitation from a saturated layer of electrolyte adjacent to the electrode surface. The saturated layer is produced by dissolution of the electrode. This precipitated, so-called type I film was later identified as ZnO by x-ray diffraction (2). Shortly after formation of the precipitated coating, another film, more coherent and skin-like than type I, becomes evident. It forms directly on the electrode surface beneath the precipitated film. This so-called type II film has also been identified as ZnO, using electron diffraction (2). It can be strongly light absorbing and is believed to contain an excess of zinc. In the presence of convection, ony the type II film was observed to form on the electrode surface (1). These findings about the nature of the anodic films forming under different hydrodynamic conditions are summarized in Fig. 1.

Hydrogen Evolution

Zinc is probably the most active metal whose oxidized species can be reduced back to the metallic state in good yield in an aqueous solution. Because the equilibrium potential of a zinc electrode is over 0.4V more active than that of a hydrogen electrode in the same KOH solution, the oxidation of zinc by the electrolyte is a spontaneous process. The complementary electron-accepting step to zinc oxidation, the reduction of water with the evolution of hydrogen, is usually sufficiently hindered that hydrogen evolution takes place at a rather slow rate. However, this latter reaction can be catalyzed.

Catalysts for hydrogen discharge on zinc can be divided into two general classes. The first is much better known and is comprised of a number of metals noble to zinc. Those of the second class are generated electrochemically and have been recognized only recently. They are based on anodic zinc oxide films.

Most metals will catalyze hydrogen evolution to some extent when in both electrolytic and electronic contact with a zinc specimen. Iron, nickel, and platinum are particularly effective, while on the other hand, mercury, thallium, lead, and tin are not catalytic. In fact, mercury and thallium impede this reaction; *i.e.*, they increase the overvoltage for hydrogen evolution on zinc (8, 9). Impurity catalysts can appear on the surface of a zinc specimen either by incorporation with the metallic zinc as impurities or alloy addition agents or by way of the electrolyte. The oxidized species of a metal noble to zinc can be reduced spontaneously to the metallic state on the zinc surface. Iron impurities in KOH solutions were found, very early in this study, to be particularly troublesome in this way.

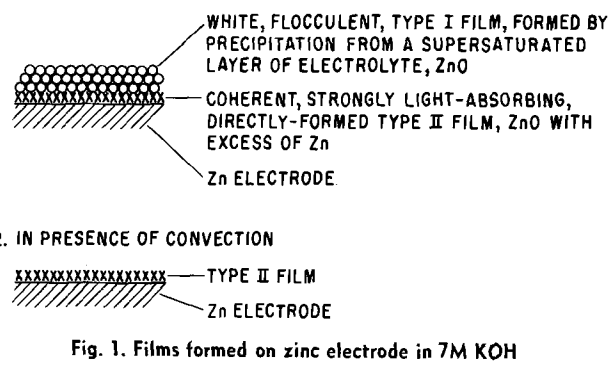

Fig. 1. Films formed on zinc electrode in 7M KOH

Although zinc oxide catalysis of hydrogenation reactions has long been known in organic chemical technology, an awareness of the catalytic activity of anodic zinc oxide films for hydrogen evolution is an achievement of only the last decade. To bring out better the nature of the phenomenon under consideration, some electrode potentials need to be cited. That for zinc in equilibrium with 0.25M zincate is −1.36V when measured against a mercury/mercuric oxide reference electrode in the same alkaline solution. That for the equilibrium between zinc and a solution saturated with respect to either zinc hydroxide or zinc oxide is −1.34V, while that for the reversible hydrogen electrode is −0.93V. Although hydrogen evolution is theoretically possible then at any potential below −0.93V, it is usually negligible in filtered 7M KOH at −1.36V. When the potential is shifted toward more positive values, the driving force for hydrogen evolution is reduced. Yet in the range from about −1.25 to −1.0V, the gas evolution rate is usually much greater than at −1.36V. The only apparent way to understand such a phenomenon is to assume the existence of a catalyst on the zinc electrode that was not present at −1.36V.

Sanghi and Fleischmann in 1959 were the first to present some evidence for the existence of this kind of catalysis (6). On applying an increasingly positive potential to a zinc electrode in a very dilute (0.01-0.1M) KOH solution, the current was anodic from the rest value until passivation ensued. However, it became cathodic over a region of more positive potentials between that for passivation and that corresponding to the hydrogen equilibrium. The current became anodic again at still more positive potentials. The cathodic current was attributed to the discharge of hydrogen catalyzed by the presence of an anodic film formed at lower potentials. Similar experimental results were observed by Kaesche working with dilute solutions of NaOH and $NaHCO_3$. Furthermore, Kaesche confirmed the existence of an electroreducible film on zinc, presumed to be zinc oxide, at potentials just slightly more positive than that for the equilibrium of zinc and zinc oxide (10). J. Oxley observed that, on subjecting zinc dendrites to a couple of hundred millivolts of anodic overpotential in 6M KOH, the dendrites turned black and a gas was evolved on them. He also observed similar phenomena on smooth zinc surfaces (11).

Tin and Lead Additions in KOH Solutions

Tin and lead salts dissolve in alkaline solutions to form the complex anions, $HSnO_2^-$ and $HPbO_2^-$, according to Garrett and his students (12). About twenty years ago, N. T. Kudryatsev reported that only millimolar concentrations of these anions in alkaline zincate baths were required to suppress zinc dendrite formation, a finding confirmed recently by Diggle and Damjanovic (13, 14). Mansfeld and Gilman report these additives give rise to microscopically smooth lead and tin films on the zinc electrode. They have observed small coral-like zinc crystallites at 200 mV of cathodic overvoltage in place of the dendrites which would otherwise have been deposited (15).

Experimental Procedure

The main technique used in this work was the observation of changes on the zinc electrode with a microscope during the passage of electric current. The experimental cell and auxiliary equipment used for simultaneous *in-situ* microscopic observations and the measurement of current density-potential curves under carefully controlled conditions have been described previously (16).

Nevertheless, the hydrodynamic conditions in the viewing cell deserve comment here. In this cell, the

specimen electrode caps the lower end of a hollow, 7.9 mm ID, Teflon polymer cylinder filled with electrolyte. The electrode is viewed through a thin window at the top of this cylinder. The specimen electrode lies in a horizontal plane facing upward with the boundary of the area exposed to electrolyte defined by the wall of the Teflon polymer cylinder. When the electrolyte is not forcibly stirred, mass transport occurs almost entirely by diffusion alone. There is little natural convection during anodic dissolution because the denser layer of solution produced by dissolution remains beneath the bulk electrolyte. Precipitation takes place from this denser layer when saturated—with little change, however, in the concentration of dissolved zincate in the bulk of the electrolyte. Thus, the hydrodynamic situation near a battery plate in proximity to a separator is simulated in the viewing cell (1, 17).

Much of the work in the present study was concerned with somewhat thicker anodic films than those studied previously (1, 2). For this reason, a Wild stereomicroscope was adapted for use with the viewing cell to complement the metallurgical microscope used exclusively in the past. The new instrument allows observation with a depth of focus and a sense of depth perception impossible with a metallurgical microscope. In addition, the ability to change magnification and size of field rapidly is most helpful in observing gas evolution. However, it has not been possible in a practical sense to photograph stereoscopically. Most of the photomicrographs shown in this paper were taken using a Leitz Ortholux microscope equipped with dark field objectives, largely because of the higher magnifications possible.

The major problems of adaption of the stereoscopic microscope were getting sufficient illumination for observing the strongly light-absorbing films that form on the alkaline zinc electrode and making provision for suitable photomicrography. A modified high-pressure mercury arc lamp, a CSI lamp, was most often used to provide the necessary high-intensity illumination. The horizontal beam from this source was projected onto the specimen in the viewing cell by means of a plane mirror and a condensing lens. In situations where less intensity was required, a quartz-iodine illuminator was used. A Leitz camera provided with a Polaroid camera back for taking 8.9 x 11.4 cm photomicrographs was suspended from a framework independent of the microscope. This type of suspension reduced vibration caused by shutter motion and eliminated the need for frequent refocusing caused by the weight of a large camera bearing down on the body tube of the microscope.

The compositions of the various electrode materials used in this study, as furnished by the suppliers, are given in Table I. Measurements and observations have been carried out on two different series of polycrystalline materials, one made up of different grades of nearly pure zinc and the other of various zinc alloys. Specimens were prepared by punching ⅞ in. diam disks from sheet stock. The surfaces of all specimens were cleaned prior to electropolishing in a 20% sulfuric acid bath. This electropolishing procedure has been described in detail elsewhere (18). While the nearly pure zinc specimens acquire a beautiful mirror finish by this procedure, the surfaces of the zinc alloys are marred by the presence of fine pits. This pitting is due to the evolution of oxygen on the alloy specimens. The last step in the polishing procedure involves subjecting a specimen to an overvoltage of nearly 8V in order to remove a gray anodic film responsible for smoothing. At this overvoltage, oxygen evolution occurs on the alloys but not on the nearly pure zinc specimens.

Because of their extraordinary mirrorlike quality which facilitates the observation of film formation, some studies were also carried out on the basal plane of single-crystal material. Such surfaces were prepared by cleavage of specimens about 3 mm thick from a larger single crystal immersed in liquid nitrogen.

Measurements were carried out with 7M potassium hydroxide solution prepared from reagent-grade chemicals and distilled water. Zinc oxide at a concentration of 0.25 mole/liter was dissolved in this solution to fix the initial zinc electrode potential and to inhibit chemical corrosion of the zinc specimens when first exposed to electrolyte. The electrolyte was filtered through Gelman Acropor microporous polymer membranes of 0.45μ pore size to remove the larger particles of iron compounds present. Experiments were carried out at 23°-25°C.

Solutions containing electrolyte additions of complex tin or lead anions were usually prepared by thorough mixing of a weighed quantity of a lead or tin salt with 100 ml of stock alkaline solution. This operation was carried out in a separate vessel equipped with a magnetic stirrer before introduction of the solution into the viewing cell. The salts used were the oxides, chlorides, and acetates. The concentration of the addition agent varied from 0.0005 to 0.01M.

The zinc electrode potentials were measured against mercury-mercuric oxide reference half cells in 7M KOH. The potential was controlled by means of a Jaissle potentiostat. The voltage required for the very low speed scanning of the zinc potential was taken from a simple potential divider network comprised essentially of a Zener diode and a multiturn potentiometer driven by a clock motor. Current-potential curves were registered on a Moseley Model 2D-2A X-Y recorder.

Experimental Results and Discussion

The results of this study are discussed under three headings: problems in observing a precipitated anodic film on zinc electrodes; hydrogen evolution and electrode reactivation; and the effects of tin and lead ions in the electrolyte on dissolution, film formation, and hydrogen evolution on zinc.

Problems in observing a precipitated film on zinc electrodes.—One of the more important findings of previous work is that the convective conditions in the electrolyte near the zinc electrode have a decisive influence on the current-potential curve and on the nature of the passivating film. Particularly relevant is the notion that passivation can be brought about by very localized precipitation of zinc oxide from a layer of electrolyte saturated with zincate without the bulk

Table I. Materials used in study

Source	Designation	Main impurities or alloying additions in per cent							
		Cd	Cu	In	Fe	Pb	Mg	Si	Ag
Cominco	69 Grade	0.00001	0.00001			0.00002	0.00001	0.00001	
Cominco	59 Grade	0.00002	0.00002		0.00002	0.0001	0.00001	0.00005	
Cominco	49 Grade	0.0005	0.0030	0.0010	0.0020	0.0030	0.0003	0.0005	0.0003
N.J. Zinc	N2261	0.007	0.0003		0.008	0.06			
N.J. Zinc	N2262	0.11	0.0003		0.013	0.041			
N.J. Zinc	N2263	0.33	0.0004		0.009	0.28			
N.J. Zinc	N2264	0.006	0.65		0.005	0.070			

Monocrystals, Inc. The single crystal was grown from zinc better than 99.999% pure.

of electrolyte in the cell being saturated. Documentation of the precipitation phenomenon has improved with time and additional experience now permits a better definition of the best conditions for its observation.

Two principal observations support the interpretation that the formation of a precipitated film gives rise to the first peak in the current observed near −1.27V (*vs.* the mercury-mercuric oxide electrode) when the potential is scanned very slowly from the rest value in a more positive direction, with convection in the electrolyte nearly absent. The first observation is that the formation of a white coating composed of very small particles coincides with this peak. On the other hand, if the electrolyte is strongly stirred, this peak is eliminated and such a white film is not observed. The latter fact is consistent with the interpretation of the first. With appreciable forced or natural convection, the formation adjacent to the electrode surface of a layer of electrolyte saturated with the dissolution product is prevented. The whole bulk of the electrolyte in the test cell would need to be saturated before precipitation could occur. The second major observation is that of slow motion of some of the small white particles or light-scattering centers. When observed, a large number of closely spaced particles can be seen traveling in the same direction. This observation indicates the particles are in the electrolyte and are propelled by small convection currents. It eliminates the possibility that these small light-scattering centers originate by direct electrochemical reaction at various numerous sites over the electrode surface.

However, both of these critical experimental facts require considerable attention to detail for their really satisfactory observation. Successful viewing of the individual particles, which when present in sufficient density form a white coating on the electrode surface, requires a special optical background. Since such particles need to be viewed under dark-field conditions, a smooth mirrorlike surface is required to provide this dark background. It is important that the darkness of the background arises from the smoothness of the surface and not because of strong light absorbance by the surface. For instance, when precipitate particles move across the electrode surface, they are almost lost from view when they cross over portions of the surface covered with so-called type II anodic film, a strongly light-absorbing electrochemically formed film. Most of the earlier work on this project was carried out with cleaved single-crystal specimens because they most nearly met this background requirement. Even with single crystals, though, there exists considerable variation in the ease with which individual precipitate particles can be documented by photomicrography. If the anodic dissolution of the specimen, required of course to produce a supersaturated layer of electrolyte, gives rise to dissolution facets on too fine a scale, light scattering from such facets makes detection of individual particles difficult. The relatively inferior documentation of precipitation provided in Ref. (1) compared to that in (2) can be attributed in part to this factor.

It has been found that chloride ion additions at low millimolar concentrations in KOH solutions cause the bunching of dissolution steps on the basal plane of zinc single crystals. This ion appears to act as a poison which reduces the rate of vertical etching of dissolution pits. Very shallow, flat-bottomed pits are produced with steep vertical walls. No other effect of chloride ion was detected. The photomicrograph shown in Fig. 2 was taken near −1.29V during an anodic scan very shortly after the motion of precipitate particles was first observed in the viewing field. An electrolyte, 0.002M in chloride ion, was used in this experiment. Some particles perhaps can be seen on the left side of this photograph against the dark field provided by the smooth bottom of the dissolution pits. This photomicrograph shows the importance of a good dark field

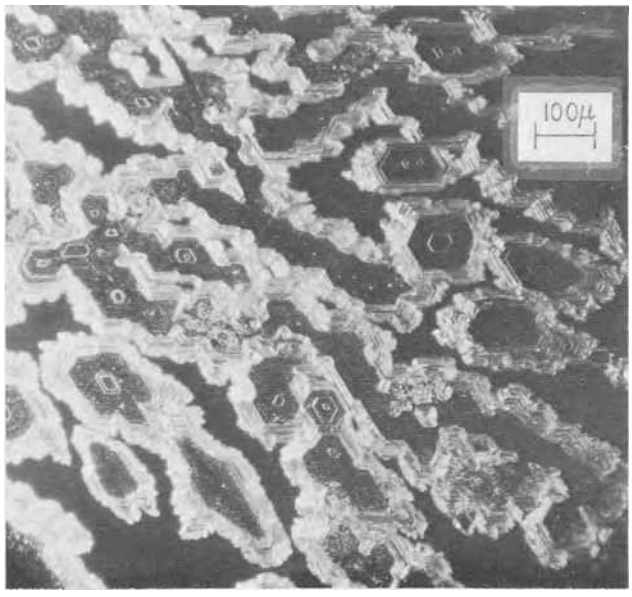

Fig. 2. Dissolution step structure on zinc single crystal associated with low concentrations of chloride ion. Dark field. 75X.

background for satisfactory viewing of the very early stages of precipitation. Since 7M potassium hydroxide prepared from reagent-grade KOH may be slightly in excess of 0.001M in chloride ion impurity, possibly the flat-bottomed dissolution pits shown in Ref. (2) owed their existence to the adventitious presence of these impurity ions (19).

Documentation of the early stages of precipitation of ZnO on polycrystalline zinc electrodes has been slightly inferior to the best obtained on single crystals. Some difficulties arise from the fact that, although electropolishing of zinc in a sulfuric acid bath produces a surface that is mirrorlike to the eye, under the microscope at about 100X, light scattering from small imperfections on such polished surfaces interferes to an extent with that from the precipitate particles. The point is illustrated below.

The ease of observation of the motion of precipitate particles varied from specimen to specimen. With some, motion could be seen in all fields of the specimen. At the other extreme, on one or two of dozens of specimens of nearly pure zinc, no motion at all was detected. It became evident that the ease of observation of particle motion was intimately related to the height of the first current peak. At the potential scan rate used in most experiments, 0.05 mV/sec, about one half of the measured heights of the first anodic peak fell in the range 42-47 mA/cm^2. However, the remainder were larger and reached 70 mA/cm^2 in a few cases. The ease of observation of the motion of precipitate particles was greatest in those cases where the peak height was large. Clearly, the small-scale natural convection, made evident by particle motion, stirs the electrolyte sufficiently to cause a larger current. Near the potential for the first current peak, −1.27V, the current is limited by the transport of zincate ions away from the electrode surface. The slight convection arises because the specimen surface is not perfectly flat. It is nearly impossible to cleave a single crystal of zinc without introducing a cleavage step. The density gradient across such a step, typically 100μ high, is evidently sufficient to produce a small convection current as particle motion is usually easiest to observe adjacent to such a surface discontinuity. Furthermore, a 2-3 mm thick single-crystal specimen is usually slightly bent during cleavage. In a few instances, the complex motion of precipitate particles was clearly associated with the small elevations and depressions in the surface associated with such bending. With polycrystalline specimens, the preferential dissolution of grain boundaries

is the largest factor giving rise to an uneven electrode surface.

In summary, the ideal conditions for observing the particles that in mass constitute so-called type I film are a mirrorlike electrode surface, a dissolution pattern that leaves large areas of electrode surface unetched or otherwise very smooth, and a small amount of convection so that motion of precipitate particles at velocities of the order of microns per second occurs over much of the electrode surface. Such velocities are smaller by a factor of 100-1000 than those usually associated with natural convection along vertical electrodes (20).

To illustrate a number of points discussed above and to introduce some new findings as well, the results of an experiment with a polycrystalline zinc specimen, 99.9999% pure, are presented in Fig. 3 and 4. These include a current-potential curve along with photomicrographs taken at different potentials. In this run, the potential was scanned in the positive direction starting at the rest value at the very slow rate of 0.05 mV/sec. The photomicrographs shown in Fig. 4 were taken with a metallurgical microscope on the same specimen field with Polaroid Type 52 film (ASA speed rating of 400) at 1 sec exposure time. Figures 4(a)-4(j) were taken with the same incident light intensity.

The initial state of the surface at the rest potential after approximately 10 min exposure to electrolyte is indicated in Fig 4(a). Even though the electropolished specimen is very smooth and appears mirrorlike to the eye, fine-scale etching is evident. This mars the dark-field background and interferes with the observation of the precipitation process to a limited degree. Figures 4(b)-4(e), which correspond to potentials along the steeply ascending portion of the current-potential curve, show that anodic dissolution occurs preferentially at the grain boundaries. These are gradually widened and deepened with time. The attack exposes macrosteps and ledges, many of which reflect so much light into the camera that individual steps are not easily discernible although they can often be seen by eye. Some, however, are so aligned that they appear black on the photomicrographs.

The first evidence of precipitation was noted shortly before the photomicrograph shown in Fig. 4(f) was taken. Figures 4(f)-4(i), taken near the first peak on the current-potential curve, show the manner in which the fine precipitate particles eventually coat the entire electrode surface. The increase in particle density on successive photomicrographs should be noted. The coating is most readily seen over the interior of the grains as illustrated over the large grain adjacent to the right border of the photographs. Actually, the grain boundaries are also coated with this precipitated type I film, although the coating there is more difficult to discern because light is so strongly absorbed at the grain boundaries.

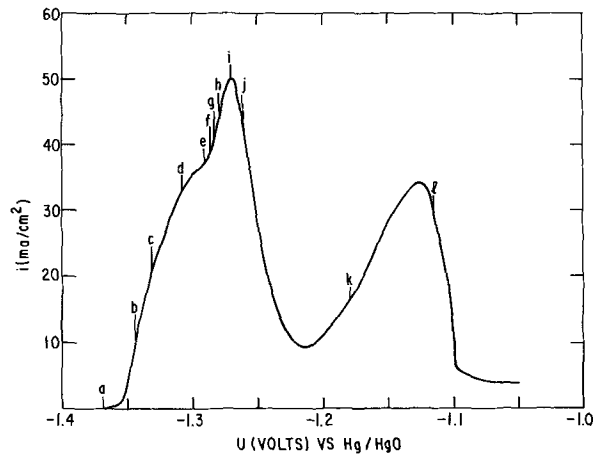

Fig. 3. Current density-potential curve for polycrystalline zinc taken during an anodic sweep at 0.05 mV/sec under nearly convectionless conditions.

In fact, the major feature of interest about the grain boundaries is their gradual darkening as shown in successive photomicrographs, Fig. 4(g)-4(j). Darkening can be noted very soon after the onset of precipitation. In experiments similar to the one under discussion, the potential scan was stopped at approximately −1.23V and the electrolyte was stirred. Stirring removes the overlying type I film on the grain boundaries and reveals the presence of another anodic film that is responsible for the grain boundary darkening. This strongly light-absorbing anodic film we have previously called type II. It is usually possible to lift up small portions of this skinlike film off the surface at irregular intervals along the grain boundaries by stirring the electrolyte. The small pieces then become particularly obvious as they flap about in the electrolyte. The sizes of pieces of type II film that have been lifted from polycrystalline specimens are very much smaller than those from single-crystal surfaces as documented previouly (1, 2). Because of the relatively good separation at 144X between areas of the specimen surface undergoing dissolution, *i.e.* the grain boundaries, and those left unattacked, *i.e.* the grain interiors, one can readily see that the formation of dark, type II film occurs only on portions of the specimen undergoing active dissolution. While this point has also been observed on single-crystal specimens, documentation is usually much more difficult because of the smaller size of active and inert areas.

Some type II film is likely present on zinc at all potentials above the zinc/zinc oxide equilibrium value. In experiments in which the electrolyte was stirred, film formation, as evidenced by multihued tinting of the specimen surface, was noted at potentials only 20 mV above this equilibrium value. These observations do pose the question whether the precipitated film is the direct or the indirect cause of the first passivation, the decline in current following the peak near −1.27V. Stated otherwise, does passivation occur by the blockage of active sites by precipitated particles or is the underlying dark type II film responsible? Conceivably, the precipitated coating could so shelter the underlying film that the formation rate of the latter exceeds its rate of dissolution. Thus, it could thicken or otherwise change its characteristics to reduce the available current. The information available does not permit a clear choice between these alternative mechanisms.

The incident light intensity needed to be increased considerably to obtain the photographs shown in Fig. 4(k) and 4(l). Two points are noteworthy and are discussed in greater detail subsequently. One is that the outermost film coarsens with time and develops considerable porosity. Many more cracks and holes are evident in Fig. 4(l) than in Fig. 4(k). The other is evidence of hydrogen evolution. Two spherical gas bubbles appear in the field in Fig. 4(l). The behavior of other grades of nearly pure polycrystalline zinc listed in the table is indistinguishable from that for 99.9999% zinc as discussed above.

Throughout this paper, the gas evolved on a zinc electrode in the potential range from approximately −1.36 to −1.00V *vs.* the Hg/HgO electrode is assumed to be hydrogen. From thermodynamic considerations, the evolution of hydrogen is possible in the range of potential under consideration. On the other hand, the potential is much too low for the gas to be oxygen. The materials deliberately added to the system comprise metallic zinc (or zinc alloys in some experiments), distilled water, reagent-grade ZnO, reagent-grade KOH, and small quantities of argon used to deoxygenate the alkaline solution. Since gas evolution has been observed to continue at an apparently unabated rate for a period of hours, it seems unlikely that the gas is derived from an impurity. Attempts to obtain a positive identification for hydrogen gas were not successful. This analysis involves working with approxi-

mately 10^{-7} moles of gas in the presence of an aqueous solution.

Hydrogen evolution and electrode reactivation.— After the surface of a zinc electrode has darkened as illustrated in Fig. (4j), the amount of additional information on film formation that can be obtained with a metallurgical microscope is usually limited. The photograph shown in Fig. 4(l) is somewhat unusual in that the film surface lies sufficiently in a horizontal plane to allow much of the field to appear in focus. However, with a stereomicroscope, more information can often be obtained both on subsequent changes in the precipitated film with time, as well as on hydrogen evolution at higher anodic potentials. Since hydrogen evolution takes place at random isolated sites over the electrode surface, it is expeditious to view it at low magnification in order to survey the entire specimen. Higher magnifications are preferred, though, for observing film formation.

Oxide film on pure zinc electrodes often appears blue to the eye. The stereomicroscope has been of great utility in examining this film property. If after the second passivation the electrolyte is circulated to dissolve the anodic film slowly, the precipitated film can be seen to have consolidated into pieces of deep-blue material. These pieces are sometimes surrounded by more reflecting type I precipitate and other times not. These consolidated masses of film substance give rise to the over-all bluish appearance of the outer film on the electrode surface. The conversion of the precipitated film into blue oxide begins near the electrode surface and proceeds away from that surface. Its for-

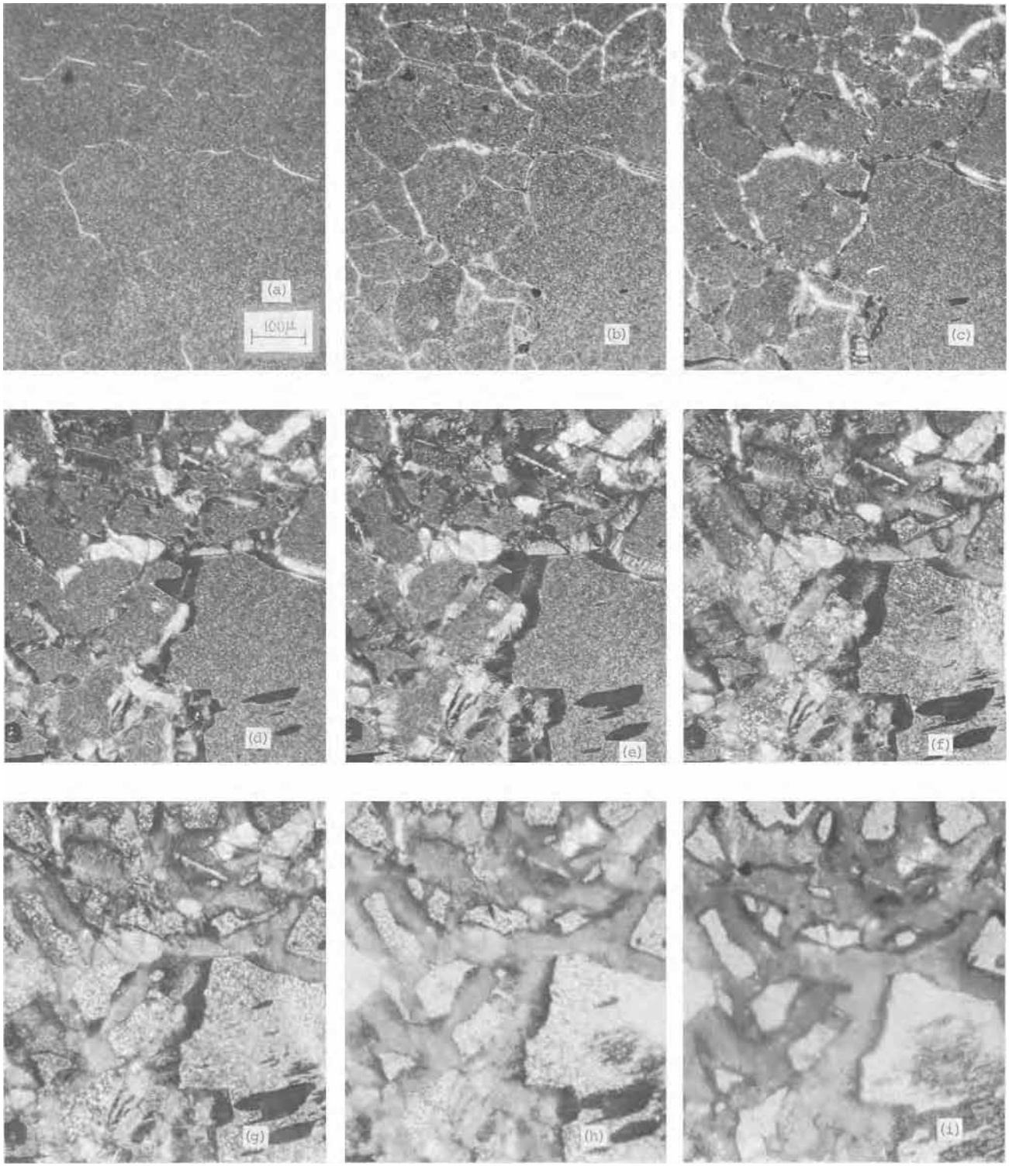

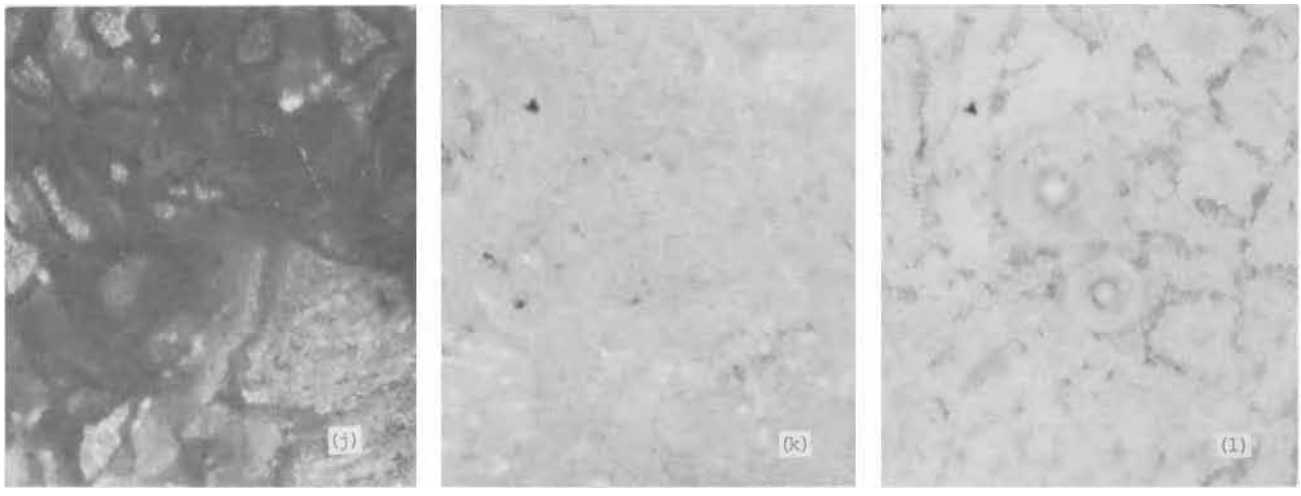

Fig. 4. Changes on a polycrystalline zinc electrode during an anodic sweep. Dark field. 90X. Letters on photomicrographs correspond to potentials indicated in Fig. 3: (a) initial surface; (b) −1.343V; (c) −1.330V; (d) −1.309V; (e) −1.292V; (f) −1.285V; (g) −1.283V; (h) −1.280V; (i) −1.273V; (j) −1.262V; (k) −1.178V, light intensity increased; (l) −1.114V, light intensity increased.

mation has often been noted in association with appreciable hydrogen evolution.

As discussed in a previous section, it is an interesting fact that after the zinc electrode is passivated near −1.24V with a coating of precipitated film it can be reactivated at still higher potentials; *i.e.*, the anodic current increases again. Surely, some change must take place in the coating to permit this to occur. One possibility is that recrystallization of the precipitate takes place to produce a more porous coating. However, on examining photomicrographs such as Fig. 4(k) and 4(l), it seems that this process takes place too late or at too high a potential to account for reactivation. The dislodging of film by the evolution of hydrogen bubbles seems the more likely cause. Hydrogen bubbles are usually first noted at a potential slightly above that for the current minimum. With but a few exceptions, this observation was noted in over a dozen runs in which an effort was made to note carefully the first appearance of gas evolution. The exceptions mainly involved runs in which the evolution rate was very low. Specimens included electrodes both of nearly pure zinc, as well as of zinc alloys. The rate of hydrogen evolution increases with potential at least up to the second current maximum. Near this potential, the accumulation of hydrogen bubbles under the window of the viewing cell often makes further microscopic observation difficult. The small bubbles so refract light that a good focus is nearly impossible. In one run in which the bubbles drifted away from the window, it was possible to observe that the rate of hydrogen evolution decreased again at still higher potentials when the electrode was passivated for the second time. Such a phenomenon is expected—the rate of hydrogen discharge must go to zero as the equilibrium potential for hydrogen at −0.93V is approached.

The underlying type II film is believed to be the catalytic site of hydrogen evolution. Bubbles must then move through the outer film before emerging from a hole in the surface. This motion is indicated in Fig. 5 where a number of only "partial" gas bubbles can be seen, owing to their incomplete emergence from holes. Many of the pores and channels evident in Fig. 4(l) were created by the motion of hydrogen bubbles. The displacement of film by bubbles has been noted frequently.

Two maxima were usually observed on the current-potential curve for the various zinc alloys studied. For example, the i-U curve for a specimen of N2263 alloy is shown in Fig. 6. From the similarity of this curve to that in Fig. 3, one would infer that duplex anodic films form on zinc alloys much as observed on nearly pure polycrystalline and single-crystal zinc electrodes. However, only indirect evidence, mostly related to the effects of hydrogen evolution, could be obtained to support this interpretation.

During the initial rapid rise in current density with potential, selective etching of grain boundaries was not observed on the alloys, but rather a more general attack took place at both grain boundaries and grain interiors. The etching of pits, without exposure of brightly reflecting crystallographic facets, could be

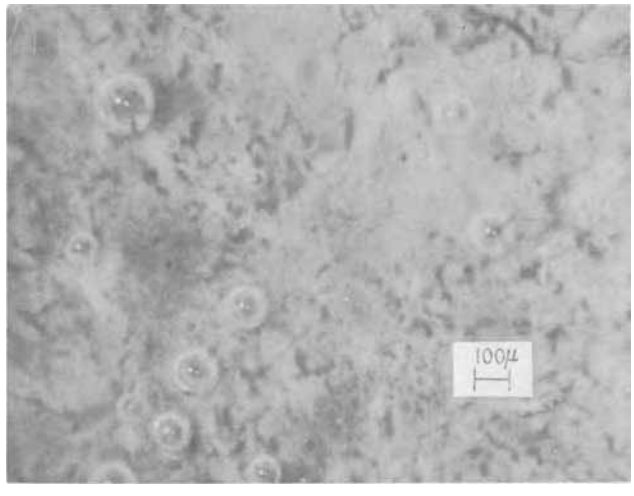

Fig. 5. Emergence of gas bubbles from overlying film. 44X

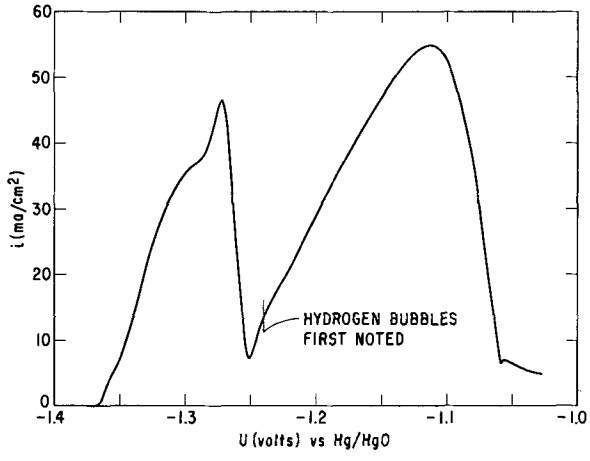

Fig. 6. Current density-potential curve for N2263 zinc alloy taken during an anodic sweep at 0.05 mV/sec under nearly convectionless conditions.

seen with the stereomicroscope but was very difficult to photograph satisfactorily. At about 80 mV above the rest potential, the initial formation of a film on the electrode was sensed. However, this film was not reflecting (white) as is the type I film formed on nearly pure zinc and, when present at some depth, channels and holes were not evident as illustrated in Fig. 4(1) for pure zinc. The outer film appeared nearly uniformly dark with little structure evident. It gradually filled the etched pits and eventually covered the electrode surface very evenly. As for specimens of nearly pure zinc, gas evolution usually was first evident near the minimum in the current potential curve. The above features were common to all the alloys studied. Nonetheless, there were differences in the behavior of individual alloys.

Films on N2262 alloy, for example, tended to blister. In one run as the second passivation was approached, observations in the stereomicroscope revealed that the film over the entire electrode surface was assuming a domed shape. When a large crack formed in the blister, the current increased and passed through a third maximum. The i-U curve taken during this run and a photomicrograph of the crack in the blister are shown in Fig. 7 and 8. This is good evidence that, as with pure zinc, hydrogen is not generated within nor at the top surface of the outer film, but rather underneath it.

The rate of hydrogen evolution on the specimens of N2262 was roughly comparable to that observed from specimens of nearly pure polycrystalline zinc. That, however, for N2263, an alloy containing about 0.3% each of cadmium and lead, appeared to be significantly less. In a run with this material, the outer film developed a small blister which did not crack, however. Following the voltage scan, the blister was punctured and a small piece of the outer film was overturned, exposing the underside to view. In contrast to the topside, the surface of the underside contained a large number of cavities as shown in Fig. 9. Such cavities were really fine channels, the mouths of which appear as dark spots on the photomicrograph. They were apparently the escape paths of small bubbles. A bubble of hydrogen still clinging to the underside of the film appears in the upper left portion of the photomicrograph. Here is additional evidence that the generation of hydrogen occurs at sites underneath the outer film.

The hydrogen evolution rate was significantly greater for the N2264 alloy, a material containing 0.6% copper, than for any other composition studied. Bubbles appeared just prior to the current minimum. The rate of evolution was sufficiently high near the second current peak that a scan of potential to the second passivation could never be completed. Hydrogen bubbles

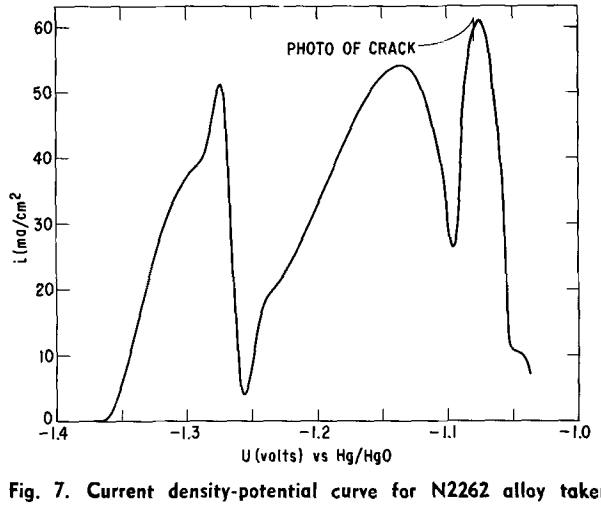

Fig. 7. Current density-potential curve for N2262 alloy taken during an anodic sweep at 0.05 mV/sec under nearly convectionless conditions.

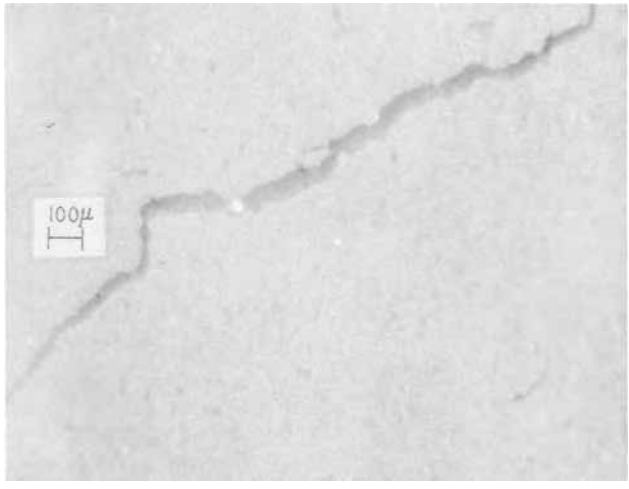

Fig. 8. Crack in blistered anodic film. 44X

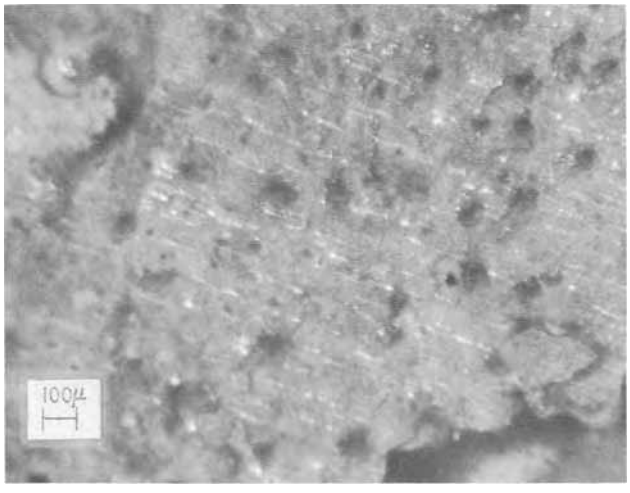

Fig. 9. Cavities in underside of anodic film on N2263 alloy. 44X

entered the sidewall capillary leading to the reference electrode compartment in the viewing cell and opened the circuit between the reference and working electrodes (16). Of course, the potentiostat could not function under this condition. Removal of the gas led very quickly to another blockage. Every run with this alloy had to be aborted near the second current peak. An indication of the gas evolution from this alloy is provided by Fig. 10, which shows the bubbles trapped below the window of the viewing cell. This photograph was obtained when the electrode potential corresponded to the second current maximum. The dark background arises from the exceedingly strong light absorption of anodic films on N2264 alloy specimens. Unlike the other alloys, this film was readily removed from the electrode surface. A bright metallic surface was found beneath it. These observations support the notion that copper in the zinc alloy enters the lattice of the type II film and thereby enhances catalysis of hydrogen evolution. It likely affects other electronic properties of this film as well. Kaesche has presented evidence that the presence of copper in anodic films on passivated zinc makes this electrode an efficient cathode for oxygen reduction in hot water (10).

When the polarization source was removed after an anodic scan on either a pure zinc specimen or on one of the alloys studied, the electrode potential dropped to that for the Zn/ZnO couple. The gas evolution rate decreased markedly from that observed near the second current peak although some hydrogen evolution continued to be noted. Much of this was likely due to gas previously trapped in the anodic coating. If this film was scratched with a pointed glass rod,

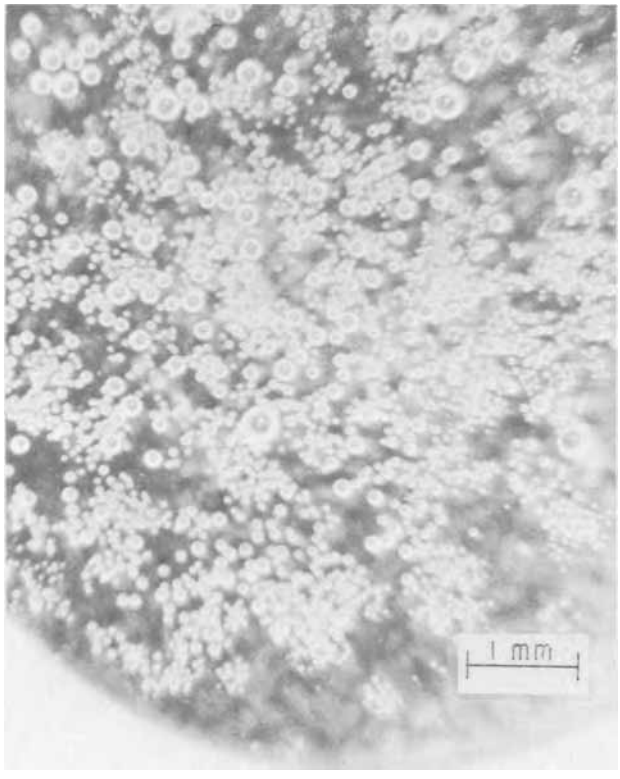

Fig. 10. Hydrogen bubbles trapped below window of viewing cell. 15X.

the release of a very large number of small bubbles could be noted under the microscope.

The viewing cell was not designed for measuring rates of hydrogen evolution. Nonetheless, a very crude estimate of the rates under consideration in this report can be obtained from the amount of gas accumulated under the window of the cell. They correspond to current densities in the range 1-10 $\mu A/cm^2$, a quantity insignificant in comparison to the rates of anodic oxidation in 7M KOH. Thus, it seems that hydrogen generated at a rate corresponding to microamperes per square centimeter can affect anodic currents about 10,000 times greater through its mechanical action on anodic films.

The effects of tin and lead anions in the electrolyte on anodic dissolution, film formation, and hydrogen evolution.—The utility of the notion that anodic films on zinc can form both by precipitation from a supersaturated layer of electrolyte adjacent to the electrode surface, as well as by a direct electrochemical mechanism on the zinc surface, is exemplified further by observations on the effects of lead and tin additions to the KOH electrolyte. The current potential curves shown in Fig. 11, along with photomicrographs corresponding to one of these curves shown in Fig. 12, indicate the sensitive effects of small concentrations of such addition agents. The three current-potential curves were obtained in KOH solutions to which various amounts of PbO were added to give the concentrations of $HPbO_2^-$ indicated in Fig. 11. The presence of lead ions in the electrolyte has practically eliminated the anodic peak near −1.27V associated with the formation of a precipitated coating.

Figure 12(A) shows a representative photomicrograph of a portion of a single crystal specimen taken before any appreciable amount of dissolution occurred. The metallurgical microscope equipped with a dark-field objective was also used to obtain the series of photographs presented in Fig. 12. The surface, which contains the basal plane, is marred by only a few traces of slip planes and by a cleavage step running from the lower left corner to the middle of the right edge of the photograph. It is not evident that the

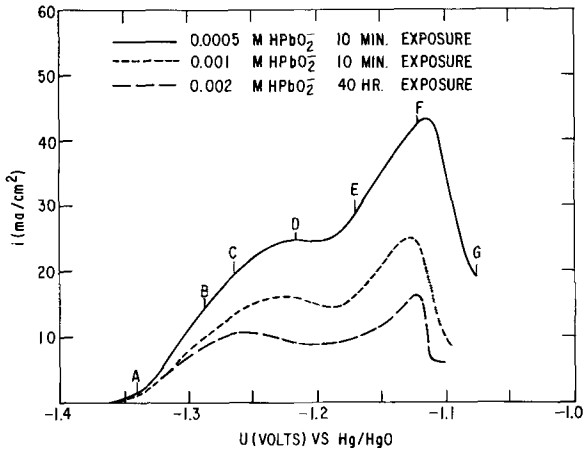

Fig. 11. Current density-potential curves for zinc single crystals taken during anodic sweeps at 0.05 mV/sec under nearly convectionless conditions with various concentrations of $HPbO_2^-$ in electrolyte.

surface is covered by a thin film of lead although the presence of such a film was indicated by x-ray diffraction carried out on another single-crystal specimen which had been immersed in a solution similar to that used in this run. In Fig. 12(B), there is a very slight indication of dissolution along the clevage step and of lifting of the lead film there. In Fig. 12(C), these events are much more evident. Just prior to taking this photograph, precipitate particles were noted moving away from the cleavage step, above which the electrolyte is saturated, toward the top of the photomicrograph. These are easy to see against the nearly perfect dark-field background. In Fig. 12(D), further spreading of precipitate particles can be observed. However, the much lower density of the particles in this coating compared to that shown in the series of photomicrographs in Fig. 4 should be noted. The lead film evidently has so restricted the amount of dissolution that a truly passivating precipitated coating does not form. Some wrinkling and buckling of the lead layer can be seen in the lower right portion of this photomicrograph.

Thus far in this series of photomicrographs, evidence of so-called type I (precipitated film) and of the lead film has been presented. In Fig. 12(E), the exposure time was increased threefold to secure evidence for the presence of type II also. The narrow areas along the cleavage step and the small, nearly circular, areas adjacent are very black because they are light absorbing. Some dissolution has occurred in these places and they are now coated with a light-absorbing film. The area in the center of this photomicrograph just above the cleavage step does not appear to have such an intense black hue. It is light reflecting because it is still coated with a smooth lead film. In Fig. 12(F), it can be seen that the circular areas have expanded. In addition, the previously wrinkled metal film in the lower right corner has gathered into a wad. In Fig. 12(G), still further spreading of the areas covered with type II film can be noted. The area in the center portion of the field has become intensely bright because the previously smooth lead film has wrinkled. Presumably, in this experiment, the passivation of the electrode surface is associated with the presence of type II film. The ability of this film to passivate a zinc electrode without the presence of a precipitated coating was shown previously in experiments where the electrolyte was stirred. Higher potentials are required, though, than those associated with a precipitated film (1).

Larger concentrations of lead ions in solution or longer exposure times of the specimen to electrolyte before the start of an anodic scan produced presumably less porous and certainly more inhibitive lead

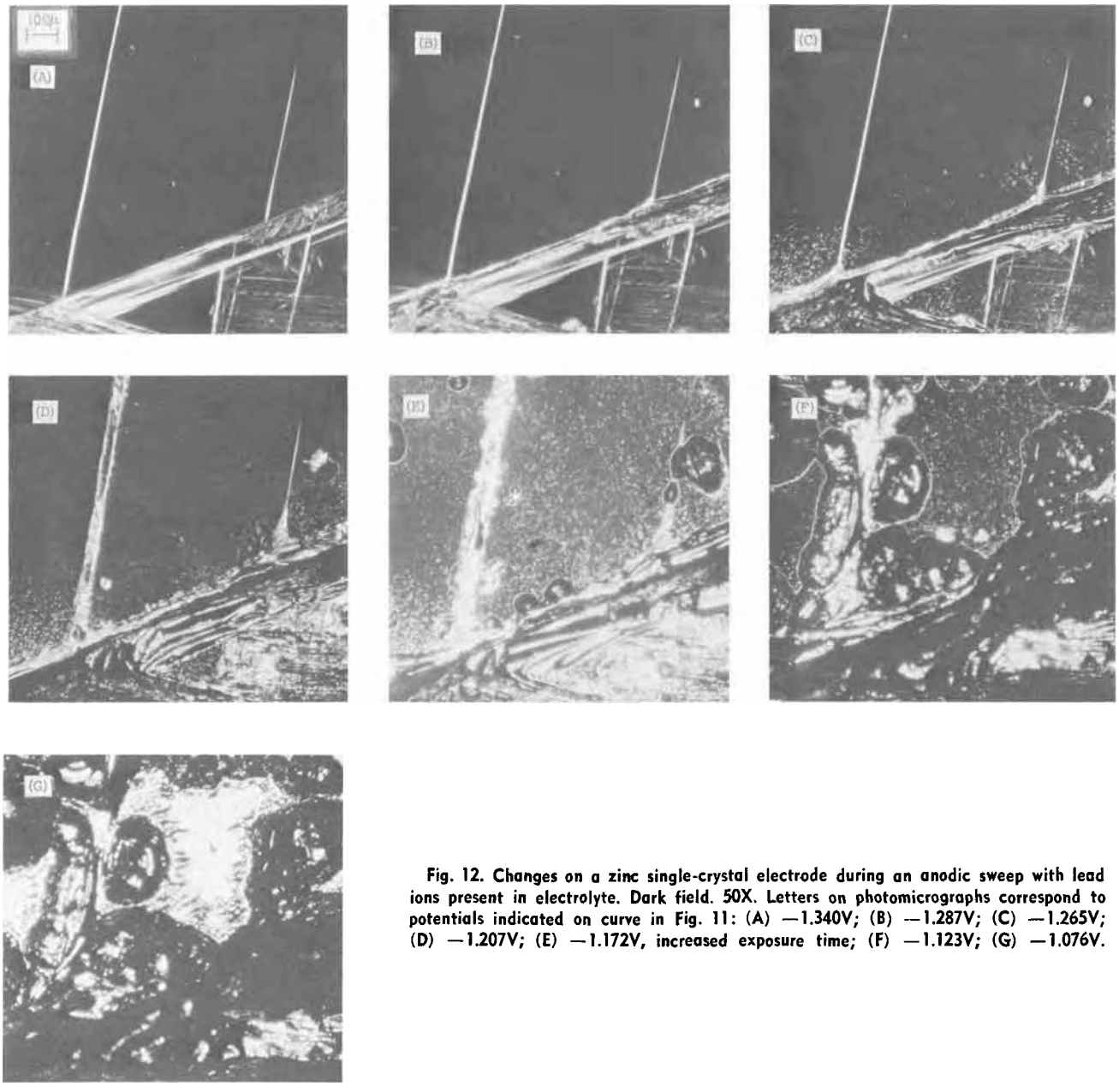

Fig. 12. Changes on a zinc single-crystal electrode during an anodic sweep with lead ions present in electrolyte. Dark field. 50X. Letters on photomicrographs correspond to potentials indicated on curve in Fig. 11: (A) —1.340V; (B) —1.287V; (C) —1.265V; (D) —1.207V; (E) —1.172V, increased exposure time; (F) —1.123V; (G) —1.076V.

films as shown on Fig. 11. When a specimen was exposed to a 0.002M lead solution for 40 hr, fine lead dendrites in addition to a smooth lead coating were noted on the zinc surface. The presence of lead dendrites suggests a lead reduction process sufficiently rapid that transport of lead ions is rate limiting. Consequently, concentrations of lead ions in excess of 0.002M were not investigated. Polycrystalline zinc specimens were usually not as effectively inhibited by a given concentration of lead ions as were single crystals.

The disintegration of tin films appeared rather similar to that for lead. They first wrinkled and then gathered into a wad. Tin films, however, were never found to be as inhibitive as those of lead. Even films, formed in 0.01M $HSnO_2^-$ after 24 hr exposure to electrolyte, did not suppress the first anodic peak as illustrated in Fig. 11 for lead films, nor correspondingly did they suppress formation of a precipitated coating. Tin films often disintegrated at much lower anodic potentials than those of lead. For example, the rumpling of a layer of tin on a zinc single crystal at —1.32V is shown in Fig. 13. This tin layer was formed by exposing a single crystal to a solution, 0.0015M in $HSnO_2^-$, for 24 hr. Actually, the rumpling of tin films has been observed at potentials below —1.34V, *i.e.* in a range of potential where type II film cannot form.

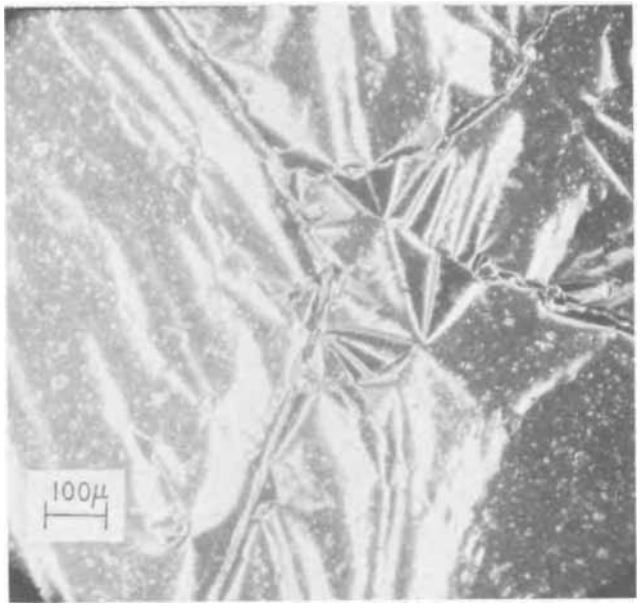

Fig. 13. Rumpling of tin layer on zinc single crystal. Dark field. 75X.

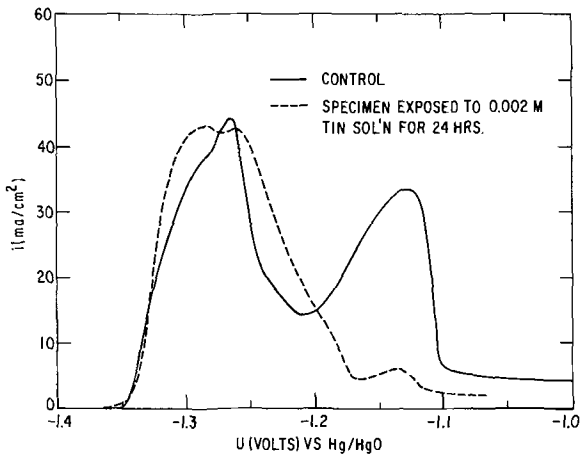

Fig. 14. Current density-potential curves for zinc single crystals taken during anodic sweeps at 0.05 mV/sec under nearly convectionless conditions with and without tin ions in the electrolyte.

The point is of some importance because type II ZnO, while very light absorbent at higher potentials, is much less so at potentials close to the zinc/zinc oxide equilibrium value. Under these conditions, it may have a metallic sheen. Consequently, care must be exercised to distinguish type II ZnO films from those of tin.

Thus, lead and tin additions to alkaline electrolyte function mainly by giving rise to smooth inert films over the zinc electrode surface. Such films inhibit dissolution until they are undercut. Apart from some effects associated with hydrogen suppression, anodic film formation on active portions of the zinc surface seems otherwise unaffected by the presence of these foreign metal anions in the electrolyte. In most of the experiments with tin anions in the electrolyte, the amount of hydrogen evolution near the second current peak appeared to be somewhat less than in control experiments. In a few, hydrogen evolution seemed to be nearly completely suppressed and the second anodic peak practically disappeared. The result of one such experiment is shown in Fig. 14. Current-potential curves are presented there for a single-crystal specimen exposed to 0.002M tin solution for 24 hr prior to the scan, as well as for a comparable specimen not exposed to tin. The results are, of course, consistent with the interpretation of electrode reactivation given above. If hydrogen evolution is suppressed, mechanical dislodging of precipitated film should not take place. Nor should electrode reactivation occur. The converse statement is not true though. In several runs, a normal second peak was observed but only a limited amount of hydrogen evolution was noted. This anomaly seems attributable to the trapping of gas inside the film as discussed above. The mechanism of this hydrogen suppression is not understood.

The findings of this paper with regard to the formation of an anodic film by precipitation are not in disagreement with those of Hull, Ellison, and Toni if the conclusions of these authors are understood to apply only to experiments with considerable forced or natural convection (4). Hull *et al.* used zinc rotating disk electrodes or vertical 0.76 mm wire electrodes. The work of Ibl has demonstrated the effectiveness of natural convection as a means of stirring electrolyte along vertical wire electrodes as well as vertical plane electrodes (21). Perhaps it should be stressed again that the notion of duplex film formation as used in this paper is applicable only to a hydrodynamic situation in which there is very little convection. Although this condition requires somewhat special arrangements to achieve in laboratory test cells, nonetheless it is of importance to battery technology where a plate is located in close proximity to a separator (21, 17).

Acknowledgments

Partial financial support for this work was provided by the International Lead Zinc Research Organization, Incorporated, New York City. Dr. M. M. Wright of Cominco Limited provided zinc sheet of different levels of purity. Dr. C. B. Tennant and Mr. S. R. Dunbar of the New Jersey Zinc Company supplied sheet stock of various zinc alloys. Doctors F. Mansfeld and S. Gilman kindly furnished the author copies of their manuscripts prior to publication.

Manuscript submitted Aug. 20, 1970; revised manuscript received *ca.* Jan. 7, 1971. This was Paper 69 presented at the Atlantic City Meeting of the Society, Oct. 4-8, 1970.

Any discussion of this paper will appear in a Discussion Section to be published in the December 1971 JOURNAL.

REFERENCES

1. R. W. Powers and M. W. Breiter, *This Journal*, **116**, 719 (1969).
2. R. W. Powers, *ibid.*, **116**, 1652 (1969).
3. R. W. Powers, Paper 369 presented at Electrochem. Soc. Meeting, Montreal, Oct. 6-11, 1968.
4. M. N. Hull, J. E. Ellison, and J. E. Toni, *This Journal*, **117**, 192 (1970).
5. G. S. Vozdvizhenski and E. D. Kochman, *Russ. J. Phys. Chem.*, **39**, 374 (1965).
6. I. Sanghi and M. Fleischmann, *Electrochim. Acta*, **1**, 161 (1959).
7. R. F. Ashton and M. T. Hepworth, *Corrosion*, **24**, 50 (1968).
8. R. Rüetschi, *This Journal*, **114**, 301 (1967).
9. T. I. Popova, V. S. Bagotskii, and B. V. Kabanov, *J. Applied Chem. USSR*, **36**, 1687 (1963).
10. H. Kaesche, *Electrochim. Acta*, **9**, 383 (1964).
11. J. Oxley, Leesona Moos Lab. First Quarterly Report to NASA, June-Sept. 1964, Contract No. NAS 5-3908.
12. A. B. Garrett, S. Vellenga, and C. M. Fontana, *J. Am. Chem. Soc.*, **61**, 367 (1939); A. B. Garrett and R. E. Heiks, *ibid.*, **63**, 562 (1941).
13. N. T. Kudryatsev, *Russ. J. Phys. Chem.*, **26**, 270 (1952).
14. J. W. Diggle and A. Damjanovic, *This Journal*, **117**, 65 (1970).
15. F. Mansfeld and S. Gilman, *ibid.*, **117**, 588 and 1154 (1970).
16. R. W. Powers, *Electrochem. Technol.*, **5**, 429 (1967).
17. U. Böhm, N. Ibl, and A. M. Frei, *Electrochim. Acta*, **11**, 421 (1966).
18. R. W. Powers and E. C. Jerabek, *This Journal*, **117**, 1099 (1970).
19. "Reagent Chemicals," 1961 edition, American Chemical Society Applied Publications.
20. N. Ibl and R. H. Müller, *This Journal*, **105**, 346 (1958).
21. N. Ibl, "Proceedings Eighth Meeting of C.I.T.C.E., Madrid, 1956," Butterworths Scientific Publications, London (1958).

Chemical Iron-Phosphorus Films

C. Ruscior and E. Croială

Polytechnic Institute of Jassy and Research Center for Physics, Jassy, Romania

ABSTRACT

Iron-phosphorus deposits on copper substrates were obtained using Brenner's method. The films (0.03-3 μm) were prepared in a bath containing ferrous ammonium sulfate, sodium citrate, and sodium hypophosphite by immersion of the copper substrate in contact with an aluminum strip. The deposition takes place at bath temperatures in the range of 25°-95°C and a *p*H higher than 9.5. For bath temperatures between 25° and ~60°C, only phosphorus-free Fe deposits are obtained. The plating mechanism is an electrochemical process due to the Cu-Al galvanic couple. Fe-P films are obtained at bath temperatures in the range of ~60° to 95°C. For these films, the plating mechanism is a combination of galvanic and chemical deposition due to reduction of the Fe cation by the hypophosphite anion accompanied by phosphorus codeposition. For the Fe-P deposit obtained at 80°C and *p*H = 10.5, the phosphorus content is 3%. The deposition conditions and some magnetic properties of the Fe-P films are investigated.

The chemical (electroless) method for the preparation of Ni-P and Co-P films, based on reduction of the Ni and Co cations by means of hypophosphite anions, was discovered by Brenner and Riddel (1) more than 20 years ago. Numerous papers have been published concerning the properties of these films. However, a method of depositing Fe-P films in this way has not yet been reported. Electrolytically obtained Fe-P films, exhibiting low coercivities (<1 Oe), are presented in (2). Ternary Ni-Fe-P films, both electrodeposited (3) and prepared by electroless technique (4), are also known.

The present paper describes a method for obtaining Fe-P deposits by chemical reduction with hypophosphite. As shown below, the Fe-P films can be obtained if the chemical reaction occurs simultaneously with an electrochemical deposition of Fe. The effects of certain plating parameters on the film thickness and some magnetic properties of these films are examined.

Experimental

Preparation of deposits.—The Fe-P films were obtained using an aqueous solution of the following composition: (*a*) ferrous ammonium sulfate, $Fe(NH_4)_2(SO_4)_2 \cdot 6H_2O$, 30 g/liter; (*b*) sodium citrate, $C_6H_5O_7Na_3 \cdot 5H_2O$, 45 g/liter; (c) sodium hypophosphite, $NaH_2PO_2 \cdot H_2O$, 30 g/liter.

The above solution was optimized after making attempts with various solution component concentrations such as (*a*) between 10 and 40 g/liter, (*b*) between 25 and 45 g/liter, (c) between 25 and 40 g/liter.

Since the deposition takes place only at a *p*H higher than 9.5, ammonia was added to increase the *p*H of the solution.

The films were plated on copper sheets (50 mm x 5 mm), after mechanical cleaning with Carborundum powder and degreasing with sodium hydroxide. To obtain the deposition, it is necessary for the copper sheet to be in contact with an aluminum, zinc, or magnesium strip. In the present work, only aluminum was used. The aluminum strip, cut from a sheet 0.5 mm thick, is clamped to the copper sheet as shown in Fig. 1. This couple is then immersed in the deposition bath (100 cm^3), whose temperature was varied from 25° to 95°C.

Under these conditions the deposition may start even at room temperature, but in this case the plating rate is very slow. The deposition rate increases with increasing bath temperature. Concurrently, the aluminum strip corrodes and Al ions pass into the solution. The same aluminum band can be used for several successive depositions.

Key words: iron-phosphorus films, magnetic coatings, electroless plating.

Thickness measurement.—The thickness was determined by the mass-density relationship assuming a bulk density of 7.8 g/cm^3 for the deposits obtained.

Analytical.—The film composition was determined by qualitative spectrographic analysis. For this purpose, the Fe-P film, deposited on pure electrolytic copper sheet, was first dissolved together with the substrate in *aqua-regia*. After evaporation, the residue was spectrochemically analyzed by means of the d-c carbon arc.

The phosphorus content was determined spectrophotometrically, using the molybdenum blue method (5).

Magnetic measurements.—In order to determine the magnetic parameters, a 50 cycle hysteresis loop tracer (6) having a maximum driving field of 300 Oe was used. The measured parameters were the coercivity, H_c, the remanence, M_r, and the magnetization, M_m, corresponding to the maximum driving field. At 300 Oe, full saturation was not attained.

Results

Film composition.—The spectrochemical analysis of the samples shows that the deposited films contain only iron as the major metallic component. The presence of aluminum was not observed, although this metal could be detected as low as 0.2% concentration in the film.

The photocolorimetric analysis showed the presence of phosphorus only for the films plated at bath temperatures in the range of ~60° to 95°C. Therefore, the films deposited below approximately 60°C are Fe films free of phosphorus, whereas those obtained above this temperature are Fe-P films. The phosphorus content of these films depends on bath temperature and *p*H. Thus, the films deposited at 80°C and *p*H = 10.5 con-

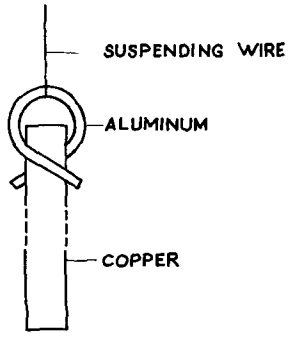

Fig. 1. Schematic drawing of the copper-aluminum couple

tain 3% P, whereas those obtained at the same temperature but at a pH = 11.4 contain only 1% P.

Properties of the Fe-P films.—The films obtained in the thickness range of 0.03-3 μm are uniform and adherent to the copper substrate. They are gray, but their aspect changes with increasing film thickness. Thus, the films below ~0.4 μm are smooth, bright, and do not oxidize in open air (during a period of many months, they did not lose their metallic luster); the films in the thickness range of ~0.4 to ~1 μm are less bright, whereas those over ~1 μm are dull and become oxidized in a few weeks.

The thickness of the deposited films depends on the plating time, bath pH, bath temperature, and the geometrical area of the copper and aluminum sheets. The effects of these parameters on the film thickness are analyzed below.

Effect of plating time.—The film thickness increases linearly with increasing plating time, at constant values of the other plating parameters. Figure 2 shows the dependence of the Fe-P film thickness on plating time, for the deposition obtained at 80°C, pH = 10.5, S_{Al} = 2 cm². In this case, the average plating rate is 2 μm/hr.

Effect of bath pH.—As mentioned above, the deposition takes place in alkaline solutions only, when pH > 9.5. At this pH value, the plating rate is small but it increases with increasing bath alkalinity. Figure 3 shows the dependence of the film thickness on the bath pH at 80°C and constant deposition time (30 min). A plating rate of 0.6-5 μm/hr is obtained as the pH varies from 10 to 11.4.

Effect of bath temperature.—The deposition takes place at bath temperatures in the range of 25°-95°C. Increasing bath temperature leads to increased deposition rate. In Fig. 4, the film thickness is plotted against bath temperature, the other plating parameters having the constant values mentioned in this figure. Two distinct temperature intervals are to be noticed with respect to plating rate change. The first one, including temperatures from 25° to ~60°C, is marked by a relatively small change of the deposition rate (0.02 μm/hr/deg). In this interval, Fe films free of phosphorus are deposited. The second interval, comprising temperatures from ~60° to 95°C, is characterized by a greater plating rate change (0.07 μm/hr/deg). In this temperature range, the Fe-P films are obtained.

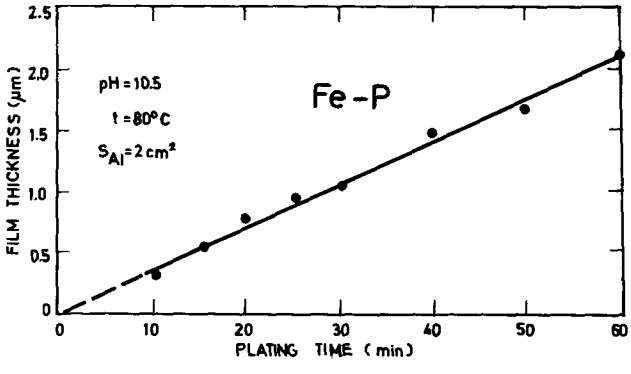

Fig. 2. Thickness of Fe-P film vs. plating time

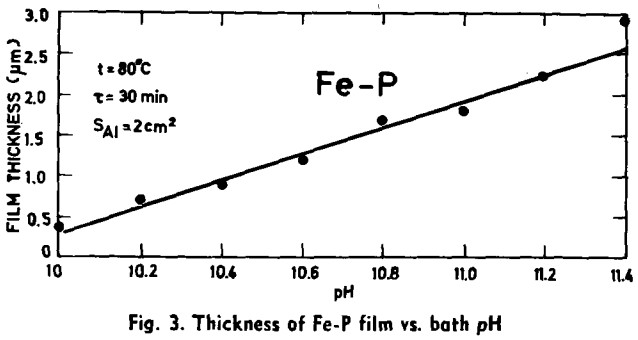

Fig. 3. Thickness of Fe-P film vs. bath pH

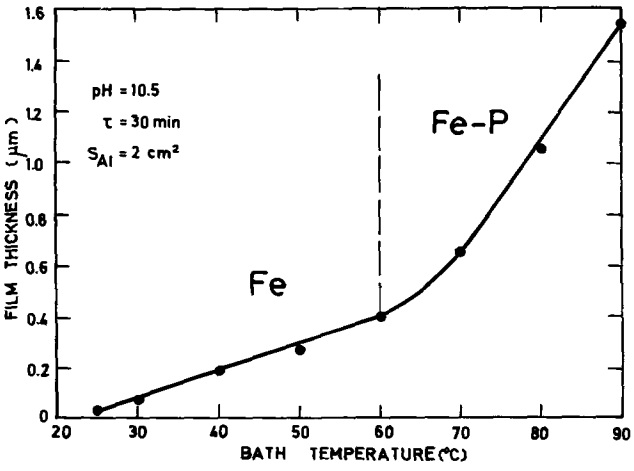

Fig. 4. Film thickness vs. bath temperature

Aluminum strip.—In order to obtain the deposition, it is necessary to bring the copper sheet in contact with metals more electronegative than Fe, *i.e.* Zn, Al, or Mg. As mentioned, only aluminum has been used in this work. During the plating process, Al passes into solution as shown by weighing the aluminum strip before and after deposition.

It is important to note that, if the aluminum contact is removed during the plating process, the deposition stops and the previously deposited film dissolves. In this respect, the Fe-P films differ from the Ni-P and Co-P films obtained on copper substrates. Indeed, for starting the deposition of these films, it is also necessary to bring the copper sheet in contact with more electronegative metals, as Al or others, but after initiation the deposition continues even if the contact is removed. In the case of Fe-P deposition, the contact between the two metals must be maintained.

The plating rate of the deposited Fe-P films depends on the area ratio of the aluminum and copper surfaces. Figure 5 shows the film thickness as a function of S_{Al}/S_{Cu} for the deposition obtained at 80°C, pH = 10.5 and τ = 30 min. It can be seen that the plating rate increases with increasing area ratio, tending to a constant value of about 3 μm/hr for area ratio higher than ~1.

Magnetic properties.—The Fe-P films deposited are ferromagnetic. The coercivity, H_c, depends on the film thickness, having high values for thin films (under ~0.5 μm) as shown in Fig. 6. For the indicated plating parameters, H_c increases from 25 to 145 Oe as the film thickness decreases from 1.2 to 0.03 μm.

In contrast with coercivity, the remanence, M_r, and the maximum value of the magnetization, M_m, increase with increasing film thickness, tending to constant values for films over ~0.5 μm. Thus, M_r approaches an almost constant value of 1100 Gs, whereas M_m reaches

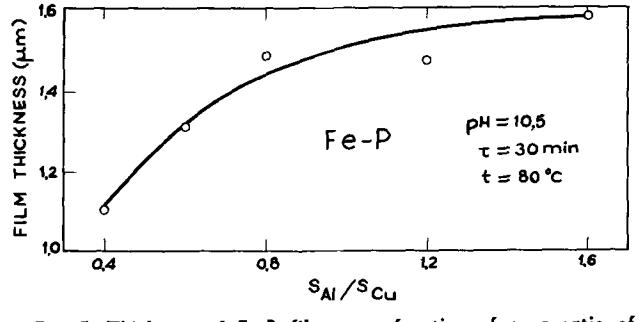

Fig. 5. Thickness of Fe-P film as a function of area ratio of aluminum and copper surfaces.

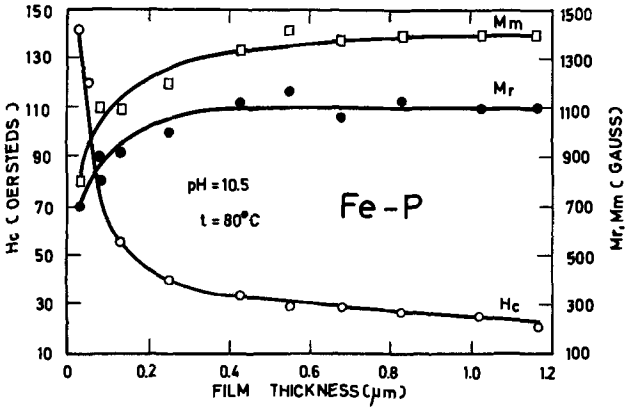

Fig. 6. Coercivity, H_c, remanence, M_r, and magnetization, M_m, at $H = 300$ Oe vs. thickness of Fe-P film.

1400 Gs. As mentioned before, full saturation is not attained at $H = 300$ Oe.

Discussion

The method of Fe-P plating described above raises the question of the mechanism of film deposition, which was investigated by performing two experiments. The first was a Fe-P deposition achieved in the usual manner, by dipping the copper substrate in contact with the aluminum strip into a plating bath containing ferrous ammonium sulfate, sodium citrate, and sodium hypophosphite. The second was a Fe deposition achieved under similar conditions, but using a bath with no hypophosphite. In Fig. 7 the masses of the two deposits obtained in this way are plotted against bath temperature, at constant plating time (30 min). As shown in this figure, for temperatures below ~60°C both depositions have practically the same mass. They are iron films free of phosphorus. For bath temperatures above ~60°C, when Fe-P and Fe films are obtained, the masses of the two deposits differ: the plating rate of the Fe-P film is higher than that of the Fe film, and it increases with increasing bath temperature. Concurrently, in both experiments the amount of aluminum dissolved can be considered identical, as shown in Fig. 8.

The results of these two experiments may be interpreted as follows.

The mechanism of the Fe deposition, obtained both from the bath containing hypophosphite and from the bath with no hypophosphite, is an electrochemical process. Indeed, the two metals, Cu and Al, connected inside the deposition bath form a galvanic couple which gives rise to internal electrolysis. As a result, the Al cations leaving the aluminum anode pass into solution and the Fe cations are reduced at the copper

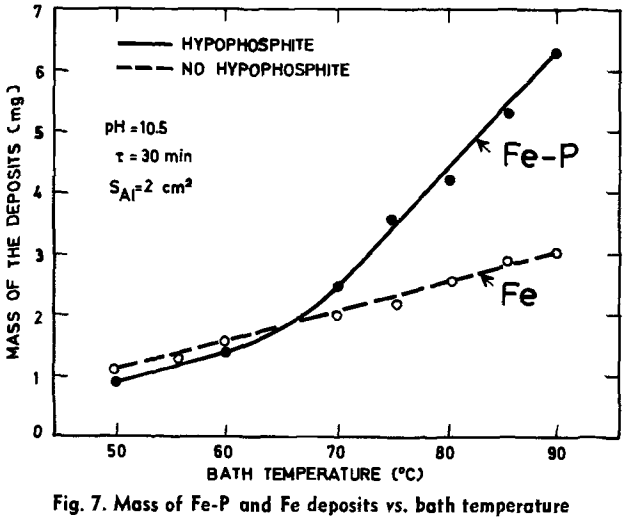

Fig. 7. Mass of Fe-P and Fe deposits vs. bath temperature

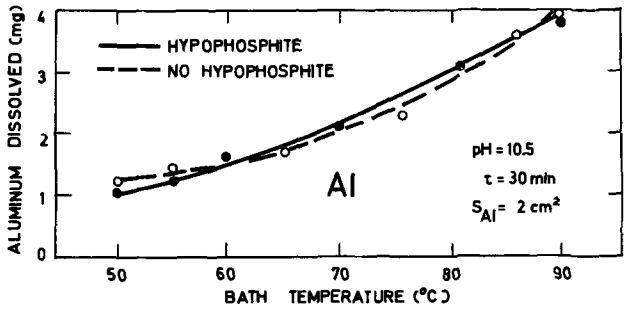

Fig. 8. Mass of aluminum dissolved vs. bath temperature

cathode forming the Fe film. This process occurs at any temperature between 25° and 95°C, the yield increasing linearly with temperature (Fig. 7).

The Fe-P deposits, obtained from the bath containing hypophosphite at temperatures in the range of ~60° to 95°C only, result as a superimposition of the above-described electrochemical process with a purely chemical process, due to reduction of the Fe cations by $PO_2H_2^-$ anions, accompanied by phosphorus codeposition. Actually, the plating rate of the Fe-P films is higher than that of the corresponding Fe films (Fig. 7) although the amount of Al ions present in the two solutions is the same (Fig. 8). Therefore, the additional deposit, leading to formation of the Fe-P films in the plating bath containing hypophosphite, must be obtained by another process which gives rise to a new iron deposition and codeposition of phosphorus, *i.e.* a chemical process.

The amount of Fe-P deposit chemically obtained depends on bath temperature, as is seen from Fig. 7. It increases linearly with increasing temperature and reaches ~50% of the total deposit at 90°C, the rest being galvanically plated iron.

The necessity of the electrochemical reduction of Fe ions as a prerequisite for the chemical reduction shows that the electrochemically plated Fe is required for the autocatalytic reduction of Fe ions by hypophosphite at temperatures greater than 60°C and a $pH > 9.5$. Consequently, the continuous electrochemical reduction of iron is necessary only to provide catalytic iron. Thus, removing the aluminum foil results in immediate dissolution and/or oxidation of the iron which eliminates the necessary catalyst for the autocatalytic reduction of iron ions by hypophosphite.

Conclusion

It has been shown that, to obtain Fe-P films by chemical reduction with hypophosphite, a concomitant electrochemical Fe deposition is necessary. It can be concluded that chemical iron-phosphorus plating is an autocatalytic process, provided that a fresh or active iron surface is present.

Acknowledgment

The authors are indebted to the reviewers of the manuscript for helpful suggestions and comments.

Manuscript submitted July 24, 1970; revised manuscript received Jan. 6, 1971.

Any discussion of this paper will appear in a Discussion Section to be published in the December 1971 JOURNAL.

REFERENCES

1. A. Brenner and G. E. Riddel, *J. Res. Nat. Bur. Std.*, **37**, 31 (1946); **39**, 385 (1947).
2. V. V. Bondar and J. M. Polukarov, *Ref. Zh. Khim. (Moscow)*, **19**, L 207 (1967).
3. W. O. Freitag, J. S. Mathias, and G. DiGuilio, *This Journal*, **111**, 35 (1964).
4. A. F. Schmeckenbecher, *ibid.*, **113**, 778 (1966).
5. W. Merz, *Mikrochim. Acta (Vienna)*, **1959**, 456 (1959).
6. D. H. Howling, *Rev. Sci. Instr.*, **27**, 952 (1956).

Primary Products of Electrochemical Oxidation of Uric Acid in Aqueous and Methanolic Solution

Glenn Dryhurst

Department of Chemistry, University of Oklahoma, Norman, Oklahoma 73069

ABSTRACT

Uric acid is oxidized in aqueous and 50% methanolic acetate buffer *p*H 3.7 in a two-electron process. In aqueous solution the primary product is uric acid-4,5-diol, which is unstable and fragments predominantly to allantoin, but a very small fraction is further oxidized to parabanic acid. In the presence of appreciable quantities (*i.e.*, 50% v/v) of methanol the greater nucleophilicity of methanol results in formation of 4,5-dimethoxyuric acid, which is apparently quite stable and cannot be further oxidized to parabanic acid, and it appears to be reasonably stable to the rather drastic conditions of hydrolysis used to determine allantoin. The results presented further confirm the site and nature of the primary product of the electrochemical oxidation of uric acid.

Uric acid (2,6,8-trioxypurine) is readily oxidized at the pyrolytic graphite electrode. Struck and Elving (1) carried out coulometry and product identification and found that in 1*M* HOAc solution a little more than two electrons were transferred in the electrochemical process and that a mixture of alloxan, allantoin (or an allantoin precursor), urea, carbon dioxide, and parabanic acid was produced. The primary product of the oxidation was proposed to be a dicarbonium ion formed by removal of two electrons from the 4,5-double bond of uric acid. Hydrolysis of the dicarbonium ion gave rise to allantoin, alloxan, CO_2, and urea, while partial further oxidation gave parabanic acid and urea. Subsequent studies (2) using fast sweep cyclic voltammetry revealed that the primary product was not a dicarbonium ion but a more stable species, probably uric acid-4,5-diol, which could be detected as a reduction peak after having first oxidized uric acid, and provided the voltammetric sweep rate was sufficiently rapid. Other purines gave a similar type of behavior which was also attributed to formation of a primary 4,5-diol product formed after having previously oxidized any unoxidized 2 or 8 position in the purine nucleus (3, 4). It has also been shown that enzymatic (5, 6), photodynamic (7, 8), and radiolytic (9, 10) oxidation of uric acid could proceed through a similar primary product to give similar ultimate products to those observed electrochemically.

Recently Matsuura and Saito (11) found that photodynamic oxidation of 1,3,7,9-tetramethyluric acid in methanol gave 4,5-dimethoxy-1,3,7,9-tetramethyluric acid which was sufficiently stable to be isolated. This, of course, provides very nice confirmatory evidence for the nature of the primary product formed in aqueous solution. A 4,5-dimethoxy (I) primary purine oxidation product would be expected to be very much more stable than the corresponding 4,5-diol (II),

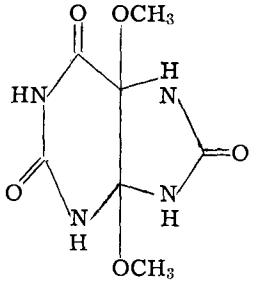

(I)

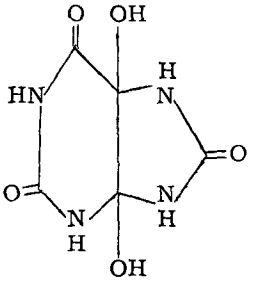

(II)

since the 4,5-diol is capable of readily decomposing to smaller stable molecular fragments, whereas the 4,5-dimethoxy- compound is not.

Accordingly, the electrochemical oxidation of uric acid in methanolic solutions has been reinvestigated with a view to understanding further the nature of the primary product in the electrochemical process.

Key words: uric acid-4,5-diol, 4,5-dimethoxyuric acid, bioelectrochemistry, pyrolytic graphite, 2,6,8-trioxypurine.

Experimental

Chemicals.—Uric acid was obtained from Nutritional Biochemicals. The *p*H 3.7 acetate buffer was prepared by diluting acetate buffer *p*H 3.7 having an ionic strength of 1*M* with an equal volume of water or with an equal volume of methanol. The *p*H 4.7 buffer used for cyclic voltammetric studies was prepared by diluting a 1*M* ionic strength solution with an equal volume of appropriate mixtures of water and methanol. All uric acid solutions were saturated in the particular background medium employed. Deaeration was accomplished with water-saturated Linde Argon without further purification.

Apparatus.—Cyclic voltammetry was accomplished with the apparatus described by Dryhurst *et al.* (12), with the triangular voltage sweeps supplied by an Exact Electronics Model 502 function generator. Current-voltage curves were recorded on a Tektronix Model 502A dual beam oscilloscope equipped with a C-27 polaroid camera. A water-jacketed three-compartment electrochemical cell was used maintained at 25° ± 0.1°C containing a saturated calomel reference electrode (SCE) to which all potentials are referred; a platinum gauze counterelectrode in saturated KCl was employed.

For controlled potential electrolysis a Wenking Model 66TA1 potentiostat was employed; current integration was performed by the usual voltage-to-frequency converter-frequency counter method. The cell used for controlled potential electrolysis and preparation of the pyrolytic graphite electrodes have been described elsewhere (13, 14).

Results and Discussion

In an attempt to define at least qualitatively the effect of methanol on the electrochemical oxidation of uric acid fast-sweep cyclic voltammetry was first performed. Although the most detailed electrochemical study has been carried out in 1*M* HOAc background (1), it was found that in the presence of appreciable amounts of methanol that the resistance of the solution was too high to permit fast-sweep cyclic studies. The most definitive data was obtained in acetate buffer *p*H 4.7 and is presented in Fig. 1, although parallel behavior was observed in acetate buffer *p*H 3.7 (Fig. 2). At a clean electrode no cathodic peaks are observed on the initial negative-going sweep. An anodic peak (peak

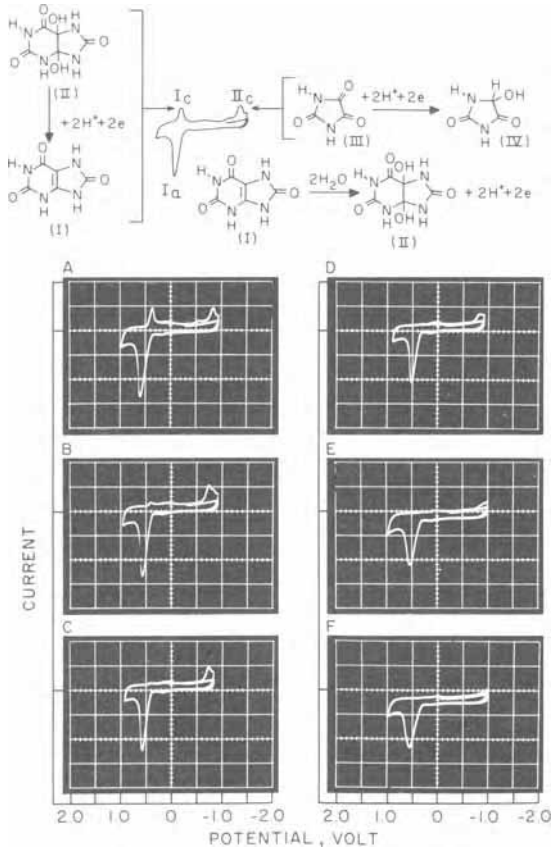

Fig. 1. Cyclic voltammograms of saturated solutions of uric acid at the stationary PGE in aqueous acetate buffer pH 4.7: A, with no methanol present; B, 5% v/v methanol; C, 10% methanol; D, 20% methanol; E, 40% methanol; F, 50% methanol. Current sensitivity 500 μA/div; calibration mark on current axis indicates zero current for each voltammogram. Scan rate, 1 Hz. Electrode area, 12.5 mm².

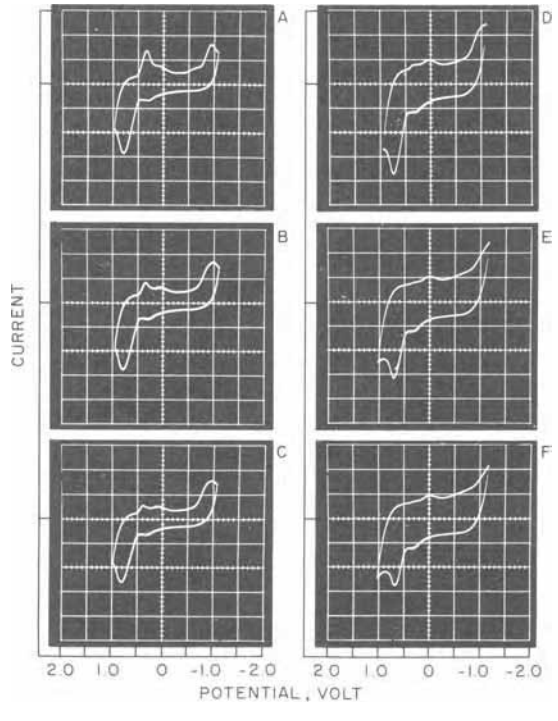

Fig. 2. Cyclic voltammograms of saturated solutions of uric acid at stationary PGE in aqueous acetate buffer pH 3.7. Methanol concentrations A through F same as for Fig. 1. Current sensitivity A, B, C, 200 μA/div; D, E, F, 100 μA/div. Scan rate, 1 Hz. Electrode area, 12.5 mm².

I_a) at *ca.* 0.6V is observed on the first positive-going sweep due to the two-electron, two-proton oxidation of uric acid (I, Fig. 1) to the corresponding 4,5-diol (II, Fig. 1). Provided the sweep rate is sufficiently rapid, part of the 4,5-diol can be reduced back to uric acid (peak I_c), the remainder being fragmented to allantoin or further oxidized to parabanic acid. The latter compound gives rise to the second cathodic peak (peak II_c) at *ca.* −0.8V, which is due to the two-electron, two-proton reduction of parabanic (III, Fig. 1) acid to 5-hydroxyhydantoin (15) (IV, Fig. 1). Upon addition of only 5% v/v of methanol the height of peak I_c (B, Fig. 1, 2) is clearly significantly reduced and at the 20% methanol level and above peak I_c is completely eliminated. Up to the 10% methanol concentration level the parabanic acid peak (peak II_c) is virtually unaffected, but at above 20% methanol concentrations peak II_c also disappears. However, peak I_a remains essentially unaffected; the slight decrease in the current value for peak I_a is no doubt related to the decreased solubility of uric acid in the mixed solvent. Thus, increasing concentrations of methanol decreases the amount of 4,5-diol produced and the amount of parabanic acid produced, although the methanol concentrations required to make these two species undetectable by cyclic voltammetry is greater in the case of the latter compound.

In order to investigate further the mechanism of the processes, coulometry of uric acid was carried out in acetate buffer *p*H 3.7 in the absence of methanol and in 50% v/v methanol solution. The *p*H of 3.7 chosen for this study was selected because alloxan, one of the products found in 1*M* HOAc electrolyses (1), is unstable above *p*H 4. After complete electrolysis, analyses were performed only for allantoin, parabanic acid, and alloxan. Data are presented in Table I where it is clear that in aqueous solution close to 90% of the uric acid oxidized results in allantoin formation with only a very small amount of parabanic acid being produced. In the 50% methanolic solution only about 20% of the uric acid oxidized results in allantoin formation, and no parabanic acid is produced. In neither the completely aqueous nor the 50% methanol solution was alloxan detected, although at *p*H 3.7 alloxan in either medium gives rise to only a very small kinetically controlled polarographic wave; accordingly, small amounts of alloxan could go undetected by the polarographic method at *p*H 3.7. Nevertheless, since experiment showed that alloxan, parabanic acid. and allantoin were reasonably stable in the 50% methanolic solution, then the bulk of the oxidized uric acid must be present in a form which cannot be produced in aqueous solution. The only reasonable major product formed is, therefore, 4,5-dimethoxy-uric acid.

Mechanism

Uric acid is clearly oxidized in aqueous and 50% methanolic acetate buffer *p*H 3.7 in a two-electron process. In aqueous solution the oxidation proceeds via a primary uric acid-4,5-diol product which predominantly simply fragments to allantoin, although a

Table I. Analysis of uric acid solutions after coulometric electrooxidation at PGE in aqueous or 50% methanolic acetate buffer *p*H 3.7

Solvent system	Millimoles uric acid oxidized	*n*	Millimoles product formed: Allantoin[a]	Parabanic acid[b]	Alloxan[c]
Aqueous	0.311	1.95[d]	0.261	0.006	ND
50% Methanol	0.313	1.90	0.064	ND[e]	ND

[a] Determined by the modified (13) Young and Conway (16) procedure.
[b] Determined polarographically by Struck and Elving (17) procedure.
[c] Method of Struck and Elving (18).
[d] Mean of replicate determinations.
[e] Not detected.

small portion is further oxidized to parabanic acid.[1] On addition of methanol to the solution cyclic voltammetry indicates that the amount of 4,5-diol is drastically decreased so that at the 50% methanol level no 4,5-diol can be detected. Under cyclic voltammetric conditions parabanic acid formation is also repressed by addition of methanol, but not at such low methanol concentrations as are required to repress the 4,5-diol detection. At the 50% methanol concentration level parabanic acid is not formed.

The mechanism of the process can thus be rationalized by assuming that, under the voltammetric conditions, the greater nucleophilicity of methanol [or methoxide ion] (19) results in preferential formation of 4,5-dimethoxy-uric acid, rather than the uric acid-4,5-diol. Since the cathodic parabanic acid peak can be observed cyclic voltammetrically even when the 4,5-diol cathodic peak is completely eliminated, then presumably most of the 4,5-diol that is produced is further oxidized to parabanic acid. At the 50% methanol concentration level no parabanic acid is observed, indicating that little or no 4,5-diol is produced in the primary oxidation process. That some allantoin can be produced (under conditions of exhaustive controlled potential electrolysis) probably result from partial hydrolysis of 4,5-dimethoxy-uric acid under the rather drastic conditions of the allantoin determination to allantoin or glyoxylic acid, which is the species actually spectrophotometrically determined (16).

It is of some interest to note that under cyclic voltammetric conditions at the stationary PGE that the cathodic parabanic acid peak (peak II_c) is much larger (Fig. 2A) relative to the principal uric acid oxidation peak (peak I_a) than would be expected on the basis of the analytical concentration of parabanic acid determined at the end of an exhaustive controlled potential electrolysis. Struck and Elving (1) found that at pH 2.3, 30% of uric acid was oxidized to give parabanic acid, *i.e.*, the lower the pH the greater the amount of parabanic acid produced. Under cyclic voltammetric conditions the peak I_a process (A, Fig. 1, 2) clearly involves liberation of protons, which must at least momentarily decrease the surface pH and presumably aid the formation of parabanic acid. Under conditions of controlled potential electrolysis the vigorously stirred solution would not be as susceptible to large changes in surface pH and, accordingly, less parabanic acid is produced.

[1] Work now in progress is being carried out with a view to elucidation of the processes leading to the uric acid-4,5-diol or 4,5-dimethoxy derivative.

Acknowledgment

The author would like to thank the National Science Foundation which supported the work described.

Manuscript submitted Sept. 30, 1970; revised manuscript received *ca.* Jan. 5, 1971.

Any discussion of this paper will appear in a Discussion Section to be published in the December 1971 JOURNAL.

REFERENCES

1. W. A. Struck and P. J. Elving, *Biochemistry*, **4**, 1343 (1965).
2. G. Dryhurst, *This Journal*, **116**, 1411 (1969).
3. G. Dryhurst and G. F. Pace, *ibid.*, **117**, 1259 (1970).
4. B. H. Hansen and G. Dryhurst, *J. Electroanal. Chem.*, In press.
5. K. G. Paul and Y. Avi-Dor, *Acta Chem. Scand.*, **8**, 637 (1954).
6. E. S. Canellakis, A. L. Tuttle, and P. P. Cohen, *J. Biol. Chem.*, **213**, 397 (1955).
7. T. Matsuura and I. Saito, *Chem. Commun.*, 693 (1967).
8. T. Matsuura and I. Saito, *Tetrahedron*, **24**, 6609 (1968).
9. J. Holian and W. M. Garrison, *J. Phys. Chem.*, **71**, 462 (1967).
10. J. Holian and W. M. Garrison, Chem. Commun., 676 (1967).
11. T. Matsuura and I. Saito, *Tetrahedron*, **25**, 549 (1969).
12. G. Dryhurst, M. Rosen, and P. J. Elving, *Anal. Chim. Acta*, **42**, 143 (1968).
13. G. Dryhurst and P. J. Elving, *This Journal*, **115**, 1014 (1968).
14. G. Dryhurst, *ibid.*, **116**, 1097 (1969).
15. G. Dryhurst, B. H. Hansen, and E. B. Harkins, *J. Electroanal. Chem.*, In press.
16. E. G. Young and C. F. Conway, *J. Biol. Chem.*, **142**, 839 (1942).
17. W. A. Struck and P. J. Elving, *Anal. Chem.*, **36**, 1374 (1964).
18. W. A. Struck and P. J. Elving, *J. Am. Chem. Soc.*, **84**, 1412 (1962).
19. A. Streitweiser, "Solvolytic Displacement Reactions," McGraw Hill Book Co., New York (1962).

Influence of the Faradaic Process on Nonfaradaic Resistance Compensation in Potentiostatic Techniques

Arthur A. Pilla*

ESB Incorporated, Research Center, Yardley, Pennsylvania 19067

ABSTRACT

The theoretical justification for the use of IR compensation in potentiostatic techniques when a faradaic reaction is present is considered in detail. It is shown that the stability of the system indeed depends on potentiostat and all electrode parameters, *i.e.*, both the double layer and faradaic time constants contribute. Under certain conditions, the faradaic contribution is not significant; however, it is difficult to determine even in an *a posteriori* manner the remaining uncompensated resistance R_u. It is concluded that IR compensation can only be employed unambiguously in the time and classical a-c frequency domains if the critical damping frequency is accurately known and the frequencies employed are sufficiently lower than this frequency. IR compensation can however be advantageously employed in combination with the transient impedance technique over the entire accessible frequency range (even those above τ_{min}) and which allows the system to be unmasked experimentally from the effects of nonfaradaic resistance. This permits the necessary kinetic and double-layer information to be extracted from the final results with a precision increased at least two orders of magnitude above the uncompensated system when high-speed circuitry is employed.

In a previous study (1), the general problem of the incorporation of IR compensation via positive feedback in a potentiostatic circuit was considered for an electrochemical system exhibiting double-layer behavior only. The system was analyzed in terms of frequency domain stability criteria and a characteristic parameter, the minimum time constant, τ_{min} was derived. This quantity is the minimum stable over-all time constant exhibited by the potentiostat-cell combination in the presence of positive feedback. It represents the maximum IR compensation beyond which damped and finally undamped oscillations may occur; τ_{min} is, in general, the sum of time constants involving both the electrochemical cell and the potentiostat, rendering the unambiguous evaluation of both the remaining uncompensated nonfaradaic resistance, R_u, and the double-layer capacitance, C_d, difficult in the time or classical (a-c) frequency domain. In addition, since τ_{min} is always a finite quantity, overcompensation in the absolute sense (*i.e.*, achieving the proper response to charge C_d in the absence of any series resistance) is physically impossible, even with the fastest state of the art potentiostats.

IR compensation is most often employed in the presence of a faradaic reaction. Essentially, the desire is to charge C_d as rapidly as possible and unmask the faradaic process for further analysis at the shortest possible times. For an extensive bibliography on IR compensation the reader is referred to ref. (1). The effect of faradaic parameters has not explicitly been considered previously. However, it has been stated that the stability of the system would most probably be increased when a faradaic reaction is present (2). This could be interpreted to mean that the degree of positive feedback might be increased above that allowable in the absence of faradaic reaction. Another approach (3, 4) has been to obtain the fastest stable system response with positive feedback at an electrode potential at which no appreciable faradaic current flows, *e.g.* at the bottom of the polarographic wave. Once this has been accomplished it is then considered that the same degree of positive feedback accomplishes the same amount of compensation when a faradaic reaction is also present. In an effort to clarify this situation and to make a previous study (1) more generally applicable an attempt will be made here to elucidate the effect of the faradaic process on the stability conditions of the total system (*i.e.*, on τ_{min}). In addition, criteria will be presented to provide guidelines for the use of IR compensation in the most general cases.

Theoretical

In order to establish a working model for the general application of IR compensation in potentiostatic techniques the same basic model as previously employed for a system exhibiting double layer behavior only will be utilized (1). This involves considering the electrochemical system as linear which allows the concept of impedance to be utilized permitting the system to be represented in shorthand notation by an aperiodic equivalent circuit (5). This circuit is then appropriately coupled to a potentiostat thereby constituting the total control circuit. Among the various types of potentiostats (3, 6) which have commonly been employed, the optimum choice when using positive feedback for high speed applications has been shown (1) to be the single amplifier variety. The incorporation of IR compensation in this type of potentiostat is achieved by voltage feedback of part of the output signal to its noninverting (+) input.

Utilizing the above considerations, a general model may now be constructed as shown in Fig. 1. Here, the electrochemical cell is shown as a series resistance, R_e, representing the electrolyte and/or working electrode nonfaradaic resistance. The working interface is shown as an arbitrary impedance, Z_E, which is valid for any electrochemical system under linear conditions. The amplifier, A_1, is the potentiostat, and A_2 is the positive feedback amplifier which is essentially a voltage follower with gain. R_o represents both the counterelectrode impedance and output impedance of A_1. IR compensation is accomplished outside the negative feedback loop of A_1 by sampling a portion of the voltage across R_1 (Fig. 1) thereby keeping τ_{min} as small as possible. This point has been discussed previously (1) and is based on the fact that the closed loop time constant of the potentiostat is smaller if the current sampling resistor is outside the negative feedback loop.

* Electrochemical Society Active Member.

Key words: positive feedback, potentiostat amplifier, impedance, frequency domain.

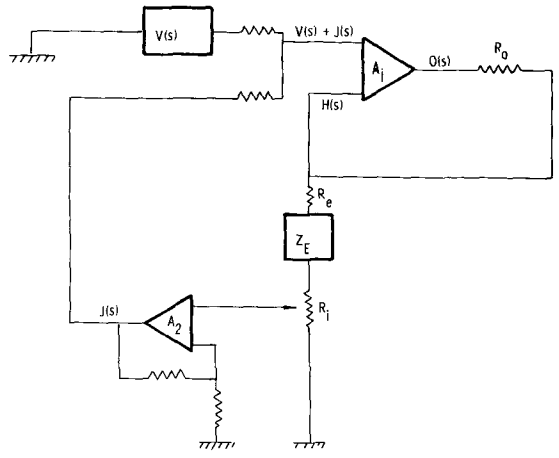

Fig. 1. Single amplifier potentiostat circuit with compensation outside the negative feedback loop: for generalized linearized electrochemical system.

All voltage signals in this model are represented in terms of their Laplace transforms (7) since this procedure allows simple algebraic expressions to be obtained which are sufficient to describe the frequency response of the system (1). The quantity necessary to examine this property is its transfer function which is defined as the ratio of the output voltage $O(s)$ (Fig. 1) to the input voltage $V(s)$ (Fig. 1). This is given by (1, 7).

$$\frac{O(s)}{V(s)} = \frac{G_1(s)}{1 + [H(s) - J(s)]\,G_1(s)} \qquad [1]$$

where $G_1(s)$ is the gain frequency function of the potentiostat, $H(s)$ is the negative feedback, and $J(s)$ is the positive feedback voltage functions. This expression takes into account the interaction of both the main and positive feedback amplifiers. Since $H(s)$ is defined as the fraction of the output voltage which is fed back to the inverting (−) input of the potentiostat, it is given by

$$H(s) = \frac{R_e + R_i + Z_E(s)}{R_o + R_i + R_e + Z_E(s)} \qquad [2]$$

The voltage at the output of A_2, which is the IR compensation signal $J(s)$ (Fig. 1) is

$$J(s) = \frac{R_i G_2(s)}{R_o + R_i + R_e + Z_E(s)} \qquad [3]$$

where $G_2(s)$ is the gain function of the IR feedback amplifier.

The essential requirements for optimum IR compensation are to keep the system order in terms of the Laplace variable s and the associated time constants as low as possible (1). For this, it is sufficient to examine the denominator of either the transfer function (Eq. [1]) or the output current, $i(s)$, or the control voltage $E(s)$ since these quantities may be obtained from the transfer function. The frequency functions which must be made explicit and which are the key factors in determining the system order are $G_1(s)$, $G_2(s)$, and $Z_E(s)$. Obviously very little can be done with $Z_E(s)$ since this is an inherent property of the electrode under study. However, the value of the time constants in $Z_E(s)$ which prevail in any given experiment are determined by the surface area of the electrode. Thus the double-layer capacitance, C_d, is smaller, as is well known, the smaller the electrode area. The same is true for parameters of the faradaic impedance such as the charge transfer resistance, R_t, adsorption capacitance, C_a, etc. It is, therefore, desirable to keep the electrode time constants as low as possible to enable optimum IR compensation conditions to be obtained.

The gain functions $G_1(s)$ and $G_2(s)$ can be determined to a certain extent by appropriate choice of amplifiers. The ideal gain function would be $G(s) = K$ indicating constant gain at all accessible frequencies. Unfortunately, in the case of the potentiostat amplifier, this function cannot be obtained since, *e.g.*, the potentiostat is not an infinite current source at infinite frequency. The various gain functions which potentiostat amplifiers may exhibit have been discussed elsewhere (1, 4). The most desirable is that of lowest order since this allows the total system order to be kept to a minimum. A first order gain function is given by

$$G_1(s) = \frac{K}{s\tau + 1} \qquad [4]$$

where K is the open loop d-c gain and τ the open loop time constant, the value of which depends on amplifier design. The fastest available potentiostats have been shown to exhibit this gain function (1). In addition external phase compensation which affects the value of τ without modification of the form of the gain function is highly desirable since this allows the total system to be stabilized without changing the over-all system order. If the positive feedback amplifier is utilized at relatively low gain and is at least one order of magnitude faster than the potentiostat amplifier under these conditions, it is then possible for it to exhibit the simple gain function $G_2(s) = K_2$. An amplifier having this characteristic when utilized for high speed IR compensation has previously been described (1).

In view of the above considerations, the transfer function now becomes, using [2], [3], and [4], and maintaining arbitrary $Z_E(s)$

$$\frac{O(s)}{V(s)} = \frac{K}{K+1}\left[\frac{R_o + R_e + R_i + Z_E(s)}{R_T\tau_p s + Z_E(s)[1 + \tau_p] + (R_T + R_u K)/(K+1)}\right] \qquad [5]$$

where

$$R_T = R_o + R_e + R_i \qquad [6]$$

$$R_u = R_e + R_i - R_i K_2 \qquad [7]$$

$$\tau_p = \tau/(K+1) \qquad [8]$$

It is convenient at this point to develop expressions for both $i(s)$ and $E(s)$. Thus

$$i(s) = O(s)/[R_o + R_e + R_i + Z_E(s)] \qquad [9]$$

from which, using [5]

$$i(s) = V(s)\frac{K}{K+1}\left[\frac{1}{R_T\tau_p s + Z_E(s)[1 + \tau_p] + (R_t + R_u K)/(K+1)}\right] \qquad [10]$$

The voltage appearing at the potentiostat control points, $E(s)$, is

$$E(s) = O(s) - i(s)R_o \qquad [11]$$

which gives, using [5]

$$E(s) = V(s)\frac{K}{K+1}\left[\frac{R_e + R_i + Z_E(s)}{R_T\tau_p s + Z_E(s)[1 + \tau_p] + (R_T + R_u K)/(K+1)}\right] \qquad [12]$$

relating the input voltage to that actually appearing across the working and reference electrodes. As has been shown previously (1, 5), the use of the transient impedance technique allows Eq. [12] to be divided by Eq. [10] in the most general case thereby markedly reducing the contribution from all parameters except those actually appearing across the potentiostat control points.

Examination of Eq. [5], [10], and [12] shows that $O(s)$, $i(s)$, and $E(s)$ are subject to the same stability conditions, as is to be expected. These conditions are determined by the roots of the denominator of the respective expressions. These roots contain, in an appropriate manner, all of the time constants present in the system including those in $Z_E(s)$. It is therefore obvious that, in the general case for which the present model is valid, the combination of time constants prevalent at the critical damping point of the system includes both potentiostat and all electrode parameters, *i.e.*, both double-layer and faradaic processes contribute.

In order to illustrate this in a somewhat more specific manner, an electrochemical system exhibiting both double-layer behavior (C_d) and charge transfer (R_t) as the faradaic process will be considered. In this case

$$Z_E(s) = \frac{R_t}{1 + R_t C_d s} \qquad [13]$$

This expression is the complex impedance of an aperiodic RC parallel electric circuit which represents a relatively classical electrochemical system [8]. Using this in, *e.g.*, Eq. [10] for $i(s)$, the following is obtained

$$i(s) = V(s)\,\frac{K}{K+1}\left[\frac{C_d s + 1/R_t}{\tau_c\tau_p s^2 + [\tau_u + \tau_c/(K+1) + \tau_p(1 + R_T/R_t)]s + 1 + 1/R_t(R_T/(K+1) + R_u)}\right] \qquad [14]$$

where

$$\tau_c = (R_e + R_i + R_o)C_d \qquad [15]$$

$$\tau_u = (R_e + R_i - R_i K_2)C_d \qquad [16]$$

and R_T, R_u, and τ_p are defined by Eq. [6], [7], and [8], respectively. Examination of [14] shows that it represents a second order system which closely resembles the result for $i(s)$ previously obtained (1) for a system exhibiting double-layer behavior only. The result is reproduced here for convenience.

$$i(s) = V(s)\,\frac{K}{K+1}\left[\frac{C_d s}{\tau_c\tau_p s^2 + [\tau_u + \tau_c/(K+1) + \tau_p]s + 1}\right] \qquad [17]$$

Comparison of [14] and [17] shows that they differ only in terms containing R_t. This difference, however, is essential since the critically damped behavior allowable for both systems is not identical. Thus, the minimum time constant, τ_{min}, corresponding to [14] is

$$\tau_{min} = \sqrt{\tau_c\tau_p[1 + 1/R_t(R_T/(K+1) + R_u)]} \qquad [18]$$

which is to be compared to τ_{min} for [17]

$$\tau_{min} = \sqrt{\tau_c\tau_p} \qquad [19]$$

Equation [18] clearly shows that, at critical damping, *i.e.*, just at the onset of damped oscillations, faradaic parameters play a role whereas these parameters are, of course, nonexistent in [19].

The above results indicate that the total electrode behavior must be taken into account when evaluating results obtained from potentiostatic techniques incorporating IR compensation. In particular, [18] and [19] clearly show that, even for the simplest of electrode systems, it is not allowable to adjust for optimum compensation in the absence of a faradaic reaction and assume that results will be unaffected in its presence. The conditions under which minimum error is made when performing the above can, however, be established by consideration of [18]. It is clear that the larger R_t is, *i.e.*, the slower the charge transfer process, the more identical [18] and [19] become since as $R_t \to \infty$, $1 >> 1/R_t[R_T/(K+1) + R_u]$. This shows that the slower the faradaic process, the less τ_{min} will be affected by it, which is entirely reasonable since this essentially means that all faradaic time constants are large compared to both the effective double-layer charging time constant, R_uC_d, and the potentiostat time constant, τ_p.

The above result may be generalized by allowing $Z_E(s)$ to be given by

$$Z_E(s) = \frac{Z_F(s)}{1 + Z_F(s)C_d s} \qquad [20]$$

which considers the faradaic impedance, $Z_F(s)$, to be arbitrary and in parallel with C_d, a valid model for many electrode systems. Using [20], $i(s)$ is then

$$i(s) = \frac{K}{K+1}V(s)\left[\frac{C_d s + 1/Z_F(s)}{R_T[C_d s + 1/Z_F(s)]\tau_p s + [R_u + R_T/(K+1)][C_d s + 1/Z_F(s)] + \tau_p s + 1}\right] \qquad [21]$$

Equation [21] reduces to that for pure double-layer behavior (Eq. [17]) when $C_d s >> 1/Z_F(s)$, which occurs if frequencies (or times) may be achieved such that the overwhelming majority of current which flows serves only to charge the double layer. It is thus only when the above condition is met that IR compensation may be employed validly in an electrochemical system exhibiting a faradaic process. Note that, in principle, a frequency range may always be achieved such that $C_d s >> 1/Z_F(s)$; however, this range may be entirely too high to be within the upper limit of stability set by τ_{min}.

It is appropriate at this point to examine the criteria which might allow the unambiguous use of a potentiostat with IR compensation in the time or classical (a-c) frequency domain. To do this, consider $Z_E(s)$ to be given by Eq. [13], *i.e.*, charge transfer in parallel with C_d. The desired current response in the absence of any potentiostat parameters is

$$i(s) = V(s)\left[\frac{C_d s + 1/R_t}{\tau_u s + 1 + R_u/R_t}\right] \qquad [22]$$

where R_u and τ_u are defined by Eq. [7] and [16], respectively. This equation allows for the fact that the potentiostat cannot be an infinite current source (1) by the existence of some uncompensated nonfaradaic resistance (R_u). Comparison of [22] with [14] shows that many conditions must be met before the two relationships become identical. However, the essential factors underlying these conditions are the speed of the potentiostat and of the faradaic reaction. Thus, [14] shows second order behavior while [22] is first order. It is therefore necessary that the term $\tau_c\tau_p s^2$ in [14] be negligible. This can be done by proper cell design and with a fast potentiostat. Cell design affects τ_c by reducing R_o (Eq. [15]) and the speed of the potentiostat affects τ_p (Eq. [8]) and R_o. It can therefore be seen that the smaller the closed loop time constant, τ_p, of the potentiostat, the more the system will behave as a first order system as predicted by [22]. Inspection of the remaining portions of [14] shows that it is essentially the relative values of potentiostat parameters which allow undesirable terms to be neglected. Thus, if the open loop d-c gain is high (>1000), the following conditions can be established: $K \cong K + 1$, $\tau_u >> \tau_c/(K+1)$ and, therefore, $R_u >> R_T/(K+1)$. The term $\tau_p(1 + R_T/R_t)$ is negligible if τ_p is small compared to τ_u and τ_c, *i.e.*, very fast potentiostat, and if $\tau_u/\tau_p >> R_T/R_t$. The latter condition is valid only if the charge transfer process (or the faradaic reaction

in general) is relatively slow and the potentiostat relatively fast. Note that when all of these conditions are met, it would not matter whether a faradaic reaction were present since the potentiostat itself no longer influences the results obtainable. It is to be remembered, however, that as critical damping is approached, indeed if present at all, then the above conditions cannot be met since a first order electrochemical system as considered here (Eq. [22]) does not predict critical damping behavior. This can be understood by considering the fact that as more and more positive feedback is employed, both τ_u and R_u become smaller, eventually rendering it more and more difficult to eliminate potentiostat parameters, *e.g.*, τ_u may approach the same order of magnitude as τ_p. In general, therefore, it is never possible to use the critical damping point as detection for optimum IR compensation in the presence or absence of a faradaic reaction if the results are to be interpreted in the time or classical a-c frequency domains at frequencies close to the critical damping frequency. The exception to the above occurs in those cases for which faradaic parameters do not contribute to τ_{min} or for sufficiently low frequencies and it is not desired to evaluate C_d in the presence of the electrode reaction. If this is so, it is then indeed advantageous to employ IR compensation so as to unmask the faradaic process for study at shorter times than possible otherwise since the upper frequency limit is higher when IR compensation is employed.

Experimental and Results

In order to illustrate the effect of the faradaic process on IR compensation, the basic circuit shown in Fig. 1 was employed. The electrode impedance Z_E is that found applicable for an electrode process involving adsorption (5) and is shown in Fig. 2. Here, the adsorption coupled charge transfer is given as a charge transfer resistance, R_t, in series with an adsorption capacitance, C_a. These are placed in parallel with the double-layer capacitance C_d. The details of the potentiostat circuit (Fig. 1) have been given in detail elsewhere (1).

Initial experiments were performed on an electrical equivalent circuit with $R_e = 500$ ohms, $R_i = 100$ ohms, $R_t = 50$ ohms, $R_o = 0$, $C_d = 0.15$ μF and $C_a = 1$ μF. The response at τ_{min} was compared with the faradaic components (R_t and C_a) both present and removed from the circuit. Representative current response curves to a potential step are shown in the photograph in Fig. 3. Here, the horizontal axis is 10 μsec per major division and the vertical axis is 20 μA per major division. The curves were obtained in the following sequence: τ_{min} was achieved with the faradaic parameters initially absent from the circuit (lower curve, Fig. 3). Note that this is normally the manner in which τ_{min} would be adjusted in an actual system, *i.e.*, in a region of the i-v curve exhibiting double-layer behavior only (3). With τ_{min} adjusted, the faradaic components were then placed in the circuit giving the upper curve in Fig. 3. It can be seen that some ringing is present indicating that the degree of positive feedback is too high. This damped oscillation is particularly

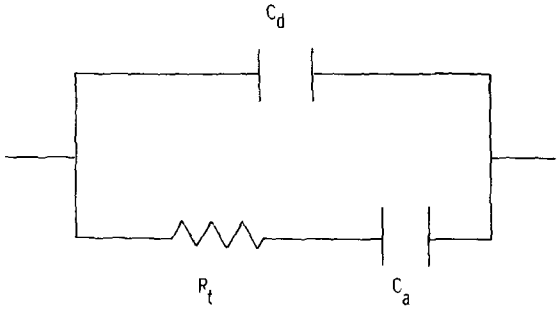

Fig. 2. Aperiodic equivalent circuit for an electrode exhibiting double layer behavior and adsorption coupled charge transfer.

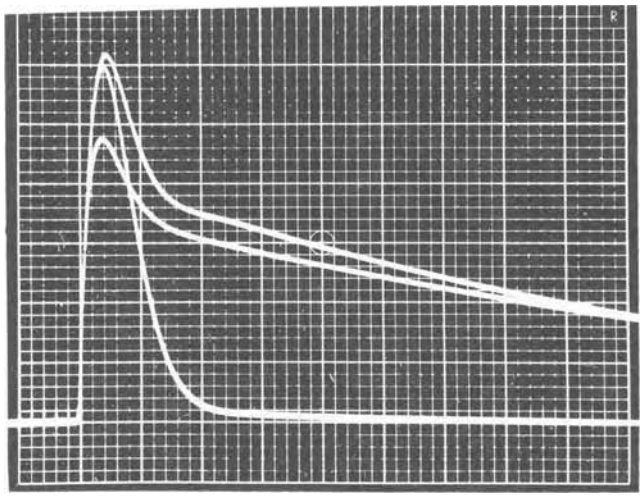

Fig. 3. Oscilloscope traces of current-time response curves to a voltage step input. Lower trace, τ_{min} with Z_F removed; upper trace, τ_{min} with Z_F replaced; center trace τ_{min} adjusted for most stable response (see text for details).

visible because a step function input perturbation [V(s)] was employed. It would be much less evident if a standard triangular or, in particular, a sinusoidal waveform were employed. In the latter case, a distortion analyzer would be needed to detect excitation of the ringing frequency, otherwise this effect would remain unnoticed with the use of, *e.g.*, standard phase sensitive detectors. The center curve in Fig. 3 is that for τ_{min} with no visible ringing in the presence of the faradaic components. It was achieved by reducing the amount of positive feedback by approximately 10% as predicted by the analysis in the previous section. The above results show that τ_{min} is indeed affected by faradaic parameters, particularly when there is significant reaction current at the ringing frequency, *i.e.*, the faradaic time constants are excited at τ_{min}.

In order to further illustrate the influence of the faradaic time constants upon IR compensation, consider the following. If τ_{min} is composed only of double layer and potentiostat parameters, then, in principle, at times longer (or frequencies lower) than τ_{min}, the system should behave as though the potential were constant across the faradaic impedance and the remaining uncompensated resistance (R_u). Thus for the circuit considered above, at all frequencies below those corresponding to τ_{min}, the impedance should appear as if it were given by

$$Z(s) = R_u + R_t + \frac{1}{C_a s} \qquad [23]$$

instead of its complete form which is

$$Z(s) = R_e + R_i + \frac{R_t C_a s + 1}{R_t C_a C_d s^2 + (C_d + C_a)s} \qquad [24]$$

The use of Eq. [23] to generate a usable $i(t)$ function requires that C_a receive no significant charge during the time required to achieve τ_{min}. In addition the time required to achieve constant potential conditions across the circuit represented by Eq. [23] must be taken into account. For this a true step function [$V(s) = V_o/s$] cannot be assumed as the input perturbation. It is, in fact, difficult to determine the exact function for this quantity, however, for evaluation of the results in the time domain, an explicit function must be employed. To a first approximation exponential behavior can be assumed. In this case $i(t)$ should be given by, for all times after the peak current (see Fig. 3)

$$i(t) = \frac{V_o}{R_u + R_t}\left[1 + \frac{1/(R_u + R_t)C_a}{a - 1/(R_u + R_t)C_a}\right] \exp\left(-\frac{t}{(R_u + R_t)C_a}\right) \quad [25]$$

where a is the reciprocal of the time constant for the rise of $V(t)$ to V_o at the current peak. Inspection of [25] shows that a linear ln $i(t)$ *vs.* t plot should be obtained having an intercept at the time of the current peak which is complex enough to render the desired quantities R_u, R_t, and C_a difficult to obtain in the most general case. In any event, linearity in ln $i(t)$ *vs.* t should be sufficient indication that faradadic contribution to τ_{min} is negligible provided that the linearity extends to times relatively close to those corresponding to τ_{min}.

In view of the above, Eq. [25] was tested for the circuit given earlier using the $i(t)$ curves shown in Fig. 3. The remaining uncompensated resistance R_u was evaluated in the absence of Z_F (lower curve, Fig. 3). This could be done with Eq. [19] as described previously (1) giving $R_u = 14$ ohms (where initially $R_e + R_i = 600$ ohms). The faradaic parameters were then inserted and ln $i(t)$ *vs.* t examined. Note that at all times from the current peak to that at which the current changes slope, this plot is not valid for the circuit corresponding to Eq. [23] since double-layer charging is also taking place during this time interval. In addition, ringing occurs in the region of slope change indicating that all times before this point relate to τ_{min}. It is, however, valid to consider that constant potential has been achieved at the current peak as far as the faradaic process is concerned. With these points in mind, it is important to note the shortest time at which nonlinearity in the ln $i(t)$ *vs.* t plots occurs. This can be seen in Fig. 4 (curve for $C_a = 1$ μF) where deviation from linearity is visible at approximately 15 μsec which is very close to that time at which $i(t)$ changes slope (see Fig. 3). The parameters calculated using Eq. [25] were $R_u + R_t = 66$ ohms and $C_a = 0.95$ μF, which is in fairly good agreement with their known values ($R_u + R_t$ should be 64 ohms). It is to be noted, however, that the most accurate results could only be achieved using the center curve in Fig. 3, *i.e.*, the most stable system response. This required, as indicated earlier, reduction of the amount of positive feedback from that for which stable response could be achieved in the absence of Z_F. Naturally, in this case the amount of positive feedback could be rendered identical; however, in an electrochemical system, this approach is not possible.

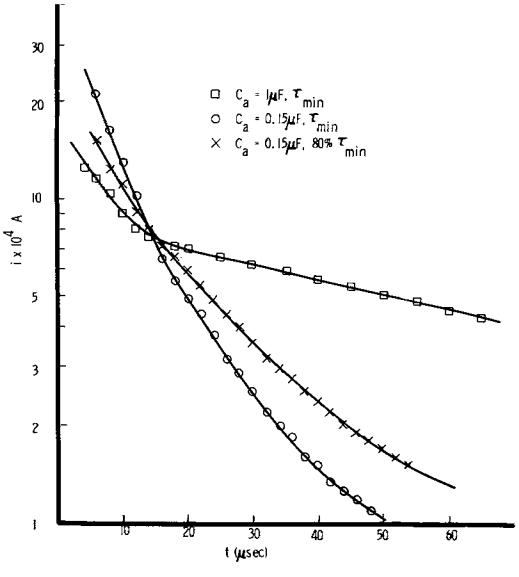

Fig. 4. ln $i(t)$ *vs.* t plots at τ_{min} for system with electrode impedance as shown in Fig. 2.

A further test of this analysis was made on the same circuit as previously employed with $C_a = 0.15$ μF, effectively changing Z_F by one order of magnitude as compared to the previous case. The procedure for determination of R_u was as above, however, as the semilogarithmic plots in Fig. 4 show, linearity was not obtained at τ_{min} or at 80% τ_{min}. This indicates the large influence of Z_F on both the over-all system stability and its response at a degree of positive feedback considerably below the ringing frequency.

The above appears to illustrate the conditions for which the faradaic contribution to τ_{min} are negligible; however, the situation is more complex than could be expected from these results. Thus, as the first case ($C_a = 1$ μF) shows, R_u was not negligible compared to R_t requiring its evaluation for meaningful values of R_t and C_a. The problem is then to evaluate R_u in every case (which would also allow knowledge of C_d). This cannot be done from a knowledge of τ_{min} alone. Thus an attempt to evaluate R_u and C_d from time domain ln $i(t)$ *vs.* t plots even in the case of pure double-layer behavior was unsuccessful (1). This is to be expected since a simple RC series circuit does not exhibit ringing except under conditions of positive feedback when potentiostat parameters become involved, as indicated earlier. The situation is even more serious when classical (a-c) impedance techniques are employed since τ_{min} is difficult to detect without distortion analysis. In principle, however, when correct detection techniques are employed R_u and C_d could be separately evaluated provided potentiostat contribution, *e.g.*, τ_p, can also be determined.

In addition to the above it is quite certain, as can be seen from Fig. 3, that τ_{min} varies somewhat, even in the best of cases, from that obtainable in the absence of Z_F. Further, since C_d generally varies with potential, τ_{min} cannot be expected to remain constant throughout the potential region of interest even when Z_F contributes negligibly. Thus as Eq. [19] shows, τ_{min} varies with τ_c which contains C_d. An example of this phenomenon has been reported recently for the $C_d(NO_3)_2$ system (9).

As can be seen from the preceding results, the use of IR compensation is subject to a great deal of ambiguity whether or not the faradaic process contributes to τ_{min}, even in the relatively simple case examined here. As the system becomes more complex, it would be necessary to derive expressions for $i(t)$ (for time domain analysis) allowing $Z_E(s)$ to take every possible form. This, of course, can be done. However, the resulting equations rapidly become unmanageable in a practical sense and would not in any case provide a good working method for the use of positive feedback. Further, in order to even develop working equations in the time domain, it is necessary to accurately know the analytical form of the input perturbation which may in general be difficult to estimate.

The above difficulties can be eliminated to a large extent by the use of the Transient Impedance Technique which allows $Z(s)$ to be examined. This quantity is obtainable in terms of the present study by the division of Eq. [12] for $E(s)$ by Eq. [10] for $i(s)$. The resulting expression is

$$Z(s) = \frac{E(s)}{i(s)} = R_e + R_i + Z_E(s) \quad [26]$$

in which it can be seen that only those quantities appearing across the potentiostat control points appear in the final results, positive feedback having no influence. This approach has been described in detail elsewhere (1, 5).

Conclusion

The above study indicates that the use of IR compensation in the presence of a faradaic reaction must be carried out with extreme caution. In general, faradaic time constants do contribute to the over-all system stability although under certain conditions their

contribution is not significant. It is, however, difficult to determine, even in an *a posteriori* manner, the amount of remaining uncompensated resistance, R_u. Thus experiments with a known system show the expected range of faradaic influence (involving considerable error even in this case if R_u had not been known); however, an unknown system certainly cannot be anticipated in such a manner. The problem now reduces to whether or not IR compensation should ever be employed. The answer depends on the manner in which the experiments are performed and, in particular, the way in which the results are interpreted. Thus, in time domain experiments, IR compensation should only be employed if it is known that the faradaic process is relatively slow and R_u can be unambiguously evaluated by using, *e.g.*, 80% τ_{min}. Note, however, that the slower the electrode reaction, the less necessary IR compensation becomes. In the classical (a-c) frequency domain, it has already been shown (1) that the use of the input perturbation $[v(s)]$ for phase reference necessitates the use of frequencies at least two orders of magnitude lower than that corresponding to τ_{min} for minimum error. This problem becomes more complex in the presence of Z_F. The use of positive feedback is rendered less ambiguous, particularly at high frequencies, if the results are interpreted using the Transient Impedance Technique (5). This is so since potentiostat parameters can conveniently be eliminated from the final impedance expression while the system is unmasked experimentally from the effects of R_e. Note that when this approach is employed, R_e is not reduced in any way in the final result; however, the experimentally accessible information content of the response function is greatly increased allowing much higher precision in the final results.

Manuscript submitted Sept. 3, 1970; revised manuscript received Jan. 18, 1971. This was Paper 310 presented at the Los Angeles Meeting of the Society, May 10-15, 1970.

Any discussion of this paper will appear in a Discussion Section to be published in the December 1971 JOURNAL.

REFERENCES

1. A. A. Pilla, R. B. Roe, and C. C. Herrmann, *This Journal*, **116**, 1105 (1969).
2. E. R. Brown, D. E. Smith, and G. L. Booman, *Anal. Chem.*, **40**, 1411 (1968).
3. E. R. Brown, T. G. McCord, D. E. Smith, and D. D. DeFord, *ibid.*, **38**, 1119 (1966).
4. R. DeLevie and A. A. Husovsky, *J. Electroanal. Chem.*, **20**, 181 (1969).
5. A. A. Pilla, *This Journal*, **117**, 476 (1970).
6. G. L. Booman and W. B. Holbrook, *Anal. Chem.*, **35**, 1793 (1963); **37**, 1322 (1965).
7. D. K. Cheng, "Analysis of Linear Systems," p. 262, Addison-Wesley, London (1959).
8. K. J. Vetter, "Electrochemical Kinetics," Academic Press, New York (1967).
9. P. Sturrock, Unpublished results.

Structural Transition in Strong-Acid Membranes

R. A. Wallace* and B. K. Jindal

Department of Materials Science and Engineering, Stanford University, Stanford, California 94305

ABSTRACT

To illustrate the effects of glass transition on ion transport in polystyrenesulfonate cation-exchange membranes, membrane d-c conductivities have been measured over a wide temperature range. Membranes were loosely crosslinked with 1% divinylbenzene and contained up to 10% by weight of styrene-sulfonic acid. Membrane conductivity obeys the Arrhenius equation with apparent activation energy values ranging from 11 to 16 kcal/mole in the glassy membrane and 15 to 22 kcal/mole in the rubberylike membrane. Computed diffusion coefficients of hydrogen ions increase with sulfonic acid content and are appreciably higher in the rubbery than in the glassy membrane states.

Membranes are widely used in electrodialytic desalting processes and electroseparation processes as ion-selective membranes and in fuel cells as solid electrolytes. Structural changes within membranes would likely cause marked changes in their mechanical and electrochemical properties. A very important structural transformation of amorphous materials, such as sulfonated polystyrene membranes, is glass transition. The temperature at which amorphous polymers when cooled solidify to a glass is called the glass transition temperature, T_g.

Above T_g, the polymeric membrane is soft and liquidlike because the chains are mobile; below T_g, it is hard and brittle on account of freezing in of chain segmental motion. Knowledge of membrane T_g and its influence on molecular rate transport might serve as a guide in improving membrane function and processes. In this paper, we present results of our T_g measurements and illustrate the effects of this structural transition on electrical transport within sulfonated polystyrene membranes of varying degrees of sulfonation.

* Electrochemical Society Active Member.

Key words: phase transition in membranes, cation-permeable membrane, hydrogen-ion transport.

For purposes of illustration, we prepared cation-exchange membranes containing up to 10% by weight of styrenesulfonic acid by sulfonating polystyrene films which were loosely crosslinked with 1% by weight of divinylbenzene. In these solid membranes, ion transport, under a d-c field, occurs primarily by migration of hydrogen ions resulting from dissociation of sulfonic acid groups (1). In correlating membrane T_g and ion conduction, the passage of mobile hydrogen ions under the influence of external electric field is considered as hopping from one sulfonate anion exchange site to the next. Ionic conduction is treated as a molecular diffusion process and is interpreted from a kinetic and thermodynamic view.

Experimental

Sulfonated polystyrene membranes containing up to 10% by weight of styrenesulfonic acid were prepared by casting a 20% solution of polystyrene (viscosity-average molecular weight of 500,000) in benzene on glass plates followed by sulfonation by the method of Chen *et al.* (2). Test membranes, 2 cm in diameter and 0.03 cm in average thickness, were dried under vacuum at 80°C prior to testing.

Membrane conductivities were measured over the temperature range 70°-170°C using a Keithley electrometer Model 610-Q, a Trigon Electronics d-c power supply Model HR40-750, and a guarded brass electrode assembly. The electrode assembly was placed in an electric oven maintaining temperatures within ±0.3°C. Membrane d-c conductivity σ was calculated from the equation $\sigma = (tI)/VA$ where t, I, V, and A are sample thickness, current, voltage, and electrode area, respectively. Tests were run at constant voltage of 10V d.c. Membranes were heated at a rate of 1°C per 2 min. Once a steady temperature was reached, current was recorded.

Results and Discussion

Membrane conductivity increases exponentially with temperature and is expressed by

$$\sigma = \sigma_0 \exp(-E_a/RT) \quad [1]$$

where E_a is the apparent activation energy of conduction and σ_0 a pre-exponential constant. Figure 1 shows the results of several membrane conductivity runs with sulfonic acid content as a parameter. Over the temperature and concentration range used, membrane conductivity obeys Eq. [1]; however, a break in the log σ *vs.* $1/T$ plot occurs to signify glass transition. Because the rate of increase of conductivity with temperature is faster above T_g than below T_g, E_a is greater in the liquid than in the glassy membrane states.

Table I lists values of apparent activation energies for the membrane ionic conduction process. These values vary from 11 to 16 kcal/mole in the glassy region and from 15 to 22 kcal/mole in the liquid region. Comparison with ionic conduction in liquid glasses yields good agreement (3). For AMF C-60 (polystyrenesulfonic acid entrapped in a polyethylene matrix) membranes, E_a is reported as 22 kcal/mole between 28° and 54 °C (1). In this temperature range, polyethylene is well above its T_g and explains why the reported E_a values agree well with our results.

Membrane T_g and conduction.—The influence of sulfonic acid concentration on membrane conduction is illustrated in Fig. 1. Membrane conduction increases with sulfonic acid content, apparently due to increasing concentration of hydrogen ions. On the other hand, membrane T_g rises with sulfonic acid content on account of progressively higher dipolar attractive forces within the membrane. T_g values are in good agreement with our correlation (2) obtained dilatometrically which is given by

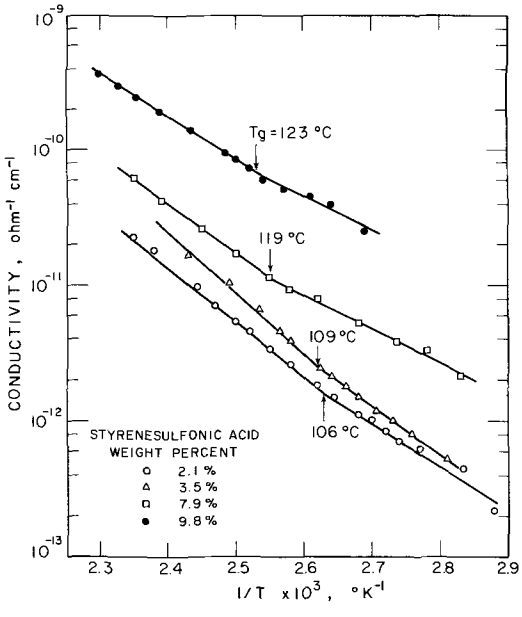

Fig. 1. Dependence of conductivity of sulfonated polystyrene membranes on temperature.

Table I. Apparent activation energies for conduction process below and above membrane T_g

Membrane T_g, °C	w/o of styrenesulfonic acid	E_g, kcal/mole	E_l, kcal/mole
100	0.0	16.4	21.0
106	2.1	14.2	17.9
109	3.5	16.3	21.8
118	8.1	15.8	21.6
119	7.9	11.2	17.5
123	9.8	11.3	15.7

$$T_g = T_{gB} + 200\, w_A \qquad (w_A < 0.15) \quad [2]$$

where T_{gB} is the glass transition temperature of loosely crosslinked polystyrene matrix and w_A is weight fraction of styrenesulfonic acid.

Ion conduction process.—The exponential temperature dependence of σ can be developed by treating the ionic diffusion process as a special case of the more general reaction rate theory for activated processes (4). Conduction under a unidirectional field involves the migration of hydrogen ions along the sulfonated polystyrene chains by hopping from one sulfonic acid site to the next. Midway between these two positions is the activated state, and hence the individual reaction to form the activated complex is: hydrogen ions (stable) → hydrogen ions (activated). Reaction rate theory provides us with the relation for diffusion coefficient of hydrogen as defined by Fick's law

$$D = \bar{\lambda}^2 \frac{RT}{Nh} \exp(\Delta S^{\ddagger}/R) \exp(-\Delta H^{\ddagger}/RT) \quad [3]$$

where λ, $\Delta H^{\ddagger}$, $\Delta S^{\ddagger}$, and N are effective jump distance of hydrogen ions in the direction of diffusion, enthalpy of activation, entropy of activation, and Avogadro's number, respectively. Combining Eq. [3] with the Nernst-Einstein relation (5) yields the expression for conductivity

$$\sigma = \frac{ce^2\bar{\lambda}^2}{h} \exp(\Delta S^{\ddagger}/R) \exp(-\Delta H^{\ddagger}/RT) \quad [4]$$

with c, e, and h as concentration of mobile hydrogen ions, electronic charge, and Planck's constant, respectively. The concentration of hydrogen ions depends on the degree of dissociation which, in turn, varies with moisture content and temperature. Dissociation is difficult for the membranes at hand because they contain only trace amounts of water. From Eq. [4] and the expression of Fuoss (6) for ion-pair equilibrium constant, we get

$$\sigma = \frac{\sqrt{c_0 K_0}\, e^2\bar{\lambda}^2}{h} \exp(\Delta S/R) \exp\left(-\frac{\Delta H^{\ddagger} + U/2}{RT}\right) \quad [5]$$

where c_0 is the total sulfonic acid concentration, K_0 is a constant, and U is the molar energy required in ion-pair separation in a dielectric. It should be noted that Eq. [5] predicts the conductivity-temperature relationship as given by Eq. [1] with

$$\sigma_0 = \frac{\sqrt{c_0 K_0}\, e^2\bar{\lambda}^2}{h} \exp(\Delta S^{\ddagger}/R) \quad [6]$$

and

$$E_a = H + U/2 \quad [7]$$

Using Eq. [6] we have estimated the transport entropy of activation of hydrogen ions (listed in Table II) in terms of the jump distance. To compute $\Delta S^{\ddagger}$, estimated values of $\bar{\lambda}$ should be used. For pure polystyrenesulfonic acid, Grubhofer (7) measured a value of 8.2 x 10^{-8} cm as the distance between adjoining sulfonic acid group. Since the chains are randomly distributed, $\bar{\lambda}$ in this case would be approximately 8.x

Table II. Estimated values of activation entropy for the membrane conduction process

T_g, °C	w/o of styrenesulfonic acid	$\bar{\lambda}^2 \exp(\Delta S^{\ddagger}/R)$ Below T_g	Above T_g
106	2.1	1.76×10^{-10}	1.81×10^{-8}
109	3.5	2.47×10^{-9}	3.9×10^{-6}
119	7.9	7.5×10^{-12}	2.51×10^{-8}
118	8.1	2.18×10^{-9}	3.32×10^{-6}
123	9.8	9.1×10^{-12}	1.08×10^{-8}

Table III. Calculated values of diffusion coefficients of hydrogen ions below and above T_g

Membrane T_g, °C	w/o of styrenesulfonic acid	$D\phi$, cm²/sec Diffusion coefficient × degree of dissociation $T = T_g - 30$°C	$T = T_g + 30$°C
106	2.1	7.4×10^{-16}	3.1×10^{-14}
109	3.5	6.8×10^{-16}	3.1×10^{-13}
119	7.9	2.5×10^{-15}	4.2×10^{-13}
118	8.1	1.2×10^{-15}	5.6×10^{-14}
123	9.8	1.4×10^{-14}	1.6×10^{-12}

$\times 10^{-8} \cos 45°$. On the assumption that the distance between sulfonic acid sites is roughly linearly proportional to sulfonic acid content, the effective jump distance in partially sulfonated membranes can be approximated. Thus for a membrane containing 9.8% of styrenesulfonic acid, $\bar{\lambda}$ is 7×10^{-7} cm and $\Delta S^{\ddagger}$ is 6.7 cal/mole $-$°K below T_g and 20.8 cal/mole $-$°K above T_g.

The highly positive values of entropy of activation of hydrogen ions within the solid charged membrane in its essentially dry state suggests that the activated state is much less ordered than the stable state. Furthermore, as pointed out by Boyd and Soldano (8), ionic diffusion may be accompanied by breakage of van der Waals bonds when $\Delta S^{\ddagger}$ is highly positive. Segmental motion above T_g would then explain the increase in $\Delta S^{\ddagger}$ as the membrane goes through its glass transition. For the wet membrane, on the other hand, ΔS tends to decrease. This is due in part to the negative contribution from the electro-restriction of water accompanying the separation of charge in forming the activated complex (8).

Table III lists values of diffusion coefficients of hydrogen ions in terms of degree of dissociation of sulfonic acid groups estimated from the Nernst-Einstein equation. These values show a rising trend in diffusion coefficients with greater sulfonic acid concentration. Glass transition results in an appreciably higher D value in the liquid state than in the glassy membrane. An estimate of D can be obtained by approximating ϕ using Fuoss's developed relation (6). For instance, for a membrane with 9.8% sulfonic acid content, setting the dielectric constant equal to 6, ϕ is 1.7×10^{-6} and D is 8×10^{-7} cm²-sec^{-1}.

Acknowledgment

The authors wish to thank the Office of Saline Water, Office of Naval Research, and the Stanford University Center for Materials Research for financial support.

Manuscript submitted Oct. 7, 1970; revised manuscript received *ca* Jan. 11, 1971.

Any discussion of this paper will appear in a Discussion Section to be published in the December 1971 JOURNAL.

REFERENCES

1. R. A. Wallace and C. S. Fadley, *This Journal*, **115**, 1264 (1969).
2. W. K. Chen, R. B. Mesrobian, P. J. Metz, and A. Glimes, *J. Polymer Science*, **23**, 904 (1957).
3. J. B. Birks and J. H. Shulman, "Progress in Dielectrics," Chap. V, McGraw-Hill Book Co., Inc., New York (1963).
4. H. Eyring, K. J. Liedler, and S. Glasstone, "Theory of Rate Processes," Chap. IV, IX, and X, McGraw-Hill Book Co., New York (1941).
5. P. G. Shewmon, "Diffusion in Solids," Chap. V, McGraw-Hill Book Co., New York (1963).
6. R. M. Fuoss, *J. Am. Chem. Soc.*, **80**, 5059 (1958).
7. N. Grubhofer, *Makromol. Chem.*, **30**, 96 (1959).
8. G. E. Boyd and B. A. Soldano, *J. Am. Chem. Soc.*, **75**, 6091 (1953).

Electrode Studies in Nonaqueous Electrolytes

III. The Sodium Electrode in $NaClO_4$-Propylene Carbonate Solutions

Stuart G. Meibuhr*

Electrochemistry Department, Research Laboratories, General Motors Corporation, Warren, Michigan 48090

ABSTRACT

The exchange current density (i_0) of smooth Na electrodes immersed in propylene carbonate solutions containing $NaClO_4$ or $NaPF_6$ was determined by galvanostatic methods. In 1*M* $NaClO_4$ the ΔH_0^* value = 14.6 kcal/mole. The i_0 value was strongly dependent on the Na^+ ion concentration, approximately 2 orders of magnitude decrease in i_0 with 1 order of magnitude decrease in Na^+. The results showed that the kinetics of the Na/Na^+ reaction in propylene carbonate are, at best, about equivalent to those for the Li/Li^+ electrode.

The number of studies of negative electrode materials in organic solutions recently has increased owing to the interest in nonaqueous electrolyte batteries. Lithium, magnesium, calcium (1-3), aluminum (2), and beryllium (4), all have been proposed and tested as negative electrode materials. Lithium amalgams in dimethylsulfoxide (DMSO) (5, 6) and calcium amalgams in propylene carbonate (PC) (7) were examined to determine both the activity of the metal in the amalgam and the standard electrode potential measured against a suitable reference electrode.

Electrode kinetic studies also have received attention. Kinetic studies of the $Li(Hg)/Li^+$ reaction in DMSO (8) yielded the standard rate constant in LiCl-DMSO solution at 25° of $(2.9 \pm 0.2) \times 10^{-5}$ cm/sec, a transfer coefficient value, α, of 0.75 ± 0.02, and an enthalpy of activation of 7.9 kcal/mole. Examination (9-11) of the solid Li/Li^+ electrode in $LiClO_4$-PC solutions resulted in values for the exchange current density (i_0) at 23° of about 0.7 mA/cm² (10, 11); α had a

* Electrochemical Society Active Member.
Key words: anodic polarization, kinetics, temperature effect.

Table I. The i_0 values for different experimental conditions

$NaClO_4$ concentration (M)	Temperature (°C)	i_0 (mA/cm²)
1.0	19	0.21
	37	0.90
	52	2.6
	66	6.77
0.5	19	0.012
0.1	19	0.0005

temperature independent value of two-thirds. These values occurred only at passivated electrodes (at low current densities). It has also been shown (12, 13) that these values are typical of Li electrodes which have been immersed into the solution for periods up to about 30 min regardless of the solute; i_0 values determined within 1 sec after a freshly cut Li surface was exposed to the solution showed higher i_0 values (12). At active electrodes, (higher current densities), i_0 was found to be equal to 1.78 ± 0.33 mA/cm² (11).

This note gives the results of a kinetic study of the previously ignored Na/Na^+ electrode in $NaClO_4$-PC solutions under experimental conditions that yielded reproducible polarization data.

Experimental

The PC solvent was purified by distillation as described before (14). The $NaClO_4$ solute was of the highest purity available (G. F. Smith Chemical Co.); it was dried at 120° in a vacuum for 4 days, cooled, and promptly transferred to a dry box. The $NaPF_6$ (Alfa Inorganics, Inc.) was used without further purification. The experimental procedure for the solution preparation, and the procedure and equipment used in making the galvanostatic polarization measurements have already been reported (10). The sodium electrodes were prepared in a dry box, manufactured by Vacuum Atmospheres Corporation, in a manner similar to a technique used for making a Pb electrode (15). A freshly polished Fe wire was used as the lead. Three such electrodes (0.06 cm²), served as test, counter, and reference electrodes.

The exchange current density was calculated for every current value with a computer program from the equation

$$i_0 = iRT/\eta_{(iR\text{-free})}F \qquad [1]$$

Reproducible i_0 values were obtained on new Na electrodes only after they were anodized for 10 min at 2 μA/cm². Electrodes so treated gave reproducible data for about 4 days before another anodization became necessary. The potential between the working and reference electrodes at open circuit remained <0.5 mV.

Results and Discussion

Figure 1 displays the linear anodic iR-free polarization data for a Na electrode in 1M $NaClO_4$-propylene carbonate solution for temperatures from 19° to 66°C. Duplicate runs yielded slopes that agreed with one another within 15%, which is somewhat poorer reproducibility than noted for the Li/Li^+ reaction (10). The i_0 variations with temperature and Na^+ ion concentration are recorded in the table. Note that the i_0 value decreased very sharply with a decrease in Na^+ ion concentration, approximately 2 orders of magnitude decrease in i_0 with 1 order of magnitude decrease in Na^+ ion. This decrease is greater than was observed for the Li/Li^+ reaction in ClO_4^- solution (10).

The solute $NaPF_6$ was considerably less soluble than the $NaClO_4$ and only very low i_0 values were obtained at Na electrodes in $NaPF_6$-PC solutions. At saturation, (about 0.3M), the i_0 value was 0.002 mA/cm² at 21°. The low i_0 values were not due to a high concentration of water because the Karl Fischer analysis showed that these solutions contained less than 30 ppm. Thus, the rapid decrease of i_0 with Na^+ ion concentration appears to be a real function of the concentration and not an artifact of some impurity such as water.

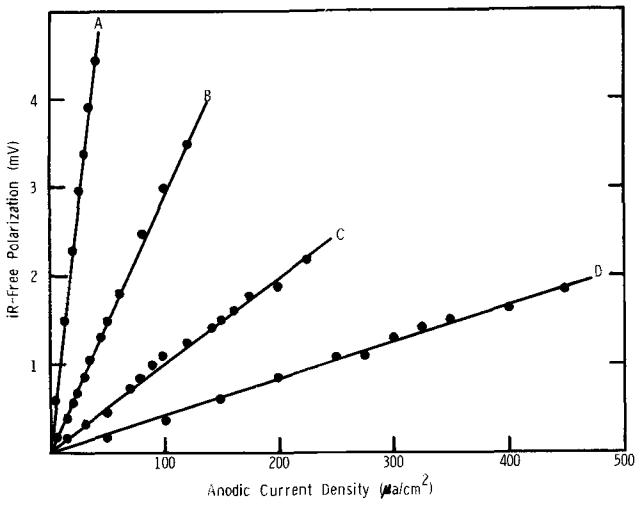

Fig. 1. Current density-iR free polarization data for a 1M $NaClO_4$ solution. Curve A, 19°C; B, 37°C; C, 52°C; D, 66°C.

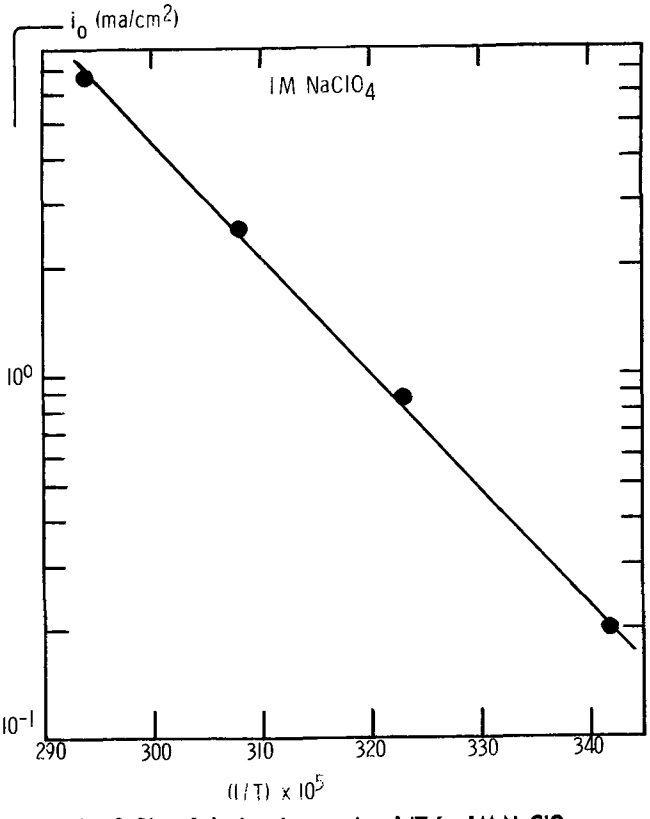

Fig. 2. Plot of the i_0 values against 1/T for 1M $NaClO_4$

The enthalpy of activation at zero polarization (ΔH_0^*) was calculated from the results of the temperature variation using the equation

$$\frac{\partial \ln i_0}{\partial (1/T)} = \frac{\Delta H_0^*}{R} \qquad [2]$$

A plot of the log i_0 against 1/T is exhibited in Fig. 2. The value for ΔH_0^* was 14.6 kcal/mole. This value, being somewhat higher than expected for metal dissolution (~10 kcal/mole), suggests that there may occur (a) reduction of the organic solvent or some other organic component such as ethylene carbonate; (b) adsorption of the solvent at the Na electrode interface; (c) some other process. However, no evidence of chemical degradation of the solvent was apparent at any temperature during the course of these experiments. No color change in the solvent, no blackening of the electrode, no gas evolution, all indicate that no chemi-

cal degradation occurred. Consequently, the unusually high ΔH_0^* value may be either real or due to adsorption.

To obtain reproducible polarization data on Na, it was necessary to anodize the test electrode. Electrodes, when immersed into the ClO_4^- solution, gave nonreproducible and very low i_0 values. A brief anodization (10 min at 2 $\mu A/cm^2$) activated the Na, perhaps by removing an oxide or hydroxide, and allowed reproducible data to be made. Subsequent brief cathodic pulses (for periods up to 10 min) did not destroy the active Na surface.

These results showed that the kinetics of the Na/Na^+ reaction in PC, at best, are about equivalent to those for lithium but are much more dependent on the Na^+ concentration than is the case for the Li reaction.

Manuscript submitted Aug. 21, 1970; revised manuscript received *ca.* Jan. 21, 1971.

Any discussion of this paper will appear in a Discussion Section to be published in the December 1971 JOURNAL.

REFERENCES

1. W. S. Elliott, S. L. Hsu, and W. I. Towle, *Proc. 18th Ann. Power Sources Conf.*, p. 82, Atlantic City, N. J. (1964).
2. J. Farrar, R. Keller, and C. J. Mazac, *ibid.*, p. 92, Atlantic City, N. J. (1964).
3. G. W. Jackson and G. E. Blomgren, *This Journal*, **116**, 1483 (1969).
4. R. E. Panzer, Paper 50 presented at the Detroit Meeting of the Society, Oct. 5-8, 1969.
5. D. R. Cogley and J. N. Butler, *This Journal*, **113**, 1074 (1966).
6. D. R. Cogley and J. N. Butler, *J. Phys. Chem.*, **72**, 1017 (1968).
7. J. N. Butler, *Electroanal. Chem. Interfacial Electrochem.*, **17**, 309 (1968).
8. D. R. Cogley and J. N. Butler, *J. Phys. Chem.*, **72**, 4568 (1968).
9. B. Burrows and R. Jasinski, *This Journal*, **115**, 365 (1968).
10. S. G. Meibuhr, *ibid.*, **117**, 56 (1970).
11. R. F. Scarr, *ibid.*, **117**, 295 (1970).
12. J. N. Butler, D. R. Cogley, and J. C. Synnott, *J. Phys. Chem.*, **73**, 4026 (1969).
13. S. G. Meibuhr, To be submitted for publication.
14. S. G. Meibuhr, B. E. Nagel, and R. Gatrell, *Energy Conversion*, **10**, 29 (1970).
15. T. F. Sharpe and S. G. Meibuhr, *J. Chem. Ed.*, **46**, 103 (1969).

Technical Notes

Differential Capacitance Study of Stress-Annealed Pyrolytic Graphite Electrodes

Jean-Paul Randin[1] and Ernest Yeager*

Chemistry Department, Case Western Reserve University, Cleveland, Ohio 44106

In recent years, high-pressure stress-annealed pyrolytic graphite has become available. This material has a near perfect orientation along the c-axis, and its structure is much more defined than that of the pyrolytic graphite used by prior workers (1). The basal plane of this material provides a rare opportunity to study the electrochemical properties of a surface in which all the surface valencies are satisfied in the plane of the surface.

The present study has been directed to the study of the differential capacity of this surface in aqueous solutions using an a-c impedance bridge.

Experimental Section

The stress-annealed pyrolytic graphite used in this study[2] showed a rocking curve whose mosaic spread is approximately 0.3° to 0.4° width at half-maximum intensity of the (002) x-ray diffraction line. The measured 2d interplanar spacing is 6.713 ± 0.002Å compared with 6.7078 ± 0.0002Å for the single crystal. The graphite electrodes were machined under compression into circular disks with a diameter of 5 mm. These graphite disks, backed with nickel to increase their mechanical strength, were then press-fitted into a Teflon holder. A fresh electrode surface was exposed for each experiment by placing a piece of plastic adhesive tape, cut to the exact size, in contact with the graphite surface and then peeling off a layer of graphite with the tape. Care was taken not to contaminate the Teflon surrounding the graphite disk with the adhesive on the plastic tape. The graphite surface so exposed had the appearance of a black mirror, and no plane other than the basal plane has been observed by microscopic examination under 800× magnification.

The electrochemical cell was made entirely of Teflon. The main compartment contained the working electrode and a 99.99% gold disk-shaped counterelectrode (9 cm diam, 0.01 cm thick), located parallel to the working electrode at a distance of about 4 cm with one side against the bottom of the Teflon cell. This electrode was used for only the a-c impedance measurements. Gold was chosen for the counterelectrode since it should not dissolve in helium-saturated sodium fluoride solutions. Two separate compartments were connected to the central compartment for the auxiliary and reference electrodes. The auxiliary electrode was used for the d-c polarization of the working electrode. Both the auxiliary and reference electrodes were 99.99% palladium foil (2.9 cm diam, 0.01 cm thick) over the rear of which was passed purified hydrogen. The reference electrode compartment was connected to the main compartment via a Luggin capillary, and the auxiliary compartment was connected to the main compartment by a short tube (1 cm diam, 5 cm long), filled with the same solution as the main compartment. The auxiliary and reference Pd electrodes were charged with hydrogen (purified with an Englehard

* Electrochemical Society Active Member.

Key words: graphite electrodes, differential capacitance, space charge, a-c impedance.

[1] Present address: Hydro-Quebec Institute of Research, Varennes, Quebec, Canada.

[2] Supplied by the Union Carbide Technical Center Research, Parma, Ohio 44130.

Industries Pd-Ag alloy diffuser) in order to form a stable H-Pd alloy, the β-phase (2).

The experiments were performed in a nitrogen atmosphere glove box to reduce contamination by atmospheric components and to minimize possible incorporation of dust and dirt in the cell. Nitrogen was continuously purged through the box.

The solutions of sodium fluoride (Baker Analyzed Reagent) were prepared by dissolution in nitrogen-saturated triple distilled water (second distillation from alkaline permanganate). Trace contaminants were removed by treatment of the electrolyte with purified active charcoal and *in situ* pre-electrolysis performed with a 50 cm^2 gold cathode in the main compartment polarized to $-0.9V$ *vs.* the H/β-Pd reference for at least 24 hr with helium bubbling. The helium was purified with copper turnings maintained at about 450°C and molecular sieves (Linde Type 3A and 13X). This gas was bubbled through the solution before and during the measurements.

The measurements of the equivalent series capacitances and resistances were carried out at 25°C with an a-c bridge and polarization circuit. This bridge has been checked with standard resistance and capacitance components and found to contribute a negligible error over the range of frequencies covered in this paper (100 Hz to 20 kHz). The a-c voltage applied to the cell did not exceed a few millivolts.

All capacitances are given in terms of apparent electrode area. The true area has not been taken into account, but the ratio of the true to apparent area should be essentially unity for the basal plane of stress-annealed pyrolytic graphite.

Results and Discussion

In a recent paper, Bauer, Spritzer, and Elving (1) studied the differential capacity of a pyrolytic graphite disk electrode whose structural characteristics were not defined in the paper. These authors observed a frequency dependence of both the series capacitance and resistance. Bauer *et al.* suggested that this frequency dispersion might be at least in part the result of the electrode geometry, since the distribution of current at a disk electrode is not uniform across the surface.

Preliminary measurements in the present study also showed a frequency dispersion. Consequently, an attempt was made to minimize the nonuniform current distribution on the disk solid electrode surface by using a Teflon hood of the type shown in Fig. 1. A circular lip, which made a line seal with the graphite electrode, was incorporated in the Teflon hood. The internal diameter of the hood (4 mm) was smaller than that of the graphite disk (5 mm). The depth of the hood was chosen to be the same as its diameter, *i.e.*, 4 mm. Preliminary tests showed that this dimension had no significant effect on the frequency dispersion.

Beside providing a more uniform current distribution on the electrode, the hood restricted the effective area of the electrode to the center of the disk and hence minimized problems associated with orientations other than the basal plane, present along the periphery of the disk where it fitted into the Teflon holder. Measurements on the edge orientation (plane perpendicular to the basal plane) indicate capacities of at least one order of magnitude higher than on the basal plane and hence even a small fraction of the surface other than the basal orientation can lead to a serious error.

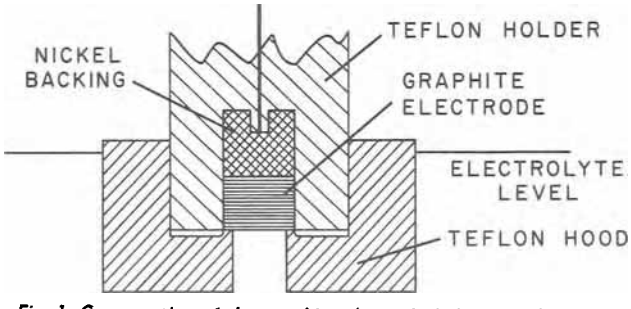

Fig. 1. Cross section of the graphite electrode holder and hood

The frequency dispersion for the basal plane of stress-annealed pyrolytic graphite in 0.9*M* NaF is shown in Fig. 2. Without the hood, the magnitude of the dispersion is comparable with that reported by Bauer *et al.* (1), although not as large. With the Teflon hood the frequency dispersion is negligible (see Fig. 2), provided the hood is slipped onto a freshly peeled dry electrode. On the other hand a small frequency dispersion is evident (see Fig. 2) if the hood is slipped onto a wet electrode, prepared by peeling off a layer from the basal plane under the surface of electrolyte in a separate container and then transferred wet within the N_2-filled glove box into the cell. This frequency dispersion is attributed to the electrolyte film between the graphite surface and the Teflon hood. When the two surfaces are dry, the small gap between the hood and the portion of the graphite covered by it does not normally fill with electrolyte because of the hydrophobic properties of the two surfaces.

Usually the capacity measured on the electrode peeled off dry was lower than that of the same electrode peeled off under the electrolyte. The reproducibility of the capacity at a given frequency also was less with electrodes peeled in either air or the nitrogen within the glove box rather than under the surface of the electrolyte. Under extreme conditions, the variation in capacity was as much as 100% with the electrodes peeled dry as compared with a variation of only 5% for electrodes peeled wet. Consequently all further measurements reported in this paper have been carried out with electrodes peeled off under electrolyte and the hood subsequently slipped on.

The lack of any appreciable frequency dispersion in 0.9*M* NaF on the basal plane of stress-annealed pyrolytic graphite with the Teflon hood is to be expected for a solid electrode provided the surface roughness is small. The mirrorlike appearance of the surface with direct visual examination as well as microscope examination (800×) both imply that surface roughness is very small. In the case of a semiconductor electrode (see the following discussion), the lack of frequency dispersion at audio frequencies also implies either that the surface electronic states contribute very little to the observed capacity on the basal plane or that the surface electronic states have very short or very long relaxation times.

The capacity measured at a fixed potential on the basal plane also decreased slowly with time. This decrease was usually smaller than 3% in 15 min with electrodes peeled wet while the series resistance remained virtually constant. This rate of decrease did not vary significantly with the applied potential in the range $+0.5$ to $-0.5V$ re NHE, with the frequency in the range 100 Hz to 20 kHz, or with stirring. The rate

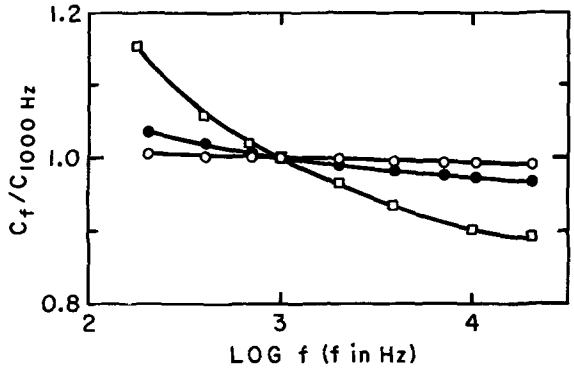

Fig. 2. Frequency dependence of capacity for the basal plane of stress-annealed pyrolytic graphite in 0.9M NaF at 25°C at a potential of +0.2V *vs.* NHE: □ without hood, layer peeled off under electrolyte; ○ with hood, layer peeled off dry; ● with hood, layer peeled off under electrolyte.

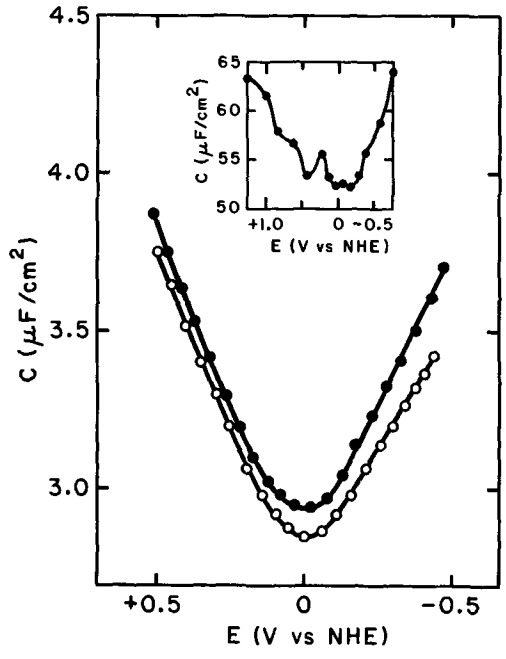

Fig. 3. Capacity-potential curves for the basal plane of stress-annealed pyrolytic graphite in NaF (pH $\simeq$ 6) at 25°C and 1000 Hz. With hood, layer peeled off under electrolyte: ●, 0.9M NaF; ○, 0.1M NaF. Insert figure: Bauer, Spritzer, and Elving (1) data in 0.5M KCl; resurfaced by polishing; frequency: 1000 Hz.

of decrease was smaller with electrodes peeled off under electrolyte than peeled dry.

Since the time dependence of the capacity on the basal plane of wet peeled electrodes was so small, the capacity-potential curves measured point by point were essentially the same regardless of whether the values were measured with increasingly anodic or cathodic potentials. The values indicated in Fig. 3 were recorded point by point with potential increasing in the anodic direction. The shape of the capacity-potential curve is nearly symmetrical with respect to the minimum, is independent of the concentration of the electrolyte at concentrations in the range 0.01 to 1.0*M*, and does not exhibit the hump usually observed on metallic electrodes. The shape of the capacity-potential curve does not depend significantly on the way the electrode surface has been renewed (peeled wet or dry).

The series equivalent resistance was also measured but is not reported. Within the accuracy of the measurements, the data showed no significant variation with potential (*i.e.*, a variation of approximately 1 to 3 ohms out of 100 ohms over the potential range +0.5 to −0.5V *vs.* NHE).

The value of the apparent capacity at the minimum of the capacity-potential curve is low, *i.e.*, ~3 μf/cm^2, compared with values usually higher than 15 μf/cm^2 for metallic electrodes. In contrast, the apparent capacity at the minimum of the capacity-potential curve is about 16 μf/cm^2 for the polished basal plane of ordinary pyrolytic graphite ($\Delta\theta_{1/2} \simeq 40°$). Furthermore, the minimum capacity is 50 to 70 μf/cm^2 for the polished edge orientation of stress-annealed pyrolytic graphite ($\Delta\theta_{1/2} \simeq 0.4°$).

Table I compares the capacity data for ordinary and stress-annealed pyrolytic graphite obtained by Bauer *et al.* (1) and in the present study. Bauer *et al.* (1) reported values ranging from ~12 μf/cm^2 for the surface prepared by cleaving to ~60 μf/cm^2 for the polished basal plane of ordinary pyrolytic graphite measured at 1000 Hz. The insert in Fig. 3 gives the capacity-potential curve based on the data reported by these authors. The minimum value of the capacity as well as the potential dependence reported by these authors deviate substantially from that found on the

Table I. Comparison of capacity data for ordinary and stress-annealed pyrolytic graphite

	Bauer *et al.* (1)	Present work
Ordinary pyrolytic graphite		
Basal plane, cleaved	12 μf/cm^2	—
Basal plane, polished	60	16 μf/cm^2
Stress-annealed pyrolytic graphite		
Basal plane, peeled off	—	3
Edge orientation, polished	—	50–70

basal plane of stress-annealed pyrolytic graphite in the present study. The minimum value of the capacity reported by Bauer *et al.* for the polished basal plane of ordinary pyrolytic graphite, *i.e.*, ~60 μf/cm^2, should be compared with ~16 μf/cm^2 found in the present study for the same orientation of polished ordinary pyrolytic graphite. The different origin and preparation of the sample are probably responsible for the discrepancy.

The capacity measured on the basal plane of the graphite specimens with very small rocking angles (*e.g.*, $\Delta\theta_{1/2} \simeq 0.4°$) should approach the value for this plane on single crystal graphite. The minimum capacity of ~3 μf/cm^2 observed on the basal plane of such stress-annealed pyrolytic graphite is far too low to be explained on the basis of the usual ionic double layer structure within the electrolyte.

The differential capacitance of a semiconductor or semimetallic electrode-electrolyte interface is composed of three series components: the capacitance of the space charge layer within the semiconductor, that of the compact double layer, and that of the diffuse ionic layer of the electrolyte. For electrolytes of high concentrations, *e.g.*, 1*M*, the capacitance of the diffuse ionic layer is usually large, *i.e.*, >100 μf/cm^2, compared with the other two components. In this case, its contribution to the total capacitance is therefore negligible. The capacitance associated with the compact layer is expected to have a value of 10 to 20 μf/cm^2 in the absence of surface states on the basis of the values encountered with metal electrodes. The capacity of the compact double layer on the basal plane of graphite may differ appreciably from this value due to the nonpolar nature of the graphite surface, but it seems quite unlikely that this difference would amount to almost an order of magnitude. Consequently, the low observed capacity is best attributed to the space charge component within the graphite.

Unfortunately, the electrical properties (resistivity, carrier concentrations, and mobilities) are not known specifically for the materials used in the present study. For similar stress-annealed pyrolytic graphite, Spain *et al.* (3) have reported a resistivity in the basal plane of ~40 μohm/cm and a charge carrier mobility of 1.2 10^4 cm^2/V-sec at room temperature. In contrast, along the c-axis the resistivity of the same material is 0.15 ohm-cm according to the same authors. For heat-treated pyrolytic graphite without stress-annealing, the charge carrier mobility along the c-axis has been reported (4) to be ~3 cm^2/V-sec at room temperature. Also at room temperature, the following total carrier concentrations have been reported: for naturally occurring graphite single crystals, 9.9 to 10.1 · 10^{18} carriers/cm^3 (5); for heat-treated pyrolytic graphite, 1.2 · 10^{19} (4), 1.1 · 10^{19} (6), and 1.4 · 10^{19} carriers/cm^3 (7). The ratio of the mobility of the electrons to that of the holes ($b = \mu_e/\mu_h$) was found to be 1.1 at room temperature (3, 5, 6) for both heat-treated and stress-annealed pyrolytic graphite.

The theory of semiconductor electrodes indicates that the capacitance of the space charge layer in a pure intrinsic semiconductor should exhibit a minimum value given by the expression (8)

$$C_o = \left[\frac{2\epsilon\epsilon_o e^2 c}{kT}\right]^{1/2} \qquad [1]$$

with the dependence of the capacity on potential given as:

$$C_{sc} = C_0 \cosh\left(\frac{\phi e}{2kT}\right) \quad [2]$$

where ϵ = dielectric constant
ϵ_0 = permittivity
e = absolute value of electronic charge
c = electronic charge carrier density
k = Boltzmann's constant
T = absolute temperature
ϕ = potential at the surface

The only values apparently available for the dielectric constant are those from optical measurements rather than at audio frequencies. According to Ergun *et al.* (9) the value of ϵ at 5461Å in the basal plane is 2.61 and along the c-axis is 3.28.

Using the value of 6.10^{18} carriers/cm^3 (mean value from Ref. 4, 6, and 7) for the electronic carrier concentration and 3 for the dielectric constant (9), C_0 is 4.5 μf/cm^2 as compared with $\sim$3 μf/cm^2 for the experimental value.

The comparison of the calculated C_0 value with the experimental value is reasonable, considering the uncertainty as to c and ϵ. The potential dependence of the space charge capacity represented by Eq. [2], however, is much greater than that observed experimentally in Fig. 3. Possible factors responsible for this discrepancy are (I) Imperfections on the exposed basal plane that give rise to sites other than those with completely satisfied valencies and result in degenerate surface electronic states. In the case of germanium electrodes, Gerischer (10) has given a theoretical treatment which shows that the space charge capacity depends relatively little on polarization in the potential region of surface degeneracy. (II) The applicability of the presently available semiconductor theory to a system such as graphite with a total carrier concentration as high as 10^{19} carriers/cm^3 and hence with Debye lengths comparable to the lattice dimensions is open to serious question.

In order to explore further the importance of the semiconductor properties of graphite in controlling the observed differential capacitance, measurements are being undertaken with boronated stress-annealed pyrolytic graphite which exhibits p-type semiconducting characteristics. Studies involving the effect of anions which normally specifically adsorb on ordinary electrodes, for example, iodide, are also in progress and will be reported later.

The data included in this paper show that the differential capacitance of the basal plane of stress-annealed pyrolytic graphite-electrolyte interface is quite abnormal and that the space charge characteristics of graphite must be taken into account in examining the electrochemical properties of this material.

Acknowledgment

The authors are pleased to acknowledge the support of this research by the U. S. Office of Naval Research. One of the authors (J.P.R.) thanks the Stiftung für Stipendien auf dem Gebiete der Chemie, Basel, Switzerland, for the award of a research fellowship. The authors also express appreciation to the Union Carbide Technical Center, Parma, Ohio and to Dr. A. Moore of that laboratory for providing the various pyrolytic graphites used in this study.

Manuscript submitted Oct. 29, 1970; revised manuscript received *ca.* Jan. 28, 1971.

Any discussion of this paper will appear in a Discussion Section to be published in the December 1971 JOURNAL.

REFERENCES

1. H. H. Bauer, M. S. Spritzer, and P. J. Elving, *J. Electroanal. Chem.*, **17**, 299 (1968).
2. D. J. G. Ives and G. I. Janz, "Reference Electrodes," pp. 112-116, Academic Press, New York (1961).
3. I. L. Spain, A. R. Ubbelohde, and D. A Young, *Phil. Trans. Roy. Soc. London, Ser. A*, **262** (1128), 345 (1967).
4. C. A. Klein, *J. Appl. Phys.*, **33**, 3338 (1962).
5. D. E. Soule, *Phys. Rev.*, **112**, 698 (1958).
6. C. A. Klein and W. D. Straub, *ibid.*, **123**, 1581 (1961).
7. C. A. Klein, *Rev. Mod. Phys.*, **34**, 72 (1962).
8. K. Bohnenkamp and H. J. Engell, *Z. Elektrochem.*, **61**, 1184 (1957).
9. S. Ergun, J. B. Yasinsky, and J. R. Townsend, *Carbon*, **5**, 403 (1967).
10. H. Gerischer, "Semiconductor Electrode Reactions," in "Advances in Electrochemistry and Electrochemical Engineering," P. Delahay, Editor, Vol. 1, p. 139, Interscience Publishers, New York (1961).

The Hydrostatic Pressure Dependence of the Ionic Conductivity of β-Aluminas

R. H. Radzilowski and J. T. Kummer

Scientific Research Staff, Ford Motor Company, Dearborn, Michigan 48121

Single crystals of Na β-alumina with the idealized formula $Na_2O \cdot 11Al_2O_3$ exhibit a specific conductivity of $\sim 3 \times 10^{-2}$ (ohm-cm)$^{-1}$ at 25°C (1) due to the rapid two-dimensional diffusion of Na^+ ions in a direction perpendicular to its hexagonal c-axis. The two-dimensional motion of the Na^+ ions takes place in a slot formed by two close-packed oxygen layers which are perpendicular to the c-axis and are held 4.76Å apart by Al-O-Al bridges. Based on the measured diffusion coefficient for various ions in ion-substituted β-alumina (1) it appears that for ions larger than Na^+ the monovalent cation diffusion coefficient is smaller than for Na^+ and the activation energy for diffusion is larger. This can be explained qualitatively by repulsion between the electron clouds of the ion and the oxygen ions above and below the mobile monovalent cation as that cation moves in the lattice. The larger the cation, the lower the diffusion coefficient. Thus, the K^+ ion diffuses slower than the Na^+ ion, and the Rb^+ ion diffuses slower than the K^+ ion. For the Li^+ ion, however, the diffusion coefficient also is smaller than for Na^+ ion. In this case the evidence (1) is that the Li^+ ion does not sit near the midplane position equidistant from the close-packed oxygen planes above and below the cation as Na^+ and the larger ions do, but because of its smaller size is located close to one or the other oxygen planes in a potential well formed by its three nearest oxygen neighbors. This position leads to an increase in the c-axis dimension, as can be seen in Table I,

Key words: potassium β-alumina, lithium β-alumina, high-pressure apparatus.

Table I. Lattice constants of β-alumina and ion-substituted β-alumina (1)

Ion radii A	Ion	a (A)	c (A)
0.60	Li^{+a}	5.593	22.570
0.95	Na^+	5.594	22.530
1.33	K^+	5.596	22.729
1.40	$O^=$		

[a] The lattice constants of Li-substituted β-alumina were determined under anhydrous conditions and differ from Ref. (1).

since the maximum force pulling the two oxygen planes together is obtained when the monovalent cation is midway between the two oxygen planes.

The motion of the Li^+ ion through the slot made by the two oxygen planes would experience, in addition to the electrostatic barriers seen by the Na^+ ion, an additional energy barrier required to move the Li^+ ion from the potential well formed by its three nearest neighbors. This picture is in agreement with the lower diffusion coefficient and higher activation energy for the Li^+ ion than for the Na^+ ion found (1) experimentally for diffusion in the β-alumina structure. This picture would also lead to the conclusion that hydrostatic pressure applied to β-alumina should decrease the diffusion coefficient or ionic conductivity of the ions larger than Na^+, which experience electron cloud repulsion when moving through the lattice, and increase the diffusion coefficient or ionic conductivity of the Li^+ ion because a closer arrangement of the two oxygen layers would enable the Li^+ ion to sit less tightly in its potential well and move towards the midplane position.

This paper reports some experiments made in an effort to support this picture by measuring the effect of hydrostatic pressure on the ionic conductivity of single crystals of Na β-alumina and K and Li ion-substituted β-alumina.

Experimental Section

The single crystals of β-alumina used in this work were obtained from fusion cast bricks, Monofrax H, Harbison Carborundum Co., Falconer, New York. The K- and Li-substituted β-aluminas were made by the ion exchange of Na β-alumina in a melt of KNO_3 and Ag-substituted β-alumina in a eutectic melt of LiCl-$LiNO_3$, respectively, as described by Yao and Kummer (1). An analysis of the crystals by atomic absorption and x-ray fluorescence spectroscopy showed that the exchanges were 99% complete. The Li-β-alumina was found to be extremely hygroscopic, and thus the crystals were handled under argon gas dried with molecular sieves.

The crystals of β-alumina were prepared for resistivity measurements by attaching Pt wire leads to the crystals (2 mm wide × 3 mm long × 0.2 mm thick) with a thin film of platinum. The platinum electrodes were formed by coating the opposite edges of a crystal with Engelhard platinum resinate solution and baking the crystal in air at 400°C for one hour. This procedure was repeated after applying a small droplet of Engelhard liquid gold over the platinum electrodes to insure good electrical contact. Excess platinum was removed from the crystals by scratching or sanding the surface of the crystals.

Hydrostatic pressures up to 4100 atm were produced by a hydraulic press acting on the piston of the assembly shown in Fig. 1. Kerosene dried with Linde molecular sieves acted as the pressure transmitting fluid. The pressure produced in the 10 cm^3 cavity of the cell was monitored with a manganin coil calibrated against the freezing pressure of mercury at 0°C. In a test run a Fe-Cu thermocouple was mounted in place of the manganin coil and the changes in temperature in the kerosene-filled cavity were followed at intervals of 500 atm up to 4000 atm of pressure. A close-fitting aluminum block surrounded the steel cell in order to help dissipate the heat generated during the compression of the kerosene. The temperature rose 3°-8°C at each pressure interval but dropped to the block temperature within 12 min. In actual runs, the manganin coil was activated for only a few seconds after the system reached equilibrium in order to prevent a rise in temperature, calculated to be small even if the coil were left on because of heat generated by the current-carrying coil. The temperature of the steel block was measured during runs with a chromel-alumel thermocouple placed in a kerosene-filled well in the top of the block.

The resistivity and capacitance of the crystals were measured on a Wayne Kerr radio frequency bridge, Type B.601 with a Tektronix Type 190B constant amplitude signal generator operated in the frequency range of 0.55-1 MHz. A tuned null detector, General Radio Type 1232-A, coupled with the IF circuit of a communications receiver, Allied Model A-2515, allowed precise balancing of the bridge. The specific resistivity of a crystal of Na β-alumina containing 5 w/o (weight per cent) Na was 44 ohm-cm at 23° with the Au-Pt electrodes. This resistivity measured at 1 MHz was 7% lower than that found at 0.55 MHz. The specific resistivities of Li- and K-substituted β-alumina at 1 MHz and 23° were 1200 and 5200 ohm-cm, respectively. The capacitance of the crystals with

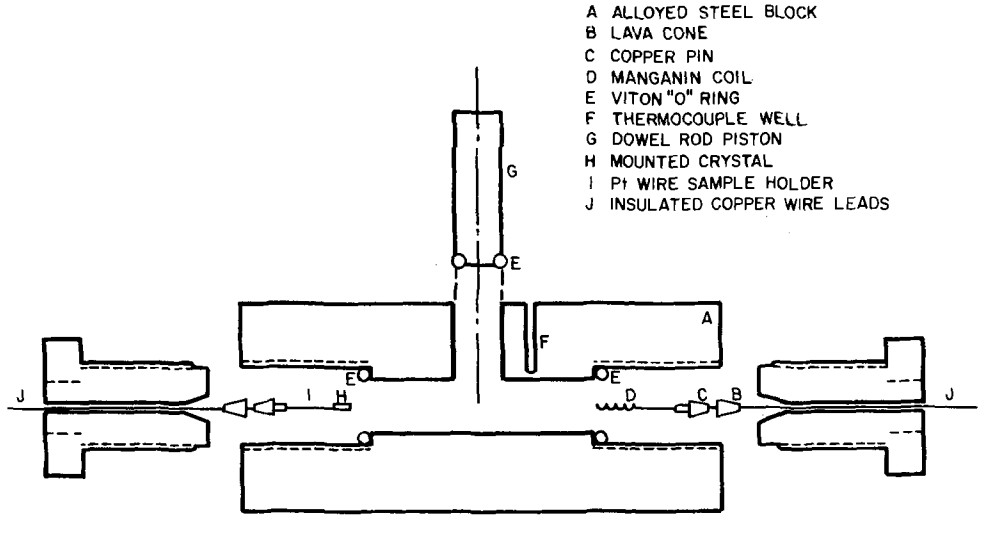

Fig. 1. A sectional view of the pressure cell

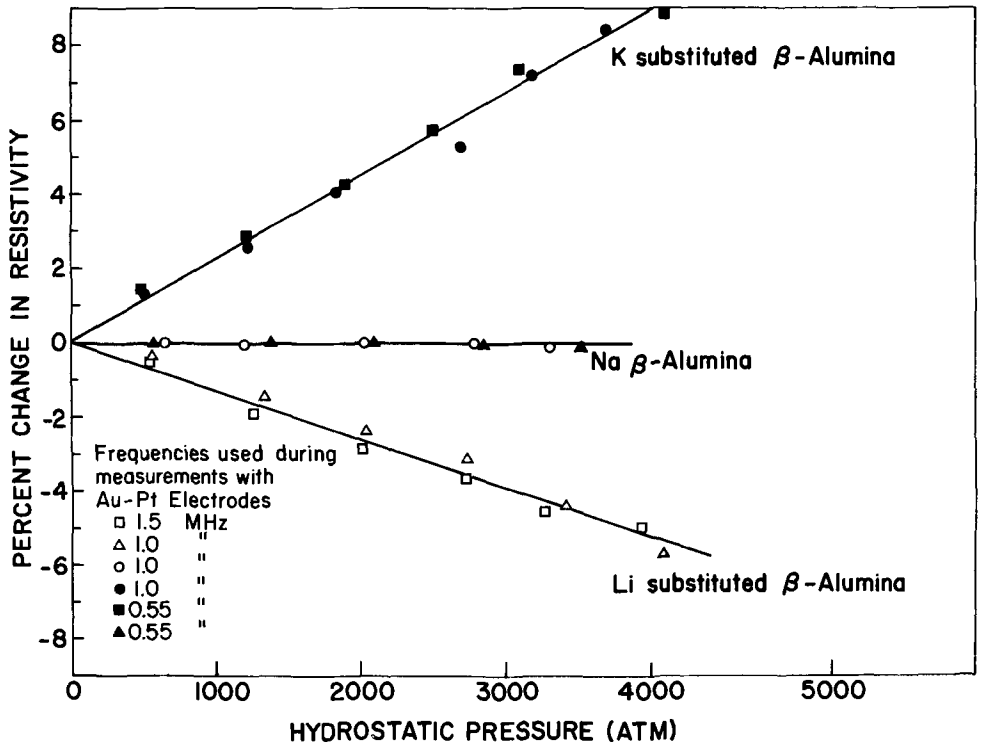

Fig. 2. The change in ionic resistivity of β-alumina and ion-substituted β-alumina with pressure

platinum wire leads varied between 9 and 23 pF at at 1 MHz.

Results and Discussion

The pressure dependence of the ionic conductivity of Na β-alumina and of the two ion-substituted β-aluminas is shown in Fig. 2. The results are qualitatively in agreement with what was expected. The activated state theory of reaction rates as applied to ionic diffusion (2) uses the concept of an activation volume of motion associated with the jump of a cation from site to site. This activation volume is the volume change due to the dilatation or contraction of the crystal lattice in the vicinity of the mobile cation when the diffusing ion sits in the saddle-point configuration.

In order for a monovalent cation to move through the β-alumina structure, it must move through the crystallographic site which is in the center of an equilateral triangle formed by nearest-neighbor normal cation sites. This point in the motion of the cation from cell to cell produces the smallest oxygen to cation distance. There are two oxygen ions above and below the cation as it moves through this site, 4.76Å apart for Na β-alumina and 4.86Å apart for K-substituted β-alumina. The Na^+ ion with an ion size of 0.95Å moves through this site without serious steric hinderance, whereas the K^+ ion (1.33Å) requires lattice expansion. The curves in Fig. 2 indicate a positive activation volume for K-substituted β-alumina and a 0 activation volume for Na β-alumina. Li-substituted β-alumina has a negative activation volume. In its motion from cell to cell it moves some distance out of its potential well toward the midplane, causing a local contraction of the lattice.

A quantitative explanation of the results in Fig. 2 cannot be made since we know only one compressibility (Na β-alumina's c-axis compressibility is $\sim 2 \times 10^{-7}$ atm^{-1}) and we lack an adequate theory. In addition, although the Pt electrodes seem quite adequate it would be desirable to cross-check the results with some electrodeless conductivity (or diffusion) measurement if this could be devised.

Manuscript received Dec. 14, 1970.

Any discussion of this paper will appear in a Discussion Section to be published in the December 1971 JOURNAL.

REFERENCES

1. Y. F. Yu Yao and J. T. Kummer, *J. Inorg. Nucl. Chem.*, **29**, 2453 (1967).
2. N. H. Nachtrieb, J. Weil, E. Catalano, and A. W. Lawson, *J. Chem. Phys.*, **20**, 1189 (1952).

JOURNAL OF THE ELECTROCHEMICAL SOCIETY

SOLID STATE SCIENCE

MAY 1971

An O^{18} Study of the Source of Oxygen in the Anodic Oxidation of Silicon and Tantalum in Some Organic Solvents

M. Croset

Centre de recherches SESCOSEM, Corbeville par Orsay-91-France

and E. Petreanu and D. Samuel

Isotope Department, The Weizmann Institute of Science, Rehovot, Israel

and G. Amsel and J. P. Nadai

Groupe de Physique des Solides de l'Ecole Normale Supérieure, Tour 23; 9, quai Saint-Bernard, Paris 5e, France

ABSTRACT

The anodic oxidation of silicon and tantalum in organic solvents containing small quantities of dissolved salts (KNO_2 and KNO_3) and water has been studied. The source of oxygen in the oxide layer has been determined using O^{18}-labeled materials. The isotopic exchange of oxygen between the various components of the electrolyte under thermal and electrolytically induced conditions was measured using mass spectrometric analysis and found to be extremely slow. Nuclear methods of analysis of isotopic oxygen were used to determine the source of oxygen in the oxide layer on both metals. It was found that over 80% of the oxygen of the oxide comes from water, the rest from the salt. The small extent of incorporation of nitrogen-containing anions in the oxide layers was also measured by a nuclear method.

A detailed study of the anodic oxidation of silicon has been undertaken in order to elucidate the phenomena occurring both in the electrolyte and in the growing oxide film. These phenomena have already received considerable attention in the literature and were first studied in 1957 in N-methylacetamide[1] solutions of KNO_3 and other salts by Schmidt and Michel (1). Since then, Duffek *et al.* have studied this process both in NMA (2) and in glycol (3) for various salt and water concentrations. In addition to the classical methods of investigation used by these authors we have resorted to a special technique developed to study anodic oxidation, *i.e.*, microanalysis by means of nuclear reactions (4-7). The latter enables the precise determination of the oxygen content of oxide films and the investigation of the mechanisms of formation using O^{18} as a tracer.

Our study was aimed primarily at determining the source of the oxygen contained in the films. This can be the solvent, the salt, or traces of water in the solution, or a combination of these. Either NMA or glycol were used as solvents, containing small quantities of KNO_3 and water. For some experiments in glycol, KNO_2 was used. Either the water or the KNO_3 used were labeled with O^{18}.

Key words: anodic oxidation, silicon, tantalum, oxygen source, O^{18} tracing, isotopic exchange, organic solution, water, salt.

[1] In what follows, the abbreviation NMA will be used for N-methylacetamide.

In addition to the anodic oxidation of silicon, the same process on tantalum was also studied in order to investigate the similarities and differences in behavior of the two metals. The reasons for using tantalum are its ready oxidation in the above electrolytes, the high current efficiency of the oxidation process, and low field of formation as compared to silicon.

Once the source of the oxygen in anodic oxidation has been determined, the mechanisms of ionic transport in the films can be elucidated. This will be the subject of a further paper, although preliminary results on field-induced self-diffusion in anodic silicon oxide has been published recently (6). The aim of the present work was also to help in determining the optimal conditions of oxide film formation so as to make anodic oxide film production competitive with thermal growth methods.

Experimental

Preparation of samples to be oxidized.—Samples of p-type silicon were used, with a resistivity of about 0.1 ohm·cm. The surface of the silicon wafers polished by a mechano-chemical process, was cleaned before oxidation using classical methods: degreasing with trichloroethylene, rinsing, removal of the oxide layers with hydrofluoric acid, and finally rinsing with hot water (of resistivity greater than 15 megohm·cm) and air drying. The tantalum samples were cut from 0.2 mm thick rolled sheets with a highly polished surface,

supplied by Fansteel Corporation, with a stated purity 99.9%. The tantalum samples were cleaned with trichloroethylene, washed with methanol, and air dried.

Preparation of labeled compounds.—O^{18}-enriched water from the Isotope Separation Plant of the Weizmann Institute was used. This water, obtained by fractional distillation, is also highly enriched in deuterium. In order to eliminate both chemical and nuclear isotope effects this water was "normalized" so as to contain less than 0.1% deuterium by the method of Zhavoronkov [see ref. (8), p. 38]. In all cases, the water was purified by distillation first from permanganate and then under reduced pressure in silica vessels. For the anodic oxidation experiments the water used had the approximate isotopic concentration 88% O^{18}, 0.5% O^{17}, 11.5% O^{16}. Various high O^{18} concentrations were used for exchange experiments.

O^{18}-labeled potassium nitrate was prepared by acid catalyzed exchange with water, by the method of Anbar *et al.* (9), and contained 77% O^{18}. The salt used was shown to be free of any O^{18}-labeled water by dissolving it in the minimum quantity of water depleted in O^{18} [*i.e.*, containing 0.007 a/o (atom per cent) oxygen^{-18}, thirty times less than natural abundance]. On distilling the water and analyzing it for O^{18}, it was found to be unchanged in isotopic content.

In certain experiments made in order to examine the effect and quantity of residual water in "dry" solvents, "washed NMA" and "washed glycol" were prepared. In each case *ca.* 2 ml highly enriched H_2O^{18} was added to *ca.* 50g organic solvent of the best quality available and the solvent dried by repeated fractional distillation, the final product having a water content of less than 0.05%.

Preparation of organic solutions.—Most of the solutions used contained 0.4% water and 0.4% salt by weight. This salt content insures that the solution has a resistivity (which appeared to be independent of the water content) convenient for easy oxidation. In addition, preliminary studies showed that the optimal water content for the formation of high-quality silicon oxide films for semiconductor devices is in the vicinity of 0.4%.

When isotopically enriched materials were used, the weight of labeled components was increased in proportion to their molecular weight, so as to insure that the same number of molecules were present in both labeled and unlabeled solutions.

In all NMA solutions KNO_3 was used. However, difficulties were encountered in oxidizing tantalum in glycol using KNO_3, when the water content was less than 2%. In particular, it was impossible to reach high anodic voltages, since breakdown occurred at about 20V. These difficulties could be overcome by using KNO_2, as was done in a number of experiments with glycol solutions.

The solvents used (NMA from Eastman Kodak and glycol from Merck) were purified by double fractional distillation at reduced pressure through a column of molecular sieves. NMA was distilled at 60° ± 0.5°C, and glycol at 55° ± 0.5°C. The final product, containing less than 0.02% by weight of water (see later), was distilled directly into the electrolytic cell. The KNO_3 was dried on a vacuum line at 100°C for 24 hr; the less stable KNO_2 *in vacuo* at room temperature for several days.

It should be noted that very small traces of impurities such as fluorides may have a deleterious effect on the anodic oxidation of silicon. These trace contaminants are not removed by the purification processes described above, so that certain batches of solvents had to be rejected, especially in the case of glycol.

Electrolyte solutions containing known quantities of O^{18}-labeled water had to be prepared with great care, since any water accidentally introduced will immediately dilute the isotopic content of the enriched water.

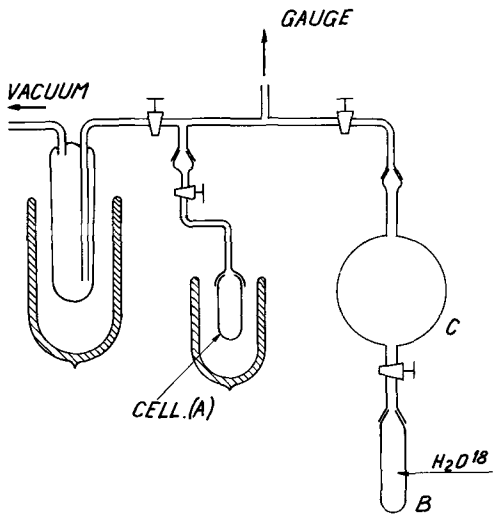

Fig. 1. Vacuum line used for transfer of O^{18} labeled water. A is electrolysis cell; B, H_2O^{18} reservoir, C, bulb for determining the quantity of water.

This could happen easily, since the solvents used were found to be very hygroscopic. It was, therefore, essential to transfer all distillable liquids on the vacuum line shown in Fig. 1. The dried, weighed salt (KNO_3 or KNO_2) is placed at the bottom of an electrolytic cell (A), which is then filled first with *ca.* 30 ml of "dry" solvent by distillation. The solvent is then carefully degassed and a given quantity of labeled water (determined by the volume of the bulb C and the saturation pressure of water at the temperature of the reservoir B maintained at 26°C) is transferred from the reservoir (B) to (A) by cooling the latter in liquid nitrogen. To prevent condensation of water vapor on other surfaces, the entire apparatus is kept at about 28°C. This enables the transfer of 60 mg of ordinary water (or its labeled equivalent) in each operation; the desired water content being obtained by repeating the above operation as many times as necessary. The problem of residual water in the solvent will be discussed later. The cell is then filled with dry argon, the cathode and samples to be oxidized are placed in position in a dry box, and the cell is ready for use.

For solutions of natural isotopic oxygen composition or for those containing an O^{18}-labeled salt, water was simply added using a microsyringe. In all cases, the total quantity of water in the electrolyte was determined just before oxidation as described below.

Method of oxidation.—The samples to be oxidized were placed as anodes opposite a platinum cathode. The solution was stirred magnetically and its temperature controlled by a thermostat. The Pyrex oxidation cell is sealed with a cover fitted with a spherical ground glass joint which supports the leads to the electrodes. Seven electrodes were placed in each cell so that successive oxidation of six samples could be performed without opening it (Fig. 2). Condensation of liquids on the walls of the cells was prevented by heating those parts not in contact with the bath.

Owing to the problems associated with maintaining electrical contact with silicon and tantalum foils, some details of the electrical connections will be given. In electrolytes where tantalum is easily oxidized (NMA + KNO_3; glycol + KNO_2) a special tantalum clamp, previously oxidized to 300V is used [see ref. (10)] with the sample totally immersed in the liquid. When glycol and KNO_3 is used to oxidize silicon, the clamp is kept above the surface of the liquid.

Oxidation was performed at a constant current of 1 mA/cm^2 up to a predetermined voltage (of up to several hundred volts), followed by a stage at constant voltage. The final current was allowed to decrease down to about 10 μA/cm^2 for all samples. The duration of this stage varied from 2 to 4 hr for silicon and 10

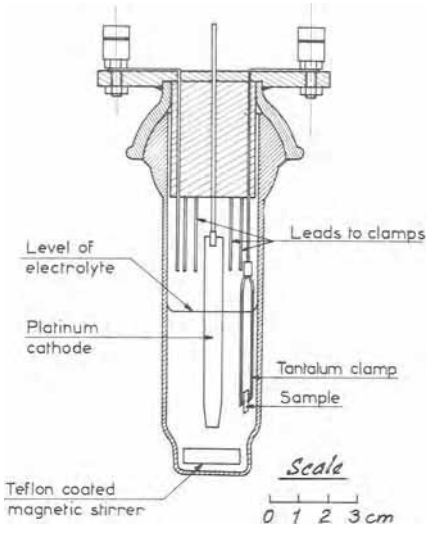

Fig. 2. Single compartment cell for successive oxidation of six samples without opening.

to 15 min for tantalum. The temperature of the solutions was maintained at about 20°C for glycol and, to avoid solidification, at around 35°C for NMA. After oxidation the samples were rinsed at 20°C in acetone, alcohol, and finally high resistivity water.

Under these conditions the thickness of SiO_2 films was measured by optical and nuclear methods and found to be about 6 Å/V, and that of Ta_2O_5 films about 16 Å/V. No gas evolution was observed at the anode during oxidation of either silicon or tantalum (see Discussion).

It was found that after a number of oxidations of silicon in glycol or NMA (consuming more than 1000 coulombs), further silicon samples cannot be oxidized satisfactorily. The solution apparently becomes poisoned by unknown decomposition products. For this reason the solutions, both isotopically labeled and unlabeled, were renewed frequently.

Exchange experiments.—Thermal isotopic exchange of oxygen between O^{18}-labeled water and glycol (or NMA) with or without added KNO_3 was examined. Various mixtures of the components of the system were heated in a sealed Pyrex tube in an oil or water bath for given times. In some cases the nitrate was labeled with O^{18}. The components were then separated and analyzed for their isotopic content, as described below.

The experiments on exchange during electrolysis were conducted at room temperature in a classical three-compartment cell with platinum electrodes. The cell consists of two electrode compartments (20 ml) and a middle compartment (15 ml), separated by sintered glass of porosity No. 1 (100 to 150μ pores). Each compartment was stirred by means of Teflon-coated bar magnets and the temperature measured by a separate thermometer. After a given number of coulombs (usually 1000) had been passed through the cell, the components of the electrolyte were separated and analyzed for their isotopic content as described below.

Chemical analysis of the solutions.—Water was determined by the Karl Fischer method. Great care was taken during the transfer of the liquids for analysis: all manipulations were done in a dry box, using oven-dried syringes and injecting the sample directly into the titration chamber through a rubber stopper. The analysis was done by back-titration. Using these precautions, the limiting sensitivity was about 0.02% (by weight) of water in NMA or glycol; reproducibility was of the same order of magnitude.

The formation of nitrite in the nitrate solutions was determined by means of the Greiss reagent. The chemical identification and analysis of other decomposition products was not attempted.

Isotopic analysis of the constituents of the solutions.—Separation of labeled compounds.—Water was removed from mixed solvents (from both exchange and electrolysis experiments) by distillation at atmospheric pressure using a 30 cm Vigreux fractionating column. The water was then redistilled in a micro still. Only when the NMA contained more than 2 ml water per 30g solvent could sufficient water of high purity for isotopic analysis be obtained. It was more difficult to isolate water from glycol, due to the formation of an azeotrope.

The organic solvent was then fractionally distilled (NMA at 80°C/4 mm; glycol at 65°C/10 mm). In order to eliminate the effect of traces of highly enriched O^{18} water in the isotopic analysis, a small quantity of unlabeled water was deliberately added to the distilled solvent and then removed by another distillation as described above. This procedure was repeated twice and the NMA or glycol dried with molecular sieves. Owing to the slow rate of isotopic exchange between NMA or glycol and water at room temperature, this procedure does not affect the isotopic content of the organic solvent at the low O^{18} concentrations found. Traces of residual water (<1%) do not affect the analysis of these isotopic concentrations.

The KNO_3 remains as a solid residue from the first fractional distillation. For the thermal exchange experiments, the heating of KNO_3 during distillation has only a negligible effect as compared to the previous much more drastic heat treatment. For the exchange during electrolysis the results on thermal exchange show that the effects of our distillation procedure was also negligible. To eliminate traces of H_2O^{18} in the salt the latter was washed and recrystallized twice with water. It was known that there is negligible isotopic exchange of oxygen under these conditions. It should be noted that recent experiments (7) using highly labeled KNO_3 in 30-times O^{18}-depleted water showed that the isotopic exchange between KNO_3 and water under similar conditions is not detectable. The traces of KNO_2 formed in the electrolytic experiments using KNO_3 are mostly removed on crystallization and do not affect the analytical result. Attempts to separate the nitrate from the organic solvent by thin layer chromatography were not successful.

For mass spectrometric analysis at least 5 mg of any compound is required for a single isotopic analysis. Quantities smaller than this give irreproducible results, due in part to exchange with traces of moisture, impurities, etc., in the glassware.

Mass spectromic analysis.—Water was analyzed by mass spectrometry using conventional methods. At low enrichments the "bromine" method was used by means of which water is converted to molecular oxygen by alkaline hypobromite (11). At high enrichments the water is equilibrated with carbon dioxide (12); at very high enrichments O^{18}-labeled CO_2 is used to avoid too great an isotopic dilution. The oxygen or carbon dioxide was analyzed by mass spectrometry. Attempts to equilibrate CO_2 directly with water mixed with either NMA or glycol were not successful.

Potassium nitrate was analyzed by two methods: a general method for pyrolysis of inorganic materials to carbon dioxide by means of a mixture of mercuric chloride and mercuric cyanide (13) and a specific method for nitrate in which the oxygen is converted to nitrous oxide by pyrolysis with ammonium chloride (14). Both methods gave the same result.

Glycol and NMA were analyzed for their isotopic content by conversion to carbon dioxide by the pyrolytic method described above. However, in order to obtain reproducible results great care must be taken to purify the carbon dioxide before mass spectrometric analysis. The gas was first passed through a column of benzoquinoline crystals in order to absorb HCl and

other acidic substances and then distilled from −80°C (dry ice acetone) to a liquid nitrogen trap. CO_2 purified in this manner gave reproducible results.

Attempts to analyze the oxygen isotopic content of NMA and glycol nondestructively by means of infrared (O^{18}) or NMR (O^{17}) were not successful owing to the low sensitivity of these methods.

Isotopic analysis of the anodic oxide films.—O^{16} was measured by the O^{16} (d,p) O^{17*} reaction and O^{18} by the O^{18} (p,α)N^{15} reaction. The technical details of these nuclear methods, devised for the study of anodic oxidation processes, are described in ref. (4) and (5). Other applications to anodic oxidation were described in ref. (6) and (7).

Results

Chemical Changes in the Electrolytes

The effects on the electrolyte of the electrochemical processes taking place during anodic treatment depend on the nature of the currents injected into the electrodes. At the cathode, by choosing a platinum electrode, we insured that this current is purely electronic. At the anode both electronic and ionic currents may pass through the oxide layer being formed. In what follows we shall discuss the various effects of the anodic current in terms of "electronic" and "ionic," it being understood that this refers to its nature in the oxide layer.

Since the current efficiency of the anodic oxidation of silicon is of the order of only 2%, it would appear that most of the current is used up in decomposing the solution, as is illustrated by the poisoning effects mentioned above. Some of the products of anodic processes have been studied by Duffek *et al.* (2, 3), who showed that the amount of silicon lost to the electrolyte is a small fraction of that contained in the oxide film formed. They also found that water was formed during the electrolysis. We have investigated some of these phenomena including the formation of water, both by effective drying of the solvents before use and also by using O^{18} as a tracer.

Measurements in a single-compartment cell.—In order to simulate the electronic current, corresponding to the small current efficiency of silicon oxidation, a given quantity of electricity was passed between platinum electrodes in the above solutions. The cell used is shown in Fig. 2. The formation of water was studied as a function of the components of the solution and of the current passed. A new solution was used for each measurement, so that each experiment is influenced in the same way by traces of water accidentally introduced. The total amount of water thus introduced into a 20 ml solution from outside sources (*i.e.*, before electrolysis) is estimated to be about 5 mg.

Figure 3 shows the results for NMA and glycol solutions containing 0.4% KNO_3. The presence of traces

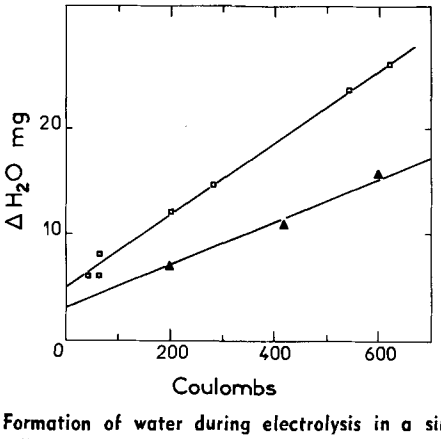

Fig. 3. Formation of water during electrolysis in a single compartment cell, as measured by Karl Fischer method: □ glycol, ▲ NMA.

Table I. Water formation in a single compartment cell

H_2O formed	Glycol	NMA
mg/1000 coulomb	40	20
mole/Faraday	0.2	0.1

of water from outside sources is shown by extrapolating the straight lines to the origin. The proportionality constant between the net increase in the amount of water and the charge passed can be deduced from these results for various solutions (Table I). The results for glycol and KNO_2 system are very similar to those for KNO_3. Thus, these two salts appear to be equivalent from this point of view.

These experiments were repeated in glycol solutions with a silicon anode, with results identical to those obtained above with platinum. This confirms that the effects in the oxidation process of silicon were indeed due to an electronic current.

Measurements in a three-compartment cell.—In order to investigate the formation of water in more detail, measurements were carried out in a three-compartment cell, using either NMA or glycol solutions containing 0.4% KNO_3 and platinum electrodes. Only hydrogen was evolved at the cathode as verified by mass spectrometry, the yield obtained by coulometric measurements being exactly 1 g-atom/Faraday. Although under normal circumstances no gas evolution was observed at the anode, precise coulometric experiments at high current densities performed with a special cell indicate that small amounts of gas may be evolved.

In NMA, after the passage of 1000 coulombs, an increase in the *p*H at the cathode was observed, which has been attributed to the formation of KOH [see ref. (2)]. Simultaneously, the *p*H at the anode fell to about 5. Further results are given in Table II.

The reduction of nitrate to nitrite is negligible as the total amount of nitrite formed corresponds to the consumption of only 0.3 coulombs, 3×10^{-4} of the quantity passed. The presence of nitrite in the anode and middle compartments can be attributed to a migration process from the cathode. Similar results were obtained in glycol. Duffek *et al.* (2, 3) also found traces of nitrite after anodic oxidation but did not estimate the extent of this process.

The amount of the water formed varies from compartment to compartment. The increase in the water content of the middle compartment could be due to transport phenomena by electrolytic migration or spontaneous diffusion from the anode compartment. Experiments have shown that the quantity of water is independent of the porosity of the sintered glass partitions for porosities of between 1 and 4 (*i.e.*, 120-10μ) indicating that migration is probably preponderant. The total amount of water formed in all three compartments is significantly greater than that found in a single-compartment cell under similar conditions for both NMA and glycol solutions. As will be discussed later, this suggests that water is probably formed at the anode and destroyed at the cathode. This suggestion is supported using O^{18} tracers and nuclear analysis of the oxide films (see below). Direct methods such

Table II. Decomposition products in a three-compartment cell

	Anode	Middle	Cathode	Total
		(a) NMA		
KNO_2 formed:				
mg/1000 coulomb	2.5×10^{-2}	2.5×10^{-2}	8.5×10^{-2}	1.3×10^{-1}
mole/Faraday	3×10^{-5}	3×10^{-5}	10^{-4}	1.6×10^{-4}
H_2O formed:				
mg/1000 coulomb	50 to 60	15 to 20	Negligible	65 to 80
mole/Faraday	~0.3	~0.1		~0.4
		(b) Glycol		
H_2O formed:				
mg/1000 coulomb	70 to 100	10 to 40	0 to 20	120 to 140
mole/Faraday	0.4 to 0.5	0.1 to 0.2	0 to 0.1	~0.7

as these eliminate the uncertainties due to transport phenomena.

Isotopic Changes in the Electrolytes

Since all the components of the solutions contain oxygen, tracer experiments by O^{18} labeling of one of the constituents can only be simply interpreted if the changes in the isotopic compositions throughout the experiment are relatively slow. Therefore the isotopic oxygen exchange between the components of the solution was studied in detail first by mass spectrometry and these results will be presented now. They will be followed by those on the labeling of the films obtained by oxidation.

Temperature induced exchange.—Solutions of NMA and glycol containing either water or nitrate labeled with O^{18} were heated to 100°C or more for times of up to 720 hr. The isotopic composition of each constituent was analyzed in a mass spectrometer before and after heating. The absolute errors on the results are taken as ±0.02% for concentrations at or near the natural abundance of O^{18} and ±0.5% for higher concentrations. The results obtained are given in Table III, where the calculated exchange ratios of the various constituents are shown. These ratios were calculated for the exchange between two constituents as follows. Since the kinetics of the isotopic exchange obey a first order kinetic law (15), the exchange ratio, ρ, after a heating time t, may be written as

$$\rho = \frac{C(o) - C(t)}{C(o) - C(\infty)} = 1 - e^{-t/\tau}$$

where $C(o)$ is the initial concentration of isotope in the constituent examined, $C(\infty)$ the concentration of isotope at equilibrium for a total exchange, and τ the mean life, characteristic of the exchange. In the three component systems (NMA + H_2O + KNO_3) the calculations were made separately for the pairs NMA + H_2O, KNO_3 + H_2O, neglecting the effect of the third component, since the extent of the exchange is small. The results indicate that in all cases studied, the exchange ratios are less than 2%. Those calculated for each constituent in glycol are in good agreement with one another, but in the case of NMA the water could not be analyzed. The mean life τ deduced from ρ is shown in Table IV.

From these results the following conclusions may be drawn:

Exchange in NMA.—The results indicate that there is a very slow isotopic exchange of oxygen between NMA and water at 100°C. Both with and without added KNO_3 the exchange ratio is of the order of 0.5%, corresponding to a mean life of 1.5 x 10^5 hr; a mechanism for isotopic exchange of oxygen between amides and water in dilute solution is known [see ref. (16)] and may operate here. The exchange at 100°C between KNO_3 and water dissolved in NMA occurs at a slightly higher rate. This exchange is known to occur but is acid catalyzed; under the drastic conditions of the experiment, the presence of traces of acid (from hydrolysis of NMA for instance) cannot be excluded. Under the considerably milder conditions used for anodic oxidation, (*i.e.*, a few hours at room temperature) thermal exchange of oxygen between the various components in the NMA system can be ruled out.

Exchange in glycol.—The isotopic exchange of oxygen between water and glycol is somewhat faster than with NMA as shown by the isotopic analysis of each component after 148 hr at 100°C. Various dehydration, hydration, and substitution mechanisms for this exchange can be posulated, but at the present time there is insufficient evidence for deciding which mechanism operates. There is virtually no exchange between glycol and nitrate, as might be expected. Here again the thermal isotopic exchange of oxygen is so slow as not to be taken into account under the considerably milder conditions of anodic oxidation.

Electrochemically induced exchange.—The isotopic labeling of a component in an electrolyte mixture under the influence of an electric current passing through the cell, could be the result of various processes:

1. the formation by electrolytic decomposition of products which can exchange oxygen rapidly with the other components of the solution;
2. the formation of nonlabeled species, chemically identical to the labeled ones; causing isotopic dilution;
3. exchange induced by the electrolysis itself.

The experiments carried out were on NMA solutions where isotopic analysis of all the components was possible, and on glycol solutions where only the glycol could be analyzed. The results obtained in the three-compartment cell may also be affected by transport phenomena; their effect on the accuracy of the results for water is smaller here than in the experiments on thermal exchange in the electrolyte, since larger quantities of labeled water are used.

The NMA-KNO_3-H_2O system.—The results of the mass spectrometric analysis are summarized in Table V. They show that:

1. there is no change in the isotopic content of the water from the middle and cathode compartments, within experimental error;
2. the isotopic content of oxygen in the water in the anode compartment decreases markedly;
3. the isotopic content of oxygen in the NMA hardly changes;

Table III. Temperature induced exchange

Bath	Exchange conditions	Oxygen content, mole	Original labeling, $C_o = \frac{O^{18}}{O^{16} + O^{18}}$ %	Equilibrium labeling, C_∞, %	Final labeling, C_t, %	Exchange ratio, ρ, %
NMA 5g	720 hr, 100°C	7 x 10^{-2}	0.2	12.4	0.28	0.65
H_2O 0.5g		2.5 x 10^{-2}	47	—	—	—
NMA 5g	720 hr, 100°C	7 x 10^{-2}	0.2	12.4*	0.28	0.65*
H_2O 0.5g		2.5 x 10^{-2}	47	—	—	—
KNO_3 0.05g		1.5 x 10^{-3}	0.2	45**	1.06	1.9**
Glycol 4g	148 hr, 100°C	1.3 x 10^{-1}	0.2	13.1	0.45	1.9
H_2O^{18} 0.5g		2.5 x 10^{-2}	81.2	13.1	80.1	1.6
Glycol 4g	148 hr, 197°C	1.3 x 10^{-1}	0.2	2.3	0.2	Negligible
KNO_3 0.15g		4.3 x 10^{-3}	59.5	2.3	59.4	Negligible

* Calculated for the couple NMA-H_2O.
** Calculated for the couple H_2O-KNO_3.

Table IV. Exchange mean life

Couple	NMA/H_2O	Glycol/H_2O	Glycol/KNO_3	H_2O/KNO_3
Exchange conditions				
Time (hr)	720	148	148	720
Temperature (°C)	100	100	197	100
Mean life (hr)	1.5 x 10^5	1.6 x 10^4	Too large to measure	8 x 10^4

4. the isotopic content of oxygen in the nitrate is unchanged (this analysis was made on KNO_3 from a solution where 500 coulombs have been passed to oxidize silicon samples). These results are compatible with those obtained is the preceding section.

In the anode compartment the change in the isotopic content of oxygen in the water does not correlate quantitatively to the change in the opposite direction of isotopic content of the NMA and nitrate. This is not, therefore, the result of exchange phenomena, but of isotopic dilution, in agreement with the production of water indicated earlier. The decrease in O^{18} content of the water in the anode compartment from 68 to 60% can be accounted for by the creation of 5×10^{-3} moles of water per 100 coulombs, *i.e.*, about 0.5 mole/Faraday. This last figure is in agreement with that obtained by the classical methods previously described. The interpretation of this result will be discussed later.

The glycol-KNO_3-H_2O systems.—Similar experiments in glycol have lead to the results given in Table V. The isotopic analysis of oxygen in glycol shows that there is again a slight change, varying from one compartment to the other.

It appears that apart from the dilution effect due to the formation of water at the anode there is little isotopic exchange between the constituents of both NMA and glycol solutions even after 1000 coulombs have been passed through the solution. Since less than 200 coulombs are required for the formation of an anodic oxide film on silicon, electrochemically induced isotopic exchanges can be neglected.

The formation of water and consequent changes in isotopic oxygen content can be examined by analyzing the oxide layers formed. Once it has been established that the isotopic exchanges between the components of the solutions are very slow, and can be neglected, one can determine the source of oxygen and the production of water with greater accuracy and care by the nuclear methods outlined above.

Isotopic Analysis of the Oxide Films

The oxygen necessary for the formation of tantalum and silicon oxides can be provided by any of the components of the solution. It is unlikely that the source of oxygen is dissolved molecular oxygen (see Discussion). The relative contribution of oxygen from each of the constituents of the solution to the oxide layer was evaluated by using labeled H_2O^{18} and $KNO_3{}^{18}$, which have been shown not to undergo isotopic exchange under a wide variety of conditions.

Both tantalum and silicon were oxidized. Because of the high yield in the anodic oxidation of tantalum and consequent minimal decomposition of the solution, tantalum oxides were considered to be characteristic of the isotopic composition of the solution at various stages. In order to verify that current density does not affect the process investigated, some experiments were made at 5 mA/cm² on silicon, in addition to all those made at 1 mA/cm². No difference was observed between them.

Table V. Electrochemically induced exchange

Bath		% O^{18} initial	Charge passed through, coulombs	% O^{18} final		
				Anode	Middle	Cathode
NMA	30g	0.2	1000	0.32	0.33	0.44
H_2O^{18}	2g	87		82.5	85.9	86.3
NMA	30g	0.2	1000	0.210	0.215	0.270
H_2O^{18}	2g	68		60	68	67.5
KNO_3	100 mg	0.2		—	—	—
NMA	30g	0.2	500	—	—	—
H_2O^{16}	100 mg	0.2				
$KNO_3{}^{18}$	100 mg	77		75.5*	75.5*	75.5*
Glycol	25g	0.2	1000	0.204	0.204	0.230
H_2O^{18}	2g	72		—	—	—
Glycol	25g	0.2	1000	0.215	0.207	0.500
H_2O^{18}	2g	72		—	—	—
KNO_3	100 mg	0.2		—	—	—

* Single compartment cell, silicon anode.

In what follows the isotopic O^{18} content, *i.e.*, the $O^{18}/(O^{16} + O^{18})$ ratio, of the oxides will be called C. In the calculations the O^{17} content, always less than 0.5%, was neglected. The quantity of interest is often the isotopic oxygen content normalized to 100% enrichment of the labeled species. This quantity will be written C^*.

O^{18}-labeled water.—It should be emphasized that during anodic oxidation it is the total amount of water produced which contributes to the isotopic dilution, since stirring mixes water from various origins completely before destruction at the cathode. In order to minimize the errors caused by dilution, the oxide layer formed in a fresh solution at the beginning of a series of oxidations (immediately after the Karl Fischer analysis) was analyzed for its O^{18} content. From this result the proportion of oxygen originating from the water can be calculated. Then, by following the isotopic content of subsequent oxide layers on a series of anodes, in the same solution, the dilution effect was measured and the rate of creation of water determined.

Experiments were carried out in the following solutions

$$\text{Glycol} + 0.4\%\ H_2O^{18} + 0.4\%\ KNO_2{}^{16}$$

$$\text{NMA} + 0.4\%\ H_2O^{18} + 0.4\%\ KNO_3{}^{16}$$

The water added to the "dry solvent" had a concentration of 88% O^{18}, but the introduction of traces of water during handling operations (as determined by the Karl Fischer method) reduced the actual isotopic concentration of the water in the solution at the start of the oxidations to 76 ± 2% O^{18}. In both NMA and glycol and for both silicon and tantalum oxidations, the isotopic content C of the first oxides produced in repeated experiments on fresh solutions was 67 ± 1%. The SiO_2 films were formed at 150V (consuming 40 coulombs) and the Ta_2O_5 films at 50V (with a consumption of less than 0.5 coulomb). A tantalum foil was oxidized before and after each silicon oxidation. Dilution of the O^{18} content due to the 40 coulombs used for the first silicon oxidation was less than 2%. When O^{18}-washed solvents (see above) were used, identical results were obtained, confirming the efficiency of our drying and analytical techniques. Calculation of the normalized isotopic content C^* shows that 88 ± 3% of the oxygen in the oxides (both silicon and tantalum in NMA or glycol) comes from the water in these conditions.

The isotopic oxygen content of a series of films formed in successive oxidations in the same bath was examined. The solutions used were similar to those decribed in preceding experiments. Ta and Si samples were alternately oxidized in NMA solutions, the cell being opened only after three pairs of oxidations. For glycol solutions the procedure was somewhat different. Si and Ta were oxidized in separate solutions. Between each oxidation of Ta, the effect of the oxidation of Si was simulated by letting a current flow between Pt electrodes so as to consume 180 coulombs. This checked the equivalence of the electrolytic effect due to the passage of electronic current with silicon or platinum anodes.

Results are shown in Fig. 4 and 5. It was found convenient to plot in these figures the quantity $\Delta(W_o{}^{18}/C)$ (where $W_o{}^{18}$ is the total amount of O^{18}-labeled water molecules present initially in the fresh solution) as a function of the number of coulombs passed through the cell. The theoretical basis for the choice of this plot is discussed below. It should be noted however that were the water the only source of oxygen and were there no destruction of water, one would have

$$C = \frac{W_o{}^{18}}{W_o{}^{18} + W^{16}}$$

where W^{16} is the amount of unlabeled water in the solution at any instant. Then

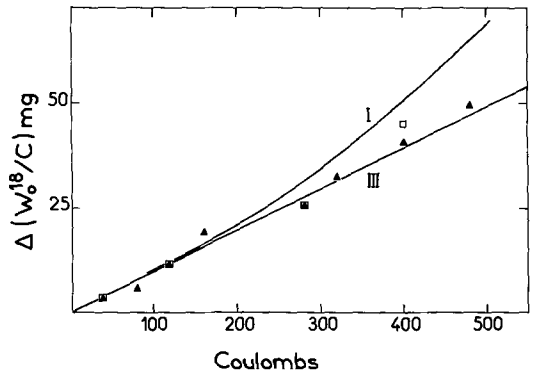

Fig. 4. Change in the isotopic content C of the oxide layer during oxidation in an NMA bath containing O^{18} labeled water. □ Silicon, ▲ tantalum. The calculated curves correspond respectively to cases I and III.

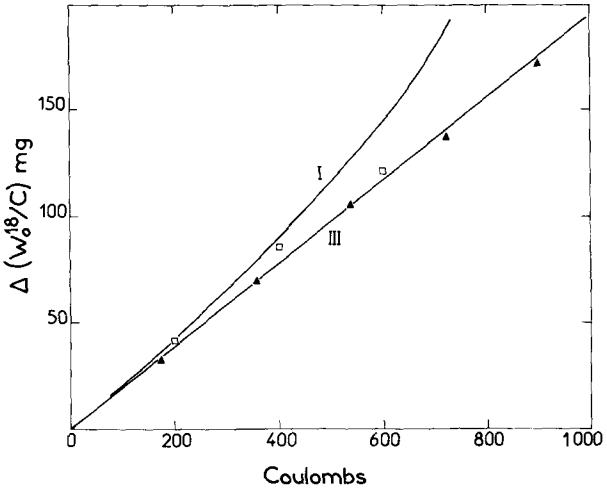

Fig. 5. Change in the isotopic content C of the oxide layer during oxidation in a glycol bath containing O^{18} labeled water. □ Silicon, ▲ tantalum. The calculated curves correspond respectively to cases I and III.

$$\Delta\left(\frac{W_o^{18}}{C}\right) = \Delta W^{16} \qquad [1]$$

and the water production could be simply deduced from Fig. 4 and 5 by measuring the slope. A more sophisticated interpretation of the results would require experiments using O^{18}-labeled KNO_3.

It is seen from Fig. 4 and 5 that the results for both silicon and tantalum oxide films fall approximately on a single line, suggesting that the source of oxygen is the same for the oxidation of both anodes.

O^{18}-labeled KNO_3.—Solutions of $KNO_3{}^{18}$ (enriched to 77% O^{18}) in either NMA or glycol and water (all of natural isotopic composition) were used to further investigate the sources of oxygen for the oxidation of silicon and tantalum.

Alternate oxidations of Si and Ta were carried out in the same NMA solution by the procedure previously described. The highest normalized O^{18}-content C* of the films obtained (both Si and Ta) in a freshly prepared 0.4% $KNO_3{}^{18}$ + 0.4% H_2O + NMA solution was 10.6 ± 1%. This value is discussed below. After a series of Ta-Si pairs of oxidations in the same solution where the change in isotopic content was very slow, successive injections of unlabeled water were added to the solution between each Ta-Si pair in order to elucidate the effect of salt to water ratio. Each injection added an increment of 0.2% of water to the system. The results are shown is Fig. 6 where the inverse of the normalized isotopic content C* of the oxides is shown as a function of the quantity of water

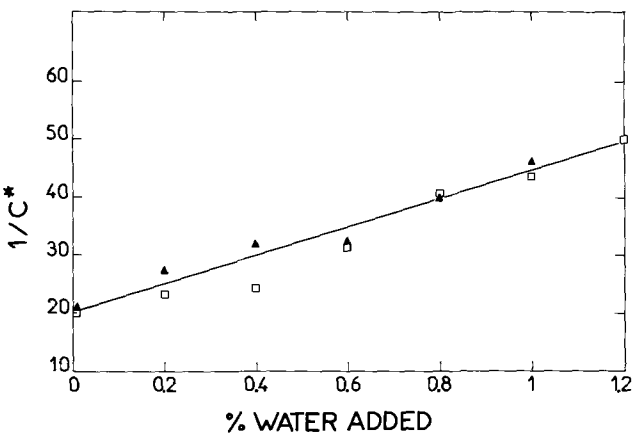

Fig. 6. Dependence of the normalized content C* of the anodic oxides on the amount of water added to NMA solutions containing O^{18} labeled KNO_3. □ Silicon, ▲ tantalum.

added (the effect of electrochemically produced water being neglected). It is seen again that the isotopic content of the silicon and tantalum oxides is very similar. The straight line obtained indicates that the relationship between O^{18} content and water added is homographic.

Similar results were obtained for SiO_2 films produced in glycol indicating that the nature of the solvent does not play a critical role in the function of the salt as a source of oxygen. On the other hand, Ta_2O_5 films produced in glycol contained slightly more O^{18} than SiO_2 films. This discrepancy may be due to the difficulties in oxidizing tantalum in glycol containing KNO_3 which produces films of bad quality and ill-defined composition, even when formed at voltages near 20V.

Incorporation of nitrate in the anodic oxide films.—One obvious reason for the presence of O^{18} in anodic oxides from labeled KNO_3 could be the direct incorporation of NO_3^- or NO_2^- anions into the film [as discussed in a similar case in ref. (7)]. It was therefore important to determine the nitrogen content of oxide films formed in NMA and glycol solutions containing 0.4% KNO_3 and 0.4% water. Nitrogen was measured using nuclear reaction microanalysis, by means of the N^{14} (d,α)C^{12} reaction as described in ref. (17). This sensitive analytical technique allowed us to assign an upper limit to the nitrogen content of the films. This limit was set by the presence of traces of nitrogen on the samples before anodic oxidation. The SiO_2 films formed in both glycol and NMA solutions were found to contain less than 0.2% nitrogen, per oxygen atom. The tantalum oxide films formed in NMA contained less than 0.8% nitrogen per oxygen atom. However, those formed in glycol containing KNO_3 contained a significant amount of nitrogen up to 2.5%, but as stated above, these films are of poor quality and results are probably not reliable.

It thus appears that direct incorporation of nitrogen containing anions accounts for less than 0.6% of the oxygen in SiO_2 and less than 2.4% in Ta_2O_5. In order to account for the 11% oxygen originating from nitrate found, a more complex mechanism of oxygen transfer from salt to oxide must be considered.

Quantitative Interpretation of Results

Empirical relationships for the sources of oxygen.—Let α, β, and γ be the relative contributions to the source of oxygen of the salt, the water, and of the solvent, respectively. We have

$$\alpha + \beta + \gamma = 1 \qquad [2]$$

For equal weights of salt and water it was found experimentally that in all cases

$$\alpha = 10.6 \pm 1\% \quad \text{and} \quad \beta = 88 \pm 3\%$$

hence

$$\alpha + \beta = 98.6 \pm 3\%$$

This shows that γ is negligible, *i.e.*, that within the experimental error the oxygen of the solvent does not constitute a direct source of oxygen.

The laws governing the contributions α and β as a function of salt and water concentrations in the solutions may be deduced from Fig. 6, using certain simple assumptions. Let V_0 be the quantity of solvent used in the labeled KNO_3 experiment, S and W the amounts of salt and water (expressed in moles) at various stages. The isotopic O^{18} content of the oxide films is

$$C = \alpha\eta$$

where η is the isotopic content of the oxygen of the salt (77% in this case). We have shown that η is constant throughout the experiment. Whereas S is constant, $S = S_0$, W varies as water is added to the solution. Hence

$$\alpha = f(W, S_0)$$

where S_0 is a fixed parameter. From Fig. 6 one can deduce, since here $C^* = \alpha$ that

$$\frac{1}{f(W, S_0)} = KW + l$$

K and l being constants.

This formula may be written in the form

$$\frac{1}{f(W, S_0)} = k\frac{W}{S_0} + l \qquad [3]$$

where k and l are now dimensionless constants.

The value of k may be obtained from Fig. 6: $k = 1.8 \pm 0.2$. Using this value and the value $10.6 \pm 1\%$ for C^* for equal weights of salt and water, one may obtain the value of l, which is not far from unity. However, this value is not well defined since it is deduced by extrapolation over a wide interval. If we assume $l = 1$, one may write

$$\alpha = f(W, S_0) = \frac{S_0}{kW + S_0} \qquad [4a]$$

and since $\alpha + \beta = 1$

$$\beta = \frac{W}{k^{-1}S_0 + W} \qquad [4b]$$

Thus, assuming $l = 1$, the amount of salt S_0 is equivalent to an amount $W_e = k^{-1}S_0$ of water. A slightly different value of l would give a more complex homographic relation for α and β, without changing the numerical values appreciably.

The above calculation was based on the hypothesis that $S = S_0$, and in principle k (like l) depends on S. If the simple equivalence law found above applies in a limited range of values of S and W (for given V_0), it is most probable that k is independent of S. This implies, in fact, the assumption that the source of oxygen depends only on the ratio W/S of the water to salt concentrations, and not on the absolute concentrations with respect to the solvent. Whereas no detailed experimental proof of the general validity of Eq. [4a] and [4b] can be given, some measurements made with 0.2% of salt by weight of solvent have confirmed the validity of these laws within the range of experimental conditions studied. Further discussion of this result is given below.

Equations [4a] and [4b] may be tested for the values of α and β measured for equal weights of salt and water with $k = 1.8 \pm 0.2$ and, assuming that $l = 1$. One finds that

$$\alpha = 9 \pm 1\% \quad \text{and} \quad \beta = 91 \pm 3\%$$

which compare well with the values $\alpha = 10.6 \pm 1\%$ and $\beta = 88 \pm 3\%$, found experimentally by independent experiments.

The production and destruction of water.—The experimental results on the production and destruction of electrolytic water (measured using O^{18}-labeled water), shown in Fig. 4 and 5, cannot be interpreted by means of the simple formula [1], since the following facts must be taken into account.

(*i*) A quantity of $q\theta$ of water is produced by θ coulombs (the number of coulombs passed through the cell), with isotopic composition identical to that of the solvent, *i.e.*, natural abundance.

(*ii*) A quantity $\hat{q}\theta$ of water is destroyed by θ coulombs; the isotopic composition of the water destroyed is the same as that of all the water in the solution, assuming isotopic homogeneity due to good stirring.

(*iii*) The O^{18} contained in the destroyed water molecules remains in the solution since the oxygen evolved as a gas at the cathode and the anode is negligible.

(*iv*) The source of oxygen is the water and the salt according to Eq. [4a] and [4b]. The water equivalent $W_e = k^{-1}S_0$ does not participate in the production or destruction phenomena and is of natural isotopic composition throughout (the salt is not labeled in this experiment).

It appears at this stage that in order to interpret the experimental results an additional assumption on the role of the O^{18} atoms which are removed from water is needed. Water is here considered to be all species detected by the Karl Fischer method in the solution. Three simple cases may be considered:

Case I. The new compounds which contain O^{18} do not oxidize the anode and do not undergo isotopic exchange with water. Hence, the corresponding O^{18} atoms do not play a role in further anodic processes.

Case II. The new compounds behave like water for anodic oxidation but are not detected by Karl Fischer titrations. In this case the amount of O^{18} atoms to be considered remains constant.

Case III. The new compounds do not act as a direct source of oxygen but are in isotopic equilibrium with the water in the solution.

The real situation may be a mixture of these various possibilities. In order to interpret our results we have calculated the theoretical curves corresponding to those three models, the calculation being given in the Appendix. The curves corresponding to case I and case III were drawn for NMA in Fig. 4, and for glycol in Fig. 5.

It thus appears that case I is not supported by the experimental results, whereas case III is in excellent agreement with the experimental points for both Ta and Si. Case II gives rise to two possibilities:

Case IIa. That the quantity W in formula [4a] and [4b] represents the total amount of oxygen-supplying compounds. In this case it appears as if there is no water destruction at all and that the phenomenon obeys Eq. [1].

Case IIb. The quantity W in Eq. [4a] and [4b] is the water detected by the Karl Fischer method. Then as shown in the Appendix, the calculated curve is identical with that of case III. These assumptions are discussed below.

It should be noted that case III leads, in the range of values studied, to a nearly linear relation, and the only difference between case III and case IIa is in the calculated value of the rate of water production.

The following rates of water production (q) are thus obtained:

Case III: 9.05 g/**F** in NMA; 17.9 g/**F** in glycol.

Case IIa: 9.85 g/**F** in NMA; 19.3 g/**F** in glycol.

Discussion

The results may be best discussed is relation to two well-defined classes of phenomena: changes induced in the electrolyte by electronic current and the anodic oxidation processes induced by ionic current.

Action of the electronic current on the electrolyte.—First, a choice should be made between case IIa and

case III which give slightly different values for the rate of water production. Case IIb, which gives the same results as case III, seems less likely as, if the decomposition products behave like water for oxygen supply they should also behave like water with respect to the salt. We have no experimental evidence to decide between cases IIa and III. However, it seems less likely that a compound behaves exactly like water for oxygen supply in anodic oxidation and not in titration by the Karl Fischer method. On the other hand, experiments have shown that in the organic solutions used, KOH is detected as water by the Karl Fischer method within experimental error, in agreement with ref. (18) (1.251). As a result the concentration of KOH is included in the amount of water formed when describing our phenomena. Under these conditions (with a 10% error if case IIa is the correct one), our results may be summed up with the statement that approximately 0.5 mole of water per Faraday is created in NMA by the electronic current and 1 mole/Faraday in glycol.

Any mechanism for this process must therefore account for the following facts:

(*a*) about 0.5 mole/Faraday of water is created at the anode in NMA, and 1 mole/Faraday in glycol; in both cases about 80% of the water produced is destroyed at the cathode.

(*b*) H^+ is produced at the anode and OH^- at the cathode.

(c) Hydrogen is evolved at the cathode. Negligible gas evolution is observed at the anode during anodic oxidation of Si and Ta.

(*d*) Slight decomposition of the nitrate into nitrite was measured.

(*e*) Isotopic exchange of oxygen between nitrate, water, and solvents is negligible. However, a very small isotopic exchange between water and the solvents was observed, mainly at the cathode.

The reactions occurring can be discussed in terms of those related to the cathode and those to the anode.

Reactions at the cathode.—The primary reaction at the cathode is probably

$$H_2O \xrightarrow{+e^-} \tfrac{1}{2}H_2 + OH^- \qquad [5]$$

Some of the hydroxide ions formed attack the organic solvent causing it to hydrolyze. While no direct evidence for hydrolysis products could be obtained, the rapid poisoning of the system quoted above may indicate the liberation of such species.

There is some evidence for nucleophilic attack of hydroxide on NMA from the slight exchange of O^{18} observed, by the mechanism involving reversible addition of OH^- to the carbonyl bond as suggested by Bender and Ginger (19). In glycol solutions there is no evidence as to the nature of the exchange reactions.

In the presence of an electric current there is the possibility of the formation of aldehydic species: acetaldehyde in the case of NMA and either acetaldehyde, formaldehyde, or a related compound in glycol. The formation of such species would account for the existence of a compound with one oxygen which rapidly undergoes isotopic exchange with the water in the solvent [ref. (8), p. 55; and ref. (20)]. Carbonyl compounds are not easily analyzed by Karl Fischer titrations and in fact formaldehyde is unaffected by the analytical reagent [ref. (18), p. 147]. Although no positive evidence for an aldehydic species has been obtained, the presence of these entities would account for most of the experimental observations.

The reduction of nitrate to nitrite at the cathode takes place according to the reaction

$$\tfrac{1}{2}NO_3^- + \tfrac{1}{2}H_2O \xrightarrow{+e^-} \tfrac{1}{2}NO_2^- + OH^- \qquad [6]$$

The quantitative measurements of nitrite showed however that this reaction accounts for such a small proportion of the current (3×10^{-4}) that its effect as a pathway for the loss of water is negligible.

Reactions at the anode.—The main reaction at the anode which must be considered is the production of water. It can be assumed that the oxygen of this water comes from the organic solvents in each case, since the only other source, nitrate, can be eliminated from the O^{18}-labeling experiments. Various condensation reactions of organic compounds (both amides and alcohols) can be suggested to account for water production (21). However, in the absence of isolatable products, no mechanism for the production of water can be suggested at the present time. It should be noted that the yield of water in glycol where there are two oxygen atoms is exactly double that in NMA where there is only one. This may be related to the mechanism, but the possibilities of a coincidence cannot be excluded. The most important reaction at the anode is of course the anodic oxidation of silicon and tantalum.

Anodic oxidation processes.—The phenomena investigated may be described as follows:

(*a*) Although their oxidation current efficiencies are very different, in all these experiments silicon and tantalum behaved in an identical manner. It therefore seems very likely that the reactions induced by the electronic current do not affect the mechanism for the supply of oxygen for anodic oxidation. Since in silicon oxidation water is produced, the similarity to tantalum indicates that this water must be immediately mixed with the bulk of the solution, so as to insure isotopic equilibrium.

(*b*) The source of oxygen in anodic oxidation does not depend on the nature (NMA or glycol) of the solution.

(c) The organic molecules do not act as a direct source of oxygen in anodic oxidation. The contribution of the two identified oxygen sources, water and nitrate, depend on their relative concentrations according to Eq. [3] and [4a] and, at least at low absolute concentrations, not on the nature of the solvent. The over-all equations for the reaction with water, which is the main source of oxygen, may be written as

$$Si + 2H_2O \rightarrow SiO_2 + 4H^+ + 4e^- \qquad [7]$$

$$2Ta + 5H_2O \rightarrow Ta_2O_5 + 10\,H^+ + 10\,e^- \qquad [8]$$

(*d*) The nitrate is also a supplier of oxygen as a direct source, since no incorporation of nitrogen or isotopic exchange with water was observed.

External molecular oxygen can play no role in the reaction since all solutions were carefully degassed before use. As was mentioned above, in cells of special geometry, some molecular oxygen may be evolved at the anode during oxidation. This however is not likely to be a source of oxygen by means of electrochemical reactions at the anode.

A tentative mechanism for the direct participation of nitrate in anodic oxidation is the following. The protons formed by the reaction [7] and [8] (and in the case of silicon, also those formed by the electronic current) could react with nitrate ions near the surface of the anode. The reaction will loosen the oxygen to nitrogen bonds possibly through a nitronium type of reaction (22), thereby providing another source of oxygen for oxide formation, the reaction being of the following type

$$NO_3^- \overset{+H^+}{\rightleftharpoons} HNO_3 \overset{+H^+}{\rightleftharpoons} (H_2NO_3)^+ \rightarrow NO_2^+ + (H_2O) \qquad [9]$$

the water species immediately reacting with the anode to form an oxide. The high local concentration of protons near the anode is such that a fixed fraction of the nitrate ions undergoes this process, independently of absolute water concentration and current density. This dependence on local protonation makes these reactions

very sensitive to possible acidity of the salt and to the environment. The two competing sources of oxygen contribute in proportion to the relative concentration of water and salt (assuming that the concentrations are the same near the anode as in the bulk of the solution). The weighting factor k of Eq. [4a] is determined by the fraction of the nitrate ions which undergoes reaction [9]. Whatever the mechanism is, the fact that k is the same for silicon and tantalum is not surprising considering their similar electrochemical properties, the oxidation reduction potentials, for reactions [7] and [8] being 0.86 and 0.81V, respectively, on the hydrogen scale.

APPENDIX

One may calculate the O^{18} content $C(\theta)$ of the oxide films as a function of the charge θ passed through the cell using Eq. [4a] and [4b] and the assumptions corresponding to cases I, II, and III. The calculations enable one to extract from Fig. 3, 4, and 5 the value of the rate of production and destruction of water, knowing the initial total water content (in moles) W_o of the solution, and the initial number of moles, W_o^{18} of the O^{18}-labeled water molecules. The total water content is for any θ

$$W(\theta) = W_o + (q - \hat{q})\theta \qquad [A\text{-}1]$$

This relation was used to extract the values of $(q - \hat{q})$ from Fig. 3, listed in Table I, which were used in the calculations below.

In all cases one may write for any θ, neglecting the O^{17} content

$$W(\theta) = W^{16}(\theta) + W^{18}(\theta) \qquad [A\text{-}2a]$$

Moreover, the new decomposition products formed contain a number of moles U of oxygen where

$$U = \hat{q}\theta \qquad [A\text{-}2b]$$

We may write

$$U(\theta) = U^{16}(\theta) + U^{18}(\theta) \qquad [A\text{-}2c]$$

and we have

$$U^{18} + W^{18} = W_o^{18} = \text{constant} \qquad [A\text{-}2d]$$

since the total number of O^{18} atoms is conserved.

Case I.—Here the only source of oxygen^{-18} is the water, and

$$C(\theta) = \beta(W)\frac{W^{18}(\theta)}{W(\theta)} \qquad [A\text{-}3]$$

where $\beta(W)$ is the fraction of oxygen in the oxide originating from the water, for fixed salt content S_o and variable water content W. We may write from [4b]

$$\beta(W) = \frac{W}{W_e + W} \qquad [A\text{-}4]$$

and

$$C(\theta) = \frac{W^{18}(\theta)}{W_e + W(\theta)} \qquad [A\text{-}5]$$

The destruction of water may be described by the equation

$$\frac{dW^{18}(\theta)}{d\theta} = -\hat{q}\frac{W^{18}(\theta)}{W(\theta)} \qquad [A\text{-}6]$$

according to assumption (*ii*) (Section on Production and destruction of water).

(*a*) If $\hat{q} = q$, $W(\theta) = W_o$ = constant and from [A-6]

$$W^{18}(\theta) = W_o^{18}\exp\left[-\frac{\hat{q}\theta}{W_o}\right] \qquad [A\text{-}7]$$

(*b*) If $\hat{q} < q$, from [A-6] and [A-1]

$$\frac{dW^{18}(\theta)}{d\theta}\Big/W^{18}(\theta) = -\frac{\hat{q}}{W_o + (q - \hat{q})\theta}$$

Simple integration yields

$$W^{18}(\theta) = W_o^{18}\left[\frac{W_o}{W(\theta)}\right]^{\frac{\hat{q}}{q - \hat{q}}} \qquad [A\text{-}8a]$$

The closer $\hat{q}$ is to q, the closer $W^{18}(\theta)$ is approximated by an exponential.

$C(\theta)$ may be conveniently expressed from [A-5] and [A-8a] by writing

$$\frac{W_o^{18}}{C(\theta)} = \left[\frac{W(\theta)}{W_o}\right]^{\frac{\hat{q}}{q - \hat{q}}}[W_e + W(\theta)] \qquad [A\text{-}8b]$$

This expression was used to calculate the curves labeled I in Fig. 4 and 5.

The values of q and $\hat{q}$ to be used in [A-8b] are readily determined by noting that from [A-8b]

$$\left.\frac{d\left[\frac{W_o^{18}}{C(\theta)}\right]}{d\theta}\right|_{\theta=0} = q + \hat{q}\frac{W_e}{W_o} \qquad [A\text{-}9]$$

Hence the second term of Eq. [A-9] is determined by measuring the initial slope in Fig. 4 and 5. Knowing $q - \hat{q}$, q and $\hat{q}$ are calculated.

Case II.—Case IIa is described by Eq. [1] as mentioned above.

Case IIb is described by assuming that the new compounds formed behave for anodic oxidation like a quantity of water U, whereas β is still given by [A-4]. Hence,

$$C(\theta) = \beta\frac{W^{18} + U^{18}}{W + U}$$

Using [A-2d] we may write

$$\frac{W_o^{18}}{C(\theta)} = \left[1 + \frac{W_e}{W}\right](W + U) \qquad [A\text{-}10a]$$

and from [A-1] and [A-2b]

$$\frac{W_o^{18}}{C(\theta)} = \left[1 + \frac{W_e}{W}\right](W_o + q\theta) \qquad [A\text{-}10b]$$

It can readily be shown that the slope of this curve for $\theta = 0$ is also given by Eq. [A-9]. Hence both case I and IIb lead to the same values of q and $\hat{q}$. On the other hand the expression [A-10b] is nearly linear in the range of values of θ considered here, as shown in Fig. 4 and 5.

Case III.—The isotopic equilibrium between the oxygen in the new compounds and the water in the solution, is expressed by

$$\frac{W^{18}}{W} = \frac{U^{18}}{U} = \frac{W_o^{18} - W^{18}}{U} \qquad [A\text{-}11]$$

the last term being deduced using [A-2d]. Solving for W^{18} one gets

$$W^{18} = \frac{W_o^{18}\,W}{U + W} \qquad [A\text{-}12]$$

and as [A-3] and [A-5] fully apply here also, according to assumption (*ii*) (Section on Production and destruction of water)

$$C(\theta) = \frac{W}{W_e + W}\frac{W_o^{18}}{U + W} \qquad [A\text{-}13]$$

hence

$$\frac{W_o^{18}}{C(\theta)} = \left[1 + \frac{W_e}{W}\right](W_o + q\theta)$$

which is identical with [A-10b]. Thus case III and IIb lead to the same result as stated above.

Acknowledgments

We wish to acknowledge the assistance of J. Diaz, P. Paimblant, and R. Venard of the SESCOSEM on

making many of the measurements reported here and of E. d'Artemare for his help in operating the Van der Graaff accelerator of E.N.S. In addition, we are grateful to Dr. J. Siejka for many enlightening discussions. The work was supported by CNRS (RCP No. 157), DGRST, and DRME.

Manuscript submitted June 19, 1970.

Any discussion of this paper will appear in a Discussion Section to be published in the December 1971 JOURNAL.

REFERENCES

1. P. F. Schmidt and W. Michel, *This Journal*, **102**, 230 (1957).
2. E. F. Duffek, C. Mylroie, and E. A. Benjamini, *ibid.*, **111**, 1042 (1964).
3. E. F. Duffek, E. A. Benjamini, and C. Mylroie, *Electrochem. Technol.*, **3**, 75 (1965).
4. G. Amsel and D. Samuel, *J. Phys. Chem. Solids*, **23**, 1707 (1962); *Anal. Chem.*, **39**, 1689 (1967).
5. G. Amsel, C. Cherki, J. P. Nadai, and J. Siejka, Extended Abstracts, New York Meeting of the Society, May 4-9, 1969, p. 20.
6. G. Amsel and M. Croset, *ibid.*, p. 24.
7. G. Amsel, C. Cherki, G. Feuillade, and J. P. Nadai, *J. Phys. Chem. Solids*, **30**, 2117 (1969).
8. D. Samuel, "Methodology of Oxygen Isotopes," in "Oxygenases," O. Hayaishi, Editor, Interscience Publisher Inc., New York (1962).
9. M. Anbar, M. Halmann, and S. Pinchas, *J. Chem. Soc.*, **1960**, 1242.
10. M. Croset, *Rev. Sci. Instr.*, **37**, 123 (1966).
11. M. Anbar, *Intern. J. Appl. Radiation Isotopes*, **3**, 131 (1958).
12. M. Cohn and H. Urey, *J. Am. Chem. Soc.*, **60**, 659 (1938).
13. M. Anbar and S. Guttmann, *Intern. J. Appl. Radiation Isotopes*, **4**, 233 (1959).
14. M. Anbar and H. Taube, *J. Am. Chem. Soc.*, **76**, 6243 (1965).
15. G. M. Harris, *Trans. Faraday Soc.*, **47**, 716 (1951).
16. D. Samuel and B. L. Silver, "Advances in Physical Organic Chemistry," Vol. 3, p. 123, Academic Press, London (1965).
17. G. Amsel and D. David, *Rev. Phys. Appl.*, **4**, 383 (1969); and in "Proceedings of Grenoble Conference on MIS Structures," June 1969, p. 243.
18. J. Mitchell and D. M. Smith, "Aquametry," Interscience Publishers Inc., New York (1948).
19. M. L. Bender and R. D. Ginger, *J. Am. Chem. Soc.*, **77**, 348 (1955).
20. P. Greenzaid, Z. Luz, and D. Samuel, *Trans. Faraday Soc.*, **64**, 2781 (1968); and previous papers cited therein.
21. D. E. Couch, *Electrochim. Acta*, **9**, 327 (1964).
22. C. K. Ingold, "Structure and Mechanism in Organic Chemistry," p. 276, G. Bell & Sons, Ltd. (1953).

A Study of the Oxygen Growth Laws of Anodic Oxide Films on Aluminum and Tantalum Using Nuclear Microanalysis of O^{16} and O^{18}

J. Siejka, J. P. Nadai, and G. Amsel

Groupe de Physique des Solides de l'Ecole Normale Supérieure, Tour 23-9, Quai Saint-Bernard, Paris 5ème, France

ABSTRACT

The oxygen growth laws of anodic oxide films on aluminum and tantalum were studied using the nuclear microanalysis of the O^{16} and O^{18} isotopes. The influence of current density and surface preparation on the growth laws has been demonstrated. The correlation of the results of nuclear microanalysis of O^{16} and of coulometric measurements allowed the determination of the dissolution current density during anodic oxidation of aluminum. This dissolution current was shown to be purely electrochemical. The values of the intercepts with the potential axis of the linear growth laws show that the overpotentials at the interfaces are smaller than 0.1V for current densities from some $\mu A/cm^2$ to 10 mA/cm^2. Measurements of isotopic exchange of oxygen using O^{18} as a tracer allowed direct estimation of the oxygen exchange current without applied field. The results show that oxygen transfer at the oxide-solution interface, enhanced by field-induced oxygen vacancies, is responsible for the growth of the anodic film.

The growth laws of anodic barrier layers on aluminum and tantalum have been carefully investigated by numerous authors (1-8) using various methods. The published results clearly indicate that the growth laws of the anodic layers are strongly dependent on the experimental conditions of sample surface preparation and of film formation, illustrating the complicated character of the mechanisms involved. It appears that the direct measurement of the oxygen content of the anodic films as a function of various parameters could contribute to the elucidation of some of the aspects of these growth mechanisms. In addition the use of tracing techniques applied to the isotopes of oxygen may yield further information, which cannot be provided directly by classical methods, on the electrochemical processes taking place during anodic treatments.

Key words: oxygen, aluminum, tantalum, anodic oxidation, growth rate, O^{18} tracing, nuclear microanalysis, exchange current, interface, surface treatment.

In this work we applied the microanalysis of the isotopes of oxygen by means of nuclear reactions to a detailed study of the anodic oxidation of aluminum and tantalum in aqueous solutions. The isotope O^{16} (natural abundance 99.758%), determined by the nuclear reaction $O^{16}(d,p)O^{17*}$, was monitored to measure the oxygen content of films formed in solutions of natural isotopic composition. In the absence of long-lived radioactive isotopes of oxygen, O^{18}-enriched compounds may be used for tracing experiments, the $O^{18}(p,\alpha)N^{15}$ reaction allowing the determination of the O^{18} isotope (natural abundance 0.204%) contained in the films. Several recent publications (9-12) deal with the application of this method to anodic oxidation processes. The techniques themselves are described in detail in ref. (13-15) and will not be pre-

sented here. These microanalytical techniques allow the determination, with a precision of the order of 1% even for oxide films some 10Å thick, of the number of O^{16} or O^{18} atoms/cm^2 they contain, with respect to an absolute oxygen standard. As an absolute oxygen standard we used here an anodic oxide film formed on tantalum in well-defined conditions, as described in ref. (9); it was shown in this reference that precise coulometric measurements allow in this case the absolute determination of the number of oxygen atoms/cm^2 in the standard with a precision of about 3%.

The oxygen growth laws were measured in both natural and O^{18}-labeled solutions for various sample surface preparation procedures. The results clarify the influence of the initial layer on the metal on the growth of the anodic films. Furthermore we have tried to estimate the value of the sum of the overpotentials at the metal-oxide and oxide-solution interfaces, by measuring the intercept of the oxygen growth law with the potential axis for various oxidation currents. For tantalum, Young (1) and Vermilyea (2) found very small overpotentials, which seems to imply a high ionic exchange current at the oxide-solution interface. We have therefore attempted to measure this exchange current directly by studying the isotopic exchange of O^{18} in order to correlate its value with those of the overpotentials, found by the nuclear method, for the two metals. In addition we have tried by the nuclear method to demonstrate the existence on the samples of layers of high ionic conductivity for various methods of surface preparation and, when such layers exist, to relate their presence to the changes observed in the corresponding oxygen growth laws. We have not attacked here the problem of the mechanism of ionic transport in the oxide itself. This was dealt with in ref. (10) and will be further studied, by O^{18} tracing, in a future publication.

Sample Preparation

The aluminum used was in the form of bright rolled and annealed sheets 0.6 mm thick, of purity 99.9%. Taking into consideration on the one hand that electrochemical polishing of aluminum is known to leave on the surface of the metal a thin film which may differ in its properties from anodic barrier layers (6, 16, 17), and on the other hand that unpolished samples, although free of contamination by chemicals, might present a less well-defined state of the surface, both polished and unpolished aluminum samples were systematically studied in this work. Unpolished samples were cleaned with acetone in a vapor degreasing set-up according to the classical procedure described by Holland (18). Electropolishing of the samples was carried out so as to avoid the deleterious effects on the anodic oxidation of aluminum of contamination by chlorine (17) or by chromates (6). On the other hand, as Godard reports that SO_4 anions are less "aggressive" to aluminum than chlorine (19) we used sulfuric acid as the main polishing agent. The procedure used consisted in: (*a*) etching in a sodium hydroxide solution (10% by weight, 10 min); (*b*) dipping into a solution containing 15% trisodium phosphate and 20% disodium carbonate (10 min); (c) anodic polishing in a solution containing 20% sulfuric acid (1 min, 5 mA/cm^2); (*d*) dipping for 10 min into the above solution; and (*e*) rinsing in triply distilled water. This procedure is used in industry and yields a highly brilliant surface; the corresponding results on anodic oxidation showed a high degree of reproducibility.

The tantalum used, 99.95% pure, was in the form of unannealed rolled sheets 0.2 mm thick. As in ref. (9) the samples were degreased with acetone and chemically polished for 15 sec in a mixture of 5 volumes of 95% H_2SO_4 2 volumes of 53% HNO_3, and 2 volumes of 45% HF. As suggested by Young (1) the samples were then dipped for 5 min in boiling tridistilled water. The assumption of Young, according to which this leaching removes fluorine traces from the surface of polished tantalum, was recently confirmed in our laboratory using nuclear microanalysis of F^{19} (20). Although for tantalum the polishing process seems to have less influence on the subsequent anodic behavior than for aluminum, here again polished and unpolished samples were compared in some cases.

All the samples were punched into 2 cm^2 rectangles by a special tool (9) insuring the reproducibility of the area. The electrical contact with the samples was made by a 0.5 mm wire as described in ref. (9) or by a special tantalum clip used by Croset (21).

The unlabeled solutions were prepared with triply distilled water of resistivity 0.5 x 10^6 ohm-cm, and high-purity salts provided by Merck. Oxidations were carried out at 22° ± 1°C in aqueous solutions of 5% by weight ammonium citrate of *p*H 6. These solutions were prepared by dissolving diammonium citrate and by adjusting the *p*H with ammonia. This yields a mixture of di- and triammonium citrate solution with good buffer characteristics.

In the tracer experiments water of nonnatural isotopic composition of oxygen was used[1]: either enriched to 80% in O^{18} (and about 0.7% in O^{17}) or depleted 30 times in O^{18} (0.007%). The isotopic composition of hydrogene was normalized near to the natural abundance (deuterium content <0.1%). The first O^{18}-labeled anodic oxide films on aluminum were produced by Amsel and Samuel (10). They encountered difficulties in oxidizing aluminum in small volumes of O^{18}-enriched water and succeeded to do so only by a massive adjunction of ammonia, up to *p*H 9 (22). It was found in this work that these difficulties were due to impurities introduced in the labeled water during the enrichment procedure: careful purification allowed the anodic oxidation of aluminum to be carried out in conditions identical to the nonlabeled case. The handling of the labeled water was carried out using a vacuum line; this allows repeated loss-free transfers of the expensive enriched water, easy purification, and prevents any isotopic exchange with the constituents of the atmosphere (23). The first stage of the purification consists of eliminating dissolved gases. The sealed ampula containing a given quantity of labeled water is broken inside a cell connected to the distillation line. This cell is placed in a mixture of solid carbon dioxide and acetone; once the water has frozen, the greatest part of the dissolved gases (O_2, CO_2, H_2, N_2) are removed by pumping. In the second stage, to eliminate traces of halogens, in particular, the water was distilled over sodium contained in a glass capillary (following the procedure developed by Dostrowsky (24) at the Weizmann Institute) from ambient temperature to that of melting ice. The transfer must be carried out in several stages, between which the hydrogen formed is pumped off at CO_2-acetone temperature. The water is then distilled from the resulting sodium hydroxide solution at ambient temperature into the oxidation cell containing the necessary quantity of salt, at the temperature of melting ice.

Salts of natural isotopic composition were used both in the O^{18}-enriched and depleted solutions: preliminary experiments using ammonium citrate enriched to 70% in O^{18} showed that at least 98% of the oxygen contained in the films formed on aluminum and tantalum in our experimental conditions come from the water in the solution used (25). In addition it was shown by Samuel (26) at the Weizmann Institute that the isotopic exchange between ammonium-citrate and water is negligible at room temperature. O^{18}-labeled solutions at *p*H 6 were prepared in the following way. Ammonium citrate was dissolved in an ammonia solution of *p*H 8 in the oxidation cell. This solution was evaporated and the remaining salt dried for 6 hr in high vacuum at room temperature. The labeled water was then distilled on the salt. This procedure yields a solution of *p*H 6-6.5. The final adjustment of the *p*H,

[1] Supplied by the Weizmann Institute, Rehovot, Israël.

if necessary, may be achieved by adding a minute amount of dry citric acid.

In all the experiments with nonnatural water a special 5 cm³ cell [described in ref. (22)] was used due to the high cost of enriched or depleted water. A special sample holder was used, described in (27), with a platinum wire cathode encircling the sample. The oxidations were carried out under atmospheric pressure, the contact with the ambients being kept to a minimum. In these conditions the drop in enrichment of the 80% O^{18} water was negligible during the duration of the experiments.

The anode potential was measured with respect to a reference electrode using a high impedance voltmeter (Keithley 610B, 10^{14} ohms). To avoid contamination of the solutions by chlorine ions from a calomel reference electrode, a mercury sulfate electrode was used. To further minimize any contamination the reference electrode was separated from the solution by a double junction of sintered glass.

For electrolytes enriched in O^{18}, reference electrodes were not used, to avoid any possibility of isotopic exchange. The anode potential was measured with respect to a platinum cathode whose current-potential characteristics had previously been measured with respect to a reference electrode.

Most of the oxidations were carried out at constant current densities, in the range of 1-10 mA/cm², using a Harrison 6209B power supply. Once the potential V_{ox} between the anode and the reference electrodes reaches a preset value, an electronic arrangement cuts the circuit. A digital current integrator (Brookhaven Instruments Corporation, Model 1000) connected to a counting scale, gives the number of coulombs consumed during the oxidation. This integrator, designed for accelerator beam current measurements, insures a precision and absolute calibration better than 10^{-3}.

In order to operate at low current densities, below 10 μA/cm², after a constant current stage (5 mA/cm²), the potential V_{ox} was maintained constant for fixed times (10 min for tantalum, 20 min and 50 min for polished and unpolished aluminum, respectively) allowing the current to decay to small final values. This procedure kept the duration of these experiments reasonably short while minimizing the perturbing effects arising at low current densities of oxidation for aluminum, which result in the formation of porous oxide or hydroxide layers as reported in ref. (4, 28, 29) (see below).

Results and Interpretation

Nuclear microanalysis gives the numbers N_{O16} or N_{O18} of oxygen atoms per square centimeter fixed on the surface of the sample; O^{17} will be neglected and hence the total number of oxygen atoms per square centimeter N_O is given in any oxide film by $N_O = N_{O16} + N_{O18}$. It should be noted that when results from nuclear microanalysis are compared with coulometric results obtained on the same sample, the effects of roughness cancel out, as has been pointed out in ref. (9). For a homogeneous oxide it is possible to introduce an equivalent geometric thickness L deduced from N_O, by assigning known values to the stoichiometry and the density of the chemical compound formed as well as to the roughness factor of the underlaying surface. Under such assumptions we may write

$$L = \lambda N_O \qquad [1]$$

where λ is a constant. This relation allows the comparison of our results on growth laws with those obtained by other authors, who measured the thickness of the films formed by various methods such as capacitance, optical, gravimetric, etc., measurements. Let us remark that the determination of the intercepts of the growth laws with the potential axis does not depend on a given normalization of the thickness, and hence neither on the roughness factor nor on the absolute oxygen standard.

Oxygen growth laws.—General characteristics.— Figures 1, 2, and 3 show the curves $N_O = f(V_{ox})$ obtained at various final current densities between some μA and 10 mA/cm², on polished tantalum and unpolished and polished aluminum, respectively. The values of the potentials are expressed in the hydrogen scale, in volts. The oxidations were carried out in unlabeled solutions; N_O is therefore given by N_{O16}. It should be noted that the quantities of oxygen in the initial layer

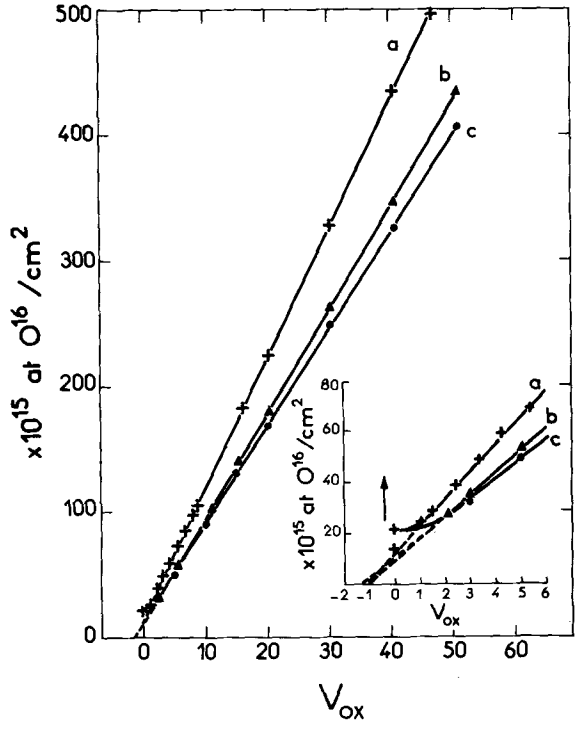

Fig. 1. $N_{O16} = f(V_{ox})$ for polished tantalum for various final current densities: curve a, of the order of 1 μA/cm² (constant potential); curve b, 1 mA/cm²; curve c, 10 mA/cm². The insert shows the detail near the origin.

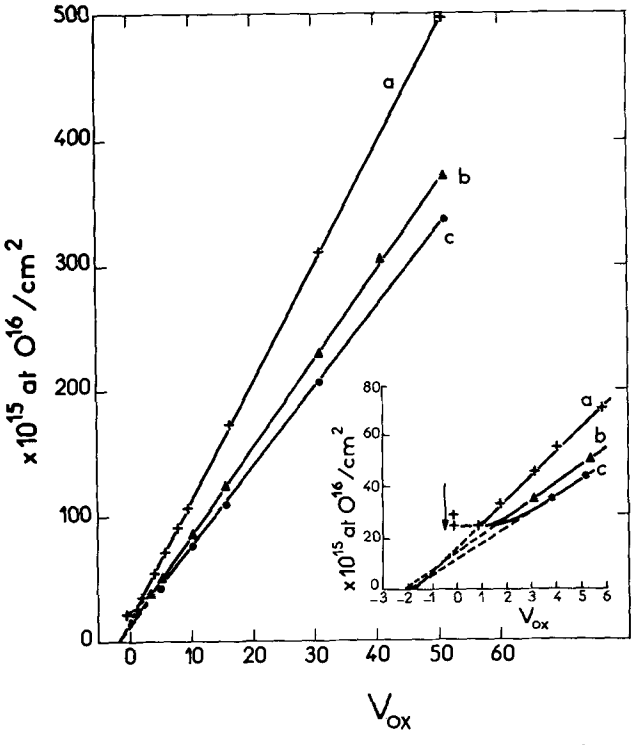

Fig. 2. $N_{O16} = f(V_{ox})$ for unpolished aluminum: curve a, below 10 μA/cm² (constant potential); curve b, 1 mA/cm²; curve c, 10 mA/cm². The insert shows the detail near the origin.

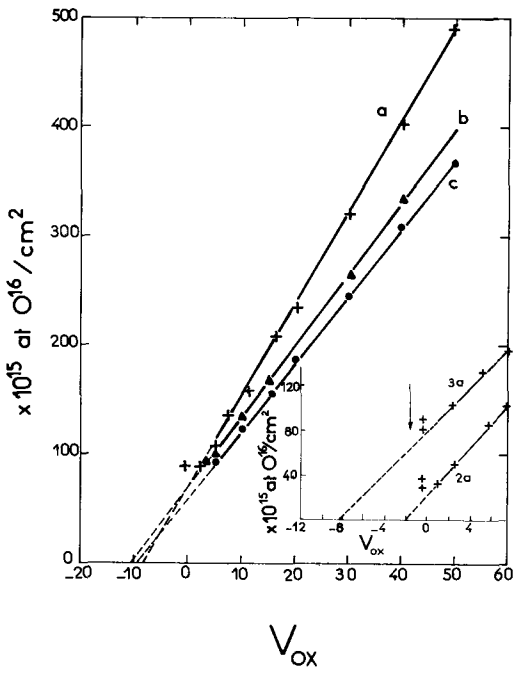

Fig. 3. $N_{O16} = f(V_{ox})$ for polished aluminum: curves a, b, c see Fig. 2. The insert compares in detail the growth laws at constant potential for unpolished (curve 2a) and polished aluminum (curve 3a).

change when the sample is immersed in the solution, before any potential is applied. This variation is shown in these figures (direction of the arrow).

The anode potential V_{ox} satisfies, according to Young (1), the relation

$$V_{ox} - V_{eq} = \eta_m + \eta_s + \eta_{ox} \qquad [2a]$$

throughout the oxidation, where η_m is the overpotential at the metal-oxide interface, η_s that at the oxide-solution interface, and η_{ox} that in the oxide. V_{eq} is the anode equilibrium potential; this potential is equal to the thermodynamic potential V_{th} for the formation of the oxide (1-3) for which the over-all reaction can be written

$$M + H_2O \rightleftarrows MO + 2H^+ + 2e^- \qquad [3a]$$

where M represents the metal.

If all the oxygen on the sample surface is contained in a highly insulating oxide film which behaves as an anodic barrier layer, we may write

$$\eta_{ox} = \lambda E_{ox} N_O \qquad [2b]$$

where E_{ox} is the electric field of formation of the oxide. If the film contains a region of high ionic conductivity, with oxygen content N_O^c, we have

$$\eta_{ox} = \lambda E_{ox}(N_O - N_O^c) \qquad [2c]$$

Hence, in the most general case we have

$$V_{ox} - V_{eq} = [\eta_m + \eta_s - \lambda E_{ox} N_O^c] + \lambda E_{ox} N_O \qquad [3b]$$

The intercept $V_{ox}(0)$ of the curve $N_O = f(V_{ox})$ with the V_{ox} axis for $N_O = 0$ is given for constant N_O^c by

$$V_{ox}(0) - V_{eq} = \eta_m + \eta_s - \lambda E_{ox} N_O^c \qquad [3c]$$

It is clear from Eq. [3c] that in the case when an initial layer of high ionic conductivity is present on the sample surface, the curve $N_O = f(V_{ox})$ is shifted toward the negative potentials. Moreover, if $N_O^c = 0$ the curves $N_O = f(V_{ox})$ for various current densities (hence various E_{ox}) intersect at one and same point, the intercept $V_{ox}(0)$ yielding the sum of the overpotentials.

In order to determine with precision the values of the parameters of Eq. [3b] it is advantageous to operate in conditions such that the curves $N_O = f(V_{ox})$ are linear. In particular E_{ox} and the overpotentials should be constant; this was insured by taking into account the following considerations. The final current density J may be decomposed in the oxide according to

$$J = J_i + J_e \qquad [4]$$

where J_i is the ionic and J_e the electronic current density, respectively. It is known that one to one relations exist between E_{ox} and J_i and between the overpotentials and J_i; furthermore these relations are of the logarithmic type. Hence E_{ox} and the overpotentials are constant if J_i is, and are nearly constant even if J_i varies slightly, owing to their logarithmic dependence on the latter. In the case of oxidations at constant current ($1 \leq J \leq 10$ mA/cm^2) J_e was always less than 5% of J (see below); this insures a good constancy of J_i by simply controlling J itself. In the case of oxidation at constant potential, at the low final current densities reached, J_e may be a large fraction of J. In this case we have no precise estimation of J_i and it appears that the control of the duration of the anodic treatment leads to a better constancy of J_i than the control of J, as illustrated by additional results below. Figures 1 to 3 clearly illustrate that operation according to these principles leads to the linear relations expected.

The experimental values of the slopes of the straight lines in Fig. 1, 2, and 3 and of the intercepts $V_{ox}(0)$ were determined by a method of least squares; they are listed in Table I. In our experimental conditions the thermodynamic potential V_{th} for the formation of tantalum oxide is equal to -1.15V (30) and for the formation of hydrated aluminum oxide or anhydrous aluminum oxide to -1.9 and -1.84V, respectively (31); over the whole range of currents investigated for polished tantalum and unpolished aluminum the values $V_{ox}(0)$ are very close to these theoretical values of V_{th}. The mean value of the difference with V_{th} is -30 mV for Ta_2O_5, and -13 or -73 mV for Al_2O_3,

Table I. Characteristic constants of the growth laws

Metal	Surface preparation	J, mA/cm^2	$dN_O/dV_{ox} = \frac{1}{\lambda E_{ox}}$ $\times 10^{15}$ at./cm^2 V	$V_{ox}(0)$ deduced from $N_O = f(V_{ox})$*	$V_{ox}(0)$ deduced from $\hat{N}_O^{18} = \hat{g}(V_{ox})$
Tantalum	Polished	10	8.20 ± 0.02	−1.20 ± 0.08	—
		1	8.79 ± 0.02	−1.15 ± 0.06	—
		~10^{-3}	10.84 ± 0.08	−1.19 ± 0.05	+0.63 ± 0.1
	Unpolished	~10^{-3}	10.52 ± 0.08	−2.13 ± 0.1	+0.63 ± 0.1
Aluminum	Polished	10	6.20 ± 0.03	−10.71 ± 0.2	—
		1	6.46 ± 0.02	−10.67 ± 0.12	—
		<10^{-2}	7.96 ± 0.1	−8.3 ± 0.2	+0.75 ± 0.1
	Unpolished	10	6.36 ± 0.03	−1.86 ± 0.17	—
		1	7.03 ± 0.03	−2.02 ± 0.12	—
		<10^{-2}	9.26 ± 0.11	−1.86 ± 0.07	+0.75 ± 0.1
	Thermally** oxidized	<10^{-2}	9.26 ± 0.11	−1.80 ± 0.1	+4.60 ± 0.1

All errors arise from the statistical spread of the nuclear countings and were calculated by the method of least squares.
* Compare with the values of the thermodynamic potentials V_{th}: −1.15V for Ta_2O_5 and −1.84V for Al_2O_3.
** At 520°C, 3 hr in dry air.

with a statistical standard deviation of 80 and 170 mV, respectively. It can be deduced that the sum of the overpotentials $\eta_m + \eta_s$ is statistically zero with the standard deviation indicated. By contrast the straight lines corresponding to polished aluminum are considerably translated toward negative potentials with respect to those for unpolished aluminum, as is shown in detail on Fig. 3. Moreover the initial layer contains about three times more oxygen on polished aluminum than on unpolished aluminum. In view of Eq. [3c] this result strongly suggests that the anodic oxides on the polished aluminum samples contain a layer of high ionic conductivity; it seems likely that this layer originates in the initial oxide layer left on the samples after the polishing procedure.

It appears also that when the growth law curve is shifted toward negative potentials the corresponding slope decreases. In the case of aluminum the ratio of the slopes for polished and unpolished samples varies between 0.98 to 0.86 as the current density varies between 10 mA/cm^2 and some μA/cm^2.

Control experiments carried out at constant potential, in electrolytes containing 0.5% by weight of salt (*i.e.*, 10 times less than above), produced the same results as those of Fig. 1-5 and Table I, within experimental error. This shows that the influence of salt concentration on the growth laws is very small, if any.

Influence of the initial oxide layer.—In order to get further insight in the phenomena induced by the presence on the sample surface of the initial oxide layer arising either from the polishing or from the spontaneous oxidation of the metal the shape of the growth laws near the origin was studied in more detail both in natural and in O^{18}-labeled solutions. As the shift of the curve $N_O = f(V_{ox})$ toward negative potentials was observed on polished aluminum samples for which the initial layer contains a relatively high quantity of oxygen, the growth laws were further studied on samples covered by an initial layer of similar oxygen content but of different origin. Unpolished aluminum was hence thermally oxidized in air at 520°C for 3 hr and then further oxidized anodically at constant potential in natural solutions. Figure 4 and Table I show the corresponding results. The growth of the anodic film starts at a potential V_1 much higher for thermally oxidized samples; nevertheless in spite of the presence of an about three times thicker initial layer, the growth law $N_O = f(V_{ox})$ shows no translation toward negative potentials.

Experiments in O^{18}-labeled solutions may give additional information on the role of the initial layers. Let $N_{O18} = g(V_{ox})$ be the growth law obtained in such solutions. In order to compare directly $N_{O18} = g(V_{ox})$ to $N_O = f(V_{ox})$, (obtained from unlabeled films) it is convenient to normalize the results to 100% enrichment of the electrolyte used. We shall call $\hat{N}_{O18} = \hat{g}(V_{ox})$ these normalized values. If the initial layer behaves like a barrier layer, and if, in addition, the oxygen atoms it contains remain in the film obtained after oxidation, undergoing no isotopic exchange (which, as we shall see, is the case), Eq. [3b] applies to N_{O18} with the following alteration

$$V_{ox} - V_{eq} = \eta_m + \eta_s + \lambda E_{ox}\hat{N}_{O18} + \lambda E_{ox}N_O^i \quad [3d]$$

for $V_{ox} > V_1$, where N_O^i is the oxygen content of the initial layer. It should be noted that the growth starting potential V_1 is equal to $\eta_m + \eta_s + \lambda E_{ox}N_O^i$ and hence slightly depends on J_i; the experiments shown here were all made at constant potential, *i.e.*, at low final current densities. Equation [3d] shows that the straight line $\hat{N}_{O18} = \hat{g}(V_{ox})$ differs from $N_O = f(V_{ox})$ only by a translation toward positive potentials. Any deviation from such a behavior indicates a more complicated role of the initial layer in the oxide growth than assumed.

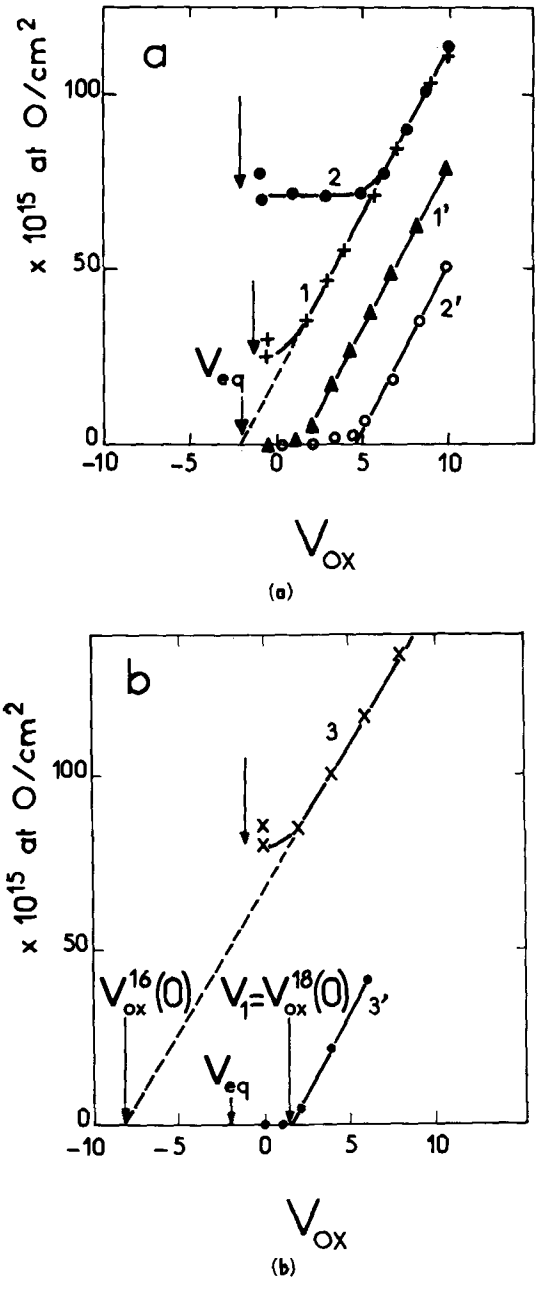

Fig. 4. Growth laws for aluminum at constant potential: (a) unpolished and (b) polished samples. Curves 1, 2, 3 represent $N_O = f(V_{ox})$, respectively, for unpolished; unpolished and thermally oxidized; polished samples. Curves 1', 2', 3' represent $\hat{N}_{O18} = \hat{g}(V_{ox})$ for samples of the safe type anodized in O^{18} enriched solutions.

Figure 4a shows $\hat{N}_O{}^{18} = \hat{g}(V_{ox})$ for unpolished aluminum, both thermally oxidized and not. It is clear that these curves strictly obey Eq. [3d], V_1 increasing with the oxygen content of the initial layer. Figure 4b shows the corresponding results for polished aluminum. We see here that, in spite of the presence of a thick initial layer, the starting potential V_1, as observed on $\hat{N}_{O18} = \hat{g}(V_{ox})$, remains small, near the value observed for unpolished aluminum.

The results of Fig. 4 and Table I suggest the following interpretation. The shift toward negative potentials of $N_{O16} = f(V_{ox})$ is not dependent on the oxygen content of the initial layer but on its nature. The initial layers of thermal origin behave like a barrier layer having no influence on the growth law and presenting no isotopic exchange of oxygen during further anodic oxidation, like anodic aluminum oxides, as shown in

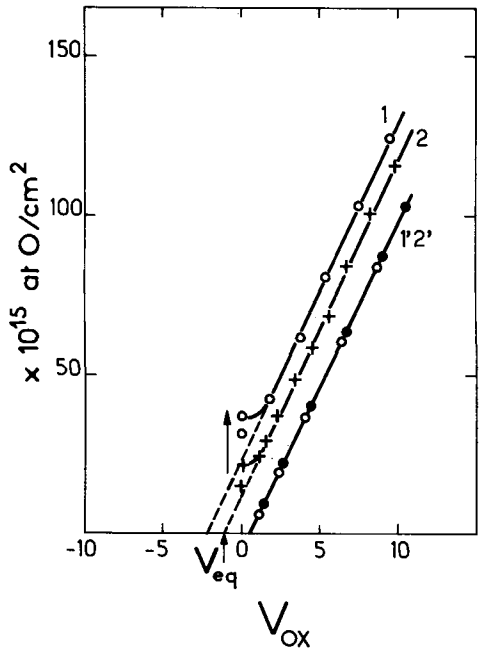

Fig. 5. Growth laws for tantalum at constant potential. $N_{O16} = f(V_{ox})$: curve 1, unpolished and curve 2, polished samples. $N_{O18} = g(V_{ox})$: curve 1', unpolished and curve 2', polished samples.

ref. (10). The initial layer on polished aluminum consists of two regions: (*a*) a region of high ionic conductivity responsible for the shift of $N_{O16} = f(V_{ox})$ by an amount $|V_{ox16}(0) - V_{eq}|$ and (*b*) a region of the barrier type responsible for the shift of $N_{O18} = g(V_{ox})$ by an amount $V_{ox18}(0) - V_{eq}$. This region has an oxygen content similar to that of the initial layer on the unpolished aluminum. The relative oxygen content of these regions is the ratio of these potential shifts, *i.e.*, 2.6 in this case. Moreover the layer of high ionic conductivity does not undergo isotopic exchange of oxygen during anodic treatment. These results indicate that the oxygen coming from the solution merely passes through the layer of high ionic conductivity, if we assume that the latter remains at the oxide-solution interface; in this case this layer would have a porous character (see Discussion).

Figure 5 shows the growth laws obtained on polished and unpolished tantalum in labeled and unlabeled solutions, and Table I shows the corresponding parameters. A translation of the curve $N_{O16} = f(V_{ox})$ toward negative potentials for unpolished tantalum seems to indicate the presence of a layer of high ionic conductivity in this case. It should be noted that the curves $\hat{N}_{O18} = \hat{g}(V_{ox})$ have the same intercept with the potential axis for both types of tantalum used.

Electric field of formation.—The values of E_{ox} were deduced from the oxygen growth laws by assigning well chosen values to λ in Eq. [3b]. It should be noted that in order to obtain a linear relation $N_O = f(V_{ox})$, when N_O^c is not vanishing, it is not necessary to require N_O^c to be a constant. In fact, if N_O^c itself varies linearly with V_{ox}, at least in a given range of potentials, the curve $N_O = f(V_{ox})$ remains linear. Such a behavior may change the value of the apparent field of formation E_{ox} as deduced from the slope of the curve $N_O = f(V_{ox})$. A decrease of N_O^c with V_{ox} may correspond to the gradual dissolution of an initial layer of high ionic conductivity or to pore-filling processes (32); an increase of N_O^c with V_{ox} may be caused by a partial formation of a hydroxide or of a porous layer during the anodic process (4). In the last case N_O^c may vanish at small V_{ox}, so that no shift of the intercept V_{ox} is observed. In what follows we shall calculate the apparent field E_{ox}; the effects of the various behaviors of N_O^c will be considered in the Discussion.

For aluminum the roughness factor was taken equal to unity; this assumption will be discussed later. Like Young (1) and Diggle *et al.* (33) we assume that the barrier layers of aluminum oxide have the formula Al_2O_3 and are amorphous. The density of such layers was measured by several authors in various conditions; the reported values range from 2.73 g/cm^3 (34) to 3.3 g/cm^3 (35). Van Geel and Schelen (36) measured 3.1 g/cm^3 for aqueous solutions; this value is near that of Bernard and Cook (5), 3.17 g/cm^3, measured in organic solutions. This is in agreement with ref. (37) in which it is assumed that barrier layers formed in organic and aqueous solutions are similar from this point of view. Our calculations were based on the value 3.17 g/cm^3.

For polished tantalum we shall take a roughness factor equal to unity in agreement with Young (1), who measured a density of 8.01 g/cm^3 for aqueous solutions; this figure was later confirmed by Schrijner and Middelhoek (38) to within 0.5% precision. We admitted here a density of 8 g/cm^3.

The calculated values of E_{ox} are listed in Table II. In order to compare our results to those of the literature, we also list in this table our values, recalculated with the densities used by the other authors quoted. For aluminum, E_{ox} is always larger on polished samples than on unpolished samples, the difference increasing with decreasing current density. Moreover our recalculated values on unpolished samples agree to within 2% with those of Harkness and Young (7), who did not use electrochemical polishing; our results on polished samples agree to within 5% with those of Bernard and Cook (5), who resorted to electrochemical polishing. These agreements might be fortuitous; nevertheless they are worthy to be noticed as Harkness and Young ascribed the difference between their values and those of Bernard and Cook to the influence of the different solutions used, whereas here the surface preparation seems to play a fundamental role. For tantalum there is excellent agreement with the values of Young (1) and good agreement for recalculated values with those of Vermilyea (39). The agreement with Young is natural for the values at high current density, as we too used coulometric measurements on tantalum to define our standard. At low current densities, where the faradaic efficiency might be less than 100%, the agreement is a good confirmation

Table II. Electric field of formation E_{ox} x 10^6 V/cm

	J, mA/cm^2	Bernard and Cook (5) [ρ = 3.17]	Harkness and Young (7) [ρ = 3.0]	This work [ρ = 3.17] Polished samples		Unpolished samples	
Aluminum	10	9.62	8.44	9.1	(8.6)	8.8	(8.3)
	1	9.10	7.77	8.7	(8.2)	8.0	(7.6)
	$\leq 10^{-2}$	—	—	7.1	(6.7)	6.1	(5.8)
	J, mA/cm^2	Vermilyea (39) [ρ = 8.74]	Young (1) [ρ = 8.0]	This work [ρ = 8.0] Polished samples			
Tantalum	10	7.1	6.6	6.6	(7.2)		
	1	6.5	6.2	6.2	(6.8)		
	$\sim 10^{-3}$	—	5.1*	5.0	(5.5)		

Values recalculated for the densities 3.0 g/cm^3 and 8.74 g/cm^3 for aluminum and tantalum respectively, are listed in brackets.
* For 1 μA/cm^2.

of the value of Young, as our value, determined by nuclear microanalysis, is not influenced by the presence of an electronic current.

Components of the current.—The ionic current density in Eq. [4] may be in turn decomposed at the oxide-solution interface according to

$$J_i = J_{ox} + J_{dis} \qquad [5]$$

where J_{ox} is the part of the current which contributes to the film growth and J_{dis} the dissolution current J_{dis} includes the current density of direct dissolution of the cations as well as that equivalent to the dissolution of oxide already formed. The one to one empirical relation between J_i and E_{ox} may be written conveniently

$$J_i = A \exp B E_{ox} \qquad [6]$$

where, for a given system A and B are temperature-dependent parameters. According to various authors (1, 40) B may slowly vary with E_{ox}, this leading for example to a quadratic term in the exponential. In what follows, at constant temperature and in the range of current densities covered, we shall consider B as constant and estimate its value from Eq. [6].

The components of J_{ox} and J_{dis} may be separated if J_i is known. This implies an estimation of J_e in Eq. [4], which might be carried out as shown below. J_{ox} is in fact given directly by the nuclear measurements. By definition the number $N_O(t)$ of oxygen atoms per square centimeter in the layer at time t is

$$N_O(t) - N_O(0) = k \int_0^t J_{ox}(\theta)\, d\theta \qquad [7a]$$

$$= k \int_0^t R(\theta)\, J(\theta)\, d\theta \qquad [7b]$$

where $R(t)$ is the oxidation current efficiency at any instant

$$R = \frac{J_{ox}}{J} \qquad [8]$$

and where the constant k is equal to 0.312×10^{19} atoms of oxygen per coulomb, if we assume that the oxygen is fixed in the film in the state O^{--}.

For oxidations carried out at constant current, the precise measurement of the number Q of coulombs per square centimeter

$$Q = \int_0^t J(\theta)\, d\theta \qquad [9]$$

consumed during oxidation allows the determination of the oxidation current efficiency from the following relation, deduced from [7b]

$$R = \frac{1}{k} \frac{dN_O}{dQ} \qquad [10]$$

This quantity is easily measured and will be used to determine J_{ox} by using Eq. [8].

Measurements at constant current.—The oxidation of tantalum and aluminum at constant current (1 to 10 mA/cm²) in presence of a redox system yields an upper limit of the electronic component J_e: 1% of the current for polished Ta in agreement with ref. (9), 2% for polished Al, 5% for unpolished Al and Ta. By difference we obtain the minimum value of the ionic current density J_i. For each type of samples used it is thus possible to estimate the value of the constants A and B in the empiric relation [6]. The approximate values of A and B obtained, using the values of E_{ox} determined at 1 and 10 mA/cm² from Table II are listed in Table III. The agreements between our results and the literature are similar to those found in Table II.

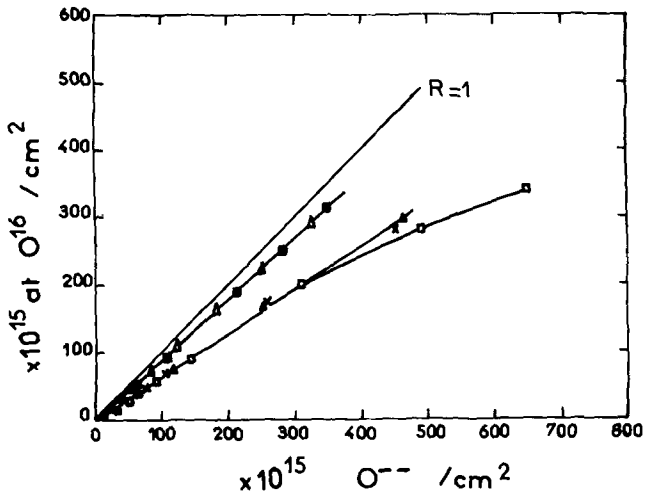

Fig. 6. Number of O^{16} atoms/cm² fixed on aluminum samples by anodic oxidation vs. electric charge consumed, expressed as a number of O^{--} anions/cm². △ polished Al, 10 mA/cm² and ■ 1 mA/cm²; ▲ unpolished Al, 10 mA/cm², × 6.6 mA/cm², and □ 1 mA/cm².

On Fig. 6 the number of O^{16} atoms per square centimeter fixed on the surface of aluminum samples by anodic oxidation at constant current (minus the initial layer) is plotted as a function of the number of coulombs per square centimeter used during formation of the film (this quantity being expressed in numbers O^{--}/cm²). The slope of the curves gives, by definition, the values of R. Here $R = 1$ for tantalum and is not considered.

For polished aluminum the current efficiency is independent of the current. For unpolished aluminum the decrease of the efficiency as the layer thickness increases and the current density decreases, is due to an increase in the dissolution current, as the electronic current is less than 5% of the total. Moreover R is much smaller for unpolished than for polished aluminum. The various components of the current as deduced from the values of J_e and R are listed in Table IV. The large values of J_{dis} found for aluminum, especially for unpolished samples, raise the question whether the dissolution currents are of chemical or electrochemical nature.

The equivalent chemical dissolution current density for aluminum oxide was measured by nuclear methods, without applied electric field (this being in fact proportional to $-dN_O/dt$); an estimated value of only about 0.3 μA/cm² for both polished and unpolished aluminum was found. It would therefore appear that the dissolution current during oxidation is purely electrochemical. This is in agreement with ref. (37). The dissolution current density on tantalum was not measurable, an estimated upper limit being 3×10^{-3}

Table III. Values of the constants A and B

	A (A/cm²)		B (10^{-6} cm/V)	
	Literature	This work	Literature	This work
Aluminum	10^{-25} to 10^{-20} (5, 6) $10^{-14.6}$ (7)	$10^{-25.7}$* 10^{-13}**	4.4 to 5.5 (5, 6) 3.2 (7)	5.8* 2.9**
Tantalum	10^{-19} to 10^{-17} (1, 38)	10^{-17}*	5 to 5.5 (1, 38)	5.28*

* Polished samples.
** Unpolished samples.

Table IV. Components of the currents for aluminum at constant current densities

Surface preparation	V_{ox}, V	J, mA/cm²	Expressed in % of J J_e	J_i	Expressed in % of J_i J_{ox}	J_{dis}
Polished	0-50	$1 \leq J \leq 10$	≤2	98	92 ± 5	8
Unpolished	0-30	1	≦5	95	68 ± 4	32
		6.6	≦5	95	68 ± 4	32
		10	≦5	95	68 ± 4	32
	30-50	1	≦5	95	42 ± 3	58
		6.6	≦5	95	65 ± 5	35
		10	≦5	95	65 ± 5	35

The values of J_e and of J_{ox} were calculated directly from measurements; the value of J_i and J_{dis} were deduced by difference.

Measurements at constant potential.—These measurements were carried out at $V_{ox} = 50$V. At the low final current densities reached in this case the electronic current density J_e may be relatively high and the value of J_i cannot be inferred from that of J. However, J_{ox} may be estimated directly from the relation (see Eq. [7a])

$$J_{ox} = \frac{1}{k}\frac{dN_O(t)}{dt} \qquad [11]$$

We may in addition estimate J_i at any instant t, by using Eq. [6], in which E_{ox} is deduced from Eq. [3b] by inserting $N_O(t)$ and where A and B are assumed to have the same values as at higher currents (Table III). This procedure implies that the nature of the films formed at low final currents is the same as at high constant current, *i.e.*, that λ and $N_O{}^c$ remain constant throughout the treatment. The values thus found should satisfy the inequality

$$J_{ox} \leq J_i \leq J \qquad [12]$$

Violation of this equation would suggest that a film of different nature from the barrier layer is formed.

Results for oxidations for various durations are listed in Table V where the values for J_i should be considered as orders of magnitude whereas the errors on J_{ox} are less than 50%. It appears that condition [12] is always satisfied, within experimental error, for the anodic oxidation of tantalum. Furthermore after 10-min oxidation the growth of the oxide is already slow and its rate tends toward zero for long periods, whereas the electronic current may represent more than 90% of the total. For the oxidation of unpolished aluminum it is only after 50 min that a current density J of less than 10 μA/cm² is reached, the film continuing to grow slowly. With polished aluminum, on the other hand, the current density J decreases very rapidly and between 17 and 90 min J_{ox} is negligible. For both types of aluminum samples the inequality [12] is satisfied until 90 min. In this case the electronic current density may be estimated to represent about 90 and 60% of the total for polished and unpolished samples, respectively. Furthermore after 13 hr at constant potential with both types of aluminum, J_{ox} is larger by orders of magnitude than the calculated J_i and an appreciable growth of the oxide layer shows up. This may be ascribed to the formation of a layer of high ionic conductivity, *i.e.*, an increase of $N_O{}^c$, which, if not taken into consideration, leads by the use of Eq. [3b] to too small values of E_{ox}. This interpretation is supported by the fact that after 60 hr under potential the films are of porous character, as proved by the stain test with an organic dye. Hunter and Towner (28) and Hoar and Yahalom (29) made similar observations.

Isotopic exchange of O^{18}.—The ionic transfer reactions at the oxide-solution interface leading to oxide formation may be written as (9, 41)

$$M_{ox}{}^{++} + (H_2O)_s \rightleftarrows (MO)_{ox} + 2H_s{}^+ \qquad [13]$$

$$(H_2O)_s \rightleftarrows (OH^-)_s + H_s{}^+ \rightleftarrows O_{ox}{}^{--} + 2H_s{}^+ \qquad [14]$$

where the index "ox" stands for ions in the oxide, "s" in the solution. Reaction [13] describes cation transfer, the oxide being formed by precipitation; reaction [14] describes oxygen transfer. If at the interface there is only one type of reaction responsible for ionic transport, the classical theory of the overpotential can be applied (27, 41) relating the ionic current density J_i during oxidation to the electrochemical exchange current J_{ex} for the reaction as follows

$$J_i = J_{ex}\left[\exp\left(\frac{\alpha ZF}{RT}\right)\eta_s - \exp\left(-\frac{(1-\alpha)ZF}{RT}\eta_s\right)\right] \qquad [15]$$

where α, Z, $\mathbf{F}$, R, and T have their usual meaning.

O^{18} tracing allows a direct determination of J_{ex} by observing the rate of isotopic exchange of oxygen between the oxide and the solution, no external field being applied. This rate depends both on J_{ex} and on the self-diffusion of oxygen in the oxide. The theory of these processes was developed in detail in papers published by our group (27, 41, 43). The slope of the curve $\hat{N}_O18(t)$ at the origin gives the values of J_{ex} independently from the oxygen self-diffusion rate.

Table V. Oxide growth during the constant potential phase

Metal	Time of oxidation*	$N_O(t)$, 10^{15} at./cm²	J, μA/cm²	J_i, μA/cm² (calculated)	J_{ox}, μA/cm²
Polished tantalum	0	406 ± 2	5000	5000	—
	10 min	530 ± 2	~1	~0.8	0.8
	50 min	536 ± 3	~1	~0.8	0.45
	13 hr	560 ± 3	~1	~0.1	0.1
	62 hr	600 ± 4	~1	~0.02	0.05
Unpolished aluminum	0	340 ± 2	5000	~5000	—
	10 min	435 ± 2	30	~20	12
	50 min	495 ± 3	10	~2	2
	90 min	500 ± 3	5	~2	0.2
	13 hr	641 ± 3	5	~0.04	0.4
	62 hr	2380 ± 10	10	$\sim 3 \times 10^{-6}$	1.6
Polished aluminum	0	385 ± 2	5000	~5000	—
	17 min	501.4 ± 3	5	~0.1	~0
	50 min	501.7 ± 3	2.5	~0.1	~0
	90 min	501.7 ± 3	1.8	~0.1	~0
	14 hr	615.5 ± 4	3.2	$\sim 10^{-4}$	0.5
	60 hr 30 min	2318 ± 10	5.1	$\sim 10^{-10}$	1.6

* After $V_{ox} = 50$V is reached, at 5 mA/cm² current density.

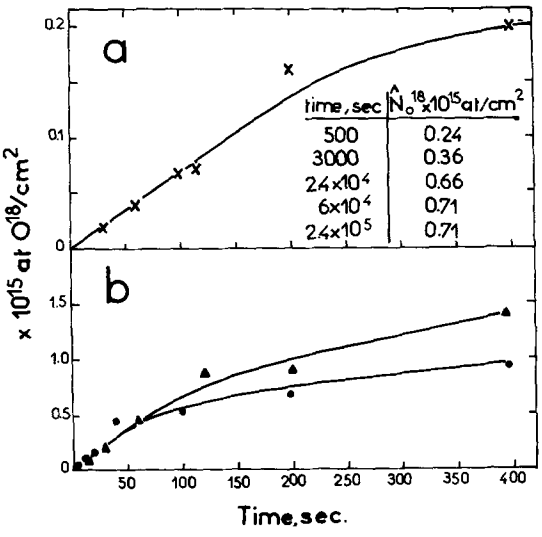

Fig. 7. Isotopic exchange in O^{18} enriched solutions as a function of time for oxides formed at 20V, 10 mA/cm^2 in O^{18} depleted solutions: a, tantalum; b, aluminum: ▲, unpolished; ●, polished samples.

The question arises whether under a high field, the growth of the anodic layer does in fact occur by transfer of oxygen at the oxide-solution interface. Comparison of the electrochemical exchange current J_{ex} of oxygen obtained by tracing with O^{18}, with the exchange currents calculated from Eq. [15] for various values of the ionic current allows the question to be elucidated. The experiments on isotopic exchange with no applied field were carried out on oxides initially formed at constant current (10 mA/cm^2) up to 20V in O^{18}-depleted water. The samples were then immersed in a solution enriched in O^{18} for increasing lengths of time t. The results are shown in Fig. 7.

In the case of tantalum, after a linear start, the exchange slows down and the saturation is reached after about 6 hr. The saturation value, 7 x 10^{14} at./cm^2 suggests that the exchange is confined to the first (or first few) molecular layer. This was confirmed by slightly dissolving the oxide. After about 15Å of oxide have been removed the O^{18} has completely disappeared. The slow dissolution of the oxide was obtained in a solution of 300g NH_4F/liter of concentrated HF as in ref. (9), according to a procedure used by Pringle (42). At 27.5°C a uniform dissolution rate of 62 ∓ 3 Å/min was observed (9, 43) in our experimental conditions. It must be verified that the observed phenomenon was not due to simple spontaneous growth of an oxide film in the enriched solution. The sample which had undergone isotopic exchange to saturation was hence immersed again in the depleted solution. The observed disappearance of O^{18} after several hours, which cannot be due to dissolution (as seen above), proved the reversibility of the phenomenon, characteristic of isotopic exchange. The observed saturation indicates a very low diffusion coefficient of oxygen in the oxide Ta_2O_5, in agreement with (43). The slope at the origin of the curve in Fig. 7a yields a value of the exchange current density of 0.3 μA/cm^2, with 15% precision.

Analogous results were obtained for aluminum for times below 10 min (Fig. 7b). For times of the order of an hour the O^{18} uptake goes on increasing slowly. Thus after 63 hr we found on polished and nonpolished samples, respectively, 15 x 10^{15} and 16 x 10^{15} at./cm^2. On the other hand a loss of the initial oxygen content of 62 and 69%, respectively, was observed, in agreement with the value of the dissolution current found above. The absence of a saturation effect on aluminum may be due to the corrosive attack of the solution; a high self-diffusion rate of oxygen in the barrier layer is unlikely taking into account the results of ref. (10). The slopes at the origin of the curves in Fig. 7b yield a value of the exchange current density of 3 μA/cm^2 with 30% precision.

From Eq. [15], using the experimental values of the overpotentials and of J_i, an order of magnitude of the electrochemical exchange current density of OH^- anions was deduced. As the sum of the overpotentials is statistically zero, we took for $\eta_m + \eta_s$ the corresponding standard deviations; this leads to lower limits for J_{ex}. These values and the results from the exchange experiments are listed in Table VI. The complete disagreement between the corresponding values of J_{ex} will be interpreted in the Discussion.

Discussion

Initial layers on aluminum samples.—The existence of an oxide layer of high ionic conductivity on the surface of polished aluminum samples clearly appears from the above results. Its presence and nature may account for some of the differences in the behavior of polished and unpolished aluminum during anodic oxidation, in particular the observed decrease of the slope dN_O/dV_{ox}, on polished samples. A first explanation could be that this layer is an unsoluble oxygen containing residue from the polishing bath. Preliminary experiments similar to that of ref. (10), using the Al^{27} $(p,\gamma)Si^{28}$ resonant reaction, indicate however that this layer has a high aluminum content. It seems therefore that the layer is a porous aluminum oxide film or perhaps a hydroxide; the use of O^{18} tracing and the localization of the O^{18} after various anodic treatments of the metal will give further insight in the nature of this film and in the mechanism of its influence on the anodic oxide formation. This conclusion may be related to the results of Hollo (16) who found by electron microscopy that electropolishing in a phosphoric acid-butyl alcohol bath yields a porous oxide film and to those of Welsh (44) who found similar results using various electropolishing baths.

Dependence of the oxygen growth law slopes on sample preparation.—The higher values of the slopes dN_O/dV_{ox} for unpolished than for polished aluminum could be explained by a corresponding difference in the roughness factor of the metal under the oxide. Under this assumption the difference would depend on the final oxidation current density J, and would be maximum for J equal to some μA/cm^2. Now, this value was reached after a stage at high current (5 mA/cm^2) at the end of which the slopes are not significantly different (Table I); hence neither are the roughness factors. It is difficult to imagine a mechanism which would lead to an increase in roughness factor during a phase at constant potential and low current. Hence we shall admit that the roughness factor of the metal backing was near unity.

Two possible explanations will now be considered:

(*i*) The anodic films formed on both polished and unpolished aluminum are pure Al_2O_3 oxides. The

Table VI. Oxygen exchange currents

Metal	$\eta_m + \eta_s$, mV	J, μA/cm^2	J_i, μA/cm^2	Minimal values of J_{ex} calculated from Eq. [15], μA/cm^2	J_{ex} deduced directly from the isotopic exchange of O^{18}, μA/cm^2
Polished tantalum	0 ± 80	10^4	~10^4	2 × 10^3	0.3 ± 0.05
Both polished and unpolished aluminum	0 ± 170	10^4	9.5 × 10^3	3 × 10^2	3 ± 1

smaller slope on polished aluminum would be due to the superposition of this oxidation mechanism and of the slow transformation of a part of the layer of high ionic conductivity initially present at the surface into a barrier layer. The growth law corresponding to unpolished aluminum would then be characteristic of barrier layer formation alone, (*i.e.*, yield the real E_{ox}). Similar assumptions may hold for tantalum. In the case of aluminum the transformation of the high ionic conductivity layer may be due to two types of mechanisms: those which do not lead to an increase of its oxygen content [for example, the transformation of $Al(OH)_3$ into Al_2O_3 by proton repulsion] and those which do (*i.e.*, pore filling process).

(*ii*) The growth law characteristic of barrier layer formation alone would correspond, according to this assumption, to polished aluminum. The higher slope for unpolished aluminum (*i.e.*, a lower apparent E_{ox}) would be due here to the simultaneous formation of a barrier layer and of a layer of high ionic conductivity (hydroxide or porous film). The ratio of the slopes would correspond then to the proportion of oxygen present in the barrier layer with respect to the total amount of oxygen in the film formed on unpolished aluminum. Polishing would appear as preventing such phenomena, the layer of high ionic conductivity remaining unchanged during treatment. This assumption cannot be applied to tantalum.

The real phenomenon could be a combination of these two mechanisms. In particular the second mechanism could play an increasing role with decreasing current densities as indicated by the porous oxidation phenomena which appear at low current densities. In any case the ratio of the slopes being close to unity, the proportion of the current J_{ox} which may contribute to the transformations of type (*i*) or (*ii*) is small.

Ion transfer at the oxide-solution interface.—The large value of the electrochemical dissolution current J_{dis} for aluminum in our solution indicates a considerable mobility of the cations at the oxide-solution interface. This is confirmed by the observations of Davies *et al.* (37) who directly determined the presence of the aluminum cations in the ammonium citrate solution. The relative values of J_{dis} with respect to J found by these authors on electrochemically polished aluminum differ from our results; in particular they found that this ratio depends on J, whereas no such dependence appears in Fig. 6. This discrepancy may be due to the different polishing procedure used and to the much higher potential V_{ox} applied (120V as compared to 50V in our case). It should be noted that these phenomena depend strongly on the solution used; in particular J_{dis} is negligible in organic solutions of the type used by Vermilyea (45).

The discrepancy by several orders of magnitude between the values of J_{ex} directly measured by isotopic exchange of oxygen without any applied field for both aluminum and tantalum and the values deduced from Eq. [15], as listed in Table VI, may be interpreted in the following way. We may define a cationic transfer current J_c at the oxide-solution interface by the relation

$$J_c = J_{dis} + \theta J_{ox}$$

where θ represents the proportion of the oxidation current J_{ox} due to cation transfer. The oxygen transfer current is hence $(1 - \theta)J_{ox}$. In what follows we shall try to estimate the values of θ.

(*i*) The large difference between the measured and calculated values of J_{ex} may be explained in two ways:

1. The two experiments are not comparable and the electrochemical exchange current of oxygen may be much greater during anodic growth than without an applied field. According to the literature (46) we can assume that the electric field will have the effect of creating oxygen vacancies which will appear at the oxide-solution interface. The presence of these oxygen vacancies will then increase the transfer current of oxygen at the interface which leads to a strong increase in the apparent electrochemical exchange current density of oxygen. This would explain the low values of the observed overpotentials and lead to $\theta \simeq 0$.

2. The low value observed for the overpotential in anodic growth may be explained by the transfer of cations predominating at the oxide-solution interface, ($\theta \simeq 1$). The chemical reaction in the double layer would be followed by precipitation thus contributing to film growth. Using relation [15] we may calculate in this hypothesis the apparent exchange current density J_{ex} for the transfer of Ta^{5+} or Al^{3+} cations. Taking $J_i = J_c = 10$ mA/cm^2 and $\eta = 0.1$V we get the minimal values of J_{ex} equal, respectively, to 0.45 and 24 μA/cm^2.

In the case of tantalum the high value of the cationic exchange current density calculated for $\theta = 1$ seems incompatible with the high chemical stability of the oxide, as well as with the observed absence of any dissolution current (Table V).

On the other hand the assumption $\theta = 1$ implies that the layer of high ionic conductivity present on polished aluminum samples should be rapidly buried in the oxide formed. If this layer is porous most of the current J_{ox} should contribute to its transformation into a barrier layer by pore filling; as seen above, this is not the case. If this layer is not porous, it should remain in contact with the metal; such a process seems unlikely. A definite conclusion may be reached only by localizing the final position of the initial layer by O^{18} tracing, an experiment which is in progress. All these considerations would appear to support the interpretation which implies that the growth of the oxide is achieved essentially by oxygen transfer at the oxide-solution interface, both for tantalum and aluminum.

(*ii*) The fact that the oxidation is chiefly due to oxygen transfer does not imply that J_c is small but only that $J_c = J_{dis}$. For aluminum the cationic transfer current density may hence be very large, up to 60% of the ionic current (Table IV) and there is no contradiction between our conclusions. The small probability of the oxide forming reaction by cation transfer might be explained by the decrease of the free energy of the cations in the oxide with respect to that in the metal, as suggested by Novakovski and Likhachev (47) in the case of iron passivity phenomena.

It should be emphasized that the fact that the growth of the oxide is mainly due to oxygen transfer at the oxide-solution interface does not imply that oxygen transport takes place in the bulk of the oxide. In fact cations migrating through the oxide, on arriving near the interface, would also create oxygen vacancies, leading to the oxidation reaction. The discussion of ion transport phenomena in the bulk of the oxide is beyond the scope of this work.

Acknowledgment

The authors wish to thank Dr. C. Cherki and Dr. G. Feuillade for enlightening discussions. They are grateful to Professor D. Samuel and Dr. S. Szapiro from the Weizmann Institute for advice in the handling of labeled water. The help of E. d'Artemare for the operation of the Van de Graaff Accelerator has been much appreciated. This work was supported by the Centre National da la Recherche Scientifique, (RCP No. 157), the DRME, and the DGRST.

Manuscript submitted July 9, 1970; revised manuscript received Dec. 1, 1970. This was Paper 12 presented at the New York Meeting of the Society, May 4-9, 1969.

Any discussion of this paper will appear in a Discussion Section to be published in the December 1971 JOURNAL.

REFERENCES

1. L. Young, "Anodic Oxide Films," Academic Press, New York (1961).
2. D. A. Vermilyea, "Anodic Films," Chap. IV, in

"Advances in Elec. and Electrochemical Engineering," Vol. 3, Interscience Publishers Inc., New York (1965).
3. T. P. Hoar, "The Anodic Behaviour of Metals," Chap. IV, in "Modern Aspects of Electrochemistry," Vol. 2, Butterworth Scientific Publications, New York (1959).
4. A. J. Brock and G. C. Wood, *Electrochim. Acta*, **12**, 395 (1967).
5. W. J. Bernard and J. W. Cook, *This Journal*, **106**, 643 (1959).
6. J. P. Ryan, Thesis, Toronto (1964).
7. A. C. Harkness and L. Young, *Can. J. Chem.*, **44**, 2409 (1966).
8. R. M. Goldstein and R. J. Lederich, *Thin Solid Films*, **5**, R 11 (1970).
9. G. Amsel, C. Cherki, G. Feuillade, and J. P. Nadai, *J. Phys. Chem. Solids*, **30**, 2117 (1969).
10. G. Amsel and D. Samuel, *ibid.*, **23**, 1707 (1962).
11. G. Amsel, C. Cherki, J. P. Nadai, and J. Siejka, Paper 12 presented at the New York Meeting of the Society, May 4-9, 1969.
12. G. Amsel and M. Croset, Paper 13 presented at the New York Meeting of the Society, May 4-9, 1969.
13. G. Amsel, L. A. L. Report, 1053, Orsay (1963).
14. G. Amsel and D. Samuel, *Anal. Chem.*, **39**, 1689 (1967).
15. J. P. Nadai, Thesis, Orsay (1967).
16. M. Gy. Hollo, *Acta Met.*, **8**, 265 (1960).
17. C. G. Dunn and L. A. Harris, *This Journal*, **117**, 81 (1970).
18. L. Holland, "Vacuum Deposition of Thin Films," p. 71, Chapman and Hall, London (1956).
19. H. P. Godard, "The Corrosion of Light Metals," John Wiley & Sons, Inc., New York (1967); H. P. Godard and E. G. Torrible, *Corrosion Sci.*, **10**, 135 (1970).
20. G. Amsel, D. Dieumegard, and B. Maurel, To be published.
21. M. Croset, *Rev. Sci. Instr.*, **37**, 123 (1966).
22. G. Amsel, *Ann. Phys.*, **9**, 297 (1964).
23. S. Szapiro, Thesis, Rehovot, Israel (1965).
24. I. Dostrovsky and D. R. Llewellyn, *J. Soc. Chem. Industry (London)*, **68**, 208 (1949).
25. C. Ortega, J. Siejka, and G. Amsel, To be published.
26. D. Samuel, Private communication.
27. G. Feuillade and R. Jacoud, *Electrochim. Acta*, **14**, 1297 (1969).
28. M. S. Hunter and P. F. Towner, *This Journal*, **108**, 139 (1961).
29. T. P. Hoar and J. Yahalom, *ibid.*, **110**, 614 (1963).
30. W. M. Latimer, "Oxidation Potentials," Prentice-Hall Inc., Englewood Cliffs, New Jersey (1959).
31. M. Pourbaix, "Atlas of Electrochemical Equilibria in Aqueous Solutions," Pergamon Press, New York (1966).
32. A. Dekker and A. Middelhoek, *This Journal*, **117**, 440 (1970).
33. J. W. Diggle, T. C. Downie, and C. W. Goulding, *Chem. Rev.*, **69**, 365 (1969).
34. G. A. Dorsey, *This Journal*, **116**, 466 (1969).
35. W. G. Burghers, A. Claassen, and J. Zernike, *Z. Phys.*, **74**, 593 (1932).
36. W. Ch. Van Geel and B. J. J. Schelen, *Philips Res. Rept.*, **12**, 240 (1957).
37. J. A. Davies, B. Domeij, J. P. S. Pringle, and F. Brown, *This Journal*, **112**, 675 (1965).
38. A. J. Schrijner and A. Middelhoek, *ibid.*, **111**, 1167 (1964).
39. D. A. Vermilyea, *Acta Met.*, **1**, 282 (1953).
40. R. J. Dreiner and T. B. Tripp, *This Journal*, **117**, 858 (1970).
41. G. Feuillade, *Electrochim. Acta*, **14**, 317 (1969).
42. J. P. S. Pringle, This was Paper 11 presented at the New York Meeting of the Society, May 4-9, 1969.
43. C. Cherki, Thesis, Paris, 1969.
44. N. C. Welsh, *J. Inst. Metals*, **85**, 129 (1956-1957).
45. D. A. Vermilyea, *Acta Met.*, **2**, 482 (1954).
46. L. Young, W. S. Goruk, and F. G. R. Zobel "Oxide Films," in "Modern Aspects of Electrochemistry," Vol. 4, Plenum Press, New York (1966).
47. V. M. Novakovsky and Y. A. Likhachev, *Electrochim. Acta*, **12**, 267 (1967).

On the Deviations from Parabolic Oxidation of Co-25 w/o Cr at High Temperature

A. Z. Hed

Battelle Memorial Institute, Columbus, Ohio 43201

ABSTRACT

Large deviations from parabolic behavior have been observed during the oxidation of Co-25 w/o (weight per cent) Cr alloys. The rate-controlling process of the oxidation at high oxygen pressures is solid-state diffusion of cobalt through CoO channels in the inner layer; thus a model decribing the deviation from parabolic behavior in terms of time dependency of the mean cross section of these CoO channels is suggested.

In a previous publication (1), the oxidation behavior of Co-25 w/o (weight per cent) Cr in the temperature range 900°-1300°C, and oxygen pressure range 0.1-760 Torr, was described. Two mechanisms of oxidation were identified for this alloy. Their occurrence depends mainly on the ambient oxygen partial pressure and temperature. At high oxygen pressures, the oxidation involved the formation of a duplex scale, the inner layer being primarily the spinel $CoCr_2O_4$, the outer layer CoO. At low oxygen pressures, Cr_2O_3 was the dominant oxidation product on the flat surfaces, while at the edges of the specimen duplex structures consisting of an inner spinel layer and an outer CoO layer were found. In both cases, the initial oxidation rates deviated markedly from parabolic. The purpose of this treatment is to describe the deviation from parabolic rates in the high oxygen pressure range by a simple mathematical model, and interpret this model on the basis of physical processes. The experimental data used in the present analysis were reported in ref. (1).

[1] Present address: Israel Product Research Company Ltd., 34/36, Itzhak Sadeh St., Tel-Aviv, Israel.

Key words: oxidation, corrosion, cobalt alloys.

Analysis of the Results

In order to determine the nature of the deviations from parabolic behavior in the high oxygen pressure range the oxidation was assumed to obey a simple parabolic rate equation after very long oxidation times, as has been shown in ref. (1), Fig. 5 and 7. The linear part of a graph of $(\Delta W/A_T)^2$ *vs.* time was extrapolated to low values of time and the experimental values $(\Delta W/A_T)^2$ were subtracted from the extrapolated ones (see Fig. 1) where ΔW and A_T are the weight gain and area of the specimen, respectively. The differences between the experimental values and the straight line $(\Delta W/A_T)^2 = k_p t - B$ may be described as an exponential function of time. The experi-

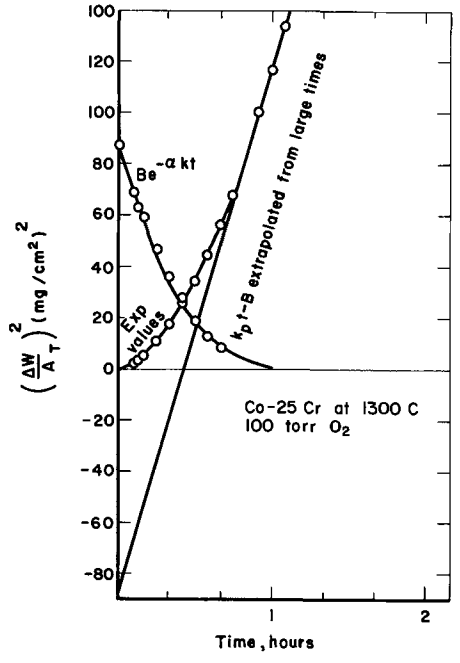

Fig. 1. Graphic representation of the calculation of the deviation from parabolic behavior for the oxidation of Co-25 w/o Cr at high oxygen pressures.

mental oxidation rate may therefore be expressed

$$\left(\frac{\Delta W}{A_T}\right)^2 = k_p t - B + Be^{-\alpha k t} \qquad [1]$$

where k_p is the "large times" parabolic rate constant, t, time, B a constant, α and k factors which will be discussed later. To test the exponential nature of the deviation from parabolic behavior the logarithms of the deviations were plotted *vs.* time for samples oxidized at 1100° and 1300°C in 100 and 760 Torr oxygen (Fig. 2). In all cases, including many not shown in this graph, a good fit to a straight line was obtained. Below a model is developed to interpret these deviations.

It has been shown (1) that the rate-determining process for the oxidation of Co-25 w/o Cr at high oxygen pressures is cobalt cation diffusion through a net-

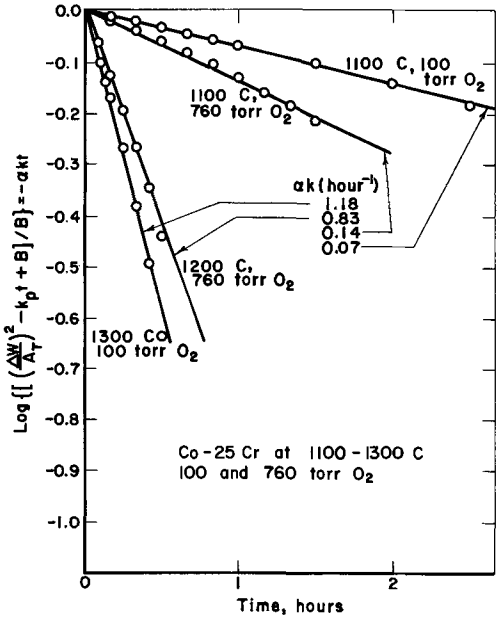

Fig. 2. Normalized deviation from parabolic behavior for Co-25 w/o Cr oxidized at temperatures between 1100° and 1300°C and high oxygen pressures.

work of CoO channels in the inner spinel layer. If the cross sectional area of this network parallel to the alloy surface is A_{eff} then the equation

$$\frac{dx}{dt} = \frac{k_p'(A_{eff}/A_T)}{x} \qquad [2]$$

describes the growth rate of the oxide scale, where k_p' is the parabolic rate constant associated with the oxidation of pure cobalt and is related to the measured k_p as discussed below. The (A_{eff}/A_T) factor is introduced to account for the fact that transport is confined to the area A_{eff} alone, the diffusion coefficient of cobalt in $CoCr_2O_4$ being three orders of magnitude smaller than in CoO (2, 3). A_{eff} is equal to the total area A_T minus the area A_s occupied by the spinel and the area $A_{Cr_2O_3}$. The experimental results suggest that A_{eff} is a function of time; however, it is sufficient to determine the variation of A_s with time.

In general, the rate of reaction for the production of spinel from Cr_2O_3 and CoO depends on the area of contact between the two oxides and the thickness of the spinel already created between the two oxides. In the case of a growing scale a gradient of cobalt cation vacancies is established from the alloy/scale interface to the outer scale/gas interface, thus creating a unidirectional movement of cobalt cations. Thus only the rate at which the cross section of spinel perpendicular to the cobalt migration path changes is important and this rate is primarily proportional to the cross section of the area occupied by Cr_2O_3. Thus as an approximation

$$\frac{dA_s}{dt} = kA_{Cr_2O_3} = k(A_o - \alpha A_s) \qquad [3]$$

where A_s = spinel cross section
$A_{Cr_2O_3}$ = Cr_2O_3 cross section
A_o = an initial cross section of Cr_2O_3 (mainly due to preferential oxidation of Cr during the holding time when the specimen is in an atmosphere ranging from 10^{-5} to about 30 Torr oxygen)
α = a factor that relates the effective cross-sectional area of the spinel formed to the cross-sectional area of Cr_2O_3 consumed
k = a surface rate constant for the formation of spinel.

By integrating Eq. [3] with the initial conditions $t = 0$, $A_s = 0$, the time dependence of A_s and $A_{Cr_2O_3}$ is found to be

$$A_s = \frac{A_o(1 - e^{-\alpha k t})}{\alpha}$$

$$A_{Cr_2O_3} = A_o - A_o(1 - e^{-\alpha k t}) = A_o e^{-\alpha k t} \qquad [4]$$

As pointed out above, the effective area for cobalt diffusion is given by $A_{eff} = A_T - A_s - A_{Cr_2O_3}$. Substituting for A_s and $A_{Cr_2O_3}$ the expressions given in Eq. [4], gives for A_{eff}

$$A_{eff} = A_T - \frac{A_o}{\alpha} - \frac{\alpha - 1}{\alpha} A_o e^{-\alpha k t} \qquad [5]$$

which in Eq. [2] produces

$$\frac{dx}{dt} = \frac{k_p'\left[\left(A_T - \frac{A_o}{\alpha} - \frac{\alpha - 1}{\alpha} A_o e^{-\alpha k t}\right) \Big/ A_T\right]}{x} \qquad [6]$$

and on integration yields

$$\frac{x^2}{2} = \frac{k_p'}{A_T}\left[\left(A_T - \frac{A_o}{\alpha}\right) t + A_o\left(\frac{\alpha - 1}{\alpha^2 k}\right) e^{-\alpha k t} + \text{const}\right] \qquad [7]$$

Where the integration constant may be calculated from the initial conditions: $t = 0$, $x = 0$, yielding $\text{const} = -\frac{\alpha-1}{\alpha^2 k} A_o$.

The weight gain, ΔW, and the thickness of the scale, x, are related by

$$\Delta W = x A_T \rho \quad [8]$$

where ρ is the mean density of the scale multiplied by the average weight fraction of oxygen in the scale, and was assumed to be constant with time. This is probably true since the ratio of the inner- to outer-layer thicknesses was constant with time [see Table I in ref. (1)].

Substituting for x gives

$$x^2\rho^2 = \left(\frac{\Delta W}{A_T}\right)^2 = \frac{2\rho^2 k_p'}{A_T}\left[\left(A_T - \frac{A_o}{\alpha}\right)t - A_o\left(\frac{\alpha-1}{\alpha^2 k}\right) + A_o\left(\frac{\alpha-1}{\alpha^2 k}\right)e^{-\alpha k t}\right] \quad [9]$$

Equation [9] has exactly the form of Eq. [1], where $k_p = 2k_p'\rho^2\left(1 - \frac{A_o}{A_T\alpha}\right)$ and $B = 2\frac{A_o k_p'\rho^2}{A_T}\left(\frac{\alpha-1}{\alpha^2 k}\right)$. We see that the square of the weight gain can be represented by the sum of a straight line, $k_p t - B$, and an exponential function, $Be^{-\alpha k t}$. Figures 1 and 2 show that this was the observed behavior.

Discussion

The analysis above describes an oxidation mechanism controlled basically by the solid-state diffusion of cobalt in CoO. An attempt was made here to account for the presence of phases in the scale which are impervious to cobalt migration, for all practical purposes, and whose morphology is time dependent. It must be emphasized that the treatment is a very simplified representation of the oxidation processes.

The basic advantage of this model is that it accounts for the decrease of the "long time" parabolic rate constants relative to those of pure cobalt, and the initial deviations from parabolic behavior. The measured parabolic rate constant at long times, k_p, is related to the theoretical rate constant, $2\rho^2 k_p'$ ($2\rho^2$ appears as a result of integration and transformation from "thickness" to "weight gain" expression of the rate equation), for the oxidation of pure cobalt by the factor $\left(1 - \frac{A_o/\alpha}{A_T}\right)$. Since A_o/α is the cross section of spinel after full reaction of Cr_2O_3 to spinel, the above weighing factor is the normalized portion of the scale able to tranport cobalt cations, after long times, as suggested in ref. (1).

This model is self-consistent but it has shortcomings related to the simplification of the parameters A_o, α, and k. These have been simplified for mathematical expediency although there is a great deal more known of their physical significance. A_o is defined as the initial cross section of Cr_2O_3; however, in the equation describing the growth rate, the cross section, A_o, should be an average over the whole of the inner layer rather than at a particular location in the layer. The surface reaction constant, k, should represent not only the effect of formation of spinel at a CoO/Cr_2O_3 interface, but also the diffusion through a $CoCr_2O_4$ interface layer, and more important, the rate of sintering of the product. Metallographic examination of the Cr_2O_3 scale at the alloy/scale interface revealed [ref. (1)] that this product is extremely porous, but the inner spinel formed is fully dense, indicating that some sintering occurred. The description of these mechanisms in a mathematical formulation is difficult and necessitates the simplified treatment.

It is theoretically possible for the constant B to be positive or negative. When $\alpha > 1$ ($B > 0$), the cross section of the resultant spinel is smaller than that of the parent Cr_2O_3 oxide, and the instantaneous parabolic rate constant will be an increasing function of time, until the CoO cross section stabilized as is found for Co-25 w/o Cr oxidized at high oxygen pressure. The fact that $\alpha > 1$ is explained by the presence of porous Cr_2O_3 and dense spinel. When $\alpha < 1$ ($B < 0$) the cross section of the resultant spinel is larger than that of the parent oxide and the instantaneous parabolic rate constant will be a decreasing function of time leading sometimes to the closing of the CoO channels and change in the oxidation mechanism to the preferential oxidation of chromium. The oxidation of Co-25 w/o Cr at low oxygen pressure could represent such a case, since we observed a decrease of the oxidation rate with time; however, further complication due to CrO_3 evaporation makes a full analysis difficult in terms of the present model.

Manuscript submitted July 30, 1970; revised manuscript received *ca.* Nov. 16, 1970.

Any discussion of this paper will appear in a Discussion Section to be published in the December 1971 JOURNAL.

REFERENCES

1. P. K. Kofstad and A. Z. Hed, *This Journal*, **116**, 1542 (1969).
2. A. Morkel and H. Schmalzried, *Z. Phys. Chem. Nege Folge*, **32**, 76 (1962).
3. R. Sun, *J. Chem. Phys.*, **28**, 290 (1958).

Kinetics and Morphological Development of the Sulfide Scale on a Nickel-20 w/o Chromium Alloy in Hydrogen Sulfide-Hydrogen Atmospheres at 700°C

G. Romeo,[1] W. W. Smeltzer,* and J. S. Kirkaldy

Department of Metallurgy and Materials Science, McMaster University, Hamilton, Ontario, Canada

ABSTRACT

The sulfidation kinetics of a Ni-20 w/o (weight per cent) Cr alloy exposed to hydrogen sulfide-hydrogen atmospheres at 700°C have been determined as a function of the sulfur pressure. The morphology and phase composition of the duplex sulfide scale formed as a corrosion product have been investigated. The kinetics appear to be controlled by diffusion of the reactants through the scale. No significant dependence of the parabolic rate constant on the sulfur pressure has been determined within the wide range 8×10^{-8} to 2×10^{-2} atm. A correlation is presented for the growth kinetics and the structural features of the nickel and chromium sulfide constituents of the scales with the ternary nickel-chromium-sulfur phase diagram.

A recent review paper by Strafford (1) points out the increasing interest during the past few years on the role of sulfur in the high-temperature corrosion of metals and alloys. Due to the difficulty of purifying natural fuels from sulfur and sulfur compounds and the inherent aggressiveness of such reagents at high temperature, considerable problems may arise in plant operations and, in general, when metal parts have to work in such environments. Although several explanations have been proposed, the fundamental mechanism underlying sulfidation phenomena is not completely understood. Comparatively few data have been collected in this field with respect to the amount of work done in the field of oxidation with air, pure oxygen, or oxygen-supplying atmospheres.

Although the sulfidation of pure metals may possibly be described in terms of comparatively simple models, the situation becomes most complicated when dealing with alloys. In an attempt to gain a better insight into sulfidation properties, we selected for the present study a nickel-base type alloy. The strengh and the high-temperature corrosion resistance of these alloys make them suitable for special applications, like turbines, jet engines, heat-exchangers, *etc.* A control of sulfur corrosion is therefore of paramount importance for these alloys.

A comprehensive investigation on the sulfidation behavior of nickel-chromium alloys has been carried out by Mrowec and co-workers (2) by using pure sulfur at the constant pressure of 1 atm. The whole range of alloy compositions was studied. We thought that it would be of interest to establish the dependence between rate of sulfidation of nickel-chromium alloys and sulfur pressure, the latter being controlled by means of hydrogen sulfide-hydrogen atmospheres. Some work with these atmospheres has already been done by Hancock (3), Davin *et al.* (4), and Seybolt (5), but to our knowledge no systematic study has been made to establish the above correlation. At the same time, we intended to determine the equations governing the kinetics in the chosen conditions and the structure and composition of the phases formed as corrosion products, for the purpose of assessing a detailed mechanism of scale formation.

[1] Present address: Physical Chemistry Laboratory, General Electric Research and Development Center, Schenectady, New York 12301.

* Electrochemical Society Active Member.

Key words: sulfidation, nickel-chromium alloys, sulfide compositions, sulfide morphologies.

Experimental

The formation of a liquid phase in the Ni-Cr-S system is possible at temperatures above 600°C as shown by thermodynamic studies (6). After a few preliminary runs, we found it convenient to carry out experiments at 700°C, since the reaction was of the gas-solid type throughout the range of employed sulfur pressures. These could be determined from the equilibrium $H_2S = H_2 + \frac{1}{2}S_2$. If the equilibrium constant is known at the fixed temperature, a definite value of sulfur potential can be obtained, by adjusting the ratio p_{H_2}/p_{H_2S}. Values of the equilibrium constant are reported by Lewis and Randall (7). The assumptions are made that the only sulfur species present in the gas phase is the diatomic molecule S_2 (7) and that there is no influence of hydrogen on the sulfidation reaction. This last point however deserves further consideration, as pointed out recently by Zelouf and Simkovich (8).

The binary phase diagram for the Ni-Cr system (9) shows that an 80 Ni-20 w/o Cr alloy consists of a solid solution over a large range of temperatures, whereas lower contents of nickel may correspond to a two-phase structure. This, together with the technical properties mentioned in the introduction, led us to choose the above alloy for study. The impurity contents of the alloy are recorded in Table I.

Cold-rolled sheets of the Ni-20 w/o Cr alloy were sheared into plates approximately 1.50 x 0.5 x 0.1 cm and weighing ~0.7g. These dimensions fulfill the requirements suggested by Romanski (10) for a "specific area" of the specimen. However we did not apply, as proposed by the same author, corrections for the area consumed during the reaction, since the over-all consumption in all our experiments was well below 10% of the initial specimen area. A suspension hole was drilled in each plate, and the specimens were then batch annealed *in vacuo* for 3 days at 1000°C. They were then ground and metallographically polished down to 1μ diamond abrasive and finally stored in ace-

Table I. Impurity contents of two alloys used in the experiments
Per cent by weight; balance = nickel

No.	C	S	Cr	Fe	Si	Mn	Al
1	0.003	<0.001	19.1	0.011	<0.05	<0.005	<0.01
2	0.003	<0.001	19.3	0.017	<0.05	<0.005	<0.01

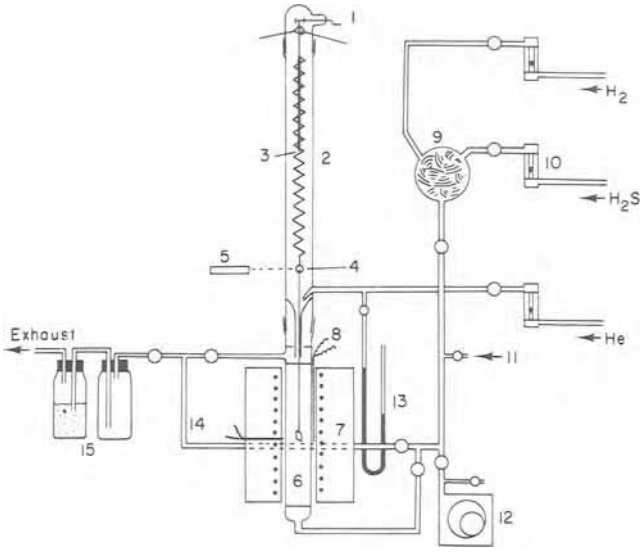

Fig. 1. Schematic of kinetic assembly: 1—winch and forks for positioning the specimen, 2—spring chamber, 3—marker, 4—target, 5—cathetometer, 6—mullite tube, 7—furnace, 8—thermocouple, 9—mixing bulb for gases filled with glass wool, 10—rotameter, 11—gas inlet to bypass the mixing bulb when using pure H_2S, 12—vacuum pump, 13—manometer, 14—bypass for adjusting the gas composition, 15—ballast and absorption flask with caustic soda.

tone. The surface area of each specimen was computed by measuring its dimensions with a micrometer.

The apparatus used for the sulfidation experiments is shown schematically in Fig. 1. A gravimetric method was employed, in which the elongation of a McBain balance could be followed by means of a cathetometer. The assembly was similar to the one described previously by Morris and Smeltzer (11). The main modification consisted in the use of inert gas (helium or argon) for purging the upper portion of the reaction column, thus avoiding condensation of sulfur in the spring chamber. The equation $f = a/A\ F$, where f and F are, respectively, the volume flow rate of the inert gas and of the reaction mixture, and a and A the cross section areas of the small inert gas outlet and of the reaction tube, demonstrated that a low flow of inert gas did not dilute the hydrogen-hydrogen sulfide atmosphere. F was of the order of 0.5 liter/min. A corresponding linear flow rate in the reaction tube of 0.6-0.7 cm/sec prevented thermal segregation of the gases.

Rotameters supplied by Brooks Instrument Division were used for metering the components of the reaction atmospheres. They consisted of interchangeable tapered glass tubes and floats of different specific gravity and were calibrated by the soap film method. Ultra-high-purity grade hydrogen, hydrogen sulfide, and helium were supplied by Matheson Company. The assembly, which could be evacuated to about 10^{-4} Torr while the furnace was brought up to temperature, was filled with helium prior to starting an experiment. The composition of an atmosphere was adjusted and the specimen was then lowered into the reaction zone a few minutes after the reaction gases had entered from the bottom of the mullite tube. This prevented the formation of a liquid sulfide phase, which was likely to happen if the equilibrium pressure of sulfur in the hot zone was not reached. Weight gains were followed for average periods of 5 hr. At the end of the run, the specimen was winched into the upper portion of the column, where the temperature drop was sufficient for quenching it. The assembly was then flushed with a stream of nitrogen.

A modification of the assembly consisted in substituting for the spring chamber a similar column equipped with four winches and four quartz rods. To these, specimens were attached and sulfidation experiments could be carried out for intervals up to 15 hr. In these experiments, continuous weight gains could not be recorded but the scale growth could be easily studied, since the four specimens could be lifted and quenched at different convenient times.

Samples of the scale formed on the specimens were removed for subsequent analyses. Specimens were cold mounted in epoxy resin and cross sections were polished and examined metallographically, both in ordinary and polarized light. Some interesting features of the scales were also examined with a scanning electron microscope. Measurements of scale thickness were made with an optical microscope equipped with a micrometer drum.

Identification of the constituents in the corrosion product was carried out by x-ray analyses, mainly with the Debye-Scherrer powder method. Nickel-filtered copper radiation was employed. Information about phase compositions and the diffusion profiles of the components in the alloy and across the scale were obtained with a CAMECA MS-64 electron microprobe. Point counts were analyzed with respect to a set of standards and corrected for atomic number and mass absorption by means of a computer program.

Results

Kinetics and scale morphology.—Kinetic measurements have been done at sulfur potentials varying approximately from 10^{-7} to 10^{-2} atm. With the exception of an initial induction period lasting for 30-40 min, the sulfidation kinetics followed a parabolic dependence in the whole range of sulfur pressure studied. In Fig. 2, parabolic plots of kinetic data, $(\Delta m/A)^2$ *vs.* t, are shown corresponding to several values of sulfur pressure for periods up to 5 hr. In Table II, values of the parabolic constants, K_p, are reported as a function of sulfur potential. For some experimental conditions, the limits of reproducibility were not better than ±25%.

At all sulfur pressures, the corrosion product appeared as a duplex scale consisting of a yellow outer layer and a gray inner layer. Both layers appeared to be compact and adherent to each other and to the alloy substrate with the exception of widely dispersed regions, where small voids were found to occur at boundaries and within the sulfide layers. These features are exemplified in Fig. 3 and 4 for two specimens sulfidized at different sulfur pressures. In Fig. 5, the observation at comparatively high magnification in polarized light demonstrates that both layers are essen-

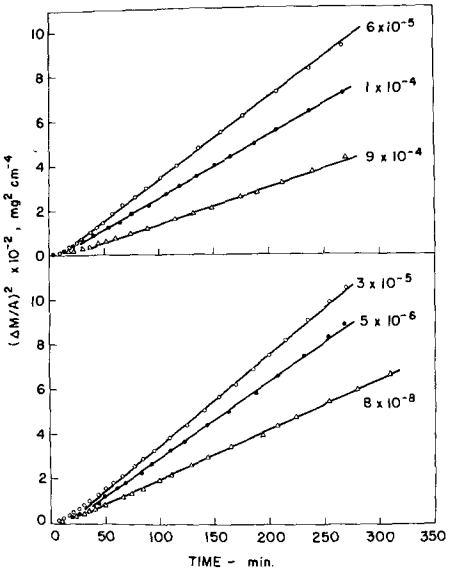

Fig. 2—Parabolic plot of weight gain vs. time for the sulfidation of a Ni-20 w/o Cr alloy at 700°C and different sulfur potentials. Values of sulfur potential in atmospheres.

Table II. Parabolic rate constants as a function of the gas composition and the sulfur potential

Different values of K_p in the same experimental conditions correspond to the limit of reproducibility of the experiments.

v/o H_2S in the mixture H_2-H_2S	p_{S_2} (atm)	K_p ($mg^2\ cm^{-4}\ min^{-1}$)
5	8×10^{-9}	2.3
		3.0
20	2×10^{-8}	3.1
30	5×10^{-8}	3.5
40	1×10^{-6}	3.3
50	3×10^{-5}	4.0
		4.4
60	6×10^{-5}	3.5
70	1×10^{-4}	2.6
		2.8
		3.9
		4.4
85	9×10^{-4}	1.6
100	2×10^{-2}	1.6
		1.9

tially compact, although a considerable difference in hardness and crystal structure can be responsible for a higher amount of polishing artifacts in the inner layer than in the outer one. These differences are exhibited more strikingly in Fig. 6 and 7, corresponding to pictures taken by scanning electron microscopy, of the outer and inner surface of the scale, respectively, and of a fractured scale cross section. A large grain size of the outer layer is matched by a much finer

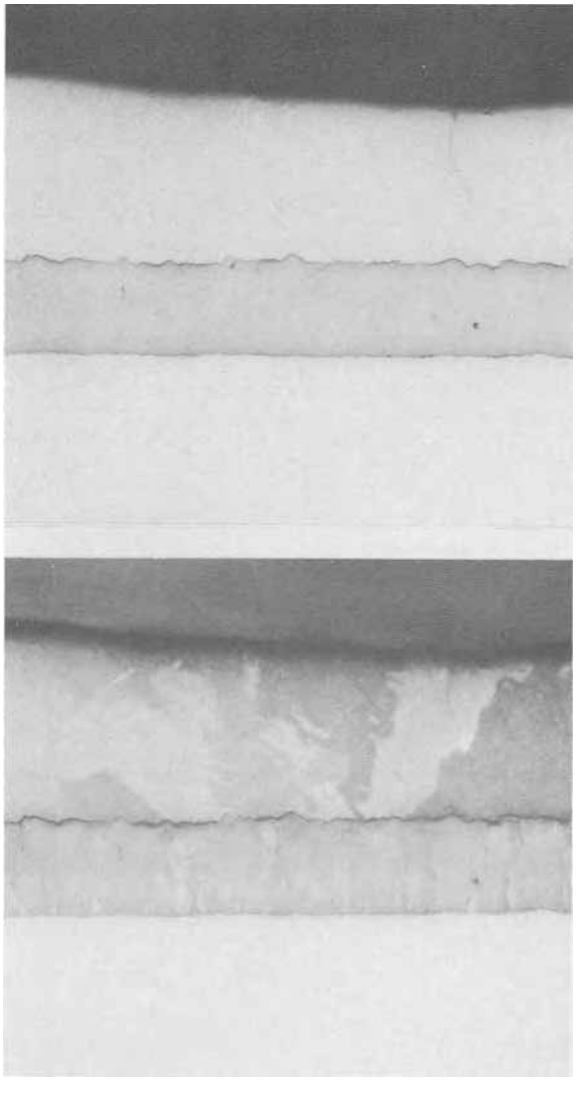

Fig. 3—Micrographs in ordinary and polarized light of the scale formed on a specimen sulfidized for 7 hr in a 5% H_2S gas mixture. Mag. 160X.

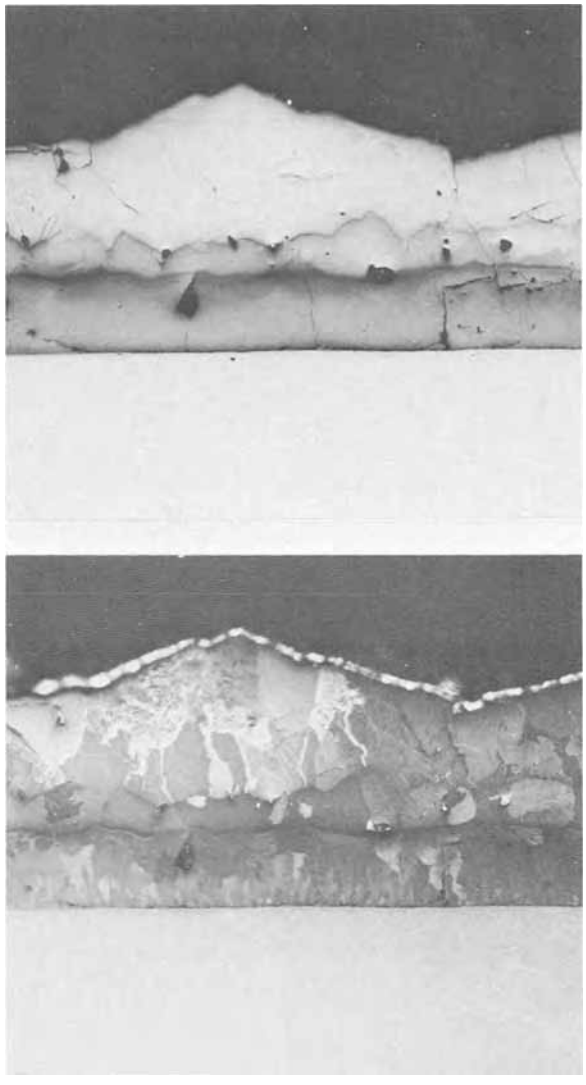

Fig. 4—Micrographs in ordinary and polarized light of the scale formed on a specimen sulfidized for 5 hr in a 50% H_2S gas mixture. A sublayer can be seen in the outer layer. Mag. 160X.

structure of the inner layer. In all cases, no evidence was found for internal sulfidation, as also reported by Mrowec and Zastawnik (12). The two layers in most cases appear to consist of one phase each, although minor features could be detected, as in Fig. 4 where a sublayer may be distinguished in the inner part of the outer layer of a scale formed in a 5% hydrogen sulfide atmosphere, and in Fig. 5 where groups of very small and preferentially oriented precipitates occur in the outer layer of a scale formed in a 50% hydrogen

A presentation of the scale growth at one sulfur potential is given in Fig. 8. Thicknesses were measured for both layers at 20 different points along the scale. The average values obtained by statistical treatment have been plotted *vs.* the reaction time up to 15 hr. Morphological irregularities were more pronounced in the outer than in the inner layer as shown by the amplitude of the errors bars, which are proportional to the probable error. It appears, however, that both layers follow the same growth kinetics. The ratio of thickness of the outer to the inner layer is constant with the time and roughly equal to 2/1.

Phase identification.—Mixed x-ray patterns for the sulfides in both the inner and outer layers were obtained by grinding samples of the scales and analyzing them with the Debye-Scherrer powder method. In all cases, it was possible to identify clearly, by comparison with ASTM cards, sulfides of nickel corresponding to the compositions NiS and Ni_3S_2, this stoi-

Fig. 5—Micrograph in polarized light of the scale formed on a specimen sulfidized for 15 hr in a 5% H_2S atmosphere. A fine needle-shaped precipitate is present in the outer layer. Mag. 800X.

chiometry varying with the conditions of sulfur pressure for the reaction, as shown in Table III. Only a few faint lines were detected that could possibly be assigned to a sulfide of chromium. Attempts to gather better information by using a chart-recording x-ray diffractometer were not successful, since a too-small amount of corrosion product was available for analysis. Flakes of the scale, on the other hand, could be examined by reflection electron diffraction. The patterns obtained from the inner surfaces of these flakes could be indexed according to the ASTM card for CrS.

Information about the composition of the duplex scale could also be obtained with the microprobe. Very little nickel [2-3 a/o (atomic per cent)] was found in the inner layer and no chromium in the outer layer, while the sulfur content varied with the phase composition of the scale. This situation is exemplified by the micrographs in Fig. 9, where the distribution of the system components is shown by the images of the corresponding x-ray radiations. Figures 10, 11, and 12 correspond to plots of point counts taken scanning with the electron beam across the alloy and the scale. The specimens were also scanned parallel to the edges, but no different results were found. The three figures are related to the lowest, medium, and highest sulfur pressure used during the experiments. It can be seen that, while the outer layer corresponds entirely to a nickel sulfide the composition of which is in agreement with the data of Table III, the inner layer composition

Table III. Results of x-ray powder method analysis

The first specimen (1% H_2S) showed liquid formation. All the other specimens underwent a gas-solid reaction. Compounds in parenthesis are present in traces.

v/o H_2S in the H_2-H_2S atmosphere	ps_2 (atm)	Composition of the outer layer of the scale
1	3×10^{-9}	Ni_3S_2
5	8×10^{-8}	Ni_3S_2
20	2×10^{-6}	Ni_3S_2
40	1×10^{-5}	Ni_3S_2(NiS)
50	3×10^{-5}	NiS (Ni_3S_2)
60	6×10^{-5}	NiS
70	1×10^{-4}	NiS
85	9×10^{-4}	NiS
100	2×10^{-2}	NiS

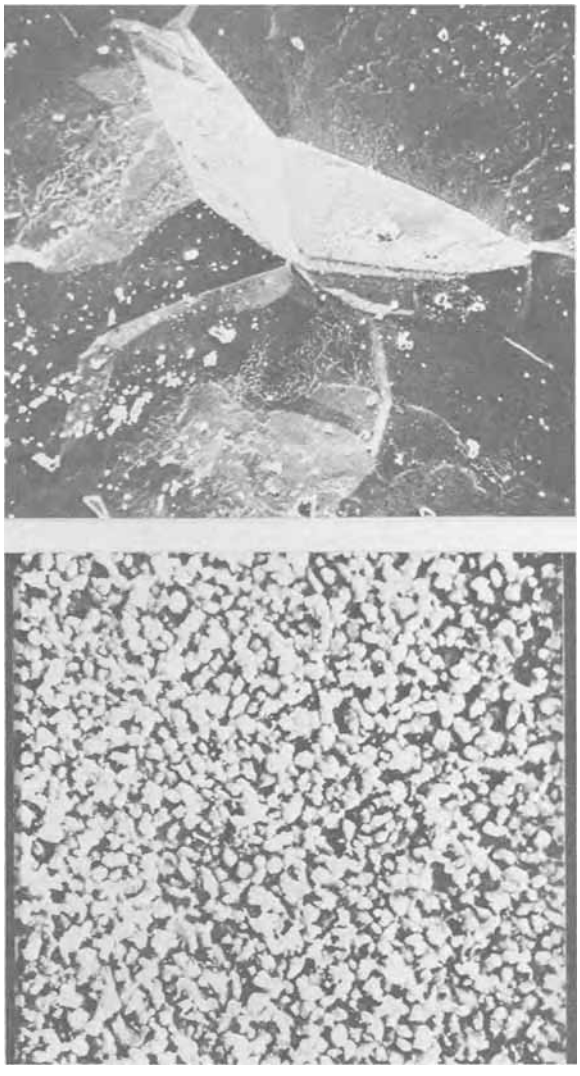

Fig. 6. SEM image of the outer face (upper micrograph) and the inner face (lower micrograph) of the sulfide scale. Tilt = 20°. Mag. of upper micrograph = ~ 180X; mag. of lower micrograph = ~ 1800X.

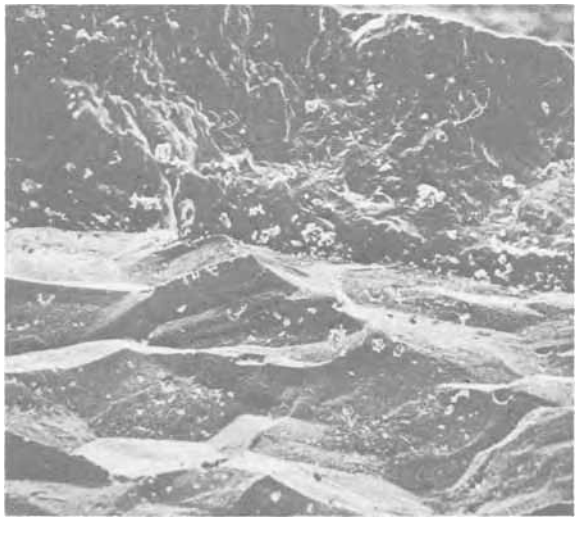

Fig. 7. SEM image of the fractured section of the sulfide scale. Tilt = 32°. Mag. ~ 500X.

seems to be less homogeneous and an average extrapolated atomic per cent ratio for chromium and sulfur would correspond to a formula close to CrS. The com-

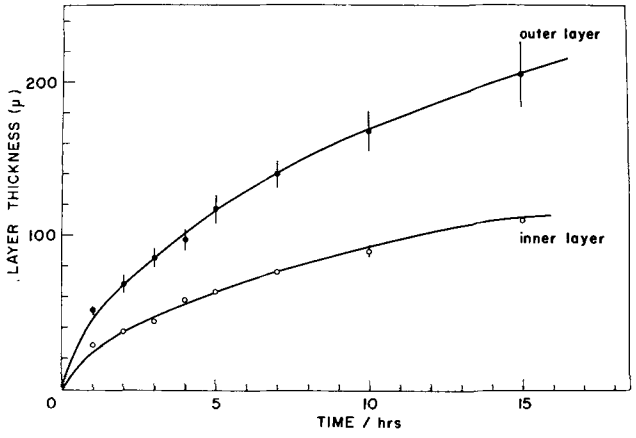

Fig. 8. Plot of the layer's growth vs. time.

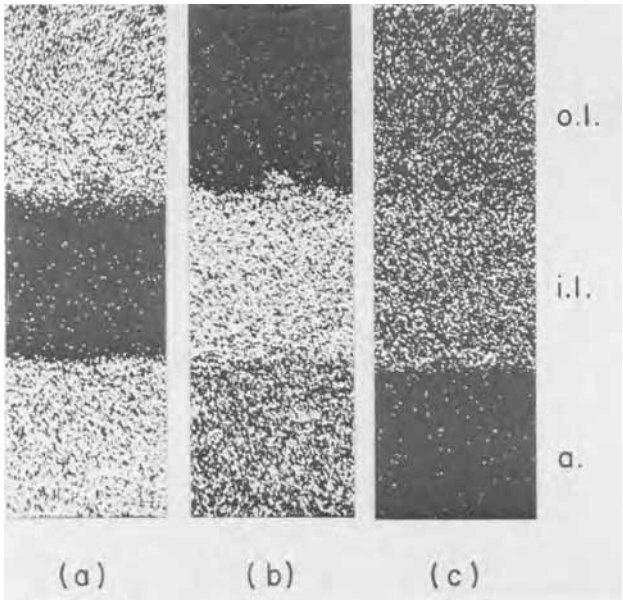

Fig. 9. X-ray images of the distribution profile after sulfidation. Mag. ~ 450X. (a) = $Ni_{K\alpha}$, (b) = $Cr_{K\alpha}$, (c) = $S_{K\alpha}$; a. = alloy, i.l. = inner layer, o.l. = outer layer.

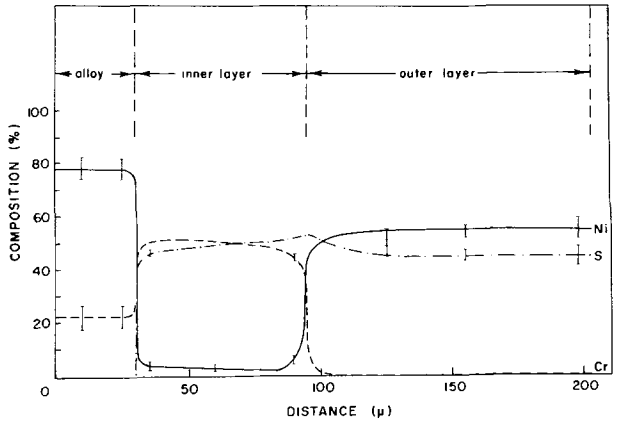

Fig. 10. Distribution profile after sulfidation in a 5% H_2S atmosphere for 5 hr. Error bars in Fig. 10, 11, and 12 show the uncertainty of the analyses.

positions of the scale layers can be related to the Ni-Cr-S ternary phase diagram, as discussed later.

Discussion

The parabolic plots shown in Fig. 2 for the over-all reaction kinetics demonstrate that sulfidation of the alloy proceeds by diffusion-controlled processes over

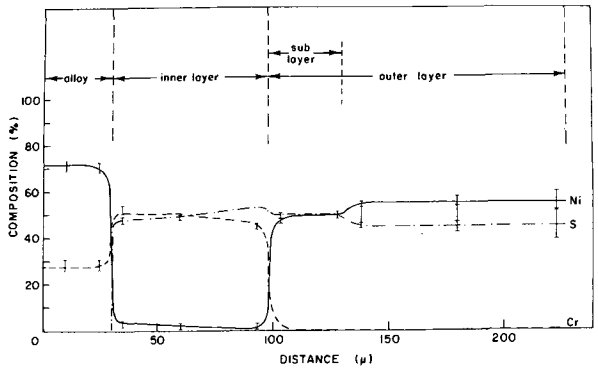

Fig. 11. Distribution profile after sulfidation in a 50% H_2S atmosphere for 5 hr.

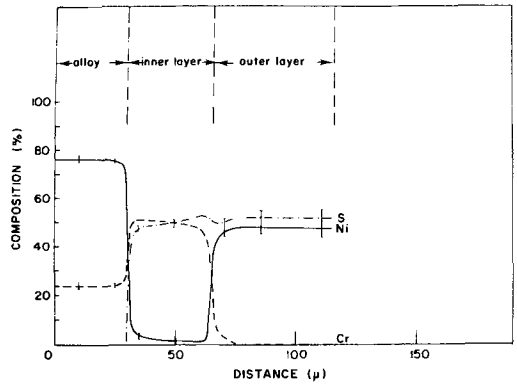

Fig. 12. Distribution profile after sulfidation in pure H_2S for 5 hr.

the whole range of sulfur potentials investigated, after a preliminary brief induction period. This result is in agreement with Mrowec's *et al.* (2) kinetic data for the sulfidation of nickel-chromium alloys with sulfur vapor. The presence, in our case, of hydrogen in the sulfidizing atmosphere has apparently not affected the basic kinetic law governing the sulfidation process. In fact, any influence of hydrogen on the defect structure of the scale would only affect the value of the parabolic rate constant. Figure 13 is a semi-logarithmic plot of K_p *vs.* sulfur pressure. One can see that the over-all variation of K_p with the sulfur potential in the range from approximately 10^{-7} to 10^{-2} atm is of the same order of magnitude as the experimental error. In other words, from a practical point of view there is no sensible dependence of the rate of sulfidation on the sulfur potential. Furthermore, Mrowec *et al.* (2) report a value of K_p equal to about 1 mg^2 cm^{-4} min^{-1} for an alloy of composition close to ours (21.8 w/o Cr) at a sulfur pressure of 1 atm. Taking this into account, we may infer that a variation of 7

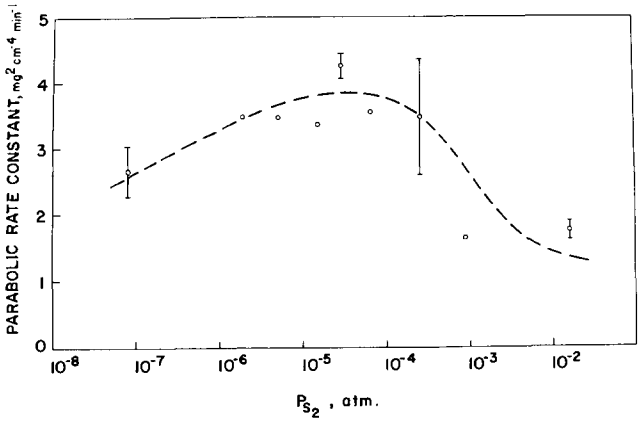

Fig. 13. Semilogarithmic plot of K_p vs. sulfur potential

orders of magnitude in sulfur potential does not have an appreciable effect upon K_p. However, the curve drawn through the experimental points shown in Fig. 13 exhibits a maximum in K_p at an intermediate sulfur pressure corresponding to a ratio of H_2S to H_2 in the atmosphere equal to 1. We ascribe this trend to the change in composition of the outer layer reported in Table III. At very low sulfur pressure (10^{-8} to 10^{-9} atm), a liquid phase is likely to be encountered. At higher sulfur pressures (10^{-7} atm), solid nickel sulfide forms with a composition corresponding to Ni_3S_2. Around 10^{-5} atm sulfur, it becomes possible to form a phase corresponding to NiS. In intermediate ranges of sulfur pressure 1-3 x 10^{-5} atm, the two solid nickel sulfide phases can coexist in a scale.

The morphology of the scale illustrated in Fig. 3 corresponds to the distribution profile of Fig. 10. The compact outer layer can be related to an atom ratio in the profile pertaining to the composition Ni_3S_2. The optically distinguishable sublayer in the outer layer of Fig. 4 appears to consist of NiS as demonstrated by the profile shown in Fig. 11. Figure 12 shows the distribution profile for a specimen which has reacted with pure hydrogen sulfide. The composition of the outer layer corresponds to NiS (no pictures of the specimen were exhibited in this case since the morphology corresponded essentially to the one shown in Fig. 3).

These findings are qualitatively consistent with thermodynamic data for the formation of nickel and chromium sulfides. Standard free energies of formation at 727°C have been reported by Rosenqvist (13), $\Delta G^\circ_{NiS} = -17{,}775$ and $\Delta G^\circ_{Ni_3S_2} = -42{,}450$ cal/mole. The standard states are the pure metal and S_2 vapor at 1 atm. For the formation of chromium sulfide, Hager and Elliott (14) propose that $\Delta G^\circ_{CrS} = -48{,}400 + 13.4\ T$ cal/mole, which is assumed to be valid in the range of temperatures 1375°-1570°K. However, extrapolating back to 700°C, we can roughly estimate the value $\Delta G^\circ_{CrS} = -35{,}360$ cal/mole, with the standard states chosen as above. No similar data have been found in the literature for higher chromium sulfides. Correspondingly, the following approximate equilibrium sulfur pressures can be derived

$$p_{S_{2(Ni_3S_2)}} = 5 \times 10^{-10} \text{ atm}, \quad p_{S_{2(CrS)}} = 1 \times 10^{-16} \text{ atm}$$

According to these values for sulfur pressures, chromium exhibits a much higher affinity for sulfur than nickel. Nickel, however, reacts more rapidly and forms concurrently a separate, thicker external layer of sulfide. Utilizing the values for the free energies of formation for NiS and Ni_3S_2, one can derive a value of $\Delta G^\circ_{NiS} = -10{,}875$ cal/mole for the reaction $Ni_3S_2 + 1/2\ S_2 = 3\ NiS$ at 727°C. This would equal an equilibrium pressure $p'_{S_{2(NiS)}} = 2 \times 10^{-5}$ atm which is within the intermediate sulfur pressure range of the diagram in Fig. 13. Thus it is possible that Ni_3S_2 and NiS may exist in a scale over appropriate sulfur potential ranges (see also Table III).

Although kinetic runs for the over-all sulfidation reaction were not followed for longer than 5 hr, results of scale growth experiments have demonstrated that the sulfidation mechanism remains basically unchanged for intervals up to 15 hr. Moreover, the same kinetic relationship controls the growth of both the inner and the outer layers. The average layer thicknesses from Fig. 8 are represented by parabolic plots in Fig. 14. It is evident that the rate of growth for both sulfide layers and the over-all reaction kinetics can be expressed by parabolic relationships. These findings are consistent with the scale morphologies shown in Fig. 3, 4, and 5, and with a prerequisite for a diffusion-controlled reaction, namely the formation of essentially compact reaction product layers within a scale. On this account, it would be possible to envisage a process for the transport of matter through the scale only in terms of lattice or grain boundary diffusion.

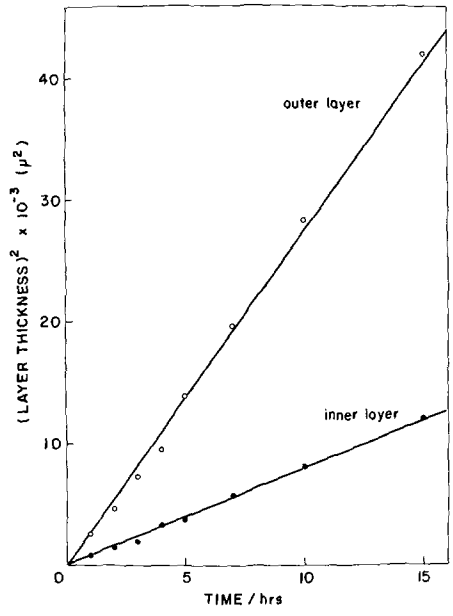

Fig. 14. Parabolic growth of the scale layers

The mechanism proposed by Mrowec *et al.* (2) for the growth of sulfide scales on nickel-chromium alloys is somewhat more complicated, since it advocates dissociation at the inner-outer layer interface, alternate building and healing of microfissures in the outer layer, and worsening of the contact between the scale and the alloy due to the growth of a chromium sulfide phase by inward sulfur transport with consequent onset of porosity. The main discrepancies between our findings and theirs consist in the relatively homogeneous and compact nature of the inner chromium sulfide layer in our case, as opposed to a pronounced porosity and the reported presence of a second phase (nickel sulfide stringers) in the inner layer in their case, for alloys of comparable composition.

The distribution profiles of Fig. 10-12 show a sharp variation in the concentration of nickel and chromium at the alloy-scale interface. Very little nickel (2-3 a/o) was found in the inner layer and no chromium in the outer layer, while the sulfur content varied with the phase composition of the scale. The outer layer was composed of Ni_3S_2 and NiS, the latter sulfide becoming predominant at sulfur pressures greater than 3 x 10^{-5} atm. A debatable point remains with respect to the stoichiometry of the chromium sulfide layer. Apparently, there is discordance in the literature on the relative stability of different chromium sulfide phases, as stressed recently by Viswanathan and Spengler (15). The compositions reported by Hancock (3), Mrowec *et al.* (2), and Seybolt (5) can vary, for instance, in the range CrS to Cr_2S_3. We mentioned earlier that in our case microprobe profiles seem to account for an average composition close to CrS. The phase diagram of Fig. 15 proposed by Bolze *et al.* (6) shows, moreover, that the chromium sulfide region may contain several chromium sulfide phases ranging from CrS to Cr_2S_3. Accordingly, the question remains open as to the exact number of phases present in the inner chromium sulfide layer.

We report in Table IV some numerical results of the microprobe analyses shown in Fig. 10-12. They refer to regions close to the interfaces present in the scale. At all sulfur pressures, the alloy is in contact with a chromium sulfide of composition close to CrS, in which about 3 a/o nickel is dissolved. The inner layer is, in turn, in contact with an outer layer corresponding closely to a composition for NiS at sulfur potentials greater than 10^{-5} atm. At lower sulfur potentials, the two nickel sulfides NiS and Ni_3S_2 may coexist in the outer layer. From the distribution profile of Fig. 11, corresponding to a sulfur pressure of about 10^{-5} atm,

Table IV. Electron microprobe analyses of sulfide scales

The table shows a set of average compositions (a/o) for the phases present in the corrosion product. The values have been determined from the corrected point counts for the different elements at the recorded distances from interfaces. The inner and outer regions correspond to distances of 5μ from the phase interfaces, represented by the vertical broken lines in Fig. 10-12. The asterisks indicate data that differ appreciably from the rest of the compositions reported for the outer region of the nickel sulfide layer.

v/o H_2S in the H_2-H_2S atmosphere	Chromium sulfide layer		Nickel sulfide layer	
	Inner region	Outer region	Inner region	Outer region
5	$Cr_{0.48}Ni_{0.03}S_{0.49}$	$Cr_{0.44}Ni_{0.06}S_{0.50}$	$Ni_{0.46}Cr_{0.01}S_{0.51}$	$Ni_{0.55}S_{0.45}$
50	$Cr_{0.51}Ni_{0.02}S_{0.49}$	$Cr_{0.45}Ni_{0.02}S_{0.53}$	$Ni_{0.48}Cr_{0.02}S_{0.50}$	$Ni_{0.54}S_{0.42}$
100	$Cr_{0.47}Ni_{0.02}S_{0.51}$	$Cr_{0.47}Ni_{0.01}S_{0.53}$	$Ni_{0.47}Cr_{0.02}S_{0.50}$	$*Ni_{0.48}S_{0.52}$
Average compositions of phases	$Cr_{0.93}Ni_{0.04}S$	$Cr_{0.82}Ni_{0.06}S$	$Ni_{0.66}Cr_{0.02}S$	$Ni_{2.5}S_2$ $*Ni_{0.93}S$

it appears that the inner region of the outer layer has a composition equal to NiS, whereas the region adjacent to the gas phase is closer to the formula Ni_3S_2, for which the ratio of sulfur to nickel is lower. The photomicrograph in Fig. 4 has illustrated that the NiS may appear as a distinct sublayer in the outer well-defined layer. This situation can be justified by the presence of a stabilizing content of chromium of about 2% in this sublayer.

The presence of the above chromium and nickel sulfide phases in the superficial scale is consistent with phase determinations for the ternary Ni-Cr-S phase diagram at 700°C (6). If the compositions shown in Table IV are superimposed on the phase diagram, tentative composition paths can be drawn, as shown in Fig. 15. In our case, tie lines have to be followed in the two-phase CrS-NiS region, because no precipitates are observed in the inner layer. Consequently, path A (1-2-3-4-5 in Fig. 15) would correspond to the formation of Ni_3S_2 (Fig. 3) or an intermediate sublayer of NiS beneath Ni_3S_2 (Fig. 4) at low and intermediate sulfur potentials, respectively. At high sulfur potentials, on the other hand, path B (1-2-3-4-6 in Fig. 15) would correspond to the presence of only NiS in the outer layer.

According to these arguments, the results of Mrowec and co-workers (2) could be described by a path similar to B, bearing in mind that a tie line has to be crossed in the region above points 3 and 4, to account for the presence of a second phase in the chromium sulfide layer. However, their experiments were carried out at a much higher sulfur pressure of 1 atm. Hence, according to the ternary phase diagram, higher sulfides both of chromium and nickel (Cr_2S_3 and NiS_2) could be present in the corrosion products, as indeed reported by these authors.

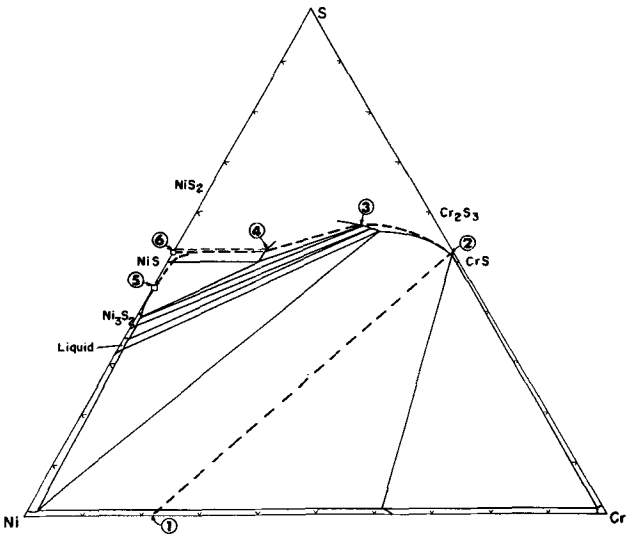

Fig. 15. Ternary phase diagram at 700°C for the Ni-Cr-S system. The dotted line represents tentative composition paths for the sulfidation process.

Conclusions

At 700°C, the sulfidation of a Ni-20 w/o Cr alloy in hydrogen sulfide-hydrogen atmospheres is governed by parabolic kinetic relationships when the reaction is entirely of the gas-solid type. The process for growth of the duplex scale is therefore diffusion controlled and, from measurements of the scale growth, one can assume that the mechanism does not vary for fairly long reaction times. A qualitative correlation can be made between parabolic rate constant and structure of the scale, although more accurate information has still to be collected about the composition of the nickel and chromium sulfide phases formed during the reaction.

Most qualitative features of the sulfidation process have been found consistent with the findings of other workers, except for the structure of the inner chromium sulfide layer of the scale. This polycrystalline layer on the nickel-20 w/o chromium alloy appears to be compact and may contain several chromium sulfide phases. An attempt has been made to correlate the microprobe analysis with the ternary phase diagram, in the form of tentative composition paths for the reaction.

Acknowledgments

This research was supported by a grant from Falconbridge Nickel Mines Limited to J. S. Kirkaldy. The authors are indebted to L. A. Morris, Falconbridge Metallurgical Laboratories, for materials and encouraging discussion, and are grateful to Khoi Nguyen for the reflection electron diffraction results.

Manuscript submitted Sept. 18, 1970; revised manuscript received *ca.* Dec. 22, 1970. This was Paper 130 presented at the Atlantic City Meeting of the Society, Oct. 4-8, 1970.

Any discussion of this paper will appear in a Discussion Section to be published in the December 1971 JOURNAL.

REFERENCES

1. K. N. Strafford, *Met. Rev.*, **138**, 153 (1969).
2. S. Mrowec, T. Werber, and M. Zastawnik, *Corrosion Sci.*, **6**, 47 (1966).
3. P. Hancock, *First International Conference on Metallic Corrosion, London, 1961*, p. 193 (1962).
4. A. Davin, D. Coutsouradis, M. Urbain, and L. Habraken, *Ind. Chim. Belge*, **30**, 340 (1965).
5. A. U. Seybolt, *Trans. AIME*, **242**, 1955 (1968).
6. G. Bolze, D. McCutcheon, and J. S. Kirkaldy, To be published.
7. G. N. Lewis and M. Randall, "Thermodynamics," p. 173, McGraw-Hill, New York (1961).
8. S. Zelouf and G. Simkovich, *Trans. AIME*, **245**, 875 (1969); *Metallurgical Trans.*, **1**, 300 (1970).
9. C. J. Bechtold and H. C. Vacher, *Trans. AIME*, **221**, 14 (1961).
10. J. Romanski, *Corrosion Sci.*, **8**, 67 (1968).
11. L. A. Morris and W. W. Smeltzer, *Acta Met.*, **15**, 1591 (1967).
12. S. Mrowec and M. Zastawnik, *Pol. Akad. Nauk, Oddzial Krakowie, Pr. Kom. Nauk Tech., Ceram.*, No. 8 (1967).
13. T. Rosenqvist, *J. Iron Steel Inst.*, **176**, 37 (1954).
14. P. Hager and J. F. Elliott, *Trans. AIME*, **239**, 513 (1967).
15. R. Viswanathan and C. J. Spengler, *Corrosion*, **26**, 29 (1970).

Preparation and Properties of Pyrolytic Zirconium Dioxide Films

R. N. Tauber, A. C. Dumbri, and R. E. Caffrey*

Bell Telephone Laboratories, Inc., Allentown, Pennsylvania 18103

ABSTRACT

Zirconium dioxide (ZrO_2) films in the thickness range of 500-8000Å have been prepared by chemical vapor deposition in the temperature range of 800°-1000°C. The films were identified as fine-grained (~325Å), nearly stoichiometric, monoclinic ZrO_2, using electron microprobe analysis, infrared absorption, and transmission electron microscopy. The films exhibited remarkable resistance to most aqueous acids and bases, although slight etching occurred in hot (220°C) phosphoric acid. The deposits had an index of refraction of 2.1 ± 0.1 at 546 nm and an optical energy gap of 5.12 eV. ZrO_2 deposited on silicon offered little resistance to Na diffusion at 600°C, while films deposited on thermal SiO_2 were a good barrier due to pile-up of the Na near the ZrO_2/SiO_2 interface. The current density, J, depended on the field, E, as $J = AE^n$, where n was 6 for the metal biased negatively and 2.75 or 5, depending on the magnitude of the field, for the opposite polarity. The dielectric constant in the frequency range of 5×10^2 to 1×10^5 Hz was relatively independent of frequency near 300°K and equal to approximately 18, however some dispersion was noted near 573°K. The a-c conductivity could be represented by $\sigma_{ac} = Cf^{\beta}$ where f is the measuring frequency and β a temperature dependent parameter, decreasing from ~1 at 300°K to ~0.5 at 573°K. The dielectric strength of the films varied between 1 to 2×10^6 V/cm, independently of thickness and polarity. High frequency (1 MHz) C-V measurements indicated the presence of negative surface charge, which varied between -6×10^{11} to -1×10^{12} cm^{-2}. The structures exhibited instability under negative bias, indicative of negative charge being injected into the insulator. C-V measurements on the double dielectric system (ZrO_2/SiO_2) showed that the presence of ZrO_2 caused a flatband voltage displacement ≈ +0.8V. In addition, the flatband voltage shifted as a function of time under negative bias and was found to obey the relationship $\Delta V_{FB} = K \log t$.

Recent developments in microelectronics, such as integrated circuit passivation and IGFET technology, have engendered extensive research in the preparation and characterization of insulating thin films (1). Much of the effort has been directed to SiO_2, Si_3N_4, and Al_2O_3. Recently, alternatives to these materials have been sought. TiO_2 (2) and Nb_2O_5 (3) have been investigated. It has been found that chemical vapor deposition (CVD) in the temperature range of 600°-1000°C produces films with the most desirable properties for the above applications.

A refractory oxide that has not been investigated in detail is zirconium dioxide (ZrO_2). This material is characterized by low electrical conductivity and extreme chemical inertness. Much of the information available on ZrO_2 has been obtained on relatively impure bulk, sintered material.

This paper reports on the preparation of ZrO_2 films by CVD, and a survey of the optical, chemical, electrical, and interfacial properties of the resulting films.

Film Preparation

The preparation of oxide films by CVD has been discussed by Powell *et al.* (4). The reaction chosen to produce the ZrO_2 films is written in over-all form as

$$ZrCl_4 + 2CO_2 + 2H_2 \xrightarrow{800°\text{-}1000°C} ZrO_2(s) + 2CO + 4HCl \quad [I]$$

which is conjectured to proceed in two steps

$$CO_2 + H_2 \rightarrow H_2O + CO \quad [a]$$

$$ZrCl_4 + 2H_2O \rightarrow ZrO_2(s) + 4HCl \quad [b]$$

where H_2O is formed near the heated substrate.

The deposition apparatus is shown schematically in Fig. 1. The substrate rests on a molybdenum susceptor, which is heated inductively. The gases are carefully metered through Brooks rotometers and are transported through stainless steel lines to the 50 mm quartz reaction chamber. The $ZrCl_4$ is transferred to the chamber by passing hydrogen through a heated saturator. A schematic of the stainless steel saturator is shown in the enlarged section of Fig. 1. The carrier gas is forced to take a tortuous path over six layers of $ZrCl_4$. All lines downstream from the saturator are heated approximately 20°C above the saturator temperature in order to prevent recondensation of the $ZrCl_4$ prior to its arriving at the heated substrate.

Successful depositions were made with substrate temperatures between 800° and 1000°C on various substrates. Most often, the depositions were done at 900°C on 3-7 ohm-cm, (100), n-type silicon using the following concentrations of reactants: $ZrCl_4$, 0.01%;

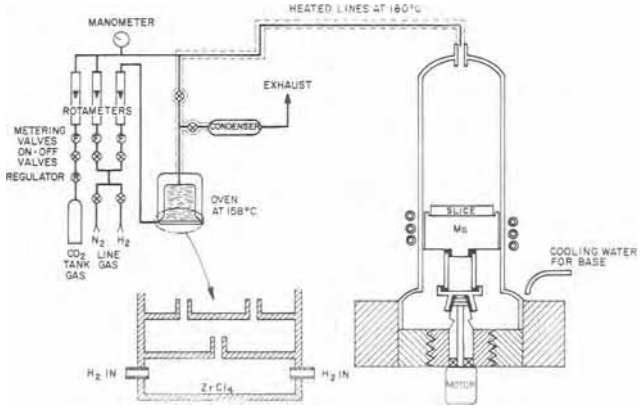

Fig. 1. Schematic representation of deposition equipment

* Electrochemical Society Active Member.

Key words: zirconium dioxide, chemical vapor deposition, dielectric properties, optical properties, insulator.

CO_2, 2.48%; the remainder hydrogen. Total hydrogen flow was ~ 3 l/min. Depositions were also made on 0.001 ohm-cm silicon, thermal SiO_2, and fused silica disks.

Identification and Structure of Films

The films were identified with respect to composition and structure using electron microprobe analysis, infrared absorption, and transmission electron microscopy.

The composition of the films was determined using a Materials Analysis Corporation Electron Microprobe at an accelerating potential of 5 kV and an x-ray emergence angle of 38.5°. The details of this technique have been described by Colby (5). Several specimens were studied at various times in the history of the experiment. A typical analysis indicated that the films consisted of 34.23 ± 0.50, 64.95 ± 0.52, and 0.81 ± 0.02 a/o (atomic per cent) zirconium, oxygen, and silicon, respectively. Silicon always appeared as an impurity. The films appeared to be slightly Zr rich, however this could be due to experimental error, since the Zr standard had a thin oxide film on its surface which would tend to cause one to overestimate the Zr concentration in the film.

The specimens for infrared absorption were prepared by depositing ZrO_2 to a thickness of 0.45 μm on 50 ohm-cm silicon slices approximately 0.63 mm thick. Spectra were taken on a Beckman IR-12 double beam spectrophotometer. A silicon slice similar to the substrate was placed in the reference beam. A typical spectrum is shown in Fig. 2. No peaks were observed at wavenumbers above 650 cm^{-1}, however six prominent peaks were observed. McDevitt and Baun (6) obtained infrared spectra from ZrO_2 pressed powders in Nujol and CsBr. The peaks shown in Fig. 2 are in good agreement with their results.

Samples were prepared for transmission electron microscopy by etching an 800Å ZrO_2 film deposited on silicon in 50:50 HF:H_2O_2 solution. The films cracked and floated free of the substrate, where they were picked up with a copper grid. The specimens were examined in a Philips 300 electron microscope at an accelerating potential of 100 kV. Figure 3 shows a transmission micrograph at 83,000 magnification. A well-defined equiaxed grain structure is observed with an average grain size of approximately 325Å. Figure 4 shows a diffraction pattern of the same area. The pattern indexes quite well to monoclinic ZrO_2 (baddeleyite) (7). Table I summarizes the indexing of the pattern shown in Fig. 4. Several weak lines were not resolved in the diffraction pattern.

The use of the electron microprobe, infrared absorption, and transmission electron microscopy has conclusively shown the films are a fine-grained, nearly stoichiometric, monoclinic ZrO_2.

Film Properties

General.—The deposits were clear, hard, crystalline films of ZrO_2 which formed a tenacious coating to the substrate. Films as thick as 8000Å did not show evidence of cracking either in the as-deposited state or after a liquid nitrogen quench and heating to room temperature.

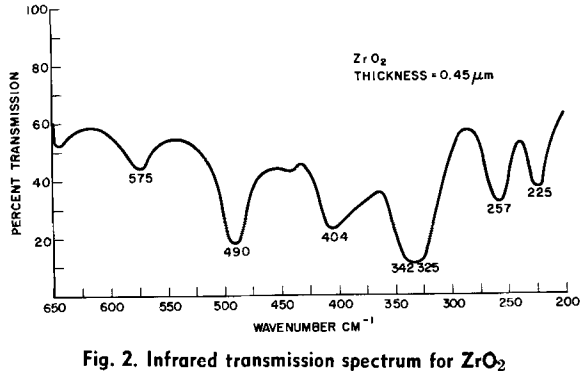

Fig. 2. Infrared transmission spectrum for ZrO_2

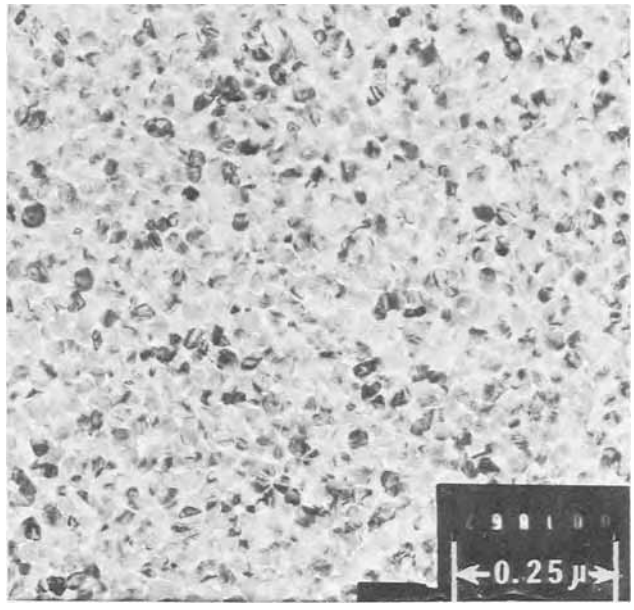

Fig. 3. Transmission electron micrograph of ZrO_2. Magnification 83,000X.

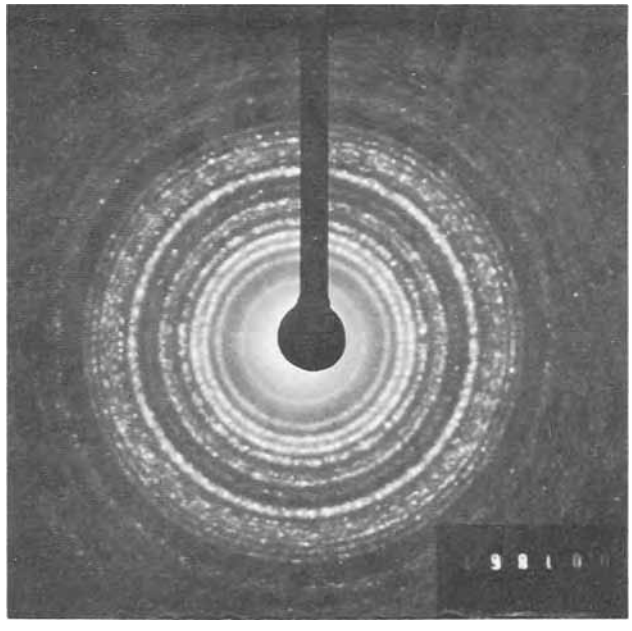

Fig. 4. Electron diffraction pattern of ZrO_2

Table I. Indexing of ZrO_2 electron diffraction pattern

Ring number	Plane (hkl)	d(hkl) theoretical	I/I_o theoretical	d(hkl) calculated	Observed intensity*
1	(100)	5.05	5	5.15	W
2	(011)	3.69	15	3.69	W
3	($11\bar{1}$)	3.16	100	3.15	VS
4	(111)	2.84	65	2.82	S
5	(002), (020)	2.62, 2.60	20, 12	2.60	W
6	(021)	2.33	5	2.31	W
7	($21\bar{1}$)	2.21	5	2.20	VW
8	($21\bar{1}$)	1.990	7	1.99	W
9	(022)	1.846	15	1.83	W
10	(112)	1.802	12	1.80	W
11	($22\bar{1}$)	1.781	5	1.77	W
12	(300), ($20\bar{2}$)	1.693	10	1.68	W

* W, weak; S, strong; VW, very weak; VS, very strong.

The films did not etch appreciably in common aqueous acids and bases such as hot H_2SO_4, boiling HCl, hot HNO_3, boiling aqua-regia, 49% HF, saturated NaOH, and KOH. The HF tended to crack the films into a "river pattern" and subsequently lift them from the substrates. The films did etch slightly in boiling phosphoric acid. The removal rates were 3 Å/min, 6 Å/min, and 50 Å/min at 180°, 190°, and 220°C, respectively. The insensitivity of the ZrO_2 films to acids and bases may render it a useful coating material in a corrosive environment.

Optical Properties

Index of refraction.—The index of refraction, n, was measured on ZrO_2 films deposited on polished silicon using a Gaertner ellipsometer at a wavelength of 546 nm. Using the analysis developed by Archer (8), both the index of refraction and the thickness were obtained. The results of approximately 75 measurements on different deposits yielded an index of refraction of 2.1 ± 0.1. This result is in excellent agreement with single-crystal results which show indices of refraction of 2.13, 2.19, and 2.20 for the a_o, b_o, and c_o axes, respectively (9). Wilkens (10), studying infrared interference of anodic and thermal ZrO_2, obtained a value for the index of refraction of 2.00 ± 0.05 in the wavelength region of 1000-7000 nm.

Optical energy gap.—Specimens were prepared for energy gap measurements by depositing 0.52 μm of ZrO_2 on optically flat fused silica substrates. Absorbance *vs.* wavelength measurements were made on a Perkin-Elmer 202 UV-VIS double beam spectrophotometer in the wavelength region of 200-750 nm. No absorption peaks were observed except for a relatively sharp edge at approximately 240 nm. It was assumed that this edge was due to the fundamental energy gap absorption.

The average transmission, T, of optical energy through a medium of thickness, x, and absorption coefficient, α, can be written as

$$T_{AV} = (1 - R)^2/[\exp(\alpha x) - R^2 \exp(-\alpha x)] \quad [1]$$

where R is the reflectivity. The $R^2 \exp(-\alpha x)$ term arises from considerations involving multiple reflections. The absolute reflectivity was measured relative to a highly polished silicon surface and found to be less than 0.03. Considering the small value of R and the relatively large values of α in the absorption edge, Eq. [1] reduces to

$$T_{AV} = \exp(-\alpha x) \quad [2]$$

The spectrophotometer used in this investigation records in absorbance, A, which is related to transmission by

$$T = 1/10^A \quad [3]$$

The largest value of A that can be measured is 1.5 which corresponds to $T = 0.0318$. Using Eq. [2] and [3], and knowing the thickness, the absorption coefficient as a function of photon energy ($h\nu$) can be obtained from the A vs. λ curve. The values of absorption coefficient measured in the region of the edge were on the order of 10^4 cm^{-1}. These values are indicative of direct optical transitions. It has been shown by Fan (11) that, for the direct allowed transition, the absorption coefficient is related to the photon energy by

$$\alpha_{(direct)} = A(h\nu - E_g)^{1/2} \quad [4]$$

where A is a constant, and E_g is the direct energy gap. Figure 5 is a plot of α^2 *vs.* $h\nu$ for a ZrO_2 film. The linearity predicted by Eq. [4] is observed and extrapolation to $\alpha = 0$ yields an energy gap of 5.12 eV.

It has been shown by Vijh (12) that a correlation exists between the energy gap and the heat of formation per equivalent for many binary semiconductors and insulators. This is expressed as

$$E_g \pm 20\% = 2\,\Delta H_f^\circ/\text{equiv.} \quad [5]$$

where ΔH_f°/equiv. is the heat of formation per equivalent. Vijh (13) gives a value of ΔH_f° (ZrO_2) equal to −64.5 kcal/equiv. Substituting this value into Eq. [5] yields an energy gap of 5.5 eV. The experimental value of 5.12 eV is within the 20% limits. Doyle and Clark (14) measured the absorption of ultraviolet radiation in ZrO_2 and noted a rise in absorption at approximately 5.5 eV. This agrees well with the value of optical energy gap obtained in this investigation.

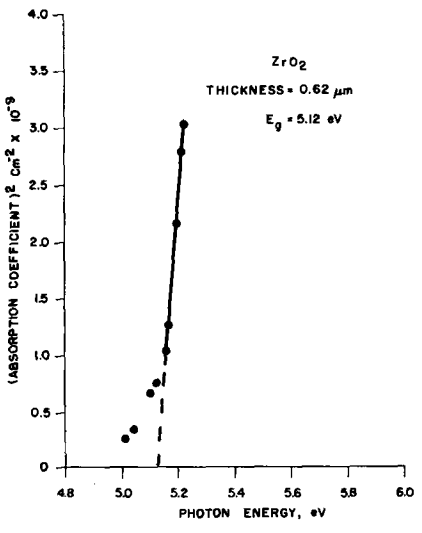

Fig. 5. (Absorption coefficient)^2 as a function of photon energy for ZrO_2.

Na *tracer diffusion.*—Radioactive sodium (Na^{22}) as NaCl along with normal NaCl was vacuum evaporated on ZrO_2 films deposited on silicon and on thermal SiO_2. The total Na was 220 times the radioactive Na^{22}. Diffusions were carried out in a forming gas atmosphere at 600°C for times of 22 and 200 hr.

After diffusion, the excess NaCl was rinsed off the surface and the Na^{22} activity measured as a function of film thickness. The thickness after each etching step was measured on an ultraviolet-visible spectrophotometer from reflectivity minima (15). Hot phosphoric acid (220°C) was used to remove ZrO_2 at a rate of 50 Å/min. The Na penetration was determined using the technique developed by Buck *et al.* (16).

Figure 6a and b are plots of Na^{22}/cm^3 *vs.* depth in angstroms for ZrO_2 on silicon, for diffusion times of 22 and 200 hr, respectively. It is apparent from these plots that ZrO_2 does not offer an appreciable barrier

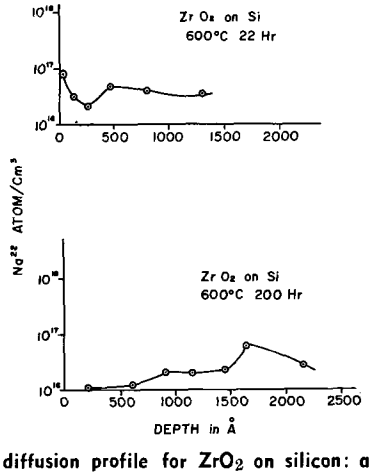

Fig. 6. Na diffusion profile for ZrO_2 on silicon: a (top), 22 hr; b (bottom), 200 hr.

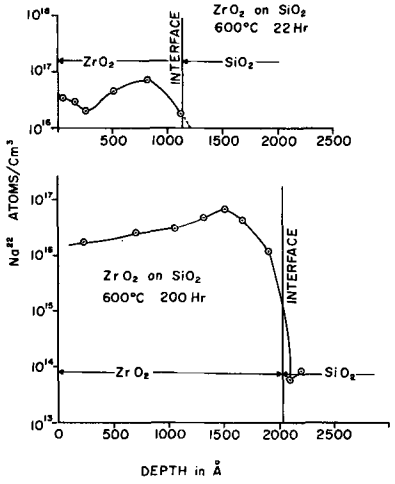

Fig. 7. Na diffusion profile for ZrO_2 deposited on thermal SiO_2: a (top), 22 hr; b (bottom), 200 hr.

to Na penetration at 600°C. For example, in the case of the 22-hr diffusion, removal of the initial 70Å of ZrO_2 leaves 91% of the Na, while similar diffusions in Si_3N_4 show only 3-10% of the Na remaining after removal of 50Å.

Figure 7a and b are plots of Na^{22}/cm^3 *vs.* depth for ZrO_2 deposited on approximately 1000Å of thermal SiO_2, diffused for 22 and 200 hr, respectively. The Na atoms show a strong tendency to pile up before the ZrO_2/SiO_2 interface. This is evidenced by the fact that 300Å from the interface, 35% of the Na remains, while at the interface, only 0.1% of the Na remains for the 200-hr diffusion.

This phenomenon of Na pile-up at a dielectric-dielectric interface has been observed by Tung and Caffrey (17) for the Al_2O_3/SiO_2 system. They describe several possible mechanisms for immobilization of the Na; however, none have been verified. A possible cause they did not consider may be the presence of a large stress gradient in the deposited dielectric, which either immobilizes the Na or serves as an effective barrier to further Na penetration. It has been shown by Tauber and Drum (18) that a large stress gradient ($\sim 2 \times 10^{15}$ dynes/cm²/cm) exists in pyrolytic Al_2O_3 deposited on thermal SiO_2 in the region of the observed Na pile-up. It is expected that a similar behavior exists in the ZrO_2/SiO_2 structure. Additional experiments are being performed to obtain better understanding of this phenomenon and to determine whether it is general to dielectric-dielectric interfaces.

Electrical Properties

The electrical measurements were performed on aluminum-zirconium dioxide-silicon capacitors fabricated by pyrolytically depositing ZrO_2 at 900°C on silicon and then filament evaporating aluminum in a vacuum of 4×10^{-7} Torr. The aluminum was evaporated through a mask in an array of dots having areas of either 2.01×10^{-3} cm² or 1.25×10^{-2} cm², depending on the particular experiment. A sheet of aluminum was evaporated on the back of the samples. The electrical properties of interest were: (*i*) d-c conductivity, (*ii*) dielectric constant, (*iii*) a-c conductivity, (*iv*) dielectric strength, (*v*) fixed surface charge, (*vi*) interface states, and (*vii*) ZrO_2-SiO_2 double dielectric layers.

D-C conductivity.—ZrO_2 films approximately 2000Å thick were deposited on $\sim$ 0.001 ohm-cm silicon. The current-voltage characteristics of the Al-ZrO_2-Si (MIS) structures were measured in a specially constructed test set. The specimen was held in place by means of a vacuum chuck and a copper probe was used to contact the aluminum dot. The specimen and probe were enclosed in a grounded copper box, which was flushed with dry nitrogen. Voltage was applied to the specimen by a Keithley Model 246 constant voltage power supply, and measured on a 610B electrometer. The current was measured by a second 610B electrometer, the output of which was connected to a time-base x-y recorder.

Several of the specimens investigated showed ohmic behavior at low voltages and had conductivities ranging from 10^{-12} to 10^{-14} (ohm-cm)$^{-1}$. A particularly resistive film having a low field conductivity of approximately 10^{-15} (ohm-cm)$^{-1}$ was investigated in detail. It was observed that the application of voltage produced a time dependent current which decayed to a steady-state value. The steady-state current was measured as a function of voltage for both the polarities (dot negative and dot positive).

The current decay was analyzed for the application of a voltage of −2.5V and found to obey the relationship (Fig. 8)

$$I(t) = At^{-0.45} \qquad [6]$$

for 20 sec $< t <$ 200 sec. It is obvious that [6] is not valid for very short, or very long times. This form of current decay has been observed previously by other investigators studying dielectric films (19) and they have related this behavior to a low frequency loss mechanism. This aspect is discussed in a later section.

Figure 9 is a plot of the current density, J, as a function of applied field, E. No ohmic behavior was observed at the lowest detectable currents ($\sim 10^{-13}$A). For the dot negative, the J-E dependence is represented by

$$J = AE^6 \qquad [7]$$

over five orders of magnitude of current. These data have been tested for a $J \propto \exp(E^n)$ dependence considering integral, fractional, positive, and negative values of n, however, no expression was found to fit as well as [7]. The data for the dot positive show considerably more scatter, however, two distinct regions are discernible. At the lower fields a $J = BE^{2.75}$ relationship was obeyed while at the higher fields a $J = CE^5$ relationship yielded the best fit.

Other investigators have observed high power dependence for various insulating films. Rand and Roberts (20) found $J \propto E^{13\text{-}15}$ for BN, while Argall and Jeacock (21) found linear, quadratic, and sixth power dependencies for anodized ZrO_2. Recently Argall (22) found linear, 3/2, and sixth power laws for anodized TiO_2.

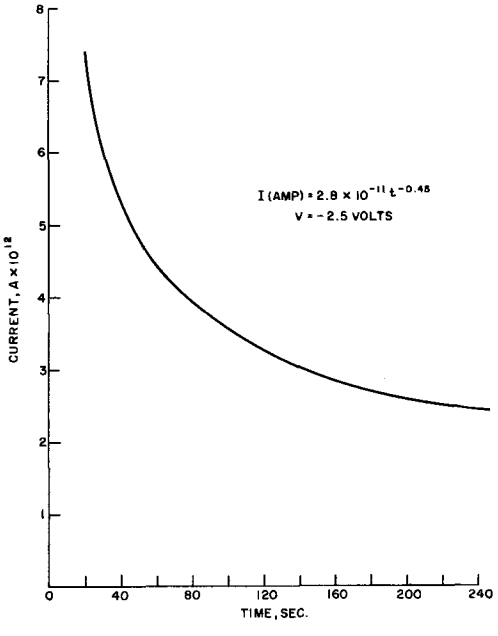

Fig. 8. Current decay for application of −2.5V

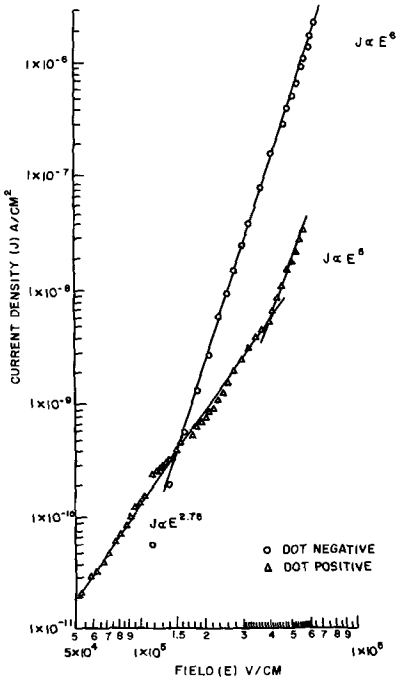

Fig. 9. Current density, J, as a function of applied field, E, for both polarities.

The present state of the theory of electronic conduction in insulators is not developed to the point where a mechanism can be assigned to a power dependence. A mechanism that may be responsible is some aspect of space charge limited conduction (SCLC). The theory of SCLC has been discussed by Lampert (23) and Rose (24). For the special cases of trap-free, or shallow trapped material, the current density is given by $J \propto E^2/l$ where l is the specimen thickness. Rose (24) has investigated the case of an exponential distribution of traps, and showed the current density is given $J \propto E^{t+1}/l^t$ where the parameter $t = T_t/T$, and T_t is a temperature characterizing the trap distribution. In the present investigation, a value of $t = 5$ is obtained which corresponds to a characteristic temperature of $T_t = 1500°K$.

The case of the reverse polarity was less amenable to analysis because of the two stages. It was observed, however, that if electrons were the conducting species, then the silicon was less injecting than the aluminum contacts.

Dielectric constant and a-c conductivity.—ZrO_2 films, approximately 2000Å thick, were deposited on ~ 0.001 ohm-cm silicon and contacted with 2.01 x 10^{-3} cm^2 area aluminum dots. The specimens were scribed, and portions were mounted on TO-18 headers. The specimens were placed in a resistance heated furnace. The capacitance and loss tangent were measured in the frequency range of 5 x 10^2 to 1 x 10^5 Hz and the temperature range of 300°-573°K. The measurements were performed on a General Radio Type 1610-B capacitance measuring assembly, using the three terminal mode at 0.7V peak-to-peak.

Dielectric constant.—The dielectric constant was determined from the film thickness and capacitance, where the thickness was determined from either ellipsometry (8) or reflectivity minima in the UV-VIS portion of the spectrum (15). Figure 10 is a plot of dielectric constant, ϵ, as a function of frequency at various temperatures. Near room temperature, ϵ was virtually independent of frequency, however, at elevated temperatures some dispersion was noted. Harrop, Wood, and Pearson (25), in a review of the a-c properties of dielectric films at room temperature, have shown that, in general, ϵ is not frequency dependent

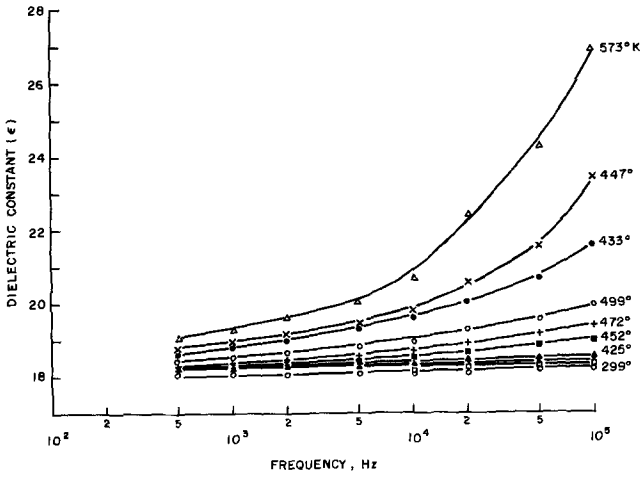

Fig. 10. Dielectric constant, ϵ, as a function of frequency with temperature as a parameter.

in the range of 10^2-10^5 Hz. Harrop and Wanklyn (26) measured the room temperature dielectric constant of single-crystal monoclinic ZrO_2 of unspecified orientation. They found a value of 22 ± 3 at 1592 Hz and observed a slight decrease with increasing frequency. We have made capacitance measurements on a Boonton capacitance bridge at 1 MHz and found a dielectric constant of 17 ± 0.5.

A-C conductivity.—The a-c conductivity was calculated from the loss tangent (tan δ), where tan δ was given by

$$\tan \delta = 1/2\pi f C_p R_p \qquad [8]$$

where f was the measuring frequency in Hz, C_p the parallel capacitance in farads, and R_p the parallel resistance in ohms. The conductivity, σ(ohm-cm)$^{-1}$, was related to the resistance and specimen dimensions by

$$\sigma = l/R_p A \qquad [9]$$

where l was the film thickness in centimeters and A the contact area in square centimeters. Combining [8] and [9]

$$\sigma = 2\pi f C_p (l/A) \tan \delta \qquad [10]$$

Figures 11 and 12 are plots of the a-c conductivity as a function of frequency over the temperature range investigated. The data over the whole temperature range can be represented by

$$\sigma = Cf^{\beta} \qquad [11]$$

where β is a temperature dependent parameter, approaching unity near room temperature and decreas-

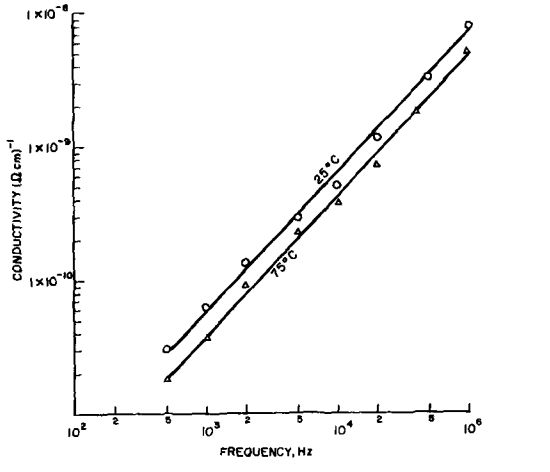

Fig. 11. A-C conductivity as a function of frequency, near room temperature.

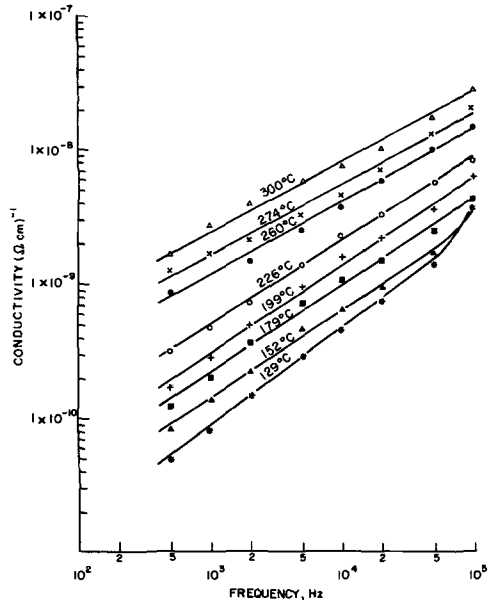

Fig. 12. A-C conductivity as a function of frequency, at elevated temperatures.

ing with increasing temperature to ~ 0.5 at 573°K. Similar conductivity behavior has been observed by Morley *et al.* (19) on vacuum deposited "silicon oxide" in the frequency range of 2 x 10^2 to 10^4 Hz and the temperature range of 273°-510°K. Argall and Jonscher (27) also found a similar behavior on evaporated "silicon dioxide" and anodized aluminum oxide films in the frequency range of 10^2 to 10^5 Hz and the temperature range of 77°-400°K. Above 10^5 Hz, they observed a $\sigma \alpha f^2$ relationship which they attributed to an electronic hopping process.

The conductivity results in the range of 10^3-10^5 Hz are not amenable to simple analysis. A possible explanation that may be considered is that the behavior results from the remanence of a low-frequency Debye-type loss mechanism. Morley *et al.* (19), when considering the Cole-Cole form of the Debye equation for frequencies greater than the relaxation frequency, have shown that the conductivity can be approximated by

$$\sigma \approx \epsilon_0(\epsilon_s - \epsilon_\infty)(2\pi)^\beta f^\beta/\tau_0{}^{1-\beta} \qquad [12]$$

where ϵ_0, ϵ_s, and ϵ_∞ are the permittivity of free space, the static, and the high frequency limits of the real part of the dielectric constant, respectively. τ_0 is the mean, or most probable relaxation time, and represents the width of the distribution of relaxation times. For a broad distribution of relaxation times, as would be expected at low temperatures, $\beta \to 1$, while as the temperature increases and the distribution narrows, $\beta \to 0$. Argall and Jonscher (27), using similar arguments concerning the remanence of a low frequency loss mechanism, have shown that a similar σ *vs.* f relationship should result.

During the course of this work, no low-frequency loss peak was observed, however, such behavior may be inferred from the current decay discussed previously. Morley and co-workers (19) in their work on silicon dioxide observed a similar current decay, except they obtained data at very short times where expression [6] is no longer applicable. Using the transform from d-c decay to dielectric loss factor, developed by Hamon (28), they showed that a loss peak should occur at 5 x 10^{-3} Hz. We can speculate that a similar behavior is applicable for the ZrO_2 films. The low-frequency dispersion is usually associated with interfacial polarization. Further measurements at lower and higher frequencies are necessary to firmly establish the conduction mechanisms in these films.

Dawson and Creamer (29) measured the temperature dependence of the a-c conductivity at 1592 Hz on anodic ZrO_2 films in the temperature range of 80°-290°C. They attempted to fit their data to an Arrhenius plot (log $\sigma \alpha 1/T$), however, except for a narrow temperature range (250° < T < 290°C), the agreement was poor. They extracted an activation energy of $\Delta E \approx 0.56$ eV from the high-temperature results. Argall (22), and Argall and Jonscher (27) have questioned the use of an Arrhenius plot for a-c conductivity. They showed that for "silicon oxide," aluminum oxide, and titanium oxide films the data can be better represented by log $\sigma \alpha T$, rather than log $\sigma \alpha 1/T$.

Figures 13 and 14 are plots of log σ *vs.* $1/T$ and log σ *vs.* T, respectively, for the ZrO_2 films for various frequencies. It is obvious from Fig. 13 that the

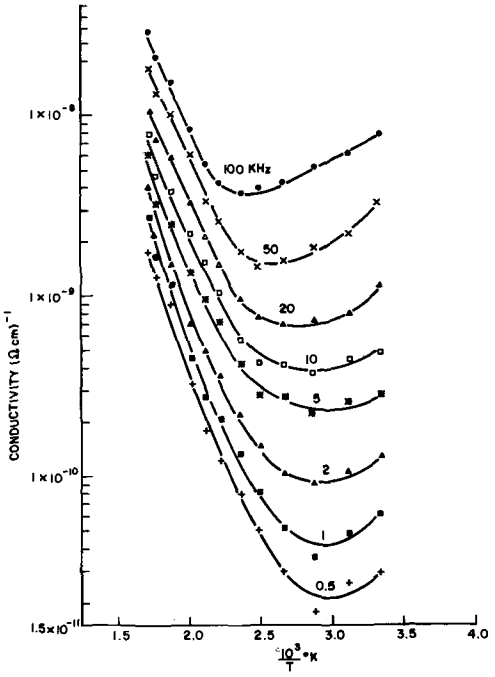

Fig. 13. Log a-c conductivity vs. reciprocal temperature

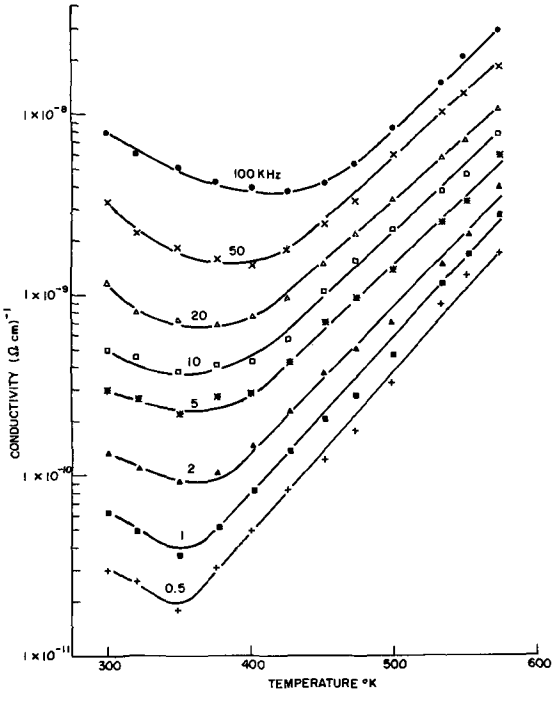

Fig. 14. Log a-c conductivity vs. temperature

data do not follow the log $\sigma \propto 1/T$ behavior below 2 x 10^4 Hz, while at higher frequencies, the Arrhenius behavior is approximated fairly well. Referring to Fig. 14 it is seen that the results can be expressed by log $\sigma \propto T$ above some temperature; the temperature at which this behavior is applicable increases with increasing frequency. At present, there is no interpretation available which readily explains the observed behavior.

The interpretation of the a-c conductivity results for ZrO_2 films prepared by CVD leaves several unexplained observations. It appears that, in general, the results are similar to those obtained from several other dielectric films prepared by various techniques.

Dielectric strength.—ZrO_2 films in the thickness range of 500 to 3600Å were deposited on 3-7 ohm-cm silicon and contacted with aluminum dots, 2.01 x 10^{-3} cm^2 in area. The breakdown voltage was measured on the capacitor structure in a capacitance-voltage (C-V) test set. A Boonton capacitance meter was connected to the y-channel of an x-y recorder, while the ramp voltage was connected to the x-channel. Voltage was increased on the metal dot at a rate of 1.5 V/sec, until an appreciable current ($\sim$ 1 μA) caused a voltage drop within the test set. The thickness of deposit under each dot tested was calculated from the accumulation capacitance.

The results of approximately 30 measurements on various slices yielded a dielectric strength varying between 1 and 2 x 10^6 V/cm, independently of thickness and polarity. This value is less than that which has been found for pyrolytic Al_2O_3, Si_3N_4, and SiO_2 (5-7 x 10^6 V/cm).

Metal-Insulator-Semiconductor (MIS) Properties

High frequency (10^6 Hz) room temperature C-V measurements were made on pyrolytic ZrO_2 deposited on 3-7 ohm-cm (100) silicon and contacted with 2.01 x 10^{-3} cm^2 aluminum dots. The resulting capacitor exhibited extreme instability with a negative bias on the field plate. To minimize the effect of the instability, the C-V traces were made between 0 and 4.8V. Figure 15 shows a C-V plot for a typical ZrO_2 deposit. In this case the film thickness was 2030Å and the flatband voltage (V_{FB}) 1.08V.

The relationship between V_{FB} and fixed surface charge density N_{FC}, is given by

$$V_{FB} = \varphi_{MS} - \frac{N_{FC} q\, l}{\epsilon \epsilon_0} \qquad [13]$$

where φ_{MS} is the work function difference between the metal and the semiconductor, q is the charge on the electron, the other quantities have been defined previously. Figure 16 shows the V_{FB} dependence on thickness, where the data were obtained on a single slice exhibiting a thickness gradient. The straight-line dependence predicted by [13] is observed. Values of

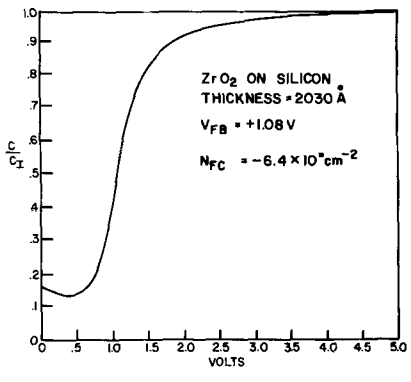

Fig. 15. Normalized capacitance as a function of applied voltage (0-4.8V).

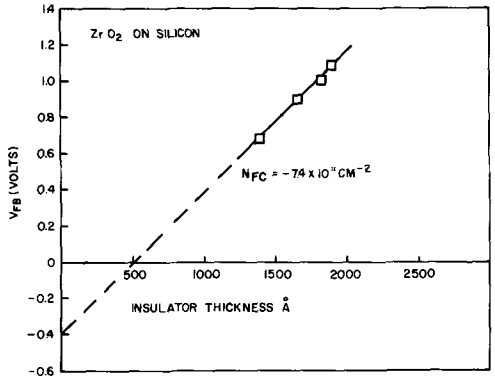

Fig. 16. Flatband voltage as a function of insulator thickness

φ_{MS} and N_{FC}, obtained from the least squares fit of the data, are −0.41V and −7.4 x $10^{11}/cm^2$, respectively. The value of φ_{MS} is in reasonable agreement with the theoretical value (−0.32V) for the silicon substrate-aluminum contacts used. Other ZrO_2 deposits resulted in values of N_{FC} ranging from −6 x 10^{11} to −1 x $10^{12}/cm^2$.

As mentioned previously, the instability under negative bias was extremely pronounced. For a field of −4 x 10^5 V/cm, the V_{FB} shifted approximately + 4V in 3 min. The direction of the shift indicates the presence of more negative charge near the interface and probably results from the trapping of injected charge in the insulator.

The distribution of interface states in the band gap was measured using the quasi-static technique developed by Kuhn (30). Figure 17 is a plot showing the distribution of interface states (N_{ss} in cm^{-2} eV^{-1}). Near the band edges the values are on the order of 10^{12} cm^{-2} eV^{-1}, while near mid-gap they approach 10^{11} cm^{-2} eV^{-1}. This is comparable to results obtained for Nb_2O_5 deposited by CVD on silicon (3). We cannot be certain that these interface states are the result of the interface between the silicon and the pyrolytic ZrO_2. They may be due to the silicon-native SiO_2 interface.

Double Dielectric (MIOS) Properties

C-V measurements, similar to those described previously, were made on sandwiches of aluminum-pyrolytic ZrO_2 ($\sim$ 2000Å)-thermal SiO_2 ($\sim$ 1000Å) and silicon (MIOS).

Values obtained for V_{FB} on this structure were approximately 0.18V. It has been well documented (31) that thermal SiO_2 grown in this laboratory and annealed in hydrogen at 900°C has a fixed charge of: $N_{FC} \approx 4 \times 10^{10}/cm^2$. Considering SiO_2 and ZrO_2 as a single insulator, and accounting for the differences

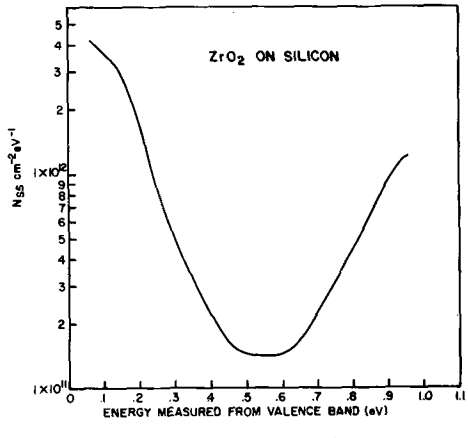

Fig. 17. Interface state density as a function of position in silicon band gap.

in ϵ, this fixed surface charge should correspond to a value of V_{FB} of ~ -0.6V. Thus, we observe a displacement in V_{FB} of 0.8V due to the presence of the second insulator. A similar displacement has been observed for Al_2O_3 deposited on SiO_2 (31). Possible causes of this displacement have been discussed by Nigh (31):

1. A sheet of negative charge near the insulator-insulator interface.
2. A contact potential or barrier energy at the insulator-insulator interface.
3. Changes in the metal-insulator barrier height when ZrO_2 is substituted for SiO_2.

It is attractive to invoke mechanism 1 to explain the observed behavior, since a sheet charge of $-1 \times 10^{12}/cm^2$ near the ZrO_2-SiO_2 interface, for a 2000Å ZrO_2 film, would account for the displacement. It has been shown by Adda and Nigh (32), from etching experiments on the Al_2O_3-SiO_2 system, that mechanism 1 cannot completely account for the behavior. It is noteworthy that the flatband displacement phenomenon is not peculiar to Al_2O_3, but occurs for other insulators as well.

The double dielectric system exhibited an instability of the V_{FB} with application of negative bias to the field plate. For an initial field of 1.7×10^5 V/cm across the ZrO_2, the V_{FB} increased $\sim$ 2.0V in 10^3 min. The V_{FB} shift depended on cumulative time at bias as

$$\Delta V_{FB} = K \log t \qquad [14]$$

Charging the MIOS capacitor to saturation at the same field, and discharging with the front and back contact shorted resulted in a discharge rate of approximately 10% of the charging rate.

Conclusions

1. A fine-grained ($\sim$ 325Å), near stoichiometric, monoclinic ZrO_2 can be produced by CVD in the temperature range of 800°-1000°C utilizing the reaction

$$ZrCl_4 + 2CO_2 + 2H_2 \rightarrow ZrO_2 + 2CO + 4HCl$$

The films were resistant to attack by most aqueous acids and bases.

2. The index of refraction of the films was 2.1 ± 0.1 at 545 nm and the optical energy gap was equal to 5.12 eV.

3. The d-c conductivity was investigated and the J-E dependence was represented by $J \propto E^n$. It is hypothesized that the behavior results from a form of SCLC with the insulator containing an exponential distribution of traps.

4. The a-c conductivity depended on frequency in the range of 5×10^2 to 1×10^5 Hz, as $\sigma \propto f^\beta$ where $\beta \approx 1$ at 300°K and $\beta \approx 0.5$ at 573°K. This behavior may result from the remanence of a low-frequency loss mechanism.

5. C-V measurements indicated that the films contained a density of interfacial negative charge which varied between -6×10^{11} and -1×10^{12} cm^{-2}. Double layer (ZrO_2/SiO_2) measurements indicated the presence of the ZrO_2 shifted the V_{FB} approximately + 0.8V.

6. The 1 MHz dielectric constant was found to be 17 ± 0.5 and the dielectric strength varied between 1 and 2×10^6 V/cm.

Acknowledgments

The authors thank J. W. Colby and D. R. Wonsidler for their assistance with the microprobe analysis and J. Drobek for his assistance with the electron microscopy. The authors also acknowledge the helpful discussions with H. E. Nigh and J. J. Curry.

Manuscript submitted Sept. 8, 1970; revised manuscript received Dec. 14, 1970. This was Paper 116 presented at the Los Angeles Meeting of the Society, May 11-15, 1970.

Any discussion of this paper will appear in a Discussion Section to be published in the December 1971 JOURNAL.

REFERENCES

1. E. S. Schlegel, *IEEE Trans. Electron Devices*, **ED-14**, 728 (1957); **ED-15**, 951 (1958).
2. D. R. Harbison and H. L. Taylor, "Thin Film Dielectrics," pp. 254-271, F. Vratny, Editor, Electrochemical Society, New York, (1959).
3. M. T. Duffy, C. C. Wang, A. Waxman, and K. H. Zaininger, *This Journal*, **116**, 234 (1969).
4. C. F. Powell, J. H. Oxley, and J. M. Blocher, Jr., Editors, "Vapor Deposition," pp. 384-403, John Wiley & Sons, Inc., New York (1966).
5. J. W. Colby, "Thin Film Dielectrics," pp. 491-520, F. Vratny, Editor, Electrochemical Society, New York (1969).
6. N. T. McDevitt and W. L. Baun, *J. Am. Ceramic Soc.*, **47**, 622 (1964).
7. X-ray Powder Data File, ASTM (1961).
8. R. J. Archer, *J. Optical Soc. Am.*, **52**, 970 (1962).
9. Handbook of Chemistry and Physics, 49th Ed., p. B-265, Chemical Rubber Co. (1968-1969).
10. N. J. M. Wilkins, *Corrosion Sci.*, **4**, 17 (1964).
11. H. Y. Fan, *Rept. Progr. Phys.*, **19**, 107 (1956).
12. A. K. Vijh, *J. Phys. Chem. Solids*, **30**, 1999 (1969).
13. A. K. Vijh, *This Journal*, **116**, 353 (1969).
14. W. P. Doyle and F. J. P. Clarke, *Brit. J. Appl. Phys.*, **12**, 574 (1961).
15. F. Reizman, *J. Appl. Phys.*, **36**, 3804 (1965).
16. T. M. Buck, F. G. Allen, J. V. Dalton, and J. D. Struthers, *This Journal*, **114**, 862 (1967).
17. S. K. Tung and R. E. Caffrey, "Thin Film Dielectrics," pp. 286-296, F. Vratny, Editor, Electrochemical Society, New York (1969).
18. R. N. Tauber and C. M. Drum, To be published.
19. A. R. Morley, D. S. Campbell, and J. C. Anderson, *J. Mats. Sci.*, **4**, 259 (1969).
20. M. J. Rand and J. F. Roberts, *This Journal*, **115**, 423 (1968).
21. F. Argall and R. Jeacock, Ref. 23 of A. K. Jonscher, *Thin Solid Films*, **1**, 213 (1967).
22. F. Argall, *Solid State Electron.*, **11**, 535 (1968).
23. M. A. Lampert, *Rept. Progr. Phys.*, **27**, 328 (1964).
24. A. Rose, *Phys. Rev.*, **97**, 1538 (1955).
25. P. J. Harrop, G. C. Wood, and C. Pearson, *Thin Solid Films*, **2**, 457 (1968).
26. P. J. Harrop and J. N. Wanklyn, *Brit. J. Appl. Phys.*, **18**, 739 (1967).
27. F. Argall and A. K. Jonscher, *Thin Solid Films*, **2**, 185 (1968).
28. B. V. Hamon, *Proc. IEEE*, **99**, 115 (1952).
29. D. K. Dawson and R. H. Creamer, *Brit. J. Appl. Phys.*, **16**, 1643 (1965).
30. M. Kuhn, *This Journal*, **116**, 249C (1969).
31. H. E. Nigh, International Conf. on Properties and Use of M.I.S. Structures, Grenoble, France, June 17-20, 1969, pp. 77-88.
32. H. E. Nigh and L. P. Adda, Private communication.

Phase Equilibria and Eu^{2+}-, Tb^{3+}-, and Mn^{2+}-Activated Luminescent Phases in the $CaO-MgO-P_2O_5$ System

R. A. McCauley and F. A. Hummel

Ceramic Science Section, Material Sciences Department, The Pennsylvania State University, University Park, Pennsylvania 16802

and M. V. Hoffman*

Lighting Research Laboratory, General Electric Company, Cleveland, Ohio 44112

ABSTRACT

The ternary subsolidus phase equilibria has been determined for that portion of the system containing less than 50 m/o (mole per cent) P_2O_5. Limits of solid solution along the orthophosphate join were determined for $Ca_3(PO_4)_2$, $Mg_3(PO_4)_2$, and $Ca_3Mg_3(PO_4)_4$. The 3:3:2 compound had a rapid, reversible inversion at 1104°C and melted incongruently at 1175° ± 5°C. $CaMgP_2O_7$ melted incongruently at 1120° ± 5°C. The Eu^{2+}- and Tb^{3+}-activated emission of $Ca_3Mg_3(PO_4)_4$ and associated solid solutions were examined under 2537 and 3650Å excitation, and the Mn^{2+}-activated emission of $CaMgP_2O_7$ was examined under cathode-ray excitation.

The binary compounds in the systems $CaO-P_2O_5$ and $MgO-P_2O_5$ have been reported by various authors to exhibit impurity-activated luminescence. This investigation was therefore undertaken to study the subsolidus equilibria in the system $CaO-MgO-P_2O_5$ and to explore for possible phosphor hosts among the ternary compounds and solid solutions.

A large volume of literature has been published on the $CaO-P_2O_5$ (1-7) and $MgO-P_2O_5$ (8-12) systems. Seven compounds, which can be prepared by solid-state reaction, have been reported for the $CaO-P_2O_5$ system and three have been reported for the $MgO-P_2O_5$ system. A convenient summary of these compounds, their various polymorphs, and symmetry data are listed in Table I.

Doman *et al.* (13) found that the CaO-MgO system was a simple eutectic type with small regions of solid solution (s.s.) at both ends, the CaO s.s. being approximately twice as extensive as the MgO s.s.

The orthophosphate join was investigated by Ando (14) and by Slawski (15). They both reported an intermediate compound $Ca_3Mg_3(PO_4)_4$, which melted incongruently at 1175°C. Ando reported a phase diagram which indicated solid-solution regions about $Ca_3Mg_3(PO_4)_4$ and at both ends of the join. The solidus line between $Ca_3(PO_4)_2$ s.s. and $Ca_3Mg_3(PO_4)_4$ s.s. was at 1175°C and that between $Ca_3Mg_3(PO_4)_4$ s.s. and $Mg_3(PO_4)_2$ was at 1120°C. With increasing amounts of magnesium, the $\beta \rightarrow \alpha$-$Ca_3(PO_4)_2$ transition temperature was raised, and the β form was stabilized. These solid-solution regions were also reported by Slawski, but, in addition, he reported two polymorphic transitions of $Ca_3Mg_3(PO_4)_4$, $\gamma \rightleftarrows \beta \rightleftarrows \alpha$, with transition temperatures of 1006° and 1104°C, respectively.

The pyrophosphate join was investigated by Bobrownicki and Slawski (16) and by Slawski (17). Bobrownicki and Slawski reported an intermediate compound, $CaMgP_2O_7$, which melted incongruently at 1127°C. The solidus line between $Ca_2P_2O_7$ and $CaMgP_2O_7$ was determined to be 1116°C and that between $CaMgP_2O_7$ and $Mg_2P_2O_7$ to be 1127°C. No data were reported for the region 90 to 100 w/o (weight per cent) $Mg_2P_2O_7$, although a $Ca_2P_2O_7$ solid solution was claimed to extend to approximately 2 w/o $Mg_2P_2O_7$. The x-ray diffraction data which were given for $Ca_2P_2O_7$ corresponded to that of the α form, which indicated that as the magnesium content increased, the α or high-temperature form was stabilized. This was just the reverse of the situation for the orthophosphate where a low-temperature form was stabilized. Slawski (17) later reported the intermediate compound to be $Ca_4Mg_2P_6O_{21}$ which melted incongruently at 1140°C. He also reported solid-solution regions at both ends of the join, the $Ca_2P_2O_7$ s.s. (7% at 1140°) being about three times as extensive as the $Mg_2P_2O_7$ s.s. (2% at 1126°). The join $Ca_3Mg_3(PO_4)_4$-$Mg_2P_2O_7$ contained a eutectic at 1056° and 24 w/o $Mg_2P_2O_7$. The composition and temperature of two ternary eutectics were given.

The fluorescence of Eu^{2+} in $Ca_3Mg_3(PO_4)_4$ has been described by Wanmaker and ter Vrugt (18). They reported an emission peak which varied between 440 and 460 nm and attributed this to the presence of more

* Electrochemical Society Active Member.

Key words: $Ca_3Mg_3(PO_4)_4$, $CaMgP_2O_7$, Eu^{2+} emission, subsolidus equilibria, Tb^{3+} emission.

Table I. Compounds in the binary systems

Compound	Composition	Polymorphs	Symmetry	Ref.
		$CaO-P_2O_5$		
Tetracalcium phosphate	$Ca_4P_2O_9$		$P2_1$	1, 2
Calcium orthophosphate	$Ca_3(PO_4)_2$	$\delta \xrightarrow{-40} \gamma \xrightarrow{35} \beta \xrightarrow{1180} \alpha \xrightarrow{1430} \alpha'$	$R3c(\beta)$, $P2_1/a(\alpha)$	1, 3, 4, 5
Calcium pyrophosphate	$Ca_2P_2O_7$	$\gamma \xrightarrow{750} \beta \xrightarrow{1150} \alpha$	$P4_1(\beta)$, Ortho(α)	1, 5, 6
Heptacalcium phosphate	$Ca_7P_{10}O_{32}$			1
Calcium metaphosphate	$Ca(PO_3)_2$	$\delta, \beta \xrightarrow{963} \alpha$	$P2_1/a(\beta)$	1, 4
Dicalcium hexaphosphate	$Ca_2P_6O_{17}$			1
Calcium tetraphosphate	CaP_4O_{11}		$P2_1/n$	1, 7
		$MgO-P_2O_5$		
Magnesium orthophosphate	$Mg_3(PO_4)_2$	$\beta \xrightarrow{\approx 1000} \alpha$ (?)		8, 9
Magnesium pyrophosphate	$Mg_2P_2O_7$	$\alpha \xrightarrow{\approx 68} \beta$	$B2_1/c(\alpha)$, $C2/m(\beta)$	8, 10, 11, 12
Magnesium metaphosphate	$Mg(PO_3)_2$			8

Table II. Compositions, heat treatments and phases in the ternary system

The $Ca_3(PO_4)_2$-$Mg_3(PO_4)_2$ join

Composition (m/o) CaO	Composition (m/o) $Ca_3(PO_4)_2$	Heat treatment (°C/hr)	Phases*
72.0	96.0	1200/12	β-C_3P (s.s)
70.0	93.4	1275/12	β-C_3P (s.s)
64.0	85.3	1100/12	β-C_3P
60.0	80.0	1150/12	β-C_3P + $C_3M_3P_2$
52.5	70.0	1150/12	β-C_3P + $C_3M_3P_2$
		1275/12	Melted
45.0	60.0	1150/12	$C_3M_3P_2$ + β-C_3P
		1275/12	Melted
41.5	55.3	1100/12	$C_3M_3P_2$ + β-C_3P
		1200/12	Melted
40.0	53.3	1100/12	$C_3M_3P_2$ (s.s.)
		1200/12	Melted
37.5	50.0	1100/12	$C_3M_3P_2$
		1150/12	$C_3M_3P_2$
33.0	44.0	1100/12	$C_3M_3P_2$ (s.s.)
		1200/12	Melted
30.0	40.0	1020/12	$C_3M_3P_2$(s.s) + M_3P
		1150/12	Melted
25.0	33.4	1020/12	$C_3M_3P_2$ + M_3P
		1100/12	Melted
15.0	20.0	1020/12	M_3P + $C_3M_3P_2$
		1100/12	Melted
11.0	14.7	1100/12	M_3P + $C_3M_3P_2$
7.5	10.0	1100/12	M_3P + $C_3M_3P_2$
3.0	4.0	1200/12	M_3P (s.s.)

The $Ca_2P_2O_7$-$Mg_2P_2O_7$ join

Composition (m/o) CaO	Composition (m/o) $Ca_2P_2O_7$	Heat treatment (°C/hr)	Phases*
60.0	90.0	1050/12	β-C_2P + CMP
50.0	75.0	1050/12	β-C_2P + CMP
40.0	60.0	1050/12	CMP + β-C_2P
35.0	52.5	1050/12	CMP + β-C_2P
33.3	50.0	1050/12	CMP + β-M_2P(Tr)
32.0	48.0	1050/12	CMP + β-M_2P(Tr)
30.0	45.0	1050/12	CMP + β-M_2P(Tr)
20.0	30.0	1050/12	CMP + β-M_2P(Tr)
10.0	15.0	1050/12	β-M_2P + CMP
5.0	7.5	1050/12	β-M_2P + CMP

The $Ca(PO_3)_2$-$Mg(PO_3)_2$ join

Composition (m/o) CaO	Composition (m/o) $Ca(PO_3)_2$	Heat treatment (°C/hr)	Phases*	Initial melting (±5°C)
45.0	90.0	600/12	β-CP + X	905
40	80.0	600/12	X + β-CP	870
35.0	70.0	600/12	X + β-CP	900
		400/24 RXG†	X′	
		600/24 RXG	X	
		850/24 RXG	X′	
30.0	60.0	600/12	X + β-CP + MP(Tr)	915
25.0	50.0	600/12	X + MP	910
20.0	40.0	600/12	X + MP	930
15.0	30.0	600/12	MP + X	950
10.0	20.0	600/12	MP + X	985
5.0	10.0	600/12	MP + X	1010

Ternary compositions

Composition (m/o) CaO	Composition (m/o) MgO	Heat treatment (°C/hr)	Phases*
43.0	42.5	1100/48	β-C_3P + M
40.0	40.0	1050/24	C_3P + $C_3M_3P_2$ + M
27.5	54.5	1100/24	$C_3M_3P_2$ + M
52.7	18.0	1000/34	β-C_3P + CMP
35.0	35.0	1050/24	$C_3M_3P_2$ + CMP
18.0	52.7	1000/34	$C_3M_3P_2$ + β-M_2P
30.0	30.0	850/12	MP + β-C_2P + CMP
28.5	28.5	900/12	MP + β-C_2P + CMP
14.0	43.0	900/12	MP + CMP
45.0	10.0	750/24	X + β-CP + β-C_2P
		400/24 RXG†	Glass
		650/48 RXG	X^1
		800/24 RXG	X + β-CP + β-C_2P
34.0	10.0	600/48	X + β-CP
		400/24 RXG	X + β-CP
		600/12 RXG	X + β-CP(Tr)
		700/12 RXG	X + β-CP

* C = CaO; M = MgO; P = P_2O_5; Tr = trace.
† RXG = recrystallized glass.
X, X^1 = unidentified phases.

than one activator site. Quantum efficiency of their material was 52%, and good brightness was maintained up to 200°C. They did not indicate that they were aware of the $Ca_3Mg_3(PO_4)_4$ solid solutions.

Experimental

Phase equilibria studies.—Reagent grade $CaCO_3$, $MgCO_3$, and $(NH_4)_2HPO_4$ were used in preparing the compositions listed in Table II. The starting materials were thoroughly mixed with acetone and then heated to 300°, 500°, 700°, and 900°C in platinum crucibles. Compositions containing 50 m/o (mole per cent) P_2O_5 or more were heated to 100°, 200°, 300°, and 500°C. The samples were remixed with acetone after each heat treatment. Pellets of ½ in. diameter were pressed to approximately ¼ in. thickness and heat treated at various temperatures and times. Several compositions containing 40 m/o or more of P_2O_5 were melted and then recrystallized at various temperatures and times.

Routine phase identification was determined by a Norelco x-ray diffractometer using nickel-filtered CuKα radiation and a scanning rate of 1° 2θ/min. For the solid-solution studies a scanning rate of 1/4° 2θ/min and silicon external standard were used.

A Model 6000 Griffin-Telin hot-stage microscope with an argon atmosphere was used to determine the melting points of the two ternary compounds and as a check for rapid, reversible polymorphic inversions.

Luminescence.—Starting materials for phosphor preparation included luminescent or reagent grade $CaHPO_4$, $CaCO_3$, basic magnesium carbonate, $(NH_4)_2HPO_4$, Eu_2O_3, Tb_4O_7, and $MnCO_3$, and especially prepared $MgNH_4PO_4$.

The compositions which contained europium were mixed in acetone and air fired in fused silica crucibles, followed by a reducing heat treatment in forming gas.

Spectral distribution curves were obtained on a direct reading spectroradiometer corrected for photocell response. The procedures for excitation and emission measurements have been previously described (19).

Results and Discussion

Phase equilibrium relationships.—The data presented in Table II were used to construct the subsolidus phase diagram given in Fig. 1. The orthophosphate and pyrophosphate joins were investigated in more detail than the remainder of the system because of the presence of the two ternary compounds.

Orthophosphate join.—The results of the present investigation agree qualitatively with the previous results of Ando (14) and Slawski (15) about the existence of solid solutions in the neighborhood of the compound $3CaO \cdot 3MgO \cdot 2P_2O_5$ (3:3:2). However, quantitatively there is considerable disagreement. Ando's diagram showed only calcium-rich solid solutions, and Slawski claimed solid solutions in the range 50-54.13

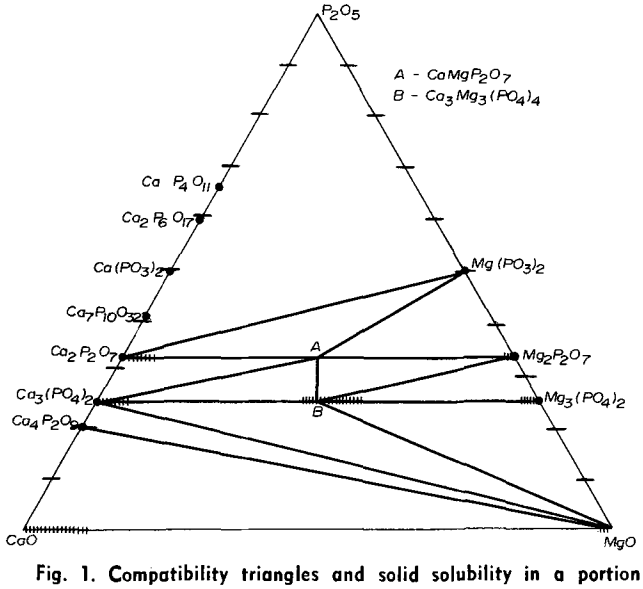

Fig. 1. Compatibility triangles and solid solubility in a portion of the system CaO-MgO-P_2O_5.

m/o $Ca_3(PO_4)_2$. It has now been shown that the solid solutions extend approximately twice as far in the direction of $Mg_3(PO_4)_2$ as in the direction of $Ca_3(PO_4)_2$. Very accurate 2θ measurements obtained by slow scanning on solid solutions along the join using silicon standardization indicated the following regions of solution:

1. 0.0 to ≈3.0 m/o CaO at 1020°C

[~0-4.0 m/o $Ca_3(PO_4)_2$]

2. ≈30.0 to ≈40.0 m/o CaO at 1020°C

[40-53.3 m/o $Ca_3(PO_4)_2$]

3. ≈70.0 to 75.0 m/o CaO at 1100°C

[~93.4-100 m/o $Ca_3(PO_4)_2$].

It should be emphasized that scanning at 1/4° 2θ/min did not reveal differences between the d spacings of these orthophosphate solid solutions and the parent compound. This is not infrequently the case in oxide systems. The limits of solid solubility were estimated rather closely by the appearance of a second phase in x-ray diffraction patterns and by the optical microscope, the latter being a more sensitive indicator in this particular system.

One polymorphic transition reported by Slawski (15) for the 3:3:2 compound was confirmed at 1104° by DTA, and it was found by quenching methods to melt incongruently at 1175° ± 5°.

Pyrophosphate join.—The data reported by Bobrownicki and Slawski (16) for the pyrophosphate join were confirmed. However, the presence of an intermediate compound with the composition $Ca_4Mg_2P_6O_{21}$ reported by Slawski (17) seems highly unlikely. The data given in Table II show that the intermediate compound was present in all the compositions. However, a change in the composition of the second phase from β-$Ca_2P_2O_7$ to β-$Mg_2P_2O_7$ occurred between the compositions containing 35.0 and 33.3 m/o CaO. The latter composition is $CaMgP_2O_7$, and all compositions near it contained large amounts of the intermediate compound, whereas the composition corresponding to $Ca_4Mg_2P_6O_{21}$ (44.5 m/o CaO, or 66.7 m/o $Ca_2P_2O_7$) was in a region where the compositions contained lesser amounts of the intermediate compound. The melting behavior of these compositions also indicated that the intermediate compound was $CaMgP_2O_7$ and not $Ca_4Mg_2P_6O_{21}$. Just above the solidus, microscopic examination showed that the compositions ranging from 60.0 to 33.3 m/o CaO contained liquid and needle-shaped crystals. The proportion of crystals increased with increasing amounts of magnesium, and the composition $CaMgP_2O_7$ yielded only crystals. Thus it was concluded that the intermediate compound had the composition $CaMgP_2O_7$. No region of solid solution surrounding $CaMgP_2O_7$ was indicated by the x-ray diffraction data, and the incongruent melting was confirmed at 1120° ± 5°C. The solidus temperatures between β-$Ca_2P_2O_7$ and $CaMgP_2O_7$ and between $CaMgP_2O_7$ and β-$Mg_2P_2O_7$ were determined to be 1115° and 1120°C, respectively, in agreement with those reported by Bobrownicki and Slawski. No attempt was made to check the extent of solid solution in $Ca_2P_2O_7$ or $Mg_2P_2O_7$. Compositions containing 50 m/o CaO or less formed glasses easily, whereas the composition containing 60 m/o CaO could not be quenched to a glass on the microscope stage. X-ray diffraction data on the ortho- and pyrocompounds are given in Table III.

Metaphosphate join.—Only cursory experiments were made in this region, and two unknown phases (X and X′) were found. One (X) was present in every composition, but it was especially prominent in the compositions containing 35.0 and 30.0 m/o CaO. The other unknown phase (X′) occurred only in the composition containing 35.0 m/o CaO which was recrystallized from a glass at 400°/24 or 850°C/24 hr. If this glass composition was recrystallized at 600°C/24 hr, it yielded the unknown phase (X) identical with that seen in compositions which were prepared by solid-state reaction. Two compositions, one on either side of the metaphosphate "join," were prepared by solid-state reaction and by recrystallization from a glass in an attempt to locate the unknown phases, but no success was achieved. All the compositions along the metaphosphate "join" were slightly hygroscopic except those containing less than 15 m/o CaO. Although the temperatures of initial melting listed in Table II are somewhat erratic, they do indicate a gradual increase in melting temperature with increasing amounts of magnesium. All these data indicated that the metaphosphate "join" was not a true join or a binary section similar to the ortho- and pyrophosphate joins and that at least one other ternary compound may exist in the system in the region near 35 m/o CaO, 18 m/o MgO, and 47 m/o P_2O_5. A major effort would have to be made to clarify the phase relations in this portion of the system, but this was not considered to be within the scope of the present work.

Table III. X-ray diffraction data for ternary compounds

$Ca_3Mg_3(PO_4)_4$ (1275°C/24 hr)		$CaMgP_2O_7$ (1050°/28 hr)	
d	I/I_1	d	I/I_1
8.42	20	4.39	10
6.11	20	4.14	8
5.01	30	3.23	15
3.87	60	3.14	5
3.75	90	3.05	75
3.25	20	3.01	85
3.11	5	2.91	10
3.05	25	2.84	100
2.82	100	2.73	8
2.75	20	2.60	5
2.71	20	2.43	5
2.51	60	2.32	8
2.17	10	2.16	8
2.14	15	2.10	10
2.02	10	2.04	8
1.877	25		
1.807	10		
1.629	10		
1.605	10		

Luminescence.—The two compounds in the system were prepared with known activators such as Mn^{2+}, Eu^{2+}, Sn^{2+}, U^{6+}, Tb^{3+}, Dy^{3+}, Eu^{3+}, and several combinations for double activation. Of these, Eu^{2+} and Tb^{3+} in the orthophosphate and Mn^{2+} in the pyrophosphate were found to be the most efficient. Compound formation and the absence of second phases were always verified by x-ray diffraction.

$Ca_3Mg_3(PO_4)_4$:Eu^{2+}.—The emission spectrum peaks in the blue region and changes slightly in position and half-width as the composition varies between the solid-solution limits. Figure 2 shows the spectral distribution of two phosphors with compositions at either end of the solid-solution region. Compositions were prepared by firing at 1100° for 6 hr, followed by a treatment at 1050°-1100° in a reducing atmosphere of about 2.5% H_2 in N_2.

Figure 3 shows the shift of the emission peak with a variation of the Ca^{2+} content in the solid solution (Eu^{2+} at 0.06 mole or lower), compared with the emission of the end member compounds. The shift is linear between $Ca_{3.00}Eu_{0.06}Mg_{2.94}(PO_4)_4$ and $Ca_{2.34}Eu_{0.06}Mg_{3.60}(PO_4)_4$. Beyond these limits, the spectra showed no shift other than that which could be attributed to the presence of the binary end member, indicating that the solid-solution limits determined by this method are in good agreement with those obtained by the phase equilibrium studies. If the Eu^{2+} is increased at the expense of Ca^{2+}, the peak emission is shifted to longer wave lengths and the half-width is increased. In both types of formulations, the absolute peak intensity decreased as the half-width increased, as shown in Table IV.

The increase in half-width is the result of an asymmetric spectral distribution, skewed toward longer wavelengths, which probably indicates that several different site symmetries are available to the Eu^{2+}

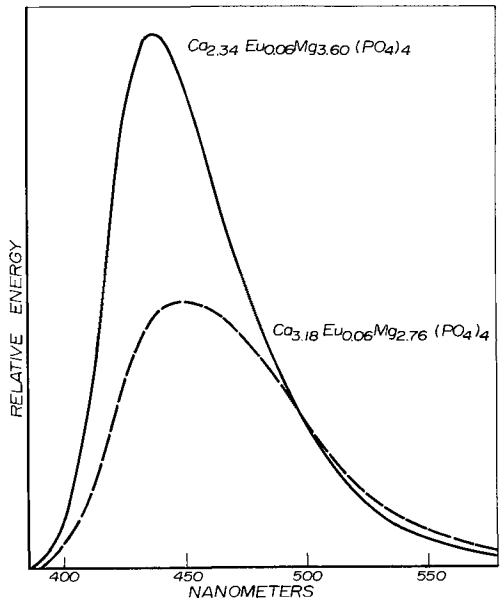

Fig. 2. Emission spectra for $Ca_{2.34}Eu_{0.06}Mg_{3.60}(PO_4)_4$ and $Ca_{3.18}Eu_{0.06}Mg_{2.76}(PO_4)_4$ under 2537Å excitation.

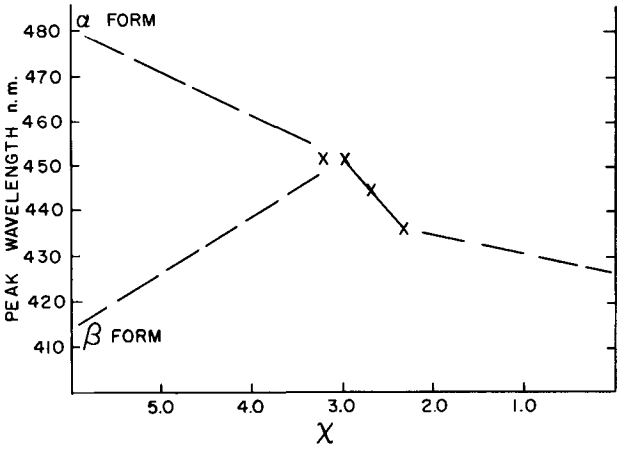

Fig. 3. Peak wavelength of $Ca_{6-x}Eu_{0.06}Mg_x(PO_4)_4$ series compared to end member orthophosphates (2537 excitation).

activator. As the sites are occupied by Eu^{2+}, broadened spectra and concentration quenching occur. The minimum Eu^{2+}-Eu^{2+} interaction occurs at the high Mg end, where considerable substitution of Mg^{2+} (radius 0.67Å) has occurred in Ca^{2+} sites (radius 0.99Å). The incorporation of Eu^{2+} (radius 1.12Å) for Ca^{2+} could occur in sites largely surrounded by the smaller Mg cations, permitting some compensation for the large size differences in the structure, and minimizing the Eu^{2+}-Eu^{2+} interaction.

Good agreement was found with the emission spectra for α-$Ca_3(PO_4)_2$:Eu^{2+} and β-$(Ca,Mg)_3(PO_4)_2$:Eu^{2+} previously reported by Wanmaker and ter Vrugt (18). The fluorescence of $Mg_3(PO_4)_2$:Eu^{2+}, with a weak emission at 425 nm, has been reported by Lagos (20), who found that the orthophosphate was the only magnesium phosphate compound which would accept Eu^{2+}.

Table IV. Spectral data for orthophosphate compositions

Composition	Intensity	Peak (nm)	½ width (nm)
$Ca_{2.00}Eu_{0.40}Mg_{3.60}(PO_4)_4$	55	450	84
$Ca_{2.20}Eu_{0.20}Mg_{3.60}(PO_4)_4$	70	443	65
$Ca_{2.30}Eu_{0.10}Mg_{3.60}(PO_4)_4$	98	440	61
$Ca_{2.34}Eu_{0.06}Mg_{3.60}(PO_4)_4$	100	439	60
$Ca_{2.35}Eu_{0.02}Mg_{3.60}(PO_4)_4$	93	433	56
$Ca_{2.94}Eu_{0.06}Mg_{3.00}(PO_4)_4$	60	452	85
$Ca_{3.18}Eu_{0.06}Mg_{2.76}(PO_4)_4$	45	452	85

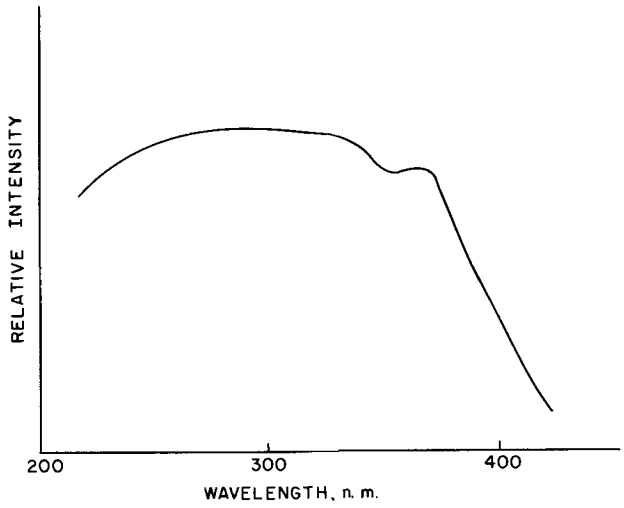

Fig. 4. Excitation curve for $Ca_{2.34}Eu_{0.06}Mg_{3.60}(PO_4)_4$ against sodium salicylate standard, detected wavelength is 440 nm.

About 4% $Ca_3(PO_4)_2$ is soluble in $Mg_3(PO_4)_2$, and apparently $Eu_3(PO_4)_2$ can also be incorporated in minor amounts.

An approximation of the quantum efficiency at 62% was made by comparing the spectra shapes of the phosphor and sodium salicylate, using a QE of 64% for the latter. The phosphor is responsive to both 2537 and 3650 excitations, as shown in Fig. 4. The optimized phosphor was tested in 40W lamps, as shown in Table V.

$Ca_3Mg_3(PO_4)_4$:Tb^{3+}.—Calculated as a substitute for Ca^{2+}, Tb^{3+} was found to require the formation of cation vacancies with the general formula $Ca_{6-x-3y}Tb_{2y}\square_yMg_x(PO_4)_4$. When charge compensation with an alkali was tried, (Na, Li, K, Rb), the brightness decreased substantially. The optimum brightness was again obtained at the magnesium end of the solid-solution range, $x = 3.60$ and $y = 0.05$ in the above formula. Emission intensities varied with Tb^{3+} concentration, and the emission from the $^5D_3$ level (blue) is quenched relative to $^5D_4$ levels (green) as the concentration is increased. This effect was found when changing the Tb^{3+} content on the magnesium end of the solid solution by increasing the value of y and also by increasing the value of x from 2.40 to 3.60 at a constant Tb concentration, which would increase the Tb^{3+}-Tb^{3+} interaction.

The absolute brightness of this phosphor is quite low, with a peak intensity of 50% of sodium salicylate, under 2537Å excitation. The excitation curve (Fig. 5) shows very poor response to the 2537Å radiation, but it is about ten times as efficient under 215 nm excitation when absorption can occur directly into the 5d band of Tb^{3+}. The phosphor is considerably more efficient under cathode-ray excitation, but the material is unstable and decreases in intensity with time. Attempts to obtain a brightness evaluation or even to record the spectra were unsuccessful due to the rapid change in the phosphor.

$CaMgP_2O_7$:Mn^{2+}.—When activated with Mn^{2+}, this phosphor responds to cathode-ray excitation, emitting in the orange-red region, with a moderately long afterglow. Partial substitution of up to 15% Zn for Mg increased the brightness. Decay measurements were made in comparison with the known phosphor

Table V. Life test on $(Ca_{2.34}Eu_{0.06}Mg_{3.60})(PO_4)_4$

Hours burned	Lumens	Color
0	1066	$x = 0.145, y = 0.092$
100	1026	
500	1020	
3000	897	$x = 0.147, y = 0.094$

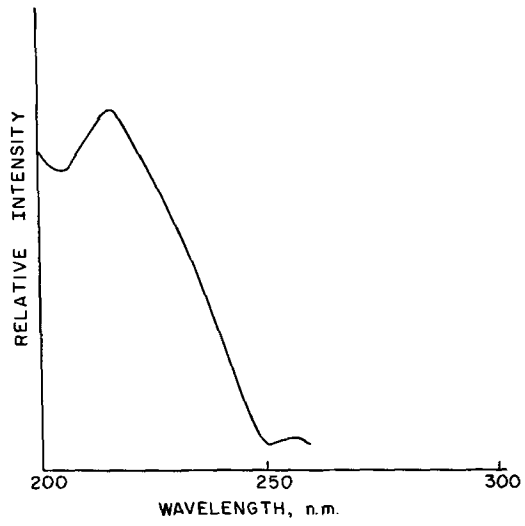

Fig. 5. Excitation curve for $Ca_{2.25}Tb_{0.10}\square_{0.05}Mg_{3.60}(PO_4)_4$ against sodium salicylate standard, detected wavelength is 549 nm.

$CaSiO_3$:Pb:Mn, P-25. $Ca_{0.99}MgMn_{0.01}P_2O_7$ has a 1/e value of 40 msec, compared with 18 msec for P-25.

Acknowledgment

The authors are grateful for the financial support of the Lamp Division, General Electric Company, Cleveland, Ohio, which made this work possible. This was Contribution No. 69-54 from the College of Earth and Mineral Science, The Pennsylvania State University, University Park, Pennsylvania.

Manuscript submitted Aug. 11, 1970; revised manuscript received *ca.* Dec. 11, 1970.

Any discussion of this paper will appear in a Discussion Section to be published in the December 1971 JOURNAL.

REFERENCES

1. E. Kreidler and F. Hummel, *Inorg. Chem.*, **6**, 891 (1967).
2. W. Brown and E. Epstein, *J. Res. Natl. Bur. Std.*, **69**, 547 (1965).
3. H. Koelmans, J. Engelsman, and P. Admiraal, *J. Phys. Chem. Solids*, **11**, 172 (1959).
4. R. Mooney and M. Aia, *Chem. Rev.*, **61**, 433 (1961).
5. A. Mackay, *Acta Cryst.*, **6**, 743 (1953).
6. P. Ranby, D. Mash, and S. Henderson, *Brit. J. Appl. Phys., Suppl. 4*, S18, 1954 (Published 1955).
7. M. Bencher, *Mat. Res. Bull.*, **4**, 15 (1969).
8. J. Berak, *Roczniki Chem.*, **32**, 19 (1958).
9. J. Sarver, M. Hoffman, and F. Hummel, *This Journal*, **108**, 1103 (1961).
10. C. Calvo, *Acta Cryst.*, **23**, 289 (1967).
11. K. Lukaszewicz, *Roczniki Chem.*, **35**, 31 (1961).
12. C. Calvo, J. Leung, and W. Datars, *J. Chem. Phys.*, **46**, 796 (1967).
13. R. Doman, J. Barr, R. McNally, and A. Alper, *J. Am. Ceram. Soc.*, **46**, 314 (1963).
14. J. Ando, *Bull. Chem. Soc. Japan*, **31**, 202 (1958).
15. K. Slawski, *Chem. Stosow., Ser. A*, **10**, 305 (1966).
16. W. Bobrownicki and K. Slawski, *Bull. Acad. Polon. Sci., Ser. Sci. Chem.*, **8**, 261 (1960).
17. K. Slawski, *Chem. Stosow., Ser. A*, **11**, 273 (1967).
18. W. L. Wanmaker and J. W. ter Vrugt, *Philips Res. Rept.*, **23**, 362 (1968).
19. M. V. Hoffman, *This Journal*, **117**, 227 (1970).
20. C. C. Lagos, *ibid.*, **115**, 1271 (1968).

Relaxation Phenomenon at Turnover in Point Contact Silicon Devices

Takashi Agatsuma* and Kiyoshi Miyake

Semiconductor and Integrated Circuits Division, Hitachi, Ltd., Kodaira-shi, Tokyo, Japan

ABSTRACT

Studies were made of the point contact breakdown or the turnover using samples of NN^+ type. Single voltage ramp with high amplitudes was applied in the reverse direction. Initially, the voltage increased with time at a constant rate corresponding to the rising slope of the voltage ramp until the voltage reached the onset of the flat part of the voltage ramp where the turnover occurred. Relaxation process was observed associated with the turnover. The relaxation process of the voltage consisted of two stages. The first stage was characterized by an exponential decay having a time constant in the range $10^{-6} \sim 10^{-3}$ sec depending on the temperature and the amplitude of the voltage ramp. The second stage was a slow process toward a steady state. The initial rate of the relaxation and the temperature dependence of the time constant suggested that the relaxation process, *i.e.* the turnover, is due to the internal field emission of electrons from shallow slow states into the conduction band of Si. A qualitative model of the emission process is discussed in terms of the rate of change in the density of occupied slow states which involves the interaction of electrons between slow states and the conduction band. A comparison of the model with experimental data showed that the slow states must be located at the energy level ~0.15 eV from the conduction band edge.

When a high voltage pulse with a short pulse width is applied in the reverse direction of a point germanium contact diode, a turnover mode different from the one observed by applying d-c or a-c voltage from a 50 Hz source is observed. Hunter (1) reported that the turnover voltage obtained by using the high-voltage pulse becomes higher than that of d-c voltage. Billig (2), Lempicki and Wood (3), and Kikuchi and Tarvi (4) also discovered that the turnover characteristic was affected by the amplitude and the wave form of the applied voltage. According to these reports, the turnover current begins to move forward with a delay of "a certain time" after the occurrence of the turnover, and this time delay varies with the amplitude and the wave form of the applied voltage.

A self-heating hypothesis has been proposed to account for this phenomenon. The idea was that, when the temperature of the point contact is increased to

* Electrochemical Society Active Member.
Key words: breakdown, point contact, semiconductor.

a certain level, a heating effect occurs followed by an emission of the current carriers. The physical significance of this model is, however, still unclear. The present author and others (5) have pointed out that the phenomenon can be understood as a relaxation effect caused by the transfer of the current carriers between surface states at the point contact and the bulk of the semiconductor. This paper describes the experiments and the qualitative analysis of the relaxation phenomenon observed for point contact silicon devices.

Experimental Samples and Procedures

An N-type silicon slice with a thickness of 5 ~ 6 mm and a specific resistivity of 0.5 ~ 10 ohm-cm and an NN^+ silicon wafer were prepared. The NN^+ silicon wafer was composed of the N^+ layer, a phosphorus-diffused layer with a high concentration and about 100μ in thickness, and the mirror-polished N layer with a specific resistivity of 13 ~ 14 ohm-cm and a thickness of 20 ~ 90μ. The wafer was separated into pellets of 2 x 2 mm. The pellet was soldered on the silver base using the gold-silicon eutectic alloy. Before the measurements, pellets were dipped into hydrofluoric acid for 1 min cleaned with deionized water, and spin dried.

The tungsten probe with a diameter of 1.0 mm was electrochemically etched to a diameter of 15-20 $\mu\phi$ at the point. The point of the tungsten probe was attached on the N layer surface with the loading pressure of $3 \times 10^6 \sim 10^7$ g/cm^2.

The arrangement of the measuring circuit has been described previously (6). The applied voltage consists of a rising part and a following flat part. The slope of the rising part was varied from 2×10^4 to 7×10^6 V/sec, and the amplitude, Va, of the flat part from 0 to 500V. The voltage was applied one time in the reverse direction through a current-limiting resistance, R_L.

Experimental Results

Figure 1 shows typical relaxation characteristics of the voltage observed on the N-type silicon slice. The voltage rises steeply with the rising slope of the applied voltage and then decreases at the rate of an exponential function characterized by a relaxation time constant, τ. This process is the first stage of Fig. 1. The voltage decreases gradually after the first stage until it almost stops to decrease and approaches a constant value, V_S, which is the second stage. The relaxation characteristic of the current was exactly equivalent to that of voltage, and the current increases with the time constant, τ, up to a constant value.

The onset of the turnover corresponds to the point where the voltage begins to decrease at the rate of an exponential function from the initially raised voltage; that is, the voltage relaxation starts. Thus, the initially raised voltage becomes the turnover voltage, V_T. As shown in Fig. 1, the turnover voltage and the relaxation time constant vary with the amplitude of the applied voltage. When the applied voltage becomes low enough to make V_T almost equal to V_S, no turnover occurs.

Figure 2 shows the relationship between the initial rate of the relaxation of the voltage $dv/dt|_{t=0}$ and the reciprocal F_{SO}^{-1} of the initial electric field strength at the point-contact surface, with W_N as a parameter. The sample used is an NN^+-type silicon device. The initial rate of the relaxation was obtained from the slope of the relaxation curves at the onset of the turnover. The initial surface field strength, F_{SO}, was calculated from the turnover voltage assuming that the depletion layer formed by applying the reverse voltage was equal to the one made by the Schottky-type junction.

The logarithm of the initial rate of the relaxation, as shown in Fig. 2, had an almost linear relationship with F_{SO}^{-1}, and the linear curves of the $dv/dt|_{t=0}$ *vs.* F_{SO}^{-1} tend to shift toward the larger portion of F_{SO}^{-1} with decreasing thickness in the N layer. This means that the turnover is initiated at the lower voltage as the thickness is decreased.

It was also found that the relaxation time constant changes largely with the ambient temperature. Figure 3 shows the effect of ambient temperature on the time constant, τ, in terms of τ *vs.* $10^3/T$, in which case the amplitude of the applied voltage was a fixed constant during measurements. In this case, the time constant, τ, was obtained by assuming that the first stage of the voltage relaxation curve was approximately repre-

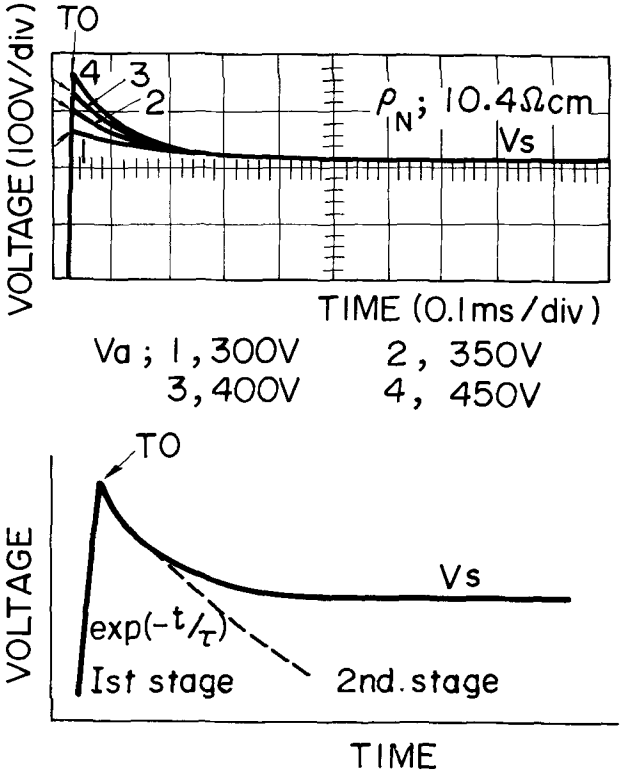

Fig. 1. Typical characteristics of voltage relaxation

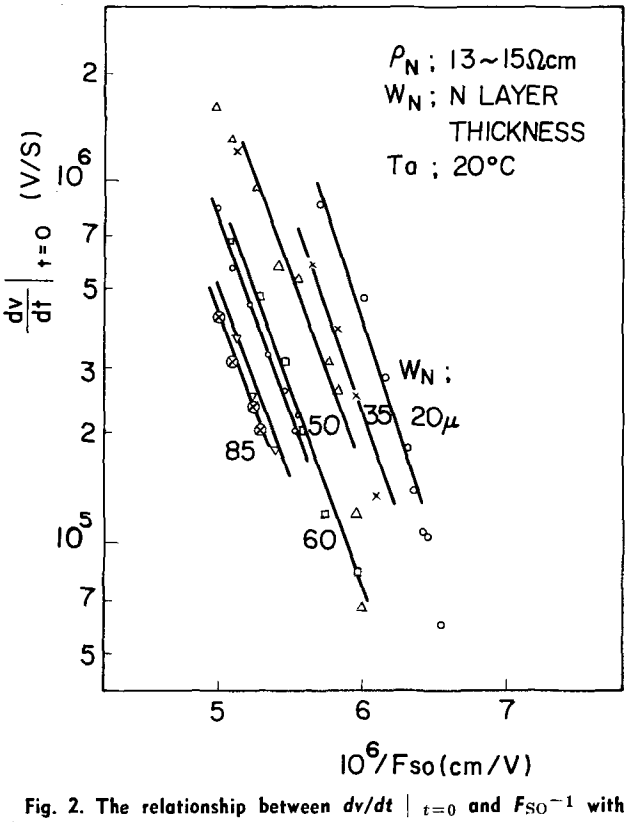

Fig. 2. The relationship between $dv/dt \mid_{t=0}$ and F_{SO}^{-1} with W_N as a parameter.

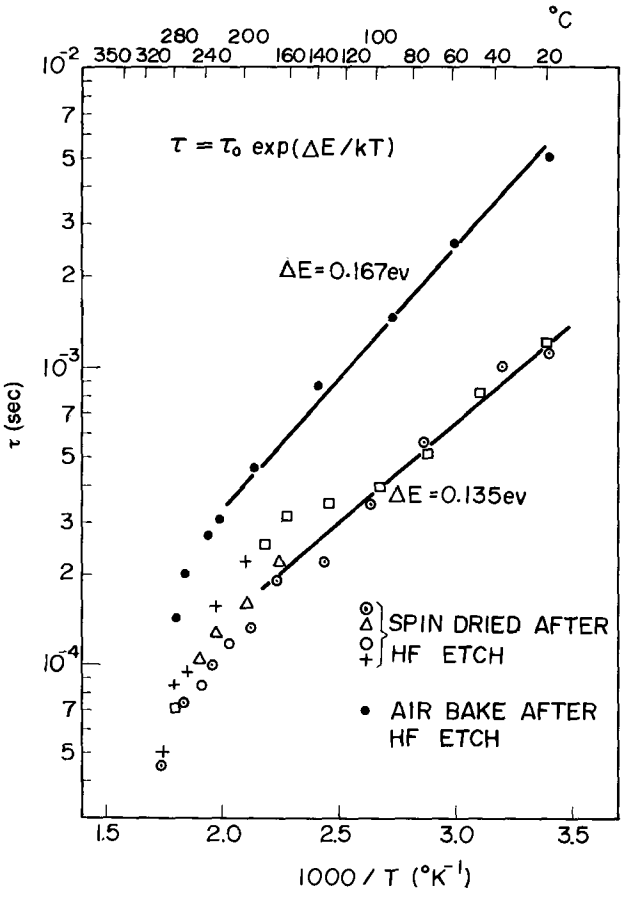

Fig. 3. The effect of ambient temperature on the relaxation time constant.

sented by the following formula

$$V = V_T \exp(-t/\tau) \qquad [1]$$

As seen in the figure, the logarithmic value of τ was approximately represented by a straight line having a slope against $1/T$, namely

$$\tau = \tau_0 \exp(\Delta E/kT) \qquad [2]$$

where k is the Boltzmann constant and ΔE is the activation energy. ΔE was slightly different from the surface treatments of the samples and was estimated on the order of 0.13-0.16 eV.

Discussion and Conclusion

As shown in the previous section, the turnover appearing in the reverse direction of the point contact silicon diode was characterized by the relaxation phenomenon of voltage and current, and the relaxation characteristic was varied by such factors as the field strength, ambient temperature, and surface treatments. This phenomenon could not be fully understood by a simple heating model. Another model of the "charge transfer mechanism between the slow surface states in the silicon dioxide and the silicon bulk" was provided in view of a close similarity of the relaxation phenomenon to the longitudinal field effect for the surface of silicon (7).

Consider the case where an electric field is applied in a form whose polarity is such that the tungsten is made negative and silicon is made positive. The energy diagram under the application of the voltage for the tungsten-silicon dioxide film-silicon system is shown in Fig. 4. The conduction electrons of the N-type silicon near the point contact will be affected by the applied electric field to repel from the N-layer surface and form a depletion layer. In this case, however, electrons trapped at the slow surface states would not be moved but frozen, and this resulted in a nonequilibrium state of electrons inside the tungsten-silicon dioxide film-silicon system. Then the relaxation phenomenon could be understood as a process of transfer of electrons from a nonequilibrium state to an equilibrium state.

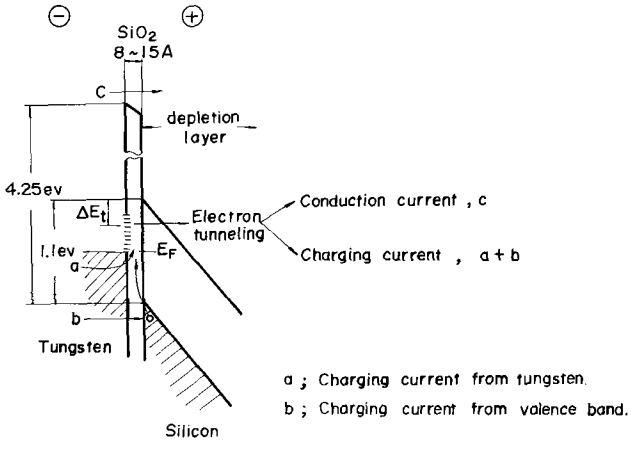

Fig. 4. The energy diagram of tungsten-silicon dioxide film-silicon during the relaxation.

With regard to the above, Rupprecht gave the time constant, τ, as a function of temperature, and Many and Goldstein (9) provided a method of solving this phenomenon by using field strength and presented a tunnel effect model. Taking into consideration the results shown in Fig. 2 and 3, however, one introduces the equation involving both temperature effect and field effect.

Thus, the relaxation process of the voltage can be expressed in terms of the rate of change in the density of occupied slow states, n_t, as follows

$$\frac{dn_t}{dt} = -C_n n_1 \{\exp(-\alpha/F_S)\} n_t + C_p p_1 (N_t - n_t) + J_t/q \qquad [3]$$

where

$$\alpha = \frac{4\sqrt{2m_e^*}}{3qh}(E_c - E_t)^{3/2} \qquad [4]$$

where q is the electronic charge, h is Planck's constant/ 2π, and m_e^* is the effective mass of electrons, being taken as the smallest mass in the conduction band (0.19 m_0, m_0: free electron mass)

$$N_t = N_0/\{1 + \exp(E_t - E_F)/kT\} \qquad [5]$$

N_t is the initial density of occupied surface states which are able to emit an electron. N_0 is the density of the slow surface states, and E_F is the Fermi-level of metal-silicon dioxide film-silicon system.

In this case, the slow surface states are assumed to consist of single charged center having the energy E_t. The temperature involves both the ambient temperature and the temperature rise induced by self-heating.

$$n_1 = N_c \exp\{-(E_c - E_t)/kt\}$$
$$p_1 = N_v \exp\{-(E_t - E_v)/kT\} \qquad [6]$$

n_1 and p_1 are the density of electrons and holes, respectively, which would be present in the oxide for the case where the Fermi level is at the level of E_t. E_c and E_v are the energy level of the edge of the conduction band and the valence band, respectively. N_c and N_v are the effective density of states for the conduction band and the valence band, respectively. C_n and C_p are the capture coefficients, the probabilities per unit time of electrons and holes, respectively, which are captured by the unoccupied slow surface states.

The first term in the Eq. [3] represents the net rate of emission of electrons from the slow surface states to the conduction band of silicon. In this case, the tunnel probability of the electrons crossing the forbidden

band of the silicon dioxide film is considered as unity, because the thickness of the silicon dioxide is in the range of 8 ~ 12Å (10). The second and third terms also represent the charging rate at which electrons are provided from the valence band and the tungsten, respectively, to fill the slow surface states being unoccupied. From its similarity to the second term, the third term may be substituted as follows

$$J_t/q = A_t(N_t - n_t) \qquad [7]$$

When the exponential term in Eq. [3] is considered as unity and the second and third terms are neglected, Eq. [3] becomes

$$\frac{dn_t}{dt} = -C_n n_1 n_t \qquad [8]$$

Equation [8] represents the thermal emission of electrons from the fast surface states into the conduction band at low temperatures and coincides with Eq. [3] given by Rupprecht (8). On the other hand, under high fields at low temperatures, Eq. [3] changes into

$$\left.\frac{dn_t}{dt}\right|_{t=0} \propto \exp\left(-\alpha/F_S\right) \qquad [9]$$

This equation corresponds to Eq. [2] presented by Many *et al.* (9).

The electrons emitted from the slow surface states will form currents, one part of which will constitute a conduction current in the conduction band of silicon bulk and the other part of which will become a charging current for the slow states being unoccupied. Accordingly, the current density may be expressed as

$$i(t) = q(N_t - n_t)^{3/2}\mu_e\bar{F} + q(N_t - n_t)C_pP_1 + J_t \qquad [10]$$

where the first term is the conduction current, in which μ_e is the electron mobility and $\bar{F}$ is the mean value of the field strength in silicon bulk. The second and third terms are the charging current from the valence band and the tungsten, respectively. The components of these currents are shown schematically in Fig. 4.

The surface field strength, F_S, observed after the turnover may be expressed as a function of time.

$$F_S^2 = F_{SO}^2 - I(t) \cdot K \cdot R_L \qquad [11]$$

where $I(t)$ is the current given by $\pi b^2 \cdot i(t)$, where b is the radius of the contact surface. K is the constant value for converting the voltage into the surface field strength, and given as $K = 4 \times 10^8/\rho_N \cdot 0.53^2$ where ρ_N is the resistivity in the N layer, and R_L is the external resistance.

Figure 5(a) and (b) show the numerically calculated curves of F_S from Eq. [3], [10], and [11] under the initial condition $t = 0$, $n_t = N_t$. Figure 5(a) and (b) are for the cases of $T = 300°K$ and $T = 400°K$, respectively. In these calculations, the following values were used; $N_o = 10^{15}$ cm^{-2}, $E_c - E_t = 0.15$ eV, $\mu_e = 4.0 \times 10^9 \cdot T^{-2.6}$ cm^2/V-sec, $C_n = C_p = 5 \times 10^{-8}$, 5×10^{-9} cm$^3 \cdot$ sec^{-1}, $\bar{F} = 200$ V/cm, $A_t = 10^{-5}$, 10^2, 10^5 sec^{-1}. A voltage relaxation curve for the silicon block with ρ_N of 10.4 ohm-cm are shown in the figures as experimental data.

In Fig. 5(a), a comparison was made between the calculations and the experimental curve by providing $C_n = 5 \times 10^{-9}$ cm$^3 \cdot$ sec^{-1}. In this case the two curves coincided for short periods of time regardless of the value of A_t, but as the time was postponed, these two curves could be matched by giving $A_t = 10^2 \sim 10^5$ sec^{-1}. In Fig. 5(b) the same condition, $C_n = 5 \times 10^{-9}$ cm$^3 \cdot$ sec^{-1}, was also provided. In this case both curves were exactly superimposed by giving $A_t = 10^{-5}$ sec^{-1} during times shorter than 2×10^{-5} sec, but no agreement of the two curves was obtained for a longer duration of time than this.

The values of physical quantities such as N_o, $E_c - E_t$, C_n, $\bar{F}$ and A_t used for the calculations mentioned above were determined as shown from the following discussion.

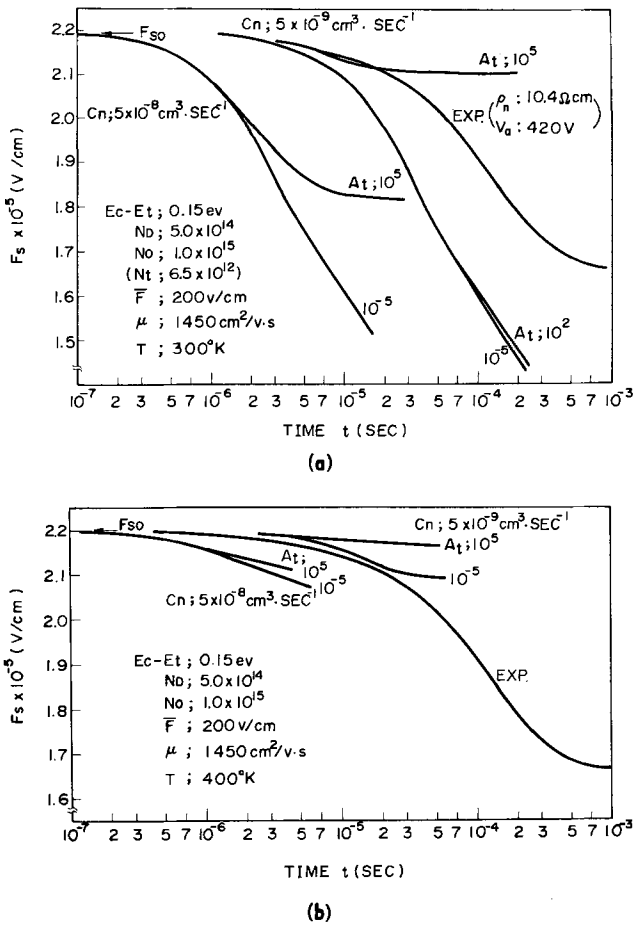

Fig. 5 (a), (b). Computed curves of F_S as a function of time

The slow surface state used in the present model were of the donor type, thus capable of emitting electrons. As the relaxation phenomenon observed quite distinctively for the samples which were cleaned in deionized water after hydrofluoric acid etching, the vapor molecules adsorbed on the silicon surface are considered to have an important role in forming the donor-type slow surface states. According to Sochanski and Gatos (11), when the vapor molecules are chemically adsorbed on the semiconductor surface, the electrons are transferred from molecules to the semiconductor, and the electrons thus transferred constitute slow surface states of the donor type. It could be deduced that, as the number of adsorption sites on the semiconductor surface is of the order of $10^{14} \sim 10^{15}$ cm^{-2}, the density of the slow surface state N_o is in the range of $10^{14} \sim 10^{15}$ cm^{-2}.

As mentioned previously, Fig. 2 and 3 describe the experimental results of the behavior of the relaxation characteristic. Figure 2 deals with this matter by using only the electric field as a responsible factor and neglecting the effect of temperature, and Fig. 3 just the opposite. Therefore, Fig. 2 may be understood by the model using Eq. [9]; Fig. 3, the model using Eq. [8]. As a result, $E_c - E_t = 0.19$ eV was obtained from the former case and, from the latter case in which $\Delta E = 0.13 \sim 0.16$ eV was previously obtained as shown in Fig. 3, these values of ΔE may be interpreted as $E_c - E_t$. As seen from the above, surface states responsible for the relaxation phenomenon have the relatively shallow energy level of the order of 0.15 eV.

This estimation of 0.15 eV as the value for $E_c - E_t$ may not deviate greatly from other reported results because in the study using an MOS-type device (12), the maximum value of the density of the interface states in the Si-SiO_2 system was found in a range as

high as 0.1 ~ 0.15 eV from the bottom of the conduction band.

According to Sclar *et al.* (13), the capture coefficient for hydrogen-like impurities in silicon and germanium was confined in the range of $10^{-9} \sim 10^{-8}$ $cm^3 \cdot sec^{-1}$. This value, applicable to slow surface states, was used for the present calculations, and F and A_t were suitably selected so that the calculation curves might not diverge from the experiment curve.

As seen from Fig. 5, the perfect matching of the calculation curves on the experiment curve was difficult to achieve because the physical quantities, such as N_o, $E_c - E_t$, and T used in Eq. [3], [10], and [11], were all dependent on a wide range of arbitrary selections. Should such a complete fit be made between the two curves, it would not be possible to decide whether the values given to physical quantities were really pertinent.

Thus it may be concluded from the above discussion that the relaxation phenomenon is due to the internal field emission of current carriers from the slow surface states in the oxide which must be located at a shallow energy level (~0.15 eV) from the conduction band edge.

Acknowledgment

The authors wish to express their sincere thanks to Dr. M. Tomono for his encouragement during this study. They are also indebted to Mr. Y. Ishikawa who performed the computer program.

Manuscript received May 14, 1970. This was Paper 81 presented at the Boston Meeting of the Society, May 5-9, 1968.

Any discussion of this paper will appear in a Discussion Section to be published in the December 1971 JOURNAL.

REFERENCES

1. L. P. Hunter, *Phys. Rev.*, **19**, 151 (1951).
2. E. Billig, *ibid.*, **87**, 1060 (1952).
3. A. Lempicki and C. Wood, *Proc. Phys. Soc. (London)*, **673**, 328 (1951).
4. M. Kikuchi and Y. Tarui, *J. Phys. Soc. Japan*, **9**, 642 (1951).
5. T. Agatsuma, *Proc. IEEE*, **54**, 1206 (1966).
6. T. Agatsuma, *IEEE Trans. Electron Devices*, **ED-13**, 748 (1966).
7. A. Many, Y. Goldstein, and N. B. Grover, "Semiconductor Surfaces," North-Holland, Amsterdam (1965).
8. G. Rupprecht, *Phys. Rev.*, **111**, 75 (1958).
9. A. Many and Y. Goldstein, *Surface Sci.*, **2**, 114 (1964).
10. R. J. Archer, *This Journal*, **104**, 619 (1957).
11. J. Sochanski and H. C. Gatos, *ibid.*, **13**, 393 (1969).
12. P. V. Gray, *Appl. Phys. Letters*, **8**, 31 (1966).
13. N. Sclar and E. Burstein, *Phys. Rev.*, **98**, 1757 (1955).

N Layer Thickness Dependence of Second Breakdown in Point Contact NN^+ Si Devices

Takashi Agatsuma* and Kiyoshi Miyake

Semiconductor and Integrated Circuits Division, Hitachi, Ltd., Kodaira-shi, Tokyo, Japan

ABSTRACT

The second breakdown phenomenon in point contact Si devices was studied using NN^+-type Si pellets having different heat sinks, where the thickness of the N layer was varied from 20 to 90μ, and the resistivity in the N layer was 13 ~ 15 ohm-cm, while the resistivity and the thickness in the N^+ layer were kept constant. Single voltage ramp was applied in the reverse direction of the devices through the current limiting resistance, R_L. The second breakdown characteristics, P_M *vs.* t_d, were found to vary depending on the thickness in the N layer and also the thermal coupling at the contact between the pellets and heat sinks. The thermal model presented showed that the second breakdown characteristics can be explained assuming that the second breakdown occurs when the temperature at the interface of N and N^+ layers reaches an initiating temperature. The initiating temperature was found to vary with the thickness of the N layer and was lowered as the thickness was reduced.

In a previous paper (1) it was shown that the turnover phenomenon observed in the reverse direction of the point contact silicon device may be caused by an injection of current carriers due to the electric field emission. In this case, however, it is predictable that, since a large amount of power is dissipated at the point contact area, the device, when held at turnover for longer periods, is subject to such a second breakdown as is seen in the P-N junction diodes, transistors, and other N^+ NN^+ devices (2).

Anupyl'd (3), who found a second breakdown phenomenon in point contact germanium diodes, has commented briefly on the frequency dependence of the applied voltage and the changes caused by the surface treatments of the device. Agatsuma (4) used point contact silicon NN^+ devices and attempted to clarify the phenomenon. The present paper is intended to describe how the delay time associated with the second breakdown varies depending on the thickness of the N layer and the thermal coupling between the pellet and the heat sink, thereby explaining this breakdown as a heat conduction phenomenon for the longitudinal direction of the device.

* Electrochemical Society Active Member.

Key words: breakdown, point contact, semiconductor.

Experimental Samples and Procedures

NN^+-type silicon wafers were prepared composed of the N^+ layer, a diffused layer of phosphorus with a surface concentration of over $10^{20}/cm^3$ and the thickness of 100μ, and the mirror-polished N layer with the specific resistivity of 13-15 ohm-cm and the thickness ranging from 20 to 90μ. The wafers were broken into small pieces (pellets) of a rectangular form to prepare the samples. The N^+ layer of pellets was attached on the heat sink (silver base) by one of the following three soldering methods. Figure 1 shows simple illustrations of the samples used.

(*a*) Vacuum-evaporate a thin layer of Mo-Ni-Ag alloy on the surface of the N^+ layer, then being welded to a silver base of 3 mm thickness through 2-5μ thick solder form.

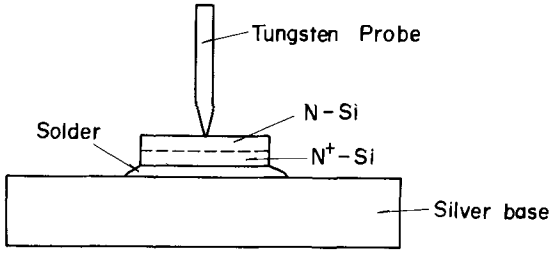

(a) Sample having heat sink of silver base

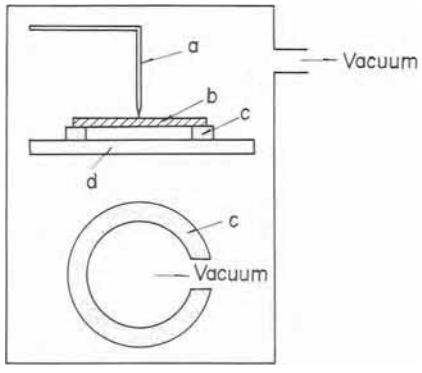

a : Tungsten probe
b : Silicon pellet
c : Ceramic ring
d : Cu plate

(b) Sample under thermally insulation

Fig. 1. Schematic drawing of the samples for the experiments

(b) Insert a gold pellet between the N^+ layer and the silver base, and heat them all to form an Si-Au eutectic alloy, thus soldering the pellet on the silver base with the thickness of eutectic layer in the range of 30-50μ.

(c) Place the pellet in a vacuum of 10^{-4} mm Hg, using a cryostat to provide the condition that the N^+ side is under thermal insulation. Before the measurements, the sample was immersed in hydrofluoric acid for 1 min, rinsed in deionized water, and spin dried.

The tungsten probe with a diameter of 1.0 mm was electrochemically etched to a diameter of 15-20 $\mu\phi$ at the point. The tungsten probe was positioned to the N side with a pressure of 3 x 10^6-10^7 g/cm^2. The arrangements of the measuring circuit are the same as in a previous paper (1). The applied voltage consisted of a rising part with a rising slope and a following flat part. The rising slope was continuously varied from 2 x 10^4 V/sec to 5 x 10^7 V/sec and the amplitude V_a of the flat part was also changed from 0 to 500V. The single voltage was applied in the reverse direction through the current limiting resistance, R_L.

Experimental Results

Figure 2 shows the typical characteristics of voltage and current transients with V_a as a parameter when a high voltage pulse is applied in the reverse direction of the device. Initially both voltage and current increased with time as shown in the figure. Then, the voltage curve arrived at its maximum value, V_T where it stopped increasing further and the current curve reached a point, I_p, where it changed the course of its progress. V_T and I_p are the turnover voltage and current, respectively (1).

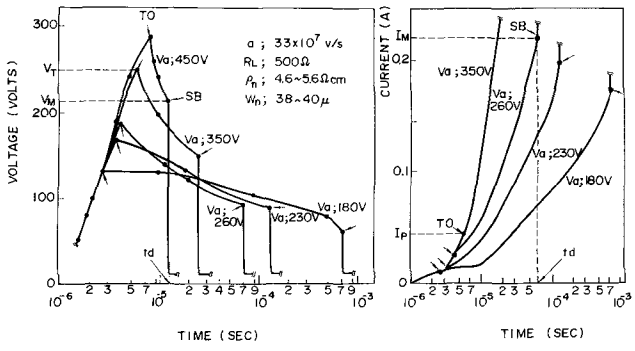

Fig. 2. Typical characteristics of voltage and current transients

After the voltage curves continued to decrease with a certain time constant, and the current curve kept on increasing, both of the curves came across a point where "the voltage reduced abruptly and the current increased suddenly." This is the occurrence of a second breakdown to which P-N junction diodes and transistors are subjected. The voltage, current, and delay time, all of which play their roles in characterizing the secondary breakdown, are defined as V_M, I_M, and t_d, respectively.

Figures 3(a) and (b) show the variations of the second breakdown characteristics with the thickness in the N layer. In the experiments, the rising slope was held at a constant value of 5.5 x 10^7 V/sec. The voltage-time and current-time characteristics were first observed and, then, the power, P_M, which is I_M multiplied by V_M and the delay time, t_d, were measured. The values of P_M and t_d were determined for each value of the applied voltage, V_a. In this manner, P_M *vs.* t_d curve for the sample with a given thickness in the N layer was obtained. This procedure was followed for all samples having the N layer ranging from 20 to 90μ. Thus, P_M *vs.* t_d curves were obtained with the thickness of the N layer as a parameter.

Figure 3(a) illustrates P_M *vs.* t_d characteristics using the soldering method mentioned previously, *i.e.* the method of soldering the surface of the N^+ layer to the silver base with Mo-Ni-Ag alloy. In the thicker samples, as seen from the figure, t_d decreases gradually with increasing P_M, while, in the thinner samples, t_d shows an appreciable decrease with no further increase in P_M.

Figure 3(b) represents the variation of P_M *vs.* t_d characteristics with the soldering methods (*a*), (b), and (c). As the delay time, t_d, became longer (in the order of ~msec), P_M *vs.* t_d characteristics were greatly changed depending on the soldering methods. For example, for the samples of 90μ thickness, the value of P_M for the constant value of t_d decreased in the sequence: Mo-Ni-Ag silver base, Au-Si silver base, and the thermally insulated sample. In the case of Mo-Ni-Ag silver base, t_d increased rapidly with no further increase in P_M. When P_M approached 40W, t_d became so long that the second breakdown was actually unobserved, while, in the case of the insulated sample, t_d did not display a saturation such as in the above case, but only a gradual reduction with the decrease of P_M. This behavior, however, became less pronounced for thinner samples.

It is to be noted that, for a range of shorter delay times, any choice of the soldering methods did not affect P_M *vs.* t_d characteristics.

The behavior mentioned above is also understood from the voltage-time characteristic and the current-voltage characteristic (relaxation curves), as shown in Fig. 4(a) and (b). As seen in Fig. 4(a), for the sample with the Au-Si eutectic silver base the voltage showed no appreciable decrease during the sweep time exceeding ~1 msec, and the second breakdown was observed at a point along the curve of this time characteristic. On the other hand, the insulated sample showed a gradual reduction of the voltage even after

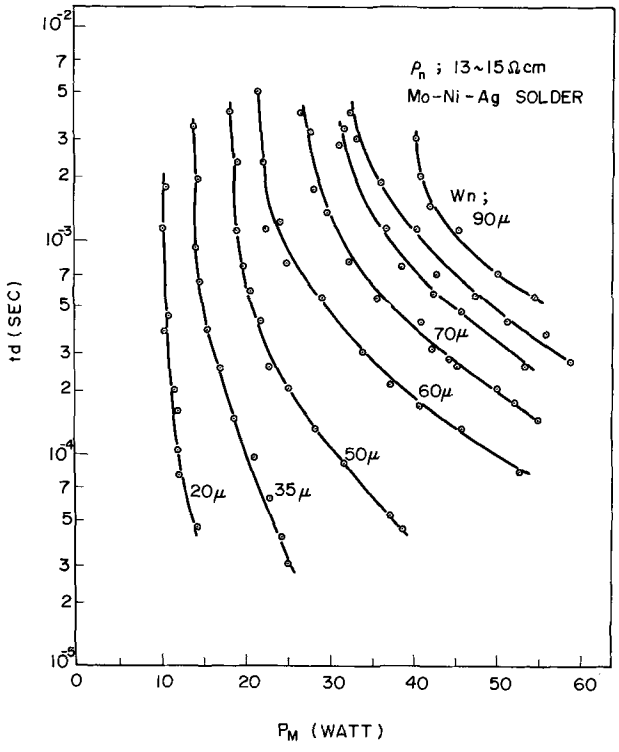

Fig. 3 (a). The dependence of P_M vs. t_d characteristics on the thickness in the N layer.

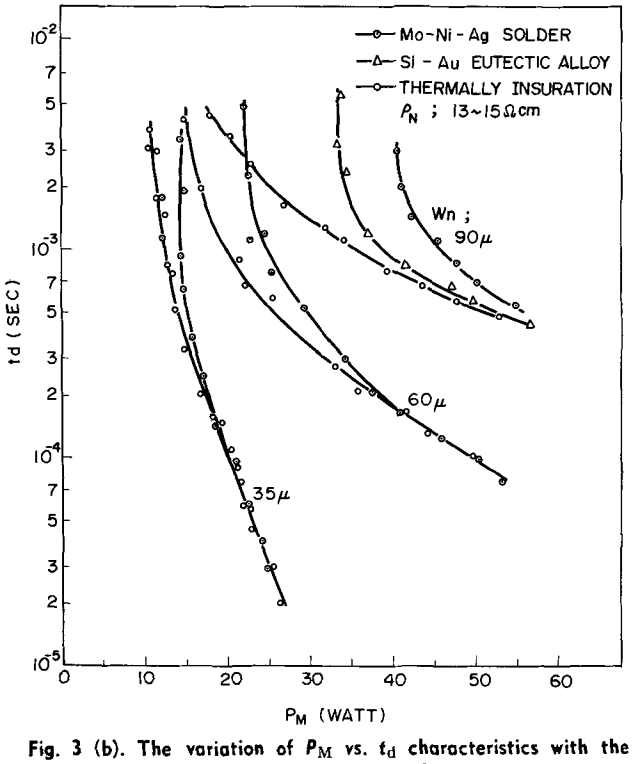

Fig. 3 (b). The variation of P_M vs. t_d characteristics with the thermal coupling between pellets and heat sinks.

the sweep time became greater than ~1 msec, and the second breakdown occurred at some point along this curve. The numbers on the curves shown in Fig. 4(b) indicate the time during which the operating points move along relaxation curves. As seen from the figure, in the case of the silver-base sample the operating point stayed at a high-power level for a long duration of time, but in the case of the insulated sample the point quickly passed over such a high-power region and reached a lower-power level where it remained for a long period of time.

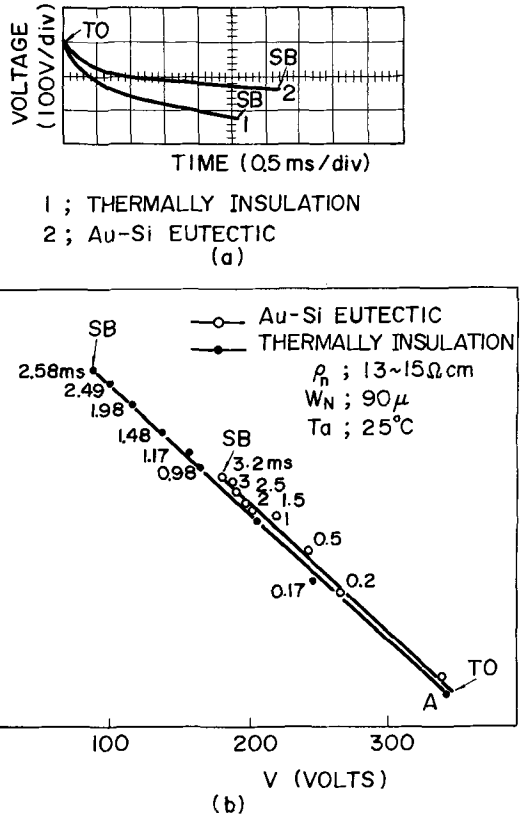

Fig. 4. The comparisons of voltage-time (a), and voltage-current characteristics (b) between samples with Au-Si eutectic silver base and under thermal insulation.

Discussions and Conclusion

As seen in the previous section the second breakdown occurred when the device was subjected to staying at the turnover for the duration of delay time, t_d. Then, the thermal model was proposed as shown diagrammatically in Fig. 5(a). This model consisted of a disk heat source having a radius b, the N-type silicon and the heat sink both extending in the direction of Z axis, and a tungsten probe. The disk heat source is positioned on $Z = 0$ plane, the surface of the contact between a tungsten point and the N-type silicon. Let us assume that the power is spread uniformly over the disk, and no heat is generated inside the N-type silicon. The heat generated may be conducted in two directions of $\pm Z$ axes, one advancing through the N-type and N^+-type silicon layers toward the heat sink and the other moving along the tungsten probe.

We consider, for simplicity, that as shown in Fig. 5(b) the whole device comprises the silicon and the heat sink, each extending to infinity, and that the heat disk is located at a distance d from the heat sink. The effect of the tungsten probe is made as a correction for this simple model.

Attention was paid to the temperature at a point of $r = 0$, $Z = W_N$, namely the boundary between the N and N^+ layers immediately under the tungsten point. Let the initial conditions be that $t = 0$, $T = 0$ and that the power $P(t)$ is dissipated from the moment of $t = 0$ to $t = t_d$. Then, the temperatures developed at the time of t_d at the point of $r = 0$, $Z = W_N$ are given by the following equation (5)

$$T(0,W_N;t_d) = \frac{1}{2\rho_1 C_1\sqrt{\pi k_1}} \left[\int_0^{t_d} \frac{P(t)}{t^{1/2}} e^{-W_N^2/4k_1t}\,(1 - e^{-b^2/4k_1t})\,dt + \left(\frac{1-K}{1+K}\right) \int_0^{t_d} \frac{P(t)}{t^{1/2}} e^{-(W_N+d)^2/4k_1t}\,(1 - e^{-b^2/4k_1t})\,dt\right] \quad [1]$$

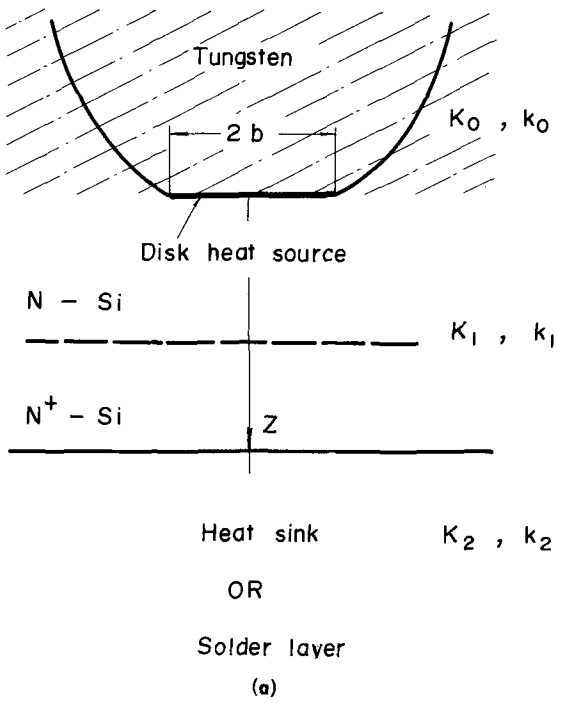

(a)

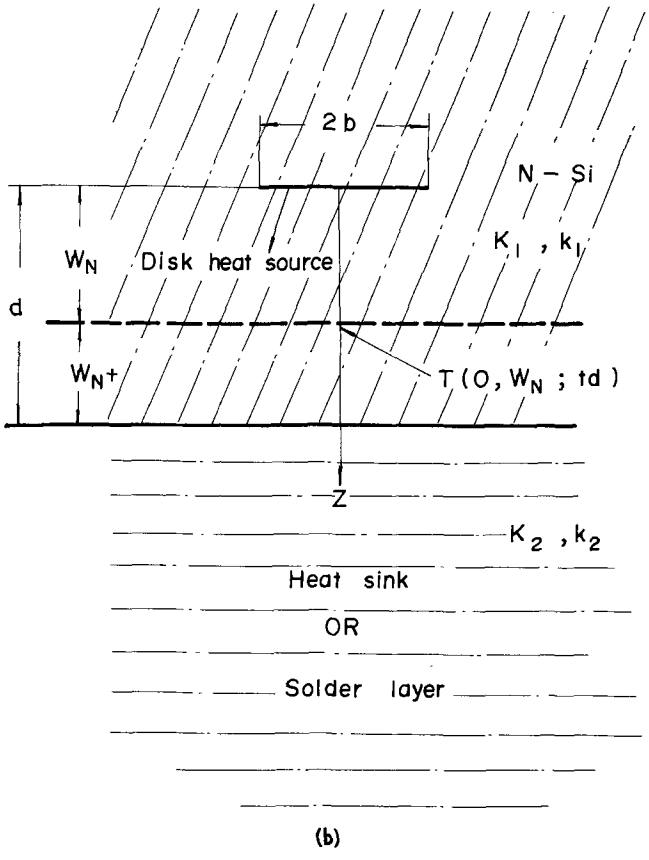

(b)

Fig. 5 (a), (b). The thermal models used

where

$$K = \frac{K_2}{K_1} \cdot \left(\frac{k_1}{k_2}\right)^{1/2}$$

$$k_{1,2} = \frac{K_{1,2}}{\rho_{1,2} \cdot C_{1,2}} \qquad [2]$$

where $K_{1,2}$, $k_{1,2}$, $\rho_{1,2}$, and $C_{1,2}$ represent the thermal conductivity, the diffusivity of heat, the density, and the specific heat, respectively, and suffix 1 refers to the silicon and suffix 2 to the heat sink. W_N and W_{N+} are the thicknesses of the N layer and N^+ layer, respectively, d is the distance between the disk heat source and the heat sink, namely the thickness of the pellet. In Eq. [1] and [2], $K = 1$ corresponds to the case where the entire region of the device was constituted by the silicon and $K = 0$ to the case where the N^+ side is under thermal insulation.

Figure 6 shows the results numerically calculated from Eq. [1] for $P(t) = P_0$ ($\equiv$ constant) as a function of P_o/T $(0, W_N; td) \cdot 2\sqrt{\pi} \cdot k_1^{1/2} K_1$, with W_N as a parameter. In this case, b is 8μ, and $K = 0$, 1, 6 are taken for each value of W_N, where $K = 6$ corresponds to the Mo-Ni-Ag silver base. As shown in Fig. 6, t_d *vs.* P_o/T curves vary depending on W_N, and these curves are slightly affected by the values of the heat sink as long as t_d is kept below 10^{-4} sec, but once t_d exceeds 10^{-4} sec, t_d *vs.* P_o/T curves are influenced by the factor of the heat sink, splitting to the different curves depending on the values of K.

The values of k_1 (=0.51 cm²/sec) and K_1 (=0.84 W/cm · deg) are constant determined for the silicon. Therefore, if it is assumed that the second breakdown occurs when the temperature $T(0, W_N; t_d)$ reaches some constant temperature T_i $(0, W_N; t_d)$, then the value of $T(0, W_N; t_d) \cdot 2\sqrt{\pi} \cdot k_1^{1/2} K_1$ can be regarded as a constant. In this connection, P_o may be identified as the power, P_M, required for the initiation of the second breakdown. Thus, Fig. 6 can be considered to represent the relationship between the power, P_M, and the delay time, t_d, in the event of the second breakdown. It is therefore considered that the calculation curves shown in Fig. 6 qualitatively explain the W_N dependency and the variations with the heat sink of the second breakdown characteristics.

The above discussion has been made on the basis of the assumption that the thermal model consisted of

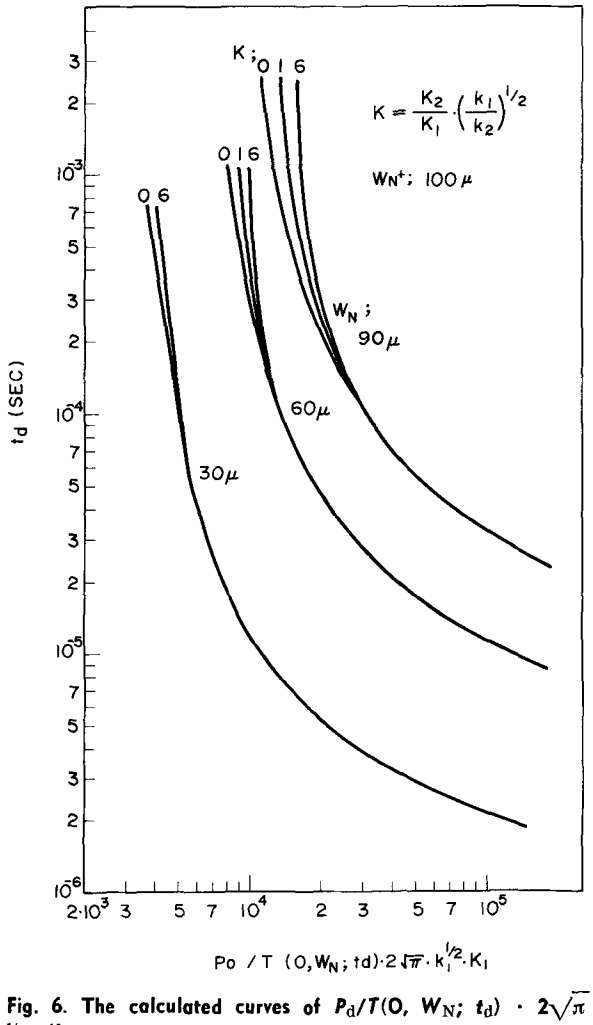

Fig. 6. The calculated curves of $P_d/T(0, W_N; t_d) \cdot 2\sqrt{\pi} \cdot k_1^{1/2} \cdot K_1$ *vs.* t_d.

the silicon extending infinitely in the $+Z$ direction and the heat sink stretching endlessly in the $-Z$ direction and that the disk heat source was embodied at the $Z = 0$ plane in the silicon. However, in the actual devices as shown in Fig. 5(a), the disk heat source was located on the surface where the tungsten probe came into contact with the N-type silicon layer. Therefore, for the quantitative estimation of the temperature of the second breakdown, it is necessary to take into consideration the effect of the tungsten probe.

The correction can be made by providing the coefficient (6), which is given by

$$\lambda = \frac{K_1 k_0^{1/2} - K_0 k_1^{1/2}}{K_1 k_0^{1/2} + K_0 k_1^{1/2}} \qquad [3]$$

where K_0 is the thermal conductivity of the tungsten and k_0 its thermal diffusivity. Using $K_1 = 0.2$ cal/cm · S · deg, $k_1 = 0.51$ cm^2/S, $K_0 = 0.346$ cal/cm · S · deg, and $k_0 = 0.56$ cm^2/S, the calculated value of λ becomes $-1/4$. This shows that the calculation values of the temperature for the thermal model as shown in Fig. 5(a) may be obtained by subtracting a 25% portion from the calculation values of the thermal model shown in Fig. 5(b).

It is to be noted that Fig. 6 represents calculation curves for the case in which the power P_0 is considered to be unchanged with time. But, in the present experiments, it was observed that the power dissipated changes considerably with time. When the sample of W_N below 80μ with a heat sink was used, the power dissipated continued to increase with a duration of time, and the second breakdown was initiated when the power reached its peak value. On the other hand, for the thermally insulated sample, as already shown in Fig. 4(b), the power dissipated was boosted during the early stage of its advancement and then reduced slowly, and the second breakdown appeared when the power was decreased to its minimum value. For the sample having a heat sink and W_N of 90μ, however, the power dissipated was almost constant at all times and the change with time was only a slight one.

Then, for a sample of 90μ in W_N thickness the estimations of T_i (0, 90μ; t_d), the initiating temperature for the second breakdown can be made from the above considerations by using calculation curves shown in Fig. 6. If we put $W_N = 90\mu$ and $t_d = 5.7 \times 10^{-4}$ sec in Fig. 3(b), P_M is read as 54W corresponding to $P_0 = 2.68 \times 10^7$ W cm^{-2}, and the value of 396°C was obtained as T_i (0, 90μ; t_d) by substituting the values of P_0, K_1 and k_1 into the equation; $P_0/\{T_i$ (0, 90μ; t_d) · $2\sqrt{\pi}$ · $k_1^{1/2}$ · $K_1\} = 1.6 \times 10^4$ sec$^{1/2}$. Considering the spread of the thickness in the N layer from 90 to 95μ, the temperature calculated becomes 370°-396°C. When the correction factor of λ is introduced, and considering that the measurements were carried out at room temperature, the initiating temperature is found to be in the range of 297°-316°C, being near the intrinsic temperature of silicon used.

For the case of the samples below 90μ, the power dissipated was observed to increase with time as mentioned previously. Then, the initiating temperature for this case was estimated by putting the average values of the power over time t_d equal to P_0. The temperatures obtained for the samples having W_N of 80, 70, 60, 50, and 20μ were 280°, 252°, 225°, 202°, and 192°C, respectively. In these estimations the calculations were made for the range of t_d below 10^{-4} sec in order to remove the effect of the heat sink on the second breakdown characteristics as shown in Fig. 3(b).

From the above discussion it may be concluded that the W_N dependence of the second breakdown and its variations with the heat sinks can be explained on the basis of the assumption that the second breakdown occurs when T (0, W_N; t_d), *i.e.* the temperature at the interface of the N layer and the N^+ layer reaches an initiating temperature. It was found that the initiating temperature varied depending on the thickness of the N layer, and was lowered as the value of W_N is reduced. When W_N is in the range of $90 \sim 80\mu$ this temperature was nearly the same as the intrinsic temperature of N-type silicon used.

The results that the initiating temperature decreases with W_N would not be explained on the basis of the thermal model. When W_N is lowered, the depletion layer associated with the reverse voltage passes through the N layer and reaches the N^+ layer. In such a case, the field effect must be added on the thermal effect, although this has yet to be studied more thoroughly.

Acknowledgment

The authors wish to express their sincere thanks to Dr. M. Tomono for his encouragement during this study. They are also indebted to Mr. Y. Ishikawa who performed the computer program.

Manuscript received May 14, 1970.

Any discussion of this paper will appear in a Discussion Section to be published in the December 1971 JOURNAL.

REFERENCES

1. T. Agatsuma and K. Miyake, *This Journal*, **118**, 759 (1971).
2. H. A. Schafft, *Proc. IEEE*, **55**, 1272 (1967).
3. A. Yu. Anupyl'd, *Radio Eng. Electron. Phys.*, **11**, 837 (1966).
4. T. Agatsuma, *Proc. IEEE*, **54**, 1206 (1966).
5. A. Sommerfeld, *Math. Ann.*, **45**, 263 (1894).
6. H. S. Carslaw and J. C. Jaeger, "Conduction of Heat in Solids," p. 364, Oxford (1959).

Selective Etching of Gallium Arsenide Crystals in H_2SO_4-H_2O_2-H_2O System

Shinya Iida and Kazuhiro Ito

Central Research Laboratory, Hitachi, Ltd., Kokubunji, Tokyo, Japan

ABSTRACT

Selective etching of GaAs in the H_2SO_4-H_2O_2-H_2O system was studied as a pretreatment to selective deposition. Flat-bottomed holes were obtained in low H_2SO_4 solutions, whereas nonplanar holes were obtained in high H_2SO_4 solutions. Differences between both cases are considered from the etching behaviors under nonselective conditions. Using low H_2SO_4 solutions, selective etching was conducted on substrates with different crystallographic orientations. Asymmetrical holes were observed in all cases except for holes on the {001} substrate with rectangular windows held parallel to the <001> direction. The possibility of the revealed planes being the wall in the hole is discussed.

Electronic devices have been developed such as the Gunn oscillator (1) and the millimeter wave diode (2) using an epitaxially grown crystal. According to their development, the requirement of integrated circuit technology in GaAs is increasing. The importance of selective deposition as an integrated circuit technology has been realized. This technique involves selective etching on a substrate. Selective etching was effected by a chemical solution consisting of the H_2SO_4-H_2O_2-H_2O system, most commonly used as a surface polishing etchant. The various etching behaviors are observed with various composition ranges in the above-mentioned system.

In this paper are described a correlation of the etching behaviors and the composition of the solution under nonselective etching conditions, favorable etching conditions to obtain flat-bottomed selective holes, and the orientation effects on hole structure.

Experimental

The substrate surfaces used here were the {001}, {111}, {110}, {112}, and {113} planes. These were sliced within 1° from the above-mentioned principal orientation and polished to a mirror-like finish.

Etching rates were measured from a step height between an etched face and a wax-coated original face, using an interference microscope. Chemical etching was accomplished in 10 ~ 60 sec and the temperature was maintained at 0 ~ 100° ± 1°C.

In selective etching, an SiO_2 mask 1000 ~ 2000Å thick was deposited on the substrate by a pyrolysis of tetraethoxy silane, and circular or rectangular windows were cut into the mask.

Structures of the holes were observed on the {110} cleavage plane perpendicular to the substrate surface under an optical microscope and under a goniomicroscope.

Etching solutions used here consisted of 98 w/o (weight per cent) sulfuric acid, 30 w/o hydrogen peroxide, and deionized water. In the following section, the volume ratios of these agents are used (35 H_2SO_4: 65 H_2O_2 means 35% by volume of 98 w/o H_2SO_4 plus 65% by volume of 30 w/o H_2O_2).

Etching Behaviors under Nonselective Conditions

Temperature and composition effects of the solutions on the etching.—Etching rates were studied on the {001} surface by varying each composition in the H_2SO_4-H_2O_2-H_2O system. The etching rates at 0°C are shown in Fig. 1 as a ternary diagram. In this case, a peak was obtained at the point of 35 H_2SO_4: 65 H_2O_2 and no etching was observed on the line of H_2SO_4-H_2O and H_2O_2-H_2O members. The etching rates were decreased by increasing H_2O at a constant ratio of H_2SO_4 and H_2O_2.

Key words: gallium arsenide, etching, semiconductor.

The diagram is roughly divided into four regions by the etched surface state. In the A region (high concentration of H_2SO_4 and H_2O_2), the etched surface became cloudy above 20° ~ 30°C. In the C (high H_2O_2) and D (high H_2SO_4) regions, mirror-like surfaces were obtained within the experimental ranges (0 ~ 70°C). In the B (high H_2O) region, a cloudy surface was frequently observed, the cloudy phenomenon due to small pits which may have been influenced by crystalline defects of the substrate.

The etching studies at various composition in the system were studied at temperatures ranging between 0° ~ 100°C. Composition ratios of the etching solutions used were as follows:

a. 1 H_2SO_4 : 4 H_2O_2 : 0 H_2O

b. 1 H_2SO_4 : 1 H_2O_2 : 1 H_2O

c. 5 H_2SO_4 : 1 H_2O_2 : 1 H_2O

d. 5 H_2SO_4 : 1 H_2O_2 : 20 H_2O

e. 40 H_2SO_4 : 1 H_2O_2 : 1 H_2O

In all cases the etching rates exponentially increased with elevating etching temperatures as shown in Fig. 2. From the slopes of the figure, the activation energies were determined to be 6 ~ 11 kcal/mole. In the high H_2SO_4 solutions, lower energies (6 ~ 8 ± 0.1 kcal/

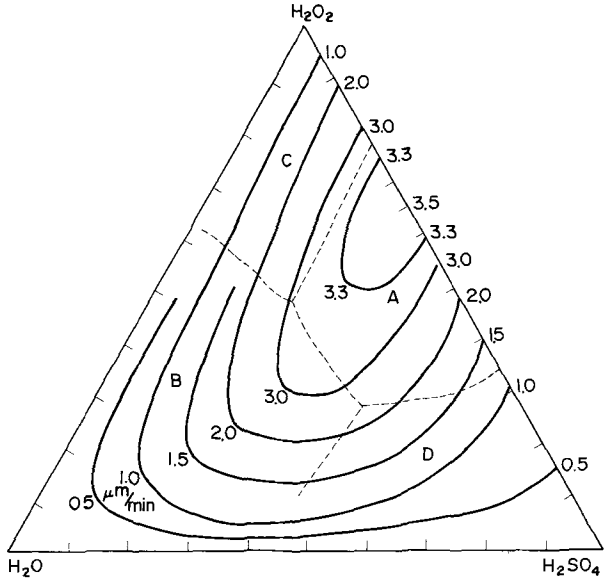

Fig. 1. Constant etching rate contours in the system of H_2SO_4-H_2O_2-H_2O obtained at 0°C. The triangle was divided into four zones (A, B, C, and D) by the etched surface state.

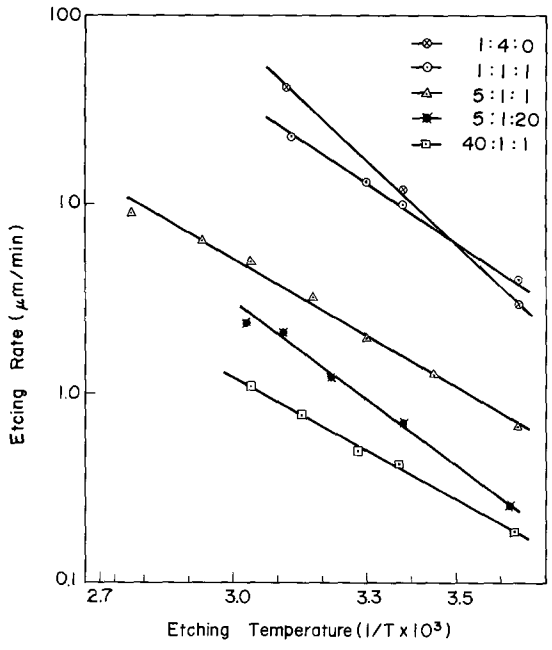

Fig. 2. Plot of the log etching rate vs. $1/T$ in various composition ratios of the solutions.

mole) were obtained, whereas larger energies ($8 \sim 11 \pm 0.1$ kcal/mole) were obtained in the low H_2SO_4 solutions. These facts may suggest that the controlling factors affecting both solutions are different.

Further, stirring effects were examined by adding ultrasonic vibration while etching. Shift of the etching rates occurred only in the high H_2SO_4 solutions. Representative data are shown in Fig. 3. It was confirmed that etching rates were invariable with carrier concentrations and impurities in the substrates.

Orientation effects on the etching rates.—Etching experiments were also conducted on the substrate with some different orientations under the same conditions. The etching solutions used here were a high H_2SO_4 solution ($8\ H_2SO_4 : H_2O_2$) and a low H_2SO_4 solution ($1\ H_2SO_4 : 8\ H_2O_2 : 1\ H_2O$), and the etching temperatures were maintained within $0 \sim 40° \pm 1°C$. Representative data are shown in Fig. 4. Etching rates are similar on the different substrates except for the {111}A plane in the former solutions; however, the etching rates depend on the substrate orientations in the latter.

Further, in depending on temperature of the etching rates on several substrates with other orientations, the slopes in the former are smaller than those in the latter, these behaviors similar to those on {001}. Under all conditions the etching rates on the {111}A surface were the slowest of all, and the etched surfaces were not shiny. For this reason, the {111}A surface was not employed as the substrate of selective etching in this work.

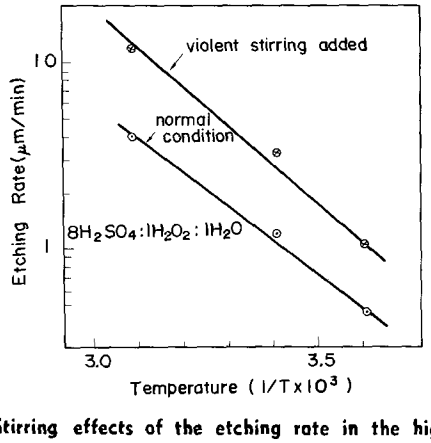

Fig. 3. Stirring effects of the etching rate in the high H_2SO_4 solutions.

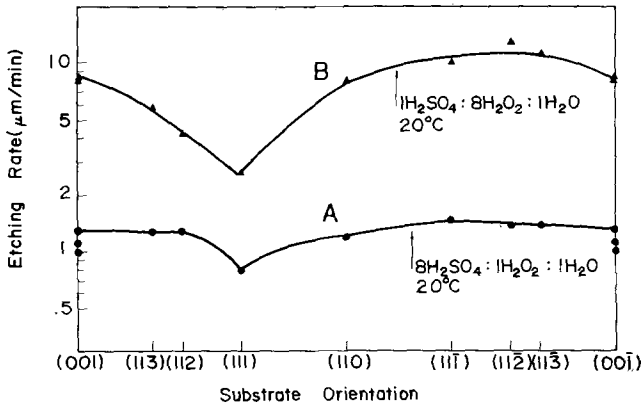

Fig. 4. Orientation dependence on the etching rates in the high H_2SO_4 (A) and in the low H_2SO_4 (B) solutions.

Selective Etching

Flat-bottomed hole on the {001} substrate.—An exposed GaAs surface bounded by an SiO_2 mask was etched by the solution in the H_2SO_4-H_2O_2-H_2O system. Flatness of the hole bottoms was examined with an interference microscope. Hole bottoms obtained by high H_2SO_4 solutions such as $8\ H_2SO_4 : 1\ H_2O_2 : 1\ H_2O$ became uneven due to deep etching near the frame of the window; while flat-bottomed holes were obtained by low H_2SO_4 solutions such as $1\ H_2SO_4 : 8\ H_2O_2 : 1\ H_2O$ or $1\ H_2SO_4 : 1\ H_2O_2 : 8\ H_2O$ solution. Representative cross sections are shown in Fig. 5. It was found from additional experiments that etching solutions with an H_2SO_4 content below one-third in overall volume were useful in obtaining flat-bottomed holes. These results agreed with those on the other substrate orientations.

Asymmetry structures of the holes.—When a side of a rectangular window was set parallel to the <110> direction and chemically etched on the {001} surface, dissimilar hole structures were observed at a right-angled intersection of two {110} cross sections perpendicular to the substrate surface as shown in Fig. 6. Thus, on one cross section, a trapezoidal structure with its short side at the bottom was formed (Fig. 6, A); whereas a trapezoidal structure with its long side at the bottom was formed on another cross section (Fig. 6, B). This difference could be explained by the remainder of the {111}A planes (Ga side), the slowest in the etching rate, although it was departing from being a precise {111}A plane.

When the side of the rectangular window was set parallel to the <100> or <010> direction, symmetrical walls were obtained (Fig. 7). These four walls were determined to be {100} planes since they were nearly perpendicular to the (001) surface, and no {111}A plane existed in these zones. These holes are available for the selected deposition described elsewhere (3).

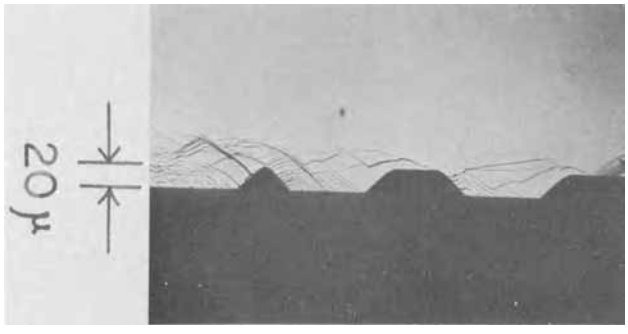

Fig. 5. Representative cross section of the flat bottomed hole

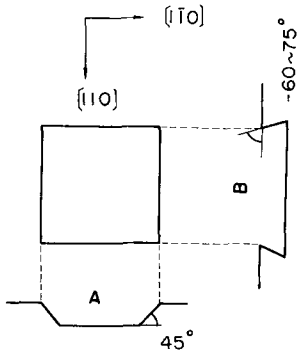

Fig. 6. Schematic hole figures on the {110} cross section on the {001} substrate with <110> rectangular window direction.

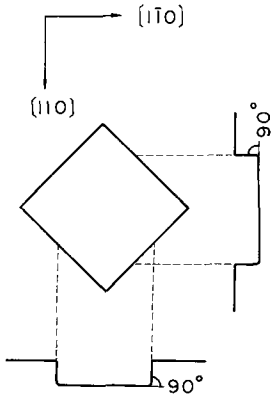

Fig. 7. Schematic cross section of the hole on the {001} substrate with <001> rectangular window direction.

Hole structures on the substrates with other crystallographic orientations.—Selective etching was carried out on the {111}B, {110}, {112}A, {112}B, {113}A, and {113}B planes in addition to the {001} previously described. An edge of the rectangular windows was set parallel to the <110> direction. Observed angles between the walls in the holes and the substrate surfaces on the vertical cross sections of the {110} cleavage plane and the plane which makes a right angle with the {110} plane are listed in Table I. In all cases, the walls in the holes show asymmetrical patterns on the right and left sides on the {110} cleavage planes, although symmetrical hole structures were observed on another cross section which was vertical to the {110} cleavage plane and perpendicular to the substrate surface. On this cross section, one could not observe the walls under a goniomicroscope in the {112}A and {113}A substrates since the hole structures displayed a trapezoidal pattern with the long side at the bottom.

Discussion

Shaw reported that the etchants most commonly used for chemical polishing of GaAs such as 5 H_2SO_4 : 1 H_2O_2 : 1 H_2O and 1000 CH_3OH: 1 Br_2 produced holes which had a nonplanar bottom (4). This was attributed to surface diffusion of the etchant molecules absorbed on the protective mask (diffusion rate-limited process). In our work, similar results were obtained by using high H_2SO_4 solutions. Facts disclosing no orientation effects on the etching rate and smaller activation energies (5) of the etching rate in the high H_2SO_4 solutions strongly support Shaw's conclusions.

While in the low H_2SO_4 solutions which produced flat-bottomed holes, the etching rates are clearly varied with different substrate orientations, and the activation energies are larger than those in the former solutions. These experimental results may suggest that the etching process in the latter is chemical reaction rate-limited, but not the diffusion rate-limited process, because a decrease of the H_2SO_4 content effects a drop in viscosity. When similar etching was done under the condition of additional ultrasonic vibration, it was recognized that the etching rate and the activation energies were increased in the high H_2SO_4 solutions, whereas no changes of etching behavior appeared in the low H_2SO_4 solutions within our experimental ranges shown in Fig. 3. Those facts reveal that a diffusion rate-limited process changes to

Table I. List of the observed and the expected angles between the revealed walls in the holes and the substrate surfaces

Substrate	Window direction	I			II			Remarks
		Observ.angle	Ident. plane	Prac.angle	Observ.angle	Ident.plane	Prac.angle	
(001)	[110]	45°	(111)	54°44′	45°	($\bar{1}\bar{1}$1)	54°44′	
	[1$\bar{1}$0]	-60~-75°	(1$\bar{1}$1)	-54°44′	-60~-75°	($\bar{1}$11)	-54°44′	
	[100]	90°	(100)	90°	90°	(0$\bar{1}$0)	90°	
	[0$\bar{1}$0]	90°	(0$\bar{1}$0)	90°	90°	(010)	90°	
(111)	[1$\bar{1}$0]	-	(00$\bar{1}$)	-54°44′	-	($\bar{1}\bar{1}$1)	-70°32′	
	[11$\bar{2}$]	-	($\bar{3}$1$\bar{1}$)	-58°31′	-	(1$\bar{3}\bar{1}$)	-58°31′	
($\bar{1}\bar{1}\bar{1}$)	[1$\bar{1}$0]	60~70°	($\bar{1}\bar{1}$1)	70°32′	50~55°	(00$\bar{1}$)	54°44′	
	[11$\bar{2}$]	59°	($\bar{1}$31)	58°31′	59°	(1$\bar{3}\bar{1}$)	58°31′	
(110)	[110]	20~35°	(111)	35°16′	85~90°	(00$\bar{1}$)	90°	
	[001]	-	(100)	45°	-	(010)	45°	
(112)	[1$\bar{1}$0]	13~26°	(111)	19°28′	83~90°	($\bar{1}\bar{1}$1)	90°	
	[111$\bar{1}$]	-	(1$\bar{2}\bar{1}$)	-60°	-	($\bar{2}$1$\bar{1}$)	-60°	
($\bar{1}\bar{1}$2)	[1$\bar{1}$0]	35°	(00$\bar{1}$)	35°16′	85~90°	($\bar{1}\bar{1}$1)	90°	
	[11$\bar{1}$]	60°	(1$\bar{2}\bar{1}$)	60°	60°	($\bar{2}$1$\bar{1}$)	60°	
(113)	[1$\bar{1}$0]	20~35°	(111)	29°30′	68~75°	($\bar{1}\bar{1}$1)	79°58′	
	[33$\bar{2}$]	-	(3$\bar{5}\bar{3}$)	-55°20′	-	($\bar{5}\bar{3}\bar{3}$)	-55°20′	
($\bar{1}\bar{1}$3)	[1$\bar{1}$0]	25°	(00$\bar{1}$)	25°14′	-88°	($\bar{1}\bar{1}$1)	-79°58′	
	[33$\bar{2}$]	53°	(3$\bar{5}\bar{3}$)	55°20′	53°	($\bar{5}\bar{3}\bar{3}$)	55°20′	

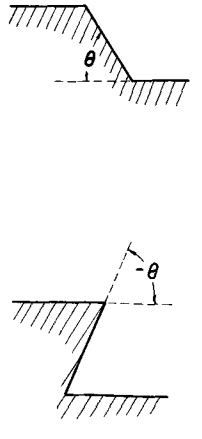

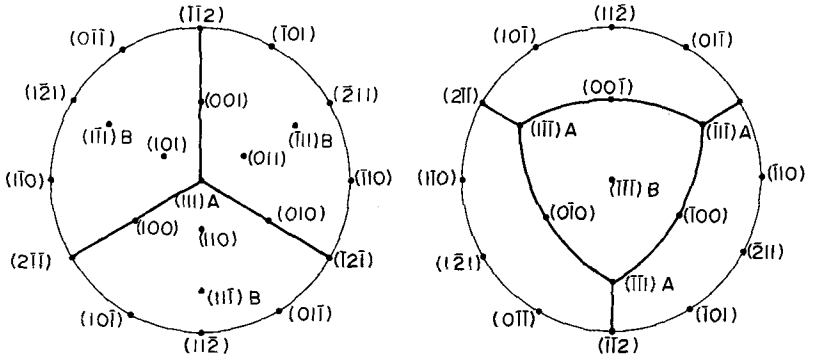

Fig. 8. Plot of possible wall planes in the hole in standard stereo projection. Revealed planes are only on the lines (great circle) connected with the four {111}A planes.

a reaction rate-limited process in chemical etching through violent stirring.

Hole structures in the rectangular selected area parallel to the <110> direction show asymmetrical patterns on the substrates of the {001}, {111}, {110}, {112}, and {113} planes except in the case of the rectangular window with a <100> direction on the {001} substrate. This phenomenon is due to the fact that the wall planes are revealed by the rule, and these planes are not present in symmetrical position.

The first plane to appear is the {111}A plane as the wall, because of its having the slowest etching rate of all. If the {111}A plane is not contained in the zone around an axis, which agrees with the side of the rectangular window, the plane appears—strongly affected by {111}A planes existing near it. In other words, the revealing plane is the intersection between the great circle through the nearest two {111}A planes, and the great circle through the substrate orientation and the parallel planes to a side of the window in standard stereo projection. From the above-mentioned interpretation the {223}A, {335}A, {112}A, {113}A, {115}A, {117}A, and {001} planes are considered as possible low-index planes, these planes all being Ga side planes with the exception of {001}. Thus these planes are always on the six arcs connected with four {111}A planes as shown in Fig. 8.

Comparing the measured angles with the predicted angles considered from the above-mentioned presumption, both cases agree well. The gaps of the angles between both cases are probably due to an uncertainty of orientation in preparing the rectangular window and substrate and/or experimental errors.

Conclusion

Selective etching was conducted on GaAs crystal surfaces with several crystallographic orientations in the H_2SO_4-H_2O_2-H_2O system. Nonplanar-bottomed holes were obtained in high H_2SO_4 solutions, whereas flat-bottomed holes were obtained in low H_2SO_4 solutions. Experimental facts show that the etching process in the former is the diffusion rate-limited process, and the latter is the chemical reaction rate-limited process.

Hole structures in the selective etching on the substrates display an asymmetrical pattern. Symmetrical holes were observed only on the {001} with <001> directional rectangular windows. These facts are well explained by the remains of the {111}A planes which constitute the slowest among the etching rates and their effects.

Acknowledgment

We thank Dr. H. Kusumoto for his continued encouragement in the course of this work. We also express our appreciation to Messrs. M. Nomura and M. Hirao for their valuable discussions.

Manuscript received July 30, 1970.

Any discussion of this paper will appear in a Discussion Section to be published in the December 1971 JOURNAL.

REFERENCES

1. D. P. Brady, S. Knight *et al.*, *Proc. IEEE*, **54**, 1497 (1966).
2. J. J. Tietjen, G. Kupsky *et al.*, *Solid State Electron.*, **9**, 1049 (1966).
3. S. Iida and K. Ito, To be published.
4. D. W. Shaw, *This Journal*, **113**, 958 (1966).
5. B. A. Irving, "The Electrochemistry of Semiconductors," pp. 256-288, Academic Press, London and New York (1962).

Epitaxial Growth of Al_2O_3 on Al_2O_3 Substrates by Chemical Vapor Deposition

Donald R. Messier and Philip Wong

Army Materials and Mechanics Research Center, Materials Research Laboratory, Watertown, Massachusetts 02172

ABSTRACT

The growth of Al_2O_3 on single-crystal and polycrystalline Al_2O_3 substrates via the net chemical reaction $2AlCl_3(g) + 3H_2O(g) = Al_2O_3(s) + 6HCl(g)$ was investigated in the temperature range from 1400° to 1600°C. Deposits that were obtained varied from polycrystalline at lower temperatures to single crystal at higher temperatures. Use of a 60° oriented substrate resulted in a higher quality, faster growing deposit compared to deposits on 0° and 90° oriented substrates.

The chemical vapor deposition (CVD) technique has several advantages that make it attractive as a method of growing single crystals of ceramic materials. Some of these advantages are: (*a*) growth occurs under isothermal conditions, the crystals obtained are thus relatively unstrained and require no annealing; (*b*) single crystals can be grown at temperatures several hundred degrees below the melting point, an advantage over melt growth techniques; and (c) because purification results from the vaporization process, the crystals obtained are of higher purity than those grown by other low-temperature methods such as hydrothermal or flux growth. A disadvantage of the CVD method is the slowness of growth rates; this is at least partially offset, however, by the fact that large crystals grown more rapidly by melt techniques are often highly strained and require long anneals.

The investigation reported here is a successor to a previous one (1) concerned with the formation of polycrystalline alumina by CVD. The only previous investigation of the growth of large single crystals of alumina by CVD that has been published in the open literature is that of Schaffer (2). He employed the reaction $2\ AlCl_3\ (g) + 3\ H_2\ (g) + 3\ CO_2\ (g) = Al_2O_3\ (s) + 3\ CO\ (g) + 6\ HCl\ (g)$, at temperatures of 1550° and above to grow single crystals weighing up to 80g. Under his conditions, the reaction rate was negligible at the lowest temperature investigated, 1550°C. A report by Schaffer (3) contains additional data on the growth of large crystals by CVD. Parker and Harding (4) reported the use of an apparatus and technique similar to Schaffer's to grow bicrystals of alumina at temperatures about 1700°C.

Earlier work at our laboratory (1) indicated that significant growth rates could be obtained via the net reaction $2\ AlCl_3\ (g) + H_2O\ (g) = Al_2O_3\ (s) + 6\ HCl\ (g)$, at temperatures considerably lower than had been previously reported. One purpose of this study was therefore to establish a low-temperature limit for the growth of single crystals at significant rates; there are numerous advantages in power and materials requirements if it is possible to work at temperatures below 1600°C. Another purpose of this investigation was to establish more clearly the effect of the crystallographic orientation of the substrate on the rate of growth and character of the resulting deposit.

Experimental Procedures

The substrates that were used in the CVD studies included both polycrystalline alumina and single-crystal sections cut to the desired orientations from Verneuil ruby and sapphire and from Czochralski sapphire. A typical substrate was 1.6 cm long x 1.6 cm wide x 0.2 cm thick. The orientations that were used were 0° ("c") corresponding to the (0001) plane, 90° ("a") corresponding to the $(11\bar{2}0)$ planes, and 60° corresponding approximately to either the $(10\bar{1}2)$ or the $(2\bar{1}\bar{1}3)$ planes[1] (see Fig. 5 for reference). The surfaces of some of the substrates were prepared by polishing with 1-5 μm diamond grit with a lead lap. Other substrates were simply used as-cut with a 220 grit diamond cutoff wheel. No obvious differences were observed between deposit layers obtained on substrates prepared in either manner.

The apparatus that was used is described in detail elsewhere (1). The furnace has a molybdenum winding and the muffle tube and all components used in the hot zone are aluminum oxide. The aluminum chloride gas is generated by the chlorination of aluminum metal. The water vapor is formed by the reaction of hydrogen and oxygen gases. Figure 1 shows the details of the rectangular box that serves as the reaction chamber. Combination of the hydrogen and oxygen to form water vapor occurs after exit of the gases from the nozzle.

Before a run, the substrates that are to be used are cemented with alumina cement to the removable floor of the reaction chamber. The system is then assembled, evacuated, and heated to the desired temperature. The reaction is begun by starting the flow of the reactant gases. The total system pressure was held at 0.5 Torr for all of the runs. Gas flow rates were maintained constant at 0.77 lpm for hydrogen, 0.57 lpm for oxygen, and 0.08 lpm for chlorine. The temperatures that were used were 1400°, 1500°, and 1600°C and run times were 6 hr. At the conclusion of a run, the system was cooled under vacuum. The specimens were removed by simply breaking them away from the floor of the reaction chamber.

Results

Kinetics of deposition.—Table I summarizes the results of deposition rate measurements on single-crystal substrates of various orientations at 1400°, 1500°, and 1600°C. Rates were determined by measuring the thickness of deposit obtained in a 6 hr run. It should be noted that the rates given are for growth on only one side of a substrate; they could easily be doubled by use of an arrangement that allowed simultaneous deposition on both sides. The maximum linear growth rate listed in Table I (60° substrate at 1500°C) is equivalent to a mass rate of 50.4 mg/cm^2 · hr. This rate compares favorably to the maximum value of 90.4 mg/cm^2 · hr quoted by Schaffer (2) for growth at 1750°C in an arrangement that allowed simultaneous deposition on all surfaces of the substrate.

Considering the complexity of the reaction mechanism and experimental difficulties, the apparent lack of temperature dependence of the reaction is not sur-

Key words: vapor deposition—chemical; vapor phases—growth; crystal growth.

[1] All of the indexes quoted in this paper refer to the structural unit cell (c_o= 12.991A) rather than the morphological one ($c = c_o/2$) sometimes used in the crystallographic literature.

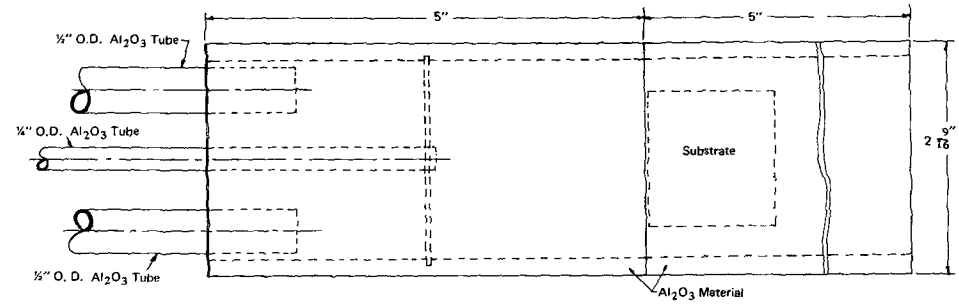

Fig. 1. Chemical vapor deposition nozzle and substrate system.

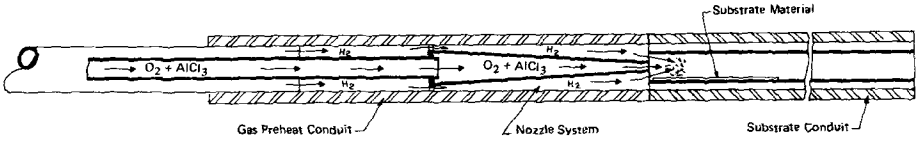

prising. That the rates are lower at 1600°C is believed to be partially a result of leakage of the reaction chamber caused by sagging of its top panel at this temperature. From a practical standpoint, the results indicate that, under our experimental conditions, close temperature control is unnecessary to obtain uniform deposits.

Characterization of deposits.—Microstructure.—The polycrystalline deposits formed at 1400°C showed interesting microstructural features that aid in their characterization. Most of the deposits formed on single-crystal substrates at 1500°C and above, however, were single crystal, and generally showed no microstructure at all. The latter were clear transparent, and indistinguishable microscopically from the underlying substrate.

Figure 2 shows a cross section of a typical deposit formed on a polycrystalline substrate at 1400°C.[2] The usual columnar grained structure with pronounced grain boundaries is clearly evident. Also notable is the considerable porosity near the interface.

Figure 3 shows deposits that formed on single-crystal substrates at 1400°C. Although further evidence shows that these deposits are still polycrystalline, the interface between deposit and substrate is cleaner, and the microstructure better than the deposit on a polycrystalline substrate. The presence of columnar grains, however, indicates that the substrate did not completely control the growth of the deposit; such grains must have resulted from nuclei formed on the single-crystal surface.

Figure 4 shows a cross section, under crossed Nicols in transmitted polarized light, of the deposit formed on a 60° oriented single-crystal substrate at 1400°C. All areas that show the same extinction behavior have the same crystallographic orientation. It is evident from the figure that certain of the columnar grains mushroom out and eventually join to form a deposit that appears single crystal. These observations are corroborated by the fact that grain boundaries were not visible in the top part of this specimen under reflected light. As far as microstructure is concerned, it thus appears that a deposit that is more nearly single crystal is obtained at 1400°C on a 60° oriented substrate than on those of the other orientations tested.

X-ray diffraction.—Figure 5 is a stereographic projection of the poles of the only five sets of plane corresponding to peaks on x-ray diffractometer traces of the surfaces of polycrystalline deposits. Various combinations of these peaks were found on material formed on single-crystal substrates (0° and 90° orientations) at 1400°C, and on polycrystalline substrates at 1400° and 1600°C. Reflections from prismatic planes and the basal plane were notably absent. Although none of the preferred orientations was observed on all of the specimens, all of the orientations occurred with about the same frequency. Furthermore, there was no apparent correlation between the orientation of the single-crystal substrates and the preferred orientation of the deposit.

The microstructural observations and x-ray diffraction data indicate that the polycrystalline deposits comprise columnar grains growing in certain preferred directions. That the directions shown in Fig. 5 are the fast growth directions for alumina follows from a discussion by Buckley (5) of the analogous case of solidification from the melt. Buckley shows that this type of microstructure results when the grain growing

[2] All of the photomicrographs were taken on unetched specimens that were prepared by relief polishing.

Table I. Growth rate vs. crystallographic orientation

(All rates are in units of mm/hr)

Orientation	1400°C	1500°C	1600°C
60°	0.128	0.127 (3)	0.102
a	0.085 (3)	0.105 (3)	0.059 (2)
c	0.087	0.058	0.053
30°			0.072

(Figures in parentheses are number of specimens evaluated.)

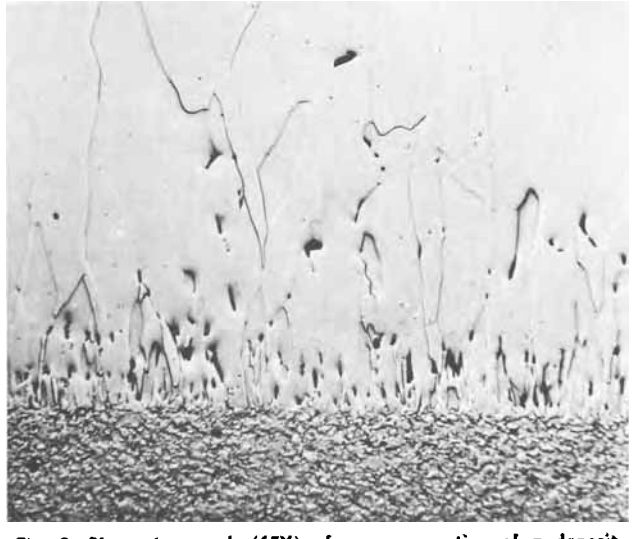

Fig. 2. Photomicrograph (65X) of a cross section of a deposit formed on a polycrystalline alumina substrate at 1400°C. The columnar grained structure and preferred growth directions are typical of such deposits.

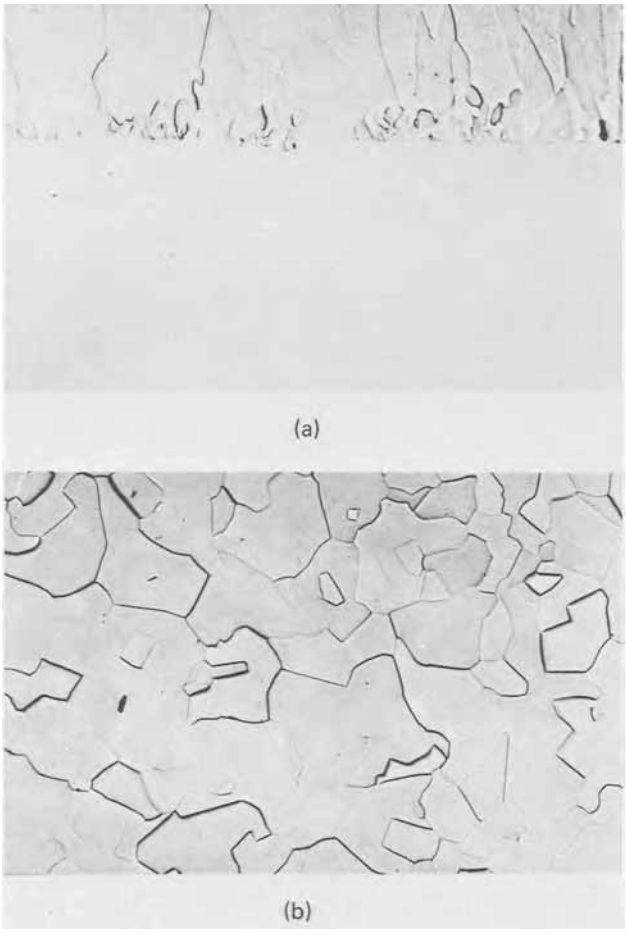

Fig. 3. Photomicrographs (80X) of deposits formed on single-crystal substrates at 1400°C: (a) cross section of a deposit on an "a" sapphire substrate and (b) top view of a deposit on a "c" ruby substrate.

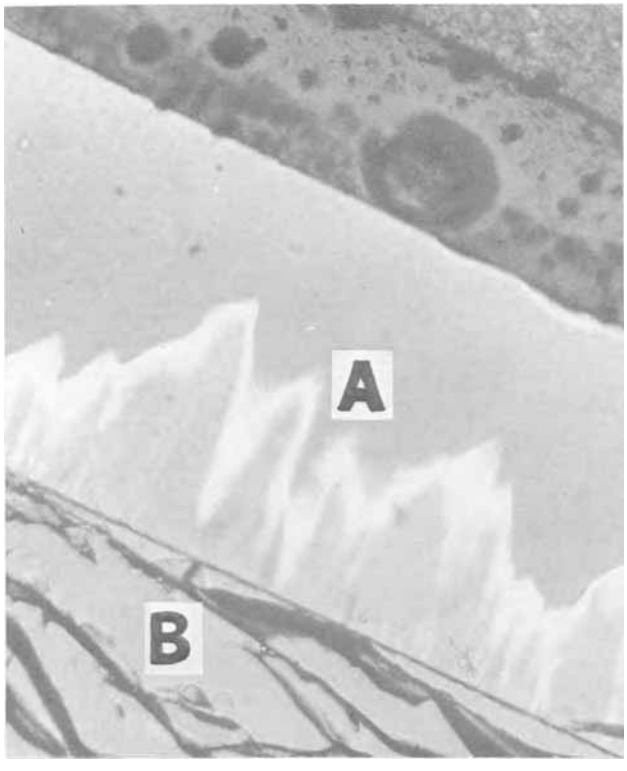

Fig. 4. Photomicrograph (175X, polarized light) of a thin section of a deposit (A) formed at 1400°C on a 60° oriented sapphire substrate (B). The deposit became virtually single crystal as it grew away from the substrate.

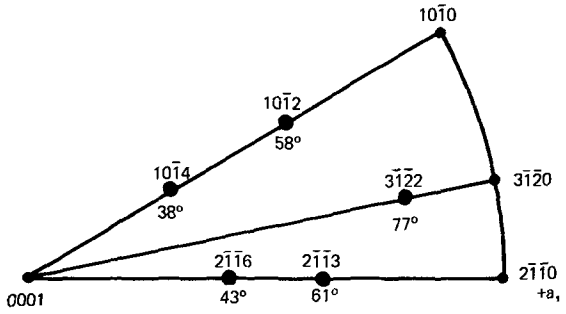

Fig. 5. Stereographic projection of poles of planes that are parallel to the surface of polycrystalline alumina deposits.

from nuclei oriented in the fast growth directions eliminate the slower growing ones. His explanation also accounts for the peculiar columnar-grained structures shown in Fig. 2-4.

The Laue back-reflection x-ray technique was used to evaluate the quality of the deposits formed on single-crystal substrates. In cases where single-crystal deposits were obtained, their orientations were the same as those of the underlying substrates. The absence of significantly misoriented subgrains on single-crystal deposits was confirmed by repeat Laue patterns on several areas of specimens and by optical microscopy using polarized light.

All of the deposits formed at 1400°C, except that on the 0° substrate showed a high degree of preferred orientation. The deposit on the latter substrate gave a polycrystalline Laue pattern. Figure 6 shows Laue patterns of deposits obtained on single-crystal substrates of several orientations at 1500°C. The substrates that were used were all cut from the same boule and run at the same time; the results should therefore reflect the influence of substrate orientation alone. The deposit on the 60° oriented substrate is single crystal and that on the 0° substrate is polycrystalline. The splitting of the spots in the pattern obtained on the 90° deposit indicates that some subgrain structure exists in this material. Deposits obtained on single-crystal substrates of all orientations tested were single crystal at 1600°C.

Dislocation density measurement.—Dislocation densities were determined on basal plane sections of the CVD deposits by an etch pit technique. The technique was that described by Sahagian (6) as a refinement of the early ones given by Alford and Stephens (7) and Scheuplein and Gibbs (8). It involved chemical polishing in orthophosphoric acid at 425°C for 2 min, followed by etching for about 5 min in the same reagent at 320°C.

Figure 7 shows an etched basal plane section of a deposit formed on a 60° substrate at 1600°C. This figure illustrates clearly the single-crystal nature of the deposit and the almost perfect match between deposit and substrate; only a partially complete line of etch pits delineates the interface between them. The distribution of dislocations in the deposit is uniform parallel to the interface and the dislocation density decreases as the distance from the substrate increases.

Another indication of the good quality of the crystal is that subgrain boundaries are absent. The dislocation densities given, 1.7×10^5 and $2.5 \times 10^5/cm^2$ for deposit and substrate, respectively, are averages of counts from several photographs including hundreds of etch pits for the areas shown in Fig. 7. The dislocation density measured on a deposit formed on a 0° substrate at 1600°C ranged from $5.5 \times 10^4/cm^2$ to $6.0 \times 10^5/cm^2$. These dislocation density values compare favorably to those of from 10^4 to $10^6/cm^2$ quoted by Sahagian (6) for basal plane sections of single crystals grown by a number of techniques.

Discussion of Results

The results concerning the dependence of the quality of the crystal on the orientation of the seed are con-

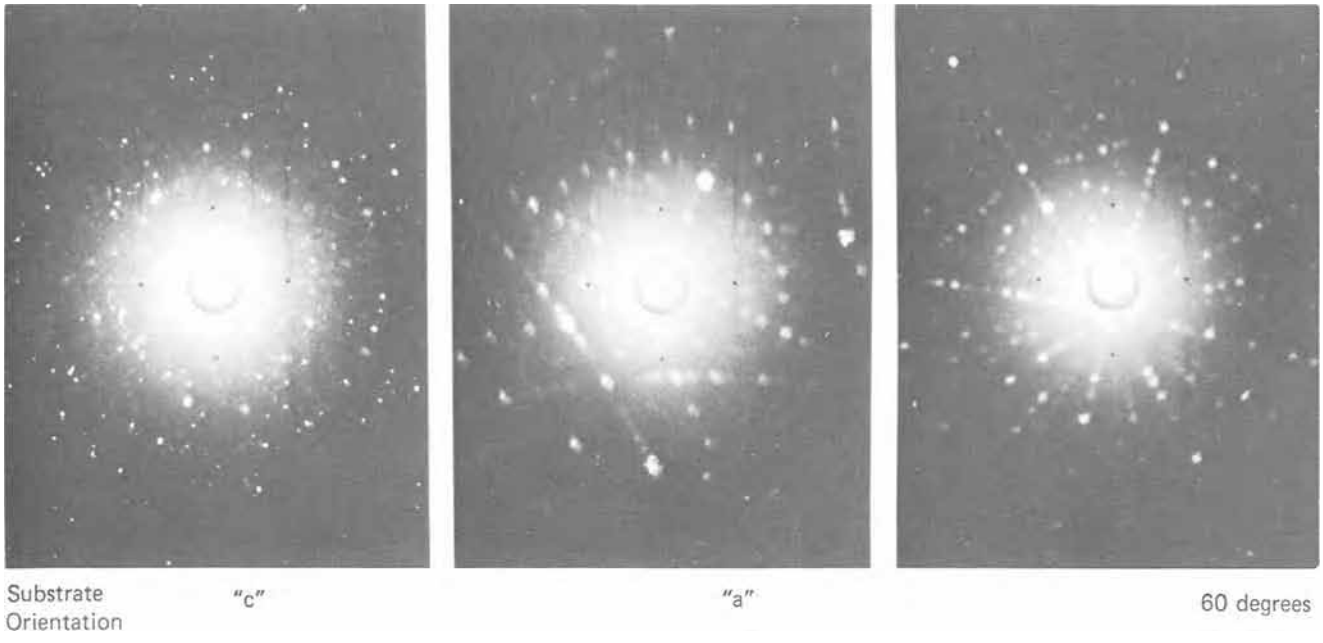

Fig. 6. Back-reflection Laue patterns of material deposited at 1500°C showing the higher perfection obtained by use of a 60° oriented substrate.

sistent with results of investigations of the growth of alumina single crystals by other techniques (9, 10). For example, Beliustin (9) found that flame-fusion single crystals grown from 60° seeds had less mosaic structure than crystals grown from seeds of other orientations. Our x-ray results indicate that the same is true for crystals grown by CVD. Beliustin states that growth is more uniform when one of the habit faces of the crystal is perpendicular to the geometric axis of the boule, and when there are other possible faces close to that face in orientation; the 60° orientation satisfied these conditions better than any other orientations we tested. The reason given by Beliustin for the lesser amount of substructure in crystals grown in this orientation is that the proximity of other faces produces growth steps that are less pronounced than they are, for example, on a 0° orientation. The latter orientation is considerably farther from possible habit faces than is the former. That a better crystal formed on the 90° seed than on the 0° seed is also consistent with this argument, for the former is closer to other potential faces than the latter.

Stephens and Alford (10) obtained results similar to ours concerning dislocations in alumina single crystals. Their specimens were crystals grown in various orientations by flux and flame-fusion techniques. They found, as did we, that growth orientation did not affect dislocation density. In addition, they observed that 0° crystals contained more substructure than 60° ones, and that 90° crystals contained the least substructure of all. Our results concur with the former observation, but not with the latter.

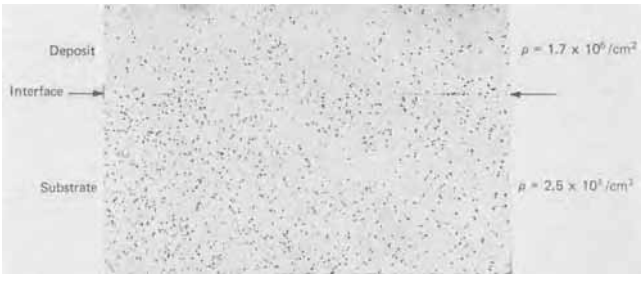

Fig. 7. Photomicrograph (48X) of an etched basal plane section of a single-crystal deposit grown on a 60° oriented sapphire substrate at 1600°C. The deposit shows a lower density of dislocation etch pits than does the substrate.

The indexes of the fast growing planes are the same as those of faces occurring on natural crystals of alumina (11). The two planes near 60° (Fig. 5) correspond to common faces and the other three planes to less common ones. Although basal and prismatic faces predominate on both natural and synthetic alumina single crystals (3, 11), our results indicate that neither face is a fast growing one. This is entirely consistent with Buckley's (5) explanation that the faces seen on a single crystal after long growth times are the slower growing, low index ones. In normal growth, the faster growing, high index faces soon grow themselves out of existence. It should be recalled, however, that the results shown in Fig. 5 pertain to the growth of columnar grained, polycrystalline deposits. For that type of growth, the fast growth directions prevail.

Consideration of phenomena involved in the CVD process leads to some qualitative conclusions about the kinetics of crystal growth. Among the phenomena involved are nucleation and growth of new material on the substrate, gas phase transport, and chemical reactions at the surface of the growing crystal.

That single-crystal deposits were obtained on single-crystal substrates of all orientations tested at 1600°C indicates that nucleation is unimportant at this temperature. The deposits merely grow on the substrates. At 1500°C, however, only the 60° deposit was single crystal. The misoriented, columnar grained deposits formed on other single-crystal substrates at and below this temperature must have resulted from nuclei formed at their surfaces. It thus appears that deposition kinetics at 1500°C and below are complicated by nucleation phenomena, and that an evaluation of growth rate as a function of substrate orientation is meaningful only for the 1600°C data.

The data on the rate of growth of the deposits at 1600°C (Table I) correlate nicely with the x-ray data on fast growing directions. Fastest growth occurs on the 60° substrate which, as seen in Fig. 5, is close to several such directions. Growth is second fastest on the 30° seed, one that is also oriented close to several favorable directions. The 0° and 90° substrates, still further from fast growth directions, yield equally slow growth rates.

The results also yield some information concerning possible rate-controlling steps in the CVD process. That the growth rate depends on the orientation of the substrate indicates that it is not solely controlled by the rate of supply of reactants, *i.e.* gas phase transport. When one considers also that gas phase nucleation is not observed, one concludes that a surface reaction of some sort is at least partially rate controlling. Although this surface process probably is some sort of surface catalyzed decomposition and oxidation of the aluminum chloride, formulation of a detailed reaction mechanism requires more data than are available at present.

In summary, it may be concluded that:

1. Single crystals of aluminum oxide can be grown by CVD at significant rates at a temperature of 1500°C, 550°C below the melting point.
2. There are five approximately equal fast growth directions for aluminum oxide, all of which lie between the basal (0001) plane and $(2\bar{1}\bar{1}0)$ and $(10\bar{1}0)$ prismatic planes.
3. Growth rate and crystal quality are both enhanced by use of a 60° substrate rather than a 0° or 90° one.

Manuscript submitted April 7, 1970; revised manuscript received *ca.* Oct. 30, 1970. This was Paper 200 presented at the Los Angeles Meeting of the Society, May 10-15, 1970.

Any discussion of this paper will appear in a Discussion Section to be published in the December 1971 JOURNAL.

REFERENCES

1. P. Wong and McD. Robinson, "Chemical Vapor Deposition of Polycrystalline Aluminum Oxide," AMMRC TR 69-24 ,Oct. 1969.
2. P. S. Schaffer, *J. Am. Ceram. Soc.*, **48**, 508 (1965).
3. P. S. Schaffer, Final Report, Office of Naval Research Contract No. Nonr-4574 (00) (1965).
4. H. S. Parker and C. A. Harding, Oral presentation at ACCG Conference on Crystal Growth, National Bureau of Standards, Gaithersburg, Md., Aug. 11-13, 1969.
5. H. E. Buckley, "Crystal Growth," John Wiley & Sons, Inc., New York (1951).
6. C. S. Sahagian, Air Force Cambridge Research Labs. Report AFCRL-66-659 (1966).
7. W. J. Alford and D. L. Stephens, *J. Am. Ceram. Soc.*, **46**, 193 (1963).
8. R. Scheuplein and P. Gibbs, *ibid.*, **43**, 458 (1960).
9. A. V. Beliustin, "Studies of the Crystallography of Al_2O_3," p. 209, Air Force Cambridge Research Labs. Translation, T-RC-25 (1968).
10. D. L. Stephens and W. J. Alford, *J. Am. Ceram. Soc.*, **47**, 81 (1964).
11. C. Palache, H. Berman, and C. Frondel, "Dana's System of Mineralogy," Vol. I, John Wiley & Sons, Inc., New York (1944).

Chemical Vapor Deposition of Iron Oxide Films for Use as Semitransparent Masks

J. B. MacChesney, P. B. O'Connor, and M. V. Sullivan

Bell Telephone Laboratories, Incorporated, Murray Hill, New Jersey 07974

ABSTRACT

Iron oxide films have been prepared by thermal decomposition of iron pentacarbonyl vapor in an oxidizing atmosphere. Optical spectra show these to be opaque in the ultraviolet but partially transparent to visible light. The nature of these deposits was studied by electron and x-ray diffraction, electron microscopy, and the Mössbauer effect. It was found that deposition at low temperatures resulted in a partially crystalline film, while films formed at higher temperatures were composed of αFe_2O_3 crystallites. The chemistry of the deposition process was considered in light of mass spectrometer analyses of species present during deposition.

Photolithographic processes for the manufacture of integrated circuits require a mask to define images on photoresist materials used to form circuit patterns. Conventional silver emulsion or chromium film masks have disadvantages. The former are easily scratched and the latter opaque to visible light, thus inhibiting registration of successive patterns. It is desirable to have a durable mask which is at least partially transparent to the visible, but opaque to ultraviolet, light used for photoresist exposure. To this end, Sinclair, Sullivan, and Fastnacht (1) considered a number of transition metal oxides suitable for mask fabrication, but settled on mixtures of vanadium and iron oxide as best able to satisfy the requirements of this mask. These they defined as: transmission of less than 1% below 4000Å, transmission of greater than 30% at 5890Å, and etchability in reagents compatible with photolithographic processing so as to provide resolution of lines separated by no more than 2μ.

Initially, our intentions were to duplicate their work using films prepared by chemical vapor deposition techniques. However, it soon became apparent that pure iron oxide films prepared by this technique differed from the sputtered films prepared by Sinclair *et al.* The principal difference was that chemically deposited films could be etched, whereas sputtered films could not. Therefore, the present study was primarily directed toward the preparation and characterization of iron oxide films prepared by chemical vapor deposition.

Key words: Fe_2O_3 (iron oxide) thin films, photolithographic masks, iron pentacarbonyl, vapor deposition.

Deposition

Iron pentacarbonyl, $Fe(CO)_5$, was selected as the source of iron in these experiments. This compound is desirable because its properties combine high vapor pressure which facilitates transport in the vapor phase and low decomposition temperature. For these reasons, use of $Fe(CO)_5$ for deposition of iron films or preparation of highly pure iron powder is well known. However, it appears to have been little used for preparation of iron oxide films, although its use is mentioned by Powell (2) and films prepared by its decomposition in microwave plasma are reported by Secrist and MacKenzie (3).

In the present studies, films were prepared using the apparatus shown in Fig. 1, which consists of a dep-

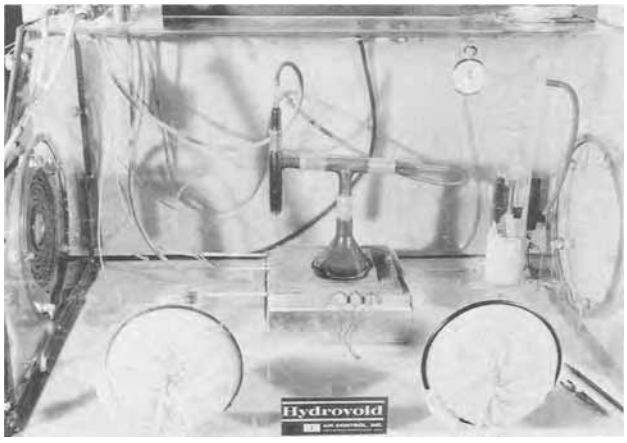

Fig. 1. Photograph of deposition apparatus as described in the text.

osition chamber resting on a hot plate. Iron pentacarbonyl vapor, generated by bubbling argon through the liquid contained in a side-arm test tube, is transported to a "T" junction where it is mixed with oxygen or other gases prior to entering the deposition chamber. Film deposition occurs by thermal decomposition of the carbonyl vapor on the surface of the heated substrate. Exhaust gases exit around the base of the deposition chamber. The apparatus was contained in a glove-box which was continuously exhausted to remove potentially toxic or explosive products.

Electronic flow meters (Hastings Raydist Model LL100) were used to monitor the flows of the different gases. Temperatures were measured by Chromel-Alumel thermocouples embedded in the plate supporting the substrate and these were recorded using a multipoint recorder. The substrate for photomask usage was a 2 x 2 x 1/16 in. soda lime glass plate which had been degreased, detergent washed, boiled in H_2O_2 (30%), blown dry, and baked. Thicknesses of iron oxide films were measured using a Tallysurf.[1]

Characterization of these deposits was accomplished by optical and Mössbauer spectra, scanning electron microscopy, electron microscopy, electron microprobe analysis, x-ray, and electron diffraction. The suitability of deposited films for mask purposes was determined by etching studies on patterned and unpatterned surfaces.

A systematic survey of deposition conditions was carried out using various flow rates, reactive gases, and deposition temperatures. These results are summarized by Fig. 2. The diagrams of this figure compare deposition rates for different flow rates of carrier gas at substrate temperatures of 120°, 140°, 160°, 180°, and 200°C in atmospheres of argon, carbon dioxide, oxygen, and oxygen-water. It is observed [Fig. 2(a)] that in an argon atmosphere little apparent change in deposition rate is occasioned by either increase in temperature or increased carrier flow. In order to check whether this behavior would occur with other nonoxidizing gases, CO_2 was introduced into the deposition chamber in addition to the argon carrier. The resulting deposition rates are shown by Fig. 2(b). Although only one flow rate was used, the similarity with the pure argon atmosphere is evident.

A dramatic change in deposition rates resulted when oxygen was used as the reactive gas [Fig. 2(c)]. Here it was observed that deposition rates, at all but the lowest temperature, were as much as an order of magnitude greater than in previous experiments. Further, these rates were approximately proportional to the carrier gas flow, *i.e.* iron pentacarbonyl concentration, and were not believed to be temperature dependent above 140°C. The final diagram of the series, Fig. 2(d), compares rates observed for oxygen-water mixtures

[1] A product of Taylor-Hobson Company, Limited.

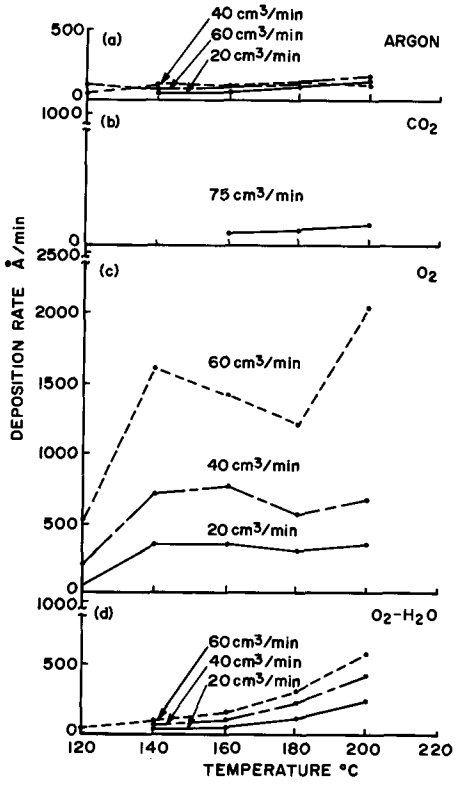

Fig. 2. Deposition rate (Å/min) vs. temperature (°C): (a) deposition in argon at carrier flows of 20, 40, and 60 cc/min; (b) deposition in CO_2 with carrier flow Ar of 75 cc/min and CO_2 flow 60 cc/min; (c) deposition on O_2, carrier flow (Ar) 20, 40, and 60 cc/min, and O_2 flow 60 cc/min; (d) deposition in O_2-H_2O, carrier flow (Ar) 20, 40, and 60 cc/min, O_2 bubbled through water at 25°C.

which were prepared by bubbling the gas through a column of water at 25°C. Although the vapor pressure of water is only 23.7 mm, this addition drastically retarded deposition, below even that of argon at the lower temperatures. The deposition rate appeared to be more temperature dependent in this case than in those where argon or CO_2 was used as a carrier.

These results can, for the most part, be rather easily summarized. When, as in the case of argon or CO_2 atmospheres, the quantity of oxygen is limited to that present as an impurity in the inert gas, to back diffusion into the deposition chamber, or desorption from the walls of the apparatus, deposition rates are low. When the supply of oxygen is plentiful, the deposition rates are high, and proportional to the quantity of iron being transported into the chamber. The role of water vapor, however, is less obvious. Even when large quantities of oxygen are supplied with it, deposition rates are low. These rates, unlike those described previously, are temperature dependent and suggest a thermally activated process. Thus, clearly either the reaction or the kinetics involving the decomposition of iron pentacarbonyl is different in a water-containing atmosphere. This point is discussed more extensively in a later section.

Etching Studies

Preparation of semitransparent photomasks requires that films with the appropriate optical spectra be etched in solvents compatible with photoresist processing materials. Furthermore, in order to achieve the desired resolution of the etched films, it is necessary that solution be accomplished uniformly without significant undercutting. Sinclair *et al.* (1) had found sputtered iron oxide films to be extremely resistant to normal etchants, and when etched they provided unsatisfactory resolution. Some of our films behaved similarly, but others could be successfully etched in

diluted HCl at temperatures between 25° and 50°C. This difference could be associated with the deposition temperatures. Films deposited below approximately 160°C could be satisfactorily etched, while those deposited at higher temperatures could not.

Optical Spectra

This observation posed the question: What is the essential difference between these two types of films? Initially, it was thought that optical spectra would provide valuable clues. Thus, extensive absorption spectra in the region between 3000 and 7000Å of films deposited under a variety of conditions were obtained using a Cary recording spectrophotometer (Model No. 14). However, for the purpose intended, this approach proved disappointing since no significant differences were observed. The point is illustrated by optical spectra (Fig. 3) of films deposited in oxygen using a carrier flow of 60 cc/min. This plot of optical density *vs.* wavelength is essentially similar for the spectra of films prepared at different temperatures, except that a somewhat sharper cutoff is exhibited by films formed at higher temperatures.

Although not particularly revealing for the purpose of characterizing the iron oxide films, these spectra do show that iron oxide films meet the criteria for semi-transparent photomasks. They are highly absorbing in the spectral range used for photoresist processing and are reasonably transparent in the visible. A typical film for photomask usage would be about 1800Å thick and would have an optical density of 2 at 4000Å and of 0.3 at 6000Å.

Scanning Electron Microscopy

A more powerful tool for the characterization of these films proved to be the scanning electron microscope. Micrographs were obtained at 10,000-20,000X using a Cambridge Stereoscan II apparatus operating in the secondary mode. The films were sufficiently conducting, $\rho \approx 10^9$ ohms/sq, so that no surface coating was needed. The resulting micrographs clearly reveal a distinction between the surface morphologies of the two types of films. Figure 4(a) shows a typical surface of a high-temperature film. Here, deposition occurred

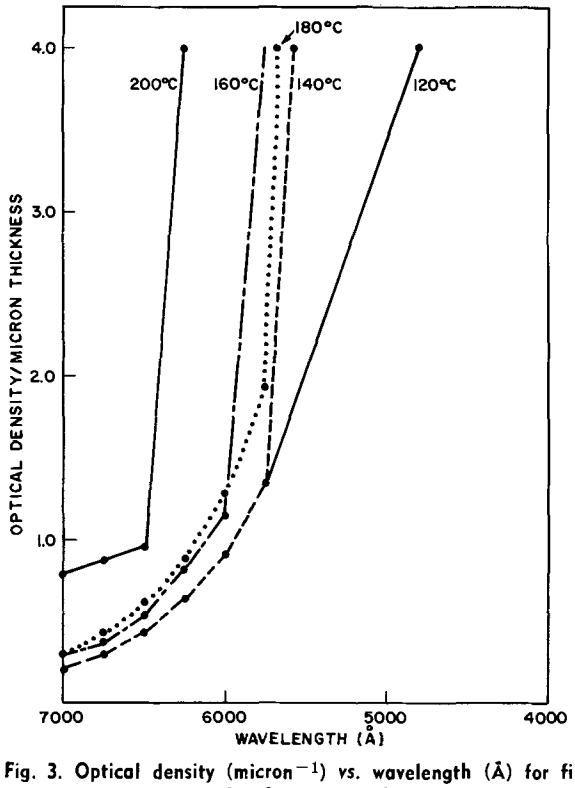

Fig. 3. Optical density (micron^{-1}) *vs.* wavelength (Å) for films formed at temperatures of 120°, 140°, 160°, 180°, and 200°C in an atmosphere of carrier (Ar) 60 cc/min, O_2 60 cc/min.

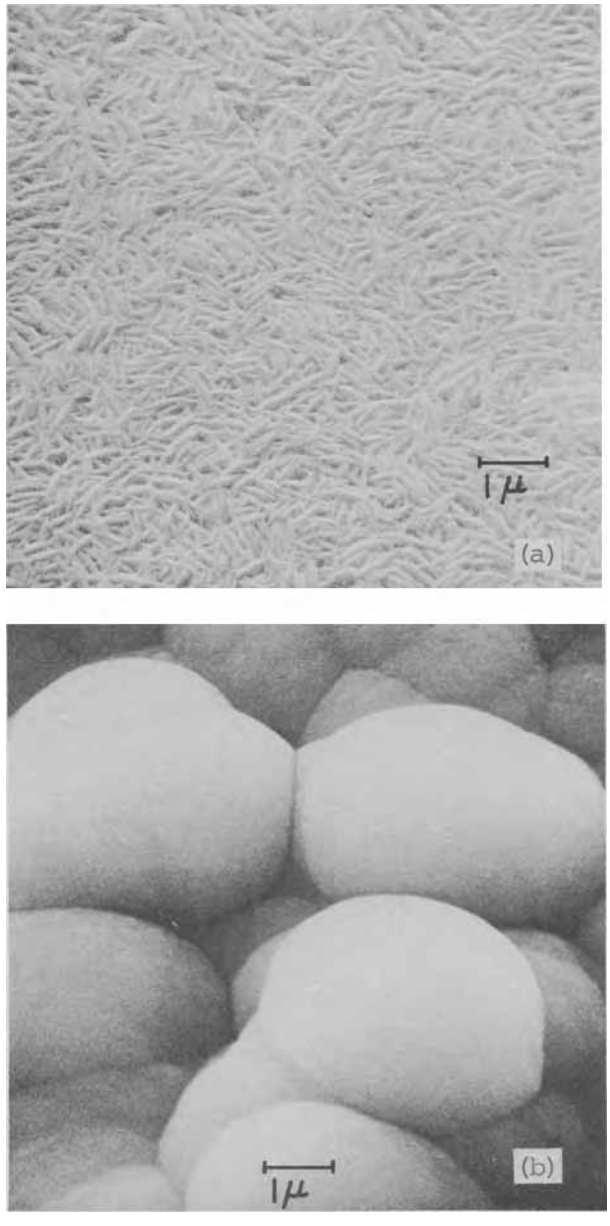

Fig. 4. Scanning electron micrographs of the surfaces of films deposited in an oxygen atmosphere carrier Ar and O_2 40 cc/min and 60 cc/min, respectively: (a) high-temperature morphology deposited at 210°C, (b) low-temperature morphology deposited at 160°C.

at 210°C in oxygen where the carrier and oxygen flows were, respectively, 40 and 60 cc/min. It is seen that the film consists of well-developed acicular crystallites with dimensions of approximately 0.1 x 0.1 x 1.0μ. A quite different appearance is observed for films formed under similar flow conditions but deposited at 160°C. An example is shown in Fig. 4(b). Component particles of this film are large, approximately 4μ in diameter, and have a rounded appearance with an absence of well-developed crystal faces. The morphology of this film is reminiscent of the reniform (4) habit frequently displayed by one variety of naturally occurring hematite. The development of this habit is associated with a low-temperature (sedimentation) process. When contrasted with the well-formed crystallites observed in the films formed at higher temperatures, it was reasonable to suspect that the difference between the two types of films involved the degree of crystallinity attained by each.

X-Ray Diffraction and Mössbauer Spectroscopy

There was little difficulty in establishing that films formed at the higher temperatures were crystalline

Table I

	155°C film, a/o	200°C film, a/o
Fe	36.60 ± 0.43	38.03 ± 0.50
O*	62.73 ± 0.39	61.88 ± 0.50
Si	0.28 ± 0.01	0.08 ± 0.09
C	0.89 ± 0.27	—

* Oxygen by difference.

and that their structure was that of αFe_2O_3. X-ray diffractometer patterns, obtained using CrKα radiation, gave reflections characteristic of this phase. In addition, Mössbauer spectra of characteristic films were obtained by methods described previously (5). One such spectrum was obtained from a 6μ film which had been deposited at 206°C and subsequently removed from the substrate. This consisted of six lines characteristic of magnetically ordered materials. Its isomer shift, obtained from the centroids of the peaks, was +0.21 mm/sec relative to ^{57}CoPd and its effective magnetic hyperfine field was 512 kOe. Both values are typical of the αFe_2O_3 phase.

Analysis of the low-temperature deposits proved more difficult. Here, x-ray diffraction, and electron diffraction as well, proved worthless. No reflections could be obtained from these films even when films several microns thick were scanned. At the same time, it was found extremely difficult to remove these deposits from glass for Mössbauer spectroscopy. However, it had been observed that films deposited on steel panels at similar temperatures had morphology identical to those deposited on glass and could thus be assumed comparable. One such film, deposited at 160°C, was removed using diluted HCl and a portion of it was retrieved from the acid for analysis. The Mössbauer spectra of this film revealed the presence of both magnetically ordered and paramagnetic-trivalent iron. The hyperfine split spectra revealed an effective field of 512 kOe similar to that observed previously. The isomer shift of the paramagnetic iron was +0.19 mm/sec. Although somewhat less than that observed previously, this value is still typical of trivalent iron. Thus, it was concluded that the low-temperature phase was composed of trivalent iron, a portion of which was present in a crystalline environment, while the remainder was either amorphous or incorporated in a phase not magnetically ordered at room temperature. It appears likely that the film was composed of crystallites having a wide range of sizes, the smaller of which were superparamagnetic and thus exhibited a range of blocking temperatures (6).

Analysis

Electron probe microanalysis was obtained from films deposited on silicon wafers. One film was deposited at 155°C using a flow of 85 cc/min argon and 80 cc/min O_2 and yielded a film 4750Å thick. A second film was deposited at 200°C to a thickness of 2250Å using an argon flow of 70 cc/min and oxygen of 50 cc/min. The mean chemical composition and two sigma limits based on 12 analyses of these films are shown in Table I.

These analyses indicate that the compositions of both films approximate that of Fe_2O_3 but are iron deficient with possible minor concentrations of carbon and silicon. This suggests the possible presence of goethite ($Fe_2O_3 \cdot H_2O$), the hydroxide $Fe(OH)_3$ or, as evidenced by the presence of carbon, a carbonate or carbonyl.

Chemistry of Iron Oxide Film Formation

The decomposition of iron pentacarbonyl in the pure state or in an inert gas atmosphere appears to be reasonably well understood. Decomposition takes place according to the over-all reaction: $Fe(CO)_5 = Fe + 5CO$. Carlton and Oxley (7) have studied equilibrium decomposition via this reaction and find that it is thermodynamically favorable, in the pure state, at temperatures above 60°C. However, the rate is limited by kinetics below approximately 200°C and by diffusion above this temperature. The rate-limiting step at lower temperatures is the decomposition of adsorbed carbonyl on the deposition surface. The activation energy for this reaction is 20 kcal/mole, but iron pentacarbonyl is only weakly adsorbed on the reaction surface ($\Delta H_{ads} = 5$ kcal/mole). Carbon monoxide, on the other hand, is quite strongly absorbed ($\Delta H_{ads} = 22$ kcal/mole). Thus, the presence of carbon monoxide in the reaction atmosphere, either as an addition or resulting from the deposition, strongly depresses the decomposition, while argon and helium which are not strongly adsorbed have little effect on the reaction rate.

In order to better understand the decomposition of iron pentacarbonyl in oxidizing atmospheres, we arranged to pass its vapor together with the argon carrier and the oxidizing gas into a CEC[2]-621 mass spectrometer. In one instance, the oxidizing gas was pure oxygen and, in another, oxygen saturated with water at 25°C. Argon (carrying the pentacarbonyl) was mixed with either of these atmospheres in the ratio of 40:60 (per cent by volume) and passed into a Pyrex manifold connected to the mass spectrometer. This was so arranged that the gas mixture could be fed directly into the instrument or first passed through a furnace packed with glass wool. Samples were analyzed for argon, oxygen, carbon monoxide, carbon dioxide, nitrogen, and iron pentacarbonyl. The results of these analyses are given in Table II. The three columns on the left give the results of direct passage into the spectrometer, while the remainder show the

[2] Consolidated Electrodynamics Corporation.

Table II. Mass spectrometer analysis of iron pentacarbonyl decomposition products, volume per cent

	Flow conditions[a]											
	Directly into spectrometer			Through packed furnace								
				25°C		146°C		176°C		210°C		
Constituents	25°C Carrier only	25°C O_2	25°C O_2-H_2O[d]	O_2	O_2-H_2O[d]	O_2	O_2-H_2O[d]	O_2	O_2-H_2O[d]	O_2	O_2-H_2O[d]
N_2[b]	0.37	0.41	0.44	0.44	0.44	0.44	0.58	0.58	0.52	0.73	0.88
O_2	0.078	61.0	61.0	61.0	61.0	62.0	62.0	58.0	57.0	57.0	59.0
Ar_2[c]	97.0	34.8	35.8	33.7	35.8	32.3	34.4	34.8	35.8	35.2	33.5
CO_2	N.D.	N.D.	0.31	2.2	0.24	2.3	0.55	1.48	1.21	2.6	1.1
CO	N.D.	N.D.	0.15	2.3	N.D.	2.3	N.D.	4.7	4.4	3.8	5.1
$Fe(CO)_5$	2.7[e]	3.3	2.1	0.27	2.0	0.10	1.7	0.031	0.24	0.008	0.007

[a] All determinations based on carrier flow-40 cc/min, O_2 or O_2-H_2O-60 cc/min.
[b] From leakage of air into apparatus.
[c] Argon flows normalized to 40 cc/min.
[d] O_2 bubbled through H_2O at 25°C.
[e] The concentration of $Fe(CO)_5$ was taken as proportional to its vapor pressure at 25°C. The mass spectra resulting from this measurement were used as a standard for subsequent determination. The absolute quantity of $Fe(CO)_5$ may be in error even though the relative quantities found are consistent.
N.D. = Not detected.

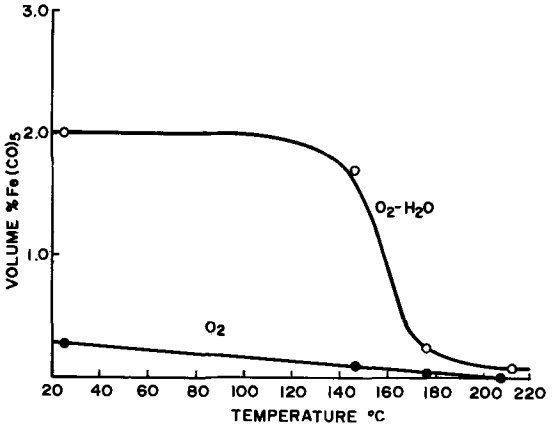

Fig. 5. Curves showing % $Fe(CO)_5$ vs. temperature (°C) obtained from mass spectrometer analyses. Mixtures of $Fe(CO)_5$ vapor, argon, and O_2 or O_2-H_2O were passed through glass wool packing before entering mass spectrometer.

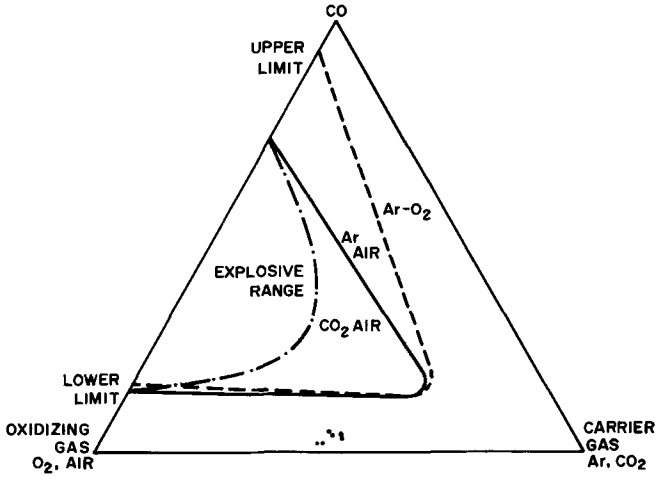

Fig. 6. Curves showing explosive ranges of various ternary gas mixtures: solid curve, CO-air-Ar; dashed curve, CO-O_2-Ar; dash-dot curve, CO-air-CO_2. Points in lower center of diagram represent analytically determined compositions of postdeposition atmospheres.

effects of passage through the glass wool. It is evident that even at low temperatures the glass wool, presumably because of its large surface area, causes decomposition of iron carbonyl. This is severe with pure oxygen but insignificant when oxygen and water are both present. These results are compared by curves of % $Fe(CO)_5$ *vs.* T (°C) in Fig. 5.

These data, combined with those derived from the deposition rate experiments represented in Fig. 2, clearly show that water inhibits the decomposition of iron carbonyl. We suggest the following rationale to explain this phenomenon: The decomposition of iron pentacarbonyl to iron oxide proceeds by a surface-catalyzed reaction. However, both oxygen and water are strongly adsorbed on the reaction surface. The heat of adsorption of oxygen on oxides is approximately 20 kcal/mole (8) and that of water on αFe_2O_3 is reported to be between 14.2 and 18.7 kcal/mole (9) at 150°C. Thus it is reasonable to think that, under the conditions of film formation, both oxygen and water compete for surface sites. In this regard, it might be mentioned that the data of Fig. 2(d) which represents deposition rates for oxygen-water mixtures, when plotted as ln R (Å/min) *vs.* $1/T(°K^{-1})$, yield a straight line whose slope is equivalent to an activation energy of 12.7 kcal/mole. This value is in reasonable agreement with that of the heat of adsorption of water on iron oxide.

The carbon monoxide concentrations determined in these analyses raise another point deserving consideration. In a process of this kind, where CO is present in an atmosphere rich in oxygen, there is the possibility of approaching the explosive range of these gas mixtures. Fortunately, the literature abounds with data on the explosive limits for mixtures of CO with O_2 and air in the presence of inert gases. From these data, we have constructed Fig. 6 which shows by means of a ternary diagram the explosive range of mixtures of CO with air or oxygen and an inert gas. The solid line of this diagram is drawn on the basis of data by van Heiningen (10) and shows the explosive range of CO-air-Ar. The range for CO-O_2-Ar is also known (11) and is represented on this diagram by the dashed curve.

In the lower center of this diagram, a series of dots are used to represent the compositions of gas mixtures tabulated in Table II. It is seen that these lie safely outside of the explosive limits. Nevertheless, the concentration of CO in deposition atmospheres could become of concern should the iron pentacarbonyl concentration, either by intent or accident, be raised significantly. In order to avoid the explosive region, the concentration of the argon carrier could be raised to greater than 60%. Alternatively, CO_2 could be substituted for argon. This causes the explosive range to shrink appreciably (12) as shown by the dash-dot curve of Fig. 6. Thus, with appropriate flow of air as the oxidizing gas and CO_2 as the carrier, the explosive range can be avoided completely.

Conclusions

This study shows that iron oxide films having optical characteristics suitable for semitransparent photomasks can be conveniently and easily prepared by decomposition of iron pentacarbonyl in an oxygen atmosphere. The substrate temperature at which the deposition is carried out is important in determining the resistance of the film to etching agents. Satisfactory films could be prepared at temperatures below approximately 160°C. These were composed of partially crystalline αFe_2O_3.

Acknowledgments

The authors are indebted to many colleagues who have provided the analytical data on which the characterization of these films is based. We are particularly grateful to G. W. Kammlott for scanning electron microscopy, P. K. Gallagher for Mössbauer spectra, G. W. Colby for microprobe analysis, F. V. DiMarcello for aid on thickness measurements, and F. Gollob, of the Gallob Analytical Service, Berkeley Heights, New Jersey, for mass spectrometer analyses. In addition, we wish to acknowledge useful discussions with W. J. Schreibeis and D. W. Johnson, and to thank W. R. Sinclair and M. D. Rigterink for both encouragement and advice, and P. A. Turner for critical reading of the manuscript.

Manuscript submitted June 19, 1970; revised manuscript received Nov. 30, 1970. This was Paper 126 presented at the Los Angeles Meeting of the Society, May 10-15, 1970.

Any discussion of this paper will appear in a Discussion Section to be published in the December 1971 JOURNAL.

REFERENCES

1. W. R. Sinclair, M. V. Sullivan, and R. A. Fastnacht, *This Journal*, **118**, 341 (1971).
2. C. F. Powell in "Vapor Deposition," C. F. Powell, J. H. Oxley, and J. M. Blocher, Jr., Editors, p. 391, John Wiley & Sons, New York (1966).
3. D. R. Secrist and J. D. MacKenzie, *Bull. Am. Ceram. Soc.*, **49**, 784 (1966).
4. C. S. Hurlout, Jr., "Dana's Manual of Mineralogy," p. 89, John Wiley & Sons, New York (1952).
5. P. K. Gallagher, J. B. MacChesney, and D. N. E. Buchanan, *J. Chem. Phys.*, **41**, 2429 (1964).
6. I. S. Jacobs and C. P. Bean in "Magnetism," Vol. 3, C. T. Rado and H. Suhl, Editors, Academic Press, Inc., New York (1963).

7. H. E. Carlton and J. H. Oxley, *A.I.ChE. J.*, **11**, 79 (1965).
8. See B. M. W. Trapnell, "Chemisorption," Butterworths, London (1964).
9. F. H. Healey, J. J. Chessick, and A. V. Fraioli, *J. Phys. Chem.*, **60**, 1001 (1956).
10. J. van Heiningen, *Rec. Trav. Chim.*, **55**, 65 (1936).
11. H. F. Coward and G. W. Jones, Bull. No. 503, Bureau of Mines (1962).
12. M. G. Zabetakis, Bull. No. 627, Bureau of Mines (1965).

The Solid Solubility Isotherms of Zn in GaP and GaAs

A. S. Jordan

Bell Telephone Laboratories, Incorporated, Murray Hill, New Jersey 07974

ABSTRACT

The solid solubility isotherms for Zn in GaP and GaAs have been calculated as a function of Zn concentration along the Ga-P-Zn and Ga-As-Zn liquidus isotherms over a wide temperature range. These calculations were based on a critical evaluation of the available solubility data, assuming regular ternary solution behavior in both ternary melts. The solubility isotherms are not only in agreement with the published data, but are also in accord with recent experimental results on the incorporation of Zn in GaP grown by liquid-phase epitaxy and liquid encapsulation pulling. In addition, the Zn surface concentrations in GaP and GaAs arising from ternary source diffusion have been estimated as a function of temperature. Finally, the enthalpies for the incorporation of Zn in GaP and GaAs according to $Zn(l) + V_{Ga} = Zn_{Ga}$ are given as approximately -2.16 and -2.29 eV, respectively.

Zinc is one of the most frequently used p-type dopants in GaP and GaAs. In particular, Zn plays a pivotal role in the formation of Zn-O complexes in red emitting electroluminescent GaP diodes (1). Several recent investigations have been devoted to the study of Zn solubility in GaP and GaAs. Most of these studies have not only provided a limited amount of solubility data at certain temperatures, but have also contributed to the present understanding of the incorporation mechanism of Zn in GaP and GaAs.

The major objective of this paper is to calculate the complete solid solubility isotherms for Zn in GaP and GaAs as a function of Zn concentration along the Ga-P-Zn and Ga-As-Zn liquidus isotherms over a wide temperature range. The temperature dependent equilibrium constants for the incorporation of Zn in these crystals required to perform the calculations are obtained by a critical analysis of the published solubility data in combination with Zn, P, and As activities taken from recent work (2). It is further shown that the approximate enthalpies of Zn incorporation are in good agreement with an independent theoretical estimate. In addition, the Zn surface concentrations as a function of temperature in GaP and GaAs resulting from ternary source diffusion are evaluated. Finally, it is demonstrated that the Zn solubility isotherms in GaP at both low and high temperatures are in accord with recent experiments on the incorporation of Zn in GaP grown by liquid-phase epitaxy and liquid encapsulation pulling.

Analysis of the Solubility Data

Trumbore *et al.* (3) have determined the solid solubility of Zn in GaP crystals, grown at about 1040°C from Ga-rich solutions by a thermal gradient technique. These authors (3) were able to relate the Zn solubility in the solid to the Zn concentration in the melt by means of a simple model, assuming the incorporation of singly and completely ionized Zn acceptors on vacant Ga sites. More recently, Panish and Casey (4, 5) and Casey *et al.* (6) have considered in some detail the ionization of Zn in GaAs and GaP and pointed out that the accepted theories for impurity incorporation, based on Fermi-Dirac statistics, required the presence of a significant amount of neutral Zn at higher concentrations. However, when the effects of high impurity concentrations on the density of states were taken into account, they have found that the merger of the localized impurity level with the valence band resulted in the total ionization of Zn.

Therefore, the incorporation of Zn in GaP or GaAs can be given by the following defect equilibria

$$O = V_{Ga} + V_P \quad [1a]$$

$$P(l) + V_P = P_P \quad [1b]$$

$$Zn(l) + V_{Ga} = Zn_{Ga} \quad [1c]$$

$$Zn_{Ga} = Zn_{Ga}^- + e^+ \quad [1d]$$

$$P(l) + Zn(l) = Zn_{Ga}^- + P_P + e^+ \quad [2]$$

where the left-hand side of Eq. [1a] represents the normal occupation in the lattice and Eq. [2] by summing over Eq. [1a] through [1d] describes the over-all incorporation process. Consequently, the equilibrium constant, K, for Eq. [2] takes the form

$$K = [Zn_{Ga}^-]\gamma_h[e^+]/a_{Zn}a_P \quad [3]$$

where the brackets signify the concentration of the enclosed species, γ_h is the activity coefficient of holes, as introduced by Panish and Casey (6), and the functions a_{Zn} and a_P are the Zn and P activities in the liquid phase in equilibrium with Zn-doped GaP. The standard states for the activities are the respective pure liquids. In writing Eq. [3] it has been assumed that the activity coefficients for $[Zn_{Ga}^-]$ and $[P_P]$[1] as well as $[P_P]$ itself are constants (Henrian and Raoultian regions, respectively). By the use of the electroneutrality condition, $[Zn_{Ga}^-] + [e^-] = [e^+]$, and the mass action relation for electrons and holes, $\gamma_h[e^-][e^+] = n_i^2$,[2] where n_i is the intrinsic concentration, one can eliminate $[e^+]$ from Eq. [3] and obtain the following relationship

$$\frac{C^{s2}_{Zn}\gamma_h}{2}\left[\sqrt{1+\left(\frac{2n_i}{C^s_{Zn}}\right)^2\frac{1}{\gamma_h}}+1\right] = Ka_{Zn}a_P \quad [4]$$

Key words: III-V compounds, doping, electroluminescent materials, semiconductor phase equilibria.

[1] The Raoultian behavior of the activity coefficient for $[P_P]$ is not seriously affected by $\gamma_h \neq 1$ as the Gibbs-Duhem equation is approximately obeyed when $[e^+]/[P_P]$ is about 10^{-3} or smaller.

[2] Note that $\gamma_e = 1$ because for Zn-doped GaP as well as for Zn-doped GaAs $[e^-] << [e^+]$.

It should be noted that in Eq. [4] the complete ionization of Zn has been introduced; thus $[Zn_{Ga}^-]$ was replaced by C^s_{Zn}, the total concentration of substitutional Zn, expressed, as usual, in units of atoms/cc.[3] Replacing the symbol P by As, Eq. [1] through [4] also hold for Zn-doped GaAs. Of course, the K's have different values for GaAs and GaP.

In determining K by Eq. [4], one must know the activities in the liquid phase, *i.e.*, $a_{Zn} = \gamma^l_{Zn} x^l_{Zn}$ and $a_P = \gamma^l_P x^l_P$ (or $a_{As} = \gamma^l_{As} x^l_{As}$), where γ^l_i and x^l_i are the activity coefficient and atom fraction of the designated component in the ternary melt, respectively. The evaluation of a_{Zn}, a_P, and a_{As} is based on work reported in ref. (2), where the liquidus data for Zn-doped GaAs and GaP in equilibrium with Ga-As-Zn and Ga-P-Zn ternary melts are fitted by means of a liquidus equation in four parameters, assuming regular solution behavior. It is demonstrated therein that the calculated ternary liquidus isotherms and component partial pressures are in good agreement with the available liquidus and pressure data. Therefore, if at a particular temperature C^s_{Zn} as a function of x^l_{Zn} has been determined, then at any x^l_{Zn} the calculated liquidus isotherm yields the corresponding x^l_{As} or x^l_P and the activity equations for regular ternary solutions provide the appropriate activities (8).

In addition, the evaluation of K from Eq. [4] also requires a knowledge of n_i and γ_h. Tabulated temperature dependent values of n_i for GaAs and GaP are available from the unpublished works of Ermanis and Casey (9) and Casey and Focht (10), respectively. Moreover, the calculated variations of γ_h on $[e^+]$ for GaAs-Zn at 700°, 800°, 900°, and 1000°C and for GaP-Zn at 1000° and 1100°C, based on the analysis of diffusion data, have been presented by Casey *et al.* (6) and Panish and Casey (4), respectively. According to these authors, γ_h departs from unity for Zn-doped GaP above $[e^+] = 3 \times 10^{19}$ and for Zn-doped GaAs above $[e^+] = 6 \times 10^{19}$. Indeed, a preliminary analysis of the extensive 1000°C Zn solubility data for GaAs of Panish and Casey (5) and Casey *et al.* (6) below this limit (where $\gamma_h = 1$ holds) by logarithmic least-squares, a method to be presented next, shows that the calculated K in combination with Eq. [4] is unable to describe the solubility isotherm in the 10^{20} range unless the γ_h of Casey *et al.* (6) is introduced. However, a similar analysis of the Zn solubility measurements of Trumbore *et al.* (3) and Panish and Casey (4) at 1040°C indicates that the experimental results, including the 10^{20} range are well represented by taking $\gamma_h = 1$ throughout. Hence, only the calculations involving Zn-doped GaAs will take into account the proposed departure of γ_h from unity at high carrier concentrations.

Since most of the experimental solubility data show a considerable scatter, it was decided to evaluate K from Eq. [4] by the method of logarithmic least squares whenever isothermal C^s_{Zn} was obtained by an investigator at more than one value of x^l_{Zn}. Briefly, by denoting at each C^s_{Zn} the logarithms of the left-hand side and $a_{Zn}a_P$ in Eq. [4] by η_i and ξ_i, respectively, one can transform this equation into

$$\eta_i = \ln K + \xi_i$$

Then, applying the method of least squares, one obtains $\ln K$ in the form

$$\ln K = \left(\sum_{i=1}^{n} \eta_i - \sum_{i=1}^{n} \xi_i \right) \Big/ n \qquad [5]$$

where n is the number of solubility determinations at a given temperature by one of the investigators.

The reported measurements of Trumbore *et al.* (3) and Panish and Casey (4) at 1040°C and Foster and Scardefield (11) at 1144°C for C^s_{Zn} in GaP as a function of x^l_{Zn} are suitable for a direct application of Eq. [4] and [5]. Likewise, the solubility data of Casey *et al.* (6) and Panish and Casey (5) at 900° and 1000°C for Zn-doped GaAs can be analyzed readily by means of the same equations. Log K *vs.* reciprocal temperature plots calculated from the above sources are shown in Fig. 1.

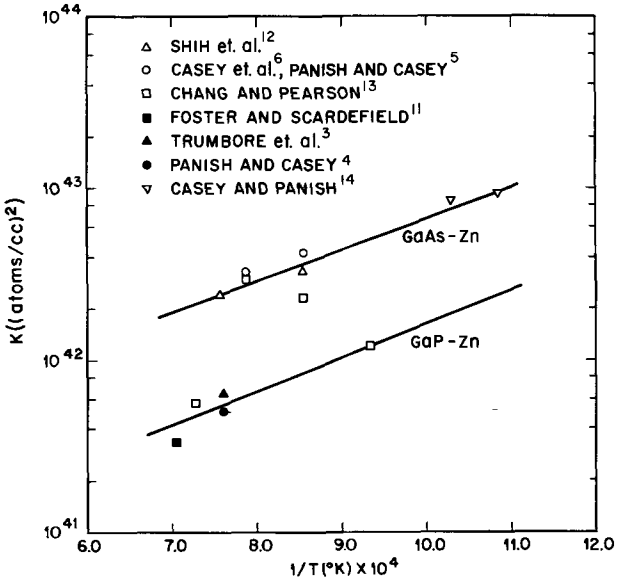

Fig. 1. Equilibrium constant *vs.* reciprocal temperature for the incorporation reactions.

$$Zn(l) + P(l) = Zn_{Ga}^- + P_P + e^+$$

and

$$Zn(l) + As(l) = Zn_{Ga}^- + As_{As} + e^+$$

Several additional K values, derived from the diffusion studies of Shih *et al.* (12), Chang and Pearson (13), and Casey and Panish (14), are also illustrated in Fig. 1. Shih *et al.* (12) have determined the surface concentrations of Zn in GaAs crystals at 900° and 1050°C, diffused from a radioactive Zn^{65} source in sealed tubes also containing an excess of As. These authors (12) have estimated the partial pressures of As, p_{As_4}, corresponding to the liquid concentrations along the ternary liquidus isotherm resulting from the presence of various known amounts of Zn^{65} and As in the ampoules. The calculation of p_{As_4} was accomplished by the use of an equation due to Furukawa and Thurmond (15) in combination with the published liquidus isotherms (16) and the earlier pressure measurements of Shih *et al.* (17).

However, to evaluate K the required variables are x^l_{Zn} and the activities instead of p_{As_4}. Therefore, these variables were derived from the raw data of Shih *et al.* (12) by a procedure completely consistent with the previously mentioned liquidus isotherm and partial pressure calculations (2), and also taking into account the presence of As_2 in addition to As_4 in the gas phase. When GaAs is heated in contact with As and an impurity in sealed tubes, ternary liquid and gas phases are formed. Since only a negligible amount of Ga is transferred into the gas phase, the total number of moles of As in the liquid (l) and gas (v) phases can be written (15) in the form

$$n^a_{As} + n^l_{Ga} = n^l_{As} + n^v_{As} \qquad [6]$$

where n^a_{As} is the number of moles of added As. Allowing for the presence of As_2 and As_4 in the gas phase and assuming the validity of the ideal gas law for the gaseous species, one has $n^v_{As} = 4n^v_{As} + 2n^v_{As_2}$ and Eq. [6] can be transformed into

[3] Consequently, the unit of K is $(atoms/cc)^2$. It can be shown that K is related to the dimensionless thermodynamic equilibrium constant, K_a, by the constant factor $K \simeq (5 \times 10^{45}/k) K_a$ where k is the activity coefficient of $[Zn_{Ga}^-]$ in the Henrian limit.

$$\frac{RT}{V}\frac{w^{a}_{As}}{M_{As}}+\frac{RT}{V}\frac{w^{a}_{Zn}}{M_{Zn}}\frac{(x^{l}_{Ga}-x^{l}_{As})}{x^{l}_{Zn}} \equiv f_1+f_2\frac{(x^{l}_{Ga}-x^{l}_{As})}{x^{l}_{Zn}}=4\left(p_{As_4}+\frac{p_{As_2}}{2}\right)+p_{Zn}\frac{(x^{l}_{Ga}-x^{l}_{As})}{x^{l}_{Zn}} \quad [7]$$

where V is the sample volume and w^{a}_{i} and M_i are the added weight and molecular weight of the designated species, respectively. For every value of C^{s}_{Zn}, the w^{a}_{i}'s and V have been given by Shih *et al.* (12); hence, f_1 and f_2 are known. Moreover, at each x^{l}_{Zn} along the Ga-As-Zn ternary liquidus isotherm x^{l}_{As} and x^{l}_{Ga} and the corresponding p_i's are available from previous work (2) is graphical and also tabulated form. Thus, for every fixed value of f_1 and f_2 a unique x^{l}_{Zn} satisfying Eq. [7] as well as a_{Zn} and a_{As} were obtained. Finally, the K's at 900° and 1050°C were evaluated from Eq. [4] and [5].

In earlier work, Chang and Pearson (13) determined the solubility of Zn in GaP and GaAs at 800° and 900°C, respectively, as a function of Zn concentration in radioactive Zn^{65}-Ga liquid alloys, used as diffusion sources. In addition, at several temperatures both compounds were diffused from a pure Zn^{65} source and the surface concentrations measured. In all cases the appropriate ternary x^{l}_{Zn} was located by intersecting the calculated liquidus isotherm, plotted on an equilateral triangle, by the straight line connecting the reported Zn composition of the source, situated on the Ga-Zn axis, with the composition representing GaP or GaAs. The evaluation of the K's from the C^{s}_{Zn} data and the derived x^{l}_{Zn} and activities followed the previously performed procedure.

It should be noted that below about 1040°C for GaP and 900°C for GaAs the liquidus composition corresponding to the pure Zn source is in equilibrium not only with solid GaP or GaAs (doped with Zn) but also with solid Zn_3P_2 or Zn_3As_2 (16, 18, 19). Therefore, in view of the uncertainty involved in locating the x^{l}_{Zn} and the activities at which both solid phases are in equilibrium with the melt, and the possibility of precipitation of Zn_3P_2 or Zn_3As_2 in the GaP or GaAs, the solubility data obtained under the above conditions were not utilized.

Recently, Casey and Panish (14) diffused Zn into GaAs at 650° and 700°C from an invariant ternary source. The composition of this source was such that at these temperatures three solid phases GaAs, Zn_3As_2, and ZnAs were in equilibrium. At both temperatures the magnitude of the solid solubility, obtained from the diffusion profile, indicates extrinsic conductivity in the crystal ($n_i << C^{s}_{Zn}$); hence Eq. [4] reduces to

$$\frac{C^{s2}_{Zn}\gamma_h}{a_{Zn}a_{As}}=K \quad [8]$$

The calculation of the $a_{Zn}a_{As}$ product is based on thermodynamic data for the decomposition of $ZnAs_2$ and Zn_3As_2, extensively discussed in a recent communication (20). Lyons (21) has shown that between 612° and 740°C $ZnAs_2$(s) dissociates according to

$$ZnAs_2(s) = 1/3\ Zn_3As_2(s) + 1/3\ As_4(g) \quad [9]$$

with the accompanying free energy change, ΔG^{o}_{1}

$$\Delta G^{o}_{1}(\text{kcal}) = 18.8 - 18.5T \times 10^{-3} \quad [10]$$

In addition, Jordan (20) has derived the free energy change, ΔG^{o}_{2}, between 328° and 478°C for the reaction

$$Zn_3As_2(s) = 3Zn(g) + \tfrac{1}{2}\ As_4(g) \quad [11]$$

Extrapolating ΔG^{o}_{2} to the mid-temperature range of Lyons (≈680°C), one has

$$\Delta G^{o}_{2}(\text{kcal}) = 136 - 95.9T \times 10^{-3} \quad [12]$$

Adding $\Delta G^{o}_{1}/4$ to $\Delta G^{o}_{2}/3$, one obtains the free energy change, ΔG^{o}_{As}, for the reaction

$$\tfrac{1}{4}\ Zn_3As_2(s) + \tfrac{1}{4}\ ZnAs_2(s) = Zn(g) + \tfrac{1}{4}\ As_4(g) \quad [13]$$

in the form

$$\Delta G^{o}_{As}(\text{kcal}) = 50.1 - 36.4T \times 10^{-3} \quad [14]$$

Since the activities of the pure solid phases in ternary source diffusion are unity, the equilibrium constant for Eq. [13], K_{As}, which can be calculated from Eq. [14] is given by

$$K_{As} = e^{-\Delta G^{o}_{As}/RT} = p_{Zn}p^{1/4}_{As_4} \quad [15]$$

Dividing Eq. [15] by the product $p^{o}_{Zn}p^{o1/4}_{As_4}$, where p^{o}_{Zn} and $p^{o}_{As_4}$ denote the vapor pressure of pure liquid Zn and As, respectively, one obtains the activity product

$$a_{Zn}a_{As} = \frac{p_{Zn}}{p^{o}_{Zn}}\left(\frac{p_{As_4}}{p^{o}_{As_4}}\right)^{1/4} = \frac{K_{As}}{p^{o}_{Zn}p^{o1/4}_{As_4}} \quad [16]$$

The pressures p^{o}_{Zn} and $p^{o}_{As_4}$ were evaluated from equations presented by Kubaschewski *et al.* (22) and Nesmeyanov (23), respectively. It should be noted that although no liquid phase exists at the conditions of these ternary source diffusion experiments, the use of pure liquid pressures in Eq. [16] is necessitated by the previous choice of referring the activities, employed in the calculation of K by Eq. [4], to the pure liquid standard states. Thus, the activities in Eq. [16] are those of a hypothetical supercooled liquid solution.

Substituting values of $a_{Zn}a_{As}$ at 650° and 700°C, obtained from Eq. [16], into Eq. [8] and taking γ_h for Zn-doped GaAs from the 800°C curve of Casey *et al.* (6) (instead of the somewhat less reliable 700°C results), K's at both temperatures from the known C^{s}_{Zn}'s of Casey and Panish (14) were derived.

Observing the positions of the discrete K values in Fig. 1 for Zn-doped GaP and GaAs, calculated by the preceding critical assessment of the available experimental data, one concludes that it is reasonable to fit them by the customary straight-line relationship between ln K and $1/T$. Therefore, using the method of least-squares the following equations were obtained for the K's

$$-RT \ln K \times 10^{-45} = -8980 + 21.7T \text{ (cal)} \quad [17]$$

for Zn-doped GaP and

$$-RT \ln K \times 10^{-45} = -8530 + 18.4T \text{ (cal)} \quad [18]$$

for Zn-doped GaAs. These lines of best fit are also shown in Fig. 1. The enthalpy changes for the GaP and GaAs incorporation reactions according to Eq. [2] are given by the constant terms in Eq. [17] and [18] (divided by 23,060 (cal)/eV) as −0.39 and −0.37 eV, respectively. These enthalpies are approximately equal which is perhaps not surprising in view of the common dopant and the similarity of the two compounds.

Calculation of the Solubility Isotherms

Solving Eq. [4] for C^{s}_{Zn}, one finds that the solid solubility of Zn in GaP and GaAs in terms of K and the activities is given by

$$C^{s}_{Zn} = \sqrt{\frac{Ka^{2}_{P}a^{2}_{Zn}}{\gamma_h\left(\frac{n^{2}_{i}}{K}+a_{P}a_{Zn}\right)}} \quad [19]$$

Therefore, substituting K from Eq. [17] or [18] into Eq. [19], one can evaluate C^{s}_{Zn} in both compounds at any temperature if the activities in the external phase are known.

In previous work (2) the liquidus isotherms and the partial pressures for Ga-As-Zn and Ga-P-Zn ternary melts in equilibrium with Zn-doped GaAs and GaP were obtained between $x^{l}_{Zn} = 10^{-6}$ on the Ga-rich sides and $x^{l}_{Zn} = 10^{-6}$ on the As and P-rich sides. As mentioned before, calculation of the pressures required a knowledge of the activities. Hence, at any

temperature for each value of x^l_{Zn} in the Ga-P-Zn or Ga-As-Zn ternary solution, C^s_{Zn} for Zn-doped GaP or GaAs in equilibrium with its respective melt can be determined.

In Fig. 2 and 3 calculated curves for C^s_{Zn} in GaAs as a function of x^l_{Zn} are presented between 600° and 1200°C in 100°C intervals and also at 1050°C, together with the previously analyzed solid solubility data. The error limits given in Fig. 2 with the 1000°C data of Panish and Casey (5) and Casey *et al.* (6) were taken from the authors.

For large values of C^s_{Zn} at 1000°C two curves are shown in Fig. 1. One of them, the dashed line, calculated in this range by setting $\gamma_h = 1$ does not, as mentioned earlier, describe the experimental results. On the other hand, the solid line obtained by substituting the 1000°C γ_h data into Eq. [19] is in good accord with the measured values. Thus, the solubility isotherms for Zn-doped GaAs were evaluated at and below 800°, at 900°, and at and above 1000°C by the use of the 800°, 900°, and 1000°C γ_h *vs.* carrier concentration curves of Casey *et al.* (6), respectively.

The lower and upper segments of the solubility isotherms describe C^s_{Zn} for a crystal in equilibrium with a Ga-rich and an As-rich liquid, respectively. To avoid crowding of the curves, only the lower segments are shown below 900°C. These isotherms are terminated at the approximate liquid composition where the secondary solid phase Zn_3As_2 appears (2, 16, 19).

The calculated solubility isotherms for Zn-doped GaP are illustrated in Fig. 4 and 5 between 600° and 1400°C in 100°C intervals and also at 1040°, 1144°, 1460°, and 1465°C. The experimentally determined solubility data, utilized in the preceding analysis, are also shown.

It has been previously indicated that for Zn-doped GaP the 1040°C isotherm even for large values of C^s_{Zn} can be described by taking $\gamma_h = 1$. Comparing the solid curve calculated by equating γ_h to unity in Eq. [19] and the dashed curve obtained by a combination of the same equation with the γ_h of Panish and Casey (4), one notices that at high Zn concentrations a somewhat better agreement with the experimental data is achieved if $\gamma_h = 1$. Therefore, all the isotherms for Zn-doped GaP were evaluated from Eq. [19] by assuming that γ_h does not depart from unity in the entire composition range.

At and above 1040°C both the lower and upper segments of the isotherms are shown. In the interest of

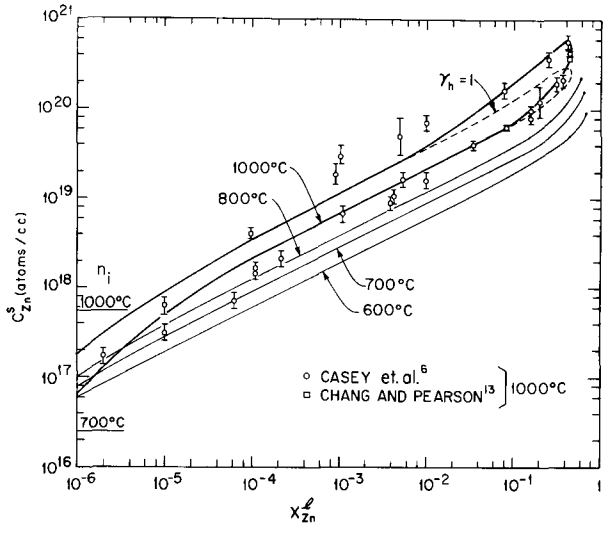

Fig. 2. Zn concentration in GaAs *vs.* x^l_{Zn} along the 600°, 700°, 800°, and 1000°C liquidus isotherms in the Ga-As-Zn system. The isotherms at 800°C and below are terminated at the approximate liquid compositions where Zn_3As_2, a secondary solid phase, appears.

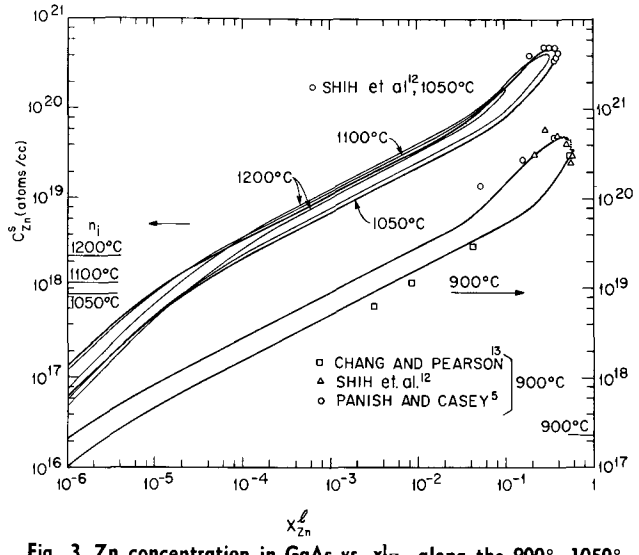

Fig. 3. Zn concentration in GaAs *vs.* x^l_{Zn} along the 900°, 1050°, 1100°, and 1200°C liquidus isotherms in the Ga-As-Zn system.

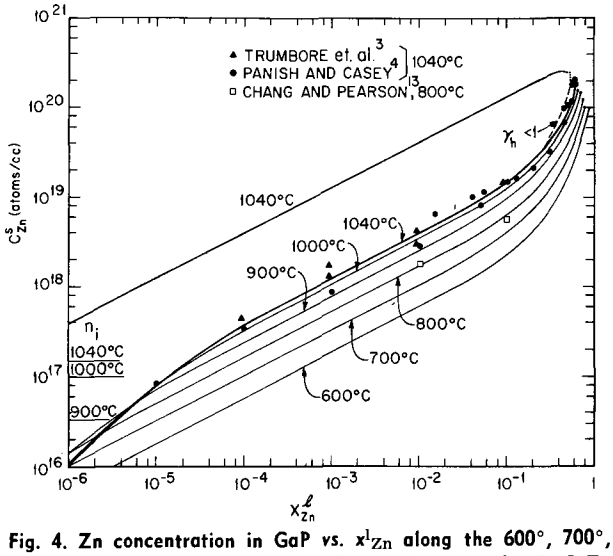

Fig. 4. Zn concentration in GaP *vs.* x^l_{Zn} along the 600°, 700°, 800°, 900°, 1000°, and 1040°C liquidus isotherms in the Ga-P-Zn system. All but the 1040°C isotherms are terminated at the approximate liquid compositions where Zn_3P_2, a secondary solid phase, appears.

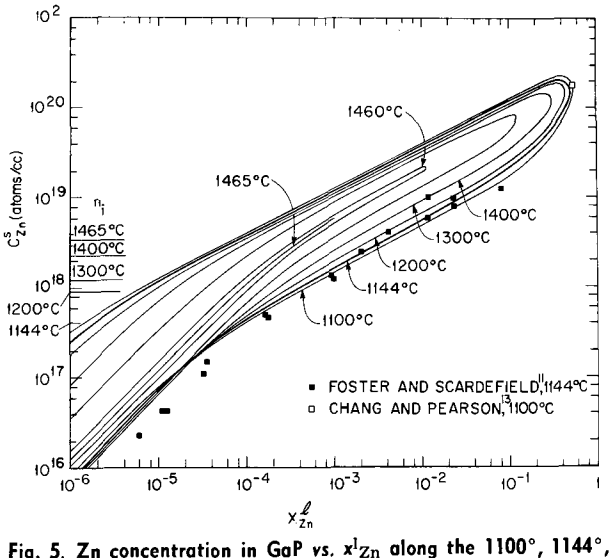

Fig. 5. Zn concentration in GaP *vs.* x^l_{Zn} along the 1100°, 1144°, 1200°, 1300°, 1400°, 1460°, and 1465°C liquidus isotherms in the Ga-P-Zn system.

clarity below 1040°C only the lower segments are presented. These isotherms were terminated at the approximate liquidus composition where the secondary solid phase Zn_3P_2 appears (2, 18).

At most temperatures, in Fig. 2 through 5, n_i for GaAs (9) and GaP (10) are also given at the edge of the diagrams. Above 800°C Fig. 2 through 5 clearly show the intrinsic region ($[e^+] \approx n_i$) with a unit slope as well as the extrinsic region ($[e^+] = C^s_{Zn}$) with a slope of 0.5. The calculated solidus isotherms for Zn-doped GaAs and GaP are generally in good agreement with the available solid solubility data.

Whenever the ternary liquid is in equilibrium only with the primary solid phase, Zn-doped GaAs or GaP, at a fixed temperature a whole range of solid solubilities is allowed as a function of x^l_{Zn}. However, if for example Zn-doped GaAs is in equilibrium with two additional solid phases, namely, Zn_3As_2 and $ZnAs_2$, as is at the surface in the case of ternary source diffusion, then at a constant temperature C^s_{Zn} is an invariant. By a combination of Eq. [8], [16], and [18], this uniquely defined surface concentration of Zn in GaAs was evaluated as a function of temperature and is presented in Fig. 6. The solid line calculated on the basis of the γ_h data of Casey *et al.* (6) agrees well with the measured surface concentrations of Casey and Panish (14). At lower temperatures and solubilities it merges with the dashed line obtained by setting $\gamma_h = 1$.

Furthermore, it is possible to estimate the C^s_{Zn} of GaP diffused from a ternary source. The composition of this source is located in a region where the three solid phases ZnP_2, Zn_3P_2, and GaP are in equilibrium. The calculation of C^s_{Zn} was accomplished by a combination of Eq. [8], equating γ_h with unity, and Eq. [18], evaluating the product $a_{Zn}a_P$ from an equation similar to Eq. [16]. This product is given by

$$a_{Zn}a_P = \frac{p_{Zn}}{p^o_{Zn}}\left(\frac{p_{P4}}{p^o_{P4}}\right)^{1/4} = \frac{K_P}{p^o_{Zn}p^{o1/4}_{P4}} \qquad [20]$$

where K_P is the equilibrium constant for the reaction

$$\tfrac{1}{4}\,Zn_3P_2(s) + \tfrac{1}{4}\,ZnP_2(s) = Zn(g) + \tfrac{1}{4}\,P_4(g) \qquad [21]$$

and the meaning of the other symbols is self-evident.

The free energy change, ΔG^o_P, for Eq. [21], obtained by adding the free energy change for the Zn_3P_2 analogue of Eq. [11], reported by Schoonmaker *et al.* (24) to the ZnP_2 analogue of Eq. [9], estimated by Jordan (20), is of the form

$$\Delta G^o_P(\text{kcal}) = 53.4 - 40.3T \times 10^{-3} \qquad [22]$$

The vapor pressure of pure liquid P was evaluated by the third-law method from data given in the JANAF tables (25).

The estimated C^s_{Zn} for GaP in contact with a ternary source is shown in Fig. 6. It is apparent from Fig. 6 that the carrier concentrations resulting from ternary source diffusion would be too high for red electroluminescent diode applications.

Discussion of Results

In the previous section the solubility isotherms for Zn in GaAs and GaP were presented between 600°C and temperatures near the respective melting points. As the measured solubilities utilized in the evaluation of the equilibrium constants for Zn-doped GaP were obtained in a somewhat restricted temperature interval, it seems desirable to show with the aid of independent information that the extrapolation over a wide temperature range is justified.

Recently, Verleur (26) has grown Zn-doped GaP crystals by liquid encapsulation pulling from a melt containing $Zn(PO_3)_2$, a glassy low melting point dopant (27) first used in liquid-phase epitaxy. The room temperature hole concentrations from Hall measurements on the seed and tail ends of these crystals were determined as a function of various $Zn(PO_3)_2$ additions to the GaP melt. It is possible to estimate the C^s_{Zn} values corresponding to these hole concentrations by means of the experimental curves of Casey *et al.* (28), relating Hall data to absolute temperature for several GaP crystals doped with a known amount of Zn[65]. In Fig. 7 the results obtained by Verleur (26) and the estimated C^s_{Zn} of the seed *vs.* x^l_{Zn} are shown for three GaP ingots. Values of x^l_{Zn} for each melt were calculated by assuming the incorporation without loss of the total amount of Zn present in the $Zn(PO_3)_2$. Figure 7 also illustrates the theoretical solubility isotherm for GaP at 1465°C, in the immediate vicinity of

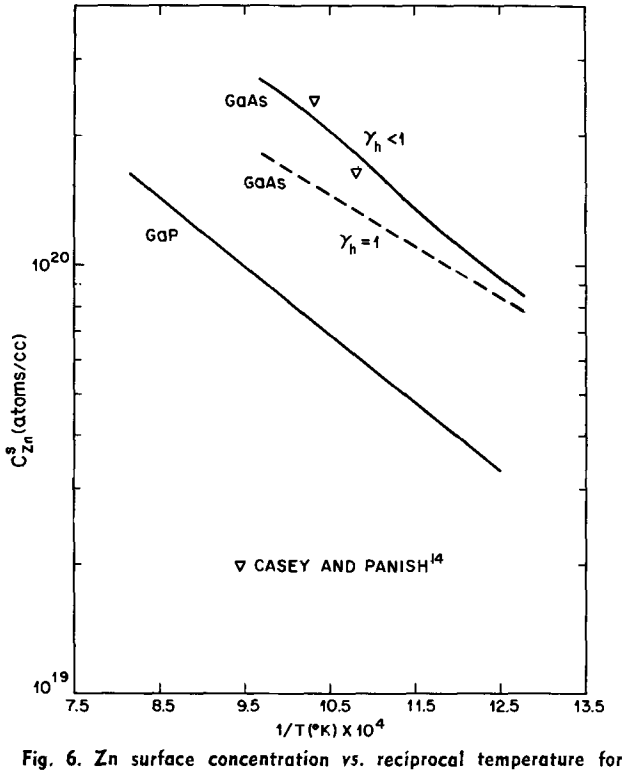

Fig. 6. Zn surface concentration *vs.* reciprocal temperature for GaAs and GaP crystals diffused from invariant ternary sources.

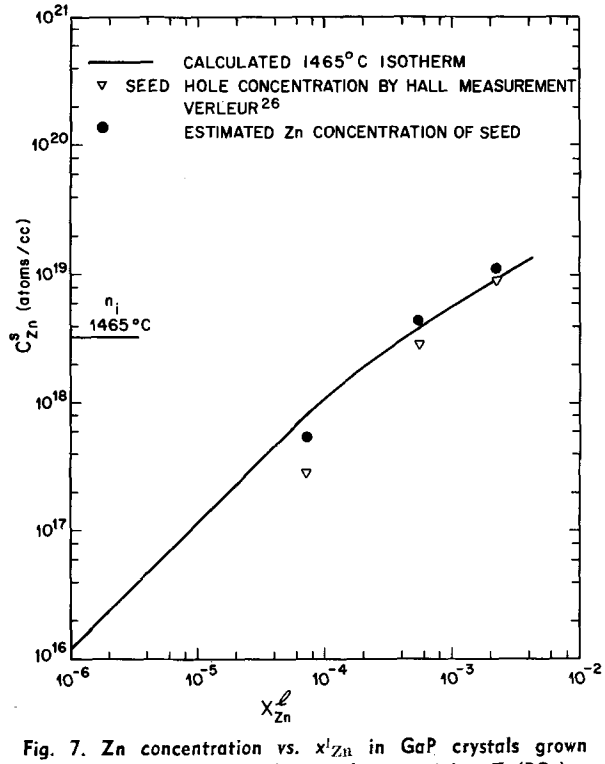

Fig. 7. Zn concentration *vs.* x^l_{Zn} in GaP crystals grown by liquid encapsulation pulling from melts containing $Zn(PO_3)_2$.

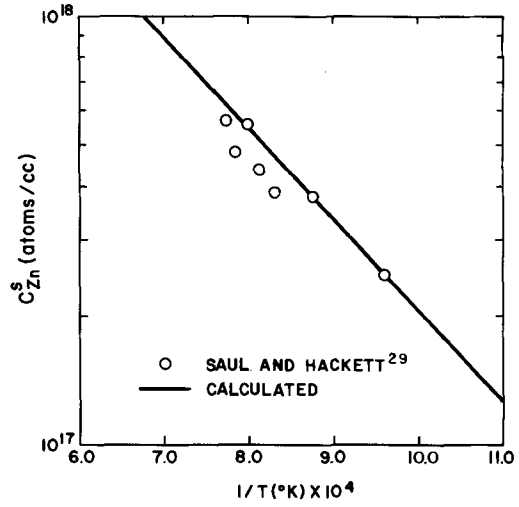

Fig. 8. Zn concentration vs. reciprocal growth temperature for a GaP layer grown by liquid-phase epitaxy from a solution containing $x^l_{Zn} = 3 \times 10^{-4}$. Only the Zn^{65} tracer data of Ref. (29) are shown.

the melting point.[4] It is seen that the calculated and experimentally derived C^s_{Zn} are in good accord.

Additional evidence to confirm the essential correctness of the low temperature isotherms is provided by the recent data of Saul and Hackett (29) on Zn incorporation in GaP, grown by liquid-phase epitaxy from an initial growth temperature of 1025°C and from a solution containing $x^l_{Zn} = 3 \times 10^{-4}$. It has been shown by these authors that the Zn solubility in GaP, obtained by surface capacitance measurements and Zn^{65} tracer analysis, decreases from the growth interface (1025°C) to the surface (≈770°C). Furthermore, Saul and Hackett (29) have demonstrated by means of a detailed analysis that their experimental Zn distribution data (C^s_{Zn} *vs.* distance from interface) compare favorably with the theoretical Zn profile calculated on the basis of the isotherms in Fig. 4. An alternative representation of the measurements of Saul and Hackett and of the calculated C^s_{Zn} can be accomplished in terms of a more commonly used thermodynamic variable by introducing equivalent growth temperatures instead of distances from the interface. Thus, it is shown in Fig. 8 that the theoretical C^s_{Zn} at $x^l_{Zn} = 3 \times 10^{-4}$, presented as a function of reciprocal temperature, provides a very good description of the tracer data of Saul and Hackett (29). The equivalent temperatures required in plotting the experimental results were obtained from Saul (30).

It should be noted that the ratio C^s_{Zn}/x^l_{Zn} divided by 4.94×10^{22} and 4.43×10^{22} atoms/cc for GaP and GaAs, respectively, yields the commonly defined distribution coefficient. In general, the distribution coefficient varies extensively along a solubility isotherm. Hence, any measurement of the variation of the distribution coefficient with temperature is meaningful only at a constant x^l_{Zn}. In particular, dividing C^s_{Zn} in Fig. 8 by the constant value $4.94 \times 10^{22} \times 3 \times 10^{-4}$ gives the temperature dependence of the distribution coefficient at $x^l_{Zn} = 3 \times 10^{-4}$, illustrating its decrease with decreasing temperature.

It can be readily seen by differentiating Eq. [8] that in the extrinsic region the sign of $d \log C^s_{Zn}/d\,1/T$, indicating whether C^s_{Zn} is increasing or decreasing with increasing T, depends on the size and sign of the temperature coefficients of the activities and K. If for different dilute solutes in GaP or GaAs the enthalpies corresponding to Eq. [2] are assumed to be roughly equal, then for a fixed dopant concentration in the melt the sign and magnitude of the derivative $d \log \gamma_{dopant}/d\ 1/T$ in the Ga-dopant binary liquid determines the sign of the temperature derivative of the distribution coefficient.

[4] At the exact melting point C^s_{Zn} approaches zero.

Having demonstrated that the temperature dependent equilibrium constants given in Eq. [17] and [18] describe the available information on the solubility of Zn in GaP and GaAs, one can estimate some other thermodynamic quantities relevant to the chemistry of Zn incorporation. Although the K's yield the enthalpy change for the over-all incorporation reaction according to Eq. [2], the energetics for the dissolution of Zn in GaP and GaAs following the defect mechanism represented by Eq. [1c] are not known. However, it is possible to estimate the enthalpy change for Eq. [1c], H_{1c}, by subtracting the enthalpy changes for Eq. [1a], [1b], and [1d], denoted by H_{1a}, H_{1b}, and H_{1d}, respectively, from that of Eq. [2], H_2. Thus, one has

$$H_{1c} = H_2 - H_{1a} - H_{1b} - H_{1d} \qquad [23]$$

Values of H_{1d} for GaP and GaAs were taken from Casey *et al.* (28) and Hill (31), respectively. In the absence of data for H_{1a} and H_{1b}, most of these enthalpies were estimated by comparison with similar quantities for Ge and Si. In order to estimate H_{1a}, the ratio of H_{1a} to the heat of atomization of GaAs and GaP into the monatomic gaseous components, H_s, was set at 0.56 and 0.52, respectively. The choice of these ratios is based on the recognition that H_{1a}/H_s are relatively constant for the covalent semiconductors Ge, Si, and CdTe (7). Hence, the ratios for GaAs and GaP were equated with those of Ge and the average of Ge and Si, respectively. Then, using the H_s data of Arthur (32) and Thurmond (33) for GaAs and GaP, respectively, the H_{1a}'s were obtained.

H_{1b} for GaAs was calculated by combining the heat, H_V(As), associated with annealing experiments of Potts and Pearson (34) according to $\frac{1}{4}\ As_4(g) + V_{As} = As_{As}$ with the heat of vaporization of As(l) (23). H_{1b} for GaP was evaluated by adding the heat of vaporization of P(l) (25) to H_V(P), estimated by the expression $H_V(P) = H_V(As)/H_V(Ge)\ [H_V(Si) + H_V(Ge)]/2$. H_V(Si) and H_V(Ge) were obtained from the known enthalpies of sublimation (35) and neutral vacancy formation (7) for these elemental semiconductors. The results of the above calculations are summarized in Table I.

The estimated enthalpies of Zn incorporation in GaP and GaAs represented by Eq. [1c] are −2.16 and −2.29 eV, respectively. The negative sign of these energies indicates that as the impurity is condensed on a Ga vacancy, as expected, heat is liberated.

An independent estimate of H_{1c} can also be derived by an adaptation of a method due to Weiser (36), previously applied to impurities in Ge and Si. Briefly, the atomistic interpretation of Eq. [1c] is based on the removal of Zn from a liquid reservoir via evaporation and its condensation on a gallium vacancy. Hence, H_{1c} is given by

$$H_{1c} = \Delta H_{vap} - E_b + E_s \qquad [24]$$

where ΔH_{vap} is the known heat of vaporization of Zn(l) (35) and E_b and E_s are the bond and strain energy contributions to the energy released by the dopant atoms upon condensation into the vacancies.

It is possible to estimate the E_b's by Allen's method (37) from the heats of vaporization of P(s), As(s), and Zn(s). The explicit expressions of E_s for Si and

Table I. Estimated enthalpies for Zn incorporation in GaP and GaAS

	GaP	GaAs
From Eq. [23]		
H_{1a} (eV)	3.84	3.77
H_{1b} (eV)	−2.13	−1.88
H_{1d} (eV)	0.06	0.03
H_2 (eV)	−0.39	−0.37
H_{1c} (eV)	−2.16	−2.29
From Eq. [24]		
ΔH_{vap} (eV)	1.20	1.20
E_b (eV)	3.91	3.72
E_s (eV)	0.38	0.13
H_{1c} (eV)	−2.33	−2.39

Ge, given by Weiser (36), are of the form $E_s = k_i(\Delta r)^2$ where k_i is a constant specific to the host (Ge or Si) and Δr is the difference in tetrahedral radius between host and impurity. Using k_{Ge} and $k_{Ge} + k_{Si}/2$ for GaAs and GaP, respectively, and taking Δr for As and Zn and also P and Zn from Pauling (38), one can find approximate values of E_s for both Zn-doped compounds. Some details of these calculations are shown in Table I. The resulting H_{1c}'s for GaP and GaAs are -2.33 and -2.39 eV, respectively, in surprisingly good agreement with the previous estimates of -2.16 and -2.29, respectively, which were partially based on the equilibrium constants.

Acknowledgments

The author expresses his gratitude to H. C. Casey and F. A. Trumbore for many fruitful discussions. Thanks are also due to H. W. Verleur and R. H. Saul for the permission to use some of their unpublished results.

Manuscript submitted July 31, 1970; revised manuscript received Jan. 11, 1971. This was Paper 145 presented at the Los Angeles Meeting of the Society, May 10-15, 1970.

Any discussion of this paper will appear in a Discussion Section to be published in the December 1971 JOURNAL.

REFERENCES

1. T. N. Morgan, B. Welber, and R. N. Bhargava, *Phys. Rev.*, **166**, 751 (1968); C. H. Henry, P. J. Dean, and J. D. Cuthbert, *ibid.*, **166**, 754 (1968).
2. A. S. Jordan, Submitted for publication to Metallurgical Transactions.
3. F. A. Trumbore, H. G. White, M. Kowalchik, R. A. Logan, and C. L. Luke, *This Journal*, **112**, 782 (1965).
4. M. B. Panish and H. C. Casey, *J. Phys. Chem. Solids*, **29**, 1719 (1968).
5. M. B. Panish and H. C. Casey, *ibid.*, **28**, 1673 (1967).
6. H. C. Casey, M. B. Panish, and L. L. Chang, *Phys. Rev.*, **162**, 660 (1967).
7. F. A. Kröger, "Chemistry of Imperfect Crystals," Interscience Publishers, New York (1964).
8. I. Prigogine and R. Defay, "Chemical Thermodynamics," Longmans Green and Co., London (1954).
9. F. Ermanis and H. C. Casey, Private communication.
10. H. C. Casey and M. W. Focht, Private communication.
11. L. M. Foster and J. Scardefield, *This Journal*, **116**, 495 (1969).
12. K. K. Shih, J. W. Allen, and G. L. Pearson, *J. Phys. Chem. Solids*, **29**, 379 (1968).
13. L. L. Chang and G. L. Pearson, *ibid.*, **25**, 23 (1964).
14. H. C. Casey and M. B. Panish, *Trans. Met. Soc., AIME*, **242**, 406 (1968).
15. Y. Furukawa and C. D. Thurmond, *J. Phys. Chem. Solids*, **26**, 1535 (1965).
16. M. B. Panish, *ibid.*, **27**, 291 (1966).
17. K. K. Shih, J. W. Allen, and G. L. Pearson, *J. Phys. Chem. Solids*, **29**, 367 (1968).
18. M. B. Panish, *This Journal*, **113**, 224 (1966).
19. M. B. Panish, *ibid.*, **113**, 861 (1966).
20. A. S. Jordan, *This Journal*, To be published.
21. V. J. Lyons, *J. Phys. Chem.*, **63**, 1142 (1959).
22. O. Kubaschewski, E. LL. Evans, and C. B. Alcock, "Metallurgical Thermochemistry," 4th Edition, Pergamon Press, Ltd. (1967).
23. A. N. Nesmeyanov, "Vapor Pressure of the Chemical Elements," Elsevier Publishing Co., Amsterdam (1963).
24. R. C. Schoonmaker, A. R. Venkitaranan, and P. K. Lee, *J. Phys. Chem.*, **71**, 2676 (1967).
25. JANAF, Interim Thermochemical Tables, Dow Chemical Co.
26. H. W. Verleur, Private communication.
27. A. S. Jordan and L. Derick, Unpublished result.
28. H. C. Casey, F. Ermanis, and K. B. Wolfstirn, *J. Appl. Phys.*, **40**, 2945 (1969).
29. R. H. Saul and W. H. Hackett, *This Journal*, **117**, 921 (1970).
30. R. H. Saul, Private communication.
31. D. E. Hill, *J. Appl. Phys.*, **41**, 1815 (1970).
32. J. R. Arthur, *J. Phys. Chem. Solids*, **28**, 2257 (1967).
33. C. D. Thurmond, *ibid.*, **26**, 785 (1965).
34. H. R. Potts and G. L. Pearson, *J. Appl. Phys.*, **37**, 2098 (1966).
35. R. Hultgren, R. L. Orr, P. D. Anderson, and K. K. Kelley, "Selected Values of Thermodynamic Properties of Metals and Alloys," John Wiley and Sons, Inc., New York (1963).
36. K. Weiser, *J. Phys. Chem. Solids*, **7**, 118 (1958).
37. T. L. Allen, *J. Chem. Phys.*, **27**, 810 (1957).
38. L. Pauling, "The Nature of the Chemical Bond," 3rd Edition, Cornell University Press, Ithaca, N. Y. (1960).

A Gravimetric Study of Nonstoichiometric MnO

I. Bransky[1]

Ohio State University Research Foundation, Columbus, Ohio 43210

and N. M. Tallan

Aerospace Research Laboratories, Wright-Patterson Air Force Base, Ohio 45433

ABSTRACT

Thermogravimetric measurements of the compositional phase diagram of MnO_{1+x} were made as a function of temperature from 1000° to 1500°C and as a function of oxygen partial pressure over most of the stable phase field. The values of x in MnO_{1+x} are presented as a function of temperature and oxygen pressure both numerically and graphically. The pressure dependence of the vacancy concentration at constant temperature was found to obey a relation of the form $x = \text{const}\ P(O_2)^{1/4}$ for $x < 0.02$. The enthalpy of solution of oxygen in this composition range is about -0.3 eV. At larger departures from stoichiometry, a sharp transition to a different defect structure is observed in the log x *vs.* log $P(O_2)$ plots, and the enthalpy of oxygen dissolution for $x > 0.02$ is $\Delta H = -0.70$ eV. Comparison of the experimental data with oxygen activities in the oxide calculated for several different defect models suggests that, for $x < 0.02$, any pairwise interaction between vacancies is less than 0.025 eV and the vacancies can be considered to be noninteracting. The behavior observed for $x > 0.02$ is believed to be due to a transition to a more complex defect at high defect concentrations and not to a change in degree of ionization of the metal vacancy. The influence of carbon dissolution, from the CO_2-CO mixtures used, on these measurements is discussed.

The iron group monoxides, MnO, FeO, CoO and NiO, exist as stable solid solutions over various ranges of metal deficiency. Small deviations from stoichiometry, at oxygen partial pressures $P(O_2) \leq 1$ atm, are found in NiO_{1+x}, where $x \leq 0.001$ (1-3), and in CoO_{1+x}, where $x \leq 0.013$ (4-6). In FeO_{1+x}, on the other hand, the departure from stoichiometry is within the range $0.045 \leq x \leq 0.19$ (7-10), and the stable phase field does not include the stoichiometric composition. In NiO_{1+x} and CoO_{1+x} the excess oxygen has been found to be incorporated primarily by the formation of either singly or doubly ionized, isolated metal vacancies (1-3, 11,12). In FeO_{1+x}, on the other hand, a more complex defect structure involving both metal interstitials and metal vacancies has been proposed on the basis of neutron diffraction studies (13) and thermodynamic considerations (14). This complex defect structure in FeO_{1+x} is plausible, in view of the large departures from stoichiometry that give rise to very large concentrations of point defects.

Unlike the foregoing iron group monoxides, MnO_{1+x} can exist over a wide range of compositions extending continuously from values of x very near zero to an oxygen excess as high as about $x \simeq 0.15$ (5, 15-19). This oxide is, therefore, an interesting material in which one might look for a transition from simple defect structure models, based on infinitely dilute concentrations of point defects, to the more complex defect structure models that can be anticipated at higher defect concentrations.

Pope and Simkovich (20) have recently reported that a considerable amount of carbon can be dissolved in MnO_{1+x} from CO_2-CO mixtures in contact with the oxide at elevated temperatures. Since CO_2-CO mixtures were used in the present study to establish the desired partial pressures of oxygen, the amount of carbon dissolution present is also considered.

Experimental Phase

In the present work, the oxygen excess in MnO_{1+x} was determined thermogravimetrically in the temperature range 1000°-1500°C at oxygen partial pressures $10^{-14} \leq P(O_2) \leq 1$ atm, using a Cahn RG electrobalance. The oxygen partial pressures used were produced by introducing constant flows of CO_2-CO or O_2-Ar mixtures into the furnace. The oxygen partial pressure, $P(O_2)$, established by the reaction

$$CO_2 \leftrightharpoons CO + \tfrac{1}{2}O_2 \qquad [1]$$

was generally calculated from the relation

$$P(O_2)^{1/2} = K_{CO_2}\,[P(CO_2)/P(CO)] \qquad [2]$$

where K_{CO_2} is the dissociation constant for Reaction [1] and is given by Wicks and Block (21), and $P(CO_2)/P(CO)$ is given by the ratio of the CO_2 and CO flows introduced into the furnace at atmospheric pressure and room temperature. In the case of very large CO_2/CO ratios, a correction must be made for the influence of the dissociation of the CO_2 on the CO_2/CO ratio actually present in the hot zone of the furnace. In this case, the oxygen partial pressure is calculated from the relations

$$P(O_2)^{1/2} = K_{CO_2}\frac{P(CO_2)}{P(CO)}\,\frac{1-\alpha}{1+\dfrac{P(CO_2)}{P(CO)}\,\alpha} \qquad [2a]$$

and

$$P(O_2) = \frac{\dfrac{\alpha}{2}\,\dfrac{P(CO_2)}{P(CO)}\,P}{1+\dfrac{P(CO_2)}{P(CO)}\left(1+\dfrac{\alpha}{2}\right)} \qquad [2b]$$

where α is the fraction of CO_2 dissociated and P is the total pressure in the furnace.

A polycrystalline sintered MnO sample, prepared from spectroscopically pure Johnson Matthey[2] Mn_2O_3 powder, was used for the majority of the measurements. Measurements were also made on a single-crystal disk, 1 cm in diameter and 2 mm thick. The agreement between the data obtained on the polycrystalline and single-crystal specimens was within experimental error. The mass spectrographic analyses of the single crystal and a representative polycrystalline specimen are shown in Table I.

[1] Visiting scientist at Aerospace Research Laboratories, Bldg. 450 (ARZ), Wright-Patterson Air Force Base, Ohio 45433.

Key words: MnO, nonstoichiometry of MnO, thermogravimetric determination of oxygen, phase diagram of MnO_{1+x}, defect structure model.

[2] Johnson Matthey Chemicals Ltd., 74 Hatton Garden, London E.C.1, England.

Table I. Mass spectrographic analyses of MnO (ppmw)

	Li	Na	Mg	Al	Si	Ca	Ti
Single crystal	2	20	20	50	200	200	15
Polycrystal			<10	20	50	10	
	Cr	Fe	Co	Ni	Cu	Mo	La
Single crystal	100	500	200	100	2	3	1000
Polycrystal		10		10	30	50	

The sample was suspended from the balance into an alumina tube furnace by means of a sapphire fiber. All weight change measurements were made at a total pressure of 200 Torr in order to minimize thermal fluctuations of the balance beam. The gas was admitted into the bottom of the furnace at a flow rate which corresponded to a linear velocity of 10 cm/sec in the vertical tube. After the sample was equilibrated in the flowing atmosphere, the flow was terminated and the weight, w, was recorded in the static atmosphere. The departure from stoichiometry, x, was calculated from the relative weight change, $w - w_0$ (the w_0 value being the indicated balance weight of the "stoichiometric" specimen, measured at 800°C in a gas mixture of the ratio $CO_2/CO = 1$), by the relation

$$x = \frac{M_{MnO}}{M_O} \frac{w - w_0}{w_s} \qquad [3]$$

where w_s is the true weight of the "stoichiometric" sample, and M_{MnO} and M_O are the molecular weight of MnO and the atomic weight of oxygen, respectively.

The balance sensitivity, at the temperatures and gas flow rates used, was about 4 μg and the reproducibility of the weight change measurements was within ± 10 μg. Evaporation was observed at high temperatures, $T > 1200$°C, especially at low oxygen pressures. The measured weight changes were corrected for the effect of evaporation by assuming the evaporation rate to be constant at constant temperature and CO_2/CO ratio. The evaporation rates at 1500°C, under the conditions of these experiments, were about 3 μg/min. The influences of buoyancy and thermomolecular flow effects were evaluated by measurements on an inert sapphire disk having the same geometry as the MnO samples used. Under the experimental conditions of this study, the required corrections for these effects were found to be less than 15 μg.

The extent of carbon dissolution in MnO as a result of high temperature exposure to CO_2-CO mixtures was evaluated on a number of polycrystalline disks. The disks, weighing approximately 7g each, were pressed from Mn_3O_4 starting powder and were sintered in air at 1200°C for 8 hr. They were then heated in CO_2-CO mixtures (where they were rapidly converted to MnO) for 8 hr, and then were quenched in the same CO_2/CO atmosphere. Low CO_2/CO ratios were used, lower in fact than those employed in the gravimetric studies, in order to have a high carbon activity. The carbon contents were then determined by combustion to CO_2 and gas chromatographic analysis. Two sintered Mn_3O_4 disks, unexposed to CO_2/CO mixtures, were analyzed as controls on the starting powder. The results for all these measurements are shown in Table II. The carbon contents of the sintered Mn_3O_4 specimens preclude any conclusions about the actual amount of carbon introduced into the MnO specimens by the CO_2-CO atmospheres or its dependence on the CO_2/CO ratio. This amount could not, however, exceed about 50 ppmw. Although any carbon introduced might influence the electrical properties near stoichiometry or in the n-type region, as suggested by Pope and Simkovich (20), it should not influence the gravimetric measurements in the composition range reported here, where

Table II. Carbon analyses of MnO and Mn_3O_4

Specimen	Heat treatment		Carbon (ppmw)
	Temp (°C)	CO_2/CO ratio	
MnO 1	1000	4.5×10^{-3}	25
MnO 2	1000	4.2×10^{-2}	31
MnO 3	1000	0.16	19
MnO 4	1200	4.5×10^{-3}	25
MnO 5	1200	4.2×10^{-2}	59
MnO 6	1200	0.16	55
Mn_3O_4-1	Starting powder	—	47
Mn_3O_4-2	Starting powder	—	102

Table III. Measured departure from stoichiometry, x in MnO_{1+x}

$x \cdot 10^2$	$\log[P(CO_2)/P(CO)]$	$-\log P(O_2)$
	1000°C	
0.037	1.000	11.85
0.038	1.171	11.51
0.050	1.379	11.09
0.059	1.630	10.59
0.076	1.790	10.27
0.100	2.000	9.85
	1100°C	
0.0535	0.464	11.27
0.0665	0.659	10.88
0.0660	0.667	10.86
0.0785	0.778	10.64
0.0982	1.040	10.12
0.105	1.081	10.04
0.111	1.134	9.93
0.139	1.294	9.61
0.179	1.547	9.11
0.225	1.804	8.59
0.254	1.977	8.25
0.283	2.047	8.11
0.348	2.230	7.74
	1200°C	
0.101	0.477	9.80
0.102	0.532	9.69
0.131	0.699	9.35
0.169	0.898	8.95
0.216	1.104	8.54
0.274	1.279	8.19
0.346	1.492	7.77
0.348	1.496	7.76
0.351	1.543	7.67
0.416	1.699	7.35
0.433	1.708	7.33
0.570	2.000	6.75
0.564	2.013	6.72
0.549	2.015	6.72
	1300°C	
0.175	0.447	8.61
0.185	0.462	8.58
0.217	0.602	8.30
0.266	0.763	7.97
0.322	0.914	7.67
0.373	1.083	7.33
0.458	1.25	7.00
0.608	1.507	6.49
0.727	1.681	6.14
0.818	1.785	5.93
0.865	1.892	5.72
1.080	2.041*	5.510
2.290	2.425**	4.65
5.150	2.861**	3.78
	1400°C	
0.317	0.505	7.39
0.467	0.845	6.71
0.545	0.959	6.48
0.672	1.173	6.05
0.777	1.316	5.77
0.947	1.486	5.43
1.26	1.663	5.07
1.66	1.909	4.58
1.91	1.967	4.47
1.90	1.996*	4.50
2.59	2.200*	4.10
2.87	2.210**	3.98
3.45	2.342**	3.72
6.25	2.755**	2.89
7.30	2.844	2.71
	1500°C	
0.763	0.804	5.84
0.930	1.005	5.44
1.16	1.201	5.05
1.38	1.382	4.69
1.68	1.543	4.36
1.88	1.681*	4.14
2.99	1.835**	3.78
2.65	1.996*	3.55
5.01	2.264**	2.92
5.88	2.315**	2.82
6.30	2.419**	2.61
6.59	2.448**	2.55
7.81	2.575**	2.30
10.17	2.771**	1.91
11.60	2.869**	1.71

* CO_2/CO ratio calculated from Eq. [2] using $P(O_2)$ calculated from Eq. [2(a)] and [2(b)].

** O_2-Ar mixture. Equivalent CO_2/CO ratio is calculated from Eq. [2].

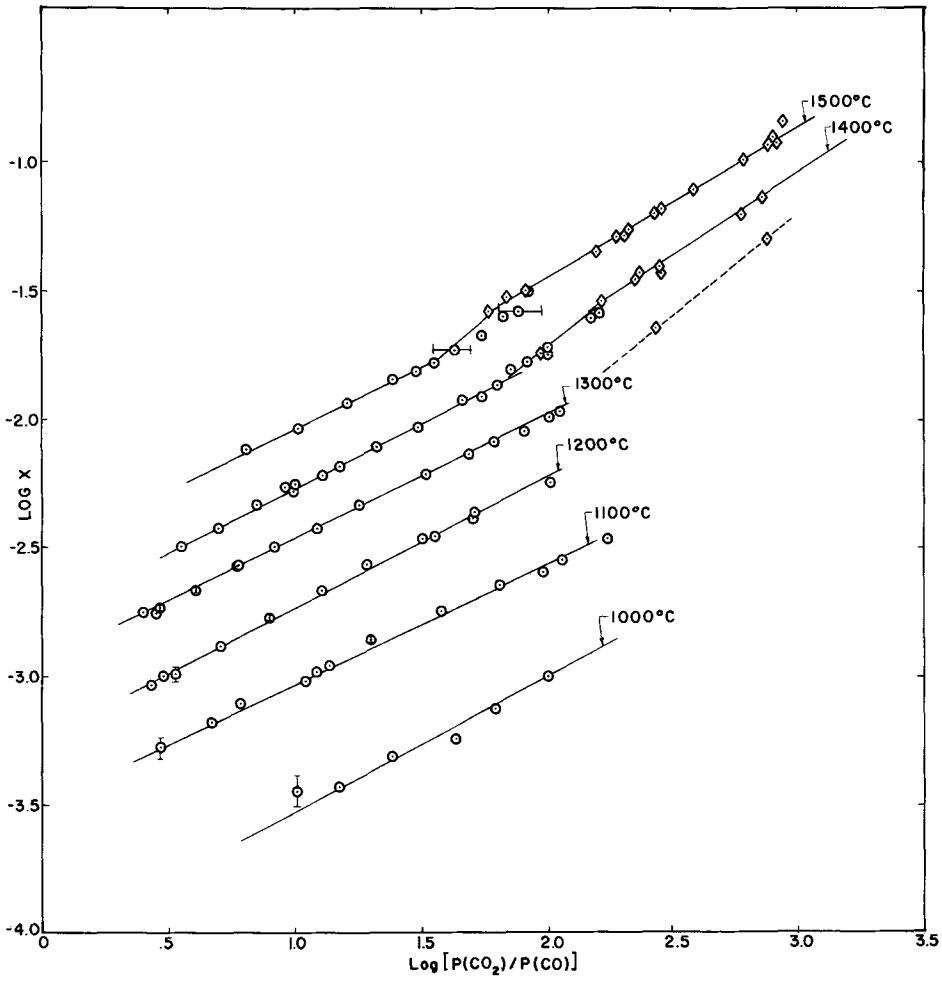

Fig. 1. Departure from stoichiometry, x in MnO_{1+x}, as a function of the CO_2/CO ratio. Extreme error bars are shown for log $\frac{P(CO_2)}{P(CO)}$ and for log x: ⊙, CO_2-CO mixtures (CO_2/CO ratios calculated from Eq. [2] using $P(O_2)$ calculated from Eq. [2a] and [2b]; ◆, O_2-Ar mixtures (equivalent CO_2/CO ratios calculated from Eq. [2]).

the departures from stoichiometry are generally very much larger than several hundred ppm.

Results

The measured departure from stoichiometry, x in MnO_{1+x}, is given in Fig. 1 as a function of the CO_2/CO ratio. The measured values are given in Table III. The total probable error in x is estimated, from the variances of the quantities appearing in Eq. [3], to be ± 0.0002. In the temperature range measured, the vacancy concentration at temperature was found by least square analysis to obey the relation

$$x = \text{const} \left[\frac{P(CO_2)}{P(CO)} \right]^{1/2.1 \pm 0.1}_{T=\text{const}} \qquad [4]$$

at small departures from stoichiometry, $x \lesssim 0.02$. At high temperatures and large departures from stoichiometry, a sharp transition to a stronger pressure dependence is observed. This transition occurs at the end of the range of experimentally accessible CO_2-CO mixtures. Its independence of the method by which the oxygen partial pressure was established, however, is demonstrated by the overlap of the data measured in CO_2-CO and O_2-Ar mixtures. The breaks observed in the log x *vs.* log $P(CO_2)/P(CO)$ plots of Fig. 1 at $x \simeq 0.02$ were observed in several polycrystalline samples as well as in the single crystal. The temperature dependences of the electrical conductance and departure from stoichiometry in constant CO_2/CO and O_2/Ar mixture ratios are given in Fig. 2. The slopes of these plots for $CO_2/CO = 22.8$ and 99, mixtures for which $x < 0.02$, are 1.30 ± 0.15 eV. The slope of the log x *vs.* $10^3/T(°K)$ plot at $P(O_2) = 10^{-3.73}$ atm (obtained in an O_2-Ar rather than a CO_2-CO mixture), for which $0.03 \lesssim x \lesssim 0.05$ over the measured temperature range, corresponds to a value of -0.70 eV.

Discussion

The departure from stoichiometry in MnO_{1+x} on the oxygen excess side may be attributed either to metal vacancies or to oxygen interstitials. Diffusion (18, 19), oxidation (22), and combined electrical conductivity and thermogravimetric studies (5, 16) support a manganese vacancy model. It is clear from Fig. 1 and Eq. [2] that at low defect concentrations, *i.e.* for $x \lesssim 0.02$,

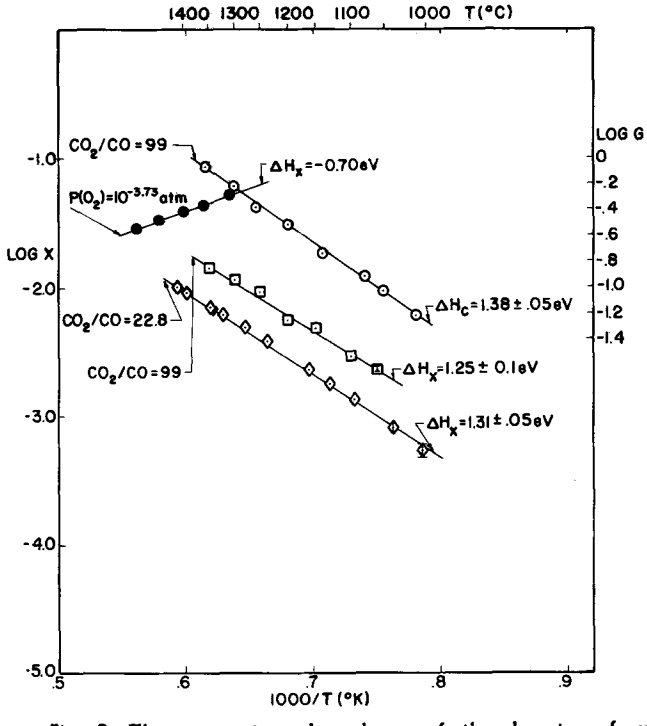

Fig. 2. The temperature dependence of the departure from stoichiometry, x, and the electrical conductance, G, in constant CO_2/CO and O_2/Ar ratios.

$$x = C(T)[P(CO_2)/P(CO)]^{1/2} = C'(T)P(O_2)^{1/4} \quad [5]$$

This is consistent with the pressure dependence expected of singly ionized metal vacancies produced by the reaction

$$\tfrac{1}{2}O_2 \rightleftharpoons O^x_O + V'_M + h^+ \quad [6]$$

where, in the usual Kroger and Vink (23) notation, the superscripts denote charge state, the subscripts denote position in the lattice, and h^+ represents an electron hole. The $P(O_2)^{1/4}$ dependence of the hole concentration is obtained by applying the mass action law to Reaction [6], approximating defect activities by defect concentrations, and assuming the charge neutrality condition

$$[V'_M] = p \quad [7]$$

For large departures from stoichiometry, the approximation of defect activities by concentrations is not satisfactory and the actual activities should be calculated.

The oxygen activity in MnO_{1+x} may be calculated by essentially the same procedure as that used by Libowitz (14) for FeO_{1+x}. Assuming that the predominant defects present are singly ionized metal vacancies and electron holes, obeying the charge neutrality condition of Eq. [7], and assuming a simple Bragg-Williams interaction between metal vacancies (*i.e.*, a pairwise interaction between nearest neighbors), then the free energy of the MnO_{1+x} crystal can be written in the form

$$G = N\mu_{MnO} + N_V g_V + N_V I_h + \frac{z}{2}\frac{N^2_V}{N}\epsilon - kT \ln \frac{N!}{(N_V!)^2 (N - 2N_V)!} \quad [8]$$

where N is the total number of Mn sites in the lattice, N_V is the number of Mn vacancies, μ_{MnO} is the free energy of an MnO formula unit in the ideal lattice, g_V is the free energy of neutral metal vacancy formation, I_h is the ionization energy of the Mn vacancy (for the removal of one positive hole), z is the coordination of the Mn site, and ϵ is the energy of interaction of the Mn vacancies. The oxygen activity in the oxide, a_O, can be calculated from Eq. [8] and the relations

$$\mu_O = \frac{\partial G}{\partial N_O} = kT \ln a_O \quad [9]$$

and

$$N = N_O = N_V + N_{Mn} \quad [10]$$

where μ_O is the chemical potential of oxygen in the MnO_{1+x} crystal and N_O and N_{Mn} are the number of oxygen and manganese atoms in the crystal, respectively. In our experiments, where a given specimen is oxidized or reduced, N_{Mn} is constant and therefore $\partial N_V/\partial N_O = \partial N/\partial N_V = 1$. The oxygen activity is obtained from Eq. [8-10]. Using Stirling's approximation and noting that the value of x in MnO_{1+x} is given by

$$x = \frac{N_O}{N_{Mn}} - 1 \quad [11]$$

the oxygen activity in MnO_{1+x} can be written as

$$kT \ln \left[a_O \left(\frac{1 - x^2}{x^2} \right) \right] = \mu_{MnO} + g_V + I_h + \frac{z}{2}\epsilon \left[\frac{2x}{1+x} - \left(\frac{x}{1+x} \right)^2 \right] \quad [12]$$

For small departures from stoichiometry, Eq. [12] can be approximated by

$$x^2 = K_{V'_M} a_O \quad [13]$$

where

$$K_{V'_M} = \exp\left[-(\mu_{MnO} + g_V + I_h + z\epsilon x)/kT \right] \quad [14]$$

Since $a_O \propto P(O_2)^{1/2}$, Eq. [13] yields the same result as Eq. [5] when $\epsilon = 0$. Equation [13] is a good approximation up to relatively large values of x, since the difference between the exact form of the oxygen activity in the crystal, given by Eq. [12], and the approximate form in Eq. [13] is less than 1% for $x < 0.1$. From Eq. [12] and a plot of $\ln [a_O(1 - x^2/x^2)]$ as a function of x, shown in Fig. 3 for data obtained at 1300° and values of $x \leq 0.01$, an upper limit for the interaction energy can be set at about $|\epsilon| \leq 0.025$ eV. This region, $x \leq 0.01$, can therefore be assumed to be a region of noninteracting defects.

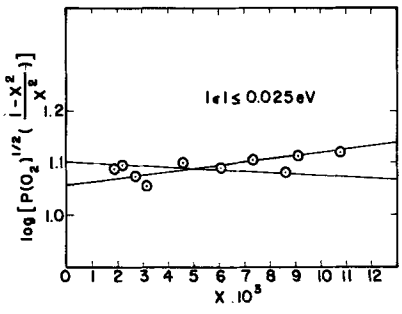

Fig. 3. Evaluation of the interaction energy $|\epsilon|$, from a plot of $\ln [P(O_2)^{1/2}((1-x^2)/x^2)]$ vs. x at 1300°C.

The oxygen activity in MnO_{1+x} was calculated from Eq. [12] at several fixed temperatures, using a value for the combined energies obtained by fitting to one experimental datum point. The resultant curves, labeled "simple," and the measured data are shown for two temperatures, 1300° and 1500°C, in Fig. 4 and 5, respectively. The oxygen activity was also calculated using an expression based on a defect complex model, involving association of two metal vacancies and a metal interstitial, derived by Libowitz (14) to fit thermodynamic data for FeO_{1+x}. The resultant curves, labeled "complex," are also shown in Fig. 4 and 5. The isolated defect and defect complex models give essentially the same results for $x < 0.02$. In this range of small departures from stoichiometry, the isolated, noninteracting, singly ionized metal vacancy model is believed to be more reasonable for MnO_{1+x} than the defect complex model, however, since no change in behavior with increasing temperature is observed even to 1500°C. If defect complexes were present, one would expect to see the effects of dissociation at high temperatures.

The enthalpy of dissolution of oxygen in the oxide, $\Delta H_{V'_M}$, in the region $x < 0.02$, can be found using Eq. [2, 13, 14] from the relation

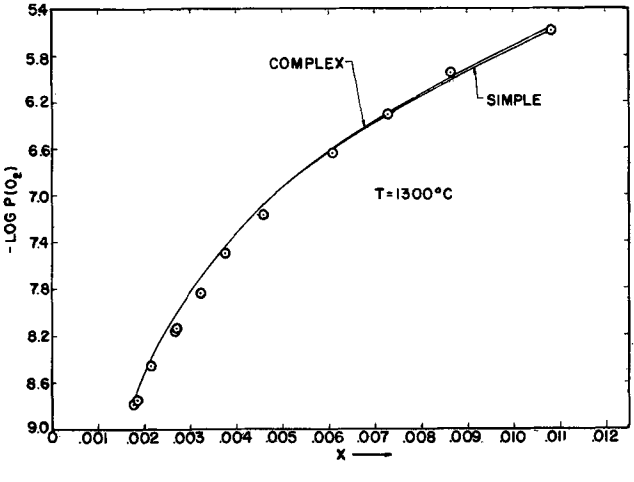

Fig. 4. Comparison of calculated oxygen activity for simple and complex defect structures with experimental data at 1300°C.

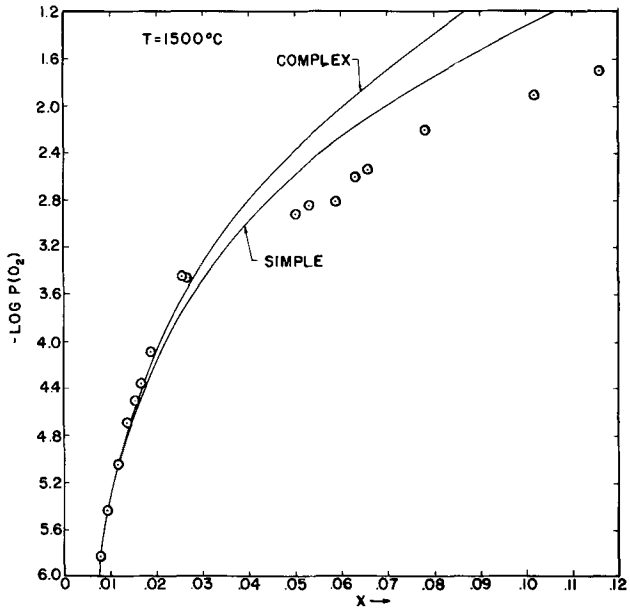

Fig. 5. Comparison of calculated oxygen activity for simple and complex defect structures with experimental data at 1500°C.

$$\Delta H_{V'_M} = -\frac{d \ln K_{V'_M}}{d(kT)^{-1}}\Bigg]_{P(O_2)=\text{const}}$$

$$= \frac{d \ln K_{CO_2}}{d(kT)^{-1}} - 2\frac{d \ln x}{d(kT)^{-1}}\Bigg]_{P(CO_2)/P(CO)=\text{const}} \quad [15]$$

The first term on the right, $[d \ln K_{CO_2}]/[d(kT)^{-1}]$, varies very little in the temperature range measured and is given by Wicks and Block (21) as −2.91 eV. The second term, $[d \ln x]/[d(kT)^{-1}]$, is found from Fig. 2 to be -1.3 ± 0.1 eV, and is found to be independent of the $P(CO_2)/P(CO)$ ratio in this range. Therefore, $\Delta H_{V'_M} \simeq -0.3$ eV. The enthalpy of dissolution of oxygen in MnO_{1+x} decreases sharply at larger departures from stoichiometry. At a given partial pressure established by an O_2-Ar mixture, $\Delta H_{V'_M}$ is given directly by $d \ln x/d(kT)^{-1}$. It may be noted in Fig. 2 that at $P(O_2) = 10^{-3.73}$ atm, $\Delta H_{V'_M} = -0.70$ eV.

The $P(O_2)^{1/3.3}$ dependence of x, found for $x > 0.02$ in Fig. 1, could be interpreted in terms of the singly ionized, noninteracting metal vacancies present at low defect concentrations associating, at higher defect concentrations, to form divacancy complexes. The formation of such complexes would be described by the reaction

$$O_2 \rightleftharpoons 2\,O^x_O + (V_M V_M)'' + 2h^+ \quad [16]$$

where $(V_M V_M)''$ denotes the complex. If the charge neutrality condition is given by $2[(V_M V_M)''] = p$, then the oxygen pressure dependences of the defect concentrations and of x are given by

$$2[(V_M V_M)''] = p = 2x = K_c P(O_2)^{1/3} \quad [17]$$

where $K_c \propto \exp(-\Delta G_c/kT)$ and ΔG_c is the free energy change for Reaction [16]. To a first approximation

$$\Delta G_c \simeq 2(\mu_{MnO} + g_V + I_h) - g_{int} \quad [18]$$

where g_{int} is the free energy of interaction of the complex $(V_M V_M)''$ and, therefore, the enthalpy of interaction of the complex, h_{int}, would be given by $h_{int} \simeq (\Delta H_c)_{x>0.02} - 2(\Delta H_{V'_M})_{x<0.02} = -0.1$ eV.

Our recent data, and that of earlier investigators (12), for CoO_{1+x} show similar behavior. The oxygen pressure dependence of the electrical conductivity of CoO_{1+x} increases from $P(O_2)^{1/4}$ at low pressures, corresponding to $x < 0.008$, to $P(O_2)^{1/3.6}$ at $P(O_2) = 1$ atm. Since the transition in oxygen pressure dependence in CoO_{1+x} occurs at about $P(O_2) = 10^{-1}$ atm, it would be experimentally very difficult to see as much of the higher defect concentration range as is visible in MnO_{1+x}. If complexes are indeed responsible for the behavior at high defect concentrations in MnO_{1+x} and CoO_{1+x}, they are more likely to be of the two-vacancy type than the two-vacancy–cation interstitial type suggested for FeO_{1+x} (13, 14). Formation of the latter type by the reaction

$$\tfrac{1}{2}O_2 + Fe^x_{Fe} \rightleftharpoons O^x_O + (V_M Fe_i V_M)' + h^+ \quad [19]$$

would lead to a pressure dependence of the hole concentration of the form $p \propto P(O_2)^{1/4}$. A higher degree of ionization of the complex or a correction based on the use of activities at high defect concentrations (14) would only decrease the oxygen pressure dependence. To observe a stronger pressure dependence, as in MnO_{1+x} and CoO_{1+x}, one would need higher order complexes if cation interstitials are involved.

It should be noted that a transition to a stronger pressure dependence, as seen in Fig. 1 for $x > 0.02$, can also be caused by a change in the ionization state of the metal vacancy. In this case, it could be due to the increasing concentration of neutral metal vacancies. In the extreme case, when the neutral metal vacancy is the predominant defect present, the oxygen activity is given by

$$\frac{x}{1+x} = K_o a_O \quad [20]$$

where $K_o = \exp[-(\mu_{MnO} + g_V)/kT]$ and, for small deviations from stoichiometry, a $P(O_2)^{1/2}$ dependence would be expected. A transition from the pressure dependence characteristic of singly ionized metal vacancies to that characteristic of neutral metal vacancies would, however, extends smoothly over a number of orders of magnitude of oxygen pressure. For example, if we define the limits of the transition region as the $P(O_2)^{1/3.85}$ and $P(O_2)^{1/2.15}$ dependences, then the transition region would extend over about seven orders of magnitude of oxygen pressure. The change in pressure dependence of x at about $x \simeq 0.02$ in Fig. 1, therefore, has more of the character of a phase transition. Similar breaks in behavior, interpreted as phase transformations, have been observed in FeO_{1+x} (8). The origin of the transition in MnO_{1+x} cannot be asserted without further x-ray and neutron diffraction study.

Manuscript submitted April 20, 1970; revised manuscript received ca. Jan. 4, 1971.

Any discussion of this paper will appear in a Discussion Section to be published in the December 1971 JOURNAL.

REFERENCES

1. S. P. Mitoff, *J. Phys. Chem.*, **65**, 882 (1961).
2. Y. D. Tretyakov and R. A. Rapp, *Trans. AIME*, **245**, 1235 (1969).
3. W. C. Tripp and N. M. Tallan, *Am. Ceram. Soc. Bull.*, **49** (1970).
4. B. Fisher and D. S. Tannhauser, *This Journal*, **111**, 1195 (1964).
5. N. G. Eror, Ph.D. Thesis, Northwestern University (1965).
6. I. Bransky and J. M. Wimmer, To be published.
7. L. S. Darken and R. W. Gurry, *J. Am. Chem. Soc.*, **67**, 1398 (1945).
8. P. Vallet and P. Raccah, *Mem. Sci. Rev. Met.*, **62**, 1 (1965).
9. H. Rizzo, R. S. Gordon, and I. B. Cutler, in "Mass Transport in Oxides," J. B. Wachtman and A. D. Franklin, Editors, pp. 129-143, National Bureau of Standards Special Publication 296 (1968).
10. I. Bransky and A. Z. Hed, *J. Am. Ceram. Soc.*, **51**, 231 (1968).
11. I. Bransky and N. M. Tallan, *J. Chem. Phys.*, **49**, 1243 (1968).
12. B. Fisher and D. S. Tannhauser, *ibid.*, **44**, 1663 (1966).
13. W. L. Roth, *Acta Cryst.*, **13**, 140 (1960).
14. G. G. Libowitz, in "Mass Transport in Oxides," J. B. Wachtman and A. D. Franklin, Editors, pp. 109-119, National Bureau of Standards Special Publication 296 (1968).

15. A. Z. Hed and D. S. Tannhauser, *This Journal*, **114**, 314 (1967).
16. A. Z. Hed and D. S. Tannhauser, *J. Chem. Phys.*, **47**, 2090 (1967).
17. F. A. Kroger, *J. Phys. Chem. Solids*, **29**, 1889 (1968).
18. J. B. Price and J. B. Wagner, Jr., *This Journal*, **117**, 242 (1970).
19. P. Lacombe, J. P. Bocquet, and M. Kawahara, *Compt. Rend.*, **265**, 1318 (1967).
20. J. M. Pope and G. Simkovich, Paper No. 111, presented at the Detroit Meeting of the Society, Oct. 5-9, 1969.
21. C. E. Wicks and F. E. Block, "Thermodynamic Properties of 65 Elements, Their Oxides, Halides, Carbides, and Nitrides," U.S. Bureau of Mines, Bulletin 605, Washington, D. C. (1963).
22. K. Fueki and J. B. Wagner, Jr., *This Journal*, **112**, 384 (1965).
23. F. A. Kroger and H. J. Vink, in "Solid State Physics," F. Seitz and D. Turnbull, Editors, Vol. 3, pp. 307-435, Academic Press, New York (1956).

Reduced Dislocation Densities in Liquid Phase Epitaxy Layers by Intermittent Growth

R. H. Saul

Bell Telephone Laboratories, Incorporated, Murray Hill, New Jersey 07974

ABSTRACT

GaP liquid phase epitaxy (LPE) layers grown using an interrupted cooling rate to induce intermittent growth, exhibit an abrupt reduction in dislocation density ρ which coincides with the interface between growth increments. Constant cooling rates interrupted by partial melt-back (heating) of the LPE layer or by isothermal annealing are both effective in reducing ρ, typically by factors of 3-6. Successive reductions in ρ could be achieved by employing several interruptions in cooling rate. These results are discussed in terms of proposed mechanisms for dislocation elimination in crystals.

A variety of liquid regrowth techniques, including liquid phase epitaxy (LPE) (1), traveling solvent method (TSM) (2), and partial back-melting (PBM) (3), are frequently employed for the fabrication of multilayer semiconductor structures. Crystals grown by these methods generally contain fewer dislocations than the substrates upon which they are grown. This improvement in crystalline perfection has been observed by etch pit or x-ray topography techniques in GaP (4, 5), GaAs (6), and GaSb (7, 8). The reported reduction in dislocation density ρ is typically by factors in the range of 3-10, and in all cases the reduction is abrupt, occurring at the initial growth interface. Because of the likelihood of slight dissolution of the substrate for LPE and TSM growth, the mechanism of dislocation elimination in these cases is probably the same as for PBM growth where the substrate is deliberately partially melted. In this paper it is shown that, in addition to the above-mentioned decrease in ρ, the dislocation density can be further (abruptly) reduced within a LPE layer by interrupting the cooling rate to induce intermittent or incremental growth. Proposed mechanisms of dislocation elimination are discussed in terms of these results and the feasibility of several step reductions in ρ is demonstrated.

Experimental Phase

The GaP LPE layers employed in this work were grown (9) from Ga-GaP solutions containing 0.01 a/o Te which provided an initial[1] doping level essentially equal to that of the Te-doped Czochralski substrates ($N_D - N_A \simeq 3 \times 10^{17}$ cm^{-3}). The layers were 25-150μ thick and were grown on a chemically polished P{111} surface. The various cooling cycles which were employed are schematically illustrated in Fig. 1. Cooling cycle I provides a constant cooling rate from A to D; cooling cycle II additionally employs a partial melt-back of the LPE layers[2] from B to C; and cooling cycle III employs a 2-hr isothermal arrest from B′ to C. The interruptions in cooling rate used in cycles II and III profoundly affect ρ as discussed below.

Each LPE layer was etched (11) on a {110} cleavage plane, normal to the growth plane, to reveal the substrate-LPE layer interface and metallurgical junction associated with the programmed changes in growth for cooling cycles II and III. Utilizing a model (10) for LPE growth which has been shown to describe adequately LPE layers similar to those used in the present work, it is readily shown that for a layer of

Key words: GaP, liquid phase epitaxy (LPE), intermittent growth, interrupted cooling, reduction in dislocations by interrupted cooling of LPE layers.

[1] The Te concentration in these layers increases along the growth direction as discussed elsewhere (10). This Te gradient is not expected to influence the effects observed in this study.

[2] This is not to be confused with the PBM method (3) in which the substrate is back-melted.

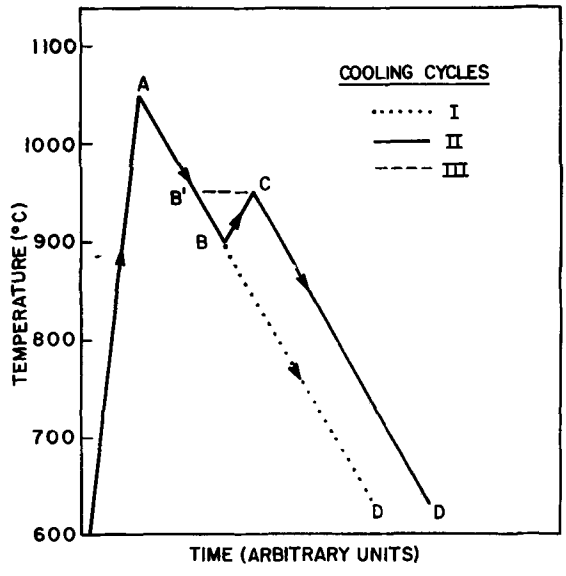

Fig. 1. Schematic representation of cooling cycles used for growth of LPE layers. Except for the initial heating rate (~20°/min), heating and cooling rates were 1°/min.

thickness t, the separation of the initial growth interface (corresponding to point A in Fig. 1) and that corresponding to point C in Fig. 1 is αt where $\alpha \lesssim 0.4$. Thus α is that fraction of the layer thickness corresponding to growth along the path ABC or AB'C. The actual value of α was determined from the cleavage-face delineation. No junction was evident in LPE layers grown using cooling cycle I. The crystals were subsequently polished at an angle of 3° to the growth surface, and the dislocation density distribution was determined by etching (4). The reduction in ρ at the substrate-LPE layer interface could not be conveniently determined in this manner because of the large disparity in etching rates of the substrate and LPE layers; however, cleavage-face x-ray topography (12) generally indicates about a 5- to 10-fold reduction in ρ over a distance less than 3μ for layers grown using cooling cycle I. Similar reductions are expected for all the cooling cycles used in this work.

Results and Discussion

Table I summarizes the results for layers grown using the various cooling cycles. For layers grown without interrupted cooling (cycle I) the dislocation density is uniform throughout the thickness of the layer, in agreement with previous observations (4-8). However, for layers grown with partial melt-back of the LPE layer (cycle II), ρ is initially constant, *i.e.*, independent of distance from the initial growth interface, but is precipitously reduced within the layer at a position coincident with the metallurgical junction delineated at a thickness αt.

Figure 2 illustrates the delineated metallurgical junction and corresponding step reduction in ρ for a layer (NT 021070) in which ρ is reduced by a factor of ~6. The rough agreement between the measured values of α (see Table I) and the value computed from the programmed cooling cycle ($\alpha < 0.4$) demonstrates conclusively that the reduction in ρ occurs at the commencement of growth (C in Fig. 1) following the partial melt-back. The last entry in Table I indicates that interrupted cooling without deliberate melt-back (cycle III) is also effective in reducing ρ. Thus it appears that the reduction in ρ is not attributable to melt-back *per se*, but rather the result of a stationary liquid-solid interface; however, the occurrence of slight melt-back resulting from thermal fluctuations during the 2-hr isothermal annealing cannot be precluded.

Table I. Effect of cooling cycle on dislocation density in LPE layers

Sample	α	ρ (initial) (10^5 cm^{-2})	ρ (final) (10^5 cm^{-2})	Cooling cycle
NT 102169-3	—	0.8	0.8	I
NT 102369-1	—	5.6	5.6	I
NT 021070	0.38	5.0	0.8	II
NT 022570	0.36	2.8	0.8	II
NT 031370-Q	0.33	2.5	0.65	II
NT 033170	0.30	4.5	1.0	II
NT 042270	0.44	6.4	2.3	III

The above results imply that the reduction in ρ within the LPE layers is a phenomenon associated with the liquid-solid interface and obviously not the result of the latter part of the epitaxial layer having been grown under conditions of reduced thermal and/or mechanical stress as previously suggested for PBM growth (7). Although it is apparent that regrowth under severe stress conditions will introduce new dislocations, it is not obvious that growth under conditions of reduced stress provides a driving force for the removal of dislocations. On the contrary, the driving force is provided by the "excess" free energy associated with these defects; dislocations are not equilibrium defects, i.e., the "equilibrium" number of dislocations in a crystal at any temperature is zero. The removal of dislocations is a problem of geometric termination, either within the crystal by mutual annihilation (formation of half-loops or networks) or at a surface by reorientation of dislocations into directions nearly normal to the growth direction (formation of partial-loops) (8).

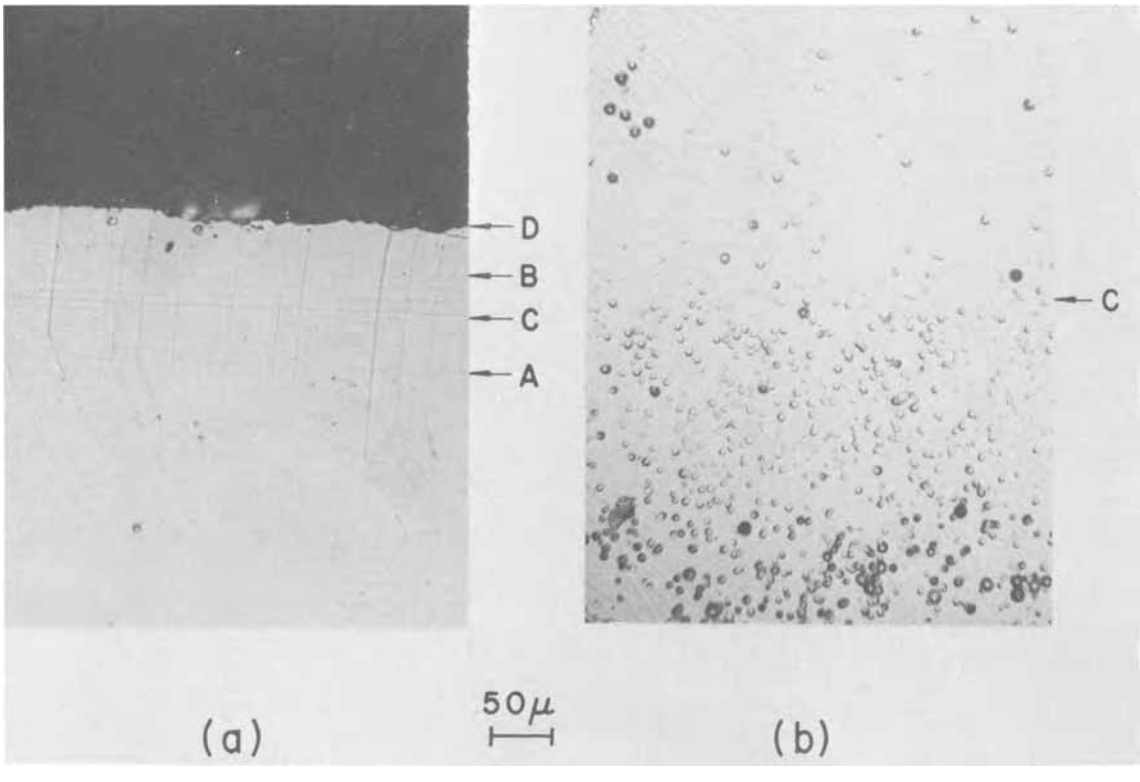

Fig. 2. Revelation of various junctions on a cleavage face (a) and dislocation etch pits on a surface lying 3° from the growth face (b) for a LPE layer grown using cooling cycle II. The arrows in the figure locate the positions corresponding to the changes in cooling rate shown in Fig. 1. (No junction is delineated at B.)

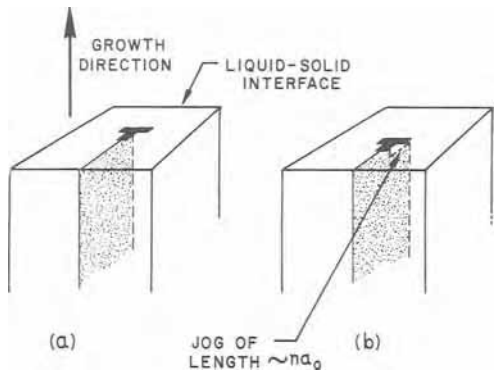

Fig. 3. Schematic illustration of an edge dislocation penetrating a liquid-solid interface (a). The shaded area represents the extra half-plane and the dashed line denotes the dislocation line. The absorption of n vacancies at the dislocation core results in a jog lying within the interface (b). (See text.)

The formation of both half-loop and partial-loop configurations requires high dislocation mobility and, for an AB compound semiconductor, climb of edge components involving both A and B vacancies (or A and B interstitials). It is postulated that the very high disorder at a liquid-solid interface provides an efficient source of the necessary point defects, and a quasi-stationary interface (which in Fig. 1 occurs in the vicinity of point B or along the path B'-C for cooling cycles II and III, respectively) provides sufficient time for reorientation of dislocations. The improvement in crystalline perfection generally observed at the initial growth interface for LPE, TSM, and PBM crystals is believed to occur by a similar mechanism.

The formation of loop or network configurations is enhanced by the tendency for dislocations to lie normal to the growth direction as discussed below. Since the dominant dislocations observed in III-V semiconductors are the so-called 60° dislocations that have substantial edge character and because we are mainly concerned about dislocations propagating along the growth direction, we consider, for simplicity, edge dislocations which are parallel to the growth direction. (The Burgers vector is thus contained in the growth plane which in practice coincides with an {hkl} glide plane.) At a stationary liquid-solid interface, the high concentration of vacancies results in dislocation climb normal to the Burgers vector so that if n vacancies are absorbed at the dislocation core, the resulting jog length is $\sim na_o$,[3] where a_o is the lattice parameter as schematically represented in Fig. 3. As the interface slowly advances, the total jogged length (and hence length of dislocation lying normal to the growth direction) is $\sum_i n_i a_o$, where n_i is the number of vacancies absorbed in each of the i "molecular" layers which have grown. One can envision rather long jogged lengths, *e.g.*, if this process occurs over a growth thickness of 1000Å and $n_i \sim 100$, then for the resulting sawtooth configuration the length of dislocation lying parallel to the growth plane is 10μ. Interaction among impinging dislocations results in network or loop formation which is confined to the region where the liquid-solid interface is quasi-stationary; the reduction in ρ occurs (abruptly) at this position.

Two questions immediately arise: (*i*) Why are not all the (removable) dislocations eliminated at the initial growth interface (point A in Fig. 1)? and (*ii*) Can further stepwise reductions in ρ be achieved? The elimination of dislocations is dictated by the random statistics of thermally induced climb and glide, and not all dislocations can be expected to terminate at the initial commencement of growth. Subsequent establishment of a stationary liquid-solid interface via interrupted cooling enables additional dislocations to terminate.

[3] A 60° dislocation can be represented by a (double-layered) {111}-oriented extra half-plane which is adjacent to the {111} slip plane containing the dislocation line and Burgers vector (13). Within this framework, climb occurs along the <110> direction lying 60° to both the dislocation line and Burgers vector. Hence, the corresponding jog length is $\frac{\sqrt{2}}{2} na_o$.

Table II. Variation of dislocation density in an incrementally grown layer

Incremental layer	Temperature range, °C	Average dislocation density (10^5 cm^{-2})
1	1060-1030	6.8
2	1030- 995	4.2
3	995- 955	3.1
4	955- 915	1.1
5	915- 600	1.3

Successive step reductions in ρ were attempted using a cooling cycle with four interruptions, with a 10-min thermal arrest between each growth increment.[4] The temperature range for each interval (see Table II) was chosen to give incremental layers of approximately the same thickness. Four nearly equispaced junctions were observed on the etched cleavage-face of a crystal grown in this manner. However, the incremental layers were so narrow that the corresponding step reductions in ρ were not apparent on the etched angle-lapped surface; rather ρ appeared to continually decrease. The value of ρ corresponding to the half-thickness of each incremental layer is given in Table II. The dislocation density appears to be reduced in all but the last of the growth increments where the thermal arrest occurred at the lowest temperature. The over-all reduction in ρ for this layer is comparable to the largest reduction observed in a single-step layer (NT 021070); however, it is believed that longer periods between growth increments may result in greater reductions in dislocation density.

The ultimate reductions in ρ that can be achieved by intermittent growth is not known, but it is likely to depend on the extent of dislocation entanglement and other factors limiting dislocation mobility rather than simply the number of these defects. The character and morphology of dislocations that can terminate at a stationary liquid-solid interface remains to be clarified.

Acknowledgment

The author is indebted to Mrs. J. Armstrong for growing the LPE layers, to G. A. Rozgonyi for topographic analysis of several of the layers, and to L. J. Varnerin for suggesting that isothermal annealing might be an alternative to partial back-melting. Helpful suggestions by W. H. Hackett, Jr., and W. A. Brantley are gratefully acknowledged.

Manuscript submitted Sept. 1, 1970; revised manuscript received Dec. 11, 1970.

Any discussion of this paper will appear in a Discussion Section to be published in the December 1971 JOURNAL.

[4] A longer thermal arrest resulted in a highly irregular surface which hampered identification of the various metallurgical junctions.

REFERENCES

1. H. Nelson, *R C A Rev.*, **24**, 603 (1963).
2. A. I. Mlavsky and M. Weinstein, *J. Appl. Phys.*, **34**, 2885 (1963).
3. D. E. Hinkley, R. H. Rediker, and M. C. Lavine, *Appl. Phys. Lett.*, **5**, 110 (1964).
4. R. H. Saul, *This Journal*, **115**, 1184 (1968).
5. I. Ladany, S. H. McFarlane, III, and S. J. Bass, *J. Appl. Phys.*, **40**, 4984 (1969).
6. M. Weinstein, H. E. LaBelle, Jr., and A. I. Mlavsky, *ibid.*, **37**, 2913 (1966).

7. R. S. Mroczkowski, A. F. Witt, and H. C. Gatos, *This Journal*, **115**, 545 (1968).
8. G. A. Wolff and B. N. Das, *ibid.*, **113**, 299 (1966).
9. R. H. Saul and W. H. Hackett, Jr., *ibid.*, **117**, 921 (1970).
10. R. H. Saul and W. H. Hackett, Jr., *J. Appl. Phys.*, **41**, 3554 (1970).
11. M. R. Lorenz and M. Pilkuhn, *ibid.*, **37**, 4094 (1966).
12. G. A. Rozgonyi and S. E. Haszko, *This Journal*, **117**, 1562 (1970).
13. J. Hornstra, *J. Phys. Chem. Solids*, **5**, 129 (1958).

Study on the Lithium Oxide-Nickel Oxide System

II. Thermodynamics of the Concentrated Solid Solutions

S. Pizzini,*,[1] G. Monari,[2] and R. Morlotti*

Reactor Material Laboratory, Thermochemistry Group,
Commission de la Commonauté Europeenne, CCR Euratom, Petten, Nederland

ABSTRACT

Thermodynamic activity measurements of dissolved lithium oxide in NiO-Li_2O solid solutions have been carried out within the homogeneity range to the solubility limit (about 33 a/o lithium). The measurements have been carried out by means of suitable galvanic cells, of the type

$$Pt/NiO\text{-}Li_2O\,(x_2)//\text{intermediate electrolyte}//NiO\text{-}Li_2O\,(x_1)/Pt$$

where α-Li_2SO_4 and β-spodumene have each been used as the intermediate electrolyte.

In a previous paper (1) and in a short note (1 bis), we dealt with the thermodynamics of the dilute solid solutions of lithium oxide in nickel oxide [from about 0.1 to 7 a/o (atom per cent) lithium]. In this range of concentrations the solution is known to be of the substitutional type, where lithium enters cationic positions and electroneutrality is maintained via an equivalent number of electron holes

$$0.5\,Li_2O\,(NiO) + 0.25\,O_2 \rightarrow Li_{Ni}' + h^\bullet + O_O^x \quad [1]$$

$$K_1 = [Li_{Ni}'][h^\bullet]/[Li_2O]^{1/2}\,p_{O_2}{}^{1/4}$$

and

$$[Li_{Ni}'] = [h^\bullet]$$

$$h^\bullet + Ni_{Ni}^x \rightarrow Ni_{Ni}^\bullet \quad [1\text{ bis}]$$

where it is assumed that electron holes are localized at nickel sites and Li_2O is considered as dissolved in NiO. At low partial pressures of oxygen, lithium enters the lattice with a different mechanism which involves, according to Deren and co-workers (2-5), either nickel vacancies

$$Li_2O + 2\,V_{Ni}'' + 2\,h^\bullet \rightarrow 2\,Li_{Ni}' + 0.5\,O_2 \quad [2]$$

at concentrations not higher than 0.01 a/o lithium, or interstitial positions

$$Li_2O \rightarrow Li_i^\bullet + Li_{Ni}' + O_O^x \quad [3]$$

at concentrations intermediate between 0.01 and 0.1 a/o lithium.

A new representation of the feature of this system was also given in ref. (1) by means of the phase diagram of Fig. 1, which shows the homogeneity region of the solid solutions along the line joining the NiO corner to the compound $LiNiO_2$. It is this line which expresses the stoichiometric 1:1 ratio between the substitutional lithium and the electron holes localized at Ni^{3+} sites.

In the same paper it was experimentally shown that the emf of concentration cells, like the following one

$$Pt/Li_2O\,(x_2)\;NiO/\alpha\text{-}Li_2SO_4/Li_2O\,(x_1)\;NiO/Pt \quad [4]$$

(operated with both electrodes under a pressure of 1 atm of oxygen) follows the Nernst law

$$\Delta E = \frac{RT}{F}\ln\frac{x_1}{x_2} \quad [5]$$

(where x_2 and x_1 are the atomic ratios of lithium in solution) up to about 2 a/o lithium, whereas at higher concentrations the departure from pure Nernstian behavior is no longer negligible.

A very general equation for the emf of cell [4] might be obtained when considering cell [4] as a double cell, with the intermediate electrolyte acting as a gas-tight diaphragm, so that the oxygen pressures above both solid solutions are those corresponding to the stoichiometry. With the electrolyte working as a pure lithium conductor, the emf of a single cell

$$Pt(O_2),\,Li_2O\;(a)/\alpha\text{-}Li_2SO_4/Li$$

could be written

$$E = E^\circ + \frac{RT}{2F}\ln\frac{a_{Li_2O}}{a^2_{Li}p_{O_2}{}^{0.5}} \quad [6]$$

being the single-cell reaction ($z = 2$)

$$0.5\,O_2 + 2\,Li \rightarrow Li_2O\;(soln) \quad [7]$$

By taking into account the equilibrium constant of reaction [1], one obtains, for the emf of cell [4]

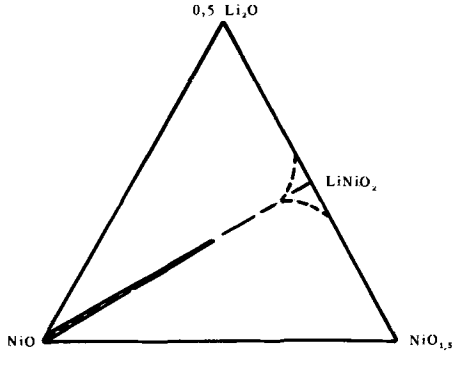

Fig. 1. Phase diagram (schematic) of the system Li_2O-Ni_2O_3-NiO. The homogeneity range lies between 0 and 33 a/o lithium.

* Electrochemical Society Active Member.
[1] Present address: Istituto Elettrochimica, Università di Milano, Via Venezian 21, Milano, Italy.
[2] Present address: Istituto di Ricerche Donegani, Novara, Italy.
Key words: activities, galvanic cells, electrical conductivity, point defects, nickel oxide.

$$\Delta E = \frac{RT}{F} \ln \frac{[Li_{Ni}']_1[Ni_{Ni}^{\cdot}]_1}{[Li_{Ni}']_2[Ni_{Ni}^{\cdot}]_2} - \frac{RT}{2F} \ln \frac{p°_1}{p°_2} \quad [8]$$

where $p°_1$ and $p°_2$ are the partial pressures of oxygen in equilibrium with the stoichiometric solutions.

In the total range of concentrations investigated, one could expect two extreme situations to occur: (*a*) the solution is a system in which both kinds of defects (*i.e.*, lithium in substitutional positions and electron holes at nickel sites) are randomly distributed, so that in the absence of interactions Eq. [8] becomes

$$\Delta E = \frac{RT}{F} \ln \frac{x_1^2}{x_2^2} - \frac{RT}{2F} \ln \frac{p°_1}{p°_2} \quad [8 \text{ bis}]$$

and (*b*) the solution is a system where only lithium is randomly distributed, whereas electron holes are localized at one of the 12 neighbor nickel ions (which form the cationic co-ordination shell of a lithium ion in the fcc lattice of the solid solution) and form stable ion pairs.

By taking into account the association reaction

$$Li_{Ni}' + Ni_{Ni}^{\cdot} \rightleftarrows [Li_{Ni}' \cdot Ni_{Ni}^{\cdot}]x \quad [9]$$

which formally accounts for the pairing of defects, one obtains

$$\Delta E = \frac{RT}{F} \ln \frac{x_1}{x_2} - \frac{RT}{2F} \ln \frac{p°_1}{p°_2} \quad [8 \text{ ter}]$$

It is worth remarking that in both cases, and independently of the degree of association, the pressure dependence of the emf is of the type

$$\Delta E = \frac{RT}{F} f\left(\frac{x_1}{x_2}\right) - \frac{RT}{F} \ln (p_{O_2}^{1/2})_1/(p_{O_2}^{1/2})_2 \quad [10]$$

The preference for one or the other situation depends on the configurational energy terms of the particular type of lattice. It has been demonstrated by means of mechanical and electrical relaxation measurements (6) that, at least at low temperatures, dilute solutions consist entirely of isolated dipoles ($[Li_{Ni}' \cdot Ni_{Ni}^{\cdot}]x$ pairs) whereas it is very likely that more concentrated solutions contain increasing concentrations of a different configuration, consisting of two neighboring lithium ions, both compensated by an electron hole at a nickel position.

Experimental results reported in the previous paper seem to confirm the van Houten and Bosman (6) view about the presence of isolated dipoles in the dilute solution and of more complex configurations in which electron holes are delocalized (or sheared with more than one nickel ion) as the lithium concentration increases.

The present paper is an attempt to extend the use of purely configurational factors when discussing the deviations of both entropy and free energy terms from ideality, in the range of more concentrated solutions.

Experimental

Electrolytes for emf measurements.—α-Li_2SO_4, which was successfully used in the range of dilute solutions (1), was shown to fail at a lithium level in the electrodes higher than 15 a/o.

Although lithium substituted β-alumina (7-9) should be a suitable electrolyte, we focused our efforts on SiO_2-base electrolytes which appear very promising[3] and which have been successfully used (12-13) for thermodynamic activity determinations.

Silica glasses[4] have been used, after a suitable doping, as intermediate electrolytes. The doping process consists of making a sandwich of three pellets (the intermediate being the silica glass and the other ones, lithium-doped NiO or Li_2SO_4) and heating it at 700°-800°C for some days. After a subsequent annealing of the SiO_2 disk at 600°C, the electrolyte is ready for operation. Analysis reveals an increase of the lithium content of about two orders of magnitude whereas the sodium content remains constant.[5]

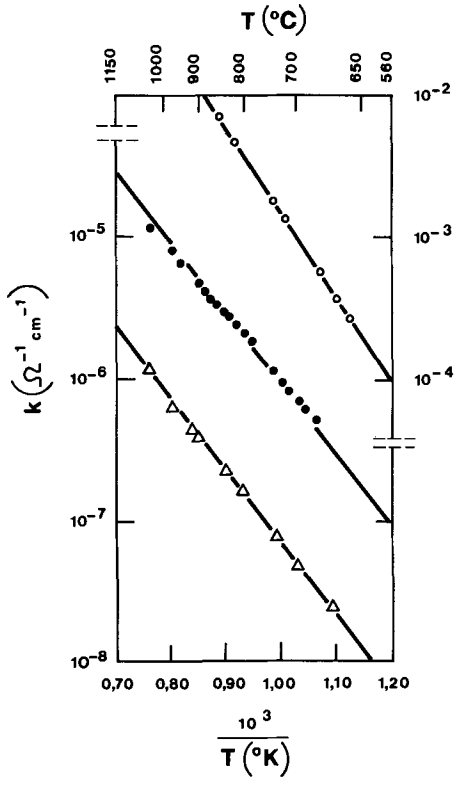

Fig. 2. Electrical conductivity of Pursil silica (△), lithium-doped Pursil silica about 100 ppm (●), and β-spodumene (○).

When comparing the results obtained with cells fitted with α-Li_2SO_4 and lithium-doped SiO_2 (see next paragraph) one recognizes that such an electrolyte could be satisfactorily used only for very dilute solutions to about 2-3 a/o lithium. A small attack of the electrolyte, at the side in contact with the more concentrated solution, is always present, and we suppose that only because of the very low reaction rate can we obtain sufficiently good results when the electrodes consist of dilute solutions.

β-spodumene (a member of a family of silico-aluminates with a composition $Li_2O \cdot Al_2O_3 \cdot 4\ SiO_2$, which expresses a one to one ratio between the aluminum and lithium) has particularly attractive structural properties (14-17) that should enhance ionic conduction. It presents channels of about 3Å diameter that run parallel to the a and b axes, similar to those present in zeolites. Along these channels lithium ions should move relatively freely when subjected to a convenient electric field. Moreover, β-spodumene is endowed with cation exchange properties, probably limited to Li^+ and H^+ (17), as with zeolites. β-spodumene was prepared by mixing SiO_2, Li_2CO_3, and Al_2O_3 in the appropriate proportions, firing the mixture and pressing it to pellets of 12 mm in diameter and finally by sintering at about 1400°C. Some a-c[6] electrical conductivity measurements have been made (18) on undoped and doped silica samples as well as on β-spodumene to have a preliminary rough idea of the carrier concentration and mobility in such a SiO_2-base compound.

The results are given in Fig. 2 as log K *vs.* $1/T$ plots which illustrate that the activation energy remains approximately constant[7] in spite of the large variation of

[3] For their ion exchange properties and purely ionic conductivity (10, 11).

[4] Pursil 453 Quarz & Silice with a total alkali content of about 20-40 ppm.

[5] A typical analysis, before and after the treatment is Li 1.4 ppm, Li 96 ppm.

[6] Carried out with a General Radio impedance bridge, Model 1608 A.

[7] 23.12 kcal/mole (pure silica), 23.32 kcal/mole (100 ppm Li-doped silica), 26.9 kcal/mole (β-spodumene).

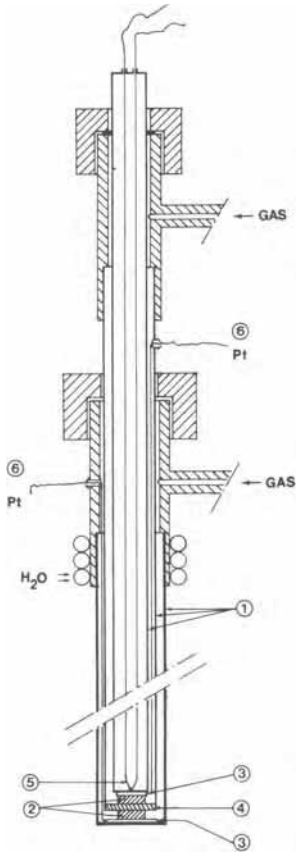

Fig. 3. Cell with separate compartments: 1, silica glass tubes; 2, electrodes; 3, platinum electrodes; 4, lithium-doped Pursil silica glass which serves as an intermediate electrolyte; 5, Pt-Pt, Rh thermocouple; 6, Pt wires to the electrodes.

the lithium concentration, whereas the absolute value of the conductivity depends on the total alkali content (and changes of about four orders of magnitude for a concentration change of the same order of magnitude). We therefore argue the same hopping mechanism as in doped silica, but with a very high level of free carriers.

Results of experiments carried out in cells of the type [1] with lithium-doped silica and β-spodumene serving as intermediate electrolytes, are illustrated in the next paragraph.

Emf measurements.—Emf measurements on solid galvanic chains of type [4] have been carried out in cells of conventional design as illustrated in previous papers (1, 19, 20) as well as on a cell with separate compartments, which is shown in Fig. 3. This cell was designed to perform measurements of emf as a function of the partial pressure of oxygen. With such a cell we should be able to determine the deviations from stoichiometry as a function of the oxygen pressure as well as the dissociation pressure of the solid solution as a function of the lithium concentration.

The requirements this cell should fulfill are the following:

1. A very limited volume of one of the two electrode compartments, to avoid sensible variations in the sample concentration due to large amounts of oxygen evolved when the external pressure is made lower than the decomposition one.
2. An intermediate electrolyte which allows a gas-tight separation between the electrode compartments.

The first requisite is satisfied by the design of the cell where the ID and OD of the silica tubes are chosen to leave the minimum dead volume.

The second requisite could be satisfied only when using lithium-doped silica glass, because the β-spodumene we prepared presents problems of gas tightness due to its relatively high porosity. One optically polished disk of Pursil silica was welded at the bottom of a silica tube (doped according to the directions given above) and used in the cell of Fig. 3. The cell is operated with two electrodes having about the same composition ($\sim$ 1 a/o lithium); one compartment is filled with pure oxygen, the other one (after a preliminary outgassing at room temperature under a vacuum of 10^{-2} Torr) is successively filled with different mixtures of oxygen-nitrogen (mass spectrometrically controlled for the oxygen content) and brought to the desired temperature under a continuous gas flow. The temperature was controlled to $\pm$ 0.1°C with a proportional temperature controller and the emf and temperature measured and recorded by a digital voltmeter and digital recorder (Hewlett & Packard, Dymec System).

Results

Comparison of the different electrolytes.—The results obtained when fitting cell [4] with lithium-doped silica, β-spodumene, and α-Li_2SO_4 at 800°C, are reported in Fig. 4. Similar results were obtained at lower temperatures. It appears that results obtained with different electrolytes fit the same curve, within experimental error, over the concentration range 0.5-7 a/o. At higher concentrations only β-spodumene works successfully. Examples of E *vs.* T curves obtained with β-spodumene are given in Fig. 5.

Cells with separate compartments.—The results of experiments carried out at 766°C with cells fitted with two electrodes containing about 1 a/o lithium are

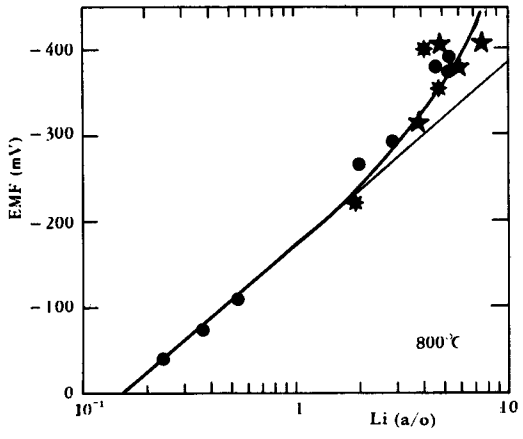

Fig. 4. EMF *vs.* concentration (in lithium atoms per cent) at 800°C: ●, α-$LiSiO_4$ as intermediate electrolyte; ✲, lithium-doped silica; ★, β-spodumene.

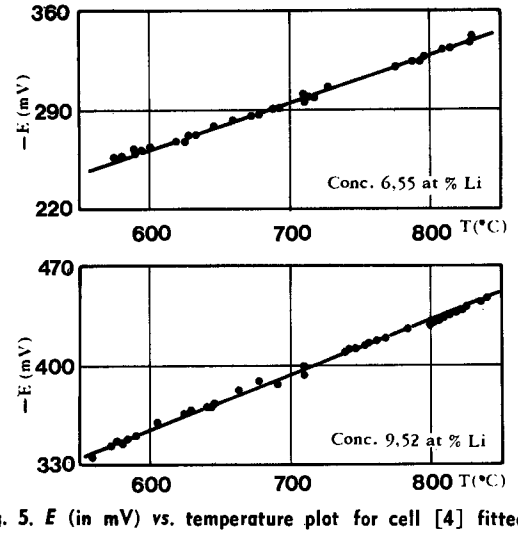

Fig. 5. E (in mV) *vs.* temperature plot for cell [4] fitted with β-spodumene as intermediate electrolyte.

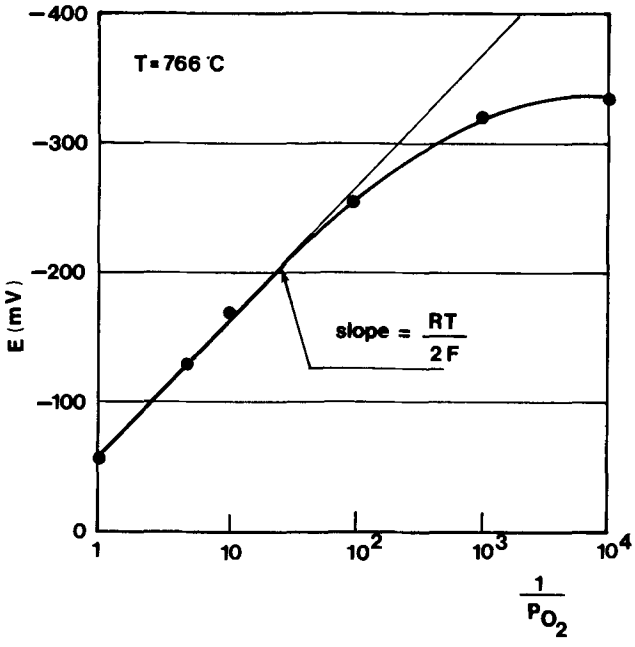

Fig. 6. EMF vs. partial pressure of oxygen plot for cell [1] fitted with lithium-doped silica glass and separate compartments.

shown in Fig. 6. The experimental points (which are an average of about 60 points printed down in more than 48 hr at each pressure investigated) present a mean square deviation of 4.05 mV and fit a curve having a slope of 104 mV.

Measurements on isobaric cells.—Results of experiments carried out on isobaric cells of type [4], when using β-spodumene as intermediate electrolyte, are reported in Table I (see also Fig. 4 and 5). This table gives the parameters which express the linear temperature dependence of the emf at different concentrations of lithium. The average number of (E, T) points used for computing the "a" and "b" values is 100. The concentration ratios quoted here have been normalized to a reference compartment concentration of 0.365 a/o lithium and correspond to concentration values iodometrically determined after completion of each high temperature experiment.

Table I. Experimental values of emf of cell [1] for different $LiNiO_2$ concentrations

$\frac{Li(a/o)_1}{Li(a/o)_2}$	E (mV) = a + b T
1.013/0.365	E = 49.37 + 0.087T
3.575/0.365	E = 46.29 + 0.287T
4.357/0.365	E = 144.64 + 0.230T
4.804/0.365	E = 2.51 + 0.379T
8.55/0.365	E = 60.96 + 0.335T
9.52/0.365	E = 120.13 + 0.390T
16.41/0.365	E = 135.65 + 0.634T
18.41/0.365	E = 11.63 + 0.691T
22.06/0.365	E = 39.05 + 0.653T
28.48/0.365	E = −1.79 + 0.772T
31.73/0.365	E = −9.46 + 0.762T

The equations reported in Table I have been used for plotting the emf isotherms of Fig. 7, 8, and 9. Here, the molar fraction ratio $x/(1-x)$ [where $(1-x)$ is the molar fraction of the NiO solvent or of the Ni_{Ni}^{x}

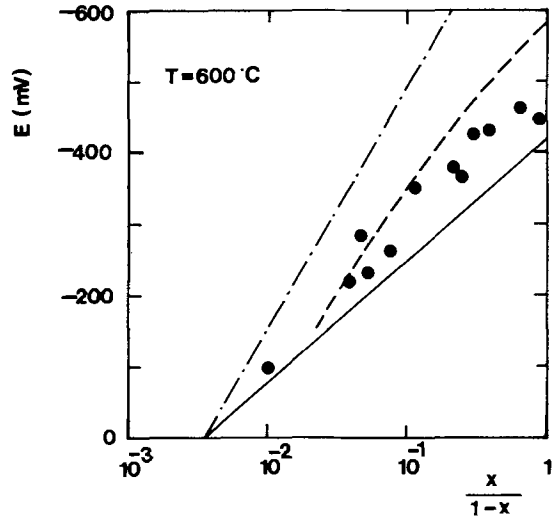

Fig. 7. Plot of the emf cell [4] fitted with β-spodumene vs. the ratio x/(1—x) of the molar fractions.

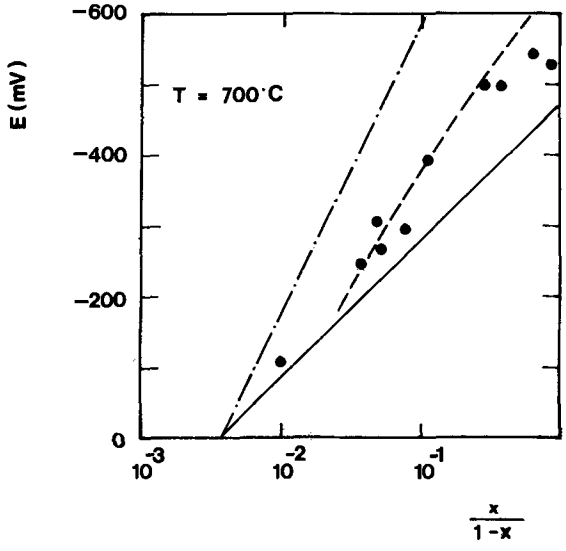

Fig. 8. Plot of the emf of cell [4] fitted with β-spodumene vs. the ratio x/(1—x) of the molar fractions.

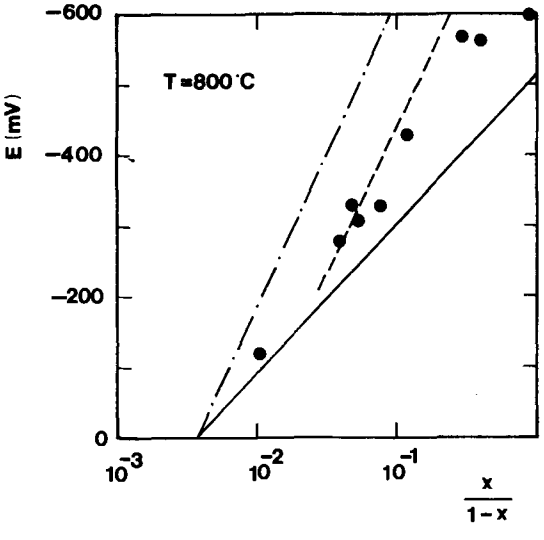

Fig. 9. Plot of the emf of cell [4] fitted with β-spodumene vs. the ratio x/(1—x) of the molar fractions.

ions] accounts for the fact that in the range of concentrated solutions, the concentration of Ni_{Ni}^{x} is no longer constant (see Eq. [1 bis]). The straight lines appearing in the same figures have been plotted according to the equations

$$\Delta E = \frac{RT}{F} \ln \frac{x_1}{1 - x_1} \Big/ \frac{x_2}{1 - x_2} \qquad [11]$$

and

$$\Delta E = \frac{RT}{F} \ln \frac{x_1^2}{x_2^2} \Big/ \frac{1 - x_1}{1 - x_2} \qquad [12]$$

where the former accounts for the theoretical emf of a solution in which pairing is 100% (solid line), and the latter for that of a solution in which pairs are 100% dissociated (dashed-dotted line).

Discussion

In the first paper of this series we discussed the thermodynamics of the dilute Li_2O-NiO solutions as that of binary system where the components are $LiNiO_2$ and NiO. In the same paper we stressed the influence of ion pairing on the thermodynamics of the solution. However, we emphasized that the use of pair concentrations (or other kind of associated species) as a measure of the $LiNiO_2$ activity does not mean that we identify a particular array of ions in the lattice with a chemical species, such as $LiNiO_2$. Nevertheless, if we do identify the activity of ion pairs with that of $LiNiO_2$, the fact that the Nernst equation holds to a deviation of less than 1 mV for $0.0015 \leq x_{LiNiO_2} \leq 0.01$, leads to the conclusion that, over this concentration range, the activity coefficient of $LiNiO_2$ is unity.[8]

Deviations from such an ideal behavior which have been observed at $x > 0.01$ were explained by considering that the statistical probability of finding configurations containing more than one lithium ion increases with the increasing of lithium content, thus affecting the entropy of the system. These entropy changes were shown to account for the over-all change of the free energy of the solution, as the enthalpy changes are, within the limits of experimental accuracy, inappreciable.

In order to avoid any possible mistake between species, coming from the different defect reactions postulated in the first part of this paper according to Eq. [1], [1 bis], and [9], and chemical components of the solution, we discuss here our present experimental results only in terms of a defect model involving ionic species, defects, and associated defects.

Measurements on cells with separate compartments show that the dependence of emf on the oxygen pressure is of the type (see Experimental section and Fig. 6)

$$\Delta E = \text{const} - \frac{RT}{2F} \ln \frac{(p_{O_2})_1}{(p_{O_2})_2} \qquad [10 \text{ bis}]$$

where the first term is essentially independent of the partial pressure of oxygen and the slope of the experimental curve equals $RT/2F$ within a few millivolts.

It is apparent that the experimental emf has the right oxygen pressure dependence required by the chosen defect model (Eq. [10]) and that the concentration of defects is not affected by the oxygen partial pressure, up to 10^{-2} atm, the first term being a constant.

This behavior indicates that the 1:1 ratio between substitutional lithium and Ni^{3+} does not appreciably change when changing the partial pressure of oxygen within the indicated range of pressures and, furthermore, that nickel vacancies, arising from reaction

$$0.5\, O_2 \rightarrow O_O + V_{Ni} \qquad [13]$$

do not play any significant role in the thermodynamics of the solution.

[8] As the standard state for NiO, the hypothetically pure and stoichiometric NiO under an oxygen pressure of 1 atm is chosen.

At the lowest partial pressures ($<10^{-2}$ atm) the deviation from linearity and the approximate independence of the emf with respect to the external pressure, indicate that the actual oxygen pressure in the electrode compartment remains constant, due to the buffering action of a decomposition reaction, that might be written as

$$[Li_{Ni}' \cdot Ni_{Ni}^{\cdot}] + 2\, O_O^x \rightarrow 0.25\, O_2 + 0.5 Li_2O + NiO \qquad [14]$$

and the system turns to be invariant.

A dissociation pressure between 10^{-2} and 10^{-3} atm, which might be inferred from Fig. 6 at 766°C, is in agreement with a figure of about 8 Torr at 800°C, reported by Hauffe (23) as the lowest pressure at which the electrical conductivity still remains independent of the pressure, for a sample of NiO doped with 1 m/o (mole per cent) lithium.

Other electrical conductivity measurements (21, 22) show that the electrical conductivity is independent of the partial pressure of oxygen. [Hauffe (23) interpreted this independence by considering that it is the chemical potential of the dissolved lithium oxide which varies with the oxygen pressure, whereas the concentration of the substituted lithium as well as of the electron holes does not.]

In order to check whether purely configurational factors account for the composition dependence of both emf and isothermal temperature coefficient of isobaric cells, we shall first consider how the entropy term should depend on the composition. When neglecting other terms but the configurational ones, the calculation of the configurational entropy of mixing could be carried out first for the two limiting situations recognized above, and corresponding to the cases: (*I*) of a mixture in which Li^+ and Ni^{3+} are associated to give stable pairs and, (*II*) of a mixture in which Li^+ and Ni^{3+} are randomly distributed.

In the first case, by using trivial statistical calculations, it could be demonstrated that the entropy of mixing results as

$$\Delta S = -R(n_{Li+} \ln x_{Li+} + n_{Ni2+} \ln x_{Ni2+}) \qquad [15]$$

and the partial molar entropy of the solute is found by differentiation to be

$$\bar{S}_{Li} - S^{\circ}_{Li} = -R \ln x_{Li} \qquad [16]$$

In the second case, the entropy of mixing could be obtained by assuming that both Li^+ and Ni^{3+} are independently arranged on N sites of the cation lattice, so that one finds

$$\Delta S = -2R(n_{Li} \ln x_{Li} + n_{Ni2+} \ln x_{Ni2+}) \qquad [15 \text{ bis}]$$

and

$$\bar{S}_{Li} - S^{\circ}_{Li} = \bar{S}_{Ni3+} - S^{\circ}_{Ni3+} = -2R \ln x_{Li} \qquad [17]$$

In Fig. 10 the straight line corresponds to the partial entropy differences (in μV/°C units) calculated from the equation

$$-\epsilon F = R[\ln x_2 - \ln (1 - x_2) - \ln x_1 + \ln (1 - x_1)] \qquad [18]$$

for the concentration cell [4] and one remarks that the experimental isothermal emf coefficients closely fit[9] the theoretical plot only in the dilute solution region. For more concentrated solutions, where deviations from the ideal behavior are apparent, it is always possible to find empirical equations which give the entropy of mixing, by replacement of the molar ratios with other suitable concentration parameters.

Then the equation for the entropy of mixing takes the form

$$\Delta S = -R(n_A \ln g_A + n_B \ln g_B) \qquad [15 \text{ ter}]$$

where $g_A + g_B = 1$.

In the case of polymer solutions (24) it has been shown that g_A and g_B are well described by the volume

[9] Thus indicating that the dilute solution is entirely constituted of undissociated pairs.

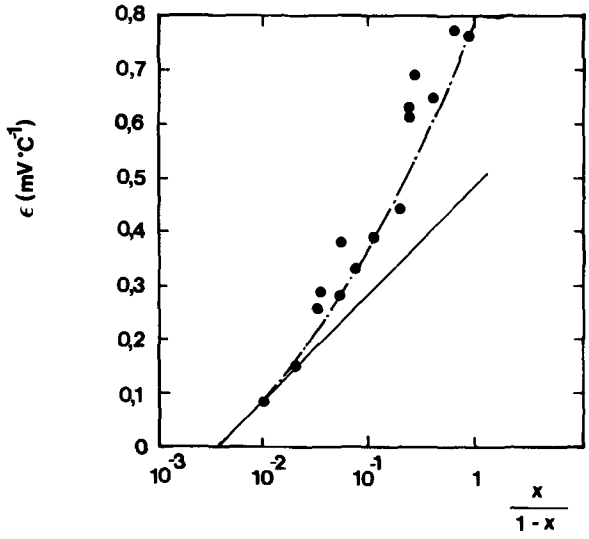

Fig. 10. Plot of the isothermal temperature coefficients of the emf vs. $x/(1-x)$. Straight line corresponds to the calculated entropy differences according to Eq. [18] and the dashed-dotted line to the entropy differences calculated according to Eq. [18 bis].

ratios ϕ_1 and ϕ_2 whereas, in our present case, it could be shown that g_A coincides with the relative statistical probability of finding those configurations containing more than two solute atoms within the nearest neighbors of a solvent atom.

Such a configurational function $g(n_i,r)$ accounts for the deviations from ideality only due to the increasing number of the contacts between like atoms as the concentration of the solute increases.

Numerical calculation of the g_A and g_B terms of Eq. [15 ter] could be accomplished by considering that in the rocksalt structure the coordination number z of cations is 12 and that each individual term $g(n_i,r)$ in the sum

$$g = \sum_{r}^{z} g(n_i,r) \qquad [19]$$

(where n_i is the number of atoms of species i in the mixture and r is the fraction of z sites occupied by cations of type i) could be calculated by the expression [see also ref. (1)]

$$g(n_i,r) = \frac{n_i!\,(N-n_i)!}{N!} \cdot \frac{z!\,(N-z)!}{r!\,(n_i-r)!\,(z-r)!\,(N-n_i-z+r)!} \qquad [20]$$

It is apparent that g_A in Eq. [15 ter] corresponds to the sum

$$g_A = \sum_{2}^{12} g(n_i,r)$$

Equation [18] could therefore be rewritten as

$$-\epsilon\mathbf{F} = R[\ln g_2 - \ln(1-g_2) - \ln g_1 + \ln(1-g_1)] \qquad [18\text{ bis}]$$

Equation [18 bis] is plotted in Fig. 10 as the dashed-dotted line and one can see that this configurational function closely fits the experimental points.

When we use, as has been done in the first paper, the values of the statistical probabilities $\sum_{r=2}^{12} g(n_i,r)$ as a measure of the activity of the solute and the values of $1 - \sum_{r=2}^{12} g(n_i,r)$ as a measure of the activity of the solvent, the calculated emf according to Eq. [11] results as

$$\Delta E = \frac{RT}{\mathbf{F}} \ln \frac{\sum_{r=2}^{12} g(n_i,r)}{x_2\left(1 - \sum_{r=2}^{12} g(n_i,r)\right)} \qquad [11\text{ bis}]$$

when substituting the molar ratios with the ratio of the statistical probabilities.

Results obtained are plotted in Fig. 7, 8, and 9 as dashed-dotted lines and show that this function accounts for the experimental results only in the range of intermediate concentrations as has been already shown (1).

We suggest, as a conclusion that the solid solutions of lithium oxide in nickel oxide are well described, in the range of dilute and intermediate concentration solutions, by a model which has the following important features:

1. Dilute solutions[10] ($0.1 \leq x \leq 2$ a/o lithium) consist entirely of undissociated [Li_{Ni}' $Ni_{Ni}^{\cdot}$] pairs. The electron holes are fully localized. This view agrees with the experimentally observed high values of the activation energy for the electrical conductivity in the same range of concentrations and are not conflicting with Deren's results reported in ref. (2, 3, 5), which show very low values of the activity coefficient of Li_2O in the same range of concentrations.[11]

2. In solutions lying in the intermediate concentration range ($2 \leq x \leq 10$ a/o lithium) interaction between like atoms leads to an apparent dissociation of ion pairs, corresponding presumably to a partial delocalization of electron holes. The entropy of the solution is always lower than the ideal one and is accounted for when calculating the (statistical) contacts between like ions. Also the activity of the components of the solutions could be approximately calculated by taking into account only statistical factors.

At the highest concentrations, however, the solution is no longer describable with the simple model illustrated in this present work.

Acknowledgments

The authors are greatly indebted to Dr. H. Rother, Professor G. Bianchi, Dr. V. Wagner, and Dr. A. Bonomi for helpful discussions and to Miss L. Oud for her kind cooperation.

This work was performed in cooperation with the Istituto di Elettrochimica, Università di Milano, and represents a part of the dissertation presented by G. Monari for the degree of chemistry at the University of Milano.

Manuscript submitted Nov. 19, 1969; revised manuscript received Jan. 5, 1971.

Any discussion of this paper will appear in a Discussion Section to be published in the December 1971 JOURNAL.

[10] In our previous paper we used the operative definition of "ideal solution" for those dilute solutions in which lithium and nickel[111] are fully associated in pairs. Note that we have used a definition which could give rise to confusion when compared with the current use of "ideality," viz., in electrolytic solutions, where "ideality" corresponds to the absence of any specific interaction between ions.

[11] In ref. (2) we have however stressed that, due to the use of electrodes consisting of a mixture of nickel metal and the solid solution, the concentrations given by Deren result in much lower concentrations of [Li_{Ni}' $Ni_{Ni}^{\cdot}$] pairs.

REFERENCES

1. S. Pizzini, R. Morlotti, and V. Wagner, *This Journal*, **116**, 915 (1969).
1 bis. S. Pizzini and R. Morlotti, *ibid.*, **117**, 1529 (1970).
2. J. Deren and G. Rog, *Bull. Acad. Polon. Sci.* (English), **16,9**, 491 (1968).
3. J. Deren and J. Ziolkowski, *ibid.*, **14,7**, 443 (1966).
4. A. Bielanski and J. Deren, from "Symposium on Electric Phenomena in Chemisorption and Catalysis on Semiconductors," K. Hauffe and

Th. Wolkenstein, Editors, W. de Gruyter & Co., Berlin (1969).
5. J. Deren and G. Rog, *Bull. Acad. Polon. Sci.* (English), **17,16**, 327 (1969).
6. S. van Houten and A. Bosman, from "Transition Metal Compounds," p. 123, E. R. Schatz, Editor, Gordon & Breach Publishing, New York (1968).
7. K. O. Hever, *This Journal*, **115**, 826 (1968).
8. K. O. Hever, *ibid.*, **115**, 830 (1968).
9. Yung Fao Yu Yao and J. T. Kummer, *J. Inorg. Nucl. Chem.*, **29**, 2453 (1967).
10. R. H. Doremus, *This Journal*, **115**, 181 (1968).
11. R. Maury, "Conductibilité électrique des tectosilicates," Thèse de Doctorat à la Faculté des Sciences de Paris, Nov. 8, 1967.
12. B. C. H. Steele, in "EMF Measurements in High Temperature Systems," pp. 1-8, C. B. Alcock, Editor, Institute of Mining and Metallurgy, London (1968).
13. W. Pluschkell and H. J. Engell, *Ber. Deut. Keram. Ges.*, **45**, (8), 388 (1968).
14. Chi-Tang Li and D. R. Peacor, *Z. Krist. Bd.*, **126**, 46 (1968); **127**, 327 (1968).
15. J. F. Schairer and N. L. Bowen, *Am. J. Sci.*, **254**, 129 (1956).
16. K. M. Finlayson and J. P. Williams, *J. Am. Ceram. Soc.*, **50**, (9), 488 (1967).
17. B. J. Skinner and H. T. Evans, *Am. J. Sci., Bradley Vol.*, **238 A**, 312 (1960).
18. V. Wagner, Private communication.
19. S. Pizzini and R. Morlotti, *This Journal*, **114**, 1179 (1967).
20. S. Pizzini, E. Romer, and R. Morlotti, *Electrochim. Metall.*, **III** (2), 151 (1968).
21. K. Hauffe and J. Block, *Z. Physik. Chem.*, **196**, 438 (1950).
22. V. D. Savin, V. T. Serebryanskii, and W. A. Fedotov, UDC 546.165, *Inorg. Mat.*, **4**, 185 (1969).
23. K. Hauffe, "Reaktionen in und an festen Stoffen" pp. 149-150, Springer Verlag (1955).
24. K. S. Pitzer and L. Brewer, "Thermodynamics," McGraw-Hill Publishing Co., New York (1961).

Diffusion of ^{51}Cr in NiO Single Crystals

M. S. Seltzer

Metal Science Group, Battelle Memorial Institute, Columbus Laboratories, Columbus, Ohio 43201

ABSTRACT

The diffusion of ^{51}Cr into NiO single crystals has been investigated as a function of temperature in the region 1100°-1250°C and under oxygen partial pressures from one to 10^{-4} atm. At high chromium concentrations the diffusion is concentration dependent, probably as a result of self-doping by the trivalent chromium cations. At 1 atm of oxygen the concentration independent diffusion coefficients can be represented by $D_{Cr}^{NiO} = 9.36 \times 10^{-5} \exp(-47.0 \text{ kcal}/RT)$. At 1150° and 1250°C chromium diffusivities decrease with decreasing oxygen partial pressure.

While self-diffusion of Ni in NiO has been studied by a number of investigators (1-8) there have been only two studies of impurity tracer migration in this compound (8, 9). Experimentally observed activation energies for nickel self-diffusion in NiO vary from 44 to 63 kcal/mole. The higher values are taken to represent diffusion in relatively pure crystals where native defects predominate over those introduced by cation impurities having valence different from the host cation, nickel. In these cases the experimentally measured activation energies include the energy of formation for the defects by which nickel migrates, as well as the energy to move the diffusing species from one equilibrium position to an adjacent site. The lower activation energies then represent only the migration energy where the concentration of defects is fixed by the impurity concentration over the temperature range investigated.

In the temperature range 1100°-1400°C, both Volpe and Reddy (7) and Crow (8) have found that nickel diffusivities decrease with decreasing oxygen pressure in the region 1 atm $> p_{O_2} > 10^{-7}$ atm, with the pressure dependence varying with temperature and p_{O_2}. The results were interpreted in terms of nickel diffusion via both singly and doubly charged nickel vacancies.

Studies of cation impurity tracer diffusion in NiO have been limited to measurements of ^{60}Co (8) and ^{55}Fe (8, 9) migration. Crow (8) found that activation energies for ^{60}Co in polycrystalline NiO containing 0.002 atom fraction chromium were about 41 kcal/mole, independent of p_{O_2} in the range 1-5 x 10^{-5} atm over the temperature range 1100°-1400°C. Diffusivities decreased slightly with decreasing oxygen partial pressure. For diffusion of ^{60}Co in "pure" NiO single crystals, activation energies of 53.1 and 52.8 kcal/mole were measured in 1 atm and 5 x 10^{-5} atm, respectively. The lower activation energies found in the doped crystals are taken to represent values for migration under conditions where the vacancy concentration is controlled by the trivalent chromium addition.

Key words: point defects, nonstoichiometry, defect pairs, vacancies.

Measurements of iron diffusion in NiO single crystals (8, 9) suggest that this species acts as a self-dopant, yielding activation energies indicative of impurity controlled diffusion. Thus Crow found that diffusion rates for ^{55}Fe in NiO were nearly independent of p_{O_2}, particularly at 1100°C, while activation energies decreased from 46 to 41 kcal/mole as the oxygen pressure decreased from 1-5 x 10^{-5} atm. Variations in the pre-exponential compensated for the activation energy changes to give the p_{O_2} diffusion independence at 1100°C. Richards and Wagstaff measured an activation energy of 44.5 kcal/mole for ^{55}Fe in nickel oxide. This value, determined in air in the temperature range 1000°-1400°C, is in excellent agreement with the values reported by Crow.

The objective of this investigation was to determine diffusion coefficients for ^{51}Cr in NiO as a function of chromium concentration, oxide composition, and temperature, in order to provide additional information necessary for an understanding of impurity migration in oxides. Such information is essential for proper interpretation of experimental results of the oxidation of alloys, sintering of oxides, and creep of scales formed during alloy oxidation.

Experimental Procedures

The NiO single crystals used in this study were obtained from Argonne National Laboratory. They were grown by the Verneuil process in an arc-image furnace. A typical analysis in ppm is Co, 200; Ag, 80; Al, 10; Cr, 30; Fe, 60; Mn, 30; K and Na, 6; Si, 10; and

Ta, 20. Several preliminary experiments were performed on single crystals grown by Marubeni-Iida. These crystals had a typical analysis in ppm of Mg, 110; Ca, 85; Co, 20; Fe, 30; Al, 10; Ti, 10; others, 15. Diffusion specimens, 4 x 4 x 2 mm were prepared by cleaving {100} parallelepipeds from the large boules and polishing parallel surfaces using 600 grit metallographic paper.

In order to obtain specimens with a desired composition prediffusion equilibrations were conducted in a platinum-rhodium wire wound resistance furnace. Equilibrations of up to two weeks duration were performed at the desired temperature with the oxygen partial pressure fixed by using premixed argon-oxygen gas mixtures in the range $1\text{-}10^{-4}$ atm p_{O_2}.

The ^{51}Cr labeled chromium was produced by neutron irradiation of high purity iodide chromium metal in the Battelle Research Reactor. In order to prepare the chromium for irradiation, approximately 1g of metal was sealed in a quartz vial under a helium atmosphere. The quartz vial was then sealed in an aluminum capsule which also contained a helium atmosphere. The chromium was irradiated for 48 hr in a thermal flux of 1×10^{13} n/cm^2/sec, which produced a specific activity of $\sim$ 100 mci/g of chromium. A gamma ray spectra was taken to check the 0.32 meV peak of ^{51}Cr.

The irradiated chromium was deposited on one side of the NiO specimens by vapor deposition using a vacuum evaporator operated at 1×10^{-6} mm Hg. The chromium was vaporized by resistance heating in a tungsten boat. The depositions were performed in three or four evaporation steps of about 30 sec each, which provided an adherent layer. The weight of chromium deposited on the specimens was 40-60 μg/cm^2 which resulted in layers about 700-900Å thick. The quantity of chromium on the diffusion specimens was determined by comparison of the ^{51}Cr activity to that of a sample of irradiated chromium of known weight.

Two chromium-plated specimens were then sandwiched into a spring-loaded Vycor specimen holder and placed in the diffusion furnace under conditions of temperature and oxygen partial pressure similar to those used in the prediffusion anneal. On completion of the diffusion anneal, side faces of the diffusion specimens were cleaved off to remove activity from rapid diffusion down the sides of the specimens. Diffusion profiles were obtained by a sectioning method (13) and by counting the residual surface activity after each sectioning step (14). Sectioning was performed by grinding the specimen on 600 grit metallographic paper which was impregnated with kerosene. For the grinding operation the specimen was glued to a stainless steel insert which fit into a micrometer-driven stainless steel grinding block. Approximate values for the thickness removed could be estimated from the micrometer settings. After the grinding operation the mounted specimen was placed in an electronic height gauge to determine more exactly the thickness removed. In this manner cuts of 3-4μ could be taken $\pm$ 0.1μ. The mounted specimen could then be placed in a counter to measure the residual activity, while the kerosene impregnated metallographic paper on which grinding had been performed was placed in a glass vial for counting the activity in the sections removed.

An end-window, gas flow proportional counter was used to radioassay the diffusion specimen after removal of each layer. The detector was operated at 1750V using P-10 counting gas. A modular scaler was used to accumulate the pulses from the detector. The efficiency of this system for counting ^{51}Cr is about 2%. A sufficient number of counts were taken to reduce counting errors to less than 1% for each section removed.

Experimental Results and Discussion

For the experimental conditions of this investigation an infinitely thin layer of ^{51}Cr can be said to have been deposited on a semi-infinite solid. For such conditions the gradient of tracer concentration C at distance x beneath the original interface is given by

$$\delta \ln C/\delta x^2 = -1/4Dt \qquad [1]$$

where D is the diffusion coefficient in square centimeters per second and t is the time in seconds. Diffusion coefficients can be obtained by plotting the logarithm of the activity against the square of the distance from the initial interface, and setting the slope of the straight line so obtained equal to $-1/4Dt$. Data obtained from diffusion anneals conducted at 1100° and 1250°C under 1 atm of oxygen are plotted in Fig. 1 as counts per minute, cpm *vs.* x^2, microns squared. Similar results were obtained using data from either the sectioning method or the residual activity technique (which were used in Fig. 1). It is seen that the initial portions of these penetration profiles do not yield straight lines. These portions of the profiles may represent concentration dependent diffusion, resulting from self-doping due to diffusing chromium ions. As the concentration of nickel vacancies due to the trivalent chromium addition drops below the concentration due to impurities already in the NiO, the diffusivities for chromium become independent of chromium isotope concentration, as represented by the latter portions of the penetration profiles in Fig. 1.

Diffusivities obtained from the straight line portions of Fig. 1 are plotted as log D *vs.* reciprocal of absolute temperature, $1/T$, in Fig. 2. A straight line can be fit to these data using the method of least squares to get the Arrhenius type equation

$$D = 9.36 \times 10^{-5} \exp\left(-\frac{47.0 \pm 3.0 \text{ kcal}}{RT}\right) \frac{\text{cm}^2}{\text{sec}} \qquad [2]$$

The activation energy of 47.0 kcal/mole is similar to the values obtained for diffusion of ^{55}Fe in NiO single crystals by Crow (8) and by Richards and Wagstaff (9). Under 1 atm of oxygen Crow reported an activation energy of 46.0 kcal/mole for iron diffusion in the temperature range of 110°-1400°C. As pointed out

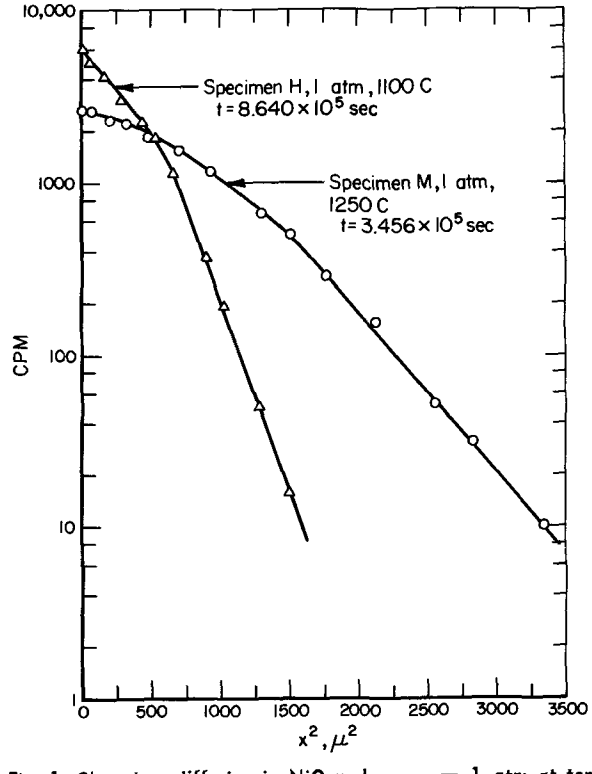

Fig. 1. Chromium diffusion in NiO under $p_{O_2} = 1$ atm at temperatures of 1100° and 1250°C. Activity in cpm vs. penetration as microns squared.

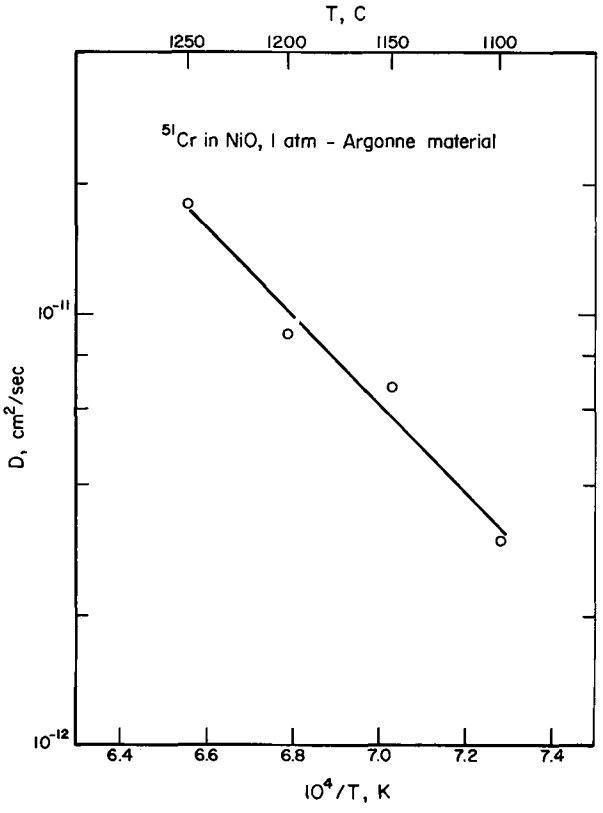

Fig. 2. Temperature dependence for diffusion of chromium in NiO at 1 atm oxygen. Log *D* vs. 1/*T*.

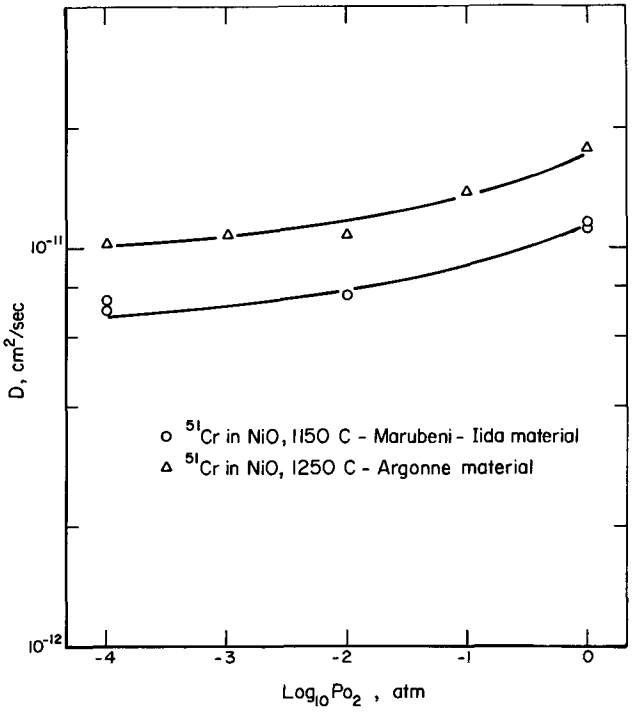

Fig. 3. Diffusion coefficients *vs.* oxygen pressure for chromium in NiO at 1150° and 1250°C.

by Crow, and discussed further below, these activation energies, which are somewhat lower than the values found for cobalt and nickel diffusion in NiO, can probably be attributed to the trivalency of the chromium and iron cations in the divalent cation host lattice.

The dependence of ^{51}Cr diffusivities on oxygen partial pressure at 1150° and 1250°C is shown in Fig. 3 as log D *vs.* log p_{O_2}. The data do not appear to be linear with log p_{O_2}. It is likely that they should be fit by curves whose slopes increase with increasing oxygen partial pressure. The diffusivities obtained from Marubeni-Iida crystals are a factor of two greater than the values determined from Argonne material (compare diffusion coefficients from Fig. 2 and 3 at 1150°C and 1 atm oxygen pressure for the two kinds of material). This may result from the fact that the net concentration of trivalent impurities is greater in the Marubeni-Iida crystals than in the Argonne material. Since trivalent additions are expected to increase the nickel vacancy concentration while monovalent impurities decrease the native vacancy concentration, the over-all effect is higher diffusivities in the NiO obtained from Marubeni-Iida.

Although the data obtained in this investigation are insufficient to develop a detailed model for the operative diffusion mechanism some suggestions can be made based on the information available.

The first possibility is that chromium diffusion occurs by a vacancy mechanism, similar to self-diffusion of nickel in NiO. The activation energy for chromium diffusion of 47 kcal/mole is, however, considerably lower than that for intrinsic self-diffusion of nickel in NiO, even where the chromium diffusivities are calculated from the concentration independent portions of the penetration profiles. It is of course likely that the NiO specimens used in this study have a high enough background concentration of electrically active impurities so that an activation energy representative of extrinsic diffusion has been obtained. In this case the penetration profiles indicate concentration independent diffusion once the chromium concentration falls below the over-all impurity level in the diffusion specimens. The similar activation energies for ^{55}Fe and ^{51}Cr in NiO could then be attributed to extrinsic diffusion where the energies for migration of iron and chromium in NiO are fortuitously similar. Crow (8) has shown that the oxygen partial pressure dependence may be expected to decrease with decreasing p_{O_2}, as is shown in Fig. 3, as the vacancy concentration becomes impurity controlled at low oxygen partial pressures. In this case the activation energy for diffusion might be expected to increase with increasing p_{O_2} as the nickel vacancy concentration becomes independent of impurity level. For ^{55}Fe in NiO Crow indeed found the activation energies to increase from 41 to 46 kcal/mole as the oxygen partial pressure increased from 5 x 10^{-5} to 1 atm. However, the value of 46 kcal/mole is still well below the value of 54.7 kcal/mole found by Crow for Ni in NiO at 1 atm.

An alternative diffusion mechanism, involves migration via an impurity-vacancy complex, in this case presumably a chromium ion-nickel vacancy pair. The theoretical basis for such a mechanism of impurity diffusion in ionic crystals has been developed by Lidiard (10), and the mechanism has been invoked to interpret experimental results for systems such as ^{109}Cd diffusion in AgBr (11).

Under the conditions of this investigation the chromium concentration over the straight portion of the penetration profile is assumed to be small in comparison with the nickel vacancy concentration, but D_{Cr} is proportional to p where p is the degree of association of the impurity. The degree of association is given (12) by the mass action equation

$$p/(1-p) = (12\,v/N^+)\exp(\Delta G/kT) = v\,K \quad [3]$$

where v is the concentration of unassociated nickel vacancies, N^+ is the concentration of nickel ion sites, ΔG is the association energy, K is an equilibrium constant, k is Boltzmann's constant, and T is the absolute temperature. Rearranging Eq. [3] gives

$$D_{Cr} = C_p = C\left[\frac{v\,K}{1+vK}\right] \quad [4]$$

where C is a constant. In this case D is seen to be nearly independent of oxygen pressure and of chromium concentration if K is large.

Acknowledgments

The author wishes to thank J. E. Howes and the late R. D. Tenaglia for invaluable assistance with various aspects of this investigation. The NiO crystals used were kindly provided by Dr. M. L. Volpe of the Argonne National Laboratory. The research was supported by the Columbus Laboratories, Battelle Memorial Institute.

Manuscript submitted July 16, 1970; revised manuscript received Jan. 11, 1971. This was Paper 149 presented at the Atlantic City Meeting of the Society, Oct. 4-9, 1970.

Any discussion of this paper will appear in a Discussion Section to be published in the December 1971 JOURNAL.

REFERENCES

1. W. J. Moore, "Complete Scientific Report on Contract Termination [on] Rate Processes in Inorganic Solids at High Temperatures [for] October 1, 1950 to August 1, 1951," ORO-78 (1951).
2. M. T. Shim and W. J. Moore, *J. Chem. Phys.*, **26**, 802 (1957).
3. R. Lindner and A. Akerstrom, *Discussions Faraday Soc.*, **23**, 133 (1957).
4. W. J. Moore, J. J. Landers, S. R. Logan, M. O'Keeffe, J. S. Choi, J. Ebisuzaki, J. Brown, and D. Mitchell, "Physical Chemistry of the Solid State," TID-11020 (1960).
5. J. S. Choi and W. J. Moore, *J. Phys. Chem.*, **66**, 1308 (1962).
6. S. M. Klotsmann, A. N. Timofeyev, and I. Sh. Traktenberg, *Fiz. Metal. i Metalloved*, **14**, 428 (1962).
7. M. L. Volpe and J. Reddy, Unpublished report, Argonne National Laboratory, Argonne, Illinois, 1969.
8. W. B. Crow, "Diffusion of Cobalt, Nickel and Iron in Cobalt, Oxide, and Nickel Oxide, Ph.D. Thesis, The Ohio State University, 1969.
9. K. J. Richards and F. E. Wagstaff, *J. Phys. Chem.*, **70**, 1553 (1966).
10. A. B. Lidiard, *Phil. Mag.*, **46**, 815, 1218 (1955).
11. J. E. Hanlon, *J. Chem. Phys.*, **32**, 1492 (1960).
12. J. Teltow, *Ann. Phys.*, **5**, 63 (1950).
13. C. Leymonie, "Radioactive Tracers in Physical Metallurgy," p. 49, John Wiley & Sons Inc., New York (1963).
14. *Ibid.*, p. 53.

Liquid Phase Epitaxial Growth of $InAs_{1-x}Sb_x$

G. B. Stringfellow and P. E. Greene†

Solid State Laboratory, Hewlett-Packard Company, Palo Alto, California 94304

ABSTRACT

Single-crystal epitaxial layers of $InAs_{1-x}Sb_x$ have been grown using a steady-state, liquid phase epitaxial growth technique. In the range of $0 < x < 0.35$ they were grown on InAs substrates from liquid compositions on the pseudobinary phase diagram and also from liquids in the In-rich corner of the ternary phase diagram at temperatures between 580° and 720°C. In the range of $0.89 < x < 1$ they were grown on InSb substrates from In-rich liquids with growth temperatures ranging from 480° to 520°C. The grown crystals are homogeneous in the region more than 4μ from the substrate. The optical absorption edges are sharp, similar to the InAs absorption edge. The 300°K energy band gap as a function of composition may be described by the following expression

$$E = 0.35 - 0.771x + 0.596x^2 \text{ eV}$$

The electrical properties of the $InAs_{1-x}Sb_x$ alloys with $x < 0.35$ are similar to those of pure InAs, *i.e.*, when $n = 2 \times 10^{16}$ cm^{-3} typical mobilities are 30,000 cm^2/V-sec at 300°K and 50,000 cm^2/V-sec at 77°K. For alloys with $x = 0.89$ typical mobilities are 67,000 cm^2/V-sec at 300°K and 50,000 cm^2/V-sec at 77°K. Incorporation of Sn during growth of $InAs_{0.92}Sb_{0.08}$ from the pseudobinary liquid at 720°C was found to give n-type doping. Under these conditions the distribution coefficient was determined to be 0.01.

$InAs_{1-x}Sb_x$ alloys are interesting semiconductor materials for two main reasons: (A) The energy band gap covers the range from 3-12μ (1) which is a range of practical interest for infrared emitting diodes and detectors. (B) They offer the prospect of having higher mobility than any presently known semiconductors (2).

The properties of $InAs_{1-x}Sb_x$ alloys were first investigated by Woolley and co-workers. They established the InAs-InSb miscibility (3), the pseudobinary phase diagram (3), and they investigated the variation of fundamental properties such as band gap (1, 4) and effective mass (5-7) with composition. Sirota and co-workers (8-10) and Kudman and Ekstrom (11) also investigated the properties of $InAs_{1-x}Sb_x$ alloys. All of the above measurements were performed on polycrystalline samples of $InAs_{1-x}Sb_x$. Basov *et al.* (12) reported the growth of single crystalline $InAs_{0.98}Sb_{0.02}$ by the Czochralski technique and the fabrication of laser diodes in this material. Neither the growth of $InAs_{1-x}Sb_x$ single crystals with $x > 0.02$ or the epitaxial growth of single crystals of the alloys have been reported in the literature, although Tietjen *et al.* (13) have grown polycrystalline layers of $InAs_{1-x}Sb_x$ with $x < 0.95$ by vapor phase chemical deposition. The electrical and optical properties, which are very dependent on structural imperfections, particularly grain boundaries, have not been investigated using single crystals.

The purpose of this paper is to describe the epitaxial growth of $InAs_{1-x}Sb_x$ ($x < 0.35$ and $x > 0.89$) single crystals and to briefly report some of their chemical, structural, optical, and electrical properties.

Crystal Growth

The In-As-Sb phase diagram which is necessary for the growth of $InAs_{1-x}Sb_x$ alloys has been calculated (14) and has been verified experimentally during the course of the present work. The calculated liquidus isotherms and experimental data obtained by solu-

† Electrochemical Society Active Member of a Sustaining Member Company.

Key words: electrical properties of InAs-InSb alloys, optical properties of InAs-InSb alloys, phase diagram In-As-Sb system, Sn doping of $InAs_{0.92}Sb_{0.08}$.

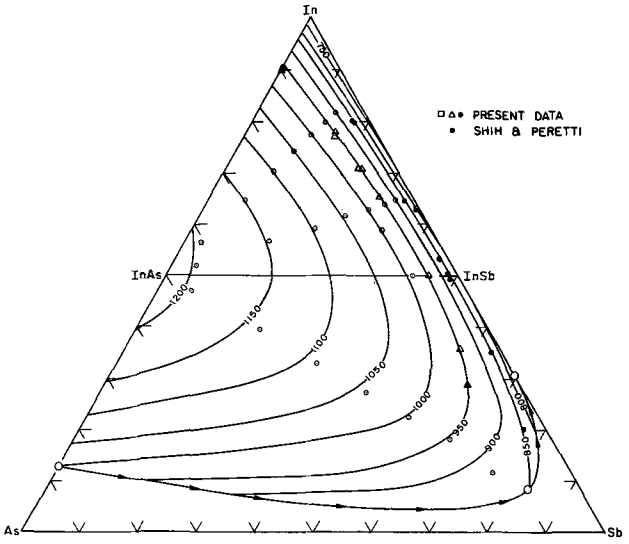

Fig. 1. Calculated liquidus isotherms for the system In-As-Sb compared with data of Shih and Peretti (21) (○) and data obtained from solubility measurements of InAs in In-Sb melts (●, △, □).

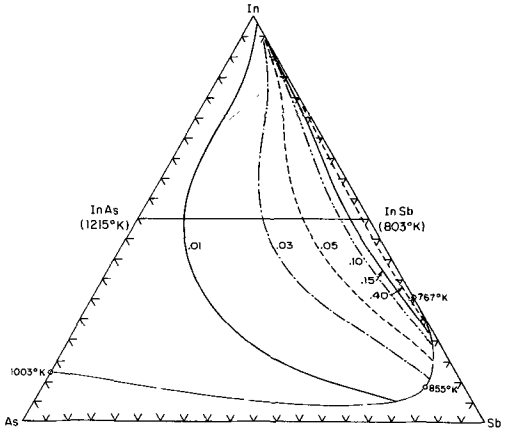

Fig. 2. Calculated iso(solid concentration) curves for the In-As-Sb system. Each curve representing the liquid compositions in equilibrium with a single solid compositon is labeled X_{InSb}.

bility measurements of InAs in In-Sb liquids are presented in Fig. 1. By comparing this with Fig. 2, which illustrates calculated iso(solid concentration) lines one can see that a solid alloy of a given composition can be grown from any liquid on the iso(solid-concentration) line but the highest growth temperature is obtained on the InAs-InSb pseudobinary. The pseudobinary, presented in Fig. 3, illustrates many of the problems encountered in the growth of single-crystal layers of $InAs_{1-x}Sb_x$ alloys:

1. The solid composition is strongly temperature dependent in the range $x > 0.1$. Thus any thermal excursion occurring during the growth of the crystal produces a large composition gradient in the grown crystal.

2. The growth temperatures are very low especially with $x > 0.2$. In fact, if InSb substrates are used, the temperature must be below 530°C.

3. The As distribution coefficient is very large causing severe kinetic problems such as constitutional supercooling during the growth of $InAs_{1-x}Sb_x$ crystals.

4. The lattice parameter of InSb is 7% larger than that of InAs, which causes difficulty in epitaxial growth of alloys of intermediate composition on either InAs or InSb especially in liquid phase epitaxial growth where compositional tapering is difficult.

These crystal growth problems necessitate a somewhat unique crystal-growth technique. During steady-

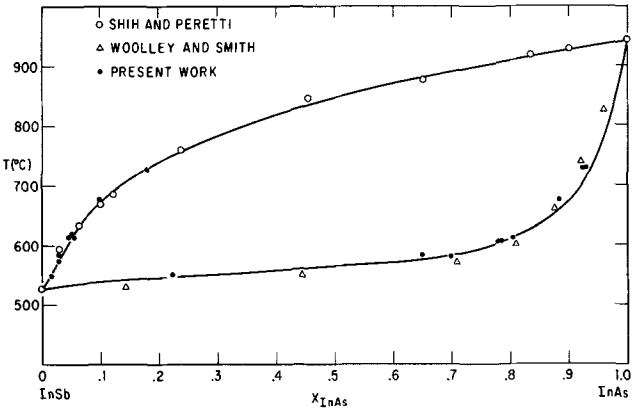

Fig. 3. Calculated pseudobinary phase diagram for the InAs-InSb system. Liquidus data points were obtained by solubility measurements of InAs in In-Sb solutions (●) and from the results of Shih and Peretti (20) (○). The solidus points were obtained by growing crystals at near equilibrium conditions. The results of Woolley and Smith (2) are presented as triangles (△).

state liquid phase epitaxial (SSLPE) growth the substrate temperature is held constant. A temperature gradient maintained in the liquid phase between the substrate and the source material acts as a driving force for the crystal growth, controls the growth and nucleation rates, and acts to stabilize the interface, thus minimizing the constitutional supercooling in the melt. The substrate may be either InAs or InSb. The source should, in principle, have the same composition as the growing epitaxial layer. Because of the large As distribution coefficient, however, the solid phase is always much richer in As than the liquid from which it is growing; thus in a system where the melt is much larger than the crystal grown, a source of As is all that is required to avoid appreciable depletion of the melt except for the growth of nearly pure InSb. InAs, a convenient source of As, was used throughout the crystal growth experiments. The apparatus for the steady-state liquid phase epitaxial growth of $InAs_{1-x}Sb_x$ is illustrated schematically in Fig. 4.

Experimental

Crystal growth was carried out in a high purity graphite crucible purged with H_2 purified by diffusion through a palladium-silver alloy membrane. The source and substrate were prepared by standard lapping and polishing procedures followed by a chemical etch in 1% Br in methanol just prior to introduction into the crystal growth apparatus. The melt was prepared by weighing appropriate amounts of 6-9's In and Sb into the graphite crucible along with polycrystalline InAs. The crucible was then heated to the

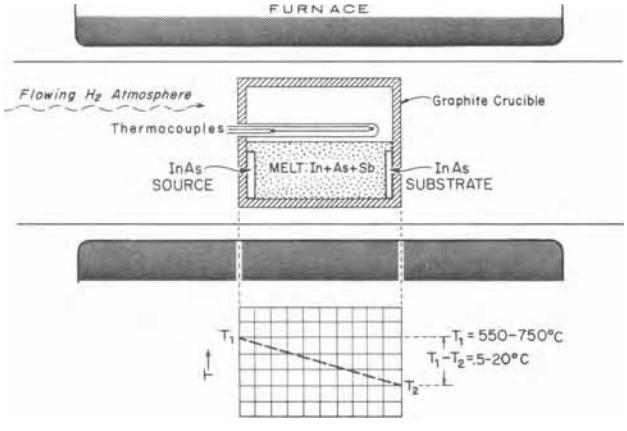

Fig. 4. Schematic diagram of the apparatus used to grow crystals of InAs-InSb alloys by the steady-state liquid phase epitaxy technique.

growth temperature for several hours to dissolve the InAs and saturate the melt. The substrate and source were then introduced into the melt by rotating the crucible. The growth was terminated by rotating the crucible again to remove the source and substrate from the melt.

The liquidus data were obtained as above using only a pure InAs substrate with no source wafer and no temperature gradient. The solubility was determined by weighing the substrate before and after the experiment, wherein the substrate was immersed in the liquid for several hours in order to completely saturate the melt. The solid compositions were determined by growing crystals using very low ΔT and, hence, low growth rates to insure that the crystal growth occurred at near-equilibrium conditions. The solid composition was found to be uniform within ± 1 a/o (atomic per cent), facilitating the determination of the phase diagram data. The alloy compositions were obtained from the lattice parameters determined from Debye-Scherrer x-ray powder diffraction patterns, using the a_0 *vs.* x data of Woolley *et al.* (3). The results are accurate to ± 0.01 in x which is equivalent to the half width of the x-ray diffraction lines.

Crystals of a given composition may in principle be grown from any of an infinite number of temperature-liquid composition pairs. In practice, the choice of the growth conditions is governed by three principles:

1. The growth temperature must be lower than the melting temperature of the substrate.
2. The As vapor pressure must be low enough to avoid appreciable loss of As from the melt during growth.
3. The growth temperature should be the highest possible which will satisfy 1 and 2 above. The highest growth temperature for a given solid is from a liquid on the pseudobinary phase diagram.

A brief summary is presented in Table I of the growth conditions used for the successful growth of $InAs_{1-x}Sb_x$ epitaxial crystals of several compositions. For growth of solids with $x = 0.04$ from liquids on the pseudobinary phase diagram the temperature-composition coordinates are such that As was lost rapidly from the melt. Crystals with $x = 0.04$ were successfully grown at 720°C from an In-rich liquid. For $x = 0.08$, 0.15, 0.20, and 0.31 the optimum growth conditions were found to be on the pseudobinary phase diagram. Crystals with $0.89 < x < 1$ were grown on InSb substrates at temperatures slightly below 530°C, the melting point of InSb. The liquid compositions were in the In-rich portion of the phase diagram.

Crystals were grown using temperature differences of 2°-15° between source and substrate. Large temperature differences of 7°-15° were usually necessary for growth with the flat liquid-solid interface necessary to avoid trapping of the melt.

Results

The experimental In-As-Sb liquidus data is plotted along with calculated results in Fig. 1. The experimentally determined solid compositions in equilibrium with a given liquid are presented in Table II for comparison with experimental results. The rms deviation of the experimental from the calculated results is 0.01, which is equal to the experimental uncertainty in x.

Photographs of typical epitaxial layers grown using the conditions set forth in Table I are presented in Fig. 5. These photographs illustrate the excellent surface morphology obtained for $x < 0.16$, which degrades as x is increased. Attempts to grow crystals with $x > 0.25$ on InAs substrates produced only polycrystalline material. The range of compositions was extended to $x = 0.35$ by growing the final epitaxial layer on a previously grown epitaxial layer having an intermediate value of x.

Table I. Conditions for the growth of $InAs_{1-x}Sb_x$

X	T(°C)	Liquid comp.	ΔT(°C)	Growth rate, μ/min	Substrate
0.04	720	$X_{In} = 0.690$, $X_{Sb} = 0.220$, $X_{As} = 0.090$	6.8	15	InAs (111)B
0.08	719.5	$X_{In} = 0.500$, $X_{Sb} = 0.416$, $X_{As} = 0.084$	8	1	InAs (111)B
0.15	670	$X_{In} = 0.500$, $X_{Sb} = 0.450$, $X_{As} = 0.050$	7.2	0.67	InAs (111)B
0.20	610	$X_{In} = 0.500$, $X_{Sb} = 0.475$, $X_{As} = 0.025$	7.6	0.3	$InAs_{0.92}Sb_{0.08}$ (111)B
0.31	579	$X_{In} = 0.500$, $X_{Sb} = 0.484$, $X_{As} = 0.016$	14.1	0.17	$InAs_{0.85}Sb_{0.15}$ (111)B)
0.89	520	$X_{In} = 0.630$, $X_{Sb} = 0.366$, $X_{As} = 0.004$	1.5	0.7	InSb (111)B

Table II. Summary of solid compositions grown from various liquids. Experimental results are compared with values calculated in ref. (14)

T(°C)	X_{In}	X_{Sn}	X_{As}	(X^c_{InAs})	(X^c_{InAs}) Calc.	ΔX
520	0.630	0.368	0.004	0.11	0.10	0.01
582	0.500	0.484	0.016	0.680	0.700	0.020
583	0.798	0.171	0.031	0.935	0.936	0.001
577	0.645	0.335	0.020	0.755	0.78	0.025
574	0.645	0.335	0.020	0.788	0.78	0.008
582	0.635	0.349	0.016	0.755	0.775	0.020
607	0.500	0.466	0.032	0.795	0.797	0.002
613	0.500	0.464	0.034	0.805	0.797	0.008
606	0.502	0.467	0.031	0.785	0.797	0.012
676	0.500	0.451	0.049	0.885	0.893	0.008
679	0.651	0.291	0.058	0.925	0.930	0.005
681	0.773	0.156	0.071	0.963	0.957	0.006
681	0.770	0.154	0.076	0.960	0.964	0.004
677	0.703	0.228	0.068	0.935	0.950	0.015
677	0.775	0.155	0.070	0.967	0.968	0.001
729	0.500	0.410	0.090	0.93	0.935	0.005

Electron microprobe scans were made of the epitaxial layers along cleaved edges in a direction perpendicular to the growth plane. A typical result is presented in Fig. 6. The composition of the epitaxial layer changes from InAs to 8% InSb in the first 4μ of growth after which the composition is nearly constant. The position $d = 0$ in Fig. 6 is the InAs substrate surface before growth. There was no evidence of substrate dissolution prior to the growth.

Another test of the homogeneity of the epitaxial layers is the width of the large angle Debye-Scherrer powder x-ray diffraction lines. Figure 7 shows the 731 and 642 lines for an $InAs_{0.92}Sb_{0.08}$ alloy and pure InAs. The alloy lines are no broader than those of pure InAs indicating that the alloy layers are homogeneous to within $\pm$ 0.01 in x.

The fact that the alloy layers were single crystalline and epitaxial was verified by Laue x-ray diffraction patterns.

Optical absorption was measured on $InAs_{1-x}Sb_x$ samples of various compositions. The transmission measurements were made using the standard sample in-sample out technique. Absorption coefficients were calculated using the relation

$$\frac{I}{I_0} = \frac{(1-R)^2}{e^{\alpha d} - R^2 e^{-\alpha d}}$$

which takes into account multiple internal reflections. Reflectivity data are not available for the alloys, so a value of $R = 0.3$, which is appropriate for pure InAs, was used for all alloys. The experimental results are plotted in Fig. 8. The absorption edge can be described using the empirical expression

$$\alpha = A \exp (h V/kT_0)$$

which has been found to describe the absorption in pure III-V compounds (15). The value of T_0, which indicates the steepness of the edge, was found to be 80°K for pure InAs and the alloys with $x < 0.20$ and

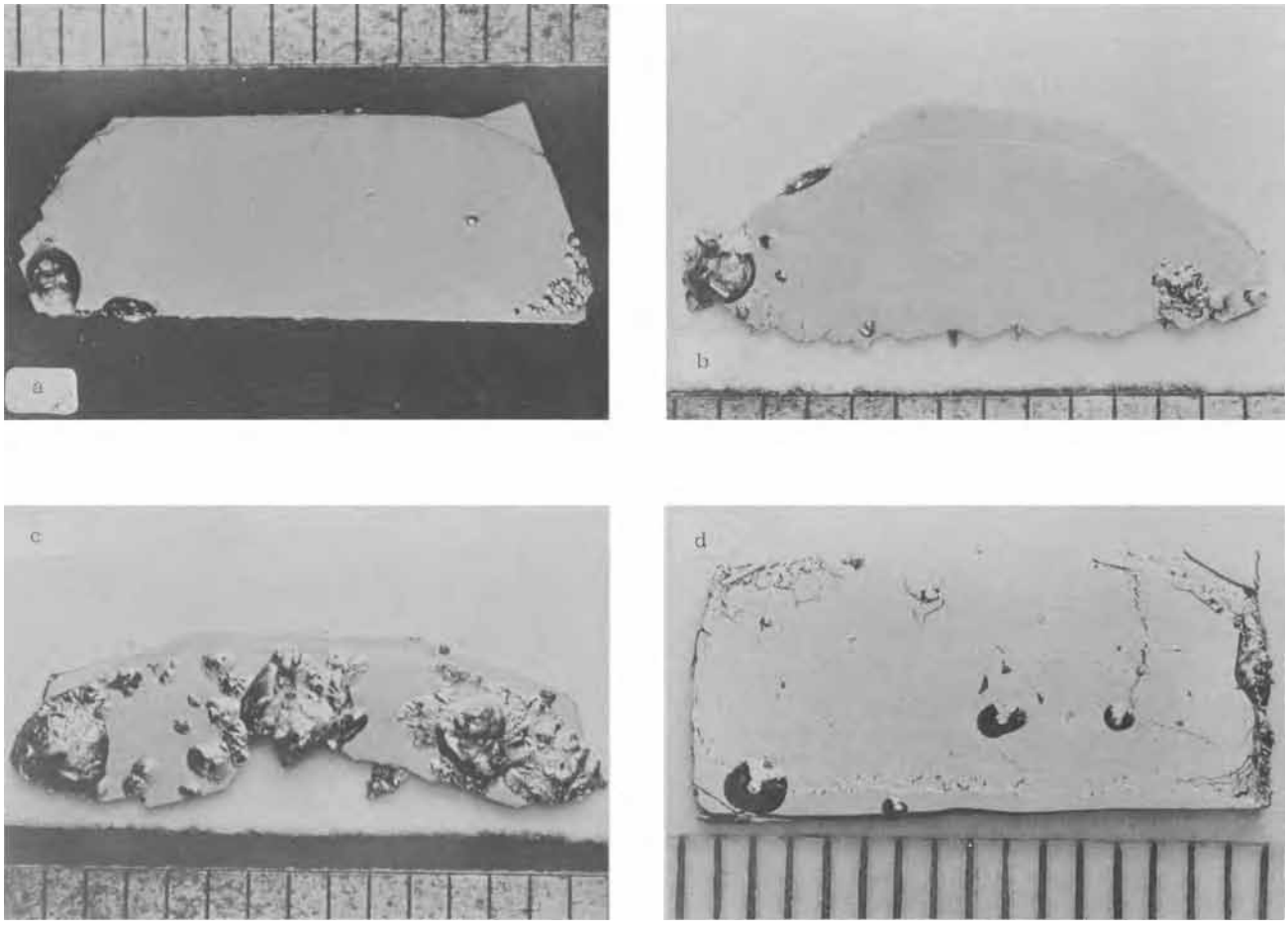

Fig. 5. Photographs of as-grown surfaces of typical epitaxial layers of $InAs_{1-x}Sb_x$ grown by SSLPE technique: (a) $x = 0.08$, (b) $x = 0.15$, (c) $x = 0.31$, (d) $x = 0.89$.

$x = 0.89$. When $x > 0.25$ the edge is slightly less sharp, with $T_o = 110°K$. It is not clear whether this is an intrinsic property of the alloys or is due to the possible slight sample inhomogeneities, within the ± 0.01 detectability limits, or within the size limits of the 1μ microprobe spot.

The band gap was determined from the absorption data as the point at which $\alpha = 300$ cm^{-1}, which gives the correct band gap for InAs and InSb. In order for absorption data to give a correct value for the energy band gap of the alloys there must be no extraneous absorptions broadening the band edge and no Burstein shift. The Burstein shift for the samples measured can be estimated from the carrier concentration data presented below, knowing the conduction band density of states. The samples measured were degenerate at room temperature; but the Fermi level was never more than 0.025 eV above the bottom of the conduction band; which is less than the value of $4\ kT$, *i.e.*, 0.1 eV necessary to produce a Burstein shift at room temperature (16). Thus, the absorption data give a reliable determination of the band gap.

The band gap *vs.* composition is plotted in Fig. 9. These results on single-crystal epitaxial layers with controlled carrier concentration are seen to agree well with earlier data of Woolley (1) obtained on poly-

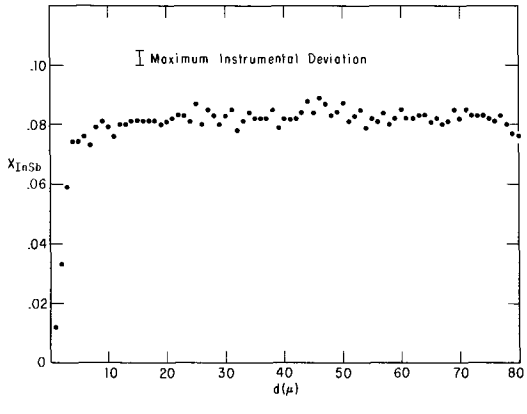

Fig. 6. Microprobe trace showing x_{InSb} along cleaved edge of epitaxial layer in a direction perpendicular to the growth plane. The d=0 position is the InAs/alloy interface.

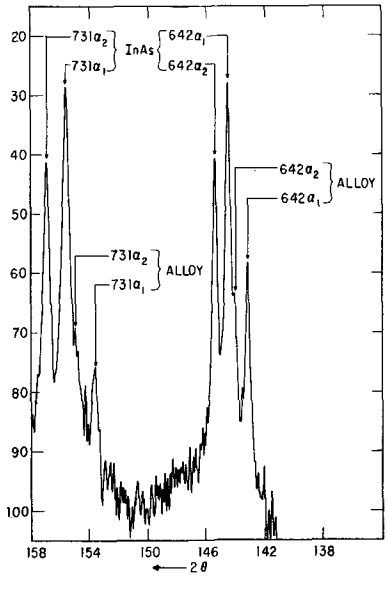

Fig. 7. X-ray powder diffraction peaks for 731 and 642 planes from $InAs_{0.92}Sb_{0.08}$ alloy and InAs substrate.

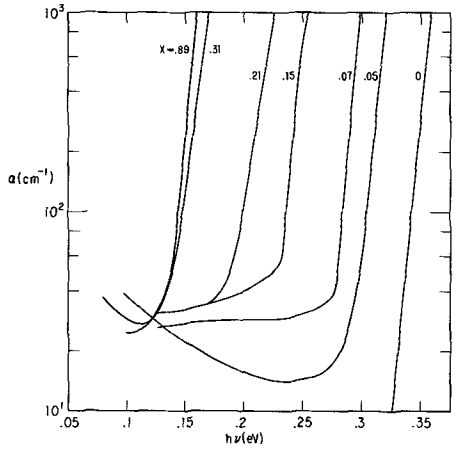

Fig. 8. Optical absorption coefficients vs. $h\upsilon$ for $InAs_{1-x}Sb_x$ samples with $x = 0$, 0.05, 0.07, 0.15, 0.20, 0.31, and 0.89.

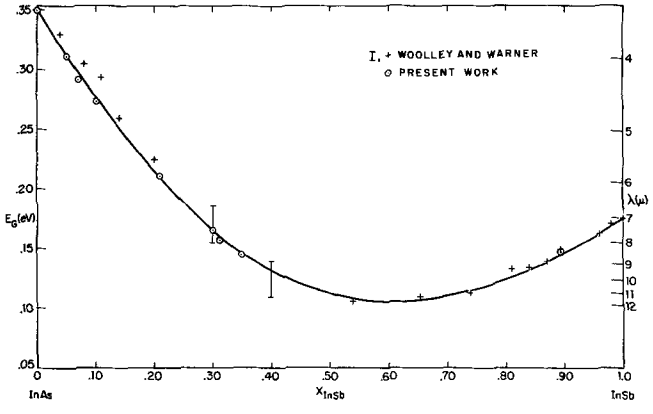

Fig. 9. Energy band gap, determined as $h\upsilon$ where $\alpha = 300$ cm^{-1}, vs. composition of alloy compared with results of Woolley and Warner (1) obtained for polycrystalline samples.

crystalline samples with higher carrier concentrations.

Conductivity and Hall effect measurements were made on single-crystal samples of $InAs_{1-x}Sb_x$ of various compositions. Hall samples of the standard rectangular parallelopiped geometry were made from $InAs_{1-x}Sb_x$ layers with the InAs substrates removed. Ohmic contacts were made by soldering indium spheres to the bar. The measurements were made using standard d-c potentiometric techniques at temperatures of 300° and 77°K. The results are presented in Table III. The carrier concentrations in undoped material can be controlled in the range $n = 2 \times 10^{16}$ cm^{-3} for all compositions. The room temperature mobilities of the alloys with $x < 0.35$ are approximately the same as for the pure InAs. The liquid nitrogen mobilities range from 20,000 to 50,000 cm^2/V-sec for undoped samples. The mobilities measured for $x = 0.89$ are 67,000 cm^2/V-sec at 300°K and 50,000 at 77°K.

The mobilities obtained are disappointingly low for samples with $x = 0.20$-0.35 and $x = 0.89$. Mobilities

Table III. Electrical properties of $InAs_{1-x}Sb_x$

Run No.	X	$n_{300} \times 10^{16}$	$\mu_{300} \times 10^4$	$n_{77} \times 10^{16}$	$\mu_{77} \times 10^4$
372	0.89	2.38†	6.72	0.17	4.9
369	0.89	3.04†	6.78	0.27	—
327	0.31	4.7†	2.7	0.5	—
283	0.31	4.7†	2.7	0.369	2.7
264	0.20	2.26	2.03	0.971	4.07
136	0.08	1.24	2.9	1.08	5.04
134	0.08	1.23	2.86	1.06	4.82
152	0.08	11.2*	2.00	10.3	2.91
154	0.08	53.0*	1.53	—	—
139	0.08	300.0*	0.87	300.0	1.0

* Sn doped.
† Intrinsic at 300°K.

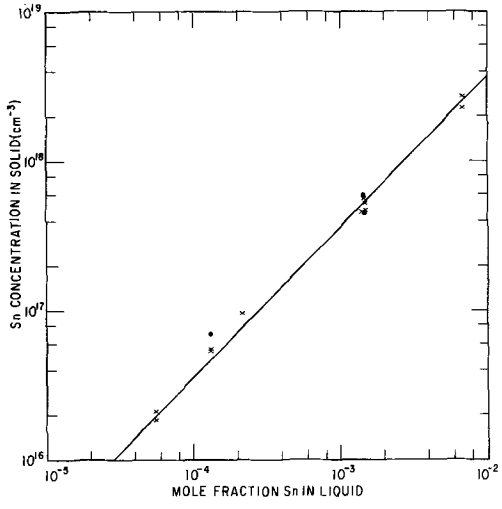

Fig. 10. Sn concentration in $InAs_{0.92}Sb_{0.08}$ solid vs. Sn concentration in the In, As, Sb liquid. Sn concentrations in the solid were obtained by Hall effect (x) and emission spectrographic analysis (●). The crystals were grown at 720°C from the pseudobinary liquid. Under these conditions the distribution coefficient is 0.01.

for $x = 0.35$, $n = 2 \times 10^{16}$, were calculated assuming a combination of polar optical and ionized impurity scattering to be 85,000 cm^2/V-sec at 300°K and 65,000 at 77°K. The low mobilities measured are probably due to imperfections in the grown crystals similar to those which cause mobilities of InAs grown on GaAs substrates to be much lower than InAs grown on InAs substrates (17).

N-type doping of $InAs_{0.92}Sb_{0.08}$ was investigated by introducing Sn during crystal growth from the pseudobinary liquid at 720°C. The Sn concentration in the solid was measured by measuring the carrier concentration and by emission spectrographic analysis. The results shown in Fig. 10 indicate the incorporated Sn is electrically active and non-self-compensating in the range of 1×10^{16} to 3×10^{18} cm^{-3}. The distribution coefficient was found to be independent of composition and equal to 0.01 under these growth conditions.

One other important method of evaluating the material is to fabricate diodes and study their properties. Wong *et al.* (18) have successfully fabricated high efficiency diodes from the $InAs_{1-x}Sb_x$ described in this paper, and reported on their properties.

Discussion

A comparison of Table 1 with Fig. 5 illustrates that the growth of $InAs_{1-x}Sb_x$ becomes increasingly difficult as x increases. The surface morphology was found to degrade, even though ΔT was increased in order to increase the growth rate and stabilize the flat interface. This seems to be due to the increasing lattice parameter mismatch as x increases. As noted above, it was not possible to grow single-crystal epitaxial layers of $InAs_{1-x}Sb_x$ with $x > 0.25$ on pure InAs substrates. A stepwise taper implemented by growing the final epitaxial layer on a previously grown epitaxial layer having an intermediate value of x resulted in successful growth of single-crystal epitaxial layers with x as large as 0.35. This indicates that the lattice parameter mismatch is the factor limiting the range of composition over which single-crystal epitaxial layers may be grown.

The free energy of a growing nucleus is increased by constraining it to stretch to fit the lattice of the substrate upon which it is growing. For this reason the lowest energy growth is in the form of columns, or, to minimize surface free energy, faceted platelets. Applying a large temperature gradient in the liquid tends to reverse this tendency and make the growth flat, but when the lattice parameter mismatch is too large, the crystals continue to grow as platelets. The

result is polycrystalline layers. The strain energy term, in addition to the chemical free energy, also perturbs the composition of the solid in equilibrium with a given liquid toward the composition of the substrate. This effect may explain the taper of composition from the substrate composition to the final chemical equilibrium composition over 4μ as seen in Fig. 6. For the growth of $Ga_{1-x}Al_xAs$ on GaAs substrates, where there is no lattice parameter mismatch, Woodall (19) reported an abrupt change in solid composition at the interface which could not be resolved using the 1μ microprobe beam size.

It should be noted that the band gaps of the alloys successfully grown by SSLPE growth on InAs substrates span the region from 0.35 eV (pure InAs) to 0.14 eV which is below the band gap of InSb. This is a region of considerable practical importance for infrared emitting diodes and detectors. These results plus the successful growth of $InAs_{1-x}Sb_x$, $x > 0.89$, indicate that the best way to cover a large range of band gaps is to grow alloys with $0 < x < 0.3$ on InAs substrates for the range 3 to 7.3μ and alloys with $1 > x > 0.6$ on InSb substrates for the range from 7.3 to 12μ.

Conclusions

Single-crystal epitaxial layers of $InAs_{1-x}Sb_x$ with $0 < x < 0.35$ and $0.89 < x < 1$ have been grown on InAs and InSb substrates, respectively, by steady-state liquid phase epitaxial growth. The crystals were found to have the following properties:

1. The solid composition remains constant after the first 4μ of crystal growth.
2. The undoped alloys have optical absorption edges as sharp as the undoped InAs edge.
3. The composition dependence of the energy band gap agrees with data of Woolley for polycrystalline $InAs_{1-x}Sb_x$.
4. The residual doping level of the undoped alloys is typically less than 2×10^{16} cm^{-3}.
5. The electron mobilities for undoped alloys range from 30,000 ($0 < x < 0.35$) to 67,000 (cm^2/V-sec) ($x = 0.89$) at 300°K and from 30,000 to 50,000 cm^2/V-sec at 77°K for all alloy compositions investigated.
6. $InAs_{0.92}Sb_{0.08}$ was Sn doped to give an electron concentration in the range 2×10^{16} to 3×10^{18} cm^{-3}. The Sn distribution coefficient at 720°C was determined to be 0.01.

Acknowledgment

The authors thank R. A. Burmeister for helpful discussions and G. Hom and R. Garcia for assisting in the experimental work.

Manuscript submitted July 31, 1970; revised manuscript received Jan. 11, 1971.

Any discussion of this paper will appear in a Discussion Section to be published in the December 1971 JOURNAL.

REFERENCES

1. J. C. Woolley and J. Warner, *Can. J. of Phys.*, **42**, 1879 (1964).
2. C. Hilsum, "Proceedings of the International Conference on Physics of Semiconductors," p. 1127, Dunod, Paris, (1964).
3. J. C. Woolley and B. A. Smith, *Proc. Phys. Soc.*, **72**, 214 (1958).
4. W. M. Coderre and J. C. Woolley, *Can. J. Phys.*, **46**, 1207 (1968).
5. E. H. Van Tongerloo and J. C. Woolley, *ibid.*, **46**, 1199 (1968).
6. M. J. Aubin and J. C. Woolley, *ibid.*, **46**, 1191 (1968).
7. J. C. Woolley and A. G. Thompson, *ibid.*, **42**, 2030 (1964).
8. N. N. Sirota and Ye. I. Bolvanovich, *Khim. Svyaz Poluprov. Termodin., Inst. Fiz. Tverd. Tela Poluprov. Akad. Nauk Belloruss, SSR*, **1966**, 267.
9. N. N. Sirota and Ye. I. Bolvanovich, *Akad. Nauk BSSR Mensk Doklady*, **11**, 503 (1967).
10. N. N. Sirota and Ye. I. Bolvanovich, *ibid.*, **11**, 593 (1967).
11. I. Kudman and L. Ekstrom, *J. Appl. Phys.*, **39**, 3385 (1968).
12. N. G. Basov, A. V. Dodenkova, A. I. Krasil'nikov, V. V. Nikitin, and K. D. Fedoseev, *Soviet Phys.-Solid State (English Transl.)*, **8**, 847 (1966).
13. J. J. Tietjen, R. Clough, A. B. Dreeben, R. Engstrom, and D. Richman, Contract No. NAS 12-538 for NASA (March 1969).
14. G. B. Stringfellow and P. E. Greene, *J. Phys. Chem. Solids*, **30**, 1779 (1969).
15. J. R. Dixon and J. M. Ellis, *Phys. Rev.*, **123**, 1560 (1961).
16. E. Burstein, *ibid.*, **93**, 632 (1954).
17. G. R. Cronin and S. R. Borrello, *This Journal*, **114**, 1078 (1967).
18. J. Y. Wong, E. E. Loebner, and K. L. Garliepp, Abs. 84, p. 232, Electrochem. Soc. Extended Abstracts, Spring Meeting, Los Angeles, May 10-15, 1970.
19. J. M. Woodall, Abs. 76, p. 208, Electrochem. Soc. Extended Abstracts, Spring Meeting, Los Angeles, May 10-15, 1970.
20. C. H. Shih and E. A. Peretti, *Trans. ASM*, **46**, 389 (1954).
21. C. H. Shih and E. A. Peretti, *ibid.*, **48**, 706 (1956).

Technical Note

The Effect of a Barrier Oxide on Evaporation of Water from a Hydrous Aluminum Oxide Film

R. S. Alwitt*

Research and Development Laboratories, Sprague Electric Company, North Adams, Massachusetts 01247

Bernard and Randall (1) have shown that a smaller weight loss results when a hydrous aluminum oxide film is heated while still in contact with base metal than when an isolated film is heated. This was found to be due to reaction of some of the water in the film with substrate aluminum to produce more oxide. There are no published results to indicate whether a barrier oxide layer between the hydrous film and the metal would block the diffusion of water to the substrate. This is of importance in analyzing thermogravimetric and differential thermogravimetric data obtained with

* Electrochemical Society Active Member.
Key words: anodic oxide films, aluminum, hydrous alumina film, water content.

Table I. Results of experimentation—specimen area equal to 17.6 cm^2

(All weights in micrograms)

V_f	Anodic oxide wt	(A) Wt gain in water	Wt Al_2O_3 hydrated	Final barrier thickness (V)	(B) Wt loss at 600°C	B/A
90	664	223	All	0	90	0.403
90	660	251	All	0	116	0.462
150	1100	186	628	64	149	0.800
150	1073	224	757	44	158	0.705
250	1933	173	585	174	164	0.948
250	1786	199	673	156	186	0.924

anodized aluminum. Such data have been used to determine the amounts of different component oxides [*e.g.*, amorphous $Al(OH)_3$, boehmite] in the anodic film with the assumption that no liberated water reacted with metal substrate (2, 3).

Experimental Procedure

Aluminum foil samples of 99.99% purity were lightly etched by immersion in 1*N* NaOH for 2 min at room temperature. The specimens were then anodized at room temperature in an electrolyte of 30% ammonium pentaborate in ethylene glycol at a current density of 1.4 mA/cm^2. Anhydrous, amorphous, barrier films are formed in this electrolyte at 100% current efficiency (4). Films were formed with thicknesses equivalent to 90, 150 and 250V. The specimens were then immersed in boiling water for 3 min to convert an outer portion of the films to hydrous oxide (5). The samples were then heated in air at 600°C for 2 hr. The quantities measured were the charge passed during anodization, the weight before and after the water reaction, and the weight after heating.

The weight of anodic oxide was calculated from the charge assuming 100% current efficiency. The amount of oxide that reacted with water was calculated assuming the hydrous oxide contained 22.8% water. This composition was determined from data of Bernard and Randall (6). The final barrier thickness was calculated from the weight fraction of the initial oxide that did not react with water.

Results and Discussion

The results are listed in Table I. The weight loss at 600°C is the sum of water evaporated and hydrogen evolved from any reaction of water with metal substrate. Some water may be trapped in the barrier oxide while diffusing toward the substrate and may not be released at 600°C (7) so it is not possible to unequivocally determine from these data the amount of water that reacted. But the entries in the last column clearly show that even a 160V film is not a sufficient barrier to permit quantitative recovery of water.

It might be noted that the capacitance of a 150V specimen was measured before and after reaction with water, and the voltage supported by the film after the water reaction was measured. Both of these measurements indicated a 60V barrier film. This agreement with the weight data indicates that hydration proceeded uniformly over the surface.

It is clear that before thermogravimetric data obtained on oxide films *in situ* can be interpreted, it is necessary to determine whether water can react with the substrate under the test conditions. Alternately, one can work with isolated films obtained by dissolving the metal in 10% bromine-methanol. It has been demonstrated that this technique permits the quantitative recovery of pseudoboehmite (1) and amorphous anodic oxide (7). Erdey *et al.* (2) reported that this treatment partially decomposed hydrargillite, but they did not give the conditions or extent of attack. It would be worthwhile to study the effect of this reagent on other forms of aluminum oxide to determine under what conditions it may be used.

Manuscript submitted Oct. 19, 1970; revised manuscript received Feb. 1, 1971.

Any discussion of this paper will appear in a Discussion Section to be published in the December 1971 JOURNAL.

REFERENCES

1. W. J. Bernard and J. J. Randall, Jr., *This Journal*, **107**, 483 (1960).
2. L. Erdey, T. Kormany, and S. Gal, *Z. Anal. Chem.*, **200**, 218 (1964).
3. G. A. Dorsey, Jr., *This Journal*, **117**, 954 (1970).
4. W. J. Bernard and J. W. Cook, *ibid.*, **106**, 643 (1959).
5. W. Vedder and D. A. Vermilyea, *Trans. Faraday Soc.*, **65**, 561 (1969).
6. W. J. Bernard and J. J. Randall, Jr., *This Journal*, **108**, 822 (1961).
7. R. S. Alwitt, *ibid.*, **114**, 843 (1967).

JOURNAL OF THE ELECTROCHEMICAL SOCIETY

ELECTROCHEMICAL TECHNOLOGY

MAY 1971

Hydrogen-Air/Lead Battery Hybrid System for Vehicle Propulsion

K. V. Kordesch*

Union Carbide Corporation, Consumer Products Division, Research Laboratory, Parma, Ohio 44129

ABSTRACT

The high energy density of a fuel cell battery and the peak current capability of a secondary battery are combined in the power plant of an electric car. The four-seat vehicle weighs 2000 lb and is powered by a 7 kW (20 kW peak) d-c motor. The 6 kW hydrogen-air fuel cell battery is connected in parallel with a 4 kWhr lead battery (84V); 660 ft^3 of hydrogen are stored in six lightweight cylinders (180 lb total weight) equivalent to 33 kWhr of actually available electric energy. The design of the fuel cell battery was aimed at very long life expectancy on intermittent duty, fast automatic starting and shutdown, reliable safety features, and use of available commercial accessories. The operation of the car is not more difficult than driving a conventional auto; the range is over 200 miles. The refilling of the hydrogen cylinders takes only a few minutes from a 2000 psig supply. The acceleration is similar to that of a small car with a combustion engine. Top speed is 55 mph.

Advantages and shortcomings of electric cars for urban transportation have been discussed extensively, mainly from the standpoint of pollution control (1). Military vehicles powered by fuel cell systems have been investigated for reasons of fuel efficiency (2). Pilot production of small electric cars with lead batteries has started in Japan, and the development of heat engine-battery hybrids has been seriously considered in the United States and Germany. For use in the vehicle which has no chance to recharge for hours and cannot have a motor generator on board (*e.g.*, taxies or "city cars" driven up to 200 miles/day), the fuel cell/secondary battery hybrid seems to offer a possible solution.

To take one more step into the future (fuel cells are not ready for production today), the *fuel* should not be derived from coal or oil for reasons of conserving fossil fuels.[1] Hydrogen seems to be a suitable energy source (compressed, liquid, or derived *in situ* from ammonia or other inexpensive chemicals), since it is the only reactant which can be easily used in high power fuel cells. The lowest present cost estimate for the noble metal catalyst requirement is $50/kW, but improved technology could eliminate or reduce this considerably. Air must be the oxidizing agent; no noble metal catalysts are needed for carbon-air cathodes.

The author has selected an alkaline fuel cell system for experimentation because, technically, it is the most advanced. Oxygen would be necessary to achieve peak performance from the fuel cell power plant (3). However, with a hybrid system, the overload capability is provided by the secondary battery and air is sufficient. The hydrogen-air/lead battery system was chosen as the most practical solution (4, 5).

The project of building a small electric car for urban transportation was actually started in 1966 by remodeling an Austin A-40 for electric propulsion by utilizing 14 lead acid batteries (84V) as the power source. The resulting vehicle (2000 lb) performed very much as predicted by many surveys made then and at later dates (6).

In 1968-1969, the car was partially converted to "fuel cell power." A 90V hydrogen-air battery replaced the seven lead-acid batteries in the rear compartment, while the seven front batteries remained as before.

No special efforts have been made to optimize components. Commercially available accessories (pumps, blowers, *etc.*) were used throughout the system. The fuel cells were hand built with electrodes of the type described in several publications (7, 8) by the author and his co-workers.

Improvements in electrode technology during the years 1967-1969 were not included because the earlier electrodes could not be mixed with the later ones for the sake of uniformity of the complete power plant, but it should be noted that the later electrodes would have allowed a design center of 100 A/ft^2 current density rather than 50 A/ft^2 (9).

This improvement was achieved by reversing the electrodes so that the porous nickel layer (nonwetproofed) faced the electrolyte, while the carbon faced the gas side, unobstructed and not subject to nitrogen blockage. The porous nickel served as an air blow-through barrier. However, due to the reduction in fuel cell activities at Union Carbide Corporation (mainly because no commercial application in the near future could be visualized), such electrodes found only limited use in hydrazine-air batteries built for the U. S. Army (10).

The experimental car, as it now exists, will have the role of a test vehicle in discovering any inherent maintenance problems, battery life expectancy, and establishing feasibility of further design improvements

* Electrochemical Society Active Member.

Key words: electric automobile, fuel cell operated vehicle, high energy density battery system, low pollution power source, parallel connected battery systems, saving of fossil fuels.

[1] At present, most of the commercial hydrogen is derived from fossil fuels, but this may change with the advent of nuclear power plants.

Fig. 1. Electric car powered by a hydrogen-air/lead battery hybrid power system.

as well as durability of materials and accessories. The vehicle is provided with safety features which should prevent any trouble due to accidental improper handling. The transportation rules governing compressed flammable gases have been carefully observed (11).

A photograph of the vehicle is shown in Fig. 1. The fuel cell system is mounted in the rear compartment together with all of the necessary accessories for automatic start-up and shutdown, including nitrogen purging. The lead battery is situated in the front next to the motor. For simplicity, the original four-gear shift transmission with clutch has been retained (it proved very beneficial for up-hill driving). "Gas pedal"-type speed control is achieved by field-winding switching.

The Hybrid Battery Concept Applied to an Automobile

The use of a fuel cell for vehicle propulsion poses problems relative to safe handling, short start-up time, avoidance of overloading and cell reversal, automatic controls in case of operating failures (electrolyte loss, overheating, *etc.*), and shutdown procedures.

Several of these problems disappear if a fuel cell battery is operated in parallel with a secondary battery. The start-up time can be stretched to several minutes while the equipment (or vehicle) is operated during that time from the secondary battery. Overloading is effectively prevented because the secondary battery takes over at the minimum voltage determined by the fuel cell characteristics. Figure 2 shows the principal wiring diagram of the hybrid automotive power plant. Seven 12V lead-acid batteries are connected in series (42 cells), and this bank is connected in parallel with a hydrogen-air fuel cell battery consisting of 15 eight-cell modules in series (120 cells). At low load levels, the fuel cell battery reaches a higher voltage than the lead-acid battery and is therefore able to charge the secondary battery. However, when the fuel cell battery is not in operation, it contains no hydrogen and has a far lower voltage than the lead-acid battery. The latter would now electrolyze water at the fuel cell electrodes and thereby cause wasteful and harmful operation. To prevent this, a diode is inserted into the connecting leads to permit current to flow only in one direction. This is one of the innovations permitting shutdown of the fuel cell battery and emptying of gases (and electrolyte) during nonoperating periods. This feature prolongs the lifetime of the fuel cells.

During start-up, however, hydrogen reaches the cells at different times and causes the activated cells to reverse the still inactive cells. This results in permanent damage to the "driven" or reversed cells. The reversed cells can be "righted" only by individually applying a pulse current (in the charging direction), a very time-consuming procedure. The difficulty can be avoided simply by applying the lead-acid battery voltage to the fuel cell battery (while the anode compartments are filled with nitrogen) by means of a resistor to bridge the diode during that period causing a small charge current to flow, which "polarizes" the cells in the "right" direction.

The nitrogen gas supply added to the fuel cell system to blanket the anodes when required can also be used for safety protection in cases of an emergency.

The Hydrogen-Air Fuel Cell System

Figure 3 shows the block diagram of the hydrogen-air fuel cell power plant as used in the automobile (the nitrogen supply is not shown).

The hydrogen-air battery contains 120 single H_2-air cells of the "duplex" or "bicell" construction. Eight such cells are arranged into a module. Figure 4 gives details of the construction of this basic 6V unit. The gas supply entry slits are on top of the batteries and the exit slits are on the bottom. Cross flow is desired. Plastic separators (network of fibers) represent the main flow resistance in the cell. The electrolyte enters

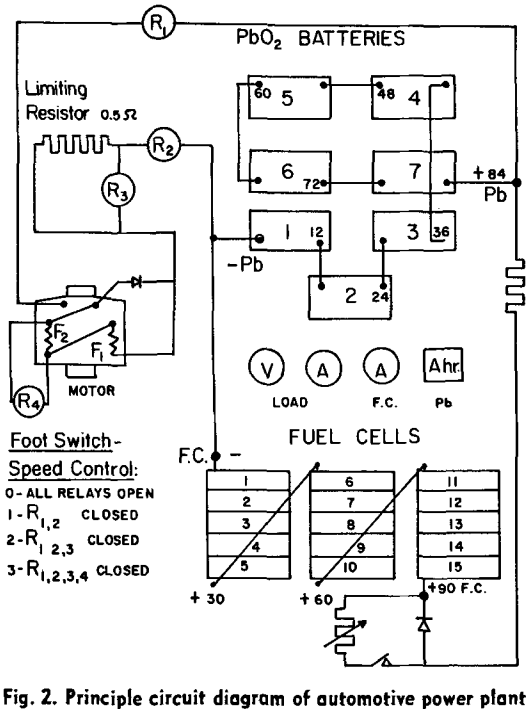

Fig. 2. Principle circuit diagram of automotive power plant

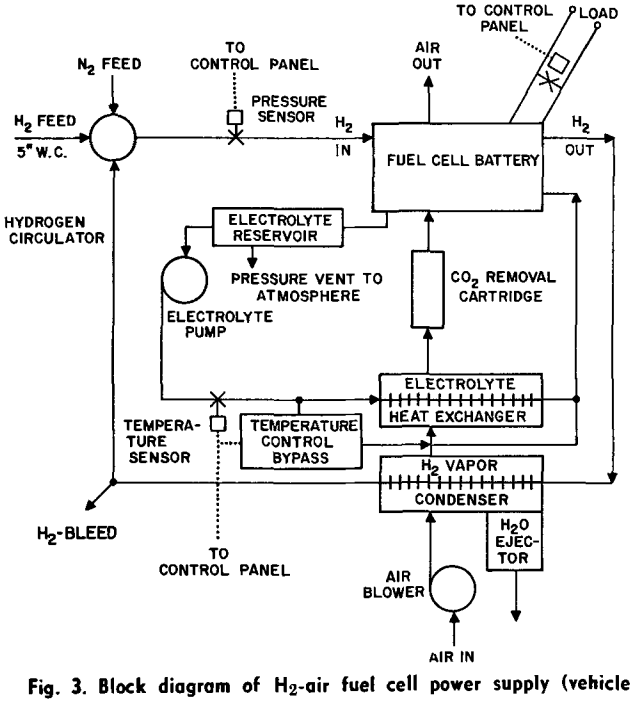

Fig. 3. Block diagram of H_2-air fuel cell power supply (vehicle concept).

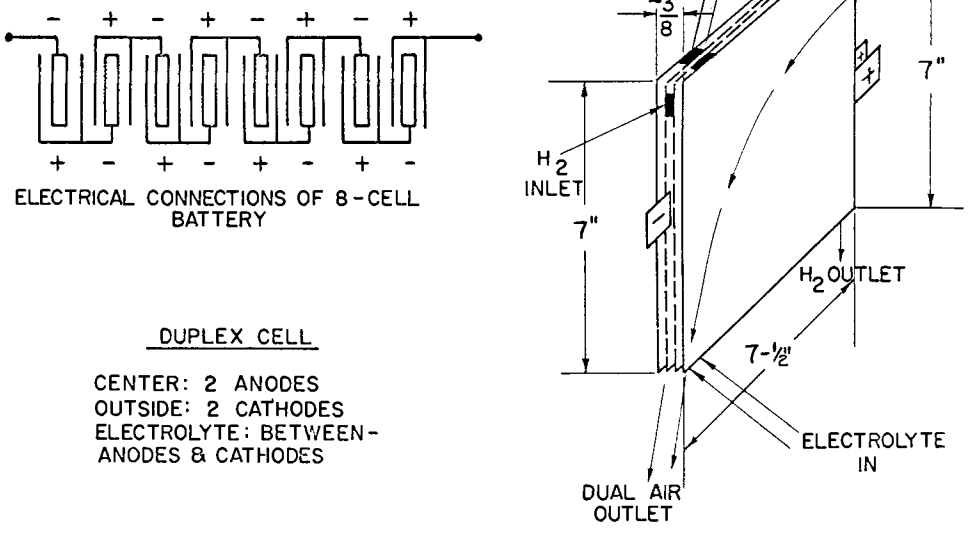

Fig. 4. Electrical connection and construction of "duplex" cell batteries.

through eight thin tubes on the bottom (not shown in Fig. 4) and leaves through two overflow tube arrangements on top. The tubing presents a relatively high electrical resistance, thus reducing parasitic current flow between cells and modules. From gas-use measurements on open circuit, it is estimated that this method of electrolyte connection reduces waste current to a level of 1-2% of the rated output. Five of such modules are connected to a "battery block," representing a power package of 2 kW at high level (100 A/ft^2) performance.

Three blocks are connected to one another by manifold networks for electrolyte, hydrogen, and air. The arrangement of the electrolyte flow pattern is critical in that it determines the magnitude of the parasitic current flow *via* the KOH conductance. The position of gas inlet and outlet ports influences the uniform distribution of the gas flow. The entire battery is mounted on a hinge so that it can be turned up to permit easy access to the bottom manifolds and electrical connections.

Figure 5 is a photograph of the modules of the hydrogen-air battery (in the turned-up position).

Figure 6 shows the battery in normal position (view from the rear of the car).

Hydrogen is stored as compressed gas in six cylinders on top of the car. The cylinders are made by the Pressed Steel Tank Company (Model No. 8RC 1500T). These lightweight tanks are made for aircraft use, scuba diving, and similar purposes.

The gas regulator and the manifold parts are standard and are fitted with the required heat and overpressure safety plugs on the cylinder valves. At the main regulator (outside the car), the pressure is reduced to 30 or 50 psig and the gas is piped through the main solenoid valve to the low-pressure regulator which delivers hydrogen at a pressure range of 2-12 in. water column (w.c.) at a high flow rate. Stainless steel traps placed after the battery collect any water before the hydrogen returns to the circulator pump; this pump is able to produce a 1 in. w.c. differential pressure across the stacks at 10-20 times the theoretical gas circulation rate at the 3 kW level (60 ft^3/hr). This amount of circulation is sufficient to remove all the water produced at 50 A/ft^2 when the battery is operating at 65°C temperature and the cooling system at 25°C.

A hydrogen-bleed value (adjustable between 0 and 5 ft^3/hr) serves as a constant inert removal device. It is usually set at from 1 to 1½ ft^3/hr hydrogen. A rapid bleed valve is activated during the start-up and shutdown sequences to exchange the battery atmosphere rapidly (N_2 for air, H_2 for N_2, and N_2 for H_2). The maximum gas flow-through rate is ~15 ft^3/min at a 10 in. w.c., which allows the exchange atmosphere to sweep the manifolds in a very short time should an emergency arise.

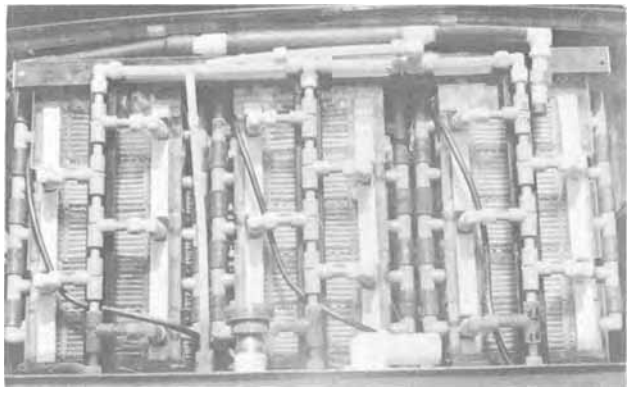

Fig. 5. Bottom view of complete 6 kW battery showing electrolyte distribution manifolds and electrical connections.

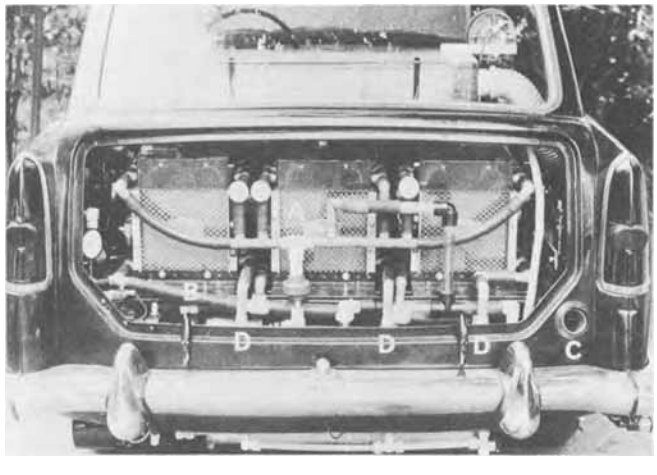

Fig. 6. Complete battery in normal position (view from rear of the car): A—electrolyte outlet manifold leading into filter, B—air outlet manifold, C—air exhaust (from water trap), D—hydrogen outlet manifold.

The hydrogen passes through a heat exchanger (water cooled) before it returns to the circulator pump (see Fig. 2). There, water vapor condenses out and passes through an automatic drain valve into the water collector tank (10 liter capacity) located under the car.

Nitrogen is stored in a cylinder mounted under the battery. The tank is of the same type as the hydrogen cylinders, but smaller (40 ft^3), and can be filled from the right rear side of the car. Nitrogen flow control is achieved by means of a solenoid valve which is energized from the dashboard sequence switch.

Air Supply System

Air is moved through the battery by a vacuum cleaner-type blower. The air intake is in the car but the blower is underneath (outside) the car to reduce noise. The pressure side of the blower is connected to the CO_2 scrubber (mounted on top of the battery) with a 3 in. flexible hose. From the CO_2 scrubber, the air is directed into three air-intake manifolds, one for each battery block. The moisture-laden air is exhausted to the outside. The blower speed is changed by depressing the footswitch in accordance with needed power requirements. With a 1 in. w.c. backpressure across the stacks, the blower can deliver 30-50 ft^3/min of air (maximum on full voltage). This is ten times the stoichiometric requirement on high level load (60A). However, to conserve the CO_2-scrubber capacity, it is normally run from lower voltage taps (24 and 32V) while still satisfying the average load of 30A and at the same time removing water vapor to such an extent that the H_2-water removal circuit has only to carry 50% of its designed capacity. This versatility assures that a satisfactory KOH normality will be maintained under all conditions (high outside temperature and high humidity are the most unfavorable conditions).

The feature of taking the air from the inside of the car and exhausting it to the outside of the car is an important safety feature because it reduces the danger of small hydrogen leaks.

The CO_2 scrubber is filled with 20 lb of soda lime; it should last at least 500 miles of average driving according to laboratory tests. Additions of Baralyme and layers of indicating Lithadsorb in the compartments close to the battery end serve as a booster and warning indicator. Intermittent driving modes seem to permit far better bed utilization than earlier continuous tests have indicated. It is interesting to note that fuel cells pick up CO_2 from the air with "inefficiency" after about 80% of the CO_2 has been removed. This becomes even more pronounced when the electrolyte dilutes under 9*N*.

The air scrubber is mounted horizontally, and five vertical buffer plates prevent bypassing of unscrubbed air when the soda lime has settled. The best particle size seems to be the 3-5 mesh range to combine low back pressure with satisfactory scrubbing.

Electrical Control Circuits

The complete start-up and shutdown procedure is sequenced by a six-position switch on the dashboard:

Position 0, System OFF

Position 1-3, STARTING

1. Open N_2 valve; bleed system rapidly.
2. Start electrolyte and air blower when pressure is sensed on the out-flow side of the fuel cells; the H_2 valve is opened; the bleed valve is also opened.
3. Connect resistor across diode; bleed reduced to small fraction of use rate.

Position 4, Normal OPERATING position of switch

All accessories are energized (but controlled by thermal switches, *etc.*)

Position 5, SHUTDOWN

De-energize everything; open N_2 valve; bleed system rapidly.

Position 6 (Same as Position 0), Fuel cell battery OFF

Since any small amount of H_2 remaining in the cells would create a reduced pressure in the anode compartments as long as the electrodes are wet and the intercell electrolyte connections are still conducting (*via* the wet manifolding), a separate negative pressure-sensitive diaphragm (−1 in. w.c.) will send nitrogen into the battery until all of the H_2 has been used up.

Control lights indicate conditions of the battery and functioning of accessories.

It is not possible to operate all circuits from the 12V accessory battery because the drain would be too high. The best solution for maintaining a separate ground is to charge the accessory battery from the fuel cell system by means of a d-c—d-c inverter with an 84-90V input and a 12-15V output.

The Lead-Acid Battery

The seven 12V batteries are all located under the hood, two in front of the motor and five above it. The batteries used were commercially available batteries manufactured by Globe Union Corporation:

Dimensions: 10¼ in. x 6¾ in. x 8¼ in. (height)
Weight: 47 lb each (329 lb total)
No. plates: 78 plates total (13 in each cell) in each battery
Capacity: 84 A-hr (20 hr rate)

Figure 7 shows a photograph of the front end of the car.

Test Results

Performance of the H_2-air battery in the laboratory.— All of the 6V modules were tested in the laboratory for at least 1 week (about 200 hr) to make sure that there were no defective cells present. If no leakage or poor intercell contacts were observed after the 5 day heat cycling (from room temperature to 70°C each day), the mechanical qualities were also considered satisfactory.

Actually, this type of battery has had a long testing history, dating back to 1966. At that time, Union Carbide Corporation tested H_2-air batteries consisting of eight Duplex cells in series, built exactly like the automobile batteries but smaller in size (4 in. x 6 in) (12).

The electrodes used in the batteries consisted of a wetproofed porous nickel layer as the backing (gas side), with a sprayed-on (plastic bonded) carbon layer on the electrolyte side (7).

The next two figures present polarization and life data for the condition that the batteries were being kept filled with electrolyte all of their life. No shut-

Fig. 7. Front-end view of the car

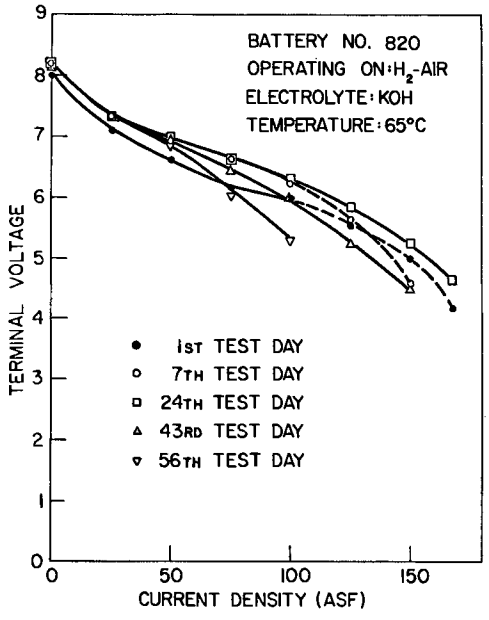

Fig. 8. Effect of aging—Battery No. 820

down procedure (as is now practiced) was used because we did not yet know of its advantages.

Figure 8 shows the performance of the 6V battery (No. 820). The effect of aging on the polarization curve should be noted.

Figure 9 gives the life history of Battery No. 820. As we now know, the capability of the battery to continue to operate after the first cell failure (after 56 days of operation) when the battery was shut down, washed with water, and restarted was very significant.

A very extensive study of water transportation as a function of gas flow, temperature, and KOH concentration was also made at that time (12). These data and others concerning mass transport and heat transfer in fuel cells (13) were very helpful in designing the automobile power plant.

Data accumulated during 1967-1969, when batteries had to be shut down on purpose (storage tests), showed that intermittent use of the batteries increased their lifetime. Note: 2000 hr continuous service is a little over 2 months; 2000 hr intermittent service may correspond to 60,000 miles driving over a three year period.

Performance of the automobile.—The hydrogen-air batteries produced over the time period 1968-1969 were washed and dried after their initial 1 week tests and were stored without any special precaution. In May 1970 the system was finished and activated for the first time as a 120 cell power plant.

Determination of polarization curves from points actually recorded during tests has been attempted in Fig. 10.

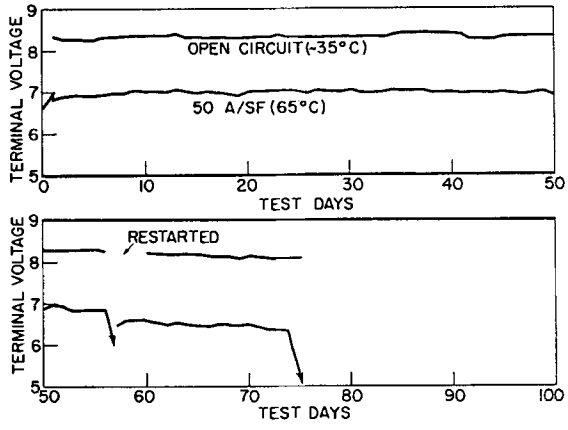

Fig. 9. Life history of Battery No. 820

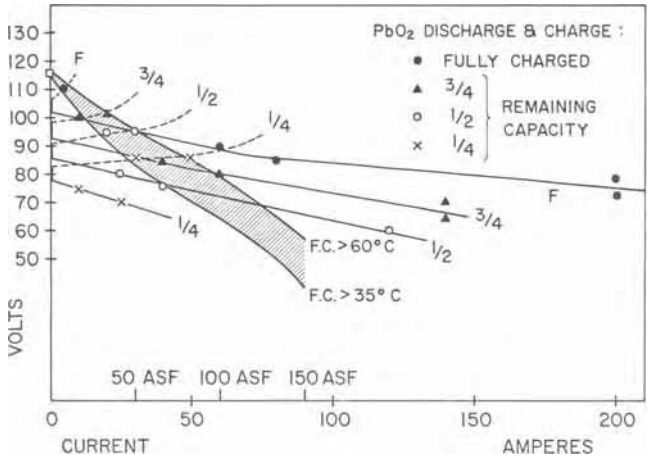

Fig. 10. Test polarization curves

Table I was compiled from instrument readings while the vehicle was moving. Road performance (acceleration and speed) and total capacity (driving range) can be readily estimated from checking its columns.

Fuel consumption.—As closely as can be estimated today, the hydrogen consumption rate is closely following that predicted (*viz.*, 1000 psi drop of tank pressure for 100 miles) for driving at mixed speeds (suburban mode). This also includes short test runs without moving the car. Since this pressure drop is about half of full pressure and the total available hydrogen volume is 660 ft^3, the figure for hydrogen consumption is therefore 330 ft^3/100 miles.

The hydrogen consumption per mile is expected to be lowest at a steady (40 mph) speed for a long uninterrupted distance. Under such conditions, about 75A

Table I. Load sharing of the hydrogen-air/lead system under different operating conditions

Power data			PbO_2 battery		H_2-air battery	
kW	V	A	State of charge	A	A	Operating conditions
11.0	85	125	Charged	80	45	55 mph, 52 mph, 48 mph, 42 mph: Full-speed driving with motor field reduced. Battery temp, >60°C.
9.5	80	115	¾	60	55	
8.0	75	105	½	40	65	
6.5	70	95	¼	25	70	
20.0	75	260	Charged	200	60	Maximum power during acceleration. Fuel cells warming up (~45°C).
14.0	65	210	¾	140	70	
12.0	60	195	½	120	75	
8.0	90	90	Charged	60	30	45 mph, 42 mph, 38 mph, 35 mph: Driving with full motor field. Battery temp, ~60°C.
7.0	85	80	¾	40	40	
6.0	80	75	½	25	50	
5.0	73	70	¼	10	60	
0.5	110	5	Charged	0	5	
2.0	100	20	¾	0	20	Fuel cell charging into PbO_2 battery. Motor not running. Battery temp, >60°C.
2.8	95	30	½	0	30	
4.2	85	50	¼	0	50	

Note: 60A from fuel cell = 100 A/ft^2 current density.

current (at 80V) are required, to which the fuel cell contributes approximately 1/2 to 2/3 until the lead batteries drop below 25% remaining capacity in their state of charge. Such a situation will be encountered if more than 2 hr of continuous driving are planned. If there is then no recharge pause available, the fuel cells will have to supply nearly all of the power (6 kW).

The parasitic (electrolytic) current within the fuel cell battery can be determined from open-circuit gas consumption measurements. These are in the order of 2 ft^3/hr, which is approximately 1½% of the 100 A/ft^2 consumption of 120 ft^3/hr. The hydrogen-bleed rate (at present set at 2 ft^3/hr) adds another 1½% waste for a total of nearly 3% of the high-level output of 6 kW. The voltage of 0.95 V/cell (7.6 V/module, or 114V for the entire battery) confirms the low parasitic current flow of about 2 A/ft^2 on open circuit. Altogether, the accessories have a power consumption of about 250-300W, or nearly 4-5% of the 100 A/ft^2 output of the fuel cell battery.

Conversion efficiency.—The fuel cell battery operates at about 0.8 V/cell. This means that the electrochemical efficiency (0.8/1.23) is 60% based on $H_2 \rightarrow H_2O$ (liquid), and the thermal efficiency (83% of this) is about 50%.

Operating costs.—The figure of 330 ft^3 H_2/100 miles is only a tentatively proposed estimate for city driving. On this basis, the cost per mile of driving is ½¢/mile if we assume that the cost of hydrogen in large quantities is 30¢/lb (220 ft^3). Liquid hydrogen storage may be considered.

Hydrogen delivered in steel cylinders, of course, is more expensive (up to ten times) than hydrogen at the plant or at large filling stations. The automobile could also be operated on liquid ammonia plus a catalytic converter. The reduction in weight would also be favorable by comparison. A 15 min time limit for getting the converter on "full stream" seems technically feasible. Only one cylinder instead of six would be needed.

Secondary battery life.—Frequent deep discharge cycles are *at present* not recommended for lead-acid batteries, but considerable improvements are expected. Of course, Ni-Cd batteries would be more suitable, but the price is high.

Conclusions

The purpose of this project was to demonstrate (*a*) that an electric automobile could be powered by a fuel cell/lead-acid battery hybrid system and retain the advantages of both battery types, and (*b*) that such a system can be easily started and shut down and is no more complicated than any other assembly of batteries with such common accessories as pumps, motors, and simple electrical circuits.

These facts were demonstrated and the electric automobile showed in driving tests that it behaved essentially like the gasoline-engine-powered automobile, except that its top speed was somewhat limited.

Summarizing the pertinent energy and power density figures, the following data are listed:

Power and energy-per-weight-figures:

Fuel cell system—6 kW (at 100 A/ft^2) output; weight, 370 lb (~60 lb/kW); 33 kWhr (actual) capacity; 90 Whr/lb; efficiency of conversion, ~50%

Lead-acid batteries—16 kW peak output; weight, 330 lb (~20 lb/kW); 3.4 kWhr (actual) capacity (at 50A); 11 Whr/lb.

Manuscript received Oct. 19, 1970; revised manuscript received *ca.* Jan. 20, 1971.

Any discussion of this paper will appear in a Discussion Section to be published in the December 1971 JOURNAL.

REFERENCES

1. "The Automobile and Air Pollution," Part II, U.S. Dept. of Commerce, Washington, D.C., Dec. 1967.
2. J. R. Huff and J. C. Orth, "Fuel Cell Systems-II," Advances in Chemistry Series 90, pp. 315-327, American Chemical Society, Washington (1969).
3. Demonstration by General Motors Corp.; cells by Union Carbide Corp.; C. Marks, E. A. Rishavy, and F. A. Wyczalek, Soc. Automobile Engrs. Paper 670176 (1967); C. E. Winter and W. L. Morgan, *ibid.*, Paper 670182; F. A. Wyczalek, D. L. Frank, and G. E. Smith, *ibid.*, Paper 670181.
4. K. V. Kordesch, Extended Abstract 273, Electrochem. Soc. Meeting, Los Angeles, Calif., May 10-15, 1970.
5. G. E. Evans, "Hydrogen-Air Fuel Cells for Vehicle Propulsion," in "Power Systems for Electric Vehicles," Symposium sponsored by the Department of Health, Education, and Welfare, Brooklyn, N. Y. (1967).
6. "Prospects for Electric Vehicles," a Study for the Department of Health, Education, and Welfare, by Arthur D. Little, Inc., Contract No. PH 86-67-108, May 15, 1968.
7. M. B. Clark, W. G. Darland, and K. V. Kordesch, *Electrochem. Technol.*, **3**, 166 (1965).
8. K. V. Kordesch, in "Handbook of Fuel Cell Technology," Carl Berger, Editor, Prentice-Hall Inc., Englewood Cliffs, N. J. (1968).
9. K. V. Kordesch, *Proc. 21st Ann. Power Sources Conf.*, **21**, 14 (1968).
10. K. V. Kordesch, *ibid.*, **24**, 207 (1970).
11. Code of Federal Regulations, Title 49, Parts 170-190 (Rev. Jan. 1, 1969), U.S. Govt. Printing Office, Washington, D.C. (1969).
12. "Thin Fuel Cell Electrodes," Final Report, Contract No. DA-28-043-AMC-01344(E), USAECOM, Fort Monmouth, N.J. (1966).
13. G. E. Evans, N. Hilvety, C. E. Winters, and R. V. Bailey, Symposium on Fuel Cell Systems, 58th Meeting of the Am. Inst. of Chem. Engrs., Philadelphia, Pa., 1965.

A Logarithmic Throwing Index for the Measurement of Throwing Powers

Der Tau Chin*

Electrochemistry Department, Research Laboratories, General Motors Corporation, Warren, Michigan 48090

ABSTRACT

A new and simple method is presented for expressing the result of throwing power measurements of electroplating solutions in terms of a logarithmic throwing index," defined as the ratio of the logarithm of linear ratios (L) to that of the metal distribution ratio (M). Graphically it is the reciprocal of the slope of a straight line obtained when M is plotted against L on log-log coordinates. The limitation of a linear throwing index method found in the literature and the advantages of the method proposed here are discussed with published results from use of the Haring-Blum cells.

In electroplating, throwing power is a measure of the extent to which a plating bath deposits a coating of uniform thickness on different parts of a cathode surface. For practical purposes, a simple and direct measurement, allowing rapid comparison of various plating solutions and operating conditions, is the use of a Haring-Blum cell (1). This device is a rectangular electrolytic cell having two metal cathodes of equal size placed vertically at either end. Between the cathodes is a flat, perforated anode having different distances from each cathode. The ratio of the anode distance from the far cathode to that from the near cathode is called the linear (or primary current distribution) ratio, L; the ratio of the rate of metal deposition on the near cathode to that on the far cathode is called the metal distribution ratio, M. The throwing power of a plating bath at a given operating condition is normally calculated from one of the following formulas:

Haring-Blum equation (1)

$$\text{Throwing power} = \frac{L - M}{L} \times 100 \qquad [1]$$

Heatley-Pan equation (2, 3)

$$\text{Throwing efficiency} = \frac{L - M}{L - 1} \times 100 \qquad [2]$$

Field equation (4)

$$\text{Throwing power (BSI)} = \frac{L - M}{L + M - 2} \times 100 \qquad [3]$$

Objection against using these equations has been raised by Jelinek and David (5) for the following reasons: first, the use of different equations would result in different numerical values for a plating bath at constant operating conditions; and second, the throwing powers computed by these equations vary appreciably with linear ratios. It is, therefore, desirable to have a single number that characterizes the throwing power of a bath over a range of linear ratios.

Jelinek and David have suggested a throwing index (5) obtained by plotting the metal distribution ratio *vs.* linear ratio on arithmetic coordinates. A straight line passing a common point ($L = 1$, $M = 1$) is drawn through the data points, and the reciprocal of the gradient of the line is taken as the throwing index. In this way a single value is obtained for a range of linear ratios which can be used to show variations of throwing power with changes in current density, temperature, and bath compositions. Since the method implies that there is a linear relationship between the metal distribution ratio and the linear ratio, a throwing index obtained this way will be called the linear throwing index in this paper. As will be shown, the linear throwing index, however, has inherent shortcomings.

This paper presents a new and simple method in terms of the logarithmic throwing index, which has all the advantages of the linear throwing index, and gives better descriptions of the characteristics of throwing power over a wide range of linear ratios.

Limitation of Linear Throwing Index

Since the linear throwing index is defined as the reciprocal of the slope of a straight line passing through the common point ($L = 1$, $M = 1$), and the experimental data in the L-M plot, there should exist the following relationship between the metal distribution and the linear ratios

$$M = 1 + \frac{1}{a}(L - 1) \qquad [4]$$

where a is the linear throwing index of a bath at constant plating conditions. Substituting this equation into the Heatley-Pan equation for the "throwing efficiency," one has

$$\text{Throwing efficiency} = \frac{L - 1 - \frac{1}{a}(L - 1)}{L - 1} \times 100$$

$$= \frac{(L - 1)\left(1 - \frac{1}{a}\right)}{L - 1} \times 100$$

$$= \left(1 - \frac{1}{a}\right) \times 100 = \text{const}$$

Similarly, by putting Eq. [4] in place of M in the Field equation, one can show that

$$\text{Throwing power (BSI)} = \frac{1 - 1/a}{1 + 1/a} \times 100 = \text{const}$$

Thus, the use of the linear throwing index results in a constant throwing efficiency and a constant "throwing power (BSI)" independent of linear ratios. This contradicts the experimental evidence, since the throwing power measurements expressed by the Heatley-Pan and the Field equations vary with linear ratios (3, 6). Apparently, the linear correlation given in Eq. [4] is not sufficient to describe the variation in the metal distribution ratios with changing linear ratios. A better relationship is therefore needed.

Logarithmic Throwing Index

In this laboratory we have made a regressional analysis for the throwing power data taken from the works

* Electrochemical Society Active Member.

Key words: throwing power, throwing index, logarithmic throwing index.

Table I. List of simple relationships that would give M = 1, when L = 1

Binomial	$M = 1 + \frac{1}{\alpha}(L-1)^{\beta}$
Exponential	$M = \exp\left\{\frac{1}{\alpha}(L-1)\right\}$
Linear	$M = 1 + \frac{1}{\alpha}(L-1)$
Parabolic	$M = 1 = \frac{1}{\alpha}(L-1) + \beta(L-1)^2$
Power	$M = L^{1/\alpha}$

Note: α and β are the regression coefficients.

of Pan (3), Jelinek and David (5), Gardam (6), and Wesley and Roehl (7). A number of functions that would give $M = 1$ when L equals unity were tested with the help of a digital computer. Table I is a partial list of the functions.

It is found that among the functions tested, the following relationship gives the best fit to the experimental data and still retains the characteristics of a single valued parameter for the measurement of throwing powers:

$$M = L^{1/A} \qquad [5]$$

The coefficient, A, in the exponent is a constant for a plating bath at constant operating conditions and will be called the logarithmic throwing index.

Accordingly, a plot of log M *vs.* log L should result in a straight line passing through the origin (0, 0). The logarithmic throwing index can be evaluated directly by taking the reciprocal of its slope. A solution with ideal throwing power would produce a horizontal line at log $M = 0$ and would therefore have a value of logarithmic throwing index equal to infinity. On the other hand, a solution with extremely poor throwing characteristics would give a vertical line at log $L = 0$, and its logarithmic throwing index equals zero.

To show the validity of this method, some of the experimental data are plotted in a log-log fashion as shown in Fig. 1. It is seen that Eq. [5] holds true for a wide variety of plating baths. Table II lists values of the logarithmic throwing index calculated from the

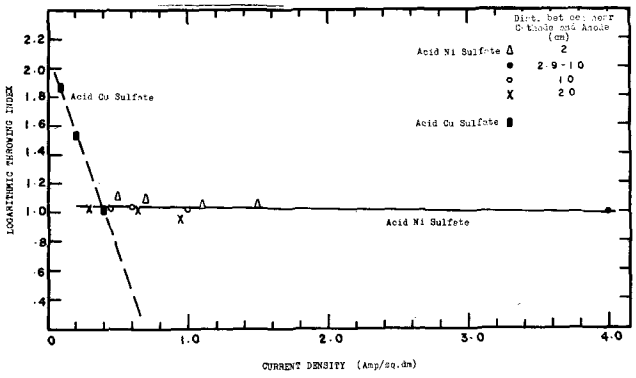

Fig. 2. Effect of current density on the logarithmic throwing index.

published results (3, 5-7) by means of regressional analysis of the linear transformation of Eq. [5]. In Fig. 2, the logarithmic throwing index of two baths in Table II is plotted against plating current densities. The dash (acid Cu sulfate) and the solid (acid Ni sulfate) curves are the regressional lines showing the tendency for the logarithmic throwing index to decrease with increasing current density.

For comparison, values of linear throwing index computed from the same data by means of regressional analysis of Eq. [4] are also given in Table II. Some of the linear and the logarithmic indexes listed are then used to calculate throwing powers in terms of Eq. [1]-[3] as functions of linear ratios. The results are compared with the values computed from the original data of metal distribution measurements. Such comparisons are shown in Fig. 3-5 for Cd-cyanide, acid-Cu-sulfate, acid-Ni-sulfate, and acid-Zn-sulfate baths. The dotted lines in the figures are the values of throwing powers calculated by replacing M in its appropriate equations with the linear throwing index and its linear relationship, Eq. [4]. The solid lines are computed by substituting into the equations, the logarithmic throwing index and Eq. [5]. The original data are indicated by the symbols ○, □, x, and △. It is seen that the calculation agrees with the previous discussion in which the use of linear throwing index would lead to a constant throwing efficiency (Fig. 4) and a constant throwing

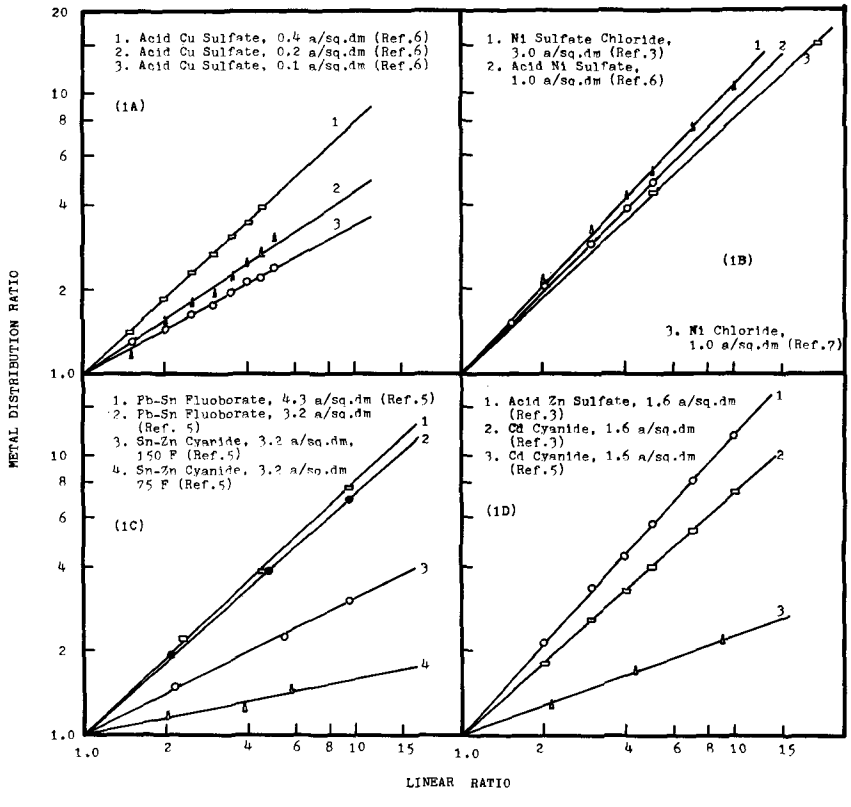

Fig. 1. Log-log plots of metal distribution ratio *vs.* linear ratio.

Table II. Values of the linear and the logarithmic index calculated from the published results

Bath	Investigators	Experimental conditions: Distance of near cathode from anode (cm)	Range of linear ratio	Temp (°C)	Current density (A/dm²)	Throwing index (calculated by regressional analysis): Linear	Logarithmic
Cd cyanide	Jelinek, David (5)			27	1.615	6.120	2.774
	Pan (3)	5-20	2-10	20	1.625	1.364	1.150
Acid Cu sulfate	Gardam (6)	2	1.5-5	18	0.1	2.733	1.867
		2	1.5-5	18	0.2	1.998	1.536
		10	1.5-5	18	0.4	1.050	1.023
Ni sulfate chloride	Pan (3)	5-20	2-10	32	3.0	0.961	0.924
	Wesley, Roehl (7)	2.9-10	5-20	54.4	4.0	1.019	1.001
Acid Ni sulfate	Wesley, Roehl (7)	2.9-10	5-20	54.4	4.0	0.993	0.995
	Gardam (6)	2	1.5-5	20	0.5	1.210	1.114
		2	1.5-5	20	0.7	1.147	1.089
		2	1.5-5	20	1.1	1.097	1.052
		2	1.5-5	20	1.5	1.098	1.053
		10	1.5-5	20	0.45	1.061	1.033
		10	1.5-5	20	0.6	1.074	1.039
		10	1.5-5	20	1.0	1.050	1.023
		20	1.5-2	20	0.3	1.029	1.027
		20	1.5-2	20	0.65	1.033	1.025
		20	1.5-2	20	0.95	0.947	0.959
Ni chloride	Wesley, Roehl (7)	2.9-10	5-20	54.0	1.0	1.347	1.099
		2.9-10	5-20	54.4	2.0	1.243	1.070
		2.9-10	5-20	54.4	4.0	1.161	1.046
Acid Zn sulfate	Jelinek, David (5)			27	1.615	0.857	0.934
	Pan (3)	5-20	2-10	25	1.625	0.837	0.927
Pb-Sn fluoborate	Jelinek, David (5)			27	3.23	1.394	1.154
				27	4.30	1.270	1.105
Sn-Zn cyanide	Jelinek, David (5)			24	3.23	9.719	4.787
				66	3.23	3.957	2.033

power (BSI), (Fig. 5) for the Heatley-Pan and the Field equations. On the other hand, the solid lines obtained with the use of the logarithmic throwing index follow the experimental values quite precisely. Even

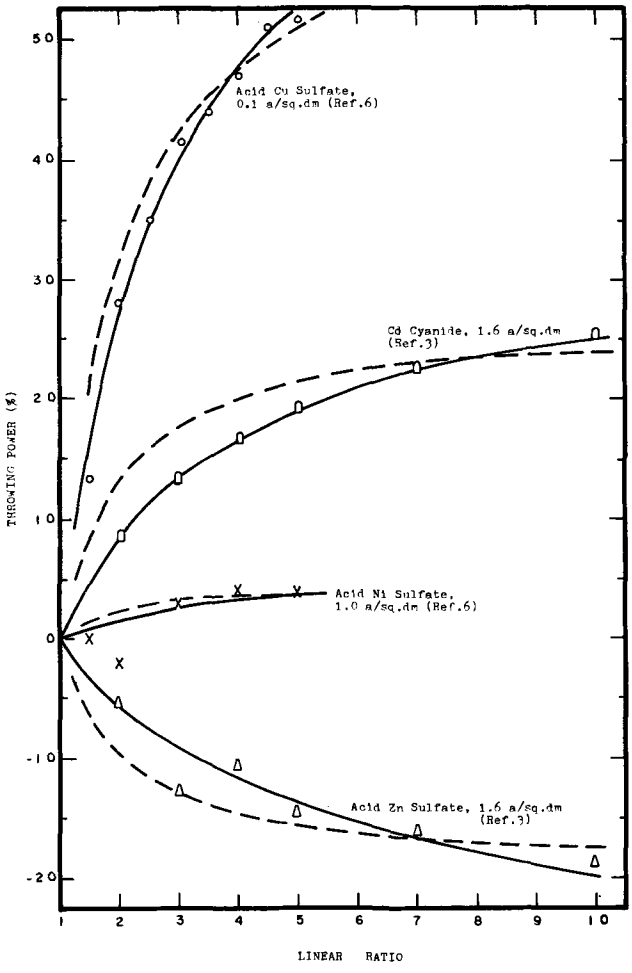

Fig. 3. Value of throwing power in terms of the Haring-Blum equation. The o, □, x, and △ are experimental data taken from the indicated references. The solid lines are the throwing power calculated from the logarithmic throwing index, and the dashed lines, from the linear throwing index.

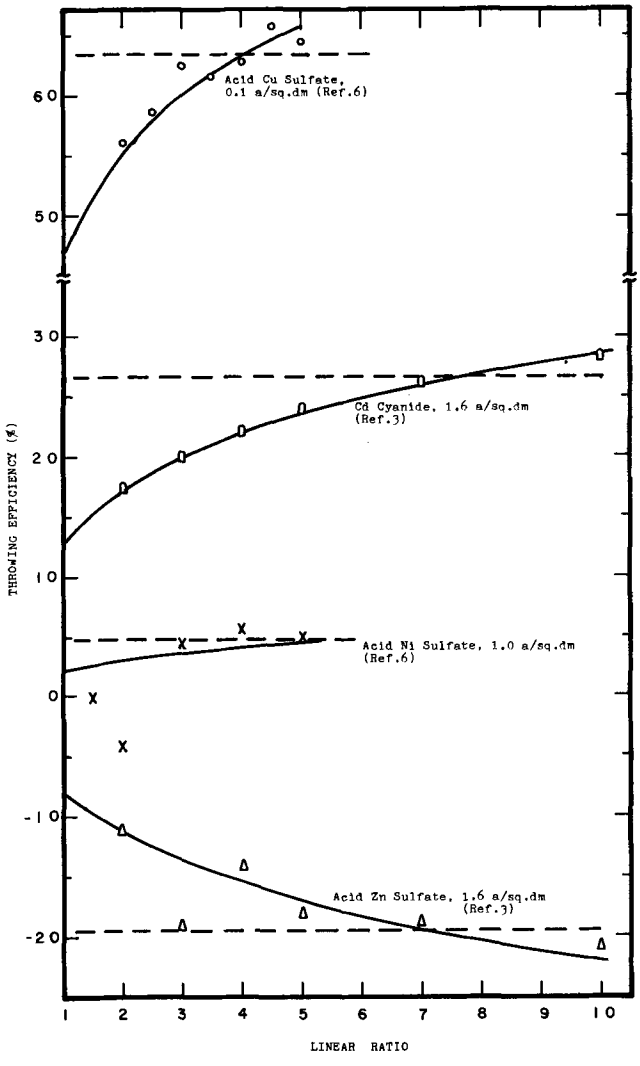

Fig. 4. Values of throwing efficiency in terms of the Heatley-Pan equation. The symbols are experimental data taken from the indicated references. The solid lines are the throwing efficiency calculated from the logarithmic throwing index, and the dashed lines, from the linear throwing index.

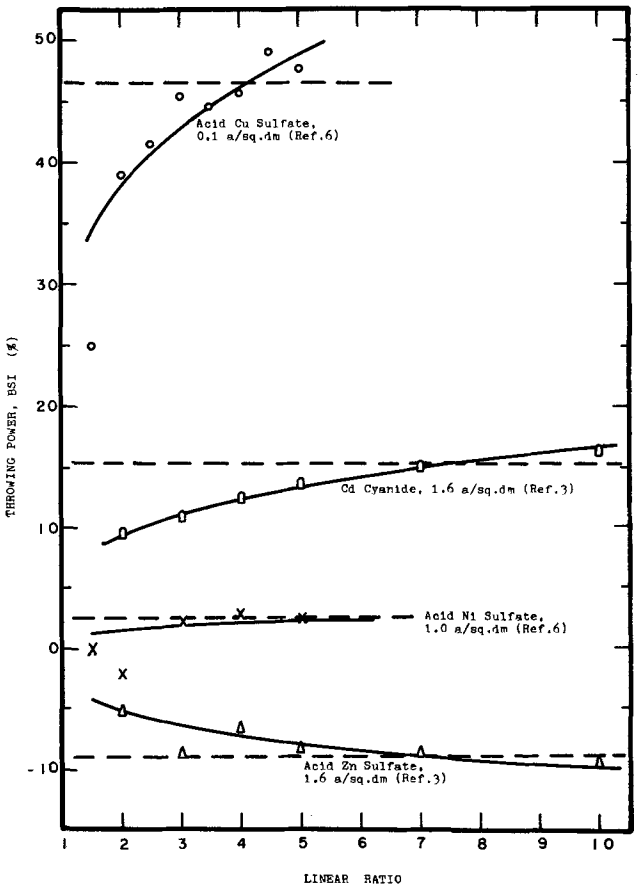

Fig. 5. Values of throwing power (BSI) in terms of the Field equations. The symbols are experimental data taken from the indicated references. The solid lines are the throwing power (BSI) calculated from the logarithmic throwing index, and the dashed lines, from the linear throwing index.

for the results expressed in terms of the Haring-Blum equation, which has thus far been omitted from the discussion, the logarithmic throwing index describes the experimental data better than the linear throwing index (Fig. 3).

Conclusions

Based on the previous discussion, it can be concluded that the logarithmic throwing index is a better tool for expressing the results of throwing power measurements of the Haring-Blum cells. For practical electroplating studies, it can be conveniently computed (by taking common logarithms on both sides of Eq. [5] from

$$\text{Logarithmic throwing index } (A) = \frac{\log L}{\log M}$$

If several experimental points are made, an average value can be assigned to a plating bath to reduce the experimental error. In this way only a single number is obtained, which represents the characteristics of a plating solution at constant operating conditions and can be used to indicate the variation of throwing powers with changes in bath temperature, composition, current density, etc.

The method is proposed principally as an empirical tool to minimize the experimental effort required for electroplating studies. It is felt that further theoretical study is necessary to clarify why the throwing power of plating baths follows the logarithmic fashion as suggested by Eq. [5].

Manuscript submitted April 27, 1970; revised manuscript received Jan. 6, 1971.

Any discussion of this paper will appear in a Discussion Section to be published in the December 1971 JOURNAL.

REFERENCES

1. H. E. Haring and W. Blum, *Trans. Electrochem. Soc.*, **44**, 313 (1923).
2. A. H. Heatley, *ibid.*, **44**, 283 (1923).
3. L. C. Pan, *ibid.*, **58**, 423 (1930).
4. S. Field, *Metal Ind. (London)*, **44**, 614 (1934).
5. R. V. Jelinek and H. F. David, *This Journal*, **104**, 279, (1957).
6. G. E. Gardam, *Trans. Faraday Soc.*, **34**, 698 (1938).
7. W. A. Wesley and E. J. Roehl, *Trans. Electrochem. Soc.*, **86**, 419 (1944).

A High-Yield Photolithographic Technique for Surface Wave Devices[1]

Henry I. Smith, Frank J. Bachner, and N. Efremow

Lincoln Laboratory, Massachusetts Institute of Technology, Lexington, Massachusetts 02173

ABSTRACT

In the fabrication of surface wave devices, standard photoresist-chemical etching techniques often provide a very low yield even at moderate resolutions, frequently cause a degradation of the substrate finish, and in many cases are incompatible with substrates of interest. A photolithographic technique is described in which metalizing is done after a photoresist image is produced on the substrate, thereby circumventing most of the problems inherent in chemical etching. It is shown by means of electron micrographs of photoresist profiles that intimate mask-substrate contact is essential. Devices with line widths of 1 μm can be produced with high yield.

This paper describes a technique of photolithography which is especially suited to the fabrication of surface elastic wave devices. In contrast to the usual technique of producing a photoresist image on a thin metallic film and etching the unprotected metal either chemically or by ion bombardment, the present technique produces the desired pattern by evaporation of the metal onto a photoresist image prepared directly on the substrate surface. The unwanted metal is separated when the photoresist is subsequently removed by organic solvents. This technique, which is depicted schematically

[1] This work was sponsored by the Department of the United States Army.

Key words: photoresist, surface waves, ultrasonics, photolithography, piezoelectric, scanning electron microscope, transducers.

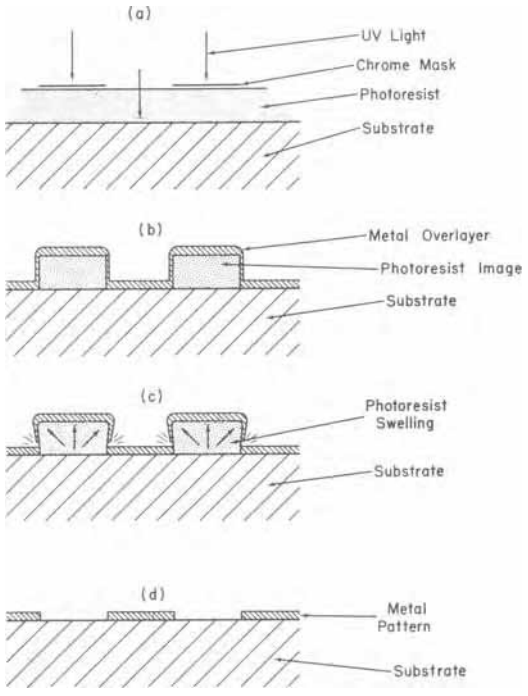

Fig. 1. Schematic representation of the steps involved in the photolithographic process.

in Fig. 1, has some distinct advantages whenever substrates present special materials processing problems, or when high resolution is required. In concept it is not new; however, published accounts either provide insufficient details (1, 2), or are not relevant to surface wave devices (3, 4), or both. In this paper, we describe the technique in detail and illustrate, by means of electron micrographs of photoresist profiles, certain critical aspects.

Photolithographic materials and techniques originally developed for use in chemical micromilling and printed-circuit board fabrication have been greatly refined and improved for use in microelectronics. However, the techniques used in microelectronics are predicated on the availability of low-cost inert substrates and selective etches. Thin film microelectronic circuits are generally formed on substrates such as ceramics or glass, and the resistive and conductive films are etched using chemicals that will attack one film but not the other and will not attack the substrate. Similarly, silicon device technology requires etches that will attack the interconnect metalization but not the oxide or the silicon, and etches that will attack the oxide but not the silicon, and *vice versa*. For microelectronic circuits involving complex patterns at line widths below about 15 μm, the availability of large numbers of essentially identical substrates at low cost is an important factor in obtaining a good yield of devices through standard photoresist-chemical etching techniques. Good yield generally requires that all the crucial process parameters (resist thickness, exposure time, baking temperature, etchant concentration, etching times and agitation, *etc.*) be optimized, and this in turn implies that many substrates are processed and many failures are discarded.

In surface elastic wave studies (5-7), typical substrates are materials such as lithium niobate, bismuth germanium oxide, lithium iodate, zinc oxide, cadmium sulfide, quartz, gallium arsenide, indium antimonide, YAG, and YIG. They are chosen for their desirable piezoelectric or acoustic loss properties, or as interesting piezoelectric semiconductors. They are specially grown, cut, and oriented (sometimes to 1/10 deg) and polished to a high tolerance. By the time a substrate is ready to be made into a device by photolithographic techniques, its preparation represents a considerable investment of time, effort, and expense. In contrast to the inexpensive and mass-produced substrates of the microelectronics field, surface wave substrates cannot generally be discarded because of a failure in the photolithographic process; they must be cleaned and reprocessed. It has been observed in this laboratory that the optically polished surfaces of many of the above-mentioned substrates are especially susceptible to degradation from such repeated processing. Scratches and pits present or nascent on the surface become augmented or revealed by the sequence of metalizing followed by chemical etching, thus requiring that the substrate be polished anew. Because optically polished surfaces do not generally have as smooth a finish as do chemically polished or glazed surfaces, one finds that surface wave device fabrication is troubled with special problems of unpredictable and nonuniform etching. Even if all process parameters are optimized, the yield of surface wave devices by chemical etching is quite low and goes down rapidly with an increase in pattern complexity and resolution. As a rule of thumb, for metal thicknesses in the 1000-2000Å range, chemical etching yields are unacceptably low for patterns involving a large number of lines and spaces of 5 μm or less in width. Sputter etching (8, 9) is capable of good yield at higher resolution but is fraught with other problems. It is difficult to control or monitor, it risks sputter etching of the substrate, and it sometimes makes the photoresist difficult to remove.

Many substrates with desirable acoustic or piezoelectric properties are incompatible with the usual metal etchants and photoresist stripping agents, and this incompatibility is intensified when such materials are in the form of polycrystalline thin films. Thus, extensive chemical compatibility tests must sometimes be performed for each desired metal-substrate combination. The technique described here does not expose the substrate to the hostile environment of chemical etching and is thus better suited for chemically reactive or easily degraded surfaces.

In surface wave work, one is frequently confronted with the problem of producing a device on a "one of a kind" substrate, a very demanding requirement for chemical etching even if chemical compatibility is no problem. The process described here provides a surprisingly high device yield in this "one of a kind" situation, even for patterns involving line widths of 1 μm.

Processing Techniques and Discussion

Figure 1 illustrates the steps of the technique. Obviously, the key element is to produce a distinct break in the metal film at the point where it leaves the substrate and begins to form a bridge over the photoresist relief pattern. To insure this, we have found that it is essential to produce a sharp vertical profile in the photoresist and to carry out the metal deposition so that atoms impinge at near normal incidence. In this way, the metal on the sides of the photoresist relief patterns is considerably thinner than the metal film on the substrate and the top of the photoresist, and the required removal of unwanted metal is readily effected by swelling the photoresist in an organic solvent.

The character of a photoresist profile depends critically on the exposure conditions, primarily on the avoidance of diffraction effects and to a lesser extent on the exposure time. In all cases, we have used contact printing rather than projection exposure (3) because of the critical focusing problems inherent in the latter and the convenience, reproducibility, and economy inherent in the former. Our masks are chromium images on Corning 0211 glass, approximately 0.2 mm thick, which are made by contact printing from 6.4 mm thick master plates. The master plates are exposed on a Model 1795[2] Photorepeater (9). In contact printing, the mask is pressed onto a substrate's photoresist coating using mechanical probes as is depicted in Fig. 2.

[2] D. W. Mann Company, Burlington, Massachusetts.

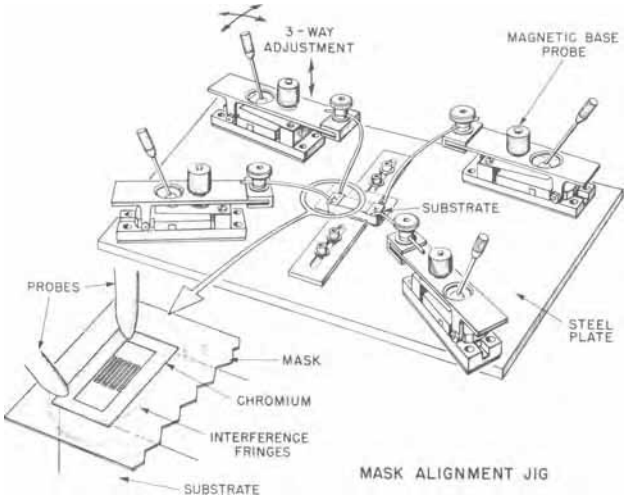

Fig. 2. Fixture for mask alignment and obtaining intimate contact.

The thin glass is quite flexible and readily deforms to the contours of the substrate or around the occasional dust particle. This work is done under yellow safelights and, when the separation between the mask and the photoresist film is reduced below about 2 μm, strong interference fringes are observed. It is a fairly simple matter to adjust the forces applied and the positions of the probes to achieve intimate or "optical" contact in the areas of the patterns. In practice, "optical contact" can be achieved quite easily over large areas without risk of damaging the substrate, the mask, or the photoresist film. The bond between mask and substrate which frequently results can be broken either by immersion in water or by peeling back the flexible mask.

Figure 3 shows that sharp vertical profiles, and in some cases undercut profiles, are obtained with the positive photoresists AZ1350[3] and AZ1350H[3] whenever intimate contact is provided. On the other hand, a marked rounding occurs even for relatively small mask-to-substrate separation. Such rounding usually makes it impossible to remove the metal bridge unless perhaps the substrate is subjected to high-power ultrasonic agitation for long periods of time, a treatment which usually damages surface wave substrates and degrades metal structures. Rounding of the profile of a photoresist pattern is of little or no concern in the case where it would be used as a chemical etching resist, and it is for this reason that the usual practice of photolithography in microelectronics does not demand such intimate contact except in the case of 1μ resolution structures (9, 10). It is noteworthy that intimate contact is necessary regardless of the resolution of the desired pattern, and this plus the care necessary to obtain intimate contact simultaneously with pattern alignment can be viewed as disadvantages of the technique. However, our experience is that these disadvantages are not significant, particularly when only a small number of prototype laboratory devices is desired.

The process did not work with negative photoresists, and this failure is attributed to a rounding of the photoresist profile. In fact, the very exposure conditions that in the case of a positive photoresist lead to the ideal undercut profile lead in the case of the negative photoresist to rounding. Moreover, since the mask must be in intimate contact with the photoresist film, standing waves are set up in the film even for nonmonochromatic exposure sources. At the nodal planes, there is insufficient exposure to cross-link the photoresist, and the subsequent development causes sections of the film to float away and redeposit elsewhere on the substrate. This phenomenon has been discussed by Altman and Schmitt for the case of projection exposure (11).

[3] Shipley Company, Incorporated, Newton, Massachusetts.

Metal deposition is carried out in an electron beam evaporator at a source-to-substrate distance of about 44 cm in order to insure that evaporated atoms arrive at the substrate at near-normal incidence. We have had some success with standard thermal evaporation from extended sources at about 20 cm source-to-substrate distance, but generally the device yield is considerably smaller than with the electron beam unit, especially for the higher resolution devices. To verify the assertion that the deposited metal must arrive at the substrate at near normal incidence, experiments were conducted in which an rf sputtering unit substituted for the electron beam evaporator. It was found that, even in the case of a very thin metal film (300-500Å of chromium), it was impossible to separate away thoroughly the unwanted metal by solvent techniques.

At the present time, in this laboratory the photolithographic process described in this paper is used for all surface wave device fabrication irrespective of pattern resolution or substrate material. For the production of interdigital electrode transducers in the range of line widths from 10 to 1 μm for $LiNbO_3$ delay lines, the following procedure is used. The substrates are thoroughly cleaned, the final rinse being in 12-18 megohm resistivity water, and dried in a jet of filtered dry nitrogen. Next, they are spin-coated with AZ1350 positive photoresist to a thickness of about 5000Å, or AZ1350H to a thickness of about 20,000Å, the choice depending on pattern resolution and the metal thickness desired. AZ1350H works quite well, at least down to 2 μm line widths. From Fig. 3, it can be readily inferred that the deposited metal thickness should not exceed about 1/3 to 1/2 of the photoresist height. Although we have not explored experimentally the limits on the metal thickness, it seems reasonable that AZ1350H would permit thicker metal films than AZ1350.

After baking in an air oven at 80°C for 10 min, the desired pattern is produced in the photoresist by contact printing using a collimated high-pressure mercury lamp and the 0.2 mm thick chromium-on-glass mask. The photoresist is developed in an aerated spray of AZ Developer for 30 sec using a nitrogen-powered artist's air brush and the recommended dilution of 1 to 1 with water. Substrates are then rinsed in high-purity water and blown dry with filtered dry nitrogen. At this point, the photoresist pattern can be inspected under a microscope for possible resist defects or residues in the open areas. If desired, the photoresist can be removed using acetone and the substrate reprocessed without fear of degradation of the surface finish. This is seldom necessary.

The photoresist is not baked after pattern development because it is not required by the process and runs the risk of rounding the photoresist profile through plastic flow. For the same reason, the substrates are not heated in the electron beam evaporator prior to the metal film deposition. The softening point of AZ1350 is about 130°C so some preheating or glow discharge cleaning to enhance metal adhesion is permissible. We have chosen to forego these in favor of double-layer metal films, the first chosen for its superior adhesion. The electron beam apparatus conveniently permits the sequential evaporation. For most surface wave devices, we deposit 300Å of titanium or chromium and 1000 to 2000Å of aluminum, the thicknesses being precisely monitored on a quartz crystal oscillator. We have substituted gold for the aluminum, on occasion used aluminum without the interface film, and in fabricating the flexible masks by this process used films of chromium or titanium 500-1000Å thick. The process works equally well for these cases. Probably any metal or combination which satisfies adhesion requirements can be used, but it has been speculated that the brittleness of the metal film and stress at its junction with the photoresist relief structure may be important factors.

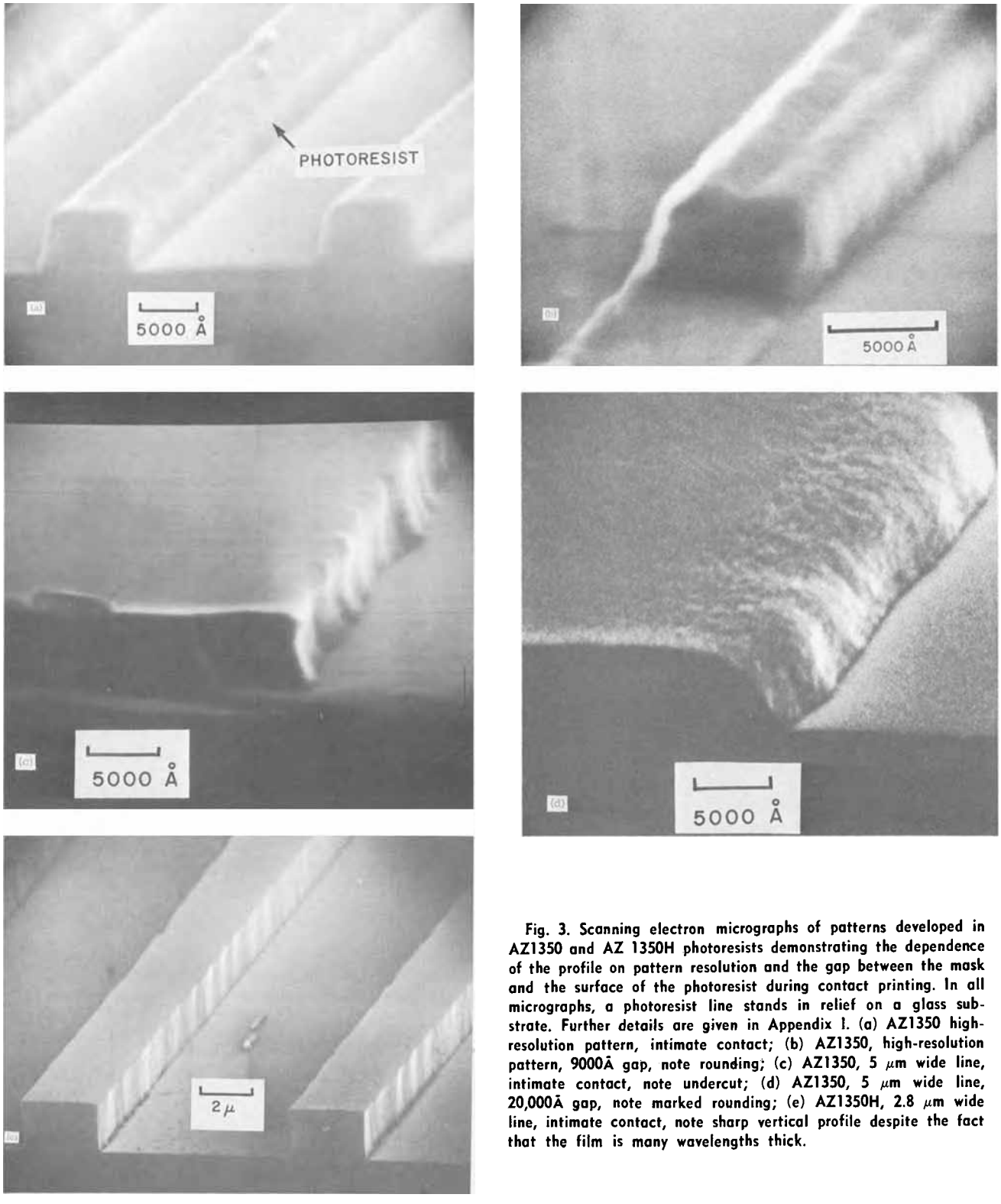

Fig. 3. Scanning electron micrographs of patterns developed in AZ1350 and AZ 1350H photoresists demonstrating the dependence of the profile on pattern resolution and the gap between the mask and the surface of the photoresist during contact printing. In all micrographs, a photoresist line stands in relief on a glass substrate. Further details are given in Appendix I. (a) AZ1350 high-resolution pattern, intimate contact; (b) AZ1350, high-resolution pattern, 9000Å gap, note rounding; (c) AZ1350, 5 μm wide line, intimate contact, note undercut; (d) AZ1350, 5 μm wide line, 20,000Å gap, note marked rounding; (e) AZ1350H, 2.8 μm wide line, intimate contact, note sharp vertical profile despite the fact that the film is many wavelengths thick.

After metal deposition, it remains only to swell the photoresist and remove the unwanted metal from the substrate. An aerated acetone spray was found to be most effective especially for 1μ resolution periodic structures. However, this is extremely hazardous because of the risk of explosion or fire and must be carried out with appropriate safety precautions.

When the procedure described above is followed, metal patterns are obtained which exhibit very nearly the same degree of edge acuity as the photoresist pattern. Figure 4 shows an interdigital electrode transducer with 1¼ μm line widths.

For substrates which have naturally rough or pitted surfaces, such as the sintered piezoelectric ceramics and some thin films, the technique described is especially valuable. There seems to be very little degradation of the edge acuity of metal patterns because of surface roughness. In contrast, when chemical etching is used on such substrates, ragged edges and discontinuities are frequently encountered.

The photolithographic technique described is similar in principle to the electron beam fabrication technique developed by Hatzakis and Broers (12, 13). They showed that an undercut profile was obtained with an electron degradable polymer film as a natural consequence of electron scattering, and that there was no continuity between evaporated metal on the substrate

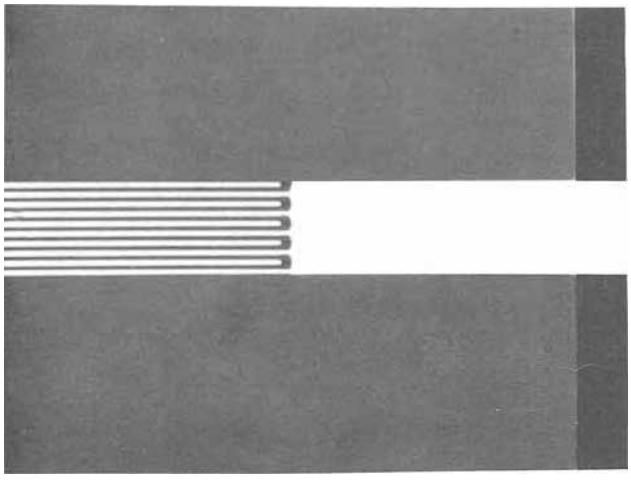

Fig. 4. Interdigital electrode transducer with 2½ μm separation between centerlines of adjacent fingers.

and metal on top of the polymer film. Our work indicates that photoresists present a more difficult problem.

Acknowledgments

The authors wish to thank R. Gray and R. Reinhard for their assistance in preparing the electron beam evaporated films.

APPENDIX I

A series of experiments were conducted on the influence of exposure time, mask-substrate separation, and pattern resolution on photoresist profiles, and the effect this had on the success or failure of the photolithographic process described in this paper. Aluminosilicate glass plates 0.15 cm thick which had been scribed on the back side were chosen as test substrates. Photoresist patterns were developed on the front sides of the glass plates opposite the scribe lines. The application of a relatively small flexural force caused the glass and the photoresist to fracture cleanly along the scribe line. Two types of interdigital electrode transducer patterns were used as masks for the experiments. Both patterns had a total of 14 fingers. The distance between centerlines of adjacent fingers was 10 μm for one pattern and 2½ μm for the other.

After coating the substrates with photoresist and baking them, the interdigital electrode patterns were exposed and developed on the substrate. The placement of the patterns was such that, when the plates were fractured in two, each half contained half of the interdigital electrode pattern. One half of the original glass plate was coated with approximately 200Å of gold so that it could be inspected in a scanning electron microscope. The other half was coated with 300Å of chromium and 1000Å of aluminum in the electron beam evaporator and then processed to remove the unwanted metal.

The exposure time and the separation between mask and substrate were varied over wide ranges, the latter being determined from the interference fringes. Referring back to Fig. 3, metal patterns with extremely sharp edge acuity, free of breaks or shorts between adjacent lines, were obtained with the other halves of the substrates in Fig. 3(a), (c), and (e). With the substrates corresponding to 3(b) and 3(d), it was impossible to separate away the unwanted metal. The rounded profile resulted in a continuous metal bridge over the photoresist. Obviously, the intimacy of mask-substrate contact is the essential element.

The range of acceptable exposure times is quite broad. We found that the threshold of complete exposure could be exceeded in many cases by a factor of 2 without any deleterious effects.

Manuscript received Nov. 2, 1970.

Any discussion of this paper will appear in a Discussion Section to be published in the December 1971 JOURNAL.

REFERENCES

1. M. K. Stelter, *J. Photochemical Etching*, **1**, 4 (1966).
2. M. K. Stelter, *SCP Solid State Technology*, **9**, 60 (1966).
3. S. Middelhoek, *IBM J. Res. Develop.*, **14**, 117 (1970).
4. S. Middelhoek, *ibid.*, **14**, 148 (1970).
5. Richard M. White, *Proc. IEEE*, **58**, 1238 (1970).
6. Ernest Stern, *IEEE Trans. Microwave Theory and Techniques*, **MTT-17**, 835 (1969).
7. Henry I. Smith, *Intern. J. Nondestructive Testing*, **2**, 31 (1970).
8. P. D. Davidse, *This Journal*, **116**, 100 (1969).
9. Henry I. Smith, *Rev. Sci. Instr.*, **40**, 729 (1969).
10. George I. Geikas and Billy D. Ables, "Kodak Photoresist Seminar Proceedings," Vol. 2, p. 47, Eastman Kodak Co., Rochester, N. Y. (1968), Kodak Publication No. P-192-A.
11. J. H. Altman and H. C. Schmitt, Jr., *ibid.*, Vol. 2, p. 12 (1969), Kodak Publication No. P-209.
12. M. Hatzakis, *This Journal*, **116**, 1033 (1969).
13. A. N. Broers, E. G. Lean, and M. Hatzakis, *Appl. Phys. Letters*, **15**, 98 (1969).

On the Czochralski Growth of GaP[1]

E. A. Miller, L. R. Weisberg,* and W. K. Liebmann[2]

RCA Laboratories, Princeton, New Jersey 08540

ABSTRACT

A high-pressure, magnetic Czochralski apparatus was built for the growth of GaP. Various operating problems were successfully overcome, such as seed-holder vibrations, poor visibility, explosions, control of solid-liquid interface shape, efficient coupling of rf power into the melt, and correcton of large temperature gradients. Experiments were carried out demonstrating the large effects of gaseous pressure on the temperature gradients. At 35-atm pressure, the autoclave behaved as if it were filled with a liquid and not a gas, both with respect to visibility and heat flow. Coarse-grained polycrystalline ingots were grown, with grains limited in size to 1 cm^3 because of spurious nucleation of new grains.

The utilization of the liquid encapsulation technique has considerably simplified the Czochralski growth of GaP (1). Prior to this, its high melting point (1470°C) and dissociation pressure (35 atm) (2) had made the growth of large single crystals a very difficult task. Several years ago (3), we had carried out experiments using the magnetic Czochralski technique (4) for GaP in an autoclave, which resulted in the preparation of coarse-grained polycrystalline ingots, with grains as large as 1 cm^3. This work should be of interest to workers in this field for three reasons.

[1] This work was supported by the Department of Defense, Advanced Research Projects Agency, Materials Sciences Office, under Contract No. SD-182.
[2] Present address: IBM Laboratories, Boeblingen, Germany.
* Electrochemical Society Active Member.
Key words: gallium phosphide, crystal growth, high-pressure growth, Czochralski growth.

First, the liquid encapsulation is not necessarily a universal technique, since compounds might exist where suitable liquid escapsulants cannot be found. For such materials, the magnetic Czochralski technique would be preferred. Second, the liquid encapsulation technique suffers in that the volatile species, here phosphorus, continually escapes from the melt, which can cause a continual change in stoichiometry. The magnetic Czochralski technique does not have this difficulty. Third, results found here can give further insight to crystal growth under high pressure, including the liquid encapsulation technique.

For people who are accustomed to crystal growth under atmospheric pressure, two main problems are encountered at 35 atm pressure: poor visibility due to convection effects, and unusual temperature gradients. Both of these problems can be "visualized" by assuming that the autoclave is filled with a liquid and not a gas. Data are given below concerning these and other problems and methods are presented to avoid them.

Experimental Apparatus

The apparatus was a standard magnetic Czochralski growth system operating within a autoclave, as shown in Fig. 1. The autoclave design was based on similar units used by Fischer (5), and was actually a predecessor of the autoclave shown by Fischer in his Fig. 10. The autoclave is divided into three sections. The crucible containing the GaP melt and the rf heating coil are located in the bottom section. The rf leads are introduced into the autoclave through a coaxial high-pressure seal which is electrically insulated from the autoclave so that, during operation, the autoclave can be grounded. The inert gas is supplied to the apparatus through a high-pressure valve. The magnet assembly for the control of the seed holder motion is located in the upper part of the autoclave. The center section contains the viewing port, which is aimed into the center of the crucible, and lines up with the viewing port on the quartz ampoule. The drive mechanism for the vertical and rotational motions of the magnets is mounted directly on top of the autoclave, and the pulling rod passes through a multiple o-ring seal. There is also a pressure safety release valve on the top of the autoclave. The walls and the lid of the autoclave are watercooled. All the controls for the furnaces and for the seed holder motion are located in a central panel which is not shown in the figure.

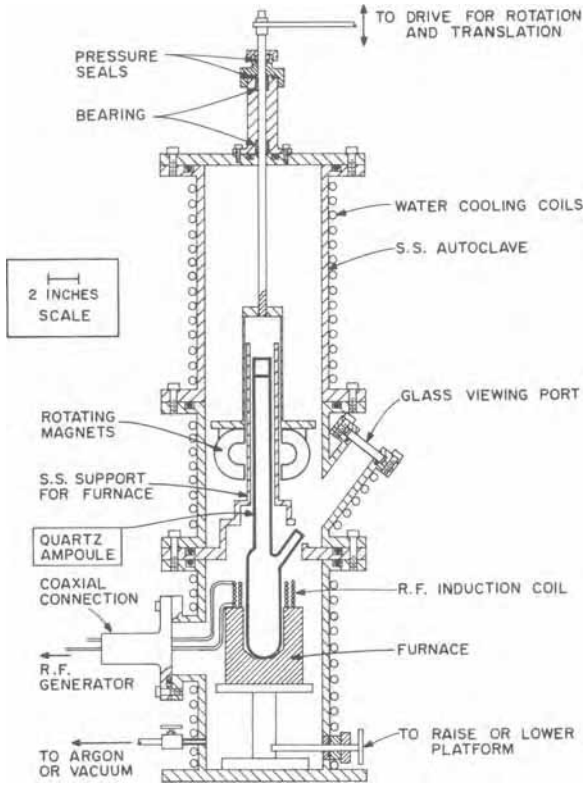

Fig. 1. Cross-sectional view of the high-pressure, magnetic Czochralski apparatus. S.S. denotes stainless steel.

Figure 1 also shows the quartz growth ampoule in the center of the autoclave, which is supported and held in position by a stainless steel piece. This support also divides the whole container into separate sections to reduce convection currents. The phosphorus reservoir is located at the bottom of the growth ampoule, and is surrounded by a furnace. Thermocouples are located at various points for temperature control. The upper section of the growth ampoule is kept at a temperature exceeding the condensation temperature of the phosphorus.

Four permanent magnets are suspended from a rod passing through the top of the autoclave, and these magnets couple to Permendur pieces within the seed holder. The weight of the seed holder is approximately 200g. The driving mechanism for the magnets is located outside the autoclave, providing a constant rotation of 16 rpm while the pulling rate is variable between 0 and 10 mm min^{-1} in a continuous fashion. The autoclave can withstand at least 60 atm internal pressure, and is also vacuum tight.

The rf generator was a 10 kW, 450 kHz unit, manufactured by the Lepel Company.

To vacuum seal the growth ampoule, a special ampoule construction was used with a side arm to contain the small lumps of red phosphorus. This allowed the entire ampoule to be vacuum baked at 600°C, including the gallium, without heating the phosphorus. Subsequent to bake-out, and without breaking the vacuum, the phosphorus was moved from the side arm into the ampoule. The ampoule was then sealed under vacuum. Directly prior to growth, the GaP was synthesized in the crucible, so that no separate synthesis step was required. The amount of phosphorus was calculated so that, during operation, all of the phosphorus was in the vapor form of P_4 molecules, which simplified determination and control of the phosphorus vapor.

Attempts were made to roughly balance the phosphorus pressure within the ampoule and the argon pressure surrounding the ampoule. However, pressure was usually maintained a few atmospheres above the phosphorus pressure within the ampoule, since it was found in separate tests that well-designed quartz ampoules could withstand implosion up to at least 40 atm of excess external pressure.

Results

Seed holder vibration.—The design of the quartz seed holder (6) is shown in Fig. 2. The Permendur slugs are sealed within and protected by the seed holder. The seed holder and attached quartz rods rotate within two BN disks, which in turn can slide up and down within the ampoule. Original problems of excessive vibration and erratic motion of the seed were virtually eliminated by constructing all the moving parts of the seed holder with high precision, including the use of precision-diameter quartz rods in the bearings, and a precision-bore quartz tube for the upper member of the ampoule. The bearings were machined from BN, with allowance in the design for differential thermal expansion.

Coupling of rf into melt.—To provide good coupling between the rf coil and the melt, it was found that an rf coil wound in a continuous double-concentric shape provided the best results. The coil is shown surrounding the ampoule in Fig. 2. The coil is easily wound into the shape without any shorting by placing quartz Fiberglas sleeving over the copper tubing.

Melt temperature control.—In this system, it was difficult to place a thermocouple into close proximity with the crucible. Also, deposition of GaP on the walls

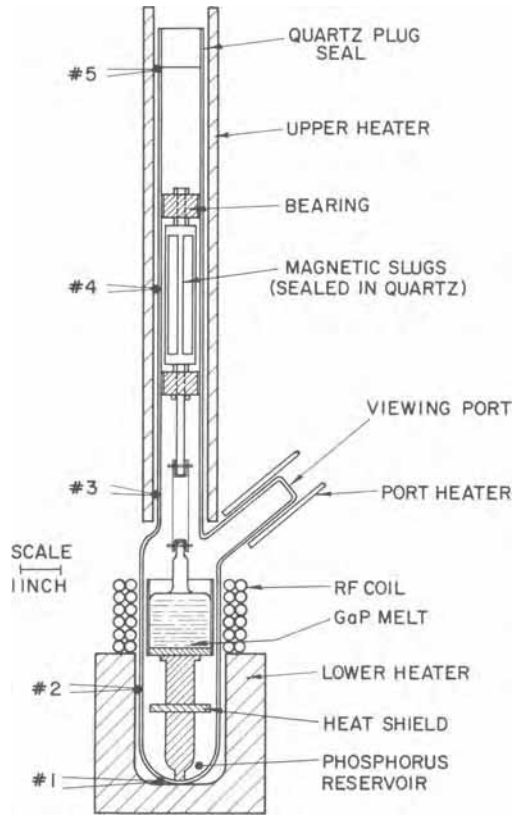

Fig. 2. Cross-sectional view of the growth ampoule for GaP, including the seed holder, crucible, rf coil, and upper and lower heaters. The numbers on the left indicate thermocouples.

prevented the use of optical temperature sensors. Instead, adequate temperature control of the melt was achieved by controlling the rf power output. A pickup coil was placed next to one of the rf input leads to the autoclave. The resulting signal was rectified and fed into a standard thermocouple control unit, which in turn regulated the saturable core reactor control in the rf generator.

Visibility problems.—Visibility can be impaired for two reasons. First, GaP can deposit on the quartz walls surrounding the crucible. Second, the fluctuations and convection currents in the argon gas give a shimmering and unsteady view of the crucible, such as the appearance of an object at the bottom of a swimming pool.

The first problem was successfully overcome by placing a side arm on the growth ampoule, as shown in Fig. 2. This is surrounded by a heater, and the temperature of the heater is held at about 1000°C. This visibility port remains clear for hours under growth conditions.

The problem of turbulence was minimized by eliminating much of the optical path through the gas with the use of a fused quartz rod acting as a light-pipe. Both ends of the quartz rod must be polished. Quartz rods were easily selected that were free of significant distortion. The quartz rod extended between the viewing port and the side arm of the ampoule, thus providing a clear view of the solid-liquid interface.

Explosion problems.—There were found to be two main causes of explosions (or implosions). The first was the formation of a "lid" of solid GaP on the top of the melt. Once this formed, as the melt was heated further, the crucible would crack and spill its contents onto the quartz ampoule, thus causing the explosion. This problem was easily avoided by keeping the phosphorus cool while first heating the gallium in the crucible to about 1500°C, and then slowly increasing the phosphorus pressure to the desired value (35 atm). Then, any GaP that forms remains molten.

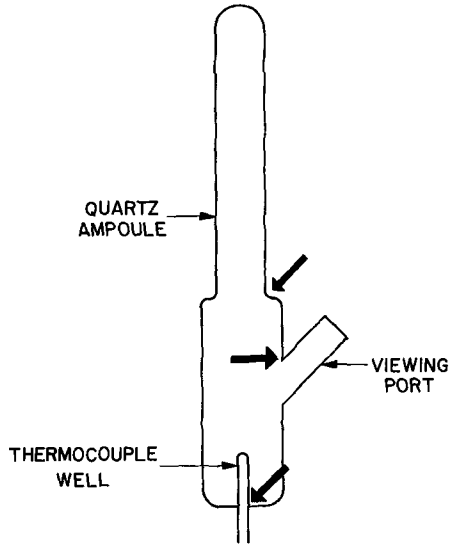

Fig. 3. Cross-sectional view of an ampoule subject to explosion. The arrows indicate weak points of construction which should be avoided.

The second and more severe problem concerned the construction of the quartz ampoule. Needless to say, the ampoule must be fully annealed after construction. However, it is also important to eliminate all sharp bends in the ampoule. Examples of a poorly designed ampoule with the weak points identified is shown in Fig. 3, in contrast to the successful design shown in Fig. 2. Using the ampoule shown in Fig. 2, explosions were reduced to roughly one in 15 runs, from the original incidence of one in two explosions.

It is noteworthy that, even in the most severe explosions, there was no damage outside of the autoclave, nor was there any damage to the large glass viewing port.

Solid-liquid interface shape.—Although direct couping of the rf energy into the melt was efficient, the resulting solid-liquid interface was invariably concave into the melt, which can be detrimental to crystal growth. In a series of experiments, the phosphorus pressure was varied between 30 and 50 atm, but no improvement was noted in either the shape of the interface or the crystallinity of the grown ingots.

Next, we tried several experiments with susceptors surrounding a crucible. In the first, a cylindrical susceptor was employed surrounding and touching the BN inner crucible. Molybdenum was unsatisfactory since it reacted with phosphorus at roughly 1300°C. Tungsten failed marginally since it reacted with phosphorus above 1500°C when gallium was present (in phosphorus vapor alone no reaction was seen). When the melt was placed in a graphite crucible, a black deposit, believed to be carbon, formed on the walls and blocked visibility, even in the side arm. However, it was found that both graphite and vitreous carbon were suitable as susceptors when a BN inner crucible was used to contain the melt.

The use of the carbon susceptors was found to change the shape of the solid-liquid interface to convex into the melt. Hence, this arrangement provided another control over the growth parameters.

Crucible materials.—Several crucible materials were tested, including quartz, SiC, graphite, vitreous carbon, and hot-pressed BN. Of those tested, the last was superior, especially because of its machinability. However, hot-pressed BN is not pure, since a binder is added, and contains B_2O_3. Extensive vacuum bake-out (over 16 hr) was used for the BN until no further deposits on the walls of the bake-out chamber were observed. Nevertheless, residual impurities in the BN might have been detrimental to the crystal growth, and pyrolytic BN is probably superior.

Insulation at high pressures.—The results on heat flow were the most unexpected feature of these crystal growth studies, especially for a person familiar with the Czochralski growth of Ge, Si, or GaAs.

We first considered the effect of insulation at elevated pressures. We performed an experiment in which a hollow tubular heater was placed vertically at the center of the autoclave, with one thermocouple inside the heater, and with thermocouples placed at various distances away. The outer diameter of the heater was about ½ in. The heater was held at 1150°C, and the temperature was measured as the argon pressure was increased. The measurements were carried out first in the absence of insulation, and again after the autoclave was filled with Fiberfrax insulation, normally considered to be an effective insulator.

Typical results are shown in Fig. 4 for one thermocouple located 1½ in. from the surface of the heater. It can be seen that the insulating effect of the Fiberfrax decreases rapidly with increasing pressure. It acts as if the autoclave is filled with a liquid, and not a gas, with the Fiberfrax floating around, doing almost nothing. Thus, at high pressures, one must use much denser insulators, such as brick insulators.

Unusual temperature gradients.—Another surprising feature of heat flow concerned temperature gradients within the growth ampoule. For example, we grew GaAs single crystals in this same apparatus as a test. When the GaAs melt was heated to above 1250°C, the reservoir below the crucible overheated, *i.e.* increased to over 600°C. In contrast, when we grew GaP at 35 atm, even when the melt was heated to 1500°C, the reservoir below the crucible remained well below 600°C.

Tests were carried out to demonstrate the effects of gas pressure on the vertical thermal gradients. A "dummy" quartz ampoule was used, containing no Ga or P, but with small holes to allow argon gas to enter. A graphite cylinder was used in place of the crucible, and the seed holder was placed in its usual position. Seven thermocouples were placed along the ampoule, five in the positions indicated in Fig. 2, and one next to thermocouples 1 and 5, but in the interior of the ampoule. The graphite was heated to 1350°C, but no power was supplied to either the upper or lower heaters.

Little difference was seen between the interior and corresponding exterior thermocouples at any pressure.

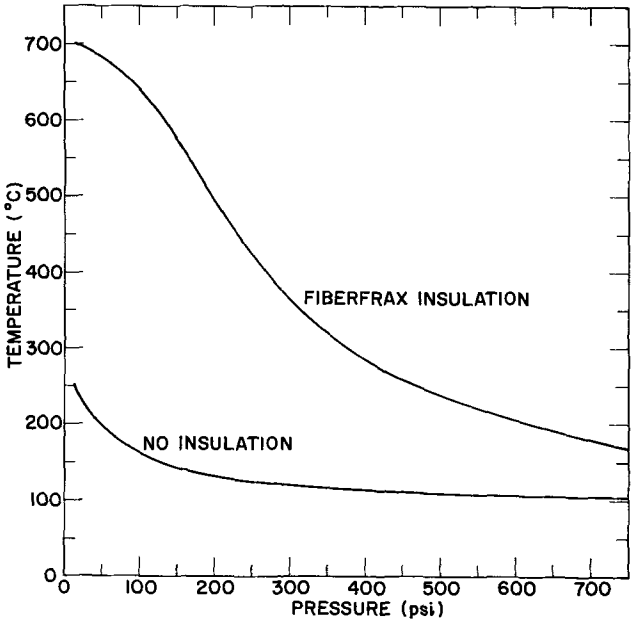

Fig. 4. Variation of temperature with pressure of a thermocouple placed 1½ in. away from the surface of a heater maintained at 1150°C.

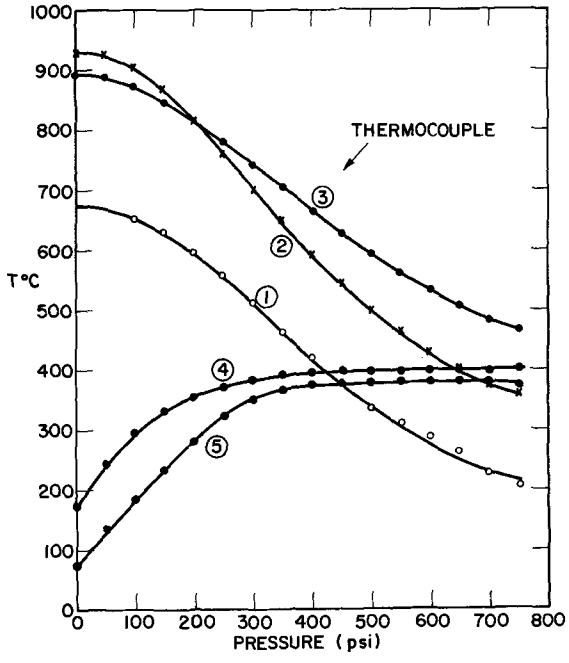

Fig. 5. Variation of temperatures along the ampoule with increasing argon pressure. Refer to Fig. 2 for the thermocouple positions. Crucible held at 1350°C, but no power supplied to upper and lower heaters.

However, the temperatures along the ampoule varied greatly with increasing pressure, as shown in Fig. 5. Thermocouples 1, 2, and 3, which at low pressures were heated mostly by radiation, dropped several hundred degrees centigrade. Thermocouples 4 and 5, in contrast, were heated probably by the convection currents in the gas. It is particularly surprising that thermocouples 2 and 3 ended up nearly 1000°C cooler than the crucible, even though they were both quite close to the crucible.

Before this effect was understood, sections of the ampoule (such as close to thermocouple 3) were below 600°C, and served as a sink for the phosphorus. In turn, this explained why, in early runs, ingots were frequently gallium rich. Proper use of solid-type insulators served to correct this problem in later runs.

GaP growth and properties.—After including the above improvements in the apparatus, coarse-grained GaP could be grown, with grains as large as 1 cm^3. GaP crystals grown in the apparatus in 1964 are shown in Fig. 6. The smoothness of these crystals shows the good temperature and mechanical control achieved. The material was always n-type as grown, with an electron concentration usually in the 10^{16} cm^{-3} range, and an electron mobility of about 150 $cm^2/V\text{-}sec$. The material grown was quite pure, although special ef-

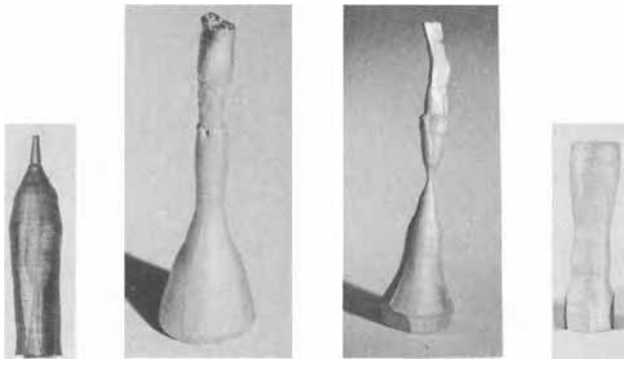

Fig. 6. GaP crystals grown in the high-pressure, magnetic Czochralski apparatus. Typical diameters of crystals at the bottom are ½-¾ in. Large single crystalline grains can be seen.

forts to maintain purity were not made. A typical emission spectrographic analysis was (ppm): Cu(<1), Si(0.1), Mg(1), B(30). The boron was probably from the BN crucible.

Large ingots of GaP could also be cast in the crucible. This cast material was close to stoichiometry, with little free gallium visible, and was very clear, with transparency possible through pieces exceeding 3 cm in thickness.

Cross-sectional examination of the pulled GaP crystals revealed that nucleation of additional grains continually occurred during growth. This occurred both at the interior and at the surface of the crystal. It was this factor that prevented the growth of larger single crystals.

The cause of this spurious nucleation was never ascertained. Single crystalline seeds were used, and the crystals were necked down after the initiation of growth. The obvious crystal growth parameters such as pulling speed, rotation rate, solid-liquid interface shape, and phosphorus pressure were all varied and optimized, but the nucleation persisted. Perhaps impurities from the hot-pressed BN crucible contaminated the melt, or maybe surface nucleation occurred due to severe fluctuations in convective heat losses at the solid-liquid interface. (Note that when liquid encapulation is used, the melt-solid interface is protected from convection heat losses.) However, the experiments were terminated because it was very time consuming to obtain data. A single run, starting from the loading of an ampoule and ending with the cleaning of the autoclave, consumed close to a week's time.

Acknowledgments

The authors are grateful to Dr. A. Fischer for valuable advice concerning construction and operation of the autoclave, and to Dr. D. Richman for important discussions during the course of the work.

Manuscript submitted July 13, 1970; revised manuscript received *ca.* Dec. 29, 1970.

Any discussion of this paper will appear in a Discussion Section to be published in the December 1971 JOURNAL.

REFERENCES

1. S. J. Bass and P. E. Oliver, *J. Crystal Growth*, **3**, 286 (1968).
2. D. Richman, *J. Phys. Chem. Solids*, **24**, 1131 (1963).
3. L. R. Weisberg and E. A. Miller in "Synthesis and Characterization of Electronically Active Solids," Tech. Reports 1-4, Contract SD-182, Advanced Research Projects Agency (1964-1965).
4. R. Gremmelmeier, *Z. Naturforsch.*, **11a**, 511 (1956).
5. A. Fischer, *This Journal*, **117**, 41C (1970).
6. L. R. Weisberg, in "The Art and Science of Growing Crystals," J. J. Gilman, Editor, p. 388, John Wiley & Sons, New York (1963).

Technical Notes

Performance Domain Analysis of Primary Batteries

R. Selim and P. Bro*

P. R. Mallory & Company Incorporated, Laboratory for Physical Science, Northwest Industrial Park, Burlington, Massachusetts 01803

The performance of primary batteries is generally given in terms of discharge curves or discharge tables for a discrete set of operating conditions. This is satisfactory for many applications, but it leaves unanswered the question of the performance of batteries under operating conditions other than those specified.

The Peukert equation (1, 2) has been used to describe the discharge of secondary batteries, and it appears to be reasonably good for this purpose. We have found that the Peukert equation can also be used for primary batteries, but only at moderate and high rates. It is not satisfactory for primary batteries at low rates.

Analyses of the discharge of cells and batteries under a variety of conditions have led to a new capacity-current correlation for primary batteries that is satisfactory for high, low, and intermediate discharge rates. In addition, the new correlation leads to the definition of a performance domain for a battery. The performance domain is a useful tool for the description of battery performance and for the analysis of the effects of design changes on battery performance.

Empirical Correlation

The search for a useful capacity-rate correlation was guided by the results of analyses of resistive network models of porous electrodes. Generally, they lead to expressions containing hyperbolic functions. It is characteristic of primary batteries that they deliver a limiting capacity at low rates, not necessarily the stoichiometric capacity, and the choice of a suitable hyperbolic function for the capacity-rate correlation should reflect this characteristic. Trial and error work with experimental data and various mathematical expressions led to the following best description of the battery performance

$$q = q_o \frac{\tanh (i/R)^{1/A}}{(i/R)^{1/A}} \qquad [1]$$

where i = battery current, mA
q = realized battery capacity, mAhr
q_o, A, R = empirical parameters

This correlation exhibits the proper capacity-rate relationship, and it approaches the Peukert equation at high rates.

The definition of the useful capacity of a battery is somewhat arbitrary, but we have found the correlation to be satisfactory for a variety of criteria defining the useful capacity provided consistency is maintained. The parameters are calculated most conveniently from the experimental data by the method of least squares applied to nonlinear expressions (3) using discharge data obtained over the entire range of discharge rates,

* Electrochemical Society Active Member.

Key words: batteries, capacity, discharge, efficiency, performance, quality control.

Table I. Comparison of observed and smoothed data* for 930-S Zn/HgO cells, 25°C

Constant current (mA)	Capacity, mAhr Observed	Capacity, mAhr Equation [1]	Error % of q_o
25	1092	1005	4.0
25	998		
50	965	995	4.3
50	940		
150	630	648	0.4
150	675		
400	120	124	6.4
400	0		
500	100	82	0.7
500	50		

* 0.80V cut-off voltage.

including low, intermediate, and high discharge rates (360 BASIC program available on request).

The empirical correlation has been tested for a wide variety of batteries: lead acid batteries, Leclanche cells of many sizes, alkaline manganese batteries, nickel-cadmium batteries, silver-cadmium cells, silver-zinc cells, and alkaline mercury cells, using performance data available from the manufacturers, e.g. (4), and a satisfactory fit was obtained in all cases. An illustration of a typical fit is shown in Table I where the observed and calculated data are compared for the discharge of 930-S Zn/HgO cells. It may be seen that the correlation fits reasonably well over the entire range of discharge rates.

The Performance Domain

The parameters q_o, A, and R can be represented graphically by a point in a three-dimensional coordinate system, and a unique prismatic region surrounding this point can be defined by the standard errors in q_o, A, and R as shown in Fig. 1. This volume is the performance domain of the battery, and it characterizes the range of battery performance to be expected due to the intrinsic variations between the cells.

Each of the three parameters that define the performance point has a simple physical interpretation. The quantity q_o is the maximum capacity obtainable from the battery. It is referred to as the standard capacity of the battery, and the deliverable capacity at any particular rate of discharge can be obtained from it using Eq. [1].

The quantity R has the dimension of current, and it is referred to as the standard rate of the battery. It is the rate of discharge beyond which the performance

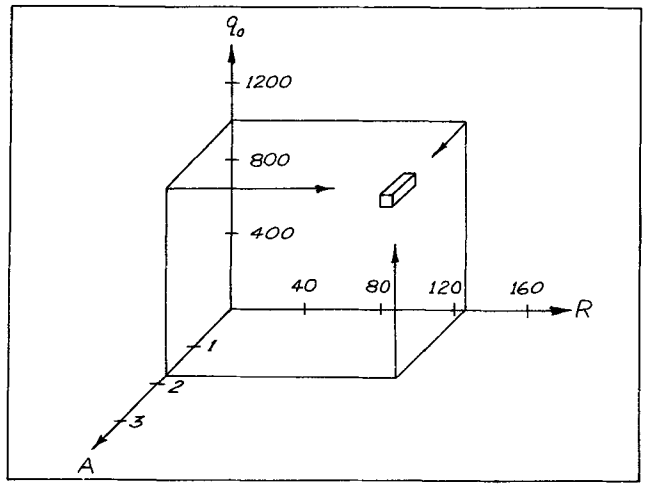

Fig. 1. Performance domain diagram of 930 S Zn/HgO cells at 25°C.

begins to become significantly rate limiting as distinct from capacity limiting. The delivered capacity is 76% of the standard capacity at the standard rate. At higher discharge rates, the delivered capacity begins to decrease appreciably.

The quantity A is the accommodation coefficient of the battery. It measures how readily the battery can accommodate high discharge rates without appreciable losses in efficiency. A small A indicates a rapid loss of efficiency above the standard rate, and a large A indicates that the battery can be operated efficiently above the standard rate. The quantity A is, therefore, a significant characteristic of the rate capability of a battery.

Discussion

The specification of the standard capacity, the standard rate, and the accommodation coefficient of a battery represents a rational and an informative means of rating battery performance that is preferable to the common practice of assigning a somewhat arbitrary rate and capacity to a battery. A table of the performance points of various batteries in conjunction with a nomograph of Eq. [1], Fig. 2, can replace bulky performance manuals.

The performance point provides an analytical tool for the evaluation of the effect of design changes on battery performance. When a design change is introduced a new performance point is established. If it

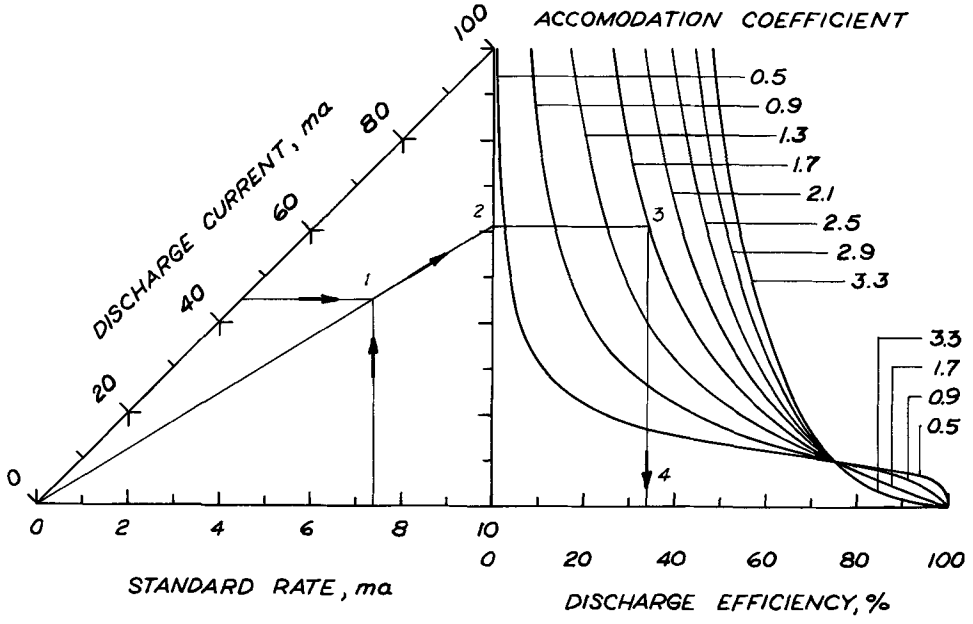

Fig. 2. Nomograph of rate-capacity relationship, Eq. [1].

falls inside the performance domain the effected change is probably of no significance. And conversely, if a significant change is obtained, the direction of change to the new performance point establishes the nature of the significant effect, whether it be a change in the standard capacity, the standard rate capability, or the accommodation capability or in a mixture of them.

The performance points of batteries also provide a means for comparing different battery systems in either the same or different structures, and the performance parameters make it possible to establish their relative merits in quantitative terms for a wide range of operating conditions.

The performance domain centered at q_o, R, and A is defined in extent by the standard errors in q_o, R, and A. For a specific batch of batteries of a particular kind and size the volume of this domain is a measure of the "quality" of the batch or what may be called the manufacturing consistency of the batch. The smaller the domain volume of a particular type of battery, the smaller the variability within the batch and the higher the quality. The qualities of different kinds of batteries may be compared in terms of the dimensionless domain volumes defined by $\Delta q/q_o$, $\Delta R/R$, and $\Delta A/A$.

The performance correlation, Eq. [1], is presented in a nomographic form in Fig. 2, and it applies to any battery. In order to use it for a particular battery it is necessary to obtain the performance parameters of the battery first. Then, the discharge efficiency can be read from the nomograph for a wide range of discharge rates.

The nomograph is independent of the mode of discharge selected by the user provided consistency is maintained in specifying the discharge rate and the standard rate. Thus, constant current or constant load or pulse load discharges may be used to any desired cutoff voltage, and the efficiency may be determined from Fig. 2, provided that q_o, R, and A were determined for the same type of discharge regime. The quantity (i/R) is dimensionless and independent of how the current or discharge rate is specified. The left-hand part of the nomograph simply performs the division (i/R), and the nomograph is equally valid if both the standard rates and the discharge rates shown in Fig. 2 are divided or multiplied by the same number or if the rates are expressed in terms other than milliamperes.

Manuscript submitted Nov. 4, 1970; revised manuscript received *ca.* Jan. 19, 1971.

Any discussion of this paper will appear in a Discussion Section to be published in the December 1971 JOURNAL.

REFERENCES

1. G. W. Vinal, "Storage Batteries," 4th Ed., p. 216, J. Wiley & Sons, Inc., New York (1955).
2. S. M. Selis and C. R. Russell, *Electrochem. Technol.*, **1**, 77 (1963).
3. G. W. Snedecor and W. G. Cochran, "Statistical Methods," 6th Ed., p. 465, Iowa State University Press, Ames, Iowa (1967).
4. Union Carbide Corp., "'Eveready' Battery Applications and Engineering Data," Consumer Products Division, New York (1968).

Electrochemical Machining: A Note on the Throwing Power of Electrolytes

D. T. Chin* and A. J. Wallace, Jr.

Electrochemistry Department, Research Laboratories, General Motors Corporation, Warren, Michigan 48090

Owing to the increasing use of hardened metals in recent years, electrochemical machining (ECM) has had a great impact on the metal removal process. One of the major problems encountered in ECM is how to obtain satisfactory dimensional control of a desired cutting geometry. To achieve this, one needs information regarding the performance of an electrolyte at various operating conditions. Such information is desirable in designing the shape of tools that would produce a desired shape on the machined work piece.

In a recent article, Brook and Iqbal (1) have suggested using the concept of throwing power to evaluate the extent of dimensional control that an electrolyte could give under constant operating conditions. They describe a modified Haring-Blum cell for measuring the throwing power of ECM electrolytes and present data obtained at a relatively low current density of 15 A/in.^{2}. The cell, in effect, is not suitable for the measurement at high current densities (300-1200 A/in.^{2}) normally used in electrochemical machining. It consists of two parallel anodes located at different distances from the cathode with no adjustment of the gap spaces while cutting is in progress. Using a normal ECM current density of 500 A/in.^{2}, for instance, experience with concentrated $NaClO_3$ indicates that for the near anode a gap space initially set at 0.01 in. will be widened to about 0.05 in. at the end of a 2-min period of machining. The cutting rate on the far anode is usually not as fast as that of the near anode; consequently, this causes a decrease of linear ratios during the experimental runs. If the initial gap for the far anode is 0.05 in., the linear ratio, as estimated from Brook and Iqbal's data, would vary from an initial value of 5 to approximately 1.2 at the end of the machining. Such a great variation in linear ratios presents a serious limitation for the accurate measurement of throwng power at high current densities.

We have developed a simple and reliable method for measuring throwing power at normal ECM operating current densities. The method consists of measuring the anode-cathode gap space as a function of time and expressing the result in terms of a logarithmic throwing index. An intense and comprehensive investigation of this new concept is being carried out at the General Motors Research Laboratories. This paper describes the results of some of these studies. A summary on the rationale of this dynamic approach is given below, and the experimental data obtained from an ECM flow cell is then presented for the sodium chlorate electrolyte.

Theoretical Background

Consider an anode and a stationary parallel cathode having an initial gap space δ_o in. The rate of cutting, r (in./sec or in./min), at any point on the anode surface is equal to the rate of increase in gap space, $d\delta/dt$

$$\frac{d\delta}{dt} = r \qquad [1]$$

where δ is the local gap space at time t after starting machining. The initial condition for the differential equation is: at $t = 0$, $\delta = \delta_o$, and $r = r_o$, where r_o is the initial cutting rate at the point where the gap is

* Electrochemical Society Active Member.

Key words: electrochemical machining, throwing power, throwing index.

measured. Introducing new variables

$$L \text{ (linear ratio)} = \frac{\delta}{\delta_o}$$

and

$$M \text{ (metal distribution ratio)} = \frac{r_o}{r}$$

Eq. [1] becomes

$$\frac{dL}{dt} = \frac{r_o}{\delta_o}\frac{1}{M} \qquad [2]$$

To solve the equation, one needs to replace M with a known function of L. A regressional analysis (2) of published throwing power data obtained from the Haring-Blum cell for various plating baths has shown that the metal distribution ratio, M, can be correlated to the linear ratio, L, by

$$M = L^{1/A} \qquad [3]$$

where A is the logarithmic throwing index and is constant for a given electrolyte at constant operating conditions. In electroplating, the metal distribution ratio is defined as the ratio of the metal deposition rates on two equipotential plane cathodes located at different distances from the anode. In ECM, however, the definition has been changed to the ratio of the rate of dissolution on the near plane anode to that on the far plane anode. Since the metal dissolution is the reverse process of electroplating, we may assume that Eq. [3] is also valid for the case of electrochemical machining. Substituting Eq. [3] into Eq. [2] and making use of the initial condition (at $t = 0$, $L = 1$), we have

$$\int_1^L L^{1/A}\,dL = \frac{r_o}{\delta_o}\int_o^t dt \qquad [4]$$

Equation [4] can be integrated to give the following expression describing the time-variation of local gap space between the anode and the cathode

$$t = \frac{\delta_o}{r_o\left(\frac{1}{A}+1\right)}\,(L^{1/A+1} - 1) \qquad [5]$$

Accordingly, if a set of L *vs.* t data is plotted in the form of t against $L^{1/A+1}$, one should obtain a straight line having a slope equal to $\delta_o/r_o(1/A + 1)$ and an intercept equal to $-\delta_o/r_o(1/A + 1)$. To find the proper exponent of L, a trial-and-error method is required: (*i*) assume a value of $1/A$, (*ii*) plot the data points in the form of t *vs.* $L^{1/A+1}$, and (*iii*) repeat steps *i* and *ii* until the data points fall on a straight line having a slope equal in magnitude to its intercept. From the slope of the straight line and the exponent of L, the initial cutting rate, r_o, and the logarithmic throwing index, A, (and thus the throwing power) can be calculated for an electrolyte at given operating conditions.

An alternative way to find r_o and A is via the graphical differentiation of the L *vs.* t curve. This can be seen if we rearrange Eq. [2] (after replacing M by $L^{1/A}$) or differentiate Eq. [5] with respect to L

$$\frac{dt}{dL} = \left(\frac{\delta_o}{r_o}\right)L^{1/A} \qquad [6]$$

This equation suggests that a straight line is obtained if log (dt/dL) is plotted against log L. The slope of the straight line is $1/A$, and its intercept equals log (δ_o/r_o). It should be noted, however, that the graphical differentiation of the L *vs.* t curve is generally not very accurate. The accuracy may be very seriously impaired by small errors in the experimental data. Unless there is a large number of data points available, this method is not recommended for the direct evaluation of the logarithmic throwing index.

Experimental Procedure

The experimental setup is similar to the flow cell system described in an earlier electrolyte study (3) with slight modifications. It consisted of a centrifugal pump, a solution reservoir, and a Lucite cell cavity. The cell and the solution reservoir were incorporated as one unit as shown in Fig. 1. The cathode was a circular copper tube, 0.251 in. OD and 0.176 in. ID, fixed on the bottom of the cell. The anodes were flat 1008 steel panels, 1 × 3 × 0.025 in., which were held in place above the cathode. The initial spacing between the anode surface and the cathode tip was 0.01 in.

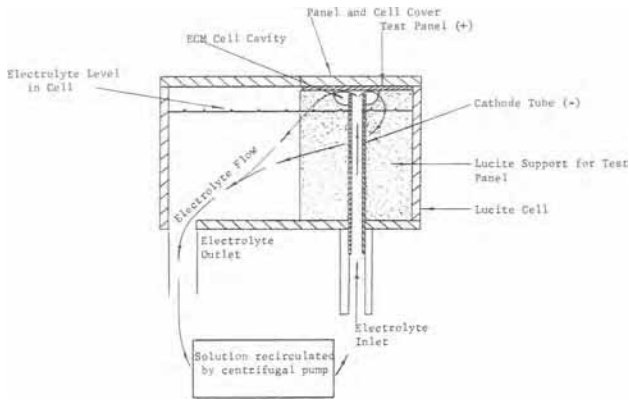

Fig. 1. Schematic illustration of the ECM test apparatus

In this study, the throwing power measurement was performed for sodium chlorate electrolytes. For each run the cell voltage was kept at 17.5V, and the electrolyte was fed through the cathode tube into the cell with a flow rate of 2.5 liters/min. The duration of machining varied from 10 to 60 sec. At the end of each test, the resulting gap space was measured as the depth of metal removed plus the initial gap space.

Result and Discussion

Figure 2 is a set of measurements of gap space expressed in the form of L *vs.* t for 320 g/liter $NaClO_3$ electrolyte at a cathodic current density of 610 A/in.^{2}. The electrolyte temperature was maintained at 18°C. It was found (using the method of trial and error) that a straight line having a slope of 8.0 sec was obtained if the data are replotted as t *vs.* $L^{1.9}$ as shown in Fig. 3. Thus the logarithmic throwing index, A, of the chlorate solution becomes

$$A = \frac{1}{1.9 - 1} = 1.11$$

For a given linear ratio, the metal distribution ratio, M, can now be computed from Eq. [3] with the known value of the logarithmic throwing index. Figure 4 is

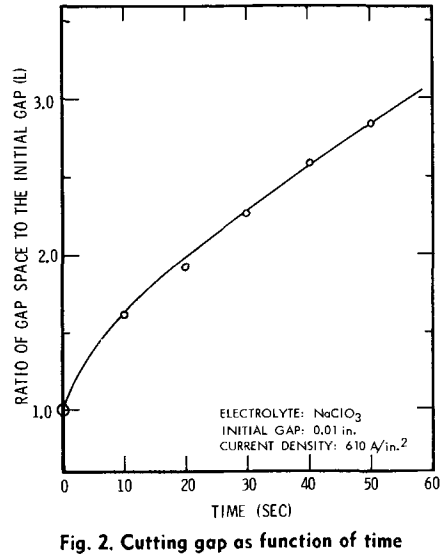

Fig. 2. Cutting gap as function of time

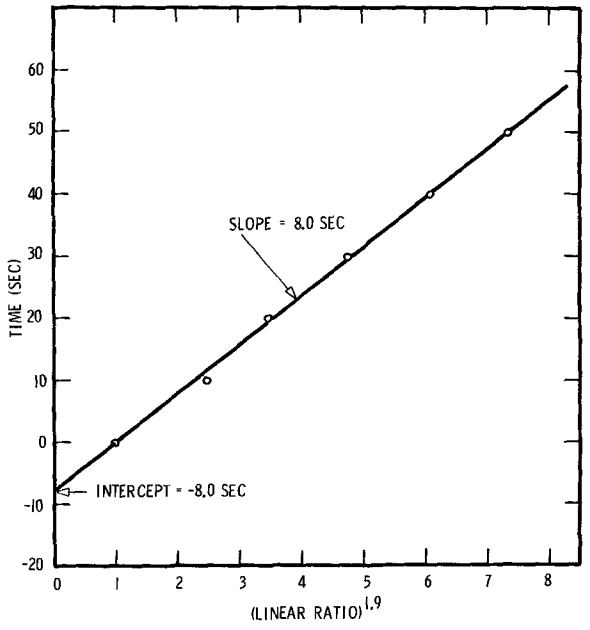

Fig. 3. t vs. $L^{1.9}$

a log-log plot of M *vs.* L for the sodium chlorate electrolyte at the above operating conditions (solid line). For comparison, Brook and Iqbal's chlorate data obtained at 15 A/in.^{2} is also plotted in the figure as circular dots. It is seen that the present measurement gives a straight line passing through the common point represented by the linear ratio equal to 1 and the metal distribution ratio equal to 1. Brook and Iqbal's data, on the other hand, also gives a reasonably straight line as shown by the dashed line; it, however, would extend to the point ($L = 1$, $M = 0.2$) instead of ($L = 1$, $M = 1$). This obviously contradicts the fact that two equipotential anodes located at the same distance from the cathode should have equal rates of metal dissolution; the deviation is probably due to the variation of linear ratios during their measurement with the modified Haring-Blum cell.

Furthermore, the present method also enables one to find precisely the initial cutting rate, r_o, corresponding to the initial gap space. For the case presented here, it can be calculated from the logarithmic throwing index and the slope of the straight line given in Fig. 3

$$r_o = \frac{0.01}{8.0 \times 1.9} \times 60 = 0.039 \text{ in./min}$$

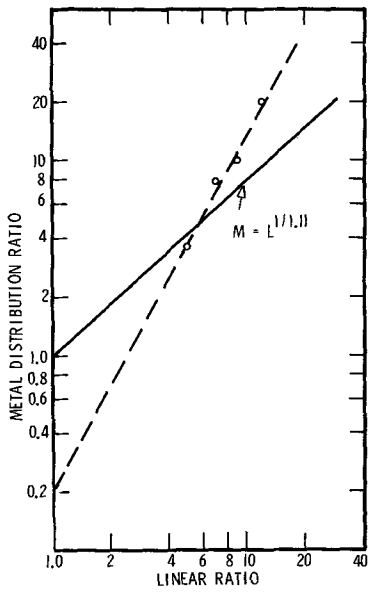

Fig. 4. Log-log plot of metal distribution ratio vs. linear ratio. The dark line is the result of present measurement from a 320 g/liter $NaClO_3$ electrolyte at a current density of 610 A/in.^{2} The circular dots connected by the dashed line are Brook and Iqbal's chlorate data at 15 A/in.^{2}.

In summary, the measurement of time variation of gap space provides simple and efficient means for obtaining the throwing power data of electrolytes under ECM operating conditions. The information thus obtained can be used directly for the tool design and in ECM practices for determining the optimum tool feed rate to maintain a constant gap space.

Manuscript submitted April 27, 1970; revised manuscript received Jan. 6, 1971.

Any discussion of this paper will appear in a Discussion Section to be published in the December 1971 JOURNAL.

REFERENCES

1. P. A. Brook and Q. Iqbal, *This Journal*, **116**, 1458 (1969).
2. D. T. Chin, *ibid.*, **118**, 818 (1971).
3. J. P. Hoare, M. A. LaBoda, M. L. McMillan, and A. J. Wallace, *ibid.*, **116**, 199 (1969).

Pulse Electroplating of High-Resistance Materials, Poorly Contacted Devices, and Extremely Small Areas

C. A. Burrus

Bell Telephone Laboratories, Incorporated, Crawford Hill Laboratory, Holmdel, New Jersey 07733

Electroplating is an accepted method of applying many metallic coatings to low-conductivity surfaces. Plating by means of current *pulses* rather than the commonly used direct current has been proposed for certain applications and a number of advantages have been reported for the pulse-deposited coatings (increased density, increased purity, reduced hydrogen embrittlement, *etc.*) (1). However, the method seems to have been little used, probably due to the added complications of providing pulsed power supplies.

Key words: pulse electroplating, semiconductor contacts.

We have employed a simple form of high-voltage pulse plating for more than 10 years in the small-scale fabrication of experimental semiconductor devices, largely to overcome the problems associated with plating high-resistance or nonuniform-resistance surfaces of small areas. Our usage has involved the plating of extremely small areas (tips of 0.003 cm wires), relatively poor-conductivity surfaces (moderately doped semiconductors), materials with poor electrical contacts (n-type GaAs held with tweezers), *etc.*—materials which, partly because of difficulties in plating

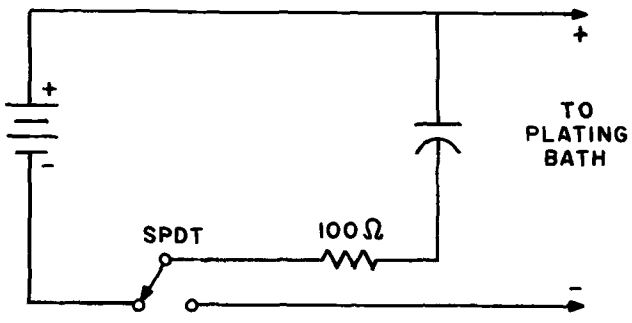

Fig. 1. Simplest form of pulse-plating circuit

by direct current, normally are coated by vacuum evaporation. This pulse-plating technique has proved to be so rapid and convenient in small-scale applications, compared to vacuum evaporation, that we wish to describe it briefly.

The plating circuit in its simplest form is shown in Fig. 1. A capacitor is charged from a battery through a normally closed SPDT microswitch. When the microswitch button is pressed, the battery is disconnected and the capacitor is discharged through the plating bath, providing a "pulse" of plating current. As a practical matter, it is convenient to provide a variable-voltage power supply and a number of capacitors which can be switched in and out of the circuit in parallel. The total charge per pulse delivered to the plating bath then can be controlled by adjusting the charging voltage and the value of the capacitance. The total metal transferred in the plating can be adjusted, additionally, by varying the number of pulses applied.

Use of such a capacitor discharge, or of a more sophisticated pulse generator, allows the starting voltage applied to the plating solution to be many times that normally used (tens of volts rather than 1-3V) but at the same time conveniently restricts the rate of charge transfer so that "burning" of the plate does not occur. The relatively high voltage aids in overcoming problems of starting a plate due to poor contacts to the object to be plated, high resistance of the object itself, thin insulating films on the surface, the presence of higher- and lower-resistance areas in parallel, and irregular shape of the surface; it often permits use of a plating solution at room temperature which normally would plate satisfactorily only at elevated temperatures; it conveniently permits plating of a surface which can be contacted only through a rectifying junction; and it easily permits the plating of extremely small areas without burning.

Wide variations in conditions have been found to be permissible, and at least two dozen different metals and metal mixtures have been plated at one time or another. A few examples which illustrate the use of the technique are listed below. Representative examples of devices fabricated with its aid can be found in the references.

1. *Very small areas.*—Plating of a dopant metal onto a pointed wire for formation of a pulse-alloyed p-n junction. For a 0.01 cm length of 0.003-0.005 cm wire: 5 μf charged at 5-7V, 3-5 pulses (2,3).

2. *Poor conductivity surface, and room-temperature use of solution normally used hot.*—Plating of tin at room temperature onto n-type GaAs for alloying as an ohmic contact, 1 cm^2 area: 80 μf, 35V, 50-100 pulses (4-6).

3. *Surface with poor electrical contact.*—Starting a gold plate on n-type GaAs held with tweezers, 1 cm^2 area: 80 μf, 45V, 20-30 pulses (4-6).

4. *Many small areas in parallel.*—Plating gold into array of 2-3 μm diameter windows on n-type GaAs to form Schottky-barrier diodes, array 1 cm on edge: 20-40 μf, 45V, groups of 5-7 pulses until desired buildup obtained (6).

5. *Surfaces in series with rectifying junction.*—Plating gold into array of p-type surfaces diffused in micrometer-diameter windows on n-type semiconductor, array 1 cm on edge: 40 μf, 45V, groups of a few pulses until desired thickness obtained (4,7).

6. *High- and low-conductivity materials in parallel* —Starting plating on p- and n-side of semiconductor chip bonded to metal stud, with metal and semiconductor immersed: 20-40 μf, 20-50V, 10-20 pulses (5).

7. *Bridging of thin insulating layer.*—As in No. 6, but semiconductor chip electrically separated from stud by thin SiO_2 layer: 80-120 μf, 50V, 30-40 pulses (5).

Some of these applications make use of the pulse-plating method to create an equipotential layer on surfaces whose conductivity is poor or nonuniform (items 2, 3, and 6) and the plating can be completed by conventional methods. Other applications (as illustrated in items 1, 4, and 5) may require that the entire job be done by the pulse technique. In all applications, use of an electronic pulse generator speeds the operation.

Manuscript submitted Dec. 4, 1970; revised manuscript received *ca.* Jan. 25, 1971.

Any discussion of this paper will appear in a Discussion Section to be published in the December 1971 JOURNAL.

REFERENCES

1. For a recent review and some previous references, see A. J. Avila and M. J. Brown, *Plating*, **57**, 1105 (1970).
2. C. A. Burrus, *J. Appl. Phys.*, **32**, 1166 (1961).
3. C. A. Burrus, *IEEE Trans. Microwave Theory and Techniques*, **MTT-11**, 357 (1963).
4. C. A. Burrus, *Proc. IEEE*, **55**, 1104 (1967).
5. C. A. Burrus and R. W. Dawson, *Appl. Phys. Letters*, **17**, 97 (1970).
6. T. P. Lee and C. A. Burrus, *IEEE Trans. Microwave Theory and Techniques*, **MTT-16**, 287 (1968).
7. C. A. Burrus and W. M. Sharpless, *Solid-State Electron.*, **13**, 1283 (1970).

Method for Producing Graded Composition Epitaxial Layers by Vapor Deposition

L. G. Bailey and G. G. Rogers

Texas Instruments Incorporated, Materials Science Research Laboratory, Dallas, Texas 75222

In recent years vapor phase epitaxial growth techniques have been used extensively for the preparation of III-V compounds for solid-state device applications. Solid-solution alloys of many of these compounds have also been produced to obtain materials with intermediate properties. The formation of graded composition alloy films, however, has received relatively little study, although such films have been considered for special device applications and for reducing the effects

Key words: $Ga_xIn_{1-x}As$ alloys, semiconductors, III-V compounds.

of lattice mismatch between substrates and heteroepitaxial layers (1, 2).

To produce graded composition epitaxial layers with chemical transport systems, the composition of the reacting vapor can be changed as a function of time by altering the relative input rates of fixed composition gases into the deposition chamber. Although this method offers the flexibility for producing any desired composition profile within the layer by suitable flow rate programming, it is difficult to execute simply if reproducible results are to be obtained. The control of very low flow rates ($\leqq$ 20 cm^3/min) is usually required during part of the growth for at least one of the input gases, and manual or even motor drive operation of needle valves to change flows is difficult at these levels because of inconsistencies in delivered flow as a function of angular rotation of the valve control shaft. In addition, techniques for accurate flow rate measurement are difficult at these levels. These problems multiply when the control of two or more flows must be coordinated to obtain a smoothly varying deposit composition.

The method reported here employs the filling and emptying characteristics of reservoirs to produce gas mixtures of changing composition at constant flow rate. The method is simple, depends on an easily reproducible physical process, and utilizes fixed gas flows at levels which are simple to measure and control. Although Tietjen and Amick have mentioned the use of a ballast vessel to smooth fluctuations in gas flows and compositions (3), their graded $GaAs_xP_{1-x}$ deposits were prepared by changing the flow rates of the input gases (2).

Experimental Procedure

A reactor of the design reported by Conrad *et al.* (4) was used to prepare epitaxial layers of $Ga_xIn_{1-x}As$ alloys on GaAs substrates. Three separate source holders were used, containing elemental arsenic, elemental gallium, and an alloy of indium and gallium. Arsenic was transported by sublimation into a carrier stream of purified hydrogen, while the group III elements were transported as chlorides by high-temperature reaction with HCl carried in hydrogen. Deposit compositions between GaAs and an alloy determined by the composition of the indium-gallium alloy were prepared by adjustment of the concentrations of HCl in hydrogen at constant flow rate entering the source holders. A gas-handling system shown in Fig. 1 was used to supply time-varying concentrations of HCl to each of these sources. This system consisted essentially of an $AsCl_3$ saturation bubbler-reduction tube combination to generate HCl-H_2 gas mixtures and a gas reservoir. This system could deliver either an increasing concentration (reservoir initially filled with hydrogen and a HCl-H_2 mixture introduced during operation) or a decreasing concentration (reservoir initially filled with a HCl-H_2 mixture and flushed during operation with pure hydrogen).

A 3-liter reservoir was used for the indium-gallium alloy source and a 0.6-liter reservoir was used for the gallium source. Flow rates of hydrogen through both systems were 50 cm^3/min, and a hydrogen flow of 33 cm^3/min was passed through the arsenic source held at 427°C. Additional flows of 39 cm^3/min and 18 cm^3/min were added to the reservoir outputs for the indium-gallium source and the gallium source, respectively. The growth temperature was 740°C, and the group III sources were held at 844°C. Growth rates were typically in the range of 15 to 25 μm/hr.

A series of tests was performed to determine directly the reservoir delivery characteristics under the same conditions of flow rate and HCl concentration as were used in the growth experiments. Gas composition was measured with a thermal conductivity cell–Wheatstone bridge combination, and its output was displayed on a strip chart recorder.

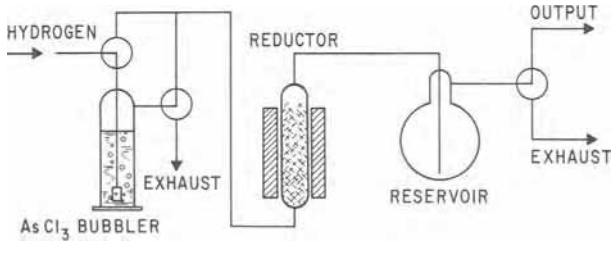

Fig. 1. System for producing time-varying concentration of HCl in hydrogen.

Results and Discussion

The reservoir delivery tests showed that both reservoirs closely followed exponential filling and emptying behavior. Figure 2 presents typical semi-log plots of gas composition *vs.* time for emptying of both reservoirs. Similar results were obtained for reservoir filling. These results indicate that under the specified operating conditions the reservoir delivery characteristics can be fairly accurately described with simple theory. Specifically for reservoir emptying, beginning with an initial concentration, C_0, of HCl in hydrogen, the output of the reservoir with time is:

$$C_t = C_0 \exp(-Ft/V) \qquad [1]$$

where C_t is the concentration at time t, F is the flow rate through the reservoir, and V is the reservoir volume. This relation follows from the assumptions of (*a*) complete reservoir mixing and (*b*) the rate of HCl loss from the reservoir as proportional to its instantaneous concentration and the gas flow rate through the reservoir.

It should be noted that the slopes of the curves in Fig. 2 will be equal to $-F/V$ if the reservoir delivery is described by Eq. [1]. Using the value of flow rate employed during the tests, the calculation of reservoir volumes yielded 3.17 and 0.60 liters which are in excellent agreement with those determined by direct measurement of water capacity, namely 3.03 liters and 0.59 liter respectively.

Figure 3 shows the variation of deposit composition with distance through a graded $Ga_xIn_{1-x}As$ epitaxial deposit formed on a (100) oriented GaAs substrate. Deposition time was 210 min, producing a layer 89 μm thick with a final composition at the surface of 46 m/o InAs. The data presented were obtained by electron microprobe analysis across a five-degree beveled section of the sample.

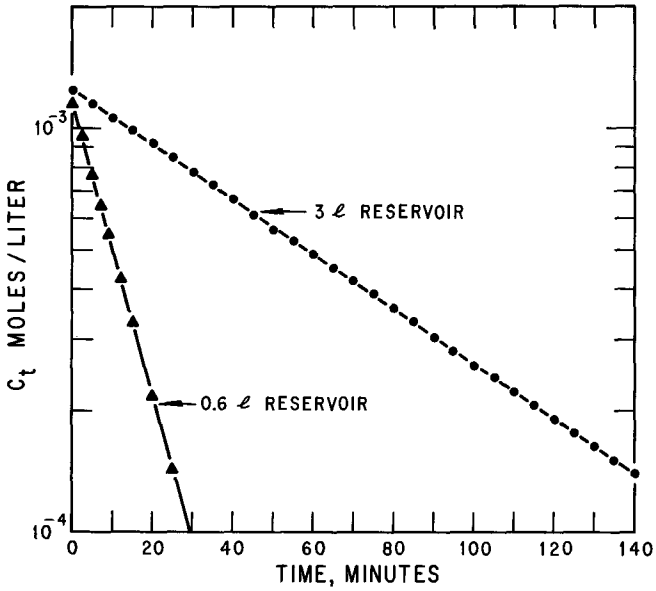

Fig. 2. Output concentration of HCl in hydrogen as a function of time for reservoir emptying.

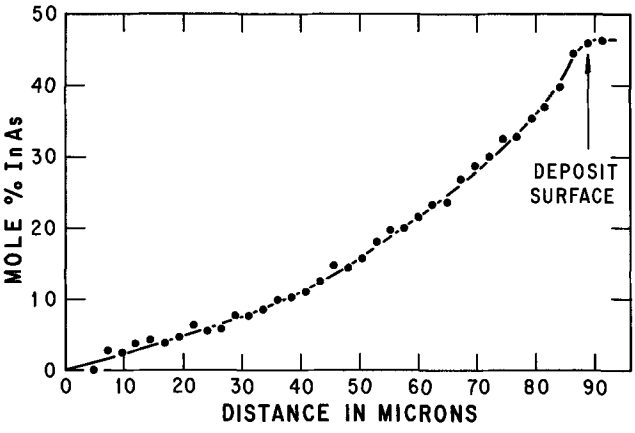

Fig. 3. Variation of $Ga_xIn_{1-x}As$ composition with depth in epitaxial deposit.

The composition of vapor-deposited $Ga_xIn_{1-x}As$ alloys is very sensitive to the relative proportions of indium and gallium chlorides in the reacting gas stream. Gallium segregates into the growing layer, and the ratio of gallium to indium in the deposit is approximately five times the ratio of the halides in the vapor for alloys in the range of 0 to 50 m/o GaAs. This phenomenon increases the difficulty of obtaining reproducible, uniformly graded layers in this alloy system, especially near pure InAs. However, as can be seen in Fig. 3, the use of an indium-gallium alloy source to fix the final deposit composition and gas reservoirs to produce slowly changing gas inputs to the group III sources has given good control on deposit composition, and the grading is very uniform.

Although the use of gas reservoirs for producing time-varying concentrations of HCl in hydrogen for grading the composition of $Ga_xIn_{1-x}As$ alloys has been discussed specifically here, we expect the technique to be a general one and applicable to many combinations of gases and alloy systems. For example, graded layers of $GaAs_xP_{1-x}$ could be prepared by using reservoir filling to increase the concentration of PCl_3 and decrease the concentration of $AsCl_3$ entering separate gallium sources.

Acknowledgments

The authors wish to thank W. W. Gartman for his assistance in preparing the epitaxial layers and Dr. J. P. Smith for his electron microprobe analysis of the beveled samples.

This work was supported in part by the Electronics Technology Division of the Air Force Avionics Laboratory under Contract F-33615-67-C-1111.

Manuscript submitted Sept. 23, 1970; revised manuscript received Jan. 8, 1971.

Any discussion of this paper will appear in a Discussion Section to be published in the December 1971 JOURNAL.

REFERENCES

1. R. H. Saul, *J. Appl. Phys.*, **40**, 3273 (1969).
2. M. S. Abrahams, L. R. Weisberg, C. J. Buiocchi, and J. Blanc, *J. Mater. Sci.*, **4**, 223 (1969).
3. J. J. Tietjen and J. A. Amick, *This Journal*, **113**, 724 (1966).
4. R. W. Conrad, P. L. Hoyt, and D. D. Martin, *ibid.*, **114**, 164 (1967).

JOURNAL OF THE ELECTROCHEMICAL SOCIETY

ELECTROCHEMICAL SCIENCE

JUNE 1971

The Zn^{2+}/Zn(Hg) Electrode Reaction in Binary Mixtures of Water and n-Propanol

M. H. Miles*

Department of Chemistry, Middle Tennessee State University, Murfreesboro, Tennessee 37130

and H. Gerischer**,[1]

Institut für Physikalische Chemie, Technische Hochschule, Munich, Germany

ABSTRACT

The kinetics of the Zn^{2+}/Zn(Hg) electrode reaction were investigated in binary mixtures of water and n-propanol. The apparent cathodic transfer coefficient increases from 0.25 in water to 0.39 in 0.04 mole fraction n-propanol, then gradually decreases to a value of about 0.3 as further alcohol is added. The apparent exchange current decreases sharply from 18 mA/cm² in water to about 1 mA/cm² in 0.04 mole fraction n-propanol, then gradually increases as the concentration of n-propanol increases. Above 0.9 mole fraction alcohol, the apparent exchange current rapidly increases as the water concentration falls below the concentration of the excess $LiClO_4$ electrolyte. These variations are interpreted in terms of specific adsorption of n-propanol on the electrode surface and preferential solvation of the Zn^{++} ions in solution by water molecules and by a change to a reaction mechanism involving $ZnClO_4^+$ as water molecules become unavailable for the preferential solvation.

Many investigations of the Zn^{2+}/Zn(Hg) electrode reaction in aqueous solutions have been made (1-6). Although the existence of Zn^+ as an intermediate in the reaction mechanism has been proposed (6-9), it is generally accepted that the charge-transfer reaction kinetics can be best described with a single two-electron step (10-12).

$$Zn^{2+} \cdot aq + 2e^- \rightleftharpoons Zn \qquad [1]$$

Since solvation and desolvation processes represent the main energy barriers in such electrode reactions, it is of interest to investigate the effect of the solvent on this reaction. The primary purpose of this study is to investigate the behavior of the apparent anodic and cathodic transfer coefficients and the apparent exchange current for the Zn^{2+}/Zn(Hg) electrode reaction in binary mixtures of water and n-propanol.

Experimental

Solutions and chemicals.—Bi-distilled water and chromatography grade n-propanol were used in preparing the binary solvent. The electrolyte concentrations were always 0.0083M $Zn(ClO_4)_2 \cdot 6H_2O$, 1.0M $LiClO_4$, and 0.02M $HClO_4$. The water content of these solutions was determined by Karl Fischer titrations. Bubbling purified nitrogen through the solutions removed dissolved oxygen. The zinc concentration in the amalgam was maintained at about 0.7M (0.01 mole fraction zinc).

Galvanostatic measurements.—Details of galvanostatic or constant current pulse measurements can be found elsewhere (13-14). The glass cell used was similar to one described previously (1) except that measurements were made with the amalgam drop hanging directly from the capillary and the current was conducted through the capillary to the drop. A magnetic hammer controlled by an adjustable timing device tapped the capillary at intervals of about 2 sec, dislodging the amalgam drop. The measurement on the fresh amalgam drop was made 1.5 sec later by delivering a short pulse of constant current to the amalgam drop and following the change in potential with time by means of an oscilloscope (14). An amalgamated zinc rod was used as the reference electrode.

A major experimental difficulty present in the galvanostatic method is the elimination of the resistance polarization, η_Ω, from the initial value of the overvoltage, $\eta(O)$, in order to obtain the charge-transfer overvoltage, η. The resistance polarization can be determined from the extremely rapid potential jump at the start of the constant current pulse. The electrolyte resistance, $R_\Omega = \eta_\Omega / i$, was found to be related to the specific conductance, k, of the solution by the expression

$$R_\Omega = 35 \text{ ohms} + 2.4 \text{ cm}/k \qquad [2]$$

Equation [2] is for experiments where the amalgam drop weighs 2.6 mg at the instant of measurement, or, assuming spherical shape, has a surface area of 0.016 cm². This size of the amalgam drop was maintained constant for all measurements. The 35 ohms was found to be the internal resistance of the closed circuit, most of this being the resistance through the amalgam thread in the capillary. As the mole fraction of n-pro-

* Electrochemical Society Active Member.
** Electrochemical Society Active Member through Deutsche Bunsen-Gesellschaft.
[1] Present address: Fritz-Haber-Institut der Max-Planck-Gesellschaft, West Berlin, Germany.
Key words: adsorption, electrode, exchange current, kinetics, n-propanol, solvation, transfer coefficients, water, zinc.

panol increases, it becomes increasingly more difficult to determine R_Ω directly, hence all calculations are based on values of R_Ω obtained from Eq. [2] using experimental values of k. The second term in Eq. [2] agrees favorably with the theoretical value calculated from the expression $R_\Omega = r \cdot A^{-1}k^{-1}a(r + a)^{-1} = 2.1$ cm/k where r is the radius of the amalgam drop, A is its surface area, and a is the distance between the surface of the drop and the reference electrode (15). For our case, $r = 0.036$ cm and $a = 0.5$ cm. Shielding by the capillary tip reducing the effective area by 12% accounts for the slightly larger experimental value of 2.4 cm.

Coulostatic measurements.—The coulostatic method used is, in principal, similar to that reported by Delahay (16-17) and details will be given elsewhere (18). A 1.0 μsec pulse of constant current charges the electrode, and the overvoltage-time curve resulting from the discharge of the double layer by the electrode reaction is recorded. By keeping the initial overvoltage small ($|\eta| < 5$ mV), linear $\log|\eta|$ *vs.* time plots are observed from which the apparent exchange current and differential double layer capacity can be determined. For all galvanostatic and coulostatic measurements, the temperature was maintained at 25° ± 0.2°C.

Results

Tafel plots of the galvanostatic measurements allow the anodic transfer coefficient, α, and the cathodic transfer coefficient, β, to be determined independently. The exchange current was determined by both extrapolation of the Tafel lines to $\eta = 0$ and determination of the charge-transfer resistance at low overvoltages. No corrections were made for the potential of the diffuse double layer; hence apparent transfer coefficients and apparent exchange currents are obtained. The variation in the apparent transfer coefficients as a function of the mole fraction of n-propanol is shown in Fig. 1, and Fig. 2 shows the apparent exchange current density as a function of mole fraction of n-propanol.

Due to the decreasing conductivity with increasing mole fraction n-propanol (Fig. 3), the effect of the resistance polarization, η_Ω, and therefore the experimental error, becomes greater as the alcohol concentration increases. The larger anodic transfer coefficient, α, is more sensitive to error introduced by η_Ω than is β. For mole fractions of n-propanol greater than 0.3, $\alpha \simeq 0.7 \pm 0.1$ and $\beta \simeq 0.3 \pm 0.05$. For high concentrations of n-propanol, $\eta_\Omega >> \eta$, and results become suspect.

The coulostatic method does not require elimination of η_Ω since there is no current flow during measurement other than the faradaic current resulting from the discharge of the double layer. The apparent exchange current densities obtained from coulostatic measurement are in excellent agreement with those determined from galvanostatic measurements (Fig. 2).

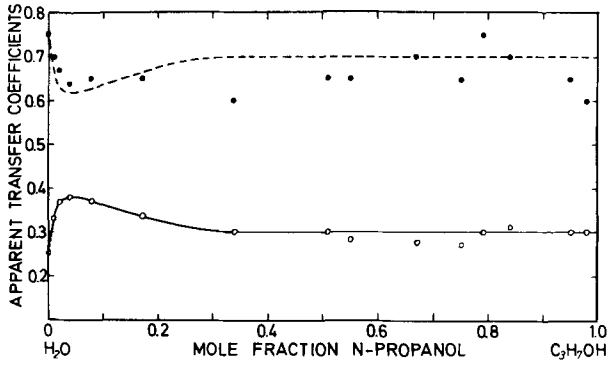

Fig. 1. Variation of the apparent transfer coefficients with mole fraction n-propanol. Dashed line represents 1 — β; ○, apparent cathodic transfer coefficients; ●, apparent anodic transfer coefficients.

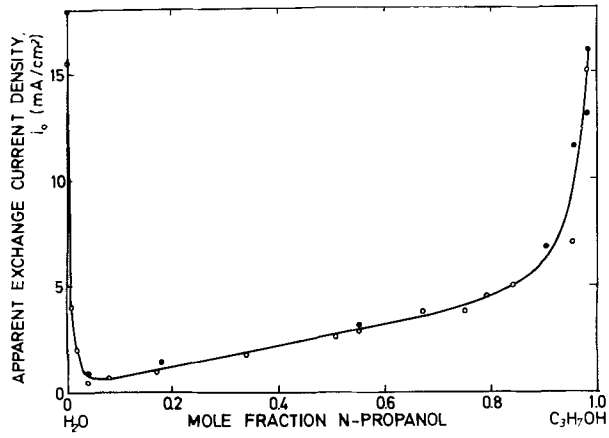

Fig. 2. Variation of the apparent exchange current with mole fraction n-propanol. T = 25.0°C; ○, galvanostatic measurements; ●, coulostatic measurements.

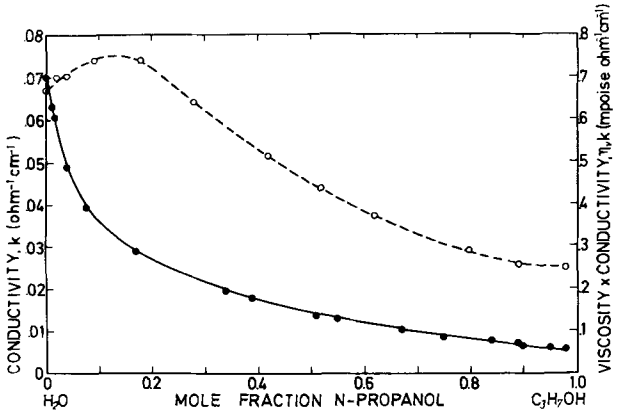

Fig. 3. Variation of the specific conductivity, k, and the product of viscosity x conductivity, $\eta_v \cdot k$, with mole fraction n-propanol at 25.0°C. ●, conductivity measurements; ○, experimental $\eta_v \cdot k$ product.

The variation of the differential capacity of the double layer with mole fraction n-propanol, as determined from the coulostatic measurements, is shown in Fig. 4.

The apparent transfer coefficients can also be obtained from coulostatic measurements using the relationships

$$\alpha = \left(\frac{\partial \ln i_o}{\partial \ln a_{Zn^{2+}}}\right)_{a_{Zn}} \quad \text{and} \quad \beta = \left(\frac{\partial \ln i_o}{\partial \ln a_{Zn}}\right)_{a_{Zn^{2+}}} \qquad [3]$$

However, undissociated $ZnClO_4^+$ or $Zn(ClO_4)_2$ in alcohol solutions may affect the determination of α. For accurate coulostatic measurements, it was experi-

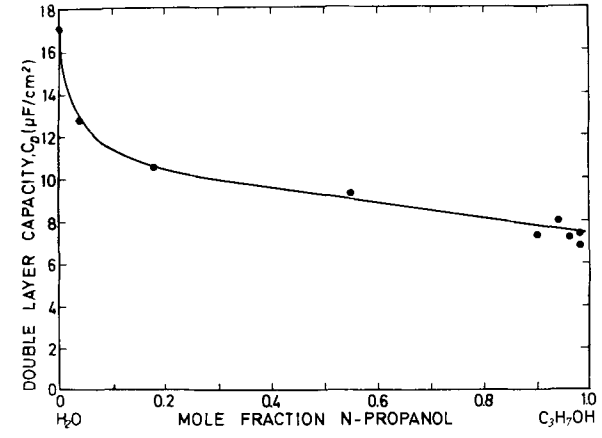

Fig. 4. Variation of the double layer differential capacity with mole fraction n-propanol at 25.0°C. The potential is the equilibrium potential of the zinc electrode.

mentally determined that the concentration of Zn in the amalgam must be between about 0.05M and 2M. Coulostatic determinations of the apparent transfer coefficients in 0.98 mole fraction n-propanol yielded approximate values of $\alpha = 0.6 \pm 0.1$ and $\beta = 0.3 \pm 0.1$, in agreement with results from Tafel plots of the galvanostatic measurements.

The equilibrium potential of the amalgamated zinc rod reference electrode was measured in the various solutions against the normal calomel electrode (NCE) using a 1M KCl salt bridge. The equilibrium potential was found to vary linearly with the mole fraction n-propanol, from −1.11V in aqueous solution to −0.84V in 0.98 mole fraction alcohol. From the Henderson equation, the liquid junction potential is estimated to be less than 5 mV for all solvent compositions.

Using the rapidly dropping mercury electrode method, the potential of zero charge, Epzc, was determined to be −0.55 *vs.* NCE in 1.0M KCl aqueous solution, while for 1.0M $LiClO_4$ in n-propanol, Epzc = −0.31V *vs.* NCE and for 1.0M $LiClO_4$ in methanol, Epzc = −0.36V *vs.* NCE. Although the addition of 0.01 mole fraction Zn to the mercury may shift Epzc about 0.2V more negative (19-20), it still appears that all measurements were made at potentials negative to Epzc. In fact for pure Zn in aqueous solution, Epzc is about −0.9V *vs.* NCE (20), or about 0.2V positive to the $Zn^{++}/Zn(Hg)$ rest potential.

A few measurements were made in methanol-H_2O and ethanol-H_2O solutions. The apparent transfer coefficients were found to be $\alpha \simeq 0.7$ and $\beta \simeq 0.3$ in these solutions. In the methanol solutions, the apparent exchange current density decreases much more gradually with mole fraction alcohol than found for n-propanol, reaching a minimum of $i_o = 3$ mA/cm² at about 0.5 mole fraction methanol.

Discussion

The $Zn^{2+}/Zn(Hg)$ electrode reaction can be described by a single two-electron step over the entire concentration range of n-propanol. The apparent exchange currents calculated from the charge-transfer resistance at low overvoltages and from coulostatic measurements assuming a two-electron step agree with the values obtained by extrapolating the Tafel plots to zero overvoltage. No assumption regarding the number of electrons involved is required in determining the exchange current from the Tafel extrapolations. Furthermore, the expected value of unity is obtained for the sum of the anodic and cathodic transfer coefficients determined from the Tafel relationship when a two-electron step is assumed, although this sum is about two if a rate-determining step involving a single electron is assumed. Similar results supporting a two-electron transfer step were found by Jaenicke and Schweitzer in other organic solvents (12).

The effect of the addition of n-propanol on the apparent transfer coefficients and apparent exchange current density (Fig. 1 and 2) may result from specific adsorption of the alcohol on the electrode surface, from changes in the potential, ϕ_2, of the diffuse double layer, or from changes in the charge-transfer reaction mechanism. Apparently all three effects are present in this complex system.

Considering the effect of the potential, ϕ_2, of the diffuse double layer, the relationship between the total current, i, and the change-transfer overvoltage, η, is

$$i = i_t^o \cdot e^{(n\beta - z)\frac{F}{RT}\phi 2} \cdot \left[e^{\frac{\alpha_t n F}{RT}\eta} - e^{\frac{-\beta_t n F}{RT}\eta} \right] \quad [4]$$

where i_t^o is the true exchange current, n is the number of electrons involved in the electrode reaction, z is the ionic valence of the oxidized species, α_t and β_t are the true anodic and cathodic transfer coefficients, respectively, and **F**, *R*, and *T* are as usual (21).

For small ϕ_2 potentials occurring in a large excess of indifferent electrolyte, $\phi_2 - \phi_2(\eta = 0) \simeq (C_D/C_d) \cdot \eta$ where C_D is the capacity of the total double layer (Fig. 4) and C_d is the capacity of the diffuse double layer (22), and Eq. [4] becomes

$$i = i_o \cdot \left[e^{\frac{\alpha n F}{RT}\eta} - e^{\frac{-\beta n F}{RT}\eta} \right] \quad [5]$$

where α and β are the apparent transfer coefficients and i_o is the apparent exchange current at $\eta = 0$. The relationship between the experimental apparent transfer coefficient, β, and the true value, β_t, is

$$\beta = \beta_t + \left(\frac{z}{n} - \beta_t \right) C_D/C_d = 1 - \alpha \quad [6]$$

In aqueous or near aqueous solutions where $Zn(H_2O)_x^{++}$ is the oxidized species, $n = z = 2$, hence

$$\beta = \beta_t + \alpha_t \cdot C_D/C_d \quad [7]$$

The correction factor, $\alpha_t \cdot C_D/C_d$, is usually less than the experimental error (5%) in aqueous solutions containing a large excess of indifferent electrolyte (22).

According to Eq. [7], the initial increase in the apparent cathodic transfer coefficient, β, upon adding n-propanol (Fig. 1) represents either an increase in the true transfer coefficient, β_t, or an increase in the correction factor $\alpha_t \cdot C_D/C_d$. Figure 4 shows a sharp decrease in C_D on adding n-propanol, probably due to specific adsorption of n-propanol on the electrode which lowers the dielectric constant of the Helmholtz double layer (23) and hence the Helmholtz capacity, C_H. In the presence of the 1.0M excess $LiClO_4$ electrolyte, the effect of the alcohol on the diffuse double layer capacity, C_d, will be small compared with the effect on C_H. An unreasonable 5- to 10-fold decrease in C_d to a value of about 50 μf/cm² is required to explain the initial increase in β in terms of the correction factor $\alpha_t \cdot C_D/C_d$. Therefore, it is concluded that the initial changes in the apparent transfer coefficients upon adding n-propanol (Fig. 1), reflect the changes in the true transfer coefficients. This is contrary to previous reports that the transfer coefficients of the $Zn^{2+}/Zn(Hg)$ electrode reaction are unaffected by the presence of alcohol (2, 12). However, it is interesting to note that values for β_t obtained by Jaenicke and Schweitzer (12) in water-tetrahydrofuran mixtures change with addition of the organic solvent very similarly to the change in β observed using n-propanol. The correction factor used by Jaenicke and Schweitzer (12) for the effect of the diffuse double layer can be shown to be equivalent to the correction factor in Eq. [7].

The increase in the true cathodic transfer coefficient, β_t, upon addition of n-propanol indicates that the transition state has moved closer to the electrode surface. In mixed water-alcohol solvents, the metal ion is preferentially solvated by water (24-26) while the alcohol tends to be specifically adsorbed on the amalgam electrode surface (2, 12, 23). In the cathodic reaction, the water molecules in the solvent shell of the Zn^{++} ion are exchanged for alcohol molecules as the Zn^{++} ion passes into the adsorbed alcoholic layer, whereupon desolvation follows as the Zn^{++} ion proceeds to the electrode surface (12). It is reasonable that the transition state occurs closer to the electrode surface in the presence of specifically adsorbed alcohol than in the case of pure aqueous solutions where only simple desolvation of Zn^{++} is involved. Figure 1 indicates that this effect relaxes as the increasing alcohol concentration reduces the contrast between the solvent composition at the electrode surface and in the bulk solution. Fundamental changes in the reaction mechanism may also occur as the solvent composition changes which may affect β_t.

The potential dependence of the electrochemical transfer coefficients (27) must also be considered in any interpretation of the behavior of β. In the cathodic

potential region where β was determined, the transfer coefficients for $Zn^{2+}/Zn(Hg)$ electrode reaction do not show any significant dependence on the potential (5, 28). In the anodic potential region where α was determined, it is reported that α tends to decrease with increasing potential (5, 28). Figure 1 does show that many experimental α values do tend to be smaller than expected, but this result is not entirely outside the experimental error.

The product of viscosity and conductivity, $\eta_v \cdot k$, shown in Fig. 3 indicates the extent of ion association in these solutions since $\eta_v \cdot k$ is roughly proportional to the ionic concentrations (12). Figure 3 indicates that about 60-70% of the salts present are undissociated in solutions with high n-propanol concentrations.

Plotting the equilibrium potential ϵ_o, *vs.* $\log[LiClO_4]$ in 0.98 mole fraction propanol gives a slope of about -30 mV (Fig. 5), suggesting from the Nernst equation that the net electrode reaction in this solution is $ZnClO_4^+ + 2e^- \rightleftharpoons Zn + ClO_4^-$, assuming that the activity of ClO_4^- is proportional to $[LiClO_4]$.

The electrochemical reaction order, P, for the ClO_4^- ion in the cathodic reaction can be determined from the relationship (29)

$$\frac{\partial \ln i_o}{\partial \ln a_k} = P + \frac{\alpha_t n\mathbf{F}}{RT}\frac{\partial \epsilon_o}{\partial \ln a_k} + (n\beta_t - z)\frac{\mathbf{F}}{RT}\frac{\partial \phi_2^e}{\partial \ln a_k} \quad [8]$$

where a_k represents the activity of the ClO_4^- ion and ϕ_2^e represents the value for ϕ_2 at $\epsilon = \epsilon_o$. The term involving ϕ_2^e is usually neglected when a_k represents some species other than the excess electrolyte. Figure 5 shows the variation of i_o *vs.* $\log[LiClO_4]$ in 0.94 mole fraction alcohol as determined from coulostatic measurements. Using the approximate relationship (30) $\partial \phi_2/\partial \ln a_k \simeq RT/\mathbf{F}$ (taking the positive sign since the Epzc measurements indicate $\phi_2 < 0$) and the relationship $z = n - P$ converts Eq. 8 to

$$\frac{\partial \ln i_o}{\partial \ln a_k} \simeq 2P - n + n\beta_t + \frac{\alpha_t n\mathbf{F}}{RT}\frac{\partial \epsilon_o}{\partial \ln a_k} \simeq 2P - 2 \quad [9]$$

where various terms were evaluated using $n = 2$ and $\beta_t = 0.3$ and estimating $\partial \epsilon_o/\partial \ln a_k$ from Fig. 5. Assuming $a_k = [LiClO_4]$ to evaluate $\partial \ln i_o/\partial \ln a_k$ from Fig. 5 yields, using Eq. [9], $P \simeq 0.75$ for $[LiClO_4] < 0.8M$ and $P \simeq 1$ for $[LiClO_4] > 0.8M$.[2] This suggests that at high $LiClO_4$ concentrations in the alcohol-rich solutions, the rate-determining step is primarily

$$ZnClO_4^+ + 2e^- \rightleftharpoons Zn + ClO_4^- \quad [10]$$

while for low $LiClO_4$ concentrations there is likely to be a parallel reaction involving the solvated Zn^{++} ion. It is interesting to note that the slope of the $\log i_o$ *vs.* $\log[LiClO_4]$ plot (Fig. 5) changes where $[LiClO_4] = [H_2O] = 0.8M$. At higher $LiClO_4$ concentrations, due to the shortage of water molecules, some of the Li^+ or Zn^{++} ions must remain completely dehydrated in the solution.

The apparent exchange current, i_o, is related to the true exchange current, i_t^o, by the expression

$$i_o = i_t^o \cdot e^{(n\beta_t - z)\frac{\mathbf{F}}{RT}\phi_2} \quad [11]$$

where $\phi_2 < 0$ since measurements are made at potentials negative to Epzc. For discharge of either $Zn^{++} \cdot solv$ or $ZnClO_4^+ \cdot solv$, $n\beta_t < z$, hence $i_o > i_t^o$. The sharp decrease in i_o upon adding n-propanol (Fig. 2) may be attributed either to a decrease in i_t^o or to ϕ_2 becoming less negative. Probably both effects are present.

Aramata and Delahay (2) showed that addition of n-amyl alcohol produces a sharp decrease in i_o for $Zn^{2+}/Zn(Hg)$ electrode reaction which they account for by ϕ_2 becoming less negative with addition of the alcohol and by the decrease in the effective surface area resulting from coverage of the electrode by the n-amyl alcohol. Their results are for 0.05M $Mg(ClO_4)_2$ electrolyte. In 1M $LiClO_4$ electrolytes, the ϕ_2 effect on the apparent exchange current will be much less.

A decrease in i_t^o upon addition of the alcohol can be attributed to the discrepancy between the solvent composition at the electrode and in the solvation shell of the Zn^{++} ion. In pure aqueous solutions, the major energy barrier to the discharge of the Zn^{++} ion is probably dehydration of the $Zn^{++} \cdot aq$ ion. With alcohol specifically adsorbed on the electrode, the dehydrated Zn^{++} must also compete with the alcohol for adsorption onto the electrode surface which increases the energy barrier. Similar arguments for an increased energy barrier upon adding an organic solvent are proposed by Jaenicke and Schweitzer (12). Their reported exchange currents are also apparent exchange currents since their corrective term for the diffuse double layer, $\eta \cdot C_D/C_d$, becomes zero at $\eta = 0$.

The steep increase in i_o above 90% alcohol (Fig. 2) probably results from complete replacement of water in the solvation shell of the Zn^{++} by propanol molecules. Calculations show that at 0.9 mole fraction alcohol there is only one water molecule available for each Li^+ and Zn^{++} ion in the solution. Both ions tend to be preferentially solvated by the water (24), hence competition for the water molecules becomes intense. As the alcohol concentration increases beyond 90 mole per cent (m/o) n-propanol, the Zn^{++} or $ZnClO_4^+$ ions may tend to become solvated solely by the alcohol. The energy barrier for desolvation of the alcoholic Zn^{++} ion is likely much less than for the aqueous Zn^{++} ion, hence i_t^o and i_o increase rapidly in this region. As the

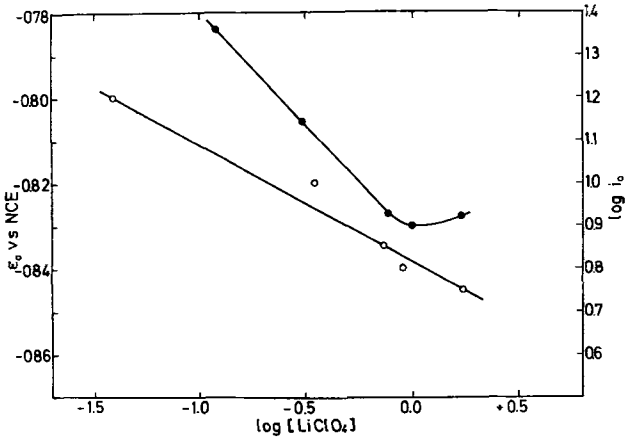

Fig. 5. Variation of the equilibrium potential, ϵ_o, and apparent exchange current density, i_o, for the $Zn^{2+}/Zn(Hg)$ electrode reaction with $\log[LiClO_4]$ at 25.0°C. The ϵ_o values were determined in 0.98 mole fraction n-propanol while the i_o values are for 0.94 mole fraction n-propanol. ○, ϵ_o measurements. ●, i_o measurements.

[2] Using the relationship $a_k = c_k\gamma$ where c_k and γ are the concentration and activity coefficient, respectively, of species k, Eq. 9 may be written

$$\frac{\partial \ln i_o}{\partial \ln c_k} = 2P - n\alpha_t + \frac{\alpha_t n\mathbf{F}}{RT}\frac{\partial \epsilon_o}{\partial \ln c_k} + (2P - n\alpha_t)\frac{\partial \ln \gamma}{\partial \ln c_k}$$

From Fig. 5, $\frac{\alpha_t n\mathbf{F}}{RT}\frac{\partial \epsilon_o}{\partial \ln c_k} = -n\alpha_t/2$. Letting $y = \frac{\partial \ln i_o}{\partial \ln c_k}$ and $x = \frac{\partial \ln \gamma}{\partial \ln c_k}$ and solving the above equation for the reaction order, P, gives

$$P = \frac{n\alpha_t(3/2 + x) + y}{2(1 + x)}$$

From the mean activity coefficient of $LiClO_4$ in aqueous solutions, generally $|x| < 0.1$. In alcohol solutions, indications are that γ decreases more markedly with salt concentration than in aqueous solutions which would give larger values for $|x|$. Nevertheless, the value of P is fairly insensitive to tne actual value of x for x values greater than -0.5. For example, using $y = 0$ from Fig. 5, P varies from only 1.4 to 0.9 in 1M $LiClO_4$ for x values ranging from -0.5 to $+0.5$. At the higher salt concentrations, $|x|$ likely decreases and approaches zero as γ approaches a minimum value. A more exact analysis awaits the actual measurement of the mean activity coefficient of $LiClO_4$ in these solutions.

remaining water molecules in the Zn^{++} ion are replaced by n-propanol molecules, the reaction mechanism probably shifts to that of Eq. [10] involving $ZnClO_4^+ \cdot solv$.

The gradual increase in i_o between 0.1 and 0.8 mole fraction n-propanol (Fig. 2) is probably due to ϕ_2 gradually becoming more negative from decreasing dissociation of the salts (Fig. 3). As long as water molecules are available, the Zn^{++} ion will apparently remain preferentially solvated by the water molecules (24-26). Partial exchange of water molecules for n-propanol molecules in the solvation shell of the Zn^{++} ion at the higher alcohol concentrations would likely contribute to this increase in i_o.

Summary

Galvanostatic and coulostatic measurements of the apparent exchange current and apparent transfer coefficients for the $Zn^{2+}/Zn(Hg)$ electrode reaction in binary mixtures of water and n-propanol are reported.

The observed changes in these quantities can be interpreted in terms of changes in the potential across the diffuse double layer, specific adsorption of the alcohol on the electrode surface and preferential solvation of Zn^{++} ions by water, and by a change to a reaction mechanism involving $ZnClO_4^+$ as the concentration of n-propanol increases.

Acknowledgment

The authors wish to thank D. Laupheimer for valuable technical assistance in the coulostatic measurements. Dr. Melvin H. Miles expresses appreciation for a NATO postdoctoral research fellowship which made this work possible.

Manuscript submitted July 10, 1970; revised manuscript received *ca.* Jan. 28, 1971.

Any discussion of this paper will appear in a Discussion Section to be published in the December 1971 JOURNAL.

REFERENCES

1. H. Gerischer, *Z. Physik. Chem. Leipzig*, **202**, 302 (1953).
2. A. Aramata and P. Delahay, *J. Phys. Chem.*, **68**, 880 (1964).
3. J. P. G. Farr and N. A. Hampson, *J. Electroanal. Chem.*, **18**, 407 (1968).
4. M. Sluyters-Rehbach, J. S. M. C. Breukel, and J. H. Sluyters, *ibid.*, **19**, 85 (1968).
5. V. K. Venkatesan. B. B. Damaskin, and N. V. Nikolaeva-Fedorovich, *ibid.*, **25**, 85 (1970).
6. L. Gaiser and K. E. Heusler, *Electrochim. Acta*, **15**, 161 (1970).
7. J. Heyrovsky, *Z. Elecktrochem.*, **59**, 802 (1955).
8. N. S. Hush and J. Blackledge, *J. Electroanal. Chem.*, **5**, 420 (1963).
9. M. Sluyters-Rehbach, A. B. Ijzermans, B. Timmer, J. G. Griffioen, and J. H. Sluyters, *Electrochim. Acta*, **11**, 483 (1966).
10. K. J. Vetter, "Electrochemical Kinetics," pp. 649-652, Academic Press, New York (1967).
11. B. Timmer, M. Sluyters-Rehbach, and J. H. Sluyters, *J. Electroanal. Chem.*, **14**, 181 (1967).
12. W. Jaenicke and P. H. Schweitzer, *Z. Physik. Chem. N.F.*, **52**, 104 (1967).
13. H. Gerischer, *Z. Elektrochem.*, **59**, 604 (1955).
14. See Ref. 10, pp. 413-417.
15. See Ref. 10, p. 395. See also pp. 385-387, 406-409.
16. P. Delahay, *J. Phys. Chem.*, **66**, 2204 (1962).
17. P. Delahay and A. Aramata, *J. Phys. Chem.*, **66**, 2208 (1962).
18. H. Gerischer and D. Laupheimer, To be published.
19. P. Delahay, "Double Layer and Electrode Kinetics," pp. 122-128, John Wiley & Sons, New York (1965).
20. J. O. M. Bockris and B. E. Conway, Editors, "Modern Aspects of Electrochemistry, No. 5," Chap. 3, Plenum Press, New York (1969).
21. See Ref. 19, pp. 153-159, 197-239.
22. See Ref. 10, pp. 144-145.
23. L. K. Partridge, A. C. Tansley, and A. S. Porter, *Electrochim. Acta*, **13**, 2029 (1968).
24. J. Padova, *J. Phys. Chem.*, **72**, 796 (1968).
25. N. A. Matwiyoff and H. Taube, *J. Am. Chem. Soc.*, **90**, 2796 (1968).
26. P. A. Zagorets, V. I. Ermakov, and A. P. Grunau, *Zh. Fiz. Khim.*, **39**, 456 (1965).
27. H. H. Bauer, *J. Electroanal. Chem.*, **16**, 419 (1968).
28. G. Salie, *Z. Physik. Chem. Leipzig.* **239**, 411 (1968).
29. See Ref. 10, pp. 436-437 and Ref. 19, pp. 183-185.
30. See Ref. 19, pp. 42-43.

An Electrochemical Oxygen and Sulfur Vapor Gauge with Pyrex as Solid Electrolyte[1]

D. Yuan* and F. A. Kröger*

Department of Materials Science, University of Southern California, Los Angeles, California 90007

ABSTRACT

Electrochemical cells W,Na|Pyrex|Pt,O_2; Pt,O_2|Pyrex|Pt,O_2; and W,Na|Pyrex|C,S_2 are found to give emf's following the Nernst formula. The emf is attributed to the formation of Na_2O or Na_2S in the glass near the glass-gas interface. After strong polarization in either direction, the cell emf returns to the value for the unperturbed system. Energies and entropies of solution of Na_2O in Pyrex are shown to be close to the corresponding values for the formation of Na_2SiO_3. Pyrex cells can be used as O_2 or S_2 pressure gauges.

Glass has been used as solid electrolyte in the cell H_2|glass|O_2 for measuring the emf's due to the formation of water from oxygen and hydrogen (1-3). Pyrex, a borosilicate glass (4), has been used as a sodium ion specific membrane in contact with molten sodium salts (5) or liquid sodium alloys (6) to measure sodium activities. The Na^+ conductor Na-βAl_2O_3 has been used as a solid electrolyte in a cell based on the reaction $Na(l) + S(l) \rightarrow Na_2S$ (7). It is of interest to see whether Pyrex can also be used to measure the oxygen and sulfur pressure in gases. To this end, emf measurements were carried out on cells of the types

$$W, Na(l) |Pyrex|Pt, O_2(g) \quad [1]$$

$$W, Na(l) |Pyrex|C, S_2(g) \quad [2]$$

and

$$Pt, O_2(I) |Pyrex|Pt, O_2(II) \quad [3]$$

The reactions underlying a possible emf are

* Electrochemical Society Active Member.

[1] This work was supported by the United States Air Force Office of Scientific Research, Directorate of Chemical Sciences, under Grant No. AF-AFOSR 68-1405.

Key words: oxygen pressure gauge, sulfur pressure gauge, Pyrex, gas cell.

$$2Na(l) + \tfrac{1}{2}O_2(g) \rightarrow Na_2O \text{ (glass)}; G^\circ (Na_2O, \text{glass}) \quad [4]$$

$$2Na(l) + \tfrac{1}{2}S_2(g) \rightarrow Na_2S \text{ (glass)}; G^\circ (Na_2S, \text{glass}) \quad [5]$$

and

$$O_2(p_{O_2})_I \rightarrow O_2(p_{O_2})_{II} \quad [6]$$

Na_2O (glass) and Na_2S (glass) indicate the state of the compounds as they are present in the glass at the glass-gas interface. If the activity of Na_2O in the glass is a_{Na_2O}, then the free enthalpy of Na_2O in the glass is

$$G^\circ (Na_2O, \text{glass}) = G^\circ (Na_2O) + RT \ln a_{Na_2O} \quad [7]$$

$G^\circ(Na_2O)$ being the standard free enthalpy of $Na_2O(s)$. A similar expression holds for G° (Na_2S, glass). A value of $a_{Na_2O} \neq 1$ must be expected to result partly from the heat and vibrational entropy of solution of Na_2O in the glass ($G_{exc.\ ox.} = H_{exc.\ ox.} - TS_{exc.\ ox.}$) and partly from configurational entropy due to the distribution of the Na_2O or its components in the glass ($a_{Na_2O,\ config.}$)

$$RT \ln a_{Na_2O} = RT \ln a_{Na_2O,\ config.} + G_{exc.\ ox.} \quad [8]$$

For simple solution behavior, $a_{Na_2O} = x^n_{Na_2O}$, n depending on the atomic structure of the solution. We expect $n = 1$ for incorporation of Na_2O in a manner in which only one defect is formed, the two Na's being close together

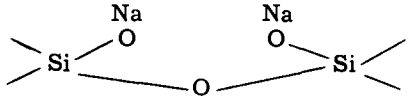

$n = 2$, if two defects are formed in concentrations larger than the native disorder

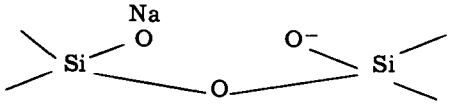

$+ Na_i^+$

and $n = 3$ if three defects are formed

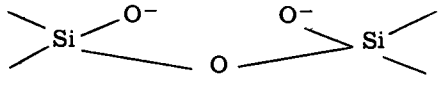

$+ 2\ Na_i^+$

Alternatively, we may have configurations involving boron

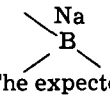

$(n = 1)$, or 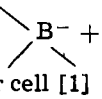

$+ Na_i^+$ $(n = 2)$

The expected emf's are for cell [1]

$$-E_1 = \frac{1}{2F}[G^\circ (Na_2O) + G_{exc.\ ox.} + RT \ln a_{Na_2O,\ config.}\, p_{O_2}{}^{-1/2}\, a_{Na}{}^{-2}] \quad [9]$$

a_{Na} being the activity of Na in the melt at the left hand side, and p_{O_2} the oxygen pressure in the gas at the right-hand side.

Similarly, for cells [2]

$$-E_2 = \frac{1}{2F}[G^\circ (Na_2S) + G_{exc.\ sulf.} + RT \ln a_{Na_2S,\ config.}\, p_{S_2}{}^{-1/2}\, a_{Na}{}^{-2}] \quad [10]$$

Cells [3] should follow the Nernst expression

$$-E_3 = \frac{RT}{4F} \ln \frac{(p_{O_2})_{II}}{(p_{O_2})_I} \quad [11]$$

Since $G^\circ = H^\circ - TS^\circ$ and $G_{exc.} = H_{exc.} - TS_{exc.}$, Eq. [9] and [10] can be rewritten as

$$-E_{ox.} = \frac{1}{2F}\left[[H^\circ (Na_2O) + H_{exc.\ ox.}] - T\left[S^\circ (Na_2O) + S_{exc.\ ox.} + R \ln \frac{a^2_{Na}\, p_{O_2}{}^{1/2}}{a_{Na_2O,\ config.}}\right]\right] \quad [12]$$

and

$$-E_{sulf.} = \frac{1}{2F}\left[[H^\circ (Na_2S) + H_{exc.\ sulf.}] - T\left[S^\circ (Na_2S) + S_{exc.\ sulf.} + R \ln \frac{a^2_{Na}\, p_{S_2}{}^{1/2}}{a_{Na_2S,\ config.}}\right]\right] \quad [13]$$

If we neglect the temperature dependence of H and S, [12] and [13] indicate that the emf's of cells [1] and [2] are of the form $E = E_o - BT$. A plot of the emf as a function of temperature is a straight line, with E_o, the intercept at $T = 0°K$, equal to $-(H^\circ_{Na_2O} + H_{exc.\ ox.})/2F$ and the slope B, equal to $-\frac{1}{2F}\left(S^\circ + S_{exc.\ ox.} + R \ln \frac{a^2_{Na}\, p_{O_2}{}^{1/2}}{a_{Na_2O,\ config.}}\right)$ with similar expressions for the sulfur case.

Experimental

Sealed sodium-filled glass cells were made as indicated in Fig. 1. The sodium was Mallinckrodt pro analysis sodium, used without further purification. As electrodes and leads, pure tungsten wires were used at the Na side, Pt wire and Pt paste at the oxygen sides (cells [1] and [3]), and graphite yarn and graphite powder at the sulfur side (cell [2]).

The sodium cell was placed inside another Pyrex tube which serves as a protection against the outside atmosphere, and the combination was mounted inside a furnace. Temperature fluctuations were kept within ±2°C by operating the furnace on a constant voltage transformer. A Chromel-Alumel thermocouple was used in measuring the temperatures. The cell emf's were measured by a Cary 31CV vibrating reed electrometer which serves as a high impedance voltmeter. When different electrode materials were used, the emf values were corrected for the small thermoelectric power of the couples these materials constitute. In the polarization experiments, outside voltages were supplied by constant voltage dry batteries and currents were measured with a Simpson meter. A digesting period is necessary for each measurement at the desired temperature in order to reach a steady state. Several gases were used to establish different oxygen activities, such as $N_2 + 10^{-5}$ atm O_2 and Ar + 10^{-7} atm O_2. For lower oxygen activities, CO/CO_2 and H_2/H_2O buffer systems were used. For the H_2/H_2O system, tank hydrogen gas is passed through water at known temperature so that the hydrogen gas is saturated with water vapor at that temperature. For the CO/CO_2 sys-

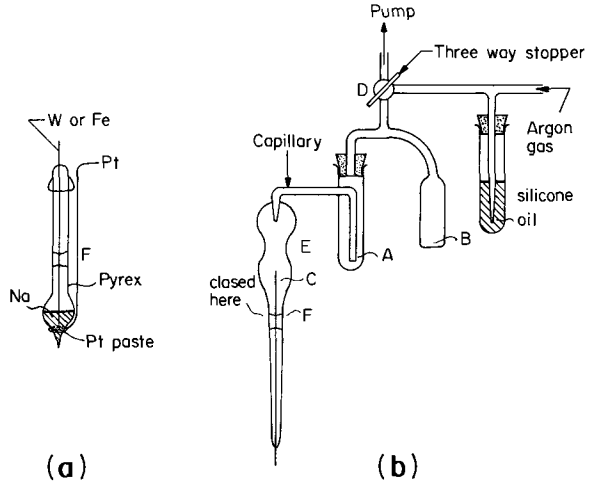

Fig. 1. The Na electrode (a) and the procedure to make it (b). 1—Introduce Na protected by toluene into A. 2—Evacuate A, B, C through D. 3—Close D. 4—Cool B to −180°C, and distill the toluene from A to B. 5—Melt Na in argon and preheat the capillary rod. 6—Let in argon at D and press the Na from A to C. 7—Evacuate through D. 8—Melt off at E.

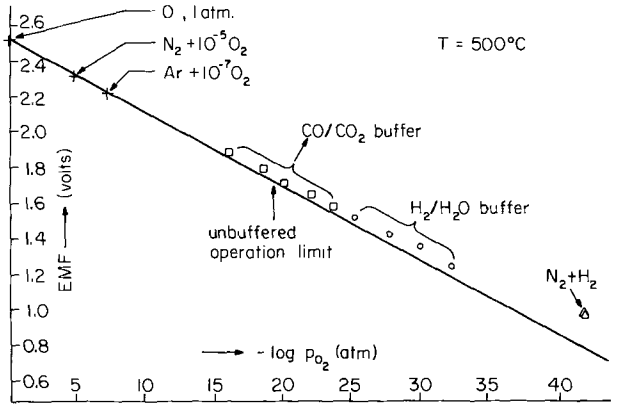

Fig. 2. Emf as $f(p_{O_2})$ for a cell W, Na(l) | Pyrex | Pt, O_2 at 500°C. The line gives the pressure dependence according to Eq. [9].

tem, tank nitrogen (containing 10^{-5} O_2) is passed over graphite which transforms the oxygen into a mixture of CO and CO_2 (8). The graphite was in a Pyrex tube inside another furnace. Different ratios of CO/CO_2 can be established by keeping the graphite at different temperatures. The "$N_2 + H_2$" mixture point was achieved by passing N_2 (containing 10^{-5} O_2) and H_2 in a 1:1 ratio through a liquid air trap to remove water, and then through a furnace at 700°C to transform the oxygen into water vapor. The oxygen pressure can be calculated from the H_2/H_2O ratio, the latter being known if it is assumed that all the O_2 in N_2 is turned into H_2O. In all cases but the latter, the oxygen pressure was determined with the aid of a cell with calcia-stabilized zirconia as solid electrolyte. For "$N_2 + H_2$," the O_2 pressure falls outside the range where the electrolyte has an ionic transference number equal to one, and therefore we have to rely on the calculated pressure. In the sulfur cells, sulfur pressures were established by various methods. In a first set of experiments, solid or liquid sulfur was present in the outer compartment of the cell and the temperatures of the sulfur and the cell were the same. In a second set of experiments, the sulfur and the cell were at different temperatures. Use of two separately controlled sections of the furnace makes it possible to vary the temperature of the sulfur source and the cell independently; *i.e.*, we can study the properties of the cell at constant T under varying sulfur pressures. In order to transfer the sulfur vapor from one compartment to the other, pure argon was used as a carrier gas. Finally, in a third series of experiments, H_2S and mixtures of $H_2 + H_2S$ were used to establish low sulfur activities.

Results and Discussion

Oxygen cells.—Figure 2 shows the emf of the oxygen cells at 500°C as a function of the oxygen activity. All the points except the "$N_2 + H_2$" point are close to the line showing the O_2 pressure dependence required by Eq. [9]. This indicates that the interpretation of the cell emf as being based on the formation of Na_2O is correct: formation of Na_2O_2 would give a dependence $\propto p_{O_2}$. In order to find the reason for the deviation of the "$N_2 + H_2$" point, let us consider the theoretical low-pressure limit for the operation of the cell. This limit is different for buffered and for nonbuffered gases. For the former, this limit is set by the oxygen pressure at which liquid sodium with $a_{Na} = 1$ is formed. In this case the cell [1] becomes identical with a cell Na(l) |Pyrex|Na(l) with $E = 0$. Extrapolation of the Nernst line in Fig. 2 to $E = 0$ gives $(p_{O_2})_{\text{limit, buffer}} = 10^{-60}$ atm—well below the 10^{-40} value of the "$N_2 + H_2$" point. In nonbuffered gases, we expect the cell to be limited by the dissociative evaporation of Na_2O

$$Na_2O\ (\text{glass}) \rightarrow 2Na(g) + \tfrac{1}{2}O_2(g); \quad G^\circ_{\text{evap. ox.}} \quad [14]$$

$$p_{Na}^2\, p_{O_2}^{1/2} = \exp\left(-G^\circ_{\text{evap. ox.}}/RT\right) \quad [15]$$

with $G^\circ_{\text{evap. ox.}} = -G^\circ(Na_2O, \text{glass}) + 2G^\circ(Na_{1\rightarrow g})$. $G^\circ(Na_2O, \text{glass})$ is given by the emf $E_1 = 2.52$V of cell [1] with pure Na(l) on one side and 1 atm O_2 on the other at 500°C: $G^\circ(Na_2O, \text{glass}) = -2FE_1 = -116.2$ kcal mole. $G^\circ(Na_{1\rightarrow g}) = 25.7$ kcal/mole (9) and, thus, $G^\circ_{\text{evap. ox.}} = 167.6$ kcal/mole and $\exp(-G^\circ_{\text{evap. ox.}}/RT) = 2.7 \times 10^{-48}$ $\text{atm}^{5/2}$. At the sublimation point, $p_{Na} = 4p_{O_2}$; then [15] leads to $(p_{O_2})_{\text{limit, unbuffered}} = 3.1 \times 10^{-20}$ atm. This is much larger than the value $\approx 10^{-38}$ atm the Nernst line indicates for the "$N_2 + H_2$" point and shows that the H_2/H_2O buffer is still active. This is to be expected. Since only reaction of H_2 and O_2 is involved, this H_2O-poor buffer should perform as well as the mixtures with more water. The deviation of the $N_2 + H_2$ point can therefore not be explained by a deviating oxygen activity in the gas phase, but must be due to a different chemical reaction having become potential determining—possibly nitride formation. Further work is necessary to solve this problem. In any case, the cell is shown to be reliable down to a pressure of 10^{-32} atm O_2.

In order to check the stability and reproducibility of the cell, it was polarized for several hours with a voltage of 12V with a Na electrode either positive or negative. Figure 3 shows the relaxation of the cell emf measured after removal of the polarizing field. For

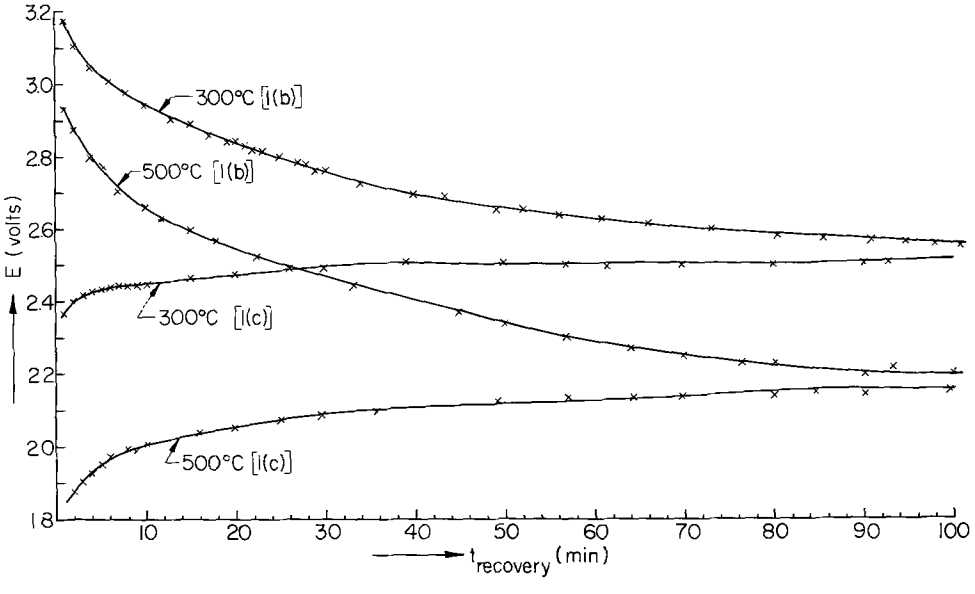

Fig. 3. Variation of the emf with time for an oxygen cell after polarization.

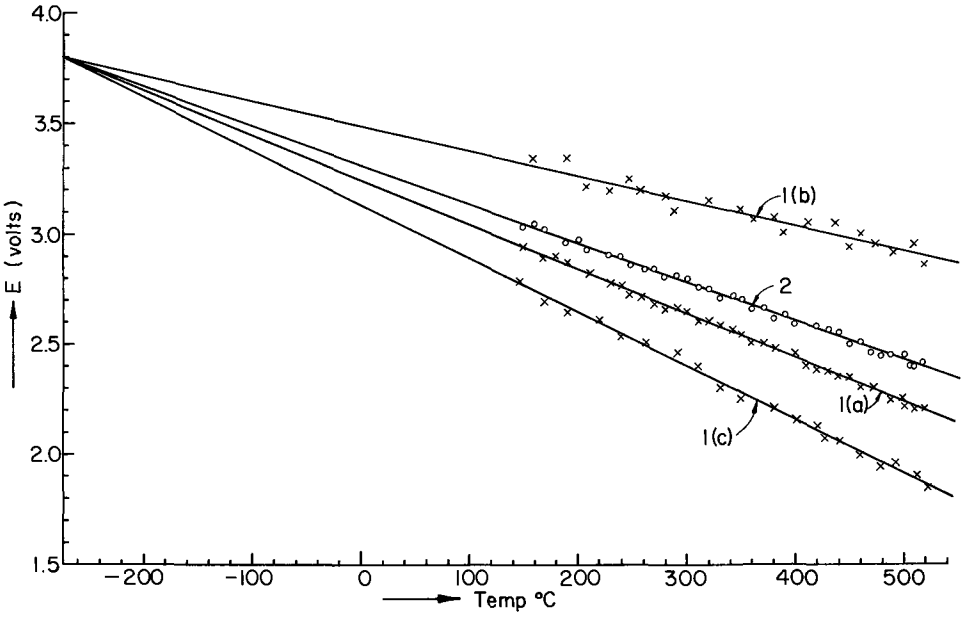

Fig. 4. Emf as $f(T)$ for a cell W, Na(l) | Pyrex | Pt, O_2, 1(a)—$p_{O_2} = 10^{-5}$ atm; unpolarized. 1(b)—As (a), but polarized (Na^+ pulled inward). 1(c)—As (a), but polarized (Na^+ pulled outward). 2—$p_{O_2} = 1$ atm.

both directions of polarization, the cell returns to its original emf in 1.5-2 hr.

Figure 4 shows the emf of the oxygen cells as a function of temperature. The lines 1(a) and 2 represent the equilibrium emf's for $N_2 + 10^{-5}$ atm O_2 and pure O_2, respectively. Lines 1(b) and 1(c) are obtained after polarization with a field of 12V at the corresponding temperature for several hours until the readings did not change with further polarization. For 1(b), the Na-side of the cell was negative; *i.e.*, sodium ions were removed from the outer surface. For 1(c), the same voltage was applied in the opposite direction; *i.e.*, sodium ions were drawn to the outer surface. In both cases the final values, taken approximately 30 sec after removal of the polarizing field, are independent of the time of polarization and the voltage used for polarization. This independence suggests for 1(b) that electrolysis has taken place with formation of a new phase (Na_2O or Na_2SiO_3) at the outer surface. Yet, as shown in Fig. 3, the original emf is restored in a comparatively short time, which suggests that true polarization, without second-phase formation, has occurred or, at least, that the formation of a second phase does not affect the emf. This is also indicated by the fact that 1(b) and 1(c) extrapolate to the same $T = 0$ value in the equilibrium lines. For all four cases [though with considerable scatter for 1(b) and 1(c)], the emf is a linear function of T: $E = E_o - BT$. The equilibrium lines 1 and 2 fit the relation

$$E = 3.80 - 1.75 \times 10^{-3}T - \frac{RT}{2F} \ln a^2_{Na}\, p_{O_2}{}^{1/2} \quad [16]$$

Interpretation of $E_o = 3.80$V on the basis of Eq. [12], neglecting the temperature dependence of H and S, leads to $H^\circ_{Na_2O} + H_{exc.\ ox.} = -173$ kcal/mole; with $H^\circ_{Na_2O,\ 298} = -100.6$ kcal/mole (10), this gives $H_{exc.\ ox.} = -72.4$ kcal/mole,[2] somewhat more negative than the enthalpy effect of the reaction

$$Na_2O + SiO_2 \rightarrow Na_2SiO_3;\ H^\circ_{298} = -56.5 \text{ kcal/mole (11)},$$

$$\Delta S = -40 \text{ cal/deg mole (11)} \quad [17]$$

The slope B for cell [2] is 1.75 x 10^{-3} V/°K. The quantity $2FB = 80.7$ cal/deg mole can be identified with $-[S^\circ(Na_2O) + S_{exc.\ ox.} - R \ln a_{Na_2O,\ config.}]$. For Na_2O made from Na(l), $\Delta S^\circ(Na_2O)_{298} \cong -37$ cal/deg mole (10); then $S_{exc.\ ox.} - R \ln a_{Na_2O,\ config.} \cong 43.7$ cal/deg mole. $S_{exc.\ ox.}$ should be close to ΔS of reaction [17].

[2] Since we neglect the temperature dependence of H and S in the interpretation of E_o and B, there is no point in distinguishing between H°_{298} and H°_0 and ΔS_{298} and ΔS°_0.

Therefore, $R \ln a_{Na_2O,\ config.}$ must be very small. Figure 5 shows the emf measurements of cell [3], with oxygen at different pressures at the two sides. The readings of the emf's have an uncertainty of ±5 mV, the flow of gas through the cell making the temperature somewhat unsteady. The readings, however, are close to the calculated values of Eq. [11].

It may be concluded that Pyrex glass cells may be used as an oxygen activity sensor. Since the large value of E_o for the sodium cell introduces a considerable source of error, it is preferable to use a cell of type [3], provided temperature effects can be eliminated. The sodium-oxygen cell can also be used to determine the Na_2O activity in sodium glasses.

Sulfur cells.—Figure 6 shows the emf of sulfur cells of type [2] as a function of the temperature of the cell for various sulfur pressures. The curve for saturated sulfur vapor corresponds to the case that the sulfur source and the cell are at the same temperature. For the other curves, the sulfur source was at temperatures different from that of the cell. When sulfur vapors, produced by evaporation of S(l) at a total pressure determined by the source temperature, reach the cell compartment with its higher temperature, the total pressure remains the same but the partial pressure of the molecular species S_2, S_3 . . . S_7, S_8 is changed. The pressure of a particular species, *e.g.* S_2, is related to those of all other species by known equilibrium constants of reactions such as $3S_2 \rightarrow 2S_3$, $2S_2 \rightarrow S_4$, *etc.* (12), and, for a given total pressure, the pressures of the various species can be calculated. Figure 7 shows the partial pressure of S_2 at different temperatures with the sulfur source at 200°, 250°, 300°, and 350°C.

By combining Fig. 6 and 7, we can construct the emf of cells of type [2] as a function of p_{S_2} at different temperatures (Fig. 8). The emf can be represented by

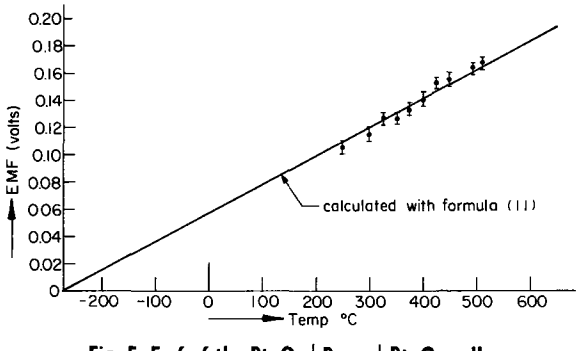

Fig. 5. Emf of the Pt, O_2 | Pyrex | Pt, O_2 cell

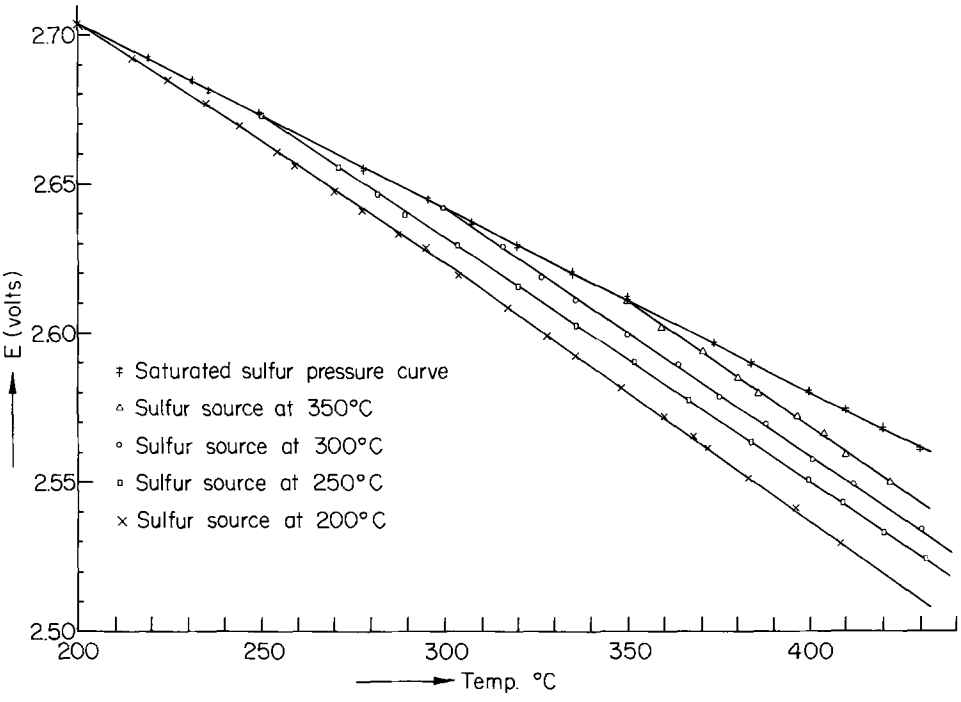

Fig. 6. Emf as function of temperature for the sodium-sulfur cell with saturated and non-saturated sulfur vapor.

$$E = E_0 - BT = 3.32 - \left(1.03 \times 10^{-3} + \frac{R}{2F} \ln a_{Na} p_{S_2}^{1/2} \right) T \quad [18]$$

The sulfur pressure dependence indicates that sulfur is incorporated at the glass surface as single ions $S^=$, as is to be expected if Na_2S is formed.

The intercept at $T = 0$ is $E_0 = 3.32$V, or $-(H^\circ_{Na_2S} + H_{exc.\ sulf.}) = 153$ kcal/mole for this reaction. As $H^\circ_{Na_2S} \cong -93$ kcal/mole (10), $H_{exc.\ sulf.} \cong -60$ kcal/mole, somewhat smaller than in the oxide case. It should be not too different from the unknown enthalpy of the reaction $Na_2S + SiO_2 \rightarrow Na_2S \cdot SiO_2$. Further, we find $S_{exc.\ sulf.} \cong -17$ cal/deg mole $+ R/2F \ln a_{Na_2S,\ config.}$

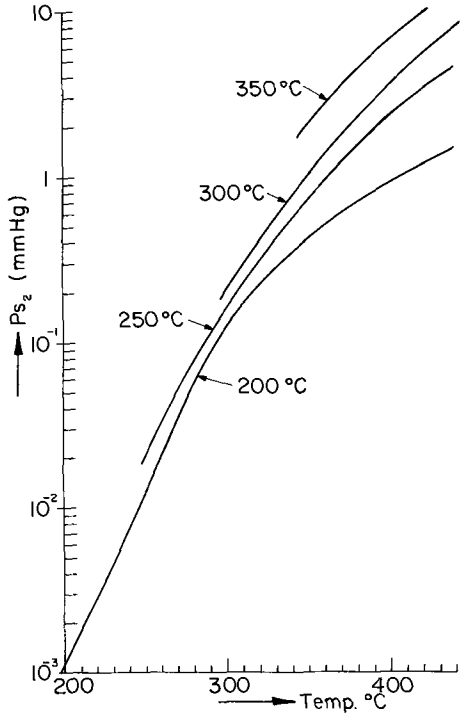

Fig. 7. Partial pressures of S_2 as a function of the temperature of overheating for sulfur vapor generated by heating sulfur at various temperatures (indicated at the curves).

The four lines in Fig. 8 fit the relation of Eq. [13]. With low sulfur pressures established with the aid of H_2S and mixtures $H_2S + H_2$, cells of type [2] give the emf as shown in Fig. 9. The reaction $H_2S \rightleftarrows H_2 + \frac{1}{2}S_2$ leads to

$$K_p(T) = \frac{p_{H_2} \cdot p_{S_2}^{1/2}}{p_{H_2S}} \quad [19]$$

with (13)

$$\log K_p(T) = -\frac{4.57 \times 10^3}{T} + 2.35 \quad [20]$$

Using Eq. [19] and [20] we can calculate values of p_{S_2} as $f(T)$, both for pure H_2S and for mixtures $H_2 + H_2S$. Then using Eq. [13] we can calculate the expected values of E of our cells and compare these to the observed emf's. There is good agreement for $T > 330$°C, but discrepancies are found for pure H_2S at $T < 330$°C. As shown in Fig. 9, these discrepancies are removed by assuming that the tank H_2S used contained an excess of sulfur equivalent to $(p_{S_2})_{extra} = 10^{-4}$ atm. This extra sulfur may have originated from persulfide ions present in the material used to generate the H_2S.

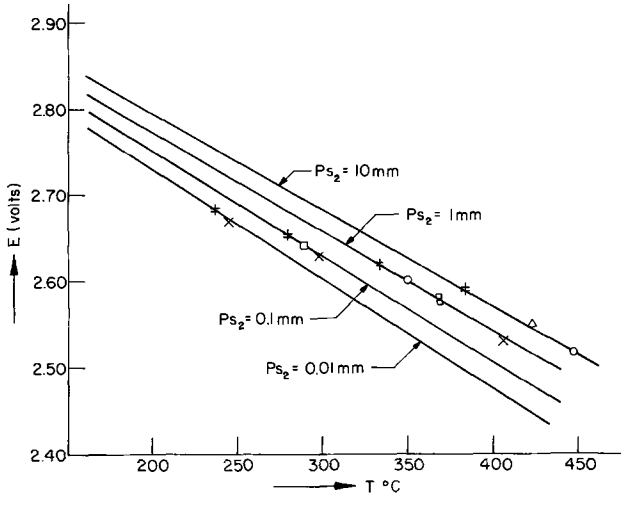

Fig. 8. p_{S_2} isobars of the sodium-sulfur cell with experimental points deduced from the data of Fig. 6.

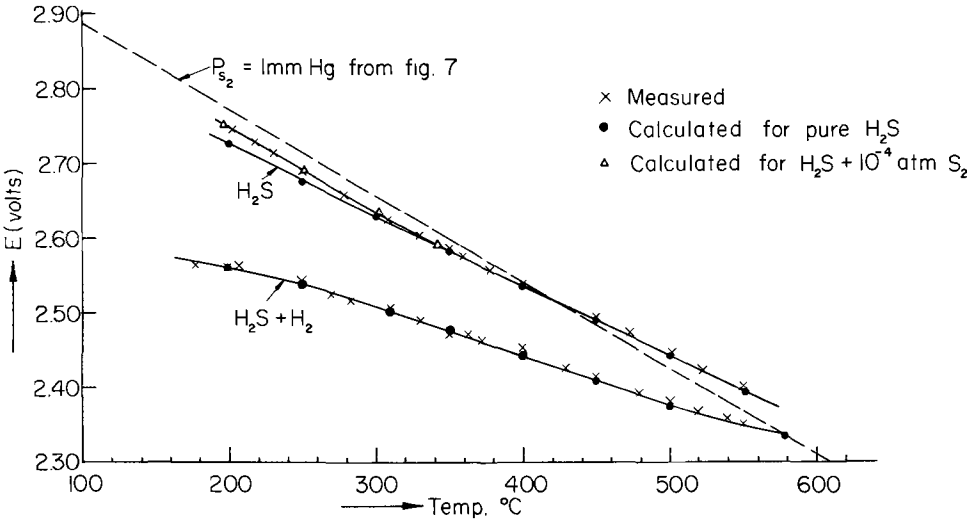

Fig. 9. Emf measurements of the sodium electrode in H_2S and an equimolar $H_2 + H_2S$ mixture compared with values calculated for pS_2 produced by pure H_2S and by $H_2S + 10^{-4}$ S_2.

It may be concluded that Pyrex glass cells may be used to measure the sulfur activity in the gases. In order to reduce errors connected with a large value of E_o, it is advisable to use cells Pt, O_2(g) |Pyrex| C, S_2(g) rather than cells [2].

Manuscript submitted May 25, 1970; revised manuscript received Jan. 18, 1971.

Any discussion of this paper will appear in a Discussion Section to be published in the December 1971 JOURNAL.

REFERENCES

1. F. Haber, *Z. Electrochem.*, **11**, 593 (1905); **12**, 415 (1906).
2. F. Haber and F. Fleischmann, *Z. Anorg. Chem.*, **51**, 245 (1906).
3. F. Haber and G. W. A. Foster, *ibid.*, **51**, 289 (1906).
4. R. W. Lee and D. L. Frey, *Phys. Chem. Glass*, **7**, 19 (1966).
5. R. H. Doremus, *This Journal*, **115**, 924 (1968). R. H. Doremus, *Phys. Chem. Glass*, **9**, 128 (1968). C. G. M. Dykhuis and J. A. A. Ketelaar, *Electrochim. Acta*, **11**, 1607 (1966); **12**, 795 (1967). J. Hladik, M. Saunier, and G. Morand, *J. Chim. Phys.*, **64**, 378 (1967). H. E. Bartlett and P. Growther, *Electrochim. Acta*, **15**, 681 (1970).
6. D. Yuan and F. A. Kröger, *J. Phys. Chem.*, **73**, 2390 (1969).
7. N. Weber and J. T. Kummer, *Proc. Ann. Power Sources Conf.*, **21**, 42 (1967); E. J. Cairns and H. Shimotake, *Science*, **164**, 3886 (1969).
8. D. Yuan and F. A. Kröger, *This Journal*, **116**, 594 (1969).
9. O. Kubaschewski and E. Ll. Evans, "Metallurgical Thermochemistry," Table B, Pergamon Press, London, New York (1955).
10. *Ibid.*, Table A.
11. *Ibid.*, Table E.
12. D. Detry, J. Drowart, and P. Goldfinger, *Z. Physik. Chem. Neue Folge*, **55**, 314 (1967).
13. F. D. Richardson, J. H. E. Jeffes, and G. Withers, *J. Iron Steel Inst.*, **166**, 213 (1967).

Ionic Conductance in Solids

I. Compounds Formed between Silver Iodide and the Cyanides of Metals of Group IA

G. W. Mellors and D. V. Louzos*

Union Carbide Corporation, Consumer Products Division, Research Laboratory, Cleveland, Ohio 44101

ABSTRACT

Compositions whose conductance is essentially ionic have been prepared in the KCN-AgI and RbCN-AgI systems. The maximum conductance is attained at a ratio of silver iodide to alkali cyanide of four to one. For example, KCN-4AgI has a conductance of 1.4×10^{-1} ohm^{-1} cm^{-1} at 25°C. The conductance has been measured as a function of temperature for KCN-4AgI and of composition for the general system. X-ray patterns and thermal analyses indicate that these new compounds are unique materials and not mixtures of their constituents.

Interest in solids that display high ionic conductance at or near room temperature arises from the fact that these materials when employed as battery electrolytes would avoid some of the difficulties associated with the conventional aqueous systems. Such shortcomings include limited shelf life, cell leakage, restricted temperature range of operation, and the difficulty of making miniaturized systems.

* Electrochemical Society Active Member.
Key words: solid electrolyte, silver iodide, conductance, KAg_4I_4CN, potassium cyanide.

It is not intended here to embark on an extensive review of the field; should the reader so desire, he may refer to a number of excellent articles (1). Very few solid materials are known possessing a specific conductance, purely ionic in nature, as high as $10^{-1} \sim 10^{-2}$ ohm^{-1} · cm^{-1}. Conductance of at least this magnitude is probably required so that cells of low internal resistance, able to deliver appreciable power, may be constructed.

The solid-state conductance of AgI (2), Ag_2HgI_4 (3), Ag_3SI (4, 5), and of the *M*I-4AgI series where *M* may

be K^+, Rb^+, or NH^+_4 (6, 7) have been reported. More recent work (8) has shown the conductance of $RbAg_4I_5$ to be 0.279 ohm^{-1} cm^{-1}, rather than the lower value of 0.21 ohm^{-1} cm^{-1} originally reported.

It was thought of interest to examine the compounds of silver iodide with the alkali cyanides and this paper describes the preparation and properties of alkali cyanide-silver iodide materials. The compounds KAg_4I_4CN and $RbAg_4I_4CN$ possess high ionic conductances very similar to those of KAg_4I_5 and $RbAg_4I_5$.

Experimental

Materials.—Silver iodide was obtained from Mallinckrodt Chemical Works. Potassium and sodium iodides and cyanides (ACS certified) were obtained from Fisher Scientific Company. Rubidium, lithium and cesium iodides, barium and silver cyanides were obtained from City Chemical Corporation. Silver metal and potassium argentocyanide were obtained from I. Miller, Incorporated, Cleveland. Argon, helium, and nitrogen were obtained from the Linde Division of Union Carbide Corporation.

All materials were stored in a dry box and wherever practicable were in addition fused and ground prior to use.

Apparatus.—Samples were made by melting together the components under argon or nitrogen in Pyrex test tubes (6 in. x 1 in.) with side arms. Pellets of samples were prepared between appropriate electrodes in a Carver Laboratory Press, Model B, and the resistance was measured with a 1000 cycle conductance bridge (Industrial Instruments, Model 216B2).

The dry box was a controlled-atmosphere laboratory Model 2C380-28R built by Kewaunee Manufacturing Company.

Differential thermal analyses were made using a Du Pont series 900 Differential Scanning Calorimeter.

Results

Preparation.—KAg_4I_4CN was prepared by melting together potassium cyanide [6.49 w/o (weight per cent)] and silver iodide (93.51 w/o) in an atmosphere of dry argon.

The procedure was as follows. The dried powders were well mixed and placed in a Pyrex tube which was flushed with dry argon for about 2 hr. After an overnight (≈16 hr) hold at 180°C, the temperature was raised to 495°C, maintained for 1 hr, and finally the tube was quenched to room temperature in a blast of cold air while the contents were protected by an argon atmosphere. (An alternative and satisfactory method of quenching was simply to pour the molten salt into liquid nitrogen.)

The material as prepared was a gray-green mass. The tube and contents were then sealed off and transferred to a dry box where the material was powdered in an agate mortar and pestle.

KAg_4I_4CN may also be prepared by heating together either KI (1 mole), AgCN (1 mole) and AgI (3 moles) or $KAg(CN)_2$ (1 mole), KI (1 mole) and AgI (7 moles). In both these cases, a material identical in all respects to that produced by the original preparation was obtained.

$RbAg_4I_4CN$ was prepared either by the reaction of RbCN (1 mole) with AgI (4 moles) or by heating a mixture of RbI (1 mole), AgCN (1 mole) and AgI (3 moles) to 400°C and quenched to room temperature. The procedure was much the same as that described previously: the reaction tube was flushed with dry nitrogen for 1 hr, heated to 130°C and held overnight, finally heated to 400°C, and quenched by plunging the tube and its contents into liquid nitrogen. The resultant solid was ground to a cream-yellow powder in a dry box.

The corresponding sodium compound was made by heating together sodium cyanide (4.96 w/o) and silver iodide (95.04 w/o). The homogenized melt was quenched from about 400° ~ 420°C to room temperature under an argon atmosphere and the material powdered in a dry box. It was dark gray-green in color.

Because of the unavailability and general difficulty of preparation of lithium cyanide, the alternative preparation starting with lithium iodide[1] (1 mole), silver cyanide (1 mole) and silver iodide (3 moles) was employed. A procedure identical to that used in the preparation of $RbAg_4I_4CN$ above was followed and the resultant compound was dark brown in color.

It should be possible to prepare $NH_4Ag_4I_4CN$ by a similar procedure but, to date, three preparations by fusing together NH_4I (1 mole), AgCN (1 mole) and AgI (3 moles) have led to gray-green solids with conductances considerably poorer than the rubidium and potassium compounds. Two preparations in sealed tubes have yielded materials of similar poor conductance.

One sample of CsCN-4AgI was made by fusion of CsI (1 mole), AgCN (1 mole) and AgI (3 moles) under argon.

One sample of the mixed potassium-rubidium compound $RbKAg_8I_8(CN)_2$ has been prepared. It is a gray solid of high conductance (see Table I). The starting materials were RbI (1 mole), $KAg(CN)_2$ (1 mole) and AgI (7 moles) and the usual heating and quenching procedures were followed.

Samples of $Ba(CN)_2$-2AgI, $Ba(CN)_2$-4AgI and $Ba(CN)_2$-8AgI were prepared by fusing together the components at 500°C under argon and quenching, still under an inert atmosphere, to room temperature. These were yellow solids of indifferent conductance (≈10^{-5} ohm^{-1} cm^{-1}).

Several compositions in the AgI-$KAg(CN)_2$ series were prepared by the above procedure with the upper temperature being in the 420°-480°C range. These materials, upon grinding in a dry box, were green-yellow powders. For conductance data on these materials, see Table I.

Table I. Conductance of cyanide-iodide materials

Material	Sp conductance (ohm^{-1} cm^{-1} at 25°C)
KCN · 4AgI	0.14
RbCN · 4AgI	0.18
NaCN · 4AgI	3.3×10^{-5}
LiCN · 4AgI	1.38×10^{-5}
NH_4CN · 4AgI	3.20×10^{-6}
CsCN · 4AgI	9.09×10^{-4}
KCN · RbCN · 8AgI	0.15
$Ba(CN)_2$-2AgI	6.6×10^{-6}
$Ba(CN)_2$ · 4AgI	1.4×10^{-5}
$Ba(CN)_2$ · 8AgI	1.3×10^{-5}
2AgI-$KAg(CN)_2$	2.9×10^{-2}
3AgI-$KAg(CN)_2$	6.7×10^{-2}
4AgI-$KAg(CN)_2$	1.2×10^{-1}
9AgI-$KAg(CN)_2$	3.8×10^{-2}
19AgI-$KAg(CN)_2$	4.5×10^{-3}

Conductance measurements.—Pellets were formed in the laboratory press at 2000 and 3000 kg/cm^2 and measured at the same pressure. It was noted that the resistance of the sample under examination decreased up to about 1000 kg/cm^2 and then remained almost constant up to the highest pressure employed (~10,000 kg/cm^2). Either platinum or silver foil electrodes were employed. The pellet was usually about 1 cm in length and 1 cm^2 in cross-sectional area; thus, the reading obtained was approximately equal to the specific resistance (or the reciprocal of the specific conductance). It was assumed that contact resistances were negligible.

Table I shows the values of the specific conductance determined for fifteen iodide-cyanide materials. From this it can be seen that the potassium and rubidium compounds possess conductances that approximate those of the MAg_4I_5 (where M is Rb, K, or NH_4) compounds previously cited (6, 7). However, the sodium and lithium versions, as in the pure iodide systems, are relatively poor conductors differing but little from silver iodide itself in this respect. Remarks on the prepa-

[1] Used as received.

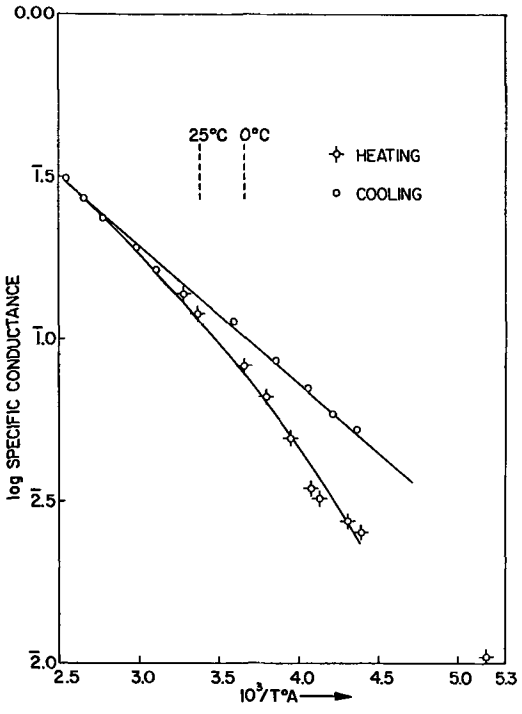

Fig. 1. Conductance of KAg_4I_4CN

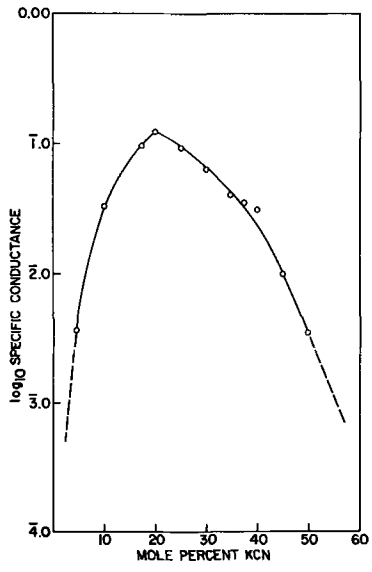

Fig. 2. Conductance as a function of composition for the KCN-AgI system at 25°C.

rations of ammonium derivative appear in an earlier section (*v.i.*) and it would appear (as yet of only one sample) that CsCN-4AgI is a borderline case vis-à-vis conductance.

In Fig. 1, the variation of conductance with temperature for KAg_4I_4CN is presented. From this graph of the logarithm of the specific conductance *vs.* the reciprocal of the absolute temperature, one may compute an apparent energy of activation of 1.94 kcal · $mole^{-1}$. Some remarks on these data are in order.

The conductance was measured at room temperature and the specimen and press were then cooled to −44°C in a large refrigeration chamber with a number of arrests, to permit attainment of equilibrium, at intermediate temperatures. Conductance measurements were obtained on the cooling cycle. During heating to 117°C, which was accomplished with a small furnace enclosing the sample, further measurements were obtained but, on the second and subsequent heating and cooling cycles, the data fell along the upper straight line of Fig. 1. It is likely that the first heating cycle causes annealing or, in general, changes to which the conductance is sensitive. Be it noted that inflections around room temperature were absent in this "annealed" material.

The conductance at 25°C of various compositions in the KCN-AgI system is shown in Fig. 2.

Nature of conductance in cyanide-iodide compounds.—It is important that the conductance of a material to be used as a solid electrolyte be essentially ionic in nature and this may be proved by demonstration of the validity of Faraday's laws.

Both KAg_4I_4CN and $RbAg_4I_4CN$ were electrolyzed under pressure between weighed silver electrodes at room temperature. In the case of the potassium salt in a run of 1 hr duration at 10 mA/cm^2 current density, anode and cathode current efficiencies of 100% were obtained. In a second experiment conducted over a 16½ hr period at 2 mA/cm^2 current density, efficiencies of 95% on the anode and 90% on the cathode were obtained. These relatively small deviations from the theoretical are probably caused by the difficulty in collecting all the cathodically deposited silver rather than by actual deviation from Faraday's laws, and for this reason it has been found preferable to weigh anode loss rather than cathode gain. The measurement of coulombs was less accurate than would have been the case had a coulometer been employed.

Measurements to determine whether a small fraction of the conductance is electronic in nature have not yet been made. It is recognized that a very small contribution ($t_e \approx 10^{-4}$) could adversely affect the behavior of the material. The deviations observed from theoretical can probably be accounted for mainly by experimental difficulty and only secondarily by an electronic contribution. Within the accuracy of the Faradaic experiments, the conductance is essentially ionic.

Although direct measurements of electronic conductance were not made, it may be inferred from the following experiment that the contribution of electrons to the total conductance is small. The emf of the cell $Ag/KAg_4I_4CN/I_2$ was 0.683V at 25°C, compared with the theoretical value of 0.687V for $Ag/AgI/I_2$ calculated from thermal data (9).

In a later experiment, electrolysis of $RbAg_4I_4CN$ between weighed silver electrodes at 0.52 mA/cm^2 current density for 94½ hr resulted in anode and cathode efficiencies of 99.7%.

X-ray patterns of iodide-cyanide materials.—Chemical analysis of the material prepared by fusion of 1 mole KCN and 4 moles AgI shows 42.65% Ag, 49.42% I, 2.33% CN and 4.1% K, compared with the theoretical values of 42.97% Ag, 47.03% I, 2.58% CN and 3.9% K. The AgI:KCN ratio of this material is computed at 3.97, and the I/CN ratio at 4.34.

The x-ray pattern of this material shows very great similarity to that observed by Bradley and Greene (6d) for $RbAg_4I_5$ and a comparison of "d" values and intensities for several of these cyanide-iodide materials and β-AgI is made in Table II.

Although certain lines are found in both the $RbAg_4I_5$ and AgI patterns, the occurrence of strong lines at "d" values of 3.74, 3.37, and 2.19 suggest that the KCN · 4AgI complex is not simply a disordered or contaminated AgI but rather a separate unique material with structure similar to the general MAg_4I_5 type of structure. However, the presence of a small impurity of AgI cannot be ruled out.

Annealing of the KCN · 4AgI complex at 190°C appears to reduce the crystallinity of the material as evidenced by the broadening and reduction in height of the x-ray peaks. This contrasts with $RbAg_4I_5$ in which annealing leads to more perfect crystallinity (and also to a higher electrical conductance). Since Raleigh (8) found no effect of annealing $RbAg_4I_5$, the material we prepared was undoubtedly not identical with his in crystallinity.

Table II. "d" Spacings and intensities for cyanide-iodide materials

$RbAg_4I_5$		KAg_4I_4CN		β-AgI**		$RbAg_4I_4CN$***		$RbKAg_8I_8(CN)_2$	
"d"	I	"d"	I	"d"	I	"d"	I	"d"	I
7.85	W*	7.9	S		Absent	7.89	M	8.0	M
3.94	W	3.99	M	3.98	M	3.99	MS	4.4	VW
—	—	3.77	M	3.75	S	—	—	4.0	W
3.72	MS	3.74	S		Absent	3.73	S	3.76	M
3.52	VW	3.53	M	3.51	M	3.50	VW	3.56	W
3.36	S	3.37	S		Absent	3.38	S	3.40	S
3.21	W	3.23	W		Absent	3.23	W	3.32	W
2.98	MW*	2.98	VW		Absent	3.15	W	3.25	W
2.79	VW*	2.79	VW	2.73	W	—	—	3.01	VW
2.71	VW*	2.71	VW		Absent	—	—	2.81	VW
2.63	W	2.63	MW		Absent	2.64	W	2.65	W
2.56	VW*	2.56	VW		Absent	—	—	2.53	VW
2.49	W*	2.50	W		Absent	—	—	2.43	VW
2.38	W	2.38	W		Absent	2.39	—	2.40	W
2.28	MW	2.30	M	2.296	S	2.29	MS	2.30	W
2.23	MW	2.23	MW		Absent	2.25	W	2.25	W
2.19	S	2.19	S		Absent	2.20	M	2.20	M
2.15	VW	2.12	MW	2.119	MW	—	—	2.16	VW
2.07	M	2.07	M		Absent	2.08	W	2.08	MW
2.04	MW	2.04	MW		Absent	2.05	W	2.05	MW
1.97	W	1.96	M	1.96	M	1.96	MW	1.99	W
1.94	W	1.94	VW		Absent	—	—	1.96	W

* These "d" spacings and intensities calculated by Bradley & Green (6d) and not observed experimentally.
** Patterns unavailable for high-temperature β-AgI. Data for β-AgI from *NBS Quarterly*, 8, 539 (1958).
*** "d" Values averaged from four patterns.

The "d" spacings of $RbAg_4I_4CN$ are shown in the fourth column of Table II. In general, these bear great similarity to those of KAg_4I_4CN and $RbAg_4I_5$ and again it is to be noted that the medium-strength 3.99 peak, present in both KAg_4I_4CN and $RbAg_4I_4CN$, is absent in $RbAg_4I_5$, the latter having only a weak peak at 3.94.

Also included in Table II are the "d" spacings of $RbKAg_8I_8(CN)_2$. On the other hand, in Table III the x-ray pattern of NH_4CN-4AgI shows only lines ascribable to β-AgI, while the pattern of CsCN-4AgI shows AgI together with some lines ascribable to the "MAg_4I_5" general structure. Refinements in the preparation of the ammonium complex may yield a material with the characteristic structure, but it is evident that at this stage the CsCN-4AgI material shows more promise.

Differential thermal analysis.—Experiments were run, on both heating and cooling cycles, with KAg_4I_4CN, $RbAg_4I_4CN$, and, for comparison, with KAg_4I_5 and $RbAg_4I_5$. Table IV shows the temperatures of solid-state decomposition and of the eutectic in each system. The differences in the incongruent melting points clearly demonstrate that the cyano iodides and iodides are indeed different materials.

Table III. "d" Spacings and intensities for NH_4CN-4AgI and CsCN-4AgI

NH_4CN-4AgI		CsCN-4AgI	
"d"	I	"d"	I
8.5	W	8.5	MW
3.98	MS	6.8	W
3.77	S	6.30	W
3.60	W	4.20	W
3.52	W	3.95	MW
2.74	W	3.72	M
2.30	S	3.52	S
2.12	M	3.35	W
1.99	W	3.16	W
1.96	MS	3.08	MW
1.92	W	2.86	MW
		2.34	M
		2.29	MS
		2.20	W
		2.15	W
		2.04	MW

Table IV. Thermal data for iodide and iodide-cyanide materials

Compound	Solid-state decomposition (°C)	Eutectic temperature (°C)
KAg_4I_4CN	230	200
KAg_4I_5	253	238
$RbAg_4I_4CN$	216	181
$RbAg_4I_5$	285	200

Discussion

At the outset of this work, it was thought that the pseudohalogenic properties of cyanide might make the addition of compounds containing this ion to silver iodide a worthwhile pursuit. However, if ionic size be the only critical factor, the CN^- ion, which has an effective freely rotating radius of 1.92Å, intermediate between that of Cl^- (1.81Å) and Br^- (2.00Å) and smaller than I^- (2.16Å) (10), might not be too interesting since mixtures of KBr(0.2)-AgI(0.8) have conductances of 1×10^{-4} ohm^{-1} cm^{-1}.

That size alone is not the overriding factor may be concluded from the highly conducting properties of KAg_4I_4CN and $RbAg_4I_4CN$. In the absence of complete structural data for these compounds analogous to that gathered for $RbAg_4I_5$ by Bradley and Greene (6d) and by Geller (11), it can only be inferred from the close similarity of the x-ray patterns that the cyanide-iodide and the pure iodide compounds have rather similar spatial distribution of component atoms.

If the aforementioned assumption is made that the CN^- ion is freely rotating thereby acquiring spherical symmetry, and that the effective radius is 1.92Å, the distance in the alkali cyanides may be computed as follows:

LiCN	2.52Å
NaCN	2.87Å
KCN	3.27Å
RbCN	3.40Å
CsCN	3.61Å
NH_4CN	3.40Å

It is known that LiCN · 4AgI and NaCN · 4AgI do not conduct, while the corresponding compounds of K and Rb are good conductors. Experiments involving Cs and NH_4 cyanides have shown tentatively that NH_4CN · 4AgI is a rather poor conductor and that CsCN · 4AgI, though more conducting than the NH_4CN · 4AgI material, is still considerably poorer than the K or Rb compounds.

Obviously, the assumption of spherical symmetry for the cyanide ion is not correct; but, as a first approximation, it is clear that a mole of cyanide can substitute for a mole of iodide in the MAg_4I_5 structure and hence will not impede the high mobility of the silver ions. More importantly, the resultant field induced by the different charge density of the CN^- ion is changed very little from that of an iodide ion coupled with K^+, Rb^+, or NH_4^+ ions.

That these materials are unique compounds and not previously prepared materials contaminated with impurities is shown by the reproducible nature of the incongruent melting points and eutectic temperatures

and by the difference of these values from those for the previously known iodide compounds. While difficulties of preparation have been met resulting in the presence of small amounts of unreacted silver iodide, there is no indication from thermal data that impurities in KAg_4I_4CN and $RbAg_4I_4CN$ consist of KAg_4I_5 or $RbAg_4I_5$.

In a series of experiments, the compositions $Ba(CN)_2 \cdot 4AgI$, $Ba(CN)_2 \cdot 8AgI$, and $Ba(CN)_2 \cdot 2AgI$ were prepared and their conductances measured. The Ba^{2+} ion was chosen because, although its ionic radius (1.35Å) is very similar to that of potassium (1.33Å), the charge density is considerably different. The conductances of all three compositions were about 10^{-5} ohm^{-1} cm^{-1}.

These materials are poor conductors and approximate the values obtained for the mixtures of AgI with LiCN or NaCN. Probably the higher charge density of the Ba^{2+} ion "tightens" up the structure reducing the mobility of the Ag^+ ion and, although structural data are lacking, it may well be that such materials do not possess the characteristic "MAg_4I_5" structure but crystallize in another form.

While as yet the only cations found useful have been K^+ and Rb^+, there is apparently considerable latitude in the cyanide-to-iodide ratio in the vicinity of that composition which gives maximum conductance. Consideration of the ionic conductor $KAg(CN)_2 \cdot 4AgI$ leads to the important observation that, although the alkali metal:cation ratio has now become 1:6, the x-ray pattern shows "d" spacings and intensities extremely similar to those of the molecularly more simple $KCN \cdot 4AgI$ compound. This would suggest that the general skeleton of these compounds based on I^- ions has a very loose structure, amenable to extensive substitution, and this additional "degree of freedom" is under investigation in more detail, since the conductance might conceivably be maximized by an altered CN/I ratio. Further it should be realized that a material which retains conductive properties despite changes in the ratio of its constituents may be valuable in a battery system where such changes may occur during service.

The stability of these highly conductive materials with respect to water vapor has been investigated both by x-ray diffraction and by differential thermal analysis and will be discussed in a later paper.

Conclusion

It may be concluded that the binary mixtures $KCN \cdot 4AgI$ and $RbCN \cdot 4AgI$ together with the ternary $KCN \cdot RbCN \cdot 8AgI$ are essentially ionic conductors. The maximum value of conductance is attained when the components are present in the ratio of 1 mole alkali cyanide to 4 moles silver iodide. The specific conductance of either binary compound, while smaller in magnitude, nonetheless approaches that for members of the family 1M Ag_4I_5 (where M is Rb, K, or NH_4) that were reported earlier (6, 7).

Acknowledgments

The authors would like to express their thanks to S. Senderoff, G. E. Blomgren, T. A. Reilly, and J. A. van Lier for enlightening discussions and to M. Soldat, G. W. Sheffield, and K. K. Maszczynski who performed much of the experimental work.

Manuscript submitted Aug. 31, 1970; revised manuscript received Jan. 22, 1971.

Any discussion of this paper will appear in a Discussion Section to be published in the December 1971 JOURNAL.

REFERENCES

1. (a) A. B. Lidiard, "Handbuch der Physik," S. Flugge, Editor, Springer-Verlag (1957); (b) R. T. Foley, *This Journal*, **116**, 13C (1969); (c) D. O. Raleigh, *Progr. Solid State Chem.*, **3**, 83 (1967); (d) J. N. Mrgudich, "The Encyclopedia of Electrochemistry," p. 84, Reinhold (1964).
2. W. Seith, *Z. Electrochem.*, **42**, 635 (1936).
3. J. A. A. Ketelaar, *Z. Physik. Chem.*, **B26**, 327 (1934).
4. B. Reuter and K. Hardel, *Naturwiss.*, **48**, 161 (1961).
5. T. Takahashi and O. Yamamoto, *Electrochim. Acta*, **11**, 911 (1966).
6. (a) J. N. Bradley and P. D. Greene, *Trans. Faraday Soc.*, **62**, 2069 (1966); (b) *idem, ibid.*, **63**, 424 (1967); (c) *idem, ibid.*, **63**, 1023 (1967); (d) *idem, ibid.*, **63**, 2516 (1967); (e) Brit. Pat. No. 1,140,398.
7. (a) B. B. Owens and G. R. Argue, *Science*, **157**, 308 (1967); (b) U.S. Pat. No. 3,443,997.
8. D. O. Raleigh, *J. Appl. Phys.*, **43**, 1876 (1970).
9. W. M. Latimer, "Oxidation Potentials," 2nd Ed., p. 190, Prentice-Hall (1961).
10. L. Pauling, "The Nature of the Chemical Bond," 3rd Ed., Cornell University Press (1960).
11. S. Geller, *Science*, **157**, 310 (1967).

Ionic Conductance in Solids

II. The Phase Diagram of the KCN-AgI System and Some Observations on the Stability of Cyanide-Iodide Compounds

G. W. Mellors, D. V. Louzos,* and J. A. van Lier

Union Carbide Corporation, Consumer Products Division, Research Laboratory, Cleveland, Ohio 44101

ABSTRACT

Some 25 compositions varying from pure AgI to pure KCN were examined. The phase diagram has an incongruent compound at the composition 4AgI-KCN with an incongruent melting point of 230°C. A eutectic occurs at the composition 45KCN-55AgI at a temperature of 200°C. The stability of KAg_4I_4CN has been examined by differential thermal analysis, conductance, and emf measurements. The effect of water vapor on both the potassium and rubidium compounds has been determined by DTA or x-ray methods.

The work of Bradley and Greene (1, 2), Owens and Argue (3), and Topol and Owens (4) on the phase relationships in the alkali iodide-silver iodide systems has shown that the conducting compounds of general formula MAg_4I_5 (where M = Rb, K, or NH_4) are incongruently melting compounds, stable with respect to temperature between about 250°C and room temperature. This present paper describes the determina-

* Electrochemical Society Active Member.

Key words: solid electrolyte, silver iodide, phase diagrams, KAg_4I_4CN, potassium cyanide.

tion of the phase relationships in the KCN-AgI system, which has been reported by the present authors (5) to contain compositions of high ionic conductance.

Experimental

Materials.—Silver iodide (99.5% pure) was obtained from Mallinckrodt Chemical Works. Potassium cyanide (98.8% pure) was obtained from Fisher Scientific Company (ACS certified). This material was fused under argon and crushed and stored in a dry box prior to use. Argon (99.996% pure) and helium were obtained from the Linde Division, Union Carbide Corporation.

Apparatus.—The compositions for thermal analysis were contained in Morganite recrystallized alumina crucibles, size XN 100. The samples were stirred by purified argon, bubbled into the melt *via* an alumina tube. The temperature was measured by a Chromel-Alumel thermocouple, encased in an alumina thermowell, provided with an external (0°C) cold junction.

The crucible and contents were placed inside a larger, deeper alumina crucible and were confined under an argon atmosphere with a Pyrex or Inconel outer vessel. Figure 1 shows the general layout of the system.

Procedure.—Each sample was about 30g in weight and the complete, sealed apparatus was flushed with argon for several hours prior to a run. The cell was then heated to a temperature about 100°C above the liquidus of the composition under examination and held at that temperature with stirring for several hours to homogenize the melt. The furnace power was switched off and a cooling curve obtained on a recorder chart, after which the temperature was again raised and the cooling curve repeated, when, if all was well, agreement with the previous inflections to about ±1°C was usually obtained. A Du Pont series 900 Differential Thermal Analyzer together with a Differential Scanning Calorimeter attachment were used in parallel determinations of the thermal inflections.

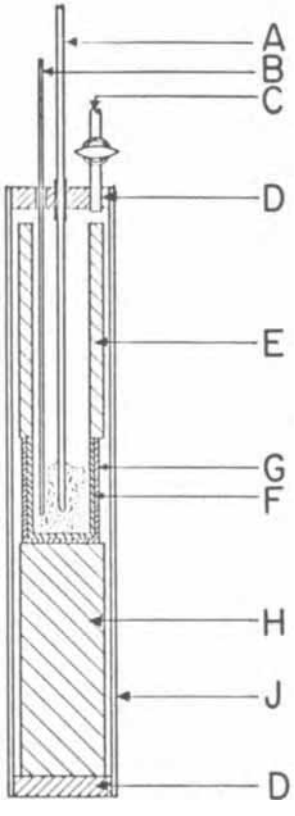

Fig. 1. Apparatus used in cooling curve studies: A—alumina thermowell, B—alumina bubbler, C—gas outlet, D—10½ rubber stoppers, E—alumina shielding tube, F—alumina crucible, G—Inconel crucible, H—Alundum crucible, J—Pyrex or Vycor envelope.

Results

The literature values for the melting points of the pure salts were reproduced to ±1°C, *viz.* 558°C for silver iodide and 634.5°C for potassium cyanide (6).

The phase diagram drawn conventionally as a binary is shown in Fig. 2 and in general aspect it appears very similar to those of the binaries of AgI with either RbI, KI, or NH_4I. An incongruently melting compound appears at the molar composition 20KCN-80AgI, the transition temperature being 230°C, and a eutectic occurs at 200°C at the molar ratio 45KCN:55AgI. The horizontal line at 146°C at the silver iodide-rich end of the diagram represents the $\alpha \rightleftharpoons \beta$ transition in this material. On the cyanide-rich side of the diagram, a maximum melting point appears to be reached at the composition 66KCN-33AgI, followed by a sharp rise of the liquidus curve from a second eutectic around 72 ~ 75KCN to the melting point of pure KCN (634.5°C).

Problems were encountered in examining compositions between 65 and 100 m/o (mole per cent) KCN, in that it proved difficult and in some cases impossible to obtain meaningful inflections. It at first appeared that there was some break in the continuity of the liquidus between 65 and 70 m/o KCN which suggested the presence of perhaps a second incongruently melting compound, possibly 2KCN · AgI or $K_2AgI(CN)_2$.

Both the RbI-AgI and KI-AgI systems contain compounds 2RbI · $AgI(Rb_2AgI_3)$ and 2KI · $AgI(K_2AgI_3)$, the former being an incongruently melting compound and the latter formed by solid-state transition below about 125°C. These are nonconductors and it became pertinent to ask whether a compound 2KCN · AgI [*i.e.*, $K_2AgI(CN)_2$] might not exist in the cyanide-iodide system. Accordingly, the composition 2KCN-AgI was made up by standard techniques, quenched, and powdered in a dry box. The x-ray pattern indicated perfect matching of "d" spacings and intensities for a mixture of $KAg(CN)_2$ and KI. It must be concluded that the following reaction had occurred

$$2KCN + AgI \rightarrow KAg(CN)_2 + KI$$

the final result being an equimolecular mixture of potassium iodide and potassium argentocyanide. A 2KCN-AgI specimen made up and slowly cooled over a 16 hr period showed an identical x-ray pattern.

In general, as the concentration of cyanide ion is increased, the greater will be the tendency to form $KAg(CN)_2$ and KI. At compositions where the KCN:AgI mole ratio exceeds 2:1, the three materials KI, KCN, and $KAg(CN)_2$ will coexist and thus the system could be represented in the most general case as a reciprocal system of KI-KCN-AgI-AgCN. However, in view of the exceptional stability of $KAg(CN)_2$ with respect to the other components of this system, it can also be considered as a pseudobinary of AgI and the (1:1) mole mixture of KI and $KAg(CN)_2$ if one wishes.

In fact, the reaction product of 0.1 mole KI, 0.1 mole $KAg(CN)_2$, and 0.7 mole AgI is equivalent in ap-

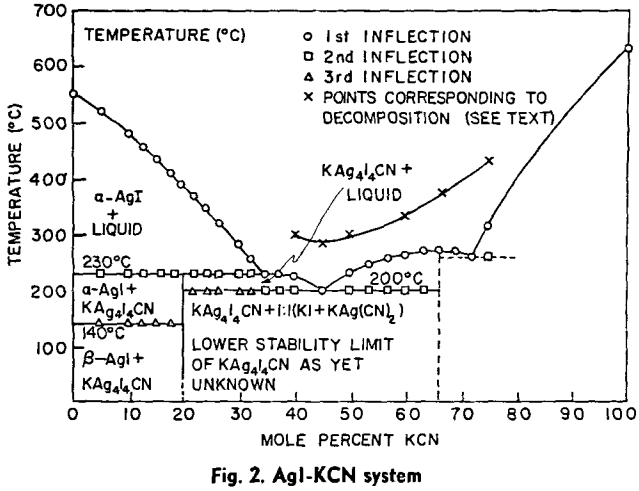

Fig. 2. AgI-KCN system

pearance, x-ray pattern, and conductance to the reaction product of 0.2KCN and 0.8AgI.

There are, it must be conceded, problems in obtaining reproducible data in this system, particularly in the KCN-rich compositions. In Fig. 2 (labeled X) are shown a number of points, corresponding to inflections consistently obtained in DTA and cooling curves. In the first instance, these were thought to represent a liquidus line, but at present it is believed that they are associated with the thermal decomposition or the products of such decomposition of the initially formed compounds on prolonged heating above the melting point. As the proportion of KCN increases, so also does that of $KAg(CN)_2$. This latter is unstable (melting point 370°C) with respect to prolonged high-temperature treatment and, as a result, silver metal appears in the melt with the probable release of cyanogen and residual KCN.

It is intended to consider, in a later publication, the detailed reactions in the KCN-AgI system and in other closely related systems. The present diagram must therefore be considered as substantially correct with respect to major solidus and liquidus lines, though in the cyanide-rich region, the nature of the true equilibrium phases has not yet been established.

Discussion

Stability of cyanide-iodide compounds.—The diagram as presented in Fig. 2 is fairly straightforward and the areas of stability of the various materials appear sharply delineated. An important point remaining unresolved by the phase diagram work is that of the lower temperature of stability of the compound KCN · 4AgI. However, this instability reaction which, in the iodides, takes the form

$$2MAg_4I_5 \rightleftharpoons M_2AgI_3 + 7AgI$$

is extremely slow and therefore difficult to determine by thermal methods. Bradley and Greene (1) in their investigation of the KI-AgI system reported that differential thermal analysis showed only a broad and indistinct peak, but that conductance measurements with a slower rate of temperature increase showed the existence of a distinct temperature (38° ± 2°C) for the onset of the above reaction. Another approach taken by these authors was to measure the emf's of the cells:

Cell I, $Ag/AgI/I_2$, the reaction for which was assumed to be

$$Ag(c) + \frac{1}{2}I_2\ (c) \rightarrow \beta\text{-}AgI\ (c) \qquad [1]$$

and Cell II, Ag/K_2AgI_3, KAg_4I_5/I_2, the reaction for which was assumed to be

$$Ag\ (c) + \frac{1}{2}I_2\ (c) + \frac{1}{7}K_2AgI_3\ (c) \rightarrow \frac{2}{7}KAg_4I_5\ (c) \qquad [2]$$

On subtracting reaction [1] from reaction [2] one obtains

$$\beta\text{-}AgI\ (c) + \frac{1}{7}K_2AgI_3\ (c) \rightarrow \frac{2}{7}KAg_4I_5\ (c) \qquad [3]$$

the free energy change for which is

$$-(E_{\text{Cell II}} - E_{\text{Cell I}})/F$$

When these emf's were plotted as a function of temperature, the straight lines intersected at about 40°C, with the quantity $(E_{\text{Cell II}} - E_{\text{Cell I}})$ positive above this temperature and negative below it. This demonstrated that if reactions [1] and [2] are the correct reactions for Cells I and II, then reaction [3] goes spontaneously to the right above 40°C and to the left below this temperature.

Cells analogous to those set up by Bradley and Greene (1) involving the KAg_4I_4CN compound would be

Cell I, $Ag/AgI/I_2$

and

Cell IV, $Ag/[KAg(CN)_2 + KI\ (1:1)]$, KAg_4I_4CN/I_2

the reaction for which was assumed to be

$$\frac{1}{7}KAg(CN)_2\ (c) + \frac{1}{7}KI\ (c) + Ag\ (c) + \frac{1}{2}I_2\ (c) \rightarrow \frac{2}{7}KAg_4I_4CN\ (c) \qquad [4]$$

On subtracting reaction [1] from reaction [4], one obtains

$$\beta AgI\ (c) + \frac{1}{7}KAg(CN)_2\ (c) + \frac{1}{7}KI\ (c) \rightarrow \frac{2}{7}KAg_4I_4CN\ (c) \qquad [5]$$

the free energy change for which is

$$-(E_{\text{Cell IV}} - E_{\text{Cell I}})/F$$

The emf's of these cells were measured and are shown in Fig. 3. It can be seen that $(E_{\text{Cell IV}} - E_{\text{Cell I}})$ is negative over the full temperature range. If reaction [4] is the correct assumption for the reaction of Cell IV, then it would appear that reaction [5] goes spontaneously to the left at all temperatures. However, while a metastable material may exist almost indefinitely at room temperature, it should convert to the stable form when heated to a reasonably high temperature. It has been found that prolonged heating of KAg_4I_4CN at 150°C does not produce any additional free AgI. It therefore seems more reasonable to conclude that reaction [4] is not the potential-determining reaction of Cell IV in the solid state.

Whereas in the experiments of Bradley and Greene (1) only one solid material, K_2AgI_3, was employed, in the present work a mixture of KI and $KAg(CN)_2$ constituted the solid phase and the presence of two solids, even though mixed intimately, may render reaction by diffusion more difficult.

In the case of the pure iodide compounds MAg_4I_5, the instability reaction involved the compounds identified in the phase diagram, *viz.* $2MAg_4I_5 \rightarrow M_2AgI_3 + 7AgI$ and, therefore, one might be tempted to conclude from Fig. 3 that the dissociation reactions in the cyanide compounds would be

$$2KAg_4I_4CN \rightarrow 7AgI + KI + KAg(CN)_2$$

or

$$KAg_4I_4CN \rightarrow 3AgI + KI + AgCN$$

but the emf experiments neither confirm nor deny this hypothesis.

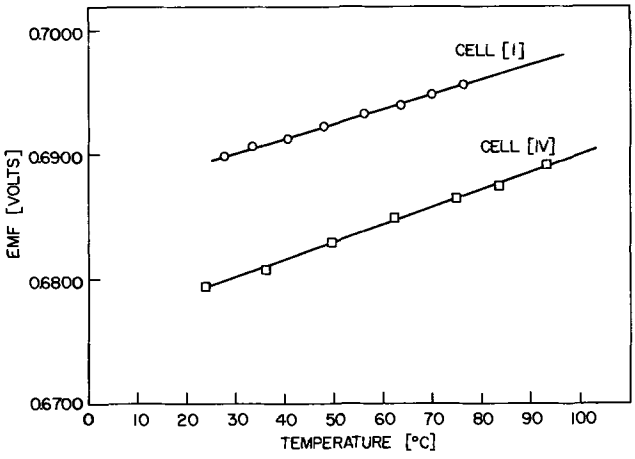

Fig. 3. EMF of silver cells

The measurement of the conductance of KAg_4I_4CN as a function of temperature has been presented in the first paper of this series and shows an absence of inflection at or around room temperature. This indicates that, if a structural change or decomposition does occur in the vicinity of room temperature, it can only be extremely small in extent and hence not readily detectable by conductance measurements.

The DTA experiments extended from room temperature up to about 300°C. Figures 4 and 5 show a typical trace obtained for KAg_4I_4CN and $RbAg_4I_4CN$ and indicate an absence of thermal arrests up to 147°C. The presence of an endothermic inflection at 147°C which is characteristic of silver iodide (Fig. 6) raises the question as to whether the source of such silver iodide is by decomposition of KAg_4I_4CN or $RbAg_4I_4CN$. Such decomposition might be an inherent property of these iodide-cyanide materials but alternative explanations are those of (*a*) incomplete reaction between the components, or (*b*) inadvertent contamination by moisture producing AgI during the course of the DTA or during transfer to the apparatus.

Since DTA is generally considered to be a sensitive indicator of structural change, it was thought worthwhile to examine KAg_4I_5 and $RbAg_4I_5$ where studies have indicated instability of the complex below 38° and 27°C, respectively. A thermogram free of inflections up to about 240°C (approximately the position of the eutectic in the KI-AgI system) was obtained from the former system, and in the latter system no significant inflections were obtained until about 200°C.

The apparent conflict between the DTA and the aforementioned thermodynamic work (4) should not be taken to indicate that water vapor was admitted inadvertently during the latter measurements. Rather it should show that the instability at 27°C in $RbAg_4I_5$ in the absence of moisture can be observed only by thermodynamic measurements and that it is too slow a process to observe in a kinetic experiment even by a method as sensitive as DTA. It should be noted that the infinitesimally slow rate of the decomposition reaction in the absence of moisture is very desirable from the viewpoint of battery "shelf life."

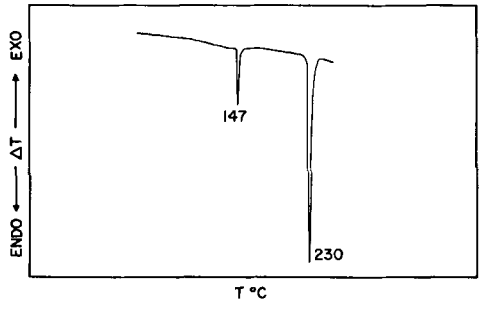

Fig. 4. DTA of KAg_4I_4CN

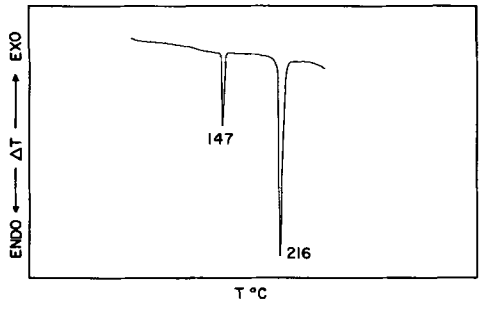

Fig. 5. DTA of $RbAg_4I_4CN$

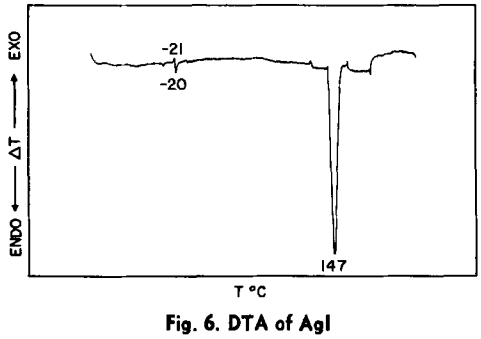

Fig. 6. DTA of AgI

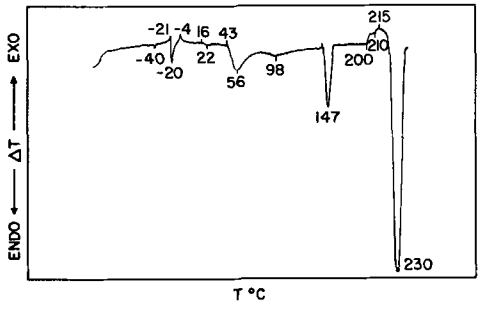

Fig. 7. DTA of KAg_4I_4CN exposed to water vapor

Some qualitative observations on the reactions of KAg_4I_4CN and $RbAg_4I_4CN$ with moisture might be made here. If either of these materials is exposed to moisture (the normal 35% humidity of the laboratory being more than adequate) for a period of time, thermograms are obtained that now show endothermic inflections between 0°C and about 150°C. These inflections vary with the amount of water and the time of exposure and Fig. 7 shows a typical result on KAg_4I_4CN. Additional evidence for the undesirable effects of water vapor is obtained from the fact that a specimen previously showing the characteristic x-ray pattern of KAg_4I_4CN, after exposure to this medium, predominantly shows lines assignable to AgI.

Qualitatively, $RbAg_4I_4CN$ would appear to possess greater stability with respect to moist air than KAg_4I_4CN. The DTA measurements show that, even after exposure to laboratory air for 12 days, additional endothermic peaks do not develop in the region of interest (approx 0°-100°C) in contrast to KAg_4I_4CN. Whereas KAg_4I_4CN on exposure to laboratory air for 24 hr gains weight and displays significant changes in its x-ray pattern, $RbAg_4I_4CN$ retains its characteristic diffraction pattern even after 6 weeks' exposure under similar conditions.

Acknowledgments

The authors wish to thank G. E. Blomgren, S. Senderoff, and T. A. Reilly for interesting and enlightening discussions; G. W. Sheffield, M. S. Soldat, P. A. Pleban, and K. K. Maszczynski who performed much of the experimental work; and S. C. Maszczynski for the x-ray diffraction data.

Manuscript submitted Aug. 31, 1970; revised manuscript received Jan. 22, 1971.

Any discussion of this paper will appear in a Discussion Section to be published in the December 1971 JOURNAL.

REFERENCES

1. J. N. Bradley and P. D. Greene, *Trans. Faraday Soc.*, **62**, 2069 (1966).
2. J. N. Bradley and P. D. Greene, *ibid.*, **63**, 424 (1967).
3. B. B. Owens and G. R. Argue, *This Journal*, **115**, 91C (1968).
4. L. E. Topol and B. B. Owens, *J. Phys. Chem.*, **72** 2106 (1968).
5. G. W. Mellors and D. V. Louzos, *This Journal*, **118**, 846 (1971).
6. "Handbook of Chemistry and Physics," 49th Ed., Chemical Rubber Co., Cleveland, Ohio (1968-1969).
7. B. B. Owens and G. R. Argue, *Science*, **157**, 308 (1967).

The Corrosion Behavior of Cu and Naval Brass in 0.5M NaCl Solutions at Ambient Temperature

A. H. Taylor

Tyco Laboratories, Inc., Bear Hill, Waltham, Massachusetts 02154

ABSTRACT

The rotating ring-disk technique was used to obtain insight into the corrosion mechanisms of pure Cu and naval brass in deaerated 0.5M NaCl at ambient temperature. The potential regions for the reactions: $Cu^{2+} \rightarrow Cu^{+}$, $Cu^{2+} \rightarrow Cu$, $Cu^{+} \rightarrow Cu^{2+}$, and $Zn^{2+} \rightarrow Zn$ have been explored to permit analysis of the products of dissolution processes occurring during galvanostatic corrosion of these materials. Pure Cu corrodes only via Cu^{+} over the range $\sim 2.5 \times 10^{-6}$ to $\sim 900 \times 10^{-6}$ A/cm^2 corrosion current (0.19 cm^2 area). No evidence is found for Cu^{2+} species or for film forming reactions. Naval brass [60.54 w/o (weight per cent) Cu, 38.70 w/o Zn, and 0.76 w/o Sn] corrodes solely via Cu^{+} and Zn^{2+} up to $\sim 450 \times 10^{-6}$ A/cm^2 corrosion current. No Cu^{2+} species are found. Experiments indicate that selective dissolution of Zn does not occur. No evidence can be found for a Cu redeposition mechanism. Data suggest the occurrence of a homogeneous solution reaction in which soluble Cu^{+} species produced on corrosion of the alloy undergo hydrolysis before reaching the zone of the ring electrode. No evidence is found for formation of CuOH or Cu_2O directly on the corroding surface.

Work described here is based on part of a program sponsored by the Office of Saline Water, United States Department of the Interior, aimed at more clearly defining the corrosion mechanisms of Cu-based alloys in saline environments. The present paper deals with preliminary work on Cu corrosion and naval brass corrosion under closely controlled conditions, subsequently outlined.

Lu *et al.* (1) has investigated the dissolution rate of Cu in H_2SO_4 at 25°C using a rotating Cu cylinder. He reports a rate-controlling step via oxidation of cuprous ion at the solution/copper interface. Thermodynamic aspects of Cu corrosion along with kinetic and electrochemical studies are reported by Ives *et al.* (2) in water containing various salts (including NaCl). Simultaneous dissolution of Cu and film growth, predominantly as Cu_2O, are indicated in the presence of O_2 and CO_2. Cl^{-} ions alter the dissolution kinetics and film growth processes causing more localized attack. Cu_2O dissolves more rapidly in Cl^{-} media. Similarly, May (3), in a study of the mechanism of pitting corrosion of Cu, noted the formation of CuCl and Cu_2O in the early stages of the process in saline solutions. Rotating ring-disk studies (4-7) by Miller (7) on a Cu electrode in NaOH solution showed that low current density dissolution proceeded via Cu^{+} with concurrent Cu_2O formation. Above 400 μA/cm^2, Cu^{2+} species were found.

Much attention has been paid to the mechanisms of brass dissolution in a range of environments and in particular on the occurrence of preferential and simultaneous dissolution. Studies have been aimed at distinguishing between dezincification by a selective dissolution mechanism as compared to an ionization-redeposition mechanism. The inhibitive effects of small As additions on the dezincification of a number of brass alloys, has also been of particular interest (8-14). A wide range of techniques have been brought to bear on this problem, ranging from x-ray (8, 11, 15-17) electron diffraction (18, 19) and metallographic observations (20) of corroded surfaces to more recent rotating ring-disk studies (21-23) of the corrosion mechanisms.

Stillwell and Turnipseed (15) used x-ray diffraction in a study of η-brass dissolution in dilute HCl and concluded that the dissolution was selective. Polushkin and Shuldener (16) observed twinning in the Cu crystals in dezincified α-brass and concluded that the Cu was residual. Lucey (11), however, observed twinning in Cu crystals redeposited from CuCl solution. He inferred from his data that simultaneous dissolution of Cu and Zn occurs followed by Cu redeposition (on α- and β-brass alloys). Bengough and May (8) found that the crystalline form of Cu produced by dezincification bore no resemblance to that in the original alloy. A Cu redeposition process was thus inferred.

Pruna *et al.* (17) and Hashimoto and Ogiva (18) both found evidence for a brass dissolution/Cu redeposition mechanism. Further support for this came from the work of Joseph and Arce (20) on 63/37 brass and Sugawara and Ebiko (19) on α- and $\alpha + \beta$-brass alloys in Cl^{-} media. The latter workers also found Cu_2O or CuCl in the early stages of corrosion. Higher Zn content alloys were more subject to dezincification.

The work of Pickering *et al.* on a wide range of alloys is of interest. Rotating ring-disk techniques (21) revealed the absence of an ionization-redeposition mechanism of preferential dissolution in a 30 a/o (atom per cent) Zn alloy in sulfate medium. Feller's rotating disk studies (22) indicated that preferential dissolution of Zn occurred more readily in the higher Zn content alloys (~80 a/o Zn) than in the Cu-rich alloys. More recently, Pickering and Byrne (24) measured partial currents during Cu and/or Zn dissolution from γ-, ϵ-, and α-brass alloys in sulfate medium. Various modes of dissolution were found depending on the potential. The ϵ-alloy (86 a/o Zn) yielded only Zn^{++} on dissolution. The γ-alloy (65 a/o Zn) dissolved first as Zn^{++} solely, followed by a potential region where dissolution proceeded in the ratio 10:1 Zn/Cu. The α-brass (30 a/o Zn) gave first of all Zn^{++} followed by an intermediate potential region where Zn and Cu dissolved to differing extents and finally in a 1:1 ratio. They also measured partial currents as a function of time during dissolution at constant potential and found a decrease in rate with time. The rate of decrease of the partial current from Zn dissolution was greater than that from Cu dissolution. X-ray examination of γ- and ϵ-brass alloys by Pickering (25) indicated a volume diffusion mechanism for preferential dissolution of these alloys.

Miller's rotating ring-disk studies (23) on 70/30 brass in Mattson (26) type solutions (~pH 7) are of interest. No evidence was found for Cu_2O film formation, in contrast to results (7) for Cu in NaOH. At low current densities (<5 mA/cm^2) corrosion proceeded

Key words: dezincification, galvanostatic corrosion, rotating ring disk.

via Cu^+ and Zn^{++} solely. Above this Cu^{++} species were produced (and no Cu^+).

Consideration of these data reveals that there is scope for further work in the field. As pointed out by Stillwell and Turnipseed (15) and Fink (9) both dezincification mechanisms can occur depending on the circumstances. It is clear also, that the composition of the alloy has a very important bearing on the mode of corrosion.

Our studies were aimed at examining the mechanism of brass dissolution and film formation in 0.5M NaCl media, the latter since we were also interested in anodically protecting the alloys in high-temperature saline solutions. Preliminary work is reported on pure Cu and naval brass corrosion in these solutions. Following the work of others (7, 21-23) this investigation has been carried out using a rotating ring-disk setup, the advantages of which have been admirably outlined by Miller (7, 23). Essential details of equipment and experimental procedures are given in the following sections.

Experimental

The rotating ring-disk assembly used in these studies was purchased from R. Disantis (Willowick, Ohio). Speed control was achieved using an electric motor (B2410) and Minarik Control unit (SL-32), Reserve Electric Company, Cleveland. This assembly was capable of rotation from 300 to 6000 rpm and was calibrated using a stroboscope. Disk materials of pure Cu (99.99%) and naval brass (60.54% Cu, 38.70% Zn, 0.76% Sn) were concentric with, but separated from, Au ring electrodes via Teflon insulating gaps. The materials were ~1/16 in. thick and were replaced as required. In a number of experiments the rings were amalgamated with Hg for reasons stated later.

Before and following each corrosion experiment, the electrodes were mounted on a lathe and polished with 600 grit silicon carbide paper followed by 5μ alumina with a polishing cloth. The electrodes were thoroughly rinsed with distilled water before use.

A concise diagram of the electrochemical cell employed is shown in Fig. 1. In the cell free rotation (up to 2000 rpm) of the electrode assembly was achieved while preventing any O_2 from contacting the solutions —the latter since O_2 is reduced at some of the potentials of interest and is particularly deleterious on an amalgamated ring (Hg/Au) in the region of Zn^{++} reduction. We employed a rotation speed of 500 rpm in most of our experiments. Solutions were flushed before use (~30 min) to remove O_2 using tagged N_2 (~4 ppm O_2 in the gas phase) in conjunction with a millipore filter (Millipore Filter Corporation, Bedford, Massachusetts) to remove extraneous dust, etc. During experiments a constant flow of N_2 was passed over the solutions. In this way no problems were found from O_2 during our measurements.

Solutions were made from an ultrapure grade NaCl (0.5M, Brinkmann Instrument, Inc., Westbury, New York). When required, the Au ring was lightly amalgamated using triply distilled Hg. This Hg/Au amalgam electrode was held at $\leq$0V *vs.* SCE at all times. In practice, solutions were replaced with new ones, suitably deaerated, prior to each new experiment.

Two sets of data are reported here. In the first case, we required information on the diffusion limited potential regions within which the various possible dissolved species, *i.e.*, Zn^{++}, $Cu,^+$ and Cu^{++} could undergo further reaction, either oxidative or reductive. To this end we used 0.5M NaCl solutions 10^{-6} to 10^{-3}M in Zn^{++} or Cu^{++} ions and scanned the ring and/or disk (0.03 V/min and 0.60 V/min) at various rotation speeds. Current/potential data were recorded on an X-Y recorder (Houston Omnigraphic Corporation, Bellaire, Texas). For these experiments an Au ring/Au disk or Hg/Au amalgam ring-disk electrode was employed. To examine the region where Cu^+ is oxidized to Cu^{++}, a different technique was used which is described in subsequent sections.

Corrosion experiments in which an Au or Hg/Au amalgam electrode was employed with a Cu or naval brass corrodible disk, were obtained in a different manner. As pointed out by Miller (7) corrosion and film formation on a rotating disk can readily be analyzed by using a constant disk anodization current to control the coulombs passed rather than sweeping the potential. In addition, such galvanostatic experiments do not require the more sophisticated electrochemical control equipment used by Bruckenstein (27) and Miller *et al.* (7, 23, 28). A conventional Wenking potentiostat, Model 61 TRS (Brinkmann Instruments Inc.) was used here to control the potential of ring or disk during cyclic scanning experiments. For corrosion measurements, the ring potential was held at the potential of interest and the disk corroded with a series of constant currents from 0.5 to ~85 μA (disk area ~0.19 cm^2). Ring currents as a function of each disk corrosion current were then measured on a Griebach milliammeter (Griebach Model 500, ½% accuracy; Griebach Instruments, New Rochelle, New York). Currents at times <2 sec are not accurate due to this method of measurement.

Collection efficiencies (29) (N) for each electrode were calculated from measurements of the various ring and disk radii using a microscope. Theoretical values were 0.3822 for Au/Au, 0.3762 for Cu/Au, and 0.3973 for naval brass/Au. Experimental and theoretical values for the Cu/Au electrode agreed to within 1%.

Results and Discussion

Cu *oxidation and reduction on* Au *in 0.5M* NaCl.— The reactions of Cu species have been well characterized in the past using rotating ring-disk systems (7, 23, 27). Typical voltage scans on the Au ring of a Au/Au ring-disk electrode in 0.5M NaCl solution containing 10^{-3}M Cu^{++} are illustrated in Fig. 2. The figure shows two plateau regions extending from 0 to −0.26V *vs.* SCE and from −0.35V to beyond −0.60V *vs.* SCE.

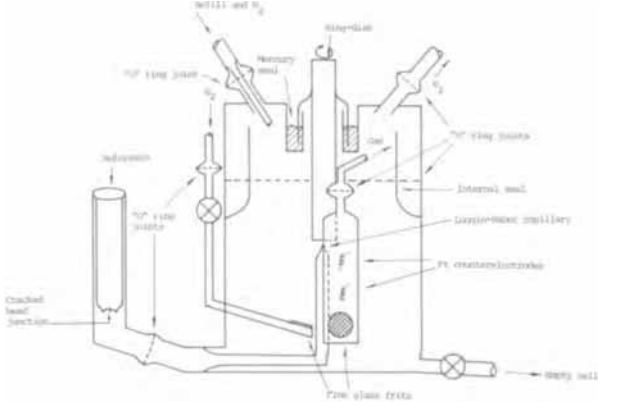

Fig. 1. Electrochemical cell for rotating ring-disk corrosion studies in "O_2-free" 0.5M NaCl at ambient temperature.

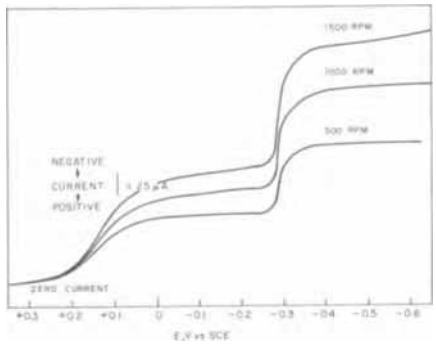

Fig. 2. Typical cyclic scans at ambient temperature on a rotating Au ring electrode in 0.5M NaCl solution containing 10^{-3}M Cu^{2+} (scan speed = 0.6 V/min).

Using reported values for the Cu^{++} diffusion coefficient (27) and a value for the kinematic viscosity (30) of KCl, a calculation of the limiting diffusion current (29) to the rotating ring electrode confirms that the first plateau corresponds to reduction of Cu^{++} to Cu^{+} and that the second plateau corresponds to reduction of Cu^{++} (and Cu^{+}) to Cu. These plateau regions were shown not to be significantly altered when the concentration of Cu^{++} in solution was reduced to 10^{-6}M and the scan rate lowered to 0.03 V/min.

Since CuCl is relatively insoluble in 0.5M NaCl, a slightly different approach was used to establish the region where Cu^{+} can be oxidized to Cu^{++} on an Au electrode under these conditions. Here, as before, the salt solution was made 10^{-3}M in Cu^{++} ions. The latter were reduced to Cu^{+} on an Au disk held at close to -0.20V by a constant current of -68.5 μA (the limiting current in 10^{-3}M Cu^{++} solution when the disk was potentiostated at -0.20V). Disk-produced Cu^{+} species were then swept into the zone of the Au ring for further oxidation back to Cu^{++}. This oxidation current should then reach a plateau level at NI_d where N is the collection efficiency of the electrode and I_d is the disk current arising from reduction of Cu^{++} to Cu^{+} (in this case -68.5 μA). At potentials less positive than those required for Cu^{+} oxidation, smaller ring currents should be observed.

Ring oxidation currents were corrected for background which was insignificant in most cases. Currents were time independent in all cases. Results plotted as ring current *vs.* ring potential are shown in Fig. 3. A plateau region was found from $\sim +0.35$ to >0.60V *vs.* SCE corresponding to oxidation of disk-produced Cu^{+} species. Moreover, this oxidation current varied from 26 to 27 μA (0.35 to 0.60V) which compared very favorably with a value of 26.0 μA calculated from the applied disk current of 68.0 μA (corrected for background) and the Au/Au ring-disk theoretical collection efficiency of 0.3822. We conclude that Cu^{+} species are oxidized to Cu^{++} at $\geq$0.35V vs. SCE in these solutions on an Au electrode.

In summary, we find that Cu^{++} is reduced to Cu^{+} between 0.00 and -0.26V *vs.* SCE and to Cu at ≤ -0.35V *vs.* SCE as detected on an Au ring electrode. Also on a Au ring, Cu^{+} is oxidized to Cu^{++} at $\geq +0.35$V *vs.* SCE. These results agree very well with those found by Napp *et al.* (27) on a Pt electrode in 0.5M KCl containing 10^{-3}M Cu^{++}. Similar data are reported by Miller also (7, 23).

Zn^{++} *reduction on an* Hg/Au *amalgam in 0.5M* NaCl. —Since the reversible potential for Zn^{++} reduction is well below that at which H_2 is evolved on an Au electrode, we amalgamated our Au ring with Hg. Cyclic scan experiments were then carried out between the limits 0.0 and -1.6V *vs.* SCE. Scan speed was varied, as was the concentration of Zn^{++} in the electrolyte ($ZnCl_2$, Baker Analyzed Grade).

In 10^{-3}M Zn^{++} solution, a plateau was observed at < -1.0V *vs.* SCE which depended on rotation speed,

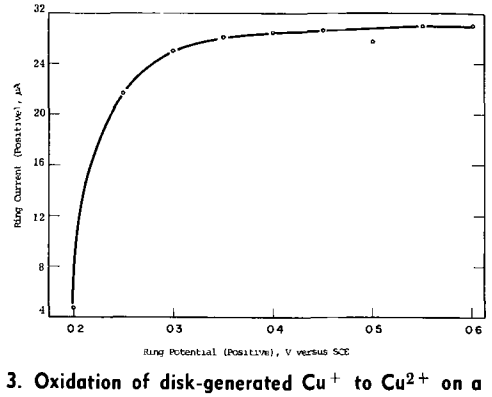

Fig. 3. Oxidation of disk-generated Cu^{+} to Cu^{2+} on a rotating Au ring electrode (500 rpm) as a function of ring potential in deaerated 0.5M NaCl containing 10^{-3}M Cu^{2+}.

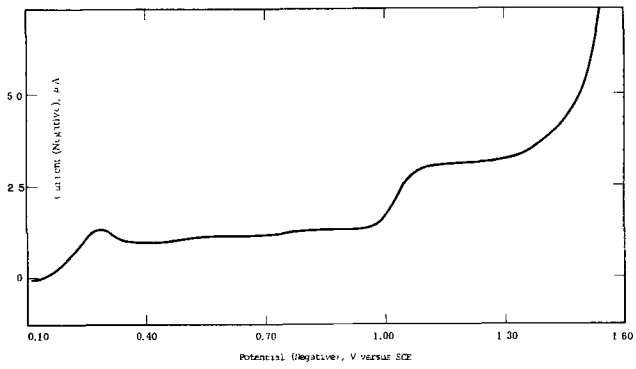

Fig. 4. Reduction of 10^{-5}M Zn^{2+} on a rotating Hg/Au amalgam ring electrode in 0.5M NaCl at ambient temperature (scan speed = 0.03 V/min).

increasing with increase in ω. Plateau currents plotted against $\omega^{1/2}$ according to the limiting diffusion equation (29) showed a straight line behavior extrapolating through the origin. Experimental and calculated currents assuming D_{Zn++} equals D_{Cu++} (the diffusion coefficients for the two species) and assuming a two-electron transfer process ($Zn^{2+} \rightarrow$ Zn), agreed very well.

Only a slight shift ($\sim$0.10V) in the potential region of the plateau current with scan speed and Zn^{++} concentration, was observed. Figure 4 shows a typical scan (0.03V/min) in 10^{-5}M Zn^{++}. The current is small to near -1.0V where a sharp increase is obtained. This levels out to a plateau at -1.1V and stays constant to -1.36V when H_2 evolution causes a sharp increase in current. The plateau current on this figure, corrected for the relatively large background value, also agreed with the calculated value.

We conclude from these data that Zn^{++} can be detected on an Hg/Au amalgam electrode at $-1.1\text{V} \geq E \geq -1.36$V *vs.* SCE which is not dissimilar from Miller's results (23) is neutral ammoniacal media.

Having confirmed these various potential regions in our solutions, we were now in a position to investigate the corrosion mechanisms of Cu and naval brass disks using Au and Hg/Au ring electrodes as detectors.

Corrosion of Cu *in 0.5M deaerated* NaCl.—Measurements were carried out at 500 rpm in unbuffered 0.5M NaCl (*p*H $\sim$ 6.5) deaerated as described. The Cu ring was normally held at $+0.60$V, -0.20V, and -0.60V to detect Cu^{+}, Cu^{++}, and both of these, respectively. The Cu disk (and ring) were polished before use as described. Disk corrosion current was varied from $+0.5$ to $+180$ μA. The disk area was 0.19 cm^2 and the theoretical collection efficiency (N) of this assembly was 0.3762.

Generally in this and in all other similar experiments, the assembly was immersed in the NaCl solution and deaeration commenced. After $\sim$30 min when the disk potential was normally constant, N_2 was passed over the solution, and the ring potentiostatted at the potential of interest. After $\sim$30 min a constant background current was observed at all potentials. The disk was then corroded and the ring current followed with time on a milliammeter. Disk potential measured in a separate experiment varied from -0.28 to -0.17V as the applied corrosion current was varied from 2.25 to 180 μA. When constant values for ring current were obtained, generally within 10 sec, the disk current was switched off and ring current followed with time. Normally this fell rapidly to its background value within 10 sec. The solution *p*H on commencement of these experiments (and those on naval brass) was $\sim$*p*H 6.5 and generally fell to $\sim$*p*H 4.7 on completion of the experiments. A typical sequence of the above events at -0.60V is shown in Fig. 5.

This indicates a sharp increase in I_r at all values of I_d. A 2-sec offset from zero time is apparent due to the cumulative effects of double-layer charging, transit time of dissolution species from disk to ring, and sim-

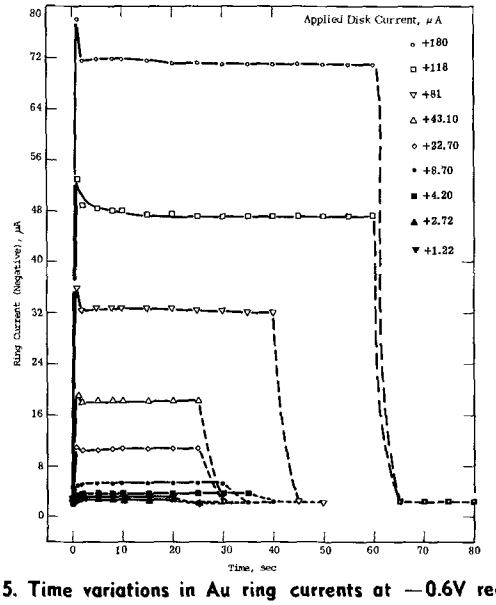

Fig. 5. Time variations in Au ring currents at −0.6V reduction of Cu^+ produced from a Cu disk during corrosion in deaerated 0.5M NaCl at ambient temperature.

ple mechanical measurement error due to overshoot in the milliammeter when first switched on. Currents, after stabilizing out to steady values in about 2 sec, were constant thereafter. When I_d was switched off, background ring values were relatively constant within 5 sec. In practice, the final background ring value was sometimes slightly larger than its initial value, especially at high I_d. This was a negligible effect here. Background ring currents were constant in the region of 2.1 μA. This is a large correction factor at small I_d, however, it was constant and as just noted, was corrected for using the value read 10 sec after each measurement. No noticeable variations in results were observed, even when the background current varied by a factor of as much as 5.

Figure 6 summarizes the results of Fig. 5 together with similar data with the ring at +0.60V *vs.* SCE both corrected for background and plotted against I_d. A linear relationship is apparent over the entire disk corrosion range. The theoretical plot assuming dissolution

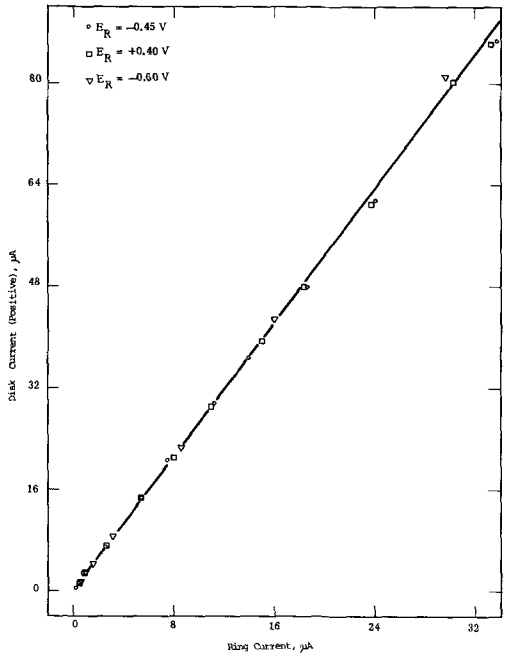

Fig. 6. Background corrected Au ring currents as a function of Cu disk corrosion currents in deaerated 0.5M NaCl at ambient temperature.

as Cu^+ solely and a value for N of 0.3762 agrees with the experimental plot exactly.

A further point may be made. Since the results at +0.60 and −0.60V (SCE) are mirror images of each other then obviously no Cu^{2+} is formed on corrosion. This was substantiated further by corroding the disk and measuring I_r with the ring at −0.20V *vs.* SCE. No increase in ring current was observed up to 180 μA I_d.

We conclude from the foregoing that in our solutions, Cu corrodes solely via Cu^+ up to ~900 μA/cm² disk corrosion current. No film formation or homogeneous solution reactions are observed.

Miller's results (7) on 70/30 brass in neutral NH_3-NH_4 salt solutions were shown to correspond to the *p*H region where Cu^{2+}-NH_3 couples begin to etch Cu (and Zn) with Cu^+-NH_3 complexes as product (31, 32). Low currents produced Cu^+ and high currents (>5 mA/cm²) produced Cu^{2+}, the polarization being a function of free NH_3 concentration and therefore of *p*H. Cu_2O formation was not observed although its possible formation was noted under less vigorous mass transport conditions. In contrast to this, Cu_2O was found during Cu corrosion in more basic, NH_3 free, 1*N* NaOH solutions (23). No film free dissolution occurred in 1*N* NaOH even at the lowest current density employed (~10 μA/cm²). Above 400 μA/cm², Cu^{2+} species were produced after the Cu_2O passivation step.

The latter observations are in accordance with the published Pourbaix (33) diagrams for Cu in aqueous solutions. Hence it is apparent from the diagrams that at sufficiently noble potentials (high anodic polarization currents) dissolution of Cu takes place as Cu^{2+} and not Cu^+. At less noble potentials (lower anodizing currents) Cu_2O formation is also indicated especially in more basic solutions. In the present experiments, as outlined above, no Cu^{2+} was found and film free dissolution of the metal occurred as Cu^+. Separate measurements showed that at each corrosion current, a single potential plateau for the metal was established immediately which had a value of < -0.17V *vs.* SCE even at the highest current employed (~900 μA/cm²). It seems unlikely that under these conditions of potential, *p*H, and salinity any Cu_2O or Cu^{2+} would be expected (33). As noted by Bertocci (34), in solutions containing halide ions, the activity of Cu^+ ions is depressed by the complexing reaction

$$Cu^+ + 2Hal^- \rightleftharpoons CuHal_2^-$$

This would then serve to facilitate dissolution of the metal via Cu^+ as is indeed observed.

The results illustrate the usefulness of the ring-disk electrode in corrosion studies. The extension of these techniques to a more complex dissolution process involving naval brass is described below.

Corrosion of naval brass in 0.5M deaerated NaCl.—More substantial data on a naval brass disk were obtained in an exactly similar manner to that for pure Cu. In this case, interpretation of the results was complicated by the dissolution of Zn^{++} also from the alloy necessitating the use of the Hg/Au amalgamated ring. Measurements in unbuffered 0.5*M* NaCl solutions are described. A theoretical value for N of 0.3973 was used in this case.

In all of these experiments the alloy potential increased linearly with the logarithm of applied current. Only a single time independent plateau was observed at each current. The disk potential, measured in a separate experiment, varied from −0.336 to −0.22V as the disk corrosion current was varied from 1.4μ to 89 μA.

Typical I_r *vs.* time curves before and after disk corrosion for a ring potential of −0.60V *vs.* SCE followed the general trends observed with pure Cu. Figure 7 summarizes the results of these data and also others at +0.60V, all corrected for background, and plotted as I_d *vs.* I_r. As with pure Cu, results at the two potentials are mirror images and fall on the same line indicating that no Cu^{++} is formed under these circumstances.

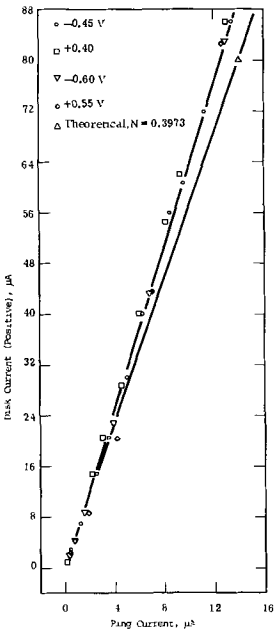

Fig. 7. Background corrected Au ring currents as a function of naval brass disk corrosion currents in deaerated 0.5M NaCl at ambient temperature.

This was further verified by results at −0.20V *vs.* SCE where no reduction of Cu^2 to Cu^+ was observed at the ring during disk corrosion.

The composition of the alloy is 60.54 w/o Cu, 38.70 w/o Zn, and 0.76 w/o Sn. Neglecting the small Sn content this corresponds to 61.15 a/o Cu and 38.85 a/o Zn. Assuming alloy dissolution in this atom per cent (a/o) ratio, *i.e.*, simultaneous dissolution of both components, we would expect that the fraction of the applied disk corrosion current (I_d) resulting in the production of Cu^+ species would equal

$$\frac{\text{a/o Cu}}{(1 \times \text{a/o Cu}) + (2 \times \text{a/o Zn})} I_d \qquad [1]$$

The calculation assumes no selective Zn^{++} dissolution, Cu^+ redeposition or film forming reactions (and of course, no dissolution as Cu^{++} as we have already shown). In addition, for a ring collection efficiency of $N = 0.3973$, the observed ring current from further ring oxidation to Cu^{2+} of corroded Cu^+ species, if dissolution proceeds in the stated a/o ratio should be

$$\frac{\text{a/o Cu}}{(1 \times \text{a/o Cu}) + (2 \times \text{a/o Zn})} \times 0.3973\, I_d \qquad [2]$$

or

$$0.1749\, I_d \qquad [3]$$

Based on the above, a theoretical line is shown also in Fig. 7 which is clearly different from the observed value. Hence at 80 μA I_d, I_r observed is 12.6 μA compared to I_r calculated of 14.0 μA, *i.e.*, 1.4 μA lower. Though this is not a large value of current, it is nevertheless almost 10% lower than the calculated value and was experimentally reproducible. It is interesting to note that the partial current for Cu^+ corrosion from the brass plotted as a function of disk potential, agreed quite well with the Cu^+ polarization curve for the pure metal. That is Cu corrosion from the alloy occurs at the same rate as in the pure metal. Similar results are reported by Pickering and Byrne (24) for γ- and α-brasses.

To examine the causes for the discrepancy between calculated and experimental Cu^+ corrosion currents, *e.g.*, selective dissolution of the Zn in the alloy, we amalgamated the ring as described and carried out exactly similar experiments, this time with the ring potentiostated at −1.3V *vs.* SCE. Here all dissolved species are plated out at the ring. I_r should therefore equal

$$0.3973\, I_d \qquad [4]$$

This holds true in the event that any preferential dissolution of Zn occurs by redeposition of Cu^+.

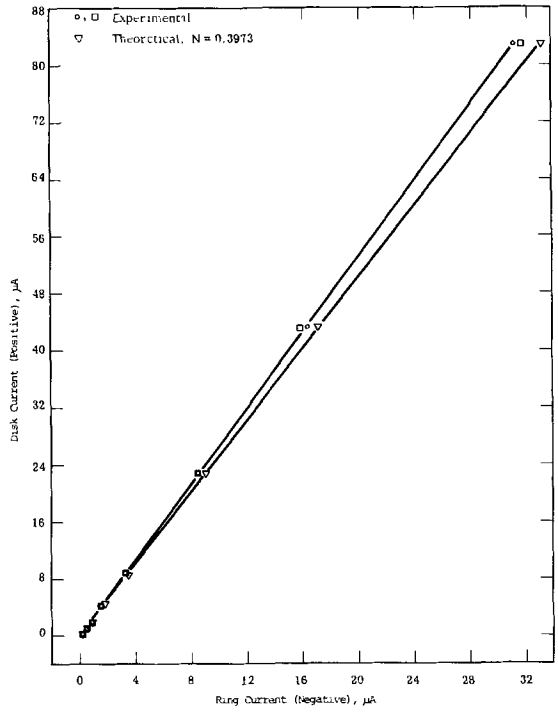

Fig. 8. Background corrected Hg/Au amalgam ring currents at −1.3 V as a function of naval brass disk corrosion currents in deaerated 0.5M NaCl at ambient temperature.

A typical I_r *vs.* time plot followed the trends outlined earlier (Fig. 5) during and after disk corrosion for a ring potential of −1.3V *vs.* SCE. The current levels were higher here as expected. Figure 8 shows the results of this experiment and a repeat of the same illustrating the I_r *vs.* I_d relationships. Also shown is a theoretical line according to Eq. [4]. Clearly, again, the data do not coincide but deviate by 1.6 μA at an I_d value of 80 μA. The calculated increase in ring current (due to $Zn^{++} \rightarrow Zn$) at a disk corrosion current of 80 μA when the ring potential is moved from ±0.60 to −1.3V, is 17.7 μA. The measured increase is 17.4 μA. This suggests that the discrepancy in the data is due to the Cu in the alloy undergoing some further reaction either at the disk or in transit to the ring and also eliminates the supposition that Zn^{++} is selectively corroded from the alloy or that Cu^+ redeposition occurs. This is in accord with Pickering (24) and Feller's (22) results which show that preferential dissolution of Zn from Cu-Zn alloys occurs more predominantly with Zn-rich than with Cu-rich alloys.

Most likely, a homogeneous solution reaction involving a fraction of the corroded Cu^+ species can account for the discrepancy between calculated and observed ring currents. Soluble CuCl can readily hydrolyze (to Cu · OH) before reaching the ring electrode and will not then be picked up there. Again, the hydrolysis product may well redeposit nonelectrochemically on the alloy surface in a manner similar to that outlined by May (35) during pitting corrosion and film formation on Cu and its alloys in Cl^- media. The second possibility is of course that some film formation, possibly Cu_2O, occurs directly on the corroding surface. In further experiments where the electrode was rotated more rapidly (2000 rpm) and the measurements repeated at −1.3V *vs.* SCE, the theoretical and experimental lines now coincided. This then substantiates the homogeneous reaction theory. In the event that a film is found on the surface, it can only be deposited there by a nonelectrochemical deposition of insoluble hydrolysis products formed from soluble corroded Cu^+ species.

It is more difficult to explain the occurrence of this phenomenon in the brass alloy as compared to pure Cu under exactly similar conditions. The explanation may be in the fact that the alloy surface offers more

favorable redeposition sites as compared to a pure Cu surface. The suggestion is very tenuous however, and the effect requires detailed experimentation in these and more basic NaCl solutions. Preliminary results in the latter media do reveal significant film forming reactions. These data and results on other alloy systems at increased temperatures will be reported subsequently.

Summary and Conclusions

1. The rotating ring-disk system has been used to investigate pure Cu and naval brass corrosion in saline solutions. The various diffusion-limited potential regions for oxidation and/or reduction of Cu^+, Cu^{2+}, and Zn^{2+} in these environments on Au and/or Hg/Au amalgam electrodes are reported.

2. The technique has been shown to be amenable to corrosion investigations. Dissolved disk species are readily identifiable at the rotating rings potentiostatted at predetermined potentials. Homogeneous and film forming reactions can also be distinguished readily.

3. Over the range $\sim 2.5 \times 10^{-6}$ A/cm^2 to $\sim 900 \times 10^{-6}$ A/cm^2 pure Cu corrodes solely via Cu^+ in 0.5*M* NaCl solutions at ambient temperature. No Cu^{2+} species are found nor is any evidence presented for film formation or homogeneous reactions of any kind.

4. Over the range $\sim 1.4 \times 10^{-6}$ A/cm^2 to $\sim 450 \times 10^{-6}$ A/cm^2, naval brass corrodes readily via Cu^+ and Zn^{2+} in these solutions. No Cu^{2+} species are found. No preferential dissolution by selective dissolution of Zn or a Cu^+ redeposition mechanism is indicated. Some evidence for a homogeneous reaction is found. Any films formed are caused by a nonelectrochemical redeposition process involving homogeneously produced species rather than direct film formation on the surface.

Acknowledgments

This work was supported by the Office of Saline Water, Department of the Interior, under Contract No. 14-01-0001-1730, with Dr. Francis Coley acting as contract monitor.

Manuscript submitted June 10, 1970; revised manuscript received Jan. 14, 1971.

Any discussion of this paper will appear in a Discussion Section to be published in the December 1971 JOURNAL.

REFERENCES

1. B. C. Y. Lu and W. F. Graydon, *Can. J. Chem.*, **32**, 153 (1954).
2. D. J. G. Ives and A. E. Rawson, *This Journal*, **109**, 447 (1962).
3. R. May, *J. Inst. Metals*, **32**, 65 (1953-1954).
4. A. N. Frumkin and L. N. Nekrasov, *Doklady Akad. Nauk, SSSR*, **126**, 115 (1959).
5. A. N. Frumkin, L. N. Nekrasov, V. Levich, and Ju. Ivanov, *J. Electroanal. Chem.*, **1**, 84 (1959)
6. L. N. Nekrasov and N. P. Berezina. *Doklady Akad. Nauk, SSSR*, **142**, 855 (1962).
7. B. Miller, *This Journal*, **116**, 1675 (1969).
8. G. D. Bengough and R. May, *J. Inst. Metals*, **32**, 81 (1924).
9. F. W. Fink, *Trans. Electrochem. Soc.*, **75**, 441 (1939).
10. G. Masing, *Wiss. Veröff-Siemens-Konzern*, **10**, 41 (1931).
11. V. F. Lucey, *Brit. Corrosion J.*, **1**, 9 (1965).
12. V. F. Lucey, *ibid.*, **2**, 53 (1965).
13. E. E. Langenegger and F. P. A. Robinson, *Corrosion*, **25**, 136 (1969).
14. G. Wranglen, *This Journal*, **108**, 1069 (1961).
15. C. W. Stillwell and E. S. Turnipseed, *Ind. Eng. Chem.*, **26**, 740 (1934).
16. C. P. Polushkin and H. L. Shuldener, *Trans. AIME*, **161**, 216 (1945).
17. M. Pruna, B. LeBoucher, and P. Lacombe, *Rev. Inst. Franc. Petrole*, **6**, 145 (1951).
18. K. Hashimoto and S. Ogiva, *Trans. Japan Inst. Met.*, **4**, 42 (1963).
19. H. Sugawara and H. Ebiko, *Corrosion Sci.*, **7**, 513 (1967).
20. G. Joseph and M. T. Arce, *ibid.*, **7**, 597 (1967).
21. H. W. Pickering and C. Wagner, *This Journal*, **114**, 698 (1967).
22. H. G. Feller, *Corrosion Sci.*, **8**, 259 (1968).
23. B. Miller, *This Journal*, **116**, 1117 (1969).
24. H. W. Pickering and P. J. Byrne, *ibid.*, **116**, 1492 (1970).
25. H. W. Pickering, *ibid.*, **117**, 8 (1970).
26. E. Mattson, *Electrochim. Acta*, **3**, 279 (1961).
27. D. T. Napp, D. C. Johnson, and S. Bruckenstein, *Anal. Chem.*, **39**, 481 (1967).
28. R. H. Sonner, B. Miller, and R. E. Visco, *ibid.*, **41**, 1498 (1969).
29. W. J. Albery and S. Bruckenstein, *Trans. Faraday Soc.*, **62**, 1920 (1966).
30. D. C. Johnson, Ph.D. Thesis, University of Minnesota, University Microfilms, Inc., Ann Arbor, Michigan. p. 87 (1967).
31. *Wash. Corr. Dialogue*, **25**, No. 272, 56 (1969).
32. G. J. L. Booker, Proc. Conf. Fund. Aspects of S.C.C. Dept. of Metallurgical Engineering, Ohio State Univ. 178, Sept. (1967) Publ. N.A.C.E. 1969.
33. M. Pourbaix, "Atlas of Electrochemical Equilibria in Aqueous Solutions," Pergamon Press, New York (1966).
34. U. Bertocci, *Electrochim. Acta*, **11**, 1261 (1966).
35. R. May, *J. Inst. Metals*, **32**, 1497 (1953-1954).

A Study of the Anodic Oxidation of Vanadium

B. H. Ellis, M. A. Hopper*,[1] and D. J. De Smet*

Department of Physics, University of Alabama, University, Alabama 35468

ABSTRACT

The anodic oxidation of vanadium in acetic acid-sodium tetraborate solutions containing small amounts of water has been studied over a potential range of 100V using the open-circuit transient analysis technique. An anodic layer which showed bright uniform interference colors was found to grow on the metal surface. Results of these experiments indicate that the dependence of the oxidation current density, i, on the formation potential, V, is expressible in the form $i = i_0 \exp(V/V_0)$, where i_0 and V_0 are parameters determined from the data analysis. The parameter i_0 is found to depend on the applied current density, while the parameter V_0 varies directly with the formation potential during galvanostatic oxidation. A result in this form implies that the electric field in the oxide is a function of the applied current density. These results show similarities to results previously obtained by others for the anodic oxidation of bismuth, tantalum, and iron.

Even though the anodic oxidation of several metals has been extensively studied (1), vanadium has received little attention. One reason for this has been the difficulty in forming an anodic film on vanadium. A study by Johansen, Adams, and Van Rysselberghe (2) of a number of metals, including vanadium, in an aqueous boric acid-ammonia solution at 25°C indicated that no anodic film would form on vanadium under these conditions. Young (1) suggests, but does not verify, that an anodic film might be formed on vanadium if a partly nonaqueous electrolyte were used. In 1965, Keil and Salomon (3) successfully formed an anodic oxide film on vanadium in acetic acid-sodium borate-water solutions. By using this almost completely nonaqueous electrolyte they overcome the problem, experienced in the past by others, of the solubility of the anodic oxide product in aqueous solutions. In a later work (4), they studied some of the chemical and electrical properties of the vanadium anodic oxide film. From these studies they concluded, among other things, that the oxidation state of the vanadium was not a function of the potential to which the vanadium was oxidized, the anodic film was V_2O_4, and, for constant current growth, a linear dependence of the growth rate on the current density necessitated that the electric field in the oxide layer be constant.

The intentions of the present study were to determine the electrical properties of vanadium oxide films by use of open-circuit transient analysis and to identify other physical properties of the oxide film. The open-circuit transient analysis technique has been used in the study of the anodic oxidation of several metals (5-10). Its use in the study of the vanadium oxide film, and a comparison of these results with results found in the studies of other metals, will help to determine the general properties of the anodic oxidation of metals.

Experimental

The samples used in this study were high-purity (99.98%) vanadium, ¼ in. diameter rods of varying lengths, purchased from Materials Research Corporation. Each sample was drilled along its axis, mechanically polished, and mounted between Teflon washers in an electrode assembly similar to the one detailed by Feller and Osterwald (11). This assembly was then immersed in a solution of 25% sulfuric acid, 70% orthophosphoric acid, and 5% nitric acid for about 30 sec. After rinsing with distilled water and drying, each sample was anodically oxidized to a potential of 50V, then the oxidation product was dissolved by immersing the electrode assembly in distilled water. This anodic oxidation and removal of the oxide was repeated several times prior to using a sample for actual measurements in order to insure reproducibility.

The electrical circuitry used was identical to that described by De Smet and Hopper (5). Current densities were calculated by dividing the applied current by the exposed macroscopic surface area of the vanadium sample. A Sanborn 7700 strip chart recorder was used to record potentials and open-circuit transients.

The electrolyte solution used in this study was similar to that described by Keil and Salomon (4) with a reduction of the water content. Nineteen grams of $Na_2B_4O_7 \cdot 10\ H_2O$ were added per liter of glacial acetic acid, this solution was heated to 60°C, and just sufficient water was added to dissolve all the salt (31 ± 1.5 ml of water per liter of acetic acid). Other nonaqueous solvents, including formamide and ethylene glycol (with various added salts), were tried but these would not sustain the formation of a vanadium oxide film. The solutions were bubbled with argon prior to and throughout the experiments.

A jacketed five-necked flask was used for the cell. The electrode assembly, a coiled platinum wire cathode, a platinum wire reference electrode, a thermometer, and a gas dispersion tube were fitted through the standard taper joints of the cell.

Preliminary experiments indicated that the vanadium anodic oxide film exhibits a photoeffect (or photoeffects) at visible wavelengths; therefore, all experiments were conducted in a darkened room, and the cell was draped with a black cloth to preclude light from reaching the cell.

The effect of temperature on the layer was also studied. The acetic acid-sodium tetraborate solution freezes at 12°C, which marks the lower temperature limit. Other experiments were conducted at temperatures of 24°, 35°, and 40°C. For experiments conducted near or above room temperature, temperatures were controlled by a Haake Model F constant temperature circulator, which circulated water through the jacket of the cell. For experiments conducted at 12°C, the electrolyte was cooled by immersing the cell in an insulated container filled with shaved ice. After the immersion, the temperature fell from 24° to approximately 10°C, then rose to 12°C. Once the temperature stabilized at 12°C, in a period of about 30 min the solution froze solidly.

Although the vanadium oxide film would not form on a clean surface using the low current densities which we were interested in investigating, a low current density will sustain growth once some oxide is present on the surface. For this reason, the following procedure was used to study the growth of the oxide at low current densities: vanadium oxide was formed on

* Electrochemical Society Active Member.
[1] Present address: Department of Physics, University of Waterloo, Waterloo, Ontario, Canada.
Key words: vanadium oxide, anodic oxide.

the clean surface at a high current density (about 500 μA/cm^2), then the current was switched to the required lower current density (10, 30, or 100 μA/cm^2) after an initial oxide film was formed. This procedure allowed open-circuit voltage decay experiments to be performed from desired current densities and formation potentials.

Results

If one considers an oxide film on a metal surface to be equivalent to a capacitor with a dielectric medium (which in some manner carries a small current) located between the capacitor plates, then the differential equation describing such a circuit is given by

$$C\,dV/dt + i = i_e \qquad [1]$$

where i is the current density through the film, i_e is the externally applied current density, V is the potential across the layer, and C is the capacitance per unit area of the layer.

The initial portions of the experimental open-circuit transients obtained for vanadium fit an expression of the form

$$V = k - V_o \log(t + \theta) \qquad [2]$$

very well. Here V_o, k, and θ are parameters which depend on the particular transient and its initial conditions. It follows, by differentiating Eq. [2] and substituting into Eq. [1], with $i_e = 0$, that the expression for the current density through the film may be written as

$$i = i_o \exp(V/V_o) \qquad [3]$$

where i_o and V_o are experimental parameters with the same dimensions as i and V, respectively. This derivation includes certain assumptions which have been discussed previously (5, 8). As the potential decays when the circuit is opened, a point in potential or time is reached where these assumptions no longer apply; hence, Eq. [2] will not describe the potential decay beyond this point. Basically, Eq. [3] is a high-field ionic conduction relation and would thus not be expected to describe the entire open-circuit potential decay, especially when the potential drop across the oxide approached zero.

Each open-circuit transient was recorded and analyzed graphically by plotting V *vs.* $\log(t + \theta)$, which was found to be a straight line for a properly chosen value of θ. Transients fit the expression of Eq. [2] over at least 1½ decades of time, corresponding to approximately a 90% decay in the potential at current densities of 100 μA/cm^2 and a 65% decay in the potential at current densities of 10 and 30 μA/cm^2. This type of analysis of open-circuit transients was described by Grahame (12), and has been used in studies of the anodic oxidation of several metals (5-10).

A series of open-circuit potential decays was recorded at intervals during galvanostatic oxidation. These transients were then analyzed to determine values for V_o and θ. To avoid confusion in terminology, we designate the current density immediately prior to the opening of the circuit as the formation current density. Also, the term formation potential designates the overpotential at which the open-circuit transient was initiated.

Figure 1 shows the values of the parameter V_o obtained from several typical sets of transients as a function of the formation potential at room temperature for three values of the formation current density: 10, 30, and 100 μA/cm^2. For each formation, current density V_o increases with formation potential and each plot is linear, at least to a formation potential of 50V (within experimental error). All lines pass through the zero of formation potential. For the largest value of the formation current density, 100 μA/cm^2, the plot of V_o *vs.* formation potential shows a noticeable change in slope at about 60V. The differences in the slopes for these three values of current density are readily apparent.

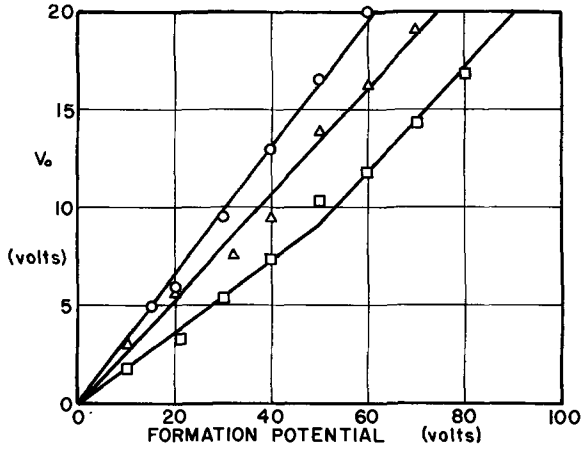

Fig. 1. Dependence of V_o on formation potential for vanadium at room temperature. The formation current density was 10 μA/cm^2 for the data represented by the circles, 30 μA/cm^2 for the data represented by the triangles, and 100 μA/cm^2 for the data represented by the squares.

A plot of the reciprocal capacitance *vs.* formation potential for current densities of 30 and 100 μA/cm^2 is shown in Fig. 2. The reciprocal capacitance is calculated from the relation $1/C = V_o/(i_e \cdot \theta)$, obtained from the boundary conditions of Eq. [1]. This result shows that the reciprocal capacitance varies with formation potential, and there are two distinct changes in slope occurring at approximately 40 and 60V. Since the parameter θ found for the open-circuit transients on vanadium can be obtained only within 10%, this error will show up directly in the reciprocal capacitance. As a result, the reciprocal capacitance-potential plots have only qualitative significance.

The plots of formation potential *vs.* time were much the same as those reported by Keil and Salomon (4) at room temperature, with the same three distinct regions of time rate of change of formation potential. This experiment conducted at various temperatures indicates a dependence of dV/dt on temperature above an overpotential of 10V. Figure 3 shows the results for a formation current density of 500 μA/cm^2 at temperatures of 12°, 24°, and 35°C. The slopes of the lines for these temperatures are 0.084, 0.075, and 0.0625 V/sec, respectively. Figure 4 shows dV/dt (above a potential of 10V) *vs.* formation current density for the same temperatures and supports the dependence of dV/dt on temperature.

The effects of visible light on the formation potential of the vanadium anode while undergoing galvanostatic oxidation is shown in Fig. 5. During galvanostatic

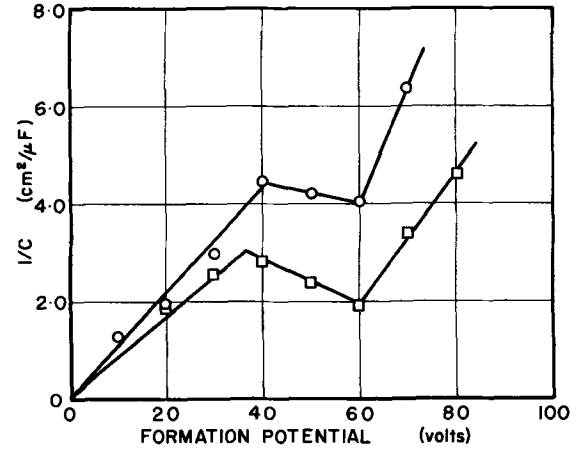

Fig. 2. Dependence of the reciprocal capacitance on formation potential. The formation current density was 30 μA/cm^2 for the data represented by the circles and 100 μA/cm^2 for the data represented by the squares.

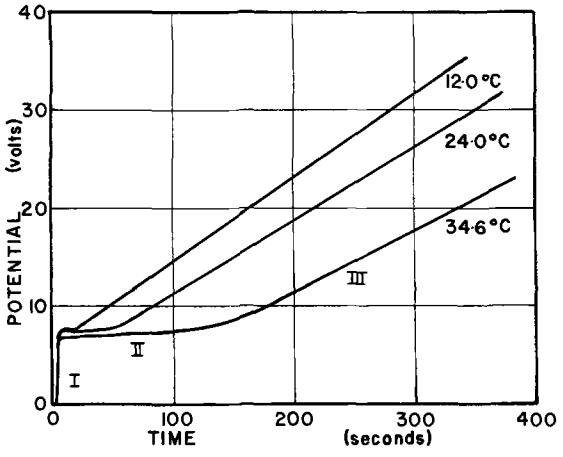

Fig. 3. Potential vs. time at a constant current density of 500 μA/cm^2 at the indicated temperatures. The vanadium sample was clean at the beginning of each experiment.

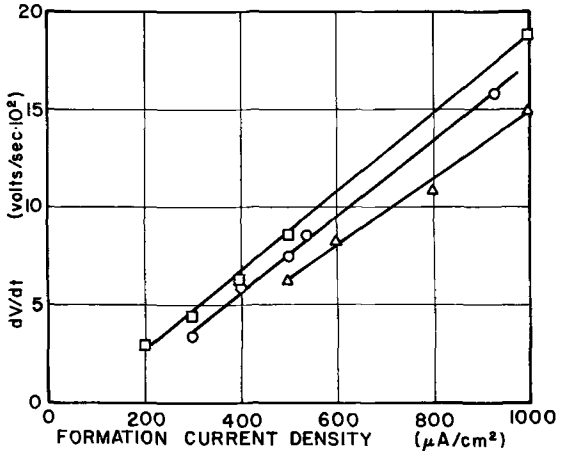

Fig. 4. The rate of change of potential (above a potential of 10V) as a function of the formation current density. The temperature was 12°C for the data represented by the squares, 24°C for the data represented by the circles, and 35°C for the data represented by the triangles.

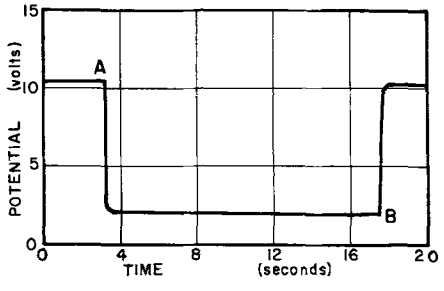

Fig. 5. Potential vs. time with an applied current density of 3 μA/cm^2. At point A the electrode was illuminated with visible light, and at point B the light was removed.

oxidation with an applied current density of 3 μA/cm^2, a high-intensity light was shone on the electrode. The light produced a sharp decrease in the potential, which returned to its original value upon removal of the light. Several experiments of this kind showed an increase of the photoeffect (that is, the voltage drop) with an increase in the formation potential under galvanostatic conditions and a decrease in the photo effect with increasing formation current densities. At a fixed current density, the per cent voltage drop when the electrode was illuminated was approximately constant. No attempt was made to vary the intensity of the illumination.

In order to facilitate the discussion which follows, a potential transient in which the applied current

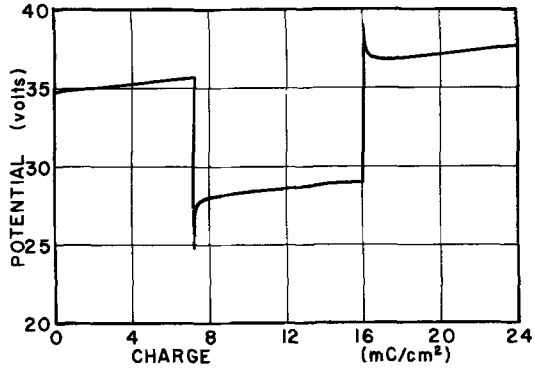

Fig. 6. Potential vs. charge for a transient in which the current density was switched from 500 to 100 μA/cm^2 and then back to 500 μA/cm^2.

density was switched from 500 to 100 μA/cm^2 and then back to 500 μA/cm^2 was recorded and is shown in Fig. 6. The speed of the strip chart recorder was slowed by a factor of five when the current density was lowered, and then switched back to its original speed when the current density was returned to its original value, thus giving a plot of potential *vs.* charge. This figure shows a potential overshoot when the current density is abruptly changed. This type of overshoot is typical of many materials undergoing anodic oxidation (1, 5, 6, 8).

Discussion

Several authors (1) interpret the theoretical relation for an exponential dependence of the current density through the anodic oxide film on the formation potential as an activation energy-controlled process. For the high-field case, this relationship is given as

$$i = 2\,anv \exp -\,(W - \lambda eaE/kT) \qquad [4]$$

where a is the half barrier width, n the density of charge carriers, ν the ion oscillation frequency, W the activation energy for the process, λ the valence of the charge carrier, and E the electric field at the activation barrier. The average electric field in the layer is the formation potential divided by the thickness of the layer (5-10). Taking the electric field at any barrier (*i.e.*, the local electric field at the barrier) equal to the average electric field in the layer, then Eq. [3] and [4] yield

$$V_0 = (kT/\lambda ea)\,D \qquad [5]$$

where D is the thickness of the layer. Therefore, if one uses this model, V_0 is directly proportional to the thickness of the oxide layer, D, assuming λ and a are constants, independent of current.

The data displayed in Fig. 1 support this type of model by showing that the values of V_0 vary directly with the formation potential for any value of the constant current density. For different values of formation current densities, the slopes of the data differ, indicating that the field in the layer depends on the formation current density. Another estimate of the thickness of the oxide layer can be seen in the data presented in Fig. 2, which shows the reciprocal capacitance proportional to the formation potential, at least for potentials below 40V. Assuming that the oxide layer acts like a parallel plate capacitor, this indicates that the capacitance of the layer is proportional to the layer thickness, as might be expected.

In Fig. 3, the data show that the potential growth pattern falls in three distinct regions, labeled I, II, and III, as reported by Keil and Salomon (4). The first region is an almost instantaneous potential rise from the zero current value to a potential value that is dependent on several factors, including the type of electrolyte used and the formation current density. This region can most likely be attributed to the ohmic voltage across the electrolyte. A second region follows

and is distinguished by a slow time rate of change of the potential. Also, the length of region II is found to depend on the formation current density and the temperature of the electrolyte. The work of Keil and Salomon (4) shows that most of the charge passed in region II goes into the production of V^{+4} ions in solution. This type of behavior is completely analogous to the active state region on the passive metals such as iron, *etc.* [see Ref. (1)], and its length is known to depend on the applied current density, the solution concentration and temperature, *etc.* This region appears to exist until the potential reaches a certain value, called the transition potential by Keil and Salomon, which is also dependent on the aforesaid factors. Once the potential reaches this value, the time rate of change of potential becomes much greater and remains at this value for the rest of the oxide layer growth.

Experiments were conducted with the photoeffects to attempt positive identification of the different types of photoeffects present in the vanadium system. Figure 5 indicates that photoconductivity is present during visible light irradiation of the oxide film. Using an accepted definition of photoconductivity as a change in the conductivity of the oxide layer due to the absorption of radiation, and using the results of Gudden and Pohl's experiments in photoconductivity as reported by Bube (13) which show photoconductivity to be a volume effect, our data clearly indicate its presence in this study. The data shown in Fig. 5 and similar data taken at varying formation potentials show the photoeffect to be dependent on the thickness of the oxide film, thus a volume effect. Similar data were reported for the photoeffect on bismuth anodic oxide films by De Smet and Hopper (5). This change in conductivity of the oxide layer is probably an electronic current added to the normal ionic current in the oxide layer. We believe that other photoeffects, perhaps including surface effects, may also be present in this system, but attempts to verify this have not been successful.

Figure 4 shows the dependence of dV/dt on the formation current density at three different temperatures. These results show that dV/dt varies approximately linearly with formation current density. This figure does not, however, imply that the electric field within the layer is independent of the formation current density. Figure 7 shows the same data as Fig. 4, this time presented in a somewhat different manner. Here we have assumed that the current efficiency of layer growth is 100%, that is all of the charge passed into layer formation (a conclusion of Keil and Salomon) and calculated $dV/dQ = (1/i) \cdot (dV/dt)$. This quantity should be proportional to the electric field within the layer. In Fig. 7, this quantity is plotted as a function of the formation current density and it is clear that dV/dQ is not a constant, independent of current density. [In Fig. 7, the lines have been drawn in merely to show the trend of the data and do not necessarily imply an exactly linear relation between dV/dQ and $\log(i)$.]

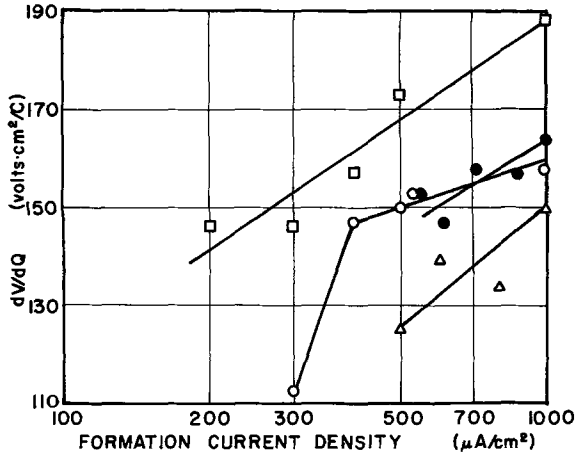

Fig. 7. Dependence of dV/dQ on the formation current density. The data represented by the squares were taken at a temperature of 12°C, the open circles at 24°C, and the triangles at 35°C. The data represented by the filled circles were taken from Ref. (4).

Figure 6, which shows potential *vs.* charge as the formation current density is switched from one value to another, demonstrates the same point. First, if the electric field were independent of formation current density, then the slopes of the linear portions of the curves at different currents would be identical. In fact, the slope of the linear portion of the curve at the lower current density is slightly smaller than that at the higher current density. Second, when the current density is lowered, the potential falls (even if the potential overshoot is ignored and the linear portion of curve is extrapolated to the point where the current was switched) and, since there is no decrease in the layer thickness, the electric field in the layer must decrease. A similar argument holds for an increase in the electric field when the current density is increased.

Until this point, we have not mentioned the parameter i_o other than to say that it has the same dimensions as i. Values of i_o for vanadium can be calculated from Fig. 1 and Eq. [3]. It is difficult to give exact values for i_o for vanadium, since the errors in individual values of i_o may be 25% or more. Nevertheless, it has been found that i_o does tend to increase with increasing formation current density. This type of dependence of i_o on formation current density has been found for several other materials, and it has been suggested that it may be possible to account for the potential overshoot such as that shown in Fig. 6 by considering the manner in which i_o changes when the formation current density is changed (5, 7,8). Similar arguments may be advanced for vanadium. We feel that the physical cause of the potential overshoot, when the current density is abruptly changed, is also the cause of the changes in i_o.

The results of the present study show many features which are strikingly similar to the results of studies of anodic films on several other metals (5-10). Experiments on the anodic oxidation of bismuth (5), iron (6, 7), and tantalum (8) show that the decays of overpotential during open-circuit transients all fit the form of Eq. [2], implying a relation between current and potential in the form of Eq. [3]. All these systems also show the same type of dependence of V_o on the formation potential fixed formation current density. The slopes of V_o *vs.* potential all depend on the formation current density. All these materials (and many others which form anodic oxide films by a high-field ionic conduction process) show potential transients similar to Fig. 6 when the current density is abruptly changed. These general features must be properties of the anodic oxidation process itself and are independent of the particular system under investigation.

Manuscript submitted Oct. 26. 1970; revised manuscript received ca. Jan. 28, 1971.

Any discussion of this paper will appear in a Discussion Section to be published in the December 1971 JOURNAL.

REFERENCES

1. L. Young, "Anodic Oxide Films," Academic Press, London and New York (1961).
2. H. A. Johansen, G. B. Adams, and P. Van Ryssel-berghe, *This Journal*, **104**, 399 (1957).
3. R. G. Keil and R. E. Salomon, *ibid.*, **112**, 643 (1965).
4. R. G. Keil and R. E. Salomon, *ibid.*, **115**, 628 (1968).
5. D. J. De Smet and M. A. Hopper, *ibid.*, **116**, 1184 (1969).
6. J. L. Ord and J. H. Bartlett, *ibid.*, **112**, 160 (1965).
7. J. L. Ord, *ibid.*, **113**, 213 (1966).

8. J. L. Ord and D. J. De Smet, *ibid.*, **116**, 762 (1969).
9. J. L. Ord, *ibid.*, **112**, 46 (1965).
10. J. L. Ord and D. J. De Smet, *ibid.*, **113**, 1258 (1966).
11. H. G. Feller and J. Osterwald, *ibid.*, **111**, 119 (1964).
12. D. C. Grahame, *J. Phys. Chem.*, **57**, 257 (1953).
13. R. H. Bube, "Photoconductivity of Solids," John Wiley & Sons, Inc., New York, London, and Sidney (1960).

Anodization of Vanadium

R. G. Keil*,[1] and K. Ludwig

Department of Chemistry, University of Dayton, Dayton, Ohio 45409

ABSTRACT

A study was made of the relationship between ion current migrating through anodic oxide films on vanadium and the electrostatic field across the dielectric over a potential range of some 100V utilizing the open-circuit transient method. The results show that the relationship between the formation current density, i, and the formation potential, V, is of the form $i = i_0 \exp(V/V_0)$, where i_0 and V_0 are parameters resulting from analysis. V_0 was found to be a linear function of the formation voltage. The quantity, θ, was found to be essentially equal to zero, a result which departs from results previously reported for other metals, for example tantalum, iron, and bismuth.

We have previously reported (1, 2) that an anodic vanadium tetroxide film, which exhibits interference colors, can be grown on vanadium metal when it is subjected to anodic polarization. An anodization solution composed of glacial acetic acid, borax, and water was used. The water concentration was not critical when below 5M (molar). These results showed that the film was vanadium IV oxide formed at 100% current efficiency at the anode. Other results suggested the film was probably porous.

In this present work, we desire to study the electrical properties of this vanadium oxide film by use of open-circuit transient analysis, a method pioneered by Grahame (3) and used in the study of the anodic oxidation of several metals (4-6). Previous experimental results indicated that the anodic vanadium oxide film was porous. We were curious during this study, therefore, to determine if θ might have an abnormal value. Ord (5) has found its value to be unity. This point and the relationship between the ion current density and the electrostatic field during film growth were the main objectives of this study.

Experimental

High-purity (>99.94%), single-pass, zone-refined vanadium rods (⅜ in. diameter) purchased from Materials Research Corporation was used for this work. The electrode was mounted and prepared for anodization by methods previously described (2). Just prior to anodization, the electrode was etched in a 1:1 water-nitric acid (70% assay) solution. The electrode was then washed, first with distilled water, then with absolute ethanol, dried, and immersed in the anodization bath.

The cell used was basically the one previously used but modified to accept a saturated calomel reference electrode in contact with the anodizing solution *via* a Luggin capillary of potassium nitrate. At extremely low water and/or sodium tetraborate concentrations, films formed showed the existence of nonhomogeneous electrostatic fields as was evidenced by nonuniform interference colors across the electrode surface. In this work, we found an acetic acid solution 2.0M in water and 0.02M in sodium tetraborate was best. This solution had a conductivity of 79 micro-(ohm-cm)$^{-1}$. These studies were all carried out at 25°C. An inert ambient of argon was maintained in the reaction flask and the anodizing solution was degassed prior to use.

An anodic film did not form on the vanadium metal surface at low current densities. Therefore, the following procedure was adopted to study the film growth at low current densities. Vanadium oxide was formed on the clean metal initially at about 1500 μA/cm^2 until the overpotential exceeded 20V. Then the current was decreased in successive steps until the desired current density (32, 71, or 352 μA/cm^2) was reached. This allowed the open-circuit transients to be obtained from desired current densities and formation voltages.

A schematic of the electrical circuitry used is shown in Fig. 1. High-input-impedance differential operational amplifiers (Philbrick SP102) were used for the galvanostat and follower. These amplifiers operate over a range of ±100V. Potentials and open-circuit transients were recorded on an oscillographic recorder (Sanborn 7701B). All potentials were recorded relative to the saturated calomel reference electrode. Overpotentials were calculated from observed voltages by subtracting the value of the open-circuit potential. Apparent current densities were obtained by dividing the applied current by the macroscopic surface area of the anode.

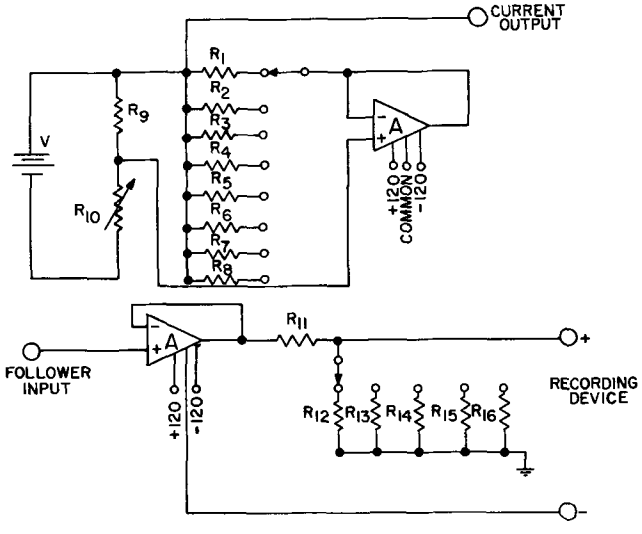

Fig. 1. Circuit schematic: A—operational amplifiers; V—Mallory TR-289, 12.6V battery; R_1—20 Mohms; R_2—2 Mohms; R_3—400 kohms; R_4—200 kohms; R_5—40 kohms; R_6—20 kohms; R_7—6 kohms; R_8—4 kohms; R_9—12.1 kohms; R_{10}—5 kohms; R_{11}—500 kohms; R_{12}—5 ohms; R_{13}—6.6 ohms; R_{14}—10 ohms; R_{15}—20 ohms; R_{16}—50 ohms.

* Electrochemical Society Active Member.
[1] Author to whom correspondence should be addressed.
Key words: vanadium, films, transients, oxide.

Results

The oxide film can be considered to be the dielectric medium of a capacitor whose plates are composed of the substrate metal and the anodizing solution. While forming, say under galvanostatic conditions, the film carries current in some manner. The external current throughout the circuit must equal the sum of the current passing through the film, plus capacitance charging. The differential equation which relates the current density through the film, i, the overpotential, V, and the external circuit current, i_e, is given by

$$i + C\,dV/dt = i_e \qquad [1]$$

Information concerning the relation between quantities in Eq. [1] can be obtained by utilizing the "open-circuit transient" method. Transients of this type (voltage *vs.* time) have been used to study the kinetics of a number of anodic oxide film systems (4-6). During an open-circuit transient, $i_e = 0$ and the differential equation describing the system becomes

$$i + C\,dV/dt = 0 \qquad [2]$$

If one can measure the change in the potential with time, the current through the anodic oxide may be determined, assuming a value for C is available.

For vanadium, the experimental voltage transients fit an expression of the form

$$V = k - V_o \ln(t + \theta) \qquad [3]$$

The quantities θ, V_o, and k are parameters which are determined by the particular transient and its initial conditions. The transient can be analyzed graphically by plotting the overpotential during open-circuit decay *vs.* $\ln(t + \theta)$ on graph paper. For each transient, θ is varied (by making a judicious choice) until a straight line is obtained for V *vs.* $\ln(t + \theta)$. This operation was performed with the aid of a digital computer. The computer was fed voltage *vs.* time data. It then performed the following functions: (*a*) it chose from a very large selection the value of θ which produced a minimum standard deviation of all data points when the data was subjected to a linear least square analysis, and (*b*) it printed out the values of k, θ, V_o, and the standard deviation. Differentiating Eq. [3] with respect to time, one obtains

$$\frac{dV}{dt} = \frac{-V_o}{(t + \theta)} \qquad [4]$$

Solving Eq. [3] for the quantity $(t + \theta)$ and substituting into Eq. [4] yields

$$\frac{dV}{dt} = -V_o \exp(-k/V_o) \exp(V/V_o) \qquad [5]$$

Substituting Eq. [5] into Eq. [2] yields the final result, an equation of the form

$$i = i_o \exp(V/V_o) \qquad [6]$$

where $i_o = CV_o \exp(-k/V_o)$. The point is that an equation of this form is the mathematical consequence of the differential equation describing the system and the experimental voltage-time profile. Here, i_o and V_o are experimentally determined parameters whose dimensions are the same as i and V, respectively. If time zero equals the commencement of the transient, the transients fit Eq. [3] for times corresponding to 80% of the potential decay at a current density of 352 μA/cm^2 and 60% of the potential decay at 32 and 71 μA/cm^2. Figure 2 shows the relationship between the parameter V_o and the formation potential. For a given formation current density, V_o is a linear function of the formation potential and all lines pass through the origin. The slope of each line is obviously a function of the formation current density and decreases with increasing current density. Studying anodization processes in a nonaqueous medium like glacial acetic acid affords one the rare opportunity of studying the effect of water concentration on the process. Figure 3 shows clearly that the quantity V_o is, for a formation current density of 71 μA/cm^2, definitely a function of the anodizing solution at a given formation potential.

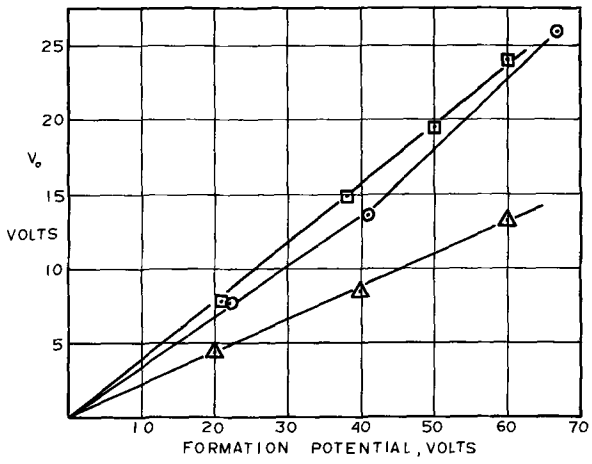

Fig. 2. Dependence of V_o on formation potential for vanadium in anodizing solution. The formation current density was 32 μA/cm^2 for the data represented by squares, 71 μA/cm^2 for the data represented by circles, and 352 μA/cm^2 for the data represented by triangles.

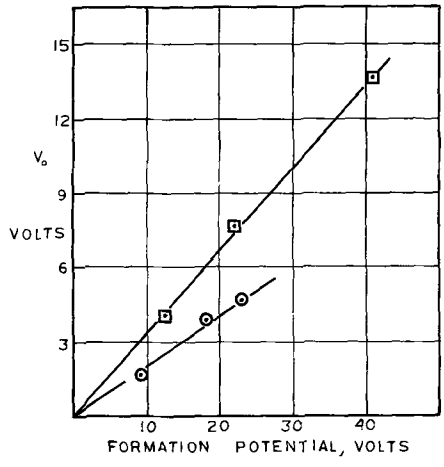

Fig. 3. Formation potential *vs.* V_o for vanadium anodized at 71 μA/cm^2 in 0.02M $Na_2B_4O_7$, 2.0M H_2O, $HC_2H_3O_2$ (squares), and 0.02M $Na_2B_4O_7$, 0.75M H_2O, $HC_2H_3O_2$ (circles) at 25°C.

From data analysis, we learned that the value of θ required to fit the transient data to Eq. [3] is quite small, with values ranging from essentially zero to as high as 0.1. A typical value is 0.02. Generally, θ increases with the formation potential of the film. Figure 4 shows the relationship between the reciprocal capacitance and the formation potential. The reciprocal capacitance is related to θ by the equation $1/C = V_o/i_e\theta$.

Discussion

An exponential dependence of the current density through the oxide film on the overpotential can be interpreted in terms of an activation-energy-controlled process (7). The theoretical relation for such a process, in the high-field case, is given in its simplest form by

$$i = 2anv \exp(-U/kT) \exp(qaE/kT) \qquad [7]$$

where a is the half-jump distance of the activation barrier, n the density of charge carriers, ν the frequency of the oscillating ions, U the activation energy for the process, q the effective charge on the mobile ions, and E the electric field at the activation barrier. The other symbols have their usual meanings. Assuming the field at the activation barrier is equal to the average electric field, a comparison of Eq. [6] and [7]

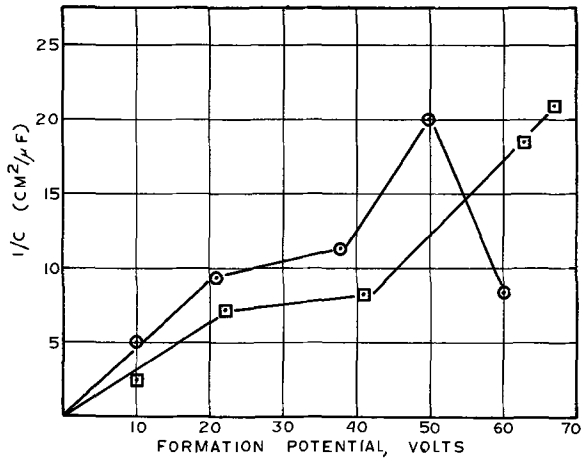

Fig. 4. Dependence of the reciprocal capacitance on formation potential. The formation current density was 32 μA/cm^2 for the data represented by the circles and 71 μA/cm^2 for the data represented by the squares.

may be made which yields the relationship

$$V_0 = (kT/qa)D \quad [8]$$

Thus, V_0 is proportional to the thickness of oxide layer, D.

The experimental data presented here verified a model of this type. Figure 2 shows that the values of V_0 are linearly proportional to the formation potential for a given formation current density over a wide range of values and that the lines intersect the origin. This result indicates that a high-field conduction process limits the current through the layer. Data taken for different formation current densities fall on lines of differing slopes, indicating that the field in the layer and i_0 both depend on the formation current density. The field in the dielectric may increase with increasing formation current density because of an increase in the ion jump distance at higher formation current densities.

As mentioned earlier, the values of θ required to linearize Eq. [3] are unusually small compared to results obtained with other metals by other investigators. We interpret this to mean that films formed in glacial acetic acid solutions containing 0.02M $Na_2B_4O_7$ and 2.0M H_2O are porous compared to those formed on, say, tantalum. These results are not at all inconsistent with our previous findings.

In an earlier work (2), we reported results which supported the existence of a porous anodic layer. First, infrared measurements showed that acetic acid, incorporated into the film during film growth, is removed from the film on standing after a very short time. Second, the final leakage current density, 0.15 μA/cm^2, was some 1000 times larger than that found for other valve metals (8). The comparative speed with which the acetic acid evaporated suggested that it might have been located along channels in the film. The onset of a porous "channel" structure during early stages of film growth would account for these experimental results. One is able to combine the values of θ, i_e, and V_0 to calculate the reciprocal capacitance through the relation, $1/C = V_0/i_e\theta$. Figure 4 shows the relationship between formation potential and $1/C$ is only roughly linear. Perhaps this is due to random defect structures like channels within the forming oxide film.

Finally, we look at Fig. 3 which shows that V_0 is, for a given formation potential, very much a function of the anodizing media. It is interesting to note that the solution containing the greater amount of water (2.0M *vs.* 0.75), yields larger values of V_0 for a given formation potential, a fact which suggests that the film formed in the solution containing the greater amount of water is thicker [recall $V_0 = (kT/qa)D$]. Perhaps this is quite correct since we reported (2) previously that film breakdown potential appears to decrease with increasing water concentration in the anodizing solution.

The results of this investigation are similar to those obtained by others studying other oxide film systems (4-6). All systems to date have shown the same type of dependence of V_0 on formation potential. The unusual results found in this study are the small values of θ necessary to linearize the transient relationship. This is believed to be due simply to the nature of the anodic oxide on vanadium.

Manuscript submitted Dec. 18, 1970; revised manuscript received *ca.* Feb. 26, 1971.

Any discussion of this paper will appear in a Discussion Section to be published in the December 1971 JOURNAL.

REFERENCES

1. R. G. Keil and R. E. Salomon, *This Journal*, **112**, 643 (1965).
2. R. G. Keil and R. E. Salomon, *ibid.*, **115**, 628 (1968).
3. D. C. Grahame, *J. Phys. Chem.*, **57**, 257 (1953).
4. D. J. DeSmet and M. A. Hopper, *This Journal*, **116**, 1184 (1969).
5. J. L. Ord, *ibid.*, **112**, 46 (1965).
6. J. L. Ord and D. J. DeSmet, *ibid*, **116**, 762 (1969).
7. L. Young, "Anodic Oxide Films," Academic Press, London and New York (1961).
8. F. Keller, M. S. Hunter, and D. L. Robinson, *This Journal*, **100**, 411 (1953).

Identification of Gold Islands on Copper-Plated Wire Surfaces by Cyclic Voltammetry

M. W. Breiter* and F. E. Luborsky

General Electric Research and Development Center, Schenectady, New York 12301

ABSTRACT

Periodic potentiostatic current-potential curves have been used to demonstrate the existence of gold islands on a copper substrate. The samples of smooth and rough copper substrates were prepared in a continuous wire plating system with an average thickness of the gold deposit of from 0 to 1400Å. Time-dependent changes in the potentiostatic curves were qualitatively explained in terms of the respective electrode reactions.

During studies concerned with the preparation of Permalloy films on wire (1), it was discovered that the application of a very low current in the gold-plating bath during the wire preparation resulted in substantial improvements in the performance of the wire as a nondestructive read-out (NDRO) element. This wire preparation and the magnetic results are described separately (2).

In this paper, we describe periodic potentiostatic measurements on the wires, without the magnetic film, which were used to obtain qualitative information about the "coverage" of the copper by the gold deposit. This technique differs from the determination of porosity of gold deposits based on measurements of the corrosion potential (3) and is sufficiently sensitive to detect the small amounts of gold present on the copper. The corrosion potential measurements were insensitive to the small amounts of gold encountered in this work. It is shown that the substrates which produce magnetic films with superior properties do contain some gold and that this gold is in the form of islands covering only a fraction of the copper substrate surface.

Experimental

The wires were prepared in the continuous wire-plating line (1, 2) by sequentially depositing a "smoothing" copper layer, a "rough" copper layer, and then a gold layer. The remainder of the plating system was not used so as to prevent contamination of the surface; *i.e.*, the NiFe cell was open, the anneal furnace "off," and the mercury removed from the test jig contact cups. Samples of various combinations of copper and gold were prepared as shown in Table I. Optimum magnetic properties, in subsequent processing, were obtained with substrates of the type represented by samples G and H. The current-voltage characteristic for the gold deposition cell is given in Fig. 1. The average gold thicknesses were determined by wet chemical analysis for samples down to 11Å. Each sample was assembled as an electrode and immersed in the 1M KOH electrolyte in a conventional cell of Pyrex glass. The electrolyte was flushed free of oxygen before use and kept agitated with the nitrogen during the measurements.

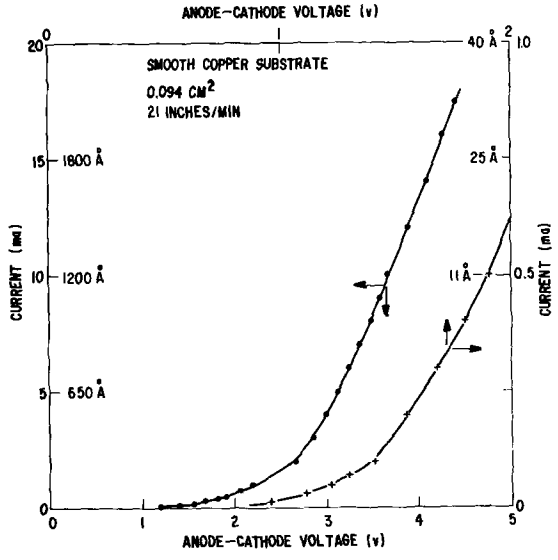

Fig. 1. Current-voltage characteristic for gold deposition in continuous plating line. Thicknesses obtained by chemical analysis. Upper and right coordinates are an expanded scale of the initial portion of the curve.

A Wenking 61TRS potentiostat and Type 255 Function Generator from Exact Electronics were used to apply periodic potential sweeps at different rates to the test electrode. The current was measured as a voltage drop across standard resistors and the current-potential curve displayed on a Tetronix 302 Oscilloscope. Potentials were measured *vs.* a hydrogen elec-

* Electrochemical Society Active Member.

Key words: electrodeposited thin films, magnetic memory, surface structure.

Table I. Characteristics of samples

Sample No.	Sample* preparation Rough Cu, mA	Au, mA	Characterization of the wire	Apparent surface, cm²	Average thickness of Au, Å
A	—	—	Solid Cu wire	0.18	0
B	n.c.**	n.c.	Smooth Cu	0.10	0
C	n.c.	0.05	Smooth Cu + partial Au layer	0.10	~11
D	n.c.	0.20	Smooth Cu + partial Au layer	0.10	~11
E	n.c.	10	Smooth Au	0.10	1400
F	20	n.c.	Rough Cu	0.10	0
G	20	0.05	Rough Cu + partial Au layer	0.10	~11
H	20	0.20	Rough Cu + partial Au layer	0.10	~11
I	20	10	Rough Au	0.10	1400
J	—	—	Solid Au wire	0.38	—

* Smooth Cu deposit at 60 mA for all samples.
** n.c.—No contact.

trode in 1M KOH. Measurements were all at room temperature.

Results

As in previous work (4, 5) concerning the surface composition of heterogeneous platinum-gold alloy wires, we have attempted to obtain information on the composition of the surface from characteristic waves in voltammetric current-potential curves. Preliminary work showed that the application of periodic potential sweeps between 0.2 and 1.2V at small rates (<1 V/sec) led to the fairly rapid destruction of the surface of some of our samples because of copper dissolution from copper patches between the gold islands. Judging only from the absence of any short-time destruction of samples made with an average thickness of the gold deposit of about 1200Å, it can be said that much thinner gold deposits do not cover the copper substrate uniformly. For the studies of the surface composition, a sweep rate of 100 V/sec was chosen. At this rate, the effect of copper dissolution is much smaller. A few results obtained at small sweep rates are mentioned later since they support the conclusions from measurements at 100 V/sec.

Voltammetric current-potential curves measured at 100 V/sec at a solid copper wire and on a smooth copper substrate are replotted in Fig. 2. The curves represent early cycles before a destructive effect was noticeable, but not the initial cycle. The shape of the I-U curves is nearly the same and the areas enclosed by the two curves are directly proportional to their apparent surface area given in Table I. The copper substrate on which the gold film was deposited in other experiments (see Table I) is uniform and thick enough to display the properties of bulk copper. The area under the anodic wave is equal to that under the cathodic wave within the experimental error (±10%). Only the anodic formation (6, 7) and cathodic reduction (6, 7) of copper oxides

$$2Cu + 2OH^- = Cu_2O + H_2O + 2e^- \quad [1]$$

$$Cu_2O + 2OH^- = 2CuO + H_2O + 2e^- \quad [2]$$

take place at the high sweep rate. A separation of the two reactions is not possible on the basis of the present results.

Voltammetric I-U curves taken in 1M KOH on a smooth gold wire at 100 V/sec are represented by curves in Fig. 3. The curves are practically symmetrical to the potential axis at U ≤ 1.1V, indicating the presence of a nearly reversible process. The formation and reduction of the oxygen layer occurs only to a small extent and is recognizable at the right side of the curves. The nature of the nearly reversible process became clear when $CuSO_4 \cdot 5H_2O$ was added in increasing amounts to the electrolyte. The height of the peaks at about 0.85V increases with the copper ion concentration (compare curves a to b). The addition of Cu^{++} in tests on the solid copper wire showed no change in the curves and no peak near 0.85V. It is suggested that the cathodic formation of absorbed copper atoms, Cu_{ad}, or of $(Cu_2O)_{ad}$ is observed during the cathodic sweep and its stripping away during the anodic sweep

$$CuO_2^{--} + 2H_2O + 2e^- = Cu_{ad} + 4OH^- \quad [3]$$

or, more likely,

$$2CuO_2^{--} + 3H_2O + 2e^- = (Cu_2O)_{ad} + 6(OH)^- \quad [4]$$

An absorbed layer of a copper-containing species is formed at potentials less positive than that for deposition of thick copper layers with bulk properties. This layer may have properties like a copper-gold alloy, but it still has to be formed on the gold substrate. The situation is similar to that encountered on platinum (8). Reactions [3] and [4] are so fast on gold that small traces of copper ions in the reagent-grade KOH can be detected. The presence of an impurity having the electrochemical properties of the Cu^{++}/Cu^+ couple was established (9) in a similar way for 0.5M HCl. The occurrence of reaction [3] which requires the presence of gold atoms is used subsequently in a qualitative way as evidence for the existence of gold patches on the surface of copper substrates. The gold patches were obtained by deposition of gold.

Three I-U curves, taken at 100 V/sec in 1M KOH with increasing average thickness of the gold deposit on top of the copper films, are replotted in Fig. 4. The conditions for the gold deposition are given in Table I. The curve for sample I in Fig. 4 with the thick gold deposit has a shape similar to curve a for the solid gold wire in Fig. 3. The gold deposit is uniform and covers the copper substrate essentially completely (except for random porosity). The enclosed areas during the anodic and cathodic sweep are about equal and proportional to the apparent surface area. The middle and the left I-U curve in Fig. 4 displayed one broad anodic wave and two cathodic waves. The cathodic wave between about 0.6 and 0.2V can be ascribed to the reduction of copper oxides, as a comparison with the curves on copper in Fig. 2 demonstrates. The narrower cathodic wave at about 0.8V appears at about the same potential as the cathodic wave of curve b in Fig. 3 and has a similar shape. It is attributed to reactions [3] and [4]. The height of this wave is a qualitative measure for the total area of the gold patches on top of the copper substrate. As expected, the height is larger for sample H with the thicker gold deposit. The presence of the cathodic wave between 0.6 and 0.2V in samples G and H represents evidence that a part of the underlying copper substrate is not covered by the gold film. This part participates in reactions [1] and [2] and, to a smaller extent, in copper dissolution.

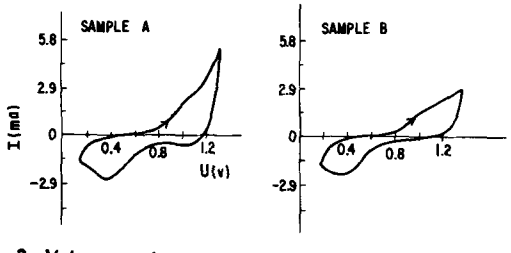

Fig. 2. Voltammetric current-potential curves at 100 V/sec on solid copper wire (sample A) and a smooth copper substrate (sample B).

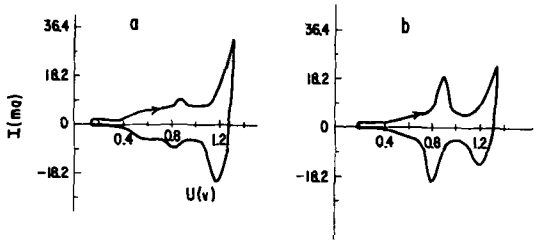

Fig. 3. Voltammetric I-U curves on solid gold wire, J, in 1M KOH + XM $CuSO_4 \cdot 5H_2O$ at 100 V/sec. Curve a: $X \approx 0$. Curve b: $X = 10^{-5}$.

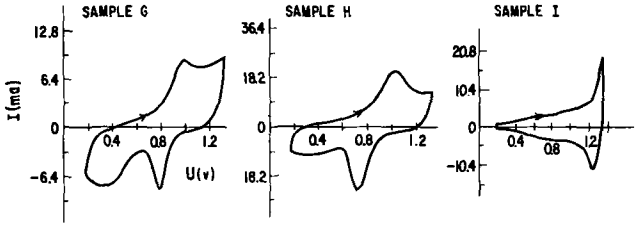

Fig. 4. Voltammetric I-U curves at 100 V/sec on 1M KOH on copper films with increasing average thickness of the gold deposit.

The occurrence of copper dissolution is evidenced by an increase with time of the height of the cathodic wave for gold at 0.8V.

It was not possible to obtain a quantitative measure for the coverage of the copper substrate with gold because thin gold films, like that on sample G, disappear from the surface during the cycling. The I-U curve of sample G was traced about 20 sec after connecting it to the potentiostatic circuit. During extended cycling, the cathodic peak at 0.8V becomes smaller and finally disappears. Then the I-U curve looks like curve b of the copper substrate in Fig. 2. The removal of the thicker gold film sample H was much slower than that of sample G. It is not known at present if the gold film is removed by anodic dissolution or by mechanical breakage because of anodic dissolution of the underlying copper substrate.

A qualitative confirmation of the preceding results is derivable from I-U curves measured at small sweep rates. The curves at 1 mV/sec have the form recently reported (10) for solid copper in 1M NaOH. The large anodic wave appearing at about 0.85V during the anodic sweep masks any other effect. However, the height of this wave increases with decreasing average thickness of the gold deposit, indicating that more copper areas become exposed to the electrolyte and participate in the anodic copper dissolution.

Conclusions

It has been demonstrated that periodic current-potential curves can be used to obtain qualitative information on the relative surface areas of copper and gold on composite samples. Differences between gold on smooth or on rough copper substrates could not be observed because of the qualitative nature of the measurements.

Acknowledgments

The authors wish to thank R. Skoda and B. J. Drummond for the preparation of the samples.

Manuscript submitted Oct. 26, 1970; revised manuscript received Jan. 20, 1971.

Any discussion of this paper will appear in a Discussion Section to be published in the December 1971 JOURNAL.

REFERENCES

1. J. S. Mathias and G. A. Fedde, *IEEE Trans. Magnetics*, **MAG-5**, 728 (1969).
2. F. E. Luborsky, R. E. Skoda, and W. D. Barber, *J. Appl. Phys.*, **42**, in process (1971).
3. R. J. Morrissey, *This Journal*, **117**, 742 (1970).
4. M. W. Breiter, *Electrochim. Acta*, **10**, 543 (1965).
5. M. W. Breiter, *J. Phys. Chem.*, **69**, 901 (1965).
6. A. Hickling and D. Taylor, *Trans. Faraday Soc.*, **44**, 262 (1948).
7. R. W. Ohse, *Z. Physik. Chem. N. F.*, **21**, 406 (1959).
8. M. W. Breiter, *This Journal*, **114**, 1125 (1967).
9. D. T. Napp and S. Bruckenstein, *Anal. Chem.*, **40**, 1036 (1968).
10. B. Miller, *This Journal*, **116**, 1675 (1969).

A New Technique for Investigating the Electrochemical Behavior of Electroless Plating Baths and the Mechanism of Electroless Nickel Plating

N. Feldstein* and T. S. Lancsek

RCA Corporation, David Sarnoff Research Center, Princeton, New Jersey 08540

ABSTRACT

The electrochemical potential of electroless nickel and electroless cobalt plating baths can be altered by the addition of a variety of chemical compounds to the baths. At the same time, the metal-to-phosphorus ratio in the deposit is altered. This behavior has been studied for a series of baths using typical accelerators including thiourea, glycine, and formate; each of these represents a different type of accelerator characteristic. A Tafel-like behavior was observed to apply for the deposition of nickel (or cobalt) and also for the deposition of phosphorus. Therefore, given a suitable reference point, the plating rate and metal-to-phosphorus ratio can be predicted from the measured potential. A model based on a modified hydride mechanism is proposed for the electroless deposition of nickel-phosphorus. With the help of this model, the hydrogen evolved during deposition can be quantitatively accounted for.

Since the discovery of the electroless plating process by Brenner and Riddell (1), many commercial processes have been developed employing this plating technique. In particular, the deposition of nickel layers by electroless techniques is widely used in the electronics industry. Although the actual structure (2-4) of nickel-phosphorus deposits formed with these baths is still unresolved, the phosphorus content in the deposit is of importance. Typical chemical and physical properties (5, 6) which are dependent on the phosphorus content are: resistivity, hardness, internal stress, corrosion resistance, magnetic moment, and electrical contacts to semiconductor material. It is thus important to control the phosphorus content through control of those parameters which affect its deposition rate.

In examining prior literature on the phosphorus content of nickel deposits, there is a general agreement on the following trends.

1. The per cent phosphorus increases with increasing temperature of operation.
2. The per cent phosphorus increases with increasing hypophosphite concentration.
3. The per cent phosphorus increases with decreasing pH of the bath.

Although considerable effort has been devoted to the study of the role played by major components of the bath (buffers, complexing agents, reducing agents, *etc.*), little attention has been focused on the possible effect(s) of stabilizers (7) and accelerators (8-10) on the phosphorus content of the deposit.

* Electrochemical Society Active Member.

Key words: electroless plating, electrochemical behavior and mechanism, role of accelerators.

In a recent investigation (11), it was demonstrated that inhibitors (stabilizers) alter the electrochemical parameters at the electrode solution interface and at the same time change the nickel-phosphorus ratio in the deposit. In the present investigation, it was decided to examine the effect(s) associated with some typical accelerators, since the use of such additives is highly desirable in practical plating. The accelerators chosen in this investigation were typical, each representing a specific class of accelerator.

Experimental Procedures

Chemicals.—All chemicals used in preparing the plating solutions were reagent grade. The water used was deionized and then distilled.

Rate.—For comparison of the relative effect(s) of the various accelerators, standard 2 in. x 2 in. alumina substrates (American Lava Corporation 614 plain) having a 40 μin. surface roughness were used. Volume of solutions was held at 200 cc unless otherwise stated. Electroless plating on these substrates was carried out using a conventional tin-palladium sensitization and activation sequence; the weight gain during plating was recorded. In most cases, initiation of plating was apparent within 30 sec; however, for solutions having the highest thiourea concentration, the initiation was sluggish. No agitation was provided during the plating.

The plating time in all cases was chosen as 10.0 min except in the case of bath C in which the deposition time was taken as 20.0 min. All plating temperatures were maintained within ±0.5°C; *p*H values were maintained within ±0.02 *p*H units at the corresponding operating temperature with the help of a Corning *p*H-controller, Model 10c. No agitation was provided during the plating cycle. In the current work, electroless Ni-P and Co-P plating baths shown in the Appendix were employed.

Subsequent to the plating, the deposits were analyzed for their nickel and phosphorus (or cobalt and phosphorus) content employing both x-ray fluorescence spectroscopy and conventional wet chemical analysis. For the wet chemical analysis, a gravimetric technique based on dimethylglyoxime was used for nickel (or cobalt), while the phosphorus was determined colorimetrically with molybdenum blue. In the x-ray technique, the net x-ray intensity (counts per second) was monitored for PKα and NiKα lines, respectively. Hydrogen evolved in the course of plating was collected by a simple displacement apparatus.

Potential measurements.—Potential measurements were carried out using a recording potentiometer (John Fluke Manufacturing Company, Model 825A). All steady-state potentials (mixed potentials) and equilibrium potentials were obtained using freshly deposited nickel or cobalt electrodes against SCE at the operating temperatures. Potential measurements were made as the concentration of the additives was varied. All reported values are within ±1 mV.

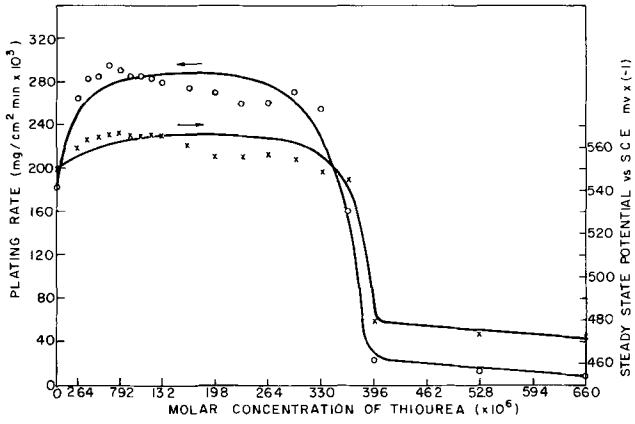

Fig. 1. Effect of thiourea on a nickel-plating bath (bath A)

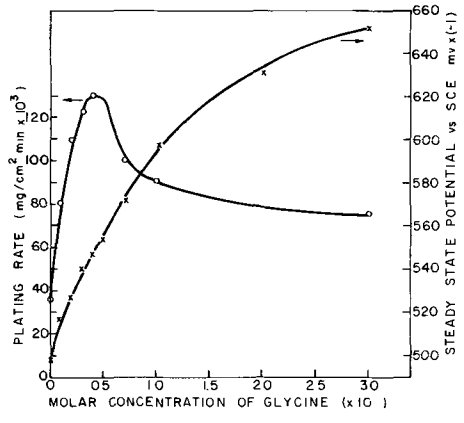

Fig. 2. Effect of glycine on a nickel-plating bath (bath B)

Results and Discussion

In examining the kinetic results shown in Fig. 1-4, the effect(s) of the accelerators may be divided into three distinct classes.

AI class (accelerator-inhibitor).—The over-all behavior of this class is demonstrated in Fig. 1 and 4. Initially, there is an increase in plating rate leading to a maximum. Further increases in additive concentration lead to inhibition of the plating rate, due to an adsorption-poisoning type mechanism. Typical materials in this class are thiourea and thiocyanate.

API class (accelerator with partial inhibition).—For this class, the over-all behavior is shown in Fig. 2. Following the initial acceleration in deposition rate, there is an inhibited range. However, the degree of inhibition is not complete; a plateau is reached at the higher accelerator concentrations. The plateau level achieved can either be below or above the initial level in the absence of additive.

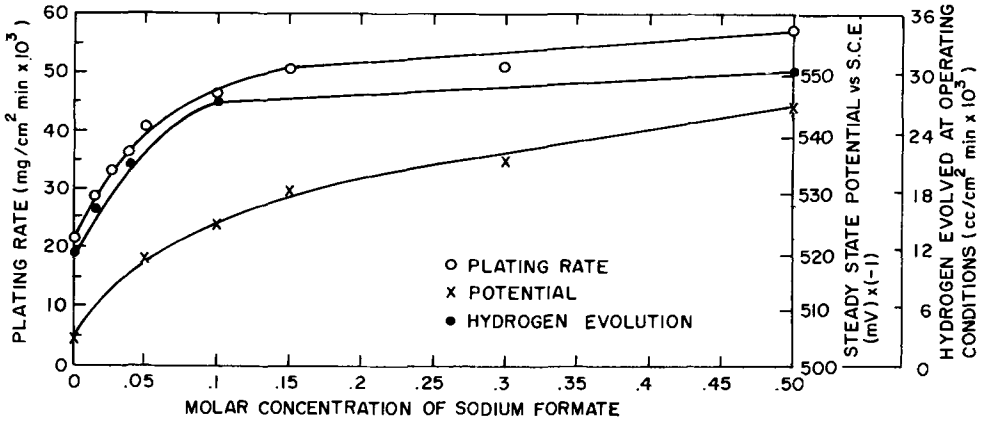

Fig. 3. Effect of formate on a nickel-plating bath (bath C).

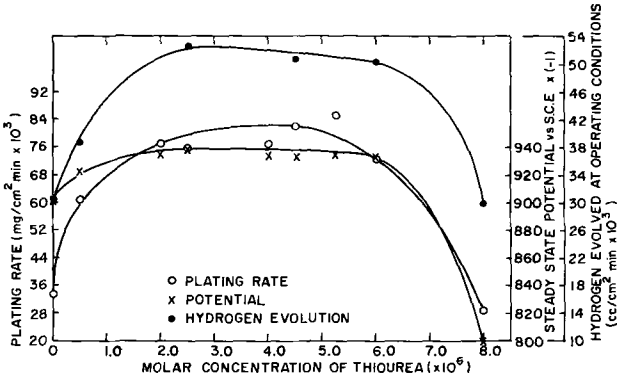

Fig. 4. Effect of thiourea on a cobalt-plating bath (bath D)

AO class (accelerator-only).—For this class, the over-all behavior is illustrated in Fig. 3. Contrary to the behavior in the above two classes, the plating rate approaches a maximum value asymptotically as the additive concentration is increased. It should be noted that the additives in this class generally do not form complexes with the metallic cation in bulk solution. Besides formate, similar behavior was noted with fluoride ion.

As reported by DeMinjer and Brenner (7), the incorporation in the bath of thiourea in low concentrations gives an accelerating effect on the plating rate. Figure 1 (bath A) shows the manner in which the plating rate and steady-state potential vary as the thiourea concentration is modified. Variations in both the plating rate and steady-state potential are similar; *i.e.*, corresponding increases or decreases in each take place as thiourea is added to the bath. It should be noted, however, that, although thiourea is known to accelerate plating from some acidic electroless nickel baths, there are cases (12) (acid-type bath) in which this anticipated acceleration does not take place. Examination of the deposits with respect to their elemental composition (Table I) shows distinct acceleration in the formation rate of both the nickel and phosphorus. At the same time, the per cent phosphorus in the deposit decreases during the acceleration part of the curve. Due to the high operating temperature, no collection of hydrogen was attempted.

In Fig. 2 (bath B), the effect of glycine on the plating rate and the steady-state potentials is demonstrated. The plating rate characteristics are in excellent agreement with the work by Holbrook and Twist (8). Furthermore, they have reported that the molar ratio of hydrogen to nickel (nickel plus phosphorus) is constant over the entire glycine range, and this determination has not been repeated in the current work. It is further demonstrated in Fig. 2 that the steady-state potential gradually increases toward more cathodic values upon the addition of glycine and leveling occurs at the higher glycine concentrations. As the glycine content varies, the equilibrium potential for the nickel redox system is altered in a regular fashion. Specifically, −384 mV *vs.* SCE and −445 mV *vs.* SCE were measured for this system in the absence of hypophosphite for 0 and 0.3M glycine, respectively. Although the potential curves for the glycine system do not follow the same characteristics as shown in Fig. 1, 3, and 4, this behavior is not surprising since glycine can complex the nickel with a *p*K value of about 5 (13). However, in view of the variations of steady-state potential with added glycine, it is not surprising to find (Table II) that both the nickel and phosphorus formation rates are altered. In addition, deposits having a different phosphorus-nickel ratio are obtained.

As seen from Fig. 3 (bath C), upon the addition of formate to the electroless nickel bath, acceleration in plating rate takes place. The plating rate, the rate of hydrogen evolution, and the steady-state potential all increase gradually leading to a plateau. As demonstrated in Table III, both the nickel and phosphorus deposition rates increase with formate addition. There is also a net decrease in the phosphorus concentration in the deposit as the formate concentration increases. Furthermore, from the data of Fig. 3 and Table III, the molar concentration of hydrogen to nickel was found to be 1.4 over the entire formate concentration range examined.

Examination of the equilibrium potential for the nickel system in the absence of hypophosphite resulted in a constant value of −383 ±4 mV. *vs.* SCE at 75°C and *p*H of 4 over the entire formate concentration range. This result, along with absorption measurements in the uv-visible range, suggests that there is no complex formation between the formate and the nickel ions in solution.

While in Fig. 1-3 electroless nickel plating baths were examined, Fig. 4 (bath D) shows the influence of thiourea on a typical electroless cobalt bath. In examining the results of Fig. 4, it is apparent that initially there is an increase in the plating rate, the rate of hydrogen evolution, and the steady-state potential with added thiourea. Further addition of the thiourea leads to a decrease in these dependent variables and the eventual cessation of the plating process. This general course of behavior closely resembles the results shown in Fig. 1. In Table IV it is clearly shown that both the cobalt and phosphorus and their respective plating rates are enhanced, however in a manner in which the per cent phosphorus is decreased in the

Table I. Effect of thiourea on the nickel-phosphorus content

Molar concentration thiourea x 10^6	Weight reclaimed[b] by analysis (mg) Ni	P	%P[c]
None	68.97	4.29	5.84
5.3	132.24	4.61	3.40
16.5	135.90	4.47	3.19
33	125.82	3.62	2.81
39.5	18.04	0.25	1.32

[b] Weight reclaimed by standard wet chemical analysis.
[c] Values calculated using weights in previous columns.

Table II. Effect of glycine on the nickel-phosphorus content

Molar concentration glycine	Net x-ray intensity counts/sec PKα	NiKα	PKα/NiKα	Weight reclaimed[b] by analysis (mg) Ni	P	%P[c]
0	1263	1177	1.07	15.61	0.66	4.05
0.01	1613	2768	0.582	34.02	2.55	6.95
0.02	1497	3325	0.450	—	—	—
0.03	1022	3737	0.273	—	—	—
0.04	802	4697	0.171	55.27	2.29	3.98
0.07	442	3631	0.122	—	—	—
0.10	411	3293	0.125	42.55	0.54	1.26
0.30	447	2852	0.157	33.65	0.52	1.52

[b] Weight reclaimed by standard wet chemical analysis.
[c] Values calculated using weights in previous two columns.

Table III. Effect of sodium formate on the nickel-phosphorus content

Molar concentration of sodium formate	Net x-ray intensity counts/sec PKα	NiKα	PKα/NiKα	Weight reclaimed[b] by analysis (mg) Ni*	P*	%P[c]
None	1425	1365	1.04	14.3	2.01	12.3
0.013	—	—	—	22.1	3.00	11.9
0.025	1640	2048	0.800	24.6	3.08	11.1
0.050	1690	2485	0.680	29.8	—	—
0.10	1671	2885	0.579	33.8	4.00	10.6
0.50	1570	3240	0.485	45.8	5.31	10.4

[b] Weight reclaimed by standard wet chemical analysis.
[c] Values calculated using weights in previous two columns.
* Samples used in this table are not the same as employed in Fig. 3.

Table IV. Effect of thiourea on the cobalt-phosphorus content

Molar conc of thiourea × 10⁶	mg of cobalt[a] reclaimed	mg of phosphorus[a] reclaimed	Per cent[b] phosphorus
None	15.86	0.81	4.86
0.50	28.69	1.41	4.70
2.50	36.83	1.50	3.92

[a] Weight reclaimed by standard wet chemical analysis.
[b] Values calculated using weights in previous two columns.

acceleration part of the curve. Examination of the equilibrium potential for the cobalt system in the absence of hypophosphite resulted in a constant value of -726 ± 2 mV *vs.* SCE for thiourea concentrations of 0-4.5 x 10^{-6}M. This behavior is exactly analogous to that exhibited by the nickel system shown in Table I. Analysis of the gaseous product evolved as related to the cobalt deposited shows that in all cases the molar concentration of the gaseous product to cobalt is in the range of 4:1 to 3:1 without any specific trend with thiourea addition. Furthermore, it was found mass spectrometrically that a substantial portion of the gas phase is ammonia.

Replotting the results of Fig. 1, 3, and 4 (and their corresponding tables) shows the manner by which the net plating rates for nickel and cobalt vary with the steady-state potentials (Fig. 5). Since the deposits formed in this work are generally quite thick, it is reasonable to assume that composition is uniform throughout the bulk of the cross section. Although in Fig. 5 the plating rate for the metals is plotted *vs.* potential, by suitable transformation (using Faraday's law) these plating rates can be converted to "deposition currents." As seen in all three cases, the logarithm of the plating rate (or deposition current) is a linear function of the potential. This behavior is characteristic of Tafel plots (14). From relating the slopes of Fig. 5 to the theoretical Tafel slope, the transfer coefficients (α) were evaluated (assuming $n = 2$). The theoretical Tafel slope is

$$-\frac{n\alpha RT}{\mathbf{F}} = \frac{d\ln i}{dE}$$

where n = number of electrons in charge transfer step
α = transfer coefficient
R = gas constant
T = absolute temperature
$\mathbf{F}$ = Faraday constant

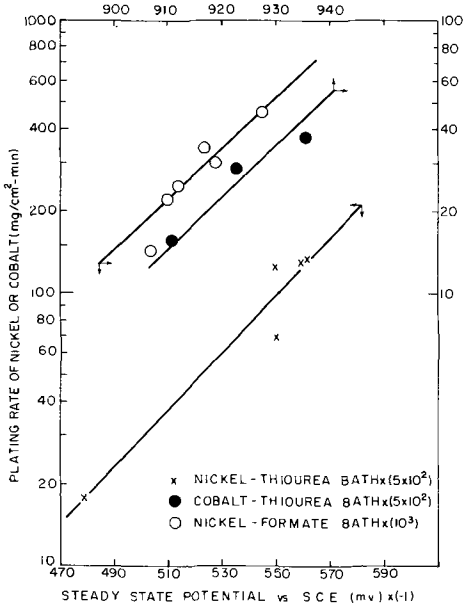

Fig. 5. Plating rate of nickel and cobalt *vs.* steady-state potential.

Specifically, the following transfer coefficients were found: 0.5 for the nickel-formate and cobalt-thiourea baths, and 0.4 for the nickel-thiourea case.

Since the Tafel type equation appears to fit the observed data, a charge transfer step can be assumed to be the slow step in the reduction of the metallic cations. Furthermore, from earlier work, this slow charge transfer step is probably due to a slow electron exchange or a slow chemical change during the course of the anodic oxidation of hypophosphite.

Figure 6 was prepared from data on the phosphorus deposition rate. As seen in all three cases, a linear relationship exists which again resembles a Tafel plot. From the slopes of Fig. 6 and the theoretical Tafel slope (n assumed to be unity), the corresponding charge transfer coefficients were found

0.71 for cobalt-thiourea bath
1.1 for nickel-thiourea bath
1.1 for nickel-formate bath

It is thus concluded that the electrochemical reduction of hypophosphite to phosphorus is also charge transfer controlled and that the kinetics of deposition may be described by the Tafel equation. However, since by definition α may have values only in the range 0-1, the value of n must be greater than 1 in the electrochemical process leading to the formation of phosphorus.

It is thus postulated that reduction of hypophosphite itself is not involved in the formation of phosphorus. Rather, another intermediate having phosphorus in a formal valence state greater than one is probably involved. This species is probably formed from hypophosphite during oxidation step(s). This intermediate species is postulated to be a metaphosphorus acid (HPO_2), which, although short-lived, could lead to the formation of either elemental phosphorus by reduction or orthophosphorus acid (H_3PO_3) by hydration.

Wieland and Winkler (15) postulated, on the basis of organic analogies, that a metaphosphorus acid is formed during the catalytic dehydrogenation of hypophosphorus acid. Based on Wieland and Winkler's postulate, Goldenstein *et al.* (2) proposed metaphosphorus acid as an intermediate in the oxidation of hypophosphite. It is interesting to note that in their work (2) the metaphosphorus acid is formed as part of an atomic hydrogen transfer mechanism rather than the hydride-type mechanism accounted in this investigation.

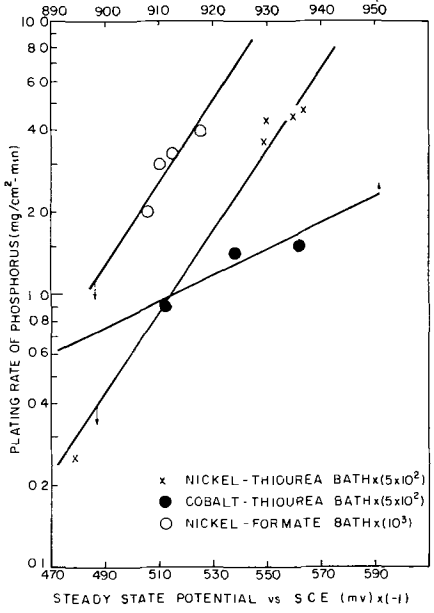

Fig. 6. Plating rate of phosphorus *vs.* steady-state potential

		REACTION TYPE
1. $H_2PO_2^- + OH^- + X$	$\longrightarrow [X\cdots H]^- + PO_2^- + H_2O$	ELECTROCHEMICAL
2. $PO_2^- + OH^-$	$\longrightarrow HPO_3^=$	CHEMICAL
3. $2[X\cdots H]^- + M^{++}$	$\longrightarrow M + 2(X\cdots H)$	ELECTROCHEMICAL
4. $2(X\cdots H)$	$\longrightarrow H_2 + 2X$	CHEMICAL
5. $[X\cdots H]^- + H_2O$	$\longrightarrow H_2 + OH^- + X$	ELECTROCHEMICAL
6. $3[X\cdots H]^- + 2H_2O + PO_2^-$	$\longrightarrow P + 3(X\cdots H) + 4OH^-$	ELECTROCHEMICAL
7. $H_2PO_2^- + OH^-$	$\longrightarrow HPO_3^= + H_2$	CHEMICAL

Fig. 7. A modified hydride transfer mechanism. For alkaline condition, X represents a catalytic site, and M represents nickel or cobalt.

In view of the results of the current investigation, and the arguments presented by Lukes (16), it is believed that a modified hydride-type mechanism (16) best accounts for general characteristics of Ni-P and Co-P type baths. Figure 7 shows the basic steps which occur in this modified hydride transfer mechanism. Reaction 1 is the rate-controlling step resulting in the charge transfer control behavior observed for reactions 3 and 6. No attempt is made in this investigation to distinguish between the two isomeric forms of hypophosphite (17). At the same time, the hydrogen evolved during the course of plating is the sum total of reactions 4, 5, and 7 (Fig. 7). Reaction 7, however, should occur only at high temperatures and in alkaline media (18). From the experimental data for the hydrogen evolved from baths B, C, and from recently reported data on an alkaline room-temperature bath (11), excellent agreement was found between the hydrogen measured and that expected, based on the composition of the deposit. Specifically, it was found that the following correlation holds fairly rigorously

$$\frac{d}{dt}[H_2] = \frac{d}{dt}[Ni] + 1.5\frac{d}{dt}[P]$$

This correlation is consistent with the over-all mechanism proposed in Fig. 7 and suggests that reaction 5 plays a minor role for the baths under examination. Furthermore, due to the competitive nature of reactions 2 and 6 with respect to PO_2^-, it can be anticipated that reaction 2 will become more important in alkaline media. This is consistent with the observation of several investigators that the phosphorus content in the deposit is lower as the *p*H is increased.

Based on the results of this investigation and the consistency of the values for the transfer coefficient (α) for nickel (or cobalt) and phosphorus, the following practical results are envisioned, all leading to greater simplicity and better control of the composition of the deposit.

1. Based on (*a*) the value found for α (transfer coefficient), (*b*) at least one deposition rate measurement, (*c*) the corresponding steady-state potential, and (*d*) the composition of the deposit, a complete deposition rate for nickel (or cobalt) and phosphorus as a function of potential may be calculated. The potential can be changed for a given bath by, *e.g.*, adding an accelerator so that a complete plating rate *vs.* accelerator concentration curve can be constructed (for class I and III only). From these data, precise bath compositions may be selected to yield the desired alloy composition and plating rate.

2. Although in the current investigation an analysis for a binary system (Ni-P or Co-P) was made, it is believed that a similar analysis can be made for ternary systems.

3. The use of thiourea in electroless plating is highly desirable since it accelerates, as well as stabilizes, such baths. There is, however, a basic limitation in the use of this material because its concentration decreases with time, due to hydrolysis and sulfur codeposition. It is thus highly desirable to have a simple analytical technique for low thiourea concentrations. Based on the potential variations (Fig. 1 and 4) with thiourea concentration, a simple potentiometric technique (19) has been conceived for the determination of thiourea in electroless plating baths.

Conclusions

In the acceleration of electroless nickel and cobalt deposition from hypophosphite-based media, three distinct classes of accelerators are observed

AI (accelerator-inhibitor)
API (accelerator with partial inhibition)
AO (accelerator-only)

In all cases, there are distinct potential changes for the bath and compositional variations in the deposit as the accelerator concentration is increased. Detailed analysis of classes I and III accelerators shows that the nickel (or cobalt) and phosphorus deposition kinetics satisfy a Tafel-like equation. This correlation with the Tafel equations implies that the electroless deposition reactions may be treated by simple electrochemical principles. From our earlier work (11), it is known that the anodic oxidation of hypophosphite is the rate-controlling step.

The hydrogen evolved is due to several chemical reactions taking place simultaneously. In acid media (or low-temperature alkaline media), we observe that the moles of hydrogen gas evolved are the sum total of the moles of nickel deposited plus 1.5 $\times$ the moles of phosphorus deposited. This leads to the hypothesis that the phosphorus originates from a short-lived intermediate such as metaphosphorus acid, rather than from the parent hypophosphite molecule. These observations are consistent with the modified hydride mechanism proposed to account for the findings of this investigation.

Acknowledgments

The authors wish to thank E. P. Bertin for his assistance in the x-ray fluorescence spectroscopy measurements and J. A. Amick for critically reviewing this manuscript.

APPENDIX

***Bath A* (7)**

$NaH_2PO_2 \cdot H_2O$, 9.45×10^{-2}M
$NiCl_2 \cdot 6H_2O$, 1.26×10^{-1}M
$C_2H_3O_3Na$, 2.54×10^{-1}M
*p*H, 4.2
Temperature, 91.5°C
CH_4N_2S, Variable

***Bath B* (8)**

$NaH_2PO_2 \cdot H_2O$, 3.63×10^{-2}M
$NiCl_2 \cdot 6H_2O$, 5.00×10^{-2}M
*p*H, 5.8
Temperature, 87°C
$C_2H_5O_2N$, Variable

***Bath C* (12)**

Ni^{++}, 0.32M
$NaH_2PO_2 \cdot H_2O$, 0.236M
*p*H, 4.0
Temperature, 75°C
HCOONa, Variable

***Bath D* (10)**

$CoCl \cdot 6H_2O$, 0.126M
NH_4Cl, 0.935M
$NaH_2PO_2 \cdot H_2O$, 0.189M
Na citrate $\cdot 2H_2O$, 0.340M
*p*H (with NH_4OH), 8
Temperature, 85°C
CH_4N_2S, Variable

Manuscript submitted Jan. 28, 1971; revised manuscript received Feb. 22, 1971. This paper was prepared

for oral presentation at the Institute of Metal Finishing, England, May 1971.

Any discussion of this paper will appear in a Discussion Section to be published in the December 1971 JOURNAL.

REFERENCES

1. A. Brenner and G. Riddell, *J. Res. Nat. Bur. Std.*, **37**, 31 (1946).
2. A. W. Goldenstein, W. Rostoker, W. Schossberger, and G. Gutzeit, *This Journal*, **104**, 104 (1957).
3. A. H. Graham, R. W. Lindsay, and H. J. Read, *ibid.*, **109**, 1200 (1962); **112**, 401 (1965).
4. J. P. Randin, P. A. Maire, E. Saurer, and H. E. Hintermann, *ibid.*, **114**, 442 (1967).
5. ASTM, Symposium on Electroless Nickel Plating, ASTM Special Tech. Publication No. 265 (1959).
6. K. M. Gorbunova and A. A. Nikiforova, "Physicochemical Principles of Nickel Plating," OTS-63-11003. Published by National Science Foundation, Washington, D.C. (1963). (Transl. from the Russian ed. of 1960.)
7. C. H. de Minjer and A. Brenner, *Plating*, **44**, 1297 (1957).
8. K. H. Holbrook and P. J. Twist, *ibid.*, **56**, 523 (1969).
9. J. S. Sallo, J. Kivel, and F. C. Albers, *This Journal*, **110**, 890 (1963).
10. J. Kivel and J. S. Sallo, *ibid.*, **112**, 1201 (1965).
11. N. Feldstein and P. R. Amodio, *ibid.*, **117**, 1110 (1970).
12. N. Feldstein, Unpublished results.
13. J. Chem. Soc., Special Publication No. 17 (1964), "Stability Constants."
14. P. Delahay, "New Instrumental Methods In Electrochemistry," Interscience Publishers, Inc., New York (1959).
15. H. Wieland and A. Winkler, *Ann. Chem.*, **34**, 198 (1923).
16. R. Lukes, *Plating*, **51**, 96 (1964).
17. W. A. Jenkins and D. M. Yost, *J. Inorg. Nucl. Chem.*, **12**, 297 (1959).
18. J. W. Mellor, "A Comprehensive Treatise on Inorganic Theoretical Chemistry," Vol. VIII, p. 875, Longmans Green & Co., New York (1928).
19. N. Feldstein and J. A. Weiner, *J. Anal. Chem.*, **43**, No. 8 (1971).

Voltammetric and Coulometric Studies of the Mechanism of Electrohydrodimerization of Diethyl Fumarate in Dimethylformamide Solutions

W. V. Childs,*[1] J. T. Maloy,[2] C. P. Keszthelyi, and Allen J. Bard*

Department of Chemistry, The University of Texas at Austin, Austin, Texas 78712

ABSTRACT

The reduction of diethyl fumarate (DEF) in tetra-n-butylammonium iodide (TBAI)-dimethylformamide (DMF) solutions at a platinum electrode has been studied by cyclic voltammetry, double potential step chronoamperometry, and controlled potential coulometry. The chronoamperometric response for several possible mechanisms of electrohydrodimerization has been obtained by digital simulation techniques, and a method for distinguishing among the mechanisms suggested. Results of double potential step chronoamperometric experiments strongly support a mechanism where the electrochemically generated anion radicals undergo a second-order dimerization reaction. Controlled potential electrolysis results give evidence for a bulk polymerization reaction in the absence of proton donor; protonation in the presence of hydroquinones; and good efficiency to the hydrodimer product in the presence of lithium perchlorate trihydrate.

The study of electrohydrodimerizations (or electrolytic reductive couplings) of activated olefins and related substances, by an over-all reaction shown in Eq. [1] has been the subject of numerous investigations, most recently especially

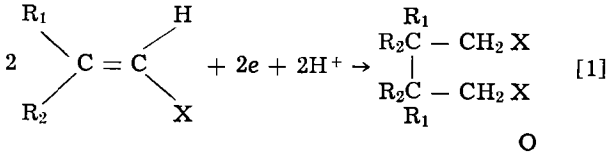

[1]

X = electron-withdrawing group, *e.g.* —CN, —C(=O)—OEt

by Baizer and co-workers [see (1-3) and references contained therein]. The reduction on acrylonitrile ($R_1 = R_2 = H$, X = CN) has been the subject of most of the investigations because of the commercial importance of the hydrodimerized product, adiponitrile. Relatively few studies have been concerned with a kinetic analysis of the mechanism of the process, however. The first papers, generally on the basis of product distribution, viewed the process as occurring with an initial two-electron reduction to the dianion, which then attacked the parent molecule to produce coupled products. Beck (4), based on an analysis of current-potential curves for the reduction of acrylonitrile, proposed a rate-determining step involving one electron and one water molecule to form a neutral radical, which is immediately reduced further to the protonated carbanion. Recently Petrovich, Baizer, and Ort (2, 3) carried out polarographic, cyclic voltammetric, and macroscale electrolysis studies of a number of diactivated olefins in N,N-dimethylformamide (DMF) solutions and concluded that dimeric products were formed by either attack of an electrochemically generated anion radical on the parent unreduced olefin, followed by further electroreduction and protonation, or by protonation of the anion radical, followed by further reduction to an anion and subsequent attack on the olefin. An alternate pathway to the dimer, that of coupling of the anion radicals, was deemed less likely.

The research described here was undertaken to investigate the mechanism of the hydrodimerization reaction using a variety of electroanalytical techniques,

* Electrochemical Society Active Member.

[1] Present address: Phillips Petroleum Company, Bartlesville, Oklahoma, 74004.

[2] Present address: Department of Chemistry, West Virginia University, Morgantown, West Virginia.

Key words: electrolytic hydrodimerization, potential step chronoamperometry, cyclic voltammetry, coulometry, computer simulation.

including double potential step chronoamperometry, cyclic voltammetry, and controlled potential coulometry. Other investigations of the mechanism by rotating ring disk electrode voltammetry and electron spin resonance spectroscopy will be reported elsewhere. The compound selected for study was diethyl fumarate (DEF), since

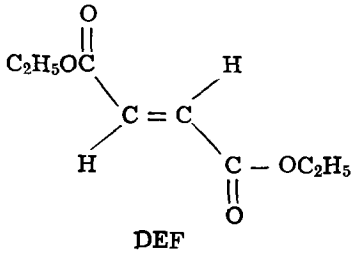

DEF

previous studies (2, 3) have shown that the following reactions of the initially formed radical anion are sufficiently slow to allow rather easy application of electroanalytical techniques.

Experimental

Materials.—Dimethylformamide (DMF) was purified as previously described (5). Tetra-n-butylammonium iodide (TBAI) was the polarographic grade supplied by Southwestern Analytical Chemicals, Austin, Texas. Diethyl fumarate (DEF) (K and K Laboratories, Inc., Plainview, New York) was used without further purification, since preliminary experiments with distilled samples showed identical behavior to that of unpurified samples.

Apparatus.—The cell used in coulometric experiments is shown in Fig. 1. It is comprised of four compartments (auxiliary, intermediate-buffer, working, and reference,) four electrodes (auxiliary, micro, macro, and reference), and a freeze-pump-thaw (F-P-T) chamber. The F-P-T chamber is used for degassing the solution by freezing at liquid nitrogen temperature, pumping to about 10^{-5} Torr, and then thawing to room temperature (with the pump off). This procedure is repeated three to five times (5).

A silver wire isolated in a compartment closed with a fine sintered glass disk was used as a reference electrode. It was found to be stable (with less than a 10 mV drift) in our TBAI-DMF systems for at least 48 hr. The reference electrode was positioned in the current path between the auxiliary and macroelectrode so that the macroelectrode would not overshoot the controlled voltage because of iR drops in coulometry experiments.

The microelectrode used for chronoamperometry and voltammetry was an 0.16 cm diameter platinum disk in glass. It was pretreated by soaking briefly in nitric acid, rinsing, and drying. The macroelectrode was two thicknesses of fine platinum gauze, 2 cm high by 10 cm long, formed into a "C." It was attached with a pin socket for easy cleaning and assembly. The auxiliary electrode was 20 cm of coiled 18 gauge platinum wire. Stirring was accomplished with a Teflon-coated stirring bar (5/16 in. diameter by 1/2 in. long). Some chronoamperometric meaurements were performed in a cell similar to the one shown in Fig. 1, but with only two large compartments (F-P-T and working), with the auxiliary electrode housed in a fritted chamber similar to that used with the reference electrode described above, but having a medium, rather than fine, sintered glass disk on the bottom.

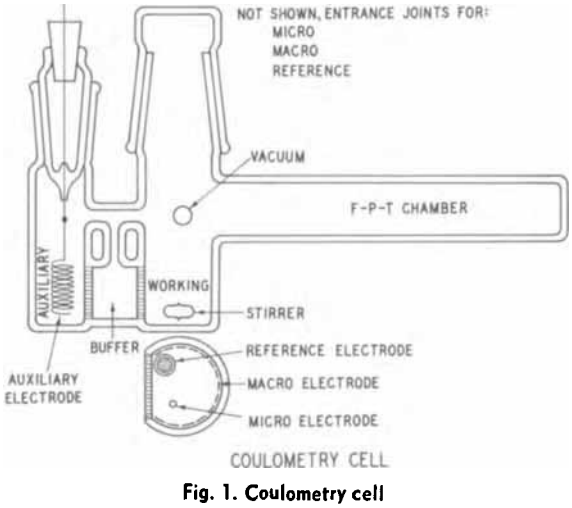

Fig. 1. Coulometry cell

Electrochemical experiments were carried out with a PAR Model 170 Electrochemistry System (Princeton Applied Research Corporation, Princeton, New Jersey). Positive feedback was generally used for resistance compensation in voltammetric experiments. In some high current situations during macroelectrolysis at high concentrations compensation was not complete because of limitations in the instrument. This does not affect the results, however, since it resulted in actual potentials less negative than those set. The various functions of the instrument were checked and calibrated periodically.

Some chronoamperometric data were also taken using a Wenking Model 61-RH potentiostat in conjunction with a Wavetek Model 114 function generator and associated switching and triggering circuitry.

Most of the chronoamperometric and chronocoulometric data were recorded using a PDP-12A computer (Digital Equipment Corporation, Maynard, Massachusetts) for data acquisition. Signals for current and coulombs from the PAR-170 system were interfaced to the analog-to-digital converters of the PDP-12A through appropriate operational amplifier followers, sense line triggers, etc. Data points were taken every 50 μsec. Techniques employed were generally similar to previous applications of digital data acquisition techniques in chronocoulometric experiments [see (6, 7) and references contained therein].

Typical experimental procedure.—A solution of DEF in DMF was prepared in a 50 ml volumetric flask. When lithium perchlorate was to be added to the electrolysis solution, a weighed amount of $LiClO_4 \cdot 3H_2O$ was added to the F-P-T chamber and 4.00g of TBAI was placed in the bottom of the working electrode compartment along with the stirring bar. The TBAI could not be mixed with the $LiClO_4$ at this stage, as lithium iodide will air oxidize to give iodine.

The cell was set up with the F-P-T chamber vertical and the DEF-DMF solution was poured in. The cell was then assembled by inserting the electrodes, closed and evacuated, and the F-P-T cycles were carried out. It was then manipulated to mix the TBAI and liquid (50 ml of DMF solution and 4.00g TBAI result in a volume of 53.0 ml).

The cell was then righted, the levels in the different compartments adjusted roughly by sloshing, and then the cell was set on a flat, stable surface and allowed to equilibrate thermally and hydrostatically; this took about 2 hr. In this cell 42% of the solution was in the working electrode compartment, as determined by removing the contents of each chamber and weighing them. The reference compartment was filled by means of a small hole just above, and a larger hole about 2 cm above, the electrolyte level. All electrochemical experiments were performed with the solution under reduced pressure. During coulometry the cell was maintained at 20°-25° and was stirred continuously. To prevent condensation in the remote portions of the cell, the liquid had to be kept cooler than the dry portions of the cell as transport through the vapor space was rapid at the reduced pressure.

Results

Cyclic voltammetry.—Cyclic voltammetric experiments were undertaken to determine the potentials for the potential-step experiments, to provide qualitative and semiquantitative information for use in

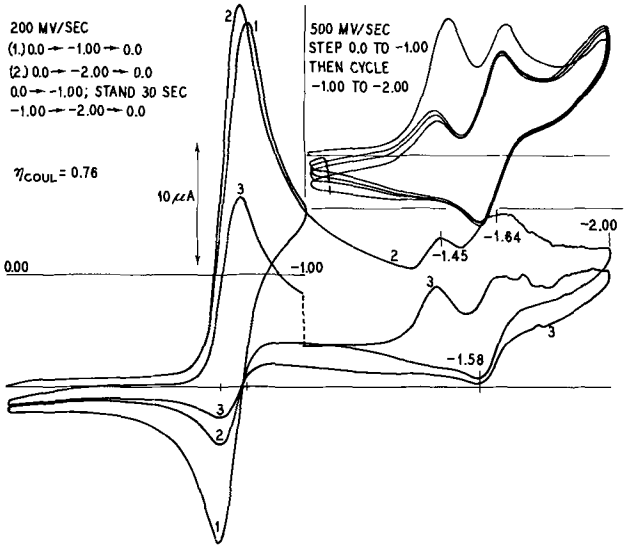

Fig. 2. Cyclic voltammograms for DEF in 0.44M TBAI-DMF solution. Potential programs and sweep rates as shown.

determining the effects of different additives (water, $LiClO_4$), and for following macroscale electrolyses. Typical cyclic voltammograms of DEF in anhydrous DMF containing 0.44*M* TBAI are shown in Fig. 2. The first peak occurs at a cathodic peak potential, E_{pc}, of −0.80V *vs.* the Ag reference electrode (Ag-RE). In all of the solutions studied the range of the peak potential was −0.78 to −0.81V with sweep rates of 100-200 mV/sec (and with positive feedback used for resistance compensation). Half-peak potentials were typically 60 mV positive of E_{pc}; $E_{pc} - E_{pa}$ values were typically 65-67 mV. Baizer and co-workers (3) gave −1.54V *vs.* an aqueous saturated calomel electrode (SCE) for the polarographic $E_{1/2}$ of the first wave in DMF −0.1*M* tetraethylammonium perchlorate (TEAP) solutions—both anhydrous and containing 1*M* water. Smaller waves following the first occur at about −1.45 and −1.64V *vs.* Ag-RE. Baizer and co-workers (3) found that a current decrease was noted during polarographic reduction of DEF at potentials about 0.6V past the $E_{1/2}$ of the first wave in anhydrous DMF. They ascribed this behavior to formation of the dianion at these potentials which reacted with incoming parent molecules in a polymerization reaction. In DMF solutions containing 1*M* H_2O a second wave, somewhat smaller than the first wave, at −2.27V *vs.* SCE, was observed. Typical data for the variation of the cathodic peak current, i_{pc}, of the first reduction with scan rate, v, and concentration, C, are given in Table I. Baizer and co-workers (3) mention a similar decrease of $i_{pc}/v^{1/2}$ C with increasing v for DEF and related compounds.

Table I. Typical cyclic voltammetric data for first reduction wave of diethyl fumarate[a]

Concentration, C (mM)	Scan rate, v (V/sec)	Peak current, i_{pc} (μA)	$i_{pc}/v^{1/2}C$
1.71	0.10	43	8.0
	0.20	60	7.8
	0.50	91	7.6
	1.00	128	7.5
	2.00	171	7.1
	5.00	262	6.8
2.03	0.02	23	8.0
	0.05	36	8.0
	0.10	51	7.9
	0.20	71	7.8
	0.50	105	7.3
3.31	0.05	62	8.4
	0.10	85	8.0
	0.20	118	8.0
	0.50	178	7.6
	1.00	247	7.5
	2.00	336	7.2
	5.00	500	6.8

[a] The solution was 0.1*M* TBAI in DMF. The platinum working electrode area was 0.11 cm². The value of $i_{pc}/v^{1/2}C$ for the reduction of azobenzene in these solutions at this electrode was 8.2, and was independent of scan rate. Experimental results of V. Puglisi.

Double potential step experiments.—To measure the rate at which the radical anion produced during the first reduction wave reacts and from these data elucidate the mechanism for the reaction, double potential step chronoamperometric experiments were undertaken. These methods, which have been used previously for reactions involving following first-order reactions (EC-mechanism) (8, 9), involve measuring the current as a function of time when the potential of the working electrode is changed.

Experimentally, the potential is first stepped to E_1, where the reaction $R + e \rightarrow R^{\cdot -}$ occurs at a mass transfer controlled rate. At a time T_F, the potential is stepped to E_2 where only the reaction $R^{\cdot -} \rightarrow R + e$ occurs. In chronoamperometric experiments, the current is measured just before T_F (I_F) and just before $2T_F$ (I_B). The ratio I_B/I_F has a value of 0.2928 in the absence of kinetic perturbations regardless of the length of T_F (8). If $R^{\cdot -}$ reacts to form nonoxdizable species, then the ratio I_B/I_F is perturbed, and will be a function of T_F. The order and rate of the perturbing reaction can be found from the variation of this ratio with T_F and concentration.

Chronocoulometric experiments are similar, except that Q_F and Q_B are measured at T_F and $2T_F$, respectively, with the unperturbed ratio Q_B/Q_F equal to 0.4142 (9).

Because the potential is stepped to values where the electrode reactions (either reduction of R or oxidation of $R^{\cdot -}$) occur at diffusion controlled rates, the measurement is unaffected by the rate of the electron transfer step. Moreover, when an adequate potentiostat and positive feedback compensation of uncompensated resistance are employed, the measurements are relatively unperturbed by double layer charging effects. These are decided advantages of these techniques over cyclic voltammetric investigations of the mechanism. Moreover, digital simulation of the different cases involving kinetic complications are somewhat easier for potential steps than for potential sweeps.

Five different reaction schemes were considered as possible in the hydrodimerization reaction scheme:

I. First order EC:

At E_1: $R + e \rightarrow R^{\cdot -}$ $\quad R^{\cdot -} \xrightarrow{k_1} X$

At E_2: $R^{\cdot -} \rightarrow R + e$

II. First order ECE

At E_1: $R + e \rightarrow R^{\cdot -}$ $\quad R^{\cdot -} \xrightarrow{k_1} R^{\cdot -\prime}$; $R^{\cdot -\prime} + e \rightarrow X$

At E_2: $R^{\cdot -} \rightarrow R + e$

III. Second order EC

At E_1: $R + 2e \rightarrow R^{2-}$ $\quad R^{2-} + R \xrightarrow{k_2} R_2^{2-}$

At E_2: $R^{2-} \rightarrow R + 2e$

IV. Second order ECE

At E_1: $R + e \rightarrow R^{\cdot -}$

$R^{\cdot -} + R \xrightarrow{k_2} R_2^{\cdot -}$; $R_2^{\cdot -} + e \rightarrow R_2^{2-}$

At E_2: $R^{\cdot -} \rightarrow R + e$

(For IVA: $R^{\cdot -} \rightarrow R + e$ and $R_2^{\cdot -} \rightarrow$ products + e)

V. Second order dimerization

At E_1: $R + e \rightarrow R^{\cdot -}$ $\quad 2R^{\cdot -} \xrightarrow{k_2} R_2^{2-}$

At E_2: $R^{\cdot -} \rightarrow R + e$

Schemes III, IV, and V represent possible alternate paths to the hydrodimer. It is assumed that R_2^{2-} is protonated rapidly, so that oxidation of R_2^{2-} at the

electrode at E_2 need not be considered. Similarly, the results would be the same in say V, if R^- first protonated in a fast reaction and then the protonated species coupled to R_2H_2. Scheme II represents the case of, for example, protonation of R^- followed by further reduction to lead to the two-electron product RH_2. Scheme I has been treated previously (8, 9) and was included here to compare with the other cases and also to serve as a check on our digital simulation procedure.

The digital simulation procedures for obtaining theoretical I-time (t) and Q-t curves generally followed methods described in detail before (10, 11). For simplicity, the diffusion coefficients of all species were taken as equal. The results are changed only slightly for reasonable differences in diffusion coefficients (*e.g.*, $D_{R^-} = 2D_{R_2^{2-}}$, etc.). The normalized currents or coulombs are determined as functions of the dimensionless parameter k_jTC^{j-1} (when $k_jT_FC^{j-1} = 1.0$), where j is the order of the reaction consuming R^- ($j = 1$ for cases I and II and $j = 2$ for cases III, IV, and V) and C is the bulk concentration of R (Fig. 3). Variations in $k_jT_FC^{j-1}$ result in variations in the ratio I_B/I_F and Q_B/Q_F for each mechanism. As a result of several simulations with other values assigned to the parameter $k_jT_FC^{j-1}$, the ratios shown in Table II were obtained. From these tabulated data the working curves for the different mechanisms are drawn. To simplify evaluation of experimental results and to establish criteria that might distinguish between the proposed mechanisms, the working curves are plotted using the dimensionless ratio I_B/I_F, normalized by dividing by 0.2928, which we will call R_I, the normalized current ratio. This ratio will vary from 1.0 in the absence of kinetic complications to zero for large values of $k_jT_FC^{j-1}$. Similarly, the Q_B/Q_F ratio is normalized to yield an R_Q which varies between zero in the absence of kinetic perturbations to 1.0 in the limit of fast kinetics. (Where comparisons with previous theoretical treatments based on solution of the partial differential diffusion equations under appropriate boundary conditions are possible, excellent agreement is obtained.) The horizontal axis is given in units of $t_{1/2}$, the real time at which $R_I = 0.5$ (Fig. 4). This value of $t_{1/2}$ can be used to calculate the rate constant of the reaction, once the mechanism is established, by the expressions given in Table II. The different mechanisms can be distinguished by comparing the shape of experimental R_I or R_Q *vs.* $t_{1/2}$ curves with the theo-

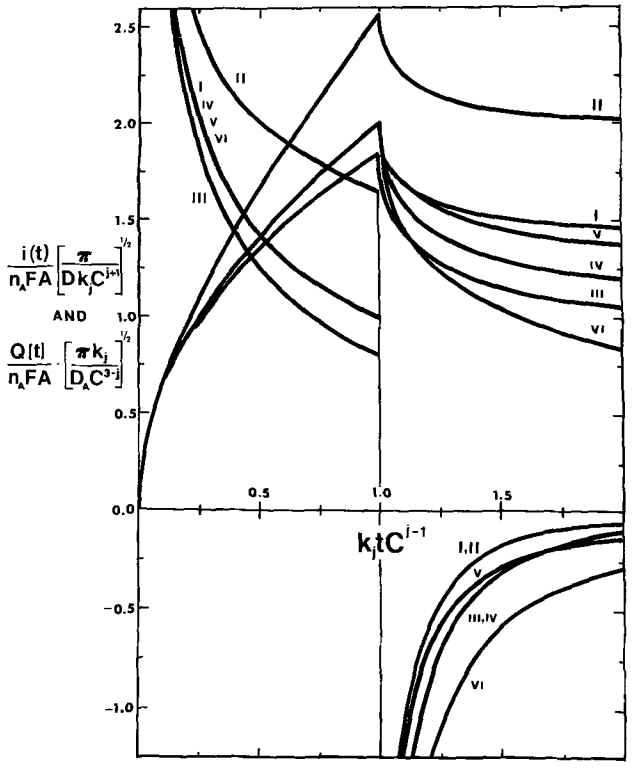

Fig. 3. Variation of current and coulombs with k_jtC^{j-1} for different mechanisms in text for double potential step chronoamperometry and chronocoulometry. VI represents system with no kinetic complications.

Table II. Values of normalized current (R_I) and coulomb (R_Q) ratios for different values of kT_FC for possible hydrodimerization reaction mechanisms[c]

k_1T_F	R_I (simulation)	R_I (lit)[a]	R_Q (simulation)	R_Q (lit)[b]
Mechanism I				
0.001	0.998		0.001	
0.050	0.917	0.918	0.043	0.029
0.100	0.842	0.844	0.083	0.082
0.200	0.709	0.711	0.157	0.154
0.300	0.598	0.601	0.223	0.219
0.400	0.505	0.508	0.283	0.278
0.500	0.427	0.429	0.337	0.332
0.700	0.305	0.308	0.430	0.423
0.900	0.219	0.222	0.506	0.499
1.00	0.186	0.188	0.539	0.532
1.30	0.114	0.116	0.621	0.612
1.70	0.060	0.062	0.701	0.693
Mechanism II				
0.001	0.997		0.002	
0.050	0.872	0.889	0.060	
0.100	0.765	0.770	0.114	
0.150	0.673	0.678	0.164	
0.200	0.595	0.603	0.211	
0.250	0.528	0.536	0.254	
0.300	0.470	0.478	0.294	
0.400	0.375	0.382	0.365	
0.500	0.302	0.309	0.427	
0.700	0.200	0.205	0.528	
1.00	0.112	0.115	0.638	
1.40	0.054	0.056	0.736	
k_2T_FC	R_I		R_Q	
Mechanism III				
0.001	0.999		0.001	
0.100	0.917		0.036	
0.250	0.812		0.085	
0.400	0.723		0.128	
0.700	0.582		0.202	
0.900	0.508		0.244	
1.00	0.475		0.263	
1.30	0.392		0.315	
1.80	0.289		0.385	
2.40	0.203		0.452	
3.50	0.110		0.543	
5.00	0.049		0.626	
Mechanism IV				
0.001	0.998		0.001	
0.100	0.893		0.045	
0.200	0.802		0.086	
0.300	0.723		0.123	
0.500	0.594		0.189	
0.700	0.495		0.246	
1.00	0.383		0.317	
1.30	0.302		0.377	
1.80	0.208		0.456	
2.90	0.099		0.577	
4.00	0.051		0.655	
Mechanism IVA				
1.25	0.249		0.526	
5.00	0.181		0.679	
10.00	0.141		0.761	
20.00	0.106		0.824	
30.00	0.090		0.852	
50.00	0.073		0.879	
100.00	0.056		0.907	
Mechanism V				
0.0005	0.989		0.001	
0.075	0.912		0.069	
0.200	0.798		0.162	
0.350	0.697		0.249	
0.500	0.619		0.316	
0.800	0.509		0.414	
1.00	0.456		0.463	
1.20	0.414		0.502	
2.00	0.306		0.608	
5.00	0.162		0.759	
12.5	0.079		0.058	
25.0	0.044		0.906	

[a] From ref. (8).
[b] From ref. (9); note, however, that a computational error appears to have been made computing the final results from the correct derived equation. The results in this column have been recomputed (J. Phelps, University of Texas at Austin, 1968).
[c] Rate constants can be calculated from the measured $t_{1/2}$-value by the following equations:

Mechanism	Rate constant
I	$k_1 = 0.406/t_{1/2}$
II	$k_1 = 0.273/t_{1/2}$
III	$k_2 = 0.922/t_{1/2}C$
IV	$k_2 = 0.690/t_{1/2}C$
V	$k_2 = 0.830/t_{1/2}C$

where $t_{1/2}$ is the value of T_F at which $R_I = 0.5$.

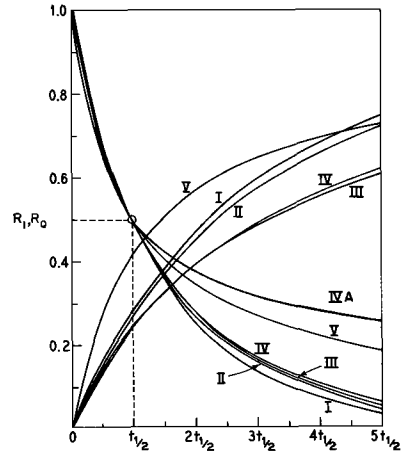

Fig. 4. Variation of normalized current and coulomb parameters as functions of $t_{1/2}$ for the different mechanisms in the text.

retical ones of Fig. 4. The following conclusions can be made about the possibility of distinguishing among mechanisms I through V: (*i*) the R_I and R_Q *vs.* T_F behavior for V is sufficiently different from the others to be distinguished; (*ii*) since I and II are independent of concentration, they may be distinguished from III and IV; (*iii*) it would be difficult to distinguish between III and IV only on the basis of potential step data; however, other information, such as the number of electrons involved in the electrode reaction determined at small times and low concentrations, or the establishment of the existence of intermediate radical ions by ESR can be used.

Double potential step chronoamperometric experiments were performed with several concentrations of DEF in DMF-TBAI solutions containing different amounts of water; typical results are given in Fig. 5 and Table III. The points shown in Fig. 5 fall along a theoretical curve characteristic of mechanism V, values of the rate constant for dimerization of the radical anions, k_2, are given in Table III. Note that the data do not fit the R_I *vs.* t behavior characteristic of the other mechanisms, particularly for times greater than several half-lives. For example, for mechanism IV, at a $T_F = 5\ t_{1/2}$, R_I is less than 0.07, whereas experimentally, R_I values of about 0.19 are found. Within the framework of mechanisms considered, the type involving formation of radical ions and then coupling of these gives the best agreement with theory. Addition of water increases the rate of this coupling reaction, but does not appear to alter the over-all mechanism.

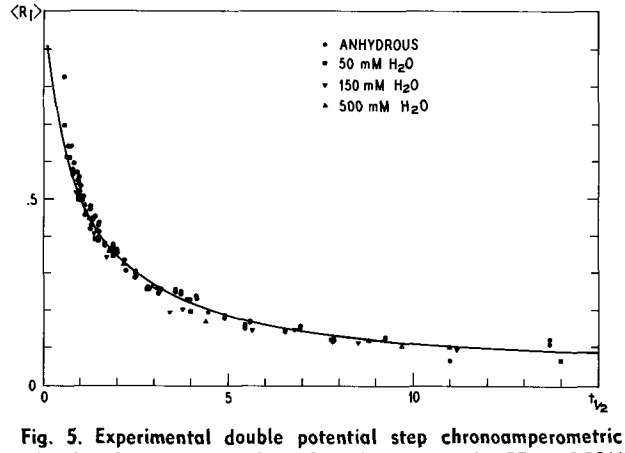

Fig. 5. Experimental double potential step chronoamperometric results for the reduction of a 10 mM solution of DEF in 0.10M TBAI in DMF solutions with different amounts of water added. The points are experimental and the line shows the simulation results of mechanism V.

Table III. Results of double potential step chronoamperometric investigation of diethyl fumarate hydrodimerization[a]

Water concentration	$-E_{p/2}$ (V *vs.* Ag reference)	k_2 [b] (l/mole-sec)	$it^{1/2}$ [c] (μA-sec$^{1/2}$)
Anhydrous	0.76	37	23
Anhydrous[d]	—	30.5	—
Anhydrous[d,e]	—	15.5	—
50 mM	0.75	46	24
150 mM	0.76	57	23
500 mM	0.74	145	23

[a] The solution contained 0.2M tetra-n-butylammonium iodide (TBAI) in dimethylformamide (DMF) and 10.0 mM diethyl fumarate (DEF). The potential program was −0.2V, −1.0V (E_1), −0.2V (E_2) *vs.* silver wire reference electrode. The temperature was 25° ± 1°C.
[b] For dimerization of $R\cdot$.
[c] For forward step.
[d] 9.75 mM DEF, 0.10*M* TBAI.
[e] Temperature was 0°C.

Table IV. Controlled potential coulometry results for the reduction of diethyl fumarate

A. Solution containing 0.43*M* TBAI in DMF

Diethyl fumarate concentration (mM)	n_{app}
4.67	0.76
6.00	0.76
10.0	0.61
17.7	0.64
24.0	0.64

B. Solution containing about 10 m*M* DEF and 0.44*M* TBAI in DMF with different amounts of $LiClO_4 \cdot 3H_2O$

$[LiClO_4 \cdot 3H_2O]/[DEF]$	n_{app}
0.0	0.61
0.50	0.80
0.50[a]	0.82
0.89	0.91
1.93	0.98
2.12	0.94
3.24	0.96
3.9	0.99

C. Solution containing 0.44*M* TBAI in DMF with other additives

[NaI]/[DEF] = 2.0[b]	0.62
[NaI + $3H_2O$]/[DEF] = 2.0[b]	0.63
[Hydroquinone]/[DEF] = 2.0[c]	1.32

[a] Added water to give $[H_2O]/[DEF] = 6.5$.
[b] [DEF] = 1 mM.
[c] [DEF] = 16.8 mM.

Coulometric experiments.—Table IVA shows the results of controlled potential coulometric reduction of DEF in anhydrous DMF, for various DEF concentrations. In all cases the apparent number of faradays per mole of DEF, n_{app}, is appreciably less than the value of 1.00 expected for electrohydrodimerization. The electrolysis times for exhaustive electroreduction were short (less than 1000 sec) and during electrolysis the working compartment solution turned yellow, while the middle compartment solution did not change color. Cyclic voltammograms taken during the exhaustive electrolysis showed that the first DEF reduction peak (Fig. 2) and the peak at −1.45V diminished with time and had disappeared by the end of the electrolysis. The peak at −1.64V persisted and at conclusion it showed a peak current of 7 μA compared to an initial peak current of 30 μA for the first reduction wave of DEF.

Effect of addition of lithium perchlorate and other substances.—As an aid in the elucidation of the mechanism of the reaction, a few preliminary experiments involving the addition of alkali metal ion salts or hydroquinone were carried out.

Table IV lists coulometric n_{app}-values obtained for reduction of solutions containing different amounts of lithium perchlorate trihydrate in addition to TBAI in DMF, for DEF of about 1 mM. These data are shown graphically in Fig. 6. As the ratio of $LiClO_4 \cdot 3H_2O$ to DEF approaches about 2.0, the n_{app}-value increases to the value of 1.0 expected for the hydrodimerization reaction as the sole reaction. For ratios of about 2.0 and

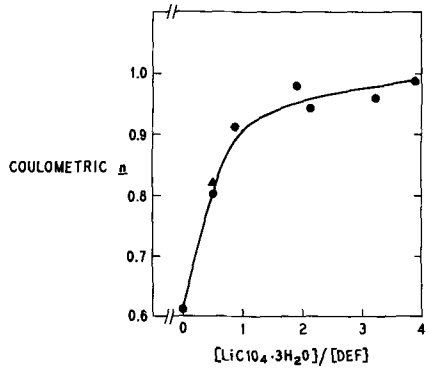

Fig. 6. Coulometric n_{app}-values for the reduction of DEF in solutions containing various ratios of lithium perchlorate trihydrate to DEF. The solutions contained 10 mM DEF. The point marked △ contained additional water to give $[H_2O]/[DEF] = 6.5$.

greater the total electrolysis times were typically 4000 sec as compared to shorter electrolysis times in anhydrous-DMF, or for low $LiClO_4 \cdot 3H_2O$/DEF ratios. The solution after reduction was water white for higher amounts of $LiClO_4 \cdot 3H_2O$, as compared to the yellow solutions characteristic of solutions containing no or low amounts of this salt. In one experiment at a $LiClO_4 \cdot 3H_2O$/DEF ratio of 0.50, water was added to give a water to DEF ratio of 6.5. This corresponds to the amount of water present in solutions with $LiClO_4 \cdot 3H_2O$/DEF ratios greater than 2.0. If the role of the lithium ion was only to catalyze a reaction with water, the coulometric n_{app} should approach 1.0. Experimentally, the n_{app}-value found was not significantly different from those found in solutions containing no additional water.

The cyclic voltammetric behavior of DEF is also altered by the presence of $LiClO_4 \cdot 3H_2O$ (Fig. 7). For $LiClO_4 \cdot 3H_2O$/DEF ratios of 1.9 or higher, no back current is observed for the oxidation of the reduction product of the first wave, for scan reversal at potentials of −1.0 to −1.7V *vs.* Ag-RE. Filming of the electrode occurs when the reduction scan is carried out to potentials beyond about −1.5V; evidence for this filming is the greatly decreased reduction currents on second and subsequent cathodic scans following reversal at these potentials. Normal (nonfilming) behavior for subsequent cathodic scans is observed for scans reversed at potentials up to −1.0V. At lower $LiClO_4 \cdot 3H_2O$/DEF ratios, some reversal current is observed after the first wave.

Controlled potential coulometry results for the addition of sodium iodide, and sodium iodide and water (Table IVC) show that lithium ion has a specific effect. The n_{app}-values with both NaI and H_2O are very close

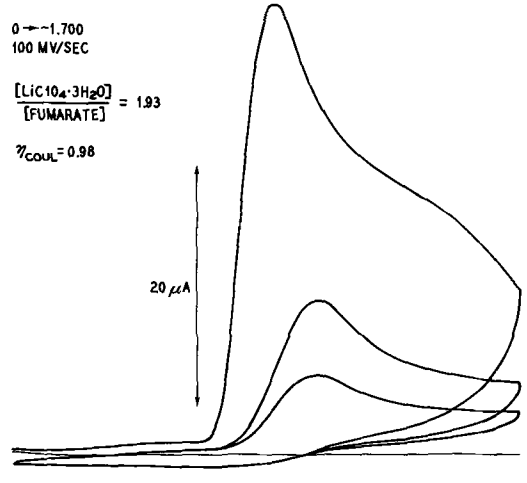

Fig. 7. Cyclic voltammograms for DEF solutions containing lithium perchlorate trihydrate.

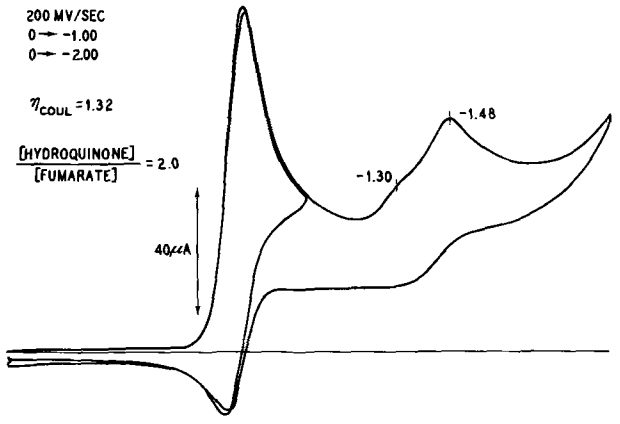

Fig. 8. Cyclic voltammograms for DEF solutions containing hydroquinone.

to those in anhydrous DMF. Cyclic voltammograms with NaI, however, are very similar to those with $LiClO_4 \cdot 3H_2O$ (Fig. 7); they show the distortion following the fumarate reduction, the absence of back current on reversal following the first reduction wave, and the apparent filming of the electrode when cycled beyond −1.5V.

When hydroquinone is added as a proton donor in a coulometric experiment, an n_{app}-value larger than one is obtained. Cyclic voltammetry in the presence of hydroquinone (Fig. 8) as compared to that in its absence (Fig. 2) shows that the peak at −1.64V is absent, the peak at −1.45V persists and may show some reversibility, and a small peak at −1.30V is clearly detectable. The peak anodic current following reversal at −1.0V is smaller for solutions containing hydroquinone at the same DEF concentrations, while the cathodic peak current for the first reduction wave is about 12% larger.

Discussion

In agreement with Baizer and co-workers (3), we find the first step of the reduction to be a one-electron transfer to form the anion radical of DEF ($R \cdot^-$). Evidence for this includes the cyclic voltammetric $i_p/v^{1/2}$ C-value, which is very near that for the reduction of azobenzene in DMF, a known one-electron reduction (12). Moreover, electron spin resonance spectra of $R \cdot^-$ have been observed (13, 14). The double potential step experiments suggest that dimerization of these radical ions is the major path to the hydrodimer for DEF. Rejection of this dimerization step in the previous study (3) was based primarily on the rather large decrease of $i_p/v^{1/2}$ values with increasing v, which the authors felt favored an ECE-type reaction. However, the particular type of ECE-reaction which might occur (a second order ECE, mechanism IV) is different from the more usual first order ECE reaction (mechanism II) in that $n_{app} = 1$ at the limit of both very large and very small values of k_2 for mechanism IV, (whereas n_{app} varies between 1 and 2 as k_1 increases, for mechanism II). Several theoretical papers on linear potential sweep and cyclic voltammetry have recently appeared (15-18) which pertain to these mechanisms. In particular they show that the dimerization mechanism (scheme V) shows a decrease of $i_p/v^{1/2}$ of up to 18% with increasing v (15, 17), while the second-order ECE mechanism (scheme IV) shows a small increase in this function with increasing scan rate. An excellent comparison of these two mechanisms can be seen in Fig. 6 of the paper of Saveant *et al.* (17). Hence, the cyclic voltammetric data in this paper and in ref. (3) are in better agreement with the dimerization mechanism, although more detailed cyclic voltammetric experiments are required to test the extent of agreement quantitatively. The free energy of activation of the coupling process was determined from the measured rate constants at 25° and 0°C to be about

−4.5 kcal/mole of R_2^{2-} formed. This rather low value may also be indicative of a radical anion coupling reaction. Dimerizations of anion radicals are known in the case of vinyl and vinylidene monomers (19) and also for ketyl anion radicals in the formation of pinacols (20). Wiemann (21) also postulated the coupling of radical anions in the hydrodimerization of esters. The relative contribution of mechanisms IV and V to the over-all hydrodimerization path must depend on the structure of the activated olefin.

We have also investigated mechanism IV including the possibility of $R_2\cdot^-$ being electroactive and oxidized at E_2. Computer simulations of this mechanism (IVA) yield an R_I curve which lies significantly above V (Fig. 4). The possibility of $R_2\cdot^-$ having diffusion coefficients significantly different from the other species was also simulated. For example, curve IV is even higher above V when D_{R_2-} is smaller than D_R, so that mechanism IVA does not agree with our experimental data.

In agreement with Baizer and co-workers (3), we find that water increases the rate of disappearance of the anion radicals. This occurs without apparently causing a change in mechanism. Although this could be ascribed to fast protonation of $R\cdot^-$ to RH· followed by dimerization, this seems unlikely, since RH· should also be reduced at the electrode (or by $R\cdot^-$) in an ECE reaction (mechanism II) and no evidence for the involvement of this reaction is observed, even in coulometric experiments. Since the amounts of water which affect the reaction are too small to change the bulk dielectric constant appreciably, the rate increase may be due to specific solvation of the anion radicals by water. Hydroquinone, a better proton donor than water, does show a contribution of the first-order ECE mechanism both in voltammetric and coulometric experiments.

Polymerization, probably by reaction of R with R_2^{2-}, can account for the low n_{app}-values in coulometry. This reaction may not be important in the potential step experiments, since the solution in the vicinity of the electrode is relatively depleted in R. Lithium ion decreases the extent of this polymerization, perhaps by increasing the rate of protonation of R_2^{2-}.

Acknowledgment

The support of the Robert A. Welch Foundation and the National Science Foundation (GP 6688X) is gratefully acknowledged. The digital data acquisition was acquired under a grant from the National Science Foundation (GP 10360). We appreciate support for one of us (W.V.C.) by the Phillips Petroleum Company.

Manuscript submitted Dec. 10, 1970; revised manuscript received Jan. 20, 1971.

Any discussion of this paper will appear in a Discussion Section to be published in the December 1971 JOURNAL.

REFERENCES

1. M. M. Baizer, J. P. Petrovich, and D. A. Tyssee, *This Journal*, **117**, 173 (1970).
2. J. P. Petrovich, M. M. Baizer, and M. R. Ort, *ibid.*, **116**, 749 (1969).
3. J. P. Petrovich, M. M. Baizer, and M. R. Ort, *ibid.*, **116**, 743 (1969).
4. F. Beck, *Chem.-Ing. Tech.*, **37**, 607 (1965).
5. L. R. Faulkner and A. J. Bard, *J. Am. Chem. Soc.*, **90**, 6284 (1968).
6. G. Lauer, R. Abel, and F. C. Anson, *Anal. Chem.*, **39**, 765 (1967).
7. G. Lauer and R. A. Osteryoung, *ibid.*, **38**, 1137 (1966).
8. W. M. Schwarz and I. Shain, *J. Phys. Chem.*, **69**, 30 (1965); **70**, 845 (1966).
9. J. H. Christie, *J. Electroanal. Chem.*, **13**, 79 (1967).
10. S. Feldberg, "Electroanalytical Chemistry," Vol. 3, A. J. Bard, Editor, Marcel Dekker, Inc., New York (1969).
11. S. A. Cruser and A. J. Bard, *J. Am. Chem. Soc.*, **91**, 267 (1969).
12. J. L. Sadler and A. J. Bard, *ibid.*, **90**, 1979 (1968).
13. S. F. Nelson, *Tetrahedron Letters*, **39**, 3795 (1967).
14. I. Goldberg and A. J. Bard, Unpublished investigation, The University of Texas, 1969.
15. M. L. Olmstead, R. G. Hamilton, and R. S. Nicholson, *Anal. Chem.*, **41**, 260 (1969).
16. R. S. Nicholson, *ibid.*, **37**, 667 (1965).
17. C. P. Andrieux, L. Dadjo, and J. M. Saveant, *J. Electroanal. Chem.*, **26**, 147 (1970).
18. J. M. Saveant and E. Vianello, *Electrochim. Acta*, **12**, 1545 (1967).
19. M. Szwarc, "Carbanions, Living Polymers and Electron Transfer Processes," p. 367 *et. seq.*, Interscience, New York (1968).
20. C. K. Mann and K. K. Barnes, "Electrochemical Reactions in Nonaqueous Solvents," Chap. 6, Marcel Dekker, Inc., New York (1970).
21. J. Wiemann, *Bull. Soc. Chim. France*, **1964**, 2545.

Limiting Local Current Densities for Electrodes Located on the Walls of a Rectangular Channel with Laminar Flow; Asymptotic Solution and Experimental Verification

I. Roušar,* J. Hostomský, and V. Cezner

Department of Inorganic Technology, Technical University, Prague, Czechoslovakia

and B. Štverák

Institute for Research, Production, and Application of Radioisotopes, Prague, Czechoslovakia

ABSTRACT

Equations were derived for calculating the local and average limiting current densities for an electrode located on the wall of a rectangular channel. The validity of the equation for the average limiting current density was checked experimentally by the deposition of Hg^{2+}. The equation expressing the local limiting current density as a function of the length and width of the electrode was verified by the deposition of Ag from an electrolyte labeled with ^{110m}Ag.

For a short electrode located on the wall of a cylindrical tube, the mass transfer rate can be evaluated using the Léveque equation (1)

$$\mathrm{Nu} = 1.62\ (\mathrm{Re\ Sc}\ D/L)^{1/3} \qquad [1]$$

where the Nusselt, Reynolds, and Schmidt number are given by

$$\mathrm{Nu} = [\bar{i}/(n\mathbf{F})]D/[D_1(c^0_1 - c^s_1)] \qquad [2]$$

$$\mathrm{Re} = \bar{u}\,D/\nu \qquad [3]$$

$$\mathrm{Sc} = \nu/D_1 \qquad [4]$$

Equation [1] is an asymptotic solution of the Graetz problem (2). Sieder and Tate (3) evaluated an empirical equation of the form

$$\mathrm{Nu} = 1.86\ (\mathrm{Re\ Sc}\ D/L)\ (\mu/\mu_s)^{0.14} \qquad [5]$$

where the factor $(\mu/\mu_s)^{0.14}$ represents a correction for the deformation of the velocity profile due to variable liquid viscosity.

Limiting current distribution on the infinite, parallel plane electrodes is well known (8). For that system, current distribution controlled simultaneously by ionic transport, ohmic drop, and electrode polarization was calculated recently by Parrish and Newman (9).

Mass transport to short electrodes located on the opposite sides of the rectangular channel has not yet been analyzed quantitatively and, therefore, is dealt with in the present paper.

Model System

An electrode of a length L and of a width $2d$ is embedded in the wall of a rectangular channel with dimensions $2b$, $2c$. The origin P(O,O,O) of the coordinates x, y, z is located in the center of the leading edge of the electrode. A counterelectrode is located symmetrically on the opposite side of the channel (Fig. 1). The electrolyte flow is laminar and fully developed; constant physical properties of the electrolyte are assumed. The concentration of the electroactive ion "1" on the whole surface of the electrode is equal to c^s_1. In the inlet solution, the concentration of the ion "1" is equal to c^0_1. Only solutions containing an excess of supporting electrolyte or single salt solutions are considered.

Velocity and Concentration Profiles in the Channel

The velocity profile for steady-state laminar flow in a rectangular channel was calculated by Love (4); the resulting equation for the velocity u in the x direction reads (5)

$$u/\bar{u} = \left\{1.5 - 1.5(y/b)^2 - 6(2/\pi)^3 \sum_{n=0}^{\infty} (-1)^n\,(2n+1)^{-3}\,[\cosh(pz/c)]\,(\cosh p)^{-1} \cos(py/c)\right\} \times \left\{1 - 6(b/c)\,(2/\pi)^5 \sum_{n=0}^{\infty} (2n+1)^{-5} \tanh p\right\}^{-1} \qquad [6]$$

where

$$p = (2n+1)\ (\pi c/2b) \qquad [7]$$

and $\bar{u}$ is average linear velocity in the channel. Equation [6] was derived for the coordinate system with the origin Q(O,O,O), see Fig. 1; the equation is valid for systems where the mass flow due to diffusion and migration is relatively small in comparison to the convective flow of electrolyte in the channel. Owing to the high Schmidt number in the electrolyte solutions (Sc $\geqq$ 1000), the diffusion layer is very thin. Hence, for the flow near the wall, the velocity profile can be considered linear inside the diffusion layer. The velocity is then given by the equation

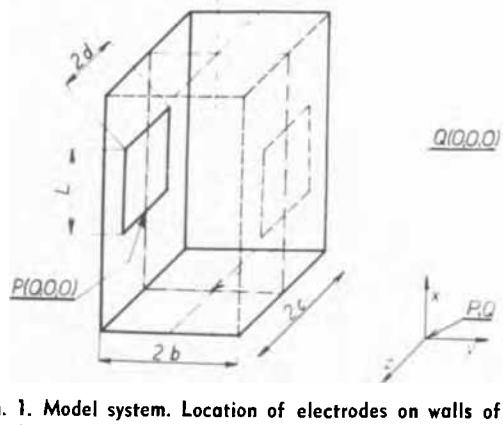

Fig. 1. Model system. Location of electrodes on walls of rectangular channel. $2b$, $2c$: channel dimensions; $2d$: width of electrode; L: length of electrode; P(O,O,O), Q(O,O,O): origins of coordinate systems; x,y,z: coordinates.

* Electrochemical Society Active Member.

Key words: laminar flow, radioactive tracers, hydrodynamic theory, metal deposition.

$$u/\bar{u} = \left(\frac{du/\bar{u}}{dy/b} \right)^s y/b \qquad [8]$$

where

$$\left(\frac{du/\bar{u}}{dy/b} \right)^s = 3f \qquad [9]$$

Substituting $u/\bar{u}$ from [6] into [9] yields the equation for f which is a function of z/c and b/c

$$f = \left\{ 1 - 2(2/\pi)^2 \sum_{n=0}^{\infty}{}' (2n+1)^{-2} \cosh(pz/c)(\cosh p)^{-1} \right\} \times \left\{ 1 - 6(b/c)\ (2/\pi)^5 \sum_{n=0}^{\infty}{}' (2n+1)^{-5} \tanh p \right\} \qquad [10]$$

It is apparent from Eq. [10] that $f \to 1$ for the flow between infinite parallel plates ($b/c \to 0$). The values of f are given in Table I.

The velocity profile can be substituted into the equations of convective diffusion

$$\vec{v} \cdot \nabla c_1 = D_1 \nabla^2 c_1 \qquad [11]$$

with boundary conditions

(*i*) $c_1 = c^s{}_1$ for $y = 0, 0 < x \leqq L$, and $0 \leqq z \leqq d$

(*ii*) $c_1 = c^o{}_1$ for $x = 0$ and $y > 0$

(*iii*) $c_1 = c^o{}_1$ for $0 < x \leqq L$ and $y \to \infty$

Equation [11] can be rewritten in the form

$$u(\partial c_1/\partial x) = D_1(\partial^2 c_1/\partial x^2 + \partial^2 c_1/\partial y^2 + \partial^2 c_1/\partial z^2) \qquad [12]$$

It can be shown by an analysis of the relative order of second derivatives at the right-hand side (6) that $\partial^2 c_1/\partial y^2 >> \partial^2 c_1/\partial x^2$. It can be also shown that diffusion in the z direction can be neglected in comparison to that in the y direction for electrodes of width d smaller than the width c of the channel (see Appendix for a detailed analysis).

After the substitution for u from [8] and [9], the equation of convective diffusion [12] is

$$\bar{u}3f(y/b)(\partial c_1/\partial x) = D_1(\partial^2 c_1/\partial y^2) \qquad [13]$$

Equation [13] can be solved by a method used in similar asymptotic cases. Introducing dimensionless variables η and C defined by

$$\eta = y[\bar{u}f/(3xbD_1)]^{1/3} \qquad [14]$$

and

$$C = (c_1 - c^s{}_1)/(c^o{}_1 - c^s{}_1) \qquad [15]$$

into Eq. [13], we obtain the differential equation

$$-3\eta^2(dC/d\eta) = d^2C/d\eta^2 \qquad [16]$$

with boundary conditions

(*i*) $C = 0$ for $\eta = 0$

(*ii*) $C = 1$ for $\eta \to \infty$

The solution of Eq. [16] is

$$C = \left[\int_0^{\eta} \exp(-\eta^3)\, d\eta \right] \Big/ \left[\int_0^{\infty} \exp(-\eta^3)\, d\eta \right] \qquad [17]$$

where

$$(dC/d\eta)_{\eta=0} = \left[\int_0^{\infty} \exp(-\eta^3)\, d\eta \right]^{-1} = 1/\Gamma(4/3) = 1/0.893 \qquad [18]$$

For calculating the local current densities at the electrode, we obtain

$$i^s/(n\mathbf{F}) = D_1(\partial c_1/\partial y)^s = D_1(c^o{}_1 - c^s{}_1)\ 0.893^{-1}\ [\bar{u}f/(3xbD_1)]^{1/3} \qquad [19]$$

Equation [19] gives the values of local current densities as a function of the x and z coordinates. The values of f needed in the calculation of i^s are given in Table I for several values of z/c and b/c.

The integration of Eq. [19] over the whole surface of the electrode yields

$$\mathrm{Nu} = 1.85\,\phi\,(\mathrm{Re\ Sc}\ D/L)^{1/3} \qquad [20]$$

where

$$D = 4bc/(b + c) \qquad [21]$$

and

$$\phi = (1 + b/c)^{-1/3}\,(c/d) \int_0^{d/c} f^{1/3}\, d(z/c) \qquad [22]$$

The values of ϕ can be found in Table II. Equation [20] represents an analogy to the Léveque equation for rectangular channels.

Experimental

Equation [20] was tested by measuring the limiting current density for the deposition of Hg^{2+} on an electrode (d = 1 cm, L = 8 cm) situated on the wall of a rectangular channel (b = c = 2.15 cm). The experiments were performed at 25°C and a Hg^{2+} concentration of 1.87 x 10^{-7} mole/cm^3, using 1*N* KOH for supporting electrolyte. The Reynolds number varied from 82 to 383. The diffusion coefficient of Hg^{2+} was determined by the Cottrel method (D_1 = 7.6 x 10^{-6} cm^2/sec) and the value of the kinematic viscosity of the electrolyte (ν = 9.66 x 10^{-3} cm^2/sec) was taken from earlier published data (7); hence, the Schmidt number was 1271.

The results of the experiments are collected in Table III. The experimental values of the Nusselt number fall into the range (−2%, +6%) as compared with the theoretical values.

The dependence of i^s on x and z was verified by the deposition of Ag from an electrolyte labeled with ^{110m}Ag. The dimensions of the channel were b = 0.5 cm and c = 1 cm; the electrode covered the entire width of the channel wall (d = 1 cm and L = 10 cm). The temperature was kept at 25°C.

Silver was activated in the thermal neutron flux of a nuclear reactor. The activated ^{110m}Ag was used for the preparation of both the silver cyanide electroplating bath and the solution used in actual mea-

Table I. Values of f as a function of b/c and z/c

z/c	b/c = 2	1	0.5	0.3333	0.25	0.2	0.1	0.05
0.000	2.1552	1.6011	1.3557	1.2475	1.1834	1.1435	1.0673	1.0325
0.100	2.1407	1.5911	1.3506	1.2454	1.1827	1.1433	1.0673	1.0325
0.200	2.0968	1.5610	1.3348	1.2386	1.1802	1.1424	1.0673	1.0325
0.300	2.0225	1.5097	1.3068	1.2258	1.1749	1.1404	1.0672	1.0325
0.400	1.9155	1.4351	1.2636	1.2038	1.1647	1.1359	1.0672	1.0325
0.500	1.7725	1.3342	1.2007	1.1677	1.1453	1.1259	1.0669	1.0325
0.600	1.5882	1.2024	1.1111	1.1092	1.1089	1.1041	1.0656	1.0325
0.700	1.3539	1.0322	0.9842	1.0143	1.0405	1.0562	1.0595	1.0325
0.800	1.0543	0.8106	0.8020	0.8587	0.9106	0.9505	1.0299	1.0310
0.900	0.6563	0.5099	0.5282	0.5927	0.6555	0.7107	0.8865	0.9963
0.925	0.5326	0.4150	0.4360	0.4962	0.5558	0.6097	0.7980	0.9531
0.950	0.3938	0.3073	0.3282	0.3796	0.4313	0.4793	0.6629	0.8577
0.975	0.2303	0.1803	0.1962	0.2316	0.2679	0.3025	0.4471	0.6414
1.000	0.0000	0.0000	0.0000	0.0000	0.0000	0.0000	0.0000	0.0000

Table II. Values of ϕ as a function of b/c and d/c

d/c	b/c = 2	1	0.5	0.3333	0.25	0.2	0.1	0.05
0.000	0.8956	0.9285	0.9668	0.9780	0.9819	0.9840	0.9899	0.9944
0.100	0.8949	0.9279	0.9664	0.9779	0.9818	0.9840	0.9899	0.9944
0.200	0.8929	0.9259	0.9652	0.9773	0.9816	0.9839	0.9899	0.9944
0.300	0.8894	0.9226	0.9630	0.9763	0.9812	0.9838	0.9899	0.9944
0.400	0.8844	0.9178	0.9598	0.9746	0.9805	0.9835	0.9899	0.9944
0.500	0.8777	0.9113	0.9552	0.9721	0.9792	0.9829	0.9899	0.9944
0.600	0.8689	0.9027	0.9489	0.9683	0.9771	0.9818	0.9899	0.9944
0.700	0.8575	0.8915	0.9403	0.9625	0.9735	0.9796	0.9897	0.9944
0.800	0.8426	0.8767	0.9281	0.9536	0.9672	0.9752	0.9890	0.9944
0.900	0.8223	0.8563	0.9099	0.9387	0.9553	0.9657	0.9859	0.9940
0.925	0.8158	0.8497	0.9039	0.9334	0.9507	0.9617	0.9840	0.9935
0.950	0.8085	0.8422	0.8968	0.9270	0.9450	0.9567	0.9811	0.9925
0.975	0.7998	0.8333	0.8882	0.9190	0.9376	0.9498	0.9765	0.9900
1.000	0.7883	0.8214	0.8760	0.9071	0.9261	0.9388	0.9671	0.9829

Table III. Experimental verification of Eq. [20]

Average limiting current densities for the deposition of Hg^{2+} ($c_1 = 1.87 \cdot 10^{-7}$ mole/cm³) in the presence of 1*N* KOH; a rectangular channel ($b = c = 2.15$ cm; $d = 1$ cm; $L = 8$ cm); Sc = 1271

$i \cdot 10^6$ (A/cm²)	Re	$\frac{Nu}{(Re\ Sc\ D/L)^{1/3}}$
4.36	82.3	1.784
4.82	135.5	1.670
5.63	217.8	1.665
6.13	282.6	1.663
6.82	327.2	1.761
7.30	383.3	1.791
Average value		1.722
Theoretical value 1.85 × 0.914		1.69

surements (~0.001m $AgClO_4$, 1m $NaClO_4$, 0.001m $HClO_4$). The silver cyanide bath served for the preparation of standards, *i.e.*, silver plates (1 mm thick) covered with a gradually changing deposit of active silver. For each standard, the weights of active Ag per cm² were known. A thin silver layer (0.2 mm) deposited on a plate 1 mm thick was also prepared using the silver cyanide bath. This silver plate served as an anode in the cell.

During the measurement, the cell voltage was kept at a constant value (*ca.* 300 mV) corresponding to the limiting current density. After finishing the electrolysis, the electrode was dried and its surface was covered with a 1 μm thick layer of polymethylmethacrylate (by mean of a chloroform solution). The electrode surface was then pressed against the AF-3 autoradiography film (ORWO Company, Wolfen, G.D.R.). The optical density of the developed film emulsion defined as log [(incident light intensity-background intensity)/(transmissed light intensity-background intensity)] was evaluated photometrically by means of a microdensitometer. The relationship between optical density and weights of ^{110m}Ag per cm² was obtained making use of the aforementioned standards; this relationship was linear.

By this method, limiting local current densities of silver deposition were obtained for $z/c = 0$ and $0 < x/L < 1$ (Fig. 2) and for $0 < z/c < 1$ and $x/L = 0.35$ (Fig. 3), 0.65, and 0.95.

For $z/c = \text{const}$, *i.e.*, for $f = \text{const}$, the relationship between i^s and x/L is of the form

$$i^s = \text{const}\ (x/L)^{-1/3} \qquad [19a]$$

For $z/c = 0$, this equation was fitted within the interval of ±6% (see Fig. 2).

For $x/L = \text{const}$, the relationship

$$i^s/i^s_{z=0} = (f/f_{z=0})^{1/3} \qquad [19b]$$

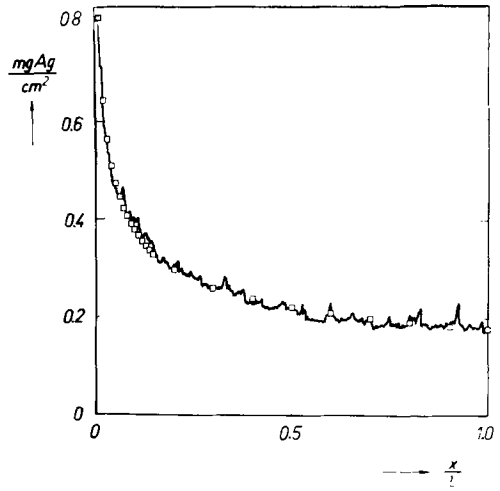

Fig. 2. Limiting local current densities (represented by mg Ag/cm²) as a function of the length of electrode for $z = 0$, $b = 0.5$ cm, $c = 1$ cm, $L = 10$ cm, $d/c = 1$, Re = 200. (Deposition of Ag^+, $c^o_1 = 10^{-5}$ mole Ag^+/cm^3, supporting electrolyte 1*N* KNO_3). □, Theoretical (Eq. [19-a]); ———, experimental.

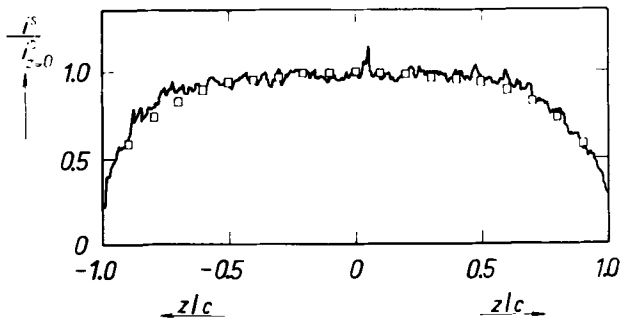

Fig. 3. Relative local current densities as a functon of width of electrode for $x/L = 0.35$, $b = 0.5$ cm, $c = 1$ cm, $L = 10$ cm, $d/c = 1$, Re = 200. (Deposition of Ag^+, $c^o_1 = 10^{-5}$ mole Ag^+/cm^3, supporting electrolyte 1*N* KNO_3.) □, Theoretical (Eq. [19-b]); ———, experimental.

was fitted within the interval of ±10% for x/L equal to 0.35, 0.65, and 0.95, respectively (see Fig. 3). The experimental lines on Fig. 2 and Fig. 3 were obtained using a microdensitometer.

Conclusions

By the asymptotic solution of the convective diffusion equation, the explicit expressions for calculating the average and local limiting current densities on the electrode embedded in the wall of a rectangular channel were derived. The expressions were checked experimentally. The agreement between experimental and theoretical average limiting current densities (Eq. [20]) was good for the system with an electrode not covering the entire channel width $d < c$. Similarly, the experimental verification of Eq. [19] for the local limiting current densities yielded good results for the region of z/c, where diffusion in the z direction can be neglected (see Appendix). For $z/c \to 1$, the difference between the predicted and experimental values increased. Therefore, Eq. [20] would give approximate values of Nusselt number for the systems with $d = c$.

APPENDIX

Concerning the validity of Eq. [13], the question is for what condition it is possible to disregard the term $\partial^2 c_1/\partial z^2$ in comparison to $\partial^2 c_1/\partial y^2$.

Concentration gradients in the z direction can be caused by the change of f values along the z axis. It follows from Table I that for the given b/c ratio, the region of z/c exists, where f decreases very slowly; therefore, in this region, mass transport in the z direction can be neglected in comparison to mass transport in the y direction. In order to investigate this point further, we shall calculate mass flows in y and z direction (averaged along the length of electrode) for the given z/c, using the solution of Eq. [13]

$$\bar{j}_y = (1/L)\int_0^L j_y\,dx = -(3/2)D_1(c^o_1 - c^s_1)\,0.893^{-1}\,[\bar{u}f/(3bLD_1)]^{1/3} \qquad [A\text{-}1]$$

$$\bar{j}_z = (L\bar{\delta}_N)^{-1}\int_0^L\left(\int_0^\infty j_z\,dy\right)dx = -(3/16)\{(1.5046/0.893^2)\,D_1\,(c^o_1 - c^s_1)\,[\partial f/\partial\,(z/c)]/(fc) \qquad [A\text{-}2]$$

In these equations, 1.5046 is the gamma function of 5/3, j_z is the local mass flow in the z direction, and $\bar{\delta}_N$ is the thickness of diffusion layer averaged along the length of electrode

$$j_z = -D_1\,(\partial c_1/\partial z) = -(1/3)\,D_1\,(c^o_1 - c^s_1)\,\eta\,(dC/d\eta)\,[\partial f/\partial\,(z/c)]/(fc) \qquad [A\text{-}3]$$

$$\bar{\delta}_N = (2/3)\,0.893\,[3bLD_1/(\bar{u}f)]^{1/3} \qquad [A\text{-}4]$$

The ratio $\bar{j}_z/\bar{j}_y$ for the given z/c is then

$$\bar{j}_z/\bar{j}_y = 0.3037\,[bLD/(c^3 Re\ Sc)]^{1/3}\,[\partial f/\partial(z/c)]/f^{4/3} \qquad [A\text{-}5]$$

Table A-I. Values of $\partial f/\partial(z/c)/f^{4/3}$ as a function of b/c and z/c
All values negative

z/c	b/c							
	2	1	0.5	0.3333	0.25	0.2	0.1	0.05
0.000	0.0000	0.0000	0.0000	0.0000	0.0000	0.0000	0.0000	0.0000
0.100	0.1053	0.1071	0.0686	0.0317	0.0121	0.0041	0.0000	0.0000
0.200	0.2193	0.2237	0.1465	0.0711	0.0292	0.0109	0.0000	0.0000
0.300	0.3528	0.3613	0.2451	0.1281	0.0586	0.0248	0.0002	0.0000
0.400	0.5225	0.5380	0.3816	0.2185	0.1130	0.0551	0.0010	0.0000
0.500	0.7578	0.7853	0.5864	0.3705	0.2177	0.1225	0.0048	0.0000
0.600	1.1196	1.1687	0.9212	0.6421	0.4273	0.2760	0.0233	0.0001
0.700	1.7593	1.8506	1.5389	1.1760	0.8772	0.6438	0.1130	0.0020
0.800	3.1739	3.3651	2.9415	2.4357	2.0046	1.6443	0.5650	0.0471
0.900	8.2468	8.8113	8.0468	7.1073	6.3167	5.6520	3.3659	1.1425
0.925	12.142	12.997	11.986	10.729	9.6824	8.8116	5.8412	2.6648
0.950	20.843	22.353	20.807	18.852	17.245	15.928	11.569	6.8063
0.975	52.057	55.965	52.553	48.143	44.568	41.687	32.605	23.394

Table A-II. Values of $\bar{j}_z/\bar{j}_y$ as a function of z/c

Calculated for Re = 200, Sc = 1000, b = 0.5 cm, c = d = 1 cm, according to Eq. [A-5]

z/c	$\bar{j}_z/\bar{j}_y$	z/c	$\bar{j}_z/\bar{j}_y$
0.000	0.0000	0.700	0.0150
0.100	0.0007	0.800	0.0287
0.200	0.0014	0.850	0.0441
0.300	0.0024	0.900	0.0786
0.400	0.0037	0.925	0.1171
0.500	0.0057	0.950	0.2034
0.600	0.0090	0.975	0.5136

Values of $[\partial f/\partial(z/c)]/f^{4/3}$ as a function of b/c and z/c are summarized in Table A-I.

Equations [A-1] to [A-5] were derived from the solution of the equation of convective diffusion [13], where the term $\partial^2 c_1/\partial z^2$ was neglected. Therefore, the values of $\bar{j}_z/\bar{j}_y$ calculated from Eq. [A-5] are only approximate; the purpose of this equation is to find the maximum value of z/c for which the ratio $\bar{j}_z/\bar{j}_y$ is sufficiently low.

As an example, the values of $\bar{j}_z/\bar{j}_y$ according to Eq. [A-5] were calculated for the geometrical and flow parameters corresponding to the deposition of Ag from the labeled electrolyte. It can be seen from Table A-II that in this case, the value of $\bar{j}_z$ can be neglected in comparison to $\bar{j}_y$ in the region $0 < z/c < 0.85$. Therefore, in this region, Eq. [20] for the Nusselt number is valid with sufficient accuracy. For the electrodes covering the entire channel width, Eq. [20] will give approximate results.

Manuscript submitted June 22, 1970; revised manuscript received Jan. 7, 1971. This was Paper 259 presented at the Los Angeles Meeting of the Society, May 10-15, 1970.

Any discussion of this paper will appear in a Discussion Section to be published in the December 1971 JOURNAL.

LIST OF SYMBOLS

- $2b$ dimension of channel (distance between electrodes), cm
- $2c$ dimension of channel (parallel to width of electrode), cm
- c_1, c^o_1, c^s_1, concentration of electroactive ion in boundary layer, in inlet electrolyte, and at electrode surface, mole/cm^3
- C dimensionless concentration, see Eq. [15]
- $2d$ width of electrode, cm
- D diameter of cylindrical tube or hydraulic equivalent diameter of rectangular channel, see Eq. [21], cm
- D_1 diffusion coefficient of electroactive ion or of binary electrolyte, cm^2/sec
- f see Eq. [10]
- $\mathbf{F}$ Faraday's constant, 96,496 coulomb/equiv
- $i^s, \bar{i}$ local and average current density at electrode surface, A/cm^2
- $j_y, \bar{j}_y, j_z, \bar{j}_z$ local and average mass flow in y and z direction, respectively, see Eq. [A-1] to [A-3,], mole/cm^2 sec
- L length of electrode, cm
- Nu Nusselt number, see Eq. [2]
- n number of electrons produced per one reactant ion or molecule
- P(O,O,O), Q(O,O,O) origins of the coordinates, see Fig. 1
- Re Reynolds number, see Eq. [3]
- Sc Schmidt number, see Eq. [4]
- $u, \bar{u}$ local and average electrolyte velocity in x direction, cm/sec
- $\vec{v}$ electrolyte velocity, cm/sec
- x,y,z length in coordinate direction, cm
- $\Gamma(4/3) = 0.8930$, $\Gamma(5/3) = 1.5046$, gamma function
- $\bar{\delta}_N$ see Eq. [A-4]
- η dimensionless coordinate, see Eq. [14]
- ϕ see Eq. [22]
- μ dynamic viscosity, poise
- ν kinematic viscosity, cm^2/sec

REFERENCES

1. I. Léveque, *Ann. Mines*, **13**, 201, 305, 381 (1928).
2. L. Graetz, *Ann. Physik*, **25**, 337 (1885).
3. E. N. Sieder and G. E. Tate, *Ind. Eng. Chem.*, **28**, 1429 (1936).
4. A. E. H. Love, "Treatise on Mathematical Theory of Elasticity," p. 129, Cambridge University Press (1927).
5. L. Rosenhead, "Laminar Boundary Layers," p. 136 Oxford Clarendon Press (1936).
6. E. Pohlhausen, *Z. angew. Math. Mechan.*, **1**, 115 (1921).
7. Spravochnik khimika, Publishing House Khimiya, Moscow, pp. 531, 719 (1946).
8. J. Newman, *Ind. Eng. Chem.*, **60**, (4), 12 (1968).
9. W. R. Parrish and J. Newman, *This Journal*, **117**, 43 (1970).

Intersolvent Potentials and the Reversible Nitrate and Sulfate Electrodes

L. G. Boxall*,[1] and K. E. Johnson*

Department of Chemistry, University of Saskatchewan Regina Campus, Regina, Saskatchewan, Canada

ABSTRACT

The standard potentials for the cells Ag/AgCl in (Li,K)Cl//$AgNO_3$ in (Li,K)NO_3/Ag at 400°C and Ag/AgCl in (Li,K)Cl//Ag_2SO_4 in (Li,Na,K)$_2SO_4$/Ag at 550°C are 0.687 and 0.718V, respectively, on the mole fraction scale. The cells Ag/$AgNO_3$ in (Na,K)NO_3//(Na,K)NO_3/NO_2, O_2, Pt, or Au and Ag/Ag_2SO_4 in (Li,Na,K)$_2SO_4$//(Li,Na,K)$_2SO_4$/SO_3, O_2, Pt show reversible behavior and good Nernstian response on variation of the partial pressures of the gases by means of a versatile gas-flow system. The standard free energy of formation of $AgNO_3$ was found to agree with published data for the range 250°-400°C. For the reaction $2Ag + SO_3 + \frac{1}{2}O_2 = Ag_2SO_4$, $\Delta G°$ was found to be -26.6 ± 0.1 kcal mole^{-1}.

One stage in the development of a unified emf series for several molten salt solvents is the measurement of the emf's of cells of the type M/MX in AX//MY in BY/M. This has already been reported with M = Ag for the cases where (*a*) X = NO_2, Y = NO_3, and A = B = Na (1) and where (*b*) X = CO_3, Y = SO_4, A = Li, Na, and B = Li, Na, K (2). In this paper we present further data for such cells with (c) X = Cl, Y = NO_3, A = B = Li, K and (*d*) X = Cl, Y = SO_4, A = Li, K, and B = Li, Na, K again using Ag as the metal of the electrodes.

In chloride melts, the chlorine electrode is of prime thermodynamic significance and its potential and stability have been established for LiCl-KCl (3). The NO_2, O_2/NO_3^- electrode has received attention for molten silver nitrate (4, 5) but not for alkali nitrate melts. We include therefore some studies of the NO_2, O_2/(Na,K) NO_3 electrode and the hitherto undeveloped SO_3, O_2/(Li,Na,K)$_2SO_4$ electrode. Of the other relevant gaseous electrodes, the CO_2, O_2/(Li,Na)$_2CO_3$ electrode has been shown to function reversibly (2) and, in the course of this study, the $NO_2/NaNO_2$ electrode has been shown not to operate reversibly.

Experimental

The preparation of the solvents has been described elsewhere (1,6,7) except that high-purity sodium pyrosulfate for use in clearing the sulfate melt was prepared according to a method described by Hotz (8) involving the controlled decomposition of copper sulfate and the absorption of the sulfur trioxide evolved by sodium sulfate. Analytical procedures for anions were as described by Ayres (9) whereas silver was determined by atomic absorption spectrophotometry (10) using a Techtron AA100 instrument. The apparatus for silver concentration cell measurements was similar to that described previously except that a double fritted compartment was used to separate the nitrate melt from the chloride.

For the gas electrodes the design and mode of operation were quite critical so will be described in some detail.

Gas electrode design.—The final design consisted of a piece of 8 mm glass tubing with a roll of platinum or gold gauze sealed in one end.

The top ¼ in. of a piece of ¾ in. x 3 in., 50 mesh platinum wire gauze (Johnson, Matthey and Mallory, Ltd.) was folded over to double the thickness. Platinum wire, 26 gauge, was then coiled in a zig-zag fashion across the upper half of the gauze and the whole rolled lengthwise. The upper portion of the gauze containing the platinum lead wire was sealed into the glass leaving approximately ¼ in. of gauze exposed below. The heavier platinum wire served to create small channels for the passage of gas.

The vertical adjustment of the electrode was made by a micrometer electrode holder (1.5 mm traverse per per dial revolution). It was placed in a compartment inserted through the central part of the 3-necked flask used for the cell. It was essential to start the flow of gas (initially nitrogen) before inserting the electrode in the melt to a point just above that needed to produce bubbling. The top of the gas electrode and the delivery tube from the gas control system were wrapped with heating tape to obtain better temperature equilibration. The gases could be readily flushed out through the tap at the top to a dry ice trap and water aspirator.

Gas control system.—Tank nitrogen was purified by passage over copper mesh at 325°C and through molecular sieve (Type 5A). Oxygen was dried by passage through molecular sieve. Liquid nitrogen tetroxide (Matheson of Canada Ltd., 99.5%) was used as supplied as was liquid sulfur trioxide (E. H. Sargent and Company).

The flows of nitrogen, oxygen, and nitrogen dioxide were controlled using stainless steel microflow valves (Matheson of Canada Ltd., Model 151) and measured using pressure differential flowmeters with n-butyl phthalate in the manometers. Flowmeters were connected in series with an open-ended n-butyl phthalate manometer to measure the excess pressure above atmospheric. The nitrogen and oxygen flowmeters were calibrated with a bubble meter and the nitrogen dioxide flowmeter, which was thermostated at 65°C, was calibrated by collecting the gas in half saturated KOH solution and back-titrating the excess base with hydrochloric acid. At the temperature of the emf measurements, the N_2O_4 is completely dissociated into NO_2 so that the calculation of partial pressures is a formality.

Since none of the normal manometric fluids is inert to sulfur trioxide, a mixture of nitrogen and oxygen of known composition was passed at a known rate from the flowmeters through liquid SO_3 in a boiling flask maintained at about 10°C hotter than the subsequent U-tube condensing column. The temperature of the latter was varied to give the desired effluent rate of SO_3, any excess SO_3 condensing in a small bulb at the bottom of the U-tube. All the tubing (1 mm ID) through which SO_3 passed was kept above 50°C by the use of heating tape or infrared lamps. The partial pressure of SO_3 was obtained from the expression

$$\log (760\, p_{SO_3}) = 10.022 \frac{-2269.4}{T}$$

* Electrochemical Society Active Member through the Faraday Society.
[1] Present address: Department of Chemistry, Colorado State University, Fort Collins, Colorado.
Key words: chloride, sulfate, nitrate, gaseous, electrode, melt.

where T°K is the temperature of the condensing column (11). The SO_3 content of the effluent gases was checked by condensing it and weighing: for four trials the calculated and experimental weights differed by 2.0%, −1.5%, −2.2%, and 0.7%.

In the cells involving gas electrodes a correction was required for the silver-platinum thermopotential. Therefore in a separate experiment the thermoelectric power of a silver-platinum thermocouple was measured using a calibrated chromel-alumel thermocouple and a sodium-potassium nitrate melt in a thermostat. The emf fitted the expression

$$E(\text{mV,Ag+}) = 0.0004 + 5.11 \times 10^{-3}t + 2.09 \times 10^{-5}t^2 - 9.74 \times 10^{-9}t^3 \quad (t \text{ in °C})$$

with values such as 0.14 mV at 25°C, 2.71 mV at 270°, and 7.51 mV at 550°C, the reference junction being 0°C. In the gas electrode studies the reference temperature was 25° ± 3°C. Thus +2.57 mV was added to the measured potential of the cell

$$\text{Ag/Ag(I) in (Na,K)NO}_3\text{/NO}_2\text{, O}_2\text{, Pt}$$

at 270°C.

Results

Chloride//nitrate potential.—The Ag(I)/Ag electrode was studied by concentration cell measurements in (Li,K)Cl and (Li,K)NO_3 (Li:K = ratio of 0.59:0.41 in each case) at 400°C and ideal Nernst behavior was observed for the concentration range 0.001 to 0.1 molal (M). The corrosion problem, encountered in activity coefficient measurements (12) did not arise here since the starting silver ion concentrations were about 10 times greater and the contact time between silver and dilute silver nitrate solutions much less.

The emf of the cell

$$\text{Ag/Ag(I) in (Li,K)Cl//Ag(I) (0.03}M\text{) in (Li,K)NO}_3\text{/Ag}$$

was determined at several temperatures as a function of silver chloride concentration. Figure 1 shows the results at 400° ± 2°C and these are summarized in column (c) of Table I. In the calculation of $E°_N$ the activity coefficients used were $\gamma_{N=0} = 2.04$ (13) for silver chloride and $\gamma_{N=0} = 1.91$ (12) for silver nitrate. The densities were taken from Janz (14) or measured separately (15).

The temperature dependence of the cell emf over the range 365°-450°C (the upper limit was dictated by nitrate decomposition) had the value

$$\frac{dE°}{dT} = (4.7 \pm 1.2) \times 10^{-4} \text{ volt deg}^{-1}$$

Table I. Potentials of the cell Ag/Ag_nX in $AX//Ag_nY$ in BY//Ag

In (a) X = NO_2, Y = NO_3, A = B = Na; in (b) X = CO_3, Y = SO_4, A = (Li,Na)$_2$, B = (Li,Na,K)$_2$; in (c) X = Cl, Y = NO_3, A = B = (Li,K); in (d) X = Cl, Y = SO_4, A = (Li,K), B = (Li,Na,K)$_2$ and n = 1 or 2.

System	(a)	(b)	(c)	(d)
Number of runs	4		5	5
Temperature, °C	309	540	400	550
Exptl. Nernst slope, V	0.1163		0.1338	0.1642
Theor. Nernst slope, V	0.1155		0.1336	0.1633
Std. dev., V	0.0033		0.0015	0.0018
$E°_M$ (measured), V	0.2455		0.687	0.718
Calc. LJP, E_J, V	0.0160		−0.003	—
$E°_M$ (chemical), V	0.230	0.253	0.690	0.718
$E°_M$ (chemical), V	0.226	0.250	0.682	0.690
$E°_N$ (chemical), V	0.219	0.237*	0.668	0.757
Error in $E°$'s	±0.003		±0.002	±0.002
Reference	1	2	This work	

M, M, and N refer to molal, molar, and mole fraction scales.
* The previous value referred to Ag(I) not Ag_2SO_4 and Ag_2CO_3.

Chloride//sulfate potential.—The Ag(I)/Ag electrode was studied by concentration cell measurements in the individual solvents (0.59 LiCl, 0.41 KCl, and 0.78 Li_2SO_4, 0.085 Na_2SO_4, 0.135 K_2SO_4) at 550°C and ideal Nernst behavior was observed for the concentration range 0.001-0.1M. The use of the ternary rather than a binary sulfate obviated the expense of silica apparatus and permitted direct correlation with the carbonate studies at 550°C.

The emf of the cell

$$\text{Ag/Ag(I) in (Li,K)Cl//Ag(I) (0.015}M\text{) in (Li,Na,K)}_2\text{SO}_4\text{/Ag}$$

at 550° ± 2°C is shown as a function of silver chloride concentration in Fig. 2 and the results are summarized in Table I. In the calculation of $E°_N$, $\gamma_{N=0}$ = 1.76 was used for silver chloride (16) but $\gamma_{N=0}$ for silver sulfate was assumed to be unity for lack of data {$\gamma_{N=0} = 0.85$ for Ag_2SO_4 in (0.8 Li_2SO_4, 0.2 K_2SO_4) (17)}. Again, densities were taken from ref. (14) or measured separately (15).

Nitrogen dioxide/nitrite electrode.—The cell Ag/Ag(I) in $NaNO_2$//$NaNO_2$/NO_2, Pt was studied at 270° ± 2°C. It was found that the cell emf was affected by the flow rate of gas and the time that the platinum electrode had been in the melt. No resemblance to Nernstian behavior was observed.

Nitrogen dioxide, oxygen/nitrate electrode.—The cell Ag/Ag(I) in (Na,K)NO_3//(Na,K)NO_3/NO_2, O_2, Pt was studied over the range 250°-325°C. The substitution of gold for platinum did not change the results. It was found that gas flow rates above 10^{-4} mole minute^{-1}

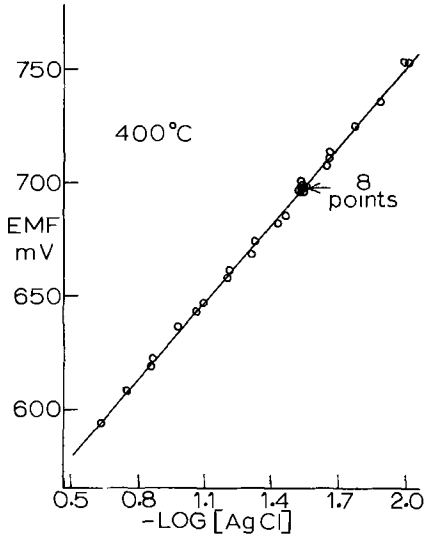

Fig. 1. Nernst plot at 400°C for the cell Ag/Ag(I) in (Li,K)Cl//Ag(I) (0.03M) in (Li,K) NO_3/Ag.

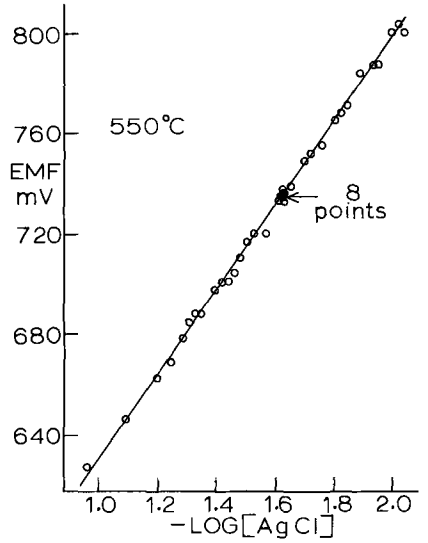

Fig. 2. Nernst plot at 550°C for the cell Ag/Ag(I) in (Li,K)Cl//Ag(I) (0.015M) in (Li,Na,K)$_2$ SO_4/Ag.

Table II. Potentials of the Pt, NO_2, O_2/NO_3^-

Number of cells	Total gas flow rate, moles minute^{-1} x 10^4	Slope of Nernst plot, V	E°, V
1	3.0	−0.0903	0.667 ± 10
1	2.0	−0.0995	0.586 ± 5
2	1.5	−0.1089	0.588 ± 3
3	1.0	−0.1102	0.552 ± 2

affected the slope of the Nernst plot and the derived standard potential, as illustrated in Table II. In subsequent runs the flow rate was kept below 10^{-4} moles minute^{-1}.

The cell potential was measured as a function of the Ag(I) concentration and the partial pressures of nitrogen dioxide and oxygen at several temperatures. The Nernst equation, corrected to a common Ag(I) molality of 0.030 takes the form

$$E = E^\circ_M - \frac{RT}{F} \ln \frac{\gamma_M\, 0.030}{p_{NO_2}\, p_{O_2}^{1/2}}$$

The activity coefficients of silver nitrate were taken from ref. (12). The data for 270°C are presented in Table III and Fig. 3 and those for five temperatures are summarized in Table IV. dE°_N/dT had the value of -0.00203 volt deg^{-1}.

Sulfur trioxide, oxygen/sulfate electrode.—The cell Ag/Ag(I) in (Li, Na, K)$_2SO_4$//(Li, Na, K)$_2SO_4/SO_3$, O_2, Pt had its emf at 550° ± 2°C measured as a function of sulfur trioxide and oxygen partial pressures. Flow rates up to 3 x 10^{-4} moles minute^{-1} gave the same potentials. The gaseous electrode required 15-30 min to stabilize after each change in gas composition and for a fixed composition remained constant to ±3 mV for 5 hr. After shorting for 5 sec, the electrode potential was reestablished within 2 min. The results are depicted in Fig. 4 and summarized in Table V.

The chloride//nitrate cell reaction is the transfer of silver ions from a nitrate to a chloride environment. From the standard chemical potential, E°_N of 0.668 ± 0.002V at 400° ± 2°C we calculate $\Delta G^\circ = -15.4 \pm 0.05$ kcal mole^{-1}. Likewise, the chloride//sulfate cell reaction is the transfer of silver ions from a chloride to a sulfate environment with ΔG°_{873} of -17.5 ± 0.05 kcal mole^{-1}.

In Ref. (1) it was suggested that the reaction for the nitrite//nitrate cell was $NaNO_2 + AgNO_2 = AgNO_2 + NaNO_3$ with E°_M corresponding to -5.30 ± 0.07 kcal mole^{-1} a 309°C. However, we should consider the standard states as the pure silver salts. In this case the meaningful quantity is E°_N (-5.05 ± 0.07 kcal mole^{-1}) but there are *no* alkali metal salts left in the reaction since they are accounted for by the activity coefficients

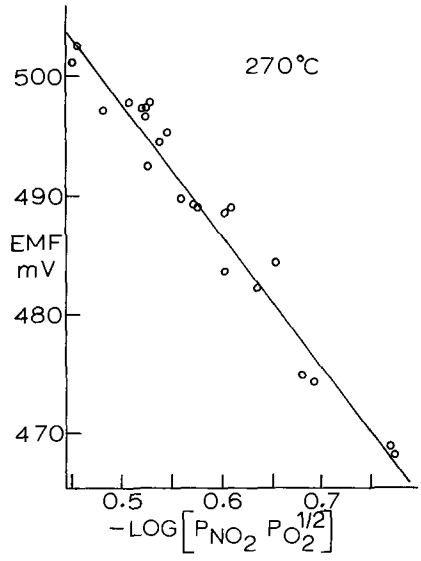

Fig. 3. EMF of cell Ag/Ag(I) (0.03M) in (Na,K)NO_3// (Na, K)NO_3/NO_2, O_2, Pt at 270°C *vs.* log $P_{NO_2}\, P_{O_2}^{1/2}$.

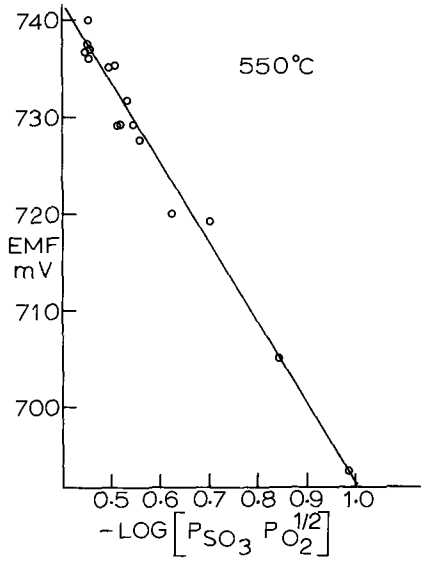

Fig. 4. EMF of cell Ag/Ag(I) (1M) in (Li,Na,K)$_2SO_4$// (Li,Na,K)$_2SO_4/SO_3$, O_2, Pt at 550°C *vs.* log $P_{SO_3}\, P_{O_2}^{1/2}$.

Table III. Cell potentials at 270° ± 2°C for the cell

Ag/Ag(I)$_{(0.03M)}$ in (Na,K)NO_3//(Na,K)NO_3/NO_2, O_2/Pt
(Total gas flow rate = 100 x 10^{-6} moles minute^{-1})

P_{N_2}, atm	P_{NO_2} atm	P_{O_2}, atm	$-\log [P_{NO_2}P_{O_2}^{1/2}]$	$-\log$ [Ag(I)], M	ΔE^*, mV	E, mV
0.330	0.489	0.119	0.770	−1.4084	12.3	468.8
0.026	0.733	0.179	0.507			498.0
0.129	0.630	0.179	0.573			488.9
0.278	0.481	0.179	0.690			474.4
0.190	0.480	0.268	0.603			488.7
0.103	0.480	0.355	0.542			494.2
0.000	0.484	0.454	0.485			497.3
0.336	0.482	0.120	0.775			468.3
0.117	0.688	0.146	0.580	−1.5732	−5.4	488.9
0.036	0.754	0.161	0.519			497.4
0.184	0.632	0.135	0.634			482.0
0.101	0.740	0.110	0.610			489.1
0.077	0.685	0.189	0.526			497.2
0.104	0.608	0.239	0.527			498.1
0.138	0.487	0.326	0.556			490.0
0.118	0.709	0.124	0.603			483.9
0.256	0.363	0.324	0.683	−1.5330	−1.1	474.7
0.099	0.519	0.325	0.527			496.9
0.007	0.616	0.320	0.456			502.9
0.094	0.610	0.239	0.524			492.2
0.000	0.631	0.312	0.451			501.5
0.117	0.623	0.203	0.549			495.0
0.193	0.628	0.122	0.657			484.5

* Potential added to cell value to convert to 0.030*M* $AgNO_3$ reference.

Table IV. Standard potential for the cell Ag/Ag(I) in (Na, K)NO_3//(Na, K)NO_3/NO_2, O_2, Pt as a function of temperature

Number of runs	Temp, ±2°C	$\gamma_{N=0}$	$E°_M$, ±0.003V	$E°_M$, ±0.003V	$E°_N$, ±0.003V	$E°_{calc.}$, V
2	250	0.95	0.443	0.473	0.334	0.3326
3	270	0.97	0.403	0.434	0.291	0.2911
2	300	1.01	0.344	0.376	0.228	0.2296
2	350	1.08	0.252	0.285	0.129	0.1280
3	400	1.12	0.159	0.194	0.028	0.0285

Table V. Standard potentials for the cell Ag/Ag(I) in (Li, Na, K)$_2SO_4$//(Li, Na, K)$_2SO_4$/SO_3, O_2 Pt

Temperature	550° ± 2°C	Partial pressure ranges:
$E°_M$ (measured), V	0.767 ± 0.002	SO_3: 0.390 to 0.842 atm
E_{Ag-Pt}, V	0.0074	O_2: 0.036 to 0.577 atm
$E°_M$ (chemical), V	0.774 ± 0.002	
$E°_M$ (chemical), V	0.827 ± 0.002	
$E°_N$ (chemical), V	0.575 ± 0.002	

(12). The $E°_N$ values are then related to the free energies of silver ions in the respective salts.

In Table IV we see very good agreement between $E°_N$ for the silver nitrate formation cell and the $E°$ value calculated for the reaction

$$Ag + NO_2 + \tfrac{1}{2} O_2 = AgNO_3$$

from published thermodynamic data (18-21). The dissociation of NO_2 into NO and O_2, although thermodynamically favored, is confirmed to be too slow (22, 23) to be of consequence in the experiments which involved short contact times between NO_2 and the melt. It should be pointed out that the results of Ketelaar and Dammers-de Klerk (4) for pure silver nitrate were also in agreement with the thermodynamic data; however the experimental arrangement used in this study was more versatile, permitting the complete testing of the Nernst equation through independent variation of the partial pressure of each gas.

Using the solid at 600°C, Hauffe and Hoeffgen (24) reported $E° = 0.555$V for the formation potential of silver sulfate

$$2Ag + SO_3 + \tfrac{1}{2} O_2 = Ag_2SO_4$$

which compares well with the value of 0.575V at 550°C (Table V) which in turn leads to a value for $\Delta G°_{823}$ of -26.6 ± 0.1 kcal mole^{-1}. We note also that $E°_M$ at 0.774V lies in the region predicted by voltammetric studies of (Li,K)$_2SO_4$ (25) and (Li,Na,K)$_2SO_4$ (26). The failure of the NO_2/NO_2^- electrode is in keeping with the findings of Topol *et al.* (27) and McCormick and Swofford (28) that the two components, as well as undergoing reversible electroreduction and electrooxidation, respectively, also react with each other thus

$$NO_2 + NO_2^- = NO_3^- + NO$$

Acknowledgment

This work was supported by the Defense Research Board of Canada under Contract No. 5412-07 and by the National Research Council of Canada through a Scholarship (to L.G.B.).

Manuscript submitted July 23, 1970; revised manuscript received Dec. 10, 1970. This was Paper 205 presented, in part, at the New York Meeting of the Society, May 5-9, 1969.

Any discussion of this paper will appear in a Discussion Section to be published in the December 1971 JOURNAL.

LIST OF SYMBOLS

T	temperature, °K
t	temperature, °C
$E°_M$	standard potential, V, on the molal scale
$E°_M$	standard potential, V, on the molar scale
$E°_N$	standard potential, V, on the mole fraction scale
$\frac{dE°}{dT}, \frac{dE}{dT}$	temperature coefficient of emf, volts deg^{-1}
$\gamma_{N=0}$	activity coefficient on the mole fraction scale, extrapolated to infinite dilution
P_x	partial pressure of x, atm
$\Delta G°$	standard free energy, kcal mole^{-1}

REFERENCES

1. L. G. Boxall and K. E. Johnson, *Anal. Chem.*, **40**, 831 (1968).
2. H. E. Bartlett and K. E. Johnson, *This Journal*, **114**, 457 (1967).
3. H. A. Laitinen and J. W. Pankey, *J. Am. Chem. Soc.*, **81**, 1053 (1959).
4. J. A. A. Ketelaar and A. Dammers-de Klerk, *Proc. Kon. Ned. Arad. Wetensch. Ser. B*, **68**, 169 (1955).
5. W. E. Triaca and A. J. Arvia, *Electrochim. Acta*, **9**, 919 (1964).
6. K. E. Johnson and J. R. Mackenzie, *This Journal*, **116**, 1697 (1969).
7. K. E. Johnson, R. Palmer, and T. S. Piper, *Spectrochim. Acta*, **21**, 1697 (1965).
8. M. C. B. Hotz, Private communication (1967).
9. G. H. Ayres, "Quantitative Chemical Analysis," Harper and Row, New York (1958).
10. A. C. Menzies, *Anal. Chem.*, **32**, 898 (1960).
11. International Critical Tables, Vol. III, McGraw-Hill, New York (1928).
12. L. G. Boxall and K. E. Johnson, Submitted to *Trans. Faraday Soc.*
13. K. H. Stern, *J. Phys. Chem.*, **60**, 679 (1956).
14. G. J. Janz, Editor, "Molten Salts Handbook," Academic Press, New York (1967).
15. L. G. Boxall and K. E. Johnson, *J. Chem. Eng. Data*, In press.
16. L. Yang and R. G. Hudson, *Trans. Met. Soc. AIME*, **215**, 589 (1959).
17. E. S. Woolner, Jr. and D. G. Hill, *J. Phys. Chem.*, **67**, 1571 (1963).
18. NBS Circular 500, Washington, D.C. (1952).
19. A. P. Altshuller, *J. Phys. Chem.*, **61**, 251 (1957).
20. Landolt-Bornstein, Editors, "Zahlenwerke und Funktionen," Vol. 2, Part 4, Berlin (1961).
21. K. K. Kelley, "Contributions to the Data on Theoretical Metallurgy," Vol. 10, Bureau of Mines, Washington, D. C. (1949).
22. M. Bodenstein, *Z. Phys. Chem.*, **100**, 68 (1922).
23. W. A. Rosser and H. Wise, *J. Chem. Phys.*, **24**, 493 (1956).
24. K. Hauffe and D. Hoeffgen, *Z. Phys. Chem.* (Frankfurt), **49**, 94 (1966).
25. C. H. Liu, *J. Phys. Chem.*, **66**, 164 (1962).
26. K. E. Johnson and H. A. Laitinen, *This Journal*, **110**, 314 (1963).
27. L. E. Topol, R. A. Osteryoung, and J. H. Christie, *J. Phys. Chem.*, **70**, 2857 (1966).
28. P. G. McCormick and H. S. Swofford, Jr., *Anal. Chem.*, **41**, 146 (1969).

Linear Sweep Voltammetry of Ni(II), Co(II), Cd(II), and Pb(II) at Glassy Carbon Electrodes in Molten Lithium Chloride-Potassium Chloride Eutectic

Wishvender K. Behl*

Power Sources Division, Electronic Components Laboratory, United States Army Electronics Command, Fort Monmouth, New Jersey 07703

ABSTRACT

The reduction of Ni(II), Co(II), Cd(II), and Pb(II) was studied at glassy carbon electrodes in molten lithium chloride-potassium chloride eutectic at 450°C using the technique of linear sweep voltammetry. Peak-shaped voltammograms were obtained at scan rates of 10 mV to 1 V/sec. Linear dependence of peak currents on metal ion concentration and the square root of voltage scan rate was obtained for all the cations studied. The diffusion coefficients of Ni(II), Co(II), Cd(II), and Pb(II) were calculated from the experimental data and found to be 1.26, 1.02, 0.98, and 1.29 x 10^{-5} cm^2/sec, respectively.

The polarographic method has been extensively applied to a study of the solute species dissolved in molten salts. These studies have been carried out both at dropping metal electrodes (mercury, bismuth, lead) and solid (platinum, tungsten, graphite) microelectrodes. The subject has been thoroughly covered in a number of reviews (1-4). At elevated temperatures, the polarographic method suffers from the use of large polarization times so that it is extremely difficult to completely eliminate the convective transport of the electroactive species to the electrode surface. Further, the metal ions which result in the deposition of a solid metal at the solid microelectrodes show an "increasing limiting current phenomenon" (1, 2, 5, 6) due to an increase in the electrode area. These difficulties can be eliminated by using the techniques of chronopotentiometry or linear sweep voltammetry (oscillographic polarography) where polarization times of only a few seconds or less are employed. The chronopotentiometric method has been widely used (1, 2) in molten salts in the past whereas the technique of linear sweep voltammetry has attracted attention only recently.

Mamantov *et al.* employed this technique to study the voltammetry of several cations in molten fluorides (7-12) at platinum wire, pyrolytic graphite, or glassy carbon electrodes and in molten $NaNO_3$-KNO_3 eutectic (13) at platinum wire electrodes. Francini *et al.* used the dropping mercury electrode to study the voltammetric behavior of several cations (14, 15), halide ions (16) and oxygen and its ions (17) in low melting nitrates. The reduction of Ag(I) at platinum wire electrodes was studied by Hills, Oxley, and Turner (18) in molten LiCl-KCl eutectic and by Kawamura (19) in mixtures of molten $NaNO_3$-KNO_3. Behl and Gaur (20) studied the reduction of Ag(I) and Pb(II) at platinum wire electrodes in molten $NaNO_3$-$Ba(NO_3)_2$ eutectic. Naryshkin and co-workers studied the reduction of several cations at platinum microelectrodes and determined their diffusion coefficients in molten NaCl-KCl (21) and LiCl-KCl (22) eutectic. They also used this method to study (23) the temperature dependence of diffusion coefficients in the latter solvent.

It was the purpose of this study to examine the applicability of the theory (24, 25) of linear sweep voltammetry to the reduction of Ni(II), Co(II), Cd(II), and Pb(II) at glassy carbon electrodes in molten lithium chloride-potassium chloride eutectic at 450°C. Since cadmium and lead metals are both liquid at the working temperature and are known (26-30) to be soluble in their halide salts, it was also of interest to see if the reduction of Cd(II) and Pb(II) was similar to the reduction of Ni(II) and Co(II) which results in the deposition of solid metals at the electrode surface.

Experimental Procedure

Reagent grade chemicals (Fischer Scientific Company) were used. The lithium chloride-potassium chloride (59:41 mole per cent [m/o]) eutectic solvent was purified by usual treatment with hydrogen chloride gas. Briefly stated it was heated at 130°C in a flowing atmosphere of hydrogen chloride gas for about 24 hr. The temperature was then slowly raised to 100 degrees above the melting point (352°C), and the bubbling of hydrogen chloride continued for another 4-6 hr. This was followed by bubbling the molten eutectic with chlorine gas for 2-3 hr. The treatment with chlorine helped to remove the black organic matter usually found in the melt after treatment with hydrogen chloride gas. The temperature was then lowered and the anhydrous eutectic so obtained was stored in an inert atmosphere of argon gas until used. Anhydrous cadmium chloride, nickel chloride, and cobalt chloride were obtained from the corresponding hydrates by heating in a flowing atmosphere of hydrogen chloride gas. Lead chloride was dried by heating under vacuum at 130°C.

The cell assembly is shown in Fig. 1. The cell consisted of a 64 mm outer diam Pyrex tubing (16 in. long) closed at the bottom and having a ground glass flange at the top. The eutectic solvent was contained in an inner Pyrex cup (57 mm outer diam and 4 in. long) and compartmented by use of Pyrex tubes (10 mm diam) with fritted-glass bottoms. The top of the cell was sealed, using an Apiezon wax, to another Pyrex flange joint assembly consisting of four standard tapered joints (19/38 $). These were used to insert the different electrodes, thermocouples, and a gas bubbling tube. The use of Teflon Swagelok fittings to introduce the electrodes into the cell helped to isolate the melt from the atmosphere. The cell also had a side arm tube with a ball joint which could either be connected to a vacuum system or to the gas outlet.

The cell assembly was heated at 450°C under vacuum for 3-4 hr before use and allowed to cool slowly to the room temperature. The top of the cell was then

* Electrochemical Society Active Member.

Key words: linear sweep voltammetry, lithium chloride-potassium chloride eutectic, nickel (II), cobalt (II), cadmium (II), lead (II), glassy carbon electrode, diffusion coefficients.

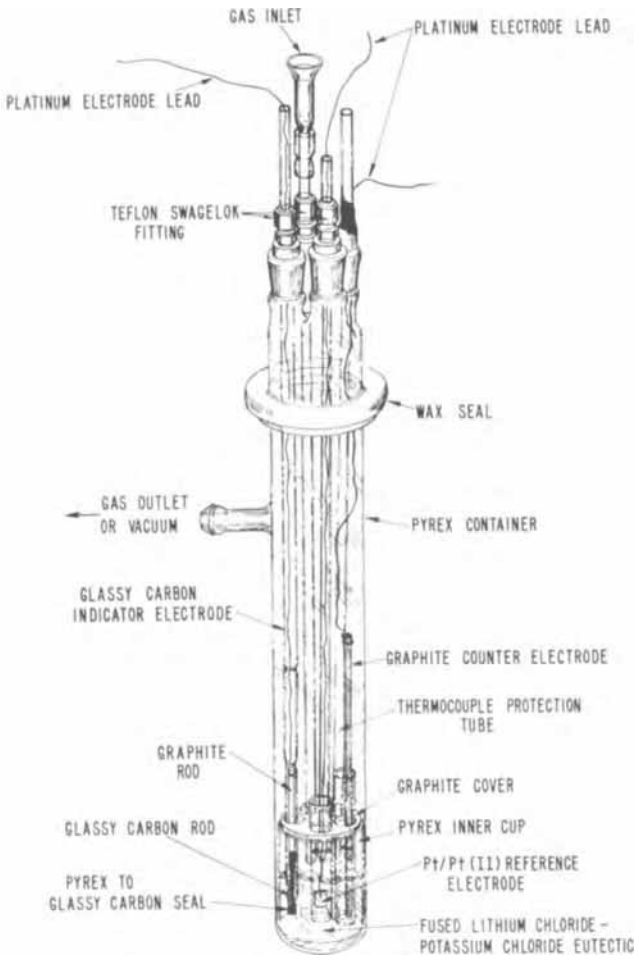

Fig. 1. Cell assembly

removed and a 100-125g solid sample of the purified eutectic transferred to the inner Pyrex container. The cell was then quickly reassembled and evacuated. The temperature was slowly raised to 450°C over a period of 10-12 hr. The eutectic melted and seeped into the Pyrex fritted disk compartments. The vacuum was then released by argon gas and a flowing atmosphere of argon maintained throughout the duration of the experiment.

The metal ion concentration in the eutectic was obtained by adding, with a small platinum scoop, weighed amounts of anhydrous salt into the main body of the eutectic (Fig. 1). Pt(II) concentration in the reference fritted disk compartment was generated *in situ* by the anodic dissolution of platinum foil at small current densities using a graphite rod in another fritted disk compartment as the counterelectrode. The exact metal ion concentration was determined at the end of each experiment by weighing the eutectic in each compartment and expressed in moles/liter. The density value (31) of 1.648 g/ml at 450°C was used for this purpose.

A three-electrode system was used for all measurements. The Pt/Pt(II) system was used as the reference electrode and a graphite rod as the counterelectrode. The indicator electrodes were made from 1.5 mm diam glassy carbon rods. A small length (3 in.) of the glassy carbon rod was tightly fitted into a ⅛ in. diam graphite rod in which a 1.5 mm hole had been previously drilled. The joint between the glassy carbon and graphite was then cemented using a Union Carbide C-9 carbon cement and the seal matured by baking in an inert atmosphere of argon gas. The electrical contact was made by tying a platinum wire around the graphite rod. The glassy carbon rod was sealed into a Pyrex tubing under vacuum and the end ground flush with the seal so as to expose the cross section of the rod. The electrode was polished to a mirror finish. The diameter of the exposed cross section was measured with an optical micrometer and the area of the electrode, unless otherwise stated, was 0.0174 cm^2.

A wire wound cylindrical furnace was used to heat the cell and the temperature of the cell was maintained at 450° ± 2°C using a SCR proportionating temperature controller (API Instruments Company). The temperature was measured with a Chromel-Alumel thermocouple.

The voltammetric scans were performed with a Tacussel Model PIT-2A potentiostat coupled with a GSTP-2 function generator. The current flowing through the cell was measured across a precision resistor in the counterelectrode circuit. The i-V curves were recorded on a Tektronix (Type 564) storage oscilloscope and photographed using a Polaroid (Type 107) film. Sweep rates were calibrated with a Tektronix (Type 184) time marker and were known with a precision of ±2%.

Results and Discussion

The theoretical treatment of linear sweep voltammetry for the electrode processes involving the reversible deposition of a soluble or insoluble product is available (24). The equations for the reversible deposition of a soluble product in the electrode or the solution were first independently derived by Randles (32) and Sevcik (33) and later rederived by Matsuda and Ayabe (34). Berzins and Delahay (35) treated the case where the reversible charge-transfer resulted in the deposition of an insoluble product. From their treatment, it can be shown that the peak current for the reversible deposition of an insoluble metal at 450°C is given by the equation

$$i_p = 236\, n^{3/2} A\, C\, V^{1/2} D^{1/2} \qquad [1]$$

where i_p is the peak current (amperes), n is the number of electrons in the charge transfer step, A is the area of the electrode (cm^2), C is the concentration (moles/liter), D is the diffusion coefficient (cm^2/sec), and V is the voltage scan rate (V/sec).

Assuming that the activity of the deposited metal is equal to unity, the peak potential, E_p, is related to the metal chloride concentration (C) by the equation (24, 35)

$$E_p = E^\circ + \frac{RT}{n\mathbf{F}} \ln f\, C - \frac{0.854\, RT}{n\mathbf{F}} \qquad [2]$$

where E° is the standard electrode potential, f is the activity coefficient of the metal chloride in solution and RT and $\mathbf{F}$ have their usual thermodynamic significance.

A similar relation can also be derived for the half-peak potential, $E_{p1/2}$, and is given by the equation (9)

$$E_{p1/2} = E^\circ + \frac{RT}{n\mathbf{F}} \ln f\, C - \frac{0.0815\, RT}{n\mathbf{F}} \qquad [3]$$

It is seen from Eq. [2] and [3] that both the peak and half-peak potentials would shift to more positive values as the metal chloride concentration is increased. Thus, at 450°C, the plots of E_p or $E_{p1/2}$ *vs.* log C would result in straight lines with a slope equal to 2.303 $RT/n\mathbf{F}$ or 0.0717V at 450°C for a two electron process.

Combining Eq. [2] and [3], the difference (ΔE) between the peak and half-peak potential is given by

$$\Delta E = E_p - E_{p1/2} = \frac{-0.7725\, RT}{n\mathbf{F}} \qquad [4]$$

Thus the difference (ΔE) is independent of the concentration as well as the scan rate.

Typical voltammograms for the reduction of 31.02, 27.32, 51.55, and 35.49 millimolar solutions of $NiCl_2$, $CoCl_2$, $CdCl_2$, and $PbCl_2$, respectively, at a scan rate of 0.095 V/sec are shown in Fig. 2. In each case, peak shaped voltammograms were obtained and on reversing

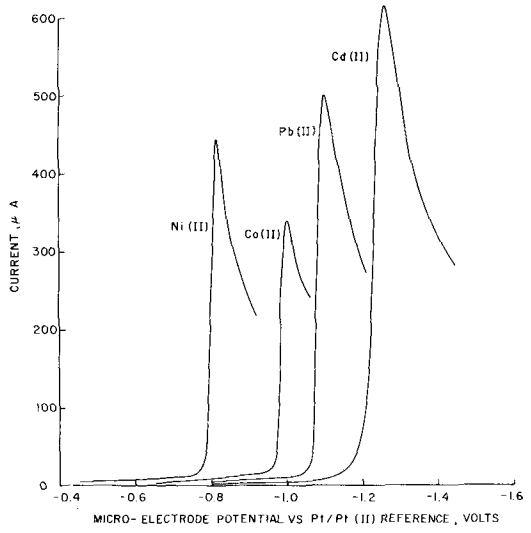

Fig. 2. Typical voltammograms for the reduction of 31.02, 27.32, 51.55, and 35.49 mM solutions of $NiCl_2$, $CoCl_2$, $CdCl_2$, and $PbCl_2$ at glassy carbon electrodes at a scan rate of 0.095 V/sec.

the direction of polarization, sharp anodic stripping peaks were observed. The potential of the working electrode was held at −0.2V *vs.* Pt/Pt(II) reference for a few minutes and the solution stirred before taking the next voltammogram. Several voltammograms were recorded at each scan rate between 10 mV to 1.0 V/sec and at several metal chloride concentrations.

The reduction of Ni(II) and Co(II) results in the deposition of an insoluble substance (solid metal) at the electrode surface at the working temperature of 450°C. Thus, the peak and half-peak potentials for the reduction of both Ni(II) and Co(II) would be given by Eq. [2-4]. The reduction of Cd(II) and Pb(II), on the other hand, results in the deposition of liquid metals at 450°C. These metals are known to dissolve in their chlorides according to the equations

$$Cd + CdCl_2 \rightleftharpoons Cd_2^{++} + 2\,Cl^- \quad (36\text{-}38) \qquad [5]$$

$$Pb + PbCl_2 \rightleftharpoons Pb_2^{++} + 2\,Cl^- \quad (39, 40) \qquad [6]$$

Thus if the deposition of cadmium and lead metals at the electrode surface is followed by their dissolution in dilute solutions of cadmium chloride and lead chloride, respectively, the activity of deposited metal will neither be equal to unity nor remain constant. The peak and half-peak potentials will, therefore, not be given by Eq. [2-4] but would instead obey the equations (24, 25, 34) for the deposition of a soluble product.

The peak and half-peak potentials of the recorded voltammograms for the reduction of Ni(II), Co(II), Cd(II) and Pb(II) were measured at all concentrations and scan rates and the data for one concentration in each case are summarized in Table I. The difference, ΔE, between the peak and half-peak potentials was found to be of the order of 20-30 mV as compared to the theoretical value of 24 mV predicted by Eq. [4] for the reversible deposition of insoluble substance at the electrode surface involving a two electron change at 450°C. Further, the peak and half-peak potentials, in each case, shifted to more positive values with increase in metal chloride concentration and the plots of $E_{p1/2}$ *vs.* log *C* resulted in straight lines with theoretical slopes predicted by Eq. [3]. Typical $E_{p1/2}$ *vs.* log *C* plots for the reduction of Ni(II), Co(II), Cd(II), and Pb(II) at a scan rate of 0.205 V/sec are shown in Fig. 3. The solid lines have the theoretical slope equal to 2.303 *RT*/2**F** or 0.0717 at 450°C and the circles represent the experimental points. Similar plots were obtained at other scan rates.

The standard electrode potentials, $E°$, for the metal ion-metal couples can also be calculated by use of

Table I. Peak and half-peak potential data for the reduction of metal ions in LiCl-KCl eutectic at 450°C

Metal ion	Concentration, mM/liter	Scan rate, V/sec	E_p	$E_{p_{1/2}}$ Volts	$E_p - E_{p_{1/2}}$
Ni(II)	22.06	0.095	−0.840	−0.820	−0.020
		0.140	−0.840	−0.820	−0.020
		0.205	−0.845	−0.825	−0.020
		0.360	−0.852	−0.830	−0.022
		0.540	−0.870	−0.845	−0.025
		0.943	−0.855	−0.825	−0.020
Co(II)	27.32	0.095	−1.000	−0.970	−0.030
		0.140	−0.985	−0.960	−0.025
		0.205	−0.995	−0.970	−0.025
		0.360	−0.995	−0.967	−0.027
		0.540	−1.000	−0.970	−0.030
		0.943	−1.010	−0.985	−0.025
Cd(II)	51.55	0.095	−1.255	−1.230	−0.025
		0.140	−1.250	−1.225	−0.025
		0.205	−1.255	−1.225	−0.020
		0.360	−1.255	−1.230	−0.025
		0.540	−1.260	−1.235	−0.025
		0.943	−1.255	−1.230	−0.025
Pb(II)	18.12	0.095	−1.120	−1.105	−0.025
		0.140	−1.120	−1.107	−0.023
		0.205	−1.125	−1.100	−0.025
		0.360	−1.125	−1.100	−0.025
		0.540	−1.125	−1.102	−0.023
		0.943	−1.120	−1.100	−0.020

Eq. [2] or [3] and compared with the reversible standard electrode potentials determined by Laitinen and Liu (41) in lithium chloride-potassium chloride eutectic at 450°C. In practice the $E_{p1/2}$ *vs.* log *C* plots shown in Fig. 3 were extrapolated to 1.0M (molar) concentration (standard state on molarity scale) of the metal chloride and the $E_{p1/2}$ values so obtained were substituted in Eq. [3] to obtain the $E°$ values for the metal ion-metal couples *vs.* the used platinum reference (≈ 5-20 mM). It was assumed that the activity coefficient of the metal chloride remains constant over the concentration range studied and the activity coefficient term in Eq. [3] is included as a constant in the $E°$ value. The $E°$ values were then converted to 1.0M platinum reference using the Nernst equation and compared with the literature values (41). The data are summarized in Table II. The standard electrode potentials obtained in the present study are within 14-59 mV of the equilibrium values determined by Laitinen and Liu (41). In view of the obvious errors involved in determining the $E°$ values from the recorded voltammograms on a Polaroid film, the above agreement is considered quite satisfactory.

Since the peak and half-peak potentials for the reduction of Ni(II) and Co(II) as well as Cd(II) and Pb(II) closely obey Eq. [2-4], it can be concluded that the reduction of these ions results in the deposition of the metal in such a way that the surface of the glassy carbon electrode is completely covered with a layer

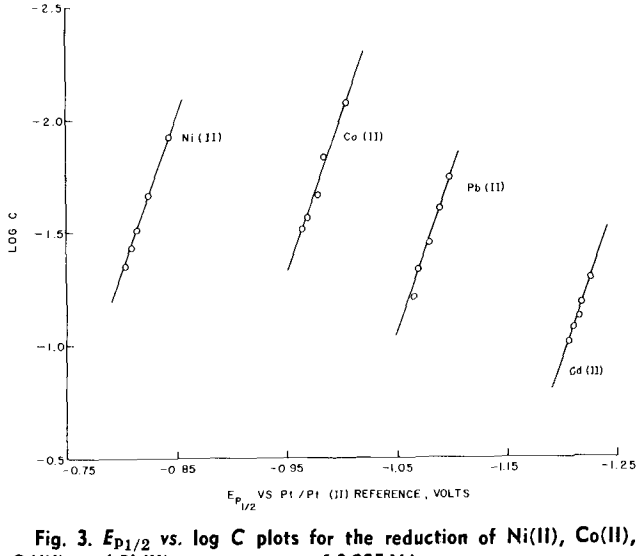

Fig. 3. $E_{p1/2}$ *vs.* log *C* plots for the reduction of Ni(II), Co(II), Cd(II), and Pb(II) at a scan rate of 0.205 V/sec.

Table II. Comparison of literature values of standard electrode potentials in LiCl-KCl eutectic at 450°C with this work

Electrode couple	Pt(II) Conc. in ref. electrode, millimolar	$E°$ vs. Pt reference, V	$E°$ vs. 1.0M Pt reference, V This work[a]	$E°$ vs. 1.0M Pt reference, V Literature values[b]
Ni(II)-Ni(O)	8.93	−0.702	−0.849	−0.795
Co(II)-Co(O)	7.80	−0.852	−1.005	−0.991
Cd(II)-Cd(O)	5.85	−0.972	−1.133	−1.101
Pb(II)-Pb(O)	17.62	−1.131	−1.257	−1.316

[a] Voltage scan rate 0.205 V/sec.
[b] H. A. Laitinen and C. H. Liu, Ref. (41).

of the metal and its activity remains constant and equal to unity. At the scan rates used, the dissolution of the liquid metals (cadmium and lead) into the dilute solutions of their respective chlorides is probably very small and slow so that the electrode is always completely covered with a thin film of the metal. Thus, on reversing the direction of polarization after the peak, a sharp anodic peak is always observed due to the dissolution of the metal film on the electrode surface. The reverse voltammograms were not studied in detail as a study of the oxidation of the thin electrodeposited metallic layers of nickel, cobalt, cadmium, and lead in molten and solid lithium chloride-potassium chloride eutectic is available in literature (42).

It was also shown by Mamantov *et al.* (9) that for the reversible deposition of an insoluble metal at the electrode surface (assuming that the activity of the deposited metals remains constant), the plots of the microelectrode potential, E, *vs.* log $(i_p - i)$ approach linearity in the range (0.5-0.9) i_p with a slope equal to $RT/2.2\ nF$ or 0.014 for a two-electron process at 450°C. Such plots for the voltammograms presented in Fig. 2 are shown in Fig. 4. Again the solid lines have the theoretical slope and the circles represent the experimental points. As expected, these plots approach linearity only in the approximate range of (0.5-0.9) i_p. Similar plots were obtained for the other voltammograms at all concentrations and scan rates.

The reduction of Ni(II), Co(II), Cd(II), and Pb(II) at glassy carbon electrodes in molten lithium chloride-potassium chloride eutectic, therefore, occurs reversibly and leads to the deposition of a metal (solid or liquid) virtually at unit activity at the electrode surface and is similar to the deposition of an insoluble substance (24, 35). The peak currents would, therefore, be given by Eq. [1]. The peak currents for the reduction of ions studied were obtained by extrapolating the residual part of the voltammograms to the peak potential and measuring the height between this base line and the peak of the voltammograms. The

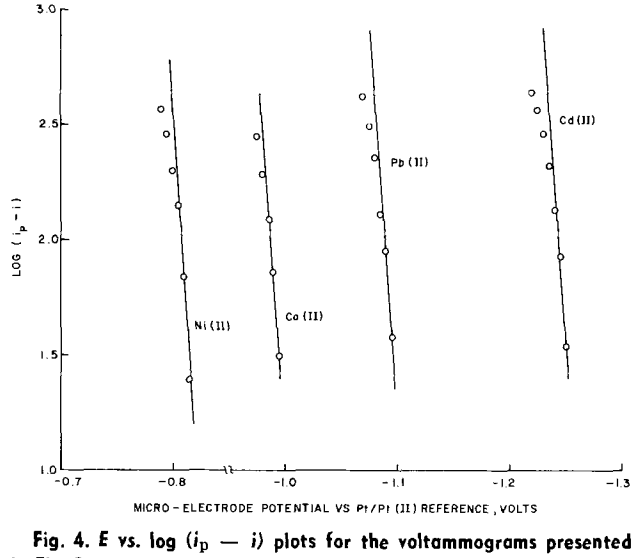

Fig. 4. E vs. log $(i_p - i)$ plots for the voltammograms presented in Fig. 2.

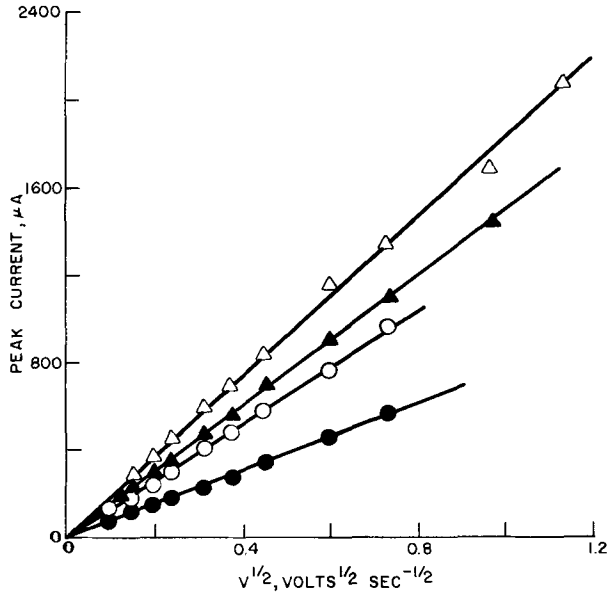

Fig. 5. i_p vs. $V^{1/2}$ plots for the reduction of 21.70 (●), 31.02 (○), 35.49 (▲), and 51.55 (△) mM solutions of cobalt chloride, nickel chloride, lead chloride, and cadmium chloride, respectively.

peak currents increased with increasing metal chloride concentration and square root of voltage scan rate and obeyed Eq. [1]. Thus, plots of peak current (i_p) *vs.* the square root of voltage scan rate ($V^{1/2}$) resulted in straight lines passing through the origin. The linear relation was observed up to an approximate scan rate of 0.8-1.0 V/sec and at higher scan rates, the peak currents tended to be lower than those predicted by Eq. [1] and showed negative deviation from the straight line plot. The typical i_p *vs.* $V^{1/2}$ plots for the reduction of 31.02, 21.7, 51.55, and 35.49 millimolar solutions of $NiCl_2$, $CoCl_2$, $CdCl_2$, and $PbCl_2$, respectively, are shown in Fig. 5. Similar plots were obtained at other concentrations.

At each concentration, the $i_p/V^{1/2}$ values were obtained from the slopes of the linear i_p *vs.* $V^{1/2}$ plots and substituted in Eq. [1] to calculate the peak current constants ($K_p = i_p/V^{1/2}\ AC$) as well as the diffusion coefficients (D) of the ions studied. These data are summarized in Table III. For most of the present work, glassy carbon electrodes with area equal to 0.0174 cm^2 were used. In case of the reduction of Co(II), an electrode of area equal to 0.0533 cm^2 was also employed and K_p values obtained with this electrode agreed very well with K_p values obtained with the former electrode. The constancy of the K_p values presented in Table III clearly demonstrates the linear dependence of peak currents on the metal chloride concentration and the electrode area as predicted by Eq. [1]. The average peak current constants (K_p) for the reduction of Ni(II), Co(II), Cd(II), and Pb(II) were respectively found to be 2.37, 2.12, 2.09, and 2.39 (10^3 A $sec^{1/2}\ V^{-1/2}$ cm per mole).

The diffusion coefficients obtained in the present study are compared in Table V with those obtained by other workers in lithium chloride-potassium chloride eutectic at 450°C by chronopotentiometry at platinum microelectrodes (43-45), polarography at dropping bismuth electrode (46) and linear sweep voltammetry at platinum microelectrodes (22). In general, the diffusion coefficients determined in the present studies are somewhat lower than the previously reported literature values for Ni(II) (22), Co(II) (44), Cd(II) (22, 43-46), and Pb(II) (22, 44, 46). However, there is a good agreement between our value for the diffusion coefficient of Co(II) and the value reported by Naryshkin *et al.* (22) and between our value for the diffusion coefficient of Pb(II) and the value found by Thalmayer, Bruckenstein, and Gruen (45).

Table III. Peak current constants and diffusion coefficients of metal ions in LiCl-KCl eutectic at 450°C[a]

Metal ion	Concentration × 10^3 (moles/liter)	$10^3 \times i_p/V^{1/2}$ (A $V^{-1/2}$ $sec^{1/2}$)	Peak current constant $K_p = i_p/V^{1/2}AC$ (10^5 A $sec^{1/2}$ cm/ $V^{1/2}$ mole)	Diffusion coefficient × 10^5 (cm^2/sec)
Ni(II)	8.48	0.355	2.41	1.30
	11.30	0.475	2.42	1.31
	12.06	0.495	2.36	1.25
	14.13	0.582	2.37	1.26
	22.06	0.915	2.38	1.27
	31.02	1.265	2.34	1.23
	37.47	1.510	2.32	1.21
			Average = 2.37	Average = 1.26
			Av. dev. = 0.03	Av. dev. = 0.03
Co(II)	6.7	0.266	2.28	1.17
	8.3	0.289	2.00	0.90
	14.8	0.554	2.15	1.04
	21.7	0.762	2.02	0.92
	27.3	1.040	2.19	1.08
	29.0	3.250[b]	2.10	1.99
			Average = 2.12	Average = 1.02
			Av. dev. = 0.08	Av. dev. = 0.08
Cd(II)	18.97	0.69	2.09	0.98
	36.90	1.35	2.10	0.99
	51.55	1.82	2.03	0.92
	65.51	2.36	2.07	0.96
	75.65	2.75	2.09	0.98
	76.10	2.77	2.09	0.98
	85.43	3.10	2.09	0.98
	89.00	3.27	2.11	1.00
	97.50	3.57	2.10	0.99
			Average = 2.09	Average = 0.98
			Av. dev. = 0.01	Av. dev. = 0.01
Pb(II)	18.12	0.787	2.50	1.40
	24.19	0.965	2.29	1.18
	35.49	1.492	2.42	1.31
	47.11	1.970	2.40	1.30
	61.16	2.510	2.36	1.25
			Average = 2.39	Average = 1.29
			Av. dev. = 0.06	Av. dev. = 0.06

[a] Area of the electrode 0.0174 cm^2.
[b] Area of the electrode 0.0533 cm^2.

Table IV. Diffusion coefficients of metal ions in molten LiCl-KCl eutectic at 450°C

Metal ion	$D \times 10^5$ (cm^2/sec) Laitinen *et al.*[a]	Thalmayer *et al.*[b]	Heus & Egan[c]	Naryshkin *et al.*[d]	This work
Ni(II)	—	—	—	1.8	1.26
Co(II)	2.42	—	—	0.9	1.02
Cd(II)	208, 1.68	1.7	1.8	1.6	0.98
Pb(II)	2.18	1.3	1.7	1.75	1.29

[a] Chronopotentiometry at platinum electrodes, Ref. 43 and 44.
[b] Chronopotentiometry at platinum electrodes, Ref. 45.
[c] Polarography at dropping bismuth electrode, Ref. 46.
[d] Linear sweep voltammetry at platinum electrodes, Ref. 22.

Summary and Conclusion

The reduction of Ni(II), Co(II), Cd(II), and Pb(II) at glassy carbon electrodes was shown to occur reversibly in molten lithium chloride-potassium chloride eutectic by the technique of linear sweep voltammetry. The reduction of Cd(II) and Pb(II), which results in the deposition of liquid metals at the working temperature of 450°C, was found to be similar to the reduction of Ni(II) and Co(II) which results in the deposition of solid metals at the electrode surface. The peak currents showed linear dependence on concentration as well as the square root of voltage scan rates in the range of 0.01 to 1.0 V/sec. The experimental results showed close agreement with the theoretical equations for the deposition of an insoluble product at the electrode surface. The diffusion coefficients for the ions Ni(II), Co(II), Cd(II), and Pb(II) were calculated and found to be 1.26, 1.02, 0.98, and 1.29 x 10^{-5} cm^2/sec, respectively.

Acknowledgment

The author is indebted to Dr. Stanley D. James of the United States Naval Ordnance Laboratory, Maryland, for supplying the glassy carbon rods used in these experiments.

Manuscript submitted Sept. 4, 1970; revised manuscript received *ca.* Jan. 8, 1971.

Any discussion of this paper will appear in a Discussion Section to be published in the December 1971 JOURNAL.

REFERENCES

1. H. A. Laitinen and R. A. Osteryoung, "Fused Salts," B. R. Sundheim, Editor, McGraw-Hill, New York (1964).
2. C. H. Liu, K. E. Johnson, and H. A. Laitinen, "Molten Salt Chemistry," M. Blander, Editor, Interscience, New York (1964).
3. Yu. K. Delimarskii and B. F. Markov, "Electrochemistry of Fused Salts," R. E. Wood, Editor, Sigma Press, Washington, D. C. (1961).
4. H. C. Gaur and R. S. Sethi, *J. Electroanal. Chem.*, **7**, 474 (1964).
5. H. A. Laitinen, C. H. Liu, and W. S. Ferguson, *Anal. Chem.*, **30**, 1266 (1958).
6. H. C. Gaur and W. K. Behl, *J. Electroanal. Chem.*, **5**, 261 (1963).
7. D. L. Manning, J. M. Dale, and G. Mamantov, *Polarography*, Vol. 2, G. J. Hills, Editor, Macmillan, London (1964).
8. D. L. Manning and G. Mamantov, *J. Electroanal. Chem.*, **7**, 102 (1964).
9. G. Mamantov, D. L. Manning, and J. M. Dale, *ibid.*, **9**, 253 (1965).
10. G. Mamantov and D. L. Manning, *Anal. Chem.*, **38**, 1494 (1966).
11. D. L. Manning and G. Mamantov, *J. Electroanal. Chem.*, **17**, 137 (1968).
12. G. Mamantov and D. L. Manning, *ibid.*, **18**, 309 (1968).
13. G. Mamantov, J. M. Strong, and F. R. Clayton, Jr., *Anal. Chem.*, **40**, 488 (1968).
14. M. Francini and S. Martini, *Z. Naturforsch.*, **23a**, 795 (1968).
15. M. Francini and S. Martini, *Electrochim. Metal.* III, **2**, 132 (1968) and **2**, 136 (1968).
16. M. Francini, S. Martini, and C. Monfrini, *ibid.*, II, **1**, 3 (1967) and **3**, 325 (1967).
17. M. Francini and S. Martini, *Electrochim. Acta*, **13**, 851 (1968).
18. G. J. Hills, J. E. Oxley, and D. W. Turner, *Silicates Ind.*, **26**, 559 (1961).
19. K. Kawamura, *Electrochim. Acta*, **12**, 1233 (1967).
20. W. K. Behl and H. C. Gaur, *J. Electroanal. Chem.*, In press; also presented at the 2nd Conference of General and Applied Physical Chemistry, Bucharest, Roumania, Sept. 1970.
21. I. I. Naryshkin, V. P. Yurkinskii, and B. S. Yavich, *Elecktrokhimiya*, **2**, 864 (1966).
22. I. I. Naryshkin, V. P. Yurkinskii, and P. T. Stangrit, *ibid.*, **5**, 1043 (1969), **5**, 1476 (1969).
23. I. I. Naryshkin and V. P. Yurkinskii, *ibid.*, **5**, 871 (1969).
24. P. Delahay, "New Instrumental Methods in Electrochemistry," Interscience, New York (1954).
25. R. S. Nicholson and I. Shain, *Anal. Chem.*, **36**, 706 (1964).
26. A. H. W. Aten, *Z. Physik. Chem.* (Leipzig), **73**, 578 (1910).
27. L. E. Topol and A. L. Landis, *J. Am. Chem. Soc.*, **82**, 6291 (1960).
28. J. D. Corbett and S. V. Winbush, *ibid.*, **77**, 3964 (1955).
29. J. D. Corbett, "Fused Salts," B. R. Sundheim, Editor, McGraw-Hill, New York (1964).
30. M. A. Bredig, "Molten Salt Chemistry," M. Blander, Editor, Interscience, New York (1964).
31. E. R. Van Artsdalen and I. S. Yaffe, *J. Phys. Chem.*, **59**, 118 (1955).
32. J. E. B. Randles, *Trans. Faraday Soc.*, **44**, 327 (1948).
33. A. Sevcik, *Collection Czech. Chem. Commun.*, **3**, 349 (1948).
34. H. Matsuda and Y. Ayabe, *Z. Elektrochem.*, **59**, 494 (1955).
35. T. Berzins and P. Delahay, *J. Am. Chem. Soc.*, **75**, 555 (1953).
36. K. Grjotheim, F. Grönvold, and J. Krogh-Moe, *ibid.*, **77**, 5824 (1955).
37. J. Farquharson and E. Heymann, *Trans. Faraday Soc.*, **31**, 1004 (1935).
38. N. H. Nachtrieb, *J. Phys. Chem.*, **66**, 1163 (1962).
39. J. J. Egan, *ibid.*, **65**, 2222 (1961).

40. J. D. Van Norman, J. S. Bookless, and J. J. Egan, *ibid.*, **70**, 1276 (1966).
41. H. A. Laitinen and C. H. Liu, *J. Am. Chem. Soc.*, **80**, 1015 (1958).
42. J. Hladik, Y. Pointud, and M. G. Morand, *J. Chimie Phys.*, **66**, 113 (1969).
43. H. A. Laitinen and W. S. Ferguson, *Anal. Chem.*, **29**, 4 (1957)
44. H. A. Laitinen and H. C. Gaur, *Anal. Chim. Acta*, **18**, 1 (1958).
45. C. E. Thalmayer, S. Bruckenstein, and D. M. Gruen, *J. Inorg. Nucl. Chem.*, **26**, 347 (1964).
46. R. J. Heus and J. J. Egan, *This Journal*, **107**, 824 (1960).

Technical Notes

The Self-Discharge Mechanism of the Li/LiI/AgI Solid Electrolyte Cell

Charles C. Liang*

P. R. Mallory & Company, Inc., Laboratory for Physical Science, Burlington, Massachusetts 01803

Investigations have been conducted in this laboratory on various high-voltage, solid-electrolyte battery systems with lithium anodes and lithium iodide electrolytes. A variety of iodine-based cathode materials such as iodine (1), metal polyiodides (*e.g.* CsI_3, RbI_3), and ammonium and organic ammonium polyiodides (*e.g.* NH_4I_3, $N(CH_3)_4I_3$) were used in the solid electrolyte cells. The initial performance of these cells was satisfactory. The cells exhibited the expected open-circuit voltages and could deliver short circuit currents of 300 $\mu A/cm^2$ at room temperatures. However, after a storage period of a few days, the internal impedance of these cells showed sharp increases indicating the diffusion of iodine through the electrolyte to react with lithium producing more resistive lithium iodide. Furthermore, the corrosive nature of the iodine-based cathodes made the selection of a satisfactory current collector and cell housing material extremely difficult.

In view of these difficulties, a metal iodide, AgI, was selected as the cathode material for the solid-electrolyte system. In addition, thin film–multilayer cell structures were designed to obtain useful discharge currents (2). The fabrication processes and the discharge characteristics of the thin film Li/LiI/AgI cells were reported in a previous publication (3). Further studies on the system revealed that the maximum discharge efficiency of the Li/LiI/AgI thin film cells was only 50% even under a drain rate as low as 5 $\mu A/cm^2$. Furthermore, the Li/LiI/AgI system was unstable. The thin film cells failed to operate after a storage period of two to four weeks at room temperatures.

The present investigation was undertaken in an attempt to determine the self-discharge mechanisms of the Li/LiI/AgI cells.

Experimental

Foote Mineral $LiI \cdot 3H_2O$ was dehydrated according to the processes reported previously (3). Mallinckrodt AgI was dried at 160°C overnight before use. Powder mixtures of anhydrous lithium iodide and silver iodide were ground in a Fisher mechanical grinding apparatus for about 1 hr. Immediately after the grinding, x-ray diffraction patterns of the mixtures were obtained at room temperatures using conventional techniques with CuKα radiation.

Pellets of lithium iodide on silver iodide were prepared by pressing prepressed lithium iodide and silver iodide pellets together under a pressure of 50,000 psi in a 7/16 in. diam steel die. These pellets were stored in individual brown glass bottles at ambient temperatures (26° ± 2°C) in a Vacuum Atmospheres Model HE-453-2 dry box. After the pellets had been stored for a predetermined period of time, they were placed in the holder of a small lathe and the silver iodide side was sectioned. The lithium content of each section was determined flame photometrically.

Results and Discussion

The x-ray diffraction patterns were obtained of the lithium iodide-silver iodide mixtures with lithium iodide contents of 20 mole per cent (m/o), 50 m/o, and 80 m/o, respectively (Table I). The diffraction pattern of the mixture containing 20 m/o of lithium iodide

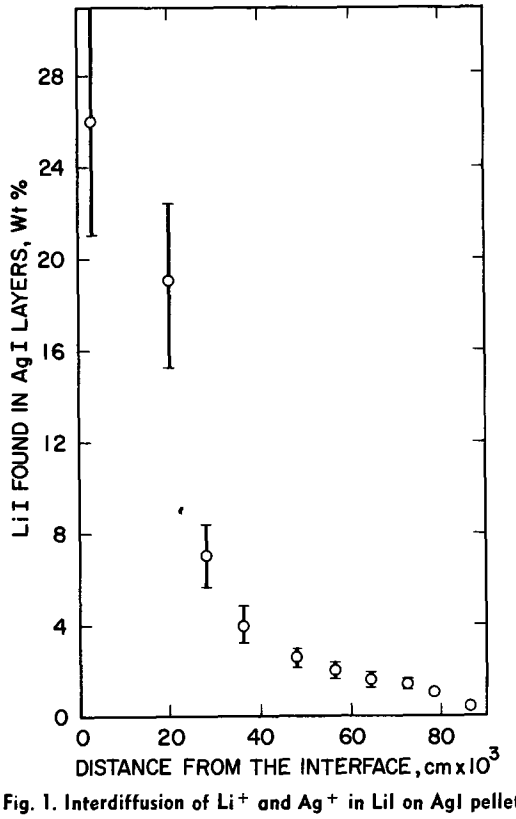

Fig. 1. Interdiffusion of Li^+ and Ag^+ in LiI on AgI pellet

* Electrochemical Society Active Member.
Key words: solid electrolytes, solid state batteries, interdiffusion, lithium/lithium iodide, lithium iodide/silver iodide.

Table I. X-ray diffraction data on (a) 80 m/o AgI + 20 m/o LiI (b) 80 m/o LiI + 20 m/o AgI*

(a) This experiment		AgI ASTM card 9-374		
d (Å)	RI	d (Å)	I/I_o	hkl
3.92	W	3.98	60	100
3.68	W	3.75	100	002
3.46	VW	3.51	40	101
2.73	VVW	2.731	17	102
2.27	S	2.296	85	110
2.10	VVW	2.119	30	103
		1.989	7	200
1.94	M	1.959	50	112
		1.9228	5	201
		1.7574	7	202
		1.5570	5	203
1.48	VVVVW	1.5031	5	210
		1.4744	3	211
		1.4535	1	114
		1.4052	5	105
1.38	VVVVW	1.3957	3	212
1.32	VVVW	1.3258	9	300
		1.2888	5	213
		1.2515	3	006
		1.2500	5	302
		1.1987	3	205
		1.1943	1	106
1.14	VVVVW	1.1480	3	220

(b) This experiment		LiI ASTM card 1-0592			AgI ASTM card 9-374		
d (Å)	RI	d (Å)	I/I_o	hkl	d (Å)	I/I_o	hkl
3.90	VVW				3.98	60	100
3.68	VVVW				3.75	100	002
3.44	VVS	3.47	100	111	3.51	40	101
2.98	VS	3.00	75	200			
2.67	VVVVW				2.731	17	102
2.26	VW				2.296	85	110
2.12	VS	2.12	40	220			
2.08	VW				2.119	30	102
					1.989	7	200
1.96	VW				1.959	50	112
1.92	VVVVW				1.9228	5	201
1.81	VS	1.81	40	311			
1.73	S	1.73	10	222	1.7574	7	202
1.53	VVVVVW				1.5570	5	203
1.50	VVVW	1.50	6	400	1.5031	5	210
1.45	VVVVVW				1.4744	3	211
					1.4535	1	114
1.38	S	1.38	15	331	1.4052	5	105
					1.3957	3	212
1.34	S	1.34	15	420	1.3258	9	300
1.27	VVVVVW				1.2888	5	213
1.23	S	1.23	8	422	1.2515	3	006
					1.2500	5	302
1.16	S	1.16	8	333, 511	1.1987	3	205
					1.1943	1	106
					1.148	3	220
					1.1029	1	310
					1.0916	1	311
					1.0831	1	304
1.06	VVW	1.06	1	440	1.0626	3	215
					1.0589	1	206, 312
1.02	M	1.02	6	531			
					1.0093	1	313
1.00	W	1.00	2	600, 442			
0.95	VW	0.95	2	620			
0.92	VVW	0.92	1	533			

* The diffraction pattern of the mixture containing 50 m/o of lithium iodide and 50 m/o of silver iodide is similar to that of (b).

showed only the silver iodide lines indicating a complete dissolution of the 20 m/o of lithium iodide in silver iodide. Both lithium iodide and silver iodide were evident in the diffraction patterns of the mixtures containing more lithium iodide. However, no third component was detected from these x-ray diffraction patterns. These results showed clearly that solid solutions were formed under the present experimental conditions.

The lithium iodide on silver iodide pellets were stored at 26° ± 2°C for three months before analysis. Figure 1 shows the lithium iodide contents in the silver iodide layers at various distances from the interface after three months. A curve was not drawn in Fig. 1 because the reproducibility of the results was poor. There were times that a variation of ±20% was observed with two similar samples. The poor reproducibility may be due to a variety of causes such as the uncertainty of the determination of the distance from the interface and the perpendicularity of the layer depth to the surface of the sample. Nevertheless, the results did show that the interdiffusion of the lithium and the silver ions did occur and occurred with rather high rates even at room temperatures.

It is known that interdiffusion of lithium and silver ions occurs when lithium iodide and silver iodide are in close contact at high temperatures. The coefficients of interdiffusion at temperatures between 200°C and 370°C are in the order of 10^{-5} cm²/sec (4). Results from this investigation showed that the interdiffusion of the cations took place in silver iodide/lithium iodide even at a temperature as low as 26° ± 2°C.

The interdiffusion of the lithium and the silver ions in the electrolyte and the cathode would result in a direct short circuit between the anode and the cathode in the Li/LiI/AgI cell, and we attributed the cell failure upon storage to the interdiffusion process.

Manuscript submitted Nov. 30, 1970; revised manuscript received March 3, 1971. This was Paper 20 presented at the Atlantic City Meeting of the Society, Oct. 4-8, 1970.

Any discussion of this paper will appear in a Discussion Section to be published in the December 1971 JOURNAL.

REFERENCES

1. M. L. B. Rao, U.S. Pat. 3,455,742, July 15, 1969.
2. C. C. Liang and P. Bro, *This Journal*, **116**, 1322 (1969).
3. C. C. Liang, J. Epstein, and G. H. Boyle, *ibid.*, **116**, 1452 (1969).
4. W. Jost, "Diffusion in Solids, Liquids, Gases," p. 199, Academic Press, Inc., New York (1960).

Electromigration of Fe and Cr in Liquid Bi[1]

S. G. Epstein[2] and J. R. Weeks

Brookhaven National Laboratory, Upton, New York 11973

The electromigration behavior of Fe and Cr in liquid Bi was investigated as part of an experimental study of the electronic phenomena that occur during the corrosion of low alloy steels in liquid Bi. The purpose of this note is to present the results obtained and to suggest their possible significance in explaining observed corrosion phenomena.

[1] This work was performed under the auspices of the United States Atomic Energy Commission.
[2] Present address: The Aluminum Association, 750 Third Ave., New York, New York 10017.
Key words: electromobility, apparent diffusion, diffusion coefficients of chromium and liquid bismuth.

Electromigration experiments were performed using the capillary-reservoir technique, which has been previously described in detail (1). Since the solubilities of Fe (2) and Cr (3) in liquid Bi are quite low (15 and 44 ppm, respectively, at 500°C), the sensitivity of this technique was put to a test. In essence, several fused quartz capillaries, normally 1 mm ID and 5 cm long with W electrodes sealed in one end, were filled in a reservoir containing liquid Bi alloyed with small amounts of either Fe or Cr. A d-c current was passed through two of the capillaries; the others sampled the

Table I. Analyses of Bi-Fe alloys after electromigration at 500°C

Experiment number	Duration (hr)	C.D.* (A/cm²)	Final Fe conc in capillary (ppm)
Fe-1	48	+250	8.5
Fe-4	24	+250	8.8
Fe-2	24	−600	217
Fe-5	28	−250	143
Fe-3	46	none	9.4
Fe-7	24	none	25

* Positive current indicates electron flow from reservoir to electrode at top of capillary (anode); negative current indicates electron flow from electrode at top of capillary (cathode) to reservoir.

alloy. Previously irradiated Fe and Cr were used in preparing the alloys, and their migration behavior was determined by radiochemical analysis. This technique is sufficiently sensitive to allow detection of the few ppm of radioactive tracer element present and precise enough to determine the actual concentration to within ±10% at these levels.

In the first experiments with Bi-Fe alloys, single capillaries with sealed-in tungsten electrodes were submerged in the liquid alloy, and a second electrode was inserted into the reservoir to complete the circuit. The results of these experiments—all performed at about 500°C—are given in Table I. In the capillaries which contained the anode, an average of only about 9 ppm Fe was found after a current of 250 A/cm² was passed for one to two days. However, in the capillaries that contained the cathode, well over 100 ppm Fe was found in the contained alloy after the current was passed. Furthermore, a greater current passed through the cathode capillary resulted in a higher concentration of Fe in the contained alloy. The neutral capillaries were intended to be samples of the melt, which should have contained a saturated solution of Fe (15 ppm). These results indicate a tendency for Fe to migrate toward the cathode, against the electron flow. Since more Fe was originally added to the charge than the 15 ppm soluble at 500°C, some particulate Fe is expected to have been present, and autoradiography revealed the presence of several large particles of Fe in the cathode and in one of the neutral capillaries. These could have formed in the capillaries because electromigration supersaturated the Bi in the capillaries with Fe so that precipitation occurred *in situ*, or they may have formed in the bath and have been carried into the capillaries by the current.

More quantitative data were obtained for Cr migration in Bi due to its somewhat greater solubility. Experiments were performed at temperatures from 310° to 605°C. The results are given in Table II. In each experiment current flowed through two of the capillaries, one containing the anode and the other the cathode. Average values of the electric mobility (U) and the coefficient of electron drag (P) were calculated from the Cr concentration changes in both current-carrying capillaries in each experiment. The scatter in data at 310°C and 405°C may be attributed to the low solubilities of Cr in Bi at these temperatures (≈2 ppm at 310° and 10 ppm at 405°). The abnormally high Cr concentration found in both capillaries at 310°C may be analogous to the high Fe concentrations in the cathode-containing capillaries in Table I. At the higher temperatures the values of U [defined in Ref. (1)] for Cr in Bi are similar to those reported (4) for Ni in liquid Bi.

In previous papers (5, 6), one of the authors has concluded that electromigration in liquid metals results from an interaction between the electron stream and the metal ions. This interaction is described by the parameter, P [defined in Ref. (6)], equal to the number of solute atoms passing through the capillary orifice per electron passing through the contained alloy.

The positive values of P indicate that Cr ions in Bi scatter electrons more strongly than the Bi ions and therefore receive a greater fraction of the momentum of the electrons. Hence, Cr is preferentially transported to the anode, displacing Bi to the cathode. Belashchenko (7) has summarized various arguments why transition metals in alloys should scatter electrons strongly, and, in addition to chromium, Ni, Co, Zr, Pd, and U have been observed (4, 7) to migrate to the anode in liquid Bi. Iron ions apparently scatter the electrons less strongly than liquid Bi and migrate to the cathode.

In a second series of experiments, the diffusion and electrodiffusion of radioactive Cr were measured from a reservoir of the Bi-Cr alloy into capillaries previously filled with pure Bi, in the apparatus shown in Fig. 1. At the desired temperature the alloy was stirred and sampled. The capillary cluster was then lowered into the pure Bi under vacuum; the capillaries were filled by pressurizing the system with purified He, removed from that reservoir, and immediately rotated and lowered into the alloy without allowing the contained Bi to solidify. Direct current was passed through two of the capillaries for a predetermined time. The capillary cluster was then removed from the reservoir and quenched by a stream of liquid nitrogen-cooled helium. The capillaries were sectioned and the contained alloy weighed and dissolved into measured amounts of acid solutions and the solutions counted for Cr^{51}. Diffusion coefficients were calculated by the average concentration technique described by Crank (8). The results of a typical experiment are given in Table III. The apparent diffusion of Cr in Bi is seen to have been enhanced approximately 3 to 4 times by the passage of 1000 A/cm² at 515°C.[3]

Any relation between these results and the selective leaching of chromium or selective attack of Cr-rich alloys during corrosion of steels in liquid bismuth is speculative at best at the present time. Preliminary

[3] Values of U and P cannot be conveniently calculated from the experiment in Table III since the boundary conditions were not those needed for these calculations.

Table II. Analyses of Bi-Cr alloys after electromigration

Temp (°C)	Duration (hr)	C.D. (A/cm²)	Cr conc in reservoir (ppm)	Final Cr conc in capillaries (ppm)		Avg $U \times 10^4$, cm²/V-sec	Avg $P \times 10^4$, atom/electron
				Anode	Cathode		
310	4	1,000	11.6	27.4	11.0	(19.7)	(11.7)
405	4	1,000	11.6	13.5	10.5	3.2	1.9_3
515	4	1,000	34.6	43.4	23.6	7.1	4.4_8
605	4	1,000	51.2	65.9	38.4	6.1	4.3_4

Table III. Diffusion coefficients and "apparent diffusion coefficients" for Cr in liquid Bi

Temp (°C)	Duration (hr)	Cr conc of reservoir (ppm)	Capillary electrode	C.D. (A/cm²)	D or "$D_{app.}$", 10^{-5} cm²/sec
~515	48	37.4	0	0	3.1
			Anode	1,000	12.3
			Cathode	1,000	1.3

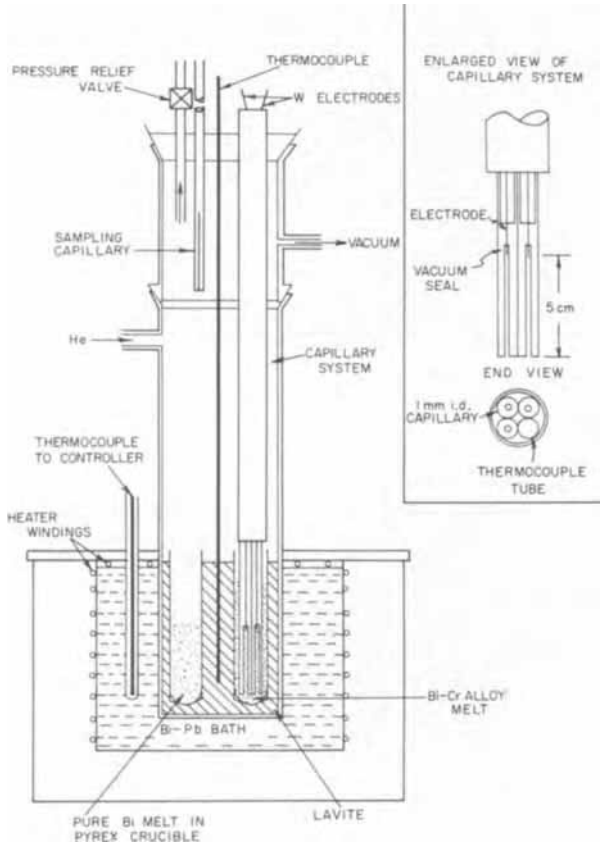

Fig. 1. Schematic representation of apparatus used in measuring diffusion and electrodiffusion of Cr in liquid Bi.

data suggest that potentials of the order of a few microvolts may exist between Cr-rich steels as the cathode and Cr-poor steels as the anode when immersed in liquid bismuth. If these potentials are substantiated, the eddy currents that possibly result from them would tend to increase the rate of dissolution of chromium and decrease the rate of dissolution of iron. Data of sufficient accuracy to demonstrate the validity of this suggestion, however, are not available at the present time.

Acknowledgments

The laboratory assistance and patience of J. E. Rutherford, Jr., in making the electromigration measurements was invaluable to this program. The work was performed under the general supervision of D. H. Gurinsky.

Manuscript submitted Nov. 15, 1968; revised manuscript received Jan. 14, 1971.

Any discussion of this paper will appear in a Discussion Section to be published in the December 1971 JOURNAL.

REFERENCES

1. S. G. Epstein, *Trans. AIME*, **236**, 1123 (1966).
2. J. R. Weeks, *Am. Soc. Metals Trans. Quart.*, **58**, 426 (1965).
3. C. J. Klamut, D. G. Schweitzer, J. G. Y. Chow, R. A. Meyer, O. F. Kammerer, J. R. Weeks, and D. H. Gurinsky, "Progress in Nuclear Energy, Series IV, Vol. 2—Technology, Engineering and Safety," p. 433, Pergamon Press, London (1960).
4. J. D. Verhoeven and E. E. Hucke, *Am. Soc. Metals Trans. Quart.*, **55**, 866 (1962).
5. S. G. Epstein, *Advan. Phys.*, **16**, 325 (1967).
6. S. G. Epstein and A. Paskin, *Phys. Lett.*, **24A**, 309 (1967).
7. D. K. Belashchenko, *Russ. Chem. Rev. (English Transl.)*, **34**, 219 (1965).
8. J. Crank, "The Mathematics of Diffusion," Clarendon Press, Orford (1956).

A Bipolar Current Interrupter for Electrochemical Measurements

P. M. Schwartz

RCA Laboratories, Princeton, New Jersey 08540

There have been some recent papers (1, 2) on the current interrupt technique as an approach to measuring and correcting for ohmic potential drops in electrochemical cells. The method introduced by McIntyre and Peck (2) is a good one, but it lacks the flexibility of being simultaneously usable with both anodic and cathodic currents. This situation is inconvenient in a-c experiments such as controlled double potential step experiments. A circuit has been introduced by Bruckenstein and Miller (3) which may be used for bipolar current interrupt measurements. Their circuit, however, establishes the zero current condition by applying the proper voltage to the cell in a feedback loop. This zero current condition is thus susceptible to errors arising from drifts in the amplifiers. In what follows, a current interrupter is described which works with both polarities of current and which establishes the zero current by switching a large resistance in series with the cell. The circuit described below also appears to have a slightly higher switching speed than the circuit of Bruckenstein and Miller.

Key words: ohmic potential measurement, double potential step, voltammetry, polarography.

In Fig. 1 a circuit is shown which works with both polarities of current. This circuit uses a field-effect transistor as the switching element to interrupt the current. In this application, the field-effect transistor operates as a voltage-controlled resistor switching from a typical resistance of >10M at cutoff to about 200 ohms at zero bias. A limitation inherent in the use of a field-effect transistor as the isolating element is that the current supplied by the circuit is limited to the saturation current of the transistor which is typically 10-30 mA for the type used. Should it be necessary to drive more current, several transistors may be used in parallel. There is also an advantage in using a field-effect transistor instead of a diode as the isolating element. McIntyre and Peck have noted that the high resistance of the diode at low current causes their circuit to oscillate when placed in a potentiostatic control circuit. This problem does not exist with the field-effect transistor since it maintains its low resistance down to zero current. Therefore, this interrupter circuit should be very useful in polarography.

The operation of the circuit is quite simple. When a negative pulse is applied to the gate input, Q_5 applies

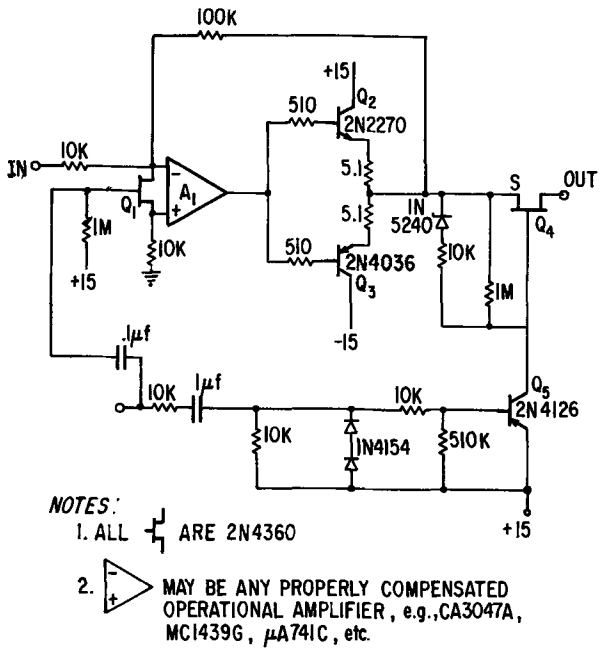

Fig. 1. Circuit diagram of the current interrupter

a large positive bias to the gate of Q_4. This action puts a large resistance in series with the electrochemical cell and prevents any current flow to the cell. The gate pulse also reduces the bias on the gate of Q_1 which shorts the inputs of the operational amplifier. This is especially necessary when the interrupter is part of a feedback loop in a potentiostat circuit for controlling electrode voltages in polarography and voltammetry, since in this case the amplifier would saturate and disturb the bias on Q_4 if Q_1 were not present. This interrupt process is quite rapid, being limited by the switching time of the transistor. In a practical configuration that included ample cable capacitance, the interrupt time was ~1 μsec.

When the gate pulse turns off, Q_5 turns off, and the bias resistors of Q_4 and Q_1 charge the gate-source voltages of those transistors to the quiescent values. Thus, Q_4 returns to the low-resistance state and Q_1 to the high-resistance state. This returns control of the output voltage to the operational amplifier. The recovery of the circuit is more complicated than the interrupt action. First, there is the time necessary to discharge the gate-source capacitance of the field-effect transistors. For the low-frequency transistors used in this circuit, that time is $\lesssim$20 μsec. Second, there is the response time of the operational amplifier. With a typical slew rate of 2.5 V/μsec, the amplifier recovery time for a typical electrochemical application would be only a few microseconds. The recovery time of the circuit was found to be ~20 μsec. This time could be improved by using higher-frequency transistors with a smaller gate-source capacitance or by decreasing the bias resistors.

The performance of the interrupter when it is acting like a voltage amplifier is shown in Fig. 2 and 3. Figure 2 shows an oscilloscope trace of the current through an electrochemical cell due to a constant applied voltage that is reversed every 13 msec. The interruptions are generated by a variable delay pulse generator (*e.g.*, Hewlett-Packard 214A) that is triggered by the voltage switching transients. Figure 3 shows, on an expanded time scale, the shape of an interrupted current pulse and the electrode voltage as measured by a reference electrode in the cell. Both the voltage and current have a recovery time constant of ~20 μsec while the fall of the current to zero takes ~1 μsec. In this mode of operation, interrupt pulses spaced as close as 200 μsec have applied without altering the over-all current waveform.

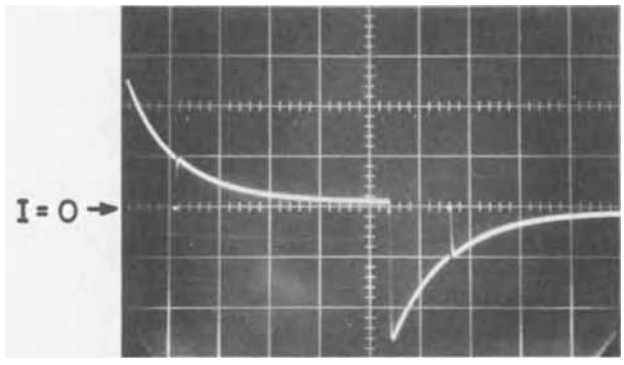

Fig. 2. Twenty-microsecond interruptions of positive and negative currents with interrupter applying a constant voltage to a cell: vertical scale 1 mA/div; horizontal scale 2 msec/div.

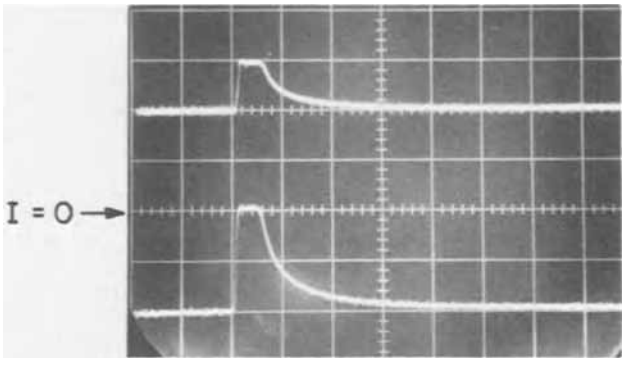

Fig. 3. Details of an interrupt pulse: upper trace—electrode voltage, 0.2 V/div; lower trace—cell current 0.4 mA/div; horizontal scale 20 μsec/div.

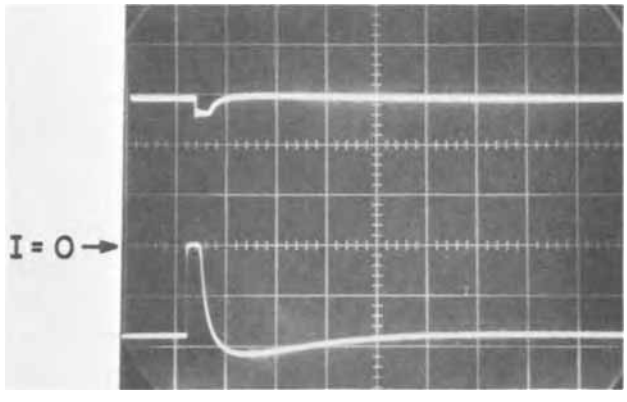

Fig. 4. Interrupt pulses in a controlled potential mode: upper trace—electrode voltage 0.5 V/div; lower trace—cell current 1 mA/div; horizontal scale 50 μsec/div.

The performance of the interrupter in controlled potential applications has also been examined. For this purpose the reference electrode potential, buffered by a voltage follower, and the signal voltage were summed at the inverting input of A1 and the 100K resistor in the feedback loop was replaced by a 0.001 μf capacitor. The results of a current interruption are shown in Fig. 4. We note that the recovery and settling time of the current has been extended to ~200 μsec. With the information provided in Fig. 4, the "uncompensated resistance" (2) in the controlled potential experiment is readily evaluated.

Acknowledgment

The author wishes to thank R. A. Blakeley for his assistance in the construction of the interrupter.

Manuscript submitted Nov. 24, 1970; revised manuscript received *ca.* Feb. 26, 1971.

Any discussion of this paper will appear in a Discussion Section to be published in the December 1971 JOURNAL.

REFERENCES

1. John Newman, *This Journal*, **117**, 507 (1970).
2. J. D. E. McIntyre and W. T. Peck, Jr., *ibid.*, **117**, 747 (1970).
3. Stanley Bruckenstein and Barry Miller, *ibid.*, **117**, 1040 (1970).

Brief Communication

A New Method of Preparation of $RbAg_4I_5$ Solid Electrolyte

Bruno Scrosati*

Istituto di Chimica Fisica, Università di Roma, Rome, Italy

$RbAg_4I_5$, silver rubidium iodide (SRI) solid electrolyte, has been so far prepared by melting a stoichiometric mixture of AgI and RbI and then quenching it (1, 2).

Recently we have discovered that SRI is soluble in acetone and in a number of other organic polar solvents and that it can be recrystallized from solutions (3). Furthermore, in a paper published in 1913 by Marsh and Rhyme, it is reported that a "rubidium silver iodide RbI,AgI" is obtained when RbI and AgI are dissolved in acetone and the solution evaporated in dry air (4).

This evidence encouraged us to suppose that SRI could simply be obtained by crystallization from a solution prepared by dissolving in acetone a mixture of silver and rubidium iodides. To test this, a known amount of AgI was added to acetone, followed by subsequent addition of RbI to the same solution. AgI, which as such is practically insoluble in acetone (see Table I), readily dissolved in the presence of RbI. The complete dissolution was obtained for an AgI/RbI molecular proportion of about 2 to 1.

The complete dissolution of the AgI-RbI mixture in acetone, however, was followed by a spontaneous precipitation of a white compound (this latter material was then identified, by x-ray powder analysis, as RbI). The acetone solution was then filtered and slowly evaporated. The resulting crystallized salt was dried at 100°C in an oven and analyzed by x-ray. The results are reported in Table II, which also includes the patterns of SRI, calculated and found by Bradley and Greene (7). All the lines of SRI are present in the acetone-crystallized compound indicating that the compound is indeed $RbAg_4I_5$.

The remaining lines found, all very weak in intensity, could probably be attributed to some impurities present in the starting materials. In fact RbI and AgI, commercial products, have been used without any further purification. This hypothesis may be confirmed by the value of the ionic specific conductivity of $RbAg_4I_5$ crystallized by acetone solution which was found to be 0.1 $(ohm\text{-}cm)^{-1}$ at 25°C. This conductivity value is somewhat inferior to that of pure $RbAg_4I_5$, which is about 0.24 $(ohm\text{-}cm)^{-1}$ at 25°C (8).

It is reasonable to suppose that starting with high purity compounds, a more conductive $RbAg_4I_5$ could also be obtained by the crystallization method described here. On the other hand it has to be considered that when SRI is used as electrolyte in a solid-state battery, its resistance represents only a small fraction of the over-all cell resistance, the major contributions being the electrode-electrolyte polarizations. Therefore, $RbAg_4I_5$ prepared by crystallization from an acetone solution of commercial AgI and RbI, may also be used as electrolyte in solid-state batteries. A difference of 0.14 $(ohm\text{-}cm)^{-1}$ in specific conductivity will affect the total resistance only by fractions of ohms.

Table I. Solubility of various salts in acetone

Salt	Solubility (w/o)	Temperature (°C)	Reference
AgI	3.2×10^{-10}	25	(5)
RbI	0.72	25	(6)
	0.65	30	
$RgAg_4I_5$	3.20	30	

Table II. X-ray powder patterns (CuK_α radiation) of $RbAg_4I_5$

Bradley and Greene (7) Calculated d	I	Observed d	I	This work d	I
				8.11	W
7.88	7.5	7.85	W	7.65	MW
6.44	0.8				
4.99	0.8				
4.55	1.2				
3.94	6.4				
				3.77	VW
3.72	51.1	3.72	MS	3.69	MS
3.53	14.8	3.52	VW	3.51	VW
3.36	96.4	3.36	S	3.34	S
3.22	32.8	3.22	W	3.20	W
3.09	1.1				
2.98	13.2				
2.79	0.1				
2.71	1.5				
2.63	24.4	2.63	W	2.62	MW
2.56	0.4				
2.49	7.1				
2.43	4.1				
2.38	21.8	2.38	W	2.36	MW
2.28	24.2	2.28	MW	2.27	MW
2.23	23.2	2.23	MW	2.23	M
2.19	100.0	2.19	S	2.20	S
2.15	13.8	2.15	VW		
2.07	49.5	2.07	M	2.07	M
2.04	31.5	2.04	MW	2.04	W
1.97	13.3	1.97	W	1.97	VW
1.94	15.3	1.94	W	1.94	VW
1.91	4.1			1.87	VW
1.88	2.0				
				1.81	W
				1.74	W
				1.66	VW
				1.42	VW
				1.39	VW
				1.38	VW
				1.28	VW
				1.13	VW

* Electrochemical Society Active Member.

Key words: $RbAg_4I_5$ solid electrolyte, preparation of.

On the basis of the reported evidence, the AgI-RbI mixture solution reaction could be tentatively represented as

$$4AgI + 2RbI \xrightarrow{\text{acetone}} 4AgI \cdot 2RbI \rightarrow RbAg_4I_5 + RbI\downarrow \quad [1]$$

To have a clearer picture of the solution mechanism, however, a more detailed study of the species in solution is necessary. This study is in progress in our laboratory.

The described new method of SRI preparation appears to be of a certain technological importance for the following reasons:

a) It is well known that the SRI decomposition, which takes place according to the reaction

$$2RbAg_4I_5 \rightarrow Rb_2AgI_3 + 7AgI \quad [2]$$

is favored by the presence of moisture. With the crystallization method of preparation in which dry acetone and pure starting materials are used, it is theoretically possible to prevent the decomposition and, ultimately, obtain a very pure material.

b) The possibility of obtaining SRI by crystallization from acetone solution allows the growing of single crystals and the deposition of thin layers of electrolyte. At the present, SRI single crystals have only been grown from nonstoichiometric melts, using the Czochralski technique (9). This method, however, is not of very easy application and presents technical problems. Single crystal growth from solution is certainly a much easier and faster procedure. In fact we have grown small octahedral SRI crystals by simple evaporation of the solutions (3). The feasibility of obtaining thin layers of film of electrolyte is also of considerable importance since it allows the development of low resistance, miniaturized solid-state batteries.

c) Finally, the solution procedure described in the case of the SRI preparation, is general and it can be applied, varying the starting materials and the solvent, for the preparation of a series of a new compound and new electrolytes. In fact at the moment a number of new solid electrolytes crystallized from solutions are under study in this laboratory.

Acknowledgments

The author would like to thank Dr. P. Cignini for the x-ray work.

Manuscript received Feb. 23, 1971.

Any discussion of this paper will appear in a Discussion Section to be published in the December 1971 JOURNAL.

REFERENCES

1. B. B. Owens and G. R. Argue, *Science*, **157**, 308 (1967).
2. M. De Rossi, G. Pistoia, and B. Scrosati, *This Journal*, **116**, 1964 (1969)
3. B. Scrosati and D. Butherus, To be published.
4. J. E. Marsh and W. C. Rhymes, *J. Chem. Soc.*, **103**, 781 (1913).
5. A. Lanung, *Z. Physik Chem.*, (A), **161**, 255 (1932).
6. C. Evertz and R. Livingston, *J. Phys. Colloid Chem.*, **53**, 1330 (1949).
7. J. N. Bradley and P. D. Greene, *Trans. Faraday Soc.*, **63**, 2516 (1967).
8. B. Scrosati, G. Germano and G. Pistoia, *This Journal*, **118**, 86 (1971).
9. L. D. Fullmer and M. A. Hiller, *J. Cryst. Growth*, **5**, 395 (1969).

DISCUSSION SECTION

This Discussion Section includes discussion of papers appearing in the *Journal of The Electrochemical Society*, Vol. 117, No. 10 and 12, October and December 1970.

The Approach to Limiting Current in a Stagnant Diffusion Cell

L. Hsueh and J. Newman (pp. 1242-1245, Vol. 117, No. 10)

L. Nanis[1]: For precise application of the stagnant diffusion cell, the authors should take into account the contribution to the over-all ohmic drop associated with the sudden change in cross section of electrolyte at the open end of the capillary. This so-called "constriction" resistance is in series with the capillary resistance given in the authors' Eq. [6]. It is of interest to note that the constriction resistance is of importance to a number of related technologies which involve the thermal and electrical resistance at metal interfaces such as electrical contacts, spot welding, and also end effects in the early definition of the ohm based on the resistance of a specified mercury column. The constriction resistance is discussed in several texts.[2-4] Calculation of the resistance of an idealized circular cross section is accomplished by solution of the Laplace equation for the field near a circular conducting opening in an otherwise insulating plane bounding the semi-infinite conducting medium. From the gradient of potential, the flux or current density normal to the disk opening is obtained, permitting application of Ohm's law to yield the resistance. The field solution for disk geometry was worked out as early as 1832 by Green[5] and in 1873 by Weber.[6] More recently, the resistance for disk geometry has also been verified by Newman.[7] By adding the end effect or constriction resistance to the resistance of the electrolyte within the capillary, the authors' Eq. [6] may be revised as

$$\Delta\phi_{ohm} = \frac{I}{\kappa_\infty a}\left[\frac{L}{\pi a} + \frac{1}{4}\right] \quad [1]$$

where I is current (A) and a is capillary radius (cm). (Remaining notation same as used by Hsueh and Newman.) According to Eq. [1] above, the end effect may be considered negligible if the capillary length to radius ratio is sufficiently large, *i.e.* $L/\pi a >> 1/4$. For vanishingly short capillaries, Eq. [1] gives the potential drop for the disk alone (cf. Eq. [9] of footnote 7). The authors report various capillary lengths, *i.e.* 7, 10, and 15 cm; and, from an electrode (and capillary) area given as 0.178 cm^2, a radius of 0.25 cm may be considererd as typical. Using these figures in Eq. [1], the ohmic potential will be consistently underestimated if the end effect is ignored, giving a 2.7% error for the 7 cm long capillary and 1.3% error for

[1] School of Chemical Engineering, University of Pennsylvania, Philadelphia, Pennsylvania 19104.
[2] J. H. Jeans, "The Mathematical Theory of Electricity and Magnetism," p. 356, Cambridge University Press, Cambridge, England (1958).
[3] F. P. Bowden and D. Tabor, "The Friction and Lubrication of Solids", p. 25, Clarendon Press, Oxford University (1954).
[4] H. S. Carslaw and J. C. Jaeger, "Conduction of Heat in Solids," p. 216, Clarendon Press, Oxford University (1959).
[5] G. Green, *Trans. Cambridge Phil. Soc.*, 5, 1 (1832).
[6] H. Weber, *Crelle J. Mathematics*, 75, 75 (1873); also to be found in "A Treatise on Bessel Functions and Their Applications to Physics," A. Gray, G. V. Matthews, and T. M. MacRobert, 2nd. Ed., p. 142, MacMillan and Co. Ltd., London (1952).
[7] J. J. Newman, *This Journal*, **113**, 501 (1966).

the 15 cm capillary. Clearly, the end effect becomes increasingly more important only for capillary lengths smaller than those reported by the authors. However, the constriction resistance should be taken into account where the capillary length (or L/a) is reduced in order to decrease time required for experiments (cf. authors' Eq. [17]).

It should be mentioned that the term ¼ in Eq. [1] is based on a boundary condition of constant potential on the disk surface.[7] An upper limit to the end effect term may be considered on the basis of uniform current density over the disk surface at the capillary opening.[8,9] Is this case, the term ¼ in Eq. [1] is replaced by $8/3\pi^2$. Since the actual capillary (open) end condition is not known, the limiting cases of constant potential and constant current density provide a lower and upper bound. The end correction term for the resistance of electrolyte in the capillary given in Eq. [1] may thus be considered as somewhat uncertain but at least bounded between 0.25 and 0.27. Finally, it should be noted that the end-effect resistance calculations relate to a capillary of infinitely large extent in the radial direction. However, from the range of the potential field,[8] the correction terms may be considered as valid for a capillary outside radius which is five to six times the inside radius or greater.

On the Relation between Standard Potentials and Activity of Interstitial Silver Ions in AgCl and AgBr

A. Hoffman (pp. 1525-1527, Vol. 117, No. 12)

F. A. Kroger[10]: In this paper, Hoffman attempted to prove that the difference in the standard potentials of Ag/AgCl and Ag/AgBr can be ascribed to the difference in activity of interstitial silver ions, Ag_i, in the respective silver halides. This would imply that the individual standard potentials depend strongly on the activity of interstitial silver and, if true, would make the standard potentials sensitive to the presence of small concentrations of aliovalent impurities and would seriously decrease their usefulness. As we shall see, this is not the case.

The potential difference under discussion is essentially due to the exchange reaction

$$AgBr + Cl^-(aq) \rightarrow AgCl + Br^-(aq) \qquad [1]$$

$Cl^-(aq)$ and $Br^-(aq)$ representing Cl^- and Br^- in aqueous solution under standard conditions. As shown in Table I of this Discussion, this reaction gives a value of $\Delta E = \Delta G^\circ/F \approx 149.2$ mV; the small difference from $\Delta E = 222.2 - 71.3 = 150.9$ mV[12] cited in the discussed paper is due to the use of slightly different values for the standard free energies.

Reaction [1] depends on the chemical potentials of the silver halides, and these in turn are equal to the sum of the chemical potentials of the basic structure elements Ag_{Ag} and Br_{Br} and Cl_{Cl}. Writing X for Cl or Br

$$\mu(AgX) = \mu(Ag_{Ag}) + \mu(X_X) \qquad [2]$$

The latter in turn depend on the concentrations (expressed as site fractions) through

$$\mu_j = \mu_j^\circ + RT \ln [j] \qquad [3]$$

j representing Ag_{Ag} or X_X.

As long as the silver halides are reasonably pure, $[Ag_{Ag}] \approx [X_X] \approx 1$, and the chemical potentials of the structure elements Ag_{Ag} and X_X are close to their standard values.

Interstitials, vacancies, and foreign impurities play a role only insofar as they affect $[Ag_{Ag}]$ and $[X_X]$; their effect is negligible as long as their site fraction is small compared to 1, say $<10^{-3}$ or 10^{-4}. Electrodes based on pure and weakly doped halides will give standard potentials differing no more than corresponds to the impurity concentration. Doping with divalent cations, on the other hand, has a marked effect on the concentration of $Ag_i^\cdot$ and V'_{Ag}. For AgBr and AgCl, the concentrations of these defects if determined by Frenkel disorder are, respectively, $\approx 10^{-8}$ [13] and 2×10^{-9}.[14] Aliovalent impurities present in concentrations larger than these values will affect the concentrations of the native defects; *e.g.*, the presence of 10^{-4} divalent cations such as Ca or Cd will increase $[V'_{Ag}]$ to this value and decrease $[Ag_i^\cdot]$ to 10^{-12} in AgBr and 2×10^{-13} in AgCl. It is very doubtful that materials used to prepare standard electrodes have ever been pure to the order 10^{-8}. Therefore, Hoffman's assumption of defect concentrations determined by Frenkel disorder is unrealistic. A more fundamental objection against the analysis as presented by this author lies in the identification

$$RT \ln [Ag_i^\cdot]_{AgBr}/[Ag_i^\cdot]_{AgCl} = \Delta\mu(Ag_i^\cdot) \qquad [4]$$

(Hoffman's Eq. [16]).

Since $\mu(Ag_i^\cdot) = \mu^\circ(Ag_i^\cdot) + RT \ln [Ag_i^\cdot]$, [4] is correct only if $\mu^\circ(Ag_i^\cdot)_{AgBr} = \mu^\circ(Ag_i^\cdot)_{AgCl}$. There is no reason why this should be so. The correspondence between the observed value of ΔE and $\Delta E = \Delta\mu(Ag_i^\cdot)/F$ as calculated in Hoffman's Eq. [18] must be fortuitous. In fact, there is no corespondence if we use more recent values for the G° of Frenkel disorder in AgCl and AgBr[14] $(G^\circ_{AgCl} - G^\circ_{AgBr})/2 = (1032 - 885)/2 = 74$ mV.

Table I. Standard free energies of reaction for various processes related to the Ag/AgX electrode potentials[11]

	Reaction	ΔG° (kcal/mole)
1	$AgBr(s) \rightarrow Ag(s) + \frac{1}{2}Br_2(l)$	22.91
2	$\frac{1}{2}Br_2(l) \rightarrow Br^-(aq) + e^-(Pt)$	−24.595
3	$Ag(s) + \frac{1}{2}Cl_2(g) \rightarrow AgCl(s)$	−26.22
4	$Cl^-(aq)\ e^-(Pt) \rightarrow \frac{1}{2}Cl_2(g)$	31.345
5	$AgBr(s) + Cl^-(aq) \rightarrow AgCl + Br^-(aq)$	3.44 (+)

[8] L. Nanis and W. Kesselman, *This Journal*, 118, 454 (1971).
[9] L. Nanis, Electrochem. Soc. Extended Abstracts I-5, Dallas, Texas, May 7-12, 1967, Industrial Electrolytic Div., Abs. No. 150, p. 27.
[10] School of Engineering, Department of Materials Science, University of Southern California, Los Angeles, California 90007.
[11] Landolt-Bornstein, "Physikalisch Chemishe Tabellen," 2nd Erganzungsband, Springer, Berlin (1931).
[12] A. J. de Bethune, Table of Standard Aqueous Electrode Potentials and Temperature Coefficients at 25°C, in "The Encyclopedia of Electrochemistry," C. A. Hampel, Editor, Reinhold Publishing Co., New York (1964).

A. Hoffman: The effect of impurities on the concentration of interstitial silver ions, (Ag^+i), is an important consideration. A plot of log ionic conductivity versus the reciprocal of temperature, reveals a break in the curve at lower temperatures for silver halides[15,16]. The temperature at which the break in the slope of the curve occurs has been used as a check on the purity of the specimens. The break reflects the condition where the concentration of impurity ions becomes significant compared to the number of thermally generated defects.

Lehfeldt[15] has shown that the break for various specimens of AgBr occurs at temperatures below room temperature. Consequently at room temperature, the uncontrolled concentration of impurities has not apparently effected the concentration of Ag^+i. For single crystal silver chloride [having a lower value of (Ag^+i) than AgBr], the break in the slope occurs well above room temperature.[16] With highly purified single crystals, the break approaches but does not reach room temperature.[16] Thus, uncontrolled impurities do effect the value of (Ag^+i) in single crystal AgCl at room temperature. The amount of uncontrolled impurities present that can effect (Ag^+i) will, of course, depend

[13] F. A. Kroger, *J. Phys. Chem. Solids*, 26, 901 (1965).
[14] Y. J. van der Meulen and F. A. Kroger, *This Journal*, 117, 69 (1970).
[15] W. Lendfeldt, Nachr. Ges. Wiss. Gootingen, Math. Physik. Kl. Fashgr. 11, (N.S.), 171 (1953).
[16] H. C. Abbink and D. S. Martin, Jr., *J. Phys. Chem. Solids*, 27, 205 (1965).

on the method of preparation. (Electrolysis, which is often used to prepare standard electrodes, might generate silver halides with lower concentrations of, for example, Cd^{++} than the procedures used in growing single crystals.)

Clearly, the extent of the effect of impurities on the value of (Ag^+i) is hard to evaluate unless the type and the concentration of these impurities are known. This represents an uncertainty in our argument.

I agree that there is no *a priori* reason why $\mu^o_{(Ag^+i)AgBr}$ should be equal to $\mu^o_{(Ag^+i)AgCl}$. I have just attempted to show that the suggestion of Awad,[17] using the model developed by Honig[18] (that the silver halide lattice can be looked upon as a solvent containing the solute cations-Ag^+i, and solute anions-silver ion vacancies) is consistent with the available data, if the assumption is made that the solvent effect can be neglected (*i.e.* that $\mu^o_{(Ag^+i)AgBr} = \mu^o_{(Ag^+i)AgCl}$).

It is possible that the correspondence between $E_2^o - E_1^o$, and $RT/n\mathbf{F} \ln {}^X(Ag^+i)_1/{}^X(Ag^+i)_2$ is fortuitous but the results for AgI suggest otherwise. I have submitted a manuscript to the *Journal*, which shows that the above equation seems to hold, within the error limits of the experimental data, for AgI also. Since AgI has a higher value of (Ag^+i) than AgBr, the break in the slope of the conductivity versus temperature should occur at even a lower temperature than that for AgBr; and hence, the effect of impurities should be more insignificant. This paper will also point out that the presence of Cd^{++} ions has a significant effect on the characteristic potential of silver halides, as determined chronopotentiometrically.

Andre J. de Bethune[19]: F. A. Kroger's critique of Hoffman's paper can, itself, be subjected to a number of objections of a formal nature. Electrochemistry, and physical chemistry to which it is intimately related, are, if anything, *algebraic sciences, i.e.* sciences based on the correct usage and manipulation of algebraic quantities. Benjamin Franklin[20] in 1752 adopted the algebraic signs (+) and (−) to represent the two physically distinct electricities discovered in 1733 by Charles Dufay: the *vitreous electricity* produced by friction in glass, porcelain, hair of animals, and wool; and the *resinous electricity* in amber, silk, thread, paper, sealing wax, and sulfur, respectively.[21]

Other areas of electrochemistry and physical chemistry have their own algebraic sign conventions.[22] Alternative "European" and "American" (so-called) conventions have been provided for the handling of "half-cell emf's." Nevertheless, the 1953 I.U.P.A.C. Stockholm convention, reaffirming a usage which goes back to Ostwald (1887) and Gibbs (1899), defines the *electrode potential* in an algebraically invariant way, *e.g.* Zn NEG, Cu POS to standard hydrogen, corresponding to the observed d-c polarities of these metals as determined from Franklin's choice of POS and NEG.

Notwithstanding these various algebraic conventions, some of them over 200 years old, Kroger brushes algebraic considerations aside and makes several statements which are in error, unless reinterpreted by the reader. Kroger's reaction Eq. [1], the displacement of Br by Cl in AgBr, has a positive Gibbs free energy change, $\Delta G^o = +3.44$ kcal $= +14.39$ kJ $= +0.1492$ volt-faradays (Kroger's Table I). The cell corresponding to reaction [1] would be, according to the 1953 I.U.P.A.C. Stockholm conventions[23]

$$(+)\ Ag/AgCl/Cl^-//Br^-/AgBr/Ag\ (-) \qquad [A]$$

where the cell voltage E(cell) is to be calculated as V(right) − V(left), and the V's are defined as in Gibbs.[24] For cell [A], therefore

$$E\ (\text{cell A}) = -\Delta G^o/(1\mathbf{F}) = -149.2\ \text{mV} \qquad [1]$$

a value very close to the difference of the electrode potentials[25]: V(right) − V(left) $= (+71.3) - (+222.2) = -150.9$ mV, as pointed out by Kroger. This writer omits several minus signs from his discussion which is, as a result, algebraically erroneous as presented by him.

The present formal critique does not affect the substance of the points in controversy between Professor Kroger and Dr. Hoffman.

Carelessness in the handling of the algebraic signs of electrochemistry causes our science incalculable harm.

[17] S. A. Awad, *J. Electroanal. Chem. Interfacial Electrochem.*, 21, 483 (1969).
[18] E. P. Honig and J. J. T. Hengst, *J. Colloid Interface Sci.*, 31, 545 (1969).
[19] Department of Chemistry, Boston College, Chestnut Hill, Massachusetts 02167.
[20] B. Franklin, Letter to Ebenezer Kinnersley, March 16, 1752.
[21] C. Dufay, *Phil. Trans. Roy. Soc.*, 38, 258 (1733-1734).
[22] T. S. Light and A. J. deBethune, *J. Chem. Education*, 34, 433 (1957).
[23] J. A. Christiansen and M. Pourbaix, *J. Am. Chem. Soc.*, 82, 5517 (1960).
[24] J. Willard Gibbs, "Equilibrium of Heterogeneous Substances, Collected Works," Vol. 1, p. 333, Yale University Press, New Haven (1949).
[25] A. J. de Bethune and N. A. Swendeman-Loud, Standard Aqueous Electrode Potentials and Temperature Coefficients, in "The Encyclopedia of Electrochemistry," C. A. Hampel, Editor, Reinhold Publishing Co., New York (1964).

JOURNAL OF THE ELECTROCHEMICAL SOCIETY

SOLID STATE SCIENCE

JUNE 1971

The Influence of an Air-Formed Film on the Nucleation and Morphology of Etch Pits in Pure Iron

G. M. Spink[1] and M. B. Ives

Department of Metallurgy and Materials Science, McMaster University, Hamilton, Ontario, Canada

ABSTRACT

Annealing pure iron in hydrogen, followed by etching in a hydrogen atmosphere is shown to develop etch features at defects in the metal itself, rather than those of an oxide film. These features are contrasted with those reported for the same etchant on unreduced samples. The influence of an air-formed film in controlling etch morphology is discussed.

The etch pitting of crystalline materials is now a well established method for pinpointing dislocations and following their movements under stress. Although much of the early work was confined to nonmetals, well authenticated examples do exist in the literature where researchers have produced etch pits at dislocation sites in metal single crystals; for example, the classical work of Livingston on copper (1) and Hibbard and Dunn on silicon iron (2). Later work included the etching of bismuth (3), tungsten (4), nickel (5), molybdenum (6), zinc (7), cadmium (8), and niobium (9). A recent review of etching methods and etchants used has been made by Robinson (10).

Subsequent research on polycrystalline metals, notably iron and iron alloys, indicated that an aging treatment was necessary in order to "decorate" the line defects with small quantities of an impurity or trace element. Suits and Low (11), for example, have shown that aging is necessary for etch pitting of dislocations in an Fe-3% Si alloy and that carbon is the principal segregating impurity. Pickering (12), again working with polycrystalline Fe-3% Si, found that a one-to-one correspondence between etch pits and dislocations is only possible when the dislocation density is below a critical value which cannot be displaced upwards by increasing the carbon content. He observed pitted areas in etched thin foils directly under the electron microscope, and saw that fresh dislocations introduced by plastic deformation were never pitted whereas aged dislocations were attacked to a degree depending on the carbon level. Pickering concluded that for a one-to-one correspondence to exist the amount of carbon in solution must be (*a*) equal to, or above, the level which is necessary to produce sufficiently large carbon atmospheres at every dislocation present in the alloy during aging; and (*b*) below that level which, by the formation of random clusters or precipitates during aging, is sufficient to cause two-dimensional nucleation of etch pits not associated with dislocations.

More recently etchants have been developed which produce etch pits without an aging treatment. Liss (13) developed etch pits in iron in what appear to be glide bands. Pelessini and Alessandrini (14), also working on iron, demonstrated the increasing density of pits with work hardening, without intermediate aging treatment, on grains of all orientations.

It is often difficult to interpret the results of etch pitting of polycrystalline metals because of the much increased density of dislocations, compared with single crystals. The processes of slip and twinning are more complex and dislocations exist in bands or tangled networks rather than as discrete defects. The pits themselves are shallow and irregular in outline and, if the dislocation density is high enough, they overlap giving an effect more like over-all surface dissolution than surface pitting.

Thus far, investigators working on polycrystalline metals have set out to show that their particular etchant will produce pits having a one-to-one correspondence with dislocations intersecting the surface etched. Sometimes this is not convincingly done, mainly because of the confusion created by the factors outlined above. No one appears to have considered the possibility that a surface film might influence the nucleation and subsequent growth of an etch pit. Yet one important difference between the surface of a nonmetallic crystal and a metallic one is the usual occurrence of an air-formed oxide film on the latter.

The present work was devised to determine how the presence or absence of an air-formed oxide film affects the nucleation and growth of etch pits in pure iron, using the etching system developed by Taoka *et al.* (15). Normally the pits produced are bounded by faces parallel to {100} and {110} planes. Each pit reflects the symmetry of the grain in which it lies, and by measuring the angles between the pit facets and the surface of the grain in a goniomicroscope the orientation of the grain can be determined.

A detailed study of the pits and the mechanisms controlling pit morphology has been discussed elsewhere (16). While the same etchants have been used here, the conditions were designed to reduce any air-formed film which might otherwise exist on the iron surface prior to etching. A significant modification in etch pit morphology was observed.

Experimental

Samples of "Ferrovac E" iron were subcritically annealed in hydrogen to reduce any surface film and

[1] Present address: Central Electricity Research Laboratories, Materials Division, Leatherhead, Surrey, England.

Key words: Surfaces, reactivity of solids, dissolution, defects in solids.

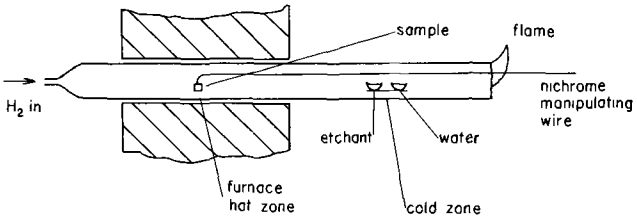

Fig. 1. Apparatus for preparing and etching oxide-free iron surfaces.

then were etched under hydrogen atmosphere in a solution containing 1 part HCl, 5 parts H_2O_2, and 100 parts H_2O. The apparatus is shown in Fig. 1. Small specimens, ½ in. diameter and ⅛ in. thick were given a standard mechanical and chemical polishing treatment and, attached to the end of nichrome wire, were pushed into the furnace hot zone through the hydrogen flame. Several investigators (17-19) have studied the reduction of oxide films on the surface of pure iron, checking for the presence or absence of a film by x-ray and electron diffraction methods. They consider that several minutes at 750°C in hydrogen is sufficient to reduce any film present. In the present experiments a standard reduction treatment of 30 min at 875°C was adopted. After reduction, the specimen was drawn back into the cold zone where its temperature eventually dropped to no more than 10 degrees above ambient.

To etch the sample in its reduced condition, two small polythene vessels fixed to a copper base plate were fed through the flame into the cold zone. One vessel contained the etchant and the other, distilled water for washing. The sample was immersed in the etchant, then washed and returned to the reduction zone to remove the reddish-brown oxide layer produced during etching. This normally took 1 hr at 875°C.

The pits produced by this technique were different both in distribution and morphology to those obtained during "normal" etching (16). Figures 2 and 3a show typical areas of a sample which before reduction had been lightly deformed in a direction parallel to its prepared surface. Two types of pits are present: (*a*) shallow depressions of irregular shape with ill-defined edges (Fig. 2b), and (*b*) conical pits having a well-defined rounded form (Fig. 3a).

In addition (Fig. 2) the shallow pits form continuous or semicontinuous grooves along slip lines. As would be expected in a body centered cubic polycrystalline metal the slip lines are "wavy" in nature and may pass through several grains, ending abruptly at the boundary of a grain unfavorably oriented for slip, to begin again on the other side of that grain.

The effect of etching time is apparent in Fig. 3 which shows the same area after etching for (a) 2 sec and (b) 4 sec. Obviously, the sample had to be removed from the apparatus for photomicroscopy, then reduced before etching a further 2 sec to obtain Fig. 3b. The pits in the two photographs demonstrate a one-to-one correspondence.

It is apparent then that the pits nucleate and grow at well-defined singularities in the surface structure. Pit counts on samples having various mechanical and thermal histories (Table I) indicate that pit densities are similar to those which would be anticipated if pits were formed at dislocation sites.

Of course, all dislocations would necessarily be in the "aged" condition, and the samples to some degree, in the annealed state, because of the reduction treatment

Table I. Pit counts

Condition of oxide free surface	Average pit density
Annealed	$0.25 \times 10^6/cm^2$
Mechanically polished surface	$0.60 \times 10^6/cm^2$
Deformed by Rockwell "brale" indenter	$0.90 \times 10^6/cm^2$

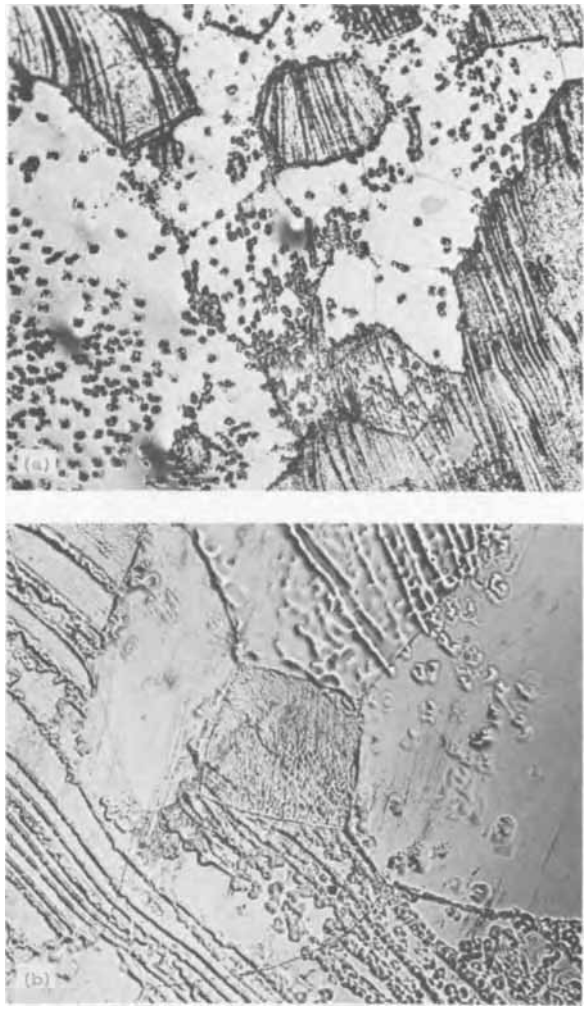

Fig. 2. Lightly deformed iron surface etched for 2 sec in oxide free condition (a) 200 X, (b) 500 X.

required before etching. In one experiment a sample was deformed *after* reduction, but prior to etching, while still in the furnace cold zone. This was achieved by allowing a pointed lathe tool, clamped to a quarter-inch diameter steel rod, to fall from a height of ¾ in. onto the surface of the sample. The impressions made on the surface were of similar size to those produced by a microhardness indentor. No increased density of pits was observed near the indentations. This suggests that the dislocations must be aged before etching will reveal their presence.

On all samples, etching for times greater than 5 sec developed crystallographic facets on the deep conical pits, identical to those on pits produced by etching in air (16). In the case of the shallow pits the rapid over-all surface dissolution seemed to overtake pit growth and they gradually faded out.

After long etching times, the appearance of the pits on oxide free surfaces was similar to that of pits produced by etching in air, followed by the reduction treatment (16). The two conditions could be distinguished by the observations that on an oxide free surface: (*a*) number of pits was independent of time, (*b*) grain boundaries were continuously attacked, and (c) there was a wide variation in pit sizes and extent of facet development.

The pits in Fig. 3b can be seen to be already developing a definite crystallography.

Discussion

Under normal metal etching procedures pits probably form at defects in the oxide film, which may or may not be related to the underlying metal. The fact that pit densities are proportional to etching time rules

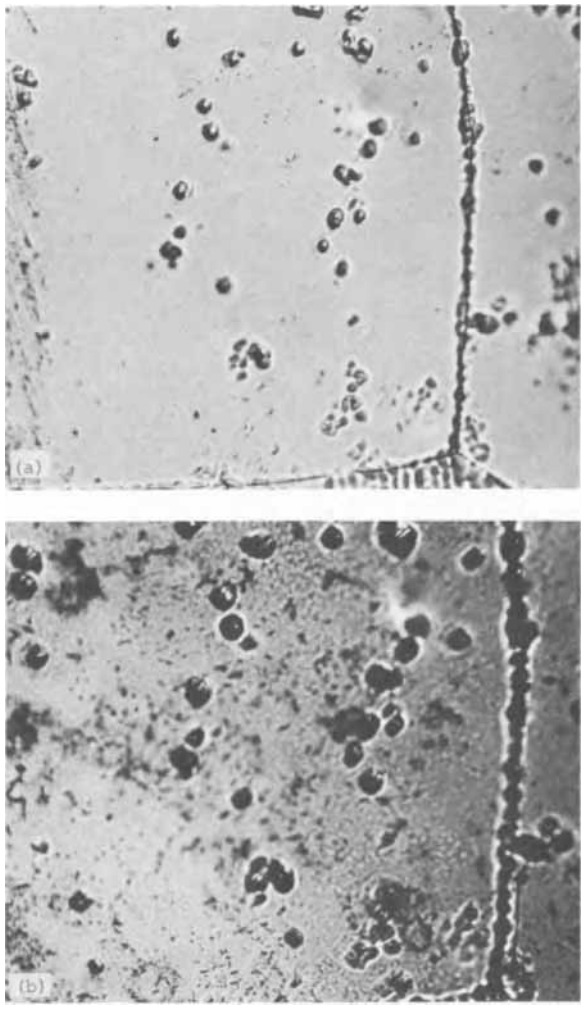

Fig. 3. (a) Annealed iron surface etched for 2 sec in oxide-free condition, 500X. (b) Same field, etched for a further 2 sec in oxide-free condition, 500X.

out a possible one-to-one correspondence with dislocations. Stresses in the film may generate flaws at which conditions for electrochemical attack are more favorable than elsewhere. Pits occasionally nucleate at grain boundaries. If the oxide film is related in orientation to the iron substrate (18) a film discontinuity may be created where the base becomes discontinuous, *e.g.* at grain boundaries.

The pits obtained by etching an oxide-free surface presumably are nucleated at defect sites in the metal. Such pit densities are independent of etching time and are similar to dislocation densities expected for annealed iron. Densities do increase with plastic deformation but this effect tended to be masked in this work because of the high-temperature reduction treatment required prior to etching. Deformation after reduction, but prior to etching, did not produce increased pit densities, indicating that an aging treatment is however necessary to decorate the dislocations.

Slip lines etched out in continuous shallow grooves, similar to those observed by Brandon and Nutting (20) and by Low and Guard (21). The "wavy" nature of the slip lines results from the ability of the screw components of dislocations to move off the glide plane easily and from the large number of slip systems. Certain arrays, presumably composed of edge dislocations, remain confined to straight lines despite the complex stress patterns which exist in polycrystalline materials.

If a dislocation network lying parallel to and just below a surface has an impurity atmosphere, and the rate of dissolution is high in the impure region, an etch groove can form along the network. The grooves observed by Low and Guard (21) were decorated with carbon. Alternatively, the local elastic strain associated with a dislocation lying parallel to and just below a surface could cause the observed differential etching effect.

It was observed here that etching an oxide-free surface produces two different types of pit. The relatively deep conical pits of Fig. 3a were never found in slip bands and constituted the majority of pits in a well-annealed, undeformed sample. They are most likely formed at aged dislocations of edge character which intersect the grain surface at a high angle. As Fig. 3b suggests, these defects extend well below the surface.

The other type of pit, however, is shallow, irregular in shape and ill-defined (Fig. 2b). Some of the slip bands in Fig. 2b are not continuous and are seen to be strings of individual pits of this type. The shallow pits are of the same nature then as the "grooved" slip lines. Cross slip of the screw component of a dislocation loop lying on or just below the surface would result in the irregular shapes observed (21).

Perhaps the most convincing evidence that the shallow pits and slip line grooves are caused by individual dislocations, dislocation loops or tangled networks parallel to and just below the surface, is the fact that after etching for 4 sec they have all but disappeared. At longer times they vanish completely, leaving only the deep pits which have started to develop crystallographic facets.

Conclusions

1. Reduction of the air-formed oxide film from the surface of iron was observed to cause a complete change in etching behavior. Instead of pits nucleating at flaws in the film, they nucleate at singularities in the base metal structure.

2. Two types of etch features are formed on a reduced surface. One is deep with conical sides and appears to be formed at the sites of intersection of aged dislocations with the surface. The other is shallow, irregular in shape and outlines slip lines. This type is probably caused by either the segregated impurity atmospheres of, or the strain fields associated with, dislocation networks lying parallel with, and just below, the surface.

Acknowledgment

This research was supported by The National Research Council of Canada.

Manuscript received Aug. 21, 1970.

Any discussion of this paper will appear in a Discussion Section to be published in the December 1971 JOURNAL.

REFERENCES

1. J. D. Livingston, in "Direct Observation of Imperfections in Crystals," p. 115, John Wiley & Sons, Inc., New York (1962).
2. W. B. Hibbard and C. G. Dunn, *Acta Met.*, **4** 306 (1956).
3. L. C. Lovell and G. N. Wernick, *J. Appl. Phys.*, **30** 234 (1959).
4. I. Berlec, *ibid.*, **33**, 197 (1962).
5. R. W. Guard, *Trans. Met. Soc. AIME*, **218**, 573 (1960)
6. G. C. Das and P. L. Pratt, *Mater. Res. Bull.*, **2**, 487 (1967).
7. M. Mikuriya, *Jap. J. Appl. Phys.*, **6**, 141 (1967).
8. P. Kratochvil and J. Homola, *Acta Met.*, **14**, 1757 (1966).
9. A. Zedler, *J. Appl. Phys.*, **38**, 2046 (1967).
10. W. R. Robinson, in "Techniques in Metal Research," Vol. 2, R. F. Bunshah, Editor, Interscience Publishers, Inc. (1968).
11. J. C. Suits and J. R. Low, *Acta Met.*, **5**, 285 (1957).
12. H. Pickering, *ibid.*, **13**, 437 (1965).
13. R. B. Liss, *ibid.*, **7**, 231 (1959).
14. D. L. Pelossini and G. Alessandrini, *Energia Nucl.*, **41**, No. 2, 99 (1967).
15. T. Taoka, E. Furubayashi, and S. Takeuchi, *Jap. J. Appl. Phys.*, **4**, 120 (1965).
16. G. M. Spink and M. B. Ives, *J. Appl. Phys.*, **42**, 511 (1971).

17. V. Laukonis and R. C. Coleman, *ibid.*, **32**, 242 (1961).
18. Sewel, Stockridge, and Cohen, *This Journal*, **108**, 933 (1961).
19. I. M. Dawson and V. Vand, *Nature*, **167**, 476 (1957).
20. D. G. Brandon and J. Nutting, *Acta Met.*, **7**, 101 (1959).
21. J. R. Low and R. W. Guard, *ibid.*, **7**, 171 (1959).

The Oxidation of Iron-Aluminum Alloys from 450° to 900°C

William E. Boggs*

U. S. Steel Corporation, Applied Research Laboratory, Monroeville, Pennsylvania 15146

ABSTRACT

The oxidation behavior of a series of iron-aluminum alloys (to 8% Al) containing up to 0.1% carbon has been investigated over the temperature range 450° to 900°C. The oxidation rate increases and then decreases with increasing aluminum content and also with increasing temperature as the result of changes in the oxide composition. The composition of the oxide is also influenced by the carbon content of the alloy, water vapor in the atmosphere, and the partial pressure of oxygen. Perforation of the protective Al_2O_3 films that form at the higher temperatures results in the formation of scattered nodes of iron oxide. The amount of nodular oxide increases with temperature, carbon content, and water vapor and decreases with increasing aluminum concentration.

It is well known that aluminum additions greatly increase the oxidation resistance of steel (1). For example, a 6% aluminum-iron alloy has about the same oxidation resistance as a 16% chromium-iron alloy at 890°C (2). Production difficulties, that is, poor hot and cold workability and fabricating difficulties when the aluminum content exceeds about 8% have limited the technological application of these alloys. In spite of these difficulties, the superior oxidation resistance of the material has prompted several investigations of the mechanisms of oxidation of iron-aluminum alloys.

The variety of experimental conditions, particularly of temperature, aluminum concentration, and oxygen pressure, under which these studies were conducted has led to a profusion of somewhat conflicting data. The pertinent investigations are those of Miyake (3), Hickman and Gulbransen (4), Scheil and Kiwit (5), Kornilov (6), Nakayama (7), Schmahl, Baumann, and Schenck (8), and Saegusa and Lee (9).

In addition, nodular oxide formation, often a limiting factor in the usefulness of oxidation-resistant alloys, has been studied in iron-aluminum (9) as well as in other ferrous alloy systems (10-15). According to Wood (16), the Cr_2O_3 layers that form on iron-chromium alloys and stainless steels in oxygen from 800°C up become detached from the alloys in random areas and tend to arch outwards because of the stresses that develop during oxide growth. Cracking of this oxide then exposes areas of chromium-depleted surface to oxygen, and iron-rich nodules begin to form. When the cavity under the lifted Cr_2O_3 film becomes filled with growing oxide, the roof could crack off and allow unimpeded growth of the nodular oxide.

In the present investigation, the effects of temperature, oxygen pressure, water vapor, and alloy composition on the oxidation of iron-aluminum alloys have been studied. Special attention has been given to factors influencing growth of iron oxide nodules on these alloys at the higher temperatures.

* Electrochemical Society Active Member.
Key words: oxidation resistance, nodular oxide, internal oxidation.

Materials and Experimental Work

The compositions of the iron-aluminum alloys used in this study are given in Table I. These alloys were vacuum-induction melted using high purity raw materials. The alloy ingots were hot- and cold-rolled to 0.15 to 0.30 mm thick sheet. This material was then vacuum-annealed at 950°C for 4 hr and cooled to room temperature at 2°C per min. Electropolished specimens were inserted in the vacuum microbalance (17), and reduced in hydrogen at 400°C for 1 hr. After evacuation to about 2×10^{-7} Torr, the oxidation experiments were begun.

The hydrogen treatment at 400°C reduces the iron oxides but not the aluminum oxides that unavoidably form during the brief manipulation of the specimen in air after electropolishing. However, the aluminum oxides apparently do not form a complete cohesive film at the start of oxygen exposure or the phenomena discussed herein could not occur.

Table I. Composition of alloys of iron and aluminum
(Per cent by Weight)

Alloy	Al	C	Mn	P	S	Si	Cu	Ni	Cr
1	0.003	0.004	<0.01	0.002	0.005	<0.005	<0.005	0.006	0.005
2	0.008	0.11	<0.01	0.001	0.002	0.006	<0.005	0.021	0.004
3	0.031	0.006	<0.01	<0.002	0.006	0.007	<0.005	0.007	0.005
4	0.095	0.004	<0.01	0.001	0.001	0.009	0.005	0.018	0.002
5	0.50	0.006	<0.01	<0.002	0.006	0.010	<0.005	0.007	0.002
6	0.72	0.004	<0.01	0.001	0.004	0.008	<0.005	0.005	0.004
7	1.14	0.004	<0.01	0.001	0.005	0.013	<0.005	0.006	0.005
8	1.49	0.005	<0.01	0.001	0.005	0.011	<0.005	0.007	0.006
9	2.35	0.004	<0.01	0.001	0.005	0.032	<0.005	0.019	0.006
10	4.94	0.005	<0.01	0.002	0.002	0.010	0.007	0.006	0.004
11	5.43	0.016	0.10	0.001	0.004	0.033	0.012	0.020	0.006
12	5.51	0.009	0.10	0.001	0.004	0.032	0.012	0.020	0.006
13	5.51	0.040	0.10	0.001	0.005	0.033	0.012	0.021	0.006
14	5.54	0.014	0.10	0.005	0.018	0.050	0.05	0.10	0.05
15	5.99	0.100	0.10	0.003	0.005	<0.005	<0.005	0.035	0.009
16	8.03	0.007	<0.01	0.007	0.005	0.010	0.010	0.007	0.006

The oxidation experiments were conducted in pure oxygen at pressures of 10 and 700 Torr, flowing water vapor at 22 Torr, or in flowing oxygen at 678 Torr saturated with water vapor at 22 Torr. The reactions were studied in the microbalances at 450° to 900°C. Additional experiments were conducted in laboratory air in muffle furnaces at 900° and 1093°C.

Alpha cyanoacrylate, an adhesive which is resistant to methanol, was used to support thin oxide films during stripping in 5 to 7% bromine in absolute methanol. Thicker films did not require a supporting layer.

Results and Discussion

The effect of aluminum concentration.—The oxidation rate of iron at 500°C in oxygen at a pressure of 700 Torr increased with increasing aluminum concentration to a maximum at about 0.092% aluminum. This may be an example of the Wagner-Hauffe effect wherein Al^{+++} replaces some Fe^{++} causing an increase in the cation vacancy concentration and thereby the rate of diffusion of iron ions through the Fe_3O_4 lattice (18).

The oxidation rate at 0.50 to 0.72% aluminum dropped to about the same as the oxidation rate of "pure" iron (0.003% Al). Further increases in aluminum concentration continued to decrease the oxidation rate under the experimental conditions used. An isometric projection of the weight-gain data obtained from the oxidation of the iron-aluminum alloys at 500°C in oxygen at a pressure of 700 Torr is shown in Fig. 1.

Two-phase scales consisting of Fe_3O_4 on the inside and αFe_2O_3 on the outside were formed on the low-aluminum alloys at 500°C (Fig. 2A) whereas three-phase scales were formed on the higher aluminum alloys (Fig. 2B). The three oxide phases were hematite (αFe_2O_3) on the outside, magnetite (Fe_3O_4) in the middle, and hercynite ($FeAl_2O_4$) next to the metal. The hercynite layer appears to develop at the expense

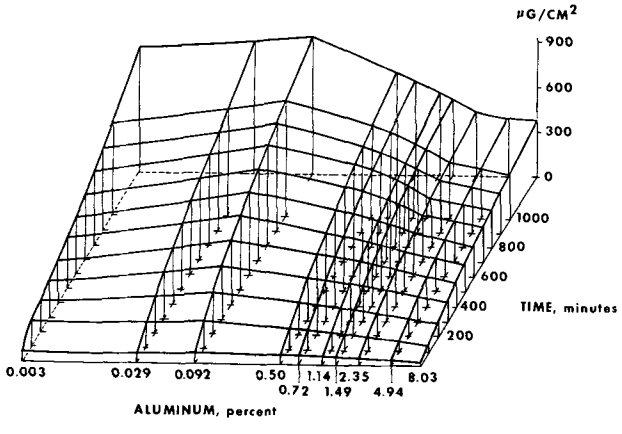

Fig. 1. Effect of aluminum concentration on the oxidation of Fe-Al alloys at 500°C in oxygen at 700 Torr.

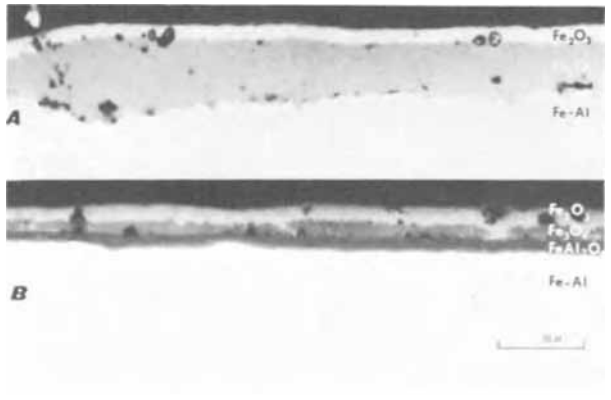

Fig. 2. Oxide formed on Fe-Al alloys in 3900 min at 500°C in oxygen at 700 Torr. (A) Fe-0.5% Al, (B) Fe-4.94% Al.

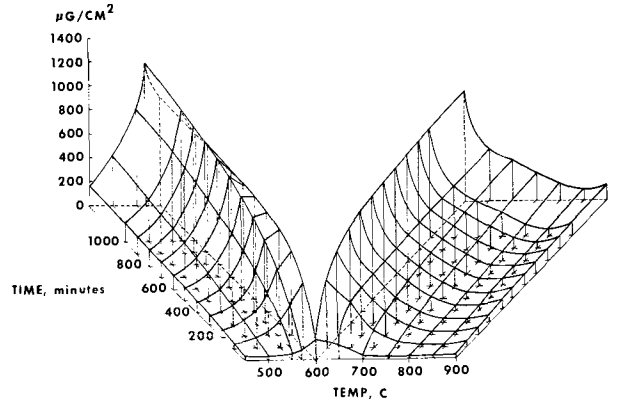

Fig. 3. Effect of temperature on the oxidation of an Fe-4.94% Al alloy in oxygen at 700 Torr.

of the magnetite layer. Whereas about 75% of the scale formed on the low-aluminum alloy shown in Fig. 2A was Fe_3O_4, less than 25% of the scale formed on the high-aluminum alloy (Fig. 2B) was Fe_3O_4. This indicates a reduction in the outward flow of iron ions. Thus, the spinel (18), $FeAl_2O_4$, constitutes a barrier to the diffusion of iron and thereby contributes to the observed oxidation resistance.

The effect of temperature.—The data obtained from the oxidation of the iron-4.94% aluminum alloy in oxygen at 700 Torr and a temperature range of 450° to 900°C are shown in Fig. 3. The time axis for temperatures up to 600°C is projected to the left and the time axis for temperatures above 600°C is projected to the right. The first data points plotted on the figure are at 10 min. The oxidation rate increased with temperature to a maximum at about 570°C and then decreased to a minimum at about 850°C. The temperature at which the maximum oxidation rate was observed, 570°C, coincides with the temperature at which FeO becomes stable (19).

The x-ray diffraction patterns from these scales indicate that the three oxide phases discussed above (hematite, magnetite, and hercynite) are formed up to 570°C in oxygen at 700 Torr. As the reaction temperature was increased above 570°C, the cubic aluminum oxide γAl_2O_3, began to appear. Concurrently, the hercynite, $FeAl_2O_4$, began to disappear. Sections of the oxide obtained at 600°C showed only two layers of oxide, αFe_2O_3 and mixed $FeAl_2O_4$-γAl_2O_3. Only a single layer can be distinguished in the sections of oxide formed at higher temperatures (Fig. 4).

It appears that the observed effect of temperature on the oxidation of the iron-aluminum alloys at 700 Torr is due to the preferential oxidation of aluminum at the higher temperature. Up to about 570°C, $FeAl_2O_4$ forms in a layer at the oxide-metal interface. The increase in oxidation rate with increasing temperature up to 570°C is probably associated with a temperature-dependent increase in iron ion diffusion rate through the hercynite layer. Above 570°C the reactions producing aluminum oxide begin to predominate. Initially the iron oxides and hercynite may form on the surface as well, when there is insufficient aluminum in the surface layer to form a complete alumina film. Subsequently aluminum atoms diffuse to the oxide-metal interface and form additional alumina by the displacement reactions with $FeAl_2O_4$ and the iron oxides. Thus, as the temperature is increased, and the mobility of aluminum atoms in the metal increases, more and more of the protective aluminum oxide is formed, less and less iron oxide and hercynite remain, and the over-all oxidation rate drops.

Two aluminum oxides have been identified in the films formed at temperatures above 600°C. These are the cubic oxide, γAl_2O_3, and the hexagonal oxide, αAl_2O_3. The γAl_2O_3 was always observed as large crystals in apparent epitaxial association with the substrate,

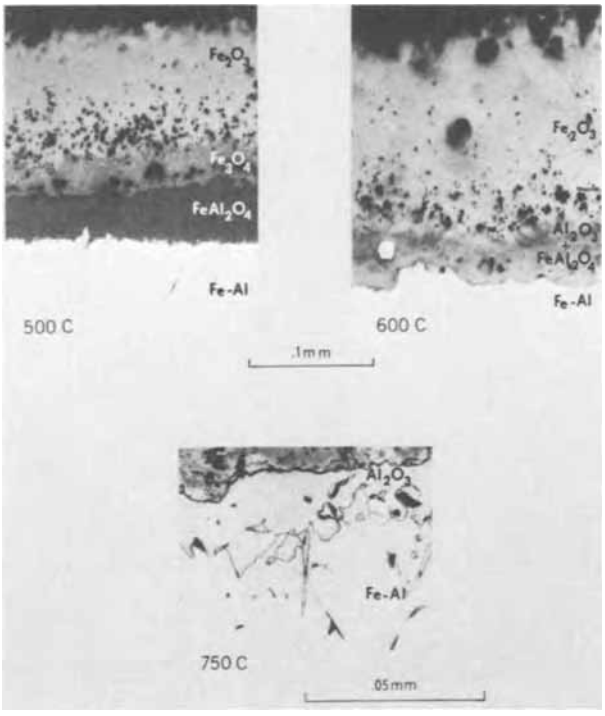

Fig. 4. Effect of temperature on oxide composition in oxygen at 700 Torr. Fe-4.94% Al (taper sections).

whereas the αAl_2O_3 was always observed as very small crystals in completely random orientation. It appears that the αAl_2O_3 results from the recrystallization of the γAl_2O_3.

The effect of oxygen pressure.—Figure 5 is an isometric projection showing the effect of oxygen pressure on the oxidation of the iron-4.94% aluminum alloy at 500°C. From 10 to 50 Torr there was only a slight increase in rate. Between 50 and 160 Torr there was a marked increase in rate. Increasing the oxygen pressure from 160 to 700 Torr produced little further increase in oxidation rate.

Several differences have been observed between the oxides formed in the two oxygen-pressure ranges. The outer layers of the films formed at 10 Torr up to about 570°C could be stripped mechanically whereas no part of the oxide formed at 700 Torr could be similarly removed. The oxide formed at 10 Torr appeared to consist of large single-crystal plates, whereas the oxide formed at 700 Torr consisted of very small randomly oriented crystals (Fig. 6). The portion of the film that could be stripped mechanically from the surface of specimens oxidized in oxygen at 10 Torr consisted mainly of αFe_2O_3. The whole film stripped chemically from specimens oxidized in oxygen at 700 Torr contained $FeAl_2O_4$, Fe_3O_4, and αFe_2O_3 but no Al_2O_3. These observations suggest that film separation occurred during oxidation of the iron-aluminum alloys at 10 Torr, but that the oxide remained in contact with the substrate at 700 Torr. This pressure-dependent phenomenon has been observed with the oxidation of pure iron, and various explanations have been proposed (20, 21).

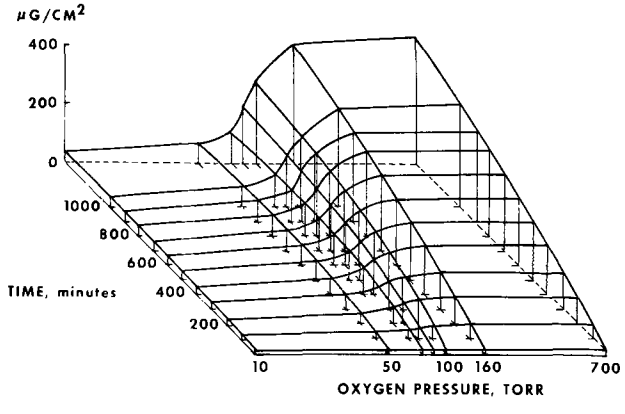

Fig. 5. Effect of oxygen pressure on the oxidation of an Fe-4.94% aluminum alloy at 500°C.

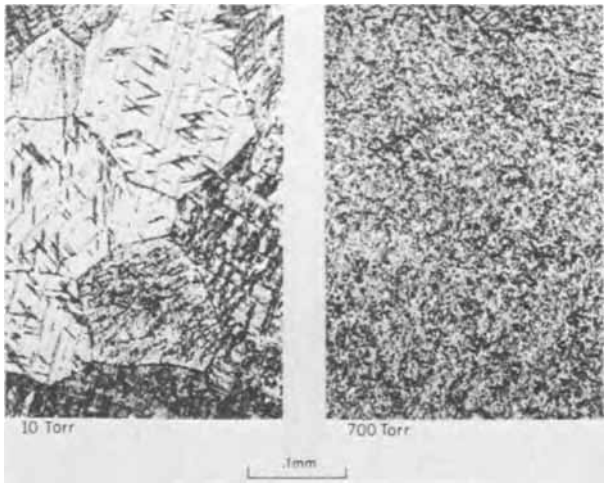

Fig. 6. Effect of oxygen pressure on crystal morphology of oxide formed on an Fe-4.94% Al alloy in 3900 min at 500°C.

It appears that the oxides of iron comprise the first major components of the films that form on the iron-aluminum alloys at temperatures up to 570°C. If the oxide is in intimate contact with the substrate, aluminum diffuses to the oxide-metal interface and reacts with the Fe_3O_4 to form a layer of $FeAl_2O_4$. When the initial oxide layer has separated from the substrate, the iron oxide in this layer is converted to αFe_2O_3. Oxygen, at reduced pressure, may enter the cavity under the separated layer and sustain oxidation of the substrate at a much reduced rate. The reduced oxidation rate allows aluminum time to diffuse from the substrate so that the concentration of aluminum in the new oxide is much higher than in scales that have formed without film separation. This argument is supported by the data given in Table II for the average iron and aluminum concentrations in some typical films. The aluminum-to-iron ratio of oxide formed at 10 Torr where separation occurs is always higher by at least a factor of 3 than the aluminum-to-iron ratio of oxide formed at 700 Torr where oxide separation apparently is not so extensive.

Table II. Concentration of aluminum and iron in oxide* formed on iron-4.94% aluminum alloy under various conditions.

Time, min	μg Al	μg Fe	Al/Fe
A. 550°C, 10 Torr			
10	11.4	22.8	0.50
20	15.8	22.8	0.70
100	19.0	29.1	0.65
300	18.6	53.8	0.35
1000	15.8	22.8	0.69
B. 550°C, 700 Torr			
Time, min	μg Al	μg Fe	Al/Fe
10	15.6	93.0	0.17
20	27.4	239.0	0.12
100	60.2	496.8	0.12
300	78.2**		0.04**
1000	382.5**		0.05**

C. 500°C, 10 and 700 Torr to "constant" weight

PO_2	Time, min	μg/cm² O_2	μg Al	μg Fe	Al/Fe
10 Torr	3900	35.6	15.8	34.8	0.46
700 Torr	59	29.5	25.6	202.6	0.13

* Total oxide, removed from substrate by chemical stripping.
** Estimated from semiquantitative spectrographic analysis of chemically stripped oxide.

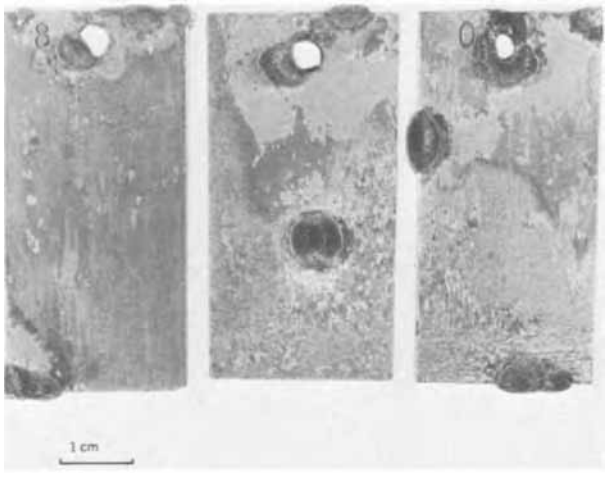

Fig. 7. Nodular oxide formed on commercial Fe-5.54% Al steel in air at 1093°C.

Nodular oxide.—Localized oxidation of iron through the protective aluminum oxide film that forms at the higher temperatures leads to the growth of corn-like nodes of iron oxide such as are shown in Fig. 7. These nodules were formed on an iron-5.54% aluminum steel in air at 1093°C for 192 hr. Nodular oxide also can occur on iron-aluminum alloys under milder conditions. Microscopic iron oxide nodules were grown on the Fe-8% Al alloy at 600°C in dry oxygen at 10 Torr.

The effect of nodular oxide growth on the over-all oxidation kinetics.—The influence of nodular growth on the over-all kinetics of oxidation of an iron-4.94% aluminum alloy in dry oxygen at 700 Torr is illustrated in Fig. 8. The oxidation rate decreases continuously at 600° and 700°C with the formation of $FeAl_2O_4$ in competition with Al_2O_3. However, at 800° and 900°C, the rate decreases for about 200 min during the growth of the protective alumina film and then increases to a maximum during the growth of iron oxide nodules before decreasing again. Examination of the surface of the alloy after the rate has begun to fall off shows that the nodules actually occupy only a small proportion of the total surface (Fig. 9). This observation, together with the decrease in oxidation rate, suggest that some mechanism operates to slow the growth or limit the size of the nodules and that new nodules do not continue to form. In general, the ultimate size seems to depend mainly on the oxidation temperature.

The morphology of nodular oxide.—A section through a typical corn-like oxide node is shown in Fig. 10. The hard outer shell is almost pure hematite, αFe_2O_3. The porous interior contains Fe_3O_4, FeO, and αAl_2O_3. (A crack through to the surface has admitted oxygen to form a hematite shell around the central cavity. Sometimes hercynite, $FeAl_2O_4$, is also detected in this region.) The metal in front of the alloy-

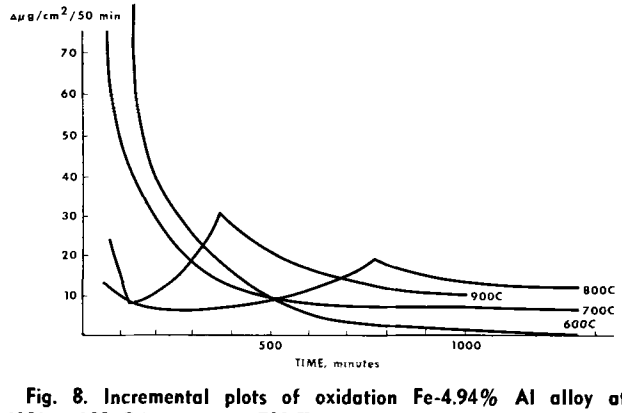

Fig. 8. Incremental plots of oxidation Fe-4.94% Al alloy at 600° to 900°C in oxygen at 700 Torr.

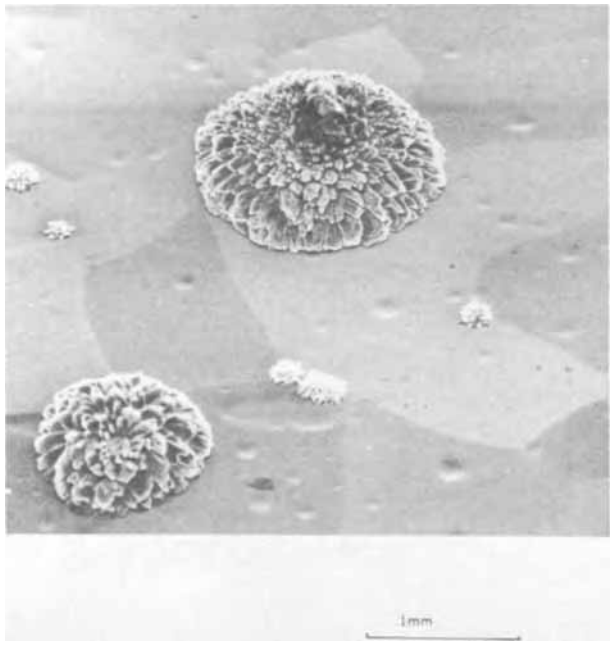

Fig. 9. Nodules formed on Fe-4.94% Al alloy in 1300 min of 800°C in oxygen at 700 Torr.

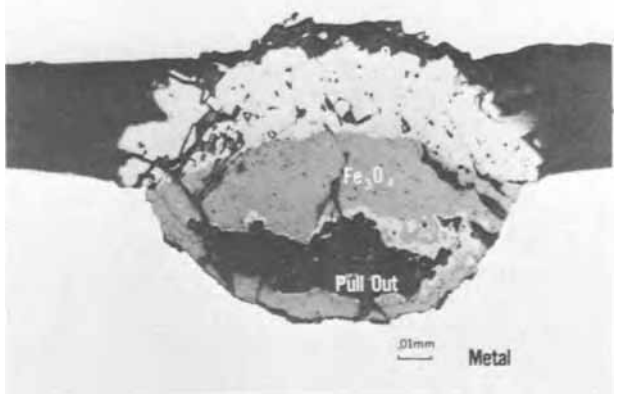

Fig. 10. Section through nodule formed on Fe-4.94% Al alloy in 3900 min at 800°C in oxygen at 700 Torr.

nodule interface polishes in relief indicating that this region is harder than the bulk of the alloy. Optical and microprobe images of an example of this region of relief polish are shown in horizontal section in Fig. 11. The oxygen image indicates a high concentration of oxygen in the relief-polished area of metal surrounding the oxide of the nodule. Aluminum is also shown

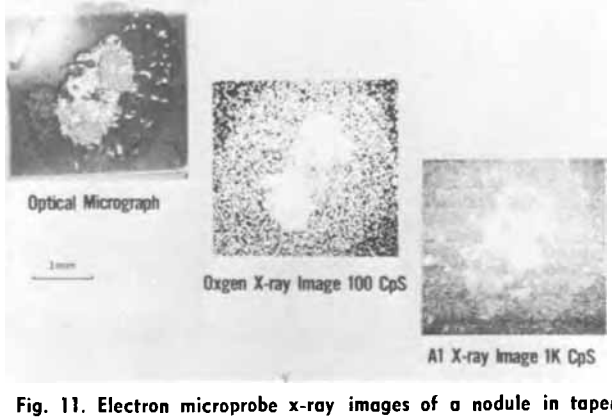

Fig. 11. Electron microprobe x-ray images of a nodule in taper section.

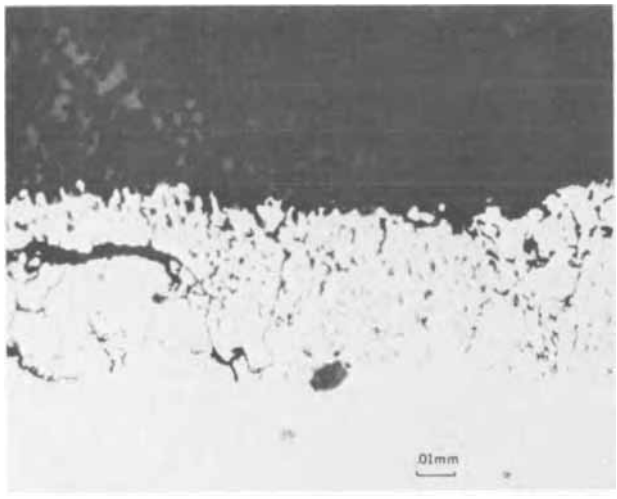

Fig. 12. Section through a nodule formed on commercial Fe-5.54% Al steel in air for 192 hr at 1093°C.

to be in higher concentrations in this area. A high magnification optical micrograph of a perpendicular section (Fig. 12), shows that the relief-polished area ahead of a nodule contains a second phase, a dispersion of small particles. The electron microprobe evidence of Fig. 11 indicates that this dispersed phase is aluminum oxide.

The nodules are apparently a localized manifestation of iron oxidation. The formation of the protective alumina film on the surface of this alloy depletes the alloy of aluminum in the region adjacent to the oxide so that this region becomes iron rich in comparison with the bulk of the alloy. When a break occurs in the alumina film, oxygen comes in contact with this iron-rich layer and nucleates an iron oxide nodule. Oxygen can diffuse through the iron oxide of the nodule into the substrate, where it then reacts with aluminum to form the dispersed alumina phase. This internal oxidation process precludes the diffusion of aluminum to the nodule-alloy interface that would be necessary to heal the crack in the original protective film.

Some oxide nodules are easily popped out of the substrate by using a sharp needle. The resulting pits contain a layer of white material found by x-ray diffraction to be αAl_2O_3. Since iron diffuses outward through the iron oxide phases that form the interior of a nodule, it seems reasonable to believe that the dispersed phase, αAl_2O_3 formed by internal oxidation, may accumulate and be compacted in sufficient quantity at the nodular oxide-metal interface during growth of the nodule to eventually isolate it from the metal substrate.

The effect of water vapor.—When oxidation experiments were conducted in the presence of water vapor, oxidation rates were substantially increased (Fig. 13), and there appeared to be little or no induction period before the beginning of nodule growth. There is relatively little difference in the oxidation kinetics in pure water vapor and in oxygen containing water vapor at 22 Torr in spite of the great difference in oxygen pressures.

Well-developed nodules could be detected with the scanning electron microscope after as little as 10 min at 800°C in the presence of water vapor. Incremental plots of the data from wet and dry oxidation experiments are shown in Fig. 14. In contrast to the behavior in dry oxygen, the oxidation rate increased continuously in the presence of water vapor, at least for the duration of the experiments. Estimates of the amount of surface containing nodules (per cent dark) after oxidation at 800°C for periods of 5 to 1000 min in oxygen dry or saturated with water vapor were made by using an Autoscan Reflectance Microscope. These

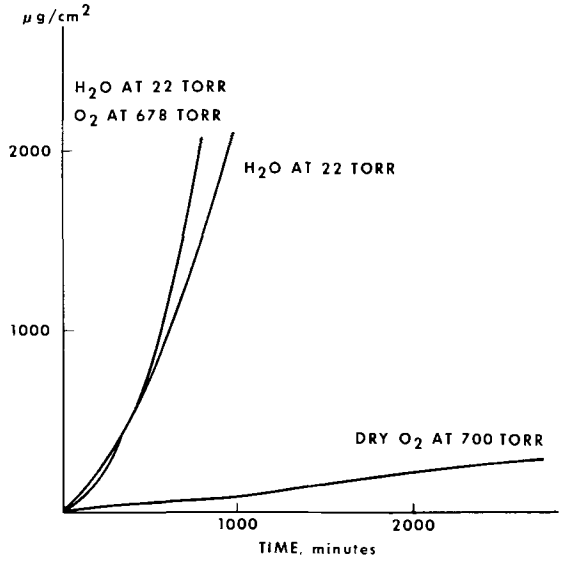

Fig. 13. Effect of water vapor on the oxidation of an Fe-4.94% Al alloy at 800°C.

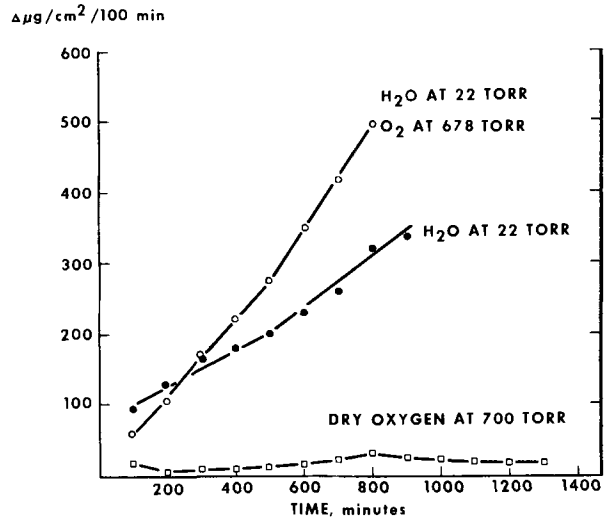

Fig. 14. Incremental plots of oxidation of an Fe-4.94% Al alloy at 800°C in water vapor and in wet and dry oxygen.

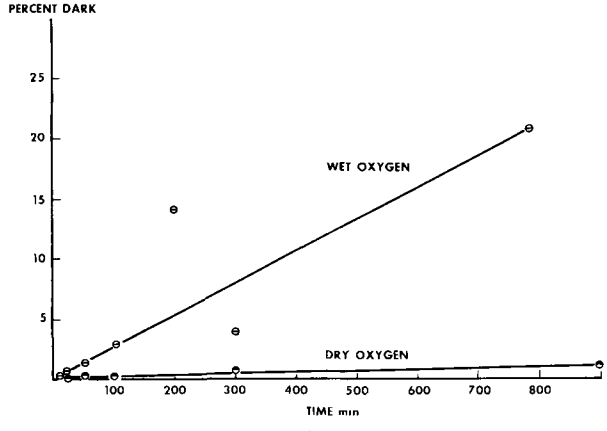

Fig. 15. Fractions of an Fe-4.94% Al alloy covered by nodular oxide at 800°C in wet and dry oxygen.

data are plotted in Fig. 15. If the data points for 200 and 300 min in wet oxygen are disregarded, the areal coverage by the nodules approximates to a linear relationship for at least the first 790 min. After 790 min at 800°C in wet oxygen, the proportion of surface involved was 20.6%. In contrast, after 1000 min in dry oxygen, the proportion of surface represented by nodules was only 1.14%.

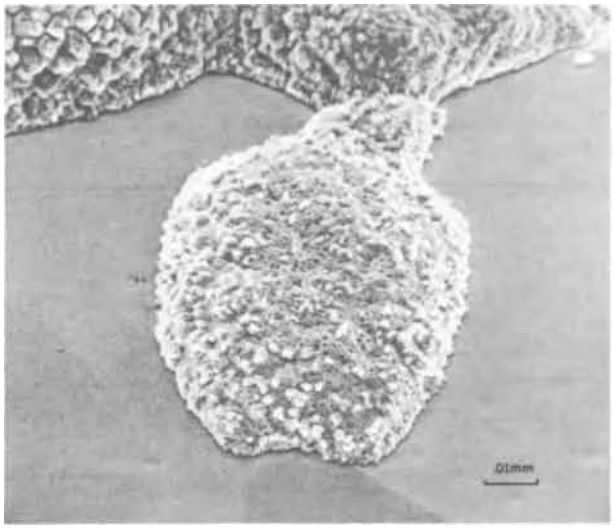

Fig. 16. Nodules formed on an Fe-4.94% Al alloy in 790 min at 800°C wet oxygen.

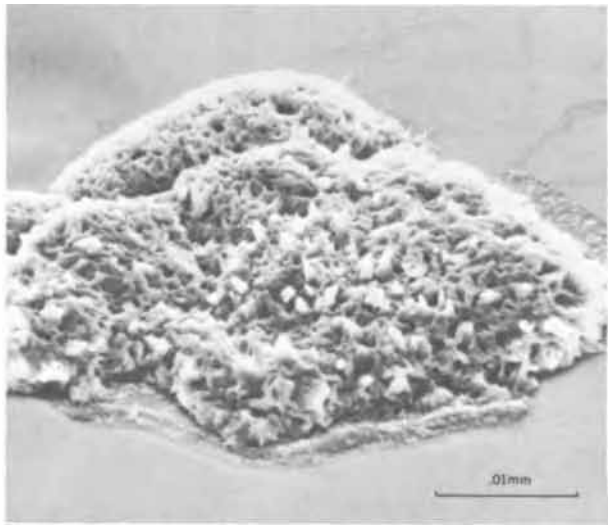

Fig. 18. Nodule formed on an Fe-4.94% Al alloy in 300 min at 800°C in wet oxygen.

Both the composition and the morphology of the oxide nodules are affected by water vapor. The major component of the nodular oxide formed in dry oxygen (Fig. 9) was cubic oxide (Fe_3O_4, γFe_2O_3, and/or $FeAl_2O_4$). The minor component was αFe_2O_3. In oxygen saturated with water vapor (Fig. 16), the major component of the nodular oxide was αFe_2O_3 and the minor component was cubic oxide. This change in composition probably resulted from penetration by oxygen deeper into the oxide nodules. Fujii and Meussner (22) have suggested that hydrogen from the dissociation of water vapor can act as a carrier to move oxygen across voids in oxide scale. A similar mechanism may account for the increase in the amount of hematite formed in wet oxygen, but it is difficult to explain the extremely high oxidation rate.

Examples of the nodular oxide formed in pure water vapor are shown in Fig. 17. The major component of these nodules was $FeAl_2O_4$, hercynite, and the minor component was cubic oxide. A nodule formed in 300 min at 800°C in water-saturated oxygen is shown in Fig. 18. This nodule is surrounded by a disturbed area that appears to result from plastic deformation of the substrate and the Al_2O_3 film to accommodate the increased subsurface volume of the oxide nodule.

At present, we have no clear explanation for the increased nucleation and growth of nodules in the presence of water vapor. The diffraction patterns of the oxides formed in wet oxygen at 800°C were more difficult to identify than the diffraction patterns from the aluminum oxides formed in dry oxygen. A hydrated form of aluminum oxide which is more easily cracked or separated from the substrate may be involved.

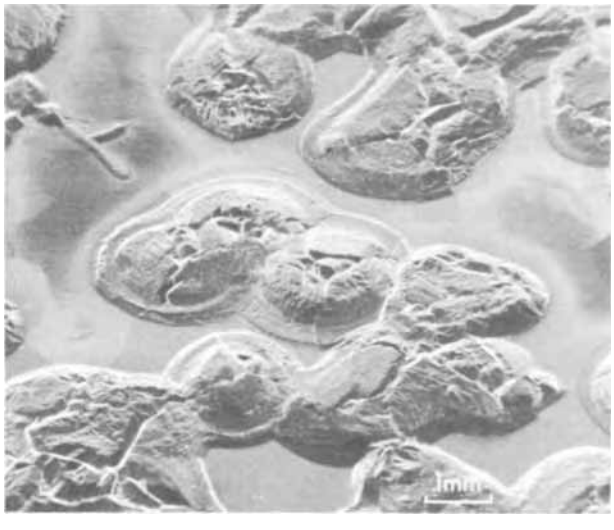

Fig. 17. Nodules formed on an Fe-4.94% Al alloy in 960 min at 800°C in pure water vapor.

The effect of carbon.—The behavior of iron-5.5% aluminum alloys containing up to 0.10% carbon at 500°C in oxygen at 10 Torr was similar to that of the iron-5% aluminum alloys. The oxide films apparently lost contact with the substrate resulting in a virtual halt of oxidation. The oxidation rate of the Fe-5.99Al-0.10C alloy was intermediate between the (low) rate of the Fe-4.94Al alloy and the (high) rate of the Fe-0.11C alloy. At the 0.1% carbon level, there are apparently enough vacancy sinks in the substrate to prevent the accumulation of vacancies at the oxide-metal interface, and the oxide remains in more intimate contact with the substrate. Carbon concentration had little effect on the oxidation rate at 700 Torr as the higher oxygen pressure prevented film separation (20, 21). The same three oxide phases, Fe_2O_3, Fe_3O_4, and $FeAl_2O_4$, that were formed on the Fe-4.94Al at 500°C were also formed on the iron-aluminum-carbon alloys under these conditions.

Above about 700°C the evolution of gas from the reactions between carbon and the iron oxides may interfere with the formation of a protective oxide film on iron-base alloys containing appreciable amounts of carbon (23). The effect of carbon concentration on the oxidation of the iron-carbon-aluminum alloys at 800°C is shown in isometric projection in Fig. 19. A sharp increase in oxidation rate with increasing carbon content is clearly evident. Microscopic examination of oxidized specimens revealed that a thin passive alumina film covered most of the surface of the alloys but that the frequency with which iron oxide nodules disrupted this film increased with increasing carbon concentration (Fig. 20). Most of the weight gain shown in Fig. 19 reflects the growth of nodular oxide, not film.

There appear to be two ways in which carbon can interfere with the protective alumina and allow nodular iron oxide to nucleate. The direct oxidation of carbon at random sites in competition with iron and aluminum might leave holes in the film at which nodules might nucleate. Alternatively, carbon from the substrate can react with iron oxides in the initial film to produce high pressure CO pockets which burst through the film and allow oxygen to reach the substrate, nucleating the nodular oxide.

Summary

As the aluminum concentration in iron-base alloys was increased from 0.003 to 0.09%, the oxidation rate

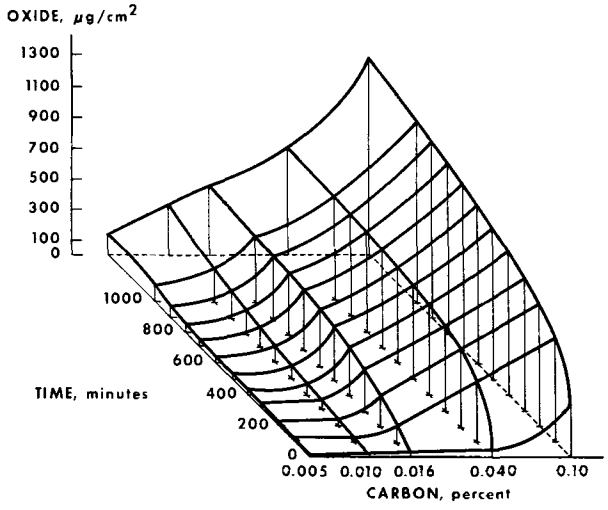

Fig. 19. Effect of carbon concentration on the oxidation of Fe-5.5% Al-C alloys at 800°C in oxygen at 700 Torr.

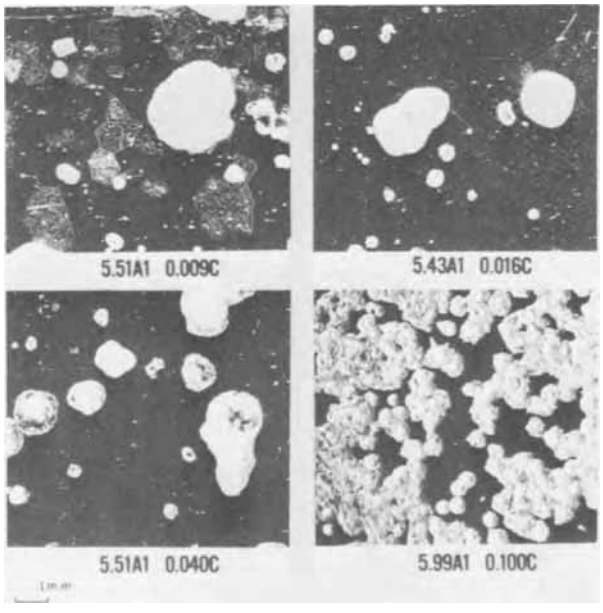

Fig. 20. Dark field optical micrographs showing effect of carbon concentration on the amount of nodular oxide formed on Fe-Al-C alloys in 1300 min at 800°C in oxygen at 700 Torr.

also increased. Above about 0.09% aluminum, the oxidation rate decreased with increasing aluminum concentration.

Up to 0.09% aluminum and at temperatures up to 570°C the scale consisted of two phases, αFe_2O_3 on the outside and Fe_3O_4 next to the metal. Above 0.09% aluminum a third phase, $FeAl_2O_4$, was found between the Fe_3O_4 and metal. This phase, hercynite, imparts oxidation resistance to the alloy.

Above 570°C, γAl_2O_3 began to appear in the scale and the oxidation rate decreased with increasing temperature. At 800° to 850°C the film was almost pure alumina and the oxidation rate was at its lowest.

As the oxygen pressure was increased at 500°C there was a slight increase in oxidation rate up to 50 Torr, a sharp increase between 50 and 160 Torr, and only a slight additional increase in rate between 160 and 700 Torr. Apparently, the initial oxide film tends to separate from the substrate during oxidation at pressures up to about 50 Torr. This creates cavities in which aluminum is preferentially oxidized to form a barrier layer under the outer iron oxide. Above 160 Torr, film separation did not appear to be a factor in the growth of the oxide, and consequently, oxidation rates were higher.

Localized oxidation of iron through the protective aluminum oxide film that forms on iron-aluminum alloys at the higher temperatures leads to the growth of corn-like nodes of iron oxide. The amount of nodular oxide increases with increasing temperature and increases in the presence of water vapor, but decreases with increasing aluminum concentration.

In dry oxygen, an initial period of γAl_2O_3 film formation precedes the increase in oxidation rate that accompanies the growth of nodular iron oxide. It is believed that the formation of an alumina film on the surface of an iron-aluminum alloy tends to decrease the concentration of aluminum in the zone near the oxide-metal interface. Any cracks or faults that may develop in the protective oxide film alloy oxygen to react with unprotected iron to form nodules. Internal oxidation ahead of the node-metal interface precipitates aluminum oxide dispersed in the iron matrix thereby preventing the healing of the protective oxide skin.

Water vapor increases the growth rate and alters the morphology and composition of the nodular oxide. Dry-formed nodules consist of an outer shell of Fe_2O_3 and a porous interior of Fe_3O_4, FeO and some αAl_2O_3. Nodules formed in wet oxygen contain a greater proportion of αFe_2O_3. The major component of the nodular oxide formed in pure water vapor is hercynite, $FeAl_2O_4$.

A three-phase scale consisting of αFe_2O_3, Fe_3O_4, and $FeAl_2O_4$ develops on Fe-Al-C alloys at 500°C. The innermost layer, $FeAl_2O_4$, causes a reduction in the oxidation rate compared with that of pure iron. Carbon at concentrations less than about 0.10% permitted film separation in oxygen at 10 Torr thereby causing abnormally low oxidation rates. Film separation did not occur at carbon level of 0.10%, and more nearly normal oxidation rates were observed. Carbon had no apparent effect on the oxidation at 500°C in oxygen at 700 Torr.

The oxidation rate of the Fe-Al-C alloys increased with increasing carbon concentration at 800°C. The thin protective film of alumina that formed on the binary Fe-Al alloy at 800°C also formed on the ternary Fe-Al-C alloy. Most of the observed weight gain was due to the growth of nodular iron oxide through this film. The frequency with which the nodules penetrated the passive alumina layer increased with increasing carbon concentration. Carbon apparently interferes with the integrity of this film so that oxygen can react with the iron in the substrate to form nodular oxide.

Manuscript submitted Oct. 12, 1970: revised manuscript received ca. Jan. 21, 1971. This was Paper 125 presented at the Atlantic City Meeting of the Society Oct. 4-8, 1970.

Any discussion of this paper will appear in a Discussion Section to be published in the December 1971 JOURNAL.

REFERENCES

1. O. Kubaschewski and B. E. Hopkins, "The Oxidation of Metals and Alloys," Second Edition, p. 234, Academic Press, Inc., New York (1962).
2. *Ibid.*, p. 233.
3. S. Miyake, *Sci. Papers, Inst. Phys. Chem. Res., (Tokyo)*, **29**, 167 (1936) and **31**, 161 (1937).
4. J. W. Hickman and E. A. Gulbransen, *Trans. AIME*, **171**, 344 (1947).
5. E. Scheil and K. Kiwit, *Arch. Eisenhuettenw.*, **9**, 405 (1936).
6. I. I. Kornilov, *Isv. Sect. Anal. Phys. Chim., Alsad. Nauk* S.S.S.R., **16**, 122 (1948).
7. T. Nakayama, *Report of Castings Research Laboratory*, Waseda University **9**, 71 (1958).
8. N. G. Schmahl, H. Baumann, and H. Schenck, *Arch. Eisenhuettenw.*, **30**, 345 (1959).
9. F. Saegusa and L. Lee, *Corrosion*, **22**, 168 (1966).
10. K. Heindlhofer and B. M. Larsen, *Trans. Am. Soc. Steels Treat.*, **21**, 865 (1933).
11. G. C. Wood, *Corrosion Sci.*, **2**, 255 (1962).
12. G. C. Wood, M. G. Hobby, and B. Vaszko, *J.I.S.I.*, **202**, 685 (1964).

13. J. W. Perrow and W. W. Smeltzer, *This Journal*, **109**, 1023 (1962).
14. J. O. Edström, *J.I.S.I.*, **185**, 450 (1957).
15. H. M. McCullough, M. G. Fontana, and F. H. Beck, *Trans. Am. Soc. Metals*, **43**, 404 (1951).
16. G. C. Wood and D. P. Whittle, *Corrosion Sci.*, **7**, 763 (1967).
17. W. E. Boggs, *Vacuum Microbalance Techniques*, **6**, 45, Plenum Press, New York (1967).
18. J. Stringer, *Met. Rev.*, **11**, 113 (1966).
19. Ref. (1), p. 109.
20. W. E. Boggs and R. H. Kachik, *This Journal*, **116**, 24 (1969).
21. D. Caplan, M. J. Graham, and M. Cohen, *Corrosion Sci.*, **10**, 1 (1970).
22. C. T. Fujii and R. A. Meussner, *This Journal*, **111**, 1215 (1964).
23. Ref. (1), pp. 231 and 232.

Characterization of Silicon Dioxide Films by the Electron Probe

B. Swaroop*

Kelsey-Hayes Research and Development Center, Ann Arbor, Michigan 48105

ABSTRACT

The morphological and compositional characterizations of thermally grown silicon dioxide films on a silicon substrate have been conducted exclusively by the use of the electron probe. The linear increase of oxygen x-ray intensity with the thickness of the films (<2000Å) demonstrates the feasibility of a quick method of finding the unknown thickness. The range of penetration of electrons in the oxide films shows 3/2 power low dependence with the accelerating potential of the beam. The quantitative analysis of oxygen content in thin as well as thick films has been obtained by using the appropriate absorption and atomic number corrections.

Silicon dioxide films have drawn great attention as dielectric in the semiconductor technology. The effectiveness of these films over the devices is very much dependent upon their purity, porosity, stoichiometry, and conductivity. Therefore, quick analysis of these films with respect to their mass thickness, contamination, stoichiometry, and valence state of their constituents is very desirable. The present investigation dealt with the compositional as well as the morphological characterization of silicon dioxide films with the use of an electron probe.

Theory

In the electron probe instrument, high energy electrons (5 to 50 keV) are brought into focus to the required diameter size of the beam spot (>1μ) on the surface of the material to be analyzed. The characteristic x-rays emitted from the sample are monochromatized by curved crystal and detected by the proportional counter. The measured x-ray intensity for a characteristic peak is used to determine the amount of the element present in a given sample. The details of the techniques involved in such measurements are elaborately given elsewhere (1, 2).

An electron beam is excited at potential energy V (keV) impinging normally on a thick specimen, as shown in Fig. 1a, and produces the characteristic x-ray until the electron energy reduces to less than excitation potential (E_c) of the given element. However, from the total number of electrons impinged on the surface, a small fraction are backscattered as shown by mode 1 (Fig. 1) and the rest of them, as shown by mode 2, are responsible for producing the x-ray. During the traverse of electrons in the specimen, the total number of ionizations (N) produced before the electron energy reduces to less than E_c is given by (3-6)

$$N_{(A)} = \frac{C_{(A)}N_0}{A} R_{(A)} \int_{E_c}^{V} (\phi_A/S_{(A)}) \cdot dE \qquad [1]$$

where C_A is the concentration of element "A" in the given compound or alloy, N_0 is the Avogadro number, A is the atomic weight, $R_{(A)}$ is the remaining fraction of ionizations when the loss due to backscattering is removed (4, 6), $S_{(A)}$ is the specific deceleration power for electrons (6), and ϕ_A is the x-ray ionization cross-section of atoms "A". The subscript (A) defines that each term corresponds to an alloy or compound.

A similar expression can be obtained for a number of ionizations obtained from pure bulk element "A". Thus, in the absence of x-ray absorption and fluorescence effects, the ratio $K_{(A)}$ is given by

$$K_A = I_{(A)}/I_A = C_{(A)}R_{(A)} \int_{E_c}^{V} (\phi_A/S_{(A)}) \cdot dE \Big/ C_A R_A \int_{E_c}^{V} (\phi_A/S_A) \cdot dE \qquad [2]$$

where $I_{(A)}$ and I_A are the observed intensities of element "A" in a given compound and in pure standard respectively. However, if pure solid standard is not available, *e.g.* oxygen in the case of silicon dioxide, then $I_{(A)}$ would be compared with a similar compound of known concentration (C_s). In the latter case, the above expression will become simply

$$I_{(A)}/I^s_{(A)} = C_{(A)}/C_s \qquad [3]$$

The above Eq. [3] is only true if compound standard is exactly of the same composition as that of unknown. Otherwise Eq. [2] still must be used but replacing C_A with C_s.

* Electrochemical Society Active Member.
Key words: thickness, stoichiometry, x-ray, thin films.

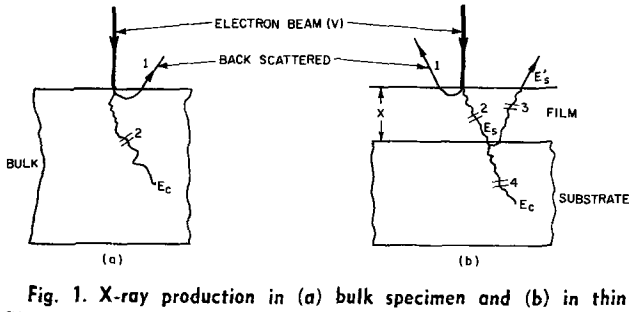

Fig. 1. X-ray production in (a) bulk specimen and (b) in thin films.

When the electrons are impinging on a thin film (7), as shown in Fig. 1b, the energy of the electrons at the interface of the substrate reduces to a value of E_s ($E_s > E_c$). In such a situation, further contributions to ionization are produced by two extra modes (modes 3 and 4 as shown in Fig. 1b). Mode 3 is due to backscattered electrons from the substrate. The number of backscattered electrons depends upon the backscattered yield (η) of the substrate. The ionization will be produced by this mode as long as the energy of the electron is above E_c potential of the given element. The fourth mode is contributed due to the penetration of electrons in the substrate, provided the element "A" is present in the substrate. Following the treatment of Colby (7) the observed x-ray intensity for element "A" is given by

$$I_{(A)} \propto C_{(A)} \left[R_{(A)} \int_{E_s}^{V} (\phi_A/S_{(A)})\,dE + \eta R_{(A)} \int_{E'_s}^{E_s} (\phi_A/S_{(A)}) \cdot dE \right] + C'_A\,(1-\eta)\,R_S \int_{E_c}^{E_s} (\phi_A/S_S) \cdot dE \quad [4]$$

where, R_s and S_s are usual terms for the substrate as explained earlier. The lower limit E'_s in one of the integrals is the exiting electron energy after producing the ionization by mode 3. When the substrate does not contain the analyzed element, the observed intensity is contributed only from the first two integrals of Eq. [4]. Such is the case for the analysis of oxygen in silicon dioxide films on the silicon substrate.

In order to calculate $C_{(A)}$ from the K ratio, the observed intensities are to be corrected for x-ray absorption, atomic number, and fluorescence effects in the sample as well as in the standard. The expressions [1], [2], and [4] given above include the atomic number effect, *i.e.* the use of terms R and S with each ionization.

In the present investigation for the determination of oxygen and silicon content, the amorphous silica and silicon dioxide films were used. The experiment results were corrected by using modified Philbert's absorption correction (8, 9) and Poole-Thomas electronic interaction correction (5) for thick films. For thin films, atomic number correction was calculated according to the treatment given by Colby (7). The modified Philbert's absorption correction is given by

$$f(\chi) = (1+h)/(1+\chi/\sigma_c)\,[1+h(1+\chi/\sigma_c)] \quad [5]$$

where, $\chi = (\mu/\rho)$ cosec θ; (μ/ρ) is the mass absorption coefficient, θ is the x-ray emergence angle, $h = 1.2\bar{A}/\bar{Z}^2$, $\bar{A}$ is the mean atomic weight, Z is the mean atomic number, and σ_c is the modified Lenard coefficient as given by Heinrich (10)

$$\sigma_c = (4.5 \times 10^5)/(V^{1.67} - E_c^{1.67}) \quad [6]$$

The mass absorption coefficient (μ/ρ) for OK_α and SiK_β emission lines are taken from the values given by Henke *et al.* (11). For thin specimen, the absorption is taken into account by replacing E_c in Eq. [6] with E_s.

Experimental Procedure

The amorphous silicon dioxide films were grown on silicon substrate as described elsewhere (12). The silicon substrate was approximately 0.012 in. thick and the thickness of the films range between 200 and 15,000Å. The thickness of the films were measured mainly by the Tolansky method (13) which gave an accuracy of ±10Å in the measurements.

The electron probe was operated between 5 and 30 keV at 0.8 x 10^{-7}A specimen current for amorphous silica and with a beam diameter of 15μ. The intensity measurement for OK_α and Si emission bands were obtained using lead stearate crystal in vacuum. A thin window flow proportional counter with flowing gas mixture of 75% methane and 25% argon at atmospheric pressure was used. The measured intensities were as the peak intensity minus the off peak background count. The spectrometer was peaked for the characteristic line of unknown films as well as standards in order to avoid the effects of wavelength shift. All counts were accumulated for a given period of time. The observed intensities were corrected for dead time of the counting circuit.

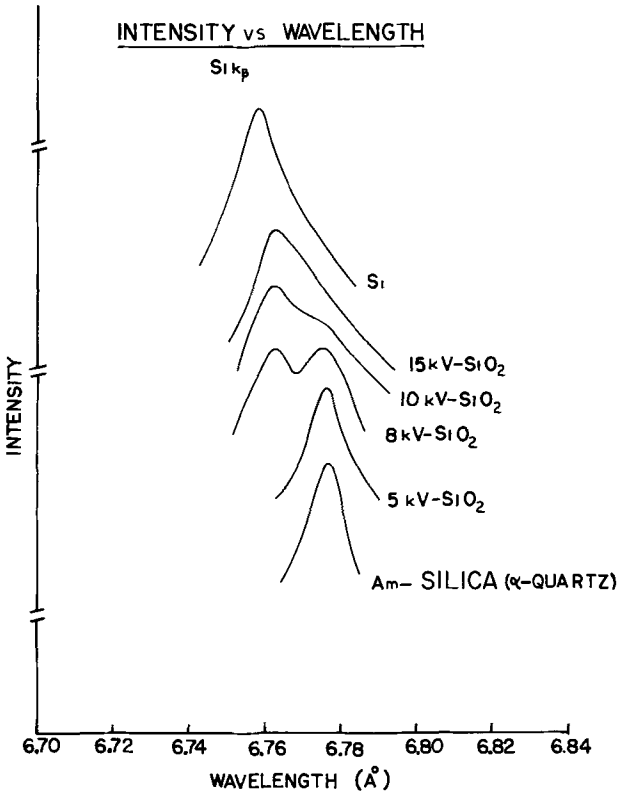

Fig. 2. Silicon (K_β) emission bands from pure silicon, amorphous silica and silicon dioxide films.

Results and Discussion

The SiK_β emission bands were first observed from bulk amorphous silica, α-quartz and 1700Å thick silicon dioxide film on the silicon substrate. Figure 2 summarizes the data obtained at various exciting potentials of the electron beam. The silicon peak position in pure silicon and amorphous bulk silica are observed at 6.758 and 6.776Å respectively. Similarly, the peak from α-quartz indicated the position very close to that of bulk silica. These emission wavelengths were observed to be almost independent of accelerating potential between 5 and 30 keV. At excitation potential of 5 keV, the peak position in the oxide film is almost coinciding with that from bulk silica; this indicates that electrons do not reach the substrate with sufficient energy to ionize the photons from the substrate. At 8 keV beam potential, there were observed two peaks of nearly equal intensities suggesting that electrons arrive with sufficient energy to excite the silicon photons from the substrate. However, at 10 and 15 keV, the silicon peak positions are close to that of pure silicon. Thus, the main contribution to the x-ray intensity is from photons being excited from the silicon substrate. These observations are very similar to that reported by Knausenburger *et al.* (14). From this data it was inferred that in order to use SiK_β emission band for analyzing the valence state of thin oxide films, or to use SiK_α peak for stoichiometric analysis of these films, one ought to work at low accelerating potentials (*i.e.* between 5 and 8 keV) so that x-rays are not excited from the substrate. On the other hand, OK_α emission band should be used in order to avoid $(1-\eta)$ substrate correction as given in expression [4]. Another important inference that can be drawn from

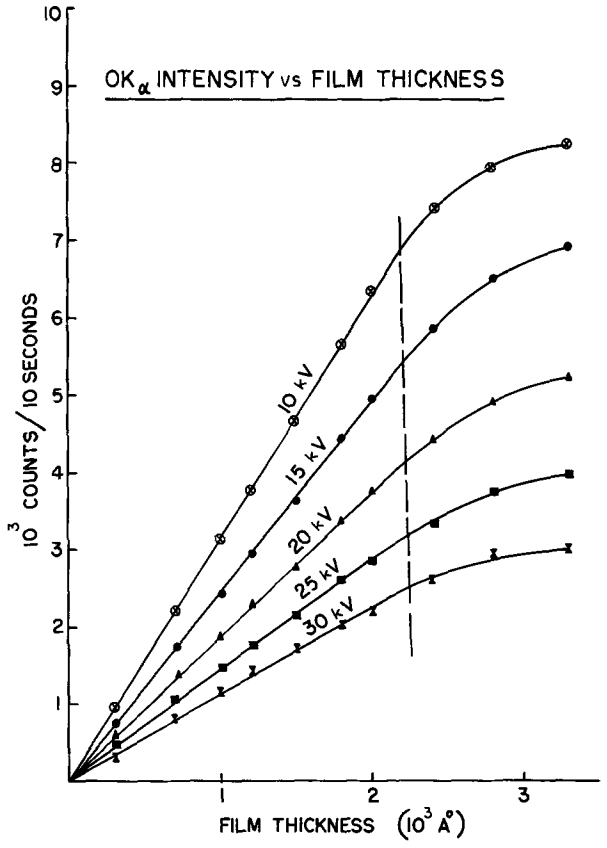

Fig. 3. Oxygen (K_α) intensity from various thicknesses of silicon dioxide films at given accelerating potentials.

these peak positions (Fig. 2) is that oxide films under investigation are essentially free from elemental silicon and that silicon is in a divalent state.

On the basis of the above analysis, the x-ray intensity for the OK_α peak from various thicknesses of the oxide films at beam potentials of 10, 15, 20, 25, and 30 keV were investigated. As shown in Fig. 3, the plots at various potentials are almost linear in the film thickness ranging from 0 to 2000Å. The intensity count rate increases linearly with the thickness. Such a linear relationship really offers a quick method of finding an unknown thickness of a given film (<2000Å) provided a calibration curve has been obtained at any given accelerating potential.

The x-ray intensity (I_F) observed from the films can also be written in terms of absorption attenuation as opposed to the atomic number effect alone as given by Eq. [1] and [4]. Such an expression is given by

$$I_F \propto \int_o^{\rho x} \phi_A(\rho x')\, e^{-\chi \rho x'} \cdot d(\rho x') + \eta \int_o^{\rho x} \phi_A(\rho x - \rho x')\, e^{-\chi \rho x'} \cdot d(\rho x') \quad [7]$$

where ρx is the mass thickness of the film, and χ is the x-ray absorption parameter. The other terms of this equation have been explained earlier. For the second integral in Eq. [7] it has been assumed that back scattered electrons are near normal to the substrate. For thin films, the x-ray excitation function $\phi_A(\rho x')$ may be approximated as (15)

$$\phi_A \approx 1 + \delta \rho x, \text{ for } \delta \rho x < 1 \quad [8]$$

where the parameter δ is the measure of electron diffusion within the film material. This parameter increases rapidly with decreasing accelerating voltage and much more slowly with increasing atomic number. The value of δ can be calculated from the initial slope of x-ray excitation curves (16) as shown in Fig. 5, or from theoretical calculations using various electron scattering theories, or from curve fitting of accurate thin film data. After substituting Eq. [8] into Eq. [7], integrating and expanding for $\delta\rho x$ and $\chi\rho x$ each being less than 1, the following expression is obtained

$$I_F \propto (1+\eta)\,\rho x\left[1 + \rho x\left(\frac{\delta}{2} - \frac{\chi}{2}\right) - (\rho x)^2\left(\frac{\delta\chi}{2} - \frac{\chi^2}{6}\right) + \ldots\right] \quad [9]$$

$$\propto \sum_1^{\infty} (1+\eta)\,(\rho x)^n\,(-1)^n \left[\frac{\delta\chi^{n-2}}{(n-1)!} - \frac{\delta\chi^{n-2}}{n!} - \frac{\chi^{n-1}}{n!}\right]$$

Relation [9] indicates that x-ray intensity is directly proportional to the mass thickness of the film as long as δ is approximately equal to χ. However, if $\delta <$ or $> \chi$, then the deviation from the linearity will be observed.

Figure 4 compares the computer analysis of expression [9] with that of obtained data. It is found that as long as $\delta \approx \chi$,the linear relationship between measured intensity and mass thickness of the films is observed. Beyond the film thickness of (50-55) 10^{-6} g/cm^2 the deviation from the linearity is evident. An excellent fit between the computer analysis and experimentally obtained data is shown in Fig. 4. For this analysis, the value of δ and η (15) were used as 1.8 x 10^4 cm^2/g and 0.16 respectively. Further, Eq. [9] predicts the negative and positive deviation for $\delta < \chi$ and $\delta > \chi$ respectively. It appears that the negative deviation is observed for silicon oxide films at all the accelerating potentials (Fig. 3 and 4).

The ratio of measured oxygen intensities from the films (I_F) to that of bulk silica (I_B) at various thicknesses of the films are shown in Fig. 5. These plots are for various accelerating potentials. Similar to that observed in Fig. 3, the normalized intensity rose linearly in the beginning. At higher thicknesses the ab-

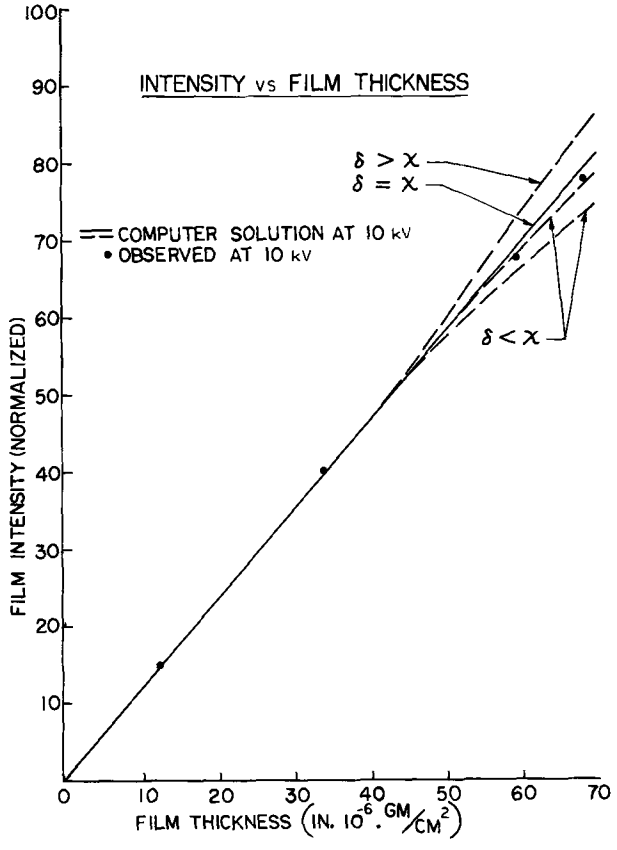

Fig. 4. Comparison between observed oxygen intensity and that calculated from the computer for various thicknesses of the films.

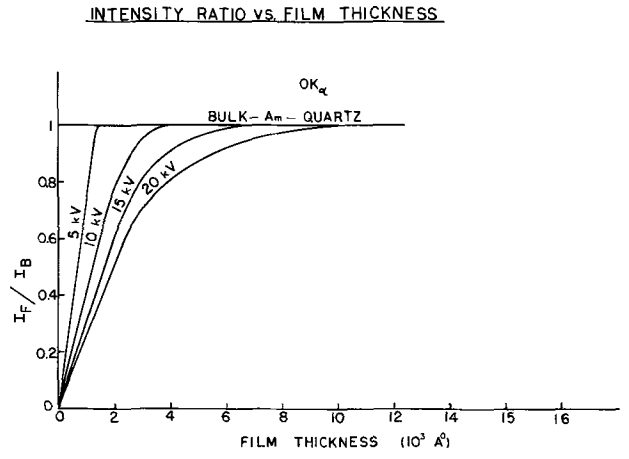

Fig. 5. Ratio of measured oxygen intensity from the films to that of bulk silica.

sorption effect, as indicated by Eq. [7], comes into play and thus an exponential rise is observed. At the thickness, where the measured intensity from the films is nearly the same as that of the bulk, the electrons are exciting the photons only from the film. In such a case, the energy of electrons before reaching the substrate reduces to less than E_c, the excitation potential of the oxygen. Therefore, this thickness level, where $I_F \approx I_B$, is then the effective penetration of electrons at the given accelerating potential. Figure 6 shows such thickness levels of oxide films at various accelerating potentials. A straight line relationship of the type

$$R_x = CE^p \qquad [10]$$

is observed, where the exponent p is found to be 1.5 and C is a characteristic constant. Cosslett and Thomas (17) have also shown that the mean as well as the extrapolated range follow the 3/2 power law. Similar dependence has also been observed by Colby (7) for various dielectric films.

The determination of the range in Eq. [10] is very important in order to calculate the energy of electrons at a given depth (x) in the films or at the interface of the substrate and film or at zero thickness when electrons are exiting with energy greater than E_c, *i.e.* via mode 3 in Fig. 1b. The simple modification of Eq. [10] in terms of energy of electrons and film thickness can be written as (17)

$$x = \frac{C'\bar{A}}{\rho\bar{Z}} V^{1.5} \qquad [11]$$

where, x is film thickness in Å, ρ the density in g/cm³, $\bar{Z}$ the mean atomic number, $\bar{A}$ is the mean atomic weight, V the accelerating potential of the electrons in keV, and C' the instrument constant which is 195 for silicon dioxide films.

Figures 7 and 8 show the measured as well as corrected OK_α intensities respectively for 3300 and 1500Å thick films at various accelerating potentials. The observed intensities in both the cases indicate decrease with increase in accelerating potential. This effect is mainly due to absorption attenuation of the x-ray and decrease in efficiency of producing photons with increase in accelerating potentials because of relatively constant volume of excitation in thin films. When these raw intensities were corrected for absorption and atomic number effects, the corrected intensities are much higher and they increase with accelerating potential. Further, it is worth noting that above 1500Å thick films (Fig. 7 and 8) the observed as well as corrected intensities show a linear relationship with accelerating potential. However, in thin films ($\leq$ 1500Å), such a linear relationship tends to show a curvature, probably owing to electrons straggling or noticeable fluorescence effect at high working potentials.

Figure 9 shows the corrected OK_α intensities for bulk amorphous silica and for oxide films of 12,000 and 2000Å thicknesses. It should be noted that the intensities for bulk and 12,000Å thick film are almost equal (within 1 to 2%) in the range of 10 to 20 keV. As observed in Fig. 5, at these potentials the 12,000Å thick film is within the penetration range of electrons. Thus, for quantitative analysis of oxygen in these films, the

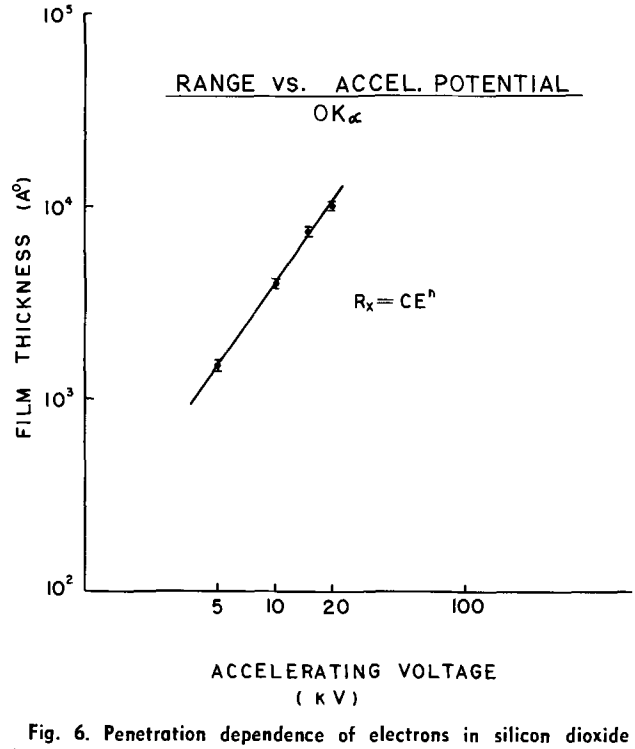

Fig. 6. Penetration dependence of electrons in silicon dioxide films at various accelerating potentials.

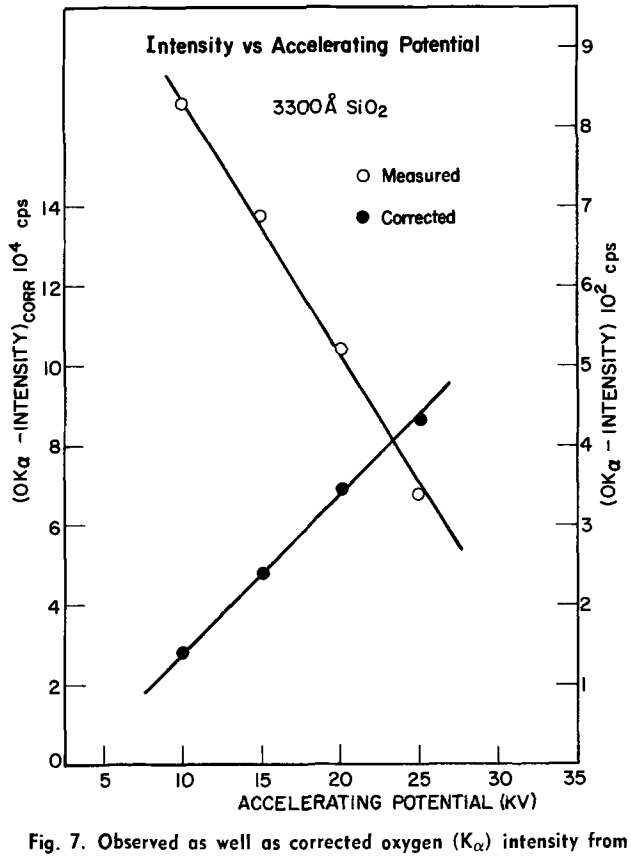

Fig. 7. Observed as well as corrected oxygen (K_α) intensity from 3300Å thick oxide film.

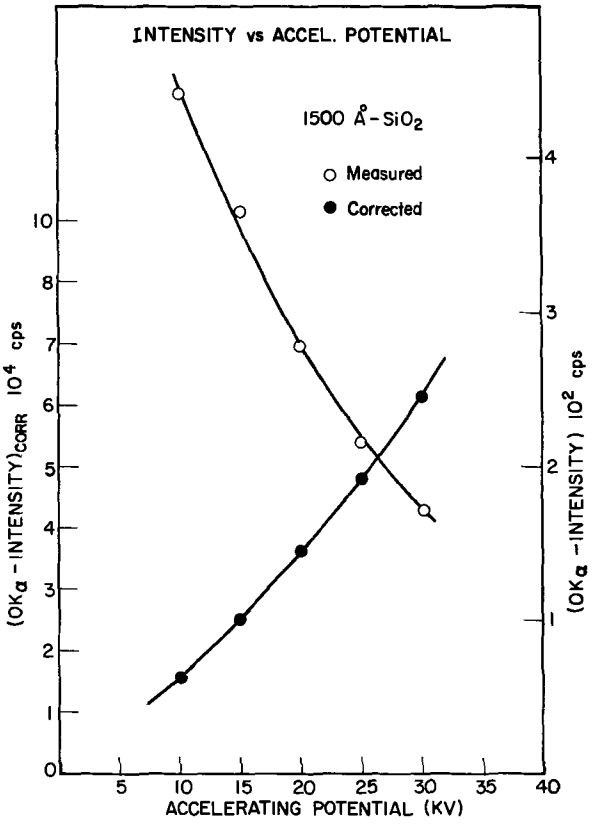

Fig. 8. Observed as well as corrected oxygen (K_α) intensity from 1500Å thick oxide film.

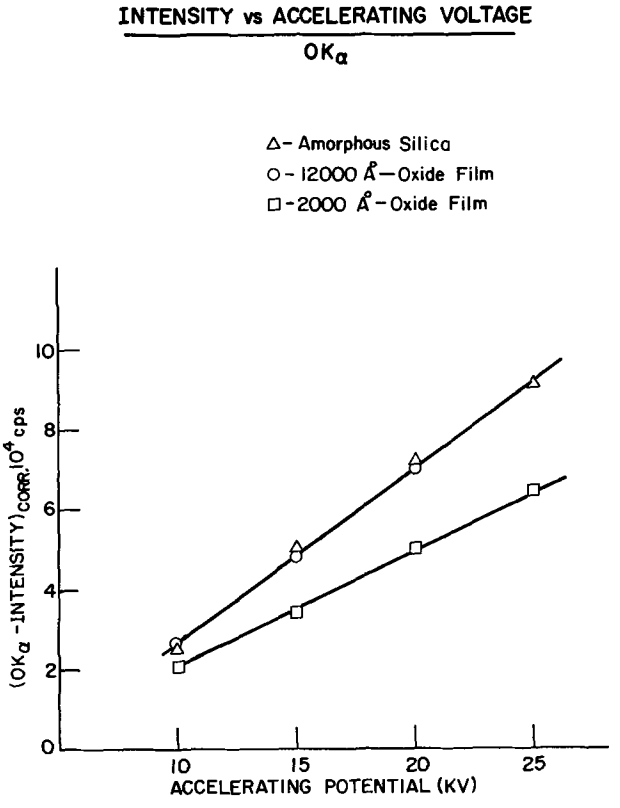

Fig. 9. Corrected oxygen (K_α) intensities from bulk silica and from oxide films (12,000 and 2000Å) at various accelerating potentials.

η-substrate correction (Eq. [4] and [7]) is not required. However, for 2000Å thick film, the actual K ratio has to be calculated after having considered the excitation of x-ray by mode 3 (Fig. 1b). Further, at any given accelerating potential, the observed intensity for 2000Å thick film is less than that of 12,000Å thick film. This is so only because in thin films the total electron energy has not been used for excitation of oxygen photons.

Table I gives the typical quantitative analysis of oxygen content in various silicon dioxide films. In arriving at the observed mass concentration given in column 4, Eq. [1] to [10] have been used. The observed mass concentration of oxygen has been found to lie within 1-2% of the theoretical mass concentration. Similarly, the silicon content of these films can also be evaluated (18). However, for thin films analyzed at high accelerating potential, the additional $(1 - \eta)$ term as given in Eq. [4] has to be considered. For the quantitative calculations the IBM 1130 computer was used.

Figure 10 shows the OK_α x-ray scan of oxide area which contains an intentionally created step of 500Å. The bright area represents the oxide thickness of 700Å and the less bright area is approximately 200Å. Such a variation in intensities could be visualized to a minimum difference in thickness of 200Å. However, to obtain a photograph of such an area containing a small difference in thickness, the scanning, pulse height, and photographic conditions have to be optimum.

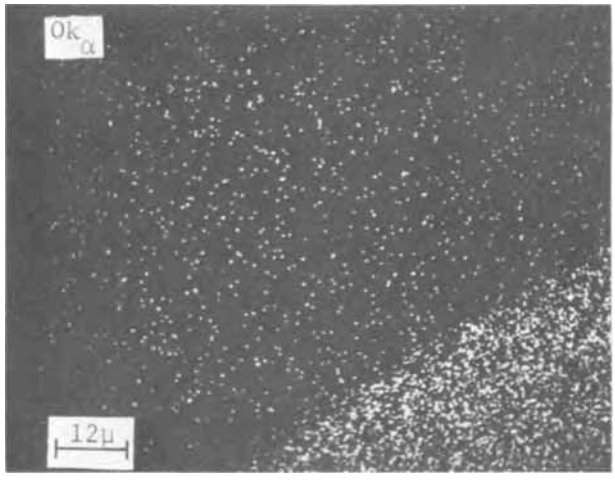

Fig. 10. Oxygen (K_α) x-ray scan from a silicon dioxide film containing a step of 500Å.

Table I. Quantitative analysis of oxygen in silcon dioxide films

Serial number	Accelerating potential (kV)	Film thickness (Å)	Intensity ratio*	Observed mass concentration	Theoretical mass concentration
1	10, 15, 20, 25	Bulk, Am—Quartz	—	53.5**	53.3
2	10	5500	0.986 ± 0.002	52.7	53.3
3	10	1250	1.008 ± 0.003	53.9	53.3
4	15	850	1.015 ± 0.003	54.3	53.3
5	20	2800	1.012 ± 0.004	54.1	53.3

* After corrections.
** From chemical analysis.

Conclusions

From the present investigation it may be concluded that characterization of silicon dioxide films or other dielectric films (19) with respect to their morphology as well as composition can be achieved by the use of the electron probe. These films may either be grown or deposited on a substrate. The mass thickness of thin films of silicon dioxide in the range of 100 to 2000Å can routinely be measured once the calibration curve has been obtained. However it should be emphasized that simultaneous determination of thickness and composition is not possible by the use of probe alone. Either one has to be supplemented by some other method. Such measurements offer a quick nondestructive method for finding the thickness, variation in thickness, and stoichiometry of the films. These techniques as explored by the use of the electron probe can be of utmost significance in semiconductor technology.

Manuscript submitted Oct. 28, 1970; revised manuscript received *ca.* Jan. 19, 1971.

Any discussion of this paper will appear in a Discussion Section to be published in the December 1971 JOURNAL.

REFERENCES

1. "The Electron Microprobe," Proceedings of the Microprobe Symposium, Washington, D. C., T. C. McKinley, *et al.*, Editors, John Wiley & Sons, Inc., New York (1966).
2. "X-ray and Electron Probe Analysis," ASTM, Special Technical Publication, No. 349, Proceedings of the Microprobe Symposium, Atlantic City (1963).
3. R. Castaing and J. Descamps, *J. Phys. Radium*, **16**, 304 (1955).
4. P. Duncumb and P. K. Shields, *Brit. J. Appl. Phys.*, **14**, 617 (1963).
5. D. M. Poole and P. M. Thomas, *J. Inst. Metals*, **90**, 288 (1961-62).
6. M. Green and V. E. Cosslett, *Proc. Phys. Soc. (London)*, **78**, 1206 (1961).
7. J. W. Colby, "Advances in X-ray Analysis," Vol. 11, p. 287, Plenum Press, New York (1967).
8. J. Philbert, in "X-ray Optics and X-ray Microanalysis," p. 379, H. H. Pattee, V. F. Coslett, and A. Engstrom, Editors, Academic Press, New York (1966).
9. P. Duncumb and P. K. Shield, in "The Electron Microprobe," p. 284, T. D. McKinley *et al.*, Editors, John Wiley & Sons, Inc., New York (1966).
10. K. F. Heinrich, "Advances in X-ray Analysis," Vol. 11, p. 40, Plenum Press, New York (1967).
11. B. L. Henke *et al.*, *Norelco Reptr.*, **14**, 112 (1967).
12. P. S. Schaffer and B. Swaroop, *Am. Ceramic Soc. Bull.*, **49**(5), 536 (1970).
13. S. Tolansky, "Multibeam Interferometry of Surfaces and Films," Clarendon Press, Oxford (1948).
14. W. H. Knausenberger *et al.*, *Appl. Phys. Letters*, **14**(2), 43 (1969).
15. G. A. Hutchins, "The Electron Microprobe," T. D. McKinley, Editor, p. 390, John Wiley & Sons, Inc., New York (1966).
16. R. Castaing, "Advances in Electronics and Electron Physics," Vol. 13, Marton, Editor, Academic Press, New York (1960).
17. V. E. Cosslett and R. N. Thomas, *Brit. J. Appl. Phys.*, **15**, 1283 (1964).
18. B. Swaroop, *This Journal*, **117**, 87C (1970).
19. B. Swaroop, To be published.

Cathodoluminescence of Ce^{3+}- and Eu^{2+}-Activated Alkaline Earth Feldspars

K. R. Laud, E. F. Gibbons, T. Y. Tien,* and H. L. Stadler*

Scientific Research Staff, Ford Motor Company, Dearborn, Michigan 48121

ABSTRACT

The compounds $MAl_2Si_2O_8$, where M = Ca, Sr, or Ba, were synthesized. Compositions in the three binary systems were also prepared. Cathodoluminescence of these compositions activated with Ce^{3+} and Eu^{2+} was studied. It was found that the Ca and Sr feldspars formed complete solid solutions. In the systems Ba-Ca feldspars and Ba-Sr feldspars, only partial solid solutions are formed. The solid solubility limits are

$SrAl_2Si_2O_8$ to $Sr_{0.6}Ba_{0.4}Al_2Si_2O_8$
and $BaAl_2Si_2O_8$ to $Ba_{0.8}Sr_{0.2}Al_2Si_2O_8$
$CaAl_2Si_2O_8$ to $Ca_{0.9}Ba_{0.1}Al_2Si_2O_8$
and $BaAl_2Si_2O_8$ to $Ba_{0.6}Ca_{0.4}Al_2Si_2O_8$

Both the Ce^{3+}- and Eu^{2+}-activated phosphors give broad emission bands under cathode-ray excitation. The peak positions of the emission for Ce^{3+}-activated phosphors are

$CaAl_2Si_2O_8$ — 355 and 490 nm
$SrAl_2Si_2O_8$ — 530 nm
$BaAl_2Si_2O_8$ — inert

and those for Eu^{2+}-activated phosphors are

$CaAl_2Si_2O_8$ — 470 nm
$SrAl_2Si_2O_8$ — 465 nm
$BaAl_2Si_2O_8$ — 375 and 500 nm

The peak position of the cathodoluminescent emission of the solid solutions for both Ce^{3+} and Eu^{2+} as activators depends on the major alkaline earth cation in the host. No significant shift from the pure compound was observed.

C^{3+}- and Eu^{2+}-activated phosphors are known to give broad-band emission under cathode-ray excitation (1). The emission peak depends on the host and is found to occur from the near ultraviolet to the yellow-red region of the spectrum. A solid solution series of isostructural end members with slightly different sized cations as hosts would be an ideal system to study the effect of crystal chemical variation

* Electrochemical Society Active Member.

Key words: phosphors, luminescence, cathodoluminescence, feldspars, cerium, europium, aluminosilicates.

on the luminescence of Ce^{3+} and Eu^{2+} ions. Moreover, it offers the possibilities of finding useful phosphors for commercial applications.

The alkaline earth aluminosilicates (known as alkaline earth feldspars) $MAl_2Si_2O_8$ (where M = Ba, Sr, Ca) crystallize in network structures and are known as stuffed derivatives of silica. The ionic radii of these alkaline earth ions are comparable to those of the Ce^{3+} and Eu^{2+}. The tabulated ionic radii (Pauling's) are Ca^{2+} = 0.99Å, Sr^{2+} = 1.13Å, Ba^{2+} = 1.35Å, Eu^{2+} = 1.12Å, and Ce^{3+} = 1.11Å. The sites available to the activators, therefore, should be those of the alkaline earth ions, since the fourfold sites in this structure are too small for the ions having a size larger than 1Å. The sites for 1Å size ions are the hexagonal structural holes in the feldspar network.

Reference to luminescence in feldspars was made as early as 1939 (2, 3). However, luminescence in binary alkaline earth feldspar systems has not been reported previously. Subsolidus phase relations in the three mutual binary systems of $CaAl_2Si_2O_8$, $SrAl_2Si_2O_8$, and $BaAl_2Si_2O_8$ have not been studied prior to this work. One would expect an extensive series of solid solutions in the three binary systems $CaAl_2Si_2O_8$-$SrAl_2Si_2O_8$, $SrAl_2Si_2O_8$-$BaAl_2Si_2O_8$, and $BaAl_2Si_2O_8$-$CaAl_2Si_2O_8$ because of the similar feldsparlike structure of the compounds and also because of the close ionic radii of the cations. These solid solutions would enable one to study the variation of cathodoluminescent emission spectra with composition.

Structural Information on the Hosts

The feldspars are a group of mineral structures based on an infinite three-dimensional silicon-oxygen framework. In alkaline earth feldspars, half of the tetrahedral positions in the framework are occupied by Al^{3+} and the other half by Si^{4+} so that, for every two Al^{3+}, one divalent Ca^{2+}, Sr^{2+}, or Ba^{2+} is introduced to neutralize the negative charge of the $(Si,Al)O_2$ framework. These large cations take the interstitial positions. The ratio of (Si + Al) to O must always be 1:2 since every Si or Al is surrounded tetrahedrally by four oxygen atoms and each of these is common to two tetrahedral groups. The silicon-oxygen framework for all of the alkaline earth feldspars is essentially the same; however, there are differences in crystal symmetries which are due to the difference in the size of the cations around which the framework closes in. Alkaline earth feldspars are $CaAl_2Si_2O_8$ (anorthite), $SrAl_2Si_2O_8$, and $BaAl_2Si_2O_8$ (celsian). According to Wyckoff (4), in anorthite ($CaAl_2Si_2O_8$) the Ca-atom has six or seven close oxygen neighbors at distances between 2.28 and 2.82Å. In celsian ($BaAl_2Si_2O_8$), the Ba-atom has nine oxygen neighbors at distances between 2.667 and 3.135Å, as well as a tenth somewhat more distant at 3.421Å. Both Ca and Sr feldspar have triclinic symmetry and the Ba feldspar is monoclinic. There are other polymorphs of these feldspars; however, they are either metastable or the stability region is outside of the temperature of preparation for this study. The polymorphs dealt with in this paper are the high-temperature phases. A brief discussion of these polymorphs follows.

Eskola (5) prepared both strontium and barium feldspars by heating oxides to 1400°C with $Sr(VO_3)_2$ and $Ba(VO_3)_2$ as fluxes and characterized the products using a petrographic microscope. He also found that a homogeneous mixture of 50 w/o (weight per cent) $SrAl_2Si_2O_8$ and 50 w/o $CaAl_2Si_2O_8$ has indexes of refraction the same as those of $CaAl_2Si_2O_8$. He postulated that Sr-feldspar formed a complete series of solid solutions with Ca-feldspar.

Davis and Tuttle (6) reported two crystalline phases of $CaAl_2Si_2O_8$ composition. One phase had a feldsparlike structure (that of anorthite). The second phase, which was metastable, had a hexagonal structure.

Sorrell (7) prepared strontium and barium feldspars in the solid state using mixtures of kaolin-type clays and Ba- or Sr-sulfates. The barium compound showed a metastable hexagonal phase which was very persistent and required prolonged heating to convert it to stable celsian (feldspar). The strontium compound also showed a hexagonal phase which was unstable and detectable only during continuous x-ray investigation. He suggested that the hexagonal phase is not a high-temperature polymorph of feldspar, but rather a metastable form produced as a result of rapid crystal growth. The stable phase of the barium feldspar had monoclinic symmetry and the strontium feldspar was triclinic.

Ito (8) determined the crystal structure of hexacelsian (a hexagonal form of $BaAl_2Si_2O_8$) and found it to consist of a double sheet of silica-alumina tetrahedra with common apexes, held together by barium ions in 12-fold coordination.

More recently Lin and Foster (9), during an investigation of $BaAl_2Si_2O_8$ polymorphism, concluded that there are four polymorphs of $BaAl_2Si_2O_8$ (*viz.*, paracelsian, orthorhombic form, hexacelsian, and celsian). Monoclinic celsian was stable from room temperature to 1590°C, where it inverted sluggishly to hexacelsian. The latter, stable to the melting point (1760°C), persisted metastably on cooling below 1590°C and inverted to the orthorhombic form through 300°C. Naturally occurring paracelsian was found to be a metastable phase which changed monotropically through hexacelsian to celsian at temperatures as low as 500°C.

Experimental

The starting materials used for the preparation of batches were $CaCO_3$, $SrCO_3$ $BaCO_3$, CeO_2, Eu_2O_3, aluminum hydroxide, and silicic acid. Except for CeO_2 and Eu_2O_3, which were phosphor grade, reagent-grade chemicals were used.

In all compositions, Ce^{3+} and Eu^{2+} concentrations were maintained at 1 and 2 m/o (mole per cent), respectively. Prior to formulation, weight loss factors for aluminum hydroxide and silicic acid were determined. Since Ce^{3+} was substituted for Me^{2+} (Me^{2+} = Ca^{2+}, Sr^{2+}, or Ba^{2+}), charge balance was accomplished as follows: for $MeAl_2Si_2O_8$:Ce, the formulation was 99 parts $MeAl_2Si_2O_8$ and 1 part $CeAl_3SiO_8$.

Weighed batches were mixed under acetone, air dried, calcined in platinum crucibles to 800°C, remixed, and finally fired at 1400°C for 24 hr. The products were ground and placed in alumina boats which were heated in an atmosphere of nitrogen with 3% hydrogen at 1100°-1200°C for 18 hr. Samples were cooled to room temperature in the reducing atmosphere.

Crystalline phases were identified by a Norelco x-ray diffractometer using a scanning rate of 2θ = 1 deg/min as a routine. For precise "d" spacing and lattice parameter measurements, a slow scanning rate of ¼ deg/min and silicon as an external standard were employed. The lattice parameters were calculated using at least 10 diffraction lines by the least-squares method using a computer program.

The cathodoluminescence (C.L.) data were obtained in a demountable electron beam gun system operated at 3 kV. Samples were mounted at the focal point of an optical system which then refocused the emitted light on the entrance slit of a ¾m Czerny-Turner spectrometer. The output from a photomultiplier (P.M.) tube, located at the exit slit of the spectrometer, was amplified by means of a synchronous detector and displayed on an x-y recorder. The required periodic signal for the P.M. tube was obtained by applying a 13 Hz square wave to the horizontal deflection plates of the electron beam gun, thus providing a 50%

excitation duty cycle on the sample. The same square-wave generator provided the reference signal for the synchronous detector.

The excitation spectra were taken in a system utilizing a xenon light source focused through a mechanical light chopper onto the entrance slit of a ¾m spectrometer. The emission from the sample, located at the exit slit, was recorded by means of a photomultiplier tube, the output of which was amplified by means of a synchronous detector and displayed on an x-y recorder. Appropriate filters were used in front of the sample and the P.M. tube and the spectra shown were corrected for system response.

Results

The compounds $CaAl_2Si_2O_8$, $SrAl_2Si_2O_8$, and $BaAl_2Si_2O_8$.—Calcium and strontium feldspars were easily prepared at 1400°C. The powders were well crystallized and produced well-defined x-ray diffraction patterns. In $CaAl_2Si_2O_8$ and $SrAl_2Si_2O_8$ compositions, Ca-feldspar and Sr-feldspar were the only phases identified. No trace of the metastable hexagonal phases was detected in each of these.

After 24 hr at 1400°C, hexacelsian was the only phase identified in the $BaAl_2Si_2O_8$ composition. Heating for 3 days at 1400°C did not convert the material to celsian, which was brought about after firing for 5 days. It is obvious, therefore, that hexacelsian when made with pure starting materials appears metastably at 1400°C and is very persistent.

The cell dimensions of the Sr- and Ba-feldspars were calculated using the least-squares method. Table I summarizes the results of this work and those reported previously. In $BaAl_2Si_2O_8$, there is good agreement between the lattice parameters calculated in this work and those reported by Sorrell (7) in the ASTM Data File. In $SrAl_2Si_2O_8$, the axial parameters *a*, *b*, and *c* of the triclinic cell agree very well with previously reported data. However, the angular parameters were somewhat different. In the ASTM File, the angle gamma (94.10°) is larger than alpha (89.43°). This work found alpha (90.18°) to be slightly larger than gamma (89.27°). A very small difference was apparent in the angle beta. The previous data for $CaAl_2Si_2O_8$ were obtained using a natural specimen of unknown chemical composition. Since anorthite is generally found to contain albite, *etc.* (10), the difference in the data presented could be due to such impurities.

The cathodoluminescent emission spectra of Ca-, Sr-, and Ba-feldspars activated by each of Ce^{3+} and Eu^{2+} are shown in Fig. 1A and 2A, respectively. Ce^{3+}-activated $CaAl_2Si_2O_8$ gave two emission peaks. The peak emission in the ultraviolet region occurred at 355 nm.

Table I. Lattice parameters of $CaAl_2Si_2O_8$, $SrAl_2Si_2O_8$, and $BaAl_2Si_2O_8$

From ASTM Data File		Present work
$CaAl_2Si_2O_8$*		
	Reduced cell	Reduced cell
a = 8.184Å	a = 7.700Å	a = 8.309Å
b = 12.865Å	b = 12.897Å	b = 12.864Å
c = 14.150Å	c = 7.555Å	c = 7.336Å
α = 92.28°	α = 91.13°	α = 89.68°
β = 115.92°	β = 115.13°	β = 119.17°
γ = 91.62°	γ = 98.37°	γ = 91.86°
$SrAl_2Si_2O_8$**		
a = 8.23Å		a = 8.312Å
b = 12.86Å		b = 12.934Å
c = 7.22Å		c = 7.129Å
α = 89.43°		α = 90.18°
β = 116.50°		β = 115.0°
γ = 94.10°		γ = 89.27°
$BaAl_2Si_2O_8$**		
a = 8.63Å		a = 8.647Å
b = 13.10Å		b = 13.071Å
c = 7.29Å		c = 7.217Å
β = 116.0°		β = 115.1°

* Cole *et al.*, *Acta. Cryst.*, 4, 20 (1951).
** Sorrel, *Am. Mineralogist*, 47, 291 (1962).

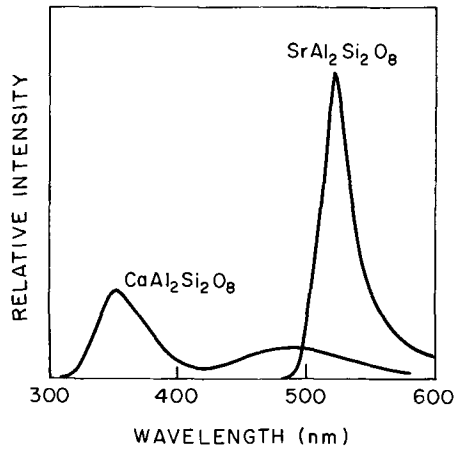

Fig. 1A. Emission spectra of Ce^{3+}-activated $CaAl_2Si_2O_8$ and $SrAl_2Si_2O_8$ due to C. L. excitation.

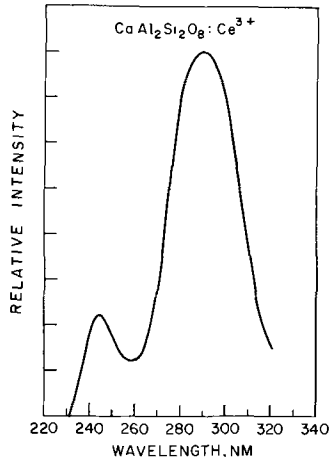

Fig. 1B. Excitation spectra of Ce^{3+}-activated $CaAl_2Si_2O_8$

Emission in the visible region was broad with a peak at 490 nm in the blue-green region. Ce^{3+}-activated $SrAl_2Si_2O_8$ gave a peak emission at 530 nm in the green region. Excitation spectra are shown in Fig. 1B and 2B. $SrAl_2Si_2O_8$:Ce^{3+} is very weakly excited by ultraviolet; only one small excitation band could be observed around 265 nm. Ce^{3+}-doped $BaAl_2Si_2O_8$

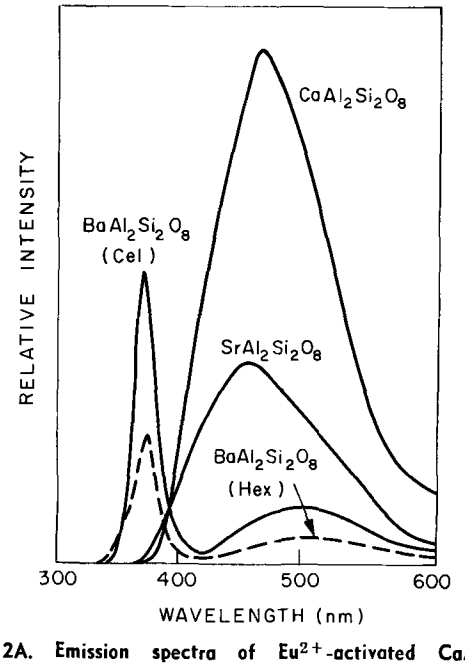

Fig. 2A. Emission spectra of Eu^{2+}-activated $CaAl_2Si_2O_8$, $SrAl_2Si_2O_8$, and $BaAl_2Si_2O_8$ due to C.L. excitation.

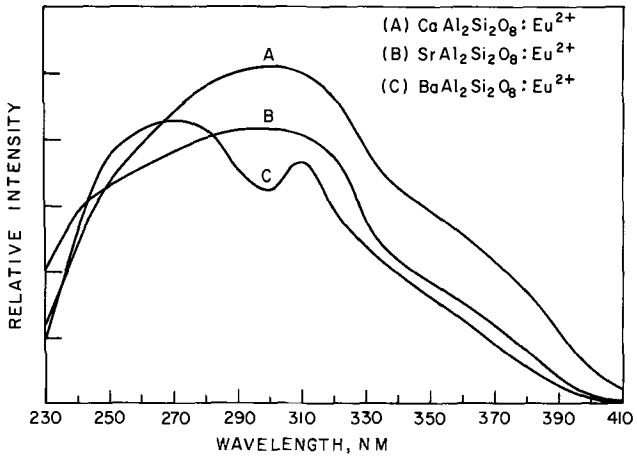

Fig. 2B. Excitation spectra of Eu^{2+}-activated feldspars

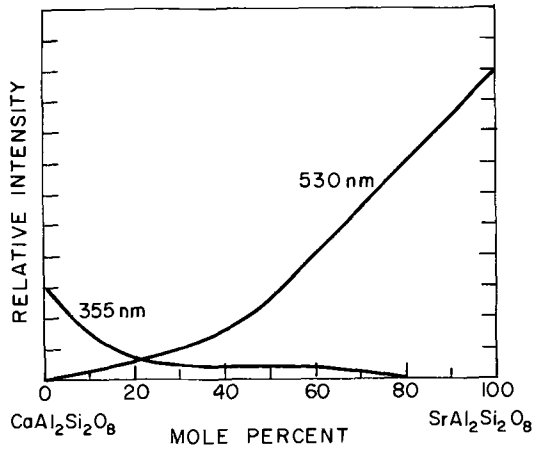

Fig. 4. A plot of relative intensity vs. composition of emission peaks in the system $CaAl_2Si_2O_8:Ce^{3+}$-$SrAl_2Si_2O_8:Ce^{3+}$ due to C.L. excitation.

(celsian) and hexacelsian were inert to C.L. excitation.

The emission of Eu^{2+}-activated $CaAl_2Si_2O_8$ and $SrAl_2Si_2O_8$ due to C.L. excitation occurred in the blue region with peak emission at 470 and 465 nm, respectively. The emission peaks were broad and there were no significant differences in their positions. The emission of Eu^{2+}-activated $BaAl_2Si_2O_8$ due to C.L. excitation occurred in the ultraviolet region and very weakly in the blue-green region with peak emission at 375 and 500 nm, respectively.

The system $CaAl_2Si_2O_8$-$SrAl_2Si_2O_8$.—Five phosphors prepared in this system were completely reacted after 24 hr at 1400°C. Only the feldspar phase was identified in each composition. X-ray diffraction patterns showed complete solid solution series between the end members. A plot of observed "d" spacing as a function of composition, shown in Fig. 3, is in good agreement with the concept of complete solid solubility.

In Ce^{3+}-activated phosphors prepared in a series of solid solutions, one frequently finds a continuous shift in the C.L. emission peak positions from one end member to the other. The Ca-feldspar and Sr-feldspar system, however, shows no such shift in the peak position. On the contrary, emission peaks of both the end members were present in the solid solution series. The 490 nm emission peak for $CaAl_2Si_2O_8$ decreases considerably at $Ca_{0.8}Sr_{0.2}Al_2Si_2O_8$ and then ceases beyond this limit. Figure 4 gives a plot of relative intensity (by peak height measurement) of emission peak as a function of composition. The peak intensity of the emission characteristic of Ca-feldspar decreases as the concentration of Sr^{2+} increases in the solid solutions. Similarly, the peak intensity of Sr-feldspar emission decreases with an increase in Ca^{2+} concentration.

Since the C.L. peak emission of Eu^{2+}-activated Ca- and Sr-feldspar occurs at 470 and 465 nm, respectively, no shifts in the positions of peak emission were anticipated in the solid solution series. The peak emission of phosphors prepared in the solid solution region occurred in the blue region at 470 nm as did those of the end members. The relative intensity (by peak height measurement) of the emission peaks as a function of composition is plotted in Fig. 5. Unlike Ce^{3+}-activated phosphors, these solid solutions have higher intensity than the end members. The phosphor with 75% Ca- and 25% Sr-feldspar has maximum intensity in the emission peak.

The system $SrAl_2Si_2O_8$-$BaAl_2Si_2O_8$.—Six compositions were prepared in this system. X-ray diffraction patterns indicated that Sr-feldspar accepted 60 m/o Ba^{2+} for Sr^{2+} in solid solution. Ba-feldspar accepted only 20 m/o Sr^{2+} for Ba^{2+}. Cell dimensions of the compositions in the system were calculated by the least-squares method. The parameters obtained, as a function of composition, are plotted in Fig. 6A and 6B. The *a*, *b*, and c parameters of $SrAl_2Si_2O_8$ all increase with the substitution of Ba^{2+} for Sr^{2+}. This linear relationship is evident up to 60 m/o Ba^{2+} beyond which the slope of the plot for $BaAl_2Si_2O_8$ solid solution region is different. Similarly, the angular parameters alpha and gamma of $SrAl_2Si_2O_8$ approach 90 deg at 60 m/o Ba^{2+}. Thereafter, they become 90 deg in the $BaAl_2Si_2O_8$ solid solution region. Between 60 and 80 m/o $BaAl_2Si_2O_8$, there exists a two-phase region.

The relative intensity (by peak height measurement) of the 530 nm peak emission *vs.* composition of Ce^{3+}-activated phosphors in the system is plotted in Fig. 7. The peak emission of $SrAl_2Si_2O_8$ increased in intensity with the substitution of Ba^{2+} for Sr^{2+} up to 40 m/o Ba^{2+} and then it dropped slowly up to 60 m/o Ba^{2+},

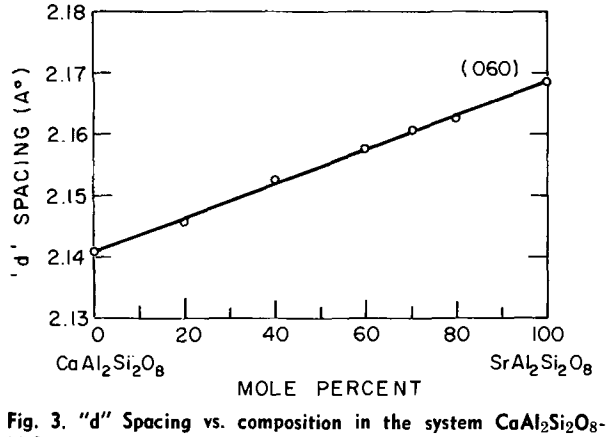

Fig. 3. "d" Spacing vs. composition in the system $CaAl_2Si_2O_8$-$SrAl_2Si_2O_8$.

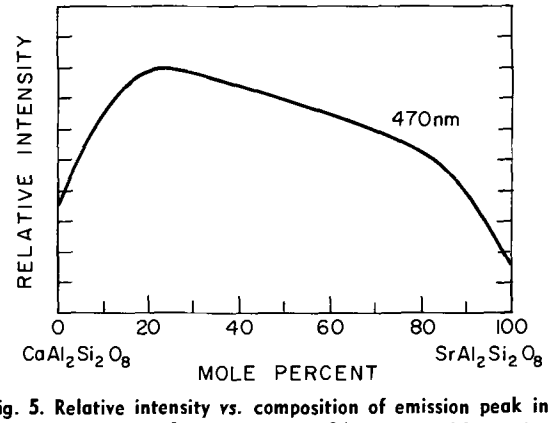

Fig. 5. Relative intensity vs. composition of emission peak in the system $CaAl_2Si_2O_8:Eu^{2+}$-$SrAl_2Si_2O_8:Eu^{2+}$ due to C.L. excitation.

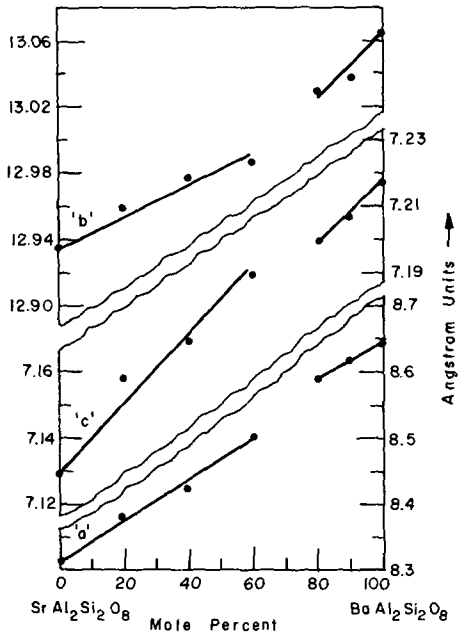

Fig. 6A. Lattice parameter vs. composition in the system $SrAl_2Si_2O_8$-$BaAl_2Si_2O_8$.

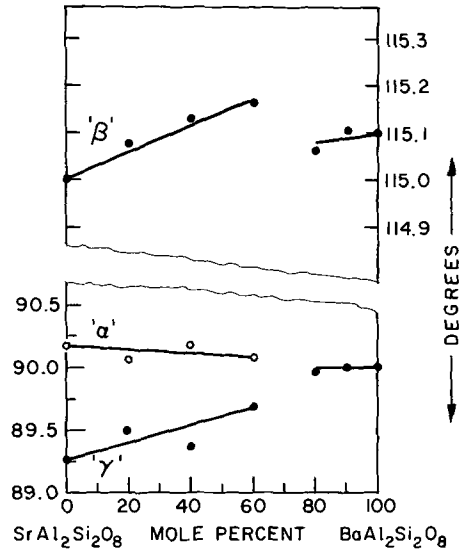

Fig. 6B. Lattice parameter vs. composition in the system $SrAl_2Si_2O_8$-$BaAl_2Si_2O_8$.

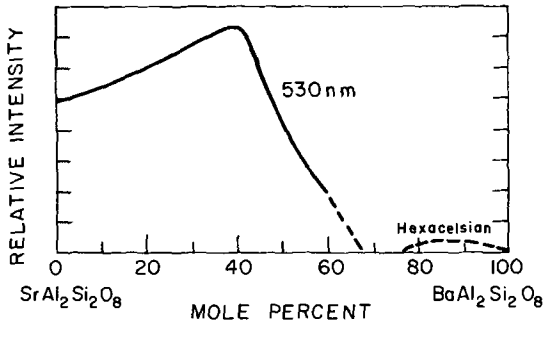

Fig. 7. Relative intensity vs. composition of emission peak in the system $SrAl_2Si_2O_8$:Ce^{3+}-$BaAl_2Si_2O_8$:Ce^{3+} due to C.L. excitation.

beyond which the luminescence ceases. Ce^{3+}-doped $BaAl_2Si_2O_8$ is inert to C.L. excitation and its solid solutions are also found to be inert. Similar results were obtained in the Eu^{2+}-activated system. Figure 8 shows a plot of the relative intensity of the 465 nm emission peak as a function of composition. The relative intensity increases with Ba^{2+} concentration up to 35 m/o Ba^{2+} and then slowly decreases up to 70 m/o Ba^{2+}. Beyond this limit, the luminescence almost ceases. The intensity of the 375 nm emission peak of $BaAl_2Si_2O_8$ decreases with increasing Sr^{2+} concentration up to 20 m/o Sr^{2+} and then ceases.

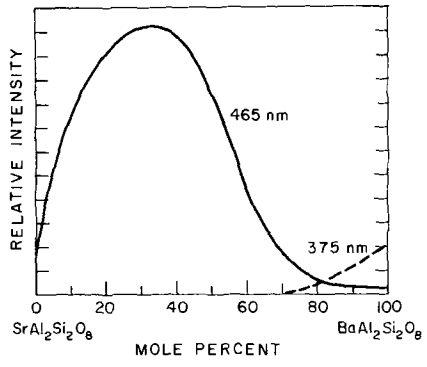

Fig. 8. Relative intensity vs. composition of emission peak in the system $SrAl_2Si_2O_8$:Eu^{2+}-$BaAl_2Si_2O_8$:Eu^{2+} due to C.L. excitation.

The system $CaAl_2Si_2O_8$-$BaAl_2Si_2O_8$.—Six compositions were prepared in this system. X-ray diffraction patterns indicate that $CaAl_2Si_2O_8$ can accept only up to 10 m/o Ba^{2+} for Ca^{2+} in solid solution. However, the $BaAl_2Si_2O_8$ solid solution is very extensive. Up to 60 m/o Ba^{2+} can be replaced by Ca^{2+} in $BaAl_2Si_2O_8$ solid solution. Between 10 and 40 m/o Ba^{2+}, Ca-feldspar and Ba-feldspar were both identified as coexisting phases. $BaAl_2Si_2O_8$ and its solid solutions were found to be inert to cathode-ray excitation when doped with Ce^{3+} and to be only very weakly excited when activated by Eu^{2+}. Therefore, the extensive solid solution of $BaAl_2Si_2O_8$ with $CaAl_2Si_2O_8$ was of no interest for luminescence studies. Since $CaAl_2Si_2O_8$ solid solution was very limited ($\leq$ 10 m/o Ba^{2+} for Ca^{2+}), it was not investigated further.

Discussion

The Ce^{3+}-activated $CaAl_2Si_2O_8$ shows two distinct peaks in the excitation spectra occurring at 34.5 x 10^3 cm^{-1} and 41 x 10^3 cm^{-1} (see Fig. 1B). These peaks are assumed to be caused by the crystal field splitting of the Ce^{3+} ion as has been previously suggested (1a). Two peaks separated by approximately 8160 cm^{-1} are also observed in the emission spectrum. In $SrAl_2Si_2O_8$:Ce, only one very weak excitation peak around 38 x 10^3 cm^{-1} could be identified. Because of inefficient pumping of the material by photons, the existence of other excitation bands cannot be ruled out. The emission spectrum also shows only one peak occurring at 18.9 x 10^3 cm^{-1}.

In forming the solid solution series between the Ca and Sr end members, the lattice parameters varied continuously as a function of composition; however, the position of the Ce^{3+} emission appears not to be affected. Instead, the emission for the solid solution samples appeared to be a combination of the two types of spectra. This would imply that the Ce^{3+} ion is probably occupying two different kinds of sites in the solid solution in which the activator environment is essentially the same as that in the end members. This may indicate that the local environment of the activator ion remains virtually unchanged, even though there is a long-range change in the crystal which is reflected in the lattice parameter variations. The decrease in the Ce^{3+} emission in the single-phase solid solution region proceeding from Sr toward Ba is also probably due to the Ce^{3+} ions occupying two sites, with the alkaline earth ion site in $BaAl_2Si_2O_8$ being inert.

With Eu^{2+} activation, both the $CaAl_2Si_2O_8$:Eu^{2+} and $SrAl_2Si_2O_8$:Eu^{2+} samples showed a broad emission throughout the visible with the peak of the band occurring at 465-470 nm. The general character of the

emission band did not change as a function of composition across the solid solution series. However, it is interesting to note that the maximum intensity occurs at a point in between the two end members. It is not known whether this increase is caused by an increased efficiency of the Eu^{2+} ion (a decrease in radiationless energy loss) or by an improvement in the energy transfer mechanism between the host and activator. A similar variation of the intensity of the 465 nm band is also observed in the Sr to Ba solid solution samples.

The $BaAl_2Si_2O_8$:Eu material shows two peaks in the emission spectra separated by approximately 6670 cm^{-1}. Again, the presence of these two bands may be caused by a splitting of the 5d level of the Eu^{2+}.

Acknowledgments

The authors are grateful to R. G. DeLosh for helpful discussion and to D. R. Peacor for the computer program for lattice parameter calculation of the triclinic crystals.

Manuscript submitted Aug. 24, 1970; revised manuscript received Jan. 8, 1971. This was Paper 51 presented at the Los Angeles Meeting of the Society, May 10-15, 1970.

Any discussion of this paper will appear in a Discussion Section to be published in the December 1971 JOURNAL.

REFERENCES

1. For example: (a) G. Blasse and A. Bril, *J. Chem. Phys.*, **47**, 5139 (1967); (b) G. Blasse, W. L. Wanmaker, and J. W. terVrugt, *This Journal*, **115** (1968); (c) W. W. Holloway, Jr., and M. Kestigan, *J. Opt. Soc. Am.*, **59**, 60 (1969).
2. H. Haberlandt and A. Koehler, *Naturwissenschaften*, **27**, 275 (1939).
3. F. A. Kröger, "Some Aspects of the Luminescence of Solids," Elsevier Publishing Co. (1948).
4. R. W. G. Wyckoff, "Crystal Structures," Vol. 4, Interscience Publication, John Wiley & Sons, New York (1968).
5. P. Eskola, *Am. J. Sci.*, 5th Ser., 4, 331 (1922).
6. G. L. Davis and O. F. Tuttle, *ibid.*, (Bowen Vol.), **250**, 107 (1952).
7. C. A. Sorrell, *Am. Mineralogist*, **47**, 291 (1962).
8. T. Ito, "X-Ray Studies on Polymorphism," Maruzen Co., Ltd., Tokyo (1950).
9. H. C. Lin and W. R. Foster, *Am. Mineralogist*, **53**, 134 (1968).
10. A. F. Wells, "Structural Inorganic Chemistry," Oxford University Press (1962).

Phase Equilibria and Tin-Activated Luminescence in the System $Ca_3(PO_4)_2$-$Ba_3(PO_4)_2$

Eric R. Kreidler

Lighting Research Laboratory, General Electric Company, Nela Park, Cleveland, Ohio 44112

ABSTRACT

The phase diagram for the system $Ca_3(PO_4)_2$-$Ba_3(PO_4)_2$ has been determined in detail. Although no intermediate compounds were found in the system, two extensive solid solution regions having the α-$Ca_3(PO_4)_2$ and β-$Ba_3(PO_4)_2$ structures were found to exist. Beta-$Ba_3(PO_4)_2$ is a newly discovered polymorph stable above 1390°C. The divalent tin-activated luminescence of various phases in the system was studied. The most efficient phosphor was α-$Ca_{2.50}Ba_{0.45}Sn_{0.02}(PO_4)_2$ which had properties similar to those of $Ca_{10}(PO_4)_6F_2$:Sb. The performance of α-(Ca, Ba)$_3(PO_4)_2$:Sn in fluorescent lamps was evaluated.

The alkaline earth orthophosphates serve as host structures for efficient luminescence and have been studied extensively in this regard. As a result of the interest in luminescence, a number of alkaline earth orthophosphate phase diagrams have been determined. The system $Ca_3(PO_4)_2$-$Ba_3(PO_4)_2$ has received some attention (1) but has not been examined in detail. Prior to the present study, two compounds, having the compositions $Ca_2Ba(PO_4)_2$ and $Ba_2Ca(PO_4)_2$, were reported to occur in the system (1, 2). These phases are found to be members of two distinct solid solution series, and no discrete compounds exist within the calcium orthophosphate-barium orthophosphate system.

The tin-activated luminescence of β- and α-$Ca_3(PO_4)_2$ and of $Ba_3(PO_4)_2$ was reported by Butler (3) in 1951. Both forms of calcium phosphate have efficient visible emissions when excited by 254 nm radiation. Under the same conditions, barium orthophosphate shows only a weak ultraviolet fluorescence. The temperature dependence of the luminescence in α-$Ca_3(PO_4)_2$:Sn and β-$Ca_3(PO_4)_2$:Sn as well as the effects of magnesium additions in β-$Ca_3(PO_4)_2$:Sn were studied by Wanmaker and Radielovic (4). Lendvay (5) speculated on the nature of the luminescence centers in β-$Ca_3(PO_4)_2$:Sn and assigned the red emission band to Sn^{2+} ions replacing Ca^{2+} ions and the green band to interstitial Sn^{2+} ions. Besides tin, many other activators have been examined in the alkaline earth orthophosphates; among these are Ce (6), Tl (7), Cu (8, 9), Sb (10), Eu (11), and Tb (12). In this study, only tin-activated luminescence is discussed.

Key words: phase equilibria, calcium-barium orthophosphates, phosphors, tin, luminescence.

Experimental

Samples were prepared by reacting mixtures of reagent-grade $CaCO_3$, $BaCO_3$, and $(NH_4)_2HPO_4$ in the solid state at temperatures of 500°, 800°, and 1050°C for times of 4, 15, and 15 hr, respectively. Between heat treatments, the samples were thoroughly remixed under acetone in glass mortars. The materials used for the phase equilibrium studies were free of tin, and were formulated to have the orthophosphate stoichiometry (*i.e.*, [Ca + Ba]/PO_4 = 1.5). Tin-activated luminescent materials were prepared by one of two methods and were intentionally made deficient in cations to facilitate incorporation of the activator. In the first method, mixtures of SnO_2, $CaCO_3$, $BaCO_3$, and $(NH_4)_2HPO_4$ were reacted in the solid state as described above. In order to obtain tin in the divalent state, these materials were then heated for 1 hr at 1050°-1100°C in a flowing atmosphere of 1% hydrogen and 99% nitrogen. In the second method, mixtures of

$Sn_2P_2O_7$ and pre-reacted $(Ca, Ba)_3(PO_4)_2$ were sealed into evacuated, fused silica capsules and heated for 2-4 hr at 1150°-1200°C. Both methods of preparation gave efficient phosphors.

The phase relationships were studied by several methods. Slow reactions were studied by the quenching technique (13) and, when possible, the equilibrium conditions were approached from two directions. Fast reactions were studied by the DTA method with a Du Pont 600 Thermoanalyzer. High-temperature x-ray diffraction measurements were done in a TemPres x-ray diffraction furnace. Phase analyses of the products were carried out on a General Electric XRD-5 diffractometer using nickel filtered copper radiation. For routine phase indentification, the diffractometer was scanned at 1 deg theta/min, but for more precise measurements the diffractometer was scanned at 0.1 deg theta/min, and the peak positions were corrected by reference to an internal aluminum standard. Index of refraction measurements were by the oil immersion method. Temperatures were measured to an accuracy of ±2°C with calibrated platinum/platinum-10% rhodium thermocouples.

Excitation and emission spectra of the phosphors were measured as described by Hoffman (14). These spectra are automatically corrected for instrumental errors and represent true relative energy per wavelength interval. The reflectance of pure α-$Ba_3(PO_4)_2$ was measured, relative to Kodak high-purity $BaSO_4$, with a McPherson Model 225 vacuum spectrometer.

Phase Equilibria

The results of the phase equilibrium study are summarized in Fig. 1. The phase diagram was constructed on the basis of quenching experiments (Table I), differential thermal analysis (Table II), and precise measurements of x-ray "d" spacings as functions of composition and temperature (Table III). The data in Tables II and III are based on multiple observations and serve to refine the approximate phase boundaries derived from the data in Table I.

Contrary to previous reports, no intermediate compounds exist within the system $Ca_3(PO_4)_2$-$Ba_3(PO_4)_2$. However, two extensive series of solid solutions do occur, and their structures correspond to those of the high-temperature polymorphs of calcium and barium orthophosphate. The compound, $CaBa_2(PO_4)_2$, reported by Lagos (2) is a member of the β-$Ba_3(PO_4)_2$ solid solutions. The x-ray pattern of $Ca_2Ba(PO_4)_2$ reported by Bobronicki *et al.* (1) is a poor approximation of the pattern of the limiting α-$Ca_3(PO_4)_2$ solid solution.

Polymorphism of $Ca_3(PO_4)_2$.—The phase transitions in pure calcium orthophosphate have been examined

Table I. Observed phase assemblages in the system $Ca_3(PO_4)_2$-$Ba_3(PO_4)_2$

Composition m/o $Ba_3(PO_4)_2$	Thermal treatment[a] °C/hr		Phases present[b]
0.0	1150/24	P	α-C_3P
	1200/88	P	α-C_3P
	1450/17	Q	α-C_3P
	1498/6	Q	α-C_3P
2.0	880/114	P	β-C_3P
	910/48	P	β-C_3P
	1000/112	P	α-C_3P + β-C_3P
	1150/24	P	α-C_3P
	1200/88	P	α-C_3P
5.0	880/114	P	β-C_3P + α-C_3P
	910/48	P	β-C_3P + α-C_3P
	1000/112	P	α-C_3P
	1150/24	P	α-C_3P
	1200/88	P	α-C_3P
	1450/17	Q	α-C_3P
	1498/6	Q	α-C_3P
10.0	793/89	Q	α-C_3P
	910/48	P	α-C_3P
	1010/72	P	α-C_3P
	1150/24	P	α-C_3P
	1200/88	P	α-C_3P
	1400/2	P	α-C_3P
15.0	793/89	Q	α-C_3P
	910/48	P	α-C_3P
	1010/72	P	α-C_3P
	1150/24	P	α-C_3P
	1200/88	P	α-C_3P
20.0	698/230	Q	α-C_3P
	793/89	Q	α-C_3P
	900/46	P	α-C_3P
	950/68	P	α-C_3P
	1010/72	P	α-C_3P
	1150/24	P	α-C_3P
	1200/88	P	α-C_3P
	1400/2	P	Melted
25.0	840/88	P	α-C_3P
	900/46	P	α-C_3P
	950/68	P	α-C_3P
	1150/24	P	α-C_3P
	1200/88	P	α-C_3P
30.0	840/88	P	α-C_3P
	910/48	P	α-C_3P
	1000/48	P	α-C_3P
	1100/24	P	α-C_3P
	1150/24	P	α-C_3P
	1200/88	P	α-C_3P + tr β-B_3P
	1270/64	P	α-C_3P + β-B_3P
	1400/2	P	Melted
35.0	840/88	P	α-C_3P + α-B_3P
	880/114	P	α-C_3P + α-B_3P
	910/48	P	α-C_3P + β-B_3P
	1000/112	P	α-C_3P + β-B_3P
	1100/66	P	α-C_3P + β-B_3P
	1200/88	P	α-C_3P + β-B_3P
	1270/64	P	α-C_3P + β-B_3P
40.0	840/88	P	α-C_3P + α-B_3P
	880/114	P	α-C_3P + α-B_3P
	910/48	P	α-C_3P + β-B_3P
	1000/112	P	α-C_3P + β-B_3P
	1100/66	P	α-C_3P + β-B_3P
	1200/88	P	α-C_3P + β-B_3P
	1400/2	P	Melted
50.0	1000/116	P	α-C_3P + β-B_3P
	1100/96	P	β-B_3P + tr α-C_3P
	1200/92	P	β-B_3P
	1400/2	P	Melted
55.0[c]	850/48	Q	α-B_3P + α-C_3P
	879/45	Q	α-B_3P + α-C_3P
	900/48	Q	α-B_3P + α-C_3P + β-B_3P
	950/72	Q	β-B_3P + α-C_3P
	1000/89	Q	β-B_3P + α-C_3P
	1200/92	P	β-B_3P
55.0[d]	850/48	Q	α-B_3P + α-C_3P
	879/45	Q	α-B_3P + α-C_3P
	900/48	Q	β-B_3P + α-C_3P
	950/72	Q	β-B_3P + α-C_3P
	1000/89	Q	β-B_3P + α-C_3P
60.0[e]	850/48	Q	α-B_3P + α-C_3P
	879/45	Q	α-B_3P + α-C_3P
	900/48	Q	α-B_3P + β-B_3P + tr α-C_3P
	950/72	Q	β-B_3P
	1000/89	Q	β-B_3P
	1200/92	P	β-B_3P
	1400/1	Q	Melted
60.0[d]	850/48	Q	α-B_3P + α-C_3P
	879/45	Q	α-B_3P + α-C_3P
	900/48	Q	β-B_3P
	950/72	Q	β-B_3P
	1000/89	Q	β-B_3P
65.0	1000/116	P	β-B_3P + α-B_3P
	1200/92	P	β-B_3P
70.0	1000/116	P	β-B_3P + α-B_3P
	1100/96	P	β-B_3P
	1200/92	P	β-B_3P
80.0	1000/48	P	α-B_3P + β-B_3P
	1100/96	P	β-B_3P + α-B_3P
	1200/92	P	β-B_3P
90.0	1000/48	P	α-B_3P + β-B_3P
	1100/48	P	α-B_3P + β-B_3P
	1200/92	P	α-B_3P + β-B_3P
	1300/18	Q	α-B_3P + β-B_3P
	1324/18	Q	α-B_3P + β-B_3P
	1353/19	Q	β-B_3P
	1395/17	Q	β-B_3P
95.0	1000/64	P	α-B_3P
	1200/64	P	α-B_3P + β-B_3P
	1300/18	Q	β-B_3P + α-B_3P
	1353/19	Q	β-B_3P
97.5	1000/64	P	α-B_3P
	1200/64	P	α-B_3P
100.0	1150/15	P	α-B_3P
	1200/68	P	α-B_3P

[a] P = pelletized sample, Q = quench sample.
[b] C = CaO, B = BaO, P = P_2O_5; thus, C_3P = $Ca_3(PO_4)_2$, *etc.*
[c] Initial phases were β-B_3P + α-C_3P + α-B_3P.
[d] Initial phase was β-B_3P solid solution.
[e] Initial phases were α-B_3P + α-C_3P.

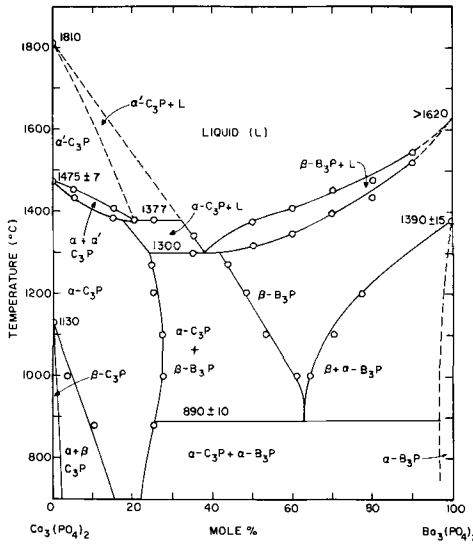

Fig. 1. The system $Ca_3(PO_4)_2$-$Ba_3(PO_4)_2$. B_3P = $Ba_3(PO_4)_2$ and C_3P = $Ca_3(PO_4)_2$.

on numerous occasions, but some disagreement over the inversion temperatures is evident in the literature. For example, the correct temperature of the $\beta \rightleftarrows \alpha$ inversion is 1130°C (15, 16), but one still finds the temperature quoted as 1180°C in the literature on luminescence. The $\alpha \rightleftarrows \alpha'$ inversion temperature was originally reported as 1430°C by Nurse *et al.* (17), but a subsequent determination by Tromel and Fix (18) gave a value of 1470°C. The temperature of the $\alpha \rightleftarrows \alpha'$ inversion was redetermined by DTA (Table II) and found to be 1475° ± 7°C which is in excellent agreement with the value of Tromel and Fix. The inversion was rapid reversible and showed neither supercooling nor superheating effects when traversed at 50°C/min. The melting point of $Ca_3(PO_4)_2$ was not determined in this study and the value used in Fig. 1 was taken from Tromel and Fix (18). The incongruent melting behavior of $Ca_3(PO_4)_2$, reported by Welch and Gutt (15), has been discussed elsewhere (19) and concluded to be an incorrect result. The low-temperature phase transitions suggested by Koelmans *et al.* (20) were not studied.

Table II. DTA study of melting and polymorphism in the $Ca_3(PO_4)_2$-$Ba_3(PO_4)_2$ system

Composition m/o $Ba_3(PO_4)_2$	Inversion temperatures (°C)	Melting temperatures (°C)
0	1475 ± 7	—
5	1434—1456*	—
15	1383—1406	—
20	1377—1395	—
25	1377—1386	—
35	—	1299—1340*
50	—	1318—1376
60	—	1345—1408
70	—	1397—1450
80	—	1431—1474
90	—	1521—1543
100	1390 ± 15	>1620

* The first temperature is the onset of the heat effect and the second is the peak of the heat effect. Temperatures were determined on the second and third melt/cool cycles to eliminate the effects of sintering. Heating (cooling) rates of 50°C/min and 15°C/min were used. The standard was α-Al_2O_3.

Table III. X-ray study of solid solubility in the system $Ca_3(PO_4)_2$-$Ba_3(PO_4)_2$

Equilibration conditions (°C/hr)	Solid solution limits—m/o $Ba_3(PO_4)_2$ Lower limit	Upper limit
	α-$Ca_3(PO_4)_2$ solid solutions*	
880/114	8.8 ± 1	26.0 ± 2
1000/112	3.5 ± 1	27.3 ± 2
1100/66	—	27.0 ± 2
1200/88	—	26.0 ± 2
1270/64	—	26.0 ± 2
	β-$Ba_3(PO_4)_2$ solid solutions**	
1000/116	61.0 ± 1	64.3 ± 1
1100/96	53.3 ± 2	70.0 ± 2
1200/92	48.0 ± 1	77.0 ± 1
1270/64	44.0 ± 1	—

* Average of values measured for five diffraction lines.
** Average of values measured for nine diffraction lines. All values fell within the indicated limits.

$Ca_3(PO_4)_2$ solid solutions.—The α-calcium orthophosphate solid solutions have a maximum barium concentration of 28 m/o (mole per cent) at 1000°C. All members of the solid solution series [including pure α-$Ca_3(PO_4)_2$] may be obtained metastably at room temperature by removing the samples from the furnace and allowing them to cool in air. A sintered sample of α-$Ca_3(PO_4)_2$, containing 5 m/o $Ba_3(PO_4)_2$, was examined under the microscope and found to have biaxial positive optic character. The optic character is in agreement with Mackay's observation of a monoclinic unit cell (21). The low symmetry helps explain the changes observed in the x-ray diffraction patterns as the α-solid solutions are traversed. Aside from the normal displacement of the diffraction peaks due to dilation of the lattice, one observes what are apparently single peaks splitting up into three or more separate peaks. One also observes large relative intensity changes among the peaks. These effects can be attributed to different rates of expansion of the crystal axes and perhaps also to a change in the monoclinic β-angle as the barium concentration increases. It is also possible that the structure becomes triclinic as barium is added. In any case, the diffraction patterns of the limiting solid solution and of pure α-$Ca_3(PO_4)_2$ are so different in appearance that, if only these two patterns were compared, they very likely would be attributed to two different compounds. However, if x-ray patterns are taken at 5 m/o intervals, a gradual change of the pure α-$Ca_3(PO_4)_2$ pattern into that of the limiting solid solution is observed. Microscopic analysis of the samples showed them to contain only one phase whose average refractive index varied with composition as shown in Table IV.

The phase boundaries of the α-solid solutions were determined by observing the points at which the x-ray "d" spacings ceased to vary as a function of composition. The details of the method are outlined by Cullity (22). The samples used for these determinations were in the form of pressed pellets (2 mm high by 10 mm diameter), which were equilibrated for several days at the temperatures indicated in Table III.

The change in the $\alpha \rightleftarrows \alpha'$ inversion temperature as a function of composition (Fig. 1) indicates considerable solid solubility of $Ba_3(PO_4)_2$ in α'-$Ca_3(PO_4)_2$ at high temperatures. The α' solid solutions rapidly revert to the α-form on cooling, and even quenching into water from 1500° is insufficient to preserve them.

The solid solubility of $Ba_3(PO_4)_2$ in β-$Ca_3(PO_4)_2$ was determined by x-ray measurements to be less than 2 m/o at 880°C.

Polymorphism of $Ba_3(PO_4)_2$.—In 1963, the author investigated the thermal behavior of $Ba_3(PO_4)_2$ by DTA and high-temperature x-ray diffraction methods. A

Table IV. Average refractive indexes of α-$(Ca_{1-x}Ba_x)_3(PO_4)_2$ solid solutions

Composition x	Index*
0.00	1.590 ± 0.001
0.05	1.593
0.10	1.595
0.15	1.595
0.20	1.597

* Measured for NaD line at 25°C. These samples were equilibrated at 1200°C/20 hr. Birefringence of the crystals was low, ~0.002.

strong, sharp endotherm was observed at about 1360°C and the high-temperature x-ray study showed the presence of a new phase at 1400°C. These results were unreported except for a brief reference by McCauley and Hummel in 1968 (23). Since 1968, more precise DTA studies have been carried out and the inversion temperature has been revised to 1390° ± 15°C. The heating and cooling rates were found to influence the inversion temperature, indicating that the transition is somewhat sluggish. At 50°C/min, the inversion occurred at 1410° on heating and at 1241°C on cooling. The corresponding temperatures observed at heating and cooling rates of 15°C/min were 1404° and 1380°C. The latter results bracket the inversion temperature to within 25°C.

Although β-$Ba_3(PO_4)_2$ can undergo considerable supercooling, this phase cannot be obtained at room temperature by rapidly quenching it into water. To the author's knowledge, the high-temperature or β form of barium orthophosphate has not been discovered previously. An x-ray pattern of β-$Ba_3(PO_4)_2$ taken at 1450° ± 10°C is given in Table V.

$Ba_3(PO_4)_2$ solid solutions.—The β-$Ba_3(PO_4)_2$ solid solutions are unstable below 890°C (the eutectoid temperature) and decompose to a mixture of α-$Ca_3(PO_4)_2$ ss and α-$Ba_3(PO_4)_2$. However, β-solid solutions having compositions between 50 and 80 m/o $Ba_3(PO_4)_2$ can be obtained metastably at room temperature by removing samples from the furnace and allowing them to cool in air. Solid solutions having compositions between 80 and 95 m/o $Ba_3(PO_4)_2$ can be preserved by water quenching. The phase boundaries of β-$Ba_3(PO_4)_2$ were determined from precise "d" spacing measurements of nine diffraction lines. The samples were in the form of cylindrical pellets and were equilibrated at the temperatures and for the times shown in Table III. The eutectoid composition, determined by extrapolation of the phase boundaries, is 63 m/o $Ba_3(PO_4)_2$ and 37 m/o $Ca_3(PO_4)_2$.

A sample of composition $(Ba_{0.6}Ca_{0.4})_3(PO_4)_2$ was crystallized from the melt and examined microscopically. This member of the β-solid solution series was biaxial negative with a small optic axial angle. The low symmetry precluded indexing of the x-ray powder patterns. Representative powder patterns of the β-solid solutions are given in Table V.

The solid solubility of calcium orthophosphate in α-$Ba_3(PO_4)_2$ was less than 2.5 m/o over the temperature range 880°-1200°C. This value was determined from precise x-ray measurements.

Table V. X-ray diffraction data for β-$Ba_3(PO_4)_2$ and its solid solutions

β-$Ba_3(PO_4)_2$* d Å	I/I_1	β-$Ba_{2.1}Ca_{0.9}(PO_4)_2$** d Å	I/I_1	β-$Ba_{1.5}Ca_{1.5}(PO_4)_2$** d Å	I/I_1
4.33	7	4.20	5	—	—
4.09	11	3.95	12	3.90	10
3.60	31	3.45	69	3.43	16
3.58	58	—	—	3.38	37
3.36	21	3.22	66	3.16	100
2.94	39	2.816	26	2.766	29
2.88	100	2.747	86	2.725	73
—	—	2.481	3	2.458	9
—	—	2.332	13	—	—
—	—	2.292	14	2.276	30
—	—	—	—	2.241	54
—	—	2.241	100	2.211	25
—	—	2.144	19	2.122	20
2.19	22	2.086	33	2.066	22
—	—	1.982	9	—	—
—	—	1.964	11	1.942	35
2.00	10	1.939	8	—	—
1.97	18	1.884	14	1.848	11
—	—	1.791	6	1.778	9
1.86	43	1.773	13	1.747	16
—	—	1.688	9	1.672	16
—	—	1.660	9	1.644	20
—	—	—	—	1.582	15
—	—	1.583	28	1.571	38
—	—	—	—	1.556	9
—	—	1.553	5	—	—

* Pattern taken at 1450° ± 10°C. Scan rate θ = 1 deg/min. CuK_α.
** Patterns taken at room temperature. Scan rate θ = 0.1 deg/min. CuK_α.

Table VI. Tin-activated luminescence of phases in the system $Ca_3(PO_4)_2$-$Ba_3(PO_4)_2$

Composition	Heat treatment* (°C/hr)	Peak λ** (nm)	Relative** intensity
$Ca_{2.94}(PO_4)_2$:$Sn_{0.02}$	1200/2 S	507	52
$Ca_{2.79}Ba_{0.15}(PO_4)_2$:$Sn_{0.02}$	1200/2 S	512	33
$Ca_{2.80}Ba_{0.15}(PO_4)_2$:$Sn_{0.02}$	1050/1 H	524	37
$Ca_{2.65}Ba_{0.30}(PO_4)_2$:$Sn_{0.02}$	1050/1 H	505	39
$Ca_{2.50}Ba_{0.45}(PO_4)_2$:$Sn_{0.02}$	1050/1 H	493	38
$Ca_{2.35}Ba_{0.60}(PO_4)_2$:$Sn_{0.02}$	1050/1 H	484	39
$Ca_{2.05}Ba_{0.90}(PO_4)_2$:$Sn_{0.02}$	1050/1 H	486	18
$Ca_{1.34}Ba_{1.63}(PO_4)_2$:$Sn_{0.02}$	1150/4 S	410	2.4
$Ca_{1.10}Ba_{1.78}(PO_4)_2$:$Sn_{0.02}$	1150/4 S	410	7.8
$Ca_{1.04}Ba_{1.93}(PO_4)_2$:$Sn_{0.02}$	1150/4 S	420	7.1
$Ca_{0.89}Ba_{2.08}(PO_4)_2$:$Sn_{0.02}$	1150/4 S	490	9.0
$Ca_{0.10}Ba_{2.85}(PO_4)_2$:$Sn_{0.02}$	1050/1 H	422	4.6
$Ba_{2.97}(PO_4)_2$:$Sn_{0.02}$	1050/1 H	426	3.8

* S = sample prepared in evacuated silica capsule, H = sample prepared by firing in 1% H_2 and 99% N_2 atmosphere.
** Only the visible emissions are listed. Intensity is relative to sodium salicylate peak heights of 100.

Melting Behavior

The melting behavior within the system was studied by the technique of differential thermal analysis. The DTA curves obtained for samples having 0-25 m/o $Ba_3(PO_4)_2$ had no distinguishable melting peaks, and those obtained for samples having 25-50 m/o $Ba_3(PO_4)_2$ were complex and difficult to interpret. Well-defined DTA peaks attributable to melting were observed for compositions having 50-90 m/o $Ba_3(PO_4)_2$ (Table II). The departure points of the DTA curves from the base line were taken as the solidus temperatures and the peaks of the DTA curves were taken as the liquidus temperatures. Considerable supercooling of the melts in this system was observed and instantaneous crystallization often occurred near or somewhat below the solidus temperatures. For this reason, only the heating curves were used in constructing the phase diagram. Although the liquidus and solidus curves in Fig. 1 were not located with high precision, their configuration is probably correct as shown.

Luminescence

The phosphors listed in Table VI were prepared and their properties measured. The phases present in the phosphors were as expected on the basis of the phase diagram, and the small amount of tin present caused no appreciable changes in the phase relationships. Of the phosphors studied, only those based on the α-$Ca_3(PO_4)_2$ structure were efficient enough for practical use. The composition of the α-$Ca_3(PO_4)_2$:Sn phosphors was optimized, and fluorescent lamp tests were made on two such phosphors. The intensity scales on all emission spectra are expressed as percentages of the peak intensity of sodium salicylate,[1] and the intensity scales on all excitation spectra are normalized to 100.

α-$Ba_3(PO_4)_2$ phosphors.—The excitation and emission spectra of α-$Ba_3(PO_4)_2$:Sn are given in Fig. 2. The emission spectrum consists of a single, nearly Gaussian band[2] centered at 426 nm. The excitation spectrum consists of two well-resolved bands at 230 and 245 nm and a broad feature extending from 215 nm to shorter wavelengths. The absorption edge of unactivated α-$Ba_3(PO_4)_2$ occurs at about 165 nm (Fig. 3) so that all features in the excitation spectrum are due to transitions involving tin.

Barium orthophosphate has two inequivalent barium positions in its structure (24) and, assuming that tin replaces barium, one might expect two emission bands. The simplicity of the excitation and emission

[1] Merck U.S.P.
[2] When plotted as a function of energy, the spectrum is Gaussian within ±2 σ of the mean, but small positive deviations from a Gaussian shape are apparent outside these limits—especially on the low-energy side of the band. According to Dexter (25), the low-energy side of an emission band is not necessarily Gaussian in shape.

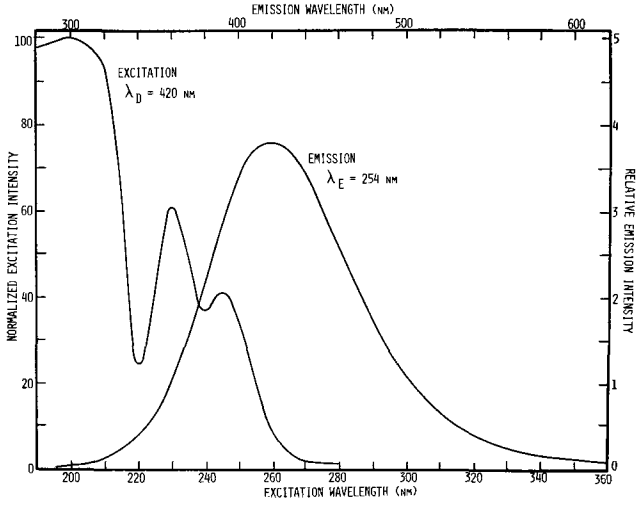

Fig. 2. Emission and excitation spectra of α-$Ba_3(PO_4)_2$:Sn. λ_D = detection wavelength, λ_E = excitation wavelength.

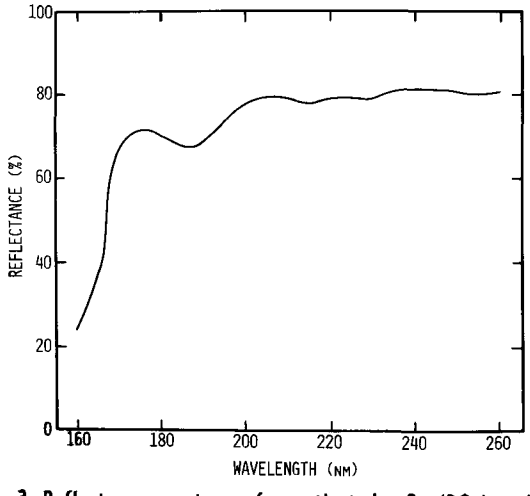

Fig. 3. Reflectance spectrum of unactivated α-$Ba_3(PO_4)_2$ relative to $BaSO_4$.

spectra indicates, however, that only one kind of luminescence center is present. The exact nature of this center cannot be determined from the data available at present. Although transitions can occur to several excited states of the stannous ion, emission apparently occurs only from the lowest excited state. A schematic configuration coordinate diagram which accounts for the observed spectra is given in Fig. 4.

β-$Ba_3(PO_4)_2$ phosphors.—The emission spectra of several β-phosphors, excited by 254 nm radiation, are shown in Fig. 5. These phosphors are inefficient and not of interest as practical materials. The emission spectra are complex and consist of bands at 300, 410,

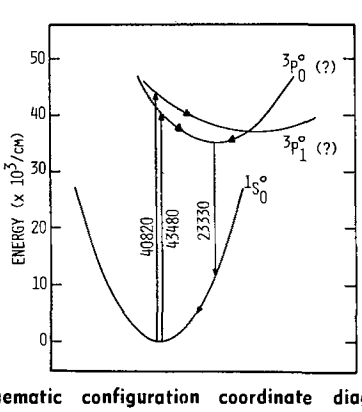

Fig. 4. Schematic configuration coordinate diagram for α-$Ba_3(PO_4)_2$:Sn.

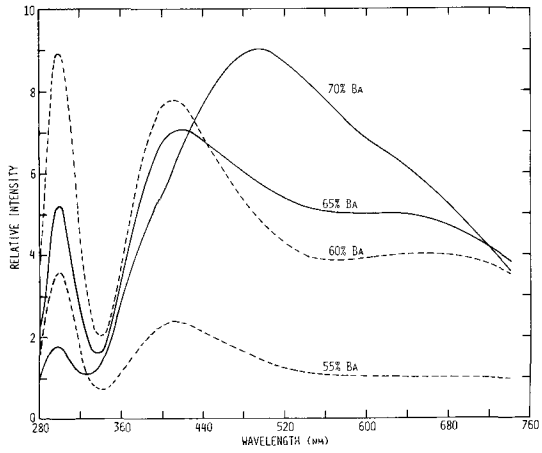

Fig. 5. Emission spectra of β-(Ba, Ca)$_3(PO_4)_2$:Sn phosphors as a function of composition. Barium concentrations are in mole percentages. Excitation = 254 nm radiation.

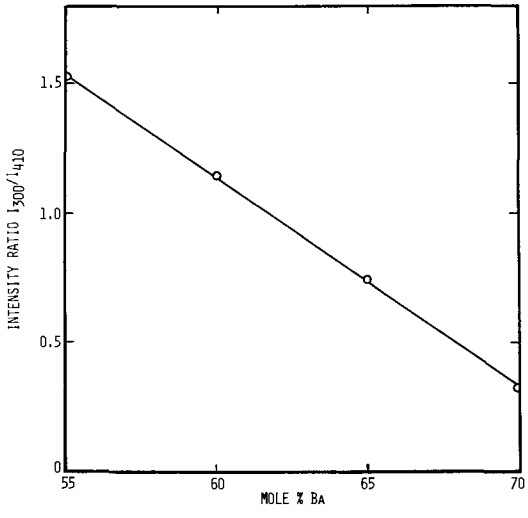

Fig. 6. Change in relative intensity of the 300 and 410 nm emission bands in β-(Ba, Ca)$_3(PO_4)_2$:Sn as a function of composition.

490, and 660 nm. The relative intensities of the bands change as a function of composition as shown in Fig. 6. This fact is taken as an indication that at least two, and possibly more, kinds of lattice positions are occupied by luminescent tin ions. The relative intensity changes can then be interpreted as due to a redistribution of tin ions over the various positions as the barium concentration is increased.

The excitation spectrum of the 490 nm emission band is shown for the most efficient β-phosphor in Fig. 7. The excitation spectrum contains at least five bands located at 205, 230, 243, 287, and 340 nm. All of these bands could be due to crystal field splitting of the J levels of the ^3P and ^1P states of the stannous ion (a maximum of 12 levels is possible). However, the emission bands at 410 and 660 nm overlap the 490 band and it is likely that the excitation spectrum has features due to these other bands.

α-$Ca_3(PO_4)_2$ phosphors.—The emission spectra of two α-$Ca_3(PO_4)_2$:Sn phosphors are shown in Fig. 8. In agreement with Butler (3), two emission bands located at 340 and 500 nm were observed. Both bands are shifted to shorter wavelengths and broadened upon incorporation of barium into the phosphor. The intensity[3] of the 340 nm band relative to that of the 500 nm band is independent of the barium concentration and has a value of 0.23. The excitation spectra of the 340 and 500 nm bands (Fig. 9) are considerably different. This might indicate that two kinds of tin centers, having

[3] Based on the areas under the bands. The areas were obtained by application of Simpson's rule.

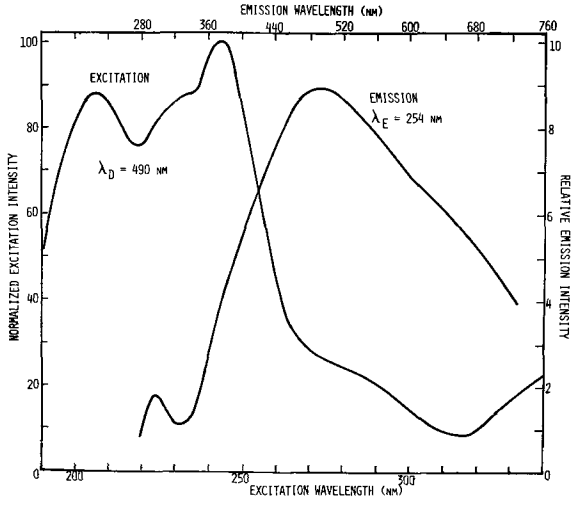

Fig. 7. Excitation and emission spectra of β-$Ba_{2.10}Ca_{0.90}(PO_4)_2$:$Sn_{0.02}$. λ_D = detection wavelength, λ_E = excitation wavelength.

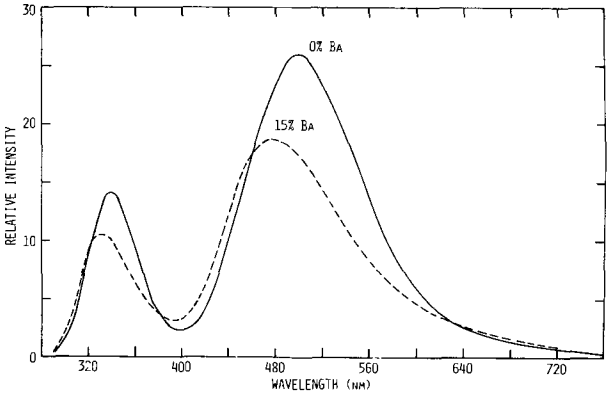

Fig. 8. Emission spectra of α-$Ca_3(PO_4)_2$:Sn phosphors as a function of composition. Barium concentrations are in mole percentages. Excitation = 254 nm radiation.

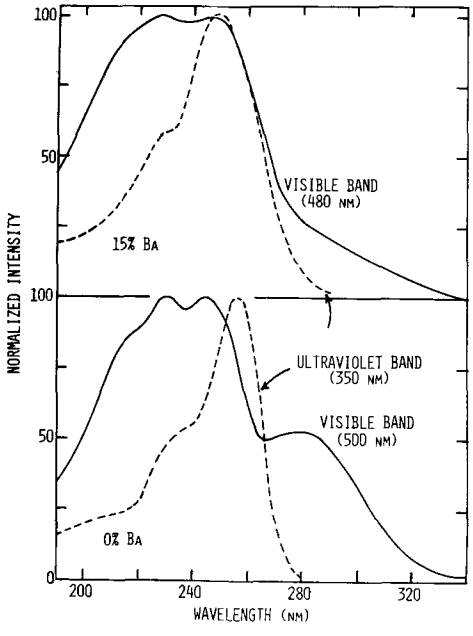

Fig. 9. Excitation spectra of the visible and ultraviolet emission bands in α-$Ca_3(PO_4)_2$:Sn.

different electronic energy structures, are present in the phosphor. However, this interpretation is at variance with the expectation that, if two centers were present, their relative emission intensities might vary as a function of composition. The question of the origin of the two emission bands in α-$Ca_3(PO_4)_2$ cannot be answered with certainty and, until such an answer is available, it is useless to attempt any interpretation of the spectra.

Optimization of α-$Ca_3(PO_4)_2$.—Suitable α-$Ca_3(PO_4)_2$:Sn phosphors can be prepared either by the sealed tube method or by the reduction firing method (see Experimental section). However, at barium concentrations lower than 5 m/o, the preparation of efficient phosphors by the reduction firing method becomes difficult due to high volatility losses of tin at the high temperatures necessary to obtain the α-$Ca_3(PO_4)_2$ structure. The phosphors low in barium were best prepared by the sealed tube method, a procedure not amenable to the production of large quantities of phosphor. The phosphors tended to have a gray body color which became darker as the limiting barium concentration was approached. Considering ease of preparation, phosphor efficiency, and phosphor appearance, the optimum barium concentration is near 15 m/o.

The efficiency of the phosphor as a function of formulated tin concentration was determined (Fig. 10). The optimum tin concentration is near 0.33 m/o, but somewhat higher values lead to only a slight loss in phosphor efficiency.

An important feature of any phosphor intended for practical application is how well it maintains its brightness as a function of operating temperature. The temperature dependence of two phosphors (Fig. 11) was measured by packing them into heated plaques and taking emission spectra at specific temperatures. The phosphor brightness is not affected by temperature up to about 150°C but thereafter brightness decreases slowly with increasing temperature. At 300°C, the phosphors are about 80% as bright as at room temperature. These results are in good agreement with those of Wanmaker and Radielovic (4). Insofar as temperature dependence is concerned, the α-$Ca_3(PO_4)_2$:Sn phosphors are well suited for application in fluorescent lamps (operating temperature ~40°C) and somewhat less well suited for use in high-pressure mercury vapor lamps (operating temperature ~300°C).

Two samples of phosphor, based on $Ca_{2.50}Ba_{0.45}(PO_4)_2$:$Sn_{0.02}$ as the optimum composition, were prepared in kilogram quantities and evaluated in 40W fluorescent lamps. These lamps are compared to a lamp made with blue halophosphate phosphor in Table VII. Although the α-calcium orthophosphate phosphors had initial powder brightnesses equal to that of blue halophosphate, when processed into lamps, they were considerably less efficient. The loss in efficiency is probably due to partial reoxidation of tin during lampmaking. In

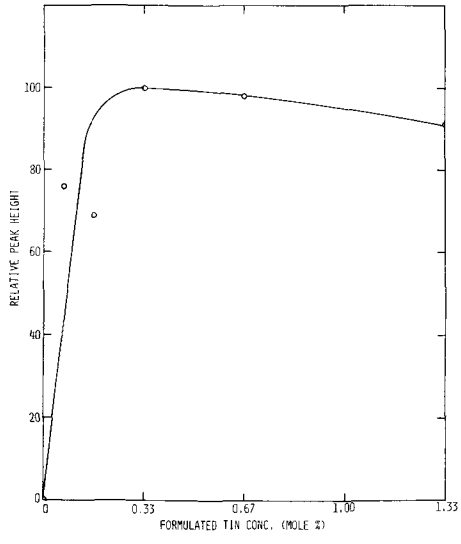

Fig. 10. Visible luminescence as a function of tin concentration in α-$Ca_{2.52-x}Ba_{0.45}Sn_x(PO_4)_2$. Mole per cent tin = 100x/3. Excitation wavelength = 254 nm.

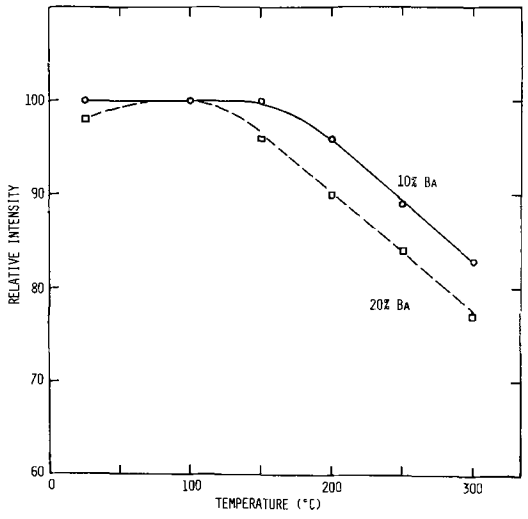

Fig. 11. Temperature dependence of visible luminescence in α-$(Ca, Ba)_3(PO_4)_2$:Sn phosphors. Barium concentrations are in mole percentages. Excitation wavelength = 254 nm.

terms of 500 hr maintenance, the α-calcium orthophosphate phosphors were as good as blue halophosphate. The color of the lamps remained stable over the duration of the tests.

Acknowledgments

The writer wishes to thank his colleagues who contributed to this work. Samples were prepared by Barbara Press and Larry Haydu. X-ray diffraction data were collected by Miss Jeannette Cooper and her staff. The measurements of optical spectra were made by Ralph Hewes, Tom Davis, and staff. Lamp tests were run by Tom Vincent.

Manuscript submitted Oct. 29, 1970; revised manuscript received Jan. 20, 1971. This was Paper 63 presented at the Los Angeles Meeting of the Society, May 10-15, 1971.

Any discussion of this paper will appear in a Discussion Section to be published in the December 1971 JOURNAL.

Table VII. Lamp tests of $Ca_{2.50}Ba_{0.45}(PO_4)_2:Sn_{0.02}$

No.*	Lumens per watt 0 hr	100 hr	500 hr	Lumen maintenance 100/0	500/100	Powder brightness
BT	56.4	55.6	53.5	97.9	95.6	100.0
E	45.9	43.3	41.9	93.9	94.9	99.7
F	46.4	44.3	42.4	94.7	95.1	100.5

No.	Color coordinates (x/y) 0 hr	100 hr
BT	—	—
E	0.238/0.321	0.249/0.329
F	0.237/0.318	0.249/0.327

* BT = standard blue halophosphate, E and F = two lots of experimental phosphor, all in F 40 T 12 lamps.

REFERENCES

1. W. Bobrownicki, K. Slawski, and J. Malik, *Roczniki Chem.*, **34**, 1833 (1960).
2. C. C. Lagos, Electrochem. Soc. Extended Abstracts, Spring Meeting, New York, May 4-9, 1969, Abs. No. 58, pp. 146-147.
3. K. H. Butler, *This Journal*, **100**, 250 (1953).
4. W. L. Wanmaker and D. Radielovic, *Electrochem. Technol.*, **2**, 16 (1964).
5. E. Lendvay, *Phys. Status Solidii*, **2**, 460 (1962).
6. H. C. Froelich, *Trans. Electrochem. Soc.*, **91**, 241 (1947).
7. R. H. Clapp and R. J. Ginther, *J. Opt. Soc. Am.*, **37**, 355 (1947).
8. Y. Uehara, Y. Kobuke, and I. Masuda, *This Journal*, **106**, 200 (1959).
9. W. L. Wanmaker and C. Bakker, *ibid.*, **106**, 1027 (1959).
10. W. L. Wanmaker, J. G. C. M. de Bres, and J. W. ter Vrugt, *Proc. Int. Conf. Lumin.*, **1966**, 2, 1370 (Pub. 1968).
11. W. L. Wanmaker, and J. W. ter Vrugt, *Philips Res. Rept.*, **23**, 362 (1968).
12. A. Bril, W. L. Wanmaker, and J. W. ter Vrugt, *This Journal*, **115**, 776 (1968).
13. G. A. Rankin and Fred E. Wright, *Am. J. Sci.*, **39**, 1 (1915)
14. M. V. Hoffman, *This Journal*, **117**, 227 (1970).
15. J. H. Welch and W. Gutt, *J. Chem. Soc.*, **1961**, 4442.
16. J. F. Sarver, F. A. Hummel, and M. V. Hoffman, *This Journal*, **108**, 1103 (1961).
17. R. W. Nurse, J. H. Welch, and W. Gutt, *Nature*, **182**, 1230 (1958).
18. G. Tromel and W. Fix, *Arch. Eisenhuettenw.*, **32**, 209 (1961).
19. E. R. Kreidler and F. A. Hummel, *Inorg. Chem.*, **6**, 884 (1967).
20. H. Koelmans, J. J. Engelsman, and P. S. Admiraal, *Phys. Chem. Solids*, **11**, 172 (1959).
21. A. L. Mackay, *Acta Cryst.*, **6**, 743 (1953).
22. B. D. Cullity, "Elements of X-Ray Diffraction," Addison-Wesley Publishing Co., Inc., Reading, Mass. (1956).
23. R. A. McCauley and F. A. Hummel, *Trans. Brit. Ceram. Soc.*, **67**, 619 (1968).
24. W. H. Zachariasen, *Acta Cryst.*, **1**, 263 (1948).
25. D. L. Dexter, "Solid State Physics," Vol. 6, p. 390, Academic Press (1958).

Optical and Electrical Properties of $SrAl_2O_4:Eu^{2+}$

Victor Abbruscato[1]

Bayside Research Center of General Telephone & Electronics Laboratories, Incorporated, Bayside, New York 11360

ABSTRACT

It has been shown that the optical and electrical properties of $Sr_{0.95\pm x}Eu_{0.05}Al_2O_{4\pm x}$ depend on composition. A composition with excess alumina was found to have the highest CR efficiency, photoconductivity, and a long-lasting persistence. A mechanism is proposed which assigns the delayed luminescence to a process involving the conduction of charged particles. Evidence is presented which indicates that holes are trapped at lattice defects and the Eu^{2+} emission is associated with thermal deactivation of these traps.

Since the introduction of $YVO_4:Eu^{3+}$ as an important commercial phosphor, there has been an increasing interest in the mechanism of transfer of energy absorbed by a host to a rare earth activator. In the ZnS and SrS systems, it has been shown that the energy transport can take place *via* electron and hole transfer (1, 2). This mechanism can also occur in fluoride hosts. For example, Banks and Schwartz (3) have shown that in the $CdF_2:Eu^{3+}$ system the Eu^{3+} acts as an electron trap, forming Eu^{2+}. On thermal deactivation of the Eu^{2+} to Eu^{3+}, the Eu^{3+} is reformed in an excited state and, as a result, the characteristic luminescence of Eu^{3+} is observed. The mechanism for thermoluminescence in the $CaF_2:Ce^{3+}$ system has also been shown to be of a charge-transfer type, involving the reduction and reoxidation of Ce^{3+} under x-ray irradiation (4). In the case of rare earth ions in oxide systems, the mechanism of transfer has been presumed to be predominantly of the multipolar type (5).

The phosphors MAl_2O_4 (M = Ba, Sr, Ca, Mg) activated by Eu^{2+} have been reported by Palilla *et al.* (6) and also by Blasse and Bril (7). The phosphor $SrAl_2O_4:Eu^{2+}$, prepared by firing Al_2O_3, $SrCO_3$, and Eu_2O_3 in H_2 at between 1400°-1700°C, has a green emission peaking at 520 nm. This phosphor has a fast decay of 10 μsec to 10% of initial brightness. The luminescent properties depend to a large extent on the conditions and stoichiometry under which the phosphor is prepared. For example, Blasse and Bril (7) prepare the phosphor by firing at 1450°C in a N_2-H_2 atmosphere and report a CR efficiency of 1.5%. Palilla *et al.* (6) fire a composition containing excess alumina at 1700°C in a H_2 atmosphere and estimate a CR efficiency of approximately 7% (8). In addition to an initial rapid decay, a high-level persistence which lasts for seconds is also observed in their samples. Since the decay of the transitions within the Eu^{2+} ion is found to be in the 10-100 μsec range (9), it was decided to investigate the electrical and optical properties of this material to determine if the long persistence is due to a trapping mechanism involving electrons or holes, and to determine to what extent this phenomenon is involved in the over-all luminescence process.

Experimental

The compositions of the samples prepared were $Sr_{0.85}Eu_{0.05}Al_2O_{3.9}$ (excess alumina), $Sr_{0.95}Eu_{0.05}Al_2O_4$ (one to one), and $Sr_1Eu_{0.05}Al_2O_{4.05}$ (excess strontium oxide). The phosphors were formed by firing the appropriate mixtures of SrC_2O_4, Al_2O_3, and Eu_2O_3 in H_2 at 1700°C for 3 hr. The products were checked using x-ray diffraction analysis and had the $SrAl_2O_4$ structure, which is distorted stuffed tridymite.

The luminescent emission spectra were recorded with a ¾m Jarrell-Ash scanning spectrometer and corrected for instrumental response.

The reflectance spectra were determined with the use of a Cary 14 spectrometer equipped with a diffuse fluorescence attachment.

The photoconductive excitation spectra were recorded with the use of a sandwich conductive cell. The front side of the sandwich was a quartz slide which had a thin conducting layer of tin oxide on the inside surface, and the back side of the cell was a thin copper plate. The cell was placed in the sample compartment of a Cary 14 spectrometer, which was used as a pulsed excitation source. The photocurrent produced a potential across a precision resistor and this voltage was measured using a PAR Model 121 lock-in amplifier tuned to the frequency of the source.

The relative conductivity measurements under long uv radiation were recorded using a gap cell, which consisted of a gold strip evaporated on a quartz slide. The gap across the strip was 20μ. In order to avoid undesirable effects resulting from differences in particle size, the distribution of particle size was established by sieving the samples. Magnified photographs showed the particles of the three samples to be of uniform size. Each sample was redeposited five times and the average value taken as the photoconductive response. The d-c voltage applied across the gap was 400V.

The Hall measurement was determined using a sintered sample of $SrAl_2O_4:Eu^{2+}$ which had an excess of alumina.

For the glow curve measurements, the phosphor was deposited on a copper plate which was then fitted into the slot of a metal block Dewar. Liquid nitrogen was introduced into the Dewar, the sample was irradiated (366) for 1 hr, and then allowed to warm up. The rise of the temperature between −125° to −75°C was linear at a rate of 0.08 deg/sec. The temperature was measured with a copper-constantan thermocouple which was in contact with the copper plate.

The long luminescence persistence and photoconductive decay times were measured simply by switching off the exciting sources while monitoring the signal from the amplifier with a H.P. 7100B strip chart recorder.

Results

The optical and electrical measurements have shown that the $SrAl_2O_4:Eu^{2+}$ high alumina sample, as compared to the other samples, has a higher luminescent intensity under uv and CR excitation, and, also, that this sample has a much higher persistence level and photoconductive response. This is shown by data in Table I.

The excitation spectra and diffuse reflectance spectra of the excess alumina, one to one, and excess SrO samples are shown in Fig. 1. The latter two correspond to the spectra previously published (5, 7), while the excess alumina sample shows a greater relative excitation response in the visible region. Figure 2 shows the glow curve spectra for the three samples, using 366 nm excitation. The photoconductive excitation spectrum of the high-alumina sample in the visible region is

[1] Present address: Alloys Unlimited, 320 Long Island Expressway, Melville, Long Island, New York 11746.

Key words: fluorescence, phosphorescence, photoconductivity, rare earth luminescence.

Table I

	Excess alumina $Sr_{0.85}Eu_{0.05}Al_2O_{3.9}$	One to one $Sr_{0.95}Eu_{0.05}Al_2O_4$	Excess strontium oxide $Sr_1Eu_{0.05}Al_2O_{4.05}$
% Persistence after 1.0 sec	0.70	0.085	0.080
Relative brightness, 366 nm excitation	100	55	61
Relative brightness, CR excitation	100	84	76
Relative photoconductive response, 366 nm excitation	100	13.1	17.3

shown in Fig. 3 and is compared to the reflectance curve for this sample. It was also observed that the samples were photoconductive under long and short uv and x-ray excitation. The Hall effect measurements showed qualitatively that holes were the conducting species under uv excitation. The decay times of the persistence and photoconductivity are similar (Fig. 4), which would indicate that the same charged species, in this case holes, is responsible for both phenomena.

Attempts were made to oxidize the Eu^{2+} activator to Eu^{3+} in portions of these samples by firing in wet oxygen at 800°C for 20 hr. These attempts met with complete success only in the high-alumina sample, while the other samples still exhibited a broad-band emission centered at 520 nm, due to Eu^{2+} (Fig. 5). It was also noted that, in the case of the high-alumina sample, the x-ray pattern showed a distinct change. The pattern changed from the distorted stuffed tridymite to very nearly "ideal stuffed tridymite," a more symmetrical structure. Therefore the Eu^{3+} emission lines in the high-alumina sample [Fig. 5(a)] are sharp and well defined, while in the one-to-one sample [Fig. 5(b)] the Eu^{3+} emission lines are broader and less defined.

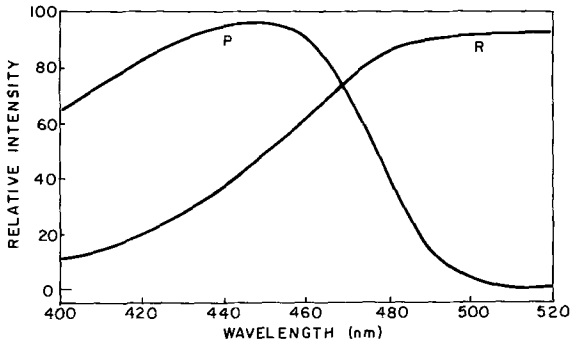

Fig. 3. The photoconductive excitation spectrum (P) and the diffuse reflectance spectrum (R) of the high-alumina sample in the visible region.

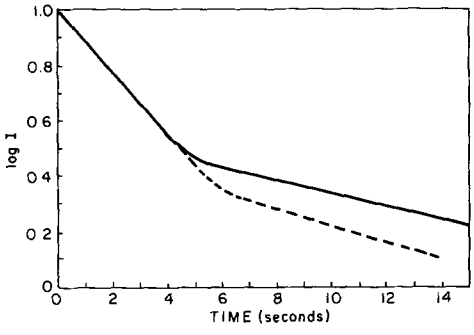

Fig. 4. The decay times of the persistence (solid line) and photoconductivity (dotted line) under 366 excitation.

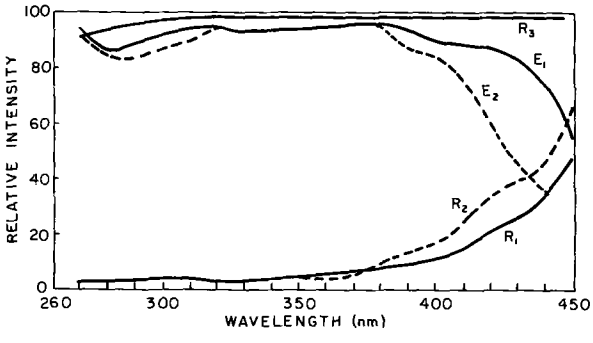

Fig. 1. Excitation spectra and diffuse reflectance spectra of $SrAl_2O_4:Eu^{2+}$ phosphors of various compositions. E_1 and E_2 represent the excitation spectra for the excess alumina and one-to-one sample, respectively. R_1, R_2 represent the diffuse reflectance spectra of the excess alumina and one-to-one phosphors, respectively. R_3 shows the diffuse reflectance spectrum of unactivated $SrAl_2O_4$ and unactivated $SrAl_2O_4$ with excess alumina, which are similar. Curve for the excess strontium oxide sample are the same as the one-to-one phosphor.

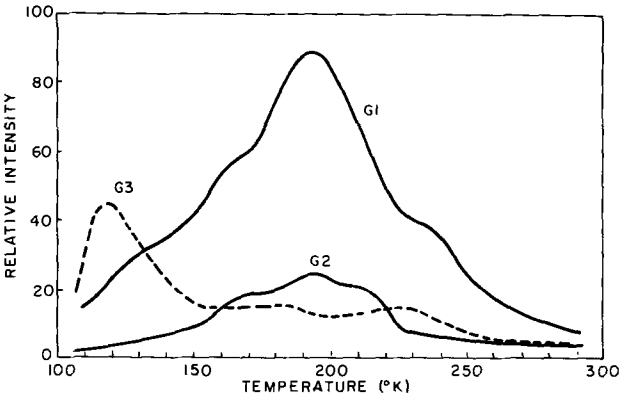

Fig. 2. The glow curves for the three samples, G1, G2, and G3 represent the glow curves for the excess alumina, one-to-one, and excess strontium oxide phosphors, respectively.

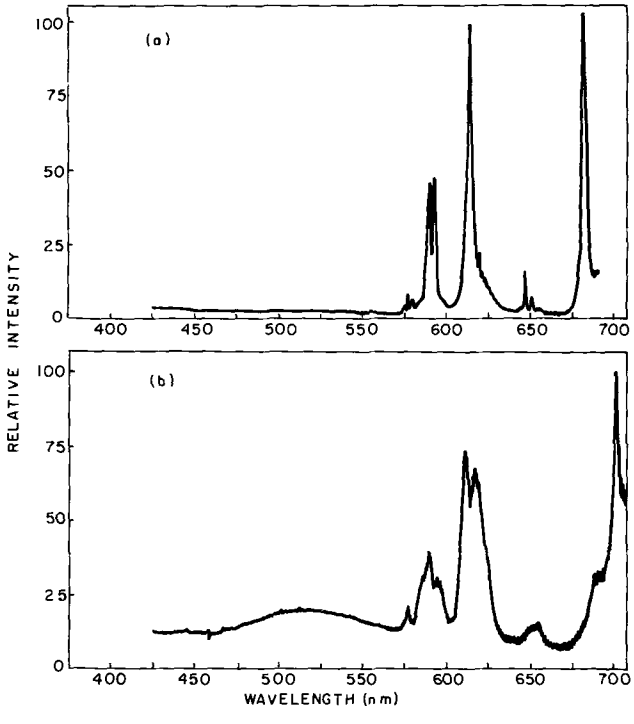

Fig. 5. The emission spectra of the reoxidized sample: (a) the excess alumina sample, exhibiting only sharp-line Eu^{3+} emission; (b) the one-to-one sample, exhibiting Eu^{2+} broad-band (520 nm) emission and Eu^{3+} emission.

Discussion

The model that is proposed to explain these results and the differences between the excess alumina sample and the other samples follows. The excess alumina incorporated into the $SrAl_2O_4$ host introduces a defect in the lattice. This defect has the property of being a hole donor, as was shown by the Hall measurement. The exact nature of this defect is not known, but it is associated with the incorporation of Eu^{2+} into the lattice, since the photoconductive absorption bands are not introduced into the $SrAl_2O_4$ host unless it is activated with Eu^{2+} (Fig. 1 and 3). The hole can migrate until it recombines or is trapped. The recombination of the charged species can cause luminescence of the Eu^{2+} ion, as shown by the fact that the photoconductivity and the Eu^{2+} luminescent persistence decay at the same rate (Fig. 4).

The glow curves show that hole trapping levels are present and are composition dependent with the high-alumina sample showing the highest concentration of traps (Fig. 2). High-alumina samples can either incorporate the alumina interstitially as Al^{3+} plus O^{2-}, or Sr^{2+} vacancies can be produced. These Sr^{2+} vacancies can be compensated by oxide vacancies or partially filled by Al^{3+} (*i.e.*, $2Al^{3+}$ for $3Sr^{2+}$). We feel that the hole traps described above are probably associated with Sr^{2+} vacancies. The ease of oxidation of Eu^{2+} in the high-alumina sample (Fig. 5) is evidence for the production of Sr^{2+} vacancies rather than the incorporation of alumina interstitially. Interstitial Al^{3+} and O^{2-} will not promote oxidation of Eu^{2+}. On the other hand, either of the Sr^{2+} vacancies described above will promote oxidation of Eu^{2+} because of the presence of O^{2-} vacancies or Al^{3+} occupying Sr^{2+} sites.

The possibility of the Eu^{2+} also acting as a hole trap was considered. This would be analogous to Eu^{3+} acting as an electron trap in the CdF_2 system (3). The high-alumina sample at liquid nitrogen temperature was irradiated for 1 hr with uv light. The emission spectrum was then recorded as the sample was irradiated at 325 nm and showed no traces of the main Eu^{3+} emission lines between 600 and 625 nm. Since Eu^{3+} would exhibit a detectable emission spectrum in $SrAl_2O_4$ (Fig. 5), it was concluded that the Eu^{2+} is most likely not acting as a trapping center.

It is therefore proposed that the charge transfer mechanism of excitation in the high-alumina sample involves the generation of a hole in the valence band. These holes can either recombine or be trapped in a lattice defect, probably a Sr^{2+} vacancy. The Eu^{2+} persistence is associated with the thermal deactivation of these traps and subsequent recombination. This mechanism of energy transfer can be an important factor in the emission intensity under CR and uv excitation. If it is assumed that the slowly decaying emission (persistence) results from a trapping phenomenon and that the initial rapidly decaying emission results from Eu^{2+} ions in an excited state, then the relative contribution of the trapping mechanism to the total emission can be obtained by an analysis of the decay curve. By comparing the areas under the curves of persistence and the total luminescence, it is estimated that in the high-alumina sample approximately 99% of the total luminescent intensity is due to activation by conducting holes.

A mechanism involving the conduction of charged species may also be operative in other rare-earth activated phosphors. For example, Pfahnl (10) has shown that, with P16 ($Ca_2MgSi_2O_7$:Ce^{3+}) ($CaAl_2Si_2O_8Ce^{3+}$) fast decay phosphors, aging under CR excitation causes the intensity and decay times to decrease. It was also shown that the decay is nonexponential in the low light level region. It is quite possible that the persistence of these phosphors is due to a trapping phenomenon. When the phosphor is aged, the probability of transfer of energy from the host to the Ce^{3+} *via* a charged species is decreased, causing a decrease in luminescence, and also a decrease of the persistence level. In another investigation, it was pointed out by Gomes de Mesquita and Bril (11) that, with certain Ce^{3+}-activated phosphors, the initial rapid decay of the Ce^{3+} luminescence is followed by an afterglow of relatively long duration. A quantity δ was defined as the percentage of cathodoluminescence 80 μsec after the end of the exciting pulse. It was found that δ could be as high as 5-10% for various gehlenite samples. When the samples were cooled down from room to liquid nitrogen temperature, δ-values increased for some samples and decreased for others. This behavior could not be explained by the authors. However, if one assumes that a trapping mechanism is responsible for the delayed luminescence, these results are easily explained. At low temperature, $kT << E_T$, (E_T = thermal energy of trap), δ will have a low value since a trap that is filled will not thermally deactivate and therefore will not contribute to an afterglow. At high temperatures, $E_T << T$, δ will again have a low value since a filled trap will rapidly deactivate, leading to a very rapid decay. Therefore, δ as a function of temperature should follow one of the hypothetical curves shown in Fig. 6; δ will decrease or increase on cooling below room temperature, depending on the depth of the trap in relation to room temperature. It is quite possible within the same host, depending on preparative and composition conditions, to have a different distribution and concentration of trapping levels.

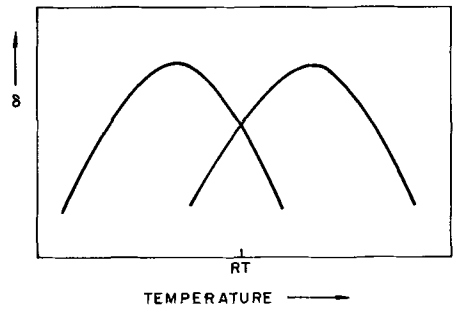

Fig. 6. Delta as a function of T

Conclusions

The optical properties of $SrAl_2O_4$:Eu^{2+}, such as efficiency under CR and uv excitation, have been shown to be dependent on composition. These differences have been correlated to the electrical properties of the phosphor. It has been shown that in this oxide system, the method of excitation of Eu^{2+} under uv and Cr excitation is predominantly of the charge transfer type.

Acknowledgments

The author is greatly indebted to V. D. Meyer for helpful discussions and to J. Ragusin for his assistance in the experimental part of the work.

Manuscript submitted Sept. 9, 1970; revised manuscript received Jan. 8, 1971.

Any discussion of this paper will appear in a Discussion Section to be published in the December 1971 JOURNAL.

REFERENCES

1. W. W. Anderson, *Phys. Rev.*, **136**, A556 (1964).
2. S. P. Keller, J. E. Mapes, and G. Cheroff, *ibid.*, **108**, 663 (1957); V. G. Dubinin and Z. A. Trapeznikova, *Opt. Spectr. (USSR) (English Transl.)*, **9**, 187 (1960).
3. E. Banks and R. W. Schwartz, *J. Chem. Phys.*, **51**, 1956 (1969).
4. J. L. Merz and P. S. Pershan, *Phys. Rev.*, **162**, 217 (1967).
5. G. Blasse and A. Bril, *This Journal*, **115**, 1067 (1968).
6. F. C. Palilla, A. K. Levine, and M. R. Tomkus, *ibid.*, **115**, 642 (1968).

7. G. Blasse and A. Bril, *Philips Res. Repts.*, **23**, 201 (1968).
8. M. R. Tomkus, Private communication.
9. G. Blasse, W. L. Wanmaker, J. W. ter Vrugt, and A. Bril, *Philips Res. Repts.* **23**, 189 (1968).
10. A. Pfahnl, *Bell System Tech. J.*, **42**, 181 (1963).
11. A. H. Gomes de Mesquita and A. Bril, *This Journal*, **116**, 871 (1969).

Alkaline Earth Aluminum Fluoride Compounds with Eu^{+2} Activation

Mary V. Hoffman*

Lighting Research Laboratory, General Electric Company, Nela Park, Cleveland, Ohio 44112

ABSTRACT

The systems MF_2-AlF_3 (M = Ca, Sr, or Ba) were investigated and the compounds and their fluorescence with Eu^{+2} were determined. In these compounds, Eu^{2+} activation results in two distinct types of emission, a band emission from 5d to 4f transitions typically found for Eu^{+2} in other matrices and line emissions from 4f to 4f transitions, similar to those of the isoelectronic Gd^{+3}.

The binary systems MF_2-AlF_3 (M= Ca, Sr, or Ba) have all been reported in the literature. The Ca system was first reported by Holm (1), and later by Ravez and Hagenmuller (2) and by Shore and Wanklyn (3). The Sr system was reported by Ravez and Hagenmuller (2) and the Ba system by Ravez (4, 5). Some fluorescence work with Mn^{+2} and other activators in the Ca and Sr systems has been reported by Smith (6) and by Wilke *et al.* (7), but these did not define the compounds in the systems.

Experimental Procedures

Two general methods were used to prepare these materials, a solid-state procedure and a precipitation method. The solid-state method is used for the calcium compounds and Sr_2AlF_7 and the precipitation procedure can be used for all barium compounds and $SrAlF_5$. For the solid-state method, AlF_3 was prepared by firing "Linde 'A' " Al_2O_3 in anhydrous HF. The alkaline earth fluoride was prepared by coprecipitation with Eu as the carbonate, followed by conversion to the fluoride by firing in anhydrous HF or by reaction with aqueous HF. The alkaline earth fluoride and AlF_3 were then combined in the stoichiometry required and fired. This method has the disadvantages of slow reaction rates and the high volatility of AlF_3 at temperatures approaching the melting points of the various compounds.

The precipitation procedure used consisted of combining the stoichiometric amounts of the alkaline earth, Eu and Al in 0.3M nitrate solutions. The pH was adjusted to 4.5-5.0 with NH_4OH and the solution heated to 80°C. A 0.3M solution of $NH_4F \cdot HF$ was added to the nitrate solution, equivalent to 95-100% of the stoichiometric amount. The resulting precipitate was heated and stirred for several hours before filtering, washing, and drying.

The firing procedure for either method consisted of a reduction firing, followed by a firing in anhydrous HF. The first firing at 750°C was in porcelain boats in an atmosphere of 1% H_2 in N_2 to reduce the activator to Eu^{+2}. The second firing was in anhydrous HF carried by N_2, utilizing a platinum tube furnace. Temperatures for this firing ranged from 700° to 900°C for 2-4 hr.

Measurements

The emission spectra were taken on a spectroradiometer previously described (8). Spectral band widths (SBW) used were 5 and 0.5Å. The detailed methods of measuring excitation and decay utilized to define the optical transitions in these phosphors have been described elsewhere (9). Quantum efficiency measurements were made by comparison of spectra with sodium salicylate, using a value of 64% for this standard. DTA measurements were made on a Du Pont Model 900, on samples which were sealed in platinum tubing, in an N_2 atmosphere. With the exception of $SrAlF_5$, all DTA measurements were made on samples containing 2 m/o (mole per cent) Eu^{+2}.

Results, Compound Formation

The binary compounds as reported in the literature and determined in this work are summarized in Table I.

CaF_2-AlF_3.—All references reported a compound at $CaAlF_5$ and found that an inversion $\alpha \rightarrow \beta$ occurs, but the exact temperature was not in agreement. The in-

* Electrochemical Society Active Member.

Key words: luminescence, spectra, calcium aluminum fluoride, barium aluminum fluoride, strontium aluminum fluoride, Eu^{+2} activation.

Table I. Binary compounds

System	Mole ratio	Compound	Ravez data [ref. (4)] Melting point, °C	Ravez data [ref. (4)] Transitions, °C	This work Melting point, °C	This work Transitions, °C
CaF_2-AlF_3	1:1	$CaAlF_5$	850 ± 10	820 ± 10		
	2:1	Ca_2AlF_7	Not found		829 ± 3	None
SrF_2-AlF_3	1:1	$SrAlF_5$	870 ± 10	None	887 ± 3	None
	2:1	Sr_2AlF_7	860 ± 10	None		
BaF_2-AlF_3	1:2	$BaAl_2F_8$	855 ± 12		Not found	
	1:1	$BaAlF_5$	895 ± 8	760 ± 8	867 ± 10	777 ± 3
	3:2	$Ba_3Al_2F_{12}$	970 ± 10	885 ± 10	883 ± 5	865 ± 3
	5:2	$Ba_5Al_2F_{16}$	905 ± 10		Not found	
	9:2	$Ba_9Al_2F_{24}$	900 ± 10			
EuF_2-AlF_3	1:1	$EuAlF_5$	845 ± 15			
[Ref. (10)]	ss	$(Eu_{0.70}Al_{0.30})F_{2.3}$	—			

vestigations by Ravez and Hagenmuller (2) were done in sealed tubes but with no mention of atmosphere control used. The other works were done in air. As prepared under conditions used in these tests, the α- and β-$CaAlF_5$ were confirmed and a second compound at Ca_2AlF_7 was found which melted at 829° ± 3°C.

SrF_2-AlF_3.—Ravez and Hagenmuller (2) reported two compounds, $SrAlF_5$ and Sr_2AlF_7, with no inversions. These were confirmed in this work.

BaF_2-AlF_3.—This system was reported by Ravez to have the compounds $BaAl_2F_8$, α- and β-$BaAlF_5$, β-$Ba_3Al_2F_{12}$, $Ba_5Al_2F_{16}$, and $Ba_9Al_2F_{24}$ (4, 5). This work was done in sealed tubes but no atmosphere control was mentioned. Identification of the compounds was both by x-ray diffraction and IR absorption (5).

In this work, utilizing an HF atmosphere, the compounds α- and β-$BaAlF_5$, α-$Ba_3Al_2F_{12}$, and $Ba_9Al_2F_{24}$ were confirmed, but the compounds $BaAl_2F_8$ and $Ba_5Al_2F_{16}$ were not found. The structure reported as β-$BaAlF_5$ was found to be metastable at room temperature, but could be quenched by rapid cooling. $Ba_5Al_2F_{16}$ was found when firing in an atmosphere containing some oxygen, but not when fired in HF. The reported $\alpha \rightarrow \beta$ inversion in $Ba_3Al_2F_{12}$ was detected by DTA at 865°C but could not be obtained by quenching. The melting point was found at 883° ± 5°C, which was reported as the inversion temperature by Ravez. No additional heat effects were found when the sample was heated to 970°C, the reported melting point.

EuF_2-AlF_3.—Ravez and Dumora (10) reported a compound at $EuAlF_5$, isostructural with $SrAlF_5$, and a solid-solution region from EuF_2 to $Eu_{0.7}Al_{0.3}F_{2.3}$. The compound was confirmed in this work, and the solid-solution region was not investigated.

Results

Eu^{+2} *emission.*—With Eu^{+2} incorporation in the alkaline earth site, the compounds in these systems give emission of two distinct types, the broad band emission associated with the 5d to 4f transition in Eu^{+2} and line emission usually found in 4f to 4f transitions of the trivalent rare earths. Some structures gave both emissions. The spectral data for these compounds are summarized in Table II. Excitations for both types of emission are broad, unstructured bands, as shown in Fig. 1.

Band emission.—All of the structures in the CaF_2-AlF_3 system and the compound Sr_2AlF_7 gave band emission of moderate efficiencies. Typical emission curves are shown in Fig. 2. The compound $Ba_9Al_2F_{24}$ also gave weak band emission, but was not investigated in detail.

Line emission.—In these systems, line emission was found in the compounds $SrAlF_5$, α- and β-$BaAlF_5$, and α-$Ba_3Al_2F_{12}$. The emission contains a band resulting from the 5d to 4f transition, with a narrow group of

Table II. Emission

Compound	Peak, nm	Type	QE, %	Peak height*
α-$CaAlF_5$	387	Band	10	11
β-$CaAlF_5$	385	Band	26	46
Ca_2AlF_7	400	Band	50	60
$SrAlF_5$	360	Band & line	65	350
Sr_2AlF_7	387	Band	60	60
α-$BaAlF_5$	358	Line	43	520
β-$BaAlF_5$	358	Line	N.D.	640
$Ba_3Al_2F_{12}$	358	Line	60	480
$Ba_9Al_2F_{24}$	390 + 405	Band	Low	—
Sodium salicylate	415	Band	64	50

* Read at 5Å SBW.

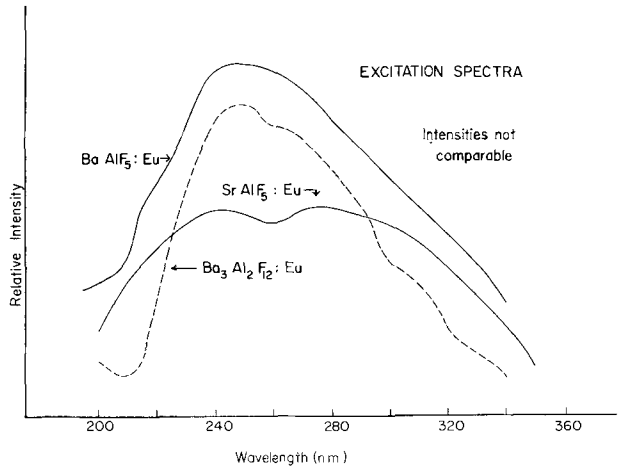

Fig. 1. Excitation spectra of Eu^{+2} line emission. Eu^{+2} band emission is similar.

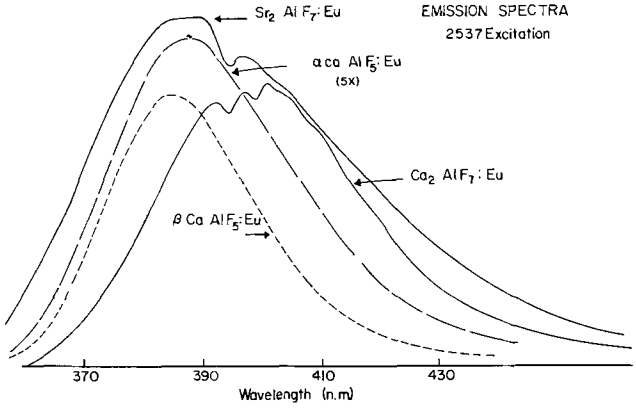

Fig. 2. Spectra of Eu^{+2} band emission, 2537Å excitation

lines superimposed on the band. The relative intensity of the band is highest in $SrAlF_5$, equaling about half of the total peak height, and is very weak in several of the barium compounds. The line emission is attributed to transitions in the 4f-4f level of Eu^{+2}, which is isoelectronic with Gd^{+3}. The major lines, which fall between 358 and 361 nm, are due to $^6P_{7/2}$ to $^8S_{7/2}$ transitions with a lesser amount of emission occurring near 355 nm from the $^6P_{5/2}$ to $^8S_{7/2}$ transition.

The number and positions of these lines are dependent on the particular structure of the compound. Spectral distribution curves are shown in Fig. 3-6, in

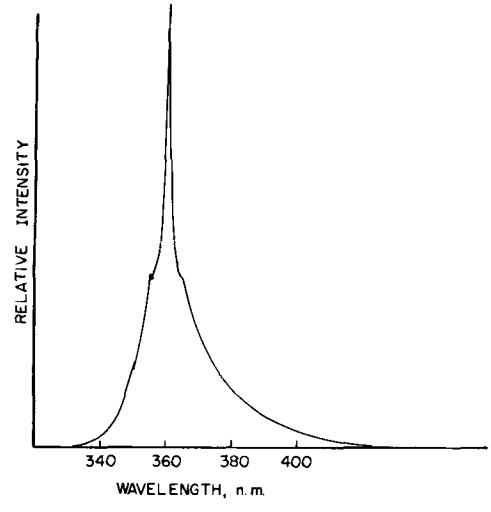

Fig. 3. Emission spectra of $SrAlF_5$:02Eu^{+2}, 2537Å excitation, 5Å SBW.

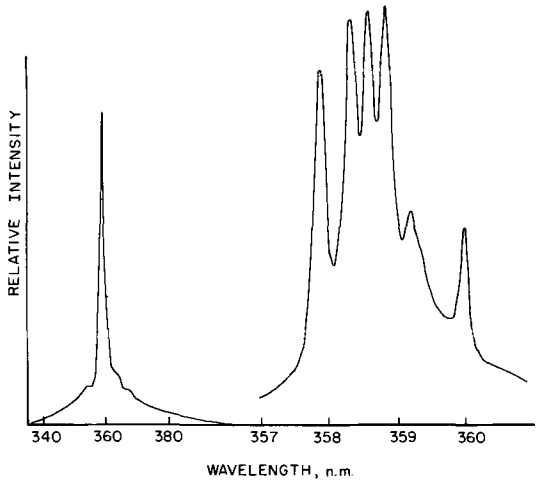

Fig. 4. Emission spectra of α-$BaAlF_5$:02Eu^{+2}, 2537Å excitation. Left curve, 5Å SBW, right curve 0.5Å SBW.

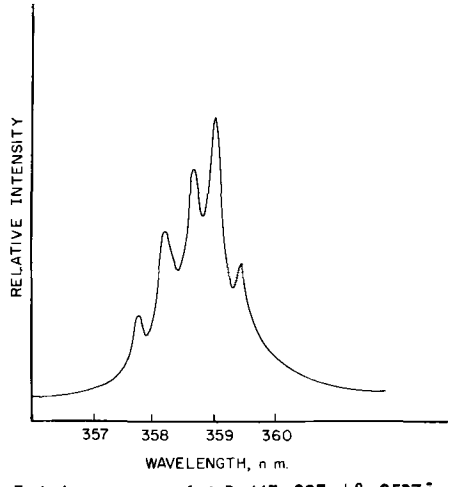

Fig. 5. Emission spectra of β-$BaAlF_5$:02Eu^{+2}, 2537Å excitation, 0.5Å SBW.

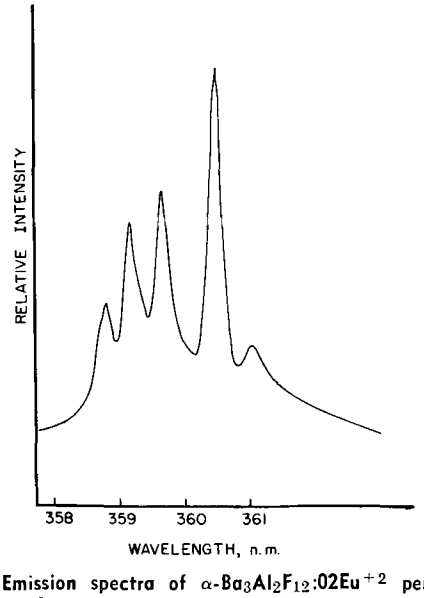

Fig. 6. Emission spectra of α-$Ba_3Al_2F_{12}$:02Eu^{+2} per Ba. 2537 excitation, 0.5Å SBW.

which α-$BaAlF_5$, β-$BaAlF_5$, and α-$Ba_3Al_2F_{12}$ are shown in expanded scale to include only the lines of the $^6P_{7/2}$ to $^8S_{7/2}$ transitions. When recorded on a resolution of 5Å SBW, the emission of β-$BaAlF_5$ cannot be distinguished from α-$BaAlF_5$ except by intensity. When recorded at 0.5Å SBW, each structure is shown to be distinctive. The peak heights shown in Table II are as recorded at 5Å SBW on the best materials obtained. The quantum efficiencies shown in the table of the three line emitters were obtained by comparing spectra taken at several different resolutions and can be considered only approximate.

The $SrAlF_5$ compound is the only line emitter which has a congruent melting and can be grown as a single crystal from the melt. Work is in progress by J. P. Meehan of this laboratory on obtaining single crystals of both unactivated and activated materials, and has provided crystals for structure analysis. The initial work has shown that the structure is more complex than reported by Ravez. The number of sites available for Eu^{+2} substitution has been confirmed as four. $SrAlF_5$ has two families of Sr^{+2} sites, one in eight-fold coordination and one in seven-fold coordination. Each family has two slightly differing arrangements (11). The number of lines in the $^6P_{7/2}$ to $^8S_{7/2}$ transition should be 16, resulting from four lines per Eu^{+2} site. Fifteen of these lines have been found. A more complete description and assignment of the lines in this and several other of these compounds was published elsewhere (9).

Substitutions of Eu^{+2} up to 30 m/o have been prepared with no change in the spectral distribution. Above about 2 m/o substitution, the emission intensity varies little with concentration. Since $EuAlF_5$ is isostructural with $SrAlF_5$, complete substitution is probable.

The extent of Eu^{+2} substitution in the barium compounds is considerably less than in $SrAlF_5$. α-$BaAlF_5$ will accept only about 12% Eu^{+2}. No change in spectral distribution has been found with increasing activator content, and above about 0.5% Eu, the intensity varies little. The β-$BaAlF_5$ form has been obtained by rapidly cooling the sample from just above the transition point, such as 800°C. The absolute intensity of the β form is highly dependent on the heating and quenching conditions. When $BaAlF_5$ is cooled from a firing temperature closer to the melting point, such as 850°C, the structure reverts to a poorly crystallized α-$BaAlF_5$, with some retention of another unknown structure. The presence of this form, which has been referred to as the γ form [ref. (9)] is detected by the addition of emission lines on the high wavelength side of the $^6P_{7/2} \rightarrow {}^8S_{7/2}$ transitions by measurements at 0.5Å SBW. The phase relations and structural changes which result in this modification have not been identified.

In $Ba_3Al_2F_{12}$, the Eu^{+2} substitution is limited to about 2%. Beyond this, the phase relations are such that α-$BaAlF_5$ and EuF_2 (or EuF_3) are stable. Ravez reported a β form, and included x-ray diffraction data, but no evidence of this structure has been found by quenching samples from an HF or N_2 atmosphere.

Solid solutions—Solid solution of Ba and Ca in the $SrAlF_5$ was determined by the shift in d spacing of the line at d = 1.959 (Fig. 7). The substitution of Ba can be made to a composition of $Sr_{0.15}Ba_{0.85}AlF_5$, and with Eu^{+2} activation, the spectral distribution changes as shown in Fig. 8. The line emission is reduced in intensity, and several additional 5d to 4f emission bands are introduced with increasing substitution. A similar change in spectral distribution is found with calcium in solid solution, which was found to extend to $Sr_{0.6}Ca_{0.4}AlF_5$ range. The presence of additional bands may indicate preferential substitution of Ba or Ca in the four Sr sites. In $BaAlF_5$, the substitution of Sr is limited to about 2%. The effect on Eu^{+2} emission is seen in increased intensity of the line emission, but no change in the 5d to 4f emission was detected when measured at 5Å SBW.

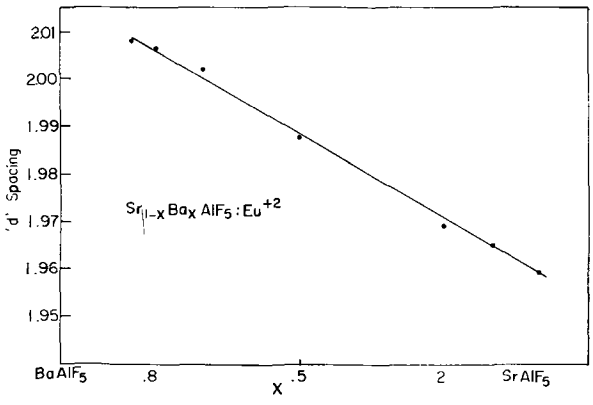

Fig. 7. Change in d spacing with Ba substitution in $SrAlF_5$

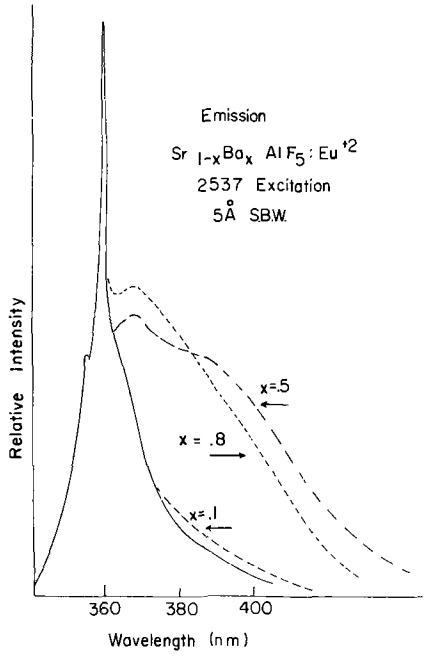

Fig. 8. Change in emission spectra of Eu^{+2} bands in solid-solution region of (SrBa)AlF_5.

Summary

The determination of compounds existing in the system aluminum fluoride-alkaline earth fluoride has disclosed structural types which result in a new type of emission from Eu^{+2}. This narrow line emission is sufficiently intense at 25°C to be potentially useful as an ultraviolet source. Spectral measurements at high resolution have shown that for a single compound, the number, position, and relative intensities of the lines are consistent, but the phase relations are such that preparative conditions can readily affect the phase purity of the material. These conditions affect the quenching of metastable phases and also possibly the volatility of the component fluorides, so that the characterization of all line-emitting compounds has not been completed.

Acknowledgments

The author is pleased to acknowledge the work of Dr. R. A. Hewes and Dr. J. P. Meehan of the Laboratory, and Dr. R. Newnham of Pennsylvania State University in contributing to this work. The optical measurements were made by Miss E. J. Wilson, and the preparative and measurements were done by Mrs. L. Funaro, Mrs. B. Burts, and Miss L. Wichert.

Manuscript submitted Dec. 2, 1970; revised manuscript received Jan. 15, 1971. This was Paper 358RNP presented at the Los Angeles Meeting of the Society, May 10-15, 1970.

Any discussion of this paper will appear in a Discussion Section to be published in the December 1971 JOURNAL.

REFERENCES

1. J. L. Holm, *Acta Chem. Scand.*, **19**, 6, 1512 (1965).
2. J. Ravez and P. Hagenmuller, *Bull. Soc. Chim. Fr.*, 7, 2545 (1967).
3. R. G. Shore and B. M. Wanklyn, *J. Am. Ceram. Soc.*, **52**, 2, 79 (1969).
4. J. Ravez, *Bull. Soc. Chim. Fr.*, 5, 1584 (1969).
5. J. Ravez, Thesis, University of Bordeaux, 1968 (Unpublished).
6. A. L. Smith, *This Journal*, **101**, 189 (1954).
7. K-Th. Wilke, K. Albers, and R. Mannheim. *Z. Physik. Chem. (Leipzig)*. Bd. 213, 191 (1960).
8. R. L. Brown, *Illum. Eng.*, **61**, 230 (1966).
9. R. A. Hewes and M. V. Hoffman, *J. Lum.*, **3**, 261 (1971).
10. J. Ravez and D. Dumora, *Comp. Rend.*, **269C**, 331 (1969).
11. R. E. Newnham, Private communication.

APPENDIX

X-ray diffraction data for all barium compounds were taken from ref. (5). Values of 2θ are for $CuK_{\alpha 1}$ radiation and were added to Ravez' data.

Ca_2AlF_7		
2θ	d	I
22.5	3.97	30
22.9	3.90	15
23.1	3.85	30
24.9	3.59	55
25.3	3.52	100
27.4	3.26	20
28.1	3.18	85
30.8	2.91	40
31.7	2.83	15
32.5	2.76	25
39.4	2.29	20
40.0	2.26	45
41.5	2.17	25
44.8	2.02	15
45.4	2.00	20
46.1	1.97	25
46.5	1.96	40
46.7	1.94	45
48.3	1.88	40
49.2	1.85	30
49.6	1.84	30
52.3	1.75	15

β-$BaAlF_5$			α-$Ba_3Al_2F_{12}$		
2θ	d	I	2θ	d	I
18.2	4.84	17	19.6	4.47	17
21.3	4.19	12	22.4	3.96	57
22.0	4.02	30	25.1	3.54	99
22.8	3.90	39	25.4	3.48	100
25.2	3.54	100			
25.6	3.48	72	26.0	3.42	77
26.1	3.41	67	26.8	3.33	54
28.2	3.17	30	27.1	3.28	53
30.6	2.93	51	27.4	3.25	65
30.9	2.88	19	27.6	3.22	60
31.7	2.83	23	28.4	3.14	80
34.3	2.61	17	29.3	3.05	41
36.9	2.43	25	29.4	3.03	33
38.2	2.36	8	30.1	2.97	44
39.1	2.30	44	30.8	2.90	22
41.1	2.20	72	32.0	2.80	9
42.1	2.15	16	36.3	2.47	10
43.1	2.10	24	37.7	2.39	48
43.7	2.07	24	37.9	2.38	72
46.4	1.95	21	38.6	2.33	20
48.5	1.87	9	39.3	2.29	18
49.4	1.84	8	40.0	2.25	62
51.7	1.76	20	41.2	2.19	55
53.0	1.73	11	42.1	2.14	20
55.9	1.64	10	42.7	2.12	28
57.6	1.60	8	43.1	2.10	32
53.8	1.58	7	44.3	2.04	16
59.4	1.56	7	44.9	2.01	24
59.4	1.55	6	45.3	2.00	22
61.1	1.52	13	46.0	1.97	43
			46.5	1.95	38
			46.7	1.94	10
			47.6	1.91	17
			48.0	1.89	47
			48.8	1.87	6
			49.6	1.84	12
			50.8	1.80	17
			51.5	1.77	26
			53.4	1.71	8
			53.8	1.70	20
			54.3	1.69	24
			54.6	1.68	11

$Ba_6Al_2F_{24}$			α-$BaAlF_5$			α-$BaAlF_5$		
2θ	d	I	2θ	d	I	2θ	d	I
16.8	5.2	3	18.1	4.86	6	37.7	2.38	2
17.8	4.97	13	21.5	4.13	5	38.0	2.37	2
22.9	3.92	5	21.9	4.05	14	38.9	2.31	15
25.3	3.52	42	22.6	3.93	19	39.7	2.27	24
26.9	3.31	100	23.4	3.80	11	40.3	2.24	22
29.2	3.05	27	24.9	3.58	13	41.1	2.20	29
31.1	2.87	13	25.5	3.50	100	41.9	2.15	22
34.0	2.63	2	26.9	3.31	2	42.9	2.11	17
37.3	2.41	21	27.7	3.22	9	43.5	2.08	16
40.1	2.24	32	28.7	3.12	3	44.3	2.04	32
42.9	2.11	6	29.0	3.05	5	46.2	1.96	6
43.8	2.07	4	31.1	2.97	9	47.1	1.93	1
44.5	2.03	59	30.3	2.94	13	48.2	1.88	4
45.5	1.99	16	30.9	2.89	8	52.2	1.75	9
48.2	1.88	15	31.4	2.84	6	54.7	1.68	4
52.8	1.74	26	34.4	2.60	5	55.4	1.66	8
54.1	1.69	7	35.0	2.56	15	56.4	1.63	9
54.7	1.67	9	36.7	2.45	3	57.4	1.60	7
61.6	1.50	7	37.1	2.42	4	58.4	1.58	4
						59.7	1.55	9

Mechanism of Flux Action in the Thermal Recrystallization of Zinc Sulfide

R. A. Brown*

RCA Electronic Components, Lancaster, Pennsylvania 17604

ABSTRACT

Electrical conductivity and electron microscopic studies on ZnS:0.015% Ag containing 2% NaCl or 10% NaCl suggest chemical interaction between zinc sulfide and flux at about 620°C. In these systems the rate of increase in particle size at 750° to 1250°C followed $D^3 = kt$, where D is the average particle diameter at a firing time t. Activation energies for particle growth were 29 ± 2 kcal at 750°-1000°C, and 58 ± 4 kcal at 1000°-1250°C. Thermal recrystallization in zinc sulfide without additives commenced at 1050°C. From 1100° to 1250°C particle growth in ZnS also obeyed $D^3 = kt$, with an activation energy of 61 ± 4 kcal. These results can be interpreted in terms of material transport by diffusion processes.

There are numerous reports in the literature regarding the effect of a fluxing agent on the thermal recrystallization and luminescent properties of zinc sulfide phosphors. Earlier workers (1-3) suggested that the purpose of the flux is to provide a liquid phase in which the zinc sulfide is soluble, so that transport of material can easily occur. Apparently, no experimental evidence has been offered in support of this hypothesis. The work of Houben (4) cast some doubts on the classical concept of the mechanism of particle growth. In studies on the ZnS-NaCl system this worker found no zinc sulfide in the fused sodium chloride phase.

Earlier studies (5-7) showed that ZnS is precipitated from aqueous solution in the form of relatively large, irregularly shaped aggregates which are made up of very fine (submicron) grains of zinc sulfide. More recently Brown (8), following previous work by Bodi and Tufts (9), has investigated changes in the particle size and morphology of zinc sulfide phosphors during the early stages of firing. These investigations demonstrated that on heating in the presence of sodium chloride as flux, the fine grains of material coalesce and grow rapidly within the aggregate, so that during the first few minutes each agglomerate becomes a single particle of zinc sulfide. Subsequently, thermal recrystallization proceeds by the growth of large particles at the expense of smaller ones.

The objectives of the present study were: a) to determine the minimum temperature at which recrystallization occurs in zinc sulfide and zinc sulfide containing sodium chloride as flux; b) to investigate the possibility of the formation of a liquid phase at temperatures below the normal melting point of the flux; c) to suggest possible mechanism(s) for the particle growth processes.

Investigation of chemical interaction and liquid phase formation between the zinc sulfide and flux was carried out by electrical conductivity methods, following the procedure of Cypres and van Ommeslaghe (10). For the particle size measurements a Coulter Counter was employed. This instrument analyzes particle size distribution by noting the change in resistance of an electrolyte caused by the volumetric change in an orifice as each particle passes through it. The rate of increase in particle size was interpreted in terms of an expression of the form $D^n = kt$ (11, 12), where D represents the average particle diameter at a firing time t. This expression is discussed more fully in the Appendix. It should be pointed out that the thermal effects depend on factors such as sample size, configuration of the firing vessel, duration of heating, and the rate of cooling. Consequently, the results obtained should be regarded as relative rather than absolute. Note that compositions are given in terms of per cent by weight.

Experimental

A detailed account of the preparation of zinc sulfide from aqueous zinc sulfate solution with hydrogen sulfide has been given previously (7). For the present work, zinc sulfide was obtained by precipitation at 25°C from 2 liter of 1M zinc sulfate solution using a hydrogen sulfide flow of 0.82 liter/min. After filtration through a Buchner funnel and washing with deionized water the precipitate was subsequently dried at 100°C for 6 hr.

For the electrical conductivity experiments, 0.6g specimens of zinc sulfide containing 2% sodium chloride were pressed into cylindrical compacts at a pressure of 800 kg/cm². The disks were placed between two

* Electrochemical Society Active Member.

Key words: phosphors, particle growth, zinc sulfide-sodium chloride, zinc diffusion in zinc sulfide.

pieces of platinum foil, to provide electrodes, and heated at a rate of approximately 10°C/min to 900°C in a stream of oxygen-free nitrogen having a flow rate of 30 cc/min. During heating, electrical conductivity of the specimens was measured at regular intervals of time by means of an Industrial Instruments Model RC 16 B conductivity bridge. For comparison, specimens of pure sodium chloride and pure zinc sulfide were pressed into disks and their electrical conductivity measured, as above.

Initially, recrystallization experiments were carried out by firing 5.5g samples in covered "Vitreosil" crucibles for various lengths of time at temperatures between 550° and 800°C in air. Systems investigated included ZnS:0.015% Ag with 2% NaCl flux, zinc sulfide without additives, ZnS containing Ag, Al, or Cu each at the level of 0.015%, and zinc sulfide containing 2% sulfur. Subsequently, specimens were examined by electron microscopic and x-ray powder diffraction methods, for the determination of particle size, morphology, and crystal structure.

For more prolonged particle growth experiments the following method was employed to prevent oxidation of the samples, and maintain a stoichiometric composition of the zinc sulfide, during heating. Test samples of 10g were placed in covered "Vitreosil" crucibles, located in a larger crucible, surrounded with zinc sulfide, and covered with a lid. Specimens were fired at temperatures in the range 750°-1250°C for periods of 1 to 10 hr. Compositions studied included ZnS:0.015% Ag with 2% or 10% sodium chloride flux, and zinc sulfide without additives. Subsequently, the materials were examined by scanning electron microscopic, x-ray powder diffraction, and Coulter Counter methods.

Results

Some representative results obtained in the initial firing experiments are given as Fig. 1 and 2. Figure 1(a) shows the appearance of the zinc sulfide precipitate after firing at 800°C for 2 hr. On heating zinc sulfide for 2 hr at 800°C in the presence of 0.015% Ag, Al, or Cu, or with 2% sulfur, there was no noticeable change in either aggregate size or morphology. This absence of change is demonstrated in Fig. 1(b) which gives only the typical result obtained for ZnS:0.015% Ag. X-ray powder diffraction data for both pure ZnS and zinc sulfide containing the various additives showed a sharpening in the diffraction patterns at firing temperatures of 700° and 800°C. Consequently, in the absence of a flux heating to 800°C apparently leads to an amorphous → crystalline lattice rearrangement, but does not give any visible change in the size or morphology of the aggregates. Figure 2 shows the influence of temperature on ZnS:0.015% Ag with 2% NaCl flux. At 550°C [Fig. 2(a)] and 600°C [Fig. 2(b)] there is no evidence of particle growth after heating for 2 hr. On firing for 2 hr at 650°C some slight coalescence occurs, as demonstrated in Fig. 2(c). Recrystallization proceeded rapidly at 700°C. Coalescence of the fine grains commenced at about 4 min [Fig. 2(d)]; after firing for 2 hr a particle size of approximately 2μ was attained, as shown in Fig. 2(e).

A plot of electrical conductivity as a function of temperature for (*a*) sodium chloride, (*b*) zinc sulfide containing 2% sodium chloride, and (*c*) zinc sulfide is given as Fig. 3. Zinc sulfide shows a gradual, slow increase in conductivity with rise in temperature. In the case of sodium chloride there is a pronounced increase in electrical conductivity at 800°C, which corresponds with the normal melting point of 801°C. Contrast these results with the behavior of the ZnS, 2% NaCl system which shows a large increase in conductivity at 620° to 720°C, followed by a further rise in the region of 800°C. This suggests the occurrence of a liquid phase or chemical reaction at temperatures as low as 620°C. Figure 4 shows the behavior of the electrical conductivity of ZnS, 2% NaCl during heating and cooling. Since the curve obtained on cooling does not follow that given during heating, it is suggested that the electrical conductivity may be due to chemical reaction, rather than a simple melting.

Results obtained in the particle growth experiments were plotted in the form of log D *vs.* log t, where D represents the average diameter of the phosphor particles (median point by weight of particles based on Coulter Counter measurements) at a firing time t. The derivation of these log D — log t plots is developed in the Appendix. Typical sets of curves, in which log D is plotted against log t at different firing temperatures, are given in Fig. 5 for ZnS:0.015% Ag, 2% NaCl, and in Fig. 6 for ZnS:0.015% Ag, 10% NaCl. These graphs show that a linear dependence does, in fact, exist. Since the measured slope of these lines is 0.33, particle growth in zinc sulfide containing sodium chloride as flux can be described by the expression $D^3 = kt$. Note that in this system an increase in the flux content leads to enhanced particle growth.

Arrhenius-type activation energy plots were derived from the data of Fig. 5 and 6, with the use of an arbitrarily chosen constant D of 10μ, and are given as Fig. 7. These plots show the occurrence of two activation energy values. In the ZnS:0.015% Ag, 2% NaCl system the results obtained were 29 ± 2 kcal at 750°-1000°C and 58 ± 4 kcal between 1000° and 1250°C. For ZnS:0.015% Ag, 10% NaCl activation energies for particle growth were 29 ± 2 kcal at 750° to 950°C and 59 ± 4 kcal at temperatures in the range 1050°-1250°C. Activation energies were calculated by means of a regression and correlation analysis carried out by G. M. Ehemann of this laboratory with the use of an RCA Spectra 70 computer program.

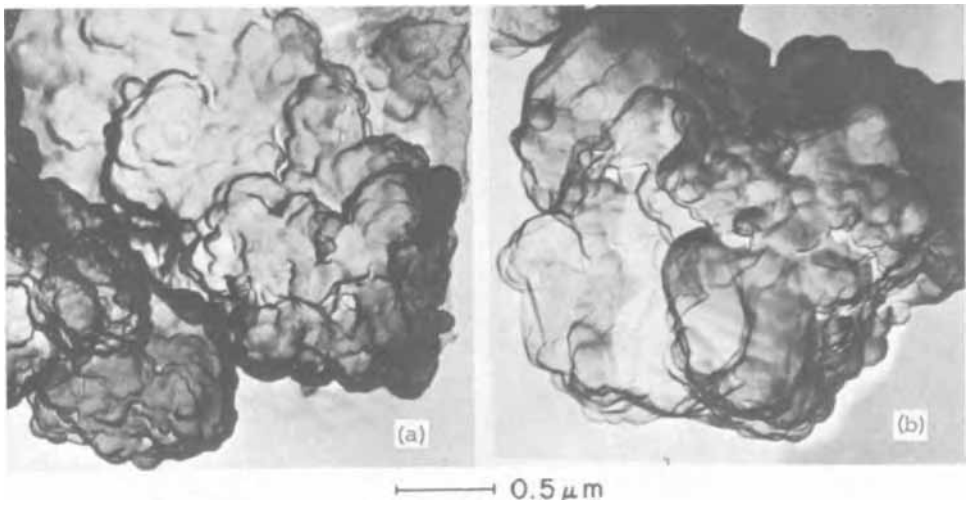

Fig. 1. Firing sequence at 800°C for 2 hr: (a) ZnS, (b) ZnS:0.015% Ag.

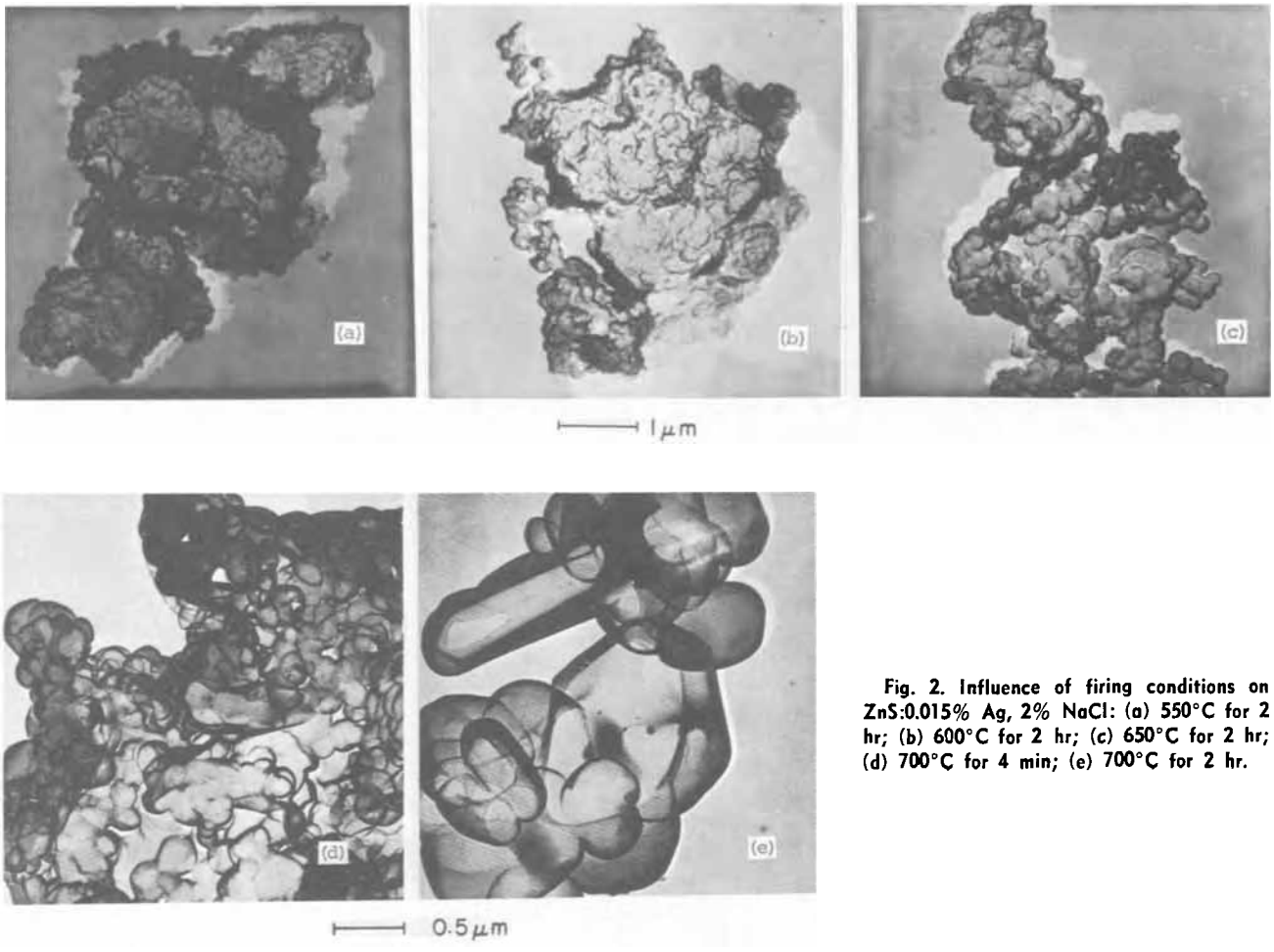

Fig. 2. Influence of firing conditions on ZnS:0.015% Ag, 2% NaCl: (a) 550°C for 2 hr; (b) 600°C for 2 hr; (c) 650°C for 2 hr; (d) 700°C for 4 min; (e) 700°C for 2 hr.

Figure 8 gives the relationship between log D and log t for zinc sulfide without additives. In this case, there was no measurable increase in particle size on heating for up to 6 hr at 800°-1000°C. Only the typical results obtained at 800° and 1000°C are given in Fig. 8. Some increase in particle size was observed at 1050°C. Between 1100° and 1250°C plots of log D *vs.* log t were linear with a slope of 0.33. Consequently, the relationship $D^3 = kt$ is also followed in zinc sulfide without flux, at temperatures above 1050°C. An Arrhenius plot was derived from the data of Fig. 8 and is given as

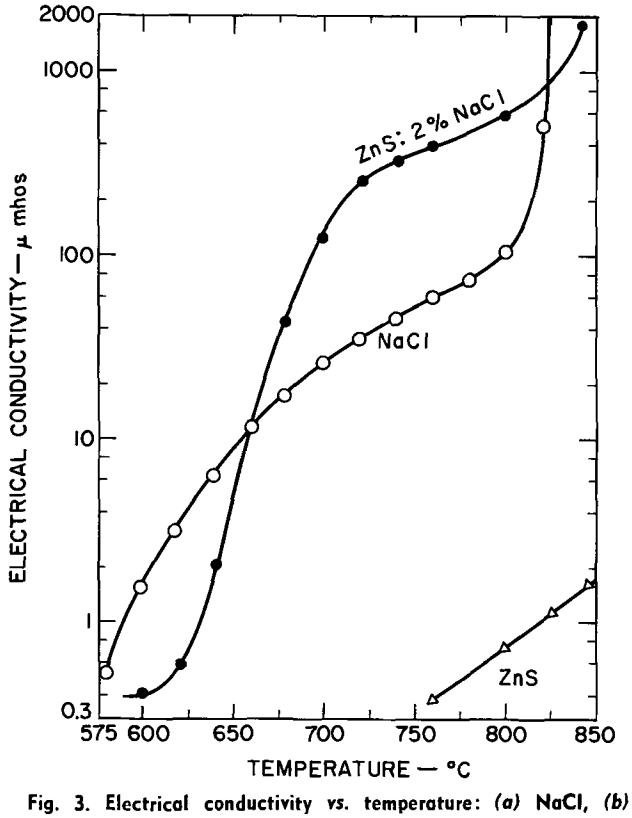

Fig. 3. Electrical conductivity *vs.* temperature: *(a)* NaCl, *(b)* ZnS-2% NaCl, *(c)* ZnS.

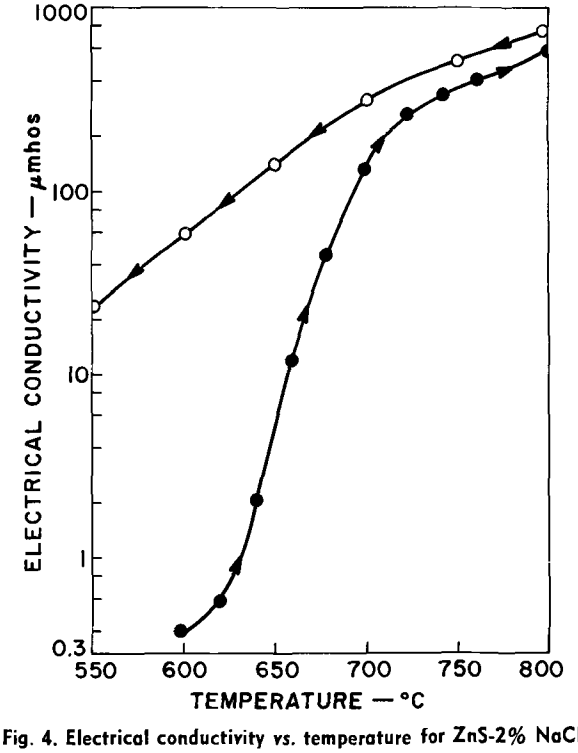

Fig. 4. Electrical conductivity *vs.* temperature for ZnS-2% NaCl

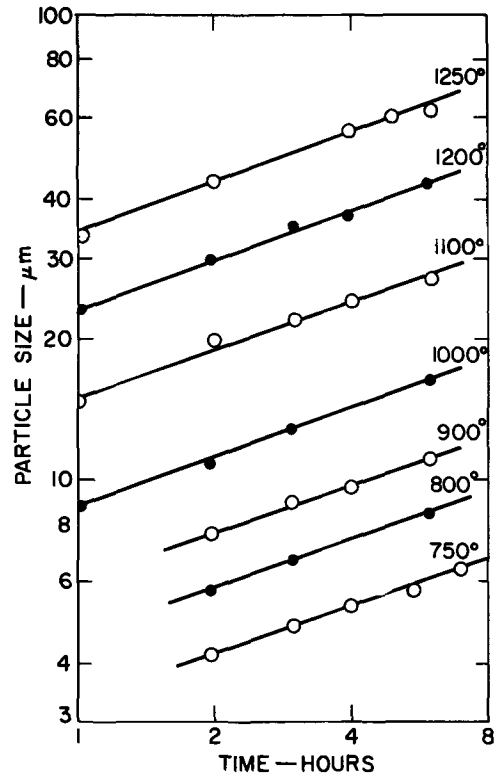

Fig. 5. Rate of particle growth in ZnS:0.015% Ag, 2% NaCl

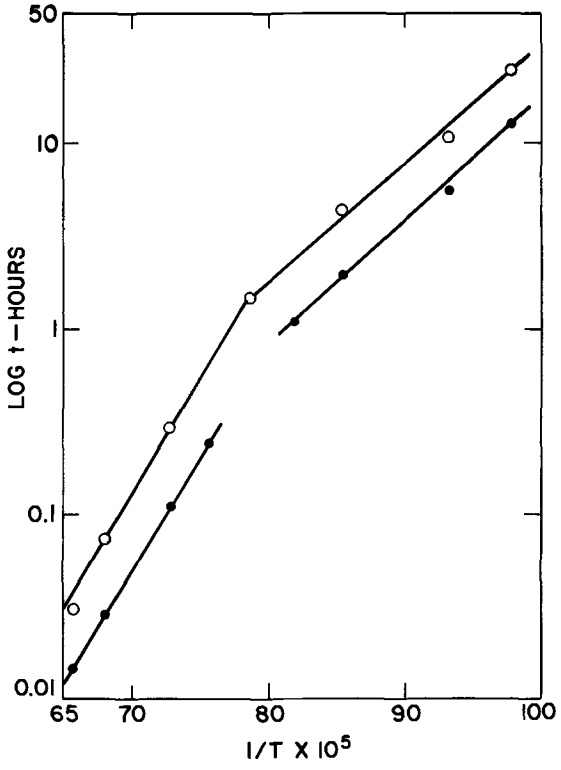

Fig. 7. Arrhenius plots for particle growth: ○—ZnS:0.015% Ag, 2% NaCl; ●—ZnS:0.015% Ag, 10% NaCl.

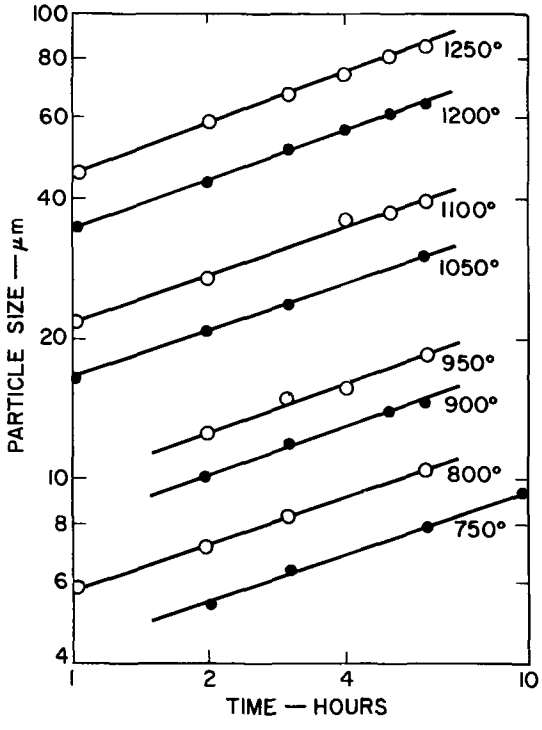

Fig. 6. Rate of particle growth in ZnS:0.015% Ag, 10% NaCl

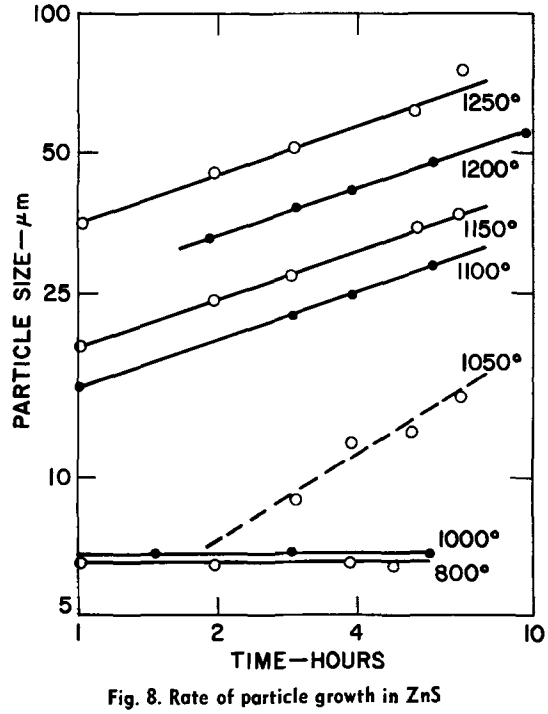

Fig. 8. Rate of particle growth in ZnS

Fig. 9. From this plot, the activation energy for thermal recrystallization in zinc sulfide at 1100° to 1250°C was calculated to be 61 ± 4 kcal.

Scanning electron photomicrographs of (*a*) unfired zinc sulfide precipitate, (*b*) zinc sulfide heated for 1 hr at 800°C, and (*c*) zinc sulfide fired at 1000°C for 1 hr are given in Fig. 10. These confirm that in the absence of a flux there is very little change in the appearance of the zinc sulfide aggregates on heating at temperatures up to 1000°C. On the other hand, these photomicrographs appear to show that some growth of the fine zinc sulfide grains occurs within the aggregate.

Discussion

On the basis of the electrical conductivity and electron microscopic studies, the onset of thermal recrystallization is suggested to occur by the following sequence of events. Heating zinc sulfide with sodium chloride to about 620°C leads to chemical interaction between the zinc sulfide and flux with the formation of a liquid phase, and the consequent introduction of defects in the zinc sulfide lattice. This sequence would explain the marked rise in electrical conductivity at 620° to 720°C. If the behavior of zinc sulfide is comparable with that of zinc oxide (13) then it is possible that the electrical conductivity may result from the presence of interstitial zinc. Other workers (14, 15)

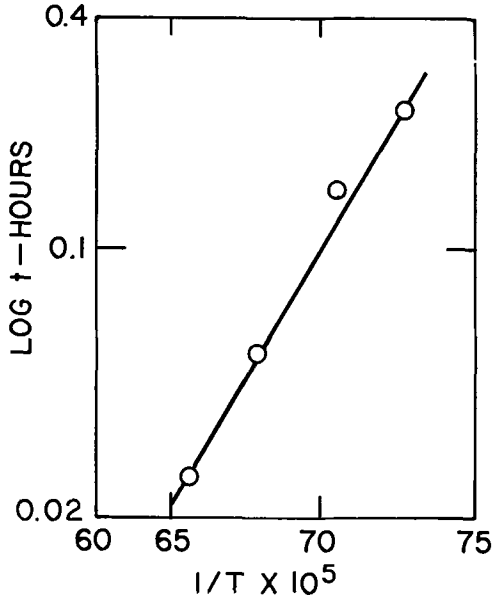

Fig. 9. Arrhenius plot for particle growth in ZnS

have established the occurrence of a chemical interaction by showing that when zinc sulfide phosphors are prepared in the presence of a metal chloride flux zinc chloride is formed according to the reaction

$$ZnS + 2MCl \rightarrow ZnCl_2 + M_2S$$

where M represents an alkali metal, such as Na. This finding was confirmed in the present study by the detection of zinc chloride in the wash water from typical phosphor preparations. Following the chemical reaction at 620°C, thermal recrystallization commences at about 650°C. Note that this temperature is considerably below the normal melting point of 801°C (16) given for the sodium chloride flux.

For ZnS:0.015% Ag with 2% NaCl or 10% NaCl the activation energy for particle growth at 750° to 1000°C was 29 kcal, whereas at 1000° to 1250°C a value of 58 kcal was obtained. Several workers (17-19) have studied the self-diffusion of atoms in polycrystalline zinc sulfide and have found movement of zinc to be the rate determining step in the diffusion processes. On the basis of radioactive tracer studies, Secco (17) gave a value of 29 kcal for the interstitial diffusion of zinc, that is movement of zinc through interstitial channels in the zinc sulfide lattice. An activation energy of 61.5 kcal was obtained by Secco (17) for the lattice diffusion of zinc, that is the movement of zinc through normal zinc sites in the zinc sulfide lattice. A similar value for a lattice diffusion mechanism was given by Bansagi and co-authors (19). The results obtained in the present study are in very good agreement with the activation energy values given by Secco (17). Consequently, particle growth in zinc sulfide containing sodium chloride is suggested to occur as follows. Chemical interaction between the host material and flux leads to the introduction of chloride into the host lattice at low temperatures (20). Although the exact nature of the resultant defects is not fully understood, several workers (21, 22) have suggested that interstitial zinc may be formed. Since the activation energy of 29 kcal is in excellent agreement with the value of 29 kcal given by Secco (17) for an interstitial diffusion mechanism, it appears that particle growth in ZnS:Ag with NaCl flux at 750°-1000°C occurs by the direct interstice-to-interstice diffusion of zinc (valency unspecified). At temperatures between 1000° and 1250°C the energy of activation of 58 kcal agrees with the value of 61.5 kcal given by Secco for a lattice diffusion process. Apparently, at higher temperatures there is sufficient thermal mobility for transport of material to occur by the lattice diffusion of zinc (valency unspecified). Note that these growth processes do not involve a solution-reprecipitation mechanism, and would require only small quantities of chloride in the zinc sulfide lattice. This conclusion is in accord with the finding of Houben (4) that fused sodium chloride does not dissolve zinc sulfide to an appreciable extent.

In the absence of a flux zinc sulfide showed no appreciable changes in aggregate size or morphology on heating at temperatures up to 1000°C. From 1100°-1250°C an activation energy of 61 kcal was obtained for the growth processes. This result suggests that at higher temperatures particle growth in zinc sulfide occurs by the same mechanism as in ZnS with NaCl flux, namely, lattice diffusion of zinc. The onset of thermal recrystallization in zinc sulfide, and perhaps also the change in mechanism for zinc sulfide with a flux, may be initiated by the cubic-hexagonal phase transformation which occurs at approximately 1020°C (23). This finding is in keeping with an observation by Morgan (24).

For both zinc sulfide and ZnS-NaCl the rate of increase in particle size can be represented by the expression $D^3 = kt$. Shionoya and Amano (25) found that a similar equation can be used to describe particle growth in ZnS:Cu and ZnS:Cu containing either 4% or 10% NaCl at 1000° to 1150°C. These workers obtained an activation energy of 30 kcal for particle growth in ZnS:Cu containing sodium chloride, and showed that the value was independent of the amount of flux used. This result is in accord with the value of 29 kcal calculated in the present study for ZnS:0.015% Ag with NaCl at lower temperatures, and again suggests an interstitial diffusion mechanism. An activation energy of 80 kcal was given by Shionoya and

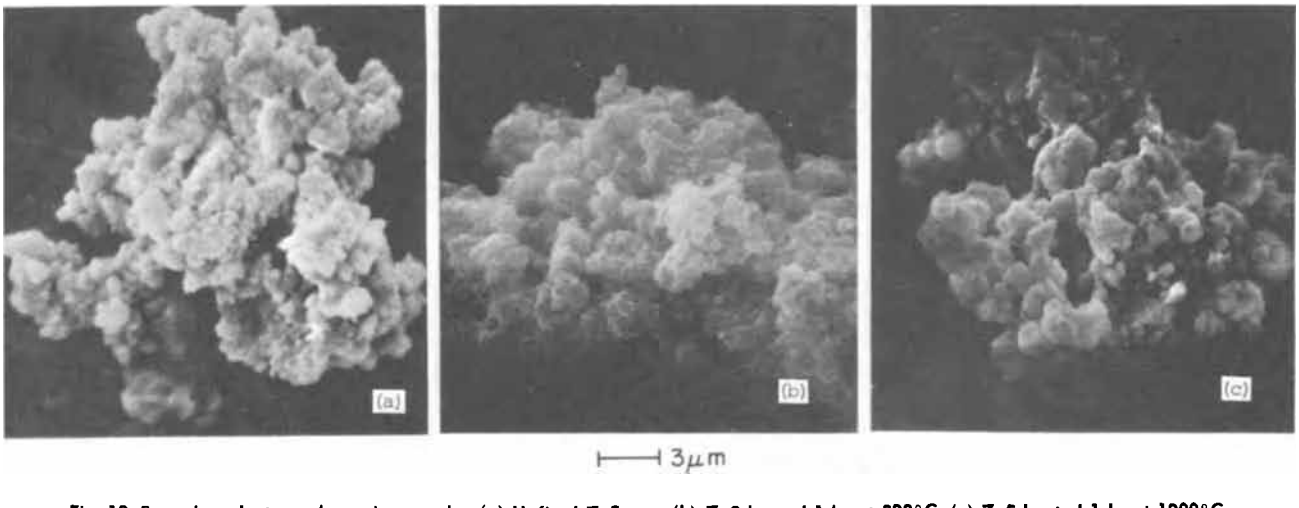

Fig. 10. Scanning electron photomicrographs: (a) Unfired ZnS ppt, (b) ZnS heated 1 hr at 800°C, (c) ZnS heated 1 hr at 1000°C

Amano for thermal recrystallization in ZnS:Cu. This value is somewhat higher than the 61 kcal found in the present work for zinc sulfide without additives.

In summary, this work has shown that chemical reaction between zinc sulfide precipitate and sodium chloride flux occurs at approximately 620°C. This temperature is considerably below the normal melting point of the flux. Subsequently, thermal recrystallization in ZnS:Ag containing sodium chloride commences at 650°C and becomes rapid at 700°C. The rate of increase in particle size of zinc sulfide or ZnS:0.015% Ag with NaCl follows the expression $D^3 = kt$, where the symbols have the meanings given above. Results obtained in the thermal recrystallization experiments can be interpreted in terms of material transport by diffusion processes. This finding is in contrast with the classical concepts of flux action, which postulated that particle growth in zinc sulfide phosphors occurred by a dissolution-reprecipitation phenomenon.

Acknowledgments

The author expresses his gratitude to E. W. Bomgardner for assistance with the preparatory work, also to Mrs. E. M. Rineer and Mrs. J. N. Shenk for providing the Coulter Counter measurements. For valuable discussions and suggestions especial thanks are due to Dr. A. L. Smith.

Manuscript received Aug. 28, 1970; revised manuscript received *ca.* Jan. 21, 1971. This was Paper 62 presented at the Los Angeles Meeting of the Society May 10-15, 1970.

Any discussion of this paper will appear in a Discussion Section to be published in the December 1971 JOURNAL.

APPENDIX

Particle Growth Dependence

Various workers have shown that the rate at which grain growth occurs in metal or ceramic systems is inversely proportional to some power of the average grain diameter, *i.e.*

$$\frac{dD}{dt} = \frac{k}{D^m}$$

or, on integrating

$$D^{m+1} - D_0^{m+1} = kt \qquad [1]$$

where D = the average diameter of a grain at a firing time t
D_0 = the grain diameter at $t = 0$
k = a rate constant

Equation [1] is usually written in the form $D^n = kt$, or as

$$D = k^{1/n} t^{1/n} \qquad [2]$$

where $n = (m + 1)$ and when $D >> D_0$. Thus, on plotting log D as a function of log t a straight line of slope 1/n is obtained. Frequently the value of 1/n lies between 0.1 and 0.5.

An activation energy for grain growth can be obtained conveniently from the log D/log t plot by measurement of the time, t', required to reach an arbitrarily chosen constant value of grain size. The reciprocal of this time value is directly proportional to the rate constant for grain growth. Consequently, the relationship between log t' and $1/T$ is, in effect, an Arrhenius plot of slope $E/2.303R$, from which the activation energy E can be evaluated.

In the present study the expressions developed for grain growth in porous compacts are applied to particle growth in zinc sulfide phosphors. Note that Eq. [2] is valid only for $D >> D_0$. This assumption is justified in the present study since the initial size of the zinc sulfide crystallites is approximately 0.02μ [ref. (7)], whereas the particle size of the fired phosphors is in the range 5μ to 50μ. For convenience, t' is taken as the time required to reach a particle size of 10μ.

REFERENCES

1. A. Schleede and H. Gantzkow, *Z. Physik. Chem.*, **106**, 37 (1923).
2. F. A. Kroeger and J. E. Hellingman, *This Journal*, **93**, 157 (1948).
3. H. W. Leverenz, "An Introduction to Luminescence of Solids," p. 78, John Wiley & Sons Inc., New York (1950).
4. J. Houben, *Mettalurgie*, **9**, 592 (1912).
5. G. R. Levi and C. G. Fontana, *Atti Accad. Naz. Lincei*, **7**, 502 (1928).
6. Y. Otomo, *Bull. Chem. Soc. Japan*, **32**, 804 (1959).
7. R. A. Brown, *Electrochem. Technol.*, **6**, 246 (1968).
8. R. A. Brown, *This Journal*, **116**, 298 (1969).
9. L. J. Bodi and C. F. Tufts, (a) *Science*, **143**, 872 (1966). (b) Proceedings of the International Conference on Luminescence, G. Szigeti, Editor, p. 1240, Akad. Kiado, Budapest (1968).
10. R. Cypres and B. van Ommeslaghe, *Bull. Soc. Franc. Ceram.*, **54**, 65 (1962).
11. P. A. Beck, J. C. Kremer, L. J. Demer, and M. L. Holtzworth, *Trans. AIME*, **175**, 379 (1948).
12. F. A. Nichols, (a) *J. Appl. Phys.*, **37**, 4599 (1966). (b) *J. Am. Ceram. Soc.*, **51**, 468 (1968).
13. P. H. Miller, *Phys. Rev.*, **60**, 890 (1941).
14. A. L. Smith, *This Journal*, **96**, 75 (1949).
15. V. M. Gugel, *Bull. Acad. Sci. U.R.S.S., Phys. Ser.*, **9**, 539 (1945).
16. R. C. Weast, Editor, "Handbook of Chemistry and Physics," 45th edition, p. B221, Chemical Rubber Co., Cleveland, Ohio (1964).
17. E. A. Secco, *Can. J. Chem.*, **42**, 1396 (1964).
18. A. J. MacKinnon, R. R. Martin, and E. A. Secco, *ibid.*, **42**, 2334 (1964).
19. T. Bansagi, E. A. Secco, O. K. Srivastava, and R. R. Martin, *ibid.*, **46**, 2881 (1968).
20. A. Kremheller, S. Faria, P. Goldberg, and D. J. Bracco, *This Journal*, **107**, 749 (1960).
21. F. Seitz, *J. Chem. Phys.*, **6**, 458 (1938).
22. H. W. Leverenz, "An Introduction to Luminescence of Solids," p. 100, Dover Publications Inc., New York (1968).
23. E. T. Allen and J. L. Crenshaw, *Z. Anorg. Chem.*, **79**, 130 (1913).
24. P. E. D. Morgan, "Sintering and Related Phenomena," G. C. Kuczynski, Editor, p. 549, Gordon and Breach, New York (1965).
25. S. Shionoya and K. Amano, *J. Chem. Soc. Japan, Pure Chem. Sect.*, **77**, 303 (1953).

The Influence of the Amorphous Phase on Ion Distributions and Annealing Behavior of Group III and Group V Ions Implanted into Silicon

Billy L. Crowder*

International Business Machines Corporation, Thomas J. Watson Research Center, Yorktown Heights, New York 10598

ABSTRACT

A study has been made of room-temperature implantations of group III and group V ions into amorphous Si layers prepared by the previous implantation of Si ions into crystalline Si substrates. Neutron activation combined with anodic oxidation and HF stripping techniques was used to determine the profiles of the implanted ions for Ga^{71} and Sb^{121}. Electrical evaluation of the implanted layers by Hall effect and sheet resistivity measurements in conjunction with layer removal techniques yielded profiles of the net electrically active species and the depth variation of mobility after annealing for 30 min in the temperature range 600°-900°C. The ion species studied were B^{11} (60-200 keV), Al^{27} (200 keV), $Ga^{69\&71}$ (140 and 280 keV), P^{31} (100-280 keV), As^{75} (280 keV), $Sb^{121\&123}$ (120 and 260 keV), and Bi^{209} (240 keV). The epitaxial regrowth of the amorphous phase at 600°C causes most of the implanted ions within this region to become electrically active and uncompensated for the ion species B, P, As, Sb, and Bi even for peak ion concentrations in excess of 10^{20} cm^{-3}. For Al and Ga implants, the number of carriers was less than the number of implanted ions. The profiles obtained for these implantations into amorphous Si were compared with predictions based on the theory of Lindhard, Scharff, and Schiott.

A dominant feature frequently observed in the annealing behavior of the electrical properties of ion-implanted Si produced at or below room temperature is the presence of a marked annealing stage at 600°C (1-4). This annealing stage has been attributed to the epitaxial recrystallization of a continuous amorphous phase onto the underlying Si substrate, a process which occurs between 550° and 600°C (5, 6). The present investigation represents a systematic study of the annealing effects that this amorphous phase has on the electrical properties of Si implanted with group III and V elements in the energy range 60-300 keV. A broader view of the electrical behavior of ion-implanted Si may be found in the article by Baron *et al.* (1) or in the review contained in the monograph by Mayer, Eriksson, and Davies (7).

For relatively high-dose implantations of heavy ions (*e.g.*, greater than 10^{15} ions cm^{-2}) at room temperature or below, most of the ions impinge on amorphous Si. Table I presents the dose required to produce a continuous amorphous surface layer as computed from a simple model (8) for the common group III and V ions in Si for very low-temperature implantations (D_0) and for room-temperature implantations (D_{300}), and as observed experimentally at room temperature (9). For light ions and/or low doses, a question arises as to whether implantation in a "random" direction is equivalent to implantation in amorphous material. Dearnaley and co-workers, who employed the convenient radiotracer P^{32}, determined that the profile for 120 keV P^{32} in amorphous Si (produced by Ne bombardment) was different from 120 keV P^{32} implanted in a "random" direction (10). The profile in amorphous Si exhibited a peak concentration at a depth 20% deeper than the profile obtained in crystalline Si in a "random" direction and no evidence of channeling. A second aim of the present investigation is to determine the ion profiles obtained in amorphous Si for several group III and V ions and to compare such profiles with the theoretical predictions of Lindhard, Scharff, and Schiott (LSS) (11).

* Electrochemical Society Active Member.
Key words: ion implantation, amorphous silicon, electrically active impurities, annealing behavior.

Table I. Ion dose required to produce a continuous amorphous Si layer (8)

Ion	D_0, cm^{-2}	D_{300}, cm^{-2}	D_{300} [measured (9)], cm^{-2}
B	9×10^{14}	4×10^{17}	$>2 \times 10^{16}$
P	2×10^{14}	8×10^{14}	$>5 \times 10^{14}$
As	1×10^{14}	2×10^{14}	2×10^{14}
Sb	6×10^{13}	1×10^{14}	1×10^{14}
Bi	4×10^{13}	6×10^{13}	5×10^{13}

Experimental Procedure

Implantations were conducted with the 300 kV accelerator used in our previous studies (3, 4, 6). The focused ion beam, after electromagnetic separation, was rastered electrostatically to provide a uniform implantation over a 2 x 2 cm^2 area. The total dose was determined by integrating the ion beam current. Dose rates employed in the present investigation ranged from 0.1 to 1.0 μA cm^{-2}, typically being 0.5 μA cm^{-2}. The substrates were wafers cut from Czochralski-grown crystals with a resistivity of 1 ohm-cm. These wafers were etch polished to provide a damage-free surface.

Hall effect and sheet resistivity measurements were made using the van der Pauw configuration previously employed. The van der Pauw pattern, defined by mesa etching, utilized contact pad regions produced by diffusion. Ions were implanted into substrates of opposite conductivity type to form p-n junctions, which provided the electrical isolation necessary for investigating the electrical properties of the implanted layer. In profiling experiments, anodic oxide growth, removal of an oxide by dilute HF, and electrical measurements were accomplished in a sample holder previously described (4).

Ion profiles were determined for P^{31}, As^{75}, Sb^{123}, and Ga^{71} by using neutron activation analysis in conjunction with layer removal by anodic oxidation and HF stripping as previously described (12). In this technique, liquid scintillation counting on the solution resulting from dissolving the anodic oxide provided the

necessary radiochemical assay. Annealing of samples was accomplished in a tubular furnace under a flowing nitrogen atmosphere.

Amorphous Silicon

A few comments are in order as to what constitutes a continuous amorphous Si phase. Investigations by Brodsky and co-workers on amorphous Si produced by several techniques provide a convenient frame of reference with which to work. These authors have determined some of the material properties associated with amorphous Si (13). Our previous investigations have demonstrated that the surface layers of Si which have received a "saturation" dose of energetic heavy ions exhibit the same optical properties and the characteristic ESR signal associated with amorphous Si (14) [the term "saturation" is used since the strength of the characteristic ESR signal increases linearly with dose (for fixed dose rate) until a critical dose[1] is reached beyond which only a small change with increasing dose is observed]. It is reasonable to conclude that such layers are completely amorphous Si.

The amorphous Si phase was produced by bombardment with 280-300 keV Si^{28} ions. For substrates maintained at or near room temperature during implantation, a dose of 3 x 10^{15} ions cm^{-2} was sufficient to produce an amorphous surface layer 0.5-0.6μ deep. In this paper, the term "amorphous Si" refers to such a surface layer.

One problem associated with the use of Si^{28} is the possible contamination of the ion beam with singly ionized molecular nitrogen. The source gas used was SiF_4, and the ratio of mass 28 to 29 to 30 was used to verify that no large amount of N_2 contamination was present. In the present experiments, the possible incorporation of relatively small concentrations of N^{14} seemed preferable to the use of large doses of "inert" species such as Ne^{20} or Ar^{40}. The use of Ar^{40} to produce amorphous Si has a deleterious effect on the annealing behavior of the electrical characteristics of Si implanted with P, even for an annealing temperature in excess of 900°C. A sample which was damaged with Ar (280 keV, 3 x 10^{15} cm^{-2}) prior to an implantation of P (280 keV, 3 x 10^{15} cm^{-2}) had, after a 600°C, 30 min anneal, a sheet resistivity of 550 ohms/sq compared to 80 ohms/sq observed after similar annealing for a control sample implanted only with P. This sample still exhibited a high sheet resistivity (160 ohms/sq) after annealing at 915°C for 30 min.

Interpretation of Hall Effect Measurements

The interpretation of Hall effect measurements obtained from ion-implanted layers has been adequately covered by a number of authors (1, 7). We briefly review some of the assumptions involved in interpreting the types of experiments presented in this paper.

The electrical measurements yield values for the sheet Hall coefficient, R_S, and the sheet resistivity, ρ_S. In experimental evaluation of the efficacy of annealing treatments, these parameters are often converted to the number of carriers per square centimeter, N_S, and the effective mobility, μ_{eff}

$$N_S = r/R_S e$$

$$\mu_{eff} = R_S/\rho_S$$

where e is the charge on the electron and r is the Hall factor expressing the ratio of Hall mobility to conductivity mobility. In most cases, the assumption is made that $r = 1$. We shall return to this point later in this section. It should be noted that both N_S and μ_{eff} are weighted averages over the impurity distribution (1, 7). In general, N_S is smaller than the true number of carriers per square centimeter since carrier mobilities are higher with lower impurity concentration. Because of this fact and the fact that the annealing behavior may differ in different portions of the ion distribution, the data obtained by isochronal annealing studies of the parameters, N_S and μ_{eff}, are only semiquantitative.

A more accurate picture of the implanted ion distribution may be obtained by combining sheet resistivity and sheet Hall coefficient measurements with layer removal techniques (1, 7). From such differential measurements, one can compute the resistivity of the ith layer, ρ_i

$$d_i\,(\rho_i)^{-1} = (\rho_S)_i^{-1} - (\rho_S)_{i+1}^{-1}$$

the mobility, μ_i, of the ith layer

$$\mu_i = \left[\frac{(R_S/\rho_S^2)_i - (R_S/\rho_S^2)_{i+1}}{(\rho_S)_i^{-1} - (\rho_S)_{i+1}^{-1}}\right]$$

and the carrier concentration, n_i, for the ith layer

$$n_i = (e\mu_i\rho_i)^{-1}$$

where d_i is the thickness of the ith layer. In this manner, a profile of the depth distribution of carrier concentration, carrier mobility, and layer resistivity can be derived.

A basic assumption involved in the above analysis is that the ratio of the Hall mobility to the conductivity mobility is unity. For lightly doped Si ($\lesssim 10^{16}$ cm^{-3}), the experimentally determined ratio is 1.2 to 1.3 for electrons and 0.7 to 0.8 for holes (15, 16). In n-type specimens, the Hall ratio, r, tends to unity for concentrations in excess of 10^{18} cm^{-3}; thus, for properly annealed n-type layers doped by ion implantation, the experimentally observed electron mobility is very nearly that determined for uncompensated bulk Si of comparable carrier concentration (1, 4). In such cases, the use of bulk data [*e.g.*, Irvin's curves (17)] in conjunction with differential sheet resistance measurements would yield a reasonable approximation to the impurity distribution.

The value of r for high concentrations of acceptors in Si is not at all well known. Irvin's data for p-type Si indicate mobility values which are significantly lower than those observed in other studies in the range 10^{17} to 10^{19} cm^{-3} (16). Furthermore, a determination of the Hall mobility in ion-implanted layers (Al, Ga implantations) (1) indicated deviations from bulk mobility values for concentrations in excess of 5 x 10^{17} cm^{-3}. Figure 1 presents a compilation of the observed Hall mobilities as a function of layer resistivity for a number of "well-annealed," boron-implanted Si wafers. Implantations were conducted at room temperature at energies of 30-200 keV. The samples were subsequently annealed for 30 min at 900°-950°C prior to stripping

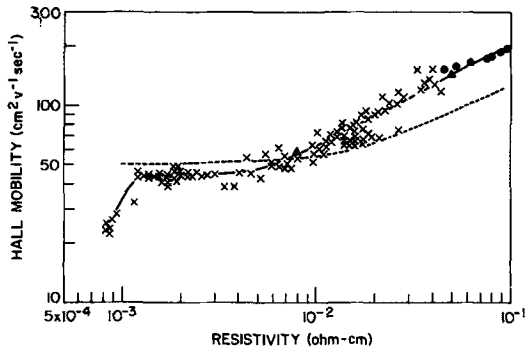

Fig. 1. Hall mobility vs. layer resistivity for B^{11} ion-implanted Si. Implantations were conducted at room temperature with ion energies between 30 and 200 keV, and the wafers were annealed for 30 min at 900°-950°C. The crosses represent data obtained for ion-implanted layers, the dashed line corresponds to the conductivity mobility of bulk Si from Irvin's curves [Ref. (17)], the triangles are Hall mobility measurements in bulk Si from Morin and Maita (Ref. 15), and the circles are Hall mobility data from Wolfstirn [Ref. (16)].

[1] The critical dose determined in this manner agrees well with published values obtained from Rutherford backscattering experiments (Table I).

for profiling. The triangles represent the Hall mobility determined in bulk Si (B-doped) by Morin and Maita (15), while the closed circles indicate the Hall mobility of Ga-doped Si given in Wolfstirn's study (16). The observed Hall mobility in these ion-implanted layers agrees well with that observed in bulk Si. In the concentration range 10^{17} to 10^{19} cm^{-3}, this agreement is an indication that the value of r is 0.7. The dashed line represents the conductivity mobility determined from Irvin's curve of resistivity as a function of impurity concentration (17). Irvin's data in the lower concentration range deviate markedly from experimental observations. The observed Hall mobility does approach a constant value in the concentration range 10^{19} to 10^{20} cm^{-3}, which is consistent with a constant conductivity mobility from Irvin's bulk data. If his bulk data in this concentration range are correct, a value of r of 0.8-0.9 would be consistent with the observed Hall mobility. For concentrations in excess of 10^{20} cm^{-3}, only limited experimental information was obtained. At concentrations greater than 1.5 x 10^{20} cm^{-3}, the observed Hall mobility decreased sharply with increasing concentration.

In interpreting the measurements of Hall effect in this paper, the assumption is made that the ratio of Hall mobility to conductivity mobility is unity. In well-annealed samples, the results discussed above indicate that such an assumption introduces errors of less than 30% in carrier concentration profiles in the range 10^{17} to 10^{20} cm^{-3}, the error being in the direction of indicating too many carriers in p-type samples and too few carriers in n-type samples.

Experimental Results and Discussion: Group III Elements

Boron.—The effect of the amorphous phase on the annealing behavior of room-temperature boron implantations is summarized in Fig. 2, which depicts the variation of N_S and ρ_S with 30 min isochronal annealing at temperatures 600°-900°C. The samples were implanted with 120 keV B^{11} ions in a "random" direction (1 x 10^{15} cm^{-2}, open triangles) or into amorphous Si (1 x 10^{15} cm^{-2}, closed circles; 1 x 10^{16}, open circles)

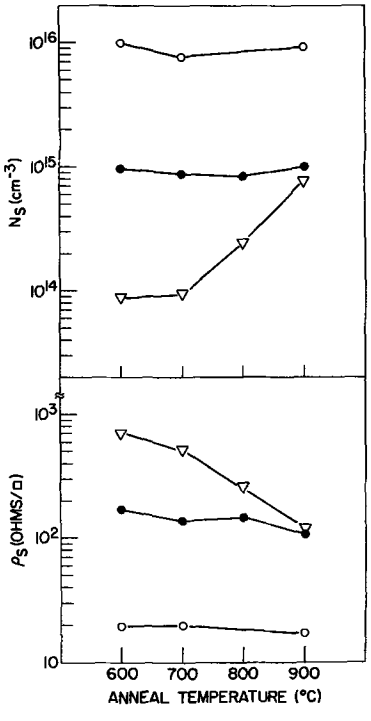

Fig. 2. N_S and ρ_S vs. annealing temperature for 120 keV B^{11} implanted into amorphous Si (circles) and into crystalline Si in a random direction (triangles). The implanted B dose was 1 x 10^{15} ions cm^{-2} (closed circles, open triangles) and 1 x 10^{16} (open circles), and implantations were conducted at room temperature. The duration of annealing was 30 min.

prepared by a sufficient dose of 300 keV Si^{28} ions (1 x 10^{16} cm^{-2}) to render the substrate amorphous from the surface to a depth of 0.6μ. The presence of the amorphous phase, which regrows epitaxially onto the Si substrate at 550°-600°C, greatly increases the number of implanted species which are electrically active and uncompensated, as previously observed by a number of authors (2, 18).

An experiment designed to establish clearly the association between the location of the amorphous phase and the region in which most of the ions are rendered electrically active and uncompensated after a low-temperature anneal was performed as follows. Damage by 300 keV Si^{28} ions was used to produce an amorphous region of a known thickness (0.53μ as determined from interference fringes in the optical absorption spectrum). This wafer was then implanted with B^{11} ions of such an energy that roughly half the ions were within this surface amorphous region and half were deeper within the crystal (*e.g.*, 200 keV ions). After annealing to recrystallize the amorphous phase, the wafer was profiled. The results of this experiment are presented in Fig. 3, which shows the depth distribution of the hole concentration and the hole mobility of 5 x 10^{15} 200 keV B^{11} ions cm^{-2} implanted under the above conditions. The carrier concentration shows a marked drop near the point at which the amorphous-crystalline interface occurs. Beyond this depth, the carrier concentration is markedly lower than the implanted ion concentration as shown by the solid line which represents the profile obtained in an annealed sample which had been implanted at 100°K with the same dose of 200 keV B^{11} ions. Implantation of B at such low temperatures produces a continuous amorphous surface layer; *cf.* Table I and Ref. (2).

The carrier mobility, on the other hand, is representative of that observed in uncompensated bulk Si of comparable carrier concentration (given by the dashed line in Fig. 3 which was derived from the experimental

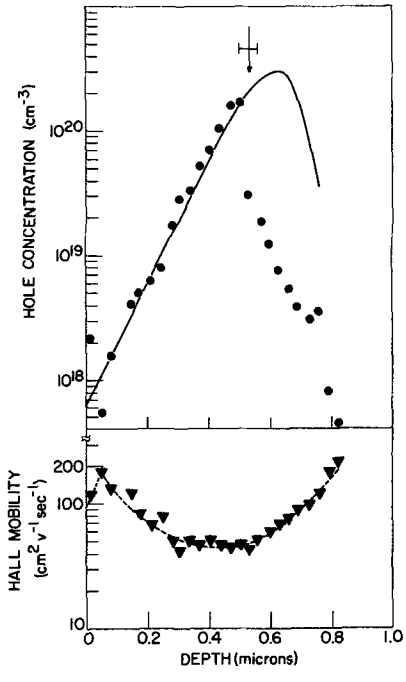

Fig. 3. Depth variation of the hole concentration and Hall mobility for 5 x 10^{15} keV B^{11} ions cm^{-2} implanted into Si with an amorphous surface layer. The depth of the amorphous layer was determined by interference fringes in the optical absorption spectrum to be 0.53μ as shown by the arrow. After implantation, the wafer was annealed at 800°C for 30 min prior to profiling. The dashed line represents the Hall mobility as determined from the solid line in Fig. 1 and the layer resistivity. The solid line is a profile obtained from a well-annealed sample implanted at 100°K with 5 x 10^{15} 200 keV B^{11} ions cm^{-2}.

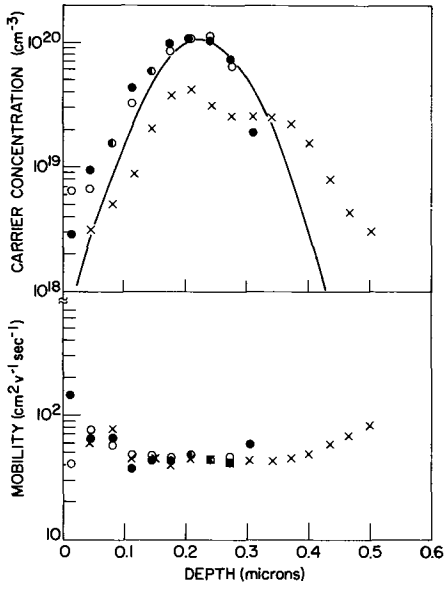

Fig. 4. Depth variation of the hole concentration and Hall mobility for 60 keV B^{11} ions implanted into amorphous Si (circles, 1.5 x 10^{15} cm^{-2}) and into crystalline Si in a random direction (crosses, 1 x 10^{15} cm^{-2}). In the latter sample, the Si was rendered amorphous to a depth of 0.5-0.6μ after B implantation by Si ion damage. The samples were annealed at 800°C for 30 min before profiling. The solid line represents a gaussian approximation to the amorphous implanted profile.

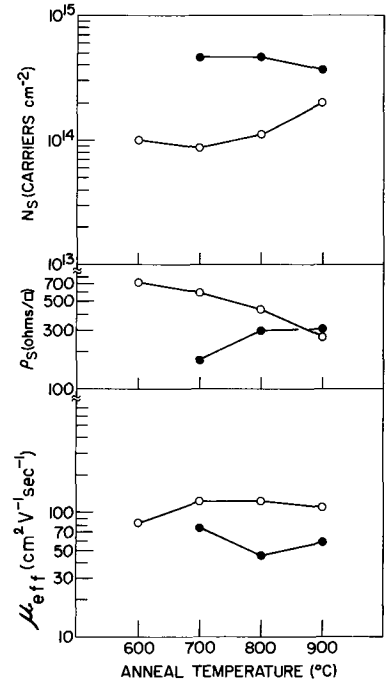

Fig. 5. Variation of N_S, ρ_S, and μ_{eff} with 30 min isochronal annealing temperature for 1 x 10^{15} 200 keV Al ions cm^{-2} implanted at room temperature into amorphous Si (closed circles) and into crystalline Si in a random direction (open circles).

layer resistivity and the data presented in Fig. 1) even in the region in which the hole concentration is markedly lower than the number of implanted B ions. This behavior is typical of B implantations (19) and indicates that nonsubstitutional B and/or compensating defect centers are neutral species.

The profile obtained by implanting into crystalline Si in a "random" direction and that obtained by implanting into amorphous Si are markedly different, as evident in Fig. 4 which presents the carrier concentration profile and variation of Hall mobility with depth for three Si wafers implanted with B and annealed at 800°C for 30 min prior to profiling. In two wafers, 60 keV B^{11} ions (1.5 x 10^{15} cm^{-2}) were implanted into amorphous Si (open and closed circles). In the third wafer (crosses), 1 x 10^{15} 60 keV B^{11} ions cm^{-2} were implanted into crystalline Si in a "random" direction (7 deg off <100>). This wafer was then damaged by Si ions to produce an amorphous phase prior to the post-implantation anneal. Implantation into amorphous Si produces a profile which is asymmetric, falling off sharply on the deep side (the value of N_S after 0.32μ was removed was only 8 x 10^{12} cm^{-2} for the sample represented by the closed circles in Fig. 4). This distribution is distinctly different from that obtained by implanting in a random direction (crosses in Fig. 4); *e.g.*, the value of N_S after 0.32μ was removed was 3 x 10^{14} cm^{-2}. The solid line in Fig. 4 is a gaussian approximation to be discussed in more detail in a later section.

Aluminum.—Isochronal annealing studies of Si implanted with Al ions are depicted in Fig. 5, which presents the annealing behavior of N_S, ρ_S, and μ_{eff} for two implantations of 1 x 10^{15} 200 keV Al ions cm^{-2}. In one case (closed circles), implantation was conducted into amorphous Si prepared by Si damage. In the other case (open circles), implantation was into crystalline Si in a "random" direction. Although the substrate in the latter case was nominally at room temperature, this dose of Al ions was not sufficient to produce a visible surface amorphous layer. The recrystallization of the amorphous phase again results in a relatively large fraction of the implanted ions being electrically active and uncompensated. In these Al implantations into the amorphous layer, however, increasing the annealing temperature decreases N_S and increases ρ_S, indicating that Al acceptors are being compensated and/or removed from substitutional sites. At this energy, a dose of 1 x 10^{15} ions cm^{-2} corresponds roughly to a peak ion concentration of 5 x 10^{19} cm^{-3} which is in excess of the solubility of Al in Si (2 x 10^{19} cm^{-3} at 1100°C). It should also be noted that previous investigations of Al implantations at significantly higher doses (1 x 10^{16} cm^{-2}) indicated that markedly higher sheet resistivities were obtained for such high doses after annealing (700°-900°C) than were obtained for 1 x 10^{15} ions cm^{-2} (19), again indicating that concentrations of substitutional Al markedly exceeding the solid solubility are not obtained by ion implantation after annealing. The behavior of 200 keV Al implanted into crystalline Si is very similar to that observed at lower energies by other authors; N_S increases smoothly with annealing temperature, while μ_{eff} approaches a constant value above 700°C (1, 19).

The profiles of carrier concentration and Hall mobility obtained for 200 keV Al implantations into amorphous Si after a 30 min anneal at 800°C (open circles and triangles) and 900°C (closed circles and triangles) are presented in Fig. 6. The observed carrier profile exhibits a "tail" relative to a gaussian approximation (dashed curve). Near the peak concentration, the observed Hall mobility is markedly lower than that expected for uncompensated bulk Si of comparable carrier concentration (the dotted line was computed from bulk mobility data and the solid line in Fig. 6). The low mobility indicates the presence of many scattering centers in addition to the implanted Al ions.

Figure 7 presents the profile obtained from implanting 1 x 10^{15} keV Al ions cm^{-2} into crystalline Si in a "random" direction and following the isochronal annealing sequence shown in Fig. 5. This profile exhibits a very long tail (channeling and/or interstitial diffusion during annealing). For the corresponding implantation into amorphous Si (closed circles, Fig. 6), the value of N_S after 0.6μ was removed was 7 x 10^{12} cm^{-2} and the value of μ_{eff} was 160 cm^2 V^{-1} sec^{-1}. The corresponding values after 0.6μ was removed for the specimen whose profile is given in Fig. 7 were 4 x 10^{13}

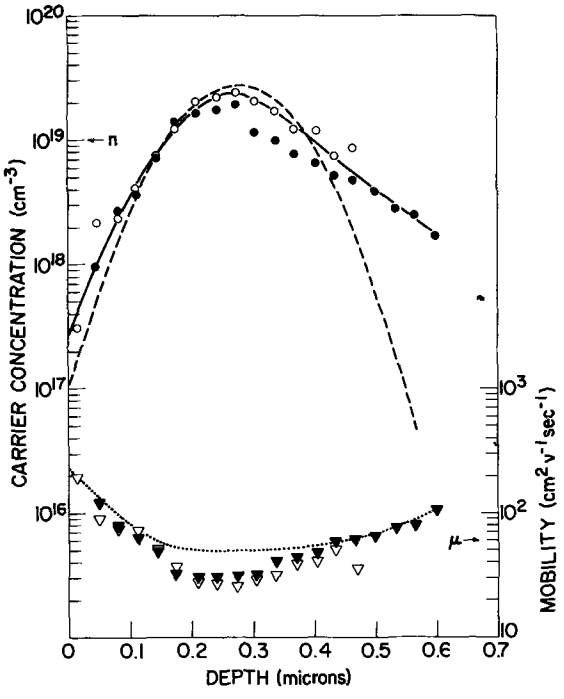

Fig. 6. Depth variation of the hole concentration and Hall mobility for 1 x 10^{15} 200 keV Al ions cm^{-2} implanted into amorphous Si. The samples were annealed for 30 min at 800°C (open points) or 900°C (closed points) prior to profiling. The dotted line corresponds to the mobility computed from the carrier concentration as given by the solid line and the bulk Hall mobility data presented in Fig. 1. The dashed line represents a gaussian approximation to the implanted profile.

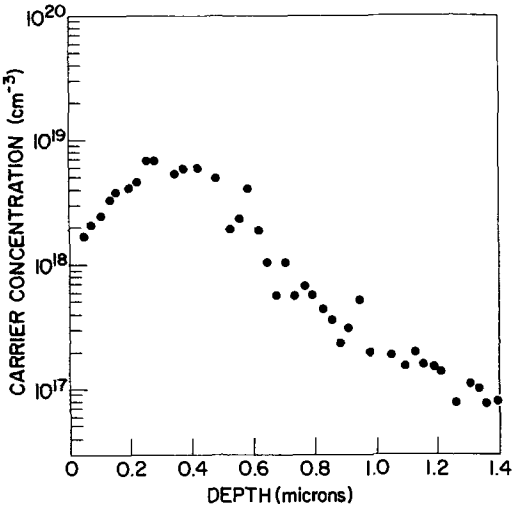

Fig. 7. Depth variation of the hole concentration for 1 x 10^{15} 200 keV Al ions cm^{-2} implanted into crystalline Si in a random direction after a 30 min, 900°C anneal.

cm^{-2} and 180 cm^2 V^{-1} sec^{-1}; *i.e.*, over five times as many carriers were present beyond 0.6μ in the "random" implant as compared to a comparably annealed amorphous implant.

At lower doses (*e.g.*, 1 x 10^{14} 200 keV Al ions cm^{-2}), the profile observed after annealing samples implanted in a "random" direction at 900°C was almost flat (7-9 x 10^{17} cm^{-3}) to a depth of 0.6μ and the mobility observed was comparable to that for bulk Si. This behavior was also noted for 30 keV Al implantations by Baron and co-workers (1) after 800°C annealing, which suggests that diffusion of Al does occur during the annealing process.

Gallium.—The isochronal anneal behavior of 280 keV Ga^{71} implanted into Si in a "random" direction is presented in tabular form in Table II. In all cases, the

Table II. Isochronal annealing behavior of 280 keV Ga^{69} implantations*

Dose (cm^{-2})	Annealing temp (°C)	ρ_s (ohms/sq)	N_s (cm^{-2})	μ_{eff} (cm^2 V^{-1} sec^{-1})
3 x 10^{15}	590	500	0.6 x 10^{15}	20
	700	412	0.27 x 10^{15}	60
1 x 10^{15}	590	215	0.44 x 10^{15}	67
	700	260	0.24 x 10^{15}	100
3 x 10^{14}	590	860	0.1 x 10^{15}	67
	700	940	0.1 x 10^{15}	60

* Duration of isochronal anneals was 30 min. Implantations were conducted at room temperature into Si substrates oriented 7 deg off the <100> axis.

dose of Ga was in excess of that required to produce a continuous amorphous surface layer (approximately 2 x 10^{14} cm^{-2}; see Table I). The value of N_s is observed to decrease with increasing annealing temperature, as observed by previous authors for 40 keV Ga (1, 20). Implanting concentrations of Ga much in excess of the solid solubility observed at high temperatures (3.5 x 10^{19} cm^{-3} at 1100°C) results in layers with a markedly higher sheet resistance than that observed for lower implantation doses (*e.g.*, compare the values for 1 x 10^{15} cm^{-2} and 3 x 10^{15} cm^{-2} in Table II). Such behavior was also noted for 40 keV Ga by Bulthuis and Tree (20). In this respect, Ga and Al behave in much the same fashion.

Since Ga^{71} is a convenient isotope for neutron activation, profiles of the Ga ion concentration as a function of depth were obtained by layer removal techniques in conjunction with radiochemical analyses. Two such profiles are presented in Fig. 8, which depicts the Ga^{71} concentration as a function of depth for implantation of 1 x 10^{15} Ga^{71} ions at 280 keV (open circles) and 140 keV (closed circles). The solid and dashed lines represent gaussian approximations to the implanted profiles. One would expect similar ranges and range straggles for Ga^{71} and As^{75}, which is indeed experimentally observed [*cf.* Fig. 10 and Ref. (12)]. One significant difference, however, is that the Ga profile shows a more pronounced tail on the distribution; the deviation from a nearly gaussian profile occurs at an order-of-magnitude-higher concentration level than that observed for As implantations [see Fig. 4 in Ref. (12)]. Since channeling is curtailed by relatively low damage levels and since one would expect the rate of damage production by 280 keV Ga^{71} and As^{75} to be comparable, this tail may be evidence

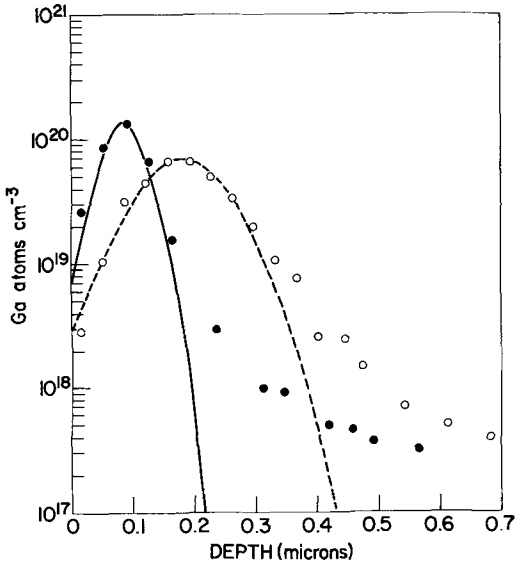

Fig. 8. Depth variation of Ga^{71} ion concentration as determined from neutron activation analysis stripping experiments for Si wafers implanted in a random direction with 1 x 10^{15} Ga^{71} ions cm^{-2} at 140 keV (closed circles) or at 280 keV (open circles).

for interstitial diffusion of Ga during implantation, neutron activation, or the 600°C, 30 min anneal which follows neutron activation.

Experimental Results and Discussion: Group V Elements

Phosphorus.—Figure 9 represents the carrier concentration profile and variation of mobility with depth of two wafers implanted at room temperature into amorphous Si with 3 x 10^{14} 280 keV P^{31} ions cm^{-2}. After implantation, the wafers were annealed for 30 min at 600°C. Prior to annealing, the location of the amorphous-crystalline interface, shown by the arrow in Fig. 9, was determined from interference fringes in the infrared optical absorption spectra of these wafers. The shape of this profile agrees quite well with that previously determined by neutron activation analysis and stripping for high-dose implantations (in which the majority of implanted P ions were actually incident on Si rendered amorphous by the damage produced by initial P ions) (12). The recrystallization of the amorphous phase does incorporate most of the implanted P ions on substitutional sites and removes most of the radiation damage defects in this region. The Hall mobility observed in this region is essentially that of bulk Si of comparable resistivity (the conductivity mobility of correspondingly doped bulk Si is shown by the solid line in Fig. 9) (17). A notable feature of these implantations is the fact that there is a transition region, as shown in Fig. 9, in which the sheet resistance and sheet Hall coefficient remained constant as layers were removed, indicating that this region is of relatively high resistivity. As the final layers were removed in this "transition region," the sheet resistance and sheet Hall coefficient actually decreased (possibly because of space charge effects). After this region was passed, layer removal resulted in normal behavior in which removing material resulted in an increase in sheet resistance and Hall coefficient. In this transition region, defects which compensate the implanted P ions are still present after a 600°C, 30 min anneal.

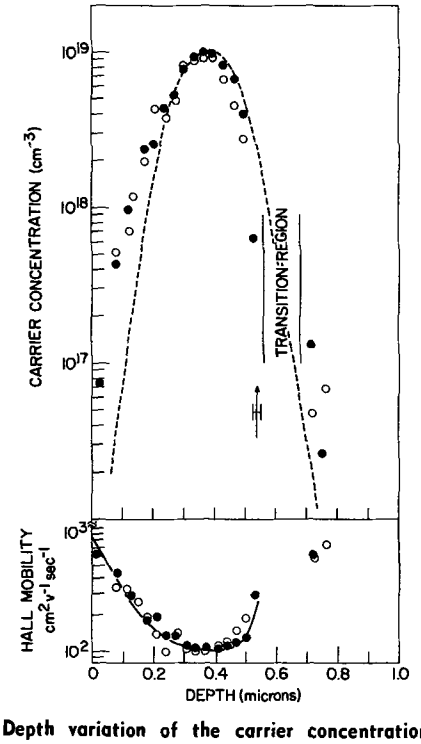

Fig. 9. Depth variation of the carrier concentration and Hall mobility for amorphous Si implanted with 3 x 10^{14} 280 keV P^{31} ions cm^{-2}. The depth of the amorphous Si layer was determined by interference fringes in optical absorption spectra as shown by the arrow. After implantation, the wafers were annealed at 600°C for 30 min. The dashed line represents a gaussian approximation to the ion profile. The solid line represents the mobility computed for bulk Si of comparable resistivity.

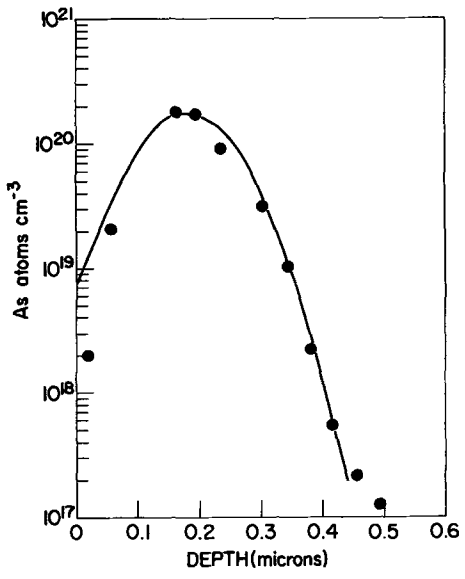

Fig. 10. Depth variation of As^{75} concentration for 280 keV As^{75} implantation into amorphous Si at room temperature as determined by neutron activation analysis. The As ion dose was 3 x 10^{15} cm^{-2}. The solid line represents a gaussian approximation to the profile.

The dashed line in Fig. 9 is a gaussian approximation to the profile. The experimental profile is asymmetric, exhibiting a larger concentration gradient (absolute value) at depths beyond the peak than at depths more shallow than that of the peak concentration.

Arsenic.—As^{75} is a sufficiently heavy ion that implantations of moderate doses (*i.e.*, greater than 3 x 10^{14} cm^{-2}) at room temperature will produce a continuous amorphous phase overlapping most of the implanted ion distribution as shown by previous studies (5, 6). Again, recrystallization of this amorphous region at 550°-600°C is the dominant factor in the observed annealing behavior (5, 6). Figure 10 presents a profile obtained by neutron activation analysis in conjunction with layer removal techniques for 3 x 10^{15} 280 keV As^{75} ions cm^{-2} implanted into amorphous Si at room temperature. This profile is essentially identical to that obtained by implanting a dose of 3 x 10^{15} 280 keV As^{75} ions cm^{-2} into crystalline Si wafers, except that channeling, which occurs during the initial stages of implantation, is not present [cf. Ref. (12)]. The solid line in Fig. 10 represents a gaussian approximation to the implanted profile.

Mayer and co-workers reported that the ratio of N_s to the implanted As dose was approximately 0.5 even after annealing to temperatures as high as 900°C (21). In that study, a low energy (20 keV) and a high dose (1 x 10^{15} cm^{-2} or higher) were employed, resulting in peak As concentrations of the order of 10^{21} cm^{-3}. At such high As concentrations, there is not a 1 to 1 correspondence between conduction electrons (measured at room temperature) and the As concentration. For example, a room-temperature implantation of 1 x 10^{16} 280 keV As ions cm^{-2} results in only 0.5 x 10^{16} carriers cm^{-2} after a 600°C, 30 min anneal. A room-temperature implantation of 3 x 10^{15} 280 keV As ions cm^{-2} results in 3 x 10^{15} carriers cm^{-2} after such an anneal. The upper limit on As concentrations at which the integrated carrier concentration equals the implanted dose is approximately (3 ± 1) x 10^{20} cm^{-3}.

Antimony.—A profile of the Sb^{123} concentration obtained by neutron activation of a sample implanted with 1 x 10^{15} 120 keV Sb^{123} ions cm^{-2} at room temperature in a direction nearly parallel to <111> is presented in Fig. 11. Implantation was started into crystalline Si, but most of the Sb ions were incident upon amorphous Si due to damage incurred from the ener-

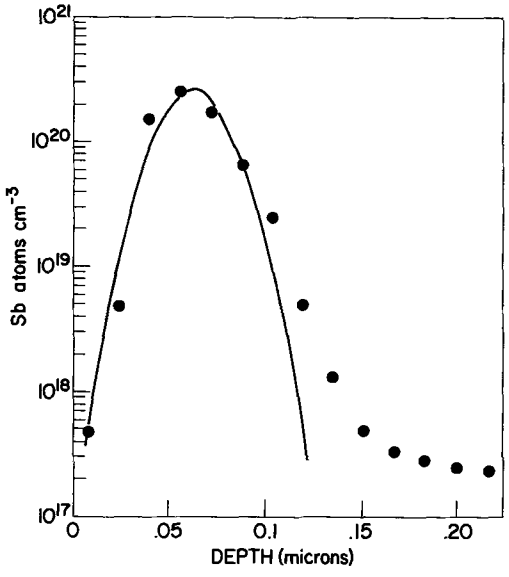

Fig. 11. Depth variation of Sb^{123} concentration in Si ion implanted with 1 x 10^{15} 120 keV Sb^{123} ions cm^{-2} as determined by neutron activation analysis. The solid line represents a gaussian approximation to the profile.

getic Sb ions in the initial stages of bombardment. The long "tail" presumably is due to channeling which occurred during that initial period before the damage density was sufficiently high to curtail it. The solid line represents a gaussian approximation to the implanted profile.

In a previous letter, we reported that the presence of the amorphous phase produced effective annealing at 600°C of even high concentrations of implanted Sb, but that implanting under conditions which prevented the formation of such an amorphous phase (*e.g.*, by heating the substrate to 500°-600°C during implantation) resulted in only a fraction of the implanted Sb as electrically active and uncompensated (3). The carrier concentration profile and depth variation of mobility for these two experimental conditions are presented in Fig. 12; the open circles and triangles were obtained from Si implanted with 3 x 10^{15} 260 keV Sb^{121} ions cm^{-2} at room temperature and annealed for 30 min at 600°C, while the closed circles and triangles represent data from a Si substrate (<111> orientation) maintained at 500°C during the implantation of 3 x 10^{15} 260 keV Sb^{121} ions cm^{-2}. The half-open circles represent "smoothed" data; the actual Hall data in this region were very noisy because of experimental difficulties. The measured sheet resistivity and an assumed mobility of 28 cm^2 V^{-1} sec^{-1} were used to compute these points.

Annealing a room-temperature implantation at 600°C, which recrystallizes the amorphous phase, results in a majority of the Sb being electrically active and uncompensated with mobilities near that of bulk Si of comparable resistivity, as shown by the dashed line in Fig. 12. The integrated carrier concentration observed in Sb implanted into Si at 500°C is about 30% of the implanted Sb, and the carrier mobility is markedly lower than that expected for bulk Si of comparable resistivity, indicating the presence of large numbers of scattering centers which limit carrier mobility. The carrier profile also indicates that implanting under these conditions results in a large fraction of the implanted ions being channeled and/or undergoing enhanced diffusion. Although no experiments were conducted to determine which process was occurring in these Sb implantations, previous research on high-temperature As implantations indicated that the largest effect was due to channeling in that the observed distribution was dependent on substrate orientation (4). The solid line in Fig. 12 represents a gaussian approximation to the Sb profile.

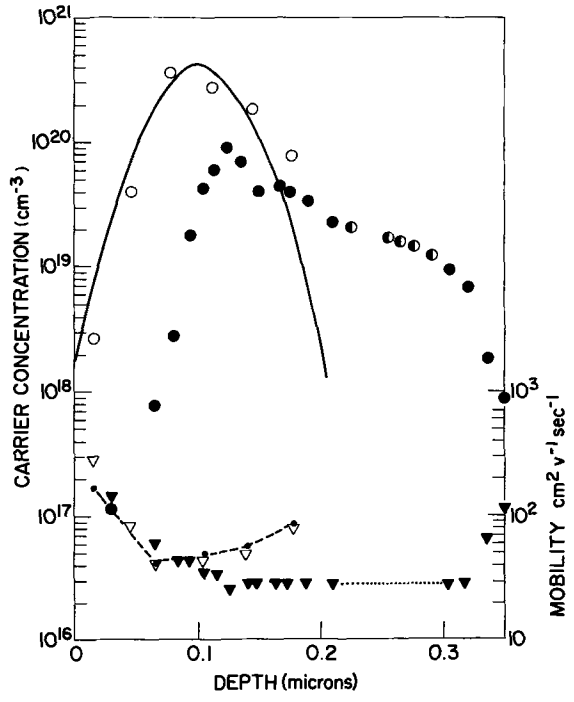

Fig. 12. Depth variation of the carrier concentration and Hall mobility of silicon implanted with 3 x 10^{15} 260 keV Sb^{121} ions cm^{-2} at room temperature followed by a 600°C anneal (open points) or 500°C anneal (closed points). The half-open points represent carrier concentrations calculated from the observed layer resistivity and an assumed constant mobility of 28 cm^2 V^{-1} sec^{-1} for the latter sample. The solid line is a gaussian approximation to the ion profile. The dashed line represents the mobility determined from bulk Si data and the observed carrier concentration in the room temperature implant.

Bismuth.—The implantation of doses of Bi^{209} in excess of 10^{14} cm^{-2} should result in the formation, at room temperature, of a continuous amorphous region, which should provide effective annealing at 600°C. This behavior is indeed observed as summarized in Table III for two different doses of 240 keV Bi^{209} ions. Table III presents the values observed for N_s and μ_{eff} as well as the integrated number of carriers per square centimeter obtained from profiling measurements and the ratio between this number and the implanted dose. For such high-energy implantations, a relatively large fraction of the implanted Bi dose can be obtained electrically active and uncompensated, in contrast to the reported behavior for 20-50 keV Bi implantations (22). For the heavy element Bi, a 20 keV implantation in Si produces a distribution with a peak concentration only slightly over 100Å from the sample surface, which may be responsible for the observed compensation at such low energies. In the 1 x 10^{15} 240 keV Bi ions cm^{-2} implantation, the peak carrier concentration was 1.2 x 10^{20} cm^{-3}, a value much in excess of the solid solubility of this species at 1100°C (2 x 10^{17} cm^{-3}).

Figure 13 presents the carrier concentration and mobility profile obtained by stripping the 3 x 10^{14} 240 keV Bi^{209} ions cm^{-2} implant. The carrier mobility is appreciably lower than that expected for bulk Si of com-

Table III. Electrical characteristics of Si layers implanted at room temperature with 240 keV Bi^{209} after a 600°C, 30 min anneal

Dose (cm^{-2})	N_s (cm^{-2})	μ_{eff} (cm^2 V^{-1} sec^{-1})	n_s (cm^{-2})*	n_s/Dose
3 x 10^{14}	1.5 x 10^{14}	88	1.8 x 10^{14}	0.6
1 x 10^{15}	6 x 10^{14}	47	6.5 x 10^{14}	0.65

* Integrated number of carriers per square centimeter obtained from profiling experiments.

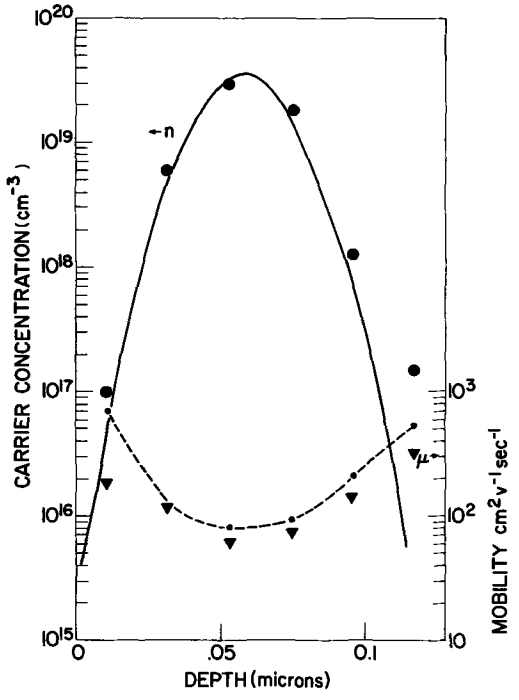

Fig. 13. Depth variation of the carrier concentration and Hall mobility of silicon implanted with 3 x 10^{14} 240 keV Bi^{209} ions cm^{-2} at room temperature followed by a 600°C anneal for 30 min. The solid line represents a gaussian approximation to the implanted ion profile. The dashed line represents the mobility computed from bulk Si data and the observed carrier concentration.

parable resistivity as shown by the dashed line. The solid line is a gaussian approximation.

A Comparison of Profiles in Amorphous Si with Lindhard Theory

It is of interest to compare the experimentally determined profiles obtained in this study for implantations into amorphous Si with the predictions of Lindhard, Scharff, and Schiott (LSS) (11), or, more specifically, with the tabulation "Projected Range Statistics in Semiconductors" by Johnson and Gibbons (23). An estimate will thereby be available as to the validity of such tables when applied to other amorphous semiconductors.

Profiles obtained by neutron activation reflect accurately the ion distribution, e.g. P^{31}, As^{75}, Sb^{123}, Ga^{71}. Profiles obtained from carrier concentration profiles are less reliable, but, when a majority of the implanted species are electrically active and uncompensated, the correspondence between carrier concentration and ion concentration should be good; e.g., the assumption that the correspondence is 1 to 1 should be good for B^{11}, reasonable for Bi^{209}, and less reliable for Al^{27}.

A basic assumption involved in applying the LSS theory in its simplest form is that the ion distribution is gaussian. This assumption was tested by comparing the observed profile with a gaussian distribution with the same peak position and a range straggle chosen so that this distribution and the observed distribution had the same full width at half maximum. The gaussian curves in Fig. 4, 6, 8, and 9-13 were determined in this manner. For light ions, e.g. B^{11} and P^{31}, the ion distribution is definitely skewed and exhibits a sharper gradient beyond the peak than before the peak[2]. The distributions observed for heavy ions implanted into amorphous Si are more nearly gaussian in shape.

[2] For such cases, the ion energies employed in the present investigation are sufficiently high so that electronic stopping becomes a significant factor in the energy loss of these ions. The additional straggle associated with this energy loss mechanism would be expected to produce a skew in the ion distribution toward the surface, since this energy loss mechanism is most important at high energies (i.e., near the substrate surface). For very light ions, wide angle scattering, which is neglected in simple LSS theory, may also distort the ion profile.

Table IV. A comparison of range parameters observed in amorphous Si with Lindhard theory calculations[1]

Ion	Energy (keV)	Range (microns) R_p (obs)[2]	Range (microns) R_p (LSS)	Range (microns) R (LSS)	Standard deviation (microns) ΔR_p (obs)[2]	Standard deviation (microns) ΔR_p (LSS)	Standard deviation (microns) ΔR (LSS)
B^{11}	60	0.23	0.244	0.346	0.07	0.071	0.059
	120	0.40	0.467	0.610	0.10	0.10	0.077
Al^{27}	200	0.26	0.297	0.360	0.08	0.070	0.084
P^{31}	100	0.12	0.123	0.155	0.048	0.035	0.046
	140	0.18	0.175	0.216	0.07	0.046	0.060
	200	0.28	0.254	0.306	0.074	0.061	0.078
	280	0.38	0.359	0.424	0.091	0.077	0.097
P^{32}	120[3]	0.16	0.149	0.185	0.06	0.041	0.054
Ga^{71}	140	0.09	0.083	0.097	0.035	0.018	0.030
	280	0.175	0.163	0.186	0.07	0.032	0.055
As^{75}	80	0.06	0.048	0.056	0.025	0.010	0.018
	140	0.095	0.079	0.091	0.040	0.016	0.028
	280	0.18	0.154	0.174	0.07	0.029	0.051
Sb^{121}	120	0.06	0.053	0.059	0.016	0.008	0.016
Sb^{123}	260	0.105	0.102	0.113	0.03	0.015	0.031
Bi^{209}	240	0.08	0.076	0.082	0.02	0.008	0.019

[1] LSS calculations from Johnson and Gibbons' tabulation [Ref. (23)].
[2] The experimental errors in these parameters are approximately ± 10%.
[3] Ref. (10).

The LSS theory provides a model from which one can compute the distance an ion travels in an amorphous material before coming to rest (the range, R) and the projection of this distance onto the direction of incidence of the incoming ion (the projected range, R_p). This theory is also used to compute the second moments or standard deviations associated with the quantities R and R_p, *i.e.* ΔR and ΔR_p. A compilation of the parameters characterizing the gaussian approximations as described in the previous paragraph for implantations into amorphous Si from this study, together with the values calculated from the LSS theory by Johnson and Gibbons for R, R_p, ΔR, and ΔR_p (23), is presented in Table IV. Also included in this table are the data obtained by Dearnaley and co-workers (10) for 120 keV P^{32} implanted into amorphous Si produced by Ne bombardment. The agreement between the observed range and the projected range is, in most cases, within the experimental errors inherent in these stripping experiments (±10%). Simple LSS theory does provide a reasonable estimate for this quantity.

The situation with respect to ΔR_p is not as clear. For very heavy ions (*e.g.*, Sb or Bi implanted in Si), for which the range and projected range are nearly equal, one would believe intuitively that ΔR and ΔR_p would be comparable (11). Surprisingly, the computations of Johnson and Gibbons indicate that, for such species, the value of ΔR_p is only about half that of ΔR (23), a result which strongly suggests that these authors made an error somewhere in their numerical analysis. Since their tabulations agree rather well with other calculations based on the LSS theory for ions lighter than the target atoms [see, *e.g.*, Ref. (24)] the origin of the error is not obvious. The error lies in the manner in which approximations were introduced into the LSS theory in order to facilitate numerical computations (see Appendix I).

Experimentally (see Table IV), it appears that the calculated values of ΔR are indeed in better agreement with the observed distribution widths than are the calculated values of ΔR_p, except for ions which are much lighter than Si (*e.g.*, B^{11}). If one adopts the simple rule of thumb that the larger of ΔR and ΔR_p should be used in estimating a gaussian approximation to an ion implantation profile, then the observed distribution widths near the peak concentrations agree with Johnson and Gibbons' LSS tabulation for B, Al, P, Sb, Bi, As, and Ga implantations into amorphous Si to within better than 30%.

Summary

In this investigation, we have demonstrated that the LSS theory does provide a reasonable estimate for the

most probable projected range of group III and group V ions in amorphous Si. The observed distribution widths, however, indicate that the detailed calculations of Johnson and Gibbons (23), although based on the LSS theory (11), erroneously predict values of ΔR_p which are much too small for heavy ions. The experimental results favor the use of their ΔR rather than ΔR_p as a reliable estimate for all but very light ions. A convenient rule of thumb is to use the larger of ΔR or ΔR_p when using these tables to estimate ion distributions.[3]

The distributions obtained in amorphous Si and in Si oriented in a random direction are not necessarily equivalent [*e.g.*, B and Al in the present study, P^{32} as observed by Dearnaley and co-workers (10)]. For heavy ions, the observed distributions in amorphous Si tend to be gaussian in shape. For light ions such as B or P, the observed distributions in amorphous Si are definitely asymmetric.

We have provided further evidence for the importance of the amorphous Si phase in determining the annealing characteristics of ion-implanted Si. The following observations are pertinent.

1. Elements with low solid solubility: For group III and V elements which have a low solid solubility at elevated temperatures (*e.g.*, Sb, Bi, Al, Ga), the maximum fraction which can be obtained electrically active for moderately high doses (*e.g.*, 1×10^{15} ions cm^{-2}) is achieved by annealing at temperatures near 600°C where the epitaxial regrowth of the amorphous phase occurs. Higher annealing temperatures tend to reduce the maximum electrical activity obtainable for these ion implanted species.

2. Group V elements: For P, As, Sb, and Bi, the epitaxial regrowth of the amorphous phase renders a majority of the implanted ions in this region electrically active and uncompensated. Peak concentrations in excess of 10^{20} electrons per cubic centimeter can be readily obtained from such species ($2\text{-}4 \times 10^{20}$ cm^{-3} observed for P, As, and Sb). Provided these peak values are not exceeded, the correspondence between the ion distribution and the electron distribution is nearly 1 to 1 for P and As and close to 1 to 1 for Sb and Bi for the atoms which lie within the region occupied by the amorphous phase before recrystallization. The discrepancy between the results reported in this work for 240 keV Bi and those reported for 20-50 keV Bi(21) probably results from the proximity of the ion distribution to the sample surface in the lower energy implantations.

3. Group III elements: No evidence of a marked increase in solubility over the solid solubility observed at high temperatures as a result of the epitaxial regrowth of the amorphous phase was obtained for ion-implanted group III ions. Only B could be obtained electrically active and uncompensated at high concentrations ($2\text{-}4 \times 10^{20}$ cm^{-3}) after implantation into amorphous Si and annealing at 600°C. The results obtained for Al implantations into amorphous Si suggest that, after 800°C annealing, charged compensating defects are present near the peak carrier concentration (reduced carrier mobility relative to bulk values). The shape of the profiles obtained for Al and Ga implantations into amorphous Si suggests that diffusion of these species may be occurring in the temperature range 600°-800°C.

4. The production of an amorphous phase by ion bombardment always results in a "transition region" composed of heavily damaged Si which is partially crystalline and partially amorphous. Annealing at 600°C does not remove all of the radiation damage defect centers in this region, and the remaining defects result in compensation and/or reduced mobility for n-type layers in this transition region.

[3] There is theoretical justification for using the larger of ΔR and ΔR_p from these tabulations. Details are given in Appendix I.

Acknowledgments

The author gratefully acknowledges the contributions of J. M. Fairfield and G. Jung in providing the neutron activation profiles, and the capable technical assistance of W. N. Hammer, N. A. Penebre, and R. A. Fiorio. The author is also indebted to W. S. Johnson for his discussion about the anomaly in the computer tabulations contained in Ref. (23).

APPENDIX I

The author contacted William S. Johnson regarding the apparent anomaly in the computer range calculations by James F. Gibbons and him contained in Ref. (23). This Appendix is a nonmathematical condensation of his private communication kindly provided to the author.

The quantity of interest, ΔR_p, can be considered to arise from two sources:

(*a*) The straggle associated with R, ΔR, projected in an appropriate fashion.
(*b*) The additional straggle associated with the uncertainty in the angle of deflection of the ions.

For very heavy ions incident upon a light substrate (*i.e.*, for those cases in which μ, the ratio of the mass of the target atom to the mass of the ion, approaches zero), one would expect that the contribution from (*b*) should tend to zero, because the angular deflection approaches zero. In this case, ΔR_p should tend to approach ΔR, as mentioned in the text. However, the tabulated values of ΔR_p contained in Ref. (23) tend to approach zero as μ approaches zero and are thus in error. The question thus arises, "What went wrong with the computer calculations?"

The origin of the discrepancy is the following. The computer calculations are based on integral equations derived from the LSS theory by applying a Taylor series expansion, keeping only first-order terms. Johnson has found that introducing this same Taylor expansion at the same point in deriving equations for the full range parameters leads to the result that, to first order, ΔR is zero! The use of higher-order terms in the Taylor expansion is thus necessary to evaluate ΔR correctly. By analogy, one may argue that it is necessary to consider second-order terms in correctly evaluating ΔR_p, particularly for those cases in which the ion is heavier than the target atoms. In a crude sense, the computer calculations of ΔR_p contained in Ref. (23) represent contributions from (*b*) to the straggle and ignore contributions from (*a*). In this case, the use of ΔR as a good approximation to ΔR_p for μ less than 1 is justified. In addition, the importance of contribution (*b*) for light ions (*i.e.*, μ greater than 1) dominates the observed straggle so that the tabulated values of ΔR_p in Ref. (23) should be reasonable estimates for this situation. This argument is certainly not conclusive but does provide some basis for using the larger of ΔR or ΔR_p as suggested in the text.

Manuscript submitted Nov. 4, 1970; revised manuscript received *ca.* Jan. 25, 1971.

Any discussion of this paper will appear in a Discussion Section to be published in the December 1971 JOURNAL.

REFERENCES

1. R. Baron, G. A. Shifrin, O. J. Marsh, and J. W. Mayer, *J. Appl. Phys.*, **40**, 3702 (1969).
2. D. E. Davies, *Appl. Phys. Letters*, **14**, 227 (1969).
3. B. L. Crowder and F. F. Morehead, *ibid.*, **14**, 313 (1969).
4. B. L. Crowder and J. M. Fairfield, *This Journal*, **117**, 363 (1970).
5. R. S. Nelson and D. J. Mazey, *Int. Conf. on Applications of Ion Beams to Semiconductor Technology, 1967, Grenoble, France*, p. 337.
6. B. L. Crowder, *This Journal*, **117**, 671 (1970).
7. J. W. Mayer, L. Eriksson, and J. A. Davies, "Ion Implantation in Semiconductors," Chap. 5, Academic Press, New York (1970).
8. F. F. Morehead and B. L. Crowder, To be published in *Radiation Effects*.
9. J. W. Mayer, L. Eriksson, and J. A. Davies, *op. cit.*, Chap. 3.

10. G. Dearnaley, M. A. Wilkins, P. D. Goode, J. H. Freeman, and G. A. Gard, AERE R 6197 (1969).
11. J. Lindhard, M. Scharff, and H. E. Schiott, *Kgl. Danske Videnskab. Selskab, Mat. Fys. Medd.*, **33**, No. 14 (1963).
12. J. M. Fairfield and B. L. Crowder, *Trans. Met. Soc. AIME*, **245**, 469 (1969).
13. M. H. Brodsky, K. Weiser, G. D. Pettit, and R. S. Title, *Phys. Rev.*, **B1**, 2632 (1970).
14. B. L. Crowder, R. S. Title, M. H. Brodsky, and G. D. Pettit, *Appl. Phys. Letters*, **16**, 205 (1970).
15. F. J. Morin and J. P. Maita, *Phys. Rev.*, **96**, 28 (1959).
16. K. B Wolfstirn, *J. Phys. Chem. Solids*, **16**, 279 (1960).
17. I. Irvin, *Bell System Tech. J.*, **41**, 387 (1962).
18. N. G. Blamires, M. D. Mathews, and R. S. Nelson, *Phys. Letters*, **28A**, 178 (1968).
19. A. H. Clark and K. E. Manchester, *Trans. Met. Soc. AIME*, **242**, 1173 (1968).
20. K. Bulthuis and R. Tree, *Phys. Letters*, **28A**, 558 (1969).
21. J. M. Mayer, O. J. Marsh, G. A. Shifrin, and R. Baron, *Can. J. Phys.*, **45**, 4073 (1967).
22. O. J. Marsh, R. Baron, G. A. Shifrin, and J. W. Mayer, *Appl. Phys. Letters*, **13**, 199 (1968).
23. W. S. Johnson and J. F. Gibbons, "Projected Range Statistics in Semiconductors," Stanford University Bookstore (1970).
24. J. W. Mayer, L. Eriksson, and J. A. Davies, *op. cit.*, Chap. 2.

Growth of Wide, Flat Crystals of Silicon Web

D. L. Barrett* and E. H. Myers

Westinghouse Research Laboratories, Pittsburgh, Pennsylvania 15235

and D. R. Hamilton and A. I. Bennett*

Westinghouse Semiconductor Division, Youngwood, Pennsylvania 15697

ABSTRACT

The temperature field and heat flow about the solidification interface of web crystals was modified by use of shaped radiation sinks. As a result, web was grown as wide as 3 cm and flat to less than 2.5 μm in 100 μm thick sheet. A qualitative extension of thermal models in dendrite growth applied to web morphology satisfactorily explains the experimentally observed results.

Silicon web growth is a modification of the controlled dendritic solidification process (1-3) in which a thin ribbon of silicon, bounded by two thicker dendrites, is pulled directly from a melt (Fig. 1). Growth is initiated by immersing a twinned [$2\bar{1}\bar{1}$] dendrite seed into an undercooled melt. Initially, growth is lateral giving the seed an inverted "T" shape; when pulling is commenced, a dendrite propagates into the melt from each end of the "T." As the solidified dendrite bridge emerges from the melt, a thin film of liquid is drawn up by surface tension between the button and the two dendrites. As growth proceeds, the dendrites grow apart, widening the web until finally a quasi-steady state is reached where the web width is constant. Web growth thus consists of seeding, widening, and finally steady-state growth during all of which the dendrites solidify slightly below the melt surface and the web section solidifies slightly above the original unperturbed melt level.

O'Hara and Bennett (3) proposed that web flatness, or rather lack of flatness, is governed by two-dimensional nucleation at the liquid meniscus-web interface so that a localized reduction in undercooling should reduce the rate of nucleation and promote flatness. Furthermore, O'Hara (4) and Tucker and Schwuttke (5) have noted that low or dislocation-free web could be grown. Our primary interest was to determine the relationships between heat sources and sinks and the crystallographic factors that determine web morphology and perfection.

There was also a practical reason for this work. We wished to determine what thermal conditions were necessary to grow wide web with flat surfaces and low dislocation content suitable for direct use in fabricating devices. Although web has been produced (6) several meters in length and a centimeter or so in width, this material must be grown wider, flatter, and of low dislocation content to be really interesting to the device fabrication industry. Greater width is desirable, for many power devices are larger than 1 cm in diameter and, while large-area rectangular-shaped web was available, this shape is not compatible with present industry tooling. In addition, photomasking requires a surface flat to 10 μm, and, although web in thin section has been reported within this tolerance (7), many devices require a thicker substrate material. Finally, dislocations which generate in the supporting dendrites accumulate within thicker web during growth (4, 7),

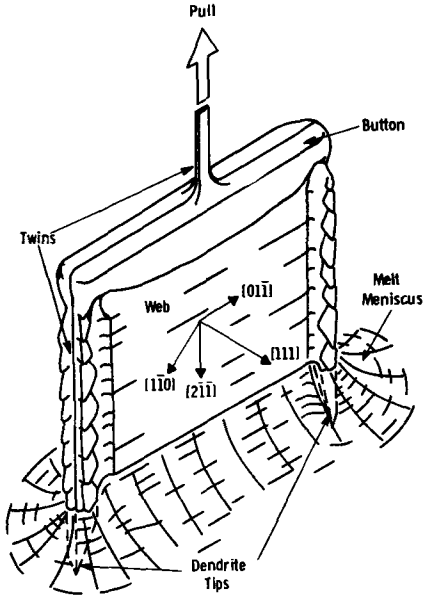

Fig. 1. A schematic drawing of a growing web crystal indicating the seed dendrite, button, and solidification interfaces of dendrites and web.

* Electrochemical Society Active Member.

Key words: silicon, webs, crystals, growth, temperature shielding, dislocations.

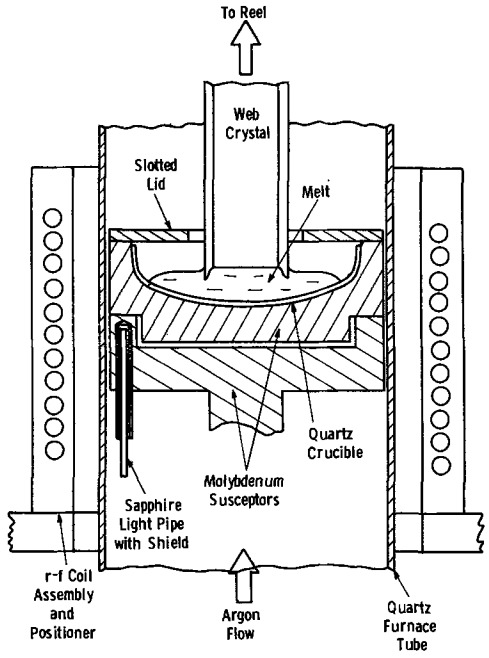

Fig. 2. Web growth furnace showing a melt and quartz crucible contained within molybdenum susceptors. A molybdenum lid covers the crucible except for a shaped slot through which the crystal is pulled. The rf coil is rigidly mounted and movable in "x,y,z" directions.

often reaching densities of 10^3-10^5 dislocation pits/cm^2. A reduction in dislocation density is essential to preparation of good device-grade web material.

In our experiments, we have altered the temperature fields about the growth interface in a controlled manner. We were able to obtain web crystals 3 cm over-all width and flat to within 2.5 μm on 100 μm thick material, with dislocation densities near 1000 cm^{-2}. We describe the experiments which resulted in these improvements and postulate crystal growth mechanisms that may be operative.

Apparatus

The apparatus used to pull web crystals is shown in Fig. 2. This system consists of a shallow quartz crucible which nests within larger molybdenum susceptors; 450 kHz, 10 kW rf heat is supplied the susceptors through a quartz furnace tube. A rapid flow of argon from the bottom of the tube and out a slot through which the crystal is pulled at the top of the system protects the melt. Pulling was accomplished by winding a leader and subsequently grown web on a large (34 in.) diameter reel. Growth rates of 1-5 cm/min could be achieved by driving the reel with a variable-speed d-c motor, regulated to about $\pm$0.01 mm/min.

The temperature of the melt was controlled by sensing radiation from a deep hole in the molybdenum support just below the melt with a sapphire light pipe and a Leeds & Northrup "Radiomatic" thermopile. The thermopile output was used to control the output of the rf generator and, although actual temperature variations within the melt were not determined, the control point variation was estimated at $\pm$0.2°C. The quality of the over-all control is indicated by our ability to grow great lengths of very small dendrites (0.1 mm diameter) without variations in size or thickness.

Maintenance of proper temperature gradients within the melt was the single most important aspect of web growth. The area of solid web crystal in contact with the melt was small and, although the heat released from the solidifying crystal must certainly dominate isotherms close to the interface, small asymmetric variations in the temperature of the surrounding melt greatly affect the growth. To maintain reproducible thermal conditions, we encased the rf coil in a castable ceramic and mounted the cast coil rigidly on a milling head positioner which could be moved in a vertical "z" direction, and the "xy" plane with respect to the susceptor. Displacements as small as 2.5 mm had marked effects on crystal growth.

As shown in Fig. 2, a slotted lid was used to cover the top of the system through which the web was pulled. The shape of this slot had much to do with defining the region of melt undercooling. Measurements showed the outer edge of the melt to be hotter than the center, thus preventing spontaneous nucleation at the melt-quartz interface, while the center region of the melt surface was undercooled as a result of radiation loss through the shield slot. Positioning the web crystal within the melt was achieved by a combination of adjustable molybdenum guide fingers and a movable flat steel plate above the slot in the lid. Proper control of the web position with respect to the undercooled center of the melt was essential to satisfactory crystal growth.

Temperature measurements in the melt were made with shielded Pt-PtRh thermocouples in fine closed-end quartz capillaries. Mechanically, it was difficult to accommodate these during web growth; thermally, their presence near the interesting region, the interface, cannot be tolerated. As in previous quantitative work (9), we were forced to rely on a melting point calibration at the melt center using a fine dendrite, and a set undercooling below this using the system's controller. The principal experimental parameter was the disposition of heat sources and sinks about the melt; and the controlled variable was the response of web growth to these.

Experimental

We altered heat flow and temperatures near the solid-liquid interface in several ways. First, we put quartz-covered, 40W resistance heaters, 0.3 cm diameter and 2.5 cm long, close to or below the melt surface and 0.2-0.3 cm away from the center of each side of the web sheet. By turning these on and off, we grew web which was thinner when heat was supplied. Since no other parameter was varied, we conclude that the undercooling of the melt near the web face was reduced and that the thinner web was a consequence of a reduction of at least the crystal growth rate and probably the nucleation rate as well, confirming the O'Hara and Bennett model (3). We were unable, however, to control the heaters sufficiently well to grow flat web surfaces and we abandoned these in favor of radiation sinks.

We modified the crucible with two kinds of radiation sinks. The simple slot in the lid (Fig. 3A) was changed by pinching in its center and by cutting out round holes at its ends (Fig. 3B). This "dog bone" slot was intended to reduce radiation loss from the center of the web and the nearby liquid, while increasing losses

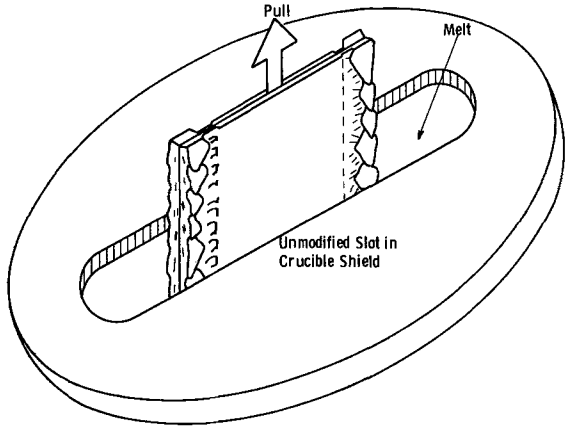

Fig. 3A. Crucible lid radiation shield showing relationship of slot shape to the crystal during pulling.

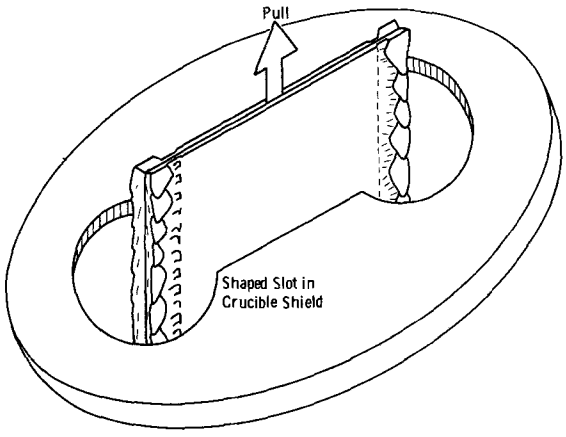

Fig. 3B. Shaped shield slot used to heat the web region while cooling the dendrite regions.

around the dendrites. For the same undercooling at the dendrites (as measured by the same dendrite size and growth velocity), the web center must be relatively hotter and growth or nucleation rates there lower.

A second and even more successful technique for radiation control is shown in Fig. 4. Two radiation ports were drilled through the bottom of the molybdenum susceptor. Each was estimated to radiate about 10W through the quartz crucible, cooling the melt beneath the dendrites. So effective was this additional cooling that solid silicon occasionally nucleated on the quartz over the ported area. Using this modification, we were able not only to improve surface flatness but also to increase greatly the initial web width and subsequent widening rate. There was one serious difficulty. Dislocations were rapidly generated and the web quickly became polycrystalline. A final modification (Fig. 5) consisted of a pair of heat shields which were put above the slot in the lid parallel to the web faces. Their function was to reduce further the temperature gradients in the web and adjacent melt by reducing radiation losses from the web after it has been pulled through the slot. This aftershield on the two-hole ported crucible was the most successful apparatus used. In it we grew the wide, flat webs of Fig. 6.

Results

Crystal width.—At constant undercooling and pull velocity, the dendrites diverge from the [$2\bar{1}\bar{1}$] growth axis and each other and the web slowly widens. The rate is sensitive to apparatus changes, and a convenient way to characterize it is to plot over-all width

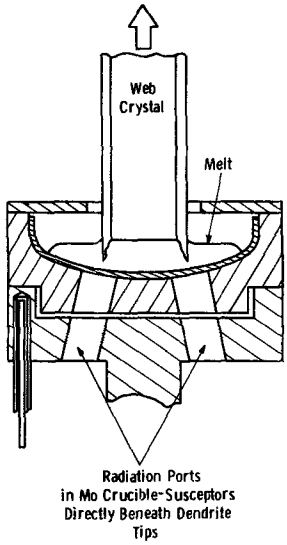

Fig. 4. Two radiation ports in crucible whereby the melt directly beneath the two dendrites is cooled.

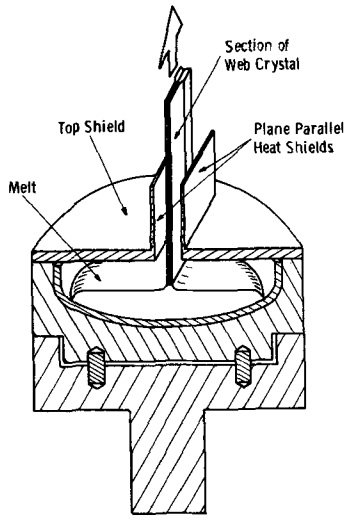

Fig. 5. Heat shields positioned parallel to the (111) web face reducing the rate of heat loss by radiation from the solidified crystal.

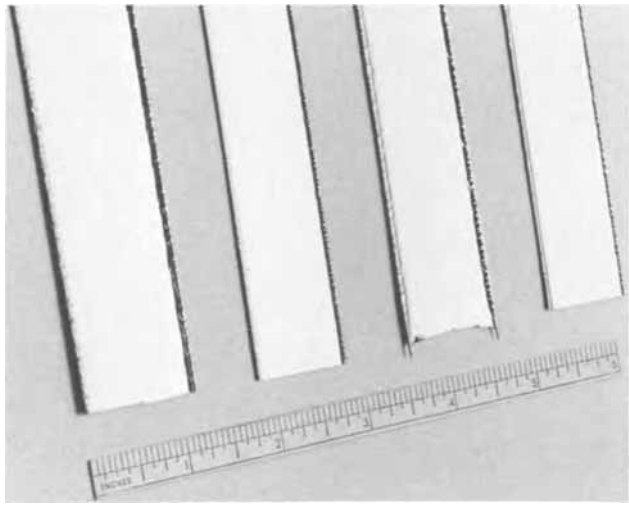

Fig. 6. Wide, flat crystals pulled from a two-hole ported crucible with aftershields.

as a function of length, Fig. 7. The three curves are averaged data of at least six crystals from each of the three furnace modifications. The first is that of Fig. 3A, the second, Fig. 3B, while the third is like the first but with the ports of Fig. 4. The widening rates increased with each change, from 0.04 to 0.1 mm/cm of length. In the ported crucible design, the limiting width was not set by approach to steady state as in the unmodified crucible but rather by the 3 cm outer diameter of the

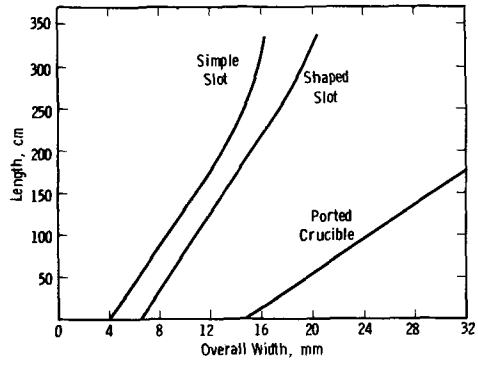

Fig. 7. Over-all crystal width as a function of web length. The widening rate in the ported crucible is about twice the simple or shaped slot rates.

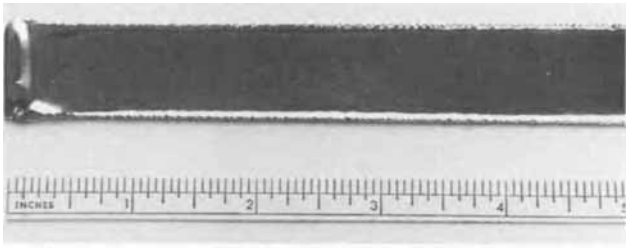

Fig. 8. Web crystal in which the initial seed button was widened to 2 cm prior to pulling. A 0.02 cm dendrite seed (not shown) was used to seed this crystal.

melt. The web was as wide as the melt. Had there been more silicon, we believe greater width could have been achieved.

These modifications changed the initial seeded width as well as widening rate. The initial widths increased from 0.4 through 0.6 to about 1.4 cm, suggesting a very real effect of apparatus upon the undercooling at the melt surface. Figure 8 shows an extreme case. The first web grown was over 2 cm wide. The seed dendrite (not visible) was about 0.02 cm diameter. Great skill was required to do this. For example, if the rf heating coil was not well positioned or if the seed was not put into the center of the undercooled region, the growth from the seed would be asymmetrical. On pulling, the tiny seed would bend under the lopsided load with subsequent loss of the meniscus and web. Although we cannot specify a detailed mechanism, we believe that the initial width and the widening rate are related to the extent to which the undercooled region was modified by the introduction of radiation sinks.

Web flatness.—Using a microscope with a calibrated micrometer eyepiece, we measured cross sections cleaved normal to the $[2\bar{1}\bar{1}]$ growth direction (Fig. 9) The distance from the intersection of the twin planes with the cleavage faces (a reference trace) to the web faces was determined at 2 mm intervals across the width to obtain the surface profile. Profiles were taken at 1 ft intervals along the web length, since both thickness and flatness vary slowly with length (providing growth conditions were not varied). The microscope measurement, referred to the twin plane trace, was sensitive not only to surface flatness but also to thickness, to bow, and to taper.

In Fig. 10, the surface profiles are plotted relative to the twin planes using a magnified and displaced vertical scale to demonstrate deviation from flatness. The total average thickness of the web was constant. The average standard deviation from flatness, σ, is shown for each profile trace. By moving the web during growth, the distance of the twins to the surface could be varied. The data shows a relationship between the flatness of the surface and its distance from the twin planes; Fig. 11 quantitatively shows this to be a linear function, with σ increasing at a rate of 10 μm for each 100 μm increase in distance from the twin plane. At a given total thickness, the closer the twin planes are to one surface, the flatter it will be but only at the expense of the reverse side. For this reason, we use the averaged standard deviation of both sides to measure web surface quality. In summary, surface flatness deteriorates as web widens. It is relatively better on whichever face is nearest to the twin planes.

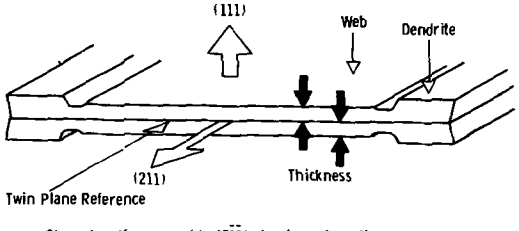

Fig. 9. Schematic cross section of web crystal normal to $(2\bar{1}\bar{1})$ showing the supporting dendrites and adjacent fillet regions. Web thickness and deviation from flatness was microscopically measured using the twin plane trace as a reference plane.

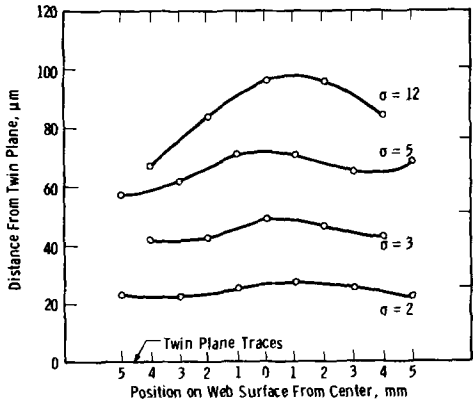

Fig. 10. Magnified profiles of web surfaces showing increased deviation from flatness (σ) with distance (thickness) from twin plane reference.

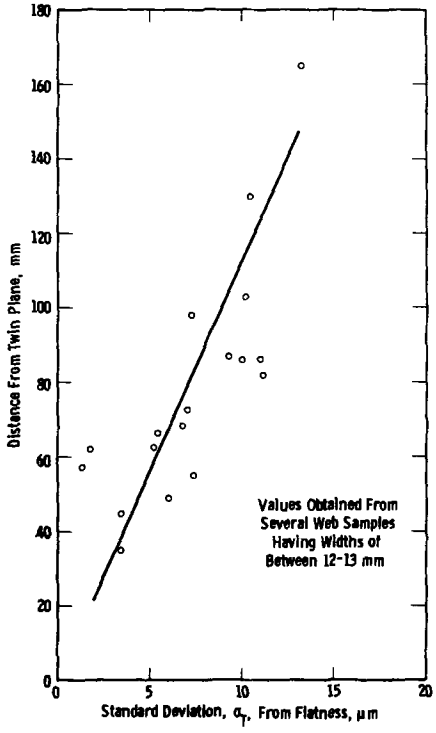

Fig. 11. A linear increase of about 10 μm deviation from flatness (σ) occurs for each 100 μm increase in thickness.

We now describe experiments with several crucibles. Figure 12 shows least-square line fits of average σ as a function of width for the three crucibles described earlier and a ported crucible with the aftershields. The flatness at given width improved regularly as the apparatus was successively modified. The web from the ported crucible with aftershields is much the flattest, even at widths greater than we could grow in others. The deviation is always less than 10 μm which is adequate for photomasking. These data confirm the efficiency of controlled heat flow in determining overall web flatness despite the observed effects of interface width and the influence of the twins.

Discussion

We can derive insight into web growth behavior by qualitative extensions of known thermal models of

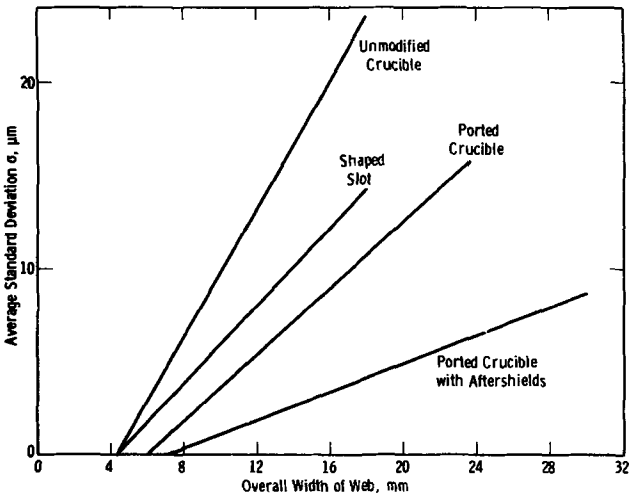

Fig. 12. Averaged values of flatness deviation are shown here as a function of over-all web width for different crystal-pulling arrangements. The ported crucible with aftershield arrangement yielded web flat to within 10 μm at 3 cm over-all width.

dendritic growth. The tip morphologies of semiconductor dendrites (8) and the theories that successfully account for their growth (9, 10) show that the thermal gradients about these are large and have almost rotational symmetry about the [2$\bar{1}\bar{1}$] growth axis. Imagine two dendrites, with a coplanar twin structure, growing side by side in an undercooled melt. Temperatures at some constant depth in the melt will in general be higher between the dendrites than at other points equidistant from one or the other dendrite. Heat flow will stagnate across the plane containing the twins. Temperature gradients thus favor growth away from the common [2$\bar{1}\bar{1}$] growth direction and the dendrites diverge. If the dendrites are joined by web, this tendency to diverge should be further increased, and the web widens. If effective heat sinks are added outside the dendrites, the widening rates will become larger. This is indeed what we observed with our lid and crucible designs. The limiting width is apparently set by the melt diameter.

The flatness of web is certainly affected by interactions with the dendrites. For example, when the dendrites are close together and the web is narrow, its middle is thin for the dendrites always dominate the heat flow about the web immediately adjacent to them. But when the dendrites are far apart, the center of the web is less influenced by them and becomes increasingly responsive to other heat sources and sinks within the system. Unfortunately, some of these other sources and sinks, the melt, the crucible, and susceptor are of overriding rotational symmetry. If only these rotationally symmetric fields were present and no attempt was made to compensate for them, the web would become round like a [211] Czochralski crystal. It is thus plausible that, when wide, web should grow thicker at its center. Since when web is narrow it is thinnest at the center, there must be some particular width at which web is flattest. As the width increases beyond this point, there should be a degradation in surface flatness. When heat sinks are added which relieve the rotational symmetry, the quantitative relationship between flatness and width should become more favorable, and the width at which the surface is flattest will become greater. The slopes of the lines in Fig. 12 show the former, and their intercepts on $\sigma \equiv 0$ the latter.

There is a correlation between surface flatness and the distance of that surface from the twin planes. Since the whole web-dendrite structure is more or less flat, there should be near the interface a stagnation plane across which no heat flows. This must also be more or less flat and certainly should be within the projection of the thickness (the [211] section) of the crystal, for the solid liquid interface is, after all, nearly isothermal. For an isolated dendrite, any plane containing the tip normal is a stagnation plane and the plane of the twins is one of these. For two coplanar dendrites the twins uniquely define it, and in our crystals it is probable that the stagnation surface will be near the twins in the web as well. Thus, if web is growing with one face near the twin planes, this face and not the other should lie nearer this surface of thermal stagnation. It is plausible that this face should be flatter, for temperatures close to the stagnation plane should be higher and nucleation and growth rates correspondingly lower after the mechanism proposed by O'Hara and Bennett (3). Thus, flatness and the distance to the twins can be plausibly related. Similarly, reversing the argument, the other side of the web should become less flat. As one side improves, the other degrades.

Dislocations.—Silicon web has a reputation for its high dislocation content, a reputation well earned for it often contains 10^3 to 10^5 dislocations/cm^2. In our web, the majority of dislocations were generated in bursts at melt entrapment centers on the dendrite surfaces (4, 7). These dislocations may slip into the web sheet and then turn and propagate in the [2$\bar{1}\bar{1}$] growth direction. If there is a sufficient number of these bursts, dislocations accumulate in the web center until eventually the web becomes polycrystalline.

In contrast to this, Tucker and Schwuttke (5) have described the growth of dislocation-free web. This web was relatively narrow, thin (45μ), and was grown with melt temperatures within 5°C of the silicon melting point. We have also grown thin web under low undercooling conditions and have confirmed that the crystal was dislocation free. Like Tucker and Schwuttke, we observed a few dislocation bursts in the dendrites, but the web was so very thin it did not intercept them and the dislocations could not propagate. However, thicker web is necessary for most conventional semiconductor devices and, hence, dislocations generated in the dendrites can and do intercept the web sheet. In the web, dislocations can be partially

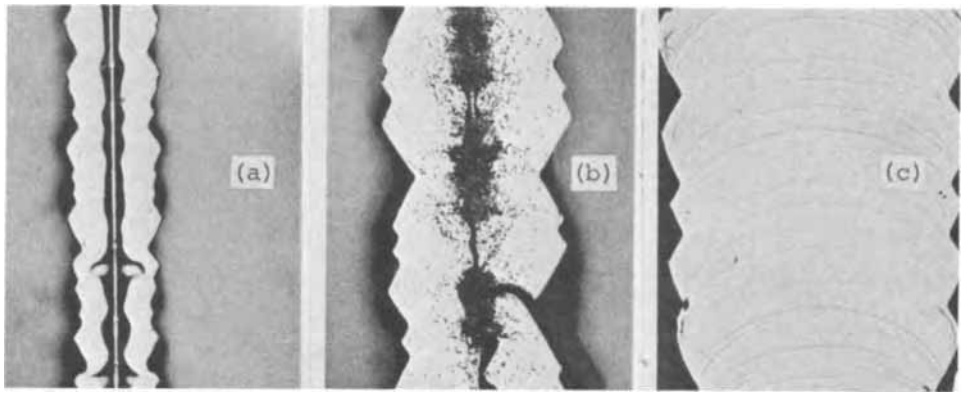

Fig. 13. Silicon dendrites grown at different depths of penetration beneath the melt surface, etched (90X).

eliminated by "necking down," or thinning the web. The dislocation density was not affected at all by the curvatures of the interface, either concave up or down to the melt. We therefore studied the formation of dislocation bursts in the dendrites and attempted to develop a technique to minimize them.

At a given undercooling, a variable pull rate can be used to produce dendrites of constant thickness but differing widths. At fast rates they are narrow, with the {111} surfaces characterized by a medial trough [Fig. 13(a)]. At lower rates, the dendrite grows deeper in the melt and the trough is partially filled [Fig. 13(b)]: Note the dislocations. At slowest rates and deepest penetration the trough is completely filled, producing good {111} surfaces without dislocations [Fig. 13(c)]. The great bursts of dislocations characteristic of the second morphology each arise at a core of silicon pushed above the adjacent {111} surface, clear evidence of both entrapment of liquid after a surface chill and subsequent deformation.

We introduced the plane parallel aftershields described earlier to slow down the freezing of any liquid droplets caught in the dendrite surfaces and also to reduce thermal strain; we also found that they forced the dendrites to grow more deeply under the melt surface as in Fig. 13(c). Using this geometry, the burst density was greatly reduced although not completely eliminated. With aftershields, the wide flat crystals previously described could be grown with a dislocation density near $10^3/cm^2$. Without these aftershields, the number of dislocation bursts was large and web from the ported crucible grew polycrystalline within a few feet.

In addition to dislocation generation in the dendrites, it was frequently observed that dislocations grew into the web from the seed button. By use of a small dendrite seed, by seeding at low undercooling, and by initially pulling at a very slow rate, we were able to minimize this source. An additional technique of "necking" was often used to advantage near the start of web growth. This was done by increasing the pulling speed for a short time until the web was thinned to about 1 mil; dislocations near the sheet surface then terminated. Those dislocations located next to the twin planes (in the last mil of web) could not be eliminated without losing the web as well. Although dislocation-free web was not grown thicker than about 100μ, careful technique and use of aftershields did result in growth of long pulls of thick, wide, flat web having low dislocation counts.

Acknowledgments

We wish to thank Dr. R. G. Seidensticker for technical suggestions and review of the manuscript, and J. J. Coleman and P. C. Mathis for assistance in crystal growth.

Manuscript submitted Aug. 10, 1970; revised manuscript received *ca.* Dec. 15, 1970. This was Paper 513 presented at the Montreal Meeting of the Society, Oct. 6-11, 1968.

Any discussion of this paper will appear in a Discussion Section to be published in the December 1971 JOURNAL.

REFERENCES

1. J. W. Faust, Jr., and H. F. John, *This Journal*, **108**, 860 (1961).
2. S. N. Dermatis and J. W. Faust, Jr., *IEEE Commun. Electron*, No. 65, pp. 94-98 (1963).
3. S. O'Hara and A. I. Bennett, *J. Appl. Phys.*, **35**, 686 (1964).
4. S. O'Hara, *ibid.*, **35**, 409 (1964).
5. T. N. Tucker and G. H. Schwuttke, *Appl. Phys. Letters*, **9**, 219 (1966).
6. T. N. Tucker, *Electrochem. Technol.*, **4**, 546 (1966).
7. S. O'Hara and G. H. Schwuttke, *J. Appl. Phys.*, **36** 2475 (1965).
8. D. R. Hamilton and R. G. Seidensticker, *ibid.*, **34**, 1450 (1963).
9. D. R. Hamilton and R. G. Siedensticker, *ibid.*, **31**, 1165 (1960).
10. R. G. Seidensticker and D. R. Hamilton, *ibid.*, **34**, 3113 (1963).

The Influence of Methane on Twin Formation During the Vapor Growth of Silicon Crystals

Lawrence D. Dyer*

Chemical Materials Division, Texas Instruments Incorporated, Dallas, Texas 75222

ABSTRACT

Single crystal silicon layers were deposited by the vapor reduction method onto <111> silicon rods with various concentrations of methane in the deposition gases. Twins appeared only at CH_4 concentrations of 100 ppm and above. In contrast to the results in the case of oxygen addition, twins were found on both $\{\bar{2}11\}$ and $\{1\bar{1}0\}$ faces; and the density of twins on the $\{\bar{2}11\}$ face increased as the 6.7^{th} power of the methane concentration. The general dependence of twin density on the methane concentration suggests that agglomerates of five to seven carbon atoms are responsible for the twin formation. A possible mechanism by which carbon or SiC chains containing less than seven atoms can cause twinning on the $\{\bar{2}11\}$ face is presented.

The growth of silicon single crystal ingots by the pyrolytic reduction of halosilane vapor (1-3) is a means of shortening the process by which single crystal silicon is obtained. One of the main problems with the growth of silicon by vapor deposition is the formation of twins in the growing material. For the <111> and <100> axial orientations that are commonly used, the size of the twins increases with the layer thickness (3); and, one twin starting from a ¼ in. diameter seed will ruin more than a 1 in. long section of a 1 in. diameter silicon rod grown from that seed. A major source of twins is impurities in the input *halo*silane-hydrogen mixture.

In a previous study oxygen was found to cause twins on $\{\bar{2}11\}$ faces if the oxygen concentration was 200 ppm or greater; but, no twins formed on $\{1\bar{1}0\}$ faces (4). The twins were attributed to the substitution of oxygen atoms in growth ledges, which causes

* Electrochemical Society Active Member.

Key words: vapor growth of silicon, twin formation, defects in Si from methane.

enhancement of the probability of deposited silicon atoms being in the twinned position. The purpose of the present study was to investigate the influence of methane on the formation of twins during vapor growth.

Experimental Procedure

Epitaxial deposition was carried out on ¼ in. diameter silicon rods, each having a <111> axis, in a manner similar to that described by Allegretti *et al.* (2), and Sirtl and Spielmann (3) using trichlorosilane as the silicon source. The rod temperature during deposition was 1250°C, and the growth rate was 2.6 μm/min. Within the first hour of deposition, the shape of the rod changed from circular to dodecahedral with the development of six {$\bar{2}11$} and six {$1\bar{1}0$} faces. The {$1\bar{1}0$} faces then gradually became narrower while the {$\bar{2}11$} faces increased in width as growth continued (2, 3).

Silicon deposition was carried out for 2 hr. Methane was then diverted into the reaction chamber at the desired concentration—either 72, 107, 143, or 453 ppm. By delaying the introduction of the methane, any {$\bar{2}11$} twins that began at the original seed crystal could be distinguished by size from those caused by the methane (4). Deposition times after the introduction of methane ranged from 1.5 to 11.0 hr. The 453 ppm run was terminated at 1.5 hr because the numerous twins on the {$\bar{2}11$} faces would have overlapped and made counting difficult.

After each run the rod was removed from the reactor, and defects were counted under an optical microscope on each of the faces {$\bar{2}11$} and {$1\bar{1}0$}.

After examination portions of the carbon-containing epitaxial layers of each rod were cut off and analyzed for total carbon by a combustion method (5). Sample size was approximately 1g. The detection limit was 10 ppm, and the accuracy was ± 10% at the 100 ppm level and above.

Results

Three main results were obtained:

1. Twins and defects were produced on the {$\bar{2}11$} and {$1\bar{1}0$} faces by the influence of methane during epitaxial growth.
2. The carbon concentration in the epitaxial layers was approximately the same as it was in the vapor phase.
3. There exists a quantitative relationship between density of twins and methane concentration.

Morphology and appearance of twins and associated defects on {$\bar{2}11$} and {$1\bar{1}0$} faces.—The defects can be divided into three categories: (*a*) twins on the {$\bar{2}11$} faces, (*b*) twins on the {$1\bar{1}0$} faces, and (*c*) chevron-shaped defects on the {$1\bar{1}0$} faces.

Twins on {$\bar{2}11$} faces.—A top view of a typical twin on the {$\bar{2}11$} face is shown in Fig. 1. (Such twins are not to be confused with those having vertical (111) twin boundaries, as shown by Faust and John (6) and Mendelson (7). The crystallography has been worked out by Sirtl and Spielmann (3). An independent check by x-ray back-reflection confirmed their results. In the figure the twin (A) is bounded on one end by the sloping coherent twin boundary (B) and on the other end by microtwin lamellae (C), which fill two trough-shaped gaps between {111} planes of the parent crystal and {111} planes of the twin crystal.

Twins on {$1\bar{1}0$} faces.—A typical twin structure on the ($1\bar{1}0$) face is shown in Fig. 2. It consists of two twins, one on the ($1\bar{1}1$) face, and one on the ($1\bar{1}\bar{1}$) face, meeting each other at a central boundary.[1] A similar twin structure is shown in Fig. 3 where two oppositely situated stacking fault tetrahedra intersect. An etched (111) cross section through this defect (A-A in Fig. 3a) is shown in Fig. 3b. The etching texture within the regions presumed to be twins is different from that outside these regions.

[1] The author is indebted to Professor Gareth Thomas at the University of California for this suggestion.

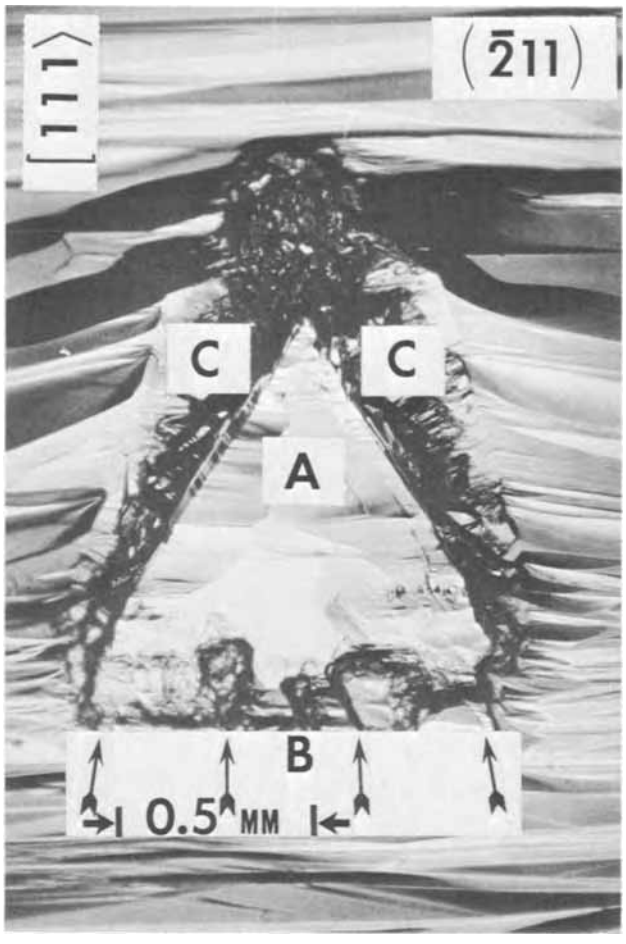

Fig. 1. Typical twin structure on ($\bar{2}11$) face

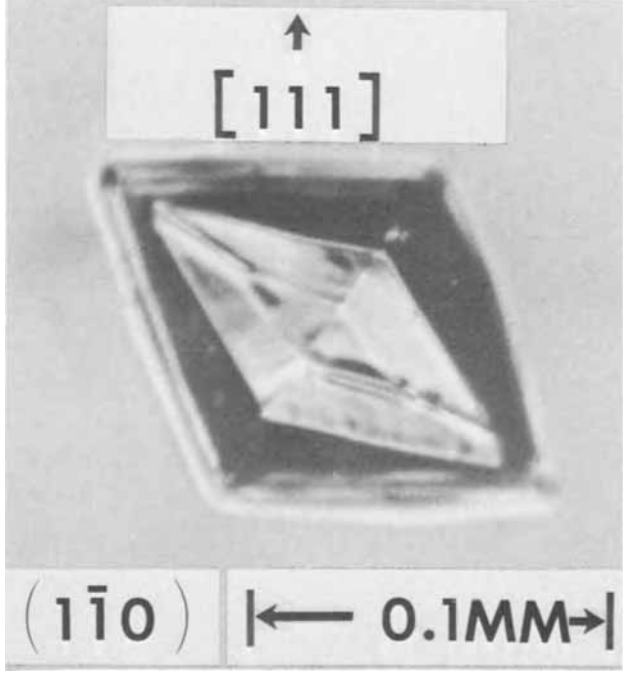

Fig. 2. Twin structure on (110) face

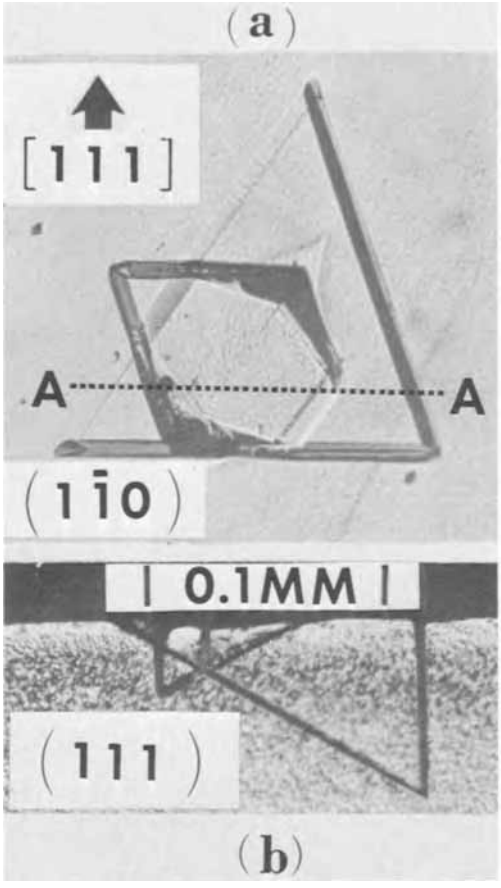

Fig. 3(a). Twin structure at intersection of two oppositely oriented stacking fault tetrahedra on (1$\bar{1}$0) face. (b). (111) Cross section of twin structure on (1$\bar{1}$0) face through A-A.

From the foregoing microscopic studies, the crystallography of the twin on the (1$\bar{1}$0) face was deduced and is shown in Fig. 4. The calculated and observed angles between the [$\bar{3}$52] and [110] directions in the twin and the parent crystal are 71.56° and 71° ± 1°, respectively.

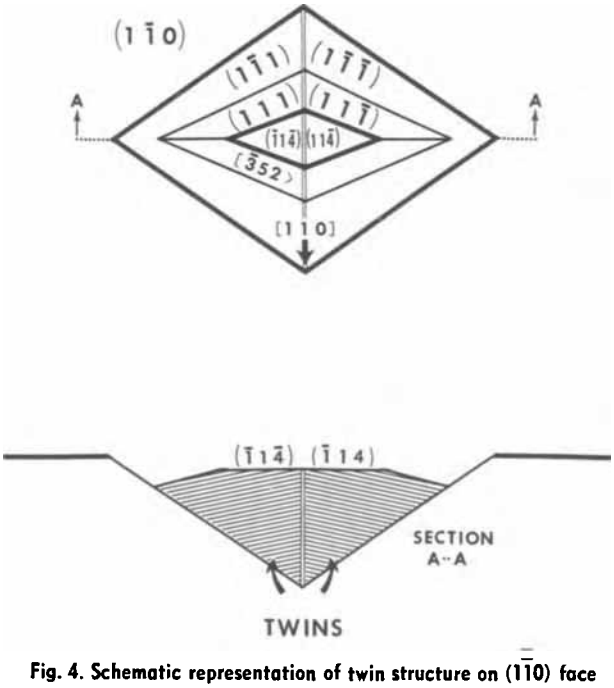

Fig. 4. Schematic representation of twin structure on (1$\bar{1}$0) face

Chevron-shaped defects on {1$\bar{1}$0} faces.—Micrographs of the layers deposited on {1$\bar{1}$0} faces at methane concentrations of 72, 107, 143, and 453-ppm are shown in Fig. 5a, b, c, d, respectively.

Several defects are evident in Fig. 5b. We have called these defects "chevrons" because their most characteristic feature is the meeting of two faults at an obtuse angle. Very often the faults are found closed into a lozenge shape, as shown in Fig. 6. A (111) cross section (B-B) of such a lozenge is given in Fig. 7, showing it to consist of vertical faults. The material enclosed by the lozenge defect is still correctly oriented, as can be seen from the dislocation etch pits in Fig. 6.

There is some connection between the chevron or lozenge faults and the twin structures because most twin structures have lozenges associated with them (8). The most likely interpretation of the chevron faults at present is that they are microtwin lamellae (9-12). As a temporary assignment the {1$\bar{1}$0} defects were counted as twins if a dark pit was seen at the apex of the chevron. Otherwise, the defects were counted as chevrons although the individual faults may actually consist of thin lamellar twins.

Defect density vs. carbon content.—Twin counts and carbon contents are given in Table I. The carbon contents in ppm were found to be approximately the same in the condensed phase as in the vapor phase. The results on twin densities are given on a time basis because of the different deposition times and because twins are produced during the entire time of exposure to methane. A defect density of 0.02 cm^{-2} hr^{-1} corresponds to 1 twin on a 20 cm rod in 2 hr.

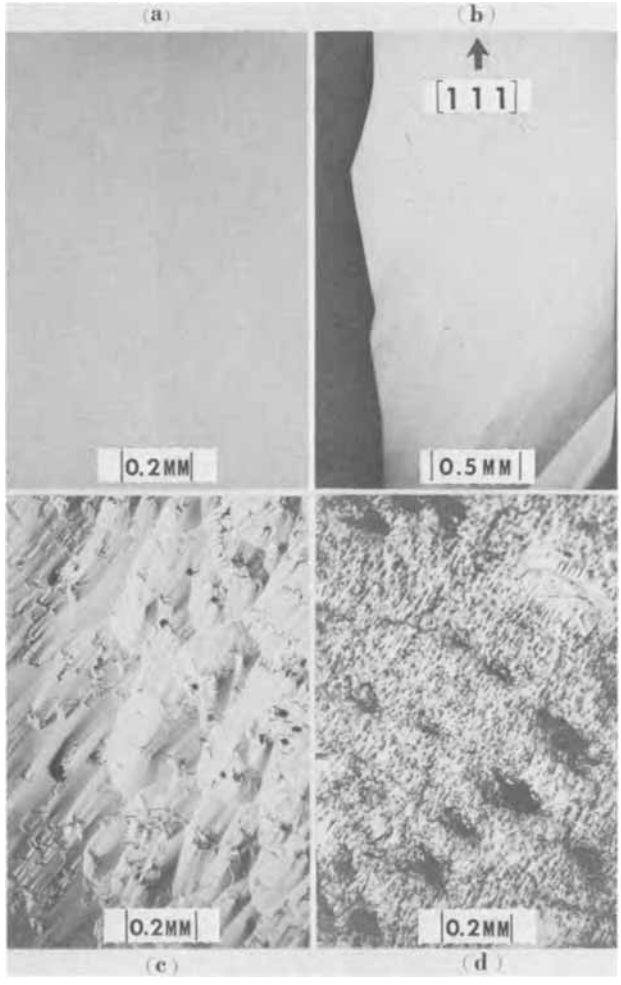

Fig. 5. {1$\bar{1}$0} Surfaces grown in the presence of methane. (a) 72 ppm, (b) 107 ppm, (c) 143 ppm, (d) 453 ppm.

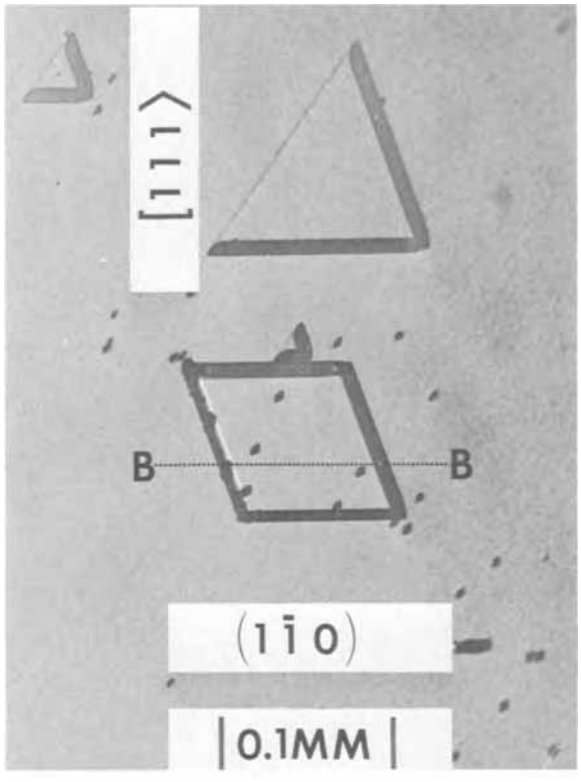

Fig. 6. Lozenge-shaped defect on (1$\bar{1}$0) face

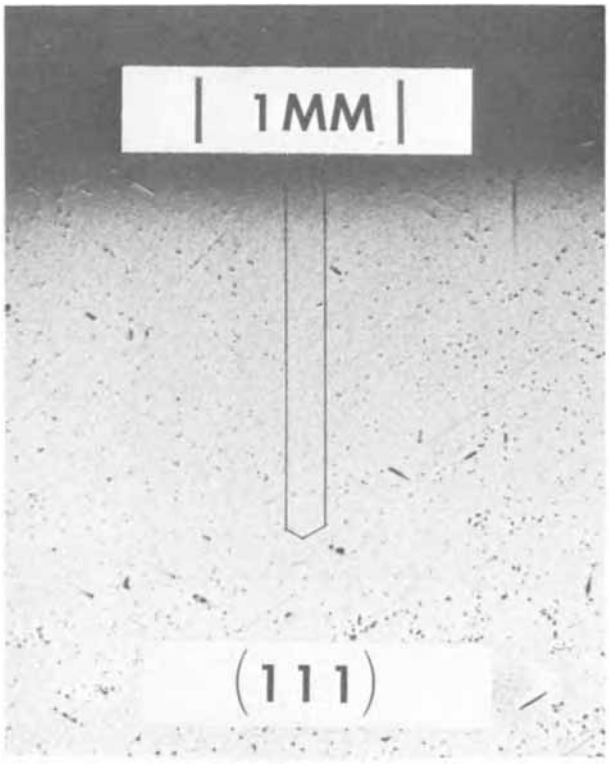

Fig. 7. (111) Cross section of defect shown in Fig. 6

From the table it appears that there is a nonlinear relationship between the density of defects and the methane concentration. Somewhere between the concentrations 72 and 143 ppm the density of each kind of defect rises significantly. The {1$\bar{1}$0} chevron defects are more numerous than the {1$\bar{1}$0} twin defects, and both are more numerous at each concentration than {2$\bar{1}$1} twins.

Table I. Twin count and carbon content at various methane concentrations

CH_4 added, ppm	Defect count/cm²/hr {211} Twins	{110} Twins	{110} Chevrons	Carbon content of layer, ppm
0	0	1.0	0.4	<10
72	0.0015	0.027	0.05	97 ± 10
72				122 ± 10
107	0.035	0.47	3.5	Not measured
143	1.2	1440	1.2×10^4	167 ± 15
453	533	Very large	Very large	395 ± 40

Figure 8 shows a plot of the twin density generated per hour on the {2$\bar{1}$1} face *vs.* the negative logarithm of the carbon or methane mole fraction. The experimental points give a slope m of 6.7 ± 0.2. Thus, we can write the empirical relationship

$$\frac{d}{T} = kC^{6.7}$$

where d is the twin density, T is the time, k is a constant, and C is the methane or carbon concentration.

Discussion

Carbonaceous contaminants have previously been found to give twinned growth centers on the {111} face during epitaxial growth (9, 13, 14). Also, twins have been shown before in epitaxial layers on the {2$\bar{1}$1} face (2, 3), and electron diffraction evidence has shown twins in {1$\bar{1}$0} epitaxial layers (15).

In the present study, a quantitative relationship between twin density and carbon content was found and should be accounted for.

There is no doubt that we could be dealing with the beginnings of the precipitation of carbon in some form. The solid solubility of carbon in silicon at 1250°C has been given as 6×10^{17} (16) and $< 3.5 \times 10^{17}$ (17) atoms/cc, whereas our 100 ppm apparent

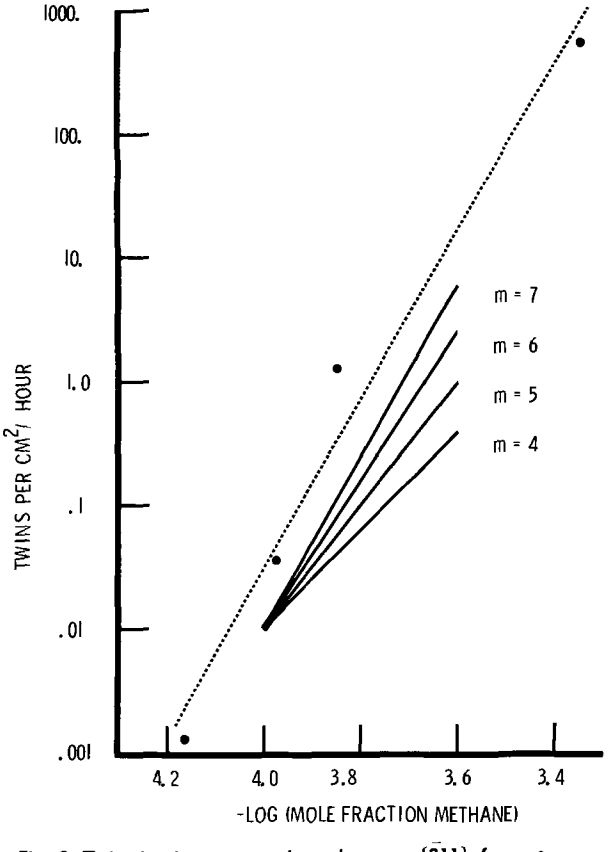

Fig. 8. Twin density generated per hour on {2$\bar{1}$1} face *vs.* negative log of methane concentration.

threshold concentration corresponds to 5 x 10^{18} atoms/cc. However, the carbon in each atom layer may not have time to aggregate to any great extent before it is covered up.

Miller *et al.* (9), and Inoue (14), attribute the twins found on {111} faces in epitaxial layers to packing effects from two extra SiC (0001) planes inserted into the crystal. While this manner of forming twins is indeed possible, it is a more stringent requirement than is necessary because of the large number of carbon atoms involved. In the present study the twin density on the $\{\bar{2}11\}$ face was proportional to the total carbon concentration to the 6.7^{th} power. This result can be interpreted to mean that only a few carbon atoms are required to come together simultaneously to cause a twin, whether 6-7 on the basis of the law of mass action, or 5-6 on the basis of the relationship derived by Walton (18). A mechanism was sought which could result naturally in the formation of a twin on the $\{\bar{2}11\}$ face and still involve the aggregation of only a small number of carbon atoms. Such a mechanism was found possible if carbon or silicon carbide groupings were in the form of chains in the $\{\bar{2}11\}$ surface in directions parallel to the $<01\bar{1}>$ ledges in each face. Twins can form when the groupings are long enough to create a mismatch between the normal silicon position and the substituted silicon position at the end of the chains sufficient to allow a twinned pair of atoms to be fixed in position in the growing row. Subsequent addition of atoms would produce the same orientation and shape of twin that were shown in Fig. 1. The smallest groupings that can create such an accumulated mismatch are chains containing three or four carbon atoms. Figure 9 shows two ways in which a twin nucleus may be formed from a silicon carbide chain of four carbons.

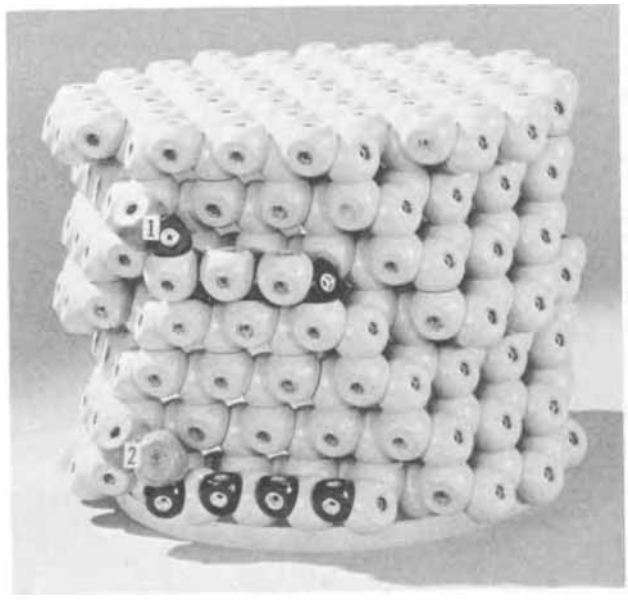

Fig. 9. Atom model of $\{\bar{2}11\}$ face showing two mechanisms by which twins would be formed by chains of carbon or SiC in $<01\bar{1}>$ steps.

Conclusions

Methane has been found to cause twins in silicon during vapor growth.

Methane causes twins on both the $\{\bar{2}11\}$ and $\{1\bar{1}0\}$ faces, in contrast to oxygen which does not form twins on the $\{1\bar{1}0\}$ face up to 600 ppm.

The density of twins on the $\{\bar{2}11\}$ face varies as the 6.7^{th} power of the methane concentration, while the density of defects on the $\{1\bar{1}0\}$ face increases even more rapidly with concentration. The formation of twins is attributed to a row growth mechanism made possible by C or SiC chains a few atoms long.

Acknowledgments

The author would like to express appreciation to Professor D. Kuhlmann-Wilsdorf at the University of Virginia for valuable discussions; to A. Ford for the sectioning studies, to Dr. A. Queen for the carbon analyses; and to P. Geminden, J. H. Smith, and D. Vanderburg for technical assistance.

Manuscript submitted Dec. 16, 1969; revised manuscript received *ca.* Jan. 25, 1971.

Any discussion of this paper will appear in a Discussion Section to be published in the December 1971 JOURNAL.

LIST OF SYMBOLS

m = the number of carbon atoms participating in a twinning event
d = density of twins in number/cm^2
T = time, hours
C = mole fraction carbon
k = constant

REFERENCES

1. R. C. Sangster, E. F. Maverick, and M. L. Croutch, *This Journal*, **104**, 317 (1957).
2. J. E. Allegretti, D. J. Shambert, E. Schaarschmidt, and J. Waldman, "Metallurgy of Elemental and Compound Semiconductors," Vol. 12, R. Grubel, Editor, Interscience, Inc., New York (1961).
3. E. Sirtl and W. Spielmann, *Z. Angew. Phys.*, **15**, 295 (1963).
4. L. D. Dyer, "Semiconductor Silicon," p. 132, R. Haberecht and E. Kern, Editors, Electrochem. Soc., New York (1969).
5. J. M. Walker, J. Spigarelli, and G. Bender, *Anal. Chem.*, **37**, 299 (1965).
6. J. W. Faust, and H. J. John, *This Journal*, **107**, 562 (1960).
7. S. Mendelson, *Acta Met.*, **13**, No. 5, 555 (1965).
8. L. D. Dyer and R. C. Bracken, *This Journal*, **114**, 145C (1967).
9. D. P. Miller, S. B. Watelski, and C. R. Moore, *J. Appl. Phys.*, **34**, 2813 (1965).
10. T. L. Chu and J. R. Gavaler, *Phil. Mag.*, **9**, 993 (1964).
11. G. R. Booker, *ibid.*, **11**, 1007 (1965).
12. S. Mendelson, *J. Appl. Phys.*, **38**, 1573 (1967).
13. G. R. Booker and B. A. Joyce, *Phil. Mag.*, **14**, 301 (1966).
14. M. Inoue, *This Journal*, **112**, 189 (1965).
15. J. M. Charig, B. A. Joyce, D. J. Stirland, and R. W. Bicknell, *Phil. Mag.*, **7**, 1847 (1962).
16. R. C. Newman and J. Wakefield, "Metallurgy of Semiconductor Materials," Vol. 15, p. 201, J. B. Schroeder, Editor, Interscience, Inc., New York (1962).
17. T. Nozaki, Y. Yatsurugi, and N. Akiyama, *This Journal*, **117**, 1566 (1970).
18. D. Walton, *J. Chem. Phys.*, **37**, 2182 (1962).

Properties of Low-Temperature Heteroepitaxial Thin Silicon Films Grown in Helium Atmosphere

J. Mercier

Section Physique des Couches Minces, Laboratoire d'Electrostatique et de Physique du Métal, Centre National de la Recherche Scientifique, Grenoble, Gare, France

ABSTRACT

Epitaxial Si layers grown by pyrolysis of silane on sapphire substrates in a He atmosphere are analyzed by x-ray diffraction, scanning electron microscopy, and the sputter-ion microprobe. Their properties are compared with those of layers grown in hydrogen at higher temperatures. A marked decrease in epitaxial temperature is observed, which is related to nucleation characteristics of the freshly deposited Si atoms. The growth rate limitations are discussed. Qualitative analysis by sputter-ion probe provides some promising results concerning impurity incorporation.

Structure defect formation and impurity incorporation are common plagues in heteroepitaxial Si films grown at high temperatures by pyrolysis of silane. It is expected that decreasing the epitaxial temperature should minimize these undesirable phenomena.

The lower epitaxial temperature in the usual silane and hydrogen system is 1025°C (1) and we succeeded in growing high-quality layers at 1030°C. Figure 1 shows an electron diffraction pattern of a 2.4 μm thick layer, the crystalline quality of which is indicated by the occurrence of Kikuchi lines. A further decrease of the temperature is hindered by the decrease of both crystalline quality and growth rate of the layer.

Obviously, hydrogen limits the silane dissociation rate (2) and is efficient in impurity transfer (3). From this standpoint (but we see later that this is not the major reason), its replacement by an inert gas is desirable.

Helium, owing to its expected high purity and good thermal conductivity, is an attractive choice. Furthermore, promising results are reported for Si growth on Si (4).

Its use, instead of hydrogen, in principle involves no major change of the deposition technique. However, in practice even the purest available He (given as 99.9995%) contains sufficient amounts of water vapor and oxygen to require further purification. Molecular sieves and liquid N_2 traps are not sufficient means, especially because of the extreme oxidizability of silane. Though special inert gas purifiers can now be purchased, they were not available when the present work started.

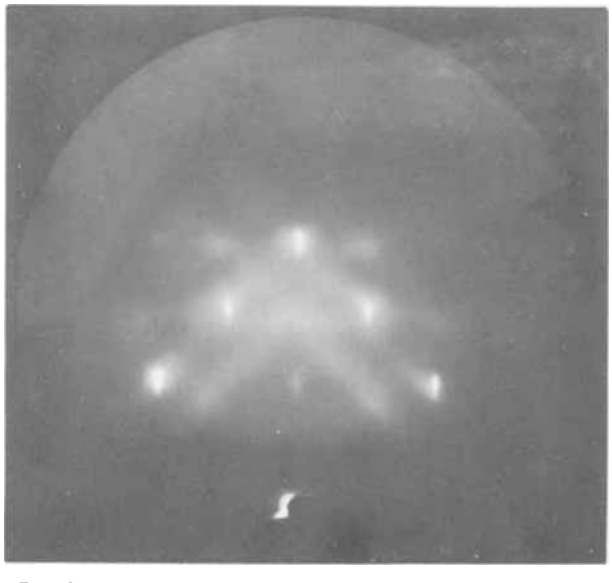

Fig. 1. Electron diffraction pattern of a (001)-Si layer grown in H_2 at 1030°C.

Expecting some balance of this oxidation reaction, we also tried experiments in a He-H_2 mixture.

Characterization Methods

These methods were chosen according to the aims of our study. We were especially interested in growing thinner layers (1-2 μm) than in our previous work and in obtaining more physical insights into interfacial processes.

Nucleation studies and chemical analyses were therefore required, using suitable techniques: scanning electron microscopy, electron replica microscopy on the one hand, and sputter-ion microprobe analysis (5) on the other, were selected.

This last method being relatively new and unusual, some comments are in order. First, infrared spectroscopy previously used by us (6) reaches its sensitivity and resolution limits for such thicknesses. The choice was to be made between the sputter-ion microprobe and the electron microprobe, but the former affords decisive advantages:

(a) A localized area to be analyzed (250 μm diameter).
(b) No limitation in atomic number of the elements, owing to the mass-spectrometry analysis.
(c) The crucial resolving power in depth (of the order of 100Å).
(d) A high sensitivity, in the 10^{-6} to 10^{-9} range of relative mass concentration.
(e) For each element, an ionic distribution image recorded on a photographic plate, resolving areas in the 1 μm range.

However, some drawbacks are also obvious:

(a) The method is destructive.
(b) Insulating layers require a metallic electrode on their surface in order to remove electric charges during sputtering.
(c) The secondary ionic current of a given element is not merely proportional to its total concentration in the matrix, but depends on several properties of this matrix. Therefore, comparative experiments are valuable.

Nucleation Experiments

Standard conditions for Si films grown in H_2 are defined as follows:

α-Al_2O_3 boules grown by the Czochralski method are cut, mechanically polished, and etched in H_2 at 1300°C for 15 min prior to epitaxy (6).
The crystalline orientation of the substrate is (01.2).

Table I. Experimental data at $T = 1100°C$

Growth conditions		Islands' properties		
Carrier gas	Time (min)	Density (cm^{-2})	Diameter (μm)	Contact angle
H_2	1	10^9	0.2-0.4	>90°
H_2	4	3×10^7	1-2	>90°
He	1	3×10^8	0.3-0.5	<90°
He	4	Continuous layer		

Silane flow rate: 5 cm^3/min.
Total flow rate: 10 liters/min.
Epitaxial temperature: $T = 11700°C$.

The nucleation steps are defined by a 1 or 4 min deposition time.

The same conditions are applied in comparative experiments, except for the replacement of H_2 as a carrier gas, during growth, by the He-H_2 mixture.

Scanning electron microscopy provides an easy measurement of the size and density of the Si islands, Fig. 2, a and b. After breaking the slice, the contact angle between the Si balls and the substrate is determined, Fig. 3, a and b.

The corresponding data are given in Table I.

Discussion.—The general trends, along with the use of He, are:

(*a*) An increase of the net reaction rate, as shown by the faster complete coverage of the substrate.
(*b*) Striking modifications of the nucleation properties—increase of the size, decrease of the density of the islands, at a given time, contact angle less than 90°.

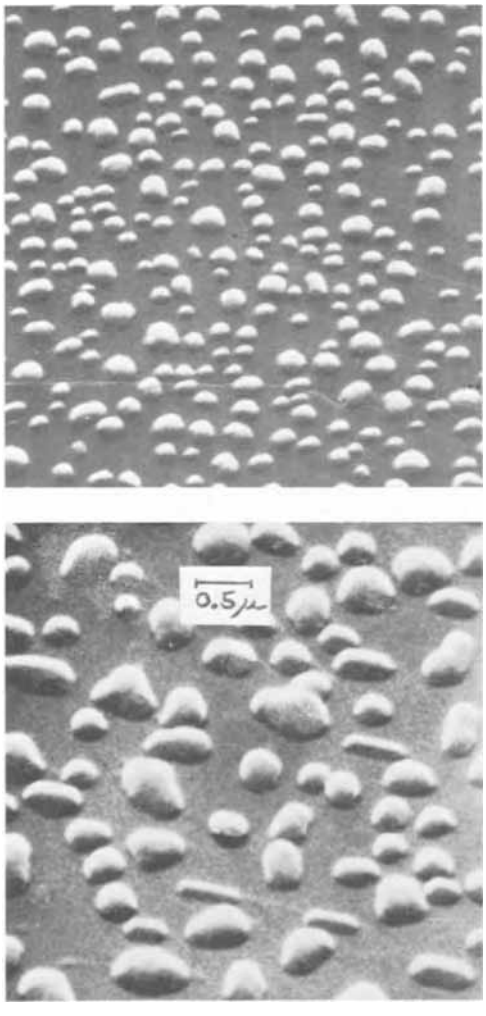

Fig. 2. Density and size of Si islands (scanning electron microscope): a (top)—ambient H_2, time 1 min (X11,000); b (bottom)—ambient He, time 1 min (X20,000).

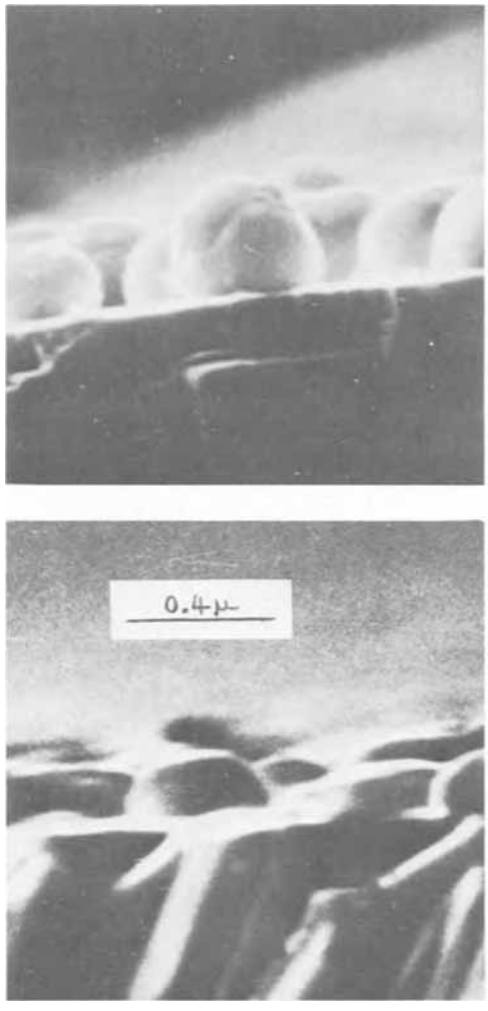

Fig. 3. Shape of Si islands: a (top)—ambient H_2, time 4 min (X26,000); b (bottom)—ambient He, time 4 min (X65,000).

These features are generally considered to be favorable to epitaxy. The contact angle value, especially, is related to defect formation during coalescence when it exceeds 90°.

Low-temperature Epitaxy

The crystalline orientation of thicker layers grown in He was checked by x-ray diffraction; a Cu-K α-radiation diffractogram is given in Fig. 4. The magnification factor is indicated for the various planes, and it is apparent that multiple orientations are found [particularly (001), as expected, and (111) orientations].

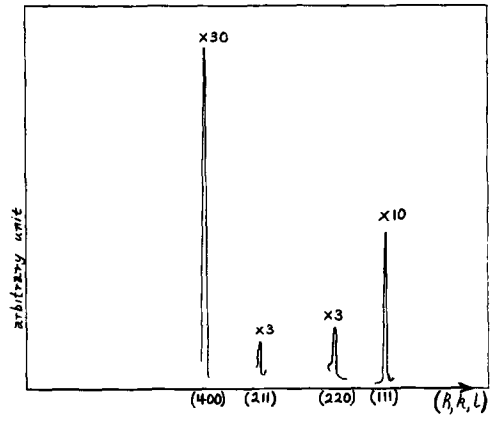

Fig. 4. X-ray diffracted intensities of a high-temperature layer grown in He. The relative height must be multiplied by the factor given at the top.

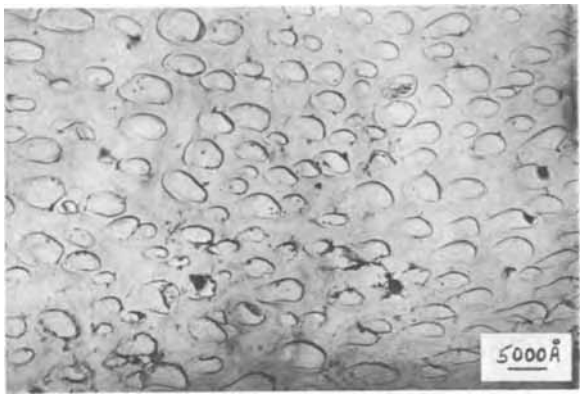

Fig. 5. Electron microscope replica of the sapphire substrate after etching the Si islands shown in Fig. 2(a) (X13,000).

Although they are not completely satisfactory, these preliminary results allow experiments at lower temperatures.

Monocrystallinity could not be achieved unless all flow rates were decreased. Ultimately, the following conditions were selected:

$T = 900°C$.
Carrier gas: He + H_2 (20% parts/volume).
Total flow rate: 2 liters/min.
Silane flow rate: 2 cm^3/min.

The decrease of total flow rate was needed because:

(a) Keeping it at its previous value gives a very different distribution of the deposit along the reaction tube. When T is decreased, the deposition area is more and more confined upstream, unfortunately in a nonuniform temperature region. This shift can be offset by decreasing the total flow rate.

(b) The crystalline quality increases, presumably due to less impurity incorporation *via* the vapor phase (see chemical analysis).

Summing up some characteristics of such films:

(a) Continuous layers are grown very rapidly, in less than 1 min.

(b) The growth rate at 900°C in helium is nearly equal to that measured at 1100°C in hydrogen (typical value: 0.1 μm/min).

(c) Non-purposely doped layers are slightly N-type and highly resistive ($\rho > 100$ ohm-cm).

(d) X-ray diffraction indicates that a quasi single orientation is achieved, but the strongest line is given by a (220) reflection instead of the expected (400) reflection. Thus, we confirm the tendency to grow (110) Si films at low temperature irrespective of the ambient, since we reported this in (6) for Si growth in H_2.

Table II. Properties of the layers to be analyzed

Layer	Growth conditions: Ambient	Growth conditions: T, °C	Thickness, μm	ρ, ohm-cm	Conductivity type	Orientation
H	H_2	1100	0.8	0.1	P	(001)
L	He	900	1.2	>100	Slightly N	(110)

Impurity Incorporation into the Films

Before describing the sputter-ion experiments, it is interesting to report direct evidence of the interaction between the substrate and the impinging Si at the early stages of the Si deposition. The method has been applied before (7) for Si grown on spinel.

Silicon islands are deposited in H_2 at 1100°C for 1 min, as shown in Fig. 1. Selective etching removes these islands only and an electron microscopy replica reveals depressed pits, outlining the previously present islands (Fig. 5).

Using He, we have also performed experiments similar to those we reported with H_2 (3) and have found aluminum transfer at a comparable level in the same high-temperature range. However, the results were not easily reproducible and were more difficult to interpret in terms of a simple diffusion process. This difficulty may be ascribed to the less pure ambient which can modify the surface conditions.

Sputter-ion Analysis

A reference is needed for this case also. A relatively thin layer is grown under standard conditions, as defined previously. Its properties are then compared with those of a layer grown in He at 900°C. The first layer is referred to as the *H* (High *T*) layer and the second as the *L* (Low *T*) layer. Their properties are given in Table II.

Prior to sputtering, a thick gold layer was evaporated in an ultrahigh vacuum system on the Si top surface.

We ascertained that no gold was incorporated into the film by selecting Au^+ ions at first. In any case, this film prevents any precise study of the Si surface itself.

We also determined that phosphorus was not detected in the *L*-layer even though it is N-type.

Aluminum (Al^+) and oxygen (O^-) were selected for the analysis since they were found previously (6) by other methods.

Silicon (Si^+) was also measured because it provided an interesting comparison with bulk material.

The three profiles (Al, O, Si) are plotted on one graph for each layer in Fig. 6, a and b.

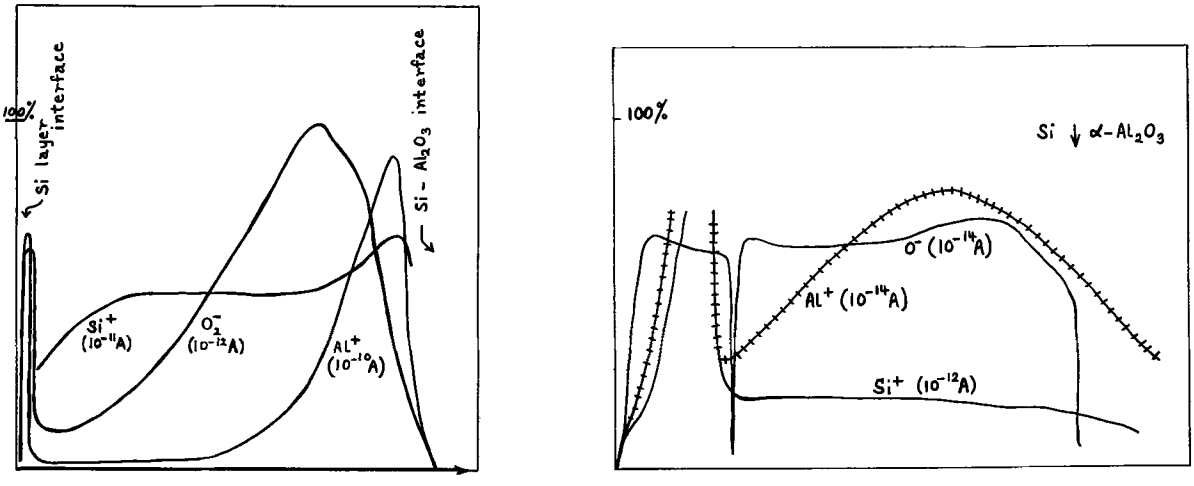

Fig. 6. Impurity profiles: a(left)—*H*-layer; b (right)—*L*-layer. The full scale (100%) corresponding to the given ionic current range is also shown.

Discussion.—As previously mentioned, the free surface properties are difficult to ascertain. In all cases, and for all elements involved, surface peaks appear. These may be explained by the phenomenon of chemical emission (8) associated with the presence of oxygen. The dip in the impurity profile of oxygen in the *L*-layer is clearly and repeatedly found and is obviously limited to the surface layer.

The outlines are somewhat different. A true diffusion profile is found in all cases (Al and O) except for the oxygen distribution in the *L*-layer, which is rather constant with depth. The O-profile, compared to the Al profile in the *H*-layer, is satisfactory because it is known that oxygen diffuses faster into Si than Al.

We conclude qualitatively that solid-state diffusion is important at high temperatures, but that oxygen incorporation *via* the vapor phase predominates at low temperatures.

Quantitatively, the results are not so understandable. To confirm the influence of the matrix, we must point out the difference between the two Si^+ secondary currents: bulk Si gives rise to a Si^+ ion current in the range of 10^{-11}A, corresponding also to that of the *H*-layer. On the contrary, the Si^+ current for the *L*-layer is only in the range 10^{-12}A. In fact, a full study must consider the influence of various parameters: the crystalline orientation, crystal perfection, and the numerous possible Si ions.

As an example, we have found that the etch rate is influenced by the crystalline perfection (9)

Bulk Si	250-300 Å/sec
Hetero Si in He	200 Å/sec
Hetero Si in H_2	80 Å/sec

Another very important point to remember is the difference in the ionization efficiency according to the chemical nature of the element; for example, bulk aluminum (Al^+ is the only ionized species) gives rise to a 10^{-10}A ionic current. However, Si and Al have almost the same atomic number, but their chemical bondings are, in fact, very different.

Taking this point into account and keeping in mind only relative figures, it is likely that:

(a) The Al content in the *L*-layer is about 10^{-4} less than in the *H*-layer.
(b) The oxygen content, likewise, is about two orders of magnitude less in the *L*-layer.
(c) Near the Si substrate interface of the *H*-layer, comparable Al-O-Si concentrations are found, which may imply a compound formation.

Some difficulties will be met in accurately defining the end of the film sputtering, especially for positively ionized species. The profile presents a long tail; by means of the specimen viewer, attached to the apparatus, we ascertained that a secondary ionic current is measured long after the primary beam reaches the bottom of the film. It is likely that, for insulating layers and due to specimen biasing, the primary ion beam shifts and etches an extended area. This hampers any firm relationship between impurity concentration and secondary current corresponding to that tail.

Last but not least, information is provided by the ionic distribution images for Al and oxygen into the *H*-layer. The apparatus records an image of a small etched region (150 μm in diameter) during sputtering, corresponding to a specific element. It therefore provides a true distribution of this element over the etched area. The difference between oxygen and Al distribution (Fig. 7, a and b) is striking: except for a small number of localized spots, the O-pattern appears uniform; conversely, Al presents a spotty pattern suggesting a localized distribution, presumably at dislocation sites. This result can be related to the beautiful photoconductivity experiments (10) on similar structures, indicating space charge distributions.

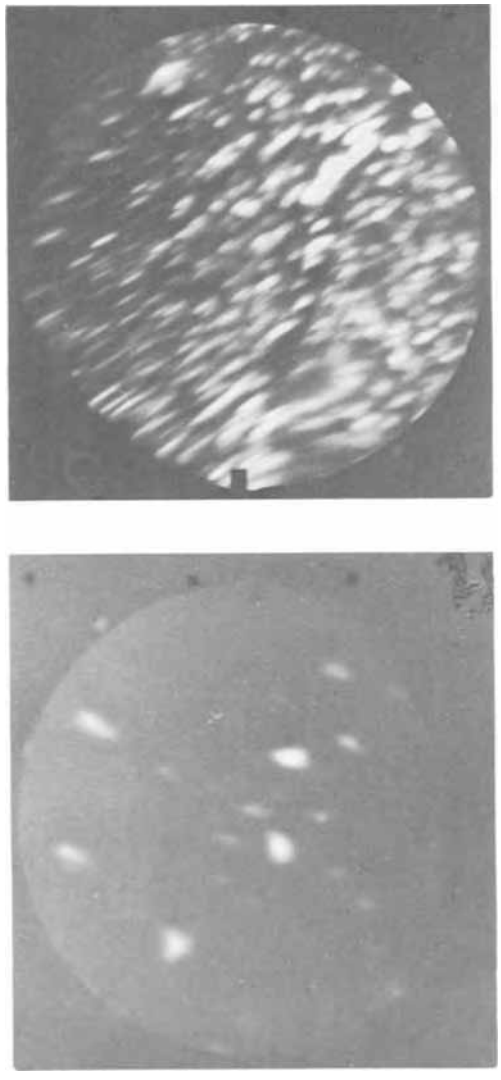

Fig. 7. Ionic distribution image (*H*-layer) of: a (top)—aluminum, b (bottom)—oxygen.

Conclusion

These first experiments were very fruitful and the main results can be summarized as follows.

1. Compatibility of low-temperature epitaxy and the He process is demonstrated.
2. Autodoping is therefore minimized.
3. The sputter-ion technique is a very promising tool for chemical analysis of such layers.

However, much work remains to be done. Several basic problems must be solved: understanding the trend toward (110) orientation, quantitative interpretation of the ion probe measurements, and, accordingly, understanding of impurity incorporation processes.

Practical problems concerning the applicability of this general technique depend on:

1. Purification conditions in order to make the layer growth procedure easier. For example, it is necessary to pump the whole system 2 days before an experiment starts.
2. Electrical characteristics (especially for doped layers). Since doping and growth conditions are related, their compatibility must be checked.

Acknowledgments

I am grateful to Professor L. Néel for allowing this research to be undertaken in his laboratory, and to Dr. B. K. Chakraverty for valuable discussions.

I express my deepest gratitude to Dr. G. Blet and his group of the L.R.G. Thomson-C.S.F. for their con-

stant scientific cooperation (IR, x-ray electron microscopy experiments). It is a pleasure to emphasize local cooperation with several laboratories of the Nuclear Center at Grenoble (C.E.N.G.). My particular thanks are addressed to Dr. Cornu in charge of DPC.SIS, who allowed the ion probe measurements. I am indebted to Dr. Blanchard for carrying out these experiments and for many interesting discussions.

Manuscript submitted June 8, 1970; revised manuscript received Dec. 17, 1970. This was Paper 197 (with the added sputter-ion analysis) presented at the Los Angeles Meeting of the Society, May 10-15, 1970.

Any discussion of this paper will appear in a Discussion Section to be published in the December 1971 JOURNAL.

REFERENCES

1. D. J. Dumin and R. H. Robinson, *J. Crystal Growth*, **3-4**, 214 (1968).
2. J. Mercier, "3rd International Mikroelektronik Tagung (Nov. 11-13, 1968), München, R. Oldenburg, Editor, p. 107 (1969).
3. J. Mercier, *This Journal*, **117**, 812 (1970).
4. D. Richman and A. H. Arlett, "Semiconductor Silicon," R. R. Haberecht and E. L. Kern, Editors, ECS Softbound Symposium Series (1969).
5. G. Slodzian, *Rev. Phys. Appl. (Supplement)*, **3**, 360 (1968).
6. J. Mercier, *This Journal*, **117**, 666 (1970).
7. Ch. Zaminer, *Z. Angew. Phys.*, **29**, 223 (1968).
8. G. Slodzian and J. F. Hennequin, *Compt. Rend.*, **263**, 1246 (1966).
9. B. Blanchard, Private communication.
10. H. Schlötterer, *Solid-State Electron.*, **11**, 947 (1968).

Ionic Contamination and Transport of Mobile Ions in MOS Structures

M. Kuhn and D. J. Silversmith

Bell Telephone Laboratories, Incorporated, Murray Hill, New Jersey 07974

ABSTRACT

A fast, simple and very sensitive technique has been developed to determine the extent of ionic contamination of oxides in MOS capacitors. The method is capable of detecting better than 10^9 mobile ions/cm^2 and is based on the measurement of the displacement current response to a slow linear ramp voltage at elevated temperatures. This yields an ionic displacement current peak whose area is proportional to the total mobile ionic space charge. The method is expected to be very useful for routine process and quality control applications. This technique has been used to study positive mobile charge behavior in silicon dioxide. The voltage dependence of the ionic displacement current indicates that trapping of ions occurs at the metal-oxide interface and that ionic transport from the metal to the silicon interface is controlled by trap emission. Ion transport from the silicon to the metal interface is characterized by a single, bulk-limited transport mechanism below 300°C with an activation energy that appears concentration dependent. Above 300°C an additional transport mechanism is observed which is slow in comparison to the primary transport mechanism.

Trace amounts of ionic contamination in thermally grown SiO_2-Si MOS structures and insulated gate field effect transistors (IGFET) are a source of instability because of ionic drift under action of an electric field. Extensive work (1-4) has traced the major source of this ionic drift instability to the presence of sodium. The extent and distribution of sodium contamination has been determined both destructively [by neutron activation analysis (5) and flame photometry (6)] and nondestructively by capacitance measurements of bias-temperature aged MOS capacitors (1-4). Flame photometry and neutron activation analysis are complicated experimental methods which are not practical for routine analysis and which lack sensitivity for sodium levels below 10^{12} atoms/cm^2. The usual high-frequency C-V measurements under bias-temperature stress indicate sodium contamination by observing shifts in the flatband voltage. These measurements are uncertain because flatband voltages are influenced by changes in the surface charge and surface state density under bias-temperature stress. Such changes make unambiguous ion concentration determinations difficult for concentrations less than 1-2 x 10^{10} ions/cm^2.

The limitations mentioned above are largely overcome if one measures the ionic displacement current in an MOS capacitor driven by a slow linear voltage ramp (7). This measurement is made at elevated temperatures, and the ionic motion is revealed by a current peak near zero bias. The total mobile ionic charge is proportional to the area of this peak, and the ionic species can be readily measured down to 10^9 ions/cm^2. The method is rapid and simple, in addition to being sensitive and independent of changes in interface properties.

The ramp method has been used to study mobile charge drift in various SiO_2-Si and Al_2O_3-SiO_2-Si MOS structures with ion concentrations spanning a range from above 10^{13} ions/cm^2 to fewer than 10^9 ions/cm^2 (8). The fraction of ionic species that is mobile depends exponentially on temperature over a range between 100°-400°C, and the shape of the ionic displacement current indicates that ionic trapping occurs at the metal-insulator interface. This suggests that ionic transport is characterized by at least two processes: a fast process at lower temperatures and a slow process at temperatures above 300°C.

This method has been independently developed by Kerr (9) and Chou (10) who have tested and confirmed its validity using the simpler and electrochemically symmetrical Si(poly)-SiO_2-Si(100) MOS structure.

Key words: ion transport, mobile ions in insulators, MOS characterization.

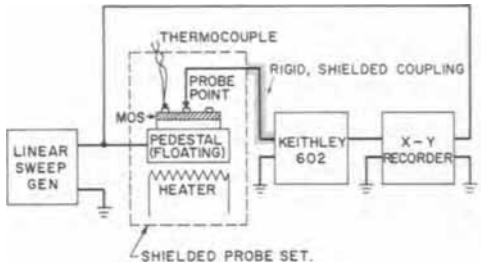

Fig. 1. Schematic diagram for mobile ion drift test set

Apparatus

The experimental test set for performing mobile ion drift measurements is shown schematically in Fig. 1. The apparatus consists of a shielded probe set containing an electrically isolated pedestal heated with a shielded resistance heater to temperatures up to 400°C and a movable probe point. The pedestal is driven with a slow linear voltage ramp obtained from an operational amplifier integrator or a slow triangular wave function generator (HP-3310A) to provide sweep rates typically 5-100 mV/sec. The displacement current flowing through the MOS capacitor on the pedestal is monitored through the probe point and is measured using a Keithley 602 electrometer operating in the "fast" mode. In this way the electrometer functions as a high gain operational amplifier, reducing the input voltage drop essentially to zero and also minimizing the response time. The output from the electrometer (unity gain) and the applied voltage ramp are recorded on an X-Y plotter to display a plot of displacement current *vs.* voltage. As typical displacement current levels are about 10^{-11}A, careful electrostatic shielding is required, and the Keithley input connector from the probe point should be kept as short and as rigid as possible to minimize stray capacitance and vibrational noise.

Analysis

The response of an MOS capacitor to a slow linear voltage ramp in the absence of any mobile charged species has been discussed (7); it was shown that under quasi-static conditions, low frequency C-V characteristics are obtained. When the oxide contains ionic impurity species which are mobile under the influence of electric field at elevated temperatures, these mobile ions contribute an additional component to the displacement current. This ionic component may be analyzed to yield the quantity of mobile ions present and may provide some additional information on their transport properties, as will be shown by the following analysis.

We consider an MOS capacitor with space charge density $\rho(x)$ in the insulator as shown below the energy band diagram of Fig. 2. The charge $Q(V)$ induced at the semiconductor surface when a voltage V volts (measured with respect to the bulk semiconductor) is applied to the field plate is given by

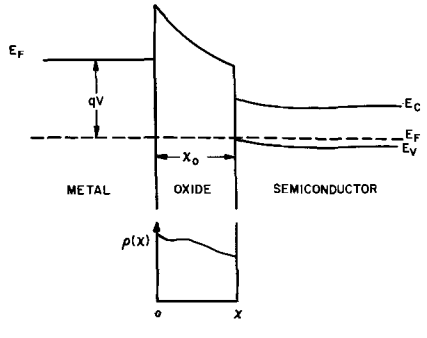

Fig. 2. Electron energy diagram of an MOS structure in accumulation. The band bending is characteristic of a P-type semiconductor. A hypothetical charge density in the oxide is shown.

$$Q(V) = -\int_0^V C(V)dV + Q_{FB} \qquad [1]$$

where $C(V)$ is the low frequency differential MOS capacitance and Q_{FB} is the induced charge necessary to establish the flatband condition. Q_{FB} may be expressed in terms of the metal-semiconductor work function difference Φ_{MS}, the space charge distribution $\rho(x)$ per unit area and the oxide-capacitance per unit area, C_{ox}, as (7)

$$Q_{FB} = C_{ox}\Phi_{MS} - \int_0^{x_o} \frac{x}{x_o}\rho(x)dx \qquad [2]$$

x is the distance into the oxide measured from the metal-oxide interface, x_o is the oxide thickness. The displacement current flowing out of the metal field plate, when the applied voltage varies with time and the space charge density is mobile, can be expressed as

$$i = -\frac{dQ(V,t)}{dt} = \frac{d}{dt}\int_0^V C(V)dV + \frac{d}{dt}\int_0^{x_o}\frac{x}{x_o}\rho(x,t)dx \qquad [3]$$

Furthermore, if we choose a linear time dependence for the applied voltage, $V = \pm\alpha t$ and using $d/dt = \pm\alpha\, d/dV$, the displacement current becomes

$$i(V) = \pm\alpha C(V) \pm \alpha\frac{d}{dV}\int_0^{x_o}\frac{x}{x_o}\rho(x,V)dx \qquad [4]$$

This expression for the displacement current as a function of applied voltages is valid under conditions of quasi-static equilibrium, that is, under sweep conditions so slow that the ionic charge distribution $\rho(x, V)$ can continuously equilibrate with the externally applied voltage. This quasi-static equilibrium may be expected to apply at elevated temperature, in the range above 150°C at sweep rates less than 100 mV/sec. Under these conditions the entire shape of the charging curve can be determined, in principle, by calculating the equilibrium charge distribution as a function of applied voltage from a solution of Poisson's equation and the general transport equations and using these to calculate the second term in Eq. [4]. We would expect these detailed calculations to yield information about the line shapes and their relation to the ionic transport properties, which might lead to a useful method for ionic spectroscopy.

It remains to show explicitly that the mobile ionic charge density is obtainable from the displacement current. This follows directly when we consider the integral of the ionic displacement current Eq. [4])

$$\int_{-V_o}^{+V_o}[i(V) - \alpha C(V)]dV = \alpha\int_0^{x_o}\frac{x}{x_o}\rho(x,+V_o)dx - \alpha\int_0^{x_o}\frac{x}{x_o}\rho(x,-V_o)dx \qquad [5]$$

This equation shows that the integral of the ionic component of the displacement current between two bias limits is equal to the difference in the weighted space-charge distribution, provided that the charge distribution is allowed to equilibrate. The mobile ionic charge density is obtained directly if the initial and final conditions are chosen so that all the mobile charge is located at an interface. For example if $-V_o$ and V_o are chosen so that $\rho(x, -V_o) \simeq \rho_o\delta(x)$, and $\rho(x, +V_o) \simeq \rho_o\delta(x - x_o)$ Eq. [5] becomes

$$\int_{-V_o}^{V_o}[i(V) - \alpha C(V)]dV = \alpha\rho_o \qquad [6]$$

In practice, at elevated temperatures, $C(V) \simeq C_{ox}$ over the entire bias range, and a practical formula for the determination of mobile ionic charge density is

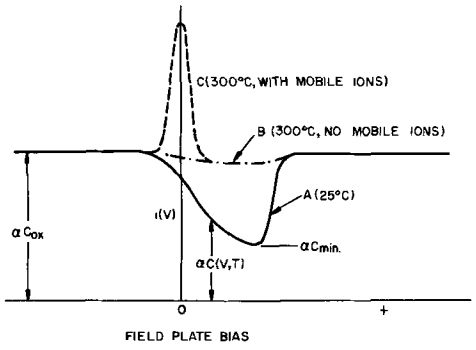

Fig. 3. Displacement current of a typical MOS capacitor (P-type substrate) in response to a d-c ramp. Curve A (25°C) and B (300°C) show the characteristic dip in capacitance near $V = 0$ due to majority carrier depletion at the Si-SiO_2 interface. Curve C (300°C) shows a peak at $V = 0$ due to the transport of mobile ions from the oxide bulk to an interface.

$$\rho_0 \simeq \frac{1}{\alpha}\int_{-V_0}^{V_0}[i(V) - \alpha C_{ox}]dV \qquad [7]$$

The mobile charge concentration is proportional to the area between the displacement current curve and the line corresponding to the oxide capacitance in a displacement current *vs.* voltage characteristic.

The idealized displacement current response as a function of the applied voltage with and without mobile ionic space charge is shown in Fig. 3. At room temperature the displacement current is proportional to the low frequency differential MOS capacitance as shown in curve A. In the absence of mobile ionic space charge an increase in the ambient temperature results primarily in an increase of C_{min}/C_{ox} until, at temperatures typically above 300°C, the displacement current is nearly constant and equal to the oxide capacitance. This behavior is a consequence of the rapid increase of the intrinsic carrier concentration with temperature which results in silicon surface capacitance much larger than C_{ox}. Such a response at elevated temperature (300°C) is shown in curve B. When ionic space charge is present in the oxide, then as the temperature is raised, redistribution may occur as a function of bias, resulting in an ionic displacement current peak near zero applied voltage; this ionic displacement current peak is superimposed on the MOS *C-V* characteristic as shown in curve C. Generally, this ionic peak is readily separable from the electronic displacement current. Therefore, this provides a simple, rapid, convenient and highly sensitive method for the investigation of ionic space charge concentrations, with the additional advantage that the method is largely independent of any of the variations in MOS interface properties ($Q_{ss} + N_{ss}$) which limit both accuracy and sensitivity of the conventional method of measuring flatband voltage shifts after bias-temperature aging. The changes in Q_{ss} and N_{ss} limit the resolution in measurement of the flatband voltage shift, and therefore limit the accuracy to no better than 10^{10} ions/cm^2.

Experiment

The experimental technique described above has been used to study ionic transport in a wide variety of MOS structures. Both P and N substrates in (100) and (111) orientations have been used with dopant concentrations ranging from 10^{14} to 10^{17}/cm^3. Oxides have been grown to thicknesses of 800-2500Å in both a plasma oxidation (8) system and a dry 1150°C oxidation furnace. Various annealing procedures after growth have been attempted, but no measurable changes in ion transport have been seen. These measurements have indicated positive ion (sodium) concentrations from below 10^9 to more than 10^{13} ions/cm^2 and give substantially the same ion concentrations as determined from flatband voltage shifts after bias aging.

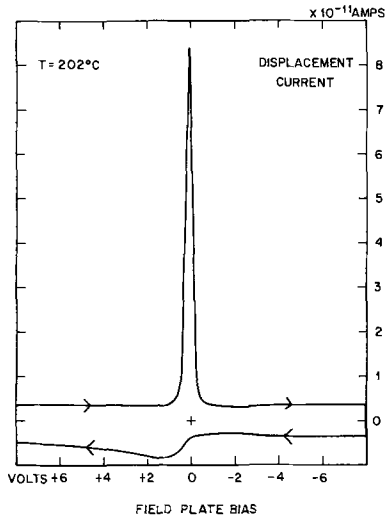

Fig. 4. Displacement current response for a heavily contaminated oxide at 200°C. The substrate consisted of a 5μ N-type, 1 ohm·cm, (111) epitaxial silicon film grown on an N-type wafer. The oxide is 1000Å thick, and is grown in an oxygen plasma system. The field plates are 15 mil dots of 200Å Cr and 2000Å Au. The sweep rate of the d-c ramp is 77.5 mV/sec.

A typical ramp response curve for a heavily contaminated oxide is given in Fig. 4. The sweep from field plate positive to negative (left to right) yields the response shown in the upper curve, while the voltage sweep from negative to positive is the lower curve. This d-c ramp *C-V* MOS measurement was taken at 202°C, and the peak above the C_{ox} baseline corresponds to 2.5 x 10^{12} mobile ions/cm^2 in the oxide. The peak is well defined with respect to C_{ox}, and the shape agrees with the model proposed earlier in this paper. During this sweep positive ions are expected to move from the Si-SiO_2 interface to the metal-SiO_2 interface, and the resulting capacitance peak, suggests that no interface trapping occurs at the Si-SiO_2 interface.

The most striking feature of these curves is the strong asymmetry of the ionic displacement current in the two sweep directions. The response when sweeping from the field plate negative to field plate positive is distorted and broadened over the entire positive voltage range, resulting in a very broad peak as shown in the lower trace of Fig. 4. This clearly indicates that ion transport is sluggish as may be expected of a transport mechanism limited by emission from ionic traps located at the metal-SiO_2 interface. Similar measurements on many MOS structures have indicated that the area under the peak and the dip are equal (with respect to the upper and lower C_{ox} baselines), showing that all the ions transported to the metal-oxide interface can be brought to the silicon-oxide interface by changing the polarity of the voltage ramp. As expected from quasi-equilibrium arguments, the area under the peak is independent of sweep rate, as long as the rate is sufficiently slow to establish the boundary conditions which approach delta functions (as described in the previous section).

The temperature dependence of the ionic displacement response is given in Fig. 5. The ionic peak does not saturate but continues to increase with temperature. At low temperature the sweep from field plate negative to positive (right to left) yields a broadened structure, resulting from the trapping-emission mechanism at the metal-oxide interface. At higher temperatures this peak sharpens and approaches more closely the ideal shape (or the shape of the peak for the opposite sweep) as expected if emission of ions from traps is more rapid at higher temperatures. Furthermore, an additional structure is observed above the C_{ox} baseline at elevated temperature ($T > 300$°C), as shown in the upper trace of Fig. 5. This structure typically takes

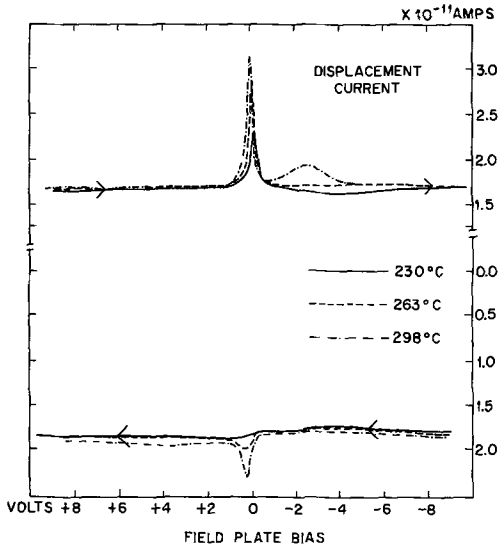

Fig. 5. Displacement current response of an MOS capacitor at 230°, 263°, and 298°C. The substrate consisted of a fresh N-type, 1 ohm·cm, (100) expitaxial film. The oxide was 2000Å thick, and was grown in a dry oxidation furnace at 1150°C. After growth, the sample was annealed in Ar at 1150°C for 30 min. Fifteen-mil dots of 200Å Cr and 2000Å Au were deposited for field plates. The sweep rate of the d-c ramp was 42.3 mV/sec.

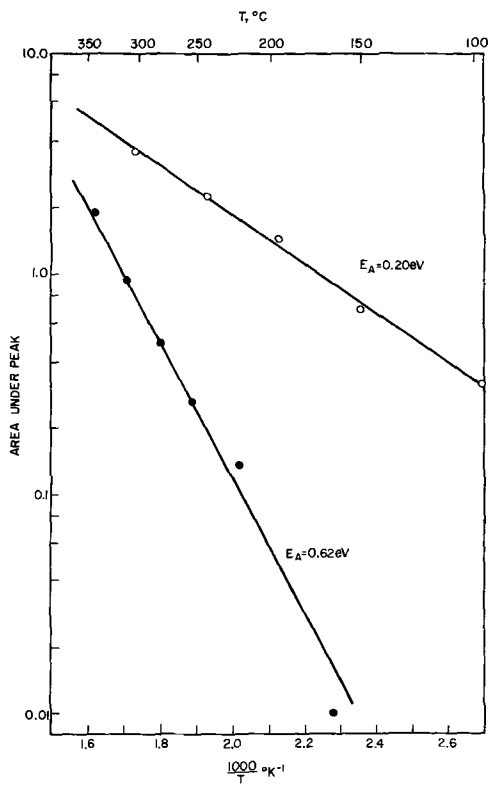

Fig. 6. Temperature dependence of the displacement current peak. The total area under the displacement current peak, above the C_{ox} baseline, is plotted on the ordinate. The open dots are data from an MOS capacitor with the same specifications as those described in the caption for Fig. 4. The closed dots are from a device fabricated on 10 ohm·cm, (100) P-type silicon. The oxide was 2000Å thick, and was grown in a dry oxidation furnace at 1150°C. After growth, 15 mil dots of 200Å Cr and 2000Å Au were deposited for field plates.

the form of a second broadened peak displaced by approximately −2V from the mobile ion peak. This may be evidence for the onset of an additional high temperature field dependent transport mechanism.

No saturation of the ionic peaks with temperature was observed. The area under the mobile ion structure increased exponentially with temperature to the limit of the experiment (370°-400°C). In Fig. 6 the temperature dependence of the area under the mobile ion structure has been plotted for two similar devices. If one can assume that the number of available mobile ions at a particular temperature can be described in terms of an activation formalism, then activation energies can be determined by plotting the area under the displacement current peak above the C_{ox} baseline *vs.* $1/kT$ where T is the measurement temperature. Applying this analysis to our experimental results we find that the activation energy, E_A, is a function of ionic concentration and is lower for higher ionic contamination. For example, a device containing about 10^{13} sodium ions/cm^2 at 300°C has an activation energy of 0.20 eV; whereas a similar device with 10^{11} sodium ions/cm^2 at 300°C has an activation energy of 0.62 eV. The increase in activation energy with decreasing ionic contamination agrees with our observation that ionic transport effects can be seen at lower temperatures only with high ionic contamination. The activation energy, E_A, is clearly a function of the impurity concentration, but no model for this behavior can be proposed at present. However, this result suggests that sodium transport in silicon dioxide may be complicated by concentration effects and may be inadequately described by a simple noninteracting single carrier model, that is, the diffusion coefficient and mobility may be concentration dependent.

As indicated in Fig. 5, we consistently observe a strong asymmetry in the shape of the ionic displacement current for a bias sweep from positive to negative voltage (silicon to metal) compared with the shape of current for a negative to positive voltage (metal to silicon) sweep. The sweep from field plate positive to negative voltage results in a sharp well-defined (fast) ion current peak near zero bias in contrast to a very broad (sluggish) ionic response associated with trap emission for the opposite sweep direction. The response of the mobile species to the voltage ramp ("fast" or "slow") appears to be independent of ramp rate below 100 mV/sec. In an electrochemically symmetric Si(poly)-SiO_2-Si(100) structure, however, the ionic displacement current is essentially independent of the sweep direction (10). Therefore, we conclude that ionic traps are associated with the metal-oxide interface and the mobile ionic species is positively charged.

The displacement current-voltage characteristic typically observed at 350°C is shown in Fig. 7. The upper curve corresponds to ion transport from the silicon to the metal interface and shows a well-defined broad peak at −2V in addition to the sharp peak structure observed alone below 300°C. After the appearance of this broad peak at 300°C (Fig. 5), the initial sharp structure saturates, and for higher temperatures the area above C_{ox} increases only under the broad peak. The total mobile charge (corresponding to the area under both peaks) follows an activation law behavior, and no change in the slope of an activation energy plot has been observed. The metal-to-silicon ionic transport above 300°C is characterized by the same sequence of mechanisms as shown in the lower curve of Fig. 7: Near zero volts a fast saturated peak is observed, and at a higher magnitude of voltage in the sweep, a slow and broad, unsaturated peak is seen. This result strongly suggests that the same positively charged ion is responsible for both peaks in the high-temperature transport. The two peaks further suggest two possible states for sodium or two transport mechanisms in SiO_2.

Discussion and Conclusions

The response of MOS capacitors to slow linear voltage ramps at elevated temperatures provides a simple, rapid, convenient, and highly sensitive method for the measurement of ionic contaminants in the oxide of the MOS structure, which is compatible with routine

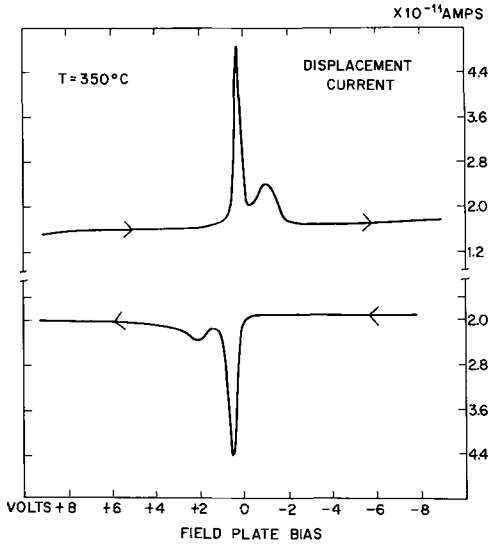

Fig. 7. Displacement current response at 350°C. The substrate of the MOS capacitor was a fresh P-type, 1 ohm·cm, (100) epitaxial film. The oxide was 2000Å thick, and was grown in a dry oxidation furnace at 1150°C. After growth, the sample was annealed in Ar for 30 min. Fifteen-mil dots of 200Å Cr and 2000Å Au were deposited for field plates. The sweep rate of the d-c ramp was 42.3 mV/sec.

process control. The method is capable of measuring ion concentrations below 10^9 ions/cm^2 and has the advantage of being largely independent of any variations in MOS interface properties (Q_{ss} and N_{ss}) with temperature. The temperature dependence of interface properties has limited both the accuracy and sensitivity of conventional methods of measuring flatband voltage after bias-temperature aging. The sensitivity of the method discussed in this paper increases with increasing oxide thickness because the ionic displacement current is superimposed upon a reduced oxide capacitance level. Using the methods of flame photometry and atomic absorption spectroscopy (6), good correlation was obtained for sodium concentrations measured by flame emission and by the high-temperature voltage ramp method discussed here.

Earlier studies by Snow *et al.* (1) on sodium ion migration in SiO_2 (using flatband shift and ionic polarization measurements after application of a positive step voltage) were interpreted in terms of a bulk-limited diffusion model and were used to extract activation energies associated with the bulk diffusion of sodium ions in SiO_2. The results presented in the previous section indicate that mobile ion transport from the metal-to-silicon interface is trap-emission controlled with the ion traps located at or near the metal-oxide interface. More recent experiments by Chou (10) have indirectly verified that the transport of mobile ions from metal to silicon is trap controlled. A comparison of our results with Chou's clearly indicates that Snow's diffusion analysis is not applicable to the sodium ion polarization measurement under positive step voltage conditions and that activation energy measurements obtained therefrom will relate to trap emission mechanisms rather than to bulk diffusion.

In contrast to ion transport from the metal-to-silicon interface, ion transport from the silicon-to-metal interface does not appear emission limited but appears controlled by bulk transport processes. Two modes of transport have been observed. A "fast" transport is observed above about 150°C and an additional "slow" transport is seen above 300°C. This observation is generally in agreement with those of Hofstein (2) who has also observed two transport modes in MOS structures heavily contaminated with sodium. Hofstein observes the onset of the "slow" transport at 200°C with a somewhat higher activation energy. Additional, more detailed studies of the mobile ion response using both the ramp and step response methods may provide the detailed information necessary to yield a correct understanding of the transport of mobile ions in MOS structures.

Manuscript submitted Sept. 14, 1970; revised manuscript received Jan. 14, 1971.

Any discussion of this paper will appear in a Discussion Section to be published in the December 1971 JOURNAL.

REFERENCES

1. E. H. Snow, A. S. Grove, B. E. Deal, and C. T. Sah, *J. Appl. Phys.*, **30**, 1164 (1965).
2. S. R. Hofstein, *IEEE Trans. Electron. Devices*, **ED-14**, 749 (1967); **ED-13**, 222 (1966).
3. E. Yon, W. H. Ko, and A. B. Kuper, *ibid.*, **ED-13**, 276 (1966).
4. M. Yamin, *ibid.*, **ED-12**, 88 (1965); **ED-13**, 256 (1966).
5. T. M. Buck, F. G. Allen, J. V. Dalton, and J. D. Struthers, *This Journal*, **114**, 862 (1967); J. F. Osborne, G. B. Larrabee, and V. Harrap, *Anal. Chem.*, **39**, 1144 (1967).
6. J. E. Barry, H. M. Donega, and T. E. Burgess, *This Journal*, **116**, 257 (1969); B. Yurash and B. E. Deal, *ibid.*, **115**, 1191 (1968).
7. M. Kuhn, *Solid-State Electron.*, **13**, 873 (1970).
8. M. Kuhn and J. R. Ligenza, Paper 144 presented at the Atlantic City Meeting of the Society, Oct. 4-9, 1970.
9. D. R. Kerr, "MIS Measurement Techniques Utilizing Slow Voltage Ramps," Conference on the Properties and Use of MIS Structures, Grenoble. France, June 1969: Paper 108 presented at the New York Meeting of the Society, May 4-9, 1969.
10. N. J. Chou, Paper 25 presented at the Los Angeles Meeting of The Society, May 10-15, 1970.

A Self-Consistent Method for Estimating Non-Step Junction Doping Profiles from Capacitance-Voltage Measurements

R. B. Fair

Bell Telephone Laboratories, Incorporated, Reading, Pennsylvania 19604

ABSTRACT

The use of the step-junction approximation for calculating the net doping density from C-V measurement data can lead to serious errors in the resulting profiles for sequentially diffused structures. Non-step junction behavior can be accounted for if the equation for the effective doping density is multiplied by a correction factor. Two approximate methods of estimating this correction factor are discussed in which the net ionized impurity density on the high side of the junction is assumed to change either linearly or exponentially with incremental changes in depletion layer depth. For both of these approximations, the net ionized impurity density on the low side is assumed to change parabolically. These net distributions of charge, which are iteratively determined in a self-consistent fashion, yield the best approximations for this functional form of the profile, according to the C-V measurements made on the junction. Comparisons between experimentally obtained doping profiles and profiles computed *via* the techniques described in this paper show good agreement.

Proper knowledge of the net impurity profiles in p-n structures is essential for the design of diodes and transistors, especially microwave transistors where the performance is limited by the net doping in the base region. High side impurity distributions can be obtained fairly accurately by carrying out anodic sectioning of the semiconductor material, and by taking resistivity measurements of the exposed surface (1). The low side doping profile of a p-n junction is usually determined by assuming a step junction, and by calculating the net ionized impurity distributions with data obtained from the diode capacitance-voltage method (2, 3). However, it is well known that in p-n junctions the depletion region extends into the high concentration side of the junction. Attempts to account for this phenomenon have resulted in analytical expressions for the symmetrical step junction, the moderately unsymmetrical step junction, and the linearly graded junction (4, 5). Experimental evidence has shown that, for a low voltage bias, the linearly graded junction yields a reasonably accurate approximation to the total depletion region thickness ($C \propto V^{-1/3}$). Conversely, as was first shown by Pritchard (6), observation of a $V^{-1/3}$ variation of capacitance is not a reliable indication of linear grading. Decker (7) has been able to determine the doping *vs.* depth in epitaxial layers in which the profile of the high side doping is assumed to be a complimentary error function. The low side doping can be determined from capacitance-voltage measurements, and from numerical integration of the assumed high side profile.

None of the aforementioned methods can be used to describe adequately nonideal doping distributions associated with shallow diffusions or implantations, while taking into account the space charge sweep into the highly doped side. Interactions between sequentially diffused impurities and incomplete ionization cause actual doping profiles to deviate from analytically assumed profiles.

In this investigation, the equation for the effective doping density, as determined by the C-V relationship, is modified for the determination of low side doping, $N_2(x)$, by the inclusion of the multiplicative factor $(1 - dx_1/dx_2)$; dx_1/dx_2 (negative) denotes the rate of change of the high side sweep-out distance with respect to the low side. Two approximate methods of determining dx_1/dx_2 are discussed in which the net ionized impurity concentration on the high side of the junction is made to change either linearly or exponentially with incremental changes in junction bias. For both of these approximations, the net ionized impurity distribution on the low side is assumed to change parabolically (see Fig. 1). The linear-parabolic and the exponential-parabolic distributions were selected because they approximate the actual net profiles in sequentially diffused structures. These net distributions of charge, which are iteratively determined in a self-consistent fashion, yield the best approximations of this type for the determination of dx_1/dx_2, according to the C-V measurements made on the junction.

Key words: C-V measurements, transistors, doping profiles.

Two-Sided Depletion Layer Sweep-Out

For an arbitrary profile on each side of a p-n junction, the relationship between the effective doping density, $N_T(x_d)$, and the net doping densities, $N_1(x_1)$ and $N_2(x_2)$, at the edges of the depletion layer is (8)

$$\frac{1}{N_T(x_d)} = \frac{1}{N_1(x_1)} + \frac{1}{N_2(x_2)} \qquad [1]$$

where x_d is the depletion layer width expressed as $x_d = (x_2 - x_1)$ (Fig. 1). $N_T(x_d)$ is a function of capacitance and voltage and is defined as

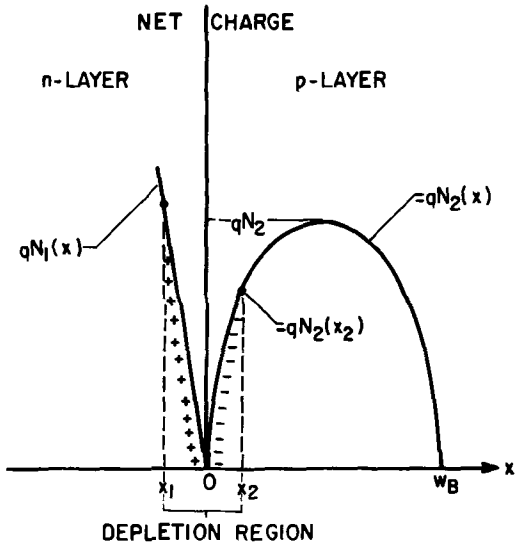

Fig. 1. Illustration of the way in which the space charge is assumed to change with applied junction voltage (linear scales). The signs of the ionized impurities in the depletion region are indicated.

$$N_T(x_d) \equiv \frac{\left(\frac{C}{A}\right)^3}{q\,\epsilon_0\epsilon_r}\left[\frac{-dV}{d\left(\frac{C}{A}\right)}\right] \qquad [2]$$

A is the area of the junction, and C is the capacitance given by the expression

$$C = \frac{\epsilon_0\epsilon_r A}{x_d} \qquad [3]$$

It can be seen from Eq. [1] that, for C-V measurements made on a particular p-n junction, it is impossible to determine uniquely the net profiles $N_1(x)$ and $N_2(x)$ which yielded these measurements. However, if the complete net profile on one side of the junction is assumed, such as $N_2(x)$, then it is possible to solve for $N_1(x_1)$ and x_1. Thus, the correctness of the estimation of the actual $N_1(x_1)$ is dependent on the correctness of the assumed profile, $N_2(x)$. In this paper, $N_2(x)$ is assumed to be parabolic, and the general form of $N_1(x)$ is either linear or exponential.

If Eq. [1] is rearranged, the net low side doping density, $N_2(x_2)$, becomes

$$N_2(x_2) = \frac{\left[1 + \frac{N_2(x_2)}{N_1(x_1)}\right]\left(\frac{C}{A}\right)^3}{q\,\epsilon_0\epsilon_r}\left[-\frac{dV}{d\left(\frac{C}{A}\right)}\right] \qquad [4]$$

Using the fact that equal quantities of charge must reside on the two sides of the junction, Eq [4] can be rewritten as

$$N_2(x_2) = \frac{\left[1 - \frac{dx_1}{dx_2}\right]\left(\frac{C}{A}\right)^3}{q\,\epsilon_0\epsilon_r}\left[-\frac{dV}{d\left(\frac{C}{A}\right)}\right] \qquad [5]$$

Therefore, for the net doping profiles which have been assumed (linear-parabolic and exponential-parabolic), it is possible to solve for the ratio $N_2(x_2)/N_1(x_1)$ (or dx_1/dx_2) for given C-V measurements. In this way a correction to the effective doping density, $N_T(x_d)$, is made which yields an estimate of the net low side doping, $N_2(x_2)$. The assumed profiles which are used in determining dx_1/dx_2 are iteratively adjusted so that the estimate of dx_1/dx_2 is self-consistent.

The Linear-Parabolic Junction

In order to calculate x_1, x_2, and hence, dx_1/dx_2, it is assumed that the change in the high side net charge density with increments of voltage is linear with distance from the junction. Thus, the charge on the high side, Q_h, is given by

$$Q_h = q\int_{x_1}^{0} m_1 x\,dx \qquad [6]$$

where m_1 (negative) is the grade constant. If the charge distribution on the low side of the junction is assumed to be parabolic with distance from the junction, then the charge on the low doped side, Q_l, is given by

$$Q_l = \frac{4q}{w_B{}^2}\int_0^{x_2} N_2(w_B x - x^2)\,dx \qquad [7]$$

where N_2 is the height of the parabola (ion/cm^3), w_B is the width of the parabola, and x_2 is the distance to the space charge edge. By setting $Q_h = Q_l$, and using the fact that

$$N_2 = \frac{N_2(x_2)w_B{}^2}{4x_2(w_B - x_2)} \qquad [8]$$

then

$$x_2{}^3 + x_2{}^2\left[w_B - x_d - \frac{2N_2(x_2)}{3m_1}\right] + x_2\frac{N_2(x_2)}{m_1}\left[\frac{4}{3}x_d - w_B\right] + \frac{N_2(x_2)x_d}{m_1}\left[w_B - \frac{2}{3}x_d\right] = 0 \qquad [9]$$

for which

$$\frac{dx_1}{dx_2} = -\frac{N_2(x_2)}{x_1 m_1} \qquad [10]$$

for charge balance at the junction.

In order to solve Eq. [9] for x_2, prior knowledge of dx_1/dx_2 and $N_2(x_2)$ is required. Thus, for each pair of C-V measurements, an iteration procedure must be performed on dx_1/dx_2 and m_1, starting with $dx_1/dx_2|_0 = -0.5$ and m_1 equal to the grade constant of the linearly graded junction. $N_2(x_2)$ can then be determined from Eq. [5]. Using these values in Eq. [9], x_2 can be determined by inverse interpolation, and then Eq. [10] can be solved for the next better value of dx_1/dx_2. This iterative process of calculating $N_2(x_2)$, x_2, and the corresponding improved estimate of the true value of dx_1/dx_2 proceeds until

$$\left.\frac{dx_1}{dx_2}\right|_{i+1} - \left.\frac{dx_1}{dx_2}\right|_i \simeq 0 \qquad [11]$$

where i refers to the i^{th} iteration.

When the condition expressed in Eq. [11] is satisfied, $N_2(x_2)$ is still not necessarily an accurate estimate of low side doping, since x_2 is not accurately known. The initially assumed value of grade constant, m_1, must be adjusted until the calculated charge distribution about the junction has associated with it a capacitance that is equal to the measured value. Thus, the calculated capacitance, $C_n{}^1$, associated with n^{th} C-V measurement can be written as

$$C_n{}^1 = \frac{(q_n - q_{n-1})A}{V_n - V_{n-1}} \qquad [12]$$

where q_n is the charge residing on the low side of the junction for the n^{th} value of bias, V_n. For the parabolic, low side profile

$$q_n = \frac{q\,N_2(x_2)\left[\frac{w_B}{2} - \frac{x_2}{3}\right]x_2}{(w_B - x_2)} \qquad [13]$$

If $C_n{}^1 \neq C_n$, where C_n is the n^{th} measured junction capacitance, then m_1 can be adjusted so as to bring $C_n{}^1$ closer in value to C_n. For each newly adjusted value of m_1, the iteration procedure for dx_1/dx_2 must be repeated and a new $C_n{}^1$ computed until

$$C_n{}^1 - C_n \simeq 0 \qquad [14]$$

Figure 2 shows the way in which the final values of m_1 (which caused Eq. [14] to be satisfied) varied as a function of applied junction voltage for a particular diode. The reference value of m_1, about which these final values of m_1 are distributed, was obtained from the C-V data as the slope of $1/C^3$ *vs.* V.

The above-mentioned procedure for calculating dx_1/dx_2 and then $N_2(x_2)$ from Eq. [5] can be performed on a computer. For each pair of C-V measurements, these iterative computations are performed with the result that each calculated point on the low side profile is adjusted to the extent that $[1 - dx_1/dx_2]$ modifies the step junction approximation.

The Exponential-Parabolic Junction

If the change in the net high side charge with voltage is approximated by an exponential curve, then the charge balance at the junction can be written as

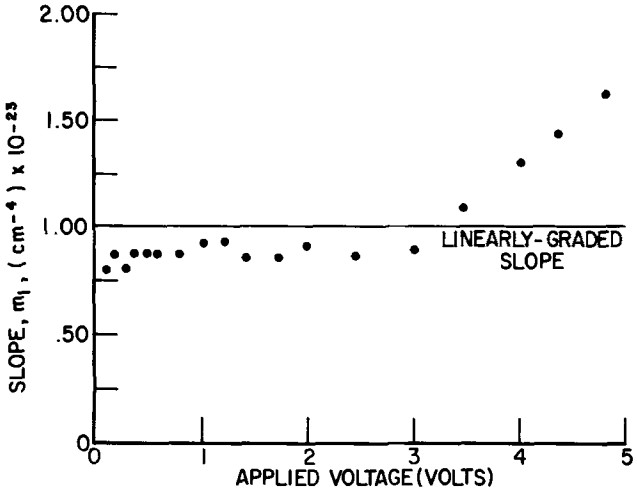

Fig. 2. Calculated values of the grade constant which give correct capacitance values for the linear-parabolic junction.

$$N_1\left[-\frac{1}{k^1}+\frac{e^{-k^1x_1}}{k^1}+x_1\right]=\frac{N_2(x_2)x_2\left[\frac{w_B}{2}-\frac{x_2}{3}\right]}{(w_B-x_2)} \quad [15]$$

where

$$N_1(x)=N_1(e^{-k^1x}-1) \quad [16]$$

k^1 is a parameter which is adjusted so that Eq. [16] initially approximates the net high side profile, and N_1 is the value of doping at which the net impurity concentration approaches the singly diffused high side concentration. dx_1/dx_2 for the exponential-parabolic junction is

$$\frac{dx_1}{dx_2}=\frac{N_2(x_2)}{N_1(1-e^{-k^1x_1})} \quad [17]$$

Figure 3 illustrates the way in which $N_1(x)$ (Eq. [16]) approximates an actual net high side profile with $N_1 = 10^{19}$ and $k^1 = 0.56 \times 10^5$. $N_1(x)$ is shown as a dashed curve (curve 3), and curve 2 represents the net high side profile which was obtained by subtracting the two singly diffused total doping profiles of opposite conductivity type (curve 4 from curve 1). Also shown is the net low side doping distribution, $N_2(x)$, (curve 5) which was calculated from Eq. [5] in conjunction with C-V measurements made on this p-n structure. The estimation of $N_2(x_2)$ and x_1 for each pair of measurements using the exponential-parabolic approximation is carried out by applying inverse interpolation to Eq. [15] for each iterated value of dx_1/dx_2. When the condition of Eq. [11] is satisfied, the capacitance associated with the calculated charge distribution can be determined from Eq. [12]. If $C_n^1 \neq C_n$, then k^1 can be adjusted so as to being C_n^1 closer in value to C_n. For each newly adjusted value of k^1, the iteration procedure for dx_1/dx_2 must be repeated until Eq. [15] is satisfied. Thus, the M data points for the computed net low side profile are modified again by the M iterated values of $(1 - dx_1/dx_2)$, which are computed from M exponential-parabolic charge profiles.

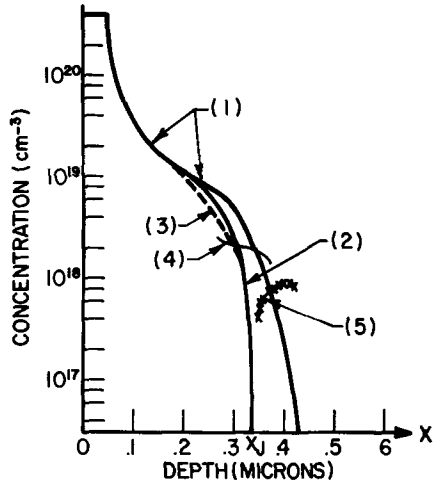

Fig. 3. Illustration of the exponential approximation to the high side net doping: (1) experimental total doping curve (phosphorus diffusion); (2) high side net doping (curve 4 from curve 1); (3) exponential approximation, $N_1(x)$; (4) experimental total doping curve (boron diffusion); (5) calculated net doping, $N_2(x)$. Curves 5 and 4 should coincide at $x = 0.42\mu$ when the compensation from the high side doping becomes negligible.

Experimental

Figure 4(a) shows the calculated net ionized impurity distributions on both sides of the junction of a sequentially diffused p-n structure (net profile symbols are on the figure). Figure 4(b) is an enlarged view of the junction region. A comparison is indicated between the net profiles which result when dx_1/dx_2 is computed from the linear-parabolic, the exponential-

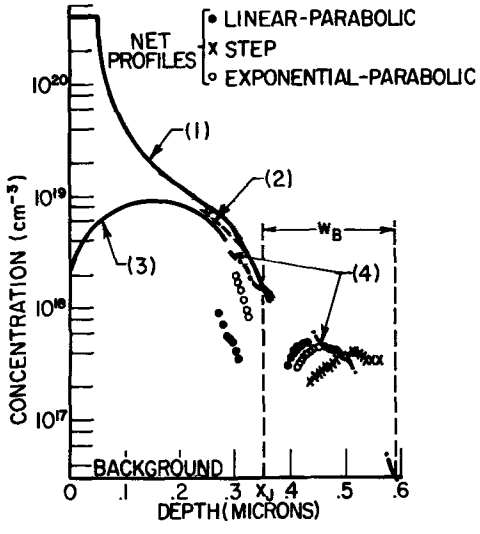

Fig. 4(a). Comparison of the calculated profiles. The $N_1(x_1)$ and $N_2(x_2)$ data points as computed from the approximations to dx_1/dx_2 are indicated by the symbols. (1) Experimental phosphorus profile (singly diffused); (2) boron profile obtained by subtracting linear-parabolic data points from (1); (3) experimental boron profile (singly diffused); (4) boron profile obtained by subtracting exponential-parabolic data points from (1).

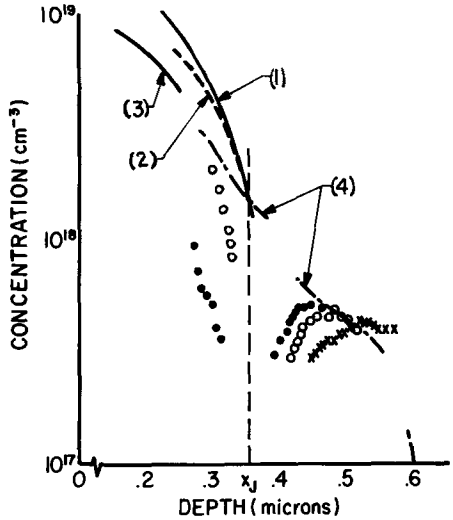

Fig. 4(b). Enlarged view of the profiles of Fig. 4(a) in the vicinity of the junction.

parabolic, and the step junction ($dx_1/dx_2 = 0$) approximations. Curve 1 is a singly diffused emitter profile (phosphorus), and curve 3 is a singly diffused base profile (boron). Curves 2 and 4 show the calculated total base doping when the base and the emitter are diffused sequentially. Curve 2 was obtained by subtracting the linear-parabolic data points from the total emitter doping profile (curve 1). Curve 4 was obtained by subtracting exponential-parabolic data points from curve 1. Because of the "emitter push-out" effect, the accuracy of the parabolic methods cannot be checked by comparing the calculated profiles with the superposition of the singly diffused emitter and base profiles. Nevertheless, it is possible to see that there is continuity on the high side between the measured singly diffused base profile (curve 3) and the calculated total doping profiles (curves 2 and 4).

Emitter push-out can be reduced by diffusing arsenic from a doped-oxide source for the emitter, and by implanting the base region with boron ions. Figure 5 shows the calculated net doping on both the high and low sides of the emitter-base junction. For this structure, dx_1/dx_2 was computed using the exponential-parabolic approximation. It can be seen that the calculated net high side doping indicates that the impurity gradient of the arsenic profile is very large in the junction region. The measured gradient from Fig. 5 is approximately 2.5 x 10^{25} cm^{-4}, which closely agrees with the value of the gradient as determined by computer simulation of the arsenic diffusion.

Curve 1 in Fig. 5 is the predicted implant profile (9). Curve 2 was drawn by subtracting the n-background doping level from the $N_2(x_2)$ data points. Good agreement with the predicted implant profile can be seen. It should be noted that the step-junction approximation ($dx_1/dx_2 = 0$) to this p-n structure would yield virtually the same values of $N_2(x_2)$ as the exponential-parabolic approximation because of the steep high side profile gradient.

Figure 6 shows the way in which dx_1/dx_2 varies with the depletion region width for the structure of Fig. 4. The values of dx_1/dx_2 which were used to plot these curves were obtained by performing the iterations required to make the charge changes with bias equal on both sides of the junction. The non-step and nonlinearly graded behavior of the linear-parabolic and the exponential-parabolic junctions can be seen ($dx_1/dx_2 = 0$ for a step junction, and $dx_1/dx_2 = -1$ for linear grading). Also shown in Fig. 6 is the fact that the dx_1/dx_2 values for the two approximations differ. Reference to Eq. [10] and [17] indicates that

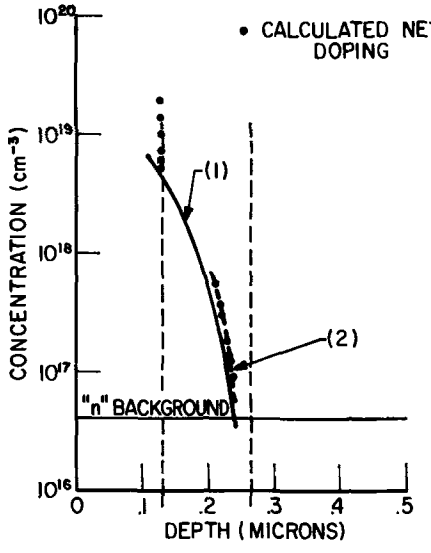

Fig. 5. Comparison of predicted and calculated profiles. (1) Predicted total implant doping, 30 keV, 1 x 10^{14} ions/cm^2, boron beam; (2) calculated total implant doping using the exponential-parabolic approximation for dx_1/dx_2.

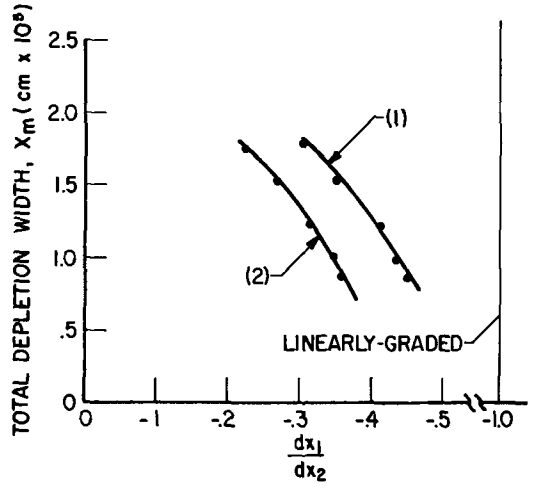

Fig. 6. Variation of dx_1/dx_2 with depletion layer width. (1) Linear-parabolic approximation; (2) exponential-parabolic approximation.

this difference is due to the functional form of the charge distributions on the high side of the junction.

Conclusion

The self-consistent methods developed here can be used for estimating doping profiles in the vicinity of the junctions of sequentially diffused or diffused-implanted structures. The linear-parabolic approximation for the determination of dx_1/dx_2 accounts for non-step junction behavior in structures for which a grade constant can be estimated. The exponential-parabolic approximation gives an improved estimate of net doping if some information can be obtained concerning the singly diffused low and high side profiles. However, because of the self-adjusting nature of these approximations, uncertainties in grade constant, m_1, or exponential constant, k^1, should not affect the precision of the computed profiles.

The accuracy errors associated with any C-V measurement technique occur in the measurement of dC and A, the area of the p-n junction, in the determination of the junction locations, and in the assumption of the form of the high side profile. While the self-consistent parabolic approximations described here do not improve on the first three sources of errors, a best fit of an assumed functional form of $N_1(x)$ can be obtained for a given pair of C-V measurements, providing that the parabolic approximation to the low side net doping is valid. Once this best fit is obtained, the correction factor ($1 - dx_1/dx_2$) can be determined so that the effective doping density, multiplied by ($1 - dx_1/dx_2$), yields the net low side doping density, $N_2(x_2)$ (Eq. [5]). This procedure is then repeated for each pair of C-V measurements. While it has not been ascertained which is the more accurate approximation (linear-parabolic or exponential-parabolic), each is clearly an improvement over the step approximation for shallow, sequentially diffused junctions.

Acknowledgments

The author would like to thank Dr. A. U. MacRae for providing the implanted samples and Dr. R. A. Moline for his helpful suggestions regarding this manuscript.

Manuscript submitted Oct. 2, 1970; revised manuscript received ca. Jan. 13, 1971.

Any discussion of this paper will appear in a Discussion Section to be published in the December 1971 JOURNAL.

REFERENCES

1. E. Tannenbaum, *Solid-State Electron.*, **2**, 123 (1961).
2. W. Schottky, *Z. Physik.*, **118**, 539 (1942).
3. T. D. Jones, Thesis, Lehigh Univ. (1969).

4. R. M. Warner and J. N. Fordemwalt, "Integrated Circuits," McGraw-Hill Book Co., New York (1965).
5. H. Lawrence and R. M. Warner, *Bell System Tech. J.*, **39**, 389 (1960).
6. R. L. Pritchard, *Semicond. Prod.*, **2**, 31 (1959).
7. D. R. Decker, *This Journal*, **115**, 1085 (1968).
8. See, for example, J. L. Moll, "Physics of Semiconductors," McGraw-Hill Book Co., New York (1964).
9. A. U. MacRae, Private communication.

Diffusion of Tin into GaAs from Doped SiO_2 Film Sources

C. F. Gibbon and D. R. Ketchow
Bell Telephone Laboratories, Incorporated, Murray Hill, New Jersey 07974

ABSTRACT

Diffusion of tin into GaAs from a doped SiO_2 source layer has produced average carrier concentrations twice as high as those previously reported in the literature for diffusions from such films. The average carrier concentration in the diffused layers was 6 to 8 x 10^{18} cm^{-3} for junctions 1 to 2 μm deep. The surface concentration appears to be nearly constant during the first hour of diffusion at 1050°C and decreases due to source film depletion. Carrier concentrations in the diffused layers were measured with both Hall effect and infrared reflectivity techniques.

High concentration n-type diffusion into GaAs is of considerable importance in the development of certain devices. Tin is a convenient n-type dopant for GaAs since it can be diffused from tin-doped SiO_2 films as suggested and carried out by von Muench (1). In addition to acting as a source of tin during diffusion, the SiO_2 films serve to protect the GaAs surface from erosion during processing at high temperatures. However, von Muench (2) found that the carrier concentration, that is, the electrically active donor tin concentration, was limited to 3 x $10^{18}/cm^3$ in diffused layers obtained using either the doped oxide film or pure tin as a diffusion source. Fane and Goss, who diffused tin into GaAs from tin deposited on the GaAs surface by electroplating, have reported that sheet resistance readings indicate about 10^{19} carriers/cm^3 were present in the resulting tin diffused layers (3).

In the present work tin diffusions into GaAs from tin-doped SiO_2 films were carried out using a different procedure from that used by von Muench. Tin-diffused layers having average carrier concentrations of 6-8 x $10^{18}/cm^3$, as measured with Hall effect apparatus, were achieved.

In the system utilized by von Muench the doped SiO_2 source film was deposited from a carrier gas which passed through a mixture of ethylorthosilicate (EOS) with 0.04 volume per cent (v/o) tetraethyl stannane (TET). In the system applied by the present authors the doping of the source solution was 2 v/o of tetramethyl stannane (TMT). TMT was used in an attempt to increase the concentration of tin in the deposited oxide. Although little information is available on the vapor pressure of TET and TMT, TET has a vapor pressure of only 10 mm at 73°C and TMT boils at 78°C (4), indicating that TMT probably has a higher vapor pressure in the room temperature source solution. The diffusions by von Muench were done in a closed ampoule with 1 atm of As pressure. During the work described in this paper diffusions were done in an open tube in forming gas (85% N_2-15% H_2).

Experimental Procedure

The GaAs substrates used were Zn-doped, p-type with hole concentrations of either 5 x $10^{16}/cm^3$ or 1 x $10^{18}/cm^3$. The doped oxide films were deposited on the substrates in a horizontal tube furnace. Forming gas was bubbled through a flask which contained the solution of TMT in EOS at room temperature and passed into the furnace tube where pyrolytic deposition occurred on the slices at 500°C. The oxide films were made as thick as possible to avoid source depletion during the diffusion. In the present cases, 5000-6000Å were deposited; oxides thicker than this could not be used because cracking of the oxide coating appeared after deposition. The diffusions were done at 1050°, 950°, and 850°C in a loosely closed quartz box which was held in a flowing forming gas atmosphere. The quartz box contained a few grams of crushed GaAs to provide some arsenic in the atmosphere and to further protect the diffusion slice from surface damage.

After drive-in the oxide source was removed from the slice with HF, the back was lapped, and Hall effect measurements were carried out on the As-diffused wafer. The Hall effect measurements were made at room temperature in the dark; the specimens were held in the fixture shown in Fig. 1. Contact to the diffused layer was made through tinned phosphor-bronze wires; the contact was formed by a high-voltage pulse from a tesla coil. On most of the specimens the contacts to the diffused layers were checked to be certain that proper rectifying properties were obtained with a fifth electrode attached to the back as a ground connection. The data were analyzed according to the technique of van der Pauw (5). The specimens were then angle lapped, and the junction depth was determined by staining with a solution of $CuSO_4$ containing a trace of HF. Some of the scatter in the data to be presented is related to difficulties in accurately measuring the junction depth. The reproducibility of a given junc-

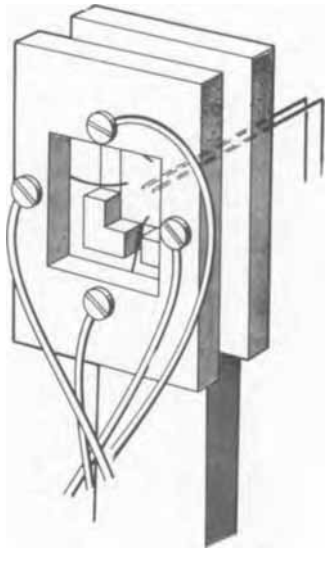

Fig. 1. Fixture for holding specimen for Hall effect measurements.

Key words: diffusion, GaAs, tin.

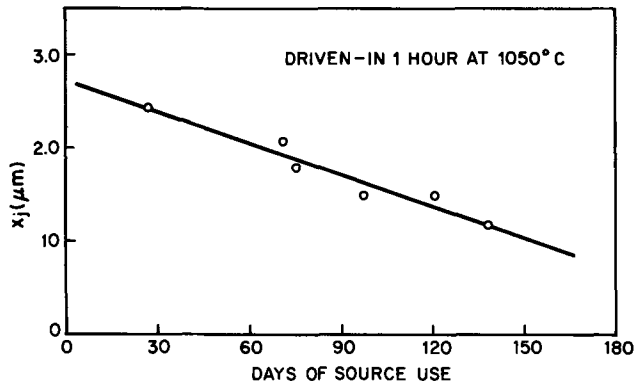

Fig. 2. Depletion of TMT from EOS source as indicated by decrease in junction depth for constant drive-in conditions after various times of source operation.

tion depth in consecutive lapping and measuring cycles is about $\pm 0.15\mu$.

One of the problems with using TMT as a dopant in EOS is that EOS has a vapor pressure of only 12 mm at 60°C and hence appears to be much less volatile than TMT which as previously noted boils at 78°C (4). Therefore, TMT probably evaporates at a higher rate than EOS in all but the most dilute solutions. This causes a slow decrease in the dopant concentration in the EOS source solution and thus in the deposited diffusion source films. Figure 2 shows the junction depths obtained for constant time and temperature diffusions from films deposited from a given 2% TMT source solution as a function of the length of time after the source was mixed. The source was being used at an approximately constant rate during the time covered. The diffusions reported herein were done over a period of approximately six weeks; thus an additional source of scatter in the results presented is due to this source solution differential evaporation effect.

Results and Discussion

Selection of source solution composition.—Doped oxide diffusion source films were deposited from EOS source solutions containing a range of TMT concentrations up to 10 v/o in an effort to optimize the source composition with respect to surface concentration. The junction depth, which should increase with increasing surface concentration since the diffusion conditions are kept constant, increases monotonically with increasing TMT dopant concentration. However, for source concentrations significantly above 2% TMT in EOS the surface of the GaAs was attacked by the doped oxide film. For this reason the 2% solution was chosen for further investigation.

Junction depth vs. time measurements.—In Fig. 3 and 4 the junction depth, x_j, is plotted *vs.* the square root of diffusion time, t, for the p-type substrates of the high and low carrier concentrations. The "error bars" in this and following graphs indicate the range of results obtained from all the specimens having the given value of the abscissa variable, and the average value of all these is the plotted point. The data in Fig. 3 indicates that x_j is roughly proportional to $t^{1/2}$ for times ranging from about 1 hr at 1050°C to 10 hr at 850°C. Beyond this time, the junction depth increase slows down markedly.

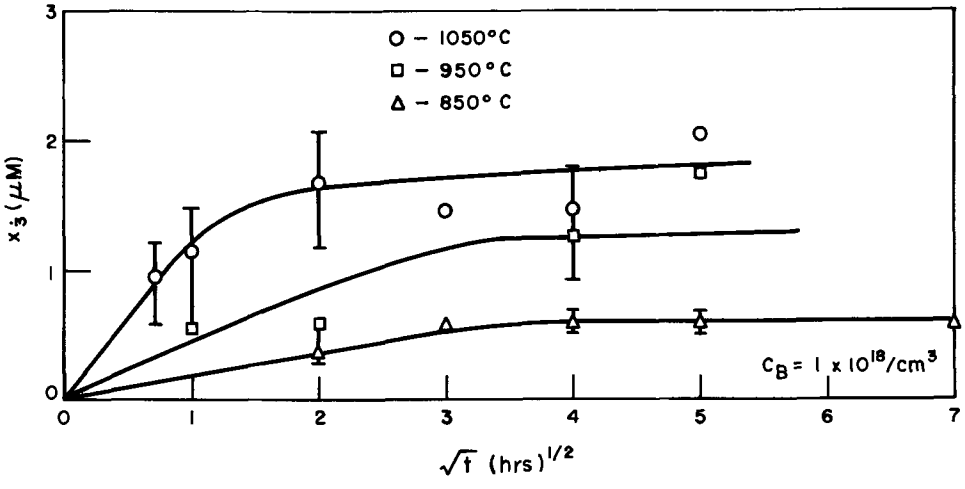

Fig. 3. Junction depth as a function of the square root of time in substrates with carrier densities of $1 \times 10^{18}/cm^3$.

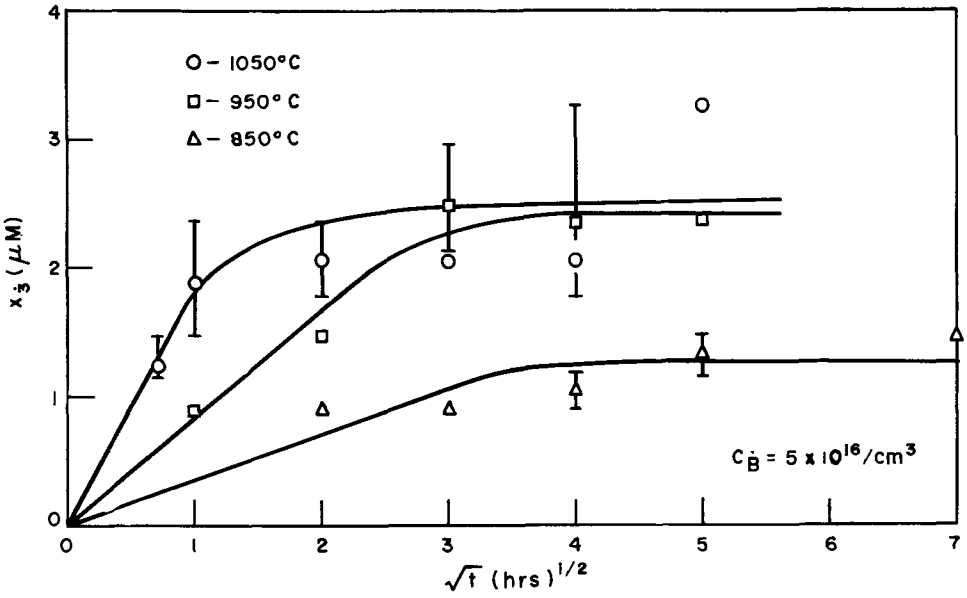

Fig. 4. Same as Fig. 1 in substrates with carrier densities of $5 \times 10^{16}/cm^3$.

This initial behavior is consistent with the presence of a constant surface concentration of tin, C_s. This would be true even if the diffusion coefficient, D, was a function of tin concentration, C, as long as this dependence could be expressed as a function of C/C_s (6). It would also not be affected by the possibility that the number of active tin donors is not equal to the chemical concentration of tin, as may be the case (2). Thus even if the diffusion coefficient of tin was a function of concentration and the active tin donor concentration was not equal to the total tin concentration, a constant C_s diffusion could give x_j proportional to $t^{1/2}$. This suggests that the doped oxide at first supports a constant surface concentration in the GaAs; then since the source is finite, it begins to deplete, and this leads to a leveling off of the x_j *vs.* $t^{1/2}$ curve.

For a finite thin film source, the long-term behavior approaches that of an instantaneous source or Gaussian diffusion (7). If this is the case, then for a Gaussian distribution

$$\frac{x_j^2}{t} = 4D \ln\left(\frac{Q}{C_j\sqrt{\pi D}}\right) - 2D \ln t \qquad [1]$$

should hold, where Q is total number of diffusing ionized tin atoms and C_j is the base carrier concentration. D here is assumed to be constant; even if D is not a constant for long diffusion times, the reduction in concentration variation across the diffused layer and the generally lower concentration throughout the layer may make Eq. [1] approximately correct with D interpreted as an effective, or average, diffusion coefficient. Thus the quantity x_j^2/t should be constant as a function of time up to the point in Fig. 3 and 4 where the curve breaks away from an approximately straight line relationship between x_j and $t^{1/2}$. For longer times x_j^2/t should become proportional to ln t as seen in Eq. [1].

Figures 5 and 6 show plots of $-x_j^2/t$ *vs.* ln t for the highest and lowest diffusion temperatures studied. It should be pointed out that the scatter at shorter times and shallower junction depths is related to the fact that the x_j values, which are already uncertain to $\pm 0.15\mu$, must be squared. The behavior predicted is fairly well obeyed for the longer times. The values of the effective diffusion coefficients for Sn in GaAs taken from the slopes of the tails of the curves are 5×10^{-13} cm^2/sec at 1050°C and 3.5×10^{-14} cm^2/sec at 850°C.

It will be noticed that particularly in the data for the slices having the lighter base carrier concentrations ($C_j = 5 \times 10^{16}$/cm^3) there is an apparent discontinuity or transition region which must be introduced between what has previously been interpreted as the constant surface concentration and depleting source regions of Fig. 5 and 6. Although the presence of this discontinuity is not well understood, it could arise if the apparent diffusion coefficient were a strong function of concentration, especially if it decreased with decreasing average concentration in the layer, finally reaching some constant value for long diffusion times and low average carrier concentrations.

Hall effect measurements.—In addition to the junction depth determinations, Hall effect measurements were also made on the diffused slices. The carrier concentration, $\bar{n}$, obtained from the Hall effect measurements is approximately the average concentration of carriers over the entire diffused layer; this corresponds to the average concentration of ionized tin donors in the layers. (Actually, some of the donor tin is compensated by zinc acceptors in the substrate and does not contribute to the carrier concentration; thus a number equal to the substrate carrier concentration should be added to $\bar{n}$ to obtain the tin donor concentration.)

Of course, this does not correspond necessarily to the total (chemical) concentration of tin in the layer; in fact, it is known to deviate from the total concentration in some cases (2). If we assume that the fraction of the total tin that is active as donors is independent of concentration of tin and that D is constant, then two limiting cases of the dependence of $\bar{n}$ on time can be considered. For a constant surface concentration, a complementary error function profile is generated and $\bar{n}$ would be constant. For a depleting source or Gaussian profile

$$\bar{n} = \frac{Q}{x_j}\,\mathrm{erf}\,\frac{x_j}{2\sqrt{Dt}} \qquad [2]$$

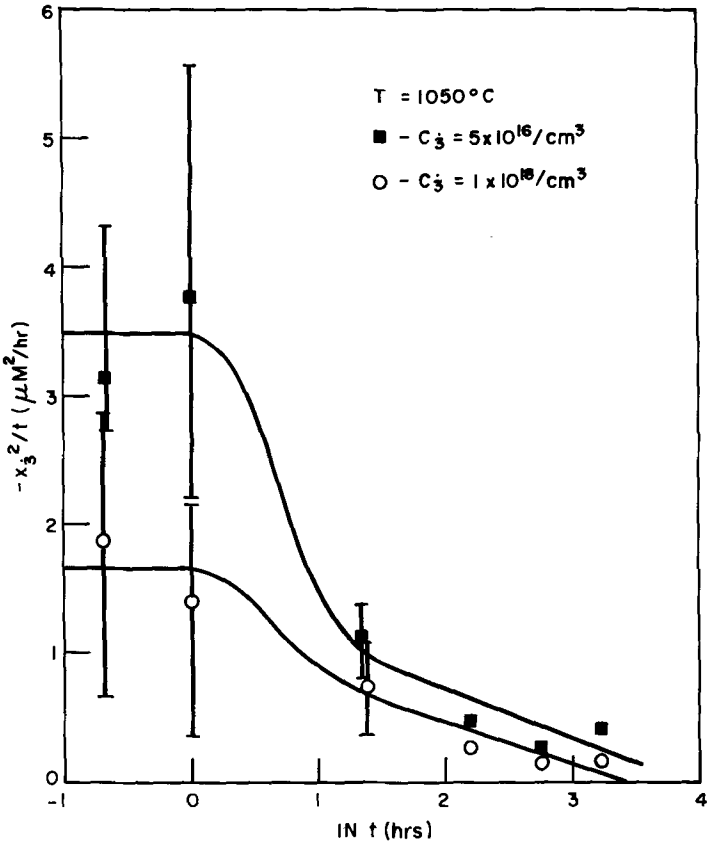

Fig. 5. Ratio of junction depth squared to diffusion time as a function of ln (diffusion time) at 1050°C.

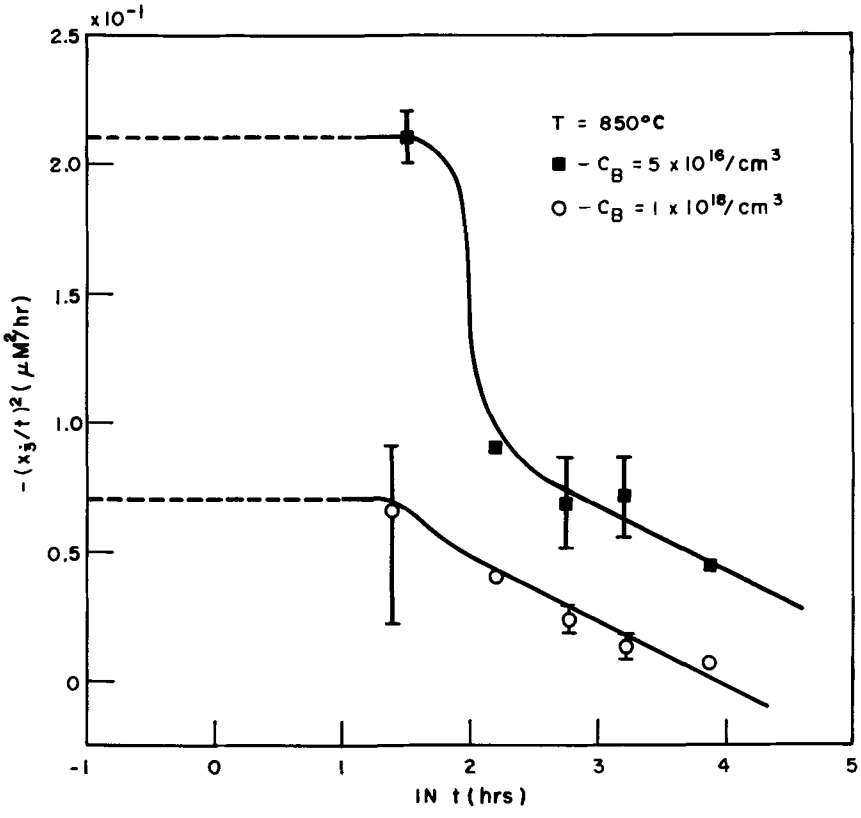

Fig. 6. Ratio of junction depth squared to diffusion time as a function of ln (diffusion time) at 850°C.

For values of $(x_j/2\sqrt{Dt})$ less than one the error function can be approximated by its argument with a maximum error of about 15%. Hence

$$\bar{n} \simeq \frac{Q}{2\sqrt{D\bar{t}}} \qquad [3]$$

For periods of 10 hr or longer this condition holds at 1050°C in the present diffusions, if the D value calculated from the slope in Fig. 5 is used in calculating $(x_j/2\sqrt{D\bar{t}})$. Figure 7 shows a plot of average tin donor concentration, $\bar{n}$, as a function of the inverse square root of time at 1050°C; also shown is similar data for a freshly prepared TMT:EOS source. The data can be fitted reasonably well with a straight line over the entire time range even though the $t^{-1/2}$ relationship was expected to hold only for longer times. The scatter in the data probably masks a change in slope of the curve at shorter times. In any event, for short diffusion times, average carrier concentrations—which are presumed to be equal to uncompensated donor tin concentrations—as high as 6-8 x 10^{18}/cm³ can be seen to be present in the diffused layers.

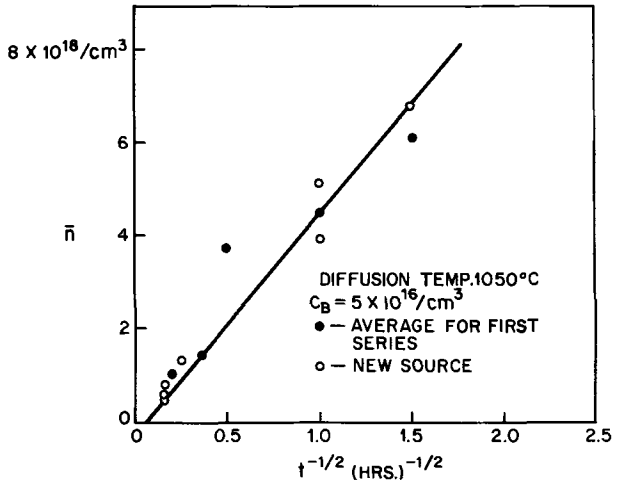

Fig. 7. Average carrier concentration in a tin diffused layer as a function of the inverse square root of the diffusion time for diffusions done at 1050°C.

Infrared measurements of surface concentration.— The surface concentrations in some of the diffused layers have also been measured by the infrared reflectivity technique (8). The positions of the reflectance minima from which these concentrations are determined are characteristic of the maximum carrier concentrations in the diffusion profiles (9). [For a complete discussion of the use of infrared reflectivity for determining surface concentrations in diffused layers, see Abe and Nishi (10).] The surface concentration data as determined from the infrared technique along with the average carrier concentrations measured with Hall effect apparatus are presented in Table I for slices diffused for 0.5 and 1 hr at 1050°C. The slice listed as having a base hole concentration of 2 x 10^{17}/cm³ is one of a few that type diffused along with the slices previously discussed. The infrared measurements support the observation that carrier concentrations in the range of 6 to 8 x 10^{18}/cm³ are present in the diffused layers, but they also indicate that the surface concentrations are equal to or no more than a factor of two larger than the average carrier density measured by the Hall technique. In particular, the fact that the average carrier concentration in the diffused layer for the slice diffused 0.5 hr is approximately equal to the surface concentration suggests that the carrier distribution may be relatively flat near the surface for the most heavily diffused layers. This would be the case if either the diffusion coefficient or the fraction of the tin ionized were appropriate functions of concentration.

In summary, regardless of the exact nature of the diffusion kinetics, the data presented in the preceding

Table I. Surface concentrations from IR reflectivity

Subst. doping (no/cm³)	Diff. time (hr)	Avg carrier conc from Hall effect (no/cm³)	C_s from IR (no/cm³)
5 × 10^{16}	0.5	8 × 10^{18}	7.4 × 10^{18}
5 × 10^{16}	1.0	3 × 10^{18}	4.8 × 10^{18}
5 × 10^{16}	1.0	3 × 10^{18}	5.9 × 10^{18}
2 × 10^{17}	1.0	4 × 10^{18}	6.0 × 10^{18}

sections indicate that the oxide source begins to deplete soon after diffusion starts. The fact that higher carrier concentrations (6-8 x 10^{18}/cm^3) were achieved in this work than had previously been observed is probably related in part to the recognition that, with an oxide source, depletion effects make short-time. shallow diffusions mandatory if high concentrations are to be obtained.

Conclusions

1. Diffusion of tin from tin-doped SiO_2 films deposited on p-type GaAs by pyrolytic decomposition of ethylorthosilicate containing tetramethyl stannane yields n-type diffused layers having average carrier concentrations of 6-8 x 10^{18}/cm^3 for short (0.5-1.0 hr) diffusion times.

2. The diffusion source appears to yield a constant surface concentration initially and then depletes. In order to obtain the high average carrier concentrations short diffusion times must be used to avoid depletion effects.

Acknowledgments

The authors wish to thank L. A. D'Asaro, J. Simpson, and T. J. Reilly for advice and encouragement. Also we wish to thank R. Berman who carried out the infrared measurements of the surface concentrations and R. L. Brown who programmed the Hall effect calculations.

Manuscript received Nov. 9, 1970.

Any discussion of this paper will appear in a Discussion Section to be published in the December 1971 JOURNAL.

REFERENCES

1. W. von Muench, *Solid-State Electron.*, **9**, 619 (1966).
2. W. von Muench, *IBM J. Res. Develop.*, **10**, 438 (1966).
3. R. F. Fane and A. J. Goss, *Solid-State Electron.*, **6**, 383 (1963).
4. H. C. Kaufman, "Handbook of Organometallic Compounds," D. Van Nostrand Co., New York (1961).
5. L. J. van der Pauw, *Philips Res. Rept.*, **13**, 1 (1958).
6. L. L. Chang, *Solid-State Electron.*, **7**, 853 (1964).
7. A. E. Owen and P. F. Schmidt, *This Journal*, **115**, 548 (1968).
8. W. G. Spitzer and H. Y. Fan, *Phys. Rev.*, **108**, 268 (1957).
9. R. Berman, Private communication.
10. T. Abe and Y. Nishi, *Jap. J. Appl. Phys.*, **7**, 397 (1968).

Preparation and Properties of $Mg_xZn_{1-x}Te$[1]

S. G. Parker,* A. R. Reinberg, J. E. Pinnell, and W. C. Holton

Texas Instruments, Incorporated, Dallas, Texas 75222

ABSTRACT

The pseudo-binary alloy system $Mg_xZn_{1-x}Te$ has been investigated for $0 = x \leq 0.8$. Compositions containing less than 53 mole per cent (m/o) Mg have a cubic structure with expanded lattice spacings of ZnTe. For Mg concentrations of 0.53-0.80 m/o the alloys have a hexagonal structure with contracted lattice spacings of MgTe. The bandgaps, as determined by electron beam bombardment, vary linearly with composition within the crystalline structure.

Numerous attempts have been made to form solid solutions from semiconductor compounds to obtain variable bandgap materials, with the aim of producing a light emitting diode whose output wavelength was thereby adjusted. Growth of solid solutions among the III-V compounds for this purpose has been rather successful; however, efficient light emission from diode structures is limited to wavelengths longer than 6000Å by the fact that at higher energies the bandgap becomes indirect. Since the II-VI compounds, principally the zinc and cadmium chalcogenides, retain a direct bandgap for the entire series, it should be possible using alloys of these, to obtain efficient light emission to wavelengths as short as the near ultraviolet. Diodes emitting in the visible have been made using ZnSe-ZnTe heterojunctions (1) and from solid solutions of $ZnSe_xTe_{1-x}$ (2). Recently solid solutions of $Mg_xCd_{1-x}Te$ were reported with light emitting diodes having been made from these alloys (3-5). This paper reports the preparation and light emitting properties of $Mg_xZn_{1-x}Te$.

Experimental

Mixtures of ZnTe, Mg and Te were melted together to give various values of x for the pseudo-binary $Mg_xZn_{1-x}Te$. Compounding was done in carbon coated quartz tubes of 8-13 mm ID by heating at 1200°C for 16-20 hr in a rocking furnace. The growth tube containing the charge was outgassed at 10^{-5} Torr and 200°C for 1 hr before sealing off for compounding. The molten charge was quenched at 50°-60°C/min to the solid state to prevent segregation (6) into solid solution of variable composition. To quench the boules the furnace power was shut off and a blast of air directed over the quartz tube. Various quench rates were obtained by changing the air flow.

The ZnTe was made by fusing 99.9999% pure Zn and Te together in He ambient while contained in a carbon-coated quartz boat. Unreacted material was removed by heating at 500°C under a vacuum of 10^{-3} Torr. The Mg metal, which was 99.99% pure, was etched with Br_2-methanol to remove oxides and carbonates from the surface and placed immediately in the compounding tube under a He ambient. The Te was 99.9999% pure and was degreased in boiling trichloroethylene before use. After compounding the quartz tube was cracked to recover the $Mg_xZn_{1-x}Te$ boule. There was no wetting of the quartz if the Mg were well-etched and if a crack-free carbon coat was obtained on the quartz tube. The boules containing Mg $\geq$ 5.0 m/o were stored in kerosene or under a vacuum to prevent reaction with H_2O or O_2. The exact composition of the material after compounding was determined by microprobe. Sometimes the compounded material was reloaded into a carbon coated quartz tube, and the Bridgman technique was used to grow large single crystals up to 1 cm on an edge. The system was heated and outgassed before sealing off as for the compounding operation.

[1] This research was sponsored in part by the Air Force Office of Scientific Research Contract No. F-44620-67-C-0073.

* Electrochemical Society Active Member.

Key words: magnesium-zinc telluride, solid solutions, crystal growth, tellurides, II-VI compounds.

Table I. Composition homogeneity of $Mg_xZn_{1-x}Te$ for different quench rates

Run No.*	Quench rate, °C/min	Position of sample in the boule†	Mole % ZnTe at random spots** 1	2	3	4	5
N10715-75	60	First to freeze	83	80	82	82	80
		Last to freeze	80	81	79	80	80
N10715-31	40	First to freeze	97	95	93	94	95
		Last to freeze	96	96	96	97	96
N10715-35	20	First to freeze	95	95	94	93	95
		Last to freeze	87	84	85	87	86
N10715-12	15	First to freeze	91	93	95	93	91
		Last to freeze	73	88	82	78	77

* The composition of the boules was not the same.
** Composition determined by microprobe.
† Boules were 8 mm in diameter and 6 cm in length.

MgTe for use as a reference was compounded by the same procedure used for the MgTe-ZnTe system except the ZnTe was omitted. A temperature of 1300°C was used for compounding with no quenching. The compounding tube was broken under kerosene so that the MgTe was not exposed to O_2 or H_2O. Samples of MgTe were taken from the kerosene bath and quickly sealed under vacuum for x-ray and DTA studies. ZnTe reference samples were obtained by vapor transport in a He ambient.

The composition of the alloys was determined by microprobe analysis using a Material Analysis Company Model 400 Electron Probe Microanalyzer. A Mg-Sn alloy was used as the Mg standard while ZnTe was used as the Zn standard. Samples were embedded in a cold, self-setting plastic and lapped in oil to expose the sample surfaces. These sample surfaces were then degreased with trichloroethylene and placed immediately in the microprobe apparatus where a vacuum of 10^{-5} Torr was pulled. An accelerating voltage of 20 kV was used for the electron beam. The precision was ±1% while the accuracy was ±2%.

Differential thermal analysis of the alloy samples was made with a Du Pont 900 Differential Thermal Analyzer. The sample size was about 25 mg and consisted of four to five chips of the material being studied. The material was removed from the kerosene storage jars or the vacuum dessicator, rinsed in boiling trichloroethylene and placed in quartz tubes, which were evacuated to 10^{-5} Torr then sealed off. Alumina powder was used as the standard reference. The thermocouple was platinum-platinum 13% rhodium. Heating rates of about 10°C/min and cooling rates of 5°C/min were used. The onset of melting was taken as the solidus temperature during heating while the liquidus points were determined by the onset of freezing during the cooling. At least two DTA runs were made for each alloy composition with a reproducibility of ±2%. Supercooling occurred occasionally but usually was not greater than 5°C.

X-ray diffraction patterns were obtained by the Debye-Sherrer method. Samples were ground to about 200 mesh under kerosene, degreased with trichloroethylene placed in a capillary tube then pumped to 10^{-3} Torr and sealed off. Copper K_α radiation for 6 hr was used to obtain the diffraction patterns.

For estimation of bandgap the luminescence stimulated by an electron gun was used. Samples of different alloy compositions prepared by the technique described above were mounted on the cold finger of a cryostat which shared a common vacuum system with a high-power electron gun. The electron gun was capable of producing pulses with a beam current of 20 mA, at a voltage up to 50 kV ranging in width from 15 to 200 nanosec at a repetition rate of 60 Hz. The recombination radiation was collected by a mirror system and focused onto the entrance slit of a ¾ meter grating spectrometer. A sampling oscilloscope was used to time resolve the observed spectra and present the data as luminescence intensity *vs.* wavelength on a recorder.

Physical Properties of the Material

Homogeneity as a function of quench rate is illustrated in Table I. It can be seen that the homogeneity, as determined by microprobe analysis of randomly selected spots in a cross sectional slice, was rather good for a quench rate of ≧20°C/min. This table also gives a comparison of the homogeneity for slices from the first and last portions to freeze. Unless freezing was rapid there was much segregation. Although rapid quench rates gave better homogeneity, coring and blow holes resulted at the higher quench rates. Above a quench rate of 75°C/min the boule was so badly cored that it was useless. Boules cooled at 20°C/min or less were not cored and did not contain blow holes, but these boules were very inhomogeneous.

The quenched material was polycrystalline but did contain single crystals up to 3 mm on an edge. The size of the single crystals decreased as the Mg content increased. Tellurium, which was determined by microprobe measurements, collected at many of the grain boundaries to make the material opaque to visible light. The amount of Te at the grain boundaries was reduced by adding 10 m/o excess Mg during compounding; this was necessary because some of the Mg was usually not available for reaction because it existed as MgO or $Mg(OH)_2$. The remainder of the Te could be removed by heating the $Mg_xZn_{1-x}Te$ in molten Zn at 850°C for several hours; this Zn treatment produced transparent material. The color of the $Mg_xZn_{1-x}Te$ varied from red-brown for low values of x to colorless for material rich in Mg. Material containing 50 m/o Mg or greater reacted with H_2O or methanol. Typical impurities present are shown in Table II.

From the differential thermal analysis results, a partial phase diagram for the MgTe-ZnTe system showing liquidus and solidus curves was constructed as shown in Fig. 1. This phase diagram indicates that solid solutions exist over a wide range for values of x in $Mg_xZn_{1-x}Te$. Linear changes in d-spacings with composition as shown by x-ray diffraction gave additional evidence that solid solutions are formed in both hexagonal and cubic structures. A pseudobinary with a cubic structure exists for Mg concentrations of 0-53 m/o. This cubic material is very similar to ZnTe with the d-spacings being expanded as the Mg concentration is increased. Table III illustrates that the d-spacings for $Mg_{0.6}Zn_{0.4}Te$ are clearly related to those for MgTe. The phase diagram is unknown in the range 0-20 m/o ZnTe since no compounds were made in this region. X-ray diffraction showed that two different hexagonal phases exist at $Mg_{0.82}Zn_{0.8}Te$ with one of these phases being similar to that for MgTe. The phase diagram in the transition region between the cubic and hexagonal structures, as bounded by the dashed

Table II. Impurities in $Mg_xZn_{1-x}Te$

Sample composition	Treatment of material	Impurities in ppm* Cu	Ni	Fe	Si	Al	Ag	Cr	Mn
$Mg_{0.4}Zn_{0.6}Te$	Compounded then quenched	5-50	10-100	10-100	10-100	5-50	0.05-5	10-100	5-50
$Mg_{0.25}Zn_{0.75}Te$	Compounded, quench and gradient freeze	10-100	0.5-5	5-50	100-1000	5-50	N.D.	N.D.	N.D.
$Mg_{0.1}Zn_{0.9}Te$	Compounded then quenched	10-100	N.D.	1-10	1000-10,000	10-100	0.1-1	N.D.	N.D.

* ppm by weight; determined by emission spectrograph.

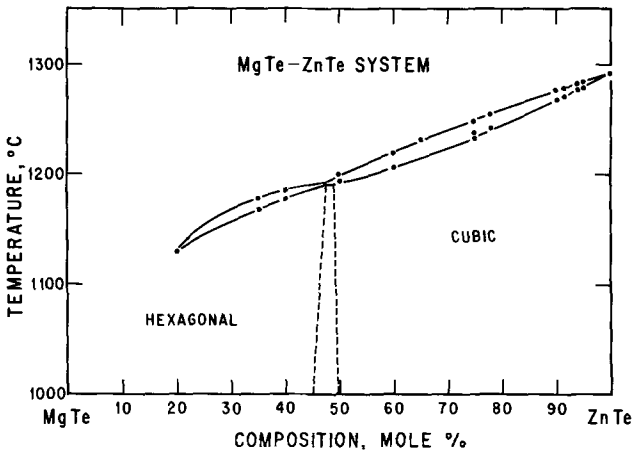

Fig. 1. Phase diagram for MgTe-ZnTe system

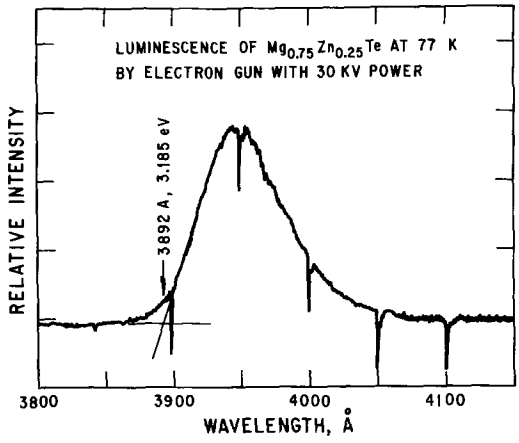

Fig. 2. Typical luminescence curve obtained by electron beam bombardment.

lines, is unknown. X-ray diffraction data did not clearly define what structures were present. Phase diagrams are based on equilibrium conditions. Because we were working with quenched samples, equilibrium conditions probably did not prevail.

It is rather difficult to explain the existence of two hexagonal phases for the composition $Mg_{0.82}Zn_{0.18}Te$ and not for MgTe. Additional study is necessary to completely determine the system in the range of 0-25 m/o ZnTe. The melting point of MgTe which is 1200° ± 5°C has not been reported previously; DTA indicates a possible phase transition in MgTe at 1170° ± 5°C. X-ray diffraction showed the MgTe to be hexagonal in agreement with work of others. It is obvious that the composition of the solid in equilibrium with the melt would be different from that of the melt; thus, Bridgman-type crystal growth would not produce material of uniform composition.

Some indication that solid solutions existed with the MgTe-ZnTe system were obtained from band edge luminescence at 77K using electron beam bombardment. A typical luminescence curve is shown in Fig. 2. Only a single luminescence line was observed which was in the region of the unexpected bandgap. Typical line widths were approximately 0.05 eV at 77K. In addition to this line, samples which had been post annealed in liquid zinc at 800°C for 24 hr exhibited a strong broad luminescence at longer wavelengths which was typically 0.250 eV in width. The broad luminescence could also be distinguished from the sharper band edge line by time resolution. That is, the sharp band edge line decayed very rapidly essentially following the electron beam current. The broad, impurity line, on the other hand, had a considerably longer decay time, typically several microseconds.

Values for the energy bandgap were estimated from the sharp, fast luminescence. We have arbitrarily chosen the high energy limit of this line as the value for the energy gap. At least in the case of pure ZnTe this gives a value of 2.37 eV which is within 0.025 eV of the accepted value for 77K. Since the sample did tend to vary somewhat in composition in a given boule and the microprobe determination of alloy composition was subject to an error of approximately 5%, it was not felt that a more careful determination would be meaningful. Figure 3 shows how the bandgap corresponding to the band edge luminescence varies with composition over the range of x = 0-80 m/o for $Mg_xZn_{1-x}Te$. A break is indicated at the region where the structure changes from cubic to hexagonal because the bandgap is expected to vary with structure. It is observed that the wavelength corresponding to the bandgap varies almost linearly, within experimental error, up to about 0.53 m/o Mg. For 0.53 to 0.80 m/o Mg the bandgap also varies linearly but with a different slope than for the smaller Mg concentrations. The

Table III. Comparison of d-spacing of $Mg_xZn_{1-x}Te$ compounds with those of ZnTe and MgTe

Indices	Cubic					Hexagonal			Indices
	ZnTe, A.S.T.M.	$Mg_{0.1}Zn_{0.9}Te$, measured	$Mg_{0.25}Zn_{0.75}Te$, measured	$Mg_{0.4}Zn_{0.6}Te$, measured	$Mg_{0.5}Zn_{0.5}Te$, measured	MgTe, measured	$Mg_{0.6}Zn_{0.4}Te$, measured	$Mg_{0.82}Zn_{0.18}Te$, measured	
111	3.523	3.50	3.54	3.57	3.57	—	—	—	—
200	3.051	3.04	3.08	3.10	3.10	3.67	3.62	3.62	002
220	2.159	2.15	2.18	2.19	2.19	3.45	3.39	3.39	101
311	1.840	1.84	1.86	1.87	1.87	2.69	2.63	2.64	102
222	1.762	1.76	1.78	—	—	2.26	2.22	2.23	110
400	1.526	1.53	1.54	1.55	1.55	2.08	2.05	2.06	103
331	1.400	1.40	1.41	1.42	1.42	—	—	—	—
420	1.365	1.37	1.38	1.39	1.39	1.93	1.92	1.94	112
422	1.246	1.25	1.26	1.27	1.27	1.90	1.87	1.90	201
511	1.175	1.18	1.19	1.20	1.20	1.85	1.86	1.87	004
440	1.079	1.08	1.09	1.10	1.10	1.74	1.70	1.71	202
531	1.032	1.03	1.04	1.05	1.05	—	—	—	—
600	1.017	1.02	1.03	—	—	1.54	1.50	1.51	203
620	0.965	0.97	0.98	0.98	0.98	—	—	—	—
533	0.931	0.93	0.94	0.95	0.95	1.46	1.42	1.46	211
622	0.920	0.92	0.93	—	—	1.43	1.40	1.43	114
444	0.881	0.88	0.89	—	—	1.38	1.36	1.37	212
711	0.855	0.86	0.86	0.87	0.87	1.31	1.28	1.29	300
642	0.816	0.85	0.83	0.83	0.83	1.27	1.25	1.26	216
731	0.795	0.82	0.80	0.81	0.81	1.24	1.21	1.22	302
—	—	—	—	—	—	1.48†	1.45†	1.68†	—
—	—	—	—	—	—	1.67†	3.84†	2.11*	—
—	—	—	—	—	—	1.96†	—	2.27*	—
—	—	—	—	—	—	3.90†	—	2.47*	—
—	—	—	—	—	—	—	—	3.77*	—
—	—	—	—	—	—	—	—	3.86†	—
—	—	—	—	—	—	—	—	4.04*	—
—	—	—	—	—	—	—	—	4.25*	—

* Second phase line.
† Not indexable using Zachariasen parameters a = 4.52A, c = 7.33A.

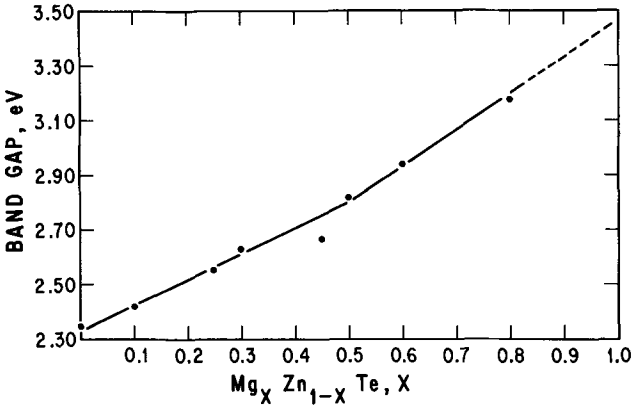

Fig. 3. Band gap as a function of composition by electron beam bombardment.

extrapolation to pure MgTe, however, leads to a value for the emission edge of 357 μm (3.47 eV) which is considerably lower energy than the value 4.7 eV previously reported (5, 7, 8).

The reference for the 4.7 eV bandgap of MgTe given by Itoh is R. H. Bube's "Photoconductivity of Solids" (7). Bube presents a table of bandgap energies of some 128 compounds including the selenides and tellurides of Mg, Sr, and Ba. Since no further references are given in this table a search was made of the literature for a primary source. The only reference to the bandgap of MgTe that could be uncovered was a measurement of the optical absorption of thin films reported by Saum and Hensley. Although these data show a maximum in the absorption coefficient occurring at about 4.7 eV, it is questionable as to whether it is appropriate to associate this value with an expected peak in band edge recombination radiation. Several sharp peaks below the maximum absorption value for the other alkaline earth chalcogenides have been tentatively identified as due to excitons. For MgTe an analogous peak is observed at 3.6 eV as reported by Saum and Hensley (8). It is possible that oxygen or H_2O reacted with the $Mg_xZn_{1-x}Te$ to form oxygen compounds which would influence the bandgap values obtained. In the absence of further detailed analysis of absorption and luminescence in these compounds it is not possible to predict where the recombination radiation should occur although it has been observed in the alkaline oxides that the cathodoluminescence generally occurs well below the fundamental electronic optical absorption (9).

Optical absorption measurements on the (Mg,Zn)Te alloys gave values for the absorption edge which were less than the bandgap values obtained by electron bombardment. This indicates that impurities or other defects caused absorption within the bandgap. The sample slices for absorption measurements were lapped to a thickness of 1 mm or less and polished.

Efforts were made to grow single crystals of (Mg,Zn)Te by the gradient freeze technique and by iodine chemical transport. Boules containing large, single crystal regions about 1 cm on an edge were obtained by the gradient freeze method while only small single crystals that were 3-4 mm on an edge were obtained by I_2 chemical transport. The homogeneity of crystals grown by both methods is illustrated in Table IV. It can be seen that the crystals grown by both methods were not very homogeneous. There was also considerable segregation of Mg and Zn in the first and later to freeze portions of the gradient freeze process. Thus, it was obvious that homogeneous crystals were not to be obtained using the gradient freeze method. Although the crystals grown by I_2 transport were rather homogeneous throughout their bulk, additional work would be needed to establish the conditions for growing larger, more uniform crystals. The chemical transport was similar to that used for growth of ZnSe crystals (10). X-ray diffraction of $Mg_xZn_{1-x}Te$ crystals grown by both methods showed that the material was cubic in structure. The compositions of these crystals ranged from $x = 0.05$-0.3.

The (Mg,Zn)Te material as produced was always p-type with resistivity of 10^4-10^5 ohm-cm. An effort was made to decrease the resistivity and to produce n-type material by doping. Aluminum metal, which was introduced during the compounding step, was used to produce n-type $Mg_{0.25}Zn_{0.75}Te$. The aluminum concentration in the (Mg,Zn)Te as determined by emission spectroscopy was 500-1000 ppm, while the resistivity was 10^7-10^8 ohm-cm. Therefore, the n-type material was probably compensated. An n-type layer was produced in (Mg,Zn)Te by diffusion of Al into the material. In the diffusion experiments Al metal was evaporated onto the surface of a (Mg,Zn)Te slice then heated at 850°C for 16 hr in the presence of Al and Zn vapors. The surface where the Al had been evaporated was n-type and could be lapped away to reveal p-type material. The resistivity of the n-type, Al diffused layer was about 10^5 ohm-cm. Attempts to measure Hall mobility both in the dark and with light were unsuccessful.

Diodes were made by diffusing Al into p-type $Mg_{0.25}Zn_{0.75}Te$ and contact to the n-type surface was made by alloying the In-Ga, while Au evaporated onto a $LiNO_3$ treated surface was used for contact to the p-type surfaces (11). The diode action was only slight, showing 1 x 10^4 ohms in the reverse direction. No light was emitted from the diode up to a breakdown voltage of 120V. Several unsuccessful attempts were made to obtain visible light from $Mg_xZn_{1-x}Te$ diodes of various composition.

Summary

The Mg-Zn-Te system produces pseudobinary alloys of $Mg_xZn_{1-x}Te$ for values of $x = 0$-0.80. Compositions containing up to approximately 53 m/o Mg have a cubic structure with expanded lattice spacings of ZnTe. Compositions richer in Mg crystallize in the hexagonal MgTe structure. Bandgaps corresponding to band edge recombination as determined by electron beam stimulation showed a linear variation with composition. The material was compounded by reaction of ZnTe, Mg, and Te in a carbon coated quartz tube at 1200°C. If quenched rapidly from the melt the boules were homogeneous but polycrystalline. The material was p-type with resistivity of 10^4-10^5 ohm-cm; aluminum diffusion produced n-type material.

Acknowledgments

The authors wish to acknowledge the assistance of Rowland E. Johnson and Don E. Ruthven.

Table IV. Homogeneity of $Mg_xZn_{1-x}Te$ single crystals

Composition of starting material	Method of growth	Position of sample	m/o ZnTe at random spots†				
			1	2	3	4	5
$Mg_{0.20}Zn_{0.80}Te$	Gradient freeze*	Slice from first to freeze	86.5	82.1	86.3	87.5	82.4
$Mg_{0.20}Zn_{0.80}Te$	Gradient freeze*	Slice from last to freeze	80.7	81.5	80.7	77.5	82.5
$Mg_{0.2}Zn_{0.8}Te$	I_2 chemical transport**	Throughout bulk	81.1	82.3	77.4	79.3	82.4

† Composition determined by microprobe analysis.
* Heated to 1280°C, then cooled at 10°C/hr.
** Feed @ 856°C, crystal growth @ 707°C, I_2 conc. = 5 mg/cc.

Manuscript submitted June 1, 1970; revised manuscript received *ca.* Feb. 5, 1971.

Any discussion of this paper will appear in a Discussion Section to be published in the December 1971 JOURNAL.

REFERENCES

1. Y. Tsujimato and M. Fukai, *Jap. J. Appl. Phys.*, **6**, 1024 (1967).
2. M. Aven and W. Garwacki, *J. Appl. Phys.*, **38**, 2302 (1967).
3. K. Itoh, *J. Phys. Soc. Japan*, **22**, 1186 (1969) and "III-VI Semiconducting Compounds," p. 1296, D. G. Thomas, Editor, W. A. Benjamin, New York (1967).
4. R. Yamamoto, M. Inoue, K. Itoh, and F. Shitaya, *Jap. J. Appl. Phys.*, **6**, 537 (1967).
5. M. Inoue, *J. Phys. Soc. Japan*, **26**, 1186 (1969).
6. S. G. Parker and H. Kraus, U.S. Patent 3,468,363, September 23, 1969.
7. R. H. Bube, "Photoconductivity of Solids," p. 233, John Wiley and Sons, Inc., New York (1960).
8. Saum and Hensley, *Phys. Rev.*, **113**, 1019 (1959).
9. H. W. Gandy, *ibid.*, **111**, 764 (1958).
10. S. G. Parker and J. E. Pinnell, *Trans. Met. Soc. AIME*, **245**, 451 (1969).
11. M. Aven and W. Garwacki, *This Journal*, **114**, 1063 (1967).

The Total Vapor Pressure of Tin Telluride under Equilibrium and Nonequilibrium Conditions

E. E. Hansen and Z. A. Munir

Department of Materials Science, School of Engineering, San Jose State College, San Jose, California 95114

ABSTRACT

The sublimation pressures of tin telluride were measured under equilibrium and free-surface conditions over the temperature range 785°-970°K. The expressions for the total sublimation pressures measured under these conditions are $\log P(\text{atm}) = (7.892 \pm 0.195) - (1.134 \pm 0.017)10^4/T$ and $\log P(\text{atm}) = (7.233 \pm 0.155) - (1.075 \pm 0.013)10^4/T$, respectively. Calculations of the thermodynamic properties associated with the reaction SnTe(s) = SnTe(g) gave, respectively, second-law ΔH_{298} and ΔS_{298} of 54.7 ± 1.3 kcal/mole and 40.8 ± 1.4 eu for the equilibrium condition, and 51.6 ± 1.1 kcal/mole and 37.4 ± 1.2 eu for the free surface condition. Third-law $\Delta H°_{298}$ associated with the equilibrium sublimation is 52.8 ± 0.5 kcal/mole. From these results, it appears that the sublimation coefficient is one in the temperature range covered in this work.

Total sublimation pressures in equilibrium with tin telluride have been measured by Knudsen cell methods (1-3), and the sublimation mode of this compound has been analyzed by mass spectrometric and optical absorption techniques (3, 4). Colin and Drowart's mass spectrometric investigation (3) has shown SnTe(g) to be the predominant species resulting from the sublimation of tin telluride. Their Knudsen cell measurements gave total sublimation pressures which are appreciably (40-70%) higher than those reported earlier by Nesterova *et al.* (1) and Hirayama *et al.* (2). Aside from this uncertainty in the published equilibrium pressures, information regarding the free-surface pressures of this compound appears to be totally lacking. In view of the desirability of such information, especially in current research efforts associated with the synthesis and control of properties of this thermoelectric material, this study was conducted for the purpose of determining both the equilibrium and free-surface sublimation pressures by means of the torsion method.

Experimental

The method and apparatus used in this work have been described in previous publications (5-8). Graphite torsion cells used in the present study had geometric designs similar to those described earlier (7, 9). Pertinent cell dimensions, reported in Table I, along with correction factors (10) and angular deflections of the cells, were used to calculate the sublimation pressure at any given temperature.

Temperatures were measured by means of a calibrated Pt-Pt/10% Rh thermocouple positioned inside a "dummy" cell which was situated about 2 cm below the torsion cell. The latter, which was suspended in the middle portion of a tungsten-mesh heating element, contained the sample to be sublimed. Thermocouple calibration techniques, as well as other calibration experiments aimed at establishing confidence in the results obtained in the present apparatus, have been discussed previously (8, 11).

Key words: tin telluride, sublimation pressure, heat of sublimation, free-surface sublimation.

Table I. Geometric characteristics of torsion cells

Cell	Sublimation area,* mm²		Moment arm, mm		Orifice depth/radius	
	a_1	a_2	q_1	q_2	$(l/r)_1$	$(l/r)_2$
Effusion-1	3 28	3.23	12.4	12.8	3.08	3.03
Effusion-2	4.46	4.46	12.9	12.8	2.60	2.60
Effusion-3	12.40	12.40	12.7	12.8	1.63	1.63
Langmuir-1	7.79	7.87	8.6	8.2	—	—
Langmuir-2	31.7	31.7	8.7	8.7	—	—

* This quantity corresponds to the orifice area of the torsion-effusion cells and to the sample surface area in the torsion-Langmuir experiments.

The purity of the tin telluride samples used in this work was established by x-ray analysis. Similar analytical methods were also employed in order to establish the congruency of sublimation of this compound. Debye-Scherrer diffraction patterns of sublimated samples which had lost up to 40% of their initial weight were identical to those obtained from unsublimated samples. However, in view of published results concerning the stoichiometry of tin telluride (12), the present x-ray results do not exclude the possibility of the existence of metallic tin in the heated samples. Within the limits of reliability of the x-ray techniques employed in this investigation, the concentration of any free tin is not likely to exceed about 3 a/o (atomic per cent). Compositional deviations toward the Te-rich end of the homogeneity range of SnTe were assumed not to have occurred since they would have resulted in

a significant change in the lattice parameter of the heated samples (13). For the torsion-Langmuir portion of this study, approximately 2 mm thick wafers were cut from tin telluride ingots which were the product of an attempt to grow single crystals. X-ray examinations of the wafers showed them to consist of a relatively small number of grains (single crystals). Because of technical difficulties, however, it was not feasible to isolate a sufficiently large single-crystalline sample for the purpose of determining its sublimation rate.

An oil diffusion pump, aided by a liquid nitrogen trap, maintained the ambient pressure inside the torsion apparatus at or below 2 x 10^{-5} Torr during all measurements.

Results

The equilibrium and free-surface sublimation pressures of tin telluride measured over the temperature range 785°-970°K are shown in Fig. 1. The least-squares expression for the equilibrium pressure covering the range 871°-970°K is

$$\log P(\text{atm}) = (7.892 \pm 0.195) - (1.134 \pm 0.017)\,10^4/T \quad [1]$$

where T is the temperature in degrees Kelvin and the shown errors are the standard deviations. Calculations of the second-law heat and entropy of sublimation at 298°K utilizing the available Cp value for SnTe(g) (14) and an assumed one for SnTe(s) (2), were based on the reaction

$$\text{SnTe(s)} = \text{SnTe(g)} \quad [2]$$

Because of lack of Cp data for solid tin telluride, the corresponding value for PbS(s) (14), an isoelectronic compound having an identical crystal structure and approximately the same molecular weight, was assumed to hold true for SnTe(s). These calculations gave the following values for $\Delta H°_{298}$ and $\Delta S°_{298}$: 54.7 ± 1.3 kcal/mole and 40.8 ± 1.4 eu, respectively.

Third-law $\Delta H°_{298}$ values for the sublimation process of Eq. [2] under equilibrium conditions, which were based on calculated free-energy functions (2) and the experimentally determined pressures, are shown in Table II. The average $\Delta H°_{298}$ value is 52.8 ± 0.5 kcal/mole.

Table III lists the free-surface sublimation pressures of SnTe. The least-squares expression for these pressures in the temperature range 785°-924°K is

$$\log P(\text{atm}) = (7.233 \pm 0.155) - (1.075 \pm 0.013)\,10^4/T \quad [3]$$

Employing Cp data cited above, changes in enthalpy and entropy accompanying the free-surface sublimation of tin telluride were calculated by the second-law method. The corresponding results at 298°K are 51.6 ± 1.1 kcal/mole and 37.4 ± 1.2 eu.

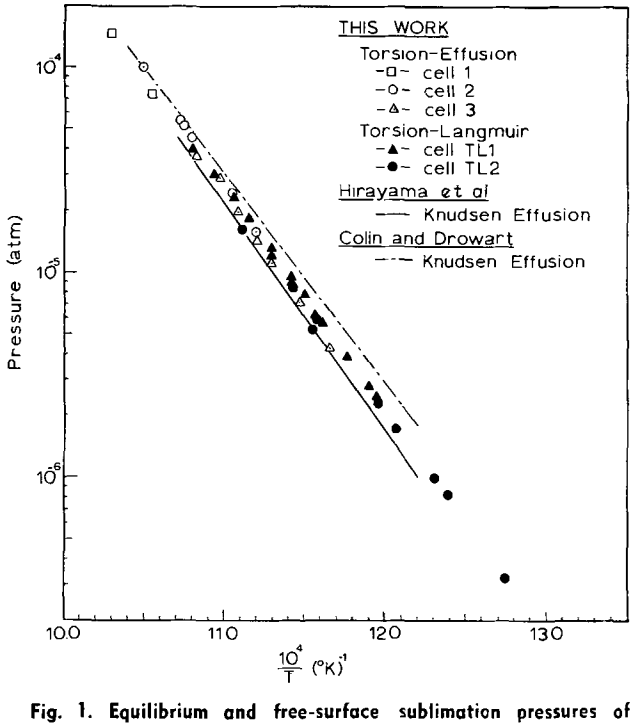

Fig. 1. Equilibrium and free-surface sublimation pressures of tin telluride.

Table II. Equilibrium sublimation pressures of SnTe

T, °K	P, atm	λ/d	ΔH°298, kcal/mole	T, °K	P, atm	λ/d	ΔH°298, kcal/mole
	Cell: Effusion-1			9.32	5.54 × 10⁻⁵	0.6	52.6
947	7.45 × 10⁻⁵	0.5	52.9	9.51	1.00 × 10⁻⁴	0.3	52.6
970	1.48 × 10⁻⁴	0.3	52.8		Cell: Effusion-3		
	Cell: Effusion-2			858	4.35 × 10⁻⁶	4.1	53.0
876	8.98 × 10⁻⁶	3.4	52.8	871	7.25 × 10⁻⁶	2.5	52.9
892	1.59 × 10⁻⁵	2.0	52.7	885	1.16 × 10⁻⁵	1.6	52.9
897	1.84 × 10⁻⁵	1.7	52.7	891	1.44 × 10⁻⁵	1.3	52.8
905	2.39 × 10⁻⁵	1.3	52.7	902	1.99 × 10⁻⁵	0.9	52.9
926	4.56 × 10⁻⁵	0.7	52.7	911	2.94 × 10⁻⁵	0.6	52.7
930	5.22 × 10⁻⁵	0.6	52.6	923	3.79 × 10⁻⁵	0.5	52.9

Table III. Free-surface sublimation pressures of SnTe

T, °K	P, atm	T, °K	P, atm
Cell: Langmuir-1		913	3.01 × 10⁻⁵
836	2.56 × 10⁻⁶	924	4.10 × 10⁻⁵
840	2.81 × 10⁻⁶	Cell: Langmuir-2	
849	3.94 × 10⁻⁶	785	3.29 × 10⁻⁷
862	5.93 × 10⁻⁶	807	8.28 × 10⁻⁷
865	6.44 × 10⁻⁶	812	1.01 × 10⁻⁶
870	7.88 × 10⁻⁶	828	1.73 × 10⁻⁶
876	9.00 × 10⁻⁶	835	2.34 × 10⁻⁶
876	9.51 × 10⁻⁶	862	5.60 × 10⁻⁶
885	1.22 × 10⁻⁵	864	5.88 × 10⁻⁶
886	1.32 × 10⁻⁵	867	5.25 × 10⁻⁶
897	1.87 × 10⁻⁵	875	8.60 × 10⁻⁶
905	2.34 × 10⁻⁵	899	1.66 × 10⁻⁵

Discussion

In agreement with published studies on the sublimation of a number of tin and lead chalcogenides (11, 15-17), the present work indicates that the sublimation coefficient of tin telluride is essentially unity in the temperature range investigated. This conclusion is made on the basis of the reasonable agreement between the pressures obtained under equilibrium and free-surface conditions (Fig. 1). The agreement between the values of the second-law ΔH_{298} calculated from the results obtained under these two conditions, within about 6%, is considered reasonable in view of the susceptibility of this method of calculation to experimental errors at either end of the range covered (18). However, because of the normal scatter in the measured pressures, the present results cannot be interpreted so as to exclude the possibility of a sublimation coefficient, α, slightly less than one, *e.g.* $0.9 < \alpha < 1.0$. Closer examination of the torsion-Langmuir results indicates that these pressures are slightly higher than those measured by the torsion-effusion method. It is believed that this discrepancy may be attributed to a temperature effect commonly referred to as evaporation-cooling (19). At a total pressure of 10^{-5} atm the temperature calculated from Eq. [3], the torsion-Langmuir results, is about 1°C less than that calculated from Eq. [1], that representing the torsion-effusion results. Similar calculations show that at a total pressure of 10^{-6} atm the corresponding temperature difference is about 4°C. Thus it is likely that, as a consequence of sublimation, the wafers used in the torsion-Langmuir experiments may have experienced a reduction in temperature, which may be, at least in part, responsible for the discrepancies cited above.

The validity of the assumed correspondence between the torsion-effusion results obtained in this work and the true equilibrium pressure values associated with the sublimation of SnTe is based on the relative lack of dependence of the values reported here on both the orifice size and the mean free path. Results obtained

with cells differing by a factor of about 4 in their orifice areas show no significant dependence on the size of the orifice. The average third-law $\Delta H°_{298}$ values calculated from the results of each of the three cells differ by only 0.2 kcal, or 0.4%. Furthermore, the present torsion-effusion results agree well with results reported in the literature based on equilibrium measurements. The third-law $\Delta H°_{298}$ value obtained in this work, 52.8 ± 0.5 kcal/mole, is in good agreement with the value reported by Hirayama *et al.* (2), 53.1 ± 1 kcal/mole which was based on identical free-energy functions. Third-law treatment of the results of Colin and Drowart (3) and of Nesterova *et al.* (2) using the free-energy functions employed in this work gave $\Delta H°_{298}$ values of 52.4 ± 0.4 kcal/mole and 53.2 ± 1.2 kcal/mole, respectively. The former authors (3) reported a value of 52.1 ± 0.4 kcal/mole based on free-energy functions which used a slightly different Cp value for SnTe(s).

The question of the existence of molecular flow conditions inside the cells, and hence the suitability of the effusion method for measuring pressures in the range reported here, is examined in light of the results listed in Table II. These results show no significant systematic increase in the measured pressures down to relatively low ratios of the mean free path-to-orifice diameter, λ/d. Earlier studies (16, 20, 21) have shown that, for molecularly subliming solids, the lower limit of λ/d in the molecular streaming range can be much less than the generally accepted value of one.

With reference to the work of Brebrick and Strauss (4), the present results indicate that, if deviations from stoichiometry in the SnTe samples utilized did exist, they would most likely be toward the Sn-rich end of the relatively narrow field of stability of SnTe, about 1 a/o (22-24). The mass-spectrometric investigations of Colin and Drowart (3), which presumably utilized Sn-rich samples, showed SnTe(g) to be predominant species in the vapor phase over a temperature range approximating that investigated in the present study. In addition to SnTe(g) and aside from gaseous species resulting from fragmentation, small concentrations of Sn_2Te_2, Te_2, $SnTe_2$, and Te were also detected. Using appropriate ionization cross sections (3), the relative partial pressures $P_{Sn_2Te_2}/P_{SnTe}$, P_{Te_2}/P_{SnTe}, and P_{SnTe_2}/P_{SnTe} were calculated to be 6.1×10^{-3}, 4.2×10^{-3}, and 4.7×10^{-3}, respectively. Although no calculations were made for Te(g), the partial pressure of this species is similarly insignificant when compared with the major component, SnTe(g). Finally, the authors of Ref. (3) indicated that, at sublimation runs where the sample had sublimed completely, small amounts of metallic tin (about 1% of the initial sample) were left behind. In view of this and other considerations regarding the nonstoichiometry of SnTe(s), it is concluded here that the total pressures measured in this work are essentially those corresponding to the maximum partial pressure of SnTe(g) which results from the incongruent sublimation of SnTe(s). Contributions of Sn(*l*) are believed to be insignificant with respect to SnTe(g). Support for this assumption comes from the observation that angular deflections, measured under the experimental conditions described above, remained constant at any given temperature for prolonged periods of time.

Acknowledgments

We are grateful for the technical assistance of A. Cooper, W. Mounts, and L. Schallberger. Our thanks to Mrs. P. Ashe and Mr. P. Enright for their help in the preparation of this manuscript.

Manuscript submitted Aug. 17, 1970; revised manuscript received *ca.* Dec. 20, 1970.

Any discussion of this paper will appear in a Discussion Section to be published in the December 1971 JOURNAL.

REFERENCES

1. Ya. M. Nesterova, A. S. Pashinkin, and A. V. Novoselova, *Russ. J. Inorg. Chem.*, **6**, 1031 (1961).
2. C. Hirayama, Y. Ichikawa, and A. M. De Roo, *J. Phys. Chem.*, **67**, 1039 (1963).
3. R. Colin and J. Drowart, *Trans. Faraday Soc.*, **60**, 673 (1964).
4. R. F. Brebrick and A. J. Strauss, *J. Chem. Phys.*, **41**, 197 (1964).
5. R. D. Freeman, in "Characterization of High Temperature Vapors," J. L. Margrave, Editor, pp. 152-192, John Wiley & Sons, Inc., New York (1967).
6. Z. A. Munir and A. W. Searcy, *This Journal*, **111**, 1170 (1964).
7. W. T. Lee and Z. A. Munir, *ibid.*, **114**, 1236 (1967).
8. R. C. Blair and Z. A. Munir, *J. Phys. Chem.*, **72**, 2434 (1968).
9. Z. A. Munir and A. W. Searcy, *J. Chem. Phys.*, **42**, 4223 (1965).
10. D. A. Schulz and A. W. Searcy, *ibid.*, **36**, 3099 (1962).
11. E. E. Hansen and Z. A. Munir, *This Journal*, **117**, 121 (1970).
12. N. Kh. Abrikosov, V. F. Bankina, L. V. Poretskaya, L. E. Shelimova, and E. V. Skudnova, "Semiconducting II-VI, IV-VI, and V-VI Compounds," Chap. 2, Plenum Press, New York (1969).
13. L. E. Shelimova and N. Kh. Abrikosov, *Zh. Neorg. Khim.*, **9**, 1879 (1964).
14. K. K. Kelley, *U.S. Bur. Mines Bull. No. 584* (1960).
15. R. C. Blair and Z. A. Munir, *J. Am. Ceram. Soc.*, **53**, 301 (1970).
16. E. E. Hansen and Z. A. Munir, *High Temp. Sci.*, **2**, 169 (1970).
17. E. E. Hansen, Z. A. Munir, and M. J. Mitchell, *J. Am. Ceram. Soc.*, **52**, 610 (1969).
18. J. L. Margrave, in "Physiocochemical Measurements at High Temperatures," J. O'M. Bockris, J. L. White, and J. D. Mackenzie, Editors, Chap. 10, Butterworths, London (1959).
19. R. S. Bradley and P. Volans, *Proc. Roy. Soc (London)*, **217A**, 508 (1953).
20. M. Lim and A. W. Searcy, *J. Phys. Chem.*, **70**, 1762 (1966).
21. R. W. Mar and A. W. Searcy, *ibid.*, **71**, 888 (1967).
22. R. F. Brebrick, *J. Phys. Chem. Solids*, **24**, 27 (1963).
23. B. B. Houston, R. F. Bis, and E. Gubner, *Bull. Am. Phys. Soc.*, **6**, 436 (1961).
24. R. Mazelsky and M. S. Lubell, in "Nonstoichiometric Compounds," p. 210, American Chemical Soc., Washington, D. C. (1963).
25. L. Y. Glukhikh and N. Kh. Abrikosov, *Zh. Neorg. Khim.*, **8**, 1792 (1963).

Sodium Ion Drift through Phosphosilicate Glass-SiO_2 Films

J. M. Eldridge

IBM Thomas J. Watson Research Center, Yorktown Heights, New York 10598

and D. R. Kerr*

IBM Components Division, East Fishkill Facility, Hopewell Junction, New York 12533

ABSTRACT

The field-assisted transport of sodium ions through phosphosilicate glass-SiO_2 composite films on silicon substrates has been investigated. The effects of P_2O_5 concentration (in the 0 to 8 mole per cent [m/o] range), sodium contamination level (between 10^{11} and 10^{15} Na^+ ions/cm^2), field, temperature, and time have been quantitatively determined. For a limited quantity of transported sodium, this quantity is approximately proportional to the square root of biasing time; exponentially dependent on temperature and field, increases linearly with the initial sodium contamination level; and decreases drastically with increasing P_2O_5 concentration. For example, seven more orders of magnitude of time are required to drift a given number of Na^+ ions through a PSG (3.5% P_2O_5 — 125Å)/2025Å SiO_2 composite layer than through a 2150Å thick layer of pure, thermally grown SiO_2. The results are consistent with a model based on the emission of Na^+ ions from traps in the phosphosilicate layer. It was concluded that phosphosilicate glass films, having negligible intrinsic polarizability, can be used to effectively stabilize IGFET threshold voltages against changes (0.1V in 10 yr at 80°C under a field of 2 x 10^6 V/cm) due to the presence of large amounts of sodium.

Phosphosilicate glass (PSG) films, formed on a thermally grown SiO_2 layer, can enhance markedly the surface stability of silicon planar junction devices and field-effect transistors (1). Without it, large shifts in the silicon surface potential can arise from field-induced drifting and accumulation of mobile sodium ions within the SiO_2 layer (2, 3). Mobile alkali ions, initially present in SiO_2 are gettered by the PSG during its formation, and those introduced subsequently tend to be trapped also in the glass (3-5).

Since the PSG itself is polarizable (6) it can by itself cause large Si surface potential instabilities, which can be minimized by decreasing the PSG-SiO_2 thickness ratio (6) and the P_2O_5 concentration (7). Since the effectiveness of the PSG as a sodium ion barrier depends on its thickness (5) and composition (8), an understanding of the extent of these dependencies is needed to optimize IGFET device performance.

In this study, both the PSG composition and the sodium ion concentrations were systematically varied in MOS structures and the sodium drift was measured as a function of applied field, temperature and time. The P_2O_5 concentrations in the PSG films were 8 m/o at most, in order to virtually eliminate their intrinsic polarizability effects. Projections were made of the lifetime stability of n-channel IGFET threshold voltages, containing various concentrations of sodium ions between the PSG and metal layers. A model for the phosphosilicate glass-sodium ion interaction will be suggested.

Experimental Procedure

Metal-PSG-SiO_2-Si capacitor structures were prepared on 2 ohm-cm, n-type, (100) oriented silicon substrates having chemically-mechanically polished surfaces. SiO_2 layers were grown in dry O_2 at 1100°C; thin phosphosilicate glass films were formed by adding P_2O_5 at 800°C in a furnace initially containing 0.14% $POCl_3$, 9% O_2, and 91% N_2 to form P_2O_5 by pyrolysis, followed by a heat treatment in N_2 at 975°C. The thicknesses and compositions of the glass films were controlled by appropriate selection of the deposition and heat treatment times, and were analyzed by plotting the total thicknesses (as measured ellipsometrically) against total elapsed etching time in a 2% solution of hydrofluoric acid at 25°C. The P_2O_5 concentrations (in mole per cent) were obtained, to within ±1%, from the etch rate-composition relationship found by Eldridge and Balk (9). By keeping the P_2O_5 concentration in the 0 to 8 m/o range with SiO_2-to-PSG thickness ratios of 7 to 1 or greater, sodium drifting could be followed without being obscured by any significant PSG polarization effects (6, 7). Sodium concentrations in the 10^{11} to 10^{15}/cm^2 range were then deposited on the oxide surfaces in a vacuum system by evaporating the residue of a drop of an aqueous solution of NaCl or NaI of appropriate normality. Kerr (10) has shown that the sodium concentration obtained in this way can be accurately calculated from the cosine distribution law when the source-substrate distance is known, and is proportional to the normality of the original solution over a wide range. An oxidized wafer without PSG was included in each salt deposition run to provide a second sodium measurement. Previous radiotracer experiments (5, 10) had shown that deposited sodium is entirely transported as Na^+ ions through SiO_2 by moderate electrothermal stressing (*e.g.* a few hundred seconds at 200°C under a field of 10^6 V/cm); during this time, the ions are detectable by current measurements. High-purity aluminum electrodes (area $\approx 5 \times 10^{-3}$ cm^2) were deposited from a source heated by an electron gun. Electrical measurements on additional control oxides that were not subjected to glassing and sodium contamination indicated a combined mobile ionic contamination level from the as-grown SiO_2 and the metallization to be less than 10^{11} ions/cm^2. After metallization, the wafers were annealed at 500°C in N_2 for 5 min to simulate the IGFET processing step used to lower contact resistance and eliminate interface states (11).

Sodium drifting through the PSG was determined in two ways. In the first, the small-signal capacitance of a given MOS structure was measured at room temperature, using a frequency of 10 kHz and a d-c ramp in order to obtain the initial silicon flatband potential (V_{FB}). Several capacitors (normally eight per wafer) were biased with the metal positive for a given time at an elevated temperature; then the wafer was quickly cooled under bias to room temperature and the C-V curves remeasured. The flux in ions/cm^2 Na^+ ions drifted through the composite PSG/SiO_2 is then: $N_I = -C_{ox}\,\Delta V_{FB}/q$ where C_{ox} is the oxide capacitance/cm^2;

* Electrochemical Society Active Member.

Key words: phosphosilicates, dielectrics, films, sodium, silicon, transport processes and properties.

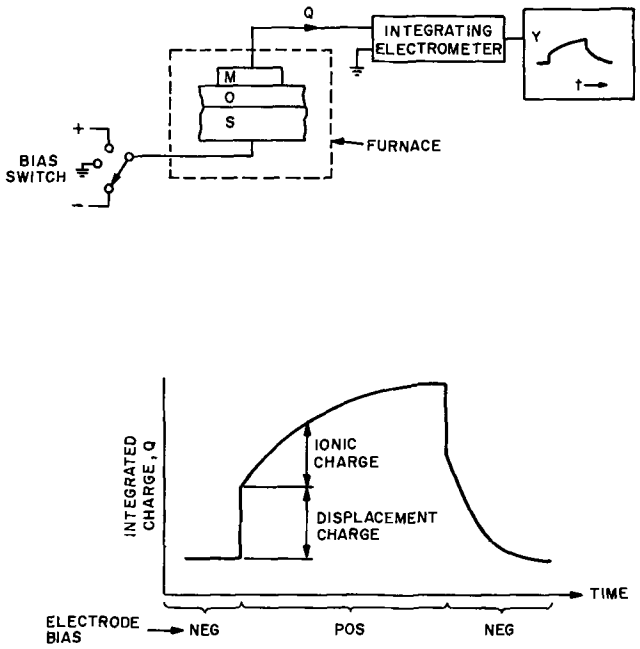

Fig. 1. Schematic diagram of electrical set-up used to measure charge transport in MOS structures, along with a typical charge vs. time trace. [After Kerr (5).]

ΔV_{FB} is the sodium-induced shift in flatband potential; q is the electronic charge. Repeated stressing and measuring cycles were used to determine the N_I *vs.* drifting time curves.

In the second method, schematically illustrated in Fig. 1, the wafer specimen is placed in a temperature cell with one capacitor that is contacted by a platinum probe from an external charge-meter (Keithley Model 610B electrometer). The silicon is initially biased positively, and is then switched stepwise to a predetermined negative value. A displacement charge step occurs instantly which is equal to the product of the oxide capacitance and the voltage change; this is followed by a much slower charge increase as the sodium ions move toward the Si. Since the electrode area is known, the density of transported ions can be directly calculated as a function of time. This technique is practical for the relatively short drift times (in the range of 1 to 1000 sec) observed at higher temperatures while the *C-V* shift method is generally useful for the much longer times encountered at ~200°C and lower. It will be shown later that the two methods yield results which are in good agreement. This agreement is expected since, to a good approximation, both techniques register only those ions which escape from the PSG to reach the SiO_2/Si interface. Later results will show that the time needed for the sodium to traverse the SiO_2 region is orders of magnitude less than that needed to pass through the PSG; hence, it follows that the Na^+ ions are either in the glass layer or the SiO_2/Si vicinity. Large SiO_2-to-PGS thickness ratios were employed so that the limited Na^+ displacements in the PSG make little impact on the *C-V* (2) and *Q-t* results. Thus, both techniques actually measure the transport-limited motion of sodium through the PSG.

Experimental Results

Even without an applied electric field, considerable amounts of sodium diffused into the phosphosilicate region during post-metallization annealing (12). The progressively larger, negative shift of the silicon flatband voltage with increasing NaCl surface contamination in Fig. 2 show this sodium ion penetration through a PSG (4% P_2O_5-125Å)/SiO_2 (900Å) composite layer during a 5 min, 500°C annealing treatment in N_2. Evidently Na^+ diffuses faster than Cl^- and I^- through the PSG, as well as through SiO_2 (3) so that the resultant uncompensated positive charge in the interior of the PSG can significantly alter the Si flatband potential.

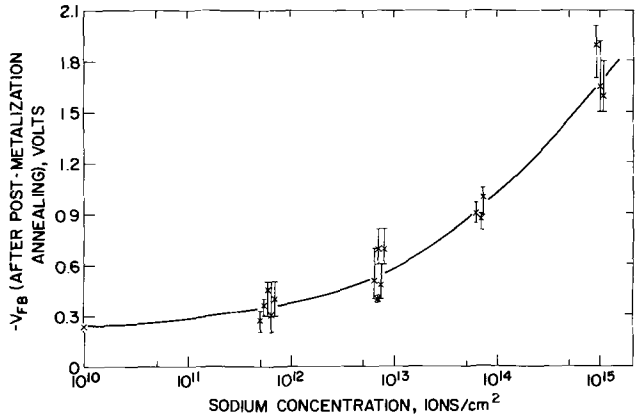

Fig. 2. Dependence of the flat band voltage on sodium contamination level in Al/NaCl/PSG (4% P_2O_5, 125Å)/SiO_2 (900Å)/Si structures after a typical post-metallization annealing treatment (5 min in N_2 at 500°C).

From the known dependence of V_{FB} on the uncompensated charge profile in the oxide (2), it was estimated that as many as 5 x 10^{12} ions-cm^{-2} penetrated approximately halfway into the glass for the 1 x 10^{15} Na^+/cm^2 specimens during the anneal. Although the effect of the PSG composition on this particular type of instability was not determined, it can still be concluded that the gate oxide region of IGFET's can withstand only moderate alkali ion contamination if the threshold values are to be held within a narrow, well-defined range of values, even when a PSG layer is present.

When typical IGFET operating fields (~10^6 V/cm) are applied at elevated temperatures, the Na^+ ions can be driven through them to the SiO_2-Si interface (5, 12, 13). The rate of displacement depends very strongly on various testing and materials parameters. Thus, from an initial surface contamination concentration of N_O (= 7 x 10^{12} NaCl/cm^2), Fig. 3 shows that the quantity (N_I) of Na^+ ions, transported

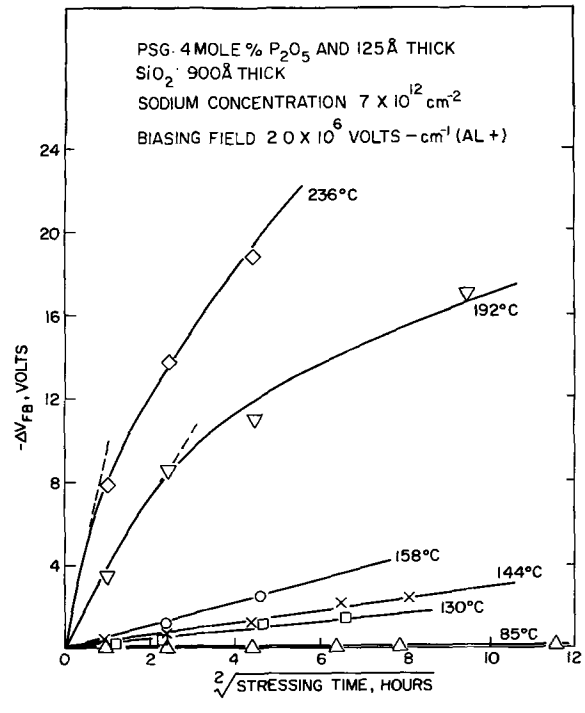

Fig. 3. Effects of time and temperature on the extent of Na^+ ion drift (α | — Δ_{FB} |) for the indicated sodium-PSG-SiO_2 system.

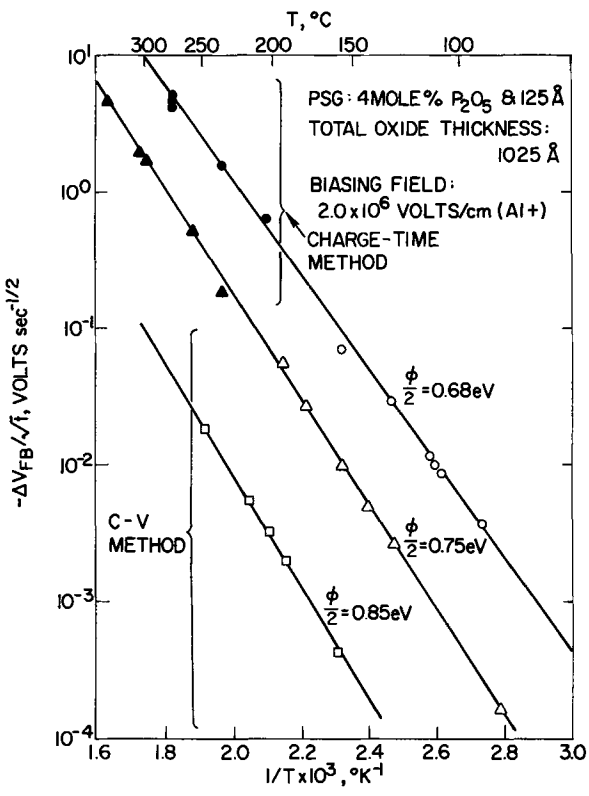

Fig. 4. Temperature dependence of $-\Delta_{FB} \cdot t^{-1/2}$ values for various sodium contamination levels: □ 6 x 10^{11}; △, ▲7 x 10^{12}; and, ○, ●7 x 10^{13} ions/cm^2. The PSG film composition and thickness are constant.

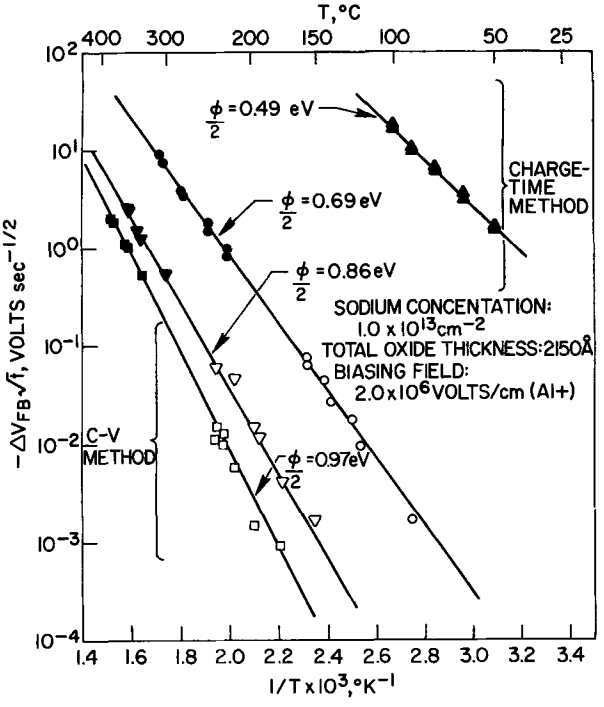

Fig. 5. Temperature-dependence of $-\Delta V_{FB} \cdot t^{-1/2}$ values for various PSG barriers: ▲ pure SiO_2; ●, ○ 3.5% P_2O_5 x 125Å thick; ▼, ▽ 6% P_2O_5 x 230Å thick; and ■, □ 8% P_2O_5 x 190Å thick. Note that the sodium concentration is constant.

through a 4 m/o P_2O_5 x 125Å thick phosphosilicate glass[1] layer is closely proportional to the square root of the stressing or biasing time (t) for $N_I \lesssim 0.2\ N_o$. The transport process is strongly thermally activated while the results of other experiments indicated that the anion (either Cl^- or I^-) used for adding sodium did not affect the Na^+ drift rate.

The rate of Na^+ drifting, as characterized by the initially constant slopes, is roughly proportional to the initial sodium contamination level, as shown in Fig. 4. These data were obtained over a time interval of ten orders of magnitude by combining the results of the two measurement techniques. It is evident that the activation energy Φ, as calculated from the slopes in Fig. 4, decreases appreciably with increasing sodium ion contaminations. The factor of ½ is used here to facilitate a direct comparison between these activation energies and those obtained earlier (14) from the slopes of log τ *vs.* $1/T$ plots, where τ is taken as the time required for a given amount of Na^+ transport. The results from the two experimental approaches are in good agreement and apparently the same Na^+ transport process is operative throughout the temperature interval from 80° to 350°C. Thus, the Φ values are characteristic of a given glass composition, sodium concentration and field.

These data indicate that a limited amount of sodium contamination, introduced after the PSG is present, can still produce appreciable threshold shifts at approximately 100°C in field-effect devices. For sodium concentrations as high as 1 x 10^{15}/cm^2, threshold shifts of several tenths of a volt occur within an hour in room temperature stressing at 2 x 10^6 V/cm.

A constant stressing field and sodium level of 1 x 10^{13}/cm^2 was used to assess the effect of P_2O_5 concentration on sodium drift. It can be seen in Fig. 5 that the rate of charge transport decreases rapidly while Φ becomes larger with increasing phosphorus oxide concentration. Although the PSG thickness of the P_2O_5-richest structures were somewhat higher (by ~50%) than that (125Å) of the lowest, the relative effects of glass thickness and composition could not be accurately separated from these data. Inspection of the 6 and 8 m/o P_2O_5 results indicates, however, that the composition parameter is the more important one. Comparison of the room temperature Na^+ drift behavior for the 2150Å SiO_2 and the PSG (4% P_2O_5-125Å)/2025Å SiO_2 structures provides a quantitative demonstration of the strong retarding power of the glass for sodium. Thus, eight more magnitudes of time are required for a given amount of sodium to drift through the date dielectric region in PSG-stabilized films than in pure silica ones. Obviously, the drift of Na^+ ions is rate-limited in the PSG layer in composite PSG-SiO_2 systems.

Discussion

Snow *et al.* (2) reported a $N_I \propto t^{1/2}$ dependence for the early stage of Na^+ transport through thermally grown SiO_2 films, deliberately contaminated in aqueous NaCl solutions. Although they proposed another model, this time-dependence can be attributed also to the temperature- and field-induced emission of Na^+ ions from trapping centers located near the metal-SiO_2 interface. These traps presumably arise from the partial chemical reduction of SiO_2 by the metal electrode. As shown by Hofstein (14), who computed the effects of small Gaussian distributed spreads (σ) in the activation energy for ion emission (Φ) from such traps, the quantity of drifted sodium is closely proportional to $t^{1/2}$ for $\sigma \simeq 3kT$ for small amounts ($N_I < 0.5\ N_o$) of Na^+ transfer. Results from the present study, such as those shown in Fig. 3, yield a σ value of $\simeq 4kT$ when fitted to the charge-time waveform curves computed by Hofstein. A $N_I \propto t^{1/2}$ dependence results for this σ value provided that $N_I \lesssim 0.2\ N_o$, in agreement with our experimental findings. This time dependence was then employed in order to reduce the number of measurements needed to complete this study. Such σ values are reasonably consistent with a proposed structural model for the polarization of phosphosilicate glass

[1] Recall at this point that the bulk polarization contributions of the PSG films to the observed ΔV_{FB} values are quite negligible, in view of the limited P_2O_5 concentrations and the large SiO_2-to-PSG thickness ratios used (7).

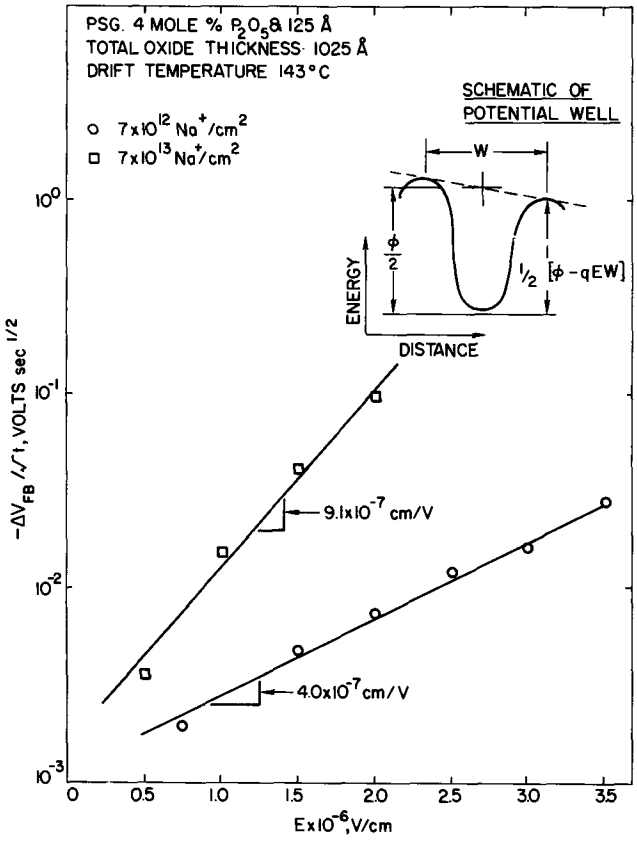

Fig. 6. Dependence of the sodium drift rate on biasing field and Na^+ concentration for a given PSG-SiO_2 barrier. A schematic diagram of a potential well has also been included to indicate how Φ is lowered by E.

where a limited spread ($\sim 2kT$) in the activation energy has been noted (6, 7).

The electric field dependence of the transport process is also consistent with a trapping model. As shown schematically in Fig. 6, the trapping center can be crudely represented by a potential energy well scheme having an average width W, and depth $\Phi/2$. To a first approximation, application of a field E lowers $\Phi/2$ by $q \cdot E \cdot W/2$. The results of this present investigation can be combined into a single, phenomenological expression

$$N_I = -C_{ox} \cdot \Delta V_{FB}/q = N_o \cdot K \cdot t^{1/2} \quad [1]$$

where N_o is the initial sodium concentration, and K is the rate constant

$$K = K_o \exp\left[(-\Phi + q \cdot E \cdot W)/2kT\right] \quad [2]$$

It follows that Φ and W may be estimated from experimental data by separating Eq. [2] into field- and temperature-dependent terms

$$\log\left[-\Delta V_{FB} \cdot t^{-1/2}\right] = \frac{1}{4.60kT} \cdot \{+ q \cdot E \cdot W - \Phi\} - \log K' \quad [3]$$

where various incidental constants have been included in K'. The data in Fig. 6 shows the expected field dependence. The simple potential energy well model is possibly too naive since the data seem to fit equally well to a log $(-\Delta V_{FB} \cdot t^{-1/2}) \propto E^{1/2}$ relationship, suggestive of a Poole-Frenkel mechanism. However, insufficient data were taken to differentiate between these two mechanisms. Based on the present model, an average trap width of ~6Å for Na^+ ions drifting through a 4 m/o P_2O_5 phosphosilicate layer from a surface source concentration of 7 x 10^{12} NaCl-cm^{-2} was calculated. An increase in the sodium level to 7 x 10^{13} cm^{-2} effectively raises W from ~6 to 13Å for this particular PSG film. Such an effect might have the following physical origin: at the higher sodium level the $Na^+ - Na^+$ distances are roughly comparable to the spacings between the trapping centers, *i.e.* ~12Å. Hence, the negatively charged, nonbridging oxygen ion can interact coulombically with more than one Na^+ ion at a time, on the average, and consequently, Φ will be lower (as found in Fig. 4). Since a range of well widths presumably exist in the glassy layer, those traps configurations having the largest W values will emit their ions first, owing to the direction proportionality between W and barrier lowering. In other words, since W values are being evaluated from data taken during a limited amount of charge transport (*i.e.* $N_I << N_o$), the field dependence reflects ion emission from the traps having the largest W values.

The results of this investigation lend support to the following structural model previously proposed to account for the intrinsic polarizability of the phosphosilicate glass (7, 12, 13). Thermally grown SiO_2 is thought to consist of a somewhat randomized, three-dimensional network of SiO_4 tetrahedra which are connected only at the oxygen sites. The addition of a P_2O_5 molecule should produce two different tetrahedral charge centers

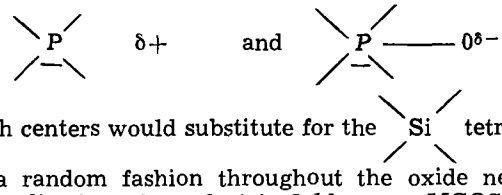

Such centers would substitute for the tetrahedra in a random fashion throughout the oxide network.

Application of an electric field across MGOS structures produces a bulk PSG polarization (6) whose magnitude is proportional to the square of the P_2O_5 concentration (7). This dependency suggests that the polarization process is favored by having the two types of phosphorus centers close to each other, in which case the nonbridging oxygen ion can jump from one to the other group. Although the polarizabilities of the films used in the present investigation were deliberately made small by limiting the P_2O_5 concentrations to $\lesssim 8\%$, the negatively charged, nonbridging oxygen ions are still present in sufficient numbers ($>10^{15}/cm^2$ in a 4% P_2O_5 x 125Å PSG layer, for example) to trap coulombically the positive sodium ions. Thus, this model can also account for the so-called "stabilization effect" of PSG films on SiO_2, as shown in Fig. 7.

As noted above, Φ decreases as progressively larger amounts of sodium are added for a given PSG layer. Thus, traps having molecular configurations with higher energy levels will be emptied first. (See Fig. 8). Although these results, taken from Fig. 4 and 5, were obtained using one field value, they support the present arguments. Since calculated Φ values are actually somewhat dependent on the field, a better anal-

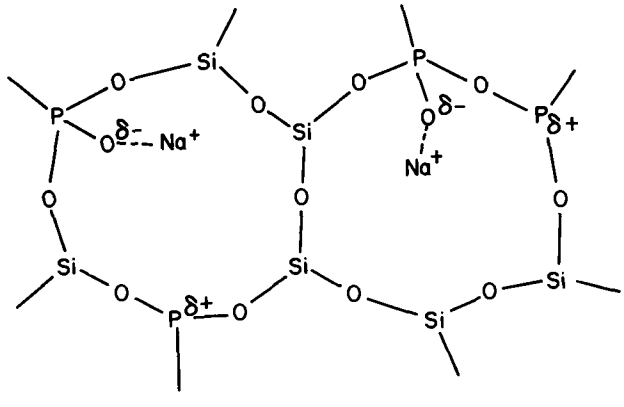

Fig. 7. Schematic two-dimensional model of the phosphosilicate glass structure, indicating the suggested mechanism of Na^+ ion trap *via* a coulombic interaction.

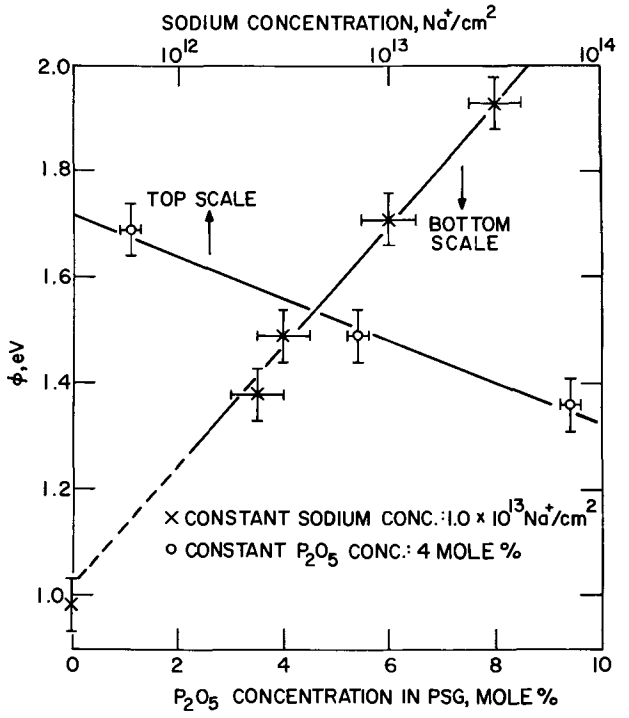

Fig. 8. Dependence of Φ on PSG composition for a constant sodium concentration and vice versa.

ysis should be developed on the field-free ion emission energies which can be obtained by extrapolation. Unfortunately, we failed to obtain enough data for such an evaluation.

In the present model, Φ increases with the P_2O_5 concentration of the PSG, when the sodium level is held constant. Thus, the approximate doubling of Φ, on going from pure SiO_2 to an 8 m/o P_2O_5 glass, results from the introduction of relatively large concentrations of nonbridging oxygen traps, some of which have lower energy configurations. This behavior also results from the simple, idealized density of states for the traps in the glasses shown in Fig. 9. In this approach, Φ is a measure of the energy difference between the released ion, that is, at the horizontal axis, and that near the top region of the filled traps. The effects of Na^+ and P_2O_5 concentrations on Φ follow directly and are consistent with the trends observed experimentally.

Based on the above experimental results, reasonably sound reliability projections can be made of the

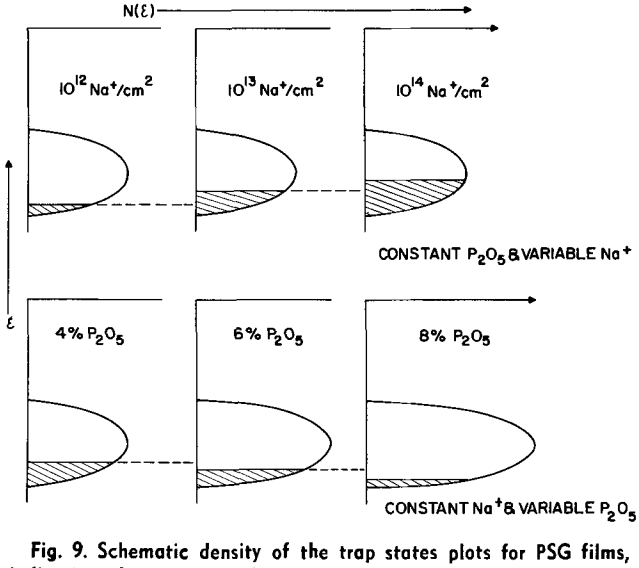

Fig. 9. Schematic density of the trap states plots for PSG films, indicating the origin of the dependence of Φ on glass composition and sodium concentration.

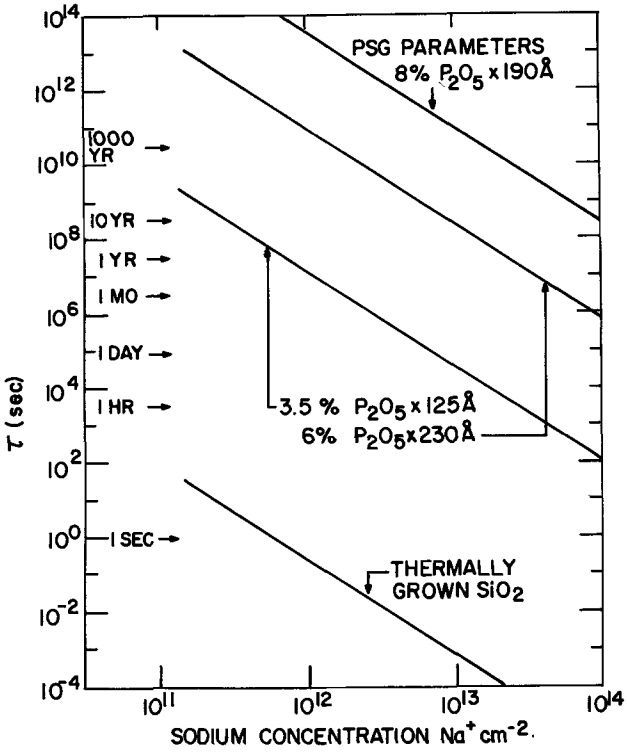

Fig. 10. Dependence of estimated time, τ (needed for a sodium-induced −0.1V threshold shift) for various PSG passivating layers. Calculated for a gate oxide thickness of 1000Å, at 80°C under a field of 2 x 10^6 V/cm with metal biased positively.

threshold voltage stability for IGFET structures, contaminated with sodium during device fabrication. A typical projection for a 1000Å thick oxide, showing the time (τ) required for sodium drift to cause a threshold shift of −0.1V at 80°C under a field of 2 x 10^6 V/cm, is presented in Fig. 10. The 3.5% P_2O_5 x 125Å thick PSG film forms an effective barrier for ion drift for sodium concentrations up to ~5 x 10^{11}/cm^2, if a device lifetime of approximately ten years at 80°C is needed. Although the use of P_2O_5 richer PSG films result in even more effective barriers, the limited but very significant Na^+ diffusion occurring during post-metallization annealing will produce an undesirably large spread in threshold values for higher ($\gtrsim 10^{13}$ cm^{-2}) contamination levels. (Recall Fig. 2.) Hence, considerable care must be taken during all IGFET fabrication steps to ensure that the PSG-stabilized gate oxide is never exposed to sodium-containing reagents, etc. By contrast, the pure SiO_2 is vulnerable to very large and fast threshold shifts, due to even a limited amount of Na^+ contamination. (See Fig. 5 and 10.) The advantages of the phosphosilicate glass stabilization, over that of the so-called "clean SiO_2" approach are evident.

Summary and Conclusions

A detailed investigation has been made of the field-induced drifting of intentionally deposited sodium ions through various phosphosilicate layers under a range of stressing conditions. It was found that the amount (N_I) of sodium initially transported through the PSG to the SiO_2-Si interface can be expressed by

$$N_I = N_o \cdot t^{1/2} \cdot K_o \exp\left[(-\Phi + q \cdot E \cdot W)/2kT\right] \quad [4]$$

where N_o is the initial Na^+ concentration; t is biasing time; K_o is a constant, dependent on the PSG thickness and composition; Φ is the activation energy for Na^+ ion emission from traps; q, the electronic charge; E is the field; and W is the average width of a trap well. These results are quite consistent with a transfer process limited by the emission of the Na^+ ions from

trapping centers in the PSG. The evidence suggests that these centers are the same as those responsible for the intrinsic polarizability of the phosphosilicate glass; namely, nonbridging oxygen ions attached to phosphorus ions in tetrahedral positions. Based on the present data, projections were made of the degree of protection against Na^+ induced threshold voltage shifts of IGFET's by various phosphosilicate films. These projections indicate that relatively thin (~4% P_2O_5) PSG layers will effectively stabilize the threshold voltage of IGFET's under typical operating conditions of temperature and field, even when significant levels of sodium ion contamination are present.

Acknowledgment

The authors are indebted to Dr. T. O. Sedgwick and Dr. A. Reisman for reviewing this manuscript and to Mr. D. Johnson and Mr. J. Petrak for their valuable experimental assistance.

Manuscript submitted Aug. 20, 1970; revised manuscript received *ca.* Jan. 25, 1971.

Any discussion of this paper will appear in a Discussion Section to be published in the December 1971 JOURNAL.

REFERENCES

1. D. R. Kerr, J. S. Logan, P. J. Burkhardt, and W. A. Pliskin, *IBM J. Res. Develop.*, **8**, 376 (1964).
2. E. H. Snow, A. S. Grove, B. E. Deal, and C. T. Sah, *J. Appl. Phys.*, **36**, 1664 (1965).
3. E. Yon, W. H. Ko, and A. B. Kuper, *IEEE Trans. Electron. Devices*, **ED-13**, 276 (1966).
4. H. G. Carlson, G. A. Brown, C. R. Fuller, and J. Osborne, "Physics of Failure in Electronics," Vol. 4, pp. 390-407, Rome Air Development Center (1966).
5. W. A. Pliskin, D. R. Kerr, and J. A. Perri, "Physics of Thin Films," Vol. 4, pp. 257-324, Academic Press, Inc., New York (1967).
6. E. H. Snow and B. E. Deal, *This Journal*, **113**, 263 (1966).
7. J. M. Eldridge, R. B. Laibowitz, and P. Balk, *J. Appl. Phys.*, **40**, 1922 (1969).
8. K. Sato, T. Abe, and Y. Nishi, Paper 98 presented at Electrochem. Soc. Meeting, Detroit, Oct. 5-9, 1969.
9. J. M. Eldridge and P. Balk, *Trans. Met. Soc., AIME*, **242**, 539 (1968).
10. D. R. Kerr, IEEE Solid State Device Research Conf., Santa Barbara, Calif., June, 1967.
11. P. Balk, Electrochem. Soc. Extended Abstracts Vol. 14, No. 2, Buffalo, Oct. 10-14, 1965, Electronics Div. Abs. No. 111, p. 29.
12. J. M. Eldridge, and D. R. Kerr, Paper 532 presented at Electrochem. Soc. Meeting, Montreal, Oct. 6-11, 1968.
13. P. Balk and J. M. Eldridge, *Proc. IEEE*, **57**, 1558 (1969).
14. S. R. Hofstein, *IEEE Trans. Electron Devices*, **ED-14**, 749 (1967).

Partial and Total Vapor Pressures over Molten Bi_2Te_3

R. F. Brebrick*,[1] and F. T. J. Smith

Lincoln Laboratory, Massachusetts Institute of Technology, Lexington, Massachusetts 02173

ABSTRACT

The total vapor pressure, P_Σ, over $Bi_2Te_3(l)$ has been determined between 980° and 1169°K by using a new manometric technique. The lower end of an evacuated, inverted, fused silica U-tube was immersed in a large reservoir of melt inside a transparent furnace. The value of P_Σ and the density of $Bi_2Te_3(l)$ were obtained at each temperature by visually observing the height to which the melt rose in the U-tube as a function of the external argon pressure applied to the reservoir surface. In separate experiments a sealed, evacuated, fused silica optical cell was maintained at 1000°C while the temperature of a sidearm reservoir containing $Bi_2Te_3(l)$ was held at a lower temperature. By measuring the optical density as a function of wavelength between 1990 and 5500Å, it was possible to determine the partial pressure of $Te_2(g)$, p_{Te_2}, and the partial optical density of BiTe(g) as functions of the $Bi_2Te_3(l)$ temperature between 943° and 1200°K. If it is assumed, consistent with all the evidence, that Te_2 and BiTe are the principal vapor species, the results of both sets of experiments are represented by

$$\log_{10}P_\Sigma(\text{atm}) = -6.4691(10^3)/T + 4.3219$$
$$\log_{10}p_{Te_2}(\text{atm}) = -6.3048(10^3)/T + 4.1396$$
$$\log_{10}p_{BiTe}(\text{atm}) = -8.978(10^3)/T + 5.4432$$

According to these expressions $Bi_2Te_3(l)$ neither vaporizes nor effuses congruently since p_{BiTe} is never more than 15% of p_{Te_2}. The density of $Bi_2Te_3(l)$ is 7.4 g/cm³ at 973°K and 7.0 g/cm³ at 1170°K.

The total vapor pressure, P_Σ, over $Bi_2Te_3(l)$ between 952° and 1265°K has been measured by using a Bourdon gauge (1). Values of P_Σ over $Bi_2Te_3(c)$ between 700° and 806°K have been determined twice (2, 3) with excellent agreement from the weight loss of a Knudsen cell on the assumption that $Bi_2Te_3(c)$ effuses congruently according to the reaction

$$Bi_2Te_3(c) \rightarrow 2\,BiTe(g) + 1/2\,Te_2(g) \qquad [1]$$

Values of P_Σ over $Bi_2Te_3(c)$ between 714° and 833°K have been determined (4) from torsion effusion data. As evidence for congruent effusion, ref. (4) cites the observation that a sample which had been subjected to a 30% weight loss by effusion was found to be single phase by metallographic examination and gave the same x-ray diffraction pattern as an unheated sample.

The temperature dependence of P_Σ found in ref. (4) is close to that of ref. (2) and (3), but the values are only about half as large. Aside from this discrepancy, the experimental situation is unsatisfactory for two more serious reasons. First, when the data for P_Σ are extrapolated to the maximum melting point of $Bi_2Te_3(c)$, 860°K, the values at this temperature derived from the low-temperature effusion measure-

* Electrochemical Society Active Member.
[1] Present address: Department of Mechanical Engineering, Marquette University, Milwaukee, Wisconsin 53233.
Key words: properties of molten salts, optical absorption, incongruent vaporization.

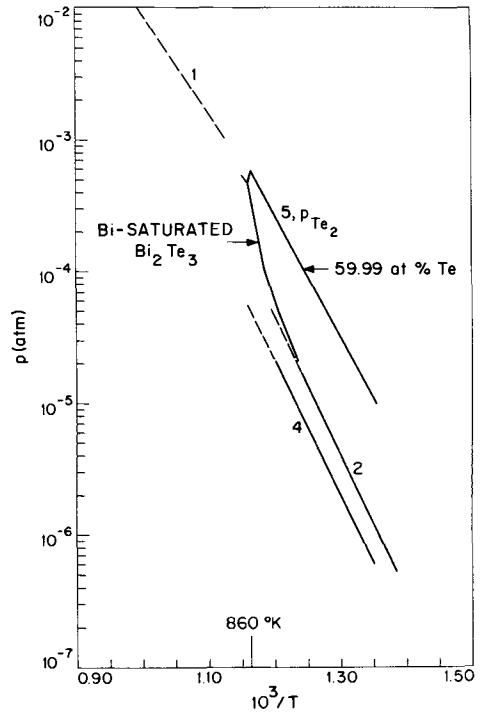

Fig. 1. Pressure in atm on a logarithmic scale plotted as a function of reciprocal absolute temperature. The numbers attached to the curves are the reference numbers. The solid portions of the lines cover the temperature range of the measurements. Lines 1, 2, and 4 give the total vapor pressure, P_Σ, for Bi_2Te_3(c, l). The loop for curve 5 gives the partial pressure of Te_2, p_{Te_2}, for the labeled compositions of Bi_2Te_3(c). The short segment attached to the high-temperature end of this loop gives p_{Te_2} for a 59.99 a/o Te melt.

ments are only 20% [ref. (2) and (3)] or 10% [ref. (4)] of the value obtained from the high-temperature Bourdon gauge measurements [ref. (1)]. Second, the results of the effusion measurements on Bi_2Te_3(c) are completely inconsistent with the values for the partial pressure of Te_2, p_{Te_2}, determined by optical density measurements (5). Thus the values of P_Σ are only 7-20% of the p_{Te_2} values measured for stoichiometric Bi_2Te_3(c) and are comparable to the p_{Te_2} values for Bi-saturated Bi_2Te_3(c). According to reaction [1], $p_{Te_2} = (1/5)(0.89)P_\Sigma$. Therefore the effusion measurements yield values of p_{Te_2} which are only 1-4% of those obtained by the optical density measurements for 59.99 a/o (atom per cent) Te Bi-Te and only 10-20% even of those for Bi-saturated Bi_2Te_3(c). The experimental results are summarized in Fig. 1. For simplicity only the values of p_{Te_2} for 59.99 a/o Te and for Bi-saturated Bi_2Te_3(c) are selected from the extensive data of ref. (5). It is seen that the extrapolated values of P_Σ obtained by the Bourdon gauge measurements are slightly higher than the values of p_{Te_2} over Bi_2Te_3(l) obtained by the optical density measurements.

The present study was undertaken in an attempt to resolve the above discrepancies. Values of P_Σ were measured for Bi_2Te_3(l) between 980° and 1169°K by using a new manometric technique involving visual observation through a transparent furnace. In separate experiments the previous optical density measurements on the vapor over Bi_2Te_3(l) were extended to higher temperatures so that the partial optical densities of Te_2(g) and BiTe(g) could be obtained at a number of wavelengths and values of p_{Te_2} could be determined from calibration experiments on Te(l). Straight lines can be drawn through the log P_Σ-$10^3/T$, log p_{Te_2}-$10^3/T$ and log (partial optical density of BiTe)-$10^3/T$ data such that the difference between P_Σ and p_{Te_2} is proportional to the partial optical density of BiTe(g). Thus on the assumption, given support later, that BiTe is the only other major vapor species, it appears that BiTe obeys Beer's law and p_{BiTe} can then be calculated.

Our results show that Bi_2Te_3(l) is not congruently vaporizing, since the vapor contains 95 a/o Te rather than 60 a/o Te. This is in agreement with an earlier (13) observation of incongruent effusion for Bi_2Te_3(l). Moreover, it appears that Bi_2Te_3(c) is not congruently subliming nor congruently effusing either, so that reaction [1] does not describe an equilibrium process. Since the vapor is Te-rich, a Bi_2Te_3(c) sample of any initial composition upon being subjected to indefinite sublimation becomes Bi-saturated and eventually enters the broad homogeneity range of the compound decomposing peritectically at 836°K and 57 a/o Te (5-7). The x-ray powder diffraction patterns for this peritectic phase and for Bi_2Te_3(c) have recently (8, 9) been shown to be remarkably similar. The patterns can easily be judged to be identical unless the low angle lines are accounted for. We therefore suggest that the workers using effusion cells were misled in concluding from x-ray diffraction patterns that Bi_2Te_3(c) effuses congruently under equilibrium cell conditions.

Experimental

Total pressure measurements.—To explain the principle of the method, we refer to the schematic of the high-temperature part of the apparatus shown in Fig. 2(a). The manometer cell, shown in detail in Fig. 2(b), consists essentially of an inverted, fused silica U-tube whose open ends are immersed in a reservoir of molten Bi_2Te_3 contained in a silica crucible. Argon pressure from an external source is applied to the surface of this reservoir via a long silica capillary. When this pressure is varied, the height of the melt in each leg of the U-tube changes until the pressure inside that leg at the level of the reservoir surface equals the pressure on the reservoir surface outside the U-tube. Provided that no residual foreign gas is trapped in the U-tube, the inside pressure is the sum of the total vapor pressure over Bi_2Te_3(P_Σ'), the hydrostatic pressure of the column of molten Bi_2Te_3 of height h above the reservoir surface, and a term due to capillary action. The outside pressure is equal to the argon pressure measured external to the cell, P_{ex}. Setting the outside and inside pressures equal gives

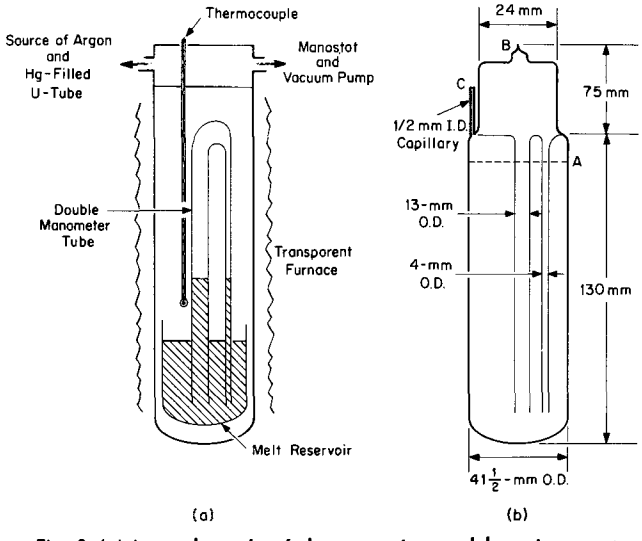

Fig. 2 *(a)* is a schematic of the apparatus used here to measure the total vapor pressure of Bi_2Te_3(l). *(b)* is a detailed drawing of the fused silica manometer cell. Access for the externally imposed argon pressure is through the capillary tube shown schematically as a straight section at the upper left hand portion of the cell ending at C. Actually this tube was about 30 cm long with 4 U-bends so that it was close to the main body of the cell and did not extend above the seal-off tip at the top of the cell, B. After loading with a pre-cast Bi_2Te_3 ingot, the bottom test-tube portion of the cell is sealed to the upper portion at A.

$$P_{ex} = P_\Sigma' + hd_M g + \frac{2\gamma_M}{r} \quad [2]$$

where P_{ex} and P_Σ' are expressed in dynes/square centimeter, and h is in centimeters. The quantities d_M (in grams/cubic centimeter) and γ_M (in dynes/centimeter) are, respectively, the density and surface tension of molten Bi_2Te_3, g is the acceleration due to gravity, and r is the radius of the U-tube leg in centimeters.

If the external measurement of argon pressure is made by means of a mercury-filled U-tube, $P_{ex} = Hd_{Hg}g$, where H is the difference in centimeters between the mercury levels in the two arms and d_{Hg} is the density of mercury. Then Eq. [2] can be rewritten as

$$H = P_\Sigma + h(d_M/d_{Hg}) + \frac{2\gamma_M}{rd_{Hg}g} \quad [3]$$

where $P_\Sigma \equiv P_\Sigma'/d_{Hg}g$ is the total vapor pressure of the melt expressed in centimeters of Hg. In principle, γ_M can be determined by comparing the values of h for different values of r when H and P_Σ are fixed. In our experiments, within the measurement accuracy of 0.005 cm the values of h were the same for the two legs of the U-tube, which had radii of 0.535 and 0.13 cm, respectively. This showed that the capillary force term can be neglected and that γ_M is less than 57 dynes/cm. Omitting this term from Eq. [3] and rewriting gives

$$h = (d_{Hg}/d_M)H - (d_{Hg}/d_M)P_\Sigma \quad [4]$$

Therefore, a plot of h as a function of H should give a straight line which yields the values of P_Σ (equal to H when $h = 0$) and d_M (equal to the reciprocal slope times d_{Hg}). If residual gas is trapped in the upper part of the U-tube, the pressure it exerts will cause deviations from linearity at sufficiently high values of H, with the slope decreasing as H increases. [In order to minimize the error due to any residual gas, the upper part of the U-tube shown in Fig. 2(b) was enlarged to a volume of about 21 cm^3.] Thus in this type of measurement, one not only gets a value of P_Σ, but also has some indication of its reliability when the experimentally observed relationship between h and H is linear and when the derived density agrees with independently measured values.

The following procedure was used to measure h as a function of H. The spectroscopically pure elements were each weighed to the nearest 0.1 mg to make a total of 361.36g of a Bi-Te mixture containing 60.00 a/o Te. The mixture was put into a previously cleaned and outgassed 40 mm OD, 25 cm long silica synthesis tube which was then evacuated to $2(10^{-6})$ Torr with a turbomolecular pump. The lower part of the tube was slowly heated to 793°K and $8(10^{-6})$ Torr. The valve to the vacuum system was closed, and N_2 at 110 Torr (passed through a liquid nitrogen-cooled trap) was admitted in order to minimize loss of material during the synthesis reaction. The sample was then heated at 893°K for 1/2 hr, at which point it was entirely molten. The temperature was lowered to 873°K, still above the melting point at 860°K, and the valve to the N_2-source closed and that to the vacuum opened in order to remove any dissolved N_2. Bubbling occurred in the melt and heavy sublimation took place to the upper parts of the tube. After about 2 min, when the pressure was about $2(10^{-6})$ Torr, the vacuum valve was closed and the melt cooled by immersing the bottom part of the tube in water. The tube was then sealed off at $5(10^{-7})$ Torr. No sublimate film was visible on the vacuum side of the seal-off point. The tube was placed in a box furnace at 773°K for 93 hr and quenched in water. (After the first 16 hr the heavy sublimate film on the upper part of the tube had entirely disappeared, having been driven into the Bi_2Te_3 ingot.)

The Bi_2Te_3 ingot was removed from the synthesis tube and slipped into the 41.5 mm OD tube forming the bottom section of the manometer cell, shown below A in Fig. 2(b). The upper part of the manometer cell, which included the two manometer legs and a 0.5 mm ID capillary 30 cm long, was then fused to the bottom part at A while the ingot was kept cool by a wet wrapping about the tube. The manometer legs fitted into holes in the BiTe ingot left by closed tubes which had been sealed to the bottom of the synthesis tube. This design of the synthesis tube decreased the dead space in the manometer cell and allowed the cell to be made shorter for a given weight of Bi_2Te_3. This in turn made it possible to establish more nearly isothermal conditions in the subsequent measurements. The capillary tube at C was closed by a close fitting silica cap held in place by a small piece of plastic tubing, and the assembled cell was then attached to a vacuum system through a seal-off constriction at B in Fig. 2(b). The lower part of the cell containing the Bi_2Te_3 ingot was outgassed by heating to 823°K for about ½ hr and the cell was then sealed off at B. The pressure reading on an ion gauge located 10 in. away on a connecting 1 in. ID glass tube was $3(10^{-6})$ Torr. There was no visible deposit of material on the vacuum side of the seal-off.

The sealed manometer cell was next placed in the apparatus shown schematically in Fig. 2(a). The cell rested on the bottom of a 76.2 cm long silica tube closed at the top with a brass cap and a Viton O-ring. The brass cap provided a central entry for a thermocouple tube and two side ports, one connecting to a mechanical fore pump through a Hg manostat, the other connecting to an argon cylinder through a silica tube packed with Ti-turnings, which during operation was heated to 973°K for gettering the argon. A side arm between this getter tube and the long tube led to a vertical Hg-filled U-tube, one arm of which was evacuated, and to a Dubrovin gauge which could be read to the nearest 0.01 cm Hg. The manometer cell, enclosed in the long silica tube, was centered in a resistance furnace consisting of three adjacent zones, each 25.4 cm long and heated by 8 equispaced, concentrically placed, vertical wires enclosed in insulators. This open-structured furnace was in turn surrounded by a 83 cm long, close fitting, open-ended Pyrex tube, the interior of which was covered by a vacuum-deposited gold film about 30-50 nm thick. The gold layer was sufficiently transparent in the visible to permit observation of the cell while simultaneously reflecting and containing most of the infrared radiation, thereby reducing the power requirements for the furnace and improving the uniformity of its temperature.

With the manometer cell in place, the containing silica tube was evacuated through the port in the brass cap and the three zones were heated to 773°K. The plastic tube holding the silica cap over the capillary tube at the top of the manometer cell decomposed and the silica cap dropped off the capillary. The manometer cell was heated to 913°K for about 2 hr to melt the ingot and seal the manometer legs while removing any residual gas and then an argon pressure of 10 cm Hg was admitted to start the measurements. At this point there was no visible deposit of material outside the manometer cell although here, as well as at previous points, a deposit of well under 200 mg should have been visible.

For each determination of the total vapor pressure the power to the three furnace zones was adjusted until the temperatures at points A and B in Fig. 2(b) and at the bottom of the manometer cell were within 3°K of each other, the uppermost point at B being the hottest. Temperatures were measured to the nearest 0.2°K using Pt, Pt, 13% Rh thermocouples, an ice reference junction, and a K-3 potentiometer. The temperature-measuring apparatus was checked using the melting points of Zn and Te. After setting the external argon pressure, the levels of the Bi_2Te_3-melt in the two legs of the manometer, the level of the melt in the crucible, and the levels in the two arms of the Hg-

manometer were read to the nearest 0.005 cm with a cathetometer to determine h and H. Below 2.0 cm Hg, H was read with the Dubrovin gauge to the nearest 0.01 cm Hg, as well as with the Hg-manometer, the two values usually agreeing within experimental precision. After a change in the argon pressure usually 30-40 min were required until the levels in the Bi_3Te_3 manometer legs became steady, the levels in the Hg manometer and the temperatures holding constant within the experimental accuracy cited above. The disadvantage of a long time constant for changes in h, caused by the restricted opening through the long capillary into the manometer cell, was accepted in order to minimize the loss of material from the cell by vaporization.

A 5W fluorescent lamp placed behind the manometer cell allowed the melt levels to be clearly seen up to 1170°K, the melt appearing black. At each temperature, readings were taken for four to seven values of the argon pressure, H, usually in order of decreasing H. When the apparatus was left overnight the temperature was lowered to 873°K and H held at 12-15 cm Hg. During the course of the measurements a black film slowly built up to opaqueness near the top of the long tube containing the manometer cell, where the temperature was about 673°K. A total of nine days was taken to complete the measurements, after which the apparatus was cooled to room temperature and the Bi_2Te_3 removed and weighed.

Optical density measurements.—The present measurements are an extension of earlier ones (5) which gave p_{Te_2} at lower temperatures for a number of compositions including some inside the $Bi_2Te_3(c)$ homogeneity range. The details of the method are given in ref (5). Essentially the experiment consists of measuring the optical density, $D = \log I_o/I$, of the vapor in a fused silica optical cell at a fixed temperature as a function of wavelength between 1990 and 7000Å and as a function of the temperature of a sidearm reservoir containing a Bi-Te melt of known composition. In the present study the composition was 59.99 a/o Te, and measurements were made with two cells having path lengths of 99.9 and 22.4 mm. The reservoir temperature was varied between about 943 and 1200°K, and consequently to prevent condensation on the windows the optical cell temperature was 1273°K rather than 1028°K as in the earlier study. The vapor over pure Te(c,l) consists essentially of $Te_2(g)$ in the range of temperatures and total Te-pressures encountered, and the spectrum at 1273°K is well characterized from an earlier study (10).

Results

Total pressure measurements.—At the completion of the experiment, after the manometer cell had been at 873°K or above for nine days, the surface of the Bi_2Te_3 appeared clean and no sign of white TeO_2 could be found anywhere in the system. The black Bi-Te sublimate of unanalyzed composition was found only on part of the apparatus where the temperature had been 873°K or below. The Bi_2Te_3 ingot had undergone a weight loss of 3.2g, putting an upper limit of ±0.5 a/o Te on the associated change in composition. Most likely the largest part of any composition change occurred during the measurements themselves.

A summary of the measurements and the results of a least squares fit to the linear relation between h and H embodied in Eq. [4] are given in Table I, in which the runs are listed in chronological order. Consistent with the observations in the preceding paragraph the temperature dependence of P_Σ does not change significantly with time. Comparison of runs 2 and 8 shows P_Σ was changed less than 3% by any change in sample composition. It is seen that a linear relationship between h and H is observed for h as large as 11.64 cm. At this value of h, the melt meniscus was in the enlarged, top-portion of the inverted U-tube.

Table I. Total vapor pressure and density of Bi_2Te_3 (l)

The total vapor pressure, P_Σ, of $Bi_2Te_3(l)$ is determined by a least squares fit of $h = \left(\frac{13.53}{d}\right)H - \left(\frac{13.53}{d}\right)P_\Sigma$ at various temperatures. H is the pressure of argon expressed in cm Hg; h is the height of $Bi_2Te_3(l)$ in the manometer tube; d is the density of $Bi_2Te_3(l)$ at the temperature in question. The runs are listed in the order in which they were taken. $\sigma(i)$ is the standard deviation in i.

Run	$10^3/T$	No. of data points	Range in h, cm	$\sigma(h)$, cm	$d \pm \sigma(d)$, g/cm³	$P_\Sigma \pm \sigma(P_\Sigma)$, atm
1	1.021	6	0.27-11.64	0.050	7.288 ± 0.068	(5.84 ± 0.34)10⁻⁶
2	0.9970	5	0.365-8.34	0.035	7.240 ± 0.081	(8.39 ± 0.31)10⁻⁶
3	0.9588	4	0.62-10.64	0.008	7.473 ± 0.013	(1.34 ± 0.009)10⁻²
4	0.9268	6	0.54-9.46	0.030	7.438 ± 0.054	(2.19 ± 0.02)10⁻²
5	0.9025	6	0.13-7.86	0.024	7.079 ± 0.054	(3.06 ± 0.01)10⁻²
6	0.8554	3	2.31-5.85	0.004	6.994 ± 0.027	(5.93 ± 0.00)10⁻²
7	0.9615	4	1.68-7.64	0.011	7.265 ± 0.027	(1.25 ± 0.02)10⁻²
8	1.000	7	0.95-9.5	0.030	7.406 ± 0.054	(8.28 ± 0.03)10⁻⁶

The densities of $Bi_2Te(l)$ obtained from the slopes of the h-H lines are plotted against temperature in Fig. 3. The error bars are placed at plus and minus one standard deviation in d. For comparison the density values obtained elsewhere using a pycnometer technique (11) are plotted as circles. Putting error bars on these data commensurate with their scatter would result in both sets of data overlapping above 700°C except for four of our points which appear to be high. The measurements giving the high densities do not show correspondingly high values of P_Σ.

Optical density measurements.—The spectrum of the vapor at 1273°K emanating from $Bi_2Te_3(l)$ at a lower temperature appears to be a superposition of the spectrum for $Te_2(g)$ and that of another species which shows vibronic bands between 2200 and 2450Å, where the $Te_2(g)$ spectrum has no structure. Runs using a pure Bi reservoir showed that the additional bands are not due to $Bi_2(g)$ or Bi(g). [These runs also showed that our detection limit for p_{Bi_2} is 10^{-5} atm. The value of p_{Bi_2} over $Bi_2Te_3(l)$ is below this limit even at the highest temperatures. The corresponding upper limit for p_{Bi}, calculated from the dissociation constant (12) of $Bi_2(g)$, is $2(10^{-4})$ atm.] We conclude that these additional bands are due to BiTe(g), which has been detected by mass spectrographic studies (13) as a major species over $Bi_2Te_3(l)$. The absorption band maxima are generally close to those obtained at higher resolution by Sharma (14), who also attributed them to BiTe(g). Between 2200 and 2345Å, Sharma reports 34 band heads with the strongest absorption at 2235Å. We observe 14 maxima in this region with the strongest absorption at 2231Å.

At the higher partial pressures of BiTe(g), p_{BiTe}, the relative optical densities of the strongest Te_2 peaks in the 1995-2056Å interval depart from the values ob-

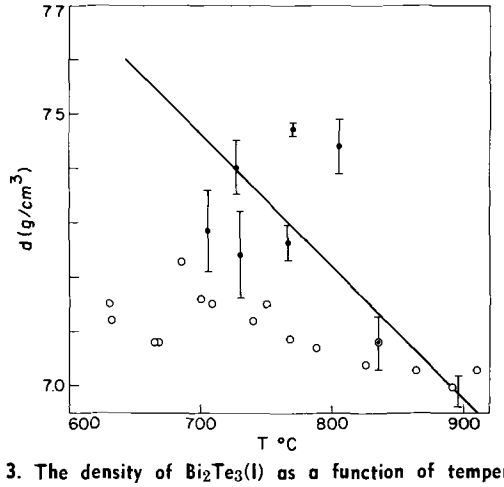

Fig. 3. The density of $Bi_2Te_3(l)$ as a function of temperature. Our points are shown with error bars at one plus and minus standard deviation. Circles are from ref. (11).

served with a pure Te reservoir (10), indicating that BiTe(g) absorbs to some extent in this interval. It does not absorb appreciably at 4357, 5000, or 5500Å, however, since the relative optical densities at these wavelengths are the same as those observed with pure Te. Therefore, the value of p_{Te_2} was obtained from the values of D at these three visible wavelengths by using the calibration curves obtained with a pure Te reservoir [Fig. 2 of ref (10)] and the vapor pressures of Te(l) given by Brooks (15) and by Ustygov (16), which are consistent with optical density measurements (17). The lowest straight line in Fig. 4 gives the values of p_{Te_2} for the 59.99 a/o Te melt plotted on a logarithmic scale against $10^3/T$. The corresponding equation is

$$\log_{10} p_{Te_2}\ (\text{atm}) = -(6.3048 \pm 0.032)\,(10^3/T) + (4.1396 \pm 0.030) \qquad 1.01 \geqq 10^3/T \geqq 0.85 \quad [5]$$

The values of p_{Te_2} calculated from Eq. [5] agree with the observed pressures to within ±2% for 17 of the 29 points obtained and to within ±3% for 22 points. The calculated and observed pressures differ by more than ±4% for only 3 points, where the differences are 4.3, 5.7, and 6.0%. Equation [5] is essentially a least squares fit of the data with the 3 high points omitted.

The partial optical densities of BiTe(g), r_λ, at four of its absorption maxima (2200, 2231, 2309, and 2319Å) were calculated by subtracting the contribution of Te_2-absorption at each wavelength from the total optical density observed. Taking the total optical density at 4357, 5000, and 5500Å as entirely due to Te_2(g), the contributions of Te_2(g) to the absorption at the wavelengths in the uv were read from a graph giving log D_λ as a function of the reciprocal temperature of a pure Te(l) reservoir [see Fig. 2 of ref. (10)]. The partial optical densities of BiTe(g) obtained in this way are shown as the upper four lines in Fig. 4, where r_λ is plotted on a logarithmic scale against $10^3/T$. Results are given for both the 99.9 mm path length cell and the 22.4 mm cell. The values of r_λ for the latter are normalized to 99.9 mm by multiplication by the factor 99.9/22.4. It is seen that the data for the four wavelengths are well represented by four parallel straight lines, consistent with the assumption that they represent absorption by a single vapor species that satisfies Beer's law. At 2231Å, 85-90% of the total absorption is due to BiTe(g). This percentage decreases with increasing wavelength to 62-68% at 2319Å. The partial optical densities of BiTe(g) satisfy the equations

$$r_{2231} : r_{2220} : r_{2309} : r_{2319} = 100 : 46.5 : 31.2 : 18.7 \quad [6]$$

$$\log_{10} r_{2231} = -(8.978 \pm 0.207)\,(10^3/T) + (8.8041 \pm 0.195) \quad [7]$$

where r_{2231} is the partial optical density at 2231Å for a 99.9 mm path length at 1273°K. The uncertainties quoted are the standard deviations of the slope and intercept obtained in a least squares fit of 65 points in which the data at the other three wavelengths were converted to the equivalent value at 2231Å using Eq. [6]. The standard deviation in log r_{2231} is 0.079.

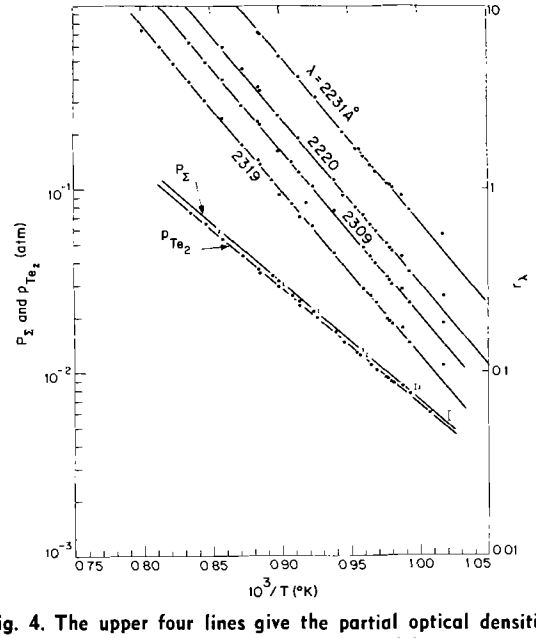

Fig. 4. The upper four lines give the partial optical densities of BiTe(g) at the indicated wavelengths for a 99.9 mm optical path length at 1273°K, plotted on a logarithmic scale (on the right side of the figure) as a function of the reciprocal temperature of Bi_2Te_3(l). The bottom two lines are semi-logarithmic plots on the same scale of the pressures over Bi_2Te_3(l) as a function of reciprocal temperature. The lower of these gives p_{Te_2} as determined by optical density measurements, and the upper gives P_Σ as determined by the manometric method.

Discussion

The values of total vapor pressure, P_Σ, for Bi_2Te_3(l) given in Table I are plotted on a logarithmic scale against $10^3/T$ in Fig. 4. The line representing the data, which for reasons discussed below was not obtained from a least squares fit, is given by

$$\log_{10} P_\Sigma\ (\text{atm}) = -6.4691(10^3)/T + 4.3219 \qquad 1.02 \geqq 10^3/T \geqq 0.85 \quad [8]$$

It is seen that this line fits five of the eight experimental points within the error bars shown (fixed at plus and minus one standard deviation in P_Σ), but the three points at the lowest temperatures lie somewhat above the line. The line is almost parallel to Ustygov's line for P_Σ, an extrapolation of which is shown in Fig. 1, but our P_Σ values are about 35% less than his. Our line for P_Σ lies just above the line for p_{Te_2} obtained by the optical density measurements and has a slope intermediate between that for p_{Te_2} and those giving the partial optical densities, r_λ, of BiTe(g).

From the discussion under Optical density measurements, the sum of the partial pressures of Bi_2 and Bi is below $2(10^{-4})$ atm and therefore is less than 3% of $P_\Sigma - p_{Te_2}$ at the highest temperatures. Consistent with this result and with extensive optical density measurements on Bi-Te melts to be published elsewhere, it appears that $p_{BiTe} + p_{Te_2}$ is within 3% of the total vapor pressure of Bi_2Te_3(l) over the entire temperature range. Therefore to a good approximation we can write

$$P_\Sigma = p_{Te_2} + p_{BiTe} \quad [9]$$

We also assume, consistent with experimental observations on a number of molecular species, that the optical absorption of BiTe(g) obeys Beer's law

$$p_{BiTe}(\text{atm}) = \alpha r_{2231} \quad [10]$$

where α is the Beer's law constant for a 99.9 mm path length at 1273°K. Using Eq. [7] for r_{2231} as a function of $10^3/T$ and obtaining p_{BiTe} by substituting Eq. [5] and [8] into Eq. [9], α as a function of temperature can be calculated from Eq. [10]. The values of α obtained in this way remain constant within about 8% over the interval 0.85-1.00 in $10^3/T$, ranging from $4.18(10^{-4})$ at the extremes of this range to $4.53(10^{-4})$ near the middle. We do not believe this variation to be excessive in view of the fact that p_{BiTe} is a small difference between the nearly equal quantities P_Σ and p_{Te_2}. Any adjustment in the P_Σ line to obtain a better fit to the experimental data at the three lowest temperatures, while still maintaining a close fit at high temperatures, leads to a significantly larger variation in α. Thus Eq. [8], rather than an equation obtained by a least squares fit, has been adopted as the best line through the P_Σ data in view of all the data. It leads to a temperature dependence for p_{BiTe} most nearly the same as that observed for the partial optical

densities for BiTe(g) given by Eq. [7]. The use of Ustygov's equation for P_Σ gives values for α that vary by more than a factor of 2 between $10^3/T = 0.85$ and 1.00.

The partial pressure of BiTe(g), p_{BiTe}, is obtained from Eq. [7] and [10] with an average value of $4.35(10^{-4})$ for α as

$$\log_{10} p_{BiTe}(\text{atm}) = -8.978(10^3)/T + 5.4432 \quad [11]$$

There are two points to be emphasized in connection with Eq. [11]. Although p_{Te_2} appears to be given to within about $\pm 3\%$ by Eq. [5] and P_Σ to within some less well-defined percentage, say $\pm 10\%$, by Eq. [8], p_{BiTe}, being the difference of these nearly equal quantities, is much more uncertain. Although the temperature dependence of p_{BiTe} is known to within 2% through Eq. [7] and [10], the absolute value could be in error by 50-100%. Second, although the total pressure must be constant throughout the optical cell and side-arm, because of the temperature difference between the optical cell and sidearm, p_{Te_2} and p_{BiTe} may vary due to the chemical dissociation of BiTe(g) and thermal diffusion. Thus p_{Te_2} given by Eq. [5] and p_{BiTe} given by Eq. [11] are the partial pressures in the 1273°K optical cell, but these may differ somewhat from the values prevailing over the Bi_2Te_3 melt in the sidearm reservoir. These differences are greatest at the lowest reservoir temperatures.

Some indication of the thermal effects can be gained by comparing the present results with our earlier measurements (5) using a 1028°K optical cell. For a 59.99 a/o Te melt at 1000°K the value of p_{Te_2} was $6.2(10^{-3})$ atm, the partial optical density of BiTe at 2231Å for a 99.9 mm path was 1.03, and the partial pressure of Bi_2 was below the experimentally detectable limit of about 10^{-5} atm. The reservoir and optical cell temperatures in this case were close enough to make thermal effects negligible, and the value of p_{Te_2} over $Bi_2Te_3(l)$ at 1000°K can be taken as the measured value of $6.2(10^{-3})$ atm. The 10% higher value of $6.83(10^{-3})$ atm obtained in the present study with a 1273°K cell is due to the increased degree of dissociation of BiTe(g) at this higher cell temperature. The values of p_{Te_2} obtained here with a 1273°K optical cell will differ even less from the actual value of p_{Te_2} over the $Bi_2Te_3(l)$ at higher melt temperatures. Therefore we can conclude that p_{Te_2} over $Bi_2Te_3(l)$ is given correctly to within 10% by Eq. [5]. Therefore $Bi_2Te_3(l)$ is not congruently vaporizing between 1000° and 1169°K. Taking the difference between P_Σ and p_{Te_2} as equal to p_{BiTe}, the vapor is more than 95 a/o Te, rather than 60 a/o Te. At 1000°K, even if the difference of $9.1(10^{-4})$ atm between P_Σ and p_{Te_2} were due to Bi_2 rather than BiTe, the vapor would be 87 a/o Te.

Extrapolation of Eq. [8] to 860°K, the maximum melting point of $Bi_2Te_3(c)$, gives $P_\Sigma = 6.4(10^{-4})$ atm. This is a factor of 4.2 higher than the extrapolated P_Σ value from ref. (2) and (3) and a factor of 11.6 higher than the extrapolated value from ref. (4), the first two obtained by effusion measurements on the assumption that effusion is congruent according to reaction [1]. It would appear from present results that serious doubt is cast on the validity of the sublimation reaction given by Eq. [1]. We suggest that this discrepancy results because reaction [1] is not valid for the Knudsen effusion nor for equilibrium sublimation of $Bi_2Te_3(c)$, and therefore the calculations of P_Σ from the effusion data are incorrect. Preliminary analysis of the earlier optical absorption results (5) and our present results supports the conclusion that $Bi_2Te_3(c)$ does not sublime congruently.

Acknowledgment

The authors wish to acknowledge the capable assistance of Mr. R. N. Capes in these experiments. This work was sponsored by the Department of the Air Force.

Manuscript submitted July 17, 1970; revised manuscript received Jan. 25, 1971.

Any discussion of this paper will appear in a Discussion Section to be published in the December 1971 JOURNAL.

REFERENCES

1. G. P. Ustygov, E. N. Vigdorovich, and I. A. Timoshin, *Izv. Akad. Nauk SSR Neorgan. Mater.*, **5**, 166 (1969).
2. Z. Boncheva-Mladenova, A. S. Pashinkin, and A. V. Novoselova, *ibid.*, **2**, 1542 (1966).
3. S. I. Gorbov and A. N. Krestovnikov, *ibid.*, **2**, 1702, 1705 (1966).
4. I. Y. Kashkooli and Z. A. Munir, *This Journal*, **117**, 248 (1970).
5. R. F. Brebrick, *J. Phys. Chem. Solids*, **30**, 719 (1969).
6. A. C. Glatz, *This Journal*, **112**, 1204 (1965).
7. J. Strassburger, *ibid.*, **116**, 640 (1969).
8. R. F. Brebrick, *J. Appl. Cryst.*, **1**, 241 (1968).
9. R. F. Brebrick, "The Chemistry of Extended Defects in Non-Metallic Solids," p. 183, L. Eyring and H. O'Keeffe, Editors, North-Holland Publishing Co., Amsterdam, (1970).
10. R. F. Brebrick, *J. Chem. Phys.*, **49**, 2584 (1968).
11. V. M. Glazov, S. N. Chizhevskaya, and N. N. Glagoleva, "Liquid Semiconductors," p. 330, Plenum Press, New York (1969).
12. R. Hultgren, R. Orr, P. D. Anderson, and K. K. Kelley, "Selected Values of Thermodynamic Properties of Metals and Alloys," John Wiley & Sons, Inc., New York (1963).
13. R. F. Porter and C. W. Spencer, *J. Chem. Phys.*, **32**, 943 (1960).
14. C. B. Sharma, *Proc. Phys. Soc. (London)*, **67**, 935 (1954).
15. L. S. Brooks, *J. Am. Chem. Soc.*, **74**, 227 (1952).
16. A. A. Kudryovtsev and G. P. Ustygov, *Russ. J. Inorg. Chem. (English Transl.)*, **6**, 1227 (1961).
17. R. F. Brebrick, *J. Phys. Chem.*, **72**, 1032 (1968).

[Note added in proof: The density of Bi-Te melts up to 993°K has been reported by A. Kestar and S. Hruska in *Met. Trans.*, **1**, 2357 (1970).]

Preparation and Electrical Resistivity of Ultrahigh Purity Niobium[1]

R. W. Meyerhoff

Union Carbide Corporation, Linde Division, Tarrytown Technical Center, Tarrytown, New York 10591

ABSTRACT

Niobium samples with residual resistivity ratios greater than 20,000 were prepared *via* a two-step process. First, a fused salt electroplating process was used to prepare niobium having an exceptionally high purity with respect to the substitutional transition metal impurities tantalum and tungsten. Second, this electroplated niobium was vacuum degassed to remove the interstitial impurities, oxygen, nitrogen, and hydrogen. The major contributions to the residual resistivity after vacuum degassing were from the impurities nitrogen, tantalum, and tungsten. The electrical resistivity of these ultrahigh purity niobium samples can be calculated from the relation

$$\rho_T = \rho(T) + 10.0 \times 10^{-6} C_{N2} + 2.49 \times 10^{-7} C_{Ta} + 11.0 \times 10^{-7} C_W \text{ ohm-cm}$$

where $\rho(T)$ represents the thermal contribution to the resistivity at the temperature T and C_{N2}, C_{Ta}, and C_W represent respectively the concentrations in atomic per cent of nitrogen, tantalum, and tungsten. The value of C_{N2} for the vacuum degassed samples is given by

$$C_{N2} = 6.2 \times 10^{-4} (p_{N2})^{1/2} \exp (23{,}000/T)$$

where p_{N2} represents the partial pressure (Torr) of nitrogen in the vacuum system and T represents the temperature (K) of the sample during outgassing.

This study of the preparation and electrical resistivity of ultrahigh purity niobium was prompted by the observation that the a-c losses in superconducting niobium wire samples decreased as the residual resistivity of these samples decreased (1). Thus, it was hoped that if those factors most strongly affecting the residual resistivity were identified it might then be possible to prepare niobium samples with lower residual resistivities and hence lower a-c losses.

In 1962 Stromberg and Swenson (2) reported the preparation of niobium with a residual resistivity ratio ($\rho 293/\rho 4.2$) of ~2,000. This value, the highest obtained prior to this work, was attained by vacuum degassing a niobium wire at a temperature close to its melting point at a pressure of the order of 10^{-9} Torr. Attempts by others to achieve significantly higher residual resistivity ratios by either vacuum degassing and/or electron beam zone refining were unsuccessful. In some cases the highest residual resistivity ratios attained were as small as 100-500. Some of these low values can be explained by the low temperatures and/or poor vacuum used to degas the niobium. One significant difference between these studies, however, was the tantalum concentration in the starting material. Stromberg and Swenson had used niobium containing less than 200 ppm tantalum while many of the other studies were made with niobium containing as much as 1,000 ppm tantalum. No attempts to attain high residual resistivity ratios have been reported in which niobium containing less tantalum than that in the niobium used by Stromberg and Swenson was used as the starting material. Two conclusions were drawn from this early work. First, electron beam zone refining of niobium does not result in any significant reduction of the tantalum content. Second, in general the highest residual resistivity ratios were reported by those investigators using niobium with the lowest tantalum content.

With the exception of cases where the impurities were present in the form of precipitates rather than in solid solution most elements previously prepared with exceptionally high residual resistivity ratios contained considerably less than 100 ppm total impurities. Previous attempts to produce ultrahigh purity niobium started with niobium containing about 200 ppm tantalum in addition to the other impurities present. This new look at the preparation of ultrahigh purity niobium was prompted in part by the development of Mellors and Senderoff (3) of a fused salt electroplating process which provided a means of preparing niobium samples containing less than 10 ppm tantalum. The work described in the remainder of this paper demonstrated that tantalum was indeed the culprit and other factors such as thermal scattering, lattice defects, dislocations, grain boundaries, *etc.* cannot account for the resistivity at 4.2K previously observed by others in "high purity" niobium.

Experimental Procedure

The first step in the preparation of the ultrahigh purity niobium samples was the formation of sheets of niobium having a low tantalum content by means of a fused salt electroplating process. Only a brief description of this process is given below since it has been described in considerable detail by Mellors and Senderoff (3). The electrolyte was prepared by melting, in a graphite crucible under an argon atmosphere, a salt mixture containing 26.2 weight per cent (w/o) LiF, 10.5 w/o NaF, 47.1 w/o KF, and 16.2 w/o K_2NbF_7. During plating this electrolyte was maintained at 775°C. Commercial niobium sheet was used for the anode and OFHC copper sheet for the cathode. The niobium was electrodeposited at a current density of 25 mA/cm^2, corresponding to a deposition rate of ~25 μ/hr. The plated niobium metal was removed from the copper cathode by dissolving the copper in a 1:1 mixture of HNO_3:H_2O. These niobium sheets were typically 3x10x0.5 cm.

The first niobium plated from a new electrolyte will contain less than 2 ppm tantalum; however, since this is considerably less than the tantalum concentration in the niobium anodes the tantalum concentration in the electrolyte will increase as plating is continued with a concomitant small increase in the tantalum concentration in the electroplated niobium. Although the as-plated niobium has a low tantalum content the concentration of interstitial impurities, especially oxygen and nitrogen, are sufficiently high to limit the residual resistivity ratio to a value less than 70. Thus, in order

[1] This work was supported in part by the Air Force Materials Laboratory under contract number AF 33 (615)-5393.

Key words: ultrahigh vacuum degassing, residual resistivity, low tantalum niobium.

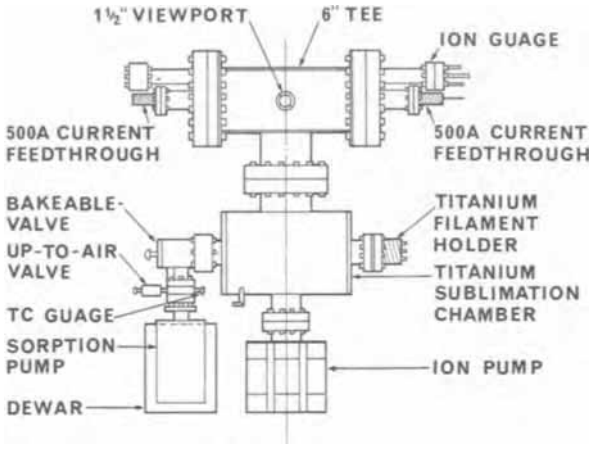

Fig. 1. Schematic of vacuum system used for degassing niobium samples.

to obtain very high residual resistivity ratios it is necessary to lower the concentration of the interstitial impurities by vacuum degassing the electroplated niobium.

The vacuum system used to degas the electroplated niobium samples is illustrated in Fig. 1. Liquid nitrogen cooled molecular sieve (Linde 5A) was used for rough pumping. The ultrahigh vacuum pumping system consisted of a 50 liter/sec ion pump and a 1,000 liter/sec titanium sublimation pump. At pressures below 10^{-4} Torr the pressure was determined from both the current *vs.* pressure calibration curve for the ion pump and a nude Bayard-Alpert gauge mounted adjacent to the sample as illustrated in Fig. 1. The sample temperature was measured with an optical pyrometer sighted on the samples through a 1.5 in. diameter view port. The samples were mounted between the ends of the two 500A electrical feed throughs by means of copper clamps such as that illustrated in Fig. 2. The only flange that had to be opened to change both the niobium samples and the titanium elements in the sublimator was that between the sample chamber and the titanium sublimator chamber.

Generally, samples in the form of ribbons 12.0 x 1.0 x 0.025 cm, cut from sheets produced by cold rolling the thicker electroplated sheets, were used. The samples were resistively heated by means of a d-c current. The samples were degassed for several days at temperatures up to 2700°K at pressures as low as 3×10^{-10} Torr. The ribbon-like shape of the samples and the use of a d-c current were chosen in the hope that some additional degree of purification could be obtained during the vacuum degassing by means of electrotransport refining. At 2700°K the d-c heating current used corresponded to a current density within the samples of $\sim 1 \times 10^4$ A cm^2 and an electric field of ~0.7 V/cm.

The following procedure was used to determine the residual resistivity ratio of the vacuum degassed niobium samples. The niobium ribbon was mounted in

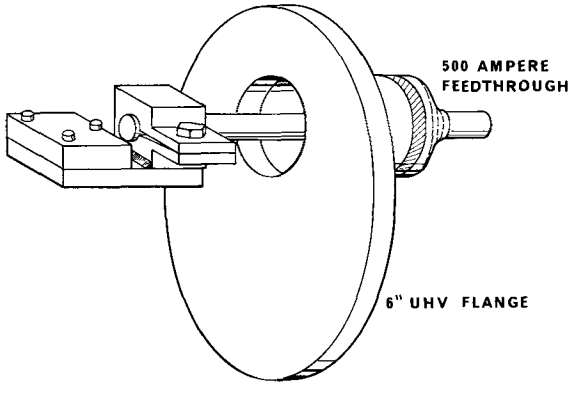

Fig. 2. A clamp used to hold samples during vacuum degassing

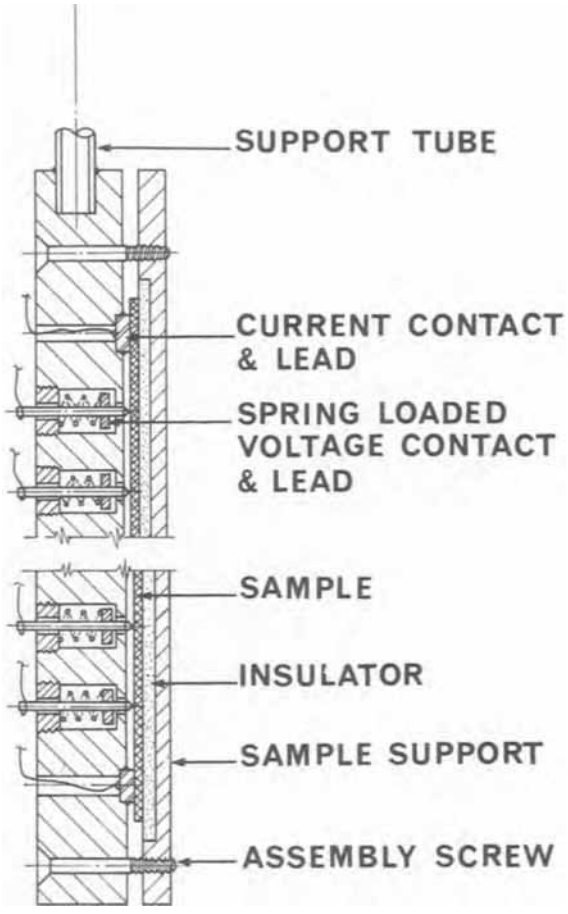

Fig. 3. Schematic of sample holder used in electrical resistivity measurements.

the sample holder illustrated schematically in Fig. 3. Current was supplied to the sample through the copper contacts at either end of the holder. The nine voltage probes are spring-loaded and were constructed from copper wire. Each of the probes was connected to two Leeds and Northrup rotary switches, the moving contacts of which were connected to one half of a Rubicon double six dial potentiometer. Thus, the voltage drop between any two of the nine voltage probes could be measured. In this way it was possible to look for any small variation in electrical resistivity along the length of a sample which might be attributable to electromigration of one or more impurities. The second half of the potentiometer was used to measure the voltage drop across a standard resistor in series with the sample. The sample current, usually $\sim 10^{-1}$A, was calculated from this voltage drop. A Keithley Model 147 Nanovolt Null Detector served as the null detector for the potentiometer.

Since niobium is a superconductor, a magnetic field large enough to destroy the superconducting state was used in all the measurements of the residual resistivity. Considerable care was taken, however, to ensure that the sample was as close as possible to being parallel to the applied magnetic field since the transverse field magnetoresistance of niobium is quite large and would lead to anomalously high values of the residual resistivity. Measurements made between 5 and 60 kg with the applied magnetic field parallel to the sample axis generally showed an increase of less than 10% in the residual resistivity over this field range.

Results and Discussion

The highest purity niobium sample prepared had a residual resistivity ratio, β, of ~22,500. This sample was prepared by vacuum degassing an electroplated niobium ribbon at ~2700°K at a pressure of $\sim 2 \times 10^{-10}$ Torr. However, while this sample had by far the

highest value of β ever reported for niobium, its residual resistivity ratio was still significantly below values which have been obtained for a few other elements. It is of interest, therefore, to examine the factors which limited the value of β for this sample.

If the electron mean free path is sufficiently short so that size effects, *i.e.* surface scattering, are negligible, Matthiessen's rule is applicable. The resistivity is then given by

$$\rho(T) = \rho_L(T) + \Sigma\, \rho_d + \Sigma\, \rho_i \qquad [1]$$

where $\rho_L(T)$ represents the temperature dependence of the electrical resistivity of the pure defect free metal. The terms $\Sigma\, \rho_d$ and $\Sigma\, \rho_i$ represent respectively the temperature independent contributions from defects and impurities. The assumption that size effects are negligible is questionable; however, the data required to calculate the electron mean free path are not known with sufficient accuracy to permit a precise calculation of the magnitude of the size effect. It is possible that the actual bulk residual resistivity ratio may be as much as five times greater than the 20,000 measured. However, measurements made on thicker samples than the 0.25 mm thick ribbons discussed in this paper invariably showed higher residual resistivities than the thin samples due to the difficulties associated with degassing these thicker samples. Thus, no direct evidence of a size effect limited resistivity was observed.

For most metals the term $\rho_L(T)$ in Eq. [1] can be calculated from the Grüneisen-Bloch relation (4)

$$\rho_L(T) = \frac{KT}{\theta_R^2}\, G(X) \qquad [2]$$

$$X = \theta_R/T$$

where K is a constant, θ_R is a characteristic temperature, and $G(X)$ is given by the relation

$$G(X) = 4\,\frac{T^4}{\theta_R} \int_0^X \frac{Z\ dZ}{(e^z - 1)(1 - e^{-z})} \qquad [3]$$

Assuming that $\theta_R = \theta_D = 240$ K and using tabulated values (4) of $G(X)$, one finds from Eq. [2], $\rho 295/\rho 4.2 = 10^6$. This relation, which predicts $\rho_L(T) \propto T^5$ at low temperatures, does not take into account the contributions at low temperature of either electron-electron scattering or Umklapp processes both of which tend to increase the value of the electrical resistivity at low temperatures. These would then lead to a smaller value of $\rho 295/\rho 4.2$ than that calculated from Eq. [2]. The results of White and Woods (5, 6), and of Webb (7) show that $\rho_L(T) \propto T^n$, where $n \approx 3$ at low temperatures. Thus, the electrical resistivity of niobium decreases less rapidly with temperature than would be expected from the Grüneisen-Bloch relation and one would not expect a value of $\rho 295/\rho 4.2 = 10^6$ even for an absolutely pure defect-free niobium sample.

Electrical resistivity measurements made on a number of samples degassed at different temperatures and pressures showed a difference in resistivity of $\sim 3.8 \times 10^{-10}$ ohm-cm between 4.2 and 1K. If one assumes that this difference is only due to the thermal contribution to the resistivity and is independent of the impurity concentrations and that the thermal contribution varied as T^3, then the first term in Eq. [1] at low temperature may be expressed as

$$\rho_L(T) = 5.14 \times 10^{-12}\, T^3 \text{ ohm-cm} \qquad [4]$$

Since $\rho 295 \approx 14 \times 10^{-6}$ ohm-cm this expression predicts values of $\rho 295/\rho 4.2$ and $\rho 295/\rho 1.0$ respectively of ~37,000 and ~5,100,000. While these values are significantly lower than those calculated from the Grüneisen-Bloch relation, they are much larger than the experimentally observed values. Thus, it is clear that thermal scattering is not limiting the value of the residual resistivity ratio measured at 1K in samples with values of $\rho 295/\rho 4.2 \approx 20{,}000$.

I will next consider the contribution of defects to the residual resistivity (the second term in Eq. [1]), in particular the contributions of dislocations, grain boundaries, and vacancies are estimated. Nordheim's concentration rule (8) states that the contribution of an impurity to the resistivity is proportional to $x(1 - x)$ where x represents the mole fraction of the impurity. In this discussion it will be assumed that the concentration of the individual impurities and defects are sufficiently low so that Nordheim's rule may be approximated by

$$\rho_i \propto x_i \qquad [5]$$

Although the effect of dislocations on the electrical resistivity of niobium has not been determined experimentally, studies of other metals (9) indicate that

$$\rho_{\text{dislocation}} \approx 5 \times 10^{-19}\, N \text{ ohm-cm} \qquad [6]$$

where N is the dislocation density in lines/cm^2. The exact value of the dislocation density in this material is not known. However, studies of the anomalous transmission of x-rays in this material by Weissman (10) showed that the dislocation density was less than 10^4 lines/cm^2. A dislocation density as high as 10^4 lines/cm^2, in the absence of other impurities or defects, would limit the residual resistivity ratio to $\sim 3 \times 10^9$. In the case of a sample with a residual resistivity ratio of 20,000 a dislocation density of 10^7 lines/cm^2 would contribute less than 1% of the measured residual resistivity. Thus it appears that the contribution of dislocations to the residual resistivity of these samples is negligible.

One approach to evaluating the contribution of grain boundaries to the electrical resistivity of metals is to treat the boundary as a region approximately 2 atomic distances wide (9) and having a resistivity equal to the resistivity of the metal at its melting point ρMP. In this way one can calculate, assuming $\rho_{MP} = 60$ μohm-cm, that each grain boundary the current must cross contributes a resistance of 3×10^{-12} ohm. In the high purity vacuum outgassed and annealed niobium samples there are approximately three grain boundaries per centimeter. Thus, the boundaries would contribute $\sim 1 \times 10^{-11}$ ohm-cm to the electrical resistivity at 4.2K, *i.e.* approximately 1% of the measured resistivity. Measurements by Andrews (11) of the effect of grain boundaries on the electrical resistivity of copper gave a value about six times greater than that obtained by assuming the grain boundary to be a layer 2 atomic distances thick with a resistivity $\sim\rho_{MP}$. In either case, the contribution of grain boundaries is still relatively small. In some of the high purity niobium samples prepared in this laboratory there were single grains large enough so that their electrical resistivity could be measured. The values measured on those single crystals were not significantly different from those measured at other positions in the sample where the resistance across one to five grain boundaries was included. Thus it appears that the contribution of grain boundaries to the residual resistivity of these samples is negligible.

Both theoretical and experimental investigations (9) of the effect of vacancies on the resistivity of metals give values of approximately 2×10^{-6} ohm-cm/atomic per cent (a/o) vacancies. The ratio of the number vacancies, n, to the number of lattice sites, N, at any temperature T is given by

$$\frac{n}{N} = \exp(-U/RT) \qquad [7]$$

where U is the energy of formation of one mole of vacancies and R is the gas constant. Although U is not known for niobium, Frenkel (12) has given a simple argument for estimating U, which shows that U should roughly be equal to the heat of vaporization.

The maximum number of vacancies one would expect to find in a well-annealed metal would be the number in thermal equilibrium at the melting point if the quench rate were high enough to retain that number. For niobium using 2733°K as the melting point and $H_{vap} = 170$ kcal/mole, one obtains

$$\frac{n}{N} = \exp(-31.1) = 10^{-13.5} \quad [8]$$

which corresponds to approximately 3×10^{-12} a/o vacancies. In order for the residual resistivity ratio to be limited by vacancies to a value of 20,000 a vacancy concentration of 3.5×10^{-4} would be required. If $U \approx 0.4\ H_{vap}$ the vacancy concentration would be this high at the melting point. It is highly unlikely however, since several seconds are required for the sample to cool below 1000°K, that an appreciable number of the vacancies in thermal equilibrium at the melting point would be quenched in by such slow cooling rates. Furthermore, as the degassing temperature was increased, and all other parameters being held constant, the residual resistivity decreased. If quenched in vacancies were a significant contributor to the residual resistivity one would see an increase rather than a decrease in this quantity as the degassing temperature was increased.

It appears, therefore, that in these niobium samples, having residual resistivity ratios as high as 20,000, the contributions to the resistivity of vacancies, dislocations and grain boundaries may be ignored. In the remainder of this section I will discuss the contribution to the residual resistivity of the last term in Eq. [1], namely the contributions to the residual resistivity by impurities.

The major substitutional impurities in these niobium samples were tantalum and tungsten. The concentrations of these two elements were respectively 7 and 1.8 ppm corresponding to 3.6×10^{-4} a/o tantalum and 9×10^{-5} a/o tungsten. Electrical resistivity measurements made on a vacuum annealed and degassed sample of niobium containing 0.08 a/o tantalum gave a value of $d\rho/dc$ of 2.49×10^{-7} ohm-cm/a/o tantalum. Similar measurements were made on a vacuum degassed sample of Cb 752, a commercial niobium alloy having a nominal composition of 5 a/o tungsten and 2.5 a/o zirconium. After vacuum degassing the sample was analyzed to determine the tungsten and zirconium concentration as a considerable fraction of the zirconium was removed during the vacuum degassing. A value of 11×10^{-7} ohm-cm/a/o tungsten was calculated from the measured residual resistivity after subtracting the contribution from the zirconium which was calculated from the measured zirconium concentration using the value of 12.0×10^{-7} ohm-cm/a/o zirconium found by Berlincourt and Hake (13). These results along with values of $d\rho/dc$ for other elements dissolved in niobium are given in Table I.

For these electroplated and vacuum degassed niobium samples the substitutional impurities tantalum and tungsten contribute 1.9×10^{-10} ohm-cm to the residual resistivity. For a sample having a residual resistivity ratio of 22,500 the residual resistivity is 6.2×10^{-10} ohm-cm. This leaves a residual resistivity of 4.3×10^{-10} ohm-cm to be accounted for by the interstitial impurities. Of the four interstitial impurities, carbon, hydrogen, nitrogen, and oxygen only the last two are of importance in this analysis since the carbon concentration is very low due to the nature of the electroplating process and hydrogen is reduced to negligible levels by the vacuum degassing. Cost and Wert (17) have found for nitrogen that

$$C_{N_2} = 6.2 \times 10^{-4} (P_{N_2})^{1/2} \exp(23{,}000/T) \quad [9]$$

where C_{N_2} is the atomic per cent nitrogen and P_{N_2} is the partial pressure of nitrogen (Torr). From Eq. [9] one finds, for a niobium sample vacuum degassed at 2×10^{-10} Torr and 2700°K, a nitrogen concentration of 4.6×10^{-5} a/o. Using this value and the value of $d\rho/dc$ for nitrogen given in Table I, one obtains a value of 4.6×10^{-10} ohm-cm for the contribution of nitrogen to the residual resistivity. This is indeed quite close to the value of 4.3×10^{-10} ohm-cm left to be accounted for in a sample degassed under these conditions. It has been often suggested that oxygen is a larger contributor than nitrogen to the residual resistivity of vacuum degassed niobium samples. However, in the present study I have found a good fit to the experimental results when I assumed the partial pressure of nitrogen was equal to the measured total pressure and used Eq. [9] to calculate the nitrogen concentration and hence nitrogen's contribution to the residual resistivity. Similar calculations based on the concentration of oxygen gave totally unsatisfactory results since at the temperatures and pressures used for the vacuum degassing the calculated oxygen concentration was considerably lower than the calculated nitrogen concentration and made a negligible contribution to the residual resistivity.

Table I. Values of $d\rho/dc_A$ for A dissolved in niobium

A	$d\rho/dc$, ohm-cm/a/o A	Ref.
Titanium	14.3×10^{-7}	Berlincourt and Hake (13)
Titanium	9.6×10^{-7}	Fietz (14)
Zirconium	12.0×10^{-7}	Berlincourt and Hake (13)
Hafnium	14.0×10^{-7}	Berlincourt and Hake (13)
Tantalum	2.49×10^{-7}	This work
Tungsten	11.0×10^{-7}	This work
Oxygen	69.0×10^{-7}	Tedmon, Rose, and Wulff (15)
Nitrogen	100.0×10^{-7}	Pasternak and Evans (16)

Summary

The analysis of the residual resistivity of niobium samples presented in the previous section showed that at low temperatures where the thermal contribution to the resistivity varies as T^3 the resistivity of electroplated and vacuum degassed samples is given by

$$\rho(T) = 5.14 \times 10^{-12} T^3 + 10.0 \times 10^{-6} C_{N_2} + 2.49 \times 10^{-7} C_{Ta} + 11.0 \times 10^{-7} C_W \quad [10]$$

where the value of C_{N_2}, which depends on the degassing temperature and pressure, is given by Eq. [9]. In Fig. 4 lines of constant nitrogen concentration calculated from Eq. [9] are shown as a function of vacuum degassing temperature and pressure. Values

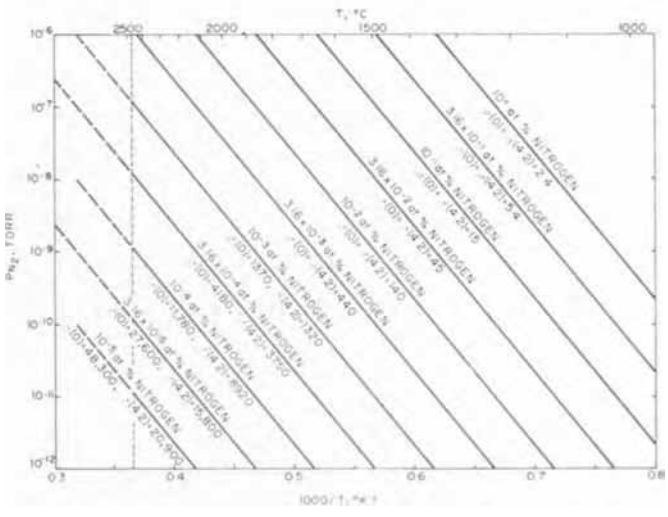

Fig. 4. Lines of constant nitrogen concentration calculated from Eq. [9] and values of resistivity ratios between room temperature and both 0 and 4.2K calculated from Eq. [10] for electroplated niobium containing 7 and 1.8 ppm respectively of tantalum and tungsten.

of the resistivity ratio, between room temperature and both 0 and 4.2K, calculated from Eq. [10] are also given in Fig. 4 for samples containing 7 and 1.8 ppm respectively of tantalum and tungsten. Although the analysis given above contains some assumptions, the agreement between calculated and measured resistivities was within 20% for the samples studied. This included samples vacuum degassed between 1400° and 2700°K at pressure in the range 10^{-7} -2 x 10^{-10} Torr.

Acknowledgments

The author wishes to express his appreciation to W. J. Runkle for his valuable assistance in the experimental part of this work and to Dr. D. C. Freeman, Jr. for his keen interest and helpful discussions.

Manuscript submitted Nov. 17, 1970; revised manuscript received *ca.* Jan. 29, 1971. This was Paper 555 presented at the Montreal Meeting of the Society Oct. 6-11, 1968.

Any discussion of this paper will appear in a Discussion Section to be published in the December 1971 JOURNAL.

REFERENCES

1. W. T. Beall and R. W. Meyerhoff, *J. Appl. Phys.*, **40,** 2052 (1969).
2. T. F. Stromberg and C. A. Swenson, *Phys. Rev. Letters*, **9,** 370 (1962).
3. G. W. Mellors and S. Senderoff, *This Journal*, **112,** 266 (1965).
4. G. T. Meaden, "Electrical Resistance of Metals," Section 4.2, Plenum Press, New York (1965).
5. G. K. White and S. B. Woods, *Can. J. Phys.*, **35,** 892 (1957).
6. G. K. White and S. B. Woods, *Phil. Trans. Roy. Soc. London Ser. A*, **251,** 273 (1959).
7. G. Webb, Private communication.
8. L. Nordheim, *Ann. Physik*, **9,** 607 (1931).
9. P. Gregory, A. J. Bangay, and J. E. Hargreaves, *Metallurgia*, **74,** 71 (1966).
10. S. Weissman, Private communication.
11. P. V. Andrews, *Phys. Letters*, **19,** 558 (1965).
12. J. Frenkel, "Kinetic Theory of Liquids," Oxford (1946).
13. T. G. Berlincourt and R. R. Hake, *Phys. Rev.*, **131,** 140 (1963).
14. W. A. Fietz, Private communication.
15. C. S. Tedmon, Jr., R. M. Rose, and J. Wulff, *J. Appl. Phys.*, **36,** 164 (1965).
16. R. A. Pasternak and B. Evans, *Trans. AIME*, **233,** 1194 (1965).
17. J. R. Cost and C. A. Wert, *Acta. Met.*, **11,** 231 (1963).

Growth, Texture, and Surface Morphology of SiC Layers

Kenneth A. Jacobson[1]

Solid State Research and Development, Dow Corning Corporation, Hemlock, Michigan 48626

ABSTRACT

Highly oriented SiC layers were grown on (001) and (111) silicon substrates by the reduction of $(CH_3)_2SiCl_2$ in an excess of hydrogen at a temperature of 1365°C. Layers up to $\approx 100\mu$ thick were grown at a rate of 4.3 μ/min. The material was predominantly β-SiC with a resistivity range of 0.5-34.5 ohm-cm, n-type. Laue x-ray analysis indicated that the degree of preferred orientation varied with thickness and that multiple orientations exist on the (001) silicon substrates. A higher degree of preferred orientation was achieved on the (001) compared to the (111) substrates. At various thicknesses, faceted grains on the order of 1-2μ in diameter were visible using the scanning electron microscope. The fact that oriented growth was achieved at higher than typical CVD rates for epitaxy suggests that detrimental effects such as substrate evaporation or impurity deposition were overcome by the higher deposition rate.

SiC has been deposited on a variety of substrates for electronic and protective coating uses. For the latter application, attempts are made to achieve high density, small grained polycrystalline deposits (1). On the other hand, noninsulating electronic applications usually require single crystalline epitaxial layers. Device quality α-SiC layers deposited on α-SiC substrates have been achieved (2, 3) and various techniques for SiC deposition on substrates other than SiC have met with some success although not enough to warrant large scale device production (4).

Approaches to the formation of β-SiC films on silicon have included vapor deposition from organosilanes or separate silicon and carbon containing compounds (5, 6), the reaction of carbon or hydrocarbons with hot silicon (6-9), and the immersion of very hot silicon into organosilane liquids (10). The failure to achieve high quality β-SiC layers on silicon substrates using chemical vapor deposition has never been formally explained. It may involve the high thermal etch rate of the silicon substrates at growth temperatures which allow enough surface diffusion for epitaxy to occur (11). Even at the growth temperature limit, the surface mobility of deposited SiC may still be too low. In addition, the role of impurities in the reactants has not been assessed for this system.

In the course of investigating SiC deposition on silicon by the reduction of $(CH_3)_2SiCl_2$, we found that at normal epitaxial growth rates (0.05 to 1.0 μ/min), some preferred orientation was achieved in the SiC film, but increasing the growth rate by a factor of 5 to 100 increased the orientation at greater thicknesses. Consequently, the growth and structure of these thicker layers was studied. Bean and Gleim (12) also studied SiC growth on silicon at higher growth rates and observed some epitaxial material; however, their interest was in polycrystalline films which were hard, chemically stable, and of high resistivity.

Growth

Deposition system and process definition.—Layer growth was done in a horizontal quartz tube epitaxial reactor. The silicon substrates were heated on a SiC coated graphite susceptor coupled to an external rf coil. The liquid feed materials, $SiCl_4$ for silicon deposition and $(CH_3)_2SiCl_2$ for SiC deposition, were va-

[1] Present address: Department of Biophysical Sciences, State University of New York at Buffalo, Amherst, New York 14226.

Key words: semiconductors, ceramics, structural analysis, chemical vapor deposition, thin films.

porized and carried through the reactor by hydrogen. Depositions were done at a total pressure of 1 atm.

The substrates ranged in surface finish from as-cut to chemically polished (15:5:2, HNO_3:HF:HAc). In the reactor, the substrate was etched first in hydrogen and then by HCl vapor, both at 1250°C. Then a 10μ thick silicon epitaxial layer was deposited via the thermal reduction of $SiCl_4$ with H_2 at 1250°C. Next, SiC was deposited by the vapor reaction of $(CH_3)_2SiCl_2$ and hydrogen. Typical SiC deposition conditions were: (*a*) mole ratio ($[CH_3]_2 SiCl_2/H_2$) = 5 x 10^{-3}, (*b*) total flow rate of 2.5 liters/min, (*c*) growth temperature of 1365°C, and (*d*) growth times of <1-40 min.

The SiC deposition was extremely sensitive to input reactant purity: oriented growth would occur only using an ultra-pure grade of hydrogen in conjunction with triply distilled $(CH_3)_2SiCl_2$. The $(CH_3)_2SiCl_2$ feed, when decomposed to yield a SiC coating on thin tungsten filaments, typically gave material with less than 2 ppma total impurities (exclusive of N_2, O_2, and Au) as measured by solid-state mass spectroscopy (13).

Oriented SiC growth was found to occur over relatively narrow deposition condition ranges:

1. Mole ratio ($[CH_3]_2SiCl_2/H_2$) : <5 x 10^{-3} to 2 x 10^{-2}
2. Total flow rate: 1 to 2.5 liters/min
3. Growth temperature: 1315° to 1400°C.

Note that substrate temperatures within 100°C of the silicon melting point were required. We found that oriented growth on the (100) as-cut silicon surface was much easier to achieve than on the (111) silicon surface; it appeared to be less sensitive to impurity concentrations in the $(CH_3)_2SiCl_2$ feed material. Rai Choudhury and Formigoni (6) have reported that in thinner SiC depositions from $(CH_3)_2SiCl_2$, growth on the (100) silicon substrates shows a single preferred orientation while growth on (111) and (110) substrates is multiple oriented. In growth from separate silicon and carbon containing compounds, Jackson (14) found that depositions on the (100) silicon substrates had far fewer inclusions of apparently polycrystalline material than those grown on (111) substrates.

To try to improve the texture of the SiC layers, a preliminary post-deposition annealing study was done. Layers having their silicon substrates removed by HF-HNO_3 etching were heat treated for 2-10 hr in argon at 2000°C. Unfortunately, an excessive coverage of large (50-100μ) crystallites grew and these had no preferred orientation.

Layer composition.—The SiC coated silicon substrate had a dark gray appearance. After the silicon substrate was removed in an HF-HNO_3 etch, the remaining SiC layer was golden yellow and translucent. The strong 795 cm^{-1} (12.6μ) infrared lattice band, characteristic of SiC (15), was observed in the infrared reflection and transmission spectra of these layers. Measurement of pinhole x-ray diffraction patterns of predominantly polycrystalline layers (Fig. 2c) identified the material as β-SiC. However, patterns obtained with the more sensitive Guinier focusing camera using monochromatic CuK_α radiation showed a few faint anomalous lines (16). These could be interpreted as trace amounts of one or several α-SiC polytypes; however, considering the nonequilibrium nature of the deposition they may derive from multiple twins and associated faults. To a spatial resolution of 10μ, electron beam microprobe analysis (17) of the top surface layers (to a depth of about 1μ) indicated the silicon content to be stoichiometric to within the detection limits of the probe [± ½ w/o (weight per cent) Si]. Using a finer electron beam diameter of 0.5μ or spatial resolution of 0.7μ, slight inhomogeneities are detected, with maximum silicon excesses or deficiencies ranging from 1.0-1.4 w/o.

Table I. Kinetic data for the SiC deposition on (001) silicon

A. Growth rate *vs.* mole ratio $\left(\frac{\text{moles } Me_2SiCl_2}{\text{moles } H_2}\right)^a$

Crystal No.	Mole ratio	Growth rate, μ/min	Layer structure
1	1 × 10^{-3}	0.4	Random polycrystalline
2	5 × 10^{-3}	4.3	Oriented
3	1 × 10^{-2}	6.8	Oriented

B. Growth rate *vs.* growth temperature[b]

Crystal No.	Growth temp, °C	Growth rate, μ/min	Layer structure
4	1250	3.0	Random polycrystalline
5	1300	3.4	Random polycrystalline
6	1315	4.4	Oriented
7	1365	4.3	Oriented

[a] For these experiments: growth temperature = 1365°C, total flow rate = 2.5 liters/min.
[b] For these experiments: mole ratio = 5 × 10^{-3}, total flow rate = 2.5 liters/min.

Deposition kinetics.—Infrared interference thickness measurements (18) of the layers as a function of growth time revealed a constant growth rate of 4.3 μ/min for the typical growth conditions defined above, using (001) silicon substrates.

Table I summarizes some kinetic data for SiC deposition on (001) silicon substrates. In the parameter range (growth temperature, reactant concentration, and total flow rate) where oriented growth occurred, the growth rate was strongly dependent on reactant concentration but insensitive to temperature. This suggests some form of mass transport or total reactant input limitation rather than a thermal activation limitation.

Texture, Surface Morphology, and Electrical Properties

Preferred orientation analysis.—Transmission electron diffraction through films grown to a thickness of about 1000Å on (001) silicon substrates yielded patterns such as shown in Fig. 1. This pattern shows strong (001) β-SiC orientation indicating that partial epitaxy [(001) β-SiC || (001)Si] is occurring. Some polycrystalline rings appear showing that nonepitaxial deposition is also occurring. This is substantiated by reflection electron diffraction patterns of initial growth

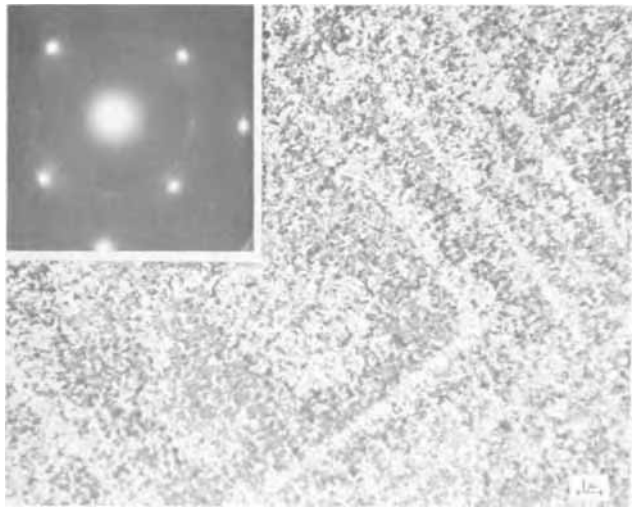

Fig. 1. Transmission electron micrograph (2950X) and corresponding transmission electron diffraction pattern (upper left) of initial SiC film (1000Å thick). The film was floated from the silicon substrate using an HF-HNO_3 etch.

which show polycrystalline β-SiC. Evidently, the early polycrystalline growth extends above the epitaxial growth and thus dominates the reflection electron diffraction pattern. The remainder of Fig. 1 is a transmission electron micrograph of the initial growth which yielded the diffraction pattern. It shows a grain structure which is considerably less than ½μ in the surface plane. Thus, a very fine grained mixture of random and epitaxial nucleation initiated the layer growth. At this thickness, these films have a greater degree of polycrystallinity than those grown from $SiCl_4$ and C_3H_8 by Jackson and Howard (5) as judged by transmission electron diffraction. Presumably, this is in part due to the 10-fold higher growth rate used in this study. However, the reactants used may also play a role as Rai-Choudhury and Formigoni (6) have noted that SiC films grown on silicon from a single organosilane, $(CH_3)_2SiCl_2$, grew faster but were less ordered than those grown from $SiCl_4$ and CH_4.

Information about the crystallography at greater layer thickness was obtained using the Laue transmission x-ray technique with molybdenum radiation and a flat plate camera. Before exposure, some of the silicon substrates were removed by $HF-HNO_3$ acid etching. Exposure times of 6 to 16 hr at tube voltages of 40 kV and currents of 18 mA were necessary to produce the patterns seen in Fig. 2. Figure 2 shows the Laue patterns from a series of films grown on (001) silicon substrates with the same mole ratio, total flow rate, and deposition temperature values but differing deposition times. Figure 2a is a pattern from a 13μ thick film (substrate removed), Fig. 2b from a 32μ thick films (substrate remaining), and Fig. 2c from an 86μ film (substrate removed). This series shows that through a thickness of 13μ, the layer is highly oriented giving rise to a Laue pattern; increasing the thickness results in more random polycrystalline β-SiC growth as evidenced by the filling in of the powder pattern rings at 32μ and the fading out of the Laue pattern. By 86μ, all the rings are nearly uniform indicating that random polycrystalline growth is the dominant contribution to the diffraction pattern.

Examination of the pattern in Fig. 2a shows that the Laue spots are elongated radially and many of the spots are close to arcs on the powder pattern rings. We think the spot enlargement is due to a small angular distribution of crystallite orientations about the preferred orientation. Some of the elongation and streaking may also be due to faults incorporated as the layer grows. These effects may be the result of the growth process itself or they may be caused by the differential thermal expansion stresses accompanying the cooling down of the layer and substrate.

To tentatively index the Laue pattern in Fig. 2a, we have made the following hypothesis: diffraction from the same set of crystallite planes generates both the enlarged Laue spots and powder pattern arcs adjacent to those spots because of an angular distribution of grain orientations about the preferred orientation. A given set of planes (hkl) within such an angular distribution of crystallites will diffract not one but a narrow spectrum of wavelengths from the continuous background resulting in a radially elongated Laue spot. When this spectrum includes the characteristic radiation, an arc will appear on an adjacent powder pattern ring (hkl) on the same radius as the spot.

We found that three orientations were required to index all the spot-arc pairs subject to the condition that the spot be formed by the same set of planes as the arc. The orientations were: (001) β-SiC || (001) Si and two (110) β-SiC || (001)Si orientations, one with [001] β-SiC || [$\bar{1}$10]Si, the other with [1$\bar{1}$0] β-SiC || [$\bar{1}$10]Si. The maximum angular range of grain orientations about the preferred orientation was found to be ±2.5°. Gnomonic projections on planes perpendicular to the [001] and [110] growth directions in the layer verified the tentative indexes given above and provided indexes for the spots not close to powder pattern rings. Figures 3a, 3b, and 3c show the identification of the Laue spots and their corresponding orientation. (For clarity, indexes of some of the weaker spots have been omitted.) Comparison of the (001) β-SiC pattern in Fig. 3a to the (001) silicon pattern underlaying Fig. 2b shows that the [100] β-SiC || [100] Si.

In summary, we conclude that the layer growth through about 50μ consists of sets of β-SiC grains having at least three orientations with the (001) orientation being epitaxially related to the (001) silicon substrate. Interspersed among the oriented grains is random polycrystalline material whose proportion increases with increasing thickness from about 12μ.

Laue patterns from SiC depositions on the (111) silicon substrates showed a similar course of growth: initial growth leading to a maximum in orientation and then a progressive decline in the amount of oriented *vs.* random growth. However, in spite of nearly equal growth rates under identical growth conditions, the strongest orientations appeared from 70 to 75μ from the substrate surface and was not as pronounced as that seen with the (001) substrates.

Surface morphology.—Information on the surface morphology was obtained using a Cambridge Stereoscan scanning electron microscope (SEM). The irreg-

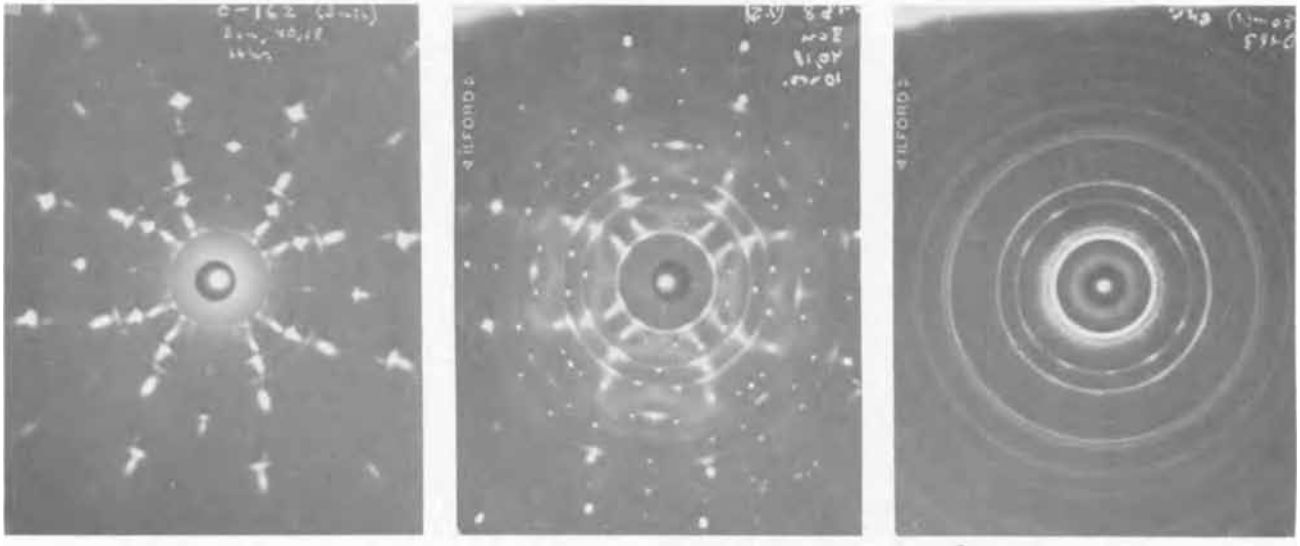

Fig. 2. Laue transmission x-ray diffraction patterns at different SiC thicknesses. a (left) 13μ thick; b (center) 32μ thick; c (right) 86μ thick.

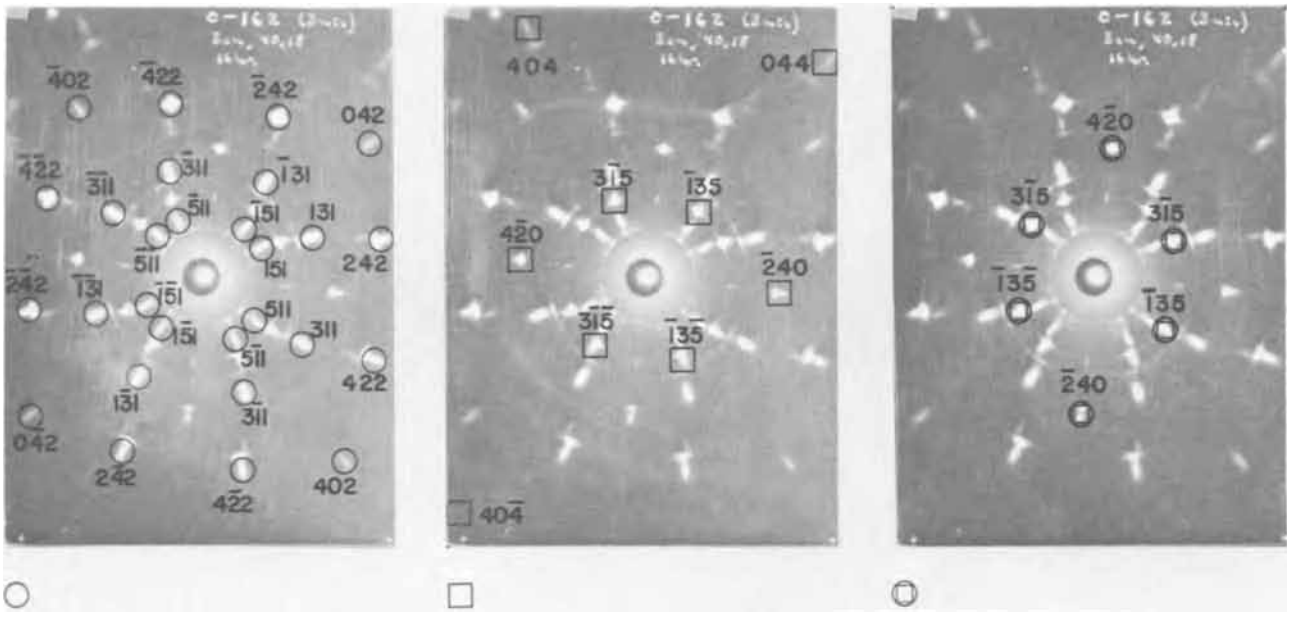

Fig. 3. Indexed components of Laue pattern in Fig. 2a. a (left): Spots, outlined by ○, arising from (001) β-SiC orientation. (001) β-SiC || (001)Si. b (center): Spots, outlined by □, arising from one (110) β-SiC orientation. (110) β-SiC || (001) Si with [001] β-SiC || [$\bar{1}$10] Si. c (right): Spots outlined by ◎, arising from second (110) orientation. (110) β-SiC || (001)Si with [1$\bar{1}$0]β-SiC || [$\bar{1}$10]Si.

ular topography and fine surface structure could be clearly observed using the SEM. Samples were conductive enough so that no metallic overcoating was required.

Figure 4 shows a series of scanning electron micrographs giving surface morphology as a function of layer thickness (growth time) for growth on (001) silicon substrates. Figure 4a (3395X) shows the surface of the 13μ thick film whose x-ray diffraction pattern is shown in Fig. 2a. Note the irregularly faceted surface and the absence of pronounced grain boundaries. In Fig. 4b, a micrograph of a 43μ thick layer at 715X, the rougher, more grainy surface that develops at larger thicknesses is shown. The grain size in the surface dimension is on the order of 5μ. Note the appearance of a few sharply faceted grains. Figure 4c is a micrograph at 720X of a layer 86μ thick whose x-ray diffraction pattern is given in Fig. 2c. By the time this layer has grown to the thickness where random, fine-grained growth strongly predominates, the deposited material has grown into larger morphological units on the order of 40μ in diameter (in the surface plane). This surface structure resembles the "growth cone" morphology seen in many polycrystalline chemical vapor depositions.

The occurrence of pips on the surfaces in Fig. 4 is of interest. These appeared in constant surface density on every grown surface examined except where strongly faceted growth had occurred. They did not appear on the fracture surfaces we examined. Thus, we do not think they are an artifact of the microscope technique. Rather, the pips represent either nucleation and early growth of additional material or are associated with the termination of the deposition.

If the growth was stopped at certain thicknesses, some of the deposited material displayed a precisely faceted grain structure. A dramatic example of this is seen in Fig. 5a which shows faceted growth of SiC polytype on (111) silicon substrates at 6080X; grain size in the surface dimension is about 1-2μ. This SiC layer is about 80μ thick. A top view at lower magnification (1200X) is shown in Fig. 5b. The surface morphology indicates that most of the polytype grains are in nearly the same orientation. The rough material

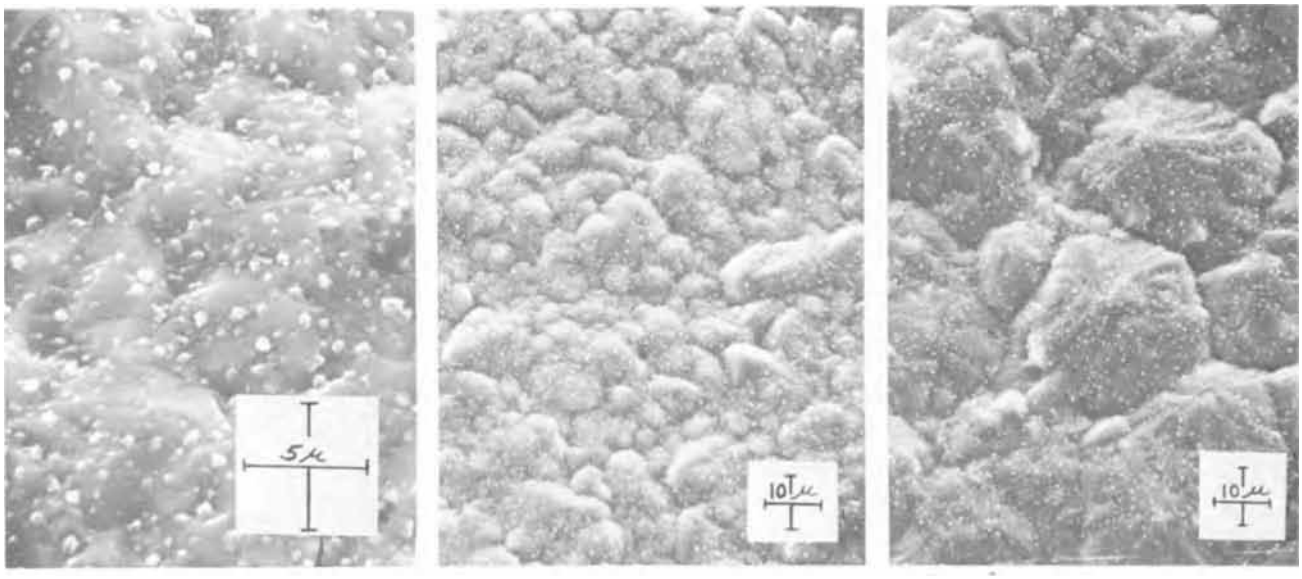

Fig. 4. Scanning electron micrographs of SiC layer surfaces at different thicknesses. a (left), 13μ thick, 3395X; b (center), 43μ thick, 715X; c (right), 86μ thick, 720X.

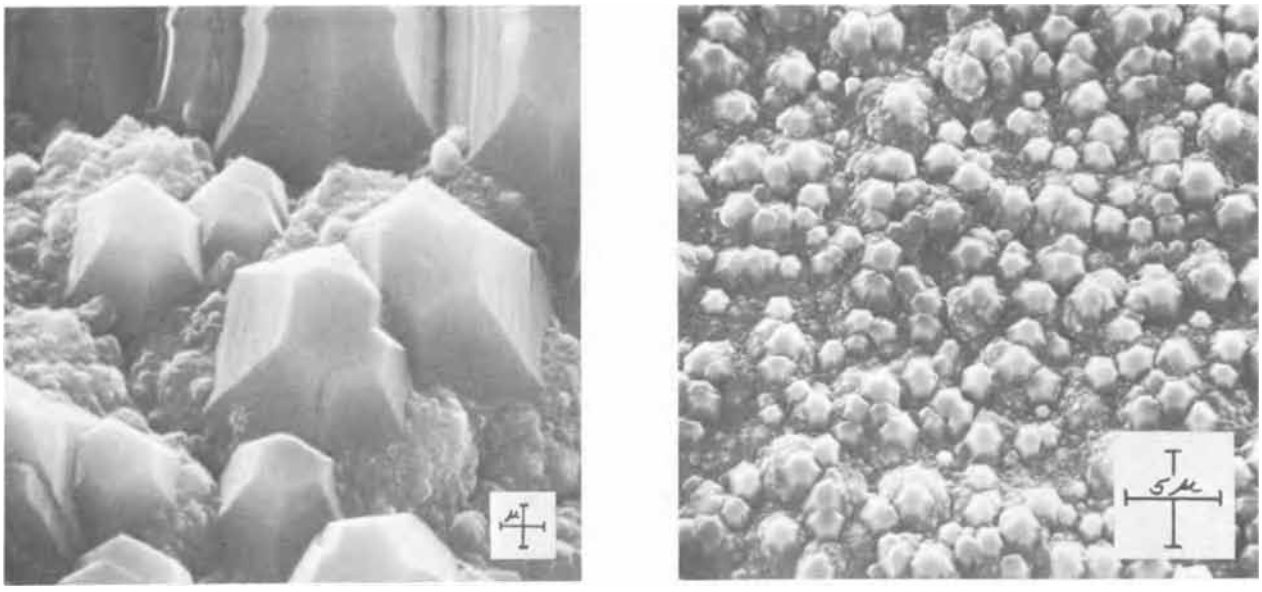

Fig. 5. Scanning electron micrographs of faceted grain structure appearing at the layer surface. a (left), 6080X; b (right), 1200X

between the faceted grains is probably much finer grained polycrystalline material.

Examination of the side facets of less perfect grains showed that they are not smooth planes but rather are composed of a series of steps; this is suggested by the striations in the side facets of the grains shown. The steps which exist are probably twin and/or polytype boundaries (lamellae). Isolated hexagonally faceted grains were also observed in growths on the (001) silicon substrates but never in such copious amounts as seen in Fig. 5.

We cannot be certain whether the hexagonal morphology indicates the presence of hexagonal or rhombohedral SiC polytypes or a multiple (111)-twinned β-SiC deposit.

Relation of layer perfection to processes occurring in growth.—The analysis of this material makes possible some speculation on the nature of SiC growth on silicon using CVD at atmospheric pressure. The faceted grain growth described above indicates that SiC single crystalline-like growth can proceed in a limited region of space and time between 1300° and 1400°C. The fact that orientation occurs at growth rates of 4 μ/min but not in the usual CVD range of 0.1-1 μ/min for epitaxy suggests that effects destroying orientation at lower growth rates are overcome at higher growth rates. These effects may include the evaporation of silicon from the substrate surface (thermal etch) or the codeposition of some impurity such as SiO_2 or carbon. At higher growth rates, partial epitaxial growth does occur and the rapidly growing epitaxial grains apparently predominate to give maximal coverage of oriented SiC at a certain thickness. However, disorienting effects such as lattice mismatch and thermal expansion and tensile strength differences (4) between substrate and film become more pronounced at greater film thicknesses perhaps accounting for the observed optimum in orientation as a function of thickness.

Preliminary electrical evaluation.—To evaluate this material electrically, the silicon substrates were removed from the SiC layers by etching in $HF-HNO_3$ mixture. Contacts were made by fusing a gold-tantalum alloy (19) into the material at 1200°-1300°C in a hydrogen ambient. All layers tested were n-type as measured by the hot probe technique. Resistivities, as measured by the van der Pauw method (20), ranged from 0.5 to 35.5 ohm-cm on layers about 25μ thick. Effective Hall mobilities for these layers fell in the range of 4-7 cm^2/V-sec. These numbers give information about the electron transport properties parallel to the layer surface. The low value of mobility probably indicates extensive grain boundary scattering due to interspersed random polycrystalline material and multiple grain orientations.

Summary

1. By increasing the CVD growth rate to 4.3 μ/min at temperatures close to the melting point of silicon (~1365°C) and by using the highest purity reagents available, SiC layers were deposited on (001) silicon which, at 12μ thick, had crystallites which were sufficiently oriented to produce a Laue x-ray pattern.

2. Such layers had both multiple orientations and inclusions of sharply faceted grains. The inclusions appeared to be more prevalent in growth on the (111) than on (001) silicon substrates.

3. The epitaxial texture changed with thickness. A mixture of random and epitaxial nucleation initiated the growth. After this, the balance between random and oriented growth varied such that the proportion of oriented growth reached a maximum and then degenerated to completely polycrystalline growth at large thicknesses (~100μ). Maximum orientation was more pronounced, reproducible, and more quickly reached in growth on the (001) silicon substrates as compared to the (111) silicon substrates.

Acknowledgments

The author thanks the late Uldis Plics of Dow Corning Corporation for the electron microscopy and diffraction analysis and Harry Baker of Dow Chemical Company for the scanning electron microscopy work. I also thank Lorenzo Sturkey of Dow and David Harker of the Center for Crystallographic Research, Buffalo, New York, for advice in interpreting the x-ray diffraction patterns. Finally, I thank Erhard Sirtl of Dow Corning and John Blocher of the Battelle Memorial Institute for their helpful comments.

Manuscript submitted March 1, 1970; revised manuscript received Dec. 18, 1970.

Any discussion of this paper will appear in a Discussion Section to be published in the December 1971 JOURNAL.

REFERENCES

1. T. D. Gulden, *J. Am. Ceram. Soc.*, **51**, 424 (1968).
2. R. B. Campbell and T. L. Chu, *This Journal*, **113**, 825 (1966).
3. J. M. Blank, *Mater. Res. Bull.*, **4S** (1969) (Proc. International SiC Conf., State College, Pa., October 1968).
4. J. J. Rohan and J. L. Sampson, *J. Phys. Chem. Solids*, Supplement No. 1, 523 (1967).

5. D. M. Jackson, Jr. and R. W. Howard, *Trans. AIME*, **233**, 468 (1965).
6. P. Rai Choudhury and N. P. Formigoni, *This Journal*, **116**, 1441 (1969).
7. N. C. Tombs, J. J. Comer, and J. F. Fitzgerald, *Solid State Electron*, **8**, 839 (1965).
8. H. Nakashima, T. Sugano, and H. Yanai, *Jap. J. Appl. Phys.*, **5**, 874 (1966).
9. I. H. Khan and R. N. Summergrad, *Appl. Phys. Letters*, **11**, 12 (1967).
10. R. Conrad, *This Journal*, **117**, 1315 (1970).
11. B. A. Joyce, Private communication, Sept. 21, 1967.
12. K. E. Bean and P. S. Gleim, *This Journal*, **114**, 1158 (1967).
13. J. A. Baker, "Mass Spectrometric Analysis of SiC" SAMPE, Advanced Techniques for Material Investigation and Fabrication, Proc. 14th Nat. Symposium and Exhibit, Cocoa Beach, Fla., November 1968, Florida Press, Orlando, Fla.
14. D. Jackson, "Research for Development of Epitaxial Techniques for Use in Fabrication of SiC Devices," AD 635 136, May 13, 1966.
15. W. G. Spitzer *et al.*, *Phys. Rev.*, **113**, 133 (1959).
16. D. Peterson and V. Ruhberg, Private communication, Dec. 1, 1968.
17. D. R. Beaman, Private communication, Nov. 18, 1968.
18. W. G. Spitzer and M. Tannenbaum, *J. Appl. Phys.*, **32**, 744 (1961).
19. H. J. van Daal *et al.*, Silicon Carbide Semiconductor Device, U.S. Pat. 3,047,439 (July 1962).
20. L. J. van der Pauw, *Philips Res. Rept.*, **13**, 1 (1958).

Technical Notes

Effect of Nitrogen on the Linear Oxidation of Niobium

C. Catella and R. Streiff*,[1]

Laboratoire de Métallurgie et Chimie du Solide associé au C.N.R.S., Faculté des Sciences, Nancy, France

Above 400°C, the oxidation of niobium exhibits typical paralinear kinetics (1, 2). The linear oxidation rate has been found to be strongly dependent on oxygen pressure, the rate decreasing with decreasing pressure (1-3). The oxidation of niobium in air should therefore be slower than in pure oxygen. This behavior has been noted in some previous investigations (5, 6) and could be purely a result of the reduction in partial pressure. Now, it has been recently shown that one cannot always assume nitrogen to be inert, especially in the oxidation of reactive metals by air (7) or at high temperature in which cases formation of oxynitrides has been observed involving changes in kinetic laws and rate values. This reaction could be possible with niobium.

Consequently, in order to determine whether or not nitrogen affects the oxidation rate, the partial pressure of oxygen has to be kept constant, in experiments both with or without nitrogen. Similar investigations, limited to the effect of small percentages of nitrogen from 1 to 10%, have already been carried out by McLintock and Stringer (4). In the present study, the effect of high percentages of nitrogen (from 10 to 90%) has been investigated.

The reaction was followed by weight gain in a microbalance. The apparatus had a large volume and the change in gas pressure was negligible. Thus, the total pressure could be assumed to be constant. The linear rate constants were determined with several experiments at each temperature in order to reduce the uncertainty of each value. The present results are shown in the form of variations of the linear constants (in micrograms per square centimeter per minute) *vs.* the reciprocal absolute temperatures. For each partial pressure of oxygen, two sets of experiments were carried out, one with pure oxygen, the other in an oxygen-nitrogen mixture with equivalent oxygen partial pressure and total pressure equal to atmospheric.

The effect of oxygen on the linear rate over the range 0.1-1 atm and at temperatures in the range 450°-1000°C is shown in Fig. 1. We observed some well-known features of the niobium oxidation behavior. The two reversals in the temperature dependence (1-2) of the oxidation rate are perceptible around 600°C and between 800° and 900°C.

The effect of nitrogen on the linear oxidation of niobium at several oxygen partial pressures is shown in Fig. 2, 3, and 4. At all temperatures, a reduction in the reaction rate in the presence of nitrogen is observed. The retardation seems not to be strongly influenced by the percentage of nitrogen. Likewise, the reduction in the rate seems not dependent on temperature ranges on both sides of the minimum rate where a stronger effect is observed. These observations are in agreement with those of Stringer (4) who noted only a very small effect of nitrogen content or variations from 1 to 10%. The present study confirms these observations over a large range of temperature and nitrogen pressure.

Besides, the presence of nitrogen does not affect the morphology of the oxide scales formed during the oxidation. The only phases observed are Nb_2O_5 with various crystal structures depending on the oxidation temperature, and the suboxides NbO_2 and NbO. Neither Kjëldhal chemical analysis nor x-ray analysis revealed the formation of nitride or oxynitride.

Microanalysis of the amount of nitrogen in the formed oxide scales by use of nuclear reaction[2] led to the same conclusions. The ratio of nitrogen is always lower than 10^{-2} $\mu g/cm^2$. Analysis of the compact scale-porous scale interface revealed a higher content of nitrogen in the porous scale than in the compact scale. This could be due to adsorption of nitrogen in

* Electrochemical Society Active Member.
[1] Present address: Laboratoire de Chimie des Matériaux, U.E.R. de Chimie—Université de Provence, Place Victor Hugo, 13 Marseille (3e), France.
Key words: niobium; oxidation; rate constant; kinetics; nitrogen, effect of.

[2] The authors are especially indebted to Dr. Beranger (Ecole des Mines—Université de Paris) for performing the nitrogen analysis by nuclear reaction, and wish to acknowledge this assistance.

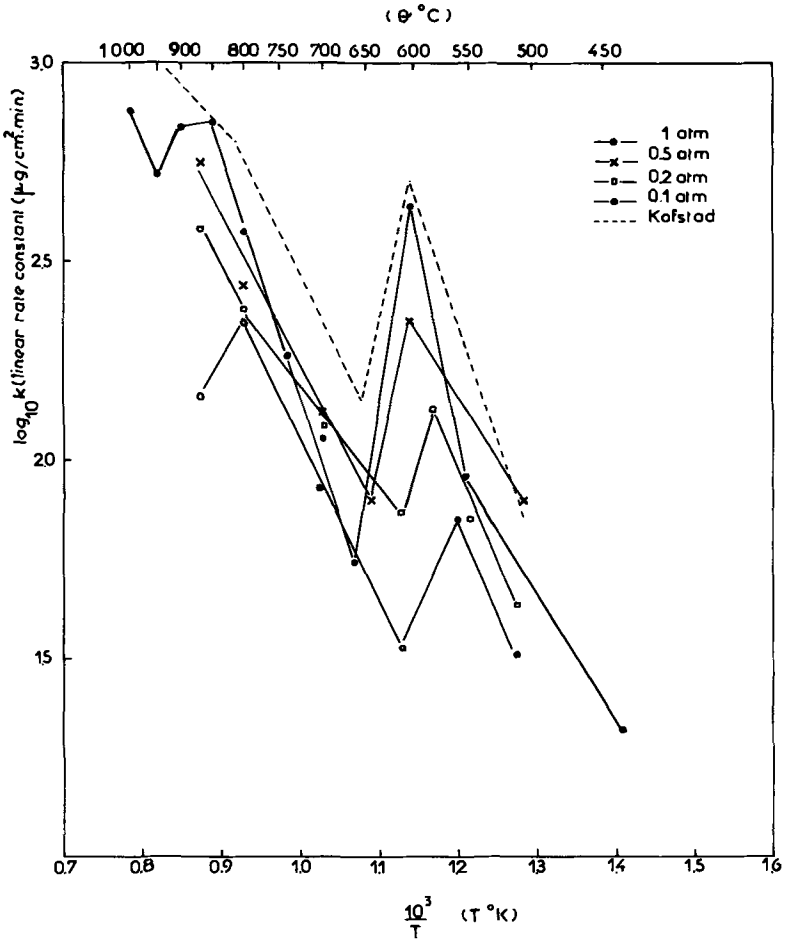

Fig. 1. Oxidation by pure oxygen at various partial pressures.

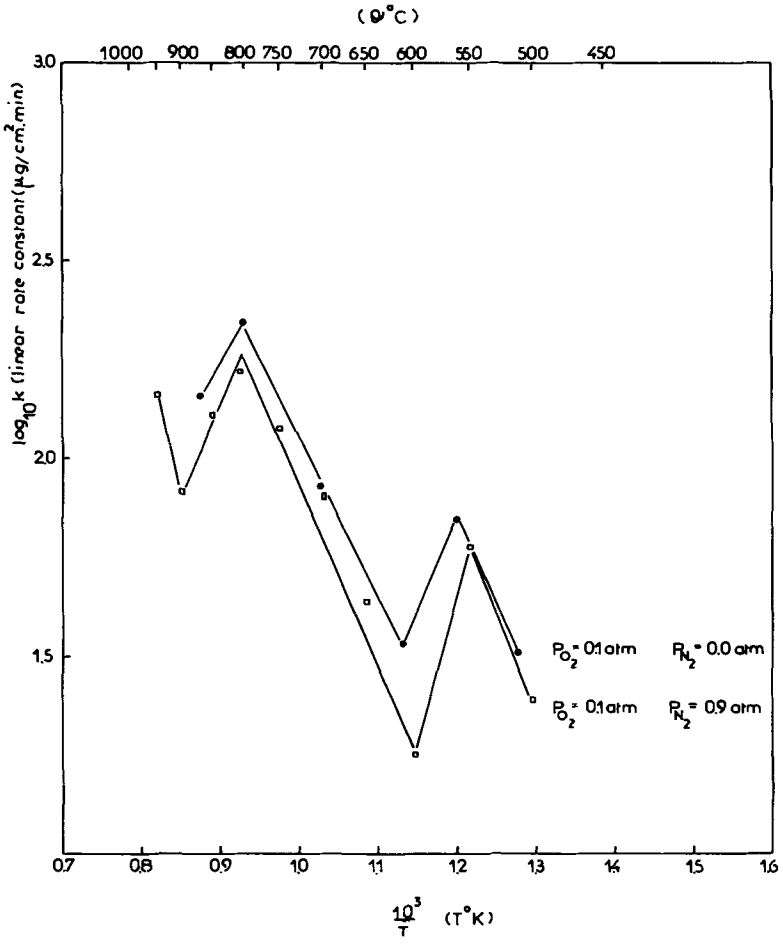

Fig. 2. Oxidation by pure oxygen at 0.1 atm pressure and by a mixture of 0.1 O_2 and 0.9 N_2.

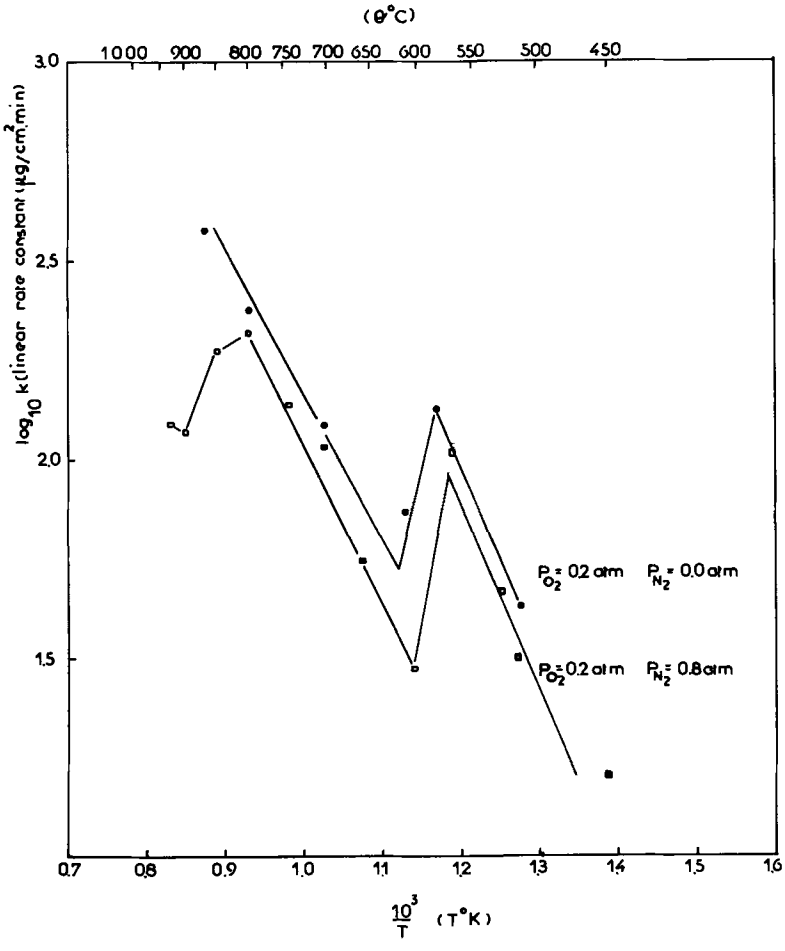

Fig. 3. Oxidation by pure oxygen at 0.2 atm pressure and by a mixture of 0.2 O_2 and 0.8 N_2.

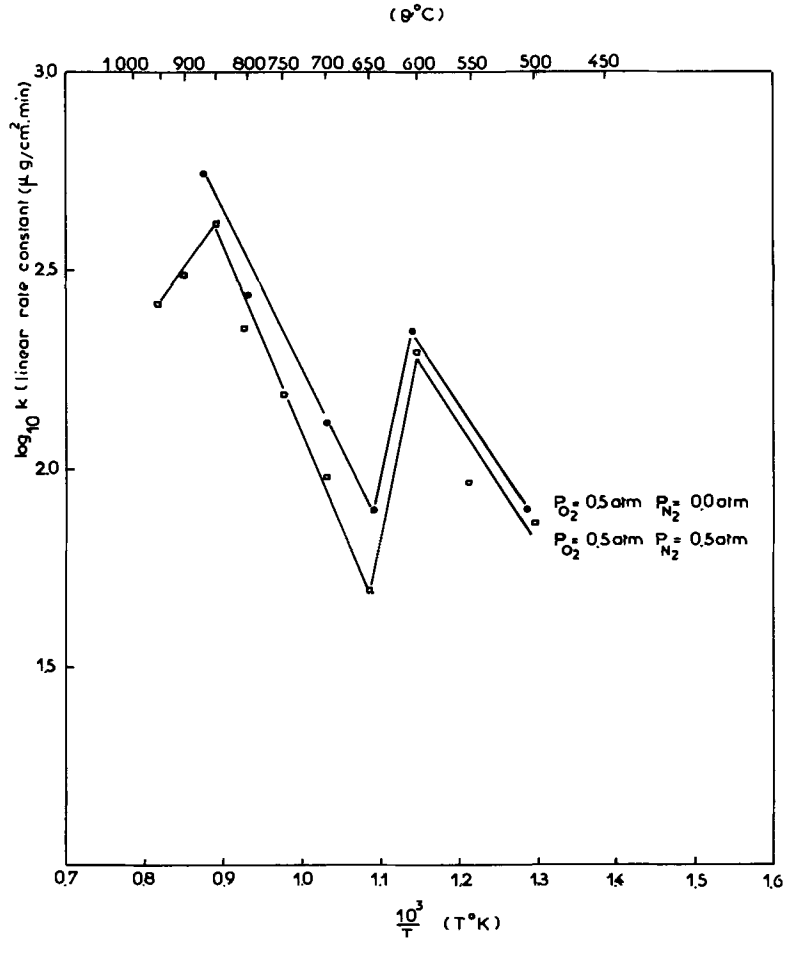

Fig. 4. Oxidation by pure oxygen at 0.5 atm pressure and by a mixture of 0.5 O_2 and 0.5 N_2.

the pores of the outer scale or at the compact scale-porous scale interface.

The decrease in the oxidation rate can therefore not be ascribed to the formation of a layer of nitride or oxynitride as formerly observed in the oxidation of calcium by air (7). It also cannot be due to the effect of a very small dissolution of nitrogen in the niobium oxide. Such a nitrogen solution in oxygen-deficient Nb_2O_5 should increase the concentration of vacancies and hence the diffusion rate in the inner compact scale, as it can be expressed in terms of the Wagner-Hauffe model, thereby increasing the over-all linear rate. That is in contradiction with Stringer's and our own observations. The nitrogen effect has to be examined with regard to an interface rate-controlled process (8). The rate of oxidation then is dependent on the oxygen concentration at some interface, this concentration being determined by an equilibrium adsorption process. The effect of nitrogen may be due to competition with oxygen on the adsorption sites at the interface compact-porous scale. The presence of nitrogen lowers the number of available adsorption sites and therefore decreases the linear oxidation rate.

Manuscript received Dec. 21, 1970.

Any discussion of this paper will appear in a Discussion Section to be published in the December 1971 JOURNAL.

REFERENCES

1. P. Kofstad and H. Kjöllesdal, *Trans. AIME*, **221**, 285 (1961).
2. F. Bollenrath and P. Poddey, *Metall*, **22**, 702 (1968).
3. C. H. McLintock and J. Stringer, *J. Less-Common Metals*, **5**, 278 (1963).
4. C. H. McLintock and J. Stringer, *J. Inst. Metals*, **90**, 190 (1962).
5. B. B. Argent and B. Phelps, *ibid.*, **88**, 301 (1959).
6. T. L. Kolski, *Trans. A.S.M.*, **55**, 1020 (1963).
7. R. Streiff, *C. R. Acad. Sci.*, **265C** 587 (1967).
8. J. Stringer, *This Journal*, **112**, 1084 (1965).
9. D. David and G. Amsel, *Rev. Phys. Appl.*, **4**, 383 (1969).

Fluorescence of Alkaline-Earth Silicates Activated with Divalent Europium

T. J. Isaacs

Westinghouse Research Laboratories, Pittsburgh, Pennsylvania 15235

The fluorescence of a number of silicates activated by divalent europium has been reported on by various authors (1-5). In this paper, a new family of silicate phosphors having the general composition $M^{2+}Al_2Si_2O_8:Eu^{2+}$, where M^{2+} can be Ca, Sr, Ba, is discussed. This family is the feldspars which are alumino-silicate framework structures with the divalent cations occupying hexagonal interstitial positions.

Experimental Procedures

Spectrographic grade starting materials from Johnson-Matthey of 5 nine's purity ($CaCO_3$, $BaCO_3$, $SrCO_3$, α-Al_2O_3, SiO_2, Eu_2O_3) were weighed in appropriate proportions, mixed in a SPEX mixer mill with approximately 10% by weight of an NH_4Cl flux for 15 min, and then fired in capped fused quartz capsules at a temperature range of 1150°-1410°C under an atmosphere of approximately 95% N_2, 5% H_2 for 2 hr. The product was ground and refired under the same conditions for the same duration of time. The run was brought rapidly to room temperature in this atmosphere. It was found that the addition of a small amount (approximately 1-2 g-atom %) of sodium (in the form of sodium carbonate) in place of strontium or calcium often brought about narrower emission peaks with greater luminous intensity. One of the three polymorphs made in this work of $BaAl_2Si_2O_8$ (celsian) was synthesized using the hydrothermal method. In this run $EuCO_3$ was used as the source of europium, and no flux was employed. The run was made at a temperature of 700°C under a pressure of approximately two kilobars; the duration was a week.

X-ray powder diffraction patterns using the Debye-Scherrer method were taken of all the compounds made to identify the materials and ascertain that they were of one phase. The exposure times varied from 8-10 hr. The x-ray diffraction pattern of the two "hexagonal" barium feldspars were very similar, and the patterns reported in the literature (6-10) were not definitive. We found that the emission spectrum gave a better indication of the number of phases present than did the diffraction patterns.

Key words: barium feldspar, strontium feldspar, calcium feldspar, emission and excitation spectra, x-ray diffraction patterns.

Emission and excitation spectra were determined at room temperature on a double-beam monochromator system designed and built by Riedel (11).

Measurements of phosphor performance of some of the materials were made at selected temperatures in the interval from room temperature to 500°C. The apparatus used was also designed and built by Riedel. An Osram HBO-100 w/2 short-arc high-pressure mercury-vapor lamp is the exciting source. The excitation wavelength is selected by using one of three interference filters with peak transmissions at 254, 313, and 365 nm respectively, and a passband of about 2 nm. The intensity of the excitation radiation, and the amount of radiation reflected from the sample are monitored by two separate photomultipliers equipped with identical interference filters. A third photomultiplier monitors the luminescence emission. A filter is used to select the desired wavelength region. The samples are kept in a stagnant nitrogen atmosphere during the runs.

Results and Discussion

The $CaAl_2Si_2O_8$ which we made corresponds to the mineral anorthite. Three polymorphs of $BaAl_2Si_2O_8$ were made, one corresponding to the mineral celsian, and the other two being similar to the so-called hexagonal celsians reported by numerous authors (6-10, 12-14). While there is some general agreement between the x-ray diffraction patterns given in the literature, and with our patterns, there are significant differences and only two of them [ref. (6, 9)] could be indexed according to hexagonal symmetry by our least squares refinement technique. One of the authors (9) reported an orthorhombic polymorph with a similar x-ray pattern to the "hexagonal" form, but using this data we were not able to index this pattern according to orthorhombic symmetry. The x-ray diffraction patterns reported in the literature and our two patterns are given in Table I for comparison purposes. The pattern given by Ito (7) has been omitted as it

Table I. *d*-Spacings and relative intensities of α-$BaAl_2Si_2O_8$

Barrer (6)		Barrer (6) ignited		Sorrell (8)		Takéuchi (9) (hexagonal)		Takéuchi (9) (orthorhombic)		Ivukina (10)		This paper (high-temp)		This paper (low temp)	
d	I/I_o	*d*	I/I_o	*d*	I/I_o	*d*	I/I_o	*d*	I/I_o	*d*	I/I_o	*d*	I/I_o	*d*	I/I_o
7.74	m	7.77	m	7.83	29	7.79	112	7.79	100	7.561	30	7.56	28	7.55	m
				4.59	7										
3.96	s	3.95	vs	3.97	97	3.963	47	3.949	43	3.968	83				
						3.901	20	3.899	18			3.902	100	3.905	s
														3.341	w
2.97	s	2.96	s	2.98	100	2.977	59	2.968	49	2.974	100	2.939	80	2.939	s
2.67	ms	2.65	ms	2.65	49	2.659	15	2.647	13	2.649	33	2.628	44	2.639	ms
						2.602	22	2.597	20			2.583	3		
				2.51	9							2.491	4		
2.31	mw	2.29	w			2.300	5	2.292	4	2.295	47	2.272	9	2.282	w
2.250	m	2.254	m	2.26	36	2.266	15	2.259	18	2.276	43	2.241	17	2.240	mw
2.215	m	2.196	ms	2.20	29	2.206	11	2.195	11			2.184	28	2.190	m
														2.070	w
1.982	vw	1.971	vw	1.95	24	1.951	60	1.947	65	1.946	43	1.965	6	1.964	mw
1.933	w	1.942	w									1.936	11	1.931	mw
1.854	m	1.850	m	1.86	31	1.860	6	1.853	7	1.846	41	1.844	17	1.845	m
				1.79	11					1.788	16	1.783	1		
1.702	m	1.690	m							1.687	18	1.687	16	1.689	m
1.592	m	1.582	m	1.58	24					1.578	31	1.578	17	1.579	m
1.561	mw	1.565	mw									1.561	10	1.563	m
1.540	w	1.526	w	1.53	9					1.530	23	1.524	9	1.530	mw
										1.472	53	1.479	1		
1.464	w	1.469	w									1.468	2	1.469	w
1.445	vw	1.440	vw							1.444	22	1.437	7	1.438	w
1.331	w	1.322	w							1.335	20	1.322	5	1.325	mw
1.319	vw											1.315	4	1.316	vw
1.282	w	1.288	mw							1.287	27	1.284	3	1.285	w
1.262	vw	1.253	vw							1.250	16	1.253	3	1.255	w
												1.247	1		
										1.204	23	1.207	6	1.209	mw
												1.200	2	1.200	w
												1.178	3	1.179	vw
										1.160	17	1.155	3	1.155	w
												1.140	<1		
												1.132	<1		
												1.128	<1		
												1.097	<1	1.096	w
												1.093	1		
										1.047	17	1.041	<1	1.043	vw
										1.024	30	1.024	<1	1.024	vw
												1.015	1		
												0.9997	1	1.003	vw
										0.9849	17	0.9839	1	0.9874	vw
										0.9590	20				
												0.9327	1	0.9342	w
												0.9254	<1	0.9246	vw
												0.9111	<1		
										0.9001	17	0.8987	1		
												0.8897	2	0.8916	vw
												0.8817	<1		
												0.8713	1	0.8716	vw
										0.8504	20				
												0.8464	2	0.8472	vw
												0.8355	<1	0.8374	vw
												0.8193	<1		
										0.8104	15	0.8086	<1	0.8073	vw
												0.8059	<1		
												0.7906	<1		

completely disagrees with all the others. The product which one obtains seems to be in good part dependent on starting materials and method of synthesis as well as temperature and duration of the run. For the sake of simplicity, we shall refer to our barium alumino silicates as celsian, and low- and high-temperature α-$BaAl_2Si_2O_8$. $SrAl_2Si_2O_8$ is reported to have both a low- and a high-temperature form (8), the former of which is hexagonal (and supposedly metastable) and the latter triclinic. We were not able to synthesize the hexagonal form as a single-phase compound but always had some of the triclinic form present.

These materials show fluorescence from the near ultraviolet to blue under 254 nm excitation. The spectra were broad with peaks at approximately 423 nm for $CaAl_2Si_2O_8:Eu^{2+}$, 427 nm for celsian, 413 nm for low-temperature α-$BaAl_2Si_2O_8$, 371 nm for high-temperature α-$BaAl_2Si_2O_8:Eu^{2+}$, 407 nm for the high-temperature $SrAl_2Si_2O_8:Eu^{2+}$, and 411-414 nm for the mixed phases $SrAl_2Si_2O_8:Eu^{2+}$. The emission spectra are shown in Fig. 1. The intensities of the curves are not drawn relative to each other as the differences in intensity are too great.

Excitation spectra of these materials show a broad band extending from approximately 213 to 390 nm for $CaAl_2Si_2O_8:Eu^{2+}$, two broad bands, one peaking at 257 nm, the other at 310 nm for celsian, a broad band with a peak at 273 nm for low-temperature α-$BaAl_2Si_2O_8:Eu^{2+}$, three bands with peaks at 202, 232, and 300 nm for high-temperature α-$BaAl_2Si_2O_8:Eu^{2+}$, and two broad bands with peaks at 260 and 330 nm for the high-temperature form of $SrAl_2Si_2O_8:Eu^{2+}$. The spectra are shown in Fig. 2. The arbitrary units are individual for each curve.

Quantum efficiency for a sample of high-temperature $SrAl_2Si_2O_8:Eu^{2+}$ containing 1 m/o (mole per cent) Eu^{2+} was determined to be 85 ± 7% at 254 nm when compared with NBS Standard $MgWO_4$ No. 1027. The other materials were not measured as this was the most intense of the compounds made.

Studies of the effects of elevated temperatures on the intensity of emission were conducted on some of

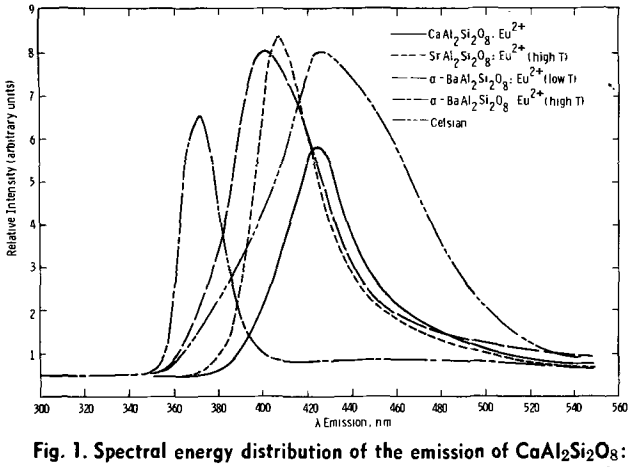

Fig. 1. Spectral energy distribution of the emission of $CaAl_2Si_2O_8$: Eu, $SrAl_2Si_2O_8$:Eu, and $BaAl_2Si_2O_8$:Eu at 254 nm excitation. The Eu^{2+} concentration is at 1%.

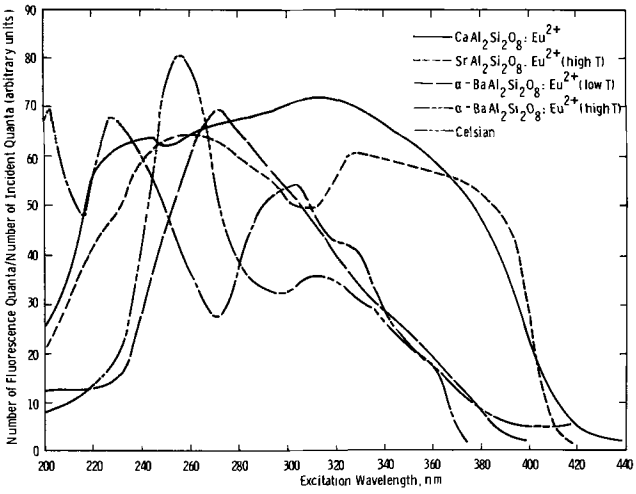

Fig. 2. Excitation spectra of Eu^{2+} fluorescence of the phosphors $CaAl_2Si_2O_8$:Eu, $SrAl_2Si_2O_8$:Eu, and $BaAl_2Si_2O_8$. The Eu^{2+} concentration is at 1%. The fluorescence wavelength was monitored at the peaks shown in Fig. 1.

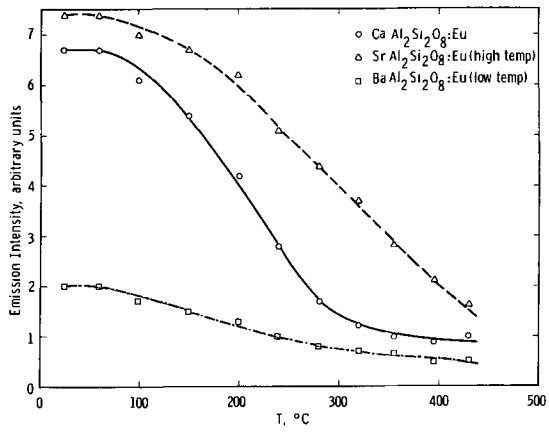

Fig. 3. Emission intensity as a function of temperature. λ_{exc} = 254 nm.

these materials, and the results are shown in Fig. 3. A Corning 3-75 filler was placed in front of the S-20 photomultiplier used to detect the fluorescence. Quenching temperatures (those temperatures at which emission intensity falls to 50% of room temperature) were approximately 225°C for $CaAl_2Si_2O_8:Eu^{2+}$, 240°C for the low-temperature α-$BaAl_2Si_2O_8:Eu^{2+}$, and 310°C for the high-temperature form of $SrAl_2Si_2O_8:Eu^{2+}$

The feldspars are complex materials and extensive work has been done on the more common members. There is confusion about the barium alumino silicates and certainly it would be desirable for us to know exactly the material we have been studying for fluorescence. Such a study would necessarily be quite extensive and therefore beyond the scope of this work.

Acknowledgments

The author wishes to thank Andrea Price for help in the preparation of the phosphors and Roy Williams for measuring the spectra and the temperature dependence. The computer program used for indexing the x-ray powder patterns was obtained from the U. S. Geological Survey.

Manuscript submitted Aug. 10, 1970; revised manuscript received Dec. 21, 1970.

Any discussion of this paper will appear in a Discussion Section to be published in the December 1971 JOURNAL.

REFERENCES

1. G. Blasse, W. L. Wanmaker, J. W. ter Vrugt, and A. Bril, *Philips Res. Rept.*, **23**, 189 (1968).
2. G. Blasse, W. L. Wanmaker, and J. W. ter Vrugt, *This Journal*, **115**, 673 (1968).
3. T. L. Barry, This was Paper 56 presented at the Boston Meeting of the Society, May 5-9, 1968.
4. T. L. Barry, This was Paper 77 presented at the New York Meeting of the Society, May 4-9, 1969.
5. W. A. McAllister and W. A. Thornton, This was Paper 79 presented at the New York Meeting of the Society, May 4-9, 1969.
6. R. M. Barrer and D. J. Marshall, *J. Chem. Soc.*, **1964**, 2296.
7. T. Ito, "X-Ray Studies in Polymorphism," Tokyo, Maruzen (1950).
8. C. A. Sorrell, *Am. Mineralogist*, **47**, 291 (1962).
9. Y. Takéuchi, *Min. J.*, **2**, 311 (1958).
10. A. K. Ivukina and Ya. I. Panova, *Kristallografiya*, **9**, 560 (1964).
11. E. P. Riedel, *J. Luminescence*, **1**, 176 (1969).
12. E. Dittler and Lasch, *Akad. Wiss. Wien., Math. Nat. Kl.*, 201 (1930).
13. B. Yoshiki and K. Matsumoto, *J. Am. Ceram. Soc.*, **34**, 283 (1951).
14. G. L. Davis and O. F. Tuttle, *Am. J. Sci.*, Bowen Vol., 107 (1952).

Mobile Ion Transfer to SiO_2 Films from Ethanol

S. I. Raider* and R. Flitsch

International Business Machines Corporation, Components Division,

East Fishkill Facility, Hopewell Junction, New York 12533

The relationship between the contamination of SiO_2 surfaces with organic reagents and the subsequent ionic drift has been interpreted in different ways. Hofstein (1), using neutron activation, ^{22}Na radiotracer analyses, electrical measurements, and tritiated ethanols in his studies, concluded that mobile protons are transferred from ethanol to SiO_2 films. Oddly, it was the less chemically reactive protons on the α- and β-carbons of ethanol, and not the hydroxyl group proton, that were correlated with the mobile species. Sunshine (2) indicated that ethanol and other organic materials, independent of alkali ions, caused ionic drift in SiO_2 films. Gregor (3) correlated shifts in flat-band voltage with contamination of oxide surfaces using high-purity organic reagents, including ethanol, as contaminants. It was suggested that the aluminum electrode reacted with the treated oxide surface to release an active positive species, but no conclusion was reached as to whether the observed ionic drift was due to mobile protons or to sodium ions. Yurash and Deal (4) measured the ionic drift in metal-oxide-silicon (MOS) structures after immersing oxides in acetone and trichloroethylene and compared these results with the number of Na^+ ions present in these solvents. The ionic drift and the Na^+ ion concentration in these two organic solvents were found to be directly related. MOS structures were also contaminated with

* Electrochemical Society Active Member.

Key words: MOS, ionic drift, mobile sodium ions, mobile hydrogen ions, organic contaminants.

Table I. Contamination of SiO_2 surface with distilled and nondistilled 100% ethanol

SiO_2 contamination	Contamination procedure	Ionic drift: Type of measurement	Ionic drift: Q/q^* × 10^{11} cm^{-2}	Na^+ in EtOH, moles/liter (Flame photometry)
Tritiated EtOH [Hofstein (1)]	15 min, EtOH drops between wafers, 75°C	Charge-time (Q-t): +50V, 250°C; d_{ox}: 6000Å	>100	—
100% EtOH [Gregor (3)]	1 Min on SiO_2 surface, room temp	Bias-temperature (C-V): +30V, 200°C, 30 min; d_{ox}: 5500Å	45-60	—
100% EtOH	5 Min immersion, room temp, 50 cc	Q-t: +40V, 250°C	84-240	2.0×10^{-5}
Control	—	C-V: +40V, 250°C, 5 min	0.5-1.2	—
100% EtOH	5 Min immersion, room temp, 50 cc	Q-t: +40V, 250°C	103-178	2.0×10^{-5}
↓	2-3 Min, EtOH (78°C) evaporated on SiO_2	C-V: +40V, 250°C, 5 min	0.4-0.7	2.0×10^{-5}
Control	—	↓	0.8	—
Distilled 100% EtOH	15 Min, EtOH drops between wafers, 75°C		1.0-1.4 0.9	3.0×10^{-8}
↓	5 Min immersion, room temp, 50 cc		0.5-1.0 1.0-1.4	3.0×10^{-8}
↓	5 Min immersion, 75°C, 50 cc		0.8	3.0×10^{-8}
Control	—	↓	0.8	

*Q = net ionic charge; q = unit charge.

organic reagents after the aluminum electrodes had been deposited and annealed. From the latter experiment, Yurash and Deal suggested that the shifts observed in the C-V plots after the MOS structures were stressed were related to ionic contaminants diffusing in from the edges of the electrodes. Reactions between the aluminum electrodes and the organic molecules which might produce mobile species were therefore considered unlikely.

In the present work, the effect of contaminating an oxide surface with ethanol was re-examined with respect to the corresponding ionic drift and the Na^+ ions present in the ethanol. Using oxygen-steam-oxygen, oxide films 5700Å thick were thermally grown on p-type, 2 ohm-cm, <100>, silicon wafers. Aluminum dots (20 mils in diameter, 5000Å thick) were evaporated through metal masks onto the oxides after contaminating the surfaces with ethanol. Aluminum was also evaporated onto the backs of the wafers. The wafers were then annealed at 400°C for 20 min in N_2 gas. Table I shows the results of flame photometric analyses of trace amounts of Na^+ ions in 100% ethanol (U.S.I. Absolute Ethanol, Reagent Grade), and also lists the number of electrically mobile ions transferred to the oxide films as a result of immersing them in ethanol.

To reduce the Na^+ content of the ethanol contacting the oxide surface, the ethanol was evaporated from a heated beaker onto an oxide film held above the beaker. The effect of contaminating an SiO_2 surface in the absence of Na^+ ions with liquid ethanol was examined after first distilling the ethanol twice, using a quartz distillation column. Hofstein's experimental procedure was stimulated by heating the distilled ethanol between two oxide surfaces at 75°-80°C for 15 min. In addition, wafers were immersed in the distilled ethanol and heated both at room temperature and at 75°-80°C for 5 min. Ionic drift results from these experiments are listed in Table I, together with those from experiments by Hofstein and by Gregor.

When the experiments described in Table I were repeated without the 400°C postmetallization anneal, similar drift results were obtained. Finally, since it had been demonstrated (5) that Na^+ impurities are most concentrated near the air surface of thermally grown SiO_2, about 250Å of each of the oxides were removed by etching with dilute HF before contaminating these surfaces with ethanol. The results of contaminating these etched oxide surfaces with distilled and nondistilled ethanol are similar to those obtained with no etching.

The results in Table I indicate that the number of electrically mobile ions found in SiO_2 films after the surfaces of these films were contaminated with ethanol appears to be related to the number of Na^+ ions present in the ethanol. Heating the distilled ethanol at 75°-80°C between two oxide surfaces had little effect on the ionic drift. Since neither the evaporated nor the distilled ethanol affected the ionic drift, it must be concluded that, contrary to Hofstein's findings, there is no evidence of mobile protons in SiO_2 resulting from ethanol contamination. The distribution of tritium that Hofstein observed in SiO_2 after he contaminated silica surfaces with tritiated ethanols does not necessarily indicate that tritium is electrically mobile in SiO_2; rather, the distribution may be indicative of a secondary effect resulting from the movement of Na^+ ions.

Acknowledgments

The authors wish to thank Drs. L. V. Gregor and D. R. Kerr for their suggestion that the question of mobile species in SiO_2 resulting from ethanol contamination be re-examined.

Manuscript submitted Nov. 4, 1970; revised manuscript received ca. March 12, 1971. This was Recent News Paper 245 presented at the Atlantic City Meeting of the Society, Oct. 4-8, 1970.

Any discussion of this paper will appear in a Discussion Section to be published in the December 1971 JOURNAL.

REFERENCES

1. S. R. Hofstein, *IEEE Trans. Electron Devices*, **ED-14**, 749 (1967).
2. R. Sunshine, "A Contamination Induced Charge in Thermally Grown Silicon Dioxide," Late News Paper, 5th Ann. Symp. on Physics of Failure in Electronics, Columbus, Ohio (Nov. 1966).
3. L. V. Gregor, Paper 12 presented at Electrochem. Soc. Meeting, Cleveland, Ohio, May 1-6, 1966.
4. B. Yurash and B. E. Deal, *This Journal*, **115**, 1191 (1968).
5. E. Yon, W. H. Ko, and A. B. Kuper, *IEEE Trans. Electron Devices*, **ED-13**, 276 (1966).

Modulation of Dopant Segregation by Electric Currents in Czochralski-Type Crystal Growth

M. Lichtensteiger, A. F. Witt,* and H. C. Gatos*

Center for Materials Science and Engineering, Massachusetts Institute of Technology, Cambridge, Massachusetts 02139

Extremely rapid modulation of dopant segregation was observed in tellurium-doped indium antimonide single crystals brought about by electric currents applied across the growth interface during Czochralski-type crystal growth. The time constant of the modulation was found to be in the millisecond range and thus orders of magnitude smaller than that encountered in diffusion-controlled processes. Abrupt changes in the microscopic growth rates associated with Peltier cooling were quantitatively determined. Concurrent changes in the facet growth were also observed.

A dual output function generator and high-speed programmable power supply were used to produce current pulses of controlled amplitude and duration. Positive current pulses were applied (from seed to melt) across the crystal-melt interface of a tellurium-doped (10^{17}/cm^3) indium antimonide system leading to Peltier cooling (see circuit diagram in Fig. 1). All results were obtained with crystals of about 1.4 cm in diameter pulled in the <111> direction without rotation [to achieve constant microscopic growth rates (1)] at a rate of 2.5 cm/hr; they were cut along the growth axis, polished, and etched. The etching rate is a sensitive function of dopant concentration (it decreases with increasing Te concentration) and the resulting surface topography reflects in detail the compositional changes in the crystal (2).

The effects of current pulses (see insert, Fig. 2), with a repetition rate of 4 sec, on dopant segregation are shown in Fig. 2. It is seen that every pulse results in an instantaneous increase in dopant concentration, the magnitude and duration of which are controlled by the pulse characteristics. It is most interesting to note that the increased dopant concentration remains at a constant level throughout the period of current flow. Similarly, upon termination of the pulse, the dopant concentration decreases instantaneously and again remains constant throughout the 3 sec interval between successive pulses (multiple beam interferograms showed that the etched regions grown with and without current flow were flat).

From the rise time of the pulses (20 msec) and the linear resolution of light microscopy ($\sim 0.2\mu$), the time constant associated with the current-induced dopant concentration change is found to be at most of the order of several milliseconds. A time constant of a similar magnitude is apparently operative during relaxation of the dopant segregation upon the termination of current pulses. From the width of the region grown during the application of pulses (800 msec), an average growth rate greater by a factor of 3.7 than the actual pulling rate was found. The regions between pulses grew at a rate which was within 5% of the pulling rate.

The effect of sloped current pulses (see insert, Fig. 3) on the dopant segregation are shown in Fig. 3; both an off-core region (right-hand side) and a core region (left-hand side) of the crystal are shown. A continuous elevation increase from top to bottom (confirmed by multiple beam interferometry) corresponding to the pulse shape is observed. It reflects the direct dependence of dopant segregation on cur-

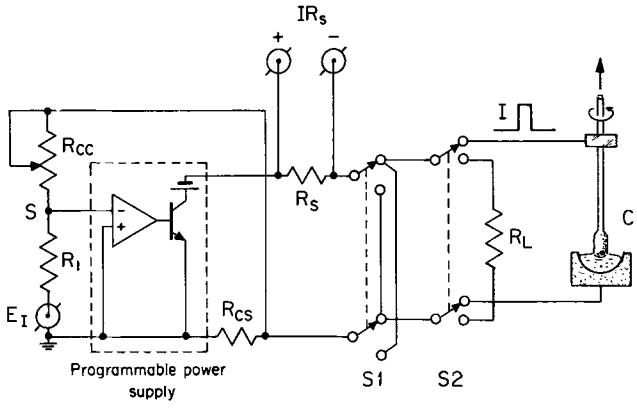

Fig. 1. Simplified diagram for programmed current pulse generator. The pulse generator signal, E_I, is fed through input resistance, R_I, to the summing point, S, of a high-speed programmable power supply (with 55V compliance) used as compensated summing amplifier. Its output, I, is controlled by a negative feedback current, IR_{CS}/R_{CC}, where R_{CS} and R_{CC} are sensing and control resistors. The voltage drop, IR_S, is used to monitor the waveform of the pulses on a differential plug-in oscilloscope. Switch S_1 permits polarity reversal of the pulses applied across the growth system, C, whose total resistance measured approximately 300 mohms for the experiments described, and switch S_2 allows current shunting across a "dummy-load," R_L, for adjusting the pulse characteristics before start of the experiment.

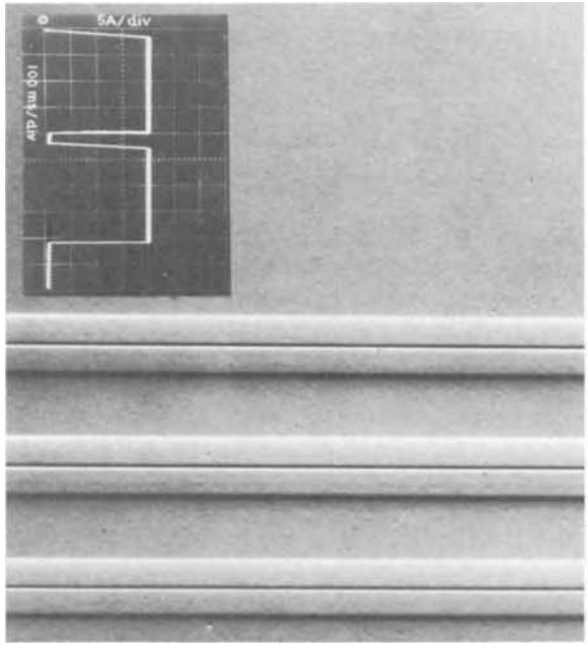

Fig. 2 (211) "Off-core" section of Te-doped InSb single crystal cut along the growth axis (grown without rotation). Composite current pulses with the characteristics shown in the figure were applied during growth. The instantaneous increase and decrease in dopant segregation associated with the onset and termination of current flow is clearly visible. Magnification 355X.

* Electrochemical Society Active Member.

Key words: crystal growth, impurity distribution, indium antimonide.

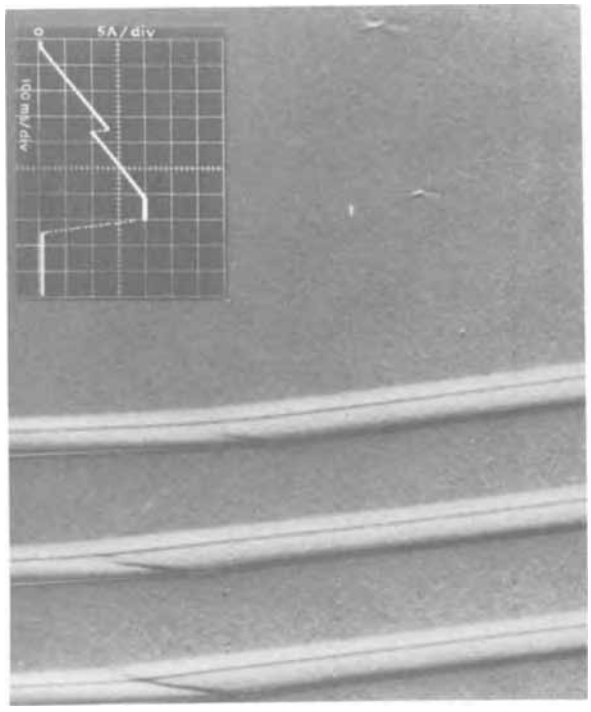

Fig. 3. (211) Section of a Te-doped InSb single crystal cut along the growth axis (grown without rotation). The long rise time of the current pulse, shown in the figure, causes a gradual increase in dopant segregation. The temporary decrease in current is reflected as a dark line (see text). Magnification 355X.

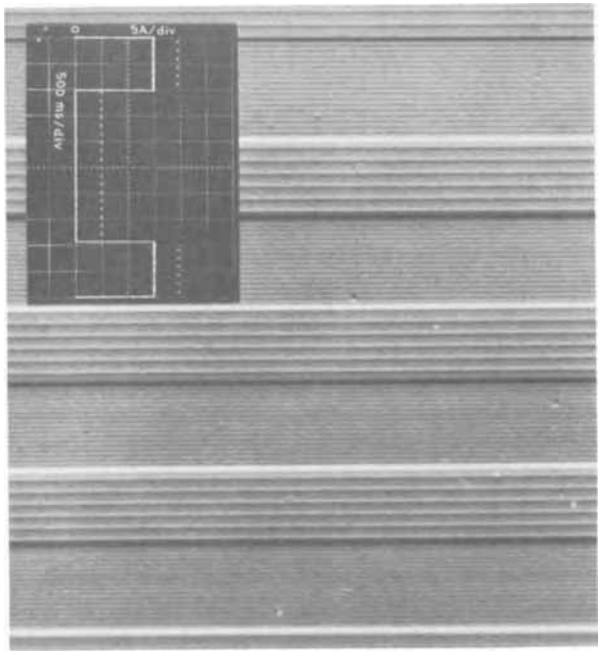

Fig. 4 (211) "Off-core" section of a Te-doped InSb single crystal cut along the growth axis (grown without rotation). The effects of superimposed 15 msec pulses (see insert) are clearly visible and are utilized as rate striations. The regions grown with current flow contain 6 and those grown between successive pulses 18 rate striations. Their relative separation shows that current flow increases the microscopic rate of growth (see text). Magnification 405X.

rent density. The asymmetric position of the dark line within the pulsed region (caused by the current reduction as shown in insert of Fig. 3) demonstrates a current-controlled growth rate. It is also seen that the current-induced increase in growth rate is greater in the off-core than in the on-core region, reflecting the differences in the prevailing growth mechanisms. Figure 3 shows further that the off-core to on-core delineation which corresponds to the transition from curved to flat growth interface is very pronounced in the regions of increased growth rate associated with current flow; it is barely visible in the parts of the crystal grown with no current flow. It is also observed that the increased growth rate associated with current flow results in a rapid facet (core) expansion into the off-core region which relaxes upon the decrease in growth rate caused by termination of the pulse. The extent of core expansion is a function of the curvature of the prevailing solidification isotherm and the magnitude and duration of the current pulse. This growth interface behavior is consistent with the spontaneous tendency of the facet to expand under unrestricted (accelerated) growth conditions. The microscopic dopant distribution in the core region adjacent to the off-core is complex and reflects the transition from one growth mechanism to another (3).

The effects of relatively long current pulses (as discussed above) on the microscopic growth rate were studied by superimposing 15 msec pulses of 5A amplitude and a frequency of 6/sec [serving as rate striations (4)]. The results are shown in Fig. 4. The regions grown with current flow (1 sec duration) can be readily differentiated from the regions grown during the 3 sec intervals between successive pulses; the former contain 6 and the latter 18 rate striations.

Measurements of the spacing of the "rate striations" show that the growth rate upon the application of the current pulses increases instantaneously by 340% and remains constant for the duration of the pulses; during the intervals between the successive pulses, the growth rate is also constant and about 8% higher than the actual pulling rate.

In the light of the instantaneous response of the growth system to the onset and termination of current flow, it is apparent that current pulses of short duration and low amplitude used for introducing "rate striations" do not interfere with the over-all growth characteristics of general concern.

The presently reported very rapid modulation of the dopant segregation cannot be explained by the prevailing theoretical treatments based on a constant interface segregation coefficient and diffusion-controlled mechanisms (5). According to these treatments, the dopant segregation readjustment to an abrupt change in growth rate should be roughly 90% completed within 1 sec, or about 0.1% completed in 10 msec. The present results show that compositional readjustment following the onset and termination of current flow takes place in less than 10 msec with no subsequent detectable composition changes for periods ranging up to 3 sec. It is evident that the presently observed dopant segregation phenomena are not diffusion controlled. We believe that they result from changes in the interface distribution coefficient which is generally assumed to be constant.

Well-defined current pulses constitute a powerful tool in fundamental crystal growth studies and in materials design, such as the formation of abrupt controlled changes in dopant concentration and the formation of dopant superlattices. Controlled crystal growth induced by Peltier cooling is currently being applied to liquid phase epitaxy.

Acknowledgments

The authors are indebted to the National Science Foundation and the Advanced Research Project Agency for financial support.

Manuscript received Jan. 14, 1971.

Any discussion of this paper will appear in a Discussion Section to be published in the December 1971 JOURNAL.

REFERENCES

1. A. F. Witt and H. C. Gatos, *This Journal*, **116**, 511 (1969).

2. D. C. Johnston, A. F. Witt, and H. C. Gatos, *ibid.*, **115**, 438 (1968).
3. See, for example, A. Trainor and B. E. Bartlett, *Solid-State Electron.*, **2**, 206 (1961).
4. R. Singh, A. F. Witt, and H. C. Gatos, *This Journal*, **115**, 113 (1968).
5. W. P. Slichter and J. A. Burton, in "Transistor Technology," H. E. Bridgers, J. H. Scaff, and J. N. Shive, Editors, Vol. 1, p. 107, D. Van Nostrand Co. Inc. (1959).

Brief Communication

The Dependence of Emission Spectrum and Efficiency of GaAs:Si Diodes on the Silicon Concentration

B. H. Ahn, R. R. Shurtz, and C. W. Trussell

Night Vision Laboratory, USAECOM, Fort Belvoir, Virginia 22060

Amphoteric GaAs:Si electroluminescent diodes are quite efficient at room temperature, and domed configuration GaAs:Si diodes have power efficiency as high as 28% (1, 2). Many investigators have made electrical absorption and photoluminescent measurements on GaAs:Si epilayers (3-5), but these parameters were not correlated to the device performance.

We present the dependence of spectral emission and power efficiency on the substrate orientation and the Si concentration in the melt. GaAs:Si diodes were fabricated by liquid phase epitaxy (6). N-GaAs substrates were used which were oriented in (100), (111)-A, and (111)-B directions and doped with Si to 2-5 x 10^{18}/cm^3. The tilt temperature was 970°C and the cooling rate was logarithmic with the fastest segment cooling at 2.5°C/min and the slowest at less than 0.5°C/min. Silicon in the melt was varied from 0.8 a/o (atomic per cent) to 2.4 a/o. The tilt temperature was high enough to have resulted in the amphoteric p-n junction growth at all the Si concentrations and all orientations. Figures 1, 2, and 3 show the emission peak dependence on the Si concentration in the melt. The longest emission spectrum (10,160Å)

Key words: amphoteric, III-V compound, electroluminescence, orientation effect.

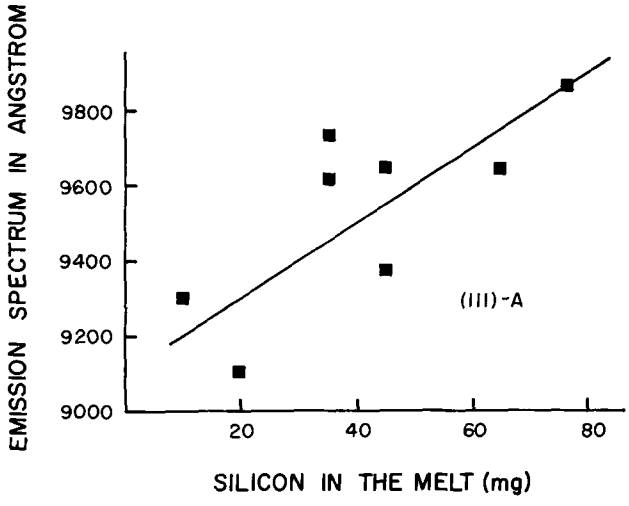

Fig. 2. Plot of emission spectrum peak *vs.* Si concentration in the melt. The GaAs substrate is oriented in (111)-A.

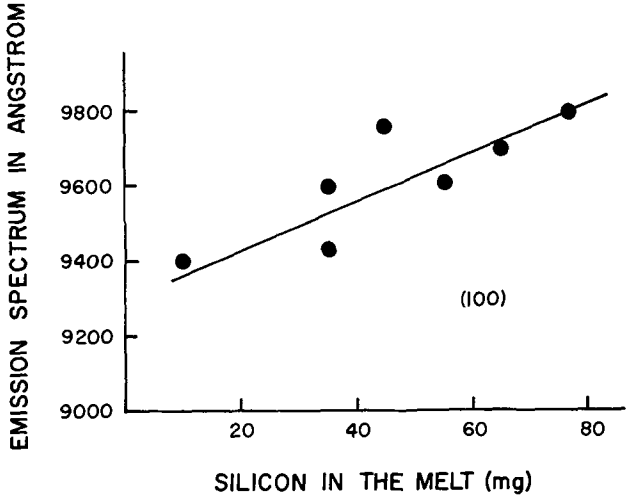

Fig. 1. Plot of emission spectrum peak *vs.* Si concentration in the melt. The GaAs substrate is oriented in (100).

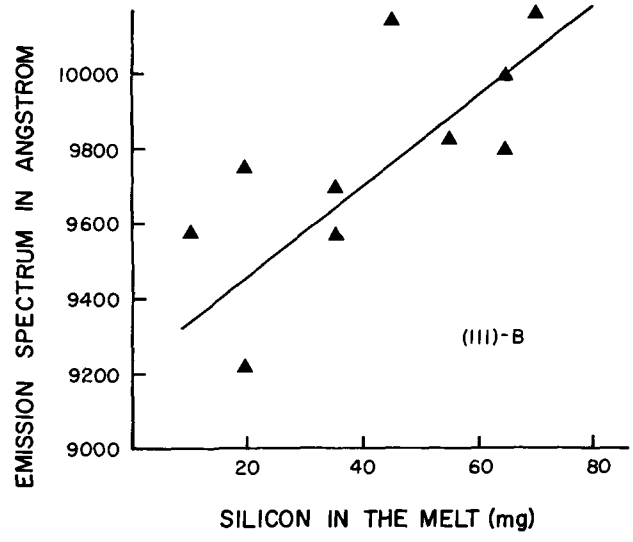

Fig. 3. Plot of emission spectrum peak *vs.* Si concentration in the melt. The GaAs substrate is oriented in (111)-B.

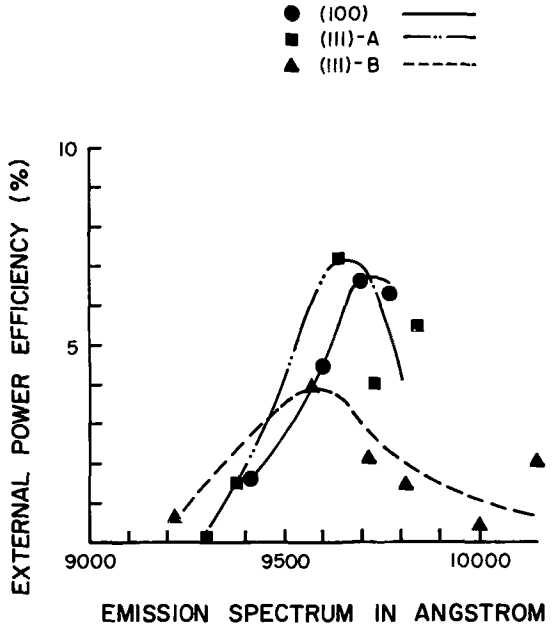

Fig. 4. Plot of the power efficiency of diodes grown at different Si concentrations on three orientations *vs.* their emission spectrum peak. Notice the (111)-B diodes are the least efficient.

was observed only in diodes grown on (111)-B oriented substrates. While there is only a small fluctuation from the straight line for (100) orientation, there exists quite a large fluctuation for the (111)-A and (111)-B. Our results indicate that Si_{As} and Si-complex atoms form a broad acceptor band, the peak of which varies as the Si in the melt is varied. The band is apparently formed by the acceptor levels seen previously by others at 0.03, 0.100, and 0.23 eV above the valence band. The Si concentration apparently changes the relative concentration of these levels.

Figure 4 shows the relationship between the spectral peak and the power efficiency. There is an optimum efficiency range between 9600 and 9700Å [these correspond to 144 and 157 meV deviation from the GaAs bandgap (7)]. We believe that lower power efficiency at shorter and longer spectral ranges is due to bulk absorption and nonradiative absorption by Si-complex atoms, respectively.

Manuscript received March 1, 1971.

Any discussion of this paper will appear in a Discussion Section to be published in the December 1971 JOURNAL.

REFERENCES

1. K. J. Linden, *Infrared Phys.*, **10**, 141 (1970).
2. N. S. Dubrovskaya *et al.*, *Soviet Physics-Semiconductors*, **3**, 1537 (1970).
3. H. Kressel *et al.*, *J. Appl. Phys.*, **39**, 2006 (1968).
4. W. G. Spitzer and M. B. Panish, *ibid.*, **40**, 4200 (1969).
5. H. Kressel and H. Nelson, *ibid.*, **40**, 3720 (1969).
6. H. Nelson, *RCA Rev.*, **24**, 103 (1963).
7. M. D. Sturge, *Phys. Rev.*, **127**, 168 (1962).

DISCUSSION SECTION

This Discussion Section includes discussion of papers appearing in the *Journal of The Electrochemical Society*, Vol. 117, No. 3 and 5 (March and May 1970).

Contact Resistance in Diffused Resistors

I. F. Chang (pp. 368-372, Vol. 117, No. 3)

H. H. Berger:[1] In his paper, Chang introduces what he calls a "Modified Transmission Line (MTL) Model" to describe the contact of a diffused resistor. He does this for two basic reasons:

(*a*) The original Transmission Line Model (TLM)[2,3] cannot consider the influence of the gap between the contact and the resistor side edges, since it is a strictly one-dimensional model.

(*b*) There are contact fabrication processes, which might modify the conductivity of the semiconductor region beneath the contact metal.

To alleviate the first problem, Chang proposes to shunt the series resistance of the TLM by the resistance of the two stripes between contact and resistor side edges. This would result in smaller end corrections than predicted by the original TLM. However, when the contact becomes smaller at a fixed resistor width, an increasing constriction resistance in the contact vicinity adds to the contact end correction, suggesting rather that the original TLM would give too small values for the total end correction. Chang's modification would make it worse.

The main issue, however, is whether for practical contacts a correction is needed at all. The maximum influence of the constriction resistance can be estimated by considering the constriction for an ideal contact as has been done theoretically (conformal mapping) by Ting and Chen[4] and experimentally (resistance paper model) by D'Andrea and Murrmann.[5] Both results suggest that the original TLM is sufficiently accurate for most practical purposes. Chang himself provides direct experimental evidence that there is indeed no need for the proposed modification: Table I of his paper shows that his samples excellently followed the inverse proportionality between contact end correction term R_{cc} and the contact width (W-2a) as the original TLM would predict. The same applies to the term R_c.

To solve the second problem, no modification of the TLM is needed either, unless a second blocking junction is formed along with the conductivity change of the semiconductor region beneath the contact. Namely, since the TLM describes the contact region only, it is self-evident that the actual semiconductor series resistance of this region must be inserted in the model. The real problem is not an inadequacy of the TLM to describe contacts with semiconductor sheet resistances different from the resistor bulk; rather it is an inadequacy of the resistor test pattern, as applied by Chang (Fig. 1 of his paper) to directly determine the series resistance for the TLM of such contacts. This test pattern was originally devised[2] for cases where the sheet resistances of the resistor bulk and the contact region remained equal. Hence it is this structure which might need a modification, not the TLM.

[1] IBM Deutschland, 703 Boeblingen, Schoenaicher Str. 220, Germany.
[2] H. H. Berger, IEEE-ISSCC Dig. Techn. Paper, pp. 160-161 (1969).
[3] H. Murrmann and D. Widmann, ISSCC Dig. Techn. Paper, pp. 162-163 (1969).
[4] C. Y. Ting and C. Y. Chen, Electrochem. Soc. Extended Abstracts, Detroit, Michigan, October 5-9, 1969, Electronics Div., Abs. No. 199, p. 525.
[5] G. D'Andrea and H. Murrmann, *IEEE Trans. Electron Devices*, ED17, 484 (1970).

In the case of Mo-PtSi-Si-contacts, the blocking action of the second (PtSi-Si) junction seems to be negligible after Chang's results. This would justify the application of the TLM to these contacts. The series resistance of the TLM could then again be directly determined with a structure according to Fig. 1 (Chang's paper), if the PtSi were applied all over the entire resistor.

On aluminum-silicon contacts, I have not found any evidence for a strong modification of the semiconductor conductivity beneath the contact.[6] Theoretically, instead of the decrease observed by Chang, one would expect an increase of the series resistance beneath the contact, since the aluminum dissolves a small layer of silicon during the sintering process.

I. F. Chang: Berger's discussion questions the two significant features of the MTL model[7]:

(*a*) The influence of the gap, *a*, between the contact and the resistor side edge (see Fig. 1 published here) in predicting contact correction for diffused resistor.

(*b*) The need of a contact sheet resistance, ρ_s', in addition to the resistor diffusion sheet resistance, ρ_s, to obtain a correct contact correction term, R_{cc}.

The MTL model introduced[7] has demonstrated clearly why these considerations are necessary. Only by considering both the existence of a gap and a contact sheet resistance, ρ_s', different from the bulk diffusion resistance, ρ_s, can one obtain good agreement with experimental data on various sizes of aluminum and molybdenum contacts to silicon. Berger has quoted

[6] Results not yet published.
[7] I. F. Chang, *This Journal*, 117, 368 (1970).

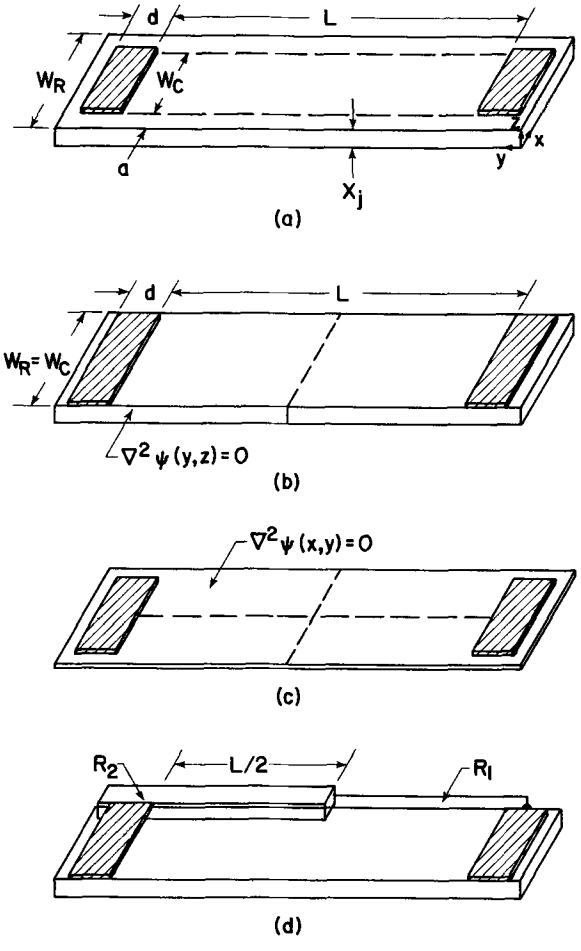

Fig. 1. (a) Diffused resistor structure, (b) resistor structure for Case 1, (c) resistor structure for Case 2, (d) resistor structure for Case. 3.

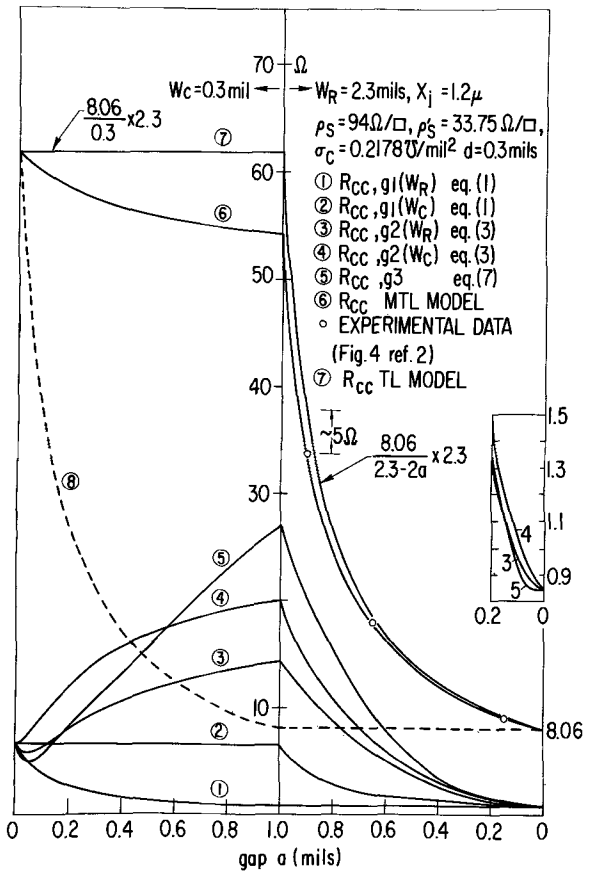

Fig. 2. Experimental data, MTL calculations, TL calculations, and other model calculation. LHS: Contact correction as a function of contact-resistor gap, a, for a constant contact width. RHS: Contact correction as a function of contact-resistor gap, a, for a constant resistor width.

other work,[8,9] and has made qualitative comparisons on their results to support his arguments. Therefore, it seems appropriate to present some detailed numerical results concerning various theoretical models to illustrate that care must be taken in making comparisons. Hopefully, these results, along with the MTL result, the TL result, and the experimental data all shown in Fig. 2 published here, will clear doubts on this subject.

I. Theoretical Modeling of Contact Correction in Diffused Resistor

Let us consider a realistic contact in a diffused resistor as shown in Fig. 1(a). The total resistance of the resistor is defined as the sum of the bulk diffusion resistance and two times the contact correction term, R_{cc} (Eq. [1] in footnote 7). R_{cc} consists of the crowding resistance of the contact (beneath the contact as well as at two sides of the contact) and the contribution from contact resistance. The latter is a fabrication process and contact geometry dependent. The former term (excluding the effect of diffusion profile on current crowding) depends mainly on contact and resistor geometry. These two types of contribution to R_{cc} cannot be separately determined by experimental measurements; thus, a correct analytical model must consider them simultaneously. However, most analytical treatments reported only deal with an ideal contact[8,10,11,12] (that is, neglecting contribution due to contact resistance) and/or a simplified contact-resistor

[8] C. Y. Ting and C. Y. Chen, Electrochem. Soc. Extended Abstracts, Detroit, Michigan, October 5-9, 1969, Electronics Div., Abs. No. 199, p. 525.
[9] G. D'Andrea and H. Murrmann, *IEEE Trans. Electron Devices*, ED17, 484 (1970).
[10] D. P. Kennedy and P. C. Murley, *IBM J. Res. Develop.*, 12, 242 (1968).
[11] Case 3 in Section I is a typical example.
[12] B. R. Chawla, *Proc. IEEE*, 59, 305 (1971).

geometry[13-15] (neglecting part of the current crowding effect due to geometry). Therefore, one should be aware of the assumptions made in each treatment and interpret their results with care. We briefly discuss a few cases below and present numerical results for each case to illustrate this point.

Case 1.—As shown in Fig. 1(b), this case assumes an ideal contact with a simple geometrical configuration (*i.e.*, the contact width, W_c, equals the resistor width, W_R). Therefore, mathematically, one can reduce this problem to a two-dimensional one. Using the Schwartz-Christoffel transformation and the definition of sheet resistance, one can solve the Laplace equation and obtain

$$R = \rho_s \frac{L}{W} + 2\left[\frac{2\rho_s X_j}{\pi W} \ln \frac{2}{(1 - e^{-\pi d/X_j})}\right] = \rho_s \frac{L}{W} + 2\,R_{cc,g1} \quad [1]$$

as given by Eq. [17] in footnote 7 and Eq. [2] in footnote 8. One notes that $R_{cc,g1}$ increases with decreasing W and increases very little with decreasing contact length, d, since $X_j << d$. The numerical result for Eq. [1] is plotted in Fig. 2 as curves 1 and 2. One notes that, because the assumption $W_R = W_c$ is made in deriving Eq. [1], it would predict ambiguous results for resistors with ideal contact of $W_c \neq W_R$. This is best illustrated in Fig. 2, curves 1 and 2, which, on LHS, presents contact correction term for a given contact (W_c = 0.3 mil) situated in resistors of various widths and, on RHS, presents R_{cc} for a given resistor (W_R = 2.3 mils) having contacts of various widths. Obviously, the constant value predicted by Eq. [1] on each side is an incorrect prediction. The varying portions of curves 1 and 2 are the approximate correction term for an ideal contact by neglecting the current distribution and crowding on the two sides of the contact.

Case 2.—Considering a thin sheet resistor (neglecting current crowding in the Z direction) shown in Fig. 1(c), Ting and Chen[8] worked out the correction term due to a current crowding in the X-Y plane alone under the assumption $d \geq 4a$ and $L/2 >> W_R$. The result is

$$R = \rho_s \frac{L}{W_R} + 2\left[\frac{\rho_s}{2\pi}\left(\frac{1}{K} \ln \frac{K+1}{K-1} + \ln \frac{K^2-1}{K^2+1}\right)\right] = \rho_s L/W_R + 2\,R_{cc,g22} \quad [2]$$

where $K = W_R/2a$. They consider that the sum of $R_{cc,g1}$ and $R_{cc,g22}$

$$R = \rho_s L/W_R + 2\,R_{cc,g1} + 2\,R_{cc,g22} = \rho_s L/W_R + 2\,R_{cc,g2} \quad [3]$$

to be a good approximation of contact correction due to current constriction. However, one notes that the assumption of $W_R = W_c$ in Case 1 is not consistent with that in Case 2, therefore, it is ambiguous whether W_R or W_c should be used for $R_{cc,g1}$ in the sum equation, or whether they can be added at all for representing the net crowding resistance. In some cases [small (a) falls within the assumption $d \geq 4a$], $R_{cc,g1}(W_c)$ and $R_{cc,g1}(W_R)$ have a difference much greater than the second correction term $R_{cc,g22}$ making it insignificant compared to the first correction term. Furthermore, $R_{cc,g2}$ or $R_{cc,g22}$ being independent of d is obviously a crude approximation. Numerical results for $R_{cc,g2}$ are also shown in Fig. 2 (curves 3 and 4). However, one should note that the valid region for $R_{cc,g2}$ (curves 3 and 4) is limited to $a < d/4$. It is worthwhile mentioning that Chawla,[12] using a numerical technique, has recently obtained analytical expression for an ideal contact in a "dog bone" resistor. The author claims that, when imposing the condition $W_R = W_c + 2a$, the expression

$$R_{cc} = \rho_s \left[0.325e^{-2.5W_c/W_R} + \left(0.834 - 0.247\frac{a}{W_R}\right)\frac{a}{W_R}\right] \quad [4]$$

should also be applicable to a straight resistor. However, one should be aware that the bulk path of the resistor considered in Chawla's case is L-$2a$ rather than L.

Case 3.—Another approach to the problem may be taken if one assumes that the actual resistor may be partitioned as shown by dotted lines in Fig. 1(a). This is a fair approximation at least in the resistor body up to the vicinity of the contact corner. Under this assumption, we can treat the resistor as two parallel conduction paths as shown in Fig. 1(d). R_1 is the main resistor whose contact correction term can be evaluated under equivalent condition of Case 1. R_2 is equivalent to two parallel resistors of two R_2 in series. The correction term for R_2 can be evaluated in a similar manner as for R_1 by recognizing the analogy $X_j \rightarrow a$, $W_c \rightarrow X_j$ and d remains unchanged (the current crowding in the Z direction in R_2 has been neglected). Thus, we have

$$R_1 = \rho_s L/W_c + 2\frac{2\rho_s X_j}{\pi W_c} \ln \frac{2}{(1 - e^{-\pi d/X_j})} = \rho_s L/W_c + 2\,R_{cc,g1}(W_c) \quad [5]$$

$$R_2 = \rho_s L/2a + 2\frac{\rho_s}{\pi} \ln \frac{2}{(1 - e^{-\pi d/a})} = \rho_s L/2a + 2\,R_{cc,g33} \quad [6]$$

$$R = R_1 // R_2$$

$$= \frac{\rho_s \frac{L}{W_R} + \frac{\rho_s \frac{L}{W_c} 2\,R_{cc,g33} + \rho_s \frac{L}{2a} 2\,R_{cc,g1}(W_c) + 2\,R_{cc,g1}(W_c) \cdot 2\,R_{cc,g33}}{\rho_s L(1/W_c + 1/2a)}}{1 + [(2\,R_{cc,g1}(W_c) + 2\,R_{cc,g33})/\rho_s L(1/W_c + 1/2a)]}$$

$$\cong \rho_s \frac{L}{W_R} + \left(\frac{W_c}{W_R}\right)^2 \cdot 2\,R_{cc,g1}(W_c) + \left(\frac{2a}{W_R}\right)^2 \cdot 2\,R_{cc,g33} = \rho_s L/W_R + 2\,R_{cc,g3} \quad [7]$$

One notes that as a approaches 0, Eq. [7] reduces to Eq. [1] indicating that Case 1 is a special case of Case 3. As W_c becomes smaller, the first correction term decreases and $R_{cc,g3}$ approaches $R_{cc,g33}$ which is a function of d/a. This may be a better representation for the contact correction term than Eq. [3] since it is independent of d/a. Numerical results of this case are plotted in Fig. 2 as curve 5. It decreases significantly as d increases.

Significance of MTL Model and Comments on H. Berger's Discussion

The above discussions are for an ideal contact. In the case of a real contact, the presence of contact resistance has the effect of spreading out the current distribution beneath the contact and along two sides of the contact. If the current distribution can be described in terms of a passive network, one may then approximate the real contact to be two parallel distributive resistance networks, one responsible for the current

[13] Case 1 in Section I is one example.
[14] H. Murrmann and D. Widmann, *IEEE Trans. Electron Devices*, ED16, 1022 (1969).
[15] H. H. Berger, IEEE-ISSCC Dig. Techn. Paper, pp. 160-161 (1969).

spreading beneath the contact and one for along the two sides of the contact (due to symmetry two sides can be combined). The MTL model is just based on this concept. The model parameters, the distributive resistance elements (ρ_s' and σ_c in addition to ρ_s) for any given fabrication process can be uniquely derived from experimental measurements using a test pattern such as shown in Fig. 1, footnote 7. The fact that the model calculation agrees very well with experimental data of various sizes of Al and Mo contacts (see Fig. 4-6, footnote 7) seems to support this concept.

To further discuss the significance of MTL model, we plot its numerical result (curve 6) in Fig. 2 for a typical resistor (width = 2.3 mil) on the RHS and for a typical contact (width = 0.3 mil) on the LHS. On the RHS curve 6 and other theoretical calculations (except curve 1) all predict the same tendency, *i.e.*, when the contact becomes smaller at a fixed resistor width, R_{cc} increases. One notes that although other calculations (curves 2, 3, 4, 5, and 7) do qualitatively indicate the trends of variation, only the MTL result agrees with the experimental data (circles in Fig. 2). This is what is expected. Now let us examine the TL model: If the contact sheet resistance, ρ_s', were not introduced, the model would predict much too high a correction (~30% too high compared with experimental data). If the proper sheet resistivity, ρ_s', under the contact were used in the TL model (Eq. [12], footnote 7), it would result in still higher end correction (curve 7) than the MTL result (curve 6) as Berger indicates in his discussion. However, the experimental data (from Fig. 4, footnote 7) seem to fit the MTL result better, particularly when a, the gap, is large (the experimental data is not inversely proportional to W-$2a$ in Fig. 4-6, footnote 7). The difference between the TL result (curve 7) and the MTL result or the experimental data is about 5 ohms for $a = 0.9$ or $W_c = 0.3$ mils.

Berger has quoted the theoretical result of Ting *et al.*[8] (curve 3 or 4 in Fig. 2) and experimental result of D'Andrea and Murrmann[9] to support the sufficiency of the TL model. However, the result of Ting and Chen does not necessarily predict the accurate maximum influence of the constriction resistance. This is due to the ambiguity in their sum equation as pointed out in Section I. Furthermore, their result plotted in Fig. 2 (curve 3 or 4) gives much lower end correction than the experimental data and the MTL prediction. The experimental result of D'Andrea and Murrmann[9] (Modelling by Resistance paper) also does not predict the maximum influence of current crowding effect since it neglects the crowding beneath the contact. Their result expresses only a partial constriction resistance and should be compared with Eq. [2] given above. Nevertheless, it is worthwhile mentioning that their calculated results using TL model (Table II, footnote 9) are much higher than their measured data for most cases except one where the calculation uncertainty is largest. This discrepancy seems to suggest that the proper contact sheet resistance and the influence on contact correction due to the existence of a gap, a, should have been considered.

Now let us turn to this question: For a fixed contact width, W_c, how does R_{cc} vary with varying resistor width, W_R, or gap, a? The answer lies in LHS of Fig. 2. The MTL model predicts that R_{cc} decreases with increasing a or W_R (curve 6) whereas the TL model predicts a constant R_{cc} regardless of the resistor size (curve 7). If one would use W_R instead of constant W_c in TL's expression (Eq. [12], footnote 7), one would obtain curve 8 on LHS and result in a constant value on RHS of Fig. 2. Note that curves 7 and 8 trace out a closed loop in Fig. 2. This closed loop is similar to that traced out by curves 1 and 2, which result from the fact that Eq. [1] was derived under the assumption $W_R = W_c$. When this assumption no longer holds, it is uncertain whether W_R or W_c should be used in the calculation. The MTL model does not have this ambiguity; it does predict correct contact correction term for various contacts in a given resistor (RHS, Fig. 2). However, it would be interesting to obtain experimental data for a given contact contained in resistors of various widths to confirm the LHS of curve 6.

It has been demonstrated in my original paper that, in order to correctly predict both R_{cc} and R_c of aluminum and molybdenum contacts, the parameter, ρ_s', has to have values much lower than the original diffusion sheet resistance, ρ_s. This may or may not have physical significance, since there is no other direct evidence verifying the physical significance of the model parameters ρ_s' and σ_c simultaneously. Therefore, it would be interesting to see Berger's unpublished data on these parameters. Nevertheless, the fact that ρ_s' and σ_c can be uniquely derived from experimental test structure (Eq. [7, 15] and Eq. [5, 16] in footnote 7—two equations with two unknowns), it warrants the necessity of introducing ρ_s' in addition to ρ_s (which is determined by another independent equation, Eq. [6], footnote 7). The fact that the model calculation does agree with experimental data (Fig. 4-6, footnote 7) suggests that MTL is at least a good phenomenological model which can give a realistic estimate of contact correction term for any given contact size and fabrication process provided the model parameters are determined experimentally. This is the purpose of MTL model.

Acknowledgments

The author is grateful to Dr. C. Y. Ting for many lengthy discussions on this work. Thanks are also due to Drs. B. Kazan and W. B. Pennebaker for their interest in this work.

The Ga-GaP-GaAs Ternary Phase Diagram

G. A. Antypas (pp. 700-703, Vol. 117, No. 5)

G. B. Stringfellow:[16] Concerning the paper by G. A. Antypas, the author uses the Darken quadratic formalism for calculating activity coefficients in the ternary liquid phase. For calculating activity coefficient ratios, *i.e.* γ_i/γ_i^{STC}, where i = A, B, or C, the Darken quadratic formalism is equivalent to the regular solution formalism. For example, in the Darken formalism

$$\ln(\gamma_B) - \ln(\gamma_B^{STC}) = \ln(\gamma_B/\gamma^\circ_B) - \ln(\gamma_B^{STC}/\gamma^\circ_B)$$
$$= -2\alpha_{AB}N_B + (\alpha_{BC} - \alpha_{AB} - \alpha_{AC})N_C + \alpha_{AB}N^2_B + \alpha_{AC}N^2_C + (\alpha_{AB} + \alpha_{AC} - \alpha_{BC})N_BN_C - (-\alpha_{AB} + \alpha_{AB}/4)$$

This can be reduced, using the relation

$$N_A + N_B + N_C = 1$$

to give

$$\ln(\gamma_B) - \ln(\gamma_B^{STC}) = \alpha_{BC}N^2_C + \alpha_{AB}N^2_A + (\alpha_{BC} - \alpha_{AC} + \alpha_{AB})N_AN_C - \alpha_{AB}/4$$

which is the expression calculated using the regular solution model (see Prigogine and Defay[17]).

The equilibrium equations used in the calculation of III-V binary and ternary phase diagrams, contain activity coefficients only in the ratios γ_i/γ_i^{STC}. Thus, the regular solution formalism is equivalent to the Darken quadratic formalism for all such calculations.

G. A. Antypas: Dr. Stringfellow observed that since the activity coefficients appear in the form of ln γ_i/γ_i^{STC}, the Darken formulation is equivalent to the regular solution in describing III-V ternary liquid solutions. An inherent assumption made in showing

[16] Solid State Laboratory, Hewlett-Packard Company, Palo Alto, California, 94304.

[17] I. Prigogine and R. Defay, "Chemical Thermodynamics," p. 257, Longmans, Green & Co., London (1954).

spreading beneath the contact and one for along the two sides of the contact (due to symmetry two sides can be combined). The MTL model is just based on this concept. The model parameters, the distributive resistance elements (ρ_s' and σ_c in addition to ρ_s) for any given fabrication process can be uniquely derived from experimental measurements using a test pattern such as shown in Fig. 1, footnote 7. The fact that the model calculation agrees very well with experimental data of various sizes of Al and Mo contacts (see Fig. 4-6, footnote 7) seems to support this concept.

To further discuss the significance of MTL model, we plot its numerical result (curve 6) in Fig. 2 for a typical resistor (width = 2.3 mil) on the RHS and for a typical contact (width = 0.3 mil) on the LHS. On the RHS curve 6 and other theoretical calculations (except curve 1) all predict the same tendency, *i.e.*, when the contact becomes smaller at a fixed resistor width, R_{cc} increases. One notes that although other calculations (curves 2, 3, 4, 5, and 7) do qualitatively indicate the trends of variation, only the MTL result agrees with the experimental data (circles in Fig. 2). This is what is expected. Now let us examine the TL model: If the contact sheet resistance, ρ_s', were not introduced, the model would predict much too high a correction (~30% too high compared with experimental data). If the proper sheet resistivity, ρ_s', under the contact were used in the TL model (Eq. [12], footnote 7), it would result in still higher end correction (curve 7) than the MTL result (curve 6) as Berger indicates in his discussion. However, the experimental data (from Fig. 4, footnote 7) seem to fit the MTL result better, particularly when a, the gap, is large (the experimental data is not inversely proportional to W-$2a$ in Fig. 4-6, footnote 7). The difference between the TL result (curve 7) and the MTL result or the experimental data is about 5 ohms for $a = 0.9$ or $W_c = 0.3$ mils.

Berger has quoted the theoretical result of Ting *et al.*[8] (curve 3 or 4 in Fig. 2) and experimental result of D'Andrea and Murrmann[9] to support the sufficiency of the TL model. However, the result of Ting and Chen does not necessarily predict the accurate maximum influence of the constriction resistance. This is due to the ambiguity in their sum equation as pointed out in Section I. Furthermore, their result plotted in Fig. 2 (curve 3 or 4) gives much lower end correction than the experimental data and the MTL prediction. The experimental result of D'Andrea and Murrmann[9] (Modelling by Resistance paper) also does not predict the maximum influence of current crowding effect since it neglects the crowding beneath the contact. Their result expresses only a partial constriction resistance and should be compared with Eq. [2] given above. Nevertheless, it is worthwhile mentioning that their calculated results using TL model (Table II, footnote 9) are much higher than their measured data for most cases except one where the calculation uncertainty is largest. This discrepancy seems to suggest that the proper contact sheet resistance and the influence on contact correction due to the existence of a gap, a, should have been considered.

Now let us turn to this question: For a fixed contact width, W_c, how does R_{cc} vary with varying resistor width, W_R, or gap, a? The answer lies in LHS of Fig. 2. The MTL model predicts that R_{cc} decreases with increasing a or W_R (curve 6) whereas the TL model predicts a constant R_{cc} regardless of the resistor size (curve 7). If one would use W_R instead of constant W_c in TL's expression (Eq. [12], footnote 7), one would obtain curve 8 on LHS and result in a constant value on RHS of Fig. 2. Note that curves 7 and 8 trace out a closed loop in Fig. 2. This closed loop is similar to that traced out by curves 1 and 2, which result from the fact that Eq. [1] was derived under the assumption $W_R = W_c$. When this assumption no longer holds, it is uncertain whether W_R or W_c should be used in the calculation. The MTL model does not have this ambiguity; it does predict correct contact correction term for various contacts in a given resistor (RHS, Fig. 2). However, it would be interesting to obtain experimental data for a given contact contained in resistors of various widths to confirm the LHS of curve 6.

It has been demonstrated in my original paper that, in order to correctly predict both R_{cc} and R_c of aluminum and molybdenum contacts, the parameter, ρ_s', has to have values much lower than the original diffusion sheet resistance, ρ_s. This may or may not have physical significance, since there is no other direct evidence verifying the physical significance of the model parameters ρ_s' and σ_c simultaneously. Therefore, it would be interesting to see Berger's unpublished data on these parameters. Nevertheless, the fact that ρ_s' and σ_c can be uniquely derived from experimental test structure (Eq. [7, 15] and Eq. [5, 16] in footnote 7—two equations with two unknowns), it warrants the necessity of introducing ρ_s' in addition to ρ_s (which is determined by another independent equation, Eq. [6], footnote 7). The fact that the model calculation does agree with experimental data (Fig. 4-6, footnote 7) suggests that MTL is at least a good phenomenological model which can give a realistic estimate of contact correction term for any given contact size and fabrication process provided the model parameters are determined experimentally. This is the purpose of MTL model.

Acknowledgments

The author is grateful to Dr. C. Y. Ting for many lengthy discussions on this work. Thanks are also due to Drs. B. Kazan and W. B. Pennebaker for their interest in this work.

The Ga-GaP-GaAs Ternary Phase Diagram

G. A. Antypas (pp. 700-703, Vol. 117, No. 5)

G. B. Stringfellow:[16] Concerning the paper by G. A. Antypas, the author uses the Darken quadratic formalism for calculating activity coefficients in the ternary liquid phase. For calculating activity coefficient ratios, *i.e.* γ_i/γ_i^{STC}, where i = A, B, or C, the Darken quadratic formalism is equivalent to the regular solution formalism. For example, in the Darken formalism

$$\ln(\gamma_B) - \ln(\gamma_B^{STC}) = \ln(\gamma_B/\gamma^\circ_B) - \ln(\gamma_B^{STC}/\gamma^\circ_B)$$
$$= -2\alpha_{AB}N_B + (\alpha_{BC} - \alpha_{AB} - \alpha_{AC})N_C + \alpha_{AB}N^2_B + \alpha_{AC}N^2_C + (\alpha_{AB} + \alpha_{AC} - \alpha_{BC})N_BN_C - (-\alpha_{AB} + \alpha_{AB}/4)$$

This can be reduced, using the relation

$$N_A + N_B + N_C = 1$$

to give

$$\ln(\gamma_B) - \ln(\gamma_B^{STC}) = \alpha_{BC}N^2_C + \alpha_{AB}N^2_A + (\alpha_{BC} - \alpha_{AC} + \alpha_{AB})N_AN_C - \alpha_{AB}/4$$

which is the expression calculated using the regular solution model (see Prigogine and Defay[17]).

The equilibrium equations used in the calculation of III-V binary and ternary phase diagrams, contain activity coefficients only in the ratios γ_i/γ_i^{STC}. Thus, the regular solution formalism is equivalent to the Darken quadratic formalism for all such calculations.

G. A. Antypas: Dr. Stringfellow observed that since the activity coefficients appear in the form of ln γ_i/γ_i^{STC}, the Darken formulation is equivalent to the regular solution in describing III-V ternary liquid solutions. An inherent assumption made in showing

[16] Solid State Laboratory, Hewlett-Packard Company, Palo Alto, California, 94304.

[17] I. Prigogine and R. Defay, "Chemical Thermodynamics," p. 257, Longmans, Green & Co., London (1954).

such equivalence, however, is that the interaction parameters (α_{ij}) are independent of composition. In calculating the interaction parameters of III-V compounds, Vieland's[18] regular solution approach has been used extensively which results in temperature-dependent parameters only. A recent analysis of available thermodynamic data of GaAs and GaP made by Rao and Tiller[19] showed that the interaction parameters of these compounds in addition to being temperature dependent are also strong functions of composition. Under this condition, the ratio of the activity coefficients based on Darken's formulation becomes

$$\ln \frac{\gamma_B}{\gamma_B^{STC}} = \alpha_{BC}N_C^2 + \alpha_{AB}N_B^2 + (\alpha_{BC} - \alpha_{AC} + \alpha_{AB})N_AN_C - \alpha_{AB} + \frac{3}{4}\alpha_{AB}^{STC}$$

[18] L. J. Vieland, *Acta Met.*, **11**, 137 (1963).
[19] M. V. Rao and W. A. Tiller, *J. Phys. Chem. Solids*, **31**, 191 (1970).

where α_{AB}^{STC} is the interaction parameter of AB at the stoichiometric composition.

A second assumption made in showing such equivalence is that the i^{th} component must be treated as a solute in both the ternary and stoichiometric binary solutions. This is the case in ternary systems having one column III and two column V elements (assuming of course that the column III element is always the solvent for both the ternary and the two stoichiometric binary solutions). However, for a ternary system, A-B-C, where A and B are column III elements and C is a column V element with B and C being the solutes, the activity coefficient ratio $\ln \gamma_B/\gamma_B^{STC}$ does not reduce to that described by the regular solution even when the interaction parameters are independent of composition. For such a system, γ°_C in A (the activity coefficient at infinite dilution of C in A), γ°_C in B and γ°_B in A are needed to describe the ternary system using Darken's formulation. None of these parameters, however, are required for the regular solution treatment.

JOURNAL OF THE ELECTROCHEMICAL SOCIETY

ELECTROCHEMICAL TECHNOLOGY

JUNE 1971

The Microstructure of Sintered Silver Electrodes

IV. Formation of AgO during Charges

Charles P. Wales*

Electrochemistry Branch, Naval Research Laboratory, Washington, D. C. 20390

ABSTRACT

Silver electrodes were cycled in 35% KOH solution and examined at various times during constant current charges. The initial formation of AgO took place on the surface of Ag_2O after charge potential rose to the Ag_2O/AgO plateau. Preferred locations for initial oxidation of Ag_2O were in the interior of the electrode, around the grid and near large Ag particles where the Ag_2O coating which formed earlier in the charge was comparatively thin. After initial AgO formation in an electrode, oxidation of nearby Ag and Ag_2O took place as the charge continued. Little or no additional Ag was oxidized in other areas of the electrode until AgO had formed there also.

The structure of silver electrodes of the type used in storage batteries is of interest, because knowledge of the structure helps in explaining the capacity changes observed when cells containing Ag electrodes are cycled. Earlier papers in this series have described changes in structure during discharges (1) and at the end of discharges (2), as well as formation of Ag_2O during charges (3). Electrodes in this work were cycled using the relatively fast 1 hr rate of discharge and the 20 hr rate of charge.

The size of Ag produced during a discharge as silver oxides are reduced depends on the rate of reduction. Fast discharges produce smaller Ag particles than slow discharges (1, 2). The electrolyte plays an important role in the formation of these particles. During a discharge, the electrolyte becomes supersaturated with dissolved Ag_2O (4). Although reduction can take place through a dissolved species, the reduction of dissolved Ag_2O is reported to be much slower than reduction of the oxide on the surface of an electrode (5). At a high discharge C.D., there are larger concentration gradients in the electrolyte and in the oxide than during slow discharges. These differing conditions promote formation of small dendritic Ag particles during a rapid discharge (2), while much larger Ag particles form during a slow discharge (6).

The size of particles produced during a discharge is very important, because in the subsequent charge small Ag particles are oxidized more readily and to a greater extent than large particles. This advantage of fast discharges in producing small particles is partially offset by fast discharges taking place at lower potentials. As a result, cells can reach the cutoff potential before all oxides have been reduced to Ag.

Experimental Procedure

Sintered Ag electrodes were cycled in 35% KOH solution at 25°C. All charges were done at the 20 hr rate of constant current, and all discharges at the 1 hr rate. Samples were cut from the electrode at various times during charges. Polished cross sections of the samples were examined using a light microscope. Details of the experimental procedure were presented earlier (1).

Results

Oxidation of Ag_2O to AgO.—All Ag particles in a porous Ag electrode had a definite Ag_2O coating by the time that potential reached the peak that ends the Ag/Ag_2O potential plateau and begins the Ag_2O/AgO plateau of a constant current charge (3). This was the condition of the active material in an electrode when AgO began to form.

The formation of AgO in a cycled electrode which had been partially charged at the Ag_2O/AgO potential is shown in Fig. 1. All photographs in this paper are cross sections through electrodes and, therefore, show cross sections through the individual crystals or particles in an electrode. After charge potential had reached the peak, the electrode in Fig. 1 was given an additional amount of charge equal to 8% of the total capacity usually accepted during a complete charge. This additional charge would have been sufficient to oxidize 21% of the Ag_2O that had formed earlier in this charge, if the reaction had consisted only of Ag_2O being oxidized to AgO. It was evident, however, that some Ag had also been oxidized after reaching the potential peak. The total charge given the electrode shown in Fig. 1 was 47% of the charge usually accepted before oxygen evolution began.

AgO had formed in many areas of this partly charged electrode, chiefly in the interior. An area where a large amount of AgO was present is in the center of Fig. 1. AgO was comparatively rare on the surface of the electrode. It had formed around all of the grid members and usually was found adjacent to the large Ag particles in an electrode. Almost all of the largest AgO particles had formed near large Ag particles. Most areas surrounding clumps of AgO crystals in the partly charged electrode were still largely Ag_2O and Ag. These areas of Ag_2O and Ag were identical in appearance to the Ag_2O and Ag present in an electrode charged to the potential peak (3), except that small AgO particles were often present in these areas. A few

* Electrochemical Society Active Member.

Key words: silver electrode, silver oxidation, silver oxide, electrode structure.

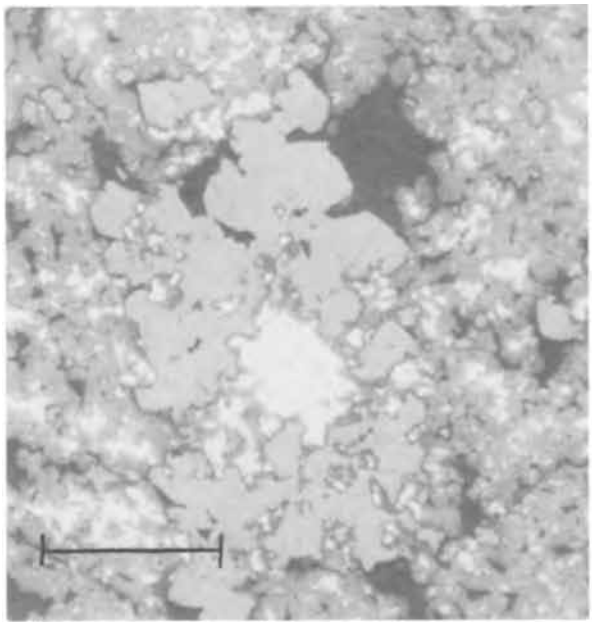

Fig. 1. Silver electrode partly charged at Ag_2O/AgO potential plateau at cycle 6, showing large AgO crystals that form after Ag_2O has formed in the electrode. Metallic Ag is white, AgO is light gray and predominates in the central areas of this photograph, Ag_2O is darker gray, and void areas are black. Marker indicates 15μ.

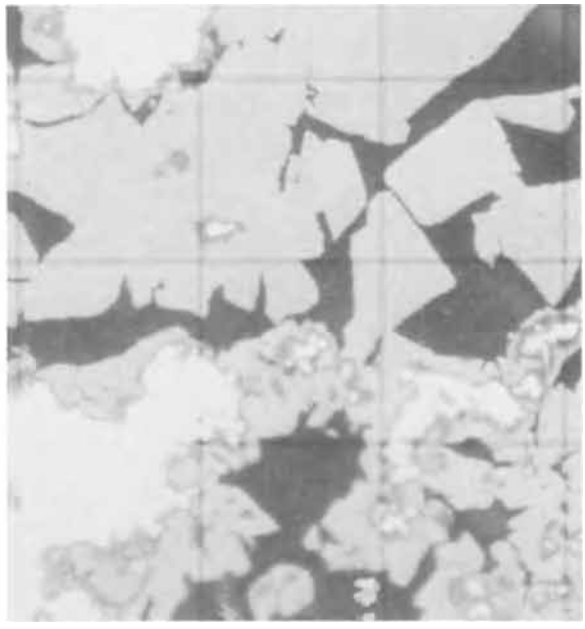

Fig. 2. Silver electrode charged to oxygen evolution at cycle 2. The majority of the active material was oxidized to AgO (light gray). Silver was the next most common form present (white). A thin layer of Ag_2O (darker gray) separated the Ag from the AgO. Small Ag_2O particles were also present at scattered sites in the AgO. Lines forming squares are 15μ apart.

small AgO particles can be seen among the Ag_2O and Ag in Fig. 1.

Charged electrode at cycle 2.—Conditions during the first charge were different from those during later charges. The average size of Ag particles in an unused sintered Ag electrode was larger than the size produced as silver oxides were reduced during a fast discharge. At cycle 2 and at later cycles, much of the oxidation was taking place on the small Ag particles which had been formed in the fast discharges. Thus the appearance of an electrode at cycle 2 is a better starting point than cycle 1 for describing the gradual changes that take place as an electrode is cycled using fast discharges.

Typical AgO formations in an electrode charged to oxygen evolution at cycle 2 are shown in Fig. 2. This electrode had accepted approximately 66% of theoretical capacity before oxygen evolution became strong. Some areas of the electrode contained large clumps of AgO crystals, such as the top of Fig. 2. The area at the bottom of Fig. 2 contained smaller AgO crystals and resembled the center of Fig. 1. In some parts of the electrode, the active material was more densely packed and contained less void space than is shown in Fig. 2. A few small areas contained several oblong AgO particles which were aligned approximately parallel to each other. Different groups of these oblong particles were aligned at random, although particles in any one group tended to be aligned in a single direction.

The Ag_2O coating that separated the remaining Ag from the AgO was thicker on small Ag particles than on large Ag particles. Although relatively little Ag_2O remained in some areas of the electrode (top of Fig. 2) Ag_2O was prominent in areas containing small Ag particles and where Ag_2O particles were present in small clumps.

Another area of the same electrode is shown in Fig. 3. This illustrates the sizes of AgO particles and voids early in the cycle life. The AgO crystals at the end of a charge were larger than the Ag_2O crystals that had formed earlier while charging at the Ag/Ag_2O potential. Many small pores had been present in the Ag_2O but, as the charge took place at the Ag_2O/AgO potential, the AgO which formed tended to fill these pores. The large voids between clumps of active material changed little in size during a charge.

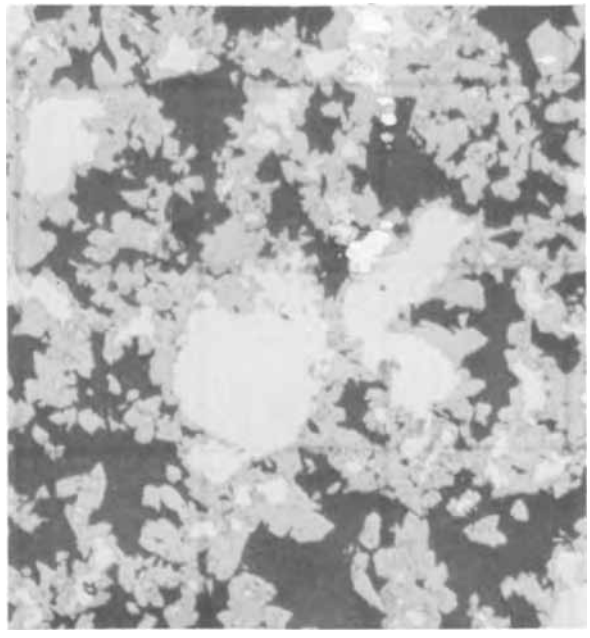

Fig. 3. Electrode charged to oxygen evolution at cycle 2. Same electrode as shown in Fig. 2, but at lower magnification. Lines forming squares are 60μ apart.

Effects of C.D. and cycling.—The capacity accepted during a charge gradually decreased as electrodes were cycled. The rate of decrease varied greatly, depending on conditions of the preceding discharges. The charges shown in Fig. 4 indicate typical potentials as electrodes were cycled. Capacity decreased slowly when all discharges were done at the 1 hr rate. Results from an electrode always discharged at the 20 hr rate are included in Fig. 4 for comparison. As can be seen by the charge curves at cycle 1, the two electrodes had accepted somewhat different amounts of capacity when the previously unused electrodes were charged for the first time. Then charge acceptance

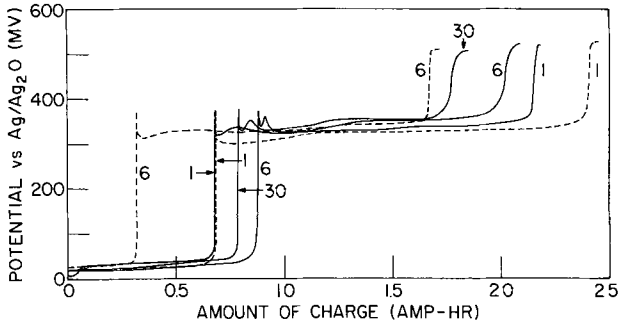

Fig. 4. Potentials at two Ag electrodes during charges at the 20 hr rate in 35% KOH at 25°C. Solid lines show charges at cycles 1, 6, and 30 of an electrode always discharged at the 1 hr rate. Dashed lines show charges at cycles 1 and 6 of an electrode always discharged at the 20 hr rate.

decreased rapidly during the first few cycles using slow discharges. As a result of this rapid decrease, the charge acceptance was less after 6 slow discharges than after 30 fast discharges.

Another change was in the shape of the potential curve at the end of a charge as potential rose to the oxygen evolution value. The final rise in charge potential was slow following rapid discharges. This can be seen in Fig 4 by comparing the gradual rise in potential shown by the solid lines at cycles 6 and 30 with the faster rise at cycle 1. Potential rise to oxygen evolution was much more rapid at the end of charges following slow discharges (dashed line at cycle 6).

The proportion of a charge that was accepted at the Ag_2O/AgO potential plateau varied, depending on discharge conditions (Fig. 4 and 5). During the first few charges that followed fast discharges, increasing amounts of Ag_2O were formed before potential reached the charge peak, while capacity accepted at the Ag_2O/AgO potential decreased proportionately. This resulted in a decrease in the per cent of a charge that took place at the Ag_2O/AgO plateau (circles, lower portion of Fig. 5).

In contrast, sharply decreasing amounts of Ag_2O formed during the first few charges that used slow discharges, while charge acceptance at the Ag_2O/AgO plateau also decreased, but more slowly. The per cent of a charge taking place at the Ag_2O/AgO potential plateau increased in this period for electrodes given slow discharges (Fig. 5). Charge acceptance became relatively constant beginning at cycle 3 when fast discharges were used, and at cycle 4 or 5 when using slow discharges.

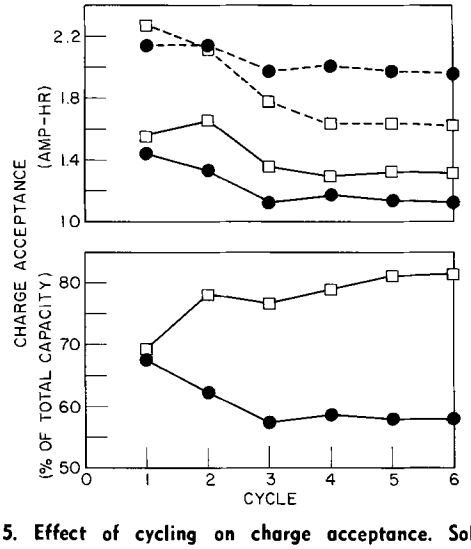

Fig. 5. Effect of cycling on charge acceptance. Solid lines, charge acceptance at the Ag_2O/AgO potential. Dashed lines, total charge acceptance. Circles are averages of 4 electrodes always charged at the 20 hr rate and discharged at the 1 hr rate. Squares are averages of 9 electrodes always charged and discharged at the 20 hr rate.

In calculating the arithmetic means shown in Fig. 5, the charge acceptance was assumed to equal the capacity given electrodes when charge potential reached 450 mV *vs.* the Ag/Ag_2O reference electrode. The computations did not include any electrodes from which samples had been removed, because of uncertainty as to the exact amount that capacity was lowered when each sample was cut. Small cracks often developed when a sample was cut and pieces of active material broke away from the electrode. A charged electrode was particularly brittle and subject to cracking when a sample was cut.

Some electrodes always accepted and delivered a greater or smaller capacity than other electrodes treated similarly. This variation in capacity resulted in the measured values being spread over a range. If a sufficiently large number of electrodes had been used, no doubt the difference in the calculated arithmetic means would have disappeared for the first charge of a previously unused electrode. The significance of the difference between the means for charge acceptance expressed as per cent was determined by the t-distribution test. These means (lower portion of Fig. 5) were not significantly different for the two sets of electrodes at cycle 1. The differences became highly significant (less than 0.1% probability that the differences were not significant) when the means for the two sets of electrodes were compared at cycles 2-6.

Charged electrode at cycle 15.—One of the most noticeable structural changes as an electrode was cycled was the gradual clumping of the active material. This change was evident in both discharged and charged electrodes (2, 3). The AgO in a charged electrode was in the form of small angular particles at cycle 2, with small voids in the AgO (Fig. 3). The active material agglomerated sufficiently rapidly that by cycle 5 large clumps of AgO were present at the end of a charge. The clumps continued to grow in size as an electrode was cycled. An example of the AgO in a charged electrode at cycle 15 is given in Fig. 6. The angular shapes typical of AgO in the early cycles (Fig. 2, 3) were less common at cycle 15. The number of small voids in the active material

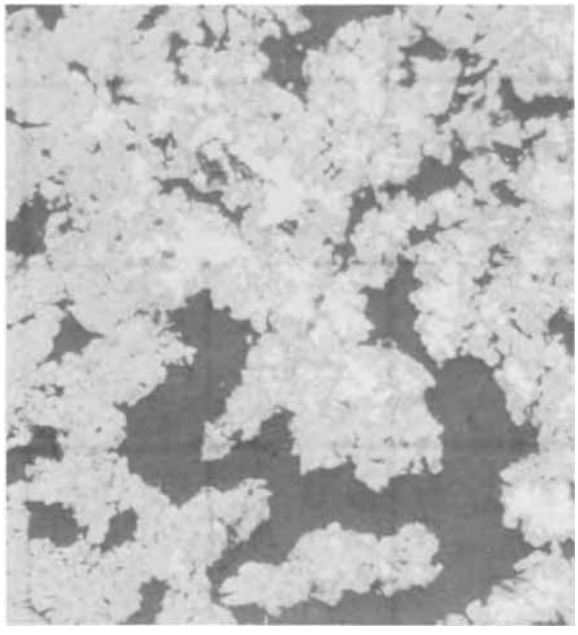

Fig. 6. Silver electrode charged to oxygen evolution at cycle 15. Lines forming squares are 60μ apart. Comparison with Fig. 3 indicates the way active material clumped as an electrode was cycled.

gradually decreased as an electrode was cycled, while the large voids were increasing in size.

Another change that took place with cycling was the increased amount of Ag_2O present at the end of a charge. Although AgO was the predominant form of oxide in an electrode charged to oxygen evolution, much Ag_2O was also present at cycle 15. The amount of Ag_2O present at the end of a charge had increased in the first few cycles which used discharges at the 1 hr rate. Little additional change in the Ag_2O was noted after cycle 5.

The oxide coating that formed on large Ag particles and on the grid gradually thickened with cycling. The grids were closer to one surface of the electrode than to the other. A charged electrode usually had a gray-colored surface but, in the sample taken at cycle 15, the grid was outlined in a shade of gray that was lighter than most of the remainder of the surface. When a cross section of this electrode was examined under the microscope, however, no difference was noted between the AgO on the surface next to a grid member and the AgO in other areas of the surface. The difference in shades of gray may have resulted from fewer voids on the parts of the surface next to grid members.

Charged electrode at cycle 28.—Many of the structural changes that had taken place between cycles 2 and 15 continued to take place as an electrode was given additional cycles. A portion of a charged electrode at cycle 28 is shown in Fig. 7. The surface of this electrode had a granular appearance and contained light and dark gray areas, with dark gray predominating slightly. The clumps of active material were larger than they had been at cycle 15 (compare Fig. 7 with 6). The size of large voids between the clumps had increased between cycles 15 and 28, but the change in size was less than the increase between cycles 2 and 15 (Fig. 3 and 6).

In a charged electrode that had been cycled many times, part of the AgO was present as large groups of crystals. An example of an area where many AgO crystals had grown together is shown in Fig. 8. Large areas that were mainly AgO were common in the early cycles (see top of Fig. 2). These areas gradually became less common as an electrode was cycled. The angular shapes typical of AgO crystals became less evident as an electrode was cycled and masses of AgO crystals tended to be more tightly packed. The oxide layer on the grid of a charged electrode gradually thickened and was much thicker at cycle 28 than at cycle 2.

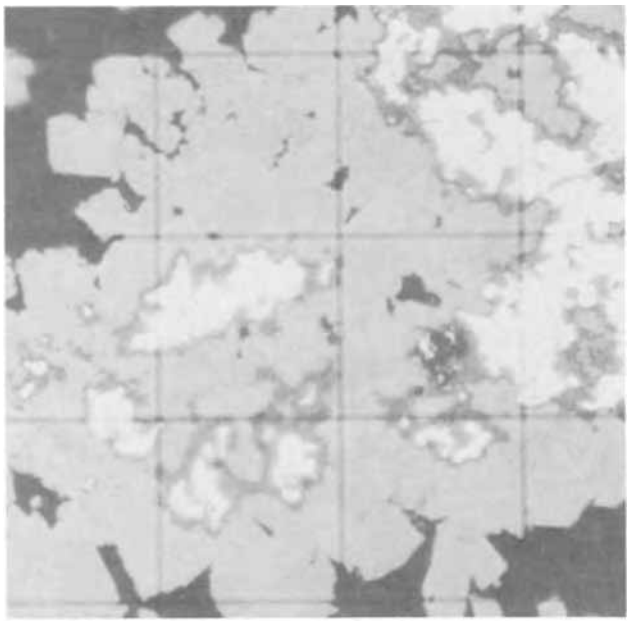

Fig. 8. Large clumps of AgO crystals present in an electrode charged to oxygen evolution at cycle 28. Same electrode as Fig. 7, but a different area and at higher magnification. Lines forming squares are 15μ apart.

Although unpolarized light was the most useful illumination for general viewing of polished cross sections of the electrodes, polarized light often gave additional information. All photographs from Fig. 1 to 8 were made using unpolarized light. The same area shown in Fig. 8 is shown in Fig. 9 using polarized light and a sensitive tint plate. Under both types of illumination, the light was at right angles to the polished surface of the electrode. The polycrystalline nature of the AgO clumps became evident when polarized light was used. This technique does not differentiate between individual Ag crystals or Ag_2O crystals. Ag_2O crystals must be smaller than AgO crys-

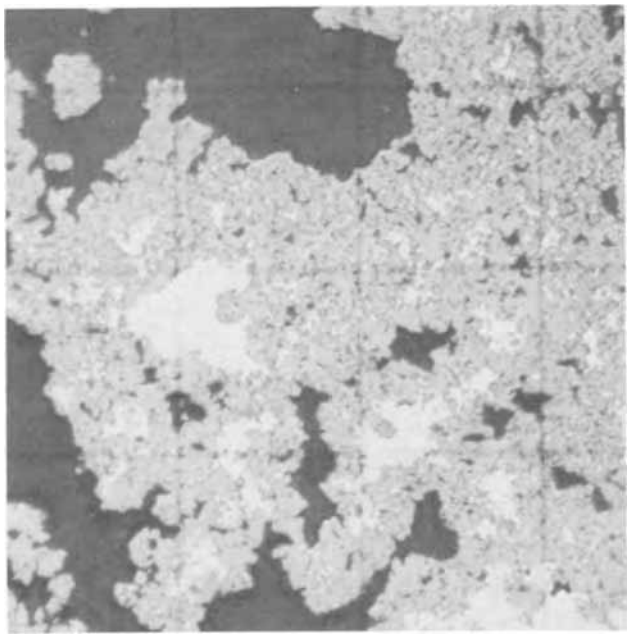

Fig. 7. Silver electrode charged to oxygen evolution at cycle 28. Lines forming squares are 60μ apart. Comparison with Fig. 3 and 6 shows that cycling resulted in a gradual increase in size of voids and clumps of active material.

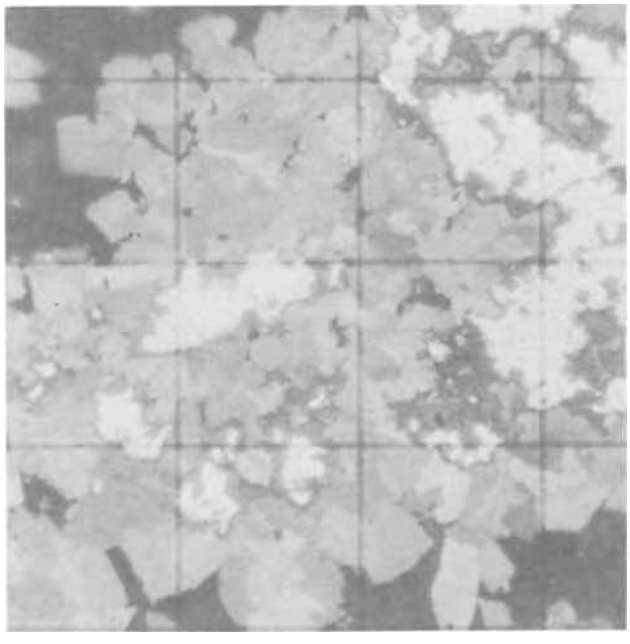

Fig. 9. Same area as Fig. 8, but using polarized light and a sensitive tint plate so that many of the individual AgO crystals can be differentiated from each other.

tals, however, because individual Ag_2O clumps were smaller than most AgO crystals.

At the end of a charge, most areas of well-cycled electrode contained more Ag_2O than the area shown in Fig. 8. A more typical area of the same electrode is given in Fig. 10. Many small Ag_2O clumps and Ag particles were present in this electrode. By the time that oxygen evolution began, all Ag was covered with Ag_2O and the Ag_2O covered with AgO. In a few areas, the Ag_2O layer that separated Ag from AgO was thicker than the layer shown in Fig. 8-10. The area shown in Fig. 10 should be compared with the bottom of Fig. 2 where a somewhat similar structure was present. Only small regions with a structure such as this were found at cycle 2.

Oxides having a particular clump size were randomly distributed in a charged electrode in the early cycles, but distribution became uneven as the cycling progressed. The surface areas of a charged electrode differed from the interior in several ways at cycle 28. AgO crystals near the electrode surface were smaller than the AgO in the interior. Ag_2O was more abundant in the surface areas than elsewhere. Clumps of particles oriented at right angles to the surface were sometimes found on the electrode surfaces at cycle 28, but were not common. None of these differences between the surface and interior were present in an electrode at cycle 2.

The particles of metallic Ag that remained at the end of a charge were not randomly distributed at cycle 28 but predominated in the interior of the electrode. Earlier work has shown that large particles of Ag gradually developed in the interior of an electrode under the cycling conditions used here (2). Many Ag particles remained in the large AgO clumps at the end of cycle 28 charge (Fig. 7 and 10). The number of intermediate-sized Ag particles had also increased.

Discussion

Anodic formation of AgO.—It is well known that Ag_2O is the first product when Ag is anodically oxidized in alkaline solution. Then, under constant current conditions, AgO begins to form after anodic potential makes a sharp rise of approximately 0.3V above the Ag/Ag_2O potential plateau. Small amounts of AgO can be detected after potential exceeds the Ag_2O/AgO equilibrium value but before potential reaches the peak (7). After reaching the peak, potential declines to the Ag_2O/AgO charging plateau and formation of AgO is the main reaction. A secondary reaction is the oxidation of additional Ag to Ag_2O. It has been established by x-ray diffraction that the initial formation of AgO takes place on the surface of Ag_2O crystals next to the electrolyte (7, 8). Observations using electron microscopy (9, 10) and light microscopy (6) have shown that AgO crystals grow to larger sizes than Ag_2O crystals when Ag electrodes are oxidized anodically in alkaline solutions. Kinetic work on the anodic oxidation of Ag_2O to AgO leaves some doubt as to the way the oxidation occurs, since the conclusions reached in different studies do not agree with each other (11, 12).

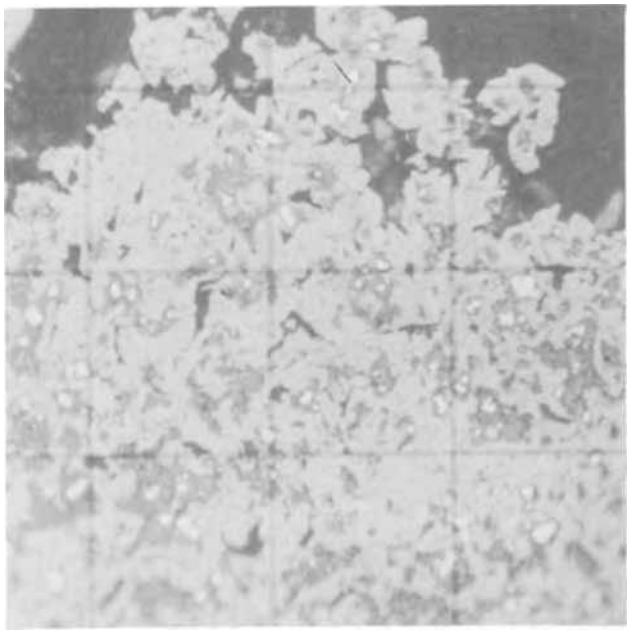

Fig. 10. Small Ag particles and clumps of Ag_2O that were present in the AgO near the surface of a charged electrode at cycle 28. Same electrode as Fig. 7-9. Lines forming squares are 15μ apart.

Microscopic examination of the electrodes indicated that the formation of AgO differed from formation of Ag_2O. Ag_2O had formed at scattered sites throughout the electrode, both at the surface and the interior (3). Ag_2O had formed preferentially and to a greater extent on the smallest Ag particles. When AgO began to form during a charge, however, AgO tended to form first near large Ag particles and around the grid members. These were places where the Ag_2O coating was thinnest.

The grid and most large Ag particles served as a conducting network in the electrode. Potential drop between the Ag_2O/solution interface and this conducting network should be smallest in places where the Ag_2O coating was thinnest. Therefore, when potential rose above the Ag_2O/AgO equilibrium value, the potential at the Ag_2O/solution interface was highest on the grid and on the large particles, and AgO nucleated here initially. The reason that AgO was comparatively rare on the surface of an electrode that was partly charged at the Ag_2O/AgO potential plateau was because most large Ag particles were in the interior of the electrode and not on the surface.

After the initial nucleation of AgO at various sites in the electrode, the AgO then spread to surrounding areas. It can be seen in Fig. 1 that metallic Ag was less common where AgO had formed than in adjacent areas where Ag_2O predominated. After AgO had formed, oxidation of neighboring Ag and Ag_2O took place simultaneously. Oxidation was concentrated near these AgO areas, with no additional oxidation of Ag to Ag_2O visible in other areas until AgO had formed there also.

Groups of AgO crystals grew together into relatively large bodies (Fig. 2, 8). Judging by the size of individual crystals in these large masses of AgO (Fig. 9), it is likely that the individual crystals formed from different clumps of Ag_2O. Many of the large masses of AgO crystals may begin forming in the way illustrated in Fig. 1, with AgO first forming a layer around Ag particles that is almost free from pores. There seems to be little additional oxidation of Ag particles after a complete coating of AgO has formed around the Ag. After a certain thickness is reached, the AgO does not thicken appreciably as a result of additional oxidation of the coated particles, but thickens as the surrounding Ag_2O and Ag are oxidized to AgO and the AgO clumps contact each other. The AgO needs only to have electronic conduction for large bodies of AgO to form in this way. Electrolyte diffusion should become increasingly hindered during a charge because AgO occupies a larger volume than Ag or Ag_2O and tends to fill the smallest voids in the electrode.

The amount of Ag_2O present at the end of a charge gradually built up as the cycling progressed (Fig. 3, 6, 7). Perhaps the reason for increased Ag_2O, and for it being more abundant near the surface of the electrode, was connected to changes in the current distribution as the active material clumped with cycling. Many of the Ag and Ag_2O particles in a charged electrode had only a thin AgO coating (less than 1μ) separating the particles from the electrolyte (Fig.

10). The fact that these particles had not been oxidized to AgO during the charge indicated that ion conduction did not take place through the solid AgO to a very great extent under these charging conditions.

Decline of capacity with cycling.—Capacity changes were the result of changes in the microstructure of these electrodes. It was mentioned earlier that larger Ag particles gradually developed as an electrode was cycled, particularly in the interior of the electrode. Since large Ag particles do not oxidize as completely or as readily as small particles, a greater amount of Ag remained in an electrode at the end of a charge at cycles 25-30 than at cycles 1-5. The increased amount of metallic Ag present at the end of a charge was reflected in a gradual decrease of the charge acceptance as an electrode was cycled. Charge acceptance usually fell in the range 60-65% of theoretical capacity at cycle 28. Earlier these electrodes had accepted 65-80% at cycle 2.

In contrast, electrodes discharged at the 20 hr rate gave a large capacity at cycle 1, since almost all oxide could be reduced during a slow discharge (Fig. 5). But, electrodes discharged at this slow rate formed Ag particles that were more than 10 times the size of the small particles which formed during a discharge at the 1 hr rate. Capacity dropped rapidly as a result of the large Ag particles not oxidizing completely in subsequent charges.

When potential fell to the cutoff value at the end of a discharge at the 1 hr rate, an electrode still contained approximately 1/10 of the oxide that had been present at the end of a charge. The proportion of oxide that was not reduced during a discharge remained approximately constant with cycling, when all cycles used the same rate of discharge. As a result of the same amount always remaining, and little oxygen evolving except at the end of a charge, beginning with cycle 2 the electrodes gave close to 100% efficiency. At cycle 1, however, efficiency averaged only 92% because part of the charge current was used in forming oxide which was not reduced during cycle 1 discharge. Judging only by charge acceptance, capacity seemed to decline 6% from cycle 1 to 6 (solid lines in Fig. 4), but the actual decrease in measured discharge capacity was only 2%. This difference between charge acceptance and discharge capacity resulted from the inefficiency of cycle 1, mentioned above.

Conclusions

1. The capacity decline with cycling was the result of changes in the microstructure. As larger Ag particles gradually developed in the electrode, mainly in the interior, a larger proportion of the active material remained in the metallic state at the end of a charge.

2. AgO formation showed a preference for sites where Ag_2O was thin, such as on the surface of large Ag particles and around the Ag grid in the electrode. This contrasted with Ag_2O forming at random sites earlier in a charge.

3. After AgO had formed, nearby Ag and Ag_2O were oxidized simultaneously, but further oxidation of Ag in other areas of an electrode did not take place until AgO had also formed in these areas.

4. AgO crystals were larger than Ag_2O crystals. Groups of AgO crystals grew together into large polycrystalline masses and tended to fill small pores in the active material.

5. As an electrode was cycled, it became less common to find large areas which were mainly AgO in a fully charged electrode. Instead, more small Ag particles and clumps of Ag_2O were present in a charged electrode.

6. At the end of a charge, the surface of a well-cycled electrode contained smaller AgO crystals and more Ag_2O than the interior.

Manuscript submitted Aug. 3, 1970; revised manuscript received *ca.* Jan. 28, 1971. This was Paper 56 presented at the Atlantic City Meeting of the Society, Oct. 4-8, 1970.

Any discussion of this paper will appear in a Discussion Section to be published in the December 1971 JOURNAL.

REFERENCES

1. C. P. Wales, *This Journal*, **116**, 729 (1969).
2. C. P. Wales, *ibid.*, **116**, 1633 (1969).
3. C. P. Wales, *ibid.*, **118**, 7 (1971).
4. B. Miller, *ibid.*, **117**, 491 (1970).
5. V. P. Galushko, E. F. Zavgorodnyaya, and Yu. P. Rodak, *Ukr. Khim. Zh.*, **34** 1075 (1968); *Chem. Abs.*, **70**, 51023 (1969).
6. C. P. Wales and A. C. Simon, *This Journal*, **115**, 1228 (1968).
7. C. P. Wales and J. Burbank, *ibid.*, **106**, 885 (1959).
8. C. P. Wales and J. Burbank, *ibid.*, **112**, 13 (1965).
9. S. Yoshizawa and Z. Takehara, *J. Electrochem. Soc. Japan*, **31**, 91 (1963).
10. G. W. D. Briggs, M. Fleischmann, D. J. Lax, and H. R. Thirsk, *Trans. Faraday Soc.*, **64**, 3120 (1968).
11. R. G. Barradas and G. H. Fraser, *Can. J. Chem.*, **42**, 2488 (1964); *ibid.*, **43**, 446 (1965).
12. M. Fleischmann, D. J. Lax, and H. R. Thirsk, *Trans. Faraday Soc.*, **64**, 3137 (1968).

General Equations for Gas Phase Compositions in Epitaxial Flow Systems

I. Amron*

Bell Telephone Laboratories, Incorporated, Murray Hill, New Jersey 07974

ABSTRACT

Equations are derived for computing the concentration of each reagent entering an epitaxial reactor from a gas train. The two basic types of systems are: (*a*) a main diluent stream, part of which is diverted through a number of parallel saturators, each containing several mutually miscible components; and (*b*) an all-gaseous system with several dilution stages. In addition, the equations for a hybrid system, which combines the two types, are also derived. The equations have no limits on the number of components or dilution stages.

Since the rate of growth of an epitaxial layer is determined by a number of factors, among which is the composition of the gas phase entering the reactor, it is necessary that the gas phase composition be known and well controlled. In order to achieve desired growth rates, the gas phase content of the epitaxial matrix source reagent must be low, usually a mole fraction less than 0.001. If the film is to be doped in a con-

* Electrochemical Society Active Member.
Key words: vapor saturators, multicomponent flow systems.

trolled manner, then the amount of dopant reagent must be even lower; in some instances, the mole fraction of dopant must be as low as 10 parts per billion in the gas phase.

The techniques, developed for attaining the low gas phase concentrations, all involve the dilution of the source reagents in a controlled manner. Gaseous source compounds may be purchased prediluted with carrier gas and used directly down to about 5 ppm. For lower concentrations, additional controlled-dilution stages must be provided in the gas supply train. With liquid reagents, sufficient dilution may be obtained by diverting a fraction of the carrier gas stream through a flow meter, which monitors the carrier flow rate through a bubble saturator. By thermostatic control of the saturator temperature, the vapor pressure of the source reagent in the diverted carrier gas stream is maintained at a constant and controlled level. The saturated carrier gas stream is then mixed with the main carrier gas stream, which serves to dilute the source vapor concentration to a moderately low level. A highly desirable feature of this technique is the wide range of concentrations which may be obtained by changing the relative flow rates of the main and diverted streams and/or changing the temperature of the saturator. This technique is sufficiently accurate and simple for use down to concentrations of the order of 1 ppm. However, the extremely low concentrations required for the lowest epitaxial film dopant levels are frequently difficult to obtain with reasonable precision, because of the very low flow rates ($\leqq$ 1 cm^3 min^{-1}) and low saturator temperatures ($\leqq$ −30°C) which must be controlled and measured. To obtain the required low dopant reagent concentrations, the saturator technique can be modified by using a dilute solution of dopant reagent dissolved in the liquid matrix reagent, *e.g.* BBr_3 dissolved in $GeBr_4$.

Practical systems may be either of the above-mentioned types or a combination of the two. As a result, once a system has been designed, it becomes essential to develop the computational equations for obtaining the gas phase compositions. This chore may become a rather frustrating one because of the extensive algebraic manipulation associated with even a moderately complex system. With the objective of reducing the required effort, this paper describes the general equations for computing the concentration of each reagent entering the reactor from a gas train, which consists of: (*a*) a main diluent stream, part of which is diverted through a number of parallel saturators, each containing several mutually miscible components; (*b*) an all-gaseous system with several dilution stages; and, finally, (*c*) a hybrid system, which utilizes both dilution methods. Thus, by starting with the most general equation appropriate for a specific system, the user may easily reduce the equation to that which applies in his case.

A Multiple-Saturator System

The model for the multiple-saturator system is shown in Fig. 1. The following assumptions are made in the derivations:

1. The ideal gas laws and Raoult's law are valid for the components used in the system.
2. The liquids in the saturators are mutually miscible at the concentrations used, and the solubility of the carrier gas in the liquids is negligibly small.
3. The saturators are capable of saturating the carrier gas at the equilibrium partial pressures of each of the liquids contained in each of the saturators.
4. The pressure drop is negligible from the point of release of the bubbles from the liquid to the reactor.
5. All of the flow meter calibrations are corrected to the same standard conditions of pressure and temperature.

The exact general solution for the model in Fig. 1 is

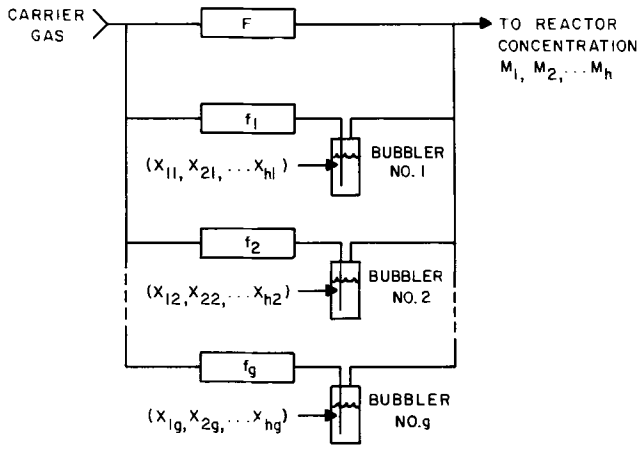

Fig. 1. Model for the multiple-saturator system

$$M_i = \frac{\sum_{j=1}^{g} \left\{ f_j (x_i P_i)_j \Big/ \left[P - \left[\sum_{i=1}^{h} x_i P_i \right]_j \right] \right\}}{F + P \sum_{j=1}^{g} \left\{ f_j \Big/ \left[P - \left[\sum_{i=1}^{h} x_i P_i \right]_j \right] \right\}} \quad [1]$$

where: M_i = the mole fraction of the i^{th} component in the gas stream entering the reactor
f_j = the volume rate of flow of carrier gas entering the j^{th} saturator
$(x_i P_i)_j$ = the partial pressure of the i^{th} component in the j^{th} saturator; x_i is the mole fraction of the i^{th} component in the liquid contained in the j^{th} saturator and P_i is the vapor pressure of pure i at the temperature of the j^{th} saturator
P = the ambient pressure downstream of the saturator
F = the volume rate of flow of diluent carrier gas being added to the vapor-saturated gas streams from the saturators

The derivation of Eq. [1] is given in the Appendix.

The following cases represent four particular applications of Eq. [1]:

A. One saturator, one pure reagent.—A by-pass carrier stream in parallel with one saturator, which contains a single pure liquid, m. The mole fraction of the vapor, M_m, entering the reactor is given by

$$M_m = \frac{P_m}{\frac{F}{f}(P - P_m) + P} \quad [2]$$

where: P_m = the vapor pressure of pure m at the saturator temperature.

B. One saturator, two reagents.—A bypass carrier stream in parallel with one saturator, which contains a solution of a dopant reagent, d, and a matrix reagent, m. The mole fractions are given by Eq. [3a] and [3b]

$$M_d = \frac{x_d P_d}{\frac{F}{f}(P - x_d P_d - x_m P_m) + P} \quad [3a]$$

$$M_m = \frac{x_m P_m}{\frac{F}{f}(P - x_d P_d - x_m P_m) + P} \quad [3b]$$

where: P_d, P_m = the vapor pressures of pure d and pure m, respectively, at the saturator temperature
x_d, x_m = the mole fractions of d and m, respectively, in the saturator

C. *Two saturators, each with one pure reagent.*—A by-pass carrier stream in parallel with two saturators, one containing pure m and the other pure d. The saturators need not be at the same temperature.

$$M_d = \frac{P_d\left[\frac{f_d}{f_m}\left(\frac{P-P_m}{P-P_d}\right)\right]}{\frac{F}{f_m}(P-P_m) + P\left[1+\frac{f_d}{f_m}\left(\frac{P-P_m}{P-P_d}\right)\right]} \quad [4a]$$

$$M_m = \frac{P_m}{\frac{F}{f_m}(P-P_m) + P\left[1+\frac{f_d}{f_m}\left(\frac{P-P_m}{P-P_d}\right)\right]} \quad [4b]$$

where: f_m, f_d = the volume flow rates of carrier gas through the pure m and d saturators, respectively

D. Two saturators, one with pure reagent and a second with two reagents.—A bypass carrier stream in parallel with two saturators, where saturator 1 contains pure m and saturator 2 contains a solution of d and m. The two saturators are at the same temperature.

$$M_d = \frac{x_d P_d}{\frac{F}{f_2}(P - x_d P_d - x_m P_m) + P\left[1+\frac{f_1}{f_2}\left(\frac{P-x_dP_d-x_mP_m}{P-P_m}\right)\right]} \quad [5a]$$

$$M_m = \frac{P_m\left[x_m+\frac{f_1}{f_2}\left(\frac{P-x_dP_d-x_mP_m}{P-P_m}\right)\right]}{\frac{F}{f_2}(P - x_d P_d - x_m P_m) + P\left[1+\frac{f_1}{f_2}\left(\frac{P-x_dP_d-x_mP_m}{P-P_m}\right)\right]} \quad [5b]$$

where: f_1, f_2 = the volume rates of flow of carrier gas through saturators 1 and 2, respectively

x_d, x_m = the mole fractions of d and m, respectively, in saturator 2. (Note: x_d and x_m for saturator 1 are zero and unity, respectively.)

A Multiple-Dilution System

The model for the multiple gas dilution system is shown schematically in Fig. 2. In this schematic, the first subscript, k, identifies the active component (*i.e.*, a particular matrix or dopant reagent) and the second subscript, n, identifies the dilution stage. The number of dilution stages, m_k, may be different for each reagent. M_{k0} is the concentration (mole fraction) of the k^{th} reagent in the supply tank, whereas M_{kn} is its concentration after the n^{th} dilution; f_{kn} represents the volume flow rate of the k^{th} reagent plus diluent from the previous dilution stage into the n^{th} dilution stage. The supply tanks may contain pure reagents ($M_{k0} = 1$), or they may be prediluted with carrier gas. F_{kn} is the volume flow rate of diluent into the n^{th} dilution stage of the k^{th} reagent.

The general equation for the concentration, M_{km_k}, of the k^{th} reagent in the gas stream entering the reactor is

$$M_{km_k} = \frac{M_{k0}\left[\prod_{n=1}^{m_k} f_{kn}\right] \Big/ \left[\prod_{n=1}^{m_k-1}(f_{kn}+F_{kn})\right]}{F + \sum_{k=1}^{p} f_{km_k}} \quad [6]$$

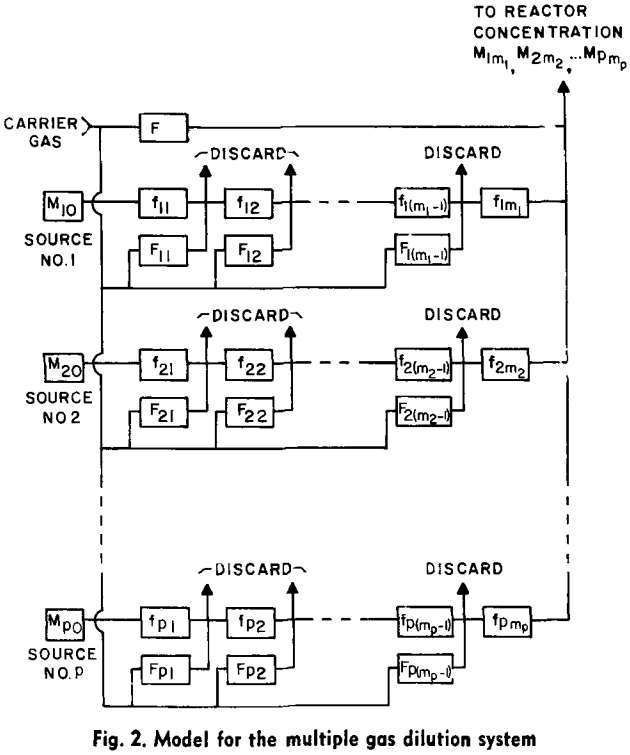

Fig. 2. Model for the multiple gas dilution system

with the detailed derivation of Eq. [6] in Appendix II.

For illustration, the reagent concentrations for a system, in which the matrix is diluted twice and the dopant reagent four times, are

$$M_{m2} = \frac{M_{m0} f_{m1} f_{m2}}{(F + f_{m2} + f_{d4})(f_{m1} + F_{m1})} \quad [7a]$$

$$M_{d4} = \frac{M_{d0} f_{d1} f_{d2} f_{d3} f_{d4}}{(F + f_{m2} + f_{d4})(f_{d1} + F_{d1})(f_{d2} + F_{d2})(f_{d3} + F_{d3})} \quad [7b]$$

Equations [7a] and [7b] may be used in a system in which, for example, SiH_4 is the source of epitaxial silicon and B_2H_6 the source of p-type dopant.

In Eq. [1] and [6], the numerator in each equation represents the partial volume rate of flow of the designated component, *i.e.* i in Eq. [1] and k in Eq. [6], and the denominator represents the total volume rate of flow of all the components into the reactor. Furthermore, each term in the denominators of Eq. [1] and [6] represents the contribution of each branch of the systems to the total flow in each system.

A Hybrid System

An example of such a system would be one in which the matrix reagent is pure liquid germanium tetrachloride, and the dopant reagents are prediluted gaseous B_2H_6 or PH_3.

The general equations for a hybrid system, consisting of h reagents supplied from g saturators, and p reagents, each supplied from a train of m_k dilution stages, are

$$M_i = \frac{\sum_{j=1}^{g}\left\{f_j(x_iP_i)_j \Big/ \left[P - \left(\sum_{i=1}^{h} x_iP_i\right)_j\right]\right\}}{F + P\sum_{j=1}^{g}\left\{f_j \Big/ \left[P - \left(\sum_{i=1}^{h} x_iP_i\right)_j\right]\right\} + \sum_{i=1}^{p} f_{kmk}} \quad [8a]$$

$$M_{kmk} = \frac{M_{k0}\left(\prod_{n=1}^{m_k} f_{kn}\right) \Big/ \left(\prod_{n=1}^{m_k-1} (f_{kn} + F_{kn})\right)}{F + P\left\{\sum_{j=1}^{g} f_j \Big/ \left[P - \left(\sum_{i=1}^{h} x_iP_i\right)_j\right]\right\} + \sum_{k=1}^{p} f_{kmk}} \quad [8b]$$

APPENDIX

Derivation of Composition Equations [1] and [6]

The volume rate of flow out of a single saturator, j, at ambient conditions is given by

$$f_j' = f_jKT \Big/ \left[P - \left(\sum_{i=1}^{h} x_iP_i\right)_j\right] \quad [A]$$

where:
- f_j = the volume rate of flow measured by the j^{th} flow meter at the standard calibration conditions, P_s and T_s
- $K = P_s/T_s$
- P_s, T_s = the standard pressure and absolute temperature, respectively, of the flow meter calibrations
- P, T = the ambient pressure and absolute temperature of the gas downstream from the saturators
- $(x_i)_j$ = the mole fraction of the i^{th} component in the j^{th} saturator
- $(P_i)_j$ = the vapor pressure of the pure i^{th} component at the temperature of the j^{th} saturator
- $\left(\sum_{i=1}^{h} x_iP_i\right)_j$ = the sum of the x_iP_i (partial pressure) terms for the j^{th} saturator only

The volume rate of flow of carrier gas at ambient conditions contributed by the bypass flow meter is given by

$$F' = FKT/P \quad [B]$$

where: F = the volume rate of flow measured on the bypass flow meter at the standard calibration conditions

The total volume rate of flow, F_t, into the reactor is the sum of the carrier gas bypass flow rate and of the sum of flow rates from all the saturators, *i.e.* Eq. [C]

$$F_t = F' + \sum_{1}^{g} f_j' \quad [C]$$

$$F_t = FKT/P + \sum_{j=1}^{g}\left\{f_jKT \Big/ \left[P - \left(\sum_{i=1}^{h} x_iP_i\right)_j\right]\right\} \quad [D]$$

$$F_t = \frac{KT}{P}\left[F + P\sum_{j=1}^{g}\left\{f_j \Big/ \left[P - \left(\sum_{i=1}^{h} x_iP_i\right)_j\right]\right\}\right] \quad [E]$$

The partial volume flow rate, f_i, of the i^{th} reagent from all the saturators into the reactor computed at ambient conditions is the sum of all the partial volume flow rates of the i^{th} reagent from g saturators, as given by Eq. [F]

$$f_i = \sum_{j=1}^{g} f'_{ij} = \frac{KT}{P}\sum_{j=1}^{g}\left\{f_j(x_iP_i)_j \Big/ \left[P - \left(\sum_{i=1}^{h} x_iP_i\right)_j\right]\right\} \quad [F]$$

where: f'_{ij} = the partial volume flow rate of the i^{th} reagent from the j^{th} saturator computed at ambient conditions.

Having determined the partial volume of the i^{th} reagent, Eq. [F], and the total volume of gas, Eq. [E], entering the reactor, the equation for the mole fraction of the i^{th} reagent, M_i, in the gas mixture in the reactor can now be written, since $M_i = f_i/F_t$.

$$M_i = \frac{\sum_{j=1}^{g}\left\{f_j(x_iP_i)_j \Big/ \left[P - \left(\sum_{i=1}^{h} x_iP_i\right)_j\right]\right\}}{F + P\sum_{j=1}^{g}\left\{f_j \Big/ \left[P - \left(\sum_{i=1}^{h} x_iP_i\right)_j\right]\right\}} \quad [G]$$

Equation [G] represents an exact general solution for a gas mixture prepared by combining a bypass carrier gas flow with the flows from g saturators, each of which contains different concentrations of each of h reagents and is maintained at a different temperature, which determines the contribution of the i^{th} component from the j^{th} saturator by the term $(x_iP_i)_j$.

A likely simplification to consider is that in which all of the saturators are maintained at the same temperature. In this case, P_i in the $(x_iP_i)_j$ term is the same for all the saturators; *i.e.*, it is the vapor pressure of the pure i^{th} reagent at the common saturator temperature. Then Eq. [G] may be rewritten as follows

$$M_i = \frac{P_i\sum_{j=1}^{g}\left\{f_jx_{ij} \Big/ \left[P - \left(\sum_{i=1}^{h} x_iP_i\right)_j\right]\right\}}{F + P\sum_{j=1}^{g}\left\{f_j \Big/ \left[P - \left(\sum_{i=1}^{h} x_iP_i\right)_j\right]\right\}} \quad [H]$$

The derivation of the composition equation for a multiple dilution system begins with the statement of the concentration of reagent in the output of each dilution stage, M_{kn}, as a function of the input concentration, M_{k0}, and the flows involved; *e.g.*, for the first dilution stage

$$M_{k1} = M_{k0}\left(\frac{f_{k1}}{f_{k1} + F_{k1}}\right)$$

where: f_{k1} = the input flow rate of gas to the first dilution stage from the source tank, which contains a mole fraction, M_{k0}, of reagent diluted with carrier gas
F_{k1} = the input flow rate of diluting carrier gas to the first dilution stage

Similarly,

$$M_{k2} = M_{k1}\left[\frac{f_{k2}}{f_{k2}+F_{k2}}\right] = M_{k0}\left[\frac{f_{k1}}{f_{k1}+F_{k1}}\right]\left[\frac{f_{k2}}{f_{k2}+F_{k2}}\right]$$

$$M_{k3} = M_{k2}\left[\frac{f_{k3}}{f_{k3}+F_{k3}}\right] = M_{k0}\left[\frac{f_{k1}}{f_{k1}+F_{k1}}\right]\left[\frac{f_{k2}}{f_{k2}+F_{k2}}\right]\left[\frac{f_{k3}}{f_{k3}+F_{k3}}\right]$$

$$\vdots$$

$$M_{k(m-1)} = M_{k0}\left[\prod_{n=1}^{m-1} f_{kn}\right] \Big/ \prod_{n=1}^{m-1}\left[f_{kn}+F_{kn}\right]$$

The equation for the last stage (the m^{th}) differs from the others, since the diluent flow in this stage contains the main carrier gas bypass flow as well as the output flows of all the other diluted reagents from their respective $(m_k - 1)$st stages (m_k is used here for clarity, since the value of m may vary from one reagent dilution train to another.) Thus, for the last stage

$$M_{km} = M_{k(m-1)}\left\{\frac{f_{kn}}{F+\sum_{k=1}^{p} f_{kn}}\right\}$$

$$= \frac{M_{k0}\left[\prod_{n=1}^{m} f_{kn}\right] \Big/ \left[\prod_{n=1}^{m-1}\left(f_{kn}+F_{kn}\right)\right]}{F+\sum_{k=1}^{p} f_{kn}} \quad [I]$$

Since the numerators of Eq. [G] and [I] represent the partial volume flow rate of the i^{th} or k^{th} reagent, respectively, and the denominators represent the total gas flow into the reactor, the derivation of the composition equations for a hybrid system, in which some of the reagents are supplied by saturators and others by multiple gas dilution trains, becomes very simple. For reagents supplied from saturators, the numerator for computing M_i is identical with that of Eq. [G], and the denominator of Eq. [G] is modified by the addition of $\sum_{k=1}^{p} f_{kn}$ to obtain the total gas flow. For reagents supplied by multiple gas dilution trains, the numerator for computing M_{kn} is the same as that in Eq. [I], and the same denominator is used as for the saturator-supplied reagents in the hybrid system.

Manuscript submitted Oct. 8, 1969; revised manuscript received Dec. 7, 1970.

Any discussion of this paper will appear in a Discussion Section to be published in the December 1971 JOURNAL.

DISCUSSION SECTION

This Discussion Section includes discussion of papers appearing in the *Journal of The Electrochemical Society*, Vol. 117, No. 8 and 10 (August and October 1970).

A Method for the Synthesis of BI_3 for Use as a Dopant Source

M. Berkenblit and A. Reisman (pp. 1100-1101, Vol. 117, No. 8)

F. E. Stafford:[1,2] Berkenblit and Reisman describe a method for reacting B_2H_6 with HI in the presence of hydrogen to generate BI_3. A fivefold excess of B_2H_6 is used. The reaction is observed to go to completion with the reactor at 250°C according to

$$6B_2H_6 + 6HI \rightleftarrows 2BI_3 + 5B_2H_6 + H_2 \quad [1]$$

They observe, however, that "At [450° and 800°C], there was no measurable trace of BI_3, indicating that K is much smaller (→ O) than the calculated value." They conclude that "these results do not appear to be due to kinetic limitations, and would indicate that the thermochemical data [given in the JANAF tabulation[3]] are in considerable error."

We disagree with this conclusion and offer the following interpretation. Diborane is unstable with respect to decomposition to boron and hydrogen, the equilibrium pressure at the temperatures in question and in the presence of 1 atm H_2 being 10^{-12} atm or less. Depending on the contact time and pressure, this decomposition is "slow" at room temperature and somewhat above, but becomes rapid with increasing temperature. (See *e.g.* Baylis *et al.*[4].) It is logical to assume, therefore, that the decomposition reaction is "slow" at 250°C under the particular conditions used by Berkenblit and Reisman and compared to the forward rate of Eq. [1].

At 450°C and above, the rate of decomposition to boron should be fast. (Whether boron containing species survive the reaction is not mentioned. Alternately, higher boranes could be formed and give a test for boron, but not react to form BI_3.) The principal net reaction then becomes

$$B + 3HI \rightleftharpoons BI_3 + 3/2\ H_2 \quad [2]$$

For 10^4 ppm HI (= 10^{-2} atm) at 700°K, and with 1 atm H_2 (or 10^{-2} atm), the equilibrium partial pressure of BI_3 is calculated to be $10^{-9.4}$ (or $10^{-6.4}$) atm, explaining the non-observation in the paper under discussion of BI_3.

In fact, the observation that Eq. [1] proceeds to the theoretical limit at 250°C, and that[5] BI_3 can be formed in appreciable yield by direct reaction of iodine with boron, indicates that the quoted[3] electron impact enthalpy of formation is essentially correct. It would be hard to change the enthalpy in a way to account for the present observations in the discussed paper.

Accordingly, control of the kinetic conditions—wall contact, contact time, B_2H_6 partial pressure—seems to be important for success of the synthesis.

M. Berkenblit and A. Reisman: Stafford begins his thesis with a misquote from our report, adds a second

[1] Department of Chemistry and the Materials Research Center, Northwestern University, Evanston, Illinois, 60201.

[2] Supported by the United States Atomic Energy Commission, Document COO-1147-39.

[3] D. R. Stull and H. Prophet, "JANAF Thermochemical Tables," The Dow Chemical Company, Midland Michigan, tables as available to June 1970.

[4] A. B. Baylis, G. A. Pressley, Jr., and F. E. Stafford, *J. Am. Chem. Soc.*, **88**, 2428 (1966).

[5] R. M. Adams, Editor, "Boron, Metallo-Boron Compounds, and Boranes," p. 276, Interscience Publishers, New York, N. Y. (1964).

misquote, uses these misquotes to argue that his logic must be accepted, and then ends with a generality which, to us, also happens to be irrelevant.

Firstly, our experiments were conducted with equal partial pressures of B_2H_6 and HI, not with a five-fold excess of B_2H_6 (see Vol. 117, p. 1101, column 1, paragraph 1). Secondly, we are quoted as stating that BI_3 can be formed in appreciable quantities from the direct reaction of boron and iodine. We made no such statement nor do we profess any knowledge of the experimental conditions needed for such a synthesis.

Our interpretation may or may not be valid. Unfortunately Stafford has not provided any new information which would enable us to reconsider our conclusion. Restated, we found that based on trivial thermodynamic calculations, the reaction shown in Eq. [1] should have yielded some BI_3 at 450°C. None was observed. One explanation is that the thermochemical data is in error, and this is the one we suggested. It is also possible that the B_2H_6 decomposes, that B drops out, and that the HI fails to react with it. Another is that B_2H_6 polymerizes etc., the products of such reaction(s) being unreactive with HI. The latter we doubt, since B_2H_6 is an effective semiconductor dopant source at elevated temperatures. Perhaps there exist ten other explanations. In lieu of proof in support of any one of them, ours is as reasonable as any and does not require invoking other obvious but more complicated conjecture.

The Effect of Several Electrode and Electrolyte Additives on the Corrosion and Polarization Behavior of the Alkaline Zinc Electrode

F. Mansfeld and S. Gilman (pp. 1328-1333, Vol. 117, No. 10)

S. M. Davis:[6] In Table III of the paper by Mansfeld and Gilman, a comparison of theoretically calculated and experimentally determined values for the corrosion potential of a pure zinc electrode in 6N KOH, containing a variable addition of ZnO, is presented. The experimentally determined values are somewhat too negative for ZnO concentrations greater than zero. No explanation is offered for this phenomenon.

Since the ZnO used in these experiments is stated to be of AR grade purity, it is likely that small but significant quantities of certain heavy metals of high hydrogen overpotential were introduced into the electrolyte solution along with the zinc oxide; notably Pb which may be present in AR grade ZnO up to 0.005%, and possibly also Sn, Cd, In, or Tl. Such additions could deposit on the zinc, raising the hydrogen evolution overpotential, thereby shifting the cathodic Tafel curve in a more negative direction and lowering the experimentally measured corrosion potential.

A simple test of this hypothesis would consist of comparing the experimentally measured corrosion potentials obtained with AR grade ZnO to those obtained with spectrographic grade ZnO in which the total metallic impurity content is <10 ppm.

F. Mansfeld and S. Gilman: The authors welcome the comment of Dr. Davis. It is not true, however, that no explanation has been offered for the fact that experimental corrosion potentials in Table III were somewhat more negative than the theoretical values. In the Discussion Section, we point out that dissolved zincate might lower the water activity according to Eq. [9] which then increases the hydrogen overvoltage which in turn leads to a decrease of corrosion rates and a shift of the corrosion potential in the negative direction. It is, of course, possible that impurities in the zinc oxide of AR grade purity like Pb or Sn increase hydrogen overvoltage as suggested by Dr. Davis. This is the effect we wanted to show in our paper. On the other hand we have shown[7] that addition of 10^{-4} M Pb to a solution of KOH + ZnO completely changes the morphology of the deposit on a zinc single crystal. Since this amount of lead ions corresponds to about 0.002%, we have to conclude that the amount of active lead in the AR grade zincate must be much smaller and, therefore, probably cannot effect the results of Table III as suggested by Dr. Davis. The same argument applies to Sn as an impurity.[8]

[6] ESB Incorporated, Ray-O-Vac Division, Madison, Wisconsin, 53703.

[7] F. Mansfeld and S. Gilman, *This Journal*, 117, 588 (1970).

[8] F. Mansfeld and S. Gilman, *This Journal*, 117, 1154 (1970).

JOURNAL OF THE ELECTROCHEMICAL SOCIETY

ELECTROCHEMICAL SCIENCE

JULY 1971

Conduction Domains for Solid Electrolytes

J. W. Patterson*

Department of Metallurgy, Iowa State University, Ames, Iowa 50010

ABSTRACT

The use of solid oxide electrolytes for determining oxygen concentrations in liquid metals has motivated much research of solid electrolyte properties over wide ranges of chemical potential and temperature. A useful scheme for assessing the electrolytic properties of solid electrolytes is that of plotting electronic and electrolytic conduction domains simultaneously with proposed application domains on chemical potential *vs.* $1/T$ diagrams. Accordingly, the concept and theoretical origins of conduction domains for solid electrolyte materials are outlined briefly. The origin and usefulness of the concept is discussed with respect to proposed applications of these solid electrolyte materials. Conduction domains for a number of known solid electrolytes are deduced from various conductivity and galvanic cell measurements and the results are presented in the form of conduction domain maps in log P_{X_2} *vs.* $1/T$ space. These maps constitute a survey of present status of knowledge regarding the materials considered. The solid electrolyte materials AgBr, AgI, CuBr, CuI, CuCl, CaF_2, $Zr_{0.85}Ca_{0.15}O_{1.85}$, and $Th_{0.85}Y_{0.15}O_{1.925}$ are discussed. Controversial implications and interpretations of conflicting data are pointed out.

The usefulness of solid electrolytes in research and other applications is based on two salient features: I. The open-circuit emf E across a solid electrolyte is a measure of a chemical potential difference; hence a solid electrolyte can function as a chemical potential (P_{X_2}) gauge. II. The charge passed through a solid electrolyte is a measure of ion transport; hence a solid electrolyte can function as a solid state ion pump.

A number of works (1-7) have reviewed research applications and have emphasized the solid electrolyte galvanic cell technique as an important quantitative method for studying the thermodynamics and kinetics of selected reactions at elevated temperatures. For the most part the solid electrolytes have been either AgI, CaF_2 or one of the oxide solid electrolytes CSZ (calcia stabilized zirconia) or YDT (yttria doped thoria) and have been employed in chemical potential (P_{F_2} or P_{O_2}) gauges in open-circuit emf measurements.[1] To a much lesser extent copper and silver halides have also been employed as solid electrolytes. Also a limited number of the reported applications have made use of the ion-pumping ability of the solid electrolytes. The most important metallurgical applications of these coulometric titration techniques involve the study of selected metal (8) and metalloid (9, 10) diffusivities in liquid and solid metallic hosts.

In contrast with these research-oriented applications, proposed application of solid electrolytes to metals technology has been almost exclusively concentrated on open-circuit emf measurements over oxide solid electrolytes. In particular, these applications involve the sensing of oxygen chemical potentials in liquid metals (11-17) at elevated temperatures. The ability to continuously monitor this thermodynamic variable is of critical importance in liquid steel refining and also in controlling the corrosivity of liquid sodium coolants to be employed in modern fast breeder reactors.

Because electronic conduction prevails in most solids, electrolytes (defined here as compounds exhibiting ionic transference numbers $t_{ion} \geq 0.99$) comprise only a very small subclass of all known compounds. More importantly, however, even the known solid electrolytes retain their predominant ionic conductivity over only limited ranges of temperature and chemical potential, *i.e.*, only over their respective electrolytic domains (18). For quantitative results from emf measurements it is most desirable that the application conditions lie within the electrolytic domain. Otherwise, the electrolytic domain boundaries must be precisely known if a quantitative interpretation of the open-circuit emf's is to be made.

The purpose of this paper is to present estimates of the electrolytic domain boundaries for several known solid electrolytes. These domains are most conveniently presented in the form of a log P_{X2}, $1/T$ map according to a scheme given by Patterson (18). The scheme is essentially an extension of an analysis first given by Schmalzreid (19, 20). It combines various conductivity and/or emf measurements in order to estimate the location of the electrolytic domain boundaries in a manner consistent with Wagner's phenomenological theory of mixed conduction (7, 21) in virtually stoichiometric compounds. Because t_{ion} is the ratio of ionic conductivity to total (ionic plus electronic) conductivity, the present definition of a solid electrolyte (namely, $t_{ion} \geq 0.99$) implies virtually exclusive ionic conduction. This definition is motivated by the desirability of reducing Wagner's general relationships (21)

* Electrochemical Society Active Member.

Key words: solid electrolytes, electrolytic domain, mixed conduction.

[1] The compositions of these electrolytes may be given by the following chemical formulas: CSZ is $Zr_{0.85}Ca_{0.15}O_{1.85}$, and YDT is $Th_{0.85}Y_{0.15}O_{1.925}$.

$$E = \phi'' - \phi' = -\left(\int_{\mu'_{X_2}}^{\mu''_{X_2}} \left[\frac{t_{ion}}{Z_x}\right] d\mu_{X_2}\right) \Big/ (2\mathbf{F})$$

$$= -\left(\int_{\mu'_M}^{\mu''_M} \left[\frac{t_{ion}}{Z_M}\right] d\mu_M\right) \Big/ (\mathbf{F}) \quad [1]$$

to the simplified version

$$E = \phi'' - \phi' = -(\mu''_{X_2} - \mu''_{X_2})/(2Z_X\mathbf{F})$$

$$= -(\mu''_M - \mu'_M)/(Z_M\mathbf{F}) \quad [2]$$

The symbols X and M in Eq. [1] and [2] denote, respectively, the nonmetal and metal components of the M_aX_b mixed conductor; whereas the double and single primes refer to the electrodes contacting the opposite ends of the compound. Z is valence, ϕ is electrostatic potential, μ is chemical potential, and $\mathbf{F}$ is Faraday's constant. In general, t_{ion} is a cumbersome function of chemical potential as well as temperature; however, within the electrolytic domain the simplified forms [2] serve as an adequate approximation to the corresponding integrals of t_{ion} on chemical potential (18-20). The chemical potential μ_{X_2} of the gaseous X_2 dimer is related to its partial pressure P_{X_2} (atm) and absolute temperature T(°K) by

$$\mu_{X_2} = \mu^o_{X_2} + 2.303\,RT \log P_{X_2} \quad [3]$$

where R is the universal gas constant and $\mu^o_{X_2}$ is the chemical potential of X_2 gas in its standard state. Equation [3] allows the variable log P_{X_2} to be used in place of the chemical potential at any given temperature. Also, most experimental or application conditions conform to finite polygons in log P_{X_2}, $1/T$ space. For these and other reasons given below it is convenient to formulate restrictions on the applications of solid electrolytes in terms of these two variables.

Conduction Domains in Log P_{X_2} $1/T$ Space

At elevated temperatures solid electrolyte materials exhibit an ionic conductivity which is virtually P_{X_2} independent. In contrast, their excess electron and positive hole conductivities, $\sigma_\ominus$ and $\sigma_\oplus$, are found to be proportional to $P_{X_2}{}^{-1/n}$ and $P_{X_2}{}^{+1/n}$, respectively, at constant temperature. The value of n is determined by the predominant defect structure of the M_aX_b solid electrolyte, but is otherwise independent of P_{X_2} and T. On the other hand, at constant P_{X_2}, all three conductivity modes exhibit an Arrhenius-type temperature dependence with apparent activation energies Q_{ion}, $Q_\ominus$, and $Q_\oplus$ that are also P_{X_2}- and T-independent. Mechanistic interpretations of these (iso-P_{X_2}) Q values do not seem to be justified beyond the point of qualitative assertions.

In view of these considerations it is possible to characterize the total conductivity σ_T in solid electrolytes as follows

$$\sigma_T = \sigma_{ion} + \sigma_\oplus + \sigma_\ominus \quad [4]$$

where

$$\sigma_{ion} = \sigma^o{}_{ion} \exp\left(-\frac{Q_{ion}}{RT}\right) \quad [5]$$

$$\sigma_\oplus = \sigma^o{}_\oplus P_{X_2}{}^{1/n} \exp\left(-\frac{Q_\oplus}{RT}\right) \quad [6]$$

$$\sigma_\ominus = \sigma^o{}_\ominus P_{X_2}{}^{-1/n} \exp\left(-\frac{Q_\ominus}{RT}\right) \quad [7]$$

and where the quantities $\sigma^o{}_{ion}$, $\sigma^o{}_\oplus$, $\sigma^o{}_\ominus$, n, Q_{ion}, $Q_\oplus$, and $Q_\ominus$ are all P_{X_2}- and T-independent. In order to discuss the nature of particular conduction domains for a given solid electrolyte, consider the log σ_T surface plotted over log P_{X_2}, $1/T$ space as shown in Fig. 1. Also shown in Fig. 1 are the surfaces corresponding to log σ_{ion}, log $\sigma_\oplus$, and log $\sigma_\ominus$ which, because of their functional form, plot as planar sheets in log σ, log P_{X_2}, $1/T$ space. Figure 1 may be thought of as the conductivity analog to a three-dimensional Kroger and Vink diagram (22, 23). It is apparent that regions or domains exist wherein only one of the conduction modes (ion, electron, or the positive hole mode) individually dominates the total conductivity of the M_aX_b mixed conductor. When this occurs, the log σ_T surface approaches coincidence with the planar sheet of the dominant conduction mechanism.

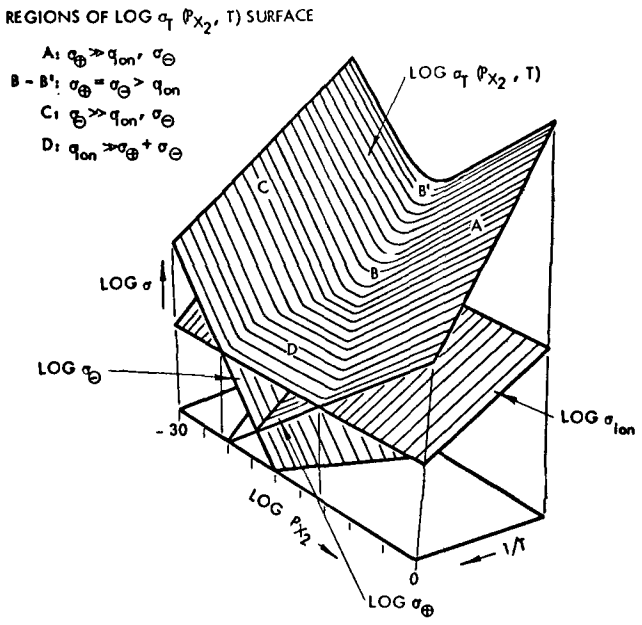

Fig. 1. Schematic representation of log σ surfaces over log P_{X_2}, $1/T$ space for $\sigma = \sigma_{ion}, \sigma_\oplus, \sigma_\ominus$, and σ_{total}.

Thus in region A of Fig. 1, $\sigma_\oplus$ is two or more orders of magnitude greater than either σ_{ion} or $\sigma_\ominus$ so that log σ_T and log $\sigma_\oplus$ are virtually identical. For the same reason, the log σ_T surface conforms to the log $\sigma_\ominus$ plane in region C whereas it conforms to the log σ_{ion} plane in region D. The projections of these regions onto the log P_{X_2}, $1/T$ plane may be called the positive hole, excess electron, and electrolytic conduction domains for the mixed conductor in question. Thus the electrolytic domain falls well within the ionic domain which is defined by the condition that σ_{ion} is simply greater than either $\sigma_\oplus$ or $\sigma_\ominus$, *i.e.*, $t_{ion} \geq 0.50$.

Various domain boundaries separate the regions where each mechanism of conduction dominates the others by at least two orders of magnitude. These boundaries represent transition conditions for the mixed conductor. Analytical expressions for them may be readily deduced by equating the appropriate conductivity expressions, taking the logarithm of the results, and then rearranging. Thus the $\sigma_\oplus$ to $\sigma_\ominus$ (p to n) transition boundary may be defined as the locus of log P_{X_2}, $1/T$ points where $\sigma_\oplus = \sigma_\ominus$. This leads to

$$\log P_{pn} = -\frac{n}{2}\left(\frac{Q_\ominus - Q_\oplus}{2.303R}\right)\frac{1}{T} + \frac{n}{2}\log\frac{\sigma^o{}_\oplus}{\sigma^o{}_\oplus} \quad [8]$$

This locus of log P_{X_2}, $1/T$ points plots as a straight line with slope $-n/2[Q_\ominus - Q_\oplus/2.303R]$ and intercept $n/2$ log $\sigma^o{}_\ominus/\sigma^o{}_\oplus$. Geometrically, it is the projected intersection of log $\sigma_\oplus$ and log $\sigma_\ominus$ planar sheets of Fig. 1. Similarly boundaries of the ionic domain may be deduced by equating $\sigma_\oplus$ and $\sigma_\ominus$ to σ_{ion} and taking the logarithm of the results; this gives

$$\log P_\oplus = -n\left(\frac{Q_{ion} - Q_\oplus}{2.303R}\right)\frac{1}{T} + n\log\frac{\sigma^o{}_{ion}}{\sigma^o{}_\oplus} \quad [9]$$

and

$$\log P_\ominus = +n\left(\frac{Q_{ion} - Q_\ominus}{2.303R}\right)\frac{1}{T} - n\log\frac{\sigma^o{}_{ion}}{\sigma^o{}_\ominus} \quad [10]$$

where the symbols $P_\oplus$ and $P_\ominus$ have been introduced in accordance with Schmalzried's usage (20).

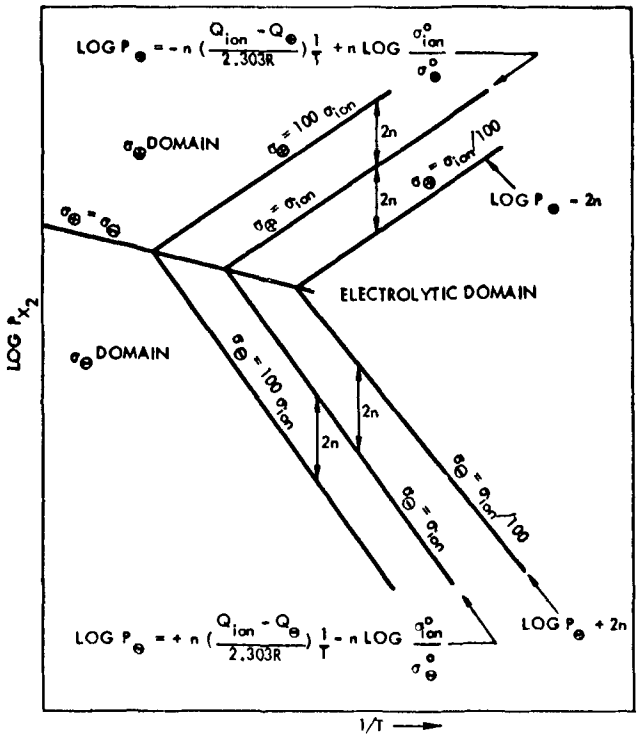

Fig. 2. Relationship between electrolytic and ionic domain boundaries in the log P_{X_2}, $1/T$ plane.

In this paper, we are mainly interested in the electrolytic domain boundaries. According to the electrolyte definition given above, these boundaries may be deduced by equating σ_{ion} to 100 $\sigma_\oplus$ and 100 $\sigma_\ominus$. In log P_{X_2}, $1/T$ space the equations for electrolytic domain boundaries are (18)

$$\log P_{X_2} = -n\left(\frac{Q_{ion}-Q_\oplus}{2.303R}\right)\frac{1}{T} + n\log\frac{\sigma^o{}_{ion}}{100\,\sigma^o{}_\oplus} = \log P_\oplus - 2n \quad [11]$$

and

$$\log P_{X_2} = +n\left(\frac{Q_{ion}-Q_\oplus}{2.303R}\right)\frac{1}{T} - n\log\frac{\sigma^o{}_{ion}}{100\,\sigma^o{}_\ominus} = \log P_\ominus + 2n \quad [12]$$

As mentioned previously, these boundaries are critical in the evaluation of a given mixed conductor for use as a solid electrolyte. Any application requiring electrolytic behavior must correspond to log P_{X_2}, $1/T$ conditions which lie between the lines corresponding to Eq. [11] and [12]. It is important to note that to a limited extent these lines may be extrapolated even if direct measurements have established their positions only over limited ranges of P_{X_2} and T. Such extrapolations are justified over ranges where the parameters Q_{ion}, $Q_\oplus$, $Q_\ominus$, $\sigma^o{}_{ion}$, $\sigma^o{}_\oplus$, $\sigma^o{}_\ominus$ remain constant. However, caution is required for polymorphic materials or materials in which more than one mechanism for σ_{ion}, $\sigma_\oplus$, or $\sigma_\ominus$ is possible. Figure 2 shows the relationships among the various domain boundaries discussed above.

It is apparent from this more or less geometrical viewpoint that experimental measurements made for a particular mode of conductivity can be used to uniquely establish its conductivity "sheet" in log σ, log P_{X_2}, $1/T$ space. Establishing the location and orientation of each of the conductivity sheets, then, serves to define their intersections and hence any of the desired domain boundaries as projected onto the log P_{X_2}, $1/T$ plane. In addition, emf measurements involving an electrode that establishes a log P_{X_2} value lying outside the electrolytic domain can be used (19, 20). The departure of the measured emf from the thermodynamic value may then be used to gain further information regarding the electrolytic domain boundaries. Permeability measurements may also be interpreted quantitatively in terms of domain boundary parameters. Patterson (18) has summarized methods for determining conduction domain boundaries from various experimental measurements.

Log P_{X_2}, $1/T$ Domain Maps for Some Known Halide Solid Electrolytes

Figure 3 is a master plot of log P_{X_2}, $1/T$ electrolytic domains of several known solid electrolytes. Only those materials are represented for which an electrolytic domain is known to exist and for which experimental data allow a quantitative estimation of the electrolytic domain boundaries. At low temperatures the chlorides, bromides, and iodides of silver and copper are represented. These compounds are characterized by an anion to cation site ratio of unity, and cations are the predominantly mobile ionic carriers in these electrolytes (1, 24). In contrast, the oxide solid electrolytes and calcium fluoride exhibit electrolytic behavior at more elevated temperatures. They have anion to cation site ratios equal to two, and anions dominate their ionic conduction modes.

Log P_{X_2}, $1/T$ diagrams for silver and cuprous halides. —The electrolytic domains of the known silver and cuprous halide electrolytes are bounded on the low P_{X_2} side by the stability limit of the electrolyte itself. Thus, in Fig. 3 the electrolytic domain of CuCl under reducing conditions is bounded by the log P_{Cl_2}, $1/T$ line corresponding to Cu, CuCl equilibrium coexistence. This boundary may be readily deduced from a tabulation (25) of the standard free energy of forma-

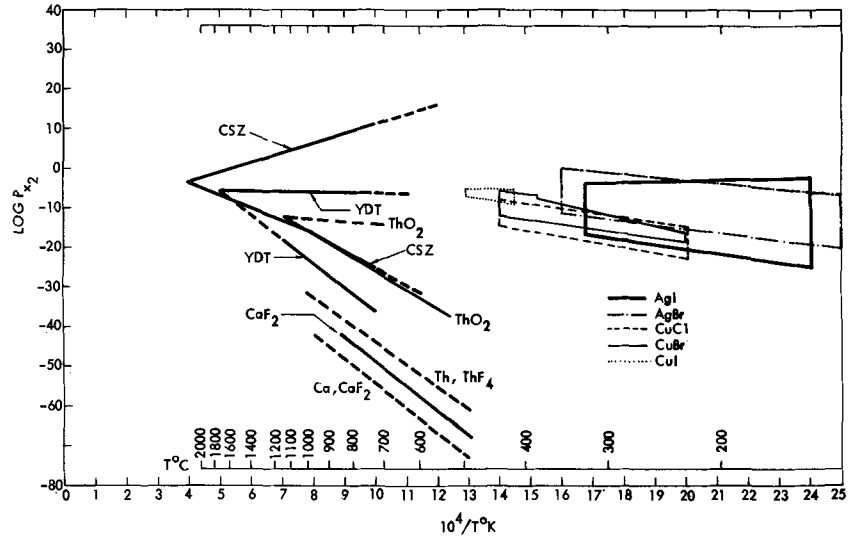

Fig. 3. Master plot of electrolytic domains in log P_{X_2}, $1/T$ space for selected halide and oxide solid electrolytes.

tion data for CuCl. The same is true for CuBr, CuI, AgCl, AgBr, and AgI. The electronic conduction in these silver and cuprous halides is dominated by positive hole (as opposed to excess electron) carriers (26-28). According to theory (7, 29, 30) and measurements (26-28), the positive hole conductivities, $\sigma_\oplus$, increase in proportion to $P^{1/2}{}_{X_2}$, where X_2 may be Cl_2, Br_2, or I_2, depending on which halide is involved. However, the ionic conductivities are found to be P_{X_2}-independent (7, 29) as suggested previously. Thus, at increased P_{X_2} values, the electrolytic domain is truncated by the onset of positive hole conduction. For the silver and cuprous halides this occurs at P_{X_2} values well below 1 atm as may be seen from Fig. 3. The following example briefly summarizes the details of determining these high P_{X_2} boundaries.

By employing d-c polarization measurements and C. Wagner's theoretical analysis (7, 29, 30), Wagner and Wagner (28) found the partial electronic conductivity of the cuprous halides to be dominated by hole conduction which in certain temperature ranges was orders of magnitude below the total (a-c) conductivity in these materials. Furthermore their observed current *vs.* d-c voltage data traverses confirmed the proportionality of $\sigma_\oplus$ to $P^{1/2}{}_{X_2}$ under conditions corresponding to Cu, CuX equilibrium coexistence. Thus from these quantitative measurements the functional dependence of log $\sigma_\oplus$ on log P_{X_2} and $1/T$ (*i.e.*, the location and orientation of the log $\sigma_\oplus$ sheet in log σ, log P_{X_2}, $1/T$ space) may be uniquely specified for each stable phase in the temperature range studied. In order to deduce the electrolytic domain boundaries at high P_{X_2} for the cuprous halides, it is only necessary to combine these results with the a-c conductivity measurements which at Cu, CuX, coexistence are an excellent approximation to only the ionic conductivity. This situation for CuCl is depicted schematically in Fig. 4. In this manner the high P_{X_2} electrolytic domain boundaries shown in Fig. 3 for CuCl, CuBr, and CuI were deduced solely from conductivity measurements. The high- and low-temperature boundaries of these same electrolytic domains are determined either by phase transformations which produce an electronic conducting phase or else by the temperature beyond which quantitative conductivity measurements have not yet been reported.

This same procedure was used in constructing the electrolytic domains for AgBr and AgI[2] shown in Fig.

[2] The electrolytic domain for AgCl is not shown primarily because of discrepancies in the d-c polarization results reported by Ilschner (27). Until further measurements resolve the presently unexplained current-voltage dependence exhibited by AgCl, quantitative determinations of the electrolytic domain boundary do not seem justified.

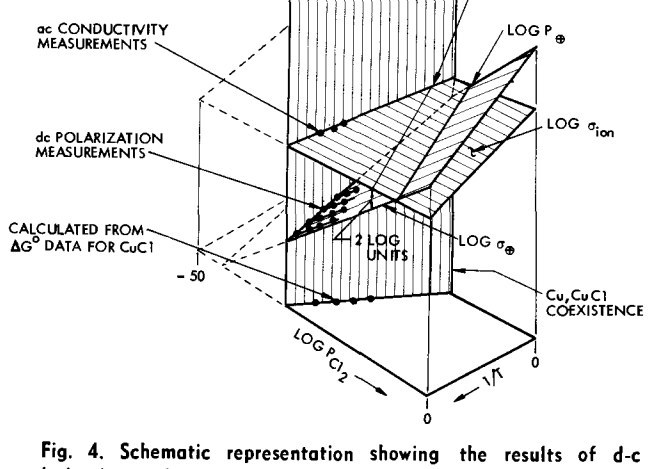

Fig. 4. Schematic representation showing the results of d-c polarization and a-c conductivity measurements in log σ, log P_{X_2}, $1/T$ space.

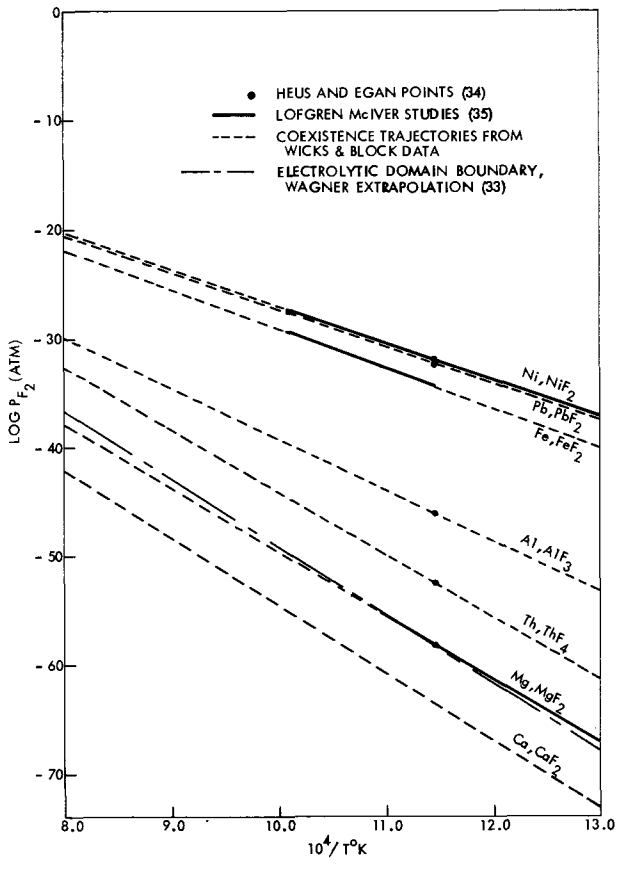

Fig. 5. Log P_{F_2}, $1/T$ diagram showing the estimated electrolytic domain boundary for CaF_2 together with selected metal, metal fluoride equilibrium coexistence loci.

3. The calculations employ the d-c polarization results of Raleigh (26) and Ilschner (27) and the a-c conductivities reported by Kurnick (31) and by Biermann and Jost (32).

Log P_{F_2}, $1/T$ diagram for CaF_2.—Figure 3 shows the proposed low P_{F_2} electrolytic domain boundary for CaF_2 to be about midway between the coexistence lines of Ca, CaF_2, and Th,ThF_4. This estimate is based on the recent analysis by Wagner (33). The practical difficulties associated with conductivity and/or emf measurements on CaF_2 in high P_{F_2} atmospheres at elevated temperatures seem to have thus far discouraged the experimental measurements required to determine the high P_{F_2} electrolytic domain boundary for this material. However, in view of the extreme electronegativity difference between $Ca^{\cdot\cdot}$ and F' ions and the correspondingly large forbidden bandgap for CaF_2 it would not be surprising if this boundary were found to be located far above 1 atm fluorine pressure. Figure 5 shows a number of selected metal, metal fluoride equilibrium coexistence trajectories superimposed on the proposed electrolytic domain for CaF_2. Only those trajectories are represented that have been studied as coexistence electrodes in conjunction with CaF_2 as the solid electrolyte at elevated temperatures (34, 35). Because of the limited number of such studies on fluoride systems, the trajectories shown can only be approximately located on such a plot at the present time.[3]

Log P_{X_2}, $1/T$ Domain Maps for Some Known Oxide Solid Electrolytes

A number of considerations serve to distinguish the known oxide solid electrolytes from the halide elec-

[3] A much more comprehensive emf study involving CaF_2 solid electrolytes is presently under way so that many more additional coexistence trajectories may be added soon. The results already indicate that CaF_2 has negligible electronic conductivity up to the Cu, CuF_2 coexistence trajectory.

trolytes treated above. Thus, the low P_{X_2} electrolytic domain boundaries of the oxide solid electrolytes CSZ and YDT are determined by the onset of excess electron (n-type) conduction rather than by the stability limit of the solid electrolyte material. Also the oxide electrolytes require comparatively large cation dopant additions before electrolytic behavior can be realized. This is in contrast with the previously discussed electrolytes that exhibit finite electrolytic domains even without the addition of selected dopant additions. Kiukkola and Wagner's solid electrolyte study (6) stimulated much of the current interest in the oxide solid electrolyte CSZ and in the application of solid electrolyte galvanic cell measurements in thermodynamic investigations. Partly on the basis of these thermodynamic studies and partly on the bases of various conductivity (36), permeability (37), and open-circuit emf studies (12, 13, 14, 19, 38, 39), Patterson (18) gave a conservative assessment of the electrolytic domain of CSZ. The results of Patterson's assessment are shown in Fig. 6. As shown in Fig. 7, the proposed electrolytic domain boundary at low P_{O_2} was placed conservatively. This was done as a safety measure to assure the validity of first-order approximations asserting the electrolytic behavior of CSZ under various experimental conditions. Thus, virtually all reported emf studies falling above that domain boundary choice had also been reported to be free from electronic conduction effects. It was apparent that other studies had suggested the true boundary might be significantly lower, but that certain investigators did not concur. In view of the uncertainties, the conservative domain boundary is retained, but it is understood that significant extension of the electrolytic domain to lower P_{O_2} values might well be possible if suitable precautions can be observed.

Evidence of electrolytic behavior for CSZ at much lower P_{O_2} values is now becoming more abundant (15, 40). On the basis of thermodynamic emf measurements in liquid iron alloys, Fruehan *et al.* (15) recently reported that the onset of electronic conduction in CSZ (*i.e.*, the electrolytic domain boundary) at

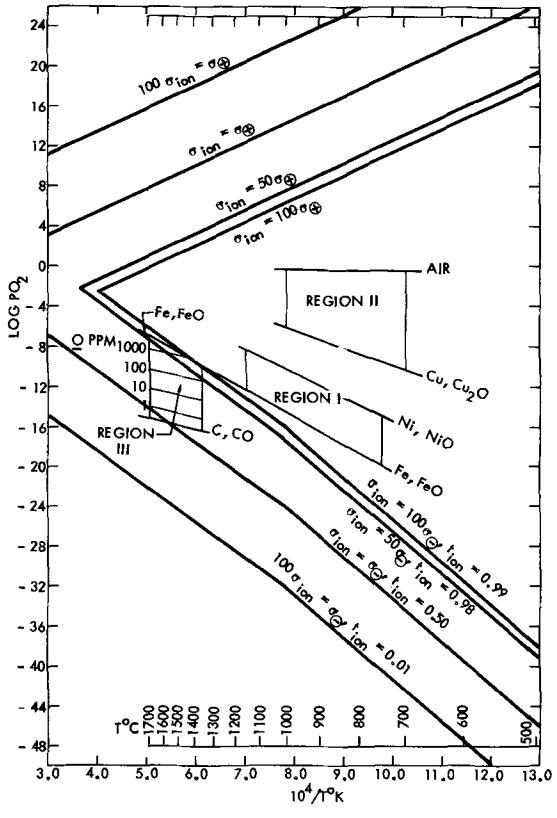

Fig. 6. Selected galvanic cell application regions with respect to the electrolytic domain of CSZ.

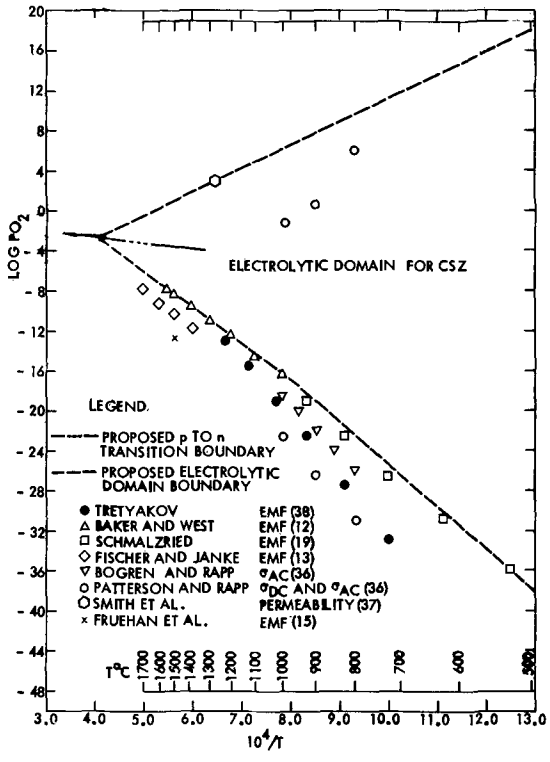

Fig. 7. Electrolytic domain boundaries and related data for CSZ

1600°C is at about 3-8 x 10^{-13} atm P_{O_2} or about down to Cr, Cr_2O_3 equilibrium coexistence. It is clear from Fig. 6 that this is well within the liquid steelmaking domain (Region III in Fig. 6). It is also well below the electrolytic domain boundary indicated by all previous assessments including Patterson's (18) and by all previous investigations including those conducted in the steelmaking domain (12-14). It is unfortunate that Fruehan *et al.* (15) did not report similar results over a range of temperatures, because then a finite boundary rather than an isolated point could be plotted in Fig. 7. Also shown on the log P_{O_2}, $1/T$ map of Fig. 6 are two additional application domains that have been investigated previously. However, these domains, (Region I) swept out by Kiukkola and Wagner (6) with the cell

Fe, FeO/CSZ/Ni, NiO (Cell I)

and that spanned by Rizzo *et al.* (39) (Region II) with the cell

Cu,Cu_2O/CSZ/Air (Cell II)

both fall entirely within the previous estimates (18) for the electrolytic domain boundaries of CSZ. Clearly much remains to be done before these estimates can be replaced with definitively established electrolytic domain boundaries.

Figure 8 shows the proposed electrolytic domain for YDT in log P_{O_2} $1/T$ space. The high P_{O_2} boundary shown in Fig. 8 was estimated by analyzing total conductivity data reported by Baurle (41) and Lasker and Rapp (42) in weighted combination with Schwerdtfeger's (40) assertion that incipient electronic (hole) conduction at 1500°C may be expected to occur at $P_{O_2} \approx 10^{-7}$ atm. The approximate temperature independence of this high P_{O_2} boundary implies that the iso-P_{O_2} activation energies $Q_{\oplus}$ and Q_{ion} for conduction in YDT are approximately equal. Because numerous open-circuit emf measurements confirm the onset of positive hole conduction as determined by conductivity studies, the electrolytic domain boundary for YDT at high P_{O_2} shown in Fig. 8 may be regarded as fairly well established.

However, as in the case of CSZ, the low P_{O_2} electrolytic domain boundary appears to be a much more controversial issue at the present time. Three recent emf

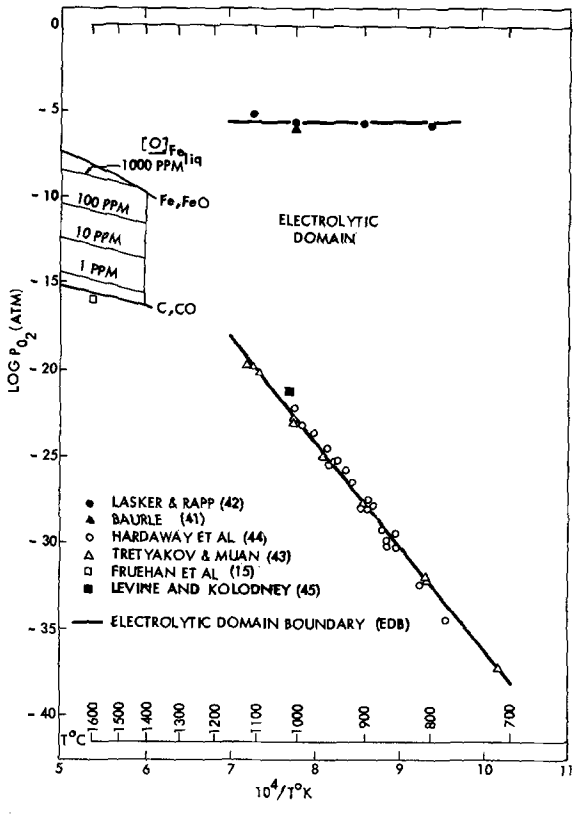

Fig. 8. Electrolytic domain boundaries and related data for YDT

studies (43-45) conducted at temperatures below the melting point of iron have been reported. These studies were performed quite independently and with significantly different means for controlling oxygen potentials. However, the electrolytic domain boundaries deduced from these studies are in substantial agreement as may be seen from Fig. 8. Extrapolating the results of these studies to the steelmaking temperature range suggests that only a small part of the steelmaking application domain lies within YDT's electrolytic domain. This is in accord with the results of Baker and West (12) who reported very substantial electronic conduction in YDT (as well as CSZ) exposed to liquid iron containing dissolved oxygen.

However, emf measurements by Schwerdtfeger (40) and by Fruehan *et al.* (15) involving YDT in liquid iron alloys indicate that a very significant portion of the steelmaking domain is within the electrolytic domain of YDT. The estimate of the onset of electronic conduction at 1600°C by Fruehan *et al.* is also shown on Fig. 8. Obviously there is much disagreement regarding the location of the low P_{O_2} electrolytic domain boundary especially at temperatures in the neighborhood of 1500° to 1600°C. For these reasons the proposed low P_{O_2} electrolytic domain boundary shown in Fig. 8 has not been extended above the 1100° point. Also, future measurements may reveal the need to modify the 700° to 1100°C low P_{O_2} boundary which is based on the works of Tretyakov and Muan (43) and Hardaway (44). However, insufficient quantitative results have been reported in the literature to justify such a modification at the present time.

Because it is beyond the intended scope of the present paper, no discussion is offered regarding the various explanations that have been given for the departures from thermodynamic emfs reported by different authors. However, the observations of Fruehan *et al.* (15) strongly suggest that at least some of the observed departures are probably not due to the onset of electronic conductivity as had been supposed. Assuming the electrolyte to be free from cracks and voids, the other major possibilities include (*a*) unreliable reference electrode behavior, (*b*) concentration polarization at the liquid metal electrode, and (c) reaction between the electrolyte and the liquid metal electrode. The present author leans to the view that explanation (c) would account for more of the discrepant emf results now in the literature than any of the other explanation possibilities.

Conclusion

In summary, the conduction domain scheme may be used to assess the useful application conditions for a given solid electrolyte. Construction of the electrolytic conduction domain on a log P_{X_2}, $1/T$ map from various conductivity data and/or emf data has been accomplished. Such domain maps are very useful for comparing observations from various investigators and for estimating the experimental conditions wherein selected solid electrolyte galvanic cell measurements may be expected to be free from deleterious electronic conduction effects. Accordingly, electrolytic domain estimates in the form of log P_{X_2}, $1/T$ maps have been given for several known electrolytes and in this context some of the more controversial domain boundaries have been pointed out and discussed.

Acknowledgment

This manuscript is submitted for publication with the understanding that no limitation will exist on the reproduction and distribution of its published or unpublished form in whole or in part for any purpose of the U. S. Goverment.

Research was sponsored by the Aerospace Research Laboratories, Office of Aerospace Research, United States Air Force, Contract F33615-68-C-1034.

Manuscript submitted Oct. 15, 1970; revised manuscript received *ca.* Jan. 27, 1971.

Any discussion of this paper will appear in a Discussion Section to be published in the June 1972 JOURNAL.

SYMBOLS

M	Metal component of the solid
X_2	Nonmetal component dimer gas molecule; *e.g.*, F_2, I_2, Br_2, Cl_2, O_2
P_{X_2}	Partial pressure in atm of X_2 gas
t_{ion}	Ionic transference number
E	Cell emf
ϕ	Electrostatic potential at electrode
μ_{X_2}	Gibbs free energy per mole of X_2 (chemical potential) at electrode
μ_M	Gibbs free energy per mole of M
Z_M, Z_X	Valence of cations and anions of the solid electrolyte
", '	Double and single primes indicate different electrodes
$\mathbf{F}$	Faraday's constant
T	Absolute temperature, °K
μ^o	Standard state chemical potential
R	Gas constant
$1/n$	Exponent of P_{X_2} in the functional dependence of $\sigma_\oplus$ on P_{X_2}
σ	Partial electrical conductivity
$\oplus$	Positive hole carriers (subscript indicator)
$\ominus$	Excess electron carriers (subscript indicator)
ion	Any or all ionic carriers (subscript indicator)
Q	iso P_{X_2} activation energy for carrier indicated by subscript
σ^0	Partial electrical conductivity extrapolated to infinite temperature and 1 atm P_{X_2}
σ_T	Total electrical conductivity
P_{pn}	P_{X_2} at which $\sigma_\oplus = \sigma_\ominus$
$P_\oplus$	P_{X_2} at which $\sigma_\oplus = \sigma_{ion}$
$P_\ominus$	P_{X_2} at which $\sigma_\ominus = \sigma_{ion}$

REFERENCES

1. R. A. Rapp and D. A. Shores, "Techniques in Metal Research," **IV**, 123, Wiley-Interscience Publishers, New York (1970).
2. C. B. Alcock, Editor, "Electromotive Force Measurements in High Temperature Systems," Proc. of 1967 Symposium, American Elsevier Publishing Co., Inc., New York (1968).
3. D. O. Raleigh, *Prog. Solid State Chem.*, **3**, 83 (1966).

4. H. Schmalzried, *Thermodyn.*, **1**, IAEA, 97 (1966).
5. B. C. H. Steele and C. B. Alcock, *Trans. Met. Soc. AIME*, **233**, 1359 (1965).
6. K. Kiukkola and C. Wagner, *This Journal*, **104**, 373 (1957).
7. C. Wagner, *Proc. Int. Comm. Electrochem. Thermo. and Kinetics (CITCE)*, 7th Meeting Lindau, 1955, Butterworth Scientific Publ., London (1957).
8. D. O. Raleigh, *This Journal*, **116**, 40 (1969).
9. H. Rickert and R. Steiner, *Z. Physik. Chem. Frankfurt*, **49**, 127 (1966).
10. R. Pastorek and R. A. Rapp, *Trans. Met. Soc. AIME*, **245** (1969).
11. G. R. Fitterer *et al.*, *J. Metals*, **18**, 961 (1966); *ibid.*, **19**, 92 (1967); *ibid.*, **21**, 46 (1969).
12. R. Baker and J. M. West, *J. Iron Steel Inst.*, **204**, 212 (1966).
13. W. A. Fischer *et al.*, *Arch. Eisenhuettenw.*, **36**, 643 (1965); *ibid.*, **37**, 43 (1966); *ibid.*, **39**, 89 (1968).
14. W. A. Fischer, *Berg. Huettenmaenn Monatsh.*, **113**, 141 (1968).
15. R. J. Fruehan, L. J. Martonik, and E. T. Turkdogan, *Trans. Met. Soc. AIME*, **245**, 1501 (1969).
16. M. Kolodney, B. Minushkin, and H. Steinmetz, *Electrochem. Technol.*, **3**, 244 (1965).
17. C. C. McPhetters, J. C. McGuire, and R. Tercovich, U. S. Pat. 3309 233 (1967).
18. J. W. Patterson, in "The Physics of Electronic Ceramics," L. L. Hench and D. B. Dove, Editors, Marcel Dekker Inc., N. Y. (1971).
19. H. Schmalzried, *Z. Elektrochem.*, **66**, 572 (1962).
20. H. Schmalzried, *Z. Physik. Chem. Frankfurt*, **38**, 87 (1963).
21. C. Wagner, *Z. Physik Chem.* B, **21**, 25 (1933).
22. F. A. Kroger and H. J. Vink, "Relations between Concentrations of Imperfections in Crystalline Solids," *Solid State Phys.*, **3**, 307 (1956).
23. F. A. Kroger, "The Chemistry of Imperfect Crystals," North Holland Publishing Co., pp. 449-456 (1964).
24. A. B. Lidiard, in *Handbuch der Physik*, **20**, 252 (1957).
25. C. Wicks and F. Block, *Thermodynamic Properties of 65 Elements—Their Oxides, Halides, Carbides, and Nitrides, U. S. Bur. Mines Bull.* 605 (1963).
26. D. O. Raleigh, *J. Phys. Chem. Solids*, **26**, 329 (1965).
27. B. Ilschner, *J. Chem. Phys.*, **28**, 1109 (1958).
28. J. B. Wagner and C. Wagner, *ibid.*, **26**, 1597 (1957).
29. C. Wagner, *Z. Elektrochem.*, **63**, 1027 (1959).
30. C. Wagner, *ibid.*, **60**, 4 (1956).
31. S. W. Kurnick, *J. Chem. Phys.*, **20**, 218 (1952).
32. W. Biermann and W. Jost, *Z. Physik. Chem. Frankfurt*, •, 139 (1969).
33. C. Wagner, *This Journal*, **115**, 933 (1968).
34. R. J. Heus and J. J. Egan, *Z. Physik. Chem. Frankfurt*, **49**, 38 (1966).
35. N. L. Lofgren and E. H. McIver, *Thermodynamic Properties of Some Fluoride Systems, U.K.A.E.A. Rep.*, 5169, 1966.
36. J. W. Patterson *et al.*, *This Journal*, **114**, 752 (1967).
37. A. W. Smith *et al.*, *J. Am. Ceram. Soc.*, **49**, 240 (1966).
38. J. D. Tretyakov, *Neorg. Materials* (USSR), **2**, 501 (1966).
39. F. E. Rizzo *et al.*, *Trans. Met. Soc. AIME*, **239**, 593 (1967).
40. K. Schwerdtfeger, *ibid.*, **239**, 1276 (1967).
41. J. E. Baurle, *J. Chem. Phys.*, **45**, 4162 (1966).
42. M. F. Lasker and R. A. Rapp, *Z. Physik. Chem. Frankfurt*, **49**, 198 (1966).
43. J. D. Tretyakov and A. Muan, *This Journal*, **116**, 331 (1969).
44. J. B. Hardaway, III, *et al.*, *J. Am. Ceram. Soc.*, **54**, 94 (1971).
45. S. R. Levine and M. Kolodney, *This Journal*, **116**, 1420 (1969).

Emf Measurements of Electrochemically Prepared Lithium-Aluminum Alloy

N. P. Yao,* L. A. Herédy, and R. C. Saunders

Atomics International, A Division of North American Rockwell Corporation, Canoga Park, California 91304

ABSTRACT

The open-circuit voltages of the cell Li(l)/LiI-KI-LiCl/Li_xAl(s) were measured over the composition range of 6.9-50 a/o (atom per cent) Li in Li_xAl alloy in the temperature range 282°-389°C. The composition of the Li_xAl alloy was varied by coulometrically charging and discharging the cell. The emf values of the cell are independent of the composition up to 47 a/o lithium in the alloy and their temperature dependence follows the relationship $E = 451.07 - 0.2202T$ ($\sigma = 0.3$), where E is in millivolts, T in °K, and σ is the standard deviation. The constant potential exhibited by the alloy is ascribed to the formation of β-LiAl phase on the alloy surface. The standard free energies of formation for β-LiAl are estimated to be −7.49, −7.24, and −7.09 kcal/mole at 300°, 350°, and 380°C, respectively. The standard enthalpy and entropy of formation are constant, −10.40 kcal/mole and −5.08 cal/mole · deg, respectively, in this temperature range. Since the electrochemically prepared lithium-aluminum alloy has a constant potential over a wide composition range and exhibits good electrochemical behavior, it can serve as a good reference electrode as well as a high energy density anode in molten salt systems containing lithium.

The use of lightweight and highly electropositive lithium metal electrodes is desirable for high energy density, high power density battery systems. Liquid lithium metal has been extensively utilized in some high power density molten salt batteries, e.g. Li/Cl_2 (1), Li/S (2, 3), Li/chalcogen (4). High self-discharge rates due to corrosion of cell components by liquid lithium coupled with some appreciable solubility (5) of liquid lithium in the molten salt electrolytes often cause difficulties in material selection and battery cell design. These difficulties, however, can be circumvented through the use of a solid alloy of lithium. One such alloy is the lithium-aluminum alloy (6) which has been utilized as the solid negative electrode in Sohio's Li/Cl_2 (7) battery. Excellent electrochemi-

* Electrochemical Society Active Member.

Key words: lithium-aluminum alloy, emf measurements, free energy, enthalpy, entropy, lithium battery anode, reference electrode, molten salt electrolytes.

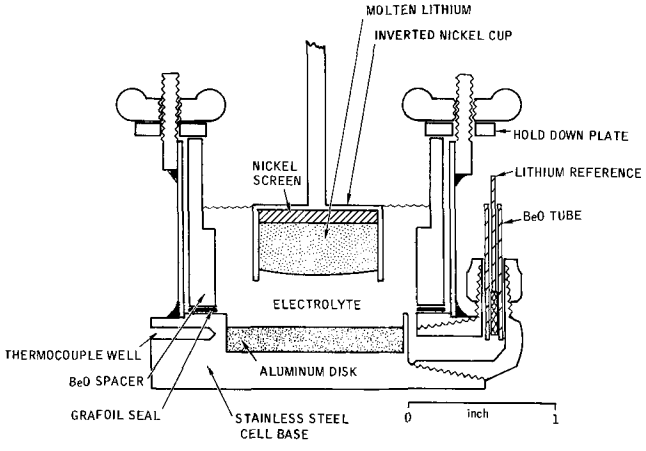

Fig. 1. A laboratory Li_xAl/Li cell

cal performances of lithium-aluminum alloy [composition range 5-30 w/o (weight per cent) Li] in molten salt systems have been reported (8-10). The lithium-aluminum alloy was shown to have a stable electrode potential during discharge and charge (10, 11) and the alloy, if properly prepared, is capable of charging and discharging at current densities up to 2 A/cm^2 (7).

In this paper, equilibrium emf measurements of an electrochemically prepared lithium-aluminum alloy in the cell Li/LiI-LiCl-KI/Li_xAl are reported in the composition range 6.9-50 a/o lithium and in the temperature range 282°-389°C. The eutectic mixture of lithium iodide, lithium chloride, and potassium iodide (12, 13) (mp 264°C) serves as the electrolyte.[1] Thermodynamic free energy, enthalpy, and entropy for the formation of the LiAl compound are calculated from the emf data.

Experimental

In order to avoid air contamination of the salts and reaction of lithium metal with air, the entire salt preparation and cell experiments were performed in an argon gas filled dry box (Vacuum Atmosphere-Allen Jones Company).

Chemicals.—Anhydrous, polarographic-grade LiI and LiCl were supplied in 200g ampoules by Anderson Physics Laboratory, Champaign, Illinois. Baker reagent-grade KI and purified LiF powder (Matheson Coleman and Bell) were vacuum dried over a 2 week period at gradually increasing temperatures up to 250°C and at 13μ Hg pressure. The eutectic mixtures of LiI-LiCl-KI (12) (59 m/o-8.5 m/o-32.5 m/o) and LiI-LiCl-LiF (15) (59.2 m/o-29.1 m/o-11.7 m/o) were prepared. The melts were colorless and clear. The melting points of the eutectic mixtures from cooling curves were 264° and 341°C, respectively, in agreement with the literature values (12, 15). Lithium metal (99.97% purity) was obtained in 1 lb ingots from Foote Mineral Company. The metal was cut and melted in a tantalum cup. It was then wetted to a nickel screen welded to the base of an inverted nickel cup current collector at 600°C. Aluminum sheet metal (99.99% purity, 0.127 in. thick) was supplied by Wilkinson Company, Santa Monica, California. The sheet metal was machined to a 1.2 in. diameter circular disk.

Apparatus.—The cylindrical cell for the electrochemical preparation of Li-Al alloy and for the emf measurements is shown in Fig. 1. The cell consists of a stainless steel cell body, an aluminum disk (0.127 in. thick, 1.2 in. diameter) welded to the cell base, and floating lithium contained in an inverted nickel cup which was supported externally. A BeO spacer was placed between the lithium electrode and the stainless steel cell wall. The annulus between the cell wall and the BeO spacer was rendered electrolyte free by the Grafoil sealing which was under compressive force transmitted by the BeO spacer. A thermocouple well and a lithium reference electrode (lithium wetted on nickel screen) were also incorporated in the cell as shown in the figure. The cell was heated at the base with a heating plate regulated with a Variac. The cell was thermally insulated by a preshaped porous alumina insulation block (1 in. thick). In this manner, the cell temperature was controlled to ±1°C. No temperature variation was observed at various depths of the molten salt electrolyte and the electrolyte temperature was within 1°C of that measured at the thermocouple well. Constant current was maintained by a d-c power supply (Hewlett-Packard 6203B) and a variable resistance pot (25 ohms, 50W) connected in series to the cell. The current was read on a Milliamperes Meter (Weston Instruments). The cell voltage and individual electrode polarizations were monitored on two strip chart recorders (Hewlett-Packard, 7100B). Equilibrium emf values of the cell were read on a Volt Potentiometer (Leeds & Northrup Company, Catalog No. 8687) and the temperature was measured with a sheathed Chromel-Alumel thermocouple. The Chromel-Alumel thermocouple was calibrated in a temperature range of 195°-505°C by intercomparison with two platinum-platinum 10% rhodium standard thermocouples certified by the National Bureau of Standards. The uncertainty for the thermocouple readings was less than 0.3°C in the temperature range.

Procedure.—The Li-Al alloy was prepared in the cell by coulometrically charging lithium into the pure aluminum disk (2.88g). The current density was 14-70 mA/cm^2 and the temperature range was 300°-390°C. On charging cathodically, the aluminum potential fell quickly to the alloy potential (about 0.3V for alloy *vs.* lithium). The initial charging current density was 14 mA/cm^2 and the current density was gradually increased as the alloy was cathodically and anodically cycled. The cell voltage during cycling was always stable and the maximum alloy polarization was less than 40 mV at the highest current density. Coulombic efficiency was greater than 93% during the repeated cyclings. The open-circuit voltage (OCV) of the cell was established to within a few millivolts of the equilibrium emf values in a period of a few minutes. The alloy composition was varied from 6.9 a/o up to 50 a/o lithium by charging and discharging it *vs.* the lithium counterelectrode, and the equilibrium OCV was determined at different compositions in the temperature range 280°-390°C. Equilibrium OCV data were normally taken after 1 hr at a constant temperature and, in some cases, the data were taken after 15 hr (overnight) and 60 hr (over a week end). The values were reproducible to within 0.1 mV in all cases.

Results and Discussion

The equilibrium emf values of lithium-aluminum alloys (*vs.* Li/Li^+) in LiI-KI-LiCl eutectic mixture are given in Table I as a function of alloy composition (in a/o and w/o lithium) and temperature. The emf values up to 46.97 a/o lithium composition were found to be independent of lithium content in the alloy and are only dependent on temperature. This is shown in Fig. 2 where the emf values (alloy *vs.* Li/Li^+) up to 46.97 a/o lithium are plotted as a function of temperature. The data in the composition range of 7-47 a/o lithium can be represented by a least-squares equation with a standard deviation $\sigma = 0.3$ mV

$$E = 451.07 - 0.2202T \qquad [1]$$

where E is emf in millivolts and T is temperature in °K. With increasing lithium content in the alloy above 46.97 a/o lithium, the emf values of the alloy (*vs.* Li/Li^+) approach zero, *i.e.* the potential of pure lithium, as shown in Fig. 3, indicating some local lithium saturation of the alloy surface. The local lithium

[1] Potassium ions of this salt mixture were not expected to interfere with the electrode reactions of lithium, on the basis of thermodynamic considerations (14). This was confirmed in the present study where the emf values of lithium-aluminum alloy (*vs.* Li/Li^+ reference) in LiI-LiCl-KI eutectic were found to be identical to those in LiI-LiCl-LiF eutectic, a pure lithium salt mixture.

Table I. Emf of lithium-aluminum alloy (vs. Li/Li^+) as a function of alloy composition and temperature in LiI-KI-LiCl eutectic salt

Alloy composition a/o Li	w/o Li	Temp, °C	Emf, mV
6.91	1.87	300	325.00
		323	320.05
		345	315.35
		350	314.50
16.19	4.73	310	323.00
		325	319.49
		351	313.60
		374	308.40
16.29	4.77	351	314.05
25.14	7.95	289	327.05
		311	322.32
		350	313.95
		382	306.75
28.79	9.42	282	328.10
		321	320.40
		350	313.96
		386	305.90
32.92	11.21	301	324.75
		326	319.13
		356	312.55
		376	307.90
36.74	13.00	299	325.35
		315	321.70
		351	313.40
		387	305.50
40.96	15.14	295	325.55
		326	218.84
		354	312.90
43.58	16.57	342	315.60
		363	310.70
		389	305.25
46.57	18.32	310	323.37
		370	309.37
46.97	18.56	309	323.43
		342	315.46
		355	313.55
		380	307.60
48.14	19.27	290	252.45
		342	241.07
		372	234.50
50.00	20.46	314	195.50
		343	189.90
		380	184.00

saturation appears to commence at approximately 46 a/o lithium composition from the extrapolation of the emf data (dotted line) as shown in Fig. 3.

The equilibrium lithium-aluminum phase diagram has been reported (6). Electrical resistivity and microhardness studies (16) of aluminum-rich alloys

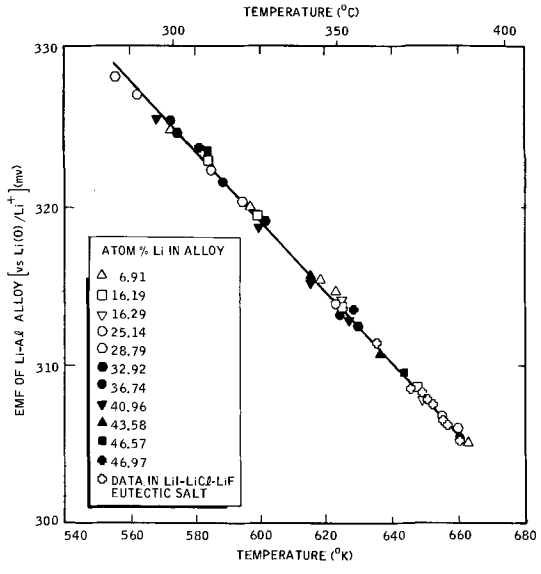

Fig. 2. Emf of lithium-aluminum alloy [vs. $Li(O)/Li^+$] as a function of composition and temperature in LiI-KI-LiCl eutectic salt.

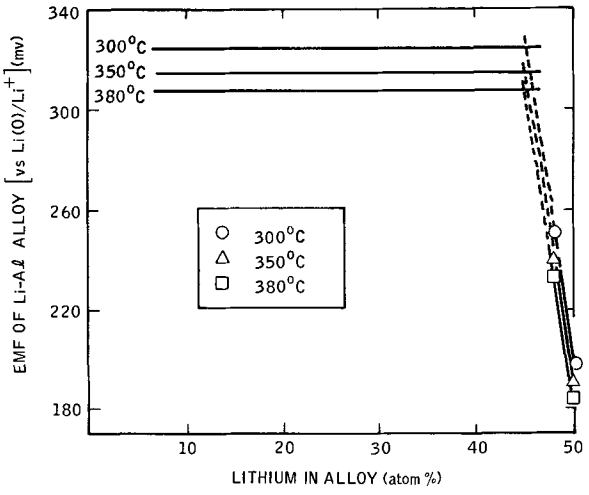

Fig. 3. Emf of lithium-aluminum alloy [vs. $Li(O)/Li^+$] as a function of temperature and composition.

showed that a solid solution of lithium in aluminum was formed up to 7.1 a/o lithium at 300°C and up to 8.5 a/o lithium at 400°C. This α phase was later confirmed by quantitative metallography and lattice-parameter measurements (17). With increasing lithium concentration at these temperatures, two phases are formed corresponding to α phase and β phase, respectively (17), where the β phase consists of the compound LiAl. The two-phase region extends to approximately 45.8 a/o lithium and has this boundary value constant over the temperature range 150°-550°C (17). In the present study, constant potential was indicated by the alloy up to 46.97 a/o lithium, which implies that a constant lithium activity exists on the alloy surface over the composition range from 6.91 to 46.97 a/o lithium in aluminum. This surface layer is likely to contain a stable compound corresponding to the β-LiAl in equilibrium with α-Al. The low emf values at 6.91 a/o lithium (in Table I) and at 8.11 a/o lithium (in Table II) seem to indicate that the surface layer of β-LiAl was formed even at these low lithium concentrations; *i.e.*, the surface concentration of lithium probably exceeded the true bulk concentration. On the other hand, further charging of lithium into the β-LiAl above 47 a/o up to 50 a/o yields a single phase, the lithium activity of which is a strong function of composition.

A duplicate run was made to prepare a lithium-aluminum alloy (up to 50 a/o lithium composition) in the LiI-LiCl-LiF eutectic mixture (mp 341°C) to assure the absence of potassium deposition. The equilibrium emf values of the alloy (*vs.* Li/Li^+) in the temperature range 362°-388°C are given in Table II, and the data up to 44.6 a/o lithium are plotted (open + points) in Fig. 2 for comparison with those obtained in the

Table II. Emf of lithium-aluminum alloy (vs. Li/Li^+) as a function of alloy composition and temperature in LiI-LiCl-LiF eutectic salt

Alloy composition a/o Li	w/o Li	Temp, °C	Emf, mV
8.11	2.22	382	306.41
		387	305.47
10.97	3.07	376	307.94
		383	306.30
19.65	5.92	378	307.66
20.80	6.33	377	308.01
25.34	8.03	377	307.68
		380	307.35
27.11	8.73	373	308.45
		380	307.41
29.84	9.86	362	311.27
		375	308.20
		377	307.80
33.67	11.55	382	306.61
37.50	13.37	379	306.73
44.86	17.31	388	304.92
47.21	18.70	382	248.00
50.00	20.46	383	171.55

LiI-KI-LiCl eutectic mixture. The two results were identical within the experimental accuracy. This shows that the potassium ion does not interfere with the lithium reaction in the temperature range studied, as was expected from thermodynamic considerations (14).

The cell reaction, in the alloy composition range 7-47 a/o lithium, is therefore the formation of solid β-LiAl compound on the surface corresponding to

$$\text{Li(l)} + \alpha\text{-Al(s)} = \beta\text{-LiAl(s)}$$

where α-Al(s) is the solid solution of lithium in aluminum (up to 7.1 a/o lithium at 300°C and up to 8.5 a/o lithium at 400°C). For practical purposes, however, the α-Al phase may be considered to be pure aluminum during the course of electrochemical alloy preparation. This is true since the reaction time of lithium and aluminum is much shorter than the solid diffusion time of lithium atoms in aluminum for α-phase formation. The diffusivity of lithium in aluminum is reported to be 1.2-1.7 x 10^{-10} cm^2/sec at 417°C (18). On this basis, the standard free energy of formation for β-LiAl saturated with α-Al from molten lithium and solid pure aluminum can be estimated from the emf data

$$\Delta G^\circ_f = -n\mathbf{F}E = -10.40 + 5.078 \times 10^{-3}\, T$$

where n is 1 equiv/mole, $\mathbf{F}$ is Faraday's constant, and T is temperature in °K. The standard enthalpy and entropy of formation are, respectively, −10.40 kcal/mole and −5.08 cal/mole · deg in the temperature range 282°-389°C. The standard free energy, enthalpy, and entropy of formation for β-LiAl at 300°, 350°, 380°C are summarized in Table III.

The lithium-aluminum alloy was prepared in the present work by constant-current cyclings in the gradually increasing current density range 14-70 mA/cm^2. As the result of expansion on charging and contraction on discharging, the alloy structure became increasingly porous. The fully charged alloy was subsequently discharged and charged at an apparent current density of as high as 150 mA/cm^2 without showing any significant polarization, presumably due to the high surface area of the alloy and an anomalous mechanism of lithium transport in the β-LiAl phase. The coulombic efficiency greater than 93% at the relatively high discharge current density would, otherwise, be impossible if the lithium atoms are transported from the alloy interior to the surface solely by solid diffusion.

The constant potential exhibited by the solid lithium-aluminum alloy over a considerable lithium concentration in LiI-LiCl-KI and LiI-LiCl-LiF eutectic salts, coupled with the good charge and discharge performance of the high surface area alloy, makes such an alloy an excellent high energy density anode material and also provides a stable reference electrode in high-temperature molten salt systems containing lithium.

Table III. Standard free energy, enthalpy, and entropy of formation for β-LiAl

T(°C)	ΔG°_f (kcal/mole)	ΔH°_f (kcal/mole)	ΔS°_f (cal/mole·deg)
300	−7.49	−10.40	−5.08
350	−7.24	−10.40	−5.08
380	−7.09	−10.40	−5.08

Manuscript submitted Nov. 4, 1970; revised manuscript received Feb. 2, 1971.

Any discussion of this paper will appear in a Discussion Section to be published in the June 1972 JOURNAL.

REFERENCES

1. D. A. J. Swinkels, *This Journal*, **113**, 6 (1966).
2. L. A. Heredy, N. P. Yao, and R. C. Saunders, *Proc. Intern. Electric Vehicle Symp., Electric Vehicle Council*, **1**, 375 (1969).
3. E. J. Cairns, M. L. Kyle, V. A. Maroni, H. Shimotake, R. K. Steunenberg, and A. D. Tevebaugh, "Development of High-Energy Batteries For Electric Vehicles," A Progress Report by Chem. Engr. Div., Argonne Nat. Lab. prepared for Nat. Air Pollution Control Administration of CPE, Public Health Service, HEW, July 1970.
4. E. J. Cairns, H. Shimotake, and A. K. Fischer, "Lithium/Chalcogen Electrochemical Cells for Energy Storage," *Argonne Review*, Oct. 1969.
5. S. B. Tricklebank, C. M. Little, and A. R. Poirier, "Li-Cl_2 Battery Power Source," Interim Tech. Report, Res. Lab. General Motors Corp., Contract No. AF 33615-68-C-1280, Project No. 3145, Jan. 15, 1969.
6. M. Hansen, "Constitution of Binary Alloys," Metallurgy and Metallurgical Engineering Series, 2nd Ed., p. 104, McGraw-Hill Book Co., Inc., New York (1958).
7. R. A. Rightmire and A. L. Jones, *Proc. Ann. Power Sources Conf.*, **21**, 42 (1967).
8. E. S. Buzzelli, "Aluminum Anode Electrical Energy Storage Device," U. S. Pat. 3,445,288, May 20, 1969.
9. H. A. Adams, "Prevention of Dendritic Growth on an Aluminum-Lithium Electrode," U. S. Pat. 3,428,493, Feb. 18, 1969.
10. W. K. Behl and D. L. Beals, "Investigation of a High-Energy Density Molten Salt Battery System," U. S. Army Electronics Command, Ft. Monmouth, N. J., Res. and Devel. Tech. Report ECOM-3166, DA Task No. ITO 61102A 34A 00, Aug. 1969.
11. J. L. Benak, "Method of Treating Aluminum-Lithium Electrode," U. S. Pat. 3,501,349, March 17, 1970.
12. C. E. Johnson and M. S. Foster, *This Journal*, **116**, 1612 (1969).
13. N. P. Yao, "Density and Electrical Conductivity of Molten Lithium Iodide-Lithium Chloride-Potassium Iodide Eutectic," To be published.
14. W. J. Hamer, M. S. Malmberg, and B. Rubin, *This Journal*, **103**, 8 (1956).
15. C. E. Johnson, "Solid-Liquid Phase Equilibria and Specific Conductivity for the Ternary Lithium Fluoride-Lithium Chloride-Lithium Iodide System," Paper M-128 presented at Am. Chem. Soc. Meeting, San Francisco, April 1968.
16. L. P. Costas and R. P. Marshall, *Trans. Met. Soc., AIME*, **224**, 970 (1962).
17. E. D. Levine and E. J. Rapperport, *ibid.*, **227**, 1204 (1963).
18. L. P. Costas, "The Diffusion of Lithium in Aluminum," USA Report, TID-16676 (1962).

Thin-Film Electrolytic Cells

John H. Kennedy* and Fred Chen**

Department of Chemistry, University of California, Santa Barbara, Santa Barbara, California 93106

ABSTRACT

Thin-film electrolytic cells have been prepared using silver bromide as the electrolyte. Deposits of silver bromide were highly oriented, (111) and (222), when deposited on silver or gold substrates at high temperature. The more random deposits obtained at ambient temperature exhibited electrical conductivities three orders of magnitude higher than the intrinsic conductivity of silver bromide. Cells of the type Ag/AgBr/Au were found to be accurate coulometers under limited conditions. The cells had a long life and could be cycled several thousand times without failing.

In the wake of the extensive amount of research being conducted on solid electrolyte materials, it has become apparent that solid electrolyte cells in the form of thin films might offer potential utility and overcome the high electrical resistance problems inherent to many of these systems. During the last few years, several articles have described the development of thin-film batteries (1-3), while our work has been aimed at developing thin-film cell configurations which could be employed as electrolytic coulometers. Although coulometers do not require extremely high conductivity, film cells also offer the possibility of cell arrays where multiple timing or integrations are required. In addition, some electrochemical systems may be coulometrically accurate, but are too resistive in conventional pellet form. Information gained from studying a known solid electrolyte coulometric system in film form could then be applied to other solid electrolytes.

Briefly stated, an electrolytic coulometer simply tabulates coulombs of charge by plating a metal (or chemical compound) on an inert indicator electrode. The counterelectrode in the cell is usually the same metal which is to be plated on the indicator electrode. A typical example is a cell consisting of a gold indicator electrode and a silver counterelectrode separated by an electrolyte containing silver ions (either solid or liquid electrolyte). Several papers have described these coulometers in detail (4-6). A thin-film electrolytic coulometer can be envisaged then by depositing a film of gold, solid electrolyte, and then silver on a substrate. Although metal films such as silver and gold are easily prepared and have been well characterized, films of solid electrolytes have not been extensively investigated. Because of its importance to the coulometer system, a detailed study of the solid electrolyte's film characteristics must be made. For initial studies, we chose silver bromide because of its simple stoichiometry and, from our pressed pellet studies (4), we knew it had a reasonable electrical conductivity of about 10^{-5} $(\text{ohm-cm})^{-1}$.

Experimental

Film depositions.—Film depositions were carried out at Sloan Technology Corporation, Santa Barbara, California. The films were vacuum deposited at several rates from 20 to 1000 Å/sec, while substrate temperatures were maintained at values from 20° to 250°C. Crystallite structure and size were controlled by the substrate temperature, and precautions had to be taken to prevent substrate temperature from increasing during the deposition. Deposition rate had to be maintained slow enough to prevent heating of the substrate.

X-ray diffraction.—X-ray diffraction studies were made with a Philips x-ray diffraction unit with CuKα radiation. A Philips Type 52572 scintillation counter with chart recorder was used for the x-ray diffractometer measurements.

Scanning electron microscopy.—Scanning electron micrographs were taken at Sloan Research, Santa Barbara, California. The samples were mounted on a sample stage with conductive silver paint. Care was taken to assure that the gold electrodes were grounded to the stage to bleed off induced charges. Some charging was still encountered due to the poor conductivity of the silver bromide. This caused focusing problems at high magnification along with some raster deflection. Overcoating the samples with a thin-film conductor will be considered for future work.

The examinations were made using a JSM-2 scanning electron microscope. A 25 kV electron beam focused to approximately 100Å diameter was rastered over the samples. All photographs were taken using the secondary electron emission mode. The samples were tilted 30° with respect to the impinging beam in order to enhance surface relief.

Constant current readout.—A Bissett-Berman Corporation E-Cell Digital Coulometer was used for constant current charging of cells and for those experiments designated as constant current readout. This unit has a built-in trigger which cuts off the constant current supply when cell voltage reaches a predetermined value.

Pulse discharge readout.—A Bissett-Berman Corporation EDR-300 E-Cell Digital Readout was used for pulse charge and discharge of cells. The unit was modified to deliver pulses of 1 μcoulomb in place of the normal 100 μcoulombs.

Temperature control.—An Associated Testing Laboratory SW-5101 environmental chamber was used for temperatures other than ambient.

Results

Silver bromide film characteristics.—Sample silver bromide films were vacuum deposited on silver, gold, silicon monoxide, and directly on a glass substrate. X-ray diffraction patterns of these films were taken, and the results are shown in Table I. Depositions were carried out at both high and low temperatures, and the

Table I. X-ray powder diffraction lines for AgBr films

Substrate	Deposition temp, °C	Film thickness, Å	Line intensity, I/I_0 Crystal plane orientation (111)	(200)	(220)	(222)
Au	280	1,450	73	0	0	100
Au	21	1,900	1	100	7	3
Au	21	3,500	4	100	9	8
Ag	280	1,450	81	32	27	100
Ag	21	1,900	11	100	31	16
Ag	180	100,000	0	100	0	23
Glass	280	1,450	0	100	11	1
Glass	280	3,200	7	100	39	7
SiO	280	3,200	7	100	6	6
Literature powder pattern			7	100	56	15

* Electrochemical Society Active Member.
** Electrochemical Society Student Associate Member.

Key words: coulometer; coulometry; electrolyte, solid; integrator, electrolytic; silver bromide; thin-film cells.

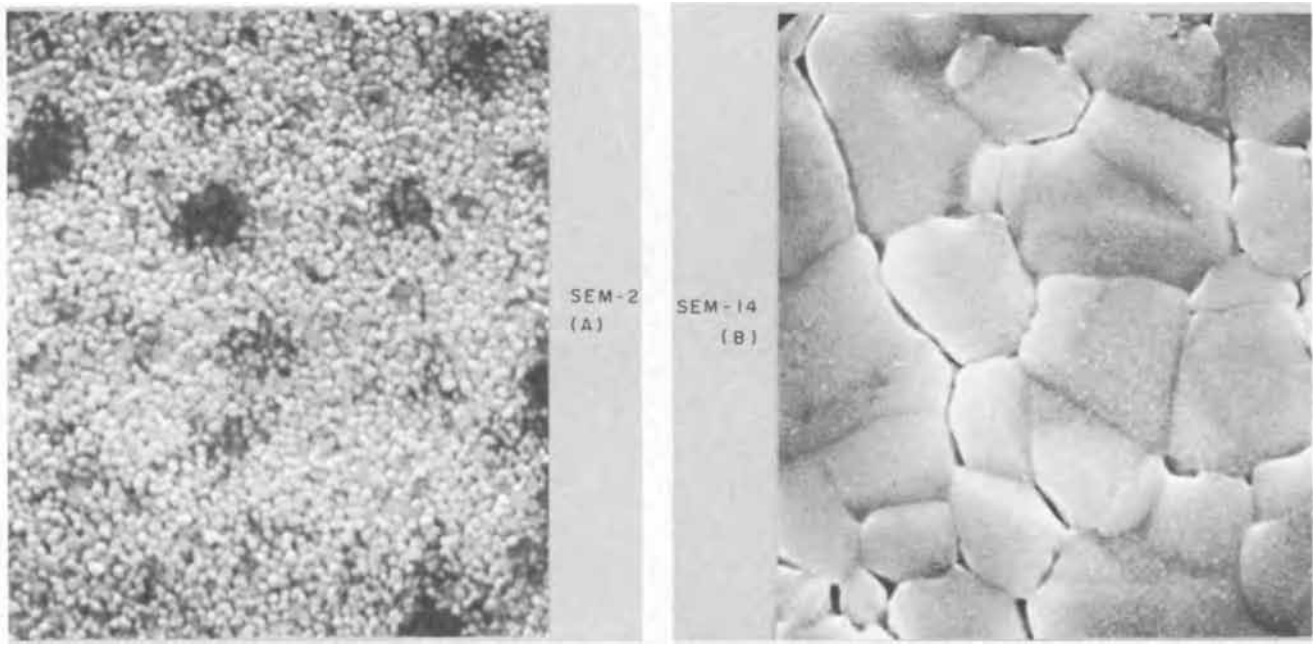

Fig. 1. Scanning electron micrographs of silver bromide films: (A)—AgBr deposited at 25°C (7600X), (B)—AgBr deposited at 250°C (7600X)

main finding was that silver bromide films were highly oriented along (111) and (222) planes when deposited at high temperature on gold or silver substrates. The primary line for powder AgBr is from the (200) reflection, and essentially the same pattern was observed for AgBr films deposited on SiO or glass. The orientation was also more random when deposited at low temperature on gold or silver and as the silver bromide film became thicker.

It appears from these results that growth along (111) and (222) planes is favored on gold and silver substrates, especially at high temperature where thermal energy allows recrystallization on the surface. Other investigators have also reported similar observations (8). This orientation is one in which a layer of bromide ions would cover the metal substrate as opposed to a surface containing both silver ions and bromide ions. This crystallite growth at high deposition temperature also meant, however, that crystallite size would be larger than films prepared at lower temperatures. This effect is readily seen in Fig. 1. Scanning electron micrograph (A) was taken of a AgBr film deposited at ambient temperature while (B) was taken of a film deposited at 250°C to gain information concerning crystallite size and shape. The crystallites formed at high temperature were 1-3μ in size, while at low temperature the crystallites were only 0.2μ.

Most of the electrolyte films for electrolytic coulometers were nominally 100,000Å thick (10μ) although several successful cells with only 20,000-30,000Å films of AgBr were prepared. Thinner layers, however, were extremely prone to electrical shorting.

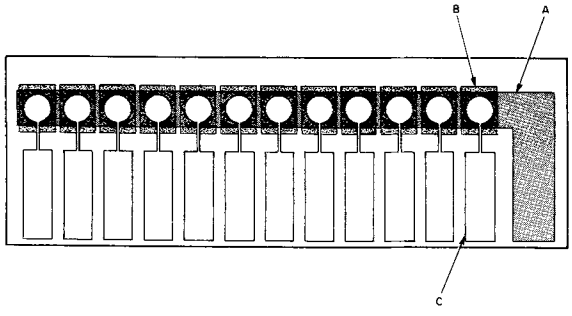

Fig. 2. Thin-film cell configuration: A—silver strip electrode (common), B—silver bromide electrolyte (12 squares), C—gold electrode (12 circles with rectangular tab for contact).

Electrolytic cell configuration and electrochemical characteristics.—The cell configuration is shown in Fig. 2. First, a set of 12 gold electrodes was deposited on the glass substrate or over a Nichrome base to obtain better adherence. Second, a set of 12 silver bromide square pads of electrolyte covered the gold electrodes. Finally, a common silver electrode strip was deposited over the entire 12 cells. The cell area was determined by the circular gold electrode which was 0.10 cm^2. The reverse deposition order was attempted, but it appeared that the silver electrode oxidized before the silver bromide deposition could be carried out. The experimental conditions were such that the films were exposed to air after each deposition.

The electrical conductivity of silver bromide films was extremely sensitive to the deposition temperature as can be seen in Table II. The conductivities of films are compared to the intrinsic conductivity of AgBr and that of pressed powder (4). In previous work, it has been shown that AgBr pressed powders gave conductivities 100 times greater than intrinsic values and that this effect appeared to be due to grain boundary conduction (4, 7). The small crystallites produced by low-temperature deposition have an extraordinary amount of grain boundaries leading to conductivities another order of magnitude higher than the pressed powder.

The conductivity was also measured as a function of temperature. The usual plot of log σ *vs.* $1/T$ was linear with an activation energy of 4.6 kcal/mole. This is considerably less than the activation energy for the intrinsic conductivity measured at high temperature which is about 20 kcal/mole. This result again emphasizes the point that the conductivity observed for AgBr films is extrinsic and probably due to a grain boundary conduction mechanism.

Although the cells made by depositing AgBr at high temperatures performed reasonably well as coulom-

Table II. Conductivity of AgBr films

Material	Deposition temp, °C	Conductivity (ohm-cm)$^{-1}$	Film resistance, ohms
Intrinsic conductivity	—	$<0.01 \times 10^{-5}$	—
Pressed powder	—	1×10^{-5}	—
Film	250	0.052×10^{-5}	19,300
Film	100	0.182×10^{-5}	5,500
Film	25	9.1×10^{-5}	130

eters, the small number of conduction paths made them highly resistive and frequently led to electrical shorting during operation. Shorting was observed with both silver plating on silver and silver plating on gold. Cells which operated several cycles usually shorted when plating silver on silver. This observation was reported earlier with pressed pellet coulometers (4). Coulometry results given below are only for cells containing AgBr deposited at ambient temperature.

After a measured amount of silver has been plated on the gold indicator electrode, the cell is a silver/silver system until all the silver is anodically stripped from the gold electrode. The open-circuit potential is essentially zero, and the applied voltage during stripping remains close to zero with just IR drop and electrode polarization contributions. After all the silver has been stripped from the gold electrode, the voltage rises steeply to the point where gold itself oxidizes or the decomposition voltage of the electrolyte is reached. A voltage/time curve during stripping for a thin-film cell is shown in Fig. 3. A charge of 150 μcoulombs of silver had been plated on the gold electrode and was then anodically stripped at 3 μA. The test equipment was set to cut off automatically when the cell reached 0.5V. Without the cutoff, the voltage rises to about 0.8V which is the decomposition voltage of AgBr. It is also in the range where gold can be oxidized to form gold bromide.

The sensitivity of a coulometer depends on how sharp this final rise curve is and can be characterized by an apparent capacitance value. The capacitance is calculated by

$$C = i \Big/ \frac{dv}{dt}$$

It must be emphasized that this is not the true capacitance since faradaic effects can also be taking place at the gold electrode as the potential changes. These faradaic effects may include oxidation of impurities at the gold surface from the silver bromide or gold and some oxidation of the gold itself at the higher voltages. After several charging and stripping cycles, apparent capacitances increased possibly due to silver residing in the gold grain boundaries being oxidized at high voltages. The thin-film cells exhibited apparent capacitances of 30-60 μf or 300-600 μf/cm². This range of values is similar to results for other AgBr studies (9). Roughness factors could also lead to high capacitance values, and no direct measurement was made on the gold films. High reflectivity and microscopic examination of the surface leads us to assume roughness factors comparable to gold foil of 1.5-4. The higher value then leads to corrected capacitance values of 75-150 μf/cm².

After silver has been completely stripped from the gold electrode, the gold indicator electrode can be held at a positive potential with respect to the silver electrode, and the current will decay to a small residual value. The gold acts as a "blocking" electrode toward ionic processes so that the residual current is a function of the electronic conductivity. Wagner (10) and Ilschner (11) have shown that silver bromide exhibits electron conductivity under these conditions, and that the following relation holds in the plateau region of residual current *vs.* applied voltage

$$i_o = \frac{RT}{LF}\sigma_o$$

where:

i_o = residual current density
L = electrode spacing
σ_o = electronic conductivity

Residual currents for most thin-film cells were <1 nanoA, and no appreciable change in residual current was observed between 0.2 and 0.5V. A plateau was difficult to demonstrate, however, since the readings were often near the low limit of our measuring equipment (0.1 nanoA). Previous work has shown that this voltage range is in the plateau region for AgBr (11). Electronic conductivity values calculated from these residual currents were $<4 \times 10^{-10}$ (ohm-cm)$^{-1}$. This would represent the maximum electronic conductivity contribution since there might still be an ionic contribution to the residual current under the experimental conditions used.

Coulometry results.—The principal function of an electrolytic coulometer is to store a charge in the form of silver atoms on the gold indicator electrode and, then, to determine this charge by anodic stripping. If a known charge is plated on the indicator electrode and stripping is carried out at constant current, the coulometer performs a timing function. Table III illustrates results for thin-film cells stripped at constant current at various temperatures. Results are within 1-2% of the true value on the average, particularly in the 200-1000 μcoulomb range. It should be noted that 2% of 200 μcoulombs is only 4 μcoulombs while a monolayer of silver atoms on the gold is about 25 μcoulombs (or greater, depending on surface roughness). The end-point or cutoff voltage was nominally picked at 500 mV. A change in cutoff voltage will only affect the first readout for the cell, provided all succeeding cycles use the same cutoff value. There was a tendency for high results at low currents and high temperatures noted (Table III: 20 sec at 1 μA at +50°C = +21.3% error) which is related to the increase in residual current as the temperature increases. Obviously, a cell can never reach 500 mV at a given current if the residual current is higher than the operating current. Under most operating conditions, the errors are usually negative. This is attributed to the migration of silver into the gold along grain boundaries to become essentially "lost." Another effect which may account for low results when large amounts of charge were used is the possibility of

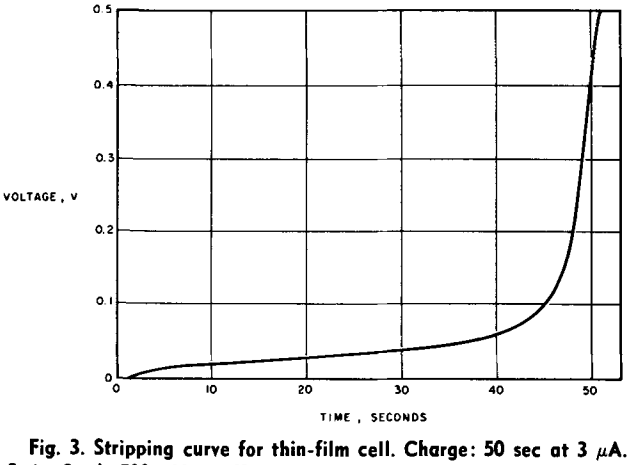

Fig. 3. Stripping curve for thin-film cell. Charge: 50 sec at 3 μA. Strip: 3 μA, 500 mV cutoff.

Table III. Timing accuracy for AgBr thin-film coulometers

Temp, °C	Current, μA	Charge time, sec: 20 Avg* error	20 Std dev	50 Avg* error	50 Std dev	100 Avg* error	100 Std dev	250 Avg* error	250 Std dev
25	1.0	+0.4	3.3	+1.1	1.0	−0.1	0.4	−3.6	1.3
	3.6	−1.1	1.9	−0.9	1.0	−1.2	1.1	−1.2	0.7
	10.0	−2.1	3.1	−0.2	0.6	−2.1	0.6	—	—
0	1.0	+4.2	2.8	+1.0	1.0	−0.3	0.3	−2.2	2.1
	3.6	+1.8	3.7	−7.7	1.1	−2.7	0.9	−5.9	2.9
	10.0	−1.4	2.0	−2.0	0.4	—	—	—	—
−20	1.0	−0.9	3.1	—	—	—	—	—	—
	3.6	−0.1	1.0	0.0	0.3	+0.4	0.7	—	—
	10.0	+0.4	0.3	+0.2	0.3	+0.4	0.2	—	—
	36.0	+0.7	0.3	+0.4	0.4	−0.4	0.1	—	—
+50	1.0	+21.3	6.0	—	—	—	—	—	—
	3.6	−1.5	3.3	−0.7	0.6	−1.3	1.4	−0.4	0.2
	10.0	−0.4	0.4	−0.2	0.3	−0.3	0.4	−9.7	7.4
	36.0	−0.1	0.5	−0.3	0.1	−6.5	3.6	—	—

* Average of 8-10 determinations.

Table IV. Coulometric accuracy for AgBr thin-film coulometers using pulse readout

Temp, °C	Charge, μcoulombs: 100 Avg* error	100 Std dev	200 Avg* error	200 Std dev	500 Avg* error	500 Std dev	1000 Avg* error	1000 Std dev
−50	−2.7	5.9	−2.2	0.7	−1.2	0.5	−0.6	—
−20	−7.4	4.3	−3.2	0.4	−1.8	0.8	−1.1	0.3
0	−2.0	5.8	−3.2	0.8	−1.1	1.3	−1.1	0.3
+25	−6.8	2.9	−2.1	0.6	−1.6	0.3	−1.4	0.4
+50	−6.7	2.1	−4.9	0.8	−1.8	0.9	−2.3	0.0

* Average of 5-8 determinations.

Table V. Open-circuit voltage stability

Voltage: 500 mV initial
Coulometry: Plate 200 μcoulombs initial

Cell No.	Function	16 Hr storage: Voltage, mV	16 Hr storage: Coulometry, μcoulombs	98 Hr storage: Voltage, mV	98 Hr storage: Coulometry, μcoulombs
3	Coulometry		171	3	170
4	Voltage	400		320	
5	Coulometry		168	3	171
6	Coulometry		145	5	151
7	Voltage	453		410	
9	Coulometry		174	3	171
10	Coulometry		174	2	185
11	Voltage	455		375	
12	Voltage	464		430	

silver losing contact with the gold electrode and becoming an island in the silver bromide electrolyte. These two effects will limit both the low and high charge capability for the coulometers.

Previous work with pressed powder cells showed that, by pulsing charge and observing the cell potential after the pulse, problems due to *IR* drop and polarization could be decreased (6). This technique was also applied to thin-film cells, and the results are given in Table IV. There was no marked improvement with errors of 1-2% observed in the range of 500-1000 μcoulombs. Somewhat greater errors were observed for charges of 100-200 μcoulombs. However, the pulsing technique could be used to apply charges of 3000-5000 μcoulombs without shorting the cells. Errors were −1 to −5% for these large charges.

The pulsing technique was also used to study charge storage capability. A charge of 1000 or 2000 μcoulombs was plated on the gold and allowed to stand for several days at ambient temperature before the stripping cycle. Figure 4 shows the results. There was a rapid loss of silver during the first day amounting to about 100 μcoulombs of charge and, then, little further loss was observed. Again, this can be explained by silver migrating into the gold along grain boundaries (bulk diffusion is much too slow to account for these results).

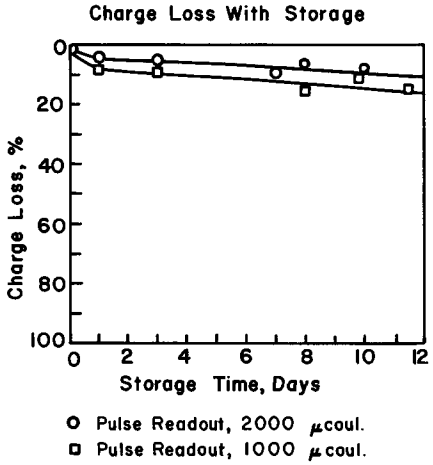

Fig. 4. Charge loss with storage

The gold surface becomes "saturated" quickly after the easily accessible sites are filled. A very slow diffusion deeper into the gold may still take place causing additional loss on long-term storage.

Memory applications.—For some applications, a coulometer must stay at the cutoff voltage after being brought to this point while the cell stands at open-circuit conditions. After a period of time, interrogation of such a cell must show it to be at a high potential, indicating that there is no silver on the gold. A slide of thin-film cells was tested for this type of application, and the results are given in Table V. Four of the cells were brought to 500 mV, while five other cells were plated with 200 μcoulombs of charge. After 16 hr, the cells were checked. Cleared cells still registered 400-464 mV, and the plated cells were read out at constant current. A loss of about 30-50 μcoulombs was noted. The coulometry cells were replated and, after 98 hr, a second check was made. Cleared cells were now 320-430 mV and, for comparison, the voltages of plated cells were 2-5 mV. Small potentials are observed for plated cells because low coverage of silver electroplated on gold has a slightly lower activity than the pure silver film. Again, the plated cells exhibited coulometric errors of 15-50 μcoulombs. As discussed above, charge loss with storage occurs within the first day and little additional loss would occur in the next 3 days.

Cell life.—The life of these cells has been surprisingly long considering the close electrode spacing. Some cells were cycled continuously with 200 μcoulombs of charge and underwent over 20,000 cycles with no apparent damage.

Resistance of pressed pellets tended to rise with time, but film cells had exactly the same resistance after 6 months. Crystallites whose boundaries have been physically pressed together appear to react slowly with time, forming fewer grain boundary conduction paths. Silver bromide films, on the other hand, exhibit no such reaction over the period of time studied. In fact, in some cases where cells were used extensively, the resistance decreased a few per cent. This was attributed to a better electrode/electrolyte contact being produced with usage.

Cell operation was not affected by light although the top of the silver electrode tarnished and some color change of the silver bromide extending beyond the electrodes was noted. It must be remembered that because of the cell dimensions only the silver bromide directly between the gold and silver electrodes will experience current flux. This part of the silver bromide is not exposed to light because of shielding by the gold and silver electrodes.

Acknowledgments

The authors thank the Bissett-Berman Corporation for financial support of this project and also Gary Breitweiser of Sloan Technology Corporation for assistance in preparing film depositions.

Manuscript submitted Nov. 2, 1970; revised manuscript received Feb. 15, 1971. This was Paper 29 presented at the Atlantic City Meeting of the Society, Oct. 4-8, 1970.

Any discussion of this paper will appear in a Discussion Section to be published in the June 1972 JOURNAL.

REFERENCES

1. O. Yamamoto and T. Takahashi, *Denki Kagaku*, **34**, 883 (1966).
2. P. Vouros and J. I. Masters, *This Journal*, **116**, 880 (1969).
3. C. Liang, J. Epstein, and G. H. Boyle, *ibid.*, **116**, 1322, 1452 (1969).
4. J. Kennedy, F. Chen, and A. Clifton, *ibid.*, **115**, 918 (1968).
5. J. Kennedy and F. Chen, *ibid.*, **116**, 207 (1969).
6. J. Kennedy, F. Chen, and J. Willis, *ibid.*, **117**, 263 (1970).

7. I. Shapiro and I. M. Kolthoff, *J. Chem. Phys.*, **15**, 41 (1947).
8. F. Trautweiler, L. E. Brady, J. W. Castle, and J. F. Hamilton, "The Structure and Chemistry of Solid Surfaces," p. 83-1, G. A. Somorjai, Editor, Proc. Fourth Intern. Materials Symposium held at Univ. of California, Berkeley, June 17-21 (1968).
9. D. O. Raleigh, "Progress in Solid State Chemistry," Vol. 3, p. 83, Pergamon Press, New York (1966).
10. C. Wagner, *Z. Elektrochem.*, **60**, 4 (1956).
11. B. Ilschner, *J. Chem. Phys.*, **28**, 1109 (1958).

Cathodic Behavior of N-Type Cadmium Fluoride

M. M. Nicholson*

Atomics International, A Division of North American Rockwell Corporation, Canoga Park, California 91304

ABSTRACT

The cathodic reduction of n-type cadmium fluoride single crystals in a 1M lithium perchlorate-propylene carbonate electrolyte was investigated by discharge at constant current densities of 0.1 and 0.2 mA/cm^2. The semiconductive cadmium fluoride was reduced through an electronic mechanism which did not occur with an undoped crystal. Bulk resistivities of the crystals were determined, and contact resistances at the boundary between the semiconductor and the indium amalgam current collector were examined. A cathodic passivation effect which limited the utilization of active material to the equivalent of a 0.1-0.2μ layer on the crystal surface was observed. Implications of the results for battery cathode performance are discussed.

Studies of faradaic processes at semiconductor electrodes have been confined mainly to the anodic dissolution of germanium and silicon (1, 2) and the charge-transfer reactions of redox systems on semiconductor substrates (3). The cathodic reduction of semiconductors with known electronic properties has received much less attention, although semiconductivity is thought to play a significant role in the discharge of certain battery cathodes containing an oxide or sulfide as the active ingredient (4-6). In this investigation, the cathodic behavior of n-type cadmium fluoride single crystals was examined galvanostatically in a 1M lithium perchlorate-propylene carbonate electrolyte. Each crystal specimen was characterized by measurement of its bulk resistivity before it was placed in the electrochemical cell. The contact resistivity at the interface between the semiconductor and the indium amalgam current collector was also investigated.

Cadmium fluoride, with an energy gap of 6.0 eV (7), is normally an insulator. Prener and Kingsley discovered that this compound can be converted to an n-type semiconductor with a resistivity of the order of 1 ohm-cm by doping with Y(III) or certain trivalent rare-earth cations and subsequent exposure to cadmium vapor at 500°C (8). Because this conversion method was available, the cathodic response of electronically conductive and nonconductive forms of cadmium fluoride could be readily compared. Such a comparison for a metal halide system is of particular interest in current efforts to develop more active cathode materials for high-energy batteries using lithium anodes and electrolytes dissolved in aprotic organic solvents. Cadmium fluoride offers a theoretical energy density of 399 Whr/lb in combination with a lithium anode, which is high enough to merit its use as a practical battery cathode material (9, 10).

Experimental Procedures

Materials.—Undoped and yttrium-doped cadmium fluoride crystals weighing 20-30g were grown by the Bridgman closed-crucible method, starting with high-purity cadmium fluoride powder from the Chemical Products Plant of the General Electric Company in Cleveland, Ohio. Prior to crystal growth, the powder was dried for several hours at 400°-600°C in a stream of anhydrous hydrogen fluoride. The yttrium fluoride dopant was introduced by fusion at concentrations from 0.01 to 1 m/o (mole per cent).

One-millimeter sections of the doped crystals, cut perpendicular to the growth axis, were washed in benzene to remove the cutting oil, polished on an abrasive stone, etched in 1:1 hydrochloric acid, and sealed into evacuated quartz or Pyrex tubes containing small pieces of cadmium metal. Heating for several minutes at 500°C produced the blue coloration characteristic of semiconductive cadmium fluoride. The colored specimens were re-etched in hydrochloric acid to remove the undoped layer which was known to form on the surface during cadmium exposure (8).

Propylene carbonate of 99% purity, manufactured by Jefferson Chemical Company, was dried by percolation through a Linde 4A molecular sieve and distilled at ~3 mm under argon at a 5:1 reflux ratio, using a 50 x 230 mm column packed with ⅛ in. Pyrex helices. The center third of the distillate had a conductivity of 2.89×10^{-8} ohm^{-1} cm^{-1} at 25°C. Gas chromatographic analysis of this fraction by the method of Jasinski and Kirkland (11) indicated 10 ppm water, 3 ppm propylene glycol, and <0.5 ppm propylene oxide.

Reagent-grade lithium perchlorate from G. Frederick Smith Chemical Company was heated 16 hr at 160°C in a stream of argon to remove traces of water. A typical weight loss of 0.33% occurred at this temperature within the first 2 hr. No further loss was observed on fusion of the dried material. The lithium metal was 99.97% pure ribbon from Foote Mineral Company. The cell materials were handled by dry box and argon-blanketing techniques.

Resistivity measurements.—Bulk resistivities of the cadmium fluoride crystal specimens and area resistivities of the indium amalgam contacts were measured by means of the conventional four-terminal arrangement shown in Fig. 1. Details are given here to clarify the notations used in reporting the results. Constant current densities ranging from 0.05 to 35 mA/cm^2 were passed between the ends of the crystal through terminals F and G by means of a 45V battery and a dropping series resistor. Electrical connections to the amalgam contacts were made with the assistance of a four-element micromanipulator assembly. Potential differences between the various terminals were measured with a Leeds & Northrup K-3 potentiometer.

The bulk resistivity, ρ, was calculated from the equation

* Electrochemical Society Active Member.
Key words: cadmium fluoride, nonaqueous electrolyte.

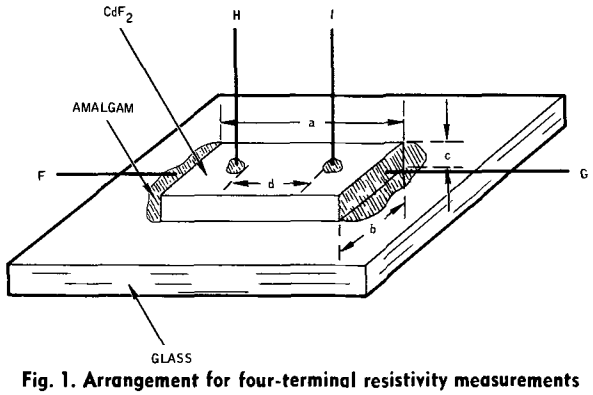

Fig. 1. Arrangement for four-terminal resistivity measurements

$$\rho = \frac{E_{H-I}}{E_s} \cdot R_s \cdot \frac{bc}{d} \qquad [1]$$

where E_{H-I} represents the potential difference between the probes at terminals H and I, E_s is the potential drop across a standard resistor, R_s, in a series with the crystal, and b, c, and d are the dimensions indicated in Fig. 1. With this technique, the bulk resistivity measurement is not ordinarily influenced by relatively large potential drops across the current-carrying boundaries. The area resistivity of the surface F was defined as

$$\rho_F = \frac{E_{F-H}}{bc} \cdot \frac{R_s}{E_s} \qquad [2]$$

and a corresponding definition was taken for the surface G.

A 50 w/o (weight per cent) indium amalgam proved more satisfactory than other contact materials that were investigated, including indium solder, several pressure-applied solid metals, and carbon paste. Acid-etched cadmium fluoride surfaces tended to produce poor contacts, even with the amalgam. Further washing in organic solvents failed to eliminate the resistive film. Amalgam contacts on freshly cleaved crystal surfaces were essentially ohmic, however.

Electrochemical measurements.—The electrochemical cell contained a single-crystal cadmium fluoride cathode mounted as shown in Fig. 2, a lithium anode, which was separated from the cathode by a glass frit, and a lithium reference electrode connected to the cathode compartment through a Luggin capillary. The crystal surface exposed to the solution was freshly cleaved and essentially parallel to the growth axis. The opposite surface was scraped to assure good contact through the amalgam to the external circuit. The exposed electrode area was typically 0.05 cm^2, and the crystal length, 0.5 cm. The cell was placed in a water bath at 25°C during the electrochemical measurements.

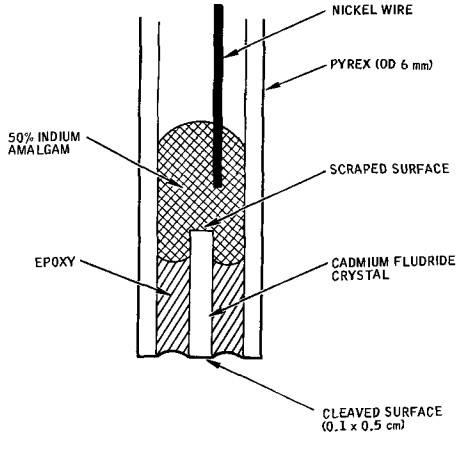

Fig. 2. Single-crystal electrode

Constant currents from an Electronic Measurements Model C633 power supply were applied between the crystal electrode and the lithium anode. The potential of the crystal was monitored with respect to the reference electrode on a General Radio Type 1230-A electrometer, with the output signal applied to a Sargent MR recorder. By means of current pulse measurements on a dummy copper electrode having the same geometry as the crystal, it was established that the solution ohmic drop between the crystal electrode and the reference was only a few millivolts.

Results and Discussion

The fluorides and chlorides of transition metals have been investigated over a period of several years as cathode materials for organic electrolyte batteries. These solids have low conductivities; their discharge apparently involves dissolution of the metal ion and its transport through the solution, followed by electron transfer at the surface of an inert current collector such as carbon. Ionic conduction in the solid state would lead, instead, to metal deposition at the boundary between the active solid material and the current collector, while electronic conduction would result in electrodeposition of the metal at the semiconductor-solution interface. In this work, it was of central importance to verify the existence of an electronic mechanism for the reduction of n-type cadmium fluoride and to determine the rate and depth of discharge obtainable by this reaction path on a known surface area. It also proved necessary to evaluate the potential drop at the interface between the semiconductor crystal and its metal contact to the external circuit.

Contact resistivities.—The contact resistivities of acid-washed and freshly cleaved surfaces on the 1.3 ohm-cm crystal are compared in Fig. 3. Notations F and G refer to the current-carrying contacts at appropriate ends of the crystal, as identified in Fig. 1. A negative current density corresponds to the passage of electrons from the amalgam into the crystal, as would occur in the cathodic reduction process. The rectification effect at this boundary, which is evident in Fig. 3, would oppose the electrochemical reaction. This problem was greatly reduced by cleaving the crystal. The area resistivity on the 1.3 ohm-cm specimen was then less than 10 ohm-cm^2 for current densities between −5 and +15 mA/cm^2. At higher Y(III) concentra-

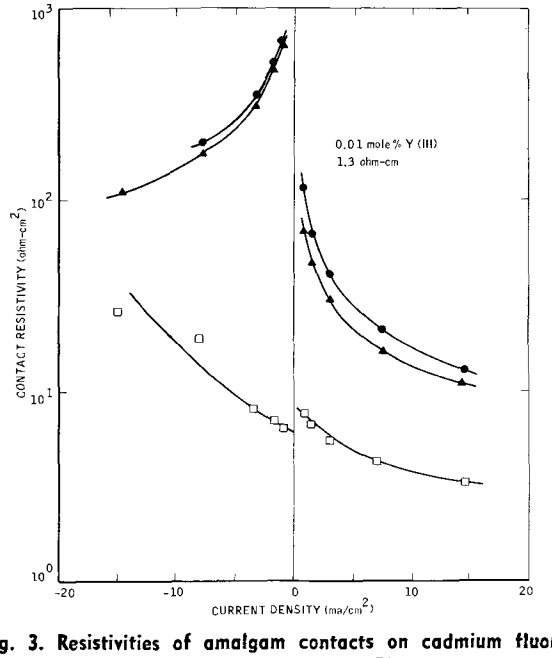

Fig. 3. Resistivities of amalgam contacts on cadmium fluoride crystal: —●—, contact F, washed in 1:1 HCl; —▲—, contact G, washed in 1:1 HCl; —□—, contact F, freshly cleaved.

tions, cleaved interfaces exhibited more ideally ohmic behavior, with a typical area resistivity of 0.3 ohm-cm^2, although the resistivities on acid-washed and benzene-washed surfaces still approached 10^3 ohm-cm^2. Since the electrochemical current density did not exceed 0.2 mA/cm^2, the potential drop at the amalgam contact on a freshly scraped surface should have been only a few millivolts. With a contaminated surface, however, this drop could easily have been of the order of 1V. These results emphasize the importance of a good electronic contact for a semiconductor electrode. The ohmic drop through the bulk of the crystal ranged from ~0.02 to 0.3 mV.

Cathodic discharge behavior.—The thermodynamic potential of a cell with the reaction

$$2Li(s) + CdF_2(s) \rightarrow Cd(s) + 2LiF(s)$$

is 2.70V. Initial open-circuit potentials determined experimentally on the doped crystals were 2.4-2.6V *vs.* Li/Li$^+$ (1M), while 1.7V were observed on an undoped crystal with a resistance >3 x 10^7 ohms.

Preliminary discharges of 1 min duration were made on each of the doped crystals at 0.1 and 0.2 mA/cm^2, to compare initial polarizations and to establish a suitable current density level for longer discharge experiments. The preliminary curves for a 0.68 ohm-cm crystal are shown in Fig. 4. Following rapid potential drops of 0.25 and 0.7V, respectively, the discharge proceeded smoothly under these conditions, and the cathode recovered within several minutes on open circuit to a new potential approaching the theoretical value. The initial drop apparently was localized at the semiconductor-solution interface, but the mechanism of its origin has not yet been determined. Corresponding curves for crystals with resistivities up to 3.2 ohm-cm differed very slightly from those of Fig. 4.

With continued discharge, a dark layer of cadmium metal became visible on the outside of the cadmium fluoride crystal, while no change was observed at the amalgam contact. A discharged electrode, when removed from the cell, washed in water, and dried, showed high surface conductance on a d-c ohmmeter. Thus, an electronic reduction mechanism was indicated for the semiconductive materials. As expected, an undoped crystal failed to pass a current of 0.1 mA/cm^2, even when 420V were applied between the anode and cathode.

Figure 5 illustrates the behavior of a doped crystal on prolonged discharge at 0.1 mA/cm^2. Data for several

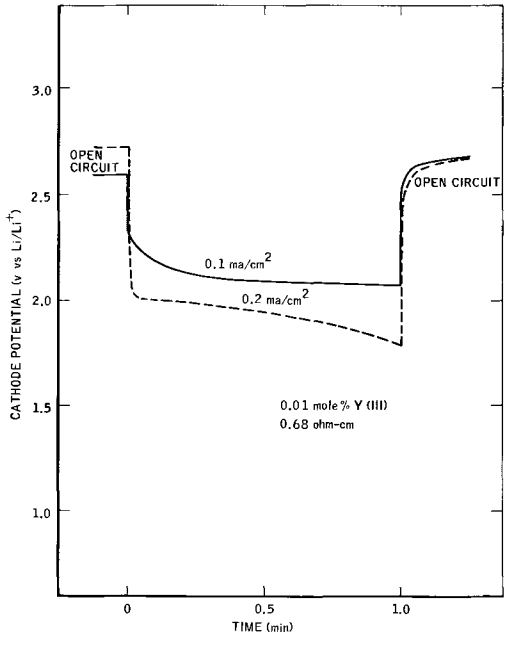

Fig. 4. Preliminary discharges of cadmium fluoride crystal

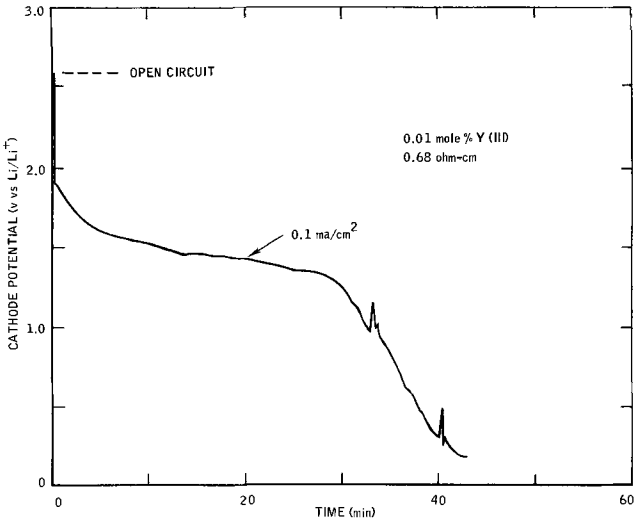

Fig. 5. First continuous discharge of cadmium fluoride crystal

crystal electrodes are given in Table I. A plateau in the potential-time curve generally occurred near 1.5V *vs.* Li/Li$^+$ (1M), followed by a transition region of the type shown in Fig. 5. A practical end of the discharge could be taken at 1.1V *vs.* Li/Li$^+$ (1M), although some minor inflections appeared at lower potentials. This cutoff corresponded to the utilization of a cadmium fluoride layer 0.1-0.2μ in thickness. Although the electrode recovered subsequently on open circuit to a potential above 2.0V, essentially no discharge capability remained, as is shown in Fig. 6. The potential dropped almost immediately when a second prolonged discharge was attempted. Cathodic activity was restored, however, by exposure of the discharged crystal to water. Two passivation mechanisms may be readily visualized—coating of the crystal by a nonporous layer of cadmium metal or by a layer of lithium fluoride. The sharp peaks in the transition region (Fig. 5) may be due to occasional fractures in the passivating film.

Implications for cadmium fluoride battery cathodes.—The preparation of secondary cathodes by anodizing cadmium metal in complex fluoride-organic solvent electrolytes has been reported by Shaw and others (9, 10). Doped crystals of the type used in the present study will not be reconstructed from the metal by anodic charging. It was of interest, nevertheless, to examine briefly the behavior of a discharged semiconductor electrode under anodic current. The results are shown in Fig. 7 and 8. At a charging current density of 0.2 mA/cm^2, the total cathode potential rose in 13 min to 8.7V *vs.* Li/Li$^+$ (1M). Of this final value, nearly 6V appeared to be a nonohmic component associated with the semiconductor/electrolyte interface. This is indicated in Fig. 7 by the immediate drop of

Table I. Discharge characteristics of *n*-type cadmium fluoride crystals

Y(III) conc (m/o)	Crystal resistivity (ohm-cm)	Initial open-circuit potential (V *vs.* Li/Li+)	Transitions Potential (V *vs.* Li/Li+)	Transitions Time (min)	Utilization thickness (μ)
1	0.44	2.43	1.08	15	0.11
			0.68	22	0.16
0.01	0.68	2.50	1.04	32	0.23
			0.72	36	0.26
			1.20[a]	49[a]	0.36
			0.79[a]	68[a]	0.50
0.01	0.68	2.60	1.17[b]	7.5[b]	0.11
0.01	3.2[c]	2.59	1.12	16	0.12
			0.69	26	0.19
0	>3 x 10^6	1.78	—	—	—

[a] Following exposure of discharged crystal to water.
[b] Current density 0.2 mA/cm^2; all other data at 0.1 mA/cm^2.
[c] Exposed to cadmium vapor 3 hr at 300°C.

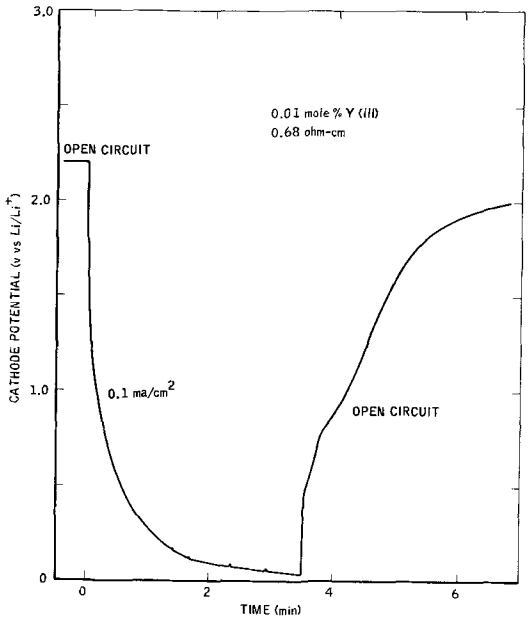

Fig. 6. Second continuous discharge of cadmium fluoride crystal and recovery on open circuit.

5.7V which occurred on interruption of the charging current. The initial voltage step in cathodic discharge at the same current immediately thereafter (Fig. 8) was only 0.25V. Such asymmetric behavior is expected for an n-type crystal, on which oxidations should be generally difficult because of the tendency to form an exhaustion layer at positive potentials (12). Although Fig. 8 indicates that some discharge capacity within the cadmium fluoride potential region resulted from charging, the anodic process occurred at low energy efficiency with the semiconductor crystal in the circuit.

In conclusion, the electronic reduction mechanism in n-type cadmium fluoride offers an alternative path for the discharge reaction, which is not available with the undoped material. In a porous electrode, this route may supplement or supplant that of another process, such as the reduction of dissolved cadmium ion. To utilize the electronic mechanism efficiently, one must provide a low-resistance contact at the semiconductor-current collector interface and control the cathodic passivation which was observed in a lithium perchlorate-propylene carbonate electrolyte. The latter problem, which may be caused by a film of cadmium or lithium fluoride, is under further investigation.

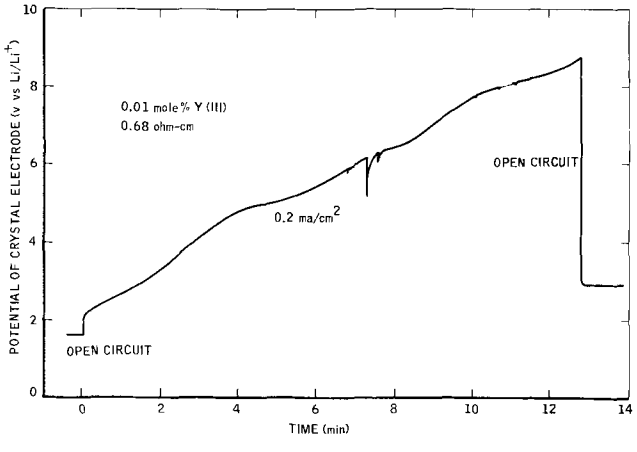

Fig. 7. Charging of previously discharged crystal electrode

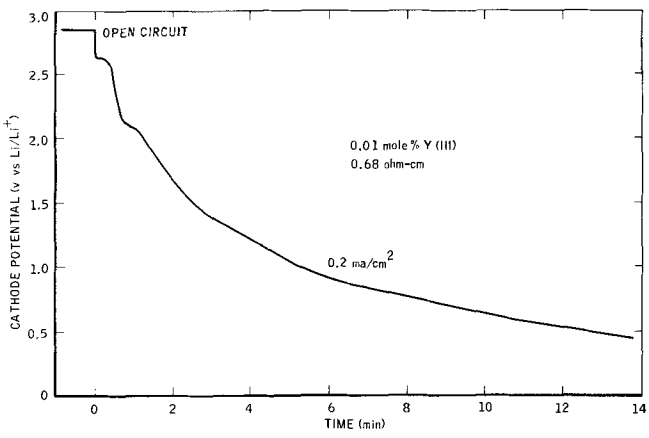

Fig. 8. Discharge of crystal electrode after charging to 8.7V vs. Li/Li⁺ (1M).

Acknowledgments

G. L. Shoop performed a major portion of the experimental work. Acknowledgments are due also to J. S. Mohl for growth of the cadmium fluoride crystals, to G. L. Hargrove for gas chromatographic analyses, and to J. O. McCaldin for advice on the doping method.

This research was sponsored by the Air Force Cambridge Research Laboratories, Office of Aerospace Research, under Contract F19628-67-C-0387, but the report does not necessarily reflect endorsement by the sponsor.

Manuscript submitted July 2, 1970; revised manuscript received March 4, 1971. This was Paper 51 presented at the Detroit Meeting of the Society, Oct. 5-9, 1969.

Any discussion of this paper will appear in a Discussion Section to be published in the June 1972 JOURNAL.

REFERENCES

1. W. H. Brattain and C. G. B. Garrett, *Bell System Tech. J.*, **34**, 129 (1955).
2. J. B. Flynn, *This Journal*, **105**, 715 (1958).
3. F. Beck and H. Gerischer, *Z. Elektrochem.*, **63**, 943 (1959).
4. H. B. Mark and W. C. Vosburgh, *This Journal*, **108**, 615 (1961).
5. R. Jasinski and B. Burrows, *ibid.*, **116**, 423 (1969).
6. J. P. Gabano, G. Gerbier, and J. F. Laurent, *Proc. Power Sources Conf.*, **23**, 80 (1969).
7. J. S. Prener and J. D. Kingsley, *J. Chem. Phys.*, **35**, 2256 (1961).
8. J. S. Prener and J. D. Kingsley, *ibid.*, **38**, 667 (1963).
9. M. Shaw and D. H. McClelland, U.S. Pat. 3,393,092, July 16, 1968.
10. M. Shaw and R. Chand, *Proc. Power Sources Conf.*, **23**, 76 (1969).
11. R. J. Jasinski and S. Kirkland, *Anal. Chem.*, **39**, 1663 (1967).
12. J. Lambe, D. K. Donald, W. C. Vassell, and T. Cole, *Appl. Phys. Letters*, **8**, 16 (1966).

Solid-State Ionics—Coulometric Titrations and Measurements of the Ionic Conductivity of Beta Ag_2Se and Beta Ag_2Te and Use of These Compounds in an Electrochemical Analog Memory Element

Takehiko Takahashi* and Osamu Yamamoto

Department of Applied Chemistry, Faculty of Engineering, Nagoya University, Nagoya, Japan

ABSTRACT

The ionic conductivities of β Ag_2Se and β Ag_2Te have been determined as a function of the metal-to-nonmetal ratio with the help of the cell Ag/$RbAg_4I_5$/β Ag_2X/$RbAg_4I_5$/Ag (X = Se or Te), and the concentrations of the ionic defects at the ideal stoichiometric composition of these compounds have been calculated to be $3.5 \times 10^{17}/cm^3$ for β Ag_2Se at 105°C and $9.7 \times 10^{18}/cm^3$ for β Ag_2Te at 97°C. The coulometric titrations have been studied with the help of the cell Ag/$RbAg_4I_5$/β Ag_2X/Pt to derive the theoretical equation in order to explain the relation between the cell voltage and the deviation from the ideal stoichiometric composition. Based on these studies, a new type of electrochemical cell, Ag/$RbAg_4I_5$/β Ag_2Te, $RbAg_4I_5$ and graphite, has been proposed. The emf of the cell is changed linearly in the range of 120 to 0 mV by the coulombs passed through the cell at room temperature. At open circuit, the emf of the cell decreases only by a few per cent in several hundred minutes.

In recent years, considerable interest has been taken in solid electrolyte galvanic cells (1-3). Electrochemical cells using solid electrolyte in place of the conventional liquid electrolyte have many advantages of achieving appreciable miniaturization and operation over a wide temperature range. However, only a little work has been reported on these devices, except for galvanic cells. One of these was a solid electrolyte coulometer reported by Yamamoto and Takahashi (4) and Kennedy and Chen (5) which consisted of the solid electrolyte held between the silver and gold electrodes. The other example was a memory with variable resistance which was proposed first by Widrow (6) and examined later by Takahashi, Yamamoto, and Kuwabara (7).

The most important problem in this field is the improvement of the low conductivity of solid electrolytes at ambient temperature. Recently, some solid electrolytes have been reported by Takahashi and Yamamoto (8), Bradley and Greene (9), and Owens and Argue (10) to have high ionic conductivity at room temperature. These were the double salts such as Ag_3SI and $RbAg_4I_5$ which show conductivities comparable to those of aqueous electrolyte solutions at room temperature. It may be possible, therefore, to develop many types of electrochemical cells with these solid electrolytes. The purpose of this paper is to examine a new type of electrochemical cell using $RbAg_4I_5$ which has a silver ion conductivity of 2.1×10^{-1} $(ohm\text{-}cm)^{-1}$ at 25°C (10).

The system investigated in this study consists of a silver electrode, electrolyte ($RbAg_4I_5$), and a silver chalcogenide such as β Ag_2Te or β Ag_2Se, the cell construction being

$$Ag|RbAg_4I_5|\text{Silver chalcogenide} \qquad \text{(I)}$$

Silver chalcogenides have been known to have nonstoichiometric composition and exhibit mixed conductivity partly ionic and partly electronic. Upon passing the current across cell (I) from right to left (charging process), a definite amount of silver is transferred from the silver chalcogenide phase to the silver electrode, decreasing the metal-to-nonmetal ratio, r, in silver chalcogenide. If the direction of current is reversed (discharging process), r increases. In silver chalcogenides, such as Ag_2Se and Ag_2Te, silver ions and electrons are both mobile so that the metal-to-nonmetal ratio becomes rapidly uniform, especially at high temperature.

$RbAg_4I_5$ is essentially an ionic conductor, and the chemical potential of silver μ_{Ag} in Ag_2Se or Ag_2Te is related to the electromotive force, E, of cell (I) by

$$\mu_{Ag} - \mu^{o}_{Ag} = -E\mathbf{F} \qquad [1]$$

where μ^{o}_{Ag} is the chemical potential of pure silver and $\mathbf{F}$ the Faraday constant. By denoting the chemical potential of excess electron, electron hole, and silver ion in β Ag_2Se or β Ag_2Te by μ_e, μ_h and μ_{Ag+}, respectively, one obtains the following expression

$$\mu_{Ag} = \mu_{Ag+} + \mu_e = \mu_{Ag+} - \mu_h \qquad [2]$$

From Eq. [1] and [2], at the ideal stoichiometric composition of β Ag_2Se or β Ag_2Te

$$\mu'_{Ag} - \mu^{o}_{Ag} = -E'\mathbf{F} \qquad [3]$$

and

$$\mu'_{Ag} = \mu'_{Ag+} + \mu'_e = \mu'_{Ag+} - \mu'_h \qquad [4]$$

are established where μ'_{Ag}, μ'_e, μ'_h, and μ'_{Ag+} are chemical potentials of each species at the ideal stoichiometric composition of β Ag_2Se or β Ag_2Te, respectively, and E' the emf of cell (I) with the ideal stoichiometric β Ag_2Se or β Ag_2Te. By combining Eq. [1], [2], [3], and [4], one obtains

$$(\mu_{Ag+} - \mu'_{Ag+}) + (\mu_e - \mu'_e) = (\mu_{Ag+} - \mu'_{Ag+}) - (\mu_h - \mu'_h) = -(E - E')\mathbf{F} = -\Delta E\mathbf{F} \qquad [5]$$

At low concentrations of interstitial silver ion and silver ion vacancy, it may be assumed that the change of chemical potential of silver ion is expressed by the following equation

$$\mu_{Ag+} - \mu'_{Ag+} = RT \ln n_o/\bar{n}_o = -RT \ln n_{\square}/\bar{n}_{\square} \qquad [6]$$

where n_o and $n_{\square}$ are the concentrations of interstitial silver ion (Ag^{+}_{o}) and silver ion vacancy ($Ag^{+}_{\square}$), and $\bar{n}_o$ and $\bar{n}_{\square}$ are those at the ideal stoichiometric com-

* Electrochemical Society Active Member.

Key words: solid electrolyte; coulometer; $RbAg_4I_5$, Ag_2Te, Ag_2Se; memory device; deviations from stoichiometry.

position. The concentrations of excess electron, n_e, and electron hole, n_h, are related to μ_e and μ_h by

$$n_e = \frac{\pi(8m_e^* \cdot kT)^{3/2}}{2h^3} \cdot \mathbf{F}(\eta_e) \quad [7]$$

and

$$n_h = \frac{\pi(8m_h^* \cdot kT)^{3/2}}{2h^3} \cdot \mathbf{F}(\eta_h) \quad [8]$$

where $\eta_e = \mu_e/RT$, $\eta_h = \mu_h/RT$, m^*_e and m^*_h are the effective mass of electron and electron hole, respectively, $\mathbf{F}(\eta)$ is the Fermi-Dirac function, and the other symbols have the usual meanings. According to the table of Fermi-Dirac function computed by McDougall and Stoner (11), the following approximation may be available for a narrow range of η values

$$\mathbf{F}(\eta) = ke^{\eta/C} = ke^{\mu/CRT} \quad [9]$$

By combining Eq. [7] and [9], or [8] and [9], one finds

$$\mu_e = CeRT \ln n_e/Ne \quad [10]$$

and

$$\mu_h = C_hRT \ln n_h/N_h \quad [11]$$

where, Ce, C_h, Ne, and N_h are constant parameters depending on the mean value of n_e or n_h within the range considered. Therefore

$$\mu_e - \mu'_e = CeRT \ln n_e/\bar{n}_e \quad [12]$$

and

$$\mu_h - \mu'_h = C_hRT \ln n_h/\bar{n}_h \quad [13]$$

are obtained where $\bar{n}_e$ and $\bar{n}_h$ are the concentrations of excess electrons and electron holes at the ideal stoichiometric composition. Substituting Eq. [6] and [12] into Eq. [5], we have

$$-\Delta E\mathbf{F} = RT \ln (n_o/\bar{n}_o)\ (n_e/\bar{n}_e)^{C_e} \quad [14]$$

If no silver atoms are present in β Ag_2Se or β Ag_2Te, the deviation from the ideal stoichiometric composition, Δr, is equal to the difference of the concentration of the two atomic imperfections or the two electronic imperfections

$$n_o - n_\square = n_e - n_h = \Delta r(No/Vm) \quad [15]$$

where Vm is the molar volume of β Ag_2Se or β Ag_2Te, and No the Avogadro number. In β Ag_2Se and β Ag_2Te, the atomic imperfection is present according to the Frenkel equilibrium

$$Ag^+ \rightleftharpoons Ag^+_o + Ag^+_\square$$

i.e.

$$n_o \cdot n_\square = \bar{n}^2_o \quad [16]$$

Further, the thermal equilibrium is established with the excess electron and electron hole

$$e + h \rightleftharpoons 0$$

i.e.

$$\mu_e + \mu_h = 0 \quad [17]$$

From Eq. [12], [13], and [17], we have

$$(n_e)^{C_e}\ (n_h)^{C_h} = (\bar{n}_e)^{C_e+C_h} \quad [18]$$

Substitution of Eq. [16] and [18] into Eq. [15] gives

$$\left(\frac{n_o}{\bar{n}_o}\right)^2 - \frac{\Delta r}{\bar{n}_o}\left(\frac{No}{Vm}\right)\left(\frac{n_o}{\bar{n}_o}\right) - 1 = 0 \quad [19]$$

and

$$\left(\frac{n_e}{\bar{n}_e}\right)^{(1+C_e/C_h)} - \frac{\Delta r}{\bar{n}_e}\left(\frac{N_o}{Vm}\right)\left(\frac{n_e}{\bar{n}_e}\right)^{C_e/C_h} - 1 = 0 \quad [20]$$

Finally, the relation between ΔE and Δr is given by

$$-\Delta E\mathbf{F} = RT \ln f(\Delta r) \cdot \{g(\Delta r)\}^{C_e} \quad [21]$$

where $f(\Delta r)$ and $g(\Delta r)$ are the solutions of Eq. [19] and [20], respectively.

The deviation from the ideal stoichiometric composition, Δr, is expressed by Faraday's law as

$$\Delta r = q/x\mathbf{F} = \frac{1}{x\mathbf{F}}\int_{E=E'}^{E} i\,dt \quad [22]$$

where q is the number of coulombs passed through cell (I), and x the number of moles of selenium or tellurium. According to Eq. [21] and [22], cell (I) must have a cell voltage depending on the deviation from the ideal stoichiometric composition of β Ag_2Se or β Ag_2Te. This means that the cell voltage is changed by the coulombs passed through the cell. This fact suggests that this cell will be able to be used as a coulometer. Further, if the cell voltage is kept constant for a certain period of time, the cell will be used as a memory device, for example as a memory with variable resistance.

It is clear from Eq. [19], [20], and [21] that the knowledge of the concentration of imperfections and the values of C_e and C_h allows the examination of the relation between Δr and ΔE. Studies on electronic imperfection have been done by Dalven and Gill (12) and Miyatani (13), and the concentration of interstitial silver ion in β Ag_2Se has been measured by Valverde (14). In this study, by measuring the ionic conductivities of β Ag_2Se and β Ag_2Te as a function of the metal-to-nonmetal ratio, the concentrations of atomic imperfection at the ideal stoichiometric composition of these compounds have been determined with the help of the theories of Koch and Wagner (15) and Stasiw and Teltow (16).

Experimental

Preparation of materials.—Silver telluride and silver selenide were prepared from the elements. A mixture of silver powder (99.999% purity) and tellurium powder (99.999% purity) or selenium powder (99.999% purity) was thoroughly ground before being sealed under vacuum in a Pyrex tube and heated at 420°C (for silver telluride) or 350°C (for silver selenide) for 48 hr. The solid electrolyte, $RbAg_4I_5$, was prepared according to the method described by Owens and Argue (10). Weighing of 0.8 mole fraction of silver iodide and 0.2 mole fraction of rubidium iodide was followed by mixing and grinding. The mixture was sealed in a glass tube under vacuum and heated at 500°C for 2 hr. Then, after being cooled abruptly, it was maintained at 160°C for 24 hr, thereby synthesizing $RbAg_4I_5$.

Ionic conductivity measurements.—The ionic conductivity measurements for β Ag_2Se or β Ag_2Te were carried out by the following cells which were similar to those used by Weiss (17)

$$Ag|RbAg_4I_5|\beta\ Ag_2Se|RbAg_4I_5|Ag \quad (II)$$
$$\uparrow$$
$$Pt$$

and

$$Ag|RbAg_4I_5|\beta\ Ag_2Te|RbAg_4I_5|Ag \quad (III)$$
$$\uparrow$$
$$Pt$$

Ag_2Se or Ag_2Te was pressed into the form of a cylindrical pellet 13 mm in diameter and 1-2 mm in thickness. In order to reduce the electrode polarization, a mixture of powdered silver and $RbAg_4I_5$ (2:5 weight ratio) was used for the silver electrode. When a d-c voltage below the decomposition voltage of $RbAg_4I_5$ and β Ag_2Se or β Ag_2Te is applied between two silver electrodes, the current is carried practically by silver ion because $RbAg_4I_5$ is a pure silver ion conductor. As the ohmic resistance of $RbAg_4I_5$ is known, the ionic resistance of β Ag_2Se or β Ag_2Te can be calculated from the total resistance. A current of 1-100 μA was used in this experiment. In order to change the cation-to anion ratio in β Ag_2Se or β Ag_2Te, the current was passed

between the silver electrode and the platinum electrode which was inserted into the pellet of β Ag_2Se or β Ag_2Te. The measurements were carried out at above 70°C, as it was necessary to wait a long period of time to obtain a steady voltage at lower temperatures.

The structure of the electrochemical cell.—A typical schematic diagram of the cell is shown in Fig. 1. A mixture of powdered silver and $RbAg_4I_5$ was used as the silver electrode. For the counterelectrode, a mixture of Ag_2Te (or Ag_2Se), $RbAg_4I_5$, and graphite was used to increase the electrode reaction area, the composition of which was selected to obtain a high performance. For example, a mixutre of 0.2g powdered silver and 0.7g $RbAg_4I_5$, 1.2g $RbAg_4I_5$, and a mixture of 0.2g powdered graphite, 1.5g $RbAg_4I_5$ and 0.4g β Ag_2Te, were pressed successively at 2 tons/cm^2 to form a pellet and it is pressed at 5 tons/cm^2 under vacuum for 10 min. The diameter of the pellet was 13 mm. A graphite block was placed on the β Ag_2Te electrode to give the electronic contact upon which a silver wire was put to make it serve as the lead wire and a silver plate was used as an electronic collector of the silver electrode. The following measurements were carried out under vacuum.

Experimental Results and Discussion

Ionic conductivity of β Ag_2Se and β Ag_2Te and the concentration of Frenkel defects at the ideal stoichiometric composition.—In 1970, the concentration of interstitial silver ion in β Ag_2Se at the ideal stoichiometric composition was measured with the help of coulometric titration (14). In this study, in order to know the concentration of ionic defects in β Ag_2Se or β Ag_2Te, the ionic conductivity was measured by a similar method proposed by Wagner (18) and examined for β Ag_2S by Weiss (17). In the study made by Weiss, AgI was used as the solid electrolyte and the measuring temperature was always above 147°C, which was the transition temperature of AgI. Below this temperature, however, the ionic conductivity of AgI was too low and in this study, therefore, $RbAg_4I_5$, which has high ionic conductivity even at room temperature, was used as the solid electrolyte to carry out the measurement at relatively low temperature.

In general, it is difficult to synthesize ideal stoichiometric β Ag_2Se or β Ag_2Te from the elements. The ideal stoichiometric compositions of these compounds were determined by coulometric titrations (19). Wagner and Schottky (20) have pointed out that in disordered crystals a point of inflection appears in chemical potential *vs.* composition curves at the ideal stoichiometric composition. The cell voltage between the platinum and the silver electrodes of cell (II) or (III) is drawn *vs.* coulombs passed through the cell and, from the maximum slope of this curve, the ideal stoichiometric composition of β Ag_2Se or β Ag_2Te was determined. For example, the maximum slope appeared at 53 mV in β Ag_2Te at 97°C and at 180 mV in β Ag_2Se at 105°C.

The current was passed between the silver and the platinum electrodes in order to change the cation-to-anion ratio in β Ag_2Se or β Ag_2Te and, at each Δr value, the ionic conductivity of these compounds was measured with the help of cell (II) or (III). The ionic

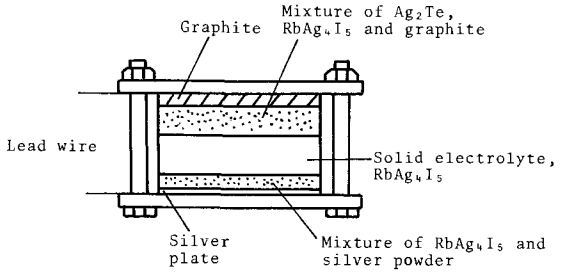

Fig. 1. Schematic diagram of the electrochemical cell

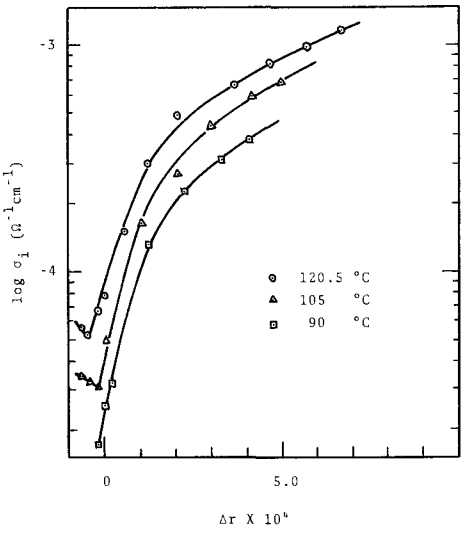

Fig. 2. The ionic conductivity of β Ag_2Se, σ_i, as a function of the deviation from the ideal stoichiometric composition, Δr.

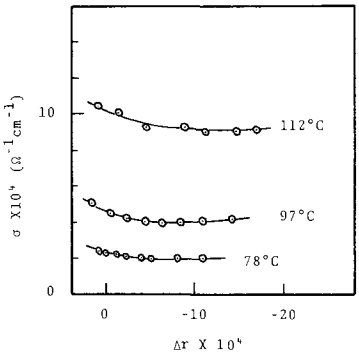

Fig. 3. The ionic conductivity of β Ag_2Te σ_i as a function of the deviation from the ideal stoichiometric composition, Δr.

conductivity of β Ag_2Se is shown in Fig. 2 as a function of the deviation from the ideal stoichiometric composition, Δr. The ionic conductivity increases rapidly with increasing Δr, indicating that the excess silver in β Ag_2Se dissociates to interstitial silver ion and excess electron. The dependence of ionic conductivity of β Ag_2Te on Δr is shown in Fig. 3. In this case, the change of ionic conductivity is not so remarkable.

The phenomenon of producing the interstitial silver ion or silver ion vacancy by removing or injecting silver from or into the lattice is considered to be similar to that of adding an impurity into a pure crystal, the theoretical approaches for which have been done by Koch and Wagner (15) and Stasiw and Teltow (16). The dependence of ionic conductivity on Δr is examined with the help of the theory of Teltow *et al.* as follows.

If the ionic carriers in β Ag_2Se or β Ag_2Te are interstitial silver ion ($Ag^+{}_o$) and silver ion vacancy ($Ag^+{}_\square$) and the other ionic defects are negligible, the ionic conductivity, σ_i is represented as

$$\sigma_i = en_o u_o + en_\square u_\square \qquad [23]$$

where u_o and $u_\square$ are the mobilities of $Ag^+{}_o$ and $Ag^+{}_\square$. The intrinsic ionic conductivity, $\bar{\sigma}_i$, at the ideal stoichiometric composition is expressd by

$$\bar{\sigma}_i = e\bar{n}_o u_o + e\bar{n}_\square u_\square \qquad [24]$$

Substituting Eq. [15] and [16] into Eq. [23] and using Eq. [24], we have

$$\frac{\sigma_i}{\bar{\sigma}_i} = \sqrt{\left(\frac{\Delta r N_o}{2\bar{n}_o V m}\right)^2 + 1} + \left(\frac{\Delta r N_o}{2\bar{n}_o V m}\right)\frac{\phi - 1}{\phi + 1} \qquad [25]$$

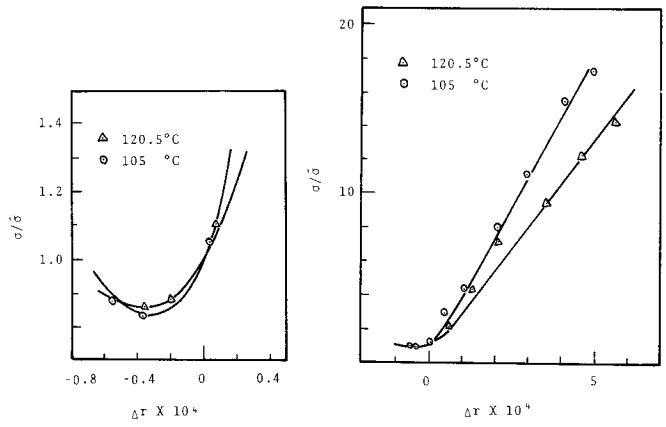

Fig. 4. The relative conductivity, $\sigma_i/\bar{\sigma}_i$ of β Ag_2Se as a function of the deviation from the ideal stoichiometric composition, Δr. The circles and triangles represent the experimental values and the lines are theoretical isotherms.

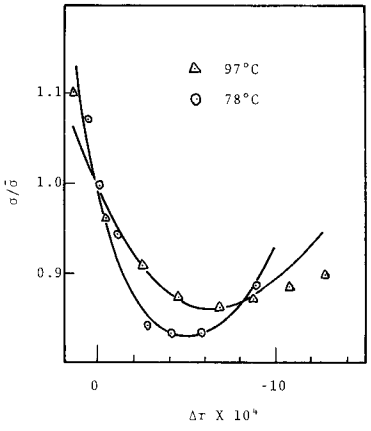

Fig. 5. The relative conductivity, $\sigma_i/\bar{\sigma}_i$ of β Ag_2Te as a function of the deviation from the ideal stoichiometric composition, Δr. The circles and triangles represent the experimental values and the lines are theoretical isotherms.

where $\phi = u_o/u_\square$. According to Eq. [25], a plot $\sigma_i/\bar{\sigma}_i$ *vs.* Δr shows a minimum at the ordinate value

$$\left(\frac{\sigma_i}{\bar{\sigma}_i}\right)_{\min} = \frac{2\sqrt{\phi}}{1+\phi} \qquad [26]$$

The relation between $\sigma_i/\bar{\sigma}_i$ and Δr is shown in Fig. 4 for β Ag_2Se and in Fig. 5 for β Ag_2Te. From these curves, ϕ can be calculated by solving Eq. [26] and $\bar{n}_o$ by substituting the numerical values of $\sigma_i/\bar{\sigma}_i$, Δr and, ϕ in Eq. [25]; ϕ and $\bar{n}_o$ obtained by this method are listed in Table I. In Fig. 4 and 5, the real lines are obtained from Eq. [25] using the numerical values of ϕ and $\bar{n}_o$. In these figures, the experimental values are found to coincide with the theoretical curves, showing that the association of interstitial silver ion or silver ion vacancy with the excess electron or electron hole is negligibly small.

Table I. Characteristic quantities of β Ag_2Se and β Ag_2Te

Substance	Temp, °C	ϕ	$\bar{n}_o$
β Ag_2Te	78	3.5	5.3×10^{18}
	97	3.1	9.7×10^{18}
β Ag_2Se	105	4.5	3.5×10^{17}
	120.5	3.1	4.8×10^{17}

ϕ is the ratio of the mobility of the Ag^+ interstitial to that of the Ag^+ vacancy; $\bar{n}_o$ is the concentration of Frenkel defects at the stoichiometric composition.

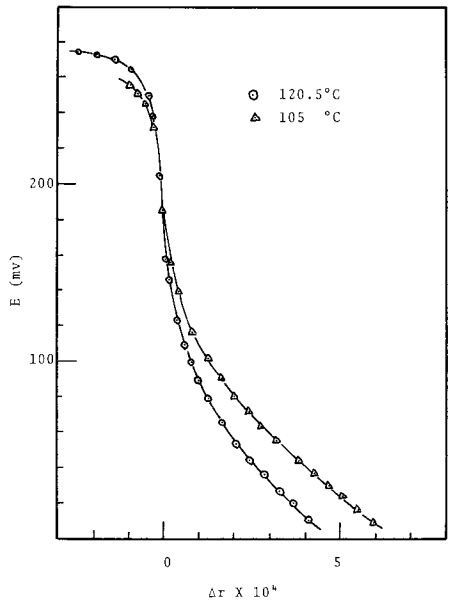

Fig. 6. The cell voltage, E, of the cell $Ag|RbAg_2I_5|\beta$ Ag_2Se *vs.* the deviation from the ideal stoichiometric composition, Δr.

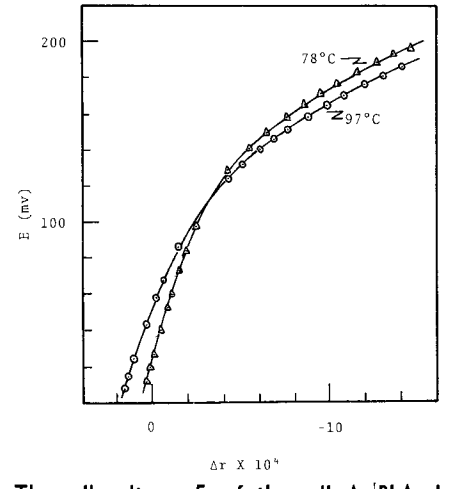

Fig. 7. The cell voltage, E, of the cell $Ag|RbAg_4I_5|\beta$ Ag_2Te *vs.* the deviation from the ideal stoichiometric composition, Δr.

The relation between the cell voltage of $Ag/RbAg_4I_5/\beta$ Ag_2Se or β Ag_2Te and the deviation from the ideal stoichiometric composition of β Ag_2Se or β Ag_2Te.—The cell voltage (E) of $Ag/RbAg_4I_5/\beta$ Ag_2Se or β Ag_2Te *vs.* the deviation (Δr) from the ideal stoichiometric composition is shown in Fig. 6 for β Ag_2Se and in Fig. 7 for β Ag_2Te. These curves were obtained passing a constant current of 10 μA between the silver and platinum electrodes in cell (II) or (III) to add or subtract silver in or from β Ag_2Se or β Ag_2Te, the cell voltage of which coincided with that kept at open circuit for 10 several minutes showing that the equilibrium was attainable immediately at as small a current as 10 μA. Δr was calculated from Eq. [22]. It is seen from Fig. 6 and 7 that E increases with decreasing Δr to reach a constant value of 270 mV for β Ag_2Se at 105°C or 190 mV for β Ag_2Te at 97°C. These values correspond to the open-circuit voltages of cell $Ag/RbAg_4I_5/Se$ and $Ag/RbAg_4I_5/Ag_{1.9}Te$ (21), respectively.

According to Eq. [21], it is necessary to know the concentration of imperfections and the values of C_e and C_h in order to examine the relation between Δr and ΔE. The numerical values of $\bar{n}_o$ and $\bar{n}_e$ are sum-

Table II. Concentrations of interstitial silver ion or silver ion vacancy ($\bar{n}_o = \bar{n}_{\square}$) and excess electron or electron hole in silver chalcogenides at ideal stoichiometric composition

Compound	Temp, °C	$\bar{n}_o = \bar{n}_{\square}$	Ref.	$\bar{n}_e = \bar{n}_h$	Ref.
β Ag_2Se	105	3.5×10^{17}	Table I	5×10^{18}	(12, 13)
	120	4.8×10^{17}	Table I	7×10^{18}	(12, 13)
	75	9.7×10^{16}	14		
	100	2.3×10^{17}	14		
β Ag_2Te	78	5.3×10^{18}	Table I	1.4×10^{18}	(12, 13)
	97	9.7×10^{18}	Table I	1.9×10^{18}	(12, 13)

marized in Table II, in which the values of $\bar{n}_e$ at the temperature considered were obtained by extrapolating the values measured at the other temperatures reported by Dalven and Gill (12) and Miyatani (13).

For β Ag_2Se, the concentration of excess electron at the ideal stoichiometric composition is distinctly larger than that of interstitial silver ions as shown in Table II, so that Eq. [21] may be reduced to a simple form of

$$\frac{\Delta r N_o}{\bar{n}_o V m} \cong \exp(-\Delta E\mathbf{F}/RT) - \exp(\Delta E\mathbf{F}/RT) \quad [27]$$

A plot of Δr *vs.* $\exp(-\Delta E\mathbf{F}/RT) - \exp(\Delta E\mathbf{F}/RT)$ should give a straight line with a slope of $\bar{n}_o V m/N_o$. This plot is shown in Fig. 8 giving a straight line from which $\bar{n}_o(\bar{n}_{\square})$ is determined to be 3.8×10^{17} at 120.5°C and 2.8×10^{17} at 105°C. These values are comparable to those estimated from the ionic conductivity measurements.

On the other hand, the difference between $\bar{n}_o$ and $\bar{n}_e$ in β Ag_2Te at the temperature investigated is not so large that Eq. [21] cannot be reduced to a simple form such as Eq. [27]. In Eq. [21], there are two unknown parameters of C_e and C_h, which may be calculated from the table of the Fermi-Dirac function if the effective masses of electron and electron hole are known. Substituting the values of $\bar{n}_e$ and m_e^*/m into Eq. [7], we have

$$\mathbf{F}(\eta_e) = 3.3 \text{ at } 97°C$$

and

$$\mathbf{F}(\eta_e) = 2.8 \text{ at } 78°C$$

where m_e^*/m was assumed to be 0.06 at both temperatures, which has been evaluated by Miyatani (13) at 100°C. According to the table of the Fermi-Dirac function, these values correspond to $\eta \cong 2.6$ and 2.2, respectively, and, substituting the values of $\mathbf{F}(\eta)$ at the vicinity of $\eta = 2.6$, and 2.2 into Eq. [9], we have $C_e \cong 2.2$ at 97°C, and $C_e \cong 2.0$ at 78°C.

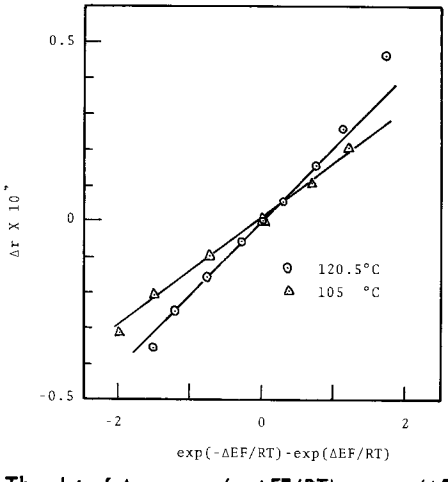

Fig. 8. The plot of Δr *vs.* $\exp(-\Delta E\mathbf{F}/RT) - \exp(\Delta E\mathbf{F}/RT)$ for β Ag_2Se.

Table III. Values of C_e and C_h

Temp, °C	$(d\Delta E/d\Delta r)_{\Delta r=0}$ (mV)	$\bar{n}_o$	$\bar{n}_e$	C_e	C_h
97	-2.6×10^2	9.7×10^{18}	1.9×10^{18}	2.2	1.6
78	-3.3×10^2	5.3×10^{18}	1.4×10^{18}	2.0	1.6

By differentiating Eq. [21] with respect to Δr, the slope of the ΔE *vs.* Δr curve at $\Delta r = 0$ is given by

$$\left(\frac{d\Delta E}{d\Delta r}\right)_{\Delta r=0} = -\frac{RT}{2\mathbf{F}} \cdot \frac{N_o}{Vm}\left(\frac{1}{\bar{n}_o} + \frac{2C_eC_h}{C_e + C_h} \cdot \frac{1}{\bar{n}_e}\right) \quad [28]$$

Substituting the values of $(d\Delta E/d\Delta r)_{r=0}$, $\bar{n}_o$, $\bar{n}_e$, and C_e into Eq. [28], C_h can be determined. The experimental values of $(d\Delta E/d\Delta r)_{r=0}$ and the values of C_h thus determined are listed in Table III. The relation between ΔE and Δr is shown in Fig. 9, where the lines are obtained by the theoretical calculation of Eq. [19], [20], and [21] using the numerical values listed in Table III. The experimental results agree with the theoretical lines in the range of Δr between 0.7×10^{-4} and -2×10^{-4} at 78°C, and 1.0×10^{-4} and -1.5×10^{-4} at 97°C. Above these ranges of Δr, remarkable differences are recognized between theoretical lines and experimental values as indicated in the figure. This discrepancy may be due to the fact that Eq. [9] is an approximate one and can be used only for certain limited ranges of η_e and η_h.

The characteristics of the electrochemical cell using β Ag_2Te electrode for a coulometer or memory device. —As described above, it has been found that the $Ag|RbAg_4I_5|\beta$ Ag_2Se or β Ag_2Te cell has a voltage depending on the deviation from the ideal stoichiometric composition of β Ag_2Se or β Ag_2Te, and the relation between the cell voltage and the deviation from the stoichiometry is expressed by Eq. [21].

For practical use, it is usually convenient to use the cell at ambient temperature. However, it has been found from preliminary experiments that β Ag_2Te could be used as the electrode material for this purpose and β Ag_2Se could not because the cell with the β Ag_2Se electrode showed high electrode polarization to give a hysteresis effect in charge and discharge processes at room temperature. A mixture of β Ag_2Te, $RbAg_4I_5$, and graphite was used for the electrode material in order to increase the electrode reaction area

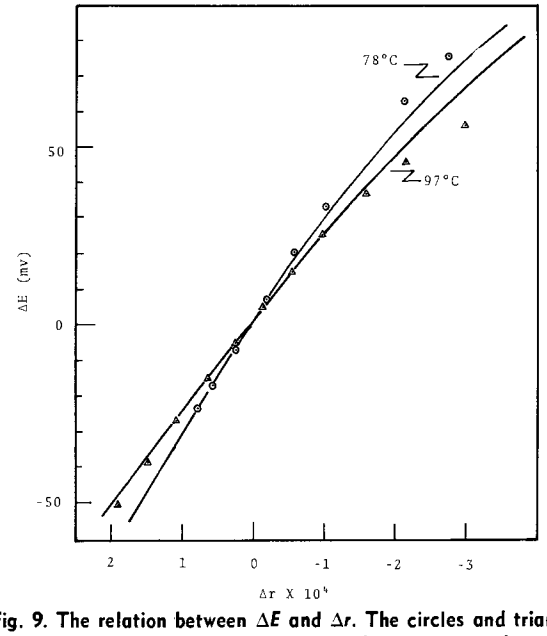

Fig. 9. The relation between ΔE and Δr. The circles and triangles represent the experimental values and the lines are theoretical curves.

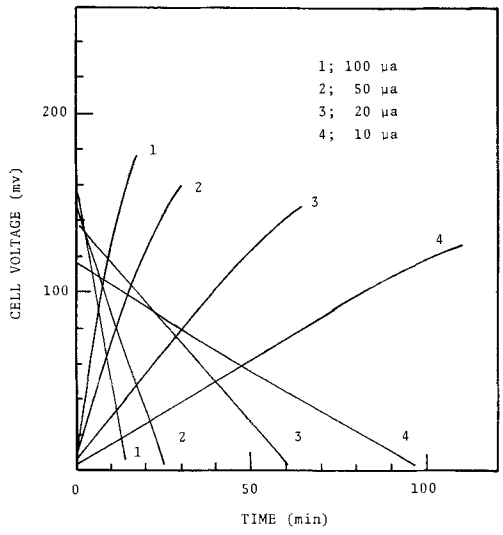

Fig. 10. The cell voltage vs. time curves of the cell Ag|$RbAg_4I_5$|β Ag_2Te (0.4g), $RbAg_4I_5$ (1.5g), graphite at 30°C.

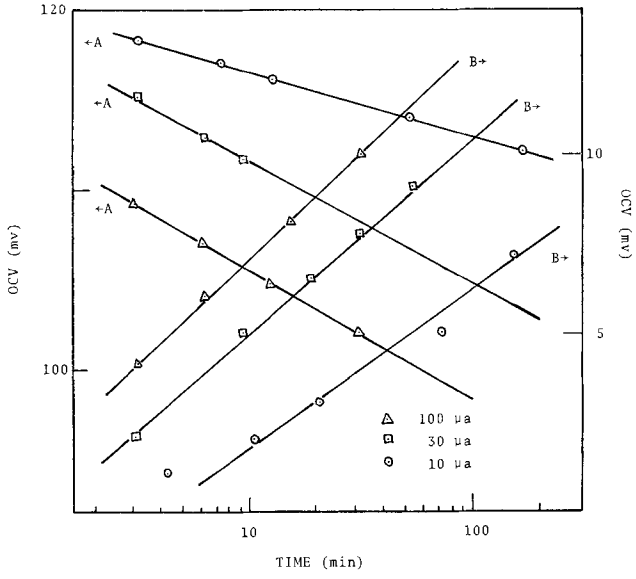

Fig. 11. The time dependence of OCV of the cell Ag|$RbAg_4I_5$|β Ag_2Te (0.4g), $RbAg_4I_5$ (1.5g), graphite (0.2g) at 22°C.

which would reduce the polarization when sufficiently high current density is used. The charge and discharge curves of the cell Ag|$RbAg_4I_5$|β Ag_2Te(0.4g), $RbAg_4I_5$ (1.5g), graphite (0.2g) were drawn at various current densities in Fig. 10. The silver telluride electrode was a mixture of 1.5g $RbAg_4I_5$, 0.4g β Ag_2Te, and 0.2g graphite. It is found in Fig. 10 that a linear relationship exists between the cell voltage (E) and time (t) in the voltage range of 0-120 mV, and the slope of the E-t curve increases with increasing current density. At higher current (>200 μA), however, the abrupt change of the cell voltage was observed immediately after a current was passed through the cell, and the slope of the E-t curve did not coincide for removing and adding silver from and to the silver telluride electrode. On the other hand, at lower current (<100 μA), the slope of the E-t curve for the charge process agreed with that for the discharge process.

The accuracy of this type of coulometer was checked with a current of 0-400 μA for a period of 0-30 min, using a triangular wave current. The relation between the cell voltage and coulombs passed through the cell was preliminarily examined by the constant current drain; and the initial and final cell voltages, after a triangular wave current was passed, were compared with the standard E vs. t curve. The error (ϵ) was calculated by the following equation

$$\epsilon = \frac{q - q_s}{q} \qquad [29]$$

where q_s is the coulombs calculated by the standard E vs. q curve. The error is less than 10% in all cases as shown in Table IV. The error decreased with decreasing current which may be due to decrease of the electrode polarization.

If the new type of electrochemical cell is charged to a certain cell voltage and the open-circuit voltage (OCV) is kept constant for a certain period of time, the cell may be used for analog memory devices. In practice, after the current was passed, OCV showed a slow change with time. The changes are shown in Fig. 11, where curves A were obtained after the cell was charged from 0 to 120 mV, and curves B after the cell was discharged from 120 to 0 mV. These results indicate that, for a limited interval of time between several minutes and several hundreds of minutes, the time dependence of OCV (E_{OCV}) will be expressed by Eq. [30]

$$E_{OCV} = A + B \log t \qquad [30]$$

where A and B are constants. The change of OCV with time is probably due to the concentration polarization and nonuniformity of the Ag-to-Te ratio through the β Ag_2Te electrode. In the case of curves A, the electronic conduction in the electrolyte $RbAg_4I_5$ is negligible for the OCV change in the short time period (<100 min) because the electronic conductivity of $RbAg_4I_5$ is less than 10^{-9} (ohm-cm)$^{-1}$ at room temperature (22). However, for the change in the long time period (>1000 min), OCV did not obey Eq. [30] but decreased linearly with time, suggesting that the electronic conductivity of the electrolyte might play a role. The change of OCV for the short time period (10-100 min) may be due mainly to the slow diffusion of silver in β Ag_2Te, and a relatively long period of time is necessary to obtain the homogeneous activity of silver in β Ag_2Te. Therefore, increase of the ionic conductivity of silver ion in β Ag_2Te is desirable to obtain a good performance cell. In general, the ionic conductivity of solids may sometimes be improved by incorporation of small amounts of various additives. In this experiment, it was found that the addition of CdTe to β Ag_2Te made the ionic conductivity of β Ag_2Te increase. For example, by the addition of 5 m/o (mole per cent) CdTe to β Ag_2Te, the ionic conductivity increased to 5×10^{-5} (ohm-cm)$^{-1}$ from that of pure β Ag_2Te which is 2×10^{-5} (ohm-cm)$^{-1}$ at 25°C. The cell using β Ag_2Te −5 m/o CdTe as the electrode material indicates the change of OCV with time as shown in Fig. 12. It is clear that the change can be greatly reduced by the addition of CdTe to β Ag_2Te. In this cell, the E vs. q curve gives a straight line in the range of 0 and 120 mV and dE/dt increases proportionally with current density. The cell using a β Ag_2Se electrode showed a larger change of OCV than that of β Ag_2Te. This may be due to the low ionic conductivity of β Ag_2Se shown in this paper.

Table IV. Accuracy of the electrochemical cell

Current, μA	Coulombs	Error, %
0—352	13.7	10.6
0—187	15.1	8.0
0—78	12.2	4.9
0—20	15.3	4.1

Conclusion

The ionic conductivities of β Ag_2Se and β Ag_2Te were measured as a function of the metal-to-nonmetal ratio. It was found from these results that the concentration of silver ion vacancy at the ideal stoichiometric composition of these compounds could be determined by the theory of Teltow *et al.* The dependence of silver

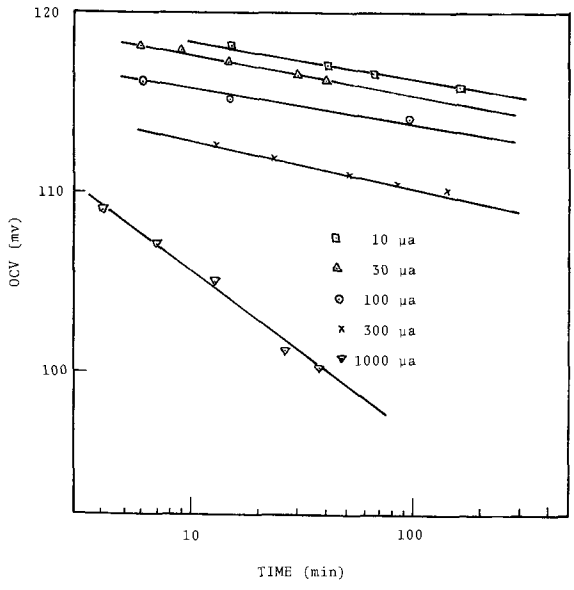

Fig. 12. The time dependence of OCV of the cell $Ag|RbAg_4I_5|\beta$ Ag_2Te-CdTe (0.4g), $RbAg_4I_5$ (1.5g), graphite (0.2g) at 25°C.

activity in β Ag_2Se or β Ag_2Se on the deviation from the ideal stoichiometric composition was determined by the concentrations of ionic and electronic imperfections. In β Ag_2Se, the activity of silver depended mainly on ionic imperfection and, in β Ag_2Te, on electronic imperfection.

Although the new type of electrochemical cell proposed in this paper may have not sufficiently high accuracy, it will have many advantages, such as attainment of appreciable miniaturization. This type of cell can be used in an electronic circuit as a coulometer or memory device.

Manuscript submitted Sept. 22, 1970; revised manuscript received Feb. 16, 1971.

Any discussion of this paper will appear in a Discussion Section to be published in the June 1972 JOURNAL.

REFERENCES

1. D. O. Raleigh, in "Progress in Solid State Chemistry," Vol. 3, pp. 83-134, H. Reiss, Editor, Pergamon Press, New York (1966).
2. T. Takahashi and O. Yamamoto, *Electrochim. Acta*, **11**, 779 (1966).
3. G. R. Argue, B. B. Owens, and I. J. Groces, *Proc. Ann. Power Sources Conf.*, **22**, 103 (1968).
4. O. Yamamoto and T. Takahashi, *Denki-Kagaku*, **36**, 894 (1968).
5. J. H. Kennedy and F. Chen, *This Journal*, **116**, 207 (1969).
6. B. Widrow, Stanford Univ., Stanford, Calif., Solid State Electronics Lab., Tech. Report No. 1553-2, Oct. 1960.
7. T. Takahashi, O. Yamamoto, and K. Kuwabara, *Extended Abstracts C.I.T.C.E.*, **17**, 397 (1966).
8. T. Takahashi and O. Yamamoto, *Denki-Kagaku*, **32**, 610 (1964).
9. J. N. Bradley and P. D. Greene, *Trans. Faraday Soc.*, **63**, 424 (1967).
10. B. B. Owens and G. R. Argue, *Science*, **157**, 308 (1967).
11. J. McDougall and E. C. Stoner, *Trans. Roy. Soc. (London)*, **A237**, 67 (1938).
12. R. Dalven and R. Gill, *Phys. Rev.*, **143**, 666 (1966); *J. Appl. Phys.*, **38**, 753 (1967).
13. S. Miyatani, *J. Phys. Soc. Japan*, **14**, 996 (1959).
14. N. Valverde, *Z. Physik. Chem.*, **70**, 113 (1970).
15. E. Koch and C. Wagner, *Z. physik. Chem.*, **B38**, 295 (1937).
16. O. Stasiw and J. Teltow, *Ann. Phys.*, **6F1**, 201 (1947).
17. K. Weiss, *Z. Naturforsch.*, **24a**, 184 (1969).
18. C. Wagner, *Z. Elektrochem.*, **60**, 4 (1956).
19. C. Wagner, *J. Chem. Phys.*, **21**, 1819 (1953).
20. C. Wagner and W. Schottky, *Z. physik. Chem.*, **B11**, 163 (1931).
21. T. Takahashi and O. Yamamoto, *This Journal*, **117**, 1 (1970).
22. T. Takahashi, O. Yamamoto, and S. Ikeda, *Denki-Kagaku*, **37** 843 (1969).

The Relevance of Accelerated Electrochemical Pitting Tests to the Long-Term Pitting and Crevice Corrosion Behavior of Stainless Steels in Marine Environments

B. E. Wilde* and E. Williams

Applied Research Laboratory, U. S. Steel Corporation, Monroeville, Pennsylvania 15146

ABSTRACT

Values of the critical breakdown potential, E_c for a series of iron-chromium binary alloys and some commercial stainless steels in aerated 3.5% sodium chloride are presented. The results are correlated with previously published data on the same materials after prolonged exposure to a marine environment. Exact correlations were obtained between the pitting performance of the iron/chromium alloys and that predicted from electrochemical tests over an exposure period of eight years. The highly beneficial influence of chromium additions on the pitting resistance of the steels is shown by the pronounced increase in the nobility of E_c over the range 12-28% chromium. Analysis of corrosion data on commercial stainless steels after 4.25 years' exposure to sea water has shown that the degree of crevice corrosion attack is directly related to the nobility of the "protection or repassivation" potential, as determined from cyclic anodic-polarization curves.

Critical breakdown potentials, E_c, have been used extensively as an index of the pitting susceptibility of alloys in halide media (1-6). Over the last few years, however, various researchers have questioned the validity of the above use, claiming that there is no correlation between electrochemically induced pitting and that induced by chemical redox systems (7), and that pitting corrosion can occur at potentials more active than E_c (8). In an attempt to clarify the situation, we have demonstrated recently (9) that in

* Electrochemical Society Active Member.

Key words: electrochemical polarization, crevice corrosion, passivity breakdown, pitting potentials, pit initiation.

Table I. Chemical composition of Fe/Cr binary alloys used in exposure tests

Alloy No.	Composition, w/o							
	C	Mn	P	S	Si	Cu	Ni	Cr
1	0.07	0.51	0.018	0.012	0.25	0.09	0.25	12.2
2	0.08	0.29	0.022	0.018	0.29	0.11	0.17	15.7
3	0.10	0.48	0.025	0.018	0.27	0.11	0.15	17.3
4	0.09	0.82	0.020	0.015	0.22	0.08	0.29	24.9
5	0.02	0.81	0.023	0.007	0.30	0.08	1.4	28.0

short-duration tests there is almost quantitative agreement between electrochemical and chemical accelerated pitting tests on stainless steels in halide media. Further, it has been shown that previous data (8), although correct, were obtained in an environment where the passive state was stabilized by the redox couple in a manner not relevant to the electrochemical tests used in comparison.

The main question of how valid are data obtained in short-term electrochemical tests, with regard to long-term exposures in a freely corroding situation, remains unanswered. Several authorities (4, 10, 11) have expressed the opinion that E_c is not a unique parameter, but varies with time and the experimental technique used in evaluating it. Little data are available on a long-term basis to either support or refute these opinions and to provide the design engineer with a satisfactory answer to the main question.

This study presents an analysis of long-term exposure data on a series of iron/chromium binary alloys and some commercial stainless steels exposed to marine environments for 8 and 4.25 years, respectively. Correlations are made between these data and parameters obtained from electrochemical polarization measurements conducted in 3.5 w/o (weight per cent) sodium chloride solutions at 25°C.

Materials and Experimental Work

The iron/chromium alloys used in this study were originally used to assess the influence of chromium on the corrosion resistance in marine atmospheres (12). Alloy compositions are shown in Table I. The ingots were hot-rolled to 0.635 cm (0.25-in) thick plate, and were heat-treated for 2.5 hr at 774°C (1425°F), followed by an air cool. Exposure samples (10.2 cm by 15.2 cm by 0.318 cm) were machined from the heat-treated plate to a number 4 finish, after being descaled in molten sodium hydroxide containing 2 w/o sodium hydride. Samples were exposed at Kure Beach, North Carolina, at the 80- and 800-ft lots in 1955. The exposure and mounting technique was the same as that recommended in the standard ASTM testing method. Samples were removed periodically to check for weight loss, and pit-density and pit-depth measurements were also made.

In another program aimed at determining the corrosion behavior of steels fully immersed in sea water, several commercial stainless steels were machined into test samples (10.2 cm by 30.5 cm by 0.635 cm) from mill-annealed plate stock. The compositions of the alloys are shown in Table II. Each sample was degreased in trichlorethylene and mounted on racks as shown in Fig. 1, with Nylon washers used to insulate the samples from the support rack. The panels were exposed to sea water at the Wrightsville Test Station so that they were totally immersed at all times. The samples were periodically inspected from 1964 to 1968 to check for weight loss.

Fig. 1. Photograph of holding assembly used for sea water immersion tests on stainless steels.

Samples for electrochemical polarization studies were machined from the same stock as the above exposure-test samples. Coupons (2.54 cm by 2.54 cm by 0.313 cm) were "potted" in an epoxy mount[1] containing a Teflon-sheathed copper conductor for electrical contact. Care was taken in the curing of the epoxy to avoid producing extraneous crevices (13). The potted samples were abraded through 600-grit silicon carbide paper, ultrasonically degreased in a detergent, washed with distilled water, and hot-air dried. The polarization equipment was the same as that described in detail elsewhere (15-17). Test samples were immersed for 60 min in the corrodent prior to polarization to allow the establishment of a steady-state corrosion potential (14). Polarization curves were constructed by running in the noble direction at a sweep rate of 0.600 V/hr.

The corrodent was prepared from reagent-grade sodium chloride diluted to 3.5 w/o with distilled water (7.4 megohm cm at 25°C). During each polarization run, the corrodent was saturated with air at a flow rate of 1.2 liters/min, resulting in a dissolved oxygen content of 7.9 ppm as measured on a Beckman Process Analyzer. It has been assumed in this work that the behavior of stainless alloys in sodium chloride solution is representative of their behavior in natural sea water. We have as yet no specific data to support this assumption. Long-term corrosion potential (E_{corr}) *vs.* time studies were conducted with samples prepared as above. The potential was measured with a saturated calomel reference electrode (SCE) connected to a L&N multipoint recorder via an electrometer switching system.

[1] Armstrong Epoxy Resin, C-4, Argonne Rd., Warsaw, Indiana.

Table II. Chemical composition of stainless steels used in sea water immersion tests

Alloy No.	Type of stainless steel	Composition w/o										
		C	Mn	P	S	Si	Cu	Ni	Cr	Mo	Ti	Al
6	USS 100	0.06	0.42	0.016	0.007	0.33	0.06	0.19	11.6	0.05	0.84	0.32
7	Type 410	0.08	0.47	0.019	0.027	0.32	0.07	0.34	12.0	0.08	ND*	ND
8	Type 430	0.06	0.61	0.018	0.012	0.54	0.05	0.20	16.4	0.03	ND	ND
9	Type 304	0.05	1.18	0.025	0.013	0.53	0.06	9.45	18.6	0.31	ND	ND
10	Type 316	0.05	1.69	0.022	0.013	0.68	0.07	13.5	17.7	2.72	ND	ND
11	Type 446	0.12	0.62	0.023	0.017	0.40	0.04	0.28	25.5	0.08	ND	ND
12	Hastelloy C	0.06	0.67	0.007	0.005	0.73	ND	56.27	15.44	3.6	ND	ND

* ND = Not determined.

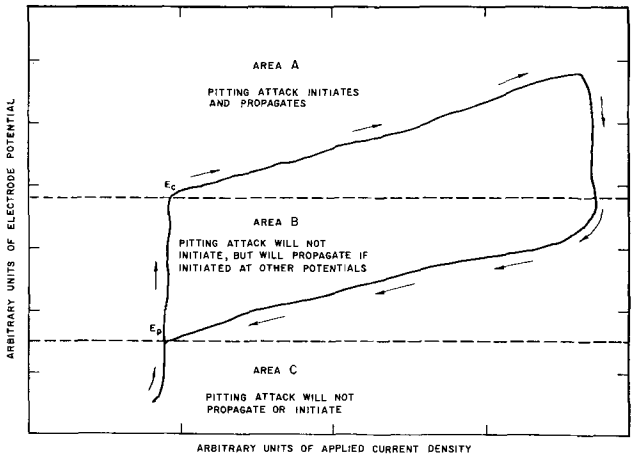

Fig. 2. Typical "cyclic" polarization curve for stainless steels in sodium chloride solutions.

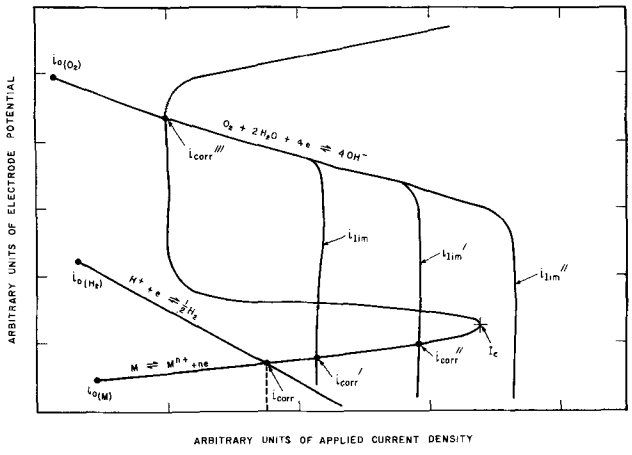

Fig. 4. Schematic representation of partial processes leading to spontaneous passivation.

Results and Discussion

In regard to our terminology used in describing the polarization curves, reference is made to Fig. 2, where a schematic of a typical "cyclic polarization curve" is shown. The point designated E_c, where a marked increase in the anodic dissolution rate occurs, will be termed the critical breakdown potential. The point E_p, where the dissolution rate again becomes equal to the passive current density, will be termed the protection potential (9, 18). We have analyzed our results on the basis that E_c uniquely relates to the process of pit initiation in the absence of crevice corrosion. Similarly, we believe that E_p relates specifically to the crevice or pit-propagation mechanism and not the initiation process.

Iron/chromium alloys.—Potentiodynamic anodic-polarization curves were obtained on each alloy shown in Table I, and typical curves are shown in Fig. 3, after submersion for 60 min in the corrodent. Very distinct breakdown potentials were observed, reproducible to ±10 mV in replicate experiments. A summary of the anodic-dissolution parameters is given in Table III. Two features in Fig. 3 are of immediate interest.

1. The changeover from active-passive behavior to one of stable passivity as the chromium content is increased over 12.2 w/o Cr. This behavior can be explained by reference to Fig. 4, where a typical anodic-dissolution curve is shown as $M \rightleftharpoons M^{n+} + ne$. Superimposed on this curve are two sets of cathodic reduction curves; one for the $H^+ + e \rightleftharpoons \frac{1}{2} H_2$ couple, the other for the $O_2 + 2H_2O + 4e \rightleftharpoons 4\ OH^-$ couple. In the latter case, the reduction rate is shown to be under various limiting diffusion conditions; for example, i_{lim}, i_{lim}'. It is known from previous work (19, 20) that a steel will spontaneously passivate when the total reduction rate exceeds the critical anodic current density I_c. The absence of an active-passive transition for alloys 2, 3, 4, and 5 (Fig. 3) indicates that they must have the condition $I_c < i_{lim} + i_{H_2}$. Similarly, alloy 1 must have an I_c greater than the limiting cathodic reduction rate.

2. The pronounced influence of chromium content on the nobility of E_c is shown in Fig. 5. Similar behavior has been noted previously (21) and also on the nickel/chromium binary alloys (22) in acidic halide media. It is apparent that chromium is very effective in stabilizing the passive state to breakdown by chloride ions.

The E_{corr} *vs.* time behavior of the alloys is shown in Fig. 6 and the final steady-state values are summarized in Table III. It is apparent that although random fluctuation in corrosion potential occurred during the first 100 hr of tests giving a quite active corrosion potential, all the alloys approached a relatively noble steady state within 300 hr. The redox potential of the corrodent, measured on bright platinum electrodes, was between +0.280 and +0.310 V_{SCE} over the 300-hr period. On the basis of the data presented in Table III, one would expect that alloys number 1, 2, and 3 would pit in an aerated sodium chloride environment because their long term corrosion potential was more noble than the value of E_c determined for these alloys. Similarly, one would not ex-

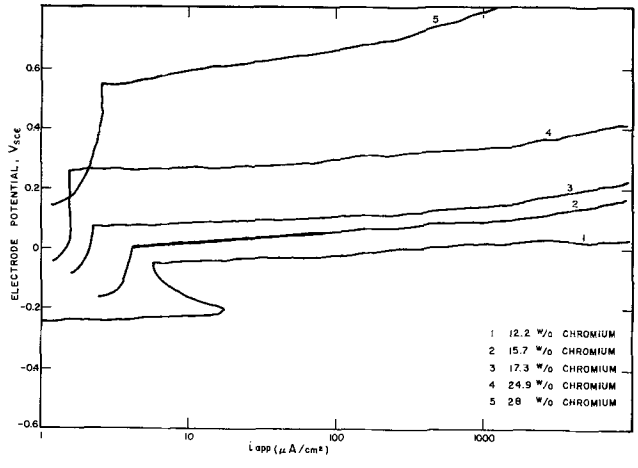

Fig. 3. Potentiodynamic anodic-polarization curves for iron/chromium alloys in aerated 3.5 w/o NaCl at 25°C sweep speed, 0.600 V/hr.

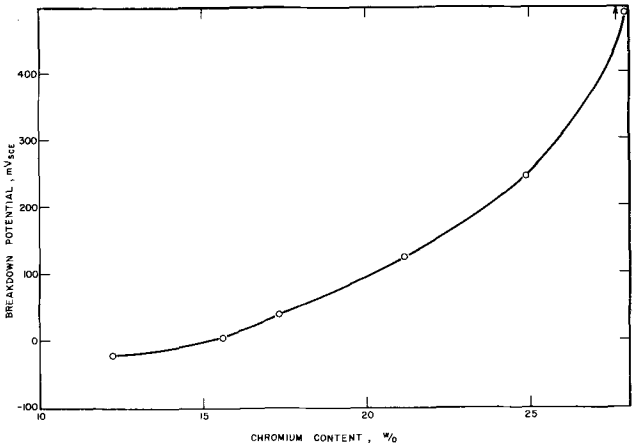

Fig. 5. Influence of chromium on the breakdown potential of iron/chromium binary alloys.

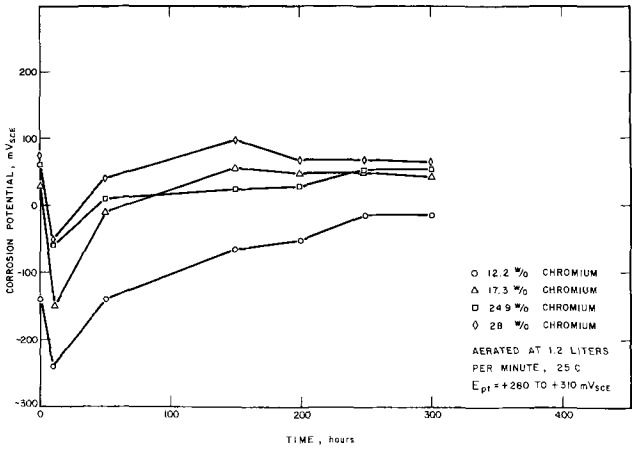

Fig. 6. Corrosion potential/time curves for a selection of iron/chromium binary alloys in aerated 3.5 w/o NaCl at 25°C.

pect alloys 4 and 5 to initiate pits, since the corrosion potential never went more noble than the corresponding E_c values.

The pitting tests on the iron/chromium binary alloys, although not originally designed for the present study, were particularly useful in that the mode of testing in salt spray eliminated any interference by crevice corrosion. We have noted many times that alloys totally immersed in sea water suffer from crevice attack around the retaining washer to the exclusion of pitting corrosion. This effect is probably due to galvanic protection of the bulk surface once a crevice anode has initiated before the onset of pitting. This phenomena is discussed in the next section. The results of the exposure tests on alloys 1 through 5 are shown in Table IV and V for the 80- and 800-ft lot, respectively. Typical pitted samples from the 800-ft lot exposure are shown in Fig. 7, where it is important to note that no crevice corrosion took place. This fact is important since the rating of alloys based on E_c is restricted to the pit-initiation process only, and not the propagation mechanism, which we believe to be identical to that of crevice corrosion. Inspection of Table V for the 800-ft lot indicates that alloys 1, 2, and 3 all pitted, whereas alloys 4 and 5 did not. Thus, the results of 8-yr exposure tests are in exact agreement with the prediction of the short-term electrochemical studies.

Inspection of Table IV for the 80-ft lot reveals that pitting corrosion occurred on all the samples,

Table III. Summary of electrochemical properties of Fe/Cr binary alloys in aerated 3.5 w/o NaCl at 25°C

Alloy No.	Chromium content, w/o	E_c, V_{SCE}	E_{corr}*, V_{SCE}
1	12.2	−0.020	−0.011
2	15.7	0.000	+0.038
3	17.3	+0.040	+0.045
4	24.9	+0.240	+0.051
5	28.0	+0.520	+0.060

* After 300 hr.

Table IV. Pitting-corrosion data for Fe/Cr binary alloys exposed for 8 yr at Kure Beach, 80-ft lot

Alloy No.	Chromium content, w/o	Average pit depth, in. × 10^{-3}	Pit density, No./in.^{2}
1	12.2	4.3	500
2	15.7	1.2	70
3	17.3	1.1	50
4	24.9	0.7	10
5	28.0	0.4	10

Table V. Pitting-corrosion data for Fe/Cr binary alloys exposed for 8 yr at Kure Beach, 800-ft lot

Alloy No.	Chromium content, w/o	Average pit depth, in. × 10^{-3}	Pit density, No./in.^{2}
1	12.2	1.2	240
2	15.7	1.0	100
3	17.3	0.6	5
4	24.9	0	0
5	28.0	0	0

although the severity of attack decreased markedly in the order predicted from electrochemical studies. The fact that pitting occurred on all samples at the 80-ft lot should not be interpreted as a conflict with the predictions of the accelerated tests without consideration of the following factors:

1. Because of the method of exposure, alternate wetting and drying possibly occurred on all samples. If such a process did occur, a build-up of chloride ion concentration would occur to levels greater than those present in the original sea-spray; for example, 3.5 w/o NaCl. In view of the greater salt "fall-out" which undoubtedly occurred at the 80-ft lot, it is reasonable to suppose that the pitting environment on these samples was more aggressive than that at the 800-ft lot. This factor would have the effect of increasing the severity of pitting over that predicted from Table III, since it has been shown previously (4) that E_c tends to become more active as the chloride ion concentration is increased.

2. It is possible in the 80-ft location, that more fluctuation in temperature occurred than experienced further inland. This behavior could also have a pronounced effect on the pitting tendencies of the alloys, since it is well known that E_c for Type 316 stainless steel, for example, is temperature sensitive.

We believe that the above data lend strong support to the long-term applicability of E_c as an index to pitting susceptibility.

Commercial stainless steels.—Typical potentiodynamic anodic polarization parameters for alloys 6 through 12 are shown in Table VI. It is clear from these data that all the alloys except numbers 8 and 12 would be expected to pit, since their steady-state corrosion potentials were more noble than their respective values of E_c, determined after a 60-min immersion in the corrodent. However, when the samples were removed from sea water after 4.25 years' immersion, pronounced crevice corrosion had taken place at the washers with little or no pitting corrosion on the general surface away from the washers, as shown in Fig. 8. This behavior demonstrates the previously mentioned fact that the induction period for

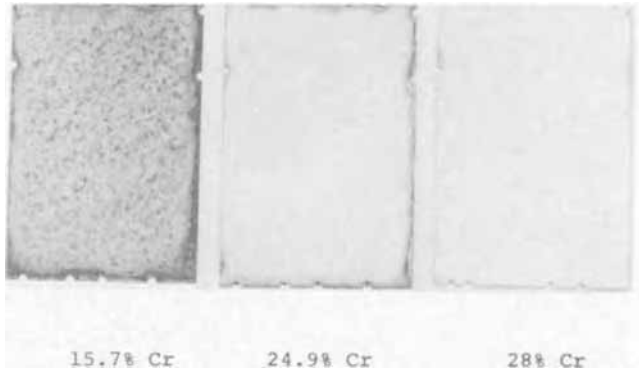

Fig. 7. Photograph indicating the condition of iron/chromium binary alloys after 8 years' exposure at the 800-ft lot at Kure Beach, North Carolina. Note the lack of crevice corrosion. Approximately 2/5 actual size.

Table VI. Polarization parameters of commercial stainless steels, in aerated 3.5 w/o NaCl at 25°C

Alloy No.	Type of steel	E_c, V_{SCE}	E_p,*** V_{SCE}	E_{corr},* V_{SCE}
6	USS 100	−0.150	−0.340	+0.012
7	Type 304	0	−0.110	+0.085
8	Type 316	+0.100	−0.020	+0.088
9	Type 410	−0.200	−0.420	−0.100
10	Type 430	−0.100	−0.260	−0.040
11	Type 446	−0.060	−0.200	+0.240
12	Hastelloy C	>+0.97**	>+0.97	+0.220
	Platinum			+0.280 to +0.310

* After 500 hr.
** Represents the potential at which oxygen evolution started with no pitting.
*** Determined by reversing the potential sweep after an applied current of 10 mA/cm² was attained.

crevice corrosion is much shorter than that of pit initiation. Further, once crevices are activated they appear to protect the bulk of the surface against subsequent pit initiation. Inspection of Table VI indicates a very important fact with regard to the behavior of alloy 8. In this case, according to the E_{corr} and E_c data, no pitting corrosion should occur, whereas in practice pronounced crevice corrosion took place. This point admirably emphasizes the fact that the applicability of E_c data is limited to situations where no crevices are present (situations of little engineering significance), and if not so limited may result in crevice corrosion.

Weight loss data obtained from the immersion tests are summarized in Table VII. Inspection of Tables VI and VII indicated that the weight loss decreased with increasing nobility of E_p. For Hastelloy C, no crevice attack was observed, and no E_p was measurable since no hysteresis was observed on cyclic polarization. It would appear, therefore, that E_p could be used as an index of susceptibility to crevice corrosion and also as a screening parameter with which to rate the severity of attack of alloys in sea-water.

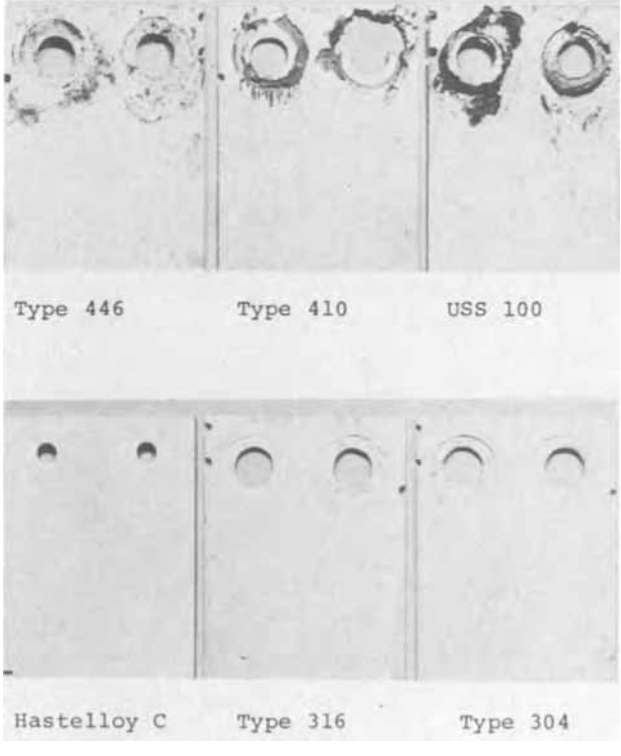

Fig. 8. Photograph of stainless steel samples after 4.25 years' immersion in sea water. Note pronounced crevice corrosion with little or no pitting.

Table VII. Corrosion weight loss data for commercial stainless steels immersed in sea water for 4.25 yr

Alloy No.	Type of stainless steel	E_p, V_{SCE}	Weight loss, mg/cm²	Comments
6	USS 100	−0.340	25.8	Crevice corrosion, no pits
7	Type 304	−0.110	10.8	Crevice corrosion, no pits
8	Type 316	−0.020	9.16	Crevice corrosion, no pits
9	Type 410	−0.420	26.7	Crevice corrosion, no pits
10	Type 430	−0.260	18.9	Crevice corrosion, a few pits
11	Type 446	−0.200	17.4	Crevice corrosion, no pits
12	Hastelloy C*	>0.97	0.25	No crevice corrosion or pits

* Exposed for 14 months.

It has been shown previously (9) that once initiated, pit propagation can be maintained at potentials more active than E_c and noble to E_p (see Fig. 2). On this basis, and in accord with previous suggestions (23), we believe that the pit-propagation mechanism and that of crevice corrosion are the same; that is, accelerated attack in a confined space due to acid hydrolysis of corrosion products. To explore the relevance of E_p to crevice corrosion, we exposed a sample of AISI Type 430 stainless steel containing an artificial crevice to 3.5 w/o aerated sodium chloride at potentials both active and noble to E_p. The crevice was made by placing a tight-fitting neoprene O-ring circumferentially around a (0.625-diam by 2-cm) sample, fitted to a Stern-Makrides gasket (24). For the sample exposed noble to E_p, crevice corrosion initiated after 27 hr, with no evidence of pitting corrosion. The sample exposed to potentials active to E_p (determined by reversing the sweep when the applied current reached 10 mA/cm²) did not evidence crevice or pitting corrosion after 230 hr. These data were qualitatively reproducible in replicate experiments.

The use of E_p in the above context, however, should be made with caution. The results of recent experiments to be published (25) indicate that E_p is not a unique parameter, but is a strong function of the number of coulombs passed after exceeding E_c during polarization. Typically, E_p approaches quite active potentials if anodic dissolution is maintaned at rates equal to or greater than 150 mA/cm²; *e.g.*, −0.400 V_{SCE} for Type 430 stainless steel.

However, we believe that to a first approximation, alloys may be screened with regard to crevice-corrosion resistance by a comparison of E_p determined in an identical manner on all samples.

Conclusions

The following conclusions may be drawn from the data presented:

1. That predictions with regard to pitting susceptibility based on accelerated electrochemical tests are valid on stainless steels exposed to a marine atmosphere for at least eight years.
2. There appears to be a direct correlation between both the susceptibility and severity of crevice corrosion of stainless steels in sea water, and the value of the protection potential determined from electrochemical polarization tests.
3. Increasing the chromium content over the range of 12-28% markedly increases the resistance to pitting corrosion, as evidenced by the increase in nobility of the critical breakdown potential.

Manuscript submitted June 16, 1970; revised manuscript received *ca.* Feb. 1, 1971.

Any discussion of this paper will appear in a Discussion Section to be published in the June 1972 JOURNAL.

REFERENCES

1. S. Brennert, *J. Iron Steel Inst.*, **135**, 101 (1937).
2. E. M. Mahla and N. A. Nielsen, *Trans. Electrochem. Soc.*, **89**, 167 (1946).
3. Ya. M. Kolotyrkin, *This Journal*, **108**, 209 (1961).
4. H. P. Leckie and H. H. Uhlig, *ibid.*, **113**, 1262 (1966).
5. W. Schwenk, *Corrosion*, **20**, 129t (1964).
6. V. Hospadaruk and J. V. Petrocelli, *This Journal*, **113**, 878 (1966).
7. R. F. Steigerwald, *Corrosion*, **22**, 107 (1966).
8. W. D. France and N. D. Greene, *ibid.*, **26**, 1 (1970).
9. B. E. Wilde and E. Williams, *This Journal*, **117**, 775 (1970).
10. T. P. Hoar and D. C. Mears, *Proc. Roy. Soc.*, **294A**, 486 (1966).
11. M. Pourbaix *et al.*, *Corrosion Sci.*, **3**, 239 (1963).
12. R. J. Schmitt and C. X. Mullen, *ASTM STP*, **454**, 124 (1969).
13. N. D. Greene, W. D. France, and B. E. Wilde, *Corrosion*, **21**, 275 (1965).
14. C. D. Kim and B. E. Wilde, Paper accepted for publication in *Corrosion Science*.
15. W. D. Henry and B. E. Wilde, *Corrosion*, **25**, 515 (1969).
16. B. E. Wilde and E. Williams, *This Journal*, **116**, 1539 (1969).
17. B. E. Wilde, *Corrosion Sci.*, **7**, 315 (1967).
18. M. Pourbaix, Private communication, CEBELCOR, Brussels, Belgium.
19. B. E. Wilde and N. D. Greene, *Corrosion*, **25**, 300 (1969).
20. C. Edeleanu, *Metallurgia*, **50**, 113 (1954).
21. J. Horvath and H. H. Uhlig, *This Journal*, **115**, 791 (1968).
22. F. G. Hodge and B. E. Wilde, *Corrosion*, **26**, 146 (1970).
23. I. L. Rosenfeld, *Proc. IVth Congress, European Coal and Steel Community, Luxembourg* (1968).
24. M. Stern and A. C. Makrides, *This Journal*, **107**, 782 (1960).
25. B. E. Wilde and E. Williams, Paper presented at the International Symposium on Passivity, Cambridge, England, July (1970).

Stress Corrosion Cracking of Pure Copper

E. Escalante and J. Kruger*

Institute for Materials Research, National Bureau of Standards, Washington, D. C. 20234

ABSTRACT

It is known that the rate of tarnish film formation is an important factor in the stress corrosion cracking (SCC) of brass. Because copper immersed in cupric acetate and sulfate solutions has tarnish film growth rates comparable to those found for brasses susceptible to SCC, it should undergo cracking in such solutions if kinetics play a role. It was found that pure copper is susceptible to cracking in cupric acetate solution but not in cupric sulfate. Light, which retards film formation on copper, but not corrosion, prevents stress cracking in the cupric acetate solution. In the absence of stress, oxide forms all over the copper surface, while stress concentrates oxide formation at the grain boundaries. These experiments point to a brittle-film rupture mechanism of stress cracking.

A recent study by Green, Mengelberg, and Yolken (1) has shown that the rate for formation of a tarnish film on copper and copper-zinc alloys in tarnishing ammoniacal solutions increases with the percentage of zinc. It is also known that the rate of cracking of α-brass in these ammoniacal environments increases significantly with increasing zinc content (2). One theory of stress corrosion cracking (SCC), the "brittle-film" model of Forty and Humble (3), suggests that the rate of tarnish film formation determines the rate of cracking. The study by Green *et al.* showed that pure copper, which is nonsusceptible, does have a low rate of film formation in the tarnishing solution they used. If the predictions of the brittle-film model are valid, pure copper should crack in an environment that produces a similar film to that in the ammonia tarnishing solutions provided the rate is comparable to that observed for the susceptible α-brasses. Such environments are the cupric ion solutions (mostly cupric acetate and cupric sulfate) studied by Miller and coworkers (4-6). These solutions produce epitaxed Cu_2O films on copper that are similar to those that form in ammonia solutions on α-brass. They also grow on pure copper at a rate that is comparable to a susceptible brass (90 Cu-10 Zn). Thus the brittle-film model would predict that pure copper should crack in Miller's solutions. This study will determine if such cracking can be observed.

If cracking of pure copper does occur in Miller's solutions, however, it is still necessary to establish whether it is "true SCC." Recently there have been two directly contradictory papers, one by Pugh, Montague, and Westwood (7) indicating that pure copper can undergo intergranular stress corrosion cracking, the other by Uhlig and Duquette (8) indicating that what was observed by Pugh *et al.* was not SCC but instead a weakening by deep intergranular corrosion. Both of these studies used a 15*N* NH_4OH solution preconcentrated with a 2.5 g/l of copper powder. However, Pugh *et al.* indicate that this solution did not produce a tarnish film. Uhlig and Duquette did observe a "dark surface oxide film." This uncertainty about tarnishing makes it difficult to ascertain whether pure copper would indeed undergo stress corrosion cracking under conditions where a tarnish film exists.

In addition to determining whether pure copper fails under conditions of rapid tarnishing, this study seeks to resolve the question of whether this film formation is an integral part of the failure process or whether simple intergranular weakening is involved.

Experimental

All experiments were carried out either in 0.4*N* cupric sulfate or 0.05*N* cupric acetate using reagent grade chemicals and deionized, double distilled water. The specimens were stressed in a constant load lever system in all but one case. Since surface cleanliness has a strong influence on the rate of oxide growth on

* Electrochemical Society Active Member.

Key words: copper, cupric acetate, kinetics, oxidation, stress corrosion, tarnish film.

a single crystal (9), initial experiments were carried out using the careful surface preparation described by Miller *et al.* (10). It was found, however, that the results were not significantly affected as long as a surface was prepared that was free of any adsorbed organic contaminants.

The following surface preparation procedure was adopted: shortly before an experiment, the specimens were immersed in a 2:1 solution of nitric acid in water for 15 sec, then rinsed in flowing distilled water for 30 sec. The specimens were then dried in a stream of warm air and installed in the testing cell. At this point the oxide forming solution was introduced into the cell. After 1 min the load was applied to the specimen.

The following materials were studied:

99.9% copper wire.—The first experiments carried out in the copper system were done using electrolytic copper having a diameter of 0.254 mm. The tensile load applied was approximately 220 meganewtons/meter (32 ksi) or just slightly more than the yield strength of the material, thus, causing some plastic deformation to occur. The copper wire was tested in both solutions.

Large grain 99.999% copper.—Continuous cast copper rods of 99.999% purity were machined to make flat tensile specimens 10 mm wide at their reduced section, 0.71 mm thick, and 19 mm long. These specimens had relatively large grains ranging from an average of 1-7 mm in diameter. This material was tested only in the cupric acetate solution.

Small grain high purity copper.— Some 99.999% Cu with large grains was reduced 50% in cross section by rolling. Specimens 6.3 mm wide, 0.36 mm thick, and 25 mm long were cut out from the resulting sheet. These specimens were recrystallized in hydrogen by heating to 700°C for 5 min then quickly cooling to room temperature at 300°C/min. The resulting grain size was of the order of 0.1 mm diameter. Surface preparation of this material was more critical because it was to be examined by electron microscopy. It was, therefore, electropolished, then carefully rinsed in distilled water before testing in the cupric acetate. Two separate sets of experiments were done with this material. One set was the tarnishing of the material in an unstressed condition, and the other set was the tarnishing of the material under stress.

Results

Morphology of attack and susceptibility.—The lower purity copper described above and the 70-30 brass were exposed to the 0.05*N* cupric acetate and the 0.4*N* cupric sulfate solutions under tensile loads exceeding the yield strength of the material. No cracking was ever observed at these loads when the specimens were not immersed in the cupric ion solutions. Failure of the 99.9% copper was observed for times as short as 18 hr in the acetate solution. Figure 1a shows that the cracks formed were always found to occur in oxide film growing into the metal. This micrograph looks similar to those published by Forty and Humble (3) for α-brass in ammonium hydroxide-copper sulfate solutions.

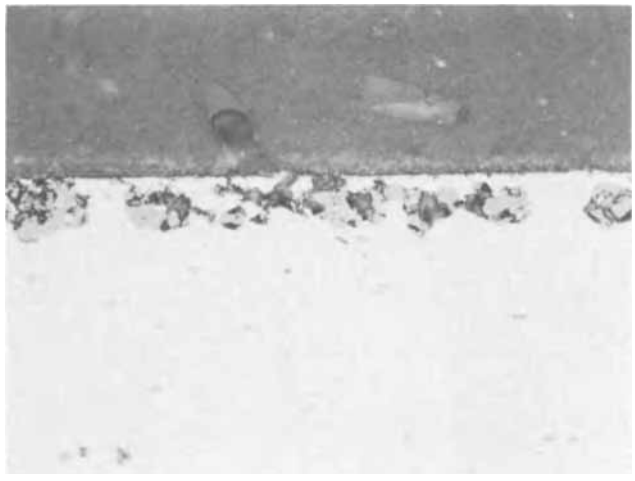

Fig. 1b. 99.9% copper specimen showing general corrosion and pitting. Stressed in 0.04*N* cupric sulfate. Magnification, 430X.

The 99.9% copper did not fail in the cupric sulfate solution. The micrographic examination indicated that oxidation was more general over the whole surface with pitting but no evidence of cracking as shown in Fig. 1b.

The large grain high-purity copper failed in as short a time as 88 hr in the acetate solution. Practically all cracks found were initiated at grain boundaries or at surface imperfections within the grain as shown in Fig. 2a and 2b. The longer time to failure may possibly be due to the fewer grain boundaries at the surface as a result of the large grain size. As Fig. 2a shows for a large-grained specimen, crack initiation would usually occur in a grain boundary normal to the stress direction, but, because the boundary did not continue in this direction, the crack would leave the boundary.

Because we were interested in locating the initiation site of the crack, the fine grain size material was made. This made it easier to locate a grain boundary at the high magnification used with the electron microscope. The grain boundaries of the unstressed and stressed material were examined. Figure 3a showing the unstressed boundaries, revealed no unusual features other

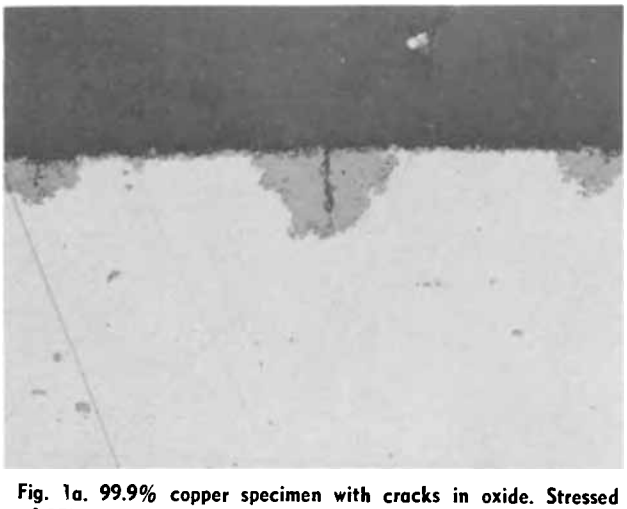

Fig. 1a. 99.9% copper specimen with cracks in oxide. Stressed in 0.05*N* cupric acetate. Magnification, 865X.

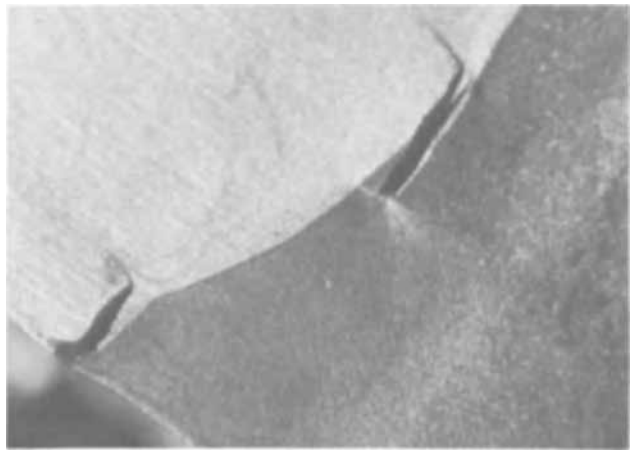

Fig. 2a. 99.999% copper specimen (large grain) showing cracks initiated at grain boundary. Stressed in 0.05*N* cupric acetate. Magnification, 45X.

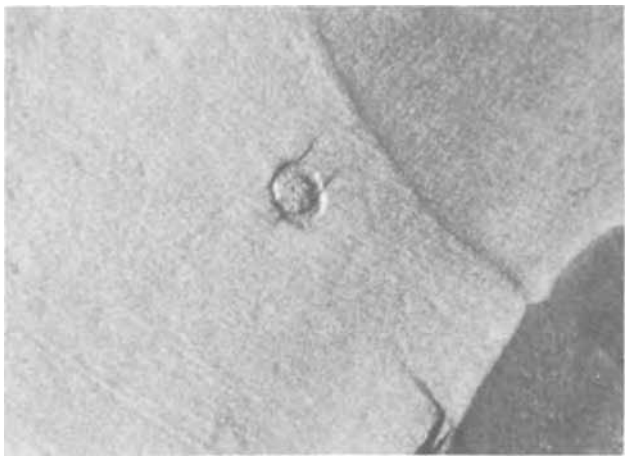

Fig. 2b. 99.999% copper specimen (large grain) showing crack initiated within grain at surface imperfection. Stressed in 0.05*N* cupric acetate. Magnification, 45X.

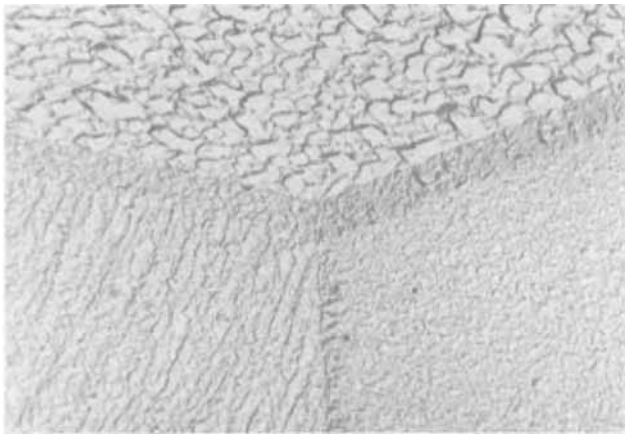

Fig. 3a. 99.999% copper specimen (small grain) showing featureless grain boundary and many crystallites in the grain. In 0.05*N* cupric acetate unstressed. Magnification, 9865X.

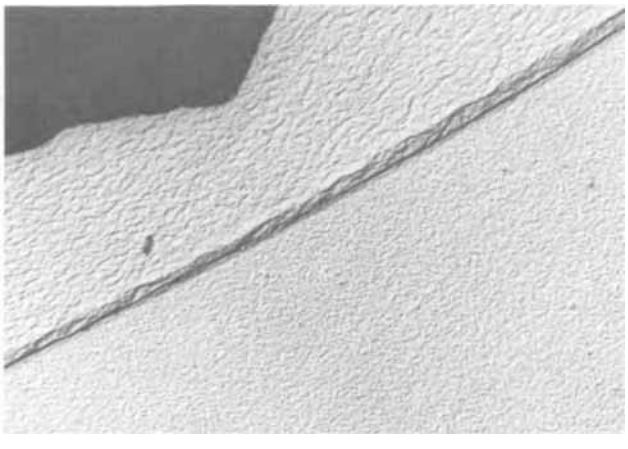

Fig. 3b. 99.999% copper specimen (small grain) showing fissures in the grain boundary with fewer crystallites in the grain. Stressed in 0.05*N* cupric acetate. Magnification, 9865X.

than the many oxide crystallites which formed on the grains, whereas the stressed material showed fissures at the boundary after 1 hr in the acetate solution and had less extensive oxidation in the grain interiors as seen in Fig. 3b. In general, the grain boundaries with fissures were perpendicular to the applied stress.

A few experiments were carried out on commercial 70-30 brass containing <0.8% Pb. This metal did not

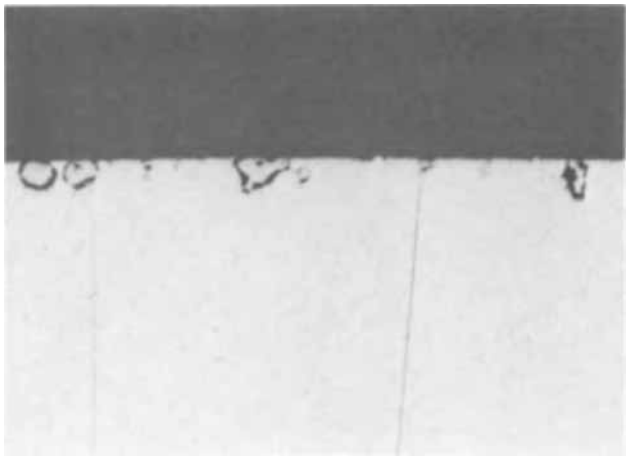

Fig. 4. 70-30 brass specimen showing intergranular attack. With little or no oxide. Stressed in 0.05*N* cupric acetate. Magnification, 85X.

fail for times as long as seven days in either solution, and as Fig. 4 shows, the morphology of attack was quite different. This attack appeared to be intergranular and involved an actual loosening of surface grains in the acetate solution. In the sulfate solution most of the attack occurred on the compression side while the tension side was relatively uncorroded.

Effect of illumination.—Because it is known that illumination retards oxide growth on copper (11), the effect of light on the failure of copper in 0.05*N* cupric acetate solution was examined. Two experiments were run in parallel. In one, the copper wire was exposed to the solution under load and illuminated on two sides by 150W high-intensity incandescent lamps. The other was carried out in an identical manner, but light was excluded. There was no measurable temperature difference between the illuminated and unilluminated tests. No failure was observed for illuminated specimens for periods as long as five days. The ones kept in the dark always failed in less than 24 hr.

Discussion

It was found that both 99.9 and 99.999% purity copper will crack in an environment where the rate of tarnish film formation is comparable or greater than the rate of tarnish for susceptible brasses. The results also indicate that cracking occurs in the oxide that forms by growth into the grain boundaries. Before considering the question of the mechanism of the failure and whether we are looking at intergranular weakening or SCC, it is useful to discuss the meanings of the phenomena observed in connection with the formation of the oxide film. In order to do this it is necessary to look at the electrochemical theory of copper corrosion as worked out by Ives and Rawson (12). They propose that the copper-cuprous oxide-solution system can be divided into three zones: zone 1 is made up of a compact, adherent film of Cu_2O and the copper substrate; zone 2 is a porous film of Cu_2O and; zone 3 is the aqueous solution containing oxygen. Each of these zones has associated with it half-cell reactions. The half-cell reaction for zone 1 is the film growth process

$$Cu^\circ + \tfrac{1}{2} H_2O \rightarrow \tfrac{1}{2} Cu_2O + H^+ + e^- \qquad [1]$$

where at 25°C $E_1 = 0.471 - 0.0592$ pH. Both film growth and film dissolution occur in zone 2 and are regarded by Ives and Rawson as constituting a hypothetical redox electrode. These reactions are

$$Cu^{2+} + \tfrac{1}{2} H_2O + e^- \rightarrow \tfrac{1}{2} Cu_2O + H^+ \text{ (film growth)} \qquad [2a]$$

$$\tfrac{1}{2} Cu_2O + H^+ \rightarrow Cu^{2+} + \tfrac{1}{2} H_2O + e^- \text{ (film dissolution)} \qquad [2b]$$

where at 25°C $E_2 = 0.203 + 0.0592\ pH + 0.0592 \log [Cu^{2+}]$. Finally, the half-cell reaction at zone 3 is

$$\tfrac{1}{4}\ O_2 + H^+ + e^- \rightarrow \tfrac{1}{2}\ H_2O \qquad [3]$$

The whole system of electrode reactions can be regarded as two cells coupled to each other, reactions [1] and [2a] are anodic and cathodic reactions, respectively, involving film growth and reactions [2b] and [3] are anodic and cathodic reactions, respectively, involving film dissolution.

We can now apply this set of half-cell reactions to four situations pertinent to the results obtained:

Film formation in the absence of light and stress.—Our results show film growth over the entire surface. The film growth observed is simply a combination of reactions [1] and [2a], as pointed out by Porterfield and Miller (6)

$$Cu^\circ + Cu^{2+} + H_2O \rightarrow Cu_2O + 2H^+ \qquad [4]$$

or if all four reactions of Ives and Rawson are used

$$Cu^\circ + \tfrac{1}{4}\ O_2 = \tfrac{1}{2}\ Cu_2O \qquad [5]$$

Both Porterfield and Miller, and Green *et al.* (1) require a porous film to provide access of Cu^{++} or O_2 to the copper substrate. If there is a compact film at the substrate (zone 1) and it is sufficiently thin, rapid solid-state diffusion through it may be a possibility.

Film formation with stress applied in the absence of light.—Our results show enhanced film growth at the grain boundaries normal to the direction of stress and diminished film growth elsewhere. To arrive at an explanation of these results it is necessary to determine which of the combinations of reactions [1], [2a], [2b], and [3] predominate in their contribution to the overall corrosion current. We can only suggest plausible ways in which the experimental results can be explained. When there is no stress and we observe growth of Cu_2O over the entire specimen, apparently the combination of reactions [1] and [2a] and/or [1] and [3] result in growth both in the grain interiors and in the boundaries. When stress is applied, very small areas of metallic copper are exposed by rupture of the Cu_2O film at the grain boundary, and reaction [1], because it involves metallic copper, predominates in the boundaries and is polarized to higher potentials than with no stress. This occurs because the current density at the bare sites must be high as a result of the small areas involved as compared to the large uncracked cathodic areas. Because stress probably makes reaction [1] the predominant growth reaction in the grain boundaries, and as our results show, causes oxide dissolution to occur in the interiors of the grains, it is reasonable to speculate that the current density for the growth reaction in the grain interiors decrease and the dissolution reaction ([2a] plus [3]) takes over. This is probably what happened in the experiments of Pugh *et al.* (7), with all the tarnishing occurring at the grain boundaries and none detectable elsewhere. Since they observed no tarnishing in the absence of stress, it must be guessed that in their solution reactions [2a] plus [3] were always predominant in the grain interiors.

Role of illumination.—Ives and Rawson (13) have shown that illumination results in enhanced corrosion of copper with greater concentrations of Cu^{2+} ions found in the corroding media. Duwell (14) also found an enhancement of corrosion rate in light. Kruger and Calvert (11) showed that the effect of the light was to cause a dissolution of a Cu_2O film present on the surface. This means that reaction [2b] predominates. Also, Duwell's work suggests the reverse of reaction [1], the production of metallic copper, can also occur. Thus, it appears that light retards or stops the growth of the Cu_2O that forms in the grain boundaries and, by doing so, retards or stops the cracking process.

Role of the anion.—Our results show that the cracking observed when cupric acetate is used is not found when sulfate is substituted. Miller and co-workers (10) found that they could separate two general types of oxide topographies, one relatively smooth, and the other composed of polyhedra. The smoother topographies are formed in acetate and formate solutions, the other in sulfate and perchlorate. They were able to show that these changes were probably due to the fact that in the sulfate and perchlorate solution, a decrease in pH occurred during the film formation process, whereas the acetate and formate ions acted as buffers and prevented any significant lowering of pH. When the pH is lowered, the dissolution reaction [2b] predominates, and oxide formation is retarded or stopped. This lowering of pH with its attendant oxide dissolution would be especially pronounced in restricted geometries such as cracks (15). Elsewhere on the surface, oxide film formation can, and does, take place. But as Miller has shown, there are sites (between polyhedra of Cu_2O) where very little film forms.

From chemical and electrochemical considerations we can conclude that failure results under those circumstances which promote oxide formation at grain boundaries. This oxide formation in a sense results in a dissolution of copper from the grain boundary but it is not the same as simple dissolution without formation of oxide. Such dissolution (probably enhanced) can occur when copper is illuminated or when sulfate ions are present. If intergranular weakening by dissolution at the grain boundaries were involved, sulfate which lowers the pH in cracks would enhance the opportunity for failure. It does not. However because oxide formation is retarded or stopped in the grain boundaries, no cracking results. Thus, intergranular weakening by simple metal dissolution is ruled out as an explanation for the cracking observed for copper in cupric acetate solutions. Because these experiments have shown that film formation is necessary, it would appear that the brittle film theory of Forty and Humble (3) fits the results better. It also seems reasonable that the complex relationships between the mechanical properties of the film, as affected by the metal and the environment, and the rate of film formation in the grain boundaries play a role. An explanation of the failure to crack brass in the cupric acetate solutions will depend on a better future understanding of these relationships.

Acknowledgment

We are grateful for the support of the Office of Naval Research under contract NAONR 18-69 NR 036-082.

Manuscript submitted Oct. 26, 1970; revised manuscript received March 4, 1971. This was Paper 132 presented at the Atlantic City Meeting of the Society, Oct. 4-8, 1970.

Any discussion of this paper will appear in a Discussion Section to be published in the June 1972 JOURNAL.

REFERENCES

1. J. A. S. Green, H. D. Mengelberg, and H. T. Yolken, *This Journal*, **117**, 433 (1970).
2. E. N. Pugh, J. V. Craig, and W. G. Montague, *Trans. ASM*, **61**, 468 (1968).
3. A. J. Forty and P. Humble, *Phil. Mag.*, **8**, 247 (1963).
4. K. R. Lawless and G. T. Miller, Jr., *Acta Cryst.*, **12**, 594 (1959).
5. R. W. Topham and G. T. Miller, Jr., *This Journal*, **113**, 421 (1966).
6. W. W. Porterfield and G. T. Miller, Jr., *ibid.*, **113**, 528 (1966).
7. E. N. Pugh, W. G. Montague, and A. R. C. Westwood, *Corrosion Sci.*, **6**, 345 (1966).
8. H. H. Uhlig and D. J. Duquette, *ibid.*, **9**, 557 (1966).
9. E. W. Young, Jr., J. V. Cathcart, and A. T. Gwathmey, *Acta Met.*, **4** (1956).

10. C. E. Guthrow and G. T. Miller, Jr., *This Journal*, **113**, 415 (1966).
11. J. Kruger and J. P. Calvert, *ibid.*, **111**, 1038 (1964).
12. D. J. G. Ives and A. E. Rawson, *ibid.*, **109**, 458 (1962).
13. D. J. G. Ives and A. E. Rawson, *ibid.*, **109**, 447 (1962).
14. E. J. Duwell, *ibid.*, **113**, 763 (1966).
15. B. F. Brown, C. T. Fujii, and E. P. Dahlberg, *ibid.*, **116**, 219 (1969).

The Influence of Chloride and Sulfate Ions on the Corrosion of Iron in Sulfuric Acid

S. E. Traubenberg[1] and R. T. Foley*

Department of Chemistry, The American University, Washington, D. C. 20016

ABSTRACT

The influence of chloride and sulfate ions on the corrosion of iron in H_2SO_4 media at pH near 3 was studied. It was shown that both ions could be either aggressive or not aggressive under definite conditions. Chloride ions accelerate corrosion considerably when the anodic reaction contributes significantly to the over-all kinetics. Sulfate ions accelerate corrosion when the reaction is under cathodic control. Chloride ions decreased the protective action of so-called anodic inhibitors ($K_2Cr_2O_7$ and NH_2-CH_2-CH_2-OH) whereas sulfate ions interfere with the action of thiourea, a cathodic inhibitor. The corrosion potential is independent of the chloride concentration but is shifted in the negative direction by sulfate, These observations are interpreted in terms of the properties of Fe-Cl^- and Fe-$SO_4^=$ complexes. The chloride complex serves simply to carry Fe^{++} away from the metal surface.

The corrosion of iron in various electrolytes is a very complex process making it difficult to separate out a single effect and demonstrating in an unequivocal way how it affects the over-all process. Bengough (1), for example, listed six metallic factors and eight environmental factors involved in the corrosion of metals in sea water. These factors do not operate independently; electrolyte concentration, oxygen concentration, temperature, and pH are all interrelated. Not withstanding the difficulty, from an experimental standpoint, of evaluating individual effects in the complex process, it is important to clarify environmental effects in iron corrosion, or, more specifically, the influence of anions. Such a clarification must come before any elucidation of the mechanism of iron corrosion which many consider to be the most important technological problem in the corrosion field.

From a review of the literature (2) it was concluded that there is no generally accepted viewpoint on the role that anions play in iron corrosion. Divergent views are held regarding the aggressive or non-aggressive nature of various anions and the manner in which the anions operate. Most discussion has been in terms of the adsorption of anions on the Fe surface or the penetration by anions of passive films. With the intent of unifying the divergent thinking on the subject, it was proposed that anions influence the corrosion rate by virtue of the type of metal-anion complex (compound) that is formed. Thus, a stable insoluble species would inhibit corrosion whereas a transitory, readily dissociable complex would accelerate corrosion. In neutral solutions or weakly acid solutions chloride ions would form a FeCl complex which under normal circumstances would dissociate and have the net effect of carrying Fe^{++} away from the surface. This would imply that Cl^- is involved in the anodic process. In most of the environments commonly encountered, Fe corrosion is controlled by the cathodic process and any influences on the anodic process are obscured in relation to the over-all corrosion kinetics. This makes it difficult to test any proposition related to the anodic process.

In the following, attempts have been made to develop the experimental conditions wherein the kinetics of the anodic process influence the over-all corrosion rate. The paper is restricted to the effect of chloride ions and sulfate ions in sulfuric acid medium at pH near 3. Both chloride ions and sulfate ions are considered "aggressive" anions.

The corrosion of Fe in its active region, at pH in the range of 2-4 has considerable technological interest. It has been shown by Rosenfel'd and Marshakov (3) that the pH within a pit or crevice in a chloride medium will stabilize at a value determined by the hydrolysis of ferrous chloride which is about 3. Herbsleb (4) also describes pitting in neutral solutions in terms of a build-up of Cl^- concentration in the pit due to transference and a decrease in pH due to hydrolysis. Recently it has been shown by direct measurements by Brown *et al.* (5) that the pH of the solution in the advancing crack of a 0.45C steel undergoing stress corrosion cracking in nearly neutral 3.5% NaCl solution is about 3.8. Thus, the behavior of iron in the pH range 2-4 is directly related to the behavior of Fe during such processes as pit propagation and stress cracking.

Several of the studies reported in the literature have dealt with chloride effects in low concentration. The present study deals with the effect of relatively high concentrations, in the range of technological interest, *e.g.*, marine environments.

Experimental

High-purity iron samples of approximately 20 cm^2 area and a thickness of 0.050 cm were used for the experiments. The preparation of the iron ingot was described by Huber (6). The reduced strip was vacuum annealed at 815°C, cut into coupons, and finally stress relieved at 500°C for 1 hr. The samples were chemically cleaned in a solution of HCl (1:1) for 1-2 min; rinsed with distilled water and immersed in a solution of concentrated H_2SO_4 and HNO_3 (1:1) for 15 sec. After rinsing with distilled water the strips were placed in a solution of NaCN (5 g/100 ml) for 5 min, rinsed with distilled water and acetone, and

* Electrochemical Society Active Member.
[1] Present address: Department of Analytical Chemistry, Moscow Technological Institute of Food Industry, Moscow, U.S.S.R.
Key words: corrosion, iron, chloride effect, inhibitors, corrosion potential, complexes.

stored under acetone. Solutions of H_2SO_4, H_2SO_4 + NaCl, and H_2SO_4 + Na_2SO_4 were used as the corrosive solutions; the pH of the solutions was about 3. The effect of chloride and sulfate ions on the corrosion of iron was studied in the concentration range from 0.1 to 3M NaCl and from 0.1 to 1M Na_2SO_4. The strips were immersed, in triplicate, in the solutions (100 ml) on glass hooks and were exposed to these solutions from 0.5 to 24 hr at 35°C. After exposure the samples were rinsed with distilled water and acetone and then dried. The weight loss was determined and the corrosion rate was expressed in terms of milligrams per square centimeter in a certain time interval or as grams per square meter per hour.

Strips of iron and copper fastened with plastic bolts were used to study the influence of chloride and sulfate ions on the galvanic process. $CuSO_4$ (0.1M) was added to the corrosive solution. The time of these experiments was from 0.5 to 6 hr.

Some experimentation was done with different inhibitors of iron corrosion. The duration of these experiments was 4-24 hr. As anodic inhibitors, potassium dichromate $K_2Cr_2O_7$ and monoethanolamine NH_2-CH_2-CH_2-OH (7) were used; as a typical cathodic inhibitor, thiourea NH_2-CS-NH_2 was used (7). The concentration of $K_2Cr_2O_7$ and NH_2-CH_2-CH_2-OH was 0.1M and the concentration of NH_2-CS-NH_2 was 0.5M. The concentration of inhibitors was chosen from the results of preliminary experiments with H_2SO_4 solutions in the absence of NaCl and Na_2SO_4. The protective action of the inhibitors was calculated according to the following accepted formula

$$H\% = \frac{\rho_0 - \rho}{\rho_0} \times 100$$

where H = protective action, ρ_0 corrosion rate in H_2SO_4 solution and ρ corrosion rate in solution with inhibitor.

A Wenking potentiostat, Fast Rise Model 61 RS, was used for the potentiostatic measurements. A conventional three electrode system was used, the working electrode a modified version of the type described by Myers *et al.* (8). The auxiliary electrode was a platinum screen and the reference a mercury-mercurous sulfate electrode. The solutions were deaerated with purified nitrogen and stirring was provided with a magnetic stirrer. The potential-current data were tabulated manually and transformed to a potential (*vs.* normal H_2 electrode)-current density plot by means of a Fortran IV E program with an IBM 1130 computer and an on-line incremental plotter. A Keithley 600A electrometer measured changes in the electrode potential of iron during corrosion (24 hr).

Results and Discussion

Effect of chloride ion and sulfate ion on corrosion kinetics.—The corrosion of iron as a function of chloride and sulfate ion concentration is given in Fig. 1.

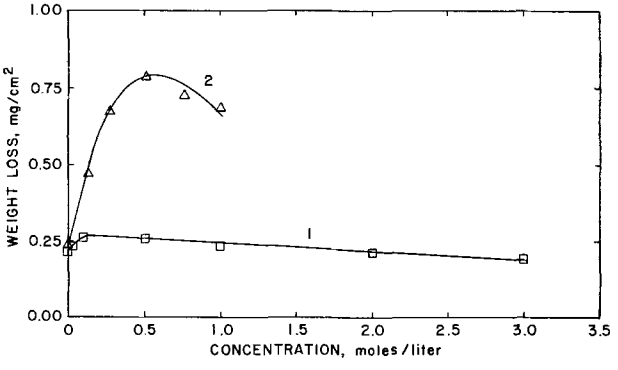

Fig. 1. Dependence of the corrosion of iron on the concentration of NaCl and Na_2SO_4 in H_2SO_4 medium. Curve 1, NaCl at pH 2.72, 35°C, for a 4 hr period. Curve 2, Na_2SO_4 at pH 2.90, 35°C, for a 6 hr period.

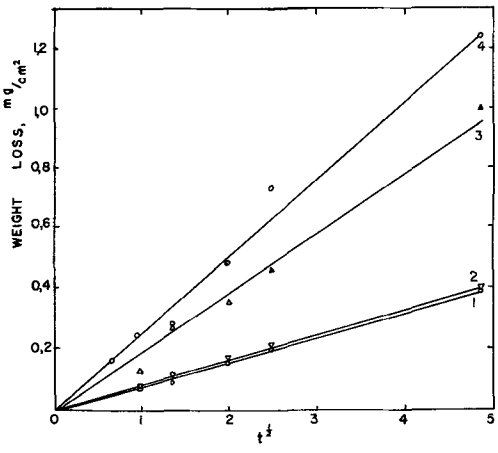

Fig. 2. Influence of Na_2SO_4 and NaCl on the kinetics of the dissolution of iron. Curve 1, $-H_2SO_4$ (pH = 2.78); curve 2, $-H_2SO_4$ + 0.5M NaCl; curve 3, $-H_2SO_4$ + 0.5M NaCl + 0.5M Na_2SO_4; curve 4, $-H_2SO_4$ + 0.5M Na_2SO_4.

These tests were conducted at 35°C at a pH of about 2.8. The weight loss as a function of concentration is similar to that previously reported in the literature for neutral salt solutions. The initial increase in corrosion which for the chloride ion is not great is usually ascribed to the increased conductivity of the solution. For concentrations greater than 0.5M the corrosion decreases and for neutral solutions this has been interpreted in terms of the decreased solubility of oxygen as discussed in detail by Evans and Hoar (9) and others. In these acid solutions it is likely that the cathodic process goes with mixed hydrogen and oxygen depolarization and a decrease in the concentration of oxygen would be expected to have a bearing on the rate. Further experimentation was done with 0.5M solutions of NaCl and Na_2SO_4 which approximated the solutions exhibiting maximum corrosion.

The effect of 0.5M additions of NaCl and Na_2SO_4 and a mixture of the two salts to H_2SO_4 solution at pH 2.78 is given in Fig. 2. The dissolution rate of Fe in these solutions follows a parabolic relationship of the type

$$W^2 = kt$$

where W is the weight loss in mg/cm², t is the time in hours, and k is a constant. The magnitude of k taken from the parabolic plot in Fig. 2 is 0.64×10^{-2} for both H_2SO_4 and H_2SO_4 + NaCl solutions (curves 1 and 2). Thus the presence of chloride ion has no great effect on corrosion over the 24 hr period investigated. This agrees with Kolotyrkin's observation (10) that addition (into acid solution) of chloride, bromide, and iodide ions has only a small influence on the dissolution of metals in the active state.

Sulfate ion on the contrary, has a very significant effect on the dissolution rate of iron in sulfuric acid solutions as shown in Fig. 2 (curve 4). The parabolic rate constant is greater, 6.5×10^{-2}, than that describing the kinetics in H_2SO_4 solution.

In the solution with 0.5M NaCl and 0.5M Na_2SO_4 the corrosion rate was higher than that in the solution with only NaCl but less than that with only Na_2SO_4. This rules out the possibility that the sulfate effect might be due only to an increase in ionic strength.

Polarization behavior.—The cathodic and anodic behavior of the iron electrode in H_2SO_4 solutions with various concentrations of NaCl is shown in Fig. 3. Curve 1, 0.001*N* H_2SO_4 without any chloride addition, reflects the low conductivity of the electrolyte requiring considerable departure from the equilibrium potential to achieve a significant current density (at 25°C). A customary procedure in an experiment of this type is to use a supporting electrolyte. However, this would introduce other anions which would interfere with the interpretation of chloride and sulfate

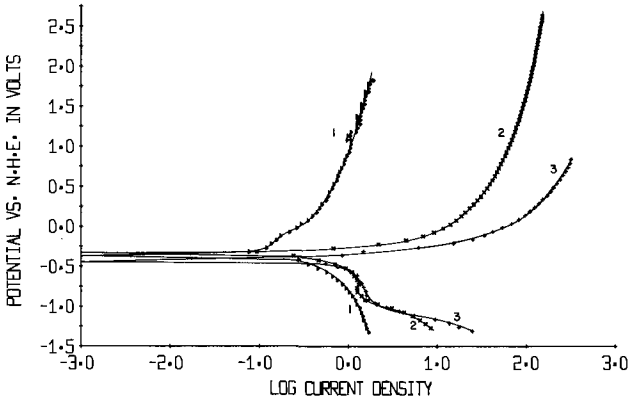

Fig. 3. Polarization behavior of the Fe electrode in H_2SO_4 solutions at pH 3 containing various concentrations of NaCl. Potential vs. normal H_2 electrode, current density mA/cm^2. Curve 1, —0.001*N* H_2SO_4; curve 2, —0.001*N* H_2SO_4 + 0.1*N* NaCl; curve 3, —0.001*N* H_2SO_4 + 0.5*N* NaCl.

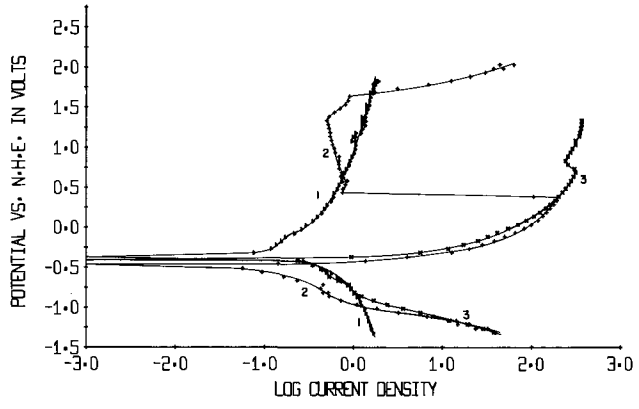

Fig. 4. Polarization behavior of the Fe electrode in H_2SO_4 solutions at pH 3 with Na_2SO_4. Potential vs. normal H_2 electrode, current density mA/cm^2. Curve 1, —0.001*N* H_2SO_4; curve 2, —0.001*N* H_2SO_4 + 1*N* Na_2SO_4; curve 3, —0.001*N* H_2SO_4 + 1.0*N* Na_2SO_4 + 0.1*N* NaCl.

effects. These curves were obtained by experiments run in deaerated solutions which means that corrosion rates, in terms of corrosion currents, cannot be obtained by extrapolation to the equilibrium potential. The distinguishing feature of the curves in Fig. 3 is the increase in the anodic current with increase in NaCl concentration. In the presence of 0.1*N* NaCl the Fe electrode is not passivated anodically, a result which has been observed previously at lower NaCl concentration (11).

Figure 4 illustrates the effect of sulfate additions to 0.001*N* H_2SO_4 solutions. In a solution containing 1.0*N* Na_2SO_4 there is a considerable increase in anodic current comparable to that realized with the chloride addition. However, in this solution anodic passivity is achieved at the appropriate potential. The potential and current density agrees well with that reported by Nobe and Tobias (11) whose pH 3 solution was prepared by neutralizing 1*N* H_2SO_4 and should agree with curve 2 in Fig. 4. The sulfate ion shifts the corrosion potential in the negative direction. The addition of 0.1*N* chloride ion to this solution essentially removes these two effects.

Bimetallic corrosion.—The corrosion rate of Fe in H_2SO_4 solution at pH 3 is controlled by a slow cathodic reaction process. Experiments wherein Cu was connected to Fe to form a bimetallic corrosion couple were performed to create the situation wherein the cathodic reaction proceeded rapidly. In a series of experiments copper and iron strips were fastened together with Nylon bolts and the couple was immersed in sulfuric

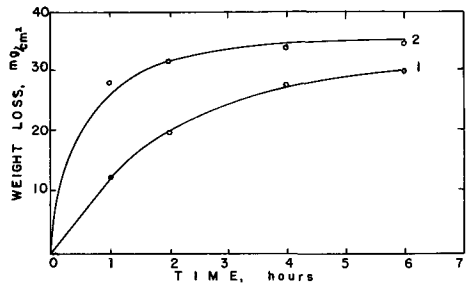

Fig. 5. Influence of NaCl on the kinetics of the dissolution of Fe in the presence of $CuSO_4$. Curve 1, —0.001*N* H_2SO_4 + 0.1M $CuSO_4$; curve 2, —0.001*N* H_2SO_4 + 0.1M $CuSO_4$ + 0.5M NaCl.

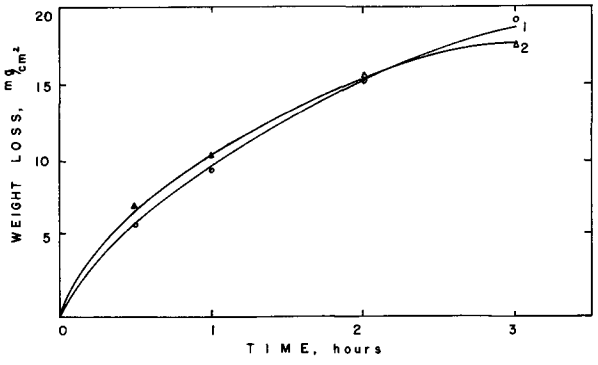

Fig. 6. Influence of Na_2SO_4 on the corrosion of Fe in the presence of $CuSO_4$. Curve 1, —0.001*N* H_2SO_4 + 0.1M $CuSO_4$; curve 2, —0.001*N* H_2SO_4 + 0.1M $CuSO_4$ + 0.5M Na_2SO_4.

acid solutions containing 0.1M $CuSO_4$ with and without NaCl. In these solutions the cathodic reaction, $Cu^{++} + 2e = Cu^\circ$ would be expected to go at a rapid rate, and in these solutions chloride ion accelerated corrosion in a significant way (Fig. 5). After 1 hr, the corrosion rate in a solution containing 0.5M NaCl was more than twice that in the control solution (283 and 124 g/m^{-2}/hr^{-1}, respectively). In a similar set of bimetallic couple experiments it was found that sulfate ion had very little influence on corrosion (Fig. 6). After 1 hr, the corrosion rate in the control solution (H_2SO_4 + $CuSO_4$) was 94 g/m^{-2}/hr^{-1} as compared with 104 g/m^{-2}/hr^{-1} in a solution containing 0.5M sodium sulfate; after 2 hr the rates were 76 g/m^{-2}/hr^{-1} and 76 g/m^{-2}/hr^{-1}, respectively. Because of the considerable amount of corrosion and deposited copper the precision of these experiments was not as good as those described above. However, it can be concluded that the chloride effect is definitely exerted when the rate of the cathodic reaction is increased to a point at which it is comparable to the anodic dissolution reaction, $Fe^\circ = Fe^{++} + 2e$.

Corrosion potentials.—The corrosion potential of Fe was measured in solutions of H_2SO_4 containing NaCl and Na_2SO_4 at several concentrations after corrosion for 24 hr. The results are given in Table I. The electrode potential was independent of chloride ion but was 25-40 mV more negative when $SO_4^=$ was present in

Table I. Potential of iron electrode in different solutions after 24 hr

Solution		pH	Potential, volts vs. NHE
H_2SO_4		2.85	—0.44
H_2SO_4 + NaCl	0.5M		—0.44
	1.0M	2.85	—0.445
	2.0M		—0.445
Na_2SO_4	0.1M		—0.48
	0.5M	2.85	—0.475
	1.0M		—0.475
Na_2SO_4	0.5M	2.85	—0.45
NaCl	0.5M		

Table II. Influence of Na_2SO_4 and NaCl on the corrosion of iron in the presence of some inhibitors

Solution	4 hr			24 hr		
	Weight loss, mg/cm²	ρ, g/m²/hr	H, %	Weight loss, mg/cm²	ρ, g/m²/hr	H, %
H_2SO_4	0.185	0.47	—	0.38	0.159	—
H_2SO_4 + 0.5M NaCl	0.185	0.47	—	0.385	0.162	—
H_2SO_4 + 0.5M Na_2SO_4	0.485	1.21	—	1.195	0.502	—
H_2SO_4 + 0.1M $K_2Cr_2O_7$	0.005	0.013	97.4	0.01	0.004	97.5
H_2SO_4 + 0.1M $K_2Cr_2O_7$ + 0.5M NaCl	0.198	0.495	−5.3	0.555	0.231	−42.6
H_2SO_4 + 0.1M $K_2Cr_2O_7$ + 0.5M Na_2SO_4	0.01	0.025	98	0.02	0.008	98.4
H_2SO_4 + 0.5M NH_2CSNH_2	0.148	0.37	21.3	0.30	0.125	21.4
H_2SO_4 + 0.5M NH_2CSNH_2 + 0.5M NaCl	0.152	0.38	19.2	0.295	0.124	22
H_2SO_4 + 0.5M NH_2CSNH_2 + 0.5M Na_2SO_4	0.408	1.02	15.7	1.025	0.428	14.7
H_2SO_4 + 0.1M $NH_2CH_2CH_2OH$	0.01	0.025	94.5	0.01	0.004	97.5
H_2SO_4 + 0.1M $NH_2CH_2CH_2OH$ + 0.5M NaCl	0.055	0.138	70.8	0.165	0.069	57.5
H_2SO_4 + 0.1M $NH_2CH_2CH_2OH$ + 0.5M Na_2SO_4	0.038	0.095	92.2	0.115	0.048	88.3

the solution. The chloride effect agrees with results obtained by Nobe and Tobias (11). The more negative value in sulfate solutions suggests a Fe-$SO_4^=$ species which is sufficiently stable to lower the Fe^{++} concentration.

Inhibitor experiments.—Experiments were conducted with three inhibitors, $K_2Cr_2O_7$, NH_2-CH_2-CH_2-OH, and NH_2-CS-NH_2. Potassium dichromate and ethanolamine are considered to be "anodic" inhibitors and thiourea a "cathodic" inhibitor (7). The mechanism of inhibition by potassium dichromate appears to be generally accepted. However, there is evidence that ethanolamine and thiourea may be involved in both the anodic and cathodic reaction depending on the *p*H of the solution (12). Nevertheless, these compounds were taken to examine the effects of Cl^- and $SO_4^=$ on inhibited solutions.

The results of the gravimetric measurements are given in Table II. Potassium dichromate inhibits corrosion in H_2SO_4 solution at a *p*H of 3 for periods of 4 and 24 hr. The efficiency of inhibition, *H*%, is not affected by the presence of 0.5M Na_2SO_4. However, in the presence of 0.5M NaCl, corrosion exceeds that in the uninhibited solution yielding negative values for *H*%. This result is in keeping with prior observations on the behavior of "dangerous" oxidizing inhibitors. To previously stated conditions such as insufficient concentration must be added the requirement for the formation of an unstable anodic complex. The anodic and cathodic polarization behavior of iron in these solutions agree with the gravimetric results (Fig. 7). There is little change in the cathodic polarization but the anodic polarization behavior indicates that the chloride ion prevents passivation from being achieved at the appropriate potential.

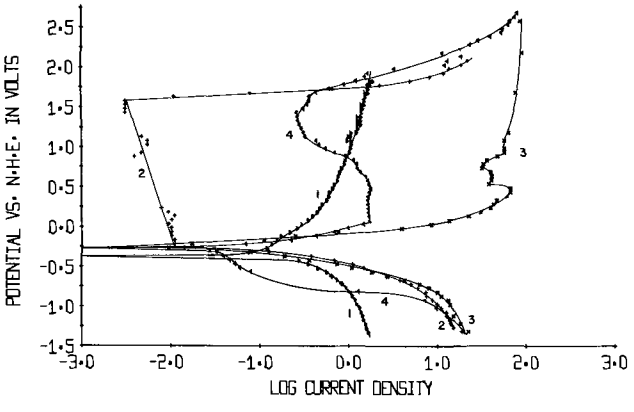

Fig. 7. Polarization behavior of the Fe electrode in inhibited solutions. Potential vs. normal H_2 electrode, current density mA/cm². Curve 1, −0.001*N* H_2SO_4; curve 2, −0.001*N* + 0.1M $K_2Cr_2O_7$; curve 3, −0.001*N* H_2SO_4 + 0.5*N* NaCl + 0.1M $K_2Cr_2O_7$; curve 4, −0.001*N* H_2SO_4 + 0.5M Na_2SO_4 + 0.1M $K_2Cr_2O_7$.

Ethanolamine, also classed as an anodic inhibitor has a high efficiency in this system at the 0.1M concentration. The efficiency in the presence of sulfate ion is also high but in the presence of chloride ion drops off. The polarization behavior of Fe in these solutions agrees with the gravimetric results. In the presence of the inhibitor anodic polarization brings Fe into the passive range. In the presence of sulfate the anodic current is reduced by two decades. In the presence of chloride there is no substantial change in the anodic behavior in the presence or absence of the inhibitor.

Thiourea, classed as a cathodic inhibitor, is much less effective than either potassium dichromate or ethanolamine with an efficiency of only 21%, under the conditions used here. Generally, cathodic inhibitors are less efficient than those of the anodic type (13). The efficiency of this compound is not substantially affected by the presence of chloride ion but the sulfate ion reduces the efficiency by about 25%. The polarization behavior of Fe in these solutions is altered by the presence of thiourea, mainly in the cathodic direction, but to a minor extent.

Conclusions

The salient observations from the experimental work comparing the effects of chloride and sulfate ions on the corrosion of iron may be summarized.

1. In the corrosion of Fe at 35°C and a *p*H of about 3 under conditions wherein the cathode reaction is rate controlling, chloride has virtually no effect, whereas sulfate increases corrosion.
2. In the presence of sulfate ion the Fe electrode is passivated by polarizing anodically (normal behavior). In the presence of chloride ion this passivation does not occur.
3. In a Cu-Fe bimetallic corrosion couple wherein a fast cathodic reaction is supplied by the reduction of copper ions, chloride greatly enhances corrosion, sulfate has little effect.
4. The corrosion potential (after 24 hr) is independent of chloride ion concentration. In the presence of sulfate ion the potential is shifted 25-40 mV in the negative direction.
5. Chloride ion will greatly reduce the efficiency of "anodic" inhibitors but does not affect the functioning of thiourea, classed as a cathodic type. Anodic inhibitors are effective in the presence of sulfate but the cathodic type drop in efficiency.

As was stated above an extended review of the literature (2) led to the conclusion that the best explanation for the effect of anions on the corrosion of iron was in terms of the formation of metal-anion complexes. Likewise these experimental results are best interpreted by assuming the formation of Fe-Cl or Fe($SO_4^=$) complexes at the reacting Fe surface.

What is postulated, and this is speculative, is that Cl ion forms a transitory Fe-Cl species of sufficient stability. In most of the usual corrosion situations investigated the anodic dissolution process is so rapid that the stability of the Fe-Cl is sufficient to enable it to remove the Fe^{++} away from the dissolving metal surface. From a mechanistic viewpoint the Fe-Cl complex can form in competition with Fe-O or Fe-OH species, thus the difficulty in achieving anodic passivity or passivity with inhibitors. Sulfate ion forms a relatively stable species as indicated by the negative shift in potential (Nernst law concentration effect). Further, it would appear that the sulfate complex in some manner assists the cathodic process (note Fig. 2.) It is postulated that this is related to the adsorption or desorption of oxygen species that would depolarize the cathode. It has been established that various anions are involved in "bridging" reactions of this type so it appears reasonable that $SO_4^=$ perhaps through the formation of HSO_4^- species can promote depolarization.

The concept of species such as Fe-Cl and $Fe(SO_4^=)$ participating directly in the corrosion of Fe must remain speculative until direct observation of these species is made. Whereas, instability constants for chloride and sulfate complexes with ferric ion are tabulated (14) there is no comparable data for ferrous complexes. These equilibrium constants would be a guide to the interpretation of kinetic data which are recognized as a measure of the rate the system attempts to attain the equilibrium condition.

These experiments, as well as many reported in the literature (2), demonstrate the specific effects of anions. Chloride and sulfate act in a manner that precludes any explanations based on ionic strength, conductivity, etc. They also argue against the significant role of such species as Fe-OH or $Fe-H_2O$ as these would be expected to be present in both chloride and sulfate solutions.

Acknowledgment

The support of the Inter-University Committee on Travel Grants for the Soviet Exchange Professor (S.E.T.) is gratefully acknowledged. A portion of this research was supported by the Advanced Research Projects Agency of the Department of Defense, ARPA Order No. 878, under Contract No. N 00014-68-A-0245. The authors would also like to acknowledge the assistance of Mr. Frederic M. Bogar in connection with the polarization work.

Manuscript submitted June 8, 1970; revised manuscript received *ca.* Jan. 28, 1971.

Any discussion of this paper will appear in a Discussion Section to be published in the June 1972 JOURNAL.

REFERENCES

1. G. D. Bengough, *Chem. Ind. (London)*, **1933**, 195-210, 228-229.
2. R. T. Foley, *Corrosion*, **26**, 58-70 (1970).
3. I. L. Rosenfel'd and I. K. Marshakov, *ibid.*, **20**, 115t-125t (1964).
4. G. Herbsleb, *Werkstoffe Korrosion*, **17** (8), 649-654 (1966).
5. B. F. Brown, C. T. Fujii, and E. P. Dahlberg, *This Journal*, **116**, 218 (1969).
6. R. W. Huber, "Preparation and Properties of Consumable-Electrode Vacuum Arc-Melted Electrolytic Iron," NRL Report No. 5928, U. S. Naval Research Laboratory, Washington, D. C.
7. I. N. Putilova, S. A. Balezin, and V. P. Barannik, "Metallic Corrosion Inhibitors," Pergamon Press, Oxford (1960).
8. J. R. Myers, E. G. Gruenler, and L. A. Smulczenski, *Corrosion*, **24**, 352-353 (1968).
9. U. R. Evans and T. P. Hoar, *Proc. Roy. Soc. (London)*, **A137**, 343-365 (1932).
10. Ja. M. Kolotyrkin, *Corrosion*, **19**, 261t-268t (1963).
11. K. Nobe and R. F. Tobias, *ibid.*, **20**, 263t-266t (1964).
12. T. P. Hoar and R. D. Holliday, *J. Appl. Chem.*, **3**, 502 (1953).
13. N. D. Tomashov, Teoria korrosii i zashchity metallov Izd. ANSSSR Moskva (1959).
14. K. B. Yatsimirskii and V. P. Vasil'ev, "Instability Constants of Complex Compounds," D. Van Nostrand Co., Princeton, N. J. (1960).

Free-Convection Mass Transfer with a Supporting Electrolyte

Jan Robert Selman* and John Newman*

Inorganic Materials Research Division, Lawrence Radiation Laboratory, and Department of Chemical Engineering, University of California, Berkeley, California 94720

ABSTRACT

Free convection and ionic migration effects are reviewed. Electrolytic free convection is treated theoretically for $CuSO_4-H_2SO_4$ solutions and for $K_3Fe(CN)_6-K_4Fe(CN)_6$ solutions without added electrolyte and with additions of KOH or NaOH. The effect of ionic migration on limiting currents is investigated. The presence of supporting electrolyte lowers the electric field, as in stagnant or forced convective systems. In addition, the concentration distributions of added electrolytes affect the density distribution, hence, the velocity profile in free convection, and, indirectly, the value of the calculated limiting currents.

Mass transfer to a vertical surface in free convection and the effect of ionic migration on limiting currents have both been studied extensively. Here, electrolytic systems are treated where both factors enter simultaneously.

* Electrochemical Society Active Member.
Key words: ionic migration, limiting current, vertical electrode, current distribution.

Free convection.—Fluid flow along a vertical wall as a result of a density gradient shows a boundary-layer structure. The pressure in horizontal planes is uniform and constant and equal to the hydrostatic pressure. The convection is caused by the difference in density along horizontal planes. By means of a similarity transformation, the fluid-mechanical and mass-transfer equations can be reduced to ordinary differ-

ential equations (1, 2), which are relatively much easier to solve than partial differential equations. The quantities of practical interest following from the solution of these equations are the mass transfer to the wall and the shear stress at the wall. For a constant density difference $\Delta\rho$ between the vertical surface and the bulk solution, these results can be expressed in dimensionless form as

$$Nu = C_b\,(ScGr)^{1/4} \qquad [1]$$

and

$$\tau_o/Lg\Delta\rho = B_b\,(ScGr)^{-1/4} \qquad [2]$$

where Nu is the average Nusselt number (defined for our systems in Eq. [32]), τ_o is the shear stress at the wall averaged over the length L, and g is the magnitude of the gravitational acceleration. Sc is the Schmidt number, Gr is the Grashof number

$$Gr = g\Delta\rho L^3/\rho_\infty\nu^2 \qquad [3]$$

and C_b and B_b are dimensionless coefficients which depend on the Schmidt number. Values of C_b and B_b for free convection in a binary fluid at a vertical surface are given in Table I.

The problem of isothermal mass transfer in a binary fluid is identical, mathematically, to that of heat transfer in a pure fluid, in which case the Prandtl number replaces the Schmidt number as a parameter in the analysis.

For free convection to a vertical surface with a constant density difference $\Delta\rho$, the local rate of mass transfer is inversely proportional to $x^{1/4}$, and the local shear stress is proportional to $x^{1/4}$, where x is the vertical distance along the surface measured from the beginning of the boundary layer.

Morgan and Warner (4) have shown how to treat this free-convection problem in the limit of an infinite value of the Schmidt number. This limit is of interest in the present context since, for electrolytic solutions, the Schmidt number is on the order of 1000. For high Schmidt numbers, the velocity profile extends to much greater distances from the surface than the region of concentration variations; that is, the hydrodynamic boundary layer is much thicker than the diffusion layer, and a singular-perturbation treatment is appropriate. Within the diffusion layer it is permissible to neglect the inertial terms in the equation of motion, and outside the diffusion layer the concentration is uniform and equal to the bulk value. It turns out that it is possible to determine the velocity and concentration distributions within the diffusion layer without carrying out the treatment of the velocity profile outside the diffusion layer.

In this manner, Le Fevre (5) determined the limiting values of C_b and B_b as given in Table I. The singular-perturbation expansions were carried out by Kuiken (6) to obtain three terms in the expansions of C_b and B_b for large Schmidt numbers. A similar perturbation treatment was given by Roy (7). Acrivos (8) has shown that this treatment can be applied, in the limit of infinite Schmidt number, to other geometries besides the vertical surface. Then, for two-dimensional geometries, the average Nusselt number is expressed as

$$Nu = C_b\,(ScGr)^{1/4}\left[\frac{1}{L}\int_0^L (\sin\epsilon)^{1/3}dx\right]^{3/4} \qquad [4]$$

Table I. Coefficients expressing the rate of mass transfer and the shear stress for free convection at a vertical plate from a binary fluid with a uniform density difference $\Delta\rho$ between the vertical surface and the bulk solution [from Ref. (1, 3, 5)]

Sc	C_b	B_b	Sc	C_b	B_b
0.003	0.1816	0.2707	1	0.5347	0.7265
0.01	0.2421	0.3528	10	0.6200	0.8434
0.03	0.3049	0.4419	100	0.6532	0.9005
0.72	0.5165	0.7045	1000	0.6649	0.9225
0.733	0.5176	0.7057	∞	0.670327	0.932835

where ϵ is the angle between the normal to the surface and the vertical. For the axisymmetric case, see Ref. (8) or (23).

The limit of small Schmidt numbers was treated by Le Fevre (5), and the problem was carried to a higher-order term by Kuiken (9).

We confine ourselves to the analysis of laminar free convection. The transition to turbulence is discussed in connection with the present results for the ferricyanide-ferrocyanide system with supporting electrolyte.

The effect of ionic migration.—The flux of an ionic species contains a contribution due to migration in the electric field as well as those due to diffusion and convection. Frequently in mass-transfer studies, a supporting or inert electrolyte is added to the solution in order to reduce this contribution of migration. In this case, the concentration of the reactant obeys the equation of convective diffusion, applicable in nonelectrolytic mass transfer. This should make the results directly comparable to those of experiments in heat transfer and nonelectrolytic mass transfer. In the case of mass transfer from a solution containing a single electrolyte, the concentration again obeys the equation of convective diffusion (10), but with the diffusion coefficient of the electrolyte rather than the reactant.

With intermediate amounts of supporting electrolyte, it is necessary to solve a more complicated set of equations. Eucken (11) has carried this out for three univalent ions in the, somewhat artificial, Nernst stagnant diffusion layer. Heyrovský (12) rejected this analysis because it did not agree with polarographic experiments for the discharge of hydrogen ions from HCl-KCl solutions and introduced an approximate correction for migration involving the transference number of the reactant.

Newman (13) solved the relevant equations numerically for a variety of electrolytic systems in the following cases: steady mass transfer to a rotating disk at large Schmidt numbers; unsteady mass transfer to a growing drop (polarography); unsteady mass transfer into a stagnant, semi-infinite fluid; and steady mass transfer in a stagnant, Nernst diffusion layer of finite thickness. Okada *et al.* (14) also solved numerically the problem for a growing mercury drop. Newman (15) showed that the case of steady migration through laminar diffusion layers generally, at high Schmidt numbers, is mathematically identical to that of migration to the rotating disk, solved earlier (13).

Newman's results (13) showed good agreement with the polarographic experiments on HCl-KCl solutions [see also Ref. (16)], thereby removing Heyrovský's objections to the methods of analysis based on the equations of electrolytic mass transfer.

Attempts to obtain an approximate solution to the problem of migration are also necessarily more restricted. Gordon, Newman, and Tobias (17) treated the rotating disk electrode by assuming a constant potential gradient in the diffusion layer. The rigorous solution by analytic means is hardly tractable (18-20), even if the velocity corresponds to a simple hydrodynamic situation.

Hsueh and Newman (21) treated the $CuSO_4$-H_2SO_4 system with no dissociation of the bisulfate ion and with partial dissociation according to its dissociation constant. The earlier treatment (13) of this system had assumed complete dissociation of bisulfate ions. This source (21) also gives the effect of migration for a stagnant Nernst diffusion layer with ions of arbitrary valence.

The migration effect is most simply expressed as the ratio I_L/I_D of the limiting current to the limiting "diffusion current," corresponding to the absence of migration, that is, with an excess of supporting electrolyte. The ratio I_L/I_D can be expressed as a function of the composition, characterized by the ratio of supporting electrolyte to total electrolyte.

Free convection in electrolytic systems.—The addition of supporting electrolyte to a solution does not make the free-convection problem directly comparable to that of heat transfer and nonelectrolytic mass transfer in a binary fluid because, while it does reduce the effect of ionic migration, the concentration variation of the supporting electrolyte affects the density variation to roughly the same extent as the reactant and thus influences the velocity profile. Nevertheless, it has frequently been assumed that the mass-transfer rate is adequately expressed by Eq. [1]. Ibl (22) has reviewed the experimental work on this problem and the applicability of Eq. [1] [see also Ref. (23)].

The evaluation of $\Delta\rho$ in the Grashof number (see Eq. [3]) has focused attention on the estimation of the concentration of the supporting electrolyte at the electrode surface, a quantity which is of secondary interest in forced convection. The method traditionally used for this estimation was originally developed by Wilke, Eisenberg, and Tobias (24) for $CuSO_4$-H_2SO_4 solutions. The papers of Wagner (25), Ibl and Braun (26), and Asada *et al.* (27) are relevant in this regard. Recently, Ravoo (28) has challenged the method of Wilke, Eisenberg, and Tobias on the basis of a bisulfate model applied to the stagnant Nernst diffusion layer [see also Ref. (21)].

Brenner (29) succeeded in quickly freezing the solution surrounding a hollow cathode and cutting slices off the frozen mass in order to analyze them. By measuring the refractive index profile, Hsueh and Newman (21) have obtained values of the sulfuric acid concentration at the electrode for unsteady diffusion into a stagnant medium.

Not all experiments in free convection have involved a supporting electrolyte and a vertical electrode. Ibl and Müller (30) have used aqueous solutions of copper sulfate. Schütz (31) experimentally investigated free-convection mass transfer to spheres and horizontal cylinders [see also Ref. (23)].

Analysis

The set of equations which determine free convection as a result of concentration variations in electrolytic solutions near a vertical electrode are the following. The equation of continuity

$$\frac{\partial v_x}{\partial x} + \frac{\partial v_y}{\partial y} = 0 \qquad [5]$$

The equation of motion

$$\nu \frac{\partial^2 v_x}{\partial y^2} + \frac{\rho - \rho_\infty}{\rho_\infty} g_x = 0 \qquad [6]$$

The mass-transfer equation for each solute species

$$v_x \frac{\partial c_i}{\partial x} + v_y \frac{\partial c_i}{\partial y} = D_i \frac{\partial^2 c_i}{\partial y^2} + z_i u_i \mathbf{F} \frac{\partial}{\partial y}\left(c_i \frac{\partial \Phi}{\partial y} \right) \qquad [7]$$

The electroneutrality equation

$$\sum_i z_i c_i = 0 \qquad [8]$$

Equation [6] is the boundary-layer form of the x-component of the equation of motion, and Eq. [7] is the boundary-layer form of the mass-transfer equation. Here y is the normal distance from the electrode. The inertial terms have been omitted from Eq. [6]. This is a valid approximation within the diffusion layer at high Schmidt numbers, as discussed in the introduction. The boundary-layer equations break down in small elliptic regions near the ends of the electrode. A detailed analysis of these regions is not attempted here.

The density is supposed to be the only variable physical property of the system, and is represented here by a linear expression in terms of the solute concentrations

$$(\rho - \rho_\infty)/\rho_\infty = \sum_i \alpha_i (c_i - c_{i\infty}) \qquad [9]$$

where α_i is a (constant) "densification coefficient." The mobility is assumed to be related to the diffusion coefficient by the Nernst-Einstein relation [see Ref. (10)]

$$D_i = RTu_i \qquad [10]$$

The boundary conditions for the velocity are

$$v_x = v_y = 0 \text{ at } y = 0 \qquad [11]$$

$$\partial v_x/\partial y = 0 \text{ at } y = \infty \qquad [12]$$

$$v_x = 0 \text{ at } x = 0 \qquad [13]$$

The boundary condition at $y = \infty$ corresponds to the matching condition for the inner region (the diffusion layer) in the first term of the singular-perturbation expansion for large Schmidt numbers (4). The inner region can be solved without treating the outer region.

A general expression for the electrode reaction is

$$\sum_i s_i M_i^{z_i} \rightleftarrows n e^- \qquad [14]$$

where s_i is the stoichiometric coefficient of species i, and M_i is a symbol for the chemical formula of species i. The current density is thus proportional to the flux of a reacting species at the electrode

$$s_i i_y = -n\mathbf{F}N_{iy} \text{ at } y = 0 \qquad [15]$$

Since the current density is not known in advance, we express the boundary condition on the species fluxes as

$$D_i \frac{\partial c_i}{\partial y} + z_i u_i \mathbf{F} c_i \frac{\partial \Phi}{\partial y} = \frac{s_i}{s_R}\left(D_R \frac{\partial c_R}{\partial y} + z_R u_R \mathbf{F} c_R \frac{\partial \Phi}{\partial y} \right) \text{at } y = 0 \qquad [16]$$

the convective contribution to the fluxes being zero at the solid electrode. Species R is a reactant called the "limiting reactant," whose concentration is taken to be constant at the electrode surface

$$c_R = c_{RO} \text{ at } y = 0 \qquad [17]$$

At the limiting current, which is of interest here, the concentration of the limiting reactant is zero at the electrode, corresponding to the maximum possible rate of mass transfer. Far from the electrode and at the beginning of the boundary layer, the concentrations have their bulk values

$$c_i = c_{i\infty} \text{ at } y = \infty \qquad [18]$$

$$c_i = c_{i\infty} \text{ at } x = 0 \qquad [19]$$

We now introduce the similarity transformation

$$\xi = y \left[\frac{3g\alpha_R (c_{R\infty} - c_{RO})}{4\nu D_R x} \right]^{1/4} \qquad [20]$$

$$\psi = \frac{4}{3} D_R x \left[\frac{3g\alpha_R (c_{R\infty} - c_{RO})}{4\nu D_R x} \right]^{1/4} f(\xi) \qquad [21]$$

where ψ is the stream function defined so that the equation of continuity [5] is satisfied identically

$$v_x = \frac{\partial \psi}{\partial y}, \quad v_y = -\frac{\partial \psi}{\partial x} \qquad [22]$$

With the dimensionless variables

$$\phi = \frac{\mathbf{F}}{RT}[\Phi - \Phi_0(x)], \quad \theta_i = \frac{c_i}{c_{R\infty} - c_{RO}} \qquad [23]$$

Eq. [5] to [10] become

$$f''' = \pm \sum_i \frac{\alpha_i}{\alpha_R} (\theta_i - \theta_{i\infty}) \qquad [24]$$

$$(D_i/D_R)[\theta_i'' + z_i(\theta_i\phi')'] + f\theta_i' = 0 \qquad [25]$$

$$\sum_i z_i \theta_i = 0 \qquad [26]$$

where the primes denote differentiation with respect to ξ. In Eq. [24], the plus sign applies if ρ_0 is less than ρ_∞, and *vice versa*.

The boundary conditions [11] to [13] and [16] to [19] become

$$\left.\begin{aligned} \theta_i' + z_i\theta_i\phi' = (s_iD_R/s_RD_i)(\theta_R' + z_R\theta_R\phi') \\ f = f' = 0,\ \theta_R = \theta_{RO} \text{ at } \xi = 0 \end{aligned}\right\} \qquad [27]$$

and

$$f'' = 0,\ \theta_i = \theta_{i\infty} \text{ at } \xi = \infty \qquad [28]$$

The densification coefficients in Eq. [9] are not unique for ionic species since the solution must be electrically neutral. The value of α_i can arbitrarily be set equal to zero for one ionic species. As a consequence of this arbitrariness, numerical values of ξ and f are not physically significant, and any results should rather be expressed in terms of the dimensionless distance η and the dimensionless stream function $F(\eta)$ defined according to

$$\eta = y\left[\frac{3g\Delta\rho}{4\nu D_R\rho_\infty x}\right]^{1/4} \qquad [29]$$

and

$$\psi = \frac{4}{3}D_R x\left[\frac{3g\Delta\rho}{4\nu D_R\rho_\infty x}\right]^{1/4} F(\eta) \qquad [30]$$

The density difference $\Delta\rho$ is not known at the outset; consequently, the calculations must be carried out in terms of ξ and f.

The principal results of interest are the mass-transfer rate or limiting current density and the shear stress at the wall. These are expressed by Eq. [1] and [2] with the coefficients C_b and B_b replaced by C and B. Here, the Schmidt number is

$$Sc = \nu/D_R \qquad [31]$$

and the average Nusselt number is

$$Nu = \frac{N_{R,avg}L}{D_R(c_{RO} - c_{R_\infty})} = \frac{s_R L\, i_{avg}}{n\mathbf{F}D_R(c_{R_\infty} - c_{RO})} \qquad [32]$$

Of interest also are the concentrations of the nonreacting ions at the electrode, θ_{iO}. These are necessary to calculate the density difference $\Delta\rho$ used in the correlation of the current density and the shear stress.

Method of Calculation

Equations [24] to [26] form a set of coupled, nonlinear differential equations with boundary conditions at zero and infinity. These equations can be linearized about a trial solution producing a series of coupled, linear differential equations. In finite difference form, these give coupled, tridiagonal matrices which can be solved readily on a high-speed digital computer (32). The nonlinear problem is then solved by iteration. For the principal results, 150 mesh points were used. A mesh width on the ξ scale of 0.0611 was used for the $CuSO_4$-H_2SO_4 system and a mesh width of 0.08 was used in the ferricyanide-ferrocyanide systems.

Ionic diffusion coefficients are calculated from limiting ionic mobilities at infinite dilution (33, 34). The densification coefficients for the various systems are given in Table II. The basis for these values can be found in Ref. (35). The $CuSO_4$-H_2SO_4 system will be considered both with complete and with no dissociation of bisulfate ions. For the ferrocyanide-ferricyanide redox system, the OH^- ions or the Na^+ ions may be absent in certain cases treated here.

As a preliminary check on the accuracy of the numerical method, calculations were carried out for a binary fluid at Sc = 1, 10, 100, 1000, and ∞ and for metal deposition from a binary electrolytic solution in the limit of large Schmidt number. Comparison of these results with those in Table I leads to the conclusion that our method is generally accurate to four significant figures. For metal deposition from a binary electrolytic solution, one can show that

Table II. Values of the densification coefficients (35) used in the calculations

Species	α_i (liters/mole)
H^+	0.02989
$SO_4^=$	0
Cu^{++}	0.13974
H^+	0.059789
HSO_4^-	0
Cu^{++}	0.19955
OH^-	0.04529
Na^+	−0.00673
$Fe(CN)_6^{4-}$	0.22591
K^+	0
$Fe(CN)_6^{3-}$	0.16727

$$C = \frac{(D_s/D_R)^{3/4}}{1 - t_R}C_b(Sc_s) \qquad [33]$$

and

$$B = (D_s/D_R)^{1/4}B_b(Sc_s) \qquad [34]$$

where Sc_s is based on the diffusion coefficient of the salt

$$D_s = \frac{D_+D_-(z_+ - z_-)}{z_+D_+ - z_-D_-} \qquad [35]$$

and t_R is the transference number of the reacting cation.

Results

$CuSO_4$-H_2SO_4.—The effect of the supporting electrolyte, sulfuric acid, can be expressed in the ratios C/C_b and B/B_b, permitting a comparison with the behavior of a binary fluid. These ratios depend on the relative amount of sulfuric acid, expressed as

$$r = \frac{c^\infty_{H_2SO_4}}{c^\infty_{H_2SO_4} + c^\infty_{CuSO_4}} \qquad [36]$$

One is also interested in the concentration of supporting electrolyte at the electrode, in particular in order to calculate $\Delta\rho$, entering into the Grashof number. This is expressed on the graphs as

$$\frac{\Delta c_{H_2SO_4}}{c_{CuSO_4}} = \frac{c^0_{H_2SO_4} - c^\infty_{H_2SO_4}}{c^\infty_{CuSO_4}} \qquad [37]$$

In view of the low value of the dissociation constant of bisulfate ions, the calculations were carried out for no dissociation of bisulfate ions as well as for complete dissociation to sulfate and hydrogen ions. To obtain an idea of the behavior when partial dissociation is considered, one should consult Ref. (21).

Results are shown in Fig. 1 for B/B_b for complete dissociation of bisulfate ions and the ratio C/C_b for both no dissociation and complete dissociation of bisulfate ions. Dashed lines show the corresponding values of I_L/I_D for a rotating disk (21).

As r approaches unity, one would expect C/C_b and B/B_b to approach unity if the appearance of $\Delta\rho$ in the Grashof number were sufficient to correlate the effect of the supporting electrolyte. The contrary behavior emphasizes the fact that these ratios express not only the effect of ionic migration but also the effect of the density profile not being similar to that for a binary fluid. Where Wilke, Eisenberg, and Tobias's correlation (24) works with $C = C_b$, this may indicate that the errors in assuming $C = C_b$ and in estimating the diffusion coefficients compensate for the error in their method of estimating $\Delta\rho$.

To be specific, the diffusion layer thickness is greater for H_2SO_4 than for $CuSO_4$ on account of the larger value of the diffusion coefficient of hydrogen ions. Thus, the density difference in the outer part of the

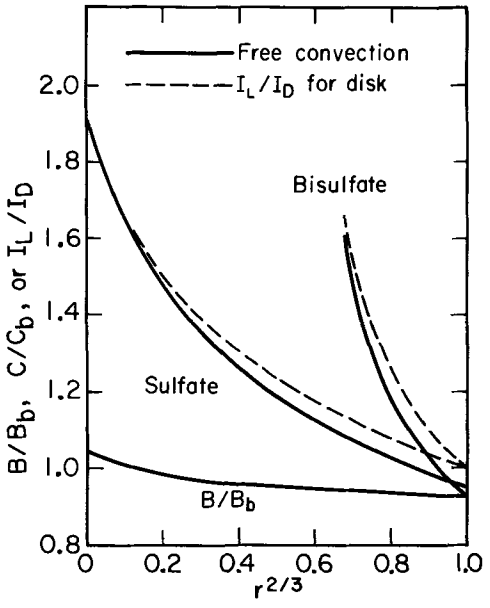

Fig. 1. Coefficients for shear stress (complete dissociation only) and mass transfer in the $CuSO_4$-H_2SO_4 system. Dashed curves show for comparison the values of I_L/I_D for the rotating disk.

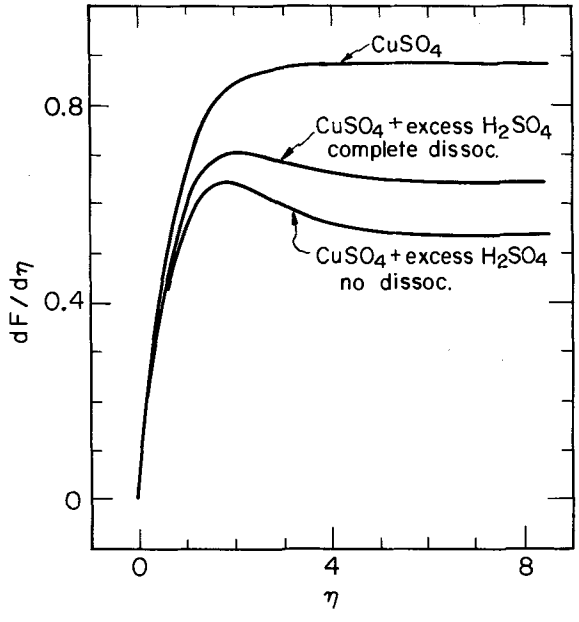

Fig. 2. Velocity profiles for binary salt solution ($CuSO_4$) and for $CuSO_4$ with excess H_2SO_4 ($r = 0.99998$) completely dissociated and undissociated.

diffusion layer is positive while it is negative near the electrode. Consequently, the value of $\Delta\rho$ does not, by itself, give sufficient information about the density profile. In fact, with added H_2SO_4, the velocity profile shows a maximum within the diffusion layer. This is shown for excess sulfuric acid in Fig. 2. The profile for a binary fluid is labeled $CuSO_4$.[1] Since these phenomena occur in a more drastic fashion in the redox systems, we shall postpone their further discussion.

The ratio B/B_b varies little since it does not involve the dominant effect of ionic migration found in the limiting currents expressed in C/C_b. Values of B/B_b for the bisulfate system are in the same range as those for complete dissociation. They extrapolate to 0.8342 at $r = 1$.

The refractive index profile is shown in Fig. 3 for complete dissociation of bisulfate ions. A slight maxi-

[1] Actually, the profile for a binary fluid would involve D_s instead of D_R in the definitions [29] and [30] of η and F.

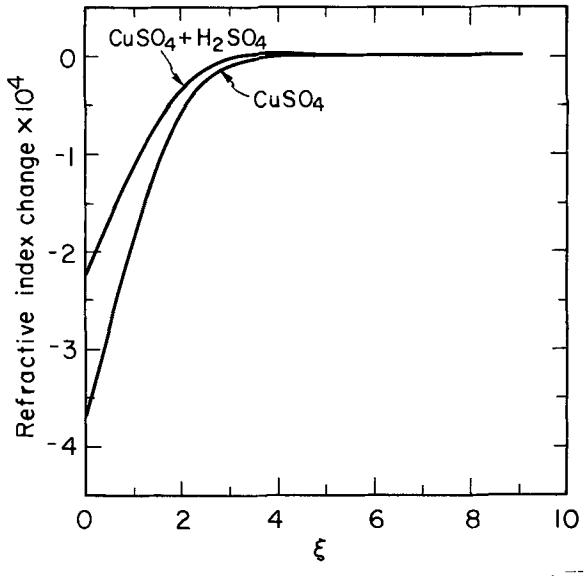

Fig. 3. Refractive index (relative to bulk) in $CuSO_4$-H_2O (0.02M bulk, 0.01M cathode) and in $CuSO_4$-H_2SO_4-H_2O (excess H_2SO_4, 0.01M $CuSO_4$ bulk).

mum occurs when sulfuric acid is present, due again to the larger diffusion-layer thickness of sulfuric acid. These can be compared with Fig. 7-12 and 7-14 in Hsueh's dissertation (36). The basis for the refractive index calculation can be found in Ref. (35).

After the actual velocity profiles have been calculated, one could separate the effect of ionic migration on C/C_b from that due to the dissimilar density profiles. Thus

$$\frac{I_L}{I_D} = (3/4)^{3/4}\, C \int_0^\infty \exp\left\{ -\int_0^\eta F d\eta \right\} d\eta \quad [38]$$

Here, the "diffusion current" I_D corresponds to the mass transfer by diffusion and convection with the actual velocity profile. Then I_L/I_D approaches unity at $r = 1$. For $r = 0$, I_L/I_D does not coincide with the value of C/C_b given by Eq. [33] unless $D_s = D_R$. However, this separation has little practical utility since the two effects cannot be separated experimentally. For a system where the diffusion coefficients of the solutes are roughly the same, one could estimate the value of I_L/I_D from calculations for other hydrodynamic situations (13) and then assume that this is equal to the value of C/C_b for free convection with little error. But if detailed calculations for free convection are carried out, one might as well report values of C/C_b, which account for both effects.

The wide range of predictions for the H_2SO_4 concentration at the electrode for the sulfate and bisulfate models and for various hydrodynamic situations is shown in Fig. 4. Also shown are some values obtained by the method of Wilke, Eisenberg, and Tobias (24). Ravoo's predictions (28) are based on the bisulfate model for a stagnant Nernst diffusion layer of finite thickness. The value 0.71 is deduced from the results of one of Brenner's experiments (29). Hsueh and Newman (21) obtained four values in the range from 0.50 to 0.57 and one value of 0.75.

$K_3Fe(CN)_6$-$K_4Fe(CN)_6$.—The redox reaction

$$Fe(CN)_6^{3-} + e^- \rightleftarrows Fe(CN)_6^{4-} \quad [39]$$

is popular in mass-transfer studies and has been used in free convection, although it is not common. The densification in this system is much weaker than in copper sulfate solutions since the excess of product ion largely compensates for the deficit of the reactant.

Results for the unsupported ferricyanide-ferrocyanide system are shown in Fig. 5. Values of I_L/I_D calculated for the rotating disk (13) are also shown. The

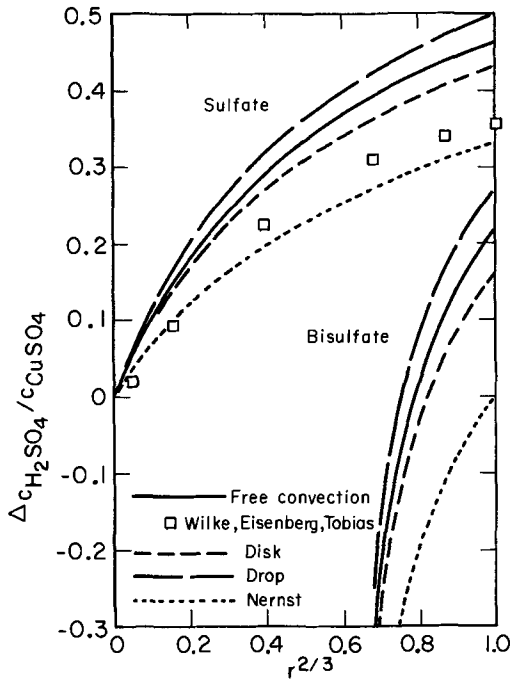

Fig. 4. Excess sulfuric acid at the electrode divided by the bulk copper concentration.

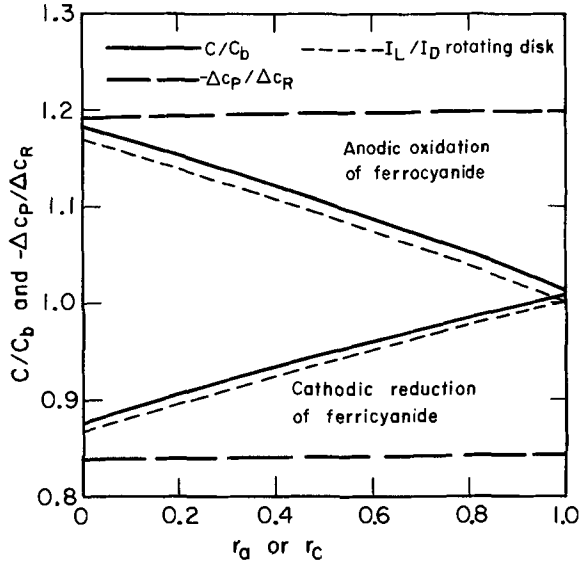

Fig. 5. Product ion concentration at the electrode and the coefficient for the limiting current in the unsupported ferricyanide-ferrocyanide system.

abscissa is the concentration ratio r_a for the anodic reaction and r_c for the cathodic reaction

$$r_c = 1 - r_a = \frac{c^{\infty}_{ferro}}{c^{\infty}_{ferro} + c^{\infty}_{ferri}} \qquad [40]$$

The product concentration at the electrode minus that in the bulk, divided by the bulk reactant concentration, is denoted $-\Delta c_P/\Delta c_R$. The effect of ionic migration on limiting currents is relatively small in this system, as observed earlier (13), since the product ion will always prevent the electric field from becoming infinite at the electrode.

By varying the densification coefficients and diffusion coefficients of the ions, we can study the importance of these factors. The relative unimportance of free convection interacting with migration is evidenced by the fact that it makes little difference for C/C_b or the product concentrations if we assign equal densification coefficients to the reacting and product ions, although the sign of the density difference $\rho_0 - \rho_\infty$ reverses and consequently the flow reverses from upward to downward, or *vice versa*. This emphasizes the fact that the density differences driving the convection in this system are very small. The consequences of this are seen below when we consider the effect of adding KOH or NaOH as a supporting electrolyte.

Supported ferricyanide-ferrocyanide.—We consider next solutions of $K_3Fe(CN)_6$ and $K_4Fe(CN)_6$ with KOH or NaOH added as a supporting electrolyte. The latter, although leading to a five-ion system with consequent complications in physical-property estimation, has been used as frequently as the former in reported investigations (37, 38).

In the results, the concentration of supporting electrolyte is expressed in the ratio

$$r = \frac{c^{\infty}_{OH^-}}{c^{\infty}_{K^+} + c^{\infty}_{Na^+}} \qquad [41]$$

Figures 6-8 give the results for these systems for equal bulk concentrations of ferricyanide and ferrocyanide ($r_a = r_c = 0.5$). Additional results for $r = 0.5$ and various values of r_a or r_c are given in Table III. In Fig. 6, values of I_L/I_D for the rotating disk with KOH supporting electrolyte (13) are plotted for comparison.

Figure 6 shows a conspicuous deviation of the values of C/C_b from the values of I_L/I_D for the rotating disk, and Fig. 7 shows a much greater variation of B/B_b than was observed for the $CuSO_4$-H_2SO_4 system. In contrast, the concentration ratios shown in Fig. 8 are essentially independent of the hydrodynamic situation, almost coinciding with results for the rotating disk (which are not shown).

Figures 6 and 7 reflect the strong dissimilarity of the density profile in the supported solutions compared to that in a binary solution. A dramatic consequence of this is shown in the velocity profiles in Fig. 9. There is a velocity maximum which becomes more pronounced as KOH is added, and the magnitude of the velocities becomes smaller. The profile for $r = 0.95$ yields a converged but physically unreasonable solution, since the velocity far from the electrode has reversed sign. Reasonable solutions were not obtained in the cathodic

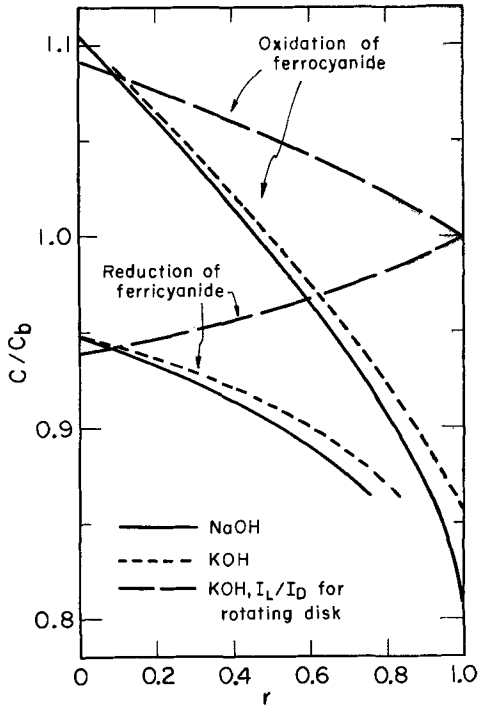

Fig. 6. Coefficient for mass-transfer rate in the supported ferricyanide-ferrocyanide systems, for equal bulk concentrations of $K_3Fe(CN)_6$ and $K_4Fe(CN)_6$.

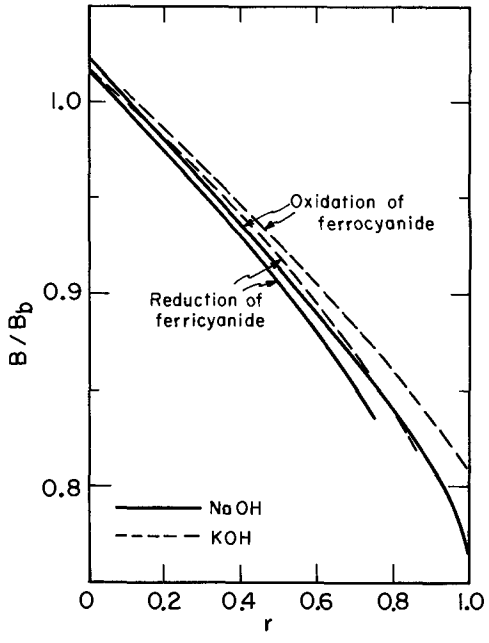

Fig. 7. Coefficient for the shear stress in the supported ferricyanide-ferrocyanide systems, for equal bulk concentrations of $K_3Fe(CN)_6$ and $K_4Fe(CN)_6$.

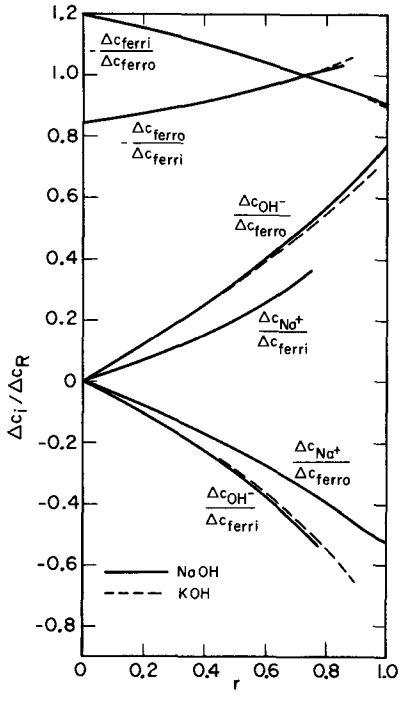

Fig. 8. Surface concentrations in the supported ferricyanide-ferrocyanide systems, for equal bulk concentrations of $K_3Fe(CN)_6$ and $K_4Fe(CN)_6$.

case for r greater than 0.85 for KOH, and 0.75 for NaOH, supporting electrolyte. The situation is different only in degree from the one encountered in the case of supported $CuSO_4$. Normalized density profiles for the two cases are compared in Fig. 10. The ferricyanide-ferrocyanide system has a weaker densification than $CuSO_4$, and consequently the addition of supporting electrolyte can have relatively a much greater effect on the density profile, as we see in Fig. 10. The velocity far from the electrode (at the outer limit of the diffusion layer) can be expressed as

$$f'(\infty) = -\int_0^\infty \frac{\rho - \rho_\infty}{\rho_\infty \alpha_R C_{R^\infty}} \xi d\xi \qquad [42]$$

Consequently, in order for there to be a flow reversal,

Table III. Results for the supported ferricyanide-ferrocyanide systems with $r = 0.5$

			Cathodic reduction of ferricyanide		
			$\frac{\Delta c_{ferro}}{\Delta c_{ferri}}$	$\frac{\Delta c_{OH^-}}{\Delta c_{ferri}}$	$\frac{\Delta c_{Na^+}}{\Delta c_{ferri}}$
r_c	C/C_b	B/B_b			
		KOH supporting electrolyte			
0.1	0.8809	0.9236	0.9278	−0.2731	—
0.25	0.8931	0.9218	0.9306	−0.2792	—
0.5	0.9117	0.9189	0.9352	−0.2890	—
0.75	0.9286	0.9165	0.9394	−0.2981	—
0.9	0.9386	0.9159	0.9419	−0.3032	—
		NaOH supporting electrolyte			
0.0003	0.8629	0.9123	0.9235	−0.2756	0.1971
0.1	0.8717	0.9111	0.9255	−0.2799	0.1990
0.25	0.8841	0.9092	0.9284	−0.2861	0.2017
0.5	0.9029	0.9063	0.9330	−0.2961	0.2059
0.75	0.9199	0.9036	0.9372	−0.3054	0.2097
0.9	0.9293	0.9021	0.9397	−0.3107	0.2119
0.9996	0.9353	0.9011	0.9412	−0.3142	0.2133
			Anodic oxidation of ferrocyanide		
			$\frac{\Delta c_{ferri}}{\Delta c_{ferro}}$	$\frac{\Delta c_{OH^-}}{\Delta c_{ferro}}$	$\frac{\Delta c_{Na^+}}{\Delta c_{ferro}}$
r_a	C/C_b	B/B_b			
		KOH supporting electrolyte			
0.0004	1.0361	0.9236	1.0583	0.3353	—
0.1	1.0294	0.9241	1.0601	0.3321	—
0.25	1.0188	0.9250	1.0630	0.3271	—
0.5	0.9995	0.9265	1.0682	0.3184	—
0.75	0.9779	0.9280	1.0737	0.3090	—
0.9	0.9638	0.9289	1.0773	0.3030	—
0.9997	0.9538	0.9296	1.0797	0.2988	—
		NaOH supporting electrolyte			
0.0004	1.0286	0.9102	1.0606	0.3433	−0.2260
0.1	1.0218	0.9108	1.0625	0.3400	−0.2248
0.25	1.0110	0.9117	1.0654	0.3350	−0.2230
0.5	0.9915	0.9133	1.0706	0.3260	−0.2197
0.75	0.9697	0.9149	1.0762	0.3164	−0.2160
0.90	0.9554	0.9160	1.0798	0.3103	−0.2137
0.9997	0.9453	0.9167	1.0822	0.3061	−0.2121

the first moment of the normalized density profile in Fig. 10 must be negative.

The boundary-layer model clearly breaks down when reversed flow occurs. But even before this happens, the velocity profile may have become unstable. It is known from the theory of hydrodynamic stability (39, 40) that boundary layers with an inflection point in the velocity profile are inherently less stable with respect to low perturbation frequencies. It follows that if transition to turbulence takes place in supported solutions, where the supporting ion has a larger diffusion coefficient, it may take place at lower Grashof numbers than for free convection in heat

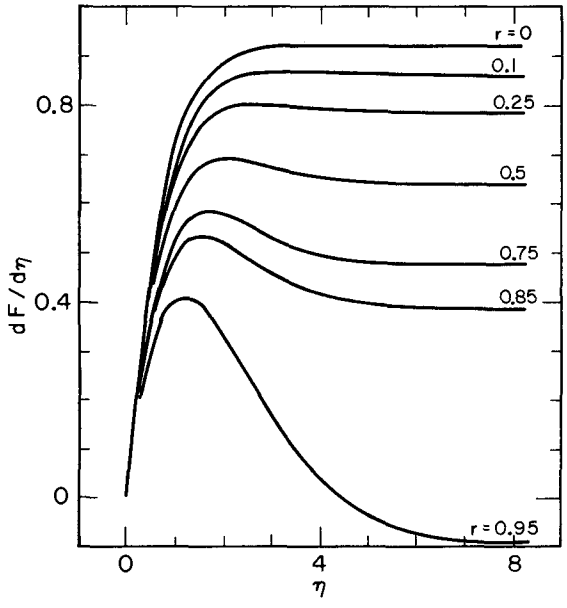

Fig. 9. Velocity profiles for various values of r for cathodic reduction of ferricyanide ions with KOH supporting electrolyte ($r_c = 0.5$).

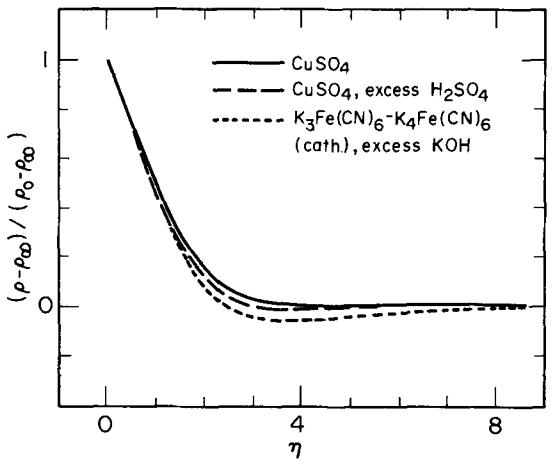

Fig. 10. Normalized density profiles for binary salt solution ($CuSO_4$), for $CuSO_4$ with excess H_2SO_4 ($r = 0.99998$), and for equimolar ferricyanide-ferrocyanide with excess KOH (cathodic reaction, $c_{OH^-}/c_{K^+} = 0.95$).

transfer or in binary solutions. This conclusion should be open to experimental verification.

Unfortunately, the experimental evidence on transition in free convection is rather confusing. Only in heat-transfer experiments with air (with a Prandtl number of 0.7) has the transition region been defined by measuring velocity and temperature fluctuations. In air, the lower limit of transition is, by agreement of several experiments (41, 42), $Gr > 2 \times 10^9$. An upper limit of transition is $Gr < 10^{10}$, above which fully turbulent heat transfer occurs.

In heat-transfer experiments (45) with water and with liquids of Prandtl numbers on the order of 100, the transition criterion was put at $Pr\ Gr = 4 \times 10^{10}$. Wilke, Tobias, and Eisenberg (46) report experiments on dissolution of organic acids in water, where laminar mass-transfer relations still hold at $Sc\ Gr = 2 \times 10^{10}$. Wagner (43), in salt dissolution experiments, observed that the flow was still laminar at $Sc\ Gr = 5 \times 10^{11}$.

Fouad and Ibl (38) place the transition in acidified $CuSO_4$ solutions, observed optically, between $2 \times 10^{11} < Sc\ Gr < 4 \times 10^{13}$. They suggest that there is a separate dependence on Sc. Wilke, Eisenberg, and Tobias (24) correlate laminar free convection in acidified $CuSO_4$ solutions up to $Sc\ Gr = 5 \times 10^{11}$. Fouad and Gouda (44) report transition in ferricyanide reduction with excess NaOH at $Sc\ Gr = 4.6 \times 10^{11}$.

One can hardly infer that destabilization had taken place in the supported solutions. However, in such solutions the density has to be estimated [usually by the method of Wilke, Eisenberg, and Tobias (24)], which can lead to appreciable errors.

Since the inertial terms in the equation of motion were neglected in this analysis, it follows that a theoretical treatment of instability in electrolytic free convection could also simplify the unsteady equation of motion, retaining only viscous and buoyancy terms. The result would be analogous in form to the so-called viscous solutions in forced flow instability (40), except for the unknown effect of coupling to the diffusion equation. No solutions are available for high-Pr free-convection instability. Gebhart (47) reports the absence in low-Pr free-convection instability of a critical layer, corresponding in forced flow to the velocity profile inflection, where the disturbance velocity equals the steady velocity. One might conclude, therefore, that the velocity profile inflection obtained in this work does not necessarily indicate instability.

At any rate, the appearance of velocity profiles which exhibit maxima within the diffusion layer can lead to values of C/C_b and B/B_b considerably different from unity so that Eq. [1] and [2] do not adequately represent the predictions of these calculations for solutions with a supporting electrolyte having a high diffusion coefficient. This is because the density difference $\Delta\rho$ does not, by itself, give sufficient information about the density profile.

Discussion and Conclusions

This investigation concerns the contribution which migration in the electric field makes to the limiting current density in free convection. The effect of migration itself (Eq. [38] is referred to here) is very similar to that calculated for other hydrodynamic situations. However, the effect of migration also leads to a nonuniform concentration of the supporting electrolyte and, here, in contrast to forced convection, this can change considerably the velocity profile and also affect the limiting current. Because this effect can be partly correlated by using the over-all density difference $\Delta\rho$ in the Grashof number, we have reported here the concentration of supporting electrolyte at the electrode.

The method of using the results of this paper to predict the limiting current density at a vertical electrode would be as follows. From the composition of the bulk solution, one estimates the composition near the electrode from Fig. 4, 5, or 8. The concentration of the limiting reactant is zero at the electrode, and the electroneutrality condition determines the concentration of the remaining ion. The density difference $\Delta\rho$ is then determined from the values of α_i in Table II, and this allows the Grashof number to be calculated from Eq. [3]. Equation [1], with C_b replaced by C, gives the Nusselt number, C being obtained from Fig. 1, 5, or 6. The limiting current density is then related to the Nusselt number by Eq. [32]. Similarly, the shear stress τ_0 at the wall can be calculated from Eq. [2], with B_b replaced by B, where B is obtained from Fig. 1 or 7.

Frequently used supporting electrolytes, acids, and bases, have higher diffusion coefficients than the reacting species. This means that the diffusion layer for the supporting electrolyte extends farther from the electrode than that for the reactants. This leads to a velocity maximum within the diffusion layer if the density difference due to the supporting electrolyte opposes that due to the reacting species, as was the case here.

The analysis applies to large Schmidt numbers. In this limit, the present results can be applied to other geometries by using the transformation of Acrivos. This means that C_b in Eq. [4] is replaced by C.

Acknowledgment

This work was supported by the United States Atomic Energy Commission.

Manuscript submitted Sept. 28, 1970; revised manuscript received Feb. 4, 1971.

Any discussion of this paper will appear in a Discussion Section to be published in the June 1972 JOURNAL.

SYMBOLS

B	Coefficient for shear stress
B_b	Coefficient for shear stress in a binary fluid
c_i	Concentration of species i (mole/cm^3)
C	Coefficient for mass transfer
C_b	Coefficient for mass transfer in a binary fluid
D_i	Diffusion coefficient of species i (cm^2/sec)
D_s	Diffusion coefficient for a binary electrolyte (cm^2/sec)
f	Dimensionless stream function
$\mathbf{F}$	Faraday's constant (96,487 C/equiv)
F	Dimensionless stream function
g	Magnitude of the gravitational acceleration (cm/sec^2)
Gr	Grashof number $= g\Delta\rho L^3/\rho_z\nu^2$
i_y	Normal component of the current density (A/cm^2)
I_D	Limiting diffusion current
I_L	Limiting current
L	Height of the vertical electrode (cm)
M_i	Symbol for the chemical formula of species i

n Number of electrons transferred in the electrode reaction
N_{iy} Normal component of the flux of species i
Nu Average Nusselt number $= s_R \mathrm{Li}_{avg}/n\mathbf{F}D_R (c_{R_\infty} - c_{Ro})$
r Ratio of supporting electrolyte to total electrolyte
r_a, r_c Ratios of ferricyanide and ferrocyanide concentrations
R Universal gas constant (joule/mole-°K)
s_i Stoichiometric coefficient of species i
Sc Schmidt number $= \nu/D_R$
t_i Transference number of species i
T Absolute temperature (°K)
u_i Mobility of species i (cm²-mole/joule-sec)
v_x Velocity component parallel to the electrode (cm/sec)
v_y Velocity component perpendicular to the electrode (cm/sec)
x Distance along the electrode measured from the beginning of the boundary layer (cm)
y Normal distance from the electrode (cm)
z_i Valence or charge number of species i
α_i Densification coefficient of species i (liters/mole)
ϵ Angle between the normal to the surface and the vertical
η Similarity variable representing dimensionless distance (see Eq. [29])
ξ Similarity variable representing dimensionless distance (see Eq. [20])
θ_i Dimensionless concentration
ν Kinematic viscosity (cm²/sec)
ρ Fluid density (g/cm³)
$\Delta\rho$ $|\rho_\infty - \rho_0|$
τ_0 Shear stress averaged over the electrode (dyne/cm²)
ϕ Dimensionless potential
Φ Electrostatic potential (volt)
ψ Stream function (cm²/sec)

Subscripts and superscripts

o At the electrode surface
∞ In the bulk solution
R Limiting reactant

REFERENCES

1. S. Ostrach, "An Analysis of Laminar Free-Convection Flow and Heat Transfer about a Flat Plate Parallel to the Direction of the Generating Body Force," Report 1111, *Thirty-Ninth Annual Report of National Advisory Committee for Aeronautics, 1953, Including Tech. Reports No. 1111 to 1157,* United States Government Printing Office, Washington (1955).
2. H. Schlichting, "Boundary-Layer Theory," 6th Ed., pp. 300-305, McGraw-Hill Book Co., New York (1968).
3. E. M. Sparrow and J. L. Gregg, "Details of exact low Prandtl number boundary layer solutions for forced and for free convection," NASA Memo 2-27-59E (1959). [*Via* Ref. (2).]
4. G. W. Morgan and W. H. Warner, *J. Aeron. Sci.*, **23**, 937 (1956).
5. E. J. Le Fevre, *Actes, IX Congrès International de Mécanique Appliquée, Brussels*, **4**, 168 (1957).
6. H. K. Kuiken, *J. Eng. Math.*, **2**, 355 (1968).
7. S. Roy, *Intern. J. Heat Mass Transfer*, **12**, 239 (1969).
8. A. Acrivos, *AIChE J.*, **6**, 584 (1960).
9. H. K. Kuiken, "Perturbation Techniques in Free Convection," Dissertation, Delft (1967).
10. J. Newman, *Advan. Electrochemistry and Electrochemical Eng.*, **5**, 87 (1967).
11. A. Eucken, *Z. Physik. Chem.*, **59**, 72 (1907).
12. D. Ilkovič, *Collection Czech. Chem. Commun.*, **6**, 498 (1934).
13. J. Newman, *Ind. Eng. Chem. Fundamentals*, **5**, 525 (1966).
14. S. Okada, S. Yoshizawa, F. Hine, and K. Asada, *J. Electrochem. Soc. Japan (Overseas Ed.)*, **27**, E51-E52 (1959).
15. J. Newman, *Intern. J. Heat Mass Transfer*, **10**, 983 (1967).
16. J. Newman and L. Hsueh, *Ind. Eng. Chem. Fundamentals*, **9**, 677-679 (1970).
17. S. L. Gordon, J. S. Newman, and C. W. Tobias, *Ber. Bunsenges. Physik. Chem.*, **70**, 414 (1966).
18. V. V. Malev and Ya. V. Durdin, *Elektrokhimiya*, **2**, 1354 (1966). [*Soviet Electrochem.*, **2**, 1240 (1966).]
19. V. V. Malev and R. V. Balukov, *Elektrokhimiya*, **4**, 348 (1968). [*Soviet Electrochem.*, **4**, 312 (1968).]
20. V. V. Malev, *Elektrokhimiya*, **4**, 1094 (1968). [*Soviet Electrochem.*, **4**, 986 (1968).]
21. L. Hsueh and J. Newman, "The Role of Bisulfate Ions in Ionic Migration Effects," *Ind. Eng. Chem. Fundamentals*, to be published.
22. N. Ibl, *Electrochim. Acta*, **1**, 117 (1959).
23. J. Newman, *Ind. Eng. Chem.*, **60**, No. 4, 12 (1968).
24. C. R. Wilke, M. Eisenberg, and C. W. Tobias, *This Journal*, **100**, 513 (1953).
25. C. Wagner, *J. (and Trans.) Electrochem. Soc.*, **95**, 161 (1949).
26. N. Ibl and U. Braun, *Chimia*, **21**, 395 (1967).
27. K. Asada, F. Hine, S. Yoshizawa, and S. Okada, *This Journal*, **107**, 242 (1960).
28. E. Ravoo, "Extended Abstracts," pp. 54-58, 20th Meeting, Comité International de Thermodynamique et de Cinétique Electrochimique, Strasbourg, France, Sept. 1969.
29. A. Brenner, *Proc. Am. Electroplaters' Soc.*, **27**, 95 (1940).
30. N. Ibl and R. H. Müller, *This Journal*, **105**, 346 (1958).
31. G. Schütz, *"Intern. J. Heat Mass Transfer*, **6**, 873 (1963).
32. J. Newman, *Ind. Eng. Chem. Fundamentals*, **7**, 514 (1968).
33. B. E. Conway, "Electrochemical Data," Elsevier Publishing Co., Amsterdam (1952).
34. B. B. Owen and R. W. Gurry, *J. Am. Chem. Soc.*, **60**, 3074 (1938).
35. J. R. Selman and J. Newman, "Migration in Supported Electrolyte Solutions with Free Convection," UCRL-20322, Jan. 1971.
36. L. Hsueh, "Diffusion and Migration in Electrochemical Systems," Dissertation, Univ. of California, Berkeley, Dec. 1968 (UCRL-18597).
37. A. J.-L. P. M. Boeffard, "Ionic Mass Transport by Free Convection in a Redox System," M.S Thesis, Univ. of California, Berkeley, Jan. 1966 (UCRL-16624).
38. M. G. Fouad and N. Ibl, *Electrochim. Acta*, **3**, 233 (1960).
39. L. D. Landau and E. M. Lifschitz, "Fluid Mechanics," Chap. IV, Boundary Layers, Pergamon Press, London (1959).
40. Ref. (2), pp. 438-446.
41. R. Cheesewright, *J. Heat Transfer*, **90**, 1 (1968).
42. A. A. Szewczyk, *Intern. J. Heat Mass Transfer*, **5**, 903 (1962).
43. C. Wagner, *J. Phys. Colloid Chem.*, **53**, 1030 (1949).
44. M. G. Fouad and T. Gouda, *Electrochim. Acta*, **9**, 1071 (1964).
45. Y. S. Touloukian, G. A. Hawkins, and M. Jakob, *Trans. Am. Soc. Mechan. Engrs.*, **70**, 13 (1948).
46. C. R. Wilke, C. W. Tobias, and M. Eisenberg, *Chem. Eng. Progr.*, **49**, 663 (1953).
47. B. Gebhart, *J. Heat Transfer*, **91**, 1 (1969).

Limiting Current on a Rotating Disk with Radial Diffusion

William H. Smyrl*

Boeing Scientific Research Laboratories, Seattle, Washington 98124

and John Newman*

Inorganic Materials Research Division, Lawrence Radiation Laboratory, and Department of Chemical Engineering, University of California, Berkeley, California 94720

ABSTRACT

The edge effect on limiting currents due to radial diffusion is calculated by a singular-perturbation technique for large Schmidt numbers, and a correction to the Levich formula is thereby obtained.

Radial diffusion, which is usually ignored, is included here in an analysis of the limiting current distribution on a rotating disk electrode. This small edge effect has created a controversy over whether or not it can cancel the correction for a finite Schmidt number. The results of this analysis are also applicable to the trailing edge of other electrodes.

Steady transfer of a solute species obeys the equation of convective diffusion

$$\underline{v} \cdot \nabla c_i = D_i \nabla^2 c_i \qquad [1]$$

if, for one reason or another, electric migration of this species can be ignored. This condition applies to a neutral solute and to a minor ionic solute in a solution with an excess of inert, supporting electrolyte. The equation also applies to a solution of a single electrolyte where the migration terms can be eliminated by means of the electroneutrality condition (1-3). In this case, D_i is replaced by the diffusion coefficient of the electrolyte.

The appropriate form of this equation for the diffusion layer on a rotating disk, including radial diffusion, is

$$Ay\left(r\frac{\partial c_i}{\partial r} - y\frac{\partial c_i}{\partial y}\right) = D_i\left[\frac{\partial^2 c_i}{\partial y^2} + \frac{1}{r}\frac{\partial}{\partial r}\left(r\frac{\partial c_i}{\partial r}\right)\right] \qquad [2]$$

where $A = a\Omega\sqrt{\Omega/\nu}$. For large values of the Schmidt number $Sc = \nu/D_i$, as encountered in electrolytic solutions, the diffusion layer is much thinner than the hydrodynamic boundary layer, and it is appropriate to approximate the normal and radial components v_y and v_r of the velocity by the first terms of their power-series expansions in the normal distance y from the disk. This introduces the rotation speed Ω, the kinematic viscosity ν, and the dimensionless constant a from the solution of the hydrodynamic problem (4-6) where it is assumed that the mass-transfer process does not influence the hydrodynamics.

The radial diffusion term is usually neglected on the basis of the thinness of the diffusion layer compared with the radius of the electrode. At the limiting current, this "diffusion-layer solution" is

$$c_i = \frac{c_\infty}{\Gamma(4/3)}\int_0^\zeta e^{-x^3}dx \qquad [3]$$

where

$$\zeta = y(a\nu/3D_i)^{1/3}(\Omega/\nu)^{1/2} \qquad [4]$$

and gives a uniform current density on the disk electrode.

We wish to consider the effect of radial diffusion on the limiting current density distribution at the downstream end of a diffusion layer, still at high Schmidt numbers. The rotating disk electrode is assumed to be embedded in an insulating plane. The region where radial diffusion is important is very small, and the problem can be treated by a singular-perturbation method similar to that used to treat the breakdown of the diffusion-layer method at the rear of a bluff body (7, 8) and at the upstream end of an electrode embedded in an insulator (9).

In the region of radial diffusion near the edge of the disk, use stretched coordinates

$$X = (r - r_0)(Ar_0/2D_i)^{1/2} \text{ and } Y = y(Ar_0/2D_i)^{1/2} \qquad [5]$$

so that Eq. [2] becomes

$$\frac{2r}{r_0}Y\frac{\partial c_i}{\partial X} - 2Y^2\left(\frac{2D_i}{Ar_0^3}\right)^{1/2}\frac{\partial c_i}{\partial Y} = \frac{\partial^2 c_i}{\partial X^2} + \frac{\partial^2 c_i}{\partial Y^2} + \frac{r_0}{r}\left(\frac{2D_i}{Ar_0^3}\right)^{1/2}\frac{\partial c_i}{\partial X} \qquad [6]$$

Neglecting terms of order $(2D_i/Ar_0^3)^{1/2}$, we obtain

$$2Y\frac{\partial c_i}{\partial X} = \frac{\partial^2 c_i}{\partial X^2} + \frac{\partial^2 c_i}{\partial Y^2} \qquad [7]$$

Since $\zeta = Y(8D_i/9Ar_0^3)^{1/6}$, ζ is small in this region, and the concentration must match the diffusion-layer solution for small values of ζ. In other words, the region of radial diffusion is embedded in the diffusion layer and

$$c_i \to \frac{c_x\zeta}{\Gamma(4/3)} = \frac{c_\infty Y}{\Gamma(4/3)}\left(\frac{8D_i}{9Ar_0^3}\right)^{1/6} \quad \text{as } X \to -\infty \text{ or } Y \to \infty \qquad [8]$$

Consequently, let us define Θ as

$$\Theta = \Gamma(4/3)\frac{c_i}{c_\infty}\left(\frac{9Ar_0^3}{8D_i}\right)^{1/6} \qquad [9]$$

Then, Θ satisfies the differential equation

$$2Y\frac{\partial\Theta}{\partial X} = \frac{\partial^2\Theta}{\partial X^2} + \frac{\partial^2\Theta}{\partial Y^2} \qquad [10]$$

and the boundary conditions

1. $\Theta \to Y$ as $Y \to \infty$
2. $\Theta \to Y$ as $X \to -\infty$
3. $\Theta = 0$ at $Y = 0, X < 0$
4. $\partial\Theta/\partial Y = 0$ at $Y = 0, X > 0$
5. $\partial^2\Theta/\partial X^2$ becomes negligible as $X \to \infty$

[11]

The coordinate stretching makes the radial and normal diffusion terms appear to be of the same magnitude in Eq. [10]. At the same time, the normal convection term disappears, and the radial convection term assumes a simpler form. From the form of the problem for Θ one perceives that by appropriate stretching of distances and concentration the problem

* Electrochemical Society Active Member.
Key words: current distribution.

for the effect of streamwise diffusion at high Schmidt numbers at the downstream end of any diffusion layer, where the electrode is embedded in an insulating surface, can be reduced to the same problem, and the results obtained here will also apply to those cases.

The ratio of the size of the region where radial diffusion is important to the thickness of the diffusion layer is $(8D_i/9Ar_0^3)^{1/6}$ or of the order of the square root of the ratio of the diffusion layer thickness to the electrode radius. Thus, the size of the region where radial diffusion is important is much smaller than the diffusion-layer thickness, whereas one might at first have assumed them to be of the same order. For a rotation speed of 300 rpm (Ω = 31.416 radian/sec), r_0 = 0.25 cm, ν = 0.01 cm^2/sec, and $D_i = 10^{-5}$ cm^2/sec, the value of this ratio is $(8D_i/9Ar_0^3)^{1/6} = 0.093$.

The fifth boundary condition means that radial diffusion again becomes negligible far downstream in the diffusion layer on the insulator. This condition can be stated more explicitly by obtaining the asymptotic solution for large X. Seek a similarity solution of Eq. [10] with the term $\partial^2\Theta/\partial X^2$ neglected and subject to the boundary conditions 1 and 4.

$$\Theta \to (9X/2)^{1/3} f(\xi) \text{ as } X \to \infty \qquad [12]$$

where

$$\xi = Y(2/9X)^{1/3} \qquad [13]$$

The function f is found to satisfy the ordinary differential equation

$$f''' + 3\xi^2 f' - 3\xi f = 0 \qquad [14]$$

with the boundary conditions

$$f' = 0 \text{ at } \xi = 0,\ f \to \xi \text{ as } \xi \to \infty \qquad [15]$$

and the solution

$$f = \xi + \frac{e^{-\xi^3}}{\Gamma(2/3)} - \frac{3\xi}{\Gamma(2/3)}\int_\xi^\infty x e^{-x^3}\,dx \qquad [16]$$

To effect a numerical solution of the problem for θ, we used parabolic coordinates in order to avoid infinite derivatives at the origin. The mass-transfer rate near the edge of the disk is shown in Fig. 1. Here the normal derivative of Θ is multiplied by $\sqrt{-X}$ in order to give an accurate representation of the results; the limiting current density becomes infinite near the edge of the disk as $\partial\Theta/\partial Y = 0.601/\sqrt{-X}$ at $Y = 0$. The recovery of the concentration on the insulating surface downstream is shown in Fig. 2; the diffusion-layer solution is given by

$$\Theta_0 = \Theta(X,0) = (9X/2)^{1/3} f(0) = (9X/2)^{1/3}/\Gamma(2/3) \qquad [17]$$

The recovery of the surface concentration is hindered by the back diffusion to the disk and is not so rapid

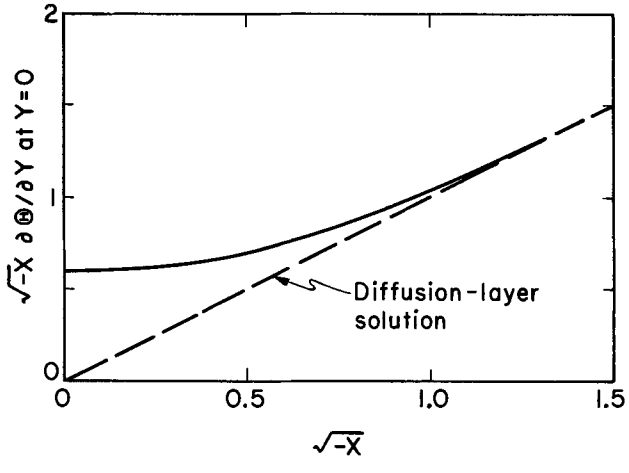

Fig. 1. Mass-transfer rate near the edge of the disk when radial diffusion is considered.

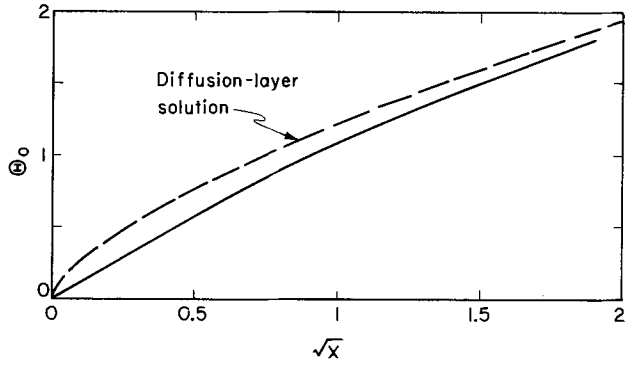

Fig. 2. Recovery of the surface concentration downstream of the disk.

as would be predicted by the diffusion-layer solution in the absence of radial diffusion. This back diffusion results in the infinite current density at the edge of the disk electrode. (This diffusion layer solution for the surface concentration beyond the disk electrode can also be obtained from Eq. [13] or [14] of Ref. (10) by letting r approach r_0.)

The mass-transfer rate shown in Fig. 1 approaches the diffusion-layer solution rather rapidly for large values of $\sqrt{-X}$ in contrast with the behavior depicted in Fig. 2 for the recovery of the surface concentration for large values of $\sqrt{X}$. The reason is that effects are propagated more easily downstream than upstream in a diffusion layer.

The correction to Levich's formula for the limiting current on a rotating disk electrode can now be obtained.

$$\frac{I_{\text{lim}}}{I_{\text{Levich}}} = \frac{1}{\pi r_0^2}\int_0^{r_0} \left.\frac{\partial\Theta}{\partial Y}\right|_{Y=0} 2\pi r\,dr$$
$$= 1 + B/Sc^{1/2}Re^{3/4} \qquad [18]$$

where $Re = r_0^2\,\Omega/\nu$ and

$$B = 4\sqrt{2/a}\int_0^\infty \sqrt{-X}\left[\left.\frac{\partial\Theta}{\partial Y}\right|_{Y=0} - 1\right] d\sqrt{-X} = 1.9193 \qquad [19]$$

The value of B is obtained from the results plotted in Fig. 1.

For the same values of the parameters as used in the last example, the correction to Levich's formula amounts to only 0.116%. For this system, the Schmidt number correction (11, 12) would be −3.1%, and the two effects cannot cancel. This comparison is of some interest since Levich (13) has discussed data which purport to support his formula rather than the Schmidt number correction. These data have since been repudiated (14).

Figure 3 indicates how a plot of limiting current *vs.* square root of rotation speed might be expected to look. Levich's solution plots as a straight line; Eq. [18] is represented by a solid curve. Levich's result is the asymptotic solution for large values of $ScRe^{3/2}$. Equation [18] gives the first correction, again valid for large values of $ScRe^{3/2}$. Additional correction terms would become necessary for smaller values of $ScRe^{3/2}$. The dotted curve represents a guess at the true solution; the intercept, $4/\pi$, is known for this curve but not its initial slope.

Conclusions

A singular-perturbation procedure allows treatment of the edge effect for the rotating disk for large values of $ScRe^{3/2}$. A large value of the Schmidt number was also assumed. The current density at the edge of the disk becomes infinite when radial diffusion is taken into account, and the recovery of the surface concentration is correspondingly less rapid than the diffusion-layer solution predicts. These results allow one to ob-

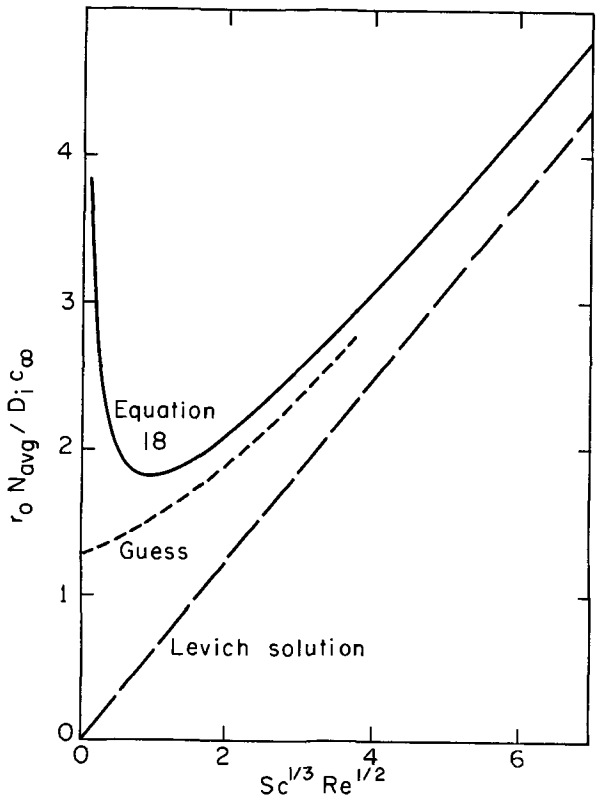

Fig. 3. Limiting current vs. the square root of rotation speed (in dimensionless form) in the absence of free convection.

tain a correction to the classical formula of Levich for the limiting current to a rotating disk electrode. The region near the edge of the disk where radial diffusion is important lies well within the diffusion layer for large values of $ScRe^{3/2}$.

Acknowledgment

This work was supported by the United States Atomic Energy Commission and by Boeing Scientific Research Laboratories.

Manuscript received Dec. 7, 1970.

Any discussion of this paper will appear in a Discussion Section to be published in the June 1972 JOURNAL.

SYMBOLS

a	0.51023
A	$a\Omega\sqrt{\Omega/\nu}$
B	See Eq. [19]
c_i	Concentration of the species of interest (mole/cm^3)
c_∞	Concentration of the species of interest outside the diffusion layer (mole/cm^3)
D_i	Diffusion coefficient of the species of interest (cm^2/sec)
f	See Eq. [12]
I	Total current to disk electrode (A)
N_{avg}	Average flux to disk electrode (mole/cm^2-sec)
r	Radial distance from the axis of the disk (cm)
r_o	Radius of disk electrode (cm)
Re	$r_o^2\Omega/\nu$, the Reynolds number
Sc	ν/D_i, the Schmidt number
v	Fluid velocity (cm/sec)
v_r, v_y	Radial and normal components of the velocity (cm/sec)
X	Dimensionless radial distance for the region of radial diffusion
y	Normal distance from the disk surface (cm)
Y	Dimensionless normal distance for the region of radial diffusion
Γ	Gamma function
ζ	Dimensionless normal distance for the diffusion layer
θ	Dimensionless concentration appropriate to the region of radial diffusion
ν	Kinematic viscosity (cm^2/sec)
ξ	$Y(2/9X)^{1/3}$
Ω	Rotation speed (radian/sec)

REFERENCES

1. W. Nernst, *Z. Physik. Chem.*, **2**, 613-637 (1888).
2. V. Levich, *Acta Physicochim. U.R.S.S.*, **17**, 257-307 (1942).
3. John Newman, *Advan. Electrochem. Electrochem. Eng.*, **5**, 87-135 (1967).
4. Th. v. Kármán, *Z. Angew. Math. Mechanik*, **1**, 233-252 (1921).
5. W. G. Cochran, *Proc. Cambridge Phil. Soc.*, **30**, 365-375 (1934).
6. E. M. Sparrow and J. L. Gregg, *J. Heat Transfer*, **81C**, 249-251 (1959).
7. P. H. Sih and John Newman, *Intern. J. Heat Mass Transfer*, **10**, 1749-1756 (1967).
8. John Newman, *Ind. Eng. Chem. Fundamentals*, **8**, 553-557 (1969).
9. John Newman, "The Graetz Problem," Lawrence Radiation Lab., Univ. of California, Berkeley, UCRL-18646, Jan. 1969.
10. W. H. Smyrl and John Newman, "Ring-Disk and Sectioned Disk Electrodes," UCRL-20379, Dec. 1970.
11. D. P. Gregory and A. C. Riddiford, *J. Chem. Soc.*, pp. 3756-3764 (1956).
12. John Newman, *J. Phys. Chemistry*, **70**, 1327-1328 (1966).
13. V. G. Levich, "Physicochemical Hydrodynamics," Sec. 11, Prentice-Hall, Inc., Englewood Cliffs, N. J. (1962).
14. V. G. Levich, Private communication. See also *Advan. Electrochem. Electrochem. Eng.*, **6**, 459 (1967).

Application of Isosurface Concentration Voltammetry at a Rotating Disk Electrode to Simple Electron Transfer Kinetics

Barry Miller,* Maria I. Bellavance, and Stanley Bruckenstein*,[1]

Bell Telephone Laboratories, Incorporated, Murray Hill, New Jersey 07974

ABSTRACT

Isosurface concentration voltammetry (ISCVA) at a rotating disk electrode has been applied to the measurement of kinetic and thermodynamic quantities of simple electron transfer steps. The technique involves scanning, or modulating, current through an electrode and measuring its potential while holding the surface concentrations of electroactive species constant. Experimentally, this is accomplished by keeping the ratio $i/\omega^{1/2}$ fixed. The theoretical basis of the procedure is outlined for the advantageous condition of a linearized rate equation. The general application of the controlled concentration polarization method to kinetic experiments is discussed.

The rate of the simple electron transfer

$$\mathrm{Ox} + ne = \mathrm{Red} \qquad [1]$$

may be written as

$$i = -i_o\,[\exp(-\alpha n\phi\eta) - \exp(1-\alpha)\,n\phi\eta] \qquad [2]$$

where[2]

$$i_o = n\mathbf{F}v \qquad [3]$$

and

$$v = k_o C_O^{1-\alpha} C_R^{\alpha} \qquad [4]$$

Anodic currents and overpotentials are treated as positive. In the case

$$\mathrm{M}^{+n} + ne = \mathrm{M} \qquad [5]$$

$$v = k_o C^{1-\alpha}{}_{\mathrm{M}^{+n}} \qquad [6]$$

The interpretation of current-potential data is frequently complicated by concentration overpotentials. The usual technique in this situation is to calculate the magnitude of this overpotential, or to obtain a function which may be extrapolated in an appropriate manner to eliminate it. The rotating disk electrode, because of its well-defined mass transfer conditions, has been used to treat the concentration overpotential problem, and several approaches are given elsewhere (2-6).

Another problem, always present when current flows, is the determination (or elimination during the experiment) of any ohmic contributions to the electrode potentials. Potentiostatic experiments are particularly sensitive to such problems and usually require real-time (*e.g.*, positive feedback) correction, in contrast to controlled-current techiques which can be corrected for ohmic effects after data acquisition.

If i-η data are interpreted under conditions such that the surface concentrations, C_O and C_R, or C_{M+n}, are constant and known, the evaluation of k_o and α from [2] and [4] is greatly simplified. As was pointed out earlier by us (7), mass transfer at the rotating disk electrode can be automatically controlled to achieve these surface concentration conditions.

While it is, in principle, possible to obtain the data corresponding to these conditions manually without automatic programming of angular velocity, the numerous practical problems encountered with the use of solid electrodes dictate that data be acquired as rapidly as possible. Our experience indicates that automatic control is far superior to other techniques.

* Electrochemical Society Active Member.

[1] Present address: Department of Chemistry, State University of New York at Buffalo, Buffalo, New York 14214.

Key words: rotating disk voltammetry, controlled concentration polarization, metal anodization.

[2] Symbols are tabulated at the end of this paper. Actually, this definition of i_o does not include the double-layer effect, activities, or stoichiometric numbers. These considerations may be incorporated in our expressions as summarized in Delahay's monograph (1).

It follows directly from the Levich equation

$$i = \pm\, 0.62\, n\mathbf{F}D^{2/3}\nu^{-1/6}\omega^{1/2}(C_j^b - C_j) \qquad [7]$$

that, in a given solution, a constant surface concentration, C, is produced for any value of $|i| \leq |i_L|$ by holding the ratio $i/\omega^{1/2}$ constant (+ sign in [7] when $j = R$, − sign when $j = O$). The latter condition is relatively easy to achieve and was used to evaluate the uncompensated ohmic potential drop in a situation where mass transfer, rather than electrode kinetics, determines the current-potential curve [method HP2 of (7)]. In this paper, we develop the theoretical basis for determining k^o, α, ohmic contributions, n, and the Nernst potential for systems described by [2], using i-E data obtained by scanning i at constant $i/\omega^{1/2}$. We now refer to the procedure of obtaining i-E curves while scanning i at constant $i/\omega^{1/2}$ as isosurface concentration voltammetry, ISCVA, since we feel this term is descriptive of the experiment.

Experimental verification of the theoretical results is given for Fe(III)/Fe(II) in 1.0M H_2SO_4 at platinum and in 0.1M HCl and 1.0M NaCl at gold. The extrapolation of the i-E curve to $i = 0$, for data obtained at constant $i/\omega^{1/2}$, yields the equilibrium potential for the system studied, free of kinetic and ohmic complications. Such data are presented for the anodic oxidation of Ag, Cu, and Hg, in addition to the Fe(III)/Fe(II) studies.

Theoretical

Separation of charge transfer overpotential from ohmic potential drops in the linear overpotential region.—As will soon become evident, the method described in this paper is particularly well suited to the study of fast electron transfer processes, *i.e.* to large values of k_o (and i_o). For the situation in which the convective-diffusion current density, i, of [2] and [7] is much smaller than i_o in [2], then

$$i = i_o\, n\phi\eta \qquad [8]$$

is a good approximation to [2] (1). In our experiment, the observed overpotential, η_{exp}, (and potential, E_{exp}) is given by

$$\eta_{exp} = \eta + iAR_u = E_{exp} - E_{eq} \qquad [9]$$

E_{eq} depends on the constant value of $i/\omega^{1/2}$ being used, and [10] gives E_{eq} for the Ox/Red system

$$E_{eq} = E_f + \frac{1}{n\phi}\ln\frac{C_O}{C_R} \qquad [10]$$

Combining [8] and [9] yields

$$E_{exp} = E_{eq} + \frac{i}{i_o n\phi} + iAR_u \qquad [11]$$

From [11], we see that the plot of E_{exp} *vs.* i gives a straight line that extrapolates to the equilibrium potential, E_{eq}. The charge transfer resistance, R_p, is defined as

$$R_p \equiv \left(\frac{\partial n}{\partial i} \right)_{i \to 0} = \frac{1}{n\phi i_o} \quad [12]$$

Hence, the slope of E_{exp} *vs.* i in [11], R_{exp}, is

$$R_{exp} = R_p + AR_u \quad [13]$$

When $R_p >> AR_u$, the experimental slope corresponds to the charge transfer resistance. If AR_u cannot be neglected, we substitute [3] and [12] into [13] to obtain

$$R_{exp} = \frac{1}{\phi n^2 \mathbf{F} v} + AR_u \quad [14]$$

We note that v is a function of k_o and surface concentrations (see [4] and [6]), so that plots of R_{exp} *vs.* the concentration-dependent part of v would yield straight lines of slope $(\phi n^2 \mathbf{F} k_o)^{-1} = 1/i_{o,s}$ and intercept AR_u. These surface concentration dependencies can be expressed explicitly in terms of the bulk concentrations, impressed current, limiting convective diffusion currents, and other parameters occurring in the Levich equation. These relations are given in Table I for a number of cases.

One simple situation, which we have experimentally investigated, occurs if only Ox is present in solution. From Table I, we write

$$v = \left[k_o \left(\frac{D_R}{D_O} \right)^{2\alpha/3} (1 - f)^{1-\alpha} f^{\alpha} \right] C_O{}^b = \frac{k_{app}}{2} C_O{}^b \quad [15]$$

where $f = i/i_c$. The factor ½ on the right side of [15] compensates for the value of $(1 - f)^{1-\alpha} f^{\alpha}$ being ½ at $i/i_c = ½$. Substituting [15] into [14] yields

$$R_{exp} = \frac{2}{\phi n^2 \mathbf{F} k_{app} C_O{}^b} + AR_u \quad [16]$$

k_{app} may be obtained from [16] by plotting R_{exp} *vs.* $(C_O{}^b)^{-1}$, while f is held constant throughout the experiment (constant f corresponds to constant $i/\omega^{1/2}$). One can then repeat the above experiment at different constant levels of f (or $i/\omega^{1/2}$) and obtain the corresponding values of k_{app}. The value of AR_u obtained in such a series of experiments will be constant, provided the Luggin capillary is reproducibly positioned with respect to the disk electrode and the solution resistance is determined solely by the supporting electrolyte.

Alternately, once AR_u has been determined for one f value, k_{app} may be directly calculated from [17]

$$k_{app} = \frac{2}{\phi n^2 \mathbf{F} C_O{}^b (R_{exp} - AR_u)} \quad [17]$$

using the experimental values of R_{exp} and $C_O{}^b$.

In the Ox/Red system, AR_u can be obtained from plots of [16] without *a priori* knowledge of α. In the M/M^{+n} system, linearization of the corresponding form of [17] requires curve-fitting to determine the value of the exponent, $(1 - \alpha)$, that appears in the current functions given in Table I.

Evaluation of k_o and α.—In the Ox/Red system when $C_R{}^b = 0$, k_o and α can be obtained from k_{app} and f by transforming equation [15] to [18]

$$\log \frac{k_{app}}{2f} = \log k_o \left(\frac{D_R}{D_O} \right)^{2\alpha/3} + (1 - \alpha) \log \left(\frac{1 - f}{f} \right) \quad [18]$$

and plotting $\log k_{app}/2f$ *vs.* $\log [(1 - f)/f]$. Provided α is not potential dependent, a straight line of slope $(1 - \alpha)$ will be obtained. At $f = ½$, $\log [(1 - f)/f] = 0$, and we obtain

$$k_o = \left(\frac{D_O}{D_R} \right)^{2\alpha/3} (k_{app})_{f=1/2} \quad [19]$$

As in all kinetic techniques involving concentration polarization, the evaluation of k_o requires the diffusion coefficients of Ox and Red. However, even for relatively large ratios of D_R/D_O, an accurately known α is not required to obtain a reliable value of k_o. For example, with $D_R/D_O = 1.25$, and $\alpha \sim 0.5$, choosing $\alpha = 0.4$ or 0.6 leads to a relative error in k_o of 1.5%, while twice as large an error in α is 3% in k_o. Hence, if only k_o is required, no serious error would be made where α is not ~0 or ~1 if k_{app} were determined at $f = ½$ and [19] were used assuming $\alpha = ½$.

Differentiating [18] with respect to f yields

$$\frac{d \ln k_{app}}{df} = \frac{\alpha}{f} - \left(\frac{1 - \alpha}{1 - f} \right) \quad [20]$$

From [20], we see that the maximum value of k_{app}, and thus i_o, occurs at $f = \alpha$. Hence, the maximum in the k_{app} *vs.* f plot might be used to determine α. Our experimental results indicate that determining the slope of [18] is preferable since i_o is relatively insensitive to f variation in the region of $f = \alpha$.

We do not explicitly state equations analogous to [15]-[20] for the other cases listed in Table I, since we do not make use of them in this paper.

Determination of E_{eq} and n.—Frequently, the thermodynamic, rather than the kinetic, parameters of a redox couple are of the most interest. In voltammetry, ohmic potential drops and η may interfere in obtaining E_{eq}. In such a case, in the linear overpotential region, E_{eq} at different points on the current potential curve can be obtained from the intercept of [11]. This extrapolation procedure will, in general, remove kinetic and uncompensated ohmic potential drop complications.

In the Ox/Red system whose kinetics were considered in detail above for $C_R{}^b = 0$, the reversible i-E curve is

$$E_{eq} = E_f + \frac{2}{3n\phi} \ln \frac{D_R}{D_O} + \frac{1}{n\phi} \ln \frac{i_c - i}{i} \quad [21]$$

Hence, using the values of E_{eq} (from extrapolation, as above) and the ordinary voltammetric plot of E_{eq} *vs.* $\ln [(i_c - i)/i]$, we obtain E_f and n. In essence, the extrapolation based on [11] allows the simple and rapid conversion of moderately irreversible, and/or IR-distorted current-potential curves to their reversible form.

The latter transformations should be valuable in a number of cases. These include measurements in nonaqueous media of moderate resistance, in Deford-Hume type (8) determinations of stability constants of slightly irreversible couples, and in situations where it

Table I. Surface concentration-current function

Reaction	Species present in bulk	Current function for v/k_o
$Ox + ne = Red$	Ox	$C_O{}^b \left(1 - \frac{i}{i_c}\right)^{1-\alpha} \left(\frac{i}{i_c}\right)^{\alpha} \left(\frac{D_R}{D_O}\right)^{\frac{2\alpha}{3}}$
	Red	$C_R{}^b \left(\frac{i}{i_a}\right)^{1-\alpha} \left(1 - \frac{i}{i_a}\right)^{\alpha} \left(\frac{D_O}{D_R}\right)^{\frac{2(1-\alpha)}{3}}$
	Ox and Red	$(C_R{}^b)^{\alpha} (C_O{}^b)^{1-\alpha} \left(1 - \frac{i}{i_c}\right)^{1-\alpha} \left(1 - \frac{i}{i_a}\right)^{\alpha}$
$M^{+n} + ne = M$	Nothing	$\left(\frac{i}{k_L \omega^{1/2}}\right)^{1-\alpha}$
	M^{+n}	$\left(C^b{}_{M^{+n}} + \frac{i}{k_L \omega^{1/2}}\right)^{1-\alpha}$

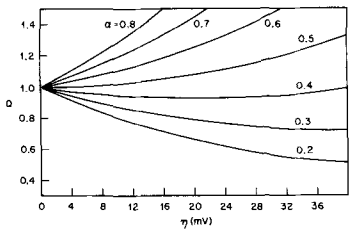

Fig. 1. Plot of $Q = \dfrac{\left(\dfrac{\partial i}{\partial \eta}\right)_{\eta}}{\left(\dfrac{\partial i}{\partial \eta}\right)_{\eta=0}}$ vs. η from Eq. [2]. Alpha values of 0.2-0.8 indicated on curves.

is convenient to electrogenerate a reactive or relatively unstable species, Ox or Red, and direct potentiometry is difficult.

Applicable range of linearized equations and their use outside these limits.—Considerable discussion of the range of validity of [8], the linearized form of the general rate equation [2] for charge transfer control, has appeared in the literature for particular experimental conditions. In Fig. 1 we have plotted

$$Q = \frac{\left(\dfrac{\partial i}{\partial \eta}\right)_{\eta}}{\left(\dfrac{\partial i}{\partial \eta}\right)_{\eta \to 0}}$$

vs. η according to [2] for α values of 0.2-0.8. The deviation of Q from unity is a measure of the departure of [8] from linearity at that particular value of η. In our method of recording E_{exp} *vs.* i at constant $i/\omega^{1/2}$, the slope of the $E_{exp} - i$ trace, R_{exp}, is the parameter of interest. The linearized form of the ISCVA method ultimately fails at large η. However, as is apparent from Fig. 1, the deviation of Q from the theoretical value becomes less the closer η approaches zero.

If an ISCVA plot shows curvature, the tangent to the *I-E* curve at the lowest value of i (and $\omega^{1/2}$) should be measured to minimize errors arising from linearization limitations. This tangent yields R_{exp}, and thus R_u and k_{exp} *via* [16], and thermodynamic quantities from the potential at which the tangent intersects $i = 0$.

Figure 1 may now be applied to obtain a practical limit for the ISCVA method by first choosing the maximum acceptable error, *i.e.* the Q value. We then determine the η level corresponding to this error (ignoring any further experimental error in drawing the tangent to the i-η curve) and express it in terms of the minimum value of k_o and other parameters occurring in the Levich equation.

For example, consider the case representing the experimental example reported in this paper, the reduction of Ox (Fe(III)) to Red (Fe(II)) at the disk. We eliminate i between [7] and [8] obtaining

$$-i_o \phi \eta = 0.62\, \mathbf{F}\, D_O^{2/3}\, \nu^{-1/6}\, \omega^{1/2}\, (C_O^b - C_O) \quad [22]$$

i_o is eliminated from [22] and k_o introduced by substituting [3], [4], and [15], yielding

$$k_o \geq \frac{0.62\, D_O^{2/3}\, \nu^{-1/6}\, \omega^{1/2}\, (C_O^b - C_O)}{2\phi |\eta_{max}| C_O^{1-\alpha}\, C_R^{\alpha}} \quad [23]$$

From [23], we see that the minimum value of k_o for which the linearization technique may be applied is determined by the value of η corresponding to the maximum acceptable error in the slope. The minimum k_o value depends on the surface and bulk concentrations, and [23] is conveniently written in terms of f. For simplicity, we assume that $D_O = D_R$; then

$$C_O = (1 - f)\, C_O^b \quad [24]$$

and

$$C_R = C_R^b + f\, C_O^b = (C_O^b - C_O) + C_R^b \quad [25]$$

The largest value of k_o (worst case) occurs if C_R^b in [25] is zero. Under these conditions, [23] becomes

$$k_o \geq \frac{0.62\, D_O^{2/3}\, \nu^{-1/6}}{2\, \phi |\eta_{max}|} \left(\frac{f}{1 - f}\right)^{1-\alpha} \quad [26]$$

At $f = 1/2$

$$k_o \geq \frac{0.62\, D_O^{2/3}\, \nu^{-1/6}\, \omega^{1/2}}{2\, \phi |\eta_{max}|} \quad [27]$$

Assuming $D_O = 8 \times 10^{-6}$ cm^2/sec, $\nu = 1/64$ cm^2/sec, and a conservative lower limit of rotation speed

$$\omega^{1/2} = 6.5 \left(\frac{\text{rad}}{\text{sec}}\right)^{1/2} \sim (400 \text{ rpm})^{1/2}$$

we obtain from [27]

$$k_o \geq \frac{41 \times 10^{-3}}{|\eta_{max}|} \text{ cm/sec} \quad [28]$$

For the solvent system we studied, Fe(III) in 1.0M H_2SO_4, $D = 4.5 \times 10^{-6}$ cm^2/sec, hence, instead of [28], $k_o \geq 31 \times 10^{-3}/|\eta_{max}|$ cm/sec. In this case, we found $k_o \sim 6 \times 10^{-3}$ cm/sec and $\alpha \sim 0.5$ using the theory based on linearization of the overpotential relation. Hence, our interpretation of the experimental data would be valid to within 1%, provided all slopes were obtained for ISCVA data at $\eta \leq 5$ mV. At 400 rpm, $\eta \cong 5$ mV when $f = 1/2$, and the use of slope data obtained under these conditions does not introduce any errors. Even at the maximum speed of our apparatus, 10,000 rpm, the error in the slope for the Fe(III)/Fe(II) system is only $\sim$ 10%, and it is difficult to detect the curvature in the ISCVA plot.

The form of [27] indicates that the optimum application of the ISCVA method requires careful choice of electrode mantle shape (11) and ω scan rate in order to maintain Levich behavior at the lowest possible $\omega^{1/2}(\eta)$.

Since the derivative $(\partial\eta/\partial i)_c$ in the limit $i \to 0$ is the value sought, other experimental approaches to improve the accuracy of its experimental estimate may be taken when k_o becomes too small (or α is very different from 0.5). For example, an angular velocity modulation procedure to be outlined below gives $(\Delta\eta/\Delta i)_c$ directly with higher precision. Plots of $(\Delta\eta/\Delta i)_c$ for different values of i can be extrapolated back to $i = 0$, rather than taking the tangent at the lowest i actually measured. If such a linear extrapolation to zero i is used, we find that there is a threefold or more reduction in the minimum error predicted by Fig. 1 for the estimate of $(\Delta\eta/\Delta i)_{i=0}$. Our present apparatus provides for superimposed angular velocity modulation (9) and has been applied to direct measurement of $(\Delta\eta/\Delta i)_c$ *vs.* i under ISCVA scanning conditions. However, in the Fe(III)/Fe(II) cases, it was not necessary to scan the current while modulating ω.

Considering [24], [25], and [26], we see that using lower f-values and having $C_R^b > 0$ will cause the linearization approximation to be valid at lower k_o-values. This approach becomes impractical as $C_R/C_R^b \to 1$, *i.e.* when the current is small enough that little or no concentration polarization occurs and the ISCVA procedure becomes superfluous.

If the values of k_o and α are such that the linear approximation is not valid, two additional cases remain. If the reaction is so slow that all the accessible Levich constants lie in the Tafel region, conventional logarithmic transformations can be used, without introducing any ambiguity arising from variations in surface concentrations. In the overpotential region lying between the Tafel and linear regimes, the data may be fitted graphically to an Allen-Hickling plot (1, 10), if an estimate of the equilibrium potential can

be made. Alternately, k_o, α, and E_f can be obtained solely from ISCVA data using a nonlinear least-squares technique.

The facile control of surface concentration *via* the ISCVA method is of substantial utility outside the linear i-η region. In contrast, most relaxation methods (12-14), whose theory is based on linearity assumptions, cannot be used when η becomes large. Thus, using the ISCVA method, steady-state data can be taken and used to calculate kinetic parameters over virtually the entire range of known reaction rates.

For extremely fast electron transfer processes, the limitations on the ISCVA method become experimental rather than theoretical. Overpotentials for high k_o-values are small, and the uncompensated ohmic potential may become greater than η. Our approach to extending the ISCVA method to very fast processes ($i_{o,s} \sim 40$ A/cm^2) involves additional refinements to the $\omega^{1/2}$-modulation method in a way that retains steady-state mathematics and will be treated elsewhere (15).

Experimental

Apparatus and materials.—The $i/\omega^{1/2}$ scanning scheme, electrode construction, cell, and electronics are similar to those described previously under method HP2 (7). A detailed description of the present motor control apparatus is given elsewhere (9), including the velocity modulation circuitry necessary to perform the step changes in $\Delta i(\Delta\omega^{1/2})$ at constant $i/\omega^{1/2}$. All data reported below refer to hydrodynamic conditions that allow the use of the Levich equation. Nonsteady-state aspects of the velocity programming are discussed in the previously cited reference (9).

Solutions were prepared from triply distilled water and reagent-grade chemicals (electronic-grade acids) without further purification. All Fe(III) solutions were analyzed volumetrically using Ce(IV). Concentration studies were made by adding increments of Fe(III) stock solutions prepared in the same electrolyte to known volumes of that electrolyte present in the cell.

Gold, platinum, silver, and copper electrodes were polished to a 0.3μ Linde A finish. A mercury disk was prepared from a gold disk of 0.317 cm^2 area by amalgamating with a drop of mercury and spinning the excess off at 10,000 rpm to provide a flat mercury surface. All other disk areas were measured to be within 1% of 0.178 cm^2. For the gold and platinum kinetic studies, the surface states of these electrodes were critical in determining the measured levels of k_o. In the 0.1M HCl-1.0M NaCl studies, the gold electrode was anodized before $\omega^{1/2}$ scans at current densities comparable to those being used in the next experiment. This pretreatment converted the electrode surface to a reproducible state, giving it a matte finish. On a surface that retained a polished appearance, the apparent rate constants were lower and less reproducible. Such surface effects are well known in the study of heterogeneous rate processes. These rate constant differences are thought to arise both from impurity adsorption and surface area changes. Similar phenomena were found for Pt in 1M H_2SO_4, but we were not able to obtain as reproducible surfaces solely by anodization. Instead, we employed a technique first used by Johnson (16) to counteract inhibition effects in oxygen reduction. If $10^{-5}M$ Pt(IV) is added to the solution, platinum deposits continually during the reduction of Fe(III) and produces a relatively reproducible surface. In the absence of Pt(IV), the rate constants we found varied over a twofold range. This variation was observed in several separate experiments over a period of time using different solutions. The largest k_o values approached that obtained with *in situ* platinizing. Johnson's technique typically increased the surface area by about 50%, as measured by comparing the coulombs used in platinum oxide reduction before and after platinization.

Procedure.—The following procedure was used to study the reduction of Fe(III) in 0.1M HCl-1.0M NaCl at gold and in 1.0M H_2SO_4 at platinum: (*a*) An increment of Fe(III) stock solution was added and the i-E curve at a constant ω (ordinarily 2500 rpm) was determined; (*b*) the limiting current, i_c, [or i_a for Fe(II)] was measured; (*c*) the apparatus was adjusted to produce the desired surface concentration of Fe(III)—*e.g.*, to obtain $f = 1/4 = C/C_b$, $i/\omega^{1/2}$ was adjusted to 3/4 ($i_c/\omega^{1/2}$); (*d*) i was scanned, holding $i/\omega^{1/2}$ constant, and E_{exp} recorded *vs.* i.

Equations [18] and [21] require the value of the ratio $(D_R/D_O)^{2/3} = i_c/i_a$. These mass transport parameters for Fe(III) and Fe(II) were determined from i_c and i_a data obtained by repeating steps (*a*) and (*b*) above at constant ω to cover the desired C_b range. Results from one typical set of such data for Fe(III) in 0.1M HCl-0.1M NaCl at 2500 rpm are given in Fig. 2.

The α determination procedures require precise estimation of R_{exp}. When it is established that $\Delta\eta/\Delta i$ accurately represents R_{exp} ([8] is valid), a significant improvement in the precision of R_{exp} is obtained by superimposing a square-wave modulation on a constant $i/\omega^{1/2}$ condition, again while holding the value of $(i + \Delta i)/(\omega + \Delta\omega)^{1/2}$ constant (9). Measurement of the modulated part of the potential and current produces $\Delta\eta$ values as a function of Δi.

This modulation technique is decidedly advantageous in solid electrode studies, where surfaces may be altered in a time-dependent manner when they are exposed to wide changes of current and potential. Modulation methods are particularly well adapted to repetitive measurements and signal averaging. The direct reading of the necessary Δi and $\Delta\eta$ values may be done numerous times within the period required for a steady-state scan determination. These factors all contribute to increased accuracy and reproducibility in the value of $\Delta\eta/\Delta i$.

Results and Discussion

Evaluation of k_o.—A set of ISCVA plots for Fe(III) in 1M H_2SO_4 for $f = 0.5$ at platinum is shown in Fig. 3. The data are linear, considering the experimental error, as predicted by [11], within the limitations suggested by [27]. They are plotted, according to [16], in the form of R_{exp} *vs.* $1/C_O^b$ in Fig. 4. The major source of deviation is the sensitivity of the surface to pretreatment. The data sets obtained with 10^{-5}M Pt (IV) present are similar except for a decrease in slope corresponding to a slightly higher $i_{o,s}$. The data in Fig. 4 represent the highest k_{exp} found when only anodic pretreatment of polished platinum electrode was used.

ISCVA kinetic data for Fe(III) in 0.1M HCl-1M NaCl for $f = 0.5$ at gold are shown in Fig. 5 and 6. The data of both Fig. 4 and 6 are linear as predicted by [16]. The least-squares values of AR_u from the intercepts of these figures are 2.5 ± 8.5 and 5.3 ± 3.6 ohms, respectively. Independent interrupter (16) estimates of AR_u (5 and 8 ohms, respectively) were within the error range of the intercepts. Values of AR_u calculated according to Newman (17) were 4 and 7 ohms, re-

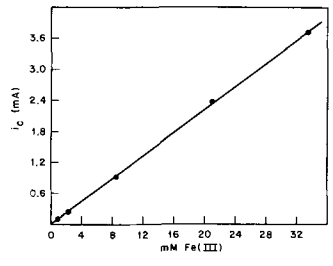

Fig. 2. Plot of i_c *vs.* Fe(III) concentration in 0.1M HCl-1.0M NaCl for 0.178 cm^2 gold disk rotated at 2500 rpm. Least-squares slope = 111 ± 3 μA/mM, $D_{Fe^{+3}} = (5.12 \pm 0.2)\ 10^{-6}$ cm^2/sec.

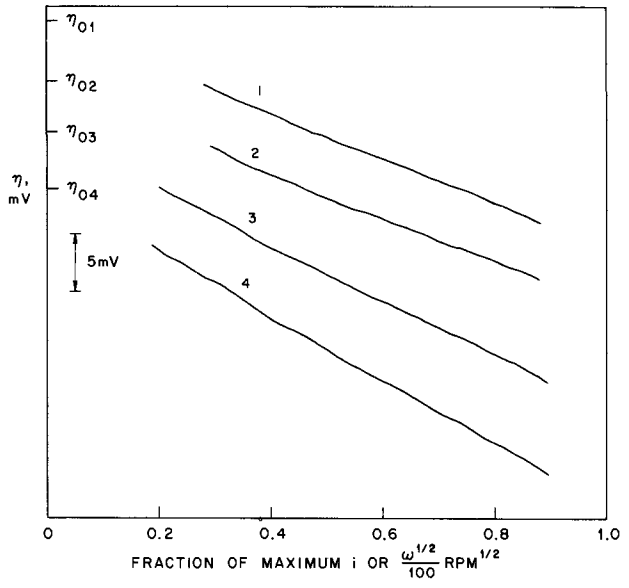

Fig. 3. Normalized ISCVA plots for the reduction of Fe(III) in 1M H_2SO_4 at Pt as a function of $C^b_{Fe(III)}$. $f = 0.5$. Tracings of actual data shown. The ordinate η is defined as $E_{exp} - (E_{exp})_{i\to 0}$. $\eta_{0,1}$ refers to η_0 for curve 1. The vertical sensitivity is 5 mV/ indicated division. Abscissa plotted as fraction of maximum current (at 10,000 rpm). Concentrations of Fe(III) are: 1—0.50, 2—0.99, 3—1.96, and 4—4.75 mM, respectively. The maximum currents are 51.2, 101.4, 232.0, and 559 μA, respectively.

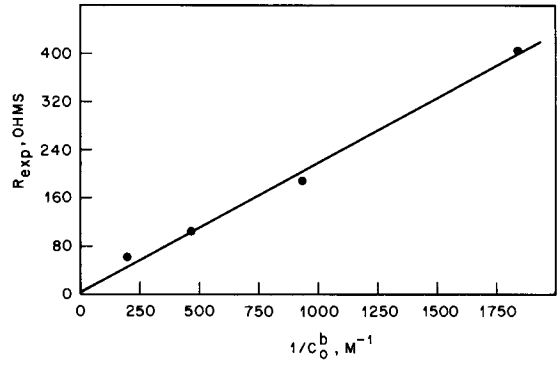

Fig. 4. Plot of R_{exp} vs. $1/C_O{}^b$ for data of Fig. 3. R_{exp} values taken from slopes of corresponding Fig. 3 traces. Least-squares intercept = 2.5 ± 8.5 ohms, slope = 0.216 ± 0.03 ohm-molar, $i_{o,s} = 0.66$ A/cm^2-molar, $k_o = 6.8 \times 10^{-3}$ cm/sec.

spectively. The uncertainties in the intercept of [16], AR_u, are not critical as long as the uncertainty in the slope, which yields k_{app}, is low. This is the case for the Fe(III) system at the 1-10 mM concentration level.

The range of k_o values obtained at polished platinum was 3-6.5 x 10^{-3} cm/sec in 1M H_2SO_4. For the platinized surface, $k_o = 7.5 \times 10^{-3}$ cm/sec. The latter value is consistent with the values we found for k_o on polished platinum after the ~50% increase in area is taken into account. Copa (17) has summarized the literature values of k_o for this system, and the range of previously reported values includes our results.

The values of k_o obtained at gold from Fig. 6 and from Fig. 8 below are 5.5 and 5.7 x 10^{-3} cm/sec, respectively. The supporting electrolyte of 0.1M HCl-1M NaCl is about the same as that of Barnartt (20) who reported the higher value of $k_o > 3 \times 10^{-2}$ cm/sec on the basis of a potential step method employing positive feedback to provide *IR* compensation. However, Bockris *et al.* (21), using a galvanostatic method, found k_o in 1M HCl at gold to be about the value found by the ISCVA technique.

Evaluation of α.—The determination of α for a 9.7 mM Fe(III) solution in 0.1M HCl-1M NaCl at a gold

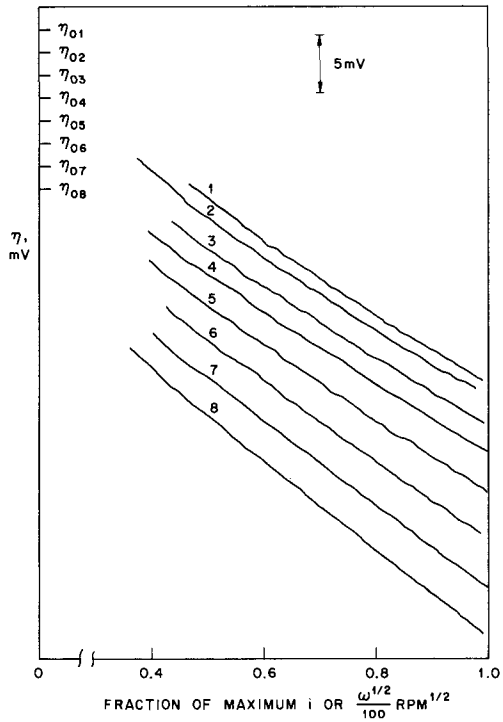

Fig. 5. Normalized ISCVA plots for reduction of Fe(III) in 0.1M HCl-1.0M NaCl at gold as a function of $C^b_{Fe(III)}$. $f = 0.50$. Concentrations of Fe(III) are (in mM): 1—1.28, 2—1.60, 3—2.22, 4—2.83, 5—4.63, 6—6.37, 7—8.03, 8—10.16. Maximum currents (in μA) are: 1—145, 2—181, 3—251, 4—320, 5—523, 6—720, 7—907, 8—1,148. Other data same as in Fig. 3.

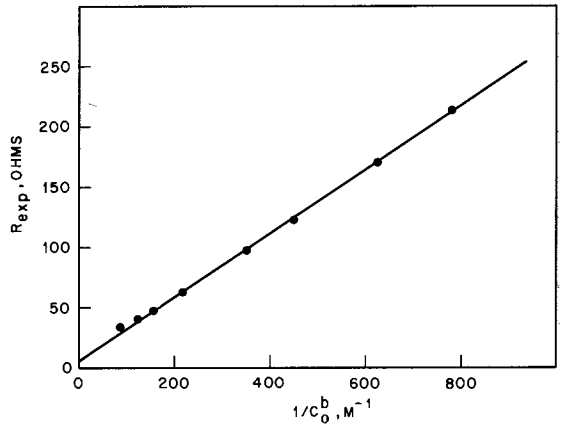

Fig. 6. Plot of R_{exp} vs. $1/C_O{}^b$ for data of Fig. 5. R_{exp} values taken from slopes of corresponding Fig. 5 traces. Least-squares intercept 5.3 ± 3.6 ohm, slope = 0.270 ± 0.024 ohm-molar. $i_{o,s} = 0.53$ A/cm^2-molar. $k_o = 5.5 \times 10^{-3}$ cm/sec.

electrode was performed in two ways: (*a*) by plotting k_{app} *vs.* f according to [20] to produce a curve with a maximum in k_{app} at $\alpha = f$, Fig. 7, and (*b*) according to [18] by plotting log $k_{app}/2f$ *vs.* log $[(1-f)/f]$ which gives α from the slope, Fig. 8. The R_{exp} data were obtained using the more precise modulation procedure as discussed earlier. All R_{exp} data were corrected to R_p values using the least-squares estimate of AR_u obtained from the intercept of Fig. 6, and k_{app} was then calculated from [17].

In Fig. 7, theoretical $i_o - f$ plots for $\alpha = 0.4$, 0.5, and 0.6 are given along with a plot of the experimental data. The maxima of the $i_o - f$ plots are broad and visual inspection of Fig. 7 leads to an estimate of $\alpha = 0.5 \pm 0.05$. The graphical procedure using [18] in Fig. 8 yields $\alpha = 0.48$ and is the preferable technique. The α-values collected by Copa (19) for 1M H_2SO_4, rather than Cl^-, range from 0.46 to 0.62. The plots in Fig. 8 deviate from linearity at values of $(1-f)/f$ re-

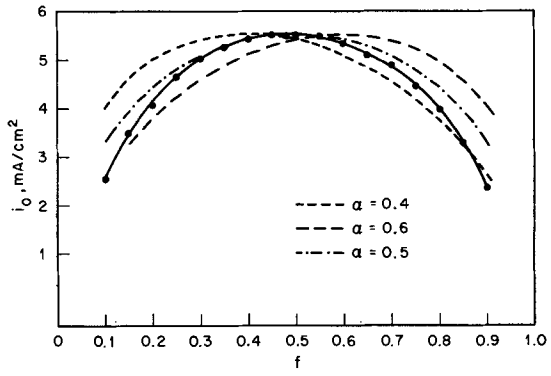

Fig. 7. Plot of i_o vs. f for 9.7 mM Fe(III) in 0.1M HCl-1.0M NaCl at gold. Data from modulation procedure, calculated as described in the text. Also shown are theoretical i_o-f plots for α = 0.4, 0.5, and 0.6 (dashed lines). The maximum of each α curve is made coincident with the experimental curve at $\alpha = f$.

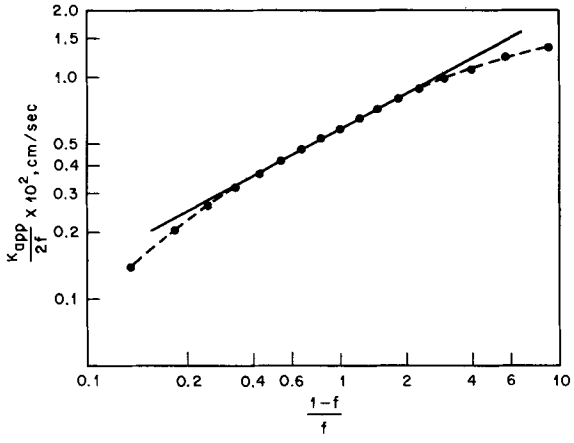

Fig. 8. Plot of log $k_{app}/2f$ vs. log $[(1 - f)/f]$ for data of Fig. 7. Slope, from linear portion, is $1 - \alpha = 0.52$. $(k_{app}/2f)_{f=1/2} = 5.85 \times 10^{-3}$ cm/sec.

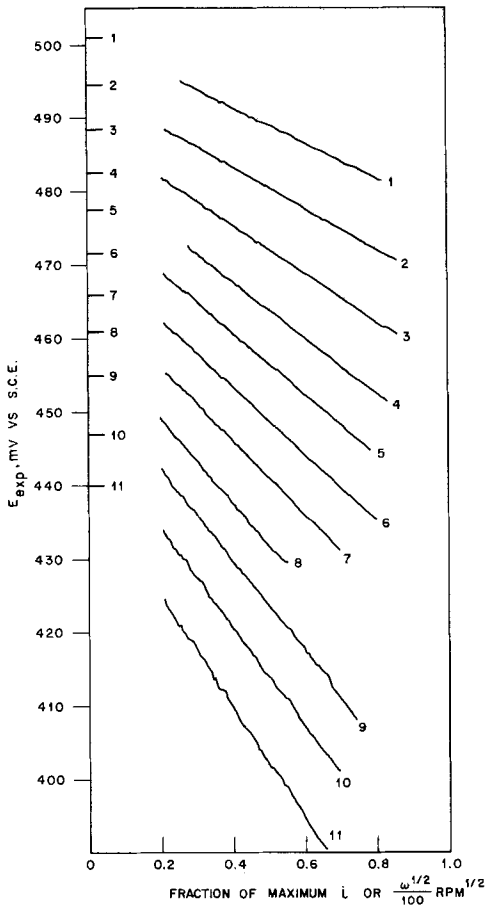

Fig. 9. ISCVA data for 9.7 mM Fe(III) in 0.1M HCl-1.0M NaCl solution at gold at different values of f. Actual data shown. E_{eq} obtained by the extrapolation to zero current of each tracing is indicated. f values for the experimental lines are 1—0.260, 2—0.312, 3—0.364, 4—0.416, 5—0.468, 6—0.520, 7—0.572, 8—0.624, 9—0.676, 10—0.728, 11—0.780.

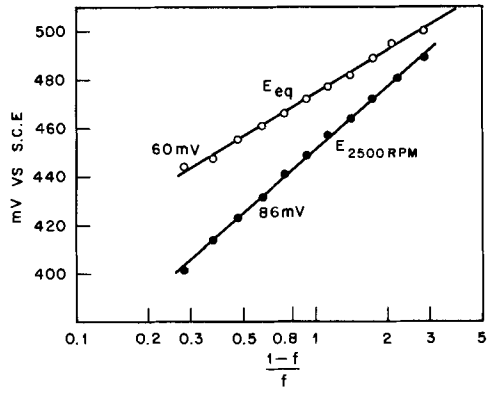

Fig. 10. Plot of E_{eq} vs. log $[(1 - f)/f]$ from zero i extrapolations of Fig. 9 traces. Experimental slope is 60 mV. A plot using E_{exp} from the 2500 rpm current points of Fig. 9 showing slope 86 mV is also included.

moved from unity. The curvature of high f is partly due to the deviation of $\Delta\eta/\Delta i$ from theoretical values, *i.e.* [26]. Changes of α over extended potential ranges, particularly when using our simplified form of the rate equation [2], may be responsible for the curvature at low f values [see Delahay (1)].

Evaluation of E_f and n.—E_{eq} was determined as a function of f using the above-mentioned 9.7 mM Fe(III) solution in the chloride electrolyte. ISCVA scan measurements were interpreted using [11], and the data used for the extrapolation of E_{exp} to zero current are shown in Fig. 9. The i-E plots in Fig. 9 are all linear, some over a relatively large E range. This is not inconsistent with the error conclusions based on Fig. 1 since (*a*) in 9.7 mM Fe(III) the IR drop represents about 25% of η_{app} and (*b*) the value of α (= 0.48) is almost optimum for minimized deviation from linearity.

The plot of E_{eq} *vs.* log $[(1 - f)/f]$ according to [21] (f is substituted for i/i_c) is given in Fig. 10. The slope of this plot yields $1/2.303\ n\phi = 60$ mV, in keeping with a one-electron redox process. Using the value of E_{eq} at $f = 1/2$, the diffusion coefficient ratio for Fe(III) and Fe(II) previously obtained from the i_c/i_a ratio, and [21], a formal potential, E_f, of 470 mV *vs.* SCE is found. The latter value is in satisfactory agreement with the values of Barnartt (20). He reported 465 and 464 mV, on the basis of potentiometric data for 40 and 200 millimolal total Fe(III) and Fe(II) solutions, respectively, in nearly the same electrolyte.

The original E_{exp} *vs.* f data were used to obtain a plot of E_{exp} at 2500 rpm *vs.* log $[(1 - f)/f]$. This conventional voltammetric plot is included in Fig. 10 and has a markedly irreversible slope of 86 mV/decade. It is apparent that a single conventional i-E curve obtained at constant ω is of little value in estimating n or E_f. *In lieu* of the ISCVA technique, the tedious manual procedure involving (*a*) the determination of i-E curves at different constant angular velocities, followed by (*b*) plotting E_{exp} *vs.* i at constant f to obtain E_{eq} at $i = 0$ could be used to obtain n and E_f by means of [21].

When the scan data in Fig. 10 were used in a plot equivalent to Fig. 7, they gave considerably more scatter and a much less precise estimate of α as com-

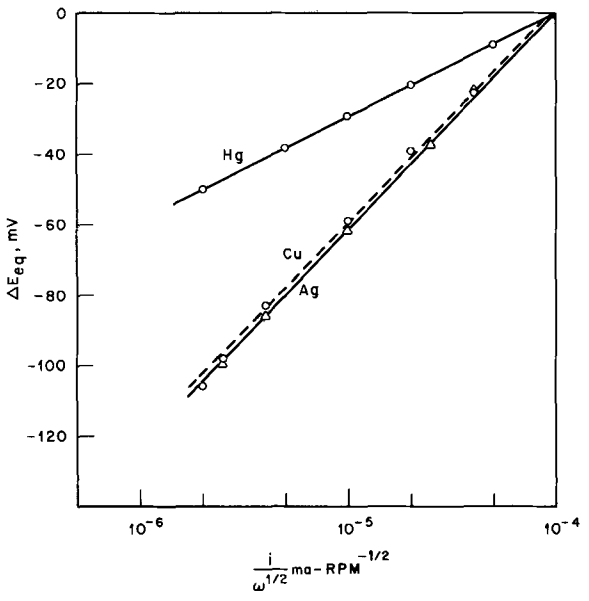

Fig. 11. Plot of ΔE_{eq} vs. log $\left(\frac{i}{\omega^{1/2}}\right)$ for oxidation in three metal/supporting electrolyte systems: Ag in 1M $HClO_4$, Cu in 1M HCl, and Hg in 1M $HClO_4$. $\Delta E_{eq} = (E_{eq})_{(i/\omega^{1/2})_{max}} - (E_{eq})_{i/\omega^{1/2}}$. Each point represents the zero current extrapolation of an E_{exp}-i plot at constant $i/\omega^{1/2}$. Slopes in mV are 62 (Ag), 62 (Cu), and 29 (Hg).

pared to the results obtained with the modulation data. The reproducibility of R_{exp} obtained by scanning was a few per cent, quite satisfactory for i_o, E_{eq}, or n determination, but distinctly less so for the α procedure.

The i-η characteristic of fast metal dissolution reactions may be curved if α is quite different from 0.5 and/or rate determining solid-state processes rather than simple electron transfer govern the kinetics. If this curvature is not extreme, extrapolation of a limiting tangent to the potential-axis ($i \rightarrow 0$) will produce relatively small errors in E_{eq}. In two cases, Ag/Ag(I) in 1.0M $HClO_4$ and Cu/Cu(I) in 1M HCl, complications produce curvature. The very fast electron transfer process for Hg/Hg_2^{+2} in 1M $HClO_4$ exhibits no curvature. Three examples of plots of ΔE_{eq} vs. log $(i/\omega^{1/2})$ are given in Fig. 11. The value of $i/\omega^{1/2}$ in each case is proportional to the metal ion concentration and the slope should be $1/2.303\ n\phi$. For $Ag \rightarrow Ag^+ + e$ and $Cu + 2\ Cl^- \rightarrow CuCl_2^- + e$, both slopes found from Fig. 11 are 62 mV, and for $2\ Hg \rightarrow Hg_2^{++} + 2e$, the slope is 29 mV, as expected.

The detailed treatment of the kinetics in these three cases involves certain refinements, either theoretical or experimental as the situation requires, beyond the scope of this discussion, and therefore will be considered elsewhere. The plots in Fig. 11 indicate that E_{eq}, n, and therefore related parameters such as stability constants for metal/electrolyte systems may be conveniently obtained by oxidation under ISCVA conditions in the appropriate supporting electrolyte. The determination of stability constants by this method requires a knowledge of the diffusion coefficients of the aquo and complexed ions. The latter data are obtainable from Levich constant determinations using a single known concentration of the ion (which can be coulometrically generated) in the two supporting electrolytes.

Summary and Conclusions

The advantages of isosurface concentration voltammetry at rotating disk electrodes have been exploited in the study of electrode kinetics. i-η data have been automatically obtained at fixed surface concentrations of all electroactive species by scanning i while holding $i/\omega^{1/2}$ constant. The variation of apparent resistance, $\Delta\eta/\Delta i$, with different constant surface concentrations (regulated by $i/\omega^{1/2}$ control) has been used to separate the charge transfer and uncompensated ohmic components of this resistance. Charge transfer rate constants and the symmetry factor, α, have been found. Equilibrium potentials and the number of electrons transferred in the electrode reaction have been established using the same data by extrapolation to zero current.

Although the kinetic systems treated were chosen to permit the ISCVA data to be interpreted on the basis of the linearized rate equation, this need not be the case. The use of the experimental scheme for automatic $i/\omega^{1/2}$ control should be of general kinetic use since the ISCVA data may be treated applying the generalized rate expression. Concentration polarization may be important even in the Tafel regime in many experimental situations, and any method depending on simultaneous electrogeneration of the potential determining species requires knowledge of the relevant surface concentrations.

The automatic scanning and modulation aspects of the ISCVA technique make available certain favorable characteristics of pulse and relaxation methods, while retaining the theoretical advantages of the steady-state regime. In ISCVA experiments, rapid changes of the equilibrium state are accomplished and measured without the necessity of considering non-steady state behavior.

Acknowledgment

Stanley Bruckenstein is grateful to the Bell Telephone Laboratories for their hospitality during the summer of 1970 when this work was done.

Manuscript submitted Dec. 9, 1970; revised manuscript received *ca.* Feb. 8, 1971.

Any discussion of this paper will appear in a Discussion Section to be published in the June 1972 JOURNAL.

SYMBOLS

A	Disk area, cm^2
C_O, C_R	Surface concentrations of Ox and Red, mole/cm^3
C_O^b, C_R^b	Bulk concentrations of Ox and Red, mole/cm^3
D_O, D_R	Diffusion coefficients of Ox and Red
E_{eq}	Potential at $i \rightarrow 0$, volts
E_{exp}	Measured potential, volts
E_f	Formal potential, volts
$\mathbf{F}$	Faraday's constant, coulombs/equivalent
f	Fraction of i_a or i_c
i_a, i_c, i_L	Anodic, cathodic, and limiting current densities, A/cm^2
i_o	Exchange current density, A/cm^2
$i_{o,s}$	Standard exchange current density, A/cm^2
k_{app}	Apparent rate constant, cm/sec
k_L	Levich constant, $i_L/\omega^{1/2}C^b$
k_o	Rate constant, cm/sec
n	Number of electrons transferred per mole of reaction
R	Universal gas constant, j/mole-deg
R_p	Charge transfer resistance, ohms-cm^2
R_u	Uncompensated ohmic resistance, ohms
T	Absolute temperature, °K
v	Reaction rate, mole/cm^2-sec
α	Transfer coefficient
η	Overpotential, volts
η_{exp}	Measured overpotential, volts
ν	Kinematic viscosity, cm^2/sec
ϕ	$\mathbf{F}/RT$
ω	Angular velocity, radians/sec

REFERENCES

1. P. Delahay, "Double Layer and Electrode Processes," Interscience Div. of John Wiley & Sons, Inc., New York (1965).
2. M. Eisenberg, C. W. Tobias, and C. R. Wilke, *This Journal*, **101**, 306 (1954).
3. D. Jahn and W. Vielstich, *ibid.*, **109**, 849 (1962).
4. A. N. Frumkin and G. Tedoradse, *Z. Elektrochem.*, **62**, 251 (1958).
5. R. N. Adams, "Electrochemistry at Solid Electrodes," Marcel Dekker, Inc., New York (1969).

6. M. Enyo and T. Yokoyama, *Electrochim. Acta*, **15**, 183 (1970).
7. B. Miller and S. Bruckenstein, *This Journal*, **117**, 1032 (1970).
8. D. D. Deford and D. N. Hume, *J. Am. Chem. Soc.*, **73**, 5321 (1951).
9. B. Miller, M. I. Bellavance, and S. Bruckenstein, To be published.
10. P. L. Allen and A. Hickling, *Trans. Faraday Soc.*, **53**, 1626 (1957).
11. A. C. Riddiford, in "Advances in Electrochemistry and Electrochemical Engineering," Vol. 4, p. 47, P. Delahay, Editor, Interscience Publishers, Inc., New York (1966).
12. D. J. Kooyman, M. Sluyters-Rehbach, and J. H. Sluyters, *Electrochim. Acta*, **11**, 1197 (1966).
13. D. M. Mohilner, N. Hackerman, and A. J. Bard, *Anal. Chem.*, **39**, 1501 (1967).
14. D. K. Roe and R. L. Birke, *ibid.*, **39**, 1501 (1967).
15. B. Miller, M. I. Bellavance, and S. Bruckenstein, To be published.
16. D. C. Johnson, Ph.D. Thesis, Dept. of Chemistry, University of Minnesota, Minneapolis (1967).
17. J. Newman, *This Journal*, **113**, 501 (1966).
18. S. Bruckenstein and B. Miller, *ibid.*, **117**, 1040 (1970).
19. W. M. Copa, Ph.D. Thesis, Dept. of Chemistry, Univ. of Minnesota, Minneapolis (1970).
20. S. Barnartt, *Can. J. Chem.*, **47**, 1661 (1969).
21. J. O'M. Bockris, R. J. Mannan, and A. Damjanovic, *J. Chem. Phys.*, **48** 1898 (1968).

Electrochemical Behavior of Substituted Oxadiazoles

G. L. Smith and J. W. Rogers

Department of Chemistry, Midwestern University, Witchita Falls, Texas 76308

ABSTRACT

An electrode reduction mechanism is reported for two aromatic-2,5-substituted oxadiazoles in DMF solvent as part of a continuing study of the electrochemistry of five-membered nitrogen oxygen heterocyclics. Polarography, cyclic voltammetry, chronoamperometry, and uv spectroscopy were techniques employed in the study. The effects of a proton donor on the stability of reduction intermediates is discussed.

Reports of the application of electroanalytical techniques to problems dealing with oxidation-reduction properties of molecules are extensive (1-3). A number represent studies dealing with heteroaromatic compounds of general chemical or biochemical importance (4-6). We wish to report in this paper the work that has continued in this laboratory on the electrochemical reduction of various oxazoles and oxadiazoles in aprotic media.

It has previously been shown that both symmetrically and nonsymmetrically 2,5-aromatic-substituted oxazoles are reduced in two polarographic steps in N,N-dimethylformamide (DMF) via the same mechanism (7). In contrast, further investigations show that the mode of reduction of 2,5-aromatic-substituted oxadiazoles is quite sensitive to the nature of the aromatic substituents. The results of polarographic, potentiostatic, cyclic voltammetric, and spectrophotometric investigations of 2,5-diphenyl-(I) and 2-(m-tolyl)-5-(1-naphthyl)oxadiazole(II) in aprotic and protic media are presented.

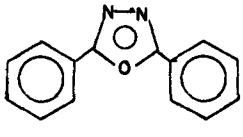

(I)

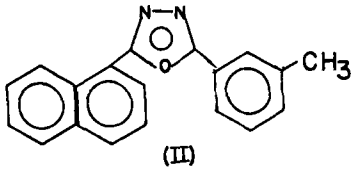

(II)

An electrochemical reduction mechanism is postulated to explain the experimental results.

Experimental

Apparatus.—The instrumentation, cells, and electrodes have been described elsewhere (7). All uv-visible spectra were recorded with a Perkin-Elmer 202 uv-visible spectrophotometer.

The product resulting from mass electrolysis of II at the third plateau was recovered from the electrolysis solution by successive benzene extractions from a 50% water electrolysis-solution mixture. The benzene was removed under vacuum and the residual brown oil was eluted from a silica gel column with chloroform. One primary fraction was observed and collected.

Key words: electrochemical reduction oxadiazole.

Chemicals.—Compounds I and II were obtained commercially from Alfred Bader Chemicals. Purification by recrystallization from pure methanol did not change the melting ranges of 138°-140° for I and 122°-127° for II. Hydroquinone was obtained from J. T. Baker Chemical Company and was recrystallized from a 50% water-ether solution before use. Spectroquality N,N-dimethylformamide containing approximately 0.03% water was obtained from Eastman Organic Chemicals. It was vacuum distilled at 70°C from anhydrous $CuSO_4$ before use. The tetra-N-propylammonium perchlorate was produced and purified as previously described (7).

Results

Polarography at a DME.—The compound 2,5-diphenyloxadiazole (I) exhibits two well-defined polarographic waves in DMF solvent at −1.87 and −2.24V *vs.* saturated calomel electrode (SCE). Behavior and characteristics of the waves (Table I) suggest that material transfer is diffusion controlled at the potential of each plateau. The first wave appears to be the result of a reversible one-electron transfer, the second also a one-electron but complicated by a coupled chemical reaction.

The compound 2-(m-tolyl)-5-(1-naphthyl)-oxadiazole (II) is reduced at a DME in three diffusion-controlled steps at −1.72, −2.11, and −2.43V *vs.* SCE in DMF solvent, Table I. The first two waves appear to represent polarographic processes analogous to those of the two waves of (I). The structure and behavior of the third wave suggest that it is the result of a complex multielectron transfer.

Voltammetry at solid electrodes.—Typical cyclic voltammograms of I are shown in Fig. 1. Voltage excursion and reversal at potentials more negative than the first $E_{1/2}$ at a planar platinum disk electrode

Table I. Polarographic data for reduction of I and II in DMF

Hg head (h) (cm)	$-E_{1/2}$ (V)	$E_{3/4}-E_{1/4}$ (mV)	$id/h^{1/2}$ (μA/cm$^{1/2}$)
		2,5-Diphenyloxadiazole (I)[a]	
		First wave	
80	1.87	56	0.60
50	1.87	56	0.66
42	1.87	56	0.63
30	1.87	56	0.67
		Second wave	
80	2.24	75	0.52
50	2.24	75	0.59
42	2.24	75	0.54
30	2.24	75	0.56
		2,5-Diphenyloxadiazole (I)[b]	
		First wave	
80	1.86	56	0.10
50	1.86	56	0.10
42	1.86	56	0.11
30	1.86	56	0.12
		Second wave	
80	2.24	87	0.15
50	2.24	87	0.15
42	2.24	87	0.15
30	2.24	87	0.15
		2-(m-tolyl)-5-(2-naphthyl)-oxadiazole (II)[c]	
		First wave	
60	1.72	59	0.43
50	1.72	59	0.44
42	1.72	59	0.46
30	1.72	59	0.46
		Second wave	
60	2.11	70	0.36
50	2.11	70	0.33
42	2.11	70	0.37
30	2.11	70	0.39
		Third wave	
60	2.43	—[d]	0.71
50	2.43	—[d]	0.75
42	2.43	—[d]	0.75
30	2.43	—[d]	0.76

[a] Solution 1 mM in I, 0.1M in TPAP supporting electrolyte in dried spectroquality DMF.
[b] Solution 0.1 mM in I, 0.1M in TPAP supporting electrolyte in spectroquality DMF used without further purification.
[c] Solution 1 mM in II, 0.1M in TPAP supporting electrolyte and in dried spectroquality DMF.
[d] Criterion not meaningful for multi-electron wave.

Table II. Cyclic voltammetric data for reduction of 2,5-diphenyloxadiazole I at a PPDE and a HMDE in DMF

Sweep rate (v) (mV/sec)	$-(Ep)c$ (v)	$(ip)c/(ip)a$[c]	$(Ep)c/2$ $-(Ep)c$ (mV)	$(ip)c/v^{1/2}$ (μA sec$^{-1/2}$)
		PPDE[a]		
		First wave[b]		
200	1.92	1.00	60	5.84
100	1.92	1.00	60	5.79
40	1.92	1.00	60	5.84
20	1.92	1.00	60	5.75
		First wave[d]		
200	1.93	0.92	75	5.81
100	1.92	0.95	72	5.95
40	1.92	0.92	65	5.92
20	1.92	0.95	68	6.04
		Second wave[b]		
200	2.42	—	—	5.53[f]
100	2.41	—	—	5.62[f]
40	2.39	—	—	6.02[f]
20	2.37	—	—	6.64[f]
		HMDE		
		First wave[d]		
200	1.93	0.90[e]	75	0.42
100	1.92	0.85[e]	69	0.42
40	1.92	0.84[e]	67	0.43
20	1.92	0.83[e]	65	0.44
		Second wave[d]		
200	2.42	—	—	0.39[f]
100	2.40	—	—	0.41[f]
40	2.39	—	—	0.46[f]
20	2.38	—	—	0.49[f]

[a] Platinum electrode was 0.78 cm^2 in area.
[b] Solution 1 mM in I, 0.1M in TPAP in dried spectroquality DMF.
[c] Scan reversal 120 mV past $(Ep)c$; ip measured by employing the potential hold method.
[d] Solution 1 mM in I, 0.1M in TPAP in spectroquality solvent used without further purification.
[e] $(ip)a$ measured from anodic diffusion peak.
[f] ip measured by extrapolating current from first peak.

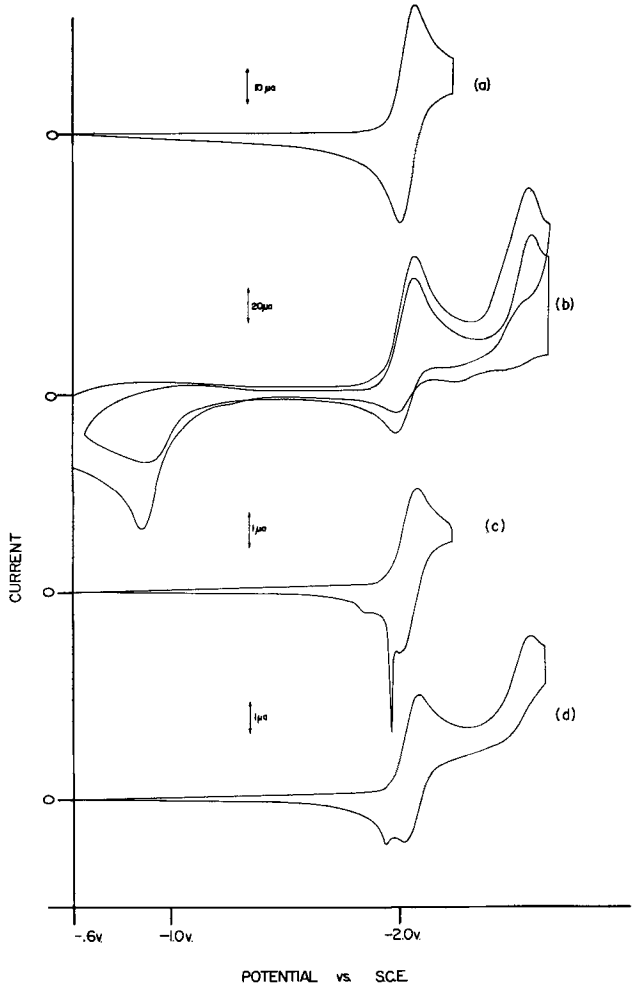

Fig. 1. Cyclic voltammograms of 2,5-diphenyloxadiazole (I) in DMF solvent at (a) a PPDE with sweep reversal 120 mV past first wave, (b) a PPDE with multicyclic sweep reversed 80 mV past second wave with 5-sec hold on second sweep, (c) a HMDE with sweep reversal 120 mV past first peak, (d) a HMDE with reversal and hold 60 mV past second wave. All solutions were 1 mM in compound (I) and 0.1M in TPAP supporting electrolyte. Spectroquality DMF was dried and distilled for experiments described in a and b only.

(PPDE) in DMF produces a voltage-current curve exhibiting properties indicative of a fast, one-electron transfer with no rapid following reactions, Table II (8). Cyclic experiments at a PPDE carried to potentials above the second $E_{1/2}$ produce a reduction current peak with no corresponding anodic current, Fig. 1. The current-peak potential, $(Ep)c$, shifts cathodic and the current function, $(ip)c/v^{1/2}$), decreases with increasing potential sweep rate (v). This behavior suggests that the electron transfer is followed by a rapid homogenous reaction (8). Cyclic experiments in which the potential is held briefly ($\sim$ 3 sec) above the second $E_{1/2}$, reveals a greatly reduced monoanion oxidation peak and an intense follow-up oxidation current at -0.75V on the anodic going segment, Fig. 1. Multicyclic experiments show that the follow-up peak has no corresponding reduction wave, Fig. 1. This behavior is analogous to that of substituted oxazoles and suggests that the product of the reaction following the second electron transfer is oxidized to the parent oxadiazole at the follow-up peak. Compound I exhibits similar behavior at a hanging mercury drop electrode (HMDE).

The influence of small amounts of water impurity on the first wave of I in voltammetric experiments conducted at solid electrodes is pronounced. The cathodic current half-peak height to full peak sepa-

ration, $(Ep)c/2 - (Ep)c$, is broadened slightly and the cathodic to anodic current ratio, $(ip)c/(ip)a$, becomes less than 1.0 at all potential sweep rates in experiments conducted in spectroquality DMF not treated with a drying agent and redistilled before use, Table II. The effect is most pronounced in experiments conducted at a HMDE, Table II. On mercury, a product adsorption peak is observed anodic of the diffusion peak representing oxidation of the anion radical, Fig. 1. The increased impurity level has no influence on the character or behavior of the second wave on platinum or mercury, Table II. The broadened cathodic wave and the enhanced anodic current at the PPDE cannot be explained totally in terms of adsorption of reactant or product or any other one electrochemical phenomenon. It does seem consistent, however, to postulate that the anion radical is protonated to a certain degree and the resulting neutral radical is adsorbed (9). This explanation for the platinum, as well as the mercury electrode, is substantiated by experiments in which the switching potential exceeds the second plateau. A diminished anion oxidation current and the absence of an adsorption peak, Fig. 1, suggest that the reaction occurring at potentials above the second $E_{1/2}$ removes any adsorbed species.

Typical voltammograms of compound II in DMF taken at a PPDE are shown in Fig. 2. The voltammetric data is summarized in Table III. The invariance of the current function, $(ip)c/v^{1/2}$, $(Ep)c/2 - (Ep)c$, and the ratio, $(ip)c/(ip)a$, of the first wave to the sweep rate is again indicative of a reversible one-electron process producing a radical species stable during the course of the experiment (8). The 30 mV cathodic shift and the 10% decrease of the current function of the second wave with a ten fold increase in sweep rate is indicative of a rapid chemical reaction following a reversible electron transfer (8). Identical to the behavior of I, the oxidation of the product of the reaction occurring at the second wave of II is noted to occur anodic of the anion radical oxidation peak, Fig. 2. These observations certainly suggest that the first two waves of II and the two waves of I represent identical electrochemical processes. Further evidence for this assertion is presented.

The cathodic peak of the third cyclic voltammetric wave of II shifts cathodic and the current function markedly decreases with an increase in potential sweep rate, Table III. The great sensitivity of the current function to the sweep rate can probably be attributed to a large n apparent.

Table III. Cyclic voltammetric data for reduction of 2-(m-tolyl)-5-(2-naphthyl)-oxadiazole II at a PPDE in DMF

Sweep rate (v) (mV/sec)	$-(Ep)c$ (V)	$(ip)c/(ip)a$[b]	$(Ep)c/2 - (Ep)c$ (mV)	$(ip)c/v^{1/2}$ (μA sec$^{-1/2}$)
		First wave[a]		
200	1.73	1.0	60	4.70
100	1.73	1.0	60	4.74
40	1.73	1.0	59	4.74
20	1.73	1.0	59	4.80
		Second wave[a]		
200	2.17	—	—	3.74[c]
100	2.16	—	—	3.85[c]
40	2.14	—	—	3.99[c]
20	2.14	—	—	4.10[c]
		Third wave[a]		
200	2.50	—	—	8.65[c]
100	2.48	—	—	9.64[c]
40	2.46	—	—	11.32[c]
20	2.45	—	—	12.80[c]

[a] Solution was 1 mM in compound II and 0.1M in TPAP in dried spectroquality DMF.
[b] $(ip)a$ was measured by employing the potential hold method. Potential was reversed 120 mV past $(Ep)c$.
[c] $(ip)c$ for waves two and three was measured by extrapolating current from previous peak.

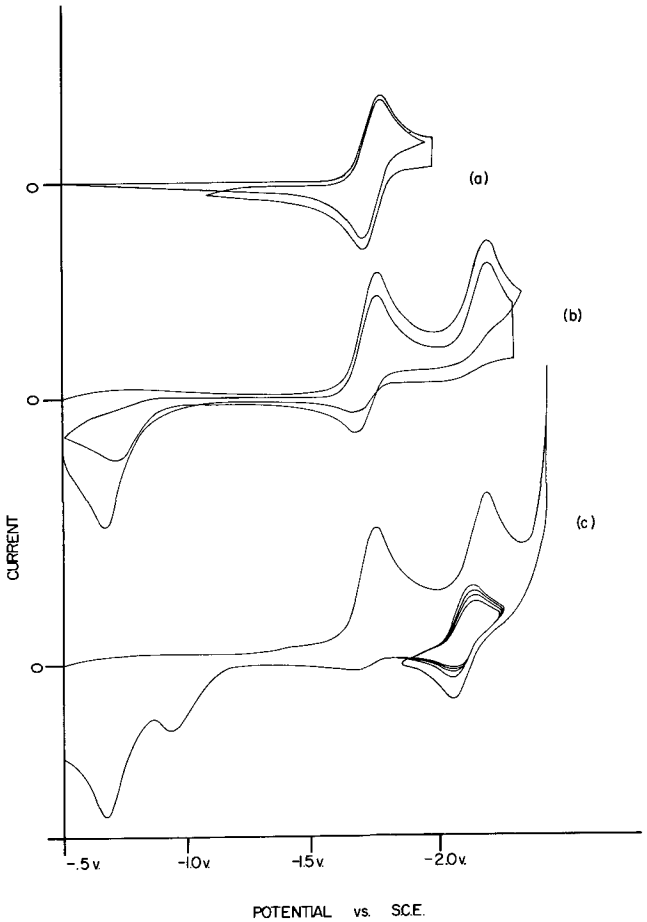

Fig. 2. Cyclic voltammograms of 2-(1-naphthyl)-5-(m-tolyl)-oxadiazole (II) in DMF solvent at a PPDE (a) with sweep reversal and reversal and hold 120 mV past first wave, (b) with sweep reversal and reversal and hold 100 mV past second wave, (c) with reversal and hold on rising portion of third wave followed by multicyclic sweep in potential region showing reversible reduction of third-wave product. All solutions were 1 mM in compound (II) and 0.1M in TPAP supporting electrolyte in dried spectroquality DMF.

Chronoamperometry.—The potential step-chronoamperometric experiment often may be simply and effectively employed in the determination of n apparent values. Plots of $it^{1/2}$ *vs.* t from diffusion current-time decay curves recorded at a constant potential corresponding to the first polarographic plateau of each compound yield straight lines of zero slope that may be employed as one-electron reference points. Similar plots from experiments carried out at potentials of the second wave of I and the second and third waves of II yield straight lines of approximately zero slope. This behavior is expected for very rapid following reactions (10). The potentiostatic data and n apparent values are summarized in Table III.

The n apparent values and the voltammetric and polarographic behavior show that the reduction of I, and the first two reduction steps of II, closely parallels that of 2,5-diphenyloxazole (7). The mechanism may be represented in the following manner:

First wave

$$R + e^- \rightleftarrows R^{\cdot -}$$

Second wave

$$R^{\cdot -} + e^- \rightleftarrows R^=$$

$$R^= + SH \rightarrow RH^- + S^-$$

Production oxidation wave

$$RH^- \rightarrow R + H^+ + 2e^-$$

The n apparent of 6.0 for processes carried to potentials above the third wave of compound II strongly suggests very rapid, complete saturation and ring opening reactions of the type:

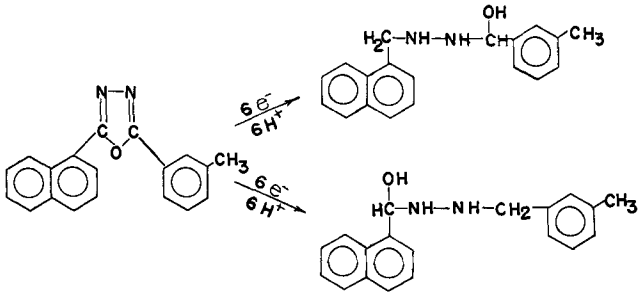

This reaction is also suggested by the work of Bezuglyi *et al.* (11) with oxadiazoles in protic solvents. The extent of the reduction process even in an aprotic solvent such as DMF reveals the great basicity of the transient intermediate reduction products of II.

Mass electrolysis.—Compounds I and II were mass electrolyzed at a mercury pool cathode in DMF solvent at predetermined potentials corresponding to various polarographic steps. The experiments were conducted to further study the stability of the postulated reduction products, $R^{-}\cdot$ and RH^{-}. The course of each electrolysis experiment was followed with uv spectroscopy and with an *in situ* three-electrode configuration employed to oxidize the mass electrolysis products (7).

Electrolysis of both compound I and II at potentials corresponding to the first polarographic plateau produces an intensely yellow solution sensitive to small quantities of O_2. The parent compound absorbance of uv spectra taken of aliquants of the electrolyzed solutions over a 2-hr period showed only a slight decrease. Oxidation of the yellow solution at a PPDE showed one intense current peak with a potential corresponding to the oxidation of the monoanion of the parent compound. This behavior exactly parallels that of oxazole compounds (7).

Electrolysis of both compounds at potentials corresponding to their second diffusion plateaus produces a purple solution that is stable in the presence of N_2 but unstable to small amounts of O_2. Oxidation of the purple solution at the *in situ* PPDE after about 1 hr of mass electrolysis shows two small current peaks, one appearing at the potential corresponding to the oxidation of the monoanion and the other at the potential corresponding to the oxidation of the EC process product, RH^{-}. The oxidation peak of RH^{-} does not increase significantly even after exhaustive electrolysis. The uv absorbance of the parent oxadiazole shows that the substance undergoes an irreversible reaction at the potential of the second wave at a rate not detectable on the time scale of the rapid cyclic or potentiostatic experiments but more rapid than similar reactions of oxazoles (7). The exact nature of the reaction product has not been determined.

Effect of proton donors.—The nature of the proposed electrochemical reactions suggests that the addition of proton donating substances should have a pronounced effect on the reduction process responsible for each voltammetric wave. Hydroquinone (HQ) has been shown to be useful in studies of this type (12).

Figures 3 and 4 illustrate the effect of added HQ on the polarographic behavior of compounds I and II. The first wave of I is only slightly perturbed by the addition of the proton source. The polarographic $E_{1/2}$ is not shifted significantly even with the addition of

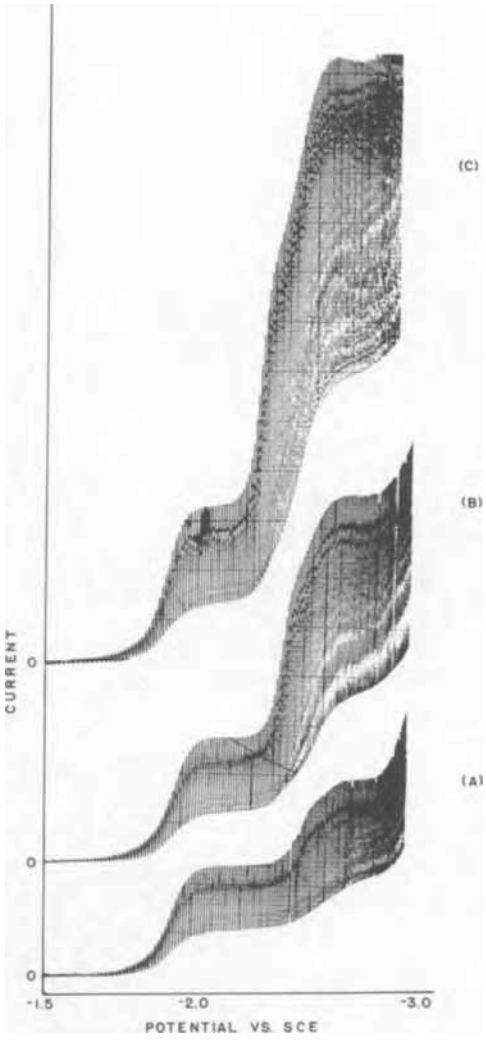

Fig. 3. Polarograms of 2,5-diphenyloxadiazole (I) in DMF showing effect of added hydroquinone (HQ). (a) No HQ, (b) 10 mM in HQ, (c) 60 mM in HQ. All solutions were 1 mM in compound (I) and 0.1M in TPAP supporting electrolyte.

enough HQ to produce a 0.06M DMF solution. However, the wave is broadened and the diffusion current is enhanced slightly by this addition of HQ, Fig. 3. The first wave of compound II is influenced in a similar manner, Fig. 4.

The second wave of compound I shifts anodically as HQ is added to the test solution, Fig. 4. There is a simultaneous, pronounced increase in the diffusion current approaching a limiting value at high concentrations of the proton donor, Fig. 3. The n apparent becomes approximately six at the higher HQ concentrations.

The great sensitivity of the diffusion current of the second polarographic wave of I to small quantities of solvent impurity is illustrated by a comparison of polarograms of I, 1 and 0.1 mM, in spectroquality DMF containing approximately 0.03% H_2O. This represents a ratio of electroactive compound to water impurity of 1/5 in the concentrated solution and 1/50 in the dilute mixture. The ratio of the first diffusion current to the second of the two plateaus is 1/1 in the more concentrated solution and 1/1.5 in the dilute. Decreasing the oxadiazole to proton source ratio in the concentrated solution to a value of 1/30 by adding HQ results in a first to second plateau diffusion current ratio of 1/1.9. This result suggests that water is almost as effective a proton donor in DMF as HQ, a result not noted in the study of aromatic hydrocarbons in aprotic media (13).

The second and third waves of compound II coalesce at low HQ concentrations (~7 mM) to one wave with

Table IV. Potential step chronoamperometric data for reduction of compounds I and II in DMF

Compound	Potential, V (V vs. SCE)	$it^{1/2}$ (μA sec$^{1/2}$)[b]	n apparent
2,5-Diphenyloxadiazole (I)	−1.96	38.86	1.0[c]
	−2.42	82.84	2.1[d]
2-(m-tolyl)-5-(1-naththyl)-oxadiazole (II)	−1.75	34.16	1.0[c]
	−2.18	71.63	2.1[d]
	−2.52	205.85	6.0[d]

[a] Solutions 1 mM in electroactive compound and 0.1M in TPAP. Experiments conducted at a PPDE having a cross sectional area of 0.78 cm^2.
[b] Values computed for times ranging from 0.75 to 4.0 sec.
[c] Assigned by various criteria discussed in text.
[d] Calculated by reference to $it^{1/2}$ value at first-wave potential.

an $E_{1/2}$ approximately the same as the second wave of II in dried DMF and with an n apparent of approximately six, Fig. 4. The diffusion current of the combination wave increases slightly with additional HQ but does not exhibit the great sensitivity noted of other waves.

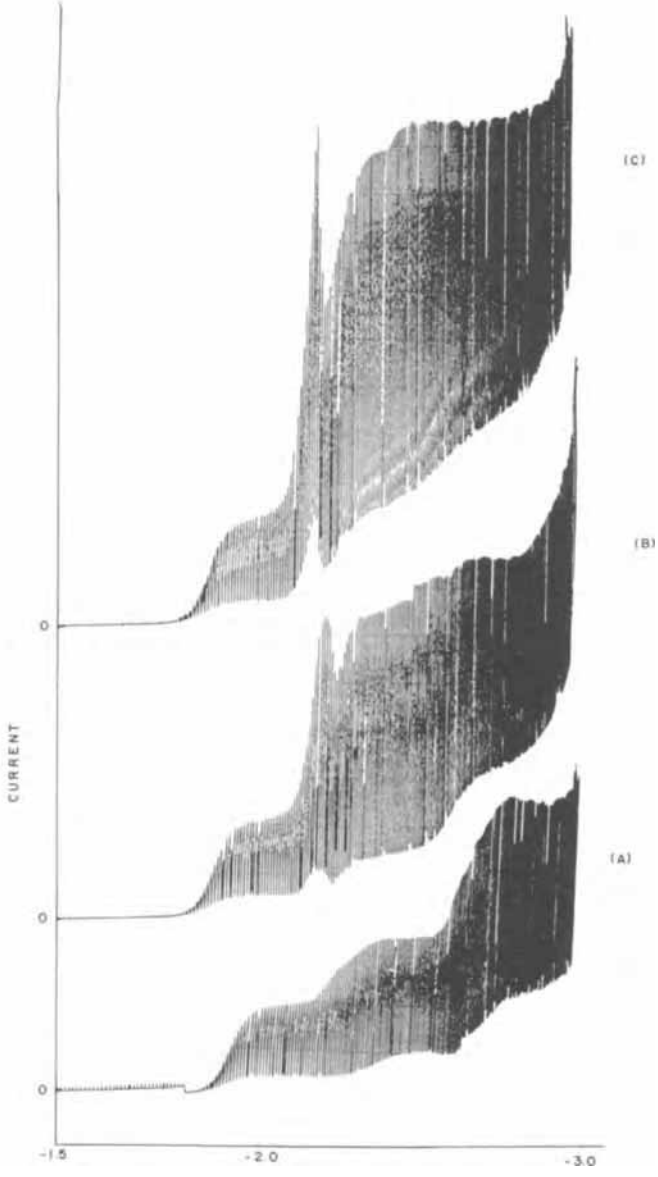

Fig. 4. Polarograms of 2-(1-naphthyl)-5-(m-tolyl)-oxadiazole (II) in DMF showing effect of added hydroquinone. (a) No HQ, (b) 6 mM in HQ, (c) 20 mM in HQ. All solutions were 1 mM in compound (II) and 0.1M in TPAP supporting electrolyte.

These results suggest the following mechanism for reduction of compounds I and II in the presence of HQ.

First wave

$$R + e^- \rightleftarrows R\cdot^-$$

$$R\cdot^- + HQ \rightarrow RH\cdot + Q^- \text{ (EC process)}$$

Second wave

$$RH\cdot + 5e^- + 5HQ \rightarrow \text{Ring opened products}$$

In contrast to oxazoles (7), other heteroaromatics and aromatic hydrocarbons (14), the protonated monoanion radical does not appear to undergo further significant reduction (an ECE process). The great dependency of the diffusion currents of the second polarographic waves of I and II is consistent with the noted instability of RH^- in the mass electrolysis experiments. This species is apparently a stronger base than the corresponding oxazole radical (7).

Summary and Discussion

Electrochemical information presented in his paper and that presented previously (7) show that aromatic-2,5-substituted oxazoles and oxadiazoles are reduced via similar mechanisms in DMF solvent. Differences in reactivity of the common reduction intermediates $R\cdot^-$ and RH^- are noted. The anion radicals of the oxadiazoles studied appear to be quite basic. These are protonated by small amounts of water. However, addition of proton donors show that the protonated radical is not significantly reduced at the potential of the first-electron addition step.

The protonated dianion of both oxadiazoles, produced by the EC process of the second polarographic step, appear to be significantly more reactive than the analogous species derived from oxazoles. The species reacts rapidly with small quantities of added hydroquinone forming saturated and ring opened products.

The nonsymmetrically substituted oxadiazole exhibits a third polarographic wave in dry DMF solvent. Addition of small quantities of HQ to the electrolysis solution shifts the $E_{1/2}$ of the wave to coincide with the second wave but does not greatly alter the n apparent of 6. This behavior is consistent with an exhaustive reductive process with a rate greatly dependent on the proton availability of the medium.

The oxidation going segment of cyclic experiments in dry DMF in which the electrolyzing potential is held at the third wave of compound II for several seconds reveals the existence of a reversible product couple with an $(Ep)c$ of −2.31V, Fig. 2C. The postulated neutral product of the third polarographic step may be thought of as a substituted naphthylene. This aromatic substance is expected to exhibit a one-electron reversible wave in DMF near the potential of the product wave, Fig. 2C (15). The existence of the reversibly reducible product may be construed as substantiation of the reduction process postulated as responsible for the polarographic wave.

More direct evidence for this postulated process is found in the IR spectrum of the product isolated from a DMF solution of II exhaustively electrolyzed at a potential controlled at the third plateau. The appearance of bands at 3200, 2900, and 3400 cm^{-1} when the product is dissolved in CCl_4 strongly suggests the electrolytic production of hydroxyl, alkyl, and secondary amine functions. The purified product melted in the range 90°-95°C.

Acknowledgment

The financial support of The Robert A. Welch Foundation (Grant No. AO-337) is gratefully acknowledged.

Manuscript submitted Jan. 14, 1971; revised manuscript received *ca.* Feb. 20, 1971.

Any discussion of this paper will appear in a Discussion Section to be published in the June 1972 JOURNAL.

REFERENCES
1. Ralph N. Adams, *Acc. of Chem. Res.*, **2**, 175 (1969).
2. K. S. V. Santhanam and A. J. Bard, *J. Am. Chem. Soc.*, **88**, 2669 (1966).
3. Ljubomir Jeftic and Ralph N. Adams, *ibid.*, **92**, 1332 (1970).
4. Salvatore Millefiori, *J. Heterocyclic Chem.*, **7**, 146 (1970).
5. G. Dryhurst, *This Journal*, **117**, 1113 (1970).
6. Borivoj Janik and P. J. Elving, *Chem. Rev.*, **68**, 295 (1968).
7. W. N. Greig and J. W. Rogers, *This Journal*, **117**, 1141 (1970).
8. R. S. Nicholson and I. Shain, *Anal. Chem.*, **36**, 706 (1964).
9. R. H. Wopschall and Irving Shain, *ibid.*, **39**, 1514 (1967).
10. C. S. Alberts and Irving Shain, *ibid.*, **35**, 1859 (1963).
11. V. D. Bezuglyi, N. P. Shimanskaya, and E. M. Peresleni, *Z. Obsh. Khim.*, **34**, 3540 (1964).
12. J. L. Sadler and A. J. Bard, *J. Am. Chem. Soc.*, **90**, 1979 (1968).
13. J. R. Jezorek and H. B. Mark, Jr., *J. Phys. Chem.*, **74**, 1627 (1970).
14. P. H. Given and M. E. Peover, *J. Chem. Soc.*, **1960**, 385.
15. A. Streitwieser, "Molecular Orbital Theory for Organic Chemists," John Wiley & Sons, Inc., New York (1962).

Dissolution of Barrier Layer of Aluminum in Sulfuric Acid Electrolyte Containing Cs^+ Ion

Michiko Shimura

Faculty of Engineering, Tokyo Metropolitan University, Fukazawa, Setagaya-ku, Tokyo, Japan

ABSTRACT

Examination of the recovery phenomenon for the anodic oxidation of aluminum in sulfuric acid electrolytes containing Cs^+ ion confirmed the suppression of the dissolution of the barrier layer. Lengths of the induction period and the current-increasing period in the recovery region were recorded. Electron microscope studies were carried out on samples taken out at the recovery region to examine the pore structure. Since the recovery currents result from the dissolution of barrier layers at the bottom of primary pores, the dissolution rates were calculated from the length of the induction period in the recovery region for $CsHSO_4$ and H_2SO_4 electrolytes. The conclusions are: (*i*) the presence of Cs^+ ions decreases the frequency factor for the dissolution process, and (*ii*) Cs-alum seals the porous layer of the oxide film and makes the steady-state current smaller.

Porous oxide film is produced by local action of electrolytes when aluminum is anodized in acid solutions. The action is temperature dependent (1, 2) and is promoted chiefly by protons in the electrolyte (1, 3) and the electric field across the barrier layer (4). The presence of an alkali metal ion such as Cs^+ improves the hardness and the coating ratio of the films (5), since an alum is deposited tightly on the porous film shortly after the beginning of the anodic oxidation. The stability of the alum increases in the order of the ionic radii of the alkali metal ions (6). The effect of Cs^+ ions on the dissolution process of the barrier layer was elucidated by examining the porous structure of the anodic films taken out at the so-called recovery period (7) during anodization.

Experimental Procedures

Observations with the oscilloscope.—Aluminum foils of 99.99% purity, 1 x 2.5 cm, were carefully electropolished in H_3PO_4-CrO_3-H_2SO_4 electrolyte and stripped in H_3PO_4-CrO_3 solution just before anodic oxidation. A 1.8*M* $CsHSO_4$ (*p*H 0.6) solution was used for the oxidation, and H_2SO_4 of the same *p*H value for a reference run. The *p*H values were adjusted to be the same since the dissolution of the film was largely dependent on the concentration of protons in the electrolyte. Parallel circuits were constructed in order to perform the oxidation simultaneously in $CsHSO_4$ and H_2SO_4. Constant voltages E_1 and E_2 were applied from two d-c power supplies. Anodization was carried out for a certain time at the higher voltage (E_1). Afterward the voltage was switched down to the lower voltage (E_2). Throughout the whole period, the I-t curves were recorded by the oscilloscope. The results were obtained in the range of 10°-40°C, E_1 = 9-15V, E_2 = 8V, length of the initial oxidation at E_1 being 90 sec to 200 min.

Examination by electron microscope.—In case of fairly thin films, anodized samples were cut off with about the size of 3 x 3 mm and immersed in CH_3OH-I_2 solution to peel off the oxide film. After rinsing with CH_3OH, the oxide films were examined by direct transmission electron microscopy using JOEL electron microscope model JEM 100. For thick films, the two-step cellulose-carbon replica technique was used. The numbers of pores were counted at a magnification of 180,000 and averaged on three different 3 x 3 cm squares. The spots were selected at random. The porosities were obtained by summing up the pore areas in the squares.

Results

Recovery effect at E_1 = 10V (5 min) and E_2 = 8V.—When the samples were anodized at 10V (E_1) in the temperature range of 10°-40°C, the current rapidly decreased to a minimum and subsequently increased to a steady-state value which became larger with the electrolyte temperature. After anodizing for 5 min under this condition, the applied voltage was switched to 8V. The current decreased suddenly to almost zero, stayed there for a while, the induction period depending on the electrolyte temperature, *i.e.*, 70 sec at 10°C, 20 sec at 25°C, and 7 sec at 40°C, and then increased to retain new steady states (Fig. 1). The existence of Cs^+ ion extended the induction period to a small extent and slightly reduced the new steady current.

Effect of prolonged anodization at the initial voltage.—In connection with the amount of alums produced, the induction period was examined as a function of

* Key words: oxide dissolution, barrier layer, aluminum.

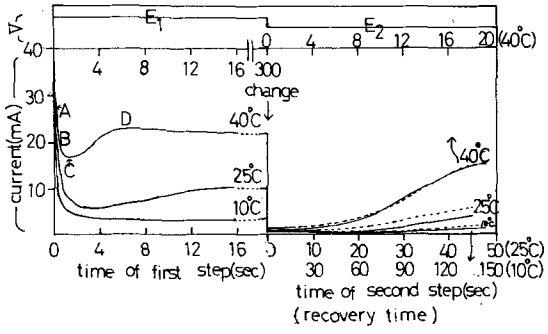

Fig. 1. I-t curves at two step oxidation, left, first step (E_1 = 10V) and right, second step (E_2 = 8V), ——— in $CsHSO_4$, – – – – in H_2SO_4.

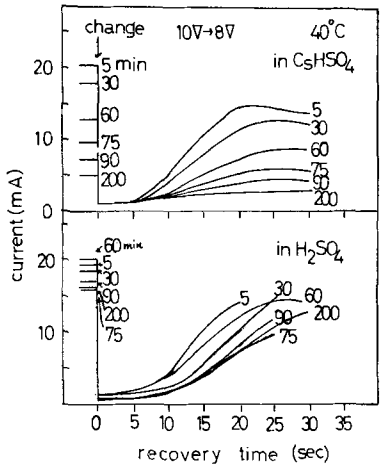

Fig. 2. Recovery behavior at various durations of E_1

the anodizing time at the initial voltage at 40°C. As is shown in Fig. 2, the induction periods did not change with the prolongation of the anodic oxidation either in $CsHSO_4$ or H_2SO_4 within 200 min. The steady-state currents at the end of the anodization both at 10V and 8V decreased with the prolongation of the oxidation in $CsHSO_4$, whereas they did not in H_2SO_4. As is discussed later with the results of the electron microscope study, the decrease of the current is explained by the sealing action of Cs-alum near the top of the pores.

Recovery effect at various voltage differences.—Figures 3 through 6 show the recovery effect at the voltage differences ΔE = 4V (12V → 8V) and ΔE = 6V (14V → 8V). The induction periods became larger with the increase of ΔE both in $CsHSO_4$ and H_2SO_4 electrolytes. The prolongation of the anodic oxidation at E_1 never changed the length of the induction period, not even at increased values of E_1. The ratio of steady-state currents, $I_{(E_2)}/I_{(E_1)}$ decreased with the anodizing time at E_1. The trend is more distinct for the increase

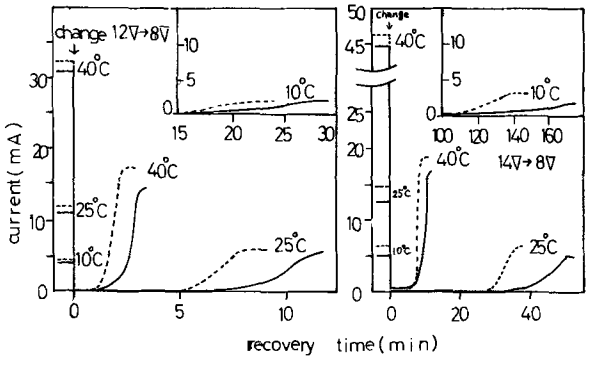

Fig. 3 (left) and Fig. 4 (right). Recovery behavior of two step oxidation; ——— in $CsHSO_4$, – – – – in H_2SO_4.

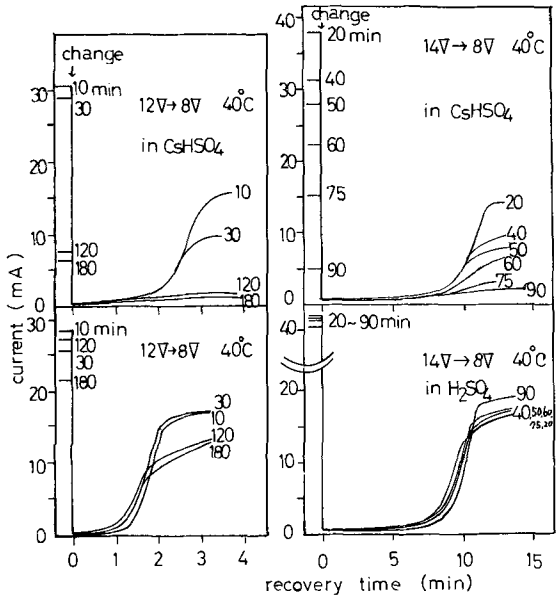

Fig. 5 (left) and Fig. 6 (right). Recovery behavior at various durations of E_1.

of ΔE at a fixed value of E_2. This suggests that the sealing of the pores with Cs-alum proceeds vigorously in the recovery region at a higher voltage E_1. The following results also confirm the sealing mechanism. The steady-state current increases exponentially with the applied voltage (8). The steady-state current is attained when the dissolution rate of the oxide at the bottom of pores is equal to the current density for the oxide formation. The rate of formation of Cs-alum is determined by the concentration of the dissolved Al^{3+} ions in the equation

$$v = k[Al^{3+}][Cs^+][SO_4^{2-}]^2$$

I-t curves plotted in a logarithmic scale are distinctly divided into an induction period and a region of increasing current. For the former region, the change of the current is too small to measure. For the latter region, the slope is nearly uniform in spite of changes of temperature, electrolytes, and voltage difference. Accordingly, the current increase should be caused by other types of dissolution than the conventional chemical dissolution. Diggle *et al.* (4) introduced field-assisted dissolution. As is shown in the next section, rapid dissolution of the film like the pore initiation at the early stage of anodic oxidation occurs at the current-increasing region.

Structure of the porous film taken out at recovery region.—Figure 7 shows the porous structure of the samples taken out at different times t in the recovery region when E_1 = 14V (90 sec) and E_2 = 8V. The structure of the anodic films formed in $CsHSO_4$ and H_2SO_4 is very similar. The size and the shape of the pores are somewhat irregular, and secondary pores are barely recognizable with the increase of magnification. The number of the primary pores in 3 x 3 cm squares on the pictures taken at 180,000X are roughly constant for all samples (Fig. 8). The tiny secondary pores, which have been observed dimly before the recovery region, become distinct with increasing time t. Therefore, the recovery effect is understood to thin the barrier layer by dissolution at the bottom of the primary pores (Fig. 9), allowing ionic current to flow again.

Porosities were examined at various times in the recovery region by summing the pore areas statistically (Fig. 8). The total pore area was almost constant in the recovery period but increased in the region of increasing current. Therefore, in the region of increasing current, the rate of the dissolution process is

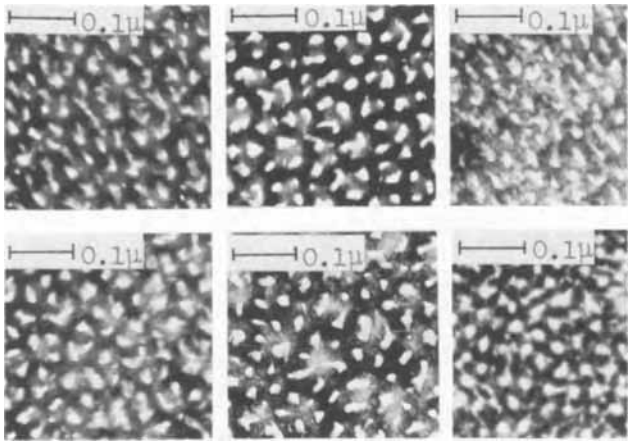

Fig. 7. Electron microscope structures of samples taken at various time scales in recovery region, 25°C, 14V-8V. Upper row; 0, 20, 45 min in $CsHSO_4$, lower row; 0, 20, 36 min in H_2SO_4.

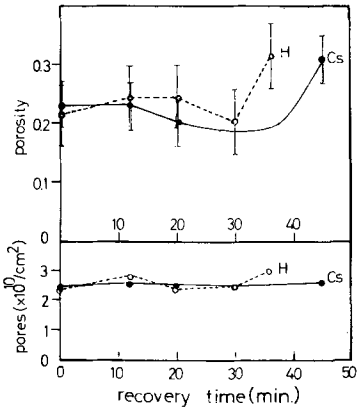

Fig. 8. Pore number and porosity vs. progress of recovery effect.

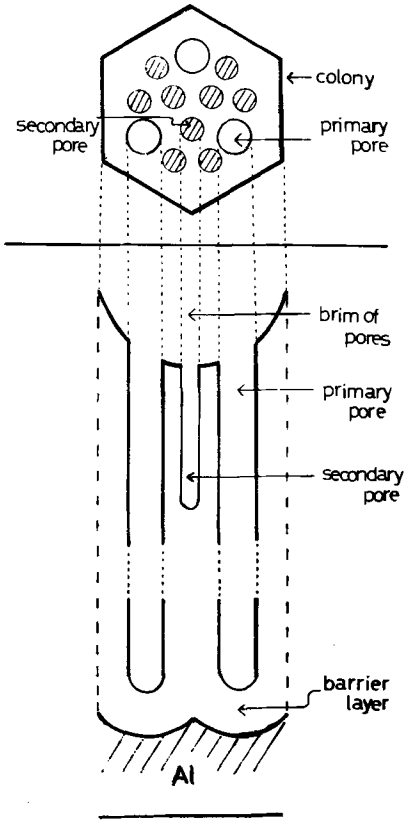

Fig. 9. Model of porous structure at the early stage. The secondary pores exist beside the primary ones.

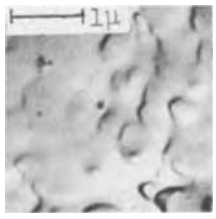

Fig. 10. Surface with Cs-alum deposits taken by replica method, 90 min, 40°C; 14V in $CsHSO_4$.

changed by some other cause than chemical dissolution.

The thickness of the oxide films differed in $CsHSO_4$ and H_2SO_4 when the initial oxidation at E_1 was longer than 5 min at 40°C. In $CsHSO_4$, the oxide film gradually thickened with time and made the direct transmission observation impossible (9). The Cs^+ ion is likely to suppress the dissolution process by decreasing the activity of the protons near the anode. After longer oxidation in $CsHSO_4$, Cs-alum was deposited and covered the surface of the oxide. It was difficult to scrape off or to dissolve by dipping in hot water (Fig. 10).

Discussion

Dissolution reaction in the recovery region.—The results of the electron microscope study clarified that the recovery effect is accompanied by the dissolution of the barrier layer at the bottom of the primary pores and that the dissolution proceeded slowly in the induction region. It was accelerated in the region where the current increased. The length of the induction period depends on the electrolyte temperature; *e.g.*, the duration at 10°C is about ten times that at 40°C in the case of $\Delta E = 2$V. Beside colorimetric analysis by Nagayama *et al.* (10) and capacitance measurements by Diggle *et al.* (4), the author's experiments (11) suggest that the dissolution is slow in the induction period, and that the concentrations of ions at the double layer of the interface oxide/electrolyte are approximately constant. Thus, the apparent reaction of the dissolution is assumed to be of zero order. Since there is an equation, $i = A \exp(B \cdot E/D)$ between current density i, applied voltage E, and the thickness D of the barrier layer, where A and B are constants, the layer thickness to be dissolved before the current begins to rise at $E_2 = 8$V is given by $D_s = (E_1 - E_2) \cdot K$, where K is a constant (*ca.* 14Å/V). The mean rate of dissolution is given by D_s/t, where t is the length of the induction period. The activation energies of dissolution were the same both for $CsHSO_4$ and H_2SO_4, Cs^+ ions having no influence on the activation energy. The frequency factor is found to decrease with the presence of Cs^+ ion. The dissolution process is governed solely by protons. Cs^+ ions are considered to decrease the local concentration of protons near the anode to some degree. Since the current tends toward a steady state some time after the pore initiation, the main role of dissolved Al^{3+} is to suppress the activity of protons.

Relation between voltage difference and activation energy of the dissolution process.—The activation energies of the dissolution process were examined as a function of the voltage difference ($\Delta E = E_1 - E_2$) when E_1 was applied for 5 min. The apparent activation energy was found higher with the decrease of the electric field across the barrier layer. The apparent activation energy W_a is the sum of the activation energy W_o and a term representing the electric field E/D

$$W_a = W_o - n \cdot F \cdot E/D \qquad [1]$$

As is shown in Fig. 11, the activation energy W_o decreases with the increase of the electric field. The electrochemically produced materials are assumed to be transformed into more soluble ones by the aid of the electric field.

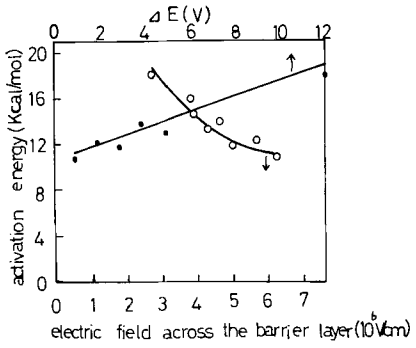

Fig. 11. Relation between apparent activation energies of dissolution process and electric field across barrier layers.

Conclusion

1. The recovery phenomenon in the induction region depends strongly on temperature while the one in the region of increasing current is independent of temperature. If the former phenomenon is regarded as zero-order dissolution, the activation energy is calculated 11-18 kcal/mole and decreases with the increase of the electric field across the barrier layer. It is in good agreement with the value obtained by Vermilyea (12) (17 kcal/mole) for the surface hydrolysis of amorphous Al_2O_3, a value close to the activation energy of diffusion for proton in many oxides. The dissolution of the barrier layer is considered to depend on the diffusion of protons through it.

2. The addition of Cs^+ in H_2SO_4 electrolyte contributes to the decrease of the frequency factor of the barrier layer dissolution.

3. Cs-alum is probably deposited at the upper part of the inner surface of pores and not at the bottom since the recovery time never changes with the prolongation of the initial oxidation when Cs-alum is deposited.

Manuscript submitted Oct. 2, 1970; revised manuscript received *ca.* Feb. 15, 1971.

Any discussion of this paper will appear in a Discussion Section to be published in the June 1972 JOURNAL.

REFERENCES

1. T. P. Hoar and J. Yahalom, *This Journal*, **110**, 614 (1963).
2. S. Tajima and M. Shimura, *J. Electrochem. Soc. of Japan*, **32**, 883 (1964).
3. M. Shimura, *ibid.*, **38**, 100 (1970).
4. J. W. Diggle, T. C. Dowine, and C. W. Goulding, *This Journal*, **116**, 737 (1969).
5. M. Shimura and S. Tajima, *J. Electrochem. Soc. Japan*, **37**, 221 (1969).
6. M. Shimura and S. Tajima, *23rd Annual Meeting, Chem. Soc. Japan*, **11**, 1029 (1970).
7. J. F. Murphy, *Proceedings of Symposium on Anodizing Aluminium*, The Aluminium Federation, April (1967).
8. M. Shimura, *J. Electrochem. Soc. Japan*, **39**, (March 1971) (In press).
9. M. Shimura, *ibid.*, In press.
10. M. Nagayama, K. Tamura, and H. Takahashi, *15th Symposium on Corrosion and Protection, Japan*, p. 131 (1968).
11. M. Shimura, T. Otsuka, and S. Tajima, *J. Electrochem. Soc. Japan*, **37**, 352 (1969).
12. W. Vedder and D. A. Vermilyea, *Trans. Faraday Soc.*, **65**, 561 (1969).

Transport Behavior in Dimethyl Sulfoxide

I. Conductance Studies

Neng-Ping Yao*,[1] and D. N. Bennion*

Energy and Kinetics Department, School of Engineering and Applied Science, University of California, Los Angeles, California 90024

ABSTRACT

Conductance of the salts $NaClO_4$, NaSCN, CF_3SO_3Na, CH_3SO_3Na, $NaB(Ph)_4$, and $(i\text{-amyl})_3BuNB(Ph)_4$ in dimethyl sulfoxide (DMSO) were determined over a concentration range 10^{-4} mole/liter to near saturation and a temperature range 25°-55°C. $NaClO_4$, NaSCN, and CF_3SO_3Na are completely dissociated while CH_3SO_3Na, $NaB(Ph)_4$, and $(i\text{-amyl})_3BuNB(Ph)_4$ appear to be slightly associated. Single-ion conductivities were determined using triisoamylbutylammonium tetraphenylboride as the reference electrolyte. The effective ionic radii for $(i\text{-amyl})_3BuN^+$, Na^+, $CF_3SO_3^-$, ClO_4^-, and SCN^- ions were determined to be 5.12, 4.32, 3.03, 2.82, and 2.37Å, respectively, at 25°C. Na^+ ion is solvated with three DMSO molecules while the $(i\text{-amyl})_3BuN^+$ ion and the anions are relatively unsolvated. The effective ionic radii in DMSO are insensitive to temperature over the temperature range studied. Activation energies for ionic conductance in dilute solutions of $(i\text{-amyl})_3BuNB(Ph)_4$, $NaB(Ph)_4$, $NaClO_4$, CF_3SO_3Na, and NaSCN are, respectively 3.50, 3.30, 3.23, 3.21, and 3.16 kcal/mole. Limiting ionic mobilities λ_o, for alkali-halide ions and other ions in DMSO at 25° are examined in the light of the Fuoss, Boyd, and Zwanzig theories of dielectric relaxation. The limiting ionic mobilities predicted by the Zwanzig theory are in qualitative agreement with the observed values, but the predicted magnitudes are low.

Dimethyl sulfoxide (DMSO) is an aprotic solvent which possesses many useful properties for applications in electrochemical systems (1) and in organic syntheses (2). Thermodynamic data which have been reported for electrolyte solutions in DMSO are some solubilities (3, 4), some acid-base equilibria (5), cryoscopic data (6), heat of solution (7, 8), and emf measurements (9-11). A few conductance studies have been reported (3, 6, 12-14). Ionic transport behavior in DMSO solutions is yet to be elucidated with systematic studies of transport parameters.

* Electrochemical Society Active Member.
[1] Present address: Atomics International Division of North American Rockwell Corporation, Canoga Park, California 91304.
Key words: conductance, dimethyl sulfoxide, ion size, limiting ionic conductance.

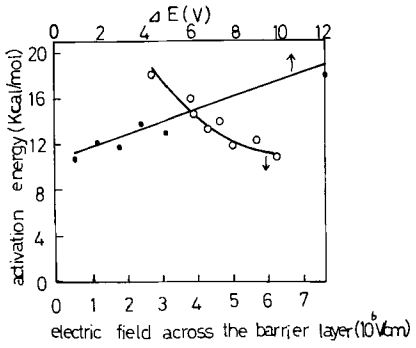

Fig. 11. Relation between apparent activation energies of dissolution process and electric field across barrier layers.

Conclusion

1. The recovery phenomenon in the induction region depends strongly on temperature while the one in the region of increasing current is independent of temperature. If the former phenomenon is regarded as zero-order dissolution, the activation energy is calculated 11-18 kcal/mole and decreases with the increase of the electric field across the barrier layer. It is in good agreement with the value obtained by Vermilyea (12) (17 kcal/mole) for the surface hydrolysis of amorphous Al_2O_3, a value close to the activation energy of diffusion for proton in many oxides. The dissolution of the barrier layer is considered to depend on the diffusion of protons through it.

2. The addition of Cs^+ in H_2SO_4 electrolyte contributes to the decrease of the frequency factor of the barrier layer dissolution.

3. Cs-alum is probably deposited at the upper part of the inner surface of pores and not at the bottom since the recovery time never changes with the prolongation of the initial oxidation when Cs-alum is deposited.

Manuscript submitted Oct. 2, 1970; revised manuscript received *ca.* Feb. 15, 1971.

Any discussion of this paper will appear in a Discussion Section to be published in the June 1972 JOURNAL.

REFERENCES

1. T. P. Hoar and J. Yahalom, *This Journal*, **110**, 614 (1963).
2. S. Tajima and M. Shimura, *J. Electrochem. Soc. of Japan*, **32**, 883 (1964).
3. M. Shimura, *ibid.*, **38**, 100 (1970).
4. J. W. Diggle, T. C. Dowine, and C. W. Goulding, *This Journal*, **116**, 737 (1969).
5. M. Shimura and S. Tajima, *J. Electrochem. Soc. Japan*, **37**, 221 (1969).
6. M. Shimura and S. Tajima, *23rd Annual Meeting, Chem. Soc. Japan*, **11**, 1029 (1970).
7. J. F. Murphy, *Proceedings of Symposium on Anodizing Aluminium*, The Aluminium Federation, April (1967).
8. M. Shimura, *J. Electrochem. Soc. Japan*, **39**, (March 1971) (In press).
9. M. Shimura, *ibid.*, In press.
10. M. Nagayama, K. Tamura, and H. Takahashi, *15th Symposium on Corrosion and Protection, Japan*, p. 131 (1968).
11. M. Shimura, T. Otsuka, and S. Tajima, *J. Electrochem. Soc. Japan*, **37**, 352 (1969).
12. W. Vedder and D. A. Vermilyea, *Trans. Faraday Soc.*, **65**, 561 (1969).

Transport Behavior in Dimethyl Sulfoxide

I. Conductance Studies

Neng-Ping Yao*,[1] and D. N. Bennion*

Energy and Kinetics Department, School of Engineering and Applied Science, University of California, Los Angeles, California 90024

ABSTRACT

Conductance of the salts $NaClO_4$, NaSCN, CF_3SO_3Na, CH_3SO_3Na, $NaB(Ph)_4$, and $(i\text{-amyl})_3BuNB(Ph)_4$ in dimethyl sulfoxide (DMSO) were determined over a concentration range 10^{-4} mole/liter to near saturation and a temperature range 25°-55°C. $NaClO_4$, NaSCN, and CF_3SO_3Na are completely dissociated while CH_3SO_3Na, $NaB(Ph)_4$, and $(i\text{-amyl})_3BuNB(Ph)_4$ appear to be slightly associated. Single-ion conductivities were determined using triisoamylbutylammonium tetraphenylboride as the reference electrolyte. The effective ionic radii for $(i\text{-amyl})_3BuN^+$, Na^+, $CF_3SO_3^-$, ClO_4^-, and SCN^- ions were determined to be 5.12, 4.32, 3.03, 2.82, and 2.37Å, respectively, at 25°C. Na^+ ion is solvated with three DMSO molecules while the $(i\text{-amyl})_3BuN^+$ ion and the anions are relatively unsolvated. The effective ionic radii in DMSO are insensitive to temperature over the temperature range studied. Activation energies for ionic conductance in dilute solutions of $(i\text{-amyl})_3BuNB(Ph)_4$, $NaB(Ph)_4$, $NaClO_4$, CF_3SO_3Na, and NaSCN are, respectively 3.50, 3.30, 3.23, 3.21, and 3.16 kcal/mole. Limiting ionic mobilities λ_o, for alkali-halide ions and other ions in DMSO at 25° are examined in the light of the Fuoss, Boyd, and Zwanzig theories of dielectric relaxation. The limiting ionic mobilities predicted by the Zwanzig theory are in qualitative agreement with the observed values, but the predicted magnitudes are low.

Dimethyl sulfoxide (DMSO) is an aprotic solvent which possesses many useful properties for applications in electrochemical systems (1) and in organic syntheses (2). Thermodynamic data which have been reported for electrolyte solutions in DMSO are some solubilities (3, 4), some acid-base equilibria (5), cryoscopic data (6), heat of solution (7, 8), and emf measurements (9-11). A few conductance studies have been reported (3, 6, 12-14). Ionic transport behavior in DMSO solutions is yet to be elucidated with systematic studies of transport parameters.

* Electrochemical Society Active Member.
[1] Present address: Atomics International Division of North American Rockwell Corporation, Canoga Park, California 91304.
Key words: conductance, dimethyl sulfoxide, ion size, limiting ionic conductance.

This paper reports the results of conductance studies of some sodium salts in DMSO over a concentration range 10^{-4}M to near saturation and a temperature range 25°-55°C. Triisoamylbutylammonium tetraphenylboride, $(i\text{-amyl})_3BuNB(Ph)_4$, was included in the present study to provide the basis for evaluating single-ion conductivities. The effective ionic radii in DMSO were obtained and the limiting ionic mobilities for various ions in DMSO were examined in the light of the theory of dielectric relaxation (15-18).

Experimental

Solvent.—DMSO was supplied by Crown Zellerbach Corporation, Camas, Washington, in five gallon size polyethylene containers. DMSO as received was purified by fractional distillation at 3.3 mm Hg pressure and 40°C. Volume of the initial charge to the boiling flask was approximately 1500 ml. The middle portion of distilled DMSO, approximately 60% of the initial charge, was collected and was stored in a nitrogen-filled dry box for subsequent use. Kolthoff and Reddy (19) reported that refluxing over CaO or BaO caused extensive decomposition and that removal of all the decomposition products, not identified, was impossible. Since the effect of the drying agents on the degree of decomposition of DMSO is not known, no special dehydration procedure was undertaken prior to the vacuum distillation. Water content in DMSO was determined to be less than 30 ±5 ppm by electrometric titration with Karl Fischer Reagent (KFR). Repeated determinations of water concentration in distilled DMSO over several months of standing showed that water content was less than 100 ppm for all cases. NMR analysis of distilled DMSO showed no detectable organic impurities peak. However, the accuracy of the NMR analysis was limited to 0.1% based on carbon 13 calibration.

Triisoamylbutylammonium tetraphenylboride, $(i\text{-amyl})_3BuNB(Ph)_4$.—This salt was prepared following the method of Coplan and Fuoss (20). The $(i\text{-amyl})_3BuNB(Ph)_4$ was thoroughly washed and then recrystallized four times from 3:1 (v/v) acetone-water (approximately 1.5g salt/100 ml solution). The recrystallized $(i\text{-amyl})_3BuNB(Ph)_4$ formed fluffy, needle-like crystals. The salt was then dried *in vacuo* at 105°C for 21 hr. Its melting point was determined to be 275°C as reported (20). Infrared spectrum analysis showed absorption peaks at 16.5, 14.2, 13.7, 13.5, 6.77, and 3.38 μm. This spectrum does not appear to have been previously reported.

Sodium trifluoromethanesulfonate, CF_3SO_3Na.—This salt was prepared by first converting $(CF_3SO_3)_2Ba$, supplied by the 3M Company, Saint Paul, Minnesota, into an acid solution of CF_3SO_3H with dilute H_2SO_4 solution, and then the acid solution was neutralized to a neutral end point with dilute Na_2CO_3 solution. The resultant solution was evaporated to dryness under reduced pressure. The dried CF_3SO_3Na was recrystallized three times from acetone. The pure white salt was dried *in vacuo* at 140°C for 42 hr. The melting point of the salt was determined to be 248° ± 1°C which is in agreement with the value of 248°C for CF_3SO_3Na as reported by Gramstad and Haszeldine (21). Infrared spectrum of the salt showed absorption peaks at 7.9, 8.6, and 9.6 μm. Gramstad and Haszeldine (21) reported absorption peaks at 7.82 and 9.60 μm for CF_3SO_3Na corresponding respectively to asymmetric and symmetric stretching of $-SO_2-$group.

Sodium methanesulfonate, CH_3SO_3Na.—This salt was prepared by neutralizing CH_3SO_3H (Eastman Organic, Reagent Grade) acid solution with basic Na_2CO_3 (J. T. Baker, Analyzed Reagent Grade) solution. As the solution was evaporated to dryness, it was filtered several times prior to precipitation of the CH_3SO_3Na. The dry salt was pure white and was insoluble in acetone, but slightly soluble in CH_3OH. The salt was recrystallized twice from 1:1 (v/v) MeOH-H_2O mixture and once from 1:1 (v/v) acetone-water mixture. The salt was then dried in a vacuum oven at 140°C for 48 hr. Infrared spectrum of the salt showed two absorption peaks at 8.3-8.5 μm and 9.5 μm. These values are in agreement with 8.37 and 9.43 μm which are assigned to the asymmetric and symmetric stretching respectively of the $-SO_2-$group as reported by Gramstad and Haszeldine (21).

Sodium tetraphenylboride, $NaB(Ph)_4$.—"Baker Analyzed" Reagent Grade $NaB(Ph)_4$ powder (minimum purity of 99.5%) was purchased from J. T. Baker Chemical Company, Phillipsburg, New Jersey. Recrystallization of the salt from 1:1 (v/v) acetone-toluene mixture (22) was unsuccessful. The dissolution of $NaB(Ph)_4$ salt had a negative temperature coefficient and positive heat of solution in the acetone-toluene mixture. The salt was, however, recrystallized three times successfully from pure acetone. The salt was then dried *in vacuo* at 80°C for 48 hr. The salt was pure white and had no phenolic odor. Infrared spectrum of the $NaB(Ph)_4$ salt showed two large absorption peaks at 13.4 and 14 μm, and four small peaks at 6.7, 7.0, 8.4, 8.7 μm all of which were identical to that shown in Sadtler Standard Spectra (23).

Sodium perchlorate, $NaClO_4$.—Anhydrous purified grade $NaClO_4$ (City Chemical Corporation, New York City) was recrystallized three times from redistilled water as done by Ames and Sears (24). The salt was dried *in vacuo* at 100°C for 66 hr and was followed by additional heating at 120°C for 7½ hr *in vacuo*. Infrared spectrum of the salt showed two absorption peaks at 8.8-9.3 μm and 16 μm which is identical to that reported (25).

Sodium thiocyanate, NaSCN.—Reagent grade NaSCN (crystals, minimum purity 99.0%, J. T. Baker) was recrystallized three times from redistilled water (12) and was dried *in vacuo* at 60°C for 29 hr. The salt is extremely hygroscopic and no reliable infrared spectrum data are available.

Potassium chloride, KCl.— "Baker Analyzed" Reagent Grade KCl (crystal, minimum purity 99.5%, J. T. Baker) was recrystallized three times from redistilled water as recommended by Daggett, Blair, and Kraus (26). The salt was dried *in vacuo* at 140°C for 40 hr. Aqueous KCl solutions of various concentrations were prepared to calibrate cell constants of conductance cells.

All purified salts were stored in vacuum dessicators over molecular sieves until used.

Preparation of solutions.—All solutions except aqueous KCl solutions were prepared in a nitrogen-filled dry box. The solutions were prepared by weights corrected to vacuum values with density data. Volume concentration was obtained from the weight concentration and density. Solutions of different concentration were prepared by successive dilution of a stock solution of near saturation.

The lowest concentration prepared for each electrolyte in DMSO was normally in the order of 10^{-4} mole/kg solution, below which solvent conductance became significant and the conductance of electrolyte solutions had to be appropriately corrected.

All glassware used in the preparation of solutions was cleaned in 1:1 ratio concentrated HCl-HNO_3 acid mixtures, followed by extensive rinse with redistilled water and reagent grade acetone. The glassware was then dried *in vacuo* at 80°C for 20 hr prior to use in the dry box.

Conductance measurements.—Conductances of the electrolyte solutions were measured with an a-c bridge (27). Sinusoidal signals of frequencies ranging from 100 Hz to 80 kHz and amplitude of approximately 15V to very low values were generated by an oscillator (General Radio Company, Type 1302-A). The cell resistance and capacitance were balanced with variable decade resistors and variable capacitors. The variable decade resistors were General Radio precision decade

Table I. Density, viscosity, and dielectric constant of distilled DMSO

Temperature, °C	Density, g/ml	Viscosity, centipoise	Dielectric constant at 80 kHz
25	1.0961	1.998	46.4
35	1.0855	1.652	44.7
45	1.0745	1.394	43.3
55	1.0637	1.192	41.9

resistors (General Radio Company, Type 510-A through Type 510-F), 0.1 ohm/step to 10 k-ohm/step with accuracies of ±0.5 to ±0.025% and with no frequency dependence up to 200 kHz. The variable precision capacitance box was of 100 to 1150 pico farad range (General Radio Company, Type 1422-N) placed in parallel with the variable decade resistors. The null point was detected by a Hewlett-Packard Model 120B oscilloscope which had a sensitivity of 10 mV/cm. All electrical wires and connections were shielded from noise by using concentrically shielded cable and BNC connectors. Further description is given elsewhere (27).

Because of the wide concentration range of electrolyte solutions to be investigated, conductance cells of various geometry were designed to give cell constants appropriate to solution resistances. Five conductance cells were designed and fabricated from Pyrex glass. The details of the cell description are given elsewhere (27). Bright platinum electrodes were utilized in these cells. Resistance measurements were made between frequency 600 Hz and 20 kHz. True resistance was obtained by linear extrapolation of resistance *vs.* reciprocal of frequency to infinite frequency. Usually resistance readings became independent of frequency when frequency was above 4 kHz.

Cell constants of the conductance cells at 25°C were determined with standard 0.1, 0.01, 0.001, and 0.0005*N* KCl solutions (28). Conductance of KCl solutions below 0.01*N* was obtained using the smoothed equation of Lind, Zwolenik, and Fuoss (29) which has an accuracy of about 0.013% at 25°C. The cell constants for the five cells were respectively 13.20, 2.676, 4.747, 0.6644, and 0.008809 cm^{-1} at 25°C. Allowing for the thermal expansion of glass and the metal electrodes, the temperature coefficients of the cell constants were calculated. At the maximum temperature, 55°C, of the present studies, the change of cell constants was negligible compared to the experimental accuracy of ±0.1%.

Filling of all solutions into the conductance cells was performed in the nitrogen-filled dry box. The cells were subsequently sealed in the dry box before being immersed in oil baths in room air. Oil bath temperature was maintained to ±0.03°C. Thermal equilibration was assumed attained when the resistance value became invariant with time, normally about 30 min.

The conductance data were reproducible to within 0.1% as the temperature was raised and lowered between 25° and 55°C. Over-all accuracy of the conductance data is estimated to be better than 0.3% based on the uncertainty of individual readings and variations between readings.

Viscosity, density, and dielectric constant measurements.—Viscosity, density, and dielectric constant of the solutions were determined respectively by modified Cannon-Ubbelohde viscometers, a two capillary relative densitometer (30), and an a-c capacitance bridge. The detailed descriptions of the apparatus and the calibration procedure have been described elsewhere (27). The over-all estimated accuracies for the viscosity, density, and dielectric constant measurements are better than ±0.1, ±0.1, and ±2%, respectively.

Data and Results

Density, viscosity, and dielectric constant of distilled DMSO at 25°, 35°, 45°, and 55°C are given in Table I. The viscosity data given in Table I represent the average value of twelve measurements of distilled DMSO. The values of density, viscosity, and dielectric constant at 25°C are in good agreement with those reported by Sears *et al.* (12), Cowie and Toporowski (31), and Lindberg and Kenttämaa (32).

Equivalent conductance of $NaClO_4$, NaSCN, $NaB(Ph)_4$, $(i\text{-amyl})_3BuNB(Ph)_4$, CF_3SO_3Na, and CH_3SO_3Na in DMSO as a function of concentration and temperature are tabulated in Tables II through VII. Solvent viscosity, η_o, and specific conductance, κ^o_{sp}, are also given in these tables.

The conductance data in the dilute concentration range, *i.e.*, $\kappa_a^o \leqq 0.2$, where the highest concentration in the dilute range was marked by an asterisk in Tables II through VII, were analyzed by the Fuoss-Onsager theoretical equation for unassociated 1-1 electrolytes

$$\Lambda = \Lambda_o - SC^{1/2} + EC \log C + (J(\overset{o}{a}) - B\Lambda_o)C \quad [1]$$

for associated electrolytes

$$\Lambda = \Lambda_o - S(C\alpha')^{1/2} + E(C\alpha') \log (C\alpha') + (J(\overset{o}{a}) - B\Lambda_o)C\alpha' - K_A C\alpha'\gamma_{\pm}^2\Lambda \quad [2]$$

Kay's least-squares computer program (33) was used for the analyses. In the computer analyses, the viscosity *B* coefficients were obtained by analyzing the viscosity data with the Jones-Dole equation (34). The

Table II. Conductance of $NaClO_4$-DMSO solutions

Λ in mho · cm^2 · Eq^{-1}. The numbers in parentheses adjoining the Λ values give the ratio of the molar concentration of the solution at the given temperature to the molar concentration of the same solution at 25°C as given in the first column.

C, mmole/liter at 25°C	Λ (25°C)	Λ (35°C)		Λ (45°C)		Λ (55°C)	
1503.4	6.213	8.478	(0.9911)	11.19	(0.9771)	14.26	(0.9643)
755.44	15.11	18.92	(0.9922)	23.14	(0.9788)	27.63	(0.9649)
380.69	21.74	26.57	(0.9895)	31.68	(0.9789)	36.96	(0.9685)
122.82	27.84	33.56	(0.9903)	39.65	(0.9802)	46.04	(0.9705)
58.252	30.41	36.64	(0.9902)	43.21	(0.9800)	50.15	(0.9704)
45.633	31.00	37.36	(0.9900)	44.11	(0.9800)	51.14	(0.9699)
16.557	33.55	40.11	(0.9900)	47.82	(0.9799)	55.39	(0.9699)
10.056	34.51	41.38	(0.9902)	49.09	(0.9803)	56.66	(0.9703)
4.4262*	35.42	42.86	(0.9903)	49.75	(0.9804)	58.57	(0.9704)
1.9806	36.48	44.08	(0.9903)	51.32	(0.9803)	60.56	(0.9704)
0.76837	37.35	44.91	(0.9904)	52.39	(0.9804)	61.95	(0.9704)
0.39829	37.70	45.49	(0.9903)	53.12	(0.9804)	62.78	(0.9704)
0.16144	37.97	45.96	(0.9904)	53.65	(0.9804)	63.48	(0.9705)
0.065889	38.26	46.18	(0.9904)	54.04	(0.9804)	63.83	(0.9705)
Solvent viscosity, η_o (centipoise)	1.998	1.652		1.394		1.192	
Solvent conductivity, κ_{sp}^o (μmho/cm)	0.367	0.440		0.524		0.616	

* Highest concentration used for theoretical conductance analysis.

Table III. Conductance of NaSCN-DMSO solutions

Λ in mho · cm² · Eq⁻¹. The numbers in parentheses adjoining the Λ values give the ratio of the molar concentration of the solution at the given temperature to the molar concentration of the same solution at 25°C as given in the first column.

C, mmole/liter at 25°C	Λ (25°C)	Λ (35°C)		Λ (45°C)		Λ (55°C)	
255.08	25.43	30.59	(0.9897)	35.96	(0.9802)	41.50	(0.9718)
56.061	34.07	40.72	(0.9900)	47.72	(0.9797)	54.99	(0.9707)
26.717	37.70	44.82	(0.9900)	51.91	(0.9800)	59.86	(0.9708)
10.772	38.49	45.92	(0.9902)	54.70	(0.9801)	63.33	(0.9711)
8.3583	38.86	46.59	(0.9902)	55.13	(0.9802)	63.72	(0.9711)
5.8229*	39.86	47.52	(0.9903)	55.64	(0.9803)	64.28	(0.9713)
3.8448	40.40	48.30	(0.9903)	56.62	(0.9803)	66.52	(0.9712)
0.53654	42.84	51.31	(0.9904)	60.44	(0.9804)	69.95	(0.9712)
0.10212	43.53	52.34	(0.9904)	61.35	(0.9804)	70.66	(0.9711)
η_0 (centipoise)	1.998	1.652		1.394		1.192	
κ_{sp}^0 (μmho/cm)	0.317	0.381		0.418		0.471	

* Highest concentration used for theoretical conductance analysis.

Table IV. Conductance of $NaBPh_4$-DMSO solutions

Λ in mho · cm² · Eq⁻¹. The numbers in parentheses adjoining the Λ values give the ratio of the molar concentration of the solution at the given temperature to the molar concentration of the same solution at 25°C as given in the first column.

C, mmole/liter at 25°C	Λ (25°C)	Λ (35°C)		Λ (45°C)		Λ (55°C)	
11.736	20.69	25.49	(0.9903)	29.51	(0.9805)	34.37	(0.9704)
7.5363	21.53	25.89	(0.9903)	30.66	(0.9804)	35.99	(0.9703)
5.4698	22.19	26.76	(0.9905)	31.87	(0.9804)	37.43	(0.9705)
3.8890*	22.56	27.19	(0.9905)	32.19	(0.9803)	37.99	(0.9705)
2.9139	23.00	27.80	(0.9904)	32.92	(0.9802)	38 84	(0.9704)
2.1963	23.16	28.03	(0.9903)	33.26	(0.9802)	39.32	(0.9704)
1.6792	23.48	28.46	(0.9904)	33.90	(0.9803)	39.81	(0.9705)
1.1955	23.78	28.76	(0.9903)	34.14	(0.9803)	40.20	(0.9703)
η_0 (centipoise)	1.993	1.648		1.387		1.191	
κ_{sp}^0 (μmho/cm)	0.281	0.365		0.476		0.572	

* Highest concentration used for theoretical conductance analysis.

Table V. Conductance of $(i\text{-amyl})_3BuNBPh_4$-DMSO solutions

Λ in mho · cm² · Eq⁻¹. The numbers in parentheses adjoining the Λ values give the ratio of the molar concentration of the solution at the given temperature to the molar concentration of the same solution at 25°C as given in the first column.

C, mmole/liter at 25°C	Λ (25°C)	Λ (35°C)		Λ (45°C)		Λ (55°C)	
113.44	12.00	14.42	(0.9908)	17.49	(0.9758)	20.60	(0.9718)
46.960	13.63	16.07	(0.9907)	19.49	(0.9783)	23.23	(0.9711)
16.677	15.81	19.12	(0.9907)	22.98	(0.9798)	27.32	(0.9707)
8.8974	17.55	21.08	(0.9905)	25.30	(0.9802)	29.96	(0.9707)
6.5546*	18.76	21.88	(0.9906)	26.20	(0.9804)	30.98	(0.9706)
4.9055	18.65	22.48	(0.9906)	26.90	(0.9802)	31.83	(0.9706)
3.6300	18.98	22.73	(0.9904)	27.31	(0.9802)	32.43	(0.9704)
1.4907	20.25	24.54	(0.9907)	29.27	(0.9806)	34.47	(0.9706)
0.38512	21.08	25.48	(0.9906)	30.30	(0.9806)	35.64	(0.9705)
η_0 (centipoise)	1.998	1.652		1.394		1.192	
κ_{sp}^0 (μmho/cm)	0.317	0.381		0.495		0.603	

* Highest concentration used for theoretical conductance analysis.

Table VI. Conductance of CF_3SO_3Na-DMSO solutions

Λ in mho · cm² · Eq⁻¹. The numbers in parentheses adjoining the Λ values give the ratio of the molar concentration of the solution at the given temperature to the molar concentration of the same solution at 25°C as given in the first column.

C, mmole/liter at 25°C	Λ (25°)	Λ (35°C)		Λ (45°C)		Λ (55°C)	
416.96	18.59	22.68	(0.9912)	26.93	(0.9829)	31.31	(0.9838)
122.04	25.33	30.59	(0.9905)	35.92	(0.9808)	41.70	(0.9715)
72.663	27.21	32.69	(0.9905)	38.58	(0.9808)	44.69	(0.9712)
42.020	28.76	34.55	(0.9903)	40.75	(0.9805)	47.23	(0.9708)
15.165	31.12	37.14	(0.9905)	44.15	(0.9803)	51.48	(0.9706)
9.0698	31.98	38.22	(0.9905)	45.54	(0.9802)	53.08	(0.9706)
6.4227	32.55	38.73	(0.9903)	46.12	(0.9801)	53.94	(0.9707)
5.7623	32.79	39.08	(0.9903)	46.36	(0.9802)	54.30	(0.9715)
4.6135*	33.14	39.51	(0.9902)	46.73	(0.9802)	54.95	(0.9705)
4.3611	33.32	39.77	(0.9903)	47.14	(0.9803)	55.12	(0.9705)
3.5867	33.60	40.14	(0.9902)	47.56	(0.9803)	55.63	(0.9705)
1.1382	34.95	42.04	(0.9903)	49.59	(0.9803)	57.70	(0.9705)
η_0 (centipoise)	1.998	1.652		1.394		1.192	
κ_{sp}^0 (μmho/cm)	0.317	0.381		0.418		0.471	

* Highest concentration used for theoretical conductance analysis.

Table VII. Conductance of CH_3SO_3Na-DMSO solutions

Λ in mho · cm² · Eq⁻¹. The numbers in parentheses adjoining the Λ values give the ratio of the molar concentration of the solution at the given temperature to the molar concentration of the same solution at 25°C as given in the first column.

C, mmole/liter at 25°C	Λ (25°C)	Λ (35°C)		Λ (45°C)		Λ (55°C)	
2.4141*	30.78	37.11	(0.9904)	43.90	(0.9804)	50.82	(0.9705)
1.4083	31.78	38.33	(0.9904)	45.36	(0.9804)	52.55	(0.9705)
1.2695	31.87	38.44	(0.9904)	45.50	(0.9804)	52.72	(0.9705)
1.2002	32.09	38.71	(0.9904)	45.83	(0.9804)	53.04	(0.9705)
1.0449	32.40	39.16	(0.9904)	46.29	(0.9804)	53.64	(0.9705)
0.97260	32.73	39.54	(0.9904)	46.84	(0.9804)	54.27	(0.9705)
η_0 (centipoise)	1.998	1.652		1.394		1.192	
$\kappa_{sp}{}^0$ (μmho/cm)	0.274	0.314		0.354		0.388	

* Highest concentration used for theoretical conductance analysis.

B values are summarized in Table VIII for each electrolyte at different temperatures. The results of computer analyses are summarized in Table IX. The conductance data were unweighted in the analyses. Solvent viscosities and dielectric constants at 25°, 35°, 45°, and 55°C used in the analyses have been given in Table I. Approximate ionic radii of 4.8Å (35), 5.0Å (36), 4.0Å (36), 4.0Å (36), 5.8Å (36), and 9.5Å (37) were initially assigned to $NaClO_4$, NaSCN, $NaCF_3SO_3$, $NaCH_3SO_3$, $NaB(Ph)_4$, and $(i\text{-amyl})_3BuNB(Ph)_4$ salts, respectively, in the analyses. Values of Λ_o for the initial evaluation of the coefficients *E* and *S* for the iteration procedure were obtained from Shedlovsky extrapolations (38) of the data. A value of zero was assigned to the association constant K_A in the initial analyses.

In Table IX, the limiting equivalent conductance Λ_o, the theoretical Onsager slope *S*, the ion size fitting parameter $\mathring{a}$ in Å, the association constant K_A, and the *J* parameter in the conductance equation are tabulated. Of the three parameters, Λ_o, $\mathring{a}$, and K_A, the value of the viscosity *B* coefficient used affects only the ion-size parameter $\mathring{a}$, and then only slightly. A 10% change in *B* changes $\mathring{a}$ by only 0.04.

Table VIII. Viscosity *B* coefficients in liters/mole for electrolyte solutions in DMSO

Salt	25°C	35°C	45°C	55°C
$NaClO_4$	0.62	0.60	0.56	0.55
NaSCN	0.62	0.60	0.56	0.58
$NaCF_3SO_3$	0.64	0.61	0.59	0.58
$NaCH_3SO_3$	0.82	0.69	0.62	0.63
$NaB(Ph)_4$	1.14	1.07	1.01	1.00
$(i\text{-amyl})_3BuNB(Ph)_4$	1.57	1.47	1.44	1.44

Table IX. Conductance parameters for electrolyte solutions in DMSO

Salt	Temperature, °C	Λ_o	*S*	$\mathring{a}$	K_A	*J*
$NaClO_4$	25	38.76 ± 0.04	54.64	4.75	0	272.1
	35	46.77 ± 0.03	66.28	5.13	0	354.8
	45	54.65 ± 0.03	78.17	4.02	0	336.4
	55	64.61 ± 0.03	91.89	3.22	0	328.5
NaSCN	25	44.14 ± 0.09	57.36	3.33	0	223.2
	35	53.01 ± 0.09	69.44	2.59	0	214.9
	45	62.28 ± 0.14	82.05	2.20	0	215.8
	55	72.02 ± 0.42	95.66	2.96	0	334.1
$NaCF_3SO_3$	25	36.82 ± 0.06	53.67	3.20	0	184.7
	35	44.39 ± 0.08	65.07	1.80	0	129.0
	45	52.32 ± 0.18	76.99	2.37	0	201.7
	55	60.71 ± 0.05	69.91	3.89	0	367.9
$NaB(Ph)_4$	25	25.39 ± 0.07	47.90	4.07	0	169.1
	35	30.81 ± 0.09	58.18	3.03	0	160.1
	45	36.68 ± 0.14	69.05	1.97	0	128.4
	55	43.10 ± 0.12	80.95	2.57	0	194.0
$(i\text{-amyl})_3BuNB(Ph)_4$	25	22.09 ± 0.16	46.24	6.24	12.4	221.8
	35	26.75 ± 0.40	56.11	8.04	19.1	338.7
	45*	32.02 ± 0.64	66.69	14.26	33.5	661.2
	55*	37.46 ± 0.46	78.08	5.44	9.93	336.6

* Weighting factor $C\gamma\pm$ was used for these two sets of data only.

Units for Λ_o, *S*, $\mathring{a}$, K_A, and *J* are given in List of Symbols.

$NaCH_3SO_3$-DMSO solutions have not been included in Table IX. The equivalent conductance of $NaCH_3SO_3$ salt solution decreased very rapidly *vs.* $C^{1/2}$, and the conductance data could not be unambiguously extrapolated to infinite dilution to obtain an initial Λ_o for analysis by the conductance equation. Even with a tentative extrapolated Λ_o for CH_3SO_3Na solution, the result of the computer analysis for the conductance data using the Fuoss-Onsager equation yielded a negative ion size, $\mathring{a}$. This conductance behavior of $NaCH_3SO_3$ solution is typical for a weak electrolyte.

Analysis of the conductance data for a weak electrolyte can be expected to follow the Ostwald dilution law and the law of mass action. An equation of the form similar to the Fuoss-Shedlovsky equation (39), except $S(z)$, can be conveniently applied. The $\gamma_\pm{}^2$ are here approximated by unity as a limiting case. The equation is of the form

$$1/\Lambda = 1/\Lambda_o + C\Lambda/K_d\Lambda_o{}^2 \qquad [3]$$

A plot of $1/\Lambda$ as a function of $C\Lambda$ for CH_3SO_3Na solution gave a straight line. Limiting equivalent conductance, Λ_o, and dissociation constant, K_d, for the solution were obtained, respectively, from the intercept and the slope. The values are summarized in Table X.

Equivalent conductances of the other electrolyte solutions in the dilute concentration range were plotted *vs.* $C^{1/2}$ at different temperatures. All electrolyte solutions approached a limiting Onsager slope at infinite dilution. $NaClO_4$, NaSCN, and $NaCF_3SO_3$ solutions showed that the conductance curves approached the Onsager slopes from above, while $(i\text{-amyl})_3BuNB(Ph)_4$ solution showed that the conductance curve approached the limiting slope from slightly below. $NaB(Ph)_4$ solution appeared to be in between the two cases. $NaClO_4$, NaSCN, $NaCF_3CO_3$ are therefore considered to be completely dissociated, while $NaB(Ph)_4$ and $(i\text{-amyl})_3BuNB(Ph)_4$ appeared to be slightly associated.

$(i\text{-amyl})_3BuN^+$ ion and $B(Ph)_4{}^-$ ion are two large nearly symmetrical ions which have been shown to possess equal limiting mobilities in methanol at 25°C (20). The assumption of equal mobilities of those two ions has been applied for different electrolyte solutions (40, 41) when transference numbers were not available. Assuming that equal limiting mobilities hold

Table X. Limiting equivalent conductance and dissociation constant of CH_3SO_3Na in DMSO solutions

Temperature, °C	Λ_o	10^2K_d
25	35.37	1.082
35	42.73	1.078
45	51.23	1.077
55	58.39	1.067

Table XI. Limiting ionic mobilities in DMSO

Ions	λ_i^o in cm²/ohm · equivalent 25°C	35°C	45°C	55°C
(i-amyl)$_3$BuN* or B(Ph)$_4^-$	11.05	13.38	16.01	18.74
Na^+	14.34	17.43	20.67	24.36
$CF_3SO_3^-$	22.48	26.96	31.65	36.35
ClO_4^-	24.42	29.34	33.98	40.25
SCN^-	29.80	35.58	41.61	47.66

for (i-amyl)$_3$BuN$^+$ ion and B(Ph)$_4^-$ ion in DMSO between 25° and 55°C, the individual ionic limiting mobilities were then obtained as shown in Table XI. The ionic limiting mobilities were obtained from the Λ_o values (tabulated in Table IX) and the application of Kohlrausch's law of independent mobility at infinite dilution. The ionic mobility increases in the order shown in the table. The mobilities of the ions have positive temperature coefficients. This appears to be due to decrease of the viscosity of DMSO with increasing temperature. The temperature coefficients of the mobilities are 0.595, 0.528, 0.462, 0.334, and 0.256 conductance unit/°C for SCN^-, ClO_4^-, $CF_3SO_3^-$, Na^+, and (i-amyl)$_3$BuN$^+$ ions, respectively, which is the reverse order of the ionic mobilities. B(Ph)$_4^-$ ion, of course, is assumed to have the same temperature coefficient as (i-amyl)$_3$BuN$^+$ ion.

Ionic Walden products, $\lambda_o\eta_o$, in cm² poise/ohm equivalent are given in Table XII as a function of temperature. Stokes' radii for these ions were calculated using the values in Table XII and the Stokes-Einstein equation (28), *i.e.*, $r_s(\text{Å}) = 0.820/\lambda^o_i\eta_o$. The calculated Stokes' radii are given in Table XIII. In the sixth column of Table XIII are given the crystallographic radii r_c which have been estimated from sources listed in the parentheses. Table XIII shows that the calculated Stokes' radius, except that of Na^+ ion, are all smaller than the corresponding crystallographic radius. Such unrealistic Stokes' radii were also observed for halide ions and ClO_4^- in sulfolane (tetrahydrothiophene-1-dioxide) (42).

An empirically modified Stokes' equation of the form

$$r_s(\text{corrected}) = \mathbf{Fe}(r_c/r_s)_{\text{corr.}}/6\pi\eta_o\lambda_o \qquad [4]$$

was proposed by Robinson and Stokes (28) to obtain more realistic hydrated ionic radii in water. Equation [4] contains a correction factor, $(r_c/r_s)_{\text{corr.}}$, which is usually obtained from the assumption that large symmetrical and low surface charge ions such as $(Et)_4N^+$, $(Pr)_4N^+$, are unsolvated. The procedure for using Eq. [4] is to first construct a calibration curve of

Table XII. Limiting ionic Walden products, $\lambda_o\eta_o$, in DMSO

Ions	$\lambda_o\eta_o$ in cm² poise/ohm·equivalent 25°C	35°C	45°C	55°C
(i-amyl)$_3$BuN+	0.221	0.221	0.223	0.223
Na^+	0.287	0.288	0.288	0.290
B(Ph)$_4^-$	0.221	0.221	0.223	0.223
ClO_4^-	0.488	0.485	0.474	0.480
SCN^-	0.596	0.588	0.580	0.568
$CF_3SO_3^-$	0.449	0.446	0.441	0.433

Table XIII. Stokes' radii, r_s, in Å calculated from Stokes-Einstein equation

References for r_c given in parentheses

Ions	Stokes Radii 25°C	35°C	45°C	55°C	Estimated crystallographic radius, r_c
(i-amyl)$_3$BuN+	3.71	3.71	3.68	3.67	4.94 (37)
B(Ph)$_4^-$	3.71	3.71	3.68	3.67	4.94 (37)
Na^+	2.86	2.85	2.85	2.82	0.95 (36)
ClO_4^-	1.68	1.69	1.73	1.71	2.4 (35)
SCN^-	1.38	1.40	1.41	1.44	2.27 (36)
$CF_3SO_3^-$	1.83	1.84	1.86	1.89	2.96 (36)

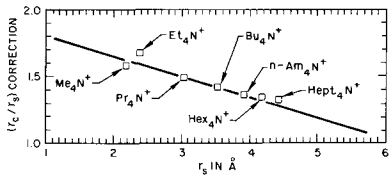

Fig. 1. Calibration curve for determining corrected Stokes' radii in DMSO at 25°C [data from Arrington and Griswold (14)].

$(r_c/r_s)_{\text{corr.}}$ *vs.* r_s based on the mobilities of $(Et)_4N^+$, $(Pr)_4N^+$, $(Bu)_4N^+$, and $(Am)_4N^+$ ions available in the particular solvent medium and subsequently using the calibration curve to obtain the corrected Stokes' radius, Eq. [4], for other ions.

In DMSO, the mobility data for a series of tetraalkylammonium ions at 25°C have been reported recently by Arrington and Griswold (14). Based on their data, a calibration curve was constructed as shown in Fig. 1. The calibration curve becomes the basis for obtaining corrected Stokes' radii for other ions in DMSO at 25°C.

For completeness, the ionic mobility data for other ions in DMSO at 25°C were collected and the Stokes' radii, r_s in Å, for these ions were calculated as given in the second column of Table XIV. In the third column $(r_c/r_s)_{\text{corr.}}$ is the correction factor obtained from Fig. 1 for the corresponding r_s. In the fourth column $r_{\text{corr.}}$ is the corrected Stokes' radius. The corrected Stokes' radii for the large ions are in good agreement with their crystallographic radii, r_c, which are given in the fifth column. Comparison of the $r_{\text{corr.}}$ and r_c for alkali and halide ions shows that alkali ions are heavily solvated while halide ions are slightly or not solvated in DMSO at 25°C.

The volume of solvation sheath surrounding an ion is approximately

$$V_{\text{solv.}} = 4\pi(r_{\text{corr.}}^3 - r_c^3)/3 \qquad [5]$$

The solvation volume for the alkali and halide ions are calculated using the values for $r_{\text{corr.}}$ and r_c given in Table XIV. The calculated solvation volume, $V_{\text{solv.}}$ in Å^3, is given in Table XV. The molecular volume of DMSO is approximately 118.4 Å^3 as obtained from the molecular weight and the density data of DMSO at 25°C. Assuming the volume contraction of the solvent molecules in the solvation sheath due to electrostriction is negligible, a solvation number for the alkali-halide ions in DMSO can be calculated. The calculated solvation number, *s*, is given in Table XV. Na^+ and K^+ ions are solvated to approximately the same extent and Li^+ ion is solvated with 4.8 molecules of DMSO. Halide ions are only slightly solvated and the order of solvation is $Cl^- > Br^- > I^-$.

Solvation volume or solvation number at 35°, 45°, and 55°C for the ions studied in the present work was not determined because of lack of a calibration curve

Table XIV. Corrected Stokes' ionic radii in DMSO at 25°C

References for r_s and r_c given in parentheses

Ions	r_s	$\left(\frac{r_c}{r_s}\right)$	$r_{\text{corr.}}$	r_c
(i-amyl)$_3$BuN+	3.71 (*)	1.38	5.12	4.94 (37)
Bu_4N^+	3.53 (14)	1.40	4.94	4.94 (37)
Li^+	3.73 (12)	1.38	5.15	0.60 (36)
Na^+	2.86 (*)	1.51	4.32	0.95 (36)
K^+	2.91 (12)	1.50	4.36	1.33 (36)
B(Ph)$_4^-$	3.71 (*)	1.38	5.12	4.94 (37)
Picrate$^-$	2.42 (12)	1.57	3.80	3.61 (37)
$CF_3SO_3^-$	1.83 (*)	1.66	3.03	2.96 (36)
ClO_4^-	1.68 (*)	1.68	2.82	2.40 (35)
SCN^-	1.38 (*)	1.72	2.37	2.27 (36)
NO_3^-	1.55 (12)	1.70	2.64	2.70 (53)
Cl^-	1.68 (14)	1.68	2.82	1.81 (36)
Br^-	1.70 (14)	1.68	2.86	1.95 (36)
I^-	1.72 (14)	1.68	2.89	2.16 (36)

* Present work.

Table XV. Solvation volume and solvation number of alkali-halide ions in DMSO at 25°C

Ion	$V_{solv.}$ in Å^3	s
Li^+	571	4.8
Na^+	334	2.8
K^+	337	2.8
Cl^-	69	0.6
Br^-	67	0.6
I^-	59	0.5

such as shown in Fig. 1 at these temperatures. However, it is clear from the temperature dependence of the limiting ionic Walden products, Table XII, that the temperature effect on solvation is practically negligible, if there is any, for the temperature range between 25° and 55°C.

Activation energies for ionic conductance, E_A in kcal/mole, were calculated as a function of concentration. The activation energies were obtained from the slopes of simple Arrhenius plots; *i.e.*, log Λ *vs.* $1/T$ at various concentrations. Linear plots were obtained for all electrolyte solutions within the temperature range studied. (i-amyl)$_3$BuNB(Ph)$_4$, NaB(Ph)$_4$, and NaSCN whose maximum solubilities are below 0.3 mole/liter have average activation energies of 3.49, 3.30, and 3.16 kcal/mole, respectively. $NaClO_4$ has an activation energy of 3.23 kcal/mole at a concentration of 0.01 mole/liter, and subsequently the activation energy increases to 4.44 kcal/mole at a concentration of 1.4 mole/liter. The average activation energy for CF_3SO_3Na below 0.3600 mole/liter is 3.23 kcal/mole. The activation energy increases for the electrolyte solutions in the order of NaSCN < $NaClO_4$ ≃ $NaCF_3SO_3$ < NaB(Ph)$_4$ < (i-amyl)$_3$BuNB(Ph)$_4$ for concentration below 0.25 mole/liter.

Discussion

Examination of the ion size fitting parameter $\mathring{a}$ in Table IX shows that a value of 4.75Å for $NaClO_4$ is reasonable and is in good agreement with a value of 4.8Å for $NaClO_4$ (35) which was found necessary to fit the data of Sears *et al.* (12). Prue and Sherrington (35) have analyzed the conductance data of $NaClO_4$ in other solvents, using the Fuoss-Onsager equation, at 25°C and the ion size fitting parameters $\mathring{a}$ found for $NaClO_4$ in dimethylacetamide, dimethylpropionamide, methanol, and water, respectively, 5.3, 5.0, 2.2, and 3.0Å. It is interesting to note that the ion size for $NaClO_4$ in the hydrogen donor solvents, *i.e.*, methanol and water, is smaller than those in dimethylacetamide, dimethylpropionamide, and DMSO.

In this present study NaB(Ph)$_4$ in DMSO has an ion size parameter $\mathring{a}$ of 4.07Å at 25°C using the Fuoss-Onsager equation; this value appears small compared to that for $NaClO_4$. This may be due to some association of NaB(Ph)$_4$ in DMSO. For example, Skinner and Fuoss (43) have studied the conductance of NaB(Ph)$_4$ in water and later Covington and Tait (22) have redetermined the conductance of NaB(Ph)$_4$ in CO_2 free water. The ion size parameter $\mathring{a}$ for NaB(Ph)$_4$ in water was determined to be 6.64 ± 0.06Å by Skinner and Fuoss (43) and 9.9 ± 0.9Å by Covington and Tait (22) for $K_A = 0$. Covington and Tait showed that the calculated ion size, $\mathring{a}$ = 6.64Å, for NaB(Ph)$_4$ as determined by Skinner and Fuoss for $K_A = 0$ can be increased to $\mathring{a}$ = 10Å if an association constant of 2.07 liters/mole was allowed using Skinner and Fuoss data. It is clear that the ion size parameter $\mathring{a}$ is not independent of the association constant in a sense that an identical set of conductance data can be fitted with a smaller $\mathring{a}$ if it is assumed there is no association. A larger $\mathring{a}$ is obtained if some association is assumed. Thus, for an electrolyte solution with a slight association such as NaB(Ph)$_4$ in DMSO, the determination of $\mathring{a}$ and K_A is not unambiguous.

(i-amyl)$_3$BuNB(Ph)$_4$ solutions at 25°C have been analyzed as an associated electrolyte. The ion size parameter $\mathring{a}$ is 6.24 with standard deviation 11.9, and K_A is 12.4 with standard deviation 28.6. The standard deviation in $\mathring{a}$ and K_A reflect partly the sensitivity of $\mathring{a}$ to experimental accuracy and again illustrate how $\mathring{a}$ can be adjusted by simply adjusting K_A. Recently Dyke *et al.* (44) obtained an ion size parameter $\mathring{a}$ = 5.3 ± 0.1Å for (i-amyl)$_3$BuNB(Ph)$_4$ salt in N-methyl-2-pyrrolidone (ϵ = 32.0) at 25°C assuming $K_A = 0$.

The ion size parameter $\mathring{a}$ for a salt varies with temperature as shown in Table IX and the variation has no systematic trend. The Fuoss-Onsager conductance equation assumes the solvent medium to be a continuum; therefore, any inadequacy of the theory due to the neglect of the solvent's role may be taken care of by the adjustable ion size parameter $\mathring{a}$. Substantially different values of $\mathring{a}$ obtained for an identical salt in different solvents (33) and the fact that $\mathring{a}$ varies with dielectric constant of the solvent (45, 46) illustrates the importance of the solvent's role. In this work $\mathring{a}$ is viewed as a fitting parameter. It remains to be seen whether greater experimental accuracy can achieve greater discrimination in K_A and $\mathring{a}$ which have been found to be mutually adjustable.

The corrected Stokes' radii for ions in DMSO at 25°C have been given in Table XIV. The values for the corrected Stokes' ionic radii are quite reasonable, although the major assumption that tetraalkylammonium ions are unsolvated in DMSO, *i.e.*, the basis for the calibration curve, has yet to be verified. Alkali ions, Li^+, Na^+, and K^+, are solvated with approximately five, three, and three DMSO molecules, respectively. The anions, Picrate$^-$, $CF_3SO_3^-$, ClO_4^-, SCN^-, and NO_3^-, are unsolvated while halide ions Cl^-, Br^-, and I^- are slightly solvated, if any. This conclusion is in general agreement with Parkers' (2) view that anions in dipolar aprotic solvents are much less solvated than in protic solvents. Maxey and Popov (47) studied the vibrational absorption bands of DMSO solutions of $LiClO_4$, NH_4SCN, NaSCN, and NaB(Ph)$_4$ and found that the absorption band is essentially independent of the nature and the mass of the anion. This again suggests that the interaction of the alkali cations with the solvent molecules exists, but for the anions the interaction is absent.

Solvation of alkali ions in DMSO is easily explained in terms of the ion-DMSO dipole interaction. The mutual electrostatic potential energy of the rigid DMSO dipole and the singly charged alkali ions is at least six times greater than the DMSO-DMSO bond strength (27) which is estimated to be 0.44 x 10^{-12} ergs, *i.e.*, one-half of the heat of vaporization of DMSO at 25°C (L_v = 12.64 kcal/mole) (48). The spherically symmetrical ions, (i-amyl)$_3$ BuN^+ and $(Bu)_4N^+$, both have unsolvated radii of approximately 5Å. The ion-dipole interaction energy for these ions is approximately equal to the DMSO-DMSO bond strength and solvation is not favored for these large ions.

Solvation of the anions by DMSO molecules is more complicated. Both the sulfur and oxygen atoms in a DMSO molecule have a lone pair of electrons available for bonding. Anions are solvated by ion-solvent dipole interactions, on which is superimposed an interaction due to the mutual polarizability of the anion and the

Table XVI. Limiting Walden product of salts in water and some nonaqueous solvents at 25°C

Salt	Solvent	ϵ	$\Lambda_0\eta_0$	Reference
(i-amyl)$_3$BuNB(Ph)$_4$	DMSO	46.4	0.4414	Present work
	Tetrahydrofuran (THF)	7.39	0.378	(41)
	Dimethoxyethane (DME)	7.20	0.421	(41)
	H_2O	78.5	0.360	(43)
	N-Methyl-2-Pyrrolidone (NM2P)	32.0	0.401	(44)
	EtOH*	24.33	0.397	(46)
	PrOH*	20.45	0.397	(46)
	MeOH	32.66	0.4005	(20)
	MeCN	35.95	0.396	(54)
NaB(Ph)$_4$	DMSO	46.4	0.5074	Present work
	THF	7.39	0.397	(41)
	DME	7.20	0.464	(41)
	H_2O	78.5	0.633	(22)
	MeOH	32.66	0.446	(55)
	Acetonitrile (MeCN)	35.95	0.462	(54)
	NM2P	32.0	0.446	(44)
$NaClO_4$	DMSO	46.4	0.7746	Present work
	N,N-Dimethylacetamide (DMA)	37.8	0.630	(56)
	Dimethylformamide (DMF)	36.71	0.655	(35)
	DMF	36.71	0.6535	(24)
	Dimethylpropionamide (DMP)	33.1	0.574	(57)
	MeOH	32.66	0.633	(58)
	H_2O	78.5	1.047	(35)
	MeCN	35.95	0.6155	(54)
	NM2P	32.0	0.6964	(44)
NaSCN	DMSO	46.4	0.8821	Present work
	DMA	37.8	0.6851	(56)
	DMF	36.71	0.712	(24)
CF_3SO_3Na	DMSO	46.4	0.7358	Present work
	Dimethylsulfite (DMSU)	22.5 (23.3 °C)	0.355	(59)

* λ_0^+ ((i-amyl)$_3$BuN$^+$) = λ_0 (B(Ph)$_4$) was assumed.

solvent molecule, which is greatest for large anions. The result obtained for the anions in DMSO is that the large anions, $B(Ph)_4^-$, and Picrate$^-$, and the unsymmetrical ions, $CF_3SO_3^-$, and SCN^-, are unsolvated while the halide ions, Cl^-, Br^-, and I^-, are only slightly solvated. This result appears to indicate that the mutual polarization and dipole-dipole interactions do not contribute significantly to the anion solvation in DMSO. Cl^-, Br^-, and I^- ions are slightly solvated and the solvation decreases slightly in the order $Cl^- \approx Br^- > I^-$ indicating that perhaps ion-dipole interactions play a role in anion solvation as was the case in cation solvation.

The temperature dependence of the ionic solvation in DMSO can be illustrated by referring to the limiting ionic Walden products as given in Table XII. It clearly shows that temperature affects ionic solvation very little in DMSO.

To illustrate further the effect of solvent properties on ionic transport, the limiting Walden product, $\Lambda_0\eta_0$, for (i-amyl)$_3$BuNB(Ph)$_4$, NaB(Ph)$_4$, $NaClO_4$, NaSCN, and CF_3SO_3Na in different solvents of varying dielectric constant are tabulated in Table XVI and are plotted as a function of dielectric constant as shown in Fig. 2.

It is observed from Fig. 2 that the effect of dielectric constant upon $\Lambda_0\eta_0$ of large ions such as (i-amyl)$_3$BuN$^+$, $B(Ph)_4^-$, and solvated Na^+ ions is small and Stokes' law is more nearly obeyed, while for smaller ions such as unsolvated ClO_4^-, SCN^-, and $CF_3SO_3^-$, the effect of dielectric constant upon $\Lambda_0\eta_0$ is greater and the limiting Walden product depends on dielectric properties of the solvent as well as other intrinsic solvent properties, *e.g.*, hydrogen bonding and perhaps acid and base properties.

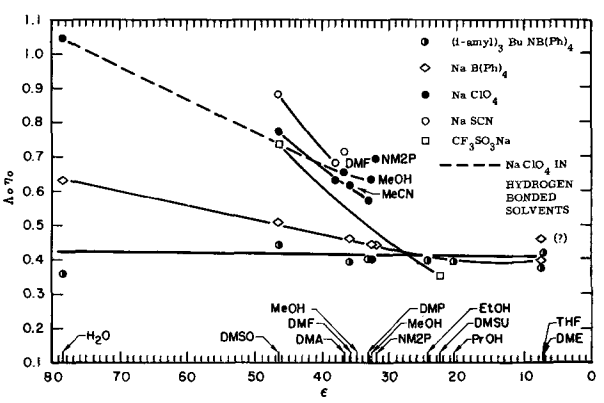

Fig. 2. Effect of solvent dielectric constant on the limiting Walden product for different salts.

Theoretical consideration of ionic mobility in a dielectric medium has been given by Boyd (16) and Zwanzig (17). The theoretical ionic mobility which accounts for the effect of dielectric relaxation is of the form

$$\lambda_i^o = Fe|z_i|/6\pi\eta_0(r_i + D/r_i^3) \qquad [6]$$

where

$$D = (2/3)z_i^2e^2\tau(\epsilon_s - \epsilon_\infty)/6\pi\eta_0\epsilon_s^2$$

Using Eq. [6], the theoretical limiting ionic mobility as a function of reciprocal of crystallographic size was calculated with the following parameter values for DMSO at 25°C: $\eta_0 = 1.998 \times 10^{-2}$ poise, $\epsilon_0 = 46.4$, $\epsilon_\infty \simeq n_0^2$ (index of refraction) (31, 49) = 2.18, and τ(DMSO) = η_0(DMSO)τ(acetone)/η_0(acetone) = 20.42×10^{-12} s where τ(acetone) is given by Boyd (16). The theoretical $\lambda_0\eta_0$ are shown in Fig. 3 by a dotted line. Experimental $\lambda_0\eta_0$ values for some ions in DMSO (open circle) at 25°C are also plotted in Fig. 3, and the values are summarized in Table XVII. Figure 3 shows that Stokes' law is at best an approximation for large ions and does not predict a maximum in $\lambda_0\eta_0$ as

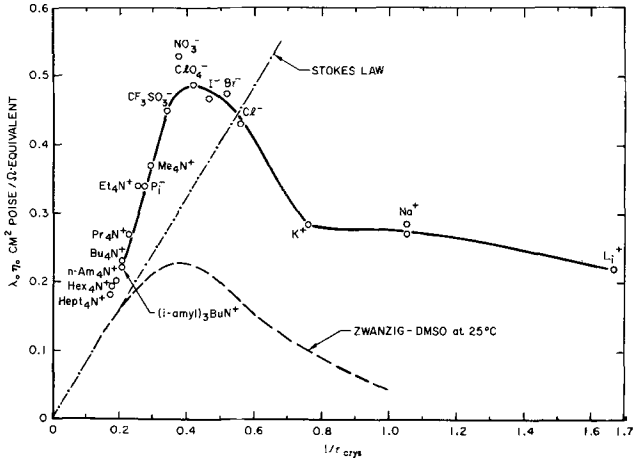

Fig. 3. Limiting ionic Walden product as a function of reciprocal of crystal radius, experimental results compared to Stokes' law and Zwanzig theory.

Table XVII. Limiting ionic Walden product in DMSO at 25°C

Ion	Estimated r_c, Å (References for r_c given in parentheses)	$\lambda_o\eta_o$	Reference
Na^+	0.95 (36)	0.285	Present work
		0.271	(12)
K^+	1.33 (36)	0.282	(12)
Li^+	0.60 (36)	0.220	(6)
Cl^-	1.81 (36)	0.461	(6)
Br^-	1.95 (36)	0.474	(12)
I^-	2.16 (36)	0.466	(12)
$(i\text{-amyl})_3BuN^+$	4.94	0.221	Present work
SCN^-	2.27 (36)	0.595	Present work
		0.572	(12)
NO_3^-	2.7 (53)	0.529	(12)
ClO_4^-	2.4 (35)	0.488	Present work
		0.482	(12)
Pi^-	3.61* (37)	0.339	(12)
$B(Ph)_4^-$	4.94	0.221	Present work
$CF_3SO_3^-$	2.96 (36)	0.449	Present work
H^+	0.53**	0.303 (at 30°C)	(19)
Me_4N^+	3.47 (28)	0.370	(14)
Et_4N^+	4.00 (28)	0.340	(14)
Pr_4N^+	4.52 (28)	0.267	(14)
Bu_4N^+	4.94 (28)	0.231	(14)
$n\text{-}Am_4N^+$	5.29 (28)	0.207	(14)
Hex_4N^+	5.61 (28)	0.195	(14)
$Hept_4N^+$	5.89 (28)	0.183	(14)

* Estimated from density data.
** Assuming 1 Bohr radius.

a function of the reciprocal of the ionic radii. On the other hand, comparison of the observed $\lambda_o\eta_o$ and Zwanzig theory in DMSO shows remarkable similarity in shape, but not in magnitude. The Zwanzig theory predicts the maximum $(\lambda_o\eta_o)_{max} = 0.231$ cm² poise/ohm equivalent at $(r_c)_{max} = 2.69$Å, *i.e.*, $(1/r_c)_{max} = 0.372$Å^{-1}, while the observed maximum in $\lambda_o\eta_o$ is about 0.49 cm² poise/ohm equivalent at 2.5Å. The observed $(\lambda_o\eta_o)_{max}$ is larger than the theoretical $(\lambda_o\eta_o)_{max}$ by a factor of about two. This is apparently due to the incompleteness of the Boyd-Zwanzig theory which considers the dielectric relaxation drag, but ignores the existence of streamlines in the medium. This in effect complements the simple Stokes law, which ignores everything but the streamlines. Recently, Atkinson and Mori (50) examined the Zwanzig theory applied to alkali ions in H_2O, D_2O, MeOH, EtOH, and MeCN solvents and to a number of ions in dioxane-water and glycerol-water mixtures. In all cases the theory gives a good qualitative description of ion mobility. A plot of $\mathbf{F}^2/N\eta_o\lambda_i^o$ as a function of $\tau(\epsilon_s - \epsilon_\infty)/\eta_o\epsilon_s^2$ for the ions as suggested by a rearranged Zwanzig's equation, Eq. [6]

$$\mathbf{F}^2/N\eta_o\lambda_i^o = 6\pi r_i + (2/3)e^2\tau(\epsilon_s - \epsilon_\infty)/r_i^3\eta_o\epsilon_s^2$$

gives a slope of $2e^2/3r_i^3$ and an intercept of $6\pi r_i$. The r_i obtained from the slope and the intercept from plots of experimental data not only disagree with each other, but are of questionable magnitude. Several possible modifications to the Boyd-Zwanzig theory have been discussed by Frank (51). These include consideration of molecular slip and microscopic local viscosity.

These possible modifications are certainly justifiable from physical intuition, but it appears that such adjustments push the theory too far. Since the theory attempts to describe the ionic motion on a molecular level, it appears that molecular jumps (52) as a mode of transport mechanism, specific solvent structure, and short range interactions will all enter in an ultimate refined form for describing ionic mobility in a dielectric medium.

Conclusions

1. $NaClO_4$, NaSCN, and CF_3SO_3Na salts are completely dissociated and $NaBPh_4$ is slightly associated. $(i\text{-amyl})_3BuNB(Ph)_4$ and CH_3SO_3Na are associated and have association constants of 12 and 100 liters/mole, respectively, at 25°C.

2. Corrected Stokes' radii for $(i\text{-amyl})_3BuN^+$, $B(Ph)_4^-$, Na^+, $CF_3SO_3^-$, ClO_4^-, and SCN^- ions are, respectively, 5.12, 5.12, 4.32, 3.03, 2.82, and 2.37Å at 25°C.

3. Alkali ions, Li^+, Na^+, and K^+, are solvated with 4.8, 2.8, and 2.8 molecules of DMSO while the halide ions Cl^-, Br^-, and I^- are only slightly solvated, if any, at 25°C.

4. Effective ionic radii are insensitive to temperature from 25° to 55°C.

5. Transport of ions in DMSO is limited principally by viscous drag.

6. The Zwanzig theory of dielectric relaxation as applied to ionic mobility in DMSO shows only qualitative agreement.

Acknowledgments

This work was supported by the U. S. Army Mobility Equipment Research and Development Center, Fort Belvoir, Virginia, under Contract No. DA-44-009-AMC-1661 (T). The authors wish to thank Mr. Laszlo Heredy, Jr., and Mr. Allan W. Dodge for their laboratory assistance.

Manuscript submitted April 15, 1970; revised manuscript received Jan. 4, 1971. This was Paper 163 presented at the New York Meeting of the Society, May 4-9, 1969.

Any discussion of this paper will appear in a Discussion Section to be published in the June 1972 JOURNAL.

LIST OF SYMBOLS

Å	angstrom, 10^{-8} cm
a^o	ion size fitting parameter, Å
B	Jones-Dole viscosity B coefficient, liter/mole
C	molar concentration, mole/liter
D	a parameter in the Zwanzig equation, cm⁴
E	conductance parameters
E_A	activation energy for ionic conductance, kcal/mole*
e	electronic charge, 4.8 x 10^{-10} statcoulomb/equivalent
$\mathbf{F}$	Faraday constant, 9.649 x 10^4 coulomb/equivalent
$J(a^o)$	a conductance parameter, (cm²/ohm-equivalent) (liter/mole)
K_A	equilibrium ionic association constant, liter/mole
K_d	equilibrium ionic dissociation constant, mole/liter
N	Avogadro's number, 6.023 x 10^{23}/mole
n_o	index of refraction
r_c	crystallographic radius, Å
$r_{corr.}$	corrected Stokes' ionic radius, Å
$(r_c/r_s)_{corr.}$	Stokes' correction factor
r_s	Stokes' radius, Å
S	theoretical limiting Onsager slope, (cm²/ohm-equivalent) (liter/mole)
$V_{solv.}$	volume of solvation sheath, Å³
α'	degree of ionic dissociation
$\gamma_\pm$	mean molar ionic activity coefficient
ϵ, ϵ_s	static dielectric constant
ϵ_o	solvent dielectric constant
ϵ_∞	dielectric constant at infinite frequency
η_o	solvent viscosity, poise or centipoise
κ	Debye-Hückel parameter, cm^{-1}
κ_{sp}	specific conductance of electrolyte solution, mho/cm
κ_{sp}^o	solvent specific conductance, mho/cm
Λ	equivalent conductance of electrolyte solution, cm²/ohm-equivalent
Λ_o	limiting equivalent conductance, cm²/ohm-equivalent
λ_o	limiting ionic mobility, cm²/ohm-equivalent
τ	Debye's dipolar relaxation time, sec

*Thermochemical kilocalorie was used.

REFERENCES

1. J. N. Butler, *J. Electroanal. Chem.*, **14**, 89 (1967).
2. A. J. Parker, *Quarterly Rev. (London)*, **16**, 163 (1962).
3. C. A. Melendres, "Solubilities, Conductances, Viscosities and Densities of Solutions of Selected Inorganic Compounds in Dimethyl Sulfoxide," *Thesis*, Univ. of California, Berkeley, 1965.
4. J. Kenttämaa, *Suomen Kemistilehti*, **33B**, 179 (1960).

5. I. M. Kolthoff and T. B. Reddy, *Inorg. Chem.*, **1**, 189 (1962).
6. J. S. Dunnett and R. P. H. Gasser, *Trans. Faraday Soc.*, **61**, 922 (1965).
7. E. M. Arnett and D. R. McKelvey, *J. Am. Chem. Soc.*, **88**, 2598 (1966).
8. C. V. Krishnan and H. L. Friedman, *J. Phys. Chem.*, **73**, 3934 (1969).
9. D. R. Cogley and J. N. Butler, *This Journal*, **113**, 1074 (1966).
10. W. H. Smyrl and C. W. Tobias, *ibid.*, **115**, 33 (1968).
11. M. Solomon, *ibid.*, **116**, 1392 (1969).
12. P. G. Sears, G. R. Lester, and L. R. Dawson, *J. Phys. Chem.*, **60**, 1433 (1956).
13. H. L. Schläfer and W. Schaffernicht, *Angew. Chem.*, **72**, 618 (1960).
14. D. E. Arrington and E. Griswold, *J. Phys. Chem.*, **74**, 123 (1970).
15. R. M. Fuoss, *Proc. Natl. Acad. Sci., U.S.A.*, **45**, 807 (1959).
16. R. H. Boyd, *J. Chem. Phys.*, **35**, 1281 (1961).
17. R. Zwanzig, *ibid.*, **38**, 1603 (1963).
18. R. Zwanzig, *ibid.*, **38**, 1605 (1963).
19. I. M. Kolthoff and T. B. Reddy, *This Journal*, **108**, 980 (1961).
20. M. A. Coplan and R. M. Fuoss, *J. Phys. Chem.*, **68**, 1177 (1964).
21. T. Gramstad and R. N. Haszeldine, *J. Chem. Soc., (London)*, 173 (1956).
22. A. K. Covington and M. J. Tait, *Electrochim. Acta*, **12**, 113 (1967).
23. Sadtler Research Laboratories, *Sadtler Standard Spectra*, Vol. 21, Spectrum No. 21429.
24. D. P. Ames and P. G. Sears, *J. Phys. Chem.*, **59**, 16 (1955).
25. Sadtler Research Laboratories, *Sadtler Standard Spectra*, Spectrum No. Y 301 S.
26. H. M. Daggett, E. J. Blair, and C. A. Kraus, *J. Am. Chem. Soc.*, **73**, 799 (1951).
27. N. P. Yao, "Transport Behavior in Dimethyl Sulfoxide," Ph.D. Thesis, Univ. of California, Los Angeles, June 1969.
28. R. A. Robinson and R. H. Stokes, "Electrolyte Solutions," 2nd Ed., Butterworths Scientific Publications, London (1959).
29. J. Lind, J. Zwolenik, and R. M. Fuoss, *J. Am. Chem. Soc.*, **81**, 1557 (1959).
30. W. J. McAuley, E. Rhodes, and A. R. Ubbelohde, *Proc. Roy. Soc., A*, **289**, 151 (1966).
31. J. M. G. Cowie and P. M. Toporowski, *Can. J. Chem.*, **39**, 2240 (1961).
32. J. J. Lindberg and J. Kenttämaa, *Suomen Kemistilehti*, **33B**, 104 (1960).
33. R. L. Kay, *J. Am. Chem. Soc.*, **82**, 2099 (1960).
34. G. Jones and M. Dole, *ibid.*, **51**, 2950 (1929).
35. J. E. Prue and P. J. Sherrington, *Trans. Faraday Soc.*, **57**, 1795 (1961).
36. L. Pauling, "The Nature of the Chemical Bond," 2nd Ed., Cornell University Press, New York (1940).
37. D. F. T. Tuan and R. M. Fuoss, *J. Phys. Chem.*, **67**, 1343 (1963).
38. T. Shedlovsky, *J. Am. Chem. Soc.*, **54**, 1405 (1932).
39. R. M. Fuoss and T. Shedlovsky, *ibid.*, **71**, 1496 (1949).
40. J. F. Coetzee and G. P. Cunningham, *ibid.*, **87**, 2529 (1965).
41. C. Carvajal, K. J. Tolle, J. Smid, and M. Szwarc, *ibid.*, **87**, 5548 (1965).
42. M. D. Monica and U. Lamanna, *J. Phys. Chem.*, **72**, 4329 (1968).
43. J. F. Skinner and R. M. Fuoss, *ibid.*, **68**, 1882 (1964).
44. M. D. Dyke, P. G. Sears, and A. I. Popov, *ibid.*, **71**, 4140 (1967).
45. J. E. Lind and R. M. Fuoss, *ibid.*, **66**, 1727 (1962).
46. D. F. Evans and P. Gardam, *ibid.*, **72**, 3281 (1968).
47. B. W. Maxey and A. I. Popov, *J. Am. Chem. Soc.*, **89**, 2230 (1967).
48. T. B. Douglas, *ibid.*, **70**, 2001 (1948).
49. R. G. LeBel and D. A. I. Goring, *J. Chem. Engr. Data*, **7**, 100 (1962).
50. G. Atkinson and Y. Mori, *J. Phys. Chem.*, **71**, 3523 (1967).
51. H. S. Frank, "Solvent Models and the Interpretation of Ionization and Solvation Phenomena," in "Chemical Physics of Ionic Solutions," B. E. Conway and R. G. Barradas, Editors, John Wiley & Sons, Inc., New York (1966).
52. Henry Eyring and Mu Shik Jhon, "Significant Structure of Liquids," John Wiley & Sons, New York (1969).
53. E. R. Nightingale, Jr., *J. Phys. Chem.*, **63**, 1381 (1959).
54. R. L. Kay, B. J. Hales, and C. P. Cunningham, *ibid.*, **71**, 3925 (1967).
55. R. W. Kunze and R. M. Fuoss, *ibid.*, **67**, 385 (1963).
56. G. R. Lester, T. A. Gover, and P. G. Sears, *ibid.*, **60**, 1076 (1956).
57. E. D. Copley and H. Hartley, *J. Chem. Soc., (London)*, 2488 (1930).
58. P. S. Albright and L. J. Gosting, *J. Am. Chem. Soc.*, **68**, 1061 (1946).
59. N. P. Yao, E. D'Orsay, and D. N. Bennion, *This Journal*, **115**, 999 (1968).

Solid Bielectrolyte Cells for Thermodynamic Measurements

David A. Shores[*,1] **and Robert A. Rapp**[*]

Department of Metallurgical Engineering, The Ohio State University, Columbus, Ohio 43210

ABSTRACT

Galvanic cells utilizing two mixed conducting solid electrolytes in intimate contact with each other, and in which transport occurs by a common ion, have been analyzed. The voltage of such cells depends on the nonmetal (or metal) chemical potential at the interface between the electrolytes. A method for calculating the chemical potential at the interface from steady-state transference conditions has been described and example calculations for a ThO_2 (Y_2O_3)-$ZrO_2(CaO)$ bielectrolyte cell have been presented. Voltages less than the thermodynamic value must be expected for bielectrolyte cells when one or both electrolytes exhibit $t_i < 1$ and their partial electronic conductivities are comparable. The bielectrolyte cell arrangement seems to offer no outstanding advantages for thermodynamic measurements over a single electrolyte cell with a properly chosen reference electrode.

Before the physicochemical details of mixed ionic and electronic conduction in solid ionic compounds were fully realized or established by experiment, Wagner (1) outlined the steady-state conditions which would exist for galvanic cells with two solid electrolytes exhibiting mixed conduction. To evaluate this theory, Wagner (1) interpreted the voltage of the galvanic cell

$$\text{Ag} \mid \text{AgI} \mid \text{Ag}_2\text{S} \mid \text{S, Pt} \qquad \text{(I)}$$

for which only average partial electrical conductivities were available for the AgI and Ag_2S "electrolytes."

More recently, zirconia- and thoria-base electrolytes have found wide application in high-temperature thermodynamic studies. Measurements of partial conductivities in these oxide electrolytes as a function of oxygen chemical potential have been reported and reviewed (2). Wagner (3) and Schmalzried (4, 5) have described and tested an analysis of the voltage of a solid electrolyte cell with a single mixed conducting electrolyte. As limiting applications of the Schmalzried theory, the "plateau" voltage of a cell may be interpreted to provide values for $P_\oplus$ or $P_\ominus$, which represent for a given electrolyte those values of P_{O_2} at which the positive hole or excess electron conductivity equals the ionic conductivity.

It was recently proposed (6) that a bielectrolyte cell involving thoria- and zirconia-base electrolytes could extend the P_{O_2} range of thermodynamic cell measurements compared to the range of either electrolyte used singly. In such a cell arrangement, the mobile oxygen ions as well as electronic carriers are common to both electrolytes, as in the cell

$$P_{O_2}', \text{Pt} \mid \text{ThO}_2(\text{Y}_2\text{O}_3) \mid \text{ZrO}_2(\text{CaO}) \mid \text{Pt}, P_{O_2}'' \qquad \text{(II)}$$

In what follows, a general analysis for the interpretation of voltages for solid galvanic cells with two mixed conducting electrolytes is presented. In particular, the voltage of cell II was selected for an evaluation of the theory. Finally, the usefulness of a bielectrolyte cell arrangement in competition with single electrolyte cells for thermodynamic measurements is discussed.

Theoretical Considerations

As a model for the calculations to follow, consider the following hypothetical cell

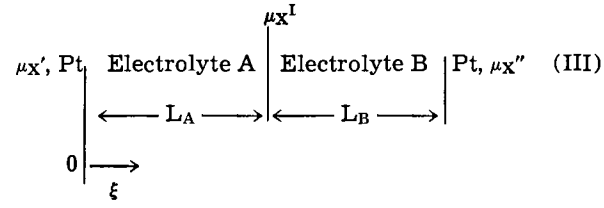

(III)

having a voltage, E, and comprised of electrolytes A and B having a common anion and thicknesses, L_A and L_B. Anions are presumed to be the predominantly mobile ionic species, and the electrodes establish chemical potentials of μ_X' and μ_X''. The electrolytes are characterized by their total electrical conductivities σ^A and σ^B, the value of n in the expressions for partial electronic conductivities $\sigma_\oplus \propto P_{X_2}^{1/n}$ and $\sigma_\ominus \propto P_{X_2}^{-1/n}$ and values of $P_\oplus^A$, $P_\oplus^B$, $P_\ominus^A$, and $P_\ominus^B$ denoting values of P_{X_2} at which the ionic transference number, t_i, equals 0.5 owing to the partial positive hole conduction at high μ_X (4, 5). The chemical potential of X at the electrolyte A/electrolyte B interface is denoted as μ_X^I. It is presumed that the two electrolytes are in intimate contact with each other, and that as a result, μ_X^I is established exclusively by electronic and ionic transport through the electrolytes and is not affected by interactions with a surrounding gas environment.

The cell voltage, E, is the sum of the voltage across each electrolyte, or for cell III (1, 3).

$$E = (1/\mathbf{F})\int_{\mu_X'}^{\mu_X^I} (t_i^A/|z_X|)\, d\mu_X + (1/\mathbf{F})\int_{\mu_X^I}^{\mu_X''} (t_i^B/|z_X|)\, d\mu_X \qquad [1]$$

where t_i^A and t_i^B are the ionic transference numbers in electrolytes A and B, respectively, and z_X is the valence of the anion X. If these ionic transference numbers are essentially unity over the individual ranges of μ_X, the integrals can be combined immediately and the resulting (thermodynamic) voltage, equal to $(\mu_X'' - \mu_X')/|z_X|\mathbf{F}$, is the same as if either electrolyte were used singly. Otherwise, a different (lower) voltage results which depends on μ_X^I and the transference numbers. One may attempt to measure μ_X^I, *e.g.* by inserting a fine Pt wire in the interface, or it may be calculated from steady-state transference conditions as described in the following.

We begin by calculating the rates of ionic and electronic transport through each electrolyte following the method of Wagner (1, 3). For two electrolytes having anions as the mobile ionic species, the steady-state rates of ionic transport and electronic transport in the

* Electrochemical Society Active Member.
[1] Present address: Materials and Processes Laboratory, General Electric Company, Schenectady, New York 12303.
Key words: solid electrolyte, galvanic cell, zirconia, thoria, silver iodide, Ag_3SI, bielectrolyte.

one electrolyte will be equivalent and equal to those in the other electrolyte if the interface is not a source or sink for ions or electrons. Thus, assuming linear cell geometry

$$-j_2^A = j_3^A = -j_2^B = j_3^B \quad [2]$$

where j_2 and j_3 are, respectively, the transport rates in equivalents per second for anions and electrons, and are given by the expression (1, 3)

$$j_{2 \text{ or } 3} = (300S\, t_2\, t_3\, \sigma / |z_X|\mathbf{F}) \mid d\mu_X/d\xi \mid \quad [3]$$

where S is the interfacial area and t_2 and t_3 are, respectively, transference numbers for anions and electrons. Substitution of Eq. [2] with integration across the thickness of the electrolytes gives

$$L_A^{-1} \int_{\mu_{X'}}^{\mu_X^I} t_2^A t_3^A \sigma^A d\mu_X = L_B^{-1} \int_{\mu_X^I}^{\mu_X''} t_2^B t_3^B \sigma^B d\mu_X \quad [4A]$$

Equivalent expressions for electrolytes exhibiting predominant cationic or mixed cationic plus anionic conduction, respectively, are

$$L_A^{-1} \int_{\mu_{Me'}}^{\mu_{Me}^I} t_1^A t_3^A \sigma^A d\mu_{Me} = L_B^{-1} \int_{\mu_{Me}^I}^{\mu_{Me}''} t_1^B t_3^B \sigma^B d\mu_{Me} \quad [4B]$$

and

$$L_A^{-1} \int_{\mu_{Me'}}^{\mu_{Me}^I} (t_1^A + t_2^A) t_3^A \sigma^A d\mu_{Me} = L_B^{-1} \int_{\mu_{Me}^I}^{\mu_{Me}''} (t_1^B + t_2^B) t_3^B \sigma^B d\mu_{Me} \quad [4C]$$

In principle, each of these equations involves only one unknown, *i.e.* the chemical potential at the interface, if the total conductivities and transference numbers of the electrolytes are known as functions of μ_X (or μ_{Me}). Then Eq. [1] could also be evaluated to obtain the voltage of the bielectrolyte cell.

Accordingly, we proceed by taking as a specific example $ThO_2(Y_2O_3)$ and $ZrO_2(CaO)$ solid electrolytes for A and B of cell III, respectively. Both electrolytes are known to be oxygen anion conductors with electronic conduction appearing at low P_{O_2} and positive hole conduction at high P_{O_2} (2). By applying the law of mass action, with the assumptions of (*a*) fully ionized defects, (*b*) concentration-independent mobilities, and (*c*) an infinitely dilute solution of electronic defects, it can be shown for such electrolytes that (4, 5)

$$\sigma_3^A = \sigma_2^A(\Delta_{A\oplus} + \Delta_{A\ominus}) \quad [5]$$

and

$$\sigma_3^B = \sigma_2^B(\Delta_{B\oplus} + \Delta_{B\ominus}) \quad [6]$$

where

$$\Delta_{A\oplus} = (P_{O_2}/P_\oplus^A)^{1/n} \quad [7A]$$

$$\Delta_{A\ominus} = (P_{O_2}/P_\ominus^A)^{-1/n} \quad [7B]$$

$$\Delta_{B\oplus} = (P_{O_2}/P_\oplus^B)^{1/n} \quad [8A]$$

$$\Delta_{B\ominus} = (P_{O_2}/P_\ominus^B)^{-1/n} \quad [8B]$$

By definition

$$t_2 = \sigma_2/(\sigma_2 + \sigma_3) \quad [9]$$

$$t_3 = \sigma_3/(\sigma_2 + \sigma_3) \quad [10]$$

Equations [5], [6], [9], and [10] may be substituted into Eq. [4A]. With the knowledge that σ_2^A and σ_2^B are independent of P_{O_2}, one obtains

$$\frac{\sigma_2^A}{L_A} \int_{P_{O_2'}}^{P_{O_2}^I} \frac{\Delta_{A\oplus} + \Delta_{A\ominus}}{1 + \Delta_{A\oplus} + \Delta_{A\ominus}} d \ln P_{O_2} = \frac{\sigma_2^B}{L_B} \int_{P_{O_2}^I}^{P_{O_2}''} \frac{\Delta_{B\oplus} + \Delta_{B\ominus}}{1 + \Delta_{B\oplus} + \Delta_{B\ominus}} d \ln P_{O_2} \quad [11]$$

With the assumption that $L_A = L_B$, upon integration the left-hand side of Eq. [11] becomes

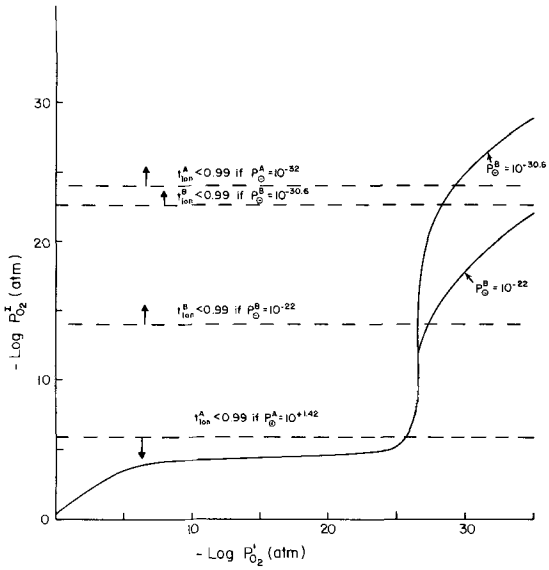

Fig. 1. Calculated values of log $P_{O_2}^I$ vs. log $P_{O_2'}$ with $P_{O_2}'' = 0.21$ atm for $P_\ominus^B = 10^{-30.6}$ and 10^{-22}, A ≡ $ThO_2(Y_2O_3)$ and B ≡ ZrO_2 (CaO).

$$\left\{ \sigma_2^A \ln P_{O_2} - n\sigma_2^A \left[w_A^{-1/2} \ln \frac{1 + 2\Delta_{A\oplus} - w^{1/2}}{1 + 2\Delta_{A\oplus} + w^{1/2}} \right] \right\} \Bigg|_{P_{O_2'}}^{P_{O_2}^I} \quad [12]$$

where $w_A = 1 - 4(P_\ominus^A/P_\oplus^A)^{1/n}$. An analogous result is obtained for the integration of the right-hand side of Eq. [11]. With the expansion of $w^{1/2}$ as a series, the dropping of higher terms, and the assumption that $P_\ominus^A$, $P_\oplus^B << P_\oplus^A$, $P_\oplus^B$, Eq. [12] may be simplified. Finally, with the substitution of the limits of integration and rearrangement, Eq. [11] becomes

$$(\sigma_2^A + \sigma_2^B) \ln P_{O_2}^I - n\sigma_2^A \ln (\lambda_1/\lambda_2) - n\sigma_2^B \ln (\lambda_3/\lambda_4) = \sigma_2^A \ln P_{O_2'} + \sigma_2^B \ln P_{O_2}'' - n\sigma_2^A \ln (\lambda_5/\lambda_6) - n\sigma_2^B \ln (\lambda_7/\lambda_8) \quad [13]$$

where the λ's are defined in the list of symbols appended to this paper.

Equation [13] can be evaluated graphically or by numerical methods to obtain $P_{O_2}^I$ for substitution into Eq. [1] and the further calculation of E for the bielectrolyte cell.

Discussion

As shown in the preceding sections, the steady-state chemical potential at the interface between the electrolytes of a bielectrolyte cell can be calculated from the ionic and electronic partial electrical conductivities of the individual electrolytes. For a cell involving $ThO_2(Y_2O_3)$ and $ZrO_2(CaO)$ electrolytes of equal thickness, *e.g.*

$$\text{Pt}, P_{O_2'} \mid ThO_2(Y_2O_3) \mid^{P_{O_2}^I} ZrO_2(CaO) \mid P_{O_2}'' = 0.21 \text{ atm (air)}, \text{Pt} \quad \text{(IV)}$$

values of $P_{O_2}^I$ have been computed for various values of $P_{O_2'}$ from Eq. [12] for $P_{O_2}'' = 0.21$ atm (air), and sets of values of the other parameters as listed in Table I. These results are shown in Fig. 1 as a plot of log $P_{O_2}^I$ *vs.* $P_{O_2'}$.

Table I. Values of $P_\ominus$, $P_\oplus$, and ionic conductivities at 1000°C for cell IV

	log $P_\ominus$	log $P_\oplus$	σ_2 (ohm-cm)$^{-1}$	Reference
Electrolyte A $Th_{0.84}Y_{0.16}O_{1.92}$	−32	+1.4	0.008	(6, 7)
Electrolyte B $Zr_{0.85}Ca_{0.15}O_{1.85}$	−30.6 or −22.0	+6.5	0.022	(8, 13)

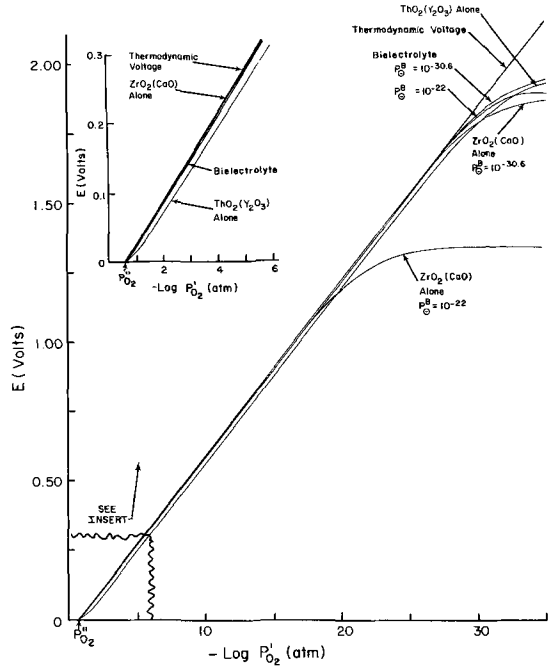

Fig. 2. Calculated values of E (volts) vs. log P_{O_2}' with $P_{O_2}'' = 0.21$ atm for single electrolytes and for the bielectrolyte arrangement of cell IV.

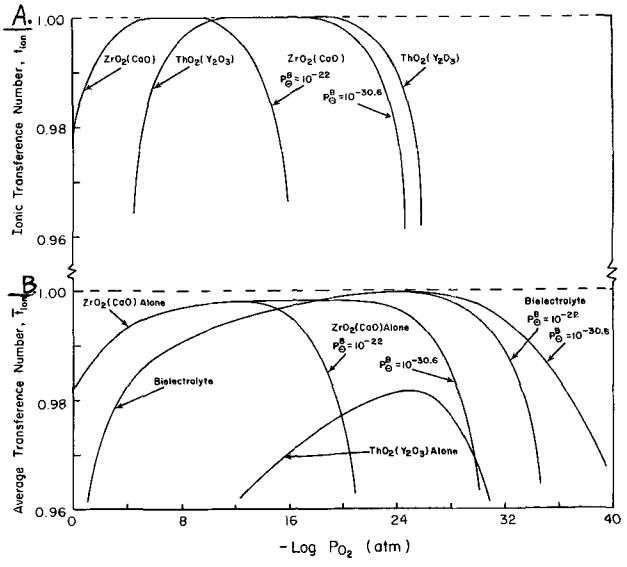

Fig. 3. A—Individual ionic transference numbers for single electrolytes; B—average ionic transference numbers for single- and bi-electrolytes in cell IV.

The values of the ionic conductivities (7-12) and $P_{\oplus}^{A \text{ or } B}$ (7, 8) and $P_{\ominus}^{A \text{ or } B}$ (6, 8, 13) chosen for Table I were taken from previously reported measurements. The most important parameter, $P_{\oplus}$ for $Th_{0.84}Y_{0.16}O_{1.92}$, was interpolated from the conductivity data of Lasker and Rapp (7). For $Zr_{0.85}Ca_{0.15}O_{1.85}$ at 1000°C, $P_{\ominus}$ has been reported as 10^{-22} (13), 10^{-23} (14), 10^{-24} (4), $<10^{-26}$ (15), 10^{-28} (16), and $10^{-30.6}$ atm (8). A recent determination of $P_{\ominus}$ for $Zr_{0.86}Y_{0.14}O_{1.93}$ by Swinkels (20) yielded an extrapolated value of $10^{-30.8}$ atm at 1000°C. The disagreement among the values of $P_{\ominus}$ is not unexpected, since the measurements are difficult experimentally and different techniques were used; further, small differences in the types and amounts of impurities may have a large effect on the electronic conductivity, and hence on $P_{\ominus}$. However, as seen in Fig. 1, values of $P_{O_2}{}^{I}$ calculated for cell IV are not sensitive to the choice of $P_{\ominus}$ for ZrO_2(CaO), until P_{O_2}' is reduced to values approaching $P_{\ominus}{}^{B}$. The two curves of Fig. 1 were calculated for the extremes in the reported values for $P_{\ominus}{}^{B}$: 10^{-22} and $10^{-30.6}$ atm.

When $P_{O_2}{}^{I}$ is known for a particular bielectrolyte cell, the expected voltage may be calculated from Eq. [1]. As an example, we may consider cell IV at 1000°C with $P_{O_2}' = 1$ atm. From Fig. 1, $P_{O_2}{}^{I} = 0.795$ atm; thus, the calculated cell voltage equals −0.0401V. This calculated value may be compared with an experimentally reported value (6) of −0.0427V. Because the $ThO_2(Y_2O_3)$ electrolyte is in a P_{O_2}-range of significant electronic conduction, the condition $P_{O_2}' = P_{O_2}{}^{I}$, *i.e.* with no chemical potential difference existing across the $ThO_2(Y_2O_3)$ electrolyte, would be required for the cell voltage to correspond exactly to the thermodynamic voltage (0.0427V), *i.e.* with an "apparent" $\bar{t}_i$ for the bielectrolyte cell equal to unity.

Voltages calculated from Eq. [1] using the data of Table I for cell IV at 1000°C are shown in Fig. 2 as a plot of E *vs.* log P_{O_2}'. For comparison, the cell voltages calculated for the single electrolytes have also been plotted. It is obvious (17) that the deviation from the thermodynamic voltage resulting from p-type conduction in the thoria electrolyte of cell IV will become a smaller fraction of the total voltage as P_{O_2}' is lowered. By calculation of this effect as illustrated in Fig. 3B, $\bar{t}_i$ for the bielectric cell becomes greater than 0.99 at about $P_{O_2}' < 10^{-6.8}$; however, for $P_{O_2} < 10^{-31.3}$, if $P_{\ominus}{}^{B} = 10^{-22}$ (or for $P_{O_2}' < 10^{-34.2}$ if $P_{\ominus}{}^{B} = 10^{-30.6}$), $\bar{t}_i$ will again decrease below 0.99 because of electronic conduction. Figure 3B is based on cell IV which specifies air ($P_{O_2}'' = 0.21$ atm) as the reference electrode in contact with the ZrO_2(CaO) electrolyte. In Fig. 3B, the bielectrolyte cell exhibits a broader range of P_{O_2} over which the average ionic transference number, $\bar{t}_i$, exceeds 0.99 than either of the two single electrolytes. However, this apparent advantage of the bielectrolyte cell must be evaluated in competition with the single electrolyte cells which may also be used to accomplish the equivalent measurement of some unknown P_{O_2}'.

Almost without exception, investigators have previously chosen to use a single electrolyte and a reference electrode well within the range of predominant ionic conduction. In Fig. 3A are plotted the ionic transference numbers of the two electrolytes described in Table I. The data of Patterson *et al.* (8) for $P_{\oplus}{}^{B}$ indicate that t_i is actually slightly less than 0.99 in air or pure oxygen. More recent and yet unpublished work by Heyne (21) and by Patterson (22) has yielded higher values for $P_{\oplus}{}^{B}$. The usual purpose of galvanic cell measurements is to determine an unknown (usually very low) P_{O_2}' as accurately as possible. For example, consider the use of a single $ThO_2(Y_2O_3)$ electrolyte cell with either a Fe-FeO or Cr-Cr_2O_3 reference electrode to measure, at 1000°C, the P_{O_2}' for the coexistence electrodes Nb-NbO or U-UO_2. It is assumed for the following calculations that any chemical attack or electrode polarization may be ignored and that the electrodes maintain their equilibrium oxygen activities (19), which are taken as: P_{O_2}(Fe,FeO) = $10^{-14.8}$, P_{O_2}(Cr,Cr_2O_3) = $10^{-21.8}$, P_{O_2}(Nb,NbO) = $10^{-25.1}$, P_{O_2}(U,UO_2) = $10^{-35.5}$ atm. This group of cells may be represented as

$$\begin{array}{c|c|c} \text{Nb, NbO} \\ \text{or} \\ \text{U, } UO_2 \end{array} \quad \begin{array}{c} \\ Th_{0.84}Y_{0.16}O_{1.96} \\ \\ \end{array} \quad \begin{array}{c|} \text{Fe, FeO} \\ \text{or} \\ \text{Cr, } Cr_2O_3 \end{array} \qquad \text{(V)}$$

In competition with cells V, we shall consider the bielectrolyte cell VI with the air reference electrode, which according to Fig. 3B might appear superior

$$\text{Nb, NbO or U, } UO_2 \mid ThO_2(+Y_2O_3) \mid P_{O_2}{}^{I} \; ZrO_2(+CaO) \mid \text{Pt, air } (P_{O_2}'' = 0.21) \qquad \text{(VI)}$$

The purpose of the comparison is, of course, to establish by calculation which cell should most accurately

Table II. Calculated values of cell voltage error and $\bar{t}_i$ for cells V and VI

Cell		E_c[a] (V)	E_t[b] (V)	Error (cal/mole)	$\bar{t}_i$[c]
Nb, NbO | $ThO_2(Y_2O_3)$ | Fe, FeO		0.6774	0.6797	106	0.997
Nb, NbO | $ThO_2(Y_2O_3)$ | Cr, Cr_2O_3		0.2159	0.2178	87	0.991
U, UO_2 | $ThO_2(Y_2O_3)$ | Fe, FeO		1.1204	1.3659	22,580	0.820
U, UO_2 | $ThO_2(Y_2O_3)$ | Cr, Cr_2O_3		0.6589	0.9040	22,540	0.729
Nb, NbO | $ThO_2(Y_2O_3)$ | $ZrO_2(CaO)$ | Pt, air ($P_{O_2} = 0.21$)	$P_\ominus^B = 10^{-22}$	1.6052	1.6116	294	0.996
	$P_\ominus^B = 10^{-30.6}$	1.6052	1.6116	294	0.996
U, UO_2 | $ThO_2(Y_2O_3)$ | $ZrO_2(CaO)$ | Pt, air ($P_{O_2} = 0.21$)	$P_\ominus^B = 10^{-22}$	1.9575	2.2978	31,300	0.852
	$P_\ominus^B = 10^{-30.6}$	2.0484	2.2978	22,940	0.891

[a] Cell voltage calculated with Schmalzried's equation for cells V, and Eq. [1] and [12] for cells VI.
[b] Thermodynamic cell voltage; *i.e.*, $E = -\Delta G^\circ/nF$.
[c] $\bar{t}_i = E_c/E_t$.

measure the low value of P_{O_2}', which in these cells is presumed to be known. The results of the calculations using Schmalzried's (4, 5) equation for cells V and our Eq. [12] and [1] for the bielectrolyte cell are listed in Table II. As seen in Table II, regardless of the higher values of $\bar{t}_i$ for the bielectrolyte cells, the more accurate measurement of P_{O_2}' is made by the single electrolyte cells. Thus, the use of $\bar{t}_i$ as a measure for the usefulness of a cell is misleading.

The calculations of Table II indicate that the least error from mixed conduction in a single electrolyte cell is realized by choosing a reference electrode whose P_{O_2} is as close as possible to that of the unknown electrode. Then, in principle, the Cr, Cr_2O_3 electrode is superior to other electrodes with higher P_{O_2}'' to measure very low values of P_{O_2}'. For a single electrolyte cell, the cell voltage may also be obtained from the graphical integration of Fig. 3A from the reference to the "unknown" electrode (7). While the area below the curve is proportional (a factor of $RT/4\mathbf{F}$) to the cell voltage, the area above the curve is proportional to the error in the measurement which results from mixed conduction. Obviously, this area and the error are minimized as the two electrodes approach each other. In the limit, an exact determination of an unknown P_{O_2}' can be made regardless of the value of t_i if a known P_{O_2}'' can be adjusted so that the cell voltage equals zero (19).

In the application of the Schmalzried (voltage plateau) technique to cell IV for the determination of an "apparent" $P_\ominus$ for the bielectrolyte, P_{O_2}' would be reduced to an extremely low value so that a limiting cell voltage is obtained. From Eq. [1], it follows that

$$E \text{ (plateau)} = E^A + E^B \qquad [14]$$

where E^A and E^B are, respectively, the voltages across electrolyte A [$ThO_2(Y_2O_3)$] and electrolyte B [$ZrO_2(CaO)$]. The interpretation of such a limiting (plateau) voltage in terms of the electronic conductivities of the individual thoria and zirconia electrolytes is as follows. If Schmalzried's equation (4, 5) for the voltage of a cell involving a mixed conducting electrolyte is applied to the thoria electrolyte of cell IV, with the condition that $P_{O_2}' \ll P_\ominus \ll P_{O_2}^I$, one obtains

$$\ln P_\ominus^A = \ln P_{O_2}^I - 4\mathbf{F}E^A/RT \qquad [15]$$

For $ZrO_2(CaO)$

$$E^B = RT/\mathbf{F} \ln (\lambda_4/\lambda_8) + RT/\mathbf{F} \ln (\lambda_7/\lambda_3) \qquad [16]$$

Substitution of Eq. [14] and [16] into Eq. [15] and neglecting the small contribution of the first term on the right side of Eq. [16] gives

$$\ln P_\ominus^A = \ln P_{O_2}^I - 4\mathbf{F}E(\text{plateau})/RT + 4 \ln (\lambda_7/\lambda_3) \qquad [17]$$

where $n = 4$.

Reported values of the plateau voltage (6)[2] for cell IV

$$E(\text{plateau}) = 2.87 - 7 \times 10^{-4}T(1000\text{-}1400\text{K}) \text{ (V)} \qquad [18]$$

may be substituted into Eq. [16] and values of $P_\ominus^A$ can be obtained if $P_{O_2}^I$ or P_{O_2}' is known. For example, at 1000°C with $P_\ominus^B = 10^{-22}$ atm, $P_\ominus^A$ is calculated to equal $10^{-32.9}$ atm if P_{O_2}' is assumed to be 10^{-34} atm and thereby $P_{O_2}^I = 10^{-21.3}$ atm (from Fig. 1), or to equal $10^{-33.6}$ atm if P_{O_2}' is assumed to be 10^{-36} atm and $P_{O_2}^I = 10^{-22.7}$ atm. Alternatively, for $P_\ominus^B = 10^{-30.6}$ atm again assuming $P_{O_2}' = 10^{-34}$ or 10^{-36} atm, $P_\ominus^A$ is calculated to equal $10^{-32.3}$ or $10^{-32.6}$ atm, respectively. These values of $P_\ominus^A$ do not differ substantially from those obtained by neglecting the contribution of $\sigma_\ominus^B$ in the bielectrolyte cell (6). It should be noted that the above calculated values of $P_\ominus^A$ depend on $P_{O_2}^I$, which is already a function of $P_\ominus^A$, and on an arbitrary choice of P_{O_2}' corresponding to the voltage plateau. An exact solution for $P_\ominus^A$ would require an iterative calculation procedure as well as a knowledge of P_{O_2}'. If values for $P_\ominus^A$ are obtained in this manner, or are otherwise available, the oxygen pressure range for which $t_i \geq 0.99$ for $ThO_2(Y_2O_3)$ alone (the usual criterion for thermodynamic measurements) may be calculated by combining Eq. [6] and [7], and setting $n = 4$, or

$$\log P_{O_2} (t_i = 0.99) \cong \log P_\ominus^A + 8 \qquad [19]$$

The foregoing general treatment of bielectrolyte cells can also be applied to cells with exchange electrodes which exhibit mixed conduction. As an example of a limiting case, the exchange electrode Ag_2S in cell I may be considered as a second electrolyte, indeed one with predominant electronic conduction. Wagner (1) has previously described this cell in which Ag is the transported species. At steady state in the absence of an external circuit, the countertransference of silver ions and electrons in AgI is extremely small because of the very low σ_e(AgI). On the other hand, because of the high $\sigma_e(Ag_2S)$, the steady-state ionic and electronic fluxes in Ag_2S are maintained with only a negligible voltage drop across Ag_2S. Thereby, the silver activity at the AgI/Ag_2S interface is virtually equal to that at the Ag_2S/S interface. Thus, the voltage across the Ag_2S "electrolyte" is zero, and the thermodynamic voltage is measured for the cell. However, as already discussed, deviations from the thermodynamic voltage must be expected for a bielectrolyte cell when one electrolyte exhibits $t_i < 1.0$ and the partial electronic conductivities of the single electrolytes are comparable.

When an electrode component reacts with the electrolyte, the cell voltage may decrease. If a compact product layer is formed, it may be considered as a second electrolyte, and information about the transport properties of the product layer may be deduced from changes in the cell voltage so long as the electrodes remain reversible. Such an interpretation of a changing cell voltage may be pertinent to the shelf life and voltage stability of a solid-state battery. Owens *et al.* (18) have questioned previous reports of the high stability of the cell

[2] These measurements may have been carried out with the oxygen activity at the thoria-zirconia interface established by coexisting Co-CoO, in which case the plateau voltage arises exclusively from electronic conduction in the thoria electrolyte.

$$Ag \mid Ag_3SI \mid I_2 \qquad (VII)$$

based on their experimental observation that Ag_3SI reacts with I_2 to form AgI and S. If AgI in the presence of I_2, or AgI doped with S, should exhibit $t_{ion} < 1$, then the mixed conducting AgI product layer would lead to a lower open-circuit voltage; if the AgI product layer is an exclusive ionic conductor, then the open-circuit cell voltage would be stable.

Acknowledgment

This research was supported under Contract No. AT(11-1)-1440 by the United States Atomic Energy Commission.

Manuscript submitted May 12, 1970; revised manuscript received Jan. 4, 1971.

Any discussion of this paper will appear in a Discussion Section to be published in the June 1972 JOURNAL.

SYMBOLS

E	EMF (volts)
$\mathbf{F}$	Faraday (96487 A s/Eq)
μ_X, μ_{Me}	Chemical potential of species X or Me
L_A, L_B	Thicknesses of electrolytes A and B
σ	Electrical conductivity (ohm-cm)$^{-1}$
ξ	Distance (cm)
z_X	Valence of species X
$P_{\oplus}^A$, $P_{\ominus}^A$, $P_{\oplus}^B$, $P_{\ominus}^B$	Schmalzried parameters for electrolytes A and B, respectively (atm)
t_i	Ionic transference number
t_2, t_3	Transference numbers of anions and electrons, respectively
j_2, j_3	Rates of transport for anions and electrons, respectively (eq/sec)
P_{O2}	Partial pressure of oxygen (atm)
$\Delta_{A\oplus}$	$(P_{O2}/P_{\oplus}^A)^{1/n}$
$\Delta_{A\ominus}$	$(P_{O2}/P_{\ominus}^A)^{-1/n}$
$\Delta_{B\oplus}$	$(P_{O2}/P_{\oplus}^B)^{1/n}$
$\Delta_{B\ominus}$	$(P_{O2}/P_{\ominus}^B)^{-1/n}$
λ_1	$[(P_{O_2}^I)^{1/n} + (P_{\oplus}^A)^{1/n}]$
λ_2	$[(P_{O_2}^I)^{1/n} + (P_{\ominus}^A)^{1/n}]$
λ_3	$[(P_{O_2}^I)^{1/n} + (P_{\ominus}^B)^{1/n}]$
λ_4	$[(P_{O_2}^I)^{1/n} + (P_{\oplus}^B)^{1/n}]$
λ_5	$[(P_{O_2}')^{1/n} + (P_{\ominus}^A)^{1/n}]$
λ_6	$[(P_{O_2}')^{1/n} + (P_{\oplus}^A)^{1/n}]$
λ_7	$[(P_{O_2}'')^{1/n} + (P_{\ominus}^B)^{1/n}]$
λ_8	$[(P_{O_2}'')^{1/n} + (P_{\oplus}^B)^{1/n}]$

REFERENCES

1. C. Wagner, *Z. Elektrochem.*, **40**, 365 (1934).
2. R. A. Rapp, "Thermodynamics of Nuclear Materials," p. 559, IAEA, Vienna (1968).
3. C. Wagner, *Z. Phys. Chem.*, **B21**, 25 (1933).
4. H. Schmalzried, *Z. Electrochem.*, **66**, 572 (1962).
5. H. Schmalzried, *Z. Phys. Chem. N.F.*, **38**, 87 (1963).
6. Y. D. Tretyakov and A. Muan, *This Journal*, **116**, 331 (1969).
7. M. F. Lasker and R. A. Rapp, *Z. Phys. Chem. N.F.*, **49**, 198 (1966).
8. J. W. Patterson, E. C. Bogren, and R. A. Rapp, *This Journal*, **114**, 752 (1967).
9. L. Heyne, Chap. in "Mass Transport in Oxides," J. B. Watchman and A. D. Franklin, Editors, NBS Spec. Publ. 296, p. 149 (1968).
10. R. E. Carter and W. L. Roth, Chap. in "Electromotive Force Measurements in High Temperature Systems," C. B. Alcock, Editor, p. 125, Inst. Min. and Metal. Publ., London (1968).
11. J. M. Wimmer, L. R. Bidwell, and N. M. Tallan, *J. Am. Ceram. Soc.*, **50**, 198 (1967).
12. E. C. Subbarao, P. H. Sutter, and J. Hrizo, *ibid.*, **48**, 443 (1965).
13. H. Yanagida, reported in D. Yuan and F. A. Kröger, *This Journal*, **116**, 594 (1969).
14. B. C. Steele and C. B. Alcock, *Trans. Met. Soc. AIME*, **233**, 1359 (1965).
15. Y. Tretyakov and H. Schmalzried, *Ber. Bunsenges. Physik. Chem.*, **69**, 396 (1965).
16. Y. D. Tretyakov, *Vsn. Mosk. Univ., Ser. II, Khim.*, In press.
17. A. A. Vecher and D. V. Vecher, *Russ. J. Phys. Chem.*, **41**, 685 (1967).
18. B. Owens *et al.*, *This Journal*, **116**, 312 (1969).
19. R. A. Rapp and D. A. Shores, "Solid Electrolyte Galvanic Cells," "Techniques in Metals Research," Vol. IV, Part 2, Interscience Publishers New York (1970).
20. D. A. J. Swinkels, *This Journal*, **117**, 1267 (1970).
21. L. Heyne, Personal communication.
22. J. W. Patterson, Personal communication.

The Effect of Anions on the Thermodynamics of Silver-Sodium Exchange between Glass and Molten Salts

Kurt H. Stern*

Naval Research Laboratory, Electrochemistry Branch, Washington, D. C. 20390

ABSTRACT

$\Delta H°$ and $\Delta S°$ were determined for the ion exchange Na^+(glass) + Ag^+(salt) = Na^+(salt) + Ag^+(glass) in mixed chloride-sulfate melts in the range 500°-600°C. The small value of the equilibrium constant K in the pure chloride melt results primarily from a negative $\Delta S°$ which is accounted for by the lower mobility of Ag^+ in the glass relative to Na^+. In the mixed anion melts both $\Delta H°$ and $\Delta S°$ contribute to K.

In previous work (1) it was shown that the equilibrium constant K for the process

$$Na^+(g) + Ag^+(s) = Na^+(s) + Ag^+(g) \qquad [1]$$

where g represents the glass and s the salt phase, is highly dependent on the melt anion, although only the cations participate in the actual exchange. For example, in mixed chloride-sulfate melts K increased by three orders of magnitude as the melt composition was changed from pure chloride to 58 mole per cent (m/o) sulfate. These results were accounted for in terms of a model in which the anionic adsorption sites on the glass and the melt anions in the double layer near the glass-melt interface "compete" for the cations. When only oxyanions are present in the melt, values of $\Delta G°$ for the exchange calculated by assuming that all cation-anion interactions are coulombic were in good agreement with experiment. However, in bromide and chloride melts, experimental values of $\Delta G°$ were much

* Electrochemical Society Active Member.
Key words: membrane potentials, glass, molten salts.

more positive.[1] This result was explained in terms of the strong tendency of halide ions to complex Ag^+, resulting in a smaller value of K than expected from electrostatics alone.

The purpose of the present work is to explore the validity of the model further by obtaining the thermodynamic functions $\Delta H°$ and $\Delta S°$ for the exchange. A comparison of the contribution these functions make to $\Delta G°$ should give further insight into the mechanism of the exchange.

Since the various oxyanions investigated previously (1) all gave similar results, only chloride-sulfate melts were studied. Membrane potentials and glass conductances were determined in the range 500°-600°C.

Experimental

The general procedures for carrying out membrane potential measurements have been described previously (1, 2). For the present work the U-shaped cells, made of General Electric Type 204 fused silica, were modified by sealing a short piece of tubing directly over the membrane so that the Platinel II thermocouple could be inserted into it with its junction in contact with the membrane. The thermocouple was calibrated initially against a National Bureau of Standards calibrated Pt-13% Rh thermocouple and recalibrated occasionally against the melting point of AgCl. The same AgCl-Ag_2SO_4 mixture was added to each side of the cell and the silver electrodes, sheathed in 3 mm OD fused silica tubing, were inserted into the cell through the top of caps through which a stream of dry helium passed continuously to reduce access of moisture to the melt. After the EMF had stabilized, usually to within a few mV of zero, sodium was added incrementally as NaCl up to ~5 m/o. Since the additions were small the Cl^-/SO_4^{-2} ratio remained approximately constant during a run. The temperature dependence of the emf was measured for each Na^+ concentration in the range 500°-600°C after the emf had become constant at each temperature. All measurements were corrected for the initial asymmetry potential.

The conductance of the membrane was measured with a General Radio 544-B Megohm Bridge, accurate to ±3%. Although AgCl is a stable liquid in the range 500°-600°C, there seems to be no sodium salt for which this is true. Several experiments were made with a NaCl-NaI eutectic which is liquid above 573°C, but this solution evolved I_2 and appeared to change the glass irreversibly since the conductance ratio with Ag^+ and Na^+ in the glass changed with the sequence of filling the cell. The most reproducible results were obtained when the cell was filled with AgCl, electrolyzed at 100-200V between Pt electrodes until the resistance became constant. The resistance was then measured as a function of temperature. The AgCl was then replaced by undried NaBr which was allowed to sinter in the cell. The electrolysis and conductance measurements were then repeated.

Treatment of Experimental Data

Since the method of calculating ion exchange equilibrium constants has been discussed in detail elsewhere (3), it is only summarized here. The emf of the concentration cell

$$Ag|AgCl, Ag_2SO_4|glass|Ag^+, Na^+, Cl^-, SO_4^{-2}|Ag \quad [2]$$

is given by $E_{cell} = E_M + E_{electrode}$, where the membrane potential E_M is (4)

$$E_M = (nRT/F) \ln [(a^{1/n} + K'^{1/n} b^{1/n})/(K'^{1/n}] \quad [3]$$

where a and b are the activities of the exchanging ions and K' is the ion-exchange selectivity constant, n is a thermodynamic factor which for the present system is near unity (3).

Since the melts in this study did not contain more than a few mole per cent sodium, the activities were replaced by mole fractions on the assumption that the activity coefficients would not vary greatly over the concentration range. The ionic activities were identified with the mole fractions of the salt components

$$a = n_{NaCl}/(n_{NaCl} + n_{AgCl} + n_{Ag_2SO_4}) \quad [4a]$$

$$b = (n_{AgCl} + n_{Ag_2SO_4})/(n_{NaCl} + n_{AgCl} + n_{Ag_2SO_4}) \quad [4b]$$

The ion-exchange selectivity constant K' can be written as the product of the equilibrium constant for reaction [1] and the ionic mobility ratio

$$K' = K(U_{Ag}/U_{Na})^n \quad [5]$$

Since it was shown previously (3) that K' is virtually independent of n, it was calculated with $n = 1$. The value of K does depend on n since this parameter appears as exponent of the mobility ratio, but it was determined that the values of $\Delta H°$ and $\Delta S°$ which are of interest in this work are affected very little by small departures (±10%) of n from unity. The K values reported in this work are therefore those with $n = 1$.

Results and Discussion

Between 500° and 600°C the conductance ($1/R$) of the glass is linear in $1/T$ for both Na^+ and Ag^+, the corresponding Arrhenius activation energies being 83.3 and 109.2 kJ, respectively. As a consequence of these different activation energies, the mobility ratio is quite temperature dependent:

t (°C)	$(U_{Na}/U_{Ag}) \pm 5\%$
500	9.8
550	7.5_0
600	5.7_6

The ratio for 570°C, the temperature of the previous study (3) is 6.4, somewhat higher than the previously reported value of 5. Linear extrapolation of the ratio in $1/T$ to 337°C gives 21 compared to 13.7 reported by Doremus (5) for fused silica at this temperature. Linear extrapolation of the plot shows that the mobilities of Ag^+ and Na^+ are expected to become equal ($U_{Na}/U_{Ag} = 1$) at 760°C.

In Table I are listed values of K' and K for the four $Cl^- - SO_4^{-2}$ melts at three different temperatures. The first two lines compare the values obtained in pure chloride melts when activity corrections are taken into account (3). For the mixed anion melts activity corrections cannot be made since the activity coefficients are not known. However, as has been pointed out elsewhere (3, 6), AgCl-Ag_2SO_4 solutions are virtually

[1] The sign of $\Delta G°_{exp.}$ in Tables II and III of Ref. 1 was inadvertently reversed. It should be positive.

Table I. K' and K values for Ag^+-Na^+ exchange on fused silica

$X_{Ag_2SO_4}$	500°C K'	500°C K	550°C K'	550°C K	600°C K'	600°C K
0.000*	5.58×10^{-5}	5.47×10^{-4}	7.22×10^{-5}	5.42×10^{-4}	9.10×10^{-5}	5.24×10^{-4}
0.000	3.62×10^{-5}	3.55×10^{-4}	4.81×10^{-5}	3.61×10^{-4}	6.21×10^{-5}	3.58×10^{-4}
0.286	2.24×10^{-3}	2.20×10^{-2}	2.58×10^{-3}	1.94×10^{-2}	3.34×10^{-2}	1.92×10^{-2}
0.500	1.16×10^{-2}	1.14×10^{-1}	1.23×10^{-2}	9.23×10^{-2}	1.62×10^{-2}	9.33×10^{-2}
0.575	1.80×10^{-2}	1.76×10^{-1}	2.04×10^{-2}	1.53×10^{-1}	1.90×10^{-2}	1.09×10^{-1}

* With activity correction.

Table II. $\Delta H°$ and $\Delta S°$ for the exchange reaction $Na^+(g) + Ag^+(s) = Na^+(s) + Ag^+(g)$

$X_{Ag_2SO_4}$	$\Delta H°$ (kJ)	$\Delta S°$ (JK^{-1})
0.000*	−2.5	−65.7
0.000	+0.2	−65.7
0.286	−7.5	−41.0
0.500	−11.0	−33.0
0.575	−27.0	−49.0

* With activity correction.

ideal, and in the ternary melt the sodium concentration range used is sufficiently small to preclude large variations of activity coefficient with melt composition. Thus, although the neglect of activity corrections affects the actual value of K (see the first two lines of Table I for the effect of the known activities in the AgCl-NaCl system), it would hardly affect the temperature coefficient of K for a particular anion composition; as pointed out previously (3) the assumption of ideality can also not account for the thousand-fold change of K with anion composition.

Values of K' at 550°C are in fairly good agreement with those determined previously (1) near that temperature. In general, the new values are somewhat lower. The marked increase of K' and K with increased sulfate concentration is apparent. With the exception of K' at 600°C for $X_{Ag_2SO_4} = 0.575$ the trend is for K' to increase somewhat with temperature. Since (U_{Na}/U_{Ag}) decreases markedly with temperature, the equilibrium constant K shows a slightly reverse trend, particularly at the higher sulfate concentrations.

The values of K can be used to calculate the enthalpy and entropy values for the cation exchange by standard thermodynamic methods. These are shown in Table II.

A comparison of the first two lines shows that the effect of neglecting the nonideality of the melts on $\Delta H°$ and $\Delta S°$ is very minor, most probably because both of these functions depend only on the temperature coefficient of K which is less sensitive to activity corrections than the absolute value of K.

The most notable feature of Table II is the fact that, particularly in the chloride-rich melts, the small values of K are almost entirely accounted for by the negative $\Delta S°$ for the exchange reaction. As the sulfate concentration increases the situation becomes more complex with both $\Delta H°$ and $\Delta S°$ contributing to $\Delta G°$, but in opposite directions: $\Delta H°$ favors the exchange process [1] as written and $\Delta S°$ opposing it. This result is surprising in terms of the model which was used to account for the increase in K (decrease of $\Delta G°$) with increasing $X_{SO_4^{-2}}$. In terms of the electrostatic interactions of the cations with the melt anions and the $AlOSi^-$ exchange sites on the glass, values of K near unity were predicted. The small values of K in halide melts were accounted for by the nonelectrostatic bonding involved in the formation of silver halide complexes which increases the activity of silver in the melt relative to that in the glass, but this effect might have been expected to be reflected in enthalpy rather than entropy changes.

The problem can be examined in more detail by writing the exchange process as the difference of two terms

$$Ag^+(s) \rightarrow Ag^+(g) \qquad (a)$$

$$Na^+(s) \rightarrow Na^+(g) \qquad (b)$$

Then

$$\Delta S° = \Delta S_a - \Delta S_b$$

$$\Delta H° = \Delta H_a - \Delta H_b$$

It seems reasonable to suppose that the entropy of the cations is greater in the melt than in the glass since they must lose at least some of their translational entropy by becoming relatively immobile on or in the glass. Therefore, ΔS_a and ΔS_b are both negative. But the experimental negative $\Delta S°$ then requires that ΔS_a be more negative than ΔS_b. If we write

$$\Delta S_a = S_{Ag(g)} - S_{Ag(s)} < 0$$

$$\Delta S_b = S_{Na(g)} - S_{Na(s)} > 0$$

this means that either one or both conditions apply

$$S_{Na(s)} < S_{Ag(s)}$$

$$S_{Na(g)} > S_{Ag(g)}$$

where the entropies are not the third law values but include only contributions to the entropy from the position of the ions. If Ag^+ is complexed in the melt, its freedom of movement should be somewhat less than that of Na^+ and the first inequality should be reversed. The argument then requires that the negative $\Delta S°$ be accounted for entirely by the second inequality which must outweigh the effect of the first. It is known that the mobility of Na^+ in the glass is much greater than that of Ag^+ so that this inequality is reasonable, *i.e.* Na^+ is less tightly bound to the glass network than Ag^+ *is*.

With increasing sulfate concentration $\Delta S°$ becomes less negative. Since the cationic mobilities are not affected by anions in the melt, it follows that this effect must arise from the first inequality, *i.e.* the interactions between the cations and SO_4^{-2} are more nearly equal than with Cl^- and $S_{Ag(s)}$ increases relative to $S_{Na(s)}$. Hence ΔS_a becomes less negative.

We next consider possible interpretations of $\Delta H°$. In chloride melts $\Delta H° \simeq 0$ and therefore $\Delta H_a = \Delta H_b$. Then,

$$\Delta H_a = H_{Ag(g)} - H_{Ag(s)}$$

$$\Delta H_b = H_{Na(g)} - H_{Na(s)}$$

where the reference state ($H_i = 0$) is the bare ion in free space. Since electrostatic attraction operates between each cation and the anions in the melt and in the glass, all the ionic enthalpies are negative. If the enthalpy terms for all interactions except $Ag^+ - Cl^-$ are identified with coulombic energies [in contrast to the previous work (1) in which they were identified with Gibbs energies] then the condition $\Delta H° = 0$ permits the calculation of $H_{Ag(s)}$ in a pure chloride melt

$$H_{Ag(s)} = H_{Ag(g)} - H_{Na(g)} + H_{Na(s)}$$
$$= (-103) - (-113) + (119) = -109 \text{ kcal}$$

But this value of $H_{Ag(s)}$ is only slightly more negative than the purely electrostatic value of −107 kcal (1). This would indicate that nonelectrostatic $Ag^+ - Cl^-$ interactions are not very significant. The experimental value of $\Delta H°$ becomes increasingly negative as the sulfate concentration is increased. In terms of electrostatics alone this is not well accounted for since the predicted value is near zero for a pure sulfate melt (1).

As a result of the present work, the ion exchange model presented previously requires some revision. The small value of K in the pure chloride melt is seen to result primarily from a negative entropy change for the exchange process. This negative $\Delta S°$ is largely accounted for by the greater mobility of Na^+ in the glass rather than the nonelectrostatic complexing of Ag^+ by Cl^- in the melt. Only the increase of $\Delta S°$ with SO_4^{-2} concentration is accounted for by the decrease of this complexing in the mixed $Cl^- - SO_4^{-2}$ melts. The major unexplained feature is the decrease of $\Delta H°$ with increasing SO_4^{-2} concentration.

Manuscript submitted July 1, 1970; revised manuscript received *ca.* Jan. 4, 1971. This was Paper 40 presented at the Atlantic City Meeting of the Society, Oct. 4-9, 1970.

Any discussion of this paper will appear in a Discussion Section to be published in the June 1972 JOURNAL.

REFERENCES

1. K. H. Stern, *J. Phys. Chem.*, **74**, 1329 (1970).
2. K. H. Stern, *ibid.*, **72**, 1963 (1968).
3. K. H. Stern, *ibid.*, **74**, 1323 (1970).
4. cf. G. Eisenman, in "Glass Electrodes for Hydrogen and Other Cations," Chapter 5, G. Eisenman, Editor, Marcel Dekker, Inc., New York, N. Y. (1965).
5. R. H. Doremus, *J. Phys. Chem.*, **72**, 2877 (1968).
6. K. H. Stern and S. Caulder, *Thermochimica Acta*, In press.

Hydrogen Embrittlement and Hydrogen Traps

J. O'M. Bockris* and P. K. Subramanyan[1]

The Electrochemistry Laboratory, The University of Pennsylvania, Philadelphia, Pennsylvania 19104

ABSTRACT

The permeation of H through iron and an iron-nickel alloy as a function of time is reported. Below a certain critical H overpotential η, the H permeation occurs as a function of time in a simple way; and can be repeated indefinitely on the same specimen. But, when $\eta > \eta_{crit}$, the permeation-time transient attains a new and characteristic shape. It is no longer repeatable on the same specimen. These characteristic differences of H permeation are seen during injection of H into the metal and after the cessation of H injection. The decay of H permeation follows simple laws before η_{crit}. At $\eta > \eta_{crit}$, the decay is complex and the permeation-time (P-t) relationship shows successive maxima. The critical overpotential is that at which microcracks begin to nucleate, spread, and provide traps for H_2. Calculated pressures, using the amount of lattice-dissolved H and adsorbed H at the cathodic surface at η_{crit}, are shown to be consistent with an H_2 pressure in voids which would cause the spreading of cracks. This leads to an electrochemical condition for the beginning of H damage: the observed critical overpotential gives reasonable values for the embrittling[2] critical pressure. Such an electrochemical condition for damage also applies during corrosion. The amount of trapped H is calculated from the permeation-time transients at overpotentials higher than η_{crit}. The H trapping constant is calculated. Distribution of hydrogen in the embrittled membrane is given. In the permeation decay transients, the first maximum represents the hydrogen in cavities and the second, H bound to chemical impurities.

Studies of embrittlement and damage to materials caused by the ingress of H are usually carried out in two ways: either by exposing the specimen to gaseous H_2, usually at relatively high temperature and pressure; and by the cathodic evolution of H_2 on the surface of the specimen, whereby H enters the metal as though its fugacity were very much above 1 atom (1). The electrochemical studies were shown to be much more convenient than the gas phase studies by Devanathan and Stachurski (2, 3). They evolved H on the cathodic side of a bi-electrode membrane and oxidized the permeating hydrogen anodically on the other side. By this simple and elegant method, the permeation, P, the diffusion coefficient, D, and the solubility corresponding to a certain fugacity (that of the overpotential, η) (1), can be quickly determined.

Permeation-time transients at constant overpotential (η) can be made repeatedly and reversibly on the same membrane (4) below a critical overpotential (η_{crit}). At higher overpotentials the shape of the permeation-time transient changes, in the sense that at constant η, the permeation of H is diminished. An attempt to repeat the permeation-time transient at lower η now shows that the metal has undergone some change of property, so that the steady-state permeation is attained at a much longer time than that which was necessary before exceeding the critical overpotential. Beck *et al.* (4) suggested that the critical overpotential corresponded to the commencement of embrittlement and produced indirect evidence that the η_{crit} was connected in some way with the dissolution of H in the metal.

In the present paper an electrochemical condition for the commencement of H damage in the metals is suggested and the anomalous behavior of the permeation at higher overpotentials is interpreted in terms of the nucleation of traps when the H fugacity reaches sufficient values to cause spreading of microcracks formed from dislocation pile-ups.

Information about the nature of the traps can be obtained from the damped oscillatory behavior of the permeation-time transient after the injection of cathodic H.

Experimental Technique

A very brief description of the experimental technique will be given here. It has been described in previous papers (2-5). A detailed description of the most recent version is given by Beck, Bockris, Genshaw, and Subramanyan (6).

Cell.—The two compartments of the cell were separated by the 0.002-0.1 cm thick metal membrane. The cathodic side of the membrane was galvanostatically controlled, while on the anodic side the H was potentiostatically ionized. The potentiostatic current (proportional to the rate of H permeation) was measured.

Membranes.—The iron specimens used were Armco Fe, (99.99%). In addition, membranes of 5% Ni, 95% Fe were used. Annealing was carried out at 600°C for 3 hr with cooling at <5°C min^{-1} in H_2.

A thin layer of Pd was electrodeposited on the anodic side of the membranes to protect them against anodic dissolution.

Solutions.—The solutions were 0.1N NaOH prepared from Baker analyzed NaOH pellets, pre-electrolyzed and deoxygenated using purified nitrogen gas. The purity of the electrolyte controls the sensitivity with which the ionization current can be determined.

Procedures.—The cathodic current used varied over a range from 5×10^{-5}-10^{-1} A cm^{-2}. During any permeation measurement a constant cathodic current was switched on and the quasi-constant cathodic overpotential observed. The permeation-time transients were

* Electrochemical Society Active Member.

[1] Present address: Materials Technology Division, Gould Laboratories, 540 East 105th Street, Cleveland, Ohio 44108.

Key words: hydrogen embrittlement, trapping, electrochemical condition of embrittlement, iron-nickel alloys.

[2] In this article, we use the word embrittlement to mean the permanent damage like cracks produced by hydrogen in metals.

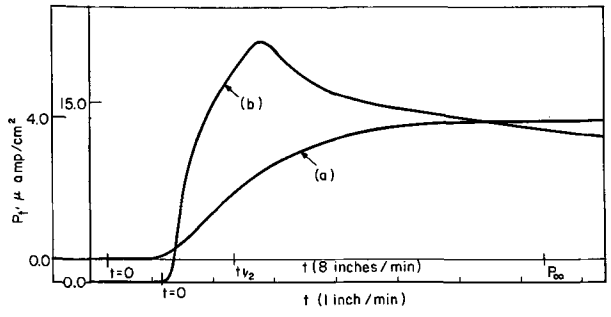

Fig. 1. Laboratory records of hydrogen permeation-time relations. (a) A typical permeation transient (for Armco iron, thickness $L = 0.106$ cm, at 60°C. Cathodic current density 10 mA/1.13 cm^2 and electrolyte 0.1M NaOH). The point $t = 0$ represents the time at which the cathodic current is switched on, $t_{1/2}$ the half-rise time of the transient, and P_∞ the steady-state permeation current. (b) An abnormal permeation transient showing the characteristic peak. (5% Ni + 95% Fe, $L = 0.09$ cm, $i_c = 108$ mA/cm^2, 50°C, and 0.1M NaOH solution.)

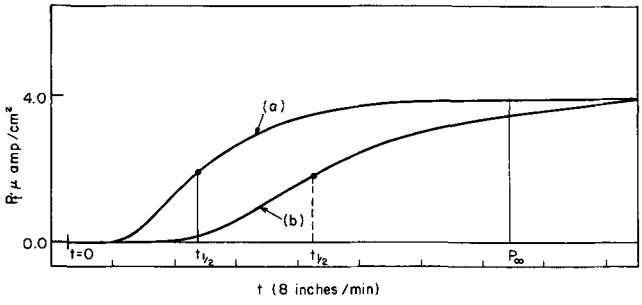

Fig. 2. Laboratory records of hydrogen permeation-time transients. (a) The typical transient shown in Fig. (1a). (b) The same transient repeated after recording a few transients at overpotentials beyond η_{crit} (cf., Fig. 1b).

followed for times up to about 30 min. Decay transients were observed over about the same period of time.

Results

The permeation-time transient at overpotentials $< \eta_{crit}$.—A typical result in shown in Fig. 1a. After switching off the injection current and waiting for the permeation decay to reach the background level, it was possible to repeat the permeation-time (P-t) transient (Fig. 1a) without noticeable difference. Repetition was possible for at least ten times and probably indefinitely.

Permeation-time transients at overpotential $> \eta_{crit}$.—It was found that there existed a threshold value of the hydrogen overpotential, η_{crit}, characterized by a cessation of the simple shape of the permeation-time transients, shown in Fig. 1b. Two differences now arise. (*i*) The P-t transient passes through a maximum. (*ii*) After the cathodic current has dropped to zero, and the permeation current on the anodic side of the bi-electrode dropped to the background level, the attempt to repeat a P-t transient at $\eta < \eta_{crit}$ failed; instead the permeation transient had a much greater rise time than that which was needed before the critical overpotential has been exceeded. These effects are shown in Fig. 2.

Decay of H *permeation.*—At situations for which $\eta < \eta_{crit}$, the decay transient is simple and is shown in Fig. 3a. However, for the decay at $\eta > \eta_{crit}$, the form of the P-t curve was radically changed and passed through one or two[3] maxima (Fig. 4).

Evaluation of P,D and C_o.—The calculation of these quantities has been described before (2, 3). The value of P is read directly from the recorded anodic current;

[3] The second maximum was seldom observed.

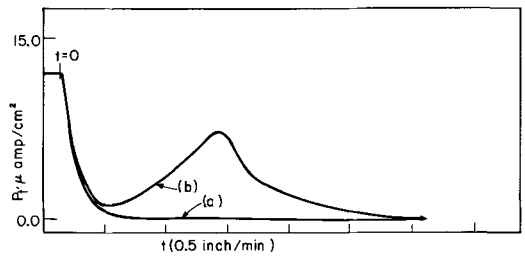

Fig. 3. Laboratory records of hydrogen permeation decay transients. (a) A typical permeation decay transient. At time $t = 0$, the hydrogen charging current is switched off. (b) An anomalous permeation decay transient with the characteristic hump. Hydrogen charging time 11 min. (5% Ni + 95% Fe, $L = 0.09$ cm, $i_c = 88$ mA/cm^2, 50°C, and 0.1M NaOH solution.)

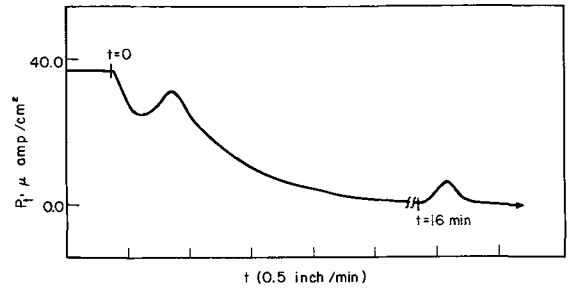

Fig. 4. A laboratory record of an anomalous permeation decay transient showing two humps. Hydrogen charging time 34 min. (5% Ni + 95% Fe, $L = 0.094$ cm, $i_c = 87$ mA/cm^2, 60°C, and 0.1M NaOH solution.)

that of D can be obtained from the half-rise time of the permeation transient; and $(C_o)_\eta$, the solubility of H at a fugacity corresponding to the η (1) can be obtained from the steady state P by means of the simple relation

$$P = (D\mathbf{F}/L)\ (C_o)_\eta \qquad [1]$$

where L is the thickness of the membrane and $\mathbf{F}$, the Faraday constant. Validity tests of these evaluations have been published elsewhere (2).

Discussion

What happens at η_{crit}?—Let it be supposed [Beck *et al.* (4)] that at η_{crit}, a critical concentration of H is dissolved and as this level is reached, some kind of change in metal lattice could occur. It is possible to assume that D remains unchanged until this internal change in the metal occurs appreciably. Therefore, just at the commencement of critical behavior

$$P_{crit} = (D\mathbf{F}/L)C_{crit} \qquad [2]$$

and hence C_{crit} can be calculated.

The minimum value of C_{crit} for Armco Fe is 1.5×10^{-7} g·atom cc^{-1}. The value is a minimum because the P-t relation should go higher (*i.e.*, higher C_{crit}) but is overtaken by the results of the change in internal properties of the metal, which decreases P.

For $C_{crit} = 1.5 \times 10^{-7}$ g·atom cc^{-1}, one obtains using a Sievert's law constant of 3.6×10^{-9} g·atom$^{-1/2}$, a value of 2×10^3 for the fugacity of H_2 which would be in equilibrium with C_{crit} and initiates the internal change.

If, now, we assume that this represents the critical pressure needed to expand a microcrack, it is easy to show that (4, 7)

$$P_{H_2,crit} = \sqrt{\frac{2Y\gamma}{\pi l(1-\nu^2)}} \qquad [3]$$

where Y is Young's modulus, γ the surface energy, $2l$ the length of the crack, and ν Poisson's ratio. With $\gamma = 1000$ ergs/cm^2, $Y = 2 \times 10^{12}$ dynes/cm^2, and $\nu =$

0.3, one obtains for a value of $l = 10^{-4}$ cm a critical pressure of 3.8×10^3 atm.

In this calculation we have not taken into account the work of plastic deformation which normally would be additive with surface energy in Eq. [3], for the following reasons:

(*i*) It is a general observation that the plastic deformation in presence of hydrogen in the metal is considerably decreased.

(*ii*) Equation [3] predicts that crack propagation can occur at such low values of pressure at which the metal cannot undergo plastic deformation. Correction for plastic work may become important in the region where $P_{H_2,crit} \gtrsim P_{P.Y}$ (stress or pressure corresponding to the yield point) but it is insignificant below $P_{Y.P}$, which for annealed iron is $\simeq 8 \times 10^3$ atm.

(*iii*) At the regions where cracks nucleate, there could be pre-existing internal stresses which modify the effective pressure to $(P_{H_2} + \sigma)$. Metals like iron start deforming when the deformation energy density exceeds 4×10^5 erg/cc and breaks when it attains approximately 4×10^6 ergs/cc. What portion of this energy is contributed as plastic work, in the process of creation of 1 cm^2 of new surface (over and above the surface energy) is not known with any degree of certainty. Some authors estimate the work of plastic deformation to be a few orders of magnitude higher than the surface energy (3000-4000 ergs/cm^2 for clean metal surfaces) (8). Tetelman has assumed the work of plastic deformation as three times the actual surface energy (9). However, for the reasons mentioned above, we think our calculation is quite meaningful. The length of the crack is assumed to be of the order of 10^{-4} cm for the reason that it represents the normal diameter of a grain.

It seems, therefore, reasonable to conclude that the process corresponding to the maximum of the *P-t* relationship is the spreading of microcracks. This is in agreement with the hypothesis of Beck *et al.* (4) and with their observation that the temperature coefficient of C_{crit} was related to the heat of solution H in Fe.

Electrochemical condition for the beginning of H-damage.—It has been shown elsewhere that the fugacity of H_2 in the metal can be related to the H_2 overpotential (1). The first critical transient was observed at $\eta \simeq -300$ mV. The evolution of H_2 on Fe occurs from alkaline solution by means of a coupled discharge-recombination mechanism. Accordingly (1), the fugacity of H_2 in cracks and internal voids are related to the overpotential by the equation

$$P_{H_2} = 10^{1.5} \exp(-\eta \mathbf{F}/2RT) \quad [4]$$

At an η_{crit} of -0.3V

$$P_{H_2} \simeq 10^{3.9} = 8 \times 10^3 \quad [5]$$

this is in reasonable accord with the pressure determined from a combination of Sievert's law and the critical concentration of the maximum in the first anomalous *P-t* graph.

We illustrate, thus, an electrochemical condition for the beginning of possible H damage. No H damage is possible until the potential of the surface of the metal is equivalent to an overpotential determined by the relation between overpotential and the fugacity of H_2 in internal cracks, with the latter exceeding the critical pressure (P_{crit}, the condition for the commencement of the spreading of cracks).

Thus, for iron, in alkaline solutions, the pressure necessary to cause damage is

$$P_{H_2} > \left(\frac{2Y\gamma}{\pi l(1-\nu^2)}\right)^{1/2} = 10^{1.5} \exp(-\eta_{crit}\mathbf{F}/2RT)^4 \quad [6]$$

The critical value for η can, hence, be found.

[4] The r.h.s. of this relationship is characteristic of the mechanism of hydrogen evolution reaction and will be different in the different cases (1).

This electrochemical limit for the possible commencement of H damage applies also to the situation in which there is no net current, *e.g.*, in corrosion. Thus, it is necessary only to know the corrosion potential. Then, one can calculate phenomenologically [knowing the solution pH and P_{H_2} (soln)] the overpotential for hydrogen evolution in the corrosion reaction, and thereby ascertain whether the situation will be embrittling or not.

Amount of trapped hydrogen.—Several investigators have observed the effect of hydrogen trapping on permeation (10-12). Some have considered the theory of hydrogen diffusion with simultaneous trapping, to various extents and in varying details (10, 11, 13, 14). Johnson and Hills (11) concluded that hydrogen trapping in cold-worked steel involved the formation of chemisorbed and molecular hydrogen at the internal crack surfaces. They assumed the existence of an equilibrium between the lattice dissolved and trapped hydrogen and obtained the lattice diffusivity from nonsteady-state measurements of hydrogen evolution from precharged specimens. Harhai *et al.* (12) observed that cold-worked steels absorbed hydrogen exothermically. From this observation, they reached the conclusion that hydrogen is trapped essentially as chemisorbed hydrogen at the internal surfaces of microcracks.

Darken and Smith (10) treated the diffusion of hydrogen with trapping in a way analogous to the problem of oxygen diffusion into copper containing small amounts of silicon (with which it could be "trapped" in the form of SiO_2). The treatment of McNabb and Foster (13) is very elaborate and involves less assumptions. However, their results are of limited use. Recently, Oriani (14) considered the theory of hydrogen diffusion with trapping with the assumption that an equilibrium exists between the lattice hydrogen and trapped hydrogen in the transient state, as assumed by Johnson and Hills. He applied this concept to obtain trap density in steels from hydrogen charging or permeation measurements. In the opinion of the present writers, the existence of an equilibrium between lattice hydrogen and trapped hydrogen especially in hydrogen charging cases in the transient state is a remote possibility.

In all these situations, the traps are uniformly distributed throughout the membrane, or the absorbing medium, before hydrogen charging. In the following we consider a unique situation in which traps do not exist (or only in insignificant numbers) until the lattice solubility C attains a value greater than a critical value C_{crit}. Before C reaches this limit, the diffusion process can be described by the familiar Fick's equation

$$\frac{\partial C}{\partial t} = D\frac{\partial^2 C}{\partial x} \quad [7]$$

where D is the diffusion coefficient of H and C its concentration. However, where C exceeds the critical solubility, C_{crit}, H begins to be trapped.

We propose the following model for a theoretical consideration of anomalous permeation. The traps are switched on only when C exceeds C_{crit}. We assume the nucleation of the traps to be a fast process. However, the filling up of the traps will be diffusion controlled. Let us consider trapping as a reaction like

$$H + \square \rightarrow \boxed{H} \quad [8]$$

When this reaction attains equilibrium

$$C_{H,tr} = K^1 C_{\square} C_{H,L} \quad [9]$$

where $C_{H,tr}$ is the concentration of H in the traps, $C_{H,L}$ the concentration of H in the lattice sites, $C_{\square}$ the concentration of unfilled traps, and K^1 the equilibrium constant. For a given concentration of lattice hydrogen, the number of filled traps at equilibrium will be

proportional to $C_{H,L}$. Hence

$$C_{H,tr} = KC_{H,L} \quad [10]$$

from which $K = K^1C_{\square}$.

However, during the transient state of diffusion, the type of relationship expressed by Eq. [10] is not true. We propose the following relationship for the transient situation

$$C_{H,tr} = \tau KC_{H,L} \quad [11]$$

where τ is a numerical constant which could have values from 0 to 1. When diffusion attains steady state or trapping is in equilibrium, $\tau = 1$ and Eq. [11] becomes identical with Eq. [10].

Let us now try to formulate a differential equation describing lattice diffusion with trapping. Consider a thin lamina of the metal membrane. It contains normal lattice sites as well as trapping sites. Diffusing hydrogen atoms enter through one side of the lamina and leave through the other. Hydrogen is supposed to enter or leave the lamina at the lattice sites. In other words, diffusion from one trapping site to another does not occur by direct jump without the intermediate stage of diffusion through the lattice sites. The rate of change of concentration in such a lamina will be the sum of the rate of change of concentration in the lattice sites and in the traps. Hence

$$\frac{\partial C_{H,L}}{\partial t} + \frac{\partial C_{H,tr}}{\partial t} = D\frac{\partial^2 C_{H,L}}{\partial X^2} \quad [12]$$

Introducing the relationship between $C_{H,L}$ and $C_{H,tr}$ from Eq. [11] into Eq. [12], we get

$$\frac{\partial C_{H,L}}{\partial t} + \tau K\frac{\partial C_{H,L}}{\partial t} = D\frac{\partial^2 C_{H,L}}{\partial X^2} \quad [13]$$

Now substituting

$$C = (1 + \tau K)C_{H,L} \quad [14]$$

we obtain

$$\frac{\partial C}{\partial t} = \frac{D}{(1 + \tau K)}\frac{\partial^2 C}{\partial X^2} \quad [15]$$

Equation [15] can be solved for the following boundary conditions

$$\text{At } X = 0, \text{ for } t > 0, C = (1 + K)C_o \quad [16]$$

because the entry of H into the lattice is a fast process (9), and the trapped H will always be in equilibrium with lattice dissolved hydrogen (C_o) and hence, $\tau = 1$.

$$\text{At } X = L, \text{ for } t > 0, C = 0 \quad [17]$$

The solution can be obtained as (15)

$$C(X,t) = (1 + K)C_o \left[\sum_{n=0}^{\infty} (-1)^n \operatorname{erfc} \frac{(X + 2nL)\sqrt{1 + \tau K}}{2\sqrt{Dt}} - \sum_{n=0}^{\infty} (-1)^n \operatorname{erfc} \frac{(-X + 2L + 2nL)\sqrt{1 + \tau K}}{2\sqrt{Dt}} \right] \quad [18]$$

and the permeability as

$$P_{t,tr} = \frac{DFC_o}{L}\frac{2}{\pi^{1/2}}\left(\frac{L^2}{Dt}\right)^{1/2} \exp\left(-\frac{L^2(1 + \tau K)}{4Dt}\right) \quad [19]$$

The additional subscript tr for P_t signifies trapping. Equation [19] shows that at relatively short times, *i.e.*, when $L^2/4Dt \cong 1$, $P_{t,tr}$ will be smaller than P_t in the absence of traps. In other words, the flux at times $t << \infty$ is reduced by the traps. As a result of this, the permeability, once the trapping is switched on, decreases from the normal permeability and gives rise to the prominent hump in the build-up permeation transients (Fig. 1b). At infinite time a steady-state

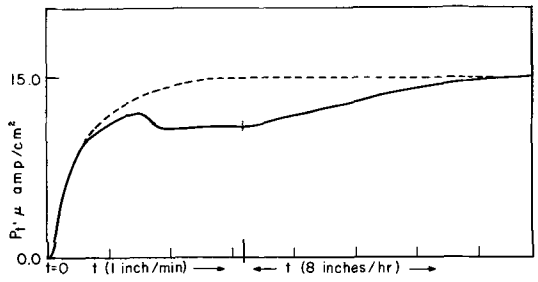

Fig. 5. A laboratory record of an anomalous permeation transient attaining a steady state. The broken line represents the expected normal course of the transient in the absence of hydrogen trapping. (5% Ni + 95% Fe, i_c = 105 mA/cm^2, L = 0.094 cm, 70°C, and 0.1M NaOH solution.)

concentration drop occurs between $X = 0$ and $X = X^1$, and another steady-state concentration drop between $X = X^1$ and $X = L$. This is in agreement with observed fact that the permeability rises again to the level $P_\infty = FDC_o/L$. The steady-state permeability, calculated from Eq. [18], would be

$$P = \frac{FD}{(1 + K)}\frac{(1 + K)C_o}{L} = \frac{FDC_o}{L} \quad [20]$$

which is the same as in the absence of traps. The permeability decreases initially when trapping begins, and then rises back to the original level. This has been found in cases where permeation with trapping was observed for sufficiently long times (*cf.* Fig. 5).

Determination of the trapping constant K.—When the trapping attains a steady state, the concentration profiles of hydrogen in the membrane are as shown in Fig. 6.[5] Corresponding to this situation we have the permeation-time relationship shown in Fig. 5. Here initially we have the permeation maximum followed by a slow increase of permeability to a final steady-state value. This steady-state value will be seen to be the same as that which the transient would have attained if it had gone the normal way. To obtain the total amount of trapped hydrogen, we extrapolate the initial part of the transient to the final steady-state value as shown in Fig. 5. The area between the extrapolated and the actual transients gives the amount of trapped hydrogen (Q_T). The amount of trapped hydrogen in the material corresponds to the triangle ABD in the concentration profile diagram (Fig. 6). We can write down a simple relation for the amount of hydrogen in the trapping region above the critical amount

$$\frac{[(1 + K)C_o - C_{crit}]}{2}AX^1 = Q_T + \frac{(C_o - C_{crit})}{2}AX^1 \quad [21]$$

where A is the permeation area. The values of C_o, C_{crit}, A, and Q_T are all known. The value of C_{crit} has to be determined from the transient which just ex-

[5] Darken and Smith (10) have reported that the distribution of hydrogen, when trapped in membranes with similar initial and boundary conditions as in the present work, is nonlinear [*cf.* Fig. 6 of ref. (10)] and is different from our results. They found that in charging a membrane by corrosion from one side and exposing the other to air (or rather a mixture of air and hydrogen), the hydrogen taken up by the membrane was 85% of the amount of the hydrogen when charged from both sides. One would expect the former to be 50% of the latter. However, there is a fundamental uncertainty involved in this study. They assumed that the concentration of H at the exit side is zero or negligibly small. In the opinion of the present writers, this boundary condition is not true. In fact, in their experimental situation there will be a good amount of H at the exit side as lattice dissolved and adsorbed H. This error invalidates their results. Second, in deriving an equation for permeability, these investigators assume that at the center of the permeation membrane, or slab, along the diffusion direction, the concentration of hydrogen is equal to the mean concentratin. This would only be true in the case of a linear distribution at steady state. They have used this derived relationship to construct the total solubility *vs.* permeability curve which they consider as the distribution of hydrogen as a function of distance. It does not uniquely follow that this curve [*cf.* Fig. 6, ref. (10)] represents the hydrogen distribution in the membrane.

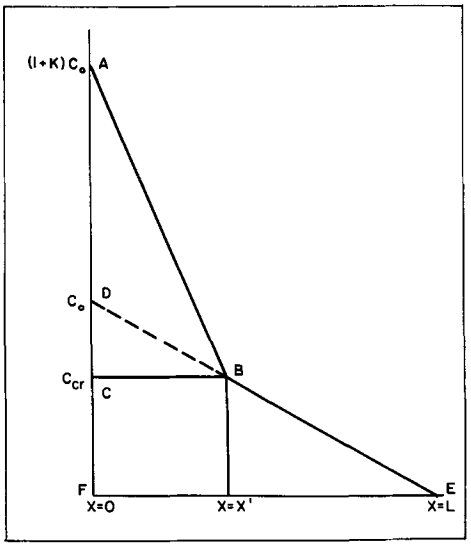

Fig. 6. Representation of the steady-state concentration profile as a function of the thickness of the membrane when hydrogen trapping is at steady state (cf., Fig. 5). Up to a thickness X^1, the concentration of hydrogen is above the C_{crit} level. K is the trapping constant.

hibits the development of the permeation maximum. However, X^1 is not yet known. This is obtained by using the properties of similar triangles (BCD and EFD)

$$(C_o - C_{crit})/X^1 = C_o/L \qquad [22]$$

For the transient in Fig. 5, we have $C_o = 2.2 \times 10^{-7}$ g-atom/cc, $C_{crit} = 1.3 \times 10^{-7}$ g-atom/cc, $A = 1.13$ cm^2, $Q_T/A = 3500$ μcoulombs ($=3.5 \times 10^{-8}$ g-atom), and $L = 0.094$ cm. From Eq. [22] we obtain $X^1 = 0.02$ cm and from Eq. [21], the value of K is found to be 16. K itself is not an equilibrium constant of trapping; it is the product of the true equilibrium constant of trapping and the concentration of the unfilled traps.

We try to obtain a reasonable value of K^1 in the following way. Let us assume that the density of microcracks or Stroh cracks formed from dislocations is 10^8/cm^2 (16). An average length of a dislocation line or of a microcrack can be taken as 10^{-4} cm. Hence, the density of the microcracks is 10^{12}/cc. The internal surface area, assuming the width to be equal to 20Å, is $2 \times 2 \times 10^{-11}$ cm^2. Therefore, the number of metal atoms at the internal surface of a microcrack is 4×10^4. Let us assume that on trapping H is adsorbed on the surface of the microcrack and that each surface atom is a potential trapping site for H. The coverage on trapping is assumed to be 99% (*i.e.*, $\theta_H = 0.99$). The trap density per cubic centimeter is then 4×10^{16}/cc or $\simeq 10^{-7}$ mole/cc. Therefore, $C_{\square} = 10^{-6}$ mole/liter. The value of K^1 which can be obtained from the relationship $K^1 C_{\square} = K = 16$ is 2×10^7. The standard free energy change of trapping, therefore, is $-RT \ln K^1 = -14$ kcal/g-atom which, in magnitude, is comparable with the standard free energy of dissolution of H_2 in iron (11.7 kcal/g-atom) at 27°C (17). The situation is that there are H_2 molecules in the microcracks, but the amount of hydrogen in the form of H_2 is much less than that of adsorbed atomic hydrogen because the volume of the microcrack is small compared to its surface area. Owing to the equilibrium between H_2 in the microcrack and the adsorbed atomic hydrogen on the surface of the microcrack, during the crack nucleation and spreading, the standard free energy change of adsorption is equal to—(the standard free, energy change of solution).[6] The experimentally evaluated (−11.7 kcal/g-atom) and the calculated (−14 kcal/g-atom) values are comparable. Hence, trapping is essentially the reverse of the dissolution of hydrogen in the metal.

The above considerations show that the model of H trapping at the internal surfaces of cracks is quite plausible. The creation of new internal surfaces ought to decrease the capability of the material to undergo plastic deformation and, therefore, it should be irreversibly embrittled.

Decay of the permeation transient; two kinds of trapped H.—Sometimes (Fig. 4) a second peak was observed (*cf.*, the decay transients). To understand the essential processes, we make the following simplifications. At regions close to cathodic surface (H input side) there are filled traps (for example, impurities) which bind hydrogen with different strengths. Monovacancies could also function as traps for atomic hydrogen. The binding energy of hydrogen will depend on the type of traps. Consider the situation represented by Fig. 5. When the steady state is attained, the concentration profile will be as shown in Fig. 7. For ease of quantitative consideration, we will assume that hydrogen in traps is uniformly distributed in the region $0X^1$. The steady-state permeation current when traps are filled can be considered as due to lattice diffusion with solubility equal to C_o. Hydrogen escaping from traps and hydrogen falling into traps occurs at the same rate at the steady state. Or

$$dn_{H,esc} = dn_{H,tr} \qquad [23]$$

when $i_c = 0$. During the transient, however, the lattice hydrogen tends to decay in the usual manner, and hence

$$dn_{H,esc} > dn_{H,tr} \qquad [24]$$

As a function of time, $(d^2n_{H,esc}/dt^2)$ goes through a maximum. Correspondingly, we have the concentration gradient of H in the lattice sites increasing to a maximum and then beginning to decrease. Here we will consider two different kinds of trapped hydrogen. An approximate relation for the flux at the anodic surface, *i.e.*, $X = L$ cm can be written as (15, 18)

$$\begin{aligned} P_t = \Bigg\{ & \left[P_o \left(1 - \frac{2}{\pi^{1/2}} \frac{Dt}{L^2} \exp - \frac{L^2}{4Dt} \right) \right] \\ & + \left[P_{\infty,P_1} \frac{2}{\pi^{1/2}} \left(\frac{D_1 t}{L^{*2}} \right)^{1/2} \exp - \frac{L^{*2}}{4D_1 t} \right]_{t=0}^{t=t_{P1}} \\ & + \left[P_{\infty,P_1} \left(1 - \frac{2}{\pi^{1/2}} \left(\frac{D_1 t}{L^{*2}} \right)^{1/2} \exp - \frac{L^{*2}}{4D_1 t} \right) \right]_{t=t_{P1}}^{t=\infty} \\ & + \left[P_{\infty,P_2} \frac{2}{\pi^{1/2}} \left(\frac{D_2 t}{L^{*2}} \right)^{1/2} \exp - \frac{L^{*2}}{4D_2 t} \right]_{t=0}^{t=t_{P2}} \\ & + \left[P_{\infty,P_2} \left(1 - \frac{2}{\pi^{1/2}} \left(\frac{D_2 t}{L^{*2}} \right)^{1/2} \exp - \frac{L^{*2}}{4D_2 t} \right) \right]_{t=t_{P2}}^{t=\infty} \Bigg\} \end{aligned} \qquad [25]$$

Here $D > D_1 > D_2$. D_1 and D_2 are the effective diffusion coefficients for H in traps of first and second kinds. P_o is the steady-state permeation current at $t \to 0$. P_{∞,P_1} and P_{∞,P_2} represent the peak permeation current of first and second humps and are approximately equal to the maximum permeation currents corresponding to the maximum concentration gradients built up by the hydrogen escaping from the different traps. L^* is the effective thickness of the membrane for the trapped H to diffuse out (*cf.*, Fig. 7), t_{P1} and t_{P2} are the times corresponding to the peak points of first and second decay humps. The following boundary conditions are assumed (*cf.*, Fig. 7). For decay

$$\text{At } X = 0,\ C = 0 \text{ for } t > 0 \qquad [26]$$

$$\text{At } X = L,\ C = 0 \text{ for } t \lessgtr 0 \qquad [27]$$

$$\text{At } X = 0,\ C = 0 \text{ for } t > t_p \qquad [28]$$

[6] This assumes that adsorption of H and formation of H_2 at the surface of the crack (which should be very clean) are always in equilibrium.

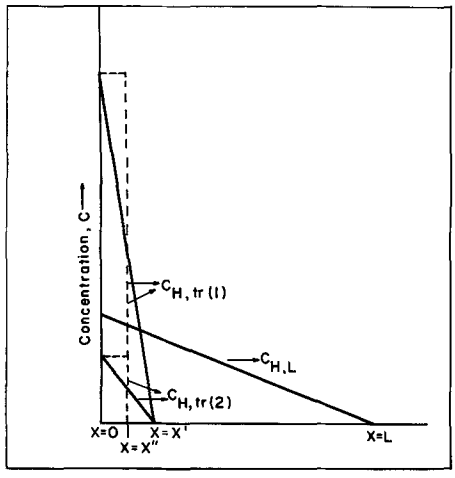

Fig. 7. Representation of the steady-state concentration profiles of hydrogen in two different kinds of traps (apart from the normal lattice hydrogen profile). The rectangles in broken lines represent the profiles assumed in the present approximate model. Beyond the range of 0 to X^{11}, there is no trapped hydrogen in the membrane. ($C_{H,L}$ means H in the usual lattice sites, $C_{H,tr(1)}$ hydrogen in traps of kind 1 and $C_{H,tr(2)}$ hydrogen in traps of kind 2.)

$$\text{At } X = L,\ C = 0 \text{ for } t \lessgtr 0 \qquad [29]$$

For the rising part of the decay transient

$$\text{At } X = X^{11},\ C = C_0 \text{ (constant) for } t \geqslant 0 \text{ up to } t = t_P \qquad [30]$$

$$\text{At } X = L,\ C = 0 \text{ for } t \lessgtr 0 \qquad [31]$$

Equation [25], if properly evaluated, will give rise to two humps in the decay transient. By incorporating appropriate number of terms in Eq. [25] the occurrence of any number of peaks in the decay transient could be understood as each being due to hydrogen in a different kind of trap.

Acknowledgments

Thanks are due to the authors' sponsor, the Naval Air Engineering Center (Warminster, Pennsylvania) under contract No. NOO156-67-C-1941; to Dr. Walter Beck and Mr. F. S. Williams for constant collaboration; and to Dr. R. A. Oriani (U. S. Steel Corporation) for sharp and stimulating discussion. We are also grateful to the U. S. Steel Corporation and particularly to Dr. R. P. Frankenthal for the membrane materials. This paper is based on work carried out by one of the authors (P.K.S.) in partial fulfillment of requirements for the Ph.D. degree of the University of Pennsylvania (1970).

Manuscript submitted July 20, 1970; revised manuscript received March 5, 1971.

Any discussion of this paper will appear in a Discussion Section to be published in the June 1972 JOURNAL.

REFERENCES

1. J. O'M. Bockris and P. K. Subramanyan, To be published in *Electrochimica Acta.*
2. M. A. V. Devanathan and Z. Stachurski, *Proc. Roy. Soc.*, **A270**, 90 (1962).
3. J. O'M. Bockris, J. McBreen, and L. Nanis, *This Journal*, **112**, 1025 (1965).
4. W. Beck, J. O'M. Bockris, J. McBreen, and L. Nanis, *Proc. Roy. Soc.*, **A290**, 220 (1966).
5. M. A. V. Devanathan, Z. Stachurski, and W. Beck, *This Journal*, **110**, 886 (1963).
6. W. Beck, J. O'M. Bockris, M. A. Genshaw, and P. K. Subramanyan, *Metallurgical Transactions*, **2**, 883 (1971).
7. I. N. Sneddon, *Proc. Phys. Soc. (London)*, **187A**, 229 (1946).
8. J. R. Low, Jr., "Fracture of Metals" in "Progress in Materials Science," Vol. 12, Bruce Chalmers, Editor, Pergamon Press (1964).
9. A. S. Tetelman, in "Fracture of Solids," D. C. Drucker and J. J. Gilman, Editors, John Wiley & Sons, Inc., New York (1963).
10. L. S. Darken and R. P. Smith, *Corrosion*, **5**, 1 (1949).
11. E. W. Johnson and M. Hill, *Trans. AIME*, **215**, 717 (1959); **218**, 1104 (1960).
12. J. Harhai, T. Viswanathan, and H. Davis, *Trans. Am. Soc. for Metals*, **58**, 210 (1965).
13. A. McNabb and P. K. Foster, *Trans. AIME*, **227**, 618 (1963); P. K. Foster and C. M. Payne, *ibid.*, **233**, 1022 (1965).
14. R. A. Oriani, *Acta Met.*, **18**, 147 (1970).
15. J. McBreen, L. Nanis, and W. Beck, *This Journal*, **113**, 1218 (1966).
16. J. S. Blackmore, *Met. Trans.*, **1**, 145 (1970); **1**, 151 (1970).
17. P. K. Subramanyan, Thesis, University of Pennsylvania, Philadelphia (1970).
18. J. McBreen, Thesis, University of Pennsylvania, Philadelphia (1965).

Thermal Diffusion Studies with the Ag/AgCl/Cl⁻ Electrode[1]

L. F. Vekens,[2] J. F. Zeeland, and J. Lin

Boston College, Department of Chemistry, Chestnut Hill, Massachusetts 02167

ABSTRACT

The initial thermoelectric powers, ϵ_0, and steady-state thermoelectric powers, ϵ_∞, of the thermocell (T)Ag-AgCl/Solution (M)/AgCl-Ag$(T + \Delta T)$ were measured for 0.01M solutions of LiCl, NaCl, KCl, RbCl, CsCl NH_4Cl, TlCl, and $CdCl_2$; 0.05M solutions of KCl and $CdCl_2$; and 0.005M solutions of KCl and $CdCl_2$. From these measurements, the entropies of transport S^* for these 12 solutions and the transported entropy of the chloride ion $\bar{S}_{Cl^-}$ were calculated. The results are compared with available literature values and discussed in terms of ion-solvent interaction and solvent structure.

Thermoelectric studies of electrolytes may yield much interesting information concerning the structure of the solvent system and other phenomena such as the ion-solvent interaction (1, 2). Physical quantities of interest in such a discussion are molar entropies of transport S^*_{salt} (or the corresponding heats of transport Q^*_{salt}) and transported entropies of ions $\bar{S}_i$. The transported entropy of an ion is defined as $\bar{S}_i = S_i +$

[1] Supported partially by OSW, U.S. Department of the Interior.
[2] NIH Predoctorate Fellow 1969-1970; NDEA Trainee 1968-1969.
Key words: thermal diffusion of some chloride salts.

S_i^*, where S_i^* is the ionic entropy of transport and S_i is the ionic partial molal entropy. Although neither of its components S_i and S_i^* may be measured experimentally (on an absolute scale), $\bar{\bar{S}}_i$ is a single ionic property which may be measured by studying the thermal diffusion process in a thermocell potentiometrically (*i.e.*, from the measurements of the initial and final thermal emf's of a thermocell). Up to the present, however, only a few thermocells have been investigated potentiometrically from their homogeneous initial states to the final (Soret) steady states. Most of them are thermocells with an electrode system reversible to the cation (3).

The purpose of this paper is to report a potentiometric study of several chloride salt thermocells using Ag/AgCl/Cl^- electrodes at a mean temperature of 25°C. Although Ag/AgCl/Cl^- electrodes have been used extensively in isothermal studies, applications in nonisothermal measurements are relatively few. Most investigations refer to the initial state (4), in which the solution is of uniform composition. Use of Ag/AgCl/Cl^- electrodes in the study of the final steady state may be found in the works of Chanu (5), and Haase and Behrend (6). In Chanu's work, Ag/AgCl/Cl^- electrodes were used in combination with the optical method and the thermal emf's were not available for comparison with the present study. In Haase and Behrend's paper, measurements were listed only for two salts, LiCl and KCl.

The initial and steady-state thermoelectric powers were measured for the thermocell:

Terminal—Ag/AgCl/Solutions (M)/
T_0 m T AgCl/Ag—Terminal (A)
$T + dT$ m T_0

where T_0 is room temperature, $T = 20$°C, $dT = 10$°, and m was platinum for the initial readings and copper for the final readings. The electrode reaction for this thermocell is

$$AgCl - Ag - Cl^- + e(m) = 0$$

and the equation governing the initial thermoelectric powers ϵ_0 may be written as

$$\mathbf{F}\epsilon_0 = [z^+ (\bar{\bar{S}}_{Cl^-} - S_{AgCl} + S_{Ag} - \bar{\bar{S}}_{e(Pt)}) - S^*_{salt}t_+]/z^+ \quad [1]$$

where $\mathbf{F}$ is the Faraday constant, $\bar{\bar{S}}_{e(m)}$ is the transported entropy of the electron in the mettal m, t_+ is the cation transference number, and z^+ is the charge on the cation. The equation governing the final thermoelectric powers ϵ_∞ is given by

$$\mathbf{F}\epsilon_\infty = \bar{\bar{S}}_{Cl^-} + S_{Ag} - S_{AgCl} - \bar{\bar{S}}_{e(Cu)} \quad [2]$$

Combining Eq. [1] and [2] yields

$$S^*_{salt} = z^+\mathbf{F}(\epsilon_\infty - \epsilon_0)/t_+ + z^+(\bar{\bar{S}}_{e(Cu)} - \bar{\bar{S}}_{e(Pt)})/t_+ \quad [3]$$

Values of $\bar{\bar{S}}_{e(Cu)}$ and $\bar{\bar{S}}_{e(Pt)}$ are available (7) and, consequently, the entropy of transport of a given salt is easily determined from the initial and steady-state thermoelectric powers, provided that the cation transference number is known. For most of the chloride salt solutions investigated, the transference numbers were readily available in the literature. However, those for 0.01M RbCl, CsCl, and TlCl were calculated from the conductance data using an equation obtained from a simple Debye-Hückel consideration (1, 8). The transport numbers used are given in Table I.

The transported entropy of the chloride ion, $\bar{\bar{S}}_{Cl^-}$, can be calculated from Eq. [2]. Since S_{AgCl}, S_{Ag}, and $\bar{\bar{S}}_{e(Cu)}$ are all known, the experimental determination of steady-state thermoelectric powers is all that is necessary.

Table I. Cation transference numbers at 25°C

All concentrations are 0.01M unless otherwise specified

Salt	t_+	Source
LiCl	0.3289	1
NaCl	0.3918	1
KCl	0.4903	1
KCl (0.005M)	0.4904	1
KCl (0.05M)	0.4899	1
RbCl	0.5049	4
CsCl	0.5029	4
NH_4Cl	0.4907	1
TlCl	0.4943	4
$CdCl_2$	0.43	2
$CdCl_2$ (0.005M)	0.43	2
$CdCl_2$ (0.05M)	0.44	3

1. Landolt-Bornstein, "Zahlenwerte und Funktionen aus Physik, Chemie, Astronomie, Geophysik, und Technik," II Band, 7 Teil, Elektrische Bigenschaften II, Springer-Verlag, Berlin (1960).
2. International Critical Tables, Vol. 6.
3. W. G. Breck and J. N. Agar, *Trans. Faraday Soc.*, 53, 179 (1957).
4. Calculated, Ref. (1, 8).

Experimental

All solutions used were prepared from analytical reagents and conductivity water. The concentration of each solution was checked by titrations with standard $AgNO_3$ solutions and density measurements.

For the purpose of measuring ϵ_0 and ϵ_∞ values during the same experiment, in the present study a mechanical stirrer was fitted into the sandwich type cell previously used by Lin (2). A similar type of cell has been used by Breck, Cadenhead, and Hammerli (9). However, the present design of the cell stirrer differs from that of Breck, Cadenhead, and Hammerli (10) in that our stirrer was driven by a variable speed motor rather than by forced air over a propeller shaft. This provision allows us to produce the initial homogeneous state for any given length of time by adjusting the speed of the motor. The stirrer consisted of a platinum axle on which a nylon mesh impeller was mounted. A variable speed d-c motor provided the stirring power. The shaft between the cell axle and motor was a flexible plastic material. One end of the plastic connector was fitted over the platinum axle, while a small circular magnet was cemented on the opposite end. This came in contact with another magnet cemented on the shaft of the motor. The flexible shaft absorbed any torque, thus preventing any leakage. To protect against any other unexpected leakage around the axle, a silicon grease reservoir in the form on a recess on the outside of the Plexiglas ring was provided along with a Teflon washer.

Many methods are available for the preparation of Ag/AgCl/Cl^- electrodes (10). In this work electrodes were prepared in two ways, one using the standard thermal method and the other by anodizing pure silver in 0.1*N* HCl. When the thermal method was used, a Ag and AgCl mixture was prepared on a thin platinum foil which was then assembled in between a Plexiglas ring and the gold disks. When the electrodes were prepared by anodizing pure silver, the following procedures were followed. Starting from metallic sheets 0.015 in. in thickness and at least 99.99% pure (supplied by A. D. Mackay, Incorporated), the electrodes were cut exactly to fit into the cells. They were then soaked several hours in concentrated NH_4OH, thoroughly rinsed with distilled water, and immersed briefly into approximately 3*N* HNO_3 until all surface contaminants were removed and a finely divided surface area formed. After again thoroughly rinsing the electrodes with conductivity water, they were anodized in 0.1*N* HCl saturated with purified argon and stirred magnetically. A current density of approximately 0.43 mA/cm^2 was maintained and approximately 2% of the silver by weight anodized. Two electrodes were always anodized simultaneously to assure as low a bias as possible. A piece of platinum wire served as the anode. The electrodes prepared in this way were reproducible to within 50 μV or better and were stable

Table II. ϵ_0 values in mV/deg at $\bar{T} = 25°C$*

All concentrations are 0.01M unless otherwise specified

Salt	This study	Goyan (4a)	Goodrich (4b)	Haase & Schonert (4c)	Khoroshin & Temkin (4d)	de Bethune *et al.* (4e)
LiCl	0.6633	0.669		0.676	0.71	
NaCl	0.6253	0.628	0.6313	0.631		0.623
KCl	0.6296	0.636	0.6407	0.643	0.67	0.621
KCl (0.005M)	0.6649			0.688		
KCl (0.05M)	0.5104			0.531		
RbCl	0.6059	0.614		0.611		
CsCl	0.6017	0.607		0.612		
NH_4Cl	0.6630	0.665		0.671	0.68	
TlCl	0.5943	0.601				
$CdCl_2$	0.5937		0.6054			
$CdCl_2$ (0.005M)	0.6512		0.656			
$CdCl_2$ (0.05M)	0.5053					

* $\bar{T}$ = Mean temperature.

over a period of weeks. $Ag/AgCl/Cl^-$ electrodes have never been prepared in exactly this manner, but the results were in excellent agreement with electrodes prepared from the thermal method.

The apparatus used for temperature control and thermal emf measurements have been described elsewhere (2). The reproducibility of ϵ_0 and ϵ_∞ values was generally within 10 μV/deg, although for $CdCl_2$ solutions it was about 15 μV/deg. The isothermal residual emf for both the sandwich cell and the N-shaped cell was small, being of the order of 50 μV and was corrected from thermal emf readings.

Results and Discussion

The measured initial thermoelectric powers are given in Table II. These have been compared with initial values determined previously. The steady-state thermoelectric powers are tabulated in Table III. The only other experimental values with which they may be compared are those for the 0.01M LiCl solution and the three KCl solutions obtained by Haase and Behrend (6). In all cases, the emf is positive when the terminal connected to the hotter electrode is positive.

The actual molar entropies of transport calculated from the experimental data using Eq. [3] are given in Table IV. The only comparisons possible are with the various conductometric and potentiometric determinations conducted at the appropriate concentrations and temperature.

Table V is a tabulation of the transported entropies calculated for the chlorides from Eq. [2]. The Third law values of 22.97 and 10.206 eu were used for S_{AgCl} and S_{Ag}, respectively.

As indicated in Eq. [2], the transported entropy of a given ion should theoretically be independent of the nature of the gegenion in dilute solutions. Applied to this particular study, this means that the value of $\bar{\bar{S}}_{Cl^-}$ should be the same for all the solutions tested in which the chloride ion concentration is 0.01M, *i.e.* in all the uni-univalent chloride salts and 0.005M $CdCl_2$. Inspection of Table V shows that this is true. On the basis of Eq. [2], this same consistency should also be displayed in the steady-state thermoelectric powers for these solutions, which it is.

Table III. ϵ_∞ values in mV/deg at $\bar{T} = 25°C$

All concentrations are 0.01M unless otherwise specified

Salt	This study	Haase and Behrend (6)
LiCl	0.6614	0.6724
NaCl	0.6652	
KCl	0.6630	0.6713
KCl (0.005M)	0.7037	0.7328
KCl (0.05M)	0.5318	0.5285
RbCl	0.6618	
CsCl	0.6614	
NH_4Cl	0.6630	
TlCl	0.6625	
$CdCl_2$	0.6170	
$CdCl_2$ (0.005M)	0.6496	
$CdCl_2$ (0.05M)	0.5217	

Examination of Table IV shows that the agreement between the S^*_{salt} values determined in this study and in previous investigations is excellent for 0.01M LiCl, NaCl, KCl, RbCl, CsCl, and TlCl. The values attributed to Agar and Turner (11), Snowdon and Turner (12), and Price (13) were all obtained using the conductometric method. The entropies of transport for 0.01M LiCl and KCl attributed to Haase *et al.* were calculated from the ϵ_0 values reported by Haase and Schonert (4) and the ϵ_∞ values reported by Haase and Behrend (6).

The agreement of the entropy of transport for 0.01M NH_4Cl determined in this study with literature values is reasonably good. Sagert and Breck (14), like Price, used the conductometric method. Although neither of them obtained a value exceptionally close to zero entropy units, all of the early investigators of the Soret effect concluded that aqueous NH_4Cl was very similar in behavior to aqueous LiCl and that both salts were essentially concentration independent and had entropies of transport very close to zero. More recently, Ikeda and Kimura (15) obtained almost identical Soret coefficients for 0.01M NH_4Cl and LiCl solutions at 25°C. In each case, the value was very small and negative.

Table IV. Entropy of transport values in eu at $\bar{T} = 25°C$

All concentrations are 0.01M unless otherwise specified

Salt	S^* (This study)	S^{*a}	S^{*b}	S^{*c}	S^{*d}	S^{*e}	S^* (Others)
LiCl	−0.28	−0.08	0.02	0.03		−0.25	
NaCl	2.20	2.58	2.35				
KCl	1.42	1.69	1.62	1.61		1.33	
KCl (0.005M)	1.67	1.88			1.76	2.11	1.80[h]
KCl (0.05M)	0.86				1.08	−0.12	1.12[h]
RbCl	2.40	2.75	2.67				
CsCl	2.59	2.78	2.77	2.71			
NH_4Cl	−0.15			0.50			1.17[f]
TlCl	3.03		3.03				
$CdCl_2$	0.95				2.95		
$CdCl_2$ (0.005M)	−0.39				3.35		
$CdCl_2$ (0.05M)	1.41						1.41[g]

[a] J. N. Agar and J. C. R. Turner (11).
[b] P. N. Snowdon and J. C. R. Turner (12).
[c] C. D. Price (13).
[d] P. N. Snowdon and J. C. R. Turner (17).
[e] Calculated from the ϵ_0 values of R. Haase and H. Schönert (4c), and the $\epsilon\infty$ values of R. Haase and H. Behrend (6).
[f] N. H. Sagert and W. G. Breck (14).
[g] W. G. Breck and J. N. Agar, *Trans. Faraday Soc.*, 53, 179 (1957).
[h] A. J. de Bethune and H. O. Daley, *This Journal*, 116, 1395 (1969).

Table V. Transported entropy values in eu at $\bar{T} = 25°C$

Salt	$\bar{\bar{S}}_{Cl^-}$
LiCl	27.97
NaCl	28.06
KCl	28.01
RbCl	27.98
CsCl	27.97
NH_4Cl	28.01
TlCl	28.00
$CdCl_2$ (0.005M)	27.70

Actually, because of the hydrogen-bonding facility of the ammonium ion, this ion would be expected to be only weakly structure altering. Consequently, an entropy of transport close to zero entropy units is quite reasonable.

The $CdCl_2$ and KCl solutions were studied at three different concentrations. Examination of Table IV shows that the only $CdCl_2$ solution for which the entropy of transport agrees well with previously reported values is the 0.05M solution. However, this S^* value is of particular interest since the literature value with which it is compared was obtained potentiometrically (16) using cadmium amalgam electrodes. Despite this, our S^* values for 0.01 and 0.005M $CdCl_2$ differ considerably from those obtained conductometrically by Snowdon and Turner (17). Previous studies made of concentration effects on entropies of transport (5, 17). for both univalent and divalent halides, all show an increase in the entropy of transport with decreasing concentration in this low concentration range. We have observed the exact opposite, a decrease in entropy of transport with decreasing concentration.

Although our results for $CdCl_2$ are in poor agreement with those of Snowdon and Turner, it must be emphasized that for these particular solutions the potentiometric method has one significant advantage over the conductimetric method. With the former, entropies of transport are measured directly, while with the latter, entropies of transport are calculated from the measured Soret coefficients, o, using the equation (11)

$$S^* = \nu RT(1 + \partial \ln \gamma_{\pm}/\partial \ln M)o \qquad [4]$$

where ν is the number of ions produced by dissociation of one molecule and $\gamma_{\pm}$ is the mean activity coefficient. Consequently, for calculation of S^* from conductimetric data, reliable activity data are necessary; but, for polyvalent electrolytes such as $CdCl_2$, this information is rather insubstantial.

In addition, $CdCl_2$ forms complexes to an unusually pronounced degree even at these quite low concentrations. The existence of species such as $CdCl^+$, $CdCl_2$, and $CdCl_3^-$ could easily lead to anomalities in the behavior of $CdCl_2$ solutions.

In contrast, the entropies of transport observed for the KCl solutions at concentrations of 0.005, 0.01, and 0.05M are in excellent agreement with the values obtained conductimetrically by Snowdon and Turner, as shown in Table IV. In this case the expected trend, an increase in entropy of transport with decreasing concentration in this concentration range, was obtained.

Both the electrostatic and electrophoretic effects on entropy that will be produced by an ion in solution have been developed theoretically (3, 18). According to Helfand and Kirkwood (18) for an uni-univalent electrolyte denoted [1, 2]

$$Q^*_{12} = Q^{*,o}_{12} + [-(e^2/6D) + (r^s_1 - r^s_2)(B_1 - B_2)]\kappa \qquad [5]$$

where $Q^{*,o}_{12}$ is the molar heat of transport at infinite dilution, e is the electronic charge, D is the dielectric constant, r^s_i is the Stokes' law radius of ion i, and κ is the Debye-Hückel parameter. This equation offers the means for calculating the transported entropy of the chloride ion at infinite dilution, $\bar{\bar{S}}^o_{Cl^-}$, although $(B_1 - B_2)$ cannot be evaluated exactly for salts such as KCl $r^s_1 \simeq r^s_2$; and, thus, this entire nonideality term is expected to be small enough to be ignored. Utilizing the average $\bar{\bar{S}}_{Cl^-}$ value for the 0.01M solutions studied, which is 28.00 eu, this equation yields an $\bar{\bar{S}}^o_{Cl^-}$ value of 18.88 eu. That this value agrees quite well with those obtained by other investigators is shown in Table VI.

Utilizing the convention of setting the entropy of transport of the chloride ion at 0.01M and 25°C equal to zero, ionic entropies of transport may be determined. On this basis, all of the cations examined are structure makers with the exception of Li^+ and NH_4^+ which are structure breakers.

Table VI. $\bar{\bar{S}}^o_{Cl^-}$ values

This study	Breck and Lin[a]	Agar[b]	Haase et al.[c]	Khoroshin & Temkin[d]	de Bethune & Daley[e]
eu 18.88	eu 19.4	eu 19.16	eu 19.3	eu 19.5	eu 18.69

[a] W. G. Breck and J. Lin, *Trans. Faraday Soc.*, **61**, 2223 (1965).
[b] J. N. Agar (3).
[c] R. Haase, K. Hoch, and H. Schönert, *Z. Physik. Chem.*, **27**, 421 (1961).
[d] A. V. Khoroshin and M. I. Temkin (4).
[e] A. J. de Bethune and H. O. Daley, *This Journal*, **116**, 1401 (1969).

Increased order in the solvent, corrsponding to a positive entropy of transport, would be expected in the vicinity of small or highly charged ions. Thus, the negative entropy of transport of Li^+ appears anomalous. However, this same high charge density would also cause the lithium ion to be heavily hydrated with firmly bound water molecules and thus act as a large ion of low surface charge. Naturally, this effect decreases with size among the alkali metal cations and there is roughly a corresponding increase in the magnitude of the entropy of transport, with the exception of K^+.

Manuscript submitted Oct. 19, 1970; revised manuscript received *ca.* Feb. 5, 1971.

Any discussion of this paper will appear in a Discussion Section to be published in the June 1972 JOURNAL.

REFERENCES

1. J. Lin and J. J. DeHaven, *This Journal*, **116**, 806 (1969).
2. J. Lin, *ibid.*, **116**, 1708 (1969).
3. See, for example, J. N. Agar, *Advan. Electrochem. & Electrochem. Eng.*, **3**, 31 (1963).
4. (*a*) F. M. Goyan, Ph.D. Thesis, Berkeley (1937); (*b*) J. C. Goodrich, Ph.D. Thesis, Berkeley (1941); (*c*) R. Haase and H. Schönert, *Z. Physik. Chem.*, **25**, 193 (1960); (*d*) A. V. Khoroshin and M. I. Temkin, *Zhur. Fiz. Khim.*, **26**, 773 (1952); (*e*) A. J. de Bethune, T. S. Licht, and N. Swendeman, *This Journal*, **106**, 616 (1959).
5. J. Chanu, *Advan. Chem. Phys.*, **13**, 1249 (1967), and the references therein.
6. R. Haase and H. Behrend, *Z. Physik. Chem.*, **31**, 375 (1962).
7. M. I. Temkin and A. V. Khoroshin, *Zhur. Fiz. Khim.*, **26**, 500 (1952).
8. R. A. Robinson and R. H. Stokes, "Electrolytic Solutions," Butterworths, London (1959).
9. W. G. Breck, G. Cadenhead, and M. Hammerli, *Trans. Faraday Soc.*, **61**, 37 (1965).
10. See, for example, D. J. G. Ives and G. J. Janz, "Reference Electrodes," p. 270, Academic Press, New York (1961).
11. J. N. Agar and J. C. R. Turner, *Proc. Roy. Soc. (London)*, **A255**, 307 (1960).
12. P. N. Snowdon and J. C. R. Turner, *Trans. Faraday Soc.*, **56**, 1409 (1960).
13. C. D. Price, U.S. Dept. Com., Office Tech. Serv., AD276 (1961).
14. N. H. Sagert and W. G. Breck, *Trans. Faraday Soc.*, **57**, 436 (1961).
15. T. Ikeda and H. Kimura, *J. Phys. Chem.*, **69**, 41 (1965).
16. J. N. Agar and W. G. Breck, *Trans. Faraday Soc.*, **53**, 179 (1957).
17. P. N. Snowdon and J. C. R. Turner, *ibid.*, **56**, 1812 (1960).
18. E. Helfand and J. G. Kirkwood, *J. Chem. Phys.*, **32**, 857 (1960).

Electrochemical Reduction of Potassium Chromate in the Presence of Zinc(II) and Cobalt(II) in Molten Lithium Chloride-Potassium Chloride Eutectic

K. W. Hanck[1] and H. A. Laitinen*

Department of Chemistry and Chemical Engineering, University of Illinois, Urbana, Illinois 61801

ABSTRACT

The electrochemical reduction of K_2CrO_4 in molten LiCl-KCl eutectic is shifted to more positive potentials by the addition of $ZnCl_2$ or $CoCl_2$. In the case of added $ZnCl_2$ three electrons are consumed per mole of K_2CrO_4 and an insoluble reduction product having the empirical formula $LiZn_2CrO_4$ is obtained. In the presence of $CoCl_2$, the reaction product depends on the electrolytic conditions, especially the cathodic potential. The limiting processes appear to be a two-electron process, favored by low cathodic potential and high cobalt(II) concentration to yield Co_2CrO_4, and a three electron process, favored by high cathodic potential and low cobalt(II) concentration to yield $LiCo_2CrO_4$. A mechanism consistent with these observations is proposed.

Laitinen and Bankert (1) used chronopotentiometry to study the electrochemical reduction of K_2CrO_4 in molten LiCl-KCl and observed a single, irreversible, diffusion-controlled, three-electron reduction step. In the presence of Mg(II), the chromate reduction potential is shifted from −1.1V *vs.* a 1M Pt(II)/Pt reference to −0.2V and a highly insoluble, chemically resistant electrode deposit is obtained at the cathode. Propp and Laitinen (2) characterized the magnesium deposit and described it as a single unstoichiometric compound having the empirical formula $Li_xMg_yCrO_4$, where $x + 2y = 5$. The values of x and y were dependent on electrolysis conditions; typically $0.3 < x < 0.5$. Popov and Laitinen (3) have recently shown that a similar deposit is obtained by electrolysis of Ni(II)·Cr(VI) mixtures. The nickel deposit is slightly more stoichiometric than the corresponding magnesium one ($0.6 < x < 0.85$) but has nearly the same lattice structure and thermal stability as $Li_xMg_yCrO_4$.

The results of an extensive characterization of the electroreduction of K_2CrO_4 in the presence of Zn(II) and Co(II) are the subject of this paper. In addition, possible mechanisms for the electroreduction of chromate in the presence of divalent metal ions are discussed.

Experimental

Reagents.—Reagent grade anhydrous $ZnCl_2$ (J. T. Baker) was further purified by fusion under an HCl atmosphere followed by scrubbing the resulting melt with dry HCl for 1 hr. After filtration through a medium porosity, sintered glass frit and scrubbing with dry argon for 2 hr, the purified molten $ZnCl_2$ was allowed to solidify. The $ZnCl_2$ prepared by this method contained 99.95% of the theoretical amount of chloride.

Anhydrous $CoCl_2$ was prepared by dehydrating the hexahydrate (J. T. Baker) in a vacuum. The temperature was slowly increased from room temperature to 150°C where it was maintained for 6-8 hr. The $CoCl_2$ prepared by this method contained 99.94% of the theoretical amount of chloride.

Anhydrous K_2CrO_4 was prepared by drying reagent grade K_2CrO_4 (J. T. Baker) at 150°C under vacuum for 6-8 hr a few days before use.

Chemicals other than those mentioned were reagent grade and were used without prior purification other than drying where required.

Molten salt procedures.—The LiCl-KCl eutectic was obtained from Anderson Physics Laboratories, Inc., Champaign, Illinois, where it was prepared and purified by the method outlined by Laitinen, Tischer, and Roe (4).

The molten salt furnace and glassware associated with the molten salt apparatus have been previously described (5). The procedures employed for cleaning glassware and handling the molten eutectic have been described in detail (5).

Electrochemical measurements.—A Pt(II)/Pt reference electrode was utilized in this work; its construction and properties have been described (6). A carbon electrode was used whenever a counterelectrode was required. The electrodes were constructed and cleaned according to the procedure outlined by Propp (7).

Both the platinum flag electrodes used in the chronopotentiometric and chronoamperometric studies and the platinum gauze electrodes used in preparative work were detachable. The construction of both the platinum gauze electrodes and the electrode holders were described by Propp (7). The platinum flag electrodes were constructed by spot welding 1 in. of 26 gauge platinum wire to a platinum foil (0.001 in. thick) approximately 5 mm on a side. The area of each flag was determined prior to spot welding by measuring its length and width with a micrometer and calculating the area by assuming the flag to be rectangular. The platinum microelectrodes used for voltammetric work were constructed as described by Lucas (8) except that soft glass was used throughout.

Voltammetric measurements were made with a Heath EUA-19-2 Polarography Module which was plugged onto a tube-type, operational amplifier manifold which has been previously described (9).

The constant current source employed for chronopotentiometric studies has been described (7). A Tektronix 502A oscilloscope and Tektronix C-12 oscilloscope camera were used to record the chronopotentiometric potential-time curves.

A Model 61 RS Wenking potentiostat was employed in the chronoamperometric experiments. A Tektronix Type 161 pulse generator supplied the desired potential pulse to the potentiostat.

A Sargent Model IV Coulometric Current Source was used in preparation of deposits and for generation of the Pt(II)/Pt reference electrode.

Analytical procedures.—In the preparative portion of this work, a number of routine analyses were performed to establish the composition of the electrode deposit as a function of various experimental parameters. The deposits were dissolved in $HClO_4$ according to the procedure described by Propp (2, 7). Chromium

* Electrochemical Society Active Member.
[1] Present address: Department of Chemistry, North Carolina State University, Raleigh, North Carolina 27607.
Key words: chromite, lithium zinc chromite, molten salt.

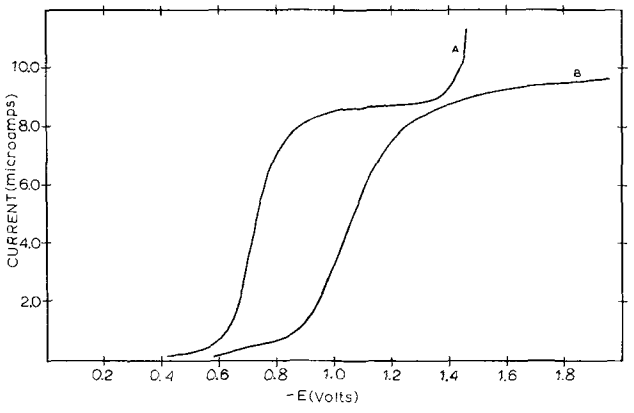

Fig. 1. Current-voltage curves for the reduction of K_2CrO_4 in the presence of $ZnCl_2$. Electrode area = 2.5 x 10^{-3} cm^2. Curve A, $[K_2CrO_4]$ = 4.51 mM, $[ZnCl_2]$ = 0.067M; Curve B, $[K_2CrO_4]$ = 4.51 mM, no $ZnCl_2$ added.

was determined by titration with coulometrically generated Cu(I); the procedure and equipment employed are described elsewhere (5). Lithium was determined by flame photometry; a detailed procedure is available (5). Zinc was determined by a spectrophotometric titration with EDTA using Eriochrome Black T as an indicator. Cobalt was also determined by spectrophotometric titration with EDTA; Xylenol Orange served as the indicator. The apparatus and procedure followed are described elsewhere (5).

Results and Discussion

Reduction of K_2CrO_4 *in the presence of* $ZnCl_2$.—As can be seen from Fig. 1, the half-wave potential for the voltammetric reduction of K_2CrO_4 is shifted in a positive direction by approximately 300 mV by the addition of anhydrous $ZnCl_2$. In the presence of $ZnCl_2$, a green, adherent film forms on electrodes polarized at potentials on the limiting plateau of the voltammetric wave. The film does not inhibit the electrode process but is extremely difficult to remove from the electrode mechanically.

Characterization of electrode deposit.—Samples of electrode deposit were prepared by constant current electrolysis using the method outlined by Propp (2, 7) and analyzed for Cr, Zn, and Li by employing the methods previously described. The average number of electrons consumed per mole of chromium was calculated to be 3.06 by comparing the micromoles of chromium found in a sample of deposit by chemical analysis to the microequivalents of current consumed in preparing the sample.

If the microequivalents of each metal are mathematically converted to an equivalent weight of metal oxide, the sample weight can be completely accounted for in terms of Li_2O, ZnO, and Cr_2O_3. Thus even though Zn(II) forms a strong chloro-complex, no chloride is found in the deposit. As with the previously reported magnesium and nickel deposits, no potassium is incorporated into the deposit.

Propp (2) and Popov (3) observed changes in the composition of the magnesium and nickel deposits as preparative parameters were changed. As can be seen from Tables I, II, and III, such was not the case for the zinc deposit. On the basis of analyses of 20 different preparations of the deposit under varying conditions an average molecular weight of 253.4 was found compared to 253.7 for $LiZn_2CrO_4$.

Table I. Composition of zinc deposit as a function of temperature

$[K_2CrO_4]$ = 0.112M Temperature (°C)	$[ZnCl_2]$ = 0.221M Empirical formula	I_o = 2 mA/cm^2 % Sample wt accounted for
400	$Li_{0.99}Zn_{1.99}CrO_{3.98}$	99.5
450	$Li_{0.99}Zn_{1.99}CrO_{3.98}$	99.8
500	$Li_{1.02}Zn_{1.98}CrO_{3.99}$	100.1

Table II. Composition of zinc deposit as a function of current density

$[K_2CrO_4]$ = 0.210M Current density (mA/cm^2)	$[ZnCl_2]$ = 0.246M Empirical formula	Temp = 450°C % Sample wt accounted for
2.16	$Li_{0.97}Zn_{2.01}CrO_{4.00}$	99.9
4.29	$Li_{0.99}Zn_{2.02}CrO_{4.01}$	99.6
8.58	$Li_{1.04}Zn_{2.01}CrO_{4.03}$	100.2
21.55	$Li_{1.01}Zn_{2.00}CrO_{4.00}$	99.1

Table III. Composition of Zn deposit as a function of $ZnCl_2$ concentration

Temperature = 450°C $[K_2CrO_4]$	$[ZnCl_2]$	Zn/Cr molar ratio	I_o = 2mA/cm^2 Empirical formula	% Sample wt accounted for
0.026M	0.276M	10.6	$Li_{1.01}Zn_{1.97}CrO_{3.98}$	99.8
0.029M	0.270M	9.27	$Li_{1.00}Zn_{2.02}CrO_{4.02}$	99.9
0.038M	0.264M	6.90	$Li_{1.00}Zn_{2.01}CrO_{4.01}$	100.3
0.059M	0.258M	4.34	$Li_{1.02}Zn_{2.02}CrO_{4.03}$	100.4
0.136M	0.252M	1.85	$Li_{1.00}Zn_{2.02}CrO_{4.02}$	100.2
0.210M	0.246M	1.17	$Li_{1.04}Zn_{2.01}CrO_{4.03}$	100.2

X-ray powder diffraction studies have shown the crystal structure of $LiZn_2CrO_4$ to be disordered face centered cubic, the length of a unit cell edge being 4.205Å (5, 10). The stoichiometry of lithium zinc chromite suggests the existence of the CrO_4^{-5} anion, but it is clear from the lattice structure that such an anion does not exist as a separate entity in the solid state.

Chronopotentiometry.—Chronopotentiograms of K_2CrO_4 in molten LiCl-KCl containing $ZnCl_2$ were found to depend on the relative concentrations of $ZnCl_2$ and K_2CrO_4. Two transitions, one at −0.76V and the other at −1.18V, were observed for solutions in which $[CrO_4^{-2}] > [Zn(II)]$. As the Zn/Cr molar ratio is increased, the first transition lengthens at the expense of the second. When the Zn/Cr molar ratio is made greater than 2, the second transition is not observed. This effect is illustrated in Fig. 2.

With the Zn/Cr molar ratio maintained at a value greater than 2.25, duplicate chronopotentiograms were obtained at 5 current densities at 5 different chromate concentrations ranging from 6.12 to 29.01 x 10^{-3}M. The reduction was found to obey the Sand equation, the value of $I_o \tau^{1/2}/C$ being 755 ± 13 A-$sec^{1/2}$ cm/mole.

The quarter-wave potential for the reduction of chromate in the presence of excess $ZnCl_2$ was found

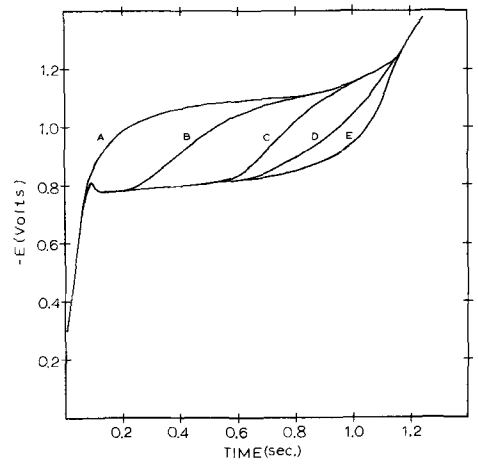

Fig. 2. Potential-time curves for the chronopotentiometric reduction of K_2CrO_4 in the presence of $ZnCl_2$. Current density = 8 mA/cm^2. Curve A, $[K_2CrO_4]$ = 11.43 mM, no $ZnCl_2$ added; curve B, $[K_2CrO_4]$ = 11.43 mM, $[ZnCl_2]$ = 7.18 mM; curve C, $[K_2CrO_4]$ = 11.43 mM, $[ZnCl_2]$ = 16.92 mM; curve D, $[K_2CrO_4]$ = 11.43 mM, $[ZnCl_2]$ = 21.60 mM; curve E, $[K_2CrO_4]$ = 11.43 mM, $[ZnCl_2]$ = 23.77 mM.

Table IV. Electrochemical oxidation of the zinc deposit

Q_f (μcoulomb)	Layers plated	Q_r (μcoulomb)	Layers stripped	Q_r/Q_f	Layers left
690	4.86	270	1.90	0.391	2.96
1190	8.37	700	4.93	0.588	3.44
2450	17.2	1570	11.1	0.640	6.10
3630	25.6	2550	18.0	0.702	7.60
5010	35.2	3650	25.7	0.728	10.5
7310	51.4	4990	35.2	0.682	16.2
8770	61.8	6460	45.5	0.736	16.3

to be independent of applied current density over the range studied (4.95-34.48 mA/cm^2); the average value being -0.764V *vs.* a 1M Pt(II)/Pt reference electrode. A quarter-wave potential of -1.18V has been reported for the reduction of pure chromate (1).

Reverse current chronopotentiometry was employed to study the ease with which the insoluble film could be electrochemically oxidized. From Table IV it is seen that Q_r/Q_f (where Q_f and Q_r are the forward and reverse coulombs) approaches the limit of *ca.* 0.7 as Q_f is increased. Microscopic examination of electrodes subjected to both forward and reverse electrolysis revealed the presence of an unoxidized film. The number of molecular layers of deposit left on the electrode after electrochemical oxidation approaches a limit of 16. The inner layers of deposit are rendered nonoxidizable by strong interaction with the Pt cathode.

Chronoamperometry.—Chronoamperograms were obtained for the reduction of chromate both in the presence and absence of Zn(II). In the presence of Zn(II) the potential was stepped from the rest potential (usually about -0.4V) to -1.15V (see Fig. 1). For the reduction of pure chromate, the final potential was -1.65V. Plots of I_o against $t^{-1/2}$ were found to be linear for both systems as predicted by the Cottrell equation.

In the absence of $ZnCl_2$, the Cottrell slope of 0.723 $\pm$ 0.009 mA sec$^{1/2}$/cm^2 gives a diffusion coefficient of 0.96 x 10^{-5} cm^2/sec based on a three-electron reduction. When $ZnCl_2$ was added a slope of 0.709 $\pm$ 0.009 was observed indicating a diffusion coefficient of 0.92 x 10^{-5} cm^2/sec. The excellent linearity of the Zn plot indicates that film formation does not adversely effect the electrode process over the time interval studied.

The important conclusion to be drawn from the chronoamperometric results, however, is that the diffusion coefficient of the electroactive species is unchanged in the presence of zinc chloride. The chronoamperometric value of D for pure chromate disagrees with the value of 1.73 x 10^{-5} cm^2/sec previously reported by Laitinen and Bankert (1). Because of higher purity starting materials, the eutectic used in this work is of slightly better quality than the eutectic used by Laitinen and Bankert. The presence of reducible impurities in the solvent causes the potential-time curve to become drawn out, consequently Laitinen and Bankert may have systematically overestimated τ. The chronoamperometric method eliminates the ambiguity associated with measuring τ and allows for convenient compensation for the reduction of impurities; consequently we conclude that the diffusion coefficient is unchanged by the addition of $ZnCl_2$ to the solvent.

Reduction of K_2CrO_4 in the presence of $CoCl_2$.—A typical current voltage curve for the reduction of K_2CrO_4 in melt containing excess $CoCl_2$ is presented in Fig. 3. During electrolysis of K_2CrO_4 solutions containing $CoCl_2$ a black, insoluble film formed on the cathode. The film was usually obtained as clumps of crystals irregularly distributed across the electrode rather than as a uniform film. Under magnification the crystals appeared to have an octahedral shape; the crystal faces were smooth with sharp edges and a metallic luster.

Characterization of electrode deposit.—Samples of electrode deposit were prepared by constant current

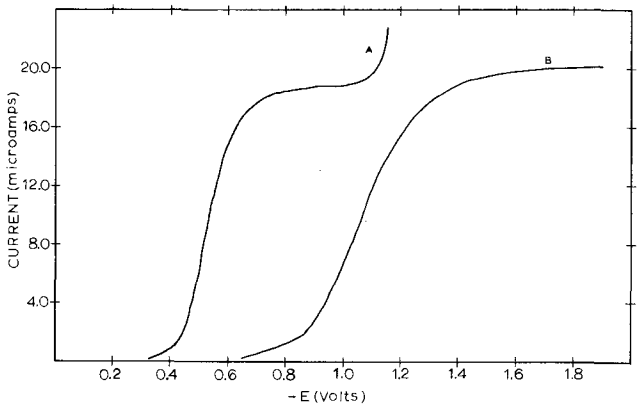

Fig. 3. Current-voltage curves for the reduction of K_2CrO_4 in the presence of $CoCl_2$. Electrode area = 4.9 x 10^{-3} cm^2. Curve A, $[K_2CrO_4]$ = 4.98 mM, $[CoCl_2]$ = 0.064M; curve B, $[K_2CrO_4]$ = 4.98 mM, no $CoCl_2$ added.

electrolysis using the method previously employed in preparing the Zn deposit; the electrode potential was not allowed to become more negative than -0.7V during preparation of the deposit. As may be seen from Table V, two electrons are consumed per mole of chromium. Deposits prepared at high Co/Cr molar ratios had n values which were consistently slightly greater than 2 but well below 3. Based on a two-electron reduction step, an oxidation number of +4 may be formally assigned to chromium.

The composition of three samples of deposit prepared under similar conditions is presented in Table VI. The sample weight can be completely accounted for in terms of the component oxides Li_2O, CoO, and CrO_2. The sample weight could equally well be accounted for if all or part of the moles of Cr were present as Cr(III) (*i.e.*, Cr_2O_3) providing an equal number of moles of Co(III) (*i.e.*, Co_2O_3) were present. Because of this interrelation of oxidation states, no oxidation states have been indicated in the empirical formulas of Table VI.

The composition of the Co deposit has been studied as a function of preparative conditions. As can be seen from Tables VII, VIII, and IX the lithium content of the deposit is very sensitive to changes in preparative parameters while the cobalt and chromium contents are not. It should be noted that except for the effect of added metal ion concentration, the compositional trends of the Co deposit are exactly the opposite of those of the previously reported Mg and Ni deposits.

Table V. Calculation of n for the case of added $CoCl_2$

μ equiv. of current passed	μmoles of Cr found	n
100.4	48.10	2.09
100.0	49.51	2.02
100.2	48.74	2.05
100.1	48.55	2.08
100.1	49.39	2.04
		$\bar{n}$ = 2.06

Table VI. Typical analyses of the cobalt deposit

A. μmoles	mg	μmoles	mg	μmoles	mg
Li	Li_2O	Co	CoO	Cr	CrO_2
3.30	0.049	99.34	7.444	50.46	4.239
3.18	0.047	99.82	7.480	49.84	4.187
3.21	0.048	100.30	7.516	49.51	4.159

B. Total mg found	Sample wt mg	% wt found	Empirical formula
11.732	11.799	99.4	$Li_{0.07}Co_{1.97}CrO_{4.00}$
11.714	11.830	99.0	$Li_{0.06}Co_{2.00}CrO_{4.03}$
11.723	11.686	100.3	$Li_{0.06}Co_{2.03}CrO_{4.05}$

Table VII. Composition of cobalt deposit as a function of temperature

$[K_2CrO_4]$ = 0.25M Temperature (°C)	$[CoCl_2]$ = 0.48M Empirical formula	I_o = 2 mA/cm² % Sample wt accounted for
400	$Li_{0.08}Co_{2.00}CrO_{4.04}$	99.3
450	$Li_{0.06}Co_{1.99}CrO_{4.02}$	98.7
500	$Li_{0.01}Co_{1.99}CrO_{3.96}$	100.3

Table VIII. Composition of cobalt deposit as a function of current density

$[K_2CrO_4]$ = 0.094M Current density (mA/cm²)	$[CoCl_2]$ = 0.18M Empirical formula	Temp = 450°C % Sample wt accounted for
2.16	$Co_{2.02}CrO_{4.02}$	100.5
4.32	$Li_{0.14}Co_{1.93}CrO_{4.02}$	99.9
8.58	$Li_{0.25}Co_{1.93}CrO_{4.05}$	99.6
21.55	$Li_{0.34}Co_{1.92}CrO_{4.09}$	99.0

Table IX. Composition of Co deposit as a function of $CoCl_2$ concentration

Temperature = 450°C $[K_2CrO_4]$	$[CoCl_2]$	Co/Cr molar ratio	I_o = 2 mA/cm² Empirical formula	% Sample wt accounted for
0.022M	0.193M	8.76	$Li_{0.50}Co_{1.97}CrO_{4.22}$	99.5
0.046M	0.189M	4.12	$Li_{0.20}Co_{1.91}CrO_{4.04}$	99.6
0.094M	0.184M	1.96	$Li_{0.14}Co_{1.93}CrO_{4.02}$	99.8
0.246M	0.481M	1.96	$Li_{0.06}Co_{1.99}CrO_{4.02}$	98.7

Samples of deposit with an empirical formula approaching Co_2CrO_4 can be prepared by using a low current density, high temperature, and high $CoCl_2$ concentration. X-ray powder diffraction studies of Co_2CrO_4 have shown it to have a diamond cubic lattice with a unit cell edge of 8.173Å (5, 10). A spinel-like structure in which the tetrahedral sites are occupied by Co(II) ions and the octahedral sites shared by Cr(III) and Co(III) ions has been proposed as the only structure consistent with both the observed x-ray data and previously established structures of multiple metal oxides of Co(II), Co(III), Cr(III), and Cr(IV) (5, 10).

Chronopotentiometry.—A typical chronopotentiogram of chromate in the presence of excess $CoCl_2$ is shown in Fig. 4. As with the case of added $ZnCl_2$ two transitions are observed at Co/Cr molar ratios below 2.09. Over the chromate concentration range studied (4.71 to 33.00 x 10^{-3}M) the reduction obeyed the Sand equation. At 450°C, $I_o \tau^{1/2}/C$ = 751 ± 7 A-sec$^{1/2}$ cm/mole, consequently $nD^{1/2}$ = 8.81 x 10^{-3} cm equiv./mole sec$^{1/2}$.

The quarter-wave potential was found to be independent of applied current density over the range 4.07-21.90 mA/cm², the average value being −0.558 ± 0.002V *vs.* a 1M Pt(II)/Pt reference. At current densities greater than 22 mA/cm² $E_{\tau/4}$ shifts in a cathodic direction as I_o is increased. Attempts to oxidize the Co deposit electrochemically were unsuccessful.

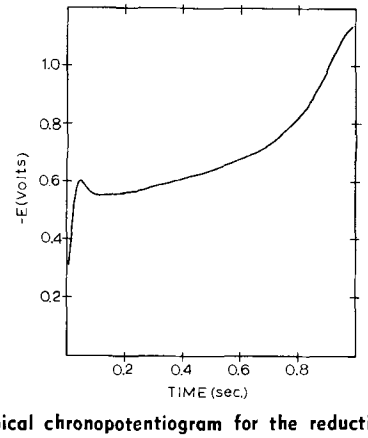

Fig. 4. Typical chronopotentiogram for the reduction of K_2CrO_4 in the presence of excess $CoCl_2$. Current density = 15.82 mA/cm². $[K_2CrO_4]$ = 17.41 mM. $[CoCl_2]$ = 0.132M.

Chronoamperometry.—Chronoamperograms were obtained for the reduction of chromate in the presence of cobalt chloride by stepping the potential of the test electrode to −0.90V (see Fig. 3) and measuring the current which flowed as a function time. Currents were measured over the time interval 20 msec to 1 sec. A plot of I_o *vs.* $t^{-1/2}$ was found to be linear as predicted by the Cottrell equation. A slope of 0.775 ± 0.13 mA sec$^{1/2}$/cm² was observed for a 4.98 x 10^{-3}M solution of K_2CrO_4 which was also 0.063M in $CoCl_2$. From the experimental slope $nD^{1/2}$ is found to be 9.06 x 10^{-3} cm equiv./mole sec$^{1/2}$.

Electroreduction mechanism.—The over-all electroreduction mechanism of chromate in the presence of a divalent metal chloride must contain a chemical reaction in order to account for the presence of the divalent metal in the reduction product. The reaction could occur before, after, or during the charge transfer process and still provide a means for incorporating divalent metal into the deposit.

If the reaction occurred prior to charge transfer, it must be analogous to the formation of a Cr(VI) complex containing the divalent metal which is more easily reduced than uncomplexed chromate. A M(II)·chromate complex would be expected to be larger in size than the uncomplexed chromate ion. Since the diffusion coefficient of chromate is unchanged by the addition of $ZnCl_2$, $NiCl_2$, or $MgCl_2$ to the melt, the size of the electroactive species in the presence of Zn(II), Ni(II), or Mg(II) must be approximately the same as in their absence and the existence of M(II)·chromate complexes may be ruled out for the cases where M = Zn, Ni, or Mg.

The initial reduction product of chromate is believed to be the oxy-anion $Cr(III)O_5^{-5}$. A chemical reaction between this anion and M(II) could also account for the presence of divalent metal in the deposit. A reaction of this type would account for the positive shift in potential as well, since the activity of the reduced form of the couple would decrease as a result of the reaction causing the equilibrium potential to become more positive.

Delahay *et al.* (11) have derived an equation relating the potential time curve of a reversible charge transfer followed by a chemical reaction to the chemical kinetic parameters. Since the electroreduction of chromate is, at best, quasireversible, Delahay's equation must be modified to take charge transfer kinetics into account. The nature of the modifications are discussed elsewhere (5). The equation is a complex one and must be solved by numerical methods

$$\frac{2k^\circ_{sh}}{D^{1/2}\pi^{1/2}}(\tau^{1/2} - t^{1/2})\theta^{-\alpha} - \frac{Kk^\circ_{sh}}{D^{1/2}(K+1)}\left\{\frac{2t^{1/2}}{\pi^{1/2}K} + \frac{\mathrm{erf}[\Delta^{1/2}t^{1/2}]}{\Delta^{1/2}}\right\}\theta^{1-\alpha} = 1 \quad [1]$$

where k°_{sh} is the standard heterogeneous charge transfer rate constant at $E = E^{\circ\prime}$, $\theta = \exp\{n\mathbf{F}/RT\ (E - E^{\circ\prime})\}$, K is the equilibrium constant of the chemical reaction, and $\Delta = (k_f + k_b)$ where k_f and k_b are the forward and reverse rate constants of the chemical reaction.

Using the data of Laitinen and Bankert (1) for the electroreduction of pure chromate, we estimate k°_{sh} to be 2 x 10^{-3} cm/sec and $E^{\circ\prime}$ to be −1.05V *vs.* a 1M Pt(II)/Pt reference electrode. Inserting these electrokinetic parameters into Eq. [1], we find that a following chemical reaction will shift the quarter-wave potential for the reduction of chromate a maximum of only 0.25 mV even if K and k_f are infinitely large. Since the ion $Cr(III)O_4^{-5}$ must have an average lifetime of at least 10^{-13} sec to be considered real (12),

the highest feasible value for k_f is 10^{13} sec^{-1}. Thus even if $k°_{sh}$ is increased by the presence of a divalent metal ion to 100 cm/sec, Eq. [1] predicts that $E_{\tau/4}$ will shift by only 202 mV. In the presence of added $ZnCl_2$, $E_{\tau/4}$ shifts by 400 mV; consequently we conclude that a simple charge transfer followed by a chemical reaction cannot be used to explain the shift in $E_{\tau/4}$ because such a mechanism requires the rate of the chemical step to be impossibly fast for reasonable values of $k°_{sh}$.

A mechanism involving an interaction between M(II) and an intermediate oxidation state of chromium remains as the only plausible way to account for the positive shift in quarter-wave potential and the incorporation of divalent metal into the reduction product.

Suppose that the reduction mechanism of pure chromate involves the following steps

$$Cr(VI) + 2e^- \overset{\text{rapid}}{\rightleftharpoons} Cr(IV) + 1e^- \overset{\text{slow}}{\rightleftharpoons} Cr(III)$$

The first step is more rapid than the second since no coordination change is involved, but the second step requires the oxygen coordination to change from tetrahedral to octahedral and is consequently slower than the first. The ion $Cr(IV)O_4^{-4}$ is a much better electron donor than $Cr(VI)O_4^{-2}$; the change in nucleophilicity of the chromium species could lead to a donor-acceptor interaction between $Cr(IV)O_4^{-4}$ and a soluble divalent metal species. The interaction would either reduce the energy required to change the oxygen coordination or change the coordination as a result of the interaction and thus allow the second charge transfer step to occur at a less negative potential than in the absence of the divalent metal. Following the second charge transfer, a second chemical step could occur to produce the solid deposit. For the case of added $ZnCl_2$

$$Cr(VI)O_4^{-2} + 2e^- \overset{\text{rapid}}{\rightleftharpoons} Cr(IV)O_4^{-4}$$

$$Cr(IV)O_4^{-4} + 2ZnCl_4^{-2} \overset{\text{rapid}}{\rightleftharpoons} Zn_2Cr(IV)O_4 + 8Cl^-$$

$$ZnCr(IV)O_4 + 1e^- \rightleftharpoons (Zn_2Cr(III)O_4)^-$$

$$(Zn_2Cr(III)O_4)^- + Li^+ \rightleftharpoons LiZn_2CrO_{4(solid)}$$

The structure of the zinc orthochromate(IV) complex has not been established, but in view of the chemistry of molten $ZnCl_2$ and ZnO it is likely to involve oxygen bridges

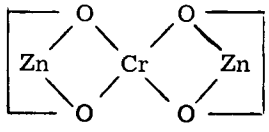

The mechanism for the electroreduction of chromate in the presence of $CoCl_2$ is similar to that proposed for the case of added $ZnCl_2$ but involves a chemical reduction path parallel to the second charge transfer step

$$Cr(VI)O_4^{-2} + 2e^- \overset{\text{rapid}}{\rightleftharpoons} Cr(IV)O_4^{-4}$$

$$Cr(IV)O_4^{-4} + 2CoCl_4^{-2} \overset{\text{rapid}}{\rightleftharpoons} Co(II)_2Cr(IV)O_4 + 8Cl^-$$

$$Co(II)_2Cr(IV)O_4 \overset{\text{path 1}}{\rightleftharpoons} Co(II)Co(III)Cr(III)O_{4(solid)}$$

$$Co(II)_2Cr(IV)O_4 + 1e^- \overset{\text{path 2}}{\rightleftharpoons} (Co(II)_2Cr(III)O_4)^{-1}$$

$$(Co(II)_2Cr(III)O_4)^{-1} + Li^+ \rightleftharpoons LiCo(II)_2Cr(III)O_{4(solid)}$$

In path 1, Cr(IV) is intramolecularly reduced to Cr(III). Based on the composition of the deposit and the fact that n is 2, path 1 is the preferred route. The second path is necessary to provide a means of incorporating Li(I) into the deposit. It, however, would predict an n value of 3.

Table X. Correlation of n with N_{Li}

Number of Li atoms per molecule (N_{Li})	Observed n	Calculated n
0.07	1.98	2.07
0.14	2.05	2.14
0.20	2.15	2.20
0.25	2.15	2.25
0.34	2.55	2.34
0.50	2.43	2.50

According to the parallel path mechanism, the value of n should equal $N_{Li} + 2$, where N_{Li} is the number of Li atoms per molecule of deposit. Several calculated and observed values of n are compared in Table X from which it may be seen that the correlation of n with the amount of lithium has some merit. When N_{Li} is small, n is nearly 2 as shown in Table X.

The changes in lithium content of the deposit may also be rationalized in terms of a parallel path mechanism. At high current density, path 1 may not be rapid enough to consume all of the $Cr(IV)O_4^{-4}$ produced by electrolysis. Consequently a significant fraction goes by path 2 and Li is found in the deposit. If the rate of the chemical path increases with temperature faster than that of the electrochemical path, very little Cr(IV) would be reduced electrochemically; hence the Li content of the deposit decreases with increasing temperature.

The rate of path 2 is potential dependent while that of path 1 is not; consequently path 2 should be favored at negative potentials. It has recently been shown by Lieto (13) that chromate is reduced via path 2 if a controlled potential electrolysis is performed at -1.07V. A deposit having a face centered cubic lattice ($a = 4.177$Å) and the empirical formula $Li_{1.11}Co_{2.22}CrO_{4.27}$ was obtained; Lieto's data were consistent with an n value of three. The increase in lithium content, the change in n from 2 to 3, and the change in lattice structure of the deposit are in excellent agreement with our mechanism.

In the case of added $CoCl_2$, the number of electrons exchanged per chromium is a function of potential. Consequently a true diffusion coefficient cannot be calculated from chronopotentiometric measurements. However, at potentials more negative than -0.90V, n is nearly equal to 3 (13) and D is calculated to be 0.91×10^{-5} cm^2/sec from our chronoamperometric results. The diffusion coefficient of the chromate ion is thus unchanged by the presence of all divalent metal ions studied.

Acknowledgment

One of the authors (K.W.H.) is indebted to the University of Illinois, Monsanto Chemical Company, and the American Chemical Society (Petroleum Research Fund) for their support in the form of fellowships. We are grateful to Dr. Louis Lieto for permission to use the results of his controlled potential electrolyses of the K_2CrO_4·$CoCl_2$ system. Financial support of this research was provided by the Army Research Office, Contract Numbers USDA-ARO-D-G586 and USDA-ARO-D-G968.

Manuscript submitted Sept. 23, 1970; revised manuscript received Jan. 16, 1971.

Any discussion of this paper will appear in a Discussion Section to be published in the June 1972 JOURNAL.

REFERENCES

1. H. A. Laitinen and R. D. Bankert, *Anal. Chem.*, **39**, 1790 (1967).
2. J. H. Propp and H. A. Laitinen, *ibid.*, **41**, 644 (1969).

3. Branko Popov and H. A. Laitinen, *This Journal*, **117**, 482 (1970).
4. H. A. Laitinen, R. Tischer, and D. K. Roe, *ibid.*, **107**, 546 (1960).
5. K. W. Hanck, Ph.D. Thesis, University of Illinois, 1969.
6. H. A. Laitinen and W. S. Ferguson, *Anal. Chem.*, **29**, 4 (1957).
7. J. H. Propp, Ph.D. Thesis, University of Illinois, 1968.
8. K. R. Lucas, Ph.D. Thesis, University of Illinois, 1966.
9. P. J. Sherwood, Ph.D. Thesis, University of Illinois, 1968.
10. K. W. Hanck and H. A. Laitinen, *J. Inorg. Nucl. Chem.*, **33**, 63 (1971).
11. P. Delahay, C. C. Mattax, and T. Berzins, *J. Am. Chem. Soc.*, **76**, 5319 (1954).
12. H. Bloom and J. O'M. Bockris in "Modern Aspects of Electrochemistry," J. O'M. Bockris, Editor, Butterworth's Scientific Publications, London, 1959, No. 2.
13. L. R. Lieto, Personal communication, unpublished results.

Technical Notes

EMF Measurements of Sodium Activity in Sodium Amalgam with Beta-Alumina

Limin Hsueh[1]* and Douglas N. Bennion*

Department of Energy and Kinetics, School of Engineering and Applied Science, University of California, Los Angeles, California 90024

Beta-alumina,[2] nominal formula $Na_2O \cdot 11Al_2O_3$, has been used as a refractory material for decades (1, 2). Recently, Ford Motor Company has used it for developing a sodium-sulfur battery system (3, 4).

Emf measurements have been performed with beta-alumina to test for behavior as a solid electrolyte for measuring sodium activity in amalgams and to test the assumption that the conductivity of beta-alumina is ionic in nature. The latter is in contrast to potassium ferrite (5), an isomorphous compound of beta-alumina, for which the electrical conductivity is partially electronic and partially ionic. Emf measurements such as this can indicate if the electronic conductivity is high enough in a practical sense to cause interference with electrochemical measurements.

Emf measurements of activity of sodium in sodium amalgams have been carried out previously by a number of workers (6-8). The early work encountered the problem of finding a solvent which is not attacked by sodium and which dissolves a reasonable amount of sodium salt to form an ionically conducting solution. A stable emf measurement with beta-alumina would enable one to develop an electrode to measure sodium content in sodium amalgams or alloys.

Present sodium amalgam analysis methods are awkward to apply accurately under many practical situations. The most commonly used techniques are:

1. The gasometric method (9) based on the volume of hydrogen evolved when sodium amalgam reacts with hydrochloric acid.

2. The potentiometric method (10) based on the potential of the cell Na-Hg|NaOH(50%)|HgO,Hg.

Experiment

Sample beta-alumina disks were obtained from Ford Motor Company (Firing No. 347) and Alcoa Company (batch 21G-5410). Physically, the Ford disks have a smooth and shiny appearance. From their physical size and weight, the density of these disks was calculated as 3.25 g/cc. Details of some transport behavior have been reported by Yao and Kummer (11). The chemical composition and crystal structure of the polycrystalline disks have been reported by Bettman and Peters (12). The analysis of beta-alumina from Alcoa was given as Na_2O 7.3%, SiO_2 0.02%, Fe_2O_3 0.03%, water 0.90%. The Alcoa disks are less smooth and have a density of 3.06 g/cc. They were fabricated and described by Francis (13).

Amalgams were prepared with triple distilled mercury and reagent-grade sodium metal (J. T. Baker Chemical Company). Sodium oxide on the metallic sodium was removed by filtering molten sodium through fritted glass. The concentrations of amalgams were determined gravimetrically (Sartorius balance, Model 2402).

Before each experiment, beta-alumina disks were heated in an alumina crucible, filled with beta-alumina powder, under an argon atmosphere at 900°C for 1 hr. The surrounding powder is used for minimizing the loss of sodium content, if any, in the disks. The measurements were made in a split U tube cell with one side arm filled with sodium and the other side with sodium amalgam as shown in Fig. 1. Experiments were carried out in an argon atmosphere dry box (Vacuum Atmosphere Corporation, Model HE-243-2 DRI-LAB). The box is equipped with a VAC Model HE-493 gas purifier for removing water vapor and oxygen and a VAC Model HE-593 titanium furnace (operated at 1600°F) for removing nitrogen. The water and oxygen content inside the box is estimated at below 1 ppm. This estimate is based on the long life (over 1 day) of a 25W tungsten light bulb filament and rate of formation of an oxide film on molten sodium. The temperature of the argon atmosphere was controlled with a thermoregulator to within ±0.2°C.

The emf of a sodium |Na-β-alumina| sodium amalgam cell was measured with a Leeds and Northrup K-3 potentiometer (catalog No. 7553) and a Hewlett

[1] Present address: Ledgemont Laboratory, Kennecott Copper Corporation, Lexington, Massachusetts 02173.
* Electrochemical Society Active Member.
Key words: electromotive force, sodium, aluminum sodium oxide (beta-alumina), sodium amalgam, ionic conduction, solid electrolyte, conduction in solid, sodium activity.
[2] The official nomenclature for $Na_2O \cdot 11Al_2O_3$ adopted by *Chemical Abstracts* are and have been: 1947-1956, β-alumina; 1957-1966, sodium-aluminate ($Al_{11}NaO_{17}$); 1966-present, aluminum sodium oxide ($Al_{11}NaO_{17}$).

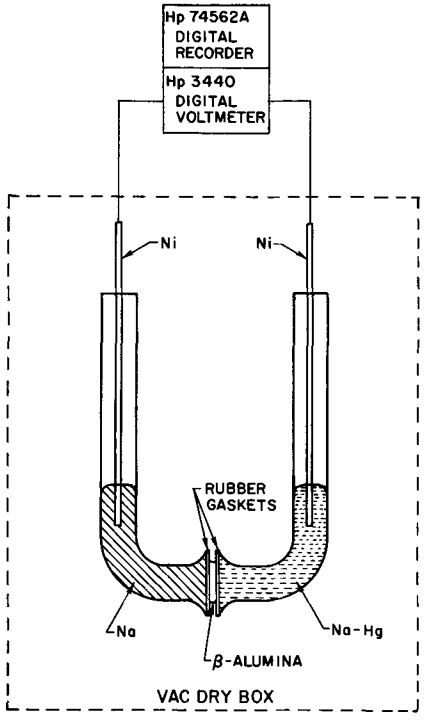

Fig. 1. Emf measurements of Na | Na-Hg cell with beta-alumina

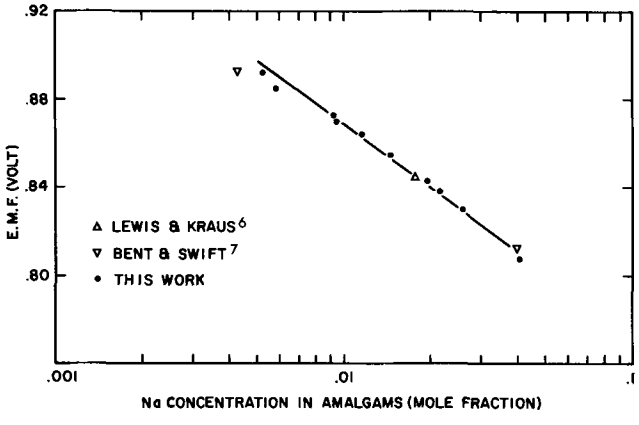

Fig. 2. Emf measurements of Na | beta-alumina | Na-Hg at 30°C

Packard Model 3440 digital voltmeter. The emf drift during a 1 hr period was less than 0.2 mV for most measurements. Both Ford disks and Alcoa disks were used for these measurements. The results for both agreed to within 0.2 mV. The measured results are tabulated in Table I.

The logarithm of activity of sodium, log a_{Na}, in amalgam is calculated from the measured emf by the relationship

$$nE\mathbf{F} = -2.303\,RT \log a_{Na} = -2.303\,RT \log \gamma x$$

where n is the number of electrons transferred, E is the measured emf, $\mathbf{F}$ is the Faraday constant, R is the universal gas constant, and T is absolute temperature. For this system, the pure sodium has been chosen as a reference state. The activity coefficients, γ, are calculated based on the mole fraction, x, of sodium in the amalgam solutions.

Table I. Observed values of emf of sodium | beta-alumina | sodium amalgam cell at 30°C

x (mole fraction of sodium)	Ford disk, volt	Alcoa disk, volt	log a_{Na}	log γ
0.005204	—	0.8923	−14.83	−12.55
0.005879	—	0.8850	−14.71	−12.48
0.009182	—	0.8730	−14.51	−12.47
0.009388	—	0.8702	−14.46	−12.43
0.01144	0.8640	0.8641	−14.36	−12.42
0.01444	—	0.8549	−14.21	−12.37
0.01911	—	0.8413	−13.98	−12.26
0.02128	0.8386	0.8387	−13.94	−12.27
0.02568	—	0.8301	−13.80	−12.21
0.04005	0.8081	0.8083	−13.43	−12.04

Table II. Inconsistency of emf measurements of Bent and Swift (7) at 25°C

Solution No.	x	Ref. to solution No. 5,* V	Ref. to pure Na, V	Solution 5— pure Na, V
3	0.0394227	0.04131	−0.81336	−0.85467
7	0.0042270	−0.04921	−0.89418	−0.84597

* Solution No. 5 has mole fraction of sodium x = 0.0177086.

Discussion

The measured results of this work are compared with some early work in Fig. 2. Lewis and Kraus (6) reported an emf measurement for the cell

Sodium|Ethylamine + NaI|Sodium amalgam

For a sodium amalgam of 0.2062 w/o (weight per cent) (x = 0.01771), the emf was 0.8456V at 25°C. The temperature coefficient they report is dE/dt = −0.0000408 V/deg. This result agrees well with this work after correction to 30°C.

Bent and Swift (7) performed the same measurements with dimethylethylamine saturated with sodium iodide as the electrolyte solution. They measured the emf of two sodium amalgam solutions (solutions No. 3 and 7) *vs.* pure sodium. However, their results were not consistent with the same two solutions *vs.* another sodium amalgam (solution No. 5) (see Table II). The deviation is 8.7 mV. This raises the question as to which, if either, measurement is correct.

The emf measurements of Iverson and Recht (8) were carried out with borosilicate glass as a separator at high temperatures (350°-400°C). No comparison is made with this work.

The agreement between the beta-alumina measurements and the results using organic solvents indicates that the electronic conduction in beta-alumina is low enough not to interfere with electrochemical measurements of this type.

Acknowledgments

We wish to thank Thomas L. Francis of the Alcoa Company and Thomas J. Whalen of the Ford Motor Company for providing beta-alumina disks.

This work was done under Contract Number DA-44-009-AMC-1661(T) to the Regents of the University of California for the U.S. Army Mobility Equipment Research and Development Center, Fort Belvoir, Virginia, DA Project/Task Area/Work Unit No. IT061102A 34A 03 013EF.

Manuscript submitted May 1, 1970; revised manuscript received Feb. 26, 1971.

Any discussion of this paper will appear in a Discussion Section to be published in the June 1972 JOURNAL.

REFERENCES

1. R. L. Ridgway, A. A. Klein, and W. J. O'Leary, *Trans. Electrochem. Soc.*, **70**, 71 (1936).
2. C. A. Beavers and M. A. S. Ross, *Z. Krist.*, **97**, 59 (1937).
3. Joseph T. Kummer and Neill Weber, U.S. Pat. 3,404,035, Oct. 1, 1968.
4. J. T. Kummer and Neill Weber, U.S. Pat. 3,404,036, Oct. 1, 1968.
5. W. L. Roth and R. J. Romanczuk, *This Journal*, **116**, 975 (1969).
6. G. N. Lewis and C. A. Kraus, *J. Am. Chem. Soc.*, **32**, 1459 (1910).

7. H. E. Bent and E. Swift, Jr., *ibid.*, **58**, 2216 (1936).
8. M. L. Iverson and H. L. Recht, *J. Chem. Eng. Data*, **12**, 262 (1967).
9. R. Ya. Ladiev and A. K. Maidannik, *Avtomatiz. Khim. Proizv.*, **1964**, 59.
10. J. A. LeDuc, C. Lurie, and J. Kourilo, *This Journal*, **112**, 870 (1965).
11. Yung-Fang Yu Yao and J. T. Kummer, *J. Inorg. Nucl. Chem.*, **29**, 2453 (1967).
12. M. Bettman and C. R. Peters, *J. Phys. Chem.*, **73**, 1774 (1969).
13. T. L. Francis, G. MacZura, and F. E. Phelps, "Sintered Sodium Beta Alumina Ceramics," Paper presented at 72nd Ann. Meeting of Am. Ceramic Soc., Philadelphia, March 1970.
14. R. Hultgren, R. L. Orr, P. D. Anderson, and K. K. Kelley, "Selected Values of Thermodynamic Properties of Metals and Alloys," John Wiley & Sons, Inc., New York (1963).

Reduction Mechanism of Thin-Film CuF_2 Electrodes in Propylene Carbonate Electrolyte

Brian Burrows*

School of Chemistry, Macquarie University, North Ryde, New South Wales, 2113, Australia

One of the principal factors limiting the utility of high energy density batteries based on organic electrolytes is the poor performance of the positive electrode. The specific causes of this poor behavior in the case of CuF_2 are not yet clear. Very little systematic work under closely controlled experimental conditions has been carried out; neither the mechanism nor the kinetics of the CuF_2 reduction process is known.

Most of the investigative work on CuF_2 has been done on electrodes of complex structure (1), *i.e.* made up from CuF_2 powder mixed with some finely divided conducting material such as graphite which acts as a current collector. An organic binder holds the structure together. The electrochemical behavior of this type of electrode, which is intended to have a large surface area, is not readily amenable to analysis. A simpler approach is to form CuF_2 on a Cu substrate in a controlled fashion and then to study the discharge of the thin film of CuF_2 in the organic electrolyte. Anhydrous HF, containing KF to improve the conductivity, was chosen as the reaction medium, and it was found to be possible to form CuF_2 of controlled thickness on a Cu substrate by electrochemical means (2).

This note presents the results of a study of the electrochemical behavior of thin-film CuF_2 electrodes in $PC/LiClO_4$ solutions under a variety of conditions.

Experimental

The CuF_2 electrodes consisted of thin porous films of CuF_2 formed on a copper wire substrate (2) by anodizing in HF/KF solution at 0.1 mA for 100 sec. The geometric electrode area was 0.33 cm^2; thus, the film thickness corresponded to 30 MHz cm^{-2}. This is equivalent to an average thickness of 24 molecular units of CuF_2. More complete details relating to the Cu/CuF_2 couple in HF-KF solutions are given in a previous paper (2).

After being formed, the CuF_2 electrodes were transferred immediately into a dry box. The CuF_2 electrodes were discharged in organic electrolyte under constant current conditions in a three-compartment cell. Unless otherwise stated, all electrodes were discharged within 5 min from time of immersion. The cell was contained inside a recirculating argon-atmosphere dry box (Vacuum Atmosphere Corporation) in which the temperature was maintained at 28° ± 0.2°C. Discharge curves (*i.e.*, potential-time curves) were recorded on a X-Y recorder (Houston Omnigraphic, Model HR-98T). A constant-current power source (Electronic Measurements, Model C623) supplied the current at voltages up to 400V. Emf's were measured with a potentiometer. A Li/Li^+ reference (3) was used in the discharge experiments.

The $PC/LiClO_4$ solutions were prepared and dried over Molecular Sieves (4A) as described elsewhere (4). The PC/Et_4NClO_4 and $THF/LiClO_4$ solutions were prepared and dried in an analogous manner. Stirring was achieved magnetically using a small Teflon-covered stirring bar in the bottom of the working-electrode compartment.

Results and Discussion

A typical discharge curve is shown in Fig. 1. The main feature is the long transition region terminating at about +2.0V. This was presumed to correspond to net CuF_2 reduction (see below). The charge recovered from the moment that constant current was applied through to the end of the major transition region was taken as a measure of the extent of net CuF_2 reduction. With increasing current density, the transition terminated at lower potentials and with less charge recovery.

As shown in the discharge curve of CuF_2, there was an initial potential drop of several hundred millivolts from the open-circuit potential of 3.4V. Fast pulse experiments were carried out to investigate whether this initial drop in potential was due to *IR* effects or to overvoltage effects. The application of a relatively high current density (3 mA/cm^2) and the simultaneous recording of the galvanostatic transient on the oscilloscope screen (1 msec/div) showed that the *IR* drop was only about 15 mV. This value is about the same as that calculated for the solution *IR* drop.

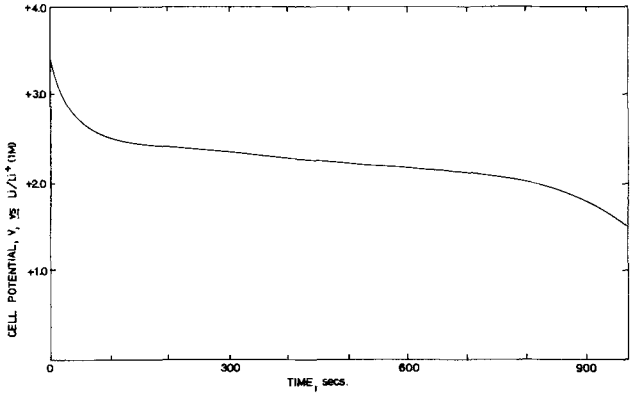

Fig. 1. Galvanostatic discharge curve for a CuF_2 electrode (30 MHz/cm^2) in $PC/LiClO_4$ (1M). Discharge efficiency was 83% to a 2V cutoff. Current density, 0.03 mA/cm^2.

* Electrochemical Society Active Member.
Key words: nonaqueous cells, copper fluoride, propylene carbonate.

Table I. Reduction of thin-film CuF_2 electrodes (30 MHz cm^{-2}) in PC/$LiClO_4$ (stirred solution)

	i, mA cm^{-2}	Q, MHz cm^{-2}
1.0M $LiClO_4$	0.03	13
	0.30	2
0.5M $LiClO_4$	0.03	10.5
	0.30	1.4
0.25M $LiClO_4$	0.03	12.2
	0.30	0.6

Table II. Reduction of thin-film CuF_2 electrodes (30 MHz cm^{-2}) in PC/$LiClO_4$ (quiescent solution)

	i, mA cm^{-2}	Q, MHz cm^{-2}
1.0M $LiClO_4$	0.03	26.3
	0.15	4.1
	0.30	3.9
0.5M $LiClO_4$	0.03	15.4
	0.15	3.8
	0.30	3.6
0.25M $LiClO_4$	0.03	11
	0.15	1.3
	0.30	1.2

Furthermore, a tenfold increase in current density caused but a fractional increase in the potential drop as observed on the X-Y recorder. This implies an overvoltage effect (kinetic and/or mass transport) as opposed to an ohmic drop, in agreement with the fast pulse measurements.

Effect of stirring.—To investigate mass transport control, discharge curves were recorded at various current densities and $LiClO_4$ concentrations in which stirring was effected by a magnetic stirrer in the bottom of the working electrode compartment. The results are listed in Table I. Comparing the results with those in Table II (static conditions), it can be seen that stirring caused a significant decrease in Q (*i.e.*, the total charge recovered) over the whole current density range and $LiClO_4$ concentration range. This is consistent with a dissolution mechanism for the reduction of CuF_2; *i.e.*, a soluble intermediate is the species which is reduced (see below). The effect of stirring would be to reduce the concentration of this species at the electrode surface, hence causing a reduction in charge recovered as compared to the case of a quiescent solution where the local concentration at the interface in viscous PC/$LiCl_4$ electrolyte would be relatively much larger.

Effect of current density and $LiClO_4$ concentration.—The results of CuF_2 reduction as a function of current density and $LiClO_4$ concentration are listed in Table II. The trend of the results is that Q decreases to a more or less constant value as current density increases. This is also consistent with a prior dissolution-reduction mechanism in that the constant Q at high i (see Table II) can be accounted for in terms of the reduction of the equilibrium amount of the intermediate present in the immediate vicinity of the electrode. At low i, Q is higher due to the ability of the dissolution process to keep supplying the electroactive intermediate at a rate sufficient to maintain reduction at about +2.5V *vs.* Li/Li^+.

The effect of decreasing $LiClO_4$ concentration is to cause a decrease in Q for a given i. This effect has also been observed by other workers using electrodes of more complex structure (1), and can be related to the proportionality between CuF_2 solubility and $LiClO_4$ concentration (5). This relationship is due to the metathetical reaction (6)

$$CuF_2\ (solid) + 2LiClO_4\ (solution) \rightarrow 2LiF\ (solid) + Cu(ClO_4)_2\ (solution) \quad [1]$$

No data are yet available on the time for this reaction to come to equilibrium.

Table III. Reduction of thin-film CuF_2 electrodes (30 MHz cm^{-2}) in PC/$LiClO_4$(1M) containing 500 ppm H_2O

i, mA cm^{-2}	Q, MHz cm^{-2}
0.03	35.0
0.15	9.8
0.30	6.3
Effect of stirring	
0.03	25
0.30	2.5

Effect of H_2O.—The solubility of CuF_2 in PC is about 10^{-4}M (5). In H_2O the solubility is of the order of 0.5M (7). Hence, the addition of H_2O to PC should increase the solubility of CuF_2 and presumably of the soluble intermediate. The discharge results obtained when 500 ppm of H_2O were added are shown in Table III. It can be seen that H_2O did indeed significantly increase Q over its corresponding value in the "dry" solution (*cf.* Table II) and stirring again caused a decrease in Q. A dry PC/$LiClO_4$ solution contains a small amount of H_2O, the last traces of which are difficult to remove (4). This trace of H_2O presumably assists the dissolution of CuF_2. On prolonged wet stand in such a "dry" solution, the CuF_2 discharge performance could be expected to worsen, as solubilized copper diffuses into the bulk of solution. The results of such an experiment showed a fourfold loss in capacity at 0.03 mA cm^{-2} over a 6 day wet stand and a 2.5-fold loss at 0.3 mA cm^{-2} over the same period. This loss in capacity has been commonly observed in experimental batteries (1).

Effect of supporting electrolyte and solvent.—Previous work indicates that LiF is a product of CuF_2 reduction (5). LiF is quite insoluble ($<10^{-5}$M) in PC (5) and its effect on the reduction of CuF_2 was investigated by replacing $LiClO_4$ with Et_4NClO_4 as supporting electrolyte. A solution of Et_4NClO_4 (at the saturation concentration of about 0.75M) in PC was prepared and dried over 4A Molecular Sieves. Discharge of CuF_2 showed no detectable transition region.

The effect of Et_4N^+ ions could be that they do not react metathetically with CuF_2 as do Li^+ ions and thus there is no mechanism for the formation of an appreciable Cu^{2+} ion concentration. The reduction of CuF_2 again became apparent after the addition of $LiClO_4$ to the Et_4NClO_4 solution.

In THF/$LiClO_4$ solution the results of the discharge of CuF_2 electrodes were not significantly different to those in PC/$LiClO_4$. It was observed, however, that well-dried THF/$LiClO_4$ solution reacted with the Li reference electrode producing a grey sponge-like film. This film was mildly explosive when impacted. When the solution contained more than about 10^{-3}M (~18 ppm) H_2O, the Li metal was stabilized, suggesting that a reaction between H_2O and Li resulted in the formation of a passive film. The presence of PC also stabilized the lithium.

Time dependence of CuF_2 dissolution.—The results thus far suggest that CuF_2 is reduced *via* a dissolution mechanism. An experiment which supported this conclusion was one in which thin-film CuF_2 electrodes (30 MHz/cm^2) were pulsed at 0.3 mA/cm^2 for 4 sec periods followed by rest periods until the end of the transition region was reached. The results are listed in Table IV in which it can be seen that, with increasing dura-

Table IV. Pulsed reduction of thin-film CuF_2 electrodes (30 MHz cm^{-2}) at 0.3 mA cm^{-2} in PC/$LiClO_4$(1M)

Rest period after each 4 sec discharge pulse (sec)	Total charge recovered to end of transition region (MHz cm^{-2})
0	5.1
10	6.9
20	9.0
30	10.8

tion of the rest period for a given electrode, there was an increasing amount of charge recovered. This is consistent with more soluble intermediate being formed as the rest period became longer, leading to an increased charge recovery.

Conclusions

This investigation of CuF_2 reduction has shown that: (*a*) the initial potential drop is not due to *IR*; (*b*) stirring causes a decrease in *Q*, the charge recovered from CuF_2 reduction; (c) a decrease in $LiClO_4$ concentration causes a decrease in *Q* in the same sense as the solubility of CuF_2 is decreased; and (*d*) an increase in H_2O concentration causes an increase in *Q* in the same sense as the solubility of CuF_2 is increased. These results point to the conclusion that CuF_2 is reduced *via* a soluble intermediate rather than through the solid state. The intermediate presumably is the cupric ion and the rate-limiting step could be either of (i) the kinetics of the Cu^{2+} ion reduction process, (ii) the rate of dissolution of CuF_2 to Cu^{2+} ions, or (iii) the mass transport of these ions to reduction sites. Until more detailed studies are carried out, it is not possible to be more specific as to the exact nature of the dissolution-reduction mechanism for CuF_2 in propylene carbonate $LiClO_4$ electrolyte.

Acknowledgments

The work reported herein was carried out at Tyco Laboratories Incorporated, Waltham, Massachusetts, and the author wishes to thank Dr. Raymond Jasinski of Tyco Laboratories for his helpful discussions and suggestions and Susan Kirkland for assisting with the experimental work. This work was carried out under Contract NOO19-67-C-0680 for the U. S. Navy Air Systems Command.

Manuscript received Jan. 25, 1971.

Any discussion of this paper will appear in a Discussion Section to be published in the June 1972 JOURNAL.

REFERENCES

1. K. H. M. Brauer and J. A. Harvey, "Status Report on Organic Electrolyte High Energy Batteries," DA Task 1CO 14501 A 34A-00-01 (May 1967).
2. B. Burrows and R. Jasinski, *This Journal*, **115**, 348 (1968).
3. B. Burrows and R. Jasinski, *ibid.*, **115**, 365 (1968).
4. B. Burrows and S. Kirkland, *ibid.*, **115**, 1164 (1968).
5. R. Jasinski, *Electrochem. Technol.*, **6**, 28 (1968).
6. M. L. B. Rao and R. W. Holmes, *ibid.*, **6**, 105 (1968).
7. R. C. Weast, Editor, "Handbook of Physics and Chemistry," 48th Ed., Chemical Rubber Co. (1967).

The Limiting Rate of Deposition by P-R Plating

H. Y. Cheh*,[1]

Bell Telephone Laboratories, Incorporated, Murray Hill, New Jersey 07974

Plating by periodically reversing the polarity of the applied current (p-r plating) is a technique used by electroplaters to reduce nodular growth, edge buildup, and surface roughness (1, 2). The instantaneous limiting current density during the cathodic part of the cycle was also known to exceed that of direct-current (d-c) plating (2). However, no satisfactory theory exists to calculate the limiting rate of deposition. In this paper we show how the diffusion model developed for plating by pulsed current (p-c plating) (3) can be extended to calculate the limiting rate of deposition by p-r plating.

The diffusion model for p-r plating is complete analogy to that of p-c plating. The only difference appears in the boundary condition involving the form of the applied current density at the electrode surface. Similar to the nomenclature used in Ref. (3), the applied current density for p-r plating can be expressed as

$$i = i_f \text{ for } 0 < t \leqq t_1, t_2 < t \leqq t_3, \text{ etc.} \quad [1]$$

and

$$i = i_r = \frac{1}{r} i_f, \text{ for } t_1 < t \leqq t_2, t_3 < t \leqq t_4, \text{ etc.} \quad [2]$$

and the cyclic period is given by

$$\theta = \theta_1 + \theta_2 = t_2 = (t_4 - t_2) = (t_6 - t_4), \text{ etc.} \quad [3]$$

where i is the applied current density, i_f is the current density during the forward part of the cycle, θ_1, i_r is the current density during the reverse part of the cycle, θ_2, r is the ratio of i_f and i_r and is always negative for p-r plating, t is time and t_n is defined in Fig. 1. The mathematical problem was solved by Rosebrugh and Miller (4), and similar to p-c plating (3), the ratio of the instantaneous cathodic limiting current density for p-r plating to that of d-c plating can be expressed as

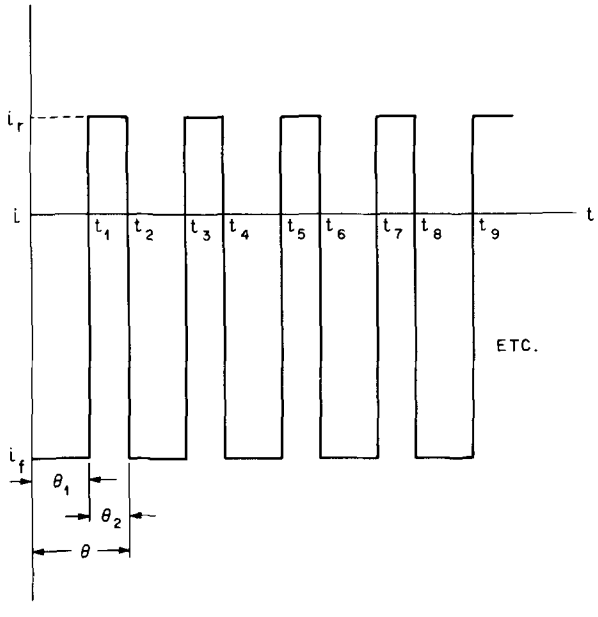

Fig. 1. Schematic diagram of applied current in p-r plating

$$\frac{(i_{p\text{-}r})_l}{(i_{d\text{-}c})_l} = \frac{1}{1 - \frac{8}{\pi^2}\left(\frac{r-1}{r}\right)\sum_{j=1}^{\infty} \frac{1}{(2j-1)^2} \cdot \frac{(\exp[(2j-1)^2 a\theta_2] - 1)}{(\exp[(2j-1)^2 a\theta] - 1)}} \quad [4]$$

where $(i_{p\text{-}r})_l$ and $(i_{d\text{-}c})_l$ are limiting current densities for p-r and d-c plating, respectively. The asymptotic form for $a\theta << 1$ is, therefore

* Electrochemical Society Active Member.
[1] Present address: Department of Chemical Engineering and Applied Chemistry, Columbia University, New York, New York 10027.
Key words: *electroplating, gold.*

$$\left[\frac{(i_{p\text{-}r})_l}{(i_{d\text{-}c})_l}\right]_{a\theta<<1} = \frac{1}{1-\left(\frac{r-1}{r}\right)\frac{a\theta_2}{a\theta}} \qquad [5]$$

The over-all rate of plating which can be calculated by integrating over the entire cycle is

$$\frac{\text{Max over-all rate of p-r plating}}{\text{Max rate of d-c plating}} = \frac{(i_{p\text{-}r})_l\left(\theta_1+\frac{1}{r}\theta_2\right)}{(i_{d\text{-}c})_l\theta} = \frac{\left(\theta_1+\frac{1}{r}\theta_2\right)/\theta}{1-\frac{8}{\pi^2}\left(\frac{r-1}{r}\right)\sum_{j=1}^{\infty}\frac{1}{(2j-1)^2}\cdot\frac{(\exp[(2j-1)^2a\theta_2]-1)}{(\exp[(2j-1)^2a\theta]-1)}} \qquad [6]$$

Numerical results of Eq. [4] and Eq. [6] for various values of $a\theta$, θ_1/θ, and $1/r = -0.20$ are plotted in Fig. 2 and Fig. 3.

Experimental investigation of Eq. [6] was carried out using the same gold plating solutions under the same experimental conditions as reported in Ref. (3). The only difference appeared in the applied current densities. A calculation on the instantaneous cathodic limiting current density was first made for $(1/r) = -0.20$ by using Eq. [3]. To ensure the fact that the cathodic limiting current density was reached, an additional current of -3 mA (*i.e.*, -9.47 mA/cm^2) was added to the calculated $(i_{p\text{-}r})_l$ value and the total value was used as i_f. $(-0.20)\cdot(i_{p\text{-}r})_l$ was used as i_r. The results for phosphate, citrate, and cyanide (corrected for chemical dissolution of gold) gold solutions were given in Fig. 4-6.

Satisfactory agreement was observed between theory and experimental results for large values of θ_1/θ for all three solutions. However, for both phosphate and citrate gold solutions, the measured limiting rate of deposition was considerably higher than that from the theory for small values of θ_1/θ. A qualitative explanation for this disagreement can be obtained by considering the anodic dissolution of gold. Gold dissolves electrochemically according to the following two reactions

In alkaline medium

$$Au + 2CN^- \rightarrow Au(CN)_2^- + e^- \qquad [7]$$

In acid medium

$$Au + 2HCN \rightarrow Au(CN)_2^- + 2H^+ + e^- \qquad [8]$$

Since the dissociation constant of $Au(CN)_2^-$ is approximately[2] 3 x 10^{-35} at 60°C, the CN^- and HCN in phosphate and citrate gold solutions must essentially come from the cathodic part of the plating cycle. The small amount of these species may cause the anodic dissolution of gold to be inefficient and consequently

[2] Calculated from standard electrode potential data from W. M. Latimer, "Oxidation Potentials," 2nd Ed., Prentice-Hall, Englewood Cliffs, N. J. (1952).

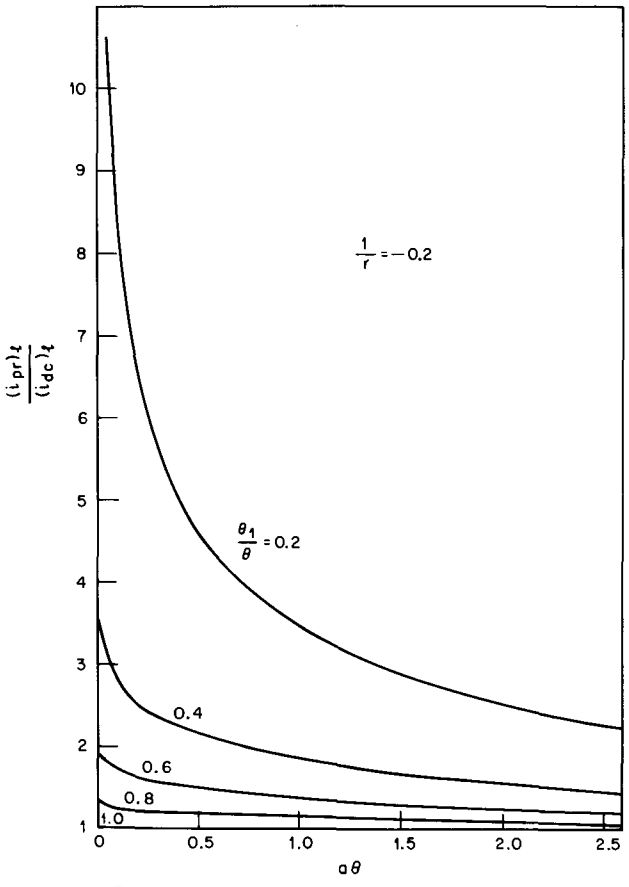

Fig. 2. Limiting current density for p-r plating

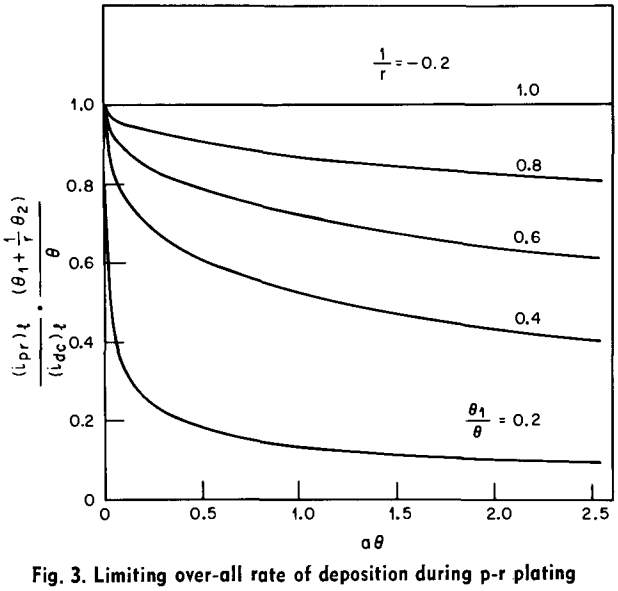

Fig. 3. Limiting over-all rate of deposition during p-r plating

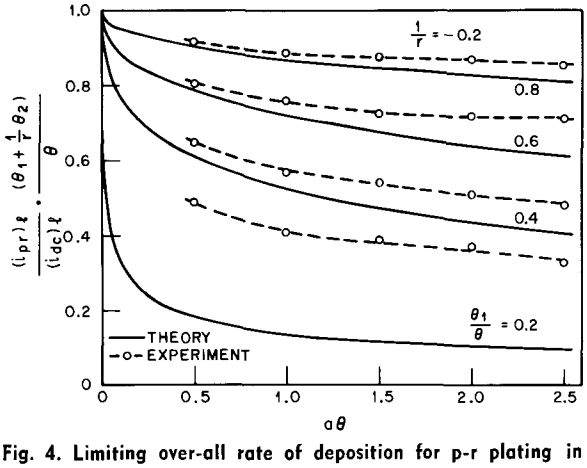

Fig. 4. Limiting over-all rate of deposition for p-r plating in a phosphate gold solution.

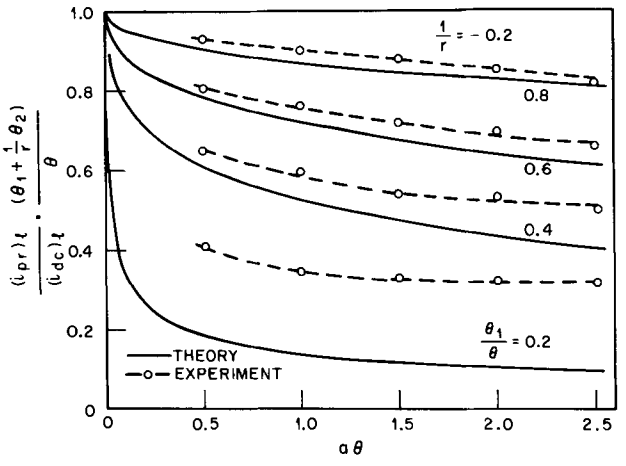

Fig. 5. Limiting over-all rate of deposition for p-r plating in a citrate gold solution.

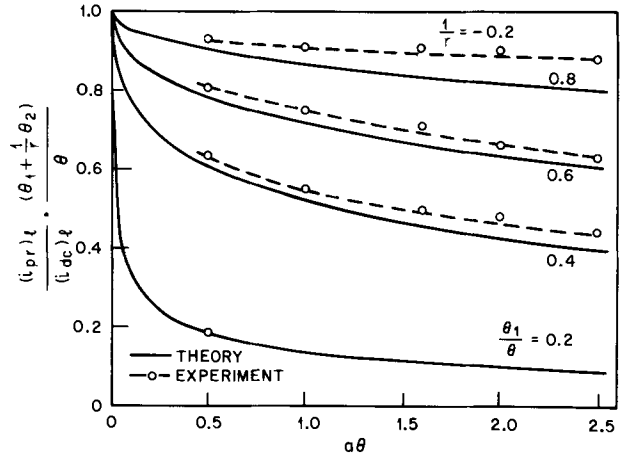

Fig. 6. Limiting over-all rate of deposition for p-r plating in a cyanide solution. Corrected for chemical dissolution of gold.

leads to a higher plating rate than that predicted from the theory. Other complexes involving citrate or phosphate with gold may also exist in the solution. However, their concentration is probably too low to cause a significant amount of dissolution of gold during the anodic part of the plating cycle. This is supported by the fact that no significant gold dissolution is found by applying an anodic current to a gold electrode in either the citrate or phosphate gold solutions.

In conclusion, the diffusion model adopted for p-r plating can be used to predict the limiting rate of deposition provided that anodic dissolution of the metal is at 100% current efficiency. A sample calculation on the application of this theory to a practical plating process is given here. Assuming the following data: $c_o = 0.1$ moles/liter, $D = 10^{-5}$ cm^2/sec, $\delta = 0.005$ cm (a typical thickness in a stirred solution), $n = 1$, $\theta = 50$ msec, $\theta_1/\theta = 0.6$, and $1/r = -0.20$, one can readily calculate $(i_{d\text{-}c})_l$, $(i_{p\text{-}r})_l$, and the limiting over-all rate of p-r plating.

$$(i_{d\text{-}c})_l = -nFD\frac{c_o}{\delta} = -19.3 \text{ mA/cm}^2$$

Since

$$a\theta = \frac{\pi^2 D}{4\delta^2}\theta = 0.0493,\ \theta_1/\theta = 0.6 \text{ and } 1/r = -0.20$$

from Fig. 2

$$\frac{(i_{p\text{-}r})_l}{(i_{d\text{-}c})_l} = 1.8$$

therefore

$$(i_{p\text{-}r})_l = -35 \text{ mA/cm}^2$$

From Fig. 3

$$\frac{\text{Limiting over-all rate of p-r plating}}{\text{Limiting rate of d-c plating}} = 0.92$$

therefore

$$\text{Limiting over-all rate of p-r plating} = -18 \text{ mA/cm}^2$$

Manuscript submitted Sept. 29, 1970; revised manuscript received *ca.* March 15, 1971.

Any discussion of this paper will appear in a Discussion Section to be published in the June 1972 JOURNAL.

SYMBOLS

a	A diffusion parameter, $a = \pi^2 D/4\delta^2$ (sec^{-1})
c_o	Concentration of the metal ion in the bulk of the solution (moles/cm^3)
D	Diffusion coefficient of the metal ion (cm^2/sec)
$\mathbf{F}$	Faraday's constant (coulomb/equiv.)
i	Current density (A/cm^2)
$i_{d\text{-}c}$	Current density for deposition for d-c plating
$(i_{d\text{-}c})_l$, $(i_{p\text{-}r})_l$	Limiting current density for d-c plating and for p-r plating, respectively (A/cm^2)
i_f, i_r	Current density during the forward and during the reverse part of p-r plating (A/cm^2)
n	Number of electrons transferred in an electrochemical reaction
t	Time (sec)
t_1, t_2, etc.	Time periods during p-r plating defined in Fig. 1 (sec)
δ	Thickness of the diffusion layer (cm)
θ	Period of a p-r plating cycle (sec)
θ_1, θ_2	Portion of the period for forward current and portion of the period for reverse current (sec)

REFERENCES

1. G. W. Jernstedt, *Ann. Proc. Amer. Electroplaters' Soc.*, **36**, 63 (1949); **37**, 151 (1950).
2. A. Hickling and H. P. Rothbaum, *Trans. Inst. Metal Finishing*, **34**, 199 (1957).
3. H. Y. Cheh, *J. Electrochem. Soc.*, **118**, 551 (1971).
4. T. R. Rosebrugh and W. L. Miller, *J. Phys. Chem.*, **14**, 816 (1910).

Contacts for Resistivity Measurements of Beta-Alumina

R. D. Armstrong, T. Dickinson, and J. Turner

Electrochemistry Research Laboratories, Department of Physical Chemistry, University of Newcastle upon Tyne, Newcastle upon Tyne, NE1 7RU, England

The determination of the conductivity of an ionic conductor is complicated by interfacial (electrode) effects. The cell impedance with two electrodes contacting the material under investigation can be represented to a good approximation (1) by the analog circuit of Fig. 1a, where the assumption is made that the interfacial regions are separated by a large number of Debye lengths.[1] In Fig. 1a, C_∞ represents the capacitance between the electrodes with the ionic conductor behaving as a dielectric material, while R_∞ is the bulk resistance. These quantities are virtually frequency independent, although C_∞ may show frequency-dependent effects due to dielectric relaxation. In solids, dipole relaxation can occur at comparatively low frequencies (kHz or less).

The interfacial impedance (Z_i) depends on the precise nature of the contacts. It can be represented as in Fig. 1b, where C_{dl}, R_{dl} represent the double layer (nonfaradaic path) and R_{ct} and W the faradaic path. It has recently been shown that these paths cannot be strictly separated since the one flux leads both to charge transfer and double-layer charging (2). The double layer is purely capacitative up to frequencies comparable with those at which the Debye-Falkenhagen relaxation occurs in the bulk material. For electrodes where charge transfer is not possible, $R_{ct} = \infty$. W is the Warburg impedance, which for β-alumina is negligible because of the high concentration of mobile species.

For $\omega \to \infty$, $Z_i \to 0$ so that for sufficiently high frequencies the cell impedance is R_∞ with C_∞ in parallel. Therefore, to determine the conductivity of the sample, it is sufficient to determine the cell impedance at such (high) frequencies that it can be represented by frequency-independent elements, R_p and C_p, which can then be identified with R_∞ and C_∞. Unfortunately, in a real cell, at high frequencies, the leads from the cell to the measuring equipment give rise to inductive effects and thus set an upper limit on the usable frequency.

In the present work, we have investigated the use of different electrodes for resistivity measurements on β-alumina. The electrodes which have been reported previously are summarized in Table I.

Key words: beta-alumina, conductivity, solid electrolyte.

[1] In β-alumina, the Debye length is ~0.1 nm.

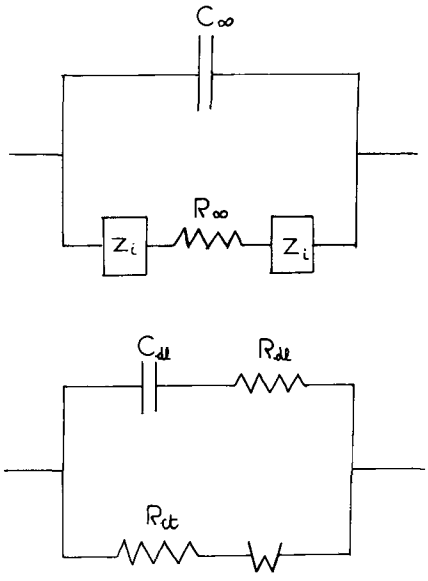

Fig. 1. Equivalent circuit for cell (a—top, b—bottom)

Experimental

Measurements were made on fully dense sintered β-alumina in the form of disks (thickness 1 mm, diameter 10 mm, English Electric) and on selected single crystals (cross section 3 mm x 0.5 mm, length 4 mm, Harbison Carborundum Company). The composition of these materials was near to $Na_2O \cdot 11\ Al_2O_3$.

Contact was made to the samples by means of

(i) molten $NaNO_3$ + Pt electrodes (320°-400°C)
(ii) molten $NaNO_3/NaNO_2$ + Pt electrodes (250°-350°C)
(iii) aqueous 5M $NaNO_3$ (30°-80°C)
(iv) evaporated gold electrodes (30°-300°C)
(v) sodium [5 w/o (weight per cent)]—mercury amalgam under an argon atmosphere (50°-300°C)

Table I. Resistivity measurements on β-alumina

Physical form	Contact	Frequency	Frequency dependence	Conductivity (ohm^{-1} cm^{-1})	Temp (°C)	Activation energy (kj mole^{-1})	Ref.
Single crystal	Indium	500 kHz	Const. from 0.5 to 1.5 MHz	$30 \pm 3 \times 10^{-3}$	25	11.1	(3, 4)
		500 kHz	—	285×10^{-3}	300		
	—	—	—	23×10^{-3}	25	14.0	This work
	—	—	—	355×10^{-3}	300		
Sintered disk (fully dense)	Na	1592 Hz	Frequency independent	36×10^{-3}	300	13.7	(5)
		1592 Hz	Frequency independent	20×10^{-3}	227	15.8	
	—	—	—	1.84×10^{-3}	25	14.0	This work
				28.5×10^{-3}	300		
Sintered disk (less than fully dense)	Ag/Ag_2O/5N NaOH	D.C.	—	$4\text{-}5 \times 10^{-3}$	25		(4)
	Na	D.C.	—	55×10^{-3}	300		
	Pt	800 kHz	—				

The sintered β-alumina was attached to within a Pyrex glass cell central glass tube with "Autostic" (Carlton Brown Limited, Elford, England), an alumina-based cement of negligible conductivity and apparently inert toward the molten salts and amalgam. The single crystals were also embedded in "Autostic," the ends of the crystal being polished flat after the cement had set. When aqueous contacts were used, the crystals were mounted in P.T.F.E. disks with "Araldite." When evaporated gold electrodes were used, spring-mounted platinum foil contacts were held against the gold; the results were not affected by increasing the pressure on these contacts. The glass cells were immersed in either an oil bath or a fluidized sand bath to control their temperature. System (iv) was held within a small temperature-controlled furnace.

Cell impedances were determined, over the frequency range 100 Hz-5 MHz, using transformer ratio-arm bridges, as equivalent R_p, C_p values (Wayne Kerr B221, B201). With systems (i)-(iii), the measured resistance was corrected for the cell resistance in the absence of β-alumina. These corrections generally amounted to less than 10%.

Results

The results obtained enable the contacts to be divided into three groups:

1. With the molten salt contacts, and the aqueous solution in contact with a single crystal, a satisfactory frequency range could be found where R_p was frequency independent ($f > 10$ kHz).
2. With Au and Na/Hg contacts at high temperatures and perhaps Au in contact with the single crystal at room temperature, R_p showed only a slight dependence on frequency at the highest usable frequencies (1 MHz).
3. With the amalgam contact, and the aqueous solution or gold in contact with the sinter, near room temperature, the highest frequency achievable (1 MHz) was obviously less than that necessary in order to identify R_p with R_∞.

We should therefore expect the conductivity measurements obtained with the systems in group 1 to be in accord with and not very different from those obtained with the members of group 2. The systems listed in group 3 should, however, show lower conductivities. This pattern of behavior is essentially confirmed by the results shown in Fig. 2 and 3. These graphs show the apparent conductivity of the single crystal (Fig. 2) and sinter (Fig. 3) as a function of temperature. The measurements were made at the highest usable frequency for each type of contact. With the single crystal, concordant results are obtained with the molten salt, aqueous, and high-temperature amalgam contacts. The results obtained with the Au contacts are in fairly satisfactory agreement with these, whereas a significantly lower conductivity was obtained with amalgam contacts at lower temperatures. With the sinter, the results obtained with the molten salt and high-temperature amalgam contacts are again

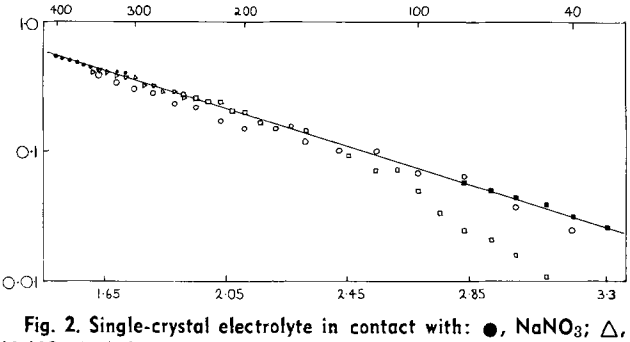

Fig. 2. Single-crystal electrolyte in contact with: ●, $NaNO_3$; △, $NaNO_3/NaNO_2$; ○, Au; □, Na/Hg; ■, aqueous $NaNO_3$. Ordinate, conductivity (ohm^{-1} cm^{-1}). Abscissa, $10^3/T$ (K^{-1}).

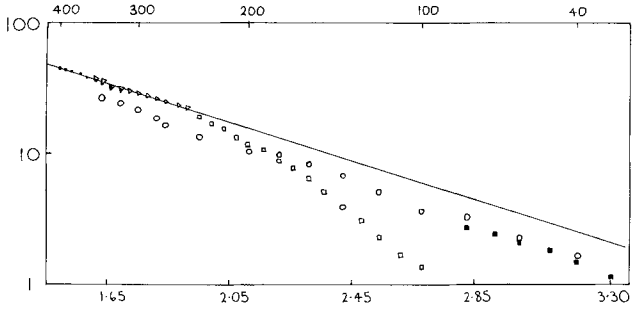

Fig. 3. Sintered electrolyte in contact with: ●, $NaNO_3$; △, $NaNO_3/NaNO_2$; ○, Au; □, Na/Hg; ■, aqueous $NaNO_3$. Ordinate, conductivity (ohm^{-1} cm^{-1}). Abscissa, $10^3/T$ (K^{-1}).

concordant. Somewhat lower conductivities are obtained with gold and aqueous contacts, assuming the graph should be linear. The amalgam contacts again gave significantly lower conductivities at lower temperatures. The lines on these graphs are believed to represent the true relation between conductivity and temperature.

Discussion

The reported results underline the need for study of the frequency dependence of the resistivity whenever conductivity measurements are being made. In the present work, the high interfacial impedance with amalgam contacts, particularly in the case of the ceramic at low temperature, gave rise to erroneously low conductivity values. This high interfacial impedance is probably due to nonwetting of the irregular surface of the ceramic by the amalgam.

The activation energies for ionic transport in the single crystal (14.0 kJ mole^{-1}) and sintered specimens (14.0 kJ mole^{-1}) are equal and in reasonable agreement with previously published values (Table I). The conductivity of the single crystal (0.355 ohm^{-1} cm^{-1} at 300°C) was considerably higher than that of the sinter (0.0285 ohm^{-1} cm^{-1}), presumably because of the lack of ordering of the crystallites in the latter. Differences of conductivity of similar magnitude have been observed previously. The conductivity values obtained for the two samples are in reasonable agreement with the published values (Table I).

Yao and Kummer (3) found an activation energy of 15.94 kJ mole^{-1} for diffusion in the single crystal, which compares well with the value of 15.86 kJ mole^{-1} for diffusion calculated from the conductivity data quoted by Weber and Kummer (4); whereas we obtain a value of 18.75 kJ mole^{-1} from our conductivity measurements.

The values of the diffusion coefficient at 300°C calculated from the Nernst-Einstein relationship on the basis of our results (3.3×10^{-5} cm^2 sec^{-1}) or those of Weber and Kummer (4) (2.66×10^{-5} cm^2 sec^{-1}) are not in accord with the value of 0.85×10^{-5} cm^2 sec^{-1} obtained by direct measurement (3). This discrepancy has been regarded as evidence supporting an interstitialcy mechanism for sodium ion migration.

Acknowledgments

We would like to thank British Rail for their support of this work, and Mr. J. L. Sudworth for helpful discussions.

Manuscript submitted Dec. 8, 1970; revised manuscript received Mar. 23, 1971.

Any discussion of this paper will appear in a Discussion Section to be published in the June 1972 JOURNAL.

REFERENCES

1. J. R. MacDonald, *Phys. Rev.*, **92**, 4 (1953).
2. P. Delahay, *This Journal*, **113**, 967 (1966).
3. Yung-Fang Yu Yao and J. T. Kummer, *J. Inorg. Nucl. Chem.*, **29**, 2453 (1967).
4. N. Weber and J. T. Kummer, *Proc. Ann. Power Sources Conf.*, **21**, 37 (1967).
5. J. L. Sudworth, Private communication.

Brief Communications

Mo-Permalloy Film Deposited on a Continuous Wire Substrate

William L. Wade, Jr., and Gordon Sands

United States Army Electronics Command, Electronic Components Laboratory, Fort Monmouth, New Jersey 07703

A nickel-iron permalloy composition containing molybdenum (79% Ni, 17% Fe, 4% Mo) has been successfully deposited on 0.005 in. diameter beryllium-copper wire. Previous attempts to electroplate (4-79) permalloy and other Mo substituted compositions have been disappointing (1). These newly developed films were deposited up to 4000Å thick using a modified continuous plating system. The development of these ternary compositions provides an additional family of plated wire materials for potential application in computer memories.

A continuous coating of magnetic molybdenum permalloy film was electroplated onto the wire in the presence of a circumferential magnetic field that established a magnetic anisotropy axis circumferentially around the wire (2, 3). Table I outlines a typical plating bath whose plating current was 22 mA. The current required to produce the preferred magnetization direction was 0.5A.

Both nondestructive readout (NDRO) and destructive readout (DRO) films were fabricated. The coercive force (H_c) ranged from 1.1 to 1.9 oersteds, and the anisotropy (H_k) ranged from 2.5 to 3.7 oersteds (4).

Key words: electrodeposition, cylindrical magnetic films, permalloy films, plated wire, magnetic film.

Qualitative determination of the presence of molybdenum was made using spectrographic instrumentation. Quantitative determination of the presence of molybdenum was made by analyzing nickel and iron spectrophotometrically, and taking molybdenum as the difference.

Manuscript received Mar. 11, 1971.

Any discussion of this paper will appear in a Discussion Section to be published in the June 1972 JOURNAL.

REFERENCES

1. S. M. Rubens, "Ferromagnetic Films," *Electro-Technol. (New York)*, **72**, 121 (1963).
2. W. D. Doyle, "Stable Permalloy Wire Memory Elements," U.S. Army Electronics Command, Ft. Monmouth, N. J., Tech. Report ECOM-0273-1, pp. 17-19, Aug. 1967.
3. W. Wade and G. Sands, "Process and Techniques for Fabrication of Magnetic Plated Wire," U.S. Army Electronics Command, Ft. Monmouth, N. J., Tech. Report ECOM-3029, Oct. 1968.
4. W. Wade and G. Sands, "Fabrication of Magnetic Plated-Wire," U.S. Army Electronics Command, Ft. Monmouth, N. J., To be published as ECOM Tech. Report.

Table I. Typical nickel-iron-molybdenum bath

Compound	Formula	Amount (grams/liter)	Cation (grams/liter)	Source
Nickelous sulfamate	$Ni(SO_3NH_2)_2$	454.8	106.4	Plating bath from Barrett Chem., Mich.
Ferrous sulfamate	$Fe(SO_3NH_2)_2$	5.84	1.3	Prepared solution from Barrett Chem., Mich.
Ferrous sulfate	$Fe(SO_4)\cdot 7H_2O$	6.46	1.3	Fisher Scientific Co.
Ammonium molybdate	$(NH_4)_6Mo_7O_{24}\cdot 4H_2O$	0.185	0.1	Fisher Scientific Co.
1, 3, 6-Naphthalene trisulfonic acid, trisodium salt	$C_{10}H_5(SO_3Na)_3$	20.0	—	J. T. Baker Co.
Boric acid	H_3BO_3	43.0	—	Fisher Scientific Co.
pH (Adjust w/sulfamic acid)	3.0	—	—	Fisher Scientific Co.
Bath temperature	50°C	—	—	—

Oxygen Reduction on Tungsten Carbide

M. Voïnov,* D. Bühler, and H. Tannenberger

Institut Battelle, Carouge-Genève, Switzerland

Tungsten carbide WC has been found to be a good electrocatalyst for the oxidation of H_2, CO, N_2H_4, HCHO, and HCOOH (1, 2).

We wish to report that on this material the exchange current for oxygen reduction is of the same order of magnitude as on platinum in an acid medium ($HClO_4$ 1M).

Nonporous WC containing 0.1% Co (3) was heat-pressed in kel-F and mounted as a rotating electrode.

Water twice distilled in quartz was used with $HClO_4$ p.a. to make the electrolyte. Potentiostatted tensions are referred to a dynamic hydrogen electrode in the

* Electrochemical Society Active Member.

Key words: oxygen reduction, electrocatalysis, tungsten carbide.

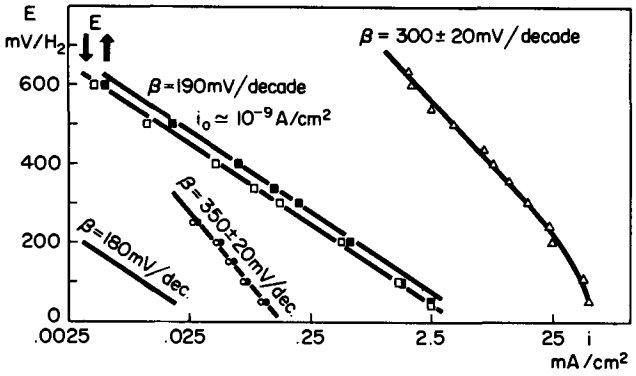

Fig. 1. Reduction of O_2 ($\simeq$ 1 atm) on WC, □ ■; Pyrocarbone, ——; and W, ○ ●. Reduction of H_2O_2 (0.04 M/liter, N_2) on WC: all measurements, $HClO_4$ 1M, 55°C, 1400 rpm.

same solution. Potential sweep (1 mV/sec) measurements were performed with nitrogen or oxygen bubbling in the thermostatted solution.

For unknown reasons, the electrode potential had to be swept at least 10 cycles between 0 and +700 mV/H_2 under nitrogen in order to obtain stable results.

The exchange current obtained by extrapolation to 1.23V of the E (log i) curve (Fig. 1) for O_2 reduction is 10^{-9} A/cm^2. The extrapolation to 1.23V is justified by the fact that H_2O_2 reduction does not appear to be rate determining in view of the relative Tafel slope for O_2 and H_2O_2 reduction on WC (Fig. 1).

The comparison between the electrocatalytic properties of WC and pure W and pyrocarbone (Fig. 1) for oxygen reduction illustrates the need for a solid-state physics approach to electrocatalysis.

Manuscript received Feb. 26, 1971.

Any discussion of this paper will appear in a Discussion Section to be published in the June 1972 JOURNAL.

REFERENCES

1. H. Binder, A. Köhling, W. Kuhn, W. Lindner, and G. Sandstede, *Nature*, **224**, 1299 (1969).
2. H. Böhm, *Electrochim. Acta*, **15**, 1273 (1970).
3. Kindly furnished by Dr. R. Funk from this laboratory.

Specific Adsorption of Sulfate Ions on Platinum

Sigmund Schuldiner* and Murray Rosen*

Electrochemistry Branch, Naval Research Laboratory, Washington, D. C. 20390

Balashova and Kazarinov (1) in an analysis of their radioactive tracer work concluded that there was some specific adsorption of sulfate ions on Pt at the potential of zero charge (p.z.c.). They further concluded that, in the potential range positive to the p.z.c., the amount of sulfate ion which is superequivalent (surface excess) to the surface charge on Pt was very slight. In the presence of adsorbed oxygen, they postulated that the bond of sulfate ions adsorbed on Pt was of a chemisorptive nature.

Accurate determinations of the double-layer capacitance, C, (2, 3) and of the potential of zero charge (1, 3,4) now give a direct method of determining the dependence of surface charge, $q_M = -\int_{p.z.c.}^{E} CdE$, on Pt with potential, E. Hence, any superequivalency of sulfate ion adsorption should be directly apparent from a comparison of q_M positive to the p.z.c. with Balashova and Kazarinov's [(1), Fig. 10] and of Schuldiner, Rosen, and Flinn's (5, 6) data on sulfate ion adsorption, $q_{SO_4^=}$, with potential. Figure 1 shows such comparisons.

The q_M curve shown in Fig. 1 is for 1M H_2SO_4 and was determined by graphically integrating under the C *vs.* E curves given in Ref. (2, 3) from the p.z.c. (0.23V) to a given E. Determination of q_M for lower concentrations of sulfuric acid would give lower values of q_M. However, for the referenced data (2, 3), the q_M values will be lowered only by less than 3 μC/cm^2. The Balashova and Kazarinov $q_{SO_4^=}$ results (1) were for 0.05M H_2SO_4 in N_2-saturated solution. All of the Schuldiner, Rosen, and Flinn $q_{SO_4^=}$ values (5, 6) were for 1M H_2SO_4 in H_2-saturated solutions. In these H_2-saturated solutions, there is no interference due to oxygen adsorption at potentials below 1.0V (6).

A comparison of the Balashova and Kazarinov $q_{SO_4^=}$ in Fig. 1 with q_M shows a superequivalency of sulfate ions at all potentials from the p.z.c. (0.23V) to 0.8V. At potentials above 0.8V, oxygen adsorption interferes with anion adsorption in the N_2-saturated Balashova and Kazarinov solution. The Schuldiner, Rosen, and Flinn $q_{SO_4^=}$ values (5, 6) generally confirm the superequivalency of sulfate ion adsorption and hence show significant specific adsorption of these anions. Oxygen atoms did not interfere for this latter case at potentials below 1.0V.

The $q_{SO_4^=}$ values for the Schuldiner, Rosen, and Flinn data represent the decrease in Pt sites available for the adsorption of oxygen atoms generated during

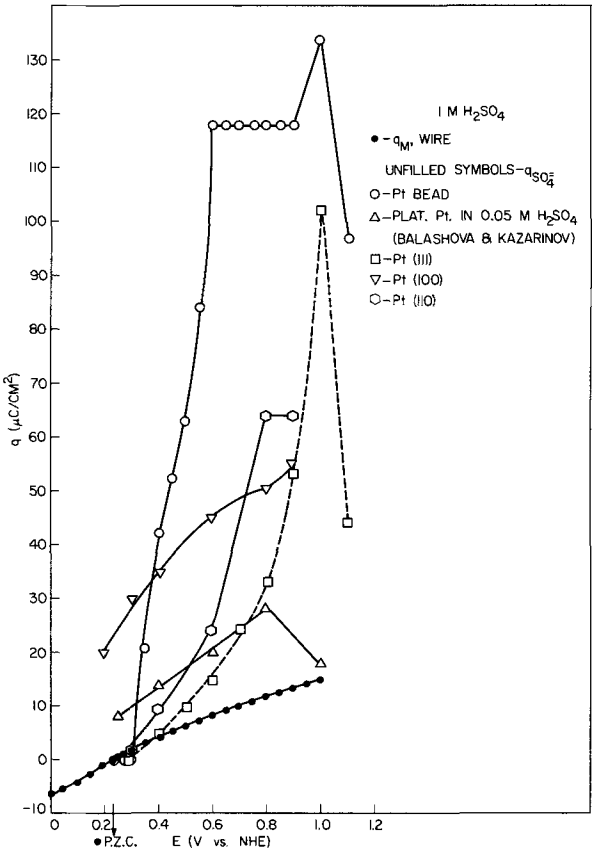

Fig. 1. Surface charge, q_M, compared to $q_{SO_4^=}$ for various Pt electrodes.

* Electrochemical Society Active Member.

Key words: anion adsorption, sulfate ion, platinum, double-layer capacitance, potential of zero charge, surface charge, surface excess.

rapid anodic charging; that is, based on the assumption that, for a bare Pt electrode, 420 $\mu C/cm^2$ of charge will be consumed to form one monolayer of oxygen atoms at 1.76V. When less charge is required, then that loss in charge is assumed to be due to the blocking of active Pt sites by $SO_4^=$ ions. The number of Pt sites which would be occupied by each sulfate ion is not known, and the assumed one-to-one correspondence may not hold, or indeed the ions may be bisulfate. If the sulfate ions are not specifically adsorbed, then the only important consideration is the net number of negative charges on the solution side of the double layer. It is difficult to see how sulfate ions which were not specifically adsorbed would block Pt sites. In any case, as high as ten times too many Pt sites are blocked as can be accounted for by q_M.

There are significant differences in the Balashova and Kazarinov data as compared to the Schuldiner, Rosen, and Flinn data. The latter not only show that the presence of H_2 increases the potential at which oxygen is first adsorbed, but also show that metallurgical factors are important. A twenty-time increase in the sulfuric acid concentration used by Balashova and Kazarinov may give a closer agreement with the 1M data shown in Fig. 1. However, there are significant variations that are due to the metallurgical differences between platinized Pt, bright polycrystalline Pt, and oriented faces of single Pt crystals. At the p.z.c. for the Pt wire, the platinized Pt shows a superequivalency of sulfate ions, as does the (100) oriented single Pt crystal. All of the other Pt electrodes show no significant excess of sulfate ions below 0.3V and, for the (111) orientation, no excess is found up to at least 0.4V. From these comparisons, it is apparent that the atom geometry, grain boundaries, dermasorbed and surface impurities associated with the metal, and stresses in the surface layers of Pt may affect both the p.z.c. and the *C vs. E* relation that thereby influences the specific adsorption of sulfate ions.

Manuscript received Jan. 25, 1971.

Any discussion of this paper will appear in a Discussion Section to be published in the June 1972 JOURNAL.

REFERENCES

1. N. A. Balashova and V. E. Kazarinov in "Electroanalytical Chemistry," Vol. 3, A. J. Bard, Editor, pp. 164-167, Marcel Dekker, New York (1969).
2. M. Rosen, D. R. Flinn, and S. Schuldiner, *This Journal*, **116**, 1112 (1969).
3. D. R. Flinn, M. Rosen, and S. Schuldiner, *Collection Czech. Chem. Commun.*, **36**, 454 (1971).
4. R. Burshtein, A. Pschenichnikov, and M. Shevchenko, *This Journal*, **113**, 1022 (1966).
5. S. Schuldiner, M. Rosen, and D. R. Flinn, *ibid.*, **117**, 1251 (1970).
6. S. Schuldiner, M. Rosen, and D. R. Flinn, *ibid.*, Paper submitted for publication.

Correction

In the paper "Electrodissolution Kinetics of Iron in Chloride Solutions, Part I. Neutral Solutions" by S. Asakura and Ken Nobe which appeared on pp. 13-18 in the January 1971 JOURNAL, Vol. 118, No. 1, on p. 18 the second paragraph under the Acknowledgment heading should read:

Manuscript received Dec. 12, 1969; revised manuscript received *ca.* Aug. 20, 1970.

JOURNAL OF THE ELECTROCHEMICAL SOCIETY

SOLID STATE SCIENCE

JULY 1971

Electrolytic Behavior of Yttria[1]

Jon Schieltz,[2,*] John W. Patterson,[*] and D. R. Wilder

Institute for Atomic Research and Departments of Ceramic Engineering and Metallurgy, Iowa State University, Ames, Iowa 50010

ABSTRACT

The electrolytic behavior of Y_2O_3 was investigated. Within the temperature range 700°-1000°C, there is no electrolytic domain ($t_{ion} \geqq 0.99$), however, a small ionic domain ($t_{ion} \geqq 0.5$) does exist and is defined within the following boundaries

$$\log P_{\oplus} = \frac{11{,}030}{T(°K)} - 15.84$$

and

$$\log P_{\ominus} = \frac{-35{,}300}{T(°K)} + 15.59$$

Yttrium sesquioxide, Y_2O_3, is the only known solid oxide of yttrium. At room temperature and under one atmosphere pressure it possesses the cubic rare earth type C structure (Ia3) (1, 2) with 16 sesquioxide formula units per unit cell. The C-type rare earth structure is almost identical to the fluorite structure (3, 4) except that the lattice points are slightly displaced and ¼ of the anions are missing to balance the trivalent cation charge. These open sites are aligned to form relatively open pathways that could serve as high conductivity paths for oxide ions. Therefore the emf measurements described below were undertaken to determine the log P_{O_2} and $1/T$ ranges, if any, wherein Y_2O_3 exhibits predominantly ionic conductivity (5-8).

Noddack and co-workers (9-11) determined the electrical conductivity of yttria, many of the rare earth oxides, and several rare earth oxide binary solid solutions and zirconia-yttria solid solutions. Their results suggested that Y_2O_3 is a predominant electronic conductor over the temperature range from 600° to 1200°C.

More carefully controlled conductivity measurements on yttria have been made by Tallan and Vest (12). The electrical conductivity of reportedly very pure, polycrystalline Y_2O_3 in controlled P_{O_2} atmospheres and temperatures from 1200° to 1600°C was obtained from guarded (3-probe) measurements with an a-c bridge. The data indicated that yttria is an amphoteric semiconductor over the temperature range 1200°-1600°C and oxygen partial pressures from 10^{-1}-10^{-17} atm. Within this region the ratio of ionic to electronic conductivity was determined to be less than 1% by a blocking electrode polarization technique. In the region of predominant hole conduction, the conductivity in ohm^{-1} cm^{-1} was expressed by the relationship

$$\sigma_{ac} = \sigma_{\oplus} = 1.3 \times 10^3 P_{O_2}^{3/16} \exp(-1.94/kT) \quad [1]$$

where 3/16 power pressure dependence was attributed to fully ionized yttrium vacancies. Polarization effects detected at lower temperatures indicated that the ionic transference number at $P_{O_2} = 10^{-15}$ atm was about 0.15 at 800°C and about 0.3 at 700°C, indicating mixed conduction in yttria below 900°C.

While investigating the defect structure of ThO_2-Y_2O_3 solid solutions, Subbarao *et al.* (13) measured the electrical conductivity of undoped yttria in air between 800° and 1400°C. The activation energy for conduction agreed quite well with that reported by Tallan and Vest (12).

In contrast to the conductivity measurements, galvanic cell emf measurements indicate a much higher ionic transference number for yttria. Such measurements by Schmalzried (6) and Tare and Schmalzried (14) indicate that the ionic domain boundaries for Y_2O_3 at 825°C are

$$\log P_{\oplus}(Y_2O_3, 825°C) = -4.2 \quad [2]$$

$$\log P_{\ominus}(Y_2O_3, 825°C) = -21.5 \quad [3]$$

These values imply that t_{ion} of Y_2O_3 is about 0.975 at $T = 825$°C and $P_{O_2} = 10^{-15}$. Subsequently Schmalzried's closed-end tube cell design (5, 6) was used by McPheeters *et al.* (15) who employed a Y_2O_3 tube as a solid electrolyte electrochemical cell for measuring oxygen activities in liquid sodium. The calibration curve given in the patent implies that Y_2O_3 has an ionic transference number of unity at extremely low oxygen activities in the temperature range from 400°-500°C.

The previously reported results for Y_2O_3 are compared in Fig. 1 which also shows the log P_{O_2} *vs.* $1/T$ trajectories corresponding to Na,Na_2O coexistence and various concentration levels of oxygen dissolved in liquid Na.[3] The log $P_{\ominus}$, $1/T$ boundary (A) is estimated conservatively from the work of McPheeters

[1] Work supported by the Aerospace Research Laboratories, Office of Aerospace Research, United States Air Force, Contract F33615 68 C 1034, and by the Ames Laboratory of the U.S. Atomic Energy Commission, Contract W-7405-eng-82.

[2] Present addriess: Tektronix Inc., Integrated Circuit Engr., P.O. Box 500, Beaverton, Oregon 97005.

* Electrochemical Society Active Member.

Key words: yttria, solid electrolyte, ionic conductivity, ionic domain.

[3] To avoid unnecessary duplication later, Fig. 1 also shows the log $P_{\oplus}$, the p to n transition and the log $P_{\ominus}$ lines deduced in the present study and discussed below.

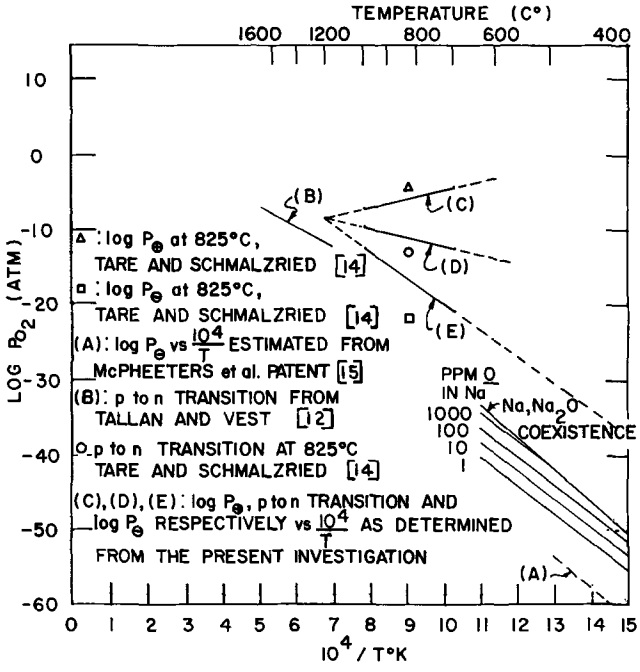

Fig. 1. Comparison of ionic domain boundary data for undoped Y_2O_3.

et al. (15) by placing (A) 7 log units below the 10 ppm trajectory. The data reported by Tallan and Vest (12) cannot be quantitatively converted into log $P_\oplus$ and log $P_\ominus$ domain boundaries without considerable additional assumptions regarding the temperature dependence of the ionic conductivity of Y_2O_3. However, the p-type to n-type conductivity transition line was deduced from their conductivity minima (12) and is shown on Fig. 1 as line (B).

Since no investigation was known to have established the ionic domain and electrolytic domain boundaries for Y_2O_3 over a range of temperatures, the present emf study was undertaken to determine the temperature dependence of the ionic domain boundaries log $P_\oplus$ and log $P_\ominus$ for Y_2O_3 over the temperature range from 700° to 1000°C.

Experimental Procedure

The yttrium sesquioxide used was supplied by the Ames Laboratory as an oxide calcination product of hydrated yttrium oxalate. A spectrographic analysis is given in Table I. The oxide was wet ground for 1 hr in a porcelain ball mill using distilled water as the liquid medium and dried to a powder. Spectrographic analysis failed to detect any contamination from the milling. Analysis showed the average agglomerate size to be 5-10μ with a crystallite size of 0.1-0.2μ. A theoretical density of 5.030 g/cm^3 was calculated from a lattice parameter of 10.6066Å which was determined from several x-ray patterns.

Table I. Spectrographic analysis of Y_2O_3

Element	Concentration (ppm)
Ca	20
Mg	20
Si	200
Fe	35
Na	Faint trace
Cu	20
Ti	30
Ta	<200
Al	100
Co	<35
Yb	<100
Er	<100
Ho	<60
Dy	<100
Gd	<100
Tb	<200
Sm	<250
Total	1570

Sample batches were prepared by four different methods:

(*a*) Samples were prepressed at 1800 psi in a ¾ in. diam double action steel die lined with tungsten carbide. The prepressed disks were isostatically pressed to 50,000 psi and sintered in a covered yttria crucible at 1850°C for 1 hr in an oxidizing atmosphere. The final bulk densities ranged from 85 to 90% of theoretical density.

(*b*) Prepressed ¾ in. diameter specimens were sintered in argon for one hour at 2000°C. Bulk densities were 90-95% of theoretical with a significant amount of closed porosity.

(c) Samples were hot pressed in graphite dies to achieve densities approaching theoretical. Densification was done at 1600°C and a pressure of 3300 psi for 15 min. After the samples were annealed (oxidized) in air at 1200°C for one week, the densities were greater than 99% of theoretical.

(*d*) Slip casting was also used to fabricate several disks. The slip was cast and allowed to stand 1 min. The slip-cast disks were prefired in air at 1000°C, and finally sintered in argon for 1 hr at 1900°C. Densities were greater than 97% of theoretical. This method gave the most reproducible densities and the specimens appeared translucent.

After firing, all specimens were diamond ground to produce parallel faces. Figure 2 shows typical microstructures for methods (*a*), (c), and (*d*). Argon sintering at 2000°C yields microstructures highly similar to air sintering at 1850°C.

The cell assembly and furnace chamber are essentially those described by Hardaway *et al.* (16). Cell assemblies employing reversible metal-metal oxide electrodes were contained in an inert atmosphere of purified helium. The tank helium was passed through a Pyrex gas purification train with the following reaction chambers in series: activated BTS Catalyst at 160°C; a mixture of activated alumina, Drierite, and Anhydrone; Ascarite; and a liquid nitrogen cold trap. For controlled atmospheres of high oxygen pressures, dried tank oxygen, dried air, and He/O_2 ratios of 10

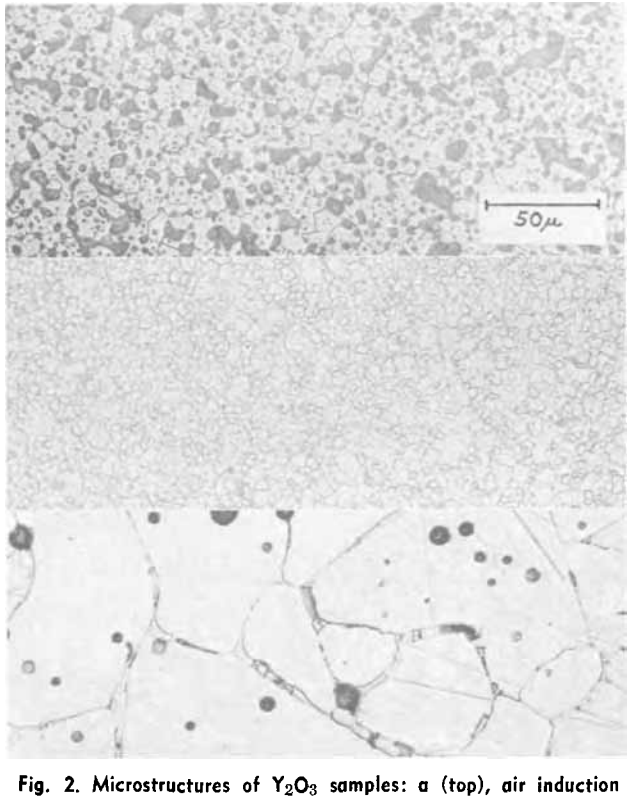

Fig. 2. Microstructures of Y_2O_3 samples: a (top), air induction fired, 280X; b (middle), hot pressed, 280X; c (bottom) slip cast, 280X.

Table II. Equilibrium oxygen activities for reversible electrodes

Electrode	Standard free energy change (cal/mole O_2)	$-\text{Log } P_{O_2}$(atm) at 1000°C	Reference
Cu-Cu_2O	$-79{,}850 + 34.2T$	6.24	17
Ni-NiO	$-111{,}930 + 40.6T$	10.34	18
Co-CoO	$-112{,}950 + 34.4T$	11.88	19
Y-Y_2O_3	$-279{,}500 + 48.1T$	37.46	20

and 100 were established with the help of a calibrated Matheson Gas Proportioner. Low oxygen partial pressures were established by CO_2-CO mixtures also controlled by the gas proportioner.

Open-circuit emf measurements were made using reversible metal-metal oxide electrodes with cells of the type

$$\text{Pt;M,MO/}Y_2O_3\text{/M',M'O;Pt} \qquad \text{(Cell I)}$$

where M,MO and M',M'O represent mixtures of dissimilar metals with their respective oxides.

The reversible electrode mixtures were prepared to give a 10:1 molar ratio of metal to metal oxide at equilibrium. Equilibrium oxygen activities for the reversible metal-metal oxide electrodes used in this investigation are listed in Table II.

Fe-FeO was eliminated as a possible electrode material since it was found to react with Y_2O_3 to form the compound $YFeO_3$ as pointed out by Worrell (21).

Results

Figure 3 shows the raw data obtained from the emf cell investigated. The distances between the dotted lines on Fig. 3 indicate the thermodynamic emf's for the corresponding reversible electrodes, *i.e.* the emf's that would result if the yttria specimen had t_{ion} unity. In all cases the measured emf's fell significantly short of the thermodynamic values.

The following cells were employed to study Y_2O_3 at low oxygen activities

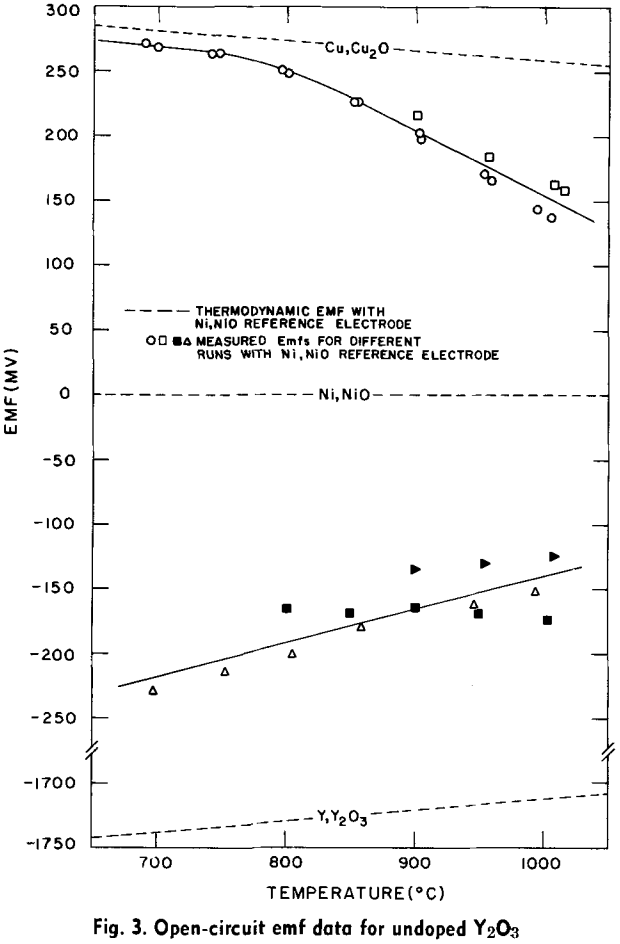

Fig. 3. Open-circuit emf data for undoped Y_2O_3

$$\text{Ni,NiO/}Y_2O_3\text{/Y,}Y_2O_3 \qquad \text{(Cell II)}$$

and

$$\text{Co,CoO/}Y_2O_3\text{/Y,}Y_2O_3; \qquad \text{(Cell III)}$$

however, reliable emf's were not obtained from Cell III. The emf data from Cell II are plotted as distances below the Ni,NiO dotted line. No data from Cell III are shown.

The cell

$$\text{Ni,NiO/}Y_2O_3\text{/Cu,}Cu_2O \qquad \text{(Cell IV)}$$

was used to study galvanic emf's from yttria under relatively oxidizing conditions. Emf's from this cell are plotted as distances above the Ni,NiO dotted line. Below 800°C the open circuit emf almost paralleled the thermodynamic emf based on Cu-Cu_2O equilibrium, whereas increasing the temperatures above 800°C caused the measured emf's to systematically decrease with respect to the thermodynamic values. Qualitatively, this behavior indicates that $P_\oplus$ is on the order of P_{O_2} for Cu,Cu_2O coexistence and, in fact, that $P_\oplus$ crosses the Cu,Cu_2O coexistence line.

To interpret the open circuit emf's quantitatively in terms of $P_\oplus$ and $P_\ominus$ values at various temperatures, an elaborate trial and error procedure was employed. The over-all procedure determines the linear function for log $P_\oplus$ and log $P_\ominus$ *vs.* $1/T$ which yields the closest fit of the observed emf data according to Schmalzried's equation (6)

$$E = \frac{RT}{\mathbf{F}w}\left\{ \ln \left| \frac{1 + w + 2\beta}{1 + w + 2\alpha} \right| + \ln \left| \frac{1 - w + 2\alpha}{1 - w + 2\beta} \right| \right\}_{P'_{O_2}}^{P''_{O_2}} \qquad [4]$$

where the reversible electrode P_{O_2} values P'_{O_2} and P''_{O_2} can be calculated from Table II and where

$$w = \{1 - 4[P_\ominus/P_\oplus]^{1/4}\}^{1/2} \qquad [5]$$

$$\alpha = [P'_{O_2}/P_\oplus]^{1/4} \qquad [6]$$

$$\beta = [P''_{O_2}/P_\oplus]^{1/4} \qquad [7]$$

A first approximation to log $P_\ominus$ was obtained from the following simplified form of Eq. [4]

$$E = \frac{RT}{4\mathbf{F}} \ln \frac{P''_{O_2}}{P_\ominus} \qquad [8]$$

where E is the emf measured from cell II, T is the temperature of the emf measurement and P''_{O_2} is the P_{O_2} for Ni,NiO coexistence. A least squares fit of these log $P_\ominus$ values to the formula

$$\log P_\ominus = A_\ominus + B_\ominus/T \qquad [9]$$

gives values for $A_\ominus$ and $B_\ominus$.

Next the measured emf's of cell IV are considered. Equation [9] was used to calculate the $P_\ominus$ value corresponding to each emf measurement from cell IV. This value of $P_\ominus$ was then inserted into Eq. [4] with P''_{O_2} and P'_{O_2} now set equal to the coexistence values for Cu,Cu_2O and Ni,NiO equilibrium respectively. The value of $P_\oplus$ was then adjusted until the calculated emf matched the value measured from cell IV at each experimental temperature. These $P_\oplus$ values were then fitted to the formula

$$\log P_\oplus = A_\oplus + B_\oplus/T \qquad [10]$$

to obtain best fit values for $A_\oplus$ and $B_\oplus$. Thus an approximate value of $P_\oplus$ could be calculated for each emf measurement made on cell II. This value of $P_\oplus$ was put into Eq. [4] with P'_{O_2} corresponding to Y,Y_2O_3 coexistence and P''_{O_2} corresponding to Ni,NiO coexistence. The value of $P_\ominus$ was then adjusted until the emf calculated from Eq. [4] matched the value measured from cell II at each temperature. This provides a new set of log $P_\ominus$ values to replace the first approximations and hence completes one full cycle of the iter-

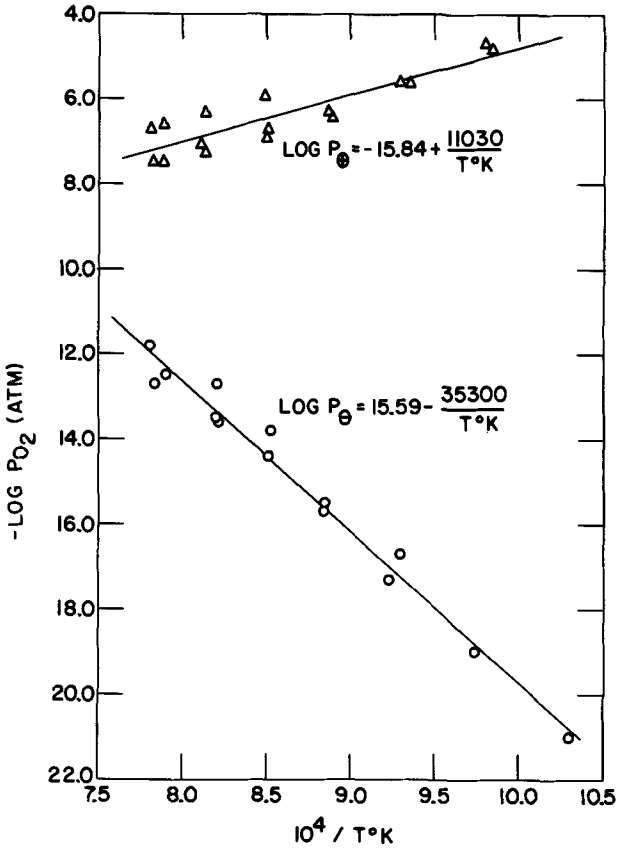

Fig. 4. Ionic domain boundaries for undoped Y_2O_3

ation scheme. This iteration cycle was repeated until the successive values of log $P_\oplus$ and log $P_\ominus$ changed by less than 0.1 at each experimental temperature. The resulting values are plotted in Fig. 4. The final least squares best fit values for the A and B parameters gave the following analytical expressions

$$\log P_\oplus = \frac{11{,}030}{T(°K)} - 15.84 \qquad [11]$$

$$\log P_\ominus = \frac{-35{,}300}{T(°K)} + 15.59 \qquad [12]$$

Values of t_{ion} of Y_2O_3 as a function of P''_{O_2} were calculated from Eq. [11], [12], and the formula

$$t_{ion} = [1 + [P''_{O_2}/P_\oplus]^{1/4} + [P''_{O_2}/P_\ominus]^{-1/4}]^{-1} \qquad [13]$$

for T = 1000°, 900°, 800°, 700°, and 400°C. The results are summarized in Fig. 5 which illustrates that t_{ion} is less than 0.99 at all P_{O_2} values between 700° and 1000°C.

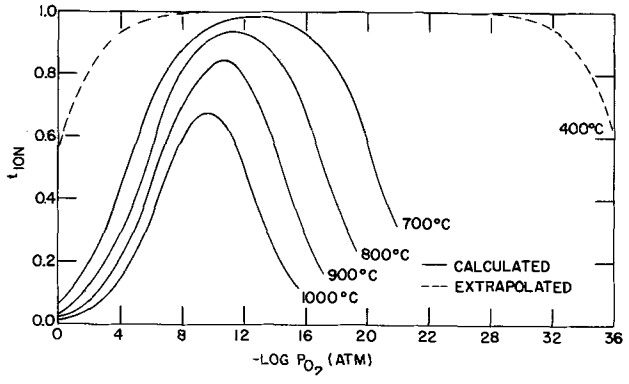

Fig. 5. Ionic transference number of undoped Y_2O_3 as a function of oxygen partial pressure determined from emf measurements.

Discussion

Figure 1 compares the ionic domain boundaries for Y_2O_3 determined by the present study with the previously reported results. The discrepancy between the present results and those reported by Tare and Schmalzried (14) is relatively minor but exceeds the scatter of points shown in Fig. 4. The p to n transition line deduced from Tallan and Vest conductivity minima (12) disagrees more significantly with the present study in which the p to n transition line is taken to be the locus of points equidistant between log $P_\oplus$ and log $P_\ominus$ at each temperature. Qualitatively the present study confirms the increase in t_{ion} with decreasing temperature that was suggested by Tallan and Vest (12). Since none of the yttria specimens used by Tare and Schmalzried, Tallan and Vest and none of those in the present study were intentionally doped, it is conceivable that the discrepancies are due to relatively minor differences in the concentrations of impurities.

The discrepancy between the present results and the results of McPheeters *et al.* (15) requires more discussion. Extrapolation of the present ionic domain boundary results to the 400°-500°C temperature range shows that the log P_{O_2} 1/T domain of liquid Na with dissolved oxygen is substantially below log $P_\ominus$. Because t_{ion} would be essentially zero, this means that no meaningful emf's should be observed from high purity Y_2O_3 electrolytes under the conditions reported by McPheeters *et al.* The following possible explanations of this discrepancy can be offered.

First of all the straight line extrapolation of log $P_\ominus$ is valid only as long as no transformations occur which can alter the conduction mechanisms for ionic and/or electronic transport. However a first order phase transformation would alter both types of conduction significantly, producing a discontinuity in the log $P_\ominus$ boundary and in its slope at the transformation temperature. Since no first order phase transformation for Y_2O_3 is known to occur in Y_2O_3 between 1000° and 500°C this possibility would seem to be ruled out at present.

However a significant change in slope of the log $P_\ominus$ line can occur if the iso-P_{O_2} activation energies of either the oxygen ion or the electronic conduction modes changes in an intermediate temperature range (8). Since this can occur without a first order phase transformation, such a possibility can not be ruled out until emf measurements of the type described above, are carried out over the intermediate temperature ranges.

Another explanation is the possibility that sodium ions from the liquid sodium electrodes dissolved as substitutional ions into the Y_2O_3 tube used in McPheeters' *et al.* study. The valence difference between Na and Y ions could greatly enhance the concentration of oxygen vacancies, much as substitutional Y ions do in the oxide solid electrolyte ZrO_2 + 7.5 m/o Y_2O_3. This would require substantial solubility and diffusivity for Na in Y_2O_3 at the low temperatures. The observed inertness of Y_2O_3 to liquid Na would seem to rule out this possibility; however a mixed conduction galvanic cell investigation of Y_2O_3-Na_2O solid solutions may be in order.

Conclusion

Undoped Y_2O_3 is a mixed conductor showing a narrow ionic conduction domain ($t_{ion} \geqq 0.5$) but no electrolytic domain ($t_{ion} \geqq 0.99$) within the temperature range (700°-1000°C) studied. The ionic domain boundaries for Y_2O_3 may be represented by

$$\log P_\oplus = \frac{11{,}030}{T(°K)} - 15.84$$

and

$$\log P_\ominus = \frac{-35{,}300}{T(°K)} + 15.59$$

Manuscript submitted Oct. 28, 1970; revised manuscript received ca. Feb. 8, 1971.

Any discussion of this paper will appear in a Discussion Section to be published in the June 1972 JOURNAL.

REFERENCES

1. J. Besson, C. Desportes, and G. Roberts, *Paris Acad. Sci.*, Ser. C, **262**, 527 (1966).
2. H. A. Johansen and J. G. Cleary, *This Journal*, **111**, 100 (1964).
3. B. G. Hyde, D. J. M. Bevan, and L. Eyring, "Intern. Conf. on Electron Diffraction and the Nature of Defects in Crystals," pp. II e 4-5, Pergamon Press, New York (1965).
4. L. Eyring, USAEC Rept. COO-1109-26, Chicago Operations Office (1966).
5. H. Schmalzried, *Z. Elektrochem.*, **66**, 572 (1962).
6. H. Schmalzried, *Z. Physik. Chem.*, NF **38**, 87 (1963).
7. R. A. Rapp and D. A. Shores, "Techniques in Metals Research IV," Chapter VI C, Interscience Publishers (1970).
8. J. W. Patterson, *This Journal*, **118**, 1039, (1971).
9. W. Noddack, H. Walch, and W. Dobner, *Z. Physik. Chem.*, **231**, 180 (1959).
10. W. Noddack and H. Walch, *ibid.*, **211**, 194 (1959).
11. W. Noddack and H. Walch, *Z. Elektrochem.*, **63**, 269 (1959).
12. N. M. Tallan and R. W. Vest, *J. Am. Ceram. Soc.*, **49**, 401 (1966).
13. E. C. Subbarao, P. H. Sutter, and J. Hrizo, *ibid.*, **48**, 443 (1965).
14. V. B. Tare and H. Schmalzried, *Z. Physik. Chem.*, NF **43**, 30 (1964).
15. C. C. McPheeters, J. C. McGuire, and R. Tercovich, U.S. Pat. 3,309,233, March 14, 1967.
16. J. B. Hardaway, III, J. W. Patterson, J. D. Schieltz, and D. R. Wilder, "The Ionic Domain for Yttria Doped Thoria at Low Oxygen Activities," *J. Am. Ceram. Soc.*, **50**, (1971).
17. F. E. Rizzo, L. R. Bidwell, and D. E. Frank, *Trans. Met. Soc. AIME*, **239**, 593 (1967).
18. C. B. Alcock, Editor, "Electromotive Force Measurements in High-temperature Systems," pp. 3-27, American Elsevier Publishing Company, Inc., New York (1968).
19. K. Kiukkola and C. Wagner, *This Journal*, **104**, 379 (1957).
20. J. P. Coughlin, U.S. Bureau of Mines Bull., 542 (1954).
21. W. L. Worrell in "Thermodynamics I," pp. 131-143 IAEA, Vienna, Austria (1966).

High-Conductivity Solid Electrolytes: C_aH_bNI-AgI Double Salts

Boone B. Owens,* J. H. Christie,[1] and G. Trent Tiedeman[2]

Gould Ionics Inc., Canoga Park, California 91304

ABSTRACT

Substituted ammonium iodides combine with silver iodide to form solid electrolytes that exhibit high ionic conductivities at ambient temperature. The formation of conductive compounds is related to the size of the organic ammonium ion. Results are given for a large number of syntheses.

With the recent discoveries of high-conductivity solid electrolyte materials (1-5) there has been a renewed interest in the field of solid-state electrolytes and related electrochemical devices. Previously, high-conductivity solid materials were known only at elevated temperatures. The largest group of solid electrolytes that has been reported is the tetraalkylammonium iodide-silver iodide group (5). Ten compounds were reported that have ionic conductivities in the range of 8×10^{-4} to 6×10^{-2} (ohm cm)$^{-1}$ at 22°C and electronic conductivities of less than 10^{-10} (ohm cm)$^{-1}$. In order to extend the area of investigation of solid electrolytes, the present study of the electrical properties of the products formed between silver iodide and hydrocarbon substituted ammonium iodides, C_aH_bNI (a and b are integers), was undertaken.

Experimental

Mallinckrodt silver iodide (nominally 99% pure) was used without further purification. The substituted ammonium iodide salts QI were obtained commercially from either Eastman Organic Chemicals, Division of Eastman Kodak Company, or Aldrich Chemical Company, Inc., or else were prepared from reagents obtained from these suppliers. The reported purities of the organic materials were in the range of 95-99%; these materials were used without further purification.

Where it was necessary to synthesize the substituted ammonium iodides, they were made by combining the suitable amine with an alkyl iodide. The conducting electrolytes were prepared by combining AgI with QI, as previously described (5), in the molar ratio of n

$$QI + n\,AgI \rightarrow Q\,Ag_nI_{n+1}$$

The method for determining the conductivity has been previously described in some detail (5, 6). The resistance cells were ½ in. diameter pressed powder pellets containing the three layers, Ag, $RbAg_4I_5$/Sample/Ag,$RbAg_4I_5$. Sample weights were normally 2g which resulted in resistance values ranging from about 4 ohms for products with specific conductivities of 0.07 (ohm cm)$^{-1}$ up to $> 10^6$ ohms for nonconductive products. Contact resistance can contribute significantly to the total cell resistance; it was reported for $RbAg_4I_5$ that 0.3 ohm (or 30%) of the cell resistance was due to contact resistance (6). The reproducibilities of the resistance measurements on identical samples of the tetraalkylammonium iodide-silver iodide salts were observed to be about 10-25%. The results of the present study (in which the contact resistance was not measured) are estimated to be accurate to about ± 30%.

The phase diagrams for the 58 binary salt systems investigated here have not been reported; therefore the selection of compositions for resistance measurements is somewhat arbitrary. The five organic ammonium iodide-silver iodide systems for which the composition-conductivity function has been determined formed conductive phases at compositions of between 80 and 90 m/o (mole per cent) silver iodide

* Electrochemical Society Active Member.

[1] Present address: Colorado State University, Chemistry Department, Ft. Collins, Colorado 80521.

[2] Present address: Weyerhaeuser Research, 3400 13th Avenue, S.W., Seattle, Washington 98134.

Key words: conductivity, quaternary ammonium iodide, silver iodide, solid electrolyte, solid-state electrochemistry, substituted ammonium iodide, tetraalkylammonium iodide.

(5, 7, 8). It was assumed in the present investigation that if conductive phases are formed, they would contain this same amount of silver iodide. In general, then, the conductive products must be assumed to contain a resistive phase as well as the conductive phase. Further detailed investigation of each of the binary systems reported here is necessary to determine the precise stoichiometry of the conducting phases. (The only structure known is that of $[(CH_3)_4N]_2Ag_{13}I_{15}$ which was reported by Geller and Lind (7).) The purpose of the present investigation was to determine the extent of the formation of conductive compounds between silver iodide and hydrocarbon substituted ammonium iodide salts as a function of the substituted ammonium ion, and did not require preparation of single-phase products.

Densities were measured only for the most electrically conductive products. This was done as previously described (5). Where the densities were not measured, the reported specific conductivities were calculated from the sample resistance and an approximate density.

Results and Discussion

The set of hydrocarbon substituted ammonium iodide salts was divided into the following subsets for the present study:

Subset 1—Completely substituted acyclic alkyl ammonium iodide (*e.g.*, Me_4NI).
Subset 2—Partially substituted acyclic ammonium iodide (*e.g.*, MeH_3NI).
Subset 3—Saturated azacyclic substituted ammonium iodide (*e.g.*, pyrrolidinium iodide).
Subset 4—Unsaturated azacyclic substituted ammonium iodide (*e.g.*, pyridinium iodide).
Subset 5—Carbocyclic, aryl, benzyl or allyl substituted ammonium iodides.

This breakdown of hydrocarbon substituted ammonium iodide salts is based partially on structural groups and partially on the availability of materials for test. The selection of compounds was sufficient to permit the testing of the extent to which conductive electrolytes $C_aH_bNI \cdot nAgI$ are formed and to form some empirical rules governing the formation of conductors.

Subset 1, the acyclic tetraalkylammonium iodide-silver iodide electrolytes, has already been reported (5). The results for our investigation of subset 2 are given in Table I. Without exception, no conductive electrolytes were formed between AgI and the partially substituted acyclic alkyl ammonium iodides, in direct opposition to what we would have expected based on results obtained with both ammonium iodide (3, 4) and the acyclic tetraalkylammonium iodides (5). Apparently, in the acyclic alkyl ammonium ions, the presence of an N-H bond introduces enough asymmetry or polarity to prevent its stabilizing the iodide anion lattice into a structure permitting high Ag^+ ion mobility (7, 8).

Subset 3 is characterized by the presence of at least one saturated azacyclic group in the ammonium ion which may be completely or partially substituted. The results are given in Table II. All of these compounds formed conductive products, relative to the silver iodide conductivity (5) of 3×10^{-4} (ohm cm)$^{-1}$. The highest value of 0.06 (ohm cm)$^{-1}$ was found with the three completely substituted ammonium ions.

Subset 4, the unsaturated azacyclic substituted ammonium ions, includes the heterocyclic pyridinium and quinolinium ions with varying numbers of alkyl groups substituted onto the rings. Results are tabulated in Table III. As shown there, eight conductors had $\sigma > 10^{-2}$ (ohm cm)$^{-1}$, eight conductors had $10^{-2} > \sigma > 10^{-3}$ (ohm cm)$^{-1}$, and seven nonconductors had $\sigma < 10^{-4}$ (ohm cm)$^{-1}$.

Subset 5 contains all remaining compounds $C_aH_bNAg_nI_{n+1}$ that were investigated and includes several groups as previously indicated. Results are given in Table IV.

Composition dependence of conductivity.—The effect of composition on the conductivity was determined for the binary system dimethylpyrrolidinium iodide-silver iodide. This study followed the procedure for binary systems that was previously reported (5). The results are given in Table V; the maximum value of 0.065 (ohm cm)$^{-1}$ occurred at 88 m/o AgI, in agreement with prior studies wherein the cation substituted silver iodide solid electrolytes contained 80-90 m/o AgI (4-8).

Temperature dependence of conductivity.—The temperature dependence of the conductivity was determined for some of the more conductive members of this group. Results for 1,1-dimethylpyrrolidinium silver iodide and 3,5-dimethylpyridinium silver iodide (at the stoichiometry QAg_7I_8) are shown in Fig. 1, with previously reported results for other solid electrolytes (5). As seen, the conductivities of these compounds are very similar to those of the tetraalkylammonium silver iodide solid electrolytes, with activation energies of 3 to 4 kcal/mole. The results for 3,5-dimethylpyridinium silver iodide, exhibit an increasing activation energy at low temperatures, which suggests

Table I. Electrical conductivity of partially substituted acyclic alkyl ammonium iodide-silver iodide compounds $C_aH_bNI \cdot nAgI$ at 22°C

Name of substituted ammonium ion	*a*	*b*	*n*	σ (ohm cm)$^{-1}$
Methylammonium	1	6	6	2×10^{-5}
Ethylammonium	2	8	6	2×10^{-5}
Trimethylammonium	3	10	6	6×10^{-5}
Diethylammonium	4	12	4	1×10^{-5}
Diethylmethylammonium	5	14	4	4×10^{-5}
Triethylammonium	6	16	6	1×10^{-6}

Table II. Electrical conductivity of saturated azacyclic substituted ammonium iodide-silver iodide compounds $C_aH_bNI \cdot nAgI$ at 22°C

Name of substituted ammonium ion	*a*	*b*	*n*	σ (ohm cm)$^{-1}$
Pyrrolidinium	4	10	8	5×10^{-3}
Piperidinium	5	12	8	2×10^{-2}
1-Methylpyrrolidinium	5	12	8	8×10^{-3}
1,1-Dimethylpyrrolidinium	6	14	7	6×10^{-2}
Quinuclidinium	7	14	6.7	6×10^{-2}
1,1-Dimethylpiperidinium	7	16	8	6×10^{-2}
N-Methylquinuclidinium	8	16	6.7	5×10^{-2}
5-Azoniaspiro[4.4]nonane	8	16	6.7	2×10^{-2}
5-Azoniaspiro[4.5]decane	9	18	6.7	6×10^{-3}
6-Azoniaspiro[5.5]undecane	10	20	6.7	6×10^{-3}
1-Butyl-1-methylpiperidinium	10	22	8	8×10^{-4}

Table III. Electrical conductivity of unsaturated azacyclic substituted ammonium iodide-silver iodide compounds $C_aH_bNI \cdot nAgI$ at 22°C

Name of substituted ammonium ion	*a*	*b*	*n*	σ (ohm cm)$^{-1}$
Pyridinium	5	6	8	4×10^{-2}
3-Methylpyridinium	6	8	6.7	4×10^{-2}
1-Methylpyridinium	6	8	6	1×10^{-2}
1,3-Dimethylpyridinium	7	10	6.7	3×10^{-2}
3,5-Dimethylpyridinium	7	10	6.7	2×10^{-2}
2,6-Dimethylpyridinium	7	10	6.7	5×10^{-3}
1,2,6-Trimethylpyridinium	8	12	6.7	2×10^{-2}
3,4,6-Trimethylpyridinium	8	12	6.7	2×10^{-5}
1,3,5-Trimethylpyridinium	8	12	6.7	1×10^{-3}
Quinolinium	9	8	8	4×10^{-3}
1,2,4,6-Tetramethylpyridinium	9	14	6.7	3×10^{-2}
1,2,3,6-Tetramethylpyridinium	9	14	6.7	2×10^{-3}
1-Methylquinolinium	10	10	4	1×10^{-2}
1-Methyl-1,2,3,4-tetrahydroquinolinium	10	14	6.7	6×10^{-3}
2-Methyl-1,2,3,4-tetrahydroquinolinium	10	14	6.7	4×10^{-5}
1-Ethylquinolinium	11	12	4	5×10^{-3}
1,2-Dimethylquinolinium	11	12	6.7	3×10^{-3}
1,2-Dimethyl-1,2,3,4-tetrahydroquinolinium	11	16	6.7	3×10^{-3}
1,1-Dimethyl-1,2,3,4-tetrahydroquinolinium	11	16	6.7	2×10^{-3}
2,2-Dimethyl-1,2,3,4-tetrahydroisoquinolinium	11	16	6.7	4×10^{-5}
1-Ethyl-2-methylquinolinium	12	14	6.7	1×10^{-4}
1-Ethyl-2,6-dimethylquinolinium	13	16	6.7	2×10^{-3}
N-Methylphenanthridinium	14	12	6.7	1×10^{-5}

Table IV. Electrical conductivity at 22°C of substituted ammonium iodide-silver iodide compounds $C_aH_bNI \cdot nAgI$ containing carbocyclic, aryl, benzyl, or allyl groups

Name of substituted ammonium ion	a	b	n	σ (ohm cm)$^{-1}$
(Saturated carbocyclic groups)				
Cyclopentylammonium	5	12	6.7	1×10^{-4}
Cyclopropyltrimethylammonium	6	14	6.7	2×10^{-2}
Cyclohexylammonium	6	14	8	8×10^{-3}
Cyclopentyltrimethylammonium	8	18	6.7	1×10^{-3}
Cyclohexyltrimethylammonium	9	20	6.7	5×10^{-1}
Butylcyclohexyldimethylammonium	12	26	8	3×10^{-5}
1-Adamantyltrimethylammonium	13	24	6.7	2×10^{-3}
(Unsaturated hydrocarbon groups)				
4-Methyl-4-azoniacyclohexene	6	12	6.7	6×10^{-2}
Allyltrimethylammonium	6	14	6.7	3×10^{-2}
4,4-Dimethyl-4-azoniacyclohexene	7	14	6.7	4×10^{-2}
(Aryl group)				
Phenylammonium	6	8	8	4×10^{-3}
Trimethylphenylammonium	9	14	4	8×10^{-3}
Ethyldimethylphenylammonium	10	16	4	5×10^{-3}
(Benzyl groups)				
Benzylammonium	7	10	4	5×10^{-6}
Benzyltrimethylammonium	10	16	8	1×10^{-2}
1-Benzylpyridinium	12	12	4	1×10^{-3}
1-Benzylquinolinium	16	14	4	1×10^{-4}

Table V. Density and specific conductivity of binary solid electrolyte system 1, 1-dimethylpyrrolidinium iodide-silver iodide at 22°C

Silver iodide, m/o	Density[a] (g/cc)	Specific conductivity[b] (ohm cm)$^{-1}$
0	1.68	~10^{-8}
66.7	3.26	~10^{-8}
75	(3.70)	1.3×10^{-3}
80	3.99	6.7×10^{-3}
85	(4.37)	4.1×10^{-2}
86	(4.45)	4.8×10^{-2}
87	(4.55)	6.2×10^{-2}
88	(4.62)	6.5×10^{-2}
89	4.69	5.4×10^{-2}
90	(4.78)	4.4×10^{-2}
100	5.76	3×10^{-4}

[a] Interpolated values are in brackets.
[b] Lower limit of measurement was ~10^{-8} (ohm cm)$^{-1}$.

that a phase transformation occurs near −50°C. However, the 1,1-dimethylpyrrolidinium iodide was still conductive at −50°C, with a value of 0.01 (ohm cm)$^{-1}$.

Size parameter.—The results that have been reported show that in this large set of AgI-QI compositions, where Q^+ is $C_aH_bN^+$, many highly conductive products are formed. It was of some interest to determine what structural parameters of the Q^+ ion determine the stability or existence of a conductive QAg_nI_{n+1} compound. The original postulate that was tested in the present study stated simply that high-conductivity solid electrolytes would be complex salts of the type $MX \cdot nAgI$ (5). Sufficient data on salts of empirical formula QAg_nI_{n+1} have now been obtained to permit a limited evaluation of the effect of Q^+ on electrical properties of the product salts.

In the group of solid electrolytes MAg_4I_5, the conductive structure was formed by $M^+ = K^+$, Rb^+, and NH_4^+ (4). Partial occupancy of the M^+ sites by Cs^+ was also permitted but no Na^+, Li^+, or $N(CH_3)_4^+$ occupancy was observed. The size of the monovalent alkali metal type cation appeared to be the parameter determining whether a stable MAg_4I_5 structure was formed. Therefore, in the present study one would logically consider the role of ionic size. However, since the Q^+ ions are complex and include species such as trimethylhexadecylammonium, pyridinium, and cyclohexyltrimethylammonium, there is considerable flexibility and ambiguity in assigning a radius to each of these ions. In the QAg_nI_{n+1} compounds formed by the homologous series of acyclic tetraalkylammonium ions there was a fairly straightforward separation of conductors from insulators. The conductivity dropped by a factor of 10^4 as the ion formula went from $C_9H_{22}N^+$ to $C_{10}H_{24}N^+$ (5). This result would indicate that there is a fairly critical volume effect in these compounds, since the ionic size would be expected to be a monotonically increasing function of molecular weight (M), with some corrections for isomer structural differences. A plot of the log of the conductivity *vs.* formula weight of QI for all of these materials investigated is shown in Fig. 2. A division between conductors and nonconductors occurs at a formula weight of about 290 g/mole for QI. As previously stated, partially substituted alkylammonium iodides formed no conductors whereas the completely substituted tetraalkylammonium iodides (up to $C_9H_{22}NI$) all form conductors. Some similarity to this apparent effect of an N-H bond is noted in subset 5 where the partially substituted cyclopentylammonium iodide and benzylam-

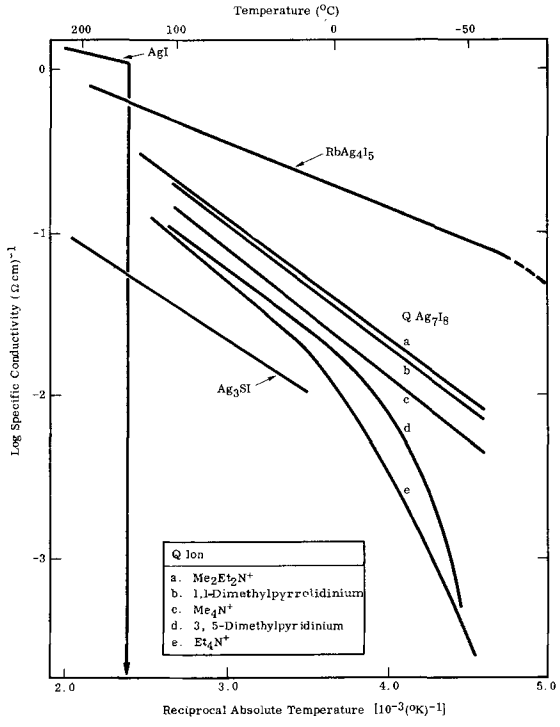

Fig. 1. Temperature dependence of specific conductivity of 1,1-dimethylpyrrolidinium silver iodide and 3,5-dimethylpyridinium silver iodide from −50° to 100°C.

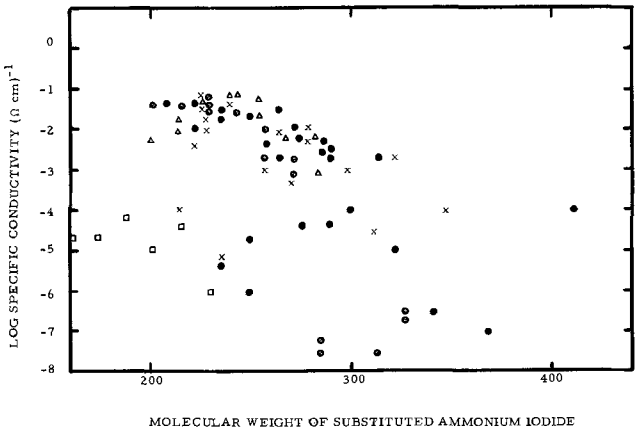

Fig. 2. Correlation between specific conductivity of QAg_nI_{n+1} and molecular weight of the QI. ⊙, Subset 1, completely substituted acyclic alkyl ammonium iodide; □, subset 2, partially substituted acyclic ammonium iodide; △, subset 3, saturated azacyclic substituted ammonium iodide; ●, subset 4, unsaturated azacyclic substituted ammonium iodide; x, subset 5, carbocyclic, aryl, benzyl, or allyl substituted ammonium iodides.

monium iodide form nonconductors whereas the completely substituted trimethyl analogs form conductors.

The four remaining nonconductive, low formula weight QI ($M < 285$ g/mole) shown in Fig. 2 are members of subset 4, the unsaturated azacyclic substituted ammonium silver iodide compounds. It was observed with several of the substituted pyridinium silver iodide electrolytes that the conductive products transformed to nonconductive structures during storage at 22°C, or on cooling to low temperatures. The compounds containing either 3-methylpyridinium, 3,5-dimethylpyridinium, or 1,2,6-trimethylpyridinium ions were conductive at ambient temperatures and became nonconductive at about −25°C. The transformations were not sharply defined but suggested a slow, solid-state reaction such as the disproportionation of KAg_4I_5 (3, 4). The 1,3-dimethylpyridinium silver iodide electrolyte increased in resistivity from 30 to 10^{+5} ohm cm during ambient storage; however, on heating the resistive product to 60°C, it transformed back into a conductive structure.

These results demonstrate that conductive solid electrolytes are formed by the combination of silver iodide with many substituted ammonium iodides. The determination of the crystal structures as well as the thermodynamic and transport properties of these compounds will be of considerable interest in the further understanding of cation substituted silver iodide solid electrolytes.

Acknowledgment

The authors wish to thank S. Geller for helpful discussions and to acknowledge the contribution of L. Hermo who performed many of the syntheses and physical measurements. The work was performed under the North American Rockwell Corporation Independent Research and Development Program.

Manuscript submitted Aug. 13, 1970; revised manuscript received Feb. 8, 1971.

Any discussion of this paper will appear in a Discussion Section to be published in the June 1972 JOURNAL.

REFERENCES

1. B. Reuter and K. Hardel, *Naturwissenschaften*, **48**, 161 (1961); *Z. Anorg. u. Allgem. Chem.*, **340**, 158 (1965).
2. T. Takahashi and O. Yamamoto, *Denki Kagaku*, **32**, 610 (1964); **33**, 346 (1965).
3. J. N. Bradley and P. D. Greene, *Trans. Faraday Soc.*, **62**, 2069 (1966); **63**, 424 (1967).
4. B. B. Owens and G. R. Argue, *Science*, **157**, 308 (1967).
5. B. B. Owens, *This Journal*, **117**, 1536 (1970).
6. B. B. Owens and G. R. Argue, *ibid.*, **117**, 898 (1970).
7. S. Geller and M. D. Lind, *J. Chem. Phys.*, **52**, 5854 (1970).
8. B. B. Owens, U.S. Pat. 3,476,606, Nov. 4, 1969.

The Effect of Sodium Oxide on the Thermal Oxidation of Silicon

Owen F. Devereux,* Rong Yau Wang, and Kuang-Ho Chien[1]

Department of Metallurgy and Institute of Materials Science, University of Connecticut, Storrs, Connecticut 06268

ABSTRACT

Polycrystalline silicon wafers coated with Na_2CO_3 were oxidized in ambient air with $P_{H_2O} = 24$ mm in the temperature range 702°-1052°C. Initial oxidation followed cubic kinetics due to the linear change in composition of the oxide film with oxidation. At longer times, the oxidation became parabolic as the concentration of and, therefore, diffusivity of hydroxyl in the oxide became nonlinear with the sodium concentration in the film. This occurs at lower concentration of sodium, where the presence of sodium is manifested in the formation of hydroxyl by an autocatalytic reaction. Activation energies for both cubic and parabolic regions were 40.8 kcal/mole; the cubic pre-exponential constant was $5.1 \times 10^6 \mu^3$/hr, and the parabolic pre-exponential constant was $6.8 \times 10^4 \mu^2$/hr. Untreated specimens oxidized as controls during these experiments showed similar behavior due to vapor phase transport of Na_2O.

There has been an increasing awareness in recent years of the deleterious effect of impurity oxides in an otherwise protective film during thermal oxidation of metals. This is commercially important in the case of high-strength, nickel-base alloys in hot gaseous environments containing sodium and sulfur compounds. The present investigation of the role of sodium oxide on silicon oxidation was initiated in order to study these effects in a simpler, better-defined oxide than that extant on the nickel alloys.

Recent papers by Deal and Grove (1) and by Revesz and Evans (2) review in large part, together with their own contribution, the status of knowledge concerning the thermal oxidation of silicon. Deal and Grove find that existing knowledge on film growth can be described as surface reaction rate limited for short oxidation times and/or low temperatures, and diffusion rate limited at long times and/or high temperatures. Combining these terms, film thickness, X, after oxidation time, t, is given by

$$X^2 + AX = B(t + \tau) \qquad [1]$$

They find an activation energy for the parabolic constant, B, of 16.3 kcal/mole under wet oxidation conditions, and 28.5 kcal/mole under dry conditions. The linear constant, B/A, has an activation energy of 46 kcal/mole in either case. The time constant, τ, which corrects for an oxide layer extant prior to the start of the experiment or for early oxidation behavior not taken into account by the linear-parabolic equation [1], has a value of zero under wet conditions, and corresponds to an initial film thickness of 230Å under dry conditions. The activation energies of B are in accord with activation energies for the diffusion of the oxidizing species, hydroxyl and superoxide ion (O_2^-),

* Electrochemical Society Active Member.
[1] Present address: Industrial Heat Treating Company, Derby, Connecticut 06418.
Key words: hot corrosion, alkali, impurity.

respectively, in fused silica, and the τ variance is explained by the variation in the thickness of the diffuse charge layer in the oxide film with the concentration of water. The parabolic constant, B, is found to vary directly with the partial pressure of the oxidant, while the value of A remains constant.

Revesz and Evans, while in agreement with the linear-parabolic rate behavior, find a considerable dependence of the reaction rates and of the activation energies on the sodium content of the oxide film. Thus their activation energies for the parabolic rate constant range from 12.45 kcal/mole for oxidation under very clean conditions in water vapor to 52.8 kcal/mole for oxidation in water vapor through a heavily sodium-contaminated oxide film. The activation energy for the linear constant varied from 44.0 kcal/mole in the clean experiment to 29.9 kcal/mole with sodium contamination. For both the linear and parabolic terms, considerable variation of the pre-exponential constants was also seen.

The present authors have conducted a further study of the oxidation of silicon with deliberate sodium contamination, using polycrystalline silicon, with moist air as oxidant. Inasmuch as the linear rate constant, but not the parabolic constant, depends on silicon orientation, some ambiguity was anticipated in the data for the linear parameters (3).

Experimental

Silicon wafers were prepared from a 1 in. diameter polycrystalline ingot of nine 9's purity. After slicing and lapping, the wafers were degreased in hot trichlorethylene followed by hot nitric acid, and rinsed in deionized water. The wafers were then chemically polished in a solution of 60 parts nitric acid, 20 parts acetic acid, and 8 parts hydrofluoric acid. After polishing, the wafers were rinsed in deionized water and stored under methanol. Final thickness was approximately 200μ.

The wafers were oxidized in a resistance-heated horizontal mullite tube furnace with an inside diameter of 1 and 11/16 in. The oxidant was ambient air saturated with water at room temperature. Flow rate was maintained at 150 cc/min, STP, with a small diaphragm pump. Saturation of the air was accomplished by bubbling it through a vessel containing water. This environment possessed a certain degree of ambiguity inasmuch as it contained both oxygen and water as oxidants; however, the oxidation rate in water vapor is sufficiently large compared to that in dry oxygen (1) that adequate control of the oxidation rate could be maintained by control of the water vapor pressure. Equilibrium water vapor pressure during the experiments was 24 $\pm$ 1 mm. The wafers were supported in a grooved ceramic combustion boat, with cylinder axis horizontal and normal to the direction of air flow. In the usual experiment two specimens were oxidized at once, a clean wafer placed upstream in the boat and a contaminated wafer placed downstream in the boat. Contamination by reagent-grade Na_2CO_3 was accomplished by dusting the surface of each specimen lightly prior to oxidation with the finely ground powder. Amounts of Na_2CO_3 applied to each contaminated specimen are given in Table I. It was anticipated that the silicon would undergo a rapid initial oxidation through partial reduction of the sodium oxide and that a uniform film across the surface would be formed quickly due to the high diffusivity of sodium ion in soda silicate glasses. This technique of applying the contaminant differed from that of Revesz and Evans, who preoxidized the silicon prior to exposing it to $NaNO_3$. However, both macroscopic and microscopic examination of the oxide films obtained during this work indicated uniformity of thickness, inferring that a homogeneous distribution of sodium in the film was obtained. Inasmuch as loss was anticipated both through the Na_2CO_3 reagent physically disengaging itself from the specimen surface and through volatility, the values recorded in Table I are not considered significant in a absolute sense, but do represent the relative amounts of sodium oxide contaminant present on each specimen during oxidation. Although the oxide films thus contained, in principle, two volatile compounds, CO_2 and Na_2O, these were not expected to evolve to any appreciable extent during the portion of the experiment subject to gravimetric analysis due to rapid dilution by SiO_2 during the early stages of oxidation. Temperature was measured at the boat and controlled to within 1°C.

Table I. Amount of Na_2CO_3 applied

T (°C)	Na_2CO_3 (mg/cm²)
702	0.02085
753	0.01945
802	0.00670
851	0.01150
903	0.01070
952	0.02000
1002 (b)	•
1002 (d)	0.01165
1052	0.04390

(b) and (d) denote different runs at the same temperature.
• Indicates measurement not made.

Oxidation rate was determined by weight change; the wafers were removed periodically and weighed with a Cahn RG electrobalance. This technique was found to be more sensitive and reproducible than continuously recording the weight of a specimen suspended in the furnace. The use of a weighing technique as opposed to the direct observation of oxide thickness that has predominated the experimental work on silicon oxidation was dictated by the more complex nature of the soda silicate oxide film. That is, color changes were not consistent with those observed on clean silicon, and a definite crystallinity in the oxide film was observed as will be noted later in the paper. It was recognized that the periodic removal of the specimens and their reinsertion in the furnace could have a decided effect on the oxidation process through stressing and possible fracture or spalling of the oxide films. For this reason, companion studies were made of specimens which were not removed but merely weighed at the end of the oxidation process. Total weight gained for these specimens scattered statistically about that for specimens oxidized for the same time, but intermittently removed, with a typical deviation of several per cent. Estimated reproducibility of individual weight measurements is of the order of 1 μg. Removal of the specimens from the furnace and their reinsertion were made as rapidly as possible to minimize the loss of heat from the interior of the furnace. Recovery time for the specimen on reinsertion as estimated by visual observation was of the order of 1 min and was neglected in considering the time of oxidation.

Tapered sections with a 10:1 ratio were made of each specimen for optical microscopy, and an x-ray diffraction pattern was obtained for each of the contaminated samples and for a representative "clean" oxidized sample.

Results

Oxidation data for the alkali-treated specimens are shown in Fig. 1. Oxidation is initially cubic and, although it is not apparent in the log-log plot shown, becomes parabolic at longer oxidation times. Defining the kinetic rate constants by means of the equations

$$X^3 = Ct \quad [2]$$

$$X^2 = Bt + \text{Const} \quad [3]$$

the cubic and parabolic regimes in terms of weight increase due to oxidation per unit area, ΔW, are given by

$$\Delta W^3 = C\rho^3 t \quad [4]$$

$$\Delta W^2 = B\rho^2 t + \text{Const} \quad [5]$$

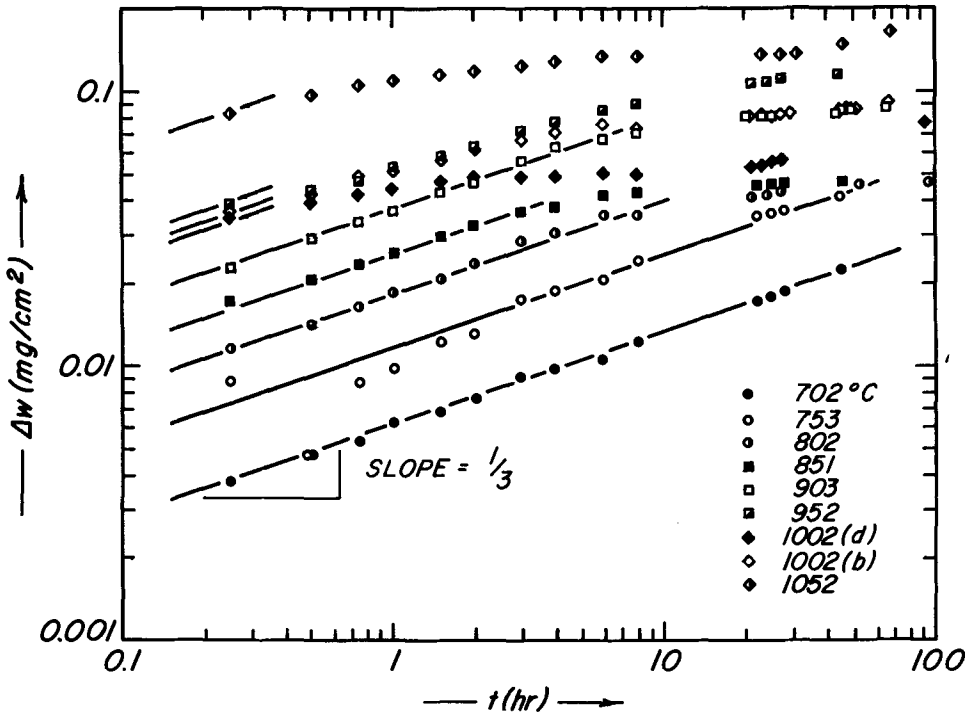

Fig. 1. Kinetic data—Na_2CO_3 treated specimens.

where ρ is the density of oxygen in the oxide film. High silica glasses have a density of the order of 2; this corresponds to an oxygen density of approximately 1 g/cm³, which has been used in this paper. Arrhenius plots of the cubic and parabolic constants are shown in Fig. 2; both are linear and exhibit the same slope, with an activation energy of 40.8 kcal/mole.

Oxidation of the untreated specimens showed similar behavior to that of the treated specimens; these data are shown in Fig. 3, with Arrhenius plots of the cubic and parabolic constants in Fig. 4. It was inferred that vapor phase transfer of a sodium oxide species had occurred and, therefore, that the untreated specimens were different from the treated specimens only in the quantities of alkali contaminant in the oxide film. Transition from cubic to parabolic oxidation occurred, in general, at thinner film thicknesses for the untreated specimens, and the cubic rate constants were considerably smaller. The rate constants plotted in Fig. 4 show more scatter than those for the treated specimens; this is especially true for the cubic constant. The line through the cubic constants is drawn with the same slope as that for the parabolic constants largely because of the apparent similarity to Fig. 2. The activation energy for these constants is 39.6 kcal/mole.

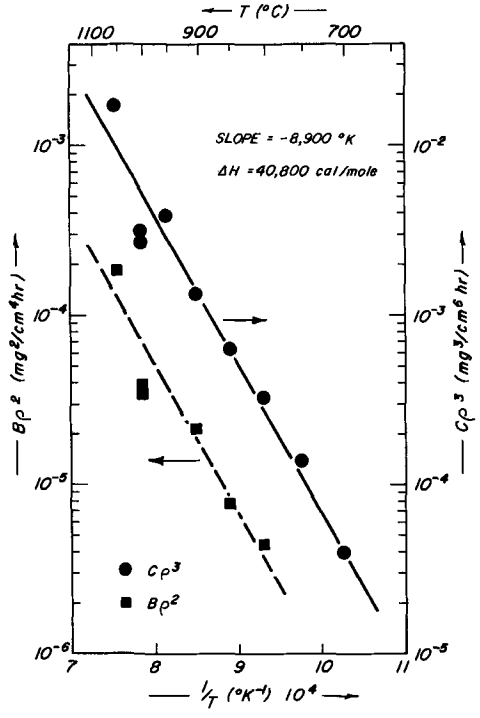

Fig. 2. Kinetic rate constants—Na_2CO_3 treated specimens

Defining the pre-exponential constants and activation energies by means of the equations

$$C = C_0 \exp(-\Delta H_C/RT) \quad [6]$$

$$B = B_0 \exp(-\Delta H_B/RT) \quad [7]$$

these parameters are shown in Table II along with values determined by Revesz and Evans. Two sets of values determined by Revesz and Evans are quoted; both were evaluated in helium with a water pressure of 24 mm. One set refers to sodium-free oxide films, and the other to films containing on the order of 10^{20} sodium atoms/cm³.

X-ray diffraction revealed only silicon peaks from the untreated, oxidized samples. Peaks other than those from silicon diffracted from the treated samples are shown in Table III. The diffraction angle, 2θ, of peaks attributed to the oxide film and the relative intensity of these peaks are reported. For each diffraction pattern, the nearest intense silicon peak was used as a 2θ standard. As seen in Table III, over the range of experimental conditions four distinct peaks were observed. These correspond to average d spacing values of 4.5135, 4.0812, 3.4717, and 3.4447Å. None of the observed combinations of these spacings corresponded to ASTM-listed values for the various polymorphs of silica or to the listed sodium silicates.

Macroscopic examination of the oxidized specimens revealed the uniform bright interference colors in-

Table II. Kinetic constants

	B_0 (μ^2/hr)	ΔH_B (kcal/mole)	C_0 (μ^3/hr)	ΔH_C (kcal/mole)
Present experiment				
Untreated	1.14×10^5	39.6	2.3×10^4	39.6
Treated	6.8×10^4	40.8	5.1×10^6	40.8
Revesz and Evans				
Clean	1.55	12.45	—	—
Na-doped	1.58×10^8	52.8	—	—

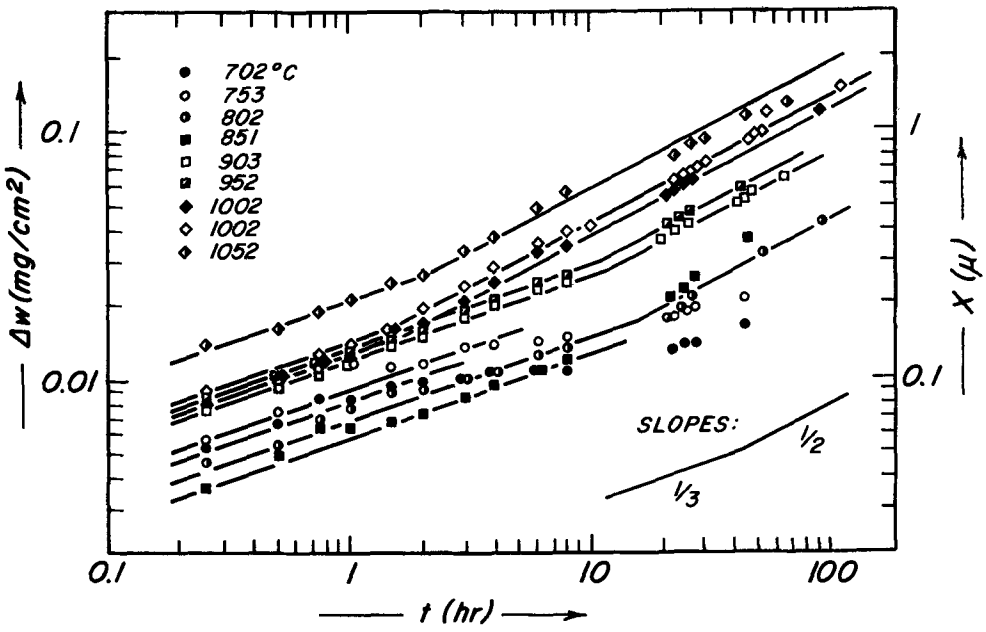

Fig. 3. Kinetic data—untreated specimens.

dicative of an amorphous film on the untreated specimens, but a gray appearance suggestive of granularity on the treated specimens. Tapered sections through the unoxidized silicon surface showed an initial surface roughness caused by preferential dissolution near the grain boundaries during specimen preparation. This roughness was retained during oxidation at low temperatures in both treated and untreated specimens, suggesting surface control of the oxidation rate. At high temperatures, particularly in the alkali-treated specimens, the surface roughness was markedly decreased, in accord with a diffusion-controlled reaction. Also visible in tapered sections of the treated specimens was a fine granularity with an apparent dendritic character at the metal/oxide interface. This appeared to be the unidentified crystalline deposit evidenced by x-ray diffraction.

Discussion

The cubic phase of the oxidation observed in these experiments was not observed by Revesz and Evans in their study of sodium-affected oxidation. This may be attributed to the method of sodium doping. Revesz and Evans preoxidized their wafers, then placed them in contact with $NaNO_3$ to permit dissolution of Na_2O in the amorphous silica film. Thus, at the onset of oxidation they had a somewhat uniform film with a Na/Si ratio on the order of 0.02. In the present experiments, the initial film may be idealized as consisting solely of Na_2O; thus, initial oxidation occurred not only through a film of high alkali content but also of changing composition.

The rate of oxidation is initially surface reaction limited; Deal and Grove have proposed that this reaction is first order with respect to the oxidant. In the presence of a high concentration of sodium oxide, the oxidant will be oxide ion and the product of the reaction will be silicate ion, the formation of which will consume oxide ions. Thus, the surface reaction rate will decrease with time according to the changing concentration. The kinetic rate expression for this mechanism may be readily calculated and is a sum of both linear and logarithmic terms; however, a comparison of the available free oxide ion, as determined from Table I, with the kinetic data in Fig. 1, shows that the available oxide ion will have been consumed in the formation of silicate during the initial oxidation period of 15 min. Therefore, this mechanism describing the initial oxidation behavior was no longer valid over the range of data taken in these experiments.

In Table IV are shown the amount of applied alkali, calculated as Na_2O, compared with the amount of oxidation, as SiO_2, after the first 15 min of oxidation, *i.e.* at the onset of the observed cubic region. Due to possible loss of the volatile Na_2O, the resulting per-

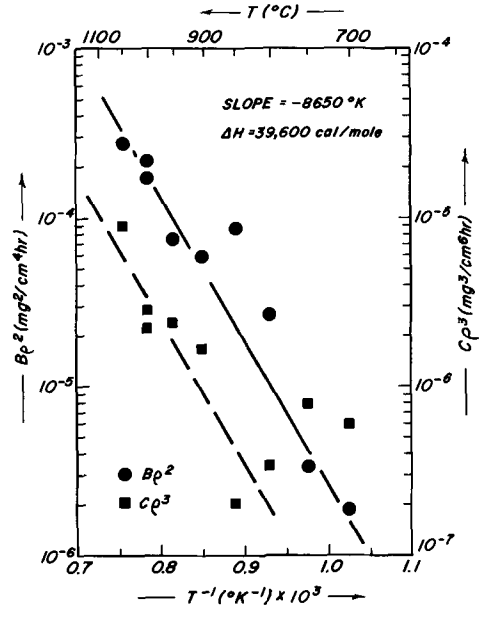

Fig. 4. Kinetic rate constants—untreated specimens

Table III. Observed 2θ/I values in oxide films (CoKα radiation)

T (°C)	2θ/I			
702			29.85	30.1
			0.5	0.05
753			29.85	30.05
			1.1	0.3
802			29.85	30.05
			0.7	0.5
851			29.83	31.01
			0.9	0.5
903		25.47	29.92	
		2.2	0.5	
952	22.87	25.32	29.87	
	1.1	0.05	1.5	
1002(b)	22.85	25.26	29.85	
	0.7	1.0	0.8	
1002(d)		25.32	29.88	
		0.4	1.35	
1052		25.3	29.9	
		1.8	0.5	

(b) and (d) denote different runs at the same temperature.

Table IV. Minimum per cent of SiO_2 in film after 15 min of oxidation

T (°C)	Na_2O (mg/cm²)	SiO_2 (mg/cm²)	Weight per cent SiO_2
702	0.0122	0.0071	36.9
753	0.0114	0.0166	59.2
802	0.0039	0.0218	84.8
851	0.0067	0.0322	82.8
903	0.0063	0.0429	87.6
952	0.0117	0.0727	86.2
1002(b)	—	0.0686	—
1002(d)	0.0068	0.0646	90.5
1052	0.0257	0.1566	86.0

(b) and (d) denote different runs at the same temperature.

centage of SiO_2 calculated in the film represents a minimum quantity. In comparing these values to the Na_2O-SiO_2 equilibrium diagram, Fig. 5, it is apparent that during observation of oxidation above 753°C the stable phases in the oxide film were a liquid and a crystalline silica, quartz at 802° and 851°C, and tridymite at higher temperatures. While there is no reason to propose that the film present during oxidation possesses an equilibrium phase structure, it is reasonable to assume that the oxidation occurs by means of transport of oxidant through a liquid phase, rather than through a solid, though amorphous, silica film. This is not the case in the experiments reported by Revesz and Evans. Their films contained only 1% Na_2O, and the appreciable effect on oxidation rate was explained by the autocatalytic reaction suggested by Charles (4), in which a relatively small quantity of Na^+ in the amorphous structure can cause a disproportionate increase in the OH^- concentration.

Due to incomplete knowledge concerning the state of the oxide layer during oxidation, it is not possible to propose a definitive mechanism. However, it is likely that the film either remains liquid throughout the cubic region, and therefore that precipitation of silica is repressed, or that the film possesses a near-equilibrium phase structure of liquid and crystalline silica. In the former case, the silica content of the liquid would increase during oxidation, and would be manifest in a corresponding increase in viscosity resulting in a decrease in diffusivity of hydroxyl as shown by the Einstein equation. Assumption of a linear change of viscosity with composition in this region leads to a cubic oxidation rate. In the latter case, a liquid phase of reasonably constant composition would persist throughout the oxidation; however, crystalline silica would precipitate in an amount proportional to the extent of oxidation. Inasmuch as the silica phase has a much lower diffusivity to hydroxyl than the liquid alkali silicate, in effect precipitation would decrease the area for diffusion in proportion to the extent of oxidation, again leading to cubic oxidation. In these proposed mechanisms, onset of the parabolic region of oxidation would, in the first case, correspond to an increase in silica content of the film to the extent that the mechanism of Charles became significant, *i.e.* formation of appreciable hydroxyl content without linear dependence on the sodium ion content. In the latter case, parabolic behavior would ensue when the liquid phase so decreased in proportion to the solid phase as to become discontinuous. Failure of x-ray diffraction to provide data to distinguish between these mechanisms may be a reflection of incomplete knowledge of the possible nonequilibrium phases in this system.

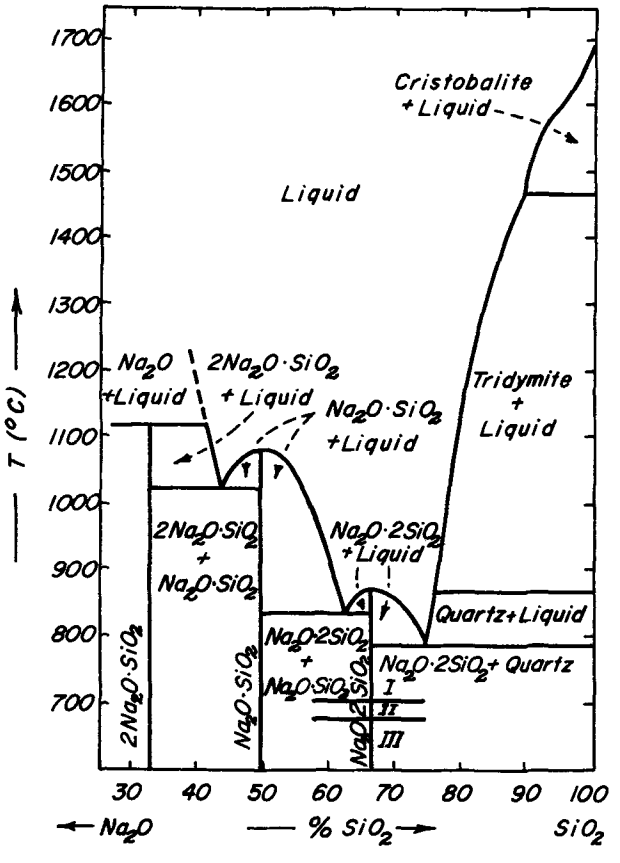

Fig. 5. Portion of the Na_2O-SiO_2 phase diagram [after Levin *et al.* (5)].

The kinetic constants of Table II are in accord with both hypotheses. The large increase in the pre-exponential constant of the treated specimens *vs.* that of the untreated is a reflection of the increased sodium content of the treated films and consequent increased diffusivity. However, in the parabolic region, the hydroxyl content and, therefore, diffusivity is determined by an autocatalytic reaction and is thus insensitive to composition. Hence the pre-exponential constants in the parabolic region are nearly the same. It is clear from the work of Revesz and Evans that a wide range of values of the kinetic constants is possible depending on experimental conditions. Thus, lack of exact agreement with their values is not surprising; however, both the activation energies and pre-exponential constants do fall with in the range reported by them.

Summary and Conclusions

Oxidation of polycrystalline silicon through a Na_2O surface film initially follows cubic kinetic behavior due to the changing composition of the film; the oxidation rate eventually becomes parabolic as transport processes in the film become insensitive to further composition changes. Activation energies for both cubic and parabolic regions are the same, approximately 40 kcal/mole. The cubic pre-exponential constant is dependent on sodium concentration in the film; however, the parabolic pre-exponential constant is relatively insensitive.

It is proposed that transport in the cubic region of oxidation is diminished by silica production due either to alteration of the viscosity of a single liquid phase, or to formation of a second phase of low diffusivity. Available data are consistent with either model. In the parabolic region of oxidation, the enhanced oxidation rate due to sodium is manifest in the production of hydroxyl ion by an autocatalytic reaction proposed by Charles (4), a process not proportional to the sodium concentration.

Acknowledgments

The authors gratefully acknowledge the support of the University of Connecticut Research Foundation and of Project Themis Contract No. F 44620-69-C-0011, "Structural Fatigue," of the Air Force Office of Scientific Research, and the use of the facilities of the University of Connecticut Computer Center.

Manuscript submitted Jan. 26, 1971; revised manuscript received Mar. 5, 1971.

Any discussion of this paper will appear in a Discussion Section to be published in the June 1972 JOURNAL.

SYMBOLS

A Linear coefficient
B Parabolic constant
B_0 Pre-exponential parabolic constant
C Cubic constant
C_0 Pre-exponential cubic constant
ΔH_B Activation energy—parabolic constant
ΔH_C Activation energy—cubic constant
I Relative intensity of diffracted beam
R Gas constant
T Absolute temperature
t Oxidation time
ΔW Weight increase due to oxidation
X Oxide film thickness
ρ Density of oxygen in oxide film
2θ Diffraction angle
τ Time correction constant

REFERENCES

1. B. E. Deal and A. S. Grove, *J. Appl. Phys.*, **36**, 3770 (1965).
2. A. G. Revesz and R. J. Evans, *J. Phys. Chem. Solids*, **30**, 551 (1969).
3. W. A. Pliskin, *IBM J. Res. Dev.*, **10**, 198 (1966).
4. R. J. Charles, *J. Appl. Phys.*, **29**, 1549 (1958).
5. E. M. Levin, H. F. McMurdie, and F. P. Hall, "Phase Diagrams for Ceramists," Am. Ceram. Soc. (1956), Fig. 19.

X-Ray Efficiency of Powder Phosphors

G. W. Ludwig†

General Electric Research and Development Center, Schenectady, New York 12301

ABSTRACT

Powder phosphors including CsI:Tl and (ZnCd)S:Ag were excited with x-rays, in the energy range 25-135 keV, obtained from radioisotope sources. The phosphor efficiency (light output per unit incident x-ray energy) was measured as a function of phosphor screen weight for each of five sources. The measured efficiencies are in reasonable agreement with theoretical curves having no adjustable parameters. The curves were calculated using tabulated x-ray energy-absorption coefficients and measured light transmission parameters, and assuming that the efficiency of conversion of absorbed x-ray energy to light energy is equal to the cathode-ray efficiency.

Powder phosphors such as (ZnCd)S:Ag and $CaWO_4$:Pb are of considerable importance for the detection of x-rays having photon energies in the region 25-135 keV. Crucial to this application is the efficiency with which incident x-ray energy is converted to useful light energy. This efficiency η may be expressed as

$$\eta = \eta_a \eta_c \eta_t \quad [1]$$

where η_a is the fraction of the incident x-ray energy which is absorbed, η_c describes the efficiency of conversion of absorbed x-ray energy to light energy, and η_t is the efficiency with which the light energy is transmitted through the powder to the detector. The detector may be a photoemissive surface, a photographic film, or the human eye.

In the work of Hamaker (1), Klasens (2), Klasens and de Groot (3), Coltman *et al.* (4), and Broser *et al.* (5), the x-ray efficiency of phosphors is discussed in the following manner. The x-ray absorption efficiency is either measured or is deduced from tabulated x-ray absorption coefficients of the elements knowing the phosphor screen weight and composition, and also the spectral distribution of the incident x-ray beam. The transmission efficiency is related to the scattering and absorption of the emitted photons by the phosphor particles within the screen, and the reflection coefficients at the screen surfaces. The measured x-ray efficiency of the phosphor screen can then be used to deduce a value for the conversion efficiency η_c. Coltman *et al.* (4) and Klasens (2) reported on $CaWO_4$ screens, while Broser *et al.* (5) presented information on some additional materials. All of these workers used for sources x-ray tubes which yielded a broad spectrum of x-ray energies, and presented no data on the possible dependence of the conversion efficiency on x-ray energy. Klasens and de Groot (3) discussed the processes involved in conversion of x-ray energy to light and concluded that the conversion efficiency should depend on x-ray energy.

Although there has been additional work,[1] remarkably little discussion of the response of powder phosphors to x-rays has appeared in the recent literature. On the other hand, there have been numerous studies of the x-ray response of scintillation crystals such as NaI:Tl, which are highly transparent to their own emitted light.

In this paper we report on the x-ray efficiency of powder phosphors such as (ZnCd)S:Ag, $CaWO_4$:Pb, and CsI:Tl. To excite the phosphors we employed a series of five radioisotopes, each of which emits x-rays at several well-defined and rather closely spaced energies in the range 25-135 keV. The phosphor response to such excitation can be conveniently analyzed, since the absorption of the beam at each x-ray energy follows an exponential law. Availability of data for a series of sources giving different x-ray energies clearly is of advantage for comparison with theory, and particularly for testing whether the conversion efficiency varies with x-ray energy.

The x-ray response was measured for a series of different phosphors, screen weights, and radioisotope sources, using a photomultiplier as the detector. The photomultiplier sensitivity to the spectrum emitted by each phosphor was calibrated by comparing the photomultiplier signal to that from a thermocouple with the phosphor excited by cathode rays. The light transmission of the screens was measured, as was the reflectivity of thick phosphor layers, in order to determine the parameters describing scattering and absorption of light within the screens.[2] The cathode-ray efficiency of the phosphors was measured. Finally, the x-ray mass absorption coefficient of each phopshor was calculated from tabulated values for the elements for each

† Electrochemical Society Active Member of a Sustaining Member Company.

Key words: luminescence, phosphors, x-rays, efficiency.

[1] See, for example, ref (6-9).

[2] The density of a powder phosphor screen is dependent on preparative techniques. For this reason we prefer discussing x-ray attenuation in terms of the phosphor mass traversed rather than the phosphor thickness traversed.

x-ray energy present in the radiation from the sources. It was then possible to compare phosphor efficiency with curves calculated from theory with no adjustable parameters.

Using the assumption that the efficiency of conversion of absorbed x-ray photon energy to emitted light is equal to cathode-ray efficiency, we find reasonable agreement between our data and a formula based on work of Hamaker (1). Thus, we find no substantiation for the assumption of Klasens and de Groot that the energy of the ions produced by x-ray absorption is less efficiently used in producing light than is that of the fast electrons. Rather it appears that Hamaker's formulas can be used together with phosphor parameters such as the cathode-ray efficiency to provide a guide to the x-ray efficiency to be expected under a wide range of experimental conditions.

Hamaker's analysis of the light output of powder phosphor screens under x-ray excitation is reviewed briefly in the following section. In subsequent sections the radioisotope sources are characterized, measurement of x-ray response and calculation of the mass absorption coefficient is described, the determination of other relevant phosphor parameters is discussed, and a comparison is made between the measured phosphor efficiency and predictions from theory. Results are also discussed.

Light Output of a Phosphor Screen

We now discuss the light output of a phosphor screen under x-ray excitation using an approach similar to that of Hamaker (1). Consider a screen which is sandwiched between media, labeled 1 and 2, which may affect its light output by reflecting or absorbing some of the emitted light (see Fig. 1). X-ray photons of energy E are incident from the left, the energy flux being N_0E. The x-ray absorption by the screen is governed by its mass absorption coefficient $\mu' = \mu/\rho$, where ρ is the phosphor density. Thus, after passing through a screen weight w the flux will be reduced to $N_0E \exp(-\mu' w)$. The flux absorbed in a weight increment dw at w is $-EdN = EN_0 [\exp(-\mu' w)]dw$ and the emitted light flux is $\mu_c EdN$, where μ_c is the efficiency for conversion of absorbed x-ray energy to light energy. We expect half of the light flux to be emitted toward the left and half toward the right.

Suppose that at w within the phosphor there is a light flux I traveling toward the right and a flux J traveling toward the left. In passing through the layer of weight dw these fluxes will be augmented by light generation (*via* x-ray absorption and phosphor fluorescence) while being attenuated by the self-absorption of the phosphor. In addition, the phosphor grains will scatter light from each flux into the other. Thus

$$dI/dw = -(a + s)I + sJ + \frac{1}{2}\eta_c EN_0 \exp(-\mu' w) \quad [2]$$

$$dJ/dw = +(a + s)J - sI - \frac{1}{2}\eta_c EN_0 \exp(-\mu' w) \quad [3]$$

Here a and s are coefficients describing the self-absorption and scattering, respectively, of the emitted light by the phosphor. Equations [2] and [3] are one-dimensional; they apply to regions sufficiently far from the screen periphery that lateral light losses and additions effectively cancel.

The solutions of Eq. [2] and [3] are of the form[3]

$$I = A(1 - \beta)e^{\sigma w} + B(1 + \beta)e^{-\sigma w} - \frac{1}{2}\eta_c EN_0 \frac{\beta\mu' + \sigma}{\beta(\mu'^2 - \sigma^2)} e^{-\mu' w} \quad [4]$$

$$J = A(1 + \beta)e^{\sigma w} + B(1 - \beta)e^{-\sigma w} + \frac{1}{2}\eta_c EN_0 \frac{\beta\mu' - \sigma}{\beta(\mu'^2 - \sigma^2)} e^{-\mu' w} \quad [5]$$

In [4] and [5] the coefficients a and s have been replaced by new parameters σ and β so defined that the expressions are simplified

$$\sigma = [a(a + 2s)]^{1/2} \quad [6]$$

$$\beta = [a/(a + 2s)]^{1/2} = \sigma/(a + 2s) \quad [7]$$

The quantities A and B in [4] and [5] are constants, the values of which are determined by imposing appropriate boundary conditions. Let r_i be the reflectivity and t_i be the transmissivity of the media 1 and 2. Then, as discussed by Hamaker (1), the light flux to the right per unit flux in the incident x-ray beam is given by [8] while that to the left is given by [9].

$$\eta_r = \frac{t_2 I(W)}{N_0 E} = t_2\eta_c\mu' \cdot \frac{(1 + \rho_2)}{2(\mu'^2 - \sigma^2)} \cdot e^{-\mu' W} \times \frac{(-\mu' + \sigma)(\rho_1 + \beta)e^{\sigma W} + (\mu' - \sigma)(\rho_1 - \beta)^{-\sigma W} + 2(\sigma\rho_1 + \mu'\beta)e^{\mu' W}}{(\rho_1 + \beta)(\rho_2 + \beta)e^{\sigma W} - (\rho_1 - \beta)(\rho_2 - \beta)e^{-\sigma W}} \quad [8]$$

$$\eta_l = \frac{t_1 J(0)}{N_0 E} = t_1\eta_c\mu' \cdot \frac{(1 + \rho_1)}{2(\mu'^2 - \sigma^2)} \times \frac{(\mu' - \sigma)(\rho_2 + \beta)e^{\sigma W} - (\mu' + \sigma)(\rho_2 - \beta)e^{-\sigma W} + 2(\sigma\rho_2 - \mu'\beta)e^{-\mu' W}}{(\rho_1 + \beta)(\rho_2 + \beta)e^{\sigma W} - (\rho_1 - \beta)(\rho_2 - \beta)e^{-\sigma W}} \quad [9]$$

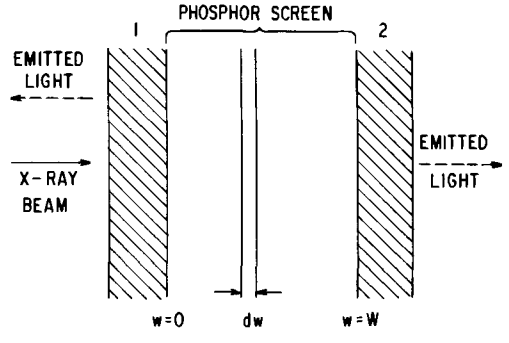

Fig. 1. X-ray excitation of a phosphor screen which is sandwiched between partially reflecting media 1 and 2.

Here W is the screen weight and the reflectivities r_i have been replaced by the related parameters $\rho_1 = (1 - r_i)/(1 + r_i)$, while η_r and η_l represent the efficiency of Eq. [1] for the detector to the right of the screen and to the left, respectively.

Equations [8] and [9] are easily generalized if the phosphor is simultaneously exposed to x-rays of several different fluxes, energies, and absorption coefficients. In particular, [8] generalizes to

$$\eta_r = (\Sigma_i N_{oi}E_i\eta_{ri})/\Sigma_i N_{oi}E_i \quad [10]$$

Simplifications of [8] and [9] which apply under special conditions have been discussed by Hamaker (1) and Klasens (2).

X-ray Generation by Radioisotopes

A number of radioisotopes which are available commercially are worth considering as sources of radiation in the x-ray region. Important characteristics, such as half-life and emitted radiations, of several isotopes which have come to our attention are listed in Table I (10). All but one of the isotopes in the table decay by capture of an electron from an inner shell to produce a daughter nucleus in an excited nuclear state. The daughter may return to its ground state with the emission of a gamma ray having an energy listed in

[3] Equation 92 of ref (1) contains a minor error.

Table I. Decay characteristics of potential x- or gamma-ray sources

Isotope	Decay mode*	Half life	Daughter	Gamma rays (keV)	X-rays (keV)
$_{26}Fe^{55}$	EC	2.6 years	$_{25}Mn^{55}$	—	~5.9
$_{50}Sn^{119m}$	IT	250 days	$_{50}Sn^{119}$	24, 65	~25
$_{53}I^{125}$	EC	60 days	$_{52}Te^{125}$	35.5	~28
$_{66}Dy^{159}$	EC	144 days	$_{65}Tb^{159}$	58	~46, ~6.7
$_{74}W^{181}$	EC	140 days	$_{73}Ta^{181}$	Weak	~58, ~11
$_{79}Au^{195}$	EC	183 days	$_{78}Pt^{195}$	31, 99, 129, 211	~68, ~10
$_{27}Co^{57}$	EC	270 days	$_{26}Fe^{57}$	14, 122, 136	6.5
$_{38}Sr^{85}$	EC	64 days	$_{37}Rb^{85}$	514	13
$_{48}Cd^{109}$	EC	453 days	$_{47}Ag^{109}$	88	22

* EC = electron capture, IT = internal conversion.

Table I. However, internal conversion of the gamma ray may also take place, whereby the photon is absorbed internal to the atom with accompanying expulsion of an electron, generally from the K- or L-shell.

Holes in the deep inner shells (K- and L-shells) of the daughter atoms are produced both by the initial electron capture and by subsequent internal conversion. Consequently, such radioisotope samples emit x-rays characteristic of the daughter element. Usually this x-ray emission is considerably more intense than the gamma-ray emission.

As an example, the decay scheme of $_{79}Au^{195}$ is depicted in Fig. 2 (11). The gold isotope decays *via* electron capture to any one of three excited nuclear states of $_{78}Pt^{195}$. Four gamma rays at 31, 99, 129, and 211 keV are reported as a result of transitions among these levels and to the ground state of Pt^{195}. However, the dominant emission in the energy region above 10 keV is the characteristic K x-ray emission of Pt at ~68 keV. This K-shell emission can be separated into four components, $K_{\alpha 1}$, $K_{\alpha 2}$, $K'_{\beta 1}$ and, $K'_{\beta 2}$ having intensity ratios 28:50:17:5 (10). The first two at 65.1 and 66.8 keV represent electronic transitions from the L-shell to the hole in the K-shell, while in the last two, at 75.7 and 77.8 keV, the electron originates in the M- or in the N-shell, respectively. There also are L-shell emissions at about 10 keV, but these low energy radiations can be effectively filtered out if desired.

Amounts ranging from 0.5 to 2 mc of the isotopes listed in Table I were obtained from commercial

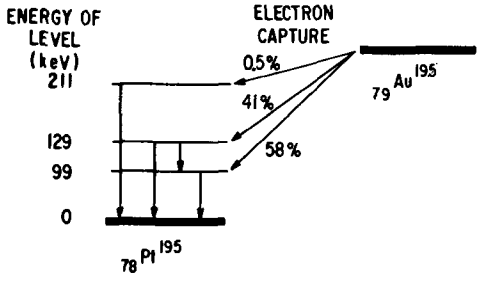

Fig. 2. Decay scheme of the radioisotope, $_{79}Au^{195}$, resulting in emission of 31, 99, 129, and 211 keV gamma rays as well as x-rays characteristic of the daughter, $_{78}Pt^{195}$ isotope [after ref. (10)].

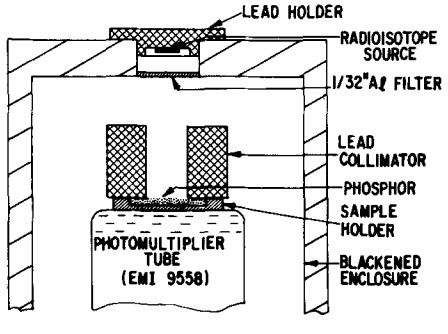

Fig. 3. Experimental arrangement used to measure x-ray response of phosphor screens.

sources.[4] The isotopes were supplied in aqueous solution. A portion of the solution was pipetted into a lead holder and evaporated to dryness. A cover was then glued over the holder to prevent escape of radioactive material while permitting passage of x-rays and gamma-rays. Beryllium foil (0.010 in. thick) was used for the low energy x-rays from the Fe^{55} sample, and 0.003 in. aluminum foil was used in the other cases.

The spectrum of the radiation from the mounted sources was examined using a Nuclear Chicago scintillation counter with a NaI crystal as the scintillator, and a pulse height analyzer. In this manner five sources were selected as yielding radiation in the range 25-135 keV of sufficient spectral purity to warrant further study. The selected sources were examined with a germanium detector and associated circuitry at substantially higher energy resolution. Taking the Au^{195} radioisotope source as an example, the $K_{\alpha 1}$, $K_{\alpha 2}$, $K'_{\beta 1}$, and $K'_{\beta 2}$ peaks of the Pt daughter were clearly resolved, as well as the weak γ-rays at 98.5 and 129.4 keV. Still weaker Pb x-rays, arriving from the irradiation of the lead holder, could also be discerned. The relative amplitudes of the K-shell components were found to be in reasonable agreement with the published values, and relative amplitudes for the γ-ray peaks could also be determined.

Characteristics of the five sources actually employed in our further experiments are summarized in Table II. In that table the $K_{\alpha 1}$ and $K_{\alpha 2}$ peaks and also the $K'_{\beta 1}$ and $K'_{\beta 2}$ peaks are lumped together and assigned an average energy and a total relative intensity.

The Nuclear Chicago scintillation counter was used to monitor the total x-ray flux from each of the mounted sources. The fluxes were measured several times during the course of the work and were found to decay in accordance with the known half-lives of the radioisotopes.

Measurement of X-ray Response

The experimental arrangement used for measurement of phosphor x-ray response is shown in Fig. 3. The radiation from the radioisotope source passed through a thin 0.031 in. Al filter and a lead collimator before reaching the powder phosphor sample. The sample was contained in a holder with a glass bottom positioned on the input window of an EMI 9558 photomultiplier tube. All parts of the enclosure about the

[4] Dy^{159}, Au^{195}, I^{125}, and Sn^{119m} were obtained from New England Nuclear Corporation, Boston, while Fe^{55}, Co^{57}, W^{181}, and Sr^{85} were obtained from International Chemical and Nuclear Corporation, Nuclear Science Division, Pittsburgh.

Table II. Characteristics of mounted x-ray sources

Isotope	Dominant emissions[a] (keV)
I^{125}	27.3(75), 31.3(17), 35.5(8)
Dy^{159}	44.1(78), 51.0(19), 58(3)
W^{181}	56.9(79), 66.1(21)
Au^{195}	66.0(71), 76.8(20), 99(9)
Co^{57}	122(90), 136,(10)

[a] The numbers in parentheses refer to the relative intensities of the emissions.

collimator, sample, and photomultiplier were blackened to minimize effects of reflected light.

Most of the phosphors investigated are available commercially. The samples were prepared by lightly pressing the powder into one of several holders which differed in depth. The screen weight was calculated from the diameter of the holder and the weight of the powder. The same screens were preserved for measurement of light transmission and of x-ray attenuation.

Originally it was thought that screens of more uniform screen weight could be prepared by settling. However, it was found that such screens tended to emit light preferentially toward the glass plate on which they were settled, presumably because of particle size separation occurring during the settling process. The use of settled screens was therefore abandoned.

The basic experimental data obtained for each phosphor were the photomultiplier currents for each source as a function of phosphor screen weight. A quantity of greater interest is the efficiency η_r as defined in Eq. [1] and given in Eq. [10], *i.e.*, the light energy emitted toward the photomultiplier per unit x-ray energy incident on the phosphor screen. The incident x-ray energy was calculated from the flux as measured with the scintillation counter taking into account the dominant emission energies from each source and their relative intensities (see Table II), and also the solid angles from the source subtended by the sample and by the counter. No corrections for attenuation by Al filter or by the Al can surrounding the scintillation crystal were required since the Al thicknesses were the same. (The Al filter served the additional useful purpose that it effectively removed low energy x-rays such as M-shell emissions at ~10 keV from the Au^{195} source.)

To convert the photomultiplier current readings to the desired values of light energy output, it was necessary to calibrate the sensitivity of the photomultiplier to the light emitted by each phosphor. This was accomplished by measuring the light output under cathode-ray excitation both with the photomultiplier and with a thermopile which gives a reading proportional to emitted light energy independent of wavelength. The photomultiplier readings had previously been calibrated in terms of emitted light energy (12). For determination of the photomultiplier sensitivity it was also necessary to compute the fraction of the emitted light gathered by the photomultiplier, taking Lambert's law into account.

A correction to the photomultiplier sensitivity was required because in the measurement of x-ray response the light is diffusely incident on the face plate, and may also undergo multiple reflections between the tube and the phosphor plaque. To estimate this basically geometrical correction readings were taken both with the arrangement of Fig. 3 and with the photomultiplier lowered to match the geometry used for cathode-ray excitation. The computed correction amounted to 20%.

Direct excitation of the photomultiplier by the sources proved to be negligible.

X-ray Cross Sections

A recent tabulation of x-ray cross sections of the elements is that of Storm and Israel (13). Of prime importance to x-ray efficiency is the total energy-absorption cross section. This cross section, labeled $(\mu/\rho)_{tot,en}$, was plotted as a function of energy for selected elements. Values at the dominant emission energies of each radioisotope source were estimated by interpolation and are given for several of these energies in Table III. Also listed in that table for convenient reference is the energy of the K-shell absorption edge (13). As the x-ray energy falls below the absorption edge for a shell, there is a sharp drop in the energy-absorption cross section, corresponding to the inability of lower energy photons to supply enough energy to ionize an electron from that shell.

Table III. Energy absorption coefficients and the K-shell absorption edge of selected elements

Atomic Number	Element	μ' in cm²/g 27.3 keV	44.1 keV	56.9 keV	66.0 keV	122 keV	K_{edge} (keV)
8	O	0.22	0.05	0.033	0.027	0.023	—
16	S	2.3	0.52	0.24	0.16	0.04	2.5
20	Ca	4.5	1.1	0.50	0.32	0.07	4.0
30	Zn	13.0	3.5	1.67	1.13	0.20	9.7
48	Cd	18.5	8.5	4.6	3.25	0.66	26.7
53	I	9.3	8.4	4.9	3.6	0.84	33.2
55	Cs	10.5	8.4	5.2	3.8	0.9	35.9
64	Gd	17.2	4.6	5.2	4.25	1.25	50.2
74	W	24.5	7.3	3.65	2.35	1.47	69.5

Table IV. Energy absorption coefficients μ', in units of cm²/g, at selected emission energies of the radioisotope sources

Phosphor \ Energy (keV)	27.3	44.1	56.9	66.0	122.0
$Zn_{0.68}Cd_{0.32}S$	11.47	3.2	2.13	1.48	0.29
$CaWO_4$	16.35	4.84	2.41	1.56	0.94
ZnO	10.48	2.82	1.35	0.91	0.16
Gd_2O_3	14.94	3.99	4.51	3.69	1.09
CsI	9.91	8.40	5.05	3.70	0.87

Energy-absorption cross sections of phosphors are readily calculated from the cross sections of their constituent elements. If μ'_i is the coefficient of an element having an atomic weight A_i, then the cross section μ'_c of a compound of molecular weight c is given by

$$\mu'_c = \sum_i \frac{A_i}{c} \mu'_i \qquad [11]$$

Energy-absorption cross sections of several phosphors, calculated from Table III and Eq. [11], are listed in Table IV.

With the apparatus available to us it was not convenient to attempt a direct measurement of the total energy-absorption cross section. However, measurements were made of the attenuation of the flux from the different sources produced by interposing phosphor screens between the source and the scintillation crystal. Values were thereby obtained for the narrow beam total cross section, labeled $(\mu/\rho)_{tot,t}$ by Storm and Israel. Each x-ray energy emitted by a source is characterized by its own cross section, and the measurement yields the average cross section provided the total attenuation is small.

The ratio between the measured and calculated average total cross section for different phosphors and sources is displayed in Fig. 4. The closeness of the

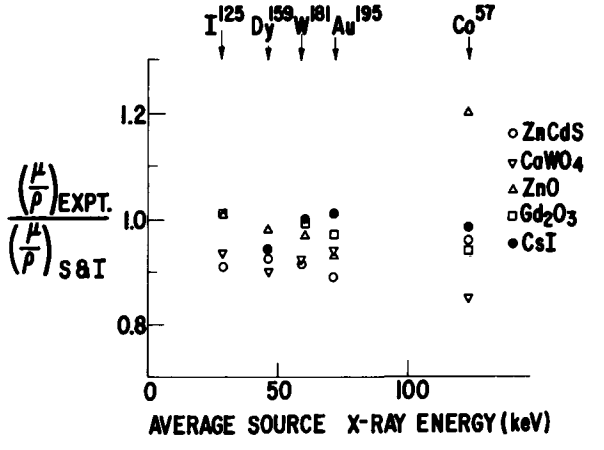

Fig. 4. Ratio of experimental and calculated values of the average total x-ray cross section of different phosphors. Calculated values were computed from the phosphor composition using $(\mu/\rho)_{tot,t}$ of ref. (13) taking into account the x-ray spectrum of the sources.

ratio to 1 tends to substantiate both our characterization of the radioisotope sources and the accuracy of the (μ/ρ) values computed for the different phosphors. The tendency for the ratio to fall below 1 may reflect insufficient collimation.

Conversion of X-ray Energy into Light Energy

A factor of prime importance to the x-ray efficiency of a phosphor is the efficiency with which it converts absorbed x-ray energy to light energy. In the region of present concern, 25-135 keV, the photoelectric process dominates x-ray energy absorption (13). In the photoelectric process the x-ray photon ionizes an electron from a deep inner shell, the excess of the photon energy over the ionization energy going to kinetic energy of an electron. We would therefore like to know the efficiency with which both the electron kinetic energy and the energy of the hole in the inner shell are converted to light energy.

In discussing the conversion of x-ray energy to light, Klasens and de Groot (3) made the assumption that only the electron kinetic energy is utilized. This assumption implies that the conversion efficiency in a compound such as NaI will have a striking dependence on x-ray photon energy. In particular, as the energy increases through the K-shell absorption edge of I at 33.2 keV, the conversion efficiency would be expected to drop by about a factor of two (the ratio of the energy absorption above the edge to that below the edge). Otherwise stated, the increase in energy absorption at the edge contributes nothing to the light output, since it represents the energy of holes in the K-shell.

Collinson and Hill (14) and more recently Aitken *et al.* (15) have studied the efficiency of NaI(Tl) and other scintillation crystals over a broad range of x-ray energies including the K-shell edge of I. They find fractional variations in efficiency of only a few per cent in the neighborhood of the K-shell edge. Collinson and Hill suggest that the energy of holes is either reradiated or is channeled via Auger transitions into electron kinetic energy. The observed efficiency variations are attributed to a dependence of efficiency on electron energy and on excitation density. Thus, they equate the efficiency under x-ray excitation to an efficiency for conversion of electron kinetic energy to light, which is the cathode-ray efficiency.

It appears reasonable to use the cathode-ray efficiency as an estimate to the efficiency with which a powder phosphor converts absorbed x-ray photons to light. Accordingly, we have measured the cathode-ray efficiency of phosphors of interest by a technique described previously (12). The values thereby obtained represent the intrinsic efficiency as diminished by light absorption within the settled plaque. The intrinsic efficiency, which is of present interest, was estimated by correcting the measured values by the factor $2/(1 + R_p)$, where R_p is the plaque reflectivity (16). Results are listed in Table V.

Table V. Cathode-ray efficiency and light transmission parameters of phosphors

Phosphor	Designation	η_{cr}	λ (Å)	β	σ (cm²/g)
(ZnCd)S:Ag	du Pont 1200	0.211	5400	0.04	5.6
(ZnCd)S:Ag	118-3-22[a] (TV green)	0.229	5400	0.015	20.0
$CaWO_4$:Pb	NBS 1026[b]	0.041	4250	0.046	20.0
ZnO	RCA 33-2-613A	0.121[c]	5400	0.052	16.0
Gd_2O_3:Eu	1327-313[a]	0.115	5400	0.005	12.3
CsI:Tl		0.137	5400	0.02	5.6

[a] Obtained from the General Electric Company, Chemical Products Business Section, Cleveland, Ohio.
[b] Obtained from the National Bureau of Standards.
[c] In the case of ZnO a 10% correction was applied to the efficiency as measured at 10 kV to take into account surface losses (ZnO has an unusually high dead voltage) (16).

Optical Properties of the Phosphor Screens

The parameters σ and β (or alternatively a and s) describing the absorption and scattering of light in a powder phosphor can be deduced from a study of screen reflection and transmission. Consider Eq. [4] and [5] with $N_0 = 0$ (no x-ray excitation) and with a light beam of intensity I_0 incident from the left of Fig. 1. Then the appropriate boundary conditions are

$$I(0) = t_1 I_0 + r_1 J(0) \quad [12]$$

$$J(W) = r_2 I(W) \quad [13]$$

and the fraction of the light transmitted is (1)

$$\frac{I_t}{I_0} = \frac{t_2 I(W)}{I_0} = \frac{\beta t_1 t_2 (1 + \rho_1)(1 + \rho_2)}{(\rho_1 + \beta)(\rho_2 + \beta)e^{\sigma W} - (\rho_1 - \beta)(\rho_2 - \beta)e^{-\sigma W}} \quad [14]$$

Similarly for $t_1 = 1$ the reflectivity R_∞ of a phosphor layer which is so thick that transmission through it is negligible is given by (1)

$$R_\infty = \frac{J(0)}{I_0} = \frac{1 - \beta}{1 + \beta} \quad [15]$$

Measurements of light transmission were made on the same samples that were examined under x-ray excitation. In one experimental arrangement light from a tungsten bulb was passed through color glass filters to select the wavelength region of interest. It was then focused through a window into an integrating sphere. The light intensity in the sphere was measured with the phosphor screen positioned in the window first so it did not and then so it did intercept the incident light beam. Data were thus acquired on I_t/I_0 as a function of W. To determine R_∞, the light was focused through a window in the sphere onto a window on the opposite end of a sphere diameter. Successive brightness meter readings were taken from the far window blocked with a thick phosphor screen and with a thick reference screen of $BaSO_4$. Grum and Luckey (17) have shown that the reflectivity of $BaSO_4$ is very close to unity in the visible. Thus, the ratio of the two readings was taken to be R_∞.

The parameter β was calculated from the relation $\beta = (1 - R_\infty)/(1 + R_\infty)$. The quantity σ was determined by matching the experimental transmissivity values to [14] using $t_1 = 0.92$, $\rho_1 = 0.85$, $t_2 = \rho_2 = 1$, and β as determined above. Values are summarized in Table V.

Using the integrating sphere the transmission of the glass holders in which the phosphors were pressed was measured to be 0.92. Thus we assume $t_2 = 0.92$ and $\rho_2 = 0.85$ in [8], while t_1 and ρ_1 were taken equal to one (the surroundings were blackened).

Comparison of X-ray Efficiency with Hamaker's Formula

We now are in a position to compare the x-ray efficiency of a series of phosphors with predictions based on other phosphor parameters. For example, the efficiency of a (ZnCd)S:Ag phosphor as a function of phosphor screen weight is summarized in Fig. 5 for each of the five radioisotope sources. The experimental points are the phosphor light output, as measured by the photomultiplier, divided by the photomultiplier sensitivity to the emitted spectrum and by the incident x-ray energy flux. The theoretical curves represent the efficiency η_r as given by Eq. [10] with appropriate values for the parameters N_{oi}, E_i, and $\mu'(E_i)$ (see, *e.g.*, Table II and IV), η_c, β, and σ (see Table V), and ρ_1, ρ_2, and t_2 (see Section on Optical Properties of the Phosphor Screens). For simplicity each curve is labeled with the average x-ray energy and average μ' for the source in question. The labels 29, 46, 59, 71, and 123 keV refer to the sources I^{125}, Dy^{159}, W^{181}, Au^{195}, and Co^{57}, respectively. The efficiency of other phosphors is summarized in Fig. 6-10.

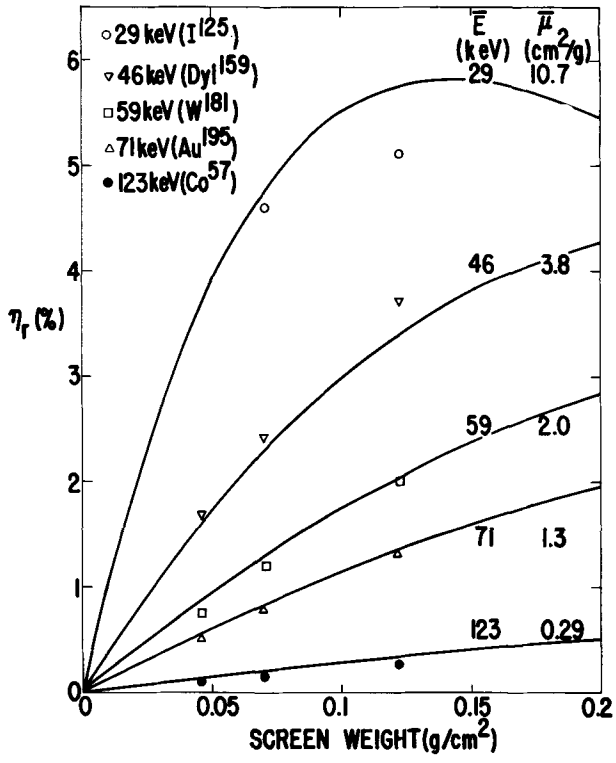

Fig. 5. X-ray efficiency of (ZnCd)S:Ag (du Pont 1200 phosphor) screens as a function of screen weight for different radioisotope sources. The experimental points represent photomultiplier readings normalized by dividing them by the product of the photomultiplier sensitivity and the incident x-ray energy. The solid lines are the theoretical efficiencies η_{lr} (see text and Eq. [8] and [10]) with η_{lc}, σ, and β as given for du Pont 1200 in Table V.

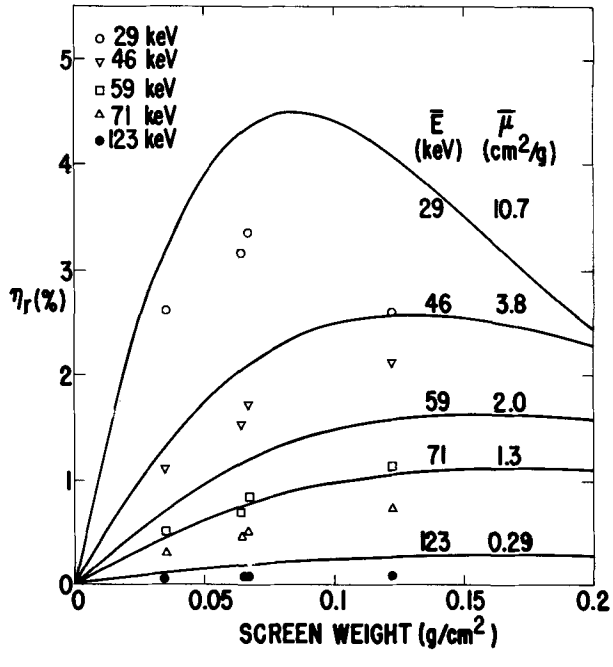

Fig. 6. X-ray efficiency of (ZnCd)S:Ag (TV green phosphor)

Discussion and Conclusions

The agreement between the experimentally determined phosphor efficiency and the theoretical curves is good for du Pont 1200 (ZnCd)S:Ag and Gd_2O_3:Eu (Fig. 5 and 9). It would be good for $CaWO_4$:Pb (Fig. 7) and much improved for the TV green (ZnCd)S:Ag (Fig. 6) if one assumed $\sigma = 30$ cm²/g in each case rather than the measured values of 20 cm²/g. Since the measured values of σ and β are quite sensitive to wavelength for $CaWO_4$:Pb and (ZnCd)S, a 50% error in σ is not unreasonable. For ZnO and CsI:Tl the experimental points tend to lie above the calculated curves.

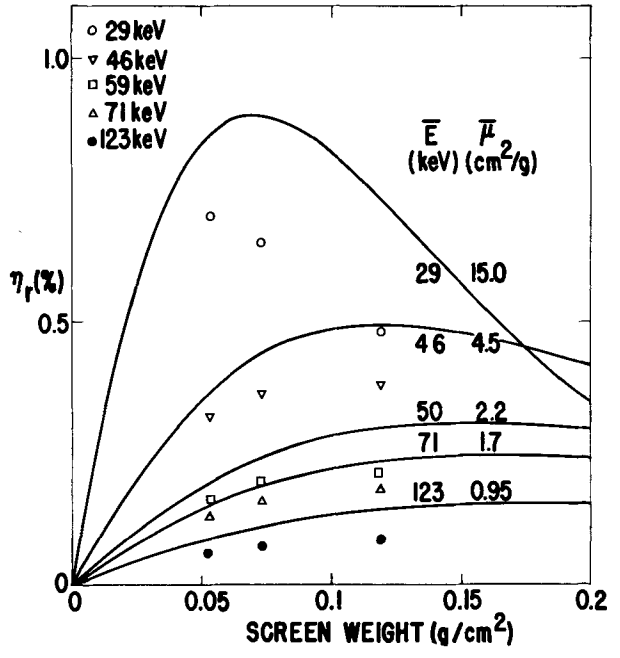

Fig. 7. X-ray efficiency of $CaWO_4$:Pb (National Bureau of Standards No. 1026 phosphor).

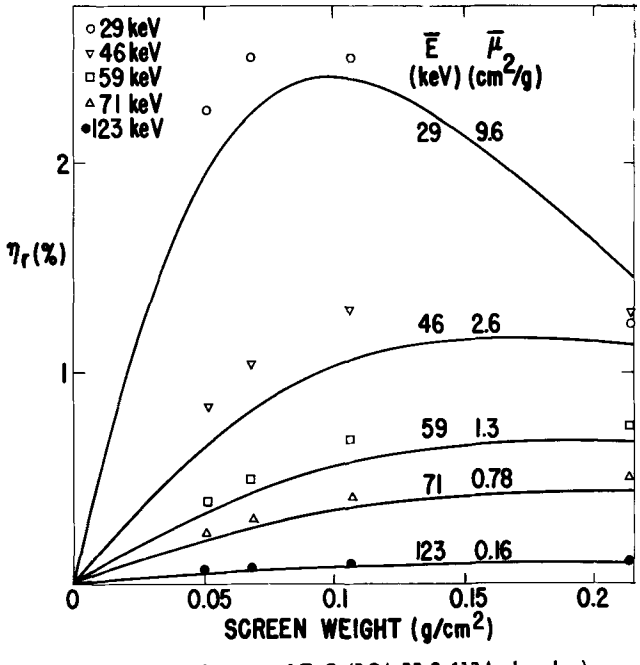

Fig. 8. X-ray efficiency of ZnO (RCA 33-2-613A phosphor)

To further explore the agreement between experiment and theory, apart from errors associated with transmission losses, the ratio $(\eta_r)_{expt}/(\eta_r)_{calc}$ was computed for the lowest screen weight of each phosphor studied. (Transmission losses are smallest at the lowest screen weight.) As shown in Fig. 11, this ratio departs from one by amounts as large as about ±30%. In most cases the ratio for a given phosphor shows a smaller scatter as the source is changed. The departure of the ratio from one would be reduced for $CaWO_4$ and the TV green phosphor if $\sigma = 30$ cm²/g had been used to compute $(\eta_r)_{calc}$.

Errors in the photomultiplier current readings, the photomultiplier sensitivity to the emitted radiation, the flux from the radioactive sources, the fraction of the flux incident on the sample, and the phosphor screen weight all affect $(\eta_r)_{meas}$. Similarly, errors in the energy-absorption cross sections, cathode-ray efficiency, and optical parameters affect $(\eta_r)_{calc}$. The scat-

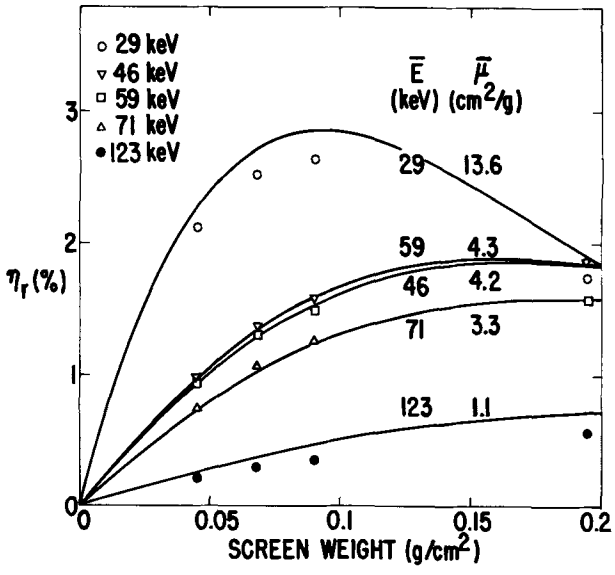

Fig. 9. X-ray efficiency of Gd_2O_3:Eu (1327-313 phosphor)

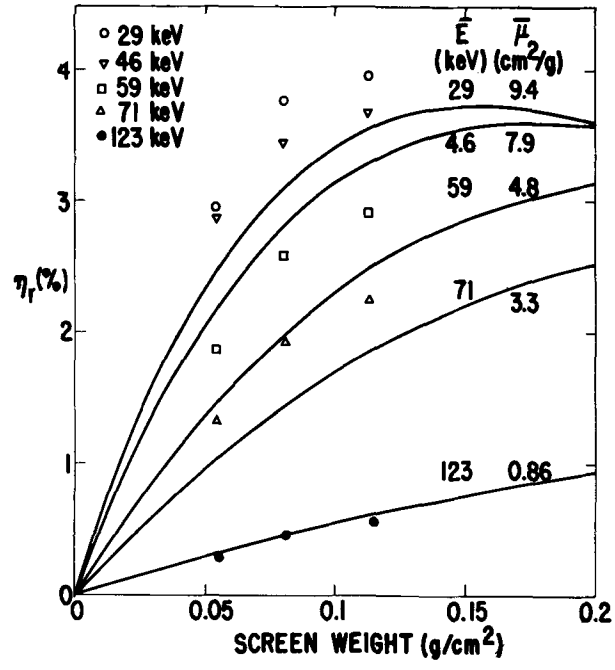

Fig. 10. X-ray efficiency of CsI:Tl

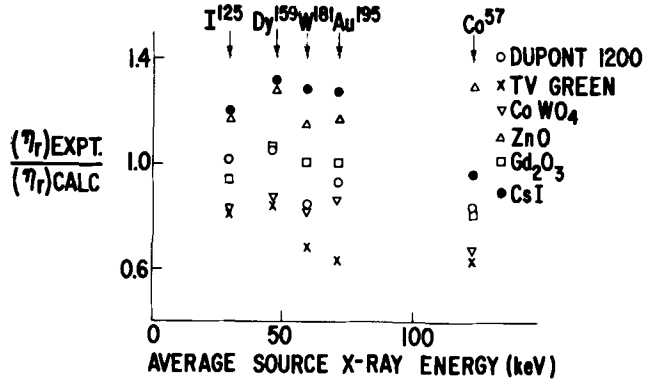

Fig. 11. Comparison of experimental and calculated values of η_r at low phosphor weight (see Fig. 5-10).

ter of ±30% may represent the composite of errors of 5-10% in half a dozen or so different measurements. Note that no adjustable parameters have been employed.

The generally good agreement between experiment and theory is evidence that the conversion efficiency for absorbed x-ray energy to light energy is at least approximately equal to the cathode-ray efficiency. Suppose, for example, only the energy of the fast electron treated on x-ray absorption were utilized [with the cathode-ray efficiency as assumed by Klasens and de Groot (3)]. Then there would be a sharp drop in conversion efficiency and in x-ray response as one increased the x-ray energy through the K-shell absorption edge of the heavy element responsible for the bulk of the x-ray absorption by the screen. For example, one would anticipate a sharp drop in the response of Gd_2O_3:Eu screens between 46 and 59 keV, associated with the K-shell edge of Gd at 50.2 eV. No such drop is observed.

The results of this paper lead us to believe that Hamaker's formulas [8] and [9] can be used together with phosphor parameters such as the cathode-ray efficiency to provide a guide to the x-ray response to be expected under a wide range of experimental conditions.

In selecting a powder phosphor for efficient x-ray detection, one obviously must optimize the three factors η_a, η_c, and η_t of Eq. [1]. Our study points to CsI:Tl and (ZnCd)S:Ag as outstanding candidates. CsI:Tl has high x-ray absorption and high cathode-ray efficiency together with good light transmission up to substantial screen weights. (ZnCd)S:Ag has a lower x-ray absorption but still higher cathode-ray efficiency. The fine-grained (ZnCd)S used as a TV green phosphor is inferior to the coarse-grained phosphor produced for x-ray detection in its transmission of the emitted light (*c.f.*, Fig. 5 and 6), particularly at the higher screen weights.

It is of interest to consider to what extent a different x-ray efficiency would be obtained for a given phosphor composition using a different phosphor lot or a different technique of screen preparation. Of the three factors in Eq. [1], the x-ray absorption would be affected the least, since it is determined solely by the phosphor composition and screen weight. The cathode-ray efficiency will vary somewhat with preparative techniques, but usually not by more than 20-30%. The transmission efficiency will depend on the grain size of the phosphor, on how tightly the grains are packed, and on the binder employed. The variation will be greater where the transmission is less, *viz.*, at the higher screen weights. Once again Fig. 5 and 6 demonstrate the kind of variation in x-ray efficiency which may be anticipated.

Acknowledgments

The author is indebted to S. J. Lubowski for carrying out many of the measurements. He wishes to thank R. A. Sieger, the Tube Department, General Electric Company, for suggesting the use of radioisotopes as x-ray sources. He is also indebted to J. D. Kingsley and J. S. Prener for valuable discussions.

Manuscript submitted May 11, 1970; revised manuscript received March 10, 1971. This was Paper 55 presented at the Los Angeles Meeting of the Society, May 10-15, 1970.

Any discussion of this paper will appear in a Discussion Section to be published in the June 1972 JOURNAL.

REFERENCES

1. H. C. Hamaker, *Philips Res. Rept.*, **2**, 55 (1947).
2. H. A. Klasens, *ibid.*, **2**, 68 (1947).
3. H. A. Klasens and W. de Groot, *Philips Tech. Rev.*, **9**, 321 (1947/48).
4. J. W. Coltman, E. G. Ebbinghausin, and W. Altar, *J. Appl. Phys.*, **18**, 530 (1947).
5. I. Broser, H. Kallmann, and U. M. Martins, *Z. Naturforsch.*, **4a**, 2041 (1949).
6. F. Grum, L. F. Costa, and J. L. Donovan, *J. Opt. Soc. Am.*, **59**, 848 (1969).
7. Y. J. Alloucherie, *Appl. Opt.*, **9**, 1403 (1970).

8. K. A. Wickersheim, R. V. Alves, and R. A. Buchanan, *IEEE Trans. Nucl. Sci.*, **NS-17**, 57 (1970)
9. L. J. Bodi, J. F. Cosgrove, and G. McIntosh, *Rev. Sci. Instr.*, **36**, 1112 (1965).
10. See C. M. Lederer, J. M. Hollander, and I. Perlman, "Table of Isotopes," Sixth Ed., John Wiley & Sons, Inc., New York (1967).
11. See ref. (10), p. 379.
12. G. W. Ludwig and J. D. Kingsley, *This Journal*, **117**, 348 (1970).
13. E. Storm and H. I. Israel, "Photon Cross Sections from 0.001 to 100 meV for Elements 1 through 100," Report LA-3753, Los Alamos Scientific Laboratory of the University of California (1967).
14. A. J. L. Collinson and R. Hill, *Proc. Phys. Soc.*, **81**, 883 (1963).
15. D. W. Aitken, B. L. Beron, G. Yenicay, and H. R. Zulliger, *IEEE Trans. Nucl. Sci.*, **NS-14**, 468 (1967).
16. A. Bril and H. A. Klasens, Philips Res. Rept., **7**, 401 (1952).
17. F. Grum and G. W. Luckey, *Appl. Opt.*, **7**, 2289 (1968).

Electronic States of Mn^{2+}-Activated Phosphors

II. Orange-to-Red Emitting Phosphors

D. T. Palumbo

GTE Sylvania Incorporated, Chemical and Metallurgical Division, Towanda, Pennsylvania 18848

and J. J. Brown, Jr.

Virginia Polytechnic Institute, Department of Metals and Ceramic Engineering, Blacksburg, Virginia 24061

ABSTRACT

The electronic states of Mn^{2+} are derived from excitation spectra for eight orange-to-red emitting phosphors: (*i*) ZnF_2:Mn, (*ii*) ZnS:Mn, (*iii*) $Zn_3(PO_4)_2$:Mn, (*iv*) $CaSiO_3$:Pb,Mn, (*v*) $CdSiO_3$:Mn, (*vi*) $Cd_{10}Cl_2(PO_4)_6$:Mn, (*vii*) $Ca_{10}F_{1.8}Cl_{0.2}(PO_4)_6$:Sb,Mn, and (*viii*) $Sr_{10}F_{1.8}Cl_{0.2}(PO_4)_6$:Sb,Mn. All eight phosphors show complete splitting of at least one electronic level. The observed splittings are compared to the expected splittings from crystal field theory. New assignments of the ZnS:Mn levels are given.

We gave in Part I (1) a description of the electronic energy levels of five green-emitting, Mn^{2+}-activated phosphors. Here we consider Mn^{2+}-activated phosphors with orange-to-red emission. We give below excitation and emission spectra for: (*i*) ZnF_2:Mn, (*ii*) ZnS:Mn, (*iii*) $Zn_3(PO_4)_2$:Mn, (*iv*) $CaSiO_3$:Pb,Mn, (*v*) $CdSiO_3$:Mn, (*vi*) $Cd_{10}Cl_2(PO_4)_6$:Mn, (*vii*) $Ca_{10}F_{1.8}Cl_{0.2}(PO_4)_6$:Sb,Mn, and (*viii*) $Sr_{10}F_{1.8}Cl_{0.2}(PO_4)_6$:Sb,Mn. Level assignments are made and compared with previously reported results where possible.

The Mn^{2+} levels in order of increasing energy in an octahedral crystal field are given by Orgel (2) as $^6A_{1g}(^6S)$, $^4T_{1g}(^4G)$, $^4T_{2g}(^4G)$, $^4A_{1g}$-$^4E_g(^4G)$, $^4T_{2g}(^4D)$, $^4E_g(^4D)$, $^4T_{1g}(^4P)$, etc., where A, E, and T refer to single, double, and triple orbital degeneracies; the free-ion-level origins are given in parentheses. In Table I, we list the crystal classes of the eight phosphors, the expected site symmetry for Mn^{2+}, and the maximum orbital degeneracy allowed in the given site symmetry. We cite, also, the appropriate references.

The energy level structure of ZnS:Mn is the subject of a number of works. Bube (11) gives excitation and absorption spectra for ZnS:0.01Mn. Ford *et al.* (15) give absorption spectra for ZnS:0.1Mn. Curie (16) comments on the reduction of the tetrahedral site symmetry of Mn^{2+} if Cl^- is introduced in the ZnS lattice, and in his text gives a summary of absorption measurements on this system. McClure (12), Ryskin *et al.* (13), and Langer and Ibuki (14) note fine structure in the absorption spectra of single crystals of ZnS:Mn; all three authors place the ^4A, $^4E(^4G)$ level at about 21,600 cm^{-1}. Mehra (38), in a recent note, also follows this assignment in his fit of McClure's observed levels.

Narita (33) calculated the energy levels of Mn^{2+} for the C_3 site in calcium fluorophosphate with change in lattice constant. Johnson (35) reports emission from both sites in the calcium halophosphates and notes that the distribution of Mn^{2+} between the two sites is a function of the halide ratio. Ryan *et al.* (39) give the optical properties of calcium fluorophosphate single crystals, giving spectra of Mn^{2+} in the C_3 and C_s sites. They also report emission from a "modified" C_s site. No detailed level assignments are given. Konstantinova-Schlezinger and Kabakova (34) gave excitation spectra for Mn^{2+} red emitters. For $Zn_3(PO_4)_2$:Mn they place the most intense band at 417 nm and show three additional excitation bands at longer wavelength.

* Electrochemical Society Active Member.
Key words: phosphors, luminescence, manganese, crystal field.

Table I. Crystal class, site symmetry, and permitted degeneracy for Mn^{2+}-activated phosphors

Phosphor	Crystal class	Site symmetry	Permitted degeneracy	References
ZnF_2	Tetragonal	D_{4h}	Double	3-5
$Cd_{10}Cl_2(PO_4)_6$	Hexagonal	C_3 and C_s	Double and single	6-9
ZnS	Hexagonal	T_d	Triple	10-16
$Ca_{10}F_{1.8}Cl_{0.2}(PO_4)_6$	Hexagonal	C_3 and C_s	Double and single	17-21
$Sr_{10}F_{1.8}Cl_{0.2}(PO_4)_6$	Hexagonal	C_3 and C_s	Double and single	19, 22
$CaSiO_3$	Triclinic	C_1	Single	23-27
$CdSiO_3$	Monoclinic	—	Single	28, 29
$Zn_3(PO_4)_2$	Tetragonal	—	Double	30, 31, 33

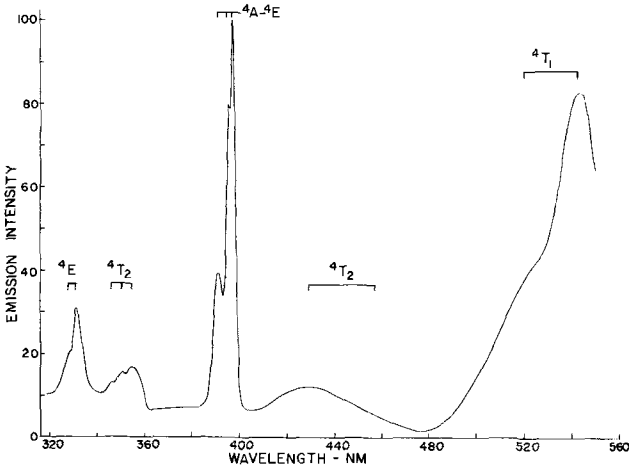

Fig. 1. Excitation spectrum of ZnF_2:0.03Mn, liquid-N_2 temperature.

Experimental Procedures

Procedures for measurement of excitation and emission spectra have been given in Part I (1). Samples were prepared by the usual solid-state phosphor synthesis. Preparative techniques are well-documented in the literature and are cited in Table I. All phosphors considered here are commercially available materials.

Experimental Results and Discussion

ZnF_2:0.03 Mn.—We use the ZnF_2:Mn excitation spectrum, given in Fig. 1, as a guide for the level assignments. The sharp triplet structure at about 395 nm is assigned as the ^4A, $^4E(^4G)$ level, the triplet indicative of complete orbital splitting of the level. Stout (36) places the $^4A(^4G)$ level of MnF_2 at 25,180 cm^{-1}; he assigns the incompletely resolved structure at 25,500 cm^{-1} to the $^4E(^4G)$ level. We assume here that the strongest excitation band in the ZnF_2, at 398.2 nm (25,113 cm^{-1}), is the ^4A (^4G) level. The triplet at about 350 nm is assigned as the split $^4T_2(^4D)$ level; the doublet at about 330 nm is assigned as the split $^4E(^4D)$ level. We would expect six excitation bands lying below the $^4A(^4G)$ level as a result of complete splitting of the $^4T_2(^4G)$ and $^4T_1(^4G)$ levels. Only three of these appear resolved, although the shapes of the bands at about 430 and 510 nm suggest the presence of additional overlapping bands.

From the barycenters of the $^4E(^4G)$ and the $^4E(^4D)$ levels, we computed values of the Racah parameters B and C, using the Tanabe and Sugano $^4\Gamma_3$ matrix, which is independent of the crystal field strength. The results are given in Fig. 2. A crystal field strength (10 Dq) of 9300 cm^{-1} gives a reasonable fit to the barycenters of the ZnF_2:Mn levels. Although in the calculations the assumption of an octahedral field is a poor approximation to the actual field (lower than octahedral), the calculated values for the barycenters of the ^4T levels are in reasonable agreement with the observations. Table II offers a comparison of our values with those reported in the literature.

$Cd_{10}Cl_2(PO_4)_6$:0.06 Mn.—Cadmium chlorophosphate exhibits more resolved structure in excitation than does the ZnF_2. Figure 3 gives the excitation spectrum. Again we attribute the sharp bands at about 405 nm to splitting of the ^4A, $^4E(^4G)$ level. While only three

Table II. Values of B, C, and 10 Dq in cm^{-1} for Mn^{2+} systems

System	B	C	10 Dq	Reference
ZnF_2:Mn	698	3678	9300	This work
MnF_2	950	3280	7800	35
$KCl{\cdot}MnCl_2{\cdot}2H_2O$	800	3200	8000	36

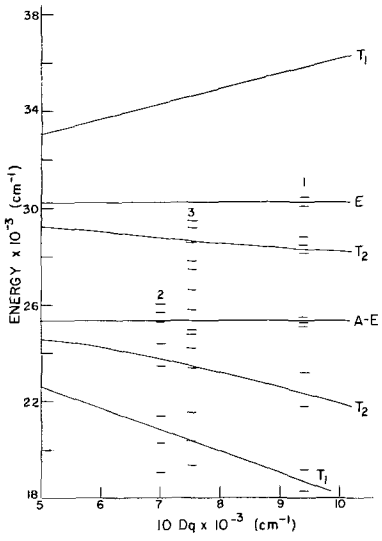

Fig. 2. Calculated energy level diagram based on position of the ^4E levels in ZnF_2:0.03Mn, for B = 698 cm^{-1} and C = 3678 cm^{-1}. Level positions shown for: 1, ZnF_2:Mn; 2, ZnS:Mn; 3, $Ca_{10}F_{1.8}Cl_{0.2}(PO_4)_6$:Sb, Mn.

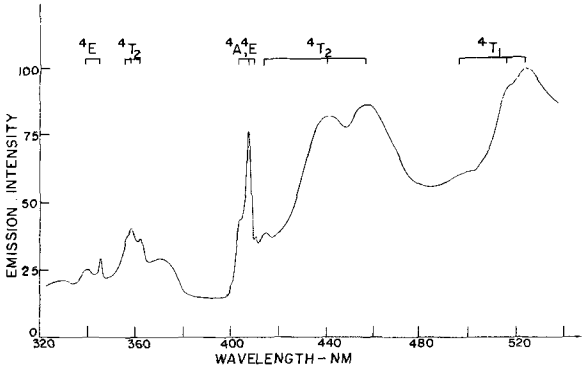

Fig. 3. Excitation spectrum of $Cd_{10}Cl_2(PO_4)_6$:0.06Mn, liquid-N_2 temperature.

bands are expected for complete orbital splitting, we observe four bands at 403.2, 405.4, 407.3, and 410.2 nm. There is also an indication of an unresolved band between the 405.4 and 407.3 nm bands. The six bands at longer wavelength are assigned to complete splitting of the $^4T_2(^4G)$ and $^4T_1(^4G)$ levels; the triplet at about 360 nm is assigned as the split $^4T_2(^4D)$ level; the doublet at about 340 nm is assigned as the split $^4E(^4D)$ level. The broad band at about 370 nm, as well as the additional levels observed in the ^4A, $^4E(^4G)$ level structure cannot be assigned unequivocally. Several possibilities exist: first, there are two possible sites for Mn^{2+} in the apatite lattice (with C_3 and C_s symmetry) and if fluorescence occurs from both sites, we could expect additional structure in the excitation spectrum; second, transitions from the $^2T_2(^2I)$ level can introduce additional structure; and third, spin-orbit coupling could produce additional splittings. Experimentally, no definitive procedure is available for differentiating among these possibilities. The structure observed, however, requires a Mn^{2+} site symmetry lower than C_3 if emission originates only from the C_3 site.

ZnS:Mn.—For ZnS:Mn we first note a previously unreported excitation band at about 410 nm. Figure 4 gives excitation spectra, measured at room temperature, for 1, 2, and 5% Mn concentrations. The intensity of the 410 nm band is seen to increase with increasing Mn concentration. The five bands shown we assign as components of the $^4T_2(^4G)$ and $^4T_1(^4G)$ levels. We would expect six bands here for complete

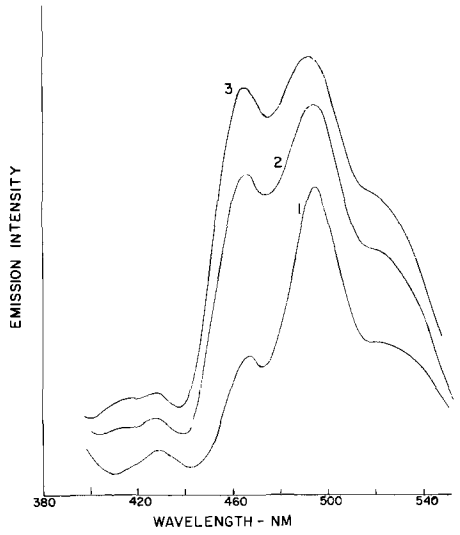

Fig. 4. Excitation spectra at room temperature for: 1, ZnS:0.01 Mn; 2, ZnS:0.02 Mn; 3, ZnS:0.05 Mn.

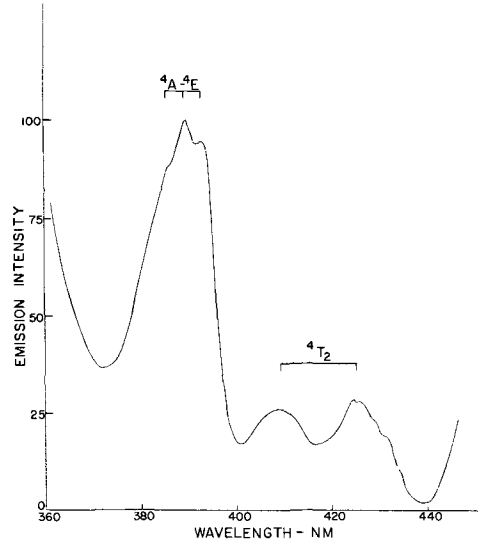

Fig. 5. Excitation spectrum for ZnS:0.008 Mn, liquid-He temperature.

splitting of the two T levels. We were unable to resolve the sixth band.

Figure 5 gives the excitation spectrum for ZnS:0.008 Mn, measured at liquid-He temperature, for the region from 360 to 450 nm. The triplet structure at about 390 nm we attribute to splitting of the ^4A, $^4E(^4G)$ level. This assignment differs with the assignments given by McClure (12), Langer and Ibuki (14), Ryskin *et al.* (13), and Mehra (38). These authors assume tetrahedral symmetry of Mn^{2+} obtains; no splitting of degenerate E and T levels is expected for this symmetry. However, the similarity of the ZnS:Mn spectrum to the ZnF_2:Mn and $Cd_{10}Cl_2(PO_4)_6$:Mn spectra, and in fact, as is developed below, the similarities in the spectra of all eight phosphors leaves little doubt that the ^4A, $^4E(^4G)$ level is found in the region from 390 to 410 nm. Curie (16) has suggested that substitution of Cl^- for S^{2-} would lower the Mn^{2+} site symmetry from T_d to C_3. We find, however, that similar splittings are observed in chloride-free samples. We conclude that substitution of Mn^{2+} for Zn^{2+} is sufficient to distort the normal T_d site symmetry.

The vibrational fine structure, reported by McClure (12), Langer and Ibuki (14), and Ryskin *et al.* (13), observed in the absorption mode is also observed in the excitation mode. We do not observe all the detailed structure reported by Langer and Ibuki (14); our results more nearly parallel those of McClure (12)

Table III. Fine structure observed in the ZnS:Mn 460 nm absorption band (in cm^{-1})

This work	McClure (12)	Ryskin *et al.* (13)
21,327	21,357	21,345
21,427	21,435	21,418
21,519	21,550	21,519
21,620	21,620	21,630
21,706	21,724	21,725
21,810	21,824	21,819
21,915	—	21,915

and Ryskin *et al.* (13), Table III lists the observed fine structure compared with McClure's and Ryskin's values.

$Ca_{10}F_{1.8}Cl_{0.2}(PO_4)_6$:0.08Sb, 0.12Mn.—Johnson (35) has noted Mn^{2+} emission from both sites (C_3 and C_s) in the apatite lattice. Our measurements of excitation spectra, while indicating more structure than is expected from a site with C_3 symmetry, do not show all the structure consistent with emission from both sites. This presumes, of course, that there is no overlapping of band positions, *i.e.*, all bands can be resolved.

Figure 6 gives the excitation spectrum for the 400 to 540 nm region and Fig. 7 gives it for the 300 to 380 nm region. The bands at about 400 and 404 nm we assign to the ^4A, $^4E(^4G)$ level and the five bands at

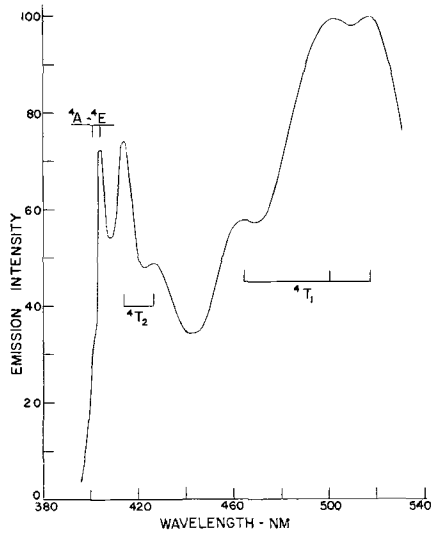

Fig. 6. Excitation spectrum for $Ca_{10}F_{1.8}Cl_{0.2}(PO_4)_6$:0.08Sb, 0.12 Mn, liquid-N_2 temperature.

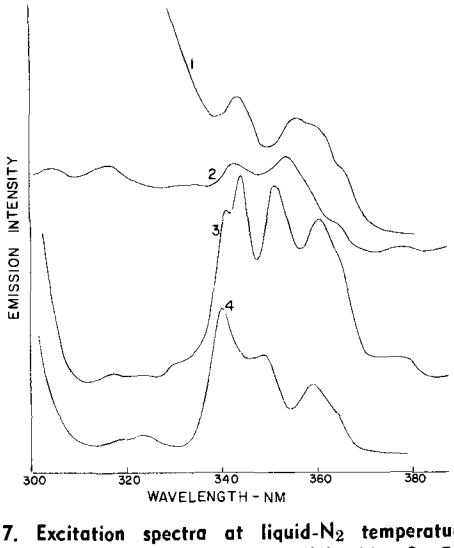

Fig. 7. Excitation spectra at liquid-N_2 temperature for: 1, $CdSiO_3$:0.03 Mn; 2, $CaSiO_3$:0.008 Pb, 0.07 Mn; 3, $Ca_{10}F_{1.8}Cl_{0.2}(PO_4)_6$:0.08 Sb, 0.12 Mn; 4, $Sr_{10}F_{1.8}Cl_{0.2}(PO_4)_6$:0.08 Sb, 0.08 Mn.

longer wavelength to the split $^4T_2(^4G)$ and $^4T_1(^4G)$ levels. The bands at 375 and 387 nm we leave unassigned; these may originate from the $^2T_2$ (^2I) level. The bands at 349, 359, and 364 nm we assign as components of the $^4T_2(^4D)$ level. The weak structure observed in the region of 320 nm we assign as the $^4T_1(^4D)$ level.

Our choice of assignment of the band at 404 nm warrants some comment. It could be argued that the band is the third component of the split $^4T_2(^4G)$ level. Our method, following Orgel, is to assign the sharpest and strongest excitation band as the $^4A(^4G)$ level. There seems little question of the validity of the method for the assignments in ZnF_2, ZnS, $Cd_{10}Cl_2(PO_4)_6$, and in the phosphors cited in Part I (1). Whether the assignment is correct in all cases, however, is not resolvable in the light of existing data.

The recent work of Ryan *et al.* (39) with single crystals of calcium fluorophosphate is a case in point. Their absorption spectra for the C_3 site suggests a band at about 510 nm. They do not observe the band in the excitation mode. As noted above, we assign a level at 517 nm as the third component of the $^4T_1(^4G)$ level; our assignments of the remaining two components of this level correspond to the levels observed by Ryan *et al.* at 487 and 461 nm. Their observation of additional structure in the $^4T_2(^4G)$ and the ^4A, $^4E(^4G)$ levels suggests complete splitting of these levels, indicative of a site symmetry lower than C_3, if we attribute the observed bands to simple orbital splittings. We would assign their level at 403.7 nm as the $^4A(^4G)$ based on the narrow band width, in correspondence with our observed level at 403.8 nm.

For the C_s site symmetry, Ryan *et al.* observe a less-structured excitation spectrum than is observed for the C_3 site. In particular, a sharp band at 400.9 nm could be assigned as the ^4A, $^4E(^4G)$ level. If so, then the band we observe at 400.5 nm may arise from the C_s site. In all, although no completely definitive assignments can be made for all the observed levels, except possibly for the $^4T_2(^4G)$ level, present data are not inconsistent with emission from a site with lower than C_3 symmetry.

Our observed levels for the calcium halophosphate show little correspondence with the levels calculated by Narita (33) for the fluorophosphate. In his first paper (33), he places the lowest energy level at 24,200 cm^{-1}; our observed value is 19,300 cm^{-1}. His second paper (33) introduces a correction in the calculation based on the ionicity of the phosphate ion. An ionicity value between two and three could place the lowest level at the observed value. However, his calculated levels show smaller separations in energy than are actually observed.

$Sr_{10}F_{1.8}Cl_{0.2}(PO_4)_6$: 0.08Sb, 0.08Mn.—The excitation spectrum of the strontium halophosphate, given in Fig. 7 and 8, is similar to that of the calcium halophosphate with some exceptions. No splitting of the ^4A, $^4E(^4G)$ level is observed; only one component of the $^4E(^4D)$ level and two components of the $^4T_1(^4P)$ level are resolved. The unassigned levels observed in the calcium halophosphate (at 375 and 387 nm do not appear in the spectrum.

$CaSiO_3$: 0.008Pb, 0.07Mn and $CdSiO_3$: 0.03Mn.—The calcium and cadmium silicates show similar features in their excitation spectra, given in Fig. 7 and 9. Both show five broad bands in the region from 420 to 540 nm, a single band for the ^4A, $^4E(^4G)$ level, a triplet at about 360 nm assigned as the $^4T_2(^4D)$ level, and doublet at about 340 nm assigned as the $^4E(^4D)$ level. The calcium silicate shows additional structure at about 310 nm assigned as the $^4T_1(^4P)$ level. From site symmetry considerations, we expect complete lifting of the orbital degeneracies in both phosphors. Although several of the levels are not experimentally observed, the spectra are consistent with complete splitting of E and T levels.

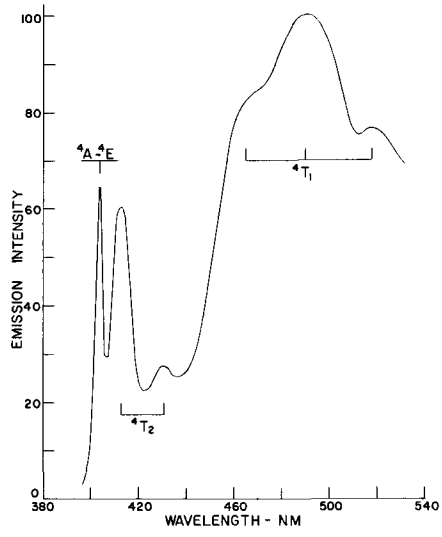

Fig. 8. Excitation spectrum for $Sr_{10}F_{1.8}Cl_{0.2}(PO_4)_6$:0.08 Sb, 0.08 Mn at liquid-N_2 temperature.

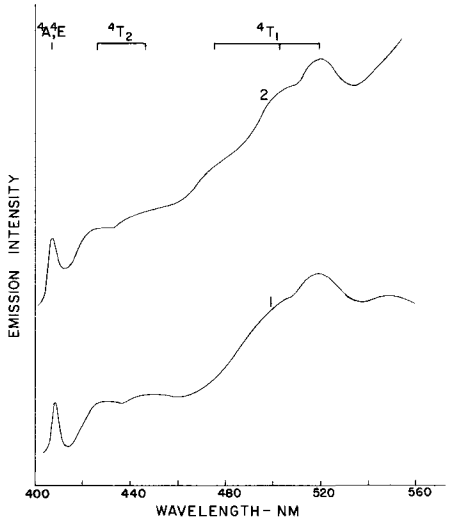

Fig. 9. Excitation spectra at liquid-N_2 temperature for: 1, $CdSiO_3$:0.03 Mn; and 2, $CaSiO_3$:0.008 Pb, 0.07 Mn.

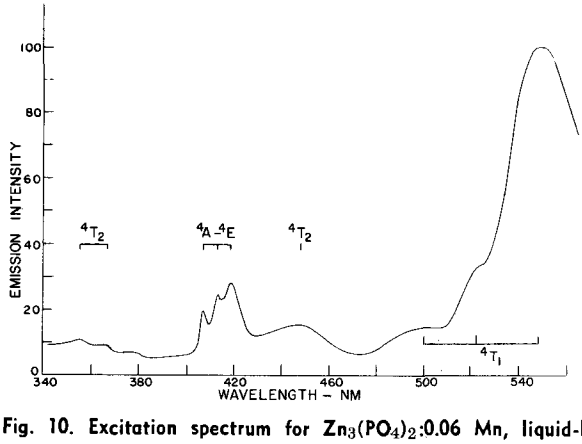

Fig. 10. Excitation spectrum for $Zn_3(PO_4)_2$:0.06 Mn, liquid-N_2 temperature.

$Zn_3(PO_4)_2$: 0.06 Mn.—The zinc phosphate shows three weak bands in the region from 350 to 380 nm. These are probably components of the $^4T_2(^4D)$ levels. The three sharp bands in the region from 400 to 420 nm we assign to the split ^4A, $^4E(^4G)$ level. Four broad bands are resolved in the region from 430 to 560 nm and are assigned as components of the $^4T_2(^4G)$ and the $^4T_1(^4G)$ levels. Konstantinova-Schlezinger and Kabakova (34)

Table IV. Mn^{2+} excitation yands (in Å and cm^{-1})

Free-ion level	Level in O_h symmetry	ZnF_2		$Cd_{10}Cl_2(PO_4)_6$		ZnS		$Ca_{10}F_{1.8}Cl_{0.2}(PO_4)_6$		$Sr_{10}F_{1.8}Cl_{0.2}(PO_4)_6$		$CaSiO_3$		$CdSiO_3$		$Zn_3(PO_4)_2$	
^4G	$^4T_{1g}$	5436	18396	5270	18975	5245	19065	5170	19342	5180	19300	5200	19231	5490	18214	5480	18248
		5210	19195	5140	19455	4930	20283	4915	20346	4900	20450	5000	20000	5190	19268	5200	19230
				4950	20202	4600	21739	4640	21552	4600	21750	4670	21413	5000	20000	4960	20161
^4G	$^4T_{2g}$	4586	21805	4575	21858	4260	23474	4270	23419	4310	23250	4450	22472	4480	22321	4505	22197
		4297	23272	4405	22701	4090	24443	4127	24231	4120	24350	4266	23441	4270	23419		
				4146	24119												
^4G	$^4A_{1g}$, $^4E_{2g}$	3982	25113	4102*	24378	3946	25342	4038	24765	4040	24800	4077	24527	4073	24552	4190	23866
		3963	25233	4073	24552	3893	25687	4005	24969							4135	24184
		3920	25510	4054	24667	3837	26062									4070	24570
				4032	24801												
^4D	$^4T_{2g}$	3550	28169	3722*	26867	Not observed		3875*	25807			3780*	26455				
		3505	28530	3630	27548			3750*	26667	3648	27400	3645	27435	3677	27196	3765*	26560
		3466	28852	3592	27839			3640	27473	3580	27950	3580	27933	3608	27716	3650	27397
				3563	28066			3590	27855	3497	28650	3530	28328	3547	28193	3550	28169
								3493	28629								
^4D	^4E_g	3322	30102	3454	28952			3428	29172	3405	29400	3420	29240	3460	28902	Not observed	
		3280	30488	3395	29455			3392	29481					3425	29197		
^4P	$^4T_{1g}$			3305	30257					3235	30912	3325	30075	Not observed			
										3190	31348	3155	31696				
												3040	32895				

* Unassigned levels.

show a single broad band for the ^4A, $^4E(^4G)$ triplet and three additional bands on the low energy side of the triplet. The observed complete splitting of the ^4A, $^4E(^4G)$ and the $^4T_1(^4G)$ levels indicates a distortion of the expected site symmetry for Mn^{2+} in $Zn_3(PO_4)_2$.

We have noted failure to resolve some of the expected levels in a spectrum, on the assumption that complete splitting of one level requires complete splitting of all levels. While this is true for transitions between levels of the same symmetry species, *e.g.*, $^4A_1 \rightarrow {}^4T_1(^4G)$ and $^4T_1(^4P)$, it is not necessarily true for transitions between levels of different symmetry species, *e.g.*, $^4A_1 \rightarrow {}^4T_1(^4G)$ and $^4T_2(^4G)$. Group theoretical arguments require that in order for electric dipole transitions to be observed the integrals, $\int \psi'_e(X, Y, \text{or } Z)\ \psi_e\, d\tau$ or $\int \psi'_v \psi'_e(X, Y, \text{or } Z)\psi_v\psi_e d\tau$, contain the totally symmetric representation, where the (ψ'_v, ψ_v) and $\psi'_e, \psi_e)$ are the vibrational and electronic wave functions, respectively, between the two states. Granted we are correct in our thesis that at least one electronic level in each of the phosphors considered above shows complete splitting, we require evaluation of the integrals for the point groups C_1, C_s, C_i, C_2, C_{2v}, C_{2h}, D_2, and D_{2h}, site symmetries consistent with complete splitting of electronic levels. Our evaluations show all the expected transitions are allowed in these symmetries. Cotton (40) gives an excellent treatment of the calculation.

We give in Table IV a summary of the wavelengths and wave numbers for the excitation bands observed for the eight phosphor systems classified according to the free-ion origin and appropriate crystal field assignment.

Emission Spectra

Only ZnS:Mn and $CaSiO_3$:Pb,Mn show structure in their emission spectra. Langer and Ibuki (14) have given the ZnS:Mn spectrum and attribute the sharp line structure to vibrational levels. Froelich (23) shows splitting of the $CaSiO_3$:Pb,Mn emission spectrum into two bands at liquid-N_2 temperature. Our results parallel these findings.

Summary

We have derived the electronic energy level structures of the two classes of Mn^{2+}-activated phosphors, *i.e.*, the green, and the orange-to-red emitters, from their excitation spectra. The position of the ^4A, $^4E(^4G)$ level is relatively constant in both classes and is found at about 23,500 cm^{-1} for the green emitters, and at about 24,800 cm^{-1} for the orange-to-red emitters. Distortion of the site symmetry is common; eight of the thirteen phosphors examined show splittings consistent with a site symmetry lower than is expected from crystallographic considerations.

Manuscript submitted Aug. 13, 1970; revised manuscript received Feb. 26, 1971.

Any discussion of this paper will appear in a Discussion Section to be published in the June 1972 JOURNAL.

REFERENCES

1. D. T. Palumbo and J. J. Brown, Jr., *This Journal*, **117**, 1184 (1970).
2. L. E. Orgel, *J. Chem. Phys.*, **23**, 1004 (1955).
3. P. D. Johnson and F. E. Williams, *ibid.*, **17**, 583 (1949).
4. J. H. Crawford and F. E. Williams, *ibid.*, **18** 775 (1950).
5. G. R. Fonda and F. J. Studer, *J. Opt. Soc. Am.*, **38**, 665, 1007 (1948).
6. A. H. McKeag and J. T. Randall, Brit. Pat. 495,706 (1937).
7. A. H. McKeag, U.S. Pat. 2,201,698 (1940).
8. R. W. Wollentin, C. K. Lui Wei, and R. Nagy, *This Journal*, **99**, 131 (1952).
9. R. C. Ropp, *ibid.*, **110**, 113 (1963).
10. F. A. Kroger, *Physica*, **7**, 92 (1940).
11. R. H. Bube, *Phys. Rev.*, **90**, 70 (1951).
12. D. S. McClure, *J. Chem. Phys.*, **39**, 2850 (1963).
13. A. I. Ryskin, G. I. Khilco, B. I. Maksakov, and K. K. Dubenskii, *Opt. Spectry.*, **16**, 149 (1965).
14. D. Langer and S. Ibuki, *Phys. Rev.*, **138**, A809 (1965).
15. R. A. Ford, E. Kauer, A. Rabenau, and D. A. Brown, *Ber. Bunsenges Physik. Chem.*, **67**, 460 (1963).
16. D. Curie, *Compt. Rend.*, **258**, 3269 (1964); "Champ Cristallin et Luminescence," Chapt. XXII, Gauthier-Villars, Paris (1968).
17. St. Naray-Szabo, *Z. Krist.*, **75**, 387 (1930).
18. A. H. McKeag and P. W. Ranby, Brit. Pat. 578,192 (1942).
19. H. G. Jenkins, A. H. McKeag, and P. W. Ranby, *This Journal*, **96**, 1 (1949).
20. R. Nagy, R. W. Wollentin, and C. K. Lui, *ibid.*, **95**, 187 (1949).
21. M. Doherty and W. Harrison, *Brit. J. Appl. Phys.*, **5**, Suppl. 4, S11 (1954).
22. A. N. Akhavan-Niaka and R. Wallaeys, *Compt. Rend.*, **246**, 1556 (1958).
23. H. C. Froelich, *This Journal*, **93**, 101 (1948).
24. G. R. Fonda and H. C. Froelich, *ibid.*, **93**, 114 (1948).
25. J. B. Merrill and J. H. Schulman, *J. Opt. Soc. Am.*, **38**, 471 (1948).
26. J. H. Schulman, R. J. Ginther, and L. W. Evans, *ibid.*, **38**, 817 (1948).
27. Kh. Mamedov and N. V. Belov, *Compt. Rend. Acad. Sci. URSS*, **107**, 463 (1956).
28. D. E. Harrison and M. V. Hoffman, *This Journal*, **106**, 800 (1959).
29. J. H. Schulman, U.S. Pat. 2,497,140 (1950).
30. G. R. Fonda, *J. Opt. Soc. Am.*, **40**, 347 (1950).
31. A. L. Smith, *This Journal*, **98**, 365 (1951).
32. F. L. Katnack and F. A. Hummel, *ibid*, **105**, 125 (1958).
33. K. Narita, *J. Phys. Soc. Japan*, **16**, 99 (1961); **18**, 79 (1963).

34. M. A. Konstantinova-Schlezinger and A. I. Kabakova, *Zhur. Prikl. Spectros.*, **6**, 632 (1967).
35. P. D. Johnson, "Luminescence of Organic and Inorganic Materials," p. 563, H. P. Kallman and G. M. Spruch, Editors, John Wiley & Sons, Inc., New York (1962).
36. J. W. Stout, *J. Chem. Phys.*, **31**, 709 (1959).
37. D. H. Goode, *ibid.*, **43**, 2830 (1965).
38. A. Mehra, *This Journal*, **118**, 136 (1971).
39. F. M. Ryan, R. C. Ohlmann, J. Murphy, G. R. Wagner, and R. W. Warren, *Phys. Rev.*, **B2**, 2341 (1970).
40. F. A. Cotton, "Chemical Applications of Group Theory," p. 231, Interscience Publishers, New York (1963).

On the Optimum Efficiency of Cathodoluminescence of Inorganic Phosphors

Willi Lehmann*

Westinghouse Research Laboratories, Pittsburgh, Pennsylvania 15235

ABSTRACT

The maximum possible efficiency of a phosphor excited by an electron beam depends primarily on the mean excitation energy required to create, by collision, a free electron-hole pair or a free carrier-ionized activator pair or an excited but nonionized activator. This energy is expressed as a multiple (factor α) of the band gap energy, E_g. Values of α measured for various phosphors scatter over a wide range depending on host material and activator and, in many cases, strongly deviating from $\alpha \approx 3$ observed in free-carrier-collection experiments in semiconductors.

The intensity of light emission of cathodoluminescence of a phosphor powder layer depends on the parameters of excitation in a fairly complex manner (1). Generally, the light intensity is not proportional to either the acceleration voltage or the current density of the exciting electron beam. The two main deviations from linearity, "dead voltage" and "current saturation," both reduce the efficiency, and it has been recognized for a long time that the highest possible efficiency of cathodoluminescence requires excitation conditions where these two deviations are minimized, *i.e.*, excitation by an electron beam of fairly high excitation voltage but of low current density. This optimum efficiency is relatively independent of voltage and current and is only a function of the particular phosphor. Some energy efficiencies of cathodoluminescence of various phosphors, believed to be measured under relatively optimized conditions by various workers, are compiled in Table I.

Experimental

We have made such measurements also on calcium sulfide and calcium oxide phosphors. The sulfides were prepared as described elsewhere (2). The oxides were made from calcium carbonate containing the desired impurities and about 1 molar-% of CaF_2 as flux by firing in O_2 at 1200°C. All phosphors were excited at room temperature, in a demountable tube, with electrons of 8 kV and a current density of approximately 10^{-6} A/cm^2 or somewhat lower. The luminescence was observed from the excited side and its intensity compared, by means of a selected silicon photodiode of very flat spectral quantum response, to several standard phosphors (P-1, P-22, $MgWO_4$) whose efficiencies were known from other sources. Division of the measured quantum intensities by the mean wavelength of the emission spectrum yields the energy efficiency in relative units. This technique delivers results reproducible to about ±5%. However, the method relies on the efficiencies of the standard phosphors and, therefore, the final results are reliable only to about ±10%. Some results so measured are given in Table II.

* Electrochemical Society Active Member.
Key words: phosphors, luminescence, cathodoluminescence, efficiency.

Table I. Some reported energy efficiencies (in %) of cathodoluminescence

	Reference 9	10	11	3
ZnS:Ag	21	21	17.8, 19.5	19.6
(Zn,Cd)S:Ag	19.5	19	12	21
ZnS:Cu	23	11	14.6, 16.6	17.5
ZnS:Mn	4			
ZnO	7			5.1
Zn_2SiO_4:Mn	8.5	6, 8	8.5	4.7
$Zn_3(PO_4)_2$:Mn	8	6		
$CaWO_4$	3	3		3.6
$MgWO_4$	2	2.5		2.9
YVO_4:Eu^{3+}				7.1
Y_2O_3:Eu^{3+}				6.4
Y_2O_2S:Eu^{3+}				13.1

Discussion

Tables I and II reveal a very pronounced difference between sulfide phosphors on the one hand, and oxygen-dominated phosphors (including oxides, silicates, vanadates, etc.) on the other. The efficiencies of good sulfide phosphors may go to about 15-20% or even higher while those of oxygen-dominated phosphors rarely come to about 10%. The question naturally arises why the various phosphors display such widely different efficiencies and what is the ultimate maximum of efficiency of a particular phosphor material prepared and excited under all imaginable optimum conditions? This problem has been attacked in the literature (1, 3) with the help of semi-quantitative considerations originally developed to describe carrier multiplication effects in semiconductors (4-7). The following reasoning is developed along the same line but

Table II. Energy efficiencies of CaS and CaO phosphors

(Highest values, measured on best samples)

		%
CaS:Mn	Yellow	16
CaS:Cu	Blue-violet	18
CaS:Sb	Yellow-green	18
CaS:Ce^{3+}	Green	22
CaS:Eu^{2+}	Red	10
CaS:Ce^{3+},Eu^{2+}	Red	16
CaS:Sm^{3+}	Yellow	12
CaS:Pb	Ultraviolet	17
CaO:Mn	Yellow	5
CaO:Pb	Ultraviolet	10

keeps open the possibility of excitations in phosphors which are not, or to a much lesser degree, possible in semiconductors.

A relatively small fraction of the primary high-energy electrons arriving from the electron gun at the phosphor surface is back scattered from the latter and does not contribute to luminescence. The amount of energy lost in this way has recently been determined by Meyer (8) to be close to 10% for typical phosphor powder layers somewhat dependent on the phosphor material and the surface texture of the layer. Hence, close to 90% of the incident energy is actually absorbed by the phosphor.

Primary electrons penetrating into the lattice of the phosphor create, by collision, avalanches of free carriers and localized excited states. One may simplify the task of a mathematical description of the complicated avalanche process and consider only the low-energy tail of it, *i.e.*, the creation of the final states of excitation which emit light quanta when they recombine afterward. Possible excitation states in a phosphor are schematically shown in Fig. 1. They include free electron-hole pairs (A), free carrier-ionized activator pairs (B), and excited but nonionized activators (C).

The mean energy required to create, by collision with hot free carriers, one of the final excitation states may be E_x. Each state delivers only the energy E_m (mean energy of the emission light) if the recombination is radiative, and nothing if it is nonradiative. Hence, the over-all energy efficiency can formally be written as

$$\eta = \eta_a \frac{CE_m}{E_x} \qquad [1]$$

where $C \leq 1$ is the probability of the recombination to be radiative and where η_a ($\approx$90% in typical phosphors) is the primary energy absorption coefficient. The mean excitation energy, E_x, may be expressed as multiple (factor α) of the band gap energy, E_g, of the material

$$\eta = \eta_a \frac{CE_m}{\alpha E_g} \qquad [2]$$

This equation has been published (in slightly different formulation) by Garlick (1) and by Ludwig and Kingsley (3).

The quantity E_g depends only on the phosphor material (*e.g.*, $E_g = 3.7$ eV for all ZnS phosphors) and E_m depends only on the emission spectrum of the luminescence (*e.g.*, $E_m = 2.75$ eV for blue ZnS:Ag). The recombination coefficient, C, may vary from sample to sample and may be responsible, to some degree at least, for the scatter in efficiency reported by different workers on different samples of the same phosphor type. The assumption is made here that C is between 80 and 100% in cases of the very best phosphor samples within each type, and this assumption is supported by measurements of the quantum efficiency of photoluminescence (3, 9-11).

The main unknown in Eq. [2] is the factor α of which no reliable measurements are available for most phosphor materials. The situation is simpler in semiconductors in which carrier multiplication by creation of free electron-hole pairs (A in Fig. 1) dominates. This

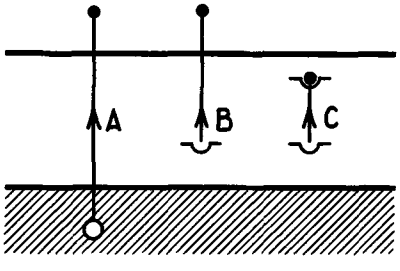

Fig. 1. Excitation transitions in phosphors

Table III. Values calculated from Eq. [3]

		η_a	C	η	E_m (eV)	E_g (eV)	α
Sulfides							
ZnS:Cu	Green	0.9	0.9	0.23	2.3	3.7	2.2
ZnS:Ag	Blue	0.9	0.9	0.21	2.75	3.7	2.9
CaS:Ce	Green	0.9	0.9	0.22	2.3	4.8	1.76
CaS:Cu	Blue-violet	0.9	0.9	0.18	2.9	4.8	2.7
CaS:Mn	Yellow	0.9	0.9	0.16	2.1	4.8	2.2
CaS:Pb	Ultraviolet	0.9	0.9	0.17	3.4	4.8	3.4
Oxides							
ZnO	Green	0.9	0.9	0.07	2.4	3.25	8.5
$ZnSiO_4$:Mn	Green	0.9	0.9	0.085	2.4	4.5	5.7
$CaWO_4$	Blue	0.9	0.9	0.036	2.9	5.0	13
YVO_4:Eu	Red	0.9	0.9	0.071	2.03	3.5	6.6
CaO:Mn	Yellow	0.9	0.9	0.05	2.1	6.5	5.2
CaO:Pb	Ultraviolet	0.9	0.9	0.10	3.45	6.5	4.3

case is accessible to theory which leads to a minimum value of α close to 3 for semiconductors of equal masses of (hot) electrons and holes (6). Direct measurements of α in Ge,Si, SiC, InSb, GaAs, GaP, CdTe, CdS, PbS, and PbO all gave the uniform result of an α slightly above 3 (12) which may be understood on the basis that effective masses of very hot carriers (in contrast to carriers in thermal equilibrium with the lattice) are nearly equal because they do not correspond to single extrema in conduction band and valence band, respectively.[1]

The excitation process in many phosphors probably is more complicated than in simple semiconductors since excitations other than the creation of free carrier pairs (transition A in Fig. 1) are possible, and since effective masses even of very hot carriers are not necessarily equal in highly ionic wide-gap compounds. Because of these unknowns, we have tried to determine values of α of common phosphor materials with the help of Eq. [2], *i.e.*

$$\alpha = \frac{\eta_a C E_m}{\eta E_g} \qquad [3]$$

from measured values of η, E_m, and E_g with the assumptions of $\eta_a = 0.9$ and $C = 0.9 \pm 0.1$. The latter requires that only the best values of η for each phosphor material can be considered. Some results are shown in Table III. Here, E_m follows from the emission spectra and values of E_g were measured from optical reflection spectra on powders. The values of α so determined in Table III are reliable only to about $\pm$20%. However, there can be little doubt that they do not cluster about 3 but scatter over a fairly wide range including values much higher and much lower than 3. It is also apparent that α-values of sulfides are consistently lower than those of oxygen-dominated phosphors.

Conclusion

We are not able to understand this result in all details but suggest the following effects to be involved and to be worth a further consideration:

(*a*) Oxides are more ionic compounds than sulfides,[2] and it is conceivable that hot free carriers, although they appear to be nearly equal in sulfides, are very unequal in oxides. This should affect the mean excitation energy required at least of transition A (Fig. 1). If so, then sulfide phosphors permit, in principle, higher efficiencies of cathodoluminescence than oxides.

(*b*) The probability factor of radiative recombination, C may be near unity for low-energy excitation characteristic of photoluminescence but may be substantially lower than $C = 0.9 \pm 0.1$ (as assumed in Table III) for excitations involving hot carriers because of competition of a nonradiative way of recombination accessible by hot but not by thermal carriers. This case probably exists in red emitting CaS:Eu^{2+} phosphors (14). If it is possible also in other phosphors it could explain some very high α-values ob-

[1] Pointed out by one of the reviewers of this paper.
[2] Electronegativities are 2.5 eV for $S^=$ and 3.5 eV for $O^=$ (13).

tained with Eq. [3] which otherwise are hard to understand. An example is $CaWO_4$ ($\alpha = 13$) in Table III.

(c) Exciting transitions B and C (Fig. 1) may compete with transition A in many phosphors. For instance, creation of free electron-ionized activator pairs (transition B) by collision with hot carriers has long been considered to take place during electroluminescence of ZnS:Cu and there is no reason to deny the possibility of this transition during cathodoluminescence. The possibility of nonionizing excitation (corresponding to internal 4f → 5d transitions) is demonstrated by a strong optical absorption band at 2.73 eV in CaS:Ce^{3+} phosphors (14), and corresponding nonionizing internal transitions within Mn^{2+} ions are well known in many Mn-activated phosphors. In either case, transitions B and C require less energy than transition A and can easily account for the very low values of α in Table III measured on ZnS:Cu, CaS:Ce, and CaS:Mn.

These three effects *a*, *b* and *c* may be present in different phosphors to various degrees and, in view of this complication, it is hardly a surprise to observe α-values to scatter over a wide range. In fact, α varies even more from phosphor to phosphor than the band gap energy, E_g, and thus is mainly responsible for variations of the optimum efficiency of cathodoluminescence in different materials.

Manuscript submitted Sept. 23, 1970; revised manuscript received Jan. 13, 1971. This was Paper 56 presented at the Los Angeles Meeting of the Society, May 10-15, 1970.

Any discussion of this paper will appear in a Discussion Section to be published in the June 1972 JOURNAL.

REFERENCES

1. G. F. J. Garlick, "Cathodo-and Radioluminescence" in "Luminescence of Inorganic Compounds," P. Goldberg, Editor, Academic Press (1966). There are also references to earlier publications.
2. W. Lehmann, *This Journal*, **117**, 1389 (1970).
3. G. W. Ludwig and J. D. Kingsley, *ibid.*, **117**, 348 and 353 (1970).
4. D. L. Dexter, Proc. Intern. Conf. Semicond. Phys., Prague, 1960, p. 122, Academic Press (1961).
5. W. Shockley, *Solid-State Electron.*, **2**, 35 (1961).
6. C. A. Klein, *J. Appl. Phys.*, **39**, 2029 (1968).
7. F. Steinrisser, *Phys. Rev. Letters*, **24**, 213 (1970).
8. V. D. Meyer, *J. Appl. Phys.*, **41**, 4059 (1970).
9. A. Bril and H. A. Klasens, *Philips Res. Rept.*, **7**, 401 (1952).
10. A. Bril in "Luminescence of Organic and Inorganic Materials," p. 479, H. P. Kollmann and G. M. Spruch, Editors, John Wiley & Sons, New York (1962).
11. G. Gergely, I. Hangos, K. Toth, J. Adam, and G. Pozsgay, *Z. Chem. Phys.*, **210**, 11 (1959); **211**, 274 (1959).
12. Fig. 3 in ref. (6). There also references to various publications.
13. L. Pauling, "The Nature of the Chemical Bond," p. 93, Cornell University Press, Ithaca, N. Y. (1960).
14. W. Lehmann and F. M. Ryan, *This Journal*, **118**, 477 (1971).

Manganese-Activated Luminescence in $SrAl_{12}O_{19}$ and $CaAl_{12}O_{19}$

Arnost Bergstein[1] and William B. White[2]

Materials Research Laboratory, The Pennsylvania State University, University Park, Pennsylvania 16802

ABSTRACT

Manganese-activated $SrAl_{12}O_{19}$ and $CaAl_{12}O_{19}$ phosphors have been prepared under oxidizing and reducing conditions, and by direct cation exchange. The red emission of oxidized phosphor and green emission of reduced phosphor confirm previous assignments to octahedral Mn^{4+} and tetrahedral Mn^{2+}, respectively. New emission bands in the yellow and orange arise from centers which are related to cation exchange, presumably the Sr^{2+} or 5-coordinated Al^{3+} sites. The behavior of the various emission bands during further oxidation and reduction provides a guide to the sites on which the activator centers are located.

The compounds $SrAl_{12}O_{19}$ and $CaAl_{12}O_{19}$ with the magnetoplumbite structure are interesting phosphor hosts because of the variety of cation sites and the effect on the luminescence of a distribution of activators among them. Our interest here is to interpret the emission spectrum of Mn in terms of the various valence states and host lattice sites available to it. To achieve this objective, phosphors have been prepared under carefully controlled oxidizing and reducing conditions. By relating the emission to the chemistry of preparation we can achieve an improved understanding of the valence state and site distribution of the activator ion.

Phosphors based on the alkaline earth aluminates were described by Kröger (1) who prepared his materials under both oxidizing and reducing conditions and so was able to show that a characteristic green emission was due to Mn^{2+} and a characteristic red emission to Mn^{4+}. Sakamoto and Hitomi (2) have investigated Tl and Ce sensitizers in Ba and Ca aluminates but did not consider the valence and site distribution of the Mn^{2+} activator itself.

The magnetoplumbite structure is known in considerable detail (3) because of the interest in the magnetic ferrites (4, 5). The structure of $CaAl_{12}O_{19}$, isomorphous with $SrAl_{12}O_{19}$, has been recently refined by Kato and Saalfeld (6). The structure of those aluminates consists of spinel-like blocks with Al^{3+} in both tetrahedral and octahedral sites. The blocks are bound with layers in which Ca^{2+} (Sr^{2+}) in 12-fold coordination replaces an O^{2-} and Al^{3+} occupies sites with 5-fold coordination. The interatomic distances and the geometry of the various sites are summarized in Table I.

Experimental

$CaAl_{12}O_{19}$ and $SrAl_{12}O_{19}$ containing a small amount of Mn were prepared as a sintered, coarse-grained mass of oriented crystals by flame fusion. The valence

[1] Visiting scientist. Permanent address: Institute of Solid State Physics, Czechoslovak Academy of Sciences, Prague.
[2] Also affiliated with the Department of Geochemistry and Mineralogy.

Key words: oxide phosphors, magnetoplumbite structure, photoluminescence, Mn^{+4} activator, Mn^{+2} activator.

Table I. Coordination numbers and cation-anion distances in $CaAl_{12}O_{19}$ [from (6)]

Cation	Coord. number	Distance from O^{2-} anion				
		O(1)	O(2)	O(3)	O(4)	O(7)
Ca	12				2.694	2.848
Al(1)	6	1.995	1.818	1.970	1.860	
Al(2)	4	1.801			1.828	
Al(3)	6		1.865			1.896
Al(4)	6	1.883				
Al(5)	5				2.187	1.839

Lattice constants of hexagonal structure: $a = 5.564$, $c = 21.892$A.

state of the Mn was adjusted in the final crystals to obtain an oxidized material, a reduced material, and an exchanged material.

$CaCO_3$ or $SrCO_3$ and Al_2O_3 were mixed in the ratio of 1:6 or 1:(6-2x), x being the mole per cent of $MnCO_3$. The activator concentration ranged from 0.012 to 0.30 m/o (mole per cent). The mixtures were homogenized and heated in air at temperatures from 1250° to 1400°C in intervals of 50°C. After each heating the homogenization was repeated and an x-ray analysis performed to check the phase composition. The annealed powder was used as starting material for growing single crystals or conglomerates of oriented single crystals by the flame fusion method, using an A.D. Little Verneuil apparatus. The ratio of hydrogen to oxygen in the flame was varied from reducing to oxidizing. The growth rate diminished when the percentage of hydrogen increased. The exact composition of the gas was not determined.

The rods from the Verneuil growth were cut into sections parallel or perpendicular to the c-axis. These sections were treated in one of the following ways:

Oxidized: Heated in air at temperatures from 900° to 1400°C for 8-100 hr.

Reduced: Heated in a reducing atmosphere of H_2 or in a carbon furnace flushed with argon at temperatures from 900° to 1250°C for 4-24 hr. The oxygen fugacity under these conditions is in the range of 10^{-5}-10^{-20}.

Exchanged: Soaked in molten $MnCl_2$ at 750°-850°C in a streaming atmosphere of purified argon and carefully washed to remove soluble chlorides.

The structure of the samples was checked by x-ray after the heat treatment. All samples showed only diffraction lines of the magnetoplumbite structure. No α-Al_2O_3 could be detected, in spite of the incongruent melting point reported by Wisnyi (7).

The chemical composition of the starting materials was checked by emission spectroscopic analysis. They contained traces of Fe, Si, Mg, and Be, about 1% Ca and an amount of Mn by which the Mn concentration in the aluminate became 0.01-0.02 m/o. Rare earths, Cr, and Na were not found.

Emission spectra were recorded on a Cary Model 14 spectrophotometer using a luminescence attachment with excitation at 254 and 365 nm. Measurements at temperatures between −168°C and room temperature were performed using liquid nitrogen and an excitation frequency of 365 nm. Qualitative cathodoluminescence and polarization experiments were performed on a luminoscope ELM-2A from the Nuclide Corporation, using 20 and 50X magnifications, and cathode rays of 6-18 kV, and on an electron microprobe. Absorption spectra were obtained on a Beckman DK 2A spectrophotometer using a diffuse reflectance attachment and a MgO reference. Some emission spectra were also obtained using the 488 nm line of an ionized argon laser as an exciting source with a Spex Ramalog spectrophotometer. In general these spectra did not show any features in addition to those observed by more conventional excitation.

Results

Emission spectra.—Emission spectra of $SrAl_{12}O_{19}$ prepared in various ways are shown in Fig. 1 and 2. These spectra are direct tracings from the Cary charts. No correction for photomultiplier response has been made and for this reason no intensity scale is shown.

Rods of $SrAl_{12}O_{19}$:Mn prepared by the flame fusion method at a very high ratio of H_2 to O_2 in the flame were white and when excited by uv radiation of both 254 and 365 nm they showed the emission spectra reproduced in Fig. 1. Five emission bands appear with their peaks at 385, 515, 560, 593, and 640 nm, the band at 640 nm being very weak.

Rods of $CaAl_{12}O_{19}$:Mn and $SrAl_{12}O_{19}$:Mn prepared under more oxidizing ratios of H_2 to O_2 were pink in their outer region and white in the center. The relative extension of the pink region increased with increasing oxygen content in the flame. The spectra were similar to the "oxidized" material in Fig. 1. There is one band with its peak at 511 nm and another intense band between ~600 and 700 nm, with sharp peaks at 643 and 657 nm.

When further manganese was introduced into such a sample by ion exchange with molten $MnCl_2$ in an inert atmosphere at 680°-750°C, emission spectra shown in Fig. 2 resulted. In addition to the green and red bands a broad band between ~520 and 600 nm with peaks at 565 and 600 nm occurred in $SrAl_{12}O_{19}$ and peaks at 562 and 590 nm occurred in $CaAl_{12}O_{19}$.

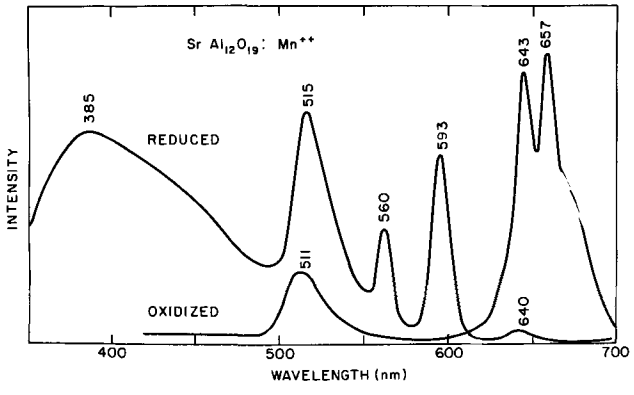

Fig. 1. Emission spectra of $SrAl_{12}O_{19}$ with 0.02 m/o Mn^{++}. "Reduced" was prepared by flame fusion with reducing (hydrogen-rich) flame. "Oxidized" was prepared by firing starting materials in air at 1400°C.

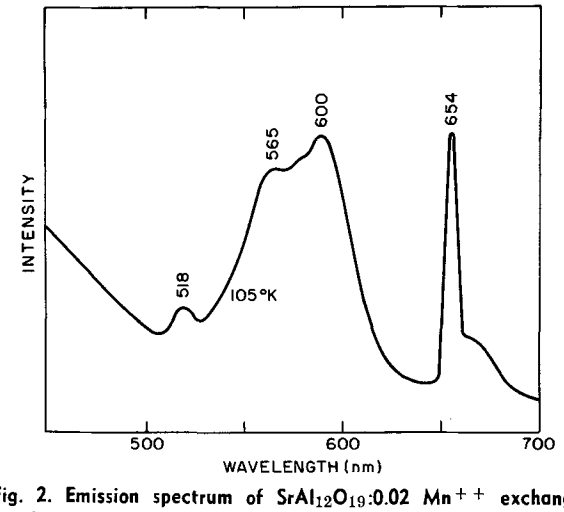

Fig. 2. Emission spectrum of $SrAl_{12}O_{19}$:0.02 Mn^{++} exchanged by soaking in $MnCl_2$ at 680°C. Excitation 365 nm. Temperature 105°K.

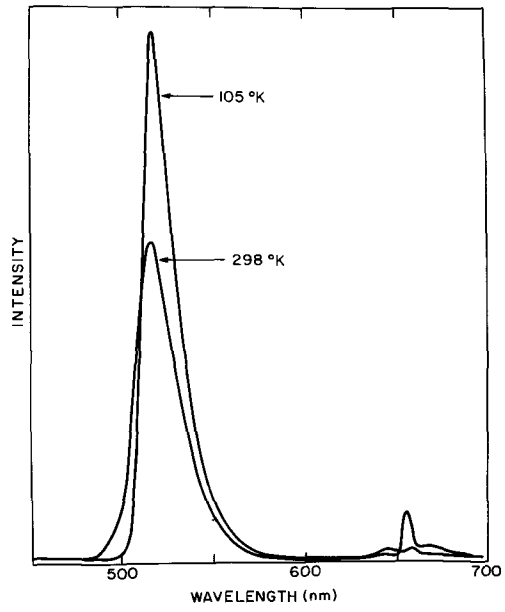

Fig. 3. Temperature dependence of the green band in totally reduced phosphor, $SrAl_{12}O_{19}$:0.2 Mn^{++} fired in hydrogen.

When $SrAl_{12}O_{19}$ is reduced by firing at 1400°C in hydrogen only the green band appears. The intermediate 560 and 590 nm bands vanish and the red band is very weak (Fig. 3).

Visual observations of cathode ray-excited samples in the electron microprobe and in the luminoscope ELM-2A showed sharp boundaries between red and green luminescent regions, corresponding to the pink and white colors without excitation. In the $MnCl_2$ exchanged samples veins of orange emission could be observed. The green and the orange emissions were polarized parallel to the c-axis; the red emission did not show evidence of polarization.

Oxidation of Verneuil-grown samples in air at 900°-1000°C for 4 hr caused a decrease of the intensity of the green emission band but no change of the intensity of the red band. Oxidation for a shorter time at 1300°-1400°C caused a decrease and eventually the disappearance of the green band and a considerable increase in the intensity of the red band. Analogously, reduction at temperatures 900°-1000°C in hydrogen or in a CO-containing argon atmosphere lead to a decrease of the intensity of the red band but to no change of the green band, whereas reduction at 1200°C made the red band decrease and disappear and the green band increase simultaneously within the same or a shorter time. The reduction of samples showing originally only the red and no green emission band at lower temperatures (900°-1000°C) produced nonluminescent samples.

Temperature dependence.—The green band present in almost completely reduced material increased in intensity with decreasing temperature (Fig. 3). However, when both the red and green centers were present, the intensity of the green band decreased with decreasing temperature (Fig. 4). The spectrum of the red center in this phosphor sharpens and the high-frequency component nearly disappears. When only the red center is present, the low-frequency component increases markedly at low temperatures while the high-frequency component becomes very weak. This effect is illustrated in Fig. 5 and the temperature dependence of the two bands is shown in Fig. 6.

Discussion

Valence state and site distribution of activator centers.—The green and the red emission bands of the alkaline earth aluminates were reported by Kröger (1) who ascribed them to Mn^{2+} activator centers and

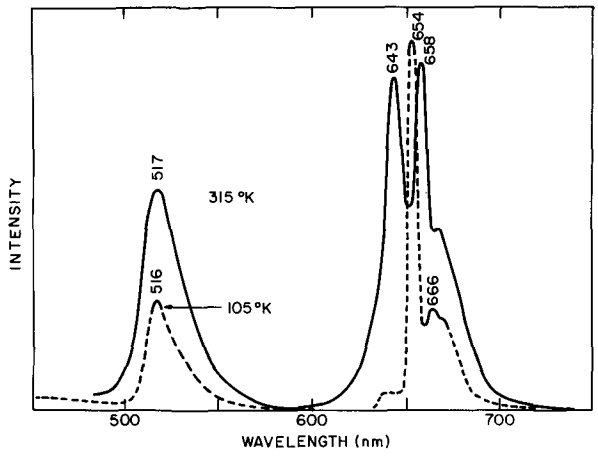

Fig. 4. Temperature dependence of emission spectra of partially reduced $SrAl_{12}O_{19}$:0.2 Mn^{++}. 365 nm excitation.

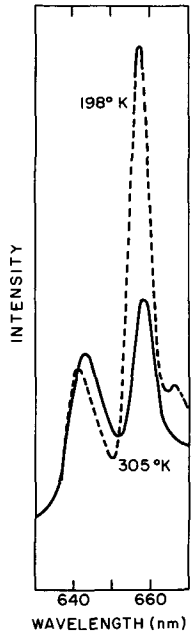

Fig. 5. Temperature dependence of the red band of highly oxidized (fired in air) $SrAl_{12}O_{19}$:0.2 Mn^{++}.

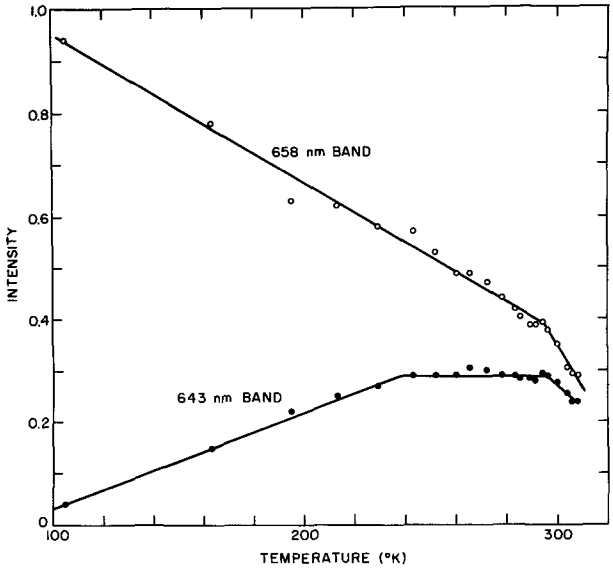

Fig. 6. Change in intensity with temperature of the two components of the red center spectrum. Typical spectra shown in Fig. 5.

to Mn with a higher valence than 2, from the dependence of their presence on the oxygen partial pressure of the atmosphere during preparation or heat treatment. The higher valence was shown to be Mn^{4+}, by chemical analysis and from the similarity of the emission spectrum to the spectra of phosphors activated with the isoelectronic Cr^{3+} ion. Since then the characteristic emission of Mn^{4+} has been identified in a large number of hosts and its identification does not seem to be in doubt (8-11).

The additional emission peaks at ~560-595 nm in the spectra in Fig. 1 and 2 must be ascribed to Mn^{2+} centers in lattice positions different from the centers causing the green emission at 500-520 nm. They appear only in reducing conditions in the hydrogen flame and in $MnCl_2$ exchanged material.

We examine first the green emission with its peak between 510-520 nm and have two experimental hints as to the location of the Mn^{2+} center to which it is linked. First, the green emission is not found in α-Al_2O_3, containing only Al^{3+} ions in octahedral coordination, but it is found in the spinel $MgAl_2O_4$ which contains both tetrahedrally and octahedrally coordinated sites but no 5-fold coordinated Al^{3+} sites nor 12-fold coordinated Sr^{2+} sites. The Mn^{2+} according to its relative site preference energy (−14.7 kcal/m) compared with Al^{3+} and Mg^{2+} (−2.5 and −5.0 kcal/m) (12) will occupy mostly tetrahedral sites. Second, the transformation of a green emitting $CaAl_{12}O_{19}$:Mn or $SrAl_{12}O_{19}$:Mn into a red emitting material requires a considerably higher temperature at equal annealing time than the mere oxidation of the Mn^{2+} centers, which means that the transformation is linked with cation diffusion and that the two kinds of centers occupy different lattice sites. All this suggests that the Mn^{2+} ions causing the green emission are situated in the tetrahedral Al(2) lattice site. The polarization of this emission may be due to deformations of the surroundings in consequence of the difference in size and charge between the Mn^{2+} ion and the Al^{3+} ion. The difference in charge should be compensated by Al^{3+} ions in interstitial positions or, less likely, by anion vacancies.

Addition of 0.02 m/o Fe as Fe_2O_3 to the starting material of the Verneuil grown samples resulted in quenching of the green emission band, whereas the red emission band was not affected contrary to the observation in Kröger (1).

It is interesting that no emission was observed that could be assigned to Mn^{2+} on the octahedral sites of the spinel block. Since the sites, Al(1), Al(3), and Al(4), are all small, the manganese emission should be pushed into the far red or near infrared. The emission is at 730 nm in MgO (13) and the AlO_6 octahedra are smaller than the MgO_6 octahedra. Either the tetrahedral site preference of Mn^{2+} has concentrated it on the tetrahedral site or the emission of octahedral Mn^{2+} lies in the near infrared beyond the range of our instrumentation.

The red bands arise from the ^2E, $^2T_1 \rightarrow {}^4A_2$ transition of Mn^{4+} · Mn^{4+} with an effective radius of 0.54Å will easily replace Al^{3+} (0.53Å) in octahedral coordination and is unlikely to substitute for the far too large Ca^{2+} or Sr^{2+} ions in any coordination. According to Table I, three kinds of oxygen octahedra around Al^{3+} ions with different anion-cation spacing and different degree of symmetry are present in the crystal lattice. From the lack of polarization of the emitted radiation the most symmetrical site, labeled Al(4) would represent the most likely location of the Mn^{4+} centers. If vicinity of the charge compensating Ca^{2+} or Sr^{2+} ions should be critical, the Al(3) sites would be preferred, which are situated on both sides of the mirror planes containing the alkaline earth ions.

The two emission peaks introduced into the Verneuil grown $CaAl_{12}O_{19}$:Mn and $SrAl_{12}O_{19}$:Mn by ion exchange with molten $MnCl_2$ in an inert atmosphere (Fig. 2) seem to be identical with peaks at 560 and 593 nm in the spectrum of a Verneuil grown sample prepared with a relatively high hydrogen ratio in the flame (Fig. 1). In both cases the Mn centers responsible for the peaks will contain Mn^{2+} in consequence of the neutral, and reducing atmosphere present during ion exchange and preparation, respectively. None of these emission peaks appeared when crystals containing only Mn^{4+} ions were reduced under any conditions of temperature or time. Thus we may assume that the Mn^{2+} centers and the Mn^{4+} centers are situated in different lattice sites. If our assignment of the tetrahedral sites to the green Mn^{2+} emission is correct and if we can eliminate the three kinds of octahedral sites in Table I on size and coordination considerations the only sites left for the yellow to orange emitting Mn^{2+} centers are the Al(5) five-fold coordinated site and twelve-fold coordinated Sr site.

There are other reasons for which Al(5) and Ca^{2+}(Sr^{2+}) lattice sites seem to be more likely than the octahedral Al^{3+} sites. Ion exchange proceeds more easily in the Sr^{2+}- and Al(5)-containing mirror planes than in the more compact Al^{3+} spinel blocks. The spacing is larger than in the Al^{3+} octahedra, the Ca(Sr)-O distance being 2.67(2.85) and 2.85(3.0)Å and the Al-O distances about 1.85 and 2.3A for the five-coordinated Al^{3+}. There are no clean-cut criteria by which to make specific assignments. Mn^{++} in either the 5-coordinated or the 12-coordinated site should emit in the green to orange range. It is interesting the $MnCl_2$-exchanged β-alumina also contains an orange band at 590 nm but no band at 560 nm (14). The structures of β-Al_2O_3 and $SrAl_{12}O_{19}$ are very similar except that the easily exchangeable Na^+ site in $NaAl_{12}O_{17}$ is 6-coordinated. The most reasonable conclusion seems to be that the orange emission at 590-600 nm arises from Mn^{2+} on the easily exchangeable large cation site (Sr^{2+}, Ca^{2+}, or Na^+) and that the yellow-emitting center is associated with the 5-coordinated Al(5) site.

It seems from our experiments that only Mn^{2+} and Mn^{3+} or Mn^{3+} and Mn^{4+} are simultaneously present in equilibrium in regions of the crystal which can be considered homogeneous thermodynamic systems, and not Mn^{2+} and Mn^{4+} or all three valences at once. This observation is in agreement with the predictions of Kröger (15). The appearance of the green and the red emission bands in one spectrum is often the result of inhomogeneous samples, containing oxidized and reduced regions, as shown by the optical microscopic observation of the cathodoluminescence.

This is of importance for the mechanism of the charge compensation assumed when tetravalent manganese is substituted for trivalent aluminum into aluminate lattices. It makes unlikely the formation of Mn^{4+} ions by disproportionation of two Mn^{3+} ions into Mn^{2+} and Mn^{4+}. As a consequence, other charge-compensating ions such as Mg^{2+} or Zn^{2+} had to be added to α-Al_2O_3 to produce the red Mn^{4+} emission (1). It is worth mentioning that no red luminescence could be obtained in $ZnAl_2O_4$, which is a normal spinel with the bivalent Zn^{2+} ions in tetrahedral lattice sites, even when treated under the same oxidizing conditions as the luminescent mixed spinel $MgAl_2O_4$, in which part of the Mg^{2+} ions are in octahedral surroundings. If, however, Zn^{2+} is dissolved in α-Al_2O_3, which contains only octahedral lattice positions, the Mn^{4+} spectrum characteristic for α-Al_2O_3 was obtained by Kröger in inhomogeneous samples containing both spinel and corundum phases. This indicates that in aluminates the valence of a cation alone is not decisive for its ability to compensate for the charge of the Mn^{4+} ions and that the coordination number might be an important factor as well. In magnetoplumbite alkaline earth aluminates, the bivalent alkaline earth ions in the mirror planes seem to provide the compensating effect, either indirectly by making possible the introduction of lattice defects like interstitial oxygen ions

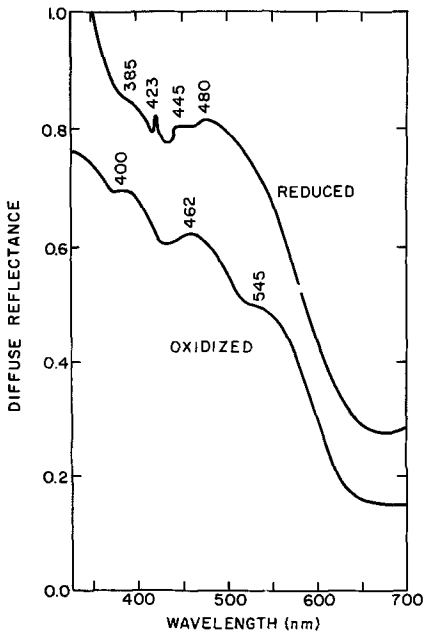

Fig. 7. Diffuse reflectance spectra of highly oxidized and highly reduced $SrAl_{12}O_{19}$:5.0 Mn^{++}.

or Al^{3+} vacancies or directly by being present in an amount exceeding stoichiometry. But here too the substitution of part of the twelve-coordinated Ca^{2+} ions by the smaller Mg^{2+} ions in six-fold (and four-fold) coordination, greatly increases the intensity of the Mn^{4+} emission.

Additional evidence for the valence state and site distribution of the manganese is provided by the reflectance spectrum in Fig. 7. The "reduced" material emits only in the green band. The absorption spectrum shows quite clearly the presence of Mn^{2+} by the characteristic sharp band at 423 nm due to the $^6A_1 \rightarrow {}^4A_1, {}^4E$ transition. Also much in evidence and obscuring the Mn^{2+} band is a broad absorption centered at 480 nm. This same band also appears in the spectrum of "oxidized" $SrAl_{12}O_{19}$ at 462 nm. The single band in this position is very characteristic of Mn^{3+}. The frequencies, 20,800 and 21,600 cm^{-1} respectively, yield a Dq value for the $^5E \rightarrow {}^5T_2$ transition of 2080 and 2160 cm^{-1} which may be compared with the value 1965 cm^{-1} measured in corundum by McClure (15). Geschwind *et al.* (11) reported a band at 21,300 cm^{-1} which they assigned to the $^4A_2 \rightarrow {}^4T_2$ transition of Mn^{4+}. However, there does not seem to be any final proof that they did not have in addition to Mn^{4+} also Mn^{3+} in their Al_2O_3 crystals. This band would place Mn^{3+}, present in both red-emitting and green-emitting materials, on an octahedral site.

New bands at 545 and 400 nm appear in the spectrum of "oxidized" phosphor. These should be the spin-allowed transitions $^4A_2 \rightarrow {}^4T_2$ and $^4A_2 \rightarrow {}^4T_1$ transitions of Mn^{4+}. The Dq value obtained from the 545 nm band is 1830 cm^{-1}, lower of course, than the value obtained by Geschwind *et al.* (11) because of the different assignment, but still a not-unreasonable value for Mn^{4+} on an octahedral site. By comparison Cr^{3+} in Al_2O_3 yields a Dq value of 1845 cm^{-1}. Dq for Mn^{4+} should have been somewhat larger because of the higher charge.

Unlike Fe^{2+} which has a similar but inverted energy level scheme, Mn^{3+} appears not to act as a killer center for luminescence. This is because the critical quintet $\rightarrow$ quintet transition lies above the emitting levels for both Mn^{2+} and Mn^{4+}, whereas in Fe^{2+} with a much smaller Dq (typically 1000 cm^{-1}) the quintet levels lie below the manganese emitting levels and so quench them.

Red-emitting bands and their temperature dependence.—The red-emitting center is generally agreed to arise from the ^2E and $^2T_1 \rightarrow {}^4A_2$ transition of Mn^{4+}. The usual Tanabe-Sugano diagram shows that these two levels are close together and essentially independent of the crystal field strength. The energies of the pair of levels are functions of the Racah B parameter, and thus of the degree of covalency of the Mn^{4+}-O bond. The emission from a wide variety of Mn^{4+}-activated phosphors including MgO (13), magnesium fluorogermanate (9), $MgSnO_3$, and magnesium arsenate (17) all fall in the range of 638-671 nm, indicating only small bond-type changes in this group of phosphors. The emission of $SrAl_{12}O_{19}$ falls directly into the range of previously known phosphors. Schläfer *et al.* (18) were able to move this emission over a range of 650-900 nm in a variety of Cr^{3+}-activated phosphors by varying the nature of the ligand and thus the degree of covalent bonding. A similar behavior would be expected for Mn^{4+}-activated phosphors.

Geschwind *et al.* (11, 19) explained the striking temperature dependence of the red emission from Mn^{4+}-activated Al_2O_3 as a thermal equilibrium between the populations of the ^2E and $^2T_1$ energy levels. A similar temperature dependence was observed in $SrAl_{12}O_{19}$ (Fig. 5). A plot of the ratio of the intensities (from Fig. 6) of the two red bands against reciprocal temperature yields a straight line spanning all points in Fig. 6 from which the energy separation was calculated as 323 cm^{-1}. Precise measurement of the red band positions at room temperature gives values of 15, 560, and 15,200 cm^{-1}. The difference, 360 cm^{-1}, is in good agreement with the thermal value. The larger energy difference compared with 82 cm^{-1} in Al_2O_3 is likely due to the increased distortion of the AlO_6 octahedra in the $SrAl_{12}O_{19}$ host.

Acknowledgment

This research was supported by the Ford Motor Company as part of a program on Crystal Chemical Controls on phosphor behavior.

Manuscript submitted Oct. 14, 1970; revised manuscript received *ca.* Feb. 1, 1971.

Any discussion of this paper will appear in a Discussion Section to be published in the June 1972 JOURNAL.

REFERENCES

1. F. A. Kröger, "Luminescence of Solids," Elsevier, Amsterdam (1948).
2. H. Sakamoto and T. Hitomi, *Jap. J. Appl. Phys.*, **6**, 1315 (1967).
3. V. Adelskold, *Arkiv. Kemi, Min. Geol.*, **12A**, 1 (1938).
4. P. B. Braun, *Philips Res. Rept.*, **12**, 491 (1957).
5. G. H. Jonker, H. P. J. Wijn, and P. B. Braun, *Philips Tech. Rev.*, **18**, 145 (1956).
6. K. Kato and H. Saalfeld, *Neues Jahrb. Mineral. Abh.*, **109**, 192 (1968).
7. L. G. Wisnyi, Card 7-85, X-Ray Powder Data File, Joint Committee on X-Ray Diffraction, Philadelphia.
8. F. A. Kröger and J. van der Boomgaard, *This Journal*, **97**, 377 (1950).
9. G. Kemeny and C. H. Haake, *J. Chem. Phys.*, **33**, 783 (1960).
10. A. H. McKeag, *Acta Phys. Hungar.*, **14**, 309 (1962).
11. S. Geschwind, P. Kisliuk, M. P. Klein, J. P. Remeika, and D. L. Wood, "Low Symposium on Paramagnetic Resonance," Vol. I, Academic Press (1963).
12. A. Miller, *J. Appl. Phys. Suppl.*, **30**, 245 (1959).
13. J. S. Prener, *J. Chem. Phys.*, **21**, 160 (1953).
14. A. Bergstein and W. B. White, *J. Inorg. Nucl. Chem.*, In press.

15. F. A. Kröger, "The Chemistry of Imperfect Crystals," North Holland Publishing Co., Amsterdam (1964).
16. D. S. McClure, *J. Chem. Phys.*, **36**, 2757 (1962).
17. S. Ibuki, K. Awazu, and T. Hata, *Proc. Internat. Conf. Lum. Budapest*, 1465 (1966).
18. H. L. Schläfer, H. Gausmann, and H. Witzke, *J. Chem. Phys.*, **46**, 1423 (1967).
19. S. Geschwind, P. Kisliuk, M. P. Klein, J. P. Remeika, and D. L. Wood, *Phys. Rev.*, **126**, 1684 (1962).

Electron Microscope Characterization of Defects on Gaseous-Etched Silicon Surfaces

E. R. Levin, J. P. Dismukes,* and M. D. Coutts

RCA Laboratories, Princeton, New Jersey 08540

ABSTRACT

Gaseous etching of silicon with HI-HF mixtures can produce mirror-smooth surfaces at temperatures as low as 900°C. Steps result when etching is too rapid. Triangular pits with plane facets can be formed, showing that etching is by a layer mechanism. Mesa-like protrusions, continuous with the silicon matrix, appear on wafers etched in the presence of SiC. The protrusions are not related to precipitated impurities, second phase inclusions, or crystallographic imperfections present in the silicon prior to etching. Rather, they are generated during the etching process by passivation of the silicon surface.

An important step in the processing of silicon wafers is the gas-phase etching to remove the SiO_2 layer and the residual work damage prior to epitaxial growth. It is desirable that this process be carried out at a relatively low temperature to simplify equipment and to reduce harmful diffusion. Both HCl (1, 2) and H_2S (3, 4) attack silicon at a rapid rate and provide smooth surfaces at the relatively high temperature of 1250°C. However, below 1100°C these reagents give typically rough surfaces.

Recent work has been directed toward etching at lower temperatures (5-11). The most critical factor in etching at low temperatures is the much decreased volatility of the SiO_2 coating (11-13). This layer is easily removed at high temperatures by the forward reaction

$$SiO_2(s) + Si \rightleftarrows 2SiO(g)$$

but at lower temperatures, the reverse reaction causes SiO_2 deposition. At 900°C, for example, SiO_2 begins to form on a bare silicon surface when the O_2 concentration exceeds 0.1 ppm. In etching with HI-HF mixtures, the HF removes the oxide film from the surface and prevents its reformation; however, other process variables must be controlled to give surfaces that are smooth and free of defects.

This paper describes the morphology of defects observed under different etching conditions. These deviations from perfectly smooth surface conditions include stepped structures, pits, and raised defects which appear under certain conditions.

Experimental

Apparatus and procedure for etching.—The apparatus and conditions of etching have been given previously (11). Typical total etchant gas flow was 10 l/min, giving an average linear flow velocity of 50 cm/sec in the reaction chamber (1 cm x 4 cm cross section). Typical concentrations of HI were 0.5-2.5%, and those of HF were 0.001-0.1%. The susceptor was usually silicon carbide-coated graphite, with, in some cases, an additional coating of silicon. The susceptor was heated by a 5 kW, 450 kHz Lepel generator; the temperature of the silicon was monitored by an optical pyrometer.

The specimens were <111> wafers, 1 in. in diameter and 0.2 mm thick, with soft-polished faces (14, 15). Wafers of both n- and p-type silicon were studied, and both high- and low-resistivity variations of each type were included. Etch rates were determined from weight loss of the wafers with a Mettler balance sensitive to 0.01 mg, and are given in Fig. 1.

Examination of etched surfaces.—The general features of the etched surfaces, including such factors as the smoothness and uniformity of the etch and the presence of gross defects or irregularities, were easily established by visual examination and by low-power optical microscopy. Details of the surface morphology of the etched wafers were studied by scanning electron microscopy in the emissive mode (16) with a Cambridge "Stereoscan." Since the SEM image is pro-

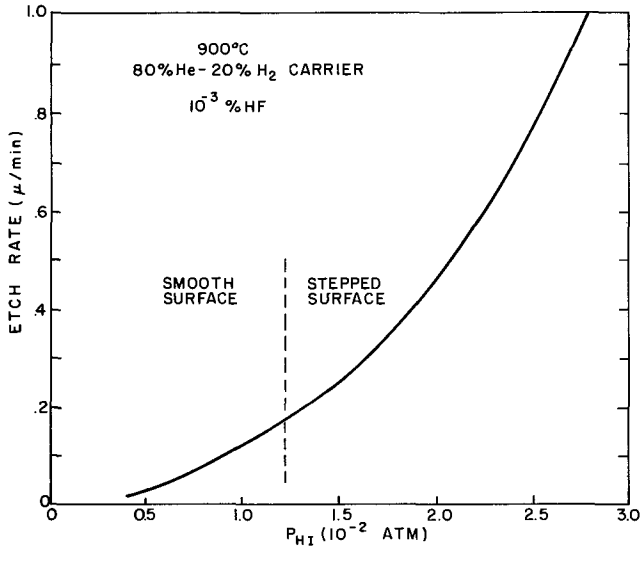

Fig. 1. The dependence of etch rate on HI concentration at 900°C. The HI is mixed with 10^{-3}% HF in a carrier gas of 80% He-20% H_2.

* Electrochemical Society Active Member.
Key words: semiconductor surfaces, surface etching, scanning electron microscopy, silicon.

duced by secondary electrons emitted from the surface under observation, no pretreatment of the silicon specimens was required.

The optical and scanning electron microscope observations were supplemented by electron microprobe analysis, x-ray topography and transmission electron microscopy and diffraction.

Results and Discussion

There was no appreciable difference in etch rate between n- and p-type wafers, nor between wafers of low and high resistivity. However, n-type wafers were generally found to etch very slightly smoother than p-type, and therefore the n-type wafers were selected for the bulk of the work.

Smooth vs. *stepped surfaces.*—An array of steps is one major cause of roughness on etched surfaces. Figure 1 shows the quadratic dependence of etch rate upon HI concentration at 900°C (11). At low concentrations of HI, smooth surfaces are obtained. As the HI concentration is increased, a transition from smooth to stepped etched surfaces is observed. At high etch rates, individual steps or arays of steps become evident, as in Fig. 2. It is significant that the stepped, rough surface in Fig. 2 does not contain pits of the kind usually encountered in preferential etching with liquid (17) or other gaseous (1) etchants.

It is useful to consider the formation of steps during etching in relation to conclusions of other studies. Joyce (18) has attributed step formation during growth to adsorbed impurities. However, in our case the steps observed after etching at high rates are apparently not related to impurities in the etchant gas, for the surface goes from very smooth to very rough over a small range of HI concentration (Fig. 1). On the other hand, since the etch rate increases with temperature, the steps could be formed by a process which is the inverse of the dendritic growth conditions described by Sirtl (9b).

Pits.—Pits are a common defect on rough or preferentially etched surfaces (1, 17). Figure 3 shows a surface etched at 900°C with 1% HI (without HF) in 95% He-5% H_2 carrier gas. The surface is made rough by a distribution of triangular etch pits and by a background array of very fine steps that are barely resolved. Somewhat similar surfaces, showing uniformly oriented triangular etch pits have been observed on (111) diamond surfaces etched with oxygen gas at reduced pressures (19). The appearance of steps and the fact that the pits have plane faces are evidence that etching proceeds by a layer mechanism, the close-packed planes being attacked relatively slowly. Thus, the etching process may be the inverse of the growth of single crystal silicon, which has been shown to take place by the propagation of submicroscopic steps (20). The pits could be "etch pits" formed in preferential attack at dislocations by oxygen or the HI reagent.

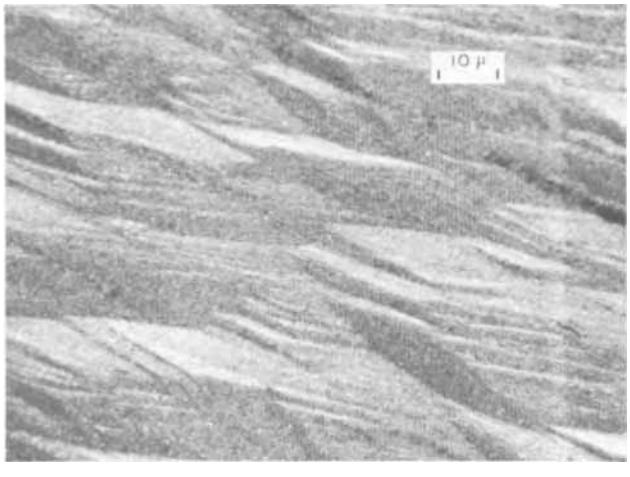

Fig. 2. Scanning electron micrograph showing surface roughness caused by large steps. The silicon wafer was etched at 900°C with 2.75% HI-10^{-3}% HF in 80% He-20% carrier (45° tilt).

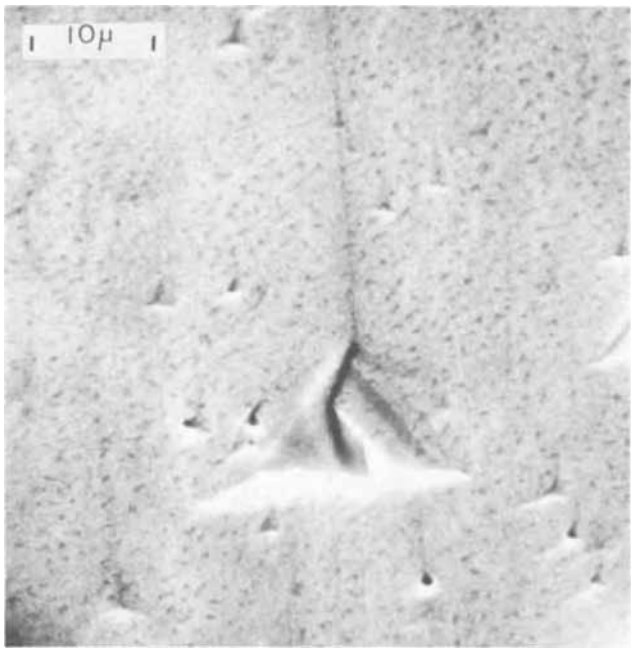

Fig. 3. Surface roughened by triangular etch pits and array of fine steps (45° tilt).

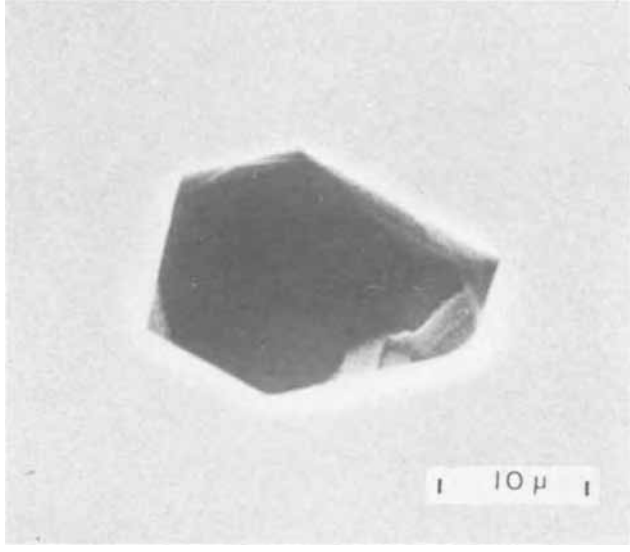

Fig. 4. Hexagonal "etch" pit with planar facets. Brightness around edge of pit suggests it is a low conductivity region (45° tilt).

Figure 4 shows a hexagonal pit in an otherwise smooth surface, etched with 0.5% HI (10^{-3}% HF) in 95% He-5% H_2 at 900°C. The area surrounding the pit is flat and featureless. Pits of this kind were relatively isolated; they occurred over only a portion of the wafer surface, with a maximum density of about 50/cm^2. The pit in Fig. 4, like those in Fig. 3, has straight edges and often planar facets which are parallel to the faces of other pits. This indicates that both the triangular and the hexagonal pits bear a crystallographic relation to the silicon matrix. It does not necessarily mean that the different pits are nucleated by the same mechanism.

The area of the surface immediately surrounding the hexagonal pit in Fig. 4 appears bright compared with the rest of the smoothly etched silicon surface. This is not the normal contrast related to enchanced production of secondaries at an edge, since this effect

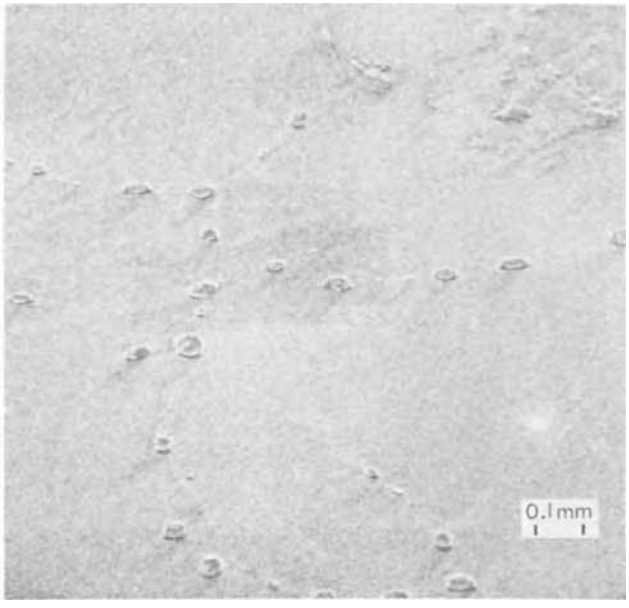

Fig. 5. Mesa-like defects on wafer etched on SiC-coated susceptor (45° tilt).

is not apparent near pits on other samples of Si and GaAs produced by growth or chemical etching. This bright contrast in the scanning electron micrograph indicates that the region may have lower conductivity or a slightly different surface composition than the surrounding matrix.

Raised defects.—Silicon wafers can be etched with HI-HF mixtures on SiC-coated graphite susceptors to produce surfaces which are smooth and free of steps and pits. However, wafers etched in this manner often exhibit defects which protrude outward from the etched surface. A low-magnification view of an etched wafer containing many such raised defects is shown in Fig. 5. This wafer was etched at 900°C with 1% HI (0.1% HF) in 80% He-20% H_2 carrier gas. These defects are present in area densities ranging from 1 to 100 per cm^2. However, they appear only when the wafer is etched on a SiC-coated susceptor: when the SiC susceptor is overlaid with a coating of silicon, the raised defects are not produced.

In Fig. 5, the defects have formed at almost regularly spaced intervals along lines which divide the surface into a cellular configuration. This arrangement suggests that the crystal may be a mosaic of slightly misoriented subgrains. Low-angle subgrain boundaries constitute very favorable sites for dislocation arrays, stacking faults, and precipitates. However, Lang x-ray topographs of this wafer showed it to be free of strain fields. No evidence was found for the existence of subgrain boundaries, dislocations, or stacking faults in the crystal. The mesa-like defects of Fig. 5 are therefore not related to strain in the crystal.

Defect features are shown in Fig. 6 at higher magnification. The defect joins the Si matrix smoothly, with no apparent boundary discontinuity. The sides are straight and prismatic, and the outer wall section is flat-topped, both of these features suggesting the structure is bounded by crystallographic facets. The central region of the mesa is flat but slightly lower than the outer wall on one side, while on the other side the plane surface is tilted downward and breaks through the outer wall. In many of the defects, the central region is completely flat and the encircling outer wall unbroken.

A similar raised defect from a different wafer is in Fig. 7. This micrograph was taken with the specimen tilted at 86° so that the wafer surface is seen at almost grazing incidence. The defect is regular in shape and extends about 1μ above the etched surface. The raised area behind the defect appears to be associated with

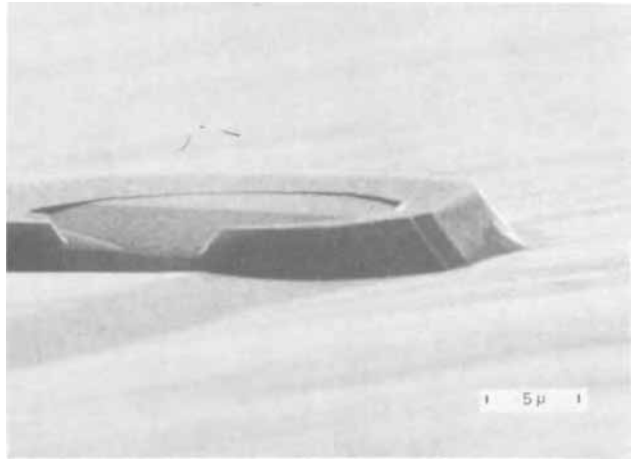

Fig. 6. Typical example of mesa defect on the surface of the wafer of Fig. 5 (80° tilt).

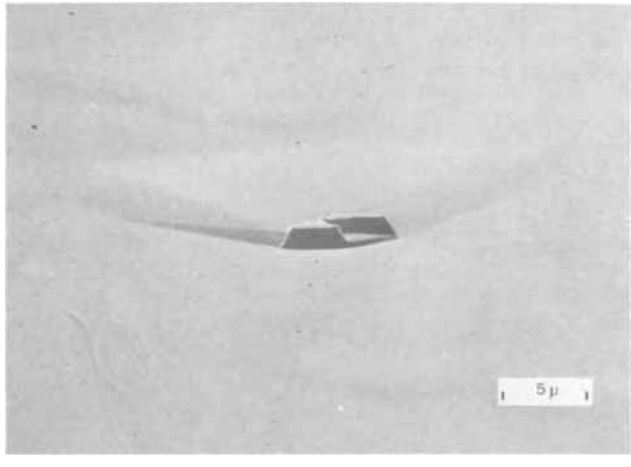

Fig. 7. A protruding defect on a different etched wafer, showing the similarity to the defects in Fig. 5-6. Note the slightly raised area spreading out behind the defect and similar smaller bumps in the foreground (86° tilt).

deflection of the etchant gas stream. The surface is otherwise featureless, except that several smaller bumps of the same general shape and orientation appear in the foreground, suggesting that smaller defects had been present but were etched away.

All of the defects in Fig. 5-7 are similar in appearance and in relation to the silicon matrix, and can evidently be attributed to the same cause. Their appearance suggests that they formed because the silicon has been etched rapidly around the periphery of the formation, while the flat central area has been etched at a slower rate. The etchant gas mixture did not attack the defect region as rapidly as the surrounding silicon, which is etched down around the defect. The slight ridging of the surfaces behind the defects in Fig. 7 may have resulted from disturbance of the gas flow pattern.

Raised defects on the surfaces of etched silicon crystals have been observed by a number of investigators (9*d*, 21-23). Although these protrusions have been attributed to precipitation of impurities with low solubility, such as carbon (β-SiC) or oxygen (SiO_2) (9*d*), no consensus has been reached on their exact nature.

It has long been recognized that oxygen in silicon can cause thermal conversion (24) of p-type silicon and precipitated SiO_2 (9c). For example, typical Czochralski-grown silicon contains up to 10^{17} oxygen atoms/cm^3 (9*e*). Similarly, typical high quality silicon can contain carbon in concentrations of 10^{18} atoms/cm^3

(25, 26), while the solubility limit for carbon in silicon is only of the order of 10^{16} atoms/cm^3 at 1000°C (25, 27). β-SiC has been identified as a second phase in Si crystals with high carbon content (27). Thus, precipitates of β-SiC or SiO_2 could be expected in even relatively high quality Si. However, electron microprobe analysis of the surface of Fig. 5 shows that the mesa-like defects are not precipitated SiO_2 or SiC. The microprobe observations indicate that there is no appreciable shift in the concentration of C or O (nor of B, N, or Sb) at or near the defects.

In further attemtps to identify and characterize the raised defects, conventional electron microscopy and diffraction were employed to study the wafer of Fig. 5. Reflection electron diffraction from the surface exhibiting the defects (Fig. 5) yielded only the well-defined single-crystal patterns to be expected from the silicon matrix. No broadening of the diffraction spots, suggestive of small misorientations, were detected. The reflection method is recognized to have limitations, in this case uncertainty in locating the exact site of electron beam interaction with the surface and in gauging the relative contributions of the matrix and defects in producing the observed patterns. However, the density of defects on the surface was great enough, and they protruded far enough out from the matrix surface to give confidence that they would make an appreciable contribution to the reflection diffraction patterns. In previous cases (31, 32) β-SiC was easily identified by transmission or reflection electron diffraction. In the present work the same techniques gave no evidence for β-SiC on the mesa-type defects.

Several pieces of the wafer containing the defects were thinned by chemical polishing and ion bombardment to allow transmission electron microscope investigations. One group of these specimens was prepared by thinning the crystal entirely from the back side, leaving the original defect surface unchanged. In these specimens, both the Si matrix and the defect areas, which were clearly defined and identifiable by the contrast alterations attendant to the thickness changes, yielded only good, sharp single-crystal silicon patterns. No shifts in orientation or quality of the patterns were detected in moving between the matrix and the defects. Very hard materials such as crystalline SiC or SiO_2 might be expected to introduce strain, which is not present in this case.

The remaining electron transmission specimens were prepared by thinning the crystal from both sides simultaneously, thereby completely effacing the original surfaces and leaving only a thin portion from the middle of the wafer. These specimens were studied by transmission microscopy and selected-area diffraction. The observations showed conclusively that no minute precipitates were present in the wafer. The specimens were also found to be completely free of dislocations and other crystallographic imperfections such as low angle boundaries and stacking faults. Only sharp, perfect single crystal diffraction patterns of Si were obtained.

These electron-optical results give further confirmation to the electron microprobe evidence and x-ray topography studies cited. Together, this body of evidence further substantiates that the mesa-like defects are not associated with precipitates or crystal imperfections present in the bulk silicon wafer before etching. Rather they must be hillocks of almost pure silicon remaining on the surface as the rest of the wafer etches down around them, perhaps with a very thin layer of possibly amorphous oxide or carbide protecting the surface.

Recently both D'Asaro *et al.* (9*f*) and Wagner (23) reported that numerous large "ridges" or "spikes" appear on single-crystal silicon surfaces after standard aqueous etching at room temperature. Using thermodynamic arguments, Wagner derived ternary phase diagrams for the Si-O-C system which are slightly revised from the earlier ones of Krivsky and Schuhmann (28), the relevant feature being inclusion of a separate "α" phase in the low carbon, low oxygen region.

There is no basis to associate the mesa-like defects observed in the present work with a second phase in the Si crystal. Rather, the evidence of the x-ray and electron-optical results demonstrates that no definite crystalline second phase is present in the HI-HF etched crystals.

Conclusions

Etching of single-crystal silicon wafers with HI-HF gas mixtures produces smooth featureless surfaces. Mesa-like defects are observed when the etching is done with a SiC-coated susceptor plate. If an additional layer of silicon is applied over the SiC plate, the raised defects do not appear during etching.

Heretofore, such defects on etched surfaces have been attributed to impurities precipitated in the silicon matrix. However, the results here are against an impurity or second-phase interpretation. The defects do not stem from the bulk silicon prior to etching. Instead, they are formed by an interaction at the surface during etching.

A plausible explanation is that the Si surface is partially passivated by trace impurities escaping from the heated SiC susceptor. The passivation might occur because of inhibition of the HI etchant by adsorbed impurity atoms or by formation of a partial and very thin overlayer on the silicon surface, probably containing oxygen or carbon. We have, for example, observed an apparent passivation of silicon during HI-HF etching where a small leak allowed a slight intrusion of oxygen. This effect also could be enhanced by attack of the SiC by the HI or HF reagents.

If it is assumed that the equations

$$2HI + SiC \rightarrow SiI_2 + C + H_2 \quad [1]$$

and

$$2HF + SiC \rightarrow SiF_2 + C + H_2 \quad [2]$$

represent the most probable reactions for attack of SiC by HI and HF, respectively, we may consider the thermodynamics of the situation as follows. The equilibrium constants estimated from thermodynamic data (29, 30) are about 5×10^{-4} for Reaction [1] and about 10 for Reaction [2]. On this basis, it appears that HI does not react with the SiC-coated susceptors, but HF does.

Thus, passivation of the Si surface by SiC-associated impurity is a reasonable mechanism for generation of the mesa-like defects. Similarly, an overlayer of silicon on the susceptor plate provides a barrier to attack by HF or a "sink" for the impurities, and thus prevents passivation of the wafer surface.

Acknowledgments

The authors thank Dr. S. H. McFarlane III for x-ray topography and Dr. E. P. Bertin for electron microprobe analysis. We are indebted to Prof. J. Bruce Wagner, Jr. for permission to cite his results prior to publication.

The research reported herein was supported in part by the Air Force Materials Laboratory, Wright-Patterson Air Force Base, Dayton, Ohio 45433, under Contract No. F33615-68-C-1331 and RCA Laboratories, Princeton, New Jersey.

Manuscript submitted Oct. 1, 1970; revised manuscript received ca. Feb. 26, 1971.

Any discussion of this paper will appear in a Discussion Section to be published in the June 1972 JOURNAL.

REFERENCES

1. G. A. Lang and T. Stavish, *RCA Rev.*, **24,** 488 (1963).
2. W. H. Shepherd, *This Journal*, **112,** 988 (1965).
3. T. L. Chu, *ibid.*, **115,** 1207 (1968).
4. P. Rai-Choudhury and A. J. Noraika, *ibid.*, **116,** 539 (1969).
5. B. A. Joyce and R. R. Bradley, *ibid.*, **110,** 1235 (1963).

6. S. Nakanuma, *IEEE Trans. Electron Devices*, **13**, 573 (1966).
7. D. C. Gupta and R. Yee, Paper 75 presented at Electrochem. Soc. Meeting, Boston, May 5-9, 1968.
8. D. Richman and R. H. Arlett, *This Journal*, **116**, 872 (1969).
9. "Semiconductor Silicon," R. R. Haberecht and E. L. Kern, Editors, The Electrochemical Society Inc., New York (1969); (*a*) D. Richman and R. H. Arlett, "Preparation and Properties of Homoepitaxial Silicon Grown at Low Temperatures from Silane," p. 200. (*b*) E. Sirtl, "Review:" Thermodynamics and Silicon Vapor Deposition," p. 63. (c) E. Spenke, "History and Future Needs in Silicon Technology," p. 1. (*d*) W. Bonsels and J. L. Lambert, "The Carbon Content of Semiconductor Silicon," p. 89. (*e*) J. A. Baker, "Oxygen and Carbon Content of Czochralski Silicon Crystals," p. 566. (*f*) L. A. D'Asaro, R. W. Landorf, and R. A. Furnanage, "Low Defect Silicon by Liquid Phase Epitaxy," p. 233.
10. R. G. Hays, "Silicon Etching by Sulfur Hexafluoride," Recent Newspaper 226 RNP, Electrochem. Soc. Meeting, Detroit, Oct. 5-9, 1969.
11. J. P. Dismukes and E. R. Levin, A.I.Ch.E. Materials Conference, Atlanta, Ga., Feb. 15-19, 1970.
12. C. Wagner, *J. Appl. Phys.*, **29**, 1295 (1958).
13. E. A. Gulbransen, K. F. Andres, and F. A. Brassart, *This Journal*, **113**, 834 (1966).
14. H. W. Gutsche, "Surface Damage in Silicon," paper presented at 6th Annual IEEE Microelectronics Symposium, Clayton, Missouri, June 21, 1967.
15. U. S. Pat. 3,170,273.
16. C. W. Oatley, W. C. Nixon, and R. F. W. Pease, "Advances in Electronics and Electron Physics," Vol. 21, p. 181, Academic Press, New York (1965).
17. F. J. Biondi, "Transistor Technology," Vol. III, p. 114, D. Van Nostrand Company, Inc., Princeton, New Jersey (1958).
18. B. A. Joyce, *J. Cryst. Growth*, **3-4**, 43 (1968).
19. J. G. Gualtieri, M. J. Katz, and G. A. Wolff, *Z. Krist.*, **114**, 9 (1960).
20. H. C. Abbink, R. M. Broudy, and G. P. McCarthy, *J. Appl. Phys.*, **39**, 4673 (1968).
21. R. C. Newman and J. Wakefield, in "Metallurgy of Semiconductors," Vol. 15, p. 201, Interscience Publishers, New York (1962).
22. J. Martin and E. Haas, *Solid-State Electron.*, **11**, 993 (1968).
23. J. B. Wagner, Jr., Private communication.
24. C. S. Fuller and R. A. Logan, *J. Appl. Phys.*, **28**, 1427 (1957).
25. H. D. Hagstrum, *ibid.*, **32**, 1020 (1961).
26. M. J. Joshi, *This Journal*, **113**, 45 (1966).
27. T. W. O'Keeffe, P. F. Schmidt, and R. Stickler, *ibid.*, **112**, 878 (1965).
28. W. A. Krivsky and R. Schuhmann, *Trans. AIME*, **221**, 898 (1961).
29. C. E. Wicks and F. E. Block, "Thermodynamic Properties of 65 Elements—Their Oxides, Halides, Carbides and Nitrides," Bureau of Mines Bulletin 60J, U. S. Govt. Printing Office, Washington (1963).
30. H. Schafer, H. Bruderreck, and B. Morcher, *Z. Anorg. Allgem. Chem.*, **352**, 122 (1967).
31. P. Rai-Choudhury and N. P. Formigoni, *This Journal*, **116**, 1440 (1969).
32. R. B. Marcus, Microscopie Electronique, Int. Conf. Grenoble, II, 379 (1970).

Thermodynamic Analysis of the III-V Alloy Semiconductor Phase Diagrams

I. InSb-GaSb, InAs-GaAs, and InP-GaP

L. M. Foster* and J. F. Woods

IBM Thomas J. Watson Research Center, Yorktown Heights, New York 10598

ABSTRACT

A thermodynamic analysis was made of the pseudobinary phase diagrams of the III-V semiconductor alloys, InSb-GaSb, InAs-GaAs, and InP-GaP. The excess free energy of mixing is expressed as Bx_1x_2, where B is a parameter characteristic of each system and x_1 and x_2 are the mole fractions of the end components. This homologous series of alloys showed consistent behavior in that all of the B/RT *vs.* composition plots were linear for both the liquids and solids. The greater part of the excess free energy of mixing of the solids appears to be in the excess entropy rather than in the enthalpy, indicating that these materials freeze with local ordering or structure rather than as homogeneous random solids. The magnitude of the departure from ideality in the solids increases from the antimonide to the arsenide and to the phosphide, which is also the order of increasing lattice mismatch between the pairs of pure components. Implications of these results in the use of the alloys in semiconductor devices are discussed.

It has been recognized for many years that the III-V alloy semiconductors might be useful for fabrication of new electronic and optical devices because of the possibility of adjusting the width of the forbidden energy gap by varying the composition of the alloys (1-3). In principle, by selecting the proper combinations of III-V compounds and adjusting the composition of the mixtures, semiconductors with band gaps ranging more or less continuously from 0.18 eV (InSb) to about 2.4 eV (AlP) could be prepared.

Whether these mixtures will be useful semiconductors will depend not only on solving such obvious problems as the growth of suitably doped single crystals, but also on whether such alloys are indeed homogeneous mixtures with properties that are smooth blends of the properties of the individual components. Thermodynamic analysis of the phase diagrams of these pseudobinary systems can give an insight into the nature of the solid alloys. This information comes from the magnitude of the departure of the systems from ideal behavior and how this depends on temperature and composition.

* Electrochemical Society Active Member.
Key words: phase diagrams, compound semiconductors, solution theory.

There are several procedures for calculating the liquidus and solidus boundaries of binary systems which depend on different basic assumptions. No attempt is made here to evaluate the relative merits of the various procedures and reference is made to standard texts (4-6). Success has been claimed for each technique in treating individual cases, but possibly in some instances this is fortuitous because of the assumptions involved (4). The most common approach is the quasi-chemical method first proposed by Guggenheim (7). It was originally intended to treat liquid solutions only, because it is based on chemical interactions between different kinds of molecules and makes no provisions for strain energy or other effects resulting from mixing molecules of different sizes in a crystalline lattice. However, this quasi-chemical approach has been employed successfully in treating some solid solutions where there is no difference in atom sizes and, hence, no lattice distortion, *e.g.* the aluminum-rich portion of the Al-Zn system (8). In most of the III-V semiconductors there is considerable difference in atom sizes, so these systems presumably are not amenable to treatment by the quasi-chemical method.

The procedure employed in the present investigation assumes that the excess free energy of mixing in a phase can be expressed as Bx_1x_2, where x_1 and x_2 are the mole fractions of the components (6). B is a parameter that contains both enthalpy and entropy contributions to nonideality, as well as distortion energy in the case of solids. In the extensive literature on phase equilibria, B seems to show some regularity in behavior only in cases of homologous series of compounds (4). Homologous series are found in the liquid and solid alloys between the group III and group V semiconductor compounds, and regularity and trends should be evident in the parameter B in these cases. These materials are isoelectronic and have the same diamond cubic crystal structure in the solid, but offer a gradation in both anion and cation size as well as in melting point and heat of fusion of the separate compounds. Trends in B should be useful in indicating which properties are important in determining the degree of nonideality in these systems.

The nine combinations of the group III metals, Al, Ga, and In, with the group V nonmetals, P, As, and Sb, give 18 possible pseudobinary systems. About half of these have been studied in some manner, although in several instances only to the extent of demonstrating that miscibility exists over the complete composition range in the solid (9). For the present study, the systems InSb-GaSb, InAs-GaAs, and InP-GaP were selected since reliable experimental data were available for both their liquidus and solidus boundaries and the melting points of the separate pure components. This provided a homologous series of three alloys differing only in the group V substituent. Additional systems will be treated as the data become available, with the objective of trying to establish trends with atom size, bond strength, *etc.*, within the group of III-V alloys and to evolve a model to describe the solid solution phase of these technologically important systems.

Detailed mathematical analysis of phase diagrams can be extremely tedious and, as a consequence, the additional effort of correlating the calculations with error limits on experimental data has seldom been made. For the present investigation, computer programs were written which provided the flexibility necessary to undertake such a correlation.

Calculation Procedure

The free energy of mixing per mole of a two-component ideal liquid is

$$\Delta F^{M(l)} = RT(x_1 \ln x_1 + x_2 \ln x_2) \quad [1]$$

where x_1 and x_2 are the mole fractions of components 1 and 2, and $-R(x_1 \ln x_1 + x_2 \ln x_2)$ is the configurational entropy of mixing. The ideal heat of mixing is zero. From $F = \mu_1 x_1 + \mu_2 x_2$, the change in the chemical potentials becomes

$$\Delta\mu_1{}^l = RT \ln x_1 \quad [2a]$$

$$\Delta\mu_2{}^l = RT \ln x_2 \quad [2b]$$

For a real solution, the heat of mixing is usually not zero because of the reforming of chemical bonds and changes in van der Waal's forces between neighbors. These effects are grouped together in the interaction parameter, B^l. Thus, for a real liquid solution, Eq. [1] becomes

$$\Delta F^{M(l)} = RT(x_1 \ln x_1 + x_2 \ln x_2) + B^l x_1 x_2 \quad [3]$$

and the change in chemical potentials becomes

$$\Delta\mu_1{}^l = RT \ln x_1 + B^l x_2{}^2 \quad [4a]$$

$$\Delta\mu_2{}^l = RT \ln x_2 + B^l x_1{}^2 \quad [4b]$$

From $\mu = RT \ln a = RT \ln x + RT \ln \gamma$, where a is the activity, the activity coefficients, γ, are obtained from Eq. [4]

$$\ln \gamma_1{}^l = (B^l/RT) x_2{}^2 \quad [5]$$

$$\ln \gamma_2{}^l = (B^l/RT) x_1{}^2 \quad [6]$$

The free energy of mixing per mole of solid solution is

$$\Delta F^{M(s)} = RT(x_1 \ln x_1 + x_2 \ln x_2) + x_1 L_1 (T/T_1 - 1) + x_2 L_2 (T/T_2 - 1) + B^s x_1 x_2 \quad [7]$$

where $L_1(T/T_1 - 1)$ and $L_2(T/T_2 - 1)$ are the changes in the chemical potentials upon fusion of a mole of the pure components. No difference is expected between the specific heats of the solid and liquid pure components so the enthalpies of fusion, L_1 and L_2, are considered constant. The parameter B^s for the solid solution is expected to be different from and larger in magnitude than B^l because of additional effects that contribute to nonideality, such as lattice distortion, that are not present in the liquid. The activity coefficients in the solid become

$$\ln \gamma_1{}^s = (B^s/RT) x_2{}^2 \quad [8a]$$

$$\ln \gamma_2{}^s = (B^s/RT) x_1{}^2 \quad [8b]$$

In order to put the relations into a form amenable to computer calculation, particularly for an iteration procedure that is required later on, the derivatives of [3] and [7] are taken with respect to the component 2 composition to give the following two expressions for straight lines on a ΔF^M *vs.* x plot

$$\Delta F^M = RT \ln(1 - x^l) + B^l (x^l)^2 + \{RT \ln [x^l/(1 - x^l)] + B^l(1 - 2x^l)\} x \quad [9]$$

$$\Delta F^M = RT \ln(1 - x^s) + B^s (x^s)^2 + L_1(T - T_1)/T_1 + \{RT \ln [x^s/(1 - x^s)] + B^s (1 - 2x^s) - L_1 (T - T_1)/T_1 + L_2 (T - T_2)/T_2\} x \quad [10]$$

where $x = x_2 = (1 - x_1)$, the mole fraction of component 2. Equations [9] and [10] are tangents to the free energy curves, Eq. [3] and [7], for the liquid and solid, respectively. When they have equal intercepts and slopes, *i.e.* when they coincide with the common tangent to both curves, the points of tangency, x^l and x^s, are compositions in the liquid and solid where the chemical potentials are equal and, hence, correspond to intersections on the liquidus and solidus boundaries of the phase diagram at temperature T. The conditions for equilibrium, then, are given by

$$RT \ln(1 - x^l) + B^l (x^l)^2 = RT \ln(1 - x^s) + B^s (x^s)^2 + L_1(T - T_1)/T_1 \quad [11]$$

for the intercepts, and

$$RT \ln [x^l/(1 - x^l)] + B^l(1 - 2x^l) = RT \ln [x^s/(1 - x^s)] + B^s(1 - 2x^s) - L_1(T - T_1)/T_1 + L_2(T - T_2)/T_2 \quad [12]$$

for the slopes.

In the special case where both liquid and solid are ideal ($B^l = B^s = 0$), [11] and [12] may be solved for x^l and x^s, giving

$$x^l_{id} = \{1 - \exp [- L_1(T - T_1)/RTT_1]\}/\{\exp [- L_2 (T - T_2)/RTT_2] - \exp [- L_1(T - T_1)/RTT_1]\} \quad [13]$$

$$x^s_{id} = \{1 - \exp [L_1(T - T_1)/RTT_1]\}/\{\exp [L_2 (T - T_2)/RTT_2] - \exp [L_1(T - T_1)/RTT_1]\} \quad [14]$$

Thus, the ideal $T - x$ phase diagram can be calculated directly in closed form if L_1, L_2, T_1, and T_2 are known.

In nonideal systems, the most useful information about the departure from ideality is expressed by the parameters B^l and B^s. These can also be given in closed form. Thus, from [11] and [12]

$$B^l = \frac{RT\{(1 - x^s)^2 \ln [(1 - x^l)/(1 - x^s)] - (x^s)^2 \ln (x^l/x^s)\}}{(x^s)^2(1 - x^l)^2 - (x^l)^2(1 - x^s)^2} - \frac{(1 - x^s)^2 L_1(T - T_1)/T_1 - (x^s)^2 L_2(T - T_2)/T_2}{(x^s)^2(1 - x^l)^2 - (x^l)^2(1 - x^s)^2} \quad [15]$$

$$B^s = \frac{RT\{(1 - x^l)^2 \ln [(1 - x^s)/(1 - x^l)] - (x^l)^2 \ln (x^s/x^l)\}}{(x^l)^2(1 - x^s)^2 - (x^s)^2(1 - x^l)^2} + \frac{(1 - x^l)^2 L_1(T - T_1)/T_1 - (x^l)^2 L_2(T - T_2)/T_2}{(x^l)^2(1 - x^s)^2 - (x^s)^2(1 - x^l)^2} \quad [16]$$

Equations [15] and [16] give the values of B^l and B^s required to fit experimental liquidus and solidus curves at compositions x^l and x^s and temperature T.

A remaining calculation that is required is to determine the liquidus and solidus points, x^l and x^s, for a given set of values of B^l, B^s, L_1, L_2, T_1, and T_2. This calculation is especially important near the two composition extremes where the calculated parameters, B, can change drastically as a result of very small variations in the way the experimental curves are drawn through the data points. It permits B's that result from different possible extrapolations from a less sensitive region to be tested for reasonableness and consistency, all with limits imposed by allowable variations in the experimental curves. An iteration procedure is required. The one used here is illustrated in Fig. 1 for a hypothetical case. Curves of the free energy of mixing for the liquid and solid at a particular temperature are drawn from Eq. [3] and [7], with $x_2 = (1 - x_1) = x$, and a set of lines tangent to the former are computed from [9] for a set of trial values of x^l. For each tangent line the difference, $\Delta F^{M(s)}$ (Eq. [7]) $- \Delta F^M$ (Eq. [9]), is calculated over a range of values of x. For a certain set of tangents, corresponding to a set of values of x^l, and a certain set of values of x, this difference will be negative (shaded area, Fig. 1). By presenting the computer calculations as an x^l/x array, the column and row in which sign change occurs is readily seen, and successive iteration determines the point of tangency of relation [9] to the two free energy curves, [3] and [7], to any arbitrary degree of precision. These points of tangency are the values of x corresponding to the liquidus, x^l, and solidus, x^s, at temperature T for the combination of B^l, B^s, L_1, L_2 T_1, and T_2 that is being tested.

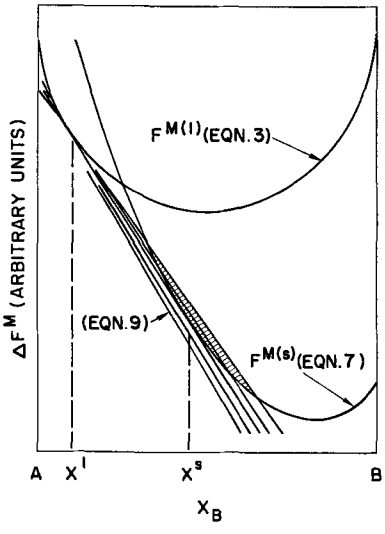

Fig. 1. Free energy of mixing of liquid and solid for hypothetical system to illustrate iteration procedure for determining liquidus and solidus points, x^l and x^s.

Procedure for Analysis of Experimental Data

Experimental data for both the liquid and solid are required. Large errors can result from assuming an ideal liquidus curve and basing calculations on an experimental solidus curve only, as has sometimes been done in literature. Recent values of L_f for the III-Sb compounds and InAs and GaAs by Lichter and Sommelet (10, 11) appear to be very reliable and are preferred to earlier literature values. Information on the enthalpies of fusion of the III-P compounds is very sparse, but values can be gotten from the entropies of fusion that can be estimated from the entropies of Si and Ge and the III-V compounds that have been measured. The assumption that L_f is constant over the temperature ranges encompassed by the phase diagrams is not on a very firm basis. Lichter and Sommelet have provided the only reliable heat content data, and only in the case of InSb and GaSb (10) are they carried sufficiently far into the liquid for an estimate of ΔC_p to be made. In those cases, the maximum change in L_f for either component is only about 4.5% over the entire temperature range of the InSb-GaSb diagram.

In making the calculations described above for an experimental phase diagram, it is generally not possible to use the actual data points since they seldom occur at the same temperature for both the liquid and solid. Therefore, a curve is drawn through the liquidus and solidus data points; values of x^l and x^s are taken from the curves at a series of temperatures; and the interaction parameters, B^l and B^s, are calculated from these values by means of [15] and [16]. The calculations of B^l and B^s are presented in two ways: as activity coefficients *vs.* composition (from Eq. [5], [6], and [8]) and as B/RT *vs.* composition.

In order to observe the effect of errors in the data on the behavior of B^l and B^s, a phase diagram was calculated for a hypothetical system by the iteration procedure described earlier, with nominal values for the parameters of $B^l = 0.5\ RT$, $B^s = 1.2\ RT$,[1] $S_1 = L_1/T_1$

[1] As will be seen when actual experimental phase diagrams are treated, the B/RT *vs.* x plots are straight lines with very small slopes, so the assumption of a constant B/RT is justified for the present purpose.

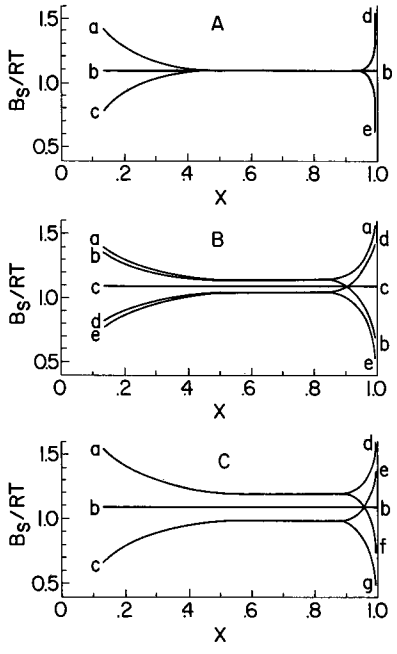

Fig. 2. Effect of errors in system parameters and data on B^s/RT for hypothetical system. A—Error in melting points of separate components: *a*, with error of +1° in component 1; *b-b*, with correct data (T_1 = 1273°K, T_2 = 1773°K); *c*, with error of −1° in component 1; *d*, with error of −1° in component 2; *e*, with error of +1° in component 2. B—Error in liquidus and solidus data: *a-a*, −5% in x^l, +5% in x^s; *b-b*, +5% in x^l, +5% in x^s; *c-c*, with correct data; *d-d*, −5% in x^l, −5% in x^s; *e-e*, +5% in x^l, −5% in x^s. C—Error in enthalpies of fusion: *a*, with error of −1 eu in L_1/T_1, and −1, 0, or +1 eu in L_2/T_2; *b*, correct data (L_1/T_1 = 14 eu, L_2/T_2 = 15 eu); *c*, with error of +1 eu in L_1/T_1, and −1, 0, or +1 eu in L_2/T_2; *d*, with error of −1 eu in L_1/T_1, and −1 eu in L_2/T_2; *e*, with error of +1 eu in L_1/T_1, and −1 eu in L_2/T_2; *f*, with error of −1 eu in L_1/T_1, and +1 eu in L_2/T_2; *g*, with error of +1 eu in L_1/T_1, and +1 eu in L_2/T_2.

= 14 eu, T_1 = 1273°K, $S_2 = L_2/T_2$ = 15 eu, T_2 = 1773°K. These parameters were then varied one at a time by small amounts to see what effect the change had on the behavior of the *B/RT vs. x* curves. This information is shown in Fig. 2 for an error in melting point of the pure components of ±1°C (Fig. 2A), an error in entropy of fusion of ±1 eu (Fig. 2B), and composition errors in the experimental curves of ±5%, where "error" in the last case is defined as 5% of x when $x \leq 0.5$, and 5% of $(1 - x)$ when $x \geq 0.5$. Figure 2 shows only the situation in the solid. Very similar results are found for the liquid with, however, a right for left reversal in the character of the curves.

The value of this information on errors is that it assists in recognizing and treating anomalous data. There is no physical model of solutions that would predict wide deviation of the *B/RT* plots at the composition extremes, and when this is encountered it must be due to errors in the system parameters or in the experimental data of the phase diagram. The sensitivity of the *B/RT* plots to error in x^l and x^s (Fig. 2B) is particularly significant. Whereas a 5% error in x near the middle of a phase diagram is probably outside the precision of a well-controlled experiment, the same error near the ends (as error is defined here; *e.g.*, ±0.0025 at x = 0.95) is quite possible. This situation is handled by extrapolating the *B/RT* plots from the less sensitive region (*i.e.*, between approximately x = 0.2 and x = 0.8) to the ends and, with these extrapolated values, recalculating the extremities of the liquidus and solidus curves by the iteration procedure described previously. It is a matter of judgment in any particular case whether the error limits on the experimental data for x^l and x^s permit redrawing of the liquidus and solidus curves acording to calculations based on extrapolated values of *B/RT*.

Considering the great sensitivity of the *B/RT* plots at the extreme ends to small errors in melting points and enthalpies of fusion, it is unlikely that a completely linear plot would be obtained the first time even if the rest of the data were precise. From the character of the anomalous curves in Fig. 2A and C, it is possible to obtain a clue as to which parameter is in error and to make a better choice. In all systems that were treated in this investigation, the final "best" parameters agreed with the most reliable literature values within the experimental precision stated by the authors.

Results

InSb-GaSb system.—Data for both the liquidus and solidus were obtained by Woolley and Lees (12). Melting points for InSb have been reported from 524° to 526°C (10, 12-16), and for GaSb from 703 to 712°C (10, 12, 13, 17, 18). Enthalpies of fusion ranging from 11.2 to 12.2 kcal/mole for InSb (10, 13, 19, 20) and from 12.0 to 16.3 kcal/mole for GaSb (10, 13, 20) were reported. Lichter and Sommelet's values (10) of 524° ± 1°C and 712° ± 1°C for the melting points and 11.414 ± 0.200 kcal/mole and 15.560 ± 0.200 kcal/mole for the enthalpies of fusion of InSb and GaSb, respectively, appear to be the most reliable.

The data of Woolley and Lees are shown as the points in Fig. 3. The solid curves were calculated by the iteration procedure, with T_1 = 523°C, T_2 = 712°C, L_1 = 11.41 kcal/mole, L_2 = 15.56 kcal/mole, and using linearity of the *B/RT* plot [shown in Fig. 4 (bottom)] as the criterion for an acceptable curve. The dashed curves are the ideal boundaries calculated from [13] and [14]. The activity coefficients of InSb and GaSb in the two phases, calculated from Eq. [5], [6], and [8], are given in Fig. 5.

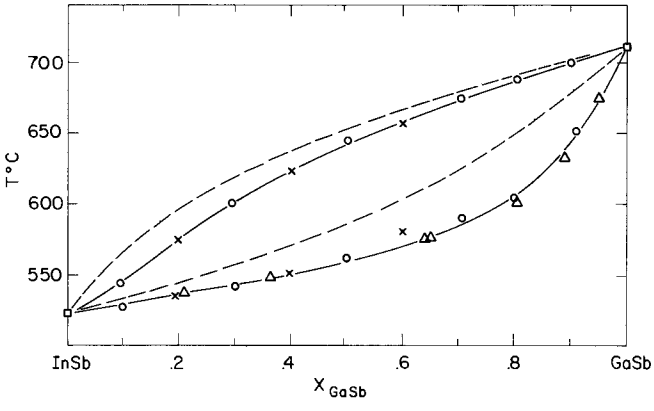

Fig. 3. InSb-GaSb system: ———, calculated; - - -, ideal; □, Ref. (10); ○, differential thermal analysis [Ref. (12)]; X, ordinary thermal analysis [Ref. (12)]; △, x-ray measurement [Ref. (12)].

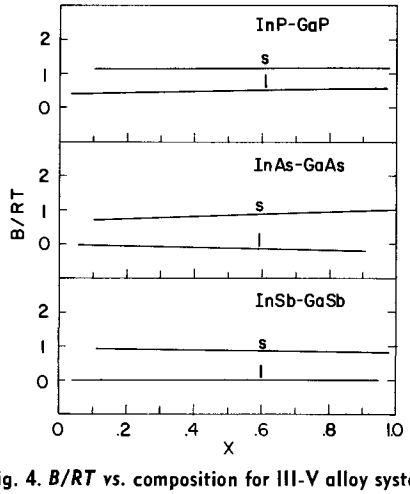

Fig. 4. *B/RT vs.* composition for III-V alloy systems

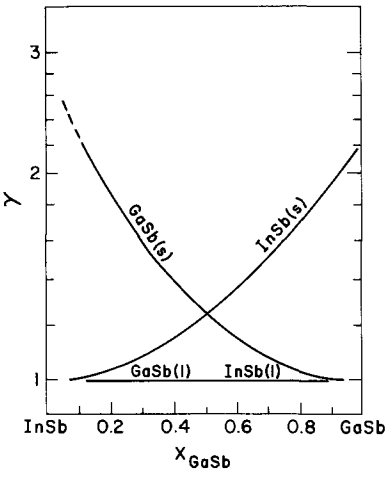

Fig. 5. Activity coefficients in the InSb-GaSb system

InAs-GaAs system.—The solidus boundary of this system was determined by Woolley and Smith (21). Three points on the liquidus boundary were determined by Van Hook and Lenken (22). Enthalpies of fusion of the pure compounds were reported at 17.58 (11), 18.2 (13), and 18.4 kcal/mole (23) for InAs, and at 25.18 (11) and 28.9 kcal/mole (13) for GaAs. The melting point of InAs has been reported at 937 (24, 11) and 942°C (13). There are many references to the melting point of GaAs, ranging from 1230° to 1255°C. Lichter and Sommelet's values (11) of 937° ± 1°C and 1240° ± 1°C for the melting points, and 17.58 ± 0.40 and 25.18 ± 0.60 kcal/mole for the enthalpies of fusion for InAs and GaAs, respectively, are taken to be the most reliable.

The experimental data points and the calculated liquidus and solidus (continuous lines) and ideal (dashed lines) curves are shown in Fig. 6. The B/RT *vs.* x plots corresponding to the continuous curves of Fig. 6 are shown in Fig. 4 (center). The activity coefficients are shown in Fig. 7. The system parameters that were used in the calculations were taken from Ref. (11).

InP-GaP system.—The solidus boundary was determined by Foster and Scardefield (25). The liquidus was determined by Panish (26) by extrapolation of isotherms from the metal-rich region of the Ga-In-P ternary to the InP-GaP pseudo-binary section. A new melting point for GaP of 1485°C was determined by Chicotka (27), which is considerably higher than that of Richman (28). The melting point of InP has been reported at 1070° (29) and 1068°C (30).

Following the same procedure as for the other two systems, the information for InP-GaP is shown in Fig. 8, 4 (top), and 9, where T_1 = 1068°C, T_2 = 1485°C, L_1 = 19.71 kcal/mole, and L_2 = 26.37 kcal/mole. The enthalpies of fusion of InP and GaP have not been

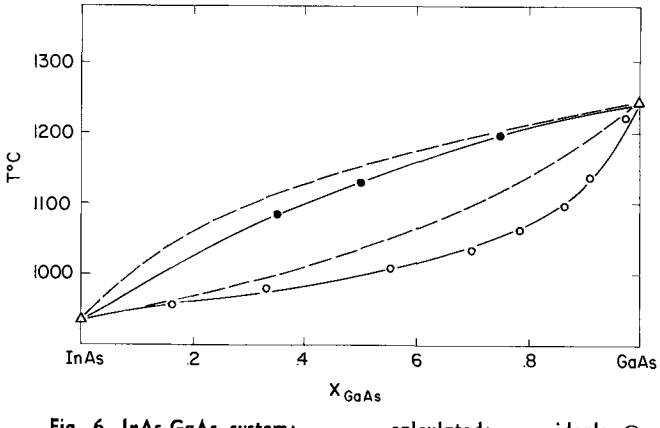

Fig. 6. InAs-GaAs system: ———, calculated; - - -, ideal; ○, Ref. (21); ●, Ref. (22); △, Ref. (11).

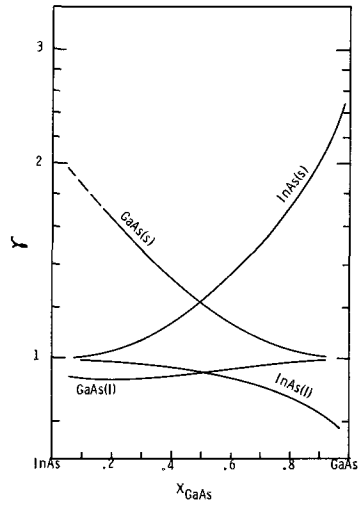

Fig. 7. Activity coefficients in the InAs-GaAs system

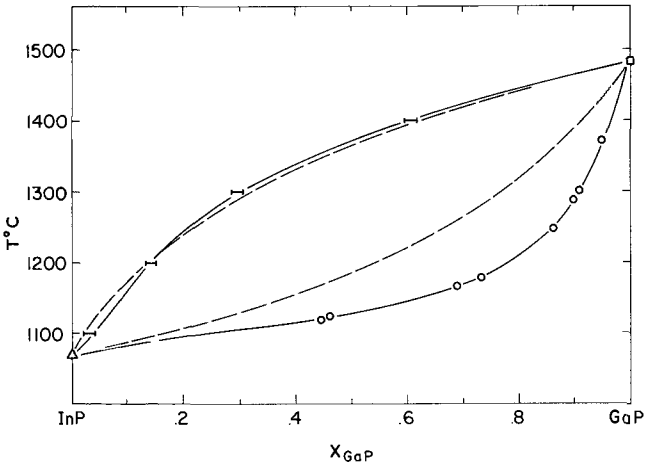

Fig. 8. InP-GaP system: ———, calculated; - - -, ideal; ○, Ref. (25); ⊢⊣, Ref. (26); △, Ref. (30); □, Ref. (27).

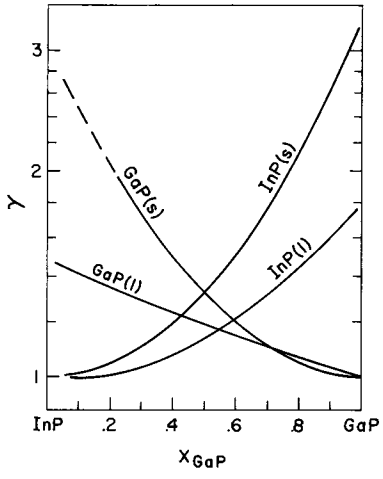

Fig. 9. Activity coefficients in the InP-GaP system

measured, and the values that were used were calculated from estimates of the entropies of fusion of 14.7 and 15 eu, respectively. The value for InP was assumed to be the same as that of AlSb, since they have approximately the same melting point and each contains an element for the third and fifth row. AlSb had been measured by Lichter and Sommelet (10). The entropy of fusion of GaP had been roughly estimated by Thurmond (31). Neither of these estimates is on a firm foundation. However, almost as satisfactory a fit to the experimental data and linear B/RT *vs.* x plots were

obtained with entropies ±0.5 eu different from those chosen.

Discussion

Thermodynamic treatment of the III-V pseudobinary phase diagrams provides information of several sorts. It makes it possible to distinguish between poor and acceptable data; it gives an insight into the nature of these semiconductor alloys, and provides a basis of comparison between members of the group. The B/RT *vs.* x plots provide the most visible indication of the quality of the data. The same information could be gotten from the activity coefficient plots, although anomalous behavior is less conspicuous in that case. The test for an "acceptable" phase diagram in the systems studied to date is taken to be linearity of the B/RT *vs.* x plot for both the liquidus and solidus. This criterion could not have been set down in advance for it was not possible to predict that these systems would exhibit such behavior. Darkin and Gurry (32) noted that many binary metal systems fall into one of three classes, where the B/RT (their α) *vs.* x plot is linear, where it shows pronounced curvature, or where it is linear with an abrupt change of slope. They pointed out that few systems seemed to exhibit intermediate or mixed behavior.

The homologous series of alloys, $Ga_xIn_{1-x}Sb$, $Ga_xIn_{1-x}As$, and $Ga_xIn_{1-x}P$, have strictly linear B/RT *vs.* x plots over the entire composition range for both liquid and solid and, hence, appear to fall into the first class described by Darkin and Gurry. On the other hand, the diagrams of several III-V systems that showed anomalous B/RT plots with wide excursions, especially near the ends, typical of those illustrated in Fig. 2, were found to be based on questionable data. Calculation of the InAs-InP system showed such anomalies when the data of Koster and Ulrich (29) were used, for example. However, recent work of Willardson *et al.* (33) suggests that the earlier data were seriously in error. The data of the InSb-InAs system, which also showed anomalous B/RT plots, are similarly suspect (34).

For the three systems treated here, the B/RT plots were almost flat (Fig. 4). If B is independent of composition, a perfectly flat plot (B/RT = constant) requires that B be directly proportional to T, or $B = AT$, where A is a constant containing R. Since $Bx_1x_2 = ATx_1x_2$ is the excess free energy of mixing, ΔF^M_{ex}, the excess entropy at constant pressure is $\Delta S^M_{ex} = -Ax_1x_2$ if there are no anomalies in the heat capacity. Then, the excess enthalpy $\Delta H^M_{ex} = \Delta F^M_{ex} - T\Delta S^M_{ex}$ is zero.

The assumption that B is independent of composition has considerable historical justification. It has as its basis the fact that this parameter can be accounted for by the difference in energy of vaporization between the two components, which should be insensitive to composition (36) or, in a parallel argument, that it involves the difference in binding energy between the possible combinations of nearest neighbors (quasi-chemical approach) (7). A considerable number of systems exhibit this "regular" behavior. It is pointed out, however, that the regular solution theory predicts that B should also be independent of temperature, which would make the excess free energy of mixing, Bx_1x_2, essentially an excess enthalpy with little or no contribution from excess entropy.

The extended quasi-chemical approach predicts a temperature dependence in B due to a loss of randomness in the distribution of unlike molecules, which involves an activation energy. However, it can be shown that according to the quasi-chemical theory the temperature-dependent part of the excess free energy, *i.e.* the entropy term, will always be substantially smaller than the enthalpy for the systems we are considering. For example, Guggenheim (7) and others have given the following approximate expressions for the excess functions

$$\Delta H^M_{ex} = x_1x_2\,\Omega(1 - x_1x_2\,2\Omega/ZRT) \qquad [17a]$$

$$\Delta S^M_{ex} = -x_1^2x_2^2\,\Omega^2/ZRT^2 \qquad [17b]$$

$$\Delta F^M_{ex} = x_1x_2\,\Omega(1 - x_1x_2\,\Omega/ZRT) \qquad [17c]$$

where Ω is the net energy change in breaking the bonds of the pure components and reforming nearest neighbor bonds, and Z is the coordination number, assumed to be 4 in the solid. (In the generalized approach used in the present investigation, Eq. [17c] is equivalent to our Bx_1x_2.) When there is a completely random distribution of molecules of the two kinds, the temperature-dependent terms are zero, and Eq. [17] reduces to the simple expressions for the excess quantities for a regular solution, $\Delta F^M_{ex} = \Delta H^M_{ex} = x_1x_2\Omega$, with no excess entropy. These relations show that, according to the quasi-chemical approach, the contribution of the entropy term to the excess free energy will always be less than half the enthalpy for all values of Ω less than $ZRT/4x_1x_2$ (approximately $4RT$).

It is apparent that there is a serious contradiction between the experimental results for the InGa-Sb, -As, and -P systems and the predictions of the regular or quasi-chemical solution theories, for it appears that the experimentally determined excess free energy is made up almost entirely of the $T\Delta S^M_{ex}$ term. This is probably not an accurate description of the make-up of ΔF^M_{ex} for it is unlikely that a real system could exhibit a substantial excess entropy of mixing and near zero excess enthalpy, since the nonrandom structure implied by the excess entropy should involve some rearrangement of chemical bonds or, at least, a change in van der Waal's forces, which should be accompanied by an enthalpy change. This change can be extremely small, however, and in some theoretical treatments (35) it is considered zero. The conclusion that the excess enthalpy of mixing is small or zero could be in error if the parameter B were not independent of composition. There is no supporting evidence for or against this contention at the present time.

The excess free energy for the three systems is plotted against composition in Fig. 10. The B parameters are shown in Fig. 11. It is seen that they are substantially larger for the solids than for the liquids, reflecting the greater departures from ideality in the former. The $Ga_xIn_{1-x}Sb$ liquid is perfectly ideal, and the $Ga_xIn_{1-x}As$ liquid is nearly so. B for the solid of $Ga_xIn_{1-x}Sb$ varies only about 6% across the entire diagram and, hence, nearly meets the criterion of a "regular" solution. However, this is because the magnitude of B^s is small in this system and trends are not conspicuous. Rather than $Ga_xIn_{1-x}Sb$ being an ex-

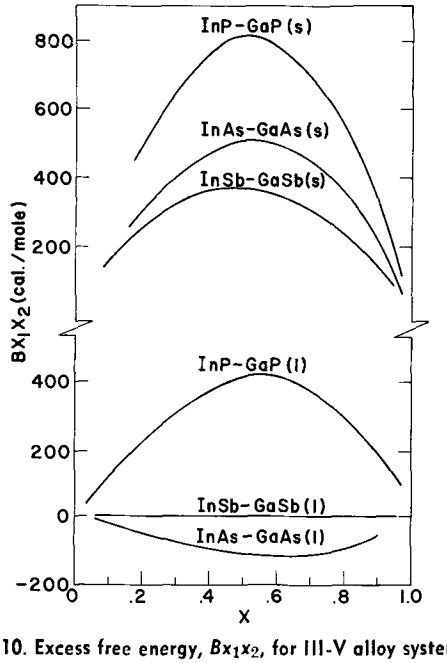

Fig. 10. Excess free energy, Bx_1x_2, for III-V alloy systems

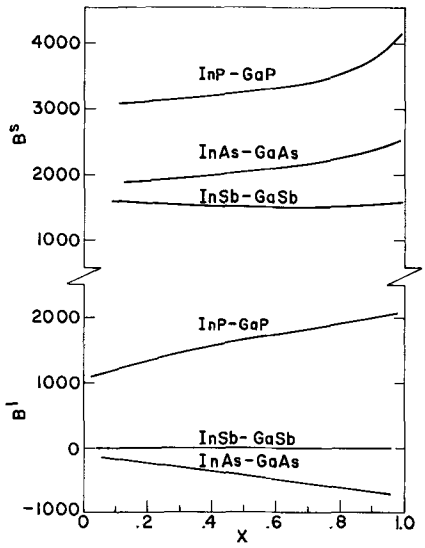

Fig. 11. The parameter, B, for the liquid and solid of III-V alloy systems.

ceptional case, it is clear from Fig. 11 that there is a gradual change in shape of the B^s *vs.* x curves, and a gradual trend in the magnitude of B^s in going from the antimonide to the arsenide and to the phosphide.

In an effort to identify the origin of the excess free energy, it is of interest to see if any parameters of these systems correlate with $\Delta F^{M(s)}{}_{ex}$. The two most obvious properties that change in going through the series InSb-GaSb, InAs-GaAs, and InP-GaP are the molecular size and the lattice binding energy, the latter being manifest in the increasing melting points, enthalpies of fusion, and shear moduli of the pure compounds. Table I lists the lattice parameters, the molar volumes, and the shear moduli for the three systems at room temperature.

The possibility that the large contribution of the excess entropy to $\Delta F^M{}_{ex}$ could result entirely from the volume change on mixing molecules of different sizes can be readily discounted. The molal excess entropy of mixing x_1 moles of molecules of one size with x_2 moles of another is given approximately by (35)

$$\Delta S^M{}_{ex} = x_1 R \ln (x_1/z_2) + x_2 R \ln (x_2/z_2) \quad [18]$$

where z_1 and z_2 are the two volume fractions. Making the calculations at $x_1 = x_2 = 0.5$ for the solid of the InP-GaP system, for which the difference in molal volumes is greatest, gives $\Delta S^M{}_{ex} = 0.012$ eu, and $T\Delta S^M{}_{ex} \approx 17$ cal/mole. This is only about 2% of the $\Delta F^M{}_{ex}$ for that system and, moreover, is of opposite sign.

Whereas a significant size-effect contribution to $\Delta F^M{}_{ex}$ appears to be excluded according to [18], that relation does not consider the concomitant strain energy that is produced in a solid lattice. Calculation of strain energy is only approximate, even in the most straightforward case of simple metals. However, a rough estimate of its expected contribution at room temperature in the present cases can be made by the procedure of Lawson (37). This yields the distortion energy, E^D, resulting from substitution of a molecule of the first kind for a molecule of the second kind in a lattice of the second kind, when the two molecules are of different size. The energy is given in terms of the shear moduli, G_1 and G_2, and the molar volumes, V_1 and V_2, as

$$E^D = 2/3[G_1/V_1(x_1) + G_2/V_2(x_2)](V_1 - V_2)^2 x_1 x_2 \quad [19]$$

where x_1 and x_2 are the mole fractions.[2] In addition to the assumptions in the original derivation, it is also assumed that there is minimal volume change on mixing, so $E^D \approx H^D$, and that the theory originally developed for metals applies to the covalently bonded mixed crystals as well.

Substitution of the appropriate quantities from Table I into [19] gives distortion energies at room temperature of 1900, 2625, and 3075 cal/mole for InSb-GaSb, InAs-GaAs, and InP-GaP, respectively, calculated at $x_1 = x_2 = 0.5$. If we identify these with the excess free energy, it is seen that they exceed $B^s x_1 x_2$ calculated from the phase diagrams (Fig. 10) by four- to five-fold. It is impossible to estimate the magnitude of the strain energies at high temperature. The shear moduli of the covalently bonded semiconductors are not greatly temperature sensitive within a few hundred degrees of room temperature where data are available, and values extrapolated to the temperatures of the solidus curves would still be of the order of 75% of the room temperature values (39). On the other hand, the moduli approach zero at the melting points and undoubtedly fall off very rapidly just short of that.

Thus, it is not possible to find a definite correlation between lattice strain and the excess free energy of mixing, even though the direction of change of the shear moduli with temperature points toward better agreement at the high temperatures than is found at room temperature.

It has been suggested (38) that an experimentally observed positive value of $B^s x_1 x_2$ might actually be the difference between a large negative $\Delta F^M{}_{ex}$, which would result when pairing or other chemical interactions between unlike atoms are favored (4), and a larger distortion energy which is always positive. That this is not the case in the systems studied here is demonstrated by the fact that the chemical effects should persist into the liquids where distortion energies are absent. This would result in large negative values for $\Delta F^{M(l)}{}_{ex}$; whereas it is seen from Fig. 11 that the liquid of the $Ga_xIn_{1-x}Sb$ system is perfectly ideal, and those of the other two systems show much smaller departures from ideality than do the solids. From the same argument, it would appear that the good agreement obtained by Stringfellow and Greene (40) between the experimental phase diagram and that calculated from a quasi-chemical approach for $Ga_xIn_{1-x}As$ might possibly be fortuitous [they used 14.7 eu for the entropy of fusion of GaAs instead of the more recent value of 16.5 (23)], since the quasi-chemical approach does not take into account the difference that would be expected between the liquid and solid as a consequence of lattice strain.

Even though the identification of $B^s x_1 x_2$ in terms of the excess thermodynamic functions is not clear, its magnitude is cause for concern in view of the rather

[2] The distortion energy calculated from [19] is ½ that given by Lawson's original relation which contained an arithmetic error (38).

Table I. Crystal properties of III-V alloys

System		Lattice parameter				Molar volume				Shear modulus* (cal. cm^{-3})	
a	b	a(Å)	b(Å)	diff. (Å)	diff. (%)	a(cm^3)	b(cm^3)	diff. (cm^3)	diff. (%)	a	b
InSb-GaSb		6.479	6.095	0.384	6.10	41.00	34.10	6.90	18.3	7.22 × 10^3	10.31 × 10^3
InAs-GaAs		6.058	5.653	0.405	6.92	33.40	27.15	6.25	20.6	9.47	14.20
InP-GaP		5.869	5.451	0.418	7.38	30.40	24.36	6.04	22.0	11.5**	15.5**

* "Semiconductors and Semimetals," R. K. Willardson and A. C. Beer, Editors, Academic Press, New York (1966), p. 110.
** Extrapolated from data for the antimonides and arsenides.

stringent requirements on materials for semiconductor device applications. A serious consequence of significant departure from ideality in multicomponent systems is the possibility of phase separation in the solid. Miscibility gaps have not been reported for any of the diagrams of the III-V alloys. However, because of the great problem in attaining equilibrium below the solidus boundaries, they cannot be ruled out. Phase separation to produce a miscibility gap will occur at temperatures less than a critical temperature given by $T_c \approx B/2R$ (41). Referring to Fig. 10, T_c, calculated at the maximum in the $\Delta F^{M(s)}{}_{ex}$ curves, is 850°, 510°, and 380°K for $Ga_xIn_{1-x}P$, $Ga_xIn_{1-x}As$, and $Ga_xIn_{1-x}Sb$ solids, respectively. This calculation assumes that the observed variation of B^s with temperature describes only the condition during solidification, and that B^s remains constant below the solidus boundary, as would be expected if it were largely due to strain.

In the case of $Ga_xIn_{1-x}P$, at least, T_c is approaching the temperature at which this material might be grown by vapor or liquid phase epitaxy, or at which it might be subsequently processed. Moreover, as was demonstrated in some other systems that were studied extensively, the critical temperature need not actually be reached for local ordering to occur. In the Al-Zn (42), Al-Ag (43), and Cu-Au (43, 44) systems, for example, segregation in the form of clustering and superlattice formation could be observed at almost 100°C above the temperature of the miscibility gaps.

As in the metal systems cited above, it is suggested that the excess free energy in the three semiconductor systems investigated here results from strain-relief processes that occur during solidification to produce local order and a decrease in entropy. This entropy change is substantial. By making the approximation, as indicated by almost flat B/RT *vs.* x curves, that all of the excess free energy is in $T\Delta S^{M(s)}{}_{ex}$, $\Delta S^{M(s)}{}_{ex}$ amounts to −0.45, −0.42, and −0.59 eu, which are about 32, 30, and 42% of the ideal mixing entropies for $Ga_xIn_{1-x}Sb$, $Ga_xIn_{1-x}As$, and $Ga_xIn_{1-x}P$, respectively.

No details about the nature of the ordering can be presented in the absence of diffuse x-ray scattering data, but the formation of stacking faults, clusters, or vacancy-stabilized defects of various sorts is a possibility. Reports of inhomogeneities in InP-GaP alloys are beginning to appear. Evidence that phase separation might be occurring during low-temperature liquid phase epitaxial growth was seen (45), and Richman (46) observed diffuse structure in x-ray patterns of this material that was produced by vapor epitaxy.

It is too early to predict the effect of possible structural inhomogeneities on the semiconductor properties of semiconductor alloy systems. The electron mobility in InAs-InP vapor-deposited alloys was found to fall much below the expected value throughout the mid-range of compositions (47), and in the InAs-GaAs system there was actually a pronounced minimum in mobility at $x = 0.5$ (48). On the other hand, in the InSb-GaSb system the mobility was essentially an additive function of the mobilities of the pure end components (49). Electrical properties can be difficult to interpret and are influenced by many factors, such as the basic conduction process, degree of compensation, *etc.*, as well as by lattice strain and inhomogeneities, all of which can vary with composition of the alloy. In electroluminescence applications, where these alloys have particular interest, structural inhomogeneities might act as trapping centers to lower the efficiency of radiative processes.

Summary

A generalized thermodynamic treatment of the pseudobinary T-x diagrams of the homologous series of III-V compound alloys, InSb-GaSb, InAs-GaAs, and InP-GaP, was carried out. These materials are all in a class characterized by linear plots of B/RT *vs.* composition, where B is defined by Bx_1x_2, the excess free energy of mixing of the two end components. The liquid phase of InSb-GaSb is perfectly ideal ($B = 0$), and the liquids of the two other systems show only small departures from ideality. The solid phases show substantial nonideal behavior, increasing in magnitude in going from InSb-GaSb to InAs-GaAs to InP-GaP. This parallels the disparity in molecular size between the two components of each pair.

The flatness of the B/RT *vs.* x plots ($B/RT \approx$ constant) indicates that the partition of the excess free energy between the entropy and enthalpy greatly favors the former. Thus, the alloys are not regular solutions and, moreover, cannot be described by a quasi-chemical approach which allows only small dependence of B on temperature. It is suggested that some of these alloys might not freeze as homogeneous random mixed crystals, but might exhibit some degree of local order in the nature of clustering, layering, or perhaps a vacancy-stabilized defect structure. Such structures would be expected to have adverse effects on the performance of some semiconductor devices that are envisioned for these alloys. The magnitude of the excess free energy in the case of InP-GaP, at least, suggests that the tendency toward inhomogeneity may be so great as to bring about phase separation in the solid at some temperatures where this alloy might be grown or processed.

Manuscript submitted Oct. 23, 1970; revised manuscript received *ca.* Feb. 15, 1971.

Any discussion of this paper will appear in a Discussion Section to be published in the June 1972 JOURNAL.

REFERENCES

1. O. G. Folberth, *Z. Naturforsch.*, **10a**, 502 (1955).
2. H. Weiss, *ibid.*, **11a**, 430 (1956).
3. C. Hilsum, *Proc. 7th Intern. Conf. on Phys. of Semiconductors, Paris, 1964*, p. 1127.
4. J. H. Hildebrand and R. L. Scott, "Solubility of Non-electrolytes," Reinhold, New York (1950).
5. L. S. Darken and R. W. Gurry, "Physical Chemistry of Metals," McGraw-Hill, New York (1953).
6. G. N. Lewis and M. Randall, "Thermodynamics," (revised by K. S. Pitzer and L. Brewer) McGraw-Hill, New York (1961).
7. E. A. Guggenheim, *Proc. Roy. Soc. (London)*, **A148**, 304 (1935).
8. J. E. Hilliard, B. L. Averbach, and M. Cohen, *Acta. Met.*, **2**, 621 (1954).
9. For a summary of data and individual references, see R. K. Willardson and H. L. Goering, "Compound Semiconductors," Vol. 1, Reinhold, New York (1962).
10. B. D. Lichter and P. Sommelet, *Trans. AIME*, **245**, 99 (1969).
11. B. D. Lichter and P. Sommelet, *ibid.*, **245**, 1021 (1969).
12. J. C. Woolley and D. G. Lees, *J. Less-Common Metals*, **1**, 192 (1959).
13. B. M. Kulwicki, Dissertation No. 64-6705, University Microfilms, Univ. of Mich., Ann Arbor, Mich.
14. T. S. Liu and E. A Peretti, *Trans. ASM*, **44**, 539 (1952).
15. J. Bednar and K. Smerous, *Czech. J. Phys.*, **5**, 546 (1955).
16. S. A Pogodin and S. A Dubinsky, *Izvest. Sektora Fiz.-Khim. Anal.*, **17**, 204 (1949).
17. W. Koster and B. Thoma, *Z. Metallk.*, **46**, 291 (1955).
18. I. C. Greenfield and R. L Smith, *Trans. AIME*, **203**, 351 (1955).
19. N. Nachtrieb and H. Clement, *J. Phys. Chem.*, **61**, 1424 (1958).
20. W. F. Schottky and M. B. Bever, *Acta Met.*, **6**, 320 (1958).
21. J. C. Woolley and B. A. Smith, *Proc. Phys. Soc.*, **72**, 214 (1958).
22. H. J Van Hook and E. S. Lenken, *Trans. AIME*, **227**, 220 (1963).
23. R. M. Cox and M. J. Pool, *J. Chem. Eng. Data*, **12**, 247 (1967).
24. J. van den Boomgard and K. Schol, *Philips Res. Rept.*, **12**, 127 (1957).

25. L. M. Foster and J. E. Scardefield, *This Journal*, **117**, 534 (1970).
26. M. B. Panish, *J. Chem. Thermodynamics*, **2**, 319 (1970).
27. R. J. Chicotka, T. J. Watson Research Center, IBM, Yorktown Heights, N. Y., Private communication.
28. D. Richman, *J. Phys. Chem. Solids*, **24**, 1131 (1963).
29. W. Koster and W. Ulrich, *Z. Metallk.*, **49**, 365 (1958).
30. M. B. Panish and J. R Arthur, *J. Chem. Thermodynamics*, **2**, 299 (1970).
31. C. D. Thurmond, *J. Phys. Chem. Solids*, **26**, 785 (1965).
32. See Ref. (5), p. 271.
33. R. K. Willardson, J. H. Winkler, and B. Ross, Bell and Howell Research Lab. Contract Rept. No. N00014-68-C-0219, O.N.R., March 1968.
34. J. A. Van Vechten, *Proc 10th Intern. Conf. on Phys. of Semiconductors, Cambridge, Mass., Aug. 1970*, p. 602.
35. S. E. Wood, *J. Chem. Phys.*, **15**, 358 (1947).
36. J. H. Hildebrand and R. L. Scott, "Regular Solutions," Prentice-Hall, New York (1962).
37. A. W. Lawson, *J. Chem. Phys.*, **15**, 831 (1947).
38. L. L. Seigle, M. Cohen, and B. L. Averbach, *J. Metals*, **4**, 1320 (1952).
39. R. K. Willardson and A. C. Beer, Editors, "Semiconductors and Semimetals," Academic Press, New York (1966).
40. G. B. Stringfellow and P. E. Greene, *J. Phys. Chem. Solids*, **30**, 1779 (1968).
41. See Ref. (6), p. 286.
42. P. S. Rudman and B. L. Averbach, *Acta Met.*, **2**, 576 (1954).
43. J. M. Cowley, *Phys. Rev.*, **77**, 669 (1950).
44. Y. Takagi, *Proc. Phys. Math. Soc. (Japan)*, **23**, 44 (1941).
45. C. Hilsum, Royal Radar Establishment, England, Private communication.
46. D. Richman and C. J. Nuese, Tech. Conf. on Prep. and Properties of Electronic and Magnetic Materials for Computers, AIME, New York, N. Y., Sept. 2, 1970.
47. H. A. Allen and E. W. Mehal, *This Journal*, **117**, 1081 (1970).
48. R. W. Conrad, P. L. Hoyt, and D. D. Martin, *ibid.*, **114**, 164 (1967).
49. W. M. Coderre and J. C. Woolley, *Can. J. Phys.*, **47**, 2554 (1969).

Substrate Surface Preparation and Its Effect on Epitaxial Silicon

P. Rai-Choudhury*

Westinghouse Research Laboratories, Pittsburgh, Pennsylvania 15235

ABSTRACT

Silicon substrates prepared carefully by chemical-mechanical techniques, such as the silicon dioxide process, are comparable with those prepared by the chemical polishing technique, which in turn, are comparable with the bulk material. Defects are found to generate on substrates during oxidation even under idealized conditions probably by migration and collapse of vacancy clusters, and some of these defects (*i.e.* the extrinsic faults) are nucleation centers for intrinsic stacking faults in the epitaxial layers. In addition to removing shallow mechanical damage, HCl etching in an rf heated system usually generates many thermally induced dislocations, which, in turn, prevent formation of defects during oxidation. The probability of stacking fault formation is significantly reduced by using (100) wafers instead of (111) wafers.

Depending on the type of device to be fabricated, chemically or chemical-mechanically polished wafers may be used as the starting material for thermal oxidation or epitaxial growth. The surface of a chemically polished wafer, although free from mechanical damage, is not flat over large distances and not mirror-like. Surface flatness over large areas is becoming increasingly important in masking operation by photolithographic techniques for devices such as photodiode arrays and many integrated circuits. Fortunately, with the development of electron beam lithography (1) such stringent requirements for surface flatness are not necessary. Among the various methods of producing very flat surfaces over large areas are the cupric ion process and the silicon dioxide colloidal suspension process (2-4). The cupric ion process takes place in an acidic medium ($pH \leq 7$) may be represented by the following reaction

$$Si(s) + 2Cu(NO_3)_2\ (soln.) + 6NH_4F\ (soln.) = (NH_4)_2SiF_6\ (soln.) + 4NH_3(g) + 2Cu(s) + 4NHO_3\ (soln.)$$

The silicon dioxide process takes place in an alkaline medium ($pH \geq 9.8$) and may be approximated as

$$Si(s) + 4NaOH\ (soln.) = Na_4SiO_4\ (soln.) + 2H_2(g)$$

Both processes being of a chemical nature, and the very small solid particles involved being either softer (*i.e.* Cu) or of hardness comparable to that of silicon (*i.e.* SiO_2), no mechanical damage is introduced during polishing (2-4). However, the possibility of introducing mechanical damage through a fractured and freed silicon particle or not removing all the prior process-induced damage exists in all these various shaping processes. Consequently, the procedure followed from sawing to the final polishing step is of importance. If the mechanical damage is shallow and the associated microstrain small then *in situ* etching at high temperature might remove the damaged layer.

Unfortunately there are some disadvantages of having a perfectly damage-free surface. Nowadays most melt-grown ingots used to prepare substrates are either free of or very low in dislocation density. As a result these crystals are supersaturated with vacancies, which may lead to the formation of vacancy clusters (5, 6), because vacancy sinks are either absent or are too far apart. Such vacancy clusters, when decorated with metallic impurities are shown to produce diodes with high leakage current (6). Fortunately these decorated vacancy clusters can be effectively cleaned by gettering, for example, with phosphorus glass at 1050°C. If, however, the surface of a dislocation-free crystal is

* Electrochemical Society Active Member
Key words: stacking faults, mechanical damage, polishing, vacancies.

mechanically damaged during shaping operation a flowed lattice with minute surface crevices results. Dislocations develop from the damaged lattice during high-temperature annealing which then act as vacancy sinks. Lawrence (7) indicated that the fault nucleation appears to occur at pinning centers in the flowed lattice provided by crevices fixed by a thermally grown silicon dioxide film. Such pinning centers increase the probability of dislocations intersecting with one another. The intersection of two dislocations which satisfies the Lomar-Cottrell conditions will form a stacking fault. These stacking faults are extrinsic and grow by vacancy emission.

The surface layers of a polished wafer can, at best, be similar to the bulk of the material from the point of view of crystallographic perfection. The Czochralski grown ingots usually contain many microinhomogeneities, which of course, become part of the surface features of a polished wafer. In the absence of any fast diffusing impurities, the importance of the substrate (when it is not an active part of a device) exists only during the initial few seconds of nucleation and growth. If the substrate microinhomogeneities are of coherent or semicoherent type, they are not detrimental to the growth of a relatively thick epitaxial layer. However, when a thin layer of epitaxial material is grown on substrates containing coherent or semicoherent type of inhomogeneities, the quality of the layers may be profoundly influenced. If the microinhomogeneities are of the incoherent type, defects such as stacking faults might be nucleated. This is, of course, a distinctly different mechanism of fault formation from that in the substrate, where stacking faults are formed by the collapse of vacancy clusters during high temperature ($\geqq$1000°C) heat treatments.

The present investigation consists of examining the substrate surface after suitable polishing in terms of surface morphology and mechanical damage. These surfaces are then compared with the bulk material in terms of microinhomogeneities. The polished wafers are subjected to tests such as oxidation and epitaxial growth to assess the quality of the starting material as well as the grown epitaxial layers. The effectiveness of *in situ* etching in removing mechanical damage and other surface contaminants are also examined.

Experimental Procedure

The polished wafers examined were of two basic types, namely, those polished by the chemical-mechanical processes, such as the silicon dioxide process, and the cupric ion process, and those chemically polished by liquid etchants. Effects of abrading with diamond and garnet particles prior to silicon dioxide polishing were also examined. The chemical polishing of the lapped wafers were performed using $HF:HNO_3:HAc::3:15:5$ mixture. Immediately before use the polished wafers were cleaned thoroughly by a special process to remove any organic and metallic contaminants from the surface. They were then Sirtl etched (8) to reveal any scratches and other crystallographic defects. Some of the shallow and isolated damages and bulk-induced defects are not always visible after Sirtl etching. Therefore, another test was performed in which cleaned wafers were oxidized in wet oxygen at 1100°C for 3 hr to give about 10,000Å of SiO_2 film and then Sirtl etched after removing the SiO_2. This is a sensitive test for revealing any defects induced by the mechanical damage and the collapse of vacancy clusters. The surfaces were examined by optical microscopy and scanning electron microscopy. The surface layers and the bulk of a number of wafers were examined by transmission electron microscopy for comparison purposes. The wafers were etched using a 1% HCl gas in palladium purified H_2 at 1270°C (corrected pyrometer temperature) for 10 min to see how effectively any damaged material can be removed from the surface. The etching was carried out in a conventional horizontal epitaxial reactor having a SiC coated graphite susceptor, heated externally by rf coils. Epitaxial layers were grown from a $SiCl_4$-H_2 system at about 1100°C. These layers were examined by optical and electron microscopy for defects and inhomogeneities that might be induced by the substrates.

Results

Ideally the silicon substrates should be prepared in such a way that the surface layer shows only the bulk features in transmission electron microscopy. Thinned surface layers from several chemically polished substrates were examined in TEM, and found to be very similar to the bulk material (from the point of view of microinhomogeneities) regardless of the doping level except when solid solubility is reached. Therefore the objective one would like to achieve is to prepare a substrate surface that has the perfection of a chemically polished surface and the flatness of a mechanically polished surface. The objective has been largely achieved as demonstrated by the test results to be presented below. However, if proper process sequence is not followed, defects can be introduced even under idealized conditions during high-temperature device processing, especially thermal oxidation.

Figure 1 shows some of the surface features of wafers, polished by the silicon dioxide process, made visible by Sirtl etching. Figure 1(a) shows the surface of a wafer that was sawed, chemically etched and then polished using an SiO_2-$NaOH$-H_2O slurry of *p*H 9.8, wheel speed 500 rpm, and a pressure of 5.5 psi. The removal or polishing rate under these conditions was approximately 0.4 mil/hr. One line defect is shown on the photograph, although most of the wafer appears flawless. A chemically polished surface is at least as good as this surface as far as the defect density is concerned, but has a typical orange peel structure. If a lapping or mechanical polishing step is introduced prior to silicon dioxide polishing then deep damage may result which is difficult to remove by such slow polishing action. Figure 1(b) shows typical surface defects caused by 12.5 micron garnet particles, and Fig. 1(c) shows scratches (made visible by Sirtl etching) from diamond abrasive particles which were not removed by the silicon dioxide polishing. It is therefore advisable not to introduce any lapping steps in the preparation of silicon substrates by the silicon dioxide process. In this regard polishing by the cupric ion process that removes typically 4 to 5 mil/hr may be preferable. Of course, the possibility of copper contamination is also increased by this process and careful procedure must be followed to remove any residual copper.

As was mentioned before, most dislocation-free or low dislocation silicon crystals contain excess vacancies and vacancy clusters, formed during cooling of the crystals grown from the melt. On subsequent annealing these vacancies will diffuse towards the surface, especially along the dislocation lines, and at pinning centers such as the SiO_2-Si interface the vacancy clusters may collapse forming stacking faults. Therefore, a more sensitive test for revealing defects induced by mechanical damage is to oxidize the wafer, remove the oxide and then Sirtl etch for about a minute or two. Figure 2 shows some of the results from this test. The diamond polishing leaves the surface severely dislocated as revealed by the etch pits [Fig. 2(a)] and since these dislocations act as numerous sinks, vacancy clusters do not grow to form stacking faults. Figure 2(b) and (c) show the faults induced by 12.5μ garnet particles. The very interesting feature is the absence of any defects in a zone surrounding the clusters of "worm-like" faults [Fig. 2(b)] or line of "saucer-like" defects [Fig. 2(c)]. Quite often such "denuded" or precipitate-free zones (P.F.Z.) are formed in the vicinity of grain boundaries in age hardened alloys. Experimental evidence (9) has shown that apart from a very narrow region immediately next to the grain boundaries, the P.F.Z.'s are depleted of vacancies

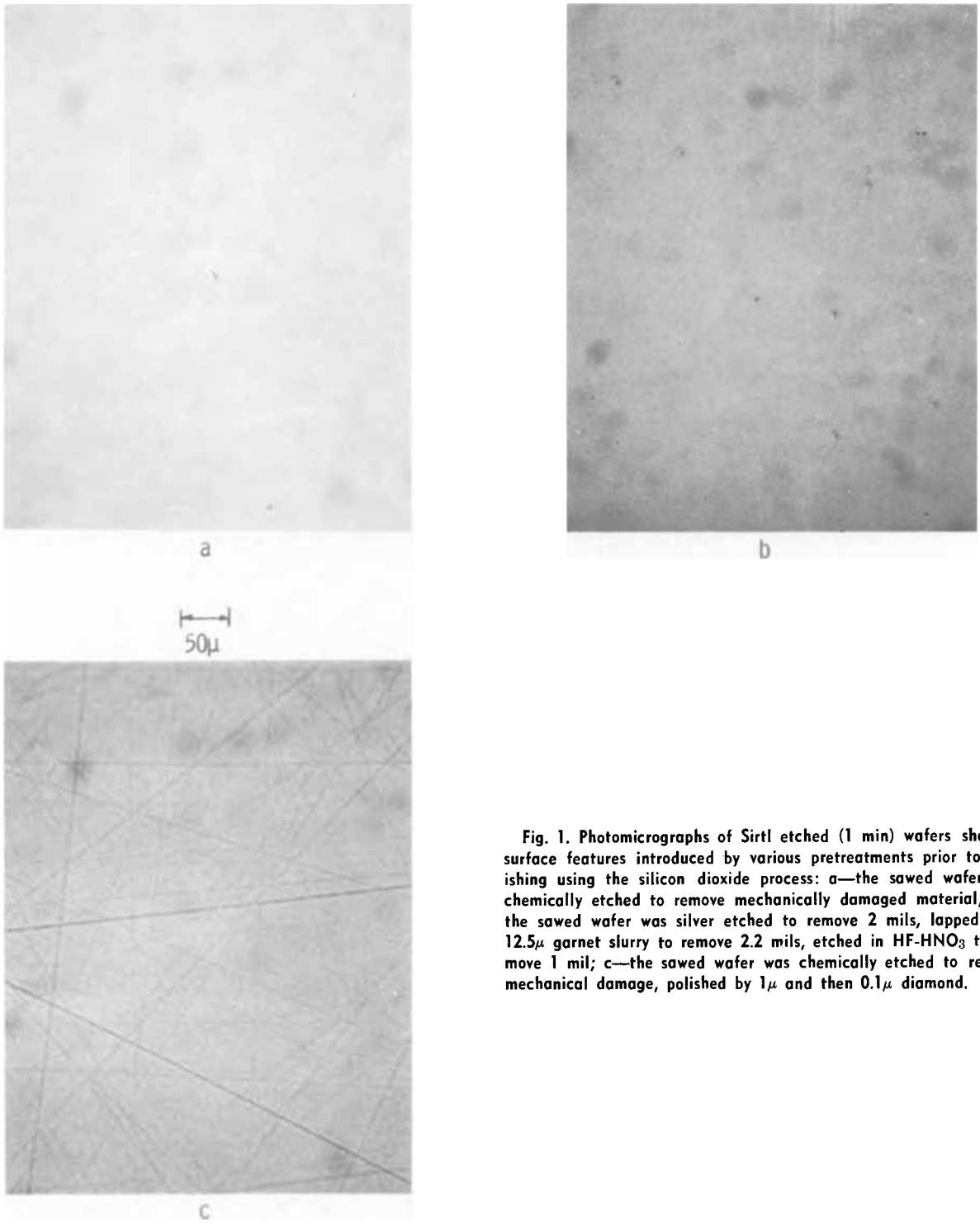

Fig. 1. Photomicrographs of Sirtl etched (1 min) wafers showing surface features introduced by various pretreatments prior to polishing using the silicon dioxide process: a—the sawed wafer was chemically etched to remove mechanically damaged material; b—the sawed wafer was silver etched to remove 2 mils, lapped with 12.5μ garnet slurry to remove 2.2 mils, etched in HF-HNO_3 to remove 1 mil; c—the sawed wafer was chemically etched to remove mechanical damage, polished by 1μ and then 0.1μ diamond.

rather than solutes. Consequently, the vacancy concentration and therefore the bulk diffusivity changes with distance from the boundary. The width of the P.F.Z. can be changed by altering the heat-treatment conditions; the zones are narrower for higher heat-treatment temperatures and faster quenching rates, both of which increase the excess vacancy content. From the above observations together with the fact that the wafer is cut from a float zone crystal, free from any precipitates and gross inhomogeneities (as examined by transmission electron microscopy), it is concluded that these faults grow by vacancy clustering and might be decorated by impurities. As will be shown later these "worm-like" and "saucer-like" defects are really dislocation etch pits and are therefore effective sinks for vacancy migration. Figure 2(d) shows some of the defects (which resemble stacking faults) induced by the sawing damage not completely removed by chemical etching and silicon dioxide polishing.

The defects shown in Fig. 2(b) and (c) could not be resolved adequately in the optical microscope. It was necessary to Sirtl etch these defects for about 3 min and any residual surface oxides removed (to prevent sample from charging) before these faults were resolved in the scanning electron microscope. Figure 3 shows the micrograph which clearly reveals these faults to be dislocation etch pits.

As mentioned before, the quality of a polished surface or the surface layer cannot be better than the bulk of the material. Therefore, several samples, polished by different techniques, were examined by transmission electron microscopy and compared with the bulk. Figure 4 shows the transmission electron micrographs of surface layers from a number of wafers. Figure 4(a) reveals some scratches not removed by

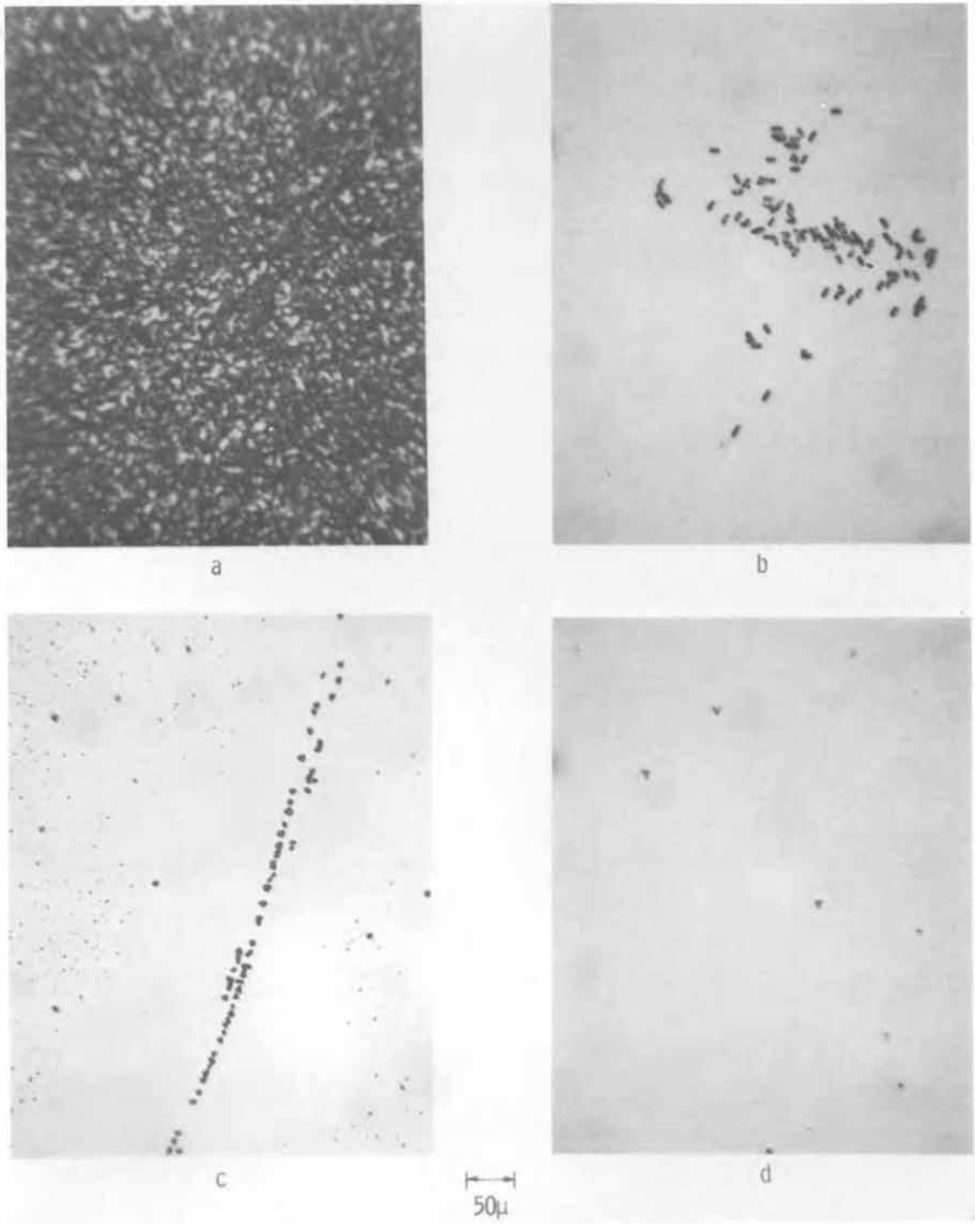

Fig. 2. Photomicrographs showing the effect of incomplete removal of the mechanical damage; the wafers were oxidized at 1100°C for 3 hr in wet oxygen followed by oxide stripping and 1 min Sirtl etching. a—Wafer showing damage from diamond abrasives (1 and 0.1μ size); b and c—wafer showing damage from 12.5μ garnet particles; d—wafer showing the effect of incomplete removal of sawing damage.

the silicon dioxide polishing. These scratches are, however, removable by HCl etching in the epitaxial reactor. Figures 4(b) and 4(c) show the surface layers of wafers polished by the silicon dioxide process and the chemical etchant, respectively. In both cases the inhomogeneities are comparable to the bulk of the respective wafers, and it is believed that these inhomogeneities are not of the type that propagate into the epitaxial layer. The characteristics and the causes of microinhomogeneities in the epitaxial layers are being investigated in detail. None of the inhomogeneities shown in the micrographs are of incoherent type, and therefore, do not contribute to the nucleation of any defects such as stacking faults. Neither are these inhomogeneities fast diffusing, because annealing in H_2 at 1220° for periods of up to 4 hr did not noticeably change their size or distribution. It can be concluded that a properly prepared wafer surface (*i.e.* avoiding any lapping steps) by the silicon dioxide process is comparable to a chemically polished surface, which, in turn, is comparable to the bulk material. A copper polished as well as an HCl etched wafer were similarly examined by TEM and the surfaces were found to be comparable to the bulk material.

If the depth of damage is shallow or the associated microstrain low, then *in situ* HCl etching might remove the damage effectively. In order to show the effectiveness in removing damaged material and surface contaminants, if any, epitaxial layers were grown on substrates with and without HCl etching. Figure 5

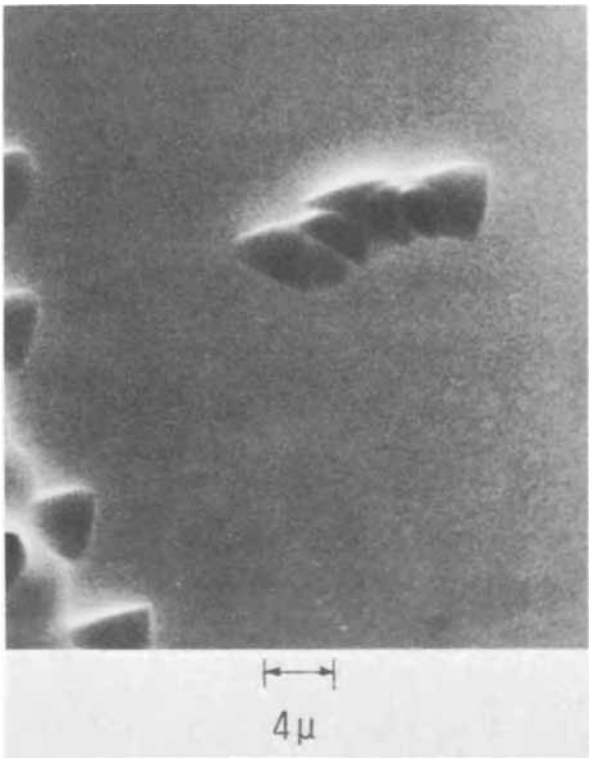

Fig. 3. Scanning electron micrograph at 45° incidence revealing dislocation etch pits; these are the same faults that appear in Fig. 2b and c.

shows that *in situ* etching does indeed remove most of the shallow damaged material. Figure 5(a) shows single stacking faults, groups of stacking faults at various stages of cancellation, line faults, and dislocation etch pits. No stacking fault interaction with incomplete cancellation is visible. All the epitaxial stacking faults are of intrinsic type, and Booker (10) has shown that they arise from small area of extrinsic fault on the (111) plane (or something equivalent). Although one fault is shown in Fig. 5(b) the entire wafer had only 4 stacking faults. Under identical growth conditions as those for Fig. 5, a 1.25 in. diam wafer, properly polished by the silicon dioxide process, gave about 115 stacking faults without HCl etching and 1 stacking fault with HCl etching. Thus *in situ* etching of the wafer before any processing reduces considerably the risk of process-induced defect formation.

As was mentioned before, all stacking faults in the substrate from vacancy collapse are of extrinsic type, and therefore are nucleation centers for the stacking faults in the epitaxial layers. The effect of the excess vacancies in causing stacking faults in the epitaxial layers was tested using (111) substrate silicon wafers that were chemically polished, dislocation free (as shown by x-ray topography) and a resistivity of 260 ohm-cm (p-type). The level of oxygen was below the detection limit of the *IR* absorption technique (<0.2 ppm), and the minority carrier lifetime was 700 μsec. All wafers were HCl etched prior to the growth of the epitaxial layers. Some of the wafers were oxidized and the oxide stripped before putting in the epitaxial reactor. The epitaxial layers were Sirtl etched to reveal the defects. The layer grown on unoxidized wafers had stacking fault density of less than 10 per wafer whereas about 400 stacking faults were found on the oxidized wafers. A possible explanation of the results is that enough dislocations are generated during the rf heating in the epitaxial reactor (11) so that the excess vacancies and vacancy clusters can be removed effectively. Absence of any effective pinning centers, such as those provided by a thermally grown SiO_2 layer makes fault nucleation difficult. Of course, in the presence of an oxide layer the vacancies will collapse to form stacking faults in the substrate (7) during oxidation, which will subsequently propagate into the grown layer. To further substantiate this point one batch of the 260 ohm-cm substrates were heat treated in H_2 to simulate the thermal cycling during HCl etching, and then oxidized along with another batch of wafers that were HCl etched. Sirtl etching of these wafers indicated practically complete absence of any oxidation-induced defects on the HCl etched wafers whereas a very few localized areas of oxidation induced defects were seen on the heat-treated wafers. Of course there was a general increase in the dislocation density of these wafers (11). Epitaxial layers were grown on some of these wafers (not Sirtl etched) after an *in situ* HCl etching. The stacking fault densities on the heat-treated wafers were ≤20 faults as compared to about 400 faults if the wafer was first oxidized. Further oxidation and examination of these epitaxial layers indicated no increase in the defect density. The results are summarized below with indicated defect densities (only to show the general trends).

Wafer treatment before oxidation	Wafer treatment after oxidation	Defects in epitaxial silicon	
		Stacking faults* No./cm²	Dislocations* No./cm²
None	HCl etch and epitaxial growth	70	300
Heat-treatment in epitaxial reactor simulating HCl etching	HCl etch and epitaxial growth	3	200
HCl etching in epitaxial reactor	HCl etch and epitaxial growth	<10	170
HCl etch and epitaxial growth	None	3	480

* Defect densities were obtained by counting all the faults in a wafer and indicate representative figures

Thus, in order to reduce the density of the stacking faults in the epitaxial layer it is not only necessary to remove any surface contaminants, but the presence or generation of a fair number of dislocations is also essential; HCl etching seems to fulfill both the requirements.

If the vacancies are present in the substrates in the form of clusters, such as, the vacancy spirals reported by deKock (6), then, these clusters cannot be removed by heat-treatment in the epitaxial reactor. When epitaxial layers were grown on such substrates the characteristic spiral pattern became visible, and consisted of numerous stacking faults (revealed by Sirtl etching) along the spiral. Thus vacancy clusters in the substrates are effective nucleation centers for stacking faults in the epitaxial layers.

Since stacking faults are nonequilibrium defects with stored energy (12) of the order of 50 ergs/cm², they can be annealed out under appropriate conditions, such as, heating in H_2 at about 1300°C for faults on (111) silicon. Hydrogen annealing causes disappearance of the characteristic fringe contrast and leave an impression of the fault on the wafer surface. However, such high-temperature annealing is not a practical solution. Segregation of impurities at the stacking faults has been observed directly by TEM. This can be interpreted as a result of the Suzuki interaction of impurity or dopant atoms with dislocations, resulting in a lowering of the stacking fault energy. Such stabilized stacking faults would be difficult to anneal, and if decorated with metallic impurities are detrimental to device performance (7, 13). Nucleation probability of stacking faults on the (111) plane is relatively high. The defects can start from an error in the stacking sequence of a single atomic plane and consist of three intrinsic faults on the inclined {111} planes. Since all the three faults are of intrinsic type there is no cancellation of (compressive and tensile) forces and the stored energy is relatively high. On the other hand the nucleation probability on the (100) plane is relatively low. In this case the formation of an (111) plane

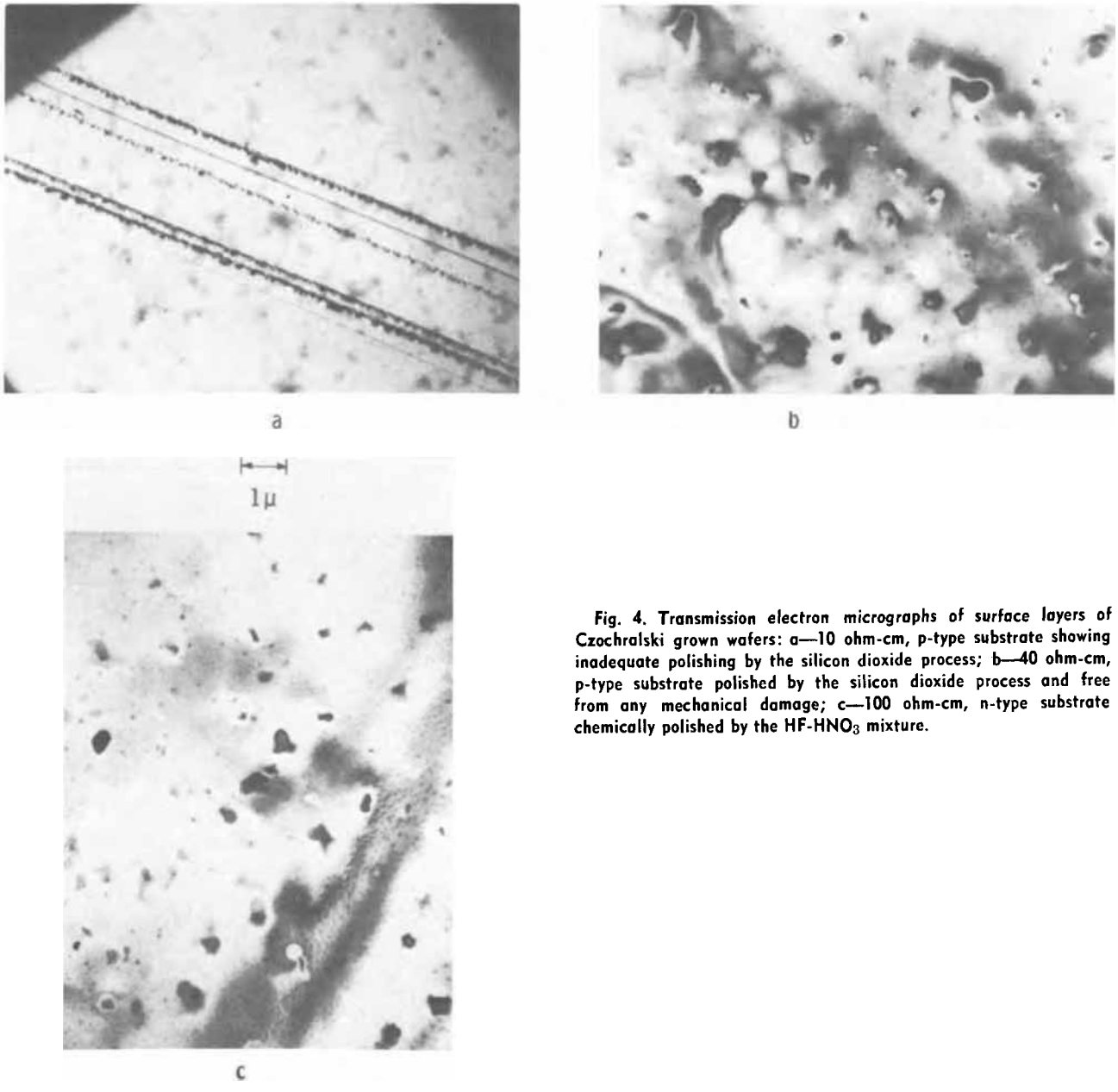

Fig. 4. Transmission electron micrographs of surface layers of Czochralski grown wafers: a—10 ohm-cm, p-type substrate showing inadequate polishing by the silicon dioxide process; b—40 ohm-cm, p-type substrate polished by the silicon dioxide process and free from any mechanical damage; c—100 ohm-cm, n-type substrate chemically polished by the $HF-HNO_3$ mixture.

must take place for which a larger error in the stacking sequence, such as, an oxide island is necessary. Also the square-type stacking faults in the epitaxial layer on (100) substrates consist of four faults as intrinsic/extrinsic/intrinsic/extrinsic on going around the defect. The total stored energy in this defect is expected to be lower than that in the (111) silicon due to some cancellation of forces, and therefore should not attract impurities as effectively as the faults on (111) silicon. Epitaxial layers were grown on chemically polished (111) as well as (100) wafers without *in situ* HCl etching. The resulting stacking fault density on the (111) wafer was about 100 faults/wafer whereas zero on the (100) wafer. It has also been observed by Thomas (14) that the stacking fault density in epitaxial silicon grown on (111) substrates was about 10^7 faults/cm^2, whereas, the density was essentially zero on the (100) silicon under identical conditions. These layers were grown at 600°C, a vacuum of 10^{-10} Torr, and at a rate of about 200 Å/min. Such large differences in the stacking fault densities between the two orientation substrates can be considered as evidence that nucleation probability of stacking faults on (100) substrates is considerably less and at sufficiently slow growth rate the mobility of the depositing atoms is high enough to prevent any errors in the stacking sequence. The preceding discussion indicates that the stacking faults are detrimental to good device performance, and in this regard (100) wafers provide a definite advantage over the (111) orientation. Therefore, (100) wafers should be preferred to (111) wafers for device fabrication.

Summary

Silicon substrates carefully polished by the chemical-mechanical processes, such as the SiO_2-NaOH-H_2O slurry possess the flatness of a mechanically polished surface and the structural perfection comparable to the bulk material. Shallow damaged material can be removed effectively from the wafer by HCl etching in the epitaxial reactor. However, if it is necessary to oxidize the wafer prior to epitaxial growth then the wafer must be free of damaged layer and should be HCl etched before oxidation. If the starting wafer is

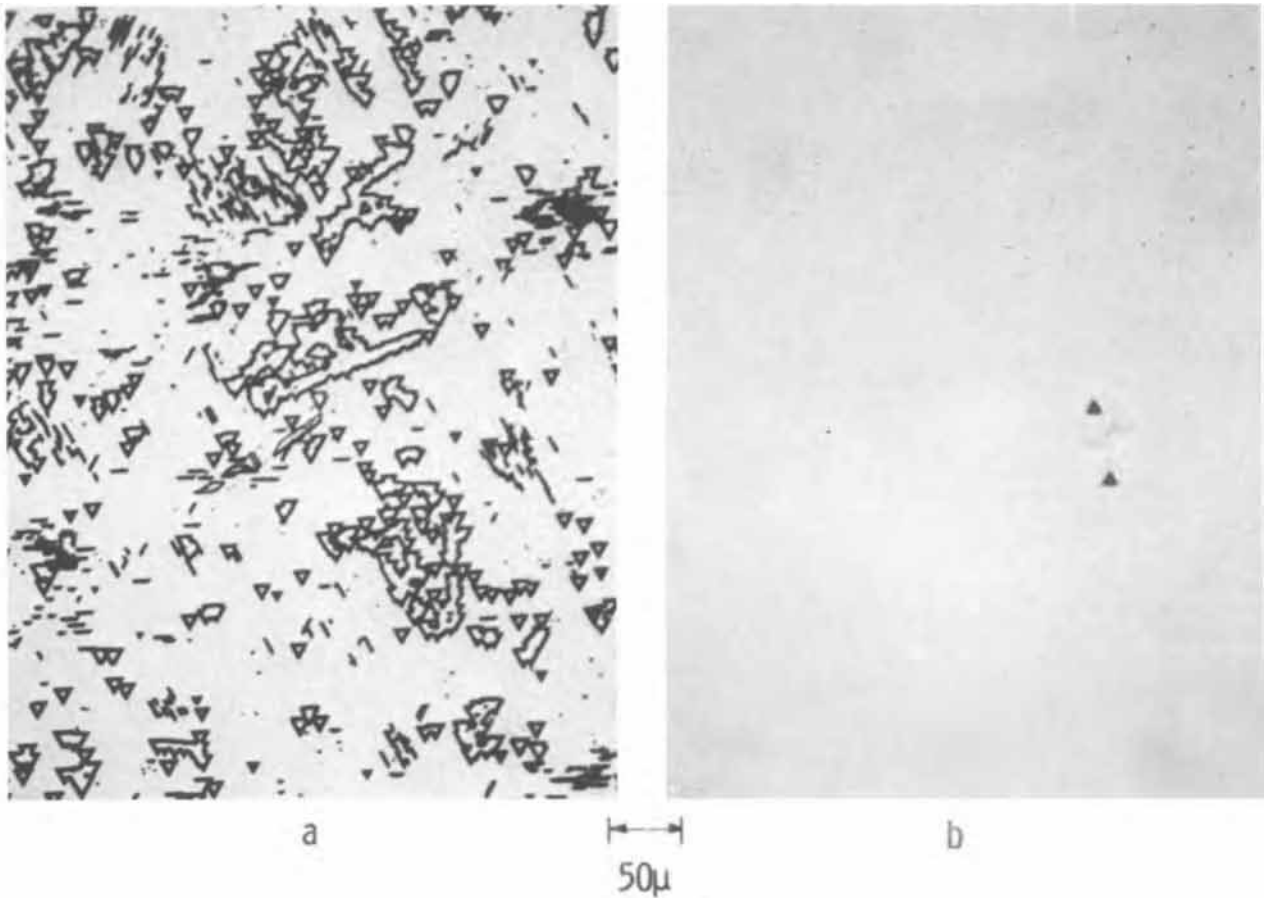

Fig. 5. Photomicrographs showing the effectiveness of HCl etching in removing mechanical damage and improving the quality of the epitaxial layers; all wafers Sirtl etched for 1 min. a—Epitaxial layer grown without *in-situ* HCl etching on the surface described in Fig. 1c; b—same as a, with HCl etching.

free from or very low in dislocation density then oxidation will generate many defects by a vacancy migration and collapse mechanism, which in turn will cause numerous stacking faults in a subsequently grown epitaxial layer. The probability and the energy of the stacking fault assembly is considerably reduced when (100) instead of (111) oriented wafers are used.

Acknowledgment

The author would like to thank W. Cifone, F. Berish, H. D. Larson, and J. H. Riefer for assistance with the experimental work, and Dr. J. E. Johnson for helpful discussions.

Manuscript submitted Nov. 9, 1970; revised manuscript received *ca.* Feb. 8, 1971.

Any discussion of this paper will appear in a Discussion Section to be published in the June 1972 JOURNAL.

REFERENCES

1. S. J. Angello, presented at the WESCON '69, San Francisco.
2. J. Regh and G. Silvey, Paper presented at the Electrochem. Soc. Meeting, Philadelphia, Oct. 9-14, 1966.
3. R. J. Walsh and A. Herzog, Monsanto Co., U.S. Pat. 3,170,273, February 23, 1965; E. Mendel, SCP and Solid State Technology, **10**, 27 (1967).
4. Siemens & Halske Aktiengesellschaft, British Pat. 987,971, March 31, 1965.
5. B. Chalmers, "Principles of Solidification", p. 55, John Wiley and Sons, Inc., New York (1964).
6. A. J. R. deKock, *Appl. Phys. Letters*, **16**, 100 (1970).
7. J. E. Lawrence, *J. Appl. Phys.*, **40**, 360 (1969).
8. E. Sirtl and A. Adler, *Z. Metallk.*, **52**, 529 (1961).
9. E. A. Starke, Jr., *J. Metals*, **22**, 54 (1970).
10. G. R. Booker and R. Stickler, *Appl. Phys. Letters*, **3**, 158 (1963).
11. P. Rai-Choudhury and W. J. Takei, *J. Appl. Phys.*, **40**, 4980 (1969).
12. E. Aerts, P. Delarignette, R. Siems and S. Amelincks, *ibid.*, **33**, 3078 (1962).
13. J. E. Lawrence, *Trans. AIME*, **242**, 484 (1968).
14. R. N. Thomas, Unpublished work.

Etching Studies of Impurity Precipitates in Pulled GaP Crystals

T. Iizuka[1]

Bell Telephone Laboratories, Incorporated, Murray Hill, New Jersey 07974

ABSTRACT

Light-emitting diodes prepared by p-tipping on n-type pulled GaP substrates are considerably less efficient than those diodes prepared by p-tipping on solution-grown substrates. The present study represents an attempt to use chemical etching and optical microscopy to determine the differences between n-type pulled GaP crystals and crystals obtained by solution- and vapor-growth techniques. Etch patterns believed to be associated with impurity precipitates were observed in large numbers in pulled crystals heavily doped (up to $N_D - N_A = 6 \times 10^{17}$ cm^{-3}) with sulfur or tellurium, and to a much lesser extent in lightly doped and undoped pulled crystals. Clusters of small etch pits attributed to isolated precipitates and short etch grooves attributed to decorated dislocations lying parallel to the surface were both observed. These etch patterns were not seen in solution-grown or vapor-grown crystals doped to approximately the same carrier concentrations.

Considerable work has been carried out on the growth and physical properties of GaP single crystals. These studies have been concerned mainly with crystals prepared by growth from gallium solution, vapor phase transport, or liquid phase epitaxial deposition. Recently, the liquid encapsulated Czochralski (LEC) technique (1-5) has become a major source of GaP crystals. However, relatively little work has been reported on defects in GaP crystals (6-11).

Crystals of n-type, doped with the elements sulfur, selenium, and tellurium, are widely used as substrates for light emitting diode fabrication. The solubility and electrical properties of these impurities in solution-grown, n-type GaP crystals have been reported by Trumbore *et al.* (12).

In this report, etching studies of impurity precipitation in n-type LEC GaP crystals are described. Etching can reveal the presence of precipitate-like defects, but there is a limitation in that it cannot directly identify the nature of the precipitate.

At present there are no standard etching solutions which reveal defects on all surfaces of GaP crystals. For example, no known etchant will reveal dislocations on {110} cleavage surfaces. However, this situation is rather useful for the study of impurity precipitation as is described later.

Experimental

Pulled GaP crystals were grown in vitreous silica crucibles with the growth axis in a <111> direction (5). Undoped, sulfur- and tellurium-doped crystals with carrier concentrations between 3×10^{15} cm^{-3} and 6×10^{17} cm^{-3} were studied. For comparison, solution-grown and vapor-grown crystals doped with sulfur and tellurium were examined.

Slices were cut parallel to the {111} plane, mechanically lapped, and then polished with Linde A. The slices were rinsed with acetone and methanol and dried. After these procedures, the slices were inspected with transmitted visible light. Then, the slices were pre-etched with chlorine-saturated methanol to remove surface damage on the P($\bar{1}\bar{1}\bar{1}$) surfaces. This pre-etching is effective for obtaining a scratch-free, smooth P($\bar{1}\bar{1}\bar{1}$) surface for detailed optical observation, but it is not effective on the Ga(111) surface. Thus, P($\bar{1}\bar{1}\bar{1}$) and cleaved {110} surfaces were mainly employed for observation. Then, a modified AB etchant [10 ml H_2O, 40 mg $AgNO_3$, 5g CrO_3, 8 ml HF for 50 min at 75°C (9, 13)] or RC etchant [8 ml H_2O, 10 mg $AgNO_3$, 6 ml HNO_3, 4 ml HF for 3 min at 60°C (14)] was used to reveal defects. The solution was occasionally stirred during etching, which was performed under ordinary room illumination. Defects on the etched surfaces were observed mainly with an interference contrast microscope (15).

[1] Present address: Electrotechnical Laboratory, Tokyo, Japan.

Key words: Defects, compound semiconductor, optical microscopy.

Results

Undoped, S- and Te-doped pulled crystals.—Etching produced the following types of etch patterns on the surfaces of n-type LEC crystals.

Dislocation etch pits.—Deep, conical dislocation etch pits were revealed on the P($\bar{1}\bar{1}\bar{1}$) surface (Fig. 1, 2, and 3). The diameters of the pits were about 5-10μ and the density was generally of the order of 10^5 cm^{-2}. The shape and the appearance of the pits in the doped crystals were not as distinct as those in the undoped crystals (Fig. 2 and 3).

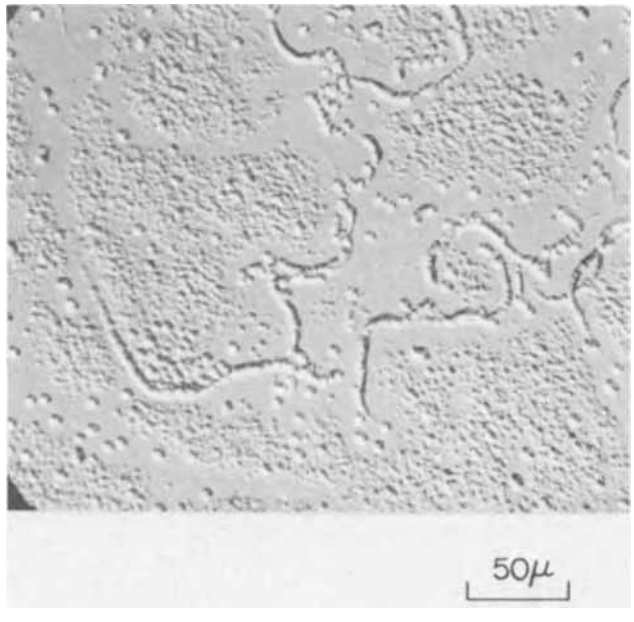

Fig. 1. Dislocation etch pits, etch grooves, and clusters of small etch pits on P($\bar{1}\bar{1}\bar{1}$) surface of S-doped crystal (N_D-$N_A \sim 6 \times 10^{17}$ cm^{-3}). Defect-free regions around the dislocation pits and grooves are seen. Etched with RC etchant.

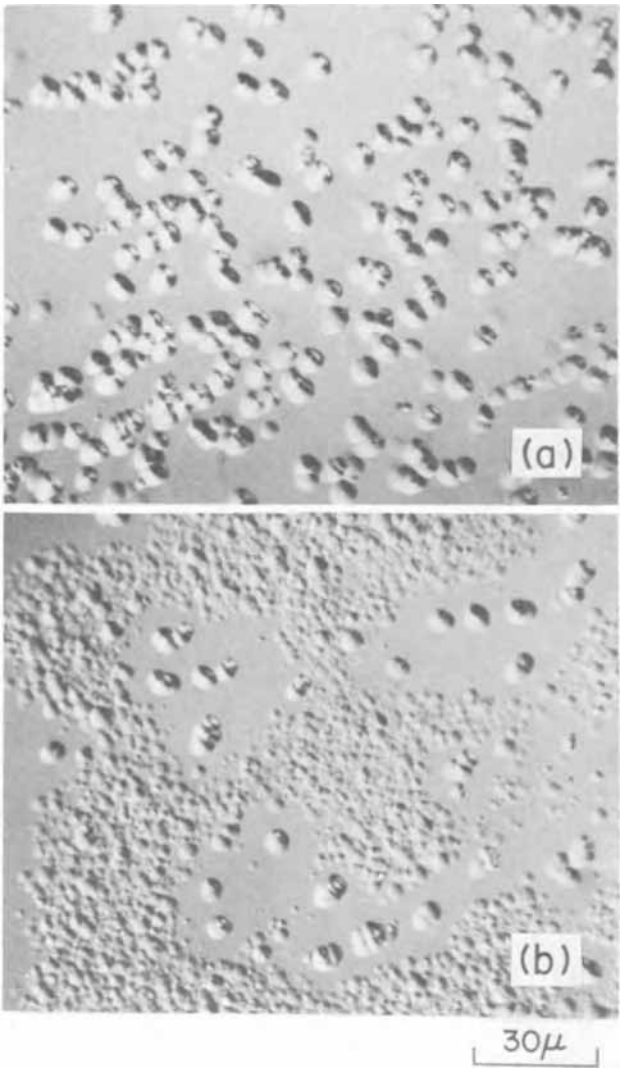

Fig. 2. Correlation between dislocation etch pit density and small-pit clusters on P($\bar{1}\bar{1}\bar{1}$) surface of S-doped crystal (N_D-N_A ~ 6x10^{17} cm^{-3}). Etched with RC etchant. (a) A peripheral region with high dislocation density (~ 8x10^5 cm^{-2}) and without small-pit clusters. (b) A central region with low dislocation density (~ 2x10^5 cm^{-2}) and with small-pit clusters, on the same slice as in (a).

Fig. 3 (a). Dislocation pits and etch grooves on P($\bar{1}\bar{1}\bar{1}$) surface of an undoped crystal. No small-pit clusters are seen. Etched with AB etchant.

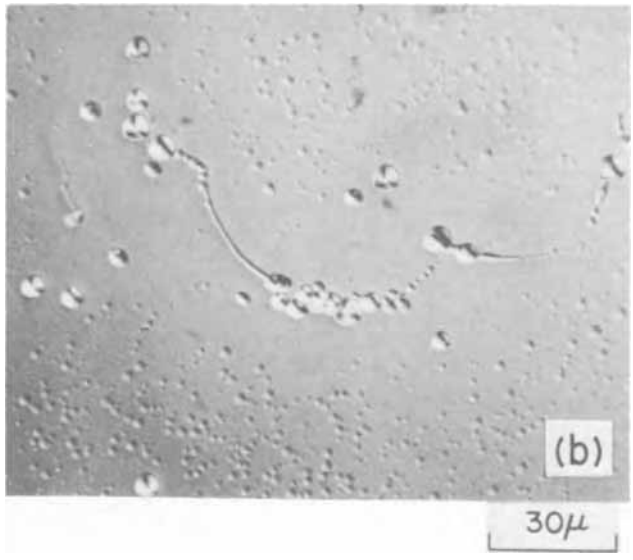

Fig. 3 (b). Another undoped crystal showing dislocation pits, etch grooves, and small-pit clusters on P($\bar{1}\bar{1}\bar{1}$) surface. Etched with AB etchant.

Clusters of small, shallow, flat-bottomed etch pits.— Clusters of small, shallow, flat-bottomed etch pits were also observed on the P($\bar{1}\bar{1}\bar{1}$) surface of one undoped crystal and all doped crystals as shown in Fig. 1, 2(b), and 3(b). However, another undoped crystal did not show these clusters on the P($\bar{1}\bar{1}\bar{1}$) surface [Fig. (3a)]. The individual pit diameter varied from approximately 0.5 to 5μ, and the density was less than 2-3 x 10^7 cm^{-2} at the clustering region on the P($\bar{1}\bar{1}\bar{1}$) surface.

These small pits were also revealed on {110} cleavage surfaces of relatively highly doped crystals ($N_D - N_A \geqq 3 \times 10^{17}$ cm^{-3}), but they were not as clearly shown as on the P($\bar{1}\bar{1}\bar{1}$) surface (Fig. 4 and 5). They were, however, readily observed by ordinary optical microscopy without an interference contrast attachment. There was always a good correspondence between the small-pit cluster distributions on the opposite {110} cleavage halves, indicating the spatial distribution of the defects responsible for the clusters in the bulk. However, even when interference contrast microscopy was employed, it was impossible to observe the small-pit clusters on the etched {110} cleavage surface of undoped ($N_D - N_A \sim 3 \times 10^{15}$ cm^{-3}) and some lightly Te-doped ($N_D - N_A \sim 1 \times 10^{17}$ cm^{-3}) LEC crystals. This result suggests that the etch patterns were related to the dopant impurity concentration.

Distribution of the small-pit clusters varied from crystal to crystal and location to location. Nonuniform distributions of the clusters were observed both in the growth direction and in the radial direction. Sometimes the distribution of the clusters was limited by growth striations on the "off-core" region of a longitudinal {110} surface including the growth axis [Fig. 5(a)]. Discontinuous distribution of the clusters was also seen on the "off-core" to "on-core" transition region as shown in Fig. 5(b). On the P($\bar{1}\bar{1}\bar{1}$) surface of the same sample cut perpendicular to the growth direction, the small-pit clusters were distributed in annular rings as shown in Fig. 6. These results suggest that the formation of the original defects responsible for the small-pit clusters is dominated by crystal growth conditions.

In general, small-pit clusters were not found at the periphery of the P($\bar{1}\bar{1}\bar{1}$) surfaces examined, but a high density of dislocation etch pits was observed [Fig. 2(a)]. In the inner region of the slice, how-

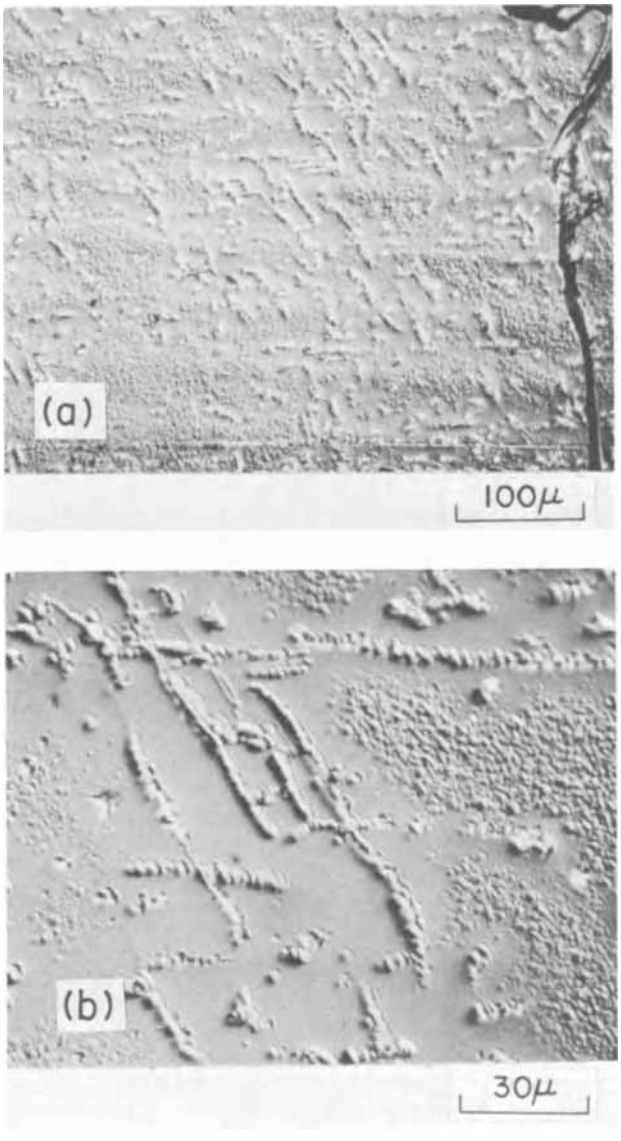

Fig. 4. Etch grooves and clusters of small etch pits on {110} cleavage surface of S-doped crystal (N_D-N_A ~ $6x10^{17}$ cm^{-3}). Defect-free smooth regions around the grooves are clearly seen. Most of the grooves are approximately parallel to either a <211> or <110> direction. Horizontal is a <211> direction. Etched with AB etchant. (a) Low magnification view. Weak striations are seen in this sample. (b) Detailed etch patterns.

ever, the dislocation pit density was lower and small-pit clusters were distributed between the dislocation etch pits [Fig. 2(b)].

Etch grooves.—Etch grooves were revealed on the P($\bar{1}1\bar{1}$) surfaces of all undoped and doped crystals (Fig. 1 and 3). While the grooves were easily revealed on the {110} cleavage surface of relatively highly doped crystals ($N_D - N_A \geq 3 \times 10^{17}$ cm^{-3}), as shown in Fig. 4 and 5, they were revealed with difficulty on the {110} cleavage surface of undoped ($N_D - N_A \sim 3 \times 10^{15}$ cm^{-3}) and lightly doped ($N_D - N_A \sim 1 \times 10^{17}$ cm^{-3}) crystals; their distribution also varied from one crystal to another. There was a correspondence between the densities of the etch grooves on the {110} cleavage surface and the dislocation etch pits on the corresponding P($\bar{1}1\bar{1}$) surface close to the cleaved edge. This correlation may indicate that the etch grooves on the {110} surface are attributed to dislocations lying on, or just under, the surface.

Smooth regions.—It is also noteworthy that there are smooth regions around both dislocation pits and etch grooves as shown in Fig. 1, 2(b), 3(b), 4, and 5.

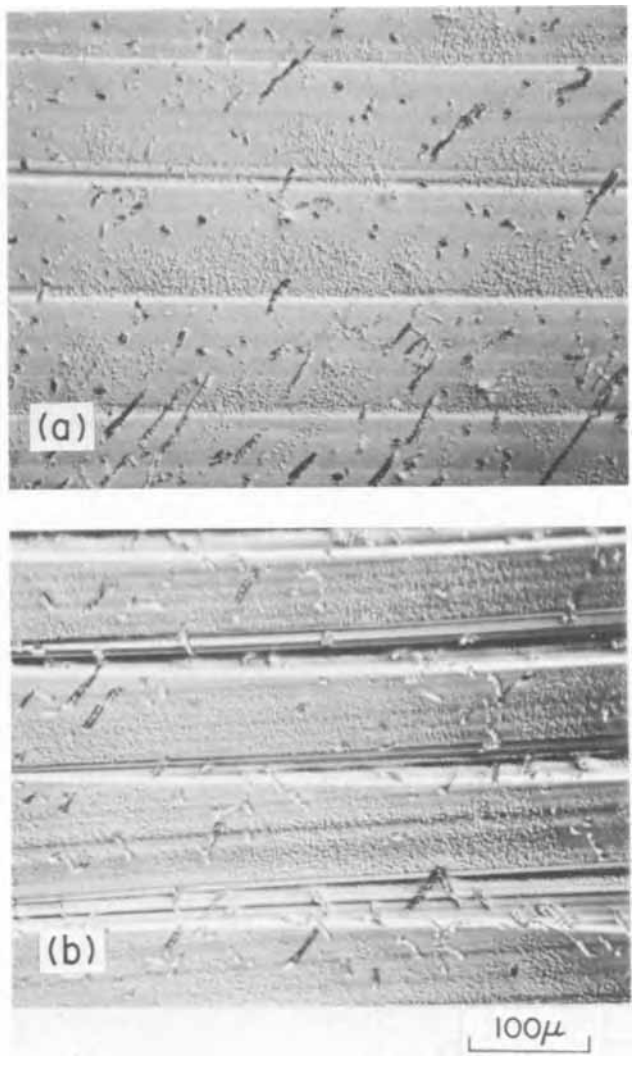

Fig. 5. Etch patterns on a {110} surface parallel to the growth axis. Striations, small-pit clusters, and etch grooves are seen. Te-doped crystal (N_D-N_A ~ $3x10^{17}$ cm^{-3}). Etched with AB etchant. (a) Off-core region. The distribution of the small-pit clusters is limited by growth striations (white lines). (b) Edge of core region (central core region is on the right-hand side of the picture). Discontinuous distribution of the clusters in the growth direction.

The width of such regions was between 10 and 30μ. The presence of similar regions has previously been observed on heavily Te- and Se-doped GaAs crystals (16-18). In Te-doped GaAs, the width of such regions was found to be 25-100μ by Casey (16), and 30-150μ (etching), and 50-200μ (x-ray topography) by the author (18). The formation mechanism of these regions is not well understood. However, it may be assumed that the mechanism is the same in both GaP and GaAs.

N-type solution-grown and vapor-grown crystals.—Neither small-pit clusters nor etch grooves were observed on any surfaces of solution-grown or vapor-grown crystals comparably doped with sulfur or tellurium.

Dislocation etch pits were observed on the {111} surfaces of these crystals. In the solution-grown crystals, they were mostly localized around impurity inclusions.

Discussion

Nature of the characteristic etch patterns of S- and Te-doped crystals.—In addition to the usual dislocation etch pits, clusters of small pits were observed on the surface of most of the donor-doped pulled crystals. The size of the individual pits is smaller than

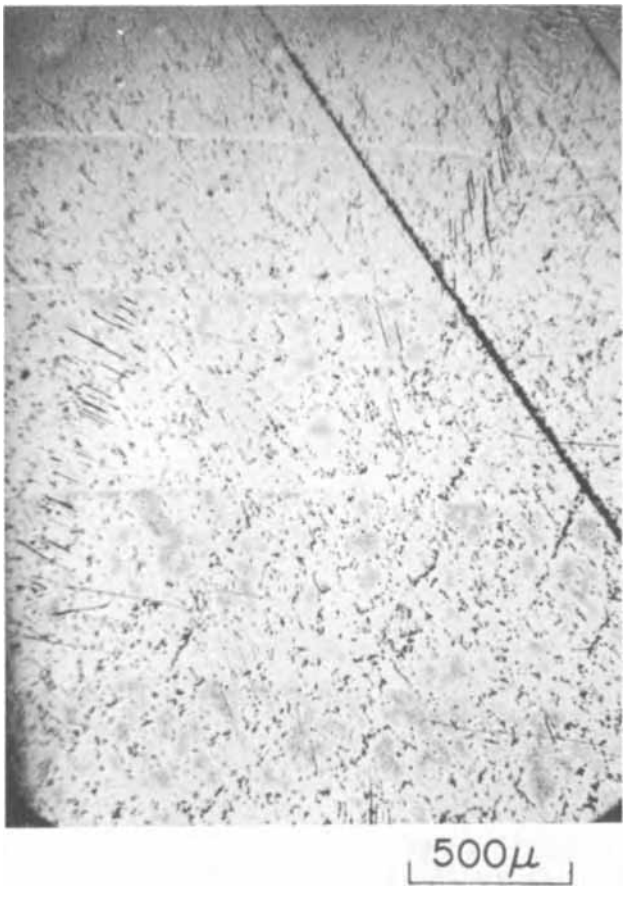

Fig. 6. Part of annular rings revealed on a P(111) surface cut perpendicular to the growth axis. The same crystal as in Fig. 5. Dark cloud-like patterns corresponding to the small-pit clusters are also limited by the annular rings. Etched with AB etchant.

that of the usual dislocation pits, and the density is larger than the usual dislocation density in pulled crystals. The small pits on P($\bar{1}\bar{1}\bar{1}$) surfaces are shallow and flat-bottomed and have no tails. These properties indicate that the small pits are not associated with the usual dislocations, but are due to defects such as impurity precipitates or vacancy aggregates, or small dislocation loops with a diameter of less than 1μ. Small etch pits not corresponding to dislocations were previously observed on Ge (19-26), Si (27, 28), and GaAs crystals (16-28, 29). They were attributed to silica (22-25), vacancies (19, 28), Te (or a Te-rich complex) (16-18), or oxygen (20, 29).

Etch pits corresponding to vacancy aggregates have been observed only in nearly dislocation-free crystals (19, 28). Thus vacancy pits were not observed in Ge crystals with dislocation densities greater than about 200 cm^{-2} (19). Therefore it is believed that dislocations serve as very effective sinks for excess vacancies. Since pulled GaP crystals have very high dislocation densities ($\sim 10^5$ cm^{-2}), it is quite improbable that the small pits observed in these crystals are due to vacancy aggregates.

The possibility that small dislocation loops are the source of the small pits is also rejected for the following reason. Dislocation can be revealed on the P($\bar{1}\bar{1}\bar{1}$) surface of GaP crystals as deep, conical etch pits, but cannot be revealed on the {110} cleavage surface. Therefore it might be thought that a small dislocation loop could be revealed on the P($\bar{1}\bar{1}\bar{1}$) surface as a small etch pit pair, but could not be revealed on the {110} cleavage surface at all. However, small-pit clusters were easily revealed on the {110} cleavage surface of highly doped n-type LEC GaP crystals. It is concluded that the small etch pits are not due to small dislocation loops.

Now we shall discuss the possibility that impurity precipitates are the origin of the small etch pits. These pits are absent from the smooth regions surrounding individual dislocation etch pits or etch grooves, and they are entirely absent from the highly dislocated areas at the periphery of the GaP slices. These observations indicate that the dislocations act as sinks for the defects responsible for the small etch pits, or in other words that the dislocations can be decorated by these defects. Decoration of the dislocations also accounts for the easy delineation of the etch grooves on P($\bar{1}\bar{1}\bar{1}$) surfaces and especially on {110} cleavage surfaces of the pulled crystals. In general, dislocations lying close and nearly parallel to the surface cannot be revealed by etching. In some cases, however, such dislocations have been revealed by etching as lines (30), channels (31, 32), trails (9, 13), or ridges (33). The delineation of these features is mainly attributed to decoration of the dislocations by impurity precipitates, which results in faster or slower etching. By analogy, formation of the etch grooves on doped GaP can be attributed to decoration by impurity precipitates. Since the defects responsible for the small etch pits can also decorate the dislocations, it seems probable that these defects are impurity precipitates, and that etching of isolated precipitates (not associated with a dislocation) leads to the formation of the characteristic flat-bottomed pits.

In pulled GaP crystals doped with S or Te, where the small-pit clusters and etch grooves are much more prominent than in undoped crystals, the impurity precipitates are formed primarily by the dopant element. Dislocation lines decorated with Se or Te have been observed with an infrared microscope as dark lines in heavily doped GaAs crystals ($n \sim 2 \times 10^{18}$ cm^{-3}) grown from the melt (17, 34). In LEC GaP crystals with carrier concentrations up to 6×10^{17} cm^{-3}, decorated lines have never been observed by transmitted visible light. Thus the dislocations are not sufficiently decorated with the dopant impurity to be detected in this manner, but are decorated enough to be revealed by preferential etching.

The appearance of the etch grooves in the doped GaP crystals varies from one groove to another and from one sample to another. Such variations are considered to be due both to different amounts of impurity precipitation and to the type of dislocation (*i.e.*, edge or screw). The difference in the appearance of the dislocation etch pits between doped and undoped crystals, as seen in Fig. 2 and 3, is attributed to a difference in the amount of impurity precipitation along the dislocations.

Etching behavior of undoped crystals.—Even in the case of undoped LEC crystals, etch grooves were revealed on the P($\bar{1}\bar{1}\bar{1}$) surface of two samples, and small-pit clusters were observed on this surface for one sample. These results also suggest the presence of isolated impurity precipitates and dislocations decorated with the same impurity. Both nondelineation of the clusters on the {110} cleavage surface and poor delineation of the grooves on this surface suggest that the degree of impurity precipitation in the undoped crystals is not as high as in the doped crystals.

The probable impurities in undoped LEC GaP crystals are considered to be boron, silicon, carbon, and oxygen (4, 5, 11) incorporated from the silica crucible, graphite susceptor, and/or boric oxide during crystal growth. Therefore it is likely that in these crystals the small pits and the etch grooves are associated with the precipitation of one or more of these impurities.

Precipitation mechanism.—Finally, some comment can be made on the mechanism of impurity precipitation in pulled GaP crystals, even though no detailed mechanism has been established. In general precipita-

tion occurs when the concentration of an impurity incorporated in the crystal lattice exceeds the solubility at a temperature where the kinetics are sufficiently rapid to permit precipitation. It would not be surprising for these conditions to be satisfied for pulled GaP crystals. First, since substitutional impurities such as sulfur and tellurium can be expected to exhibit retrograde solubility (35), the concentrations incorporated at the melting point, 1470°C, could exceed the solubilities at lower temperatures. Second, since the initial cooling rates after solidification are relatively low, the crystal spends an appreciable time at temperatures high enough for the precipitation rate to be rapid. In contrast, the vapor- and solution-grown crystals are prepared at much lower temperatures, approximately 900° and 1140°C, respectively, where the precipitation kinetics would be extremely slow.

Such a difference in precipitation behavior between LEC crystals and solution-grown or vapor-grown crystals leads to a difference between them in etching behavior.

Summary

1. Characteristic clusters of small etch pits, etch grooves, and cluster-free regions around dislocations were revealed on the surface of pulled GaP crystals by etching techniques.

2. There is a distinct difference in etching behavior between pulled crystals and solution-grown or vapor-grown crystals.

3. The delineation of these etch patterns is attributed to impurity precipitation followed by preferential etching.

4. The impurity which is mainly responsible for the formation of etch patterns in doped crystals is the dopant element (sulfur or tellurium).

5. In undoped crystals, the impurity responsible for precipitation is thought to be boron, silicon, carbon, or oxygen incorporated during crystal growth.

6. The easy formation of precipitates in the pulled crystals is attributed to retrograde solid solubility and crystal growth at a high temperature.

Acknowledgments

The author is indebted to several people for contribution to this paper. The pulled crystals were supplied by H. W. Verleur. The solution-grown crystals were supplied by L. Derick and M. Kowalchik. L. C. Luther provided the vapor-grown crystals and reviewed the manuscript. Thanks are also due to A. A. Bergh, B. Schwartz, F. A. Trumbore, G. A. Rozgonyi, and R. H. Saul for their help in improving the manuscript and comments. Thanks are also due to Dr. A. J. Strauss of Lincoln Laboratory for his helpful comments.

Manuscript submitted Sept. 8, 1970; revised manuscript received *ca.* March 2, 1971.

Any discussion of this paper will appear in a Discussion Section to be published in the June 1972 JOURNAL.

REFERENCES

1. E. P. A. Metz, R. C. Miller, and R. Mazelsky, *J. Appl. Phys.*, **33**, 2016 (1962).
2. S. J. Bass, P. E. Oliver, and F. E. Birbeck, *J. Crystal Growth*, **2**, 169 (1968).
3. J. B. Mullin, R. J. Heritage, and C. H. Holliday, *ibid.*, **3, 4**, 281 (1968).
4. S. J. Bass and P. E. Oliver, *ibid.*, **3, 4**, 286 (1968).
5. S. F. Nygren, C. M. Ringel, and H. W. Verleur, *This Journal*, **118**, 306 (1971).
6. M. Gershenzon and R. M. Mikulyak, *J. Appl. Phys.*, **35**, 2132 (1964).
7. N. A. Shestakova, M. A. Gurevich, L. I. Marina, and A. Ya. Nashelskii, *Soviet Phys.-Solid State (English Transl.)*, **6**, 3367 (1964).
8. M. I. Val'Kovskaya and Yu. S. Boyarskaya, *ibid.*, **8**, 1976 (1967).
9. R. H. Saul, *This Journal*, **115**, 1184 (1968).
10. H. Shiraki, *Japan. J. Appl. Phys.*, **8**, 279 (1969).
11. I. Ladany, S. H. McFarlane, III, and S. J. Bass, *J. Appl. Phys.*, **40**, 4984 (1969).
12. F. A. Trumbore, H. G. White, M. Kowalchik, R. A. Logan, and C. L. Luke, *This Journal*, **112**, 782 (1965).
13. M. S. Abrahams and C. J. Buiocchi, *J. Appl. Phys.*, **36**, 2855 (1965).
14. J. L. Richards and A. J. Crocker, *J. Appl. Phys.*, **31**, 611 (1960).
15. G. Nomarski and A. R. Weill, *Rev. Met.*, **52**, 121 (1955).
16. H. C. Casey, Jr., *This Journal*, **114**, 153 (1967).
17. M. G. Mil'vidskii, V. B. Osvenskii, V. I. Fistul, E. M. Omelyanovskii, and S. P. Grishina, *Soviet Phys.-Semiconductors (English Transl.)*, **1**, 813 (1968).
18. T. Iizuka, *Japan. J. Appl. Phys.*, **7**, 490 (1968).
19. A. G. Tweet, *J. Appl. Phys.*, **30**, 2002 (1959).
20. J. R. Dale and J. C. Brice, *Solid State Electron.*, **3**, 105 (1961).
21. M. Shoji, S. Tauchi, T. Mitsuishi, and M. Tomono, *J. Phys. Soc. Japan*, **16**, 1253 (1961).
22. T. Abe and T. Dhashi, *Acta Met.*, **9**, 1072 (1961).
23. H. Kato, H. Muraoka, and T. Abe, *Toshiba Rev.*, **7**, 24 (1961).
24. D. H. Lyon, *Western Electric Eng.*, **7**, 3 (1963).
25. A. A. Bergh and L. P. Adda, Paper No. 84 presented at the Toronto Meeting of the Society, May 3-7, 1964.
26. S. Sh. Shil'shtein and T. I. Simonova, *Soviet Phys.-Cryst. (English Transl.)*, **10**, 490 (1966).
27. T. Abe, T. Samizo, and S. Maruyama, *Japan. J. Appl. Phys.*, **5**, 458 (1966).
28. A. J. R. de Koch, *Appl. Phys. Letters*, **16**, 100 (1970).
29. J. C. Brice, J. A. Roberts, and G. Smith, *J. Mater. Sci.*, **2**, 131 (1967).
30. W. W. Tyler and W. C. Dash, *J. Appl. Phys.*, **28**, 1221 (1957).
31. W. C. Dash, *ibid.*, **29**, 705 (1958).
32. E. M. Pell, "Solid State Physics in Electronics and Telecommunications," Vol. 1, p. 261, M. Désirant and J. L. Michiels, Editors, Academic Press, London (1960).
33. S. O'Hara, *J. Appl. Phys.*, **35**, 409 (1964).
34. H. Kressel, H. Nelson, S. H. McFarlane, M. S. Abrahams, P. LeFur, and C. J. Buiocchi, *ibid.*, **40**, 3587 (1969).
35. C. D. Thurmond and J. D. Struthers, *J. Phys. Chem.*, **57**, 831 (1953).

[Note Added in Proof: Recently it has been shown (36) that local variations in the photoluminescence efficiency of p-type LEC material are inversely related to the S-pit density. Also, the improvement of red-emitting electroluminescent diodes fabricated on n-type LEC substrates by *double* layer liquid phase epitaxial growth has been attributed (37) to moving the active p-n junction away from the high S-pit density LEC substrate to a low or zero S-pit density n-type liquid phase epitaxial layer. 36. G. A. Rozgonyi and Martin A. Afromowitz, Paper to be presented at Electrochem. Soc. Meeting, Cleveland, Oct. 3-8, 1971. 37. G. A. Rozgonyi, T. Iizuka, and S. E. Haszko, Paper 86 presented at Electrochem. Soc. Meeting, Washington, D. C., May 9-13, 1971.]

Thermogravimetric Study of the Oxidation of ZrB_2 in the Temperature Range of 800° to 1500°C

W. C. Tripp

Systems Research Laboratories, Dayton, Ohio 45440

and H. C. Graham

Aerospace Research Laboratories, Wright Patterson Air Force Base, Dayton, Ohio 45433

ABSTRACT

A thermogravimetric system is described for the determination of the total oxygen consumption, sample weight-change, and vaporization rate during the oxidation of $ZrBr_2$. The results show an increasing deviation from parabolic kinetics with increasing temperature at 250 mm oxygen pressure. The following equation is used to describe the total oxygen consumption in the temperature range of 800°-1500°C

$$\frac{\Delta n_{O_2}}{A}\left(\frac{\text{moles } O_2}{\text{cm}^2}\right) = 5.41 \times 10^{-4} \exp\left(\frac{-25{,}000}{2RT}\right) t^{1/2} + 2.86 \exp\left(\frac{-47{,}000}{RT}\right) t$$

Because ZrB_2 is oxidized stoichiometrically, this result can be converted to the recession of ZrB_2 as follows

$$\delta\,(\text{cm}) = 4.06 \times 10^{-3} \exp\left(\frac{-25{,}000}{2RT}\right) t^{1/2} + 2.10 \times 10^{1} \exp\left(\frac{-47{,}000}{RT}\right) t$$

The total oxygen consumed in the oxidation of ZrB_2 has been investigated by Berkowitz (1) over the temperature range of 1150°-1550°C. Parabolic oxidation was reported in that study as well as in the study by Kuriakose and Margrave (2), who measured sample weight change over the temperature range of 950°-1250°C. In both of these studies, the effect of oxygen partial pressure on the oxidation behavior was investigated at 1056°C. Kuriakose and Margrave found the increase in the parabolic rate constant to be directly proportional to the oxygen pressure over the oxygen partial pressure range of 100-740 Torr. Berkowitz substantiated this finding but found no oxygen pressure dependence at 1287°C over the range of 8-40 Torr or at 1557°C over the range of 20-700 Torr. Clougherty *et al.* (3) have measured recession rates of ZrB_2 at temperatures up to 1900°C and reported their data on the basis of a parabolic time dependence.

In view of the current technological need for materials with good oxidation resistance at high temperatures, this study was undertaken to obtain additional quantitative data on the oxidation of ZrB_2 by independent determinations of sample weight-change, total vaporization, and total oxygen consumption. These measurements allow the evaluation of the amount of ZrO_2 and B_2O_3 formed.

Experiment

A common method of studying the kinetics of an oxidation process is by continuously recording weight-change at constant temperature. For many materials this method has proved to be very successful. However, in the study of the oxidation of some alloys and high-temperature refractory materials, care must be used in interpreting weight-change data because of the formation of volatile oxides. Weight-change measurements indicate only the amount of oxide products remaining on the sample.

If volatile oxides are formed, then other methods, such as the measurements of total oxygen consumed by means of pressure changes or volume changes, must be used to determine reaction rates. Thermal conductivity measurements of the gas stream before and after reaction have been used successfully (4). Some experimental difficulties are encountered in all of these methods, particularly at very high temperatures.

The techniques described here are designed for the thermogravimetric measurement of total oxygen consumption for materials that form a volatile oxide which is condensable at temperatures below the reaction temperature. Slight modifications of the system can be made to measure separately the vaporization rates and sample weight-change.

During this study of the oxidation of ZrB_2, three methods were used to separate into parts the oxidation processes which occur simultaneously. These methods were:

1. Sample weight-change—conventional weight-change measurements in which only the weight increase due to the oxidation products remaining on the sample are recorded.
2. Oxygen consumption—measurement of the weight increase of the sample plus the weight of any volatile oxides that are condensable within the temperature range of the system.
3. Vaporization—only the weight of the condensable oxides is measured.

Measurements of sample weight-change were made with an Ainsworth FV-AU-1 recording microbalance. The capacity of the balance is 10g and the sensitivity is ±3 μg. A total weight-change of 100 mg can be recorded. In the conventional weight-change measurements, the gaseous B_2O_3 collected on the cooler parts of the furnace and represented an unknown weight loss. Single-crystal sapphire rods were used to suspend the samples, and measurements were made only to 1500°C.

At 1500°C and above, it was not possible to complete a run because of a reaction which destroyed the sapphire rods. It was observed that the reaction product of ZrB_2, probably B_2O_3, reacts quite destructively with most materials at high temperatures. Rh, Pt, Ir, Al_2O_3, ThO_2, ZrO_2 were tried without success in attempts to

Key words: thermogravimetric, oxidation, oxygen consumption, vaporization, ZrB_2, B_2O_3, paralinear.

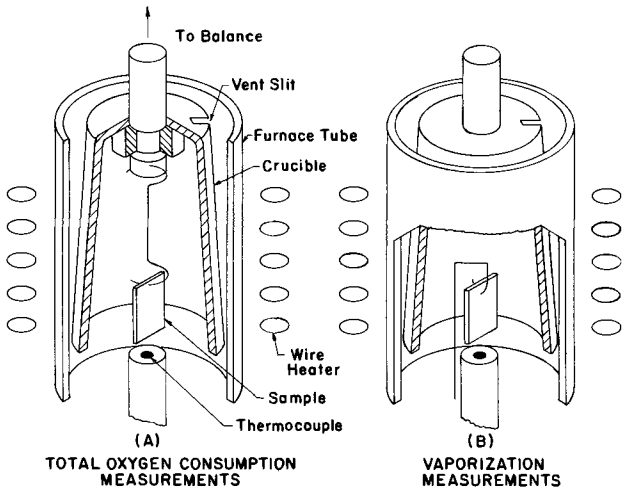

Fig. 1. Sample suspension for measuring total oxygen consumption and vaporization rates of a condensable oxide.

suspend a specimen in the temperature range of 1500°-2000°C (5).

The oxygen consumption and vaporization measurements were made with a Cahn RH Electrobalance which has a capacity of 100g and a sensitivity of ±10 μg. The total weight-change that can be recorded with this balance is variable but can be as much as 20g. Figure 1 is a diagram of the methods used to measure total oxygen consumption and vaporization. ZrB_2 oxidizes to form both ZrO_2 and B_2O_3. Since B_2O_3 is a liquid above 450°C and has an appreciable vapor pressure above 1000°C (6), some vaporization of this oxide is expected. In Fig. 1(a) is shown the method used for measuring total oxygen consumption. An inverted crucible 100 mm long is suspended from the balance with the specimen hanging inside. A modification of this, as shown in Fig. 1(b), is used to directly measure vaporization rates. Here the sample is not connected to the balance but is again inside the crucible. In this case, only the vapor condensed on the crucible is measured. In both arrangements, the top of the crucible is considerably cooler than the specimen so that any condensable products will collect there. The total load on the balance is about 50g in either case.

The furnace system used in this study has been described previously (7). Sample temperature was measured by a thermocouple placed just below the sample. The temperature profile of the furnace showed that the specimen should be within 10°C of the measured temperature. All the temperatures reported are thermocouple temperatures.

The ZrB_2 material was supplied by Manlabs Incorporated as a hot-pressed billet about 75 mm in diameter and 25 mm thick. The major impurity in this material is ZrO_2 and the B/Zr ratio is slightly less than two. Small rectangular coupons weighing about 1g and with an area of approximately 4 cm^2 were cut from the billet with a diamond saw. The specimens were ground smooth with a 150 grit diamond wheel and ultrasonically cleaned in alcohol.

The samples used to measure weight change were annealed in a vacuum of 10^{-5} Torr at 600°C for about 15 hr before the start of each run. In the oxygen consumption experiments, argon at a pressure of 20 Torr was used for the annealing environment. These different annealing methods did not appear to affect the kinetics in any way. After annealing, the sample was heated to the desired temperature and oxygen was introduced into the system as quickly as possible. During the time of heating to the temperature of the run, the weight was observed to be constant up to 1100°C. Small weight gains were observed above this temperature.

The dependence of the oxidation rates on gas flow was measured. In the temperature range covered and

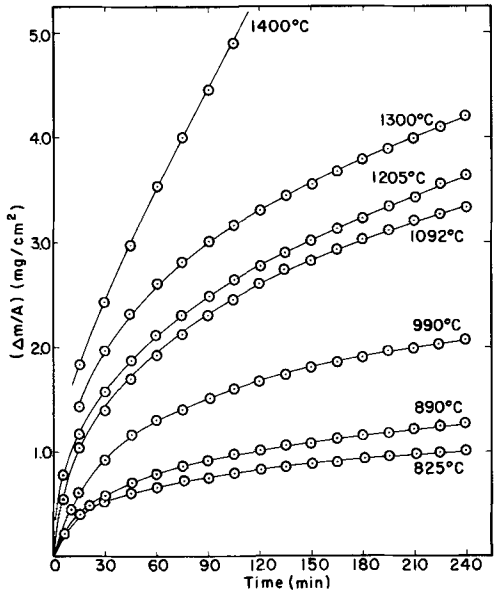

Fig. 2. Sample weight change, ZrB_2 at 250 Torr O_2

for the size of specimens that were used, a flow rate of 0.5 cm/sec was found to supply enough oxygen so that the reaction rate was not flow dependent. All the measurements reported here were made at a total pressure of 250 Torr in pure oxygen.

Results

The measurements of sample weight change are presented in Fig. 2. Since B_2O_3 has an appreciable vapor pressure above 1000°C, some vaporization of this oxide will occur. At the higher temperatures, the data, therefore, represent both a gain in weight from the addition of oxygen forming ZrO_2 and B_2O_3 and a loss in weight due to a loss of boron in the vaporization of B_2O_3.

The B_2O_3 left on the sample after an oxidation run at 250 Torr O_2 could be vaporized by heating at 1100°C in a vacuum of 10^{-5} Torr until a constant weight was recorded. With the assumption that all of the B_2O_3 had evaporated, the weight-change measured after this vacuum treatment represented the total oxygen consumed in the formation of ZrO_2 minus the boron lost in the vaporization of B_2O_3. From this weight-change, the total oxygen consumption can be calculated if it is assumed that ZrB_2 oxidized stoichiometrically.

The direct measurements of total oxygen consumption agreed quite well with these calculations particularly for temperatures of 1100°C and below. Specimens oxidized above this temperature were cooled to 1100°C before the furnace was evacuated. Consequently, some excess oxide was formed and the agreement between the calculations and experiments was not as good. However, because of the agreement between calculated values of total oxygen consumed and measured values, ZrB_2 must oxidize stoichiometrically within the conditions of these experiments.

Using the second method described, *i.e.*, the weighing of the sample plus the condensed vapor species, the data presented in Fig. 3 were obtained. Since any B_2O_3 that evaporates will condense at the cool end of the crucible, these data represent the total oxygen consumed during the oxidation process.

A measure of the rate of vaporization can be obtained from the difference between the total oxygen consumed (Fig. 3) and the specimen weight-change (Fig. 2). The vaporization rate was also measured directly by the third technique described. The results of all three measurement methods at 1200° and 1300°C are shown in Fig. 4 and 5, respectively.

The curves labeled "sample weight" are the net specimen weights observed in conventional weight-change measurements of oxidation kinetics. The "oxy-

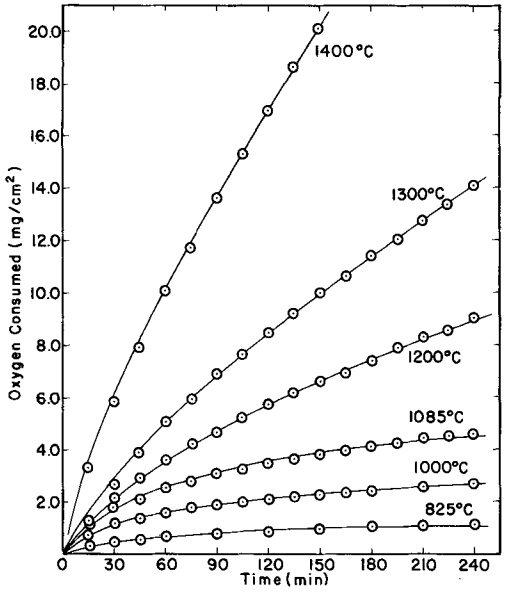

Fig. 3. Total oxygen consumption, ZrB_2 at 250 Torr O_2

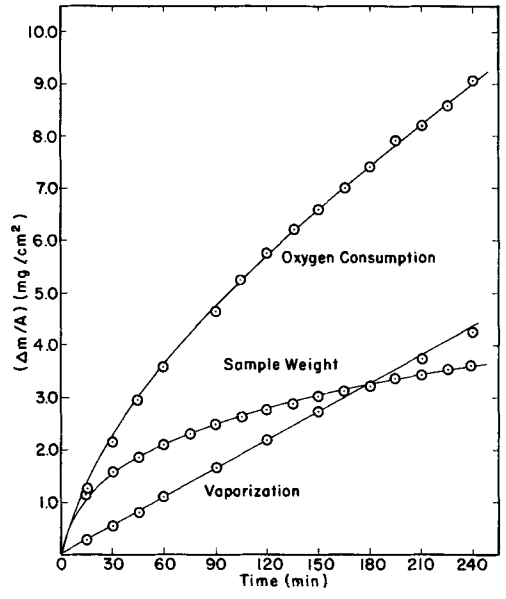

Fig. 4. Three types of measurements of the oxidation rate of ZrB_2, 1200°C, 250 Torr O_2.

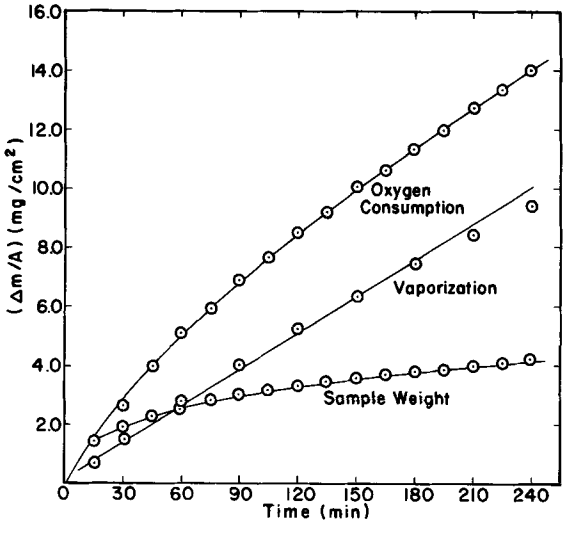

Fig. 5. Three types of measurements of the oxidation rate of ZrB_2, 1300°C, 250 Torr O_2.

gen consumption" curves describe the total oxygen consumed when all of the oxidation products are collected and weighed. Since this study indicates that ZrB_2 oxidizes stoichiometrically, the values of oxygen consumption can be converted directly into material consumed, or recession rates.

The third curve in the figures, vaporization, was determined by weighing only the condensable oxides formed, using the technique shown in Fig. 1(b). This curve can also be determined by simply subtracting the sample weight values from the total oxygen consumption values at any time. The agreement between all three measurement methods was found to be quite good at all temperatures.

Discussion

Previous investigators (1-3) have interpreted measurements of boride recession, oxygen consumption, and weight-change as being a parabolic process and therefore have suggested that the reaction is controlled by diffusion through a continuously growing oxide layer. Because of the evaporation of B_2O_3, weight-change measurements alone are of questionable value when used to determine a time dependence for the oxidation process. Measurements of the total amount of oxygen consumed will not be influenced by vaporization and are, therefore, more suitable for use in the determination of reaction kinetics. Since ZrB_2 oxides stoichiometrically, oxygen consumption measurements can be converted directly to boride recession.

Berkowitz (1) has presented evidence from microstructural examination of the oxide layer formed in the neighborhood of a crack that intersected the surface, that the oxide must grow by the inward diffusion of oxygen. The original surface of the crack was replaced by the oxide, and there was no indication of the crack closing due to an outward diffusion from the boride. There are no known ternary compounds formed in the Zr-B-O system and B_2O_3 is the predominant species detected during the vaporization of boron oxide (6). The condensed oxide layer formed on ZrB_2 will consist of a mixture of both $B_2O_3(l)$ and $ZrO_2(s)$. If the temperature is high enough or the reaction time long enough, $B_2O_3(l)$ can vaporize as quickly as it is formed and the oxide layer will contain only ZrO_2.

The measurement of a linear vaporization rate for times less than 4 hr at temperatures between 800° and 1400°C indicates that liquid B_2O_3 is present under these conditions. Figures 4 and 5 show the relationship between the amount of oxygen consumed and the amount of vaporization. Because the oxygen consumption data show a decreasing time dependence and the vaporization is linear, the amount of $B_2O_3(l)$ in the scale is decreasing with time. Since the scale consists of a mixture of B_2O_3 and ZrO_2, it would be expected that the inward diffusion of oxygen would occur at a much faster rate through $B_2O_3(l)$ than through $ZrO_2(s)$. The length of the diffusion path for the inward diffusion of oxygen is, therefore, decreasing with time as the thickness of $B_2O_3(l)$ is reduced through vaporization. The reduction in the diffusion barrier would certainly be expected to increase the rate of recession and, therefore, truly parabolic recession behavior would not be expected.

When the oxygen consumption data are plotted as weight-gain squared *vs.* time, an increasing deviation from parabolic behavior is observed as the temperature is increased. Figure 6 shows these data from 1095° to 1400°C. At 1095°C and for temperatures less than 1095°C, a straight line is observed, indicating that the reaction rate is parabolic and limited by diffusion through a barrier layer which does not suffer significant vaporization. The data below 1095°C are not shown because of the relatively small magnitude when plotted on the scale used in Fig. 6. Above 1095°C, a positive curvature is observed and the curvature in-

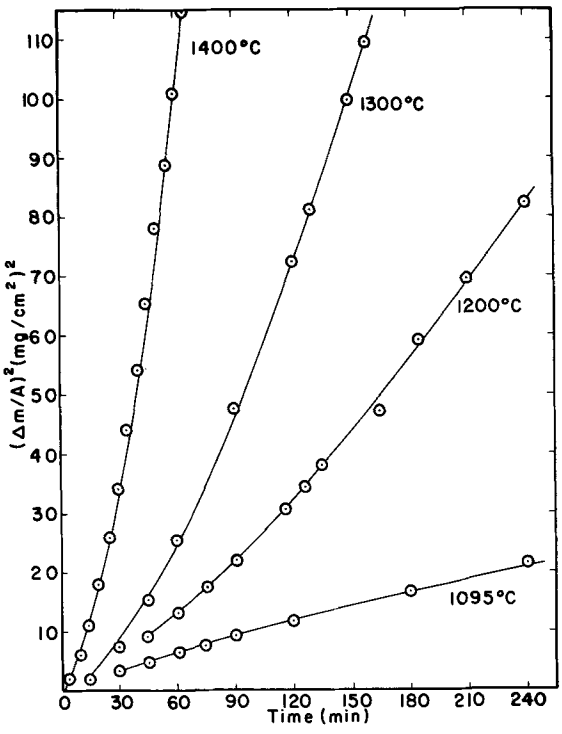

Fig. 6. Parabolic plot of the total oxygen consumption data, ZrB_2, 250 Torr O_2.

creases with increasing temperature. In this temperature range, the rate of oxygen consumption is faster than parabolic because of a decreasing thickness of the barrier layer caused by the evaporation of B_2O_3 (1).

The increase of the reaction rate with temperature can also be shown if it is assumed the oxygen consumption rate is dependent on time in the following manner

$$\left(\frac{\Delta n_{O_2}}{A}\right)^x = kt$$

Values of x are shown in Table I and clearly indicate that above 1100°C the scale is no longer an effective barrier for oxygen diffusion.

Previous investigators have interpreted their measurements of oxygen consumption and weight-change of ZrB_2 as a diffusion-controlled reaction obeying a parabolic rate equation. Although the measurements made in this study do not show a parabolic time dependence at temperatures above 1095°C, a comparison can be made between the results presented here and those of previous studies. An "apparent" parabolic rate constant was determined from a least-squares value of the slope when the oxygen consumption and weight-change data were plotted as in Fig. 6. These "forced" rate constants are shown on the Arrhenius plot in Fig. 7 together with the parabolic rates for oxygen consumption obtained by Berkowitz (1) and the parabolic rates for weight-change obtained by Kuriakose and Margrave (2). The close agreement of the data from the three separate studies indicates that equivalent measurements have been made on similar material. However, it must be emphasized that simple parabolic behavior is not the interpretation of the measurements presented here.

Table I. Values of x in the Eq. $\left(\frac{\Delta n_{O_2}}{A}\right)^x = kt$

Temp, °C	x
885	2.2
1000	2.1
1095	2.0
1200	1.5
1300	1.3
1400	1.3

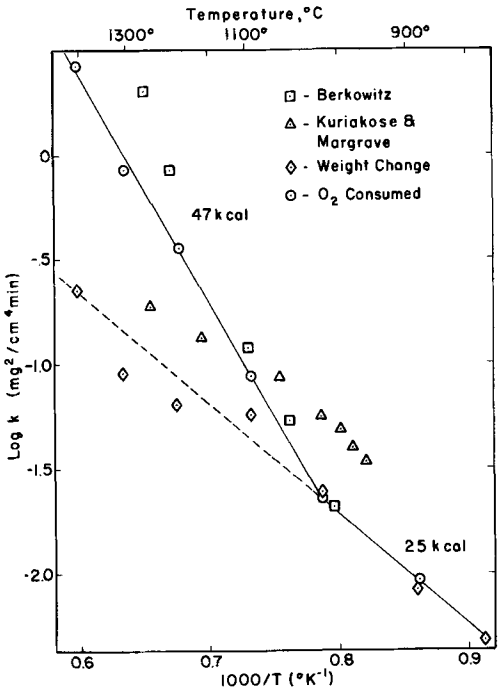

Fig. 7. Arrhenius plot of the parabolic rate constants, ZrB_2

The vaporization of B_2O_3 from the oxide layer influences the rate of oxygen consumption and is the reason for the deviation from parabolic kinetics. A paralinear-type equation having the form

$$\frac{\Delta n_{O_2}}{A} = at^{1/2} + bt \qquad [1]$$

is a better representation of the oxygen consumption data. If the linear rate constant for vaporization, b, is plotted as shown in Fig. 8, a slope can be calculated which will represent the temperature dependence of the vaporization. This can be combined with the temperature dependence of the weight-change, Fig. 7, and an equation can then be written to represent the total oxygen consumption. The following equation is found to represent the total oxygen consumption

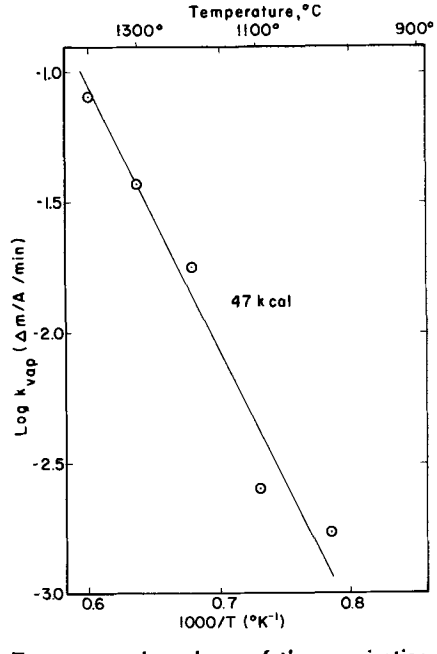

Fig. 8. Temperature dependence of the vaporization of B_2O_3 on oxidizing ZrB_2 at 250 Torr O_2.

$$\frac{\Delta m}{A}\left(\frac{\text{mg}}{\text{cm}^2}\right) = 17.65 \exp\left(\frac{-25{,}000}{2RT}\right) t^{1/2} + 9.15 \times 10^4 \exp\left(\frac{-47{,}000}{RT}\right)_t \quad [2]$$

or

$$\frac{\Delta n_{O_2}}{A}\left(\frac{\text{g moles } O_2}{\text{cm}^2}\right) = 5.41 \times 10^{-4} \exp\left(\frac{-25{,}000}{2RT}\right) t^{1/2} + 2.86 \exp\left(\frac{-47{,}000}{RT}\right) t \quad [3]$$

where T is the temperature in degrees Kelvin and t is the time (min). The first term on the right approximates the net sample weight-gain and is parabolic. The second term is derived from the vaporization data and is linear with time. Since stoichiometric oxidation occurs, recession rates can be calculated from this equation by assuming that 40% of the total oxygen consumed forms ZrO_2 and 60% forms B_2O_3. From these values, the amount of zirconium and boron consumed, and therefore the amount of ZrB_2, can be calculated

If 6 g/cm^3 is used for the density of ZrB_2, then the total oxygen consumed, as calculated from Eq. [2], can be multiplied by 2.3 x 10^{-4} to give the amount of boride recession

$$\delta(\text{cm}) = 4.06 \times 10^{-3} \exp\left(\frac{-25{,}000}{2RT}\right) t^{1/2} + 2.10 \times 10^1 \exp\left(\frac{-47{,}000}{RT}\right) t \quad [4]$$

It can also be seen from Eq. [3] that for sufficiently long times, the second term representing the constant vaporization rate will eventually exceed the rate of formation of $B_2O_3(l)$. Therefore, this equation can only be true over the temperature-time range where $B_2O_3(l)$ is present at the surface.

The heat of vaporization of B_2O_3 is about 90 kcal, whereas the vaporization energy measured in these oxidation experiments is only 47 kcal. Vaporization of liquid B_2O_3 would involve mass transport through a gas phase, thus there is no reason to expect the temperature dependence to be a measure of the heat of vaporization. However, a separate experiment was performed to measure the temperature dependence of the vaporization of B_2O_3 under these same experimental conditions. The energy measured was 50 ± 10 kcal, in very close agreement with the oxidation results.

Equation [2] for total oxygen consumption is plotted together with the experimental data in Fig. 9. The agreement can be seen to be quite reasonable. As can be noted, the data at 1100°C and below agree very closely. In this region, the parabolic term is the predominate term in the equation and the reaction rate is controlled by diffusion of oxygen through $B_2O_3(l)$. Excellent agreement is also observed at 1400°C where the linear term will predominate after short times. At this temperature, there will no longer be a protective barrier layer of $B_2O_3(l)$.

Summary

A system has been described that allows the thermogravimetric determination of total oxygen consumption, sample weight-change, and vaporization rate of a material that oxidizes with the formation of volatile products that are condensable at temperatures below the reaction temperatures.

This system has been used to study the oxidation of ZrB_2 at 250 Torr O_2 over the temperature range of 800°-1500°C. The volatile oxide formed is B_2O_3 which is a liquid above 450°C and vaporizes readily above 1100°C.

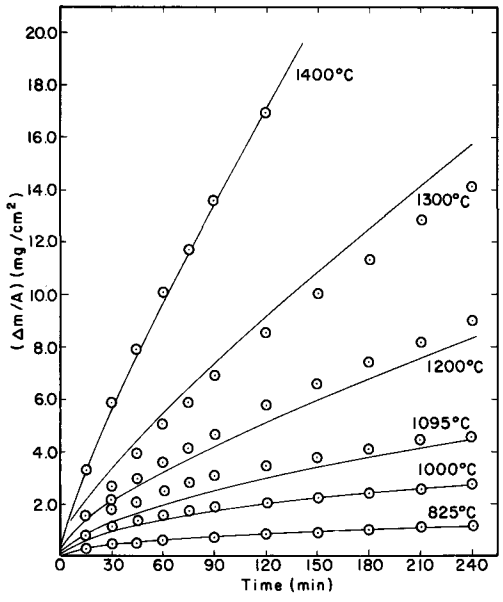

Fig. 9. Comparison between calculated and measured oxygen consumption values; solid line, calculated; circle, measured.

The vaporization of B_2O_3 influences the kinetics of the oxidation process. At temperatures below 1100°C measurements showed the vaporization to be negligible. The scale, composed of a mixture of $B_2O_3(l)$ and $ZrO_2(s)$, formed a barrier layer and the rate of oxygen consumption was controlled by diffusion through the $B_2O_3(l)$.

At higher temperatures the vaporization of $B_2O_3(l)$ became significant and the influence of this on the kinetics was clearly demonstrated by separate measurements of oxygen consumption, weight-change, and vaporization.

A paralinear equation was derived to describe the rate of oxygen consumption within the range of these measurements. Since ZrB_2 oxidizes stoichiometrically this equation can be converted into boride recession rates.

Acknowledgments

The authors wish to thank Mr. Joseph Henry for assistance with the thermogravimetric measurements; Professor Robert Rapp, Ohio State University, for his many helpful suggestions and discussions; and Mr. John Fenter, Air Force Materials Laboratory, for supplying the material. This work was performed at the Aerospace Research Laboratories under contract No. F33615-69-C-1017.

Manuscript submitted March 16, 1970; revised manuscript received *ca.* March 1, 1971.

Any discussion of this paper will appear in a Discussion Section to be published in the June 1972 JOURNAL.

REFERENCES

1. Joan B. Berkowitz-Mattuck, *This Journal*, **113**, 908 (1966).
2. A. K. Kuriakose and J. L. Margrave, *ibid.*, **111**, 827 (1964).
3. E. V. Clougherty, D. Kalish, and E. T. Peters, "Research and Development of Refractory Oxidation-Resistant Diborides," AFML-TR-68-190, July 1968.
4. Joan B. Berkowitz-Mattuck, *This Journal*, **111**, 908 (1964).
5. H. C. Graham and W. C. Tripp, "Vacuum Microbalance Techniques," vol. 6, pp. 63-75, Plenum Press (1967).
6. J. R. Soulen, P. Sthapitanonda, and J. L. Margrave, *J. Am. Chem. Soc.*, **59**, 132-136 (1955).
7. W. C. Tripp, R. W. Vest, and N. M. Tallan, "Vacuum Microbalance Techniques," vol. 4, pp. 141-157, Plenum Press (1965).

Gallium Nitride Films[1]

T. L. Chu*

Electronic Sciences Center, Southern Methodist University, Dallas, Texas 75222

ABSTRACT

The thermal decomposition of a gallium tribromide-ammonia complex in an ammonia, argon, or nitrogen atmosphere has been used for the deposition of gallium nitride films on silicon and hexagonal silicon carbide substrates in a gas flow system. The substrate temperature and the nature of the ambient are the most important parameters of the deposition process. Adherent and transparent films of gallium nitride have been deposited at substrate temperatures up to about 600°C in an ammonia atmosphere and up to about 750°C in a nitrogen or argon ambient. At higher temperatures, the deposit became contaminated with gallium. The gallium nitride films deposited on {111} oriented silicon substrates at 600°-700°C were found to show a (110) fiber orientation. Epitaxial, single crystalline gallium nitride films have been grown successfully on the basal plane of hexagonal silicon carbide substrates at 520°-600°C. These films are of high resistivity indicating that the thermal decomposition of gallium nitride is negligible. Thus, the thermal decomposition of the gallium tribromide-ammonia complex provides a new promising technique for the crystal growth of gallium nitride.

Gallium nitride, one of the less-known III-V compounds, has an energy gap of 3.2 eV at room temperature (1). Because of this relatively large energy gap, gallium nitride has potential applications for high-temperature devices and for visible-light opto-electronic devices.

Gallium nitride crystallizes in the wurzite structure with lattice parameters $a = 3.18$A and $c = 5.16$A (2). Polycrystalline gallium nitride has been reported to dissociate into its elements at temperatures above 600°C, and the rate of dissociation is decreased by the presence of nitrogen (3). This thermal instability suggests that lower temperatures are preferred for the preparation and crystal growth of gallium nitride. Gallium does not combine directly with nitrogen to yield gallium nitride. Various chemical techniques, such as the reaction of gallium oxide with ammonia (3) and the thermal decomposition of gallium trichloride-ammonia complex (4), have been used for the preparation of polycrystalline gallium nitride. Gallium nitride produced by the reaction of gallium oxide with ammonia in the temperature range 600°-1100°C varied from light yellow to gray in color, depending on temperature; the gray color produced at 1100°C was due to the formation of free gallium (3). Recently, the reaction between gallium monochloride and ammonia in a hydrogen atmosphere has been used for the epitaxial growth of gallium nitride on the basal plane of sapphire at 825°C (5). The room-temperature energy gap of the deposited material has been determined to be 3.39 eV from optical-absorption measurements. The undoped crystals, though colorless, have a very high inherent electron concentration, 1 to 5 x 10^{19} cm^{-3}, which was attributed to nitrogen vacancies due to the thermal dissociation of gallium nitride. Epitaxial gallium nitride films have also been deposited on the basal plane of sapphire and {111} faces of gallium arsenide at 550°C by the evaporation of gallium in a nitrogen discharge (6). Films prepared in this manner were low-resistivity n-type and had an absorption edge at about 3.4 eV.

In general, the group V nitrides can be prepared by the ammonolysis of their halides at high temperatures. Since the Ga-Br bond is of lower energy than the Ga-Cl bond, the formation of gallium nitride by the ammonolysis of gallium tribromide is expected to be more feasible than that of gallium trichloride. Due to the hygroscopic nature of gallium tribromide, it is more convenient to use a gallium tribromide-ammonia complex which is stable in the laboratory ambient. In this work, the thermal decomposition of a gallium tribromide-ammonia complex has been used for the deposition of gallium nitride on {111} oriented silicon and the basal plane of hexagonal silicon carbide substrates. This reaction can produce gallium nitride at temperatures considerably below those required for reactions used by previous authors (3-5) so that its thermal dissociation can be minimized. Hexagonal silicon carbide was chosen as a substrate because its basal-plane lattice parameter ($a = 3.08$A) is similar to that of gallium nitride. The deposition process and the properties of the deposited gallium nitride are discussed below.

Experimental

The decomposition of a gallium tribromide-ammonia complex in an ammonia, argon, or nitrogen atmosphere was used for the deposition of gallium nitride on {111} oriented silicon and the basal plane of hexagonal silicon carbide substrates. Gallium tribromide and anhydrous ammonia, each of better than 99.99% purity, were used for the preparation of the complex. Molten gallium tribromide was saturated with ammonia at about 150°C, and the resulting mass was distilled in an ammonia atmosphere to yield a white crystalline solid. Its composition, deduced from the analysis of its bromine and ammonia contents by conventional chemical analysis, corresponds to $GaBr_3:4NH_3$. The silicon substrates were in the form of slices with main faces of {111} orientation and were chemically polished with a nitric acid-hydrofluoric acid mixture before use. Hexagonal silicon carbide substrates were in the form of thin platelets, the main faces of which were parallel to the basal plane. They were heated in a sulfuric acid-nitric acid mixture followed by treating with hydrofluoric acid. To minimize contaminations, the rinsing and drying of the substrates were carried out in a laminar flow bench.

The apparatus used for the deposition of gallium nitride is shown schematically in Fig. 1. The reaction was carried out in a 25 mm ID fused silica tube. The gallium tribromide-ammonia complex was placed in a fused silica container in the reaction tube and was heated externally by a resistance heater. The substrates were supported on a gallium nitride-coated graphite susceptor in the reaction tube, and the susceptor was heated by an rf generator. Ammonia, nitrogen, argon, or hydrogen, at a flow rate of 2 liters/min, was used to carry the vapor of the gallium tribromide-ammonia complex to the substrate surface. The rate of vaporiza-

* Electrochemical Society Active Member.

[1] This research was supported by the Robert A. Welch Foundation, Houston, Texas, under Grant N-298.

Key words: crystal growth, deposition, epitaxy, films, gallium nitride, substrates.

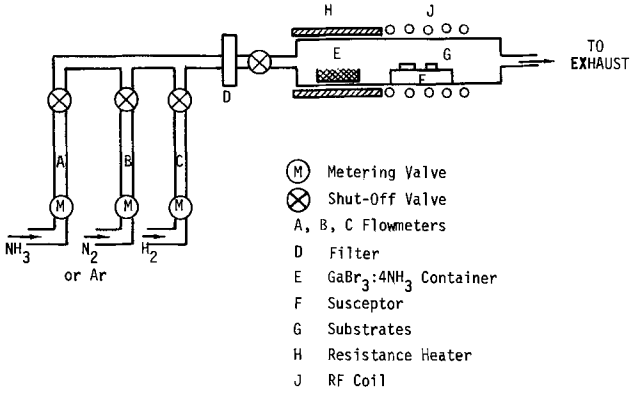

Fig. 1. Schematic diagram of the apparatus for the deposition of gallium nitride films by the pyrolysis of a gallium tribromide-ammonia complex.

tion of the complex was varied by adjusting its temperature, which was in the range of 200°-240°C.

The thickness of gallium nitride films deposited on silicon and silicon carbide substrates was measured directly on the angle-lapped surface with an optical microscope.

To measure the electrical properties of gallium nitride films, aluminum-gallium nitride-silicon structures were made from gallium nitride films deposited on 0.01 ohm-cm n-type silicon substrates by vacuum evaporation of aluminum through a metal mask. The aluminum electrode on the gallium nitride film was 1.3×10^{-2} cm^2 in area. The resulting structure was annealed in argon at about 400°C and mounted on a TO-5 header, and its d-c current voltage characteristics were measured from room temperature to about 500°C.

Results and Discussion

The deposition of gallium nitride by the decomposition of the gallium tribromide-ammonia complex was carried out in ammonia, argon, nitrogen, and hydrogen atmospheres at substrate temperatures in the range of 400°-900°C. Ammonia was used with the objective of preventing nitrogen deficiency in the deposit. Argon and nitrogen are chemically inert under the conditions used here and are expected to have similar effects on the deposition of gallium nitride. The nature of the carrier gas was found to have a pronounced effect on the deposition process. By using a carrier gas containing the gallium tribromide-ammonia complex at a flow rate of 2 liters/min, adherent and transparent films were deposited on silicon and silicon carbide substrates at 430°-600°C in an ammonia atmosphere and at 600°-750°C in a nitrogen or argon ambient. These deposits, after removing the silicon substrate with a hydrofluoric acid-nitric acid mixture, were identified as gallium nitride from their Debye-Scherrer patterns. As the substrate temperature was increased above the stated temperature limits, the deposit became gray and then black due to the formation of free gallium. Furthermore, no adherent deposits were obtained in a hydrogen atmosphere in the temperature range 400°-600°C. These results indicate the reactivity and instability of gallium nitride at high temperatures. The decomposition of gallium nitride in ammonia takes place at lower temperatures than that in argon. Since ammonia is thermodynamically unstable at temperatures above 500°K (7), it is likely that the hydrogen liberated from the thermal dissociation of ammonia has hindered the formation of gallium nitride. Similarly, gallium nitride cannot be formed in the presence of a large excess of hydrogen under the conditions used here. Thus, the thermal decomposition of the gallium tribromide-ammonia complex is quite different from the ammonolysis of gallium monochloride since clear gallium nitride has been deposited by the latter at temperatures as high as 825°C.

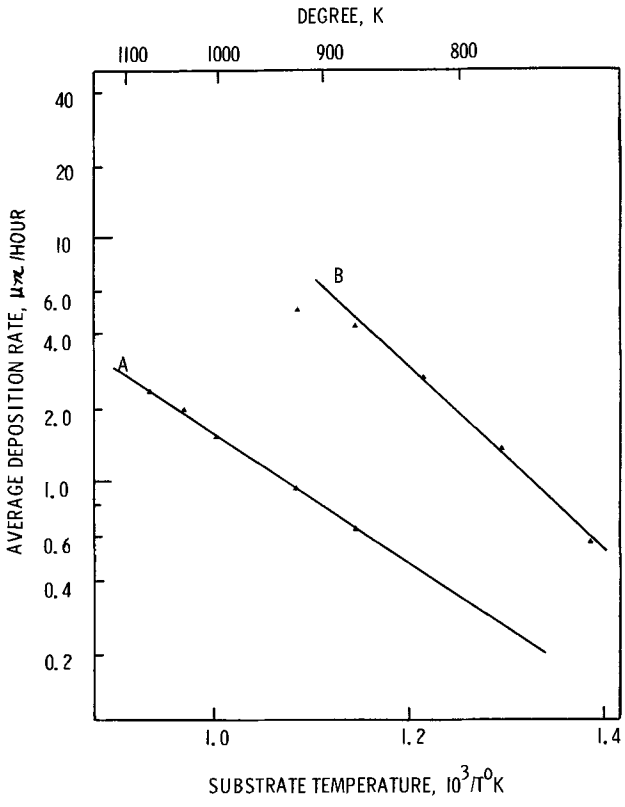

Fig. 2. Temperature dependence of deposition rate of gallium nitride on silicon substrates in argon (A) and ammonia (B) ambients.

This difference must be due to the widely different reaction kinetics.

The deposition of gallium nitride in ammonia and argon atmospheres was studied in more detail. Using the carrier gas at a flow rate of 2 liters/min, the temperature dependence of the deposition rate of gallium nitride on silicon substrates is shown in Fig. 2. It is noted that, at the same temperature, the deposition rate of gallium nitride in argon is considerably less than that in ammonia, as expected from the mass-action law. At 600°C, for example, the average deposition rates of gallium nitride in argon and ammonia are 0.65 and 4.3 μm/hr, respectively. The deposition rate in argon was negligible at temperatures below 500°C. Furthermore, the apparent activation energy of the deposition process is approximately 12.4 kcal/mole in the argon atmosphere in the temperature range 600°-800°C and is approximately 17.6 kcal/mole in the ammonia atmosphere in the temperature range 400°-600°C. This difference in activation energy is presumably related to the heat of adsorption of ammonia on the silicon surface.

Gallium nitride films deposited on silicon substrates in ammonia and argon atmospheres were highly adherent to the substrates; however, those deposited on silicon carbide substrates frequently cracked, particularly in films greater than 5 μm in thickness. This cracking is due to the large difference in thermal expansion coefficients of gallium nitride and silicon carbide. All gallium nitride deposits exhibited no structural features when examined with an optical microscope. They were examined by the reflection electron diffraction technique. Figure 3 shows the electron diffraction pattern of a gallium nitride film, approximately 2 μm thick, deposited on the basal plane of a hexagonal silicon carbide substrate at 530°C in an ammonia atmosphere. This pattern, obtained with the electron beam azimuth in a $<1\bar{1}0>$ direction, indicated that the grown film is single crystalline gallium nitride and is of parallel orientation with respect to the substrate, *i.e.* of {001} orientation. Figure 4 shows the elec-

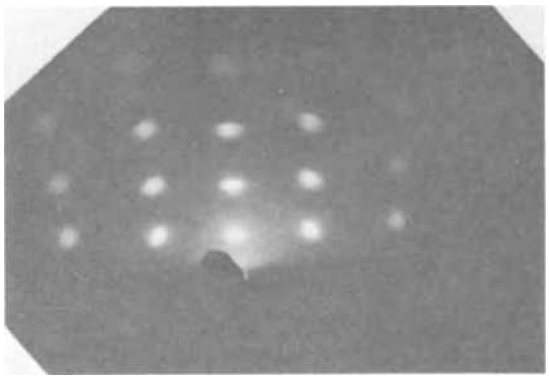

Fig. 3. Reflection electron diffraction pattern of a gallium nitride film deposited on a hexagonal silicon carbide substrate.

Fig. 4. Reflection electron diffraction pattern of a gallium nitride film deposited on a {111} oriented silicon substrate showing a (110) fiber orientation.

tron diffraction pattern of a gallium nitride film, approximately 5 μm thick, deposited on a {111} oriented silicon substrate at 700°C in a nitrogen atmosphere. This pattern indicated that the deposited gallium nitride showed a (110) fiber orientation. The lack of three dimensional epitaxial growth is apparently related to the large difference in lattice parameters of gallium nitride and silicon. The fiber structure was not observed when gallium nitride was deposited at lower temperatures.

The deposited gallium nitride films are relatively inert, insoluble in common acids at room temperature. For example, silicon substrates can be removed from gallium nitride-silicon structures by using a hydrofluoric acid-nitric acid mixture, leaving behind gallium nitride films. Gallium nitride dissolves slowly in aqueous solutions of sodium hydroxide. Figure 5 shows the dissolution rate of gallium nitride films, deposited in argon at 600° and 760°C and in ammonia at 450° and 550°C, in a 50% aqueous solution of sodium hydroxide in the temperature range 5°-90°C. The temperature of deposition has a very pronounced influence on the dissolution rate of gallium nitride films, as shown in Fig. 5. At a given temperature of the etchant, the dissolution rate increases rapidly with decreasing deposition temperature, due presumably to the higher density of the films deposited at higher temperatures. (The densities of gallium nitride deposited at 650° and 750°C are 5.7 and 6.1g cm^{-3}, respectively, as compared with a theoretical density of 6.1g cm^{-3}.) For a film deposited under a given set of conditions, the dissolution rate also increases with increasing dissolution temperature. The activation energy of this dissolution process is 18 $\pm$ 1 kcal/mole for all films studied.

The room-temperature, d-c current-voltage characteristics of an aluminum-gallium nitride-silicon structure, prepared from a gallium nitride film of 4 μm thickness deposited on a 0.01 ohm-cm n-type silicon substrate at 650°C in argon, are shown in Fig. 6. The

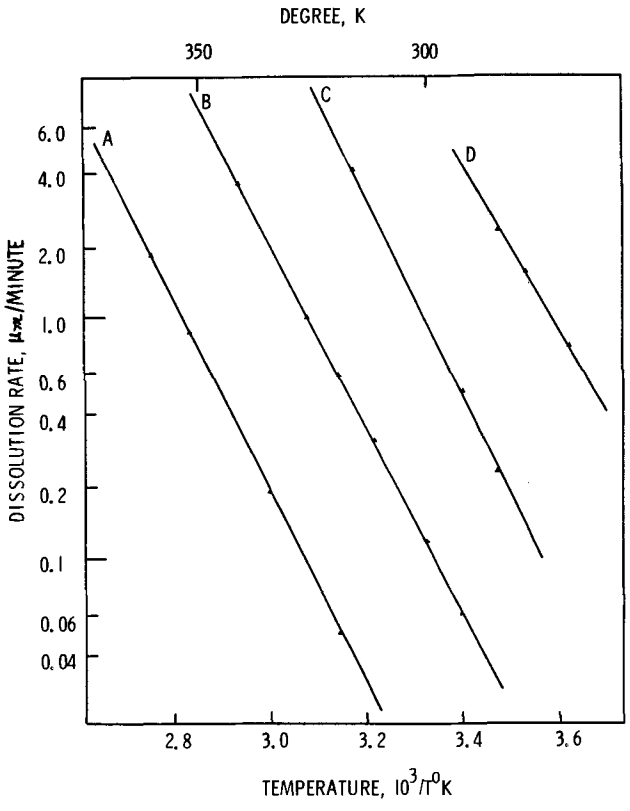

Fig. 5. Dissolution rate of gallium nitride films in a 50% aqueous solution of sodium hydroxide as a function of temperature. Gallium nitride was deposited in argon at 760°C (A) and 600°C (B) and in ammonia at 550°C (C) and 450°C (D).

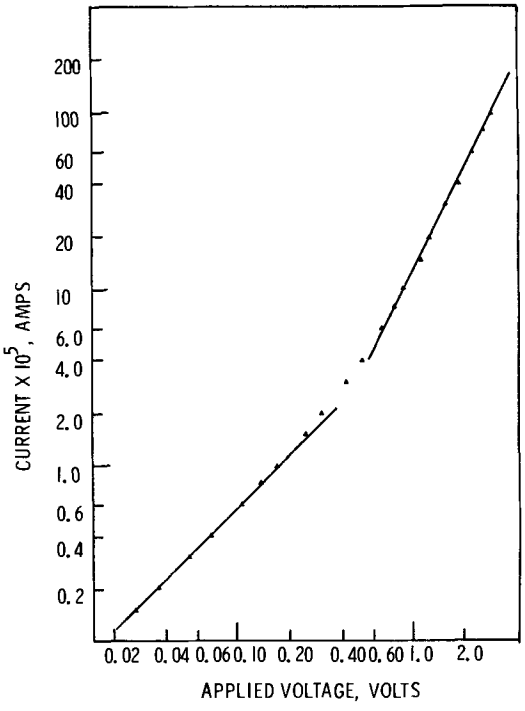

Fig. 6. Current-voltage characteristics of an aluminum-gallium nitride-silicon structure.

measured characteristics were essentially polarity independent, indicating the ohmic nature of the aluminum contacts. Two regions may be distinguished in the log I *vs.* log V plot. Ohmic behavior prevails at low bias levels, 500 V/cm or less, and the electrical resistivity of gallium nitride is approximately 10^6 ohm-cm. As the bias is increased, the slope of the log I *vs.* log V plot increases to two, indicating a space-charge-

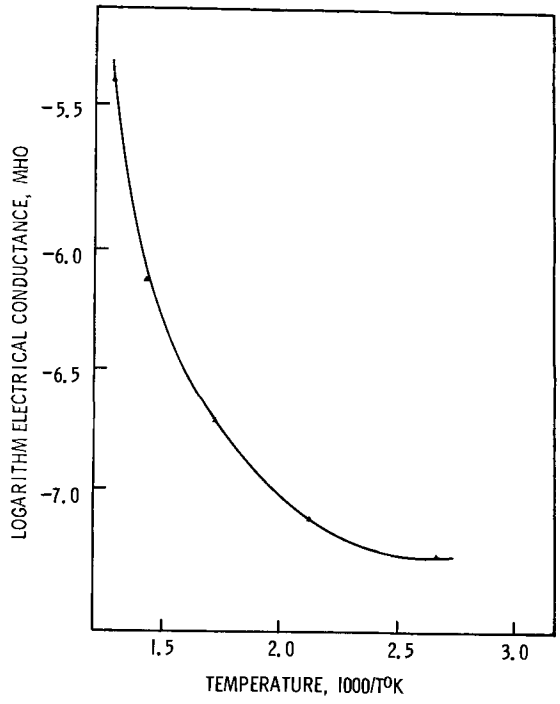

Fig. 7. Electrical conductance of an aluminum-gallium nitride-silicon structure as a function of temperature.

limited current situation. This is expected because of the high resistivity of gallium nitride. The current-voltage characteristics of the aluminum-gallium nitride-silicon structure were also measured in the temperature range 100°-500°C. The logarithm of the conductance is plotted *vs.* the reciprocal absolute temperature in Fig. 7, where a large variation of conductance with temperature is shown. The contact resistance is concluded to be insignificant as compared with the bulk resistance since the contact resistance is relatively insensitive to temperature. The activation energy deduced from the high-temperature region of Fig. 7 is approximately 1.1 eV, indicating the presence of a deep-lying impurity.

The gallium nitride films deposited on silicon carbide substrates were also of high resistivity at room temperature, similar to those deposited on the silicon substrates. Intrinsic gallium nitride is expected to be of high resistivity at room temperature because of its relatively large energy gap. On the other hand, the gallium nitride prepared by the ammonolysis of gallium monochloride at 825°C was n-type with a room-temperature resistivity of 0.001-0.005 ohm-cm (5). This low resistivity has been attributed to the nitrogen vacancies produced at the high temperature used in the deposition process. The low resistivity of the gallium nitride films deposited by the vacuum evaporation of gallium in a nitrogen discharge is presumably also associated with nitrogen vacancies. The high resistivity of gallium nitride achieved in this work indicates that the decomposition of the gallium nitride prepared from the gallum tribromide-ammonia complex is negligible compared with that prepared by other techniques. Thus, the thermal decomposition of the gallium tribromide-ammonia complex provides a new promising method for the crystal growth of gallium nitride.

Summary

The reaction between gallium tribromide and ammonia has been used for the preparation of a gallium tribromide-ammonia complex, $GaBr_3:4NH_3$. This complex is stable in laboratory ambient and decomposes at 450°C and above to yield gallium nitride. Gallium nitride films have been deposited on silicon and hexagonal silicon carbide substrates in this manner in an ammonia, argon, or nitrogen atmosphere. Adherent and transparent films have been deposited in ammonia atmospheres at temperatures up to 600°C and in argon or nitrogen atmospheres at temperatures up to 750°C. At higher substrate temperatures, the deposit became contaminated with gallium.

Gallium nitride is relatively inert at room temperature, insoluble in common acids, and dissolves slowly in aqueous alkalies. The gallium nitride films deposited on {111} oriented silicon substrates were found, by the electron diffraction technique, to have a (110) fiber orientation, and epitaxial, single crystalline gallium nitride films have been deposited on the basal plane of hexagonal silicon carbide substrates. Gallium nitride films were found to have high electrical resistivity at room temperature, indicating the negligible decomposition of the nitride. Thus, the thermal decomposition of the gallium tribromide-ammonia complex provides a new promising method for the crystal growth of gallium nitride.

Acknowledgments

The author wishes to thank Messrs. F. Y. Jou, A. E. Hyslop, and J. M. Jackson for their contributions in various phases of the experimental work.

Manuscript submitted Sept. 14, 1970; revised manuscript received *ca.* Mar. 1, 1971.

Any discussion of this paper will appear in a Discussion Section to be published in the June 1972 JOURNAL.

REFERENCES

1. E. Kauer and A. Rabenau, *Z. Naturforsch.*, **12a**, 942 (1957).
2. R. Juza and H. Hahn, *Z. Anorg. Allgem. Chem.*, **239**, 282 (1938).
3. M. R. Lorenz and B. B. Binkowski, *This Journal*, **109**, 24 (1962).
4. T. Renner, *Z. Anorg. Allgem. Chem.*, **198**, 22 (1959).
5. H. P. Maruska and J. J. Tietjen, *Appl. Phys. Letters*, **15**, 327 (1969).
6. B. B. Kosicki and D. Kahng, *J. Vacuum Sci. Technol.*, **6**, 593 (1969).
7. JANAF Interim Thermochemical Tables, The Dow Chemical Co., Midland, Mich.

Condensation Coefficients of Refractory Materials

I. AlN and BN

M. Hoch and D. Ramakrishnan

Department of Materials Science and Metallurgical Engineering, University of Cincinnati, Cincinnati, Ohio 45221

ABSTRACT

A method was developed for determining the condensation coefficient β of component B in reactions of the type

$$AnBm \rightarrow nA\,(g \text{ or } s) + \frac{m}{2} B_2(g)$$

β is measured by studying the rate of exchange of isotopically marked $B^*_2(g)$ on the surface of $AnBm$. For the method to be applicable, component B must be present as a dimer (or higher) in the gas. The condensation coefficients of AlN and BN were measured using this method, employing N^{15} nitrogen isotope. The condensation coefficients thus measured, $\beta = 5 \times 10^{-3}$ for AlN, and $\beta = 1 \times 10^{-2}$ for BN, compare favorably with values obtained by conventional methods where the kinetic pressure is compared with the equilibrium pressure.

The kinetics of vaporization of nitrides such as AlN and BN are of interest in the study of vaporization mechanisms. Metal nitrides decompose primarily to the elements. Current (1, 2) theories of the evaporation and condensation of solids postulate that evaporation and condensation are processes which involve several steps. The vaporization of metal nitrides include a slow step which results in a low vaporization coefficient α, the ratio of the rate of vaporization at the experimental conditions to the rate at the equilibrium conditions. α is generally determined by measuring the Langmuir pressure P_L, using the Langmuir free evaporation technique (3), and the equilibrium pressure P_{eq}, as obtained by the Knudsen effusion technique (4); α is then given by P_L/P_{eq}.

In the Knudsen effusion method under steady-state conditions, the rate of vaporization equals the rate of condensation plus the rate of effusion so that $\alpha C\, P_{eq} = \beta C\, P_{cell} + C\, P_{cell} \cdot h/S$ or

$$\alpha P_{eq} = P_{cell}\left(\beta + \frac{h}{S}\right) \qquad [1]$$

where β is the condensation coefficient, h/S is the ratio of the areas of the effusion hole and the vaporizing solid. In all work where only the weight loss is measured, it is usually assumed that $\alpha = \beta$. Thus

$$P_{eq} = P_{cell}\left(1 + \frac{h}{\alpha S}\right) \qquad [2]$$

It is possible in favorable cases to evaluate P_{eq} and β using Eq. [2] by measuring P_{cell} as a function of h/S. Hoch and White (5) as well as Hildenbrand and Hall (6) used Eq. [2] to evaluate α for AlN and BN by measuring P_{cell} as a function of h/S. However, it is feasible to measure β, the condensation coefficient, separately in a Knudsen experiment if, instead of the total effusion rate, the isotope exchange rate of the vaporizing species with the solid is measured. In the research reported here, an isotopic exchange technique has been developed to determine the condensation coefficients of AlN and BN.

Mathematical Treatment

The experimental set-up developed to study the isotopic exchange reactions between AlN^{14} and AlN^{15} is shown in Fig. 1. Pellets of AlN^{14} and AlN^{15} of equal size are placed in the Knudsen cell so that they do not make physical contact. On heating the cell to a high temperature, the two pellets vaporize independently:

Key words: aluminum nitride, boron nitride, condensation, isotope exchange, vaporization.

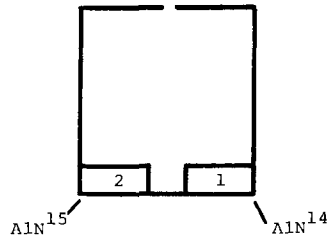

Fig. 1. Schematic arrangement of samples in Knudsen cell

pellet 1 reacts as $AlN^{14} \rightarrow Al(g) + \frac{1}{2} N_2^{14}(g)$, and pellet 2 as $AlN^{15} \rightarrow Al(g) + \frac{1}{2} N_2^{15}(g)$. Within a few microseconds, a steady-state pressure P_{cell} will build up in the cell. The gas in the cell will be composed of Al(g) and equal amounts of $N_2^{14}(g)$ and $N_2^{15}(g)$. The Al(g), however, does not enter into subsequent considerations so it will not be discussed further.

Inside the cell, exchange collisions of $N_2^{14}(g)$ with AlN^{15} pellet and $N_2^{15}(g)$ with AlN^{14} pellet will generate $N^{14}N^{15}(g)$ molecules. This will increase the $N^{14}N^{15}(g)$ concentration with time and decrease the $N_2^{14}(g)$ and $N_2^{15}(g)$ concentrations in the gas until a steady-state is reached, *i.e.*, the concentration of each species in the gas phase remains constant. A certain amount of gas will effuse from the hole of the Knudsen cell. $AlN^{14}(s)$ and $AlN^{15}(s)$ will vaporize to compensate the effusion loss. Exchange reactions between the gas molecules and the solid pellets will contaminate $AlN^{14}(s)$ by $AlN^{15}(s)$ and vice versa. This contamination will also increase with time. The increase in $N^{14}N^{15}(g)$ concentration in the gas will be followed by analyzing the effusion flow with a mass spectrometer. The contamination of the $AlN^{14}(s)$ by $AlN^{15}(s)$ will be determined by interrupting the exchange experiment, removing the $AlN^{15}(s)$ and vaporizing the original $AlN^{14}(s)$ pellet alone. The fraction of $AlN^{15}(s)$ in $AlN^{14}(s)$ can then be calculated from the composition of the gas.

It is assumed here that exchange between nitrogen molecules takes place only on the surface of the AlN pellets. This assumption is justified by work of Clusius (7) which showed that the exchange reaction

$$N_2^{14}(g) + N_2^{15}(g) \rightarrow 2N^{14}N^{15}(g) \qquad [3]$$

does not occur on platinum wires even at 1000°K. In fact, the reaction could be initiated only after the dissociation of nitrogen molecules to nitrogen atoms in discharge tubes. This suggests, though, that the exchange reaction could take place in the ion source of the mass spectrometer, but fragmentation of N_2 mole-

cules in the ion source is minimized by using a low ionizing electron energy.

At high temperatures where isotopic effects can be neglected and each atom or molecule has an equal probability to react, the equilibrium constant for Eq. [3] has a value of 4 (7, 8), that is

$$\frac{(N^{14}N^{15})}{(N_2{}^{14}\,N_2{}^{15})} = 4 \qquad [4]$$

Since only nitrogen molecules are present in the gas phase, the subscript (g) is omitted, and $N_2{}^{14}$ means $N_2{}^{14}(g)$. In the solid, only atoms are present, and hence, $N^{14}(s)$ means nitrogen bound in the solid AlN. Thus, if a vaporizing solid contains a fraction γ of N^{15}, and $(1-\gamma)$ of N^{14}, the concentration of the various species in the gas will be

$$(N^{14}N^{15}) = 2\alpha(1-\alpha);\ (N_2{}^{14}) = (1-\alpha)^2,$$

$$\text{and } (N_2{}^{15}) = \alpha^2$$

The reactions which contribute to the N^{15} enrichment of the AlN^{14} pellet (and vice versa) and to the build-up of $N^{14}N^{15}$ are as follows

$$N_2{}^{14} + N^{15}(s) \rightarrow N^{14}N^{15} + N^{14}(s) \qquad [5]$$

$$N_2{}^{15} + N^{14}(s) \rightarrow N^{14}N^{15} + N^{15}(s) \qquad [6]$$

$$N^{14}N^{15} + N^{14}(s) \nearrow N^{14}N^{15} + N^{14}(s) \qquad [7a]$$

$$\qquad\qquad\qquad\quad \searrow N_2{}^{14} + N^{15}(s) \qquad [7b]$$

$$N^{14}N^{15} + N^{15}(s) \nearrow N^{14}N^{15} + N^{15}(s) \qquad [8a]$$

$$\qquad\qquad\qquad\quad \searrow N_2{}^{15} + N^{14}(s) \qquad [8b]$$

Equations [7] and [8] have to be written in this split fashion: $N^{14}N^{15}$ has the same probability to react as $N_2{}^{14}$ but because it is asymmetric, it can react either way, each having the probability ½.

Enrichment of solid.—Let us consider the AlN^{14} pellet and assume that after a certain time, t, it contains a fraction γ of AlN^{15}. (Similar considerations apply to the AlN^{15} pellet.) The change of γ with time is then, from Eq. [5]-[8]

$$\frac{d\gamma}{dt} = k\,[(1-\gamma)(N_2{}^{15}) + \tfrac{1}{2}(1-\gamma)(N^{14}N^{15}) - (N_2{}^{14})\gamma - \tfrac{1}{2}\gamma(N^{14}N^{15})] \qquad [9]$$

In the gas phase

$$(N_2{}^{15}) + (N_2{}^{14}) + (N^{14}N^{15}) = 1 \qquad [10]$$

and

$$(N_2{}^{15}) = (N_2{}^{14}) \qquad [11]$$

thus

$$\frac{d\gamma}{dt} = k \cdot \left(\frac{1-2\gamma}{2}\right) \qquad [12]$$

This expression contains only the enrichment due to Eq. [5]-[8]. A certain amount of $N^{15}(s)$ is removed because the pellet is constantly vaporizing due to the gas effusing through the hole. Thus

$$\frac{d\gamma}{dt} = k \cdot \left(\frac{1-2\gamma}{2}\right) - k'\gamma \qquad [13]$$

where

$$k = \frac{F \cdot S/2 \cdot n_g}{n_o \cdot S/2 \cdot z}\beta \text{ and } k' = \frac{F \cdot S/2 \cdot n_g}{n_o \cdot S/2 \cdot y} \cdot \frac{h}{S} \qquad [13a]$$

$(F \cdot S/2 \cdot n_g)$ is the number of gas molecules hitting the surface per second. $(n_o \cdot S/2)$ is the total number of nitrogen atoms in a single layer.

The reaction between gas and solid will take place on a monolayer surface of the solid. Though diffusion of $N^{15}(s)$ from the monolayer is very slow, a certain amount will accumulate in the adjacent layers. This is taken into account by expanding the thickness of the reacting zone, z, expressed in atoms of nitrogen. Thus, $(n_o \cdot S/2 \cdot z)$ is the number of nitrogen atoms in the reaction layer. If diffusion is absent, the reacting zone is a monolayer and $z = 1$; if diffusion is extremely rapid and the composition of the whole solid uniform, z is large (but varies with time as the solid sample gets thinner due to vaporization). Similar considerations apply to the vaporization process. However, since all vaporization will take place from the surface (monolayer), $y \simeq 1$.

β is defined as the efficiency of a gas molecule collision with the surface and thus is identical to the condensation coefficient.

Equation [13] can be rewritten

$$\frac{d\gamma}{dt} = A \cdot \frac{\beta}{z}\left(\frac{1-2\gamma}{2}\right) - A \cdot \frac{h}{yS}\gamma \qquad [13b]$$

Both Eq. [13] and [13b] express the rate of N^{15} increase in the AlN^{14} pellet as a function of the condensation coefficient β. Assuming constant z and y, Eq. [13b] can be integrated, with the boundary conditions of $\gamma = 0$ at $t = 0$

$$\gamma = \frac{1}{2}\,\frac{1 - e^{-\left(\frac{\beta}{z} + \frac{h}{yS}\right)At}}{1 + \frac{z}{y} \cdot \frac{h}{\beta \cdot S}} \qquad [14]$$

Change of composition of gas.—Let us now calculate the change in $N^{14}N^{15}$ concentration of the gas. Consider the reaction on the AlN^{14} pellet which again contains γ AlN^{15} after at time t.

From Eq. [5]-[8]

$$\frac{d(N^{14}N^{15})}{dt} = k''\,[(N_2{}^{14})\gamma + (N_2{}^{15})(1-\gamma) - \tfrac{1}{2}(N^{14}N^{15})(1-\gamma) - \tfrac{1}{2}(N^{14}N^{15})\gamma] \qquad [15]$$

combining [15] with Eq. [10] and [11]

$$\frac{d(N^{14}N^{15})}{dt} = k''\left[\frac{1 - 2(N^{14}N^{15})}{2}\right] \qquad [16]$$

where $k'' = F \cdot (S/2)/V \cdot \beta$ and $F \cdot (S/2)/V$ is the number of times a molecule hits the surface per second.

An equation similar to [16] applies to the AlN^{15} pellet; thus the total will be

$$\frac{d(N^{14}N^{15})}{dt} = \frac{F \cdot S}{V}\beta\left[\frac{1 - 2(N^{14}N^{15})}{2}\right] \qquad [17]$$

Equation [17] takes into consideration only the change in concentration of $(N^{14}N^{15})$ due to reaction of the gas with the pellet. A certain amount of $(N^{14}N^{15})$ is lost by effusion through the hole, and a certain amount gained by vaporization of the pellet to replace the effused gas. Taking these facts into account, the final equation becomes

$$\frac{d(N^{14}N^{15})}{dt} = \frac{F \cdot S}{V}\beta\left[\frac{1 - 2(N^{14}N^{15})}{2}\right] - \frac{F \cdot h}{V}[(N^{14}N^{15}) - 2\gamma(1-\gamma)] \qquad [18]$$

with $F \cdot h/V$ $(N^{14}N^{15})$ the $(N^{14}N^{15})$ lost due to effusion, and $F \cdot h/V$ $2\gamma(1-\gamma)$ the amount gained by vaporization of the solid. γ can be obtained from Eq. [14].

1. At the beginning of an experiment when γ and the $N^{14}N^{15}$ concentration in the gas are small, $[(N^{14}N^{15}) - 2\gamma(1-\gamma)] \simeq 0$, and the integration of Eq. [18] results in

$$\ln[1 - 2(N^{14}N^{15})] = -\frac{F \cdot S}{V}\beta t \qquad [19]$$

Equation [19] thus expresses the initial increase of the $(N^{14}N^{15})$ content of the gas as a function of β.

2. After a period of time, the system reaches steady state both in the solid and gas phases, which means

$$\frac{d\gamma}{dt} = \frac{d(N^{14}N^{15})}{dt} = 0$$

Under those conditions, Eq. [13b] can be rearranged to give

$$\gamma = \frac{1}{\beta + \left(\frac{z}{y} \cdot \frac{h}{S}\right)} \cdot \frac{\beta}{2} \qquad [20]$$

Equation [18] under the same conditions becomes

$$\frac{d(N^{14}N^{15})}{dt} = \frac{F \cdot S}{V}\beta\left(\frac{1 - 2N^{14}N^{15}}{2}\right) - \frac{F \cdot h}{V}[(N^{14}N^{15}) - 2\gamma(1-\gamma)] = 0 \qquad [21]$$

Introducing Eq. [20] and rearranging we get

$$(N^{14}N^{15})\left[\frac{S\beta}{h} + 1\right] = \frac{S\beta}{2h} + \frac{\beta\left(\frac{\beta}{2} + \frac{zh}{yS}\right)}{\left(\beta + \frac{zh}{yS}\right)^2} \qquad [22]$$

Given the steady-state value of $(N^{14}N^{15})$, and the quantities S, h, and z/y (which are fixed), β can be evaluated numerically. Two limiting cases can be formulated more simply

1. If $z/y \cdot h/S >> \beta$, then

$$\beta = \frac{h}{S}\frac{(N^{14}N^{15})}{\left[\frac{1}{2} - (N^{14}N^{15}) + \frac{y}{z}\right]} \qquad [23]$$

The limits on y/z are $0 < y/z < 1$.

2. If $z/y \cdot h/S << \beta$, the solution gives $(N^{14}N^{15}) = \frac{1}{2}$. Thus if the condensation coefficient is high, equilibrium will be attained in the Knudsen cell.

Now Eq. [18] predicts that the mass spectrum as a function of time should appear schematically as in Fig. 2. In that figure, N_2 indicates the sum of the intensity of the 28, 29, and 30 peaks (corresponding to the total amount of N_2), Al corresponds to the peak of aluminum, and R corresponds to the concentration of the $N^{14}N^{15}$) molecule; thus, $R = I_{29}/N_2$. The Al and N_2 are given on the ordinate scale in arbitrary intensity units whereas R is given as a fraction. When starting with AlN^{15} and AlN^{14} at constant temperature, N_2 and Al do not change with time whereas R should increase from 0 to the steady-state value given by Eq. [18]. While R is small (near $t = 0$) Eq. [19] indicates that it increases linearly with t. When the steady-state value of R is reached, Eq. [22] and [23] specify its magnitude.

If, after a certain time, t, the sample is cooled to room temperature so that no vaporization takes place and the gas in the Knudsen cell is pumped out, then N_2 and Al will become zero. On retreating the system to the same temperature as before, N_2 and Al will again quickly reach constant value while R will rise from a value close to zero toward its steady-state value. The second starting point for R is not zero because the samples now are each somewhat contaminated. If a change in temperature occurs during the run, then N_2 and Al should increase or decrease together.

It should be clear that the equations derived above for AlN, must also apply to BN, NiO, and any other compound which decomposes according to the reaction

$$AnBm \rightarrow nA(g \text{ or } s) + \frac{m}{2}B_2(g)$$

Equation [19] then indicates that R will start as a small number and increase rapidly to its steady-state value. However, this predicted rapid rise was not observed experimentally for AlN and BN. All the exchange runs of AlN and BN made with fresh samples showed a gradual rise of R with time. On reheating the same set of pellets next day, though, R rose rapidly to the steady-state value.

The condensation coefficients of AlN and BN were calculated using Eq. [23] with z as a parameter. The reported values of β are those where z is large and $y/z \simeq 0$ in Eq. [23].

Materials

AlN.—Several methods (9-13) of preparation of AlN are known. AlN^{14} samples used in this work were prepared by reacting about 100-500 ml of high purity NH_3 gas with about 400 mg of aluminum metal at 1400°K. Aluminum wire of 99.99% purity was supplied by Alcoa (No. Cl-44311-C). AlN^{15} samples were prepared in the same way using $N^{15}H_3$ obtained from Bio-Rad Laboratories, Richmond, California. Two purity levels of N^{15} (97.8 and 99.3%) were used. The description of the apparatus and the details of the method of preparation is given elsewhere (14). The AlN^{14} and AlN^{15}

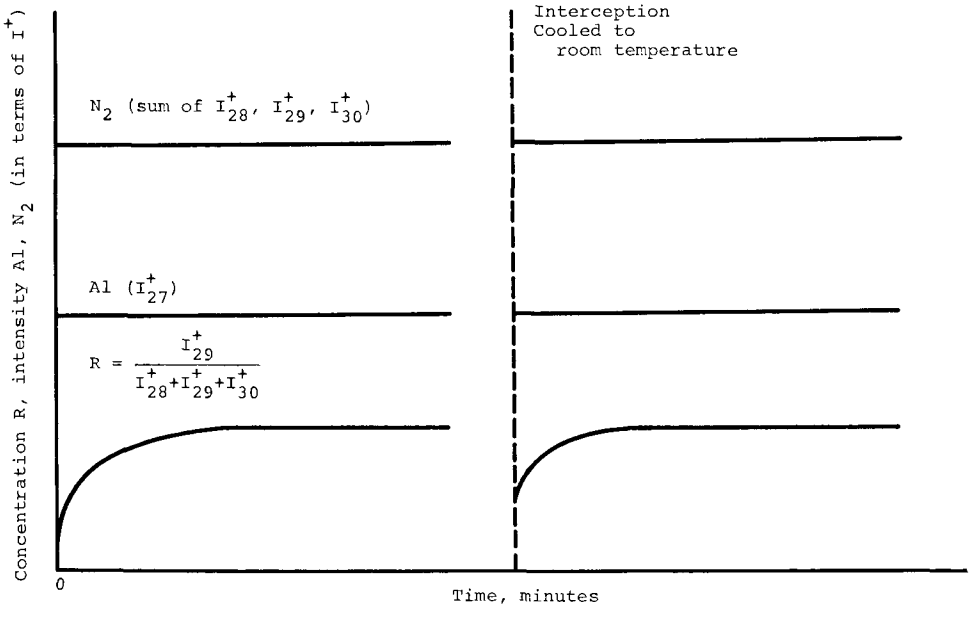

Fig. 2. Expected change $(N^{14}N^{15})$ concentration (R) with time.

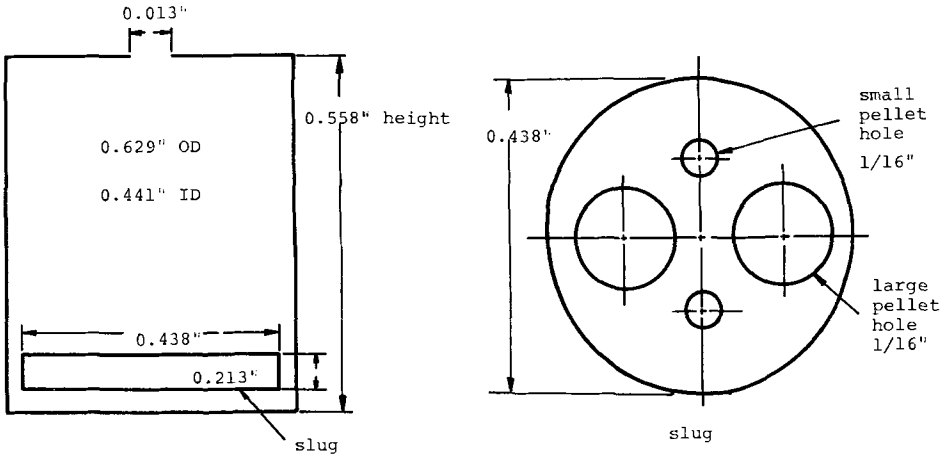

Fig. 3. Knudsen cell and tungsten slug assembly (schematic).

samples were purified by heating in chlorine atmosphere (15) at 1000°K for 90 min to remove any unreacted Al as $AlCl_3$. X-ray diffraction studies showed only the sharp lines of recrystallized AlN. The purified powder was pressed into 3/16 in. diameter pellets and degassed in vacuum at 1800°K for 60 min.

BN.—A general survey of the known methods of preparation of BN is given by Giardini (16). Attempts to react elemental boron with NH_3 or N_2 gave poor yields. BN^{14} and BN^{15} samples for this work were prepared by forming the addition product $BCl_3 \cdot NH_3$ using 99.9% pure BCl_3 and its subsequent decomposition to BN and other decomposition products. The details are given elsewhere (14). A fluffy white solid was obtained after decomposition. The white product was first heated to 1400°K in argon to remove the volatile impurities. The residue was then boiled in dilute HCl, washed with distilled water, and dried. To recrystallize the product, the powder was passed into 3/16 in. diameter pellets and heated in vacuum at 1900°K for 3 hr first and for 2 hr subsequently. The first heating resulted in 40% weight loss. The weight loss was about 2% after the second heating. An x-ray diffraction pattern showed the sharp lines of hexagonal BN.

Knudsen cells.—A tungsten Knudsen cell fitted with a tungsten slug was used to study the exchange reactions of AlN samples. The dimensions of the cell and the slug are shown in Fig. 3. The slug contained four holes, two of 3/16 in. diameter, and two of 1/16 in. diameter. The degassed AlN^{14} and AlN^{15} pellets were either introduced into the large holes or introduced into the small holes. In this manner, the surface area S of the evaporating surface could be varied, keeping the other properties of the cell constant. Some runs were made without using the slug. In that case, each pellet was cut into half and the two half pellets were placed in the bottom of the cell facing each other's cut edges. One drawback in this arrangement is that the area S is not well defined.

The exchange reactions between BN^{14} and BN^{15} were studied in a graphite cell fitted with a graphite slug. The dimensions of the cell and slug were essentially identical to the dimensions of the tungsten cell assembly except that the graphite cell had a 0.025 in. diameter hole in the lid.

Experimental Procedure and Results

AlN.—The exchange runs were made by heating the AlN^{14} and AlN^{15} placed in the tungsten Knudsen cell. The cell was heated by electron bombardment in the Bendix (Model 12) Time-of-Flight mass spectrometer. The temperature was measured by a L&N disappearing filament optical pyrometer sighted through a prism and a window on the black-body hole of the cell. The pyrometer readings were corrected for the window and prism absorptions. To reduce the background interference at mass 28 corresponding to the N_2^{14} ion, the mass spectrometer was baked for several days. The mass spectrometer was also fitted with an extended flight tube to improve its resolution. Fragmentation and recombination of nitrogen molecules in the ion source was minimized by operating the mass spectrometer with only 20V electron energy.

In a typical exchange run, the cell with the pellets was heated gradually in the mass spectrometer to the operating temperature. When a fresh sample was introduced into the Knudsen cell, it took approximately 3 hr to reach this temperature due to outgassing of the samples. After reaching the temperature of the run, the intensities of signals (I_{27}, I_{28}, I_{29}, and I_{30}) corresponding to Al, N_2^{14}, $N^{14}N^{15}$, and N_2^{15} ions were recorded at 15-min intervals. All runs made with a fresh pair of sample pellets are designated as "a." The subsequent runs made with the same pellets are designated as b, c, d, etc.

The data on run 17 shown in Fig. 4a and 4b are representative of the exchange runs made without using the tungsten slug. At the beginning of run 17a, the temperature was high (1840°K) and then dropped to the steady-state values (1818°K). This is shown by the parallel variation of Al and N_2 intensities. It can be seen that $R = \dfrac{I_{29}}{I_{28} + I_{29} + I_{30}}$ rises very slowly from 0.1 to the steady-state value of 0.4. This was characteristic of all "a" runs, suggesting some difficulty in the reactivity of the material.

The run was continued the next day (run 17b). The temperature was fairly constant at 1819°K in run 17b as indicated by the constant N_2 and Al intensities. R started at 0.25 and rose as expected to 0.4 again. In contrast to run 17a, only 15 min was required to reach the temperature in run 17b. After run 17b, the cell was opened. The contamination of the half-pellet of AlN^{15} by N^{14} was determined by vaporizing it separately at 1819°K in run 17c. The concentration of N^{14} in AlN^{15} pellet was calculated from the ratio (17) of intensities of mass 29 and mass 30 peaks. Similarly, the N^{15} concentration in AlN^{14} was calculated from the ratio of mass 29 and mass 28 peak intensities by vaporizing AlN^{14} half pellet in run 17d. These results are shown in Fig. 5. At the start, both half-pellets show a large amount of contamination, but it decreases with time as the top layers are eliminated by the vaporization of the sample pellets. Only after a substantial amount of time had elapsed were the contaminated layers completely removed, indicating that for this configuration $z = 1$.

Run 22, an extremely long run using the large holes of the slug, was made at 1808°K. The results show the same characteristics as run 17, *i.e.*, a fairly slow buildup of R at the beginning, culminating in a steady-state value of 0.33. Results of exchange run 29 made with samples in the small holes of the slug were unsatisfactory, because it was very difficult to obtain constant N_2 and Al intensities.

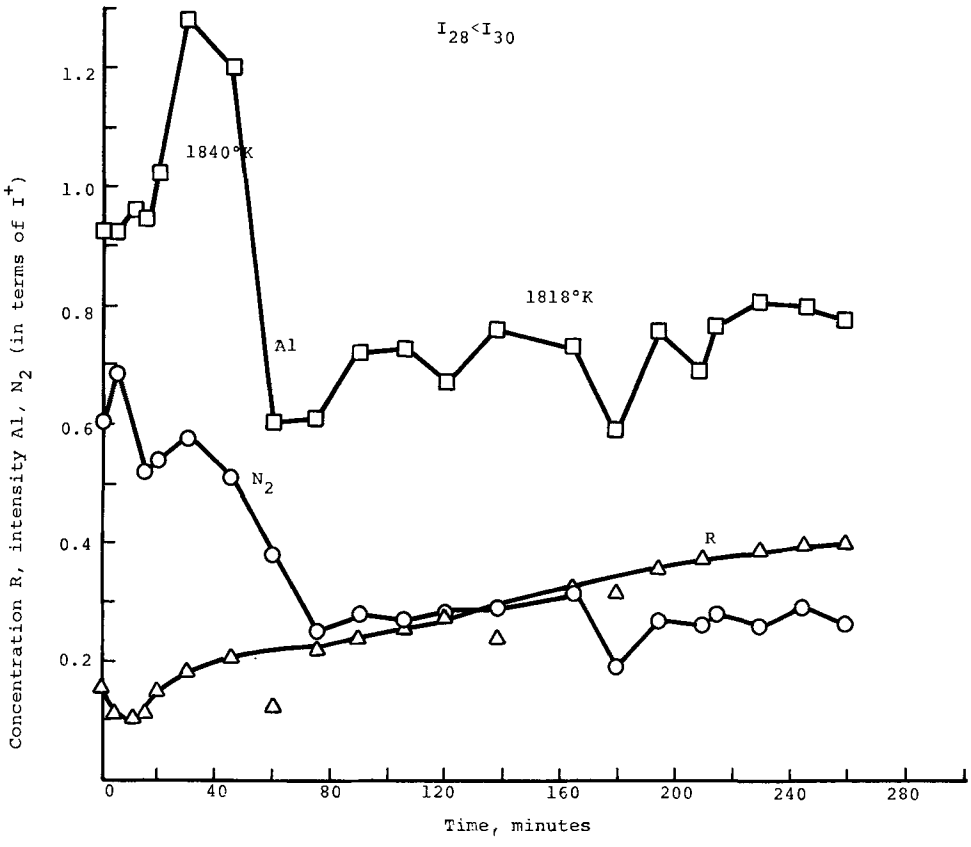

Fig. 4a. Run 17a. AlN^{14}, AlN^{15} half pellets, no tungsten slug.

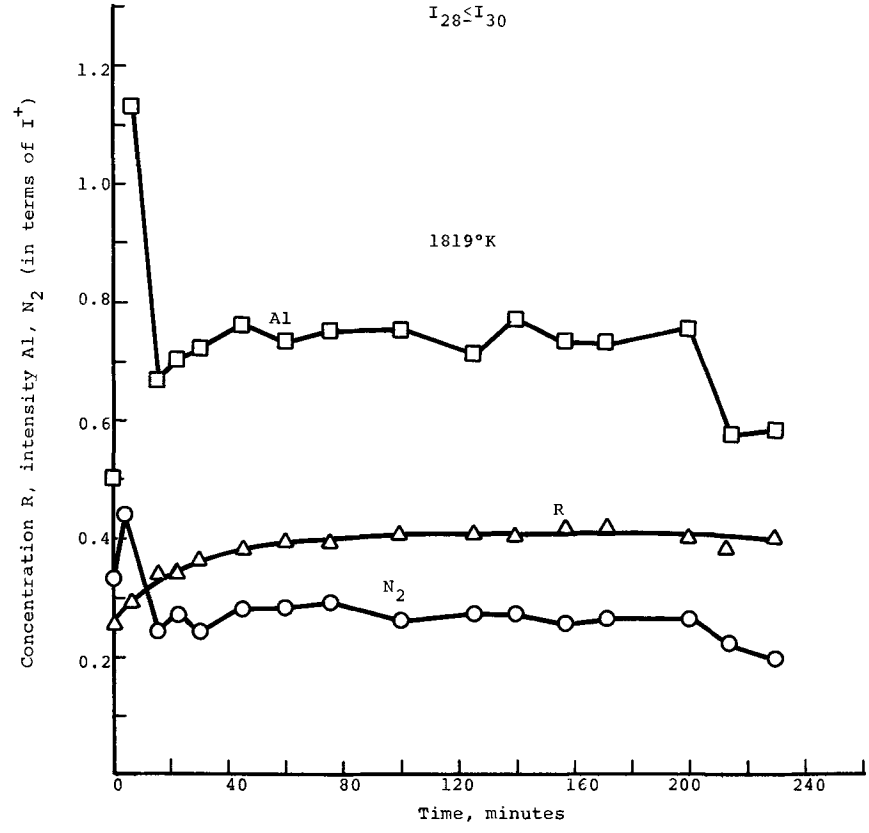

Fig. 4b. Run 17b. AlN^{14} half pellets, no tungsten slug.

In one of the runs made with sample pellets in large holes, the Knudsen cell was exposed to air (after interrupting the run) in order to study the effect of absorbed nitrogen on the exchange reaction. No great influence was observed. To study the effect of free aluminum at the beginning of the exchange reaction, a piece of aluminum was put into both holes at the end of an exchange run. When the cell was reheated, the aluminum vaporized but no effect on the steady-state value of R was detected.

The temperature variation of R was studied in run 35. The data is shown in Fig. 6, run 35e. As before, R increased from a small value to the steady-state value of 0.34. When the temperature was raised or lowered, Al and N_2 increased and decreased together while R remained practically constant.

Finally, an equimolar mixture of AlN^{14} and AlN^{15} was prepared. The powder containing AlN^{14} and AlN^{15} was pressed into two pellets. Exchange run 36 was made after placing the two pellets in the large holes of

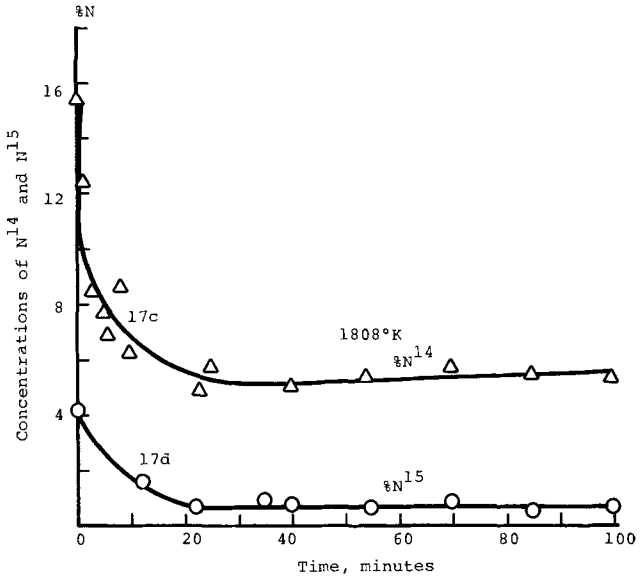

Fig. 5. Runs 17c and 17d. Separate pellets (AlN^{14} and AlN^{15}) to determine contamination.

the tungsten slug. At this moment, a "mixed crystal" is not present. A mixed crystal is defined as a material where within each grain N^{14} and N^{15} (present in equal amounts) are distributed at random. Vaporization of such a sample would yield a value of $R = 0.5$ irrespective of β value because both pellets are equal: no gas exchange between the two pellets is required to buildup ($N^{14}N^{15}$). In the present experiment, however, each pellet contained separate grains of AlN^{14} and AlN^{15}; therefore, at the start of the run, the system was not different from the one with separate pellets. During the experiment, however, diffusion between the two types of grains and sintering should take place in the pellets so that the material progressively approaches the status of a mixed crystal. Thus, experimentally, R should first reach a steady-state value and then increase slowly due to interdiffusion between the grains. Run 36a confirmed these expectations. R reached a steady-state value of 0.34, but on repeated heatings in runs 36b, 36c, and 36d, it increased linearly with time to a maximum value of 0.46.

Equation [23] could be used to calculate β, the condensation coefficient. In that calculation, it is assumed that $y = 1$ (only the top surface vaporizes), whereas z is assumed to vary with $S/2$. The rate of diffusion of nitrogen in the pellet is fixed; but the rate of surface recession of the pellet due to vaporization depends on its surface area. For a large surface area, the rate of vaporization per unit area will be small, the rate of recession of the surface will be small; thus a large amount of diffusion will take place resulting in large z. A small surface area, on the other hand, will recede faster. Hence, before a large amount of diffusion can take place, the material vaporizes. In this case, z will be small. In either case, y/z is the significant parameter in the calculation of β using Eq. [23].

Table I summarizes our results. For the "no slug" configuration and the runs where the sample was placed in the 3/16 in. holes, z is large, so $y/z \simeq 0$. For the small holes configuration, where $S/2$ is only 1/20 of its value when no slug is used, z will be nearly 1. Thus, $y/z \simeq 1$. Using these approximations, the calculations give an average value of $\beta = 5 \times 10^{-3}$ for the temperature range of 1800°-1900°K where the measurements were carried out.

BN.—Preheated BN^{14} and BN^{15} pellets were loaded into the large holes of the tungsten slug and the exchange run[51] was made at 1952°K using the tungsten Knudsen cell. In this run, R started from an unusually large value of 0.37, rose to 0.45 within 60 min and remained constant. At the end of the run, examination of the pellets and the cell revealed evidence of chemical reaction between the samples and tungsten metal. The pellet had shrunk in size and the tungsten slug was welded to the body of the cell. Therefore, subsequent exchange runs were made with a graphite Knudsen cell and a graphite slug containing two 3/16 in. diameter holes.

The empty graphite cell assembly was degassed in vacuum at 2100°K for several hours. Later, in order to

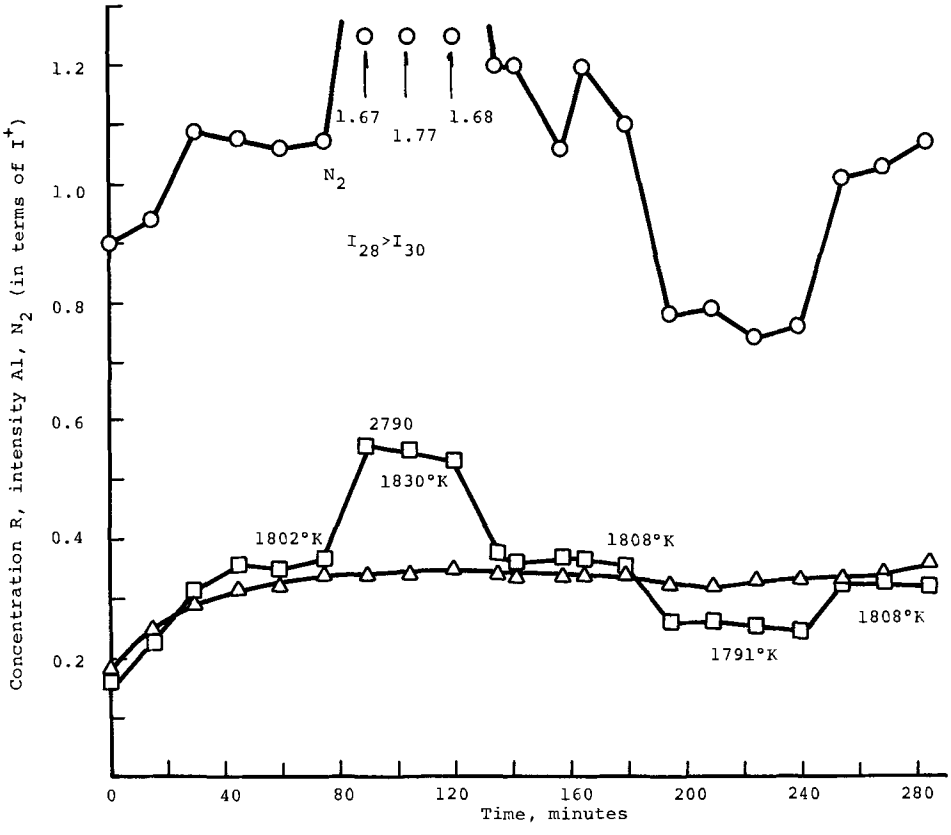

Fig. 6. Run 35E. AlN^{14}, AlN^{15} in large tungsten holes, to study influence of temperature variation.

Table I. Calculation of the condensation coefficients from the steady-state $N^{14}N^{15}$ concentration at various surface areas

Run	Temp, °K	Samples	Cell	Configuration	S, cm²	h, cm²	R,* steady-state	β $y/z = 0$	β $y/z = 0.5$	β $y/z = 1$
17	1840	AlN^{14} & AlN^{15}	Tungsten	No slug	0.72	8.55×10^{-4}	0.4	4.75×10^{-4}	7.9×10^{-4}	4.3×10^{-4}
22	1808	AlN^{14} & AlN^{15}	Tungsten	Large holes	0.36	8.55×10^{-4}	0.33	4.75×10^{-3}	1.2×10^{-3}	6.9×10^{-4}
29	1819	AlN^{14} & AlN^{15}	Tungsten	Small holes	0.04	8.55×10^{-4}	0.3	3.2×10^{-2}	9×10^{-3}	5.3×10^{-3}
36	1824	AlN^{14} & AlN^{15} mixed	Tungsten	Large holes	0.36	8.55×10^{-4}	0.34-0.46	—	—	—
41	1791	Commercial AlN^{14} & lab. made AlN^{15}	Tungsten	Large holes	0.23	3.2×10^{-3}	0.14	5.4×10^{-3}	2.2×10^{-3}	1.4×10^{-4}
42	1865	Commercial AlN^{14} & lab. made AlN^{15}	Graphite	Large holes	0.36	3.2×10^{-3}	0.2	6×10^{-3}	2.3×10^{-3}	1.4×10^{-4}
52	2112	BN^{14} & BN^{15}	Graphite	Large holes	0.36	3.2×10^{-3}	0.2	6×10^{-3}	2.3×10^{-3}	1.4×10^{-4}
53	1963	BN^{14} & BN^{15}	Graphite	Large holes	0.36	3.2×10^{-3}	0.23	1.2×10^{-2}	2.6×10^{-3}	1.7×10^{-3}
					0.36	3.2×10^{-3}	0.27**	1×10^{-2}	3.3×10^{-3}	2×10^{-3}

* $R = \dfrac{I_{29}}{I_{28} + I_{29} + I_{30}}$.

** $R' = \dfrac{I_{29}}{I_{29} + 2I_{30}}$.

estimate the contribution of CO contamination to the mass 28 readings, the cell was heated in the mass spectrometer to 1963°K. The measured background at the intensity mass 28 peak, was as expected, much higher than with the tungsten cell.

With this in mind, exchange run 52a was carried out at 2112°K and run 52b at 2050°K. In each case, 4-5 hr of preheating was needed to reach the operating temperature. In run 52a, R rose rapidly from an initial value of 0.09 to a steady-state value of 0.23 which remained constant in the two subsequent runs. At the end of run 52c, the cell was opened and the contamination of BN^{14} and BN^{15} by the other isotope species was determined by heating each pellet separately in the mass spectrometer. The results, which resembled those obtained for the AlN pellets, are shown in Fig. 7.

In all the runs, however, the intensity of the peak at mass 28 was much larger than the peak intensity of mass 30. That deviation from predicted behavior seems to be due to the evolution of CO from the graphite cell. This was inferred from the fact that at 70V electron energy, two intense peaks at mass 14 and 15 were observed in the spectrum, with $I_{15} > I_{14}$. In contrast, if the intensity of the mass 28 peak in run 52 was entirely due to N_2^{14} ions, then $I_{15} < I_{14}$. Moreover, the calculated ionization efficiency curves for mass 28 and mass 30 peaks were not identical as they should be if only N^{14} and N^{15} ions were involved.

To minimize this background interference, the empty graphite cell assembly was reheated in vacuum to 2300°K for 4 hr. Runs 53a and 53b were then made with a fresh pair of BN^{14} and BN^{15} pellets. In run 53a (1963°K), R rose from 0.03 to 0.14. At the beginning, $I_{28} > I_{30}$; but after 135 min, I_{28} became nearly equal to I_{30}. In run 53b the temperature was raised to 2018°K; the value of R rose to 0.21 and remained constant, but I_{28} stayed larger than I_{30}.

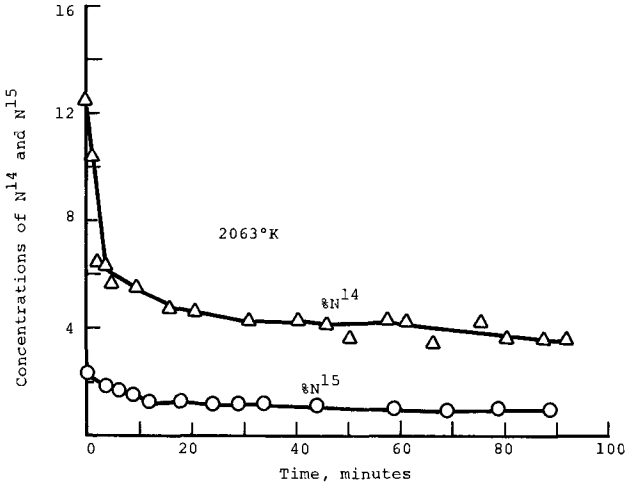

Fig. 7. Runs 52d and 52e. Separate pellets (BN^{14} and BN^{15}) to determine contamination.

To correct for the background contribution to the 28 peak, R was calculated assuming $I_{28} \simeq I_{30}$. Thus, $R = I_{29}/(I_{29} + 2I_{30})$. The steady-state value calculated on this assumption was 0.27. The condensation coefficient β of BN was calculated using Eq. [23], and the results are given in Table I.

Comparison of data from runs 52a, 52b, and 52c with that from runs 53a and 53b indicates that the steady state is reached much more rapidly when the run is made at a higher temperature. The steady-state value of R, however, is not influenced by temperature. At the end of run 53b, the temperature was decreased from 2018° to 1952°K; and though the intensity of N_2 peaks decreased correspondingly, R remained nearly constant.

Discussion

The condensation coefficient of $N_2(g)$ on AlN determined by this work ($\beta = 5 \times 10^{-3}$) is in good agreement with earlier work of Hoch and White (5), Hildenbrand and Hall (6), and Dreger *et al.* (18) which is summarized in Table II. The condensation coefficient of Al cannot be determined by the isotopic exchange technique because Al(g) exists as a monomer.

It is well established (5, 6) that AlN vaporizes congruently evolving Al(g) and $N_2(g)$ in stoichiometric ratio. One might expect, however, different values for the condensation coefficients of Al(g) and $N_2(g)$ on an AlN surface. On the other hand, Dreger, Dadape, and Margrave (18) found by x-ray studies that the lattice constant of AlN did not change during evaporation. Therefore, a large difference in the two condensation coefficients may not be present, and the value of β for $N_2(g)$ on AlN may be a good approximation for the β of Al(g) on AlN. The condensation coefficient of N_2 on BN determined by this work and the values of the vaporization coefficients determined by earlier workers are summarized in Table II.

In the BN vaporization-condensation equilibrium, a layer of amorphous boron forms on the BN surface. However, Knudsen effusion studies on BN by Hoch and White (5), as well as Hildenbrand and Hall (6), established that this boron layer did not block the subsequent escape of nitrogen molecules during vaporization of AN. Moreover, in the present work, the total intensity of all the nitrogen peaks in the exchange runs remained nearly constant with time even though the thickness of boron layer over BN was increasing with time. These observations are in contradiction with the work of Dreger *et al.* (18) who found that in Lang-

Table II. Vaporization and condensation coefficients of AlN and BN

Author	Method	Temperature, °K	AlN*	BN*
Hoch & White (5)	Knudsen	1660-2196	$\alpha = 1 \times 10^{-4}$	$\alpha = 1 \times 10^{-4}$
Hildenbrand & Hall (6)	Knudsen	1780-1970	$\alpha < 2 \times 10^{-3}$	—
	(Torsion effusion)	1850-2160	—	$\alpha < 2 \times 10^{-3}$
Dreger, Dadape & Margrave (8)	Langmuir	1450-1870	$\alpha = 10^{-2}$-10^{-3}	—
		1421-2031	—	$\alpha = 10^{-2}$-10^{-3}
This work	Isotope exchange	1800-1900	$\beta = 5 \times 10^{-3}$	—
		1950-2100	—	$\beta = 1 \times 10^{-2}$

* α is vaporization coefficient, β is condensation coefficient.

muir evaporation of BN, the rate of weight loss decreased as a function of time until it approached a constant rate determined by the vapor pressure of boron.

The formation of a boron layer on BN, thus raises the question of where the exchange reaction takes place. There are two possibilities: (*i*) on the boron layer, or (*ii*) on the BN. If the exchange reaction is taking place on the boron layer, then the value of R should increase continuously with time because the boron surface area increases as the BN sample is progressively decomposed. In these experiments, though, R was found to be constant with time after reaching a steady-state value. The contamination of the BN^{14} pellet by N^{15} and vice versa (shown in Fig. 7) also supports the conclusion that the exchange reaction takes place not on the boron surface layer, but on the boron nitride.

Acknowledgment

This work was supported in part by the Air Force Materials Laboratory, Wright Patterson Air Force Base, Ohio 45433, under Air Force Contract No. AF 33(615)9048.

Manuscript submitted Jan. 12, 1970; revised manuscript received ca. March 1, 1971. This was Paper 212 presented at the Detroit Meeting of the Society, Oct. 5-9, 1969.

Any discussion of this paper will appear in a Discussion Section to be published in the June 1972 JOURNAL.

LIST OF SYMBOLS

A $A = \dfrac{F \cdot n_g}{n_o}$

Al intensity of 27 peak in mass spectrometer corresponding to aluminum

C conversion factor, from atm to g cm^{-2} sec^{-1}

F the volume of gas which strikes an area of 1 cm^2 in 1 sec, $F = 3638\sqrt{T/M}$ cm^3 cm^{-1} sec^{-1}

G rate of effusion, g cm^{-2} sec^{-1}

h area of effusion hole in cm^2 (including Clausing correction)

M molecular weight, $M \simeq 29$

n_o number of nitrogen atoms in 1 cm^2 of AlN, or BN

n_1 number of nitrogen atoms along 1 cm in solid AlN, or BN

N_2 intensity of sum of 28, 29, and 30 peaks in mass spectrometer corresponding to nitrogen

n_g number of nitrogen molecules in 1 cm^3 gas

P_{cell} gas pressure in the Knudsen cell

P_{eq} equilibrium pressure for the reaction studied

P_L Langmuir pressure

R concentration of $N^{14}N^{15}$, in mole fraction $R = \dfrac{(N^{14}N^{15})}{(N_2^{14}) + (N^{14}N^{15}) + (N_2^{15})}$

$S/2$ area of AlN^{14} (and also AlN^{15}) pellet "exposed to gas" in cm^2 (also BN)

t time in sec

T temperature in °K

V volume of Knudsen cell in cm^3

y thickness of layer of solid, in nitrogen atoms, which takes part in vaporization reaction

z thickness of layer of solid, in nitrogen atoms, which takes part in condensation (exchange) reaction

α vaporization coefficient

α' accommodation coefficient

β fraction of gas molecules which hits the surface, sticks, and enters the solid lattice; condensation coefficient

γ atom fraction of N^{15} in a pellet of AlN^{14} (and vice versa) at time t (also BN)

REFERENCES

1. O. Knacke and I. N. Stranski, *Progr. Metal Phys.*, **6**, 181 (1958).
2. J. P. Hirth and G. M. Pound, *J. Chem. Phys.*, **26**, 1216 (1957).
3. I. Langmuir, *Phys. Rev.*, **2**, 329 (1913).
4. R. Speiser and H. L. Johnston, *Trans. Am. Soc. Metals*, **42**, 282 (1950).
5. M. Hoch and D. White, MCC-1023-TR-214 Ohio State University Research Foundation, Columbus, Ohio (October 1956).
6. D. L. Hildenbrand and W. F. Hall, *J. Phys. Chem.*, **67**, 888 (1963).
7. K. Clusius, *Helv. Chim. Acta*, **33**, 2134 (1950).
8. M. Hoch and H. R. Weisser, *ibid.*, **33**, 2128 (1950).
9. F. Weston and H. Ellis, *Trans. Faraday Soc.*, **4**, 61 (1908).
10. A. J. Sofianopoulos, *Bull. Soc. Chim.*, **5**, 616 (1909).
11. R. A. Périéres and R. Bollack, U.S. Patent No. 2,962,359, November 29, 1960.
12. T. Reuner, *Z. Anorg. u. Allgem. Chem.*, **298**, 22 (1958).
13. K. M. Taylor and C. Lenie, *This Journal*, **107**, 308 (1960).
14. D. Ramakrishnan, Ph.D, Thesis, University of Cincinnati, 1967.
15. I. Adams, T. R. Aucoin, and G. A. Wolff, Ultra Purif. Semicond. Mater., Proc. Conf., Boston, Mass., 1961, p. 186 (Publ. 1962).
16. A. A. Giardini, U.S. Bur. Mines Inform. Circular No. 7664 (1953).
17. G. P. Barnard, "Modern Mass Spectrometry," p. 264, Institute of Physics, London (1953).
18. L. H. Dreger, V. V. Dadape, and J. L. Margrave, *J. Phys. Chem.*, **66**, 1556 (1962).

Condensation Coefficients of Refractory Materials

II. NiO

D. Ramakrishnan and M. Hoch

Department of Materials Science and Metallurgical Engineering, University of Cincinnati, Cincinnati, Ohio 45221

ABSTRACT

The condensation coefficient of oxygen in NiO was studied using the isotope exchange technique applied earlier for aluminum nitride and boron nitride. Experiments were carried out in a platinum Knudsen cell and in an aluminum oxide Knudsen cell. Using the aluminum oxide Knudsen cell, the condensation coefficient β for NiO was found to be 1.1×10^{-1} in the temperature range 1700°-1750°K. Using the platinum Knudsen cell, the exchange coefficient reached an equilibrium value of 0.5 because oxygen exchange also took place on the hot platinum surface. It was found also that NiO exchanges with oxygen in the air very slowly at room temperature.

The isotopic exchange technique in combination with the time-of-flight mass spectrometer has been used to determine the condensation coefficients of AlN and BN (1, 2). The purpose of these experiments was to determine whether the method of isotopic exchange devised for nitrides works with oxygen on NiO. The problem was to determine the condensation coefficient of oxygen on NiO. A large number of diffusion experiments are reported in the literature where the oxygen exchange is used to determine the diffusion coefficient of oxygen in metal oxides. The diffusion of oxygen in an oxide of a metal is expected to be a two-step process (3): (*i*) oxygen exchange on the surface, and (*ii*) migration of oxygen into the solid. Experimenters have assumed that the first step takes place faster than the second and that instantaneous equilibrium exists at the solid-gas interface (isotopic composition of oxygen in surface is equal to that in the gas). This assumption will be tested by applying the isotopic exchange technique to nickel oxide. The vaporization of nickel oxide has been the subject of several investigations (4-7). The most recent work is that of Grimley, Burns, and Inghram (8). They used a molybdenum Knudsen cell with an inner liner and lid made of recrystallized morganite alumina. The effusing beam was analyzed by a mass spectrometer. In the temperature range 1575°-1710°K, Ni^+ and O_2^+ were the predominant species in the vapor. They also reported the presence of free nickel on the lids of their Knudsen cells used for vaporization of NiO. Free nickel on the lids of the cell was also observed in this work. The authors concluded that NiO vaporizes primarily by dissociation to the elements.

Theory

The theory and the mathematical treatment of the experimental data of the isotopic exchange technique which is applicable to nitrides and oxides of metal was reported by Hoch and Ramakrishnan in the earlier report cited. The condensation coefficient, β, was obtained from an analysis of the steady-state conditions in the isotopic exchange reactions. First, expressions were derived which define the fractional changes in the solid and vapor compositions resulting from the exchange reactions. Second, a relationship was then established for the time rate of change of γ, the concentration of the contaminating isotope on the surface of the solid. Finally, a relationship was obtained between the concentration of the mixed isotope in the vapor and γ.

The isotopic exchange technique employs a Knudsen effusion cell which contains two samples of the solid which is to be vaporized, each containing a high concentration of a particular isotope. In this work, the solids are NiO^{16} and NiO^{18}. The samples are of equal size and are physically separated. When the cell is heated, the samples vaporize producing a gas with equal concentrations of O_2^{16} and O_2^{18}. The oxygen recondenses, with some of the O_2^{16} condensing on the NiO^{18} sample and becoming incorporated into the solid and vice versa. Since some of the vapor escapes through the orifice, equilibrium is not established and the solids continue to vaporize. Each sample contains some of the other isotope and subsequent vaporization produces gaseous $O^{16}O^{18}$ molecules. The concentration of $O^{16}O^{18}$ increases and the concentration of O_2^{16} and O_2^{18} decreases with time. If the temperature of the cell is held constant, a steady state is obtained. The condensation coefficient, β, can then be calculated from the steady-state values of vapor composition using the relationship

$$\beta = h/S \frac{(O^{16}O^{18})}{[\frac{1}{2} - (O^{16}O^{18}) + y/z]} \quad \text{if} \quad \frac{zh}{yS} >> \beta \qquad [1]$$

where: h = area of effusion hole (cm^2)
S = total exposed area of two pellets in Knudsen cell (cm^2)
$(O^{16}O^{18})$ = steady-state concentration of mixed isotopic molecule in vapor
y = thickness of layer of solid, in oxygen atoms, which takes part in vaporization reaction
z = thickness of layer of solid, in oxygen atoms, which takes part in condensation (exchange) reaction.

No attempt was made to convert to absolute pressures because the isotopic exchange technique does not depend on the knowledge of absolute pressure.

Preparation of Nickel Oxide

Use of the isotopic exchange technique for determining the condensation coefficient of nickel oxide requires a nickel oxide sample with a very high concentration of the atomic weight 18 isotope of oxygen. Commercially available NiO^{18} was obtained from Volk Radiochemicals Company, Burbank, California, and tested in the mass spectrometer. The sample was found to be unsuitable since it was essentially $NiCO_3$ which decomposed on heating to NiO and CO_2 gas. The mass spectrum was characterized by an intense peak at mass 44 which corresponds to CO_2^+. Therefore, it was necessary to prepare NiO^{18} in the laboratory.

Several preparation techniques for NiO are described in the literature (10). The most common method of preparation of NiO is the precipitation of $NiCO_3$ from a nickel salt solution and the thermal decomposition of nickel carbonate to nickel oxide. These wet methods were found unsuitable and the direct oxidation of nickel metal was selected as the most expedient prep-

Key words: nickel oxide, condensation, isotope exchange, vaporization.

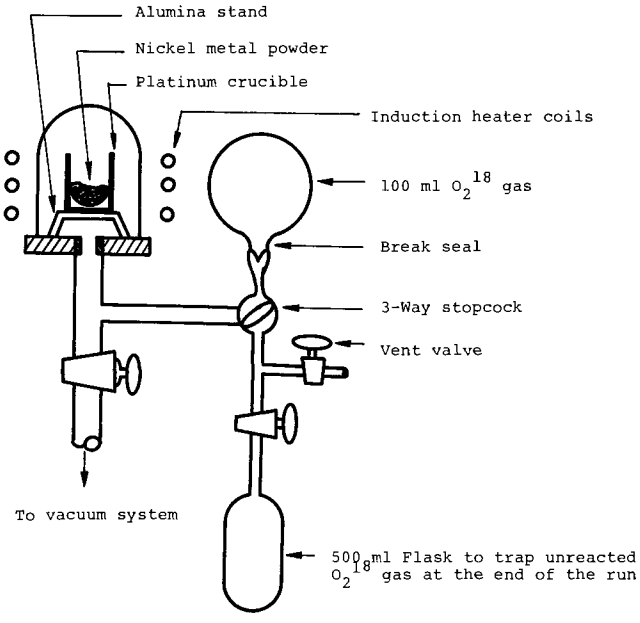

Fig. 1. Apparatus for the preparation of NiO^{18}

aration technique. Since O_2^{18} is available only in limited quantities, it was necessary to develop a preparation technique which would yield a maximum amount of NiO using 100 ml of O_2^{18} gas.

Initial studies indicated that the oxidation of compressed nickel metal powder in a limited volume of oxygen gas at 1 atm pressure is slow at 1300°K. Hence nickel powder was reacted with 100 ml of O_2 gas at NTP in an apparatus shown in Fig. 1 which was constructed to prepare NiO^{16} and NiO^{18}. The apparatus consists of a small quartz bell jar, a vacuum system, a gas inlet, a 500 ml flask to collect unreacted O_2 gas, and a sample heating system. The volume of the system was kept small to conserve oxygen. The nickel powder was placed in an open platinum crucible fabricated from platinum foil. The crucible was heated by an induction heater while sitting on an alumina stand. The alumina stand was coated with platinum paste to avoid any loss of O_2^{18} due to exchange with oxygen atoms in alumina.

Procedure.—Nickel oxide was prepared by introducing 400 mg of nickel metal powder into the platinum crucible, evacuating the whole system to below 5×10^{-5} Torr, degassing the powder under vacuum, admitting the oxygen gas after closing the stopcock connecting the 500 ml flask to the system, and heating the crucible. Within a few minutes of the start of the induction heating, the reaction set in as indicated by a glow inside the crucible. After 5 to 10 min, the glow disappeared and the surface temperature was slowly increased to 1300°K and held for about 2 hr. The surface temperature was corrected for surface emissivity and absorption of the quartz bell jar. The total correction is 108° at 1300°K. At the end of the run, any unreacted oxygen gas was collected in the evacuated flask.

X-ray diffraction powder patterns of the samples were made, which showed the sample was nickel oxide. No nickel lines were present in the powder pattern. Samples for the exchange runs were ground in an agate mortar and were pressed into pellets by using either a 3/16 or a 0.15 in. die. The pellets were degassed in vacuum at 1173°K for 105 min. Generally about 500 mg of the product nickel oxide was obtained starting with 400 mg of nickel metal and 100 ml O_2 gas at NTP. The yield was nearly 100%.

Bogatski (11) reports that NiO exists over the composition $Ni_{0.998}O$-$N_{0.758}O$. Our samples were green in color indicating lower oxygen content in our samples as compared to the oxygen-rich black oxide. Using the equation for vacancy concentration in NiO

$$\frac{Nv}{N} = 0.055\, P_{O2}^{1/6} \exp \frac{-17{,}800}{RT}$$

given by Mitoff (12) and $P_{O2} = 4.22 \times 10^{-6}$ atm (oxygen partial pressure over NiO at 1707°K measured by Grimley *et al.*), one has $x = 3.7 \times 10^{-5}$ in $Ni_{1-x}O$. Thus the deviation in stoichiometry in our samples is believed to be very small. Since R remained constant in the exchange runs, it is believed that the excess Ni(s) in the partially vaporized samples did not affect the results.

Knudsen Cells

Two different Knudsen cells were used to study the exchange reaction. A schematic sketch of the two cells and their inserts for holding the samples is shown in Fig. 2. One of the Knudsen cells was made of platinum. It was 11/16 in. tall and had an ID of ½ in. The thickness of the walls of the cell was 1/32 in. The lid of the cell was 1/16 in. thick and had a hole whose diameter was 0.025 in. The samples were placed in the two platinum inserts.

The other Knudsen cell had an outer cell of molybdenum and a molybdenum lid (1/16 in. thick) and an inner cell fabricated from 97% pure Al_2O_3. The alumina inner cell was ¾ in. tall and had an ID of 7/16 in. The diameter of the hole in the 1/16 in. thick alumina lid was 0.028 in. The samples were placed in an alumina insert.

Materials

Pure nickel metal powder (99.9%) was supplied by Gallard Schlesinger Chemical Manufacturing Corporation, Carle Place, New York.

The isotopic oxygen gas containing 99.6% O^{18} was obtained from Bio-Rad Laboratories, New York, New York.

The platinum Knudsen cell was fabricated by Engelhard Industries, Inc., Newark, New Jersey, and the

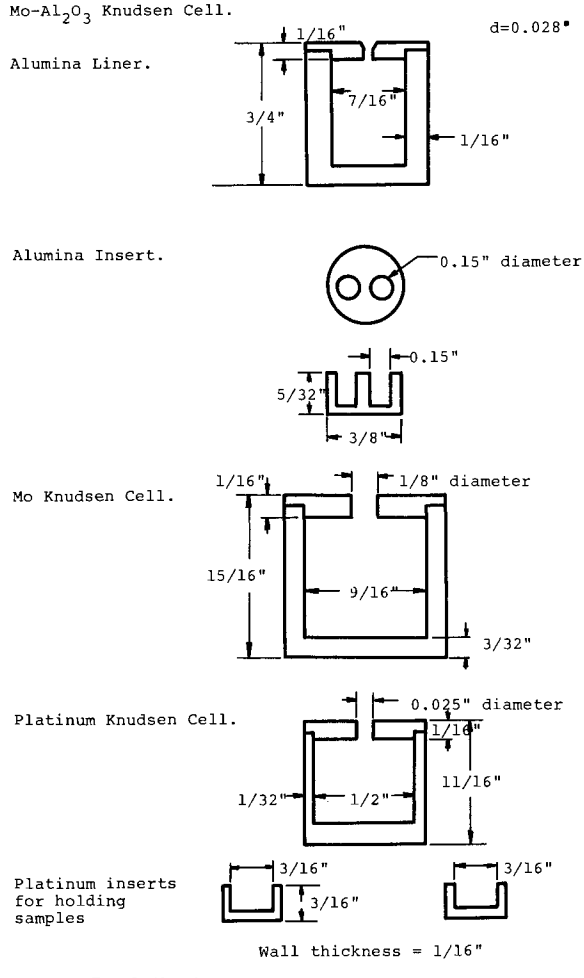

Fig. 2. Knudsen cells and inserts (schematic)

alumina Knudsen cell was supplied by McDanel Refractory Porcelain Company, Beaver Falls, Pennsylvania. The molybdenum Knudsen cell used with the alumina cell was machined in our machine shop.

To prepare NiO^{16} samples, commercial oxygen gas was used which was purified by passing through a liquid nitrogen trap.

Preliminary Experiments

Commercial nickel oxide was heated in the mass spectrometer using the platinum Knudsen cell to identify the vaporizing species. Above 1600°K, the only species detected was O_2^+ at mass number 32. Ni^+ peaks were absent in the mass spectrum. It was concluded that the nickel atoms in the vapor stuck to the walls and the lid of the platinum cell, and thus, they did not effuse through the hole in the lid. When NiO^{16} sample was heated in the molybdenum Knudsen cell with alumina liner, Ni peaks at mass numbers 58, 60, and 62 appeared in the spectrum along with O_2^+ peak at mass 32.

The intensity of O_2^+ (I_{32}) at mass 32 and the intensity of the peak at mass 16 (I_{16}) corresponding to O_2^{++} or O^+ were studied as a function of electron energy. Below 20 eV electron energy, the mass 16 peak disappeared completely. To minimize the dissociation of oxygen molecules to atoms and their recombination in the ion source, the exchange runs were made with 20 eV electron energy. The apparent temperature of the Knudsen cell was measured in degrees Fahrenheit by a disappearing filament type optical pyrometer sighted on the effusion hole through a glass prism and window. The correct temperature was obtained by converting the optical pyrometer readings in degrees Fahrenheit to degrees centigrade and adding the correction for the absorption due to the glass prism and the window. This correction was about 20°C at 1400°C. Sighting on the hole eliminated the need for an emissivity correction.

Experimental Results and Discussion

The first exchange run 1a was made using the platinum Knudsen cell (the detached mass spectrometric data can be obtained from the authors). The degassed NiO^{16} and NiO^{18} pellets were placed in tightly fitted holes drilled in an insert for the cell, and the cell was loaded in the mass spectrometer. The temperature was slowly raised to 1470°K and held there for about 20 min before increasing to 1703°K. The exchange reaction was studied to 1703°K and the intensities of mass peaks 32, 34, and 36 [I_{32}, I_{34}, and I_{36}] corresponding to O_2^{16}, $O^{16}O^{18}$, and O_2^{18} ions were recorded and the temperature measured at 15 min intervals. I_{34} was larger than I_{32} or I_{36} from the beginning of the run. The ratio $R = I_{34}/I_{32} + I_{34} + I_{36}$ was very close to 0.5 right from the beginning of the run and remained constant throughout the run which lasted 135 min. The run was continued (run 1b) the next day for 100 min and R was nearly 0.5 from the start to the end of the run. In both run 1a and run 1b, $I_{32} \approx I_{36}$, which suggests that the background interference at mass 32 was insignificant.

After run 1b, the cell was opened and the contamination of the half-pellets NiO^{16} and NiO^{18} by the other oxygen isotope were investigated. This was done by heating each half-pellet separately and observing the decrease in O^{16} concentration (or O^{18} concentration) with time. The concentration of O^{16} in NiO^{18} pellet was calculated from the ratio of the intensities of mass 34 and mass 36 peaks. Similarly, the O^{18} concentration in NiO^{16} pellet was calculated from the ratio of the mass 34 and 32 peak intensities. At the start, both half-pellets showed a large amount of contamination which decreases with time. For some reason the decrease in contamination in run 1c is not as fast as it is in run 1d.

The value of R was nearly 0.5 initially and it remained constant during the runs 1a and 1b. If every impact of the oxygen gas molecules with the solid nickel oxide results in exchange producing the mixed molecule $O^{16}O^{18}$, the R will be nearly 0.5 and remain constant. The second possibility is that the exchange reaction $O_2^{18}(g) + O_2^{16}(g) \rightarrow 2(O^{16}O^{18})(g)$ would take place on the hot platinum surface (13) of the cell. In either case, equilibrium will be achieved in the cell and R will be 0.5

To investigate the two possibilities, exchange runs 2a and 2b were made using the molybdenum Knudsen cell lined with alumina. In these runs, Ni^+ peaks at mass 58 and 60 were recorded along with mass 32, 34, and 36 peaks. In both the runs, $I_{32} \approx I_{36}$. R started with an initial value of 0.28 and reached a steady-state value of 0.43 after 30 min. The runs were made at an average temperature of 1697°K. During run 2b, the temperature was increased to 1753°K and held for 10 min. R remained constant at 0.43. The results are shown in Fig. 3. At the end of run 2b, the NiO^{16} pellet was removed. Run 2c was made to determine the amount of contamination of the NiO^{18} pellet by O^{16}. Similarly, run 2d was made to determine the amount of contamination of NiO^{16} pellet by O^{18} The results are given in Fig. 4. Both pellets showed a high degree of contamination in the beginning of the runs and then dropped to a nearly constant value. The cell was examined at the end of the run. The inner walls of the alumina cell and the lid developed a bluish coloration.

The Mo-Al_2O_3 cell was heated in the mass spectrometer (run 3) without any sample inside to find the reason for the bluish color of the liner. The mass spectrum consisted of mass 32, 34, and 36 peaks corresponding to the oxygen species and mass 58 and 60 peaks corresponding to the nickel species. Throughout run 3 the ratio R was nearly 0.5. It seems that the metal and the oxygen species adhered to the walls of the alumina liner and desorbed when heated. This desorption could have affected the results of the contamination runs 2c and 2d since oxygen may have desorbed from the walls of the cell while either of the nickel oxide pellets were being heated. If desorption takes place, it makes the data incorrect. Examination of the intensities of the oxygen peaks in runs 2c and 2d shows that desorption did not take place when the cell was heated with the specimen in it. When NiO^{18} pellet alone was heated, I_{36} was several times larger than I_{32} and the intensities of the oxygen peaks were consistent with the extent of contamination by O^{16} that was expected. If the walls of the alumina cell were contributing to the effusion flow, the amount of contamination

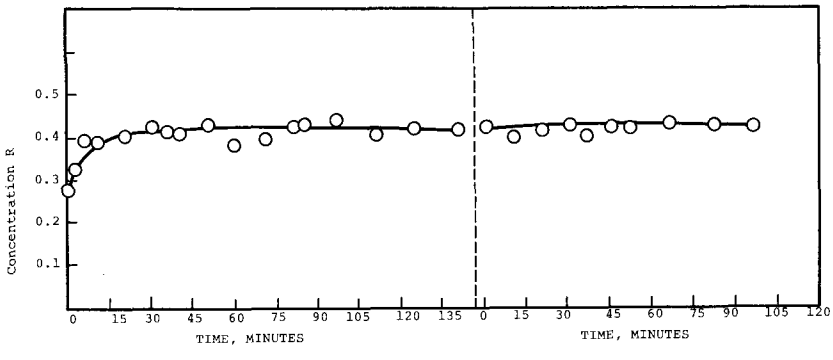

Fig. 3. Runs 2a and 2b. NiO^{16}, NiO^{18} pellets in alumina inserts (Mo-Al_2O_3 cell).

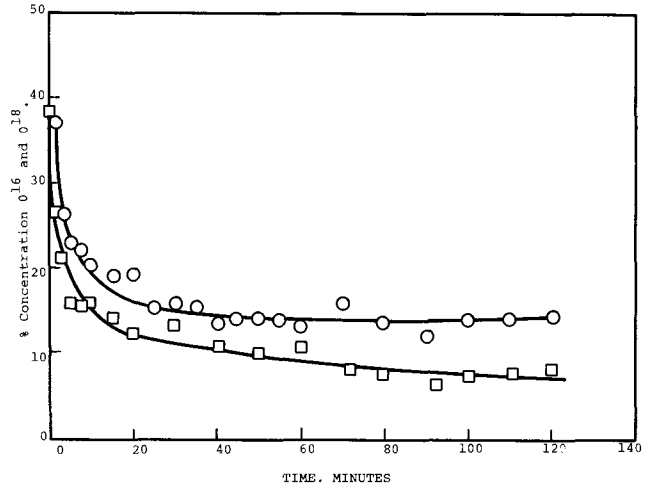

Fig. 4a. Runs 2c and 2d. Separate pellets (NiO^{16} and NiO^{18}) to determine contamination.

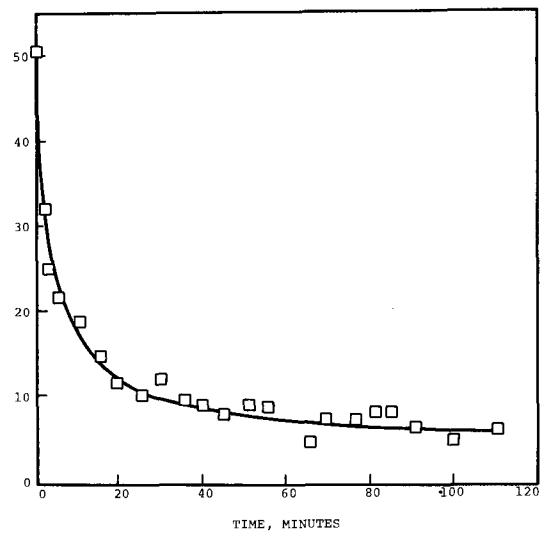

Fig. 4c. Run 1d. NiO^{16} pellet to determine contamination

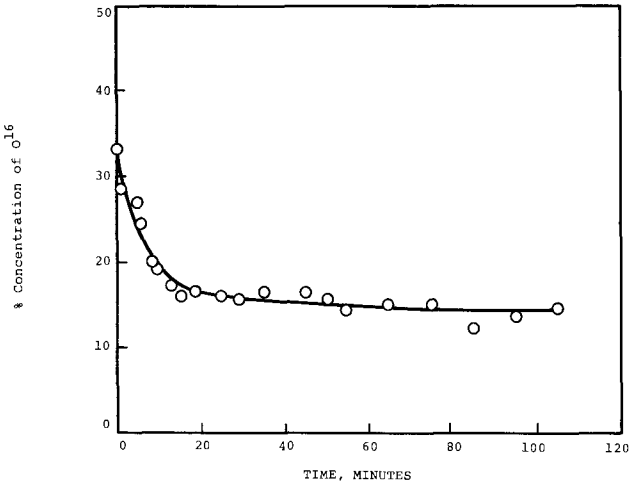

Fig. 4b. Run 1c. NiO^{18} pellet to determine contamination

would have been larger. The decrease in contamination as a function of time would have been less than that observed. Based on these observations, it is reasonable to conclude that any vapor species which stick to the alumina liner desorb only when the empty cell is heated. When the nickel oxide sample is heated in the cell, the sorbed species do not desorb and contribute to the effusion flow.

The O^{18} concentration in NiO^{16} sample was determined immediately after a pellet was made from NiO^{16} powder which was prepared sometime earlier. Run 4 was made by heating the NiO^{16} pellet in the mass spectrometer using the platinum Knudsen cell. This pellet was not used in any of the exchange runs and hence should contain only about 0.2% of O^{18} (natural abundance of O^{18} in oxygen). The O^{18} concentration was 2% at the start of the run and it decreased to less than 1% after 20 min. The same procedure was repeated in run 5 for an NiO^{18} sample (freshly made from NiO^{18} powder) using the platinum cell. The initial concentration of O^{16} in the NiO^{18} sample was 17% which decreased to 6% in the first 20 min of the run. The average concentration of O^{16} was 3-4% throughout the latter part of the run. The $O_2{}^{18}$ gas with which the NiO^{18} powder was prepared may have been contaminated with O^{16} isotope, or the NiO^{18} sample may have picked up some O^{16} during its preparation. In either case, the concentration of O^{16} in the NiO^{18} sample would have remained constant as a function of time in run 5. But the O^{16} concentration in the NiO^{18} sample was initially high and it decreased rapidly to a steady-state value. This decrease suggests that NiO^{18} exchanges slowly with atmospheric oxygen even at room temperature. The rapid decrease in the O^{16} content with time was due to the elimination of the surface layers contaminated with O^{16} isotope because of vaporization of the NiO^{18} sample.

Since the steady-state value of R in runs 2a and 2b made with the Mo-Al_2O_3 cell was 0.43 and not 0.5, it is improbable that each impact of the oxygen molecule with NiO solid results in the exchange. The reason for R being equal to 0.5 in runs 1a and 1b made with the platinum cell is that the exchange was taking place on the hot platinum surface.

The condensation coefficient of NiO was calculated taking the steady-state value of R as 0.43 and substituting the values of h (the area of the effusion hole) and S (the surface area of nickel oxide exposed to gas) in Eq. [1]. The results are given in Table I. The diffusion of oxygen in the solid NiO is fast; and hence, the depth of penetration z will be large, in which case $y/z \simeq 0$. The value of β (the condensation coefficient) is 1.1×10^{-1}.

Conclusions

1. The isotopic exchange technique is applicable to solids like oxides which have larger condensation coefficients than nitrides like AlN and BN.

2. A method has been developed to prepare required amounts of NiO^{18} by heating nickel metal powder in a limited volume of $O_2{}^{18}$ gas.

Table I. Calculation of the condensation coefficient of NiO from the steady-state $O^{16}O^{18}$ concentration

Sample	Cell	S, cm^2	h, cm_2	R,* steady-state	β $y/z = 0$	β $y/z = 0.5$
NiO^{16} and NiO^{18}	Mo-Al_2O_3	0.23	3.97×10^{-3}	0.43	1.07×10^{-1} 1.1×10^{-1}	2.31×10^{-2} 2.3×10^{-2}

* $R = \dfrac{I_{34}}{I_{32} + I_{34} + I_{36}}$.

3. The condensation coefficient of NiO is 1.1×10^{-1} in the temperature range 1697°-1753°K.

4. The exchange reaction $O_2^{18}(g) + O_2^{16}(g) \rightarrow 2(O^{16}O^{18})$ takes place on a hot platinum surface.

5. NiO^{18} when exposed to air at room temperature slowly exchanges oxygen and picks up O^{16}.

6. Under the conditions obtained in this investigation on the NiO system, the assumption that instantaneous equilibrium exists at the solid-gas interface (isotopic composition of oxygen in the surface is equal to that in the gas) is not valid.

Acknowledgment

This work was supported in part by the Air Force Materials Laboratory, Wright Patterson Air Force Base, Ohio 45433, under Air Force Contract No. AF 33(615)3420.

Manuscript submitted Jan. 12, 1970; revised manuscript received ca. March 1, 1971. This was Paper 212 presented at the Detroit Meeting of the Society, Oct. 5-9, 1969.

Any discussion of this paper will appear in a Discussion Section to be published in the June 1972 JOURNAL.

REFERENCES

1. M. Hoch and D. Ramakrishnan, *This Journal*, **118**, 1204 (1971).
2. D. Ramakrishnan, Ph.D. Thesis, University of Cincinnati, 1967.
3. H. S. Edwards, A. F. Rosenberg, and J. T. Bittel, Thorium Oxide-Diffusion of Oxygen, Compatibility with Borides, and Feasibility of Coating Borides by Pyrohydrolysis of Metal Halides, ASD-TDR-63-635, Air Force Materials Laboratory, Aeronautical Systems Division, Wright-Patterson Air Force Base, July 1963.
4. L. Wohler and O. Balz, *Z. Electrochem.*, **27**, 406 (1921).
5. R. N. Pease and R. S. Cook, *J. Am. Ceram. Soc.*, **48**, 1199 (1926).
6. A. Skapski and J. Dabrowski, *Z. Electrochem.*, **38**, 365 (1932).
7. H. L. Johnston and A. L. Marshall, *J. Am. Chem. Soc.*, **62**, 1383 (1940).
8. R. T. Grimley, R. P. Burns, and M. G. Inghram, *J. Chem. Phys.*, **35**, 551 (1961).
9. Ref. (1), Eq. [23].
10. C. A. Jacobson, "Encyclopedia of Chemical Reactions," Vol. IV, Reinhold Publishing Corp., New York (1948).
11. D. P. Bogatski, *Zh. Obshch. Khim.*, **21**, 9 (1951).
12. S. P. Mitoff, *J. Chem. Phys.*, **35**, 882(1961).
13. K. Clusius and G. Dickel, *Z. Physik. Chem.*, **193**, 274 (1944).

Analysis of the Exchange Reaction Between Nitrogen and Aluminum Nitride

Emile Rutner and E. J. Rolinski

Materials Physics Division, Air Force Materials Laboratory Wright-Patterson Air Force Base, Ohio 45433

ABSTRACT

A model has been proposed to simulate the rate of isotopic exchange of a solid with a gas formed by its decomposition. The model considers the effect of the vaporization and condensation reactions, accompanied by effusion of the gas from a Knudsen cell, on the measured rate of exchange. The reaction rate constants for the vaporization of nitrogen from AlN and the condensation of N_2 and gaseous Al on solid AlN, at near equilibrium conditions, have been calculated. The condensation and the vaporization coefficients have been formulated in terms of the kinetic processes. The model has been applied to data of Hoch and Ramakrishnan (1) for the isotopic exchange reaction of nitrogen on aluminum nitride.

In the study of vaporization and condensation reactions it is desirable to determine the kinetics of such reactions at the equilibrium pressure since in many cases the reaction rates are dependent on the pressure of the gas in contact with the solid. One method for doing this is to study the isotopic exchange reaction between the gas and the solid. Such a reaction was carried out by Hoch and Ramakrishnan (1), who studied the time rate of isotopic exchange of N_2 gas with AlN and calculated an exchange coefficient from their data which they equated to a vaporization coefficient.

To fully utilize the data generated in (1) a kinetic model is proposed herein which takes into account the kinetics of the solid-gas reactions taking place. Since models for the vaporization and condensation of solids cannot be formulated in general terms, because the particular forms which the rate equations assume are determined by the kinetics of the reactions taking place, it is necessary in formulating a model to express the exchange reaction rates in terms of the kinetics of the processes involved. For the particular experimental arrangement utilized in (1), this required a model which described the processes involved in the vaporization of the solid, the condensation of the gas to form the solid, and the flow of the gas from the Knudsen cell.

Key words: Knudsen cell, vaporization, condensation, isotopic exchange, model.

Model for Isotopic Exchange of N_2 with AlN Accompanied by Flow from a Knudsen Cell

Utilizing an experimental arrangement as shown in Fig. 1, Hoch and Ramakrishnan (1) measured mass

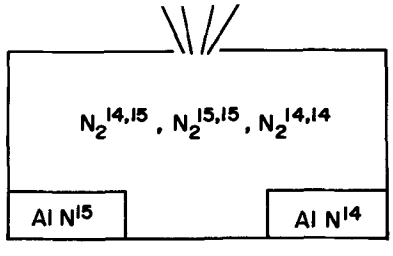

Fig. 1. Arrangement of aluminum nitride pellets in the Knudsen cell. AlN^{14} and AlN^{15} are pellets initially composed of the N^{14} isotope and N^{15} isotope, respectively.

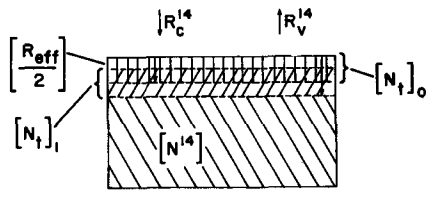

Fig. 2. Relation between the positions of reaction zone $[N_t]$ at time zero, $[N_t]_o$, and at some later time, $[N_t]_1$. Rate of mass motion of the zone is equal to one half of the rate of effusion of nitrogen plus aluminum.

spectrometrically, as a function of time, the fraction of N_2^{29} molecules, $[N_2^{29}]/[N_2^{28}] + [N_2^{29}] + [N_2^{30}]$, in the gas phase generated by the decomposition of two pellets of AlN in a Knudsen cell. Originally, one of the pellets was composed entirely of AlN^{14}(I) and the other pellet was composed of AlN^{15}(II). When the pellets were heated in a Knudsen cell a gas phase was generated which at zero time was composed of equal concentrations of N_2^{28} and N_2^{30}; and which during the course of time of the experiment became enriched with N_2^{29}, as a result of isotope exchange between the two pellets. The model proposed herein accounts for the time rate of change of the isotopic distribution of N atoms in the N_2 molecules.

Since the change in the isotopic composition of the gas is accompanied by a change in the isotopic composition of the solid any model proposed must account for the simultaneous changes in the composition of the gas and the solid. The change in the composition of the solid is actually limited to a region defined as a reaction zone as shown in Fig. 2. The reaction zone is assumed to be of constant volume. The zone recedes into the unreacted portion of the solid as the sample evaporates, and thus becomes enriched by N^{14} in the case of pellet I and N^{15} in the case of pellet II. The actual thickness of the zone is physically determined by the volume of the solid confined to the gas-solid interface. The gas-solid interface is determined by the control volume in which diffusion is fast enough so that there is thorough mixing between (*a*) the nitrogen that is in the zone, (*b*) the nitrogen that is added to it by the motion of the zone into the unreacted solid, and (*c*) the nitrogen that condenses from the gas phase into the zone. The total change in the composition of the zone can therefore be attributed to the following factors, assuming that the nitrogen gas is composed of N_2^{28}, N_2^{29}, and N_2^{30} molecules:

A. Vaporization of nitrogen from the zone.

B. Condensation of nitrogen from the gas phase onto the pellet.

C. Addition of nitrogen to the zone from unreacted solid.

On the other hand the change in gas phase composition is due to:

A'. Vaporization of nitrogen from each of the pellets into the gas phase.

B'. Condensation of nitrogen from the gas phase onto the pellets.

C'. Flow from the gas phase through the orifice of the Knudsen cell.

Change in Composition of the Solid

Reaction [1] represents the exchange of nitrogen isotope (j) with AlN^i, solid, where i and j represent the two different nitrogen isotopes

$$AlN^i + N_2^{jj} \rightarrow AlN^j + N_2^{ij} \quad [1]$$

To obtain a rate expression for the vaporization process [1] above, the over-all reaction must be represented by a mechanism. The mechanism is depicted by the following steps

$$[Al]_s \rightleftarrows [Al]_{ads} \quad [2]$$

$$[N^i]_s \rightleftarrows [N^i]_{ads} \quad [3]$$

$$[Al]_{ads} + [N^i]_{ads} + [N^j]_{ads} \rightleftarrows [AlN_2^{ij}Al]_{ads}^* \quad [4]$$

$$[AlN_2^{ij}Al]_{ads}^* \rightarrow [Al]_g + [N_2^{ij}]_g \quad [5]$$

Steps [2] and [3] represent the motion of (Al) and (N) atoms, respectively, from a lattice site in the solid (s) to an adsorbed site (ads) on the surface of the solid. Step [4], represents the formation of an activated complex involving N_2, which is required to satisfy the activated complex model for the reaction rate [2]. Step [5] represents the dissociation of this complex to form Al and N_2^{ij} in the gas phase. It should be noted that the nature of the complex requires that the adsorption site for $[N_2]$ on $[AlN]_s$ be Al atoms.

The steps in the condensation process (*B* and *B'* above) are given as follows

$$[Al]_g \rightleftarrows [Al]_{ads} \quad [6]$$

$$[Al]_{ads} + [N_2^{ij}]_g \leftrightharpoons [AlN_2^{ij}Al]_{ads}^* \quad [7]$$

$$[AlN_2^{ij}Al]_{ads}^* \rightarrow [Al]_s + [N^i]_s + [N^j]_s \quad [8]$$

Reactions [6] and [7] represent the adsorption of aluminum and nitrogen on the surface of aluminum nitride. Reaction [8] represents the over-all reaction leading to reverse of reactions [4], [3], and [2]. To utilize the data, the observed rates must be expressed as the rates of the reversible phenomenological reactions [9] for vaporization and condensation.

$$[Al]_s + [N^i]_s + [N^j]_s \underset{c}{\overset{v}{\rightleftarrows}} [Al]_g + [N_2^{ij}]_g \quad [9]$$

The rate of formation of $[N_2^{ij}]_{gv}$ by vaporization from a single pellet of solid AlN is given by Eq. [10].

$$\left(\frac{d[N_2^{ij}]}{dt}\right)_{gv} = \frac{1}{\sigma_{ij}} k_v[N^i]_s[N^j]_s[Al]_s^2 \frac{A_s}{V_c} \quad [10]$$

In Eq. [10], t is time, k_v is the rate constant for vaporization, σ_{ij} is the symmetry number of ij-th species; the bracketed quantities represent concentration, the subscript (s) refers to the solid phase, A_s represents the area of a single pellet, and V_c represents the gas volume of the Knudsen cell. All symbols are defined in Table I.

The condensation reaction can be expressed as Eq. [11] where the symbol (gc) represents change in gas phase concentration due to condensation, and k_c represents the reaction rate constant for condensation

$$-\left(\frac{d[N_2^{ij}]}{dt}\right)_{gc} = k_c[N_2^{ij}]_g[Al]_g^2 \frac{A_s}{V_c} \quad [11]$$

Defining $\gamma = [N^{14}]_s/([N^{14}]_s + [N^{15}]_s)$, the fraction of nitrogen atoms present in the solid reaction zone as N^{14} isotope, the time rate of change of γ is given by [12], letting $[N_t] = [N^{14}]_s + [N^{15}]_s$, the total number of atoms of nitrogen per square centimeter of reaction zone, and $\gamma_o = \gamma(t = 0)$.

$$[N_t]_s \frac{d\gamma}{dt} = -k_v[Al]_{ads}^2([N^{14}]_s^2 + [N^{14}]_s[N^{15}]_s) + k_c[Al]_{ads}^2([N_2^{14,15}]_g + 2[N^{14,14}]_g)K_a^2 + B\frac{W_h A_h \gamma_o}{A_s}([N_2^{14,15}]_g + 2[N_2^{14,14}]_g) \quad [12]$$

The last term in Eq. [12] represents the mass loss rate of nitrogen from the pellets due to effusion of nitrogen molecules from the Knudsen cell. In Eq. [12], K_a is the equilibrium constant for Eq. [6]; W_h is the Clausing factor for the Knudsen cell effusion [3], A_h is the area of the effusion hole, and $B = (2\pi M/RT)^{-1/2}$, M being the molecular weight of the effusing species, R the gas constant, and T the temperature, °K. Dividing by $[N_t]$, using the ratio $(\gamma/1-\gamma) = [N^{14}]_s/[N^{15}]_s$, and the stoichiometric relation for the concentration of N^{14} as atoms in the gas phase in terms of nitrogen molecules,

Table I. Symbols and values of experimental and calculated quantities

Symbol	Definition	Value
ads (subscript)	adsorbed	
[Al]	Aluminum atom concentration	
A_c	Cross-sectional area of Knudsen cell	0.986 cm^2 [a]
A_h	Area of Knudsen cell effusion hole	8.55×10^{-4} cm^2 [a]
A_s	Area of sample per pellet	0.180 cm^2 [a]
B	$RT(2\pi MRT)^{-1/2}$	2.85×10^4 cm × sec^{-1} at 1786°K [a]
e (subscript)	Denotes equilibrium conditions	
g (subscript)	Refers to gas phase	
h (subscript)	Related to effusion hole	
h	Planck's constant	6.63×10^{-27} ergs × sec [b]
I	Ratio $([N_2^{14,15}]/[N_2^{14,15}] + [N_2^{14,14}] + [N_2^{15,15}])_g$	
$I(\infty)$	I at $t = \infty$	0.4 [a]
k	Boltzmann constant	1.38×10^{-16} ergs × $(°K)^{-1}$ [b]
k_c	Reaction rate constant for condensation	2.08×10^{-27} $molecules^{-2}$ × cm^7 × sec^{-1} at 1786°K
k_v	Reaction rate constant for vaporization	2.84×10^{-43} $molecules^{-3}$ × cm^6 × sec^{-1} at 1786°K [c]
K_a	Equilibrium constant	$K_a = [Al]_{ads}/[Al]_g$
L	Lodschmidt's number	6.06×10^{23} molecules/mole [b]
M	Molecular weight	As given in text
N_1	Molecules in single layer	2.4×10^{15} atoms × cm^{-2} [e]
N_t	Total molecules in reaction zone	2.4×10^{20} [c]
$[N_2^{ij}]_g$	Concentration of nitrogen molecules of isotopic mixture of atomic weight i and j	
$[N^i]$	Refers to concentration of atoms of isotope of atomic weight i	
$[N_2]_g$	Concentration of N_2 molecules in the gas phase	2.58×10^{13} molecules × cm^{-3}
$[N_2]_{ge}$	Concentration of N_2 molecules in the gas phase at equilibrium	1.12×10^{14} molecules × cm^{-3} at 1786°K [ref. (6)]
$(P_e)_{1786}$	Equilibrium pressure at 1786°K	8.1×10^{-5} atm [ref. (6)]
$(P_c)_{1786}$	Pressure measured at 1786°K	1.9×10^{-5} atm [ref. (6)]
R	Gas constant	erg × $mole^{-1}$ × $(°K)^{-1}$
s (subscript)	Refers to solid sample	
sI (subscript)	Refers to original pellet which was AlN^{14}	
sII (subscript)	Refers to original pellet which was AlN^{15}	
t	Time	sec
T	Temperature	1786°K [a]
V_c	Volume of cell	0.836 cm^3 [a]
W_h	Clausing factor for hole	0.323 [a,d]
α_c	Condensation coefficient	2.7×10^{-3} [e]
α_v	Vaporization coefficient	2.7×10^{-3}
γ	Fraction of atoms which are N^{14} in reaction zone	$[N^{14}]_s/[N_t]_s$

[a] Observed experimentally in ref. (1).
[b] Physical constants.
[c] Obtained from calculations reported herein.
[d] Calculated according to ref. (3).
[e] Calculated from physical properties, ref. (13).

i.e., $[N^{14}]_g = \gamma_0([N_2^{29}]_g + 2[N_2^{28}]_g)$, Eq. [12] can be solved to give [13]. The concentration of $[N^{14}]_g$ is independent of time, if the temperature is a constant

$$\gamma = \frac{K_4}{K_1}\exp -(K_1 t) + \frac{K_3 + K_2}{K_1} \quad [13]$$

Where the constants are defined as

$$K_1 = k_v[N_t]_s[Al]_{ads}^2 \quad [14]$$

$$K_2 = \frac{BW_hA_h[N^{14}]_g}{[N_t]A_s} \quad [15]$$

$$K_3 = k_cK_a^2[Al]_{ads}^2[N^{14}]_g \quad [16]$$

$$K_4 = K_1\gamma_0 - K_2 - K_3 \quad [17]$$

Change of Gas Phase Composition

Relation [13] can now be used in the determination of the gas phase composition as a function of time. Referring to steps *A'*, *B'*, and *C'* above, the contributions of these processes must be added to determine the total rate of change in gas composition. If the fraction of N_2^{29}, nitrogen molecules in the gas phase is defined as $I = [N_2^{29}]_g/\Sigma[N_2^{ij}]_g$, where $\Sigma[N_2^{ij}]_g = [N_2^{28}]_g + [N_2^{29}]_g + [N_2^{30}]_g$, the change in I with time due to the effects of both pellets can be expressed as Eq. [18]

$$\frac{dI}{dt} = \frac{2k_v[Al]_{ads}^2[N_t]^2A_s}{V_c[\Sigma N_2^{ij}]_g}(\gamma - \gamma^2) - \frac{[N_2^{29}]_gA_s}{V_c[\Sigma N_2^{ij}]_g}\left[2k_c[Al]_g^2 + \frac{BW_hA_h}{A_s}\right] \quad [18]$$

A solution of this equation is obtained by substituting Eq. [13] for γ, and integrating to obtain Eq. [19]

$$I = \frac{1}{[\Sigma N_2^{ij}]_g}\left(\frac{K_5K_8}{2K_1 - K_9}\exp -(2K_1t) + \frac{K_8K_6}{K_1 - K_9}\exp -(K_1t) + K_{10}\exp -(K_9t) + \frac{K_8K_7}{K_9}\right) \quad [19]$$

where the constants are defined in terms of quantities used previously.

$$K_5 = \frac{K_4^2}{K_1^2} \quad [20]$$

$$K_6 = \frac{K_4}{K_1} - \frac{(K_3 + K_2)^2}{K_1^2} \quad [21]$$

$$K_7 = \frac{K_3 + K_2}{K_1}\left[1 - \frac{K_3 + K_2}{K_1}\right] \quad [22]$$

$$K_8 = \frac{2k_v[Al]_{ads}^2[N_t]^2A_s}{V_c} \quad [23]$$

$$K_9 = \frac{2k_c[Al]_{ads}^2K_a^2A_s}{V_c} + \frac{BW_hA_h}{V_c} \quad [24]$$

Utilizing the initial condition, *i.e.*, $I_0 = ([N_2^{29}]/[\Sigma N_2^{ij}])_g = 0$ at $t = 0$, an expression for K_{10} can be obtained. The measured value of I at $t = \infty$, *i.e.*, $I(\infty) = 0.4$, is the steady-state value which is less than the equilibrium value of I; *i.e.*, $I_e(\infty) = 0.5$.

Referring to Eq. [13], on substituting the equilibrium value of $\gamma = \gamma_e = 0.5$ obtained at $t = \infty$, a relation between the equilibrium gas concentration, $[\Sigma N_2^{ij}]_{ge}$, and the reaction rate constants can be obtained. The expression is

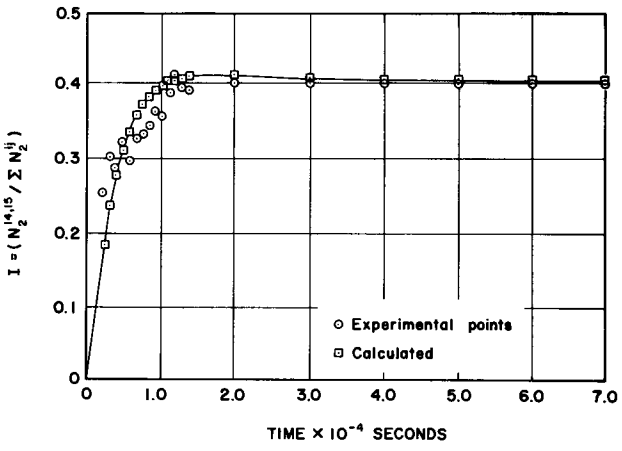

Fig. 3. Best fit to experimental data from ref. (1). Utilizing Eq. [19] or for $I(t)$, at a pressure equal to the equilibrium pressure of nitrogen, 8.1 x 10^{-5} atm at 1786°K, and k_c = 2.08 x 10^{-27}.

$$\frac{k_v}{k_c} = \frac{2[\Sigma N_2^{ij}]_{ge} K_a^2}{[N_t]^2} \qquad [25]$$

Utilizing Eq. [25], the number of unknown parameters in Eq. [19] is reduced to two; *i.e.* N_t and k_c.

Discussion

The best fit for the values of k_c and N_t utilized to reproduce the experimental results are given in Table I and Fig. 3. The value of $[N_t]$ indicated that the reaction zone is a region 10^5 atoms thick per square centimeter, or that a zone containing this number of atoms per square centimeter is required to give a rate of exchange with the gas phase nitrogen which is rapid enough to reproduce to experimental data. It should be noted that if the actual zone becomes too thick the rate of exchange approaches zero due to the slow mixing by diffusion of the atoms in the unreacted portion of the solid with the atoms already in the zone.

Estimation of the reaction rate constant for vaporization.—In order to determine the value of k_v it was necessary to estimate the concentration of $[Al]_{ads}$ on the surface on the AlN. This was done by utilizing the activated complex reaction rate theory (4) and applying it to adsorption of atoms on the surface.

$$\text{Velocity of desorption} = [Al]_{ads} \frac{kT}{h} \frac{F+}{F_a} \exp - E_2/RT \qquad [26]$$

where h is Planck's constant, $F+$ is the partition function for the activated complex, F_a is the partition function for the adsorbed species, and E_2 is the energy of activation for desorption. If it is assumed that $F_a = F+$ then the rate of desorption is equal to the rate of vaporization, and they may be estimated from the vapor pressure of [Al] over the [AlN]. If it is further assumed that the rate of vaporization is the equilibrium rate, and that a stoichiometric relation exists between the rate of desorption of N_2 and Al, the rate of vaporization per square centimeter of sample is given by

$$-\left(\frac{d[Al]}{dt}\right)_{ve} = 2k_c[N_2]_{ge}[Al]_{ge}^2/V_c \qquad [27]$$

$$= \frac{8k_c[N_2]_{ge}^3}{V_c} \qquad [28]$$

Utilizing the constants in Table I the rate of vaporization was found to be 2.8 x 10^{16} atoms x cm^{-2} x sec^{-1}.

The value of E_2 (50 kcal/mole) was estimated by taking one-half of the heat of atomization of Al from AlN. This value was obtained by considering that an adsorbed Al atom is bound by only three bonds as required by the form of the activated complex. The calculated concentration of adsorbed aluminum atoms was: $[Al]_{ads}$ = 1.03 x 10^9 atoms x cm^{-2}. Utilizing this value in Eq. [25] a value of k_v = 2.84 x 10^{-43} was obtained.

Values of the vaporization coefficient (α_c) and condensation coefficient (α_v) were found by using the following relations (5)

$$\alpha_v = \frac{\text{observed rate of vaporization}}{\text{maximum possible rate of vaporization}} \qquad [29a]$$

$$\alpha_c = \frac{\text{rate of condensation}}{\text{rate of molecular collision with the surface}} \qquad [29b]$$

The maximum rate of vaporization is the equilibrium rate which is equal to the condensation rate at equilibrium. The maximum possible condensation rate is the rate of collision with the surface.

Considering the vaporization and condensation of N_2 molecules the following expressions can be written for α_c and α_v

$$\alpha_v(N_2) = \frac{2k_v[Al]_{ads}^2\,[N_t]^2}{B[\Sigma N_2^{ij}]_{ge}} \qquad [30]$$

$$\alpha_c(N_2) = \frac{k_c[Al]_{ads}^2 K_a^2 [\Sigma N_2^{ij}]_g}{B[\Sigma N_2^{ij}]_g} \qquad [31]$$

The calculated value of α_v equals α_c = 2.7 x 10^{-3}. These compared with the values of α_c estimated in ref. (1) to be 5 x 10^{-3}, and in ref. (6) to be 2 x 10^{-3}. In general, equal values for α_c and α_v are obtained when the activated complex is the same for the vaporization reaction as for the condensation reaction. This is so, as noted in Eq. [4] and [8] for AlN.

Thermodynamics of reactions used.—An examination of the significance of the thermodynamic quantities involved in the reactions which were used to determine the equilibrium concentrations and to guide the formulations of the kinetics led to the following results. The value of the equilibrium constant for the gas phase isotopic equilibrium is derived in the manner described in Eq. [7]. The only difference in the partition functions of the molecules N_2^{ij} is that the rotational partition function differs by the value of the symmetry number; *i.e.*, σ_{ij} equals 1 for $i \neq j$ and equals 2 for $i = j$. This leads to a value of the equilibrium constant K_p = 4 for reaction [32].

$$N_2^{30} + N_2^{28} \rightleftharpoons 2N_2^{29} \qquad [32]$$

The equilibrium ratio then becomes I_e = 0.5. The measured value of $I(\infty)$ = 0.4, is less than I_e. This difference is due to flow from the Knudsen cell which maintains the steady-state pressure in the cell lower than the equilibrium pressure.

The binding energy of Al atoms to the surface of AlN was estimated as follows: To maintain congruency in the vaporization processes over a temperature range, the heat of vaporization per Al atom must be equal to one-half the heat of vaporization per nitrogen molecule. Therefore, the heat of reaction for [33] which equals to the heat of vaporization of Al atoms plus half of the heat of vaporization of nitrogen molecules must be equal to 1.5 times the heat of vaporization of Al from AlN. Reference (6) gives a value of 150.11 kcal for $\Delta H°$ for [33] at 1786°K, the temperature of the experiments.

$$[AlN]_s \rightarrow [Al]_g + \tfrac{1}{2}[N_2]_g \quad \Delta H°_{1786°} = 150.11 \text{ kcal} \qquad [33]$$

The heat of vaporization of $(N_2/2)$ from AlN must, therefore, be 50 kcal. Half of the heat of vaporization of Al from AlN is assumed to equal the binding energy of Al atoms on the surface of AlN and, therefore, is equal to 50 kcal. The fraction one-half is based on the

assumption that only one-half of the normal bonds in $[AlN]_s$ are binding the Al atom to the surface.

An examination of the results (Fig. 3) indicates that the mechanism proposed which involves the activated complex $[AlN_2Al]^*$ is consistent with the experimental results, and that the value of the vaporization and condensation coefficients obtained, $\alpha = 2.7 \times 10^{-3}$, is in agreement with that obtained in ref. (1); *i.e.*, $\alpha = 2 \times 10^{-3}$, and compares reasonably well with that found in ref. (6); *i.e.*, $\alpha = 5 \times 10^{-3}$. The model also predicts a variation in condensation rate of N_2 with the partial pressure of Al, and that the condensation and vaporization coefficients are a function of the pressures of Al and N_2. Although not shown in Fig. 3, the variation of the parameter $[N_t]$ indicated that the model may give results which are not physically possible for very large values of N_t.

Use of the Motzfeldt equation for Knudsen cell flow.— The calculation was extended to include the Motzfeldt formulation to describe the flow from a Knudsen cell (9). These equations take into account the effect of the Clausing factor of the cell on the pressure distribution inside the cell. By combining the Motzfeldt equations with the equations describing the kinetics of the reaction taking place as proposed by Rutner (10), the results obtained did not significantly differ from those shown in Fig. 3, and as noted in Table I. A complete solution of these equations is given in ref. (11).

Conclusions

A model which simulates the change in isotopic compositions of a gas in a Knudsen cell due to vaporization from and condensation on a solid, accompanied by effusion from the cell has been proposed and applied to the data in ref. (1) for the exchange of N_2 on AlN. This model was able to give reaction rate constants for the vaporization and condensation reactions, and vaporization (α_v) and condensation (α_c) coefficients. The value of the coefficients found $\alpha_c = \alpha_v = 2.7 \times 10^{-3}$ agree with previously reported values. It can, therefore, be concluded that the model describes the processes involved in the isotopic exchange reaction of N_2 on AlN.

Acknowledgment

The authors wish to thank Professor M. Hoch for discussions during the course of this research, and for providing the experimental data before publication; and to Mr. Thomas E. Duvall for programming the computations (12).

Manuscript submitted Jan. 12, 1970; revised manuscript received *ca.* Sept. 22, 1970. This was Paper 210 presented at the Detroit Meeting of the Society, Oct. 5-9, 1969.

Any discussion of this paper will appear in a Discussion Section to be published in the June 1972 JOURNAL.

REFERENCES

1. M. Hoch and D. Ramakrishnan, U.S. Air Force Materials Laboratory Report No. AFML-TR-65-359 (1965).
2. S. Glasstone, K. J. Laidler, and Henry Eyring, "The Theory of Rate Processes," Chap. I, p. 1, McGraw-Hill Book Co., New York (1941).
3. R. D. Freeman, "Molecular Flow and the Effusion Process in the Measurement of Vapor Pressures," ASD-TR-63-754, AFML, WPAFB, Ohio 45433.
4. Ref. 2, pp. 353-355.
5. O. Knacke and I. N. Stranski, "Progress in Metal Physics," B. Chalmers and R. King, Editors, Vol. 6, chap. 5, Pergamon Press, Ltd., London and New York (1956).
6. D. L. Hildenbrand and W. F. Hall, *J. Phys. Chem.*, **67**, 888 (1963).
7. J. E. Mayer and M. G. Mayer, "Statistical Mechanics," pp. 209-213, John Wiley & Sons, Inc., New York (1940).
8. D. R. Stull, Editor, "JANAF Thermochemical Tables," Advanced Research Projects Agency, Washington, D. C.
9. K. Motzfeldt, *J. Phys. Chem.*, **59**, 139 (1955).
10. E. Rutner in "Condensation and Vaporization of Solids," p. 159, E. Rutner, P. Goldfinger, and J. P. Hirth, Editors, Gordon and Breach, New York (1964).
11. E. Rutner and E. J. Rolinski, U.S. Air Force Materials Laboratory Report No. AFML-TR-68-120 (1970 rev.).
12. T. E. Duvall, "A Least Squares Fit with an Approximation Function that Requires a Large Range of Numbers," Report ASNCD I.M.-68-001, Directorate of Computation Services, Wright-Patterson AFB, Ohio 45433.
13. C. D. Hogness, Editor, "Handbook of Chemistry and Physics," Chemical Publishing Co., Cleveland, Ohio (1964).

An Analysis for Si Contamination in GaP

L. C. Luther

Bell Telephone Laboratories, Incorporated, Murray Hill, New Jersey 07974

and H. W. Verleur

Bell Telephone Laboratories, Incorporated, Reading, Pennsylvania 19604

ABSTRACT

Chemical transport of solid GaP using HCl as reactant often results in the formation of a voluminous residue conforming to the shape of the initial charge. Analysis by x-ray fluorescence showed such residues to consist primarily of silicon, probably as SiO_2. It was shown that the transport reaction did not introduce extraneous SiO_2 from vapor phase reactions with the quartz liner. In addition it was demonstrated that silicon dissolved in gallium could be almost completely recovered as a SiO_2 residue. Thermodynamic considerations are presented to show that unintentional or deliberate moisture contamination of the reactants is required to prevent SiO_2 losses. The method is proposed as a quantitative tool for determination of Si content in Ga, GaP, and GaAs with a sensitivity of $\geq 5 \times 10^{16}$ atoms/cc. It was applied to analyze polycrystalline GaP and single crystals of GaP grown from this material by the Liquid Encapsulated Czochralski (LEC) technique. The analysis confirmed that Si doping of the LEC crystals by the quartz crucibles does not occur and undoped LEC crystals normally contain less than 5×10^{16} Si atoms/cc. Moreover, most of the Si contained in Si-doped melts is "gettered" by the B_2O_3 encapsulant, probably through oxidation.

When GaP or GaAs is chemically transported by reaction with gaseous HCl a white or sometimes gray residue is formed at the site of the original material. Silicon-doped GaP or GaAs in the shape of a large compact ingot leaves a voluminous "ghost" residue reproducing the original shape (Fig. 1). Frosch (1) has made similar observations on evaporation of Si-doped GaP in a wet hydrogen transport system. Moest (2) observed residues after evaporating GaAs and obtained a mass spectrometric analysis indicating that the residue was mainly SiO_2.

Present analytical procedures for determining the total Si content in GaP are unsatisfactory. The sensitivity limit for wet chemical analysis is $2 \times 10^{18}/cm^2$ [Trumbore (3) and Kometani (4)]. Neutron activation analyses have been performed in GaAs but not in GaP because matrix phosphorus is converted to Si during the activation (5). Electrical measurements are not definitive because silicon is an amphoteric dopant in GaP. Although spark source mass spectrometric measurements have been shown to give accurate analytical results for Si at the 10^{21} atom/cm^3 level (6), it is not clear what accuracies may be expected on the parts per million level. Interference from hydrocarbon lines raise serious problems of interpretation.[1] Thus in view of the generally expected contamination of GaP by Si, a simple unambiguous analytical method is needed. The present study shows that impurity enrichment by matrix evaporation is a reliable quantitative tool for silicon and potentially applicable to other elements that form refractory oxides.

Key words: GaP, impurities in; GaP, Czochralski growth; Si, in GaP; halogen transport of GaP.

Material Preparation

The analytical method, to be described in more detail in the next section, was applied to study the Si content of both polycrystalline and single-crystal GaP. The polycrystalline GaP was prepared both at the Bell Lab-

[1] Survey analyses are routinely performed claiming a sensitivity limit of 1 ppm Si. In the absence of standards an uncertainty factor of 3 is attached to all analytical results (7).

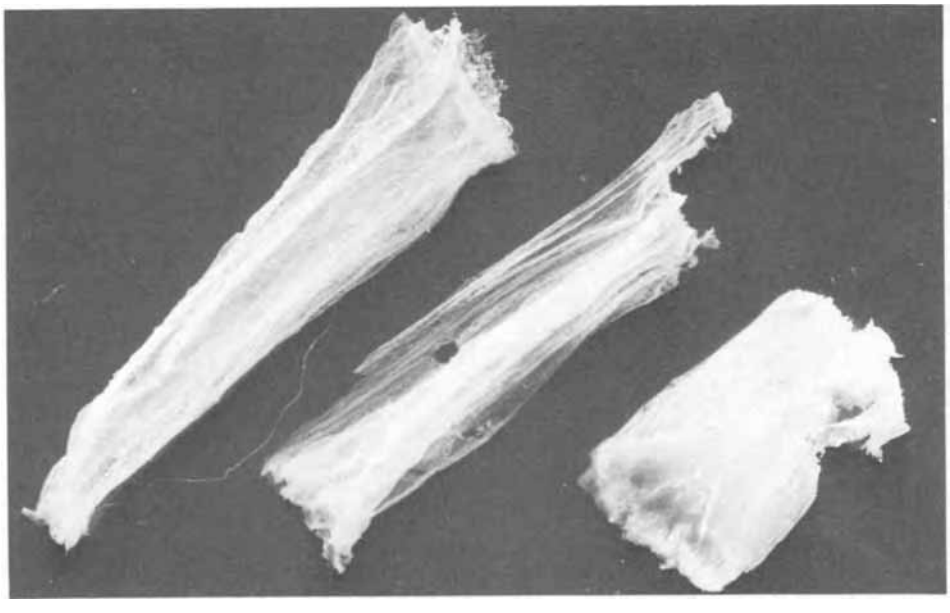

Fig. 1. Residues obtained by evaporating GaP single crystals.

oratories and by an outside supplier by dissolving phosphorus, obtained from the dissociation of PH_3, in Ga at temperatures near 1150°C. The details of this technique are described by Ringel (8). The material supplied from the outside was prepared in an all BN system, *i.e.*, pyrolytic BN liner tubes and boats. The material preparation at Bell Laboratories employed BN boats and quartz liners.

Both kinds of polycrystalline GaP were used as starting material in the Liquid Encapsulated Czochralski (LEC) growth of single crystals. In this method, which has been described elsewhere (9, 10), B_2O_3 was used as the liquid encapsulant and the melt was contained in quartz crucibles. The crystals analyzed were either undoped or doped with Ga_2O_3, C, Si, or B. All dopants were added in the crystal puller, while the polycrystalline starting material was undoped except for unintentional contamination from the boat or liner material.

The pulled crystals to be analyzed were etched for a few minutes in hot aqua regia, rinsed in deionized water and methanol, and weighed after drying.

Analytical Technique

The vapor transport apparatus used in these experiments was originally designed and used for the vapor growth of GaP single crystals and has been described elsewhere (11). The temperature of the Ga or GaP source material was 930°C. Pure hydrogen chloride used to transport the source material was derived from reaction of PCl_3 with carrier hydrogen. The hydrogen flow rate was kept at 60 ml/min, which in our apparatus corresponds to a flux of 10 ml/min-cm^2. a much lower value than was used during crystal growth runs, when the flow rates varied from 300 to 500 ml/min. The HCl partial pressure, however, was increased to 7.8 x 10^{-2} atm from a value of 5 x 10^{-2} atm existing during the crystal growth runs. The transport took place in vitreous SiO_2 furnace tubes except in certain control experiments when a pyrolytic BN liner was used. Pyrolytic BN boats were used to contain the source material to be analyzed except in those runs when the reaction between Ga and silica was studied. Under the above conditions 1 cm^3 of analytical sample can be evaporated in 1 hr.

During the early runs, the importance of complete evaporation of the Ga and GaP was realized. While in principle it would be possible to weigh the residue (ranging from several milligrams to a few micrograms), treat it with HF to dissolve the SiO_2 and subtract the weight of the remaining particles, in practice this can lead to considerable inaccuracies.

The SiO_2 residue from GaP crystals was judged to be amorphous SiO_2 on the basis of Laue back scattering experiments.

Qualitative analysis of the residues by x-ray fluorescence showed the major constituent to be Si. Other elements found by this analysis were Ga, Al, and Ca. While only trace quantities of Al and Ca were detected, Ga was found to be a major constituent only in the residue resulting from the transport of polycrystalline material. In all residues derived from pulled crystals only trace quantities of Ga were found. The presence of Ga in the polycrystalline GaP is to be expected. While the polycrystalline ingots are etched in hot HNO_3 or HCl after growth to remove excess gallium, some Ga inclusions can remain or be converted to α-Ga_2O_3, or $Ga(NO_2)_3$ unless the material is crushed prior to etching, which was not done for any of the material analyzed in these experiments. The β-form of Ga_2O_3 is formed from various compounds containing Ga and O on heating above 650°C (12). Thus, Ga $(NO_3)_3$, α-Ga_2O_3, etc., contained in aqua regia etched and poorly washed, porous GaP may be converted to β-Ga_2O_3 on heating to transport temperature (930°C). Once formed it may react relatively slowly with HCl compared to GaP. Elemental Ga, however, would not be oxidized in the reducing atmosphere of the transport system and hence not yield Ga-rich residues.

Reliability and Sensitivity of Analytical Technique

To determine whether SiO_2 is introduced in the residue from either the boats or the liner tubes, several control experiments were carried out. When gallium was placed in an SiO_2 boat and transported through reaction with HCl, films of SiO_2 were detected in the boat. No such residues were ever formed with BN boats. At temperatures near 1100°C, used for synthesis of GaP by saturation of gallium with gaseous phosphorus, it is well known that severe Si contamination occurs if SiO_2 liner tubes are used, even when Ga is contained in a BN boat. Under these conditions reactions between hydrogen and the silica furnace tubes produce gaseous Si species which are dissolved in the gallium (8).

To check that no such reactions occurred in our system at 930°C two samples from the same GaP ingot were evaporated separately in two runs. One evaporation was carried out as usual using a BN boat placed in a SiO_2 furnace tube. The other sample was evaporated from a BN boat placed in a BN tube. In both cases the amounts of residues were extremely small (a few micrograms) and yielded comparable Si levels.

These results indicate that the SiO_2 residues are indeed derived from the GaP and not from the container materials. As additional proof, we note that not all GaP material evaporated in SiO_2 tubes left residues. Polycrystalline material prepared in an all BN system as well as several pulled crystals yielded no detectable SiO_2 residues.

Several control experiments were performed to ascertain the reliability of the method as a quantitative analytical tool. Pure gallium[2] was doped with small quantities of elemental silicon and evaporated from BN boats in SiO_2 furnace tubes under the same conditions as the GaP. The weights of the SiO_2 residues recovered are listed in Table I. SiO_2 losses are calculated by subtracting the recovered amounts from the known contamination converted to SiO_2. The deviations from the known amount of Si always correspond to a loss of Si, again indicating that no extraneous Si is introduced in the process.

Silicon, in the material to be analyzed, can be lost by vapor transport in a reaction with HCl to form $SiCl_4$. The suppression of $SiCl_4$ depends on the amount of residual oxygen contained in the incoming hydrogen carrier gas in the form of both O_2 and H_2O. For the reaction

$$SiO_2 + 4HCl \rightarrow SiCl_4 + 2H_2O \qquad [1]$$

an equilibrium coefficient

$$K_1 = \frac{p_{SiCl_4} p_{H_2O}{}^2}{p_{HCl}{}^4}$$

was calculated for 1200°K from data given in the JANAF Tables (13). From K_1 one can make reasonable estimates of the theoretical Si losses through conversion to $SiCl_4$ during the transport reaction. K_1 at 1200°K is 4 x 10^{-11} atm^{-1}.

Thermodynamic considerations presented in ref. (11) indicate that the partial pressure of HCl in equilibrium with the GaP source is 7.8 x 10^{-2} atm. The partial pressure of H_2O derived from impurities in

[2] Which according to manufacturer's mass spectrometric analysis contained less than 0.04 ppm Si.

Table I. Recovery of silicon from gallium

Wt. of Ga, g	Wt. of Si dopant, μg	Wt. of SiO_2 residue, μg	Loss of SiO_2, μg	% Recovery
39.41	21,100	40,200	5000	89
4.87	92	135	62	69
3.53	421	834	69	92

the dry H_2 and the PCl_3 is not known. An analysis provided by the supplier of PCl_3 indicates a $POCl_3$ content of 0.2 m/o (mole per cent). From this number we can calculate an H_2O partial pressure of 8×10^{-5} atm. This pressure is expected to increase with increasing enrichment of the PCl_3 in the higher boiling $POCl_3$ as the reaction proceeds. Experiments with GaP and GaAs transport in the dry H_2 used as a carrier gas indicated a H_2O residual partial pressure of 2×10^{-5} atm.

A reasonable estimate of the total partial pressure of H_2O in the system is, therefore, 1×10^{-4} atm. Inserting this value together with $p_{HCl} = 7.8 \times 10^{-2}$ atm into the equation for K_1 (1200°K) we find a partial pressure of $SiCl_4$ equal to 1.5×10^{-8} atm.

From this estimate of the partial pressure of $SiCl_4$ one can calculate that during an experiment in which 1 cm^3 of GaP is evaporated over 1 hr into a carrier gas flow of 60 ml/min an amount of 0.1 μg of SiO_2 will be lost. This estimate is to be increased, however, because toward the end of the run almost all the GaP is consumed and the p_{HCl} rises to the value of the incoming HCl pressure. Since p_{SiCl_4} increases with the fourth power of p_{HCl}, SiO_2 consumption increases drastically and will after complete evaporation of the GaP sample rise to 1.3 μg/min. It is therefore useful to provide an auxiliary GaP source downstream from the analytical sample.

In the above it was assumed that the only source of SiO_2 in the system is the sample. Considering the finely divided state of the SiO_2 residues this is likely to be true. However, the reaction between HCl and the quartz furnace tube walls used in all our routine analytical runs may have served to reduce the Si_2O losses.

The actual SiO_2 losses observed in the control experiments using Si-doped Ga indicate SiO_2 losses ranging from 5000 to 60 μg, roughly proportional to the amount recovered. It is concluded that these losses represent both mechanical losses occurring during transfers and the expected theoretical losses. It is also possible that convection currents in the transport tube carry away small amounts of the extremely light SiO_2.

On the basis of these considerations it is suggested that the Si concentrations in GaP deduced by this method present a lower limit to the actual Si content. The method yields a total silicon content regardless of distribution. Due to the increased importance of mechanical losses when the residues are small, we would expect this method to yield values that are only about 50% of the actual concentrations. Since a convenient sample size in view of running time is about 5g, Si concentrations less than 5×10^{16} atoms/cc (1 ppm) yield residues less than 5 μg. Such small quantities become extremely hard to handle accurately. Consequently, the sensitivity limit of this method should be considered to be 5×10^{16} atoms/cc.

Discussion of Analytical Procedure and Results

The procedure as presented was derived from crystal growth experiments and relies on an unintentional moisture content of the reactants. The experimenter can control the moisture content of the reactant gas by saturating part of the incoming hydrogen with water vapor by passing it through a temperature controlled water bubbler as described by Kamath and Bowman (14).

The results of the analysis of the various GaP samples are listed in Table II. For a comparison we have included spark source mass spectrometric data on the same or similar material measured by Malm (7). In comparing the two methods it must be borne in mind that the sampling procedures for the two methods differ radically. The evaporation method measures the total silicon content of a large sample (~5g), regardless of distribution inhomogeneities. The spark source mass spectrometric analysis yields a value pertaining to a very small crystal volume. The discrepancy between the silicon content values given by the two methods can be quite large (*e.g.*, RD 111 and RD 117 in Table II).

With the limitations of both methods in mind, two significant conclusions may be drawn from Table II. First, the silicon content of LEC grown ingots which are not intentionally doped with silicon is less than or equal to 5×10^{16} atoms/cc or about 1 ppm (atomic).[3] This is comparable to the Si concentrations in the polycrystalline starting material. Hence, no significant contamination from the quartz crucibles occurs.

Second, in both cases where the polycrystalline material contained silicon, either by direct addition of elemental Si to the melt (RD 117) or because of its preparation in SiO_2 liners (RD 111), the Si concentration in the LEC grown ingot dropped by nearly two orders of magnitude. This confirms the gettering action of B_2O_3 with respect to silicon as already reported by Bass and Oliver (15, 16), who suggested

[3] One cubic centimeter of GaP weighs 4.13g and contains 4.9×10^{22} atoms. One part per million (atomic) corresponds to 4.9×10^{16} atoms/cc. One part per million (by weight) of Si would correspond to 8.8×10^{16} atoms/cc.

Table II. Si content in polycrystalline GaP and LEC grown single crystals of GaP

Sample No.	Type material	Dopant	Growth conditions	Weight of sample, g	Weight of residue, μg	Si content, atoms/cc	Mass spec. analysis, atoms/cc
BP	(Outside supplier)	—	All BN system	3.00	0	$<5 \times 10^{16}$	10^{17}**
BP	(Outside supplier)	—	All BN system	8.50	0	$<5 \times 10^{16}$	
CR 28	Poly (BTL)	—	All BN system	6.11	0	$<5 \times 10^{16}$	$<5 \times 10^{15}$**
CR 32-34	Poly (BTL)	—	SiO_2 liner BN boat	6.11	2140	1.5×10^{19}	
RD 110	LEC single	—	Grown from undoped poly (outside supplier)	6.16	0	$<5 \times 10^{16}$	5.5×10^{16}
RD 117	LEC	Si (1.47×10^{20} atoms/cc in melt)	Grown from undoped poly (outside supplier)	7.22	230	1.3×10^{18}	$2\text{-}4 \times 10^{17}$
RD 111	LEC single	Si (1.5×10^{19} atoms/cc in melt)	Grown from poly CR 32-34	5.59	33	2.4×10^{17}	4×10^{16}
RD 107	LEC single	Ga_2O_3	Grown from undoped poly (outside supplier)	6.59	8	5×10^{16}	—
RD 107	LEC single	Ga_2O_3	Grown from undoped poly (outside supplier)	4.29	<5*	$<5 \times 10^{16}$	—
RD 114	LEC single	C	Grown from undoped poly (outside supplier)	7.42	0	$<5 \times 10^{16}$	$2.5\text{-}30 \times 10^{16}$
RD 116	LEC single	BP	Grown from undoped poly (outside supplier)	6.18	0	$<5 \times 10^{16}$	$2\text{-}20 \times 10^{16}$
RD 103	LEC	$Zn(PO_3)_2$	Grown from undoped poly (outside supplier)	4.89	7	6×10^{16}	$<2 \times 10^{16}$
RD 112	LEC	Ga_2O_3		5.60	22	1.8×10^{17}	$0.5\text{-}2 \times 10^{17}$

* Analysis performed in all BN system.
** These data were not obtained on the same material, but on material from same source, grown under similar conditions.

that B_2O_3 might be reduced by elemental Si. Malm's (7) mass spectrometric analysis of RD 117, a Si-doped crystal, shows a considerable amount of boron, *i.e.*, 20-30 ppm as compared to 1 ppm in undoped ingots. While this confirms that some of the Si is removed, through reduction of B_2O_3, Weiner has pointed out that the residual water content of the B_2O_3 is primarily responsible for oxidation of the elemental Si into SiO_2 which then dissolves in the B_2O_3 (17).

Acknowledgments

We gratefully acknowledge the mass spectrometric analysis work performed by D. L. Malm as well as the use of his unpublished data. We also thank C. M. Ringel for supplying some of the polycrystalline material, Mrs. M. Reed for the x-ray study of the SiO_2 residue, and Miss S. Vincent for x-ray fluorescence analysis. It is a pleasure to acknowledge valuable discussions with F. A. Trumbore.

Manuscript submitted July 10, 1970; revised manuscript received *ca.* Jan. 10, 1971.

Any discussion of this paper will appear in a Discussion Section to be published in the June 1972 JOURNAL.

REFERENCES

1. C. J. Frosch, Bell Telephone Laboratories, Murray Hill, N. J., Private communication.
2. R. R. Moest, Bell Telephone Laboratories, Reading, Pa., Private communication.
3. F. A. Trumbore, H. G. White, M. Kowalchik, C. L. Luke, and D. L. Nash, *This Journal*, **112**, 1208 (1965).
4. T. Y. Kometani, Bell Telephone Laboratories, Murray Hill, N. J., Private communication.
5. C. K. Kim, Bell Telephone Laboratories, Murray Hill, N. J., Private communication.
6. A. J. Ahearn, F. A. Trumbore, C. J. Frosch, C. L. Luke, and D. L. Malm, *Anal. Chem.*, **39**, 350 (1967).
7. D. L. Malm, Bell Telephone Laboratories, Murray Hill, N. J., Private communication.
8. C. M. Ringel, Paper presented at the Los Angeles Meeting of the Society, May 10-15, 1970, Extended Abstract 67. The method was first described by P. J. Dean, C. J. Frosch, and C. H. Henry, *J. Appl. Phys.*, **39**, 5631 (1968).
9. E. P. A. Metz, R. C. Miller, and R. Mazelsky, *J. Appl. Phys.*, **33**, 2016 (1962).
10. J. B. Mullin, B. W. Stranghan, and W. S. Brickell, *J. Phys. Chem. Solids*, **26**, 782 (1968).
11. L. C. Luther and D. D. Roccasecca, *This Journal*, **115**, 850 (1968).
12. I. A. Sheka, I. S. Chaus, and T. T. Mityureva, "The Chemistry of Gallium," p. 33, Elsevier Publishing Co., New York (1966).
13. JANAF Thermochemical Tables, U.S. Dept. Commerce, Natl. Bureau Standards Clearing House, Springfield, Va.
14. G. S. Kamath and D. Bowman, *This Journal*, **114**, 192 (1967).
15. S. J. Bass and P. E. Oliver, "Gallium Arsenide," *Proc. Int. Sym., Reading, 1966, Institute of Physics and Physical Soc. Conference Series No. 3*, p. 41 (1967).
16. S. J. Bass and P. E. Oliver, *J. Crystal Growth*, **3**, 4 (1968).
17. M. E. Weiner, Bell Telephone Laboratories, Murray Hill, N. J., To be published.

Crystallization Studies of Nickel-Tellurium Oxide Films

M. L. Lieberman,[1] B. Boller, and R. C. Medrud

Research and Development Laboratories, Corning Glass Works, Corning, New York 14830

ABSTRACT

Crystallization of amorphous nickel-tellurium oxide films prepared by multicathodic reactive sputtering has been studied by x-ray diffraction. Devitrification resistance is maximized for films with an atomic ratio (Te/Ni) near 0.47. A new compound has been prepared which has a structure resembling that of rutile. It has been identified as $Ni^{+2}Te^{+6}O_4$. The identification of this compound, the preparation of similar known mixed-oxides by the same method, and other evidence indicates that amorphous tellurate films can be prepared by reactive sputtering.

Previous work in multicathodic reactive sputtering has shown that amorphous mixed-oxide films can be prepared over a wide composition range (1). Crystallization of amorphous bismuth-tellurium oxide films produced unidentified phases which are probably bismuth tellurates (compounds with Te^{+6}), but identification has not been possible because no structural data on bismuth-tellurium oxides have been reported.

To continue the work on multicathodic reactive sputtering and to obtain stronger evidence for tellurate formation, we have studied the nickel-tellurium-oxygen system in which at least one well-characterized compound, trinickel tellurate, Ni_3TeO_6, exists (2). This report deals primarily with the preparation and identification of phases in nickel-tellurium oxide films. Other similar systems have also been studied.

Experimental

Multicathodic reactive sputtering was used to deposit mixed-oxide films on rotating, liquid-nitrogen cooled glass substrates in a 1:1 Ar-O_2 gas mixture. Deposition parameters and film compositions are given in Table I. The apparatus has been described elsewhere (3). Film composition was varied in different deposition experiments by changing the cathode voltages. Seven different compositions were prepared over the atomic-ratio range 0.049_1-2.02 g-atom Te/g-atom Ni.

Films were deposited simultaneously on four substrates during each deposition experiment. Different films from each deposition experiment were used for phase identifications and for chemical analyses. Phase identifications were based on x-ray diffraction analyses, as in previous work (1, 3). A G.E. diffractometer was used with CuKα radiation. Chemical analyses were obtained by spectrophotometric methods. The uncertainties in the mass values are estimated as $\pm$ 3% for mass values greater than 1 mg; for smaller mass values, the uncertainties are larger.

Discussion and Results

Film crystallinity.—Under the experimental conditions outlined in the previous section, films with low

[1] Present address: Sandia Laboratories, Albuquerque, New Mexico, 87115.

Key words: amorphous tellurate films, reactive sputtering.

Table I. Deposition parameters and film compositions

Deposition experiment	175	176	177	178	179	180	181
Nickel voltage, V	3600	3600	3600	3600	3600	3000	2400
Nickel current, mA	170	170	170	170	170	150	100
Tellurium voltage, V	600	900	1200	1500	1800	1800	1800
Tellurium current, mA	24	33	45	60	66	76	75
Total gas pressure,* μ	20	19	19	18	17	20	20
Deposition time, min	150	150	150	150	150	150	100
Film thickness,† A	4490	5110	6030	8610	—	11300	9900
Mass of nickel, mg	3.30	3.30	3.54	3.49	3.42	2.67	1.57
Mass of tellurium, mg	0.35_2	0.74_9	1.76	3.58	3.47	7.66	6.88
Atomic ratio, g-atom Te/g-atom Ni	0.049_1	0.10_3	0.229	0.472	0.736	1.32	2.02

* 1:1 Ar-O_2 gas mixture.
† Measured with a Proficorder; uncertainty estimated at ±250A.

atomic ratios (Te/Ni) are black, as are nickel oxide films (3). With increasing atomic ratio (Te/Ni), the films progressively approach the virtually colorless character of as-deposited tellurium oxide films (3). After heat treatments at 350°C or higher, the black films turned olive green. Nachman, Cojocaru, and Ribco (4) have attributed the black color in NiO to the presence of Ni^{+3} ions. Such ions are present in NiO as charge compensation for nickel vacancies which occur with an excess of oxygen. Nearly stoichiometric NiO is pale green. Consequently, it seems likely that when the films are heated, the Ni^{+3} ions are reduced to Ni^{+2} ions, and the excess oxygen is eliminated.

Previous work (1) in multicathodic reactive sputtering has indicated that amorphous, mixed-oxide films of some systems can be prepared at all compositions if each of the metal oxides involved forms amorphous single-oxide films. Since nickel oxide films prepared in the present apparatus are crystalline and those of tellurium oxide are amorphous (3), it was anticipated that crystallinity in the nickel-tellurium oxide films would depend on composition. That this was the case is shown by the diffractometer traces of Fig. 1. All curves show the broad peak from the glass substrates at about 22° in 2θ. As the atomic ratio Te/Ni) increases, the three NiO peaks decrease in intensity. For films 178-181 with atomic ratios (Te/Ni) equal to or greater than 0.472, no crystalline NiO is observed. Instead, the films appear to be amorphous.

Diffractometer traces from films heated for 3 hr at different temperatures showed variations with both temperature and atomic ratio. The portions of the diffractometer traces which exhibited the most intense peaks are presented in Fig. 2. Films with atomic ratios (Te/Ni) of 0.736 and 1.32 crystallized with the formation of a new phase. The film with an atomic ratio (Te/Ni) of 2.02 crystallized with the formation of a mixture of the new phase and tetragonal TeO_2. The latter film became a white-tan, opaque film on crystallization and exhibited the "splatter" marks characteristic (1, 3) of TeO_2 formation from TeO_{2+x} ($0 < x \leq 1$). Crystallization of the films with an atomic ratio (Te/Ni) of 0.472 was not possible because the films peeled off the substrates when heated at 550°C. It is significant to note, however, that they were still amorphous after a 500°C heat treatment.

In all samples the only phases obtained on crystallization were tetragonal TeO_2, the new phase, and what appeared to be cubic NiO. The true symmetry of NiO is actually rhombohedral but the distortion of the structure from cubic is very slight and the breadth of the diffraction lines from these films was sufficient to make the symmetry appear to be cubic. In no case was trinickel tellurate, Ni_3TeO_6, obtained on crystallization. It was formed by reheating pieces of the crystallized films 177, 179, and 180 to 700°C in air. X-ray fluorescence analyses indicated that the quantity of tellurium in the films decreased after the 700°C heat

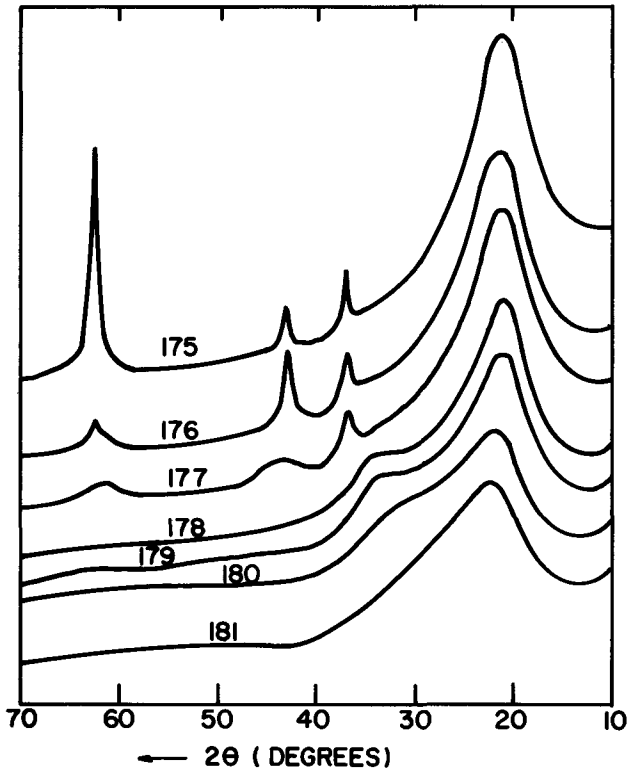

Fig. 1. Diffractometer traces of nickel-tellurium oxide films heated at 400°C for 3 hr. These traces are identical to those obtained from as-deposited films. Films are identified by deposition experiment number. The broad peak on the right is from the glass substrate.

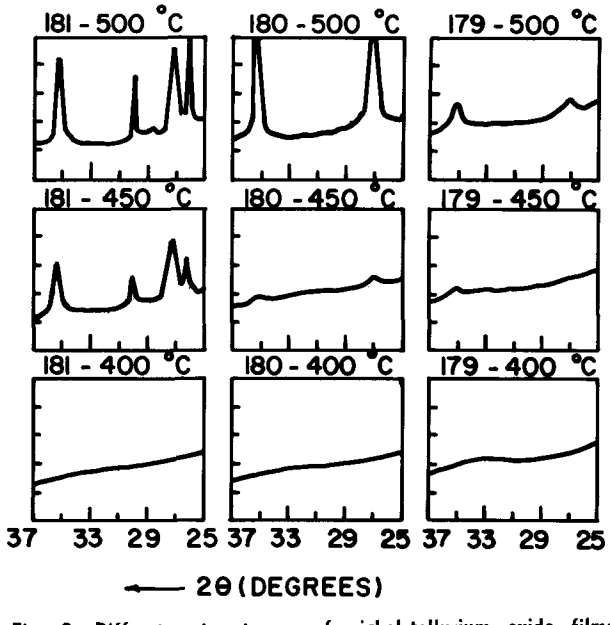

Fig. 2. Diffractometer traces of nickel-tellurium oxide films heated at various temperatures for 3 hr. Films are identified by deposition experiment numbers and temperatures of heat treatments.

treatment. This loss was undoubtedly due to vaporization of some tellurium species.

The x-ray diffraction data show that devitrification resistance of the nickel-tellurium oxide films depends highly on composition. The greatest devitrification resistance was exhibited by a film with an atomic ratio (Te/Ni) of 0.472. Films with either higher or lower atomic ratios (Te/Ni) exhibited less devitrification resistance. This suggests a region of glass formation in the nickel-tellurium-oxygen system, although no such bulk glasses have been reported.

Tellurate formation.—Whether tellurates are formed in the amorphous films must be considered further. No evidence of gas evolution or any other physical change was visible when the new phase formed upon crystallization of the amorphous films. This suggests that the oxidation state of tellurium in the new phase is the same as that in the amorphous films. Therefore, if this phase is shown to be a tellurate, it can be concluded that amorphous tellurate films have been prepared. This would also suggest that the amorphous TeO_{2+x} ($O < x \leq 1$) and bismuth-tellurium oxide films reported earlier (1, 3) represent amorphous TeO_3 and bismuth tellurate(s), respectively.

The new phase gives an x-ray diffraction pattern whose strong lines resemble those from compounds having the tetragonal rutile-type structure. Table II shows a comparison between the diffraction data from RuO_2, which is isostructural with rutile, and of the new phase which we believe to be $NiTeO_4$. The compound RuO_2 was chosen for comparison because of similarities to $NiTeO_4$ with respect to ionic radius and atomic number as well as atomic arrangement. The intensities for RuO_2 were calculated from the data of Cotton and Mague (5) using the computer program of D. K. Smith (6). The additional, weak lines in the $NiTeO_4$ data indicate that deviations from the atomic arrangement in the rutile-type structures exist which require a larger unit cell and/or lower symmetry in order to fully describe the structure.

Our first choice for comparison was the trirutile structure which Fe_2TeO_6 possesses (7, 8). The trirutile unit cell is obtained from the rutile unit cell by tripling the c axis, $c = 3c_R$, where the subscript R denotes the rutile unit cell dimensions. However, the only observed Fe_2TeO_6 diffraction lines that agree with our data in either position or intensity were those from the rutile-type subcell.

Table II. X-ray diffraction data for $NiTeO_4$ and for RuO_2

$NiTeO_4$				RuO_2		
d (obs.)	d (calc.)	I (obs.)	hkl	hkl	d	I
5.1	5.35	6	201			
4.24	4.335	5	102			
3.97	3.956	4	301			
3.29	3.286	100	400	100	3.176	100
3.05	3.057	5	003			
2.83	2.855	2	322			
2.80	2.799	2	421			
2.72	2.713	4	213			
2.68	2.672	4	402			
2.55	2.554	90	223	101	2.555	83
2.47	2.475	5	422			
2.37	2.359	3	521			
2.33	2.323	12	440	200	2.246	20
2.24	2.238	9	403	111	2.221	5
2.08	2.078	3	620	210	2.008	1
1.97	1.971	2	513			
1.95	1.955	3	612			
1.79	1.799	4	115			
1.72[0]	1.719	42	623	211	1.687	61
1.69	1.692	8	305			
1.64[2]	1.643	10	800	220	1.588	14
1.52[8]	1.528	10	006	002	1.554	8
1.49[5]	1.494	3	515			
1.47[5]	1.474	4	653			
1.46[8]	1.469	8	840	310	1.420	13
				112	1.395	14
1.44	1.442	2	901			
1.38[4]	1.381	18	663	301	1.349	17
1.27[6]	1.277	6	446	202	1.278	7
Tetragonal				Tetragonal		
$a = 2\sqrt{2}a_R = 13.1^4$ (.65) A				$a = 4.491$ A		
$c = 3c_R = 9.17$ (3.06)				$c = 3.107$		

The next possibility which we examined was that the structure of $NiTeO_4$ might be similar to that of NbO_2 (9). The NbO_2 unit cell is obtained by making $a = 2\sqrt{2}a_R$ and $c = 2c_R$. This model accounts for intensity and position of the rutile-type subcell lines and the position of some of the additional lines. We then succeeded in indexing all observable diffraction lines in the $NiTeO_4$ data by choosing $a = 2\sqrt{2}a_R$ and $c = 3c_R$. The agreement between observed and calculated line positions is shown in Table II and is within the precision of the data. However, the intensity agreement between the weak lines of $NiTeO_4$ and related lines of NbO_2 and Fe_2TeO_6 is not good, indicating that the atomic arrangement of $NiTeO_4$ is similar to either NbO_2 or Fe_2TeO_6 in gross features only. Since there are no other similar known structures to use as models, neither the quality nor the quantity of our experimental data permits more detailed analysis.

Bayer (10) has surveyed materials with the rutile-type structure and cites examples with the following general formulas: $A^{+4}O_2$, disordered $A^{+3}B^{+5}O_4$, and the two trirutile types, $A_2^{+3}B^{+6}O_6$ and $A^{+2}B_2^{+5}O_6$. Corresponding formulas in this system are then: $Ni^{+3}Te^{+5}O_4$, $Ni_2^{+3}Te^{+6}O_6$, and $Ni^{+2}Te_2^{+5}O_6$. It is probable that Te^{+5} would actually be a combination of Te^{+4} and Te^{+6}. This has been postulated but not substantiated for Te_2O_5 (11). There are apparently no reported $A^{+2}B^{+6}O_4$ compounds with the rutile-type structure, but we consider $Ni^{+2}Te^{+6}O_4$ to be the most likely formula for the new compound for the following reasons. The number of compounds in which nickel appears exclusively in the plus three state is very small and the majority of these compounds are coordination complexes, not simple salts (12). The presence of Te^{+6} in a compound with the rutile-type structure is much more likely than Te^{+4} or a combination of the two species. The ion Te^{+6} has thus far been found only in octahedral coordination (13-15), while Te^{+4} has been found only in three or fourfold coordination (16). As Zemann has pointed out in the paper just cited, oxides of Te^{+4}, which has fourfold coordination, tend to have relatively low densities when compared with oxides which have ions of similar size but with a coordination number of six. This difference also appears in unit cell size. Table III gives some data taken from Bayer (10) showing ionic radii and unit cell dimensions for several compounds which have the rutile-type structure and also for TeO_2. It is obvious that TeO_2 has a much larger c unit cell dimension. This causes a large volume difference which is primarily due to the differences in coordination, fourfold for Te^{+4} in TeO_2 and sixfold for both A and B ions in the compounds with the rutile-type structure. The close similarity between the data for $NiTeO_4$ and for the rutile-type compounds (such things as unit cell dimensions, x-ray intensities, and cation radii) lends further support to our conclusions. If either Te^{+4} or a combination of Te^{+4} and Te^{+6} were present, we would expect a larger unit cell, closer to that of TeO_2. The $NiTeO_4$ stoichiometry is also favored over the other possibilities because Film 180 with an atomic

Table III. Comparison of ionic radii and unit cell dimensions for some rutile-type compounds and for tetragonal TeO_2 After Bayer (10)

	r_A*	r_B*	a	c
GeO_2	0.53 Å		4.39 Å	2.86 Å
RuO_2	0.67		4.491	3.107
TiO_2	0.68		4.594	2.958
SnO_2	0.71		4.74	3.19
TeO_2	0.70		4.796	7.594 (3.797)**
$NiTeO_4$	0.69	0.56 Å	13.14 (4.65)**	9.17 (3.06)**
$AlSbO_4$	0.51	0.62	4.51	2.96
$FeNbO_4$	0.64	0.69	4.68	3.05
Fe_2TeO_6	0.64	0.56	4.59	9.12 (3.04)**

* Ionic radii after Ahrens (19).
** Rutile-type subcell dimensions.

ratio (Te/Ni) of 1.32 gives the most intense diffraction pattern, much stronger than would be expected just from thickness considerations (see Table I and Table II). Film 181 also gives a strong diffraction pattern but TeO_2 is present in an equivalent amount to $NiTeO_4$. Film 179 gives a diffraction pattern which contains only $NiTeO_4$ but it is considerably weaker than the previous two and the pattern from Film 178 is weaker still.

We obtained additional supporting evidence on the identity of the new phase by studying mixed-oxide films in systems in which similar bulk compounds have been reported. Films prepared by multicathodic reactive sputtering were thermally crystallized and examined by x-ray diffraction. Nickel-tantalum and nickel-antimony oxide films crystallized in the range 500°-700°C and yielded diffraction patterns of the known rutile-like $NiTa_2O_6$ and $NiSb_2O_6$ phases, respectively (10, 17). The crystallization of iron-tellurium oxide films at 500°-600°C produced the known (7, 8, 10) rutile-type tellurate, Fe_2TeO_6, without any visible change in the films. There is one difference between the diffraction patterns obtained from the films and those reported for the bulk compounds. The films appear to be in the disordered form because of the absence on the diffraction pattern of all super-lattice lines which distinguish the ordered trirutile form from the disordered form. A calculation of x-ray intensities for the bulk forms of these three compounds was made using the computer program of Jeitschko and Parthé (18). The results indicate that some of the super-lattice lines should be of sufficient intensity to appear in our data if the films were fully ordered. Partial ordering cannot be ruled out by our data, however. In the phases $NiTa_2O_6$, $NiSb_2O_6$, and Fe_2TeO_6, the nickel and tellurium atoms are in the +2 and +6 oxidation states, respectively. There is no reason to believe that the oxidation states differ in the nickel-tellurium oxide films. From the evidence just presented, we believe that the most likely formula for this new phase is $Ni^{+2}Te^{+6}O_4$.

Three attempts were made to prepare the new compound in bulk form. The first attempt used pressed pellets of NiO plus TeO_2 with atomic ratios (Te/Ni) of 2.0, 1.0, and 0.5. The pellets were heated in air at 500°C for 66 hr and 700°C for 24 hr. NiO and TeO_2 were seen in all samples and those heated at 700°C also contained large amounts of Ni_3TeO_6 and an unidentified phase not seen before. No evidence of $NiTeO_4$ was found. The second attempt used pellets of NiO plus a mixture of H_6TeO_6 and H_2TeO_4 with the same atomic ratios as above. These pellets were heated at 350°C for 120 hr to drive off water, repressed, and again heated to 350°C for 160 hr. The only crystalline phase seen in these mixtures was NiO, but there was also a substantial amorphous peak on the patterns. This indicates that the tellurium is in the amorphous phase which has been reported previously (11). We also attempted to grow crystals by evaporating a dilute nitric acid solution of NiO, H_2TeO_4, and H_6TeO_6. Again the product was only NiO.

Conclusions

Crystallization studies have been performed on nickel-tellurium oxide films prepared by multicathodic reactive sputtering. The devitrification resistance of the films is greatest at a composition intermediate to the two component oxides. Crystallization of the amorphous mixed-oxide films produced a new compound with a structure resembling that of rutile which has been identified as $Ni^{+2}Te^{+6}O_4$. We conclude that amorphous tellurate films have been prepared in this and in earlier (1, 3) work.

Acknowledgments

The authors wish to thank Dr. Y. S. Su for the chemical analyses and Mr. Oliver W. Kendall for technical assistance in preparing the films and bulk materials. Helpful discussions with Dr. Peter R. Segatto are gratefully acknowledged.

Manuscript submitted July 6, 1970; revised manuscript received *ca.* Jan. 4, 1971.

Any discussion of this paper will appear in a Discussion Section to be published in the June 1972 JOURNAL.

REFERENCES

1. M. L. Lieberman, *J. Appl. Phys.*, **40**, 2659 (1969).
2. R. E. Newnham and E. P. Meagher, *Mater. Res. Bull.*, **2**, 549 (1967).
3. M. L. Lieberman and R. C. Medrud, *This Journal*, **116**, 242 (1969).
4. M. Nachman, L. N. Cojocaru, and L. V. Ribco, *Phys. Status Solidi*, **8**, 773 (1965).
5. F. A. Cotton and J. T. Mague, *Inorg. Chem.*, **5**, 317 (1966).
6. D. K. Smith, "A Revised Program for Calculating X-ray Powder Diffraction Patterns," UCRL-50264, Lawrence Radiation Laboratory, Livermore, California, 1967.
7. W. Kunnmann, S. LaPlaca, L. M. Corliss, and J. M. Hastings, *J. Phys. Chem. Solids*, **29**, 1359 (1968).
8. M. C. Montmory, M. Belakhovsky, and R. Chevalier, *Solid State Commun.*, **6**, 317 (1968).
9. A. Magneli, G. Andersson, and G. Sundkvist, *Acta Chem. Scand.*, **9**, 1402 (1955).
10. G. Bayer, *Ber. Deut. Keram. Ges.*, **39**, 535 (1962).
11. J. Rosicky, J. Loub, and J. Pavel, *Z. Anorg. Allgem. Chem.*, **334**, 312 (1965).
12. J. M. Dale and C. V. Banks, "Nickel," *Treatise of Analytical Chemistry*, Part II, Sect. A. Vol. 2, p. 384, John Wiley and Sons, Inc., New York (1962).
13. G. Bayer, *J. Less-Common Metals*, **12**, 326 (1967).
14. H. M. Kasper, *Mater. Res. Bull.*, **4**, 33 (1969).
15. R. E. Newnham, J. F. Dorrian, and E. P. Meagher, *ibid.*, **5**, 199 (1970).
16. J. Zemann, *Z. Krist.*, **127**, 319 (1968).
17. A. Bystrom, B. Hok, and B. Mason, *Arkiv·Kemi Mineral Geol.*, **15B**, 1 (1941).
18. W. Jeitschko and E. Parthé, "A FORTRAN IV Program for the Intensity Calculation of Powder Patterns," University of Pennsylvania, Philadelphia, Pennsylvania (1965).
19. L. H. Ahrens, *Geochim. Cosmochim. Acta*, **2**, 155 (1952).

Technical Note

The Use of Plated Metal Films for Semiconductor Oxide Parameter Measurements

Don L. Cannon

Department of Electrical Engineering, University of Texas at Arlington, Arlington, Texas 76010

In order to measure oxide charge levels or oxide thickness by interferometer techniques, a metal film must be formed on the wafer. For many experiments, such as etch rate measurements, vacuum evaporation becomes unfeasible from the standpoint of turnaround time and the requirements for whole wafers. An alternative to such expensive and time-consuming processing is to chemical plate the metal films on the experimental wafers. While there are many electroless plating procedures, the examples described are the well-known silver plating mirror process and an electroless nickel plating procedure. In actual practice one may prefer a more immobile element nickel especially when MOS C-V measurements are to be made at high temperature. The actual plating procedures used in the experiment described are given in Ref. (1), (silver plating solution), and Ref. (2) (nickel plating). The plating procedures are summarized in the appendix for quick reference.

The technique has been verified by performing the following sequence of measurements. The oxide thickness and MOS flat-band voltages of several wafers were measured using evaporated aluminum films. The aluminum was then removed, and the silver films were chemically plated on the oxide. The oxide thickness was again measured, again using interferometry techniques. Areas of the silver located over the oxide were isolated by mechanically scraping the silver with a tungsten probe. Then the capacitance-voltage curves were traced, and the parameters shown in Fig. 1 were recorded. Then the procedure was repeated with new samples only with nickel used as the electrode instead of silver. The results of these measurements are shown in Table I. These results demonstrate that the plated films yield the same data as do the evaporated aluminum films when the measurements are conducted at room temperature. When temperature-bias measurements are required, the nickel or some other immobile (in oxide) metal element should be used.

Key words: oxide charge, interferometry.

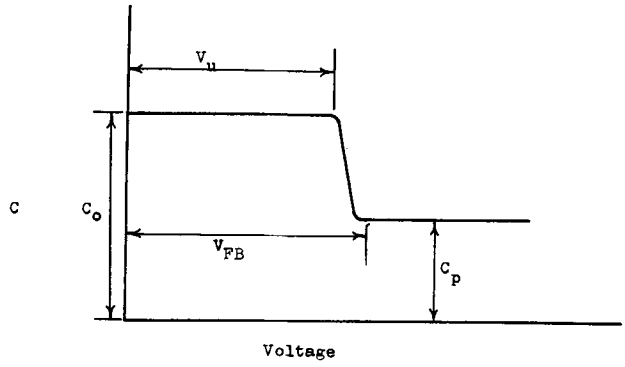

Fig. 1. Capacitance vs. voltage measurement parameters

In summary, in-process or experimental oxide parameter measurements that require the use of metal film deposits can be made accurately and simply by using a chemically plated metal film. Such metallization is then readily removed chemically, leaving the wafers ready for their next processing step. Since plating baths may be rich in alkali ions, care must be exercised in using such techniques on production wafers. In such cases, use of test wafers for the measurement of samples would be advisable.

Manuscript received Feb. 15, 1971.

Any discussion of this paper will appear in a Discussion Section to be published in the June 1972 JOURNAL.

Table I. Summary of results

A. Silver films

Film	Aluminum film				Plated silver film			
Parameter / Units	V_{FB} Volts	V_u Volts	C_o/C_p —	t_{ox} fringes[b]	V_{FB} Volts	V_u Volts	C_o/C_p —	t_{ox} fringes[a]
Wafer 3-1	7	25	1.25	2.1, 1.9	5, 6.5	20, 30	1.33	2.0
Wafer 3-2	15	35	1.20	2.0	13, 15	33, 35	1.33	2.0
Water 3-3	8	27	1.25	2.0	7	25	1.33	2.0

B. Nickel films

Film	Aluminum film			Plated nickel film		
Parameter / Units	ΔV_{FB}[c] Volts	C_o/C_p —	t_{ox} fringes[a]	ΔV_{FB} Volts	C_o/C_p —	t_{ox} fringes
Wafer 4-1	0	1.25	2.0	0	1.37	2.0
Wafer 4-2	1	1.20	2.0	0	1.31	2.0

[a] All measurements at room temperature.
[b] 1 fringe = 2.23μ.
[c] ΔV_{FB} is the change in the band voltage after applying +25V bias (+ on the aluminum) for 10 min.

REFERENCES

1. Wm. Blum and G. B. Hogaboom, "Principles of Electroplating and Electroforming," McGraw-Hill, New York (1949).
2. T. D. Schlabach and K. Rider, "Printed and Integrated Circuitry—Materials and Processes," p. 140, McGraw-Hill, New York (1963).

APPENDIX A

Silver Plating Solutions

Sensitizer Solution

10 g/liter $SnCl_2 \cdot 2H_2O$
40 ml/liter HCl

Reducing Solution

90 g/liter granulated sugar
4 ml/liter HNO_3
Boil for 5 min

Solution A

50 g/liter $AgNO_3$
25 g/liter KOH

Solution B

65 g/liter $AgNO_3$

Plating Solution

Add enough NH_4OH to solution A to dissolve precipitate. Add enough solution B to this to slightly darken.

Plating Procedure

1. Clean wafers: (*a*) rinse in Acetone, (*b*) rinse in running DI water, (*c*) hot HNO_3, (*d*) rinse and store in DI water.
2. Place wafers to be plated in Sensitizer Solution for 1 min.
3. Place sensitized wafer in beaker and pour in 1 part reducing solution to 4 parts plating solution. Leave wafer in this solution for at least 1 min.
4. Rinse plated wafers with DI water and blow dry.

APPENDIX B

Nickel Plating Solution

Sensitizer Solution

Same as for Silver Plating.

Activator Solution

Palladous chloride solution 2 g/liter

Plating Solution

30 g/liter Nickel Chloride
10 g/liter Sodium Hypophosphite
10 g/liter Sodium Citrate

Plating Procedure

1. Clean wafers as in silver plating procedure.
2. Place wafers to be plated in sensitizer solution for 1 min.
3. Place sensitized wafers in activator solution for 1 min.
4. Place activated wafers in plating solution at 60°C and plate for 1 min (longer if a thicker film is desired).
5. Rinse wafers in 60°C DI water and blow dry.

Brief Communication

The Influence of Dopant Concentration on the Oxidation of N-Type GaAs in H_2O

B. Schwartz* and S. E. Haszko

Bell Telephone Laboratories, Incorporated, Murray Hill, New Jersey 07974

and D. R. Wonsidler

Bell Telephone Laboratories, Incorporated, Allentown, Pennsylvania 18100

In a recent communication (1), Schwartz described the results of exposing GaAs and GaP to various oxidizing media. He showed that when n-type, silicon-doped GaAs with an $N_D - N_A = 1.5 \times 10^{18}$ was exposed to warm (60°C) water for 6 days, a readily observable crust was formed that was identified by x-ray diffraction as $Ga_2O_3 \cdot H_2O$. Figure 1 shows the as-polished surface (bottom) and the oxidized surface (top) of that sample; this was a (100)-oriented slice cut from a <111>, Czochralski-grown ingot. The observation that the oxide was nonuniform in thickness and striated over the surface of the sample called for further investigation. The series of photographs in Fig. 2 shows the one-to-one correlation between the oxide striae and strain fields in the slice, determined by reflection x-ray topography[1]; this analysis was done on a portion of the oxidized region shown in Fig. 1.

Figure 3 shows the two halves of an identical slice of GaAs, one half of which had been boiled in water for 2 hr (top), while the other half was suspended over a beaker of boiling water in air for 2½ hr (bottom). One can see the randomly oriented scratch lines left

* Electrochemical Society Active Member.
Key words: gallium arsenide, oxidation, impurity striations.

[1] Note that the x-ray topographic technique results in a mirror image of the optical photomicrograph.

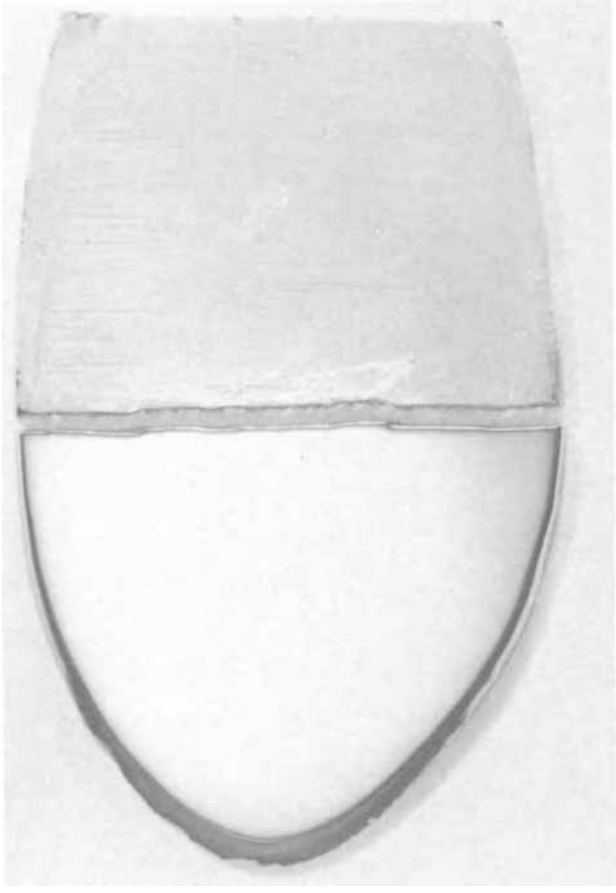

Fig. 1. Photomicrograph of (100)-oriented, Si-doped, $N_D - N_A = 1.5 \times 10^{18}$ slice of GaAs. Bottom, as-polished in Br_2-CH_3OH; top, after immersion in 60°C H_2O for 6 days (~7X magnification).

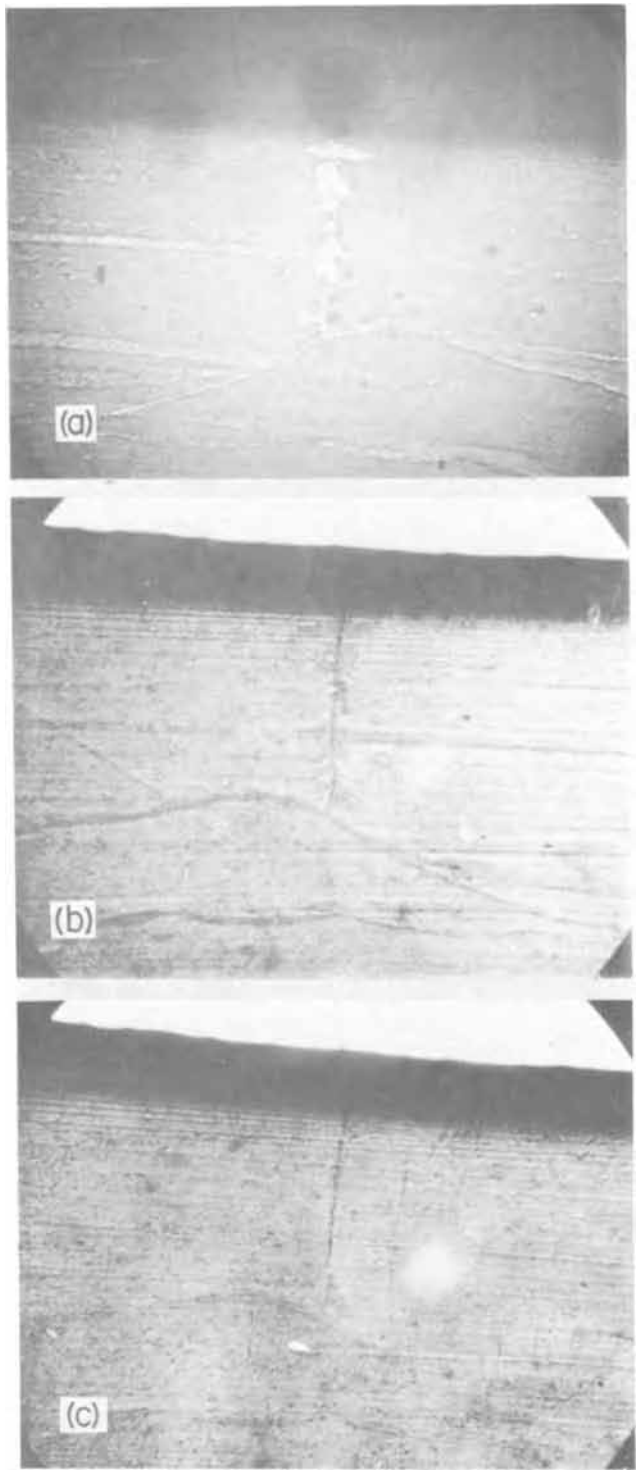

Fig. 2. Photomicrograph of portion of same sample as Fig. 1 top, showing correlation of strain fields and oxide striae: (a) optical photograph of as-deposited film (~30X magnification); (b) x-ray topograph of same area with oxide still in place; (c) x-ray topograph of same area after oxide film was removed.

in both samples from the polishing operation. Nonuniform oxidation has taken place on both pieces, and the immersed sample contains thicker oxide regions than does the sample exposed to water vapor. Note that the very clearly delineated striations are regions of lines which alternate in tilt from the horizontal. This is the two-dimensional representation one would expect to find on looking at a (100) plane cutting through an inhomogeneous medium, with the inhomogeneity being basically a helical plane, with the <111> as the major axis of the helix (2, 3). Obviously, the fact that the major striae are made up of groups of parallel striae indicates that there is also a radial inhomogeneity as well as the vertical helix to be considered.

An electron beam microprobe analysis of a portion of the oxidized sample shown in Fig. 3 (top) established: (a) that the Ga:O ratio is 1:2, a finding consistent with the formula $Ga_2O_3 \cdot H_2O$ found by x-ray analysis; and (b) that, where the oxide was thick, the integrated silicon concentration was high and, where it was thin, the integrated silicon concentration was low (see the schematic in Fig. 4). As Fig. 4 shows, at the surface of the GaAs, the silicon content was relatively uniform, while, only a short distance below the surface (about 7000Å), it was again high in the region of the thick oxide.

When these data are coupled with the fact that an attempted oxidation of GaAs doped at 2×10^{17} in boiling water for 5 hr produced an oxide only about 50-100Å thick, it becomes clear that free carrier concentration greatly influences the oxidation rate of GaAs in water. The strong striation effect seen in Fig. 3 merely reflects the free carrier inhomogeneity caused by the nonuniform distribution of the dopant, when Czochralski growth of GaAs is attempted at silicon concentrations above about 1×10^{18}.

Lest one conclude that this striation effect might be due strictly to the silicon in the samples, we can report that striated oxide growth has also been observed in the oxidation of boat-grown, n-type, Te-doped GaAs with an $N_D - N_A = 3 \times 10^{18}$, where the silicon concentration was known to be extremely low.

Manuscript received Apr. 12, 1971.

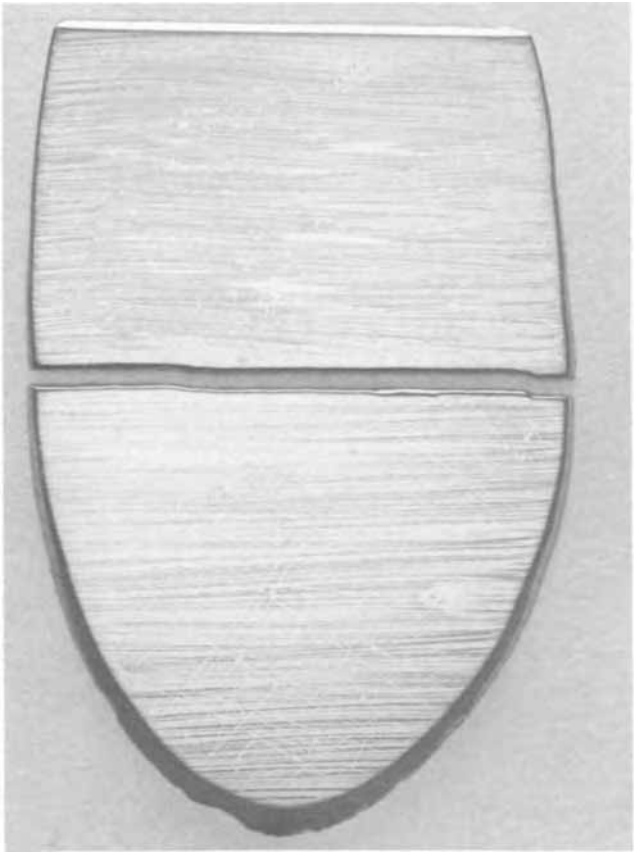

Fig. 3. Photomicrograph of (100)-oriented, Si-doped, $N_D - N_A = 1.5 \times 10^{18}$ slice of GaAs. Bottom, after exposure to boiling-water vapor for 2½ hr. Top, after immersion in boiling water for 2 hr (~7X magnification).

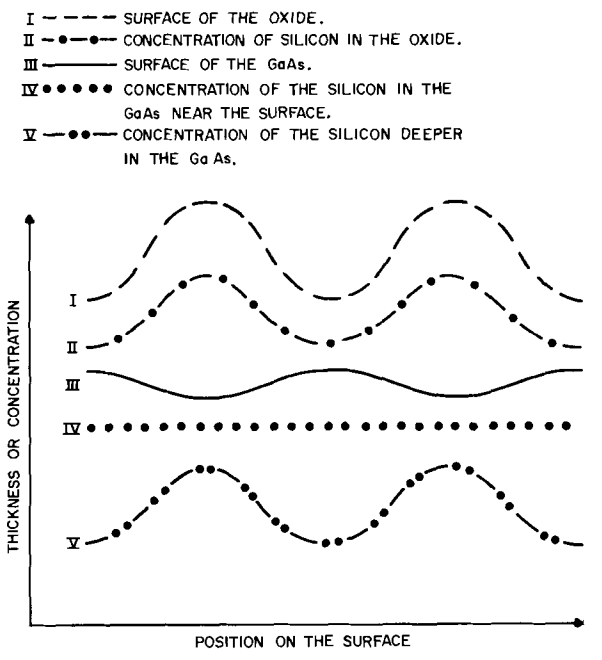

Fig. 4. Schematic to show the conditions at the surface of the sample shown in Fig. 3, top.

Any discussion of this paper will appear in a Discussion Section to be published in the June 1972 JOURNAL.

REFERENCES

1. B. Schwartz, *This Journal*, **118**, 657 (1971).
2. J. A. M. Dikhoff, *Solid-State Electron.*, **1**, 202 (1960).
3. K. Morizane, A. F. Witt, and H. C. Gatos, *This Journal*, **114**, 739 (1967).

Correction

In the paper "The Use of Metal-Organics in the Preparation of Semiconductor Materials," two parts of which appeared in the April 1971 JOURNAL, Vol. 118, No. 4 (part II, "II-VI Compounds," by H. M. Manasevit and W. I. Simpson, pp. 644-647; part III, "Studies of Epitaxial III-V Aluminum Compound Formation Using Trimethylaluminum," by H. M. Manasevit, pp. 647-650), Fig. 1 of part II (p. 644) was transposed with Fig. 1 of part III (p. 647).

JOURNAL OF THE ELECTROCHEMICAL SOCIETY

ELECTROCHEMICAL TECHNOLOGY

JULY 1971

The Operation of an Ion-Membrane Fuel Cell with Microbially-Produced Hydrogen

G. C. Blanchard

Laboratory Service, Veterans Administration Hospital, Boston, Massachusetts 02100

and R. T. Foley*

Department of Chemistry, The American University, Washington, D. C. 20016

ABSTRACT

A consideration of various methods of converting the energy associated with biochemical or microbiological reactions to electrical energy indicates that the most practical approach is the indirect whereby products produced by enzymatic reactions are fed to an electrochemical converter. Hydrogen can be produced by the action of *Clostridium perfringens* on glucose and natural product substrates in technologically significant quantity and purity. The hydrogen produced by the action of *Clostridium perfringens* on glucose and bananas (as an example of natural products) has operated an ion-membrane H_2-O_2 fuel cell for periods of 24-48 hr with no evidence of detrimental reactions. Such systems operate at power densities order-of-magnitude greater than direct biochemical fuel cells wherein the enzymatic reaction takes place on the electrode. They would offer advantages for operation in remote areas.

In the last decade there has been a renewed interest in utilizing biochemical or microbiological reactions for energy conversion. Aside from scientific curiosity, the new emphasis has been derived from the desire to use cheap and readily available fuels for the production of electrical energy.

There are three general methods by which microorganisms or enzyme solutions can convert chemical energy into electrical energy: *1*) Synthesis of metabolic products which either increase or decrease the potential of the medium with respect to its original state (bioanodes); 2) Depolarization of cathodes, thus permitting spontaneous galvanic cells (*i.e.* Mg-Fe couple) to function at a reasonable rate (biocathodes); *3*) Synthesis of gaseous products (H_2, CH_4, NH_3) which can be subsequently fed to some electrochemical converter.

The purpose of this paper is to report on work employing the third conversion method, the utilization of microbially-produced hydrogen in a hydrogen-oxygen fuel cell.

Pioneering work on the utilization of microbiological reactions for energy conversion was done around 1910 by Potter (1). More precise work was done in 1931 by Cohen (2). Also, at this time Boyd and Reed (3), Clifton, Cleary, and Beard (4), and Johnstone (5) conducted experiments which were successful in clarifying the oxidation-reduction relationships developed in *E. coli* cultures. In the early 1960's the field dealing with the utilization of microorganisms to produce electrical power was revived. Sisler (6), Rohrback, Scott, and Canfield (7), and Wilson (8) described the operation of "biochemical fuel cells" based on the sulfate reduction capability of *Desulfovibrio desulfuricans,* the latter author clarifying the cathode depolarizing role of the bacteria. In this period, several attempts were made to use natural products, an objective related to the present investigation. Silverman (9) reported on a cell which involved the oxidation of formic acid produced from coconut milk, and Perry and Christopulos (10) a cell involving the oxidation of ethanol produced by the action of yeast on glucose.

From a survey of these and other reports (11) it may be concluded that no system possessing significant electrochemical capacity derived only from microbiological energy has been developed to the working state. The cells that have operated at practical power levels, derived their capacities from sacrificial anodes (*e.g.* Mg). The so called "direct" biochemical fuel cell which would have the enzyme-substrate electron transfer reaction occur on the metallic electrode has been limited by colloid chemistry considerations. Specifically, in bacterial systems the electron transfer process takes place within large molecules or within cell structures which are separated from the electrode by distances very large when compared with atomic (electron transfer) dimensions. This then suggests that the energy associated with the microbiological process might be best converted by the employment of the low molecular weight products formed during the growth of microbial cells. This has led to the investigation of the production of hydrogen by microorganisms and the utilization of microbiologically produced hydrogen in a hydrogen-oxygen fuel cell.

Blanchard *et al.* (12, 13), and May *et al.* (14) examined 18 different microbial species and showed that *Clostridium perfringens* (ATCC 10873) produced hy-

* Electrochemical Society Active Member.

Key words: fuel cell, biochemical fuel cell, microbial hydrogen, clostridium perfringens, energy conversion.

drogen at a greater rate and quantity than any of the other species. The present report deals with the utilization in an ion-membrane type fuel cell of hydrogen produced by *Clostridium perfringens* with glucose and natural product substrates.

Experimental Materials and Methods

The microorganism used in this study, *Clostridium perfringens* ATCC 10873 was obtained from the American-type culture collection, Rockville, Maryland. Stock cultures were maintained with 2% deep liver medium (15). Inocula for fermentors and Warburg flasks were prepared by growing the cells in 2% glucose deep liver medium for 18 hr at 37°C. Cells were harvested in a Sharples-type centrifuge, washed twice by centrifugation and suspended in 0.1M phosphate buffer at pH 6.5. The number of bacterial cells being studied was determined microscopically with a Petroff-Hausser counting chamber and by a standard plate count on Brewer Anaerobic Agar (BBL). The number of cells used for inoculation varied depending on the experiment being performed. In the fuel cell experiments a cell suspension sufficient to yield 5 x 10^9 cells/ml in the final fermentation broth was used.

The ability of *Cl. perfringens* to produce hydrogen from fruits and vegetables was evaluated by Warburg respirometry. The natural product resulting in the greatest rate and yield of hydrogen was then evaluated in a fermentation system. The fermentation studies were performed in tightly closed glass carboys especially adapted with sampling ports for the addition and removal of either gas or liquid samples during the fermentation. The medium (medium 1) for the glucose experiments contained 10 liters of Quinns (16) D-58 salts solution [10.9g $(NH_4)_2SO_4$, 21.8g $MgCl_2 \cdot 6H_2O$, 60.5g $K_2HPO_4 \cdot 3H_2O$, 12.0g KH_2PO_4, 1.3g $CaCl_2$ and 10 liters of tap water], 200g glucose, 100g tryptone, 100g yeast extract and 50 ml of salts B (17). Fermentors containing banana suspensions were prepared by homogenizing 2000g of bananas in 20 liters of D-58 salts solution (16) and salts B (17). The banana medium was sterilized in an autoclave deaerated with helium and inoculated by the same procedures as used for the glucose fermentors.

Gas evolution from the fermentors was recorded in a wet test meter (Precision Scientific Company). The composition of evolved gas was determined by gas chromatography using a cross-section ionization detector with 25 x ⅛ in. column of 100/120 mesh, 13 x molecular sieve and a 7 x ⅛ in. column of 200/230 mesh, silica gel as previously described (12, 13, 18). This system easily separated H_2, O_2, N_2, CH_4, CO_2, and CO and detection was in the parts per million range.

The hydrogen-oxygen ion-exchange membrane fuel cell was supplied by the Direct Energy Conversion Operation of the General Electric Company. This fuel cell which uses air as the oxygen source, and operates at one atmosphere of pressure was assembled with the instrumentation as shown in Fig. 1. The input gas line to the fuel cell was attached to a three-way valve which permitted operation of the system first on tank helium to flush the cell, then on tank hydrogen to calibrate, and then on hydrogen supplied by the microbial generator. The unit was cooled by flowing tap water. The cell was flushed with helium for 15 min before and after use, and stored under helium. The exposed membrane was kept moist during use by occasional wetting with distilled water. During storage the exposed membrane was moistened and sealed.

Results and Discussion

Hydrogen generation from glucose and natural products.—The objective of the microbiological studies was to develop a hydrogen generator which would produce hydrogen of sufficient quantity and purity to operate a hydrogen-oxygen fuel cell at a practical level. To accomplish this objective, studies were performed to determine the factors which limit the rate

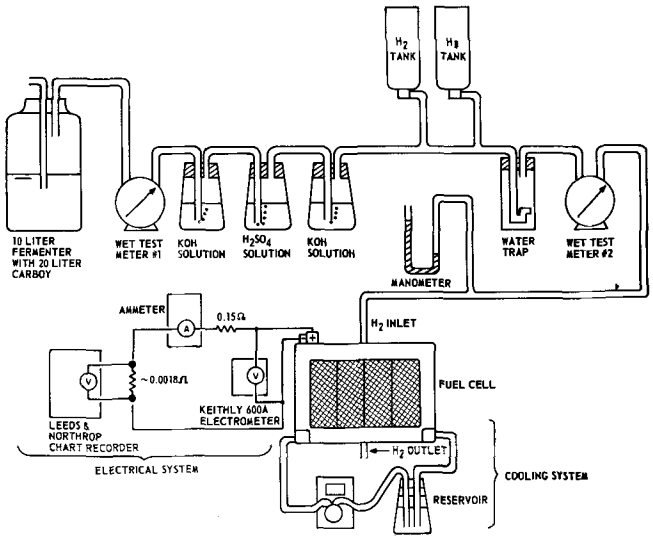

Fig. 1. Experimental arrangement with ion-membrane fuel cell utilizing microbially-produced hydrogen.

and total yield of hydrogen production as well as to establish the conditions required for maintaining continuous hydrogen evolution and power production by the microbial fermentor system. These studies will be reported in detail elsewhere (19) but certain observations can be made to summarize the pertinent findings as follows:

1. Hydrogen evolution was proportional to cell number between 3 x 10^8 and 3 x 10^9 cells. Beyond this number a lower hydrogen yield per cell was obtained.
2. Both the initial pH and the incubation temperature were important in the synthesis of the hydrogen evolving system. The greatest activity per (resting) cell was obtained at 30° to 35°C in a medium with an initial pH of 5.0-6.5. Essentially no hydrogen was formed by cells grown at 40°C at any pH.
3. For growing cells the optimum pH for growth was between pH 5.9 and 7.5, whereas the optimum pH for hydrogen generation was between pH 5.9 and 6.9.
4. Hydrogen production in the fermentors appeared to be directly related to the glucose concentration; the bacterium produced 34 liters or about 1.5 moles of hydrogen from 0.77 moles of glucose.
5. It appeared possible to obtain continuous gas production in the fermentors by using a large inoculum, a nonlimiting substrate concentration, and a pH between 5.5 and 7.0.
6. Using optimized conditions hydrogen could be produced at a constant rate of about 10 liters per hour.
7. The study of the ability of *Cl. perfringens* to metabolize fruit and vegetable homogenates, as tested in a Warburg respirometer, showed that the resting cells produced hydrogen without lag and that the rate of production and total yield was greater with banana, cucumber, squash, and grapes than with glucose or other natural products (Fig. 2).

Fuel cell studies with microbial hydrogen generators.—After demonstrating that hydrogen production by microbial generators could be maintained at a uniform rate the power output by the hydrogen-oxygen fuel cell was studied using microbially-produced hydrogen. The system used for fuel cell calibration and for determining power production by the microbial fermentors is shown in Fig. 1. For calibration, the fuel cell was first flushed with helium for 15 min and then flushed with tank hydrogen. Tank hydrogen was allowed to flow through the fuel cell at a rate in excess of the fuel cell consumption. The input hydrogen rate was measured but no attempt was made to measure the excess output hydrogen except by visually observing it bubble through approximately ½ in. of water. The helium flush was used to remove oxygen

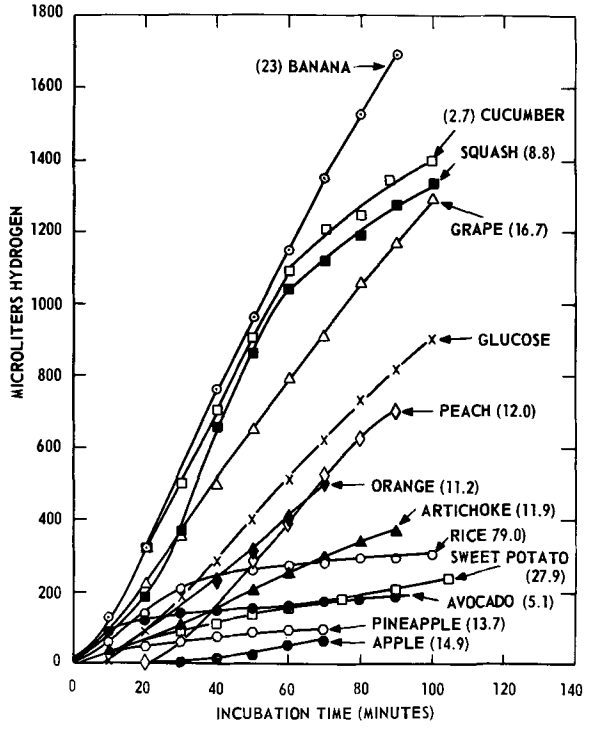

NUMBERS IN PARENTHESIS REPRESENT APPROPRIATE CARBOHYDRATE COMPOSITIONS ON BASIS OF WET WEIGHT (WOOSTER AND BLANDS)

Fig. 2. Production of hydrogen from natural products

which might have entered the internal membrane surface during storage.

After demonstrating that the fuel cell was performing properly, a microbial generator containing 10^{14} cells in medium 1 was assembled as shown in Fig. 1. The microbial generator was permitted to incubate and thus flush with microbial hydrogen for 2 hr before connection to the fuel cell. During these 2 hr the fuel cell was flushed with helium for about 30 min, followed by hydrogen for 90 min. Hydrogen from the microbial generator was allowed to flow through the fuel cell at a flow rate of 7 liters/hr. In the initial experiments hydrogen generation decreased during the periods when glucose and NH_4OH were added to the fermentation mixture. However, these problems were overcome by the use of glucose solutions, previously deaerated by nitrogen flushing and by slow addition of the glucose and NH_4OH to the bottom of the fermentor. Although some fluctuations were observed in hydrogen production during the 22 hr experiment, power production was steady between the 3.1 and 3.3W (Fig. 3). Glucose and NH_4OH were added periodically to maintain a nonlimiting substrate concentration and a pH between 5.6 and 6.8. At the end of the experiment the fuel cell was tested with tank hydrogen to make certain that no loss in efficiency had occurred.

The microbial generator system used for demonstrating power production from bananas was identical to Fig. 1 except two 10 liter fermentors were used to make certain that hydrogen production would be in excess of the fuel cell requirement. Each of the two fermentors were prepared as described above and contained 2000g of homogenized bananas in D-58 salts solution and an inoculum of 10^{14} cells of *Cl. perfringens*. The microbial generator was flushed with its own gas for 3 hr while the fuel cell calibration was being performed. The hydrogen line from the microbial generator was clamped off for 10 min prior to connection to the fuel cell. This step partially eliminated the fluctuation in pressure which occurs when the microbial generator is connected to the fuel cell. The results in Fig. 4 show that the 2000g of bananas added initially contained sufficient quantities of fermentable carbohydrate to maintain the hydrogen evolution rate relatively constant for 24 hr. As a result of this, the power output was maintained between 3.1 and 3.5W for the 24 hr. It is believed that the fluctuations which did occur in the hydrogen evolution rate were due to changes in the pH of the medium and that an automatic pH controller would eliminate this variation.

These studies demonstrate the feasibility of using microorganisms to convert natural products into hydrogen for use in a hydrogen-oxygen fuel cell. No serious problem was found in coupling the biochemical hydrogen generator to a commercially available fuel cell. Although no problems were observed in 24 to 48 hr operation, studies of greater duration would be needed before conclusions could be drawn about long-term performance. However, the gas chromatographic analysis of the gas does not indicate the presence of compounds such as CO which are known to poison the catalytic electrodes of the fuel cell.

The ability to use hydrogen from fruits and vegetables suggests that this approach for utilizing microbiological energy offers potential for use in remote areas, because the unit can operate on natural products obtained on-site. This, of course, offers certain logistic advantages over most of the other presently available hydrogen generators.

A comparison of these results with those reported for the direct approach (methods 1 and 2 above) indicates that the indirect biochemical fuel cell approach for generating energy from biological materials is far more successful than the direct approach. A good direct

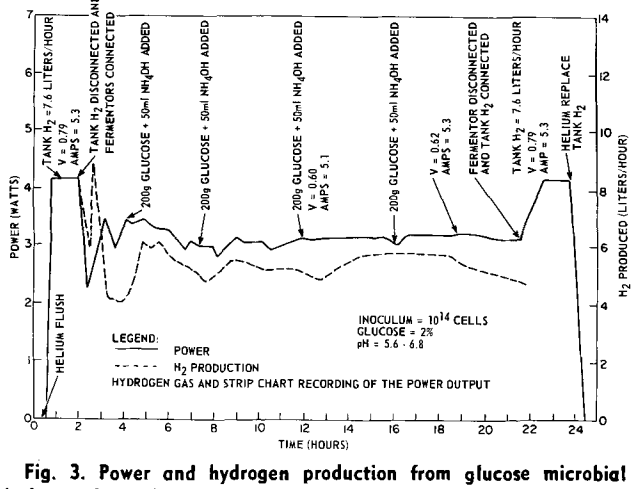

Fig. 3. Power and hydrogen production from glucose microbial hydrogen fuel cell system.

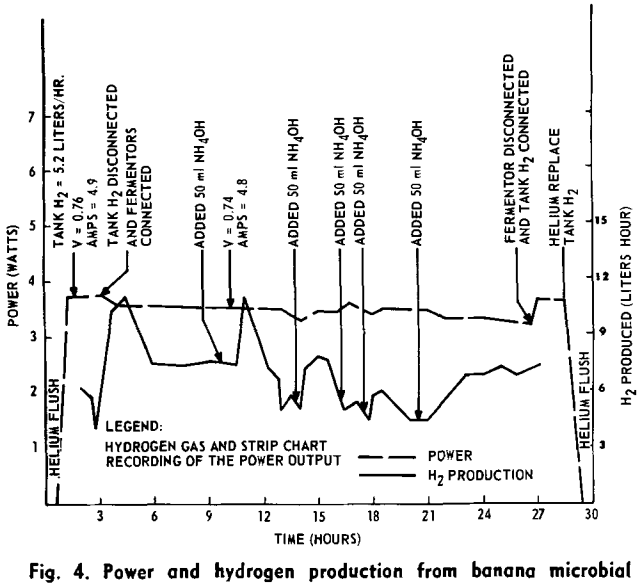

Fig. 4. Power and hydrogen production from banana microbial hydrogen fuel cell system.

biochemical fuel cell will produce about 10 mA at 0.3V with a 100 cm^2 electrode, or a current density of 0.1 mA/cm^2 at 0.3V. Microbially produced hydrogen in the H_2-O_2 fuel cell produced about 5A at 0.78V with an air electrode size of 272 cm^2. This is about 18 mA/cm^2 at 0.78V. Thus, the indirect approach has given 100 to 500 times greater current densities than the direct approach, and has bypassed all the nettling electrochemical difficulties which followed from the direct approach. In using the indirect method of utilizing microbiological processes the limitation in the electrochemical sense is imposed by the hydrogen-oxygen fuel cell rather than the microbiological process. Until the problems associated with electrode reaction in solution are solved, the direct approach will probably always give much lower current densities than the indirect approach. Because there are no obvious solutions to these problems, it would appear that future effort can be more profitably directed to the indirect approach.

Acknowledgments

This study was supported by the U. S. Army Electronics Command at Fort Monmouth, New Jersey, under contract number DA 36-039-SC-90878. The authors are grateful to Melpar, Inc. of Falls Church, Virginia, for permission to publish this work.

Manuscript submitted Aug. 26, 1970; revised manuscript received Feb. 23, 1971.

Any discussion of this paper will appear in a Discussion Section to appear in the June 1972 JOURNAL.

REFERENCES

1. M. C. Potter, *Proc. Royal Soc. (London), Ser. B*, **84**, 260-276 (1911).
2. B. Cohen, *J. Bacteriology*, **21**, 18-19 (1931).
3. E. M. Boyd and G. B. Reed, *Can. J. Res.*, **4**, 605-613 (1931).
4. C. E. Clifton, J. P. Cleary, and P. J. Beard, *J. Bacteriol.*, **28**, 541-559 (1934).
5. K. I. Johnstone, *J. Pathol. and Bacteriol.*, **54**, 25-38 (1942).
6. F. D. Sisler, *New Scientist*, **12**, 110-111 (1961).
7. G. H. Rohrback, W. R. Scott, and J. H. Canfield, Paper presented at the 16th Annual Power Sources Conference at Atlantic City, N. J., May 22-24, 1962, sponsored by the U.S. Army Signal Research and Development Laboratories, Fort Monmouth, N. J.
8. B. J. Wilson, "Experiments with a Magnesium Seawater Cell Incorporating a Bacterial Colonized Cathode" NRL Report 5998, October 4, 1963.
9. H. P. Silverman, Biochemical Fuel Cell, Contract DA 36-039-SC-90866, July 1962 to July 1965.
10. J. Perry, Jr. and J. Christopulis, "Biochemical Fuel Cells," Proceedings of the 19th Annual Power Sources Conference, pp. 19-23, May 18-20, 1965.
11. K. Lewis, *Bacteriol. Rev.*, **30**, 101-113 (1966).
12. G. C. Blanchard, R. T. Foley, and M. J. Allen, "Biochemical Fuel Cells." Proceedings of the 17th Annual Power Sources Conference, May 1963.
13. G. C. Blanchard, C. R. Goucher, and M. A. Mitz, "Biogeneration of Hydrogen from Waste for Fuel Cell Utilization." Paper presented at the 149th American Chemical Society Meeting, Detroit, Michigan, April 4-9, 1965.
14. P. J. May, G. C. Blanchard, and R. T. Foley, "Biochemical Fuel Cells," Proceedings of the 18th Annual Power Sources Conference, May 1964.
15. W. C. Haynes, L. J. Wickerham, and C. W. Hesseltine, *Applied Microbiol.*, **3**, 361 (1955).
16. L. Y. Quinn, Personal communication (1964).
17. M. I. Krichevsky, I. Friedman, M. F. Newell, and F. D. Sisler, *J. Biol. Chem.*, **236**, 2520-2525 (1961).
18. K. Abel, *Anal. Chem.*, **36**, 954 (1964).
19. G. C. Blanchard, To be published.

Electroless Copper Plating as an Image Amplifier for Electrolytic Printing

Dennis R. Turner* and Catherine Wolowodiuk

Bell Telephone Laboratories, Incorporated, Murray Hill, New Jersey 07974

ABSTRACT

Electroless copper plating was found to be an effective image amplifier for silver electrolyzed into paper. An amplification factor of up to one million times was demonstrated. The small amount of silver required to produce an image makes high-speed electrolytic printing feasible. This was demonstrated with 1 μsec-20V pulses used to electrolyze silver into a moving paper, followed by electroless copper plating.

Electrolytic printing is an old art. The first record of its use or recording facsimile was in 1843. The technique was used for many years in telephone and radio facsimile recording where immediate visual observation of the result was more important than the print quality (1). Electrolytic printing has also been used for qualitative analysis of a metal by electrolytically dissolving the metal into paper containing a specific reagent capable of producing a colored reaction product with the metal ions (2).

To our knowledge, the only present-day commercial application of electrolytic printing for facsimile application is in the Stewart-Warner System known as Datafax. In Datafax printing, an electrolyte premoistened paper is slowly pushed between two electrodes. The cathode is mounted on a drum in a spiral fashion so that, as the drum rotates once, the cathode area which contacts the paper moves across the entire width of the paper. The anode is a strip of silver on the opposite side of the paper. Silver is electrolyzed into the paper from the anode bar where it is reduced to the metallic form by a chemical reducing agent contained in the paper. The entire image is composed of finely divided silver particles which appear black in the paper. The speed of printing is relatively slow since the rate of anodic silver dissolution is limiting. An 8½ by 11 in. page of print is reproduced in about 6 min. The silver anode bar must be replaced periodically as it is consumed. The Datafax technique cannot be speeded up to produce 1 page of printed copy in about 2 sec as is required for some applications. The cathode drum rotation speed becomes too high and it is not

* Electrochemical Society Active Member.

Key words: silver electrolysis, pulse anode dissolution, paper-supported electrolyte, catalytic sensitivity, hard copy.

practical electrochemically to electrolyze enough silver into the paper in the time required.

This paper describes a new process in which relatively small amounts of silver are electrolyzed into the paper from stationary multiple electrodes. This silver serves as a catalyst to carry out electroless copper metal deposition which serves to amplify the latent silver image. Since very small amounts of silver are required, the process is sensitive and high writing speeds can be achieved. A prime advantage of electrolytic printing over electrostatic printing is that it can be carried out at relatively low voltages between 2 and 20V as compared to 300-600V for electrostatic methods. One important consequence of this is that cheaper solid-state electronic devices can be used for accessing individual electrodes of multiple arrays when low voltages are involved.

Over-all Description of Electrolytic Printing Technique

A schematic view of the electrolytic printing process is shown in Fig. 1. The paper is preimpregnated with electrolyte, rolled tightly, and kept in a confined compartment. This arrangement keeps the paper moist for long periods of time—months. As printing is required, the paper is passed over an electrode assembly. Good image resolution can be achieved with an electrode array 8 in. wide and segmented into about 1700 individual electrodes. These can be accessed by electronic means, so that pulsed printing signals are fed into individual electrodes as the paper moves by. Counter-electrodes can be placed on the opposite side of the paper but, for very rapid paper transport, it is more practical that both anode and cathode electrodes are on the same side as illustrated in the printing electrode detail shown in Fig. 1. Very small amounts of silver are electrolyzed into the paper with each pulse and this is amplified with an electroless plating solution. Finally, the paper is cut into suitable length to provide the hard copy required. A detail of the electrode assembly is shown in cross section indicating one silver anode electrode and one platinum cathode. Electronic techniques are available so that it is not necessary to provide a separate cathode electrode for each anode.

All the common metals available were tried as anode electrodes; however, silver proved to be most effective. Other materials were also tried in place of platinum; nickel was found to be suitable. Most of the exploratory work was done with pairs of electrodes—one silver and one platinum spaced 12 μm apart with Mylar film and potted in epoxy resin.

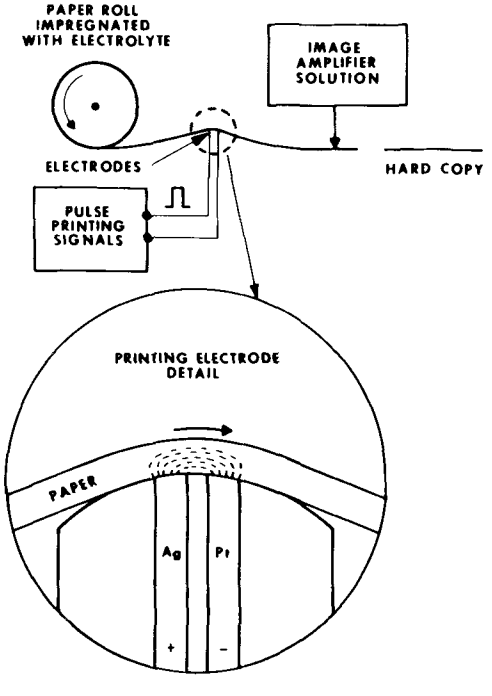

Fig. 1. Schematic of electrolytic printing process

The paper used for electrolytic printing must meet certain requirements: (*a*) high absorbency to electrolyte and development solutions, (*b*) good wet strength, (*c*) reasonably smooth surface, (*d*) long-term stability to solutions and residues, and (*e*) low cost. The paper industry has developed papers which meet these requirements. They are mainly cellulose-base papers containing an organic polymer (usually melamine-formaldehyde resins). Most of our work was done with paper developed for the Datafax printing process.

The paper was preimpregnated with either sodium or potassium nitrate solutions, 0.1-1 normal. Current flows between the silver and platinum electrodes through the paper as a voltage pulse is applied. Silver dissolution occurs at the anode and nitrate reduction takes place at the cathode. It is not clear at this point whether the silver enters the paper as silver ions or a silver oxide is formed which is wiped off by the moving paper. In either case, the silver is reduced to metallic silver in the presence of the reducing agent used in the electroless copper plating solution. The cathode reaction involves the reduction of nitrate ions. This is a low cathode polarization reaction with no gas evolution to complicate the printing process. One reason silver is such a good anode electrode material is that the kinetics of silver dissolution are extremely favorable as illustrated in Fig. 2. The Tafel relation was constructed from exchange current data reported by Price and Vermilyea (3), 7 A/cm^2 and a transfer coefficient of 0.32 as determined by Gerischer (4). Typical current densities using 20V pulses of 1 μsec duration are about 80 A/cm^2. Even at this high current density, as seen in Fig. 2, the polarization voltage is only slightly more than 0.3V. Therefore, silver dissolution does not appear to be a limiting process. Most of the applied potential appears as an *IR* drop in the paper between the electrodes.

An oscilloscope recording of the voltage pulse applied to the electrodes and the resulting current pulse are shown in Fig. 3. The top curve is the voltage pulse. The vertical axis is 2V per large division; thus, the applied pulse is 11.2V. The time axis is 1 μsec per large division so that the pulse is about 2 μsec long. The corresponding current pulse reaches a maximum of 30 mA and decreases slightly with time. This corresponds to a current density of about 55 mA/cm^2 at the silver anode. The electrolyte used in this experiment was 0.5*N* sodium nitrate solution.

Assuming a double-layer electrode capacitance of 20 μf/cm^2, the number of coulombs required to charge the double layer to the full voltage of 11.2V is about 1000 times less than the total coulombs in the current pulse. Thus, most of the current flowing during each pulse electrolyzes silver into paper.

Study of Electroless Plating Process

Preliminary results indicated that an electroless copper plating solution could be used as an image amplifier. However, it was necessary to optimize the process so that image amplification could be maximized. Previous work (5) indicated that there is a minimum amount of catalysis which will initiate plating for a given electroless metal plating solution and conditions.

A simple technique was developed to test the effect of modifying the electroless copper bath composition and temperature on the ability of the process to develop a latent silver image in paper. Strips of No. 1 Whatman filter paper about 1.4 cm wide and 7 cm long were ruled into five sections 1.4 cm long. A 0.05 drop of silver nitrate solution from a microsyringe was placed in the center of each section. By varying the silver nitrate concentration of the drop placed in each section, a range of silver concentrations was achieved in each paper strip. Silver ions probably were reduced to metallic silver by room light; however, the reducing agent in the electroless plating solution would convert

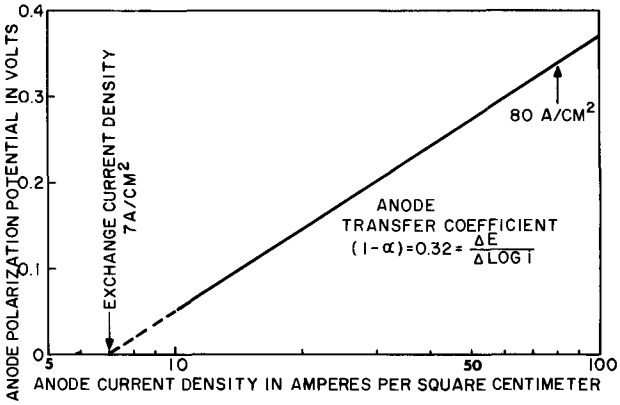

Fig. 2. Silver anode polarization relation from kinetic parameters: $i_o = 7$ A/cm² and $(1 - \alpha) = 0.32$.

any unreduced silver. The paper strips could be made up in quantity, dried, and stored for later use.

The effect of temperature on electroless copper plating sensitivity with various amounts of silver is illustrated in Fig. 4. The total amount of silver placed in each section ranged from 5×10^{-12} to 5×10^{-8}g. The area of the developed spot varied from about 0.16 to 0.33 cm². The images were black or dark brown and permanent-ideal for hard copy. Thus, the amount of silver per unit area ranged from about 3×10^{-11} g/cm² for the lowest to 1.5×10^{-7} g/cm² for the highest in Fig. 4. It is well known (6) that increasing bath temperature increases the electroless copper plating rate. The results of Fig. 4 show that increased temperature also increases copper plating sensitivity to small amounts of silver catalyst. The optimum bath (to be described later) was used in this experiment. A 10 deg increase in temperature (50°-60°C) results in a 100 times increase in sensitivity. The over-all image amplification capability of electroless copper plating at 60°C is about one million times. This was determined by increasing the silver concentration in each drop until a visible image in reduced silver was observed. This occurred at a silver concentration of 5×10^{-5} g/cm² on the paper.

At 60°C, an unstabilized electroless copper bath decomposes in a few minutes. However, the copper image on silver develops in a few seconds at 60°C so there is a margin of safety. Furthermore, a fast development time is desirable for a practical printing process and the hot solution facilitates drying.

The composition of the electroless copper bath was studied to optimize it for maximum sensitivity without premature bath decomposition. Copper ion concentration, complexing ion and its concentration, reducing

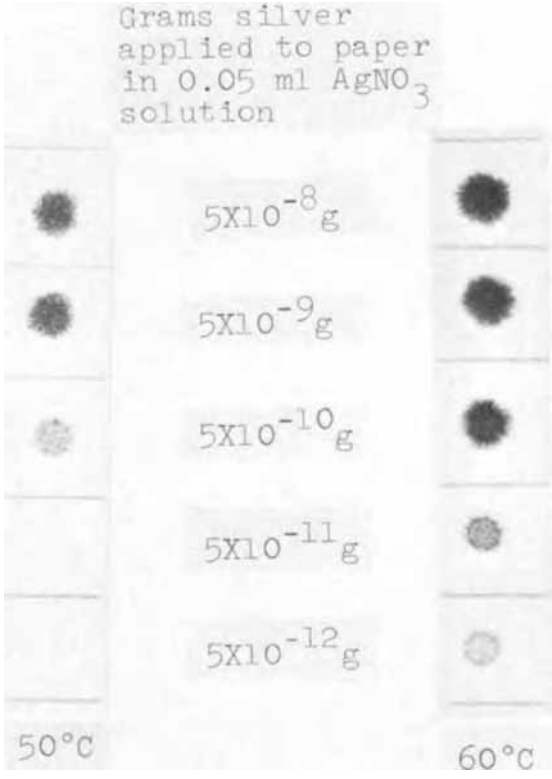

Fig. 4. Effect of electroless copper solution temperature and silver concentration in paper on image development sensitivity.

agent concentration, and *p*H were varied. The calibrated silver spots on paper strips[1] were used to observe the effects of bath composition changes. The effect of copper concentration is shown in Fig. 5—between 10 and 60 g/liter copper sulfate—$CuSO_4 \cdot 5H_2O$. In these experiments, Rochelle salt complexing agent concentration was 2½ times the copper concentration. KOH concentration was equal to the copper concentration and development time was 5 sec. The temperature was 60°C. At 10 g/liter, the image was just visible at 5×10^{-10}g of silver. Whereas, at 60 g/liter copper sulfate, a dark image is visible at 5×10^{-12}g silver but

[1] This idea of a catalyst-impregnated paper strip is considered to be a simple and convenient way of monitoring the condition of any electroless metal plating bath and particularly one that must initiate plating on surfaces containing a relatively small amount of catalyst. This work also suggests that, under certain conditions, two electroless baths may be desirable: one which initiates metal deposition with very small amounts of catalyst present but has a short life, and a second which deposits that bulk of the metal with good physical properties and has a long bath life.

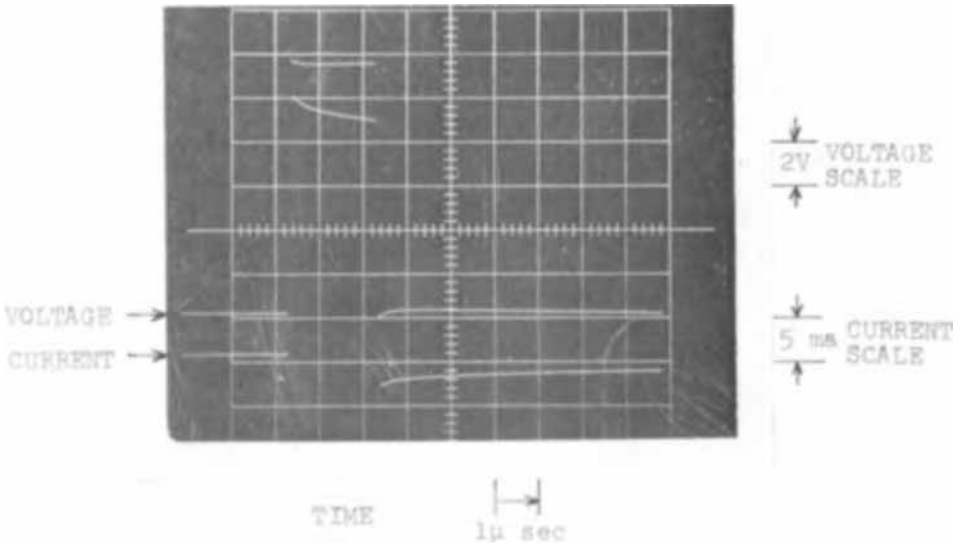

Fig. 3. Typical voltage pulse and corresponding current pulse. Silver anode and platinum cathode. Electrolyte 0.5*N* $NaNO_3$.

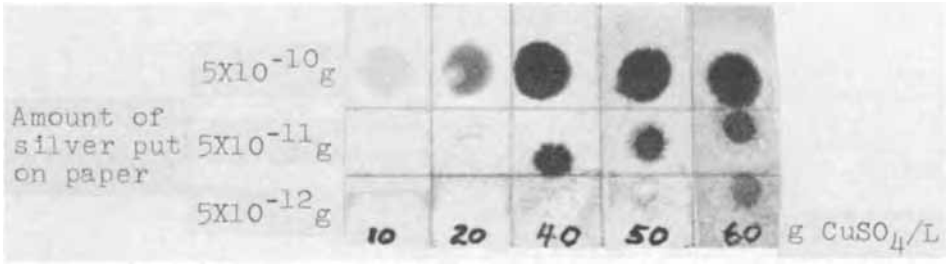

Fig. 5. Effect of copper sulfate concentration on sensitivity of the electroless copper amplification process.

the bath decomposes and darkens the paper. On the basis of this study, 20-40 g/liter copper sulfate were considered optimum.

Rochelle salt was found to be better than EDTA[2] as the copper complexing agent, and paraformaldehyde was better than formaldehyde as the reducing agent since it left less residual odor in paper. The optimum solution composition arrived at is as follows:

Electroless Copper Image Amplifier Solution

Part A	g/liter
Copper sulfate ($CuSO_4 \cdot 5H_2O$)	40
Rochelle salt ($NaKC_4H_4O_6 \cdot 4H_2O$)	100
Potassium hydroxide (KOH)	40
Part B	
Paraformaldehyde $(HCHO)_3$	130
Potassium hydroxide (KOH)	120

The bath is made up in two parts. As an image amplifier, an equal volume of each part is mixed together so that the final concentration of each constituent is one half that shown above (for example, 20 g/liter copper sulfate, *etc.*). It is estimated that, to develop an 8½ by 11 in. page of print, about 5 cc of electroless copper solution are required.

Over-all Feasibility Study

The initial phase of a feasibility study on the over-all technique was carried out using stationary electrodes consisting of one silver and one platinum electrode. Later, a multiple electrode array was used. The problem of moving paper past the electrodes at the required speed to simulate printing 1 page in 2 sec without resorting to a large expensive machine was resolved by adapting a record player capable of turntable rotation speed of 16 rpm. A strip of premoistened Datafax paper, 2 cm x 5 cm, attached to a 12 in. long-play record about 5 in. (12 cm) from the center moves at about the right speed at 16 rpm. The spacing between microgrooves on an LP record is 0.17 mm which is about the spacing desired between electrodes across a page, and between scan raster lines down the page. The electrode assembly was fastened to the record player needle transport head and, while the record needle tracked in the microgrooves, the electrode assembly moved over 0.17 mm each revolution. An E-H Research Laboratories, Incorporated, electronic pulser generated a 1 μsec 20V pulse with 1000 μsec between pulses. These pulse trains were interrupted with a mechanical switch made by attaching a gold foil to the edge of the record and masking off sections of gold with Scotch tape. A spring contact then was placed on the record at that point and, as each conducting strip moved past the contact, voltage pulses were applied to the printing electrodes.

After a latent image of silver is printed into the paper, the image is made visible with electroless copper plating as previously described. Success of the printing process with very short pulses down to 1 μsec and 1000 μsec between pulses is illustrated in Fig. 6.

[2] Ethylenediamine tetra acetic acid-sodium salt.

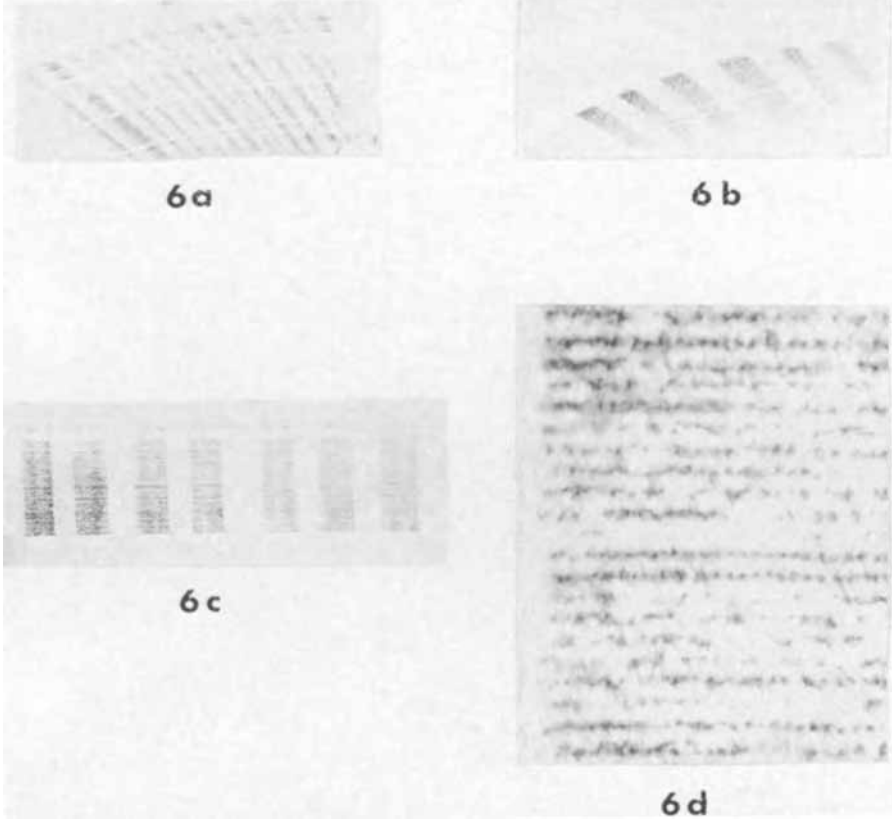

Fig. 6. Examples of high-speed electrolytic printing with electroless copper image amplification. a—Image with 1 μsec-20V pulses 1000 μsec apart; paper moistened with 0.1*N* HNO_3; paper speed ~ 14 cm/sec. b—Same as in a; paper allowed to dry while printing. c—Image with multiple electrode printing head; electrodes 0.1 mm wide and 0.1 mm between electrodes; 30 μsec-20V pulses 1000 μsec apart. d—Magnified view of c.

The total time required to record the entire image in Fig. 6a and 6b was about 15 min. In that time, the paper tended to dry out. Therefore, in Fig. 6a the paper was kept moist with 0.1*N* HNO_3 solution. In a real electrolytic printing system, the paper would move by the electrodes only once and drying would not be a problem. The dampness of the paper is an important variable in determining the current through the paper and the amount of silver electrolyzed into the paper when voltage pulses are used. Therefore, constant current pulses are more desirable to maintain a uniform image density. Figure 6b shows the effect of drying as the paper is rotated on the record player with constant voltage pulses. The image becomes lighter with each revolution since the electrolysis current is decreasing. The result does show that the technique has a gray scale potential. In practice, the image darkness could be varied by modulating the current level of printing pulses.

Experiments were also carried out with multiple silver electrodes. These were made using standard thin film device technology. The silver electrodes were 0.1 mm wide with 0.1 mm spacing between them. Typical images formed with these multiple electrode printing heads are shown in Fig. 6c. The 1.3 cm wide electrode array contained 65 individual electrodes. For these experiments they were connected together, but for printing useful information each electrode would need to be accessed electronically. In this arrangement, a common platinum cathode was placed on the opposite side of the paper. Premoistened paper was moved past the electrodes only once at the same speed as before, 1 page length in 2 sec. The image in Fig. 6c was printed with 30 μsec-20V pulses spaced 1000 μsec apart and intensified with electroless copper plating.

A magnified view of part of Fig. 6c is given in Fig. 6d. The image introduced with the 30 μsec pulse is evident as dark spots and the spacing between spots is 1000 μsec. The spacing between the center of each row of dots is 0.2 mm. Image quality at the magnification in Fig. 6d is poor, but it is comparable with many commercial copying processes. Image resolution could be improved if the paper were smoother without individual fibers protruding. Gelatin coated papers were tried and they did improve image resolution. However, gelatin absorbs copper solution during image intensification, causing the paper to darken.

Summary and Conclusions

Electrolytic hard copy printing with electroless copper plating image amplification is capable of high-speed printing. Extremely small amounts of silver introduced into paper by whatever means are capable of initiating electroless copper plating. Image intensification by the process can be as high as one million times.

Advantages of the process are: (*a*) it is capable of high-speed facsimile printing, (*b*) it operates with relatively low voltage pulses, (c) the image is dark and permanent, and (*d*) an inexpensive paper may be used.

The disadvantages include: (*a*) image development is a wet process, (*b*) paper contains residual salts, and (c) the silver printing electrodes erode and must be renewed periodically.

Finally, electrolytic printing with electroless copper amplification may have some application for printed circuit pattern generation. Computer generated pulse trains could print any desired metallic pattern. Techniques developed for computerized drafting should be useful here. The substrate must be somewhat porous to retain electrolyte and provide mechanical adhesion for the image and electroless metal deposit.

Acknowledgments

The authors wish to thank M. L. Olmstead for help in interpreting silver dissolution results with pulsed currents, J. T. Early for his advice on papers, and L. N. Schoenberg and Y. Okinaka for their support in the electroless copper plating work.

Manuscript received Nov. 30, 1970. This was Paper 205 presented at the Atlantic City Meeting of the Society, Oct. 4-8, 1970.

Any discussion of this paper will appear in a Discussion Section to be published in the June 1972 JOURNAL.

REFERENCES

1. R. M. Schaffert, "Electrophotography," p. 118, The Focal Press, New York (1965).
2. H. W. Hermance and H. V. Wadlow in "Physical Methods in Chemical Analysis," p. 155, W. G. Berl, Editor, Academic Press, New York (1951).
3. P. B. Price and D. A. Vermilyea, *J. Chem. Phys.*, **28**, 720 (1958).
4. H. Gerischer, *Z. Elektrochem.*, **62**, 256 (1958).
5. D. R. Turner, Abs. 137, p. 368, Electrochem. Soc. Extended Abstracts, Fall Meeting, Detroit, Oct. 5-9, 1969.
6. W. Goldie, "Metallic Coating of Plastics," Vol. 1, p. 61, Electrochemical Publications Ltd., Hatch End, Middlesex, England (1968).

Electrochemically Thinned N/N$^+$ Epitaxial Silicon—Method and Applications

Ronald L. Meek*

Bell Telephone Laboratories, Incorporated, Murray Hill, New Jersey 07974

ABSTRACT

The method of thinning n/n$^+$ epitaxial silicon wafers by selective anodic dissolution of the substrate in aqueous HF is described. Some of the properties of the system are discussed and applications are presented. It appears the technique is best suited for use where the material has not had extensive prior processing, especially n$^+$ diffusions, and/or where the epitaxial layer is of high resistivity. The most promising areas of application appear to be: (*a*) fabrication of thin films for experimental purposes, (*b*) thinning of simple diode arrays, and (c) solid dielectric isolated IC fabrication. Considerable impediments to use of the process are the necessity of having epitaxial layers of unusual perfection and the fact that local anodic etching occurs at sites of high carrier generation.

While thin silicon ($\sim 1\mu$) is of interest for some high-frequency, high-power device applications (1, 2), its primary impact is expected to be in the field of air or solid dielectric isolated integrated circuitry where thin slices lead to small junction-junction spacing and potential economic advantages. Selective etching techniques have seemed a natural method for thinning, as it has been known for some years that silicon may or may not be anodically dissolved depending on the type and resistivity of the silicon, its electrical potential, and the properties of the solution. In particular, it is well known that n$^+$ and p-type silicon readily dissolve when anodically biased in HF solution, whereas n-type does not (3). This knowledge has led to a method for removing the substrate of an n/n$^+$ epitaxial wafer leaving the thin n-epi layer (4, 5).

Method

The basic method of wafer thinning is, in principle, rather straightforward: an n/n$^+$ epitaxial wafer, which might have previously received some or all of the normal planar device processing, is mounted with acid-resistant wax on a sapphire plate with the n$^+$ side exposed. The silicon is then biased anodically relative to a platinum mesh cathode and the electrodes are lowered into a 5 w/o (weight per cent) aqueous HF solution; the n$^+$ substrate is selectively dissolved, leaving the thin n-type epitaxial layer.

There has apparently been some confusion as to an appropriate way to make electrical contact to the slice. Contact should not be made across the n-side of the wafer since, as will be seen shortly, it is unwise to maintain the n-material at a higher potential than necessary for an extended time period. Furthermore, if p-diffused regions are present in the n-layer and if electrical contact is made to them, which will be practically unavoidable, areas will be etched through on the slice since the forward-biased p-n junctions will inject holes into the n-layer allowing it to dissolve electrochemically.

If a wire is simply clipped to the n$^+$ side, an irreproducible and likely nonlinear contact resistance will result and the actual cell potential will be unknown. A simple method of circumventing this and maintaining a constant silicon potential regardless of current or contact resistance is illustrated in Fig. 1. Two platinum wires are clipped to one edge of the n$^+$ side of the wafer. An operational amplifier implemented as shown then maintains the cell voltage constant at the power supply setting, V_c. For applications where potential control is extremely critical, the potential sensing lead may instead be connected through a buffer amplifier to a reference electrode with the silicon grounded and amplifier output to the cathode, thereby achieving potentiostatic control. (In Fig. 1, the reference electrode serves only as a monitor, and may be omitted for routine work.)

The apparatus used for silicon thinning is schematically shown in Fig. 2. It consists essentially of a gear-driven raising and lowering mechanism. The apparatus is contained in a light-tight box (not shown)

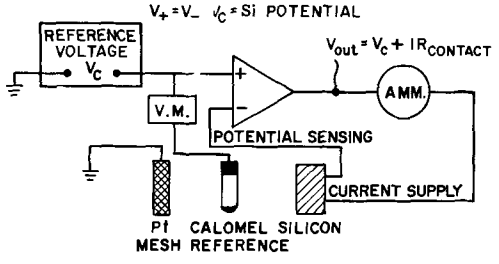

Fig. 1. Circuit to maintain constant cell potential

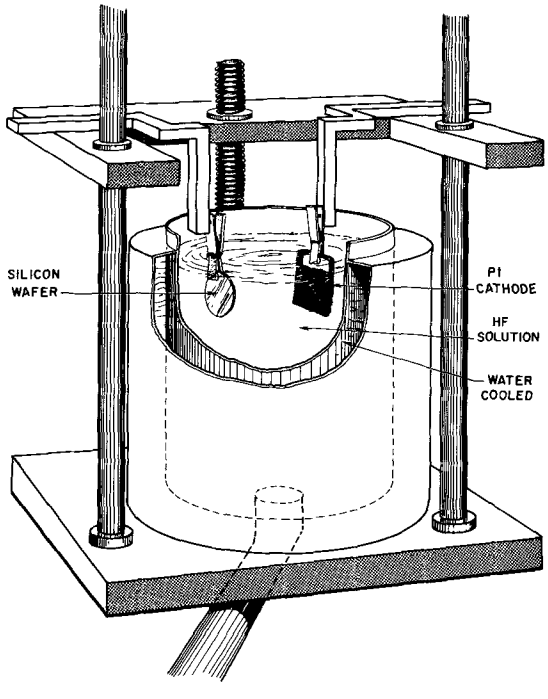

Fig. 2. Lowering apparatus for wafer thinning

* Electrochemical Society Active Member.

Key words: silicon electrochemistry, thin silicon, integrated circuits, anodic dissolution, selective etching.

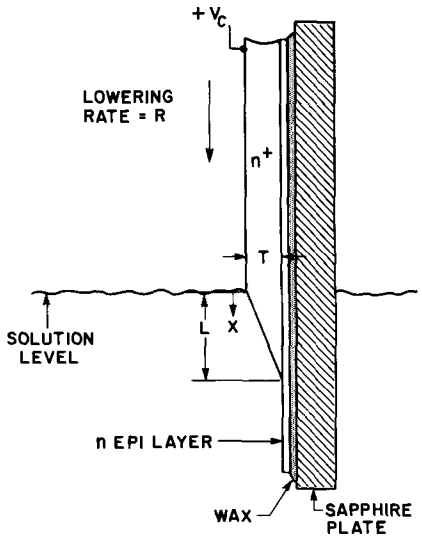

Fig. 3. Expanded view of silicon wafer being thinned

and the electrolyte container is water cooled. The platinum mesh cathode has a projected area of 25 cm² and is 1 cm from the silicon wafer.

Discussion of the lowering is facilitated by reference to Fig. 3. The wafer may not simply be completely immersed initially as the impedances involved are such that the current will flow from the silicon into the solution over an area close to the contact, or the solution-air interface as the case may be; and, consequently, only this area will be thinned. Rather, suppose the wafer is lowered into the solution producing the wedge-shaped remnant of n^+ material below the solution surface ($x = 0$) as illustrated in Fig. 3. Now, if the lowering rate is too large, the potential distribution will be such that sufficient current will not reach the bottom of the wedge ($x = L$) to electropolish it; consequently, in time, L will increase and the material will not be totally removed.

For steady state and $L >> T$, the lowering rate, R, is related to the etch rate, E, by

$$R = \frac{L}{T} E \qquad [1]$$

For n^+ material, the etch rate is approximately 0.02 cm/hr (6).

The determination of the maximum L which can be tolerated is not readily amenable to analysis but has been determined experimentally to be in the range 0.1-0.5 cm, depending on the substrate resistivity, the applied potential, and on the substrate thickness, T. The following table summarizes the experimentally determined R_{max} for various substrate thicknesses at $V_{cell} = 6V$ for $\rho = 0.001$ ohm-cm and <111> orientation.

T (mil)	R_{max} (cm/hr)
10	0.2
5	1.0
3	3.0

These values supply a sufficiently good design criterion for $\rho = 0.01$-0.001 ohm-cm, $V_{cell} = 5$-$10V$, and <111> or <100> orientation, as it has been found that R_{max} depends most strongly on the thickness, T.

Most satisfactory results have been obtained with substrate thicknesses in the range 3-7 mils and $R \simeq 0.7 R_{max}$. It is often desirable to mechanically thin (lap) or chemically etch thicker wafers to this range to minimize wax deterioration due to extended exposure to HF and also to reduce time-dependent attack on the n-layer (6).

To permit selection of an appropriate cell potential for a given substrate resistivity and orientation, the

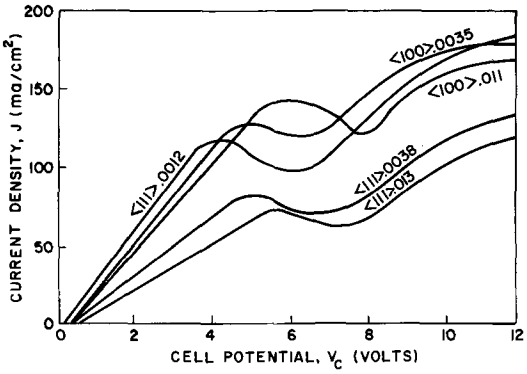

Fig. 4. Current density vs. cell potential for n^+ silicon

data of Fig. 2 of Ref. (6) are replotted *vs.* cell potential in Fig. 4. The optimum operating point is a potential just beyond the maximum in a J-V curve; that is, just into the electropolishing range. Smaller cell potentials require considerably reduced lowering rates because the current density *vs.* potential decreases so rapidly that values of L as discussed in the preceding paragraph cannot be maintained. Only slightly higher potentials actually result in a slower etching; and much larger potentials, while yielding a somewhat greater removal rate, result in an extensively degraded epi layer.

Results

Figure 5a shows a wafer which was partially masked during thinning so that a window was cut through the substrate to the epitaxial layer which is <111>, 2 ohm-cm, 6μ thick. The window size is 6 by 10 mm. The

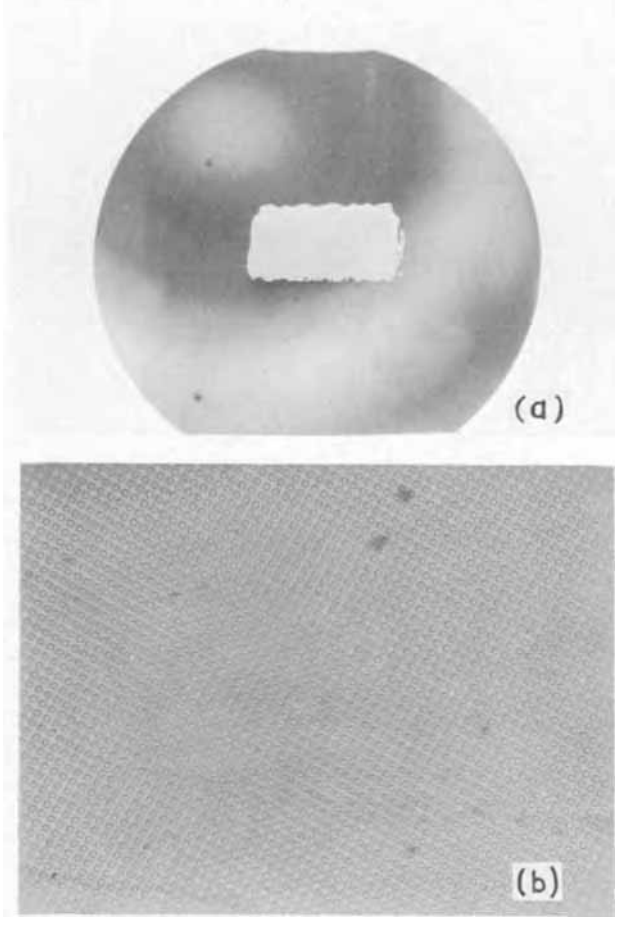

Fig. 5. Wafer with window etched to epi layer: (a) low magnification—window is 10 mm x 6 mm x 6μ; (b) high magnification—showing diffused diode array.

remaining thin silicon membrane is structurally sound, is not buckled or wrinkled, and contains no pinholes when examined at 400X. Thin membranes having thicknesses as small as 1μ have been prepared for use in channeling studies. The thin membranes may be further processed without adverse effect. For example, they have been steam oxidized (1μ oxide each side of 2μ silicon), the oxide stripped in buffered HF, and they have also been rf sputtered. Further evidence of the resultant film quality can be drawn from the aforementioned channeling experiments, the preliminary results of which indicate that the material is crystallographically sound (7).

The particular slice in Fig. 5a had a camera tube diode array diffused into it before thinning (steam oxide, 1050°C, 45 min; boron diffusion, 1140°C, 20 min) as is apparent at higher magnification in Fig. 5b. The dot size is 8μ diam on 15μ centers. In light of the comments of the previous paragraph, application to diode array thinning seems promising. Also, it appears possible to thin the wafer before the array is fabricated.

Early attempts to thin integrated circuits were unsuccessful because etch-through occurred around the periphery of each chip as illustrated in Fig. 6a and b which show a slice (epitaxial layer: <100>, 3 ohm-cm, 8μ thick) upon which phototransistor arrays had been fabricated. Both views are from the etched side; 6a is reflected, and 6b is transmitted, light. The reason for this etch-through behavior was determined to be the fact that in normal processing the base and emitter diffusion are applied also to the grid area around the chips. In fact, it has been found that if either an n^+ [Fig. 6c (8μ epi, <100>, 3 ohm-cm nominal)] or a p [Fig. 6d (8μ epi, <100>, 3 ohm-cm nominal)] grid is present, etch-through of the n-layer results.

The reason for etch-through at p-grids at first seems apparent as the p-regions would be able to inject holes, if they were forward biased, into the n, allowing its dissolution. However, a reverse-biased junction also seems to exist in the circuit as contact has been made to the n^+. It has been found that etch-through occurs below p-diffused areas only if the area diffused extends over the edge of the wafer. It is perfectly possible to retain 1 ohm-cm n-epi layers which have had an area 1 cm on a side p-diffused as long as the diffused area does not extend to the wafer edge. If the p-diffusion extends over and around the slice edge, no effective junction is formed and the p is at the cell potential. Of course, the p-material is, itself, not in contact with the electrolyte. (The junction which does exist is an n^+p^+ surface junction and is very leaky.) The n-material is then etched due to hole injection from the p-diffusions.

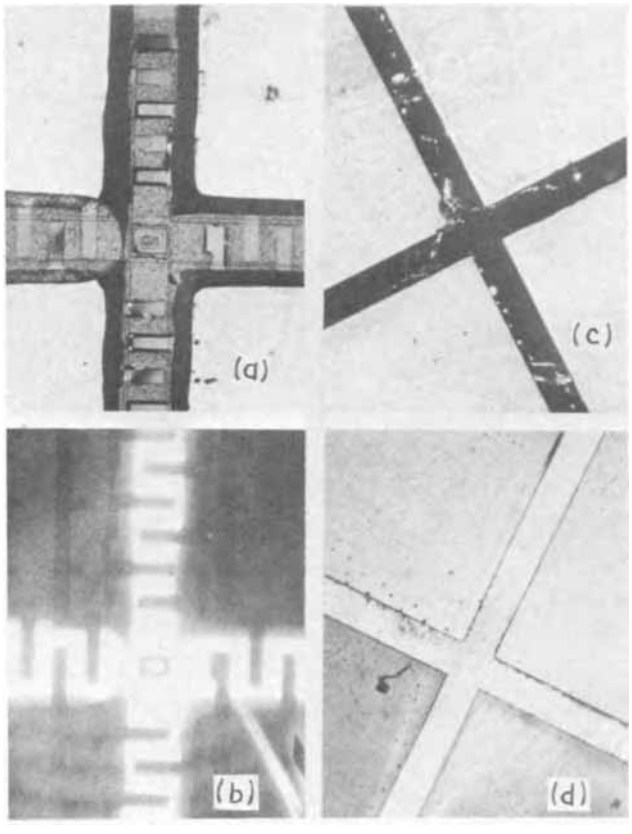

Fig. 6. Etch-through of layers with diffused grids: (a) phototransistor array—reflected illumination; (b) phototransistor array—transmitted illumination; (c) N^+ grid, 1 mil wide; (d) P^+ grid, 1 mil wide.

The mechanism of etch-through at n^+ is considerably more interesting. The effect can best be discussed by reference to a particular example (see Fig. 7). These micrographs are of a thinned slice containing diffused areas. The large squares contain p-diffusion (boron, 1140°C, 20 min), while the rectangular areas and the small squares in the upper-right corner of each large square are n^+ diffusions (phosphorus, 925°C, 36 min; 1000°C, 20 min). The photographs are of the etched side of the layer which is 3 ohm-cm, 8μ thick, and was thinned at 6V and a lowering rate of 0.7 cm/hr. In the first photograph, the slice is shown as it appears only 10 min after the n^+ substrate has been etched away. One of the lines of n^+ rectangles is just beginning to etch. (The residual n^+ substrate in each case is off the bottom of the pictures.) After 20 min considerable etching has taken place, and after 30 min the epi layer has been etched through. (In this particular case, the etching has produced a residual "brown film" but sometimes clean etch-out occurs; see, for example, Fig. 10 which also shows other features to be discussed later.)

The explanation for this must be carrier generation at or below the surface of the n^+ diffused areas, perhaps due to diffusion-induced defects or due to incorporation of large numbers of impurities which act as generation centers. The band diagram through the epi layer to the electrolyte interface appears qualitatively as in Fig. 8, demonstrating that any holes generated would be driven toward the electrolyte interface. The electrons are attracted along the slice to the contact. A local large number of generation centers would thus allow the n-material in the vicinity to etch.

We note that p-diffused areas do not in general etch, even though they surround n^+ diffusions, because the built-in biases retard any extra hole migration to the interface.

This etch-through is enhanced for large-area n^+ diffusions because the adjacent n is maintained at a higher potential for a long time. The current voltage data of Ref. (6) for n-silicon are presented with cell potential as abscissa in Fig. 9. As has been discussed (6), when the initial current density (which is the value plotted in Fig. 9) exceeds 0.05 mA/cm^2, an increase of current with time is observed and pitting of the surface occurs. Above 1 mA/cm^2, current fluctuations are so large that meaningful measurement cannot be made. When n-silicon is held at the potential necessary to electropolish the substrate (about 6V), after an initial induction period the current will increase and pitting will occur.

A number of other etching and staining phenomena are observed both before and after processing. A stain film is sometimes found on the surface but its thickness and the coverage of the surface is variable. The occurrence seems to depend in some undefined way on the material, being fairly consistent within a batch of epitaxial slices but varying widely from batch to batch. The fact that it is sometimes completely absent is attested to by the success of channeling experiments which would reveal the existence of a disordered surface layer. It is to be noted, however, that, if a wafer is partially thinned, removed from the etch and dried,

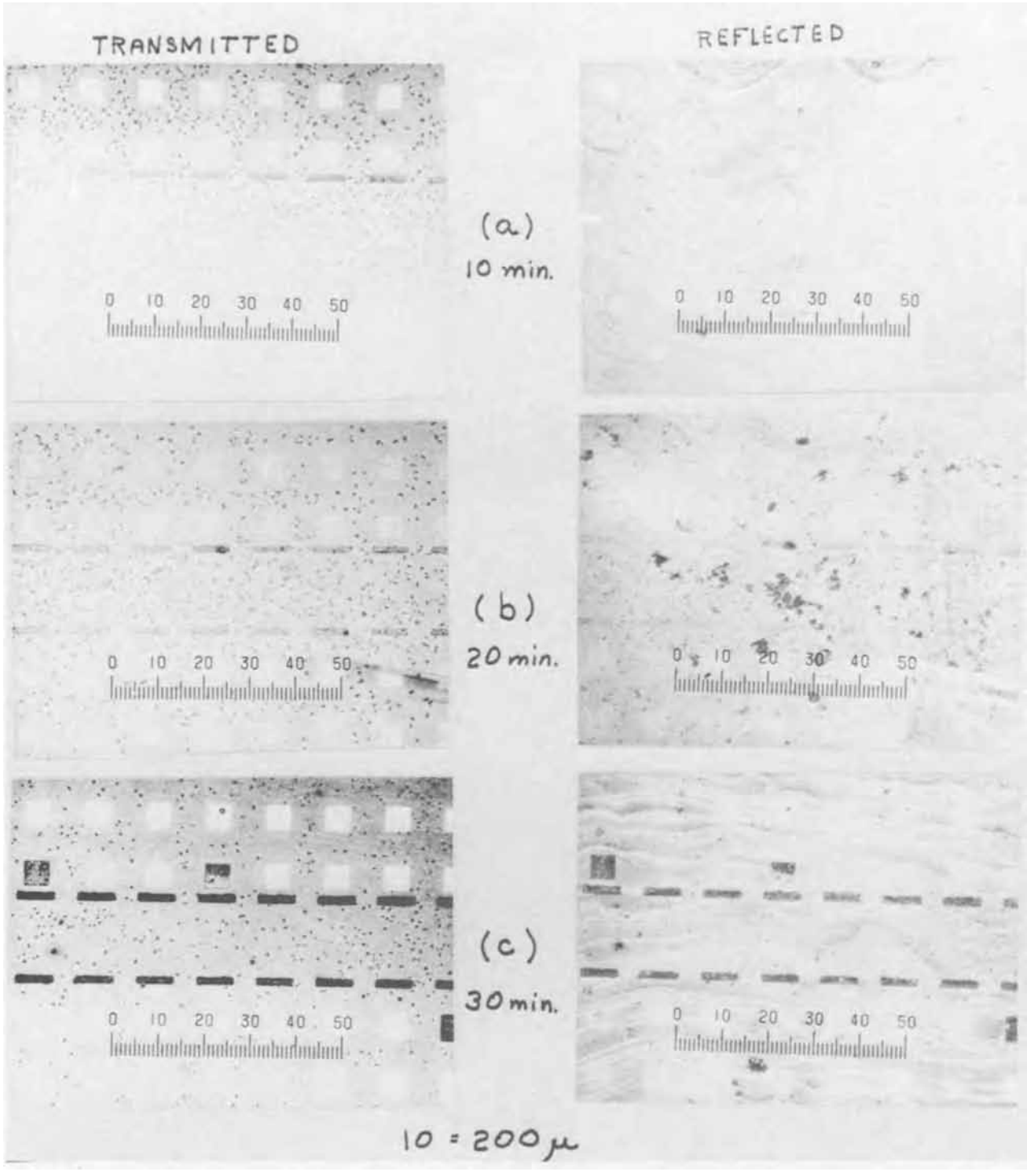

Fig. 7. Etch-through at isolated n^+ diffusions

and the rest of the substrate removed, a film will form on the previously thinned part of the wafer.

The wafer of Fig. 10, although it has received processing, illustrates features often found both before and after processing. The material is severely wrinkled along the right edge of the photograph and a curved line along which etching and staining have occurred also appears. In Fig. 11, we see that holes have etched through the epi layer and, furthermore, etching has been so accelerated that they extend even through the n^+ material where it has been thinned to 20-30μ. These are believed to be dislocations. Only about one batch of epitaxial material in ten has been found to be substantially free of all of these problems.

Two additional types of defects have been observed after "good" epitaxial layers are processed (oxidized and diffused). These are illustrated in Fig. 12. It is very interesting to note that they have not formed in areas which were p-diffused. (The same kinds of defects, but much less dense, have occasionally been observed before processing.) The identity of either defect is not known but those of Fig. 12a have the appropriate morphology to be stacking faults.

It is also noted, parenthetically, that the etch-through at diffused grids (Fig. 6) produces very precisely sized silicon elements. This may be of use as a separation technique where chips or arrays of precise size and/or spacing are desired, as the tolerance depends only on the masking tolerance; consequently, the element edge is in very precise registry with the device diffusions, as the grid and emitters and/or bases are diffused at the same time.

Another interesting etch-through problem may now also be interpreted sensibly. Suppose in Fig. 3 that

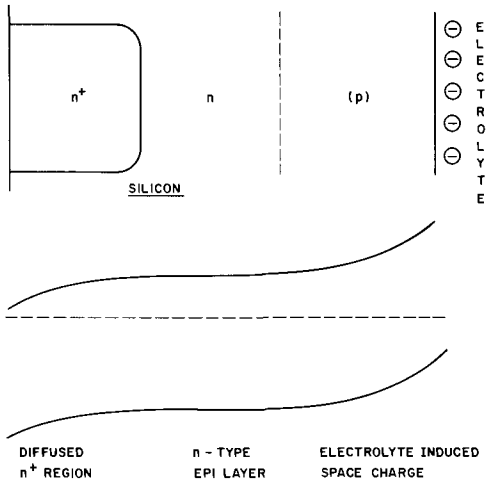

Fig. 8. Qualitative band diagram laterally across the positively biased epitaxial layer in the presence of an n^+ diffusion and the electrolyte.

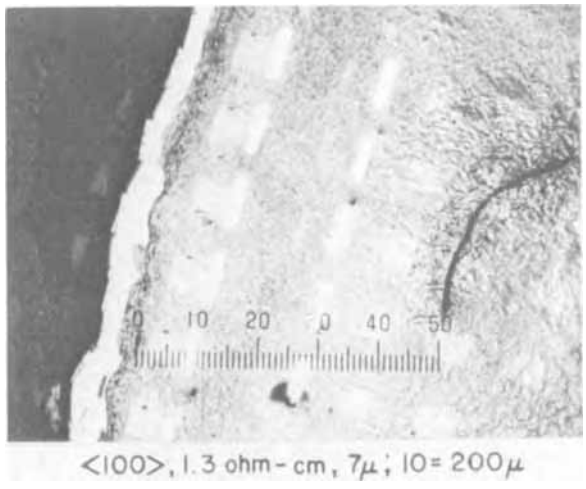

Fig. 10. Thinned layer showing complete etch-out of n^+ diffused areas, etch-through at a window edge, wrinkling, and a line defect.

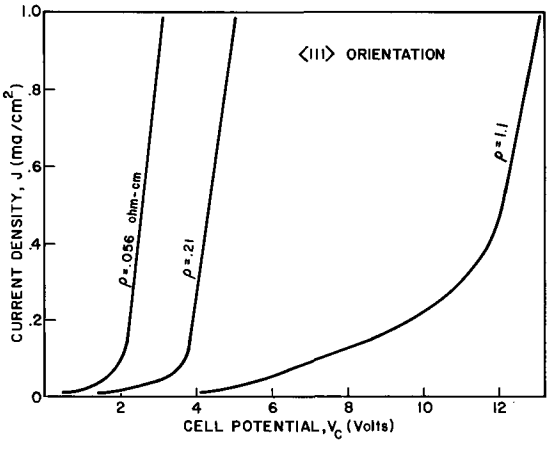

Fig. 9. Current density *vs.* cell potential for n-silicon

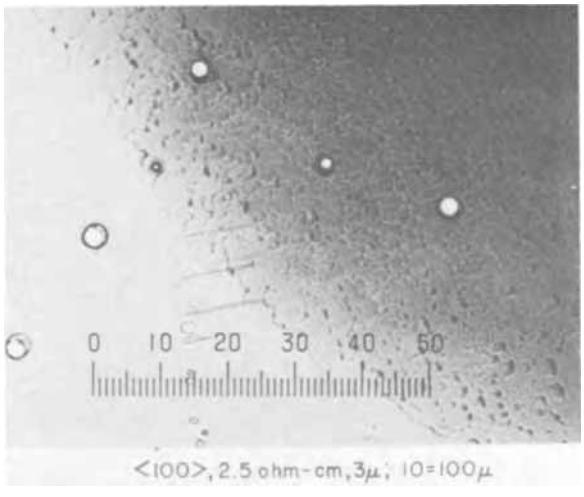

Fig. 11. Pinholes in the epitaxial layer after thinning

$L \rightarrow 0$. Now the n^+ is etching at a very slow rate; or, from a frame of reference attached to an exposed point on the n-material, the n^+ is receding very slowly. This is the case, for example, if $R = 0$ or when the window edges are approached for a structure such as that of Fig. 5. The experimental observation is that the n-material etches through on a stripe about 100μ wide adjacent to the stationary edge of the n^+ material in something like 10 min. (Figure 10 also serves to illustrate this, along the left side of the picture.) The obvious explanation is diffusion of holes into the n, allowing etching within about a diffusion length. The question is, of course, where do the holes come from? It appears from recent C(V) measurements (8) that they are generated at the n^+ surface.

Clearly, if one expects to retain windows as shown in Fig. 5, either great skill must be exercised in removing the wafer at the appropriate time or it must be mechanically preshaped so the n^+ is still receding at an appropriately large rate when etching is terminated.

Application to Integrated Circuits

Although certain performance advantages might be designed into specialized p-n junction isolated IC's, the main impact of thin silicon is on the junction spacing (and, consequently, the economics) of dielectric-iso-

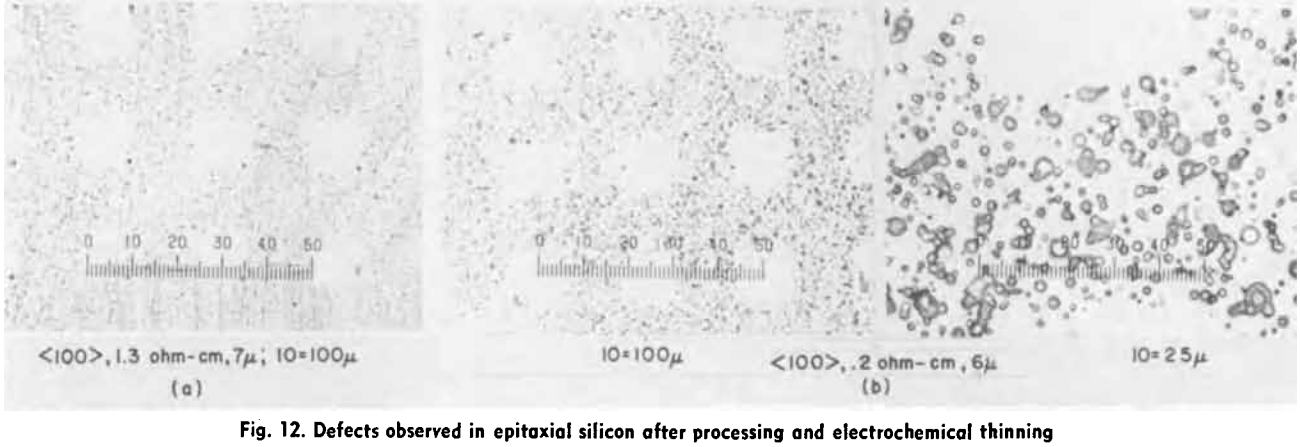

Fig. 12. Defects observed in epitaxial silicon after processing and electrochemical thinning

lated circuits. Consequently, only dielectric isolation is considered here, and an entirely arbitrary distinction is made between air (AIM) and solid dielectric isolation because of the importance of Beam Lead Technology (9) to the Bell System.

Dielectric isolation of integrated circuits has attracted increasing interest in past years for the following reasons: (a) very high breakdown voltages are possible, (b) parasitic capacitances are very much reduced compared to p-n junction isolation, (c) complementary transistors of comparable quality may be produced, and (d) circuits are resistant to nuclear (gamma radiation) effects.

The two principal difficulties with dielectric isolation have been that a difficult and expensive precision mechanical shaping step has been necessary, and that isolation etch channels are of such a depth (~ mils) that utilization of available wafer area is poor. Both these difficulties will be seen to be eliminated by use of the electrochemical thinning procedure.

Consideration of the economics (10) of integrated circuit processing, in conjunction with data on defect density, leads to the conclusion that the cost per unit useful area is a minimum if the chip is about 30 mils on a side. For a complex circuit, then, the area occupied by each element should be minimized.

At present, slices are back-etched (or ground or polished) down to 1 or 2 mils, masked, and finally an isolation etch is performed. To do this, a stripe of 2-4 mils, depending on slice thickness, around the active element must be allowed. This means the total chip area must be 2-4 times the active device area to allow for isolation. Clearly, then, if the wafer could be uniformly thinned to a few microns, instead of mils, the number of active elements per circuit chip could be doubled or even quadrupled.

Air-Isolated IC

When electrochemical etching is substituted for mechanical thin-down on a completed air-isolated structure, there arises, of course, the problem of etch-through at n^+ diffused areas. Three ways can be thought of to eliminate the n^+ etch-through:

1. Have no n^+ diffusions.
2. Ion-implant and thin before the impurities are activated.
3. Zone-etch so the n-layer is exposed to the electrolyte for only very short times after the n^+ substrate is etched away. (That is, confine the etchant to a zone slightly greater than L on the wafer.)

Number 1 requires no comment. The latter two methods have both been applied successfully.

AIM structures thinned by this method would suffer from a high series collector resistance, since it is not possible to retain an n^+ area on the back of the chips. This can, perhaps, be eliminated by metallization of the back of the slice. Such a procedure would have a number of additional advantages:

1. To supply structural integrity to very thin devices.
2. To allow possible electrical contact to back of chip.
3. To permit face-up handling and mounting of chips.

It appears that Turner's (11) method of nickel plating silicon could be incorporated, as it would simply entail addition of certain chemicals to the etching bath after the wafer is thinned and subsequent plating as the slice is withdrawn. Preliminary results of this procedure appear promising (12).

Dielectric Isolated IC

Numerous detailed process sequences have been proposed to produce material suitable for fabrication of dielectric isolated circuits. These may, however, be divided into two general categories (13): (a) those which involve two polycrystalline silicon, or other "handle" material, depositions but which utilize the original wafer surface for device fabrication, and (b) those which require only one polycrystalline silicon deposition and which therefore use the back-etched or polished surface for device diffusions.

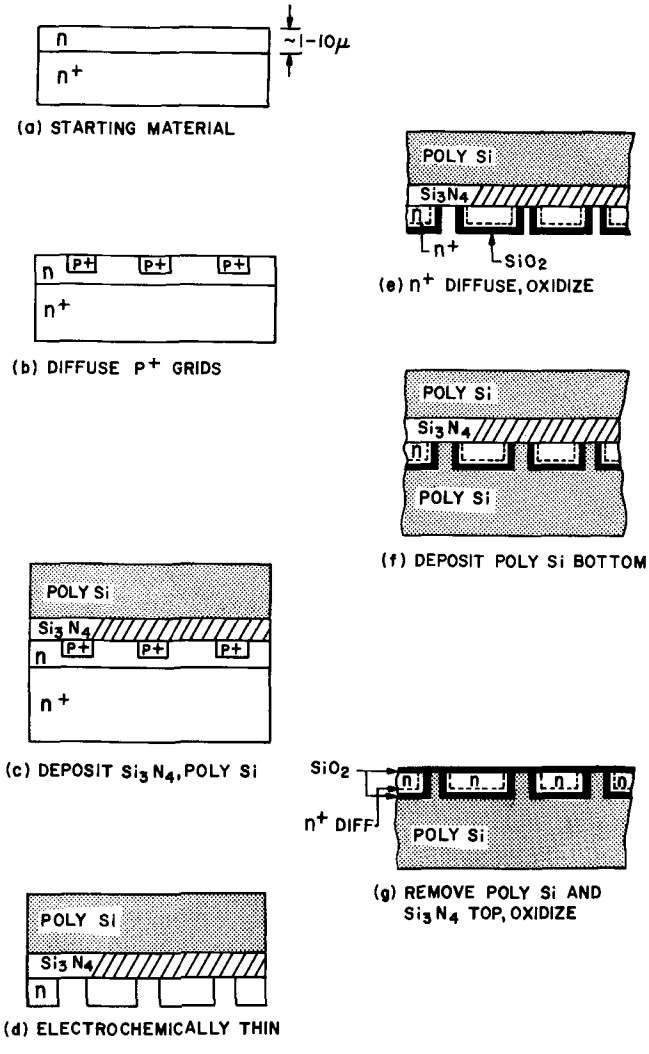

Fig. 13. Dielectric isolated IC fabrication—double poly process

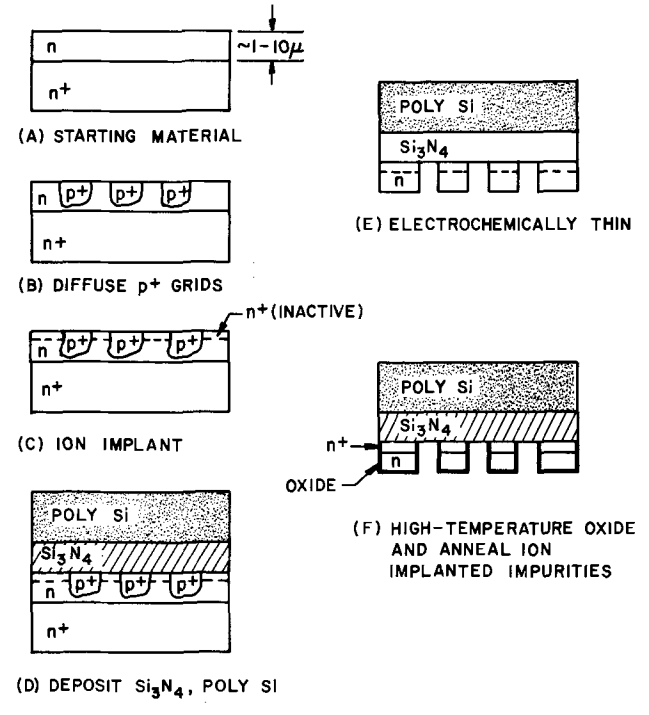

Fig. 14. Dielectric isolated IC fabrication—single poly process

Figure 8 illustrates a process sequence typical of the first category. A total of 10 steps is needed to prepare the starting material for device fabrication, but only one mask is used and the original slice surface is reclaimed. The phenomenon of grid etch-through is utilized to separate the islands as the wafer is thinned.

Figure 9 illustrates the second method. Again, grid etch-through is utilized as well as ion implantation to reduce series collector resistance. The ion-implanted impurities are not activated, annealed in, until after electrochemical thinning so that complete etch-through of the wafer does not occur. Here, the electrochemically etched substrate-epitaxial layer interface is to be the device surface. Six steps and again only one mask are needed.

It may also be noted that material of any orientation may be used since anisotropic etching is not utilized.

Summary

The process for electrochemically thinning n/n^+ epitaxial silicon wafers in HF solution yields satisfactory results when the n-layer is of high resistivity and defect free and where either no n^+ diffusions are present or they are otherwise prevented from causing accelerated etching. Most promising applications seem to be: (*a*) preparation of thin films for experimental study, (*b*) thinning of simple diode arrays, (c) solid dielectric isolated integrated circuit fabrication, and (*d*) perhaps specialized AIM circuits. Principal limitations on the method are availability of very perfect epitaxial layers to be thinned and the fact that etching takes place at local areas of carrier generation.

Acknowledgments

R. H. Braun performed many experiments and constructed the apparatus involved. The author would like to thank M. P. Lepselter and P. J. Boddy for advice and encouragement.

Manuscript submitted Sept. 14, 1970; revised manuscript received Jan. 25, 1971.

Any discussion of this paper will appear in a Discussion Section to be published in the December 1971 JOURNAL.

REFERENCES

1. R. Edwards *et al.*, "Silicon Millimeter Wave IMPATT Diodes," Washington IEEE Meeting, Oct. 1969.
2. *Electronics*, **41**, 170 (1968); D. H. Mash *et al.*, *J. Phys. D*, **3**, 1199 (1970).
3. D. R. Turner in "The Electrochemistry of Semiconductors," P. J. Holmes, Editor, p. 176, Academic Press, London (1962).
4. H. J. A. van Dijk and J. de Jonge, *This Journal*, **117**, 553 (1970).
5. M. J. J. Theunissen *et al.*, *ibid.*, **117**, 959 (1970).
6. R. L. Meek, *This Journal*, **118**, 437 (1971).
7. W. M. Gibson, Private communication.
8. R. L. Meek, *Surface Science*, **25**, 526 (1971).
9. M. P. Lepselter, *Bell System Tech. J.*, **45**, 233 (1966).
10. G. R. Madland *et al.*, "Integrated Circuit Engineering," p. 162, Boston Tech. Pub., Cambridge (1966). B. T. Murphy, *Proc. IEEE*, **52**, 1537 (1964).
11. D. R. Turner, *This Journal*, **106**, 786 (1959).
12. W. H. Craft, Private communication.
13. U. S. Davidsohn and F. Lee, *Proc. IEEE*, **57**, 1532 (1969).

Electrochemical Fluorination

H. M. Fox,* F. N. Ruehlen, and W. V. Childs*

Research and Development Department, Phillips Petroleum Company, Bartlesville, Oklahoma 74003

ABSTRACT

A new process is described for continuous and efficient electrochemical fluorination. The description is supported by detailed data on the fluorination of ethane and qualitative information on some other paraffins and aliphatic chlorides. The preferred anode material is porous carbon, and the electrolyte is composed of approximately one mole of potassium fluoride and two moles of hydrogen fluoride. The cell is operated at about 100°C. An essential feature of the process is that the feed to be fluorinated is kept confined to the pores of the porous carbon and is not permitted to break out into the bulk electrolyte. This is achieved by control of the permeability and pore size distribution of the porous carbon. It is necessary that the electrolyte not wet the anode (contact angle greater than 90°) under electrolysis conditions. Aliphatic hydrocarbons, typified by results on ethane reported herein, fluorinate smoothly and give the hydrogen substituted derivatives predominantly. Over 95% of the ethane converted was recovered as fluoroethanes. This yield did not vary significantly when conversion of ethane was between 31 and 85% per pass or conversion of total hydrogens in the ethane feed was between 10 and 65% per pass. Other products were predominantly various fluorobutanes. The quantity of products obtained by carbon-carbon scission was negligible. Some aliphatic halides also were fluorinated. The chlorides gave even higher efficiencies to hydrogen-substituted derivatives than did the hydrocarbons. The chlorides were subject to scrambling of the halide atoms, the extent of which depended on the compound being fluorinated. Like the hydrocarbons the halides produced a negligible quantity of carbon-carbon scission products. The yield of dimers and other telomers was even smaller.

Shortcomings of conventional fluorination methods have led investigators to seek more effective approaches to electrochemical fluorination. Direct fluorination with elemental fluorine is both expensive and hazardous. Unless elaborate and costly measures are taken to moderate the reactions, poor yields are generally obtained. Fluorination by milder fluorinating agents such as metal fluorides requires elemental fluorine to regenerate the fluorinating agent, and this is expensive. Substitution of fluorine for another halo-

* Electrochemical Society Active Member.

Key words: electrochemical fluorination, hydrocarbons, chlorohydrocarbons, fluorocarbons, porous carbon anode, hydrogen fluoride, potassium fluoride, molten salt, high efficiency, high current density, moderate temperature, wide application.

gen such as chlorine is unsatisfactory because of the limited range of materials which can be made, and the inefficiency resulting from weight loss of feedstocks. Thermodynamic considerations exclude oxidative processes analogous to oxychlorination.

The well-known Simons electrochemical fluorination process (1) is reported to be in commercial use by the 3M Company (2) to produce perfluoro compounds. While his process is primarily suitable for feeds that are soluble in the electrolyte, Simons also disclosed methods for fluorination of insoluble compounds, and other investigators have further refined the process. Radimer (3), and Ashley and Radimer (4) used porous anodes to sparge the feed to be fluorinated into the electrolyte in proximity to the suface of the electrode where fluorine is generated.

The present work is a new approach to electrochemical fluorination (5), distinguished by a novel method of feeding a reactant to a porous electrode. The reactant to be fluorinated, which is insoluble in the electrolyte, is fed continuously to the anode where it remains while it is fluorinated, and the fluorinated products and unreacted feed are recovered continuously from the anode. The process is characterized by its applicability to a wide range of feedstocks and by its high efficiency in producing fluorinated derivatives at conversion rates that approach 100% per pass. In most cases carbon-carbon bond scission does not take place.

Basic Concepts

An essential feature of the process is that the feed and fluorinated products while in the cell remain within the pores of the anode and do not break out into the bulk electrolyte. This occurs if the electrolyte does not wet the anode material and if the permeability of the anode is such that the pressure drop due to feed flow is less than the hydrostatic head of the electrolyte. Ideally, there should be no pores in the anode large enough to be flooded by the electrolyte. However, a substantial proportion of total porosity can be in pores which will flood without causing the feed to break out into the electrolyte. A practical limitation on permeability or porosity is reached when the carbon is too weak mechanically or has too high an electrical resistance to be used as an electrode.

It is known that the nonaqueous electrolyte used in commercial fluorine cells, composed of about 1 mole of potassium fluoride to 2 moles of hydrogen fluoride ($KF \cdot 2HF$), does not wet carbon during electrolysis. Rudge (6) reports that when carbon is made anodic in the $KF \cdot 2HF$ electrolyte, the contact angle increases from 0° to 140° and the anode is no longer wetted by the electrolyte.

Operation of the anode reactor is readily understood in terms of capillarity, as discussed recently by Schwartz (7). In a solid-liquid-vapor capillary system such as porous carbon in a nonwetting liquid, the capillary pressure, P_c, is derived from Young's equation

$$P_c = \frac{2\gamma \cos \theta}{R}$$

where γ is the surface tension of the liquid, θ is the contact angle between the solid and liquid surfaces at the point of contact (Fig. 1), and R is the radius of the capillary.

When a porous material is immersed in a liquid, the smallest pore will fill when P_c equals the negative of P_h (hydrostatic head of the liquid, defined as the product of height of the liquid, density of the liquid, and the gravitational constant)

$$\frac{2\gamma \cos \theta}{R} = -\rho g h$$

or

$$R = -\frac{2\gamma \cos \theta}{\rho g h}$$

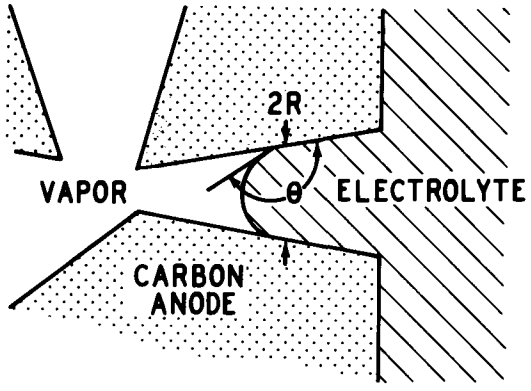

Fig. 1. Idealized pore

In the porous carbon-$KF \cdot 2HF$ system at about 100°C considered herein, γ is approximately 100 dyne cm^{-1}, $\rho = 1.91$ g cm^{-3}, and $g = 981$ cm sec^{-2}. Under electrolysis conditions, θ is reported by Rudge to be about 140°. Calculations of minimum pore size to flood with electrolyte at various depths of immersion can serve as a basis for selecting porous carbons that can be used at different depths of immersion. For example, at 10 cm immersion, the smallest pore that will fill with electrolyte has a radius of about 81 μm.

As mentioned previously a certain amount of filling of electrode pores with electrolyte can be tolerated if there is enough permeability in the unfilled porous structure for the feed flow rate desired. If these conditions are met, the porous carbon acts like a chimney. A gas will flow from one end to the other and will not break out into the electrolyte. Typically, an anode for this process is a cylindrical or rectangular piece of porous carbon immersed vertically with feed at the bottom; products are taken from the top. However, the direction of feed flow could be horizontal if the carbon is completely immersed and suitable inlet and outlet ports are provided.

Experimental

Cell.—Figure 2 is a schematic drawing of the experimental cell used in this study. The cell case, which was jacketed for heating and cooling purposes, and the cathode were of mild steel. The cell lid and anode support were cut from ½ in. and 1 in. Teflon sheeting. The electrolyte level was controlled by means of a level probe extending through the lid to the desired level. When contact between the probe and electrolyte was broken, HF was added automatically until contact was reestablished. The cell temperature was maintained near 100°C by adjusting the temperature of the coolant. This was done automatically by means of a temperature-sensing electronic controller which controlled the water rate to an in-line heat exchanger. The coolant was General Electric SF-96(20) silicone fluid which was circulated from a steam-heated reservoir through the heat exchanger and cell jacket. The steam-heated reservoir was necessary to maintain the cell temperature above the freezing point of the electrolyte during shutdowns. Electrolyte flow as indicated by the arrows on Fig. 2 was due to lift by hydrogen generated at the cathode.

Anode.—A schematic representation of the anode, the mounting assembly, and path of feed flow are given in Fig. 2. The porous carbon was 6 in. long and 1¾ in. in diameter. It was drilled and tapped (½-20) to a depth of 5½ in. to receive a copper stem which served as current collector and feed tube. The data reported were obtained where the electrolyte level was maintained at 5 in. immersion. The lateral surface area was 167 cm^2. The arrows in Fig. 2 illustrate the flow of feed down to the bottom of the electrode and up through the porous structure of the anode. Unreacted feed and fluorinated products left the anode at or slightly above the surface of the electrolyte. Products are mixed with

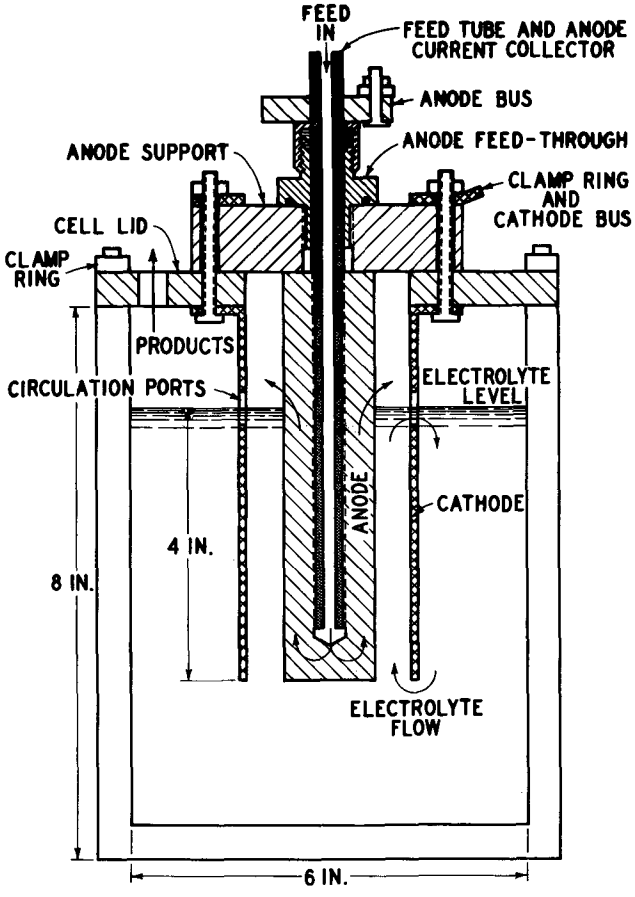

Fig. 2. Experimental fluorination cell

cathode hydrogen before leaving the cell. By a slight modification of the cell, products can be extracted from the anode before they are mixed with cathode hydrogen.

A variety of porous carbons have proven successful. Stackpole Carbon Company SD-139 exhibits little or no flooding of its largest pores at deep immersions. However, the permeability of this carbon is so low that at appropriate flow rates there is break-out of gas into the electrolyte at depths greater than 3 in. National Carbon Corporation PC-60 permits a greater depth of immersion to a limit of about 12 in. Great Lakes Carbon Corporation B-303 and National Carbon Corporation PC-45 give good feed distribution throughout the carbon structure to depths of at least 24 in. Carbon B-303 was used in the runs on ethane to be discussed. These carbons are readily available and have an acceptable combination of pore properties and mechanical properties.

Electrolyte.—Nominal composition of the electrolyte was KF · 2HF containing 0.05 weight per cent (w/o) LiF. Hydrofluoric acid content was maintained at 41-42 w/o. The electrolyte was described by Cady (8) and Schumb *et al.* (9). It was prepared by cautious addition of anhydrous HF to KF · HF rather than to KF, because the reaction is less violent. Hazards of preparation and handling the electrolyte are discussed in Saunders (10). Analysis was done by adding excess base and back-titrating with 1M HCl to a phenolphthalein end point.

Organic feedstocks.—Ethane used was Phillips Pure Grade Product (99.0+ % ethane). Other reactants were high grade products from various sources.

Power supply—Two Sorenson DCR40-125A power supplies were used They were set to operate at constant current with crossover to voltage control at 20V when an "anode effect" occurred (6). An anode effect was relieved by allowing the voltage to rise to 45-70V at constant current for 1-3 min. When the power supplies were turned off and restarted the cell resumed normal operation at about 8V.

Product analysis.—Total cell effluent except hydrogen was collected in one or more receivers cooled with liquid nitrogen. A weighed quantity of sodium fluoride (⅛ in. pellets) was placed in the receiver(s) to remove HF from the cell product. The product was flash-evaporated from the sodium fluoride pellets. Its weight was checked against feed flow and fluorine generated as calculated from the current passed. Mass balances determined in this way were usually within 1 or 2% of unity. The increase in weight of sodium fluoride was taken as the amount of HF removed and was usually in agreement with that calculated based on the vapor pressure of HF over the electrolyte.

Products were analyzed by gas chromatography. The peaks were identified by a GC-mass spectrograph combination and comparison with authentic samples where available. A Perkin-Elmer F11 machine was used with a hot wire detector. Flame ionzation detectors give widely varying responses and poor sensitivity with highly fluorinated materials. The column used was a 20 ft by ⅛ in. Porapak Q. He flow was 40 cc/min. The oven temperature was programmed as follows: temperature was held at 100°C for 8 min; then temperature was increased at 6°C/min to 220°C; then temperature was held at 220°C until heavies eluted.

Results and Discussions

Chemical efficiency.—Data are given in Table I for a series of runs of varying feed rate on ethane. The limiting rate at which the feed will not break out of the B-303 carbon into the electrolyte at 5 in. immersion is about 60 liters/hr; thus the maximum rate evaluated in this series of runs, 35 liters/hr, is considerably below the breakout point. The variations in flow rate were such as to give a range of Faradays of current passed per hydrogen equivalent fed between 0.21 and 1.30. At 2.00**F** per hydrogen equivalent, perfluoroethane would be the sole product if only hydrogen substitution occurred. Stated in another way, 10.5% of the hydrogens in the ethane feed would be converted at the highest flow rate, and 64.8% at the lowest feed rate, if hydrogen substitution accounted for all of the current used.

Product yield is the ratio of the moles of product or products specified to the total moles of ethane converted, multiplied by one hundred. Efficiency is the ratio of moles of fluorine-substituted ethanes to the total moles of ethane converted, multiplied by one hundred.

Table I. Electrochemical fluorination of ethane

Feed rate, liter/hr*	35.3	10.5	10.9	7.8	5.7
Cell potential, V	8.0	7.9	8.0	8.0	7.9
Cell current, A	53	53	53	53	53
Current density, A/dm²	30	30	30	30	30
Electrolyte temperature, °C	101	100	101	101	102
Theoretical hydrogen conversion, %	10.5	18.0	33.9	47.3	64.8
Faradays per hydrogen equivalent	0.21	0.36	0.68	0.95	1.30
Product distribution, mole per cent					
CH_3-CH_3	69.4	55.2	34.7	23.3	15.3
CFH_2-CH_3	13.0	16.7	13.6	7.5	7.1
CFH_2-CFH_2	4.6	6.5	6.5	5.8	5.0
CF_2H-CH_3	3.0	4.4	4.3	3.9	3.3
CF_2H-CFH_2	3.6	5.8	13.6	12.9	10.9
CF_3-CH_3	0.5	0.9	2.2	2.4	2.1
CF_2H-CF_2H	1.2	2.1	6.6	10.5	8.6
CF_3-CFH_2	0.8	1.4	4.4	7.0	5.8
CF_3CF_2H	0.9	1.9	4.4	9.4	11.5
CF_3-CF_3	1.1	3.8	7.1	13.9	27.7
CF_4	0.2	0.3	0.5	0.6	0.7
C_3^+ fluorides**	1.7	1.0	2.1	2.8	2.0
Ethane conversion, %	31.4	45.1	65.7	77.1	84.9
Current efficiency, %	98.1	99.4	97.3	100.0	91.5
Chemical efficiency, $\frac{C_2 \text{ fluorides}}{\text{Ethane converted}}$, %	91.4	96.5	95.4	95.1	96.6

* Gas flow reduced to standard pressure.
** Assumed fluorine content same as theoretical hydrogen conversion.

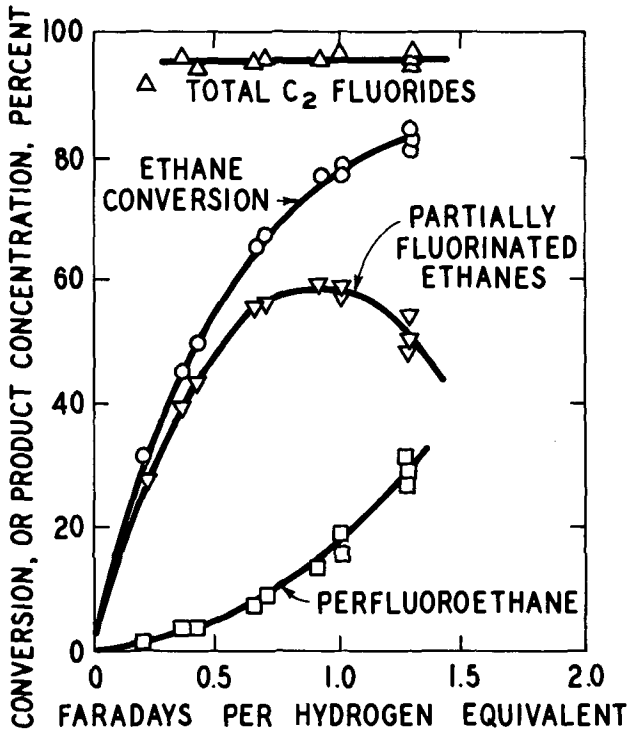

Fig. 3. Effect of Faradays per hydrogen equivalent (feed flow varied) on conversion or product concentration.

Figure 3 is a plot of the results as a function of Faradays per hydrogen equivalent. The proportion of total products represented by the higher fluorinated derivatives increases with increasing Faradays per hydrogen equivalent, while the proportion of ethane and less fluorinated derivatives decreases. The efficiency to C_2 fluorocarbons, or the efficiency to fluorine-substituted products of ethane, is insensitive to Faradays per hydrogen equivalent (thus hydrogen conversion) or to ethane conversion within the range investigated.

Major products obtained are those which can be formed by a radical process such as

$$CH_3\text{-}CH_3 + [F] \rightarrow CH_3\text{-}CH_2\cdot + HF \quad [1]$$

$$CH_3\text{-}CH_2\cdot + [F] \rightarrow CH_3\text{-}CFH_2 \quad [2]$$

The major by-products from ethane fluorination are fluorobutanes. Trace amounts of olefins, especially ethylene and vinyl fluoride, are observed. They are believed to be derived from radical disproportionation reactions, such as

$$2CH_3\text{-}CH_2\cdot \rightarrow CH_3\text{-}CH_3 + CH_2{=}CH_2 \quad [3]$$

Rather than a combination of two radicals, the butanes appear to come from the reaction of an olefin and a radical such as

$$CH_3\text{-}CH_2\cdot + CH_2{=}CH_2 \rightarrow CH_3\text{-}CH_2\text{-}CH_2\text{-}CH_2\cdot \quad [4]$$

At low conversions 1-fluorobutane is present in much higher concentration than any other, including butane itself.

Very small amounts of one-carbon compounds are produced.

Table II qualitatively summarizes data on some other compounds fluorinated by this process. A variety of low-boiling paraffins, up to and including isooctane, all fluorinated smoothly. Scission products in all cases were low. Dimerization of fluorides or chlorides was usually lower than that obtained on the corresponding hydrocarbon. For example, the fluorination efficiency (to the fluorine-substituted derivatives) of 1,1-difluoroethane was above 98%.

Disproportionation of chlorine was observed during the fluorination of the chlorine substituted paraffins.

Table II. Summary of results on various feedstocks

Feedstocks	Efficiency to expected substitution products (%)	Types of major by-products observed
Methane	90	Fluoroethanes
Ethane	95	Fluorobutanes
Propane	95	Heavies—probably fluorohexanes
1,1-Difluoroethane	98	Fluorobutanes
1,2-Dichloroethane	85	Fluoromonochloroethanes and fluorotrichloroethanes
1,1,2-Trichloroethane	75	Fluorodichloroethanes and fluorotetrachloroethanes
Chloroform	99	—
Methylene chloride	60	Fluoromonochloromethanes, fluorochloroform, and fluorochloroethanes

For example, ethylene dichloride produced some fluorinated monochloroethanes and trichloroethanes in addition to the main products, fluorinated 1,2-dichloroethanes. The products of disproportionation of halogen can occur by reactions such as the following

$$CClH_2\text{-}CClH_2 + [F] \rightarrow CClH_2\text{-}CClH\cdot + HF \quad [5]$$

$$2(CClH_2\text{-}CClH\cdot) \rightarrow CH_2{=}CClH + CClH_2\text{-}CCl_2H \quad [6]$$

$$CH_2{=}CClH + 2[F] \rightarrow CFH_2\text{-}CClFH \quad [7]$$

Products of these reactions and analogous reactions of the partially fluorinated derivatives were observed.

Monochlorides and trichlorides could disproportionate accordingly to give the tetrachlorides and compounds without any chlorine which were observed in trace quantities in some cases.

Chloroform is an example of a chloride which fluorinated almost quantitatively to the fluorine-substituted derivative, trichlorofluoromethane. Methylene chloride disproportionated chlorine to a considerable extent.

Electrical efficiency.—As mentioned previously, the electrical efficiency of this process approaches unity. The total current consumed was accounted for by fluorine in the product as determined by gas chromatographic analysis. This has been confirmed by analysis of product for total fluorine by the Wickboldt method. Careful measurement of the amount of hydrogen produced gave the predicted amount based on current passed indicating no internal shorting such as by oxidation of H_2 or reduction of F_2.

Manuscript submitted Jan. 25, 1971; revised manuscript received *ca.* March 11, 1971. This was Paper 117 presented at the Washington, D. C., Meeting of the Society, May 9-13, 1971.

Any discussion of this paper will appear in a Discussion Section to be published in the June 1972 JOURNAL.

REFERENCES

1. J. H. Simons, Electrochemical Process of Making Fluorine-Containing Carbon Compounds, U.S. Pat. 2,519,983 (1950).
2. W. A. Sheppard and C. L. Sharts, "Organic Fluorine Chemistry," W. A. Benjamin, Inc., New York (1969).
3. K. J. Radimer, Process for the Production of Fluorine-Containing Compounds, U.S. Pat. 2,841,544 (1958).
4. P. E. Ashley and K. J. Radimer, Fluorination Process, U.S. Pat. 3,298,940 (1967).
5. H. M. Fox and F. N. Ruehlen, Electrochemical Fluorination of Organic Compounds, U.S. Pat. 3,511,760 (1970).
6. A. J. Rudge, "The Manufacture and Use of Fluorine and Its Compounds," Oxford University Press, New York (1962).
7. A. M. Schwartz, *Ind. Eng. Chem.*, **61**, 10 (1969).
8. George Cady, *J. Am. Chem. Soc.*, **56**, 1431 (1934).
9. W. C. Schumb, R. C. Young, and K. J. Radimer, *Ind. Eng. Chem.*, **39**, 244 (1947).
10. B. C. Saunders, "Advances in Fluorine Chemistry," Vol. 2, M. Stacey, J. C. Statlow, and A. G. Sharp, Editors, Butterworth Inc., Washington, D. C. (1961).

JOURNAL OF THE ELECTROCHEMICAL SOCIETY

ELECTROCHEMICAL SCIENCE

AUGUST 1971

Analysis of Porous Electrodes with Sparingly Soluble Reactants

John S. Dunning,** Douglas N. Bennion,* and John Newman*

Department of Energy and Kinetics, School of Engineering and Applied Science, University of California, Los Angeles, California 90024

ABSTRACT

A model is developed for the operation of a porous electrode in which slightly soluble reactants are present. Numerical techniques are used to predict current distribution and total electrode polarization for the case of a uniform porous structure. This technique is extended to the case where nonuniformities in reactant conversion are produced by a nonuniform current distribution within the electrode. In addition, a simulation of electrode behavior on repeated cycling is obtained. The implications of nonuniform reactant conversion and mass transfer limitations for real battery electrodes are discussed. The results of the numerical calculations indicate that diffusion-limited currents within the porous electrode are possible for certain input parameters. The high polarization at constant current corresponding to a limiting current may be obtained after some time of discharge, but before all of the theoretically available active material is used. In the cycling simulation, significant changes in the relative distribution of reactants and products were observed as a function of depth in the electrode. These changes caused differences in the total electrode polarization from cycle to cycle.

Various idealized mathematical models have been proposed to explain the operation of porous electrodes. The ultimate aim of such studies is the formulation of a model which predicts the performance of practical electrodes. With such a model the optimum design of new cells, particularly power cells of high energy density, may be achieved. Previous work in this field is extensive and has been reviewed elsewhere (1). In general, efforts have been made to determine the effects of ohmic, activation, and diffusion overpotentials (2-4). In addition, changes in porous structure as a result of the passage of current have been investigated for the case of a dissolving metal electrode (5).

In this study a new model is developed which considers transport of active species within the porous electrode itself. The transport of species to and from the bulk solution is not considered, so the model represents a rather special case. It is assumed that the active material is stored within the electrode in the form of small, dispersed crystallites of low solubility. The reactants and products of the electrochemical reaction tend to diffuse out of the porous structure at a very low rate. The model thus corresponds somewhat to the situation in a lead-lead sulfate negative or cadmium hydroxide negative electrode in an actual battery. During operation, the active material dissolves and is transported by diffusion to an electrochemically active site. After reaction, the products diffuse from a region of supersaturation to a saturated region where conditions are favorable for the precipitation of product crystallites

Description of the Model

The general model is formulated using a macroscopic approach. The electrode is assumed one dimensional as shown in Fig. 1. An electronically conducting matrix phase is interspersed with small pores which contain electrolyte solution. The current density in the matrix phase is given by Ohm's law

$$i_1 = -\sigma \frac{d\phi_1}{dx} \qquad [1]$$

The symbols are defined at the end of this paper. In the presence of supporting electrolyte, the current density in solution is given by

$$i_2 = -\kappa \frac{d\phi_2}{dx} \qquad [2]$$

An equation describing the kinetics of the electrochemical reaction which takes place at the solution-matrix interface is necessary. A fairly general equation describing an oxidation-reduction reaction which is first order with respect to both reactants and products is

$$\frac{di_1}{dx} = -ai_o \left\{ \frac{c_1}{c_1^o} \exp\left[\beta(\phi_1 - \phi_2)\right] - \frac{c_2}{c_2^o} \exp\left[-\beta(\phi_1 - \phi_2)\right] \right\} \qquad [3]$$

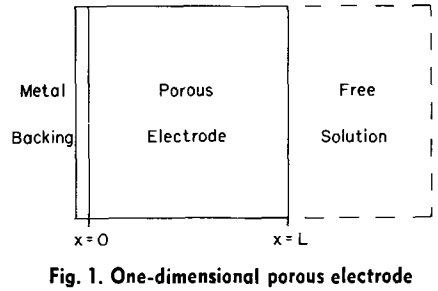

Fig. 1. One-dimensional porous electrode

* Electrochemical Society Active Member.
** Electrochemical Society Student Associate.
Key words: secondary batteries, porous electrodes, transient behavior, mathematical model, sparingly soluble reactants.

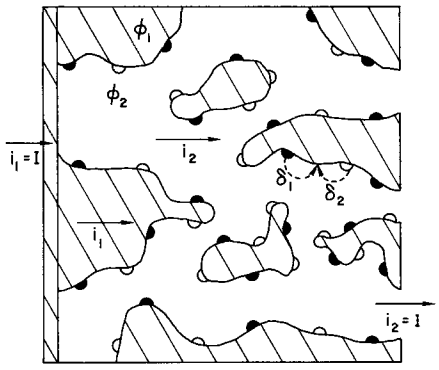

Fig. 2. Detailed structure of porous electrode showing small crystallites of active species: ● anodic reactant, ○ cathodic reactant.

The quantity di_1/dx is the cathodic reaction rate per unit volume of electrode at a point within the electrode. In general, the factor β appearing in the exponential terms can be different for the forward and backward reactions. However, using just one parameter simplifies the mathematics, and most features of the model will not be affected.

The model to this point is essentially the same as those of other workers, in particular that of Newman and Tobias (2). The new feature incorporated into this model is the consideration of diffusional transport of active species stored within the electrode. In Fig. 2 the detailed structure of the model is shown. The anodic reactant crystallites (species 1) are shown as solid dots on the matrix structure while the cathodic reactant crystallites (species 2) are represented as white dots. The active materials are nonconductors and react only when they diffuse to the surface of the conducting matrix. The saturation concentration of the reactant is so low that diffusion out of the porous matrix is slow. However, since the crystals may be small and highly dispersed, the diffusion paths within the electrode may be short and reasonable reaction rates may be possible. Similarly, the reaction products are assumed to be only slightly soluble and to be nonconductors. The reaction product concentration will build up at the reaction site until supersaturation occurs. Then the product will diffuse a short distance to small product crystallites or other preferred nucleation sites and precipitate. An effective diffusion path δ_i is assumed for each species. This represents a typical distance between a storage site and an active site at which the charge transfer reaction takes place. It is an averaged property which depends on the local geometry of the pores and crystallites within the electrode. In general it is expected that δ_i would be the order of one tenth of the average pore diameter. A typical pore diameter of 10μ would therefore indicate a value of δ_i the order of 10^{-4} cm.

A mass transfer coefficient k_{mi} is also defined for each species i. The flux of active material to the reaction site is assumed to be given by

$$N_i = k_{mi}\,(c_i^o - c_i) \qquad [4]$$

The mass transfer coefficient may be approximated by

$$k_{mi} \cong D_i/\delta_i \qquad [5]$$

If a diffusion coefficient of 10^{-5} cm^2/sec is taken as typical, a reasonable estimate of the mass transfer coefficient would be 0.1 cm/sec. The exact value of the average diffusion path is difficult to estimate. A precise estimate requires solution of the 3-dimensional species conservation equation for a given pore wall and crystallite geometry to establish the boundary conditions. An effective mass transfer coefficient could then be determined by averaging the flux and diffusion path over a given area of pore wall. Qualitatively, a high mass transfer coefficient is expected for small crystallites and a low mass transfer coefficient for larger crystallites. Thus, the mass transfer coefficient depends on crystallization dynamics and the crystallite and pore morphology. In this paper these subtleties are not explicitly considered, and an average value of k_{mi} is used as a variable parameter.

A general expression for an electrochemical reaction is

$$\sum_i s_i M_i^{z_i} \rightarrow ne^- \qquad [6]$$

where the s_i are stoichiometric coefficients and the z_i are ionic charges for each species taking part in the reaction. For simplicity, in this paper we will restrict ourselves to the case where s_1 is 1 and s_2 is -1. Using this notation the local reaction rate is related to the flux of active material toward the active site by

$$\frac{di_1}{dx} = \frac{-n\mathbf{F}aN_i}{s_i} \qquad [7]$$

for each species.

As current is passed, there is assumed to be a change in the sizes of reactant and product particles with time. Such changes cause variations in the diffusion path length and, correspondingly, in the mass transfer coefficient. In order to account for this phenomenon, it is necessary to assume a functional form for the dependence of the mass transfer coefficient on the amount of active material present in any part of the electrode. A function of the form

$$k_{mi} = k_{mi}^{max}\left(\frac{w_i}{\Sigma w_i}\right)^p \qquad [8]$$

satisfies the initial and long-time conditions. That is, as the amount of active material remaining, w_i, vanishes, the mass transfer coefficient and local reaction rate must fall to zero. Of course, this applies only to the species which is diffusing toward the electrode. The fact that only a small amount of product may be present cannot be allowed to hinder the reaction. For this reason a lower limit of 0.1 was placed on the ratio k_{mi}/k_{mi}^{max} for the product species in the actual calculations. The upper limit on the mass transfer coefficient, k_{mi}^{max}, is attained when all of the material present has been converted to the form of species i. It is to be noted that the value of Σw_i is a constant which corresponds to the capacity of the electrode in the fully charged state. The exponent p in Eq. [8] depends on the local geometry of the crystallites and is essentially an adjustable parameter. In this work p has been set equal to unity.

The amount of any species remaining at a point within the electrode depends on the history of that point. In terms of the reaction rate, the remaining amount of material is given by

$$w_i = w_i^o + s_i \int_o^t \frac{di_1}{dx}\,dt \qquad [9]$$

The condition of charge conservation requires that

$$i_1 + i_2 = I \qquad [10]$$

or

$$\frac{di_1}{dx} + \frac{di_2}{dx} = 0 \qquad [11]$$

where I is the total apparent current density in the electrode. In this paper all results are reported for galvanostatic polarization.

Equations [1], [2], [3], [4], [7], and [11] represent a set of coupled, nonlinear, first-order differential equations at a time t. The boundary conditions are

$$\begin{aligned} &\text{at } x = 0,\ i_1 = I \\ &\text{at } x = L,\ i_2 = I \text{ and } \phi_2 = 0 \end{aligned} \qquad [12]$$

The condition on ϕ_2 represents the choice of a zero point of potential. The total electrode overpotential, which is of primary importance to battery design, is

given by the quantity $\phi_1(0) - \phi_2(L)$. All results of this paper are presented in terms of the total electrode overpotential.

It is convenient to transform the set of differential equations into dimensionless form. The following set of definitions were used for this purpose

$$\begin{aligned} j &= i_1/I \\ y &= x/L \\ \xi_1 &= c_1/c_1^0 \\ \xi_2 &= c_2/c_2^0 \\ \psi &= \beta(\phi_1 - \phi_2) \end{aligned} \qquad [13]$$

The following dimensionless groups were defined

$$\begin{aligned} z_1 &\equiv nFaL\, c_1^0\, k_{m1}^{max}/s_1 I \\ z_3 &\equiv nFaL\, c_2^0\, k_{m2}^{max}/s_2 I \\ z_5 &\equiv LI\beta/\sigma \\ z_6 &\equiv LI\beta/\kappa \\ z_7 &\equiv La i_0/I \end{aligned} \qquad [14]$$

As a result of these transformations, Eq. [1], [2], and [10] become

$$\frac{d\psi}{dy} = z_6 - (z_5 + z_6)j \qquad [15]$$

Equation [3] becomes

$$\frac{dj}{dy} = -z_7\{\xi_1 e^{\psi} - \xi_2 e^{-\psi}\} \qquad [16]$$

Equations [4] and [7], when combined and written for the two species considered here, become

$$\frac{dj}{dy} = -z_1(1 - \xi_1) \qquad [17]$$

and

$$\frac{dj}{dy} = -z_3(1 - \xi_2) \qquad [18]$$

The boundary conditions on the above four equations are

$$\begin{aligned} &\text{at } y = 0,\ j = 1 \\ &\qquad y = 1,\ j = 0 \end{aligned} \qquad [19]$$

The above equations were solved numerically for the current in each phase, the local concentrations, and the local overpotential as functions of position in the electrode for the case of a constant imposed current density. The following computational procedure was used:

1. Equations [15], [16], [17], and [18] were solved for the initial conditions using the technique of Newman (6).
2. New values of the mass transfer coefficients were calculated after a short time interval, Δt, by assuming that the reaction rate at any point was constant during the time interval. Equations [8], [9], and [10] were used for this calculation.
3. The new values of the mass transfer coefficients were used to solve Eq. [15], [16], [17], and [18]. In this manner the transient behavior of the electrode could be followed.

Results

It was necessary to select numerical values for the constants appearing in the differential equations. In all cases presented here, a single electron transfer ($n = 1$) was assumed. In addition the value of β was taken to be 19.55 V^{-1}. The exchange current density, i_o, was assumed to be 10^{-5} A/cm^2 in all cases. The value of the matrix conductivity, σ, was assumed to be 10^3 mho/cm. The thickness of the electrode, L, was taken to be 1 mm. The values of w_1^0 and w_2^0 were both taken to be 720 coulomb/cm^3 in all cases. The other parameters of interest were chosen as reasonable guesses for organic electrolyte systems. For each set of results given, the values of the important parameters appear in the figure captions.

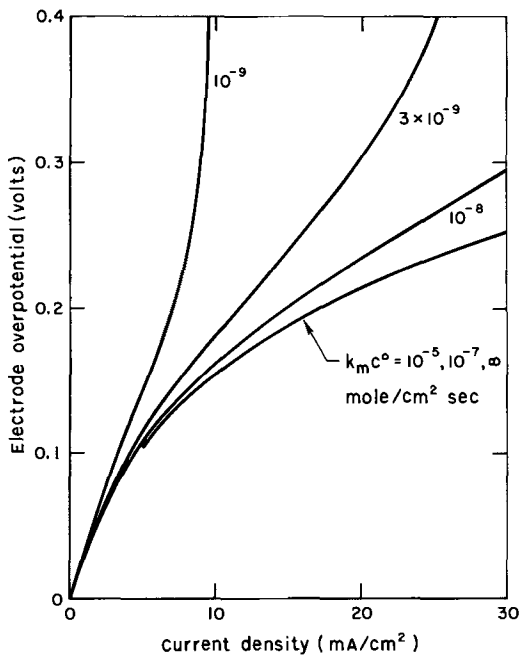

Fig. 3. Overpotential vs. current density for different values of $k_m c^0$. $a = 10^3$ cm^{-1}, $\kappa = 7\times10^{-3}$ mho/cm. Initial conditions.

Initial behavior.—The time-dependent behavior of the model proposed in this paper is conveniently introduced by an examination of the initial behavior of the model, *i.e.* for time equal to zero. A semianalytic solution for this case has been presented previously for relatively high local overpotentials where the back reaction can be neglected (7). The present numerical treatment allows for the inclusion of both forward and back reaction terms of Eq. [3] and thus represents a more complete description of the entire range of local overpotentials. Figure 3 shows the dependence of the calculated electrode overpotential, $\phi_1(0) - \phi_2(L)$, as a function of the applied current density for a specific set of electrode parameters. The various curves are for different values of the product of the mass transfer coefficients and the saturation concentrations of reactants and products. In this figure we have let $k_{m1} = k_{m2} = k_m$ and $c_1^0 = c_2^0 = c^0$ so that the parameter of interest is $k_m c^0$. At high current densities, activation control is represented by an infinite mass transfer coefficient. This corresponds to an analytic solution given by Newman and Tobias (2) for a constant concentration within the pores. As the quantity $k_m c^0$ decreases, the overpotential increases until a mass transfer limiting current is obtained. This is indicated by the rapid increase in electrode overpotential with current density near 9.5 mA/cm^2 for $k_m c^0$ equal to 10^{-9} mole/cm^{2}sec.

The approach to limiting current is accompanied by increasing uniformity of transfer current distribution within the electrode. In Fig. 4 the dimensionless volumetric reaction rate distribution, dj/dy, is shown as a function of position in the electrode for a given current density, 20 mA/cm^2. For large values of $k_m c^0$, the major portion of charge transfer takes place near the free solution edge of the electrode, $y = 1$. For this situation mass transport effects are not important compared with the interplay between activation control and ohmic drop in the solution. However, for lower values of $k_m c^0$ the reaction distribution becomes more uniform and approaches -1 throughout the electrode. This is a result of the surface concentration of reactant being driven to zero due to the difficulty of transporting active species from storage sites. This phenomenon is not explicitly dependent on the amount of charge stored in the electrode. A mass transfer

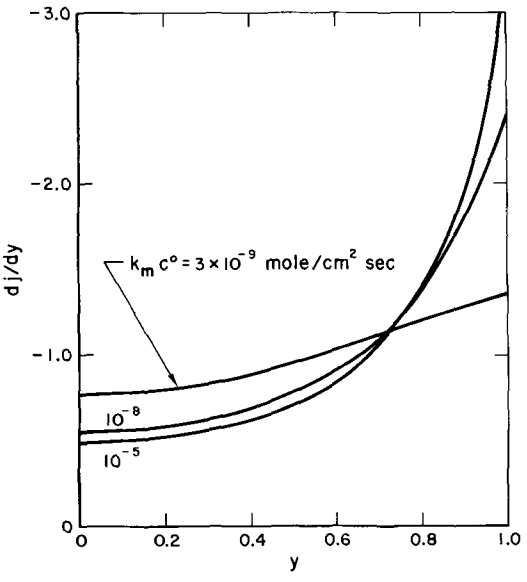

Fig. 4. Dimensionless volumetric reaction rate vs. dimensionless distance from backing plate for various values of $k_m c^o$. $I = 20$ mA/cm², $a = 10^3$ cm^{-1}, $\kappa = 7 \times 10^{-3}$ mho/cm.

limitation may occur even in fully charged electrodes so that high power densities may not be possible.

Transient behavior.—Let us now consider the time-varying behavior of the electrode overpotential under conditions of constant current. Equation [8] was used to give the form of the variation of mass transfer coefficient with the charge remaining at any point. Figure 5 shows the calculated overpotential as a function of discharge time for various saturation concentrations of active species. An initial capacity of 0.2 A-hr/cm³ was assumed present at zero time. That is, the equivalent of 0.2 A-hr/cm³ of the species to be oxidized was present, distributed uniformly throughout the electrode. In addition, another 0.2 A-hr/cm³ of species already oxidized was assumed to be present initially. If the oxidation were carried to completion, there would eventually be 0.4 A-hr/cm³ of oxidized species present, and none of the reduced species.

A number of phenomena are apparent from the different curves. Curve A, representing high saturation concentrations, has three distinct sections. For short times the overpotential is nearly constant. At some intermediate time the overpotential begins to rise almost linearly with time. At this point all of the reactant at the free solution-electrode interface has been converted to product. The reaction then begins to "eat" its way back into the electrode. At a later time the third section of the curve becomes apparent. This is when, as the reaction is driven further into the electrode, the local reaction rate becomes too large for the mass transfer mechanism to accommodate. The result is a rapid rise in overpotential indicating approach to limiting current conditions. The constant and linearly varying types of overpotential behavior have recently been reported in experimental cells using slightly soluble reactants (8). This type of polarization behavior was also obtained by Winsel (3) as a consequence of his assumption of a limited amount of reactant at each point. The difference between the results presented here and those of Winsel is the presence of diffusion-limiting current regimes in curves B, C, and D in Fig. 5. For comparatively low values of saturation concentrations, mass transfer effects become apparent at earlier times. Thus it is possible that, even if the initial polarization of a practical electrode is not prohibitively high, it may become so after a relatively short time, *i.e.* before a large fraction of the active material is consumed. The result is that the effective capacity (and true energy density) of the electrode must be sacrificed if a high current density drain is insisted upon. For example, curve A represents a discharge such that essentially all of the available reduced species is oxidized before the overpotential reaches 0.4V. Curve B shows 0.4V being reached before 93% of the active species is used. Curve D indicates that 0.4V overpotential is reached before only 68% of the active species present initially has been reacted.

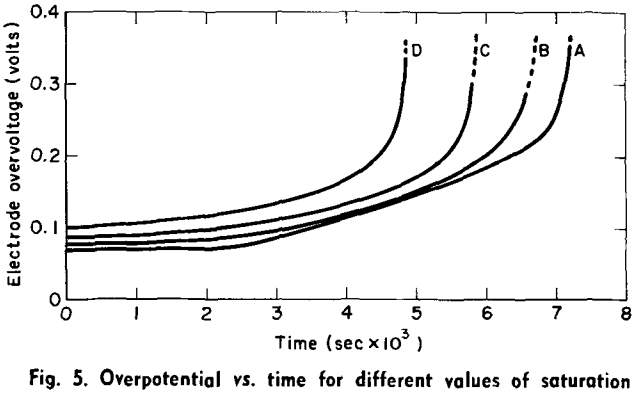

Fig. 5. Overpotential vs. time for different values of saturation concentration. $I = 10$ mA/cm², $a = 10^4$ cm^{-1}, $k_m^{max} = 0.2$ cm/sec, $\kappa = 10^{-3}$ mho/cm. Values of c^o are: (A) 5×10^{-8}, (B) 10^{-8}, (C) 5×10^{-9}, (D) 3×10^{-9} mole/cm³.

In Fig. 6 the reaction distribution is shown for the set of operating conditions represented by curve A in Fig. 5. The different curves represent the distribution at various stages of discharge. The percentage discharged is based on the theoretically available capacity of 0.2 A-hr/cm³. For the initial conditions (0% discharged), the curve shows a monotonically increasing nonuniform distribution similar to those in Fig. 4. However, as time progresses the initial nonuniform nature of the reaction distribution has the effect of reducing the mass transfer coefficient more near the free solution interface than in the interior of the electrode. This results in a maximum in the reaction distribution. After about 37% of discharge has been reached (curve not shown), the outer part of the electrode becomes converted entirely to product, and the reaction maximum slowly works its way into the electrode. When the maximum has moved beyond the backing plate, a limiting current condition is obtained.

Cycling behavior.—The nonuniform conversion of active species, resulting from the long time discharges

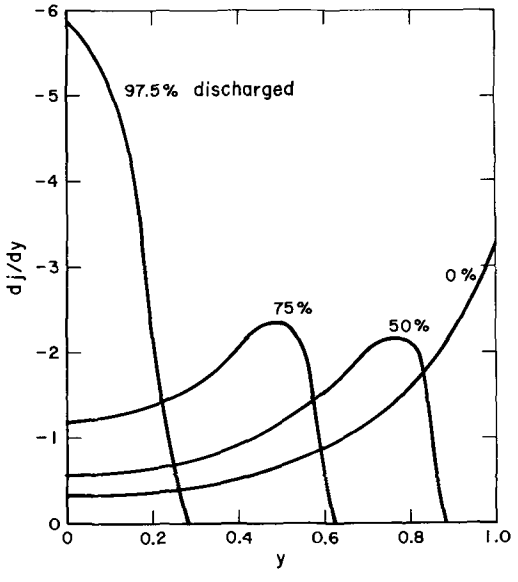

Fig. 6. Dimensionless volumetric reaction rate vs. dimensionless distance from the backing plate for different states of discharge. $I = 10$ mA/cm², $a = 10^4$ cm^{-1}, $k_m^{max} = 0.2$ cm/sec, $\kappa = 10^{-3}$ mho/cm, $c^o = 5 \times 10^{-8}$ mole/cm³. This sequence of curves corresponds to curve A in Fig. 5.

discussed above, suggests that significant redistribution of the proportion of oxidized and reduced species might occur on repeated cycling of the electrode with positive and negative currents. This was investigated by applying current densities of 10 mA/cm^2 alternately anodically and cathodically. The distribution of active material between the oxidized and reduced species at the end of one half-cycle was used as the initial distribution for the following half-cycle of opposite polarization. In order to prevent an unrealistic contribution to the overpotential due to a small amount of product present at the beginning of each half-cycle, the value of k_{mi}/k_{mi}^{max} for the product species was not allowed to fall below 0.1. Initially, the species were dispersed throughout the electrode as a uniform, equimolar mixture of reactant and product. In other words, the electrode was 50% charged, based on the total possible capacity, which was assumed to be 0.4 A-hr/cm^3. The duration of each half cycle was such that the state of charge varied between 50 and 75% of the total capacity. The computer program can be easily modified to accommodate any combination of initial conditions and duty cycles, but the above set was chosen for illustrative purposes.

Figure 7 shows the electrode overpotential as a function of time for the various cycles. The anodic cycles (positive overpotentials) show gradually increasing overpotential as a function of time during a half-cycle. Each successive anodic half-cycle shows a lower over-all overpotential at a given time. The cathodic half-cycles show very flat potential-time curves, with overpotentials increasing slightly in magnitude with cycle number.

Figure 8 shows the relative distribution of cathodic reactant at the end of each charge and discharge. It is to be recalled that the total amount of material at each point is constant. In addition the problem was formulated such that $w_1^o = w_2^o$. The above two facts imply that $w_1/w_1^o = 2 - w_2/w_2^o$, so that the amount of anodic reactant at any point can also be calculated from Fig. 8. Initially the distribution is uniform at 1, but after each whole cycle the conversion is such that

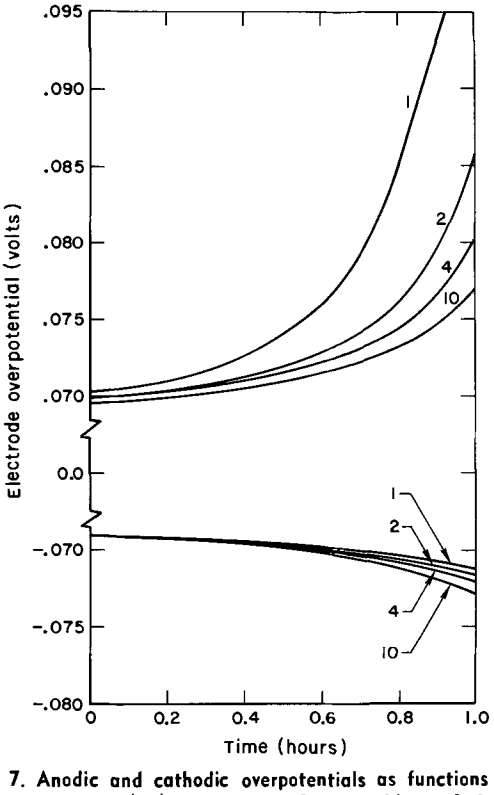

Fig. 7. Anodic and cathodic overpotentials as functions of time for different cycles. $|I| = 10$ mA/cm^2, $a = 10^4$ cm^{-1}, $k_m^{max} = 2.39 \times 10^{-2}$ cm/sec, $\kappa = 0.005$ mho/cm, $c^o = 10^{-7}$ mole/cm^3. Anodic part of cycle precedes cathodic part of cycle.

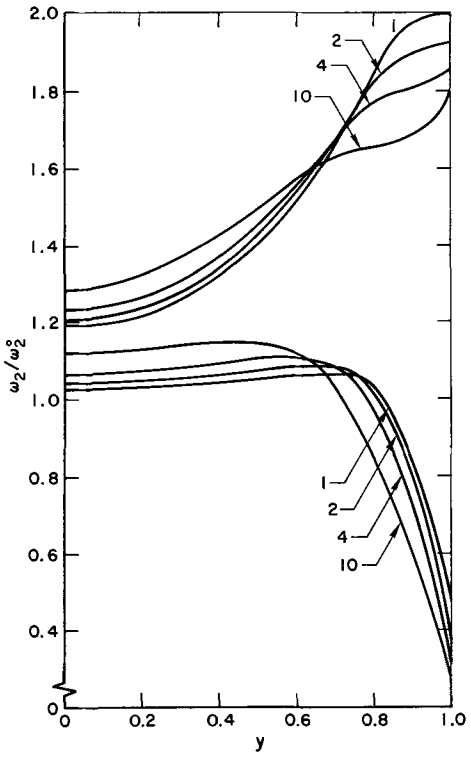

Fig. 8. Distribution of cathodic reactant at the end of each half-cycle. Parameters are the same as for Fig. 7.

there is relatively more of the oxidized species (w_2) near the backing plate and relatively less near the pore mouth. This, in effect, makes the free solution side of the electrode depleted in cathodic reactant and forces the discharge (cathodic) potential curves downward. The symmetry of the roles of reactants and products is such that another conclusion can be drawn from Fig. 8. If the electrode were cycled between 50 and 25% of total capacity (instead of 50 and 75%), the discharge curves would show lower overpotentials and the charge curves would show higher overpotentials with increasing charge number. It is important to note that these changes occur as results of nonuniform conversion of reactants as predicted by the combined kinetic and transport equations and are not due to side reactions, formation of soluble complexes, or other strictly chemical or mechanical problems.

Discussion and Conclusions

The model which has been described in this paper is necessarily idealized, but it could be applied to practical electrodes presently in use with suitable modifications. One possible improvement would be to consider explicity ionic transport in solution and to replace Eq. [2] with a more general expression. In this manner such phenomena as $SO_4^=$ transport in lead acid negatives and OH^- transport in cadmium negatives could be included. The present treatment does not consider actual changes in the total amount of active species present (*i.e.*, Σw_i is constant). However, for actual cells the movement of active species, induced by temperature differences resulting from nonuniform current distributions, should be considered.

In spite of these shortcomings, the model does point out a possible mode of failure caused by an internal mass transfer limitation of electrodes with sparingly soluble reactants. It also suggests an important criterion by which possible new electrode systems could be evaluated in terms of the solubility and diffusivity of the active species. These quantities must be small enough to ensure that the self-discharge of the cell is slow and they must be large enough so that mass transfer limitations do not cause unacceptably high overpotentials at reasonable discharge rates. For ex-

ample, from Fig. 5 one might decide that a solubility of 5×10^{-5} molar is the minimum acceptable for good battery performance for that particular system. Let us assume a minimum acceptable shelf life of two years and calculate a maximum acceptable solubility. If the capacity of the electrode is 0.2 A-hr/cm^3 and the electrode thickness is 1 mm (these are conditions assumed for Fig. 5), then the total capacity of the electrode is 2×10^{-2} A-hr/cm^2. We will also assume a 1 mm separation between plates. Based on these assumptions, a solubility of 11.4×10^{-5} molar will give a two-year shelf life. Thus, for this particular set of assumptions, the acceptable range of solubilities is rather narrow, *i.e.* between 5×10^{-5}M and 11.4×10^{-5}M. The lower limit of the range is quite sensitive to the choices of physical constants made for the model. This is especially true of the mass-transfer coefficient which is roughly estimated and may be good only to an order of magnitude. Nevertheless, it is interesting to note that the solubility of $PbSO_4$ in 10% sulfuric acid solutions is about 2.25×10^{-5}M (9) which is near the range predicted for a successful battery electrode involving a sparingly soluble reactant.

Acknowledgment

This work was supported by the U. S. Naval Air Systems Command under contract No. N00123-70-C-0188. Computer time was donated by the UCLA Campus Computing Network on an IBM 360/91 digital computer.

Manuscript submitted Sept. 30, 1970; revised manuscript received Feb. 26, 1971. This was Paper 274 presented at the Los Angeles Meeting of the Society, May 10-15, 1970.

Any discussion of this paper will appear in a Discussion Section to be published in the June 1972 JOURNAL.

LIST OF SYMBOLS

- a Specific surface area of porous electrode, cm^2/cm^3
- c_1 Local concentration of oxidant, mole/cm^3
- c_1^o Saturation concentration of oxidant, mole/cm^3
- c_2 Local concentration of reductant, mole/cm^3
- c_2^o Saturation concentration of reductant, mole/cm^3
- D_i Effective diffusion coefficient of species i, cm^2/sec
- $\mathbf{F}$ Faraday's constant, 96,500 coul/equivalent
- i_1 Current density in matrix phase (based on over-all apparent porous electrode area), A/cm^2
- i_2 Current density in solution phase, A/cm^2
- I Total apparent current density applied to porous electrode, A/cm^2
- i_o Exchange current density, A/cm^2
- j Dimensionless current (i_1/I)
- k_{mi} Mass transfer coefficient of species i, cm/sec
- k_{mi}^{max} Maximum possible value of mass transfer coefficient of species i; occurs when all active species have been converted to species i, cm/sec
- L Thickness of porous electrode, cm
- M_i Symbol for chemical species i
- N_i Flux of active species i to local active site, moles/cm^2 sec
- n Number of electrons transferred in electrochemical reaction
- p Dimensionless parameter
- s_i Stoichiometric coefficient of species i
- t Time, sec
- w_i Amount of active material i stored at a point within the electrode, coulombs/ cm^3
- x Distance coordinate from backing plate of porous electrode, cm
- y Dimensionless distance (x/L)
- z_i Ionic charge on species i
- β A convenient reciprocal voltage ($n\mathbf{F}/2RT$), V^{-1}
- δ_i An effective diffusion path length from crystallite of active species i to electrochemically active site, cm
- κ Effective conductance of solution inside porous electrode, mho/cm
- ξ_i Dimensionless concentration (c_i/c_i^o)
- σ Effective electrical conductivity of matrix phase, mho/cm
- ϕ_1 Potential in the matrix, V
- ϕ_2 Potential in solution, V
- ψ Dimensionless overpotential [$\beta(\phi_1 - \phi_2)$]

REFERENCES

1. R. de Levie, *Adv. Electrochem. Electrochem. Eng.*, **6**, 329 (1967).
2. J. S. Newman and C. W. Tobias, *This Journal*, **109**, 1183 (1962).
3. A. Winsel, *Z. Electrochem.*, **66**, 287 (1962).
4. E. A. Grens and C. W. Tobias, *Ber. Bunsen. Physik. Chem.*, **68**, 236 (1964).
5. R. C. Alkire, E. A. Grens, and C. W. Tobias, *This Journal*, **116**, 1328 (1969).
6. J. Newman, *Ind. Eng. Chem. Fundam.*, **7**, 514 (1968).
7. J. S. Dunning and D. N. Bennion, *Proceedings of the Advances in Battery Technology Symposium*, Southern California—Nevada Section of the Electrochemical Society, Vol. 5, p. 135 (1969).
8. S. Lerner and H. N. Seiger, *This Journal*, **117**, 574 (1970).
9. G. W. Vinal, "Storage Batteries," 4th ed., John Wiley & Sons, Inc., New York (1955).

Electrolytic Behavior of Yttria-Stabilized Hafnia[1]

Jon D. Schieltz,*,[2] John W. Patterson,* and D. R. Wilder

Institute for Atomic Research and Departments of Ceramic Engineering and Metallurgy, Iowa State University, Ames, Iowa 50010

ABSTRACT

X-ray analysis and electrical conductivity measurements (800°-1000°C) on yttria-hafnia solid solutions between 2 and 20 m/o (mole per cent) Y_2O_3 were made to locate the cubic phase and to select the composition best suited as a solid electrolyte. The phase boundary is located near 7 m/o Y_2O_3. Total conductivities obtained from the cubic phase solid solutions appear to be ionic. The 8 m/o Y_2O_3-HfO_2 composition showed the highest conductivity (log $\sigma_T = -1.57$ at 1000°C), and lowest activation energy (16.9 kcal/mole), and was selected as the optimum composition for a solid electrolyte. Open-circuit emf, electrical conductivity, and Wagner d-c polarization measurements between 800° and 1000°C were made to determine the electrolytic domain of the 8 m/o Y_2O_3 composition. The electrolytic domain width at 1000°C extends from log P_{O_2}(atm) $= -16.6$ to $+0.4$. The 8 m/o yttria-stabilized hafnia composition does appear suitable as a solid electrolyte. Its electrical properties are very similar to those of calcia-stabilized zirconia.

The investigation of solid electrolytes has been influenced by the proven behavior of the fluorite solid solutions of zirconia and thoria. Fluorite solid solutions of hafnia are obvious potential materials (1-3). The relationships between the cubic fluorite structure and the C-type rare-earth oxide structure suggest applications of C-type rare-earth oxides. The present study was undertaken to study the best Y_2O_3-HfO_2 solid electrolyte and to determine if its electrolytic domain (4) includes conditions not covered by other presently known oxide solid electrolytes.

Johansen and Cleary (3) measured the electrical conductivity of CaO-HfO_2 solid solutions from 800° to 2000°C. The conductivity was assumed to be ionic, based on previously reported investigations of CaO-ZrO_2 solid solutions. The oxygen potential was not reported but must have been limited to low or intermediate oxygen partial pressures, since a graphite resistance furnace with an argon atmosphere was used. The maximum conductivity was found to be at 12.5 m/o CaO or 6.25% anion vacancies.

Oxygen permeability studies by Smith (1) show a 1/4-power oxygen pressure dependence of the permeability of 13.5 m/o CaO-HfO_2 with an activation energy for hole conduction of 58.5 kcal/mole. The transport mechanism was attributed to the migration of oxygen vacancies and electron holes.

Most of the studies involving rare earth oxides (Re_2O_3) and hafnia deal with the structural determination of solid solutions, the existence of a pyrochlore compound $Re_2Hf_2O_7$, and the determination of phase diagrams (5, 6). Caillet *et al.* (7) have examined the HfO_2-Y_2O_3 system from 0 to 50 m/o Y_2O_3. From x-ray diffraction analyses, a two-phase region was reported between 0 and 8 m/o Y_2O_3, and only the cubic fluorite phase was present above 8 m/o Y_2O_3. The lattice parameter showed an anomaly at 33.3 m/o Y_2O_3. Along with the electrical conductivity studies by Besson *et al.* (2) which showed a minimum in conductivity and a maximum in activation energy at 1000°C for the 33.3 m/o Y_2O_3 composition, the existence of the pyrochlore compound $Y_2Hf_2O_7$ was predicted but never observed. An a-c two-probe method was used to measure the electrical conductivity of various yttria-hafnia solid solutions in a controlled atmosphere. The 8 m/o Y_2O_3 composition exhibited a maximum conductivity, which was pressure independent, and a minimum activation energy. Oxygen pressure dependence of the conductivity was observed with compositions containing less than 8 m/o Y_2O_3 and was interpreted as the electronic contribution from the monoclinic solid solution within the two-phase region. Open-circuit emf values across various cubic fluorite compositions between Ni-NiO and Fe-FeO electrodes agreed with thermodynamic values verifying that the electrical conductivity remains ionic down to oxygen pressures fixed by those electrodes.

Preparation of Samples

Spectrographic-grade hafnium oxychloride obtained from the Wah Chang Corporation (Lot SP10684B) and previously described yttria powder (8) were the starting materials. Spectrographic analysis supplied with the hafnium oxychloride is given in Table I.

The hafnium oxychloride was dissolved in distilled water and the hafnium oxide content determined analytically to establish a standardized concentration. Yttria was dissolved in hot concentrated HCl and the solution was standardized. These two solutions were mixed and slowly added to an equal stirred volume of 10*N* NH_4OH. The gelatinous coprecipitate was filtered, washed, dried, and calcined.

Calcination appeared to have an influence on the final sintered state. Dried precipitates were calcined at 600°, 800°, and 1000°C for various lengths of time. Those calcined at 1000°C possessed the highest sintered densities, while those calcined at 600°C possessed the

Table I. Spectrographic analysis of hafnium oxychloride spectrographic-grade powder

Element	Concentration (ppm)
Al	<25
B	<0.2
Cb	<100
Cd	<1
Co	<5
Cr	<10
Cu	<40
Fe	<50
Mg	<10
Mn	<10
Mo	<10
Ni	<10
Pb	<5
Si	<40
Sn	<10
Ta	<200
Ti	<20
V	<5
W	<20
Zr	64
Total	635.2

* Electrochemical Society Active Member.

[1] Work supported by the Aerospace Research Laboratories, Office of Aerospace Research, United States Air Force, Contract F33615 68 C 1034, and by the Ames Laboratory of the United States Atomic Energy Commission, Contract W-7405-eng-82.

[2] Present address: Tektronix Incorporated, Integrated Circuit Engr., P. O. Box 500, Beaverton, Oregon 97005.

Key words: solid electrolytes, d-c polarization, ionic conductivity, electronic conductivity, open-circuit emf, yttria-stabilized hafnium.

lowest sintered densities. Calcination times were not controlled sufficiently to produce an observable effect on the sintered samples. The calcination temperature used in the present investigation was 1000°C.

X-ray diffractometer traces of calcined compositions known to be within the single-phase region indicated that the calcined material was a one-phase fluorite solid solution.

The calcine was ground to −325 mesh in a mortar and pestle, prepressed to 1800 psi in a ¾ in. diam tungsten carbide lined steel die, isostatically pressed to 50,000 psi, and fired in a Centorr furnace for 1 hr at 2000°C and 30 min at 1500°C. The lower temperature was employed to stabilize the expected anion vacancies as demonstrated in the calcia-zirconia system (9). Disks of identical composition were placed in a covered yttria crucible, and rhenium metal was used to separate the individual disks within the crucible. The hafnia solid solutions investigated ranged from 2 to 20 m/o Y_2O_3 in 2 m/o intervals and were light brown in color after firing, indicating partial reduction. Annealing the disks for several hours in air at 1000°C produced a color change to white. The bulk density (total mass divided by total volume including open and closed pores) of the sintered yttria-hafnia samples varied from 80 to 94% of theoretical density as the calcination temperature was increased from 600° to 1000°C. Figure 1 shows the typical microstructure of an 8 m/o Y_2O_3 sample of 92% theoretical density.

Apparent densities (bulk densities corrected for open pore volume but not for closed pore volume) were used to determine the defect model for Y_2O_3-HfO_2 solid solutions as discussed below. The apparent densities were obtained by a water displacement-water saturation method for specimens of various Y_2O_3 concentrations but with approximately the same bulk density. Thus, systematic variations of closed porosity with Y_2O_3 content are not expected. Also, only the high total porosity (low bulk density) sintered disks were used for apparent density determinations because they contain almost no closed pores. Thus, the apparent density of the low bulk density disks is expected to be very close to, but slightly less than, the true density of the solid solution phase; the difference is due to closed pores in the sintered disk.

An x-ray analysis of the yttria-hafnia system was made to determine the lattice parameter as a function of composition. Diffraction patterns for the YSH (yttria stabilized hafnia) disks were recorded before and after each conductivity run. Lattice parameters were determined by Cohen's extrapolation method as modified by Vogel and Kempter (10). The monoclinic hafnia solid solution was identified by comparing the diffraction patterns with the monoclinic HfO_2 ASTM card. The fluorite structure of the YSH solid solutions was confirmed by comparing intensities and 2θ values to those obtained for erbia stabilized hafnia solid solutions which have been identified as possessing the calcium fluoride structure with anion vacancies.[3]

[3] J. K. Johnstone, "The Erbia Hafnia System," Unpublished thesis, Iowa State University, Ames, Iowa.

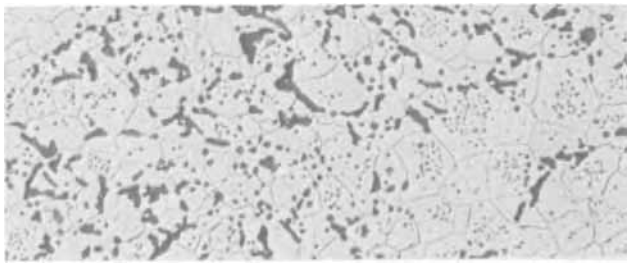

Fig. 1. Microstructure of 8 m/o Y_2O_3-92 m/o HfO_2 fluorite solid solutions of 92% theoretical density, 270X.

Results and Discussion

Structural system.—Sintered hafnia solid solutions with 2-20 m/o Y_2O_3 annealed at 1500° were subjected to x-ray analysis to determine the 1500°C solubility limit of HfO_2 in the cubic fluorite structure. The presence of both the monoclinic HfO_2 and the cubic fluorite peaks on the diffractometer traces indicated that the system is two phase between 2 and 6 m/o Y_2O_3. Between 8 and 20 m/o Y_2O_3, only the cubic fluorite phase appeared; consequently, the phase boundary lies between 6 and 8 m/o Y_2O_3 at 1500°C. The temperature dependence of the phase boundary was not investigated.

The variation in fluorite phase lattice parameter with composition is shown in Fig. 2. This can be accounted for by the size of the ions, since the ionic radius of Y^{+3} (1.02Å) (11) is larger than that of Hf^{+4} (0.83Å) (11). The lattice parameters are based on all the observed peaks for the two-phase compositions and only those peaks for which $2\theta > 60°$ for the single-phase compositions. The lattice parameters obtained are in good agreement with published values (7).

As Y_2O_3 is added to HfO_2, charge neutrality is maintained by one of two defect structures. Either the cation sublattice remains completely filled and the appropriate number of anion vacancies are created, or the anion sublattice remains filled and the excess cations occupy interstitial sites. The difference between the two models is the addition of extra cations or the absence of oxygen ions within a unit volume and should be reflected by a difference in densities. A comparison between the measured apparent densities and the theoretical densities for each model calculated from the lattice parameter data is shown in Fig. 3. On the basis of these data and the similarity between YSH and CSZ, it was concluded that the single-phase cubic solid solutions possess a fluorite-type structure with a filled cation sublattice and anion vacancies.

Electrical conductivity.—Electrical conductivity was measured as a function of composition and oxygen partial pressure. Figure 4 is a plot of $\log \sigma$ *vs.* $1/T$(°K) for compositions from 6 to 20 m/o Y_2O_3; apparent activation energies deduced from the slopes of these plots are given for each composition.[4] The a-c conductivities shown in Fig. 4 were measured at 1592 Hz in

[4] If $\log \sigma T$ *vs.* $1/T$ slopes are used instead, all the activation energies reported above are increased by the amount $-R[d\ln T/d(1/T)]$. In the temperature range 800°-1000°C, this averages out to an increase of +0.05 eV for each of the Q values.

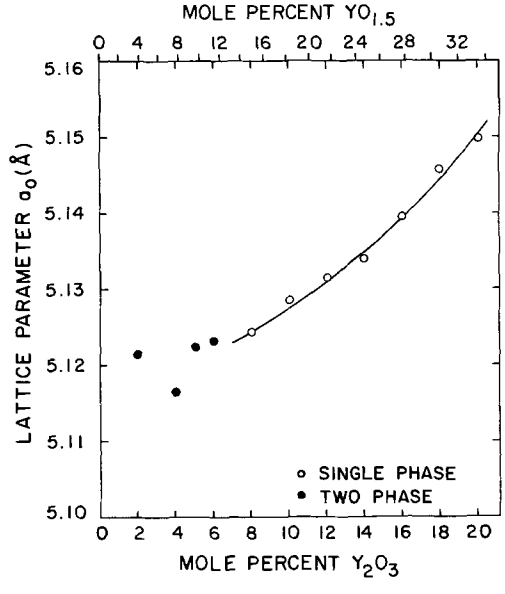

Fig. 2. Variation of the fluorite phase lattice parameter with composition in the Y_2O_3-HfO_2 system annealed at 1500°C.

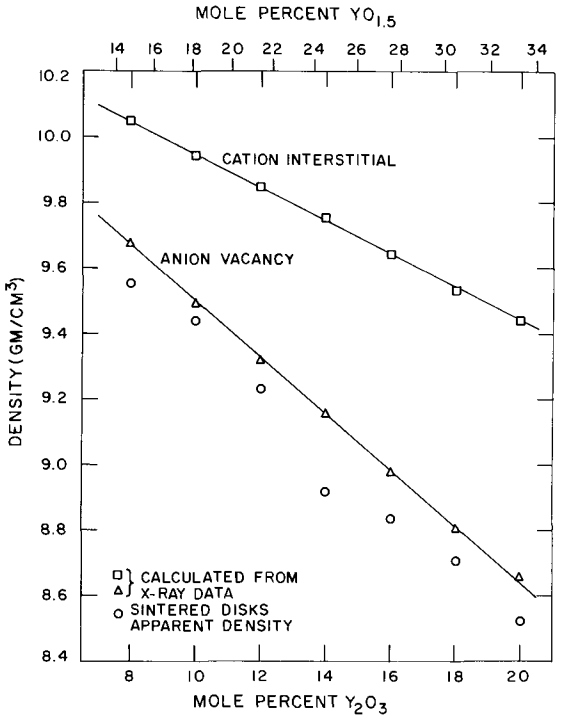

Fig. 3. Theoretical and measured densities of Y_2O_3-HfO_2 solid solutions annealed at 1500°C.

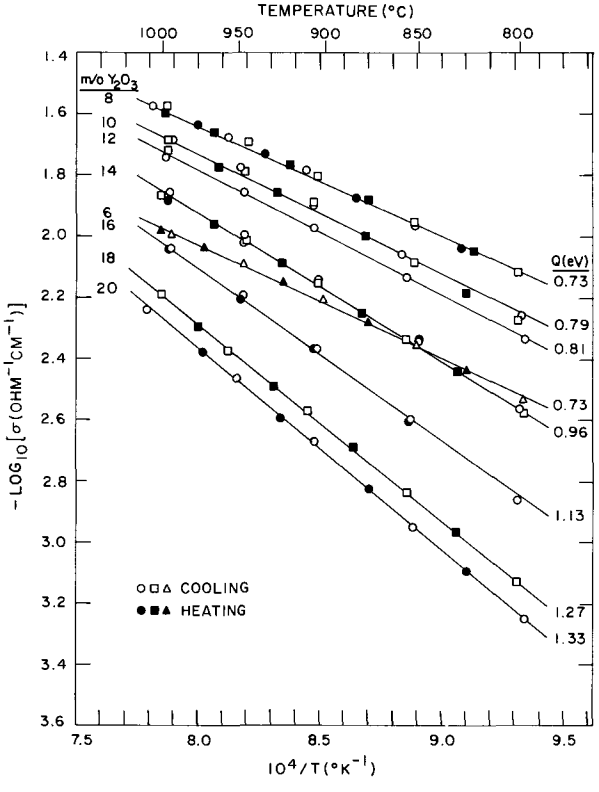

Fig. 4. Total conductivity in dry air as a function of temperature for Y_2O_3-HfO_2 specimens of different compositions; previously annealed at 1500°C.

dry air using a guard ring technique (12) with porous platinum electrodes.

At 1000°, the conductivities remained unchanged in pure oxygen, air, He/O_2 at ratios of 10 and 100, and purified helium in which log P_{O_2} was found to be < -10 as measured by an *in-situ* solid electrolyte oxygen gauge. This behavior indicates that all the compositions investigated were ionic conductors. In the low P_{O_2} range where He-O_2 and CO-CO_2 mixtures give overlapping P_{O_2} values, conductivities measured in CO-CO_2 mixtures were significantly lower than those measured in the above atmospheres. No explanation for this type of behavior is offered; however, other independent experiments supported the presence of a pressure-independent ionic conductivity.

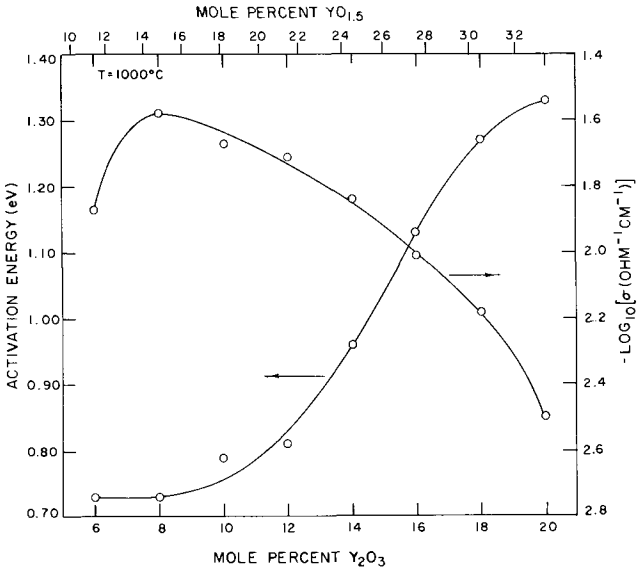

Fig. 5. Activation energy and 1000°C isothermal conductivity as a function of composition in the Y_2O_3-HfO_2 system.

The electrical conductivities agree well with values previously reported (2) at 900°-1000°C. However, the previously reported activation energies (2) are approximately 0.25 eV higher than those obtained from this work.

Because the 8 m/o Y_2O_3 composition possessed the highest conductivity and the lowest activation energy as shown in Fig. 5, it was chosen for further investigation as a possible electrolyte. The fact that the 6 m/o composition had the same activation energy as the 8 m/o composition, but a lower total conductivity, supports the x-ray studies in placing the phase boundary between these two limits. If there are two phases present at the 6 m/o composition, the monoclinic HfO_2 solid solution would be present as small islands in a continuous cubic fluorite host with a composition corresponding to the solubility limit of HfO_2 in the fluorite structure. Indications are that the conductivity is much lower in the monoclinic phase (2) than in the fluorite phase; consequently, the measured conductivity and activation energy would correspond to the continuous fluorite host with a reduced cross-sectional area. Thus, the effect of the nonconducting islands would be to decrease the total flux and thereby decrease the apparent total conductivity without altering the activation energy.

Figure 5 shows a trend of increasing activation energies and decreasing conductivities for increasing Y_2O_3 content above 8 m/o. This trend has been previously observed for the fluorite phase of the Y_2O_3-HfO_2 system (2, 13) and in similar systems (3, 14, 15). It has been suggested that this trend is due to ordering of anion vacancies (16).

Open-circuit emf measurements on 8 m/o Y_2O_3 hafnia.—Open-circuit emf measurements were made on the cells: Ni,NiO/YSH/Co,CoO and Cu,Cu_2O/YSH/Ni,NiO. The results of these measurements as a function of temperature are given in Fig. 6. The measured emf's are slightly lower than the calculated thermodynamic emf's. However, the pressure independence of the conductivity in the high oxygen pressure region and the magnitudes of $\sigma_\oplus$ and $\sigma_\ominus$ deduced from polarization experiments, described below, suggest that the low emf values are not the result of a perceptible electronic transference number. The emf discrepancies

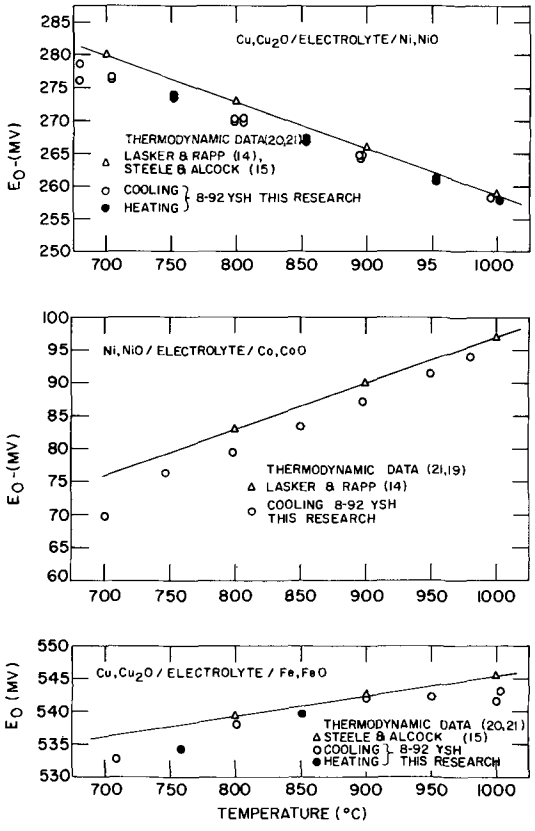

Fig. 6. Comparison of previously reported data with open-circuit emf's measured with 8 m/o Y_2O_3-HfO_2 solid electrolyte.

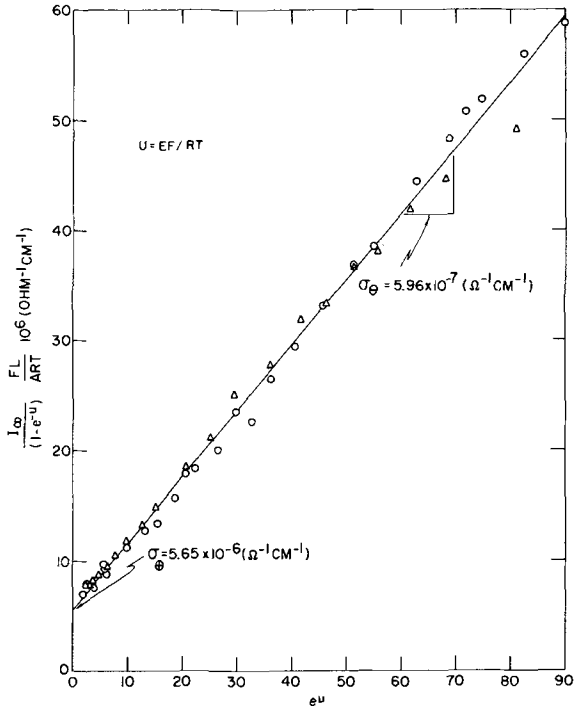

Fig. 7. Converted data plot according to Patterson (18) for d-c polarization measurements with the cell Cu, Cu_2O/8 m/o Y_2O_3-HfO_2/Au, Pt at 1000°C.

are presumed to be due to minor polarization effects associated with molecular or atomic transport through the electrolytes which were relatively porous.

In fact, emf cells such as Cu,Cu_2O/YSH/Fe,FeO and Fe,FeO/YSH/Hf,HfO_2, and Co,CoO/YSH/NbO,NbO_2, which involved large oxygen potential gradients, did not produce stable emf's. It was believed that the open porosity in the samples allowed molecular or atomic oxygen to be transferred through the electrolyte causing polarization and eventual failure of the electrodes to maintain a fixed oxygen potential. To combat this problem and rejuvenate the cell, an appropriate voltage was applied to the cell to titrate oxygen from the low to the high oxygen potential electrode. The titrations were deliberately designed to "overrestore" the apparently polarized electrodes. The titration current leads were then disengaged and the open-circuit emf was recorded as a function of time. The open-circuit emf's dropped almost instantaneously to a value which remained essentially constant for perceptible periods of time (on the order of minutes) before rapidly dropping once again. In all cases, these emf *vs.* time arrests fell very slightly below the thermodynamic emf's.

Representative samples taken after the sintering process, the conductivity, and the emf investigations were submitted for electron microprobe and wet chemical analyses to verify the composition of the solid solutions and to check for contamination resulting from the electrodes used in the emf studies. Results showed that the compositions remained unchanged and equaled the calculated compositions based on the standardized yttria and hafnia liquid solutions. As expected, the microprobe analysis indicated that the Fe-FeO electrode reacted slightly with the fluorite solid solutions, probably due to the presence of Y_2O_3. No reaction zones could be detected for the other electrodes used.

D-C polarization measurements.—An electrolyte of 8 m/o Y_2O_3 was subjected to Wagner d-c polarization measurements (17) at 1000°C to determine the magnitude of the electronic conductivity. A voltage was applied across the cell Cu,Cu_2O/YSH/Au,Pt forcing the oxygen ions to migrate to the reversible electrode. The steady-state current, assumed to be entirely electronic, was recorded as a function of the applied voltage. The data were analyzed by the method of Patterson *et al.* (18) and the results are shown in Fig. 7, where $\sigma_\oplus$ and $\sigma_\ominus$ represent the hole and excess electron conductivity, respectively, at the Cu-Cu_2O electrode.

The total conductivities of the 8 m/o Y_2O_3 were assumed to be ionic conductivities. The hole and excess electron conductivities were extrapolated based on a $+\frac{1}{4}$ and a $-\frac{1}{4}$ oxygen pressure dependence until they intersected the ionic conductivity. These intersections define the ionic domain (4) at 1000°C and are given by log $P_\oplus = +8.4$ and log $P_\ominus = -24.8$. Moreover, the lower domain limit of log $P_\ominus = -24.8$ is in excellent agreement with that of log $P_\ominus = -24.4$ obtained by open-circuit emf measurements.

Figure 8 compares this YSH electrolyte with other oxide solid electrolytes by showing the relative location of their respective ionic domain ($t_{ion} \geq 0.50$) boundaries. Because log $P_\oplus$ for YSH is higher (at 1000°C) than that for YDT (yttria-doped thoria), the ionic and hence the electrolytic domain for YSH is superior to that for YDT on the high P_{O_2} side. However, using Patterson's assessment (4) for CSZ (calcia-stabilized zirconia), YSH is found to be inferior to SCZ at high P_{O_2} values.

On the low P_{O_2} side, the ionic domain for YSH is about the same as that estimated by Patterson (4) for CSZ but is substantially inferior to (*i.e.*, has a much higher log $P_\ominus$ value than) YDT (8). Hence the ionic domain of YSH at 1000°C does not extend beyond conditions already covered by the previously known solid electrolytes CSZ and YDT. Using Patterson's analysis (4) and $+\frac{1}{4}$ and $-\frac{1}{4}$ oxygen pressure dependences for positive hole and excess electron conductivities implies that the electrolytic domain ($t_{ion} \geq 0.99$) for YSH extends from log $P_{O_2} = -16.8$ up to log $P_{O_2} = +0.4$ at 1000°C.

Conclusions

1. The cubic fluorite phase of yttria-stabilized hafnia is stable from about 7 m/o Y_2O_3 to compositions greater than 20 m/o Y_2O_3 at 1500°C.

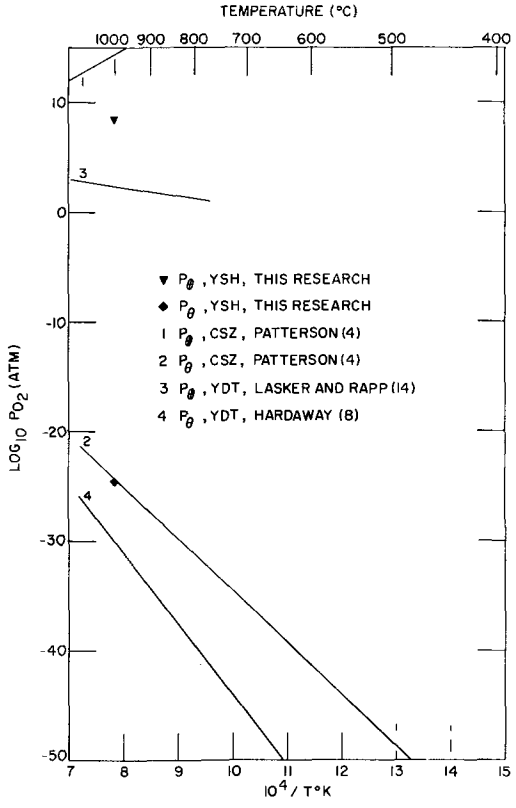

Fig. 8. Ionic domain boundaries for various oxide materials

2. The fluorite phase is an anion defective structure with substitutional replacement of hafnium with yttrium. Charge neutrality is maintained by fully ionized anion vacancies.

3. All yttria-hafnia solid solutions between 6 and 20 m/o Y_2O_3 exhibit a predominant ionic conductivity over the temperature range from 800° to 1000°C as evidenced by the oxygen pressure independence of the total conductivity.

4. Within the yttria-stabilized hafnia fluorite phase, activation energies increase and total conductivities decrease with increasing Y_2O_3 content. These trends suggest a tendency toward anion vacancy ordering.

5. The 8 m/o Y_2O_3-HfO_2 composition is a solid electrolyte over finite oxygen pressure and temperature ranges. The electrolytic domain width ($t_{ion} \geq 0.99$) for this composition at 1000°C is from log P_{O_2}(atm) = −16.6 to 0.4. It does not extend beyond conditions already covered by the previously known solid electrolytes CSZ and YDT at 1000°C.

Manuscript submitted Oct. 29, 1970; revised manuscript received Feb. 8, 1971.

Any discussion of this paper will appear in a Discussion Section to be published in the June 1972 JOURNAL.

REFERENCES

1. A. W. Smith, F. W. Meszaros, and C. D. Amata, *J. Am. Ceram. Soc.*, **49**, 240 (1966).
2. J. Besson, D. Deportes, and G. Robert, *Acad. Sci. Paris, Ser. C*, **262**, 527 (1966).
3. H. A. Johansen and J. G. Cleary, *This Journal*, **111**, 100 (1964).
4. J. W. Patterson, in "The Physics of Electronic Ceramics," L. L. Hench and D. B. Dove, Editors, Marcel Dekker, Inc., New York (1971).
5. L. M. Komissarova, W. Ken-shih, V. I. Spitsyn, and Y. P. Simanov, *Russ. J. Inorg. Chem.*, **9**, 383 (1964).
6. F. M. Spiridinov, V. A. Stepanov, L. N. Komissarova, and V. I. Spitsyn, *J. Less-Common Metals*, **14**, 435 (1968).
7. M. Caillet, C. Deportes, G. Robert, and G. Vitter, *Rev. Hautes Temp. Refract.*, **4**, 269 (1967).
8. J. B. Hardaway, III, J. W. Patterson, D. R. Wilder, and J. D. Schieltz, *J. Am. Ceram. Soc.*, To be published (1971).
9. A. M. Diness and R. Roy, *Solid-State Commun.*, **3**, 123 (1965).
10. R. E. Vogel and C. P. Kempter, *Acta Cryst.*, **14**, 1130 (1961).
11. R. D. Shannon and C. T. Prewitt, *ibid.*, **B25**, 925 (1969).
12. R. W. Vest, USAEC Rept. ARL-67-0010, Aerospace Research Lab., Wright-Patterson AFB, Ohio (1966).
13. E. Aleshin and R. Roy, *J. Am. Ceram. Soc.*, **45**, 18 (1962).
14. M. F. Lasker and R. A. Rapp, *Z. Physik. Chem.*, **49**, 198 (1966).
15. B. C. H. Steele and C. B. Alcock, *Trans. Met. Soc. AIME*, **233**, 1359 (1965).
16. R. E. Carter and W. L. Roth, in "Electromotive Force Measurements in High-Temperature Systems," C. B. Alcock, Editor, pp. 125-144, American Elsevier Publishing Co., Inc., New York (1968).
17. C. Wagner, "Proceedings of 7th CITCE Meeting," p. 361, Butterworth Scientific Publications, London (1957).
18. J. W. Patterson, E. C. Bogren, and R. A. Rapp, *This Journal*, **114**, 752 (1967).
19. K. Kiukkola and C. Wagner, *ibid.*, **104**, 379 (1957).
20. F. E. Rizzo, L. R. Bidwell, and D. E. Frank, *Trans. Met. Soc. AIME*, **239**, 593 (1967).
21. B. C. H. Steele, in "Electromotive Force Measurements in High-temperature Systems," C. B. Alcock, Editor, pp. 3-27, American Elsevier Publishing Co., Inc., New York (1968).

Differential Capacitance and Linear Sweep Voltammetry Studies on Polycrystalline Lead and Electrodeposited Lead Dioxide

J. P. Carr and N. A. Hampson

Chemistry Department, Loughborough University of Technology, Loughborough, Leicestershire, England

ABSTRACT

Impedance and linear sweep voltammetry (LSV) studies are reported on polycrystalline Pb and electrodeposited PbO_2 (α and β) in aqueous NaOH. The impedance studies indicate a pzc of -0.62 ± 0.01V (NHE) for Pb and $+1.15 \pm 0.01$V (NHE) for β-PbO_2. The LSV studies indicate that the anodic oxidation of Pb and cathodic reductions of α-PbO_2 involve mass transport of OH^- ions by diffusion in solution. Reduction of β-PbO_2 is complicated by modification to α-PbO_2.

Studies of lead dioxide electrodes in acid media are numerous. PbO_2 exists as two polymorphs, the orthorhombic α-form and the tetragonal β-form (1-3). It has been established that in acid media β-PbO_2 is the more stable polymorph (4, 5), however, α-PbO_2 has been observed in positive plates of lead acid batteries (6) and other investigations (7-10) have shown that α-PbO_2 is the main constituent of the anodic corrosion product on Pb.

Thermodynamically α-PbO_2 is the more stable polymorph in alkaline solutions (11) and recent work (12) has established the production of basic conditions in the interior of positive plates in the lead acid battery during the initial stages of formation which would provide the conditions conducive to the formation of α-PbO_2.

In spite of this few electrochemical measurements have been made on polycrystalline lead and lead dioxide in alkaline media. In this work we present differential capacitance and fast linear sweep voltammetry (LSV) data on polycrystalline lead and electrodeposited PbO_2 (α and β) in aqueous NaOH.

Previous Work in Alkali

Venstrem and co-workers (13, 14) studied the variation of hardness, with potential, of lead electrodes in NaOH (1M) and report the potential of zero change (pzc) at -0.55V (NHE). This confirms differential capacitance determinations in other aqueous solutions (15-21).

Following earlier work by Jones, Thirsk, and Wynne-Jones (22), Elbs and Forssell (23), and Glasstone (24), Farr and Hampson (25) studied the anodic behavior of polycrystalline lead in aqueous KOH and showed that the anodic oxidation of lead is complicated by transitions between the processes

$$Pb + 2\,OH^- = PbO + H_2O + 2e \qquad [i]$$

$$PbO + 2\,OH^- = PbO_2 + H_2O + 2e \qquad [ii]$$

$$\text{discharge of } OH^- \text{ on the } PbO_2 \text{ layer} \qquad [iii]$$

It was concluded that during oxidation, part of the oxidized lead was incorporated into a film of tetragonal lead oxide while the remainder dissolved in the electrolyte until the electrolyte in the immediate vicinity of the electrode became saturated with the anodic product, and orthorhombic lead oxide was deposited on the electrode blocking reaction [*i*]. α-PbO_2 was formed by oxidation of the tetragonal lead oxide on the electrode surface.

In previous differential capacitance studies (26) on time stable lead dioxide electrodes in aqueous KNO_3, we reported the pzc as 1.06 ± 0.01V (NHE) (α-PbO_2) and 1.15 ± 0.01V (NHE) (β-PbO_2). Other workers (27-29) have reported the pzc at 1.5-1.85V (NHE), but in the latter cases the results were for short electrode/electrolyte contact times.

In an earlier galvanostatic study (30), it was established that in alkaline solutions containing Pb(II), α-PbO_2 is the stable polymorph. PbO is adsorbed at the α-PbO_2 electrode surface and, at potentials near the equilibrium, the charge transfer reaction involves a simultaneous two-electron transfer between adsorbed PbO and two OH^- ions in solution whereas at higher overpotentials the exchange involves two consecutive electron steps.

Chartier and co-workers (31, 32) have studied the cathodic reduction of α- and β-PbO_2 in alkali. For β-PbO_2 they suggest that the electrode reaction involves two mechanisms
(*a*) a solution reaction

$$\beta\text{-}PbO_2 + H_2O + 2e = HPbO_2^- + OH^- \qquad [iv]$$

and (*b*) a solid phase reaction

$$\beta\text{-}PbO_2 + H_2O + 2e = PbO + 2\,OH^- \qquad [v]$$

Experimental

Double layer capacitance measurements.—The experimental technique and electrolytic cell have been described previously (33, 34). Charcoal purification of electrolytes (AR NaOH and doubly distilled water from deionized stock) was used, each electrolyte solution being continuously circulated through the cleaned activated charcoal for at least 14 days before making measurements. Potential measurements were made against a saturated calomel electrode using an electrometer (Keithley Type 610B). The counterelectrode was platinum gauze of high surface area. PbO_2 test electrodes were of α- and β-PbO_2 deposited on platinum bases (35, 36). Comparative x-ray studies were made in order to establish the freedom of each deposit from the unrequired polymorph [Phillips Diffractometer Type P.W. 1015 (36)]. Pb test electrodes were prepared by drawing molten Pb (99.999% pure supplied by Johnson Matthey Company Ltd.) into a glass capillary while under an atmosphere of N_2. The end was cut square and polished on a diamond wheel. Before each set of readings on Pb the electrode was mechanically polished on roughened glass using conductivity water as a lubricant, electrochemically etched in perchloric acid (20%), and finally chemically etched in the perchloric acid for 30 min.

LSV experiments.—Potential sweep measurements were carried out at $23° \pm 0.5°$C using a fast response potentiostat in conjunction with a linear sweep generator (Chemical Electronics Ltd.). The current was recorded on an x/y plotter (Bryant Instruments Ltd.). No parasitic interaction between the potentiostat and recorder was observed.

The test electrodes were as above. The counter and test electrodes were always of identical material. The

Key words: lead, lead dioxide, linear sweep voltammetry, differential capacitance, alkaline electrolytes.

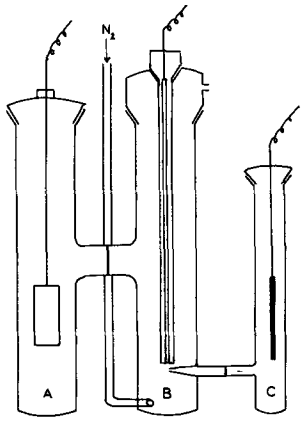

Fig. 1. Electrolytic cell: A—counterelectrode compartment, B—test electrode compartment, C—reference electrode compartment.

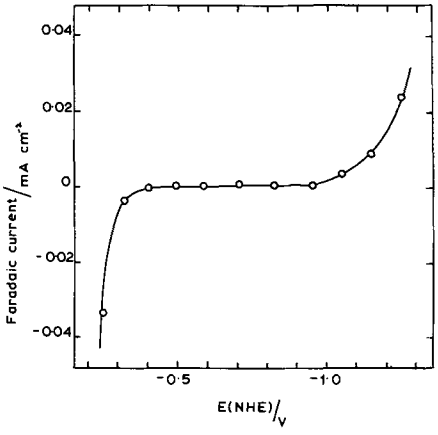

Fig. 2. Typical faradaic current-bias potential curves for polycrystalline lead in NaOH (0.0149M), 23°C.

reference electrode was a saturated calomel electrode. The electrolytic cell, Fig. 1, consisted of three compartments separated by glass frits. The reference electrode was joined to the test electrode compartment by a Luggin capillary and in all sweeps it was ensured that the test electrode was within 1 mm of the Luggin capillary tip, in order to minimize IR drop which was small in all the experiments. The Luggin capillary was finely drawn out at the tip to minimize shielding of the electrode.

Results and Discussion

Differential Capacitance Studies

Polycrystalline lead.—Figure 2 shows a characteristic faradaic current-bias potential curve for polycrystalline lead in NaOH electrolytes. The experimental polarizable region extends from ~ -0.25 to -1.0V,[1] the limits being governed by hydrogen evolution at the negative extremity and lattice dissolution at the positive extremity. Figure 2 indicates that for Pb the polarizable region is not ideal; however, the extent of the deviations from ideality is not very different from that observed for other metals (34).

Stable electrode impedances were obtained after 2 hr electrode/electrolyte contact. Readings taken at very short times showed a certain amount of drift but once stability had been achieved the system remained stable at potentials within the polarizable region for at least 24 hr without significant change. Replicate electrode impedances indicated an 8% variation about a mean.

Hysteresis was observed at both the negative and positive extremes of the polarizable region but for potential excursions within these limits no hysteresis

[1] All potentials are reported with respect to the normal hydrogen electrode.

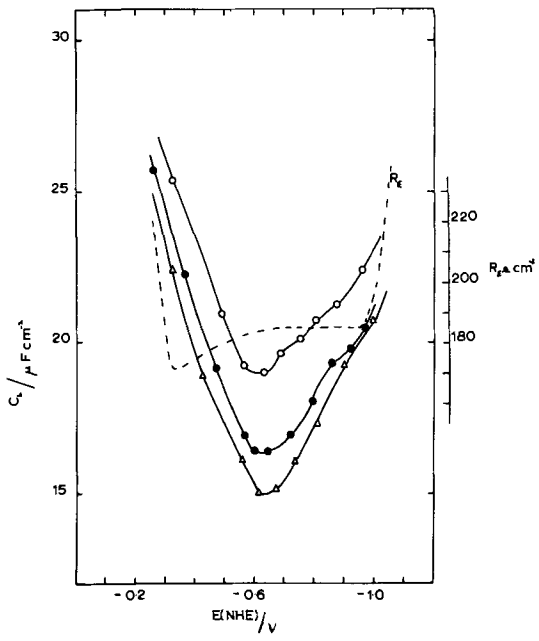

Fig. 3. Differential capacitance curves for polycrystalline lead in NaOH electrolyte, 23°C, 1000 Hz, (○) 0.401; (●) 0.091; (△) 0.0148M.

was observed. Electrodes forced to potentials outside the polarizable region and then returned to the polarizable region never reverted to their original electrode conditions indicating that irreversible electrode changes had occurred.

Figure 3 shows differential capacitance curves at 1 kHz for the range of concentrations investigated. (The separation of the anodic branch of the differential capacitance curves with $[OH^-]$ is a consequence of the equilibrium reaction

$$Pb(OH)_3^- + 2e \rightleftarrows Pb + 3\ OH^-$$

which predicts that E° shifts by ~ -90 mV for each decade in $[OH^-]$). On the same diagram is plotted the electrode resistance, R_E. A well-defined minimum in the differential capacitance curves, which increased with dilution, appears at -0.62V. This minimum is characteristic of the potential of zero charge, pzc, and compares with the work of Venstrem and co-workers (13, 14) who reported the pzc as -0.56V. R_E is potential dependent to some extent, a maximum occurring at ~ -0.41V, however, at potentials more negative R_E is reasonably constant indicating that at the pzc of Pb indicated (~ -0.6V) the true Pb/NaOH interphase is being observed.

Figure 4 shows a typical frequency dispersion of the differential capacitance. The extent of the dispersion amounted to less than 5% for a frequency change 1 kHz to 120 Hz. The dispersion observed is similar to that expected for solid metal electrodes and is most probably due to a certain amount of surface roughness as discussed by De Levie (37).

Electrodeposited PbO_2.—Figure 5 shows characteristic faradaic current-bias potential curves for α- and β-PbO_2 in NaOH electrolytes. The experimental polarizable region extends from $\sim$ 0.6 to 1.25V for α-PbO_2 and $\sim$ 0.6 to 1.20V for β-PbO_2, in each the limits are governed by oxygen evolution at the positive extremity and lattice dissolution at the negative extremity. A small change in the potential of zero current flow was observed for the two polymorphs, $\sim$ 0.65V for α-PbO_2 and $\sim$ 0.76V for β-PbO_2.

For α-PbO_2 electrodes stable electrode impedances were obtained within 1 hr of electrode/electrolyte contact, however, for β-PbO_2, 10-hr contact times were required. Impedance readings taken at short contact times showed a certain amount of drift. Once stability

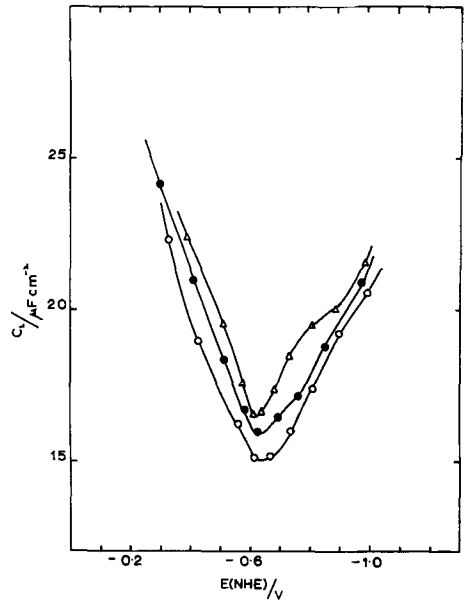

Fig. 4. Typical frequency dispersion of differential capacitance curves for polycrystalline lead in NaOH electrolyte (0.0149M), 23°C; △, 120 Hz; ●, 300 Hz; ○, 1000 Hz.

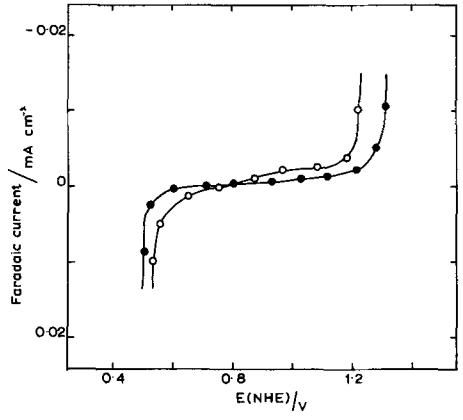

Fig. 5. Typical faradaic current-bias potential curves for electrodeposited lead dioxide in NaOH electrolyte (0.1M), 23°C; ●, α-PbO_2; ○, β-PbO_2.

had been achieved however the α-PbO_2 system remained stable at potentials within the polarizable region for at least 24 hr without significant change, the β-PbO_2 system was stable for only a relatively short time (1-2 hr). Replicate impedances indicated a 5% variation about a mean. No hysteresis was observed for potential excursions within the polarizable region, however, forcing the potentials outside this region caused serious irreversible changes at the electrode and it was found impossible to return to the original electrode condition.

Figures 6a and 6b show differential capacitance curves for α- and β-forms, respectively, at 1 kHz for the concentration of NaOH electrolytes investigated. On the same diagram is plotted the electrode resistance, R_E, which was satisfactorily constant in all electrolyte concentrations over the experimental polarizable region, for both polymorphs.

The differential capacitance curves shown for α-PbO_2 (Fig. 6a) were flatter than similar curves for β-PbO_2 (Fig. 6b) and the capacitance minimum was less well defined. For β-PbO_2 a minimum in the capacitance curves, taken to be the potential of zero charge, E_z, appears at 1.15V. Figures 7 and 8 show the typical frequency dispersion of capacitance which was observed in all experiments and appeared to be an inherent property of the electrode. The extent of the

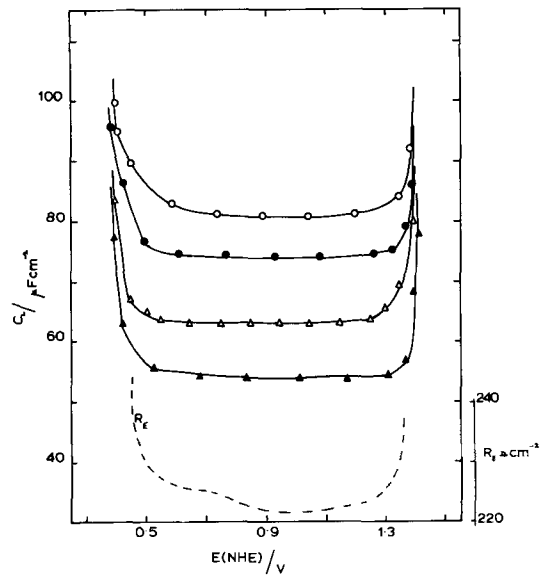

Fig. 6a. Differential capacitance curves for electrodeposited α-PbO in NaOH electrolytes, 23°C, 120 Hz; ○, 0.105; ●, 0.0405; △, 0.007; ▲, 0.0023M.

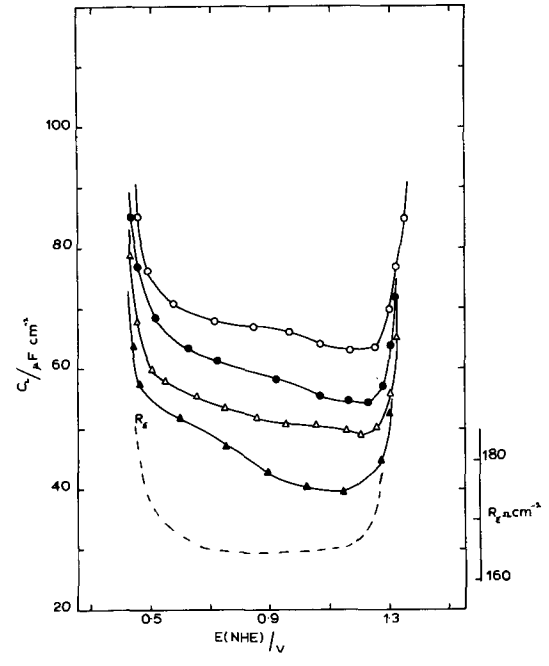

Fig. 6b. Differential capacitance curves for electrodeposited β-PbO_2 in NaOH electrolytes, 23°C, 120 Hz; ○, 0.105; ●, 0.0405. △, 0.007; ▲, 0.0023M.

dispersion, which was similar for both polymorphs, amounted to ~ 10% variation for a frequency change 1 kHz to 500 Hz.

Fast LSV Studies

LSV has been widely used for the examination of surface phenomena at electrodes (38-40). The general theory was developed by Randles (41) and Ševčik (42). In the case of the formation of a soluble substance at the electrode the current limitation is caused by a progressive removal of the reacting species in the immediate vicinity of the electrode. The magnitude of the maximum current (I_m) is proportional to the concentration of the rate-controlling species. Considering the general electrode equation

$$O + Ze = R \qquad [1]$$

and an ideal system in which the transport of reacting species at the electrode surface is by linear diffusion,

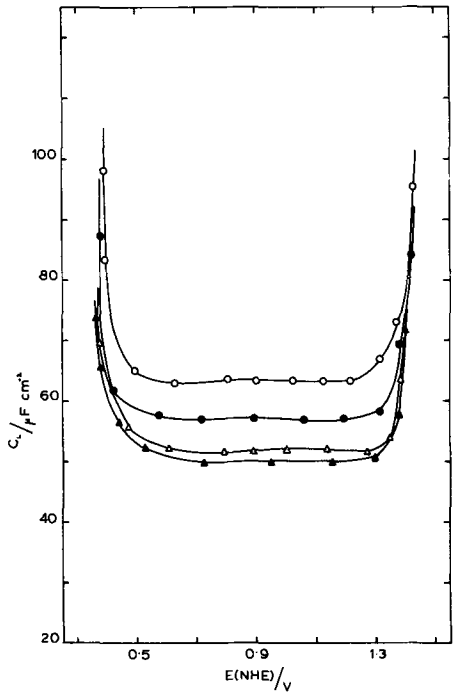

Fig. 7. Typical frequency dispersion of differential capacitance curves for electrodeposited α-PbO_2 in NaOH electrolyte (0.007M), 23°C; ○, 120 Hz; ●, 300 Hz; △, 500 Hz; ▲, 1000 Hz.

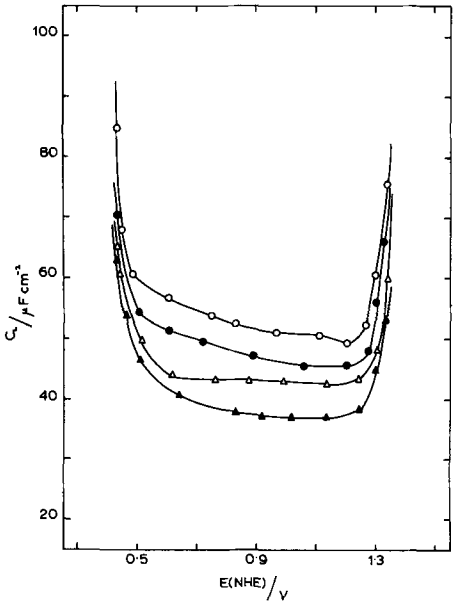

Fig. 8. Typical frequency dispersion of differential capacitance curves for electrodeposited β-PbO_2 in NaOH electrolyte (0.045M), 23°C; ○, 120 Hz; ●, 300 Hz; △, 500 Hz; ▲, 1000 Hz.

Delahay (43) has shown that at 25°C

$$I_m = 2.72 \times 10^5 \cdot Z^{3/2} \cdot A\, D^{1/2} \cdot C \cdot v^{1/2} \qquad [2]$$

where Z is the number of electrons involved in the reaction, A is the area of the electrode, D the diffusion coefficient, C the concentration of the rate-controlling electroactive species, and v the potential sweep rate.

Similarly for the reversible formation of an insoluble substance at the electrode and assuming linear diffusion Delahay (43) has shown that at 25°C

$$I_m = 3.67 \times 10^5 \cdot Z^{3/2} \cdot A\, D^{1/2} \cdot C\, v^{1/2} \qquad [3]$$

Experiments with solid metals are complicated by difficulties which prevent quantitative measurements being made, for example, doubt concerning the true

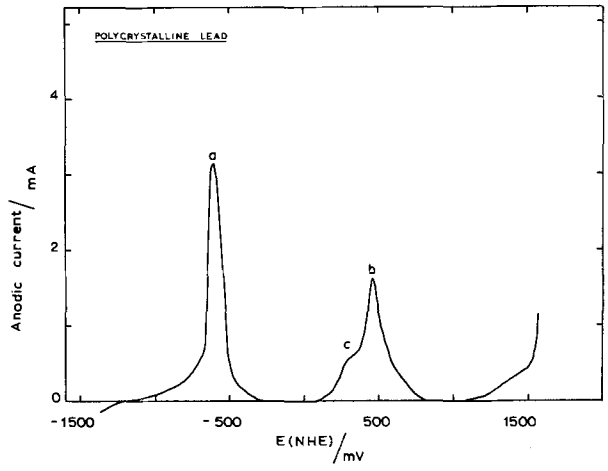

Fig. 9. Typical fast anodic potential sweep on polycrystalline lead in NaOH (3.45M), 23°C, 58.3 mV sec^{-1}.

surface area, true concentration of electroactive species, and the exact value of the diffusion coefficient. Also the problem arises of what proportion of the total current flowing is due to the capacitive component (I_c) where

$$I_c = X_c \left(\frac{d\eta}{dt}\right) \qquad [4]$$

where X_c is the double layer capacitance.

It is however, possible to obtain qualitative information concerning the controlling modes of diffusion occurring.

Polycrystalline lead.—Figure 9 shows the results of a typical fast anodic potential sweep. The experimental potential range (~ −1300 mV to ~ +1700 mV) was limited by hydrogen evolution at the negative extremity and oxygen evolution at the positive extremity. Between these potential limits two clearly defined, sharp current peaks (*a* and *b*) were observed and a minor peak *c* appeared as a shoulder on peak *b*. Peak *a* occurred at approximately the Pb/PbO redox potential (−585 mV NHE) and corresponded to the anodic oxidation of Pb to PbO as given by the general reaction

$$Pb + 2\,OH^- = PbO + H_2O + 2e \qquad [5]$$

Peaks *b* and *c* occurred at a potential approximately corresponding to the PbO/PbO_2 redox potential. Later experiments with the separate polymorphs of PbO_2 indicated that peak *b* was due to formation of α-PbO_2 and peak *c* due to formation of β-PbO_2.

Figure 10 shows the effect of sweep rate on the anodic peak height (peak *a*). A linear relationship between I_m and $\sqrt{v}$ was observed, the I_m-$\sqrt{v}$ line passing through the origin throughout the experimental concentration range. Figure 11 shows the effect of [OH^-] on I_m (peak *a*). I_m is directly proportional to [OH^-] in agreement with Eq. [2].

From Fig. 10 and 11 it is clear that the process which controls the flow of current is a diffusion process in solution and that the OH^- ion is the species which is involved in the diffusion process. Since I_m is directly proportional to [OH^-], Eq. [2] and [3] indicate that only one OH^- ion is involved in this process. It is suggested that a possible sequence of reactions at the electrode is as follows

$$Pb + 2\,OH^- = Pb(OH)_2 + 2e \qquad [6]$$

$$Pb(OH)_2 + OH^- = Pb(OH)_3^- \qquad [7]$$

$$Pb(OH)_3^- = PbO + OH^- + H_2O \qquad [8]$$

where [7] and [8] occur subsequently to produce a PbO phase at the electrode and, at the same time, [7] occurs in absence of [8] to form plumbite ions in

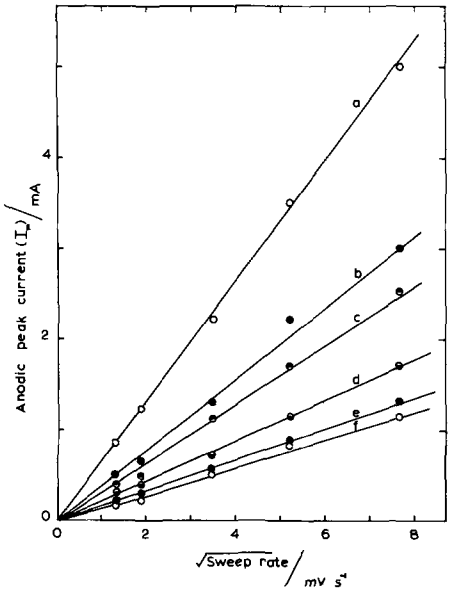

Fig. 10. Anodic peak current (I_m) vs. (sweep rate)$^{1/2}$ for formation of PbO on polycrystalline lead (peak *a* of Fig. 9) in NaOH, 23°C. (a) 4.7; (b) 3.45; (c) 2.53; (d) 1.79; (e) 1.39; (f) 1.02M. Electrode area 3.3 x 10^{-2} cm^2.

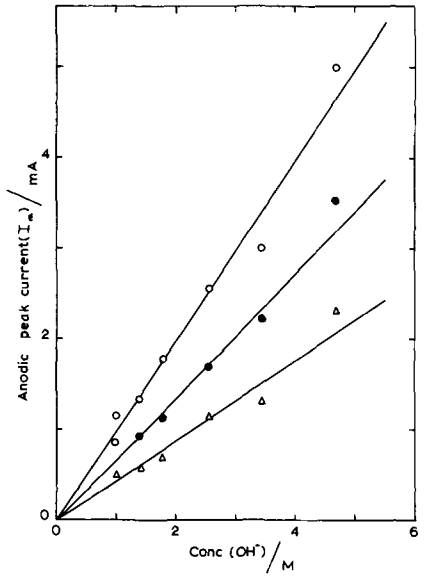

Fig. 11. Anodic peak current (I_m) vs. [OH^-] for formation of PbO (peak *a* of Fig. 9) on polycrystalline lead, 23°C. ○, 58.3 mV sec^{-1}; ●, 29 mV sec^{-1}; △, 12 mV sec^{-1}. Electrode area 3.3 x 10^{-2} cm^2.

solution. This mechanism is similar to that proposed by Farr and Hampson (25) on the basis of an electron microscopic study of the electrode surface coupled with a galvanostatic electrometric investigation.

The apparent diffusion coefficient of the OH^- ion calculated from the slopes of the I_m *vs.* $\sqrt{v}$ lines (Fig. 11) indicates a mean value of $\sim 10^{-7}$ cm^2 sec^{-1}. This value is considerably smaller than published data (46) for the diffusion coefficient of the OH^- ion in aqueous solution. A possible explanation of this is that diffusion of OH^- ions must occur through a layer of anodic products and the diffusion coefficient involved is that of the diffusing ion in the product phase. An alternate explanation is that the true surface area of the electrode available for diffusion is very much less than the apparent area due to the presence of a solid phase of PbO (25). It is difficult to decide which of these two explanations is formally correct but both indicate the well-established fact that in the region of the dissolution of a lead electrode in alkali a layer of solid products exists at the electrode surface (25). (It is not likely that a transpassive dissolution occurs at the electrode since the potential region at which peak *a* is observed is too low and in any case a transpassive dissolution would be expected to yield ions of a higher valence state.)

Linear relationships between I_m and $\sqrt{v}$ were not obtained within the experimental concentration range for peaks *b* and *c* indicating that the rate-controlling reaction mechanism is more complex than simple diffusion. The fact that I_m of peak *b*, which corresponded to the formation of α-PbO_2, was always greater than I_m of peak *c* (β-PbO_2), indicated that at high anodic potentials, although α-PbO_2 was the major product formed, traces of β-PbO_2 were always present. If the PbO_2 deposit was scraped from the electrode surface after a complete anodic potential sweep the presence of an orange brown colored deposit of PbO underneath the PbO_2 was observed. This would be in agreement with Farr and Hampson (25) that PbO_2 overlays a layer of PbO.

Nonreproducible relationships between I_m and sweep rate for peaks *b* and *c* indicate the possibility of formation of PbO_2 by more than one mechanism as observed previously by Rüetschi and Cahan (44) who suggest simultaneous oxidation of PbO and underlying Pb.

A slight negative shift of the potential of peak *b* and *c* occurred with increasing sweep rate indicating that the reaction occurring was significantly irreversible. For such a reaction Delahay (43) derived the relationship

$$E_p = E - \frac{RT}{a\,z\,\mathbf{F}}\left[0.77 - \ln k_f^{i}\,(\beta D\cdot)^{1/2} + \frac{1}{2}\ln\frac{a\,\mathbf{ZF}}{RT}\,v\right] \quad [9]$$

where E is the initial potential and E_p the potential at sweep rate v, α is the charge transfer coefficient for the electrode reaction, β is given by the expression

$$\beta = \frac{a\mathbf{ZF}}{RT}\,v$$

and k_f^{i} a reaction constant. Although theoretically α should be obtainable from $E_p - v$ data, in practice the uncertainties in the study of solid electrodes prevent this.

Electrodeposited α-PbO_2.—Figure 12 shows the results of a typical fast cathodic potential sweep. Between the two potential limits two clearly defined peaks (*d* and *e*) were observed. Peak *d* occurred at a potential representing reduction of the α—PbO_2 to PbO.

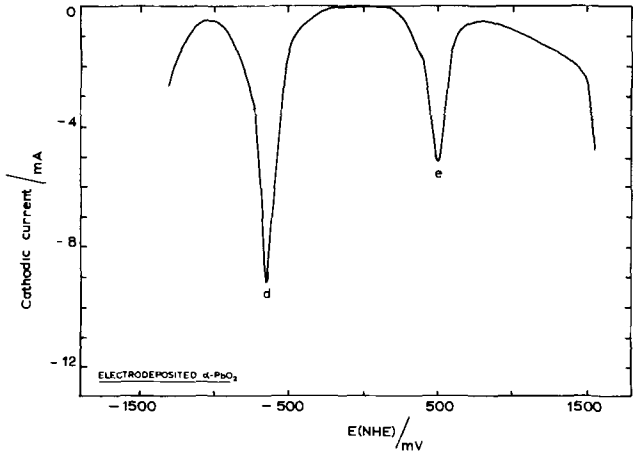

Fig. 12. Typical fast cathodic potential sweep on electrodeposited α-PbO_2 in NaOH (4.7M), 23°C, 58.3 mV sec^{-1}. Electrode area 4.9 x 10^{-2} cm.

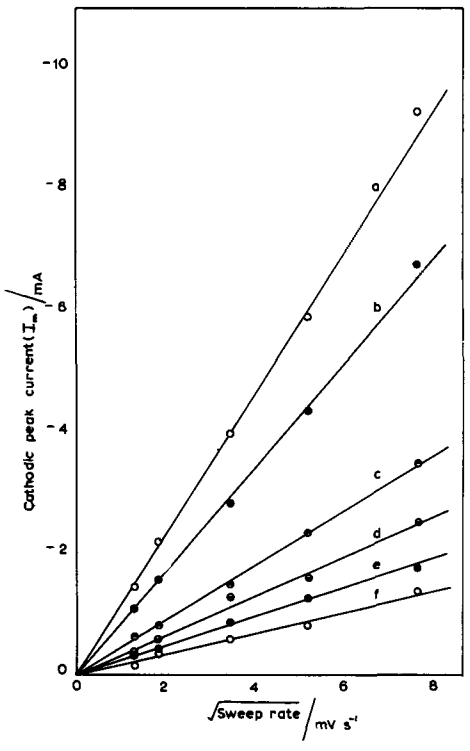

Fig. 13. Cathodic peak current, I_m, vs. $\sqrt{\text{sweep rate}}$ for formation of PbO (peak *d* of Fig. 12) on electrodeposited α-PbO_2 in NaOH, 23°C. (a) 4.7; (b) 3.45; (c) 2.53; (d) 1.79; (e) 1.39; (f) 1.02M. Electrode area 4.49 x 10^{-2} cm^2.

A shift of the potential of peak *d* to more negative values with increasing v indicated some irreversibility of this reaction. Peak *e* appeared at the Pb/PbO redox potential and represented reduction of PbO to Pb.

Figure 13 shows the effect of sweep rate on the cathodic peak height (peak *d*). A linear relationship between I_m and $\sqrt{v}$ was observed and within the experimental concentration range the I-$\sqrt{v}$ curves passed through the origin indicating that the current-limiting reaction is the diffusion of OH^- ions in solution.

Figure 14 shows the variation of I_m with concentration of OH^-; a linear relationship was not observed, the slope of $\log_{10} I_m$ *vs.* $\log_{10}$ [OH^-] having a value of ~1.4. The results confirm our previous work (30) indicating that adsorption of the electrode reaction products intrudes in the electrode reaction. The following sequence represents the electrode reaction

$$PbO_2 + H_2O + 2e = PbO_{ads} + 2\,OH^- \quad [10]$$

$$PbO_{ads} = PbO_{aq} \quad [11]$$

$$PbO_{aq} + OH^- + H_2O = Pb(OH)_3^- \quad [12]$$

Calculation of the diffusion coefficient using Eq. [2] and the initial part of the curves in Fig. 14 yields a value of ~10^{-7} which is far too small to be the true diffusion coefficient of the OH^- ion in aqueous solution. As previously suggested for the case of lead in alkali these data can be interpreted by either of the two explanations previously outlined, however, in this case it seems that the presence of an adsorbed layer through which the OH^- ion must diffuse is better supported by previous experimental work (30) than the postulation of an incomplete oxide film.

For peak *e*, a linear relationship of I_m *vs.* $\sqrt{v}$ was not observed indicating a duplex reaction system depending on prior reactions.

Electrodeposited β-PbO_2.—Figure 15 shows the results of a typical fast cathodic potential sweep. Between the potential limits three peaks were observed (*f*, *g*, and *h*). Peak *h* occurred at the Pb/PbO redox potential. Peak *g* occurred at the α-PbO_2/PbO redox

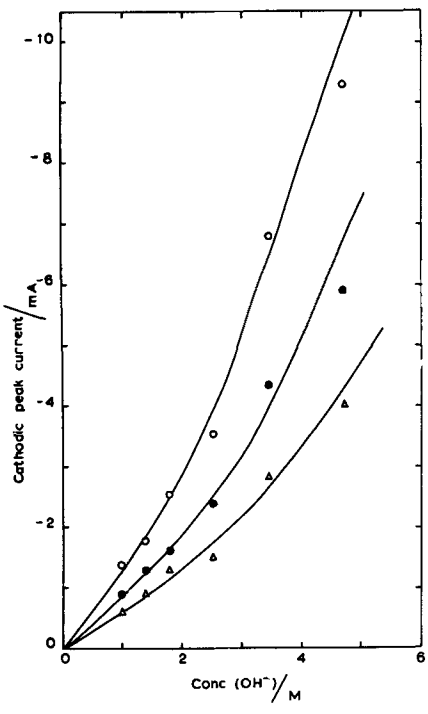

Fig. 14. Cathodic peak current (I_m) vs. [OH^-] for formation of PbO (peak *d* of Fig. 12) on electrodeposited α-PbO_2, 23°C; ○, 58.3 mV sec^{-1}; ●, 29 mV sec^{-1}; △, 12 mV sec^{-1}. Electrode area 4.49 x 10^{-2} cm^2.

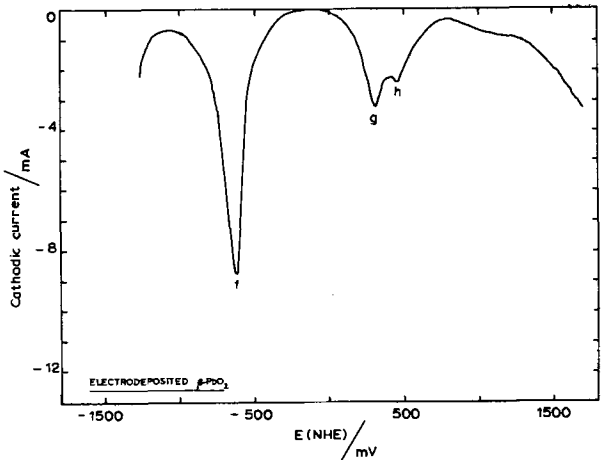

Fig. 15. Typical fast cathodic potential sweep on electrodeposited β-PbO_2 in NaOH (4.7M). 23°C, 58.3 mV sec^{-1}. Electrode area 4.9 x 10^{-2} cm^2.

potential indicating the presence of α-PbO_2 in the deposit. Peak *f* was observed only for β-PbO_2 and must be due to the β-PbO_2/PbO redox reduction. Continuous cathodic cycling showed a decrease in peak *f* but increase in peak *g* indicating a possible modification of the β-PbO_2 on the electrode surface to α-PbO_2 confirming earlier work (30) the reverse of which was observed in acid solutions (45), *i.e.*, modification of α-PbO_2 to β-PbO_2.

Conclusions

1. Differential capacitance studies
   (*a*) The pzc of Pb in aqueous NaOH is −0.62 ± 0.01V (NHE). The differential capacitance-bias potential curves show a distinct minimum.
   (*b*) The pzc of β-PbO_2 in aqueous NaOH is 1.15 ± 0.01V (NHE). The differential capacitance-bias potential curves show a broad minimum.
   (c) The pzc of α-PbO_2 could not be estimated.
2. Fast LSV studies

(a) The anodic oxidation of Pb to PbO in aqueous NaOH involves mass transport control by diffusion of OH^- ions in solution.
(b) The cathodic reduction of α-PbO_2 to PbO in aqueous NaOH involves mass transport control by diffusion of OH^- ions in solution but is complicated by adsorption of PbO at the electrode surface.
(c) The cathodic reduction of β-PbO_2 is complicated by a modification of surface β-PbO_2 to α-PbO_2.

Acknowledgments

We thank the Science Research Council for financial support (to J.P.C.). Professor Phillips is thanked for his interest.

Manuscript submitted Dec. 18, 1970; revised manuscript received March 23, 1971.

Any discussion of this paper will appear in a Discussion Section to be published in the June 1972 JOURNAL.

REFERENCES

1. N. Kameyama and I. Fukumoto, *J. Soc. Chem. Ind. Japan.*, **49**, 1946 (1946).
2. A. I. Zaslavsky, Y. D. Kondrashev, and S. S. Tolkachev, *Dokl. Akad. Nauk, SSSR*, **75**, 559 (1950).
3. A. I. Zaslavsky and S. S. Tolkachev, *Uch. Zap. Leningr. Gos. Univ., Ser. Khim. Nauk*, **12**, 186 (1953).
4. P. Rüetschi, J. Sklarchuk, and R. T. Angstadt, *Electrochim. Acta*, **109**, 177 (1963).
5. S. J. Bone, K. P. Singh, and W. F. K. Wynne-Jones, *ibid.*, **4**, 288 (1961).
6. E. Bode and E. Voss, *Z. Electrochem.*, **60**, 1053 (1956).
7. J. Burbank, *This Journal*, **103**, 87 (1956).
8. J. Burbank, *ibid.*, **104**, 693 (1957).
9. P. Rüetschi and B. D. Cahan, *ibid.*, **104**, 407 (1957).
10. S. Ikari and S. Yoshizawa, *J. Electrochem. Soc. Japan*, **E192** (1960).
11. P. Rüetschi, C. J. Venuto, and R. T. Angstadt, *This Journal*, **109**, 177 (1962).
12. D. Pavlov, *Electrochimica Acta.*, **13**, 2051 (1968).
13. E. K. Venstrem and P. A. Rehbinder, *Dokl. Akad. Nauk. SSSR*, **68**, 329 (1949).
14. E. K. Venstrem, P. A. Rehbinder, and V. Likchtman, *ibid.*, **107**, 105 (1956).
15. T. Borisova, B. Ershler, and A. N. Frumkin, *Zh. Fiz. Khim.*, **22**, 925 (1948).
16. N. V. Nikolaeva, N. S. Shapino, and A. N. Frumkin, *Dokl. Akad. Nauk. SSSR*, **86**, 581 (1952).
17. G. M. Deriaz, Ph.D. Thesis, University of Birmingham, 1951.
18. D. I. Leikis and B. N. Kabanov, *Tr. Inst. Fiz. Khim. Akad. Nauk. SSSR, 6 Nauye Metody Fiz. Khim Isslebovanii*, **2**, 5 (1957).
19. Ya. Kolotyrkin, C.I.T.C.E. Rept., 9th Mtg., p. 406, Butterworths, London (1958); *Trans. Faraday Soc.*, **55**, 455 (1959).
20. A. N. Frumkin, *J. Res. Inst. Catalysis, Hokkaido Univ.*, **15**, 61 (1967).
21. K. Rybalko and D. I. Leikis, *Electrokhimiya*, **3**, 383 (1967).
22. P. Jones, H. R. Thirsk, and W. F. K. Wynne-Jones, *Trans. Faraday Soc.*, **52**, 1003 (1956).
23. K. Elbs and J. Forssell, *Z. Electrochem.*, **8**, 760 (1902).
24. S. Glasstone, *J. Chem. Soc.*, 1459 (1922).
25. J. P. G. Farr and N. A. Hampson, *Electrochem. Technol.*, **6**, 10 (1968).
26. J. P. Carr, N. A. Hampson, and R. Taylor, *J. Electroanal. Chem.*, **27**, 109 (1970).
27. B. N. Kabanov, I. G. Kiseleva, and D. I. Leikis, *Dokl. Akad. Nauk. SSSR*, **99**, 805 (1954).
28. G. A. Kokarev, N. G. Bakhichisaraits'yan, and V. V. Panteleeva, *Tr. Mosk. Khim. Tekhnol. Inst.*, **54**, 161 (1967).
29. D. J. Leikis and E. K. Venstrem., *Proc. Acad. Sci. USSR Phys. Chem. Sect. (English Transl.)*, **112**, 17 (1957).
30. J. P. Carr, N. A. Hampson, and R. Taylor, *Ber. Bunsenges*, **74**, 557 (1970).
31. P. Chartier, *Bull. Soc. Chem. France.*, **7**, 2250 (1969).
32. P. Chartier and R. Poisson, *Bull. Soc. Chim. France.*, **7**, 2255 (1969).
33. J. P. G. Farr and N. A. Hampson, *Trans. Faraday Soc.*, **62**, 3494 (1966).
34. D. Armstrong, N. A. Hampson, and R. J. Latham, *J. Electroanal. Chem.*, **23**, 361 (1969).
35. N. A. Hampson, P. C. Jones, and R. F. Phillips, *Can. J. Chem.*, **47**, 2171 (1969).
36. N. E. Bagshaw, R. L. Clarke, and B. Halliwell, *J. Appl. Chem.*, **16**, 180 (1966).
37. R. De Levie, *Electrochim. Acta.*, **10**, 113 (1965).
38. J. Vogel, "Progress in Polarography," Vol. 2, chap. 20, Interscience Publishers Inc., New York (1962).
39. G. Mamantov and D. L. Manning, *J. Electroanal. Chem.*, **18**, 309 (1968).
40. N. White and F. Lawson, *ibid.*, **25**, 409 (1970).
41. J. E. B. Randles, *Trans. Faraday Soc.*, **44**, 327 (1948).
42. A. Ševčik, *Collection Czech, Chem. Commun.*, **13**, 349 (1948).
43. P. Delahay, "New Instrumental Methods in Electrochemistry," chap. 6, Interscience Publishers Inc., New York (1954).
44. P. Rüetschi and B. D. Cahan, *This Journal*, **105**, 369 (1958).
45. N. A. Hampson, P. C. Jones, and R. F. Phillips, *Can. J. Chem.*, **47**, 2171 (1969).
46. J. Heyrovsky and J. Kuta, Zaklady Polarografie, Nakladatestui Československé Akademie Věd, Prague, 1962.

Effects of Carbonate on the Anodic Dissolution and the Passivation of Zinc Electrode in Concentrated Solution of Potassium Hydroxide

Yuichi Sato, Hirokazu Niki, and Tsutomu Takamura

Toshiba Research and Development Center, Tokyo Shibaura Electric Company, Ltd., Kawasaki, 210, Japan

ABSTRACT

The effect of carbonate ions on the anodic behavior of a horizontal zinc anode in concentrated KOH solutions has been investigated by measuring the passivation time at constant current. Anodic dissolution of zinc was found to be associated with the diffusion-controlled zincate ion saturation near the electrode and the passivation time of the electrode, which is defined to be a period until the passivation occurs, was reduced with increasing concentration of carbonate ions at constant concentration of KOH. The phenomenon was explained from the linear relationship between t_p and $1/\eta$ as a result of the increase in viscosity η of the solution.

Although many authors have studied the anodic behavior of zinc electrodes in alkaline electrolyte (1, 2), few papers appear to have been published regarding the effect of carbonate ion on the zinc electrode reactions. Preliminary experiments showed that the presence of carbonate accelerates the passivation of the zinc electrode during the anodization in alkaline solution. Carbonate may be introduced in the solution when it is in contact with atmospheric air in the process of alkaline battery production. The knowledge of the effect of carbonate, therefore, appears valuable from the practical standpoint. The present study was initiated in order to determine the effect quantitatively and to establish a mechanism.

Of the many possible experimental approaches, measurements of the time for passivation at constant current with a horizontal plane electrode seem most suitable for obtaining a direct correlation between the battery performance and the carbonate concentration. In the present paper, passivation time of the zinc electrode was measured at constant anodic current and the relation between the passivation time and the carbonate concentration was investigated.

Experimental

The zinc electrode used was a disk of 20 mm diameter, that was cut from a rolled zinc sheet of 0.3 mm thickness and of about 99.99% purity. The electrode was cleaned by immersing in dilute HCl for about 5 min and rinsed in a stream of distilled water until the chloride ion was not detected by the $AgNO_3$ test. The sample treated by nitric acid (1) gave nearly the same results as that treated by hydrochloric acid. After being dried at room temperature, the electrode of lustrous surface was placed in an electrolysis cell. A H-type electrolysis cell of acrylic acid resin was used. The diameter of each compartment of the cell was about 30 mm. The solution volume of the sample compartment, 25 ml, was sufficient to prevent the concentration change during the anodic dissolution of zinc. The bottom of the sample compartment had a hole of 1.28 cm^2 and the zinc plate was sandwiched between the outer face of the bottom and a nickel plate which was covered by a thick plate of acrylic resin. The sandwich was tightened by screws to prevent any liquid leak. The actual working area of the zinc electrode was the same as that of the hole. The nickel plate was used as an electric contact. The potential of the zinc electrode at constant anodic current density was monitored through a Luggin capillary *vs.* a mercury-mercuric oxide electrode in pure KOH of the same concentration as that in the test cell. In another compartment of the cell, a nickel gauze of large area was placed and used as a counterelectrode. A constant anodic current of $\pm 0.3\%$ accuracy was supplied to the test electrode from a regulated power supply (Showa Electronics Model VSA 710S) until the onset of passivation on the surface. The passivation time, t_p, of the electrode was determined from the potential-time curves recorded on an electric polyrecorder (Toa Electronics Ltd. Model EPR-2TB) as illustrated in Fig. 1. The electrolysis was carried out in a thermostat kept at 25° ± 0.1°C, and oxygen dissolved in the electrolytic solution was removed by bubbling pure nitrogen gas through the solution for about 15 min. Ten minutes of nitrogen bubbling was found satisfactory for the complete removal of dissolved oxygen, which was checked polarographically. During the electrolysis, nitrogen gas was passed over the solution. Electrolysis was started 15 min after the immersion of the specimen electrode into the solution.

The base electrolytic solution was prepared by dissolving a known amount of reagent grade KOH pellet into doubly distilled water, the concentration being determined by titration. A solution containing the required concentration of ZnO or K_2CO_3 was prepared by dissolving a known amount of ZnO or K_2CO_3 of reagent grade into the base solution. All the procedures were carried out in a glove box filled with flowing nitrogen gas.

Viscosity and density measurements at 25°C were made for the electrolytic solution by conventional methods in a constant temperature bath controlled to ± 0.05°C. The white precipitate formed on the test electrode during the anodization was determined by x-ray and IR analysis. Samples for the analysis were collected as white leaves from the passivated electrode surface which, in advance, was washed with distilled water and dried in air. IR reflection spectra measurements were also made for the surface of the anodized zinc electrode which was washed with water and dried.

Results

The anodization was carried out at various current densities. The passivation time, t_p, was found dependent on the electrolysis conditions as has been pointed out (1, 2), and, of course, it increased when the solution was agitated during the electrolysis. Therefore, all the values cited below were obtained by keeping the solution quiescent. The reproducibility of t_p was excellent with the experimental error of $\pm 5\%$.

A typical potential-time curve at constant current is reproduced in Fig. 1, from which the passivation time of the electrode is determined as indicated in the figure.

Key words: alkaline batteries, viscosity, constant current electrolysis, zinc oxide.

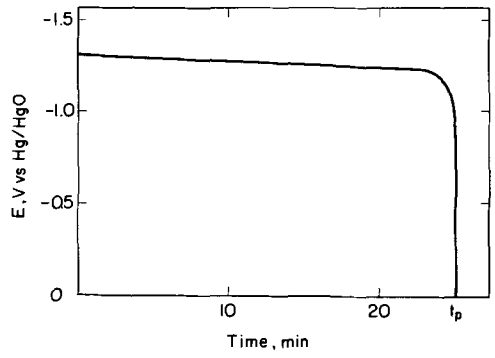

Fig. 1. Typical potential-time curve for horizontal zinc anode in a solution of 7.84M KOH containing 0.5M dissolved ZnO. Current density is 40 mA/cm^2.

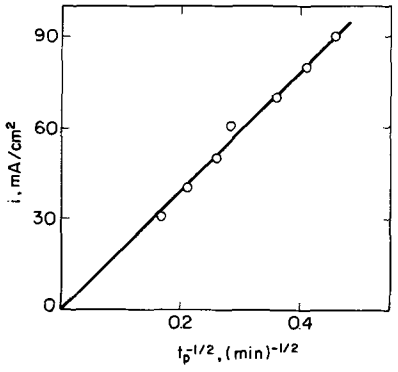

Fig. 2. Passivation time and current density relationship in a solution of 7.84M KOH containing 0.5M dissolved ZnO.

Figure 2 shows the relation between the anodic current density and the passivation time of the electrode for the solution of 7.84M KOH containing 0.5M dissolved ZnO at 25°C. As is seen in the figure, $t_p^{-1/2}$ increased linearly with the increase of applied anodic current.

When K_2CO_3 was added to KOH solution, t_p was found to be reduced in a linear manner and the slope was dependent on the concentration of dissolved ZnO. Figure 3 shows the variation of t_p in the solution of KOH against varied concentration of K_2CO_3 with and without 0.5M dissolved ZnO. The effect of ZnO can also be seen in the figure: at constant concentration of K_2CO_3, t_p was decreased by the addition of 0.5M ZnO, indicating the same tendency as with K_2CO_3. Addition of K_2CO_3 or ZnO may decrease the OH^- activity resulting in the decrease of t_p. In order to check whether there is a factor other than OH^- activity acting on t_p, t_p was measured in the system of KOH-NaOH where the OH^- concentration was kept constant. In Fig. 4, the relation between t_p and the gram equivalent fraction of KOH in the solution is given, where a marked reduction of t_p is shown to be caused by the increase of Na^+ concentration in spite of keeping the OH^- concentration constant.

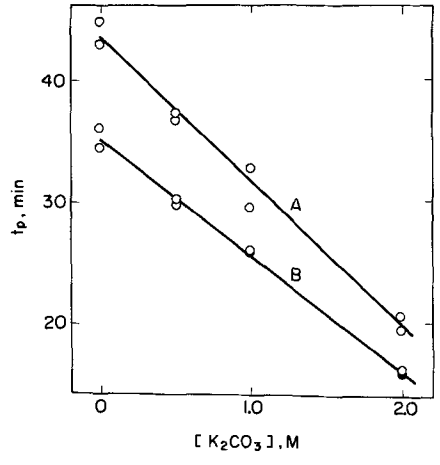

Fig. 3. Effects of carbonate ions on the passivation time in both 7.86M KOH (plot A) and 7.83M KOH + 0.5M dissolved ZnO (plot B). Concentration of K_2CO_3 was varied from zero to 2M and the current density was kept at 30 mA/cm^2.

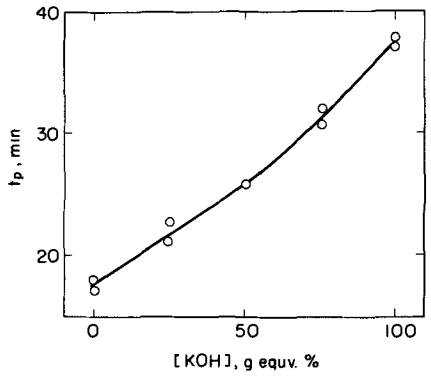

Fig. 4. Relation between the passivation time and gram equivalent fraction of KOH in the 8M alkaline solution whose total alkaline concentration was adjusted with NaOH and contained 0.5M ZnO. Current density is 30 mA/cm^2.

Density and viscosity data for the various solutions used in these experiments are tabulated in Tables I-III. The viscosity of the solution is increased with increasing the concentration of K_2CO_3 or the fraction of NaOH.

One may ascribe the decrease in t_p in the presence of CO_3^{2-} to the formation of $ZnCO_3$ film which retards further dissolution of zincate ion by covering the electrode surface. Low solubility of $ZnCO_3$ in water (3) appears to support this explanation. In order to detect the presence of $ZnCO_3$, the reaction product formed during the anodization was determined by x-ray and IR analyses. The x-ray analysis of the reaction products showed that the products consist of ZnO and do not contain $ZnCO_3$ and $Zn(OH)_2$. Neither IR spectra of the reaction products nor the reflection spectra of the surface of the zinc electrode after the electrolysis gave signals characteristic of $ZnCO_3$ (4).

Table I. Density and viscosity of the solutions of 7.86M KOH containing K_2CO_3 at 25°C

K_2CO_3, M	ρ, g/cm^3	η, centipoise
0	1.3220	2.285
0.5	1.3591	2.700
1.0	1.3962	3.224
2.0	1.4658	4.688

Table II. Density and viscosity of the solutions of 7.83M KOH containing 0.5M of dissolved ZnO and K_2CO_3 at 25°C

K_2CO_3, M	ρ, g/cm^3	η, centipoise
0	1.3512	2.523
0.5	1.3860	2.989
1.0	1.4218	3.560
2.0	1.4901	5.209

Table III. Density and viscosity of the 8M alkaline solutions containing 0.5M of dissolved ZnO at 25°C

KOH, M	NaOH, M	ρ, g/cm^3	η, centipoise
0	8.02	1.3065	6.726
2.03	6.04	1.3202	5.264
4.02	3.95	1.3304	4.017
6.05	1.93	1.3465	3.250
7.95	0	1.3578	2.583

Discussion

Since longer t_p favors the better discharge performance of the battery, solution contact with atmospheric air should be avoided during the production process of alkaline batteries. It is well known that the dissolution of carbon dioxide in caustic alkali causes a decrease in OH^- activity resulting in the decrease of t_p. An additional disadvantage due to the presence of CO_3^{2-}, however, has been shown to exist in the present study even if OH^- concentration is kept constant. Clear indication of lowering t_p due to increased concentration of CO_3^{2-} is seen in Fig. 3, where OH^- concentration is kept constant.

We wish to consider the mechanism of accelerated passivation due to CO_3^{2-}. For a situation in which ions generated at the anode diffuse away, time and current density are related by the following form of the diffusion equation (5, 6)

$$i = \frac{n\mathbf{F}\pi^{1/2}D^{1/2}\Delta C}{2t_p^{1/2}} \qquad [1]$$

where ΔC is the concentration difference of zincate ions between the electrode surface and the bulk solution, other symbols have the usual meaning. Figure 2 shows that the present experimental conditions satisfy the diffusion-controlled condition where anodic current is inversely proportional to the square root of the passivation time. Thus, the passivation is associated with a diffusion-controlled zincate ion saturation or supersaturation of the solution layer adjacent to the electrode resulting in the deposition of ZnO.

Of the oxide films formed by the anodic polarization in alkaline solution, existence of two different types has been reported by several authors (1, 2): the type 1 film is white, loose, and flocculent and the type 2 is a more adherent, compact, and protective film. According to Powers and Breiter (1), the former is formed at about −1.27V and influences the polarization, but it is not so strong as to cause the complete passivation, whereas the latter is of predominant importance in controlling the active to passive transition. The potential at which the type 2 film begins to form is uncertain but is considered to be more anodic than that of type 1. The potential-time curve in Fig. 1 begins to fall at about −1.25V, indicating the type 1 film forms initially, followed by the formation of the type 2 film, which passivates the zinc electrode. The passivation time, t_p, is shown to decrease linearly with the increase of CO_3^{2-} concentrations (Fig. 3). Two factors in Eq. [1] can contribute to the reduced t_p, *i.e.*, the decrease in ΔC or D.

First, we consider the reduction in ΔC. If the solubility of zincate ion which is formed as a result of the anodic dissolution is lowered by some reasons, ΔC should be decreased. If the solubility of $ZnCO_3$ is smaller than that of ZnO in alkaline solution, the passivation time would be shortened by the formation and the deposition of $ZnCO_3$ on the surface. This possibility, however, is denied by the analytical results of the passivation film, where $ZnCO_3$ could not be identified. This is in accordance with the solubility consideration in which the effect of OH^- activity is taken into account. The solubility product of $ZnCO_3$ in water is very small ($K = [Zn^{2+}][CO_3^{2-}] = 1.6 \times 10^{-11}$, at 25°C) (3), but the solubility in alkaline solution is shown to be very much increased as follows. The equilibrium constant of the equation (3) is a measure of the solubility of $ZnCO_3$ in alkaline solution

$$ZnCO_3 + 4\,OH^- \rightleftarrows [Zn(OH)_4]^{2-} + CO_3^{2-} \qquad [2]$$

$$K_1 = \frac{[Zn(OH)_4^{2-}][CO_3^{2-}]}{[ZnCO_3][OH^-]^4} \qquad [3]$$

Since the following equilibrium constants are known

$$Zn^{2+} + 4\,OH^- \rightleftarrows [Zn(OH)_4]^{2-} \qquad [4]$$

$$K_2 = \frac{[Zn(OH)_4^{2-}]}{[Zn^{2+}][OH^-]^4} = 1.4 \times 10^{15}\ (7) \qquad [5]$$

$$ZnCO_3 \rightleftarrows Zn^{2+} + CO_3^{2-} \qquad [6]$$

$$K_3 = [Zn^{2+}][CO_3^{2-}] = 1.6 \times 10^{-11} \qquad [7]$$

K_1 can be calculated by assuming the activity of $ZnCO_3$ as unity. The calculated value of K_1 is 2.2 x 10^4, showing that $ZnCO_3$ is very soluble in concentrated alkaline solution and would not deposit before the deposition of ZnO on the electrode.

Now we have to take into consideration the other factor, *i.e.*, the decrease in D which is reasonably expected to be caused by the increasing viscosity of the solution with increasing concentration of K_2CO_3. Because the anodic dissolution of zinc electrode is diffusion controlled as discussed above, the increase in viscosity would retard zincate ions to diffuse away from the electrode and facilitate the passivation of the electrode.

The relation between the passivation time and the viscosity of the solution will be derived for the purpose of explaining the present experimental data. According to Stokes' law, a particle of radius r moving through a homogeneous medium of viscosity η under the influence of a force f will maintain a velocity v, given by $v = f/6\pi\eta r$. When the definition of equivalent ionic conductance λ is introduced, the following relation holds

$$\lambda = \frac{|z|\mathbf{F}^2}{6\pi\eta r N} \qquad [8]$$

where N is Avogadro's number. The diffusion coefficient is given by Eq. [9]

$$D = \left(\frac{RT}{|z|\mathbf{F}^2}\right) \cdot \lambda \qquad [9]$$

By using these relations, Eq. [1] is rewritten as

$$t_p = \frac{n^2\mathbf{F}^2RT\Delta C^2}{24\,i^2N\pi} \cdot \frac{1}{\eta} \qquad [10]$$

Equation [10] shows that passivation time should be inversely proportional to the viscosity of the solution if the other factors are kept constant. Mean values of t_p at a given concentration of K_2CO_3 shown in Fig. 3 are plotted *vs.* the reciprocal of η cited in Tables I and II. As shown in Fig. 5, the experimental values fall on a straight line going through the original point, indicating the mechanism can be elucidated in terms of the viscosity increase. Equation [10] shows that ΔC can be calculated from the slope of the plot if the ionic radius is known. The values of ΔC for both cases of A and B, namely in the absence and the presence of 0.5M ZnO, can be calculated from the slopes of Fig. 5. Calculated values are 5.5M for the case of plot A, and

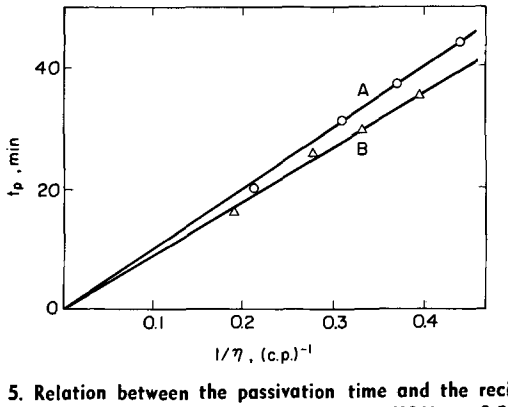

Fig. 5. Relation between the passivation time and the reciprocal viscosity in 7.86M KOH (plot A) and in 7.83M KOH + 0.5M dissolved ZnO (plot B). Viscosity was changed by adding K_2CO_3 (see Tables I and II).

5.1M for B, where the ionic radius of zincate ion is assumed to be the same as the literature value of 3.5A for Zn(II) aquo ion (8). The calculated concentration difference seems to be too large in comparison with the solubility of ZnO in concentrated KOH solution, which is about 0.9M in 8M KOH solution at 25°C (9). However, initial zincate ion concentrations have been found fairly higher than the equilibrium solubility when zincate ion is dissolved by anodization in caustic alkali, the tendency being explained by the feasibility of supersaturation (5, 10). This evidence justifies the higher values obtained here. It is obvious from Eq. [10] that the value of ΔC is dependent on r whose accuracy determines the validity of ΔC. The difference of ΔC obtained by the calculation for two sorts of solutions with and without ZnO is 0.4M which is nearly coincident with the experimental concentration difference of 0.5M. This would be an indication of the validity of the present treatment, which will provide one possible method for determining the concentration of dissolved material in the vicinity of the electrode.

Another factor influencing t_p is the activity of OH^-. The solubility of ZnO decreases with decreasing concentration of OH^- (9) and the OH^- activity may be lowered by the addition of K_2CO_3. But the slight lowering of the activity seems not enough to reduce to half the passivation time. The data given in Fig. 4 and 6 support the present argument. The solubility of ZnO in 8M KOH is 0.9M (9), and about 1.3M in 8M NaOH (11). If the passivation time is governed by the solubility of ZnO only, it must be longer in NaOH solution than in KOH, which contradicts the experimental results in Fig. 4. Figure 6 shows that t_p is mainly controlled by the viscosity of the solution. The slight downward departure from a straight line in Fig. 6 would be explained in terms of the solubility of ZnO. The solution of low viscosity was prepared by mixing a smaller amount of NaOH and a larger amount of KOH, where the solubility of ZnO is lower. In such a solution, the deposition of ZnO is facilitated resulting in the shorter t_p. A nondiffusional process like convection cannot explain the downward departure because t_p is expected to increase at the high $1/\eta$ value region, where the effect of convection seems to be more significant if convection occurred in the present case. Migration is not considered because of the high concentration of the electrolyte as compared to the electrolysis current.

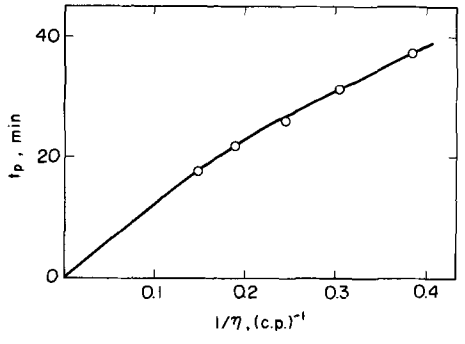

Fig. 6. Relation between the passivation time and the reciprocal viscosity in 8M (KOH + NaOH) solution containing 0.5M dissolved ZnO. Viscosity was changed by varying the ratio of KOH to NaOH as shown in Table III.

Manuscript submitted Nov. 12, 1970; revised manuscript received April 6, 1971.

Any discussion of this paper will appear in a Discussion Section to be published in the June 1972 JOURNAL.

REFERENCES

1. R. W. Powers and M. W. Breiter, *This Journal*, **116**, 719 (1969).
2. M. N. Hull, J. E. Ellison, and J. E. Toni, *ibid.*, **117**, 192 (1970).
3. Gmelins Handbuch der anorg. Chem., 8 Auflage, System No. 32, Zink, (1956), p. 973.
4. J. M. Hunt, M. P. Wisherd, and L. C. Bonham, *Anal. Chem.*, **22**, 1478 (1950).
5. M. Eisenberg, H. F. Bauman, and D. M. Brettner, *This Journal*, **108**, 909 (1961).
6. C. W. Tobias, M. Eisenberg, and C. R. Wilke, *ibid.*, **99**, 359C (1952).
7. T. P. Dirkse, *ibid.*, **101**, 328 (1954).
8. R. A. Robinson and R. H. Stokes, "Electrolyte Solutions," 2nd ed., p. 126, Butterworths Scientific Publishers (1959).
9. T. P. Dirkse, *This Journal*, **106**, 154 (1959).
10. T. P. Dirkse, *ibid.*, **102**, 497 (1955).
11. R. Scholder and G. Hendrich, *Z. anorg. allgem. Chem.*, **241**, 76 (1939).

Electrode Behavior of Iron in 2M HCl Containing Oximes or Quinuclidine

Erwin Laengle[1] and Norman Hackerman*[,2]

Department of Chemistry, The University of Texas at Austin, Austin, Texas 78712

ABSTRACT

Galvanostatic anodic and cathodic potential measurements were carried out with pure iron in 2M hydrochloric acid plus aliphatic and aromatic oximes and quinuclidine at different concentrations. Inhibition of both the anodic iron dissolution and the cathodic H_2-evolution by oximes and quinuclidine was caused by adsorption of the organic molecules on the metal surface. The cathodic polarization curves were interpreted quantitatively by the assumption of two rate-determining charge transfer reactions in a combined Volmer-Heyrovský mechanism. Anodic polarization curves were S-shaped with small Tafel regions around the rest potential. A change to less polarizable behavior at large polarizations was explained as due to desorption of adsorbed Cl^- and inhibitor molecules. The anodic Tafel slopes changed continuously from 120 to 30 mV with increasing inhibitor concentration and were interpreted by proposing a reaction mechanism on the basis of the combination of two limiting cases, namely the iron dissolution in inhibitor-free and in concentrated inhibitor-HCl solution.

The efficiency of nitrogen-containing organic compounds (amines, amides, pyridines, quinolines, acridines, thiourea, etc.) as inhibitors of iron in acid solutions has been extensively studied (1-5). It was clearly established that inhibition in a system without oxygen and oxidizing agents must be caused by the adsorption of the organic molecule on the iron surface (6). Enhanced inhibition can be attributed to improved adsorption due to the functional group and the polarizability of the inhibitor molecule.

In this study some aliphatic and aromatic oximes were investigated. In addition quinuclidine was studied in order to provide a comparative substance which is expected to adsorb without complications, such as different possibilities of orientation on the iron surface, etc.

Anodic and cathodic galvanostatic polarization measurements of pure iron in 2M HCl solution at 25° ± 1°C were made with several concentrations of the inhibitors. Metal dissolution rates were determined colorimetrically for dissolved iron. Kinetic parameters of the iron dissolution and the hydrogen evolution with and without inhibitors were sought in order to propose a mechanism for the inhibition.

Experimental

Chemicals.—Triple-distilled water prepared by redistilling standard laboratory water through a two-stage still (Model E-1, Barnstead Still & Sterilizer Company) was used in the preparation of the test solutions. All chemicals used were analytical reagent grade. Test electrodes were machined from a stock of zone-refined iron supplied by Battelle Memorial Institute with the following impurities in ppm: total nonmetallic, 8; total metallic, 38.

Polarization measurements.—The test electrode was a cylindrical iron rod pressed into a cylindrical Teflon plug with one flat edge (0.125 cm^2) exposed to the solution. A brass center rod was screwed into both the Teflon plug and the glass support. After abrading with 0, 1, and 4/0 emery papers the electrode was electropolished immediately before use in a mixture of 70-72% perchloric acid and glacial acetic acid (4:1 by volume) for 3 min at 150 mA/cm^2 and finally cleaned with pure acetone and water.

A glass cell in which the anode and cathode compartments were separated by fritted glass was used for the polarization measurements. A platinum sheet served as auxiliary electrode and the reference electrode was a Ag/AgCl electrode fitted into a Haber-Luggin capillary filled with 2M HCl solution. The potential of the reference electrode was found to be +195 mV *vs.* SHE, checked periodically with a saturated calomel electrode. The polarization current was supplied by a 90V battery and a series of variable resistances. The potentials and applied currents were determined with two Model 610B Keithley electrometers.

The measurements were carried out with 150 ml of test solution. Purified helium gas was bubbled through the solution for at least 15 hr before each experiment was started. Readings were started 2 hr after immersion of the test electrode. Upon application of a constant current, the potential required between 4 and 10 min to reach a steady value.

Colorimetric measurements.—After immersing in 50 ml of deareated test solution in a glass cell, the test electrode, pretreated in the same way as described above, was prepolarized for 1 hr with a constant cathodic current of 0.2 mA/cm^2. This procedure was used to reach a stable rest potential without iron dissolution. The circuit was then opened and after 6 hr the electrode was removed from the solution. The colorimetric iron determinations were carried out with 1,10-phenanthroline (7) and a student-type Bausch & Lomb colorimeter.

Results

Anodic and cathodic polarization measurements were conducted separately. The polarization curves in 2M HCl solution without inhibitor were measured several times and showed well-defined Tafel regions extending over about a decade of the current axis. Reproducibility of the cathodic Tafel slopes was somewhat better than those of the anodic slopes (±5 mV/decade and ±10 mV/decade, respectively). For uninhibited 2M HCl, the corrosion current (Table I) and the rest potential were given by the intersection of extrapolated anodic and cathodic Tafel lines. (When an inhibitor was added, the rest and corrosion potentials were not necessarily the same.) The rest potential was found to be −240 ± 5 mV; the corrosion current density was reproducible to ±3%.

Cathodic galvanostatic polarization curves.—All experimental curves with inhibitor solution showed a

* Electrochemical Society Active Member.
[1] Present address: Swiss Federal Institute of Technology, Zurich, Switzerland.
[2] Present address: Department of Chemistry, Rice University, Houston, Texas 77001.
Key words: corrosion, polarization curves, inhibition, adsorption.

Table I. Corrosion rates and inhibitor effectivenesses ($E = (i_{\text{uninhibited}} - i_{\text{inhibited}})/i_{\text{uninhibited}}$) of iron in 2M HCl solutions with and without inhibitors extrapolated from anodic polarization curves (i_{corr} and E_1), and the inhibitor effectivenesses calculated from colorimetric iron determinations (E_2)

	i_{corr}, mA/cm²	E_1	E_2
2M HCl	4.5×10^{-2}	0	0
1×10^{-3}M acetone oxime	2.9×10^{-2}	0.36 ± 0.03	0.31 ± 0.04
1×10^{-3}M 2-butanone oxime	2.5×10^{-2}	0.44 ± 0.03	0.37 ± 0.04
1×10^{-3}M acetophenone oxime	2.2×10^{-2}	0.51 ± 0.03	0.51 ± 0.04
1×10^{-3}M benzaldoxime	1.9×10^{-2}	0.58 ± 0.03	0.59 ± 0.04
1×10^{-3}M benzophenone oxime	1.5×10^{-2}	0.67 ± 0.03	0.63 ± 0.04
1×10^{-3}M quinuclidine	3.0×10^{-2}	0.33 ± 0.03	0.31 ± 0.04

characteristic shape as given in Fig. 1. The same polarization curves were obtained whether the solution was stirred by bubbling helium during the measurements or not. The intersection of the linear portions of the cathodic curves with the potential axis at the rest potentials indicates that quinuclidine and all oximes act as accelerators. However, the intersection of the linear portions of the anodic curves with the potential axis at the rest potentials indicates that these compounds showed inhibition. Colorimetric determinations of the dissolved iron in solutions with and without inhibitors proved that the real corrosion currents were those derived from the anodic curves, as shown in Table I.

In the concentration range between 1×10^{-4}M and 1×10^{-1}M, no relation was found between the rest potentials and the corrosion rates for any inhibitor investigated here. The rest potentials were all between −223 and −261 mV with a maximum error of ±10 mV for each experiment.

The characteristic shape of the cathodic polarization curves can be explained by the assumption of the following two rate-determining charge transfer reactions in a combined Volmer-Heyrovský mechanism

$$H^+ + e^- \rightarrow H_{ad} \quad \text{Volmer}$$

$$H^+ + H_{ad} + e^- \rightarrow H_2 \quad \text{Heyrovský}$$

Vetter (8) derived a theoretical expression for the current-potential relation of the Volmer-Heyrovský mechanism.

$$i_{H_2} = 2i_{0,V} \exp\left[-\frac{(1-\alpha_1)\mathbf{F}}{RT}\eta_{H_2}\right] \frac{1 - \exp\left(\frac{2\mathbf{F}}{RT}\eta_{H_2}\right)}{1 + \frac{i_{0,V}}{i_{0,H}} \exp\left[\frac{(1+\alpha_1-\alpha_2)\mathbf{F}}{RT}\eta_{H_2}\right]} \quad [1]$$

where

i_{H_2} = total current density
η_{H_2} = overvoltage
$i_{0,V}$ = exchange current density of the Volmer reaction
$i_{0,H}$ = exchange current density of the Heyrovský reaction
α_1 = transfer coefficient of the Volmer reaction
α_2 = transfer coefficient of the Heyrovský reaction

Without the factor 2 and by using polarization π instead of η_{H_2} this formula can be used for the calculation of all cathodic polarization curves measured in this study.

$$i_{H_2} = i_{0,1} \exp\left[-\frac{(1-\alpha_1)\mathbf{F}}{RT}\pi\right] \frac{1 - \exp\left(\frac{2\mathbf{F}}{RT}\pi\right)}{1 + \frac{i_{0,1}}{i_{0,2}} \exp\left[\frac{(1+\alpha_1-\alpha_2)\mathbf{F}}{RT}\pi\right]} \quad [2]$$

$i_{0,1}$ and $i_{0,2}$ are now not exchange current densities at the equilibrium potential of the hydrogen electrode, but current densities at the rest potential. Kaesche (9) also explained his cathodic curves for iron in acid perchlorate solutions with phenylthiourea by the Volmer-Heyrovský mechanism. He used Eq. [2] in a simpler form by setting $[1 - \exp(2\mathbf{F}/RT\ \eta_{H_2})] = 1$. The experimental results described in the present study were found to fit the complete expression [2] better.

Representative examples of calculated polarization curves by using Eq. [2] are shown in Fig. 1-4. The values of the parameters $i_{0,1}$, $i_{0,2}$, and α_1 were graphically extrapolated from the experimental data by determining the cathodic and anodic Tafel lines. Values for α_2 were selected to give the best fit of the experi-

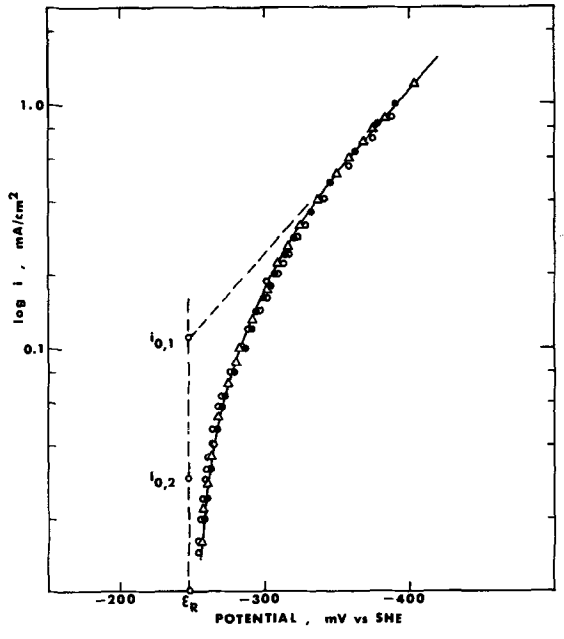

Fig. 1. Cathodic polarization curves of iron in 2M HCl solution containing 1×10^{-3}M acetone oxime. With stirring, Δ; without stirring, ○, ●; ——— from Eq. [2] calculated curve.

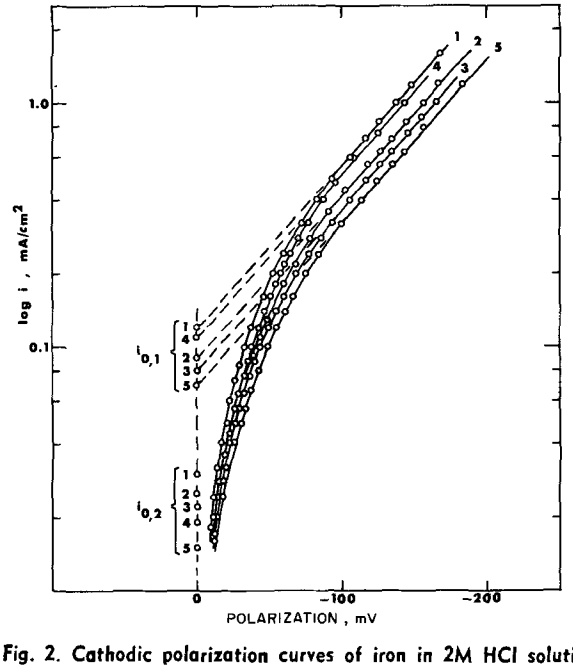

Fig. 2. Cathodic polarization curves of iron in 2M HCl solutions containing 1×10^{-3}M: quinuclidine, 1; 2-butanone oxime, 2; acetophenone oxime, 3; benzaldoxime, 4; and benzophenone oxime, 5. Experimental values, ○; ——— from Eq. [2] calculated curves. $i_{0,2}$ extrapolated from anodic polarization curves.

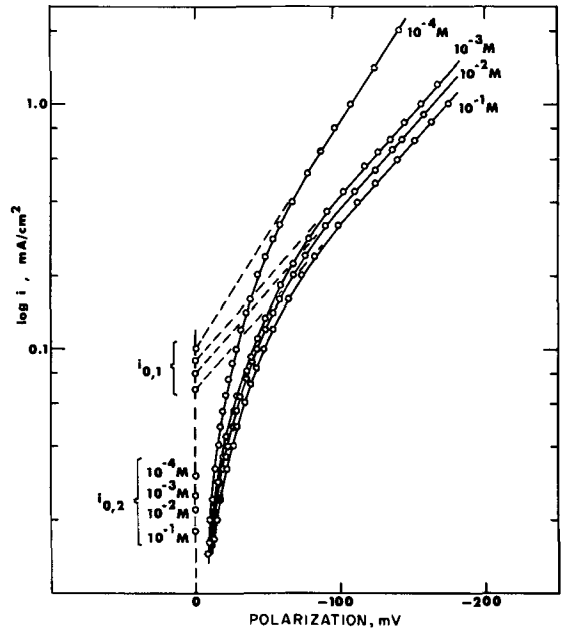

Fig. 3. Concentration dependence of cathodic polarization curves of iron measured in 2M HCl solutions with 2-butanone oxime in a concentration range between $1x10^{-4}$ and $1x10^{-1}$M. Experimental values, ○; ——— from Eq. [2] calculated curves. $i_{0,2}$ extrapolated from anodic polarization curves.

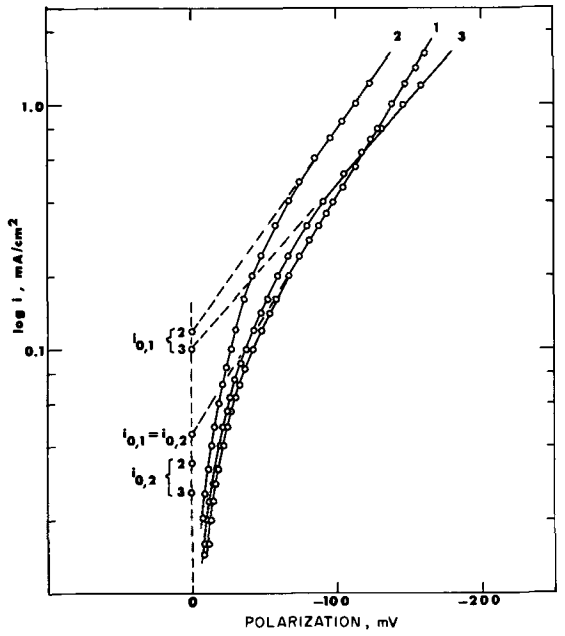

Fig. 4. Cathodic polarization curves of iron in 2M HCl solutions: without inhibitor, 1; with $1x10^{-4}$M acetone oxime, 2; and with $1x10^{-2}$M acetone oxime, 3. Experimental values, ○; ——— from Eq. [2] calculated curves. $i_{0,2}$ extrapolated from anodic polarization curves.

mental data to the curves which Eq. [2] provides theoretically.

Table II lists the concentration dependence of the α_1 and α_2 values obtained from cathodic polarization curves of all investigated inhibitors. All experimental curves with benzophenone oxime, acetophenone oxime, and benzaldoxime fit theoretical curves with constant values of the parameters α_1 and α_2. Benzophenone oxime could not be investigated at concentrations higher than 1×10^{-3}M because of the limited solubility. For acetone oxime and 2-butanone oxime within a concentration range of 1×10^{-3} to 1×10^{-1}M and also for quinuclidine between 5×10^{-4} and 1×10^{-2}M, the same α values were obtained. At very small concentrations, the aliphatic oximes and quinuclidine fit curves with smaller transfer coefficients. In uninhibited 2M HCl solution the cathodic curve can be calculated by using the following parameters: $\alpha_1 = 0.42$, $\alpha_2 = 0$ (*e.g.*, infinitely small) and $i_{0,1} = i_{0,2}$. This result can be interpreted by the assumption that transfer coefficients obtained from measurements at very low inhibitor concentrations are very similar to those determined in uninhibited solutions (Fig. 4).

The current densities $i_{0,1}$ and $i_{0,2}$ at the rest potential as functions of the inhibitor concentration are shown in Fig. 5 and 6, with $i_{0,2}$ corresponding to the measured corrosion rate at the rest potential. The inhibitors can be divided into two groups (one in Fig. 5 and the other in Fig. 6) according to their concentration dependence. The group in Fig. 5 exhibits linear relations of the log $c/i_{0,1}$ and log $c/i_{0,2}$ plots of the aliphatic oximes and quinuclidine. The corrosion rates ($i_{0,2}$) as well as the current densities of the Volmer reaction at the rest potential ($i_{0,1}$) became smaller with increasing inhibitor concentrations, as shown in Fig. 5 and 6. Acetone oxime and quinuclidine had the same corrosion rates. For the log $c/i_{0,2}$ plot of 2-butanone oxime the current densities decreased by 4×10^{-3} mA/cm² but this plot was still parallel to that of acetone oxime and quinuclidine. The slope of both lines is about -4×10^{-3} mA/cm²/decade on the concentration axis. Slopes of the $i_{0,1}$ plots increase in the series: acetone oxime, 2-butanone oxime, quinuclidine. The other group (Fig. 6) includes acetophenone oxime and benzophenone oxime for which concentration independent values of $i_{0,1}$ and $i_{0,2}$ were obtained at high concentrations. The concentration dependence of benzaldoxime is very close to that of the first group (Fig. 5). In relation to $i_{0,2}$ it shows the same behavior as the aliphatic oximes with the same linear slope of the log $c/i_{0,2}$ line.

Table II. Kinetic parameters of all measured polarization curves of iron in 2M HCl solutions with and without inhibitors

α_1 = transfer coefficients of the cathodic Volmer reaction. α_2 = transfer coefficients of the cathodic Heyrovský reaction. b_1 = Tafel slopes extrapolated from cathodic Tafel lines in mV/decade. b_3 = Tafel slopes extrapolated from anodic Tafel lines in mV/decade.

	b_1	α_1	α_2	b_3		b_1	α_1	α_2	b_3
1×10^{-4}M acetone oxime	120	0.5	0.1	100	2M HCl	103	0.42	0.0	120
5×10^{-4}M acetone oxime	120	0.5	0.2	—	1×10^{-4}M acetophenone oxime	150	0.6	0.4	70
1×10^{-3}M acetone oxime	150	0.6	0.4	86	3.55×10^{-4}M acetophenone oxime	150	0.6	0.4	—
5×10^{-3}M acetone oxime	150	0.6	0.4	—	1×10^{-3}M acetophenone oxime	150	0.6	0.4	48
1×10^{-2}M acetone oxime	150	0.6	0.4	40	5×10^{-3}M acetophenone oxime	150	0.6	0.4	—
5×10^{-2}M acetone oxime	150	0.6	0.4	—	1×10^{-2}M acetophenone oxime	150	0.6	0.4	39
1×10^{-1}M acetone oxime	150	0.6	0.4	31	5×10^{-2}M acetophenone oxime	150	0.6	0.4	—
1×10^{-4}M 2-butanone oxime	109	0.45	0.1	92	10^{-4}M benzaldoxime	150	0.6	0.4	85
5×10^{-4}M 2-butanone oxime	120	0.5	0.3	—	5×10^{-4}M benzaldoxime	150	0.6	0.4	—
1×10^{-3}M 2-butanone oxime	150	0.6	0.4	80	1×10^{-3}M benzaldoxime	150	0.6	0.4	52
5×10^{-3}M 2-butanone oxime	150	0.6	0.4	—	5×10^{-3}M benzaldoxime	150	0.6	0.4	—
1×10^{-2}M 2-butanone oxime	150	0.6	0.4	63	1×10^{-2}M benzaldoxime	150	0.6	0.4	32
5×10^{-2}M 2-butanone oxime	150	0.6	0.4	—	5×10^{-2}M benzaldoxime	150	0.6	0.4	—
1×10^{-1}M 2-butanone oxime	150	0.6	0.4	50	10^{-4} quinuclidine	109	0.45	0.1	80
1×10^{-4}M benzophenone oxime	150	0.6	0.4	54	5×10^{-4}M quinuclidine	150	0.6	0.4	—
1.5×10^{-4}M benzophenone oxime	150	0.6	0.4	—	1×10^{-3}M quinuclidine	150	0.6	0.4	60
4.1×10^{-4}M benzophenone oxime	150	0.6	0.4	—	5×10^{-3}M quinuclidine	150	0.6	0.4	—
1×10^{-3}M benzophenone oxime	150	0.6	0.4	42	1×10^{-2}M quinuclidine	150	0.6	0.4	41
					5×10^{-2}M quinuclidine	120	0.5	0.4	—

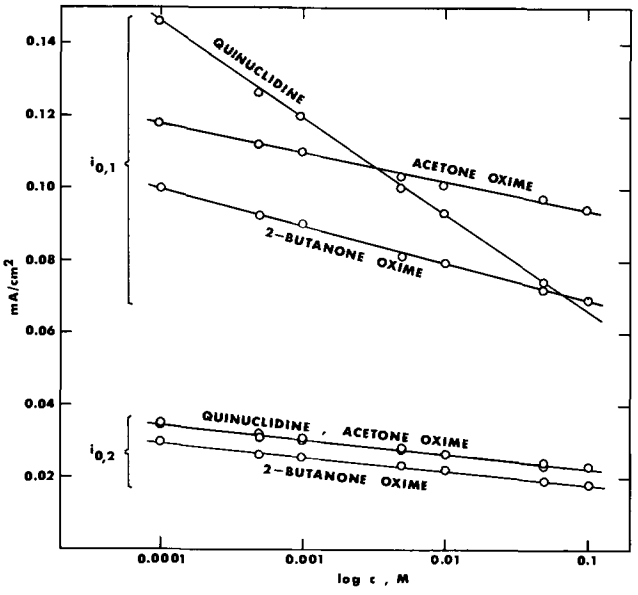

Fig. 5. Concentration dependence of the current densities $i_{0,1}$ and $i_{0,2}$ at the rest potential of iron measured in 2M HCl solutions containing acetone oxime, 2-butanone oxime and quinuclidine.

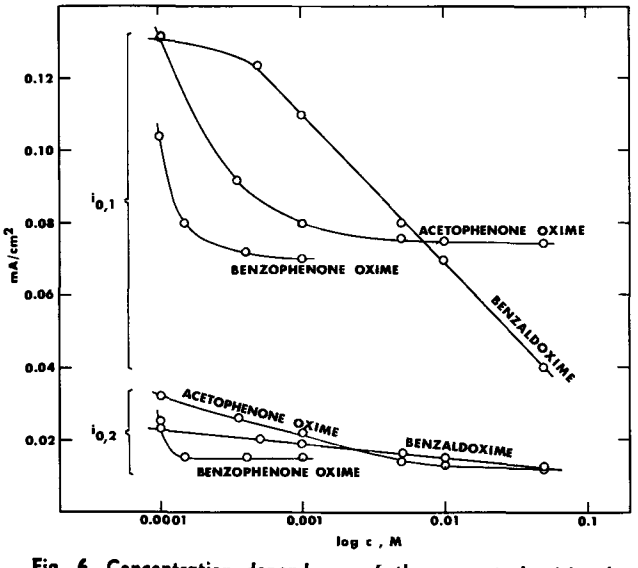

Fig. 6. Concentration dependence of the current densities $i_{0,1}$ and $i_{0,2}$ at the rest potential of iron measured in 2M HCl solutions containing acetophenone oxime, benzophenone oxime, and benzaldoxime.

Anodic galvanostatic polarization curves.—Anodic polarization measurements in 2M HCl solutions with and without inhibitors resulted in S-shaped polarization curves as shown in Fig. 7 and 8. Stern (10), and more particularly Schwabe and Voigt (11), found the same type of polarization curves for dissolution measurements of iron in acid solutions containing Cl^-; the less polarizable behavior of the anodic curves at high polarizations was probably due to Cl^- desorption.

While the anodic polarization curve of iron in 2M HCl solution shows a well-defined Tafel region extending to over 1 mA/cm² with a Tafel slope of 120 mV/decade, addition of inhibitor effected a drastic reduction of the Tafel region. In Fig. 7 and 8 the concentration dependence of the anodic polarization curves of two representative examples are shown. With increasing inhibitor concentration the Tafel regions decrease from about +0.4 mA/cm² at 1 x 10^{-4}M inhibitor to +0.15 mA/cm² at 1 x 10^{-2}M inhibitor. As can be seen

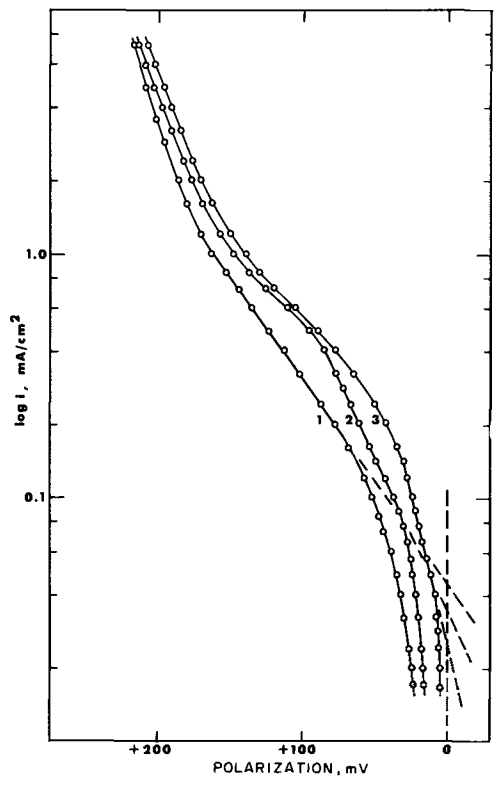

Fig. 7. Anodic polarization curves of iron in inhibitor-free 2M HCl solution, 1; in 2M HCl solution with 1x10^{-4}M quinuclidine, 2; and 1x10^{-2}M quinuclidine, 3.

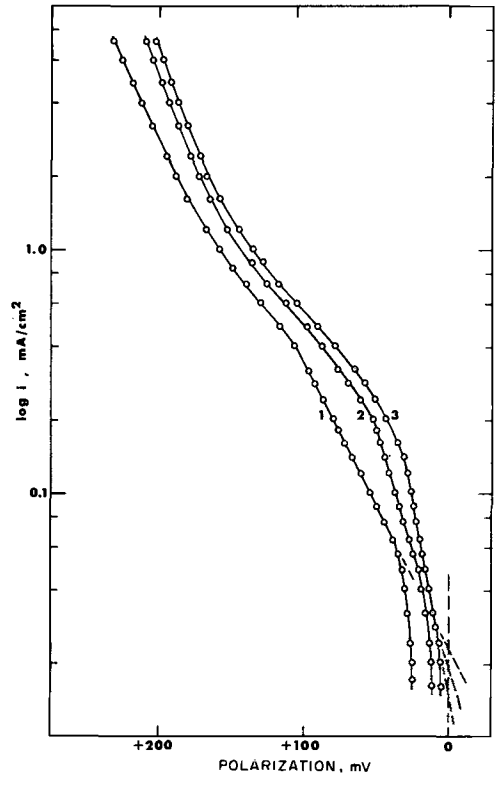

Fig. 8. Concentration dependence of anodic polarization curves of iron measured in 2M HCl solutions with benzaldoxime at 1x10^{-4}M, 1; 1x10^{-3}M, 2; and 1x10^{-2}M, 3.

in Table II the Tafel slopes, b_3, decreased with increasing inhibitor concentrations from 100 to 31 mV/decade.

It should be noted that the cathodic partial current density cannot be neglected when the linear portions of the anodic polarization curves extend to less than 20 mV from the rest potential. Therefore, the corrosion

effectivenesses, E_1, are not completely correct when they are derived only from the anodic curves. Nevertheless, the E_1 values are reasonable because the corresponding $i_{0,2}$ values can be used in Eq. [2] for the calculation of the cathodic polarization curves.

Discussion

The relative order of inhibitive effectiveness of the ketoximes at 1 x 10^{-3}M (Table I) is acetone oxime < 2-butanone oxime < acetophenone oxime < benzophenone oxime. Replacing methyl by ethyl or phenyl increases molecular polarizability and therefore increases the corrosion effectiveness of the ketoximes. Benzaldoxime does not fit this relation (it should be less effective than acetophenone oxime). This may be because only benzaldoxime exhibits both the syn- and anti-isomers in HCl solution (12), that is, *cis* and *trans* position of the OH group in relation to the planar carbon-nitrogen double bond. Quinuclidine and acetone oxime produce the same corrosion rate in 2M HCl solution. Alkyl groups increase the electron density on the nitrogen atom of amines and lead to better inhibition (13). Because the alkyl portion of the double ring compound quinuclidine consists of 7 CH_2-groups, compared with two methyl groups of acetone oxime, it can be assumed that oxime compounds have a relatively better inhibitive effect than corresponding amines. However, the relative area of metal surface which the two molecules would effectively cover in the adsorbed position has also to be considered. A comparison is not possible here because the position of adsorbed acetone oxime is uncertain.

No relationship was found between the rest potentials and the corrosion rates in inhibited solutions and all corrosion potentials were found to be within a range of 40 mV. Therefore it can be assumed that all inhibitors investigated exhibit anodic as well as cathodic inhibition effects.

Reaction mechanism of the cathodic H_2 evolution.— For large cathodic polarizations Eq. [2] is reduced to

$$i_{H_2} = i_{0,1} \exp\left[-\frac{(1-\alpha_1)\mathbf{F}}{RT}\pi\right] \qquad [3]$$

This is the equation for the cathodic polarization curve of the Volmer reaction, $H^+ + e^- \rightarrow H_{ad}$.

For very small cathodic polarizations, exp ($2\mathbf{F}/RT\,\pi$) in Eq. [2] is much smaller than 1 and can be neglected. Under the additional assumption $i_{0,1}/i_{0,2} >> 1$, Eq. [2] simplifies to the current-polarization relation of the Heyrovský reaction, $H^+ + H_{ad} + e^- \rightarrow H_2$ (9)

$$i_{H_2} = i_{0,2} \exp\left[-\frac{(2-\alpha_2)\mathbf{F}}{RT}\pi\right] \qquad [4]$$

Since the corrosion current density corresponds to $i_{0,2}$, the cathodic polarization behavior of iron in inhibited 2M HCl solution can be explained in the following manner. At the rest potential and at very small polarizations, the charge transfer of the Heyrovský reaction is rate-determining. With increasing cathodic polarization the Volmer reaction starts to control the reaction rate of H_2 evolution after a transition range with two consecutive electron transfer reactions. As shown in Fig. 1-4, for $\pi > 100$ mV the polarization curves fit the Tafel equation with slopes required by the Volmer reaction.[3]

Except for very low concentrations of acetone oxime, 2-butanone oxime plus possibly 5 x 10^{-2}M quinuclidine, constant values of the parameters α_1 and α_2 (therefore constant Tafel slopes) were found for all inhibitors at all concentrations. The inhibition effect for both the Heyrovský and Volmer reactions is attributed to adsorption of inhibitor molecules on the iron surface. Under the assumption that the concentration of adsorbed hydrogen on the metal surface is diminished by adsorbed inhibitor molecules, the inhibition of iron dissolution around the rest potential is understandable because the concentration of H_{ad} (and H^+) determines the reaction rate of the Heyrovský reaction.

The combined Volmer-Heyrovský mechanism also fits quinuclidine and the less effective aliphatic oximes, but smaller values for α_1 and α_2 were measured in less concentrated inhibitor solutions. With decreasing inhibitor concentration α_2 tends to 0 and α_1 to the value extrapolated from the Tafel slope measured in inhibitor-free 2M HCl solution (Table II). With respect to α_1 and α_2, the cathodic polarization behavior of iron at low inhibitor concentrations becomes more like the limiting case of inhibitor-free 2M HCl solution (Fig. 4). However, this should not be overrated because the polarization curve of the cathodic H_2 evolution of iron in HCl solution can also be interpreted on the basis of the Volmer reaction as the only rate-determining step instead of a combined Volmer-Heyrovský mechanism.

Reaction mechanism of the anodic iron dissolution.— S-shaped anodic polarization curves were measured in both inhibited and uninhibited 2M HCl solutions; this type of polarization behavior for iron in Cl^- containing acid solutions has been explained by the desorption of Cl^- at higher polarizations (10, 11). In inhibited solutions both Cl^- and organic inhibitor molecules are adsorbed on the iron surface, and both the organic species and Cl^- will desorb at large polarizations. As inhibitor concentrations increased, shorter linear regions and smaller Tafel slopes were measured, as shown in Fig. 7 and 8. The change of the Tafel slopes and the shorter linear portions of the polarization curves during anodic polarization indicate a possible acceleration of the metal dissolution by complex formation of iron with Cl^- and/or organic molecules. Table II shows that for all inhibitors investigated Tafel slopes decreased as inhibitor concentrations increased. Therefore it can be assumed that the iron dissolution, similar to the combined Volmer-Heyrovský reaction for H_2 evolution, apart from the desorption effect, is characterized by a change in the dissolution mechanism depending on the inhibitor concentration. On a qualitative basis, it is possible to propose a reaction mechanism composed of two limiting cases, (*i*) the dissolution of iron in 2M HCl solution and (*ii*) in high inhibitor-concentrated solution. However, a quantitative description is too difficult because the anodic polarization curves are not as reproducible as the cathodic curves.

In inhibitor-free 2M HCl solutions, anodic Tafel slopes of approximately 120 mV have been measured. Under the assumption of two one-electron charge transfer reactions followed by hydrolysis of the intermediate, the following reactions are possible

$$\mathrm{Fe} + \mathrm{Cl_{ad}^-} \rightleftarrows \mathrm{FeCl_{ad}} + e^- \qquad [a]$$

$$\mathrm{FeCl_{ad}} \rightarrow \mathrm{FeCl^+} + e^- \qquad [b]$$

$$\mathrm{FeCl^+} + \mathrm{H^+} \rightarrow \mathrm{Fe^{+2}aq} + \mathrm{H^+} + \mathrm{Cl^-} \qquad [c]$$

$$\mathrm{Fe} \rightarrow \mathrm{Fe^{+2}aq} + 2e$$

The corresponding current-potential expression for the rate-determining reaction (*a*) is

$$i_+{}^0 = \mathrm{K}\, q^0{}_{\mathrm{Cl-ad}} \exp\left(\frac{\alpha\mathbf{F}}{RT}\epsilon\right) \qquad [5]$$

(q = surface concentration) with a Tafel slope $b = d\epsilon/d(\log i) = 2.303\ RT/\alpha\mathbf{F} = 120$ mV for $\alpha = 0.5$.

Heusler (14) and Lorenz *et al.* (15) discussed the reaction mechanism of anodic iron dissolution in acid solutions and proposed a multistep reaction where hydroxyl anions react to give catalytic intermediates. In a similar partial reaction sequence, using Cl^- and adsorbed inhibitor molecules X instead of OH^-, the iron dissolution reaction mechanism at low polariza-

[3] No Tafel lines of the Heyrovský reaction could be measured because $i_{0,1}$ and $i_{0,2}$ were found to be in the same order of magnitude and therefore the assumption $i_{0,1}/i_{0,2} >> 1$ for getting Tafel lines at small polarizations was not valid.

tions (*e.g.*, where the Tafel behavior is valid) in more concentrated inhibitor solutions may be as follows.

Adsorbed Cl^- and X species react with the iron in two steps followed by a fast electron transfer reaction and decomposition of the intermediates in acid solution

$$Fe + Cl_{ad}^- \rightleftarrows FeCl_{ad} + e^- \quad [d]$$

$$Fe + X_{ad} + FeCl_{ad} \rightleftarrows FeX^+ + FeCl^+ + 2e^- \quad [e]$$

$$FeX^+ \rightarrow FeX^{+2} + e^- \quad [f]$$

$$FeX^{+2} + FeCl^+ + 2H^+ \rightarrow 2Fe^{+2}aq + 2H^+ + Cl^- + X \quad [g]$$

$$2Fe \rightarrow 2Fe^{+2}aq + 4e^-$$

For reaction (*e*) the current-potential relation is given by

$$i_+ = K_1 q_{X_{ad}} q_{FeCl_{ad}} \exp\left(\frac{2\alpha F}{RT}\epsilon\right) \quad [6]$$

Considering the potential dependence of Cl^-_{ad}, the Nernst relation for reaction (*d*) is

$$\epsilon = \epsilon^0 + \frac{RT}{F} \ln \frac{q_{FeCl_{ad}}}{q_{Cl^-_{ad}}} \quad [7]$$

$q_{FeCl_{ad}}$ can then be calculated as

$$q_{FeCl_{ad}} = K_2 q_{Cl^-_{ad}} \exp\left(\frac{F}{RT}\epsilon\right) \quad [8]$$

Elimination of $q_{FeCl_{ad}}$ from Eq. [6] and [8] gives the final expression for the two rate-determining steps (*d*) and (*e*)

$$i_+ = K_3 q_{X_{ad}} q_{Cl^-_{ad}} \exp\left[\frac{(1+2\alpha)F}{RT}\epsilon\right] \quad [9]$$

Comparison of the current densities in inhibited and uninhibited solution at the rest potential by using Eq. [5] and [9] gives

$$i_+ = K_4 i_+^0 \frac{q_{Cl^-_{ad}}}{q^0_{Cl^-_{ad}}} q_{X_{ad}} \quad [10]$$

Assuming Cl^- is partially replaced by X on the metallic surface ($q^0_{Cl^-_{ad}} = q_{X_{ad}} + q_{Cl^-_{ad}}$), Eq. [10] becomes

$$i_+ = K_4 i_+^0 \frac{q_{Cl^-_{ad}} \cdot q_{X_{ad}}}{q_{Cl^-_{ad}} + q_{X_{ad}}} \cong K_4 i_+^0 q_{Cl^-_{ad}} \quad [11]$$

The inhibitive effect of the organic molecules depends therefore on the surface concentration of Cl^- which decreases with increasing inhibitor concentration.

For $\alpha = 0.5$ the corresponding Tafel slope (Eq. [9]) is calculated to be 30 mV which is, within the error limit, in good agreement with the experimentally determined Tafel slopes for inhibitors at concentrations above 1×10^{-2}M.

Acknowledgments

The authors wish to express their appreciation to The Robert A. Welch Foundation of Houston, Texas, for financial support of this work, and to Battelle Memorial Institute, Columbus, Ohio, for providing the zone-refined iron.

Manuscript submitted Oct. 28, 1970; revised manuscript received Feb. 22, 1971.

Any discussion of this paper will appear in a Discussion Section to be published in the June 1972 JOURNAL.

REFERENCES

1. C. A. Mann, *Trans. Electrochem. Soc.*, **69**, 115 (1936).
2. K. Aramaki and N. Hackerman, *This Journal*, **115**, 1007 (1968).
3. H. Kaesche and N. Hackerman, *ibid.*, **105**, 191 (1958).
4. K. C. Tsai, Ph.D. dissertation, The University of Texas at Austin, 1969.
5. J. Elze and H. Fischer, *This Journal*, **99**, 259 (1952)
6. N. Hackerman, "Comptes Rendus du Symposium European sur les Inhibiteurs de Corrosion," p. 99, Ferrara, Italie (1960).
7. E. B. Sandell, "Colorimetric Determination of Traces of Metals," p. 374, Interscience Publishers, Inc., New York (1950).
8. K. J. Vetter, *Z. Elektrochem. Ber. Bunsenges. physik. Chem.*, **59**, 435 (1955).
9. H. Kaesche, *Z. Elektrochem.*, **63**, 492 (1959).
10. M. Stern, *This Journal*, **102**, 609 (1955).
11. K. Schwabe and C. Voigt, *Electrochim. Acta*, **14**, 853 (1969).
12. W. Theilacker and L. H. Chou, *Ann. Chem.*, **523**, 143 (1930).
13. N. Hackerman and A. C. Makrides, *Ind. Eng. Chem.*, **46**, 523 (1954).
14. K. E. Heusler, *Z. Elektrochem.*, **62**, 582 (1958).
15. W. J. Lorenz, H. Yamaoka, and H. Fischer, *Z. Elektrochem.*, **67**, 932 (1963).

Hydrogen Overpotential on Pure Metals in Alkaline Solution

T. S. Lee*

Union Carbide Corporation, Consumer Products Division, Research Laboratory, Cleveland, Ohio 44101

ABSTRACT

Hydrogen overpotentials on pure Zn, Cd, Fe, and Pb were measured in 6*N* potassium hydroxide solution at 2°, 25°, and 50°C. Measurements were also made in 9*N* potassium hydroxide solution at room temperature. Exchange current densities, transfer coefficients, and heats of activation for the hydrogen solution process were obtained, and the mechanism for process in the solution is discussed. The transfer coefficients in the alkaline solutions are compared with these in acid solutions.

The hydrogen overpotential in alkaline solutions on mercury has been measured by Bockris and Watson (1), on nickel by Lukovzev, Levina, and Frumkin (2), Legran and Levina (3), and Bockris and Potter (4); and on copper by Bockris and Pentland (5). All of these workers have made the measurements in dilute alkaline solutions. Zholuder and Stender (6) have measured hydrogen overpotentials on a number of metals in 6*N* sodium hydroxide solution in an open

* Electrochemical Society Active Member.

Key words: hydrogen overpotential, hydrogen overvoltage, hydrogen evolution process in alkaline solution, electrode kinetics hydrogen evolution process.

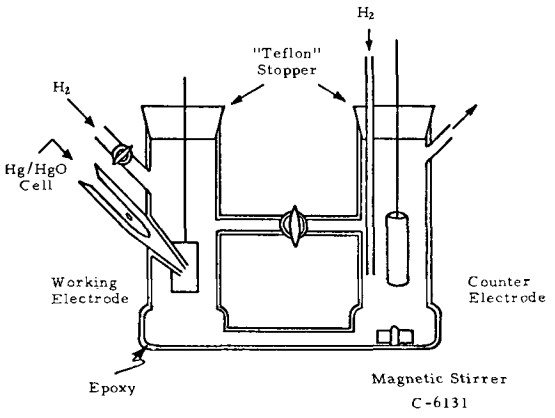

Fig. 1. Schematic drawing of the cell

vessel. Iofa, Komlev, and Bagotskii (7) have measured the same property at a zinc surface in different concentrations of potassium hydroxide solutions. The purpose of this paper is to report the measurement of hydrogen overpotentials on high purity metals in highly purified 6*N* and 9*N* KOH solutions. The results will be interpreted by a theoretical treatment of the hydrogen evolution process.

Experimental

The cell used for this study is shown schematically in Fig. 1. The cell is made from epoxy-lined Pyrex. The purpose of using the epoxy lining is to prevent the introduction of impurities into the solution through attack on the cell walls.

The epoxy used in this study is made from Union Carbide products ERL-2793 and ERL-2774. The procedure is as follows: 1 part (by volume) of ERL-2793 and 3 parts of ERL-2774 are slowly mixed together. In about 10 to 15 min, the mixture changes from a relatively thick mass to a less viscous liquid. At this time, the well-mixed liquid is poured into the Pyrex cell. By rotating the glass apparatus, the inside wall is coated with a layer of the liquid epoxy, which will solidify in another 15 to 20 min. The apparatus is kept at room temperature for a few hours. Finally, the apparatus is placed in an oven at 65°-75°C and baked for 4 hr. Before it can be used, the epoxy-lined apparatus is soaked in distilled water and 35% KOH solution for a few days. If the lining is not too thick, the wall is somewhat opaque, yet semitransparent. In a closed system, the semitransparent wall could enable the operator to see where the electrode and reference electrode are placed.

To make sure no epoxy had leached into the alkaline solution during a reasonable length of time, the following experiment was conducted. Epoxy-lined glass beakers were used to store 9*N* and 12*N* KOH solutions for 4 to 5 weeks. These KOH solutions were extracted with organic solvents. The extracts were then evaporated and their IR spectra were examined. Epoxy exhibits good IR spectra with powder as well as extracts. One IR spectrum for epoxy is shown in Fig. 2 and the spectrum for the extract from 12*N* KOH solution which was in contact with epoxy for 4 weeks, is shown in Fig. 3.

The typical IR adsorption peaks for epoxy are observed at 8 and 12μ. In Fig. 3 there is no evidence that even a trace of epoxy is present in the residue. However, there might be a very small amount of epoxy that could go into the solution which would not be detected by the IR technique, but still could affect the electrochemical measurement. Thus, the operation of soaking the cell in concentrated KOH solution for a few days is important. The feasibility of this system for high-purity electrochemical measurement is emphasized by the fact that the hydrogen overpotentials are highly reproducible (within a few millivolts) and quite linear over a five decade range of current densi-

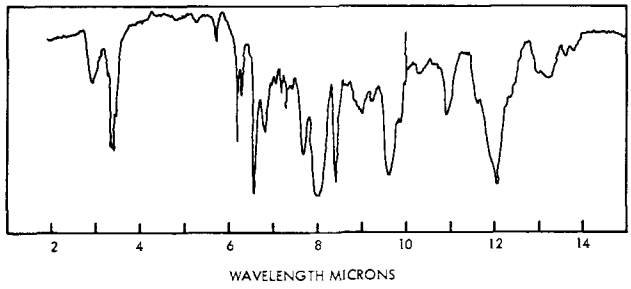

Fig. 2. IR spectra of chloroform extract of the epoxy

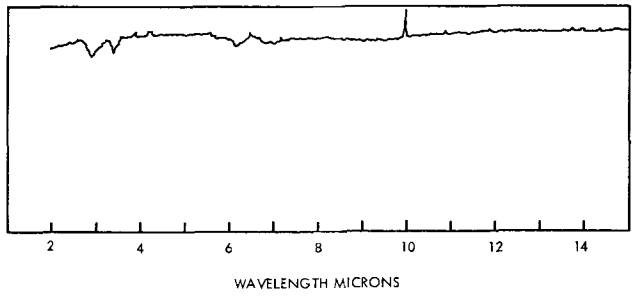

Fig. 3. IR spectra of chloroform extract from 12N KOH which has been contacted with epoxy for 4 weeks.

ties, regardless of whether the measurements are begun at high or low current densities.

The cell is a closed system with a slightly positive hydrogen pressure to prevent air entry. There is a separate compartment for both anode and cathode. A stream of high-purity hydrogen is passed through the anode compartment during the measurement to carry away the oxygen produced at the anode.

The reference electrode is a Hg/HgO electrode in the same solution in a separate tube. The Luggin capillary, which has an ID of about 0.1 mm, contacts the electrode being measured. In designing the cell, attention was given to the reference electrode compartment, such that the possibility of contamination from Hg/HgO to the solution in the measuring cell is kept to a minimum. The counterelectrode, which is made of pure nickel sheet, has an area of about eight to ten times that of the metal electrode. The purity of the Zn, Cd, and Pb electrodes is 99.999+% and the Fe electrode is spectroscopically pure.

The potassium hydroxide solution is made from AR grade chemical and conductance water. This solution is kept in KOH preleached high-density polyethylene bottles. Occasionally, the KOH solution is made in a Teflon bottle. The results do not show any difference. The solution is pre-electrolyzed in the cell each time for several days before the measurement is started.

The back and edges of the metal electrodes are covered with the same epoxy coating as the glass vessel and are subjected to the same treatment as the cell. The exposed area of the electrode is about 1 cm^2. The surface of the electrode (except lead) is prepared by successive abrasion with emery paper, ending with 000 paper. The lead electrode is prepared by light abrasion with 00 paper or by scratching with a stainless steel knife edge.

After a smooth surface is obtained, the electrode is washed well with a jet of distilled water to remove any particles which may have become attached during the process of abrasion. The electrode is then placed in a separate cell of the same type to be cathodized against the counterelectrode for at least 30 min at a current density of 30-50 mA/cm^2. The main purpose of this cathodization in a separate cell is to leave any impurities introduced during the preparation of the surface in the separate cell. Finally, only the working electrode is transferred to the measuring cell, which

Table I. Reversible potential for hydrogen evolution process

KOH	Temp, °C	E_{rev} (V) measured	E_{rev}, calculated
6N	2	−0.9376	−0.937
	25	−0.9306	−0.932
	50	−0.9245	−0.924
9N	25	−0.9396	−0.938

has been degassed with "Ultra Pure" hydrogen[1] for a couple of hours, and the same cathodization process is continued for another half hour with a different counterelectrode before measurement begins. Care is taken to avoid the possibility of dissolution of active metals into the KOH solution by connecting both working and counterelectrodes to the current source before the working electrode is introduced into the solution. The constant current is supplied by a Harrison Laboratories Model 855C power supply through a series of variable power resistors. The potentials are measured by a Keithley Model 630 potentiometric electrometer which has a minimum input resistance of 10^{13} ohms. The measurements are carried out from the high current density to the low current density region and back again; this process is then repeated. The steady potential is recorded at each current density. Variations of only a few millivolts are observed in the steady potential even though the potentials are occasionally observed as long as 30 min to 2 hr at certain current densities. There is no sign of hysteresis in any of the measurements.

The data reported here are the average values of four or more runs for each point. After each run, the electrode is washed, dried, and examined under a microscope. Except for lead, the surfaces are still shiny and appear unchanged. The lead surface appears darker after the measurement.

The temperature of the cell is kept constant by placing it in a water bath in which the temperature is controlled by a Lauda K-2/R constant temperature circulator. The accuracy of the temperature control is within 0.02°C.

In order to obtain the values of overpotential, the reversible potential for hydrogen evolution under the specific conditions is needed. This is obtained by measuring the potential of the platinized platinum hydrogen electrode against the Hg/HgO electrode in the solution. The values of the reversible hydrogen potential under various conditions are listed in Table I. In most cases, the measured potential is within 1 mV of the theoretically calculated value based on the best available activity data in the literature (8). At 25°C the reversible hydrogen potential is calculated from the equation

$$E = -0.920 + 0.0296 \log a_{H_2O}$$

where a_{H_2O} is the activity of water in the solution. At other temperatures, the reversible potential is calculated through temperature coefficients given by de Bethune (9).

Results and Discussion

The hydrogen overpotentials and the logarithm of current density plots for Zn, Cd, Fe, and Pb in 6N KOH at various temperatures are shown in Fig. 4-7. The plots for these metals in 9N KOH at 25°C are shown in Fig. 8. The transfer coefficients (α) and the exchange current densities (I_0) for the reaction are obtained from these plots. The standard activation energy (ΔH°) for the process is obtained through the rate of change of the overpotential with temperature at constant current. To obtain the numerical value, an equation derived by Bockris (10) assuming that the transfer coefficient is constant with temperature is used. That is

[1] Produced by Linde Division of Union Carbide, the purity is 99.999% and the oxygen content is less than 1 ppm.

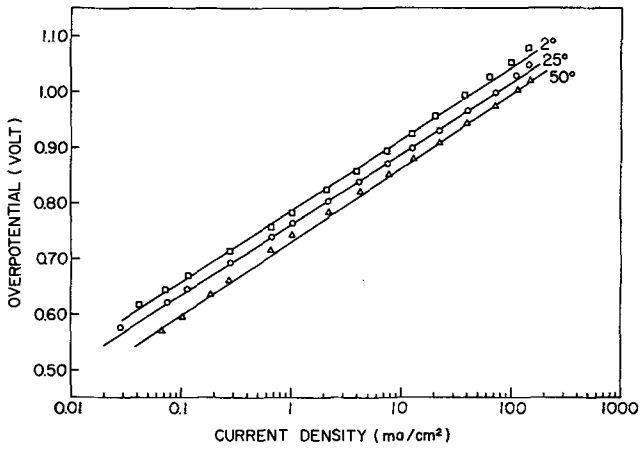

Fig. 4. Hydrogen overpotential on Zn in 6N KOH

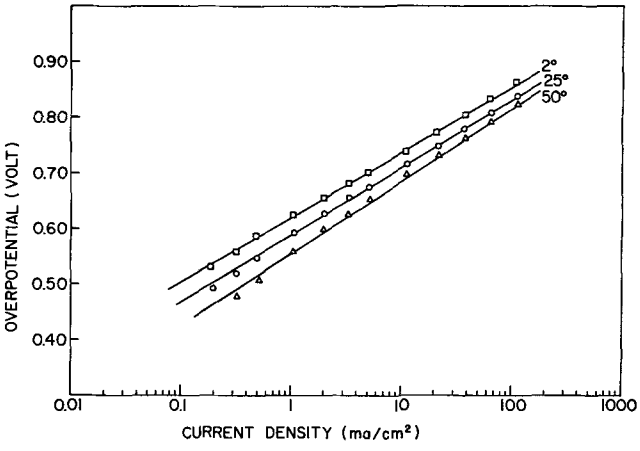

Fig. 5. Hydrogen overpotential on Cd in 6N KOH

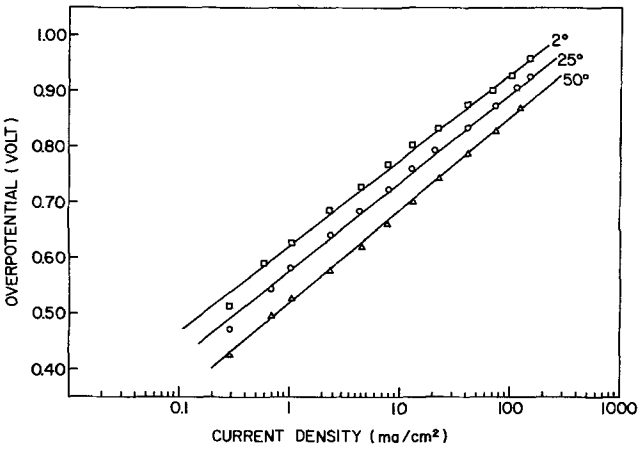

Fig. 6. Hydrogen overpotential on Fe in 6N KOH

$$\left(\frac{\partial \eta}{\partial T}\right) i_c = (\alpha \eta F + \Delta H^\circ + RT)/\alpha F T$$

The electrochemical parameters for those metals in 6N KOH are listed in Table II and those in the 9N KOH are listed in Table III. The Tafel slopes in Tables II and III are at 25°C. It is also interesting to note in Fig. 4-7 that the Tafel slopes for different metals at various temperatures in 6N KOH vary slightly with temperature.

It is known that the over-all reaction for the process in this medium is

$$2H_2O + 2e = H_2 + 2\,OH^- \qquad [1]$$

There are three possible rate determining steps

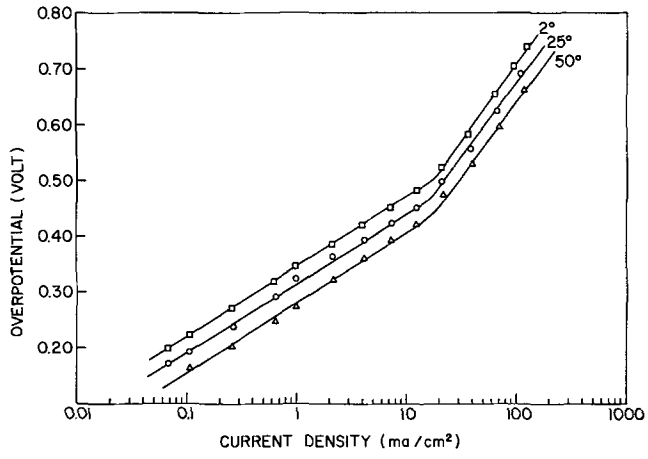

Fig. 7. Hydrogen overpotential on Pb in 6N KOH

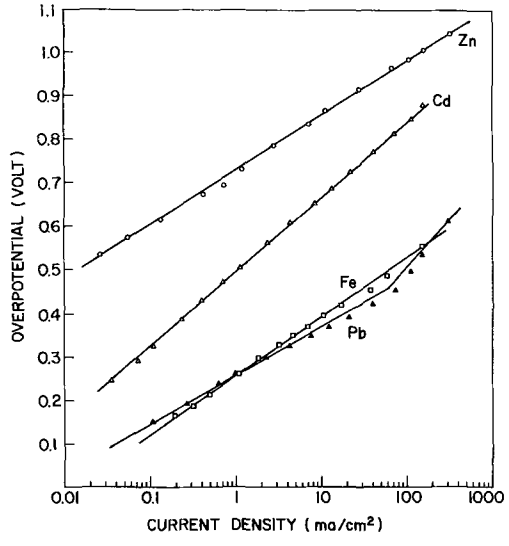

Fig. 8. Hydrogen overpotential on Zn, Cd, Fe, and Pb in 9N KOH at 25°C.

$$H_2O + e = H_{ad} + OH^- \text{ (Volmer)} \quad [2]$$

$$H_{ad} + H_2O + e = H_2 + OH^- \text{ (Heyrovsky)} \quad [3]$$

$$2H_{ad} = H_2 \text{ (Tafel)} \quad [4]$$

and each one of the three steps could lead to Eq. [1].

Table II. Electrochemical parameters for hydrogen evolution process in 6N KOH

	Tafel slope	α	I_o (A/cm²)	$\Delta H°$ (kcal/mole)
Zn	0.124	0.48	8.5×10^{-10}	13.4
Cd	0.157	0.38	3×10^{-7}	14.3
Fe	0.120	0.49	1×10^{-8}	12.5
Pb*	0.121	0.49	4×10^{-6}	8.8

* For the low current density region.

Table III. Electrochemical parameters for hydrogen evolution process in 9N KOH

	Tafel slope	α	I_o (A/cm²)
Zn	0.124	0.48	1.5×10^{-9}
Cd	0.168	0.35	1×10^{-6}
Fe	0.126	0.48	6×10^{-8}
Pb*	0.120	0.49	1×10^{-7}

* For the low current density region.

Since all measurements are in concentrated solutions, no double layer correction[2] has been made. Referring to reaction [2], one can write the following rate equation by neglecting the back reaction

$$\text{rate} = K_f \exp(-n\alpha \mathbf{F}\phi/RT) \quad [5]$$

where ϕ is the potential between the metal electrode and the bulk of the solution and K_f is the rate constant for the forward reaction. The other symbols have the usual meanings. Omission of the back reaction is justified here, since all of the measurements are made at relatively high overpotentials. The current per unit area (I) of the reaction surface can be written as

$$I = n\mathbf{F}a_{H_2O} \text{ rate} \quad [6]$$

where a denotes activity. From [5] and [6]

$$\phi = K_f' + \frac{RT}{\alpha\mathbf{F}}(\ln a_{H_2O} - \ln I) \quad [7]$$

One can also write the Nernst equation for [1] at 1 atm of H_2

$$\phi_{eq} = E° + \frac{RT}{\mathbf{F}} \ln (a_{H_2O}/a_{OH^-}) \quad [8]$$

and the overpotential η is

$$\eta = \phi - \phi_{eq} \quad [9]$$

From [6], [7], [8], and [9] one obtains

$$\eta = \text{const.} + [(1-\alpha)/\alpha]\frac{RT}{\mathbf{F}} \ln a_{H_2O} + \frac{RT}{\mathbf{F}} \ln a_{OH^-} - \frac{RT}{\alpha\mathbf{F}} \ln I \quad [10]$$

if $\alpha = \frac{1}{2}$.

$$\eta = \text{const.} + \frac{RT}{\mathbf{F}} \ln a_{H_2O}\, a_{OH^-} - \frac{2RT}{\mathbf{F}} \ln I \quad [11]$$

The experimental data show that, for the same KOH concentration, the numerical values of the overpotential are higher (less negative) at a higher temperature. It also shows that, at the same temperature, the numerical values of the overpotential are higher (less negative) in a lower KOH concentration. In connection with this, Eq. [11] indicates that, in the concentration range of this study, the activity of H_2O and OH^- is smaller at a higher temperature in the same concentration of KOH. It also indicates that the activity of H_2O and OH^- is smaller in a lower KOH concentration solution at the same temperature. This is consistent with the experimental trend found by Akerlof and Bender (8).

At a definite KOH concentration and a definite temperature, the first two terms of Eq. [11] are constant, so that the equation then becomes the familiar Tafel equation. At 25°C, a plot of η against log I will have a slope of 120 mV per decade. By examining the experimental data, one can conclude that the one-electron transfer is the rate-determining step in the process.

The high slope for lead in the higher current density region might be due to other processes occurring simultaneously with the reduction of water. It is plausible that the formation of some kind of lead hydride occurs at the higher potential (12). Since no hysteresis loop is observed in moving up and down the curve, the formation of a hydride must be potential dependent and unstable.

The reason for the slightly higher slope on Cd in both 6N and 9N KOH is not completely clear yet. It may be due to the formation of a thin layer of hydrated oxide on the cadmium surface.

Finally, it is interesting to compare the transfer coefficients obtained in this study to those obtained in acid solution by others (13, 14). This comparison is

[2] Double layer correction sometimes called Frumkin correction, for example, see Delahay (11).

Table IV. Comparison of transfer coefficient of hydrogen evolution process in acid and alkaline solutions

Metal	α
Zn	0.5 (0.01-1*N* H_2SO_4) (14) 0.48 (6, 9*N* KOH)
Cd	0.3 (1*N* HCl, 2*N* H_2SO_4 (13) 0.38 (6*N* KOH), 0.35 (9*N* KOH)
Fe	0.4 (1*N* HCl), 0.5 (2*N* H_2SO_4) (13) 0.49 (6*N* KOH), 0.48 (9*N* KOH)
Pb	0.48 (0.01-8*N* HCl, 0.1*N* H_2SO_4) (13) 0.49 (6, 9*N* KOH)

shown in Table IV, where the value of α is followed in parenthesis by the solutions in which the hydrogen overpotentials are measured. One can see that there is not much difference in α in the hydrogen evolution process from dilute acid solutions to concentrated alkaline solution.

Acknowledgment

The author wishes to express his thanks to Professor E. B. Yeager and Professor H. A. Laitinen for valuable discussions.

Manuscript submitted Nov. 30, 1970; revised manuscript received ca. Mar. 25, 1971. This was Paper 65 presented at the Detroit Meeting of the Society, Oct. 5-9, 1969.

Any discussion of this paper will appear in a Discussion Section to be published in the June 1972 JOURNAL.

REFERENCES

1. J. O'M. Bockris and R. G. H. Watson, *J. Chim Phys.*, **49**, 1 (1952).
2. P. Lukovzen, S. Lavina, and A. N. Frumkin, *Acta Physicochim.*, **11**, 21 (1939).
3. A. Legran and S. Lavina, *ibid.*, **12**, 243 (1940).
4. J. O'M Bockris and E. C. Potter, *This Journal*, **99**, 169 (1952).
5. J. O'M Bockris and N. Pentland, *Trans. Faraday Soc.*, **48**, 833 (1952).
6. M. B. Zholuder and V. V. Stender, *Zh. Prikl. Khim.*, **31**, 711 (1958).
7. Z. A. Iofa, L. V. Komlev, and V. S. Bagotskii, *Zh. Fiz. Khim.*, **35**, 1571 (1961).
8. G. C. Akerlof and P. Bender, *J. Am. Chem. Soc.*, **70**, 2366 (1948).
9. "The Encyclopedia of Electrochemistry," C. A. Hampel, Editor, p. 414, Reinhold Publishing Co., New York (1964).
10. Natl. Bur. Std. Cir. 524, p. 250 (1953).
11. P. Delahay, "Double Layer and Electrode Kinetics," p. 197, John Wiley & Sons, Inc., New York (1965).
12. J. W. Mellor, "A Comprehensive Treatise on Inorganic and Theoretical Chemistry," Vol. VII, p. 562, Longmans (1927).
13. B. E. Conway, "Electrochemical Data," p. 347, Elsevier Publishing Co., New York (1952).
14. A. A. Rotinyan, N. P. Fedotev, and Li Un Sok, *Zh. Fiz. Khim.*, **31**, 1295 (1957).

Corrosion Inhibition and Hydrogen Adsorption in the Case of Iron in a Sulfuric Aqueous Medium

I. Epelboin,* P. Morel, and H. Takenouti

Groupe de Recherche du C.N.R.S., Physique des Liquides et Electrochimie, Université de Paris VI, Paris 5e, France

ABSTRACT

The corrosion process for two iron samples of different purities in a molar solution of sulfuric acid has been studied by means of a rotating disk electrode. This study supports the previously formulated hypothesis which assigns the hysteresis, observed when corrosion is low, to the partial coverage (θ_H) of the electrode surface by adsorbed hydrogen $(FeH)_{ads}$. The decrease of the cathodic reaction rate is then accounted for by a slow diminution of the number of active sites due to this coverage. The hydrogen adsorption is favored by the presence of 2-butyne 1,4-diol. At potentials more anodic than the corrosion potential, the same coverage persists. The study of the θ_H variation with potential, in the presence of 2-butyne 1,4-diol, shows that θ_H, close to unity near the corrosion potential, diminishes when the anodic potential increases and tends toward zero for potentials above which hysteresis is no longer observed. All these results tend to confirm the role of $(FeH)_{ads}$ as a corrosion inhibitor.

In a previous work (1), it was reported that the current-potential characteristics obtained in sulfuric acid for certain samples of very pure iron, whose corrosion rates were low, showed hysteresis. This phenomenon occurred even with a pure industrial iron, characterized by a higher corrosion rate, provided that an acetylenic-type corrosion inhibitor, such as 2-butyne 1,4-diol, was added to the sulfuric medium. This hysteresis of the current-potential curve and the inhibiting action of acetylenic alcohols were then attributed to a partial coverage of the iron surface by adsorbed hydrogen. In this article, we intend to present new information on the relation between corrosion inhibition and hydrogen adsorption.

* Electrochemical Society Active Member.

Key words: 2-butyne 1,4-diol, dissolution mechanism, faradaic impedance, hydrogen evolution reaction, hysteresis, polarization curve.

Polarization curves (2) and faradaic impedance (3, 4) studies showed that two of the iron samples used in the above-mentioned investigation (1) followed the same anodic dissolution mechanism, *i.e.* one of the mechanisms proposed by Bockris, Drazič, and Despič (5). According to this mechanism, OH^- would be adsorbed in a first step, I

$$Fe + OH^- \rightleftharpoons (FeOH)_{ads} + e^- \qquad \text{I}$$

to give rise to $(FeOH)_{ads}$. In a second step, II

$$(FeOH)_{ads} \rightarrow FeOH^+ + e^- \qquad \text{II}$$

the iron would leave the metallic lattice as a $FeOH^+$ cation which would finally undergo the rapid chemical reaction III

$$FeOH^+ \rightleftharpoons Fe^{++} + OH^- \qquad \text{III}$$

This anodic mechanism is still valid when the sulfuric acid solution contains 2-butyne 1,4-diol (6).

In order to understand the corrosion inhibition and the hydrogen adsorption mechanisms, it is important also to study the cathodic reaction kinetics for these two iron samples in a sulfuric acid medium with and without addition of acetylenic alcohol.

Experimental

This investigation was carried out in an air-free medium for which it can be supposed that the cathodic process is limited to the mere hydrogen evolution. One of the two metal samples studied here is a spectroscopically pure iron provided by Johnson-Matthey (denoted in this paper as iron I); the second sample, Holzer iron provided by Compagnie des Ateliers et Forges de la Loire (iron II), has a corrosion rate 25 times as great as that of iron I when measured in a molar solution of sulfuric acid. The main impurities of the two irons are: Iron I—C, 0.03%; Si, 0.0004%; Mn, 0.0003%; Mg, 0.0002%; Iron II—Si, 0.33%; Mn, 0.06%; S, 0.018%; C, 0.003%. Iron I was cold worked, while iron II was wrought in a furnace under vacuum and subjected to a treatment of standardization at 900°C.

We used a molar solution of sulfuric acid prepared from concentrated acid (Merck) diluted in water of resistivity greater than 2 megohms/cm. The solution was maintained at 25° ± 0.1°C, and was deoxygenated by argon bubbling (Ultrapure Argon, provided by Air Liquide).

For the study of the two iron samples, we employed disk electrodes oriented downward. So as the gas bubbles resulting from the cathodic process did not remain on the electrode surface, the electrode was turned at a speed of at least 1000 rpm. Under our experimental conditions, the cathodic current does not depend on the disk rotation speed, which confirms the complete deoxygenation of the solution (7).

Except for the separation of cathodic current from the over-all current, the potential of the working electrode is controlled by a fast potentiostat built in our laboratory (8). The methods of impedance measurements have been described elsewhere (3).

Results and Discussion

Study of the cathodic process in a deoxygenated sulfuric acid medium.—Absence of a steady-state $I = f(V)$ polarization characteristic.—We have not been able to obtain any steady-state $I = f(V)$ polarization curve, since the successive potentiokinetic traces cannot be superposed. As a matter of fact, when the potential V is fixed at a certain value, a slow evolution of the cathodic current I is observed, whose rate and behavior depend on the iron nature.

As an illustration, Fig. 1 shows, as a function of time, a current variation which is characteristic of iron I, the apparent area of the electrode being 0.2 cm². Curves 1, 2, and 3, respectively, correspond to the polarization potentials of −0.5, −0.55, and −0.6 V/SCE. The current decreases very rapidly just after immersion of the electrode, then more and more slowly, and after some 3 hr reaches a stationary value. During this evolution, the metal, practically, does not dissolve, and the surface remains bright.

In the case of iron II, when the electrode is polarized at −0.5 V/SCE, the current decreases just after immersion of the electrode (Fig. 2), goes through a minimum after some 3 min, and then increases during more than 4 hr up to a relatively stationary value. The metal then appears to be strongly attacked, even to the naked eye. On the other hand, when the electrode is polarized at a higher potential, we can obtain one or the other of the types of evolution represented in Fig. 1 and 2, according as the electrode is polarized at potentials higher or lower than −0.55 V/SCE. In the first case, the surface remains unaltered; in the second, it is markedly attacked.

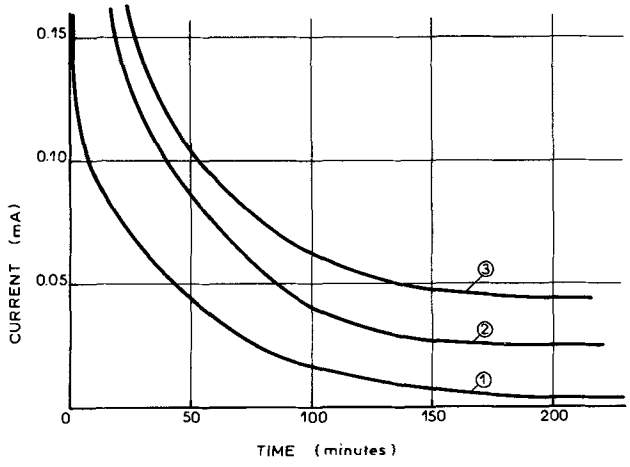

Fig. 1. Variation of the cathodic current with time: iron I, 1M H_2SO_4. Curve 1, $V = -0.50$ V/SCE; Curve 2, $V = -0.55$ V/SCE; curve 3, $V = -0.60$ V/SCE.

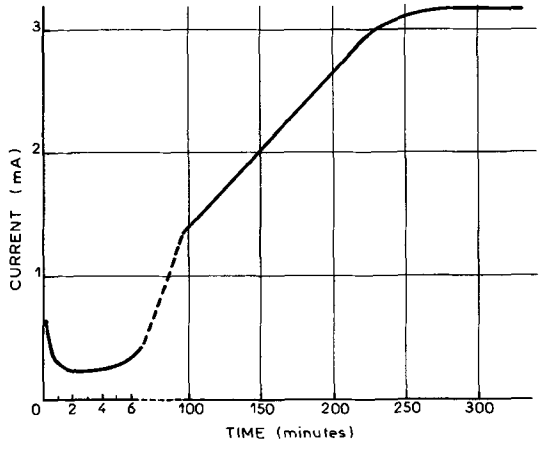

Fig. 2. Variation of the cathodic current with time: iron II, 1M H_2SO_4. $V = -0.50$ V/SCE.

It is well known that the hydrogen adsorbed at the iron surface penetrates into the metal. This absorbed hydrogen considerably modifies the state of the electrode surface, especially in the case of iron II, and plotting the steady-state $I = f(V)$ curve becomes impossible. It is therefore difficult to study the cathodic reaction kinetics at the corrosion potential by means of a $I = f(V)$ characteristic obtained point by point, at least for high cathodic polarizations. Now, acetylenic alcohols are known to inhibit hydrogen absorption into iron (9). We therefore studied for iron I and iron II the influence on the current variation, in the cathodic range, of 2-butyne 1,4-diol, one of the most representative inhibitors of the family of acetylenic alcohols.

Influence of 2-butyne 1,4-diol.—When 2-butyne 1,4-diol is added in the electrolyte, there is always a decrease of the above-defined stationary current (see first paragraph under Results and Discussion). This inhibiting effect increases with increasing acetylenic alcohol concentration up to 10^{-3}M, the concentration chosen for the experiments described here. Furthermore, whatever the moment the inhibitor is introduced into the sulfuric acid solution (before the metal sample —*i.e.*, "previous addition"—or after the polarization current has reached its stationary value—*i.e.*, "subsequent addition"), after the introduction the current evolves up to a stationary value very slowly.

In the case of iron I, whatever the method of the 2-butyne 1,4-diol addition, the stationary current decreases by only 30% and the inhibiting effect is not very obvious.

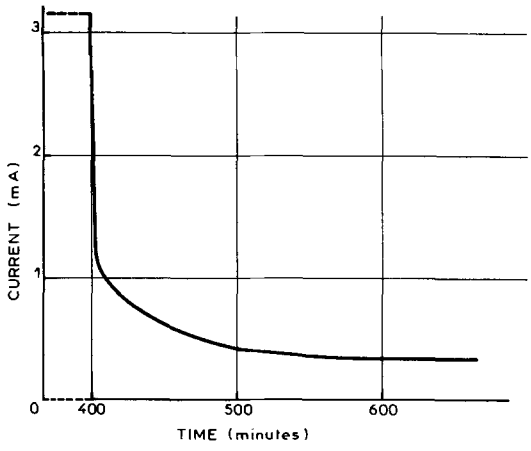

Fig. 3. Variation of the cathodic current with time after introduction of 10^{-3}M 2-butyne 1,4-diol. ("Subsequent addition": see *Influence of 2-butyne, 1-4 diol* under Results and Discussion). Iron II, 1M H_2SO_4. $V = -0.50$ V/SCE.

For iron II and a "previous addition," the current continually decreases even at −0.5 V/SCE, which is contrary to the case presented in Fig. 2. After about 5 hr, the current reaches a stationary value which is 50 times as low as that reached in the absence of an inhibitor. Visual examination of the electrode surface then reveals no trace of corrosion. In the case of a "subsequent addition" (and at the same polarization potential of −0.5 V/SCE) carried out after 400 min under the conditions of Fig. 2, the current rapidly diminishes as soon as the inhibitor is introduced. This decrease carries on more and more slowly for several hours until the current reaches a new stationary value, as shown in Fig. 3. This value is higher than that obtained in the case of a "previous addition." The observed difference can be explained by a change in the state of the surface during corrosion without an inhibitor.

The problem of the stationary current having been specified, we will now examine whether impedance measurements allow us to explain the influence of the nature of the iron sample on the cathodic reaction rate in a sulfuric acid medium with and without the acetylenic alcohol.

Measurements of the frequency dependence of the cathodic impedance.—Such measurements have been performed only when the direct current I could reach a stationary value. We have plotted the impedance diagrams in the complex plane $Z = R - jG$ in which frequency is the parameter. All these diagrams, obtained with and without inhibitor, for iron I as well as for iron II have the same shape, *i.e.* that of a capacitive arc.

As an example, in Fig. 4 is given a diagram obtained at −0.5 V/SCE with iron II in the absence of an inhibitor. From this diagram, a value of 2.3 ohms is found for the electrolyte resistance R_e which is the impedance limit at infinite frequency; this value is in good agreement with that determined by an interrupter method

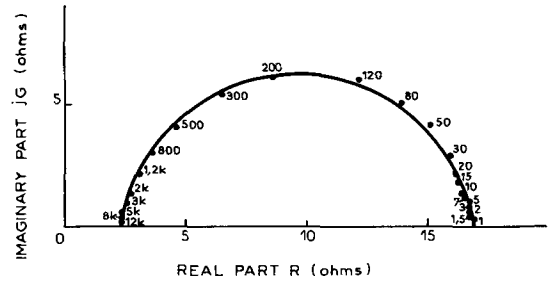

Fig. 4. Cathodic impedance diagram (parameter = frequency in Hz): iron II, 1M H_2SO_4. $V = -0.50$ V/SCE.

(2). It can also be seen that, at zero frequency, the impedance tends to become a resistance whose value is about 16.8 ohms.

Furthermore, a least-squares analysis of our impedance diagrams, carried out on an IBM 360/75 computer, reveals that the impedance Z variations with frequency can be represented by a capacitive time-constant τ which obeys a Cole-Cole-type distribution law (10) to the exclusion of any other time constant

$$Z = \frac{R_t}{1 + (j\omega\tau)^\gamma}$$

where R_t is the transfer resistance and γ, a dispersion parameter, is a nondimensional number between 0 and 1.

Now, in the case of a simple transfer reaction, the calculation of the impedance also involves only one time constant which is due to the transfer resistance R_t, the product R_tI being independent of the current. We therefore calculated the product of the current I and the limiting value of the impedance at zero frequency: we verified that it is the same for all the diagrams, its value being close to 52 mV, as can be seen in Table I which gathers together as an example the results from five diagrams. Note lastly that this product, in the case of a single electrochemical step obeying Tafel's law, allows an indirect measurement of the Tafel slope (which, in the case of our experiments, would be 120 mV/decade).

Discussion of results.—It is generally accepted that the hydrogen evolution occurs in two steps implying the intermediate species $(FeH)_{ads}$. The faradaic impedance calculation, in this case, predicts that the relaxation of the coverage θ_H by $(FeH)_{ads}$ introduces a further time constant which is expressed either by an inductive term or by a capacitive term (11). The fact that such a reactive term could not be detected during our measurements indicates that, under our experimental conditions, the potential variation causes no θ_H variation. This lack of variation can be accounted for by one of the following hypotheses: (*a*) the hydrogen adsorption step is rate determining ($\theta_H \simeq 0$), (*b*) the hydrogen desorption step is rate determining ($\theta_H \simeq 1$), and (*c*) the steps are both electrochemical and have the same Tafel slope ($0 < \theta_H < 1$). According to Gerischer and Mehl (11), in the case of iron and other transition

Table I. Results from cathodic impedance measurements

R_t = transfer resistance
γ = dispersion parameter
(The two methods of addition are defined in the paragraph "Influence of 2-butyne 1,4-diol" under Results and Discussion.)

Sample	Iron I	Iron I	Iron II	Iron II	Iron II
V(V/SCE)	−0.55	−0.55	−0.50	−0.50	−0.50
Concentration of 2-butyne 1,4-diol (M)	0	10^{-3}	0	10^{-3}	10^{-3}
Method of addition	—	Subsequent	—	Subsequent	Previous
Stationary current I(mA)	0.026 ± 0.001	0.017 ± 0.001	3.3 ± 0.2	0.31 ± 0.02	0.058 ± 0.002
R_t(ohms)	2120 ± 40	3280 ± 140	14.5 ± 0.2	172 ± 70	900 ± 10
IR_t(mV)	55 ± 3	56 ± 6	48 ± 4	53 ± 5	52 ± 2
γ	0.931 ± 0.005	0.921 ± 0.015	0.967 ± 0.015	0.908 ± 0.018	0.928 ± 0.017

metals, the second hypothesis in highly probable, due to the high strength of the bond between H_{ads} and the metal. This statement has been confirmed by the recent work of Bockris *et al.* (12): the electrochemical desorption step actually determines the hydrogen evolution rate for the transition metals, and in this case $\theta_H \simeq 1$. Furthermore, according to the recent work of Tomashov and Vershinina (13), in the case of iron the Tafel slopes corresponding to these two steps would be equal and θ_H would be close to unity.

The results from impedance measurements (Table I) seem to show that the reaction mechanism remains unchanged, although the cathodic reaction rate may depend on the electrode nature and on the presence or absence of 2-butyne 1,4-diol. As it is known on the other hand (3) that the product R_tI is independent of the reacting surface, the observed differences in rates must be attributed only to a variation of this surface.

The decrease of the reaction rate, revealed by the current-time curves (Fig. 1 and 3), would correspond to a slow diminution of the number of active sites caused by the adsorbed hydrogen. In the absence of 2-butyne 1,4-diol and at −0.5 V/SCE (Fig. 2), the passage into the solution of impurities contained in iron II [sulfur, in particular (14)] increases the number of active sites (15, 16) and thus gives rise to the marked corrosion mentioned above. This would also explain the observed increase of current with time at this potential.

These results strongly support the hypotheses that we put forward (1, 2) during the last several years in order to interpret the hysteresis phenomenon: they tend indeed to indicate that $(FeH)_{ads}$, resulting from the cathodic reaction and covering almost all the surface, has an inhibiting effect. We shall now show that in the anodic range near the corrosion potential the θ_H variation with the potential is responsible for the hysteresis phenomenon.

Mixed kinetics of the iron corrosion process.—Near the corrosion potential, two reactions occur simultaneously: cathodic hydrogen evolution and anodic iron dissolution. The former leads to coverage of a fraction θ_H of the electrode surface by $(FeH)_{ads}$, and the latter to coverage of a fraction θ_{OH} of the same electrode by $(FeOH)_{ads}$. Having no common intermediate, these two reactions compete and, hence, give rise to mixed kinetics.

In the literature, many authors (17-20) consider that at the corrosion potential almost the whole electrode surface is covered by $(FeH)_{ads}$. Now, the coverage fraction θ_H, close to 1 at cathodic potentials, must decrease when the anodic polarization is increased. Nevertheless, it does not seem that this θ_H variation has been systematically studied. In this paper, the analysis of the hysteresis phenomenon allows us to carry out such a study.

The hysteresis phenomenon.—In the anodic range near the corrosion potential and in a molar solution of sulfuric acid, the potentiokinetic traces carried out for iron II exhibited no hysteresis (1, 2). On the other hand, for iron I and under the same conditions, a narrow cycle is observed, much narrower than that observed with a single-crystal iron (2). However, in the presence of 2-butyne 1,4-diol and for both iron I and iron II, the hysteresis cycle becomes more obvious. This phenomenon has also been observed on iron samples of different natures (2). Moreover, even for the lowest sweep rates compatible with good reproducibility of the measurements (dissolution alters the state of the surface little by little), the curves recorded successively at increasing anodic potential (forward trace), then at decreasing potential (backward trace), remain distinct. We have shown elsewhere (6) that at frequencies close to 10^{-3} Hz the impedance tends, in this potential range, to become a pure resistance that must be considered as the slope of a steady-state polarization curve independent of the sweep conditions.

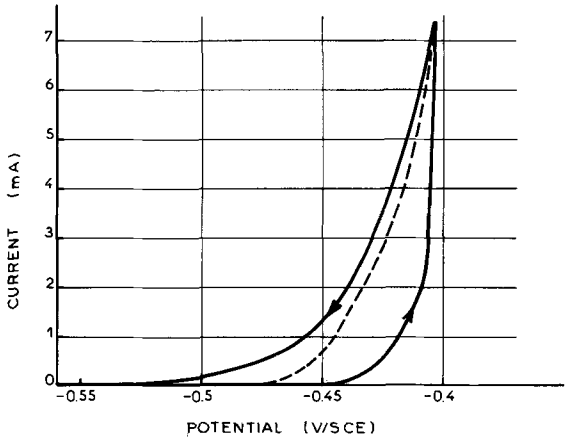

Fig. 5. Anodic polarization curves: iron I, 1M H_2SO_4 + 10^{-3}M 2-butyne 1,4-diol. Solid line: potentiokinetic trace; dV/dt = 0.2 V/min (the arrows show the sweep direction). Dotted line: steady-state trace.

In other words, there must exist only one $I = f(V)$ characteristic.

According to this result, the observed hysteresis would be caused by the fact that the surface coverage by $(FeH)_{ads}$ cannot reach a steady-state, even for the lowest sweep rates used here, because of the slowness of the hydrogen adsorption-desorption process.

Steady-state $I = f(V)$ polarization curve.—We obtained this curve by immersing the electrode, then by waiting at each point for the stabilization of the current. In order to check that there is only one $I = f(V)$ curve, we stopped the potential sweep during either the forward trace or the backward trace, and recorded the subsequent evolution of the current. We then confirmed that the value toward which the current tends depends only on the potential where the sweep was stopped, and that the curves obtained by these two methods are identical. As an illustration, we give in Fig. 5 the steady-state curve (dotted line) obtained point by point for iron I in a molar solution of sulfuric acid containing 10^{-3}M of 2-butyne 1,4-diol. In the same figure is shown the quasi-steady-state potentiokinetic curve (solid line) recorded at a speed of 0.2 V/min. The arrows indicate the sweep direction. The time needed to stabilize the current after the sweep is stopped is about 10-30 min, depending on the anodic potential; then we again obtained the $I = f(V)$ characteristic shown in dotted line. It can be seen that the steady-state curve is identical with the forward trace near the corrosion potential and with the backward trace at potentials above −0.4 V/SCE. As these curves here represent the over-all current I, *i.e.* the difference between the anodic current I_a and the cathodic current I_c, we wanted to separate its two components before attempting any interpretation.

Separation of the cathodic component I_c from the over-all current.—In an acidic medium, iron dissolves as a divalent ion. If iron is assumed to undergo no disaggregation, the measurement of weight loss allows the separation of I_a and I_c at a given current I. We have determined them in the case of the dissolution of iron I by means of Faraday's law in a molar solution of sulfuric acid containing 10^{-3}M of 2-butyne 1,4-diol. The constant current I is supplied by a wide-band galvanostat built in our laboratory by C. Gabrielli. The dissolution time is limited to 1 hr in order to avoid pitting. The dissolved iron is determined by colorimetry with o-phenanthroline as an indicator.

Table II summarizes, for each value of I, the values of I_a and I_c with their confidence interval calculated on the 10% level of significance from 8 experiments for I = 0.1 and 0.2 mA, and from 4 experiments for I greater than 0.2 mA. From this table, it can be noted

Table II. Results from the measurements of weight loss: iron I, 1M H_2SO_4 + 10^{-3}M 2-butyne 1,4-diol

R_t = Measured transfer resistance
R_{ta} = Anodic transfer resistance
θ_H^* = Surface coverage by $(FeH)_{ads}$
I = Over-all current
I_a = Anodic current
I_c = Cathodic current

I(mA)	$-I_c$(μA)	I_a(μA)	V(mV/SCE)	R_t(ohms)	$R_{ta}I_a$(mV)	θ_H^*
0.1	45 ± 6	145 ± 6	−470	221 ± 17.5	37 ± 3.8	0.78
0.2	47 ± 12	247 ± 12	−464	133 ± 5	38.4 ± 4.0	0.70
0.3	37 ± 10	337 ± 10	−460	101 ± 8	38.1 ± 4.0	0.62
0.5	54 ± 29	554 ± 29	−454	65.3 ± 1.6	38.7 ± 3.2	0.54
0.7	44 ± 28	744 ± 28	−450	50.2 ± 1.8	39.0 ± 1.6	0.45
1	42 ± 20	1042 ± 20	−445	36.7 ± 2.5	39.7 ± 2.2	0.40

that I_c is independent of I. Although the polarization potential varies only by 25 mV when I passes from 0.1 to 1 mA, a marked variation of the surface available for the cathodic reaction can be expected. Therefore, we may consider that the reaction responsible for the term I_c merely occurs on particular sites. Besides, this interpretation is corroborated by the microscopic observation, *in situ*, of the electrode through an objective immersed in the electrolyte: the gas bubbles always appear on well-determined sites whose positions depend on the structure of the surface.

The obtained I_a (V) values do not correspond to the anodic dissolution mechanism (5) which is applicable at higher currents (2). We shall now show that this deviation, which cannot be attributed to the cathodic current, may be explained by the coverage of the surface by $(FeH)_{ads}$.

Evaluation of the coverage fraction θ_H.—Column 5 of Table II shows the transfer resistance R_t, deduced from anodic impedance measurements (6) carried out during the dissolution experiments themselves. It hence can be seen that the product R_tI, which elsewhere (3) was shown to be constant for high currents ($\simeq$40 mV), diminishes for currents lower than 2 mA. If we take into account that R_t has an anodic component R_{ta} and a cathodic component R_{tc}, we can write that

$$\frac{1}{R_t} = \frac{1}{R_{ta}} + \frac{1}{R_{tc}}$$

The product R_{ta} I_a is constant (Table II, Col. 6) within the precision of measurements, even at the lowest polarization, and is equal to the value of R_tI found for currents higher than 2 mA. Consequently, it can be considered that the dissolution mechanism (5) remains valid even for very low anodic currents, although we have found an obvious difference between the variations of I_a and of its density J_a with the potential (6). Since R_{ta} I_a does not depend on the reaction surface, this difference can be attributed only to a variation of the area of cathodic coverage by the hydrogen (θ_H) and perhaps by the inhibitor (θ_{inh}). However, according to Mayer *et al.*, the inhibiting effect of 2-butyne 1,4-diol appears only when the electrode surface is covered by H_{ads} (21). In the same way, referring to the polarization curves obtained in the presence and absence of the inhibitor, it can be seen that 2-butyne 1,4-diol has the same effect as H_{ads} and that θ_H and θ_{inh} cannot be distinguished. Consequently, we may write

$$I_a = J_a\,(1 - \theta_H^*)$$

where θ_H^* is the cathodic coverage in the presence of 2-butyne 1,4-diol.

The last column of Table II presents the values of θ_H^* as a function of I. The values of J_a were obtained from the extrapolation of the anodic Tafel line corresponding to step I of the iron dissolution reaction (5). Figure 6 represents the variation of θ_H^* as a function of the potential V. From this figure it can be seen that θ_H^* tends toward 1 near the corrosion potential, which is in agreement with the results obtained at the

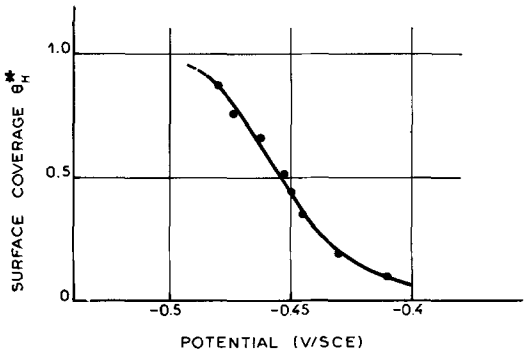

Fig. 6. Variation of the surface coverage θ_H^* with the anodic polarization potential: iron I, 1M H_2SO_4 + 10^{-3}M 2-butyne 1,4-diol.

cathodic range (see first section under Results and Discussion). On the other hand, θ_H^* tends toward zero for anodic potentials close to −0.4 V/SCE. These results explain the hysteresis of the potentiokinetic curve presented in Fig. 5. According to our interpretation (1, 2), the forward trace corresponds to an almost complete coverage by $(FeH)_{ads}$ and the backward trace to an almost uncovered surface. Moreover, it can be noted that the −0.4 V/SCE value is close to that above which hysteresis is no longer observed (2) with a single-crystal iron (−0.38 V/SCE).

Finally, it is to be noted that further support for this interpretation of the observed hysteresis is given by the impedance measurements within the anodic range (6). As a matter of fact, in the (R,jG) diagram, there appears a second inductive loop which is clearly distinguished from that caused by the relaxation of the coverage by $(FeOH)_{ads}$ and which can be assigned to the relaxation of the cathodic coverage (22). In this latter case, if there were two distinct coverages, θ_H and θ_{inh}, one might expect to observe two different time constants. We should observe, on the whole, three time constants, which is not the case here. We may therefore conclude that there is only one coverage, that of hydrogen, 2-butyne 1,4-diol having only the effect of reinforcing the bond between H_{ads} and the metal.

Conclusion

We have been able to elucidate the influence on the cathodic phenomenon of an acetylenic alcohol, namely 2-butyne 1,4-diol, during the corrosion of iron in a sulfuric acid medium. From our results, it appears, indeed, that 2-butyne 1,4-diol increases the surface coverage by $(FeH)_{ads}$ by reinforcing the Fe-H bond.

This coverage causes, in the cathodic range, a decrease with time of the reaction rate, probably by diminishing the number of active sites. In the anodic range, the persistence of the coverage by $(FeH)_{ads}$ at potentials much higher than the corrosion potential reduces the surface available for the dissolution reaction. Consequently, the variation of the hydrogen coverage θ_H with the potential is at the origin of the hysteresis phenomenon.

Lastly, for a highly pure iron, even in the absence of 2-butyne 1,4-diol the presence of $(FeH)_{ads}$, which leads to a very low corrosion rate, would explain the observed low inhibiting efficiency.

Manuscript submitted Dec. 1, 1970; revised manuscript received *ca.* Mar. 1, 1971. This paper was presented at the 3e Symposium Européen sur les Inhibiteurs de Corrosion, Ferrare, Italy, Sept. 1970 (and appeared in French in the Abstracts of the symposium proceedings).

Any discussion of this paper will appear in a Discussion Section to be published in the June 1972 JOURNAL.

REFERENCES

1. I. Epelboin, "Proceedings of the 2° Symposium Européen sur les Inhibiteurs de Corrosion," p.

663, The University of Ferrara, Ferrara, Italy (1966).
2. Ph. Morel, Thèse de Doctorat d'Etat, Paris (1968), No. d'Enregistrement C.N.R.S.: A.O. 2346; *idem., Traitements de Surface,* No. 89, 9 (1969) and No. 91, 37 (1970).
3. M. Keddam, Thèse de Doctorat d'Etat, Paris (1968), No. d'Enregistrement C.N.R.S.: A.O. 2192; *idem., Traitements de Surface,* No. 95, 39 and No. 96, 3 (1970); I. Epelboin and M. Keddam, *This Journal,* **117,** 1052 (1970).
4. M. Keddam and H. Takenouti, *Compt. Rend. Acad. Sci. Paris Serie C,* **270,** 283 (1970).
5. J. O'M. Bockris, D. Drazič, and A. R. Despič, *Electrochim. Acta,* **4,** 325 (1961).
6. I. Epelboin, M. Keddam, and H. Takenouti, Communication at the 3° Symposium Européen sur les Inhibiteurs de Corrosion, Ferrara (1970).
7. I. Epelboin, M. Keddam, and H. Takenouti, Communication at the 17th Meeting of C.I.T.C.E., Tokyo (1966).
8. M. L. Boyer, I. Epelboin, and M. Keddam, *Electrochim. Acta,* **11,** 221 (1966).
9. R. M. Hudson and K. J. Riedy, *Metal Finishing,* **62,** 48 (1964).
10. K. S. Cole and R. H. Cole, *J. Chem. Phys.,* **9,** 341 (1941).
11. H. Gerischer and W. Mehl, *Z. Elektrochem.,* **59,** 1049 (1955).
12. J. O'M. Bockris and P. K. Subramanian, *Corrosion Sci.,* **10,** 435 (1970).
13. N. D. Tomashov and L. P. Veshinina, *Electrochim. Acta,* **15,** 501 (1970).
14. P. Jolly and C. Goux, *Mém. Sci. Rev. Métal.,* **66,** 605 (1969).
15. B. Le Boucher, Thèse de Doctorat d'Etat, Paris (1963); *idem., Rev. Inst. Pétroles,* **18,** No. 4 (1963).
16. G. Wranglen, *Corrosion Sci.,* **9,** 585 (1969).
17. E. McCafferty and A. C. Zettlemoyer, *J. Phys. Chem.,* **71,** 2452 (1967).
18. T. P. Hoar and R. D. Holliday, *J. Appl. Chem.,* **3,** 502 (1953).
19. P. J. Hillson and E. K. Rideal, *Proc. Roy. Soc. (London),* **A199,** 295 (1949).
20. L. J. Antropov, "Proceedings of the 1st International Congress on Metallic Corrosion," p. 147 Butterworths & Co., London (1962).
21. C. Mayer, W. J. Lorenz, and H. Fischer, *Z. Phys. Chem. N.F.,* **52,** 193 (1967).
22. H. Takenouti, Thèse d'Université, Paris (1971); I. Epelboin, Plenary Lecture at the 21st Meeting of C.I.T.C.E., Prague (1970).

Low Defect Density Electrodeposits on Copper Single Crystals[1]

U. Bertocci and C. Bertocci

Solid State Division, Oak Ridge National Laboratory, Oak Ridge, Tennessee 37830

ABSTRACT

The electrodeposition of layers of copper over 100 μm thick on copper single crystals has been carried out on highly perfect copper single crystal substrates, having {111} orientation. Conditions for the achievement of low defect density deposits have been investigated. The defects present in the deposit have been studied by Borrmann topography and other x-ray techniques as well as optical microscopy and dislocation etching. In the most perfect deposits produced, no mosaic structure has been found, and the concentration of defects visible by Borrmann topography did not increase substantially the absorption of the x-ray beam. Small loops or point defect clusters in concentrations of the order of $10^6/cm^2$ have been detected by etching. The orientation of the substrate has been found to affect the perfection of the deposits. It is concluded that random nucleation is likely to be the mechanism for step generation where the orientation is very close to {111}.

Epitaxial growth of copper single crystals by electrodeposition is very well documented, particularly from sulfate solutions (1-8). Not so well known, however, is the degree of perfection which can be attained by electrodeposition, as well as the characteristics of the defect structure.

Among the structural studies reported in the literature, many are concerned with the preferential orientation of polycrystalline deposits (9-13), since knowledge on this topic is of considerable practical interest. Epitaxial growth on single crystal substrates has been examined by x-rays (14), but most of the information is not topographic in nature (3, 5, 15) and gives only a general idea of the defects in the deposit. When sensitive techniques have been employed, the use of substrates having a substantial defect density tended to obscure the significance of the results (16).

A more detailed picture of the defects present in electrodeposits has been obtained employing transmission electron microscopy (10, 12, 13, 17). Although very valuable, this method is in general limited to examination of very thin deposits. The substrate, usually produced by evaporation, tends to contain a high number of defects. Electron microscopy has been mostly used to study the deposition of a metal on a substrate of different composition; this gives rise to defects peculiar to the difference in lattice parameters of substrate and deposit.

In recent years, because of the availability of metal crystals of high perfection and the improvement of x-ray techniques, Borrmann topography has been developed as a powerful tool for the examination of defects in crystals, and copper has been extensively studied (18-21). This technique is based on the phenomenon known as anomalous transmission. If a single crystal is so perfect that changes in orientation of the lattice are no more than a few seconds of arc, a monochromatic collimated x-ray beam will travel through it in certain directions with an absorption coefficient 10 to 20 times smaller than the ordinary value. For copper, specimens up to about 1 mm can be examined by transmission. If defects such as dislocations are present inside the crystal, images of them can be

[1] Research sponsored by the U.S. Atomic Energy Commission under contract with Union Carbide Corporation.
Key words: electrodeposition, x-rays, anomalous transmission Borrmann topography.

formed on the topographs, and by means of stereo pairs, the spatial arrangement of the defects inside the crystal can be determined. Intensity sufficient for obtaining a useful topograph can be transmitted only if no mosaic structure is present and the dislocation density is not more than about $10^4/cm^2$. As far as resolution is concerned, defects smaller than a few microns do not form an image, although contributing to the absorption.

Since specimens hundreds of microns thick are well suited as electrodes, Borrmann topographs can be used to gather information about the perfection of the deposits and about the relationships between defects in the substrate and in the deposit. The method allows examination of much thicker layers than possible by transmission electron microscopy, so that no doubt exists that the deposits were obtained in steady-state conditions.

The aim of the work described here has been to investigate the conditions for obtaining high perfection deposits and to contribute to the knowledge of the nature and spatial distribution of defects in the deposit, as well as the influence of perfection and orientation of the substrate on the deposit perfection. The experimental method employed has been the correlation of Borrmann topographs and other x-ray data with optical microscopy and dislocation etching.

Experimental Methods

The depositions were carried out on crystals of purity 99.999% approximately 10 x 10 mm, whose thickness ranged from 0.2 to 0.5 mm. The two main surfaces had {111} orientation. The crystals had been irradiated with 10^{17} fast neutrons/cm^3 in order to increase their hardness so as to withstand handling (20). The specimens were electropolished in a phosphate bath, rinsed in 10% H_3PO_4 for a minute and finally under flowing distilled water for several minutes. This preparation technique produces surfaces reasonably free of contamination. In particular, phosphorus is not present (22). The specimens were kept under water during the time (approximately 30 sec) necessary to transfer them into the cell.

The solution, whose composition was 0.5M $CuSO_4$, 0.2M H_2SO_4, was prepared by dissolving recrystallized reagent grade $CuSO_4$ and adding reagent grade H_2SO_4. The solution was filtered several times through fritted glass, and care was taken that particulate matter could not be detected by observing scattered light under a low power microscope.

The cell was all Pyrex glass, with Teflon stoppers and magnetic stirrer. The anodic and cathodic compartments were separated by fritted glass disks, and the solution was introduced into the cell from the anodic compartment so that a final filtration was achieved for the solution filling the cathodic compartment. The closed cell was swept with pure argon and kept permanently under an argon blanket at slight, positive pressure. Further purification was achieved by preelectrolysis on high purity copper cathodes, the current density being about five times larger than that used for the depositions. Stirring was employed only during pre-electrolysis.

All depositions were carried out at room temperature, about 23°C. The thickness of the deposits ranged from 30 to 120 μm.

Some depositions were made with periodic current reversal by means of a Hewlett-Packard 6823A Power Supply in the constant current configuration modulated by a signal generator. A cathode ray oscilloscope was used for measuring amplitude and duration of the pulses. The average c.d. calculated from pulse shape was checked against the weight gain of dummy specimens; the differences were of the order of 2 or 3%.

Borrmann topographs were taken using MoK_α radiation, the diffraction vector being either $\bar{1}\bar{1}\bar{1}$, $\bar{1}11$, or $1\bar{1}\bar{1}$, considering the crystal surface where the x-rays enter as (111). As a faster method for checking the perfection of the deposits, the measurement of the half-width of the 444 Bragg peak was chosen. Since the theoretical value for a perfect crystal, using MoK_α radiation, is 2″ of arc (23), small deviations from a perfect crystal, corresponding to a few seconds of arc, can be detected. The measurements were carried out by means of a double crystal spectrometer.

The deposits were also examined by optical microscopy, both as obtained after deposition and after electropolishing and etching with a dislocation etch (24). The orientation of the facets developed during deposition, particularly at the edges of the specimens, was determined by means of a two circle goniometer.

By sectioning some specimens and measuring the thickness of the deposits, it was deduced that the current density on high index planes was not more than three times that on close-packed ones. Since the flat crystals used as electrodes had their main faces oriented within a few degrees from {111} and at the edges—which accounted at most for 10% of the total surface area—slowly growing facets soon developed, it was concluded that the average current density did not differ from the actual current density on the {111} planes by more than 20%. Optical measurement of the thickness of the electrodes before and after deposition supported this conclusion.

Production of low defect density deposits.—By examining the deposits, standards for assessing their quality were developed. In the course of the work it became apparent that trace impurities affected both surface structure and perfection; repeated pre-electrolysis was generally beneficial. However, particulate matter suspended in solution was very detrimental, as was shown during preliminary work in cells without separation between cathodic and anodic compartment. During pre-electrolysis copper powder is generated at the anode by preferential attack at grain boundaries. If the powder reaches the cathode, abnormal growth protrusions are formed, often misoriented with respect to the substrate.

The features marking deposits whose perfection was considered unsatisfactory, because they were unsuitable for Borrmann topography, were a tendency for the surface steps to aggregate, forming steep ledges exhibiting crystallographic character (see Fig. 1). These ledges developed into {210} facets which broke up the {111} surface into areas often of different height. The same facets also bound hexagonal pits, which tended to cover large areas of the surface.

Visual examination was therefore sufficient for detecting unsatisfactory deposits. Their appearance correlated well with x-ray data; the half-width of the

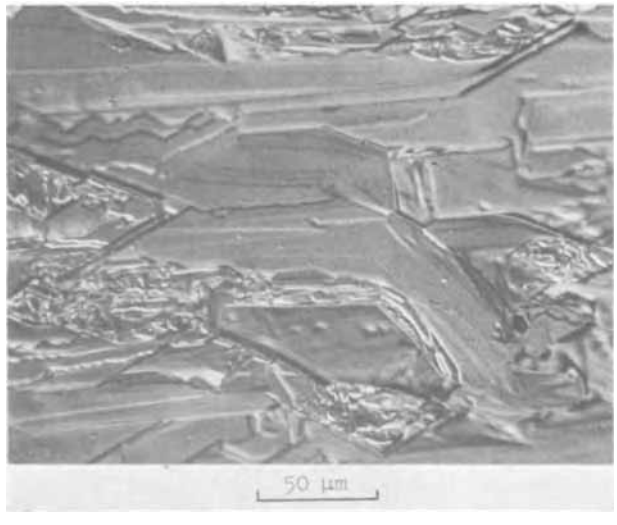

Fig. 1. Deposit of unsatisfactory perfection. (111) surface after deposition of 45 μm at 0.5 mA/cm^2. Nomarski interference contrast.

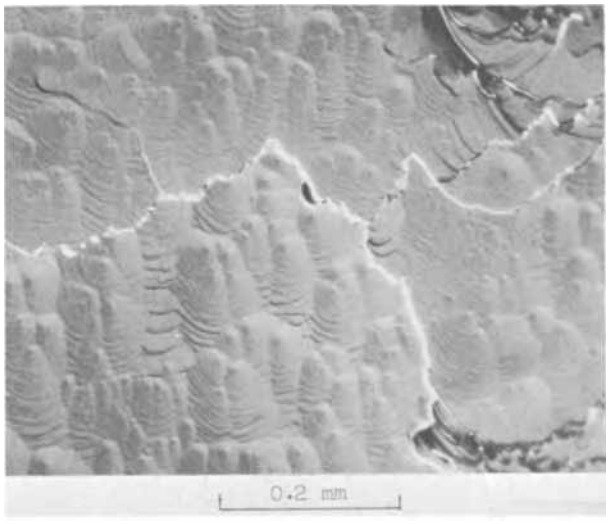

Fig. 2. Deposit of high perfection. (111) surface after deposition of 50 μm at 0.5 mA/cm^2. Nomarski interference contrast.

444 reflection on such surfaces varied from 10″ of arc up to 1′, indicating the angular range of the mosaic structure in the deposit. The transmitted x-ray intensity was so low that Borrmann topographs could not be taken.

More perfect deposits were characterized by regular arrays of macrosteps about 10-12 μm apart, if the surface was more than about 1°10′ to 1°30′ from {111}, and by randomly distributed hillocks as shown in Fig. 2 for smaller misorientations. The transition between the two surface structures is quite sharp. The slope of the hillocks, as measured by means of a modified Nomarski interference contrast microscope (25) is between 6′ and 10′ of arc. Steeper ledges such as those crossing Fig. 2 (see also Fig. 6) reach misorientations of 4° to 5°. The tendency to form pits bound by {210} facets was largely suppressed. The half-width of the 444 peak was from 4″ to 5″ of arc. Borrmann topographs could be taken and areas of higher or lower perfection could be observed and examined.

The experiments at constant current density showed that consistently good deposits could not be obtained at current densities higher than about 0.5 mA/cm^2. At 1 mA/cm^2, Borrmann topographs showed that most of the deposit had a high defect density, and the half-width of the 444 peak was of the order of 20″.

Some depositions were carried out with periodic current reversal using either sinusoidal or square wave signals. In the present experiments no improvement over constant current deposition was found, either in the perfection of the deposits or in the possibility of increasing the deposition rate without increasing the defect density.

In a series of tests a sinusoidal signal was superimposed on a direct c.d. of 0.5 mA/cm^2. The conditions were the following: 500 Hz, 1.8 mA/cm^2 rms; 2000 Hz, 2 and 5 mA/cm^2 rms. The appearance of the deposit was substantially different compared with d-c deposition, particularly at the lower frequency, showing formation of large triangular hillocks on the {111} faces. The perfection was low, half-width was 30″ to 1′, and the topographs were opaque, except in very few isolated patches. Subsequent electropolishing and etching showed a pit density greater than 10^6/cm^2.

Some experiments were carried out using rectangular current pulses. The current density, both anodic and cathodic, varied between 0.6 and 0.9 mA/cm^2, the duration of the anodic pulse being 20 msec and that of the cathodic pulse 180 msec. Longer pulse durations have also been tested. This work is still in progress, but preliminary observations have given little indication that higher deposition rates and/or highly perfect deposits can be achieved in this way. This method, however, seems to affect the growth habit so that facets different from those observed with d-c depositions are formed.

Experimental Results

The experimental evidence to be analyzed principally consists of photographs recording x-ray or visible light intensity patterns, and their analysis mainly consists in comparing topographs with different diffraction vectors, as is necessary in order to examine line defects, or in correlating spatially x-ray pictures with photomicrographs, both before and after etching. The experimental data, therefore, do not lend themselves to being presented in compact form as with numerical tables or graphs. An effort has been made to show some of the most significant examples, but it must be understood that only a small part of the evidence can be presented.

Figures 3 and 4 show stereo pairs of topographs of the same area of a specimen before and after deposition. The thickness of the deposit on each side is approximately 130 μm, and the total thickness is 430 $\pm$ 30 μm. The main faces of the crystal are misoriented about 5° from {111}. In the deposit very few defects can be seen except on the edges of the crystal (lower left corner), where they are associated with growth of facets other than {111}.

Some dislocations ending at the surface of the substrate can be recognized. For the comparison between the dislocation network in Fig. 3 and 4, it must be remembered that after taking Fig. 3, the specimen had to be electropolished immediately before the deposition, as described in a preceding section. Therefore some dislocation lines were shortened, particularly those intersecting the surface at a low angle.[2] In all cases, instead of a clear dislocation line continuing into the deposit, only a faint line starting from the end of the dislocation line in the substrate can be seen. Also, series of small spots roughly aligned so as to cross the deposit perpendicularly to the surface are visible.

Figure 5 shows a topograph of another specimen; the deposit obtained at 0.5 mA/cm^2 is approximately 50 μm thick. The orientation of the surface, very close to {111}, is shown in Fig. 6, a composite photomicrograph of the same area (Nomarski interference contrast and

[2] Defects close to the exit surface for the x-ray beam exhibit reverse contrast, producing a black and white double image, instead of a simple black image (on positive prints). The reader should notice that the dislocation lines showing reverse contrast in Fig. 3 have been in general removed by the electropolishing and no longer appear in Fig. 4.

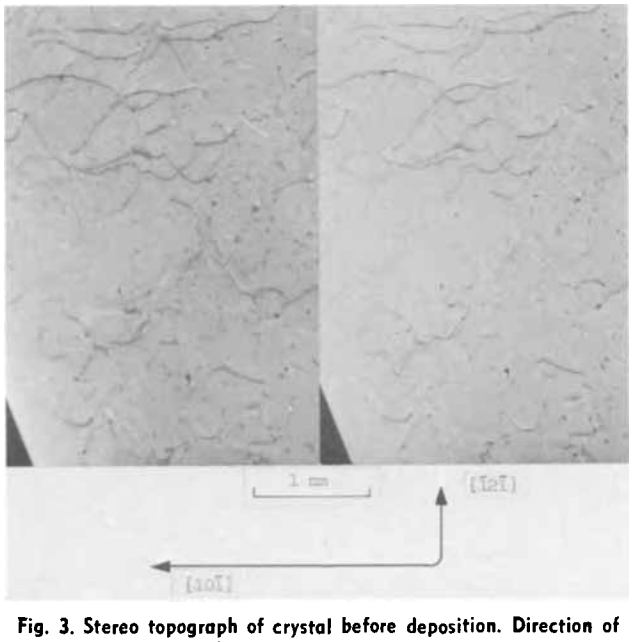

Fig. 3. Stereo topograph of crystal before deposition. Direction of diffraction vector = $\bar{1}\bar{1}\bar{1}$.

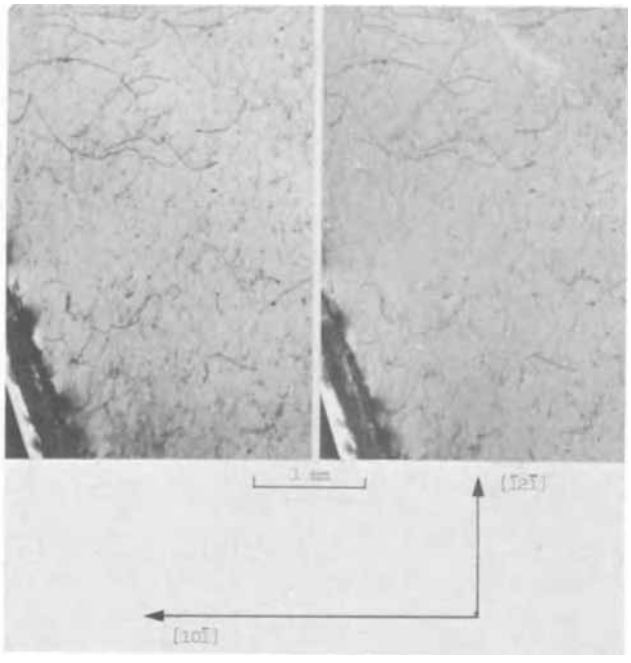

Fig. 4. Stereo topograph of crystal shown in Fig. 3 after deposition of 130 μm at 0.7 mA/cm^2. Direction of diffraction vector = $\bar{1}1\bar{1}$.

a low magnification objective were used so as to obtain high contrast; the surface is actually fairly smooth). In Fig. 5 a number of defects can be seen, but many cannot be resolved as either dislocation lines or point defect clusters. Areas of higher defect density, as revealed by the topograph, correspond on Fig. 6 to areas where closely spaced hillocks grew together or where surface ledges were pinned, bent sharply, or bunched. The correspondence between higher defect regions and recognizable surface features is, however, not complete: the defect regions appear to be at different levels inside the deposit; this can be seen by comparing Fig. 5 with Fig. 7, a topograph of the same region of the crystal taken after electropolishing the specimen so as to remove most of the deposit, and

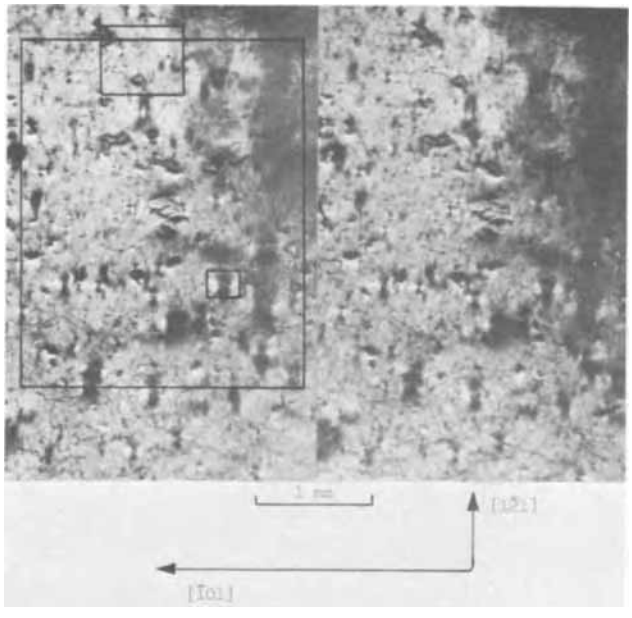

Fig. 5. Stereo topograph of crystal after deposition of 50 μm at 0.5 mA/cm^2. Direction of diffraction vector = $\bar{1}1\bar{1}$. Black lines show outlines of Fig. 6. (large rectangle), Fig. 8 (lower rectangle) and Fig. 9 (upper rectangle).

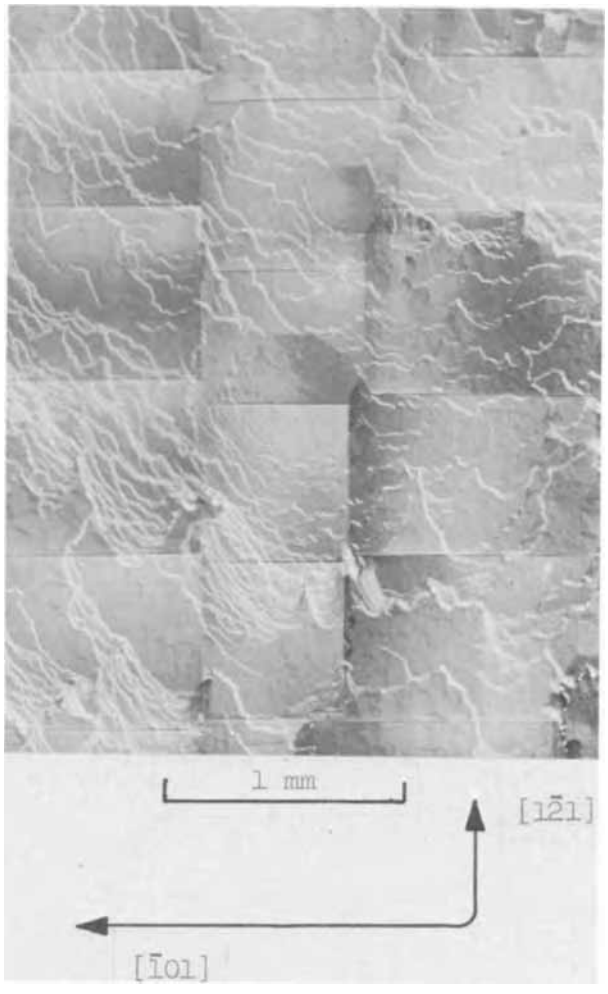

Fig. 6. Composite photomicrograph of surface of deposit shown in Fig. 5. Nomarski interference contrast.

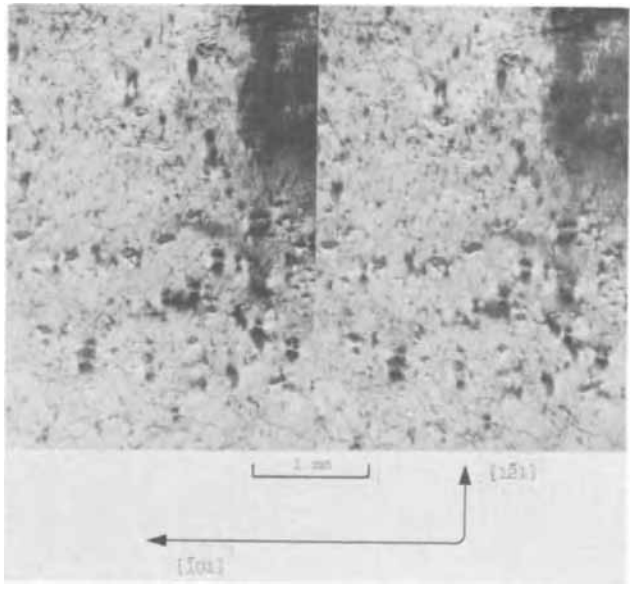

Fig. 7. Stereo topograph of area shown in Fig. 5 after removal of about two-thirds of deposit. Direction of diffraction vector = $\bar{1}1\bar{1}$.

etching with a dislocation etch (23). A number of the high defect regions have completely disappeared but others are now at the surface, as can be inferred from the strong black-white contrast. Microscopic observation of the etch-pits shows that tight clusters of pits are found in positions corresponding to the black spots

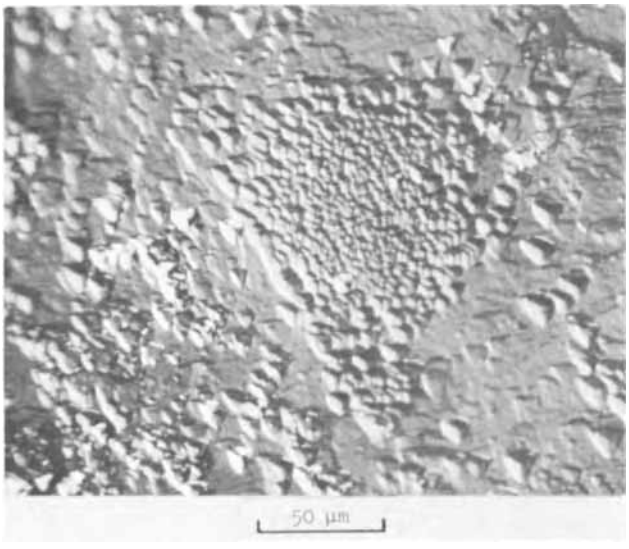

Fig. 8. Photomicrograph of part of crystal shown in Fig. 5 after electropolishing and etching. Nomarski interference contrast.

seen on the topograph (see Fig. 8). However, pit densities (of the order of $5 \cdot 10^5$ per cm^3) higher than in the substrate could be seen also where the x-ray topograph did not show a significant defect density. Figure 9 shows clearly the difference between substrate and deposit, which had been completely removed in some areas. It is noteworthy that the etch-pits produced have different sizes, a number of them being small and flat-bottomed. This feature is generally not associated with long dislocation lines, but rather with small dislocation loops (26).

In some instances, growth of isolated pyramids has been observed. The steps on the side of the pyramid, although bunching to form multi-atomic ledges clearly visible by optical microscopy, generated only relatively few defects detectable in the x-ray topographs. At the center of the pyramid a rather diffuse spot showing black-white contrast can be seen. The isolated pyramid, therefore, is not associated with a single dislocation line. Figures 10 and 11 show a stereo topograph and a micrograph of an area containing isolated growth pyramids. The slope of the steepest one (bottom left in Fig. 11) is about 2°. The others are less than 1°.

Some information about the nature and location of defects present in deposits considered of unsatisfactory perfection was obtained by electropolishing and etching. As is clearly visible in Fig. 12, etch-pits are often

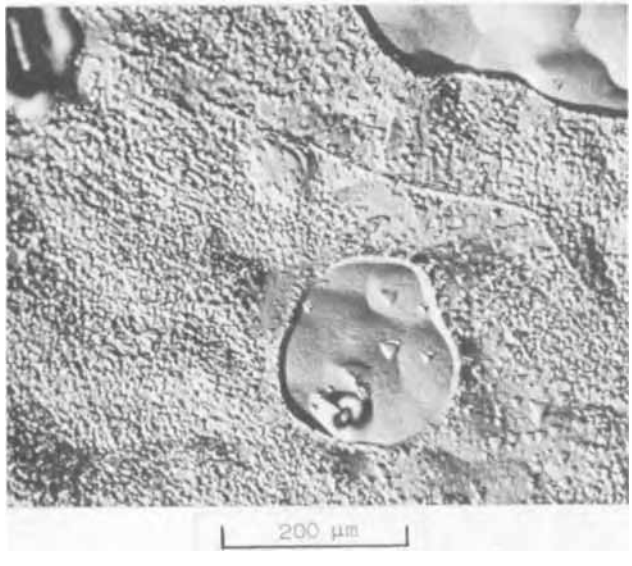

Fig. 9. Photomicrograph of part of crystal shown in Fig. 5 after electropolishing and etching. Nomarski interference contrast.

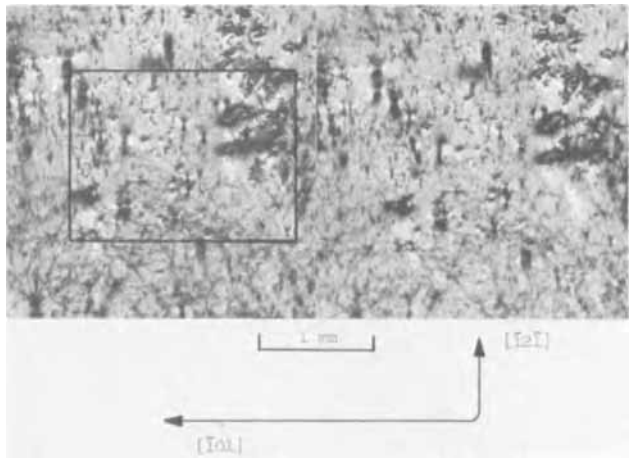

Fig. 10. Stereo topograph of crystal after deposition of 35 μm at 0.5 mA/cm². Direction of diffraction vector = $1\bar{1}1$. Black line shows outline of Fig. 11.

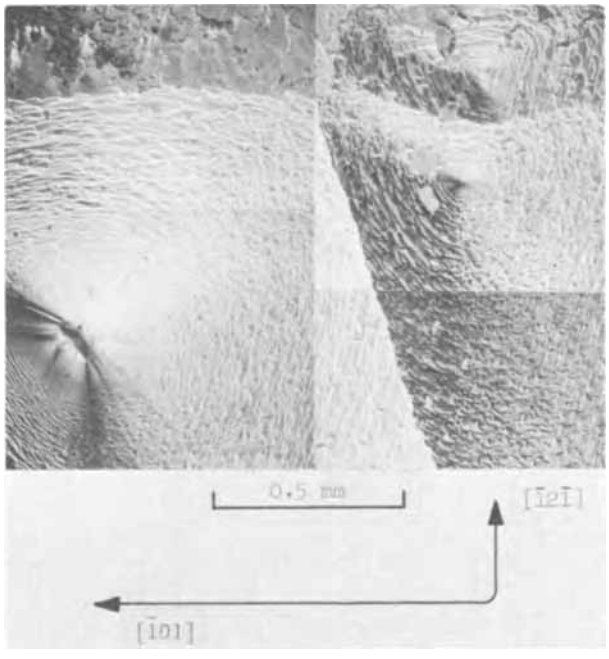

Fig. 11. Composite photomicrograph of deposit shown in Fig. 10. Nomarski interference contrast.

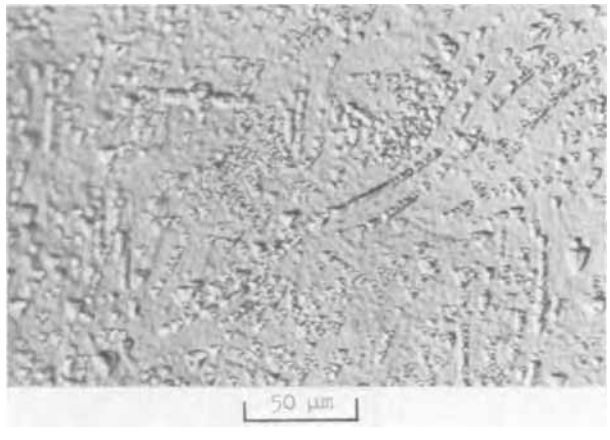

Fig. 12. Photomicrograph of {111} surface of deposit of unsatisfactory perfection after electropolishing and etching in HCl-HBr-$FeCl_3$ mixture. Half-width of 444 Bragg peak after electropolishing = 9″ of arc. Nomarski interference contrast.

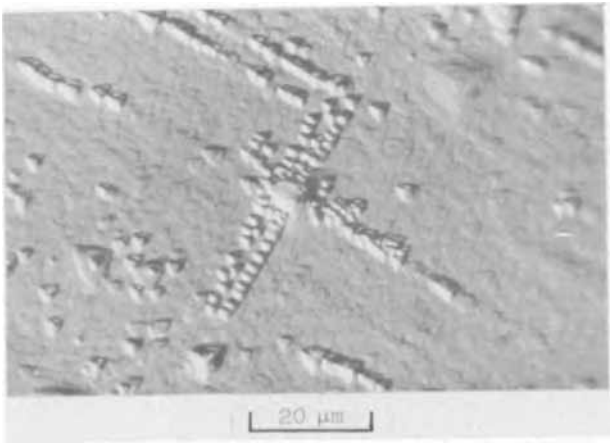

Fig. 13. Hollow strain center surrounded by punched out loops. Same specimen and treatment as in Fig. 12. Nomarski interference contrast.

clustered in lines. The lines follow approximately the contour of the steep ledges observed on the surface of the deposit. Furthermore, strain centers surrounded by etch-pits and seemingly having a hollow core are fairly numerous (see Fig. 13, where double rows of pits, revealing punched-out prismatic loops, are shown).

In the course of this work data about the growth habit of electrodeposited copper were gathered by measuring the orientation of the facets formed at the edge of the specimens. These data were supplemented by depositions carried out on hemispherical crystals (see Fig. 14). The results can be summarized as follows: The tendency to form flat and well-oriented facets (deviations being generally less than 1°) is exhibited only by {111} and {110}. The latter orientation, however, is not a preferred one, and only small facets are formed, generally at the intersection of two {210} facets (see Fig. 15). An orientation which develops preferentially is {210}. Large facets are formed by deposition on hemispherical crystals, as Fig. 14 shows. The facets are not very smooth; the reflections at the goniometer indicate that most of the surface is oriented about 4° from {210} toward the nearest {110}, but slightly off the <001> zone. The results of the goniometer readings agree with microscopic observations (see Fig. 16), where considerable variations in orientation can be seen. The growth seems to occur by motion of ledges or facets, visible in Fig. 16, and whose orientation is approximately {320}.

It is remarkable that all areas close to <100> poles never develop {100} faces but orientations varying from

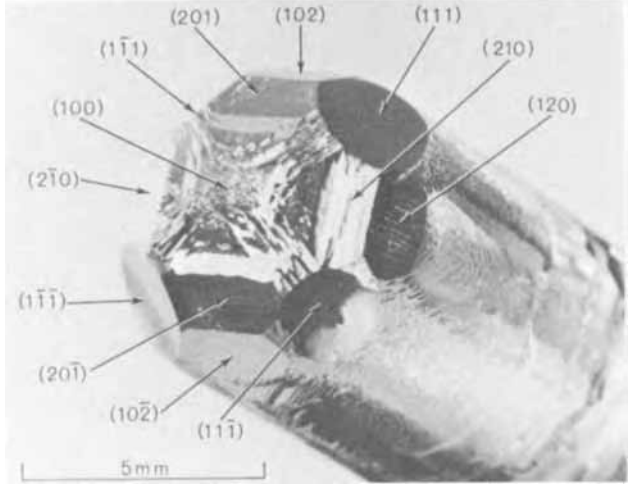

Fig. 14. Photomicrograph of deposit obtained on hemispherical crystal. Current density = 0.3 mA/cm^2. Average thickness 230 μm.

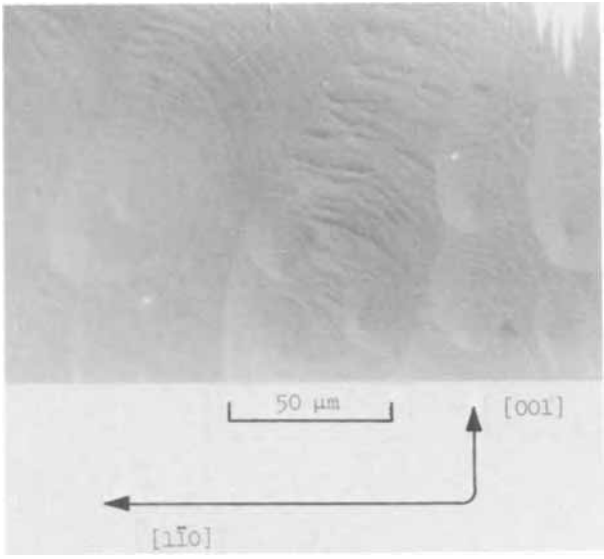

Fig. 15. Photomicrograph of {110} facet developed during deposition at 0.5 mA/cm^2. Nomarski interference contrast.

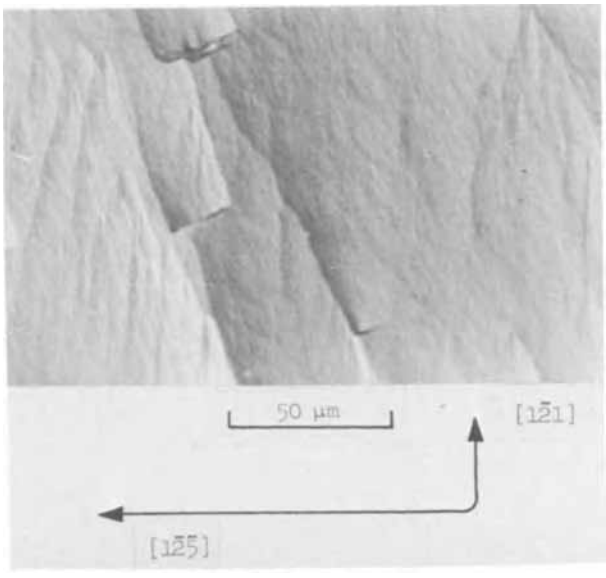

Fig. 16. Photomicrograph of {210} facet developed during deposition at 0.5 mA/cm^2. Nomarski interference contrast.

{710} to {15,1,0}. The goniometer reflections are rather diffuse, in agreement with the structure seen under the microscope: terraced pyramids tending to have {15,1,0} at the base and {710} at the tip (see Fig. 17). The pyramids very often have a core which is not epitaxially oriented, as was determined by x-ray examination.

Discussion

From the results presented it can be concluded that in carefully controlled conditions it is possible to electrodeposit copper from sulfate solutions in layers over 100 μm thick with a high degree of perfection. It is, however, clear that the orientation of the surface plays an important role, and so far only for orientations close to {111} have conditions leading to good deposits been found.

Since the sensitivity of a method for detecting defects varies with their nature, only correlating different results can give an accurate picture of the defect structure of a crystal. The measurement of the half-width of the 444 Bragg peak, although more sensitive than Borrmann topography in detecting mosaic structure (the half-width of the anomalously transmitted beam is of the order of 15" of arc) is little affected by individual defects. The broadening of the 444 peak is

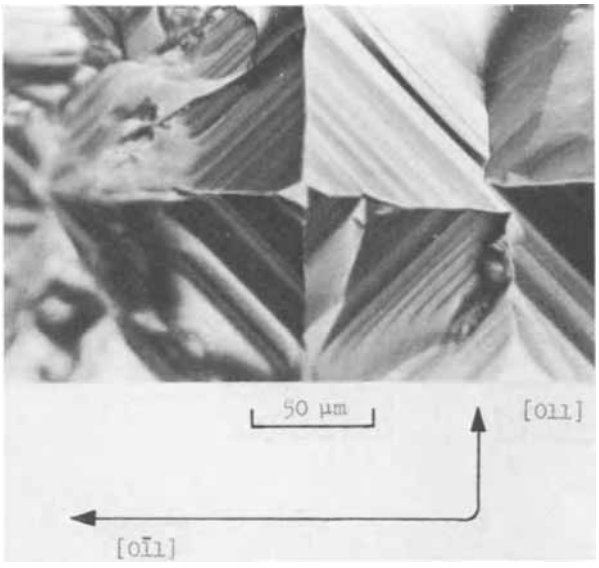

Fig. 17. Pyramidal growth bound by {710} and {15,1,0} facets. Deposition at 0.5 mA/cm². Nomarski interference contrast.

barely noticeable when Borrmann topographs show the presence of a substantial number of defects. Topography is extremely sensitive in detecting dislocations as well as small loops or point defect clusters having dimensions down to few μm. However, in the restricted case of a fairly flat and well-oriented surface, etch-pit observations have shown a density of defects of the order of 10^5 to 10^6 per cm² in crystals which appeared nearly perfect if examined by x-ray methods. Analogous results have been obtained in the case of copper specimens irradiated with fast neutrons (26); this leads to the conclusion that the defects detected here as etch-pits are mostly point defect clusters or very small dislocation loops.

In the rare instances where a dislocation line could be seen continuing in the deposit, the image in the topograph exhibited less contrast than in the substrate; this cannot be easily understood, since no change in the Burgers vector of the dislocation can be expected. This observation has to be left for the moment unexplained. It is, however, interesting that the faint lines extending from the dislocations in the deposit tend to be more or less perpendicular to the surface. This is in contrast with the observations in the electrolytic growth of silver (27), where it was reported that most dislocations tended to grow along <110>.

Among the factors affecting the perfection of the deposits, the defect density in the substrate does not seem to be as important as the presence of impurities in solution or the orientation of the surface; for misorientations of less than 1° from {111}, a substrate with a dislocation density up to about $5 \cdot 10^4$/cm² would contribute very little to Bragg peak broadening (28) or etch-pit density, compared with defects generated during deposition. As the deposit shown in Fig. 4 seems to indicate, however, the lowest defect density in the deposit might be achieved for misorientations in the range of 3° to 6° of arc.

It has been suggested that defects intersecting the surface influence the kinetics of electrodeposition, providing sources of steps (29). The present observations show that about 10^6 defects per square cm, as detected by etch-pits, should be expected on a growing {111} surface. When the misorientation is higher than 1° to 1°30′, that is when the step density $d \geqq 10^6$/cm, the surface appearance changes drastically, and the regularity of the step arrays suggests that steps due to misorientation are sufficient to maintain the current density. Since there is no indication that local current density is much higher than the average value, a step velocity between 10^{-6} and $2 \cdot 10^{-6}$ cm/sec can be deduced from the formula

$$v = \frac{i V_m}{zFdh}$$

where i is the current density, $V_m = 7.11$ cm³/mole is the molar volume, $z = 2$ is the charge, **F** is the Faraday constant, and $h = 2.09 \cdot 10^{-8}$ cm is the height of a step on a {111} plane. On the surfaces close to zero average misorientation such as those shown in Fig. 2 and 6, it is difficult to estimate step density; however, by measuring the slope of the hillocks a step density of the order of 10^5/cm can be deduced. Under the conservative assumption that local current density can be as low as 0.3 mA/cm², a step velocity of the order of $5 \cdot 10^{-6}$ cm/sec can be calculated. From studies on the interaction between random nucleation and step motion (30), the nucleation rate R_n which would insure a current density of about 0.3 mA/cm² on a perfect {111} is given by

$$R_n = \frac{vd^3}{2}$$

resulting in a value of the order of $2 \cdot 10^9$ nucleations/cm² sec. It is therefore unlikely that nucleation occurs only at defect sites; with a defect density of the order of 10^6/cm², about 10^3 close-packed layers per second would be generated at the same place, giving a vertical growth rate of $2 \cdot 10^5$ cm/sec. Since the horizontal rate v is smaller, very steep hillocks should be observed. On the contrary, even when a system of defects is capable of enhancing growth so that a large pyramid results (Fig. 11) the slopes measured never exceed 2°. Most of the nucleations therefore occur randomly, and relatively few result in extended defect formation. The evidence indicates that defects in electrodeposited copper are a consequence of the growth process rather than its cause.

From these considerations one would conclude that the range of conditions in which defect density in the substrate can influence the kinetics may be very limited; also the dependence of the reaction rate on misorientation postulated by the classical treatment of electrocrystallization kinetics (31) might be difficult to observe. Nevertheless, defects generated during deposition could influence anodic dissolution; it is interesting to remember that differences in anodic overvoltage between electrodeposited and grown from the melt material have been observed both in silver (32) and copper (33, 34). Also, isolated point defects would not have been detected in the present investigation, and their influence on the kinetics is unknown.

The principal mechanism for the formation of the defect clusters which can be detected by Borrmann topography seems to be interaction between steps meeting and annihilating; accordingly, higher defect density is found where the orientation is so near to a close-packed plane that new steps have to be generated by nucleation, moving then in every direction. Similarly, on slightly misoriented areas multi-atomic steps are sometimes pinned so that step pile-up occurs at one point. The steps then bend and bypass the obstacle, and so meet and annihilate locally. In these points both x-ray topographs and etching techniques show high defect concentration. On the other hand when the misorientation is larger than a few degrees, the chances of interaction between the moving multiatomic steps are high because of the small spacing, and defect concentration tends to increase again.

As comparison between Fig. 4 and 5 shows, the areas containing a high defect density do not continue indefinitely in the deposit and can be buried by a layer of more perfect crystal. This also shows that no long dislocation lines tend to be formed. The complexity of the situation and of the defects formed by deposition is further illustrated by Fig. 10 and 11; even in the case of well developed hillocks, the defect found in their center is not simply one or a few dislocation lines, but

a strain center giving an image several tens of μm in diameter.

Examination of the deposits of unsatisfactory perfection indicates also that hindered motion of steps on the {111} surface is responsible for the formation of defects, many of which are found in long lines where the steps had been blocked. The piling up of the steps is responsible for the development of {210} facets. There is evidence of overgrowth, presumably at the bottom of pits, leaving cavities and giving rise to considerable strains as Fig. 13 shows; prismatic loops are evidently punched out from these strain centers.

The observations about the crystal habit of copper are in general agreement with the findings of other workers (1, 35), although most previous depositions had been carried out at higher current density; the main differences are that in the present work a more pronounced tendency to form {210} facets was found and that {100} was never observed in d-c deposits. On this last point it is not clear, however, if the difference is due to different deposition conditions or if the measurement of the orientations was carried out in previous work carefully enough to distinguish between facets differing by a few degrees. Orientations similar to those observed here have been reported previously for both anodic attack and cathodic deposition in chloride solutions (33, 36).

Since convex crystals tend to be bound in growth by slowly growing faces, the {110} orientation has no tendency to develop because growth in this direction is fast, as shown by x-ray (11) and electron microscope observation (12) of the texture of polycrystalline deposits. Also exchange current densities on {110} have been found to be higher than on other close-packed orientations (7).

In the present work, periodic current reversal has not proved to be helpful in growing more perfect crystals. However, preliminary results seem to show that it can influence crystal habit; for instance, well-developed and smooth {100} facets have been produced by low frequency rectangular pulses. The method could, therefore, be interesting for developing surfaces of various orientations for the purpose of making kinetic measurements.

Acknowledgments

The authors wish to thank F. W. Young, Jr. and B. C. Larson for many helpful suggestions, and F. A. Sherrill for taking the x-ray topographs.

Manuscript submitted Dec. 18, 1970; revised manuscript received *ca.* March 15, 1971.

Any discussion of this paper will appear in a Discussion Section to be published in the June 1972 JOURNAL.

REFERENCES

1. G. Tammann and M. Straumanis, *Z. Anorg. Chem.*, **175**, 131 (1928); H. Leidheiser and A. T. Gwathmey, *Trans. Electrochem. Soc.*, **91**, 95 (1947).
2. G. I. Finch, H. Wilman, and L. Yang, *Discussions Faraday Soc.*, **1**, 144 (1947); H. Seiter and H. Fischer, *Z. Elektrochem.*, **63**, 249 (1959).
3. H. J. Pick, G. G. Storey and T. B. Vaughan, *Electrochim. Acta*, **2**, 165 (1960).
4. T. B. Vaughan and H. J. Pick, *ibid.*, **2**, 179 (1960); S. C. Barnes, G. G. Storey, and H. J. Pick, *ibid.*, **2**, 195 (1960); N. A. Economou and D. Trivich, *ibid.*, **3**, 292 (1961).
5. I. Giron and F. Ogburn, *This Journal*, **108**, 842 (1961).
6. S. C. Barnes, *Electrochim. Acta*, **5**, 79 (1961); A. Damjanovic, M. Paunovic, and J. O'M. Bockris, *J. Electroanal. Chem.*, **9**, 93 (1965); L. Peraldo Bicelli and G. Poli, *Electrochim. Acta*, **11**, 289 (1966).
7. A. Damjanovic, T. H. V. Setty, and J. O'M. Bockris, *This Journal*, **113**, 429 (1966); T. Hayashi, S. Higuchi, H. Kinoshita, and T. Ishida, *J. Electrochem. Soc. Japan*, **37**, 64 (1968).
8. D. W. Hardesty, *This Journal*, **117**, 168 (1970).
9. R. Glocker and E. Kaupp, *Z. Physik*, **24**, 121 (1924); H. Fischer, H. Matschke, and F. Pawlek, *Z. Elektrochem.*, **56**, 477 (1950); H. I. Matthews, T. deS. Mutucumarana, and H. Wilman, *Acta Cryst.*, **16**, 636 (1960); N. A. Economou, H. Fischer, and D. Trivich, *Electrochim. Acta*, **2**, 207 (1960); G. G. Storey and S. C. Barnes, *Trans. Inst. Metal Finishing*, **37**, 11 (1960).
10. S. Steinemann and H. E. Hintermann, *Schweiz. Arch. Angew. Wiss. Tech.*, **26**, 202 (1960); B. C. Banerjee and P. L. Walker, *This Journal*, **108**, 449 (1961).
11. F. Ogburn and C. Newton, *This Journal*, **110**, 1148 (1963).
12. H. Schlötterer, *Metalloberflaeche*, **18**, 33 (1964).
13. E. M. Hofer, L. F. Chollet, and H. E. Hintermann, *This Journal*, **112**, 1145 (1965).
14. T. B. Vaughan, *Electrochim. Acta*, **4**, 72 (1961).
15. D. Shanefield and P. E. Lighty, *This Journal*, **110**, 973 (1963).
16. P. E. Lighty, D. Shanefield, S. Weissmann, and A. Shrier, *J. Appl. Phys.*, **34**, 2233 (1963); J. J. O'Connor, B. Rubin, and R. Spector, AFCRL-66-538. Office of Aerospace Research (1965).
17. T. G. Stoebe, F. H. Hammad, and M. L. Rudee, *Electrochim. Acta*, **9**, 925 (1964); K. R. Lawless and L. B. Garmon, 5th Int. Congress Electr. Micr. Paper DD-7 (1962); K. R. Lawless, *J. Vacuum Sci. Technol.*, **2**, 24 (1965).
18. F. W. Young, Jr., F. A. Sherrill, and M. C. Wittels, *J. Appl. Phys.*, **36**, 2225 (1965).
19. F. W. Young, Jr., T. O. Baldwin, A. E. Merlini, and F. A. Sherrill, "Advances in X-Ray Analysis," Vol. 9, p. 1, Academic Press, 1966.
20. F. W. Young, Jr., "Crystal Growth," H. S. Peiser, Editor, p. 789, Oxford University Press, 1967.
21. U. Bertocci, C. Bertocci, and F. W. Young, Jr., *J. Appl. Phys.*, **40**, 1674 (1969).
22. L. H. Jenkins and M-F. Chung, *Surface Sci.*, **24**, 125 (1971).
23. M. C. Wittels, F. A. Sherrill, and F. W. Young, Jr., *Phys. Letters*, **5**, 183 (1963).
24. F. W. Young, Jr., *J. Appl. Phys.*, **32**, 192 (1961); U. Bertocci, L. D. Hulett, and L. H. Jenkins, *This Journal*, **110**, 1190 (1963).
25. U. Bertocci and T. S. Noggle, *Rev. Sci. Instr.*, **37**, 1750 (1966).
26. F. W. Young, Jr., *J. Appl. Phys.*, **33**, 749 (1962).
27. R. Kaischew and E. Budevski, *Contemp. Phys.*, **8**, 489 (1967).
28 T. O. Baldwin, F. A. Sherrill, and F. W. Young, Jr., *J. Appl. Phys.*, **39**, 1541 (1968); K. J. Bachmann, T. O. Baldwin, and F. W. Young, Jr., *ibid.*, **41**, 4783 (1970).
29. W. K. Burton, H. Cabrera, and F. C. Frank, *Phil. Trans. Roy. Soc. London Ser. A.*, **243**, 299 (1951); D. A. Vermilyea, *J. Chem. Phys.*, **25**, 1254 (1956).
30. U. Bertocci, *Surface Sci.*, **15**, 286 (1969).
31. W. Lorenz, *Z. Electrochem.*, **57**, 382 (1953); *Z. Naturforsch.*, **9A**, 299 (1954).
32. W. M. Krebs and D. K. Roe, *This Journal*, **114**, 892 (1967).
33. U. Bertocci, *ibid.*, **113**, 604 (1966).
34. L. H. Jenkins, *ibid.*, **117**, 630 (1970).
35. E. Budevski and V. Bostanov, *Izv. Inst. Fiziokhim. Bulgar. Akad. Nauk*, **2**, 65 (1962).
36. T. Erdey-Gruz and E. Frankl, *Z. Physik. Chem.*, **178A**, 266 (1937).

Laplace Plane Analysis of the Impedance of Faradaic and Nonfaradaic Electrode Processes

Arthur A. Pilla*

ESB Incorporated, Research Center, Yardley, Pennsylvania 19067

ABSTRACT

A unified theory of the impedance of electrode processes is presented. It is shown that the expression of impedance in terms of the Laplace variable, s, permits all cases of interest to be treated. The basic equations developed allow a finite rate for both charge transfer and adsorption, as well as mass transport, in a system of uniform potential distribution. The question of coupling of faradic and charging currents is treated in detail.

The use of impedance as a characteristic function of electrochemical systems has long been recognized (1, 2). It was recently pointed out (3) that its expression in terms of the Laplace transform variable, s, enables impedance to be considered as a real ($s = \sigma$) or complex ($s = j\omega$) function allowing both less ambiguity in mechanism detection and an increased frequency range to be achieved.

The necessary quantities can be obtained by starting with the following general relation

$$i_T(s) = i_f(s) + i_c(s) \qquad [1]$$

where $i_f(s)$ is the faradaic current (*i.e.*, that which involves the passage of charge across the interface) and $i_c(s)$ is the interfacial charging current (*i.e.*, that which does not require the passage of charge across the interface). Equation [1] can be misleading, as has recently been pointed out (4-11), since both partial currents may contain double-layer and faradaic parameters if strong reactant adsorption is present. However, their expression in terms of s to develop impedance clearly shows how coupling may or may not exist and allows some interesting and usable limiting cases to be determined, which heretofore do not appear to have been described.

General Theory

To illustrate this approach, it will be assumed that only the oxidized species need be taken into account (*e.g.*, metal-metal ion electrode). Extension to any number of electroactive species is a trivial matter.

The quantities $i_f(s)$ and $i_c(s)$ in [1] must first be written in explicit form. For the former, the most general approach would be to express it in terms of the appropriate independent variables. Since the treatment below will assume finite kinetics for both charge transfer and adsorption, it is rigorous to pick both C_0 and Γ_0 as well as E for these variables. However, since the (linearized) rate expression given below for Γ_0 allows its dependence on C_0 (as well as E) to be established, it is sufficient to use only C_0 and E to describe $i_f(s)$. (Note that this does not require C_0 and Γ_0 to be in equilibrium.) It is to be remembered, nevertheless, that the variation of C_0 at the interface can in fact be obtained only if both charge transfer and adsorption (finite or otherwise) are taken into account. For the purposes of this study, the standard linearized rate expression is employed realizing, however, that the most general form for $i_f(s)$ does in fact consist in its expansion involving the well-known partial derivative coefficients. Note that, in the latter case, the parameters are lumped in such a way that the frequency variation of C_0 is no longer separable from either the dependence of i_f on E (*i.e.*, charge transfer) or on C_0. In order to express $i_c(s)$ [$=s\,q(s)$] in an explicit manner, it is convenient (12) to consider it in terms of Γ_0 and E. This takes into account the fact that q may vary not only with E, as in classical systems, but also with Γ_0 when specific adsorption is present. Of course, Γ_0 is related to C_0 *via* the (linearized) rate expression given below.

Using the above considerations, [1] can now be written

$$i_T(s) = i_o[-\Delta C_0(0, s)] + n\mathbf{F}i_o\eta(s)/RT + q_{\Gamma_0}s\Delta\Gamma_0(s) + q_E s\eta(s) \qquad [2]$$

where

$$q_{\Gamma_0} = (\partial q/\partial\Gamma_0)_E \qquad [2a]$$

$$q_E = (\partial q/\partial E)_{C_0} \qquad [2b]$$

$$\Delta C_0(0, s) = (C_0(0, s) - C_0)/C_0 \qquad [2c]$$

$$\Delta\Gamma_0(s) = (\Gamma_0(s) - \Gamma_0)/\Gamma_0 \qquad [2d]$$

and $\Gamma_0(s)$ and $C_0(0,s)$ are, respectively, the frequency variation of the surface excess and interfacial concentration of the reacting species, and the other terms have their usual meaning.

Equation [2] can be solved to obtain an expression for the impedance of the system, provided both $\Delta\Gamma_0(s)$ and $\Delta C_0(0,s)$ are known. These quantities are related by allowing finite adsorption kinetics given by (3, 12)

$$\Delta\Gamma_0(s) = (v_0/s\Gamma_0)\,[\Delta C_0(0,s) - \Delta\Gamma_0(s) + a\eta(s)] \qquad [3]$$

where v_0 is the exchange adsorption rate and a is a coefficient representing the potential dependence of Γ_0. Note that [3] does not presuppose an *a priori* form of adsorption kinetics, merely that any kinetic expression can be linearized. Fick's second law can now be employed to obtain $\Delta C_0(0,s)$. For this, the remaining necessary equation (boundary condition) can be written as

$$s\Gamma_0\Delta\Gamma_0(s) = \sqrt{D_0}C_0\sqrt{s}\,\Delta C_0(0,s) + i_f(s)/n\mathbf{F} \qquad [4]$$

which simply states, as is well known (5), that the surface excess of the reacting species can vary either by mass transport (in this case semi-infinite linear diffusion), or by charge transfer, or by both.

Utilizing [2], [3], and [4], the following is obtained for the generalized faradaic [$Z_F(s)$] and charging [$Z_C(s)$] impedance

$$Z_F(s) = \frac{RT}{n\mathbf{F}i_o}\,\frac{b\sqrt{D_0}C_0\sqrt{s} + b\Gamma_0 s/(1 + \Gamma_0\, s/v_0)}{b\sqrt{D_0}C_0\sqrt{s} + (b\Gamma_0 + an\mathbf{F}\Gamma_0)\,s/(1 + \Gamma_0\, s/v_0)} + \frac{1}{b\sqrt{D_0}C_0\sqrt{s} + (b\Gamma_0 + an\mathbf{F}\Gamma_0)\,s/(1 + \Gamma_0\, s/v_0)} \qquad [5]$$

in which $b = n^2\mathbf{F}^2/RT$, and

* Electrochemical Society Active Member.

Key words: adsorption, double layer, electrode kinetics, frequency domain.

$$Y_C(s) = 1/Z_C(s) =$$

$$\frac{q_{\Gamma_0} s[nFi_o/RT + a(nF\sqrt{D_0}C_0\sqrt{s} + i_o)]}{(1 + \Gamma_0 s/v_0)(nF\sqrt{D_0}C\sqrt{s} + nF\Gamma_0 s(1 + \Gamma_0 s/v_0) + i_o) + q_E s} \quad [6]$$

Both Z_F and Z_C are in parallel and do not readily lend themselves to interpretation *via* aperiodic equivalent circuits, although the number of parameters is not too great for numerical analysis to be attempted. Some general observations can, however, be made as is shown below.

Negligible Adsorption Potential Dependence

Inspection of [5] shows that as $a \to 0$ (*i.e.*, as the potential dependence of adsorption becomes negligible), then [5] can be written

$$Z_F(s) = \frac{RT}{nFi_o} + \frac{1}{b\sqrt{D_0}C_0\sqrt{s} + b\Gamma_0 s/(1 + \Gamma_0 s/v_0)} \quad [7]$$

In addition, as $a \to 0$, $q_{\Gamma_0} \to 0$ as thermodynamics requires (13) for the conditions under which [3] is valid, and [6] reduces to

$$Z_C(s) = 1/q_E s \quad [8]$$

Comparison of [5] and [6] with [7] and [8] shows that in the latter cases Z_F depends only on charge transferred across the interface (*i.e.*, represents solely a faradaic process), while Z_C does not require faradaic current. In contrast, the former cases show how the faradaic and charging processes are intercoupled.

Use of [7] and [8] allows the aperiodic equivalent circuit shown in Fig. 1 to be constructed where R_e is the electrolyte resistance and

$$C_d = (\partial q/\partial E)_{\Gamma_0} \quad [9]$$

$$R_t = RT/nFi_o \quad [10]$$

$$Z_D = 1/b\sqrt{D_0}C_0\sqrt{s} \quad [11]$$

$$C_a = b\Gamma_0 \quad [12]$$

$$R_a = 1/b\,v_0 \quad [13]$$

This case differs from classical Randles-Ershler (1, 2) behavior by the presence of the adsorption terms R_a and C_a. In fact, if R_a and C_a are not present (*i.e.*, no reactant adsorption), then it can readily be seen how classical behavior is obtained, since in this case both $a = 0$ and $\Gamma_0 = 0$.

Equations [5] and [6] can also be used to establish the conditions for infinitely fast adsorption kinetics,

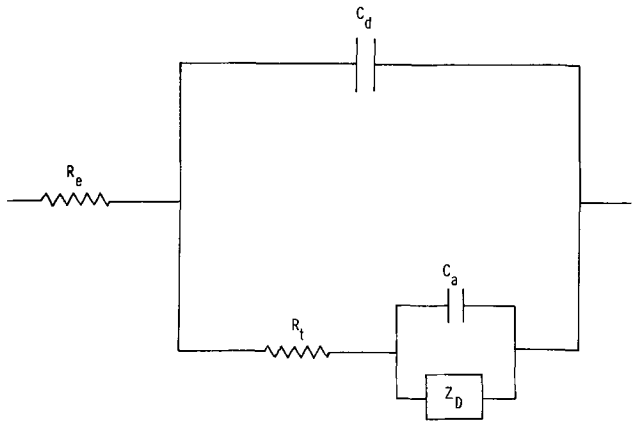

Fig. 2. As Fig. 1, except for infinite adsorption kinetics

since $v_0 \to \infty$ and $R_a \to 0$. If, in addition, $a \to 0$, then the aperiodic equivalent circuit shown in Fig. 2 may be employed. This is exactly the same result which would have been obtained if a kinetic expression for adsorption (Eq. [3]) had not been employed, but rather the expansion (6) for $d\Gamma_0/dt$, since Γ_0 is related to $(\partial\Gamma_0/\partial C_0)_E$ (*i.e.*, an isotherm) and a is similarly related to $(\partial\Gamma_0/\partial E)_{C_0}$. It can thus be seen that this is merely a special case of the more general approach given above, as expected.

Infinite Charge Transfer Kinetics

The case of infinitely fast charge transfer (*i.e.*, $i_o \to \infty$) can now be considered. Inspection of [5] and [6] shows that, when this limit is set, then

$$Z_F(s)_{i_o \to \infty} = \frac{1}{b\sqrt{D_0}C_0\sqrt{s} + (b\Gamma_0 + anF\Gamma_0)s/(1 + \Gamma_0 s/v_0)} \quad [14]$$

and

$$Z_C(s)_{i_o \to \infty} = \frac{1}{\frac{q_{\Gamma_0}(nF/RT + a)s}{1 + \Gamma_0 s/v_0} + q_E s} \quad [15]$$

which results in the aperiodic equivalent circuit shown in Fig. 3 where

$$C_a' = q_{\Gamma_0}(nF/RT + a) \quad [16]$$

and

$$R_a' = \Gamma_0/v_0\, q_{\Gamma_0}(nF/RT + a) \quad [17]$$

Diagnostic analysis is possible particularly if Z_D and C_d can be isolated by study over a wide frequency range, and the two remaining time constants are sufficiently different. It can easily be seen that, if adsorption is infinitely fast, $R_a \to 0$ and $R_a' \to 0$ and the cir-

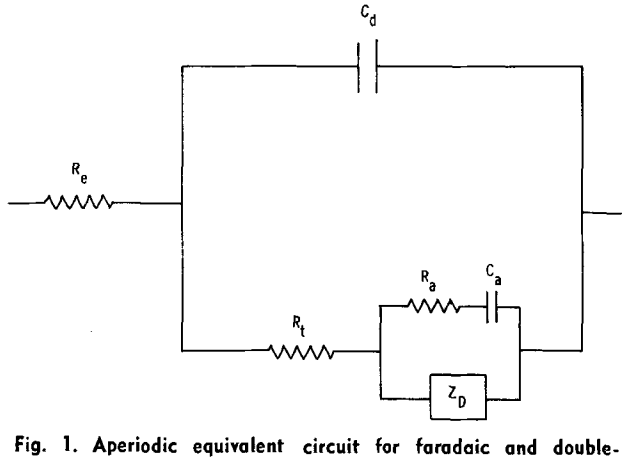

Fig. 1. Aperiodic equivalent circuit for faradaic and double-layer processes in the case of finite adsorption and charge transfer kinetics (potential dependence of adsorption negligible).

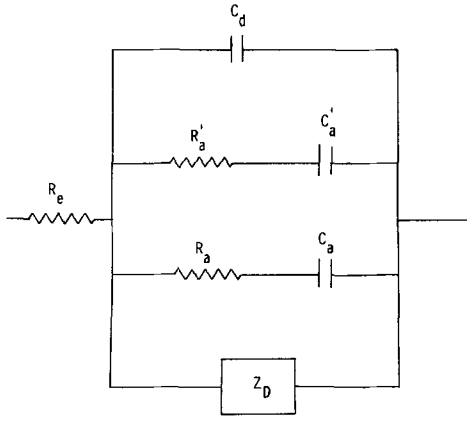

Fig. 3. Aperiodic equivalent circuit for infinite charge transfer and finite adsorption kinetics (potential dependence of adsorption not negligible).

cuit reduces to one which looks classical with the parallel capacitance composed of C_d, C_a, and C_a'.

Negligible Charge Transfer

The case of infinitely slow charge transfer $i_o \rightarrow 0$ can now be considered. With this restriction, $Z_F(s) \rightarrow \infty$ as can be seen by inspection of [5]. Equation [6], however, now becomes

$$Y_C(s) = 1/Z_C(s) = \frac{q_{\Gamma_0} s (an\mathbf{F}\sqrt{\bar{D}_0 C_0 \sqrt{s}})}{(1 + \Gamma_0 s/v_0)(n\mathbf{F}\sqrt{\bar{D}_0 C_0}\sqrt{s} + n\mathbf{F}\Gamma_0 s/(1 + \Gamma_0 s/v_0) + q_E(s)} \quad [18]$$

for which the aperiodic equivalent circuit is shown in Fig. 4, where

$$Z_D' = \Gamma_0/q_{\Gamma_0} an\mathbf{F}\sqrt{\bar{D}_0 C_0} \quad [19]$$

$$R_a'' = \Gamma_0/q_{\Gamma_0} av_0 \quad [20]$$

and

$$C_a'' = 1/q_{\Gamma_0} a \quad [21]$$

This is, of course, the well-known result for the adsorption of electroinactive species with a slow adsorption step (12, 14). Again, when adsorption is infinitely fast, $v_0 \rightarrow \infty$ and $R_a'' \rightarrow 0$ and the circuit reduces to that originally proposed for this situation (15).

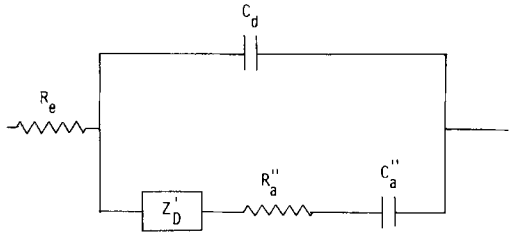

Fig. 4. Aperiodic equivalent circuit for adsorption of electroinactive species with slow adsorption step.

Negligible Mass Transport

Finally, it is of interest to consider the case for which mass transport is negligible (high reactant concentration). For this

$$Z_F(s) = \frac{RT}{n\mathbf{F}i_o} + \frac{1}{(b\Gamma_0 + an\mathbf{F}\Gamma_0)s/(1 + \Gamma_0 s/v_0)} \quad [22]$$

and

$$Z_C(s) = \frac{1}{q_{\Gamma_0} as/(1 + \Gamma_0 s/v_0) + q_E s} \quad [23]$$

Inspection of [22] and [23] shows that they can be represented by the aperiodic equivalent circuit given in Fig. 5 which shows adsorption with slow kinetics involved in both the faradaic and charging processes as expected. Similar to the above cases, if $a \rightarrow 0$, then the circuit becomes that given in Fig. 6 where R_T may be equal to R_t, R_a, or $R_t + R_a$ depending on the value of v_0. A circuit of this type has in fact been found for the Pt/1M H^+ system (16, 17) where diffusion is negligible.

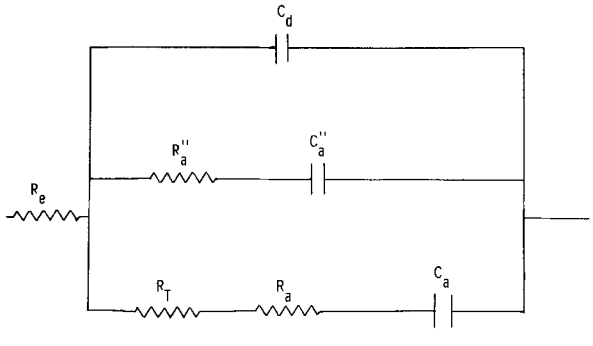

Fig. 5. Aperiodic equivalent circuit for finite charge transfer and adsorption kinetics and negligible diffusion (potential dependence of adsorption not negligible).

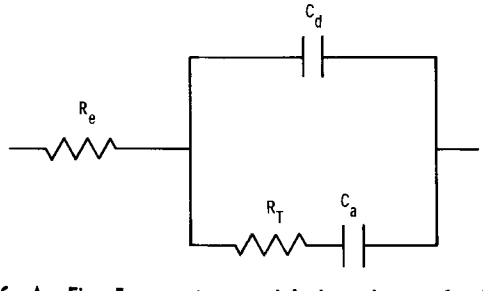

Fig. 6. As Fig. 5, except potential dependence of adsorption negligible.

Conclusion

In summary, the expression of impedance in terms of s starting with the general case allowing both finite charge transfer and adsorption, as well as mass transport in a system of uniform potential distribution, has been performed. The basic equations developed allow essentially all cases of interest in this general scheme to be treated. In particular, the coupling of faradaic and charging currents is clearly shown, as well as the manner in which relatively simple behavior can be obtained when the potential dependence of adsorption, which is the essential coupling parameter, is negligible.

Manuscript submitted Feb. 18, 1971; revised manuscript received *ca.* Mar. 26, 1971.

Any discussion of this paper will appear in a Discussion Section to be published in the June 1972 JOURNAL.

REFERENCES

1. J. E. B. Randles, *Discussions Faraday Soc.*, **1**, 11 (1947).
2. B. V. Ershler, *ibid.*, **1**, 269 (1947).
3. A. A. Pilla, *This Journal*, **117**, 467 (1970).
4. P. Delahay, *J. Phys. Chem.*, **70**, 2373 (1966).
5. K. Holub, G. Tessari, and P. Delahay, *ibid.*, **71**, 2612 (1967).
6. P. Delahay and K. Holub, *J. Electroanal. Chem.*, **16**, 131 (1968).
7. R. Parsons, in "Advances in Electrochemistry and Electrochemical Engineering," Vol. 7, P. Delahay and C. Tobias, Editors, Interscience, New York (1970).
8. M. Sluijters-Rehbach and J. H. Sluijters, in "Electroanalytical Chemistry," Vol. 5, A. J. Bard, Editor, Marcel-Dekker, New York (1970).
9. R. deLevie and L. Pospisil, *J. Electroanal. Chem.*, **22**, 277 (1969).
10. W. H. Reinmuth, *Anal. Chem.*, **40**, 185 R (1968).
11. F. Anson, *Ann. Rev. Phys. Chem.*, **19**, 83 (1968).
12. W. Lorenz and F. Mockel, *Z. Elektrochem.*, **60**, 507 (1956).
13. D. M. Mohilner, in "Electroanalytical Chemistry," Vol. 1, p. 288, A. J. Bard, Editor, Marcel-Dekker, New York (1966).
14. R. D. Armstrong, W. P. Race, and H. R. Thirsk, *J. Electroanal. Chem.*, **16**, 517 (1968).
15. A. N. Frumkin and V. I. Melik-Gaikazyan, *Dokl. Akad. Nauk SSSR*, **77**, 855 (1951).
16. A. A. Pilla, J. H. Christopulos, and G. J. DiMasi, Paper 235 presented at Electrochem. Soc. Meeting, New York, May 4-9, 1969.
17. P. Dolin, B. V. Ershler, and A. N. Frunkin, *Acta* Physicochim, URSS, **13**, 779, 793 (1940).

The Electrode Potential of Zinc Amalgam in Alkaline Zincate Solutions

D. P. Boden,* R. B. Wylie, and V. J. Spera*

ESB Incorporated, Research Center, Yardley, Pennsylvania 19067

ABSTRACT

The electrode potential of zinc amalgams has been measured in potassium hydroxide solutions containing dissolved zincate. Curvature in the Nernst plots was observed at high zincate concentrations in agreement with the results of other workers. The curvature is explained as being due to the dependence of the hydroxyl and zincate ion activity on concentration in strong potassium hydroxide solutions. The data yield a value of −1.205V (*vs.* SHE) for the standard potential of the zinc, zincate ion electrode (I.U.P.A.C.—Stockholm convention) and −205.86 kcal for the free energy of formation of the zincate ion at 25°C.

The potential of the zinc electrode in alkaline solutions has been studied previously but there is still no general agreement as to the nature of the ionic species to which the electrode is reversible.

Bodländer (1) and Kunschert (2) measured the electrode potential of cells containing solutions of zinc in sodium hydroxide. Their data were interpreted to show that the zinc existed as the $Zn(OH)_4^{2-}$ ion in strongly alkaline solutions. Later, Dirkse (3) reported measurements on cells of the type

$$Zn(s)/KOH + ZnO/KOH, H_2, Pt \qquad [A]$$

It was concluded that the species existing in solution was the $Zn(OH)_4^{2-}$ ion and that water participated in the reaction to form an aquotetrahydroxy zincate ion. This conclusion was based on the observation that plots of E *vs.* log $a(OH^-)$ at constant zinc concentration showed curvature at high hydroxyl ion concentrations. Recently, Hampson, Herdman, and Taylor (4) studied the zinc amalgam electrode in KOH solutions containing zincate ion and confirmed the curvature in the logarithmic plots reported by Dirkse. They found that the curvature could be reduced by allowing for the participation of two to four water molecules in the reaction but, even then, a completely linear relationship was not obtained. It was suggested that the electroactive zinc species in solution was the six coordinated diaquotetrahydroxy zincate ion. It was also found that the electrode potential was insensitive to the zincate ion concentration from 0.2 to 1.0*M* (molar), the highest concentration studied. This led them to propose that, at high zincate concentrations, the zinc species becomes $[ZnO_2aq]^{2-}$.

Raman and infrared spectral studies (5) of solutions of zinc oxide in potassium hydroxide indicate that the predominant species is $Zn(OH)_4^{2-}$ in agreement with studies using proton magnetic resonance (6). However, Okinada (7) and Jost (8) do not rule out the presence of $Zn(OH)_3^-$ in dilute solutions.

In this work, the electrode potential of zinc amalgam electrodes has been measured as a function of the hydroxyl ion and zincate ion concentrations.

An attempt has been made to relate the potential dependence to the change in activity of the electroactive species as the concentration is changed.

Theory

When zinc oxide is dissolved in KOH solution, it is possible for the following solute species to be present: Zn^{++}, $Zn(OH)^+$, $Zn(OH)_2$, $Zn(OH)_3^-$, $Zn(OH)_4^=$ ----- $Zn(OH)_n^{(n-2)-}$.

These are formed according to the general equation

$$Zn^{++} + n\,OH^- = Zn(OH)_n^{(n-2)-} \qquad [1a]$$

$$\beta_n = [Zn(OH)_n^{(n-2)-}]/[Zn^{++}][OH^-]^n \qquad [1b]$$

Assuming that no complexes higher than $Zn(OH)_4^=$ are present, the mass balances are given by ($N = 4$)

$$C(Zn) \Big| = \sum_{n=0}^{N} \beta_n [Zn^{++}][OH^-]^n \qquad [2]$$

and

$$C(OH^-) \Big| = [OH^-] + \sum_{n=0}^{N} n\,\beta_n [Zn^{++}][OH^-]^n \qquad [3]$$

where $C(Zn)$ and $C(OH^-)$ are the analytical concentrations of zinc and hydroxyl ion, respectively, and $[OH^-]$ is the equilibrium concentration.

The equilibrium constants for zinc hydroxy complex formation are not known at high ionic strengths; therefore, the concentrations of the various zinc species cannot be calculated with a high degree of certainty. Approximate values can be obtained, however, by use of stepwise complex formation equilibrium constants at zero ionic strength. Butler (9) gives the constants for the stepwise complex formation equilibria of zinc hydroxy complexes

$$[Zn(OH)^+]/[Zn^{++}][OH^-] \qquad K_1 = 10^{4.15} \qquad [4]$$

$$[Zn(OH)_2]/[Zn(OH)^+][OH^-] \qquad K_2 = 10^{6.0} \qquad [5]$$

$$[Zn(OH)_3^-]/[Zn(OH)_2][OH^-] \qquad K_3 = 10^{4.1} \qquad [6]$$

$$[Zn(OH)_4^=]/[Zn(OH)_3^-][OH^-] \qquad K_4 = 10^{1.26} \qquad [7]$$

Therefore, the cumulative complex formation constants have the values $\beta_1 = 10^{4.15}$, $\beta_2 = 10^{10.15}$, $\beta_3 = 10^{14.25}$, $\beta_4 = 10^{15.51}$.

Assume, as a first approximation, that only OH^-, $Zn(OH)_3^-$, and $Zn(OH)_4^=$ are present to any appreciable extent; then

$$C(Zn) = \beta_3[Zn^{++}][OH^-]^3 + \beta_4[Zn^{++}][OH^-]^4 \qquad [8]$$

$$C(OH^-) = [OH^-] + 3\beta_3[Zn^{++}][OH^-]^3 + 4\beta_4[Zn^{++}][OH^-]^4 \qquad [9]$$

Since, in general, the concentration of $Zn(OH)_3^-$ is small compared to the concentration of $Zn(OH)_4^=$ and since the $[OH^-]$ is much larger than the concentration of zinc, Eq. [9] can be approximated by

$$C(OH^-) = [OH^-] + 4C(Zn) \qquad [10]$$

The solubility of zinc oxide in KOH has been deter-

* Electrochemical Society Active Member.

Key words: electrode potential, zinc amalgam, zincate solutions, activities, Davies equation, standard potential.

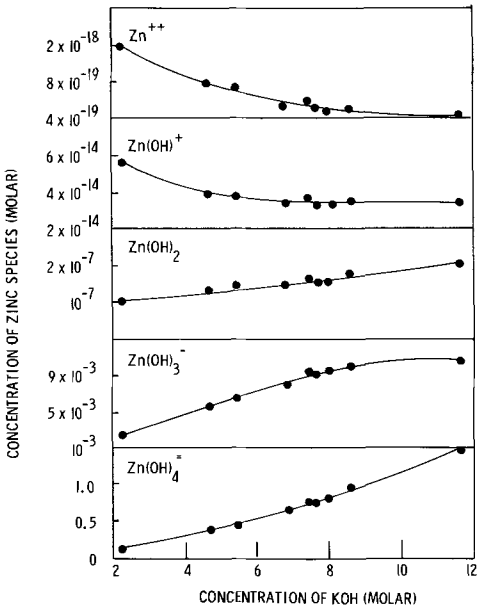

Fig. 1. Plot showing variation in concentration of various zinc hydroxy species in KOH solutions saturated with zincate.

mined (10, 11) and, therefore, it is possible to solve Eq. [8] and [10] and, by use of the mass action equilibria, obtain the concentrations of the various zinc hydroxy complexes as a function of the KOH concentration. The results are shown in Fig. 1. The only zinc species present to any appreciable extent is the $Zn(OH)_4^=$ ion. Therefore, even though the above calculations are only approximate, it was assumed that only $Zn(OH)_4^=$ is present.

In a cell of the type

$$Hg,HgO/KOH(a_1)//KOH(a_2),Zn(OH)_4^=/Zn(Hg) \quad [B]$$

the emf is given by

$$E = E^\circ(Zn) - E^\circ(HgO,Hg) - (RT/2\mathbf{F}) \ln \frac{a^4(OH^-)_2 \cdot a(Zn)}{a(Zn(OH)_4^=)} + (RT/2\mathbf{F}) \ln a^2(OH^-)_1 \quad [11]$$

Since the activity of the zinc in the amalgam and of the hydroxyl ion in the reference compartment remained constant during the experiment, Eq. [11] can be written as

$$E = E^{\circ *}(Zn) - (RT/2\mathbf{F}) \ln \left(a^4(OH^-)_2 / a\left(Zn(OH)_4^=\right) \right) \quad [12]$$

where

$$E^{\circ *}(Zn) = E^\circ(Zn) - E^\circ(HgO,Hg) - (RT/2\mathbf{F}) \ln a(Zn) + (RT/\mathbf{F}) \ln (OH^-)_1 \quad [13]$$

Therefore, a plot E *vs.* $\log \left(a^4(OH^-)_2 / a\left(Zn(OH)_4^=\right) \right)$ should be a straight line wtih a slope of 0.0295V and an intercept which can be used to obtain $E^\circ(Zn)$, provided that the activity of hydroxyl ion in the reference compartment and the activity of zinc in the amalgam are known.

Since the activity coefficients of zincate ion and hydroxyl ion in the presence of each other are not known, these were calculated from the Davies (12) equation. This equation which has the form

$$-\log \gamma_\pm = Az^+z^-[I^{1/2}/(1 + I^{1/2}) - BI] \quad [14]$$

has been successful in predicting the activity coefficients of a number of electrolytes up to fairly high concentrations. Here, A is the usual Debye-Hückel coefficient, 0.509, in aqueous solutions. I is the ionic strength, expressed in moles per liter of solution. Although this equation does not have a sound theoretical

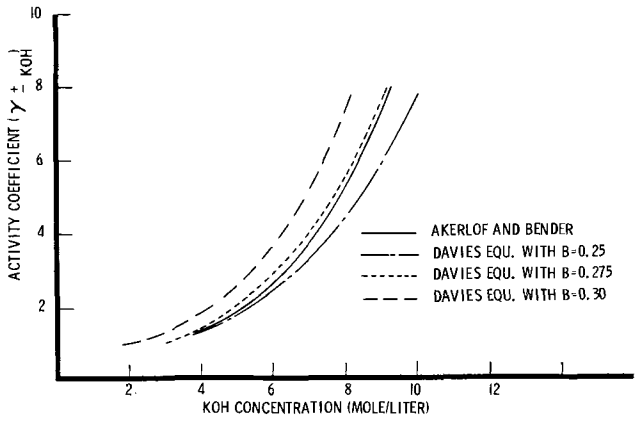

Fig. 2. Activity coefficients of concentrated KOH solutions calculated from the Davies equation with various values for *B* compared to the experimental values of Akerlof and Bender.

basis, it has been applied to a large number of electrolytes with good success. It has not been applied, however, to solutions having concentrations as high as those used in the present work. To gain some insight into the effectiveness of the equation in predicting the activity coefficients of concentrated KOH solutions, calculated activity coefficients have been compared to those determined experimentally by Akerlof and Bender (13). The results are shown in Fig. 2. In the concentration range of interest in this work, *i.e.* around 7.0M, the data of Akerlof and Bender are fitted quite well by the Davies equation with B = 0.275. It was therefore thought permissible to use this equation in calculating activity coefficients of zincate solutions in this range of ionic strengths.

Experimental

Materials.—The potassium hydroxide solutions were prepared by dissolving Fisher "Certified" reagent-grade pellets of KOH in twice-distilled water. A stock solution of 7.03M (moles KOH per liter of solution) was used for all the experiments. The zincate solution was prepared by saturating a KOH solution with zinc oxide (Baker Analyzed Reagent) so that the final concentration of free hydroxyl ion was 7.03M calculated by means of Eq. [10].

A 1% zinc amalgam was prepared by electrodeposition from a saturated zincate solution into triple-distilled, instrument-grade mercury.

Method.—The experiment was carried out in the cell shown in Fig. 3. The working electrode was 1% zinc amalgam which was placed in the working compartment of the cell. Solid zinc was not used because trouble was encountered with fluctuations in the electrode potential, caused apparently by the hydrogen generated as a result of the zinc dissolving.

The working compartment, salt bridge, and reference compartment were filled with 7.03M KOH solution and the zincate concentration was varied by adding a solution of 7.03M free KOH and 1.28M zincate from a burette. In this way, the concentration of KOH was kept constant during the experiment and only the zincate concentration was varied. The liquid junction potential due to the zincate was judged to be very small and was neglected. The reference electrode was Hg/HgO/7.03M KOH in water.

The measurements were made to ±0.01 mV using a Rubicon precision potentiometer. The test cell was immersed in a constant temperature bath controlled at 25° ± 0.1°C.

Results and Discussion

The results of a typical experiment are shown in Table I. In Fig. 4 the emf is plotted *vs.* the logarithm of the zincate ion concentration. At low concentrations, the graph is linear with a slope of 0.0275V. At higher concentrations, however, the plot shows con-

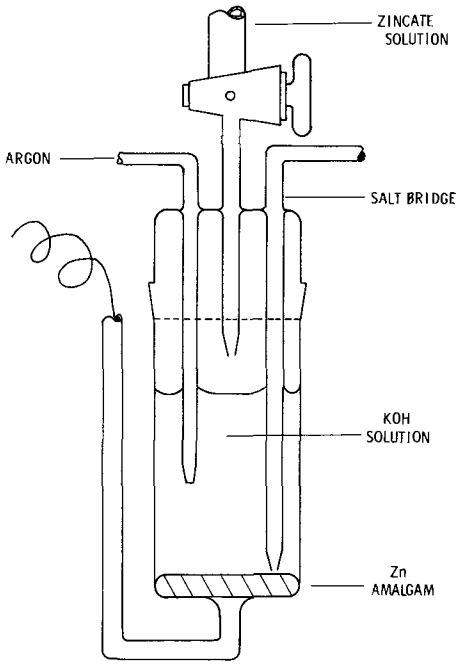

Fig. 3. Cell for emf measurements on zinc amalgam electrodes

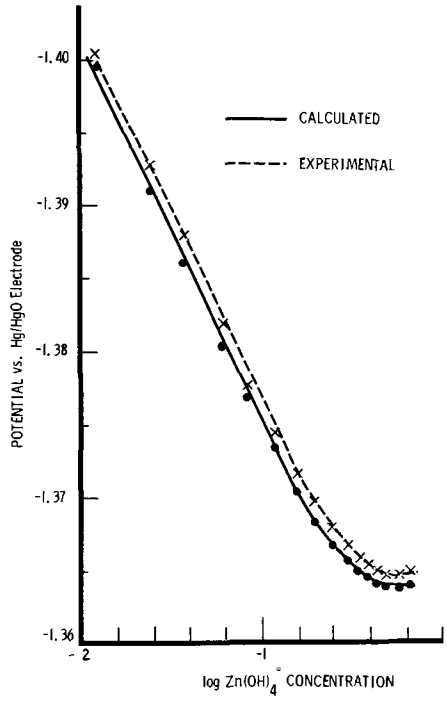

Fig. 4. Plot of zinc amalgam electrode potential vs. the logarithm of the zincate ion concentration in moles per liter: ●, calculated points (see text); ×, experimental data. Potential of Zn amalgam/zincate ion electrode in 7.03M KOH supporting electrolyte referred to Hg/HgO electrode in 7.03M KOH, at 25°C.

siderable curvature and eventually passes through a minimum. This curvature has been observed previously by Dirkse (3) and by Hampson *et al.* (4) although no minimum has been reported. It seems unlikely that the curvature in the data is caused by the presence of other hydroxy complexes apart from $Zn(OH)_4^=$ since their concentration is probably negligible. The curvature could be attributable to the participation of water in the reaction as proposed by Dirkse (3) or it could also be a consequence of the behavior of the activity coefficients of zincate and hydroxyl ion in the solution studied.

In making a plot of the emf *vs.* the logarithm of the concentration, a number of assumptions are made: first, that the activities in Eq. [12] can be replaced by concentrations and, second, that the activity of the hydroxyl ion in the working electrode compartment is constant. The first of these assumptions is probably not too bad at low zincate concentrations but it cannot be expected to hold over the entire concentration range studied. It is also incorrect to assume that the activity of the hydroxyl ion is constant, since, as the zincate is added, the ionic strength will change even though the hydroxyl ion concentration remains constant.

Table I. Experimental electrode potential of zinc amalgam as a function of the concentration of zincate ion, referred to mercury-mercuric oxide electrode, both electrodes in 7.03M KOH (25°C)

$C(Zn(OH)_4^=)$ moles/liter	$\log a(Zn(OH)_4^=)$	$\log a(OH^-)$	$\log[a^4(OH^-)/a(Zn(OH)_4^=)]$	E (volts)
0.0126	−0.6606	1.4660	6.5246	−1.40053
0.0250	−0.3535	1.4708	6.2367	−1.39275
0.0372	−0.1710	1.4758	6.0742	−1.38797
0.0609	0.0617	1.4851	5.8787	−1.38185
0.0837	0.2182	1.4944	5.7594	−1.37813
0.1163	0.3868	1.5703	5.6424	−1.37453
0.1571	0.5501	1.5237	5.5447	−1.37173
0.1952	0.6821	1.5390	5.4739	−1.36981
0.2477	0.8206	1.5599	5.4190	−1.36790
0.2953	0.9350	1.5790	5.3810	−1.36672
0.3380	1.0280	1.5961	5.3564	−1.36598
0.3785	1.1095	1.6124	5.3401	−1.36546
0.4260	1.1991	1.6315	5.3269	−1.36502
0.4800	1.2945	1.6533	5.3187	−1.36478
0.5680	1.4383	1.6888	5.3169	−1.36477
0.6400	1.5483	1.7177	5.3225	−1.36503

Activities calculated from concentrations *via* the Davies equation, Eq. [14], with $A = 0.509$ and $B = 0.275$. For zincate ion, the activity coefficient calculated from the Davies equation is that for the salt $K_2Zn(OH)_4$.

In order to determine whether the curvature results from the concentration dependence of the OH^- and $Zn(OH)_4^=$ ions, one would require the activities of zincate and hydroxyl ion in the presence of each other and, unfortunately, these have not been determined. Therefore, it was decided to attempt to calculate the activity coefficients by use of the Davies equation which, as has been shown earlier, gives fairly good agreement with experimental data for KOH alone with $B = 0.275$. This equation was used to calculate the activity coefficients of the hydroxyl and zincate ions [*i.e.*, of KOH and $K_2Zn(OH_4)$] from which the activities could readily be obtained. The calculated activities are shown in Table I and a plot of E *vs.* $\log a^4(OH^-)/a(Zn(OH)_4^=)$ is shown in Fig. 5. It can be seen that a straight line is obtained over the entire concentration range studied, giving an intercept of −1.207V and a slope of 0.030V. Furthermore, it can be seen from the activity values in Table I that the variation of $\log a^4(OH^-)/a(Zn(OH)_4^=)$ with concentration, passes through a minimum at 0.5680M in zincate concentration. That the electrode potential also passes through a minimum at this concentration gives additional confirmation that the activities calculated from the Davies equation are reasonably accurate. The intercept of −1.207V gives $E°$ for an electrode at unit activity of OH^- and zincate ions, referred to the Hg/HgO/7.03M KOH reference electrode. This intercept is $E°*(Zn)$ in Eq. [12].

Using the value $E°(HgO,Hg)$ given by Latimer (15), the data of Akerlof and Bender (13) for the activity of the hydroxyl ion in the reference compartment, and those of Walls and Upthegrove (14) for the activity of zinc in the amalgam, $E°(Zn)$ was calculated to be −1.205V from Eq. [13], referred to the SHE. This value is somewhat more positive (*i.e.*, more noble) than the values of −1.211 reported by Dirkse (3) and −1.216 reported by Latimer (15). Dirkse (16) has suggested that, in 7M KOH, the partial molal free energy of H_2O is about 0.2 kcal lower than in dilute solutions and that this would result in a shift in the reference electrode potential, making it about 6 mV more negative. If this correction is applied, our value

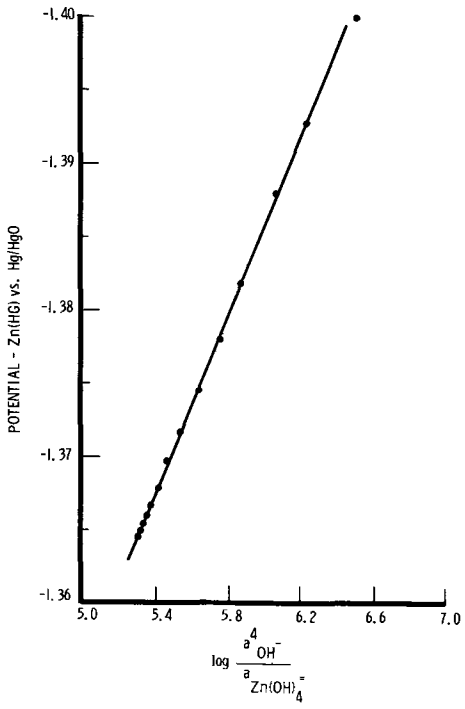

Fig. 5. Potential of zinc amalgam electrode as a function of log $a^4(OH^-)/a(Zn(OH)_4^=)$. The activity coefficients were calculated with the aid of the Davies equation with $B = 0.275$. Supporting electrolyte 7.03M KOH. Reference electrode: Hg/HgO/7.03M KOH.

of −1.205V is made to coincide exactly with Dirkse's.

The free energy of formation of the zincate ion is found to be −205.86 kcal. Previous values include −206.2 (Dirkse) and −206.41 (Latimer).

When the calculated activities are used in conjunction with the experimentally determined value of $E°$ to calculate the electrode potential as a function of the zincate ion concentration, the calculated points shown in Fig. 4 are obtained. The agreement between the experimental and calculated curves is generally within 1 mV over the whole concentration range studied. Thus, the curvature in the plot of the electrode potential *vs.* the log of the zincate ion concentration can be explained in terms of the variation in the activities of the hydroxyl and zincate ions with concentration. As was shown by Hampson *et al.* (4), the curvature in log plots of this type cannot be entirely explained by taking account of the participation of water in the electrode reaction as was suggested by Dirkse (3). It appears, therefore, that the behavior of the zinc amalgam electrode can be more adequately explained in terms of the values of the activities of the ions to which the electrode is reversible.

Manuscript submitted Mar. 5, 1970; revised manuscript received Jan. 4, 1971.

Any discussion of this paper will appear in a Discussion Section to be published in the June 1972 JOURNAL.

REFERENCES

1. G. Bodländer, *Chem. Ber.*, **36**, 3933 (1903).
2. F. Kunschert, *Z. Anorg. Chem.*, **41**, 337 (1904).
3. T. P. Dirkse, *This Journal*, **101**, 328 (1954).
4. N. A. Hampson, G. A. Herdman, and R. Taylor, *J. Electroanal. Chem.*, **25**, 9(1970).
5. J. S. Fordyce and R. L. Baum, *J. Chem. Phys.*, **43**, 843 (1965).
6. G. H. Newman and G. E. Blomgren, *J. Chem. Phys*, **43**, 2744 (1965).
7. Y. Okinaka, Paper 48 presented at Electrochem. Soc. Meeting, Philadelphia, Oct. 9-14, 1966.
8. E. Jost, *ibid.*, Paper 49.
9. J. N. Butler, "Ionic Equilibrium—A Mathematical Approach," Addison-Wesley (1964).
10. T. P. Dirkse, *This Journal*, **106**, 154 (1959).
11. G. T. Baker and T. Trachtenberg, *ibid.*, **114**, 1045 (1967).
12. C. W. Davies, "Ion Association," Butterworths (1962).
13. G. C. Akerlof and P. Bender, *J. Am. Chem. Soc.*, **70**, 2366 (1948).
14. H. A. Walls and W. R. Upthegrove, *J. Chem. Eng. Data*, **9**, 194 (1964).
15. W. M. Latimer, "Oxidation Potentials," 2nd Ed., Prentice Hall, Inc. (1952).
16. T. P. Dirkse, Private communication (1970).

Thermodynamics of Hydrochloric Acid in Glycerol-Water Mixtures from EMF Measurements between 5° and 45°C

Rabindra N. Roy and William Vernon

Department of Chemistry, Drury College, Springfield, Missouri 65802

and Alfred L. M. Bothwell

Department of Chemistry, Washington University, Saint Louis, Missouri 63100

ABSTRACT

Electromotive force measurements were made of cells of the type Pt/H_2(g, 1 atm)/HCl(m), glycerol(X), H_2O(Y)/AgCl-Ag where X = 20, 40, 70, and 90 w/o (weight per cent) glycerol at 5°, 15°, 25°, 35°, and 45°C and also in 10 w/o glycerol at 25°C. The cell has been used to calculate, (*a*) the standard emf, (*b*) the mean molal activity coefficients of HCl, (c) the primary medium effect, (*d*) the relative partial molal enthalpy, and (*e*) the standard thermodynamic functions ($\Delta G°_t$, $\Delta S°_t$, and $\Delta H°_t$) for the transfer of HCl from the aqueous standard state to the standard state in the respective mixed solvents. The electrostatic part of the total free energy, entropy, and enthalpy of transfer has been computed using Born's model. The nonelectrostatic contribution (the chemical effect) of the thermodynamic quantities has been evaluated by subtracting the electrostatic contributions from the total values. The values of $E°_m$ obtained by a theoretically justified polynomial curve fitting technique have been expressed as a function of temperature. The significance of these results in relation to the acid-base behavior and the breakdown of the structure of water is discussed.

The properties of dilute strong electrolytes in mixed solvents have long been of interest. Standard potentials of the silver-silver chloride electrode in dipolar aprotic solvents such as tetrahydrofuran-water (1, 2) and in amphiprotic solvents like isopropanol-water (3) have been useful in the investigation of chemical equilibria. In the present work, the binary mixtures of water + glycerol were chosen, because these mixtures are often used as solvents in studies of ionization constants (4) and acid-base properties of compounds slightly soluble in water.

The emf measurements on hydrochloric acid solutions in 50 w/o (weight per cent) glycerol in the temperature range 0°-90°C have been reported earlier (5). The solvent mixtures containing 10 and 30 w/o glycerol were studied by Knight *et al.* (6), through the temperature range 0-40°C. Lucasse (7) also studied the same cell in 3.06 and 21.2 w/o glycerol at 25°C, but none of these investigators provided data for the associated thermodynamic quantities.

In the present work, measurements of the emf of the cell

$$Pt/H_2(g.\ 1\ atm)/HCl(m),\ glycerol(X),\ H_2O(Y)/AgCl\text{-}Ag \quad [A]$$

were made from 5° to 45°C at intervals of 10°C in several glycerol-water mixtures (X = 20, 40, 70, and 90 w/o) and also in 10 w/o glycerol at 25°C with the concentration range 0.005 to 0.2 molal hydrochloric acid. The present paper reports our results on the thermodynamic properties of dilute hydrochloric acid solutions. As is demonstrated below, the values of the standard electrode potential, the activity coefficient, primary medium effect, and the related thermodynamic quantities provide useful insights with regard to the acid-base behavior and the changes in structural aspects of the solvents.

Experimental

Glycerol (Fisher certified ACS) was used without further purification, after the preliminary measurements had shown that the difference in emf for solutions made with purified glycerol (8) and for solutions made from untreated glycerol was no greater than the experimental error (±0.1 mV). The stock solution of hydrochloric acid was prepared from a twice-distilled sample of the acid. The specific conductance of the water used in the preparation of the solutions was less than 0.7×10^{-6} mho/cm. The solvent mixtures of various percentages were made by weight. All solutions were freshly prepared before taking measurements. All concentrations are accurate to within ±0.02%.

The general experimental procedures employed in the present work were the same as those described previously (2). The silver-silver chloride electrodes were of thermal electrolytic type (9).

Measurements were made at 5°, 15°, 25°, 35°, and 45°C by means of a K-3 Universal Type Potentiometer. An Eppley standard cell having low temperature coefficient and the mirror-type galvanometer having a sensitivity of ±0.02 mV per division was used in conjunction with the potentiometer. The water bath in which the cells were immersed was regulated within ±0.01°C. The cell was constructed so as to permit the use of two Ag-AgCl electrodes and two hydrogen electrodes. The equilibrium was reached in 3-4 hr after the initiation of hydrogen bubbling. The criterion for equilibrium was a stable reading within ±0.1 mV over a period of about 1 hr. The emf at 25°C was recorded three times, namely at the start, middle, and end of the temperature run. The individual readings for the same solution, at 25°C, agreed within ±0.08 mV, and the average is given in Table I.

Total vapor pressures (p) of the solvents at the respective temperatures were obtained from data of Carr, Townsend, and Badger (10), and by the method of extrapolation and interpolation, which utilized the straight-line plots of log p as a function of $1/T$, where T is in Kelvin. The dielectric constants, D, of the solvent mixtures used for the calculation of the electrostatic free energy were derived from the data of Åkerlöf (11).

Key words: activity coefficient, glycerol, mixed solvent, thermodynamics, standard emf, medium effect.

Table I. Electromotive force (V) of the cell Pt/H_2(g, 1 atm)/HCl(m), glycerol(X), H_2O(Y)/AgCl-Ag at different temperatures in °C

X and Y are weight percentages

X = 10		X = 20					
^mHCl	25	^mHCl	5	15	25	35	45
0.00498	0.4924	0.00509	0.4773	0.4807	0.4836	0.4826	0.4879
0.01000	0.4585	0.01005	0.4478	0.4499	0.4516	0.4540	0.4524
0.0300	0.4049	0.0300	0.3964	0.3960	0.3960	0.3958	0.3947
0.0400	0.3908	0.0402	0.3830	0.3829	0.3817	0.3817	0.3793
0.0498	0.3801	0.0500	0.3736	0.3722	0.3717	0.3710	0.3691
0.0598	0.3702	0.0603	0.3652	0.3648	0.3639	0.3623	0.3601
0.0798	0.3572	0.0801	0.3527	0.3510	0.3497	0.3482	0.3456
0.1063	0.3423	0.1069	0.3407	0.3397	0.3380	0.3357	0.3327
0.1595	0.3218	0.1629	0.3213	0.3190	0.3170	0.3145	0.3117
0.2061	0.3083	0.2093	0.3093	0.3071	0.3045	0.3012	0.2969

^mHCl	5	15	25	35	45
		X = 40			
0.00504	0.4644	0.4663	0.4690	0.4705	0.4712
0.01011	0.4336	0.4344	0.4356	0.4351	0.4348
0.0272	0.3897	0.3900	0.3883	0.3875	0.3868
0.0405	0.3730	0.3711	0.3701	0.3672	0.3657
0.0500	0.3629	0.3617	0.3597	0.3580	0.3554
0.0607	0.3540	0.3517	0.3507	0.3478	0.3451
0.0802	0.3427	0.3397	0.3380	0.3352	0.3323
0.1074	0.3292	0.3256	0.3239	0.3212	0.3179
0.1656	0.3088	0.3038	0.3013	0.2999	0.2938
0.2138	0.2961	0.2917	0.2893	0.2855	0.2809
		X = 70			
0.00491	0.4296	0.4309	0.4313	0.4245	0.4276
0.00989	0.3992	0.3998	0.3993	0.3972	0.3932
0.0298	0.3529	0.3514	0.3492	0.3458	0.3424
0.0395	0.3404	0.3380	0.3360	0.3335	0.3293
0.0500	0.3303	0.3284	0.3261	0.3222	0.3183
0.0594	0.3234	0.3205	0.3184	0.3151	0.3113
0.0793	0.3105	0.3081	0.3050	0.3015	0.2966
0.0968	0.3024	0.3006	0.2947	0.2919	0.2885
0.1531	0.2802	0.2768	0.2730	0.2684	0.2626
0.2010	0.2681	0.2642	0.2600	0.2556	0.2492
		X = 90			
0.00479	0.3791	0.3821	0.3826	0.3798	0.3781
0.00957	0.3484	0.3523	0.3511	0.3480	0.3454
0.0319	0.3001	0.3008	0.2995	0.2947	0.2896
0.0383	0.2940	0.2937	0.2894	0.2846	0.2788
0.0510	0.2818	0.2811	0.2775	0.2731	0.2669
0.0638	0.2729	0.2710	0.2670	0.2613	0.2552
0.0830	0.2613	0.2597	0.2545	0.2491	0.2421
0.0925	0.2567	0.2547	0.2490	0.2441	0.2364
0.1499	0.2350	0.2321	0.2253	0.2194	0.2122
0.1978	0.2224	0.2195	0.2119	0.2065	0.1982

Results

Standard electrode potentials.—Evaluation of the standard potential of the reversible cell reaction is the primary step in the computation of the thermodynamic quantities. The commonly used linear graphical extrapolation technique for the evaluation of the standard potentials, using the Gronwall, LaMer, and Sandved (12) extension of the Debye-Hückel theory involves data such as the density and dielectric constants of the mixed solvents, an appropriate estimate of the ion-size parameter for the linear plot (13), and the Debye-Hückel constants, whereas this information is not necessary when the extrapolation of emf data is made by a theoretically justified polynomial curve fitting technique as demonstrated below.

The emf of the cell studied is expressed by the Nernst equation

$$E + (2RT/\mathbf{F}) \ln m = E^\circ - (2RT/\mathbf{F}) \ln \gamma_\pm \quad [1]$$

For electrolytes of symmetrical valence types, the extended equation for ln $f_\pm$ is given by the equation (12, 14)

$$\ln f_\pm = -\frac{\epsilon^2 z^2}{kTDa}\,\frac{.1.}{2}\,\frac{x}{1+x} + \sum_{m=1}^{\infty}\left[\frac{\epsilon^2 z^2}{kTDa}\right]^{2m+1}\left[\frac{1}{2}X_{2m+1}(x) - 2mY_{2m+1}(x)\right] \quad [2]$$

where D is the dielectric constant of the solvent, T is in Kelvin, $x = \zeta a$ and $\zeta^2 = 8\pi N\epsilon^2 z^2 c/10^3 kTD$, N is Avogadro's number, k is the Boltzmann constant, ϵz is the charge on the ions, c is the molar concentration, and a the ion-size parameter. In the case of symmetrical valence type electrolytes, the even order terms vanish, and the contribution of the terms $X_{2m+1}(x)$ and $Y_{2m+1}(x)$ have been evaluated by Gronwall, LaMer, and Sandved (12) up to the fifth order. After appropriate expansions, integrations, and some tedious algebraic manipulations, Eq. [2] can be expressed as (15)

$$\ln f_\pm = A_1''x + A_2''x^2 + A_3''x^3 + \ldots \quad [3]$$

The use of the molality scale changes the molar activity coefficient by some constant value and Eq. [3] is rewritten as

$$\ln \gamma_\pm = A_1'm^{1/2} + A_2'm + A_3'm^{3/2} + \ldots \quad [4]$$

where the first term on the right hand side of Eq. [4] represents the Debye-Hückel limiting law. Substitution of Eq. [4] into Eq. [1] yields

$$E + (2RT/\mathbf{F}) \ln m = E^\circ + A_1m^{1/2} + A_2m + A_3m^{3/2} + \ldots \quad [5]$$

If a good set of experimental data is available, the coefficients E°, A_1, *etc.*, can be evaluated by means of a polynomial curve fitting program of the form

$$y = A_0 + A_1X + A_2X^2 + A_3X^3 + \ldots \quad [6]$$

Equations [5] and [6] are of identical form. Hence, such a method is theoretically sound and yields excellent results as was shown in our earlier paper (16) by comparison of E°_m data with those obtained from the best linear extrapolations for various solvent systems. The theoretical validity of Eq. [5] has been further corroborated by Dill *et al.* (17, 18).

The observed potentials for the cell, corrected to a hydrogen fugacity of 1 atm, are presented in Table I. Each value in the table indicates the mean value from three or four replicate cells. The lowest and highest values for replicate cells did not differ by more than 0.12 mV.

Table II gives the values of the standard potentials on the molality (m) and mole fraction (N) scales in glycerol-water mixtures. The standard cell potentials for water-glycerol (X weight per cent) solvent mixtures were found to fit the equations given below, together with the equation for water as the solvent (13)

Table II. Standard cell potentials of the silver-silver chloride electrode in glycerol-water media at different temperatures (uncertainty ±0.0003V)

X = weight per cent glycerol; M_{xy} is the mean molecular weight of the solvent

X	t/°C = 5		15		15		35		45		
	E°_m	E°_N	E°_m	E°_N	E°_m	E°_N	E°_m	E°_N	E°_m	E°_N	M_{xy}
20	0.2220	0.0379	0.2150	0.0242	0.2090	0.0117	0.2020	−0.0019	0.1920	−0.0186	21.47
40	0.2070	0.0330	0.1995	0.0192	0.1900	0.0036	0.1846	−0.0081	0.1744	−0.0246	26.56
70	0.1670	0.0141	0.1570	−0.0013	0.1490	−0.0148	0.1390	−0.0303	0.1260	−0.0489	41.23
90	0.1108	−0.0200	0.1041	−0.0315	0.0947	−0.0456	0.0818	−0.0632	0.0693	−0.0803	65.26
10					0.2166[a]	0.0146					19.59
10					0.2165[b]						

[a] From the present study.
[b] From ref. (6).

$$E^\circ_m(X = 0) = 0.2224 - 6.396 \times 10^{-4}\,(t - 25) - 3.18 \times 10^{-6}\,(t - 25)^2 \quad [7]$$

$$E^\circ_m(X = 20) = 0.2090 - 7.300 \times 10^{-4}\,(t - 25) - 5.00 \times 10^{-6}\,(t - 25)^2 \quad [8]$$

$$E^\circ_m(X = 40) = 0.1900 - 8.010 \times 10^{-4}\,(t - 25) - 0.93 \times 10^{-6}\,(t - 25)^2 \quad [9]$$

$$E^\circ_m(X = 70) = 0.1490 - 9.999 \times 10^{-4}\,(t - 25) - 5.71 \times 10^{-6}\,(t - 25)^2 \quad [10]$$

$$E^\circ_m(X = 90) = 0.0947 - 10.526 \times 10^{-4}\,(t - 25) - 10.63 \times 10^{-6}\,(t - 25)^2 \quad [11]$$

The standard potentials on the mole fraction scale have been calculated with the equation

$$E^\circ_N = E^\circ_m - (2RT \ln 10/\mathbf{F}) \log_{10} (1000/M_{xy}) \quad [12]$$

where M_{xy} is the mean molecular weight of the solvent and is listed in Table II.

The stoichiometric mean activity coefficients of hydrochloric acid, $\gamma_\pm$, at round molalities were calculated from the following equation

$$\log_{10} \gamma_\pm = [E^\circ_m - \{E + (2RT/\mathbf{F}) \ln m\}]/(4.6052RT/\mathbf{F}) \quad [13]$$

using the values of E°_m given in Table II. The values of $\{E + (2RT/\mathbf{F}) \ln m\}$ at round molalities were obtained from Eq. [5]. The term $\gamma_\pm$ measures the difference in the "nonideal" part of the chemical potential of the HCl acid at finite concentration and at infinite dilution of the mixed solvent.

The primary medium effect is a measure of the energy involved in the transfer of HCl from infinite dilution in one solvent to infinite dilution in another solvent. This effect ($\log {}^s_w\gamma^\circ_\pm$(HCl)) of glycerol-water mixtures was computed by the equation

$$ {}^wE^\circ_m - {}^sE^\circ_m = \lim_{m \to 0} (4.6052RT/\mathbf{F}) \log_{10} {}^s_w\gamma_\pm \quad [14]$$

and the values are tabulated in Table III. The superscript, s, on the mean activity coefficient, $\gamma_\pm$, indicates that the measurements are carried out in a mixed solvent; whereas, the subscripts, w and s mean that $\gamma_\pm$ is measured relative to unit value at infinite dilution in water and in a mixed solvent, respectively. The limiting value ${}^s_w\gamma^\circ_\pm$ represents the activity coefficient of hydrochloric acid at infinite dilution in a mixed solvent (s) referred to unity at infinite dilution in water.

Relative partial molal quantities.—For each round molality in the respective media, $\log_{10} \gamma_\pm$ was fitted to a power series of the form

$$-\log_{10} \gamma_\pm = a + bT + cT^2 \quad [15]$$

where T is in Kelvin. The values of the relative partial molal enthalpy, $\bar{L}_2 = \bar{H}_2 - H_2^\circ$, of hydrochloric acid was evaluated by the equation

$$\bar{L}_2 = (-4.6052RT^2)\, d(\log_{10} \gamma_\pm)/dT \quad [16]$$

which after proper substitution of the constants of Eq. [15] yields

Table III. Primary medium effect ($\log {}^s_w\gamma^\circ_\pm$) of glycerol-water media upon hydrochloric acid at 5°, 25°, and 45°C

X = w/o glycerol

X	t/°C = 5	25	45
20	0.1096	0.1174	0.1299
40	0.2455	0.2727	0.2690
70	0.6078	0.6196	0.6529
90	1.0685	1.0789	1.1009

Table IV. Relative partial molal enthalpy, $\bar{L}_2$, in cal[a]/mole

X = w/o glycerol

m(mole/kg)	t/°C =	X = 40 5	25	45	X = 90 5	25	45
0.005		41	61	87	161	192	225
0.01		92	103	115	186	216	295
0.02		113	122	146	200	224	335
0.05		131	169	214	310	363	424
0.1		169	209	255	345	441	678

[a] 1 thermochemical calorie = 4.1840 joules.

$$\bar{L}_2 = (2RT^2 \ln 10)\,(b + 2cT) \quad [17]$$

The values of $\bar{L}_2$ are shown in Table IV.

Thermodynamic quantities.—The standard thermodynamic quantities (ΔG°_t, ΔS°_t, and ΔH°_t) for the transfer process (t)

HCl (in H_2O) → HCl (in various glycerol-water media)

can be obtained from the standard emf of the cell in water and in the respective glycerol-water mixtures and the variation of E°_m with temperature together with Eq. [12] for E°_N. The use of the mole fraction scale eliminates the energy changes due to concentration changes.

For the transfer process, we can now calculate the thermodynamic functions by applying the customary thermodynamic relations to Eq. [8-11] in combination with Eq. [12]

$$\Delta G^\circ_t = \mathbf{F}({}^wE^\circ_N - {}^sE^\circ_N) \quad [18]$$

$$\Delta S^\circ_t = -\,d(\Delta G^\circ_t)/dT \quad [19]$$

and

$$\Delta H^\circ_t = \Delta G^\circ_t + T\Delta S^\circ_t \quad [20]$$

The values of these quantities are given in Table V.

For HCl, the protolytic reaction involves the transfer of protons from water to another amphiprotic solvent (SH)

$$H_3O^+ + SH \rightleftarrows SH_2^+ + H_2O$$

This reaction depends not only on the specific chemical interactions (nonelectrostatic effect or acid-base properties), but also depends on the change of the dielectric constant of the medium (electrostatic effect). The chemical interactions involve the destruction of one type of solvation shell and the creation of another (20). Thus, the related thermodynamic quantities comprise two parts: electrostatic (el) and chemical or nonelectrostatic (non). For the change of the free

Table V. Standard thermodynamic quantities[a] accompanying the transfer of HCl from water to glycerol-water mixtures

X = w/o glycerol

X	ΔG°_t	$\Delta G^\circ_{t,el}$	$\Delta G^\circ_{t,non}$	ΔH°_t	$\Delta H^\circ_{t,el}$	$\Delta H^\circ_{t,non}$	ΔS°_t	$\Delta S^\circ_{t,el}$	$\Delta S^\circ_{t,non}$	D
20	99	141	−42	−312	−219	−93	−1.4	−1.2	−0.2	72.99
40	286	322	−36	−468	−375	−93	−2.5	−2.3	−0.2	67.13
70	711	787	−76	−798	−706	−92	−5.1	−5.0	−0.1	55.67
90	1421	1393	28	115	−878	993	−4.4	−7.6	3.2	45.54

[a] ΔG° and ΔH° are in (cal/mole) and ΔS° in (cal/°K-mole).

energy of transfer

$$\Delta G^\circ_t = \Delta G^\circ_{t,el} + \Delta G^\circ_{t,non} \quad [21]$$

and similar equations exist for the other thermodynamic functions, ΔS°_t and ΔH°_t. The contribution to the electrostatic part of the free energy change can be calculated from the well-known Born equation

$$\Delta G^\circ_{t,el} = \{Ne^2/2\}\{1/D_s - 1/D_w\}\{1/r_+ + 1/r_-\} \quad [22]$$

where r_+ is the radius of the "solvated hydrogen ion" and is arbitrarily taken as 2.76Å (21) for all of the mixed solvents, and r_- is the radius of the chloride ion taken as 1.81Å (22). The values of $\Delta G^\circ_{t,non}$ have been obtained by the difference between ΔG°_t and $\Delta G^\circ_{t,el}$. All these data are shown in Table V.

The electrostatic contribution of the entropy change can be evaluated by differentiating Eq. [22] with respect to temperature and subsequent substitution of the resulting equation into the empirical equation (23)

$$D = D_0 e^{-T/\theta} \quad [23]$$

gives

$$\Delta S^\circ_{t,el} = (-Ne^2/2)(1/D_s\theta_s - 1/D_w\theta_w)(1/r_+ + 1/r_-) \quad [24]$$

In Eq. [23], D is the dielectric constant at temperature T, and D_0 and θ are the constants characteristic of the medium. To use Eq. [24], the values of $1/\theta_s$ and $1/\theta_w$ can be obtained by differentiating Eq. [23]

$$d(\ln D)/dT = -1/\theta \quad [25]$$

Thus, from the slopes of the linear plots of log D *vs.* T for the respective glycerol-water media, the following values of θ were calculated

w/o glycerol	0	20	40	70	90
θ	220	208	203	197	203

The chemical or nonelectrostatic contribution of the entropy of transfer, $\Delta S^\circ_{t,non}$, can then be obtained by subtracting $\Delta S^\circ_{t,el}$ from ΔS°_t. All these computed values are given in Table V.

From a knowledge of $\Delta G^\circ_{t,el}$ and $\Delta S^\circ_{t,el}$, the electrostatic part of the enthalpy change, $\Delta H^\circ_{t,el}$, has been evaluated and hence the nonelectrostatic part of the quantity, $\Delta H^\circ_{t,non}$, has also been obtained. The values so calculated at 25°C are presented in Table V.

Discussion

A direct comparison of the value of E°_m for $X = 10$ was made with that of ref. (6). Our value (at 25°C) of E°_m determined by the polynomial curve fitting technique is equal to 0.2166V compared to 0.2165V by Knight *et al.* The agreement is excellent.

The values of the activity coefficient for $X = 40$ and 90 at all experimental temperatures are given in Table VI. In a given system and at a given temperature the increase in the value of the mean activity coefficient corresponds to the decrease in the molality

Table VI. Activity coefficients ($^s\gamma_\pm$) of hydrochloric acid in 40 and 90 w/o glycerol at different temperatures

m, moles/kg	t/°C = 5	15	25	35	45
		X = 40			
0.005	0.871	0.870	0.868	0.867	0.865
0.01	0.834	0.831	0.829	0.827	0.824
0.02	0.792	0.789	0.787	0.784	0.782
0.05	0.740	0.737	0.733	0.730	0.726
0.1	0.717	0.713	0.709	0.705	0.701
		X = 90			
0.005	0.728	0.725	0.722	0.720	0.718
0.01	0.664	0.660	0.657	0.654	0.651
0.02	0.605	0.602	0.598	0.594	0.590
0.05	0.562	0.554	0.548	0.542	0.535
0.1	0.542	0.536	0.529	0.522	0.516
0.2	0.506	0.498	0.492	0.484	0.478

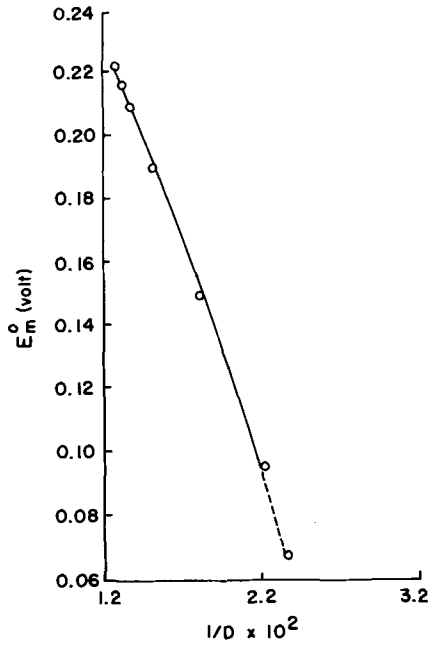

Fig. 1. Plots of the standard potential (E°_m) *vs.* $1/D$ at 25°C

of hydrochloric acid. As expected from Debye-Hückel theory, the value of $\gamma_\pm$ at a given molality decreases with increasing proportions of glycerol, because the dielectric constant of the medium is lowered. An average uncertainty of ±0.08 mV in emf values corresponds to an error of 0.003 in the values of $\gamma_\pm$.

It is evident from Table III that the primary medium effect (ion-solvent interaction) of glycerol-water mixtures on hydrochloric acid becomes greater as the concentration of glycerol is gradually increased. This also expresses the well-known fact that the escaping tendency of HCl is greater in glycerol-water mixtures than in the pure aqueous solutions.

It is interesting to see how the values of E°_m change with the dielectric constant of the media. The Born equation predicts that the plot of E°_m *vs.* $1/D$ should be linear. In Fig. 1, it is rather remarkable that the predictions of the Born equation are qualitatively correct. The dashed line represents the slight curvature for 95 w/o glycerol (24). It should be mentioned, however, that the Gibbs energy calculations based on the Born model may be acceptable, but the uncertainties in the computed values of the entropy and enthalpy are greater, mainly because of the arbitrary choice in the ionic radii and the dielectric constant of the medium. Hepler's equation (25), which takes into account the dielectric saturation in the ionic force field, may be better, but still the uncertainty factor in the radius of the solvated proton would remain. The values of ΔG°_t are presumably correct within ±8 cal.

It is evident from Table V that the transfer Gibbs energy appears to be positive for all solvent compositions in the glycerol-water systems, while the chemical part of the free energy change, $\Delta G^\circ_{t,non}$, is negative up to $X = 70$. The positive value of ΔG°_t indicates that HCl appears to be in a lower Gibbs energy state in water than in glycerol-water mixtures. The fairly uniform negative values of $\Delta G^\circ_{t,non}$, signify that it is favorable for the transfer process from water to glycerol-water mixtures as far as the chemical interaction or solvation is concerned. But, the electrostatic factors are important and predominate over the chemical interaction causing an unfavorable effect in the over-all transfer process. The nonelectrostatic contribution appears to be a solvent parameter which is possibly characterized as a measure of the increase in basicity of the medium as glycerol is added up to a composition of $X = 70$. The positive value of $\Delta G^\circ_{t,non}$ for $X = 90$ does have a real significance. This result shows that water

has a greater chemical affinity for the proton than the mixed solvent if it is assumed tentatively that very little free energy change (due to chemical interaction or solvation) is involved in the transfer of the accompanying chloride ion.

The dissociation behavior of some cation acids in methanol-water mixtures (26, 27) and in ethylene glycol-water mixtures (28), support the above view that as the respective alcohol is added to water, the basicity increases passing through a maximum ($X = 80$). The reason for this apparent anomaly was suggested by Braude and Stern (29) that the addition of alcohol may gradually destroy the water structure, thus the basic centers of the oxygen in water molecules become free for the attachment of incoming protons. This reasoning may apply equally well for glycerol-water media.

Beside the less discriminating free energy changes which are not affected by structural factors, the changes in enthalpy and entropy might offer some limited interpretation of structural changes (30, 31) involved in the over-all process. The values of ΔH^o_t and ΔS^o_t appear to be negative and decrease with the increasing proportion of glycerol up to $X = 70$ and indicate a gradual breakdown of the structure in water (30) with further addition of glycerol to highly polar water molecules. Moreover, the glycerol molecules decrease their rotational freedom in the high electric field of an ion and contract their volume due to electrostriction, giving negative values of entropy. The increasing values of ΔS^o_t (still negative) and ΔH^o_t for $X = 90$ might be due to a number of diverse phenomena. For instance, the order created by HCl in this solvent composition relative to pure water begins to increase (31) as far as the structural effect is concerned. Another factor might involve a proton solvation effect. The basicity falls off past the minimum and glycerol may begin substituting for water causing a serious disturbance in the hydration sphere of the ions (28).

When the electrostatic factors are taken into consideration, the contributions of $\Delta H^o_{t,non}$ and $\Delta S^o_{t,non}$ from the chemical interaction follow a general trend and appear to be negative up to $X = 70$ and then positive for $X = 90$. Further analysis of the results, however, should wait for similar studies in different amphiprotic solvent + water mixtures.

Acknowledgments

The authors thank Professor J. Greene for assistance with computer calculations, Mrs. Margaret Lindquist for assistance with preliminary experiments, and Dr. J. Padron for providing the facility for this experimental work as well as for his comments and criticisms about the manuscript.

Manuscript submitted Sept. 10, 1970; revised manuscript received Mar. 16, 1971.

Any discussion of this paper will appear in a Discussion Section to be published in the June 1972 JOURNAL.

SYMBOLS

1 cal	4.1840 joules (defined thermochemical calorie)
${}^wE^o_N$, ${}^sE^o_N$	Standard electrode potentials in water and in a mixed solvent (mole fraction scale), V
${}^wE^o_m$, ${}^sE^o_m$	Standard electrode potential in water and in a mixed solvent (molal scale), V
a	Ion-size parameter, Å
x	Weight per cent glycerol in a mixture with water
$f_\pm$	Mean ionic activity coefficient, molar scale
$\gamma_\pm = {}^s\gamma_\pm$	Mean ionic activity coefficient of HCl (molal scale) in a mixed solvent (superscript, s) relative to unit value at infinite dilution in a mixed solvent (subscript, s)
${}^s{}_w\gamma_\pm$	Mean ionic activity coefficient of HCl (molal scale) in a mixed solvent (s) relative to unit value at infinite dilution in water (w)
${}^s{}_w\gamma_\pm{}^o$	Mean ionic activity coefficient of HCl (molal scale) at infinite dilution in mixed solvent (s)
D_s, D_w	Dielectric constant of the mixed solvent and water, respectively
M_{xy}	Mean molecular weight of the solvent, kg mole^{-1}
r_+, r_-	Radius of the cation (H^+) and anion (Cl^-), respectively, Å
$\bar{L}_2$	Relative partial molal enthalpy, cal/mole
A_0, A_1, ...	The constants of Eq. [6]
a, b, ...	Empirical constants of Eq. [15]
D_o, θ	Constants of Eq. [23]

REFERENCES

1. R. N. Roy and B. Sen, *J. Chem. Eng. Data*, **13**, 79 (1968).
2. R. N. Roy and B. Sen, *ibid.*, **12**, 584 (1967).
3. R. N. Roy and A. Bothwell, *ibid.*, **15**, 548 (1970).
4. H. S. Harned and F. H. M. Nestler, *J. Am. Chem. Soc.*, **68**, 966 (1946).
5. H. S. Harned and F. H. M. Nestler, *ibid.*, **68**, 665 (1946).
6. S. B. Knight, H. D. Crockford, and F. W. James, *J. Phys. Chem.*, **57**, 463 (1953).
7. W. W. Lucasse, *J. Am. Chem. Soc.*, **48**, 627 (1926).
8. G. Åkerlöf, *ibid.*, **54**, 4128 (1932).
9. R. G. Bates, "Determination of pH," p. 281, John Wiley, New York (1964).
10. A. R. Carr, R. E. Townsend, and W. L. Badger, *Ind. Eng. Chem.*, **17**, 643 (1925).
11. G. Åkerlof, *J. Am. Chem. Soc.*, **54**, 4125 (1932).
12. T. H. Gronwall, V. K. LaMer, and K. Sandved, *Physik. Z.*, **29**, 358 (1928).
13. R. G. Bates and V. E. Bower, *J. Res. Nat. Bur. Std.*, **53**, 283 (1954).
14. H. S. Harned and B. B. Owen, "The Physical Chemistry of Electrolytic Solutions," 3rd ed., p. 67, Reinhold Publishing Corp., New York (1958).
15. R. N. Roy, Ph.D. Dissertation, Louisiana State University, Baton Rouge, 1966.
16. B. Sen, D. A. Johnson, and R. N. Roy, *J. Phys. Chem.*, **71**, 1523 (1967).
17. A. J. Dill and O. Popovych, *J. Chem. Eng. Data*, **14**, 240 (1969).
18. A. J. Dill, L. M. Itzkowitz, and O. Popovych, *J. Phys. Chem.*, **72**, 4580 (1968).
19. R. A. Robinson and R. H. Stokes, "Electrolytic Solutions," 2nd ed., p. 35, Butterworths, London (1965).
20. J. L. Kavanau, "Water and Solute-Water Interactions," p. 73, Holden-Day, Inc., San Francisco (1964).
21. M. Paabo, R. G. Bates, and R. A. Robinson, *J. Phys. Chem.*, **70**, 247 (1966).
22. L. Pauling, "The Nature of the Chemical Bond," 3rd ed, p. 521, Cornell University Press, New York (1960).
23. R. W. Gurney, "Ionic Processes in Solution," p. 16, McGraw-Hill Book Co., Inc., New York (1953).
24. R. N. Roy, W. Vernon, and A. L. M. Bothwell, Unpublished data.
25. L. G. Hepler, *Aust. J. Chem.*, **17**, 587 (1964).
26. H. Strehlow, *Z Physik. Chem., Frankfurt*, **24**, 240 (1960).
27. E. E. Sager, R. A. Robinson, and R. G. Bates, *J. Res. Natl. Bur. Stand.*, **68A**, 305 (1964).
28. J. H. Stern and J. M. Nobilione, *J. Phys. Chem.*, **72**, 3937 (1968).
29. E. A. Braude and E. S. Stern, *J. Chem. Soc., London*, 1976, 1982 (1948).
30. D. Feakins, in "Physico-Chemical Processes in Mixed Aqueous Solvents," F. Franks, Editor, Elsevier Publishing Co., New York (1967).
31. F. Franks and D. J. G. Ives, *Quart. Rev., London*, **20**, 1 (1966).

Thermodynamics of the Molten AgCl-RbCl-NaCl System by Electromotive Force Measurements

A. D. Pelton and S. N. Flengas

Department of Metallurgy and Materials Science, University of Toronto, Toronto 5, Ontario, Canada

ABSTRACT

Electromotive force measurements have been made using the reversible formation cell

$$\text{Ag} \mid \underset{\text{(liquid)}}{\text{AgCl-RbCl-NaCl}} \mid \text{graphite, } Cl_2$$

Partial molar excess free energies, enthalpies, and excess entropies of mixing of AgCl have been measured over the entire composition range of the AgCl-RbCl-NaCl ternary system. Partial properties of mixing of RbCl and NaCl and integral properties of mixing have been calculated using an analytical solution of the Gibbs-Duhem equation. The partial properties of RbCl and NaCl can be explained on the basis of simple considerations of regular solution behavior. The partial properties of AgCl, however, cannot be explained in this way.

There have been very few systematic studies made of ternary fused salt systems. In no such system are complete free energy, enthalpy, and entropy data simultaneously available.

In a previous publication (1), emf measurements using the cell

$$\text{Ag} \mid \underset{\text{(liquid)}}{\text{AgCl, alkali chloride}} \mid \text{graphite, } Cl_2 \qquad [A]$$

were described. Properties in the AgCl-*A*Cl (where A = Na, K, Rb, or Cs) binary systems were measured. In the present investigation, the formation cell was used to obtain partial molar excess free energies, enthalpies, and excess entropies of mixing of AgCl at several compositions over the entire composition range of the AgCl-RbCl-NaCl ternary system. Above 800°C, one homogeneous liquid phase exists at all compositions in this system.

In the AgCl-NaCl binary system (1), excess free energies, enthalpies, and excess entropies of mixing are all positive. In the AgCl-RbCl system (1), however, all these excess properties are negative. By studying the ternary system, it is possible to see how the properties vary between the two extremes as the ratio of NaCl to RbCl is changed, and so the competing effects of the RbCl and NaCl can be examined.

As is discussed later, if this ternary system is to be studied fully, it is necessary to have "end point" thermodynamic data in the RbCl-NaCl binary system. Enthalpies of mixing are available in this binary system from the calorimetric studies by Hersh and Kleppa (2). The phase diagram of the RbCl-NaCl system has been measured (3), and free energies of mixing have been calculated from the phase diagram with good precision (3). The availability of these "end point" data was one of the considerations in the decision to study the AgCl-RbCl-NaCl system.

Data Treatment

To be able properly to analyze the experimental data in a ternary system, it is essential that a method of applying the Gibbs-Duhem relation must be available so that partial properties of all components and integral properties of mixing can be calculated. In a previous publication (4), an analytical solution of the Gibbs-Duhem equation in ternary systems was developed. It was shown that the analytical method overcomes the many problems inherent in the older graphical Gibbs-Duhem integration techniques. The analytical method has also recently been extended (5) to apply to systems of any number of components.

The composition variables chosen (4) were designated y and t, where

$$y = (1 - X_1) \qquad [1]$$

$$t = X_3/(X_2 + X_3) \qquad [2]$$

where X_1, X_2, and X_3 are the mole fractions of the three components.

In the composition triangle of an isothermal ternary system, t is constant along quasi-binary lines of constant X_3/X_2 ratio. The variable can assume values from $t = 0$ in the 1-2 binary system to $t = 1$ in the 1-3 binary system. The variable y is constant along lines parallel to the 2-3 binary line, and can assume values from $y = 0$ for pure component 1 to $y = 1$ in the 2-3 binary system. This is shown on the ternary composition triangle in Fig. 1.

When the method is applied later to the AgCl-RbCl-NaCl ternary data, component 1 will be AgCl for which the partial molar properties have been measured. Components 2 and 3 will be RbCl and NaCl, respectively.

The partial and integral molar properties of mixing are expressed as power series in y and t as follows

$$f_1 = \sum_{j=2} \sum_{k=0} a_{jk} y^j t^k \qquad [3]$$

$$f_2 = \sum_{j=0} \sum_{k=0} b_{jk} y^j t^k \qquad [4]$$

$$f_3 = \sum_{j=0} \sum_{k=0} c_{jk} y^j t^k \qquad [5]$$

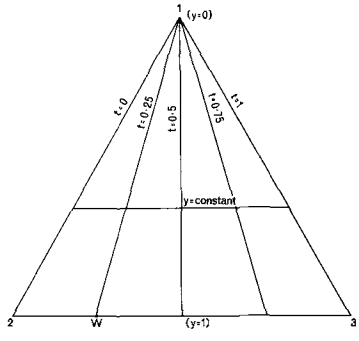

Fig. 1. Quasi-binary lines in a ternary system (in AgCl-RbCl-NaCl system: 1 = AgCl, 2 = RbCl, 3 = NaCl).

Key words: silver chloride, rubidium chloride, sodium chloride, fused salts, molten salts, ternary systems, thermodynamics, emf measurements, formation cell, silver electrode, chlorine electrode.

$$f = \sum_{j=1} \sum_{k=0} \phi_{jk} y^j t^k \quad [6]$$

where f_1, f_2, and f_3 are the partial molar properties of mixing of components 1, 2, and 3, and f is the integral property of mixing. In order that such series expansions can be written for f_1, f_2, f_3, and f, the properties and their derivatives must be continuous and finite functions in and on the boundaries of the entire composition range of the system. Excess properties of mixing will always satisfy these conditions.

Equation [3] may be written in expanded form as

$$f_1 = (a_{20} + a_{21}t + a_{22}t^2 + \ldots)y^2 + (a_{30} + a_{31}t + a_{32}t^2 + \ldots)y^3 + \ldots\ldots\ldots\ldots\ldots \quad [7]$$

Along a line of constant t, each of the bracketed factors in Eq. [7] becomes constant, and f_1 is simply a power series in $y = (1 - X_1)$ starting with the y^2 term, which is the well-known type of expansion first suggested by Margules (6) for binary systems. It is in this sense that the lines of constant t are called "quasi-binary" lines.

The expansion [3] for f_1 starts with the $j = 2$ term. That the missing coefficients a_{0k} are zero for all values of k follows from the condition that $f_1 = 0$ when $y = 0$. That the missing coefficients a_{1k} are all zero follows from the Gibbs-Duhem relation as is discussed shortly. In the expansion [6] for f, the missing coefficients ϕ_{0k} for $j = 0$ must all be zero because of the condition that $f = 0$ when $y = 0$.

Experimental values of f_1 may be fitted by a least-squares technique to an expansion of the form of Eq. [3]. In the present case, the partial molar excess free energies, enthalpies, and excess entropies of mixing of AgCl may be fitted to such an expansion. The coefficients b_{jk}, c_{jk}, and ϕ_{jk} in the expansions [4], [5], and [6] for f_2, f_3, and f may then be calculated from the following relationships which have been derived (4) from the Gibbs-Duhem equation

$$b_{jk} = a_{jk} - \frac{j + 1 - k}{j} a_{(j+1)k} \quad j \geqq 1 \quad [8]$$

$$c_{jk} = a_{jk} - \frac{j + 1 - k}{j} a_{(j+1)k} - \frac{k + 1}{j} a_{(j+1)(k+1)} \quad j \geqq 1 \quad [9]$$

$$a_{jk} = (1 - j)\,\phi_{jk} \quad [10]$$

(For $j = 1$, it may be seen from Eq. [10] that $a_{1k} = 0$ for all values of k, since the coefficients ϕ_{1k} must be finite. This proves the assertion made previously.)

The use of end point data.—From Eq. [8] and [9], the coefficients b_{jk} and c_{jk} of the expansions for f_2 and f_3 may be determined from a knowledge of the coefficients a_{jk} except when $j = 0$. The coefficients b_{0k} and c_{0k} cannot be calculated from the Gibbs-Duhem equation and must be determined from boundary values.

Equation [4] for f_2 may be expanded as follows

$$f_2 = \left(\sum_{k=0} b_{0k} t^k \right) + \sum_{j=1} \sum_{k=0} b_{jk} y^j t^k \quad [11]$$

The undetermined term, $\left(\sum_{k=0} b_{0k} t^k \right)$, is constant along a quasi-binary line where t is constant. The knowledge of one end point value of f_2 along a quasi-binary line is thus sufficient to give values of f_2 at any point on that line.

Consider the specific case in which values of f_2 in the 2-3 binary system are available from independent measurements in this system. (In the present case, partial molar properties of NaCl and RbCl in the RbCl-NaCl system are available as has been mentioned.) Let $f_{2(1,t)}$ be the value of f_2 at some value of t in the 2-3 binary system where $y = 1$. Then

$$f_{2(1,t)} = \left(\sum_{k=0} b_{0k} t^k \right) + \sum_{j=1} \sum_{k=0} b_{jk} t^k \quad [12]$$

Let $f_{2(y,t)}$ be the value of f_2 at any value of y for the same value of t. Substitution of Eq. [12] into Eq. [11] then gives

$$f_{2(y,t)} = f_{2(1,t)} + \sum_{j=1} \sum_{k=0} b_{jk}(y^j - 1)t^k \quad [13]$$

In Fig. 1, then, values of $f_{2(y,t)}$ at any point along the quasi-binary line 1-W are given from a knowledge of the end point value of f_2 at point W.

An equation completely analogous to Eq. [13] may be written for f_3

$$f_{3(y,t)} = f_{3(1,t)} + \sum_{j=1} \sum_{k=0} c_{jk}(y^j - 1)t^k \quad [14]$$

For calculating the integral property f, it may be seen from Eq. [10] that the coefficients ϕ_{jk} may be calculated from a knowledge of the coefficients a_{jk} for all values of j and k except for $j = 1$. The coefficients ϕ_{1k} cannot be determined from the Gibbs-Duhem equation, and end point values of f are required. By a derivation similar to that just given for f_2 and f_3, values of $f_{(y,t)}$ may be shown (4) to be given by the equation

$$f_{(y,t)} = y \cdot f_{(1,t)} + \sum_{j=2} \sum_{k=0} \phi_{jk}(y^j - y)t^k \quad [15]$$

where $f_{(1,t)}$ is an end point value of f in the 2-3 binary system.

If f_2, f_3, and f have been measured in the 2-3 binary system as functions of concentration, then $f_{2(1,t)}$, $f_{3(1,t)}$, and $f_{(1,t)}$ may be written as power series expansions in t (where $t = X_3$ in the 2-3 binary system from the definition [2]). Equations [13], [14], and [15] would then be complete analytical expressions for f_2, f_3, and f in the ternary system.

Experimental

The experimental apparatus and technique have been fully described elsewhere (1). An all-quartz experimental cell was used. The precision of the results obtained in the binary systems (1) was believed attributable in part to the use of a very high resistance "asbestos diaphragm" between the Ag and Cl_2 half cells.

Reagent-grade AgCl and NaCl were used. The RbCl (Matheson) was of 99+% purity. All salts were dried under vacuum and with dry HCl gas at 400°C in the case of AgCl and at 550°C for NaCl and RbCl. All salts were stored in a vacuum desiccator. The silver electrode was of 99.9+% purity. The graphite electrodes were special spectroscopic-grade graphite, pretreated [see ref. (1)] in chlorine gas. The chlorine was Matheson "high-purity" grade.

All readings reported have been corrected to a Cl_2 pressure of 1 std atm (101,325 newton/m^2), and all voltages are given in absolute volts.

Cell temperatures reported here have been shown (1) to have a probable accuracy of ±1°K.

The standard cell potential, $E°$, obtained with pure AgCl electrolyte, was found (1) to be given by the equation

$$E°\,(\text{mV}) = 1227.0 - 1.5973T + 0.182T\ln T - 4.48(10^{-5})T^2 \quad [16]$$

where T is in kelvins, and where the correction for the thermoelectric potential of the Ag-C couple has been applied.

AgCl, RbCl, and NaCl are numbered components 1, 2, and 3, respectively. Thus, $y = (1 - X_{AgCl})$, and $t =$

$X_{NaCl}/(X_{RbCl} + X_{NaCl})$; $t = 0$ in the AgCl-RbCl binary system, and $t = 1$ in the AgCl-NaCl binary system.

Results

Cell potentials, E, were measured with electrolytes at several compositions along quasi-binary lines where $t = 0.25$, $t = 0.50$, and $t = 0.75$. This was done primarily to facilitate presentation of the data. Values of $(E - E°)$ were calculated for each experimental point using Eq. [16] for $E°$. Results are shown in Fig. 2a-c. In all cases, the points were well fitted by straight lines. Least-squares lines are shown in Fig. 2a-c, and the equations of the lines are given in Table I along with the mean and maximum deviations for each line. The values of t for each composition, as in Table I, while not always exactly 0.2500, 0.5000, or 0.7500, differ only insignificantly from these values.

Also given in Table I are the equations of the least-squares lines for $(E - E°)$ *vs.* T obtained (1) at compositions in the AgCl-RbCl ($t = 0$) and AgCl-NaCl ($t = 1$) binary systems.

The partial molar excess free energy of mixing of AgCl at 800°C as well as the partial molar enthalpy and excess entropy of mixing of AgCl as calculated from the fitted curves are listed in Table I for each composition studied (1 cal is defined as 4.1840j). (For the composition at $X_{AgCl} = 0.1043$ in the AgCl-NaCl system, there are only two data points, and it was felt that the slope of this line is not sufficiently well defined for partial enthalpies and excess entropies to be calculated.)

Excess free energies of mixing.—Experimental values of the partial molar excess free energy of mixing of AgCl, $\Delta\bar{G}^E_{AgCl}$, at 800°C are plotted *vs.* X_{AgCl} along the three quasi-binary lines where $t = 0.25$, $t = 0.50$, and $t = 0.75$, as well as along the AgCl-RbCl ($t = 0$) and AgCl-NaCl ($t = 1$) real binary lines in Fig. 3. In Fig. 4 is a similar plot of the parameter $\Delta\bar{G}^E_{AgCl}/y^2$.

The 36 data points were fitted by a 9-coefficient equation of the form of Eq. [3]. The equation is given in Table II. Mean and maximum deviations were 17 and 54 cal. The fitted curves for the five lines of constant t are shown in Fig. 3, and as the solid lines in Fig. 4. It must be remembered when examining the

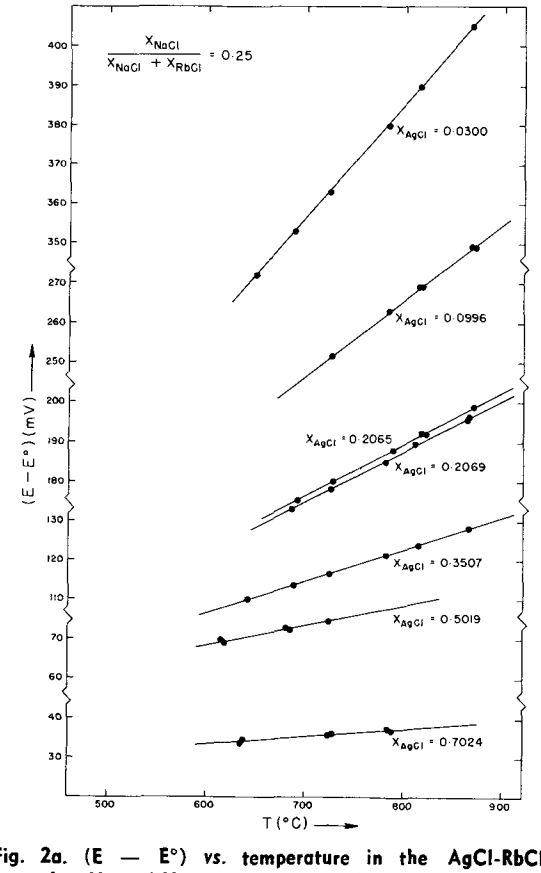

Fig. 2a. $(E - E°)$ *vs.* temperature in the AgCl-RbCl-NaCl system when $X_{NaCl}/(X_{RbCl} + X_{NaCl}) = 0.25$.

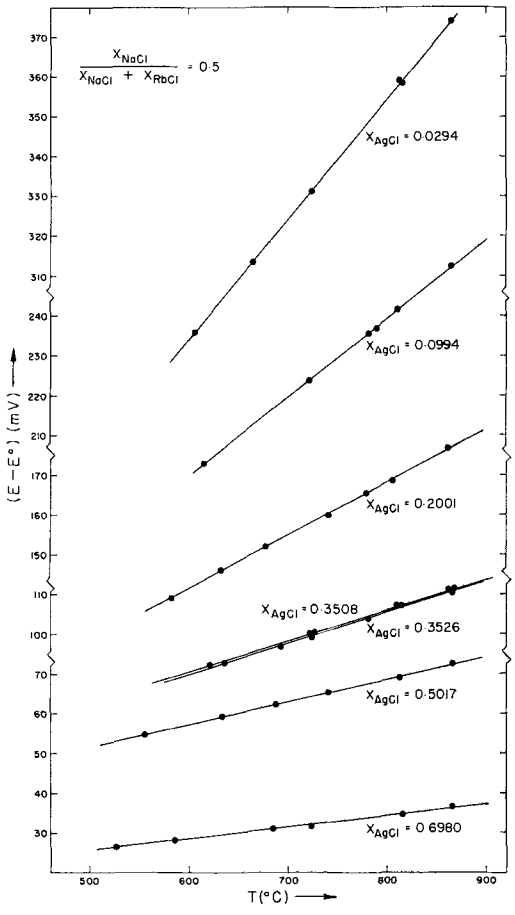

Fig. 2b. $(E - E°)$ *vs.* temperature in the AgCl-RbCl-NaCl system when $X_{NaCl}/(X_{RbCl} + X_{NaCl}) = 0.50$.

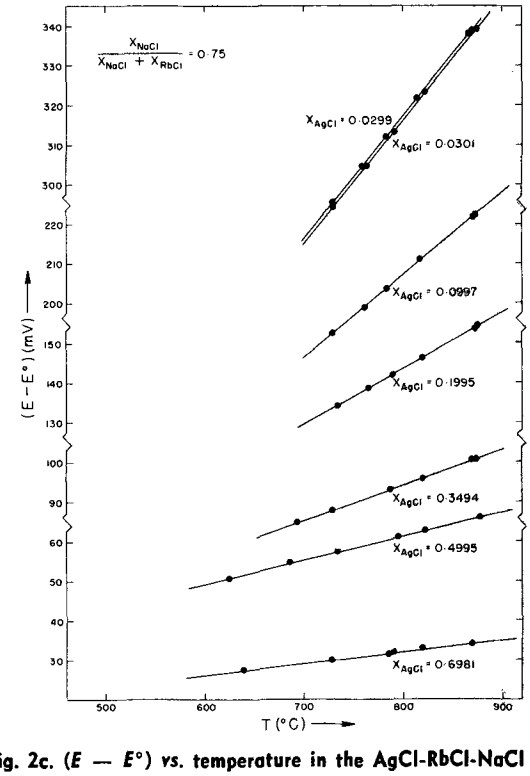

Fig. 2c. $(E - E°)$ *vs.* temperature in the AgCl-RbCl-NaCl system when $X_{NaCl}/(X_{RbCl} + X_{NaCl}) = 0.75$.

Table I. Least-squares fits for $(E - E^\circ)$ vs. temperature at compositions in the AgCl-RbCl-NaCl ternary system

$t = \frac{X_{NaCl}}{X_{RbCl} + X_{NaCl}}$	X_{AgCl}	$(E - E^\circ)$ (mV) (T = kelvins)	Mean deviation (mV)	Maximum deviation (mV)	$\Delta\bar{S}^E_{AgCl}$ (cal/°K-mole)	$\Delta\bar{H}_{AgCl}$ (cal/mole)	$\Delta\bar{G}^E_{AgCl}$ at 800°C (cal/mole)
0.2501	0.0300	75.4 + 0.2889T	0.1	0.2	−0.31	−1739	−1411
0.2499	0.0996	60.2 + 0.1917T	0.1	0.3	−0.16	−1389	−1213
0.2500	0.2065	48.8 + 0.1312T	0.2	0.5	−0.11	−1125	−1008
0.2500	0.2069	48.9 + 0.1292T	0.2	0.4	−0.15	−1128	−968
0.2501	0.3507	35.3 + 0.0816T	0.1	0.1	−0.20	−915	−599
0.2501	0.5019	23.9 + 0.0509T	0.1	0.2	−0.20	−551	−341
0.2500	0.7024	15.2 + 0.0208T	0.1	0.2	−0.22	−350	−112
0.5001	0.0294	30.4 + 0.3017T	0.3	0.4	−0.05	−702	−648
0.5001	0.0994	27.0 + 0.1978T	0.2	0.3	−0.03	−623	−595
0.5003	0.2001	25.4 + 0.1329T	0.2	0.4	−0.13	−587	−444
0.5000	0.3508	22.9 + 0.0772T	0.1	0.2	−0.30	−528	−205
0.5002	0.3526	20.9 + 0.0788T	0.2	0.5	−0.25	−481	−209
0.5001	0.5017	8.3 + 0.0561T	0.1	0.2	−0.08	−192	−109
0.4999	0.6980	3.7 + 0.0284T	0.1	0.3	−0.06	−86	−23
0.7499	0.0299	−14.3 + 0.3088T	0.1	0.1	0.15	329	171
0.7500	0.0301	−18.9 + 0.3122T	0.1	0.1	0.24	437	182
0.7500	0.0997	−15.3 + 0.2072T	0.1	0.3	0.20	352	142
0.7500	0.1995	−7.8 + 0.1409T	0.1	0.1	0.05	180	131
0.7500	0.3494	−1.5 + 0.0891T	0.1	0.2	−0.04	34	72
0.7500	0.4995	−3.5 + 0.0604T	0.1	0.1	0.01	81	67
0.7500	0.6981	0.3 + 0.0296T	0.1	0.1	−0.03	−6	27
$t = 0$	0.0297	120.2 + 0.2796T	0.2	0.4	−0.54	−2771	−2191
(AgCl-RbCl system)	0.0997	111.2 + 0.1750T	0.3	0.6	−0.55	−2654	−1978
	0.1999	90.6 + 0.1198T	0.1	0.3	−0.44	−2089	−1622
	0.3509	63.6 + 0.0766T	0.3	0.6	−0.31	−1467	−1129
	0.5007	33.5 + 0.0536T	0.3	0.5	−0.14	−772	−623
	0.5995	20.0 + 0.0407T	0.1	0.1	−0.08	−462	−377
	0.7007	10.7 + 0.0299T	0.1	0.4	−0.02	−247	−229
$t = 1.0$	0.0515	−72.0 + 0.2875T	0.4	0.6	0.74	1661	870
(AgCl-NaCl system)	0.1032	−54.2 + 0.2163T	0.2	0.5	0.47	1251	741
	0.1043	−49.5 + 0.2101T					765
	0.2058	−45.5 + 0.1553T	0.2	0.4	0.44	1050	579
	0.3580	−24.9 + 0.0968T	0.1	0.1	0.19	574	368
	0.5080	−12.8 + 0.0625T	0.2	0.5	0.10	294	191
	0.7073	−6.4 + 0.0331T	0.3	1.0	0.07	147	67
	0.8548	−5.2 + 0.0182T	0.3	0.9	0.11	119	4

(1 cal = 4.1840 j).

plots of $\Delta\bar{G}^E_{AgCl}/y^2$ in Fig. 4 that dividing $\Delta\bar{G}^E_{AgCl}$ by y^2 greatly magnifies the discrepancy between the fitted curve and the experimental points when y is small. When $y = 0.3$, for instance, errors are magnified about 11 times more than when $y = 1$ ($X_{AgCl} = 0$). The least-squares fit is done on the values of $\Delta\bar{G}^E_{AgCl}$, not on the values of $\Delta\bar{G}^E_{AgCl}/y^2$. In Fig. 4, the fitted curves for small values of y (*i.e.*, large values of X_{AgCl}) are shown as broken lines to indicate this uncertainty.

In Fig. 4 are shown, as dashed lines, the curves which would result if $\Delta\bar{G}^E_{AgCl}$ varied linearly (additively) with t, as t varied from 0 to 1 at constant X_{AgCl}. That is, the three dashed lines in Fig. 4 are ¼, ½, and ¾ of the way between the two experimental curves for the binary systems at $t = 0$ and $t = 1$. It is seen that when $X_{AgCl} = 0$, such additive (linear) behavior is very closely followed by the experimental curves, but as the solutions become richer in AgCl there occur progressively larger positive deviations of the experimental curves from this additive behavior.

Enthalpies of mixing.—The experimental values of the partial molar enthalpy of mixing of AgCl, $\Delta\bar{H}_{AgCl}$, are plotted *vs.* X_{AgCl} for the five values of t in Fig. 5. In Fig. 6 are similar plots of the parameter $\Delta\bar{H}_{AgCl}/y^2$. The 35 data points were fitted by a 6-coefficient equation of the form of Eq. [3]. The equation is given in Table III. Mean and maximum deviations were 63 and 147 cal. Fitted curves are shown in Fig. 5 and as the solid curves in Fig. 6. For large values of X_{AgCl}, the curves are again shown as broken lines in Fig. 6 to

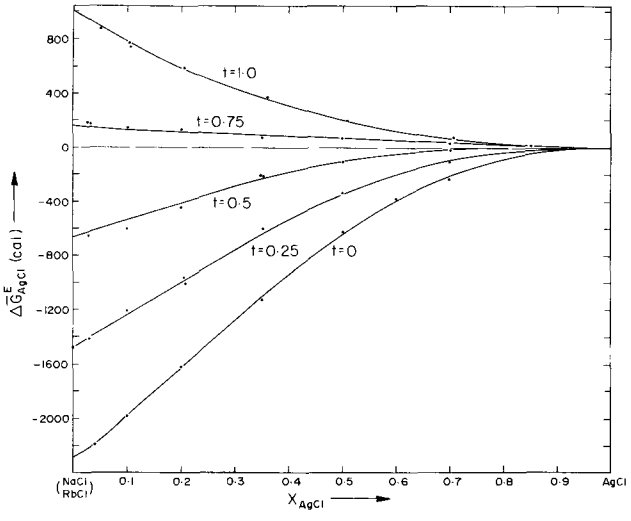

Fig. 3. $\Delta\bar{G}^E_{AgCl}$ at 800°C in the AgCl-RbCl-NaCl system (lines are from least-squares fit). $t = X_{NaCl}/(X_{RbCl} + X_{NaCl})$.

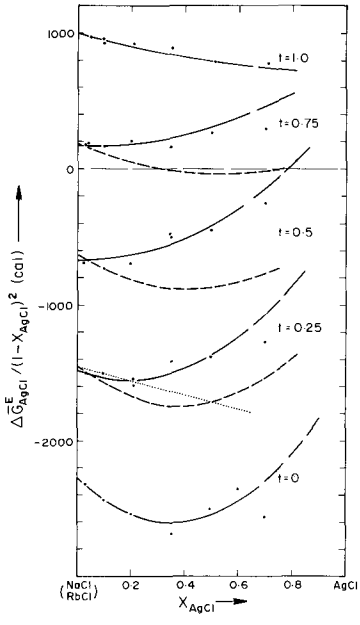

Fig. 4. $\Delta\bar{G}^E_{AgCl}/(1 - X_{AgCl})^2$ at 800°C in the AgCl-RbCl-NaCl system. $t = X_{NaCl}/(X_{RbCl} + X_{NaCl})$. ———, Least-squares fit. – – –, Assuming linearity with t at constant X_{AgCl}. [. . . . . , AgCl-KCl binary system (1).]

Table II. Least-squares fit for $\Delta\bar{G}^E_{AgCl}$ at 800°C vs. composition in the AgCl-RbCl-NaCl ternary system and other partial free energies and integral free energy of mixing as calculated analytically from the Gibbs-Duhem equation

$y = (1 - X_{AgCl})$ $\quad t = X_{NaCl}/(X_{RbCl} + X_{NaCl})$

Mean deviation = 17 cal Maximum deviation = 54 cal

$$\Delta\bar{G}^E_{AgCl} = (-1527 + 5702t - 3485t^2)y^2 + (-3368 + 478t + 3013t^2)y^3 + (2618 - 3018t + 590t^2)y^4$$

$$\Delta\bar{G}^E_{RbCl} = [-632t^2] + (3054 - 5702t)[y - 1] + (3525 + 5224t - 4992t^2)[y^2 - 1] + (-6859 + 3496t + 2620t^2)[y^3 - 1] + (2618 - 3018t + 590t^2)[y^4 - 1]$$

$$\Delta\bar{G}^E_{NaCl} = [-632 + 1264t - 632t^2] + (-2648 + 1268t)[y - 1] + (3286 + 2211t - 4992t^2)[y^2 - 1] + (-5853 + 3103t + 2620t^2)[y^3 - 1] + (2618 - 3018t + 590t^2)[y^4 - 1]$$

$$\Delta G^E = [-632 + 632t^2]y + (1527 - 5702t + 3485t^2)[y^2 - y] + (1684 - 239t - 1507t^2)[y^3 - y] + (-873 + 1006t - 197t^2)[y^4 - y]$$

Table III. Least-squares fit for $\Delta\bar{H}_{AgCl}$ vs. composition in the AgCl-RbCl-NaCl ternary system and other partial enthalpies and integral enthalpy of mixing as calculated analytically from the Gibbs-Duhem equation

$y = (1 - X_{AgCl})$ $\quad t = X_{NaCl}/(X_{RbCl} + X_{NaCl})$

Mean deviation = 63 cal Maximum deviation = 147 cal

$$\Delta\bar{H}_{AgCl} = (-3714 + 5490t - 3411t^2 + 2476t^3)y^2 + (702 + 268t)y^3$$

$$\Delta\bar{H}_{RbCl} = [-690t^2 - 160t^3] + (7428 - 5490t + 0 + 2476t^3)[y - 1] + (-4767 + 5222t - 3411t^2 + 2476t^3)[y^2 - 1] + (702 + 268t)[y^3 - 1]$$

$$\Delta\bar{H}_{NaCl} = [-770 + 1380t - 450t^2 - 160t^3] + (1938 + 1332t - 7428t^2 + 2476t^3)[y - 1] + (-4901 + 5222t - 3411t^2 + 2476t^3)[y^2 - 1] + (702 + 268t)[y^3 - 1]$$

$$\Delta H = [-770t + 690t^2 + 80t^3]y + (3714 - 5490t + 3411t^2 - 2476t^3)[y^2 - y] + (-351 - 134t)[y^3 - y]$$

indicate the uncertainty resulting from division by y^2 when y is small. The lines which would result if $\Delta\bar{H}_{AgCl}$ varied linearly (additively) with t at constant X_{AgCl} are shown in Fig. 6 as the dashed lines. These lines lie ¼, ½, and ¾ of the way between the two experimental curves at $t = 0$ and $t = 1$.

Excess entropies of mixing.—Experimental values of the partial molar excess entropy of mixing of AgCl, $\Delta\bar{S}^E_{AgCl}$, are plotted *vs.* X_{AgCl} for the five values of t in

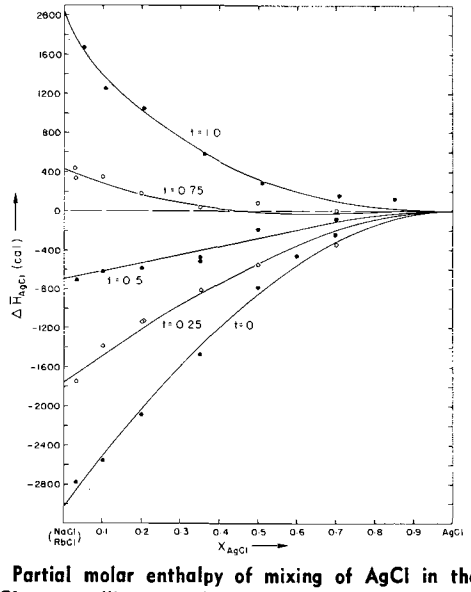

Fig. 5. Partial molar enthalpy of mixing of AgCl in the AgCl-RbCl-NaCl system (lines are from least-squares fit). $t = X_{NaCl}/(X_{RbCl} + X_{NaCl})$.

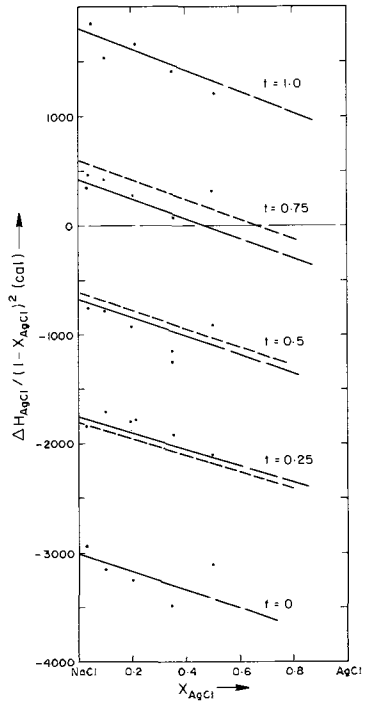

Fig. 6. $\Delta\bar{H}_{AgCl}/(1 - X_{AgCl})^2$ in the AgCl-RbCl-NaCl system. $t = X_{NaCl}/(X_{RbCl} + X_{NaCl})$. ———, Least-squares fit. – – –, Assuming linearity with t at constant X_{AgCl}.

Fig. 7. Also shown as solid lines are the fitted curves obtained using a 6-coefficient equation of the form of Eq. [3]. The equation is given in Table IV. Mean and maximum deviations were 0.05 and 0.17 cal/°K-mole. The lines which would result if $\Delta\bar{S}^E_{AgCl}$ varied linearly (additively) with t at constant X_{AgCl} are also shown in Fig. 7 as dashed lines. These lines represent entropies of mixing lying ¼, ½, and ¾ of the way between the two experimental curves for $t = 0$ and $t = 1$.

Calculation of partial properties of RbCl and NaCl and of integral molar properties.—The coefficients, (b_{jk}, c_{jk}, and ϕ_{jk}) in the expansions [4], [5], and [6] for the partial excess free energies $\Delta\bar{G}^E_{RbCl}$ and $\Delta\bar{G}^E_{NaCl}$, and for the integral molar excess free energy of mixing, ΔG^E, were calculated from the fitted coefficients, a_{jk}, of $\Delta\bar{G}^E_{AgCl}$ given in Table II. Equations [8], [9], and [10], respectively, were used for this purpose. The resulting expansions for $\Delta\bar{G}^E_{RbCl}$, $\Delta\bar{G}^E_{NaCl}$, and ΔG^E are given in Table II in the form of Eq. [13], [14], and [15]. In Table II, end point values, $\Delta\bar{G}^E_{RbCl(1,t)}$, $\Delta\bar{G}^E_{NaCl(1,t)}$, and $\Delta G^E_{(1,t)}$ as functions of t in the RbCl-

Table IV. Least-squares fit for $\Delta\bar{S}^E_{AgCl}$ vs. composition in the AgCl-RbCl-NaCl ternary system and other partial entropies and integral entropy of mixing as calculated analytically from the Gibbs-Duhem equation

$y = (1 - X_{AgCl})$ $\quad t = X_{NaCl}/(X_{RbCl} + X_{NaCl})$

Mean deviation = 0.05 cal/°K-mole
Maximum deviation = 0.17 cal/°K-mole

$$\Delta\bar{S}^E_{AgCl} = (-1.049 + 1.418t - 3.079t^2 + 2.489t^3)y^2 + (0.482 + 0.576t)y^3$$

$$\Delta\bar{S}^E_{RbCl} = [-0.208t^2] + (2.098 - 1.418t + 0 + 2.489t^3)[y - 1] + (-1.772 + 0.942t - 3.079t^2 + 2.489t^3)[y^2 - 1] + (0.482 + 0.576t)[y^3 - 1]$$

$$\Delta\bar{S}^E_{NaCl} = [-0.208 + 0.416t - 0.208t^2] + (0.680 + 4.740t - 7.467t^2 + 2.489t^3)[y - 1] + (-2.060 + 0.842t - 3.079t^2 + 2.489t^3)[y^2 - 1] + (0.482 + 0.576t)[y^3 - 1]$$

$$\Delta S^E = [-0.208t + 0.208t^2]y + (1.049 - 1.418t + 3.079t^2 - 2.489t^3)[y^2 - y] + (-0.241 - 0.288t)[y^3 - y]$$

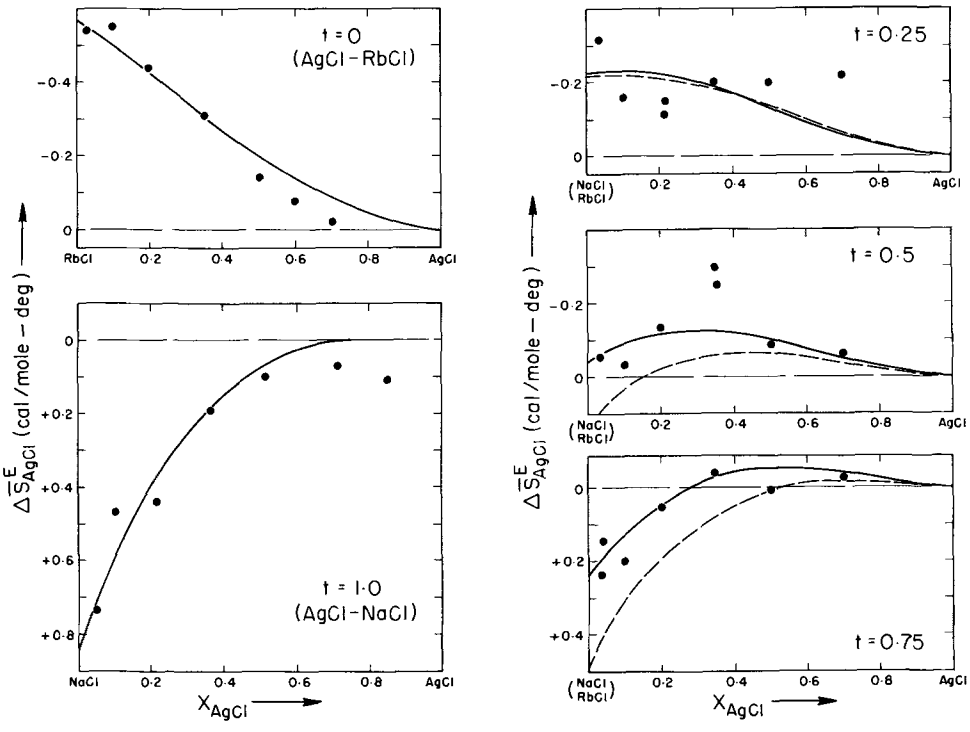

Fig. 7. $\Delta\bar{S}^E_{AgCl}$ in the AgCl-RbCl-NaCl system. $t = X_{NaCl}/(X_{RbCl} + X_{NaCl})$. ———, Least-squares fit. – – –, Assuming linearity with t at constant X_{AgCl}.

NaCl binary system are used. *Viz.*:

$$\Delta\bar{G}^E_{RbCl(1,t)} = -632t^2 \quad \text{cal/mole} \quad [17]$$

$$\Delta\bar{G}^E_{NaCl(1,t)} = -632(1-t)^2$$
$$= -632 + 1264t - 632t^2 \quad \text{cal/mole} \quad [18]$$

$$\Delta G^E_{(1,t)} = -632t(1-t)$$
$$= -632 + 632t^2 \quad \text{cal/mole} \quad [19]$$

(where $t = X_{NaCl}$ in the RbCl binary system from definition [2]). These are the values obtained from the phase diagram calculations (3).

Similar calculations were performed to give the partial molar enthalpies and excess entropies of mixing of RbCl and NaCl, and to give the integral molar enthalpies and excess entropies of mixing. The resulting equations are given in Tables III and IV. The end point values, $\Delta\bar{H}_{RbCl(1,t)}$, $\Delta\bar{H}_{NaCl(1,t)}$, and $\Delta H_{(1,t)}$ as functions of t in the RbCl-NaCl binary system were calculated from the data of Hersh and Kleppa (2). End point values of the excess entropies were calculated by combining the free energies calculated from the phase diagram with the calorimetric enthalpies (3).

The accuracy of all the end point data has been shown (3) to be quite good.

The calculated integral molar properties of mixing, ΔG^E, ΔH, and ΔS^E, are shown in Fig. 8, 9, and 10 in the form of iso-ΔG^E, iso-ΔH, and iso-ΔS^E plots. The analytical Gibbs-Duhem technique is very useful in the preparation of such 'iso-plots." With an equation for ΔG^E as in Table II, for example, one can calculate values of ΔG^E at hundreds of composition points within the ternary system using a computer, and one can then easily trace out lines of constant ΔG^E.

It may be noted that the lines of zero ΔG^E, zero ΔH, and zero ΔS^E in Fig. 8, 9, and 10 follow approximately the same composition path for all three properties.

Graphical plots of the partial molar properties of RbCl and NaCl are shown and discussed later.

As seen in Fig. 4, the quantity $\Delta\bar{G}^E_{AgCl}/y^2$ exhibits almost perfectly additive behavior as t varies from zero to unity at constant X_{AgCl} when$X_{AgCl} = 0$. Progressively increasing positive deviations from additivity occur, however, as X_{AgCl} increases. Guion *et al.* (7) made some similar measurements of $\Delta\bar{G}^E_{AgCl}$ using formation cells in the AgCl-KCl-NaCl and AgCl-CsCl-NaCl systems. Plots of $\Delta\bar{G}^E_{AgCl}/y^2$ at 800°C *vs.* X_{AgCl} at several values of t are shown in Fig. 11 (where t is defined as $t = X_{NaCl}/(X_{ACl} + X_{NaCl})$ where A = K or

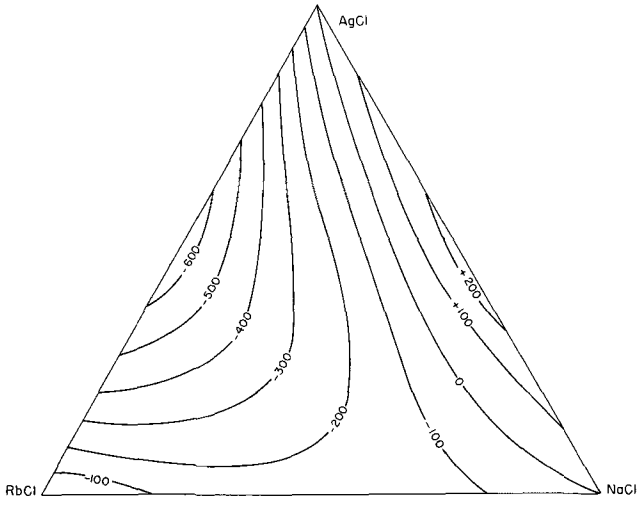

Fig. 8. Iso-ΔG^E lines at 800°C

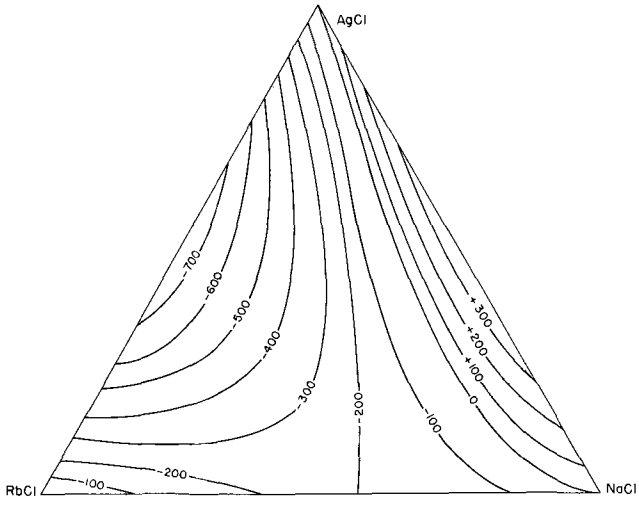

Fig. 9. Iso-ΔH lines

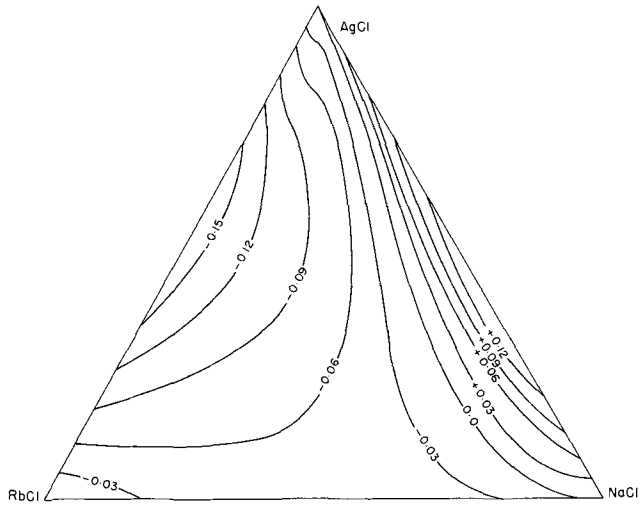

Fig. 10. Iso-ΔS^E lines

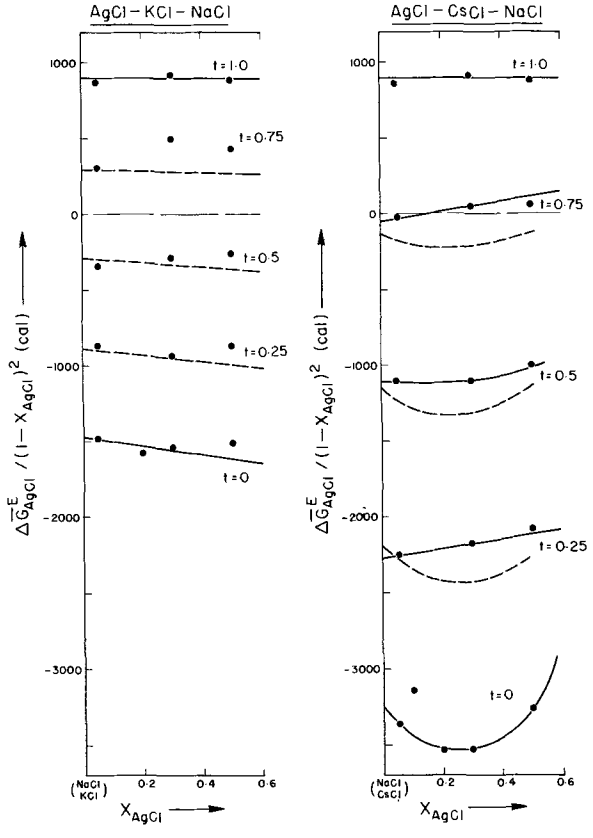

Fig. 11. $\Delta\bar{G}^E_{AgCl}/(1 - X_{AgCl})^2$ at 800°C in the AgCl-KCl-NaCl and AgCl-CsCl-NaCl systems [Guion et al. (7)]. $t = X_{NaCl}/(X_{ACl} + X_{NaCl})$ where A = K or Cs. – – –, Calculated assuming linearity with t at constant X_{AgCl}.

Cs). From the plots for the AgCl-CsCl-NaCl system, it is seen that behavior very similar to that observed in Fig. 4 is exhibited. For the AgCl-KCl-NaCl system, there is perhaps some evidence of positive deviations from additivity, although these deviations are certainly much less than in the other two systems.

In Fig. 4 is a plot of $\Delta\bar{G}^E_{AgCl}/y^2$ for the AgCl-KCl binary system (1). The shape of the curve for this real binary system is much different from the shape of the curve for the quasi-binary system where $t = 0.25$, even though the values of $\Delta\bar{G}^E_{AgCl}$ are similar in magnitude in the two cases.

In Fig. 6, it may be seen that $\Delta\bar{H}_{AgCl}/y^2$ exhibits nearly additive behavior within experimental error limits as t is varied at constant X_{AgCl}. In the plots of $\Delta\bar{S}^E_{AgCl}$ in Fig. 7, it is seen that there is evidence of quite large negative deviations from additivity in this property. A negative deviation from additivity in $\Delta\bar{S}^E_{AgCl}$ will, of course, cause a positive deviation in $\Delta\bar{G}^E_{AgCl}$. Thus, there is evidence that the deviations from additivity in $\Delta\bar{G}^E_{AgCl}$ as seen in Fig. 4 may be largely due to deviations from additivity in the excess entropy and not in the enthalpy. However, in attempting to separate the deviations from additivity in Fig. 4 into entropy and enthalpy effects, one is working near the limits of the experimental accuracy.

Enthalpies and excess entropies calculated from the results of Guion *et al.* (7) in the AgCl-KCl-NaCl and AgCl-CsCl-NaCl systems were too scattered for trends to be observable.

Discussion

In simple regular solution theory (8, 9) ΔG^E in a ternery system may be described by an equation of the form

$$\Delta G^E = X_1X_2b_{12} + X_1X_3b_{31} + X_2X_3b_{23} \quad [20]$$

where b_{12}, b_{31}, and b_{23} are concentration-independent parameters which have the same values in the ternary system as in the 1-2, 1-3, and 2-3 binary systems. Such an equation is usually derived assuming random mixing, and assuming constant, additive, pairwise interactions between particles. For simple molten salt solutions with a common anion, such as the AgCl-RbCl-NaCl system, the simple regular solution approach takes the major contribution to the energy of mixing to be due to second-nearest neighbor cation-cation pairwise interactions. For instance, in this theory (9), b_{23} is given by

$$b_{23} = \tfrac{1}{2}(2E_{23} - E_{22} - E_{33}) \quad [21]$$

where E_{23}, E_{22}, and E_{33} are the energies of 2-3, 2-2, and 3-3 second-nearest neighbor cation-cation "bonds," respectively.

From Eq. [20], the partial free energy of mixing of component 1 may be calculated, and is given by

$$\Delta\bar{G}^E_1 = y^2(1 - t)b_{12} + y^2tb_{31} - y_2t(1 - t)b_{23} \quad [22]$$

which may be written as

$$(\Delta\bar{G}^E_1/y^2) = y^{-2}[(1 - t)\Delta\bar{G}^E_{1(12)} + t\Delta\bar{G}^E_{1(13)})] - \Delta G^E_{23} \quad [23]$$

where $\Delta\bar{G}^E_{1(12)}$ and $\Delta\bar{G}^E_{1(13)}$ are values of $\Delta\bar{G}^E_1$ in the 1-2 and 1-3 binaries at the particular value of y in question, and ΔG^E_{23} is the integral excess free energy of mixing in the 2-3 binary at the end of the line of constant t in question. That is, in Fig. 12, $\Delta\bar{G}^E_1/y^2$ at point P is given by taking a linear variation in $\Delta\bar{G}^E_1$ between points a and b, and then subtracting the integral excess free energy of mixing at point c in the 2-3 binary. Equation [23] was first derived in the form given here by Alcock and Richardson (10), who had

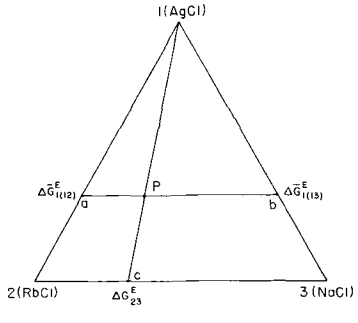

Fig. 12. Ternary relationships in Eq. [23]

much success with the equation in predicting the properties of liquid alloy systems dilute in component 1.

In most cases, the parameters b_{12}, b_{23}, and b_{31} will not be independent of concentration even in the binary systems. For instance, the present experimental results show that b_{12} and b_{31} in the AgCl-RbCl and AgCl-NaCl binary systems are not independent of concentration. Nevertheless, the geometrical relationship of Eq. [23] might still reasonably be expected to be a fairly good approximation.

In the RbCl-NaCl binary system, $\Delta G^E_{23} = -632 X_{NaCl} X_{RbCl}$ (1). In Fig. 4, then, Eq. [23] predicts a constant positive deviation from additivity at $t = 0.5$ of about +158 cal. This deviation should be independent of X_{AgCl}. No such constant deviation is seen in Fig. 4. In the solutions dilute in AgCl, where Eq. [23] should be expected to hold best (10), nearly perfectly additive behavior is observed, as if the final term in Eq. [23] were not present. As the concentration of AgCl is increased, positive deviations from additivity are observed, and these rapidly become much greater than 158 cal.

A similar relationship to Eq. [23] should also hold for the quantity $\Delta \overline{H}_{AgCl}/y^2$. In the RbCl-NaCl binary system at $X_{RbCl} = X_{NaCl} = 0.5$, ΔH_{23} is about −200 cal (2), and the model thus predicts a constant positive deviation from additivity of +200 cal at $t = 0.5$. Once more, as may be seen in Fig. 6, this behavior is not observed. Within the experimental error limits, actually, it would seem that the system exhibits nearly additive behavior everywhere.

So it is seen that Eq. [23] does not explain the observed partial properties of AgCl. This would indicate that the regular solution theory is not applicable to the present system. However, if the partial properties of RbCl and NaCl are examined, Eq. [23] does appear to explain the observations quite well, as will now be shown.

Behavior of partial properties of RbCl and NaCl.— In Fig. 13 are plots of $(\Delta \overline{G}^E_{RbCl}/(1 - X_{RbCl})^2)$ *vs.* the parameter $X_{AgCl}/(X_{NaCl} + X_{AgCl})$ at constant values of X_{RbCl}. The parameter $X_{AgCl}/(X_{NaCl} + X_{AgCl})$ assumes constant values along lines radiating from the "2-corner" of the composition triangle. It is seen that negative deviations from additivity occur along the paths of constant X_{RbCl}.

The Alcock-Richardson equation may be applied to component 2 (RbCl) to give an equation for $(\Delta \overline{G}^E_{RbCl}/(1 - X_{RbCl})^2)$ similar to Eq. [23]. This would predict

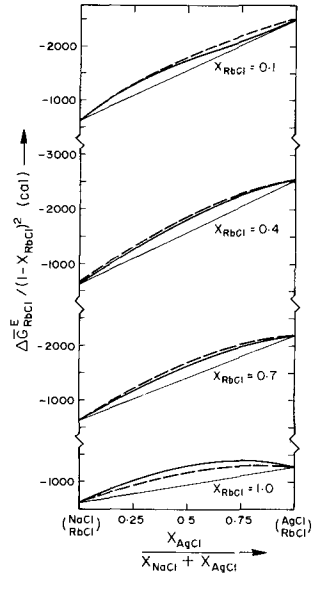

Fig. 13. $\Delta \overline{G}^E_{RbCl}/(1 - X_{RbCl})^2$ vs. $X_{AgCl}/(X_{NaCl} + X_{AgCl})$ at constant values of X_{RbCl} at 800°C. ———, Experimental. – – –, Calculated.

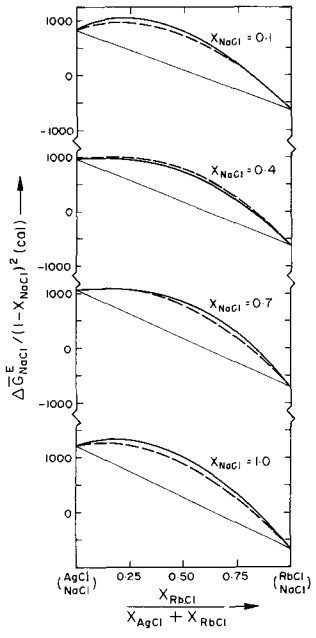

Fig. 14. $\Delta \overline{G}^E_{NaCl}/(1 - X_{NaCl})^2$ vs. $X_{RbCl}/(X_{AgCl} + X_{RbCl})$ at constant values of X_{NaCl} at 800°C. ———, Experimental. – – –, Calculated.

that in Fig. 13, at any value of $X_{AgCl}/(X_{NaCl} + X_{AgCl})$, there should be constant deviations from additivity, independent of X_{RbCl}, equal to $(-\Delta G^E_{13})$, where ΔG^E_{13} is the integral excess free energy of mixing in the 1-3 (AgCl-NaCl) binary system at the end of the line of constant $X_{AgCl}/(X_{NaCl} + X_{AgCl})$ ratio. Since ΔG^E_{13} in the AgCl-NaCl system is positive, negative deviations from additivity are expected. The actual predicted curves are shown in Fig. 13. Agreement with the experimental curves is very good.

In Fig. 14 are plots of $(\Delta \overline{G}^E_{NaCl}/(1 - X_{NaCl})^2)$ *vs.* the parameter $X_{RbCl}/(X_{AgCl} + X_{RbCl})$ at constant values of X_{NaCl}. Positive deviations from additivity occur. The Alcock-Richardson equation predicts that these deviations should be equal to $(-\Delta G^E_{12})$, where ΔG^E_{12} is the integral molar excess free energy of mixing in the 1-2 (AgCl-RbCl) binary system at the end of the line of constant $X_{RbCl}/(X_{AgCl} + X_{RbCl})$ ratio in question. The deviations should be positive, since ΔG^E_{12} in the AgCl-RbCl system is negative. Predicted curves are shown in Fig. 14, and are in very good agreement with the experimental curves.

In Fig. 15 and 16 are plots similar to those in Fig. 13 and 14, respectively, except that the partial enthalpy functions rather than the partial free energy functions are plotted. The curves predicted by the Alcock-Richardson equation are also shown. In view of the greater experimental errors in the enthalpy measurements, the agreement with experiment is good.

The experimental errors in the excess entropies are great enough that it is not possible to draw any conclusions regarding deviations from additivity in plots $\Delta \overline{S}^E_{RbCl}$ and $\Delta \overline{S}^E_{NaCl}$.

So, it may be seen that the simple considerations of regular solution behavior used in the derivation of Eq. [23] are sufficient to explain the observed partial properties of RbCl and NaCl quite satisfactorily, even though these same considerations completely fail to explain the partial properties of AgCl. This is evidence that the bonding of AgCl in these solutions is of different character than that of the alkali chlorides. Evidence from measurements on the binary systems that silver-chlorine bonds have a partially covalent nature has been presented previously (1).

The advantages of examining the partial properties of all the components when studying a ternary system can be seen.

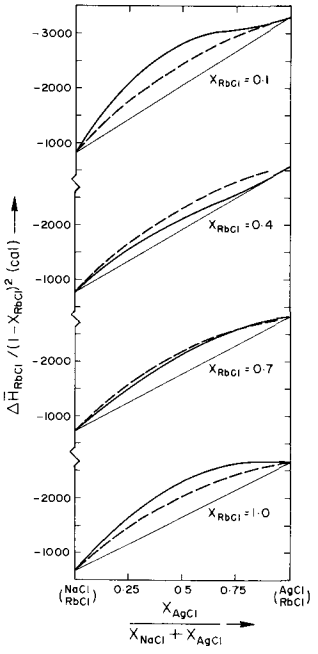

Fig. 15. $\Delta\bar{H}_{RbCl}/(1 - X_{RbCl})^2$ *vs.* $X_{AgCl}/(X_{NaCl} + X_{AgCl})$ **at constant values of** X_{RbCl}. ———, **Experimental.** – – –, **Calculated.**

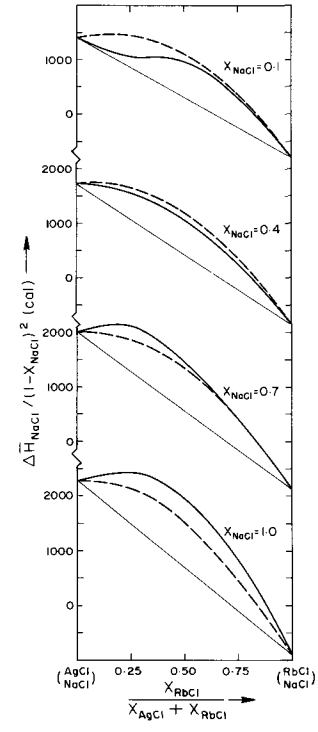

Fig. 16. $\Delta\bar{H}_{NaCl}/(1 - X_{NaCl})^2$ *vs.* $X_{RbCl}/(X_{AgCl} + X_{RbCl})$ **at constant values of** X_{NaCl}. ———, **Experimental.** – – –, **Calculated.**

At high dilutions in the RbCl-NaCl binary, it has been shown that $\Delta\bar{G}^E_{AgCl} = RT \ln \gamma_{AgCl}$ varies almost linearly with t (γ_{AgCl} = activity coefficient of AgCl). It may be noted, however, that a corresponding plot of γ_{AgCl} *vs.* t exhibits negative deviations from linearity. AgCl is more stable (γ_{AgCl} is lower) in dilute solution in RbCl than in NaCl. Because γ_{AgCl} exhibits negative deviations from linearity with t, AgCl dissolved, say, in an equimolar mixture of RbCl and NaCl will have an activity closer to that which it would have in pure RbCl. For any solute dissolved in a mixture of two solvents in which ($RT \ln \gamma_{solute}$) varies approximately linearly as t (where t is the molar ratio of the two solvents), γ_{solute} will show negative deviations from linearity. The greater the difference in the values of γ_{solute} in the two individual solvents, the greater will be the deviations. Therefore, if the solute were not particularly stable in solvent A, but were quite stable in solvent B, the addition of a relatively small amount of B to a solution of the solute in A would have a very large stabilizing effect.

Acknowledgments

A maintenance fellowship for one of us (ADP) from Shell Canada Limited, and financial assistance from the National Research Council of Canada are gratefully acknowledged.

NOMENCLATURE

X_i	Mole fraction of component i
y	$(1 - X_1) = (1 - X_{AgCl})$
t	$X_3/(X_2 + X_3) = X_{NaCl}/(X_{RbCl} + X_{NaCl})$
f_i	Some excess partial molar property of mixing of component i
f	Some excess integral molar property of mixing
a_{jk}	Coefficients in power series expansion of f_1
b_{jk}	Coefficients in power series expansion of f_2
c_{jk}	Coefficients in power series expansion of f_3
ϕ_{jk}	Coefficients in power series expansion of f
E	Cell potential (mV)
$E°$	Standard cell potential (with pure AgCl electrolyte) (mV)
T	Temperature (°K)
$\Delta\bar{G}^E_i$	Partial molar excess free energy of mixing of component i (cal/mole)
$\Delta\bar{H}_i$	Partial molar enthalpy of mixing of component i (cal/mole)
$\Delta\bar{S}^E_i$	Partial molar excess entropy of mixing of component i (cal/°K-mole)
ΔG^E	Integral molar excess free energy of mixing (cal/mole)
ΔH	Integral molar enthalpy of mixing (cal/mole)
ΔS^E	Integral molar excess entropy of mixing (cal/°K-mole)
b_{12}, b_{31}, b_{23}	"Interaction parameters" (cal/mole)

Manuscript submitted Sept. 14, 1970; revised manuscript received March 16, 1971.

Any discussion of this paper will appear in a Discussion Section to be published in the June 1972 JOURNAL.

REFERENCES

1. A. D. Pelton and S. N. Flengas, *This Journal*, **117**, 1130 (1970).
2. L. S. Hersh and O. J. Kleppa, *J. Chem. Phys.*, **42**, 1309 (1965).
3. A. D. Pelton and S. N. Flengas, *Can. J. Chem.*, **48** (1970).
4. A. D. Pelton and S. N. Flengas, *ibid.*, **47**, 2283 (1969).
5. A. D. Pelton and S. N. Flengas, *ibid.*, **48**, 752 (1970).
6. M. Margules, *Sitz-Ber. Math-Naturw. Kl. Bayer. Akad. Wiss. München. IIa*, **104**, 1243 (1895).
7. J. Guion, M. Blander, D. Hengstenberg, and K. Hagemark, *J. Phys. Chem.*, **72**, 2086 (1968).
8. E. A. Guggenheim, "Mixtures," Oxford University Press, New York (1952).
9. T. Førland, Chap. 2 in "Fused Salts," pp. 74-78, B. Sundheim, Editor, McGraw Hill, New York (1964).
10. C. B. Alcock and F. D. Richardson, *Acta Met.*, **6**, 385 (1958).

The Effect of Competition with Water on the Kinetic Parameters in Electrode Reactions

E. Gileadi*

Institute of Chemistry, Tel Aviv University, Ramat Aviv, Israel

and G. E. Stoner

Department of Materials Science, School of Engineering and Applied Science, University of Virginia, Charlottesville, Virginia 22901

ABSTRACT

The effect of competition with water on electrode kinetics as well as the kinetics of chemical reactions catalyzed by metals in solution has been determined theoretically. The model of Bockris, Devanathan, and Muller was taken into account and shown to play a considerable role for large molecules and for potentials far removed from the potential of zero charge.

The importance of adsorbed intermediates (*e.g.*, hydrogen atoms or OH radical) in the mechanism of electrode reactions has been recognized early in the development of mechanistic studies of electrode kinetics (1). Detailed discussions of the Tafel slopes which should be obtained under limitingly low or limitingly high values of the fractional surface coverage, where the Langmuir adsorption isotherm is applicable, are available (2-4). The case of intermediate values of the coverage on a heterogeneous surface, where the Temkin or Frumkin isotherm is applicable has also been worked out in detail for various reactions (5, 6).

Butler (7, 8) considered the role of the energy of adsorbed water molecules as important in the adsorption process. Replacement of adsorbed water on solid electrodes was treated by Barradas and Conway (9). Mott and Watts-Toben (10) introduced a model for the potential dependent orientation of water molecules which has been recently applied by Bockris, Devanathan, and Muller (11) and Muller (12) for the derivation of an isotherm. Thus, it is now realized that adsorption from solution onto the surface of an electrode is a replacement reaction, the energetics of which depend mainly on the difference between the energy of adsorption of the adsorbent and the energy of desorption of an appropriate number of water molecules (13). The potential dependence of adsorption of neutral organic molecules has been interpreted alternatively as being due to the change of energy of the double layer capacitor (14-16) and as due to the dependence of energy of adsorption of water molecules on the field across the metal/solution interface (11, 13). More recently it was shown (18) that this type of effect should be taken into consideration when discussing the charge-transfer adsorption of organic species. Changing the potential has two effects in this case: Equilibrium is shifted toward a higher degree of adsorption due to charge transfer, while competition with adsorbed water tends to decrease the extent of adsorption. In a study of the anodic oxidation of hydrazine on gold electrodes (19) this effect was also taken into account to explain the observed Tafel slope, which deviated markedly from any simple multiple of $(2.3\ RT/\mathbf{F})$.

In the present paper the value of the Tafel slope has been calculated for a number of commonly occurring mechanisms. Competition between adsorbed intermediates and water molecules for sites on the surface affects the kinetics of the reaction in two ways. On the one hand the degree of coverage by adsorbed intermediates and its rate of change with potentials $d\theta/d(\Delta\phi)$ is altered, and has been shown previously (18). On the other hand the specific rate constant for the rate-determining step (rds) is affected, increasing in the case of a desorption step and decreasing in the case of an adsorption step. The relationship between the dependence of the apparent standard free energy of adsorption and the apparent standard free energy of activation on potential (*i.e.*, between the dependence of the equilibrium constant and the specific rate constant on potential) is similar to that calculated for the dependence of the same quantities on coverage under Temkin conditions, as discussed elsewhere (5, 6).

The isotherm of Bockris, Devanathan, and Muller (11) has been employed. This was criticized recently by Damaskin (16) for not taking into account the contribution due to the change of energy of the double layer capacitor, as proposed by Frumkin (14). However, it was shown recently by Gileadi (20) that this is a relatively small contribution, which does not exceed *ca.* 10% in most cases of practical interest. Thus, including this correction does not alter the results presented below qualitatively.

Calculation of Tafel Slopes

The bromine evolution reaction.—General considerations.—A simple anodic process, the bromine evolution reaction has been chosen to exemplify the method of derivation of Tafel slope. This reaction takes place in two steps. The initial charge transfer

$$Br^- \underset{k_{-1}}{\overset{k_1}{\rightleftharpoons}} Br_{ads} + e \qquad [1]$$

followed by a surface recombination of two adsorbed atoms

$$2Br_{ads} \xrightarrow{k_2} Br_2 \qquad [2]$$

or by further charge transfer according to the equation

$$Br_{ads} + Br^- \xrightarrow{k_3} Br_2 + e \qquad [3]$$

Surface recombination rds.—If the surface recombination step (Eq. [2]) is assumed rate determining, with the preceding charge transfer step at quasi-equilibrium, the rate equation at limitingly low coverage is commonly written as

$$i = n\mathbf{F}k_2\theta^2 = n\mathbf{F}k_2 K_1^2 C_{Br}^2 - \exp(2\Delta\phi\mathbf{F}/RT) \qquad [4]$$

giving rise to a Tafel slope of $b = 2.3RT/2\mathbf{F}$.

The dependence of adsorption on potential at high values of the field is obtained from the equations de-

* Electrochemical Society Active Member.

Key words: adsorption, electrode kinetic, water competition.

rived by Bockris *et al.* (12) as a variation of the equilibrium constant K_1, with potential (18).

$$K_1 = K_{1,o} \exp - \left(\frac{m\mu}{e_o\nu}\right)\left(\frac{\Delta\phi \mathbf{F}}{RT}\right) \qquad [5]$$

where m is the number of water molecules replaced by each molecule of adsorbed intermediate, μ is the dipole moment of water, e_o is the electronic charge, and ν is the thickness of the compact part of the double layer, taken in this case to be equal to the diameter of a water molecule on the surface. The minus sign in the exponent arises from the assumption that the anodic oxidation takes place at a high positive rational potential, *i.e.*, far anodic to the potential of zero charge, where the competition with water causes a decrease in fractional coverage with increasing potential.

Equation [5] may also be written in the form

$$\Delta G^\circ = \Delta G^\circ_o + \left(\frac{m\mu}{e_o\nu}\right)\Delta\phi \mathbf{F} \qquad [6]$$

Where ΔG° is the apparent standard free energy for the adsorption equilibrium and ΔG°_o is its value at $\Delta\phi = 0$. It was shown both experimentally and theoretically (20, 21) that the change in apparent standard free energy of activation (22) for a given reaction is proportional to the change in the apparent standard free energy of the reaction. Thus

$$\Delta G^{\circ\neq} = G^{\circ\neq}_o - \left(\frac{m\mu}{e_o\nu}\right)\beta\Delta\phi \mathbf{F} \qquad [7]$$

where β is a symmetry factor the value of which is commonly taken to be near 0.5, and $\Delta G^{\circ\neq}$ and $\Delta G^{\circ\neq}_o$ are the apparent standard free energies of activation at some potential $\Delta\phi$ and at $\Delta\phi = 0$, respectively. Equation [7] has a negative sign because the energy of activation for the desorption process (Eq. [2]) is decreased with increasing potential.

From Eq. [7] one has for the rate constant k_2 the expression

$$k_2 = k_{2,o} \exp \frac{m\mu}{e_o\nu}\left(2\beta \frac{\Delta\phi \mathbf{F}}{RT}\right) \qquad [8]$$

where the factor 2 has been introduced because two adsorbed species are desorbed in each act of the rate-determining step. Using the values of K_1 and k_2 in Eq. [4] one has

$$i = K^1 C^2_{Br^-} \exp\left(\frac{2\Delta\phi \mathbf{F}}{RT}\right) \exp - \left(\frac{m\mu}{e_o\nu}\right)\left(\frac{2\Delta\phi \mathbf{F}}{RT}\right) \exp\left(\frac{m\mu}{e_o\nu}\right)\left(\frac{2\beta\Delta\phi \mathbf{F}}{RT}\right)$$

$$= K^1 C^2_{Br^-} \exp\left(\frac{2\Delta\phi \mathbf{F}}{RT}\right)\left[1 - \frac{m\mu}{e_o\nu}(1-\beta)\right] \qquad [9]$$

The numerical values to be used in Eq. [9] are: $\mu = 1.8 \times 10^{-18}$ esu; $e_o = 4.8 \times 10^{-10}$ esu; $\nu = 2.7 \times 10^{-8}$ cm, and $\beta = 0.5$. With these, Eq. [9] becomes

$$i = K^1 C_{Br^-} \exp(2\Delta\phi \mathbf{F}/RT)(1 - 0.07m) \qquad [10]$$

The Tafel slope will depend on the size and mode of adsorption of the intermediate species, which determines the number of water molecules replaced from the surface. For the case of bromine discussed here a value of $m = 2$ would seem reasonable, giving rise at room temperature to

$$b = (2.3RT/2\mathbf{F})(1 - 0.07m)^{-1} = 35 \text{ mV}$$

to be compared to a value of 30 mV obtained for the same mechanism, neglecting the effect of competition with water.

In the other extreme case, when θ approaches unity, the rate equation is commonly written as

$$i = n\mathbf{F}k_2 \qquad [11]$$

Table I. Values of the Tafel slope (in mV) calculated for different mechanisms in the bromine evolution reaction

Mechanism	$\theta \ll 1$		$0.2 < \theta < 0.8$		$\theta \to 1$	
	$m = 0$	$m = 2$	$m = 0$	$m = 2$	$m = 0$	$m = 2$
$Br^- \rightleftharpoons$ [Br] + e; 2 [Br] $\xrightarrow{rds}$ Br_2	30	35	60	60	∞	214
$Br^- \rightleftharpoons$ [Br] + e; [Br] + $Br^- \xrightarrow{rds} Br_2 + e$	40	42	60	64	120	93
$Br^- \xrightarrow{rds}$ [Br] + e; [Br] + [Br] $\rightarrow Br_2$	120	167	—	—	—	—

which leads to a limiting current behavior.[1] If the dependence of k_2 on potential according to Eq. [8] is taken into account one finds, however

$$i = K^1 \exp \frac{m\mu}{e_o\nu}\left(\frac{2\beta\Delta\phi \mathbf{F}}{RT}\right) \doteq K^1 \exp 0.14m(\Delta\phi \mathbf{F}/RT) \qquad [12]$$

yielding a Tafel slope of

$$b = (2.3RT/\mathbf{F})/0.14m = 214 \text{ mV}$$

At intermediate values of the coverage, assuming the Frumkin isotherm (23) to prevail, the rate equation will be written in the form (5, 6)

$$i = n\mathbf{F}K_1\theta^2 \exp(2\beta mr\theta/RT) \qquad [13][2]$$

and the equilibrium in step [1] can be represented by the isotherm

$$\frac{\theta}{1-\theta} \exp\left(\frac{mr\theta}{RT}\right) = K_1 C_{Br^-} \exp \frac{\Delta\phi \mathbf{F}}{RT} \qquad [14]$$

in which the pre-exponential term in θ may be neglected in comparison with the exponential term (Temkin's approximation). Thus from Eq. [14] one has

$$\exp \frac{r\theta}{RT} = K_1^{1/m} C_{Br^-}^{-1/m} \exp \frac{\Delta\phi \mathbf{F}}{mr\theta} \qquad [15]$$

combining Eq. [15] and [13], and introducing the potential dependence of K_1 and k_2 from Eq. [5] and [8], respectively, one has

$$i = K^1 C^2_{Br^-} \exp(\Delta\phi \mathbf{F}/2\beta RT) \qquad [16]$$

yielding a Tafel slope of

$$b = 2.3RT/2\beta\mathbf{F} = 60 \text{ mV}$$

It is thus found that for this mechanism under Temkin conditions the calculated Tafel slope is not affected by taking into account the competition with water. This, however, is not always the case under Temkin conditions, as shown in Table I.

Ion-atom step rate determining.—It will now be assumed that reaction [3] is rate determining, with reaction [1] still at quasi-equilibrium. The rate equation can be written under Langmuir conditions, in the form

$$i = n\mathbf{F}k_3 C_{Br^-}\theta \exp \beta\Delta\phi \mathbf{F}/RT \qquad [17]$$

and the rate constant will depend on potential according to the equation

$$k_3 = k_{3,o} \exp(0.14\beta m\Delta\phi \mathbf{F}/RT) \qquad [18]$$

[1] This is called the reaction limited current, to distinguish it from the diffusion limited current observed when the over-all reaction rate is controlled by the rate of mass transport of reactions to the surface.

[2] The parameter r in this paper is defined in a slightly different manner tnan in previous publications (5, 6). It is the rate of change of the apparent standard free energy of adsorption with coverage per mole of adsorption sites. The product mr is the same parameter per mole of adsorbed species.

Substituting θ for low coverage conditions as in Eq. [4] and taking into account the variation of k_3 and of K_1 with potential (Eq. [18] and [5], respectively), the rate equation becomes

$$i = K^1 C^2_{Br^-} \exp [0.14\beta m + (1 - 0.14m) + \beta]\Delta\phi\mathbf{F}/RT$$

$$= K^1 C^2_{Br^-} \exp [1 + \beta - 0.14m(1 - \beta)]\Delta\phi\mathbf{F}/RT \quad [19]$$

which gives rise to a Tafel slope of

$$b = (2.3RT/\mathbf{F})/(1.5 - 0.07m) = 42 \text{ mV}$$

to be compared with a value of 40 mV obtained for the same mechanism when the effect of competition with water is not taken into account.

Considering the same mechanism for limiting high coverage ($\theta \to 1$). The rate equation is obtained by combining [17] and [18]

$$i = K^1 \exp \frac{\beta\Delta\phi\mathbf{F}}{RT} [1 + 0.14m] \quad [20]$$

The resulting Tafel slope is

$$b = (2.3 \times 2RT/\mathbf{F})/(1 + 0.14m) = 93 \text{ mV}$$

to be compared with a slope of 0.12V obtained when m is put equal to zero.

In the intermediate coverage range, under Temkin conditions, the rate equation will take the form

$$i = n\mathbf{F}k_3\theta C_{Br^-} \exp (\beta mn\theta/RT) \exp (\beta\Delta\phi\mathbf{F}/RT) \quad [21]$$

The exponential term in θ is substituted from Eq. [15] and the potential dependence of K_1 and k_3 from Eq. [5] and [18], respectively, to give

$$i = K^1 C_{Br^-}{}^{1+\beta} \exp \frac{\Delta\phi\mathbf{F}}{RT} [0.14\beta m + \beta + (\beta - 0.14m)]$$

$$= K^1 C_{Br^-}{}^{1+\beta} \exp \frac{\Delta\phi\mathbf{F}}{RT} [2\beta - 0.14m(1 - \beta)] \quad [22]$$

hence

$$b = (2.3RT/\mathbf{F})/(1 - 0.07m) = 64 \text{ mV}$$

as compared to 60 mV for $m = 0$.

Initial discharge rate determining.—Consider now the case where the initial discharge step (Eq. [1]) is rate determining. The rate equation

$$i = n\mathbf{F}k_1 C_{Br^-}(1 - \theta) \exp (\beta\Delta\phi\mathbf{F}/RT) \quad [23]$$

The rate constant in this case decreases with increasing anodic potential because it relates to an adsorption process, thus

$$k_1 = k_{1,o} \exp - \left(\frac{m\mu}{e_o\nu}\right)\left(\frac{\beta\Delta\phi\mathbf{F}}{RT}\right) \quad [24]$$

Only the low coverage case needs to be considered when formation of the intermediate is the rds. Thus

$$i = n\mathbf{F}k_{1,o}C_{Br^-} \exp (\beta\Delta\phi\mathbf{F}/RT)(1 - m\mu/e_o\nu) \quad [25]$$

and hence

$$b = 2(2.3RT/\mathbf{F})/(1 - 0.14m) = 167 \text{ mV}$$

compared to 0.12V for $m = 0$.

It is interesting to note that this model can, for the first time, predict Tafel slopes that are higher than 2 x 2.3$RT/\mathbf{F}$ for a simple mechanism.

Table I summarizes the Tafel slopes obtainable for various mechanisms of the bromine evolution reaction assuming $m = 2$. The usual Tafel slopes calculated when the effect of change of free energy of adsorption due to competition with water is not taken into account ($m = 0$) are given for comparison.

Electroorganic reactions.—From the discussion above it can be seen that the effect of change of apparent standard free energy of adsorption with potential on the Tafel slope increases with the size of the molecule or the number of sites it occupies on the surface. Thus, it would seem most appropriate to apply the above considerations to the interpretation of kinetic parameters observed in the study of electrode reactions of organic compounds. In Table II a number of typical mechanisms for the stepwise anodic oxidation of an organic compound is shown with the corresponding Tafel slopes for low, intermediate, and high coverage. The numbers of water molecules replaced by the substrate, the first and the second intermediate are denoted m, l, and p, respectively. The method of derivation of these Tafel slopes is similar to that shown above for the bromine evolution reaction, and will not be reproduced here. The choice of mechanisms is somewhat arbitrary and Table II is mainly intended to illustrate the type of results which may be expected under somewhat more complex situations than the bromine evolution reaction. The usual Tafel slope can be obtained in each case by setting m, l, and p equal to zero.

Table II. Tafel slope derived for different typical organic oxidation reactions at an electrode

	Mechanism	$b/(2.3RT/\mathbf{F})$ $\theta << 1$	$0.2 < \theta < 0.8$	$\theta \to 1$
I.	$A \rightleftharpoons [A] + mH_2O$			
	$[A] \xrightarrow{rds} [B] + (m - l)H_2O$	$[0.07(m + l)]^{-1}$	∞	$[0.07(m - l)]^{-1}$
II.	$A \rightleftharpoons [A] + mH_2O$			
	$[A] \xrightarrow{rds} [B] + H^+ + e + (m - l)H_2O$	$2[1\cdot0.14(m + l)]^{-1}$	2	$2[1 + 0.14(m - l)]^{-1}$
III.	$A \rightleftharpoons [B] + H^+ + e = mH_2O$			
	$[B] \xrightarrow{rds} [C] + (m - l)H_2O$	$[1\text{-}0.07(m + l)]^{-1}$	$2\left[\frac{m - l}{m}\right]^{-1}$	$[0.07(m - l)]^{-1}$
IV.	$A \rightleftharpoons [B] + H^+ + e + mH_2O$			
	$[B] \xrightarrow{rds} [C] + H^+ + e + (m - l)H_2O$	$[1.5\text{-}0.07(m + l)]^{-1}$	$2\left[1 + \left(\frac{m - l}{m}\right)\right]^{-1}$	$2[1 + 0.14(m - l)]^{-1}$
V.	$A \rightleftharpoons [B] + H^+ + e + mH_2O$			
	$[B] \rightleftharpoons [C] + H^+ + e + (m - l)H_2O$			
	$[C] \xrightarrow{rds} [D] + (l - p)H_2O$	$[2\text{-}0.07(l + p)]^{-1}$	$\left[\frac{l - p}{l}\right]^{-1}$	$[0.07(l - p)]^{-1}$

Discussion

Scope and applicability of the method.—The theory for the calculation of Tafel slopes presented above applies to an anodic reaction taking place at potentials for anodic to the potential of maximum adsorption or for a cathodic process taking place at potentials for cathodic to the potential of maximum adsorption. In an inverse case, *i.e.*, a reduction taking place at very positive potentials or vice versa, the effect of competition with water will be just the opposite. The values of the Tafel slope can be calculated in this case in a straightforward manner following the derivations given above with a change in sign in the exponential dependence of the equilibrium constants and specific rate constants on potential. These equations will therefore not be derived here.

The competition with water affects the calculated value of the parameter b to a lesser degree if the reaction considered is taking place at potentials in the vicinity of the potential of maximum adsorption. The Tafel lines in this region are expected to be nonlinear, changing from the value derived when the competition with water is neglected to the values obtained in Table I and II.

Quasi Tafel relationship in heterogeneous catalysis in solution.—The first mechanism presented in Table II is of some special interest, since the reaction rate is potential dependent although no charge transfer occurs. A quasi Tafel slope can be defined in this case as $b \equiv \partial(\Delta\phi)/\partial \log r$, where r is the rate of the chemical reaction. Thus, chemical reactions catalyzed in solution by metals can be controlled by controlling the potential of the catalyst. The rate may be expected to depend strongly on potential at low values of the fractional surface coverage; it will be independent of potential at intermediate values of the coverage (under Temkin conditions); and it will depend somewhat on potential again at full coverage. Thus, changing the potential may serve as a convenient means of starting up or stopping a chemical reaction which occurs on the surface of an electronically conducting catalyst in solution.

Conclusions

The adsorption of intermediates formed in electrode processes is controlled on the one hand by the charge transfer process and on the other hand by competition with water. A new isotherm which takes into account both effects has been developed elsewhere (18). It is used here to calculate Tafel slopes for a number of typical mechanisms, particularly relevant to electrode reactions of organic compounds which replace a large number of water molecules from the surface per reactant molecule adsorbed. The Tafel slopes calculated are seen to depart markedly from simple multiples of $2.3RT/\mathbf{F}$. In particular a value of $b > 2 \times 2.3RT/\mathbf{F}$ is calculated when a first charge-transfer adsorption step is rate determining.

These considerations probably do not apply to the hydrogen and the oxygen evolution reactions because in these cases the reactant (i.e., H_3O^+, H_2O, or OH^-) does not have to replace water molecules from the surface.

The rate of purely chemical reactions catalyzed by metals in solution can be controlled by setting the potential with respect to an appropriate reference electrode in the same solution.

Acknowledgment

One of the authors (E.G.) wishes to thank the Center of Advanced Studies of the University, sponsored by the National Science Foundation, for the award of a University Lecturership. This work was supported by the National Institute of Dental Research, Grant DE-2111-02.

Manuscript submitted Oct. 12, 1970; revised manuscript received March 23, 1971.

Any discussion of this paper will appear in a Discussion Section to be published in the June 1972 JOURNAL.

REFERENCES

1. A. N. Frumkin, "Advances in Electrochemistry and Electrochemical Engineering," Vol. III. Chap. 5, P. Delahay, Editor, Interscience Publishers Inc., New York (1963).
2. J. O'M. Bockris, "Modern Aspects of Electrochemistry," Vol. I, Chap. IV, J. O'M. Bockris and B. E. Conway Editors, Butterworths, London (1954).
3. J. O'M. Bockris, *J. Chem. Phys.*, **24**, 817 (1956).
4. S. Srinivasan, Ph.D. Dissertation, University of Pennsylvania (1964).
5. B. E. Conway and E. Gileadi, *Trans. Faraday Soc.*, **58**, 2493 (1962).
6. E. Gileadi and B. E. Conway, "Modern Aspects of Electrochemistry," Vol. III, Chap. 5, J. O'M. Bockris and B. E. Conway, Editors, Butterworths, London (1964).
7. J. A. B. Butler, *J. Phys. Chem.*, **34**, 2286 (1932).
8. J. A. V. Butler, *Proc. Roy. Soc.*, **135**, 348 (1932).
9. R. G. Barradas and B. E. Conway, *J. Electroanal. Chem.*, **6**, 314 (1963).
10. N. F. Mott and R. J. Watts-Toben, *Electrochim. Acta*, **4**, 79 (1961).
11. J. O'M. Bockris, M. A. V. Devanathan, and K. Muller, *Proc. Roy. Soc.*, **A274**, 55 (1963).
12. K. Muller, "Electrosorption," Chap. VI, E. Gileadi, Editor, Plenum Press, New York (1967).
13. E. Gileadi, *J. Electroanal. Chem.*, **11**, 137 (1966).
14. A. N. Frumkin, *Z. Physik*, **35**, 792 (1926).
15. A. N. Frumkin and B. B. Damaskin, "Modern Aspects of Electrochemistry," Vol. III, Chap. 3, J. O'M. Bockris and B. E. Conway, Editors, Butterworths, London (1964).
16. B. B. Damaskin, *J. Electroanal. Chem.*, **23**, 431 (1969).
17. J. O'M. Bockris, E. Gileadi, and K. Muller, *Electrochim. Acta*, **12**, 1301 (1967).
18. T. Bejerano, Ch. Forgacs, and E. Gileadi, *J. Electroanal. Chem.*, In press.
19. U. Eisner and E. Gileadi, *ibid.*, In press.
20. E. Gileadi, *ibid.*, In press.
21. M. I. Temkin, *Zh. Fiz. Khim.*, **15**, 296 (1941).
22. R. Parsons, *Trans. Faraday Soc.*, **47**, 1332 (1951).
23. A. N. Frumkin, *Z. Phys. Chem.*, **116**, 466 (1925).

Technical Notes

Electrode Studies in Nonaqueous Solvents

II. Anion Effect on the Kinetics of Li/Li^+ in Propylene Carbonate

Stuart G. Meibuhr*

Electrochemistry Department, Research Laboratories, General Motors Corporation, Warren, Michigan 48090

A number of different electrolytes are being used in lithium organic electrolyte batteries. These include propylene carbonate (PC) (or mixtures containing it), as the organic solvent and a solute containing as anion either ClO_4^-, $AlCl_4^-$, or PF_6^- (1).

The electrochemical kinetics of a smooth lithium electrode in PC solutions of either $LiAlCl_4$, $LiPF_6$, or $LiBF_4$ at temperatures up to 60°C are reported here. Two types of experiments were performed. The lithium reference electrode in $LiAlCl_4$-PC solutions was evaluated by measuring the potential of a Li/Li^+ concentration cell at ambient temperature; and the Li/Li^+ electrode kinetics were studied by analyzing the anodic and cathodic polarization of Li electrodes.

Experimental

The PC solvent was vacuum distilled as described before (2) and contained < 20 ppm H_2O. The solutes were used as they were obtained without further attempt to purify or dry them. The $LiAlCl_4$ was obtained on special order from Lithium Corporation of America in a 14 lb lot. The elemental analysis provided by the manufacturer was 1.02, 0.97, and 0.86% theoretical for the Li, Al, and Cl, respectively. The $LiPF_6$ obtained from K & K Laboratories and Agri-Chemicals, Inc., was extremely hygroscopic. The $LiBF_4$ was from the Research Inorganic Chemical Corporation. Solutions of 1M were prepared by weighing in a dry box sufficient solute to add to 100 ml of PC. The $LiPF_6$ solution, after having been stored over Li for several weeks, contained 60 ppm water. The water content in the $AlCl_4^-$ solution could not be determined by the Karl Fischer method; however, because of the similarity of the i_o value and its behavior with immersion time for both $AlCl_4^-$ and ClO_4^- solutions, it will be assumed that the water content of 1M $LiAlCl_4$ was the same as in 1M $LiClO_4$—about 20 ppm. The 1M $LiBF_4$ solution contained 180 ppm water. Less concentrated solutions were prepared by dilution and contained less water than the more concentrated 1M solutions. Details regarding the solutions, electrode preparation, and equipment have already been given (3).

The experimental procedure was similar to that described previously (3), except that the polarization measurements were made within 1-2 min after the polished electrode was immersed into the solution. The solution resistance measurements were made in the previously described way but at the conclusion of the polarization run instead of before the run as was done in the earlier work (3). The exchange current densities were calculated with a computer program from the equation

$$i_o = IRT/\eta_{IR\text{-free}}\mathbf{F}$$

where

$$\eta_{IR\text{-free}} = E_{exptl} - E_{oc} - IR$$

Under all experimental conditions with all solutions, the C.D.-polarization plots were linear. In the several instances when cathodic data were taken, the polarization plot agreed with the anodic plot within 5%. Duplicate anodic runs on freshly repolished electrodes produced slopes that were within 10% of each other.

The value for the *IR* drop varied from 10-50% of either the measured voltage or the polarization value. For example, in 0.5 $LiAlCl_4$, a value for the *IR* drop was 1.6 mV whereas the measured voltage and the polarization was 4.75 and 3.0 mV, respectively, at 55 $\mu A/cm^2$. In the PF_6^- and BF_4^- solutions, the *IR* drop was regularly only 10% of the measured voltage and about 50% of the polarization value.

The potential of the concentration cell

$$Li/LiAlCl_4\ (c_1) - PC/LiAlCl_4\ (c_2) - PC/Li$$

was measured for values of c_1 = 1.0 and 0.5M and c_2 = 1.0, 0.5, 0.25, and 0.1M. Included in the measured emf was an unknown junction potential which was estimated using the Henderson equation (4)

$$E_j = RT/\mathbf{F}\,\frac{\lambda_+^\circ - \lambda_-^\circ}{\lambda_+^\circ + \lambda_-^\circ}\ln\frac{c_1}{c_2}$$

where λ_+° and λ_-° are the limiting ionic mobilities of Li^+ and $AlCl_4^-$, respectively. The value for λ_+° in PC solutions was calculated as 8.7 (3) and was reported as 7.3 (5); hence, in this equation, an average value of 8.0 was used for λ_+°. The value for λ_-° was calculated from

$$\Lambda_o = \lambda_+^\circ + \lambda_-^\circ$$

The value for Λ_o in $LiAlCl_4$ solutions was determined to be 32.5 at 25° (6), consequently, λ_-° is 24.5.

Results and Discussion

Concentration cell studies.—Table I shows the measured emf values for the cell together with the calculated E_j values and the corrected emf values. A plot of the concentration *vs.* the corrected emf values has a slope of 57 mV. Considering the assumptions that were made in calculating the E_j values, the potential responded to the changing Li^+ ion concentration in good agreement with the Nernst equation. Thus, a solid lithium electrode immersed in solutions of $LiAlCl_4$ behaved satisfactorily for a reference electrode. These results in $AlCl_4^-$ solutions agreed with similar results regarding the use of Li as a reference electrode in ClO_4^- solutions (3, 7). Because of the Nernstian agree-

Table I. Concentration cell studies

c_1 (M)	c_2 (M)	Measured cell potential (V)	E_j (V)	Corrected emf (V)
1.0	1.0	0.0000	—	0.0000
0.5	0.5	0.0000	—	0.0000
1.0	0.5	0.0385	0.0208	0.0177
1.0	0.25	0.0760	0.0416	0.0344
0.5	0.25	0.0380	0.0208	0.0172
0.5	0.1	0.0880	0.0483	0.0397

* Electrochemical Society Active Member.

Key words: lithium electrode, nonaqueous cells, propylene carbonate.

Table II. The i_o values for different experimental conditions

Solute concentration (M)	Temperature (°C)	i_o (mA/cm²)
M $LiAlCl_4$	19	0.40
	35	1.05
	46	1.49
	55	2.35
0.5M $LiAlCl_4$	19	0.45
	29	0.86
	45	1.65
	56	2.90
0.1M $LiAlCl_4$	19	0.37
	40	0.79
	51	1.10
0.05M $LiAlCl_4$	19	0.29
	41	0.40
M $LiPF_6$	20	0.29
	31	0.52
	46	0.53
	57	0.65
M $LiBF_4$	20	0.50
	48	0.72
	55	0.88
	65	0.97

ment for both $AlCl_4^-$ and ClO_4^- solution, it will be assumed that similar behavior exists in the other two Li^+ ion containing solutions used in this study.

Polarization studies.—The i_o variations with temperature, Li^+ ion concentration, and type of anion are summarized in Table II. From the results of the temperature effect on the polarization, the enthalpy of activation at zero polarization (ΔH_o^*) was calculated from the plot of the log i_o against $1/T$. These plots are displayed in Fig. 1 for $AlCl_4^-$ solutions and in Fig. 2 for PF_6^- and BF_4^- solutions. The ΔH_o^* values were 9.9 kcal/mole for $LiAlCl_4$ concentrations > 0.5M; 6.4 kcal/mole for the 0.1M $LiAlCl_4$, and 5.1 kcal/mole for the 0.05M $LiAlCl_4$. No such change of ΔH_o^* with Li^+ ion concentration occurred with the ClO_4^- solutions (3).

The ΔH_o^* value for 1M solutions of $LiPF_6$ and $LiBF_4$ was 3.5 kcal/mole, a value considerably lower than the ΔH_o^* value for 1M solutions of $LiAlCl_4$ or $LiClO_4$. Two possible reasons for this striking difference in ΔH_o^* value are: (*a*) the water contents of the $AlCl_4^-$ and the ClO_4^- solutions were lower (the solutions that were analyzed showed lower water and were stored over Li for long times), or (*b*) fluorine-containing anions clearly influence the kinetics of the lithium/lithium ion reaction to the extent that the observed difference in ΔH_o^* is real.

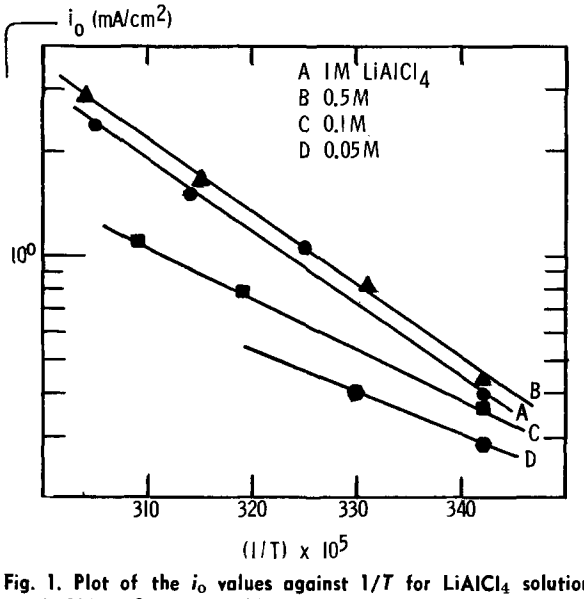

Fig. 1. Plot of the i_o values against $1/T$ for $LiAlCl_4$ solutions. Curve A, 1M; B, 0.5M; C, 0.1M; D, 0.05M.

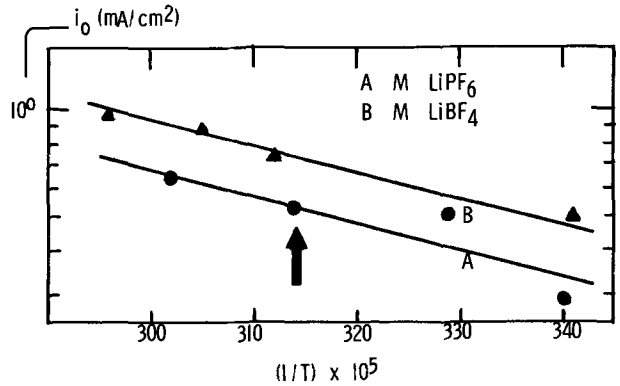

Fig. 2. Plot of the i_o values against $1/T$. Curve A, 1M $LiPF_6$; B, 1M $LiBF_4$.

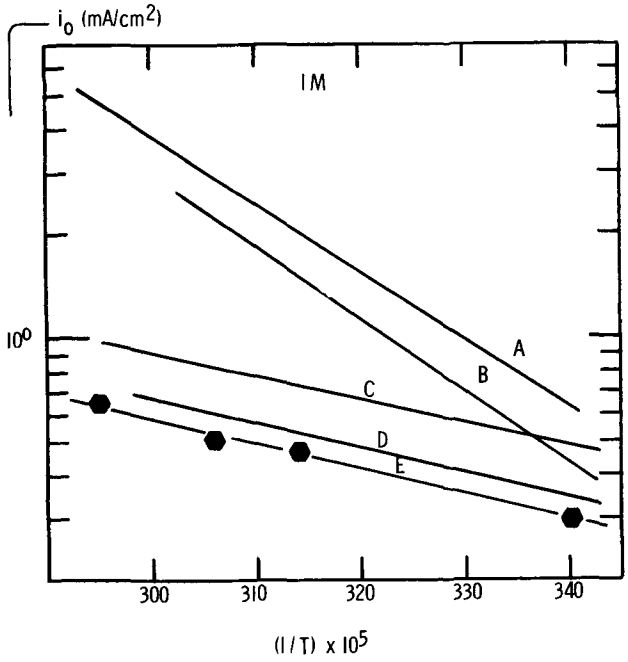

Fig. 3. Plot of the i_o values against $1/T$ for 1M solutions. Curve A, dry $LiClO_4$; B, $LiAlCl_4$; C, $LiBF_4$; D, $LiPF_6$; E, wet $LiClO_4$ (1800 ppm water).

To distinguish between these two causes, the following experiment was performed. To a solution of 1M $LiClO_4$ (containing about 20 ppm water) was deliberately added water to a concentration of 1800 ppm. The polarization runs were repeated in duplicate at 4 temperatures. The results (log i_o *vs.* $1/T$) appear in Fig. 3 where curve A corresponds to the dry 1M solution and curve E corresponds to the solution that contains the water. The other plots depict other 1M solutions shown in Fig. 1 and 2. Indeed, the wet solution exhibited a ΔH_o^* value virtually identical to the BF_4^- and PF_6^- anion containing solutions identified as curves C and D. The solute $LiPF_6$ is thermally unstable, and it etched the glass container in which it was stored. This etching implied the presence of water. The BF_4^- solution contained about 180 ppm water. These data confirm that the BF_4^- and PF_6^- solutions contained sufficient water to affect the electrode kinetics probably by film retardation of the electron transfer reaction (8). These data also suggest that in dry lithium salt solutions, the kinetics of the lithium/lithium ion reaction may be relatively independent of the nature of the anion of that salt. Hence, the selection of a specific solute (for a battery operation) should depend less on electrode kinetics, than on factors such as cost, ease of drying the solute, stability of the solution, and compatibility with other cell components.

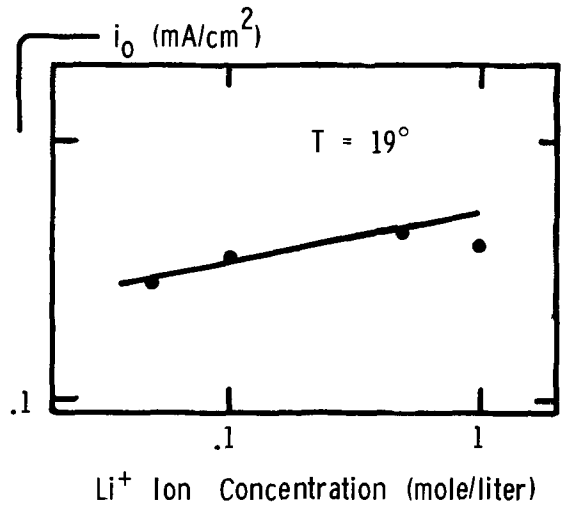

Fig. 4. Determination of the $(1 - \alpha)$ value from $LiAlCl_4$ solutions. Temperature = 19°C.

The transfer coefficient, α, was calculated indirectly from the slope of the plot $\partial \log i_0/\partial \log C_{Li}$ (9). Such data were taken only with $LiAlCl_4$ solutions. The data in Fig. 4 yielded a value for α of about 0.8. This value is somewhat higher than the 0.67 value reported for solid Li electrodes in $LiClO_4$-PC solutions (3, 10), or the 0.75 value reported for Li amalgams in LiCl-dimethylsulfoxide solutions (11). Whether these differences in value are real or whether the present value has been influenced by the presence of trace amounts of water in the dilute solutions of Li^+ ion, cannot be resolved.

Acknowledgments

I am grateful to the following members of the Electrochemistry Department: Dr. James P. Hoare for his suggestions during the preparation of the manuscript, and Charles R. Wiese for his assistance with this work.

Manuscript submitted Aug. 3, 1970; revised manuscript received *ca.* March 15, 1971. This was Paper 280 presented at the Los Angeles Meeting of the Society, May 10-15, 1970.

Any discussion of this paper will appear in a Discussion Section to be published in the June 1972 JOURNAL.

REFERENCES

1. R. Jasinski, *Electrochem. Technol.*, **6**, 28 (1968).
2. S. G. Meibuhr, B. E. Nagel, and R. Gatrell, *Energy Conversion*, **10**, 29 (1970).
3. S. G. Meibuhr, *This Journal*, **117**, 56 (1970).
4. P. Henderson, *Z. Phys. Chem.*, **59**, 118 (1907); S. Glasstone, "Introduction to Electrochemistry," p. 213, D. Van Nostrand, Inc., Princeton, N. J. (1956).
5. R. Keller, J. N. Foster, D. C. Hanson, J. F. Hon, and J. S. Muirhead, NASA Report CR-1425, Aug. 1969.
6. F. W. Breivogel and M. Eisenberg, *Electrochim. Acta*, **14**, 459 (1969).
7. B. Burrows and R. Jasinski, *This Journal*, **115**, 365 (1968).
8. J. N. Butler, D. R. Cogley, and J. C. Synnott, *J. Phys. Chem.*, **73**, 4026 (1969).
9. P. Delahay, "Double Layer and Electrode Kinetics," p. 165, Interscience Publishers, Inc., New York (1965).
10. R. Scarr, *This Journal*, **117**, 295 (1970).
11. D. R. Cogley and J. N. Butler, *J. Phys. Chem.*, **72**, 4568 (1968).

On Causes of Error in Multiple Specular Reflection Studies

B. D. Cahan, Jean Horkans,* and Ernest Yeager**

Chemistry Department, Case Western Reserve University, Cleveland, Ohio 44106

Recent studies in the laboratory have revealed that substantial errors were introduced in the earlier work (1) using multiple specular reflection to investigate the gold-electrolyte interface. While the earlier work was essentially correct in those trends which are independent of wavelength, significant errors occur in the wavelength dependence because of the large number of reflections used. These errors have been traced to scattering (primarily from imperfections in the electrode surface) and to impurity wavelengths from the monochromator. Both sources of error may become important when the number of reflections is sufficiently large and can be made negligible by using a small number of reflections. The purpose of this note is to call attention to these errors and to present some corrected results for gold.

Gold is of special interest for optical studies because of its absorption edge in the visible. The reflectivity of gold is close to unity in the red but drops off to ~30% in the blue. This edge can be used as a probe in studying the electronic properties of the metal surface (2).

The original work was done using mechanically polished bulk gold electrodes spaced to give 19-21 reflections. A large number of reflections was used to enhance the small relative change of light intensity occurring at each single reflection. Current work is being done using low numbers of reflections (1-7) from electrodes made by evaporating gold films onto smooth glass substrates.[1] The stability and noise level of the source and detection system have been improved to a point where a large number of reflections is no longer needed to enhance the sensitivity, and in fact, a single reflection is generally used.

Several factors contribute to the total intensity I of the light entering the photomultiplier after passing between two parallel electrodes spaced to give n reflections. These are represented as follows

$$I = R(\lambda_1)^n I_0(\lambda_1) + \int_{\lambda \neq \lambda_1} R(\lambda)^n I_0(\lambda)\, d\lambda + S_{eff} R(\lambda_1)^m I_0(\lambda_1) + C \quad [1]$$

where λ_1 represents the wavelength of interest, λ (unsubscripted) represents all other wavelengths, $R(\lambda)$ is the reflectivity of the surface at λ, and $I_0(\lambda)$ is the intensity of the incident light at λ.

The first term corresponds to the final intensity after an incident light of intensity I_0 undergoes n specular reflections, and is generally assumed to be the only significant term. However, recent work in this laboratory has shown that when a large number of reflections are used, other factors can become important. The second term represents the effects of any light impurity of other wavelengths, caused chiefly by scattering within the monochromator. The third term represents

* Electrochemical Society Student Member.
** Electrochemical Society Active Member.
Key words: electroreflectivity, electromodulation, specular reflection, gold.

[1] The two substrate materials used were microscope slides and slides cut from a drawn sheet of Corning 7059 glass. The results were found to be the same for both.

that fraction of the light which is scattered (rather than reflected) down the optical path between the electrodes such that it enters the photomultiplier. The symbol S_{eff} designates the fraction of the incident light scattered to the photomultiplier. The scattering originates primarily from nonspecular reflection caused by such things as scratches on the electrode surface, particulate matter that may be present in the solution, and small surface irregularities. Because of the geometry of the cell, light scattered from the entrance window undergoes essentially the same number of reflections as the direct light. The term C is included to represent all other stray light which does not pass through the optoelectrochemical system and hence is not electromodulated.

The scattering term is a gross oversimplification, since the number of reflections undergone by the scattered light is dependent on the scattering angle and where the scattering occurs. Some of the rationale for the form of this term may be seen from the following. Consider the scattering occurring at the j^{th} reflection. Let S_{eff} be the fraction of the light scattered so as to undergo k more reflections before entering the detection system. Then the intensity of this scattered component is

$$I_s = [R(\lambda_1)^j I_o(\lambda_1)]S_{eff}R(\lambda_1)^k$$
$$= S_{eff}R(\lambda_1)^m I_o(\lambda_1) \quad [2]$$

where $m = j + k$, and S_{eff} and m are to be viewed as effective average values and are wavelength dependent. Specific values of m can range from j to infinity, depending upon the angle the scattered light makes with the surface. The rapid attenuation of intensity with multiple reflection when $R(\lambda_1) < 1$, however, results in the lower values of m being much more heavily weighted than large values of m. Hence the effective average value for m would be expected to be substantially smaller than n. The scattered component of the light will still be electromodulated through the dependence of $R(\lambda_1)$ on potential.

Experimentally, the reflectivity is recorded while a triangular sweep is applied to the electrode. The quantity $(1/R)(\partial R/\partial E)_\lambda$ is sensitive to processes occurring at the electrode-electrolyte interface and is related to the shape of the reflectivity-potential (I *vs.* E) curves through

$$\frac{1}{R}\left(\frac{\partial R}{\partial E}\right)_{\lambda_1} = \frac{1}{n}\frac{1}{I}\left(\frac{\partial I}{\partial E}\right)_{\lambda_1} \quad [3]$$

with the assumption that only the first term in Eq. [1] is important. If other terms in Eq. [1] are also significant, Eq. [3] will no longer be valid. The way in which these other terms will affect the value of $(1/R)(\partial R/\partial E)_{\lambda_1}$ will now be examined for the case of a gold electrode with $n \simeq 19$.

Case I. High reflectivity region: $\lambda_1 > \lambda_{edge}$

For wavelengths in the red, where the reflectivity of gold is high (*e.g.* $R \simeq 0.9$), the intensity of the light reaching the photomultiplier after n reflections is still relatively large (*e.g.* $0.9^{19} = 0.135$) and the first term in Eq. [1] is generally predominant. Impurity wavelengths and the nonelectrochemically modulated stray light (*e.g.* light scattered from the cell windows) should be negligible. A significant contribution, however, can be made by the scattering term, particularly with mechanically polished or etched surfaces. As discussed above, scattering results in a lowering of the effective number of reflections to some value $m < n$. Thus, from Eq. [3], the value of $(1/R)(\partial R/\partial E)_\lambda$ found by assuming n reflections based on the geometry of the system is too small, since n is too large.

Case II. Low reflectivity region: $\lambda_1 < \lambda_{edge}$

For wavelengths in the blue, where the reflectivity is < 0.5, the quantity $R(\lambda_1)^n I_o(\lambda_1)$ is very small for large n (*e.g.* $0.5^{19} \simeq 10^{-6}$ and $0.25^{19} \simeq 10^{-12}$). With the emergent light being of such low intensity, the other terms in Eq. [1] can become significant.

Light impurities from the monochromator (caused chiefly by internal scattering) should also be considered. When the primary wavelength is heavily attenuated through many reflections, the impurity wavelengths can become important. The error is worst when the primary wavelength is in the blue, and there are impurity wavelengths in the red. The observed electromodulation will be caused by a distribution of wavelengths, and the value of $(1/R)(\partial R/\partial E)_\lambda$ will thus be in error.

The situation with respect to light scattered within the cell is the same in the blue as in the red. However, the magnitude of the effect is much larger in the blue due to the small size of the first term in Eq. [1]. Scattering causes the experimental values of the quantity $(1/R)(\partial R/\partial E)_\lambda$ to be too low in general. At wavelengths less than the wavelength of the absorption edge of gold (where R becomes small), the apparent $(1/R)(\partial R/\partial E)_\lambda$ drops off sharply.

When $\lambda_1 < \lambda_{edge}$, even such factors as incompletely compensated dark current and stray, nonelectromodulated light can become significant relative to the intensity of the specularly reflected light. In the evaluation of $(1/R)(\partial R/\partial E)_\lambda$ with Eq. [3], the experimental value for the total intensity I includes the background levels. When the background levels are small compared to the first term in Eq. [1], the error is negligible. When the background level is appreciable compared to the first term, as when $\lambda_1 < \lambda_{edge}$, the quantity I in the denominator of Eq. [3] is too large, and the apparent value of $(1/R)(\partial R/\partial E)_\lambda$ rapidly becomes much smaller than the true value.

The effects of these errors is illustrated in Fig. 1, which shows the dependence of $(1/R)(\partial R/\partial E)_\lambda$ on wavelength. The data were obtained for an evaporated gold film electrode using a single reflection. The data obtained with $\sim$ 19 reflections (1) are also included for comparison. The differences in shape between these two sets of data can be explained in terms of the above discussion. All of the values for $(1/R)(\partial R/\partial E)_\lambda$ obtained using multiple reflection are lower than those values from the single reflection data. The general shape of the two sets of curves is seen to differ most drastically at wavelengths where the reflectivity is no

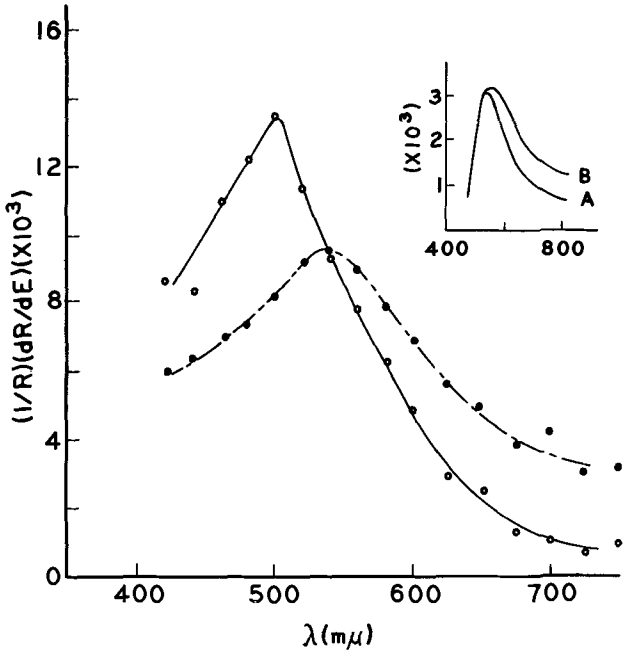

Fig. 1. $(1/R)(\partial R/\partial E)_\lambda$ at 0.2V (———) and 1.0V (———– – ———). The inset is the multiple reflection data of Ref. (1): A is at 0.52V, B is at 1.03V.

longer near unity. In the red the deviation is principally a result of a lowering of the effective number of reflections due to scattering. In the blue end of the spectrum even small amounts of light impurities, scattering, and background light levels can become important when the intensity of the reflected light is heavily attenuated through the use of a large number of reflections. Thus, the invariance of the peak in $(1/R)(\partial R/\partial E)_\lambda$ with respect to potential and the sharp dropoff in the blue obtained from the multiple reflection work appear to be artifacts.

Equation [3] can be used as a criterion for evaluating the importance of these spurious effects in a real system. If the only important term is the first term in Eq. [1], then for n reflections the slope of the reflectivity-potential curve, $(1/I)(\partial I/\partial E)_\lambda$, should be n times the slope of the curve obtained for a single reflection. Experimental data obtained using 1 to 7 reflections from evaporated films (2) showed that within experimental error the shape of the $(1/R)(\partial R/\partial E)_\lambda$ curve is independent of the number of reflections used.

The conclusions based on the multiple reflection work (1) need re-examination in light of the corrected $(1/R)(\partial R/\partial E)_\lambda$ data. As stated above, the peak at 550 mμ is artifactual. The position of the peak is actually dependent upon the potential at which the slope of the reflectivity-potential curves is obtained. The linearity of these curves at $\sim$ 550 mμ reported in the earlier work (1, 2) is fortuitous. This linearity is altered by adsorption of either ionic or nonionic species even at 550 mμ.

The actual peak in $(1/R)(\partial R/\partial E)_\lambda$ in Fig. 1 is much broader than that reported earlier using multiple reflection (1). The width of the peak casts doubt upon the hypothesis that a change in electrode potential produces a simple shift of the reflectivity curve along the wavelength scale as the electrode potential is changed. An attempt has been made (2) to observe this shift directly by recording the reflectivity *vs.* wavelength curve of an electrode potentiostated at various potentials from 0.0 to 1.4V *vs.* NHE. These curves were fitted to high order polynomials (5th to 15th degree), and the position of the inflection point was found to be invariant within $\sim$ 6 x 10^{-4} eV/V compared to the postulated shift (3) of 0.0108 eV/V. Present indications are that the primary effect of a change of potential is a distortion of the reflectivity-wavelength curve.

Acknowledgment

The authors are pleased to acknowledge the support of this research by the U.S. Office of Naval Research and also the Electrochemical Society through the Edward Weston Fellowship to one of the authors (J.H.).

Manuscript submitted Dec. 3, 1970; revised manuscript received *ca.* April 10, 1971.

Any discussion of this paper will appear in a Discussion Section to be published in the June 1972 JOURNAL.

REFERENCES

1. T. Takamura, K. Takamura, W. Nippe, and E. Yeager, *This Journal*, **117**, 626 (1970).
2. B. D. Cahan, J. Horkans, and E. Yeager, Faraday Soc. Symp., Dec. (1970).
3. W. N. Hansen and A. Prostak, *Phys. Rev.*, **174**, 500 (1968).

JOURNAL OF THE ELECTROCHEMICAL SOCIETY

SOLID STATE SCIENCE

AUGUST 1971

SSS

The Initial Oxidation Rates of Single-Crystal Copper and the Effect of Gaseous Pretreatment

A. W. Swanson** and H. H. Uhlig*

Department of Metallurgy and Materials Science, Massachusetts Institute of Technology, Cambridge, Massachusetts 02139

ABSTRACT

Submicroscopic faceting occurs when any Cu surface is heated in H_2 or N_2, favoring, according to oxidation rate data, the (111) and (100) faces, respectively. The subsequent thin film oxidation rate in O_2, 1 atm at 200°C, is determined by the rearranged surface rather than by the original orientation of the underlying single crystal. This accounts for an observed large effect of gaseous pretreatment on oxidation of single-crystal or polycrystalline Cu, and suggests one important reason for typical lack of agreement between previously reported thin film oxidation rates of many metals. Electropolished or faceted single-crystal Cu of original (100), (110), or (111) orientation follows the two-stage logarithmic oxidation equation. The present data are interpreted in terms of a model based on control of thin film oxidation rates by transfer of electrons from metal to oxide surface.

A review of the literature on oxidation behavior of Cu was presented by Rönnquist and Fischmeister (1). Although many papers on oxidation of Cu appear in the literature, only a limited number deal with quantitative data. This is especially true of results on the effect of crystal face. Furthermore some of the limited results previously reported are subject to question because of high-temperature surface treatment which may have seriously disturbed surface structure and orientation. Results are presented herewith in which such disturbing effects are both studied and avoided, and which serve as a more reliable basis for evaluating the mechanism of thin film oxidation kinetics.

The high-temperature pretreatment of Cu specimens in H_2 previous to oxidation studies is commonly practiced both to anneal specimens and to chemically reduce air-formed oxide films. It was shown by previous experiments (2), however, that pretreatment of this kind applied to a polycrystalline Cu surface at 450°C for 30 min can markedly influence the subsequent oxidation rate in O_2 at 200°C. The observed effects were found, on further examination, to depend on gas atmosphere and on crystal face. Nitrogen pretreatment of the (111) face increased the subsequent thickness of oxide formed in O_2 at 200°C (20 min) by a factor of 5, whereas pretreatment with H_2 had no effect within experimental error. For the (100) face, on the other hand, just the opposite effect resulted: N_2 pretreatment had no effect whereas H_2 pretreatment reduced the subsequently formed oxide thickness by a factor of 4. It was shown that the observed effects were not reasonably caused by (*a*) surface impurities or (*b*) by hydrogen dissolved in the Cu lattice. Instead it was proposed that submicroscopic faceting (not visible at 1000X) occurs during pretreatment schedules, the metal surface becoming rearranged so as to favor either rapidly or slowly oxidizing faces depending on the pretreatment atmosphere. The predominant face that develops is apparently that of lowest surface energy for the particular gas adsorbed on its surface. Accordingly, it was concluded that hydrogen adsorbed on Cu favors facets of slowly oxidizing approximate (111) orientation, whereas N_2 whose effect was ascribed to traces of oxygen in the metal or gas, favors the more rapidly oxidizing approximate (100) orientation.

Electron micrographs are now presented to show that faceting does indeed take place at pretreatment temperatures. The present investigation also carries out in further detail oxidation rate studies of the three close-packed faces (100), (110), and (111). These include thin film oxidation rates (up to 3500Å total oxide thickness) for untreated surfaces at 175°, 200°, and 225°C and for surfaces pretreated under a variety of temperatures and times.

Experimental

Copper single crystals (purchased from Virginia Institute of Scientific Research) were cut from a 2.5 cm diameter boule into specimens having a thickness of about 0.6 cm. Their final alignment was checked by x-ray. The specimens were mounted so that one face made contact with a spiral Nichrome wire heater employing mica sheet insulation and a back-up plate of thin 18-8 stainless steel. Temperature was measured by an insulated Chromel-Alumel thermocouple placed in a small hole carefully drilled in the side of the specimen.

Oxidation studies were carried out on the surface of the single crystal opposite to the side in contact with the heating element. Electropolishing a previously

* Electrochemical Society Active Member.
** Electrochemical Society Student Associate.
Key words: logarithmic oxidation, single crystal copper, faceting, thin film oxidation.

metallographically polished surface (with heating element removed) provided a surface of essentially unit roughness factor. The electrolyte consisted of 70 v/o (volume per cent) of 85 w/o (weight per cent) orthophosphoric acid at 0°C to which 10 g/liter of cupric orthophosphate were added. Initial and final current densities ranged from 0.04 to 0.02 A/cm^2, respectively, over a period of about 20 min. The specimen was then taken out of the electrolyte without interrupting the current, immersed immediately in 10 v/o orthophosphoric acid, and subsequently washed in deaerated distilled water. The acid-water rinse was repeated until all copper reaction products remaining on the surface from the electropolishing operation were removed; final washing was carried out in five consecutive bottles of distilled H_2O through which CO_2 passed continuously. A stream of nitrogen gas was used to dry the specimens.

The oxidation runs, as described previously (2), were immediately carried out in a spherical Pyrex vessel measuring 9 cm diameter. This vessel containing the specimen was fitted by means of a ground glass joint (omitting grease) to a glass holder through which thermocouple and heating current wires were connected through tungsten seals. Nitrogen, O_2, or H_2 was admitted to the oxidation chamber by opening appropriate stopcocks. Nitrogen and H_2 were dried over $CaCl_2$, passed over Cu turnings at 400°C, and then through a liquid N_2 cold trap. Oxygen was only dried using $CaCl_2$.

Two oxidation procedures were followed. One involved pretreating the H_2-reduced electropolished specimen surface in N_2 or H_2 before oxidation in O_2 at 1 atm. The other involved direct oxidation in O_2 at 1 atm after electropolishing and cleaning; in this case the specimen surface was covered by a superficial oxide film which developed within the brief time the specimen was exposed to air at room temperature during assembly of the apparatus. In detail, the procedure was to rapidly heat the specimen to temperature (2 min to reach 200°C) in purified flowing N_2, then switch to O_2 at 1800 ml/min maintaining the temperature manually to within ±1°C. At the end of the oxidation period, the heating current was turned off and the cell flushed with purified N_2 at an initial flow rate of 4000 ml/min which was later reduced to 2000 ml/min. No visible surface changes occurred during heating in N_2 no matter how long the time, indicating that O_2 contamination was negligible.

Nitrogen pretreatment was carried out by heating to 450°C in purified N_2, switching to H_2 at 1 atm, 1000 ml/min at temperature for 5 min (to reduce the air-formed oxide film), shifting to the prescribed temperature in H_2, changing again to N_2 at 1000 ml/min, and holding for a definite time after which the temperature was lowered to 200°C and held. The cell was then flushed with O_2 at a rate of 1800 ml/min and oxidation allowed to proceed for 20 min. The cooling procedure was the same as that described previously for oxidation runs. Hydrogen pretreatment was carried out at specified temperatures and times analogous to N_2 pretreatment. Flushing with N_2 at 200°C previous to O_2 exposure, which was necessary for H_2 pretreatment in order to avoid explosive mixtures, was shown by experiment to be too low a temperature for occurrence of any surface rearrangement subsequent to faceting produced by H_2 at higher temperatures.

Oxide thickness was determined by coulometric reduction in N_2-saturated 0.1N KCl in accord with the technique described by Campbell and Thomas (3). The oxdized specimen was attached by springs to a small inverted glass cell separated by a rubber gasket lightly covered with stopcock grease. A silver-silver chloride reference electrode was mounted inside the cell near the specimen surface. The potential change of the specimen surface during reduction at constant current (0.2-0.8 mA/cm^2) was followed using a d-c amplifier and a chart recorder. From the time required to completely reduce the Cu_2O film (density = 6.0 g/cm^3), the oxide thickness was calculated, assuming a roughness factor of unity, to within ±10Å. Although the roughness factor was undoubtedly often greater than unity, the primary effects of gaseous pretreatment far overshadowed any accompanying effects on oxidation introduced by surface roughening.

Electron micrographs of the Cu surfaces were prepared from replicas obtained by applying a 1% Parlodion solution in distilled n-butyl acetate. To assure that the replicas reproduced the actual pretreated metal surface and not an air-formed oxide film, the plastic solution was applied to the specimen surface in the pretreatment cell at room temperature under a purified N_2 atmosphere and then dried in flowing N_2. The replicas were shadowed with Cr at an angle of 15° before photographing using a Siemens electron microscope.

Results

Oxidation rate data for the (100), (110), and (111) faces follow the direct logarithmic equation $y = k_1 \log (t/\tau + 1)$ where y is oxide thickness, t is time, and k_1 and τ are constants. Specifically, the three faces all show two-stage logarithmic behavior as shown in Fig. 1-3. Two-stage logarithmic behavior was shown previously to apply to single-crystal Cu by Lustman and Mehl (4), to single-crystal and to

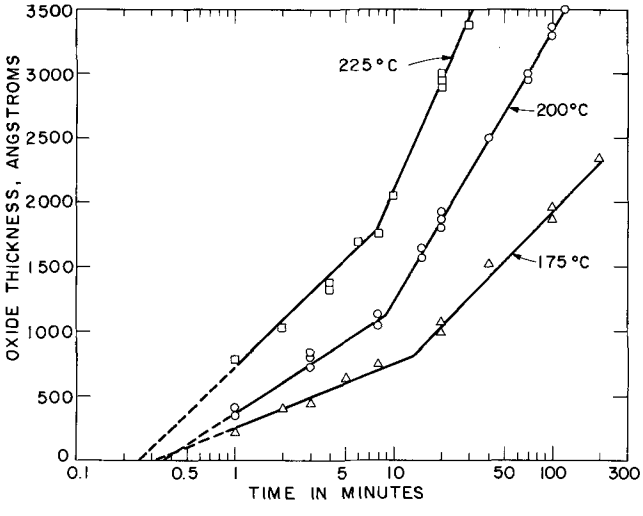

Fig. 1. Oxidation of electropolished (100) Cu in O_2, 1 atm, at various temperatures (air-exposed specimens).

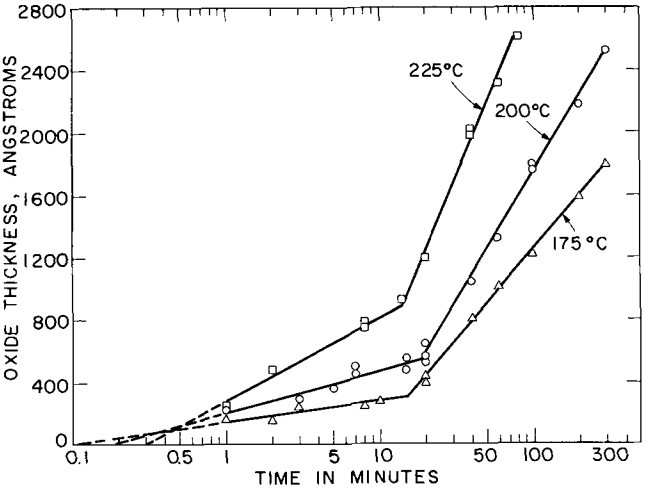

Fig. 2. Oxidation of electropolished (111) Cu in O_2, 1 atm, at various temperatures (air-exposed specimens).

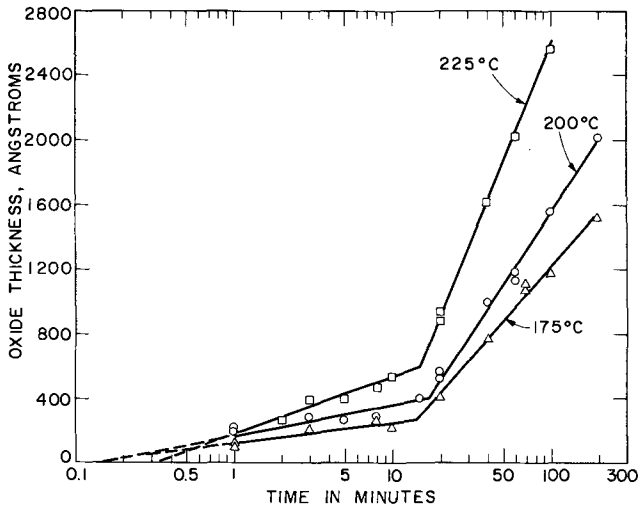

Fig. 3. Oxidation of electropolished (110) Cu in O_2, 1 atm, at various temperatures (air-exposed specimens).

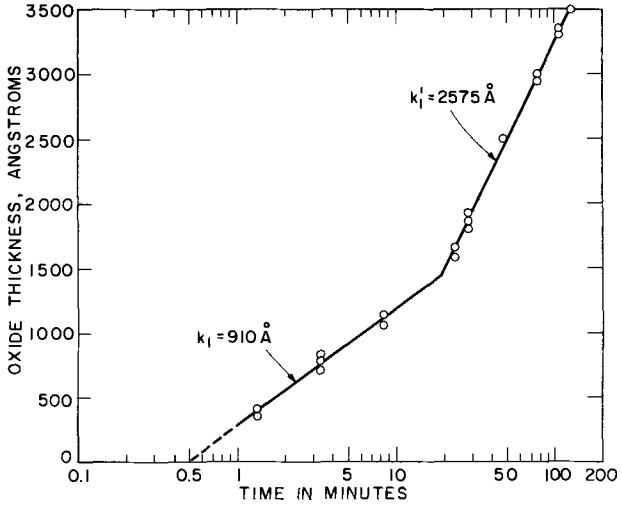

Fig. 4. Oxidation of electropolished (100) Cu in O_2, 1 atm, 200°C, plotting log $(t + \tau)$ and log $(t + \tau')$ instead of log t. Data from Fig. 1.

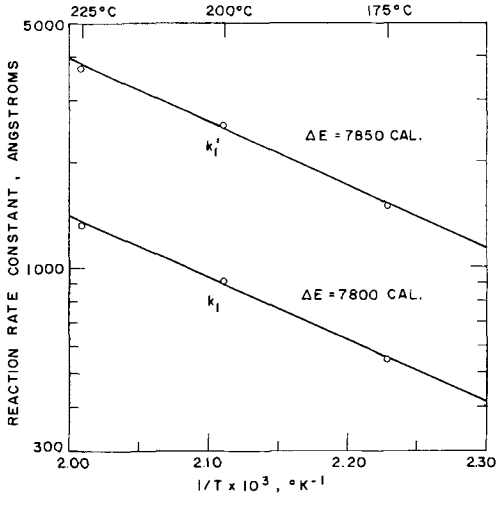

Fig. 5. Log first- and second-stage reaction rate constants for (100) Cu plotted with reciprocal absolute temperature.

polycrystalline copper by Bradley and Uhlig (2), and to polycrystalline Cu by Tylecoat (5), and by MacNairn and Uhlig (6). Two-stage logarithmic behavior can also be found in thin film oxidation data reported for Zn (7), Ni (8), and Fe (9).

Values of τ are obtained from data of Fig. 1-3 by extrapolating y *vs.* log t plots to $y = 0$, emphasizing points for which $t >> \tau$. Values of τ' for second-stage oxidation can be obtained on the basis that the following relation holds: $y - L = k_1' \log (t/\tau' + 1)$ where L is the thickness of oxide at the transition to second-stage kinetics. The value τ' is then the time at which y equals L. Values of k_1 and k_1', in turn, are obtained by plotting y *vs.* $k_1 \log (t + \tau)$ or y *vs.* $k_1' \log (t + \tau')$ which are also linear as shown by a typical plot of oxidation rate data for the (100) face at 200°C (Fig. 4) taking data from Fig. 1. Values of k_1 or k_1' obtained in this way are more precise, although not much different from corresponding values obtained by the usual plot of y *vs.* log t. Values of k_1, k_1', τ, and τ' as well as L [obtained from y *vs.* log $(t + \tau)$ plots] are listed in Table I.

By plotting log k_1 *vs.* $1/T$, where T is the absolute temperature, the activation energy of oxidation is obtained for each crystal face. A typical plot is shown in Fig. 5. Activation energies so obtained for 1st and 2nd stage oxidation are listed in Table I. From these values, it is apparent that the activation energies for first-stage oxidation decrease in the order of (100) > (110) > (111). Differences between (111) and (110) are small, but it is of interest to note that the reverse order of oxidation rates for these two faces is obtained comparing actual oxide thickness at a given time (see Fig. 2 and 3; also Table II). Oxide thickness leads to the order of oxidation rate: (100) > (111) > (110) in accord with the order previously reported by Gwathmey and co-workers (10-12), by Ali and Wood (13), and by Bradley and Uhlig (2). This suggests that the pre-exponential factor of the Arrhenius rate equation also differs with crystal face, accounting for an order of oxide thickness differing from the order of activation energies. It should be noted that activation energies for second-stage oxidation are approximately the same for all crystal faces. Accordingly values of k_1' also do not vary greatly with crystal face.

Oxide thickness plotted with log time in O_2 at 200°C for the (100) face pretreated 30 min in H_2 at 450°C is shown in Fig. 6. Note that the data accurately follow

Table I. Oxidation rate parameters

Face	Temp, °C	k_1 (Å)	τ (min)	k_1' (Å)	τ' (min)	L (Å)	ΔE, cal/mole 1st Stage	ΔE, cal/mole 2nd Stage
(100)	175	550	0.32	1520	13.0	1000	7800	7850
	200	910	0.34	2575	8.8	1440		
	225	1300	0.25	3690	8.0	2290		
(111)	175	140	0.11	1470	15.5	350	12,800	7330
	200	270	0.19	2070	18.5	600		
	225	565	0.30	3340	14.0	1080		
(110)	175	120	0.14	1330	14.0	280	11,000	7850
	200	200	0.14	1900	17.0	450		
	225	410	0.33	3190	15.0	720		
(100) Pretreated in H_2	200	270	0.11	2120	17.0	700		
(111) Pretreated in N_2	200	850	0.15	2550	14.0	1950		

Table II. Effect of H_2 pretreatment at 450°C, 30 min on oxide thickness formed subsequently at 1 atm O_2, 200°C, 20 min

Crystal face	No pretreatment, A*	H_2 pretreated, A*
(100)	1860 ± 59	715 ± 40
(111)	580 ± 51	620 ± 37
(110)	400 ± 13	585 ± 25

* Averaged for three or four specimens. Deviations are maximum values.

two-stage logarithmic kinetics and that the parameters of oxidation parallel those of the slowly oxidizing (111) face at the same temperature (Table I). Similarly, the (111) face pretreated 30 min in N_2 at 450°C follows two-stage logarithmic kinetics paralleling that of the (100) face. Pretreated surfaces accurately follow the two-stage logarithmic equation up to and including a total oxide thickness of 3200Å. In this connection, it should be noted that similarly pretreating the (100) face in N_2 or the (111) face in H_2 at 450°C (Table II) has no effect on subsequent oxidation rates in O_2 within experimental error of such measurements. On the other hand, pretreating the (110) face in H_2 increases the subsequent oxidation rate to that characteristic of (111) (Table II). Hence in accord with previous conclusions, N_2 pretreatment produces surface facets favoring the (100) orientation whereas H_2 pretreatment produces surface facets favoring the (111) orientation.

Electron Micrographs of Faceted Surfaces

The appearance of facets on Cu surfaces after low-temperature heat treatment in the order of 350°-450°C was missed in early work by other investigators probably because the facets are not visible under an optical microscope. Any observed effect of pretreatment on oxidation rate was typically ascribed to surface impurities. However, Parlodion replicas of electropolished (111) Cu, which show a smooth surface at 100,000X, show definite reproducible roughening typical of striations or faceting after N_2 pretreatment (Fig. 7). Similarly, H_2-pretreated (100) Cu also shows roughening with formation of facets of somewhat smaller dimensions than those produced in N_2-pretreated (111) (Fig. 8). The background facets for either face have dimensions in the order of 100Å; N_2-pretreated (111) shows a superimposed formation of larger areas in the order of 500Å. Their over-all small dimensions account for lack of sharp definition at 100,000X. Important was the observation that surface roughening accompanying facet formation is reversible, depending on the adsorbed gas, as is shown in the micrograph of Fig. 9. Here (100) Cu

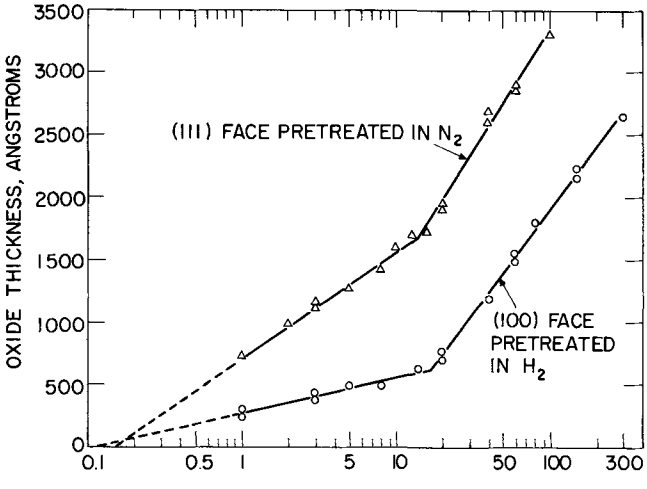

Fig. 6. Oxidation in O_2, 1 atm, 200°C, of electropolished (111) Cu pretreated in N_2 and of (100) Cu pretreated in H_2, 450°C, 30 min. (Initially H_2-reduced surfaces, not air-exposed.)

Fig. 7. Electronmicrograph of electropolished (111) Cu pretreated in N_2, 1 atm, 450°C, 30 min.

Fig. 8. Electronmicrograph of electropolished (100) Cu pretreated in H_2, 1 atm, 450°C, 30 min.

Fig. 9. Electronmicrograph of electropolished (100) Cu pretreated in H_2, 1 atm, 450°C, 30 min, then in N_2, 1 atm, 450°C, 30 min, showing reversible faceting.

was first faceted in H_2 at 450°C for 30 min, followed immediately by exposure to N_2 at 450°C for 30 min. The first gas produced faceting as in Fig. 8, but the latter gas favoring the original (100) face again produced a relatively smooth surface. The relatively larger oxide crystals which form on H_2-pretreated (100) Cu oxidized in O_2, 1 atm, at 200°C for 20 min is shown in Fig. 10. Electron micrographs, therefore, support the premise that faceting results from gaseous pretreatment; in turn, the large effect of gaseous pretreatment on subsequent oxidation rates leaves little doubt that faceting is the cause.

Faceting produced at temperatures in the order of 450°C is plausibly the result of surface rearrangement resulting from surface diffusion of Cu atoms. The effect

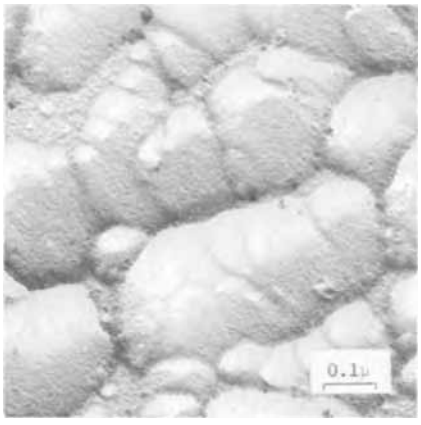

Fig. 10. Electronmicrograph of electropolished (100) Cu pretreated in H_2, 1 atm, 450°C, 30 min then oxidized in O_2, 1 atm, 200°C, 20 min.

of temperature and time on faceting, as measured by oxidation rates of pretreated surfaces, is shown in Fig. 11 and 12. It is apparent that surface rearrangement or faceting does not occur appreciably below 300°C within 30 min. Comparatively, at 450°C, it requires 10 min for optimum faceting of (111) in N_2 or analogously 20 min for (100) in H_2. The data for N_2 pretreatment provide a calculated activation energy of 9700 cal/mole and a similar but higher value for pretreatment in H_2. These low values are consistent with a surface diffusion process. It was also concluded by Tucker (14) that faceting of (210) Rh in 10^{-6} Torr O_2 at 350°C to form (100) and (110) surfaces, as revealed by low energy electron diffraction, occurs by surface diffusion.

Discussion

The close correspondence of the reaction rate constants k_1 and k_1', at 200°C for the H_2-treated (100) face with those for the untreated (111) face (Table I) plus the effects of H_2 pretreatment of all faces (Table II) indicate that (*a*) the oxidation rate is established by the specifically oriented facets that form during gaseous pretreatment and (*b*) the predominant orientation of the facets which form on exposure to H_2 at 350°-450°C is (111). Similar conclusions are drawn on comparing the oxidation parameters for the N_2-treated (111) face and the untreated (100) face, the corresponding predominant orientation of facets being (100). Not only do the faceted surfaces exhibit two-stage logarithmic behavior, similar to untreated surfaces, but the linear relation between oxide thickness and logarithm of time is valid up to oxide thicknesses of at least 3200Å which lie well beyond the equivalent dimensions of facets (100-500Å) as estimated from Fig. 7 and 8. The thickness of copper consumed in forming a 3200Å film of Cu_2O, for example, is 1920Å. Hence, it appears that the oxidation rate established by a faceted surface may continue beyond the time that the facets themselves are consumed. This suggests that the oxide-metal orientation relationships at the interface become stabilized soon after oxidation begins and hence orientation of facets dominates the oxidation process for an appreciable time within the thin film region. If the interface were not stabilized, the oxidation rate should gradually revert to that characteristic of the original crystal orientation, which rate can be either higher or lower than the initial rate. There is no evidence from thickness *vs.* log time plots that this reversion occurs.

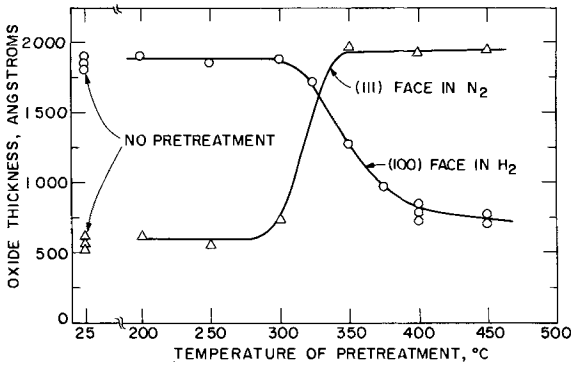

Fig. 11. Effect of temperature of pretreatment for 30 min on subsequent oxidation of Cu in O_2, 1 atm, 200°C, 20 min.

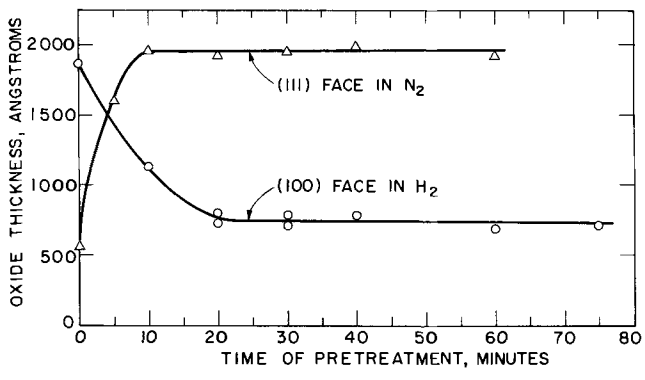

Fig. 12. Effect of time of pretreatment at 450°C on subsequent oxidation of Cu in O_2, 1 atm, 200°C, 20 min.

Actually, since the rates in second-stage oxidation tend to be the same and independent of crystal face, the influence of a faceted surface need extend only to the maximum oxide thickness characteristic of first-stage oxidation or to a thickness equal to L. Maximum values of L at 225°C range from 720Å for (110) to 2290Å for (100). Differences of roughness factor of the faceted compared to the equivalent nonfaceted surfaces may account for an increase in values of L for treated surfaces, but experimental variations of L are too large for any quantitative interpretation.

The reversible nature of faceting presently observed for copper surfaces, and which was also observed by Moreau and Bénard (15) for an 18% Cr-Fe alloy in H_2-H_2O atmospheres, reasonably results from a surface diffusion process stimulated by gas absorbed on the metal surface. The tendency is to form a surface of adsorbed gas-metal atoms of lowest free energy, the orientation of the resulting surface depending on the gas. The rate at which such a surface forms probably also depends on the nature of the adsorbed gas. This is suggested by results of Rhead (16) who reported that surface diffusion of Ag and Cu is enhanced by adsorbed oxygen. The apparently larger dimensions of facets which form on N_2-treated Cu compared to H_2-treated Cu (Fig. 7 and 8) can be explained accordingly by a higher surface diffusion rate of the Cu-O complex compared to the Cu-H complex.

After such time as oxide nuclei form and grow into a continuous film [within seconds at 500°C, 1 Torr O_2 (17); still less time at 200°C, 1 atm O_2], the surface orientation of metal with respect to oxide probably becomes "frozen," effectively blocking any further tendency for the surface to rearrange itself to form facets of orientation differing from that of the metal in contact with oxide. Hence, the oxidation rate is firmly established by the orientation relationships which exist at such time as the three-dimensional oxide film becomes continuous and the two-stage logarithmic equation is found to apply. After the oxide film grows to a thickness such that diffusion of ions or vacancies through the oxide becomes rate determining, the effect of metal face is no longer an important factor in establishing the oxidation rate, and the usual parabolic equation applies instead. This was shown by similar oxidation rates (within 20%) of various Cu faces at 900°C reported by Bénard and Talbot (18). The differing rates for Cu crystal faces at 600°C,

1 Torr O_2, reported by Ali and Wood (13), despite the parabolic equation being obeyed, suggest that conditions were intermediate between logarithmic and parabolic kinetics, and hence some of the effects of crystal orientation persisted.

The large effect of faceting on thin film oxidation behavior of Cu suggests that faceting should exert important effects quite generally. In this regard, it is of interest to note that work functions measured by Underwood (19) for the (100) Cu surface, on continued heating in vacuum approached the work function of (111) Cu presumably because facets of approximate (111) orientation slowly developed on the (100) face. Similarly, work function measurements by Köhler (20) on a copper single-crystal sphere cooled from the melting point in high vacuum showing no effect of crystal face, is probably explained by a faceted surface, all portions of the sphere having the same approximate orientation. The lack of good agreement in the thin film region for oxidation rates of metals in general, as reported by various investigators, suggests that uncontrolled faceting was probably a contributary cause in addition to any important effects of impurities. It is probable in the case of Cu that perturbations caused by surface treatment were sometimes minimized by a usual final vacuum treatment which reversed in part any faceting caused by an initial pretreatment of specimens in hydrogen. The observed effect of pretreatment of Cu surfaces with CO_2 at 250°C causing accelerated oxidation rates of the (111) face in O_2, as reported by Cathcart *et al.* (21), suggests that the effect of pre-exposure may have been one of submicroscopic faceting produced by the CO_2 atmosphere. The temperature in this case was somewhat below the minimum temperature found presently to produce faceting in H_2 or N_2 atmospheres. Similarly, the accelerated oxidation rate of pure Zr reported by Demant and Wanklyn (22) following vacuum annealing at 800°C for ½ to 48 hr, an effect which could be erased by electropolishing less than 10μ from the metal surface, is plausibly ascribed to faceting produced by the vacuum anneal. The authors sought in vain for a likely surface contaminant.

Based on the model of logarithmic oxidation kinetics according to which the rate is controlled by electron transfer from metal to oxide (6) it is possible to calculate the work function (w.f.) ϕ for each Cu face at the oxide-metal interface, as well as the density n of imperfections in Cu_2O at which electrons become trapped. The latter produce a growing uniform density negative space charge within the growing oxide next to the metal surface which impedes electron transfer, accounting for a slowing down of oxidation. The w.f. is calculated from the derived relation ΔE (activation energy, 1st stage) $= \phi - 3.6$ (electron volts) where ϕ is the metal w.f. as modified by contact with oxide and 3.6 eV is the electron affinity of O adsorbed on Cu_2O. The density of sites n at which electrons become trapped can be calculated from the reaction rate constant $k_0 = k_1/2.3 = \epsilon kT/4\pi nle^2$ and $3.6 = 2\pi nel^2/\epsilon$ where ϵ is the dielectric constant of Cu_2O (equals 10.5), e is the charge on the electron (4.80×10^{-10} esu), l is a parameter, which cancels out, equal to the calculated thickness of uniform charge density oxide at which the Fermi levels in oxide and metal become equal, k and T are the Boltzmann constant and absolute temperature, respectively. Calculated values of ϕ and n are listed in Table III using values of ΔE and k_1 listed in Table I.

Table III. Calculated values of Cu work function ϕ at oxide-Cu interface, and density n of electron trap sites in Cu_2O

Face	ϕ (V)	n (cm^{-3}) 175°C	200°C	225°C
(100)	3.95	2.1×10^{14}	0.86×10^{14}	0.47×10^{14}
(111)	4.08	34.5	9.8	2.5
(110)	4.16	44.5	17.8	4.7

The w.f. for polycrystalline Cu in vacuum (4.47V) is about 0.6V higher than for the value modified by contact of metal with oxide as calculated from oxidation rate data (8). The corresponding modification of present values, however, is expected to vary with crystal face. This can be seen from the fact that, since ΔE is the work necessary to transfer an electron from metal to oxygen absorbed on oxide, ϕ is made up of several terms, *e.g.*, $\phi_0 + X_0 - X_1 + X_2$ where ϕ_0 is the w.f. of metal in vacuum, X_0 is the increase of w.f. caused by immediate contact of metal with oxygen atoms, X_1 is the w.f. of oxide at the metal-oxide interface, and X_2 is the w.f. of oxide at the oxide-O_2 interface. Under equilibrium conditions, $X_1 = X_2$, but, in an actively growing oxide, defect structure differs at the two interfaces, altering corresponding values of w.f. Since crystal face determines the oxidation rate, which in turn influences the defect structure, it is logical to expect that X_1 and X_2 will also vary with crystal face. The value X_0 probably also varies with crystal face as was shown for Ni by MacRae (23). A fractional ¼ coverage of O on (111) Ni increased the w.f. by 1.2V whereas on (100) Ni the same ¼ coverage by O increased the w.f. by only 0.25V, indicating that (111) Ni in contact with O has a higher w.f. than (100) Ni similarly exposed to O. The modified w.f. probably explains why (111) is the face of Ni which oxidizes least in the thin film region as reported by Lawless *et al.* (24). A similar effect may explain why the order of w.f. for Cu in vacuum: $\phi_0(100) > \phi_0(111)$ as measured by Underwood (19) and Rose (25) is opposite to the order shown in Table III: $\phi(111) > \phi(100)$, and that (111) Cu correspondingly oxidizes at a lower rate than (100) Cu despite the order of w.f. values in vacuum.

Values of n, the density of electron trapping centers in Cu_2O, also vary with crystal face, being much larger for the slowly oxidizing (110) and (111) faces than for the more rapidly oxidizing (100) face. The average values are consistent with 10^{14} to 10^{15} holes or defect sites per cubic centimeter at >100°C in Cu_2O formed from commercial copper as calculated by Brattain (26) from conductivity and mobility measurements, although the values reported in Table III are obviously kinetic values and do not refer to an equilibrium state. For this reason, the observed imperfection densities in Table III vary with oxidation rates which in turn vary with crystal face.

The observed activation energies for second-stage oxidation, corresponding to growth of a diffuse space charge oxide, are largely independent of crystal face, being in the range 0.32 to 0.34 eV. According to the theory cited earlier (6) the activation energy for second-stage oxidation is equal to

$$-4\pi ne^2lL/\epsilon - e(\phi - v) + 4\pi e^2/\epsilon kT\left(\frac{d\,nlL}{d\,1/T}\right)$$

where v equals the electron affinity of adsorbed O (3.6V), and other terms have already been defined. In the original derivation, the third term above was inadvertently omitted. In view of the fact that observed values of nl decrease whereas observed values of L increase with temperature, the third term can sometimes be neglected, but this is probably not true generally. Since the values of ϕ, l, n, and L are all dependent on crystal face, the assumption can be made that these factors interact in such a manner as to result in the same approximate second-stage activation energy for the three crystal faces. One can also assume that continued oxidation beyond the first stage produces surface rearrangement and hence essentially the same metal-oxide orientation relations; the operating work function ϕ may then become independent of crystal face. Further consideration of Cu_2O semiconducting properties and of the detailed nature of the energy barrier at the Cu_2O-Cu interface are needed for further useful evaluation of such effects on the mechanism of thin film oxidation.

Conclusions

1. Submicroscopic faceting of Cu surfaces occurs during gaseous pretreatment, having a major effect on subsequent oxidation rates. Electron micrographs confirm that faceting occurs and that it is a reversible process.

2. Gaseous pretreatment in H_2 favors facets of slowly oxidizing predominately (111) orientation, whereas in N_2, the effects of which are ascribed to traces of O_2, the rapidly oxidizing predominately (100) orientation is favored.

Activation energies (9700 cal/mole) for facet formation are in accord with a surface diffusion process.

3. Oxidation rates, according to oxide thickness measurements, decrease in the order: (100) > (111) > (110), but, according to activation energies, in the order: (100) > (110) > (111).

4. All three faces follow two-stage logarithmic kinetics at 175°, 200°, and 225°C. This is also true of treated (100) and (111) faces oxidized at 200°C.

5. Work functions calculated from activation energies of oxidation indicate that modification of the metal work function at the metal-oxide interface is orientation dependent.

Acknowledgment

The authors express their appreciation to the National Steel Company for financial support. They are grateful to John Breedis and Robert Goss for guidance in preparing the electron micrographs.

Manuscript submitted Nov. 4, 1970; revised manuscript received ca. March 20, 1971. This was Paper 98 presented at the Atlantic City Meeting of the Society, Oct. 4-8, 1970.

Any discussion of this paper will appear in a Discussion Section to be published in the June 1972 JOURNAL.

REFERENCES

1. A. Rönnquist and H. Fischmeister, *J. Inst. Metals*, **89**, 65 (1960-1961).
2. W. Bradley and H. Uhlig, *This Journal*, **114**, 669 (1967).
3. W. Campbell and U. Thomas, *Trans. Electrochem. Soc.*, **76**, 303 (1939).
4. B. Lustman and R. Mehl, *Trans. AIME.*, **143**, 246 (1941).
5. R. Tylecoat, *J. Inst. Metals*, **78**, 327 (1950).
6. Quoted by H. H. Uhlig, *Acta Met.*, **4**, 541 (1956).
7. V. Nwoko and H. Uhlig, *This Journal*, **112**, 1181 (1965).
8. H. Uhlig, J. Pickett, and J. MacNairn, *Acta Met.*, **7**, 111 (1959).
9. B. Lustman, *Trans. Electrochem. Soc.*, **81**, 359 (1942).
10. A. Gwathmey and A. Benton, *J. Phys. Chem.*, **46**, 969 (1942).
11. F. Young, J. Cathcart, and A. Gwathmey, *Acta Met.*, **4**, 145 (1956).
12. W. Harris, F. Ball, and A. Gwathmey, *ibid.*, **5**, 574 (1957).
13. S. Ali and G. Wood, *Corrosion Sci.*, **8**, 413 (1968).
14. C. Tucker, Jr., *Acta Met.*, **15**, 1465 (1967).
15. J. Moreau and J. Bénard, *Compt. Rend. Acad. Sci. Paris*, **242**, 1724 (1956).
16. G. Rhead, *Acta Met.*, **11**, 1035 (1963); **13**, 223 (1965); *Trans. Faraday Soc.*, **61**, 797 (1965).
17. F. Gronlund, *J. Chim. Phys.*, **53**, 660 (1956).
18. J. Bénard and J. Talbot, *Compt. Rend. Acad. Sci. Paris*, **225**, 411 (1947).
19. N. Underwood, *Phys. Rev.*, **47**, 502 (1935).
20. P. Köhler, *Z. Angew. Phys.*, **21**, 191 (1966).
21. J. Cathcart, G. Petersen, and C. Sparks, Jr., Proc. Nucléation Dans Les Réactions des Gaz Sur Les Métaux, p. 11, Centre National de La Recherche Scientifique, Paris 1965.
22. J. Demant and J. Wanklyn, *Corrosion*, **22**, 60 (1966).
23. A. MacRae, *Surface Sci.*, **1**, 319 (1964).
24. K. Lawless, F. Young, and A. Gwathmey, *J. Chim. Phys.*, **53**, 667 (1956).
25. B. Rose, *Phys. Rev.*, **44**, 585 (1933).
26. W. Brattain, *Rev. Modern Phys.*, **23**, 203 (1951).

The Chlorination Kinetics of Tungsten, Molybdenum, and their Alloys

A. Landsberg, C. L. Hoatson, and F. E. Block

Albany Metallurgy Research Center, Bureau of Mines, U. S. Department of the Interior, Albany, Oregon 97321

ABSTRACT

The chlorination kinetics of tungsten, molybdenum, and three of their binary alloys have been studied as part of a Bureau of Mines effort to provide information of value when considering chlorine metallurgy processes. Tungsten and molybdenum were used for this initial investigation of alloys because they are chemically similar, form a complete range of solid solutions, and have been shown to chlorinate at temperatures sufficiently different so as to facilitate the determination of temperature dependency of reactivity by experiments based on the measurement of weight loss as the volatile chlorides are formed. Both the pure metals and alloys containing 22, 48, and 72 atomic per cent (a/o) molybdenum were found to chlorinate between 400° and 775°C at rates of 10^{-7} to 10^{-5} mole per square centimeter per minute, with the reaction rate dependent upon the 0.6 power of chlorine pressure. Molybdenum exhibited the highest reactivity, tungsten was the least reactive, and the alloys showed intermediate reactivity with respect to temperature. Single crystals of the pure metals showed marked anisotropy upon chlorination. When chlorinated, the polycrystalline alloy specimens of 22 and 72% molybdenum tended to show the crystalline anisotropy exhibited by the major component, while the 48% molybdenum specimen developed no pattern similarity to the pure metals.

Chlorine reacts with all metals at appropriate temperatures and pressures. Some of the chloride products of such reactions volatilize at the temperatures at which detectable reaction occurs, leaving a clean metal surface during chlorination. Tungsten and molybdenum exhibit this characteristic. Their chlorination kinetics, studied previously in our laboratory (3), show a temperature difference of over 200°C for equal chlorination rates of the two pure metals. Simple removal of reaction products, a wide range of reaction

Key words: alloy chlorination, tungsten-molybdenum chlorination, molybdenum-tungsten chlorination, morphology of chlorination.

Table I. Spectrographic analysis of samples, ppm

Sample	Al	Ca	Cu	Fe	Mg	Mo	Ni	Si	Sn	Ti	W	Zr
W	5	20	1	5		100	5	500	5			
W-22 Mo	5	20	0.5	5			1	400	1	1		
W-48 Mo	5	10	0.5	5				200	5	1		
W-72 Mo	20		5	80	10		5	500	100			20
Mo	20			80	5			30			100	

No analysis was made for nonmetallic impurities.

temperatures, and the fact that these chemically similar metals form solid solutions in all proportions (2) suggest that the determination of temperature dependency of chlorination rate might be used conveniently for studying the effects of alloying on reactivity.

Experimental Work

Sample preparation.—The starting materials for the samples used in this study were metal powders supplied by the General Electric Company with average particle diameters of 3μ for the tungsten powder and 5μ for the molybdenum powder. Preweighed powders for each sample composition were mixed in a twin-V-shell blender for 15 min, passed through a 60-mesh screen, again mixed for 15 min, screened for a second time, and finally mixed for a third 15 min. Each blended composition was compacted isostatically, and the compacts were sintered in hydrogen at 2200°C for 10 hr. The resulting sintered bars of 90 to 95% of theoretical density were then consumable-arc-melted into ingots which were machined to a diameter of 1.5 in. and extruded at 1900°C to rectangular bars ⅜ x ¾ in. in cross section. These bars, after being conditioned by sand blasting to remove surface defects, were hot-rolled. A rolling temperature of 1450°C was used for the tungsten and the alloys, with a reduction of 20% per pass. The molybdenum was hot-rolled at 800°C, with a reduction schedule of 10% per pass. The final rolled thickness was 0.25 cm on all specimens. To reduce oxidation, all heating was done in an argon atmosphere. Sample specimens measuring 2.5 x 2.0 x 0.25 cm were machined from this rolled stock. Table I shows the impurity analysis for the samples used, and Table II shows the variation of sample composition from point to point as determined by an electron microprobe.

Single-crystal specimens were obtained from Materials Research Corporation. These materials were pure tungsten and molybdenum which contained no spectrographically detectable impurities. Crystal orientation was determined by x-ray reflection methods.

Table II. Typical electron microprobe analysis of sample surfaces*

Sample	Atomic per cent molybdenum			
	Before reaction		After reaction	
W-72 Mo	68.8		68.2	
	71.6		68.5	
	70.1		67.4	
	68.4		66.8	
	70.9		68.4	
	Average	70.0	Average	67.9
W-48 Mo	44.7		42.0	
	45.6		44.1	
	43.5		44.1	
	43.3		44.5	
	43.9		42.0	
	Average	44.2	Average	43.3
W-22 Mo	24.1		20.7	
	21.8		20.7	
	23.5		20.7	
	23.6		20.6	
	—		20.4	
	Average	23.2	Average	20.6

* These analyses were made randomly on highly polished sample surfaces with the electron beam of 1μ diameter to a depth of approximately 1000A. After reaction the surfaces were slightly roughened. Chemical analysis of large portions of the samples gave 22, 48, and 72 a/o molybdenum which reflect the composition changes in samples fabricated from the same ingot.

Procedure.—Chlorination-rate measurements were begun by weighing and measuring a metal sample. Weights were determined to the nearest 0.1 mg, and the rectangular measurements were made to the nearest 0.01 cm. The sample was then placed horizontally so that it rested slightly below center in a 28-mm Vycor[1] reaction tube which was held in a 3 x 30 cm tube furnace. C. P. grade argon and chlorine passing through control needle valves and calibrated rotameters were scrubbed in a bubbler containing sulfuric acid before entering the reaction tube. Gases leaving the reaction tube passed through another such bubbler and were vented via a laboratory hood. With the metal sample in place, argon was passed through the apparatus at the rate of 500 cc/min while the furnace was brought to operating temperature. The reaction-zone temperature was measured by a Chromel-Alumel thermocouple in a small Vycor tube positioned directly over the sample. After the reaction zone had been held at the desired operating temperature for several minutes, the reaction was started by substituting chlorine for part of the argon to give the desired chlorine concentration at a total gas flow of 500 cc/min. All work was done at 20% chlorine (approximately 152 Torr) except where noted. Reaction times ran from 15 min to 1 hr, during which the temperature remained constant to within ±2°C, and the gas flows were held to within 2% of the desired values. At the end of a run the chlorine flow was stopped and the argon flow increased while the entire reaction tube was cooled. When cool, the sample was removed and weighed. The weight loss was used to calculate the rate of reaction as moles of metal per minute per cm^2 of surface based on the geometric area and the average tungsten-molybdenum composition of the sample.

Results

The measured rates of chlorination, as moles of metal/cm^2 min, are shown graphically in Fig. 1. Data for each of the metal compositions given by open, filled, and partially filled symbols represent the experimental results from the three samples of each metal composition. Also each data point is the average of at least three replicate runs using an individual sample. The data show reproducibility from sample to sample, and the lines derived from a least squares analysis of the data according to the Arrhenius relationship agree quite well with our previous work on commercially prepared sheets of the pure metals. The least squares analyses are given in Table III. All samples changed in appearance as chlorination proceeded. Initially the surfaces appeared dull because of their sandblasted finish but became shiny as they reacted. The reaction rates increased during the two or three initial reaction experiments and then remained constant for an extended period of chlorination during which the experiments were made for the reported data. After the constant rate period of chlorination the samples were rough on all surfaces and very jagged on the edges in the direction of rolling and the reaction rate decreased slightly. These decreasing-rate data are not reported here. The composition of the sample sur-

[1] Reference to trade names is made to facilitate understanding and does not imply endorsement by the Bureau of Mines.

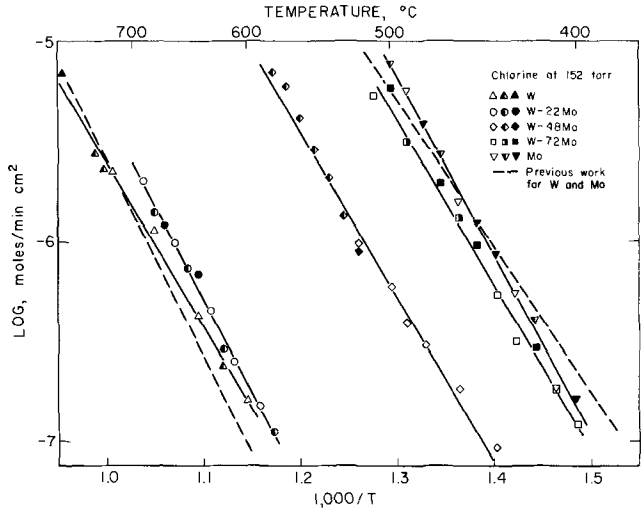

Fig. 1. Arrhenius plot for W-Mo chlorination

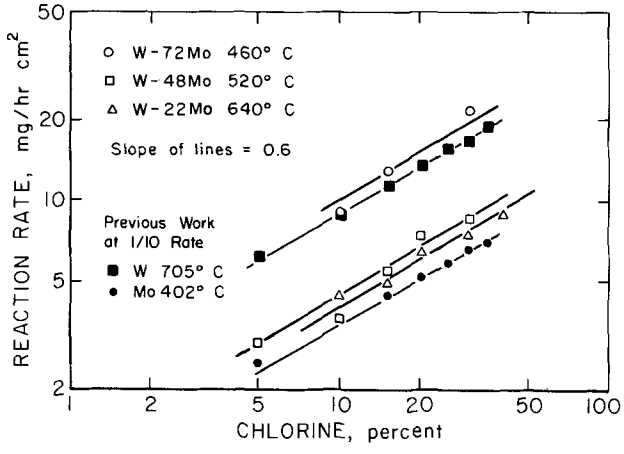

Fig. 2. Effect of chlorine pressure on reaction rate

faces showed slight preferential loss of molybdenum upon chlorination, as indicated by the electron microprobe measurements in Table II. The data, although presented in the table in pairs of analyses for before and after reaction, do not necessarily represent exactly the same location on the surface before and after reacting. These surfaces were only slightly reacted before the final microprobe analyses were made. Other tests in which over half of the entire sample was removed by chlorination showed no depletion of molybdenum. The resulting, very rough surfaces hindered accurate microprobe analyses.

The effect of chlorine pressure on the reaction rate is shown in Fig. 2. As in our previous work with the pure metals, the alloys showed a rate of chlorination

Table III. Least square equations for chlorination rates

Material	A*	B*
W	8254	2.65
W-72 Mo	9350	4.00
W-48 Mo	8295	4.51
W-22 Mo	8322	5.44
Mo	8961	6.48

* Constants for the equation

$$\log R = -\frac{A}{T} + B$$

where R is the chlorination rate in moles per cm² min with 20% chlorine and T is the absolute temperature in °K.

approximately dependent upon the 0.6 power of chlorine concentration. At the highest rates of chlorination measured, changes of total gas flow rates from 500 to 1000 cc/min produced no change in measured chlorination rates demonstrating that true chemical reaction was the rate-limiting factor.

Upon chlorination all samples changed in appearance because of the anisotropic attack of chlorine. The polycrystalline metals and alloys developed ridges and troughs running in the direction in which the samples had been hot-rolled. Figure 3 shows the trimmed ends of the molybdenum sample before and after chlorination. Interestingly, a sample which had been reacted at 1200°C did not develop the deep ridges and troughs but remained rather smooth with the individual grains becoming very evident. Microscopic views of these reacted samples are not of high quality because of the deep etching and low depth of field at high magnification. Nevertheless, in Fig. 4 these views do reveal a similarity between the reacted textures of tungsten and tungsten-22 molybdenum, and between molybdenum and tungsten-72 molybdenum with the tungsten-48 molybdenum texture being distinct. The molybdenum after chlorination at higher temperatures shows

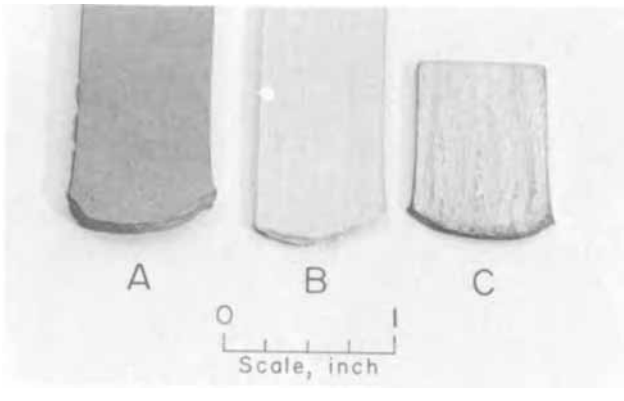

Fig. 3. Polycrystalline molybdenum samples. A is an unreacted molybdenum strip, B had been reacted at 480°C with 20% chlorine, and C had been reacted at 1200°C with 20% chlorine.

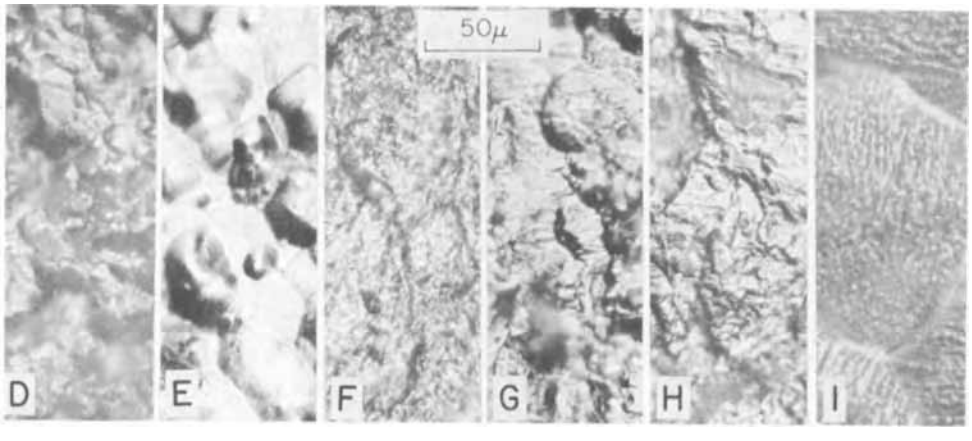

Fig. 4. Photomicrographs of chlorinated polycrystalline samples. D. Tungsten, 700°C., E. W-22 Mo, 700°C., F. W-48 Mo, 580°C., G. W-72 Mo, 480°C., H. Molybdenum 480°C., I. Molybdenum, 1200°C. Direction of rolling ↕.

Fig. 5. Single-crystal specimens after chlorination. J. Tungsten, 700°C., K. Tungsten, 700°C., L. Molybdenum, 1200°C.

reaction produced rows of small circles running in different directions on adjacent crystals. This produces crystal differentiation on a macroscopic scale.

Single crystal samples show the anisotropic attack of chlorine quite clearly. Figure 5 is a photograph of two tungsten single crystals which have been extensively chlorinated at 700°C and a molybdenum crystal chlorinated at 1200°C. These specimens were cylindrical before reaction occurred. Because of the high reaction rate of molybdenum at 1200°C, gaseous diffusion limited the reaction rate, causing the somewhat rounded corners on the single crystal; however, close examination shows distinctive surface characteristics at 90° intervals. Electron microscope views in Fig. 6 of a molybdenum single crystal show surfaces in the early stages of attack by chlorine, and Fig. 7 and 8 show surfaces parallel or nearly parallel to the {100}, {110}, and {410} planes which have developed after extensive chlorination. Nomarski interference-contrast microscopic views of similar surfaces are shown in Fig. 9. Similar surface configuration resulted from chlorination at all chlorine concentrations and temperatures studied (except for the high-temperature experiments specifically noted).

Tungsten single-crystal surfaces developed similarly upon extensive chlorination. Two planar surfaces which formed on an originally cylindrical crystal were parallel to the {100} and {210} planes. Electron microscope

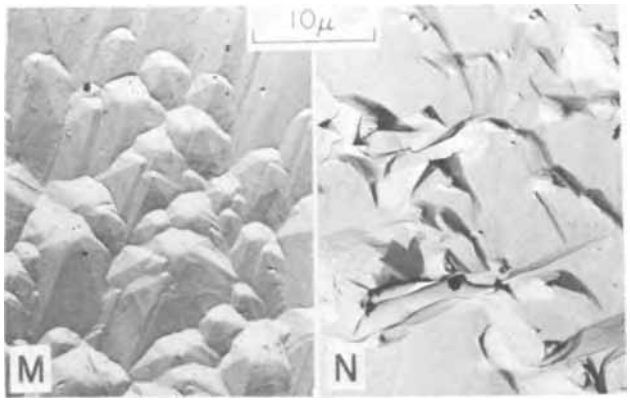

Fig 6. Electron micrographs of single-crystal molybdenum at the onset of chlorination. M. Reacting surface, N. Nonreacting area.

views of these surfaces are shown in Fig. 10. Optical microscope views of the surfaces which developed parallel to the {100}, {210}, and {320} planes are shown in Fig. 11.

The molybdenum crystal reacted with chlorine at 1200°C showed a series of microscopic rod-like depressions over the entire surface. These cylindrical pits were all parallel. Viewing the crystal microscopically from various angles revealed that the pit spacing varied periodically every 90° on surfaces parallel to their length, but perpendicular to their length the pits appeared as round holes in the metal surface.

Discussion

The chlorination of tungsten and molybdenum in the temperature range studied shows striking similarity to certain oxidation reactions of these metals. Perkins, Price and Crooks (5) have shown that within boundaries defined by temperature and oxygen pressure tungsten is oxidized without formation of an oxide scale at a rate proportional to the 0.59 power of the oxygen pressure. Single-crystal tungsten used by these investigators shows anisotropic attack by oxygen in this region. Other investigations (4, 7) have shown that oxygen attacks both tungsten and molybdenum with a similar fractional exponential dependence on oxygen pressure. Like the oxidation of these metals, the appearance of the chlorination-reaction-produced surfaces changes as the temperature rises. This was shown clearly for molybdenum chlorinated at 1200°C, the maximum temperature obtainable in our equipment (see Fig. 3 and 5). Tungsten surfaces chlorinated at 1200°C showed some dissimilarity to surfaces chlorinated at lower temperatures.

The marked anisotropy of the chlorination of tungsten and molybdenum as evidenced by the resulting morphology of single crystals demonstrates that certain crystal surfaces are reactive and also the fact that certain crystal planes are not chlorinated. This

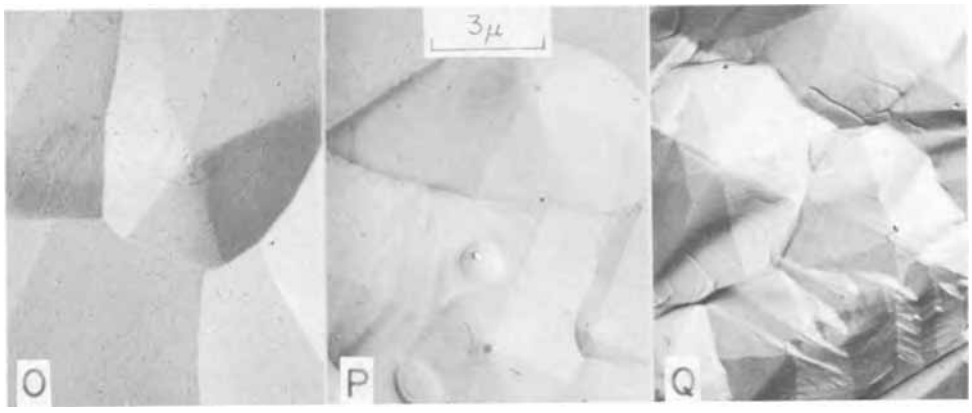

Fig. 7. Electron micrographs of chlorinated molybdenum single-crystal surfaces parallel to the {100} plane.

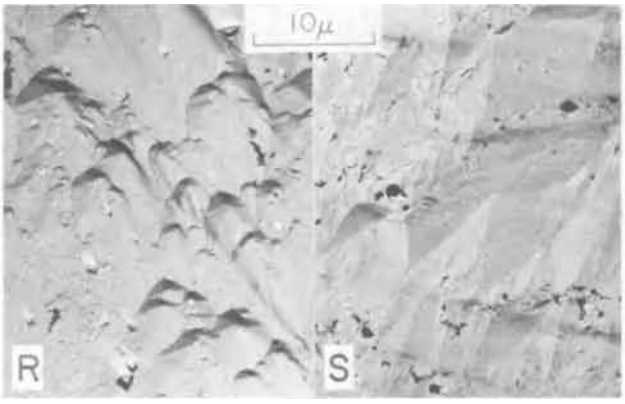

Fig. 8. Electron micrographs of chlorinated molybdenum single crystal surfaces. R is a {410} surface; S is a {110} surface.

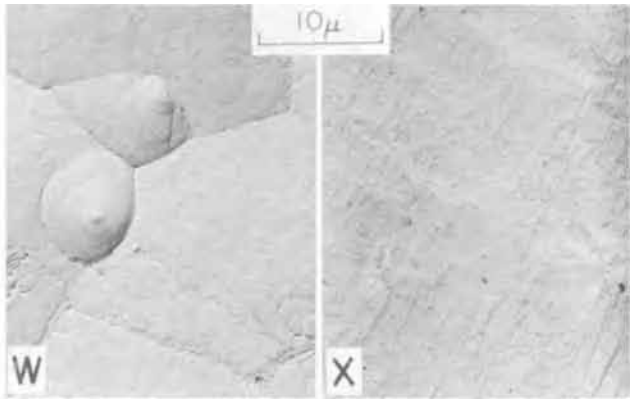

Fig. 10. Electron micrograph of chlorinated tungsten single-crystal surfaces. W is a {100} surface; X is a {210} surface.

is clearly shown in Fig. 5 by the very sharp corners on the reacted tungsten single crystals. Figure 6 also illustrates a contrast between the reactive and nonreactive faces of a single crystal. Even though the surfaces shown had only been exposed to chlorine for a few minutes, it is very clear that a marked pattern had already developed on one face while an adjacent area showed no change from the unreacted surface. Such areas alternated around the cylindrical crystal every 45°.

Examination of Fig. 7, 8, and 9 reveals a system of pyramids developed by chlorination on {100} molybdenum surfaces and surfaces close to {100}. The large surface area resulting from these pyramids (*e.g.* frame T) gives an indication as to why molybdenum upon chlorination recedes rapidly perpendicular to {100} planes. On some higher order planes similar pyramids appear slanted, and a pencillike structure is noted with the pyramid being in the sharpened-point position. A trisoctahedron form best correlates with the single-crystal morphology developed as the result of molybdenum chlorination.

Tungsten crystals also produce an octahedral form when chlorinated. The square pyramids shown in the electron photomicrograph of Fig. 10, W are severely rounded, but photomicrographs in Fig. 11 of the chlorinated {100} and {320} surfaces depict a sharper series of angular faces. The {210} faces, which reacted rather rapidly, show no clearly defined geometric pattern other than a series of shallow lines. The best geometrical shape that conforms to these chlorination-developed surfaces is a tetrahexahedron with faces made up of {210} planes.

From these tentative identifications of the reactive planes of tungsten and molybdenum, a difference in surface reactive geometry may be postulated for the two metals even though the over-all chemical mechanism may be similar. Indeed, this is observed in the chlorination-produced faceting under equal magnification and developed on materials which had a similar crystal texture due to rolling. [Reference (1) gives a rolled texture of (100) <011> for both tungsten and molybdenum.] The alloys rich in one metal develop a chlorination faceting similar to that of the pure metal and show a chlorination dependency on temperature similar to that of the high-content metal, but the alloy with nearly equal numbers of tungsten and molybdenum atoms develops a surface quite different from either of the pure metals. Dependency of chlorination rate on the nearly half power of the chlorine pressure may be attributed to the breakup of the chlorine molecule on the metal surface, and others (6) have shown that atomic chlorine is more reactive towards molybdenum; indeed it may be the only reactive chlorination species.

Positive identification of the reacting metal surfaces needs to be made, and a correlation between the various temperature-dependent regions of chlorination and the role of the metal surface must be determined before a complete understanding of the chlorination of tungsten and molybdenum and their binary alloys is realized. Such determinations would answer the question as to whether a certain crystal-oriented morphology develops on tungsten, molybdenum, and their alloys because of the atoms present or because of the temperature-chlorine pressure region of the reaction.

Manuscript submitted Dec. 23, 1970; revised manuscript received *ca.* March 25, 1971.

Any discussion of this paper will appear in a Discussion Section to be published in the June 1972 JOURNAL.

REFERENCES

1. C. S. Barrett and T. B. Massalski, "Structure of Metals," 3rd Edition, pp. 558-561, McGraw-Hill Publishing Co., New York (1966).
2. Max Hansen, "Constitution of Binary Alloys," 2nd

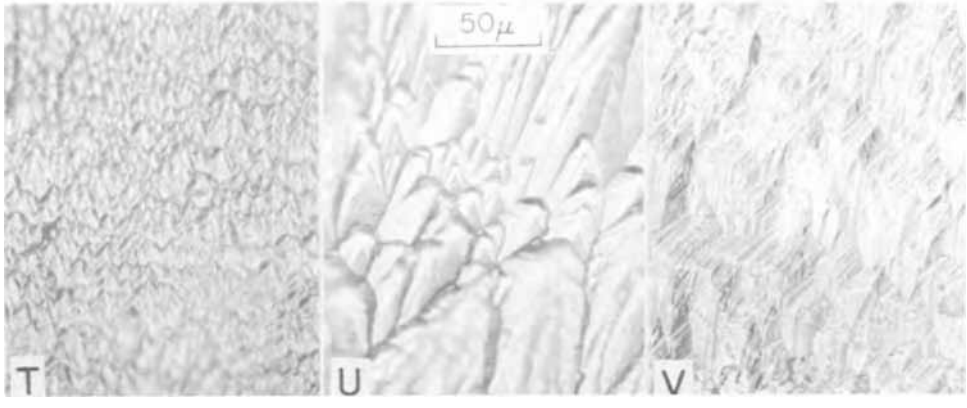

Fig. 9. Photomicrograph of chlorinated molybdenum single-crystal surfaces. T and U show {100} surfaces; V is a {110} surface.

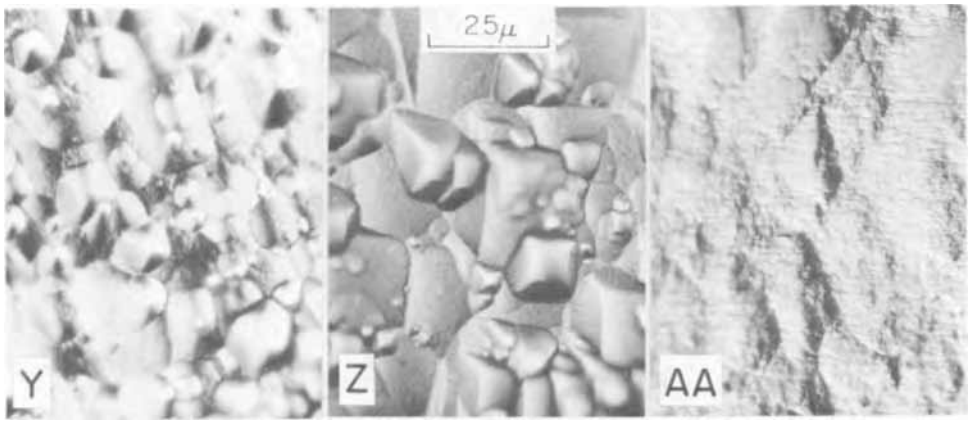

Fig. 11. Photomicrographs of chlorinated tungsten single-crystal surfaces. Y is a {100} surface; Z is a {320} surface; AA is a {210} surface.

Edition, p. 980, McGraw-Hill Publishing Co., New York (1958).
3. Arne Landsberg and F. E. Block, A Study of the Chlorination Kinetics of Germanium, Silicon, Iron, Tungsten, Molybdenum, Columbium, and Tantalum. *U. S. Bur. Mines, Rept. Invest.* 6649 (1965).
4. North American Aviation, Inc., Materials Research Department (Downey, Calif.) "High Temperature Oxidation of Molybdenum Under High Altitude Conditions." Rept. AL-2617, Sept. 1, 1957, ASTIA AD 147 839.
5. R. A. Perkins, W. L. Price, and D. D. Crooks, Oxidation of Tungsten and Other Refractory Metals, NASA Accession No. N66-13738, Report No. AFML-TR-64-162, April 1965.
6. D. E. Rosner and H. D. Allendorf, *J. Phys. Chem.*, **69**, 4290 (1965).
7. D. E. Rosner and H. D. Allendorf, *This Journal*, **114**, 305 (1967).

Mechanism of Sulfidation of Nickel-Chromium Alloys at 700°C as Inferred from Inert and Radioactive Marker Techniques

G. Romeo,*,[1] W. W. Smeltzer,* and J. S. Kirkaldy

Department of Metallurgy and Materials Science, McMaster University, Hamilton, Ontario, Canada

ABSTRACT

Sulfidation experiments have been carried out on a Ni-20 w/o Cr alloy using platinum markers and the tracer S^{35} to elucidate the transport mechanism for the diffusion-controlled formation of the duplex sulfide scale. It is concluded that outward diffusion of nickel and chromium accounts entirely for the growth of both layers. Chromium sulfide, being more stable than nickel sulfide, is formed by decomposition of the latter at the boundary between the two layers. This process is compensated for by a rapid growth of nickel sulfide at the gas-scale interface. It has been unequivocally demonstrated that sulfur diffusion does not contribute significantly to scale growth.

The results of a kinetic and morphological study of the scale formation on nickel-20 w/o (weight per cent) chromium alloys in hydrogen sulfide-hydrogen atmospheres were presented in an earlier publication (1). We report in this paper the results of a further series of experiments designed to elucidate the mechanism of the process. In particular, platinum markers and radioactive sulfur have been used to establish the contribution of the different species to the net transport of matter across the sulfide scale formed as a corrosion product. Such techniques have been widely employed in the past few years. We refer the reader to the papers by Mrowec and Werber (2-4) for further information and to an extensive and up-to-date bibliography on this subject in a recent paper by Holt and Himmel (5).

Experimental

Platinum marker experiments.—Specimens approximately 1.5 x 0.5 x 0.1 cm were cut from sheets of Ni-20 w/o Cr alloys. Details on composition and metallographical preparation prior to sulfidation have been reported in our earlier publication (1). In the same publication, the assembly was described for the concurrent sulfidation in hydrogen sulfide-hydrogen atmospheres of four specimens. The specimens could be raised to a relatively cold zone of the assembly and quenched after different reaction times. All experiments were carried out at 700°C which, as discussed in the previous work, was convenient for avoidance of the formation of a liquid phase. H_2S/H_2 atmospheres were used that ranged from 5 to 60 v/o (volume per cent) in hydrogen sulfide it being previously established that the pressure of sulfur has a negligible effect on the reaction mechanism.

Short pieces of 50μ diameter platinum wire were stretched across the surface of the specimens and electrically spot welded at several points and to the edges. Satisfactory adhesion to the surface of most markers was attained and the specimens could be sulfidized in the upright position. During later examinations of scale cross sections comparison of the relative positions of

* Electrochemical Society Active Member.
[1] Present address: Physical Chemistry Laboratory, General Electric Research and Development Center, Schenectady, New York 12301.
Key words: sulfidation, nickel-chromium, markers.

the different markers in a given specimen allowed one to recognize those with poor adhesion and to ignore them in the subsequent analysis. Specimens were mounted in epoxy resin as cross sections, polished, and examined metallographically.

Radioactive marker experiments.—Radioactive sulfur S^{35} is a convenient isotope for studies on the mechanism of sulfide scale formation. The advantages consist in its commercial availability, its comparatively long half-life (~90 days), and its decay with the emission of β^- radiation only. The latter characteristic sensibly reduces the number of precautions that have to be taken in handling the radioactive material.

The experiments consisted in first sulfidizing the alloy specimens with normal sulfur and subsequently with the radioactive isotope, or vice versa. It is assumed that the mechanism of reaction is the same for sulfur obtained from the decomposition of H_2S or directly from sulfur vapor (1, 7).

An assembly was designed (Fig. 1) similar to that used by Meussner and Birchenall (6) in which the specimens could be exposed to a sulfur atmosphere containing a small amount of S^{35}. A few coils of platinum wire were wound around the specimens to prevent contact with their containers. One or more specimens could be located in pockets at one end of a Vycor cell. At the opposite end was located a bulb containing remelted sulfur flowers. Some drops of a benzene solution of S^{35}, supplied by Amersham/Searle Company, corresponding to a total activity of approximately 1 mC were added to the normal sulfur. The reaction vessel was then sealed off in vacuo, and the sulfur-containing bulb was rapidly heated up to about 200°C, corresponding to a sulfur vapor pressure of roughly 3×10^{-3} atm. Finally the end of the vessel bearing the specimens was inserted into a furnace previously brought up to 700°C. The sulfidation was allowed to proceed for a selected time at the end of which the Vycor cell was quickly cooled down to room temperature and opened. The specimens could then be given further treatment with ordinary sulfur at the same temperature, either in a similar cell or in the assembly used for the platinum marker experiments.

Alternatively, sulfidation with normal sulfur could be followed by treatment with the radioactive isotope. In this experiment the reaction had to be stopped for a time at the end of the first stage for transfer of the specimens from the reaction vessel containing the isotope to the one containing ordinary sulfur or vice versa. This could have affected the experiments insofar as the thermal shocks may have caused strains and cracks in the sulfide scales. However, a critical appraisal of the results indicates that these artifacts do not seriously confuse the interpretations.

Cross sections of the specimens were prepared metallographically and their autoradiographs taken, exposing Kodak "contrast process ortho" films by contact with the radioactive surface. This technique is in general use and details can be found in several publications (8).

Results

In Fig. 2, micrographs are given of the cross sections of four specimens sulfidized at $\sim 10^{-7}$ atm sulfur for

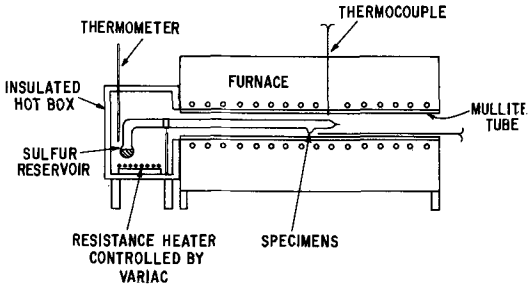

Fig. 1. Apparatus for sulfidation with radioactive sulfur

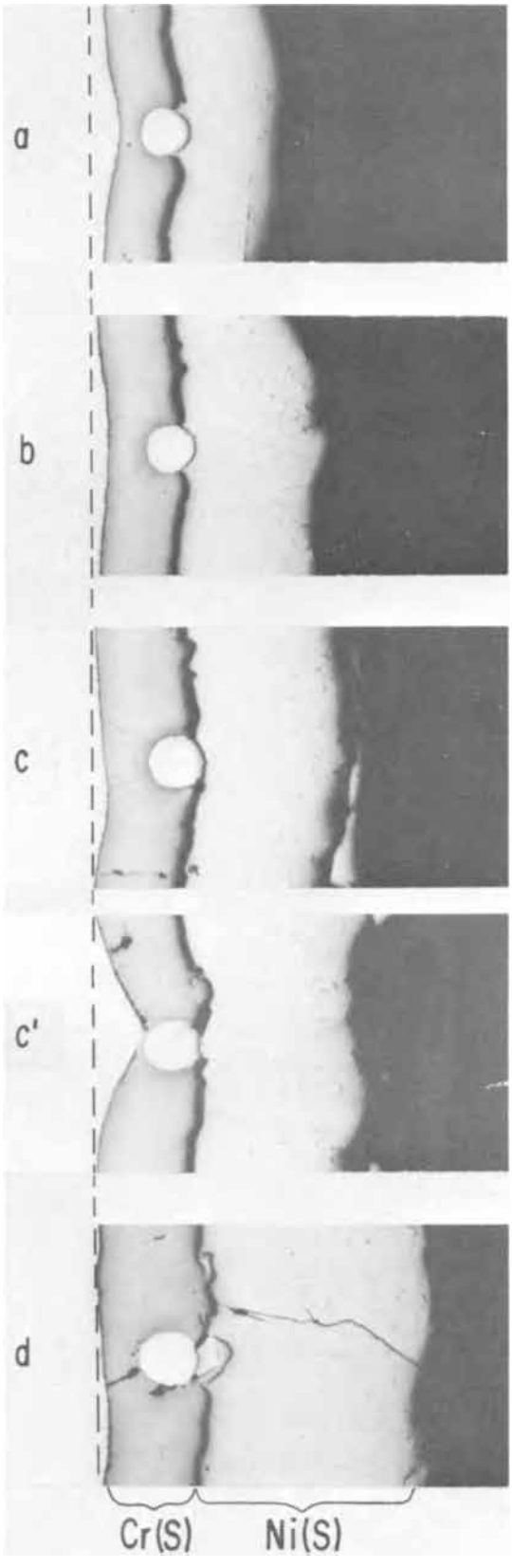

Fig. 2. Positions of the platinum markers after different reaction times. Micrographs a, b, c and c', d correspond to 5, 7, 10, 15 hr sulfidation at 700°C and $\sim 10^{-7}$ atm sulfur, respectively. Micrograph c' is indicative of the "undercutting mechanism." Magnification 135X.

5, 7, 10, and 15 hr, respectively. In addition to the remarkable compactness of the scale, one can observe that the platinum markers are situated in the inner chromium sulfide layer close to the adjacent nickel sulfide layer. This position leaves some space between

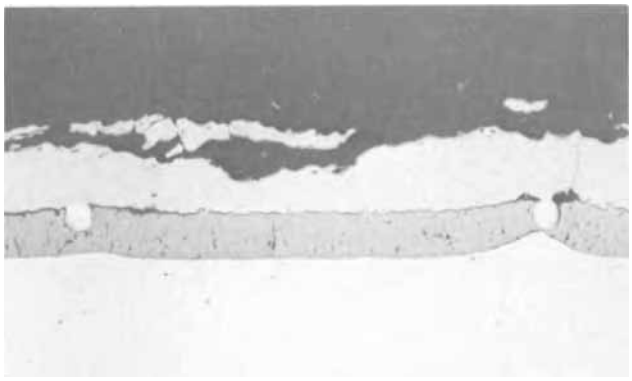

Fig. 3. Morphology of alloy and sulfide scale with relation to two platinum markers. Specimen sulfidized for 15 hr. Magnification 85X.

the bottom of the platinum marker and the metal interface. The thickness of this space is constant with the time within the limits of accuracy of our metallographical observations as suggested by the dashed line. Micrograph c' in Fig. 2, and Fig. 3, exemplify the "undercutting mechanism" (6) that takes place during the scaling of the alloy. The platinum marker acts as a barrier to the outward transport of metal ions thus impeding scale formation at this point. The space progressively made available by lateral depletion of the metal is apparently filled with chromium sulfide by plastic deformation until the "hill" under the marker disappears. The marker is gradually imbedded in chromium sulfide as the reaction proceeds. This observation indicates that thickening of the inner layer involves outward diffusion of chromium. It is also evident that the faster growth of the outer nickel sulfide layer must occur above the platinum marker by the outward diffusion of nickel.

The results of the tracer tests are perhaps even more definitive. Using the assembly of Fig. 1, specimens were sulfidized first with normal sulfur and then with the radioactive isotope. Figure 4 shows a beveled section of one of these specimens, which underwent treatment for 5 hr with normal sulfur and for 7 hr with S^{35} at 700°C. The layer of nickel sulfide grown during the second stage of the reaction on top of the pre-existing scale can be clearly seen. In Fig. 5, the micrograph of a specimen which had reacted for 6 hr with normal sulfur and for 10 hr with S^{35} is exhibited together with the corresponding autoradiograph.

Radioactive tracers have an advantage over other types of markers, primarily because they do not cause surface damage and take part in the reaction without interfering mechanically with the growth of corrosion products. However, this kind of macro-autoradiography has its limitation in the diffuseness of the radioactive trace. This is due to the fact that not all the radiation coming out of the specimen cross section hits the film perpendicularly. It is nonetheless clear from Fig. 5 that the radioactive isotope does not move into the layer of nickel sulfide grown in the first stage of the reaction except when, through cracks in the scale, it can reach and react with the metal core.

The results of the reverse two-stage sulfidation experiment are presented in Fig. 6. Here the ends of the cross sections of three specimens are shown, their characteristic features being easily comparable with the corresponding autoradiographs mounted opposite in a mirror-like arrangement. A comparatively low magnification has been chosen in order to include in the micrograph a large area of the specimen and at the same time keep the enlargement of the original autoradiograph within suitable limits. The magnification is identical for specimens and autoradiographs. All three scales exhibit under the optical microscope the familiar duplex structure, although this does not show in the picture for specimen (a). An intermittent gap

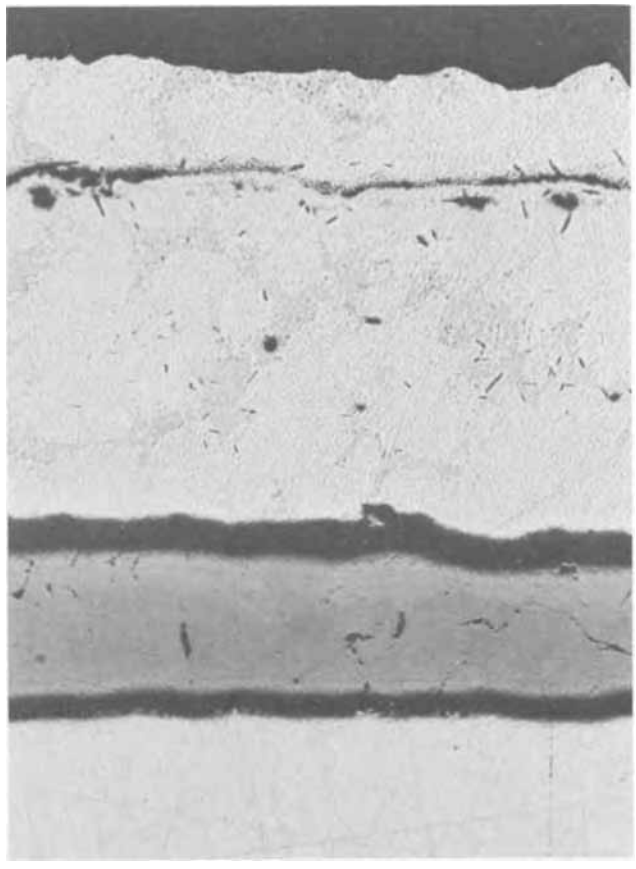

Fig. 4. Beveled section of a specimen treated for 5 hr with normal sulfur and 7 hr with radioactive sulfur at 700°C. At the top is the nickel sulfide layer grown in the second stage of the reaction. The inner layer boundaries are not properly focused, due to pronounced rounding off of this area during polishing. Magnification approx. 160X.

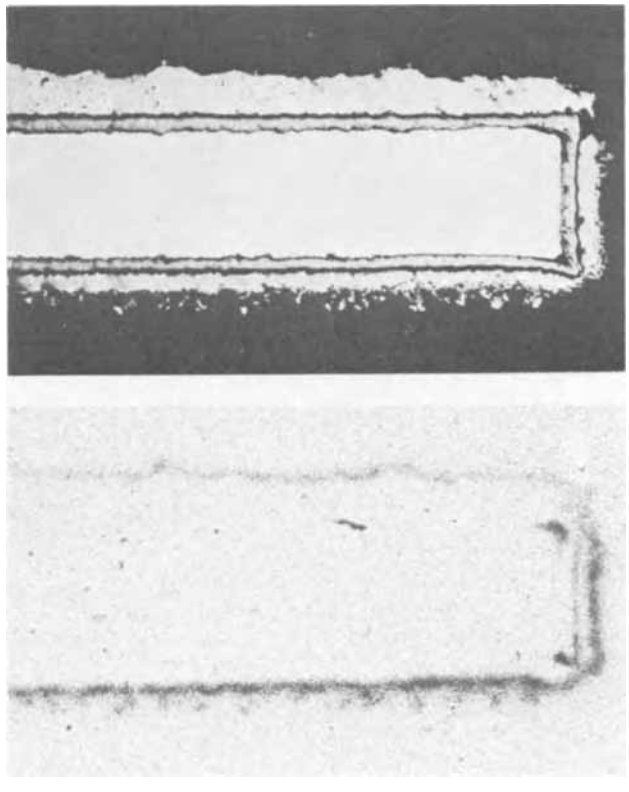

Fig. 5. Cross section of specimen treated for 6 hr with normal sulfur followed by 10 hr with radioactive sulfur at 700°C. At the bottom is the corresponding autoradiograph. Magnification 21X.

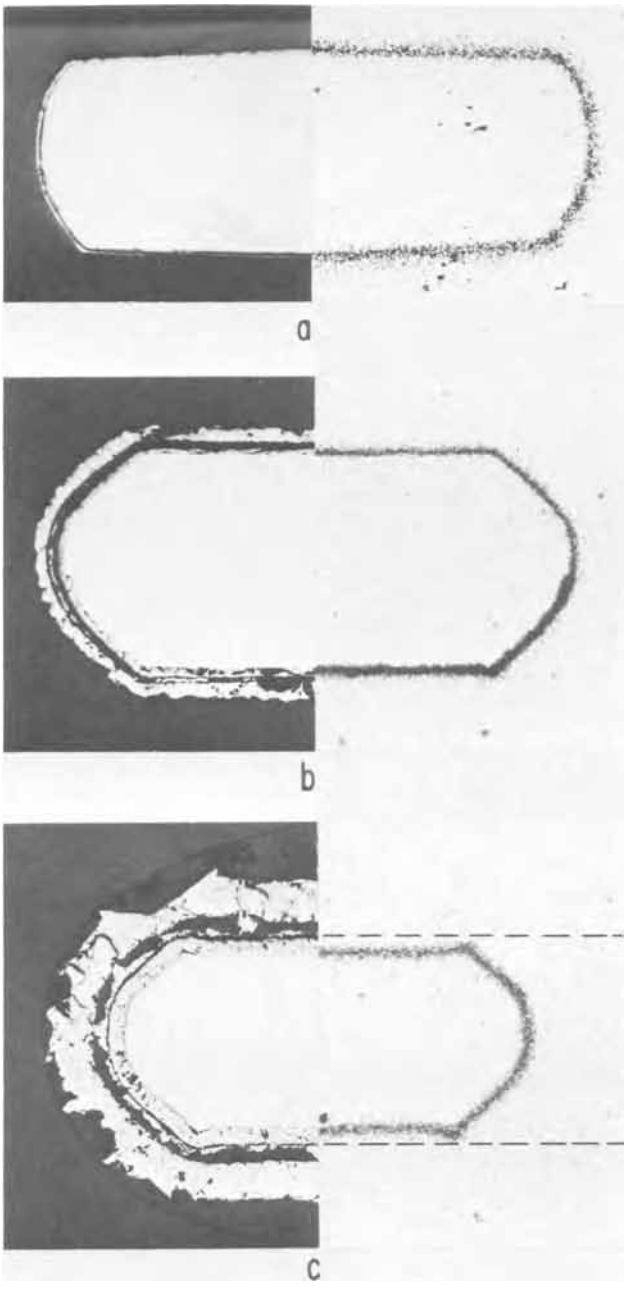

Fig. 6. Micrographs and autoradiographs of specimens sulfidized first with radioactive, then with normal sulfur. The three specimens have been treated for 15 min with S^{35}. Subsequently specimens (b) and (c) have been sulfidized with normal sulfur for 2 and 8 hr, respectively. Mounted opposite to the cross sections are the corresponding autoradiographic traces. Inner and outer layer in (b) and (c) are separated by an intermittent gap. This gap formed not as a general sulfidation feature but during the final quench in this particular type of experiment. Magnification 27X.

between the two scale layers has developed, as seen in specimens (b) and (c). Specimen (a) was treated for 15 min at 700°C with only radioactive sulfur, while specimens (b) and (c) after identical treatment underwent further sulfidation at the same temperature in H_2S/H_2 atmosphere (sulfur pressure $\cong 10^{-6}$ atm) for 2 and 8 hr, respectively. It is evident, upon comparing (a) and (c), that after 8 hr the tracer is no longer present in the outer nickel sulfide layer. The thickness of trace (a) looks wider than that of the other two traces because in this case no layer of inactive sulfide is absorbing the side scattered radiations. It can be seen that the inner border of the radioactive traces always coincides with the metal interface. Moreover, for specimen (c) part of the chromium sulfide layer lies outside the tracer perimeter, as indicated by the dashed lines. In conclusion, the distribution of radioactive sulfur remains essentially of constant width in the vicinity of the alloy surface, irrespective of scale thickness, clearly indicating that sulfur anions do not ostensibly diffuse in either of the sulfide phases.

Discussion

This section aims to synthesize a reaction mechanism for the formation of sulfide scales on nickel-chromium alloys. We shall base our arguments on the analysis of kinetic data, metallography, platinum marker positions, and radioactive sulfur distribution in the scales.

In our previous investigation (1), it was shown that parabolic relationships describe the growth of the individual sulfide layers and the duplex scales. Prerequisites for this type of kinetics are compactness and adherence of individual sulfide layers. Although in our case these conditions were satisfied, a certain amount of mechanical breakdown of the scale did occur, especially where the specimen geometry restricted plastic deformation. This led, after a prolonged reaction time, to the formation of preferential channels at the edges of specimens through which sulfur reached the metal surface by transport through the gas phase. Nonetheless, on the basis of our observations it appears valid to set up a model for the scale growth over a flat alloy surface in terms of solid diffusion of its components alone.

The stoichiometries of the nickel and chromium sulfide phases, have been shown to vary with sulfur pressure within somewhat large ranges (1, 9). We shall assume, in agreement with these results, that the composition of the outer layer is Ni_3S_2 or NiS if the reacting sulfur pressure is below or above 10^{-5} atm, respectively. We ascribe the formula CrS to the inner chromium sulfide layer, although phases lying within the composition range $CrS\text{-}Cr_2S_3$ could possibly be present in this region.

It is evident from Fig. 2, 5, and 6 that outward movement of nickel ions is entirely responsible for the growth of the outer nickel sulfide layer. Diffusion probably occurs via vacancies in the cation sublattice, since both NiS (10-12) and Ni_3S_2 (13) exhibit characteristics of metal deficit (p-type) semiconductors. The formation of these lattice defects, nickel vacancies and positive holes, can be expressed by the equations

$$S \rightleftarrows NiS + Ni\square'' + 2\oplus \qquad [1]$$

and

$$2S \rightleftarrows Ni_3S_2 + 3Ni\square'' + 6\oplus \qquad [2]$$

Since we have no evidence of a nickel sulfide phase dispersed in the chromium sulfide layer, we assume that a similar mechanism accounts for the transfer of nickel ions across the inner chromium sulfide layer, with nickel-substituting chromium ions in the cation sublattice. Microprobe analysis has in fact shown nickel in solution to about 3 a/o (atom per cent) (1). Therefore, the diffusion of nickel through the chromium sulfide layer must be a rather fast process.

The growth of the inner layer must be controlled by a similar mechanism. Microscopic examination has shown that from the very beginning of the reaction the corrosion product has the duplex structure. The position of the inert platinum markers, taking into account the above-mentioned "undercutting mechanism," indicates concurrent outward diffusion of chromium and nickel ions. The anion lattice being everywhere inert, Fig. 6 and its interpretation in Fig. 7 make this conclusion unassailable.

Figure 5 shows clearly that radioactive sulfur did not penetrate into the compact outer layer. Furthermore, it has been reported that the diffusivity of nickel in nickel sulfide is much higher than that of sulfur (14). Our observations show that the boundary between the inner and the outer layer in Fig. 3 moves outward with respect to the platinum marker and the metal interface with increasing reaction time. We con-

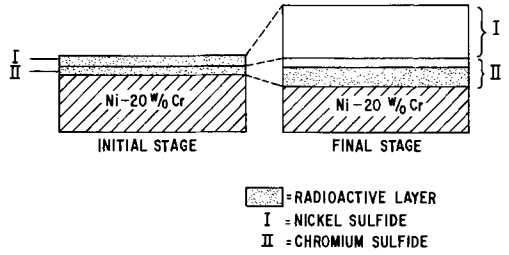

Fig. 7. Schematic representation of the two-stage sulfidation depicted in Fig. 6. The dashed lines connecting the two models show the relative displacement of the interfaces during the reaction.

clude therefore, that the inner layer grows at the expense of the nickel sulfide layer, with the displacement reaction NiS + Cr $\rightleftarrows$ CrS + Ni occurring at its inner boundary. This process results in a decrease in thickness of the outer layer, but it is balanced by a much faster growth rate at the gas phase interface.

The driving force for the conversion of nickel sulfide into chromium sulfide is the difference in the free energy of formation of these compounds. Extrapolated standard free energy variations for the formation of 1 mole of reaction product from pure metal and S_2 at 1 atm are, respectively, $\Delta G°_{NiS} = -17{,}775$ cal/mole, $\Delta G°_{Ni_3S_2} = -42{,}450$ cal/mole at 727°C (10), and $\Delta G°_{CrS} = -35{,}360$ cal/mole at 700°C (15). The growth of chromium sulfide at the expense of nickel sulfide is clearly favored. If this reaction occurs at the inner-outer layer interface, chromium must be transferred to this region. Unfortunately no data are available, to our knowledge, on the defect structure of CrS. Assuming that this compound is a p-type semiconductor, chromium from the alloy could reach the interface via cation vacancies, formed according to the equation

$$S \rightleftarrows CrS + Cr\square'' + 2\oplus \qquad [3]$$

where sulfur is supplied by the dissociation of nickel sulfide.

The proposed over-all reaction mechanism is summarized in Fig. 8. The nickel ions and electrons are transported across the scale from the alloy to the gas phase interface, where they react with adsorbed sulfur to form the nickel sulfide layer. This transport occurs via cation vacancies in the inner and in the outer layer, both of which are supposed to have a p-type structure (16). This model does not require the presence of a second nickel sulfide phase within the chromium sulfide layer, as previously reported in the literature (7). Although the composition of this layer has not been characterized generally for our experimental conditions the formula CrS can be adopted. The growth of this layer is attributed to outward diffusion of chromium to react with nickel sulfide at the interface between the two layers.

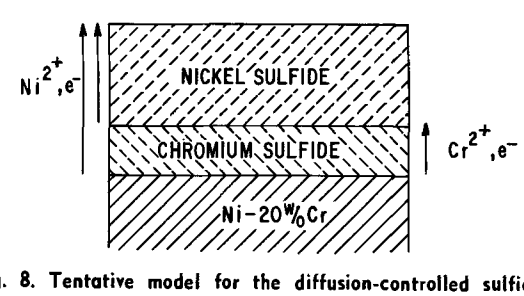

Fig. 8. Tentative model for the diffusion-controlled sulfidation of a Ni-20 w/o Cr alloy at 700°C.

Summary

On the basis of kinetic and morphological data and with the help of markers, we have been led to propose a mechanism for the sulfidation of a Ni-20 w/o Cr alloy. The model is based entirely on diffusion of metal across the scale under conditions for high-temperature corrosion phenomena, although concurrent mechanisms can contribute to the scaling of the alloy when mechanical breakdown of the scale takes place. This model stands on a few hypotheses which should be checked by further experimentation. Information should be gathered on the composition and the defect structure of the phases involved in the sulfidation, as well as on the lattice and boundary diffusivities of the scale components. Notwithstanding, the results of this investigation disprove the prevalent view that nickel sulfide stringers in chromium sulfide are essential for transfer of nickel across the scale and that sulfur migrates as sulfur vapor or hydrogen sulfide through fissures in the nickel sulfide and chromium sulfide layers to form chromium sulfide at the alloy interface.

Acknowledgment

This research was supported by a grant from Falconbridge Nickel Mines Ltd. to J. S. Kirkaldy. The authors are grateful to Falconbridge Metallurgical Laboratories for providing materials. A number of useful and encouraging discussions were held with Dr. L. A. Morris and Dr. M. J. Lavigne of that company.

Manuscript received Feb. 8, 1971.

Any discussion of this paper will appear in a Discussion Section to be published in the June 1972 JOURNAL.

REFERENCES

1. G. Romeo, W. W. Smeltzer, and J. S. Kirkaldy, *This Journal*, **118**, 740 (1971).
2. S. Mrowec and T. Werber, *Acta Met.*, **8**, 819 (1960).
3. S. Mrowec, *Z. Phys. Chem. Neue Folge*, **29**, 47 (1961).
4. S. Mrowec and T. Werber, *Werkstoffe Korrosion*, **19**, 944 (1968).
5. J. B. Holt and L. Himmel, *This Journal*, **116**, 1569 (1969).
6. R. A. Meussner and C. E. Birchenall, *Corrosion*, **13**, 677 (1957).
7. S. Mrowec, T. Werber, and M. Zastawnik, *Corrosion Sci.*, **6**, 47 (1966).
8. M. D. Adams and R. K. Steunenberg, "Some Metallurgical Applications of Autoradiography," ANL-6412 Technical Report, Office of Technical Services, Department of Commerce, Washington, D. C. (1961).
9. G. Bolze, D. McCutcheon, and J. S. Kirkaldy, To be published.
10. T. Rosenqvist, *J. Iron Steel Inst.*, **176**, 37 (1954).
11. S. Mrowec and H. Rickert, *Z. Phys. Chem. Neue Folge*, **28**, 422 (1961).
12. M. Laffitte, *Rev. Nickel*, **25**, 79, 109 (1969).
13. G. Liné and M. Laffitte, *C. R. Acad. Sc. Paris*, **256**, 3306 (1963).
14. K. Fueki, Y. Oguri, and T. Mukaibo, *Bull. Chem. Soc. Japan*, **41**, 569 (1968).
15. P. Hager and J. F. Elliott, *Trans. AIME*, **239**, 513 (1967).
16. E. Lifshin, A. U. Seybolt, and J. B. Hudson, Report No. 70-C-134, General Electric Research and Development Center, Schenectady, N. Y. (1970).

Characterization of Silicon Nitride Films

E. A. Taft

General Electric Research and Development Center, Schenectady, New York 12301

ABSTRACT

Various "silicon nitride" films have been prepared from SiH_4, N_2, NH_3, and N_2O in an rf-promoted glow discharge reaction. These films are described primarily through the use of infrared absorption. Aided by ultraviolet absorption, the inclusion of excess silicon or of oxygen in the films is readily followed. Changes in index of refraction, etch rates in HF acid, and electrical conductivity of the films are correlated with the optical absorption study. Comparisons of these films with those formed by pyrolysis or by reactive sputtering are made. Some reproducible physical properties of an amorphous Si_3N_4 film are stated.

After an initial group of manuscripts on silicon nitride thin films in 1967, there have appeared reports on new processes or variations of old processes in preparing these amorphous layers. Evaluations of the prepared films have been made through physical, chemical, or electronic methods depending on the particular interest of the investigator. The general interest has been toward the development of an impervious dielectric film to replace or to supplement silicon oxide films which serve in various capacities in silicon device technology. Because of these different methods of preparation and the individual emphasis on a property of a film, there has been on real basis for assuming that only one material was undergoing investigation. On the other hand, a common set of evaluations of variously prepared films could serve to establish an identity for silicon nitride.

Three general methods are used to form these nitride films. The most used system is the pyrolytic decomposition of mixtures of gases of silicon compounds and nitrogen compounds (1-5); typically these gases are SiH_4 and NH_3 decomposed on a substrate at 1000°C (6-8). Other work describes the reactive sputtering of silicon in nitrogen onto a cold or heated substrate (9-11). Radio-frequency (rf) sputtering of Si_3N_4 is not generally used as high-purity cathodes are not readily available. The third method utilizes a rf glow discharge to ionize gases and form films on cold or heated substrates (12-14). A more recent report describes the action of ultraviolet light on SiH_4 and H_4N_2 mixtures (15). The general properties of many of these films have been described in terms of their surface structure, optical absorption, or x-ray diffraction. An interest in mechanical stresses, etch rate in HF acid, or resistance at elevated temperatures to diffusion of specific atoms through the films appears in some papers (16-20). The electrical conductivity or "leakage" of these dielectric films is discussed in other papers (21-23), and the silicon-silicon nitride interface has received much study (3, 7, 23, 25).

This report is based on optical absorption studies of silicon nitride films formed in a glow discharge of $SiH_4 + NH_3$ or $SiH_4 + N_2$. (Pyrolytic films from $SiH_4 + NH_3$ prepared by F. K. Heumann and reactively sputtered films of Si in N_2 prepared by L. F. Cordes were available for comparison.) The index of refraction and the etch rate in HF acid is determined for many of the films. Variations in properties of glow discharge films are explained and an amorphous Si_3N_4 film is identified. Silicon oxynitride films obtained from glow discharges in SiH_4, N_2O, and N_2 are also measured. In addition, comparisons are made with other nitride and oxynitride (25-29) films to show a continuous variation in properties as the composition of the amorphous film is changed. [X-ray and electron diffraction work (7, 25) especially that of Tombs *et al.* (28) shows no long range order on ½μ thick deposited films. The films used here, deposited at low temperatures, are therefore also described as amorphous.]

Key words: thin dielectric films, rf glow discharge, infrared absorption.

Experimental

The reaction chamber was a 2-in. ID Pyrex tube which was initially evacuated to less than 1×10^{-3} Torr with a mechanical pump. The flow of gases was controlled by needle valves or by capillaries. A simple nichrome wire spiral heater supported a carbon sample holder. Several turns of copper wire or tubing were wound over the Pyrex tube and rf current was passed through the coil. At the usual gas pressure of 0.05-1 Torr, monitored by a thermistor vacuum gauge, a discharge was readily started with a small oscillator at frequencies from 0.5 to 30 MHz. Power absorbed by the discharge was usually less than 10W, and an unheated substrate was warmed slightly. The experimental setup used appears to be much like that described by Joyce (30). The procedure was normally limited to fixing a flow rate of SiH_4, setting a substrate temperature, adjusting the flow of NH_3, N_2, or N_2O, and then starting a discharge. Substrates were either thin silicon wafers for infrared absorption or disks of sapphire for the ultraviolet absorption. The thickness and the index of refraction of the films on silicon were determined from the wavelengths of interference minima for reflected light. While this method requires measurement at two different angles of incidence and films at least several fringes thick, the substrate need not be an optical flat. A Cahn electrobalance was used for density measurements.

The infrared absorption spectrum was recorded on a Perkin-Elmer 337 grating spectrophotometer. Films on sapphire disks were observed in ultraviolet absorption on a Perkin-Elmer 202 grating spectrophotometer. The etch rate in 48% hydrofluoric acid was recorded for some films.

Results

Glow discharge SiH_4-N_2-NH_3.—As most of the discussion will include data from infrared absorption, a composite spectrum is drawn in Fig. 1 to indicate the bands which are observed and band strengths which may be encountered. The Si-N bonds (31) appear in absorption at 11.5 and 21μ and are typically of the strength shown. The N-H and Si-H modes have been seen with absorption coefficients as high as those shown, but they are often not detectable. The log scale emphasizes the sharpness of the bands. Figure 2 shows only the region of major absorption for the Si-N bonds on a linear absorption scale. Si_3N_4 crystalline powder (β-phase) in a KBr pressed disk exhibits sharp structure in comparison to amorphous silicon nitride films formed by any of the three different methods. These spectra shown are typical, though variations will be shown later, and the slightly sharper peaks of the pyrolytic material formed at 1000°C is perhaps the only notable feature. The absorption coefficients of the

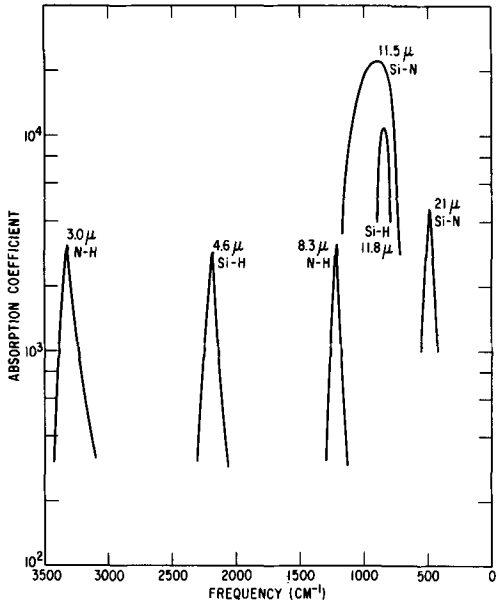

Fig. 1. Infrared absorption bands in silicon nitride films formed in a rf glow discharge.

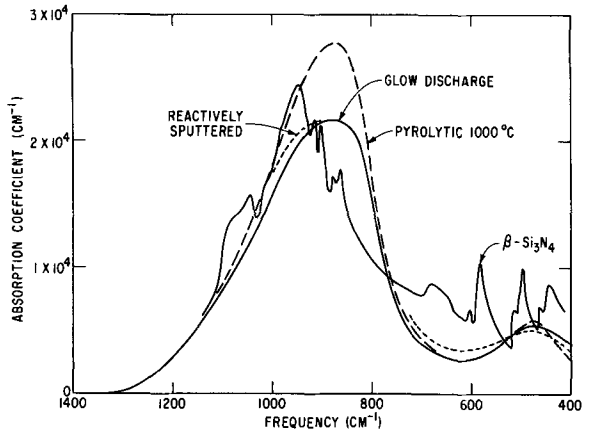

Fig. 2. Comparison of crystalline and amorphous silicon nitride infrared absorption.

films are not accurately determined but they should be within 20% of these values.

Starting with a fixed silane pressure in the glow discharge system, anhydrous ammonia was run through at different rates in a series of runs. The substrate was held at approximately 400°C while films of ½ to 1μ in thickness were deposited. Variations of the peak amplitudes of the infrared absorption coefficients in three different bands are given in Fig. 3 for changing ammonia pressure. When nitrogen rather than ammonia is used, quite a different pattern is obtained, as seen in Fig. 4. The index of refraction and deposition rate variations for the nitrogen runs appear in Fig. 5. It was found that moving the position of the rf coil, changing the temperature of the substrate, or moving the injection point of the silane caused changes in the curves presented in Fig. 3, 4, and 5. Therefore, these data are shown to illustrate the variations which do occur, but which cannot be readily reproduced in detail in a separate system. They do serve to emphasize the ease with which films of different properties can be formed. Even the main Si-N band absorption is subject to considerable shift in peak position and to change in intensity. Figure 6 shows this change with three examples and the index of refraction for each. The Si-N absorption at 21μ in 1μ thick films is even more variable as indicated in the spectrograph tracings in Fig. 7. The pyrolytic deposit of curve B contains the well-defined

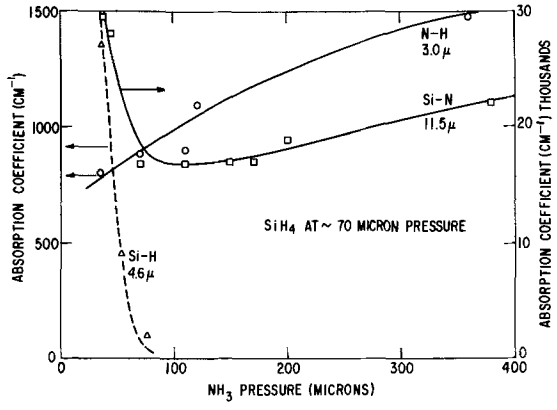

Fig. 3. Change in infrared absorption coefficients with ammonia gas pressure.

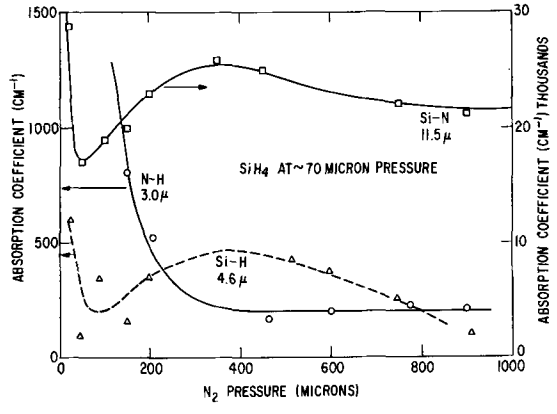

Fig. 4. Change in infrared absorption coefficients with nitrogen gas pressure.

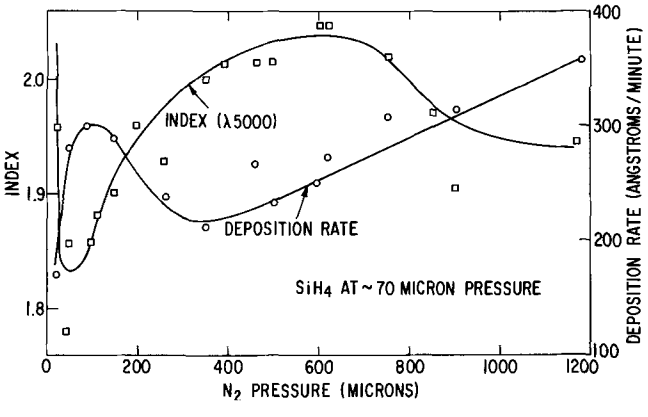

Fig. 5. Variation of index of refraction and deposition rate with nitrogen pressure.

absorption at 21μ typical of films formed at 1000°C. Curve A represents a low-temperature glow discharge film containing large N-H fractions. In curve C the 21μ absorption peak is nearly obliterated. The film giving curve C, also from a low-temperature glow discharge, shows small N-H but large Si-H absorption bands. The 21μ peak is the symmetric stretching mode in Si-N absorption (31), and it is clear that there is enough Si-H bonding (the absorption coefficient at 4.6μ is 3000 cm^{-1}) made at the expense of Si-N bonds to greatly disturb the Si-N absorption normally localized in this region.

Figure 8 shows tracings of a portion of spectrographs for 1μ thick films in the higher energy range. Absorption coefficients as high as 3000 cm^{-1} have been observed in each of the bands shown. The 4.6μ band, while a little sharper than the one at 3.0μ, does not

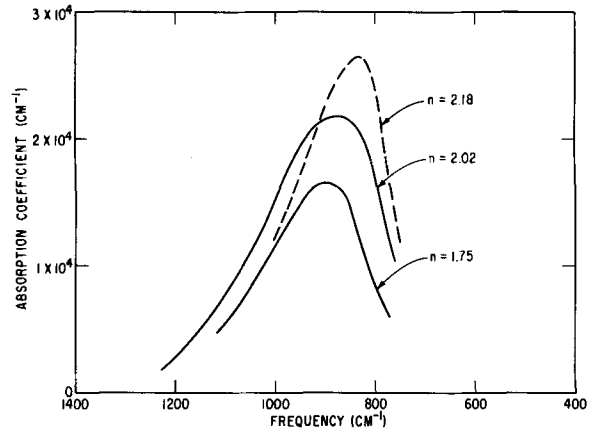

Fig. 6. Shift of peak position and index of refraction in silicon nitride glow discharge films.

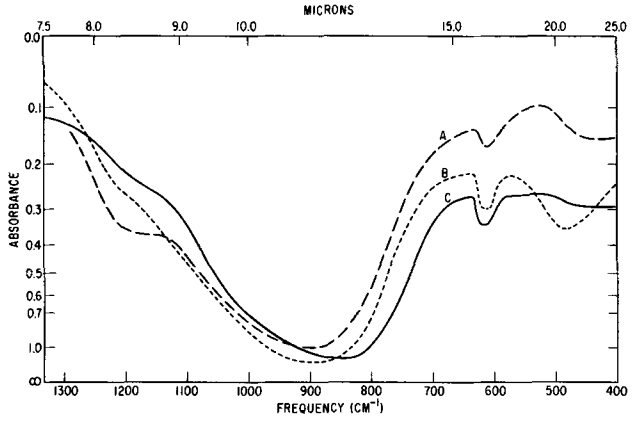

Fig. 7. Variations in the 21μ absorption band in silicon nitride glow discharge films.

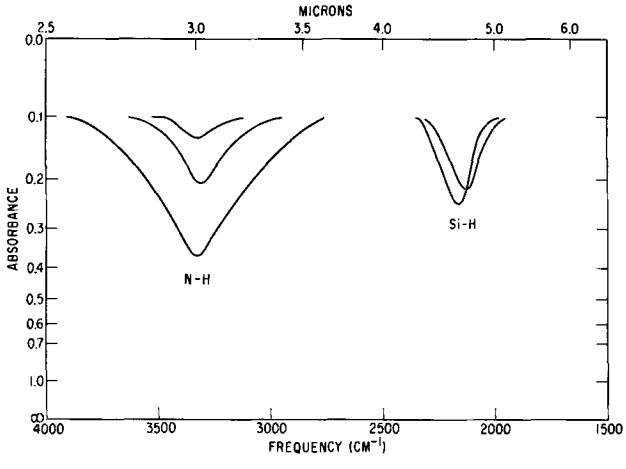

Fig. 8. Tracings of the hydrogen bond absorbance in glow discharge films of silicon nitride.

appear to be so definitely fixed in peak position. The 3.0μ band seems always to be accompanied by an absorption of about the same strength at 8.3μ in the tail of the main Si-N band. The 4.6μ band also seems to be accompanied by absorption near 11.8μ indicating a second stronger Si-H mode. This mode is often evidenced through an apparent shift in the peak position of the main Si-N band, as for example in curve C of Fig. 7. This shift toward lower energy has been found in all films having appreciable 4.6μ absorption. The observation of this second absorption of Si-H was initially made on films formed from SiH_4 and N_2O.

Glow discharge SiH_4-N_2O.—In film formation from SiH_4 and N_2O gases there is observed, in addition to

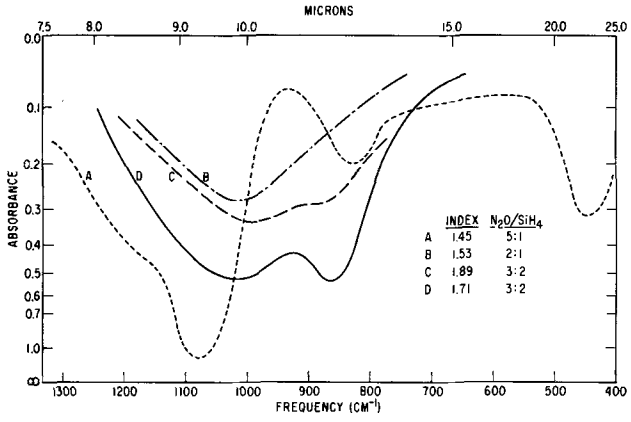

Fig. 9. Infrared absorbance with change in nitrous oxide/silane ratio in glow discharge.

the bands previously discussed, absorption of O-H at 2.74μ, and the prominent Si-O bands at 9.3, 12.4, and 22μ. Figure 9 gives the trend in infrared absorption of ½-1μ thick films as the SiH_4/N_2O ratio is increased. Curve A appears to be much like that for normal absorption of a silicon dioxide film, and the index of refraction is that expected of the oxide. Curve B (for a film of different thickness) appears to belong to an intermediate of silicon oxide and silicon nitride. This film has a small band at 2.98μ—apparently the N-H absorption slightly shifted; whereas curve A has a small O-H absorption at 2.74μ. The index of refraction of the film of curve C approaches that of a nitride, but the absorption still indicates an intermediate oxynitride composition, although a second peak near 11.8μ is beginning to rise. The film of curve D was deposited under the same gas conditions as film C, but the substrate was not heated. The second peak is now much larger. The absorption at 4.6μ is also found to be larger. In this series of films, the second peak near 11.8μ always corresponds in strength to the Si-H absorption at 4.6μ. At higher SiH_4/N_2O ratios the films become more and more silicon rich.

Glow discharge SiH_4-N_2-N_2O.—Some films were deposited in SiH_4 and N_2 or SiH_4 and NH_3 with small amounts of N_2O added. An illustration of the effect of the added oxidizing gas is given in Fig. 10 for films 1½μ thick. Curves A and B show a shifting and broadening in the 9-12μ region of absorption as oxygen is incorporated in the film. Curve C shows features of the sharper and stronger bands associated with silicon oxide. However, a small absorption occurs at 2.95μ and indicates that the N-H band is still present but slightly shifted in position. When coupled with the index of refraction value, it appears that there is still a fraction of silicon-nitrogen bonding in the composite film.

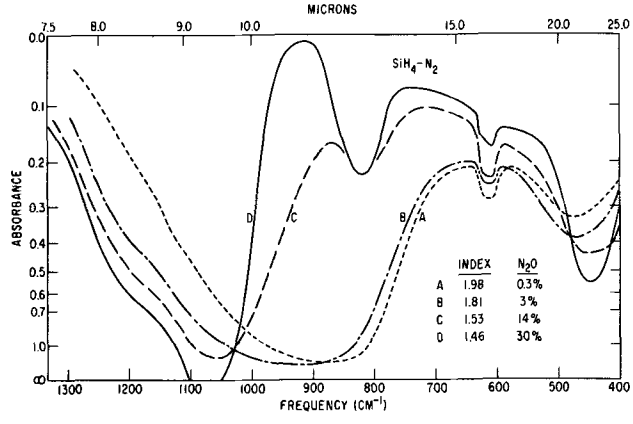

Fig. 10. Infrared absorbance with added nitrous oxide in silane-nitrogen glow discharge.

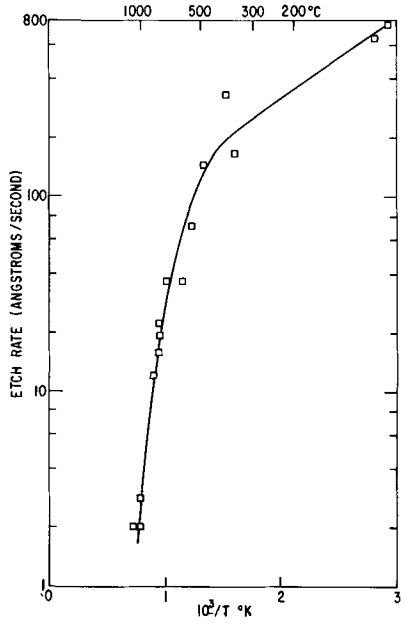

Fig. 11. Etch rate in 48% hydrofluoric acid vs. substrate temperature for silane-ammonia glow discharge films.

In curve D, the Si-O absorption bands are clearly separated and the greater peak values of absorption are evident. The N-H band near 3.0μ has now disappeared to be replaced by the O-H band at 2.74μ.

Etching in hydrofluoric acid.—Some of the samples deposited at various substrate temperatures from the SiH_4-NH_3 glow discharge were placed in 48% hydrofluoric acid and the film removal rate observed. For films with low deposition temperatures the etch rates are very high, but the rates decrease to about 6000 Å/min for substrate temperatures of 500°C. (See Fig. 11.) The rates then drop rapidly with increasing temperatures until at temperatures above 800°C the films are, of course, indistinguishable from pyrolytic films formed without the glow discharge. The infrared absorption at 3.0μ indicative of N-H bonds was found to exhibit some correlation with the etch rate. The general trend is given in Fig. 12, although some films prepared at other gas pressures or other gas ratios did not fit this curve well. The films formed in the SiH_4-N_2 system appear to fit to an entirely different curve with respect to the 3.0μ absorption strength. This curve

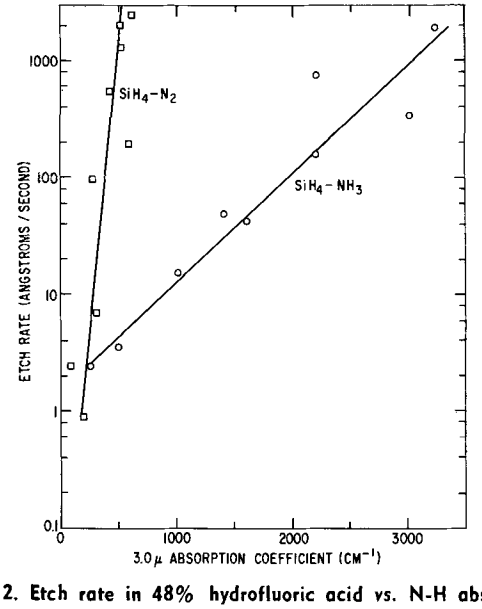

Fig. 12. Etch rate in 48% hydrofluoric acid vs. N-H absorption coefficient at 3.0μ for silane-ammonia and silane-nitrogen glow discharge films.

is also shown in Fig. 12 and again represents the general trend.

Data on the index of refraction and the density were taken for films deposited at various substrate temperatures from SiH_4 and NH_3. Deposition at room temperature produced films with a density of 2.4. This density is much lower than the 3.1 found for high-temperature films. The decreased density and the usual high hydrogen content accompanying it are factors in the lack of resistance of these films to hydrofluoric acid attack. The index of refraction of a film is much easier to obtain than the density. These index values were found to range from 1.8 to 2.1 for the same group of films which varied in density from 2.4 to 3.2. A change of this order is predicted by the Lorenz-Lorentz law (32), so the index can be used (at least for silicon nitride films in this range) to estimate the density.

Ultraviolet absorption.—A number of films were deposited on sapphire substrates. Tracings of data from the spectrophotometer are shown in Fig. 13. For films about 1μ thick the absorption coefficient where the curves intersect the base line (absorbance = 1.5) is 3×10^4 cm^{-1}. Curve 1 is typical for a film containing excess silicon. The reactively sputtered films of Cordes (11) show curves of this shape and near this wavelength position. Pyrolytically formed films (25) at high NH_3/SiH_4 ratios show absorption at higher energies near curve 2. The more rapid increase in absorption at higher energies as compared with curve 1 is always observed. Curves 3 and 4 are included to show the smooth shift of the absorption edge to higher energies as small amounts of oxygen are added to the film. Continuous shifts to lower energies are observed as the N_2/SiH_4 ratio is reduced in the glow discharge. A film having an index of 2.8 gives a base line intercept at 420 mμ and an amorphous film prepared from pure SiH_4 has moved to 570 mμ.

Discussion

Resistance to corrosion, great hardness, and low thermal expansion made crystalline Si_3N_4 an attractive high-temperature refractory (33). The work of Turkdogan *et al.* (34) firmly established the formula as Si_3N_4 and set the density at 3.19 ± 0.01. Additional work on the properties was reported by Popper and Ruddlesden (35). The solubility and electrical activity of nitrogen in silicon have been studied by Kaiser and Thurmond (36). These few papers on crystalline material are a background to the many papers on the amorphous thin film. To summarize a few figures on crystalline Si_3N_4, first the old density figure of 3.44 (37) should be replaced by 3.19 (34). The dielectric constant value of 9.4 often appears, but the source is not apparent. If the Lorenz-Lorentz approximation (32) is made using the measured density (3.11) and the dielectric constant (7.4) of amorphous material (25), a value of 8.0 is obtained for the dielectric constant of crystalline material. Also, if the index of re-

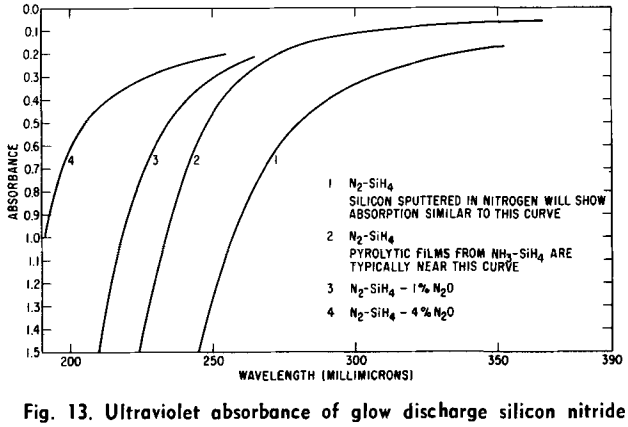

Fig. 13. Ultraviolet absorbance of glow discharge silicon nitride films 1μ thick.

fraction of the film at 4500Å is 2.03 (25), the index of the crystal is calculated to be 2.06. These numbers will be considered as those representing crystalline Si_3N_4 and an amorphous material with similar bonding.

The reactively sputtered films deposited by Cordes (11) were highly reproducible and quite insensitive to system parameters. Because of this invariable behavior, it was first assumed that this must be the stoichiometric material. This assumption was in part based on the observation that the pyrolytic films of Heumann (25) contained hydrogen and were of slightly lower index of refraction. However, the conclusions of Cordes (11) seem valid, and a slight excess of bonded Si is built into the lower substrate temperature sputtered deposits. Cordes found that high-temperature annealing decreased the index but not the thickness of the film. This observation agrees with the assumption that Si-Si bonds were replaced with Si-N bonds. The etch rate of the reactively sputtered films moved from ~120 to 150 Å/min after heating and the index of refraction changed from 2.06 to 2.03. These values are like those of a pyrolytic film. As the sputtered film does not contain hydrogen, the small amount of N-H bonding seen in infrared absorption in the higher temperature pyrolytic films therefore has no discernible effect on the index or the etch rate.

If excess conductivity is assumed to indicate Si-Si bonding in films, again the pyrolytic film with the lowest conductivity should be more nearly the Si_3N_4 composition. Cordes (11) uses conductivity to describe Si excess in a sputtered silicon nitride lattice by comparing to the pyrolytic films of D. M. Brown (25). Hu (24) also used sputtered films. Doo (16), G. A. Brown (22), and Yeargan (21) show pyrolytic film conductivity. Deal (23) measured a slightly different film formed from $SiCl_4$ and NH_3. Parnell (38) gives a comparable conductivity for rf glow discharge dielectrics in capacitors. A comparison of these data (Fig. 14) shows that the pyrolytic deposits of many investigators seem to approach a common minimum conductivity at voltages near the breakdown strength of the dielectric. Doo (16) and G. A. Brown (22) found their curves to represent the minimum conduction observed as the ratio of silane to ammonia was decreased.

The ultraviolet absorption edge also appears to be a relatively sensitive indicator of excess silicon or of oxygen contamination, and an absorption increase accompanies a conductivity increase. The addition of small amounts of oxygen to either the pyrolytic or glow discharge systems gives a continuous shift of the ultraviolet edge to higher energies. This again indicates that the assignment of the 2290Å wavelength to a 10^4 cm^{-1} absorption coefficient for amorphous silicon nitride is approximately correct.

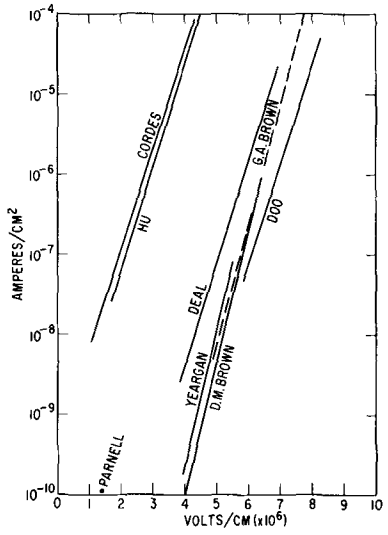

Fig. 14. Conductance in pyrolytic and sputtered silicon nitride films.

Two types of investigation which have received some attention are film structure (28, 39, 40) and the electrical behavior of the film with a silicon interface. Because of the already diverse properties of films prepared in this work and early recognition of silicon nitride as a leaky insulator (25), no use of the C-V behavior of the films was attempted in this study. Throughout the infrared work when the effects of quantities of oxygen, hydrogen, or silicon could be observed as part of the silicon nitride film, there gradually built up the impression that the composition of these films can be made continuously variable. The data on the oxynitrides, in particular, appears to agree with the work of Tombs *et al.* (28), and their description of the films as solid solutions appears to fit as well to the wider range of films discussed here. Drum and Rand (29) also suggest this continuous range of properties and refer to their films as oxynitride polymers.

Conclusions

An amorphous film of silicon nitride of Si_3N_4 composition has an index of refraction of 2.03 at a wavelength of 4500Å, a dielectric constant of 7.4, and ultraviolet absorption edge with an absorption coefficient of 10^4 cm^{-1} at wavelength 2290Å. Its broad infrared absorption band with an absorption coefficient of 2 x 10^4 cm^{-1} peaks near 11.5μ with a smaller band at 21μ. The etch rate, in 48% hydrofluoric acid at room temperature, is 150 Å/min, and the resistivity is 10^{16} ohm-cm at 4 x 10^6 V/cm.

Pyrolytic films formed at 900°-1100°C with very dilute SiH_4 in NH_3 appear to approach this description except for the small added hydrogen content. At formation temperatures below 900° most of the hydrogen remaining in the film is correlated with a lowering of the index of refraction and an increase in the etch rate. With low (<10:1) ammonia-silane ratios excess silicon appears in the films. Reactively sputtered films always form with a slight silicon excess indicated by the increased index of refraction of 2.06 and lowered etch rate of 120 Å/min. No hydrogen appears in these films. Glow-discharge-promoted deposits can be made at room temperature, but the resultant films have a high hydrogen content accompanied by a greatly lowered index of refraction and almost no etch resistance. Films formed at higher temperatures can be made which approach pyrolytic material in etch resistance and dielectric strength. These films are usually obtained by adjusting the gas ratio and allowing the films to become slightly silicon rich. The hydrogen content then appears to switch from the N-H bond to the Si-H bond and the dielectric constant increases while the etch rate decreases.

If N_2O is added to the gases, a range of oxynitrides can be made using the glow discharge. These films also retain hydrogen, especially at the lower substrate temperatures, and can be made to contain excess silicon. The range of index of refraction is from that of silica at 1.45 to that of silicon-rich films at >3.

Acknowledgments

The data and discussions contributed by F. K. Heumann and L. F. Cordes are gratefully acknowledged.

Manuscript submitted Sept. 28, 1970; revised manuscript received *ca.* Feb. 10, 1971.

Any discussion of this paper will appear in a Discussion Section to be published in the June 1972 JOURNAL.

REFERENCES

1. C. R. Barnes and C. R. Geesner, *This Journal*, **107**, 98 (1960).
2. T. L. Chu, C. H. Lee, and G. A. Gruber, *ibid.*, **114**, 717 (1967).
3. M. J. Grieco, F. L. Worthing, and B. Schwartz, *ibid.*, **115**, 525 (1968).

4. S. Yoshioka and S. Takayanagi, *ibid.*, **114**, 962 (1967).
5. J. A. Aboaf, *ibid.*, **116**, 1736 (1969).
6. V. Y. Doo, D. R. Nichols, and G. A. Silvey, *ibid.*, **113**, 1279 (1966).
7. S. M. Hu, *ibid.*, **113**, 693 (1966).
8. K. E. Bean, P. S. Gleim, R. L. Yeakley, and W. R. Runyan, *ibid.*, **114**, 733 (1967).
9. S. M. Hu and L. V. Gregor, *ibid.*, **114**, 826 (1967).
10. A. R. Janus and G. A. Shirn, *J. Vacuum Sci. Technol.*, **4**, 37 (1967).
11. L. F. Cordes, *Appl. Phys. Letters*, **11**, 383 (1967).
12. H. F. Sterling and R. C. G. Swann, *Solid State Electron.*, **8**, 653 (1965).
13. R. C. G. Swann, R. R. Mehta, and T. P. Cauge, *This Journal*, **114**, 713 (1967).
14. Yukinori Kuwano, *Jap. J. Appl. Phys.*, **8**, 876 (1969).
15. M. G. Collet, *This Journal*, **116**, 110 (1969).
16. V. Y. Doo, *IEEE Trans.*, **ED-13**, 561 (1966).
17. Y. Watanabe, *Japan J. Appl. Phys.*, **7**, 960 (1968).
18. V. Y. Doo, D. R. Kerr, and D. R. Nichols, *This Journal*, **115**, 61 (1968).
19. A. N. Saxena and O. Tkal, *ibid.*, **115**, 227 (1968).
20. P. J. Burkhardt and R. F. Marvel, *ibid.*, **116**, 864 (1969).
21. J. R. Yeargan and H. L. Taylor, *ibid.*, **116**, 273 (1969).
22. G. A. Brown, W. C. Robinette, Jr., and H. G. Carlson, *ibid.*, **116**, 948 (1969).
23. B. E. Deal, P. J. Fleming, and P. L. Castro, *ibid.*, **116**, 300 (1969).
24. S. M. Hu, D. R. Kerr, and L. V. Gregor, *Appl. Phys. Letters*, **10**, 97 (1967).
25. D. M. Brown, P. V. Gray, F. K. Heumann, H. R. Philipp, and E. A. Taft, *This Journal*, **115**, 311 (1968).
26. T. L. Chu, J. R. Szedon, and C. H. Lee, *ibid.*, **115**, 318 (1968).
27. C. R. Barnes and C. R. Geesner, *This Journal*, **110**, 361 (1963).
28. N. C. Tombs, F. A. Sewell, Jr., and J. J. Comer, *ibid.*, **116**, 862 (1969).
29. C. M. Drum and M. J. Rand, *J. Appl. Phys.*, **39**, 4458 (1968).
30. R. J. Joyce, H. F. Sterling, and J. H. Alexander, *Thin Solid Films*, **1**, 481 (1968).
31. U. Wannagat, "Advances in Inorganic Chemistry and Radiochemistry," p. 232, Academic Press, New York and London (1964).
32. J. C. Slater and N. H. Frank, "Introduction to Theoretical Physics," p. 280, McGraw-Hill Book Co., New York and London (1933).
33. J. F. Collins and R. W. Gerby, *J. Metals*, **7**, 612 (1955).
34. E. T. Turkdogan, P. M. Bills, and V. A. Tippett, *J. Appl. Chem. London*, **8**, 296 (1958).
35. P. Popper and S. N. Ruddlesden, *Trans. Brit. Ceram. Soc.*, **60**, 603 (1961).
36. W. Kaiser and C. D. Thurmond, *J. Appl. Phys.*, **30**, 427 (1959).
37. L. Weiss and T. Engelhardt, *Z. Anorg. Chem.*, **65**, 38 (1910).
38. M. Parnell and H. F. Sterling, *Electron. Commun.*, **43**, 63 (1968).
39. J. V. Dalton and J. Drobek, *This Journal*, **115**, 865 (1968).
40. M. V. Coleman and D. J. D. Thomas, *Phys. Status Solidi*, **25**, 24 (1968).

Evaluation of a New Polish for Gallium Arsenide Using a Peroxide-Alkaline Solution

J. C. Dyment and G. A. Rozgonyi

Bell Telephone Laboratories, Incorporated, Murray Hill, New Jersey 07974

ABSTRACT

It has recently become necessary to obtain a high-quality, strain-free polish on the (111) Ga-face of GaAs. Previous techniques using a bromine-methanol (BM) solution or a Syton-bromine-methanol (SBM) solution were found to be inadequate. The BM and SBM solutions were also subject to undesirable aging characteristics which resulted in nonreproducible polishing rates with time. In this report we show that a new solution containing H_2O_2 and NH_4OH, referred to as the PA solution for peroxide-alkaline, overcomes the limitations of the BM and SBM solutions. A comparative study of the three polishes has been made relating the optical quality, crystal orientation dependence, polishing rates and stability, ohmic contact resistance to the polished surfaces, and residual surface damage, as determined by high-resolution x-ray topography of polished surfaces and cleaved cross sections. In each case the PA solution equals or improves on the BM or SBM solutions. In addition, it is found that PA polished substrates yield diffused junction lasers with threshold current densities comparable to the best BM and SBM data.

Chemical polishing of GaAs wafers is recognized as a crucial step in the fabrication of many device structures. Because of the excellent results obtained on the (100) face and the $(\bar{1}\bar{1}\bar{1})$ As-face of GaAs with the bromine-methanol solution (BM), first described by Sullivan and Kolb (1) in 1963, it has been widely used in GaAs technology. However, several limitations still exist with the BM solution that are becoming increasingly important in order to meet the stringent requirements of recent advances in GaAs devices. For example, the single-heterostructure junction laser (2-4) often requires that the n-type substrates of these devices be polished on the (111) Ga-face to within a few microns of the p-n junction. These procedures are employed to reduce the thermal resistance between the junction and a suitable heat sink and thereby permit improved continuous or high duty-cycle operation.

Two of the limitations of the BM solution are its inability to polish the (111) Ga-face nonpreferentially, and its aging characteristics which result in nonreproducible polishing rates with time. It was found that adding Syton to the BM solution, hereafter SBM, improved the optical quality of the (111) face, but it still was not completely satisfactory for many devices, and its aging characteristics were worse than the BM solution. We have therefore made a detailed study of a

Key words: gallium arsenide, polishing, x-ray topography.

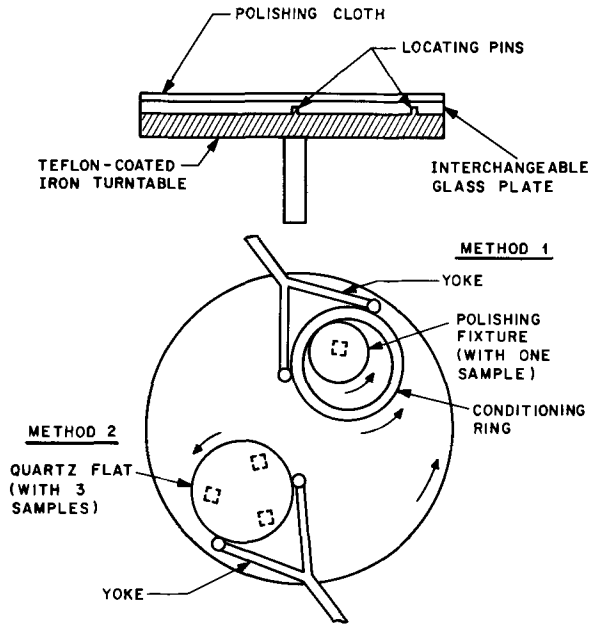

Fig. 1. Top: Schematic of polishing machine turntable and interchangeable glass plate. Bottom: Diagram illustrating the two methods used for polishing samples. In method 1, the single sample rotates about its own center. The sample and polishing fixture turn inside a conditioning ring which is positioned by a yoke. In method 2, several samples are polished simultaneously by mounting them on a large quartz flat. As the flat turns inside the yoke, samples receive a translational motion across polishing cloth.

new polishing solution for GaAs which contains H_2O_2 and NH_4OH and was first used by Sayko (5) of these laboratories. In the present paper, we show that this peroxide-alkaline (PA) solution overcomes the limitations associated with both the BM and SBM solutions.

Several properties of the PA solution were investigated as follows:

a. Optical quality and crystallographic dependence.
b. Polishing rates and reproducibility.
c. Surface damage and residual strain due to polishing.
d. Metallic contact resistance to polished layer.
e. Fabrication of diffused junction lasers from PA-polished substrates.

The results of these studies are reported and, where applicable, comparisons are made with the BM and SBM polishes. Finally, a critical evaluation of the PA solution and some areas which still require further investigation are outlined.

Experimental Procedures

The apparatus used for polishing is shown schematically in Fig. 1. It consists of a Teflon-coated iron turntable and several interchangeable flat Pyrex glass plates. These plates can be used with any desired polishing cloth or, alternately, without a cloth during lapping operations. For PA and SBM polishing we used Politex Supreme cloths,[1] while PAW scientific cloths[2] were employed for BM polishing. Both of these cloths have adhesive backings which are pressed onto the Pyrex plates.

Two methods of mounting wafers are used depending on the number of available samples as illustrated in Fig. 1 (bottom). In method 1, a single wafer is mounted in a polishing fixture similar to one reported by Mash *et al.* (6). The wafer is first waxed to a flat quartz or stainless steel disk which is then attached to a plunger. The movement of the plunger is constrained by a linear bearing to maintain the surface of the wafer parallel to the plane of the turntable. The polishing pressure is varied by adjusting a compression spring located inside the center shaft of the plunger. With method 2, on the other hand, three or more wafers must be mounted simultaneously on a large quartz flat. Although it is not possible to polish one wafer at a time, method 2 does have the advantage of producing a more desirable polishing motion since each sample is translated back and forth across the polishing cloth rather than turning only about its own center as in method 1. Further discussion of these aspects is given in Experimental Results.

Most of our polishing experiments have been performed on n-type wafers with electron concentrations in the low 10^{18} cm^{-3} range, which is a typical doping for junction lasers. Before polishing, the wafers were always lapped with 5 μm alumina abrasive. Each of the polishing solutions was mixed in the proportions given in Table I and applied at rates of 800-1400 ml/hr. The pressure applied during polishing with methods 1 and 2 was approximately 400 and 120 g/cm^2, respectively. After the removal of a few microns of material the lapping damage was usually not visible, but the polishing was always continued until about 50 μm of material had been removed.

Experimental Results

Optical quality and crystallographic dependence.— Polishing of the (100), (111) Ga-rich, and $(\bar{1}\bar{1}\bar{1})$ As-rich faces has been investigated. For all three solutions, highly polished surfaces were achieved on the (100) and $(\bar{1}\bar{1}\bar{1})$ faces with little evidence of any preferential etching, although the BM polished surfaces sometimes revealed a slight lemon-peel undulation[3] which was not observed with either the PA or SBM surfaces. On the other hand, only the PA and SBM solutions polished the (111) face nonpreferentially. Initial results with a scanning electron microscope failed to reveal any features of the surface topography. Additional measurements with a Talysurf[4] showed the PA topography to be flat and uniform with no elevated features greater than about 100Å which is the resolution limit of the instrument. This value is also consistent with

[1] Obtainable from Geoscience Instruments Corporation, Mount Vernon, New York.
[2] Obtainable from Pellon Corporation, New York, New York.
[3] Similar undulations have been produced on germanium by the CP4 etch [see ref. (7)].
[4] Model 4 Talysurf, manufactured by Rank Taylor Hobson Division, Leicester, England.

Table I. Comparison of three polishing solutions for GaAs

Polishing solution	Composition*	Nonpreferential polish (100)	(111)	$(\bar{1}\bar{1}\bar{1})$	Polishing rates** (μm/hr) Initial	Final	Contact resistance (ohm-cm²)	Residual surface damage
Peroxide-alkaline (PA)	1 ml NH_4OH 700 ml H_2O_2	Yes	Yes	Yes	18	19	$\leq 3.9 \times 10^{-5}$	Not detected
Bromine-methanol (BM)	1 ml Bromine 2000 ml Methanol	Yes	No	Yes	12	4	$\leq 3.9 \times 10^{-5}$	Not detected
Syton-bromine-methanol (SBM)	1 ml Bromine 20 ml Methanol 300 ml Syton	Yes	Yes	Yes	12	1	—	Moderate

* Chemical assays NH_4OH (29.5%), H_2O_2 (29-32%, superoxol), bromine (99.8%), methanol (99.9%), Syton (Monsanto Company).
** Final rate determined 8 hr after preparation of polishing solution.

another measurement obtained with a multiple beam interferometer.

In order to achieve a nonpreferential polish on the (111) face with the PA solution, we found that the motion of the samples on the polishing cloth is an important factor. In this regard, method 2 is notably superior to method 1 apparently because the samples have increased translational motion and a correspondingly increased contact with the polishing cloth. To understand the importance of the motion, it is first necessary to describe how the PA polishing mechanism differs from conventional etching mechanisms. When a GaAs wafer is in contact with the PA solution, a thin film, which probably contains gallium and/or arsenic oxides, forms on the GaAs surface. The exact composition of the film is still undetermined but, since the film is very soft, it is continually removed by the cloth during polishing. In contrast with most etching solutions, the PA solution contains no second component which chemically dissolves the film as it forms. Thus, the PA solution by itself cannot be used to etch a GaAs substrate and polishing will only proceed when the GaAs is in contact with the cloth. This has two advantages. First, the film is removed from the high regions of the wafer before the low regions and this improves the over-all flatness. Second, the formation of any preferential polishing effects, which are sometimes observed on the (111) face, will also be inhibited.

The lack of translational motion associated with method 1 sometimes leads to a situation where small preferential pimples are observed near the center of the (111) slice being polished. In accordance with the above discussion, these pimples are not usually observed at the outer edges of the slice which do have some translational motion. With method 1, a nonpreferential (111) surface can still be obtained by slightly increasing the amount of NH_4OH to raise the *p*H value from its initially measured value of about 7.0. However it is important not to increase the *p*H value too much since this may cause a shallow pitting of the surface. Therefore, in summary, the (111) orientation of GaAs can be polished with the PA solution, but both the sample motion and NH_4OH concentration are important factors which determine the quality of the polished surface.

Polishing rates and reproducibility.—Initial observations with the PA solution indicated that the polishing rate was essentially constant over durations of several hours which is in marked contrast with either of the solutions containing bromine. To substantiate these results, three identical $(\bar{1}\bar{1}\bar{1})$ wafers were selected and then individually polished by method 1, using one wafer for each solution. All solutions were mixed as in Table I and applied at a constant rate (1000 ml/hr). The turntable speed was maintained at 70 rpm and each wafer was polished at a pressure of approximately 400 g/cm^2. The results of these controlled experiments are plotted in Fig. 2. Each point represents 30 min of polishing time with the exception of the initial points which are for 20 min of polishing beginning with the lapped surfaces. These initial points have been plotted for completeness only and are not indicative of the true polishing rates since a lapped surface polishes more rapidly. The main conclusion from Fig. 2 is that the polishing rate for the PA solution is remarkably stable during the 8-hr test period, whereas the rates for BM and SBM solutions are reduced by factors of 3 and 12, respectively. The evaporation of bromine is believed to be the main cause of these reduced polishing rates.

Surface damage and residual strain due to polishing.—A further evaluation of the three solutions has been made using a series of high resolution reflection x-ray topographs of the actual polished surfaces. Again, $(\bar{1}\bar{1}\bar{1})$ wafers were examined so that the BM solution could be included. X-ray topographs were obtained

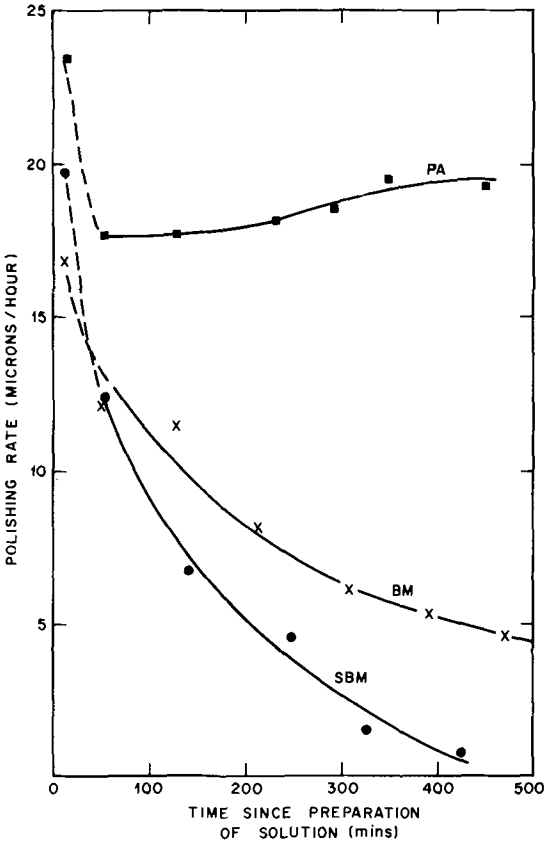

Fig. 2. Polishing rate as a function of time for each of the three solutions (see Table I for composition). All solutions were applied at a constant rate (1000 ml/hr) and each of the identical $(\bar{1}\bar{1}\bar{1})$ wafers was polished at a pressure of ≃400 g/cm^2. The initial point where curve is dashed is for a 20 min polish on a lapped surface. All other points present 30 min of polish. Estimated accuracy on each rate is ±1.5 μm/hr.

with Cu $K_{\alpha 1}$ radiation using a (422) reflection from samples polished with PA, BM, and SBM solutions. The results are presented in Fig. 3a, b, and c, respectively. Notice in Fig. 3a and b that there is excellent diffraction contrast between the perfect or defect-free regions of the polished surface (*i.e.*, the uniform gray background) and the defect dislocations (*i.e.*, the short dark lines uniformly distributed throughout the bulk of the sample). These observations are typical for Czochralski-grown ingots (8) and, from these topographs, it is estimated that there are approximately 5 x 10^4 dislocation lines per square centimeter. In marked contrast to Fig. 3a and b, Fig. 3c shows that, due to the residual strain present in the SBM surface, contrast at the dislocations has essentially been eliminated. Note, however, that some heavy tweezer damage does show up very clearly in three places in the lower central portion of Fig. 3c. These photographs clearly demonstrate the superior quality of the PA and BM polished surfaces.

A qualitative explanation for the loss of contrast in Fig. 3c is presented in Fig. 4 where we schematically compare the diffracted X-ray intensity expected from a "perfect" strain-free area, I_p, containing a dislocation line, I_d, with a comparable region on a strained surface, I_s. It can be seen that, because damaged surfaces give rise to enhanced diffracted intensity, *i.e.*, $I_s > I_p$, the contrast difference $(I_d - I_s)$ will suffer when compared to the perfect region where it is $(I_d - I_p)$. In the extreme cases, when $I_s \simeq I_d$, the reflection topographs are uniformly dark and featureless.

The residual strain fields at the surfaces of the above samples have also been examined by obtaining x-ray topographs from (110) cleavage faces using procedures described by Rozgonyi and Haszko (9). The cleavage

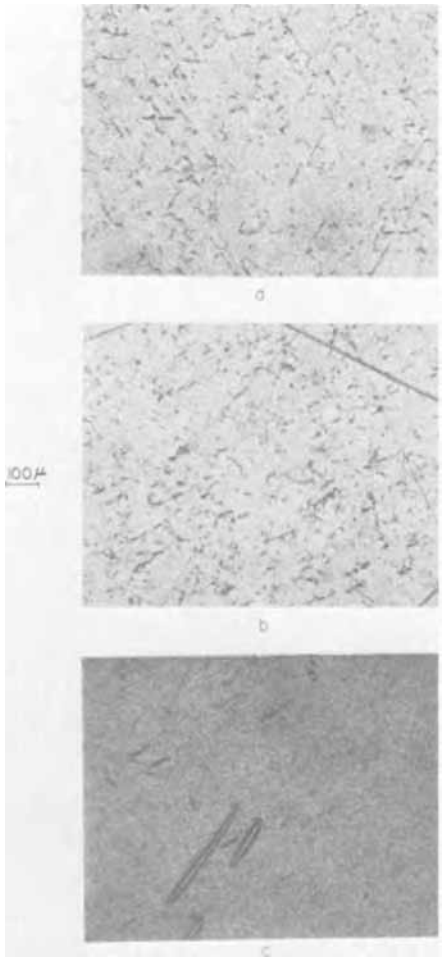

Fig. 3. High resolution reflection x-ray topographs of (a) PA, (b) BM, and (c) SBM polished GaAs wafers. See text and Fig. 4 for explanation of these photographs.

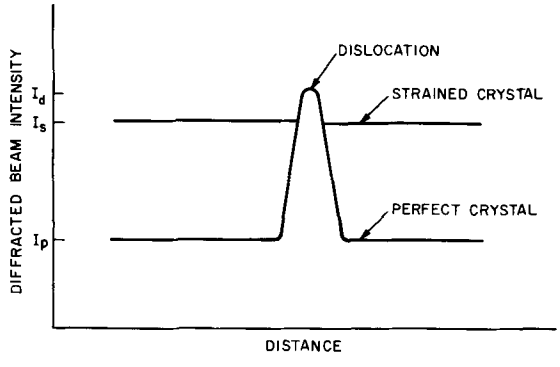

Fig. 4. Schematic representation of diffracted x-ray intensities I_p at a perfect strain-free surface compared to I_s at a strained surface and I_d for a bulk dislocation. The contrast difference ($I_d - I_p$) is greater than ($I_d - I_s$) which accounts for the increased contrast found in Fig. 3a and b compared to Fig. 3c.

face x-ray topographs of PA and BM polished surfaces showed excellent dislocation contrast uniformly distributed from the interior of the wafers to the outer (polished) edge of the cleavage face, see Fig. 5a and b. However, for the SBM polished sample, see Fig. 5c, a thin uniformly black area was observed at the edge of the cleavage face corresponding to the polished surface at the right-hand edge of the photograph. The black area again indicates there is residual surface damage associated with the SBM polish. The enhanced diffraction at the left-hand edge of these topographs is primarily due to the saw cutting and lapping operation.

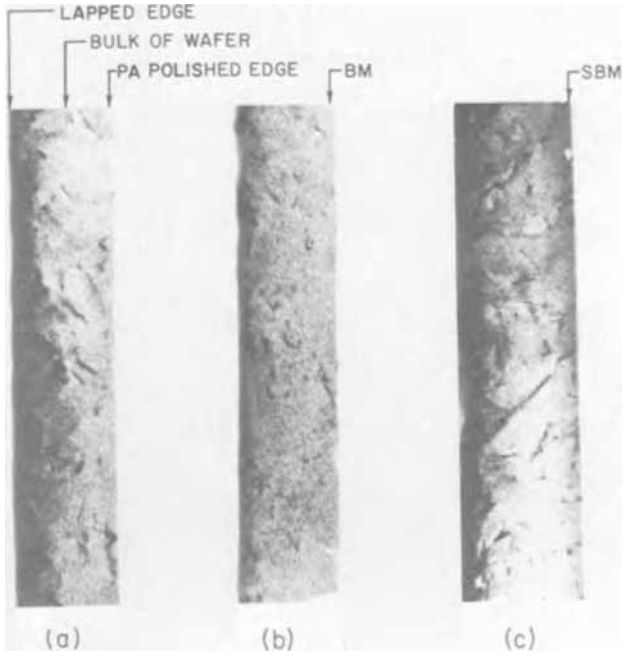

Fig. 5. Cleavage face x-ray topographs for the three samples of Fig. 3.

Thus the cleavage face topographs are consistent with the $(\bar{1}\bar{1}\bar{1})$ surface topographs presented in Fig. 3.

We believe that the results reported here explain some of our previous data regarding the threshold current densities of diffused junction laser diodes. These lasers were prepared by diffusing Zn to a depth of 2 μm into BM and SBM polished surfaces using procedures described previously (10). The standard stripe geometry contacts (11) were then applied. It was found that the threshold current densities were at least 30% higher for SBM than for BM polished wafers. This was observed for three separate ingots. One possible explanation for the higher thresholds associated with SBM would be increased diffraction losses due to photons propagating through the strained material near the surface. Another explanation might be that the strained surface somehow affects the diffusion of the Zn to produce a more ragged junction or one that does not have the optimum gradient. After the discovery that it required higher thresholds, the SBM polish was discontinued as a prediffusion substrate polish. However, until the discovery of the PA solution, the SBM solution was still used whenever the (111) surface had to be polished, *e.g.*, to thin the n-GaAs substrates of single-heterostructure lasers.

Metallic contact resistance to polished layer.—In view of the above discussion, it seems probable that some film which is not completely removed by the cloth will remain on the GaAs surface after PA polishing. The thickness of this residual film has been estimated (12) to be about 70Å from ellipsometer measurements. This is to be compared to a film thickness of only 20Å on a BM polished slice. It is found, however, that the PA film thickness is reduced to less than 20Å after HF cleaning. Nevertheless, for any device application, it is essential to determine whether the remaining layer prevents the achievement of a good ohmic electrical contact to the polished slice. We performed several contact resistance experiments using our standard contact to n-type GaAs which is an alloy containing Sn-Pd-Sn (13). With the polished GaAs substrate held in vacuum at 150°C, 2000Å of Sn and 500Å of Pd were successively evaporated onto the surface. These two metals were then alloyed in vacuum at 525°C for 30 sec. On cooling the substrate to 150°C again, the final 7000Å thick layer of Sn was evaporated. Good ohmic contacts were reliably formed on

PA polished slices with the Sn-Pd-Sn contact and the results are virtually the same as found for the BM case. The numerical values given in Table I were obtained by measuring the total resistance of several n-type GaAs samples of known dimensions and subtracting off the bulk contributions. We conclude, therefore, that any layer which does remain on the surface after PA polishing does not prevent an ohmic contact.

Fabrication of diffused junction lasers from PA polished substrates.—Since PA and BM polished ($\bar{1}\bar{1}\bar{1}$) surfaces both appear to be of comparable quality, it was expected that diffused junction lasers should also be comparable in performance. At the present time, two different sets of PA and BM polished wafers have been compared. For each set, shallow 2 μm junctions were diffused (10) and stripe geometry contacts (11) applied in the usual manner. It was found that the average laser threshold current densities were essentially equal. Some devices from the PA polished substrates had slightly lower thresholds but this is not thought to be significant due to the complicated nature of the junction laser. Nevertheless, these results support our findings and again indicate that the PA solution produces a high quality surface.

Discussion

Our results, which are tabulated in Table I, demonstrate that the new PA polish is highly useful for GaAs technology. In summary, the PA solution provides satisfactory microtopography for all GaAs orientations of interest to device engineers, constant polishing rates, essentially strain-free surfaces, and ohmic metallic contact characteristics. The PA solution is much more predictable than either the BM or SBM solutions since these both deplete rapidly with time. In addition, the PA solution would be preferred over the BM solution because the latter will not polish the (111) faces. Sullivan and Kolb (1) have shown that if the bromine content is reduced to 0.0025% (*i.e.*, a factor of 20 smaller than used in this paper) then the (111) faces can be polished. However, as Iiyama *et al.* (14) have noted, the polishing rate is then so slow that it is no longer practical. Although the SBM solution will polish the (111) faces, it has the disadvantage that it is somewhat messy to use and leaves a strained surface which we believe has contributed to higher thresholds in diffused junction lasers. The presence of strain in a substrate may also be detrimental if one subsequently deposits vapor or liquid phase epitaxial layers. Such a situation has been reported by Weinstein *et al.* (15) for GaAs and Rozgonyi and Saul (16) for GaP.

There are several areas which we feel warrant further investigation. For example, we have not tried to optimize the over-all flatness of our wafers. In some cases with polishing method 1 of Fig. 1 we have achieved flatnesses of approximately 1 μm over a linear dimension of 1 cm. In this measurement a fairly large wafer is required since a rounding effect occurs at the outer 2 or 3 mm of the wafer. This rounding is considerably reduced by polishing method 2. However, it is expected that further improvements in flatness could be achieved by using some of the recently reported discal polishing techniques (14).

It would also seem important to determine optical quality and polishing rates as the volume percentage of NH_4OH is varied up or down from the value used by us which provides an essentially neutral solution ($pH \simeq 7.0$). In addition to the experimental results reported in this paper, we have performed two additional experiments using NaOH and KOH in place of NH_4OH. These were mixed with H_2O_2 to again produce a $pH \simeq 7.0$. In each case a test slice of n-type GaAs yielded a polish which appeared comparable in quality to the PA results of this paper when examined microscopically. These two solutions have not been investigated in detail but many possibilities are suggested of using these and other alkalines in conjunction with oxidizers other than H_2O_2.

It may also be of interest to study the effects of PA solutions on n-type and p-type GaAs as functions of the substrate doping levels. We can report that 10^{16} cm^{-3} n-type GaAs has been polished in addition to the $\simeq 10^{18}$ cm^{-3} GaAs used in most of the above experiments. We have also polished p-type $Ga_xAl_{1-x}As$ but extensive measurements on flatness, rate of removal, etc., are still to be made. Finally, it should be verified whether III-V compounds other than GaAs can be polished in PA solutions.

Acknowledgments

The authors thank R. E. Albano for expert technical assistance during the course of these investigations including the effects of motion and solution *p*H on the optical quality of the polished surface. We also thank A. P. Pisarchik and V. Decker for furnishing the original designs of the polishing machine and polishing fixture, A. J. Sayko for informing us of the existence of the PA solution, W. R. Costello for the scanning electron microscope study, V. J. Albano for assistance with the *p*H measurements, and S. E. Haszko for the x-ray topographs. Useful discussions have also been held with F. Vratny and M. V. Sullivan during the course of this work. Finally, we thank J. H. Rowen, L. A. D'Asaro, B. Schwartz, J. E. Ripper, and E. A. Ulmer for comments on the manuscript.

Manuscript received Nov. 30, 1970.

Any discussion of this paper will appear in a Discussion Section to be published in the June 1972 JOURNAL.

REFERENCES

1. M. V. Sullivan and G. A. Kolb, *This Journal*, **110**, 585 (1963).
2. M. B. Panish, I. Hayashi, and S. Sumski, *IEEE J. Quantum Electron.*, **QE-5**, 210 (1969).
3. I. Hayashi, M. B. Panish, and P. W. Foy, *ibid.*, **QE-5**, 211 (1969).
4. H. Kressel and H. Nelson, *RCA Rev.*, **30**, 106 (1969).
5. A. J. Sayko, Personal communication.
6. D. H. Mash, G. D. Henshall, and B. A. Eales, *J. Phys. D: Appl. Phys.*, **3**, 1199 (1970).
7. "Transistor Technology," Vol. 1, p. 355, H. E. Bridges, J. H. Scaff, and J. N. Shive, Editors, D. Van Nostrand Co., Princeton, N. J., (1958).
8. E. S. Meiran, *Trans. Met. Soc. AIME*, **242**, 413 (1968).
9. G. A. Rozgonyi and S. E. Haszko, *This Journal*, **117**, 1562 (1970).
10. J. C. Dyment and L. A. D'Asaro, *Appl. Phys. Letters*, **11**, 292 (1967).
11. J. C. Dyment, *ibid.*, **10**, 84 (1967).
12. A. C. Adams and B. R. Pruniaux, Personal communication.
13. R. E. Albano, Personal communication.
14. S. Iiyama, I. Ida, and S. Furumoto, *Rev. Elect. Commun. Lab.*, **17**, 1022 (1969).
15. M. Weinstein, R. O. Bell, and A. A. Menna, *This Journal*, **111**, 674 (1964).
16. G. A. Rozgonyi and R. H. Saul, *ibid.*, **117**, 259C (1970).

Neutron Activation Analysis of Epitaxial Silicon

Graydon B. Larrabee* and Joseph A. Keenan

Texas Instruments Incorporated, Central Research Laboratories, Dallas, Texas 75222

ABSTRACT

A neutron activation analysis technique has been developed for the analysis of epitaxial silicon. The technique is described in detail along with a table of detection limits. Impurity and dopant concentrations have been profiled through epitaxial films on boron- and antimony-doped substrates. These data along with experience in routine analyses show a factor of 10 to 40 higher impurity concentrations in the outer layer of silicon epitaxial films. Autoradiography combined with profiling has been shown to be a powerful tool for studying doping uniformity.

The production of epitaxial silicon for device fabrication has increased markedly in the last few years. Marketing personnel estimate that close to 80% of the total dollar production of single-crystal silicon will be epitaxial material in the 1972-1974 time period. This pronounced change in the mix of silicon product has focused attention on the development of new techniques for the characterization of this material.

The characterization of epitaxial material, for any parameter, is complicated by the physical form and size of the sample. Epitaxial silicon samples can generally be described as thin, lightly doped, single-crystal films, 2-30μ in thickness, on heavily doped 200-300μ thick single-crystal substrates. There are many techniques available for growing these single-crystal films (1, 2) but usually they are vapor grown at high temperatures (1050°-1250°C) on highly polished substrates from $SiCl_4$ as shown in Eq. [1]

$$SiCl_4 + 2H_2 \rightarrow Si + 4HCl \qquad [1]$$

Current silicon production is on 2-in. slices, which means that the amount of epitaxial silicon sample available for analysis ranges from 1 to 15 mg, depending on the thickness of the film. Both intentionally added and adventitious impurities in these films range in concentration from about 1 ppm down to the sub-ppb level. As can be seen a highly sensitive characterization technique is required to analyze these films because of the combined effects of sample size and small impurity concentration.

Neutron activation analysis meets both of these requirements and has been used for the analysis of bulk silicon (3, 4). However, bulk silicon is readily available as large single crystals with samples in the 1-10g size. Further, there is no problem in sample handling whereas with epitaxial silicon it is necessary, before radioassay, to physically separate the film from the substrate without sampling the substrate as part of the film. This is accomplished by masking and etching techniques.

Abe and Sato (5) used activation analysis to determine the distribution of arsenic atoms in epitaxial films deposited on heavily doped arsenic substrates. Interpretation of the data which they obtained was difficult because the distribution could not be fitted to an error-function diffusion profile. Perezhogin and Meshcheryakov (6) determined the distribution of phosphorus in an epitaxial film on a boron-doped substrate and antimony in an epitaxial film on an antimony-doped substrate. This work is concerned with the determination of adventitious impurities in epitaxial films.

Experimental

Neutron activation analysis of epitaxial silicon can be described as a three-step process; irradiation, source preparation, and radioassay. Most of the radioactive isotopes produced in neutron bombardment decay by β-γ emission. Some pure β-emitters such as ^{32}P must be studied by β-spectroscopy. Chemical separations are usually required for β-spectroscopy both because of the polyenergetic β spectrum and because a thin source must be counted in order to minimize absorption of β particles within the source. The greater penetrating power of γ-rays makes it possible to identify impurities in solutions and solid samples by γ-ray spectroscopy. Since γ-rays are monoenergetic and specific for the isotope considered, most elements can be identified in a single sample without resorting to chemical separations. The simplicity of source preparation for γ-ray spectroscopy is counterbalanced, however, by the complexity of data reduction. In this laboratory computer reduction of data is used to achieve rapid analysis by γ-ray spectroscopy.

Irradiation

In earlier work (7) on the neutron activation analysis of SiO_2 films and silicon for sodium it was shown that both the amount and the location of this impurity in the sample was strongly dependent on the pre-irradiation packaging. As a result of that work, a standard quartz dish was designed, as shown in Fig. 1. These dishes have an inside diameter slightly larger than a 2-in. silicon slice and are approximately 0.5 in. in height.

In this work, epitaxial silicon samples were stacked into the dishes with specially cleaned ultrapure silicon spacers between them. Flux monitors were included with the slices. The dishes were fitted with quartz tops, wrapped in aluminum foil, and shipped to the reactor.

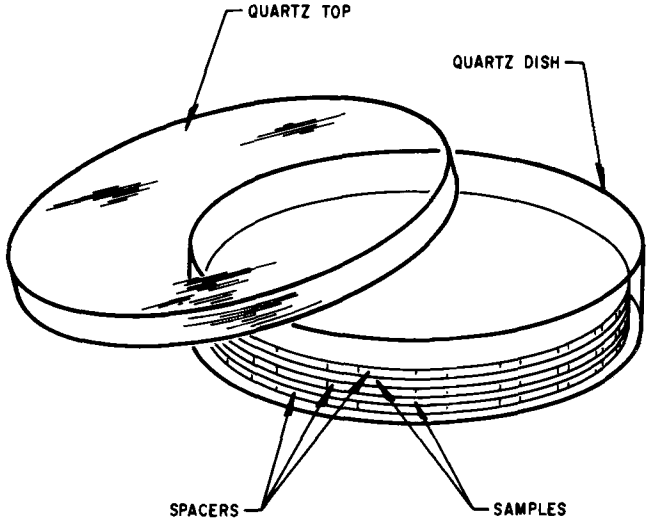

Fig. 1. Quartz dish used for the irradiation of silicon samples

* Electrochemical Society Active Member.

Key words: impurities, neutron activation, epitaxy, silicon, autoradiography.

Irradiations were performed in a fixed position on the face of the Texas A&M University reactor at a flux of 1.5 x 10^{13} n/sec/cm^2 for 14 hr. Normally the irradiation ended at midnight. The samples were shipped to our laboratory the following morning, processed for counting that afternoon, and counted the following morning. This 36 hr delay allowed the 2.6 hr ^{31}Si arising from activation of the matrix to decay sufficiently to make a negligible contribution to the γ-spectrum.

Source Preparation

Once returned to our laboratory, the quartz dish was opened, the monitors were placed to one side, the spacers were discarded, and the samples were stored in individual plastic boxes. Each slice was given three successive 2-min washes in 50 ml of 50:50 HCl:CH_3OH in plastic beakers to remove surface contamination. After these washings, the slices were rinsed twice in methanol, once in acetone, and air dried. The back of each slice was then masked with 2-in. polyethylene tape.[1]

It should be pointed out at this time that when the epitaxial film is grown on the substrate it effectively "wraps around" the edges of the slice. This "wrap-around" has been confirmed by angle lap and stain techniques. Therefore, the substrate is completely isolated from the etch solution once the tape has been applied to the back.

The masked slices were etched to remove the desired thickness of epitaxial material. The etches used were either an 8 μ/min "planar" etch ($HF:HNO_3:CH_3COOH$, 2:15:5, vol/vol) or a 1μ/min etch ($HF:HNO_3:CH_3COOH$, 1:40:1, vol/vol). The amount of material removed is readily determined by infrared interferometry spectroscopy (8). The etch rate for each etch composition has been found to be constant and reproducible.

In order to minimize sample handling and retain constant counting geometry, the slices were etched in the same 250 ml beaker in which the etchant was to be γ-counted. After the desired amount of epitaxial silicon had been removed the slice was taken from the solution with tweezers and rinsed with water into the same beaker. Finally the etch solution was diluted to a standard volume of 20 ml and the beaker was sealed for counting.

Monitors that were included in the irradiation were processed in the standard manner after all samples had been prepared for radioassay. Generally this involved crushing the small quartz vial with the monitor in the acid solution that was to be used to dissolve the monitor. After dissolution, the solution was diluted to volume in a volumetric flask, an aliquot removed and diluted to 20 ml in a 250 ml plastic beaker. This assures the same counting geometry for monitors and samples.

Gamma-ray Spectroscopy

Both low-resolution NaI(Tl) and high-resolution Ge(Li) γ-ray spectrometers were used in this work. The less efficient Ge(Li) system was used predominately as a pilot detector in order to identify the components of complex spectra for the linear-least squares computer analysis of the NaI(Tl) data.

The Ge(Li) system consisted of a 16 cc coaxial lithium-drifted germanium detector, a Tennelec TC135 preamplifier, TC200 shaping amplifier, and a Nuclear Data Model 2200 4096-channel multichannel analyzer. Energy resolution for the system was 3.7 keV at the 1333 keV peak of ^{60}Co. The multichannel analyzer was equipped with CRT display and teletype print and punched paper tape output.

All the detectors had plastic collars fitted to them to ensure that the 250 ml beakers containing the 20 ml of etch solution were held in a fixed-reproducible geometry. Typically NaI(Tl) spectra were accumulated for 100 min. Due to the lower efficiency of Ge(Li) detectors, these spectra were accumulated for as long as the intensity of the sources permitted (typically 20 hr) in order to obtain the best possible counting statistics.

Data Reduction

An IBM Model 047 tape to card converter was used to convert the BCD paper tape information from the NaI(Tl) detectors to IBM cards. For the bulk of the time covered by this work, the data from the Ge(Li) detector were analyzed by hand. More recently Ge(Li) data have been analyzed on a Texas Instruments Model 861 computer via a direct interface between the Nuclear Data Model 2200 and the computer.

The computer programs used to analyze the NaI(Tl) data were operated in a multiprogramming mode in a CDC 6400 computer. The two program system is outlined in Fig. 2. The first program (H 137) is a modified form of a linear least squares analysis developed by Helmer *et al.* (9). The second program converts the γ-intensities obtained from H137 to concentrations of the impurities in the sample.

In addition to the selection of various options, the input required for H137 consists of a background spectrum, the experimental data, and standard spectra of all the elements contributing to the experimental spectrum. These standard spectra are kept in a library which is updated at frequent intervals.

In order to derive impurity concentrations, H092 uses the γ-intensity from the monitor to account for

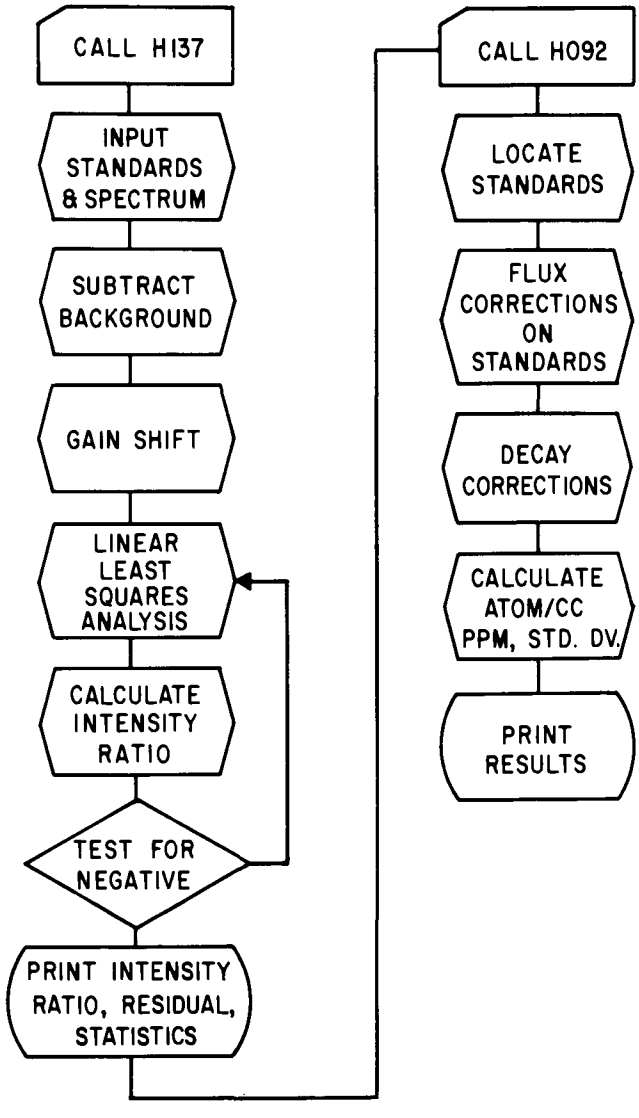

Fig. 2. Outline of the computer programs used to analyze the gamma spectra.

[1] Arno Adhesive Company, Fort Worth, Texas.

the difference in flux for the standards and for the experimental source. The additional inputs required by H092 are γ-intensity of the monitor, the weight of the sample, and the time after irradiation at which the sample was counted. Typically eight to ten samples can be processed through these computer programs to obtain final results as parts per million or atoms per cubic centimeter in 20 to 30 sec of central processor computer time.

The γ-intensities derived by H137 are expressed as the ratio of the experimental intensity to the standard intensity. Ratios as small as 0.001 have been detected with highly consistent results. The detection limits for a 100 min count, 36 hr after a 14-hr irradiation, at 1.5 x 10^{13} n/sec/cm^2 are given in Table I. These limits are based on counting a 10μ film etched off a 2-in. slice. A 10μ film was used in the calculations to simplify normalization of these detection limits to any other thickness removed. As can be seen the detection limits are good, with 50 elements having sensitivities less than one ppma and 33 less than 10 ppba. It must be remembered that these sensitivities are based on a 10μ film and any change in the thickness analyzed will proportionally affect the sensitivity. These sensitivities can be readily improved by an order of magnitude by going to a higher flux in another reactor and/or increasing the irradiation time.

A relative standard deviation of $\pm$5.3% for five impurities over a concentration range of 0.65 ppb to 415 ppm has been established for this technique applied to bulk silicon (3). The absolute accuracy was shown to be in the $\pm$6.1 to $\pm$35% range when compared to electrical measurements. There is no reason to believe that this precision and accuracy should change significantly, if at all, for epitaxial material.

Results

Epitaxial silicon.—Neutron activation analysis of epitaxial silicon has been in routine use in these laboratories for about 18 months. The most commonly observed impurities are those generally seen in all semiconductor grade silicon; gold, copper, sodium, arsenic, and antimony. A statistical analysis of the gold, copper, and sodium contents of the surface (outer 4μ) and epitaxial film (remaining film after removal of the outer 4μ) gives clear evidence that the surface concentrations are a factor of 10 to 40 higher than in the film. An example of this is shown in Table II.

Table I. Detection limits for impurities in silicon epitaxial material etched off for analysis assuming a 2 in. slice, analyzing 10μ. Sample counted on a 3x3 NaI spectrometer. 14.00 H irradiation at 1.50E + 13 neutrons/cm^2/sec. 36.00 H decay

Element	Atoms/cc	Element	Atoms/cc
Antimony 122	6.949E + 12	Neodymium 147	1.957E + 14
Antimony 124	1.759E + 14	Osmium 191	4.525E + 13
Arsenic 76	6.377E + 12	Palladium 109	5.105E + 13
Barium 131	1.084E + 16	Phosphorus 32 beta	3.389E + 13
Barium 133	6.971E + 17	Platinum 197 0.2 meV	5.380E + 14
Bromine 82	1.338E + 13	Platinum 197 77 keV	1.286E + 14
Cadmium 115	1.854E + 15	Potassium 42	3.839E + 15
Cadmium 115M	2.982E + 16	Praseodymium 142	1.002E + 14
Calcium 45 beta	4.690E + 15	Rhenium 188	1.328E + 12
Cerium 141	1.862E + 14	Rubidium 86	2.364E + 15
Cerium 143	1.419E + 14	Ruthenium 97	7.149E + 14
Cesium 134	1.087E + 14	Ruthenium 103	3.421E + 14
Chromium 51	1.006E + 15	Samarium 153	3.270E + 11
Cobalt 60	7.392E + 14	Scandium 46	2.207E + 13
Copper 64	1.519E + 13	Selenium 75	1.555E + 15
Dysprosium 165	7.031E + 15	Silver 110M	7.782E + 14
Erbium 171	4.041E + 13	Sodium 24	7.254E + 13
Gadolinium 159	7.954E + 13	Strontium 85	4.938E + 16
Gallium 72	1.295E + 13	Sulfur 35 beta	3.174E + 15
Germanium 77	4.587E + 15	Tantalum 182 0.1 meV	5.480E + 13
Gold 198	1.289E + 11	Tantalum 182 1.0 meV	1.147E + 14
Hafnium 181	3.520E + 13	Tellurium 127	3.495E + 17
Holmium 166	1.318E + 12	Terbium 160	1.163E + 13
Indium 114	2.157E + 14	Thallium 204 beta	1.110E + 14
Indium 116	1.447E + 22	Thulium 170	4.120E + 13
Iridium 192	1.796E + 12	Tin 113	4.138E + 16
Iridium 194	1.094E + 12	Tungsten 187 0.1 meV	4.985E + 12
Iron 59	1.542E + 17	Tungsten 187 0.7 meV	4.988E + 12
Lanthanum 140	4.467E + 12	Ytterbium 169	1.061E + 13
Lutecium 177	3.973E + 12	Yttrium 90M	2.364E + 18
Manganese 56	2.698E + 15	Zinc 65	1.634E + 16
Mercury 197	2.492E + 13	Zinc 69M	8.500E + 14
Mercury 203	1.145E + 14	Zirconium 95	4.215E + 16
Molybdenum 99	1.426E + 15	Zirconium 97	1.510E + 16

Table II. Concentrations of three impurities in epitaxial silicon showing distribution

Impurity	Concentration (atoms/cc) Surface (4μ)	Epitaxial film (>4μ)
Gold	1 x 10^{13}	1 x 10^{12}
Copper	7 x 10^{14}	6 x 10^{13}
Sodium	3 x 10^{15}	7 x 10^{13}

Other impurities have been observed in epitaxial films including those elements present in the lapping compounds such as zirconium and hafnium. This occurs when the slices have not been properly cleaned. Other impurities that have been observed sporadically include molybdenum, tungsten, lanthanum, bromine, chromium, gallium, cerium, and the rare earths. There appears to be no explanation for the random appearance of these latter impurities but the evidence for their presence is strong since they were confirmed by both NaI(Tl) and Ge(Li) gamma-ray spectroscopy.

Impurity Profile Through the Film

Impurities.—The distribution of impurities through two epitaxial films was determined by incremental etching followed by gamma-ray spectral analysis of the etch solutions. The results of these profile analyses are shown in Fig. 3 for a 20μ film on a boron substrate and in Fig. 4 for a 20μ film on an antimony-doped substrate. As can be seen the concentration of impurities tends to be high at the surface and then becomes level through the epitaxial film. In the case of the film on the antimony substrate, the outdiffusion of the antimony into the film is easily seen. Since boron does not have a detectable radioactive species, similar data are not available for the boron-doped substrate.

An understanding of the location of the impurities in epitaxial film could provide valuable insight for device processing (10). Generally, devices are fabricated in the first few microns of the epitaxial film where the highest concentration of impurities exist. This would suggest that a cleanup procedure which removes a micron or more of the epitaxial film might be beneficial.

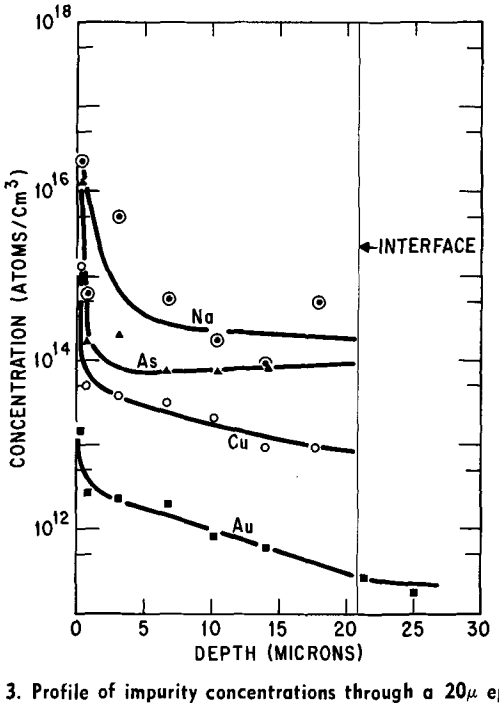

Fig. 3. Profile of impurity concentrations through a 20μ epitaxial film on a boron-doped substrate.

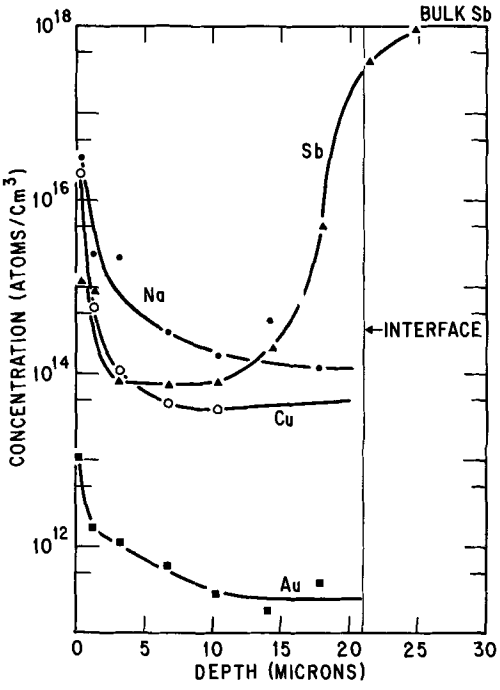

Fig. 4. Profile of impurity concentrations through a 20μ epitaxial film on an antimony-doped substrate.

Dopant.—Two samples of 0.11 ohm-cm arsenic-doped epitaxial film (12.5μ thick) on a p-type boron-doped substrate were irradiated and profiled. The arsenic distributions for both slices are shown in Fig. 5. As can be seen good agreement was obtained. The depth of penetration of arsenic was considerably deeper than anticipated and may have been caused by indiffusion of the arsenic dopant during epitaxial deposition.

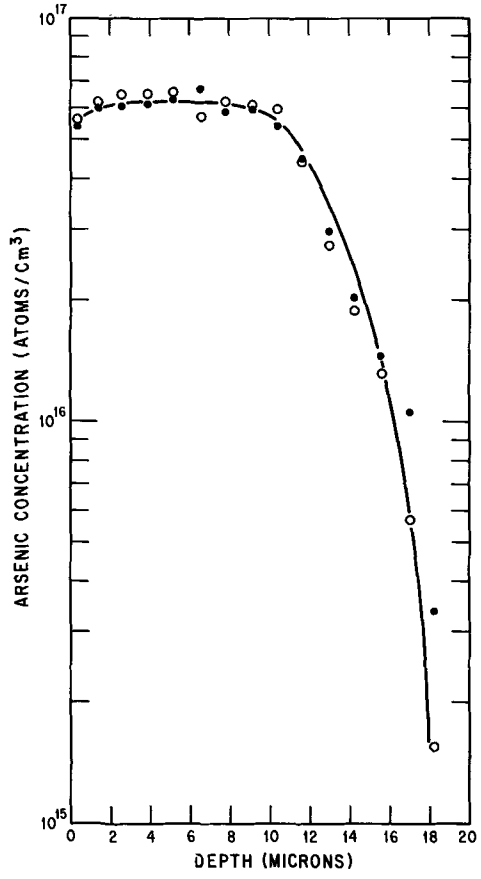

Fig. 5. Profile of arsenic distribution through a nominal 12.5μ arsenic-doped epitaxial film.

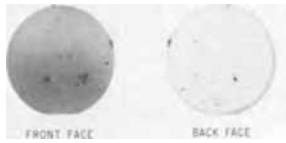

Fig. 6. Autoradiogram of arsenic distribution on the front and back face of a silicon slice with a 12.5μ arsenic-doped epitaxial film.

The surface distribution of the arsenic was also studied using autoradiography. A typical autoradiogram is shown in Fig. 6. By simultaneously taking autoradiograms of the front and back of the slice it is possible to differentiate between front and back face radioactivity. Activity exposing the film through the slice will form a diffuse image. Notice that on the back face autoradiogram the arsenic distribution shows that the epitaxial film, when grown, wraps around the edges. It can also be seen that, on this particular slice, there are areas of high arsenic concentration in the epitaxial film.

This combination of autoradiography and profiling provides a valuable tool for the study of doping uniformity in epitaxial films. Information can be obtained on the doping uniformity both across the slice and through the film.

Conclusions

Neutron activation analysis is a powerful characterization technique with high sensitivity and with the capability to analyze epitaxial films for chemical impurities in depth. The analytical procedure described in this work, utilizing computer reduction of the gamma spectra immediately followed by the calculation and print out of impurity concentrations, has been shown to be a versatile and efficient method. While the irradiations must be performed at a remote location, a 36-hr wait is required to allow the 2.6-hr ^{31}Si matrix activity to decay. This allows adequate time for the return of the samples from the reactor to the laboratory and sample preparation for radioassay. Sample preparation, including masking the back of the slice, etching and diluting to volume for counting takes typically 2 hr for six to eight samples. Radioassay generally takes 100 min to acquire sufficient counting statistics in the gamma spectrum.

A profile of the impurity concentrations through the epitaxial films indicate higher concentrations at the surface. This observation is supported by the historical data on the routine analyses and shows about 10 to 40 times higher concentrations on the surface than in the bulk. This phenomenon is particularly important in device fabrication because all devices are built in the outer surface of the epitaxial film. Doping uniformity, both radially and in depth can be readily studied by combining autoradiography and these profiling techniques.

Impurities that do not form detectable isotopes in (n,γ) reactions, *e.g.*, boron, carbon, oxygen, aluminum, etc., cannot be determined by neutron activation. These elements can be detected by other techniques such as charged particle activation, ion microprobe mass analysis, and spark source mass spectroscopy (11).

Acknowledgments

This work would not have been possible without the assistance of personnel from both the Components and Materials Groups. T. George originated much of this work and has generously provided samples. O. Cecil grew the epitaxial films used for the profiling work and has given us substantial help in the interpretation of the results. We are especially indebted to J. King for his diligence in performing the radiochemistry involved with this work.

Manuscript submitted Jan. 19, 1971; revised manuscript received April 6, 1971.

Any discussion of this paper will appear in a Discussion Section to be published in the June 1972 JOURNAL.

REFERENCES

1. P. F. Kane and G. B. Larrabee, "Characterization of Semiconductor Materials," pp. 298-333, McGraw Hill Book Co., New York (1970).
2. W. R. Runyan "Silicon Semiconductor Technology," pp. 65-78, McGraw Hill Book Co., New York (1965).
3. K. G. Heinen and G. B. Larrabee, *Anal. Chem.*, **38**, 1853 (1966).
4. W. Gebauhr, J. Martin, and E. Haas, *Z. Anal. Chem.*, **200**, 266 (1964).
5. T. Abe and K. Sato, *Japan J. Appl. Phys.*, **4**, 70 (1965).
6. G. A. Perozhogen and V. G. Mescheryakov, *Zavodskaya Lab.*, **35**, No. 7, 816 (1969).
7. J. F. Osborne, G. B. Larrabee, and V. Harrap, *Anal. Chem.*, **39**, 1144 (1967).
8. "1969 Book of ASTM Standards," ASTM, Philadelphia (1969).
9. R. G. Helmer, R. L. Heath, D. D. Metcalf, and G. A. Cazier, IDO, 17015 Idaho Falls, Idaho (1964).
10. G. B. Larrabee and H. G. Carlson in "Silicon Device Processing," p. 375, C. P. Marsden, Editor, NBS Special Publication 337, U.S. Government Printing Office, Washington, D. C. (1970).
11. J. B. Clegg, E. J. Millett, and J. A. Roberts, *Anal. Chem.*, **42**, 713 (1970).

Vapor Growth and Properties of AlAs[1]

M. Ettenberg, A. G. Sigai,* A. Dreeben,* and S. L. Gilbert

RCA Laboratories, Princeton, New Jersey 08540

ABSTRACT

Aluminum arsenide epitaxial layers on GaAs substrates have been prepared by a continuous flow vapor transport technique employing AlCl and AsH_3. It has been found that for all practical experimental conditions the reaction of AsH_3 and AlCl takes place at the point of mixing of the reactive gases. This behavior is consistent with a thermochemical analysis of the AlAs growth. The bandgap of AlAs was determined by optical absorption to be 2.17 eV and indirect. Hall and resistivity measurements made on epitaxial layers removed from the substrates indicate that the as-grown material is n-type with electron concentrations ranging from 6×10^{18} to 4×10^{17} cm^{-3} with corresponding room-temperature mobilities varying between 75 and 280 cm^2/V-sec. The value of 280 cm^2/V-sec is the highest measured electron mobility yet reported for AlAs. While the material does degrade in air, it has been found stable enough to allow ample time for device fabrication and protection.

The large bandgap (> 2.1 eV) (1) of AlAs makes it an especially interesting material for high-temperature device applications or optical applications in the visible region of the spectrum. The high melting point of this compound and the reactivity of aluminum have created problems in its high-purity preparation. The major limitation to material characterization or device fabrication, however, has been the instability of AlAs in air. Reported complete degradation of grown layers in 10 min (2) would indicate a limited usefulness.

This study was made using the open flow vapor growth system (3) employing the Group V hydride and the Group III chloride, modified to accommodate the growth of aluminum III-V compounds. In this system growth takes place at temperatures significantly below the melting point of the compound grown, thus reducing many of the problems associated with the reactivity of aluminum and general contamination. This technique has yielded n-type AlAs having increased stability and the highest electron mobilities yet reported (4, 5).

Experimental

The growth system, shown in Fig. 1, consists of a quartz tube which accommodates a pure alumina liner containing alumina boats filled with 99.999% aluminum. The alumina is 99.7% Al_2O_3 with 0.05% SiO_2, 0.1% Fe_2O_3, 0.2% Na_2O, and 0.05% K_2O as major impurities. Aluminum monochloride is formed by passing Pd-diffused H_2 carrier gas containing 0.2% HCl by volume over the liquid aluminum at 1000°-1050°C. The AlCl is then mixed with AsH_3, and the AlAs formed was deposited on GaAs substrates at a temperature between 1000°-1050°C. The AsH_3, which contains < 1 ppm total impurities determined by mass spectrometry, is 2% by volume in the H_2 carrier gas. This configuration (Fig. 1) includes provision for a gallium boat so that $Al_xGa_{1-x}As$ alloys may be grown as well as pure AlAs by simultaneously passing HCl over gallium. This basic system may also be employed to grow AlN using NH_3 instead of AsH_3 and AlP using PH_3. The long aluminum zone, containing up to six aluminum-filled boats, allows the first two aluminum boats to act as getters removing any traces of H_2O, O_2, or other impurities contained in the HCl and H_2 stream. The remaining boats serve to insure complete equilibration of the HCl with aluminum. The exposed quartz in the deposition zone is protected from attack by the initial deposits of AlAs. More recently, a tungsten liner has

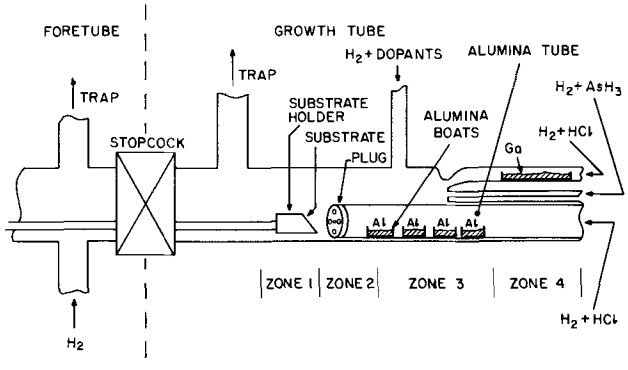

Fig. 1. Aluminum arsenide vapor growth system

* Electrochemical Society Active Member.

[1] The research reported in this paper was sponsored in part by the National Aeronautics and Space Administration, Electronic Research Center, under Contract No. NAS 12-538.

Key words: mobility of AlAs, thermochemical analysis of AlAs vapor growth.

Table I. Impurity analysis

Sample	Technique	Fe	Cr	Si	Cu ppma
Interfacial layer	Mass spec[1]	2	2	31	6
Cr-doped GaAs	Mass spec[1]	0.1	2	0.5	0.1

[1] In all the mass spectrographic analyses, impurity levels of C, O, and F were consistently observed. These levels are thought to be associated with surface contamination since their concentrations decreased as more of the surface is removed during analysis.

been employed in the deposition region to facilitate cleaning and to further reduce Si contamination.

Reaction of the AsH_3 and AlCl to form AlAs takes place at the point of mixing of the two gases, independent of reactive gas concentrations up to at least changes of a factor of five in AlCl or AsH_3 concentrations. Furthermore, the location of the reaction zone does not change for various combinations of aluminum and reaction zone temperature between 850° and 1050°C. In order to move the reaction zone from the mouth of the alumina tube, an alumina plug (99.7% Al_2O_3), with small holes (1/16 in. diam) drilled through it, was added to the mouth of the alumina tube, decreasing the effective cross section and thus increasing the gas velocity at the point of reaction. This spread the reaction over a 4 in. length, allowing a suitable substrate to be conveniently placed in the reaction zone.

Growths were usually made on chemically polished GaAs substrates oriented 3° from the (100) plane. Substrates were cleaned for 20 min in Caro's acid etch (5 H_2SO_4, 1 H_2O, 1 H_2O_2) and 1 min in 1% Br-methanol solution just prior to insertion in the system. Growth rates could be varied between 10 and 100 μm/hr depending on reactant concentrations and volumes. Depositions at growth rates less than 60 μm/hr on GaAs substrates at temperatures exceeding 980°C were invariably good single-crystalline layers as evidenced by Laue back-reflection photographs. Layers grown at temperatures below 980°C or at high growth rates (> 60 μm/hr) were usually highly oriented large-grain polycrystals.

AlAs Properties

One of the significant factors limiting the potential usefulness of AlAs is its reported instability in air (2); contrary to this report, some of the single-crystalline epitaxial layers reported here were stable in air for periods of up to 1 month and could be maintained in vacuum indefinitely. Unprotected diffused diodes fabricated from this material (6) maintained their I-V characteristics for several weeks. This stability is attributed to the higher purity and good crystallinity of the AlAs prepared by this technique.

The optical bandgap for the material has been ascertained to be indirect and 2.17 ± 0.02 eV at 300°K, in good agreement with prior studies (1, 6, 7). This value has been obtained by analysis of optical absorption data from several AlAs layers from which the GaAs substrate was removed. Similar results were obtained with polycrystalline layers grown on (0001) sapphire substrates.

Hall effect and resistivity measurements made on epitaxial aluminum arsenide layers, while still on semi-insulating Cr-doped GaAs substrates (> 10^5 ohm-cm), yielded mobility values which were inordinantly high for a large indirect bandgap material (in excess of 3000 cm²/V-sec). Attempts to remove the AlAs from the substrate were hampered by cracking of the sample as it was thinned. By preferential removal of the AlAs in aqueous HCl, it was ascertained from Hall measurements that there existed, in some samples, a thin layer of highly conducting GaAs at the surface of the semi-insulating GaAs substrate. The Hall mobility of such a layer was measured to be ~ 2000 cm²/V-sec. By sandblasting the GaAs surface with alumina powder, the conducting GaAs layer could be removed; it was estimated, by further etching, that the thickness of these interfacial layers were between 2 and 10 μm. In Table I the impurity concentrations at the surface of a Cr-doped GaAs substrate are compared before and after removal of the interfacial conducting layer by sandblasting.

As can be seen from the table, there is a high concentration of impurities at the interfacial layer. These impurities probably have diffused into the GaAs from the AlAs during growth. The impurity concentration of silicon is sufficiently in excess of the Cr compensation to make the semi-insulating Cr-doped GaAs n-type. Furthermore, calculations, assuming a reasonable value for the diffusivity, have shown that typical growth rates may be comparable to the diffusion rate of Si at growth temperatures, indicating that the Si contamination of the semi-insulating GaAs substrate could arise from Si impurities present in the AlAs. Thus, it may be concluded that, contrary to the results for other III-V compounds, electrical measurements on vapor-grown AlAs cannot be made on compensated semi-insulating substrates when diffusion of impurities is likely.

As a result, emphasis was placed on electrical data derived from thicker AlAs layers (> 4 mils) from which the GaAs substrates could be removed. Ohmic contacts were made to the AlAs by a combination of ultrasonic soldering with indium followed by an anneal in H_2 at 800°C for 2 min. In Table II are listed electrical properties and impurity analyses of AlAs epitaxial layers with the GaAs substrates removed. Table II indicates that silicon is the main donor in this vapor-grown AlAs.

The room-temperature electron mobility of 280 cm²/V-sec obtained for sample C is higher than the highest previously reported value of 180 cm²/V-sec obtained by Whitaker (5). The higher mobility value found in this study may still be representative of compensated material, perhaps due to Si self-compensation such as found in $Al_{1-x}Ga_xAs$ grown from Ga solution (8). This hypothesis is consistent with the mass spectrographic analysis which shows that the amounts of species which are probably compensators (Fe, Cu, Mg) are quite low in sample B, while the silicon contamination is quite high.

The cracking of the thinner epitaxial AlAs layers upon attempts to remove the GaAs substrate is indicative of strain at the interface. It is noteworthy that at the growth temperature the lattice match between AlAs and GaAs is almost perfect (9), indicating that this is not the source of the strains. Instead, the strain is probably due to the differential thermal contraction

Table II. Electrical properties and chemical analyses of vapor-grown AlAs removed from GaAs substrates

Sample	Temp, °K	N_D-N_A electrons/cm³	μ cm²/V-sec	Impurity analysis technique	Fe	Cu	Mg	Si	
A	298	1.4×10^{18}	95	Mass spec[1]	1.7	0.6	1.0	110	ppma
B	298	6.4×10^{18}	75	Mass spec[1]	1.2	1.0	1.6	200	ppma
	77	2.0×10^{17}	18						
C	298	3.6×10^{17}	280	Emission spec	2	2	15	30	ppma
D	298	5.4×10^{17}	220						

[1] In all the mass spectrographic analyses, impurity levels of C, O, and F were consistently observed. These levels are thought to be associated with surface contamination since their concentrations decrease as more of the surface is removed during analysis.

(9). This hypothesis is consistent with the fact that the dislocation densities found by electron microscopy in the grown AlAs layers are comparable to that of the starting substrates ($\sim 10^5/cm^2$).

Thermochemical Analysis

Analysis of the thermochemistry of the aluminum arsenide vapor growth was made to better understand the growth of AlAs and provide a compiled data source to give insight for the future growth of $Al_xGa_{1-x}As$ and other mixed aluminum compounds.

Three primary sources of data were employed. The JANAF tables (10) were used for data on AlCl, $AlCl_3$, and HCl; the values derived from this source for the important reactions present in the system are shown as solid lines in Fig. 2 and 3. Values derived from recent work by Kikuchi *et al.* (11), more in agreement with the bulk of previous measurements, are indicated as dashed lines in Fig. 2 and 3. The free energy of formation of AlAs is given by Hoch and Hinge (12), who used a Knudsen effusion cell to measure vapor pressures between 1350° and 1530°K. On this basis, the extrapolated values are estimated to be reliable within ± 50°C about the measured temperature range. The free energy of formation was reduced to the liquid aluminum standard state by taking values for the free energy of evaporation from Hultgren *et al.* (13).

Although there are some discrepancies between the various sources of thermodynamic data, certain conclusions may still be drawn. It is assumed that the volume fractions of the various gases, in the growth tube, are equal to their partial pressures. This is a valid assumption since the system is held at a constant pressure of 1 atm by a small head of silicone oil at the gas exit, and the volume fractions of the gases are all measured at room temperature.

It must first be ascertained what gaseous species enter the growth or mixing chamber. If it is assumed that the various species have come to equilibrium, according to data accumulated by Ruehrwein, at 1000°C and an incoming AsH_3 pressure of 2×10^{-2} atm (14), the AsH_3 has completely decomposed ($<<$ 0.01% undecomposed) and the amounts of As_2 and As_4 coexisting are 20 and 80%, respectively. Employing the data of Stull and Sinke (15), 70% As_2 and 30% As_4 exist at 1000°C at equilibrium. In both cases, little of the As species is present ($<$ 0.1%). Even though the calculations do not clearly indicate the predominant arsenic species, As_2 is used as the standard state for the reactions considered in Fig. 2 and 3. The assumption is justified because departures from equilibrium will tend to favor the simpler As_2 molecule; also, as shown in Fig. 2, there is only a small difference in free energy of formation of AlAs between the As_2 and As_4 standard states.

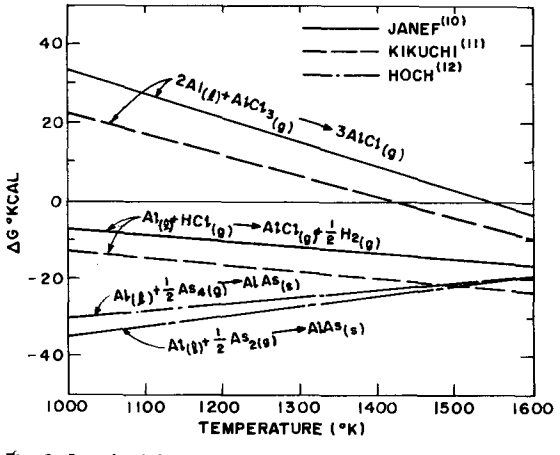

Fig. 2. Standard free energy changes for aluminum reactions

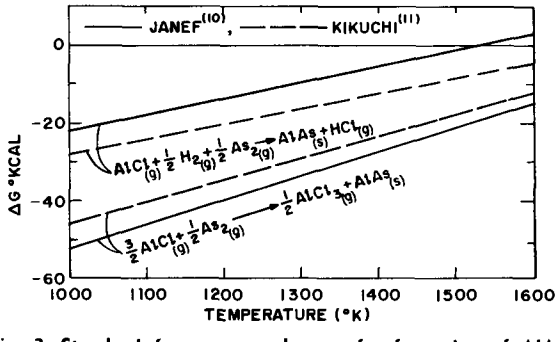

Fig. 3. Standard free energy changes for formation of AlAs in vapor-growth system.

In the aluminum zone, the picture is much clearer; in equilibrium at 1000°C and an incoming HCl pressure of 2×10^{-3} atm, AlCl is the predominant species. Using the JANAF tables, calculations show that 99.5% is AlCl and 0.5% is $AlCl_3$, while from the data of Kikuci 99.8% of the reactive gas is AlCl. Calculations with both data indicate that a negligible amount of HCl will remain unreacted at equilibrium.

The equilibrium products for the reactions taking place on mixing of the As_2 and AlCl at 1000°C can now be calculated. The two possible reactions forming AlAs are

$$AlCl + \frac{1}{2}H_2 + \frac{1}{2}As_2 \rightarrow AlAs + HCl \quad [1]$$

$$3AlCl + As_2 \rightarrow 2AlAs + AlCl_3 \quad [2]$$

Ignoring the small diluent effect of mixing the As_2 and AlCl from the JANAF data, both reactions will result in almost complete reaction of AlCl to form AlAs, 85% if HCl is the only product and 96% for $AlCl_3$ product. Kikuchi's data indicate 99% conversion for HCl and 90% for an $AlCl_3$ product. Due to the differences in free energies from the two sources, a dominant reaction cannot be chosen. The over-all reaction in the mixing zone is

$$5AlCl + 2As_2 + H_2 \rightarrow 4AlAs + 2HCl + AlCl_3 \quad [3]$$

This reaction does go to completion but the ratio of HCl to $AlCl_3$ is ambiguous from the available data.

It should be noted that, for the various reactions taking place in the AlAs growth system, an examination of the signs of the free energy changes alone will not lead to proper conclusions about the gaseous species involved. One of the major factors controlling these reactions is the low partial pressures of the reactive gaseous compounds. Only if all the gases are in their standard states, 1 atm, can the sign or magnitude of the various free energy changes be used as a criterion for choosing dominant reaction.

Although it is difficult to make precise quantitative statements from the available data, it should be possible to predict some temperature range where, at the present flow rates, the reactants forming AlAs should not react completely. The reactive gases may then be mixed in one temperature zone and the product deposited at some lower temperature as is done for the growth of GaAs. By examination of Fig. 3, it may be seen that at temperatures in excess of 1300°K the dominant reaction is the one that yields HCl as the product. An arbitrary temperature to employ as a mixing temperature would be the point at which the reaction only proceeds 25% to completion. This temperature is ~1160°C from the JANAF data and ~1300°C from Kikuchi's data. The temperatures necessary to test this hypothesis were not attainable in the present growth system; and, in use, equilibrium was only approached. Although quantitative data are difficult to derive from this growth system, it has nevertheless been observed that as the temperature is raised in the reaction zone the growth region tends to spread out. Thus, as indicated by the equilibrium anal-

ysis, complete reaction is not taking place at the point of mixing of reactive gases.

In summary, the vapor growth of AlAs from AsH_3 and AlCl, in the temperature range accessible in the present experiments and reactant concentration necessary for single-crystal growth, occurs at the point of mixing of the two reactant gases. This is distinct from GaAs vapor growth where mixing occurs at one temperature and deposition occurs at some lower temperature. This immediate deposition of AlAs is consistent with the given thermochemical analysis. Furthermore, AlAs has been shown to be a wide band gap semiconductor with a higher electron mobility than GaP and a stability which allows sufficient time for device fabrication and protection.

Acknowledgments

Acknowledgments are to W. L. Harrington and H. Whitaker for mass and emission spectroscopy, respectively, M. S. Abrahams for electron microscopy, W. M. Anderson for technical assistance, and D. Richman, L. R. Weisberg, and R. Enstrom for helpful discussion.

Manuscript submitted Jan. 20, 1971; revised manuscript received *ca.* April 13, 1971. This paper, in part, was Paper 102 presented at the Los Angeles Meeting of the Society, May 11-15, 1970.

Any discussion of this paper will appear in a Discussion Section to be published in the June 1972 JOURNAL.

REFERENCES

1. V. W. Kischio, *Z. Anorg. Allgem. Chem.*, **328**, 187 (1964).
2. H. M. Manasevit, Electrochem. Soc. Meeting, May 4-9, 1969.
3. J. J. Tietjen and J. A. Amick, *This Journal*, **113**, 724 (1966).
4. D. E. Bolger and B. E. Barry, *Nature*, **199**, 1287 (1963).
5. J. Whitaker, *Solid-State Electron.*, **8**, 649 (1965).
6. C. J. Nuese, A. G. Sigai, M. Ettenberg, J. J. Gannon, and S. L. Gilbert, *Appl. Phys. Letters*, **17**, 90 (1970).
7. M. R. Lorenz, R. Chicotka, and G. D. Pettit, *Solid-State Commun.*, **8**, 693 (1970).
8. H. Kressel, F. Z. Hawrylo, and N. Almeleh, *J. Appl. Phys.*, **40**, 2248 (1969).
9. M. Ettenberg and R. J. Paff, *ibid.*, **41**, 3926 (1970).
10. Chow. JANAF Thermochemical Tables (1964).
11. T. Kikuchi, T. Kurosawa, and T. Yagihashi, *Trans. Japan Inst. Metals*, **122**, 5 (1964).
12. M. Hoch and K. S. Hinge, *J. Chem. Phys.*, **35**, 451 (1961).
13. R. Hultgren, R. L. Orr, P. D. Anderson, and K. K. Kelley, "Selected Values of Thermochemical Properties of Metals and Alloys," John Wiley & Sons, New York (1963).
14. R. A. Ruehrwein, Monsanto Research Corp., Tech. Rpt. AFML-TR-68-319 (1968).
15. D. R. Stull and G. C. Sinke, *Advan. Chem. Series*, **18** (1956).

The Phase Diagrams of the Systems $PbCl_2$-UCl_4 and $PbCl_2$-UCl_3

J. L. Borowitz, R. Rafaeloff,[1] and A. Roy[2,*]

Soreq Nuclear Research Centre, Yavne, Israel

ABSTRACT

The phase diagrams of the salt mixtures UCl_4-$PbCl_2$ and UCl_3-$PbCl_2$ have been investigated by means of thermal analysis. There is a single eutectic at 50 mole per cent (m/o) UCl_4 and 346°C in the UCl_4-$PbCl_2$ system. A compound with incongruent melting point, of a composition $6PbCl_2$:$1UCl_4$ decomposing at 386°C is apparent. The melting points of the pure salts, as measured, are 503°C for $PbCl_2$, 590°C for UCl_4. The UCl_3-$PbCl_2$ system has a single eutectic at 11 m/o UCl_3 and 470°C, with no peritectic reaction. A heat effect at 342°C was noted. The melting points of the pure salts, as measured are for $PbCl_2$ 502°C for UCl_3 841°C. X-ray diffraction analyses gave no indication of solid solution in either system. Analysis of both the phase diagrams according to the Van't Hoff equation indicates that both systems behave like ideal mixtures [in accordance with Temkin's (1) model] oversignificant concentration ranges.

Phase diagrams of mixtures of UCl_4 and alkali metal chlorides have been investigated by Barton *et al.* (2), by Kuroda and Suzuki (3), and by Bogacz and Trzebiatowski (4). The last showed the mixtures to be nonideal due to the formation of complexes in the melt. Kuroda and Suzuki also examined the UCl_4-alkaline earth chloride systems.

The present research shows that melts of uranium and lead chlorides approach ideality, indicating that the different charges on the cations do not cause irregularity in the molten salt structure (5).

Experimental

Materials.—Reagent grade (Baker Analyzed) $PbCl_2$ of specified purity 99.5% was dried by heating under vacuum. The temperature was raised at approximately 100°C per hr until just below the melting point.

UCl_4 specified as chemically pure, obtained from A. D. Mackay, Inc., U.S.A., was purified by vacuum sublimation. This was done in an apparatus consisting of four tubes 250 mm long and 36 mm in diameter joined end-to-end horizontally by tubing of smaller diameter. The UCl_4 was placed in one end tube, and this end was sealed. The apparatus was evacuated from the other end to 10^{-3}-10^{-4} mm Hg. The tube containing the UCl_4 was heated to 500°C, the second tube to 325°C, and the third to 250°C, and the sublimation carried out at these temperatures. UCl_4 sublimed into the second tube, while more volatile impurities condensed mainly after the third tube. A 120g batch could be purified in this way in 6-8 hr, dark green crystals of UCl_4 being obtained. At the end of the run the tube containing the sublimed UCl_4 was sealed at both ends and opened in a dry box. This material normally had

[1] To whom correspondence should be addressed.
[2] Present address: University of The Negev, Beer-Sheva, Israel.
* Electrochemical Society Active Member.
Key words: uranium chloride, lead chloride, phase diagram, uranium tetrachloride, purification.

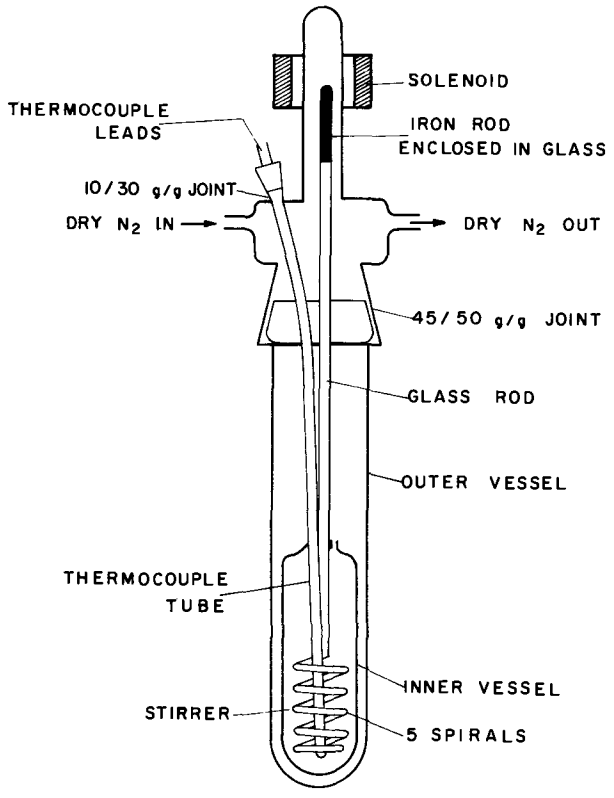

Fig. 1. Thermal analysis cell

a chlorine to uranium ratio of 4.00 ± 0.02. The original material, analyzed spectroscopically contained less than 0.07% metal elements other than uranium. UCl_3, obtained from the same source, was used as received, after analysis.

Nitrogen gas for the inert atmosphere was passed through a column of copper chips at 550°C to remove traces of oxygen, and then through a drying tube containing Linde "Molecular Sieve 5A."

Apparatus.—The thermal analysis cell used was very similar to that described by Solomons and Janz (6), and is shown in Fig. 1. The melt was contained in a Pyrex test tube, 25 mm in diameter and 70 mm long, closed except for a 9 mm hole at the top through which the stirrer passed. The space between the stirrer and the hole was used for filling the test tube, and was afterwards closed by wrapping a piece of platinum foil around the opening, in order to prevent loss of UCl_4 by sublimation. The thermocouple well was sealed into the top of the test tube, as shown.

The stirrer was a glass helix with five spirals extending over a length of 30 mm. A piece of iron rod was encased completely in glass at the top of the stirrer extension rod, and by means of a solenoid a vigorous up-and-down movement of the stirrer could be induced, thus overcoming the high viscosity of the melts.

The test tube was kept in an atmosphere of dry nitrogen gas in the outer vessel. This gas was dried and purified by passing over copper chips at 550°C to remove traces of oxygen, and then through a drying tube containing Linde molecular sieve 5A.

The test tube was made of Pyrex for the UCl_4 experiment and of quartz for experiments with the higher melting UCl_3. The melts did not appear to affect the test tube in any way, even after a few days contact, provided moisture was rigidly excluded.

Temperature measurement.—The temperature of the melt was measured by a Chromel-Alumel thermocouple. The thermocouple was calibrated before, during, and after the measurements at the freezing points of tin, cadmium, lead, and zinc. The melting points of these metals were obtained with a reproducibility of ±0.5°C. Both temperature-time cooling and heating curves were obtained on most samples. The liquidus temperature of a salt mixture was usually taken by extrapolation across the supercooled region. Reproducibility was approximately ±1°C. The temperature was continuously recorded on a recording potentiometer and the thermocouple electromotive force was periodically checked on a Leeds and Northrup precision potentiometer.

Analysis of melts.—A freshly prepared mixture was used for the determination of each temperature-composition point on the phase diagram. After recording cooling curves some mixtures were analyzed using the procedure detailed below. The compositions were found to correspond, within the limits of accuracy of the analysis, to those based on the known weights of the compounds introduced into the reaction vessel. The latter were thus taken as the compositions of the mixtures.

The analytical procedure was to dissolve the mixture in nitric acid and to determine the chloride by the Votocek and Volhard titration methods (7).

For determination of lead and uranium, another sample was dissolved in nitric acid and evaporated twice to white fumes. The lead was then precipitated as lead sulfate by sulfuric acid. Since nitric acid dissolves lead sulfate, the solution was evaporated twice with sulfuric acid until dense white fumes were evolved. In order to separate the lead from coprecipitated UO_2Cl_2, the sulfate was dissolved in ammonium acetate solution, and reprecipitated with ammonium para-molybdate. The lead was weighed as $PbMoO_4$ (8). The separated uranium was precipitated from solution as ammonium uranate (9).

Experimental procedure.—The apparatus, which had been filled in a dry box, was placed in a tube furnace. It was evacuated at 10^{-3}-10^{-4} mm for one hour, purged with dry nitrogen for an hour, and then heated to 150°C under vacuum for one hour. After this the apparatus was cooled to room temperature under vacuum and flushed again with nitrogen. While heating and cooling curves were being obtained, a very small flow of nitrogen was maintained so that the vessel was always slightly above atmospheric pressure.

The mixture was slowly heated until it became liquid, when the stirrer was turned on. After adequate agitation to homogenize the melt, a cooling curve was obtained by lowering the power input to the furnace. Liquidus and transition points were deduced from breaks in the cooling curves. Repeated cooling curves confirmed the points with variation not greater than ±1°C.

Results and Discussion

Figure 2 is the phase diagram for the UCl_4-$PbCl_2$ system. The melting point of the pure compounds as given on the figure were found at 503°C for $PbCl_2$ and 590°C for UCl_4. A eutectic of composition 50 mole per cent (m/o) of UCl_4 is evident at 346°C, and a peritectic line at 388°C was found. This line is due to a compound of incongruent melting point and composition near 6 $PbCl_2$:1 UCl_4. The existence of this compound was confirmed by x-ray diffraction. Solidified melts of composition between 14% and 50% UCl_4 revealed diffraction lines corresponding to *d*-values of 4.08, 4.00, 2.45, and 2.05Å. These are quite distinct from the lines of pure UCl_4 and pure $PbCl_2$ as checked by us.

An attempt to isolate the $PbCl_2$-rich compound was made as follows. A mixture of 40% UCl_4, 60% $PbCl_2$ was placed in a vessel similar to the ordinary phase diagram vessel, but for two changes: (*i*) The inner vessel, containing the mixture, had a perforated bottom. (*ii*) This vessel was inserted into a close-fitting test tube. The fit here was good enough to prevent molten material leaving the vessel to any large extent until the vessel was lifted out of the test tube.

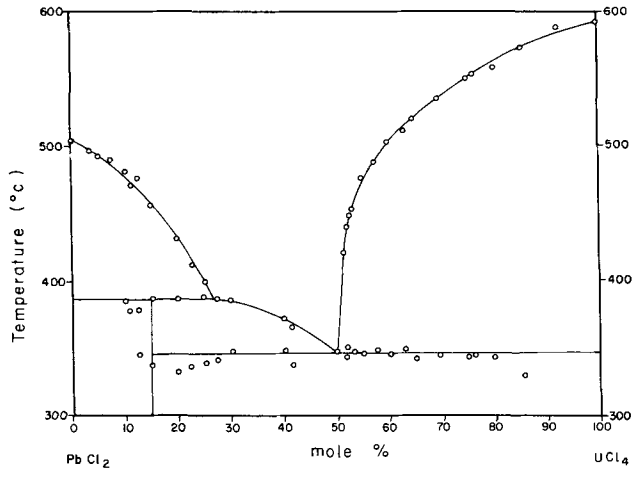

Fig. 2. Phase diagram—UCl_4-$PbCl_2$

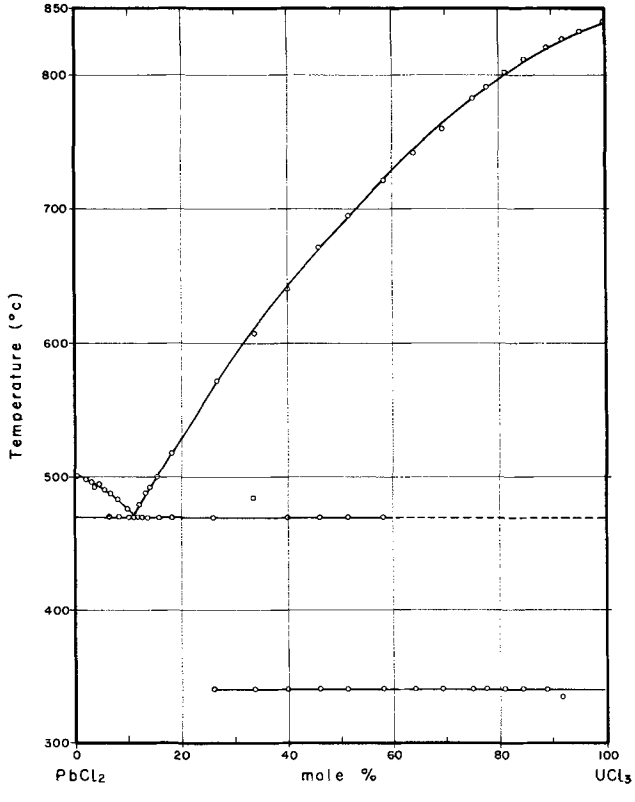

Fig. 3—Phase diagram—UCl_3-$PbCl_2$

The material was melted under the conditions used for cooling curves, stirred, and then held at a temperature between its liquidus and the eutectic temperature for two hours, while stirring. At the end of this period the inner vessel was lifted out of the test tube, filtration took place, and the system was then cooled rapidly.

An analysis of the material left in the vessel indicated a composition of 14.4% molar UCl_4, or an approximate ratio of UCl_4 to $PbCl_2$ of 1 to 6.

Comparison of the lines characteristic of $PbCl_2$ and UCl_4 obtained from solidified melts, with those of the pure compounds gave no indication of solid solution.

The phase diagram of the UCl_3-$PbCl_2$ system is shown in Fig. 3. A single eutectic at 11 m/o UCl_3 and 470°C was found. X-ray diffraction analyses on solidified melts showed no signs of solid solutions.

The heat effect at 342°C does not appear in the literature. It is shown on the diagram as it was a marked effect, but the possibility that it is an impurity (UCl_4) effect may not be excluded.

A simple thermodynamic analysis of the two phase diagrams investigated was attempted using the Van't Hoff equation.

$$\ln a_A = \frac{\Delta H_A}{R}\left(\frac{1}{T_o} - \frac{1}{T_m}\right) + \frac{\Delta C_p}{R}\left(\frac{T_o}{T_m} - 1 - \ln\frac{T_o}{T_m}\right)$$

where a_A is the activity of component A

ΔH_A is the latent heat of fusion of pure A

T_o is the melting point of pure A

T_m is the liquidus temperature.

$$\Delta C_p = C_L - C_S$$

where C_L is the specific heat of the liquid at T_m

C_S is the specific heat of the solid at T_m.

The ΔC_p correction has been neglected in the analyses on the basis that, within the concentration ranges considered, it is unlikely to exceed significantly the experimental error (10).

Figures 4 and 5 are plots of $\ln X_A$ against $1/T_m \cdot 10^3$.

Ideal behavior is seen in the UCl_4-$PbCl_2$ system between 100% and 88% $PbCl_2$ and between 100% and 85% UCl_4. In the UCl_3-$PbCl_2$ system the mixtures are approximately ideal from 100% to about 48% UCl_3.

The ideal behavior found shows the activity a_A to be equal or almost equal to the concentration X_A. This equality is in accord with Temkin's (1) model for ideal behavior of molten salts. In this model the charge of a cation does not affect its distribution on cation sites which is random. The activity thus tends to equal the concentration.

Allowing for vacancies introduced into the "lattice" of the melt by the inequality of the cation valencies,

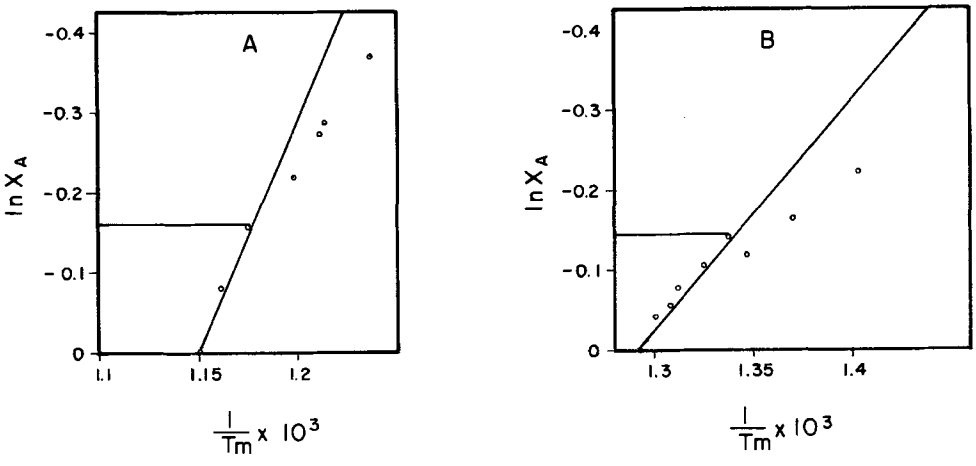

Fig. 4. Analysis of UCl_4-$PbCl_2$ for ideality. (A) $A = UCl_4$, slope $= \Delta H_f/R = 5400$ (11). Horizontal line segment denotes limit of ideality which corresponds to $PbCl_2 = 15$ m/o. (B) $A = PbCl_2$, slope $= \Delta H_f/R = 2930$ (12). Horizontal line segment denotes limit of ideality which corresponds to $UCl_4 = 12.5$ m/o.

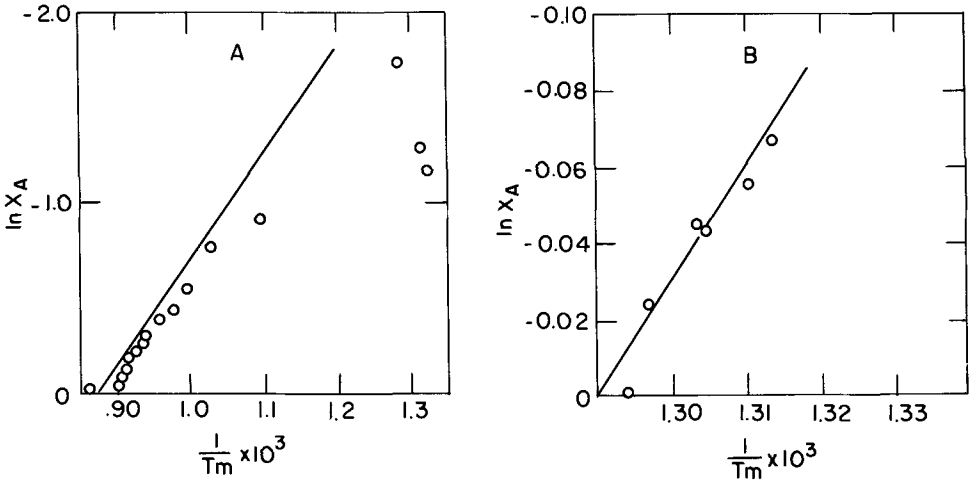

Fig. 5. Analysis of UCl_3-$PbCl_2$ for ideality. (A) $A = UCl_3$, slope $= \Delta H_f/R = 5600$ (11). (B) $A = PbCl_2$.

according to Flood, Forland, and Grjotheim (5), one arrives at the equation

$$a_{PbCl_2} = \frac{X_{PbCl_2}}{X_{PbCl_2} + 2X_{UCl_4}}$$

for the $PbCl_2$-UCl_4 system. The "equivalent" activity is thus lower than the ordinary activity. It is clear from Fig. 5 that the experimental concentrations of UCl_3 are almost always larger than the ideal concentrations, *i.e.* the activity is greater than 1. In other words, even when the behavior is not ideal, it does not tend in the direction of the "equivalent" model but in the opposite direction.

The systems investigated thus behave in a more-or-less ideal fashion, indicating that the different valencies of the cations do not cause vacancies in the lattice, *i.e.* the lead and uranium cation positions in the lattice should be interchangeable.

Manuscript submitted Jan. 5, 1970; revised manuscript received *ca.* April 5, 1971.

Any discussion of this paper will appear in a Discussion Section to be published in the June 1972 JOURNAL.

REFERENCES

1. M. C. Bell and S. N. Flengas, *This Journal*, **113**, 27 (1966).
2. R. E. Thoma, Phase Diagrams of Nuclear Reactor Materials ORNL-2548 (1959).
3. T. Kuroda and I. Suzuki, *Electrochem. Soc. Japan*, **26**, 140 (1958).
4. A. Bogacz and W. Trzebiatowski, *Roczniki Chem.*, **38**, 723 (1964); *ibid.*, **38**, 729 (1964).
5. H. Flood, T. Forland, and C. Grjotheim, quoted in ref. (1).
6. C. Solomons and G. J. Janz, *Rev. Sci. Instruments*, **29**, 302 (1958).
7. C. J. Rodden, "Analytical Chemistry of the Manhattan Project," 1st ed., Vol. VIII, p. 292, McGraw-Hill Book Co., New York (1950).
8. A. I. Vogel, "Quantitative Inorganic Analysis," p. 420, Longmans Green, London (1955).
9. C. J. Rodden, "Analytical Chemistry of the Manhattan Project," 1st ed., Vol. VIII, p. 46, McGraw-Hill Book Co., New York (1950).
10. T. Forland, "Thermodynamic Properties of Fused Salt Systems in 'Fused Salts,'" B. S. Sundheim, Editor, p. 102, McGraw-Hill Book Co., New York (1964).
11. M. H. Rand and O. Kubaschewski, "The Thermochemical Properties of Uranium Compounds," p. 69, Oliver and Boyd, Edinburgh and London (1963).
12. JANAF Thermochemical Tables. Clearinghouse for Federal Scientific and Technical Information, U.S. Dept. of Commerce, Washington, D.C.

Some Thermodynamic Properties of Zn_3As_2, Cd_3As_2, and ZnP_2

A. S. Jordan

Bell Telephone Laboratories, Incorporated, Murray Hill, New Jersey 07974

ABSTRACT

By analogy with the known mode of vaporization of Zn_3P_2, Cd_3As_2 and Cd_3P_2, the Knudsen cell pressure measurements on Zn_3As_2 of Nesmeyanov *et al.* between 601° and 751°K have been reinterpreted according to the reaction

$$Zn_3As_2(s) = 3Zn(g) + \tfrac{1}{2}As_4(g)$$

The derived free energy change for this reaction, given by

$$\Delta G^\circ(\text{kcal}) = 139 - 99.8 \times 10^{-3}T$$

is consistent with the fragmentary thermochemical data for Zn_3As_2. In addition, the free energy change for the dissociation reaction

$$ZnP_2(s) = 1/3\ Zn_3P_2(s) + 1/3\ P_4(g)$$

has been estimated as

$$\Delta G^\circ(\text{kcal}) = 21.4 - 18.4 \times 10^{-3}T$$

Finally, the entropies of fusion of Zn_3As_2 and Cd_3As_2 have been evaluated by applying the Clausius-Clapeyron equation to recent data, yielding 28.7 and 29.5 eu/g-mole, respectively.

The importance of the group II-V compounds $ZnAs_2$, Zn_3As_2, ZnP_2, and Zn_3P_2 in the interpretation of the Ga-As-Zn and Ga-P-Zn ternary phase diagrams has been emphasized by Panish (1, 2). Recently, Casey and Panish (3) lacked thermodynamic data for Zn_3As_2 in their analysis of Zn diffusion in GaAs from an invariant ternary source. Moreover, thermodynamic data for Zn_3P_2 and ZnP_2, if available, are thought to be useful to design and interpret Zn diffusion experiments in GaP from a ternary source. The diffusion of Zn into $Ga_xIn_{1-x}P$ from Zn_3P_2 has been accomplished by Hakki (4).

In addition, there is also an intrinsic interest in the properties of the II-V compounds. For example, Rubenstein and Dean (5) have very recently observed the luminescence of ZnP_2. Other semiconducting II-V compounds such as $ZnAs_2$, $CdAs_2$, Zn_3As_2, and Cd_3As_2 have also been investigated (6-8).

The volatilities of $ZnAs_2$, $CdAs_2$, Cd_3As_2, and Zn_3P_2 have been the subjects of several thermochemical studies. However, there are no thermodynamic data for ZnP_2 and the information on Zn_3As_2 is fragmentary and incorrectly interpreted. The primary objective of this paper is the derivation of consistent thermodynamic data for Zn_3As_2 by the reinterpretation of available measurements. Then, the standard heat of formation and entropy of ZnP_2 are estimated by comparison with the properties of other arsenides and phosphides. These thermodynamic data for Zn_3As_2 and ZnP_2 were found to be useful in recent work (9) concerned with the solid solubility of Zn in GaP and GaAs. In addition, the entropies of fusion of Zn_3As_2 and Cd_3As_2 are evaluated by the Clausius-Clapeyron equation from existing pressure-temperature and density data. Finally, the entropies of fusion of $ZnAs_2$, ZnP_2, and Zn_3P_2 are estimated.

The Vaporization and Some Thermodynamic Properties of Zn_3As_2

Nesmeyanov *et al.* (10) have measured the vapor pressure of Zn_3As_2 between 601° and 751°K by means of a Knudsen cell. The analysis of the resulting condensate, containing radioactive Zn and As, led these authors to believe that the predominant mode of evaporation of Zn_3As_2 proceeds according to

$$Zn_3As_2(s) = Zn_3As_2(g) \qquad [1]$$

Consequently, Nesmeyanov and his associates (10) expressed the observed pressure of $Zn_3As_2(g)$, denoted by p_{obs}[1] in the present paper, in the usual form as

$$-RT \ln p_{obs} = 39.7 - 28.3 \times 10^{-3}T \qquad [2]$$

in units of kcal. These authors have also proposed a mode of evaporation similar to Eq. [1] for Cd_3As_2.

However, comparing Bourdon gauge and dew-point measurements on Cd_3As_2, it was demonstrated by Lyons and Silvestri (11) that this compound, which is also in the group II-V family together with Zn_3As_2, thermally dissociates according to the reaction

$$Cd_3As_2(s) = 3Cd(g) + \tfrac{1}{2}As_4(g) \qquad [3]$$

The mass spectrometric work of Westmore *et al.* (12) has confirmed the above result.

Recently, mass spectrometric studies by Schoonmaker *et al.* (13) have revealed that at elevated temperatures Zn_3P_2 also decomposes into the component gases (*i.e.*, into $\tfrac{1}{2}P_4(g)$ and $3Zn(g)$. Likewise, Cd_3P_2 (14) follows the aforementioned sublimation process.

Therefore, it is reasonable to propose that, contrary to the interpretation of Nesmeyanov *et al.* (10), Zn_3As_2 dissociates according to

$$Zn_3As_2(s) = 3Zn(g) + \tfrac{1}{2}As_4(g) \qquad [4]$$

The reinterpretation of Nesmeyanov *et al.*'s data, represented by Eq. [1], for the correct mode of evaporation, as expressed above, is possible by the extension of a procedure established by McCabe (15) and also by Goldfinger and Jeunehomme (16) for the analysis of the Knudsen evaporation of II-VI compounds. Ac-

Key words: II-V compounds, vaporization, heat of fusion, heat of formation.

[1] Nesmeyanov *et al.* (10) utilized the usual Knudsen equation to calculate p_{obs} from their experimental data. Although the actual orifice area for each vapor pressure determination was not tabulated, these authors have emphasized that the orifice area was varied from run to run and, in addition, the sample area was at least 1000 times larger than the orifice area. The resulting ln p_{obs} plotted as a function of reciprocal temperature showed no systematic variation from a straight line, indicating that the measurements were insensitive to changes in the orifice area. Hence, even if the condensation coefficient departs from unity, it is reasonable to assume that the experimental arrangement of Nesmeyanov *et al.* (10) leads to p_{obs} which nearly equals the equilibrium pressure in the temperature range under study.

cordingly, if the effusing species were $Zn_3As_2(g)$, then in Knudsen evaporation p_{obs} would be given by

$$p_{obs} = \frac{\alpha w}{\sqrt{M}} \quad [5]$$

where α is a constant of proportionality incorporating T, the time of the experiment and the "effective" orifice area, and M is the molecular weight of Zn_3As_2 of total weight loss w. However, if the predominant effusing species, as suggested in Eq. [4], are Zn(g) and $As_4(g)$, then the partial pressures of these species, denoted by p_{Zn} and p_{As4}, respectively, are of the form

$$p_{Zn} = \frac{\alpha}{\sqrt{M_{Zn}}} \frac{3M_{Zn}w}{M} = 3\left(\frac{M_{Zn}}{M}\right)^{1/2} p_{obs}$$

and

$$p_{As4} = \frac{\alpha}{\sqrt{M_{As4}}} \frac{M_{As4}w}{2M} = \frac{1}{2}\left(\frac{M_{As4}}{M}\right)^{1/2} p_{obs} \quad [6]$$

where the M_i's are the molecular weights of the designated species.

The equilibrium constant, K, for Eq. [4] is given by

$$K = p_{Zn}{}^3 p_{As4}{}^{1/2} \quad [7]$$

Substituting Eq. [6] into Eq. [7] and taking the logarithms of both sides, one finds

$$-RT \ln K = -3.5\, RT \ln p_{obs} - RT \ln \frac{27 M_{Zn}{}^{3/2} M_{As}{}^{1/4}}{M^{7/4}} \quad [8]$$

Introducing the p_{obs} of Nesmeyanov *et al.* (10) from Eq. 2 into Eq. [8], one obtains the following free energy change, $\Delta G°$, for Eq. [4]

$$\Delta G°\,(\text{kcal}) = 139 - 99.8 \times 10^{-3} T \quad [9]$$

where $\Delta H° = 139$ kcal and $\Delta S° = 99.8$ eu are the second law enthalpy and entropy changes for Eq. [4], respectively, at 676°K (mid-temperature of Nesmeyanov *et al.*) (10).

The free energy equation given in Eq. [9] is reasonable in comparison with the free energy determination of Schoonmaker *et al.* (13) by means of torsion effusion and torsion surface vaporization measurements between 620°-820°K for the reaction

$$Zn_3P_2(s) = 3Zn(g) + \tfrac{1}{2}P_4(g)$$

which was reported to be

$$\Delta G°\,(\text{kcal}) = 144 - 107 \times 10^{-3} T \quad [10]$$

In particular, one finds combining the values of $\Delta S°$ in Eq. [9] and [10] with the standard entropies of gaseous species involved, obtained from Stull and Sinke (17), that the standard entropies of $Zn_3As_2(s)$ and $Zn_3P_2(s)$ at 676°K are 73 and 61.2 eu/g-mole, respectively. The corresponding entropies derived by the Neumann-Kopp rule are 72.9 and 65.9 eu/g-mole, respectively. Therefore, taking into account the reported ±6 eu uncertainty in the entropy given by Schoonmaker *et al.* (13), one concludes that the entropy of Zn_3As_2 is consistent with that of Zn_3P_2.

It can further be shown that Eq. [9] is also consistent with the available fragmentary thermodynamic data for Zn_3As_2. According to the calorimetric measurement of Ariya *et al.* (18), the enthalpy change at 298°K for the reaction

$$Zn_3As_2 = 3Zn(s) + 2As(s) \quad [11]$$

is 30.5 kcal. $\Delta H°$ for Eq. [4] at 298°K can be readily calculated by means of Kirchhoff's equation from the known $\Delta H°$ at 676°K and the appropriate heat capacity functions. If it is assumed that the heat capacity of Zn_3As_2 obeys the Neumann-Kopp rule,[2] then taking the heat capacity functions for the solid and gaseous elements from Kelley (19), one obtains 141.9 kcal for $\Delta H°$ of Eq. [4] at 298°K by an essentially second law procedure. Adding the heats of condensation of 3Zn(g) and $\tfrac{1}{2}As_4(g)$, tabulated by Stull and Sinke (17), to this result, one finds that $\Delta H°$ at 298°K for Eq. [11] is 31.1 kcal, in very good agreement with Ariya *et al.*'s (18) measurement. An alternative third law treatment of the raw data of Nesmeyanov *et al.* (10) results in $\Delta H° = 30.4 \pm 1$ kcal for Eq. [11] at 298°K.[3] By an analogous second law procedure, starting with the $\Delta S°$ for Eq. [4] taken from Eq. [9], one gets $\Delta S° = 0.5$ eu for Eq. [11] at 298°K, in almost complete accord with the Neumann-Kopp rule; hence, the recommended $S°$ of Zn_3As_2 is 47 eu/g-mole at 298°K.

Sirota and Smolyarenko (20) have recently reported that emf measurements between 700°-800°K for the reaction $3Zn(l) + 2As(s) = Zn_3As_2(s)$ yield $\Delta G° = -31.0 \pm 4$ kcal. This result presumably refers to the middle of their temperature range, 750°K. An extrapolation of Eq. [9] to 750°K in combination with the pertinent free energies of condensation as tabulated by Stull and Sinke (17) gives $\Delta G° = 29.2$ kcal for the above reaction, in reasonable agreement with the value of Sirota and Smolyarenko (20). Unfortunately, the derived $\Delta H°$ and $\Delta S°$ values of these authors are inconsistent; hence, in the absence of any information on the temperature dependence of the emf, no further comparisons can be made.

Estimated Thermodynamic Properties of ZnP_2

Having analyzed the dissociation pressure of $ZnAs_2$ as determined by Bourdon gauge and dew-point techniques, Lyons (21) has concluded that this compound dissociates according to

$$ZnAs_2(s) = 1/3\, Zn_3As_2(s) + 1/3\, As_4(g) \quad [12]$$

and

$$\Delta G°\,(\text{kcal}) = 18.8 - 18.5 \times 10^{-3} T$$

between 885°-1013°K. Likewise, it has been demonstrated by Lyons and Silvestri (11) that the decomposition of $CdAs_2(s)$ follows the above reaction.

Unfortunately, as yet there have not been any measurements either on the mode of decomposition or the thermodynamic properties of ZnP_2. However, there is no reason to doubt that its decomposition in analogy with Eq. [12] proceeds according to

$$ZnP_2(s) = 1/3\, Zn_3P_2(s) + 1/3\, P_4(g) \quad [13]$$

In order to estimate the free energy change at elevated temperatures, say at 700°K, for Eq. [13], it is at first necessary to estimate the heat of formation and standard entropy of ZnP_2 at 298°K.

In Table I the heats of formation per g-atom at 298°K, $\Delta H°$, of $CdAs_2$, $ZnAs_2$, Cd_3As_2, Zn_3As_2, and Zn_3P_2 from their solid elements are listed together with their respective standard entropies per g-atom, $S°$. Noting that the atoms in the semiconducting compounds ZnP_2 and $ZnAs_2$ are tetrahedrally coordinated (22), one would expect periodic trends in the thermodynamic properties of $CdAs_2$, $ZnAs_2$, and ZnP_2, in comparison with the III-V compounds obtained by replacing Cd and Zn with group III elements in the same row of the periodic system. Therefore, the most recent or best values of $\Delta H°$ and $S°$ for InAs, GaAs, and GaP are also listed in Table I. In addition, $\Delta H°$ and $S°$ for the II-VI compounds CdSe, ZnSe, and ZnS are given.

The tabulated values of $\Delta H°$ and $S°$ for the Zn and Cd arsenides and phosphides had to be derived from the available high-temperature data. $\Delta H°$ and $S°$

[2] According to Robinson and Bever (33), this assumption holds within better than 4% for Mg_3Sb_2, a similar II-V compound.

[3] As the free energy function ($FEF = G°(T) - H°(298)/T$) of Zn_3As_2 is not known, a rough estimate of the FEF had to be obtained. By a combination of the known heat capacity equation of Zn_3N_2 (19) with an *a priori* estimate of the $S°$ of Zn_3As_2 at 298°K, the FEF was computed following the usual thermodynamic procedure (34). The $S°$ was estimated by the averaging of the $S°$'s of Zn_3Sb_2 (19) (63.6 eu/g-mole) and Zn_3P_2 (36 eu/g-mole from Table I) at 298°K. Taking the FEF's for the gaseous species from Stull and Sinke (17), the third law method yields the $\Delta H°$ for Eq. [4] at 298°K which can be readily converted to the desired $\Delta H°$ for Eq. [11].

Table I. Enthalpies of formation and standard entropies at 298°K of some arsenides and phosphides

	$-\Delta H°$ (kcal/g-atom)	Ref.	$S°$ (eu/g-atom)	Ref.
$CdAs_2$	1.6		9.8	
$ZnAs_2$	6.5		6.7	
ZnP_2	8.1[a]		4.8[a]	
Cd_3As_2	2.6		11.4	
Zn_3As_2	6.2		9.4	
Zn_3P_2	7.6		7.2	
InAs	7.4	(32)	9.05	(28)
GaAs	10.4	(31)	7.67	(28)
GaP	12.2	(29)	5.98	(29)
CdSe	16.2	(16)	11.5	(16)
ZnSe	19.5	(30)	9.9[b]	(16)
ZnS	24.6	(30)	6.9	(25)

[a] Estimated.
[b] May be 1.5 eu/g-atom too high as in the case of ZnTe (34).

for Zn_3As_2 have been evaluated in the previous section. A similar procedure has been followed in the calculation of the standard values for Cd_3As_2 and Zn_3P_2. In the case of $ZnAs_2$, Lyons' (21) pressure data between 885°-1013°K yield $\Delta H° = 18.8$ kcal and $\Delta S° = 18.5$ eu for Eq. [12] at 950°K. Assuming the validity of the Neumann-Kopp rule for the specific heat of $ZnAs_2$ and Zn_3As_2 and taking the C_p of $As_4(g)$ from Kelley (19), one obtains $\Delta H° = 20.3$ kcal and $\Delta S° = 21$ eu for Eq. [12] at 298°K by an application of Kirchhoff's equation. This in combination with the data for Eq. [11] and the heat of condensation and standard entropy of 1/3 $As_4(g)$ yields $\Delta H° = 19.5$ kcal at 298°K for the reaction

$$ZnAs_2(s) = Zn(s) + 2As(s) \qquad [14]$$

and $S° = 20.1$ eu/g-mole. The data of Lyons and Silvestri (11) for $CdAs_2$ have been analyzed by a similar procedure.

The periodic trends in $\Delta H°$ and $S°$ per g-atom of the triads of compounds listed in Table I are immediately obvious. Therefore, it is suggested that $\Delta H°$ for

$$ZnP_2(s) = Zn(s) + 2P(s) \qquad [15]$$

at 298°K should be estimated by adding to the $\Delta H°$ per g-atom of $ZnAs_2$ the average of the $\Delta H°$ differences between Zn_3As_2 and Zn_3P_2 and between GaAs and GaP. An analogous procedure is proposed for the estimation of $S°$ of ZnP_2. Carrying out the calculations, one finds $\Delta H° = 24.3$ kcal for Eq. [15] and $S° = 14.4$ eu/g-mole.

Finally, based on the above values for Eq. [15] and the data of Schoonmaker *et al.* (13) for Zn_3P_2, reversing the method used to evaluate $\Delta H°$ and $S°$ for Eq. [14] from Eq. [12], one obtains for Eq. [13] at 700°K

$$\Delta G°(\text{kcal}) = 21.4 - 18.4 \times 10^{-3}T \qquad [16]$$

which is comparable with Lyons' (21) $\Delta G°$ (Eq. [12]) for $ZnAs_2$.

The Entropies of Fusion of Zn_3As_2 and Cd_3As_2

Recently, Jayaraman *et al.* (23) have investigated the dependence of the melting points, T_f, of Zn_3As_2 and Cd_3As_2 on the total pressure, p, and have given measured values of dT_f/dp for these compounds. In addition, Glazov and Kasymova (24) have reported the densities of solid Zn_3As_2 and Cd_3As_2 and of their respective melts. Thus, the entropy of fusion, ΔS_f, of these compounds can be readily computed from the Clausius-Clapeyron equation written in the form

$$\Delta S_f = \frac{dp}{dT_f}\Delta V_f = \frac{dp}{dT_f}\left(\frac{M}{d_l} - \frac{M}{d_s}\right) \qquad [17]$$

where ΔV_f is the volume change of fusion, d_l and d_s are the liquid and solid densities, and M is the molecular weight of the compound. Substituting the required variables into Eq. [17], one obtains

Table II. Heats and entropies of fusion of some arsenides and phosphides

	ΔS_f (eu/g-atom)	ΔH_f (kcal/g-mole)
Zn_3As_2	5.74,[a] 5.30[b]	36.9[a]
Zn_3P_2	5.3[c]	40.0[c]
Cd_3As_2	5.94,[a] 5.25[b]	28.6[a]
$ZnAs_2$	6.5[c]	20.4[c]
ZnP_2	5.9[c]	22.2[c]

[a] Experimentally determined, based on Eq. [17].
[b] Calculated from Eq. [19].
[c] Estimated by adding 0.3 eu/g-atom to Eq. [19].

$$\Delta S_f = 28.7 \text{ eu/g-mole} = 5.74 \text{ eu/g-atom} \quad \text{for } Zn_3As_2 \qquad [18]$$

and

$$\Delta S_f = 29.5 \text{ eu/g-mole} = 5.90 \text{ eu/g-atom} \quad \text{for } Cd_3As_2$$

The corresponding heats of fusion, ΔH_f, taking T_f from Jayaraman *et al.* (23), are

$$\Delta H_f = 36.9 \text{ kcal/g-mole} \quad \text{for } Zn_3As_2$$

and

$$\Delta H_f = 28.6 \text{ kcal/g-mole} \quad \text{for } Cd_3As_2$$

The above ΔS_f's seem to be reasonable in comparison with the theoretical estimate calculated by a method recommended by Kubaschewski *et al.* (25). According to these authors, the entropy of fusion/g-atom for an ordered compound of formula A_mB_n is given by

$$\Delta S_f = \frac{m\Delta S_f(A) + n\Delta S_f(B)}{m+n} - R\left(\frac{m}{m+n}\ln\frac{m}{m+n} + \frac{n}{m+n}\ln\frac{n}{m+n}\right) \qquad [19]$$

in units of eu/g-atom where $\Delta S_f(A)$ and $\Delta S_f(B)$ are the entropies of fusion of the pure elements A and B, respectively. Substituting the ΔS_f's of the elements from Stull and Sinke (17) into Eq. [19], one finds $\Delta S_f = 5.30$ eu/g-atom and 5.25 eu/g-atom for Zn_3As_2 and Cd_3As_2, respectively, which compare favorably with the values in Eq. [18].

Estimated Entropies of Fusion of $ZnAs_2$, ZnP_2, and Zn_3P_2

Noting that the above-calculated ΔS_f of Zn_3As_2 based on Eq. [19] is approximately 0.3 eu/g-atom less than the experimentally determined result (Eq. [17] and [18]), it is suggested that the ΔS_f's of ZnP_2, $ZnAs_2$, and Zn_3P_2 should be estimated by adding $\approx$0.3 eu/g-atom to the theoretical value calculated from Eq. [19]. The estimated ΔS_f's and ΔH_f's of ZnP_2, $ZnAs_2$, and Zn_3P_2 are presented in Table II together with the experimentally determined quantities of Zn_3As_2 and Cd_3As_2. In performing these calculations, the ΔS_f of P(red) was taken from the JANAF (26) tables. The melting points of $ZnAs_2$ and ZnP_2 were obtained from Hansen (27) and the recent work of Rubenstein and Dean (5). Finally, the melting point of Zn_3P_2 was estimated to be 1240° $\pm$ 20°C by adding to the melting point of Zn_3As_2 the average of the relatively constant difference between the melting points of ZnP_2 and $ZnAs_2$ (214°C) and of GaP and GaAs (227°C).

Manuscript submitted Aug. 21, 1970; revised manuscript received Feb. 24, 1971.

Any discussion of this paper will appear in a Discussion Section to be published in the June 1972 JOURNAL.

REFERENCES

1. M. B. Panish, *J. Phys. Chem. Solids*, **27**, 291 (1966).
2. M. B. Panish, *This Journal*, **113**, 224 (1966).
3. H. C. Casey and M. B. Panish, *Trans. Met. Soc. AIME*, **242**, 406 (1968).
4. B. Hakki, Abs. 74, p. 204, Electrochem. Soc. Extended Abstracts, Spring Meeting, Los Angeles, May 10-15, 1970.

5. M. Rubenstein and P. J. Dean, *J. Appl. Phys.*, **41**, 1777 (1970).
6. G. A. Silvey, *ibid.*, **29**, 226 (1958).
7. W. J. Turner, A. S. Fischler, and W. E. Reese, *Phys. Rev.*, **121**, 759 (1961).
8. G. A. Silvey, V. J. Lyons, and V. J. Silvestri, *This Journal*, **108**, 653 (1961).
9. A. S. Jordan, *This Journal*, **118**, 781 (1971).
10. A. N. Nesmeyanov, B. Z. Iofa, A. A. Strelnikov, and V. G. Fursov, *Zhur. Fiz. Khim.*, **30**, 1250 (1956).
11. V. J. Lyons and V. J. Silvestri, *J. Phys. Chem.*, **64**, 266 (1960).
12. J. B. Westmore, K. H. Mann, and A. W. Tickner, *ibid.*, **68**, 606 (1964).
13. R. C. Schoonmaker, A. R. Venkitaranan, and P. K. Lee, *ibid.*, **71**, 2676 (1967).
14. R. C. Schoonmaker and K. Rubinson, *ibid.*, **71**, 3354 (1967).
15. C. L. McCabe, *J. Metals*, **6**, 969 (1954).
16. P. Goldfinger and M. Jeunehomme, *Trans. Faraday Soc.*, **59**, 2851 (1963).
17. D. R. Stull and G. C. Sinke, "Thermodynamic Properties of the Elements," Advances in Chemistry Series, No. 18, Am. Chem. Soc.
18. S. M. Ariya, M. P. Morozova, Khuan Tszi-tao, and E. Volf, *J. Gen. Chem. U.S.S.R.*, **27**, 325 (1957).
19. K. K. Kelley, U.S. Bur. of Mines Bull. 584 (1960); and K. K. Kelley and E. G. King, U.S. Bur. of Mines Bull. 592 (1961), U.S. Govt. Printing Office, Washington, D.C.
20. N. N. Sirota and E. M. Smolyarenko, in "Chemical Bonds in Semiconductors and Thermodynamics," Consultants Bureau (Plenum Publishing Corp.), New York (1968).
21. V. J. Lyons, *J. Phys. Chem.*, **63**, 1142 (1959).
22. I. J. Hegyi, E. E. Loebner, E. N. Poor, Jr., and J. G. White, *J. Phys. Chem. Solids*, **24**, 333 (1963).
23. A. Jayaraman, T. R. Ananthraman, and W. Klement, Jr., *ibid.*, **27**, 1605 (1966).
24. V. M. Glazov and M. Kasymova, *Proc. Acad. Sci. U.S.S.R. (Dokl.), Phys. Chem. Sect.*, **183**, 803 (1968).
25. O. Kubaschewski, E. LL. Evans, and C. B. Alcock, "Metallurgical Thermochemistry," 4th Ed., Pergamon Press Ltd. (1967).
26. JANAF, Thermochemical Tables, Thermal Labs., Dow Chemical Co.
27. M. Hansen, "Constitution of Binary Alloys," McGraw-Hill Book Co., Inc., New York (1958).
28. D. Lichter and P. Sommelet, *Trans. Met. Soc. AIME*, **245**, 99 (1969).
29. C. D. Thurmond, *J. Phys. Chem. Solids*, **26**, 785 (1965).
30. "Selected Values of Chemical Thermodynamic Properties," NBS Technical Note 270-3, Washington, D.C. (1968).
31. J. R. Arthur, *J. Phys. Chem. Solids*, **28**, 2257 (1967).
32. W. Schottky and M. B. Bever, *Acta Met.*, **6**, 320 (1958).
33. P. M. Robinson and M. B. Bever, in "Intermetallic Compounds," J. H. Westbrook, Editor, John Wiley & Sons, Inc., New York (1967).
34. A. S. Jordan and R. R. Zupp, *This Journal*, **116**, 1264 (1969).

Vaporization in the PbTe-SnTe System[1]

David A. Northrop

Sandia Laboratories, Albuquerque, New Mexico 87115

ABSTRACT

The vaporization of three alloys in the PbTe-SnTe system has been investigated thermogravimetrically. The vaporization is noncongruent as SnTe, the more volatile component, is lost preferentially. Due to the similarity of the PbTe and SnTe vapor pressures, the observed differences in total effusion rates between the alloys and changes in rate expected due to noncongruency are of the magnitude of the experimental error and the vaporization appears to be congruent in gravimetric experiments. Effusion rates, composition changes, and approximate vapor pressures have been determined with the results falling between the limits given by PbTe and SnTe. The results for a commercial, (Pb,Sn)Te thermoelement are given for comparison with this work and previously published investigations.

Vaporization of alloys in the PbTe-SnTe system has been investigated as part of a continuing study of vaporization in the (Pb,Sn,Ge)Te system (1). Considerable interest has been shown in the PbTe-SnTe pseudobinary system as these alloy compositions are in use as the p-junction in several isotope power generator systems. The vaporization of three compositions was studied: $Pb_{0.91}Sn_{0.09}Te$, $Pb_{0.72}Sn_{0.28}Te$, and $Pb_{0.50}Sn_{0.50}Te$. In addition, the results for a commercial, p-type thermoelement are given which were obtained with the same effusion cells and procedures so that a direct comparison could be made.

Commercial p-type thermoelements of nominal $Pb_{0.50}Sn_{0.50}Te$ composition were used for the free surface vaporization rates given by Bates and Weinstein (2), and in the mass spectrometric effusion studies by Winchell (3). The latter investigator concluded that the vaporization was either congruent or "pseudocongruent" and occurs by the loss of SnTe and PbTe molecules in the same relative concentrations as in the solid. Sokolov *et al.* (4), on the other hand, found a SnTe-rich vapor over a $Pb_{0.52}Sn_{0.48}Te$ material, which would indicate noncongruency and a progressively Pb-enriched alloy composition. These studies are discussed in more detail later in this report.

Other studies in the PbTe-SnTe system have been concerned with determination of the phase relations (5-8), examination of the variation of lattice parameter with composition (5-7, 9-12), growth and characterization of single crystals (7, 8, 13), and investigation of electrical properties (6-8, 14, 15). The over-all results show that PbTe and SnTe form a complete range of solid solutions which exhibit nearly ideal behavior. The temperature-composition phase relations are in the shape of a simple lens with end points given by the melting points of 917° and 806°C for pure PbTe and SnTe, respectively, and a maximum difference between the liquidus and solidus of ~18°C at 45 m/o (mole per cent) SnTe (5). Lattice parameters show slight positive deviations from Vegard's law when the exact tellurium concentration is considered. The single-phase (Pb,Sn)Te compositions are all p-type and thus the field lies on the Te-rich side of the PbTe-

[1] This work was supported by the U.S. Atomic Energy Commission.

Key words: lead telluride, tin telluride, vapor pressure, effusion, thermoelement.

SnTe binary join (13). The liquidus surface of the Pb-Sn-Te ternary system has also been determined (16).

Experimental Details and Results

General.—A detailed description of the apparatus, methods, and sources of error is given elsewhere (1), and only specific details are reported here. An automatic recording balance was used and its continuous weight, time, and temperature record is particularly suited for the investigation of noncongruent vaporizations where changing rates of loss are expected.

Three alloys were made from the elements (of stated purity > 99.99%) by reaction at 950°C in evacuated quartz ampoules. The ampoules were air quenched from this temperature, and the samples were reground finer than 240 mesh and annealed at 600°C for 48 hr, also in evacuated quartz ampoules. The lead concentration was determined by polarography and the alloy composition was calculated assuming an exact $Pb_xSn_{1-x}Te$ stoichiometry. The initial alloy compositions are, to ±0.01 a/o (atomic per cent), $Pb_{0.91}Sn_{0.09}Te$, $Pb_{0.72}Sn_{0.28}Te$, and $Pb_{0.50}Sn_{0.50}Te$. Powder x-ray diffraction analyses indicated that only the alloy phase was present.

Graphite and alumina effusion cells were used, and their effective orifice areas were determined by effusion of a lead standard (1). Three types of effusion experiments were made: Type 1: Isothermal runs in which ~80 mg were effused until a constant cell weight was observed. Type 2: isothermal runs which were quenched at successive stages of vaporization and samples taken for x-ray and polarographic analyses. The initial amount of sample was ~1200 mg and two cuts and a final residue were obtained for each run. For each cut, the sample was removed from the cell, reground and mixed thoroughly, ~100 mg removed permanently for analysis, and the remainder replaced in the cell for further vaporization. Type 3: effusion runs of ~20 rate-temperature data points for the vapor pressure calculations. The initial sample weight was 800-900 mg and no more than a third was vaporized in a single run.

Vapor species.—No direct determination of the vapor species was made in this investigation. It is assumed that (Pb,Sn)Te vaporizes by the loss of molecular SnTe(g) and PbTe(g), and this assumption is based on the results for the pure end members and the following reported mass spectrometric data for the alloys. Winchell (3) observed approximately equal intensities of $SnTe^+$ and $PbTe^+$ but no Te_2^+ or higher molecular weight ions for a thermoelement of approximate composition $Pb_{0.5}Sn_{0.5}Te$. Sokolov *et al.* (4) examined the effusion of a $Pb_{0.52}Sn_{0.48}Te$ sample at 760°C and identified the following parent ions with relative intensities given in parentheses: $SnTe^+$ (132), $PbTe^+$ (100), Te_2^+ (~1), $SnTe_2^+$ (~1), and lesser amounts of $Sn_2Te_2^+$, $PbSnTe_2^+$, and $PbSnTe^+$. Unambiguous determination of the equilibrium vapor is hindered by electron impact dissociation in the mass spectrometer ion source, and atomic ions produced by fragmentation were observed in both studies.

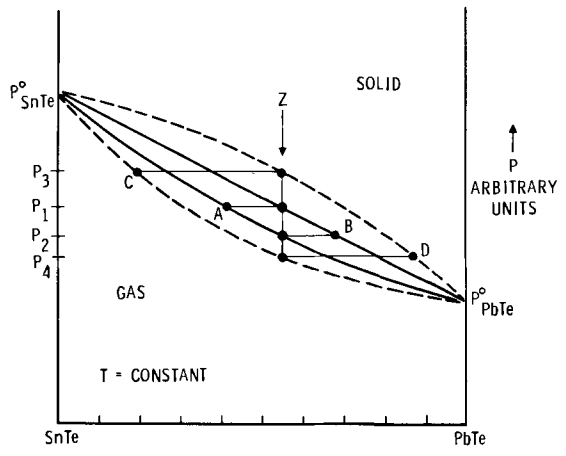

Fig. 1. Possible pressure-composition phase relations for the PbTe-SnTe system showing the compositional relations for the ideal (solid lines) and a typical nonideal (dashed lines) solid solution.

Congruency.—A noncongruent vaporization of (Pb,Sn)Te alloys was expected and was confirmed by several experiments. The prediction was made by examination of the schematic pressure-composition phase relations shown in Fig. 1 for a binary alloy system exhibiting a complete range of solid solutions. In addition, while PbTe vaporizes congruently, SnTe vaporizes noncongruently with the loss of a slight excess of Te which first produces a two-phase, Sn-SnTe assemblage, and then a very small amount of pure Sn as a final phase (1). Thus noncongruency has to be examined from two standpoints: the relative loss of SnTe with respect to PbTe and also the possibility of the formation of a metal second phase.

The results for the type 2 effusion runs are given in Table I. Each cut was analyzed polarographically for total lead content and an alloy composition was calculated on the assumption that only a stoichiometric $Pb_xSn_{1-x}Te$ phase was present. The results are semiquantitative with the uncertainty arising from both the analytical technique and possible inhomogeneities and minor phases present in the cut. Each alloy was investigated at 625°, 700°, and 825°C, but the three results were averaged in each case as no general temperature dependence could be observed.

A small portion of each cut (<1 mg) was examined by x-ray diffraction utilizing the Debye-Scherrer technique and Ni-filtered, CuKα radiation. From published reports (9), the alloy lattice constant can be related to its composition provided that the exact Te stoichiometry is known from the carrier concentration or other measurements. The lack of this information and the uncertainty that such a small portion of the total sample would accurately reflect the bulk composition precluded any quantitative analysis by x-ray methods. Qualitatively, however, comparative line shifts in the back-reflection region indicated that in every case the observed *d*-spacings became greater (increased PbTe concentration) with increased vaporization.

Table I. Alloy composition as a function of amount vaporized

Material	Initial composition	Cut A		Cut B		Residue	
		Amt lost, w/o	Composition	Amt lost, w/o	Composition	Amt lost, w/o	Composition
Type 2 effusion runs:							
$Pb_{0.91}Sn_{0.09}Te$	91/09	18	94/06	39	96/04	59	99/01
$Pb_{0.72}Sn_{0.28}Te$	72/28	19	77/23	36	78/22	63	82/18
$Pb_{0.50}Zn_{0.50}Te$	50/50	22	54/46	48	58/42	75	64/36
Residue from the type 3 effusion runs:							
Curve 1, Fig. 2	91/09					22	92/08
	91/09					22	93/07
Curve 2, Fig. 2	72/28					24	78/22
	72/28					25	77/23
Curve 3, Fig. 2	50/50					32	52/48
	50/50					31	54/46

The residues from the type 3 effusion experiments were also analyzed by the two methods. The results are also given in Table I and the same trend is found.

The possibility of the formation of a metallic second phase is more difficult to assess. If the original stoichiometric concentrations of the elements were maintained, the initial alloys should be two-phase, (Pb,Sn) and (Pb,Sn)Te, as the single-phase alloy compositions lie on the Te-rich side of the PbTe-SnTe binary join (13). However, a metal second phase could not be detected in x-ray powder patterns of either the initial alloys or any cuts from the special effusion runs. Isothermal effusion runs (type 1) to constant weight with pure SnTe resulted in a Sn residue of ~0.3 w/o. Similar experiments with the $Pb_{0.50}Sn_{0.50}Te$ alloy produced a trace residue (<0.1 w/o) which was identified by x-ray diffraction as SnO_2, and its exact origin is unknown. Pb would not be expected in the residue at a constant observed weight as its vapor pressure is of the same order of magnitude as lead telluride. In the type 1 effusion runs, care was taken to insure that the cell temperature did not overshoot the intended run temperature. During the first 5 w/o of loss, the maximum observed rate decreased by ~7% to an essentially constant rate for the balance of the run. In the noncongruent vaporization of GeTe, this rate-time behavior was interpreted as the rapid loss of excess Te to drive the over-all composition into a Ge-GeTe two-phase region (1). The same interpretation could be applied in this case, and further evidence is found in the parent Te_2^+ contribution reported by Sokolov *et al.* (4).

To summarize, the vaporization of (Pb,Sn)Te is noncongruent. The primary composition change is a decrease in the SnTe/PbTe ratio due to the preferential loss of SnTe(g). There is inconclusive evidence for the loss of additional tellurium but in amounts that should not affect the results and discussions in this report.

Effusion rates.—Two type 3 effusion runs were made with different graphite cells for each alloy. Unless assumptions are made concerning the relative vapor composition and its change due to noncongruency, the total vapor pressure cannot be calculated from the total rate of weight loss as is usually done *via* the Knudsen equation

$$P_T = \sum_i P_i = \sum_i \left(\frac{1}{A}\right) x_i \left(\frac{dw}{dt}\right)_T \sqrt{\frac{2\pi RT}{M_i}} \quad [1]$$

where A is the effective orifice area, $(dw/dt)_T$ is the total observed rate of weight loss, and x_i and M_i are the weight fraction and molecular weight of the ith vapor species. Alternatively, a quantity Q_T has been defined

$$Q_T = \left(\frac{1}{A}\right)\left(\frac{dw}{dt}\right)_T \sqrt{2\pi RT} \quad [2]$$

which is essentially proportional to the observed effusion rate and is related to the total vapor pressure by

$$P_T = Q_T \sum_i x_i \sqrt{\frac{1}{M_i}} \quad [3]$$

The reason for presenting the data in terms of Q_T is to emphasize the similarity of the observed effusion rates for this alloy system.

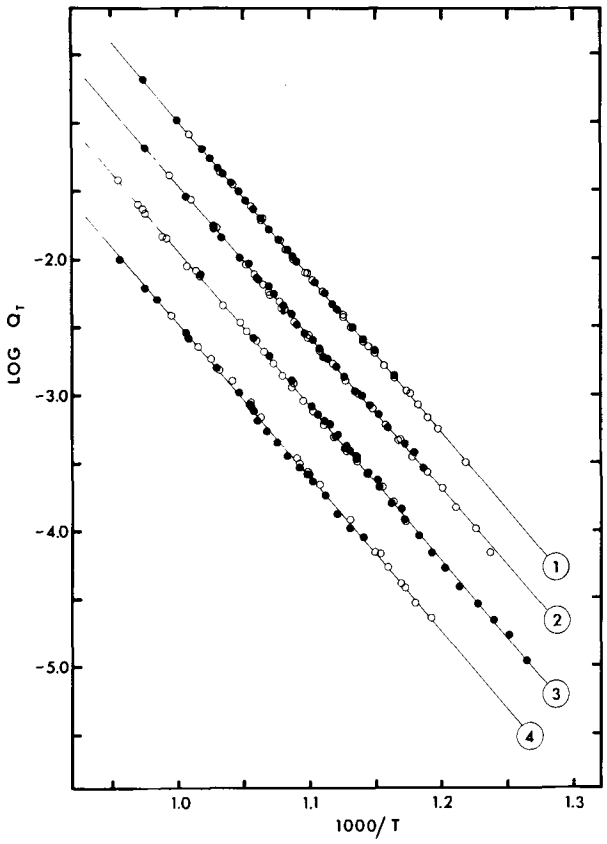

Fig. 2. Experimental data for the type 3 effusion runs expressed as log Q_T *vs.* reciprocal temperature: curve 1, $Pb_{0.91}Sn_{0.09}Te$; curve 2, $Pb_{0.72}Sn_{0.28}Te$; curve 3, $Pb_{0.50}Sn_{0.50}Te$; curve 4, thermoelement. Ordinate scale applies to curve 4; each of the other curves has been offset from the other by log Q_T = 0.50 for clarity.

If the summed term is relatively constant during an effusion run, as in the case of a large sample and small over-all weight change, then Q_T is directly proportional to P_T and a plot of log Q_T *vs.* reciprocal temperature should be essentially linear with a slope equal to the enthalpy of vaporization. Linear least-squares fit of log Q_T as a function of $1/T$ resulted in equations of the form

$$\log Q_T = (A \pm \sigma_A) + (B \pm \sigma_B)(1000/T) \quad [4]$$

where σ_i are the standard deviations associated with the constants. The results for the two effusion runs for each of the three alloys and the thermoelement are shown in Fig. 2 and summarized in Table II. Values of Q_T for PbTe and SnTe have been calculated from the average summary equation given in Tables III and V, respectively, of Ref. (1).

Steady state and equilibrium.—In these experiments, the effective orifice areas of the effusion cells ranged from 4.49 x 10^{-4} to 5.64 x 10^{-3} cm^2 and the sample was

Table II. Effusion results expressed in terms of log Q_T and the experimental enthalpy of vaporization

Material	Average temp (°C)	log $Q_T = A + B(1000/T)$ A	B	ΔH_{vap} (kcal/mole)
PbTe[1]	634	8.837 ± 0.058	−11.294 ± 0.177	51.68 ± 0.81
$Pb_{0.91}Sn_{0.09}Te$	640	9.026 ± 0.024	−11.506 ± 0.022	52 65 ± 0.10
$Pb_{0.72}Sn_{0.28}Te$	634	8.781 ± 0.038	−11.236 ± 0.035	51.42 ± 0.16
$Pb_{0.50}Sn_{0.50}Te$	634	8.989 ± 0.042	−11.426 ± 0.038	52.29 ± 0.17
SnTe[1]	635	8.972 ± 0.083	−11.360 ± 0.182	51.98 ± 0.83
Thermoelement	654	8.836 ± 0.071	−11.310 ± 0.065	51.75 ± 0.30

[1] Calculated from data given in Ref. (1).

Table III. Calculated values of log Q_T and specific effusion rates at 650°C

Material	log Q_T	Specific effusion rate (g/cm² sec)	σ[1]	$\sigma\%$[2]
PbTe[3]	−3.394	5.89×10^{-4}	0.037	±9
$Pb_{0.91}Sn_{0.09}Te$	−3.435	5.36×10^{-4}	0.009	±2
$Pb_{0.72}Sn_{0.28}Te$	−3.388	5.97×10^{-4}	0.016	±4
$Pb_{0.50}Sn_{0.50}Te$	−3.385	6.01×10^{-4}	0.021	±5
SnTe[3]	−3.331	6.81×10^{-4}	0.045	±11
Thermoelement	−3.413	5.64×10^{-4}	0.024	±6

[1] σ is the standard error of the estimate of the linear least-squares fit of log Q_T *vs.* reciprocal temperature. σ applies to the log Q_T values shown.
[2] $\sigma\%$ is σ expressed as a per cent difference between Q_{calc} and Q_{obs} and applies to the rates shown.
[3] Calculated from data given in Ref. (1).

always ground finer than 340 mesh (<75μ). The vaporization coefficients for PbTe and SnTe are greater than 0.2 (1) and the attainment of steady-state conditions is not hindered by a low α_v or a low sample surface area/orifice area ratio as discussed by Motzfeldt (17). The observed effusion rates for all compositions were essentially constant during the type 1 effusion runs to greater than a 99 w/o loss. The rates then broke essentially discontinuously to zero (a constant cell weight). Thus, as little as 1 mg of material was sufficient to produce steady-state conditions in the cell. Surface enrichment of the less volatile phase (PbTe in this case) would normally tend to hinder vaporization and the attainment of steady-state conditions and would increase the apparent activity and vapor pressure of this phase. The results of the type 1 effusion experiments and the similar vapor pressures of PbTe and SnTe show that such effects are not detectable in these gravimetric experiments. In addition, the observed effusion rates and calculated pressures appear to be independent of orifice area within the range given above and, thus, a case can be made that these results represent the equilibrium values.

Discussion

The alloy vaporization can be described in terms of the P-X phase relations given in Fig. 1, where the solid and dashed lines indicate the phase boundaries for an ideal and a typical nonideal solid solution, respectively. In the ideal case, the exact boundaries can be calculated from the solid composition and the vapor pressures of the pure end members since, by definition, $P_i = x_i P_i^\circ$. The initial equilibrium vapor composition over an alloy of composition Z is given by A at a total pressure of P_1. As vaporization proceeds, both the vapor and solid compositions shift toward the less volatile component with Z and B becoming the concentrations of vapor and solid as the last solid vaporizes. Note that the vapor is always rich in the more volatile component and has the initial alloy composition only at the end of vaporization. The equilibrium total pressure decreases from P_1 to P_2 in the course of the vaporization. The representative nonideal case shown indicates that greater compositional and pressure changes would be expected: C going to Z for the vapor, Z going to D for the solid, and P_3 decreasing to P_4.

Table III gives values of log Q_T and specific, total rates of weight loss (g/cm² sec) calculated at 650°C. The similarity in these values is striking and can perhaps explain why these alloys have been interpreted as vaporizing congruently or "pseudocongruently" (3). The rate-temperature effusion data gave no systematic changes in observed rate with total weight loss up to losses of ~30 w/o. Furthermore, in the type 1 effusion runs, a continuous, over-all decrease in rate could not be definitely identified for any of the alloy compositions outside of the small initial decrease described earlier in the congruency discussion.

Several factors combine to explain this apparent congruency in these gravimetric experiments, and the over-all result is that the expected decrease in rate due to noncongruency is less than the over-all precision of the experimental procedure. First, the standard error of the estimates between log Q_{calc} and log Q_{obs} range from 0.009 to 0.045 which correspond to uncertainties of approximately ±2 to ±11% in Q_T. These uncertainties in themselves practically cover the entire range of calculated values given in Table III. Second, the temperature can be controlled to ±½°C during the isothermal effusion runs, and a 1° temperature change varies the observed rate by ~2.5% at these values of ΔH and temperature. Finally, only small changes in observed total rate are expected due to the similar vapor pressures of SnTe and PbTe. At a given temperature, the relative effusion rates for pure SnTe and PbTe are given by

$$\frac{\left(\frac{dw}{dt}\right)_{SnTe}}{\left(\frac{dw}{dt}\right)_{PbTe}} = \frac{P^\circ_{SnTe}}{P^\circ_{PbTe}}\sqrt{\frac{M_{SnTe}}{M_{PbTe}}} \qquad [5]$$

This rate ratio has the values of 1.133 and 1.171 at 550° and 725°C, respectively. Thus, an approximate 15% decrease in rate would occur during a hypothetical effusion run in which the solid composition would change from SnTe to PbTe. It is clear from Fig. 1 that a considerably smaller decrease would be observed during the vaporization of a given alloy composition. This change during a complete isothermal effusion can be calculated exactly if it is assumed that the system behaves ideally. For a 50/50 m/o alloy at 700°C (where $P^\circ_{SnTe}/P^\circ_{PbTe} = 1.359$), the ratio of initial to final rate is 1.0222; this is a decrease of approximately 2%.

Table IV shows the maximum composition changes that can be expected for a complete equilibrium vaporization if the alloy system is ideal. In every case, the observed composition changes are greater, suggesting nonideality and phase relations similar to those given by the dashed lines in Fig. 1. The observed changes eliminate the possibility of a more complicated double-lens type of phase diagram in the composition range $Pb_{0.5}Sn_{0.5}Te$ to PbTe. However, the possibility of a pressure maxima and a congruently subliming indifferent point (18) at the SnTe-rich end of the phase diagram is still compatible with the data.

It is desirable to calculate apparent total vapor pressures from the experimental data. As the vapor composition is continuously changing and has not been measured directly at any point in these experiments, an arbitrary, "average" molecular weight has been selected for this calculation. The initial vapor composition for an ideal alloy (Table IV) was selected and

Table IV. Calculated and observed composition changes at 700°C

Material	Calculated for an ideal solid solution[1]		Observed solid composition (from Table I)
	Initial vapor composition	Final solid composition at end of a complete vaporization	
$Pb_{0.91}Sn_{0.09}Te$	88/12	93/07	99/01 after a 59 w/o loss
$Pb_{0.72}Sn_{0.28}Te$	65/35	78/22	82/18 after a 63 w/o loss
$Pb_{0.50}Sn_{0.50}Te$	42/58	58/42	64/36 after a 75 w/o loss

[1] $P^\circ_{SnTe}/P^\circ_{PbTe} = 1.359$ at 700°C.

Table V. Approximate total vapor pressures based on an arbitrary average molecular weight

Material	Selected vapor composition	Average molecular weight	Log $P_T = A + B(1000/T)$ A	B	Calculated pressure at 650°C (atm)	σ%[2]
PbTe[1]	—	—	7.575	−11.294	2.21×10^{-5}	±9
$Pb_{0.91}Sn_{0.09}Te$	88/12	324.2	7.771	−11.506	2.04×10^{-5}	±2
$Pb_{0.72}Sn_{0.28}Te$	65/35	303.8	7.540	−11.236	2.35×10^{-5}	±4
$Pb_{0.50}Sn_{0.50}Te$	42/58	283.5	7.763	−11.426	2.45×10^{-5}	±5
SnTe[1]	—	—	7.776	−11.360	2.97×10^{-5}	±11
Thermoelement	42/58	283.5	7.610	−11.310	2.30×10^{-5}	±6

[1] From Ref. (1).
[2] See Table III.

the total weight loss has been ascribed to a vapor with this average molecular weight. For this comparative calculation, the error introduced by the arbitrary choice of vapor composition and not treating the data rigorously by Eq. [1] is less than the over-all experimental uncertainty. The equations for log Q_T in Table II can then be converted to log P_T by the addition of log $(M^{-1/2})$ to the A term. The results are given in Table V and the total vapor pressure curves presented in Fig. 3. Pressures calculated at 650°C given in Table V show more clearly the relative total vapor pressures for these materials. While a variation of pressure with alloy composition is evident, these pressures are practically indistinguishable within the limits set by the pure PbTe and SnTe when the experimental uncertainties are considered. It should be emphasized that the observed effusion rates are even more similar (see Table III) than the pressure curves given in Fig. 3; the molecular weight in the pressure calculation produces much of the vertical separation.

Thermoelements

3P,[2] p-type thermoelements were used in the studies of Winchell (3) and Bates and Weinstein (4), and were examined for comparative purposes in this work. While the exact composition is proprietary, this p-type material contains PbTe, SnTe, and MnTe in approximately 47/47/06 m/o proportions. MnTe is less volatile than the other two tellurides and can be identified as a residue in both effusion and free surface vaporizations. However, its accumulation did not affect the effusion results as seen in Fig. 2, curve 4. As for the alloy compositions discussed in an earlier section, no systematic variation of rate with time or amount vaporized was observed. Winchell did not detect any form of Mn in the vapor during his investigation (3).

The results have been calculated and presented along with the "pure" alloy materials, and they are closest to those for the 72/28 and 50/50 compositions. The approximate vapor pressure curve is given in Fig. 4 relative to pure SnTe and PbTe and the previously reported results of Winchell (3), Bates and Weinstein (2), and Sokolov *et al.* (4). Thus, the near-equilibrium vaporization behavior of this complex material is determined by the behavior of the major constituent and is relatively unaffected by minor phases or dopants added to enhance its electrical properties. Unpublished data from this laboratory indicate that this is also true for 3N[3] and TAGS[4] thermoelements where the near-equilibrium vaporization behavior is essentially identical to that of the major phase, PbTe and GeTe, respectively.

[2] The 3M Company, St. Paul, Minnesota 55101.
[3] The 3M Company, St. Paul, Minnesota 55101.
[4] Isotopes, Incorporated, Timonium, Maryland.

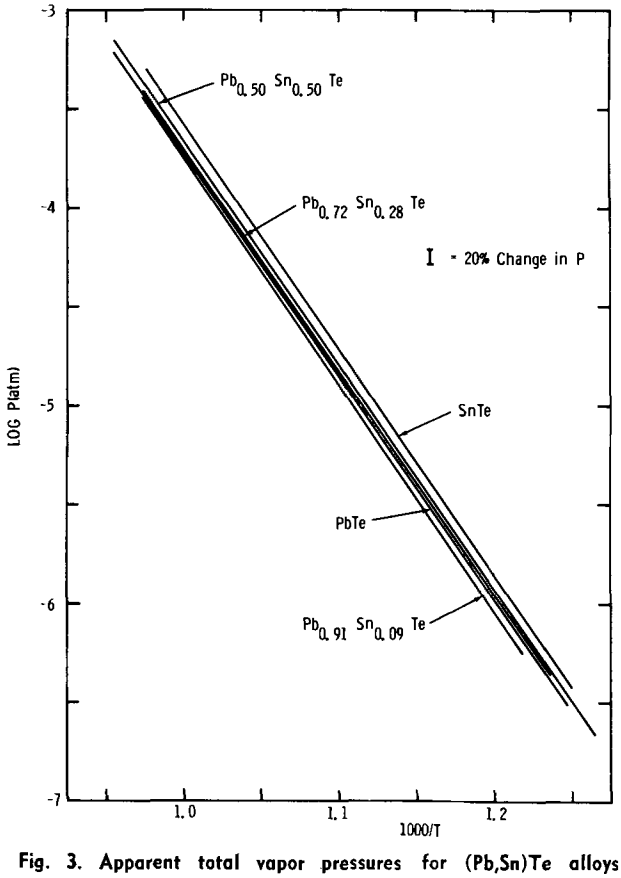

Fig. 3. Apparent total vapor pressures for (Pb,Sn)Te alloys calculated with the assumptions described in detail in the text. The over-all experimental uncertainty is of the order of the error bar given.

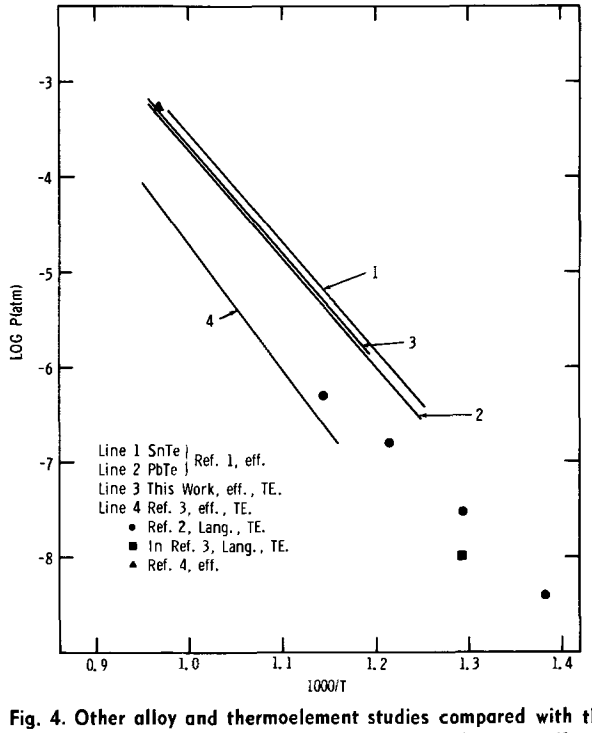

Fig. 4. Other alloy and thermoelement studies compared with the results of this study: TE = commercial thermoelement; eff. = effusion method; Lang. = free surface or Langmuir method.

Manuscript submitted Nov. 16, 1970; revised manuscript received Feb. 22, 1971.

Any discussion of this paper will appear in a Discussion Section to be published in the June 1972 JOURNAL.

REFERENCES

1. D. A. Northrop, *J. Phys. Chem.*, **75**, 118 (1971).
2. H. E. Bates and M. Weinstein, *Advan. Energy Conv.*, **6**, 177 (1966).
3. P. Winchell, *Energy Conversion*, **8**, 81 (1968).
4. V. V. Sokolov, V. I. Belovsov, V. B. Shol'ts, and L. N. Sidorov, *Russ. J. Phys. Chem.*, **40**, 885 (1966).
5. J. W. Wagner and J. C. Woolley, *Mater. Res. Bull.*, **2**, 1055 (1967).
6. N. K. Abrikosov, K. A. Dvul'dina, and T. A. Danilyan, *Russ. J. Inorg. Chem.*, **3**, 1632 (1958).
7. J. W. Wagner and R. K. Willardson, *Trans. Met. Soc. AIME*, **242**, 366 (1968).
8. A. R. Calawa, T. C. Harman, M. Finn, and P. Youtz, *ibid.*, **242**, 374 (1968).
9. R. F. Bis and J. R. Dixon, *J. Appl. Phys.*, **40**, 1918 (1969).
10. A. M. Reti, A. K. Jena, and M. B. Bever, *Trans. Met. Soc. AIME*, **242**, 371 (1968).
11. R. Mazelsky, M. S. Lubell, and W. E. Kramer, *J. Chem. Phys.*, **37**, 45 (1962).
12. N. R. Short, *Brit. J. Appl. Phys. (J. Phys. D)*, **1**, 129 (1968).
13. J. F. Butler and T. C. Harman, *This Journal*, **116**, 260 (1969).
14. A. A. Machonis and I. B. Cadoff, *Trans. Met. Soc. AIME*, **230**, 333 (1964).
15. R. N. Tauber and I. B. Cadoff, *J. Appl. Phys.*, **38**, 3714 (1967).
16. K. J. Kinden and C. A. Kennedy, *ibid.*, **40**, 2595 (1969).
17. K. Motzfeldt, *J. Phys. Chem.*, **59**, 139 (1955).
18. E. M. Levin, H. F. McMurdie, and F. P. Hall, "Phase Diagrams for Ceramists," p. 12, American Ceramic Society, Columbus, Ohio (1956).

Technical Notes

Formation of 20-25Å Thermal Oxide Films on Silicon at 950°-1140°C

J. A. Aboaf*

IBM Components Division, East Fishkill Facility, Hopewell Junction, New York 12533

Recent papers on MNOS (metal-Si_3N_4-SiO_2-Si) memory transistors, in which charge can be stored at or near the interface between the two insulators (1-6), classify them as either Fowler-Nordheim devices or direct tunneling devices, the only difference being that the latter have thinner oxide layers. For oxide layer thicknesses up to 37Å (3), the interface traps are charged by direct tunneling through the SiO_2 layer. Direct tunneling devices consequently exhibit great sensitivity of the so-called "write" characteristics to the oxide layer thickness (4, 7). Since the growth rate of SiO_2 on silicon is relatively high in oxygen or water vapor ambients (8) at high temperatures, low temperatures and/or diluted oxygen atmospheres should be used when very thin (about 20Å) films are necessary. While Wallmark and Scott (3), in their MNOS studies, prepared SiO_2 films in steam at 600°C, the present paper shows that very thin films of SiO_2 (less than 50Å) can be formed on silicon in ambient mixtures of NO and H_2 at 950°-1140°C.

P-type silicon wafers (<100>, 10 ohm-cm) were first cleaned in ammonia, hydrochloric acid, hydrofluoric acid, and deionized water, and then blown dry in nitrogen. The residual SiO_2 covering the wafers was then measured by ellipsometry (9, 10) and found to be 10 ± 1Å. The reactions were carried out using rf induction heating of a conventional horizontal quartz tube (59 mm in diameter) with a graphite susceptor encased in a fused silica envelope and attached to the cap of the reactor. High-purity hydrogen and nitric oxide gases (Matheson Corporation) were used without further purification.

The growth of oxide on these silicon wafers at 1000°C in various gas ambients is shown in Fig. 1. The oxide thickness, measured by ellipsometry, increased linearly above 25Å but probably logarithmically below 25Å.

The oxidation of Si by NO (curve A) probably occurs by the reaction of silicon with the oxygen formed while the NO gas is decomposing. The mechanism of thermal decomposition of NO in nitrogen and

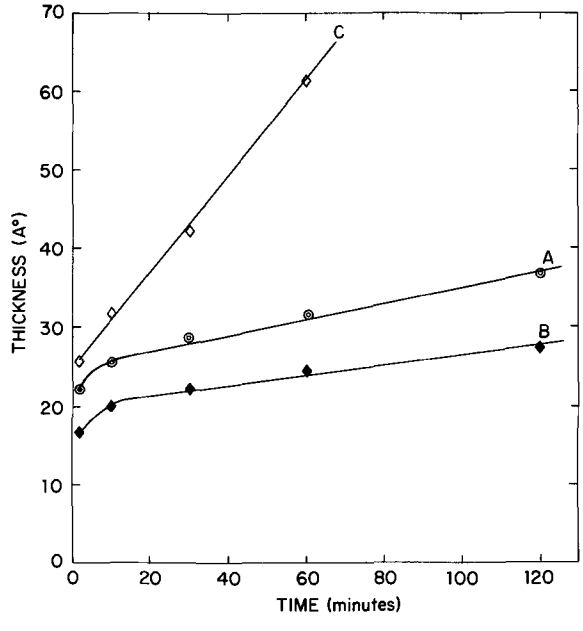

Fig. 1. Oxide growth as a function of time at 1000°C in the following gas ambients: A—6%NO, 94% N_2 in volume (total flow: 4.5 liters/min); B—6% NO, 94% H_2 in volume (total flow: 4.5 liters/min); C—0.3% O_2, 99.7% N_2 in volume.

* Electrochemical Society Active Member.

Key words: oxidation, silicon, thin films.

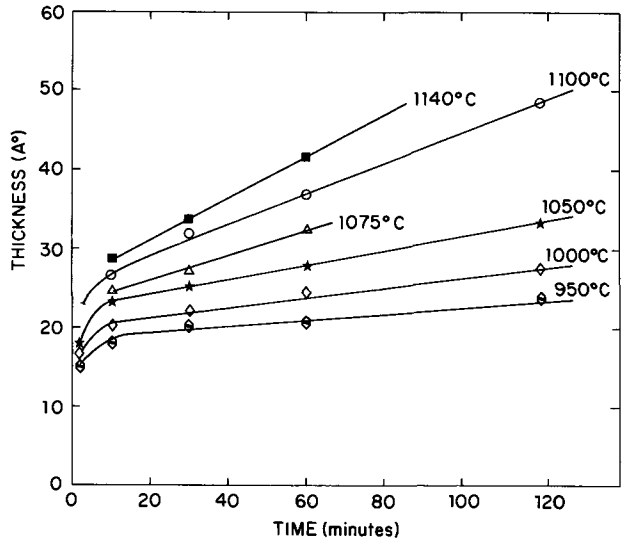

Fig. 2. Oxide thickness as a function of time at several temperatures: 6% NO, 94% H_2 in volume (total flow: 4.5 liters/min).

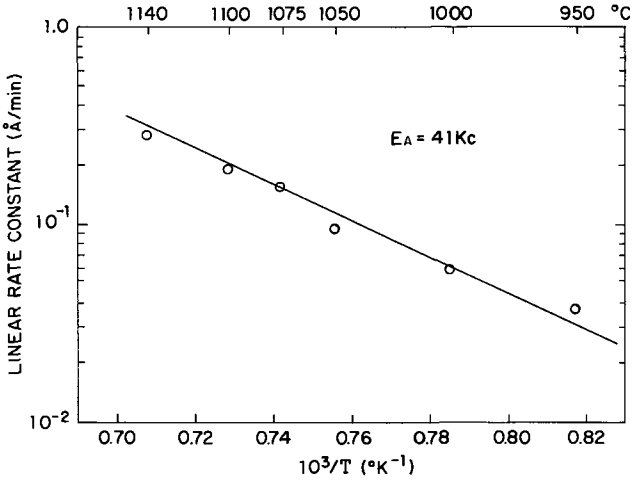

Fig. 3. Effect of temperature on the linear rate constant

oxygen involves a complex chain propagated by the atomic species (O, N) formed during the reaction (11, 12).

In the 6% in-volume NO + 94% in-volume H_2 ambient (curve B), the growth rate in the linear region is very nearly the same as in the NO + N_2 ambient, but lower absolute values of oxide thickness are obtained. For comparison, note the much faster oxide growth rate in even a very dilute oxygen ambient, 0.3% in-volume O_2 + 99.7% in-volume N_2 (curve C).

Oxide growth rate in NO + H_2 mixtures is strongly thermally activated. Figure 2 shows the thicknesses of oxide films at various temperatures, between 950°C and 1140°C as a function of time. The growth rate is linear with time except for the earliest stages of the oxidation process. Reproducibility of the thickness measurements was ± 1Å for the lowest temperature of oxidation and ± 2Å for the highest temperature of oxidation. Figure 3 shows the effect of temperature on the linear rate constant. An activation energy value of about 41 kcal/mole was calculated from the slope of the line. This energy value approximates the 45.3 kcal/mole obtained by Deal and Grove (8) for the direct oxidation of silicon in oxygen and/or water vapor.

The kinetics of the NO + H_2 reaction were studied by Graven (13) in the range of 840°-1060°C, and a homogeneous chain mechanism including intermediates such as NOH, O_2H, and OH was proposed. Kohout and Lange (14), using a mass spectrometric method, showed that NOH was the primary product of the H_2-NO reaction, and that N_2O and small amounts of NH_2OH were also formed. The films grown in the present study were not oxynitrides, no nitrogen was detected at the electron microprobe, and the index of refraction of 1000Å thick films grown at 1100°C was found to be that of thermal oxide of silicon, 1.46.

Acknowledgments

The author is grateful for the cooperation and support of J. F. Shepard and Dr. J. M. Eldridge, as well as the technical assistance of S. Neumann. He also wishes to thank Drs. B. Vromen and Y. van de Muelen for their helpful discussions concerning the ellipsometrical measurements.

Manuscript submitted Jan. 28, 1971; revised manuscript received April 15, 1971.

Any discussion of this paper will appear in a Discussion Section to be published in the June 1972 JOURNAL.

REFERENCES

1. H. C. Pao and M. O'Connell, *Appl. Phys. Letters*, **12**, 260 (1968).
2. F. A. Sewell, Jr., H. A. R. Wegener, and E. T. Lewis, *ibid.*, **14**, 45 (1969).
3. J. T. Wallmark and J. H. Scott, Jr., *RCA Rev.*, **30**, 335 (1969).
4. E. C. Ross and J. T. Wallmark, *ibid.*, **30**, 366 (1969).
5. D. Frohman Bentchkowsky, *Proc. IEEE*, **57**, 1190 (1969).
6. E. C. Ross, M. T. Duffy, and A. M. Goodman, *Appl. Phys. Letters*, **15**, 408 (1969).
7. E. C. Ross, Reliability Symposium, Las Vegas, April 1970.
8. B. E. Deal and A. S. Grove, *J. Appl. Phys.*, **36**, 3770 (1965).
9. A. C. Adams and R. H. Kaiser, Abs. 134, p. 343, Electrochem. Soc. Extended Abstracts, Los Angeles, May 10-15, 1970.
10. E. Passaglia, R. R. Stromberg, and J. Kruger, Editors, "Ellipsometry in the Measurement of Surfaces and Thin Films," Nat. Bur. Stds. Misc. Pub. #256, Washington, D.C. (1963).
11. H. Wise and M. F. Frech, *J. Chem. Phys.*, **20**, 22 (1952); **20**, 1724 (1952); **21**, 752 (1953).
12. F. Kaufman and J. R. Kelso, *ibid.*, **21**, 751 (1953); **23**, 1702 (1955).
13. W. M. Graven, *J. Am. Chem. Soc.*, **76**, 3697 (1957).
14. F. C. Kohout and F. W. Lange, *J. Chem. Phys.*, **46**, 4075 (1967).

Electric Field Effects on the System Oleyl Cholesteryl Carbonate-Cholesteryl Chloride

Werner Haas* and James Adams

Xerox Research Laboratories, Webster, New York 14580

The study of induced phase transitions from the cholesteric to the nematic mesophase has recently been of interest to a number of investigators. Sackmann, Meiboom, and Snyder (1) reported a magnetically induced phase transition, and Wysocki *et al.* (2, 3) described an electric field induced phase transition. Theoretical work by De Gennes (4) and Meyer (5) resulted in mathematical expressions which described the fields required to induce the phase transition, and the threshold fields were found to be inversely proportional to the pitch of the unperturbed cholesteric helix. Experimental work designed to confirm the theory was carried out by Durand (6) for magnetic fields and Baessler and Labes (7) for electric fields.

In the experiments described here, the electric fields required to induce the cholesteric-nematic phase transition were measured in the system cholesteryl chloride (right handed)-oleyl cholesteryl carbonate (left handed) and were correlated with the reciprocal pitch which is a function of composition.

Mixtures in 10% steps ranging from 0 to 100% content by weight of cholesteryl chloride (CC) were prepared by dissolving the components in petroleum ether. The films were cast from the solvent and heated in order to remove as much solvent as possible.

A preliminary examination of the mixtures under the polarizing microscope showed that mixtures with contents higher than 70% cholesteryl chloride crystallize quickly and mixtures with oleyl cholesteryl carbonate contents larger than 90% were isotropic at room temperature. Somewhat surprising was the observation that 50-50% mixtures deposited onto a slide without cover glass spontaneously adopted a uniaxial configuration with positive sign. Oriented areas as large as 1.0 cm^2 were observed. Positive signs are characteristic of smectics and nematics, but the textures which were observable at the borders of the preparation appeared nematic in nature.

The pitch of the mixtures was measured at room temperature on aligned free surface liquid crystals. Monochromatic light was incident at an angle ϕ_i measured from the normal, and the maximum reflection was detected by a photodiode at an angle ϕ_s also measured from the normal; ϕ_i, ϕ_s and the index of refraction n of the liquid crystal were correlated by Fergason's (8) formula with the pitch of the helical structure. Details of the instrumentation were given elsewhere (9).

A plot of the reciprocal pitch *vs.* composition is shown in Fig. 1; around the 50% point, the reciprocal pitch value approaches zero which is in agreement with the observed positive conoscopic figure.

The electric field strengths required to induce the phase transition were measured with cells as shown schematically in Fig. 2. The gap between the electrodes was about 200μ and was measured for each cell with a micrometer. Results were checked by focusing the microscope on the lower and upper slides. The accuracy of these measurements was $\pm 10\%$.

The geometry of the cell is such that pressure effects are largely eliminated. The liquid crystal material after introduction into the gap generally assumed, after some relaxation time, a texture of optically active areas surrounded by birefringent regions which

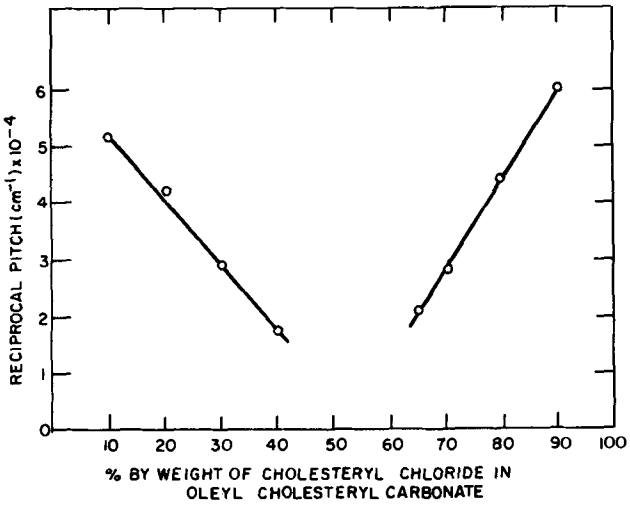

Fig. 1. Reciprocal pitch *vs.* composition

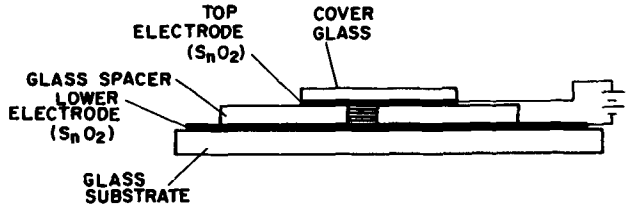

Fig. 2. Measuring cell

form a focal-conic-like texture. In the optically active areas, the liquid crystal adopted the Grandjean plane texture which is optically negative. This is somewhat surprising for the 50% mixture which, as mentioned previously, was optically positive on an uncovered slide. The film on the open glass slide, however, was about 50 times thinner than the layer in the cell, and deposition of a "thick" film on an uncovered slide also produced a cholesteric texture. The conclusion drawn from this experiment was that in the compensated region the liquid crystal is very labile and, depending on film thickness, substrate, or other factors affecting the ordering, can adopt either the cholesteric or nematic molecular arrangement.

When an electric field was applied to the mixed cholesterics in the measuring cell at field strengths substantially below the transition field, the optically active areas disappeared (2) and the film broke off into a number of small birefringent domains. The film became totally focal-conic and scattered light strongly. Without a microscope, the film appeared frosted and the over-all aspect was similar to dynamic scattering (10) without the violent turbulence associated with that effect.

The disappearance of the optically active areas is associated with a realignment of the optic or helical axes to a position perpendicular to the electric field and is due to the sign of the anisotropy of the dielectric susceptibility. This type of realignment is not only observed in the system studied but is characteristic of many other cholesteric systems.

* Electrochemical Society Active Member.

Key words: liquid crystals, mesomorphism, phase transition.

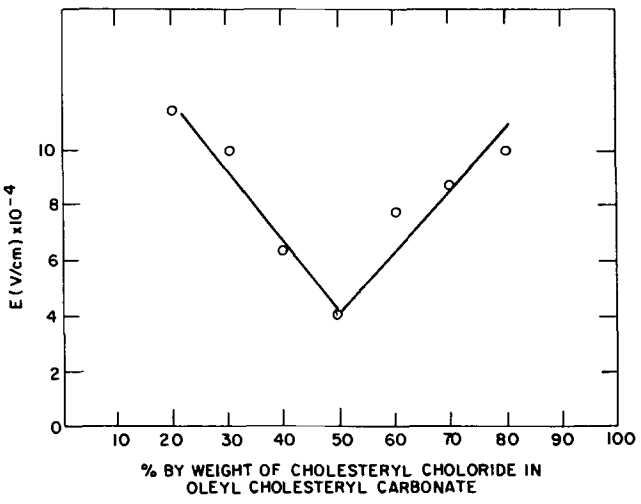

Fig. 3. Transition field vs. composition

This effect precludes the observation of the transition for the case in which the electric field is applied parallel to the optic axis. Thus, Meyer's formula (5) $F_c = 2\pi/Z_0 \ (K_{22}/\Delta\epsilon)^{1/2}$, where F_c is the critical electric field, Z_0 the pitch of the unperturbed cholesteric helix, K_{22} an elastic constant, and $\Delta\epsilon$ the anisotropy of the dielectric constant, is not applicable. The appropriate formula to be used is the electric analog of the prediction by De Gennes, $H_c = \pi^2/2Z_0 \ (K_{22}/\Delta\chi)^{1/2}$, for magnetic fields applied perpendicular to the helical axis. H_c is the critical magnetic field and $\Delta\chi$ the anisotropy of the magnetic susceptibility. This expression probably also applies to the measurements by Baessler and Labes (7).

In the measurements described here, once the layer had become focal-conic, the field was always normal to the helical axes. With increasing voltages, scattering and domain sizes underwent quantitative changes. Below the transition, turbulence increased and dark regions appeared which correspond to areas in which the film was already nematic and aligned. In time the film became darker until the field was totally extinguished. At this point the interference figure was very sharp and scattering ceased completely.

The criterion used in the measurements of the field strength required to produce the transition was total darkness 2 min after application of the field. The results are plotted *vs.* composition in Fig. 3. The threshold field is linear in reciprocal pitch as predicted by the theory for the magnetic analog (4). From the reciprocal pitch measurements or from the thin film experiment, one would have expected that the value for the 50% composition would have been very small. This was not the case. The value is relatively low but still considerable. Since the data were taken in 10% steps, the absolute minimum was, of course, not precisely determined.

If the field is removed when the liquid crystal is in the aligned nematic state, the film breaks into a number of unaligned domains. The conoscopic figure appears to become temporarily biaxial and then vanishes rapidly. In parallel light between crossed polarizers, the light output increases and a number of colors appear in sequence. These phenomena were recently studied in detail by Wysocki *et al.* (11). Scattering increases strongly as the film settles into the focal-conic texture and after 20 min the first optically active areas become visible again.

In summary, the pitch of cholesteryl chloride-oleyl cholesteryl carbonate mixtures was measured and correlated with critical fields required to induce the cholesteric-nematic phase transition. The critical field was found to vary linearly with reciprocal pitch for the case of field perpendicular to the helical axis which is in agreement with the magnetic analog (4). Optically active areas whose helical axes are parallel to the field realign at fields smaller than required for the transition. The realignment is due to the sign of the anisotropy of the dielectric susceptibility.

Acknowledgment

The authors thank Bela Mechlowitz for technical assistance.

Manuscript submitted Jan. 14, 1971; revised manuscript received April 15, 1971. This was Paper 157 presented at the Detroit Meeting of the Society, Oct. 5-9, 1969.

Any discussion of this paper will appear in a Discussion Section to be published in the June 1972 JOURNAL.

REFERENCES

1. E. Sackmann, S. Meiboom, and L. C. Snyder, *J. Am. Chem., Soc.*, **89**, 5981 (1967).
2. J. J. Wysocki, J. Adams, and W. Haas, *Phys. Rev. Letters*, **20**, 1024 (1968).
3. J. Wysocki, J. Adams, and W. Haas, *Mol. Crystals*, **8**, 471 (1969).
4. P. G. De Gennes, *Solid-State Commun.*, **6**, 163 (1968).
5. R. B. Meyer, *Appl. Phys. Letters*, **12**, 281 (1968).
6. G. Durand, L. Leger, F. Rondelez, and M. Veyssie, *Phys. Rev. Letters*, **22**, 227 (1969).
7. H. Baessler and M. M. Labes, *ibid.*, **21**, 1791 (1968).
8. J. L. Fergason, *Mol. Crystals*, **1**, 293 (1966).
9. J. Adams, W. Haas, and J. J. Wysocki, *J. Chem. Phys.*, **50**, 2458 (1969).
10. G. H. Heilmeier, L. A. Zanoni, and L. A. Barton, *Proc. IEEE*, **56**, 1162 (1968).
11. J. J. Wysocki, J. Adams, and D. J. Olechna, "Liquid Crystals and Ordered Fluids," Plenum Press, New York (1970).

Ge-Esperite—A New Mn-Activated Phosphor

A. Wachtel* and C. K. Lui Wei

Westinghouse Electric Corporation, Bloomfield, New Jersey 07003

A recent paper by Ito (1) describes a number of Zn, Ca, Pb silicates, among which $Zn(Ca_{1-x}Pb_x)SiO_4$ (Calarsenite, recently renamed esperite) is known for its bright Mn-activated luminescence in the yellow-green (2). Owing to low stability, however, this compound is difficult to prepare in pure form, especially as a well-crystallized phosphor. In this connection, we noted that the analogous germanate which we propose to call Ge-esperite (GESP) is considerably more stable and amenable to synthesis.

The purpose of this note is to report on some of the properties of GESP and to describe efforts to ascertain its composition.

* Electrochemical Society Active Member.

Key words: luminescence, phosphors, germanates, calcium larsenite, esperite.

Experimental

Compounds activated by 0.01 Mn replacing Zn were prepared by appropriate heat treatment of raw materials obtained by different techniques as will be described. Luminescence under 254 nm excitation was

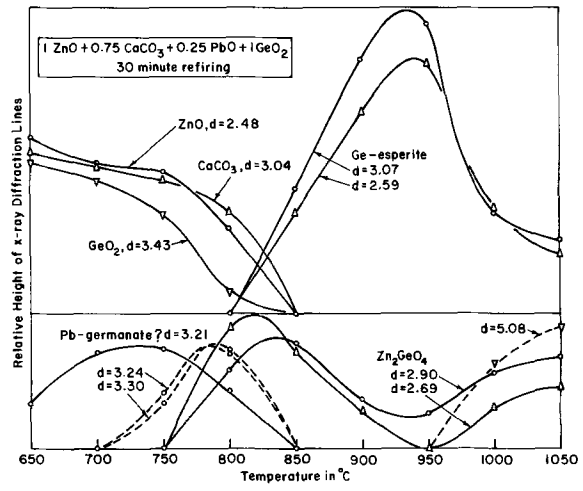

Fig. 1. X-ray powder diffraction analyses of a dry mix after 30 min firings at increasing temperatures.

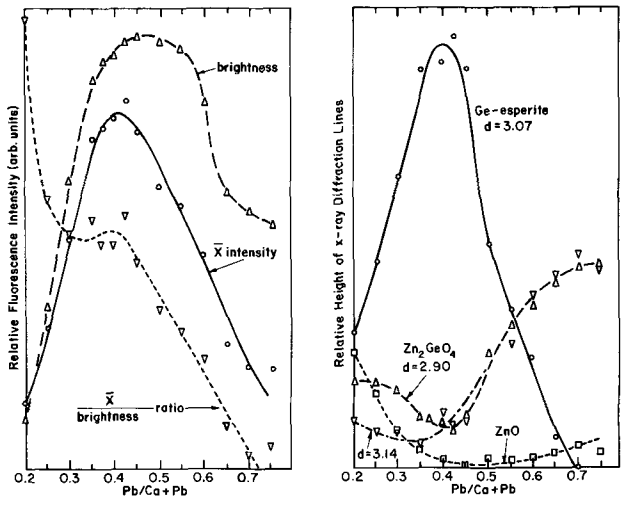

Fig. 2. Luminescence (left) and x-ray powder diffraction analyses (right) of hydroxide slurries, dried and fired at 820°C, as a function of composition. Use of $\bar{x}$ and $\bar{y}$ filters was to distinguish between the luminescence of different phases.

observed microscopically as well as measured in powder plaques. X-ray powder diffraction analyses were performed with a Philips x-ray diffractometer, operated at 35 kV and 15 mA, using a Cu target and Ni filter.

Results

Solid-state reaction between component oxides and carbonates proceeds *via* formation of Zn_2GeO_4 above 750°C, followed by GESP above 800°C. Above 950°C, GESP begins to decompose to Zn_2GeO_4 and other products, at least one of which displays a weak orange-red luminescence and is unidentified. Prolonged annealing of the fused (1000°C) product at lower temperatures, *e.g.* 850°C, again causes formation of GESP. Microscopic examination of the luminescence showed that the Pb/Ca+Pb ratio (x) of the compositions strongly influences the relative yield of the various phases obtained: below $x = 0.25$, a red luminescent phase[1] is noted together with GESP even at moderate temperatures; while, above $x = 0.25$, it disappears but the amount of Zn_2GeO_4, which is always present, increases. Maximum formation of GESP (about 50%) obtains at $x = 0.25$. Figure 1 shows the course of the reaction, as monitored by x-ray diffraction analyses, on products obtained from this composition in heating steps of 30 min and 50° increments. To avoid crowding, the figure is divided in two portions, and unidentified phases are indicated only by the most prominent d-spacing. It essentially confirms the results already noted by microscopic examination of activated materials. The extremely complex pattern obtained on high-temperature decomposition products was not suitable to identify the red luminescent phase, as this was often associated with d-spacings other than that at 5.08Å. Note that Zn_2GeO_4 goes through a minimum at the temperature of maximum GESP formation, at which point the initially strongest reflection at 2.69Å disappeared, while the second strongest reflection at 2.90Å has increased in relative intensity. This curious observation was reproducible in similar experiments.

Considerably higher yields of GESP resulted from wet slurries of component hydroxides which seemed to partially react prior to drying and firing. Figure 2 shows the luminescence (left) and x-ray diffraction line heights (right) of products obtained at 820°C as a function of x. Note that, in contrast to previous results, x is clearly optimized at 0.4. The relative concentration of side products is lower, and is also minimized at $x = 0.4$; however, their presence still casts some doubt on the actual composition of GESP at this point.

[1] Presumably some Zn,Ca germanate, and not necessarily the same orange-red emitting phase previously mentioned.

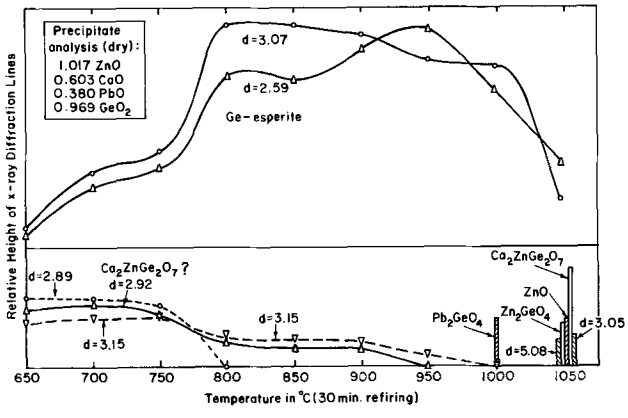

Fig. 3. X-ray powder diffraction analyses of a coprecipitate after 30 min firings at increasing temperatures. Bars denote phases observed at only one temperature.

The most rapid formation of GESP resulted from firing of coprecipitates derived from mixed nitrates and Na_4GeO_4. The purest and most strongly luminescent preparations resulted from initial compositions of $x = 0.35$ and Ge = 1.04 but, owing to small losses of Ca and Ge, the final compositions were somewhat richer in Pb and more stoichiometric in Ge. Figure 3 shows the thermal reaction of a typical precipitate of this composition. Comparison with Fig. 1 shows some important differences: GESP is observed already at 650°C and reaches maximum near 800°C, and no Zn_2GeO_4 is formed prior to decomposition of GESP at higher temperatures. The small amount of side products between 800° and 1000°C is due only to the short firing times employed, and single-phase preparations of GESP were readily obtainable by this technique by firing at 850°-900°C for a few hours. Table I shows the powder diffraction pattern of one of these in comparison to that of esperite as reported by Moore and Ribbe (3). It can be seen that the agreement is excellent, and also that the observed specific gravity was in good agreement with that calculated from the x-ray data on the basis of 12 Ge atoms/unit cell. It was, however, interesting to note that within the precision afforded by the sharpness of the lines our d-spacings were independent of x; *i.e.*, no lattice expansion due to Pb replacing Ca could be observed.

Figure 4 shows the emission and excitation spectra of GESP as compared to those of two specimens of esperite from Franklin, New Jersey. It can be seen

Table I. X-ray powder diffraction patterns

Esperite (3) hkl	d_{calc}	d_{obs}	I	Ge-Esperite hkl	d_{calc}	d_{obs}	I
002,101	7.63	7.62	45	002,101	7.78	7.79	47
112	4.73	4.73	10	112	4.82	4.82	12
200,103	4.41	4.41	15	200,103	4.49	4.49	5
				201	4.31	4.34	3
				020*	4.21	4.21	8
				210*,113	3.96	3.97	6
004,202	3.81	3.82	15	004,202	3.89	3.90	10
211	3.77	3.76	7	211	3.84	3.84	8
				120	3.81	3.81	8
121,022	3.64	3.64	15	121,022	3.70	3.70	10
				212*,014	3.53	3.53	5
122	3.360	3.363	23	122	3.42	3.42	18
023	3.208	3.216	17	023	3.27	3.27	14
220	3.017	3.017	100	220,123	3.07	3.07	100
221	2.958	2.958	22	221	3.01	3.01	16
105,204	2.884	2.884	33	105,204	2.94	2.94	34
222	2.805	2.805	4	222,024	2.87	2.86	4
124	2.672	2.675	8	124	2.72	2.72	9
006	2.543	2.543	75	006,303	2.59	2.59	76
132	2.487	2.490	4	132	2.53	2.53	4
313	2.432	2.434	8	313	2.48	2.48	8
				320	2.44	2.44	3
224	2.366	2.367	40	224,321,125	2.41	2.42	19
				230,133	2.38	2.38	13
231	2.310	2.314	4	231	2.35	2.35	7
314	2.240	2.237	4				
400	2.207	2.205	4				
323	2.169	2.169	8	323,026	2.21	2.21	5
225	2.145	2.145	4				
402	2.118	2.118	8	402,107,305	2.16	2.16	10
				411	2.15	2.15	5
		2.051	13	041	2.085	2.086	5
		2.015	10	140	2.048	2.050	4
		1.994	4				
		1.944	45	420,226,142	1.981	1.982	26
				127	1.920	1.922	5
				235	1.890	1.892	5
				227	1.801	1.804	5
				243	1.788	1.788	7
				511	1.748	1.745	6
				250,153	1.576	1.576	29
$a = 8.814$				$a = 8.99$		$spgr_{calc} = 5.02$	
$b = 8.270$				$b = 8.43$			
$c = 15.26$				$c = 15.52$		$spgr_{obs} = 5.03$	

* hkl agrees with Ito's pattern (1).

that, within the range displayed by the minerals, the emission is not significantly different. Despite the high luminosity of the emission, however, we could obtain only about 40% of the brightness of Zn_2GeO_4:Mn in our best samples.

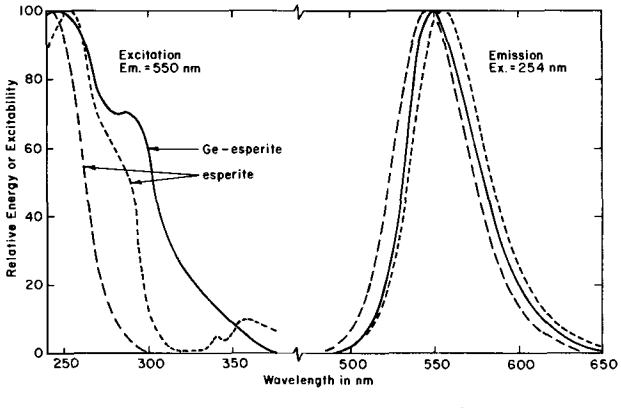

Fig. 4. Excitation and emission spectra of GESP (solid lines), and of two specimens of esperite from Franklin, New Jersey (dashed lines).

Discussion

The present data show that, unlike esperite, GESP can form by solid-state reaction between conventional oxide or carbonate raw materials, although the much better results with homogeneous coprecipitates suggest that the reaction is slow. This, as well as comparison of the decomposition temperature with that of esperite (1), shows that the germanate is considerably more stable.

Comparison between the germanate and silicate concerning their x-ray diffraction patterns, and their agreement between actual and calculated specific gravities when both are calculated on the basis of the same number (12) of Si or Ge atoms/unit cell, shows that the two substances are isomorphous.

The unit cell model proposed by Moore and Ribbe (3) contains 16 Ca sites, 4 Pb sites, and 4 sites which may be occupied by either ion. This corresponds to a range of 4-8 Pb/24 cation sites ($x = 1/6$ to $1/3$). Our values of x, leading to maximum formation of GESP depended on the technique of preparation: in solid-state reactions, it was 0.25 which is the mean of this range; while, in the more homogeneous wet preparations, the much higher values (0.35-0.4) would require that some of the sites proposed for Ca alone be occupied by Pb. However, our data are uncertain, either because the presence of side products makes it impossible to equate the composition of GESP with the over-all composition or, in the case of homogeneous preparations, because of the formation of single-phase solid solutions over a range of compositions. Finally, the value of $x = 0.4$, suggested by Fig. 2, would require a basic unit cell according to $Ca_3Pb_2(ZnGeO_4)_5$, in violation of the presently assumed model (3).

In the near future, we hope to resolve this question by means of reaction products obtained by fluxing component oxides with KCl at 850°C and leaching in water. Microscopic examination of such powders, under 254 nm excitation, reveals well-crystallized needles of Zn_2GeO_4:Mn (green), plates of GESP (green-yellow), and aggregates of inert and weak red luminescent matter. Using the cathodoluminescence of the particles for identification, we expect to be able to ascertain the composition of GESP by electronmicroprobe analyses and, in particular, to note whether it is a function of the over-all raw material composition. These results will be reported in a separate communication.

Acknowledgments

The authors wish to thank Miss I. Walinski for sample preparations and measurements, and Dr. W. B. White for helpful discussions.

Manuscript submitted Apr. 1, 1971; revised manuscript received April 28, 1971.

Any discussion of this paper will appear in a Discussion Section to be published in the June 1972 JOURNAL.

REFERENCES

1. Jun Ito, *Am. Mineralogist*, **53**, 231 (1968).
2. C. Palache, L. H. Bauer, and H. Berman, *ibid.*, **13**, 142 (1928).
3. P. B. Moore and P. H. Ribbe, *ibid.*, **50**, 1170 (1965).

Oxidation of Vapor Deposited Aluminum in Air at 23°C

D. L. Kinosz and D. L. Belitskus

Aluminum Company of America, Alcoa Research Laboratories, New Kensington, Pennsylvania 15068

Hart (1) has summarized early work on oxidation of nascent aluminum surfaces in air or oxygen at room temperature. The quartz crystal microbalance provides a method of obtaining rapid, accurate oxidation data for vapor deposited metal films from early stages of oxidation. Kirk and Huber (2) used this technique to study the oxidation of aluminum in dry oxygen at

Key words: quartz, crystal, microbalance, kinetics, dew point.

pressures ranging from 10^{-3} to 10 Torr, finding a pressure dependent, direct logarithmic film growth. The present work employed this method to determine the growth laws applicable in dry and moist air at atmospheric pressure.

Experimental

Weight gains were measured with a Westinghouse Model 701 Quartz Crystal Microbalance coupled with a Hewlett-Packard Model 521C Counter. The crystal head was mounted in a conventional bell jar assembly in a room held at 23° ± 1°C (−5° to 0°C dew point). Aluminum films were evaporated onto the exposed gold covered quartz crystal from 99.999% Al on a tungsten helix fitted with a beam collimator. A shutter between the exposed crystal and the vaporization source was kept closed until the vaporization was constant to minimize any radiant heat effects. Films averaging 1000Å were deposited at 15 Å/sec. The pressure, maintained by an oil diffusion pump and a liquid nitrogen trap, was typically 3-5 x 10^{-7} Torr, as measured by a hot filament cathode gauge before the start of vaporization. After film deposition, about 10 min was required for the balance to stabilize.

For four experiments in −75°C dew point air, a ballast tank was filled from a commercial cylinder to sufficient pressure to equal one atmosphere when the gas was expanded into the bell jar assembly. Gas expansion required about 90 sec. Four experiments at −5° to 0°C dew point used room air vented into the system. Finally, two experiments were conducted in 23°C dew point air produced by bubbling air through water before entering the ballast tank.

The reversible correction in balance beat frequency produced by admitting an air atmosphere to a gold coated crystal (3) was determined and applied to the oxidation data.

Results and Discussion

Average weight gains per unit geometric area are shown in Fig. 1 as a function of the log of oxidation time. There is no significant difference between the kinetics in air at −75°C dew point and in air at 0°C dew point for up to 10 hr (3.6 x 10^4 sec). Only one run in air at 0°C dew point was carried out beyond 5 x 10^3 sec. Weight gain in moisture-saturated air was more rapid but is also best represented by a direct logarithmic oxidation rate.

The direct logarithmic oxidation rate in moisture-saturated air agrees with the results of Hart (1), who studied the oxidation of electropolished aluminum by anodic polarization. The direct logarithmic oxidation rate in dry air agrees with the results of Kirk and Huber (2) and Eley and Wilkinson (4) in dry oxygen at reduced pressures and with Boggio and Plumb (5) in dry air at one atmosphere but is contrary to the results of Hart in dry oxygen at one atmosphere. While the mechanism of oxide formation may differ in dry air and dry oxygen at atmospheric pressure, it is possible that because of the absence of data during very early oxidation in the investigation of Hart [*cf.* Fig. 5 of Ref. (1)], an incorrect assignment of the oxidation kinetics was made. After about 10 hr, oxidation in air at either −75°C or 0°C dew point oxidation became more rapid, departing from a direct logarithmic rate. While data were insufficient to determine the rate law beyond this point, it may be the inverse logarithmic rate found by Hart. Boggio and Plumb (5) found no deviation from a direct logarithmic law in up to 10^6 seconds. The reason for this difference is not obvious but may be related to differences in substrate or in aluminum film thickness, purity, or porosity.

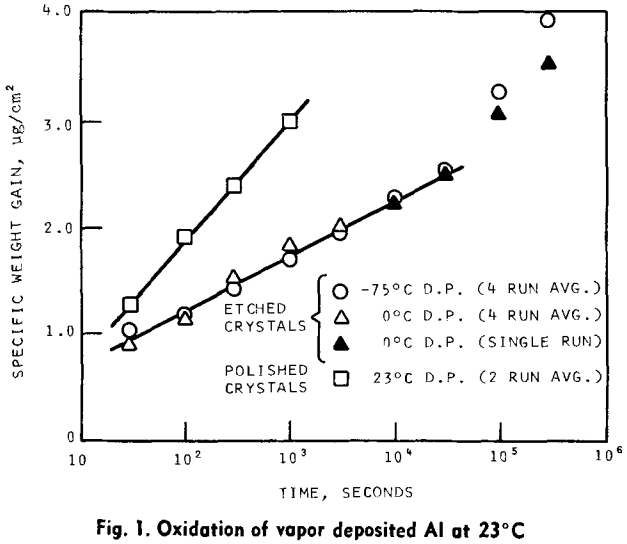

Fig. 1. Oxidation of vapor deposited Al at 23°C

Several theories predict a logarithmic time law for the initial oxidation. Hauffe and Ilschner (6) assume that the rate of electron tunnelling determines the initial rate, resulting in a direct logarithmic law, and that the rate of ionic transfer determines the rate with thicker films, resulting in an inverse logarithmic law. Lanyon and Trapnell (7) assume a two-stage reaction involving oxygen chemisorption and a place-exchange reaction between the chemisorbed oxygen and the underlying aluminum atoms which leads to the pressure-dependent, direct logarithmic law found by Kirk and Huber (2) and Eley and Wilkinson (4). Boggio (8) showed that electron tunnelling and reaction with adsorbed oxygen atoms leads to the same growth law.

The experiments in dry air and in air of 0°C dew point employed etched gold coated quartz crystals as received from the manufacturer. Reproducibility was good for the four runs in air of 0°C dew point, with the highest rate about 15% greater than the lowest, but poor for the runs in dry air, with the highest rate nearly 100% greater than the lowest. Nonetheless, each of the individual curves followed the direct logarithmic time law and the average curve is considered reasonable. Lack of reproducibility is attributed primarily to variability in surface roughness of the quartz crystals, which may have been accidentally greater for the runs in dry air. An attempt to measure surface roughness by stripping the oxide film from aluminum coated crystals by a radioactive chromate-phosphate solution (9) failed when the vapor deposited aluminum coating was also removed. Handy and Waters (10) have estimated the surface area of similar crystals as 2.5± 0.2 times the geometric area.

The two runs in moisture-saturated air used polished crystals obtained from Reeves-Hoffman (Carlisle, Pennsylvania). Scanning electron micrographs (2000X) of oxidized aluminum surfaces on an etched and on a polished crystal are shown in Fig. 2. The difference in slopes of the two curves in Fig. 1 increases from twofold to fivefold after correction for surface roughness (taking the roughness of a polished crystal as unity). This should not be taken as quantitative since part of the difference could be due to the change in the base crystals. In air at 23°C dew point some condensation may occur on the crystal, giving rise to higher oxidation rates. More experiments using a common type of quartz crystal substrate (preferably polished) are required.

Assuming the oxide formed in dry air is amorphous Al_2O_3 of density 3.5 g/cc and a 2.5 roughness factor, oxide thickness after 24 hr is about 35Å. This is close to the 30-40Å range found by Hart (1) in 1 atm of dry oxygen and the 30Å found by Madden, Canfield, and Hass (11) in 1 atm of air but is higher than the 19Å found by Boggio and Plumb (5). The thickness of the oxide cannot be accurately determined with a quartz crystal microbalance until information on the identity and density of the film is available. Quartz crystal microbalance studies in conjunction with tech-

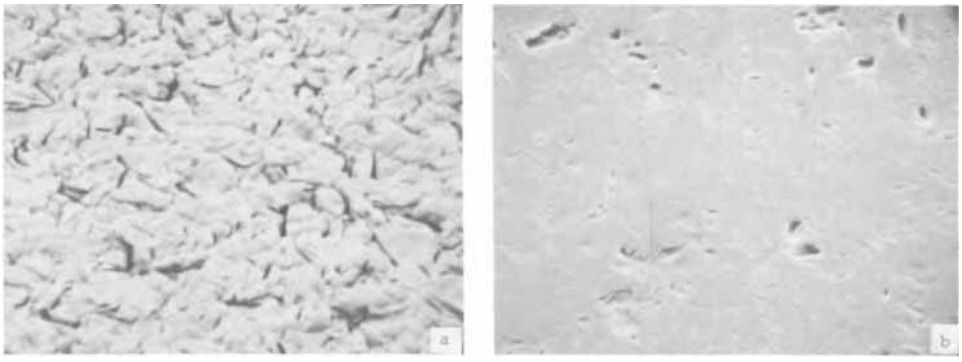

Fig. 2. Scanning electron micrographs (2000X) of oxidized Al surfaces. (a) etched crystal and (b) polished crystal.

niques which provide accurate information on film thickness would provide interesting information on the density and composition of these thin films.

Acknowledgment

The authors would like to thank R. J. Campbell for his technical assistance and J. Ptasienski for the scanning electron micrographs.

Manuscript submitted Feb. 24, 1971; revised manuscript received April 16, 1971.

Any discussion of this paper will appear in a Discussion Section to be published in the June 1972 JOURNAL.

REFERENCES

1. R. K. Hart, *Proc. Roy. Soc. (London), Ser. A*, **236**, 68 (1956).
2. C. T. Kirk and E. E. Huber, Jr., *Surface Sci.*, **9**, 217 (1968).
3. W. H. Lawson, *J. Sci. Instr.*, **44**, 917 (1967).
4. D. D. Eley and P. R. Wilkinson, *Proc. Roy. Soc. (London), Ser. A*, **254**, 327 (1960).
5. J. E. Boggio and R. C. Plumb, *J. Chem. Phys.*, **44**, 1081 (1966).
6. K. Hauffe and B. Ilschner, *Z. Elektrochem.*, **58**, 382 (1954).
7. M. A. H. Lanyon and B. M. W. Trapnell, *Proc. Roy. Soc. (London), Ser. A*, **227**, 387 (1955).
8. J. E. Boggio, *Surface Sci.*, **14**, 1 (1969).
9. J. E. Lewis and R. C. Plumb, *Intern. J. Appl. Radiation Isotopes*, **1**, 33 (1956).
10. R. M. Handy and P. M. Waters, Westinghouse Scientific Paper 65-1F1-FILMD-P1, not published.
11. R. P. Madden, L. R. Canfield, and G. Hass, *J. Opt. Soc. Am.*, **53**, (1963).

JOURNAL OF THE ELECTROCHEMICAL SOCIETY

ELECTROCHEMICAL TECHNOLOGY

AUGUST 1971

The Response of the Stabilized Zirconia Galvanic Cell to Methane-Oxygen Mixtures

Y. L. Sandler*

Westinghouse Research Laboratories, Pittsburgh, Pennsylvania 15235

ABSTRACT

The voltage response of the stabilized zirconia galvanic cell to varying concentrations of methane-air mixtures in their combustion products was studied, using air as a reference gas. It is shown that the cell can be operated in two distinct ways, the equilibrium and the nonequilibrium mode. In the former case, the electrode equilibrates the mixture completely and registers a Nernst potential corresponding to the oxygen partial pressure in the equilibrated mixture. With active porous platinum electrodes, this condition is realized. In the nonequilibrium case, the cell registers the Nernst potential corresponding to the true oxygen partial pressure in the mixture. This condition is realized with silver electrodes; exact oxygen potentials were obtained at temperatures as high as 800°C with mixtures containing up to 27% methane in air. By means of a combination of nonequilibrium and equilibrium electrodes, both oxygen and methane concentrations can be determined. A methane gauge is described that can measure methane in air without the use of a reference gas.

The solid electrolyte high-temperature cell is ideally suited for the rapid and accurate potentiometeric determination of oxygen in gas mixtures. The electrolyte used in the present study is a stabilized zirconia tube containing 15 m/o (mole per cent) calcia. Within wide limits of temperature and oxygen pressure, the conductivity (1) of the electrolyte is due solely to the mobility of the oxygen ions. With suitable electrodes, reversible oxygen potentials are obtained at open circuit. Cells of this type have therefore come into use as oxygen gauges (2, 3) for determining oxygen pressures or oxygen partial pressures in inert gas mixtures. In equilibrium mixtures (4, 5), such as H_2/H_2O, CH_4/H_2O, or CO/CO_2, the cell is capable of indicating accurately the potential corresponding to the equilibrium oxygen partial pressure. An air or oxygen electrode is usually used as a reference electrode.

In the present paper, the response of the cell is more closely examined when a nonequilibrium mixture containing both oxygen and a fuel, methane, passes the cell. The complete equilibration of the mixture and the correct response to the oxygen partial pressure cannot be taken for granted under all conditions. The response will depend on the catalytic activity of the electrode material as well as on physical characteristics, such as porosity and size, flow rate, and temperature. In the present work, methane-air mixtures were used with and without combustion products present. As will be shown, the proper choice of the electrode makes it possible to operate the cells under conditions of either complete equilibrium or complete nonequilibrium. In intermediate cases, the cell voltage is often difficult to interpret.

Experimental

The electrolytic tubes were made of zirconia doped with 7 w/o (weight per cent) calcia and were supplied by the Zirconium Company of America. Their dimensions were 4 mm ID, 5 mm OD, and 18 cm length. Platinum or silver electrodes were made from metal paste as provided by Engelhard Industries. The outside electrode was in contact with the atmosphere as a source of constant oxygen partial pressure. The gas to be analyzed was passed through the inside.

The furnace heating the electrolyte tube had a temperature zone constant to 3°C over about 2 cm length. When platinum was used, to maximize the catalytically active area, the electrode extended over almost the entire length of the electrolyte tube, as shown in Fig. 1(a). No voltage deviation due to the colder parts of the tube (having a higher ohmic resistance) was noticed. When no catalytic activity was desired, with

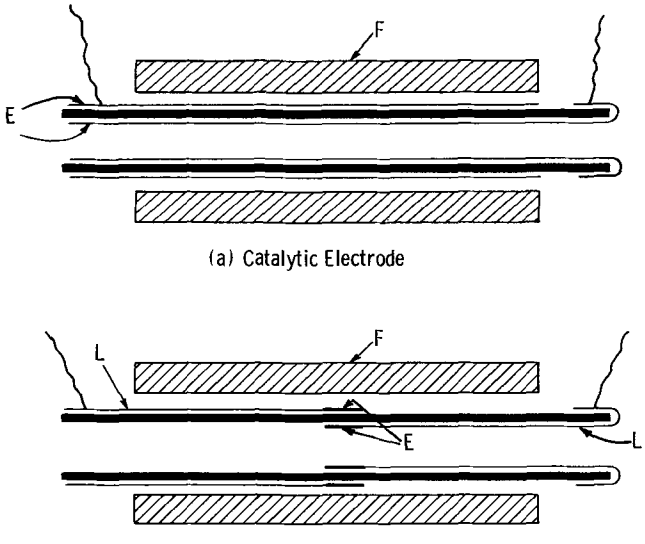

Fig. 1. Solid oxide cells in furnace with (a) catalytic electrodes, (b) noncatalytic electrodes. *E* = electrodes, *F* = furnace, *L* = leads to cold end of electrolyte tube.

* Electrochemical Society Active Member.

Key words: oxygen, methane, catalyst, silver, zirconia, gauge, electrode.

silver electrodes, a small electrode of about 1 cm length at the center of the tube was used. Electrical connections to the cold end of the tube were made by narrow lines consisting of the same material [Fig. 1(b)].

The pure or premixed gases were taken from cylinders supplied by Matheson Company. After passing through separate flowmeters, the combined gases passed a water vapor saturator which was kept in an oil bath thermostated to within 10^{-2}°C. The gas lines beyond the saturator were kept hot by means of a heating tape to prevent the condensation of water vapor. Gas samples were taken off before and after passage of the gas through the furnace. Analyses were carried out by means of a mass spectrometer, Consolidated Electrodynamics, Model 620-A. Cell voltages were measured with a Keithley 660 Differential Voltmeter.

The partial pressure of water vapor was determined from the temperature of the water saturator and by taking into account the water formed in the cell by oxidation of the fuel. Control experiments were performed to check the reliability of this procedure. Water and carbon dioxide were absorbed by passing gas mixtures through two absorption tubes containing Drierite and Ascarite, respectively. The molar ratio of water to carbon dioxide absorbed agreed to at least 5% with the ratio calculated from the water saturation temperature and the mass spectrometric value for the CO_2 concentration, corrected for the presence of the water vapor.

Results and Discussion

The equilibrium potential, E, of the oxygen electrode with respect to an air reference electrode is given by the Nernst equation

$$E \text{ (in volt)} = 4.95 \times 10^{-5} \times T \log (0.20/p) \quad [1]$$

p is the oxygen pressure in atmospheres at the electrode-electrolyte interface. 0.20 was the partial pressure of oxygen in the air at the reference electrode[1]; T is the absolute temperature.

When possible, the output voltage was compared directly to the oxygen partial pressure as found by mass spectrometric analysis. With fuel in excess, in the equilibrium experiments, p was calculated from the known equilibrium constants for the oxidation of the fuels.

Platinum electrodes.—Two typical results with platinum electrodes are summarized in examples 1 and 2 of Table I. Dilute methane-oxygen mixtures were used that contained an excess of nitrogen, carbon dioxide, and water vapor. Given are the temperature and the flow rate; the water vapor pressure given is the equilibrium vapor pressure at a certain measured temperature of the water saturator (see Experimental section). The mass spectrometric analyses are given for samples entering and leaving the cell and do not include the water vapor. The partial pressures of the individual gases are obtained by multiplying the given concentrations by a factor $(1 - p_{H_2O}) \times 10^{-2}$. In the last two columns of the table, the measured cell output is compared with the output calculated from the oxygen partial pressure of the outgoing gas unless indicated otherwise.

Generally, good agreement was obtained between measured and calculated values as demonstrated in examples 1 and 2; this was expected on the basis of previous work (4, 5). In the first example, there was an excess of oxygen in the fuel mixture; in the second, an excess of methane. In either case, the methane was consumed completely within the error of the mass analysis for methane. In example 1, an excess of oxygen was left in the emerging gas. In example 2, no measurable amount of oxygen was left and hydrogen was found. It may be formed by the two reactions

$$CH_4 + 1H_2O = CO + 3H_2 \quad [2a]$$

and

$$CH_4 + 2H_2O = CO_2 + 4H_2 \quad [2b]$$

Both reactions are of importance at 800°C where the equilibrium constant for the water gas shift reaction $CO + H_2O = CO_2 + H_2$ is approximately equal to 1.[2]

Silver electrodes.—When it is desired to measure the correct partial pressure of oxygen in the presence of a reactive gas, an electrode material must be used that does not catalyze the oxidation of the fuel. Obviously such factors as contact time, temperature, electrode porosity, and surface area will also affect the degree of oxidation during passage of the gas through the cell.

Relatively little information is available on the catalytic oxidation of saturated hydrocarbons (6) at high temperatures. On general grounds, one would expect that the transition metals are not suited for the present purpose. In view of the vacancies in their d-orbitals, they strongly chemisorb hydrogen and they also chemisorb methane dissociatively because enough energy is gained for breaking the C-H bond by the bonding of the split off hydrogen. On the other hand, silver is an s-metal and does not chemisorb hydrogen at low temperatures. [Strictly, this holds true only for oxygen-free silver (7).] The chemisorption of methane on silver would be expected to be very slow. On the other hand, silver is known to provide an excellent oxygen electrode. The reason for this is that the oxygen chemisorption, as well as the diffusion to the electrode-electrolyte interface, is fast. This also holds for electrodes of low porosity because of the relatively high diffusion rates of oxygen through the bulk or along the grain boundaries of the silver film.[3]

No oxidation of methane was observed in any experiment with silver electrodes up to 800°C. The gas analyses of samples taken before and after transfer of the mixtures through the cell were the same.

In Tables II and III, some typical results are presented. In Table II, a single oxygen mixture was used containing 0.85% methane and 2.34% oxygen (excluding water), at temperatures between 550° and 800°C, with and without water present. The only slightly lower oxygen concentration found in the "out"-sample at the highest temperature of 795°C is at least partly

[1] Strictly, the fraction of oxygen in dry air is 0.2094. The value 0.200 was used in the calculations for the oxygen reference pressure. It is an empirical average value chosen to offset the effect of humidity in the reference air and of the excess pressure of the gas to be analyzed over atmospheric pressure at an average flow rate.

[2] The CO formed in example 2 of Table I could not be reliably analyzed. It contributed less than 1% to the mass peak 28 which it shares with N_2. With $K = [CO_2][H_2]/[CO][H_2O] = 0.877$, the CO formed is found to be 0.6%. The error in the analyses is up to 3% and is higher for the low methane concentrations.

[3] These properties are important even at open circuit; otherwise, in the presence of a reducing gas, cell voltages may be observed that seem abnormally high. (Y. L. Sandler, Unpublished results; also cf. Abs. 328, p. 732, Electrochem. Soc. Extended Abstracts, Spring Meeting, Los Angeles, May 10-15, 1970.)

Table I. Typical results with platinum electrodes

Example No.	Temp, °C	Approx flow rate, cc/min	H_2O pressure, atm		Mass spectrometer analysis m/o (H_2O excluded) CH_4	O_2	N_2 (+ CO)	CO_2	Other	Cell output, mV Measured	Cell output, mV Calculated
1	847	40	0.148	In	0.08 ± 0.03	2.11	88.1	9.67			
				Out	~0.02	2.03	88.1	9.83		59.6	59.0
2	850	120	0.134	In	0.98	0.87	89.2	8.93			
				Out	0.00	0.00	89.7	9.11	1.20 H_2	790	792*

* $E_{calc} = 0.916 - 0.114 \log (P_{H_2O}/P_{H_2})$.

Table II. Results with silver electrodes: dilute fuel-oxygen mixture

Flow rate 65 cc/min

Temp, °C	p_{H_2O}, atm		Analysis m/o without H_2O CH_4	N_2	O_2	CO_2	Output, mV Meas	Calc
795	0	(Out)	0.86	88.46	2.16	8.52	51.8	51.5
645	0.163						48.4	47.7
645	0						44.5	44.1
556	0.163						43.5 → 44.0	43.1
556	0						40.5	39.8
743	0	(In)	0.85	88.40	2.34	8.41	47.2	47.4
743	0.163						52.2	51.4

Table III. Results with silver electrodes: methane + air (undiluted)

Temp, °C	Flow, cc/min	p_{H_2O}, atm		Analysis m/o without H_2O CH_4	N_2	O_2	Output, mV Meas	Calc	Ratio O_2/N_2
649	100	0	Out	7.31	74.05	18.55	1.55	1.58	0.250
750	100	0					1.78	1.75	
750	100	0.037					2.75	2.57	
696	30	0	In	19.70	64.42	15.88	4.88	4.92	0.247
696	30	0.037					5.75	5.60	
697	15	0.033	Out	26.99	58.54	14.47	7.85 ± 0.1	7.90	0.247
697	15	0					7.02	6.87	

due to fluctuations in the gas composition that occurred in this set of experiments.

In Table III, similar experiments are presented with relatively high concentrations of methane in "air," actually a mixture of 20% oxygen in nitrogen. Three different mixtures were used near 700°C at flow rates varying from 15 to 100 cc/min. The results appear particularly striking[4]: with mixtures containing up to 27% methane, the gauge indicated the correct oxygen partial pressure in the mixture entering the gauge, with and without the presence of water vapor. As may be seen, the ratio of oxygen to nitrogen is the same before and after passage through the gauge, showing that no oxidation of methane occurred. The maximum deviation of only 0.2 mV between measured and calculated voltages corresponds to an error of about 1% in the oxygen concentration, which is below the error of the mass spectrometric oxygen determination.

When the gas supply was stopped and the exit of the tube was closed by a plug, the potential gradually rose, as shown in Fig. 2 for one example. This is caused by slow catalytic combustion of the methane and the resulting loss in oxygen.

The experiment sets the approximate temperature limit of 700°C at which silver can be used as a nonequilibrium electrode in static systems. In the present flow system, accurate voltages were obtained to 800°C. Small positive deviations from theoretical voltages were observed at 850°C at low flow rates indicating some catalytic activity. At any rate, the use of such high temperatures is not practical because of the high vapor pressure of silver and the resulting short life of the electrodes.

[4] Methane is explosive in concentrations above 5.5% in air. The absence of any gas phase reaction is due to the large surface-to-volume ratio in the narrow electrolyte tube. [F. B. Lewis and G. von Elbe, "Combustion, Flames and Explosions of Gases," Second Ed., p. 103, Academic Press, New York (1961).]

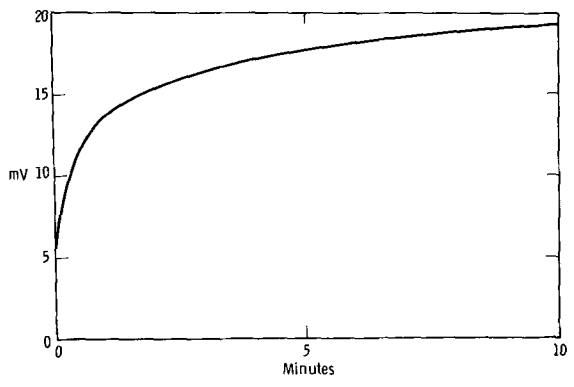

Fig. 2. Change in cell voltage with time for a stationary mixture of 19.7% CH_4 and 80.3% air at 696°C.

A methane gauge.—It has been demonstrated for methane-air mixtures that, by the use of appropriate electrodes, the zirconia high-temperature cell can accurately indicate the chemical potential of the oxygen either in the totally equilibrated state or in the totally unequilibrated state. The nonequilibrium cell measures the true oxygen partial pressure, or concentration, in the mixture, while the equilibrium cell indicates the excess oxygen pressure or concentration after complete equilibration of the mixture. Thus, the difference in the oxygen content indicated by the two cells gives the oxygen required for the combustion of the methane, which is equal to one half the amount of the methane in the mixture. The combination of the two cells therefore allows the determination of both the oxygen and the methane in the mixture.

The situation may arise that the amount of oxygen in the mixture is known, for example, when methane is present as an impurity in air. Then a single measurement is sufficient to determine the methane concentration. This can be achieved by the use of a cell having one equilibrium and one nonequilibrium electrode. One version of this type of cell is indicated in Fig. 3. The air stream containing methane is split in two parts. One part passes through a catalyst bed where the mixture is equilibrated and subsequently comes in contact with one silver electrode, the anodes of the cell. The other part passes directly over the cathode which is also made of silver. The same metal is used for both electrodes to avoid the thermoelectric potential set up between dissimilar metals. (The potential of a platinum-silver couple was measured to be 13 mV at 800°C.)

Suppose that the mixture initially consists of a moles CH_4 and b moles O_2. At the equilibrium electrode, the mixture will be

$$a\,CO_2 + 2a\,H_2O + (b - 2a)\,O_2$$

The cell voltage then is

$$\Delta E = (RT/4F)\ 2.30 \log [b/(b - 2a)] \qquad [3]$$

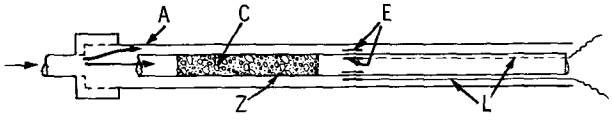

Fig. 3. Methane gauge. A = alundum sheath, Z = zirconia cell, E = electrodes, L = leads to cold end of Z, C = catalyst.

Table IV. Results with 2-cell arrangement

Methane + (19.8% O_2 + 80.2% N_2). Flow rate 30 cc/min

1		2				3	4	5	6	7	8	9
Temp, °C	CH_4	Analysis of gas at exit of cell II (incl H_2O) N_2	O_2	CO_2	H_2O	% CH_4 in, from analysis	Cell I (noneq) E_1 (mV)	% O_2	Cell 2 (eq) E_2 (mV)	% O_2	ΔE (mV)	% CH_4 from E_1,E_2
800	0.0	79.7	17.3	1.0	2.0	1.0	0.9	19.3	3.0	17.6	2.1	0.8_5
800	0.0	78.6	13.8	2.5_5	5.1	2.5_5	1.4	18.8	8.5	13.8	7.1	2.5
800	0.1	76.9	9.0	4.7	9.4	4.8	2.1	18.3	18.7	8.9	16.6	4.7
700	0.1	79.7	16.7	1.2	2.4	1.3	0.7	19.4	3.3	17.1	2.6	1.1_5
700	0.1	78.2	13.1	2.9	5.8	3.0	1.3	18.8	8.9	13.1	7.6	2.8_5
700	0.1	76.7	8.3	5.0	10.0	5.1	1.9	18.3	18.8	8.2	16.9	5.0_5

The ratio of the partial pressures in the Nernst equation can be replaced by the number of moles or by concentrations because the number of molecules does not change during the combustion of methane.

Then,

$$b/(b - a) = \log^{-1}[(4\mathbf{F}/2.30\,RT)\,\Delta E] = A$$

or

$$a = b/2\,[(A - 1)/A] \qquad [4]$$

giving the methane concentration in terms of the known oxygen concentration and the measured cell voltage.

It is desirable to use a catalyst that is effective in small amounts so that it can be inserted directly into the electrolyte tube. A platinum catalyst supported on porous alumina fragments of 2-3 mm diameter was found adequate. The support was soaked in chloroplatinic acid and reduced with borohydride to give a platinum content of 1% by weight. After careful washing and steaming, the catalyst was densely packed into the electrolyte tube between two retaining nickel nets about 4 cm apart.

The method was tried out in a system shown in Fig. 4 which allowed the test of different combinations. It consists of a nonequilibrium gauge and an equilibrium gauge in series. All electrodes were made of silver paste. The outer electrodes, the cathodes, were exposed to air and were electrically connected. The gas mixtures used consisted of methane and a premixed gas containing 19.8% oxygen in nitrogen. The results are presented in Table IV. Only the mixture emerging from the second cell was analyzed by mass spectrometer. The analyses, as given in column 2 of the table, already include the water content; it must be twice the amount of CO_2 which is formed by the reaction $CH_4 + 2\,O_2 = CO_2 + 2H_2O$. The concentration of methane initially present, as given in column 3, is equal to the amount of CO_2 formed plus the small amount of residual methane found in some of the exit samples. Columns 4-7 give the nonequilibrium and the equilibrium voltages, E_1 and E_2, and the oxygen concentrations derived from these voltages. ΔE in column 8 is the voltage between equilibrium and nonequilibrium electrode which is equal to the difference between the two cell voltages, E_1 and E_2. The methane concentrations given in the last column are one half of the difference of the oxygen concentrations in the two cells (columns 5 and 7). The same methane concentrations are obtained when calculated from the initial oxygen concentrations and ΔE by the use of Eq. [4], without the use of E_1 and E_2 individually. As may be seen, the methane concentrations obtained from the cell measurements are in satisfactory agreement with the data derived from the mass-spectrometric analyses (column 3).

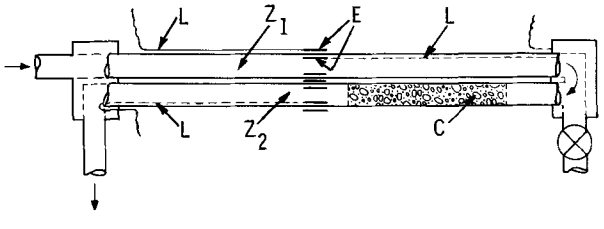

Fig. 4. Combination gauge. Z_1 = nonequilibrium cell, Z_2 = equilibrium cell, E = electrodes, L = leads to cold end of Z, C = catalyst.

It should be possible to improve further the sensitivity and accuracy of the method, particularly at low methane concentrations, by the use of a larger amount of catalyst, to oxidize the methane more completely before it reaches the anode, and by compensating for asymmetries in the cell with the use of pure air or oxygen on both sides of the cell.

No pure air or oxygen is required when determining the methane content of air from ΔE and the known initial-oxygen concentration. A device as depicted in Fig. 3 therefore should be well suited as a methane detector in applications such as coal mine safety devices or gas leak detectors.

Acknowledgment

The author is much indebted to Mr. D. D. Durigon for his efficient help with the experiments.

Manuscript submitted Mar. 13, 1970; revised manuscript received Mar. 3, 1971.

Any discussion of this paper will appear in a Discussion Section to be published in the June 1972 JOURNAL.

REFERENCES

1. C. Wagner, *Naturwiss.*, **31**, 265 (1943).
2. J. Weissbart and R. Ruka, *Rev. Sci. Instr.*, **32**, 593 (1958).
3. W. M. Hickam, "Vacuum Microbalance Techniques," Vol. 4, p. 47, Plenum Press (1965).
4. H. Peters and H. H. Möbius, *Z. Physik, Chem.*, **209**, 298 (1958).
5. J. Weissbart and R. Ruka, *This Journal*, **109**, 723 (1962).
6. G. C. Bond, "Catalysis by Metals," p. 451, Academic Press (1962).
7. Y. L. Sandler, S. Z. Beer, and D. D. Durigon, *J. Phys. Chem.*, **70**, 3881 (1966).

An Intercell Planar Heat Pipe for the Removal of Heat During the Cycling of a High Rate Nickel Cadmium Battery[1]

E. T. Mahefkey

Air Force Aero Propulsion Laboratory, Wright-Patterson AFB, Ohio 45433

and M. M. Kreitman[2]

Physics Department, University of Dayton, Dayton, Ohio 45409

ABSTRACT

Two 22 A-h nickel-cadmium cells were continuously cycled at a 1c charge rate and a 2c discharge rate, with cooling provided by an intercell planar (rectangular cross section) heat pipe. For purposes of comparison, thermocouple measurements were also taken with an aluminum conduction fin substituting for the heat pipe. The aluminum fin and heat pipe were cooled, by room temperature forced air. Thermally insulated cells were also cycled at the same rates. Cell case temperatures were measured during cycling, and a maximum of 29°C with a 5°C thermal excursion was noted with the heat pipe under conditions of thermal equilibrium which were observed after 3 complete cycles. For the aluminum fin configuration a maximum of 42°C with a 7°C thermal excursion was obtained near thermal equilibrium after 5 complete cycles. The insulated configuration yielded a battery case temperature of 83°C after 5 cycles, and thermal equilibrium was never reached. Coulombic efficiency values for the heat pipe cooled battery were found to be several per cent greater than ~95% which was recorded for the aluminum fin configuration. The specific heat of the cells was measured to be 0.27 cal/g°C. From this and the measured values of the total heat generated per cycle, the effectiveness of the heat pipe in removing battery heat was calculated to be approximately 26% greater than the aluminum fin at or near equilibrium. It is surmised that the significantly lower operating temperatures produced by the heat pipe should lead to an important lengthening of battery cycle life and an associated reduction of capacity degradation.

The use of a heat pipe for the transfer of a large amount of heat with a small temperature drop is well known (1) and it has shown promise of being immediately useful in many areas of technology (2). High thermal conductance is achieved by transferring heat via evaporation and condensation of a fluid within a wick lined pressure vessel (see Fig. 1). The evaporation of the fluid (termed working fluid) occurs at one end of the device and vapor transport carries the heat (of vaporization) to another section where condensation and heat rejection occur. The condensed vapor is returned to the evaporator section via wick forces (capillary pumping). The heat pipe is closely analogous to the ordinary steam heating-radiator system, where the wick serves as the condensate return mechanism rather than gravity. Within certain limits, the heat pipe is capable of transferring heat energy from one point to another point with very small temperature differences.

One of the most important technological applications of a heat pipe is the efficient removal of waste heat from power sources. In the following paragraphs, we wish to discuss and compare the cooling of an advanced two cell nickel cadmium battery at high charge and discharge rates by (*a*) the use of a planar heat pipe; and (*b*) an aluminum conduction fin.

Although the literature on heat pipes deals chiefly with cylindrical geometry, planar type heat pipes are not only important because their flat configuration is highly adaptable to many requirements, but in addition, since their rectangular cross section can offer much more perimeter than circular cross sections of the same area, they can offset significant limitations on the thermal conductance of cylindrical heat pipes by presenting much larger surface areas to the heat source. In this way, lower thermal fluxes through the heat pipe surface can be realized and the possibility of local overheated areas is decreased. Recently, in discussing thermal control of spacecraft batteries, Coggi (3) has considered the optimization of the conduction path between the battery and the heat sink. In order to be compatible with rectangular case configurations of battery cells, and to achieve maximum heat transfer between the cell case wall and the heat pipe, a planar heat pipe was developed and tested with electrical heaters serving to simulate the battery heat source (4). We now report on measurements associated with the application of this heat pipe to the removal of battery waste heat.

Apparatus

Heat Pipe.—The planar heat pipe employed for these experiments was fabricated from thin (0.635 mm) Type 304 stainless steel sheet with over-all dimensions of 12.7 mm x 88.9 mm x 304.8 mm. In addition to its outer shell, a heat pipe normally consists of a porous wick and enough working fluid to saturate the entire wick. Although a variety of working fluids, ranging, for example, from ammonia to silver, have been found suitable (5), water was used for the working fluid

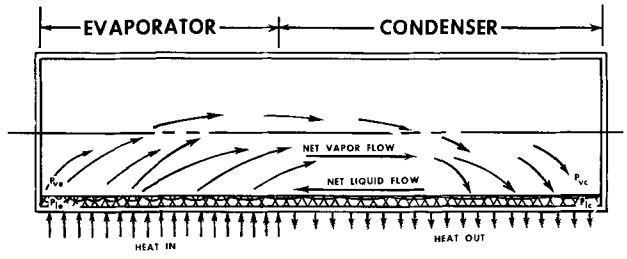

Fig. 1. A schematic drawing of a planar heat pipe

[1] This manuscript is submitted for publication with the understanding that no limitation shall exist on the reproduction and distribution of its published or unpublished form in whole or in part for any purpose of the United States Government.

[2] Supported by Aerospace Research Laboratories, OAR, USAF, Contract No. F 33615-67-C-1027.

Key words: NiCd battery, heat pipe, heat transfer, heat generation.

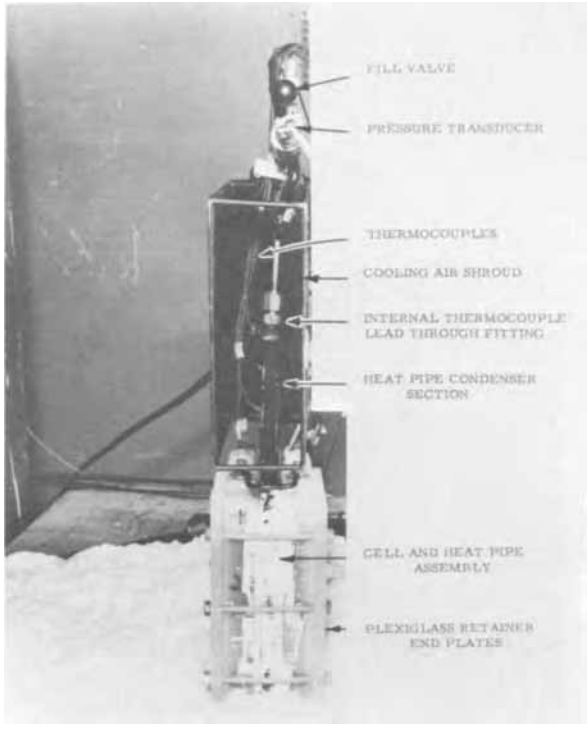

Fig. 2. Assembled battery, intercell heat pipe, and cooling shroud (with insulation removed).

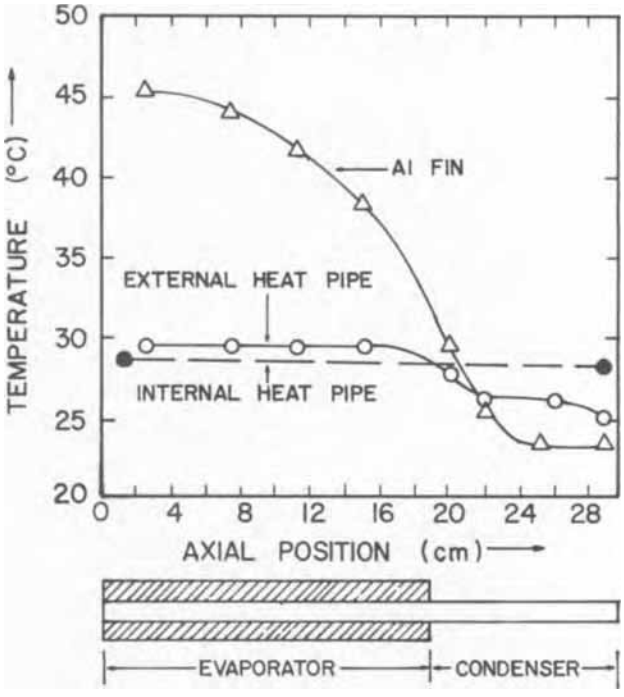

Fig. 3. Axial temperature profile of battery-heat pipe and battery-aluminum fin after five continuous cycles.

because it presented fewer experimental difficulties and offered an abundance of thermophysical data. Thirty grams of singly distilled, deionized, demineralized water was introduced into the heat pipe through the fill valve shown in Fig. 2. Two unbonded layers of 100 mesh stainless steel screen were used as capillary material. The stainless steel surfaces were passivated by soaking in 10% Na-OH solution for 12 hr prior to loading the working fluid. The heat pipe weighed approximately 570g. No attempt was made to minimize weight or volume of this prototype device. Further construction details of the heat pipe have been described in Ref. (4).

Battery.—The two nickel cadmium cells employed for these tests were new, unsealed, and flooded. Nominal capacity of each cell was 22 A-h, although the actual capacity was approximately 26 A-h. Design features of the cell (6) included thin (0.508 mm) plates, with a nickel, rather than iron, current-carrying substrate. The plate combs and terminals were nickel plated heavy copper. Cell internal resistance was 0.5-0.8 milliohms. The cell case material was nylon and the separator material was nonwoven nylon. Over-all dimensions of each cell were 26.7 mm x 79.4 mm x 194.1 mm and each weighed 1139g.

Assembly.—The heat pipe was located between the cells and held in place by two 9.5 mm thick Plexiglas retainer plates, which were bolted together. See Fig. 2. A thin layer of heat sink compound was spread on the cell face to promote good thermal contact. With the exception of the heat pipe condenser section (the part of the heat pipe protruding above the cells), the cell-heat pipe-Plexiglas assembly was insulated with a 15 cm thickness of ceramic fiber insulation. The top of each cell was uninsulated, but was covered with a 1.6 mm thick Teflon cover plate (not shown in Fig. 2) to minimize heat losses. For comparative purposes, the two cell battery was also tested with a 3.18 mm thick intercell aluminum thermal conduction fin which was assembled in the same manner as the heat pipe. The heat rejection portion of the fin (3.18 mm x 88.9 mm x 101.6 mm) was similar to that of the condenser end of the heat pipe (12.7 mm x 88.9 mm x 101.6 mm). Cooling was provided by placing the uninsulated part of the fin or heat pipe condenser section into an air duct into which a small centrifugal blower supplied room temperature (20°-22°C) cooling air.

Instrumentation.—Instrumentation of the heat pipe included internal and external copper-constantan thermocouples (±0.5°C accuracy) and a pressure transducer to monitor working fluid vapor pressure (±0.01 psia). Four No. 36 copper-constantan thermocouples were attached to the centerline of the evaporator (heat input) section of the heat pipe at axial positions corresponding to the abscissa values of data plotted in Fig. 3. The aluminum fin was instrumented in a similar fashion. For measurements on a third configuration (in which neither the heat pipe nor the aluminum fin were included), five thermocouples were located between the cells at approximately the same axial positions (see Fig. 4), and the heat accumulation without cooling was investigated with a 15 cm thick blanket of ceramic fiber insulation surrounding the battery assembly.

Procedure

The cells were cycled at nearly constant current conditions, 26A charge and 48A discharge. Charge and discharge currents were manually controlled by adjustment of individual power supplies. Cell case (heat pipe evaporator) temperatures and internal heat pipe temperatures were measured and recorded during cycling, as were charge and discharge currents and voltages. The 26A charge was terminated at one hour and discharge was initiated immediately. Discharge was terminated when the battery voltage reached 1.8V (0.9V/cell). Thus, the depth of discharge was nearly 100%. Five continuous cycles were run for each configuration in an attempt to establish equilibrium conditions in the cell.

The heat pipe and batteries were tested in both the vertical position (reflux mode), with condenser section uppermost and in the near horizontal position. In the near horizontal position, the evaporator section was purposely elevated one inch with respect to the condenser to insure liquid return was by capillary pumping. In preliminary experiments, the effect of gravity had little influence on heat pipe or battery performance for these test conditions. However, some difficulty was experienced due to leakage of electrolyte

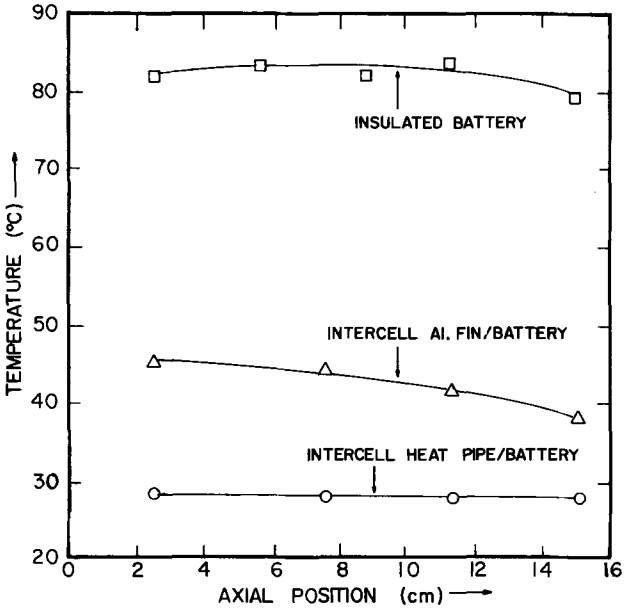

Fig. 4. Axial temperature profile of Ni-Cd cell case after 5 continuous cycles. (Cell case temperature ≡ temperature of the portion of the heat pipe or the aluminum fin in contact with the cell case.)

through the battery outgassing seals, and it was decided to limit further experiments to the vertical position only.

In general, the heat pipe may be designed to operate in a gravity environment, such as encountered in a spinning spacecraft. The effect of gravity is to reduce the maximum transportable heat flux, therefore, the device is more attractive for zero gravity or reflux mode (condensate return aided by gravity) applications.

Results

Figure 4 shows the cell case temperature profile at the end of discharge after five continuous cycles for the three configurations investigated. Table I summarizes the measured electrical parameters for the cycles indicated. Current and voltage data given are average values. These results show the heat pipe cooled battery efficiency to be several per cent better than that of the aluminum fin cooled configuration. Both the heat pipe and aluminum fin cooled configurations are markedly superior in efficiency to that of the uncooled, insulated battery.

The axial temperature profile of the entire length after 5 complete cycles with the aluminum fin and heat pipe are shown in Fig. 3. Characteristically the heat pipe cooled cells exhibit a near isothermal axial temperature profile, while the aluminum fin cooled cells are subjected to a 15°C axial temperature gradient. It may be noted that the evaporator section of the heat pipe is significantly cooler than the aluminum fin, while the condenser section of the heat pipe is hotter.

To assist in the analysis of the results, the specific heat of the cell was measured using a water calorimeter. The cell was heated in a furnace to a known temperature, typically between 50° and 60°C, then removed from the furnace and immersed in a water bath which was initially at a temperature of 5° to 10°C. The equilibrium temperature of the cell and bath were measured and the cell specific heat was calculated. Five separate determinations were performed and the mean specific heat of the cell was found within 3.4% to be 0.27 cal/g°C at approximately 25°C. The specific heat of a brass sample was measured in the same manner and found to be within 4% of the accepted value.

Table I. Electrical performance of battery at or near thermal equilibrium

Cycle description	Cycle number	Charge Amps (avg)	Charge Volts (avg)	Discharge Amps (avg)	Discharge Volts (avg)	Efficiency η_{A-h} %	Efficiency η_{W-h} %
Insulated battery	Cycle 4	26.0	2.80	47.5	2.37	59.3	50.4
	Cycle 5	26.1	2.83	47.9	2.32	52.4	44.3
Battery with Al-fin	Cycle 3	26.9	2.84	48.4	2.45	96.3	83.0
	Cycle 5	27.1	2.82	48.0	2.45	94.6	82.2
Battery with heat pipe	Cycle 4	26.4	2.85	48.1	2.45	97.8	84.0
	Cycle 5	26.4	2.82	48.4	2.47	98.4	86.0

Discussion

Two important thermal related properties of battery performance are cell cycle life and cell capacity (7). Reference (7) discusses the logarithmic decrease of cell cycle life with an increase of depth of discharge for different temperatures. For an 80% depth of discharge, it has been observed that the cell cycle life is approximately doubled when the operating temperature is decreased from 49° to 24°C. Based on the temperature dependence of the cell cycle life given in Ref. (7), the data in Fig. 4 indicate that operation of the battery at the lower temperatures provided by the heat pipe should yield significant improvements in cell cycle life.

Another temperature dependent property of cell operation is cell capacity, the ability of a cell to store charge. Marked decreases in cell capacity have been observed with these cells as a result of extended cycling at elevated (>40°-50°C) temperatures (8). In Fig. 5, the end of charge heating observed for the in-

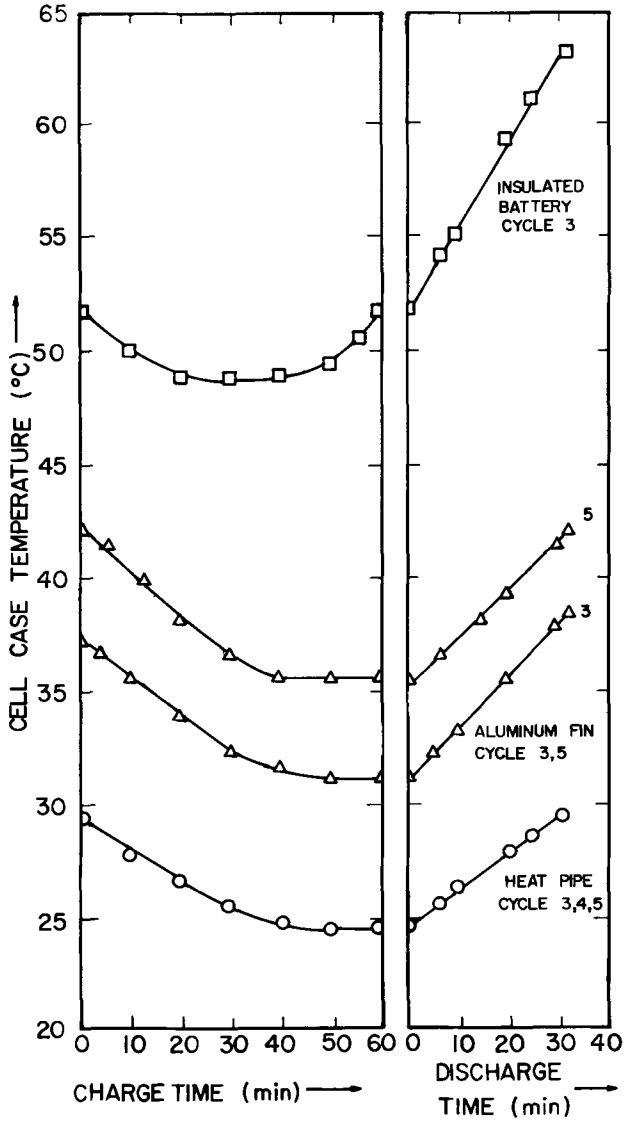

Fig. 5. Comparison of mean cell case temperature during charge and discharge.

sulated battery configuration can be partly attributed to faradaic inefficiency (reduction in cell capacity) because of operation at higher temperatures. Similar end of charge heating was also observed for cycles 4 and 5, but, these data are not shown because they lie beyond the scale of the graph.

Mean battery case temperatures (average of ordinate values of Fig. 4) were also plotted as a function of charge time in Fig. 5 for the heat pipe and aluminum fin cooled battery configurations and a nearly linear temperature change was observed during the first 40 min of charge. The cell temperatures were then observed to remain nearly constant until completion of the 26A, 1 hr charge. Cycle 4 for the aluminum fin configuration is omitted in Fig. 5 (and in Table I) because the cells were deliberately overcharged by 10% (~6 min) in an attempt to examine the thermal response. Rapid end of charge heating was observed similar to that noted above with the insulated battery configuration, and this was used as a check on the actual A-h capacity of the battery. Similar overcharge results were obtained in separate experiments (not reported here) with the heat pipe configuration.

On discharge, the mean cell case temperature change as a function of time was linear for all three configurations. It was observed that the thermal excursion undergone by the heat pipe cooled cell is approximately 5°C as compared to 7°C for the aluminum fin configuration. It is expected that reduction in the thermal excursion (with the heat pipe configuration) could be realized by various improvements of the heat pipe design, specifically, by employing a sintered screen or porous metal capillary wick instead of an unbonded layered wick (4). No such attempts were made. It was found that the thermal excursions of the heat pipe-cooled battery reached dynamic equilibrium after 3 cycles, while the aluminum fin cooled battery appeared to approach equilibrium after 5 cycles. Dynamic equilibrium was assumed when the temperature dependence of the charge discharge results for successive cycles was found to be approximately identical.

In order to estimate the net heat transferred by the heat pipe and aluminum fin, the heat generated by the cells was compared to the heat accumulated in the cells. The heat generated during charge is given by the first and second laws of thermodynamics (9)

$$Q_C = \int_C I\Delta E dt + T\Delta S \Big|_C \quad [1]$$

The heat generated during discharge is given by

$$Q_D = \int_D I\Delta E dt + T\Delta S \Big|_D \quad [2]$$

For high A-h efficiencies, the chemical reaction can be assumed reversible such that

$$T\Delta S \Big|_C \simeq -T\Delta S \Big|_D \quad [3]$$

Adding Eq. [1] and [2] and integrating yields the total heat generated per cycle, given by

$$Q_{\Delta E} = I_C \Delta E_C t_C + I_D \Delta E_D t_D \quad [4]$$

where recorded charge and discharge current and voltage data was averaged and used to calculate $Q_{\Delta E}$. The heat accumulated in the cells per cycle is given by

$$Q_{\Delta T} = m\, C_P\, \Delta T \quad [5]$$

and the net heat transferred per cycle by the heat pipe and aluminum fin is

$$Q_R = Q_{\Delta E} - Q_{\Delta T} \quad [6]$$

The above analysis neglects end of charge heating and thermal losses through the power leads and insulation. A small amount of end of charge heating was observed on some cycles, characterized by a slight (0.5°-1.0°C) increase in cell case temperature. For the first two cycles of the insulated battery configuration where it was assumed that $Q_R \approx 0$ and where the measured amp hour efficiencies were greater than 95%, it was found that $Q_{\Delta E}$ exceeded $Q_{\Delta T}$ (calculated from the measured specific heat) by only 8%. This result indicates that the effects of thermal lag and external heat losses cannot be more than 8%. Thus, the Q_R for the heat pipe and aluminum fin configuration can be computed to within 8%.

Table II. Comparison of heat transferred and fin effectiveness for the heat pipe and aluminum fin for heat accumulated over n cycles (where $1 \leq n \leq 5$)

	$\Sigma Q_{\Delta E}$	$\Sigma Q_{\Delta T}$	ΣQ_R	ξ
Aluminum fin/battery				
Cycle 1	11.42	8.54	2.88	0.252
Cycle 2	22.12	11.90	10.22	0.462
Cycle 3	32.32	12.70	19.62	0.607
Cycle 4	44.02	15.30	28.72	0.652
Cycle 5	53.76	15.85	37.91	0.705
Heat pipe/battery				
Cycle 1	11.93	4.56	7.37	0.618
Cycle 2	22.60	5.55	17.05	0.754
Cycle 3	32.48	5.84	26.64	0.820
Cycle 4	42.92	5.84	37.08	0.864
Cycle 5	52.81	5.84	46.97	0.889

Table II summarizes the thermal performance of the heat pipe and aluminum fin battery configurations during cycling. These data are based on the total heating values, obtained by addition of the per cycle heating parameters described by Eq. [4], [5], and [6] respectively. Comparison at equilibrium conditions, cycle 5, shows the heat pipe to be approximately 26% greater in fin effectiveness, or relative heat transfer capability, as compared to the aluminum fin. Heat accumulated in the cells with heat pipe cooling was approximately 11% (5.84 W-h) of the total heat generated in 5 cycles, as compared with 29% (15.85 W-h) for the aluminum fin cooled configuration.

Conclusions

It was demonstrated that the heat pipe limited maximum temperatures of the cell case during cycling to 29°C for the 1C/2C charge/discharge rates. Thermal equilibrium was achieved after three complete cycles, during which the thermal excursion of the cell case was limited to 5°C. By comparison, after five complete cycles the temperature of the aluminum fin cooled battery case reached 42°C, near thermal equilibrium was achieved, and the thermal excursion was 7°C. However, for the insulated battery, the case temperature ascended to 83°C after five cycles, and thermal equilibrium was never attained.

At or near thermal equilibrium, the electrical efficiency of the heat pipe cooled battery was found to be several per cent greater than approximately 95% which was recorded for the aluminum fin configuration. After two cycles the efficiency of the uncooled, insulated battery, decreased rapidly due to heat accumulation, and at 5 cycles it was measured approximately 52%.

The mean specific heat of the cell was measured to be 0.27 cal/g°C and this result was used to show that the fin heat transfer effectiveness with the heat pipe is approximately 26% greater than that with the aluminum fin at or near equilibrium. It is surmised that the heat transfer effectiveness of the heat pipe could be improved further by capillary design refinements, thus lowering the evaporator and condenser radial temperature gradients. It is expected that the weight and volume of the prototype heat pipe (570g, 344 cc) could be halved by such design optimization with no adverse effects on heat transport capability. These experiments demonstrate the ability of the heat pipe to minimize heat accumulation and thermal excursion in the battery during cycling, thereby allowing operating conditions at significantly lower temperatures. Such improved operating conditions should lead to an important lengthening of the battery cycle life and an associated reduction of capacity degradation.

Acknowledgments

We would like to acknowledge valuable information and assistance obtained from Dr. J. J. Lander and technical help provided by Mr. Stanley Douple of the Air Force Aero Propulsion Laboratory. Thanks are also due to Mr. Earl Roeger of the Battelle Memorial Institute for his assistance.

Manuscript submitted Nov. 30, 1970; revised manuscript received *ca.* March 29, 1971.

Any discussion of this paper will appear in a Discussion Section to be published in the June 1972 JOURNAL.

NOMENCLATURE

ΔT	Cell temperature increase during cycling, °C
m	Cell mass, g
C_p	Average specific heat of cell, cal/g°C
I	Current, A
ΔE	Difference between open circuit voltage, taken as 1.32 V/cell, and charge or discharge voltage, V
$Q_{\Delta E}$	Heat generated by cell (averaged over a cycle) due to internal resistance and polarization losses, W-h
$Q_{\Delta T}$	Heat accumulated in cell during cycling, W-h
Q_R	Net heat transferred by fin per cycle, W-h
ξ	Fin heat transfer effectiveness, ratio of heat transferred to heat generated $\Sigma Q_R/\Sigma Q_E$
C, D	Subscripts denote charge and discharge respectively
t	time, hours
$\eta_{A\text{-}h}$	Ampere-hour efficiency
$\eta_{W\text{-}h}$	Watt-hour efficiency

REFERENCES

1. G. M. Grover, T. P. Cotter, and G. F. Erickson, *J. Appl. Phys.*, **35**, 1990 (1964).
2. G. Y. Eastman, *Sci. Am.*, **218**, 38 (1968).
3. J. V. Coggi, Intersociety Energy Conversion Engineering Conference, McDonnell Douglas Corp., Las Vegas, Nevada, Sept. (1970).
4. E. T. Mahefkey, "An Experimental Investigation of a Planar Heat Pipe for Cooling Large Capacity Batteries," M.S. Thesis, Physics Department, University of Dayton, Dec. (1970).
5. K. T. Feldman, Jr., and G. H. Whiting, *Mech. Eng.*, **89**, 30 (1967).
6. E. Kantner, R. Tarantino, P. Ritterman, R. C. Shair, Technical Report AFAPL-TR-66-77, AD 489830, Sept. (1966).
7. P. Bauer, "Batteries for Space Power Systems," p. 102, NASA SP-172, Library of Congress Catalogue Card No. 68-61302 (1968).
8. Private communication with Dr. J. J. Lander, Air Force Aero Propulsion Laboratory, Wright-Patterson AFB, Ohio.
9. "The Encyclopedia of Electrochemistry," p. 744, Clifford A. Hampel, Editor, Reinhold, New York (1964).

Sintered Zirconia Electrolyte Films in High-Temperature Fuel Cells

N. J. Maskalick* and C. C. Sun

Energy Storage Department, Westinghouse Research Laboratories, Pittsburgh, Pennsylvania 15235

ABSTRACT

Thin-film fuel cells employing stabilized cubic zirconia as an oxygen anion-conducting electrolyte depend on an effective separation of fuel gas and air by the dense zirconia electrolyte layer. Fully stabilized solid-zirconia electrolyte films have been prepared by reactive sintering of zirconia, ZrO_2, and calcium zirconate, $CaZrO_3$. Such films are employed as the electrolyte in high-temperature fuel cells. Electrolyte film conductivity is at least 50% of that expected from the geometry of test cells. The films are sufficiently pure and gastight to allow near-theoretical open-circuit voltages to be displayed.

The high electrical conductivity of the oxide mixture $(ZrO_2)_{0.85}(Y_2O_3)_{0.15}$ was first observed by Nernst (1) in 1900. Solid electrolytes were studied in oxygen concentration cells by Haber (2) in 1905. The electromotive force, E, of an oxygen concentration cell having a solid zirconia electrolyte, as derived from the work of Wagner (3), is

$$E = -\frac{1}{4\mathbf{F}}\int_{\mu'_{O_2}}^{\mu''_{O_2}} (t_{ion})\, d\mu_{O_2}$$

where $\mathbf{F}$ is Faraday's constant; μ'_{O_2} and μ''_{O_2} are the chemical potentials of oxygen in the reversible cathode and anode, respectively. Assuming ideality, the chemical potentials, μ_i, are related to partial pressures, p_i, by

$$\mu_i = \mu^\circ_i + RT \ln p_i$$

where R is the gas constant per mole and T is the absolute temperature. The maximum emf of such cells, as defined by the ratios of the oxygen partial pressures

$$E = (t_{ion})\frac{RT}{4\mathbf{F}} \ln \frac{p'}{p''}$$

is not obtained unless t_{ion}, the oxygen ion transference number, is equal to unity. As shown by Neuimin *et al.* (4) dispersed electronically conductive phases, such as NiO, and dissolved compounds, such as Fe_2O_3, can each contribute to considerable lowering of t_{ion} in calcia-stabilized zirconia electrolyte if present in sufficient quantities.

The transference number of the oxygen ion in the pure electrolyte is near unity for $(ZrO_2)_{0.85}(CaO)_{0.15}$, as demonstrated by Kingery *et al.* (5). The same electrolyte was used in a fuel cell by Weissbart and Ruka (6) to measure near-theoretical voltages for the hydrogen-oxygen reaction. Archer *et al.* (7) demonstrated that 20-cell batteries using stabilized zirconia electrolyte could develop open-circuit voltages within 3% of theoretical values using hydrogen as fuel. Twenty of these batteries were assembled into a unit which employed coal gas as fuel (8). Maximum power, when loaded so that its terminal voltage was 50% of open-circuit voltage, was 110W.

The electrolyte employed by Archer was in self-supported bell-and-spigot geometry. To decrease internal resistance as much as possible, the active cell region of the electrolyte was machined to a minimum practical thickness of approximately 0.04 cm. White

* Electrochemical Society Active Member.

Key words: solid electrolytes, zirconia, fuel cells, thin films, sintering.

(9) has reported the successful plasma-arc spray fabrication of fuel cells with electrolyte having comparable electrolyte thickness. White employed an iron-oxide-doped, Y_2O_3-stabilized zirconia and a final sintering step to accomplish densification. Both the machined electrolyte and the plasma-sprayed electrolyte are comparatively thick structures, wasteful of power due to excessive voltage dropped across large internal resistances.

Recent work has employed electrolyte having considerably less thickness to further decrease internal resistance and also to minimize the cost of dense zirconia for the particular case where yttria rather than calcia is the stabilizing agent. Maskalick (10) constructed sputtered cells with stabilized zirconia electrolyte less than 5μ thick. Low sputtering rates limited the economic feasibility of this type of cell. Isenberg (11) evaluated a fuel cell with zirconia-yttria electrolyte formed by chemical vapor deposition approximately 30μ thick which developed near-theoretical open-circuit voltage and 0.45 W/cm^2 when loaded to a terminal voltage which was 50% of open-circuit voltage. Thickness control, high-temperature masking, chemical attack of cell materials, and a temperature limitation of 1100°C for processing of subsequently applied layers all contributed to make adoption of this technique in mass production difficult.

To overcome these disadvantages, Maskalick investigated sintering of thin films using layers of fine-particle, fully stabilized zirconia with and without iron oxide additions. Such films, if doped with iron oxide, were dense, though cracked and poorly bonded to the porous zirconia substrate. Extensive and rapid migration of iron led to contamination and volume changes in the porous support tube itself. Containment of iron solely in the sintering electrolyte film did not appear to be feasible, so that component structures applied in later sintering operations (*e.g.*, interconnections and air electrodes) could also be subject to iron contamination. Without iron oxide, adequate densification of fully stabilized zirconia did not occur.

The reactive sintering process $x\ ZrO_2 + y\ CaZrO_3 \xrightarrow{\Delta} (ZrO_2)_{x+y}\ (CaO)y$ was developed to form dense, well-bonded, and continuous thin films of stabilized zirconia electrolyte. This electrolyte contributes no contaminants to the surrounding fuel cell components and can be cycled repeatedly up to 1400°C for sinter-processing of successively applied component layers. Fuel cells employing this electrolyte were constructed and tested. This paper discusses the performance of such cells and aspects of the fabrication method.

Experimental

Preparation of electrolyte films.—Zirconia and calcium zirconate react quickly and completely at 1400°C to yield a dense, sintered film suitable for use as the electrolyte. The term reactive sintering is used because of the phase changes consequent to the mechanism: monoclinic zirconia and calcium zirconate in the proper proportions can react to form stabilized cubic zirconia. This is a specific example of the general reaction between monoclinic zirconia and zirconia containing stabilizing agents, *e.g.* CaO, Y_2O_3, to form cubic zirconia. Such reactions, if they occur during sintering, improve the densification of the electrolyte layer with enhanced grain growth and improved bonding to the substrate.

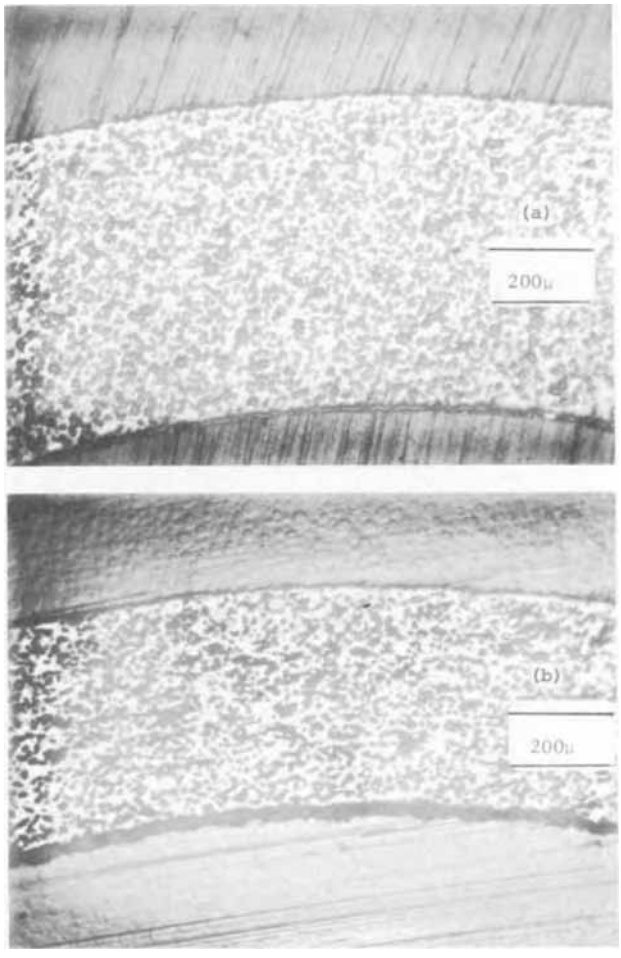

Fig. 1. Typical cross section through one wall of (a) extruded tube and (b) slip-cast tube of calcia-stabilized zirconia.

Slurries of the reactive mixture equivalent to an over-all composition of $(ZrO_2)_{0.85}(CaO)_{0.15}$ can be made by ball-milling 76 w/o (weight per cent) of submicron ZrO_2 with 24 w/o of −325 mesh $CaZrO_3$ and sufficient butyl acetate to produce a free-flowing suspension. Ball-milling times vary from 1 to 20 hr. With longer ball-milling times, the probability of the appearance of flaws due to the presence of coarse agglomerates is diminished.

Preparation of fuel cells.—The electrolyte and the working electrodes are all fabricated in sequence on the outer surface of a porous zirconia support tube. The throughgoing porosity of these tubes is displayed in Fig. 1.

In order to realize a cell geometry, the porous support tube is first coated with a sintered layer consisting of a coarse two-phase mixture of cobalt and stabilized zirconia (Fig. 2). Sintering of this layer is

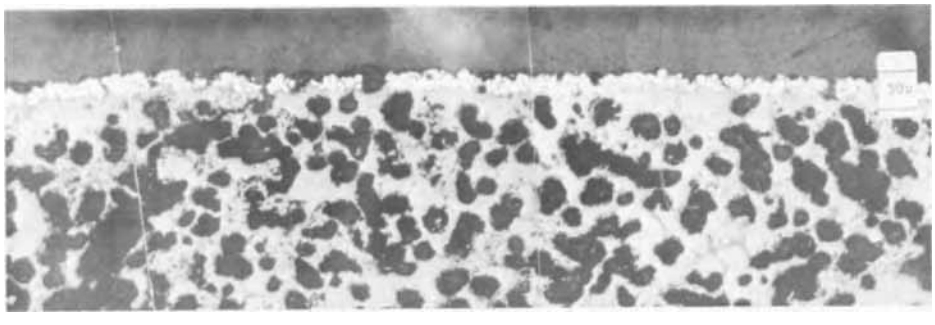

Fig. 2. Slip cast cobalt-zirconia fuel electrode over porous zirconia tube.

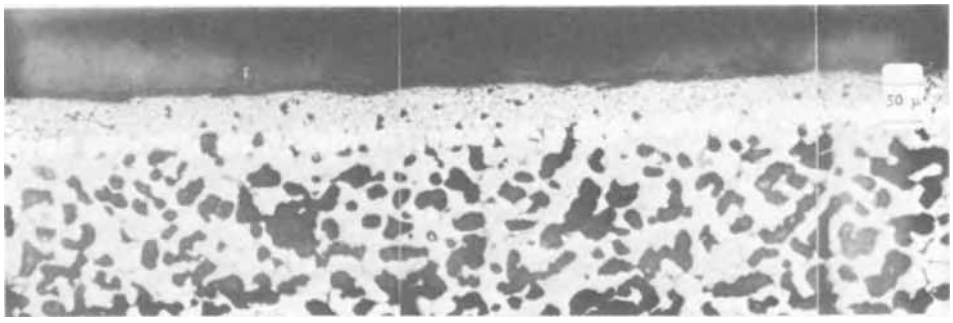

Fig. 3. Reactively sintered stabilized zirconia electrolyte over fuel electrode.

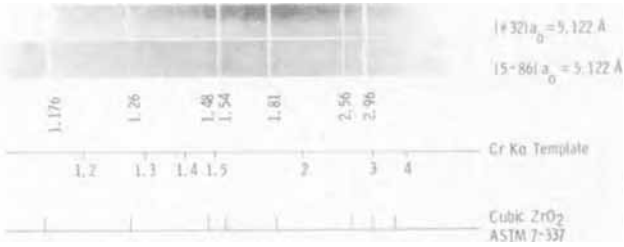

Fig. 4. Cubic structure demonstrated by thin-film reactively sintered ZrO_2-CaO electrolyte. Two-radian Debye-Scherrer powder pattern.

carried out in N_2, 5% H_2 saturated with H_2O at 26°C. This layer functions as a porous, electronically conductive fuel electrode and as the surface to which the electrolyte must sinter. The stabilized zirconia electrolyte layer must form a thin, dense, adherent film over this fuel electrode.

Electrolyte slurries may be applied to the tube and to the fuel electrode surface either by slip-casting or by spraying. Typical weight gains, after the butyl acetate has been completely removed, are 10-30 mg/cm².

Sintering is conducted in atmospheres which do not tend to oxidize the metal in the fuel electrode, so that disruptive phase changes are avoided. Either reducing mixtures of H_2/H_2O in an inert carrier gas or inert gases scrubbed to low oxygen content are employed. Sintering is carried out at temperatures which do not permit excessive migration of the cobalt metal in the fuel electrode. Experience has shown that this constraint establishes a practical limit at approximately 1430°C. Sintering times at 1400°C have been varied from 1 to 15 hr. Film grain sizes of 5-10μ are observed after 1 hr and up to 50μ after 10-15 hr.

The microstructure of a reactively sintered zirconia electrolyte film is displayed in Fig. 3. This film covers the fuel electrode layer which, in turn, is sintered to the base tube of porous zirconia. The electrolyte films at present are produced with approximately 5% apparent pore volume. Air (S.T.P.) leak rates of 6×10^{-7} moles/min at present can be demonstrated over 40 cm² with a 10^{-2} Torr initial vacuum on one side of the sintered electrolyte film. The reactively sintered electrolyte crystal structure is cubic as determined by powder method x-ray diffraction (Fig. 4). The observed range of lattice parameter is 5.122-5.123Å for films containing 17 m/o (mole per cent) calcia over-all. These data are compared with a lattice parameter of 5.11Å observed by Duwez *et al.* (12) who cooled their specimens rapidly from 2000°C. Since the lattice parameter is a function of sintering history as well as calcia content, no attempt is made to claim a particular stoichiometry for these films. They are completely cubic within a 5% limit of detection for the x-ray method. Therefore, $t_{ion} \rightarrow 1$ should be demonstrated if bulk electrolyte properties are obtained. Two test specimens were prepared, specimen A embodying two separate cells, and specimen B, also with two separate cells. In the tests reported here, the electrolyte was applied and fired on in four successive steps. Total weight gain of applied electrolyte was 33 mg/cm² and total time at 1400°C was 6 hr (specimen B) and 7.5 hr (specimen A). The sintered electrolyte films were about 60μ thick.

Electronically conducting interconnection oxide material was applied in two bands and sintered concurrently with the electrolyte. The interconnection bands served as potential taps to determine fuel electrode ρ/δ (resistivity/thickness) by the four-terminal method.

The air electrode structure of specimen A consisted of plasma-sprayed In_2O_3, 2 m/o SnO_2. The air electrode structure of specimen B was more complex, consisting of 24 mg/cm² of an intermediate porous layer of submicron $(ZrO_2)_{0.9}(Y_2O_3)_{0.1}$ fired on at 1400°C for 2 hr. This layer was then covered with plasma-sprayed In_2O_3, 2 m/o SnO_2, and finally impregnated with 0.5-1.0 mg/cm² of $CoPrO_3$.

A summary of the processed layers is given in Table I. A schematic of these layers, and their orientation on the completed device, is given in Fig. 5.

Testing of fuel cells.—Figure 6 shows the individual load circuits for each of the two cells on the test device. Contacts were established with platinum wires. Pt, Pt 10% Rh thermocouples were employed on all cells as potential taps. The geometry permits the testing of two independent cells on each specimen device. The oxide potential taps are employed to measure the voltage drop in the fuel electrode. Gold gaskets contacted the fuel electrode at both ends of the test specimen.

Cell operation was conducted with air flowing on the outside of the tubular cells and hydrogen saturated with water at 68°C flowing through the inside of the tube as depicted schematically in Fig. 6(a). Calculations of the theoretical emf are based on the H_2/H_2O ratio obtained by assuming the fuel gas mixture to be hydrogen at 0.7 psi gauge pressure containing water at the partial pressure expected at equilibrium over $H_2O(l)$ at 68°C. Two oxygen gauges served to detect

Table I. Summary of sample preparation

	Specimen A	Specimen B
Support tube	100% Cubic zirconia	100% Cubic zirconia
Fuel electrode	Air-sprayed Co-ZrO_2 cermet—sintered in reducing atmosphere of N_2 5% H_2 saturated with H_2O at 26°C	Air-sprayed Co-ZrO_2 cermet—sintered in reducing atmosphere of N_2 5% H_2 saturated with H_2O at 26°C
Electrolyte	Air-sprayed $(ZrO_2)_{0.85}$ $(CaO)_{0.15}$ Sintered in reducing atmosphere of Ca-gettered argon	Air-sprayed $(ZrO_2)_{0.85}$ $(CaO_{0.15}$ Sintered in reducing atmosphere of Ca-gettered argon
Fuel electrode potential taps	Painted, electronically conducting oxide—sintered concurrently with electrolyte	Painted, electronically conducting oxide—sintered concurrently with electrolyte
Air electrode	Plasma-sprayed In_2O_3, 2 m/o SnO_2, 32 mg/cm²	(1) $CoPrO_3$ impregnated in stabilized ZrO_2 porous skeleton (2) Plasma-sprayed In_2O_3, 2 m/o SnO_2, 81 mg/cm²

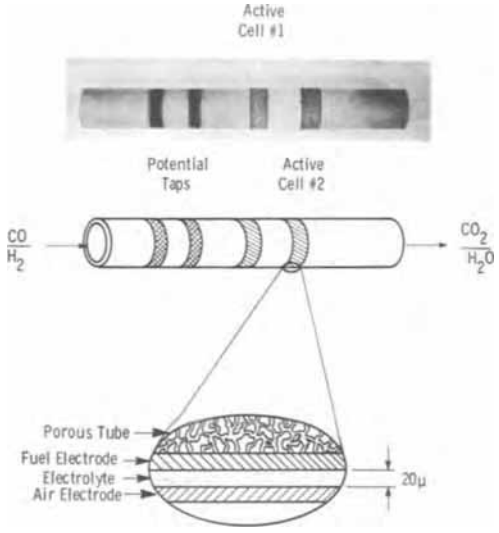

Fig. 5. Thin film fuel cell—active cell region

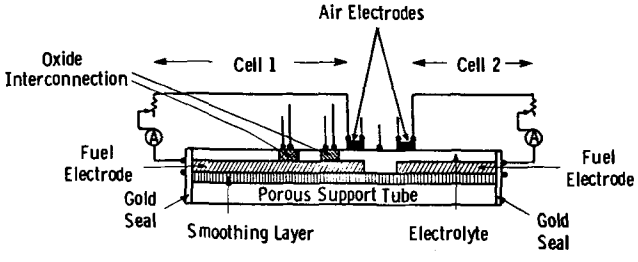

Fig. 6. Cross section of component specimen with electrical leads.

system leaks both upstream and downstream of the test cells.

Results

Both cells of specimen A developed open-circuit voltages which were 96% of theoretical over a period of 12 days. The test was terminated prematurely due to test equipment malfunction in which fracture of the upstream oxygen gauge led to contamination of the fuel stream and oxidation of the fuel electrode. Performance of these cells is displayed in Fig. 7 and 8. The cell resistances were high due to the high resistance ($\rho/\delta = 5$ ohms) of the flame-sprayed indium oxide air electrode. As a consequence, effective cell area was much less than the over-all area which was used to compute current density.

Specimen B employed an improved air electrode with a greater proportion of active cell area. The high surface area porous zirconia component of the air electrode served to increase the area of contact with the In_2O_3. The $CoPrO_3$, a conductor of both electrons and oxygen anions, was provided to improve the introduction of oxygen anions into the zirconia lattice and reduce air electrode polarization. The resulting cells developed 100% of the theoretical open-circuit voltage and showed significantly improved performances (Fig. 9 and 10). Fast and slow polarization processes observed during interruption of the current in the cell test circuits were recorded by photographing oscilloscope traces of voltage change *vs.* time. Analysis showed that the air electrode resistance and fuel electrode polarization are the two most significant voltage losses.

By measuring the fast portion of the current interruption pictures using an oscilloscope, individual contributions of total cell resistance were obtained. Referring to Fig. 6, the total cell resistance is equal to the sum of the resistance measured from the air side and the resistance on the fuel side. The resistance on the air side consists of air electrode resistance (R_a) and one half of the electrolyte resistance ($\frac{1}{2} R_b$), and the resistance measured from the fuel side includes the fuel electrode resistance (R_f) plus one half of the electrolyte resistance. Table II compares the measured resistances with values expected from the geometry of the cells on samples A and B. Cell resistances are computed assuming that the electrode resistances are low compared with that of the electrolyte. However, as pointed out earlier, due to the high air electrode resistance, $(\rho_e/\delta_e)_a = 5$ ohms, the effective cell area is lessened. This is in agreement with the higher cell resistance and polarization losses observed.

The test of specimen B was terminated on the fourth day when the open-cell voltage dropped below 0.3V. Axial cracks in the electrolyte were observed after testing. Cross sections showed that the electrolyte was lifted up from the cobalt fuel electrodes and had axial cracks where it was lifted but, in the intercell area where no fuel electrode was underneath, the electrolyte remained dense and well attached to the support tube.

A circumferential crack broke the tube open on cell No. 2. A microscopically visible circumferential crack on cell No. 1 appeared to be directly underneath the

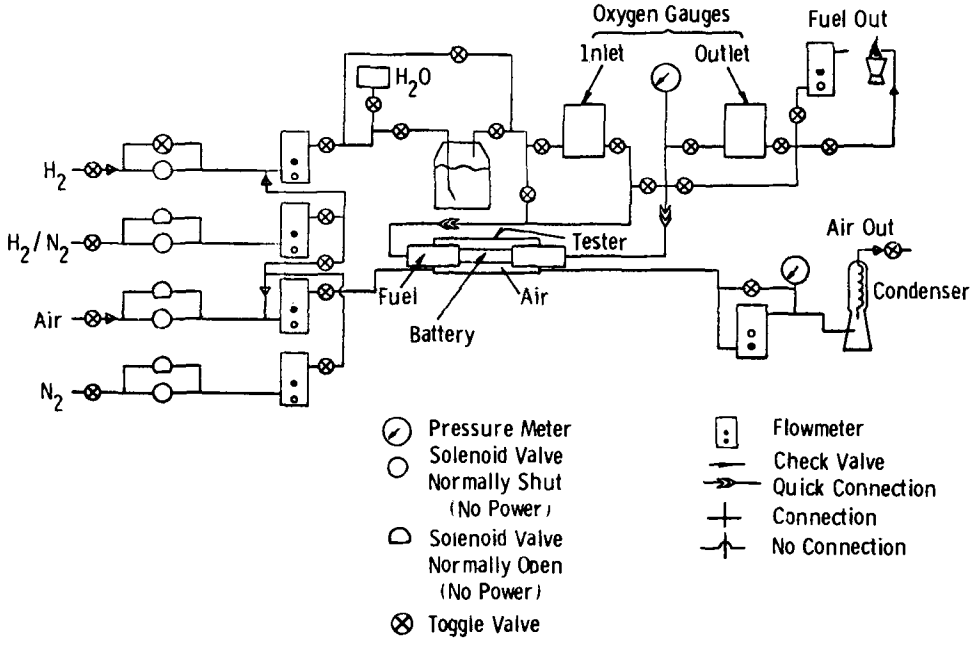

Fig. 6(a). Schematic diagram of testing system for thin-film fuel cells.

Table II. Comparison of the observed and expected cell resistances

Resistance	Observed/expected	Cell A-1 ohms	Cell A-2 ohms	Cell B-1 ohms	Cell B-2 ohms
$(\rho_e/\delta_e)_f$	Observed	0.15		0.06	
R_f	Expected	0.18	0.12	0.07	0.04
	$R_f = \left(\frac{\rho_e}{\delta_e}\right)_f \left(\frac{1}{\pi D}\right)\left(l_f + \frac{1}{2} l_c\right)$				
$R_{fuel\ side}$	Expected	0.21	0.15	0.10	0.07
	$R_{fuel\ side} = R_f + \frac{1}{2} R_b$				
	Observed	0.30	0.25	0.20	0.10
$(\rho_e/\delta_e)_a$	Observed	5	5	5	5
R_a	Expected	0.08	0.08	0.08	0.08
	$R_a = \frac{1}{8}\left(\frac{\rho_e}{\delta_e}\right)\left(\frac{l_c}{\pi D}\right)$				
$R_{air\ side}$	Expected	0.11	0.11	0.11	0.11
	$R_{air\ side} = R_a + \frac{1}{2} R_b$				
	Observed	4	3	0.60	0.40
R_{cell}	Expected	0.32	0.26	0.21	0.18
	$R_{cell} = R_a + R_f + R_b$				
	Observed	4	3	0.7	0.5
R_b, i.e. resistance of electrolyte in the cell	Expected	0.06	0.06	0.06	0.06
	$R_b = \frac{\rho_b \delta_b}{\pi D l_c}$				
	Observed i.e. $2(R_{fuel\ side} - R_f)$	0.24	0.26	0.26	0.12

Definition of Symbols:
D — Diameter of support tube (centimeters).
δ_b — Thickness of electrolyte (centimeters).
δ_e — Thickness of electrode (centimeters).
ρ_b — Resistivity of the electrolyte (ohm-centimeters).
l_c — Length of active cell (centimeters).
l_f — Length of fuel electrode lead (centimeters).
ρ_e — Resistivity of the electrode (ohm-centimeters).
R_a — Resistance of the air electrode (ohms).
R_f — Resistance of the fuel electrode (ohms).
R_b — Resistance of the electrolyte (ohms).

platinum wire leads. Because of the poor In_2O_3 current collector ($\rho/\delta \simeq 5$ ohms) employed on these cells, high current densities prevailed in the immediate contacted region of the platinum wire, causing hot spots and mechanical stresses.

From the test results of the four cells comprising specimens A and B, one can conclude the following:

1. Hydrogen-oxygen cells generating full theoretical open-circuit voltage at 960°C may be prepared using reactively sintered $(ZrO_2)_{0.85}(CaO)_{0.15}$ electrolyte 60μ thick. Such films must therefore have an oxygen ion transference number which approaches unity.
2. Electrolyte film resistivity approaches 50% of bulk, fully stabilized resistivity.
3. Air electrode resistance and fuel electrode polarization limit cell performance.
4. Mechanical stability of the entire structure also limits cell performance. The observed stresses were due to nonuniform current distribution arising from a poorly conductive air electrode.

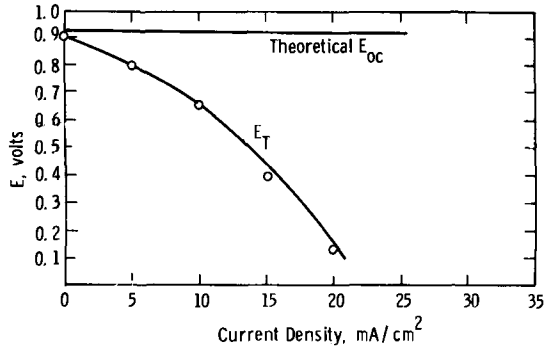

Fig. 7. Cell 1 performance, at 1000°C (specimen A)

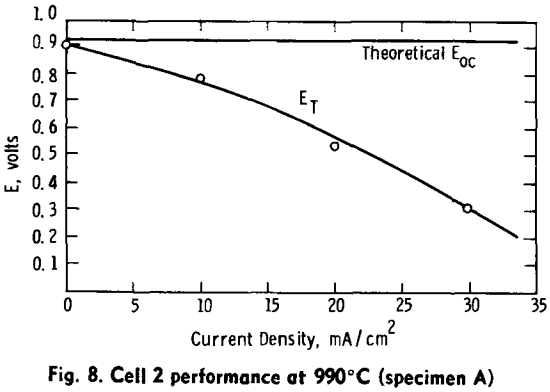

Fig. 8. Cell 2 performance at 990°C (specimen A)

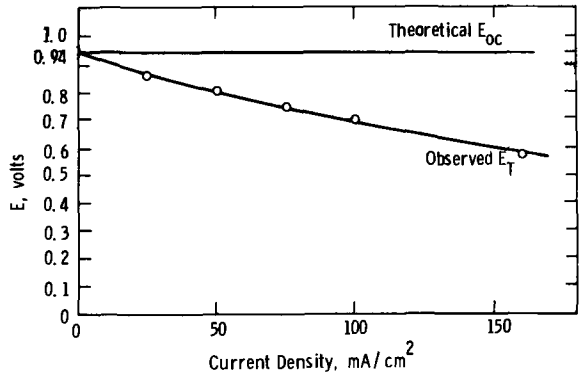

Fig. 9. Cell 1 performance at 960°C (specimen B)

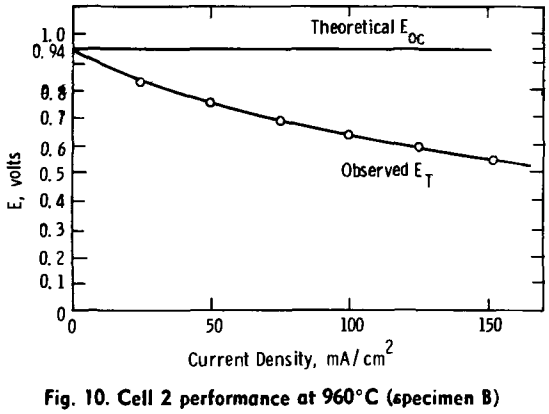

Fig. 10. Cell 2 performance at 960°C (specimen B)

Summary

A reactive sintering process has been developed to produce films of calcia-stabilized zirconia. This process involves spraying of a butyl acetate slurry of fine particle monoclinic zirconia and calcium zirconate. Subsequent sintering at 1400°C causes the formation of fully cubic electrolyte films of sufficient purity, density, and impermeability to gas flow to allow near-theoretical open-circuit voltages to be obtained in complete cell structures. The ability to display theoretical voltages implies that t_{ion} approaches unity, a critical property of fully stabilized bulk zirconia electrolyte. Initial measurements also indicate that sintered electrolyte film resistivity agrees with bulk resistivity values within the uncertainty introduced by estimates of active cell area.

By employing the reactive sintering process to fabricate the thin-film analog of bulk stabilized zirconia, the problems of thickness uniformity, high-temperature masking, and restrictive temperature limitations in processing are avoided. The economies associated with producing all-sintered practical fuel-cell batteries become available, though further development of all component structures is needed to improve device performance.

Reactive sintering is an effective and economical way to form thin-film electrolyte in a dense, well-bonded cubic structure.

Acknowledgment

This work was sponsored by the Office of Coal Research, Department of the Interior, under Contract No. 14-01-0001-303.

Manuscript submitted Dec. 7, 1970; revised manuscript received March 22, 1971.

Any discussion of this paper will appear in a Discussion Section to be published in the June 1972 JOURNAL.

REFERENCES

1. W. Nernst, Z. *Electrochem.*, **6**, 41 (1900).
2. F. Haber and A. Moser, Z. *Elektrochem. Angew. Physik. Chem.*, **11**, 593 (1905).
3. C. Wagner, Z. *Phys. Chem.*, **21**, Abt. B, 2 (1933).
4. A. D. Neuimin, S. F. Pal'guev, V. N. Strekalovskii, and G. V. Burov, Tr. Inst. Elektrokhim. Acad. Nauk SSSR, Ural'sk. Filial, **4** (1964).
5. W. D. Kingery, J. Pappis, M. E. Doty, and H. C. Hill, *J. Am. Ceram. Soc.*, **42**, 393 (1959).
6. J. Weissbart and R. Ruka, *This Journal*, **109**, 723 (1962).
7. D. H. Archer, R. L. Zahradnik, E. F. Sverdrup, W. A. English, L. Elikan, and J. J. Alles, *Proc. Ann. Power Sources Conf.*, **18**, 36 (1964).
8. D. H. Archer, L. Elikan, and R. L. Zahradnik, "Hydrocarbon Fuel Cell Technology," p. 51, Academic Press Inc., New York (1965).
9. D. W. White, Abs. 354, p. 187, Electrochem. Soc. Extended Abstracts, Fall Meeting, Montreal, Oct. 6-11, 1968.
10. N. J. Maskalick, Abs. 7, p. 17, Electrochem. Soc. Extended Abstracts, Battery Division, Vol. 11, Fall Meeting, Philadelphia, Oct. 9-14, 1966.
11. A. O. Isenberg *et al.*, "A Thin-Film Solid Electrolyte Fuel Cell," Div. of Fuel Chemistry, Paper No. 24, 158th ACS National Meeting, New York, Sept. 8-11, 1969.
12. P. Duwez, F. Odell, and F. H. Brown, Jr., *J. Am. Ceram. Soc.*, **35**, 107 (1952).

Technical Note

High-Stability Cathodes for Fuel Batteries

D. C. Constable

CSIRO, Division of Mineral Chemistry, P.O. Box 124, Port Melbourne, Victoria 3207, Australia

The use of noble metals, notably platinum, for the cathodic reduction of oxygen in acid electrolyte fuel cells is well known, and many methods of catalyst preparation and electrode fabrication have been published. Catalysts of two main types have been used—unsupported metal blacks (1-3) and metal blacks deposited on an inert support (3-6).

The electrodes are fabricated by mixing the catalyst material with a polymeric binder, spreading onto a conducting substrate material, and pressing at a temperature sufficient to accomplish sintering of the binding material. In some cases a wetproofing layer of polymer is applied to the surface by spraying or applying a coherent polymer film.

Commercial electrodes[1] of the PTFE and platinum black sinter type have been available for some time, but supply was uncertain and their long-term performance was found to be poor. For these reasons it was necessary to initiate a program to develop and produce electrodes for our own use.

We have found that electrodes prepared by a method similar to the above (3) but using Adams' Catalyst (7) (platinum dioxide) have shown excellent stability for over 2000 hr when used as cathodes in low-temperature fuel cell batteries employing ion exchange membrane separators and water-soluble fuel. The use of Adams' Catalyst was suggested by the work of Cairns and McInerney (8), who found that electrodes of reduced platinum oxide and sintered PTFE showed a 3.5-fold increase in activity for propane oxidation over electrodes prepared with commercial platinum black. For oxygen reduction, we found a two-fold increase in activity, using platinum dioxide in place of commercial platinum black.[2]

Electrode Fabrication

Electrodes were prepared by a method similar to that described by Christopher (3). The required quantity of platinum dioxide was blended with an aliquot of Fluon GP30[3] (PTFE) dispersion to form a doughlike mass which was spread uniformly onto a 145 cm^2 degreased 4/0 or niobium mesh,[4] using a metal blade. After drying, the electrodes were pressed between aluminum foils for 2 min at 2000 lb and 300°C. The aluminum foils were dissolved in sodium hydroxide solution (400 g/liter) and the electrodes washed with distilled water. Finally, reduction of the platinum dioxide was carried out in 5% formaldehyde solution.

[1] American Cyanamid Type AA1.
Key words: fuel cells, platinum dioxide, ion-exchange membrane, air electrode.

[2] Engelhard Corp. Platinum Black, "Special for Fuel Cells."
[3] John Crane, Mauri, Melbourne, Australia.
[4] Exmet. Corp., Tuckahoe, N. Y.

When using an ion exchange membrane, the application of polymer to the electrode surface is unnecessary.

The first electrodes prepared by this method performed erratically. Generally poor performance could be correlated with a high ohmic loss attributable to surface oxide on the metal substrate, an effect previously observed by Christopher (3).

Two methods have been tried in an attempt to overcome this difficulty: (*a*) chemically etching the substrate using 10% hydrofluoric acid before spreading the catalyst layer and (*b*) plating an inert metal onto a cleaned substrate.

The first method yielded substrates that had low ohmic losses but became brittle after etching, thus limiting substrate life. The second method, employing a gold coating, yielded substrates with low ohmic losses without affecting substrate life. This approach was also taken by Christopher (3), who used electroplated gold at 4 mg/cm^2. The gold was applied by vacuum evaporation onto the substrate cleaned by heating to 1200°C at a pressure of 2×10^{-4} Torr. A coherent gold deposit was obtained at a loading of 0.5 mg/cm^2. In the case of low platinum loadings, to enable an even spread of the small quantity of catalyst involved, a layer of graphite (10 mg/cm^2) and PTFE (2.8 mg/cm^2) was spread on the substrate and pressed for 1 min at 300°C and 10,000 lb before application of the catalyst.

Electrode Testing

To check reproducibility electrodes were tested as cathodes in a half-cell (Fig. 1) based on the design of Cathro *et al.* (9). The materials and components of the test module were polypropylene frames, chlorobutyl rubber seals, and tantalum bipolar plates and current collectors. These same components were used for the construction of the fuel cell batteries used for the long-term testing of the electrodes. To enable comparison of data, all half-cell tests were carried out using an electrolyte containing formaldehyde. The electrolyte, maintained at a temperature of 60°C by a glass-sheathed immersion heater, was circulated by a Hypalon-lined oscillating pump. Air was supplied at atmospheric pressure, and flow rate was measured by a laboratory flowmeter. Polarizing current was supplied from a direct current source, and the potential of the cathode was measured *vs.* a mercury/mercurous sulfate reference electrode in contact with the circulating electrolyte. The ohmic contribution to the potential was determined by a current interrupter technique and the appropriate correction made.

Electrodes, selected at random from each batch prepared, were tested in the half-cell before and after extended fuel battery operation; the polarization values reported are mean values for electrodes when tested in the half-cell.

Results and Discussion

The platinum and PTFE loadings, together with the type of substrate used for the electrodes tested, are

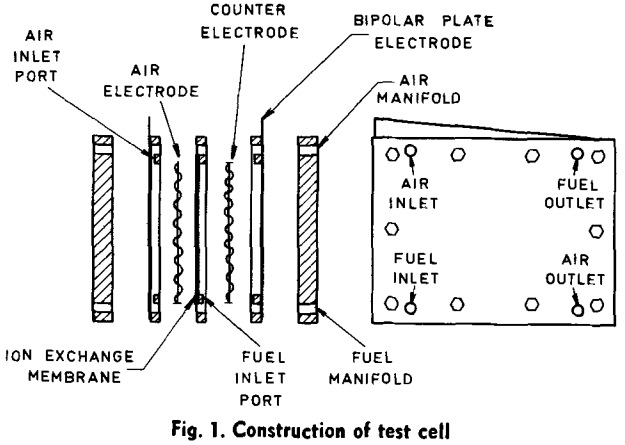

Fig. 1. Construction of test cell

Table I. Composition of electrodes tested

Electrode number	Preparation number	Platinum mg/cm^2	PTFE mg/cm^2	Substrate	Application
DL 3,5,9	1	10	1.4	Graphite 4/0 Nb mesh	6-cell methanol battery
DL 6,7,8	2	20	2.8	Graphited 4/0 Nb mesh	6-cell methanol battery
DL 11,12	3	20	2.8	4/0 Nb mesh	40-cell formaldehyde battery
DL 13,14	4	20	7.5	Graphited 4/0 Nb mesh	40-cell formaldehyde battery
DL 18,20,22	5	20	6.8	4/0 Nb mesh	40-cell formaldehyde battery
DL 24	6	20	3.3	4/0 Nb mesh	40-cell formaldehyde battery
Cyanamid air electrodc		10	3.8	Ta gauze	Single formaldehyde cell

shown in Table I. In order to determine the effect of platinum loading on performance, two sets of electrodes were prepared, using a graphited substrate with Pt loadings of 10 and 20 mg/cm^2 (Preparations 1 and 2). These six electrodes were tested for 1293 hr at a current density of 30 mA/cm^2 in a methanol-fueled battery at 60°C, using air.

The initial and final performance curves for these electrodes are shown in Fig. 2. It can be seen that increased platinum loading decreases electrode polarization and improves stability. The loss in performance of these electrodes, however, indicates a definite limitation in useful life. This decline in performance was attributed to either a change in PTFE character with a consequent change in wettability or to a change in electrode structure due to oxidation of the graphite substrate or to both factors. To ascertain which of these effects controls electrode stability, forty electrodes were prepared for use in a formaldehyde-fueled battery, using platinum and PTFE loadings as shown in Table I. The formaldehyde battery was operated as a fully self-contained system for a period of 2250 hr, after which the cathodes were retested in the half cell.

The initial and final polarization curves of the electrodes tested are shown in Fig. 3-6. In all cases except one, the stability of these electrodes was superior to that of Preparations 1 and 2 electrodes. The exception was Preparation 4 (Fig. 4) which was prepared for comparison with Preparation 2, using PTFE loading of 7.5 mg/cm^2 on a graphitized substrate to determine whether higher concentrations of PTFE would decrease the rate of loss of wetproofing. It appears in fact that an excessive concentration of PTFE was used and loss of catalyst surface has occurred due to occlusion, since these electrodes still appeared to be hydrophobic after 2250 hr use. It is possible that a synergistic effect, due

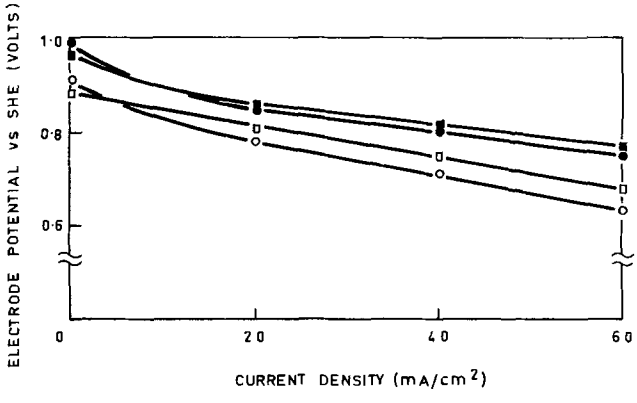

Fig. 2. Effect of time on performance. Preparation 1: Pt 10 mg/cm^2 PTFE 1.4 mg/cm^2 on graphited 4/0 mesh substrate. Preparation 2: Pt 20 mg/cm^2 PTFE 2.8 mg/cm^2 on graphited 4/0 mesh. Electrolyte 2M H_2SO_4 0.5M HCHO 60°C; air 500 ml/min; ● new performance Preparation 1; ■ new performance Preparation 2; ○ performance after 1293 hr Preparation 1; □ performance after 1293 hr Preparation 2.

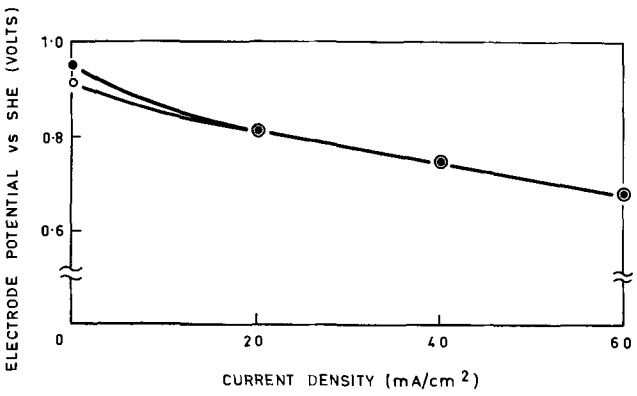

Fig. 3. Effect of time on performance, Preparation 3. Pt 20 mg/cm² PTFE 2.8 mg/cm² on graphited 4/0 mesh. Electrolyte 2M H_2SO_4 0.5M HCHO 60°C; air 500 ml/min; ● new performance; ○ performance after 2250 hr.

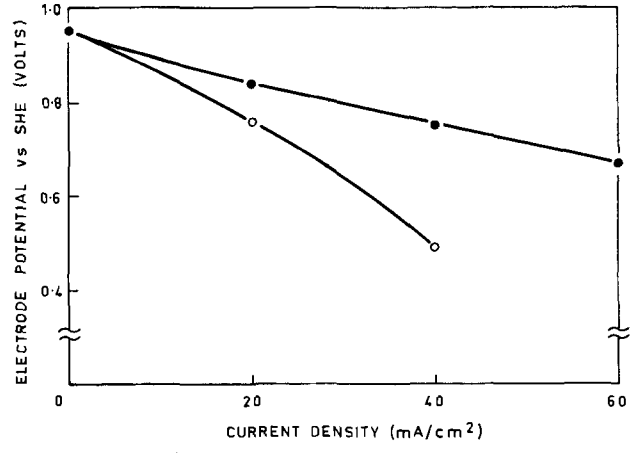

Fig. 4. Effect of time on performance, Preparation 4. Pt 20 mg/cm² PTFE 7.5 mg/cm² on graphited 4/0 mesh. Electrolyte 2M H_2SO_4 0.5M 60°C; air 550 ml/min; ● new performance; ○ performance after 2250 hr.

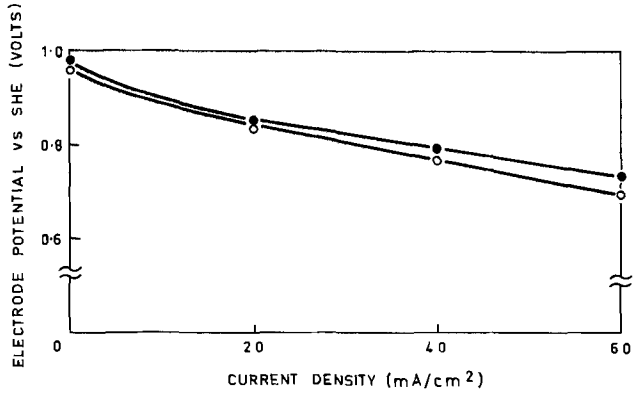

Fig. 5. Effect of time on performance, Preparation 5. Pt 20 mg/cm² PTFE 6.7 mg/cm² on 4/0 mesh. Electrolyte 2M H_2SO_4 0.5M HCHO 60°C; air 500 ml/min; ● new performance; ○ performance after 2250 hr.

to the graphite substrate, may exist since Preparation 5 electrodes with a PTFE loading of 6.8 mg/cm² show excellent stability (Fig. 6).

The stability of the electrodes prepared without graphite is excellent (Fig. 3, 5, 6) and is markedly superior to that of commercial electrodes (Fig. 7). The performance of these electrodes is quite uniform despite a wide variation in PTFE loading.

Conclusions

The production of stable cathodes for use in fuel cell batteries using acid electrolyte and soluble organic

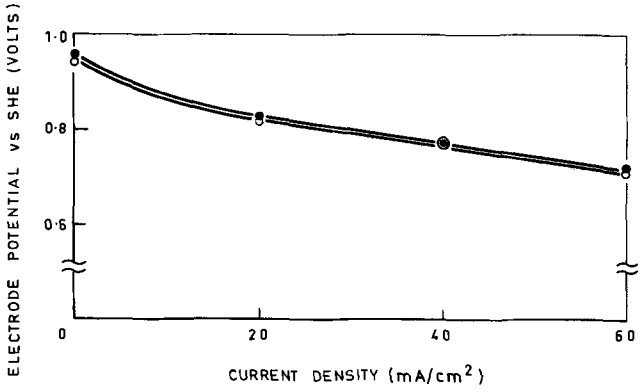

Fig. 6. Effect of time on performance, Preparation 6. Pt 20 mg/cm² PTFE 3.3 mg/cm² on 4/0 mesh. Electrolyte 2M H_2SO_4 0.5M HCHO 60°C; air 500 ml/min; ● new performance; ○ performance after 2250 hr.

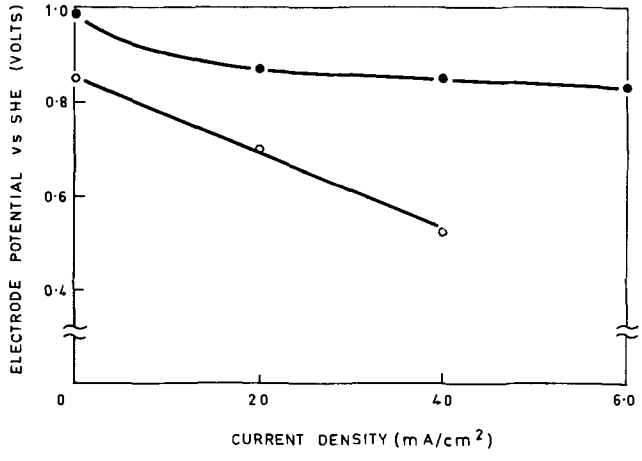

Fig. 7. Effect of time on performance, commercial air electrode. Pt 10 mg/cm² PTFE 3.8 mg/cm² on Ta gauze. Electrolyte 2M H_2SO_4 0.5M HCHO 60°C; air 500 ml/min; ● new performance; ○ performance after 1000 hr.

fuel has been demonstrated. A high platinum loading has been shown to contribute markedly to the long-term stability of electrodes under battery-operating conditions. Results show that electrodes prepared with only platinum and PTFE show stable performance with a PTFE content of 2.8–6.7 mg/cm². Electrodes prepared on a graphited substrate show inferior stability especially when high PTFE loadings are used.

Acknowledgment

The author gratefully acknowledges the assistance of Mr. W. Ihle and Dr. K. J. Cathro during the conduct of this work.

Manuscript received Feb. 26, 1971.

Any discussion of this paper will appear in a Discussion Section to be published in the June 1972 JOURNAL.

REFERENCES

1. L. W. Niedrach and H. R. Alford, *This Journal*, **112**, 117 (1965).
2. J. Giner, J. M. Parry, S. Smith, and M. Turchan, *ibid.*, **116**, 1692 (1969).
3. H. A. Christopher, *Proc. 20th Power Sources Conf.*, pp. 18-21.
4. H. I. Zeliger, *This Journal*, **114**, 236 (1967).
5. W. T. Grubb and D. W. McKee, *Nature*, **210**, 193-4 (1966).
6. H. I. Zeliger, *J. Catalysis*, **7**, 198 (1967).
7. V. L. Frampton, J. D. Edwards, Jr., and H. R. Henze, *J. Am. Chem. Soc.*, **73**, 4432 (1951).
8. E. J. Cairns and E. J. McInerney, *This Journal*, **114**, 980 (1967).
9. K. J. Cathro, D. F. A. Koch, and H. R. Skewes, *Mech. Chem. Eng. Trans. Inst. Engineers Australia*, **3**, 17 (May 1967).

JOURNAL OF THE ELECTROCHEMICAL SOCIETY

REVIEWS AND NEWS

JUNE 1971

Electroluminescent II-VI Heterojunctions[1]

A. G. Fischer*

Westinghouse Research Laboratories, Pittsburgh, Pennsylvania 15235

ABSTRACT

D-C electroluminescence in II-VI films is still in its infancy and could become of great technical importance if the problem of efficient hole injection in the absence of p-n homojunctions can be solved, which is possible through systematic efforts. A survey is given of the existing methods of hole injection and of the available materials combinations. Their advantages and shortcomings are listed, and as a conclusion a new method is proposed.

The Present Situation of Industrial Electroluminescence

The industrial significance of electroluminescence in America has undergone some metamorphoses. In the fifties, when the internal mechanism of the a-c electroluminescence of ZnS type embedded powders (Destriau effect), then in its heyday, was not yet fully understood but when brightness and efficiency figures improved almost daily due to empirical development, we thought of electroluminescence as the light source of the future. Prematurely, production facilities were set up. When this rapid progress reached an unexpected plateau, and when the mechanism was begun to be understood, II-VI electroluminescence work (mainly carried out by phosphor chemists) fell into undeserved oblivion, including the work on some promising still-undeveloped aspects of it.

With the upsurge of III-V semiconductor research (mainly carried out by another group, the semiconductor scientists), electroluminescence took a different turn. Whereas before one had aimed for large-area panels for general illumination purposes, the new light sources were tiny single-crystalline p-n diodes emitting infrared and red light, to be used for punch card readouts, control lights, and small alphanumeric displays. An enormous amount of research was expended and impressive progress was made, especially recently with gallium phosphide lamps, but it is clear that this is a relatively limited application. By analyzing the market, one finds that there is only one potential big-scale application of electroluminescence which can justify the large previous and coming research expenditures: multielement image display panels.

With this in mind, the outlook is different. To compete with other displays which dominate the market, the cost of one electroluminescent element, plus addressing and storage circuitry, has to be far less than one penny. This prosaic requirement deflates the exaggerated expectations for individually fabricated monolithic p-n junction diodes, even the simplified mass-production versions which we have explored (1), and brings back the former II-VI electroluminescence in its various forms.

From past mistakes, we have now learned to look at the whole intended system, not just at electroluminescence *per se*. In a separate study, we have concluded that the best way to provide addressing and storage for a multielement display system (the most desirable system would be flat television) is by large-scale-integrated thin-film-transistor (TFT) circuitry (2). Since the Destriau type of a-c electroluminescence requires high-voltage, audio-frequency drive power which presents impedance matching problems to TFT circuitry (which, admittedly, could be overcome), the most favorable type of electroluminescence would be low-voltage, d-c electroluminescence. Since we ruled out the single-crystal approach, we have to investigate polycrystalline layers. III-V polycrystalline layers do not luminesce well and cannot easily be made by vacuum deposition. Therefore, we have to concentrate on polycrystalline II-VI layer structures, which is the topic of this paper. II-VI layer structures have the well-known advantage that they can be produced easily and cheaply and that they show highly efficient photo- and cathodoluminescence throughout the visible spectral range, even at low excitation densities, which shows that they do not have many nonradiative transitions which have to be swamped before luminescence can occur. The task is to achieve the luminescence we now have by photo- or cathodoexcitation by minority carrier injection through contacts. This is a very worthwhile task and should be pursued even though progress so far has been slow, and even though the spectacular success of monolithic III-V diodes tends to divert attention from it at the present time.

Minority Carrier Injection in II-VI Compounds

Difficulties of producing II-VI p-n homojunctions.— Due to the phenomenon of self-compensation of added doping impurity ions by the formation of lattice vacancies on nearby lattice sites (3), wide-band gap semiconductors with partially ionic ("soft") lattices can be prepared only n- or p-type depending on the material, but not in both types. This inherent tendency can be combated by using thermodynamic nonequilibrium methods. Procedures tried or suggested so far are: squeezing out the compensating vacancies under extreme pressure (*e.g.*, 10^4 atm) at elevated temperature and then cooling while still under hydrostatic pressure (4), doping at low temperature using ion implantation (5), and film preparation by means of reactive sputtering with simultaneous incorporation of acceptor ions (6). These methods have, however, not yet been reduced to practice sufficiently, and some may be too expensive to become of industrial importance. Therefore, we consider in this paper only

* Electrochemical Society Active Member.

[1] Work done while author was associated with RCA Laboratories, Princeton, New Jersey 08540. The research for this paper was sponsored by the U.S. Army Electronics Command, Fort Monmouth, New Jersey, under contract DAAB07-69-C-0290.

Key words: electroluminescence, II-VI compounds, heterojunction structures, polycrystalline films, multielement display panels, addressing by thin-film transistors, semibarrier injection electroluminescence.

those methods where the properties of existing materials in thermodynamic equilibrium are utilized.

Problems with II-VI quasihomojunctions.— A quasihomojunction is defined as a p-n junction between two materials, one being n-type, the other p-type, which form a complete series of alloys so that there is no abrupt transition from one material to the other, but a gradual one. This is in contrast to a heterojunction in our nomenclature, where the two materials are not, or not completely, miscible, so that a vertical step occurs within the junction. Commonly, the word heterojunction is used to cover both types.

We have the following II-VI materials at our disposal, with their (direct) bandgaps listed: ZnS (3.7 eV), ZnSe (2.7 eV), ZnTe (2.2 eV), CdS (2.4 eV), and BeS (5.5 eV), BeSe (4.5 eV), BeTe (3.5 eV) (7), and MgTe (4.7 eV) (8). (The other alkaline-earth-chalcogenides are very humidity-sensitive, and not of zinc blende or wurtzite structure.)

Since ZnTe, and possibly BeTe and MgTe, are the only materials with native p-type properties, only a limited number of combinations are feasible. This is the first comprehensive review.

n-CdS/p-ZnTe junction.—This junction is self-suggestive since CdS readily comes n-type and ZnTe is natively p-type. It is unworkable, however, because CdS and ZnTe do not form a continuous alloy series (9) and hence form an abrupt heterojunction full of nonradiative interface states (Fig. 1). Besides, injection into ZnTe is predominant due to the bandgap relations, and ZnTe films are known to be poorly luminescent at room temperature for reasons not fully understood. This junction is mentioned mainly as a negative example.

n-ZnSe/p-ZnTe quasihomojunctions.—ZnSe and ZnTe are fully miscible (10). Polycrystalline ZnSe films cannot be made as highly n-type conducting as CdS films, notwithstanding the high n-type conductivity obtainable in ZnSe:Al, Zn single crystals (0.1 ohm-cm). This is due to high intergranular Schottky barriers (11) in ZnSe films. These are much shallower, or completely absent, in CdS films since CdS has a higher work function than ZnSe (11).

We have found that, even with highly n-type ZnSe single-crystal substrates, epitaxially grown n-ZnSe/p-ZnTe junctions, although light emitting (12), are inherently inefficient. This may be caused by the 8% lattice mismatch between ZnSe and ZnTe leading to a high concentration of lattice defects in the junction and by the anomalous dip in the bandgap of these alloys (10). The latter is now explained by intermediate bands formed by isoelectronic traps (13) which form a "sump" within the junction coinciding with the disturbed crystal area (Fig. 2), thus enhancing nonradiative recombination. In addition, it is known that even homogeneous $ZnSe_{0.60}Te_{0.40}$ single crystals are poorly luminescent at room temperature (14).

n-CdS/i-ZnSe/p-ZnTe n-i-p quasihomojunctions.—In this sandwich structure, designed to avoid the former pitfalls, one can envision electrons being injected into the central ZnSe layer from the CdS electroding layer, and holes from the ZnTe electroding layer, with radiative recombination occurring in the insulating ZnSe layer which can be doped optimally for efficient luminescence since it does not have to compromise with conductivity requirements.

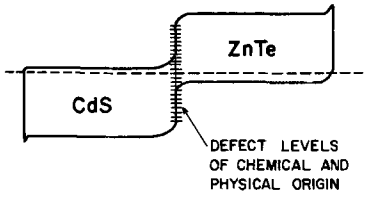

Fig. 1. n-CdS/p-ZnTe heterojunction

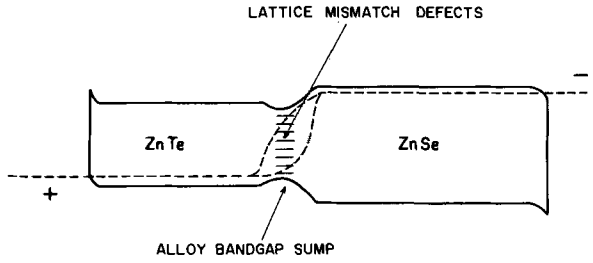

Fig. 2. n-ZnSe/p-ZnTe quasihomojunction (forward voltage applied).

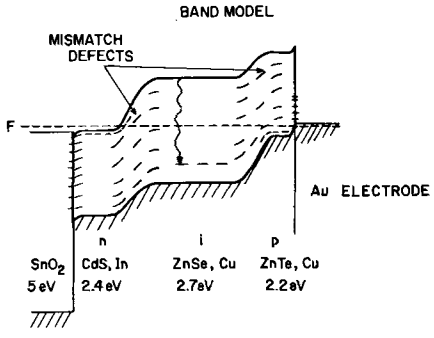

Fig. 3. n-CdS/i-ZnSe/p-ZnTe quasihomojunction

We found that a true p-i-n structure with an i-layer thicker than a diffusion length (about 2μ) tends to be blocking and then breaks down suddenly at increasing voltage, with current constriction at points, revealing a strongly negative I-V characteristics. This is a basic, not much publicized, flaw which even follows from theory in any space-charge-limited double-injection p-i-n structure with deep traps and strong recombination, especially in the case of "uphill" injection where the i-part has a higher bandgap than the n- and p-electrodes. It occurs even if the junctions are made gradual, not steep (15).

This undesirable condition can be avoided by making the i-layer so thin that currents through it are diffusion limited, not field driven, and/or by giving the central ZnSe layer a weak conductivity. This structure has been suggested recently by Lehmann (16) (Fig. 3).

A possible drawback of this structure is that the ZnTe electrode absorbs that emission of the ZnSe which has a shorter wavelength than red light.

n-ZnSe/i-$ZnSe_{0.4}Te_{0.6}$/p-ZnTe n-i-p quasihomojunctions.—In the desire to overcome the previously recognized obstacles by a suitable materials combination, the following structure was conceived (Fig. 4). Starting with a polycrystalline ZnSe:Al,Zn layer (bandgap 2.7 eV) in which the n-type conductivity has been enforced by heating in Zn vapor, we superimpose an almost intrinsic $ZnSe_{0.4}Te_{0.6}$ layer (bandgap 2 eV) by flash evaporation, to be followed by a p-type ZnTe layer (bandgap 2.2 eV). Thus, we have the converse case of a graded p-i-n junction, namely one where carriers are injected "downhill." Theory shows that such a structure allows very high double-injection carrier density in the i-region (17), a condition which is essential in order to "swamp" nonradiative recombination centers and to avoid negative resistance regions with the concomitant current constriction into filaments resulting in burnout. This structure also permits easy escape of the bandgap radiation of the i-layer through the electroding layers which act as "windows" (17).

However, an important shortcoming of this structure is that light emission is limited to 2 eV and that

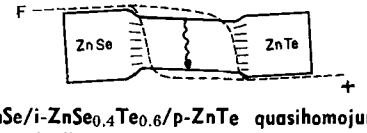

Fig. 4. n-ZnSe/i-$ZnSe_{0.4}Te_{0.6}$/p-ZnTe quasihomojunction. Band model (voltage applied).

$ZnSe_{0.4}Te_{0.6}$, in its present state of perfection, is a poor phosphor at room temperature.

Abrupt II-VI heterojunctions.—Carrier injection from sharp spikes.—The a-c electroluminescence of ZnS type powder particles (Destriau effect) is caused by the fortunate peculiarity of the ZnS-Cu_2S composite system that ZnS, due to its zinc blende-wurtzite polymorphism, develops linear defects. These act as nucleation sites for excess copper sulfide as the crystals are slowly cooled during preparation. The copper sulfide forms conductive thin long needle-shaped precipitates. (These can now be made directly visible by transmission electron microscopy. Before, they could only be seen by optical microscopy at very high copper concentration where the electroluminescence was almost concentration quenched.)

When an a-c field is applied, it relaxes in the conducting needles and concentrates at the tips, where bipolar nonohmic carrier injection into the surrounding near-insulating phosphor matrix takes place, with trapping of the holes in the deep luminescence centers for half a cycle, and recombination with the then injected electrons, in the form of comet-shaped sheaths around the conducting needles, in the next half cycle (18).

A remarkable fact has to be emphasized here, since it gives strong support to our contention that d-c electroluminescence in II-VI compounds has a promising future: the local brightness in these light-emitting comets (which constitute only about 1/1000th of the total volume of the electroluminescent capacitor) is on the order of 100,000 ft-L (19). The quantum efficiency is near unity (18) and can actually exceed 100% if particles are arranged in a string between the electrodes (20). The over-all power efficiency is low (but still on the order of 1%), due to the high ohmic losses of the currents oscillating back and forth in the near-insulating crystallites.

"All we have to do" is to achieve these conditions in contiguous large areas, in low-resistivity layers driven by d-c current.

Impact-excitation or impact-ionization electroluminescence in back-biased Schottky barriers.—Impact-ionization of the lattice by electrons emerging from a superficial copper sulfide precipitate, and accelerated in the high field of a back-biased Schottky barrier between the n-type ZnS interior and the Cu_2S surface, was postulated early to be the acting mechanism of the Destriau effect. Electroluminescence occurs as the impact-created excess electrons return to their ionized centers at field reversal (21, 22). D-C electroluminescence based on this effect (Fig. 5) was observed early in SiC and was found also in electrolyte-ZnO contacts (green EL) (23) and in silver paint or Aquadag-(n)ZnS:Al contacts (blue EL), from 5-7V on (24), always with the metal electrode negative. [Strangely, n-type CdS does not exhibit this effect, possibly due to a peculiarity in the conduction band structure which prevents electrons from heating up (25).]

Cusano found strong d-c electroluminescence (1000 ft-L) in his n-type, vapor-deposited ZnS, CdS, ZnSe, and ZnCdS films when the superficially applied Cu_2S surface layer was biased negatively (26). The half life of these films was too short for practical applications, probably due to copper migration.

Vecht prepared bright d-c electroluminescent cells using ZnS:Cu, Mn powder particles with Cu-rich surfaces, embedded into a minimum of organic binder (20). Since electrolytic currents are unavoidable in this scheme and copper is used, the life of these cells is limited, even though several hundred hours are claimed. The acting mechanism is probably a combination of several of the effects described here.

Though easy to obtain, impact ionization electroluminescence is inherently inefficient: only a very small fraction of the electrons passing the high-field region is accelerated up to ionization energy (about 3/2 bandgap energy); the rest produce nothing but heat. In cases where impact ionization was clearly the active mechanism, electroluminescent efficiencies never exceeded 10^{-4} photons/electron, as theory demands. Inversely, if higher efficiencies are observed, impact ionization cannot be the sole acting mechanism. Therefore, impact ionization or impact excitation schemes have no practical importance.

Minority carrier injection through physical inversion layers.—By placing a very high work function metal electrode such as Pt (5.4 eV), Au (5.1 eV), or C (4.6 eV), onto an n-type conducting luminescent crystal of low electron affinity (ZnS and ZnSe about 3 eV, CdS 4 eV), the resulting Schottky barrier becomes so steep that a physically induced p-type surface layer is formed (Fig. 6). For instance, carbon deposited onto an n-type ZnSe:Al crystal leads to light emission (yellow, hv ~ 2.1 eV) from only 1.5V on (contact positive) (27). The effect is enhanced if a thin insulating film is interposed, for instance by using Aquadag (graphite dust which has a trace of silicate binder). Green light emission has ben obtained in an electrolyte-ZnS contact using fuming sulfuric acid (oleum), which has a "work function" of 7 eV and does not attack ZnS (28).

We have obtained blue injection electroluminescence ($h\nu$ ~ 2.6 eV) from only 2V on when we contacted

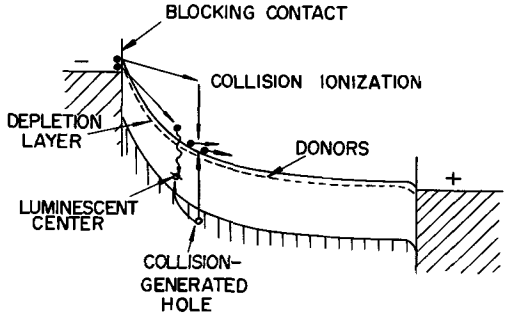

Fig. 5. Impact ionization electroluminescence in back-biased Schottky barrier.

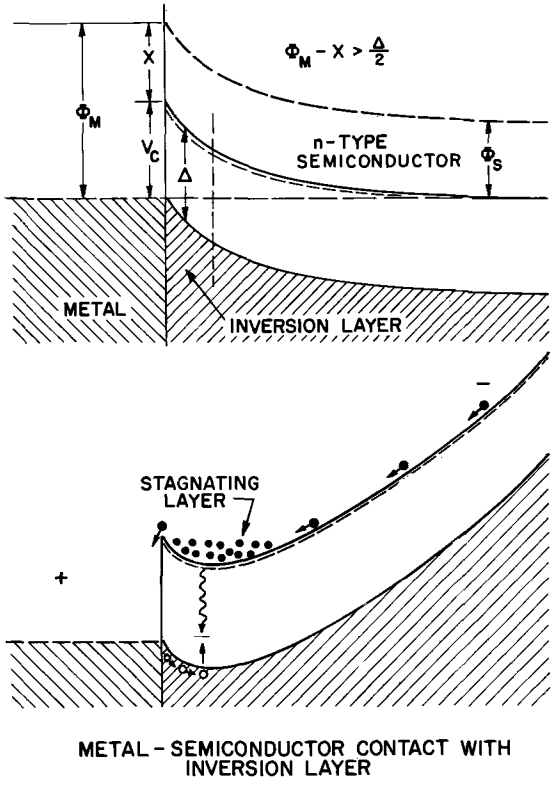

METAL - SEMICONDUCTOR CONTACT WITH INVERSION LAYER

Fig. 6. (a)—top and (b)—bottom, Electroluminescent physical inversion layer.

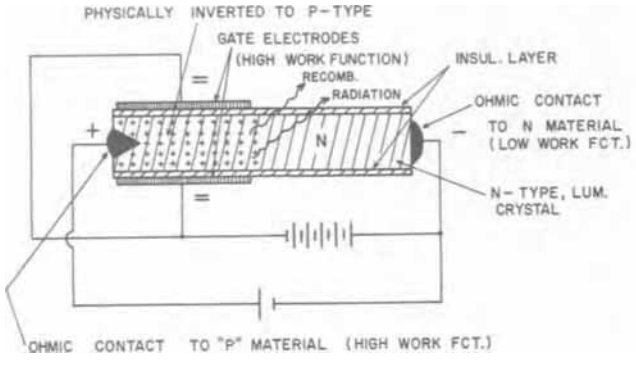

Fig. 7. Field-effect electroluminescent device

highly n-type ZnS:Al crystals (1 ohm-cm)[2] with Aquadag. The blue light emission was brighter, and the efficiency higher, than similar blue light obtained from GaAs LED's coated with up-conversion phosphors. The discrepancy between the energy of the emitted light and the applied voltage is explained in Ref. (27).

If one uses a p-type luminescent semiconductor such as ZnTe, the relations are inversed: by contacting the crystal with a low work function metal such as Ba (2.5 eV), light emission is obtained from very low voltages on (metal negative). Again, the effect is enhanced if a thin insulating layer is interposed, which can be an intrinsic surface layer of the host crystal itself (30). The efficiency is lower than with n-type crystals since ZnTe has poor luminescent properties at room temperature in its present state of development.

The decisive shortcoming of this scheme is that the number of injected minority carriers is by far exceeded by the number of majority carriers which flow out of the crystal into the metal electrode.

Field-effect electroluminescence.—The formation of a superficial physical inversion layer due to the work function difference between contacting metal and luminescent semiconductor can be enhanced artificially by using the field effect. If one interposes an insulating film between metal and semiconductor, one can apply an external potential in the same way as it is done in MOS and TFT transistors, except that one has to make the field effect so strong that conversion to the opposite type, not just to the insulating state, is achieved.

Whereas an a-c scheme based on this idea has been proposed by Kahng (31), a d-c structure which holds definite promise has been proposed, and reduced to practice using silicon as a model substance, by A. M. Goodman[3] (Fig. 7). A strong depletion layer induced by the negatively biased gate electrodes drives the n-type conducting luminescent semiconductor layer toward p-type. A high work function "source" electrode injects holes into this inverted channel. As soon as these holes drift toward the "drain" electrode and emerge from the inverted region into the n-type region, they recombine with electrons radiatively. A structure simpler than shown in Fig. 7 has been designed so that, in principle, a multielement panel could be fabricated by successive vapor deposition through masks.

A drawback of this interesting scheme is that the carrier density of the injected holes can at best come close to that of the charge on the gate, due to $Q = C \cdot V$.

Thornton's method.—An amazingly bright d-c electroluminescent structure (more than 1000 ft-L) was empirically developed by Thornton (32). At the present time it is still the best II-VI d-c EL scheme available, even though it was abandoned due to its limited half life. Only now, after a long dormancy period, is work on this scheme being resumed.

A ZnS:Mn,Cu,Cl film is vacuum deposited onto a heated or after-baked transparent conducting glass substrate. The back electrode must be applied in such a way that there is a very thin insulating interlayer. Aluminum or Mg is best, because they form this interlayer by solid-state electrolysis. After a "forming period," bright yellow light typical of the manganese center is emitted at the anodic metal contact. This is an indication that hole injection takes place, even though the I-V characteristics show that this is not the "ohmic" injection known from p-n junctions. Rather, it is a form of high-field injection in which the insulating film and the needle-shaped copper sulfide precipitates play an important role. Aging occurs if the insulating film becomes too thick (33) and is due to migration of copper ions which are mobile in high fields even at room temperature.

Light emission has been observed from 2V on (32), which rules out impact ionization as the sole mechanism.

Thin-film tunnel injection electroluminescence.—This scheme is a logical development from the preceding one. If a very thin insulating film is interposed between the luminescent semiconductor and the metal electrode, the potential drop across this film leads to a shift between the Fermi levels in such a way that holes from the metal can now tunnel through the insulating film into the valence band of the semiconductor, where they can recombine with electrons from the conduction band [Fig. 8(a)]. Light emission is observed, but this principle (34, 35) never became very popular due to low quantum efficiency and frequent breakdown of the insulating film. The reasons for this failure are scrutinized here for the first time.

The main shortcoming which must be explained is the low ratio of minority carrier injection over majority carrier extraction. The relations of the bandgaps and electron affinities of the materials in contact play an important role. Figure 8(a) shows a case

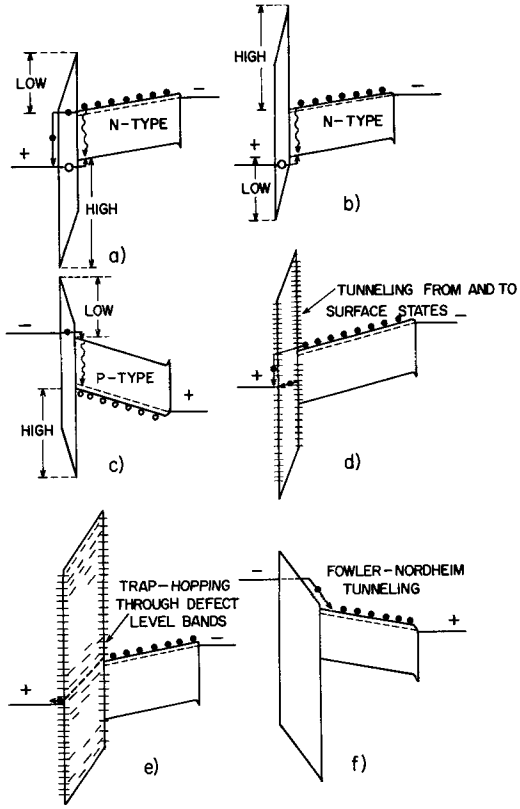

Fig. 8. Possible conditions in thin-film tunnel-injection electroluminescence.

[2] Insulating ZnS:5000 ppm Al (Eagle Picher Company) crystals were treated in Zn using the Aven method (29): the crystals were heated for 12 hr at 850°C submerged in Zn in a sealed quartz ampoule, the liquid Zn shaken off the crystal before solidification to prevent cracking of the crystals.

[3] Personal communication.

where majority carrier out-tunneling is stronger than minority carrier in-tunneling, simply because the barrier for holes is higher than that for electrons. The case in Fig. 8(b) is more desirable. These relations at the contact can now be determined experimentally by the use of internal photoemission (36).

However, Fig. 8(a),(b),(c) describe an idealized situation which may never occur in reality. It is more likely that the thin insulator film is thoroughly disturbed: Fig. 8(d) shows tunneling to and from surface states within the forbidden gap of the luminescent semiconductor; Fig. 8(e) shows tunneling through defect level bands. Apparently, these situations in which the injected carriers do not arrive in the respective conduction or valence band but somewhere within the bandgap occur most of the time. It was always a puzzle why tunnel injection electroluminescence could only be obtained with films of 300Å thickness or more, which should be completely impervious to tunneling (theory demands that 80Å be the maximum thickness).

Apart from the possibility of injection through defect level bands, another explanation for the penetration through relatively thick films may be "Fowler-Nordheim tunneling" [Fig. 8(f)]: if the applied voltage is high enough, the carriers do not have to penetrate the whole film but emerge from the tunnel into the conduction band of the insulator. There they are accelerated by the field and then penetrate into the luminescent semiconductor conduction or valence band.

Improved II-VI heterojunction structures.—As we have seen, all the successful schemes described so far have been developed quite empirically. With the better surview that we now have gained, we should be able to design a better structure which avoids the recognized pitfalls and uses all the advantages.

The envisioned optimized structure should have the following features.

(*a*) Use a highly n-type luminescent layer, to avoid ohmic losses. ZnS:Mn,Al,Cl, ZnSe:Al,Zn, and $Cd_xZn_{1-x}S$:In,Cl can be made quite conducting while retaining their luminescent properties (37).

(*b*) Avoid strong copper doping to prevent rapid deterioration.

(c) For hole injection, use a high-work-function back electrode with a superimposed thin film with low electron affinity to build a barrier for harmful electron extraction and a bandgap which eases hole injection. The material must be chemically very stable to prevent changes by solid-state electrolysis.

(*d*) The transparent conducting front electrode must make good ohmic contact to the conduction band of the luminescent layer.

As a result of this study, we have conceived a new structure, "semibarrier injection electroluminescence," for which several possible materials combinations exist (38). One possible configuration is shown in Fig. 9 (2).

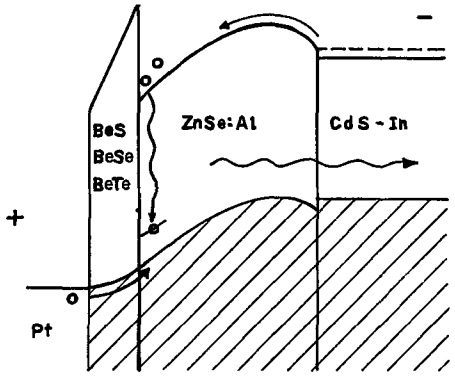

Fig. 9. One possible configuration of our new semibarrier electroluminescent structure. The Be-chalcogenide film can be prepared by reactive sputtering.

The insulating film is made so thick (*e.g.*, 5000Å) that tunneling through it, even by means of defect level bands, becomes impossible. The electron affinity is so low that this barrier also becomes insurmountable. In this way, majority carrier extraction is curbed.

To ease hole injection, the bandgap of the insulator and the work function of the contacting metal are so chosen that the holes can flow through this film as single-carrier, space-charge-limited current. Thereby, they attain a high velocity so that they penetrate into the luminescent layer, away from the surface states. The materials have to be selected so that these surface states are harmless.[4] Active work is in progress to realize this structure.

Conclusion

The problem of injecting holes into n-type, luminescent II-VI films in the absence of p-n junctions is still not solved in a satisfactory way. The solution is of great technical importance. For the first time, the many existing attempts are surveyed here systematically and their advantages and shortcomings discussed. New solutions are proposed. It is hoped that this will stimulate further progress. The most important requirement is a consistent well-staffed, long-term research effort. Up until now, work in this field has lingered along in many scattered, one-man, part-time programs, mainly depending on serendipity.

Acknowledgment

The author wishes to express his gratitude to Dr. W. Lehmann of Westinghouse Research Laboratories, Pittsburgh, Pennsylvania, for his competent review of this paper.

Manuscript submitted Oct. 13, 1970; revised manuscript received Feb. 9, 1971.

Any discussion of this paper will appear in a Discussion Section to be published in the December 1971 JOURNAL.

[4] We have found, for instance, that the interface n-CdS/i-ZnS, which has a step of 0.8 eV between the respective conduction bands, does not introduce radiationless transitions, despite the mismatch in lattice constants (1). This test was made observing photoluminescence at a ZnS-covered CdS interface excited by 4200Å radiation.

REFERENCES

1. A. G. Fischer, 2nd Quart. Rept., Contract DAABO7-69-C-0290, U.S.A. ECOM, Ft. Monmouth, N. J.
2. A. G. Fischer, 3rd Quart. Rept., same contract, Presented at the IEEE Conf. on Display Devices, New York, Dec. 1970, and submitted to *IEEE Trans. Electron. Devices.*
3. See, *e.g.*, A. G. Fischer, Chap. 10 in "Luminescence of Inorganic Solids," p. 566, P. Goldberg, Editor, Academic Press, New York (1966).
4. A. G. Fischer, Final Rept. AFCRL-67-0005, Contract AF19(628)-3866 (1966), and Unpublished work.
5. A. G. Fischer, *Z. Physik.*, **149**, 107 (1957); A. Robinson and B. Kun, *Appl. Phys. Letters*, **15**, 371 (1969).
6. M. Lichtensteiger *et al.*, *Appl. Phys. Letters*, **15**, 418 (1969).
7. W. M. Yim, J. P. Dismukes, E. Stofko, and R. J. Paff, To be published.
8. R. Yamamoto *et al.*, *Japan. J. Appl. Phys.*, **6**, 537 (1967); W. Lehmann, Westinghouse Res. Labs., Personal communication.
9. A. G. Fischer and R. J. Paff, *J. Phys. Chem. Solids*, **23**, 1479 (1962).
10. S. Larach, R. E. Shrader, and C. F. Stocker, *Phys. Rev.*, **108**, 587 (1957).
11. A. M. Goodman, *This Journal*, **116**, 364 (1969).
12. A. G. Fischer, in "Radiative Recombination in Semiconductors," p. 259, Dunod, Paris (1965).
13. S. Bloom, *J. Appl. Phys.*, **41**, 1864 (1970).
14. M. Aven, II-IV Conf., Providence, R. I., Aug. 1967, Proceedings.
15. M. A. Lampert and P. Mark, "Current Injection in Solids," Academic Press, New York (1970).
16. W. Lehmann, U.S. Pat. 3,510,715 (May 1970); T.P. Brody *et al.*, Tech. Report AFAL-TR-67-85, May 8, 1968.

17. A. G. Fischer, *Solid-State Electron.*, 2 232 (1961); H. Kroemer, *Proc. IEEE*, **51**, 1782 (1963).
18. J. L. Gillson, Jr., and F. J. Darnell, *Phys. Rev.*, **125**, 149 (1962); A. G. Fischer, *This Journal*, **109**, 1043 (1962); **110**, 733 (1963).
19. A. G. Fischer, in "Photoelectronic Materials and Devices," p. 39, S. Larach, Editor, Van Nostrand, Princeton (1965).
20. A. Vecht, N. J. Werring, and P. J. F. Smith, *Brit. J. Appl. Phys., Sec. 2*, **1**, 134 (1968).
21. W. W. Piper and F. E. Williams, *ibid., Suppl. No. 4*, **S39** (1955).
22. P. Zalm, *Philips Res. Repts.*, **11**, 353, 417 (1956).
23. A. G. Fischer, *Z. Naturforsch.*, **8a**, 756 (1953).
24. A. G. Fischer, Rept. AFCRL 65-524, Contract AF 19(628)3866 (1966).
25. R. Williams, *This Journal*, **114**, 1173 (1967).
26. D. A. Cusano, in "Luminescence of Organic and Inorganic Materials," p. 494, J. Wiley & Sons, New York (1962).
27. A. G. Fischer, *Phys. Letters*, **12**, 313 (1964).
28. L. J. Van Ruyen and F. E. Williams, *Phys. Rev. Letters*, **16**, 889 (1966).
29. M. Aven, U.S. Pat. 3,146,204 (1964); *Phys. Rev.*, **137**, A228 (1965).
30. M. G. Miksic, G. Mandel, F. F. Morehead *et al.*, *Phys. Rev. Letters*, **11**, 202 (1964).
31. Y. S. Chen, M. V. DePaolis, Jr., and D. Kahng, *Proc. IEEE*, **58**, 184 (1970).
32. W. A. Thornton, *J. Appl. Phys.*, **33**, 3045 (1962); U.S. Pat. 3,044,902 (1962); Electrochem. Soc. Meeting, Pittsburgh, April 15-18, 1963, Enlarged Abstract No. 23.
33. P. Goldberg, Chap. 7 in "Luminescence of Inorganic Solids," P. Goldberg, Editor, Academic Press, New York (1966).
34. R. C. Jaklevic, D. K. Donald, J. Lambe, and W. C. Vasell, *Appl. Phys. Letters*, **2**, 7 (1963).
35. A. G. Fischer and H. I. Moss, *J. Appl. Phys.*, **34**, 2112 (1963).
36. A. M. Goodman, *This Journal*, **115**, 276C (1968).
37. A. G. Fischer, 5th Quart. Report, Contract DAABO7 [see Ref. (1)].
38. For other materials combinations, see Ref. (2).

Connections between Color Center Phenomena and Luminescence Phenomena in General

Herbert N. Hersh*

Zenith Radio Corporation Laboratories, Chicago, Illinois 60639

ABSTRACT

Alkali halide research has occupied a central position in solid-state physics. Its teachings are transferable to other fields. A modern synthesis of alkali halide research relevant to luminescence phenomena in general is presented. The relationship between the mechanisms of coloration and luminescence in alkali halides is described. The concepts of nonmoving excitons and of self-trapping are discussed and used to explain intrinsic luminescence in all alkali halides and the scintillation mechanism in thallium-activated alkali halides in an atomistic way. The possible importance of self-trapping, lattice relaxation, internal metastable states, molecules in crystals, *etc.*, in the luminescence of some conventional phosphors is pointed out.

When preparing this paper, I thought it might be of interest to choose a topic that bordered on luminescence but was one field away. For almost 30 years, physicists and physical chemists have spent millions of dollars per year and millions of man-hours studying color centers in alkali halides. The sponsors of this research have supported it, not because color centers are beautiful (which they are) or useful (which they are not), but on the grounds that what they would learn about them would be applicable to technologically more useful materials. By and large, the research has gone on but the implicit promise to apply the acquired knowledge was never really kept. I would like to examine some of the outcomes of alkali halide research and point out those concepts which come through strongly in this field and may have relevance to luminescence in general. This will touch on the detailed work of many people in a wide but selected variety of topics (1) but, more importantly, I shall be striving to extract broad but simple ideas which may be useful in other fields of work.

We start with a definition of an *F* center: an electron trapped at a halide ion vacancy (1). In the first approximation, this is an ionic model, since the electron occupies a lattice site of positive potential. In reality, however, the electron is shared among surrounding neighbors. This latter picture of the *F* center is absolutely established by EPR and ENDOR experiments. The *F* center gives rise to a characteristic absorption in the crystal which is responsible for the various colors and other properties seen in different alkali halides. *F* centers may be made in a number of ways, such as irradiating the crystal with neutrons, x-rays, or electrons, or chemically doping with a stoichiometric excess of alkali.

When ionizing radiation is used, holes are also generated and these give rise to additional absorption at shorter wavelengths than the *F* band which do not appear when only electron-donating alkali atoms are chemically added. After being colored, the crystals exhibit such properties as photoconductivity, paramagnetism, luminescence and optical absorption, photochromism, *etc.* Figure 1 shows a typical absorption spectrum of an x-rayed crystal.

Although a lot of effort has successfully gone into identifying and explaining the properties of color centers, the big problem plaguing color center workers is not how electrons and holes are shuffled around by the radiation; it is the fact that the radiation produces halogen ion *vacancies*. The generation of these vacancies would be conceptionally simple if neutrons had been used to knock halogen ions into the interstices, but x-ray photons and low-energy electrons are also effective and these have almost no momentum to transfer to the heavy halogen ion to cause it to move to an interstitial position. We shall come back to this point, but first I would like to make a few general comments.

It is well known that most alkali halides crystallize in the NaCl structure, are good insulators, have large binding energies and bandgaps, and are transparent

* Electrochemical Society Active Member.
Key words, alkali halide crystals, luminescence, color centers, excitons, scintillators.

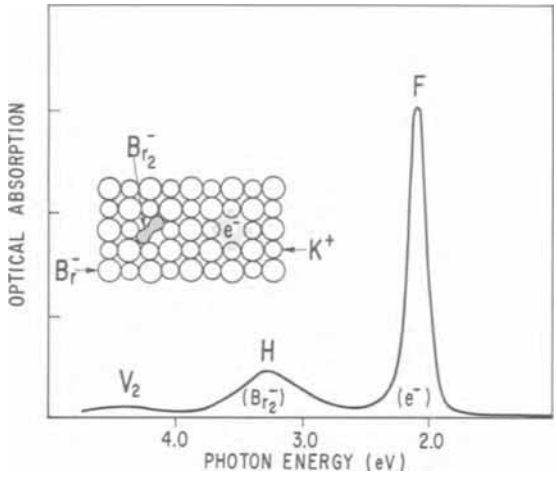

Fig. 1. Absorption bands produced by x-raying KBr at 2°K. The x-rays result in *(a)* the displacement of a bromide atom which then forms an interstitial Br_2^- molecule (called the *H* center), and *(b)* the simultaneous formation of a bromide vacancy which traps an electron to form the *F* center.

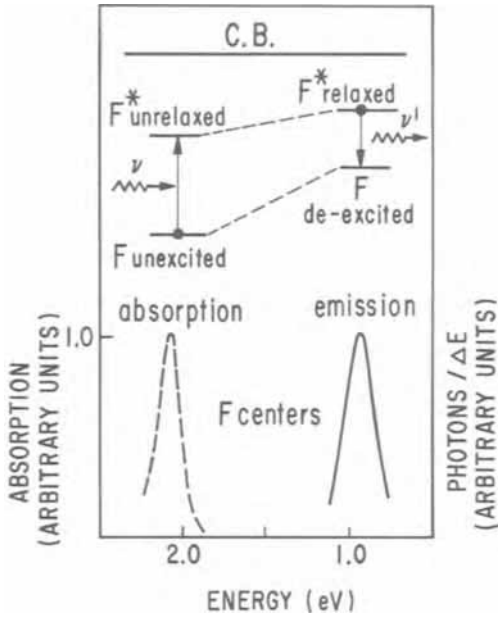

Fig. 2. Excitation and emission spectra (lower), and schematic representation of the luminescence of a relaxed *F* center. The relaxation is caused by the outward motion of neighboring ions and the delocalization of the excited electron.

from the near ultraviolet to the far infrared. Simplified representations of the energy bands of an alkali halide have been used to explain many of the optical and electrical properties of these insulators (*1*). The transitions to the exciton levels and the conduction band are believed to be responsible for the strong absorptions in the ultraviolet region. However, we note (*a*) that the energy band representation has not been a very useful one in explaining coloration processes or in predicting or understanding the nature of the intrinsic luminescence, and (*b*) it is more useful to regard the positive hole as a halogen atom (as will be seen).

The most decisive experimental technique in the radiation physics of alkali halide has been electron spin resonance, developed only in the later stages of the long history of color center studies. The most radical departure from conventional points of view has been the idea that not all color centers are ionic as formerly supposed; some of them, the so-called *V* centers, are stabilized by strong covalent forces which operate between atoms and ions in ionic crystals.

As shown below, *F*-center luminescence studies have revealed the importance of *relaxed* excited states, while impurity luminescence studies have exposed the nature of so-called metastable states; and studies of the intrinsic luminescence of undoped alkali halides have illustrated the importance of covalent bonding and of the competitive relationship between luminescence and one kind of nonradiative de-excitation (*viz.*, color center formation).

F Center Luminescence and Relaxed Excited States

The luminescence properties of an electron trapped at an unoccupied lattice site are quite pertinent to the general theory of solid-state luminescence. The usual EPR studies describe the *F* center electron only in its ground state (*2*). It is the optical excitation of the electron from this S-like state to higher excited states that gives rise to the characteristic colors of the various alkali halides. At low temperatures, irradiation in the *F* band efficiently excites luminescence at longer wavelengths (*3*). In KBr, the emission spectrum has a maximum at about 1.2μ, corresponding to a Stokes shift of almost 1 eV. The luminescence is very easily quenched by other impurities and by *F* centers themselves. In KCl, the quantum efficiency is approximately unity at temperatures below 78°K but drops off sharply with temperature in a small temperature region between 90° and 125°K. In this same temperature region, there is a sharp increase in photoconductivity due to the fact that the *F* center can either be thermally ionized from its excited state or emit light.

Faraday rotation experiments (*4*) show that the excited state of the *F* center is P-like but the individual P states are unresolved. However, the fluorescence lifetime of 1 μsec is too long for a simple allowed P-to-S downward transition. It is therefore generally believed that the *F* center in its excited state strongly interacts with the surrounding ions to form a new, *relaxed-excited state,* as indicated in Fig. 2. It is presumed that, after excitation to the bound P state, the surrounding positive ions immediately move outward to new equilibrium positions; and, during this process, the P state crosses an excited state quite different in physical character and symmetry, from which the transition, a quasi-S-to-S transition, proceeds with lower probability and hence longer lifetime. The concept which has been developed is this: an excited electronic system in a polarizable crystal will, in general, give rise to dynamic adjustments of the ions (as well as the electrons) resulting in relaxed-excited states; these states may be physically different from the initial excited states in character and symmetry. Thus, *two* configuration coordinate models are needed (as in Fig. 2), one to describe the absorption and the second to describe the emission. Substances like Ge or GaAs are not sufficiently polar to give rise to obvious effects caused by lattice relaxation but sulfides and oxides might be. Substances having radical ions such as molybdates, tungstates, and vanadates are probably important candidates for built-in nuclear relaxation processes and relaxed-excited states.

It is interesting that one can distinguish two kinds of electron centers in alkali halide crystals, exemplified by the *F* center (intrinsic to the pure crystal) and by the electron which is trapped at an impurity (and which is often the basis of photochromism in inorganic materials). Chemically speaking, they both correspond to the reduction of a cation. In the case of the *F* center, the electron resonates among identical alkali ions; in the case of an impurity, *e.g.* Tl^+ or Ag^+, the electron is in the immediate vicinity of one impurity ion and usually more tightly bound. The *F*-center electron (whose center-of-charge is at a halide ion site) is shared among the neighboring surrounding alkali ions; it is thus an "inside-out" atom as contrasted, say, to a silver atom in an alkali halide, where the electron

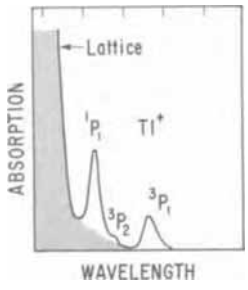

Fig. 3. Absorption bands of Tl^+ in an alkali halide. The cross-hatching indicates the lattice absorption (after Seitz).

surrounds (or is on the outside of) the Ag ion. Unlike the alkali atoms, the $P_{1/2}$ level is above the $P_{3/2}$ in the *F* center. This inversion of the P levels is a property of an electron in a cage of surrounding nuclei rather than of an electron surrounding a nucleus (as in the case of Tl^o or Ag^o) and gives rise to a negative spin-orbit coupling which has been inferred from Faraday rotation and circular dichroism experiments (5). (In the case of the cesium halides, the spin-orbit splitting is sufficiently large to give rise to resolved structure in the *F*-band optical absorption which is absent in the other alkali halides.)

Impurity Luminescence and Metastable States

The phosphor usually described as archetypical in most solid-state physics books is KCl:Tl. Thallium-activated bromides and iodides are completely analogous in their properties, and similar phenomena occur in a variety of doped crystals such as KBr:In, KCl:Ag, *etc.* Figure 3 shows the well-known schematic optical absorption spectra of a thallium-activated alkali halide. The energy levels of Tl^+ are analogous to those of atomic Hg and are split by spin-orbit interactions in the crystal. The ground state is $^1S_0$ and the first excited states are $^3P_{0,1,2}$ (the $J = 0, 2$ states being metastable) and $^1P_1$. The $^1S_0$-$^1P_1$ transition is ordinarily the strongest (*C* band). The selection rules are not strictly obeyed and the $^1S_0$-$^3P_1$ is also a strong transition as in the case of Hg (*A* band absorption); the $^1S_0$-$^3P_2$ also is weakly allowed (*B* band). When excited optically in the *A*, *B*, or *C* bands or with x-rays, fluorescent emissions occur at longer wavelengths. KCl:Tl is usually classified as a nonphotoconducting phosphor (6) but it is not; in some luminescence processes, free electrons and holes play a major part (as will be seen). The object of this section is to show that recent research does away with the idea of internal metastable states such as the $^3P_0$ and $^3P_2$ functioning as traps, a concept which had been invoked to explain phosphorescence effects noticed at low temperatures (7). Extensive and very detailed experiments prove that such intra-atomic states are not responsible for the phosphorescence and that there is a real separation of charge giving rise to this energy storage (8). This is illustrated by the following example in which an infrared image is converted to a visible one in a KI:Tl crystal without electro-optic scanning or high voltages.

If one takes a transparent crystalline plate of a Tl-activated alkali halide at dry ice or liquid nitrogen temperature, energy can be stored in it by irradiating for a few seconds with x-rays. Then the crystal is in the infrared-stimulable or "pumped" state. If an infrared image is focused on the surface of the crystal, it is transduced to a visible image with high sensitivity and resolution (Fig. 4). So long as the temperature is maintained below a certain value, the crystal remains in the "pumped" state and is ready for use. The color of the emission depends on the activating impurity and the host. What is the physical nature of such a light-storing crystal? It was previously thought this was due to some metastable states of Tl^+ but this is not so. In the case of KI:Tl, work has been performed (9) which yields the following answer:

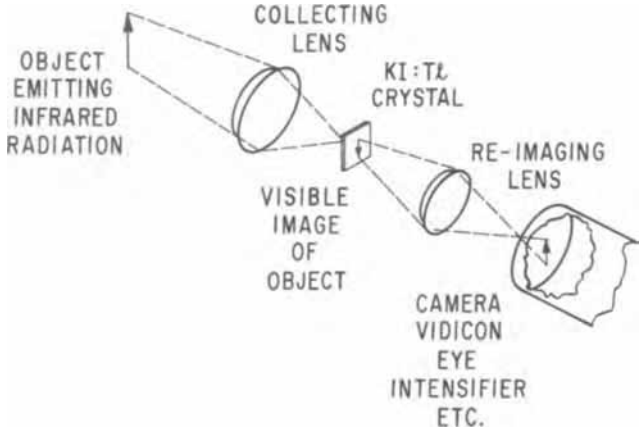

Fig. 4. Schematic of *IR* image converter using a thallium-activated alkali halide.

1. Before pumping, the crystal contains K^+, I^-, and a small percentage [say 1 a/o (atom per cent)] of Tl^+ occupying K^+ sites. After pumping, there are some neutral thallium atoms as a result of electron trapping and some Tl^{+2} as a result of hole trapping.

2. Irradiation with infrared light releases electrons from the Tl atoms which recombine with the trapped holes, restoring the crystal to its former condition with the emission of light (Fig. 5). These processes of storage and infrared stimulation may be summarized by the following equations:

$$\text{KI:Tl} \xrightarrow{\sim} e + h \qquad [1]$$

$$\vec{e} + Tl^+ \rightarrow Tl \qquad [2a]$$

storage

$$h + Tl^+ \rightarrow Tl^{+2} \qquad [2b]$$

$$Tl + h\nu_{IR} \xrightarrow{\sim} Tl^+ + e \qquad [3a]$$

stimulation

$$\vec{e} + Tl^{+2} \rightarrow Tl^{+*} \rightarrow Tl^+ + h\nu \qquad [3b]$$

(The broken arrow indicates a photoreaction.)

This picture of what happens is supported by detailed studies of the energy-storing state, using techniques of optical absorption, electron spin resonance, thermoluminescence, photoconductivity, and emission and excitation spectroscopy (10). The above over-all reaction is the direct antithesis of the concept that internal metastable states of the Tl^{+1} ion ($^3P_0$ and $^3P_2$) are responsible for energy storage.

On the basis of these detailed low-temperature studies, which isolate the individual recombination and retrapping steps, the atomistic mechanism by which thallium-activated gamma ray detectors operate at room temperature has been pieced together (11). This is based on the reasonable assumption that the scintillation mechanism at room temperature is simply

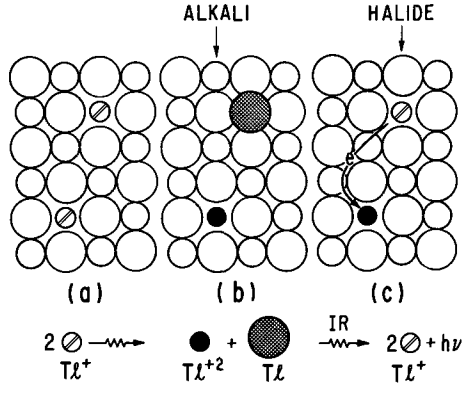

Fig. 5. Heavily doped KI:Tl crystal *(a)* before x-irradiation, *(b)* after x-irradiation, and *(c)* during *IR* excitation, at 78°K.

the appropriate time-sequential composite of the steps frozen out and studied at low temperatures which lead to emission.

The above reactions apply only to a heavily doped phosphor, *e.g.* 10^{-1}-1 a/o Tl^+. If more lightly doped, the hole is not only trapped at a Tl^{+1} but is self-trapped as well, *i.e.* trapped at an I^- ion. The hole (which is chemically equivalent to a halogen atom) immediately forms a molecular bond with a halide ion; the resulting X_2^- molecule (where X is any halogen) has been unambiguously identified by EPR. Electrons may recombine with X_2^- centers as well as Tl^{+2} ions. The generation of the self-trapped hole (X_2^- center) is of great significance. The over-all reaction is indicated by the following for a lightly doped KCl:Ag crystal exposed to x-rays or cathode rays (12).

$$KCl{:}Ag^+ \xrightarrow{\sim} Ag + Cl_2^- \qquad [4]$$

It is basically an electron transfer followed by a dark reaction between the chlorine atom and a neighboring chlorine ion, *viz.*

$$Cl^- \xrightarrow{\sim} Cl^0 + e \text{ (electron transfer)} \qquad [5a]$$

$$\vec{e} + Ag^+ \rightarrow Ag \qquad [5b]$$

$$Cl^0 + Cl^- \rightarrow Cl_2^- \qquad [6]$$

The identification of this center (also called the V_K center) was the first positive proof (*a*) that molecules could exist in ionic crystals and (*b*) that simple holes cannot exist in alkali halides. The molecule formed by the atom and a neighboring ion has a unit positive charge with respect to the crystal and occupies ordinary substitutional lattice sites of the halide sublattice (although it is pulled together by the covalent bond) (13). With alkali halides, the concept of self-trapping is seen in very simple terms as the forming of a chemical bond with a neighboring ion. It is easy to see that a moving electron trapped by the molecular center will restore the crystal to its original condition: *i.e.*, the X_2^- acts like a hole. The reason simple holes cannot stably exist is that they are trapped by surrounding halogen and impurity ions.

The important concepts to arise from these studies of impurity luminescence in alkali halides are these: (*a*) internal metastable states of atoms do not act as long-lived traps: (*b*) for all practical purposes, holes in alkali halides are equivalent to halogen atoms; and (c) covalently bonded atoms can exist in ionic crystals.

Intrinsic Luminescence

Only a few years ago, it was shown conclusively that undoped alkali halides are phosphors, excitable by ultraviolet radiation and x-rays (14). The existence of this intrinsic luminescence (which occurs only at very low temperatures) is of fundamental significance and leads to some interesting concepts, the most provocative of which is that in alkali halides simple excitons cannot move far and probably cannot move at all.

It has been shown that, when electrons interact with self-trapped holes (X_2^- molecules), there is a characteristic luminescence which is identical to that produced by ultraviolet irradiation (15, 16) in accordance with

$$\vec{e} + X_2^- \rightarrow 2X^- \pm h\nu \qquad [7]$$

Process [7] occurs only at sufficiently low temperatures. The recombination has been conceived to be due to a transitory excited molecule, $X_2^{=*}$, composed of an X_2^- molecule and a more loosely bound electron, as indicated in [7]. This has been conclusively proved using EPR and polarized luminescence techniques (15) (since the X_2^- is anisotropic as well as paramagnetic).

It is useful to consider the various ways in which the $X_2^{=*}$ center can be formed. Theoretically, an $X_2^=$ molecule must be derived from two nonequivalent X^- ions for there to be net binding (*i.e.*, one of the X^- ions must be excited); it follows therefore that it can be formed without first forming a free electron (*i.e., without recombination*). We may thus write down the process of intrinsic luminescence in undoped alkali halides excited by ultraviolet, nonionizing light as

$$X^- + h\nu \xrightarrow{\sim} X^{-*} \text{ (Frenkel exciton)} \qquad [8]$$

$$X^{-*} + X^- \rightarrow X_2^{=*} \rightarrow 2X^- + h\nu \text{ (intrinsic luminescence)} \qquad [9]$$

The exciton is thus explicitly identified atomistically as an excited (localized) X^- ion. Because there is always an unexcited halide ion next to it, the exciton in such polar crystals will probably *never* move but be trapped instead. The $X_2^{=*}$ molecule is thus a self-trapped excitonic molecule. When self-trapped at low temperatures, it relaxes radiatively and the constituent halide ions simultaneously resume their normal separation on the halide sublattice. An interesting fact about the intrinsic luminescence center in the alkali halides is that it is produced *by* the irradiation, and does not exist prior to it. Its existence points up the importance of ionic relaxation processes as well as exchange forces in luminescence processes. It has even been suggested that the onset of photoconductivity in a solid does not necessarily imply the onset of interband transitions because relaxation can take a bound excited state, *i.e.* an excitonic state, above the conduction band (17).

Intrinsic Luminescence and Coloration

The recognition of the existence and origin of intrinsic excitonic luminescence in alkali halides has played a very important role in studies of color center formation. As stated above, when F centers are produced by x-rays, halogen ion vacancies are also produced. Now vacancies can only be produced by vacating lattice ions. X-ray photons have insufficient momentum to cause this motion, even though they have plenty of energy. Thus, creating a negative-ion vacancy is like moving a billiard ball by hitting it with a pea. EPR studies show that an interstitial halogen atom is ejected and forms a molecule with a neighboring ion somewhat like the X_2^- center. This interstitial molecule is called the H center (18). Chemically, the H center, like the self-trapped hole, is composed of a halogen atom and ion but occupies one halide site rather than two (see Fig. 1). The important fact is that the interstitial atom leaves behind a vacancy plus an electron, *i.e.* an F center. How does this come about? In particular, where does the momentum come from (19)? A reasonable mechanism is now available based on the observation made only a few years ago that there is an inverse relationship between intrinsic luminescence and coloration (20, 21).

In KI, in a certain temperature region it is now known (22) that, while the radiation is on, the most pronounced phenomenon is the generation of intrinsic luminescence; after the radiation is turned off, stable color centers, such as F and the X_2^- interstitial center, are seen, the characteristic luminescence centers having disappeared.

It was natural to ask if the luminescence centers are responsible in any way for the color centers which are produced. The answer is, they are. In many photochemical systems, the onset of reaction is accompanied by a drop-off in luminescence. KI exhibits this characteristic. There is virtually no color center formation below 90°K and the luminescence is very high; above 90°, there is no luminescence and the coloration rate is high. In photochemical systems, a luminescence center is often known to be the first product of photon absorption and then the source of subsequent photochemical products. In the same way, the luminescence center in KI can be looked on as the generator of the color center, leading to the following description of color center formation:

During x-ray (and even ultraviolet excitation as described above), there exists in the crystal a high

steady-state population of $X_2^{=*}$ luminescent molecules, some of which radiatively decay to the ground state. What happens to those that do not? It has been proposed that the $X_2^{=*}$ molecules are all initially formed in, or excited to, a predissociative state, that the successful dissociation of *some* of them generates vacancies and halogen interstitials with sufficient kinetic energy that they are separated, and that radiative transitions of *undissociated molecules* generate the intrinsic emissions. At very low temperatures, we get intrinsic luminescence; at high temperatures, color centers instead, as is found experimentally.

It is explicit in the mechanism (21) that alkali halides can be colored by *nonionizing* light as well as by ionizing rays; *i.e.*, the threshold energy is of the order of 6-10 eV, and not thousands of electron volts as previously thought. Near ultraviolet light is nonionizing. Ultraviolet colorability experiments are in accord with this (22). EPR evidence has recently come forth (23) which shows directly that, when an electron combines with a self-trapped hole (X_2^-) at sufficiently high temperatures, an interstitial halogen atom and a vacancy are formed. This provides fairly conclusive evidence for an excitonic mechanism in accordance with the following (21)

$$X^- + X^- \xrightarrow{\text{uv}} X_2^{=*}$$

formation of self-trapped exciton [10]

$$X_2^{=*} \rightarrow X_i + \boxed{e} + X^- \quad \text{formation of } H \text{ and } F \text{ centers} \quad [11]$$

Thus, through the formation of a covalent bond between the excited and a normal halide ion, the potential energy imparted to the ion by an almost momentless photon can be converted into kinetic energy: sufficient momentum has been gained to move a massive ion. We can thereby explain both color center formation (a special type of nonradiative process) and intrinsic luminescence by one general mechanism and see clearly the relationships between them.

Applications of Alkali Halide Research

We now know a good deal about color centers in alkali halides. The proof of this is that, as described above, we know what atoms are involved and their configurations; also how the atomic configurations come about and how they give rise to the observed electrical and optical properties. Thus, a good understanding of color center production and intrinsic luminescence in alkali halides has been achieved. How can this knowledge be used? The following points suggest some possible relevance to other fields.

1. Excitons and self-trapping.—In alkali halides, it has been shown that excitons intrinsically do not move because of self-trapping. Self-trapping has been hypothesized in oxygen-dominated phosphors (24) and recently has been observed in tungstates (25).

2. Lattice relaxation.—The luminescence of F centers and the existence of the X_2^- molecule show the importance of lattice relaxation. In these cases, even the symmetry of the excited state is changed by lattice ion relaxation. Relaxation phenomena certainly play a role in the excited states of groups such as vanadate ions, and the concept of a relaxed-excited state probably has general applicability in luminescence.

3. Covalent bonding in ionic crystals.—The existence of color centers and luminescence centers that are molecular indicates the importance of covalent bonding in ionic solids and in luminescence processes. Even a trapped electron is bound partially covalently in a defect.

4. Cathodoluminescence at low electron energies.—It has been shown in alkali halides and also in YVO_4 that uv photons can produce the same excited state for luminescence as electrons. Thus, it is clear that energy packets too much in excess of the necessary minimum will lead to inefficiency; *i.e.*, it is obvious that the threshold energy is physically more significant than the average energy to produce an event (which for high-energy excitation is about 3 E_g per electron-hole pair). It has recently been shown (26) that electrons having only bandgap energy (1 E_g) above the conduction band of CdS can give rise to direct individual pair production and recombination luminescence in which the momentum is conserved without phonon participation. Low-voltage cathodoluminescence (below the plasmon energy) is not only an intrinsic expectation of solids but an experimentally rewarding research area.

5. Isoelectronic traps.—Even when they come from the same group in the periodic table, impurities such as Ag^+ and Br^- added to alkali halides can act as electron and hole traps (27) (as well as activators). This is because of their electron affinity relative to the host ions. Similar effects may occur in sulfide phosphors at very low doping levels, as the properties of oxygen-containing ZnSe scintillators suggest (28).

6. Internal metastable states.—Such states exist in Tl^+ but they do not play any role as trapping states in low-temperature phosphorescence. It is likely that all long-lived metastable states in inorganic phosphors involve separation of charge; this is entirely different physically from an internal metastable state of an impurity.

7. Penetration of fast electrons with matter.—This has been studied experimentally by examining the profiles of luminescence generated as a function of electron energy. Even using good photographic techniques, it is difficult to get precise data because of internal reflections, *etc.* (29). Color center generation should provide a good way of examining electron penetration in matter and of having a permanent record of the experiments.

8. MOS and MIS devices.—It is known that metal oxide semiconductor devices are affected by radiation. Trapped charges in the oxide can affect the electrical properties. It should be possible to compare the radiation effects in bulk silica (amorphous and crystalline) and alumina with effects in the oxide layer of the device and then, just as with alkali halides, one can do experiments such as measuring thermally stimulated current and luminescence on MOS devices themselves, and determine imperfection content, propose models to explain radiation effects, and devise ways of decreasing radiation sensitivity.

9. Electroluminescence.—A frequently proposed model for a-c-excited electroluminescence in ZnS is based on field-released primary electrons from imbedded specks of Cu_2S. Recently it has been possible to obtain electroluminescence from single crystals of KI at low temperatures as well as from KI:Tl at room temperature (30). It is possible to prepare heat-treated, additively colored alkali halide single crystals in such a manner that they contain evenly dispersed colloidal specks of alkali metal. These could serve as sites of field emission and it should be possible in such a well-characterized specimen to excite electroluminescence and test the validity of proposed mechanisms (31).

Conclusion

An attempt has been made to present an eclectic picture of alkali halide research in highly abbreviated form, that might be relevant to luminescence and other fields. In alkali halides, the mechanics of intrinsic luminescence and color center formation are competitive. Self-trapping of holes and excitons is a prominent feature and it leads to the probability that, in alkali halides at least, excitons do not and cannot move. Considering the great variety of materials and phenomena many of us are working on, it is possible that these ideas which come through so strongly in alkali halide research may be applicable to other fields.

Acknowledgments

The author wishes to acknowledge the critical comments of G. Kaufman and W. Hadley of the Zenith Research Laboratories in the preparation of this paper.

Manuscript received Nov. 16, 1970; revised manuscript received *ca.* Jan. 22, 1971. This paper was prepared as the basis for a Keynote Address (Paper 38) presented before the Electronics (Luminescence) Division at the Los Angeles Meeting of the Society, May 10-15, 1970.

Any discussion of this paper will appear in a Discussion Section to be published in the December 1971 JOURNAL.

REFERENCES

1. J. H. Schulman and W. D. Compton, "Color Centers in Solids," The MacMillan Co., New York (1962).
2. W. C. Holton and H. Blum, *Phys. Rev.*, **125**, 89 (1962).
3. Th. P. J. Botden, C. Z. van Doorn, and Y. Haven, *Philips Res. Repts.*, **9**, 469 (1954).
4. J. Mort, F. Luty, and F. C. Brown, *Phys. Rev.*, **137**, A566 (1965).
5. D. Y. Smith, *ibid.*, **137**, A574 (1965).
6. D. Curie, "Luminescence in Crystals," J. Wiley & Sons, New York (1960).
7. F. E. Williams and P. D. Johnson, *Phys. Rev.*, **113**, 97 (1959); F. E. Williams, *J. Phys. Chem. Solids*, **12**, 265 (1960).
8. W. B. Hadley, S. Polick, R. G. Kaufman, and H. N. Hersh, *J. Chem. Phys.*, **45**, 2025 (1966).
9. W. B. Hadley and R. G. Kaufman, *ibid.*, **44**, 1311 (1966).
10. C. J. Delbecq, A. K. Ghosh, and P. H. Yuster, *Phys. Rev.*, **151**, 599 (1966).
11. R. B. Murray and A. Meyer, *ibid.*, **122**, 815 (1961); R. Gwin and R. B. Murray, *ibid.*, **131**, 508 (1963); R. G. Kaufman, W. B. Hadley, and H. N. Hersh, *IEEE Trans. Nucl. Sci.*, **NS-17**, 82 (1970).
12. C. J. Delbecq, W. Hayes, M. C. M. O'Brien, and P. H. Yuster, *Proc. Roy. Soc. (London)*, **271**, 243 (1963).
13. T. G. Castner and W. Kanzig, *J. Phys. Chem. Solids*, **3**, 178 (1957).
14. K. Teegarden, Halide Lattices, Chap. in Goldberg, "Luminescence of Inorganic Solids," Academic Press, New York (1966).
15. M. N. Kabler, *Phys. Rev.*, **136**, A1296 (1964); R. B. Murray and F. J. Keller, *ibid.*, **137**, A942 (1965).
16. H. N. Hersh and R. Jarka, *Bull. Am. Phys. Soc.*, **9**, 542 (1964); H. N. Hersh and A. Cocco, *Phys. Rev.*, **161**, 834 (1967).
17. R. F. Wood, *Phys. Rev. Letters*, **15**, 449 (1965).
18. W. Kanzig and T. O. Woodruff, *J. Phys. Chem. Solids*, **9**, 70 (1959); W. H. Dueriz and J. J. Markham, *Phys. Rev.*, **88**, 1043 (1952).
19. J. Crawford, *Advan. Phys.*, **17**, 93 (1968).
20. D. Pooley, *Proc. Phys. Soc.*, **87**, 257 (1966).
21. H. N. Hersh, *Phys. Rev.*, **148**, 928 (1966); C. B. Lushchik, I. K. Vitol, and M. A. Elango, *Soviet Phys.-Solid State*, **10**, 2166 (1969).
22. J. Konitzer and H. Hersh, *J. Phys. Chem. Solids*, **27**, 771 (1966).
23. F. J. Keller and F. W. Patten, *Solid-State Comm.*, **7**, 1603 (1969).
24. S. G. Polick and H. N. Hersh, Paper 69 presented at Electrochem. Soc. Meeting, Dallas, May 7-12, 1967; H. N. Hersh and H. Forest, *J. Luminescence*, **1**, 2, 862 (1970).
25. G. Born, A. Hofstaettler, A. Scharman, and G. Schwarz, International Conference on Luminescence, 1969, Abs. H-5 (in *Bull. Am. Phys. Soc.*, Series 11, Vol. 14, No. 8, Aug. 1969).
26. F. Steinrisser, *Phys. Rev.*, To be published.
27. J. W. Wilkens and J. R. Gabriel, *Phys. Rev.*, **132**, 1950 (1963); D. Schoemaker, *ibid.*, **149**, 693 (1966).
28. T. C. Madden, J. L. Merz, G. L. Miller, and D. G. Thomas, *IEEE Trans. Nucl. Sci.*, **NS-15**, 47 (1968).
29. W. Ehrenberg and D. E. N. King, *Proc. Phys. Soc.*, **81**, 751 (1963).
30. A. G. Fischer, *This Journal*, **110**, 733 (1963).
31. S. Unger and K. Teegarden, *Phys. Rev. Letters*, **19**, 1229 (1967); H. Hersh, Unpublished [Note added in proof: the colloid experiment has been performed by C. Paracchini and G. Schianchi, *Phys. Stat. Sol.*, **36**, K1 (1969).]

JOURNAL OF THE ELECTROCHEMICAL SOCIETY

REVIEWS AND NEWS

JULY 1971

The Scientific Society and National Materials Problems[1]

N. E. Promisel

National Materials Advisory Board, National Research Council, Washington, D. C. 20418

For some years now, I have been absorbed with the need for viewing, in broad perspective, materials science and engineering as an interdisciplinary force involved in a very significant way in our major national issues and our individual interests. Now this statement can be made about other subjects, for example, chemistry. Chemistry, however, is a relatively cleanly bounded area, recognized in its fullest interactions by everyone. This is not true about materials, for which there is not even a generally accepted definition. For the most part, the subject of materials is described by a nondefinition; *i.e.*, it is defined as "everything except," and the exceptions depend on the immediate purpose at hand. Electrochemistry is certainly an important aspect of materials, and I was encouraged to think that it would be appropriate and provide an opportunity to discuss materials science and engineering, particularly in terms of national issues and problems, and the related importance of a learned society such as this.

It may be useful to review briefly, at least as I see it, the genesis of materials science and engineering as it is recognized today. I would then like to discuss relevant national issues; some efforts toward providing a national forum, if not a national policy, with respect to materials; and, finally, the position and role of the learned and professional societies in this scenario. Please keep in mind that, whenever I use the word "materials," I consider that the word "electrochemistry" may either be substituted for it or forms a vital part of it.

First, to build up our ego a bit, I will quote from Sir George Thomson, who won the Nobel Prize in Physics in 1937. He said: "We have for some time labeled civilizations by the main material which they have used: The Stone Age, The Bronze Age, and The Iron Age. . . . . A civilization is both developed and limited by the materials at its disposal . . . . Today, man lives on the boundary between The Iron Age and a New Materials Age."

As a result of the impressive developments in electrochemistry, chemistry, physics, solid state science, metallurgy, ceramics, and other disciplines (all of which, when integrated, become the field of materials), there has grown up a materials science and a materials engineering which are having a profound impact on industry, government, and academia, and are, therefore, receiving more and more attention at all levels. We must recognize, however, that materials as a total concept, or as an identifiable segment of science and engineering, is really relatively new.

In the United States, materials science and engineering were given their stimulus in World War II, primarily with Federal funding. We had, of course, the mono-disciplines of metallurgy, chemistry, physics, *etc.*, and a storehouse of fairly classical materials from which the designer and product developer drew. Background and experience were major influences on his material selection. Those with metal backgrounds stayed with metals, those with chemical backgrounds stayed with plastics when they could, *etc.* For example, asked how to protect steel from corrosion, an electrochemist would recommend electrochemical protection and a chemist would recommend an organic coating. The boundaries of the disciplines were barriers rather than interfaces. Communication between designers and metallurgists or chemical engineers was grossly inadequate.

The drastic demands of defense and, later, nuclear energy and space forced a change in this attitude. Now the requirements tended to be expressed in terms of performance; for example, a *material design* to withstand "*x*" temperature degrees, for "*y*" hours, with "*z*" creep under "*s*" stress, without specifying whether it be metal, ceramics, intermetallic compounds, a combination of these, or these combined with built-in cooling; or one would specify a certain electrical performance, whether it use vacuum tubes, solid state devices, or special electronic concepts. Thus there grew the concept of materials as a system and the concept of the multidisciplined materials engineering. Simultaneously, inspired by such demanding fields as electronics and progress in solid-state science as in single crystals and synthetic polymers, a clearer understanding was being developed of the relation between the properties or behavior of a substance and its basic electronic, atomic, and molecular structure. It became evident that this relationship was essentially fundamental, thus establishing a kind of commonality in certain attributes of various materials and minimizing the real differences between various types of materials. There also grew a materials science, indigenous to the behavior of many kinds of materials, that tended to break down the barriers between metallurgy, chemistry, and other disciplines.

It was natural that a concern for increasing the availability of material scientists and engineers should also develop. Obviously, universities had not been producing this type of individual. Attention was focused on promoting university courses, curricula, and research for educating and training students in this direction. The first step was a major effort by the United States Government to create interdisciplinary laboratories in 17 universities. Approximately a 10-year program was created, which cost in the neighborhood of a quarter of a billion dollars. This program is now nearing its end. Clearly the Ph.D.'s and other graduates in this field have increased substantially, at least a fewfold. Some universities have created very effective materials science departments, in many cases, as an outgrowth of their metallurgy departments. At the same time, the interdisciplinary efforts in some uni-

[1] This paper is based on the Plenary Electrochemical Society Lecture presented at the Atlantic City, N. J., Meeting of the Society, October 5, 1970.

versities have been only in name; the old barriers between departments really still existed.

It is interesting to note that the onset and trend toward materials science and engineering also had their impact on industry, where diversification has become common and materials-producing and materials-system industries have grown. Many of the larger companies, as in aerospace, also have established their own laboratories of materials science and engineering.

The effect has been felt even in technical and professional societies: our metal societies deal with plastics; our chemical societies include metals; our electrical societies include materials; *etc.* The Electrochemical Society could, as justifiably as some others, be termed a materials society; a review of the Society Divisions shows coverage of many materials, material processes, and material behavior phenomena.

It is worth emphasizing also that, while enormous contributions have continued to be made by the more conventional materials industries (such as those concerned with metals, ceramics, and textiles), recent progress in solid-state science and engineering has shown that the most subtle new insights (such as quantum electronics concepts, statistical mechanics applied to changes in polymers, and the lattice-defect theories of metallic aggregates) can be applied effectively to a host of practical problems which were heretofore treated only with empiricism.

In summarizing the above, I would say that the past 20 years have seen a transition from the single disciplines of metallurgy, chemistry, *etc.*, to the multidiscipline concept of materials, which includes all of these subjects and more. The single disciplines, of course, still exist (as they should) because they are vital. This change has had profound effect in industry, government, and universities. It has been an important step forward in optimizing design and production, by forcing open-minded consideration of many competitive materials, techniques, and concepts, permitting wider choice based on both improved performance and improved economy. It has established communication and transition between science and engineering. Finally, and of extreme importance, it has made possible the concept of tailor-making or custom-making materials to satisfy very difficult and complex requirements which could not be satisfied by the more conventional approaches.

Electrochemists, as such, perhaps may be referred to as a vanishing group. This may be an exaggeration; I have not attempted to document it. But my "gut" feeling is supported, for example, by some correspondence. As a further example, in the hundreds of contacts representing a wide variety of disciplines which we annually make in our own Advisory Board, I cannot recall a single individual who calls himself an electrochemist. I myself, although basically an electrochemist by training and many years of practice, call myself either a materials scientist or a materials engineer, depending on my audience and what I want to achieve. Yet, as I have already indicated, electrochemistry has many of the same interdisciplinary aspects as materials science, although not on so comprehensive a scale. Just as the devotees of materials have felt (at least until fairly recently) that their subject was not being appreciated in terms of its true significance and importance, that it was being neglected and not being assigned an adequate priority in the family of scientific and technological subjects, so the charge is now being made that electrochemistry as a field is waning both in terms of academic interest and industrial support. It is claimed that the annual production of only 5-10 Ph.D.'s in electrochemistry in this country is far out of balance with the annual production of about $4 billion of electrochemical products; that, under these conditions, the United States will fall behind in industrial disciplines as compared to Europe, where electrochemistry still commands substantial interest and respect in universities and laboratories; that the United States will deprive itself of important technical contributions to our societal problems. This is an important indictment of science in our country which, if completely real, could have far-reaching implications. At the same time one can ask, without meaning to imply any bias whatsoever, a number of questions: Is much or even most of the work that should be done in electrochemistry actually being done but not under the name of electrochemistry; for example, under the heading of materials science, or physical chemistry, or surface chemistry? If so, should we let these trends continue their course so that eventually electrochemistry will exist primarily as a concept and series of principles serving as important adjuncts of other fields of science and technology but not in itself be classed as a separate, identifiable entity in the same sense as metallurgy, chemistry, or physics? If this is not desirable, what priority should be given this field, considering the financial strain currently being imposed on science as a whole and the needs of other scientific and engineering fields? Where are the opportunities and potential payoffs greatest? For we hear the same plaint in other technical areas. For example, in the recent Orton Memorial Lecture of the American Ceramic Society, Dr. Osborn stated: "The position of the U. S. in ceramic science and technology rose to one of world leadership during the past few decades. . . . A recent study . . . concludes that the U. S. is rapidly losing this leadership. . . . How in the future will we fund the basic research our industry will need . . . . ? Basic research in ceramics has at present a precarious future." I do not pretend to have adequate answers to these and similar questions but I believe they are important, and I suggest that this Society is a logical place to start developing some facets of a national, documented position for consideration. Perhaps you are already doing so.

I have injected this topic at this stage because I believe it is a fitting introduction to the next subject, namely, national problems which interface with materials and related topics. The question of the status and future policy with respect to electrochemistry is but one of a series of major issues with which this country is not organized to cope in a deliberate, efficient, comprehensive manner. So I would now like to spend some minutes on these national situations and the related importance of materials and, directly or indirectly, electrochemistry. These issues are tabulated in Table I.

The materials problems of societal needs.—By societal needs is meant those now quite commonly recognized: pollution and environment control, transportation, low-cost housing, urban development, *etc.* Examples of materials problems in these areas are numerous. Already millions of pieces of metal are being implanted in human beings annually and yet there has been no major concerted effort to develop optimum materials for these specialized and literally vital applications. Mostly, implant materials have been "borrowed" from other technologies, and such effects as corrosion and electrochemical behavior under the particular conditions obtaining in the body still need vigorous attack. Many of the biological interactions involved depend on electrochemical reactions. Progress in high-speed transportation by trains is being hampered by materials problems in wear, friction, and brake applications; aggressive approaches through surface chemistry and coatings are obviously needed. Environment control demands refined approaches to proc-

Table I. Some major national materials issues

- The Materials Problems of Social Needs
- The Challenge of the Materials Explosion
- The National Posture in Technology
- The Life Cycle of Materials
- The Mobilization, Operation and Control of R&D
- Miscellaneous: Forecasting; Government Interaction; Diffusion, Storage and Use of Information; Public Safety; etc.

essing materials, utilizing them, converting from one form of energy and power to another (batteries and fuel cells are important approaches), minimizing waste and reclaiming value from it, perhaps designing the ultimate industrial products to facilitate salvage or disposition. These are only a few of the more obvious material and electrochemical aspects of societal problems.

The challenge of the materials explosion.—The materials explosion of the past two decades has contributed to probably all branches of science and engineering: from cryogenics to ultrahigh temperatures; from automobiles to space travel; in computer technology, food processing, communications, man-made fibers for textiles, clothing, and massive structures; *etc.* The challenge is to take advantage of this explosion now and to insure its continuation in the future. The scientific understanding must be converted to engineering application; the technology in sophisticated areas—in the United States notably in defense, space, and nuclear energy—must be transferred to other areas. Recognition must be given to the tremendous potentials in the ever-increasing nonmetallics areas such as plastics, inorganic engineering materials, ceramics and glass for industry and for the nation. Electrochemical syntheses are often basic to some of these products.

National security and national posture in technology.—I have grouped under this heading such pursuits as defense, space technology, commerical nuclear power, and other items which require strong government involvement and support and are often inter-related in other ways. Government involvement is justified when industrial risks are too high (as in the SST), when there is political or military significance (*e.g.* space and computers), or when there is lack of profit incentive (as in electric cars). As an illustration, let me cite the birth and development of a whole new industry, titanium, in less than two decades, as a result of close government/industry interaction springing from a deliberate national policy. Many features of this industry are electrochemical in nature; for example, the electrochemical production of magnesium (the main reducing agent for titanium tetrachloride) and the electrode processes in melting.

Material life cycle.—This topic has been mentioned earlier. We consider this cycle as proceeding from natural resources (raw materials), to preparation and transformation into products, to utilization, to disposal (waste), to recovery for reuse, thus closing the cycle. Such a cycle does, in fact, include all the problems I have enumerated: materials availability, pollution, efficient use of resources, export/import balance and economics, and many more. There is an international aspect as well, since all countries are in some respects "have-not" nations and must depend on imports and exchange of commodities to meet their internal needs. The increasing industrialization in so many countries will create extreme competition for these materials throughout the world, with peculiar situations possible. For example, it is conceivable that a country some day might be faced by the unpleasant necessity of choosing between a mineral shortage and a food shortage, since one can be bartered for the other.

Mobilization, operation, and control of materials research and development (R&D).—The U. S. is spending on the order of $1 billion per year in materials research and development. The estimate of this amount varies depending on how one defines the scope of materials. Perhaps half of this amount is furnished by the government directly or indirectly, and the rest is mainly provided by industry.

If we normalize the budgets over the last five years to correct for inflation, the annual effort is not increasing and probably is tending to decrease.

A number of questions, therefore, can immediately be asked. Is this annual rate adequate? How was the government effort determined? Is it properly distributed in proportion to priorities and defined goals? Is the technical manpower adequate? How about equipment and facilities? What is the relation to university educational programs? And many more questions. You see, the previous question of the adequacy of the national effort in electrochemistry and its priority fits into this category of issues.

I wish I could say that years ago we defined our national goals and priorities in materials and were now following an up-to-date grand plan. Unfortunately, this is not the case. I am not saying that our present fragmented programs are not good or logical. Perhaps they are; but I am emphasizing that we have not had a mechanism in the past for forecasting needs in materials and processes in such a way, and with such conviction, that we could define our goals and design national programs to achieve these goals most efficiently.

Other problems.—There are a number of other problem areas that could be presented if time were available. Now there is the need to define (forecast) both our opportunities and major problem areas in the next 10 to 20 years; to establish long range strategies, necessary for guidance of university curricula, for industry operation, and indeed to maintain our economic position in the world; the problem of optimizing the exchange and use of information generated by the annual billion dollar effort, and the important role that the professional society should play here; the task of improving public safety by taking advantage of new understanding of material behavior; the challenge to take advantage of electronic data processing to deal adequately with materials as a system on a national basis. And there are many more issues requiring a national forum for planning.

Thus, over the years, materials have moved from being an individual problem, to an industrial problem, to a government involvement problem. There is hardly any major national situation in which materials do not play a significant role. Therefore, no piecemeal, fragmented, haphazard activities can provide the answers and actions that are needed to deal nationally with these situations. There must be a national mechanism for focusing on these problems and creating policy. Otherwise, there is confusion, inefficiency, and big, unfilled gaps demanding attention. My earlier statements about assessing the needs for national action in the field of electrochemistry, *vis-à-vis* other national scientific needs, is an example of such a gap.

At the moment, I see three important contributory assists to this situation: one is at the Federal Government level; the second is the organization which I represent, namely, the National Materials Advisory Board; the third is the scientific and professional society, working either as an individual society or in consort with other societies, preferably the latter. These approaches, by the way, are not mutually exclusive; in fact, I see them as a strong coalition. Let me discuss them in a little detail.

Mainly as a result of the Government's concern with pollution, waste, recovery, and control of the environment in general, it has been possible to stimulate, in the Senate, a bill for the formation of a Presidential Commission on Materials. Some of you will recall that in the early fifties there was a Presidential Commission on natural resources, chaired by Mr. W. M. Paley of the Columbia Broadcasting System. The resulting Paley Report dealt with a number of resource issues in the country and included recommendations, some of which were implemented, and others, including the establishment of a continuing national body to monitor problems, which were not. In any case, the Paley studies are certainly out of date, and many of us have felt for several years that a new, comprehensive study was needed. The bill that was introduced in the Senate in mid-1970 was designed to set up a seven-man commission, to be appointed by the President, to conduct a study to be completed within three years, financed by

Table II. Proposed subjects for a national commission on materials policy

- Materials requirements, priorities, objectives and economic projections
- Relationship of materials policy to population size and environmental quality
- Recommended means for extraction, development and use of materials susceptible to recycling, reuse, or self-destruction, to enhance environmental quality and conserve materials
- Means of exploiting scientific knowledge in the life cycle of materials and encouraging research and education
- Means to enhance coordination and cooperation among Federal agencies
- Feasibility and desirability of establishing computer inventories of materials requirements, supplies and alternatives
- Other subjects as may be developed

Congress up to $2,000,000, with the objectives shown in Table II. The bill has now become law. In the meantime, another group has been authorized to inventory United States requirements and supplies of raw materials until the year 2000. Another act is also in process which would require annual reporting on mining, minerals reclamation, utilization trends, *etc.* Clearly Congress and the Executive Department are worried about materials resources for the next 30 years.

The second force that I mentioned in connection with national materials problems was my own organization, the National Materials Advisory Board (NMAB); and I would like to briefly describe this. The NMAB is a unit of the National Academy of Sciences and the National Academy of Engineering (which essentially are honorary groups of distinguished scientists and engineers), and the National Research Council (which is the operating arm of these two academies). In accordance with the principles and charter of the two academies, NMAB, therefore, is a nongovernment activity, supported by both government and private funds, for the advancement of the science and engineering of materials in the best interests of the country. It works with government agencies, industry, professional societies, universities, and trade associations. For national problems and opportunities in materials, and for transfer of technology to nonmaterials areas, it provides the functions of analyzing, defining, planning, balancing, cross-fertilizing, integrating, monitoring and coordinating, both for government and nongovernment. It operates mainly by assembling the best available talent in the country, and sometimes from abroad, for a given problem or objective. The functions of NMAB are abbreviated in Table III. The NMAB, therefore, provides a neutral, unbiased forum and focal point for discussing and providing implementable

Table III. Objectives and functions of NMAB

- Provide assistance to government and non-government
- Provide studies on national problems and opportunities and on action to be taken
- Identify problems and approaches in interacting materials with other functions
- Cooperate in development of advanced educational approaches
- Promote cooperation among professional societies
- Disseminate information
- Be aware of advancing technology, emphasize opportunities and roadblocks, and promote advanced concepts

approaches to national issues, embracing the three major sectors of the materials community: government, industry, and academia. Its role with respect to technical societies will become clear in a moment.

The Board itself, besides its permanent staff, consists of between 25 and 30 outstanding, top level scientists and engineers, representing many professional views: metallurgy, chemistry, physics, ceramics, economics, management, *etc.* They come from industry, government, and universities throughout the country.

The organization of NMAB is shown in Fig. 1. I do not intend to discuss this organization in detail but do want to emphasize a few of its facets. First, note that there are three councils, to permit focusing on the problems and interests of each of the three sectors I have mentioned. However, each council contains representatives of all three sectors, to insure balanced input and interaction. In addition to these three councils, we have an Interagency Council which includes all the government agencies concerned with materials; that is, not only DoD, AEC, and NASA, but the National Science Foundation, Department of Transportation, the National Institutes of Health, Housing, and Urban Development and a half dozen more, thus assuring good interaction between materials and other government problems.

Note also that we have essentially three types of operational groups or committees, not including various administrative committees. These are the Ad Hoc Technical Committees, dealing with fairly specific technical studies of limited duration, such as a year or two. The Standing Committees are intended to deal with broad issues and have no finite termination date. The third group are special committees of finite life but dealing with broad subjects, not specifically technical. Let me illustrate these three types. In Fig. 1 are examples of some technical topics that the Ad Hoc Technical Committees deal with. The Standing Committees or Technical Councils could deal with fracture prevention or corrosion, for example, on a continuing,

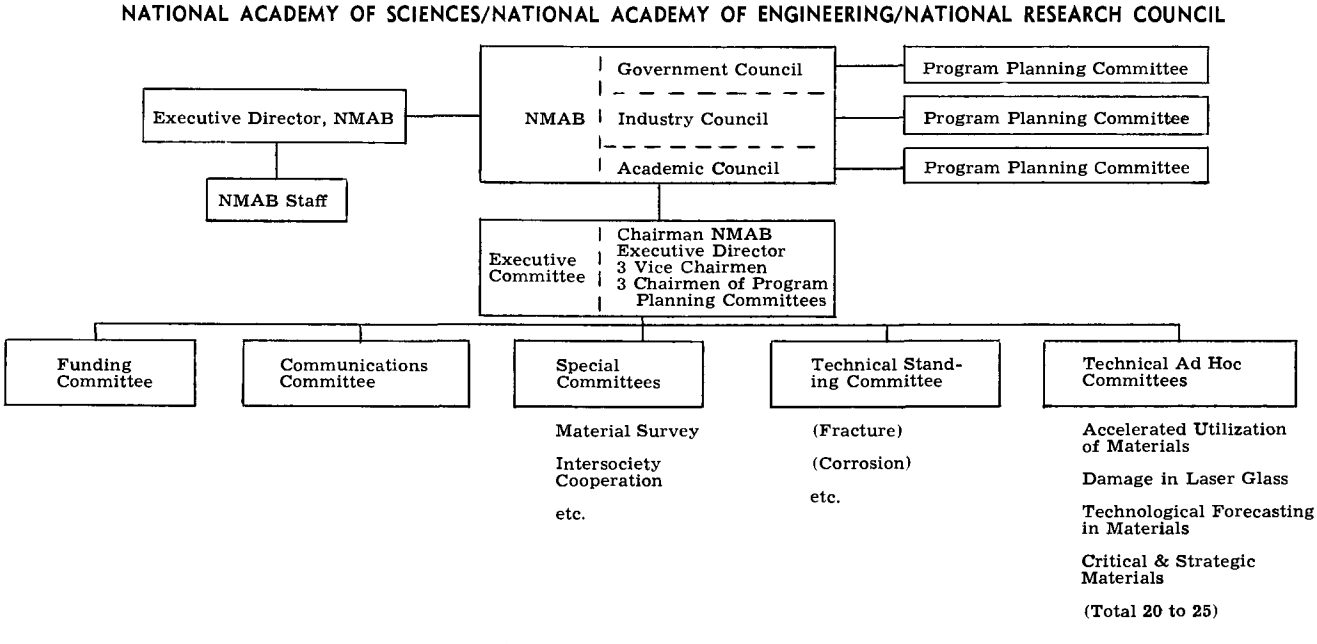

Fig. 1. The organization of NMAB

Table IV. Tentative objectives of national materials survey

- Identify and define the field of materials science and engineering.
- Identify past accomplishments and future potential and role.
- Determine gaps in materials R&D
- Examine national manpower needs.
- Examine educational structure in this field.
- Identify approaches for improving interaction between science and engineering.
- Plan future goals, strategies and priorities.

comprehensive basis. For the Special Committees, I want to mention two subjects in particular.

Some of you may be familiar with a series of reports produced by the National Academy of Sciences covering broad surveys of technical areas. There is such a report on chemistry (The Westheimer Report), on physics (The Pake Report), on life sciences, *etc.* The NMAB has been active in stimulating and planning such a survey on materials, with the objectives shown in Table IV. Certainly as one component of materials, a number of aspects of electrochemistry will be included. Nevertheless, you might want to consider a separate survey of electrochemistry as such, with objectives parallel to those described, if indeed you are concerned about the status and future direction of electrochemistry.

The second special topic I want to describe has to do with the broad group of scientific, technical, and professional societies.

In the United States we have about 35 technical and professional societies significantly concerned with materials in one way or another. The Electrochemical Society is one of these. Without questioning at this time the justification for all of these societies (although I have personal reservations), it is clear that this multiplicity does result in unnecessary duplication of meetings, lectures, symposia, *etc.*, on the one hand; and, on the other hand, no one society is able to cope with certain broad national problems, providing an integrated view on national materials issues when such a view is sought, *etc.*

A few years ago, during the annual meeting of the National Research Council on which are represented most of the societies involved, we decided to explore with these representatives several possibilities for concerted action. From this beginning, through a sequence of task forces, committees, and individual actions, there has evolved the conclusion that these societies can work best and to mutual advantage in the form of a society federation, analogous but not identical to the American Institute of Physics, the American Geological Institute, and others.

Let me emphasize immediately certain basic tenets of this proposal for a federation. No new society is intended here, only the voluntary cooperative effort of existing societies. No merger of any societies is being sought; conceivably, in the future, something in this direction could spontaneously occur. No society is being asked to yield its autonomy, its prerogatives, or its individuality. The federation will in no sense be a political lobby but it could respond technically and in a coordinated way to government requests. The major thrust of this effort is to provide a deliberate, positive opportunity and mechanism for a number of societies to work together, efficiently, toward common goals and to mutual advantages, with better service resulting to the scientific and technical community and to the nation as a whole. The NMAB is serving only in a catalytic role in this activity; once the objective is achieved in whatever form is desired by the societies, it does not intend to have any continuing function.

At a meeting called at the NMAB in August 1970 to discuss plans for a conference to determine the next moves toward forming such a federation, 18 selected societies were invited with almost 100% response; rather amazing and quite significant, in my opinion. Although no commitments were requested and none made, the group reaction was most favorable and encouraging, with a decision to proceed with the drafting of a charter. This has been done and drafts of a Constitution and Bylaws have been circulated to all of the societies involved. At the planned conference, held on February 11, 1971 at the National Academy of Sciences, the society representatives formed a steering group to define available options for an intersociety operating mechanism or federation. In the meantime, the steering group itself is authorized to plan appropriate coordinating and cooperative society activities. I continue to be hopeful, therefore, that by this or other means we can move forward to expanded intersociety activity on a firm, deliberate, continuing basis.

I personally consider that the scientific and professional societies in the fields we are discussing have been too modest for too long. The talent and technical resources which reside in the hundreds of thousands of members could make valuable contributions to the many vital problems and situations which confront the nation. More than one member of Congress, for example, has exhorted societies to act in this way. The societies are needed to help in these national issues and, in turn, can demonstrate the significance and importance of the technical areas they represent. In a sense, I think we can look on a society such as this one as a fourth dimension, a vital adjunct and contributor to the other three: industry, academia, and government.

In conclusion, I would recapitulate by stating that materials science and engineering, including electrochemistry under this broad spectrum, have made dramatic strides in the past few decades. Simultaneously, however, this country has awakened to, or has created, some massive national issues to which materials can make valuable contributions. The expanded National Materials Advisory Board is providing a forum and a mechanism to assist in making these contributions feasible and in providing guidance. In addition to this national effort of NMAB, one or more President's Commissions are being established. In every sense, a society such as The Electrochemical Society can provide valuable inputs and accomplishments, simultaneously ensuring that the field for which it is responsible to its membership receives proper attention and priority. Particularly today, when science and technology have lost some of their luster in the public's mind and yet, ironically, when the public needs science and technology perhaps more than ever before, it is important that each society assess its position and capability and join in an integrated effort for the common good.

Manuscript received Feb. 9, 1971.

Any discussion of this paper will appear in a Discussion Section to be published in the June 1972 JOURNAL.

JOURNAL OF THE ELECTROCHEMICAL SOCIETY

REVIEWS AND NEWS

AUGUST 1971

Anion Bridging and Anion Electrocatalysis on Mercury

Robert de Levie

Department of Chemistry, Georgetown University, Washington, D. C. 20007

ABSTRACT

The rate-enhancing effect of some specifically adsorbed anions on the kinetics of several electrode reactions greatly exceeds that predicted by the Frumkin correction. The literature on this effect is critically reviewed, including Heyrovský's 1947 hypothesis of ligand bridging and the pioneering work of Aikens and Ross on the oxidation of Cr(II). Two current theoretical interpretations are discussed and several related comments are made regarding ionic adsorption.

The double layer at the electrode-electrolyte interface has long been known to exert a significant effect on the kinetics of electrode reactions. Frumkin (1) was the first to point out that electrode reactions are driven by the effective potential $E - \phi$ (where ϕ is usually associated with the so-called "outer" Helmholtz potential) rather than by the applied potential E. He also introduced a Boltzmann correction for the interfacial reactant concentrations, which are modified by coulombic attraction or repulsion of ions by the double-layer field. Since anion specific adsorption alters the value of ϕ, such adsorption may significantly change the rates of electrode reactions.

A second type of double-layer influence is that of blocking. Adsorbed organic molecules often severely suppress electrode reactions. This interference is usually much larger than can be accounted for on the basis of a mere change of ϕ resulting from the adsorption. Of course, the influence of ϕ is present as well, and the two effects can sometimes be distinguished when they work in opposite directions (2).

Many adsorbed organic molecules, like proteins, alkaloids, and pyridines, are known to catalyze the reduction of hydrogen on mercury. This effect has been studied extensively for several decades, and the reader is referred to recent reviews (3, 4) for details.

Of more recent date is the realization that adsorbed inorganic ions can act as catalysts as well. The ion adsorption is of course accompanied by a change in ϕ, but the observed acceleration of electrode reaction rates is often much too large to be accounted for solely on that basis. Another factor which sometimes complicates the interpretation is the possibility of complex formation between the reduced cation and the added anion. However, the rate enhancement is often much more pronounced with I^- than with Cl^-, even when the tendency for the cation to form complexes is greater with Cl^- than with I^-.

Heyrovský was the first to notice the pronounced effect of halides on the reduction of Sn(II), Bi(III), Sb(III), and In(III) (5). These observations he explained, as early as 1947, with electron transfer through a bridge mechanism. Many more examples have since been reported, and it now appears that electrocatalysis by adsorbed anions is a fairly general phenomenon.

Key words: adsorption, catalysis, isotherms, kinetics, ligand bridging.

In this review, discussion is restricted to electrode processes on mercury. This should not be taken to imply that similar effects are not operative on other electrodes, but merely to reflect the fact that, for a variety of reasons, sufficiently detailed double-layer data on solid electrodes are virtually nonexistent. Our present understanding of both electrode kinetics and double-layer structure stems largely from experiments on mercury, and the same applies to electrocatalysis, which represents a close interplay between kinetics and double-layer structure.

So far, two cases of rate enhancement by anion bridging have been worked out in fair detail: the oxidation of Cr(II) and the reduction of In(III). Since quite different and largely complementary approaches were taken in these two cases, we will consider them separately. Subsequently, some more or less scattered data from the literature and from our own research are discussed in order to illustrate the fairly common occurrence of such effects on mercury.

Chromium(II)

After several investigators (6, 7) had noticed that the addition of chloride accelerates the oxidation of Cr(II), Aikens and Ross (8) examined this reaction in detail. They measured the oxidation rate constants as a function of solution composition and electrode potential. The oxidation rate is enhanced more by I^- than by Br^-, and Br^- in turn is a more efficient accelerator than Cl^-. This sequence runs parallel with the adsorbabilities of these anions, but counter to the tendency of Cr(II) to form complexes with halides. Also, the rate enhancement is much more pronounced at more positive potentials, where halide anions are more strongly adsorbed, suggesting again that the adsorbed rather than the bulk anions cause the effect.

Aikens and Ross (8) also performed large-scale electrolytic oxidation of Cr(II) in the presence of chloride, and found that the electrolysis, when performed at rather positive potentials, almost exclusively produced chloropentaquochromium(III). All the above data are consistent with two parallel oxidation pathways in the presence of chloride ions:

$$Cr^{2+} \rightarrow Cr^{3+} + e^- \qquad [1]$$

and

$$Cr^{2+} + Cl^-_{ads} \rightarrow CrCl^{2+} + e^- \qquad [2]$$

Finally, Aikens and Ross (8) pointed out that $CrCl_2^+$, even if initially formed, would react rapidly with Cr^{2+} as long as there would still be some Cr^{2+} left:

$$Cr^{2+} + CrCl_2^+ \rightarrow Cr^{2+} + CrCl^{2+} + Cl^- \quad [3]$$

Consequently, product analysis in this case cannot indicate whether one or two adsorbed halides are involved in the halide-assisted charge transfer.

The observations of Aikens and Ross (8) have been confirmed extensively by Kemula and Rakowska (9), Anson *et al.* (10, 11), and Watanabe *et al.* (12). Recently, Anson *et al.* (13) have extended the measurements to the oxidation of Cr(II) in the presence of thiocyanate ions. In this case, $Cr(NCS)_2^+$ and $Cr(NCS)_3$ are the predominant oxidation products over a wide range of conditions. The dependence of the product distribution on potential, and the preferential formation of the cis-isomer of $Cr(NCS)_2^+$, are clear evidence that adsorbed SCN^- is involved in the oxidation, and apparently acts as ligand bridge between cation and electrode.

In the oxidation of Cr(II), direct chemical product analysis provides convincing evidence for the involvement of adsorbed ions in the electrode process, because the reaction products are quite substitution-inert, *i.e.*, they do not quickly exchange coordinated solvent molecules or ions with the surrounding solution. In the case of substitution-labile products, we must rely on less direct evidence, an example of which will be given in the next section.

Indium(III)

Heyrovský (5) noticed that the presence of halides rendered the oscillopolarographic reduction of indium reversible, and explained this observation in terms of electron transfer through a halide bridge. Earlier, Lingane (14) had observed a minimum on the polarographic wave for In(III) in halide solutions; but it remained for Cozzi and Vivarelli (15) to correlate the occurrence of this minimum with anion desorption. Similar minima (*i.e.*, regions in which the polarographic reduction current decreases as the potential is made more negative) are observed also with, e.g., tartrate (15), oxalate (16), thiocyanate (17, 18), and with several organic sulfur and nitrogen compounds (19).

Shirai (17) noticed that the a-c polarogram of In(III) in thiocyanate solutions exhibits a negative admittance. Tanaka *et al.* (20) pointed out that the sign of the faradaic admittance is determined by the sign of dk/dE, where k is the reduction rate constant and E the applied potential. This correlation was given a more precise formulation by de Levie and Husovsky (21), who also demonstrated that the polarographic minimum and the negative faradaic admittance are indeed manifestations of the same phenomenon, namely a decrease of the over-all reduction rate when the electrode potential is made more negative. Finally, Pospíšil and de Levie (22) showed that all data can be accounted for quantitatively by the following reaction sequence

$$In^{3+} + 2\,SCN^-_{ads} \xrightarrow[\text{slow}]{} In(SCN)_2^+{}_{ads} \xrightarrow[\text{fast}]{+\,3e^-} In^\circ + 2\,SCN^-_{ads} \quad [4]$$

This represents a truly electrocatalytic mechanism, since there is no net consumption of the bridging ligands. Whether the thiocyanate ions act as electron conductors (5) or merely labilize the hydration shell of the hexaquo indium ions is not yet clear. Hexaquo indium(III) itself, in the absence of hydrolysis or electrocatalysis, appears not to be reducible polarographically.

That two adsorbed thiocyanate ions partake in reaction [4] follows from the dependence of the reduction rate constants on the surface activity of adsorbed SCN^-, see below. That the reacting indium(III) species is probably In^{3+} rather than one or more indium-thiocyanate complexes, can be deduced from measurements at very low thiocyanate concentrations (22) and also from the dependence of the rate constants on bulk thiocyanate concentration, at constant surface activity. In view of the equilibrium data of Sundén (23), the Frumkin correction (1) does not affect the analysis since the average charge of thiocyanato-indium complexes is essentially zero for $[SCN^-] \geq 1M$.

The polarographic minimum, then, is caused by the gradual desorption of the electrocatalyst, SCN^-_{ads}, as the potential is progressively made more negative (15). In more concentrated NaSCN solutions, the minimum becomes more pronounced, despite the larger amount of adsorbed SCN^-, because extensive bulk complexation sharply reduces the availability of hexaquo In(III).

The polarographic minimum in chloride solutions is not quite as pronounced as that in thiocyanate. Analysis similar to that for SCN^- indicates (24) that, most probably, two chlorides are involved in the electrocatalytic reduction of In(III) in solutions containing 0.1-2.5M NaCl. In much more dilute (10^{-4}-10^{-2}M) NaCl solutions there are indications that the reduction can also proceed through one adsorbed halide, though not as efficiently.

In bromide and iodide solutions, the data (24) are not so simple to interpret, with slopes of log rate constant *vs.* log βa of 1.5 to 2. It is not yet clear whether this is an indication of more than one catalytic pathway or whether it is merely a reflection of the imprecision of available surface activity data.

Surface Activity

In the preceding section, the concept of surface activity (22) was introduced. We will now show how it is defined, and subsequently how it can be obtained experimentally. Assuming equilibrium between adsorbed and bulk particles (indicated by subscripts a and b, respectively), one can write for their electrochemical potentials, μ

$$\mu^\circ_a + RT \ln a_a = \mu_a = \mu_b = \mu^\circ_b + RT \ln a_b \quad [5]$$

where a denotes an activity ratio and the superscript $^\circ$ a standard state. Consequently

$$a_a = a_b \exp\left[\frac{\mu^\circ_b - \mu^\circ_a}{RT}\right] \quad [6]$$

which can be written in a more compact notation as

$$a_a = a_b\beta \quad [7]$$

$$\beta \equiv \exp\left[\frac{\mu^\circ_b - \mu^\circ_a}{RT}\right] = \exp\left[\frac{-\Delta G^\circ_{ads}}{RT}\right] \quad [8]$$

The above formalism is extremely simple, yet the application of Eq. [7] is not all that straightforward, and several difficulties arise, especially with adsorption of ionic species.

In the case of ion adsorption, a_a represents the bulk ion activity. As long as no reliable methods have been developed to estimate single ion activities, we have to resort to the conceptually less satisfactory, but at least measurable, salt activities or related mean salt activities. Secondly, thermodynamic measurements of surface tension, surface charge density or double layer capacitance yield surface excesses rather than surface activities, in contrast with thermodynamic measurements of bulk properties, which yield activities rather than concentrations. Ion adsorption is further complicated by the fact that the measured surface excesses contain contributions from both short-range and long-range interactions with the electrode. Since we are interested here in specific ("contact") adsorption, the contribution due to long-range, coulombic forces must be corrected for, using a theoretical model (*e.g.* that

of Gouy-Chapman) for the diffuse double layer contribution. The resulting specifically adsorbed surface excess still varies with the chosen electrical parameter: applied potential, surface charge density, etc. There is still considerable controversy about the most meaningful choice of electrical parameter but, within the framework of any such choice, β could in principle be estimated from Eq. [7] by using

$$\lim_{\Gamma \to 0} a_a = \Gamma \qquad [9]$$

so that

$$\beta = \frac{a_a}{a_b} = \lim_{\Gamma \to 0} \frac{\Gamma}{a_b} \qquad [10]$$

if, in this limit, β were to depend solely on adsorbate-adsorber interactions. For ions, this appears not to be the case and, moreover, the experimental precision needed for the direct application of Eq. [10] is not yet available, so that less straightforward techniques must be used. See the Appendix for some related comments.

For only relatively few ions, has the specific adsorption onto mercury been studied quantitatively. For these ions, to a first approximation, β appears to be (25) an exponential function of both the electrode charge density Q and of the effective electrode potential, $E - \phi$. This is a very useful property, since it allows us to extrapolate β values to regions where direct measurements are not available. The uncertainties inherent in such an extrapolation should of course be appreciated.

Zinc

Randles and Somerton (26) observed that the presence of halides or thiocyanate significantly increased the rates of the reactions

$$Zn(II) + 2e^- \rightleftharpoons Zn(Hg) \qquad [11]$$

Such behavior cannot be explained by a simple ϕ effect.

Oscillopolarographic measurements by Heyrovský (27) established the presence of two quite distinct reduction peaks in fairly concentrated KI solutions; one at the potential at which zinc is oxidized from its amalgam, the other at that at which Zn(II) is reduced from acidic sulfate solution. Polarographic measurements on a streaming mercury electrode (28) confirmed the presence of two separate reduction waves in the presence of I^-. Consequently, two separate processes must be considered, one related to the presence of I^- and the other not. Since Zn(II) has a greater tendency to form complexes with Cl^- than with I^-, whereas the rate enhancing effect is larger with I^-, Tamamushi *et al.* (29, 30) concluded that anion adsorption rather than complex formation is involved in the halide-related process. A similar conclusion was reached by Blackledge and Hush (31).

More recently, Sluyters *et al.* (32-36) have published extensively on the Zn(II)/Zn reaction. They found that the standard rate constant is an exponential function of the amount of specifically adsorbed halide ions (35, 36). However, Sluyters *et al.* considered only one single reaction pathway. The observed (35) exponential dependence of the rate constant on the amount of specifically adsorbed anions is quite compatible with a linear dependence on βa similar to that found for indium. Another explanation, in terms of the activity coefficient of the activated complex, was given by Parsons (37).

In summary, the available evidence strongly suggests the presence of halide electrocatalysis in the reduction of Zn(II), although no satisfactory quantitative analysis has yet been given.

Other Cations

The reduction of nickel(II) to some extent resembles that of In(III): the reduction of the hexaquo ion appears to involve a preceding destabilization of the hydration shell (38) and, in the presence of SCN^-, a polarographic minimum and the associated negative faradaic admittance are observed (39-41). Quantitative measurements are hindered, however, by the appearance of a polarographic maximum which is possibly related to the the formation of a nickel film on the mercury surface rather than amalgamation. Adsorbed organic amines (42-45) and thiourea (46) can also catalyze the reduction of Ni(II).

Moorhead *et al.* have reported extensively (47-50) on the SCN^- catalyzed reduction of Ga(III) in aqueous solutions of high ionic strength. Their experiment with competitive adsorption (49) clearly suggests that adsorbed rather than bulk thiocyanate is involved.

Polarographic minima have been observed in the reduction of Sn(IV) (51), V(V) (52), and Mo(VI) (53), and these systems have been shown to exhibit negative faradaic admittances (54), see Fig. 1 and 2. It is highly probable that bridging by adsorbed ligands is involved in these instances.

The reduction of Bi(III) from a noncomplexing medium like 1M $HClO_4$ takes place at a positively charged electrode, so that the addition of small amounts of halides changes ϕ considerably. However, the reduction of Bi(III) is accelerated so much (55)

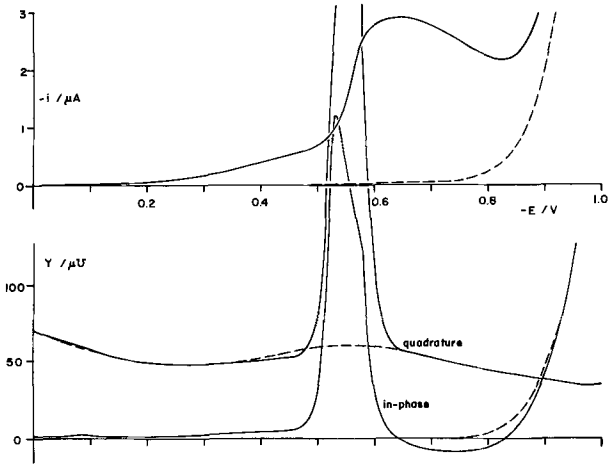

Fig. 1. D-C (top) and a-c (bottom) polarograms of 1 mM $SnCl_4$ in 0.5M oxalic acid, 0.45M Li_2SO_4 and 0.05M H_2SO_4, showing a negative faradaic admittance (54). Replacing all or part of the Li_2SO_4 by H_2SO_4 does not affect the curves, which appears to indicate that the electrocatalyst in this case is the undissociated acid, $C_2O_4H_2$. A-C signal: 5 mV top-to-top at 15.9 Hz. Note that the capacitive component of the faradaic admittance around −0.55V exceeds the resistive component, indicating pronounced reactant specific adsorption. Dashed line: same curves in absence of electroactive species.

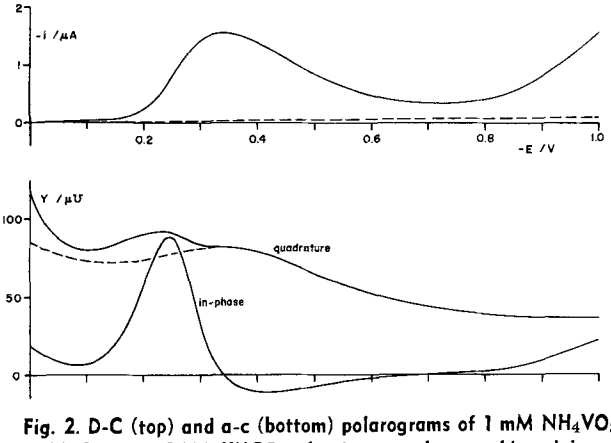

Fig. 2. D-C (top) and a-c (bottom) polarograms of 1 mM NH_4VO_3 in 0.5M $C_2O_4K_2$, 0.5M $KHCO_3$ showing a polarographic minimum (52) and the associated negative faradaic admittance (54). A-C signal: 5 mV top-to-top at 15.9 Hz. In this case, as well as that of Fig. 1, the negative faradaic impedance coincides with the decreasing part of the polarographic minimum, as one would expect for a negative charge transfer resistance (21).

that ligand bridging appears likely. Quantitative analysis is complicated (24) however, by uncertainty about the chemical species present in solution (needed for reliable application of the Frumkin correction) and especially, by coupling (56) of kinetic and adsorption phenomena. The latter leads to extremely complicated mathematical analysis when, as in this case, the electrode reactions are not "infinitely fast." Vlček and Kůta (57) showed that the polarographic reduction of pentamine cobalt(III) is catalyzed by adsorbed halides. This catalysis is complicated by the direct, chemical involvement of Hg in the reduction process (58), in a reaction sequence like (59)

$$2Co(NH_3)_5^{3+} + 10\,H^+ + 2X^-_{ads} + 2Hg \xrightarrow[\text{slow}]{} 2Co^{2+} + 10\,NH_4^+ + Hg_2X_2 \quad [12]$$

$$Hg_2X_2 + 2e^- \xrightarrow[\text{fast}]{} 2Hg + 2X^-_{ads} \quad [13]$$

A somewhat similar mechanism had been suggested as early as 1953 by Laitinen *et al.* (60) for the halide-catalyzed polarographic reduction of $Co(NH_3)_6^{3+}$. In these cases, the actual reduction process is a heterogeneous chemical reaction, whereas the electrochemical step [13] serves to remove Hg_2X_2 and to regenerate the catalyst, X^-_{ads}. Such a situation can readily be distinguished from the cases discussed earlier since reaction [13] yields a reduction wave which rises, without inflection, from the anodic mercury oxidation wave (59).

Interesting but not yet quite understood results were obtained by Anson (61) in the oxidation of the Co(II)-EDTA complex at Pt, the rate of which is greatly enhanced by the presence of halides. This paper (61) serves to illustrate some of the difficulties involved in explaining, even if only qualitatively, results obtained on electrodes other than Hg.

Finally, halide electrocatalysis has also been indicated in the reduction of protons on mercury (62). Especially noteworthy was the observation that the basic rate constant for the halide-catalyzed reaction pathway is the same for Cl^-, Br^- or I^-, within the accuracy of the data. This suggests a common slow mechanism, probably labilization or loss of coordinated water.

An Alternative Interpretation

An interesting alternative explanation for the effects of halides on, *e.g.*, the reduction of hydrogen and zinc ions on Hg, was given by Parsons (37). He interprets the rate enhancement as resulting from the effect of specifically adsorbed ions on the activity coefficient of the activated complex of the charge transfer reaction. This model requires that the activated complex be present inside the compact (Helmholtz) double layer. Of course, such a physical interpretation cannot account for the chemical incorporation of halides during the oxidation of Cr(II). Also, the physical nature and especially, the charge of the activated complex invoked in this model, are rather undefined as a consequence of the Franck-Condon principle. On the other hand, the model yields behavior which may often be rather similar to that predicted by our chemical interpretation, making it difficult to distinguish experimentally between the two (101). Interestingly, Parsons' model also provides for an interpretation of the blocking effect of organic compounds (37, 101).

Discussion

(A) In the foregoing, the term anion bridging has been used to describe a molecular mechanism whereby the anion adsorbed in the electrode/solution interface appears to be involved directly in the electron transfer between metal ion and electrode. On the other hand, anion electrocatalysis is used to denote an over-all stoichiometry. Thus, in all examples given, anion bridging is presumed to be present, but only in some are the bridging anions incorporated into the final reaction products. In the oxidation of Cr(II), adsorbed anions are built into the resulting substitution-inert species, and therefore the reaction is not really catalytic. In such a reaction, chemical analysis of the reaction products provides an unambiguous indication of the chemical involvement of adsorbed ions in the reaction process. Such direct chemical evidence is not available when the reaction product is either a metal atom or a substitution-labile ion, and less straightforward electrochemical evidence must be used. In the latter case, the term "bridging" is not to be taken in the strict sense of Libby (103) and Taube (104), since no distinction between, *e.g.*, inner or outer sphere activated complexes can yet be made.

(B) When the reaction rate increases markedly in the presence of some strongly adsorbed anions, ligand bridging may be involved. However, the observed effects might also be due to a change in ϕ or to complex formation, or both. It is therefore likely that cases of weak halide bridging will not be readily distinguishable, especially when the tendency of the cation towards complexation with anions parallels the tendency for anion adsorption, *e.g.*, $Cl^- < Br^- < I^-$.

(C) When the rate-enhancement resulting from ligand bridging is very pronounced, and especially when the reaction in the absence of bridging is very slow, polarographic minima and associated negative faradaic admittances may be observed, as with In(III), Ni(II), and Sn(IV). Such minima are not likely to be due to double layer repulsion when they occur at potentials far away from the potential of zero charge, and when they persist at high ionic strengths. This criterion must of course be applied with caution since at least one minimum (63) and the associated negative faradaic resistance (64) is known to be caused by still another quite different mechanism.

(D) The concept of surface activity, as defined in the section on Surface Activity, can be used to obtain more precise, stoichiometric information on the reaction mechanisms. So far its application has been restricted to only a few relatively simple cases (22, 62), although it could readily be extended to more complicated situations in which, *e.g.*, several complexes are reduced simultaneously, as soon as more and better surface activity data become available. However, as the number of adjustable parameters (standard rate constants, transfer coefficients, stoichiometric numbers) increases, so does the speculative nature of the interpretation, and one quickly reaches the point of futility, especially in view of the large inherent uncertainties of surface activity data.

(E) The reaction sequence during electrocatalysis can be represented by a scheme like

$$M^{m+} + pX^-_{ads} \rightarrow MX_p^{(m-p)+} \quad [14]$$

$$MX_p^{(m-p)+} + ne^- \rightarrow M^{(m-n)+} + pX^-_{ads} \quad [15]$$

with possible modifications including metal complexes as starting material and or product. For oxidations, n is a negative quantity.

When the chemical reaction [14] is much slower than the electron transfer step [15], then the over-all reaction rate will be simply proportional to the activity of M^{m+} and to the pth power of the surface activity of X^-_{ads}. Thus, the rate is given by

$$\text{rate} = k\beta^p a_x^p a_M \quad [16]$$

where k is the rate constant of the chemical reaction [14] and is independent of the electrical parameter, whereas β usually varies as an exponential function of potential (or charge density). Thus, the formalism for an oxidation with rate-determining ligand bridging, Eq. [14], and fast subsequent charge transfer [15], misleadingly resembles that for a slow electron transfer step!

The reduction of hexaquo indium(III) from thiocyanate solutions is an example of rate-determining

ligand bridging, quite analogous to several bulk chemical reactions of hexaquo vanadium(II) which are also limited by the rate of formation of the "precursor complex" (65, 66, 102).

When reaction [14] is much faster than [15], then [14] may be considered to be in equilibrium. The overall rate equation will then follow the usual electrochemical formalism, but in terms of the interfacial activity of MX_p, which in turn is proportional to the activities a_M and $(\beta a_x)^p$, so that

$$\text{rate} = kK\beta^p a_x^p a_M \exp\left[\frac{\alpha n\mathbf{F}(E - E^\circ)}{RT}\right] \quad [17]$$

where

$$K = \frac{a_{XM_p}}{a_M\,(\beta a_x)^p} \quad [18]$$

This is the situation observed in the reduction of hydrogen ions (62).

(F) Electrocatalysis or ligand bridging, if present, will go unnoticed when the uncatalyzed reaction is already near the limit of accurate measurements (at present, $k_{sh} \gtrsim 0.1$-1 cm sec^{-1}). The fact that electrocatalysis or ligand bridging has so far been established mostly in cases in which the uncatalyzed reactions are very slow [In(III), Cr(II), Ni(II), H(I)], may therefore be merely a reflection of the limitations of our present measurement techniques. On the other hand, it is tempting to speculate that many electrode reactions involving a drastic change in coordination are slow because the cations involved have low rates of exchange of coordinated water (67), and that the ligand-bridging pathway is effective in labilizing the hydration shell. Such a hypothesis is quite compatible with the observation that the reduction of Zn(II) becomes faster in concentrated perchlorate solutions (68), in which the "inert" electrolyte competes for coordination water, or with somewhat similar observations with Ni(II) (69).

(G) By its very nature, ligand bridging depends strongly on the adsorbability of the bridging anions. However, there seems to be no direct relation between the effectiveness of ligand bridging and the adsorbability of the cations or cationic complexes involved (73). For instance, cis-$Cr(NCS)_2(H_2O)_4^+$ is very strongly adsorbed on mercury (13), like its tetramine analog, cis-$Cr(NCS)_2(NH_3)_4^+$ (70), but there is no evidence that $CrCl(H_2O)_5^{2+}$ or $CrBr(H_2O)_5^{2+}$ are strongly adsorbed, although the oxidation pathways are similar. Likewise, In(III) is not measurably adsorbed on Hg in chloride solutions (71, 72), yet the reaction mechanism seems to be quite similar to that in thiocyanate, where In(III) is markedly adsorbed (72, 73).

(H) In the foregoing we have tried to emphasize some purely chemical double layer effects, as distinct from the well-known, more physical influences like those of the ϕ potential or of blocking. Somewhat analogous cation-bridging effects have been proposed by, *e.g.*, Delahay and Mattax (105) and Schmid and Reilley (106). Clearly, ligand bridging in homogeneous solution has its interfacial analog, the study of which is interesting both for our fundamental understanding of charge transfer processes and for its obvious practical applications.

APPENDIX 1: THE ELECTROCHEMICAL PARAMETER

Experimentally, adsorption on electrodes varies with the applied potential. Consequently, in order to study e.g. the dependence of the amount adsorbed on the bulk activity of the adsorbable material, the analysis must be made at constant electrochemical parameter. Stern (74) proposed to use as such the effective potential $E - \phi$, which, incidentally, is the same parameter introduced subsequently by Frumkin (1) in the description of electrode kinetics. Grahame (75, 76), in his work confirming and extending the ideas of Stern, used electrode charge density Q as the electrochemical parameter, a choice later rationalized by Parsons (77).

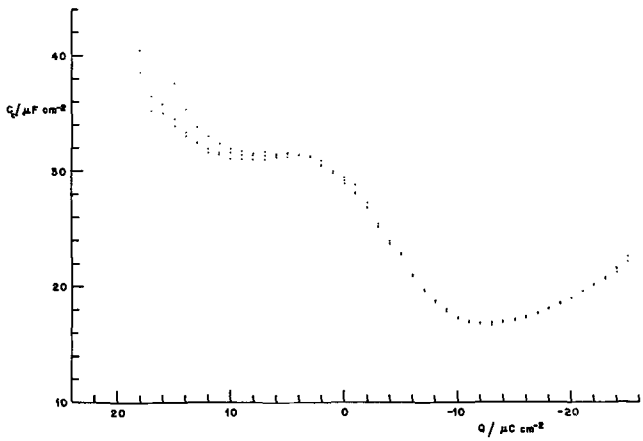

Fig. 3. The compact double-layer capacitance, C_c, as a function of electronic charge density, Q, from Grahame's experimental data (87) of Hg in 0.01, 0.10, and 0.916 M NaF, calculated from the measured capacitance, C, according to $C^{-1} = C_c^{-1} + C_d^{-1}$ where the diffuse double-layer capacitance, C_d, is given by $C_d^2 = (zFQ/2RT)^2 + (\epsilon\kappa/4\pi)^2$ and κ is the Gouy-Chapman reciprocal length, ϵ the macroscopic solvent dielectric constant.

Several arguments pro and con this choice have been given (78-81) and need not be repeated here. A few observations may be added.

The potential ϕ of the (outer) Helmholtz plane is not directly measurable, and its calculation depends on the model chosen for the description of the diffuse double layer. Consequently, the values of the effective potential, $E - \phi$, also depend on such model assumptions,[1] though to a lesser extent since the range of values of ϕ is about an order of magnitude smaller than that of E.

In the absence of electrode reactions, the electrode charge density Q is a directly measurable, "thermodynamic" quantity. However, Q becomes thermodynamically undefined when adsorbable species are involved in electrode reactions (82-86). Under those circumstances, ϕ can still be evaluated from the surface excess of a nonadsorbed ion which is not participating in the electrode reactions, like *e.g.* Na^+ or K^+ from the inert electrolyte. In the case of anion bridging or electrocatalysis, where adsorption phenomena and kinetics are intertwined, the measurability of the electrochemical parameter is obviously important, quite apart from the convenience of using the same parameter, $E - \phi$, for the description of both adsorption and kinetics.

Experimentally, the two choices, $E - \phi$ and Q, appear to be rather equivalent (25). For instance, Grahame showed (75, 76, 87) that, for Hg in aqueous NaF solutions, the capacitance C_c of the compact double layer is independent of the NaF concentration, but that C_c still is a function of Q, see Fig. 3. The same conclusion holds when Q is replaced by $E - \phi$, see Fig. 4. Similarly, adsorption isotherms which are congruent (see below) when plotted at constant Q are equally congruent, though not necessarily of the same shape, when considered at constant $E - \phi$, unless the argument is changed halfway from $E - \phi$ to E (88).

APPENDIX 2: THE ISOTHERM FOR ADSORPTION OF IONS

Adsorption is conveniently described by the adsorption isotherm, *i.e.* the dependence, at constant temperature, pressure and electrochemical parameter, of the surface excess Γ on the logarithm of the bulk activity a of the adsorbable material. Often, neutral molecules exhibit so-called "congruent" isotherms, that is, the isotherms obtained for the same substance but at different values of the chosen electrochemical parameter ($E - \phi$ or Q) can be made to superimpose by a mere shift along the log a axis. Of course, congruence applies likewise to the integrated form of the

[1] For ion adsorption, the dependence of $E - \phi$ on a diffuse double layer model does not introduce any additional uncertainty, since the necessary prior subtraction of the contribution of ions "non-specifically" held in the diffuse double layer depends on the very same model.

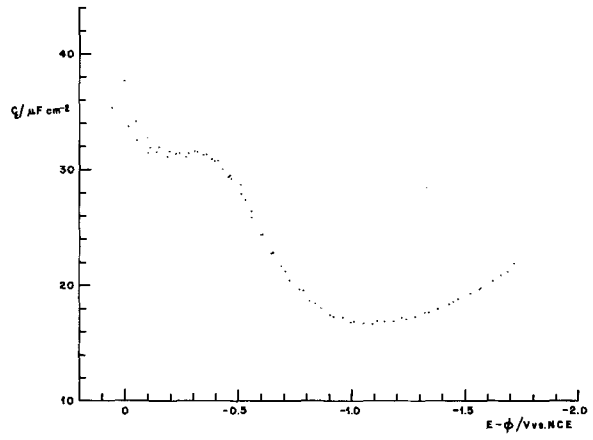

Fig. 4. The same compact double-layer capacitance data as in Fig. 3, but now plotted as a function of the effective potential $E - \phi$. The potential ϕ was calculated using $\phi = 0.05139$ arcsinh $[Q/11.74\ c^{1/2}]$. Note that the data for the three NaF concentrations fit equally well for both choices of the electrical parameters, $E - \phi$ or Q. A similar plot as a function of the applied potential, E, leads to clearly noncoinciding curves.

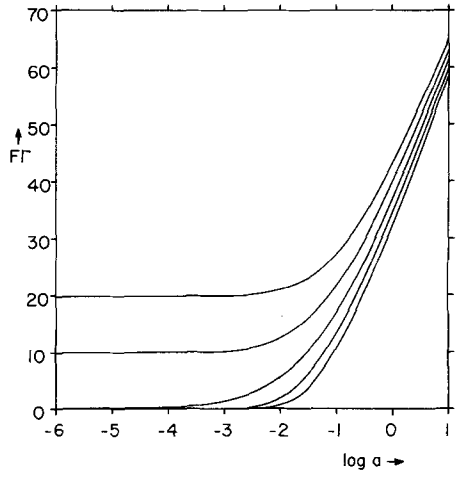

Fig. 5. Adsorption isotherms, at constant electrode charge density, Q, calculated from Eq. [19] using the following parameters: $\beta = 10^{-6}$ cm, $\Gamma_s = 10^{-9}$ moles cm^{-2}, and $A = 10^{10}$ cm^2 mole^{-1}. Curves calculated for electrode charge densities of (from top to bottom) +20, +10, 0, −10, and −20 μC cm^{-2}, respectively. For ease of comparison, β is kept constant despite the variation of Q. The potential ϕ is calculated according to $\phi = 0.05139$ arcsinh $[(Q + zF\Gamma)/11.74\ c^{1/2}]$. In the calculation of ϕ, the difference between bulk concentration, c, and bulk ionic activity, a (both in moles liter^{-1}), is neglected. For $Q > 0$, the curves tend to approach $F\Gamma \approx Q$ at low salt activities, and no Henry region (where Γ is proportional to a) is observed in the activity range shown. Units: $F\Gamma$ in μC cm^{-2}, a in M.

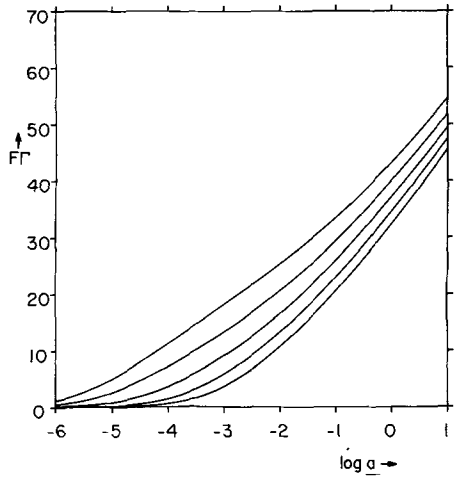

Fig. 6. The same adsorption isotherms as in Fig. 5, but at constant ionic strength (1M) maintained with a nonspecifically adsorbed electrolyte. Note that the curves differ substantially from those in Fig. 5, and appear to be much more congruent, since the double-layer influence has been reduced significantly for the larger part of the curves (log c < 0).

adsorption isotherm, *viz.* the plot of surface pressure, $\pi = RT\int P\ d\ \ln a$, *vs.* log a, for which it was first observed (89). This fairly general rule of congruence is reflected in the fact that many of the proposed equations for adsorption isotherms, *e.g.* all those listed in Ref. (90), correspond to congruent ones, *i.e.*, βa is a function solely of Γ.

Experimentally, ionic adsorption isotherms are usually noncongruent. There is one apparent exception, that of I^-, which is congruent over the entire range studied by Grahame (91), although noncongruence shows up even here when the measurements are extended to lower concentrations (92). A typical example of a noncongruent ionic adsorption isotherm is that of chloride (93).

The noncongruence shows most clearly at low bulk activities, with correspondingly small values of Γ. This rules out effects due to changing mutual interaction of adsorbed ions. The only interactions which do not tend to vanish at low bulk activities, and which also are not accounted for by any of the congruent adsorption isotherms, are those between specifically adsorbed and nonspecifically adsorbed ions.

Adsorption isotherms which include a Boltzmann term in ϕ, like those of Stern (74), Levine *et al.* (94, 95), and Devanathan and Tilak (96), sometimes fit the trends of ionic adsorption isotherms better than do congruent adsorption isotherms (25). Extension could of course be made to Flory-Huggins statistics (97, 98) if the introduction of still another adjustable parameter is warranted. Figures 5 and 6 show the Frumkin isotherm (99) as modified by the inclusion of the Boltzmann term

$$\beta a = \frac{\Gamma_s\Gamma}{\Gamma_s - \Gamma} \exp\left[A\Gamma + \frac{z\mathbf{F}\phi}{RT}\right] \qquad [19]$$

Note that Frumkin (99) proposed his isotherm for adsorption of uncharged substances, and that Eq. [19] indeed reduces to that isotherm for $z = 0$. An isotherm similar to Eq. [19], but using the "inner Helmholtz" potential ϕ_i instead, was used by Grahame (91) and by Parry and Parsons (107).

In some cases, as with chloride, Eq. [19] appears to overemphasize the effect of the diffuse double layer; and better agreement with experiment is obtained with only a fraction of the term $z\mathbf{F}\phi/RT$ in the exponent.

Interestingly, the inclusion in the isotherm of a term in ϕ leads to behavior like that observed by Dutkiewicz and Parsons (100), without the need to invoke salt activities rather than ionic ones, as can clearly be seen by comparison of Fig. 5 and 6.

APPENDIX 3: THE DETERMINATION OF β

For systems exhibiting congruent adsorption isotherms, β, and consequent surface activity βa, and surface activity coefficient $\beta a/\Gamma$, can be obtained from the surface pressure either at constant effective potential or at constant electrode charge density. When the isotherm is not congruent, then curve fitting to a theoretical or empirical adsorption isotherm appears to be the only available alternative. Although ΔG°_{ads} would seem to be a thermodynamic quantity, there is as yet no purely thermodynamic way to determine ΔG°_{ads} or β for ions.

Acknowledgments

Extensive assistance with various aspects of this work by Dr. L. Pospíšil, Miss J. C. Kreuser, and Mr. J. K. Corless, and helpful discussions with Dr. Roger Parsons and Professor Fred C. Anson are gratefully acknowledged, as is the financial support of this work by the National Science Foundation (Grant GP 8575), the Air Force Office of Scientific Research (OAR,

USAF, Grant 68-1344), and the Office of Naval Research.

Manuscript submitted Nov. 6, 1970; revised manuscript received ca. Feb. 26, 1971.

Any discussion of this paper will appear in a Discussion Section to be published in the June 1972 JOURNAL.

REFERENCES

1. A. N. Frumkin, *Z. Physik. Chem.*, **164**, 121 (1933).
2. L. Gierst, J. Tondeur, R. Cornelissen, and F. Lamy, *J. Electroanal. Chem.*, **10**, 397 (1965).
3. J. Heyrovský and J. Kůta, "Principles of Polarography," Chap. XVIII, Academic Press, New York (1966).
4. S. G. Mairanovskii, "Catalytic and Kinetic Waves in Polarography," Plenum Press, New York (1968).
5. J. Heyrovský, *Discussions Faraday Soc.*, **1**, 212 (1947).
6. R. L. Pecsok and J. J. Lingane, *J. Am. Chem. Soc.*, **72**, 189 (1950).
7. K. M. Abubacker and W. U. Malik, *J. Indian Chem. Soc.*, **36**, 463 (1959).
8. D. A. Aikens and J. W. Ross, *J. Phys. Chem.*, **65**, 1213 (1961).
9. W. Kemula and E. Rakowska, *Roczniki Chem.*, **36**, 203 (1962).
10. J. G. Jones and F. C. Anson, *Anal. Chem.*, **36**, 1137 (1964).
11. J. Jones Ulrich and F. C. Anson, *Inorg. Chem.*, **8**, 195 (1969).
12. I. Watanabe, E. Habashi, and S. Ikeda, *ibid.*, **7**, 1920 (1968).
13. D. J. Barclay, E. Passeron, and F. C. Anson, *ibid.*, **9**, 1024 (1970).
14. J. J. Lingane, Thesis, Univ. of Minnesota (1938); I. M. Kolthoff and J. J. Lingane, "Polarography," p. 275, Interscience Publishers, New York (1941).
15. D. Cozzi and S. Vivarelli, *Z. Elektrochem.*, **57**, 408 (1953); **58**, 907 (1954).
16. M. Bulovová, *Collection Czech. Chem. Commun.*, **19**, 1123 (1954).
17. H. Shirai, *J. Chem. Soc. Japan, Pure Chem. Sect.*, **81**, 1248 (1960).
18. K. Z. Brainina, *Dokl. Akad. Nauk SSSR*, **130**, 797 (1960).
19. A. J. Engel, J. Lawson, and D. A. Aikens, *Anal. Chem.*, **37**, 203 (1965).
20. N. Tanaka, T. Takeuchi, and R. Tamamushi, *Bull. Chem. Soc. Japan*, **37**, 1435 (1964).
21. R. de Levie and A. A. Husovsky, *J. Electroanal. Chem.*, **22**, 29 (1969).
22. L. Pospíšil and R. de Levie, *ibid.*, **25**, 245 (1970).
23. N. Sundén, *Svensk Kem. Tidskr.*, **66**, 50 (1954).
24. R. de Levie and L. Pospíšil, Unpublished work.
25. R. de Levie, Unpublished work.
26. J. E. B. Randles and K. W. Somerton, *Trans. Faraday Soc.*, **48**, 951 (1952).
27. J. Heyrovský, *Z. Elektrochem.*, **59**, 802 (1955).
28. J. Koryta, *Electrochim. Acta*, **6**, 67 (1962).
29. R. Tamamushi, K. Ishibashi, and N. Tanaka, *Z. Physik. Chem.*, **35**, 209 (1962).
30. R. Tamamushi and N. Tanaka, *ibid.*, **39**, 117 (1963).
31. J. Blackledge and N. S. Hush, *J. Electroanal. Chem.*, **5**, 435 (1963).
32. A. B. IJzermans, M. Sluyters-Rehbach, and J. H. Sluyters, *Rec. Trav. Chim.*, **84**, 767 (1965).
33. M. Sluyters-Rehbach, A. B. IJzermans, B. Timmer, J. B. Griffioen, and J. H. Sluyters, *Electrochim. Acta*, **11**, 483 (1966).
34. B. Timmer, M. Sluyters-Rehbach, and J. H. Sluyters, *J. Electroanal. Chem.*, **14**, 181 (1967).
35. P. Teppema, M. Sluyters-Rehbach, and J. H. Sluyters, *ibid.*, **16**, 165 (1968).
36. M. Sluyters-Rehbach, J. S. M. C. Breukel, and J. H. Sluyters, *ibid.*, **19**, 85 (1968).
37. R. Parsons, *ibid.*, **21**, 35 (1969).
38. J. Dandoy and L. Gierst, *ibid.*, **2**, 116 (1961).
39. H. Shirai, *J. Chem. Soc. Japan, Pure Chem. Sect.*, **81**, 1248 (1960).
40. T. Takahashi and H. Shirai, *Rev. Polarog. (Kyoto)*, **11**, 155 (1963).
41. R. Tamamushi and K. Matsuda, *J. Electroanal. Chem.*, **12**, 436 (1966).
42. H. B. Mark, *ibid.*, **7**, 276 (1964); **8**, 253 (1964).
43. H. B. Mark, L. R. McCoy, E. Kirowa-Eisner, and H. C. MacDonald, *J. Phys. Chem.*, **72**, 1083 (1968).
44. L. R. McCoy, H. B. Mark, and L. Gierst, *ibid.*, **72**, 4637 (1968).
45. Ya. I. Tur'yan and O. N. Malyavinskaya, *J. Electroanal. Chem.*, **23**, 69 (1969).
46. Ya. I. Tur'yan and O. E. Ruvinskii, *ibid.*, **23**, 61 (1969).
47. W. M. MacNevin and E. D. Moorhead, *J. Am. Chem. Soc.*, **81**, 6382 (1959).
48. E. D. Moorhead, *ibid.*, **87**, 2503 (1965).
49. E. D. Moorhead and G. M. Frame, *Anal. Chem.*, **40**, 280 (1968).
50. E. D. Moorhead and G. M. Frame, *J. Electroanal. Chem.*, **18**, 197 (1968); *J. Phys. Chem.*, **72**, 3684 (1968).
51. A. J. Bard, *Anal. Chem.*, **34**, 266 (1962).
52. J. J. Lingane and L. Meites, *J. Am. Chem. Soc.*, **69**, 1021 (1947).
53. E. P. Parry and M. G. Yakubik, *Anal. Chem.*, **26**, 1294 (1954).
54. J. C. Kreuser and R. de Levie, Unpublished work.
55. J. E. B. Randles and K. W. Somerton, *Trans. Faraday Soc.*, **48**, 951 (1952).
56. P. Delahay, *J. Phys. Chem.*, **70**, 2069, 2373 (1966).
57. A. A. Vlček and J. Kůta, *Nature*, **185**, 95 (1960).
58. N. Tanaka, Y. Sato, and R. Tamamushi, *Rev. Polarog. (Kyoto)*, **12**, 127 (1964).
59. F. C. Anson and T. Chang, *Inorg. Chem.*, **5**, 2092 (1966).
60. H. A. Laitinen, A. J. Frank, and P. Kivalo, *J. Am. Chem. Soc.*, **75**, 2865 (1953).
61. F. C. Anson, *This Journal*, **110**, 439 (1963).
62. R. de Levie and L. Pospíšil, *J. Electroanal. Chem.*, **25**, 340 (1970).
63. L. Gierst, L. Vandenberghen, and E. Nicholas, *ibid.*, **12**, 462 (1966).
64. R. de Levie, J. C. Kreuser, and H. Moreira, *Anal. Chem.*, **43**, 784 (1971).
65. B. R. Baker, M. Orhanovic, and N. Sutin, *J. Am. Chem. Soc.*, **89**, 722 (1967).
66. H. J. Prince and H. Taube, *Inorg. Chem.*, **7**, 1 (1968).
67. J. E. B. Randles and K. W. Somerton, *Trans. Faraday Soc.*, **48**, 937 (1952).
68. B. Behr and J. Malyszko, *Roczniki Chem.*, **41**, 1589 (1967).
69. M. Pavlik, *Collection Czech. Chem. Commun.*, **3**, 223 (1931).
70. N. Tanaka, E. Kyuno, G. Satô, and R. Tamamushi, *J. Phys. Chem.*, **66**, 2707 (1962).
71. G. C. Barker and R. L. Faircloth, *Adv. Polarog.*, **1**, 313 (1960).
72. G. W. O'Dom and R. W. Murray, *J. Electroanal. Chem.*, **16**, 327 (1968).
73. B. Timmer, M. Sluyters-Rehbach, and J. H. Sluyters, *ibid.*, **19**, 73 (1968).
74. O. Stern, *Z. Elektrochem.*, **30**, 508 (1924).
75. D. C. Grahame, *Chem. Rev.*, **41**, 441 (1947).
76. D. C. Grahame, *J. Am. Chem. Soc.*, **76**, 4819 (1954).
77. R. Parsons, *Trans. Faraday Soc.*, **51**, 1518 (1955).
78. R. Parsons, *J. Electroanal. Chem.*, **7**, 136 (1964).
79. R. Parsons, *ibid.*, **8**, 93 (1964).
80. A. N. Frumkin, *ibid.*, **7**, 152 (1964).
81. B. B. Damaskin, *ibid.*, **7**, 155 (1964).
82. A. N. Frumkin, *Z. Physik. Chem.*, **103**, 55 (1922).
83. D. C. Grahame and R. B. Whitney, *J. Am. Chem. Soc.*, **64**, 1548 (1942).
84. D. M. Mohilner, *J. Phys. Chem.*, **66**, 724 (1962).
85. R. de Levie, *J. Electroanal. Chem.*, **20**, 332 (1969).
86. A. Frumkin, O. Petry, and B. B. Damaskin, *ibid.*, **27**, 81 (1970).
87. D. C. Grahame, Tech. Report No. 14 to the Office of Naval Research, Feb. 18, 1954.
88. E. Dutkiewicz, J. D. Garnish, and R. Parsons, *J. Electroanal Chem.*, **16**, 505 (1968).
89. R. Parsons, *Proc. Roy. Soc.*, **261A**, 79 (1961).
90. P. Delahay, "Double Layer and Electrode Kinetics," p. 83, John Wiley & Sons, New York (1965).
91. D. C. Grahame, *J. Am. Chem. Soc.*, **80**, 4201 (1958).
92. P. Delahay and D. J. Kelsh, *J. Electroanal. Chem.*, **18**, 194 (1968).
93. D. C. Grahame and R. Parsons, *J. Am. Chem. Soc.*, **83**, 1291 (1961).

94. S. Levine, G. M. Bell, and D. Calvert, *Can. J. Chem.*, **40**, 518 (1962).
95. S. Levine, J. Mingins, and G. M. Bell, *J. Electroanal. Chem.*, **13**, 280 (1967).
96. M. A. V. Devanathan and B. V. K. S. R. A. Tilak, *Chem. Rev.*, **65**, 635 (1965); *Proc. Roy. Soc. (London)*, **290A**, 527 (1966).
97. P. J. Flory, *J. Chem. Phys.*, **10**, 51 (1942).
98. M. L. Huggins, *J. Phys. Chem.*, **46**, 151 (1942); *Ann. N.Y. Acad. Sci.*, **43**, 1 (1942).
99. A. N. Frumkin, *Z. Physik.*, **35**, 792 (1926).
100. E. Dutkiewicz and R. Parsons, *J. Electroanal. Chem.*, **11**, 100 (1966).
101. R. Parsons, To be published.
102. J. M. Malin and J. H. Swinehart, *Inorg. Chem.*, **7**, 250 (1968).
103. W. F. Libby, *J. Phys. Chem.*, **56**, 863 (1952).
104. H. Taube, H. Meyers, and R. L. Rich, *J. Am. Chem. Soc.*, **75**, 4118 (1953).
105. P. Delahay and C. C. Mattax, *ibid.*, **76**, 5314 (1954).
106. R. W. Schmid and C. N. Reilley, *ibid.*, **80**, 2101 (1958).
107. J. M. Parry and R. Parsons, *Trans. Faraday Soc.*, **59**, 241 (1963).

JOURNAL OF THE ELECTROCHEMICAL SOCIETY

ELECTROCHEMICAL SCIENCE

SEPTEMBER 1971

Formation of $PbSO_4$ Crystallites on Pb in the Lead-Acid Cell

Takewo Chiku* and Koichi Nakajima

Toyota Central Research and Development Laboratories, Inc., Nagoya, Japan

ABSTRACT

Formation of lead sulfate crystallites on lead during the electrochemical reaction has been examined by electron microscopy and x-ray diffraction techniques. It was found (*i*) that lead sulfate as the active material nucleates preferentially on the crystal surface of lead and grows dendritically, depending on the condition of discharging; also that the crystallographical relation shows a tendency to have Pb [100]//$PbSO_4$ [100] for the (001) plane and Pb [$1\bar{1}0$]// $PbSO_4$ [010] or [111] for the (111) plane of Pb, and (*ii*) that the morphology of the lead sulfate as the active material seems to be different from the lead sulfate not transformed to Pb, even in a fully charged condition.

Burbank (1, 2) studied lead oxide and the three basic sulfates of the lead-acid cell by x-ray and electron microscope techniques and found that these basic sulfates were transformed into prismatic and nodular particles of PbO_2 by anodic oxidation. She (2) also observed that crystals of PbO_2 in a state of discharge varied from prismatic individuals to complex spherulitic formations, depending on how the electrode plates were prepared and the progress of the electrochemical reaction.

The electrochemical reaction which occurs on the positive plate is characterized by the formation and consumption of H_2O during the reaction. It may be important to consider this in the mechanism of nucleation and formation or decomposition of PbO_2 and the basic sulfates in the positive plate, since it suggests that the characteristics of the reaction process produce complicated substances similar to those obtained by Burbank.

Formation of active material in the negative plate during anodic oxidation depends directly on the existence of sulfate ions; therefore, the formation of lead sulfate should depend considerably on the concentration of sulfate ions along the surface of the plate during the progressive reaction.

Recently it has been shown (3, 4) that lead sulfate crystallites grow dendritically on lead crystal surfaces, especially on the (100) and (111) planes. The purpose of this study was to determine how lead sulfate crystallites nucleate and grow onto Pb during the process of discharging.

Experimental Procedure

Single crystals of Pb were prepared in the form of cylindrical rods 10 mm in diameter, which were cut parallel to the (111) and (100) planes by the modified Bridgman method. A Servomet spark erosion machine was used for the cutting. Part of the cut surface was then removed by chemical polishing in a solution containing four volumes of CH_3COOH and one volume of H_2O_2 (30%).

* Electrochemical Society Active Member.

Key words: electron microscopy, x-ray diffraction, nucleation.

The specimens were annealed at 300°C for 3 hr in vacuum and then used as electrode plates which were charged and discharged under conditions shown in Table I. The specific gravity of the electrolyte was 1.260 at 20°C. These electrode plates were then washed thoroughly with distilled water and dried at room temperature under reduced pressure.

Extraction replicas were prepared from the surfaces by a standard two-stage plastic carbon replication technique. Chromium was used as the replica shadowing material to determine the crystallographical relationship between $PbSO_4$ and Pb as the active material. Electron microscopic observations were made with a JEOL (JAPAN) JEM-6A electron microscope at 100 kV.

Crystallographic orientation was determined by the x-ray diffraction technique. Shadowing by chromium was carried out from the direction of the projection parallel to [100] direction for the specimen cut parallel to (001) and [110] direction for the specimen cut parallel to (111). The glancing angle was 28.5°.

Samples used for x-ray measurements were taken from a commercial battery at various stages of discharge (Fig. 1). At each stage they were put into a small polyethylene bag together with the electrolyte solution of the battery and then mounted on a specimen holder.

Table I. Condition of electrolysis on the specimens of Pb single crystal

Reflecting plane	Cathodic reduction	Anodic oxidation
(111)	0.2 mA 30 sec	0.2 mA 300 sec
		0.2 mA 30 sec
		0.05 mA 1200 sec
		0.05 mA 120 sec
	0.8 mA 30 sec	0.8 mA 20 sec
(200)	0.2 mA 30 sec	0.2 mA 300 sec
		0.2 mA 30 sec
		0.1 mA 600 sec
		0.1 mA 60 sec
		0.05 mA 1200 sec
		0.05 mA 130 sec
	0.8 mA 30 sec	0.8 mA 20 sec

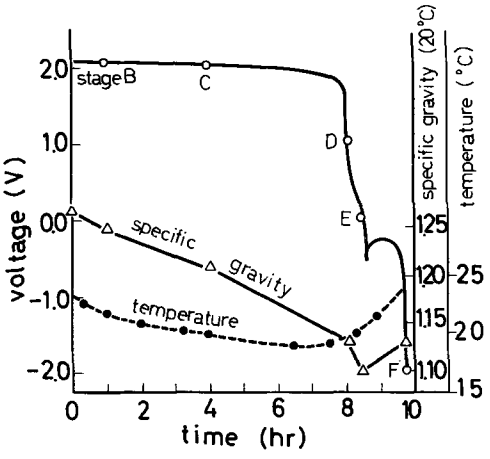

Fig. 1. Characteristic curves of discharge (at 4A) in the battery examined.

Results

Observation of the crystal surface of lead crystal dipped in the electrolytic solution.—Figure 2 shows an example of the electron micrographs and the selected area diffraction patterns obtained from the (001) plane dipped in the electrolytic solution for 2 hr. From the diffraction patterns, the materials extracted were found to be $PbSO_4$. Prismatic individuals of $PbSO_4$ are observed irrespective of the orientation of the surface of the lead crystal.

To obtain a clean surface of Pb single crystals, the surfaces of each of the specimens were polished chemically and then reduced cathodically at 200 or 800 μA for 30 sec. No extracted materials were observed after this treatment, but in some cases small amounts of the materials were found to exist on the surface and were determined to be $PbSO_4$ crystallites. These were thought to be caused by the deoxidization of the lead oxides during the cathodic charging.

Nucleation and growth of lead sulfate crystallites during discharging.—Figures 3-6 show morphological changes of the $PbSO_4$ crystallites. Results obtained after discharging at 200 μA for 30 sec and 800 μA are shown in Fig. 3 and 4, respectively. These electron micrographs show a dendritic $PbSO_4$ formed from Pb during the process of discharging. The formation condition of the $PbSO_4$ dendrite on a definite lattice plane of a Pb crystal can be determined from the analysis of an electron micrograph and the corresponding diffraction pattern. It should be noted first that the electrochemical reaction does not proceed homogeneously over the whole surface of the electrode plate but locally, depending on the crystal orientation. Second, the relationship between crystallographical orientation of the surface of the lead crystals and the

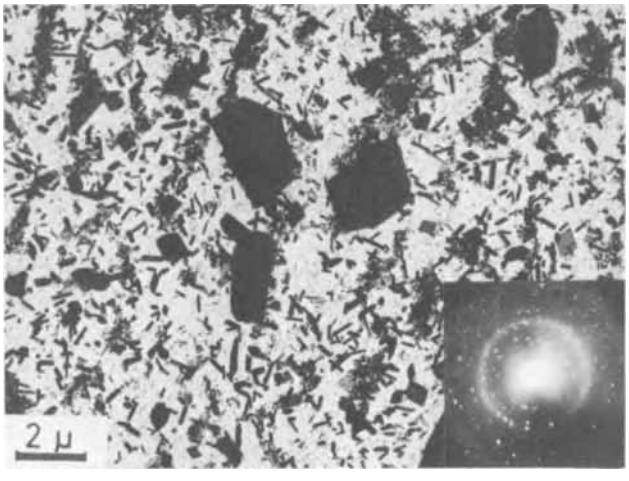

Fig. 2. Electron micrograph of an extraction replica taken from (100) plane of Pb single crystal merely dipped in the electrolytic solution for 2 hr.

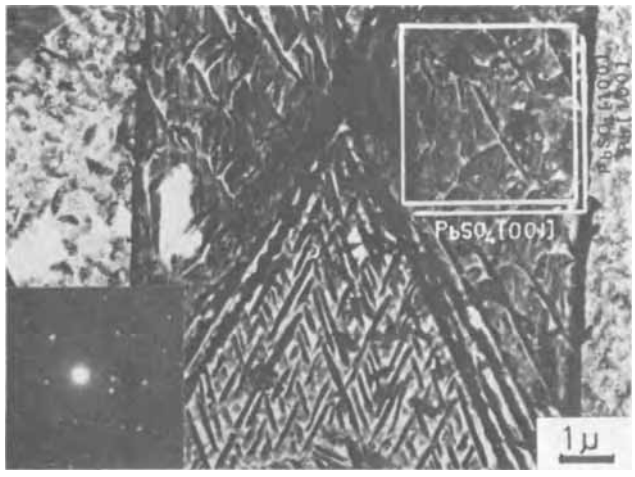

Fig. 3. Electron micrograph of an extraction replica taken from (100) plane of Pb single crystal discharged at 200 μA for 30 sec in the electrolyte solution.

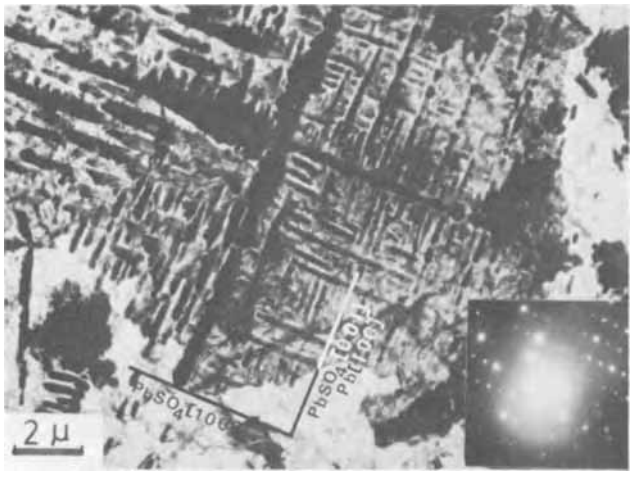

Fig. 4. Electron micrograph of an extraction replica taken from (100) plane of Pb single crystal discharged at 800 μA for 20 sec in the electrolyte solution.

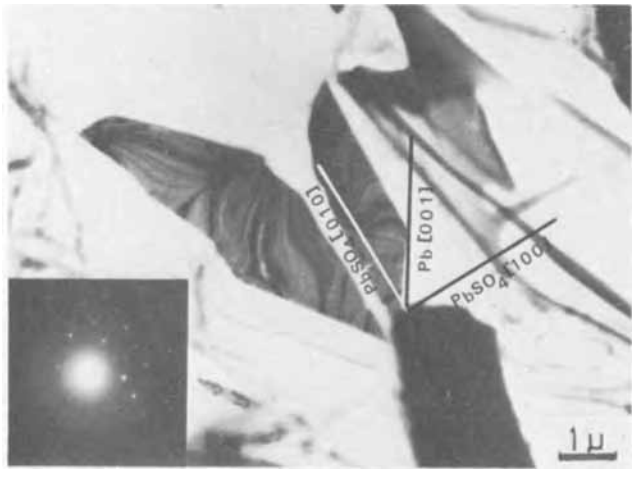

Fig. 5. Electron micrograph of an extraction replica taken from (100) plane of Pb single crystal discharged at 100 μA for 60 sec in the electrolyte solution.

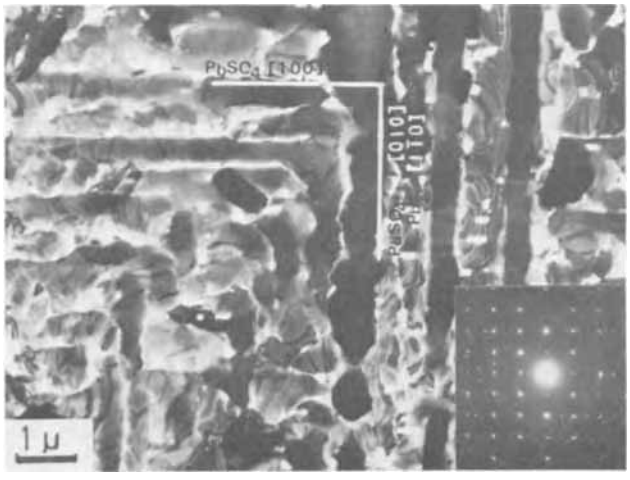

Fig. 6a. Electron micrograph of an extraction replica taken from (111) plane of Pb single crystal discharged at 200 μA for 300 sec in the electrolyte solution.

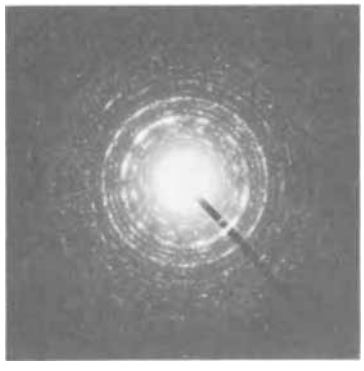

Fig. 6b. Diffraction photograph of the same sample obtained by using a high resolution diffraction technique. The area irradiated was taken to be about 0.1 mm in diameter.

$PbSO_4$ clearly depends on the condition of anodic oxidation. Figure 5 shows the result obtained with the (001) plane of Pb crystals after discharging at 100 μA for 60 sec; dendritic growth of $PbSO_4$ crystallites can hardly be observed.

With an increase of discharge current, the formation of $PbSO_4$ crystallites appears to give rise to a typical dendrite having an immediate connection with the crystal orientation of Pb. Figure 4 is an example of the type of formation of $PbSO_4$ referred to as the dendritic growth. This is found more frequently on the (001) plane of Pb crystal and results from discharging at 800 μA for 20 sec. The crystallographic relation yields to Pb [100] // $PbSO_4$ [100], and in some cases to Pb [100] // $PbSO_4$ [211]. Figure 6a illustrates the dendritic growth of $PbSO_4$ on the (111) plane of Pb crystals, showing a somewhat different crystallographic relation compared with that in the (001) plane. The relationship is determined by Pb [$1\bar{1}0$] // $PbSO_4$ [010] or Pb [$1\bar{1}0$] // $PbSO_4$ [111].

To correlate these crystallographic relationships with crystal structures it is necessary to know the detailed structure of the $PbSO_4$ crystal. It is orthorhombic in structure, having $a_o = 8.48$Å, $b_o = 5.40$Å, and $c_o = 6.96$Å, and contains four molecules per cell. The positions of Pb and S in the unit cell are given (7) but those of the O atoms are not as yet clear.

A high resolution diffraction technique was applied in order to investigate a wide region of the extraction replica. Figure 6b shows the diffraction obtained. The area irradiated was approximately 100μ in diameter. It can be seen that the $PbSO_4$ crystallites cluster around

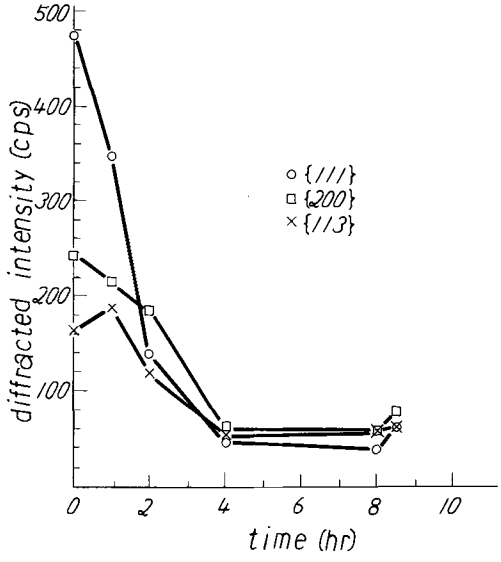

Fig. 7. Changes in the negative plate of the diffracted intensity of some diffraction lines of Pb and $PbSO_4$.

certain orientations. It is interesting to note that the diffraction pattern shown is identical with that of $PbSO_4$, but the selected area diffraction pattern obtained from the same specimen shows some extra diffraction where the spots correspond to the forbidden reflection, *i.e.*, (100), (010), and (100). This suggests that these spots appear due to double reflection.

X-ray diffraction analysis for the transformation of Pb to $PbSO_4$.—Figure 7 shows the change in diffracted intensity of the {111}, {200}, and {113} planes in Pb with increase in time of discharging. It can be clearly seen that (*i*) the diffracted intensity from each plane decreases rapidly and (*ii*) the relative intensity of these reflecting planes deviate greatly from that in the normal state. For example, the relative $I_{111}:I_{200}:I_{113} = 100:50:32$ in the initial stage becomes 8:12:11 after discharging at 4A for 8 hr, indicating that the nucleation and growth of $PbSO_4$ on the surface of Pb becomes more dense on the crystal surface of a definite orientation.

The diffracted intensity from each plane decreases with the time of discharging, but the rate of decreasing depends on the crystal orientation. The results obtained here were about 1/12 for {111}, 1/4 for {200}, and 1/3 for {113}, respectively, in the nearly zero terminal voltage stage. This suggests that the {111} plane of Pb may be a habit plane for the nucleation of $PbSO_4$ during discharging. The electron micrographic observations also show that the lead sulfate grew dendritically on the Pb crystal surface, especially on the (100) and (111) planes.

An interesting result was obtained by analysis of diffracted intensity from various planes of Pb composed of the negative plates of new and old fully charged batteries. As shown in Table II, the intensity of {111} reflection from the new battery differs greatly from that in the old battery, but not for those of other

Table II. Diffracted intensity from various lattice planes of Pb and $PbSO_4$ crystallites in fully charged batteries

Miller indices		ASTM	Diffracted intensity New battery		Old battery	
Pb	111	100	100	(820 Hz)	100	(210 Hz)
	200	50	58	(476 Hz)	116	(244 Hz)
	311	32	26	(213 Hz)	125	(262 Hz)
$PbSO_4$	112	35	13	(13 Hz)	39	(82 Hz)
	020	46	13	(13 Hz)	64	(134 Hz)
	211	100	100	(100 Hz)	100	(210 Hz)
	102	71	52	(52 Hz)	85	(179 Hz)
	210	86	74	(74 Hz)	106	(223 Hz)
	002	33	65	(65 Hz)	37	(78 Hz)
	201	23	17	(17 Hz)	29	(61 Hz)

reflecting planes. This was probably caused by preferential nucleation and growth of $PbSO_4$ on the {111} plane of Pb. Diffracted intensities from various lattice planes of $PbSO_4$ and age of the battery are given in Table II. It can be seen from this table that $PbSO_4$ crystallites formed on Pb with a preferred orientation.

X-ray examinations were carefully carried out to distinguish crystallographically between $PbSO_4$ as the active material and the other type of $PbSO_4$ not being transformed to Pb. No change of crystal structure could be observed in either of them. The present study points up an important lead in determining how the amounts of $PbSO_4$ in the electrode plate increase with the age of batteries, even in the fully charged state. The morphological change of $PbSO_4$ crystallites on the electrode plate must be intimately related as to whether or not the $PbSO_4$ formed is effective as the active material. Lead sulfate formed in connection with the crystallographic relation (Fig. 3) transforms completely to Pb as a result of cathodic charging, while the other type of $PbSO_4$ formed during soaking in electrolytic solution (Fig. 2) keeps its configuration, even in the fully charged state.

As shown in Table II, a considerable decrease of diffracted intensity is clearly seen in the {111} and {200} planes of Pb in the negative plate, depending on how much the battery is used. This suggests that these planes in Pb crystallites are exhausted with the aging of the battery by the formation of $PbSO_4$. In other words, the age of the battery is estimated roughly from the total residual area of {111} or {100} planes in each particle composing the electrode plate.

The integral breadth of diffraction lines of Pb as the active material was observed to increase [or decrease (3)] gradually with the time of charging (or discharging), approaching the value of metallic Pb when the terminal voltage became nearly zero. The highly strained state produced during cathodic charging may be explained in terms of hydrogen impregnation occurring during the charging. The elastic stored energy was estimated to be about 0.05 cal/g (3). In fact, hydrogen adsorption is known (5) to reduce the surface tension of metal, and the adsorbed hydrogen slows down the discharge of metallic ions (6) with increasing polarization and results in occurrence of a strained state in the matrix.

Summary

Nucleation and growth of lead sulfate crystallites as the active material on an electrode plate were examined by electron microscopy and x-ray diffraction techniques. The results were as follows:

1. In the early stage of anodic oxidation, lead sulfate crystallites nucleate preferentially on the crystal surfaces of Pb having low indices, especially the (001) and (111) planes, and grow dendritically depending on the condition of discharging. The crystallographic relation between them is given by $Pb[100]//PbSO_4[100]$ for the (001) plane of Pb, and $Pb[1\bar{1}0]//PbSO_4[010]$ or [111] for the (111) plane of Pb.
2. The crystal structure of lead sulfate as the active material could not be distinguished from that of the other type of $PbSO_4$. It was not transformed to Pb even in the fully charged state, but a morphological change could be seen in both forms of $PbSO_4$.

Acknowledgment

The authors wish to express their thanks and appreciation to Mr. A. Isogai, Mr. T. Ishiguro, and Mr. and Mrs. H. Kojima for their diligent aid throughout the course of the work.

Manuscript submitted Nov. 24, 1970; revised manuscript received May 12, 1971.

Any discussion of this paper will appear in a Discussion Section to be published in the June 1972 JOURNAL.

REFERENCES

1. J. Burbank, *This Journal*, **113**, 10 (1966).
2. J. Burbank, *ibid.*, **116**, 125 (1969).
3. T. Chiku, *ibid.*, **115**, 12 (1968).
4. T. Chiku *et al.*, "The 8th Batteries Symposium," p. 88 (1967) (in Japanese).
5. N. I. Petch, *Phil. Mag.*, **1**, 331 (1956).
6. V. I. Likhtman and Ye. D. Shchukin, *Usp. Fiz. Nauk*, **66**, 213 (1958).
7. R. W. G. Wyckoff, "Crystal Structures," Vol. 2, Interscience Publishers, Inc., New York (1960).

Performance Characteristics of Solid Electrolytes under Steady-State Conditions

N. S. Choudhury* and J. W. Patterson**

Deparmtent of Metallurgy and Engineering Research Institute, Iowa State University, Ames, Iowa 50010

ABSTRACT

Parametric integral equations for the steady-state terminal voltage and external current of a solid electrolyte energy conversion device are derived under the assumption that the anode and cathode chemical potentials remain invariant. Plots of terminal voltage, power delivered, and efficiency *vs.* external current are generated for yttria-doped thoria at 1600°C by first inserting the appropriate functional dependencies for the ionic and electronic conductivities into the parametric equations and then systematically eliminating the common parameter. The formulas are also used to calculate and plot the chemical potential profiles inside the yttria-doped thoria solid electrolyte under applied voltage (charging) as well as under load (discharging) conditions.

The feasibility of an electrochemical energy conversion device (*e.g.* battery, fuel cell, etc.) for any particular application depends on its voltage-current characteristics. Once the relationship between terminal voltage and external current is known, the delivered power and efficiency of the device may be estimated for proposed operating conditions. Such operating characteristics are usually obtained empirically by merely observing device response to preselected charge and discharge conditions.

Observed variations in terminal voltage with external current may be rationalized in terms of various

* Electrochemical Society Student Member.
** Electrochemical Society Active Member.
Key words: solid electrolytes, mixed conductors, d-c polarization, open circuit emf, thermodynamic emf, electrochemical potential, chemical potential, charge-discharge characteristics, electronic conductivity, hole conductivity, ionic conductivity, ionic transference number, chemical potential profile, interface polarization, electrode polarization.

polarization effects associated with (*a*) mass and charge transport through the electrodes and electrolyte, and (*b*) transfer reaction kinetics at the electrodes. Although extensive experimental and theoretical effort has been directed to the polarization effects associated with electrodes and electrode-electrolyte interfaces, polarization effects within the bulk of the electrolyte have received much less attention.

The present paper concerns polarization effects within solid electrolytes. In particular, Wagner's theory of mixed conduction (1, 2) is used to obtain quantitative methods for calculating terminal voltage, external current, delivered power, efficiency, and chemical potential profiles (3) for virtually stoichiometric solid electrolytes under steady-state conditions of charge and discharge.

Expressions for Current and Voltage for Solid Mixed Conductors at Steady-State

Consider the electrochemical system depicted schematically in Fig. 1. For generality the M_aX_b solid electrolyte is presumed to exhibit a perceptible amount of electronic conductivity σ_3 in addition to the cationic and anionic conductivities σ_1 and σ_2. Chemical conditions in electrodes 1 and 2 serve to fix the nonmetal chemical potentials μ_{X_2}' and μ_{X_2}'' in the respective electrode compartments.

The chemical potentials $\mu_{X_2}(O)$ and $\mu_{X_2}(L)$ prevail just inside the electrolyte at the corresponding electrode-electrolyte interfaces. If mass transfer polarization effects external to the electrolyte can be neglected, $\mu_{X_2}(O) = \mu_{X_2}'$ and $\mu_{X_2}(L) = \mu_{X_2}''$ even under load or discharge conditions. Because we are considering only losses within the electrolyte, this assumption of completely reversible behavior is employed below. Departures from these equalities are the subject of electrode and interface polarization effects external to the electrolyte (4).

The electronic leads connecting the electrode-electrolyte interfaces to the external circuit in Fig. 1 are assumed to be of identical composition so that the electrochemical potential difference $\eta_3'' = \eta_3'$ for electrons in leads 2 and 1 is related to the terminal voltage V_T by

$$\eta_3'' - \eta_3' = -\mathbf{F}\,V_T \qquad [1]$$

where $\mathbf{F}$ is Faraday's constant. Electronic polarization effects outside the solid electrolyte are neglected by assuming the electrochemical potential of electrons $\eta_3(O)$ and $\eta_3(L)$ just inside the electrolyte at the O and L interfaces are respectively equal to η_3' and η_3''.

According to Wagner's theories (1, 2), the local charge fluxes I_1 (due to cations), I_2 (due to anions), and I_3 (due to electrons) may be written in terms of the corresponding partial conductivities σ_i, electrochemical potential gradients $\nabla\eta_i$ and valences Z_i as follows

$$I_i = -A(\sigma_i/Z_i\mathbf{F})\nabla\eta_i; \quad i = 1, 2, 3 \qquad [2]$$

where $\mathbf{F}$ is Faraday's constant, and A is the cross sectional area of the solid electrolyte. The assumptions of local equilibria involving neutral atoms, ions, and electrons—and the condition of virtual stoichiometry combined with the Gibbs-Duhem relation between the species M and X—facilitates the elimination of the nonmeasurables η_1 and η_2 in favor of the variables μ_{X_2} and η_3 whose differences can be measured and controlled in physical systems. There results

$$I_{ion} = -A\,\sigma_{ion}(\nabla\mu_{X_2}/2Z_2\mathbf{F} + \nabla\eta_3/Z_3\mathbf{F}) \qquad [3]$$

and

$$I_3 = -A\,\sigma_3\,\nabla\eta_3/Z_3\mathbf{F} \qquad [4]$$

where $I_{ion} = I_1 + I_2$ and $\sigma_{ion} = \sigma_1 + \sigma_2$.

The condition of steady-state requires that I_1, I_2, and I_3 must individually be independent of location. Therefore the ratio

$$r = I_{ion}/I_3 \qquad [5]$$

is also independent of location. In this paper the parameter r is used to characterize the steady-state condition of the solid electrolyte because for fixed values of μ_{X_2}', μ_{X_2}'', and temperature T, each value of r corresponds uniquely to a particular external current I_{ext} and terminal voltage V_T. The quantitative formulas for I_{ext} and V_T in terms of σ_i, μ_{X_2}', μ_{X_2}'', and r may be readily derived by appropriate integration under the assumptions of steady-state conditions and negligible polarization outside the electrolyte phase.

Substitution of Eq. [3] and [4] into [5] solved for $\nabla\eta_3$ gives

$$\nabla\eta_3 = \frac{Z_3}{2Z_2}\left(\frac{\sigma_{ion}}{r\sigma_3 - \sigma_{ion}}\right)\nabla\mu_{X_2} \qquad [6]$$

Integration of Eq. [6] from one end of the electrolyte to the other, division by $\mathbf{F}$, and use of Eq. [1] yields

$$V_T = \int_{\mu_{X_2}'}^{\mu_{X_2}''}\left(\frac{\sigma_{ion}}{r\sigma_3 - \sigma_{ion}}\right)\frac{d\mu_{X_2}}{2Z_2\mathbf{F}} \qquad [7]$$

as the explicit formula for the terminal voltage in terms of r, μ_{X_2}', μ_{X_2}'' and appropriate transport parameters for the M_aX_b phase. For any given value of r the integrand in Eq. [7] is a function of μ_{X_2} only and the integral may be evaluated explicitly when the dependence of σ_{ion} and σ_3 on μ_{X_2} are known for the electrolyte in question.

The external current I_{ext} is simply the sum of I_{ion} and I_3. Thus I_{ext} may be written as

$$I_{ext} = I_3 + I_{ion} = -\frac{A(1 + r)\sigma_{ion}\sigma_3}{(r\sigma_3 - \sigma_{ion})}\frac{\nabla\mu_{X_2}}{2Z_2\mathbf{F}} \qquad [8]$$

where Eq. [3], [4], [5], and [6] have been used to eliminate I_{ion}, I_3, and $\nabla\eta_3$ in favor of the variables σ_{ion}, σ_3, $\nabla\mu_{X_2}$ and the parameters A, Z_2, r, and $\mathbf{F}$. Integration of Eq. [8] under the assumption of linear flux geometry and the steady-state implication that I_3 and I_{ion} are independent of location in the electrolyte yields

$$I_{ext} = -\frac{A}{L}\int_{\mu_{X_2}'}^{\mu_{X_2}''}\frac{[1 + r]\sigma_{ion}\sigma_3}{(r\sigma_3 - \sigma_{ion})}\frac{d\mu_{X_2}}{2Z_2\mathbf{F}} \qquad [9]$$

In Eq. [9] as in [7] the integral may be evaluated explicitly if the dependences of σ_{ion} and σ_3 on μ_{X_2} are known from independent measurements and if the values of μ_{X_2}', μ_{X_2}'', and r are specified.

The functional dependences of σ_{ion} and σ_3 on μ_{X_2} (or equivalently log P_{X_2}) may be determined experimentally from a-c conductivity, d-c polarization, and open circuit emf measurements on appropriate cell arrangements involving M_aX_b specimens (2, 5). Alternately the dependences may at least in part be inferred from law of mass action considerations involving the species believed to dominate the defect struc-

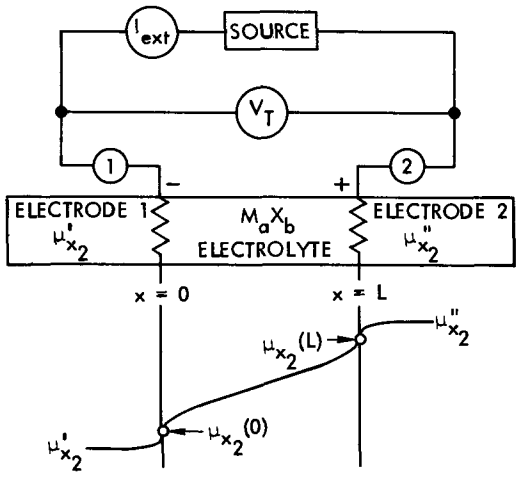

Fig. 1. Schematic representation of a solid electrolyte energy conversion device.

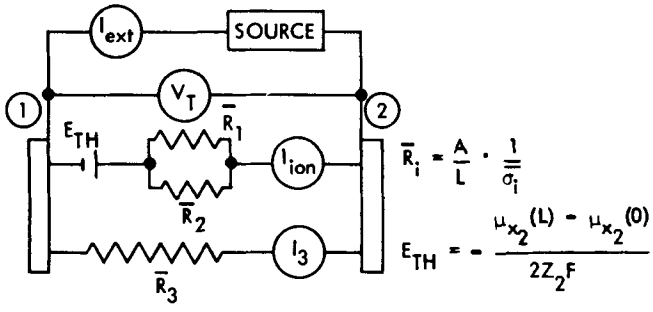

Fig. 2. Linear circuit analog for a solid electrolyte energy conversion device.

ture of the M_aX_b compound (6-9); in the present context, however, the dependences of σ_{ion} and σ_3 on μ_{X2} are assumed to be available from independent sources. We may therefore turn to the task of generating the voltage-current characteristics with the help of Eq. [7] and [9] which are parametric in r.

In principle the procedure is quite simple. One merely ranges r over as many values as desired. For each r, V_T and I_{ext} are evaluated from Eq. [7] and [9] and then plotted *vs.* one another to form the voltage-current characteristic curve. However, the range of r values to be chosen for a given assessment may not be too obvious at first glance. Thus the equivalent circuit shown in Fig. 2 is offered for assistance. Because the values of $\bar{\sigma}_i$ and hence of $\bar{R}_i$ may depend on the applied current and voltage, the equivalent linear circuit shown in Fig. 2 is only a very crude way to approximate the behavior of the physical system depicted in Fig. 1. Nevertheless, Fig. 2 provides some insight into the ranges of r that correspond to particular modes of steady-state behavior.

If the source is a load resistor of infinite impedance or a battery with an appropriate bucking emf, I_{ext} vanishes, and the electrolyte is said to be functioning in the open circuit mode. Inspection of the circuit diagram in Fig. 2 indicates that neither I_{ion} nor I_3 vanish in the open circuit case but rather $I_{ion} = -I_3$, *i.e.* $r = -1$. Figure 2 also indicates that the open circuit magnitudes of I_3 and I_{ion} depend not only on the overall ionic and electronic resistances but also on the magnitude of the thermodynamic voltage E_{TH} (indicated as a battery in Fig. 2) generated by chemical conditions of the electrodes. The magnitude of E_{TH} is given by

$$E_{TH} = -(\mu_{X_2}'' - \mu_{X_2}')/2Z_2F \qquad [10]$$

It is easy to demonstrate that the above assertions are in accordance with Wagner's tarnishing theory by substituting $r = -1$ into Eq. [9] to get $I_{ext} = 0$ and into Eq. [7] to get Wagner's well-known result

$$E_W = -\int_{\mu_{X_2}''}^{\mu_{X_2}''} \frac{t_{ion}}{2Z_2F} d\mu_{X_2} \qquad [11]$$

where the ionic transference number t_{ion} is defined as $t_{ion} = \sigma_{ion}/[\sigma_{ion} + \sigma_3]$.

If the source in Fig. 1 is a battery with the same polarity and emf as E_{TH}, I_{ion} vanishes and $I_{ext} = I_3$ only. In this case $r = 0$, and the physical situation corresponds to the stopping voltage for scaling of metals (9, 10) or to the conditions corresponding to the Hebb-Wagner (2, 11, 12) d-c polarization technique for studying the electronic conductivity of mixed conductors. If the source battery polarity remains the same but its emf is increased, the M_aX_b electrolyte is said to be in the charging mode. By inspection, the charging mode corresponds to r values greater than zero.[1]

If the source voltage is less than E_W as given by Eq. [11] the electrolyte is said to be discharging under load.

[1] Because it is of such little interest in practical cases, we omit consideration of another $r > 0$ mode that results when the polarities of the source voltage and E_{TH} are not opposed.

By inspection of Fig. 2 it is seen that I_{ion} and I_3 will flow in opposite directions, and it is found that the range of r from -1 (open circuit) to $-\infty$ (dead short) covers all possible load conditions. This mode of operation (*i.e.* steady-state discharge) will be examined below to demonstrate the use of Eq. [7] and [9] to calculate current, voltage, power, and efficiency.

Analogous calculations and characteristic curves can also be made for the charging mode ($r > 0$) of operation but this case is not analyzed in detail. Chemical potential profiles are calculated and plotted below for linear geometry solid electrolytes in the charge ($r > 0$), discharge ($r < -1$), and open circuit ($r = -1$) modes.

Calculations for Special Cases

Specific calculations for a given electrolyte require that the dependences of σ_3 and σ_{ion} on μ_{X2} (or equivalently on log P_{X_2}) be known in some detail for the temperature and electrolyte of interest. Unfortunately, information of this type is available for only a few solid electrolytes and for only limited temperature ranges (5, 13). Furthermore, because of the discrepancies reported from investigator to investigator, those data which now exist can only yield an approximation to the functional dependences required. Nevertheless it is useful to demonstrate the calculation of the various characteristic curves by analyzing a solid electrolyte for which the required data (however approximate) are presently available.

The oxide solid electrolyte YDT (yttria-doped thoria $= Th_{0.85}\ Y_{0.15}\ O_{1.925}$) has been chosen for the calculations. By combining the results of various conductivity measurements (8), emf measurements (14), and assumptions regarding the defect structure of YDT, the following dependences of σ_3 and σ_{ion} for YDT may be used

$$\sigma_3 = \sigma_{ion}[(P_{O_2}/P_\oplus)^{1/4} + (P_{O_2}/P_\ominus)^{-1/4}] \qquad [12]$$

The ionic conductivity σ_{ion} is due to oxygen ion vacancies and is fixed at a given temperature by the dopant. Hence σ_{ion} is independent of P_{O_2} but exhibits an Arrhenius temperature dependence which at 1600°C gives a value of

$$\sigma_{ion}(1600°C) = 0.10\ \text{ohm}^{-1}\ \text{cm}^{-1} \qquad [13]$$

The Schmalzried parameters $P_\oplus$ and $P_\ominus$ in Eq. [12] also exhibit an Arrhenius temperature dependence (13) and for YDT at 1600°C they have the values

$$P_\oplus(1600°C) = 100\ \text{atm} \qquad [14]$$

and

$$P_\ominus(1600°C) = 10^{-19}\ \text{atm} \qquad [15]$$

Equations [7] and [9] may be evaluated for any r value by substituting Eq. [12] and [13] into the integrands and changing the variable of integration to P_{O_2}. Calculations at other temperatures merely require knowledge of the temperature dependences of σ_{ion}, $P_\oplus$, $P_\ominus$ and the end points of integration P_{O_2}' and P_{O_2}''.

Calculation of Discharge Characteristic Curves

Under load conditions the power P_d delivered by the electrolyte is simply I_{ext} times V_T which may be readily evaluated from Eq. [7] and [9] for various values of r. The consumption rate P_c of chemical energy stored in the electrodes is simply $I_{ion} = I_{ext}\ r/(r+1)$ times the thermodynamic emf E_{TH}. Thus the power P_d, the efficiency $e = P_d/P_c$, and the terminal voltage V_T for the electrolyte under steady-state discharge conditions may be calculated along with I_{ext} for any values of r in the range -1 to $-\infty$. The plots of P_d, e, and V_T *vs.* I_{ext} in this range of r values comprise the discharging characteristic curves for the electrolyte in question.

Figure 3 shows the results of the calculations for P_{O_2}' and P_{O_2}'' values corresponding to $P_\ominus$ and $P_\oplus$ respectively. Because the electrode chemical potentials extend well beyond the electrolytic domain (5, 13) for the electrolyte, the parasitic effects of electronic conduction on the efficiency add significantly to the in-

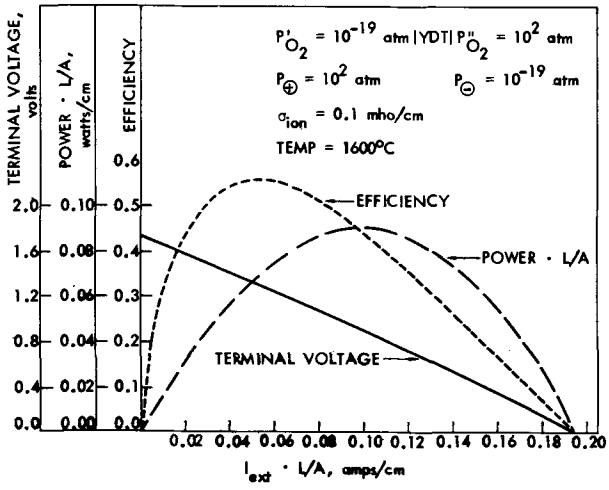

Fig. 3. Plot of terminal voltage, power, and efficiency vs. external current for yttria-doped thoria electrochemical cell having cathode $P_{O_2} = P_\oplus$ and anode $P_{O_2} = P_\ominus$.

escapable loss associated with the ionic resistance of the YDT solid electrolyte. In order to avoid special assumptions regarding the geometric factor L/A, external current and power quantities were calculated and plotted as $I_{ext}(L/A)$ A/cm and $P_d(L/A)$ W/cm. The efficiency e and terminal voltage V_T are independent of the L/A ratio.

In order to demonstrate the parasitic effects of electronic conduction the following four pairs of end points of integration were investigated:

	P_{O_2}' atm	P_{O_2}'' atm
Case 1	$10^{-10.5}$	$10^{-6.5}$
Case 2	$10^{-14.5}$	$10^{-10.5}$
Case 3	$10^{-18.5}$	$10^{-14.5}$
Case 4	$10^{-22.5}$	$10^{-18.5}$

In Fig. 4-6 respectively, the power delivered, the efficiency, and the terminal voltage *vs.* the external current are shown for each of the above cases. Although the thermodynamic voltage is the same for each of the cases, the figures show that P_d L/A, e, and V_T all decrease as the electrode P_{O_2}' and P_{O_2}'' values are shifted to lower values. This is due to the increase in excess electronic conduction in YDT at reducing conditions. A symmetric effect would also result if the P_{O_2}' and P_{O_2}'' value were similarly shifted upward, due

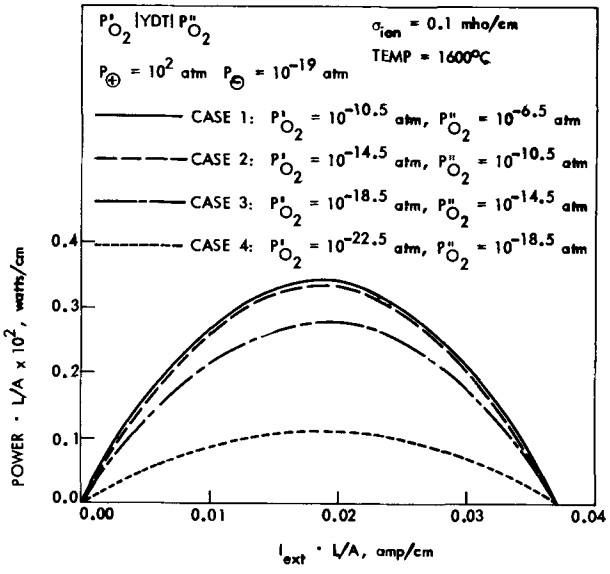

Fig. 4. Power vs. external current plots for cases 1 through 4

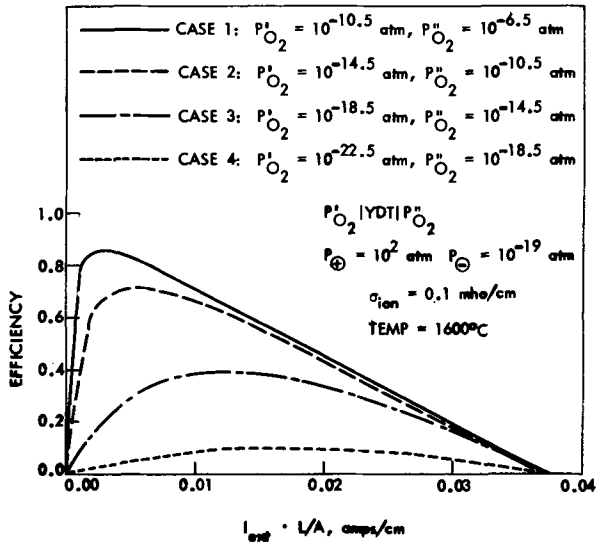

Fig. 5. Efficiency vs. external current plots for cases 1 through 4.

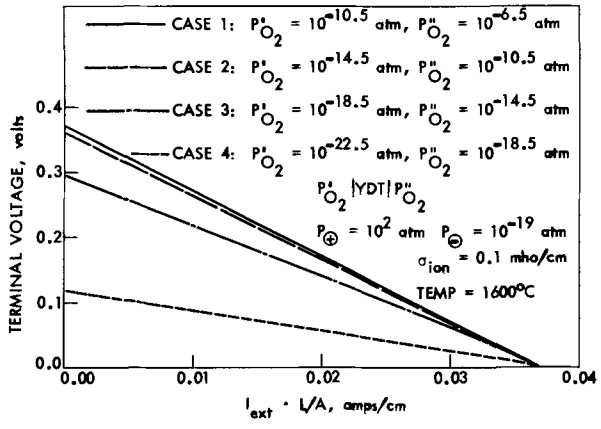

Fig. 6. Terminal voltage vs. external current plots for cases 1 through 4.

to increased positive hole conduction at oxidizing conditions. Because both these forms of electronic conduction detract significantly from the efficiency, the most efficient operation results (for a given difference between log P_{O_2}'' and log P_{O_2}') if the values of log P_{O_2}' and log P_{O_2}'' are chosen symmetrically about the log P_{O_2} at which the excess electron conductivity $\sigma_\ominus$ equals the positive hole conductivity $\sigma_\oplus$; *i.e.* the point of minimum electronic conductivity log P_{np}.

Chemical Potential Profile Calculation

In a recent paper Choudhury and Patterson (3) demonstrated a method for calculating chemical potential profiles in solid electrolytes under open circuit ($r = -1$) and ion blocking ($r = 0$) steady-state conditions. To supplement those results the chemical potential profiles for a range of charging ($r > 1$) and discharging ($r < -1$) conditions are given below for YDT at 1600°C.

The basic idea in generating these profiles is the conservation of some appropriate flux throughout the electrolyte's interior. Conserving I_{ion} yields

$$I_{ion} = -\frac{A}{x}\int_0^x \sigma_{ion}\,\nabla\eta_2 dx \qquad [16]$$

where

$$\eta_2 = \mu_{X2} + (Z_2/Z_3)\,\eta_3 \qquad [17]$$

Substitution of Eq. [17] into [16], integrating from O to x and then from O to L, and assuming σ_{ion} to be constant yields

$$I_{ion} = \frac{\sigma_{ion} A}{x} \{[\mu_{X_2}(x) - \mu_{X_2}'] + 2\mathbf{Z}_2\mathbf{F}V_T(r,x)\} \quad [18]$$

and

$$I_{ion} = \frac{\sigma_{ion} A}{L} [(\mu_{X_2}'' - \mu_{X_2}') + 2\mathbf{Z}_2\mathbf{F}V_T(r,L)] \quad [19]$$

where $V_T(r, x)$, the voltage drop from $x = 0$ to x, and $V_T(r, L)$, the voltage drop across the entire length, are evaluated for a particular value of r with the help of Eq. [7]. Division of Eq. [18] by Eq. [19], rearrangement, replacement of X_2 with O_2, and elimination of μ_{O_2} in favor of P_{O_2} yields

$$\frac{x}{L} = \left[\frac{\log|P_{O_2}/P_{O_2}'| - 4\mathbf{F}V_T(r,x)/RT}{\log|P_{O_2}''/P_{O_2}'| - 4\mathbf{F}V_T(r,L)/RT}\right] \quad [20]$$

where R is the gas constant and T the absolute temperature. By selecting r and any value of P_{O_2} between the endpoint values P_{O_2}' and P_{O_2}'', the corresponding x/L value is readily calculated with the help of Eq. [7]. Repeating this procedure for a constant r and plotting the corresponding log P_{O_2}, x/L values yields the desired chemical potential profile in the form of a log P_{O_2} *vs.* x/L plot.

The profiles shown in Fig. 7 were generated in this way for the values of r indicated. The value of V_T for each r is also shown. Figure 7 supplements the earlier results of Choudhury and Patterson (3) which applied only to the open circuit ($r = -1$) and ion blocking ($r = 0$) conditions. It is seen that a dead short ($V_T = 0$) over the electrolyte yields a linear chemical potential profile. Applying an emf V_T of the same polarity

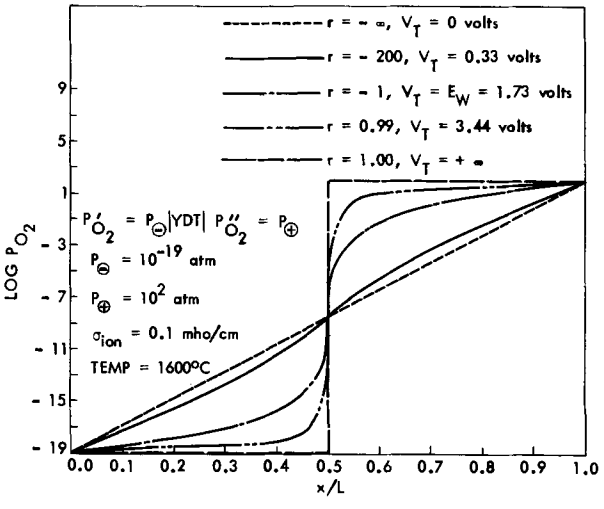

Fig. 7. Steady-state chemical potential profiles in yttria-doped thoria while holding $P_{O_2}' = P_\ominus$ and $P_{O_2}'' = P_\oplus$ constant.

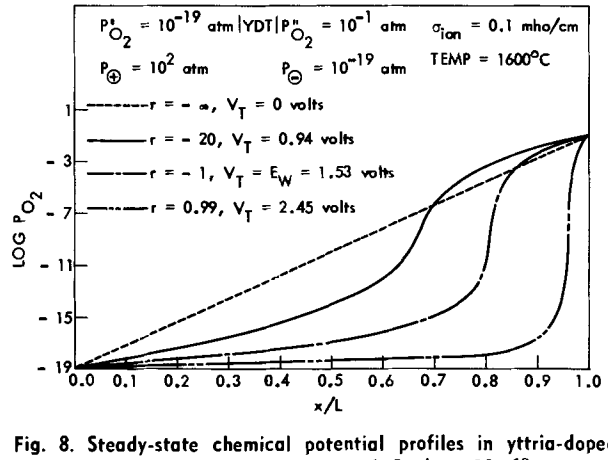

Fig. 8. Steady-state chemical potential profiles in yttria-doped thoria for different terminal voltages with $P_{O_2}' = 10^{-19}$ atm and $P_{O_2}'' = 10^{-1}$ atm.

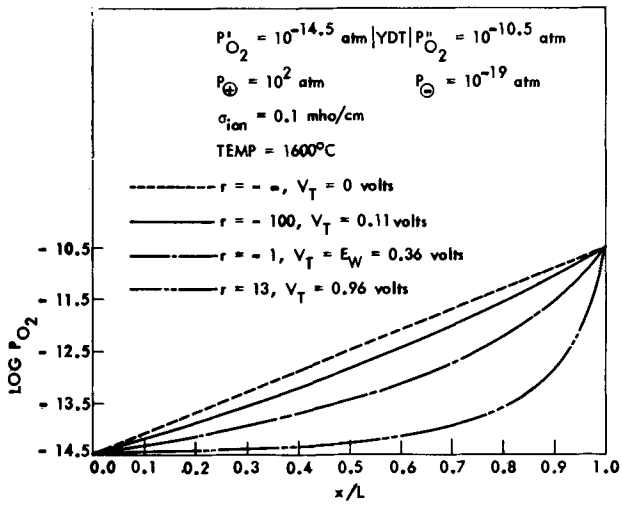

Fig. 9. Steady-state chemical potential profiles in yttria-doped thoria for case 2 and various values of terminal voltage.

as E_W but much greater in magnitude causes the profile to become increasingly abrupt. The limiting profile is a step function.

Interestingly, the inflection points (which always occur at log P_{np}) all superpose at $x/L = 0.5$ in Fig. 7. This somewhat fortuitous circumstance is a result of the symmetrically chosen endpoints of integration as well as the linear cell geometry. However, when the values of log P_{O_2}' and log P_{O_2}'' are not chosen symmetrically about log P_{np}, the inflection points are displaced for each value of r. Figure 8 shows a family of profiles for which this is the case. As an extreme case of asymmetry, P_{np} may not lie between P_{O_2}' and P_{O_2}''. In these cases the profiles exhibit no inflection points but will possess a maximum slope either at $x = 0$ or $x = L$. Figure 9 shows a family of profiles for which P_{np} does not lie intermediate between P_{O_2}' and P_{O_2}''. The general rule (1) according to Eq. [8] and the assumption of steady state, is that the profile slope (or equivalently $\nabla\mu_{X_2}$) is a maximum at the point where the "conductivity factor" $(1 + r)\sigma_{ion}\sigma_3/(r\sigma_3 - \sigma_{ion})$ is a minimum and *vice versa*.

Acknowledgment

Research was sponsored by the Engineering Research Institute at Iowa State University through funds provided by the Aerospace Research Laboratories, Office of Aerospace Research, United States Air Force, Contract F33615-68-C-1034.

Manuscript received Feb. 16, 1971.

Any discussion of this paper will appear in a Discussion Section to be published in the June 1972 JOURNAL.

SYMBOLS

A	cross-sectional area
e	efficiency
E_{TH}	thermodynamic emf
E_W	open circuit emf
$\mathbf{F}$	Faraday's constant
I_1	steady-state electrical current conducted by the cations
I_2	steady-state electrical current conducted by the anions
I_3	steady-state electrical current conducted by the electrons
I_{ext}	steady-state external current
I_{ion}	$I_1 + I_2$
L	total length of the solid-electrolyte
P_c	rate of consumption of chemical energy
P_d	delivered power
P_{np}	P_{X_2} at which $\sigma_\oplus = \sigma_\ominus$
P_{O_2}	partial pressure of oxygen gas
P_{X_2}	partial pressure of nonmetal gaseous dimer (X_2 gas)

$P_\oplus$ P_{X_2} at which $\sigma_{ion} = \sigma_\oplus$
$P_\ominus$ P_{X_2} at which $\sigma_{ion} = \sigma_\ominus$
r ratio of I_{ion}/I_3
R gas constant
t_{ion} ionic transference number
T temperature, °K
V_T terminal voltage
x distance coordinate inside the solid electrolyte
Z_1 valence of cation
Z_2 valence of anion (a negative integer)
Z_3 valence of electrons
η_3 electrochemical potential of electrons
μ_{X_2} chemical potential/mole of nonmetal gaseous dimer (X_2 gas)
σ_{ion} total ionic conductivity
σ_1 cationic conductivity
σ_2 anionic conductivity
σ_3 total electronic conductivity
$\sigma_\oplus$ hole conductivity
$\sigma_\ominus$ excess electronic conductivity

APPENDIX: INTEGRATED FORMULAS

Evaluation of the parametric Eq. [7] and [9] for special assumptions regarding the P_{X_2} dependences of σ_{ion}, $\sigma_\oplus$, and $\sigma_\ominus$ leads to somewhat awkwardly integrated formulas and requires that attention be restricted to r values that have physical meaning. Let us assume σ_{ion} is a constant, and σ_3 is given by Eq. [12] where exponents $\pm\frac{1}{4}$ are replaced by $\pm 1/n$ and where P_{O_2} is replaced by P_{X_2}. In this case Eq. [7] may be transformed to a standard form and integrated to yield

$$V_T = -\left(\frac{RT}{2Z_2\mathbf{F}}\right)\cdot\left(\frac{n}{\sqrt{w}}\right) \cdot\left[\ln\left|\frac{1-2r(P_{X_2}/P_\oplus)^{1/n}-\sqrt{w}}{1-2r(P_{X_2}/P_\oplus)^{1/n}+\sqrt{w}}\right|\right]_{P_{X_2}'}^{P_{X_2}''};\ w>0 \quad [21]$$

or

$$V_T = \left(\frac{RT}{2Z_2\mathbf{F}}\right)\cdot\left(\frac{2n}{\sqrt{-w}}\right) \cdot\left\{\arctan\left[\frac{2r(P_{X_2}/P_\oplus)^{1/n}+1}{\sqrt{-w}}\right]\right\}_{P_{X_2}'}^{P_{X_2}''};\ w<0 \quad [22]$$

where

$$w = 1 - 4r^2(P_\ominus/P_\oplus)^{1/n} \quad [23]$$

Also under these assumptions, I_{ext} $[L/A]$ may be written in terms of V_T as follows

$$I_{ext}(L/A) = \sigma_{ion}\left(\frac{r+1}{r}\right)\cdot(E_{TH} - V_T) \quad [24]$$

where E_{TH} is given by Eq. [10] above. Numerous limiting cases may be used to simplify Eq. [21] and [22] for practical applications.

It may appear that evaluation of Eq. [21]-[24] can be carried out for any r values in the interval from $-\infty$ to $+\infty$. However, physically meaningful results are found only for those ranges of r in which the denominator of the integrand in Eq. [7] cannot vanish. For the functional dependences assumed above, two such ranges, R_1 and R_2, exist

$$R_1:\ -\infty \leqq r < \frac{\sigma_{ion}}{\sigma_3(\max)} \quad [25]$$

and

$$R_2:\ \frac{\sigma_{ion}}{\sigma_3(\min)} < r \leqq \infty \quad [26]$$

In these relationships, $\sigma_3(\max)$ and $\sigma_3(\min)$ are respectively the maximum and the minimum values of $\sigma_3 = \sigma_\oplus + \sigma_\ominus$ occurring between the limits of integration P_{X_2}' and P_{X_2}''. $\sigma_3(\max)$ will be $\sigma_3(P_{X_2}'')$ or $\sigma_3(P_{X_2}')$, whichever is larger. $\sigma_3(\min)$ will be the smaller of these two values unless P_{np} (the P_{X_2} where $\sigma_\oplus = \sigma_\ominus$) lies between P_{X_2}' and P_{X_2}''. In the latter case $\sigma_3(\min)$ is given by $\sigma_3(P_{np})$.

Only calculations for r values in the range R_1 have been considered above because this range covers all the cases of practical interest within the scope of this paper. Values of r in R_2 correspond to the uninteresting cases where E_{TH} and V_T are not bucking each other. Calculations for r values in the interval $[\sigma_{ion}/\sigma_3(\max)] < r < [\sigma_{ion}/\sigma_3(\min)]$ are without physical meaning in the present context.

REFERENCES

1. C. Wagner, *Z. Physik. Chem.*, **B21**, 25 (1933).
2. C. Wagner, Proc. Int. Comm Electrochem. Thermo. and Kinetics (CITCE). 7th meeting Lindau (1955), Butterworth Scientific Publications, London (1957).
3. N. S. Choudhury and J. W. Patterson, *This Journal*, **117**, 1384 (1970).
4. R. L. Zahradnik, *This Journal*, **117**, 1443 (1970).
5. J. W. Patterson, Chap. 5 in "The Physics of Electronic Ceramics," L. L. Hench and D. B. Dove, Editors, Marcel Dekker Inc., New York (1971).
6. H. Schmalzried, *Z. Electrochem.*, **66**, 572 (1962).
7. H. Schmalzried, *Z. Phys. Chem. (Frankfurt)*, **38**, 87 (1963).
8. M. F. Lasker and R. A. Rapp, *Z. Physik. Chem. N. F.*, **49**, 198 (1966).
9. F. A. Kroger, "The Chemistry of Imperfect Crystals," North Holland Publ., Amsterdam (1964).
10. P. J. Jorgenson, *J. Chem. Phys.*, **49**, 1594 (1968).
11. M. Hebb, *J. Chem. Phys.*, **20**, 185 (1952).
12. J. W. Patterson, E. C. Bogren, and R. A. Rapp, *This Journal*, **114**, 752 (1967).
13. J. W. Patterson, *This Journal*, **118**, 1033 (1971).
14. J. B. Hardaway, J. W. Patterson, D. R. Wilder, and J. D. Schieltz, *J. Am. Ceram. Soc.* To be published in the January 1971 issue.

Aggressive Ion Accessibility and the Morphology of Corrosion Pits

T. Tokuda[1] and M. B. Ives

Institute for Materials Research, McMaster University, Hamilton, Ontario, Canada

ABSTRACT

Corrosion pits were formed under potentiostatic conditions on {100}, {111}, and {110} surfaces of nickel in 1*N* H_2SO_4 or (0.5*N* $NiSO_4$ + 0.01*N* H_2SO_4) solution by adding Cl^- ions at passive potentials. The morphologies of the pits obtained were analyzed using a model based on the atomistic mechanics of dissolution. It is found that a simulation, which removed atoms one by one according to the principle that atoms more accessible to the aggressive ions are removed more easily, approximates the morphologies of pits obtained experimentally. Observed morphological changes with the reaction rate (dependent on the degree of passivation, the potential of chloride addition and the acidity of the solution) could also be accounted for by appropriate modification of the simulation procedure. The simulation also is shown to predict the morphology of corrosion pits in body-centered cubic metals reported by other workers. It is proposed that the state of close-packing of a crystal surface is not the only factor to be considered in determining the relative dissolution rates of crystallographic surfaces when aggressive ions are present.

The pitting corrosion of metals has usually been investigated from the standpoint of electrochemistry and very rarely from the standpoint of surface morphology. However, a morphological study can provide important clues to the mechanisms of crystal dissolution, evaporation, and growth. For example, evaporation spirals have been accounted for by a mechanism in which atoms are removed from the surface step emanating from the intersection of a screw dislocation with a free crystal surface (1, 2). The pitting of single crystal metal surfaces under potentiostatic control usually results in a small number of pits which grow to sizes sufficient for ready observation of their morphology. Also, these pits are obtained on most crystal orientations due to the fact that the surface outside the pits is always in a more passive state than the interior of the pits. This is in contrast to those etch pits which can be obtained at defects on a wide variety of materials, but usually only on crystal orientations within a small angle of low-index planes (3-6). Analysis of the morphology of etch pits has been attempted by considering the relative dissolution rates of various crystal orientations (7-11). For example, Batterman (7) and Irving (8) have considered the conditions for the stability of etch hillocks and pits on germanium. Frank (9) developed a kinematic theory to relate the orientation dependence of crystal dissolution rate to the dissolution morphology obtained, and this was successfully applied (10) to the dissolution morphologies obtained by Batterman (7). This approach to the morphology of dissolution features requires, however, a large number of dissolution measurements and is applicable only to dissolution shapes resulting from starting conditions of macroscopic dimensions.

The approach used in this work is closer to the principles employed to analyze dissolution at screw dislocations (2), and extends the approach to account for the atom-atom relationships resulting from the crystal structure. This truly atomistic model of pitting provides an opportunity to simulate the removal sequences of atoms subject to specific constraints, supposed to be appropriate to the particular experimental conditions existing during pitting corrosion under potentiostatic control. The extent to which a particular simulation approaches the pit morphologies observed is taken as a measure of the appropriateness of the assumed conditions.

[1] Present address: Showa-Denko Co. Ltd., Yokohama, Japan.

Key words: nickel, simulation, breakdown of passivity.

Morphology of Corrosion Pits on Nickel

Garz *et al.* (12) have studied the morphology of corrosion pits formed in 0.5*N* $NiCl_2$ on {111}, {100}, and {110} surfaces of nickel. They state that faces of high atomic density constitute the facets of pits obtained at high anodic potentials. They observed pit facets to be composed of {310}, {110}, and {111}. No other definitive study of corrosion pits on nickel has come to our attention.

For the present work, 99.9% nickel was used to grow single crystals of <110> and <111> axes by the Czochralski technique under argon atmosphere. Disk samples of approximately 8 mm diam were prepared of {100}, {111}, and {110} orientations by cutting the crystals in a multiple-wire seesaw system and polishing to a 0.1μ diamond finish. The polarization cell has been described in detail elsewhere (13) and consisted of a Wenking potentiostat, platinum counterelectrode, Luggin capillary connected to a saturated calomel reference electrode, and Teflon specimen holder arranged for *in situ* microscopic observation.

Pits were formed by passivating the samples in 1*N* H_2SO_4 or in (0.5*N* $NiSO_4$ + 0.01*N* H_2SO_4) for 30 min at various potentials followed by the incremental addition of chloride ion (as NaCl solution) until pitting was initiated at the chosen potential for pitting. The two electrolytes were adopted to permit a study of morphological change with acidity.

In addition to the *in situ* optical observations, scanning electron microscopy was performed on samples after removal from the cell and goniomicroscopy was used to assist the determination of pit facet orientation.

The shape and structure of typical pits observed on the various crystallographic surfaces and at both low and high "reaction rates" (*i.e.* high and low anodic current during pitting) are presented in Fig. 1-6. Pit densities were always low, being less than 20 cm^{-2}. In many cases pit facets were stepped and the orientations quoted below are the mean crystallographic orientations.

Figure 1 is representative of the only type of pit morphology observed on {100} nickel surfaces in this work. The side facets of the pits were determined to be {111} orientations and the pit bottoms were usually mottled. All efforts to change the morphology by changing the reaction rate (*e.g.* changing the degree of passivation; adopting different activation potentials)

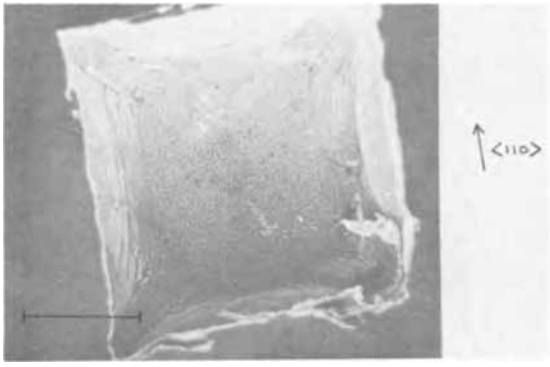

Fig. 1. Scanning electron micrograph of a typical pit formed on the {100} surface of nickel following passivation in 1*N* H_2SO_4 for 30 min at 500 mV, and activation with NaCl addition at 500 mV. The marker represents 50 μm.

were unsuccessful and only one morphology could be obtained on this orientation.

The {111} surfaces developed pits which tended to vary in external geometry from hexagonal toward triangular as the reaction rate was decreased. For example, Fig. 2 shows a pit formed in 1*N* H_2SO_4 at 800 mV after passivating at 500 mV and Fig. 3 a pit formed in (0.5*N* $NiSO_4$ + 0.01*N* H_2SO_4) at 500 mV after passivating at 500 mV. In the latter case the dissolution rate within the pit should be less, since the potential of activation is lower and the degree of passivation is higher in the less acidic solution. In Fig. 3 the pit facets are close to {111} and {210}.

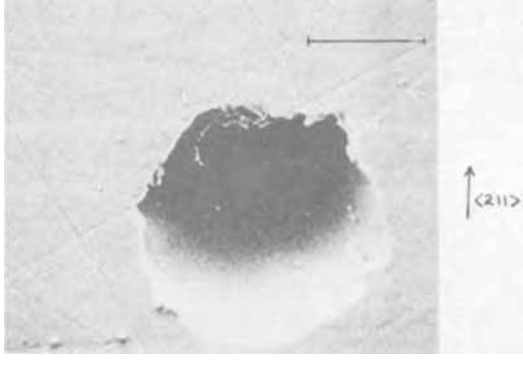

Fig. 2. Scanning electron micrograph of a pit on {111} nickel following passivation in 1*N* H_2SO_4 for 30 min at 500 mV, and activation with NaCl addition at 800 mV ("high reaction rate"). The marker represents 50 μm.

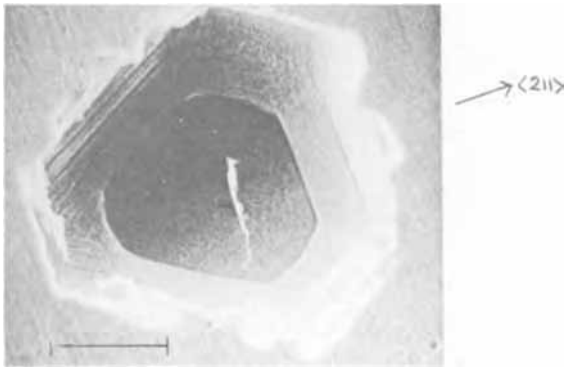

Fig. 3. Scanning electron micrograph of a pit on {111} nickel following passivation in (0.01*N* H_2SO_4 + 0.5*N* $NiSO_4$) for 30 min at 500 mV, and activation after NaCl addition at 500 mV ("low reaction rate"). The marker represents 50 μm.

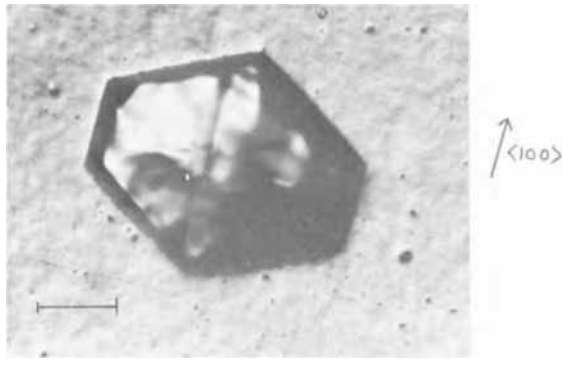

Fig. 4. Optical micrograph of pit observed during formation in the electrolytic cell on {110} nickel surface following passivation in 1*N* H_2SO_4 for 30 min at 500 mV, and activation after NaCl addition at 800 mV ("high reaction rate"). The marker represents 50 μm.

Fig. 5. Optical micrograph of a pit formed on {110} nickel surface following passivation in 1*N* H_2SO_4 for 30 min at 800 mV, and activation following NaCl addition at 500 mV (low reaction rate). The marker represents 50 μm.

Pits obtained on {110} surfaces also exhibited a dependence on the passivating potential, and an independence of the activation potential. The external geometry changed from hexagonal toward rhombohedral when the passivating potential was increased. For example, Fig. 4 shows a pit formed at 800 mV after passivation at 500 mV in 1*N* H_2SO_4 and Fig. 5 a pit obtained at 500 mV after passivation at 800 mV. The reaction rate would be lower in the latter case, due to the greater degree of passivation (13). On the {110} surfaces regular faceting of the pits was rare.

Certain of the crystals prepared for this study were found to be much more susceptible to pitting than most. Such crystals showed no difference in the shape of pits on {100}, and {111} surfaces but, on {100} surfaces rectangular pits (Fig. 6) were obtained at low potentials in less acidic solution, although in other conditions pit shapes were as in Fig. 4. These samples exhibited Laue x-ray diffraction patterns which suggested a mosaic subgrain structure. Whereas Garz *et al.* (12) reported observing rectangular pits on {110} regularly, in the present work only the "anomalous" crystals exhibited pits of this shape.

Simulation of Pitting

Simulation of pitting on the three major low-index planes of the face-centered cubic structure was carried out by a process of atom-by-atom removal, following the arbitrary subtraction of a single surface atom. It is supposed that this arbitrary subtraction corresponds to the point at which the passivating film is broken and pitting initiated. We assume that the extent of the phenomenon is such that in the area simulated there will be no further such surface nucleation event, since all other atoms remain covered with the passivating

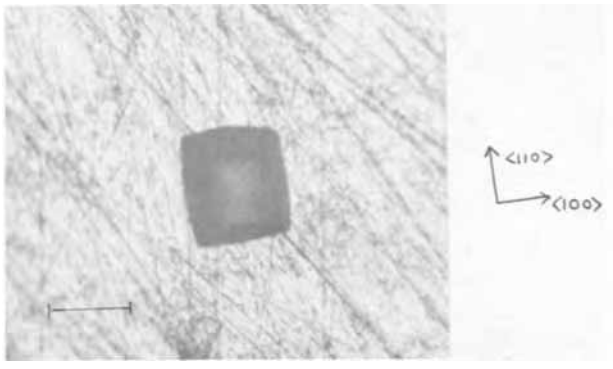

Fig. 6. Optical micrograph of a rectangular pit typical of those observed on {110} nickel surfaces of some crystals following passivation in (0.01*N* H_2SO_4 + 0.5*N* $NiSO_4$) for 30 min at 300 mV, and activation after NaCl addition at 150 mV. The marker represents 50 μm.

film until they are removed as a consequence of the expanding pit.

Simulation based on bonding.—The simplest model for the removal of surface atoms is that which assumes that an atom is removed preferentially if it has less bonds (nearest neighbors) than all other atoms. It is necessary to suppose that initially all the atoms, including the surface atoms in contact with the passive film, have the same number of bonds. Thus, the number of bonds broken is used as the criterion for priority of removal. After the initial arbitrary removal it is possible to simulate pit formation by atom-by-atom removal. The result of this procedure for the {100} surface of a face-centered cubic crystal is shown in Fig. 7. Only two layers are considered because it was found that a second layer atom is never in a position

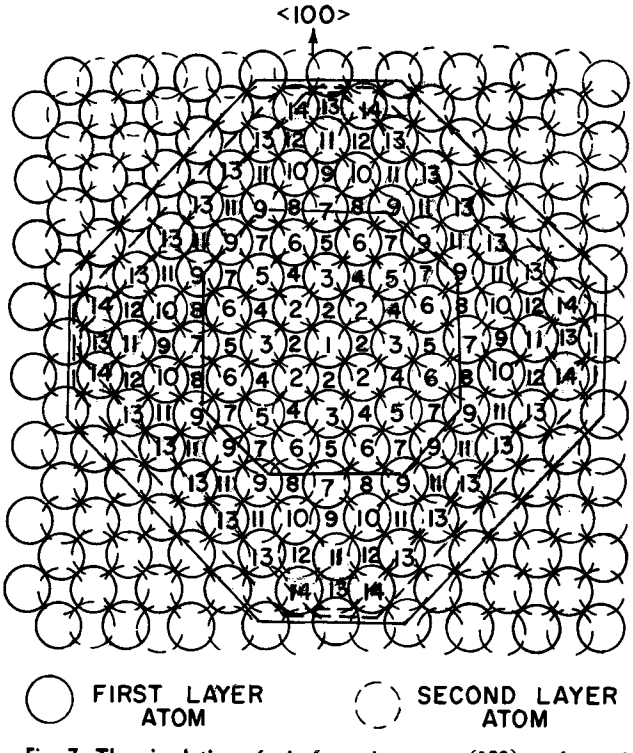

Fig. 7. The simulation of pit formation on a {100} surface of a face-centered cubic crystal, incorporating removal priorities dependent on the number of nearest neighbors. Atoms are designated with numbers corresponding to the removal sequence. The continuous lines refer to the removal boundaries for the first layer atoms following removal sequences 6 and 14: outer and inner dotted lines indicate removal boundaries for the second and third layer, respectively, following removal sequence 14.

to lose a bond with a third layer atom before it is itself removed. The numbers assigned to the atoms correspond to the order in which they were removed during the simulation. If more than one atom has the same number, these atoms had at one time the same number of nearest neighbors and, therefore, were removed simultaneously. The shape of the pit immediately following the fourteenth removal sequence is shown by the heavy solid line for first layer atoms and the outer dotted line for second layer atoms. Comparing this shape with that existing following the sixth removal sequence, (inner full line) it can be supposed that when grown to macroscopic dimensions the pit will appear square with sides along <110> directions.

Third layer removal for this case would commence, if the simulation rules are followed, by removal of the third layer atom immediately below atom "1" after the removal of atoms "2." The third layer removal will then be continued simultaneously with the upper layer removal.

The relative positions of the removal boundaries for each layer permits a prediction of the orientation of the pit facets which will be developed to macroscopic size, presumably when additional layers are subsequently removed. Thus the pit so simulated in the {100} surface has four {111} facets. The macroscopic morphology of such a pit is shown schematically in Fig. 8 (a).

In a similar manner, morphologies of pits developed on {111} and {110} surfaces can be readily obtained using the same "rules." Pits simulated for these two surfaces are shown in Fig. 8 (b) and 8 (c) respectively.

Comparing these morphologies with those obtained experimentally it is seen that there is some correspondence in the case of {100} and {111} pits, but there is considerable discrepancy for {110}.

Simulation based on the accessibility of aggressive ions.—The inability of the simple bonding model to generate the observed pit morphologies suggests that the factors controlling dissolution morphology during pitting are more complex, and we conclude the previous model is too simple. Kolotyrkin (14, 15) has considered the part played by anions in anodic dissolution and has suggested that the aggressive ions (in this case Cl^-) play an important part in assisting the removal of atoms. This concept leads to dissolution control through the ability of such aggressive ions to bond effectively with the atoms to be removed. Access of the aggressive ions during pitting corrosion is obtained only through the spaces produced by previous atom removal, and this factor must be considered in any simulation.

Since the number of spaces is coincident with the number of bonds broken, a simulation taking the number of spaces for the criterion of removal would give the same morphologies as those obtained in the "bond breaking" simulation already discussed. But the aggressive ions are unlikely to be of the same size as the metal ions of the lattice (called "atoms" here to avoid confusion) and could well be hydrated. What-

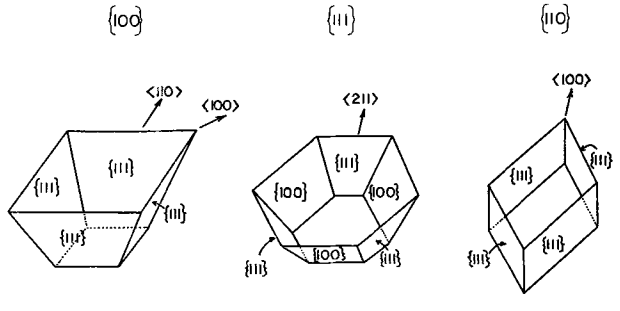

Fig. 8. Morphologies obtained by simulation using the "broken bond model" on {100}, {111}, and {110} surfaces.

ever form they may take, the configuration of those spaces adjacent to an atom will play an important role, if accessibility is the controlling factor. Hereafter the accessibility has been taken as the sole criterion of the ease of removal of atoms, since it successfully predicts the observed shapes. This necessitates considerable refinement to the rules of removal during simulation.

At low reaction rate.—At low reaction rates we assume time not to be important and that if there is a space large enough to accommodate the aggressive ions they will have time to reach that space. This leads to the following factors determining the accessibility:

(*A*) The total number of spaces adjacent to a given atom is the primary consideration (this factor corresponds to that used in the simple bonding simulation).

(*B*) There is a decrease in the contribution of a space if that space is shared among more than one adjacent atom.

(*C*) If a space is overlapped by an atom or atoms on an upper layer the accessibility of that space is reduced (In the simulation it is discounted completely for the atoms lying on the same layer as the space).

(*D*) The geometric configuration of a given number of spaces can determine the effective space they provide.

Factor (*B*) considers that when a space is shared among more than one atom the ability of the aggressive ion to remove these atoms is less than if it were adjacent to only a single atom. Factor (*C*) supposes the aggressive ions will have more difficulty in penetrating beneath an existing atom, and though this will render the lower layer space ineffective for the removal of atoms in that layer, the existence of that space does contribute to the removal of the upper (overlapping) atom. Factor (*D*) takes account of the effective volume of a set of adjacent spaces, and will be further elaborated when the individual simulations are described.

The factors noted above must be translated into "rules" which govern the progress of the simulation. We denote these rules for low reaction rates below:

L-1: Let N_1 be the number of spaces adjacent to an atom [factor (*A*)].

L-2: Let N_2 be the number of the adjacent spaces which lie on the same layer as the atom and are subject to overlap of atoms remaining in the upper layer [factor (*C*)].

L-3: Remove the atom with the largest $(N_1 - N_2)$. If more than one atom has the same $(N_1 - N_2)$ distinguish between them as follows:

L-4: Let n be the number of those $(N_1 - N_2)$ spaces which are shared with other atoms having $(N_1 - N_2)$ spaces [factor (*B*)].

L-5: Remove the atom with smallest n. If more than one atom has the same n, proceed as follows:

L-6: Let m be the number of those $(N_1 - N_2)$ spaces which have two of the other $(N_1 - N_2)$ spaces for the same atom adjacent to them [factor (*D*)].

L-7: Remove the atom with the smallest m.

These rules were applied to each of the three low-index fcc surfaces and if an appropriate morphology was not obtained, modifications were made to the rules consistent with the general factors (*B*), (*C*), (*D*) which are dependent on the specific surface structure and can be expected to result in different rules for different surfaces. It was found for all surfaces that only two layers need be considered in the simulation because second layer atoms are never in a position to possess spaces on the third layer, though the first layer atoms do possess spaces on the second layer. The morphology is determined by the first two layers.

The removal sequence for a pit in the {100} surface is summarized in Table I which also shows the instantaneous values of the various parameters used in applying the removal rules. In this case factor (*B*) (or the value of n) has no effect throughout the simulation. Until the sequence 7 the atoms with largest $(N_1 - N_2)$ have the same n, m values and are removed simultaneously. At sequence 8, atoms "8" and "9" have the same $(N_1 - N_2)$ and n values but different values of m. Thus, atoms "8" are removed in preference to atoms "9" by involving factor D. Figure 9 shows the development of this simulation and notes the removal boundaries after sequence 8 by full and dotted lines for the first and second layers respectively. The removal boundary for the third layer is indicated by the inner dotted line if the same simulation is applied to the third layer atoms. It is readily seen that the square shape is maintained as the pit expands. The simulation also predicts the development of {111} pit facets if successive layers are removed in a uniform manner. Such a macroscopic morphology appears to be coincident with the morphology obtained experimentally on {100} surfaces at low reaction rates.

Table I. Simulation 100-L

Removal sequence	Atoms Z(N_1,N_2,N_1-N_2,n,m) prior to removal
1	1 (arbitrary removal)
2	*2(1,0,1,1,0)*, 3(0,0,0,ND,ND)
3	*3(3,0,3,2,1)*, 4(2,1,1,ND,ND)
4	*4(3,0,3,3,3)*, 5(1,0,1,ND,ND)
5	*5(3,0,3,0,3)*, 6(2,0,2,ND,ND)
6	*6(3,0,3,2,1)*, 7(3,2,1,ND,ND)
7	*7(5,0,5,0,3)*, 8(2,0,2,ND,ND)
8	*8(3,0,3,2,1)*, 9(3,0,3,2,3), 9(2,1,1,ND,ND)

Atoms removed at each sequence are in italics.
Z is designation of atom in Fig. 10.
N_1,N_2,n,m are defined in text.
ND indicates that the value was not determined.

The same removal rules, "L," when applied to a {111} surface predict the triangular pit on the left hand side (a) of Fig. 10. The simulation sequence for this surface is summarized in Table II. (Atom designation for this surface has been modified for clarity.) In this case, factor (*D*) (the value of m) has no influence throughout the simulation, but factor (*B*) (value of n) is required at sequences 9, 10, and 12. This simulation suggests {111} pit facets and can be considered an effective simulation for the morphology approached by pits on {111} at low reaction rates, although no triangular pit has in fact been observed on the nickel surfaces in this work.

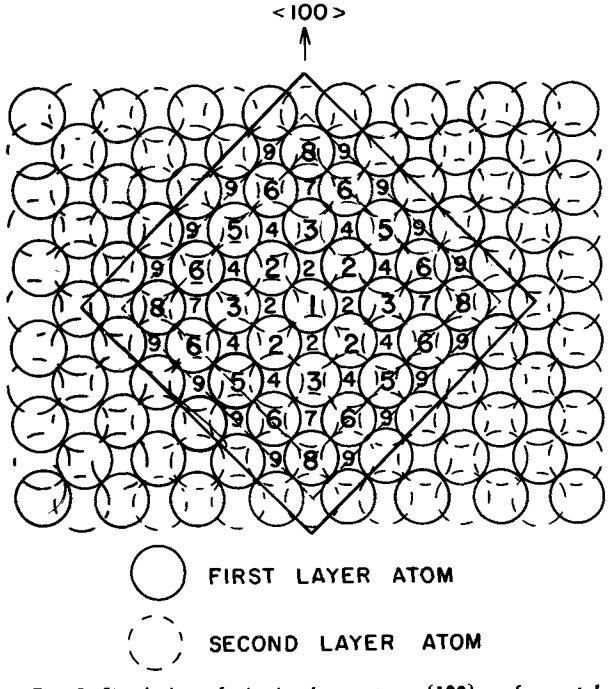

Fig. 9. Simulation of pit development on {100} surface at both low and high reaction rates. Removal boundaries are shown for the first, second, and third layers following removal sequence 8 (Tables I and IV).

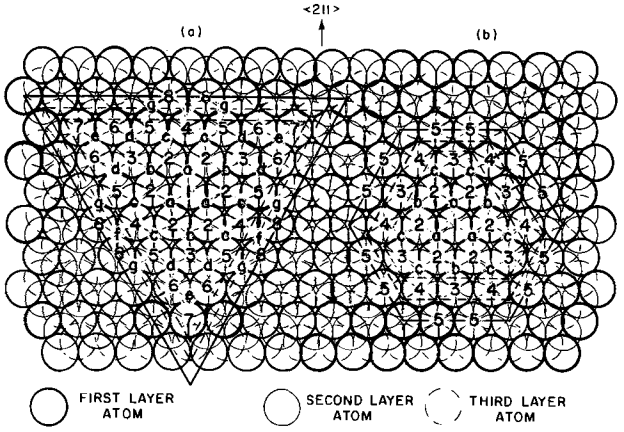

Fig. 10. Pit development on {111} surfaces at (a) low reaction rate with removal boundaries shown following removal sequence 12 (Table II); (b) at high reaction rate with removal boundaries shown following removal sequence 5 (Table V).

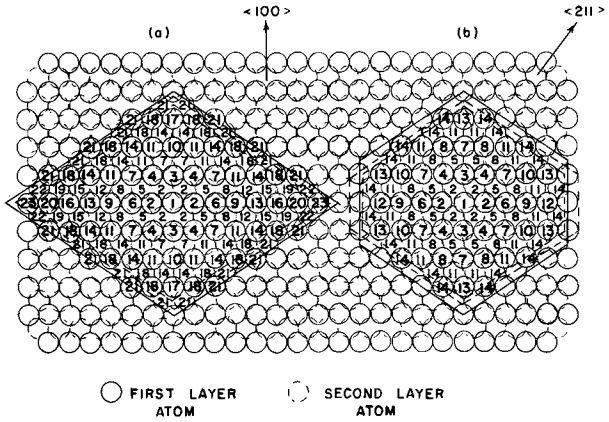

Fig. 11. Pit development on {110} surfaces for (a) low reaction rate, with removal boundaries shown following removal sequence 20 (Table III), and (b) for high reaction rate, and removal boundaries following removal sequence 14 (Table VI).

The results of the simulation of pitting on {110} surfaces at low reaction rates are summarized in Table III and the left hand side (a) of Fig. 11. In this case, in order to simulate the observed rhombohedral shape of the pits, it was found necessary to interpret rule L-5 in a less rigid manner than originally formulated. In order to simulate the observed shape it was necessary to make no distinction with respect to the accessibility of aggressive ions if $n = 1$ or 2. Therefore $n = 0$ was always taken in preference to any other value of n, but no distinction was made between $n = 1$ and $n = 2$. This modification appears at sequences 7, 10, 14, and 17 in Table III. The removal boundaries in the case of the simulated pits at low reaction rate in {110} surfaces predict pit facets to be composed of other {110} orientations.

The simulations at low reaction rate predict well the observed pits on {100} and {110} surfaces, and in the case of {111} indicate, at least, the tendency exhibited by pit shapes at low reaction rates. The prediction of the pit facets also seems accurate, subject to the complicating factor of ledges observed within the pits which will be discussed later.

At high reaction rate.—In order to simulate the pit morphologies observed at high reaction rate, it was necessary to modify the rules for atom removal which, in hindsight, result in the following amendments to the factors being considered.

At high reaction rates, it is reasonable to suppose that the accessibility of the aggressive ions to the spaces adjacent to lower layer atoms will be reduced more than that for the upper layer atoms. We have already assumed, even at low reaction rate, that the accessibility to lower layer atoms will always be less than that to the upper layer atoms [factor (C)], and it is now supposed that at high reaction rates an additional blocking effect will be provided by aggressive ions already adsorbed at the upper layer spaces. Consequently, we replace factor (C) with a new factor, namely,

(E) spaces occupied by adsorbed ions in upper layers will block spaces in lower layers, and consequently the latter will not be counted.

Table II. Simulation 111-L

Removal sequence	Atoms Z(N_1,N_2,N_1-N_2,n,m) prior to removal
1	*1* (arbitrary removal)
2	*2(1,0,1,0,0)*, *a(1,0,1,0,0)*, 3(0,0,0,ND,ND)
3	*b(4,0,4,2,4)*, 3(2,0,2,ND,ND)
4	*3(3,0,3,0,3)*, 4(2,0,2,ND,ND,) c(3,1,2,ND,ND)
5	*c(3,0,3,2,3)*, 4(2,0,2,ND,ND)
6	*4(4,0,4,0,4)*, 5(3,0,3,ND,ND)
7	*5(4,0,4,2,2)*, d(4,1,3,ND,ND)
8	*d(4,0,4,2,4)*, 6(2,0,2,ND,ND)
9	*f(3,0,3,0,3)*, 6(3,0,3,1,ND)
10	*6(3,0,3,2,3)*, 8(3,0,3,3,ND), g(4,2,2,ND,ND)
11	*e(4,0,4,0,4)*, 8(3,0,3,ND,ND)
12	*7(3,0,3,0,3)*, 8(3,0,3,ND,ND), g(4,1,3,1,ND)

Atoms removed at each sequence are in italics.
Z is designation of atom in Fig. 11(a); 1,2—first layer atoms; a,b—second layer atoms.
N_1,N_2,n,m are defined in text.
ND indicates that the value was not determined.

Table III. Simulation 110-L (fcc)

Removal sequence	Atoms Z(N_1,N_2,N_1-N_2,n,m) prior to removal
1	*1* (arbitrary removal)
2	*2(1,0,1,1,0)*, 3(0,0,0,ND,ND)
3	*3(2,0,2,0,0)*, 4(1,0,1,ND,ND), 5(2,1,1,ND,ND)
4	*4(2,0,2,1,0)*, 5(2,1,1,ND,ND)
5	*5(3,0,3,1,1)*, 6(1,0,1,ND,ND)
6	*6(3,0,3,0,1)*, 7(2,0,2,ND,ND)
7	*7(2,0,2,1,0)*, *7(2,0,2,2,0)*, 8(2,1,1,ND,ND)
8	*8(3,0,3,1,1)*, 9(1,0,1,ND,ND)
9	*9(3,0,3,0,1)*, 10(2,0,2,ND,ND)
10	*10(2,0,2,0,0)*, 11(1,0,1,ND,ND), 11(3,1,2,1,0,), 11(2,0,2,1,0)
11	*11(2,0,2,1,0)*, *11(3,1,2,1,0)*, 12(2,1,1,ND,ND)
12	*12(3,0,3,1,1)*, 13(1,0,1,ND,ND)
13	*13(3,0,3,0,1)*, 14(2,0,2,ND,ND), 14(3,1,2,ND,ND)
14	*14(2,0,2,2,0)*, *14(2,0,2,1,0)*, *14(3,1,2,1,0)*, 15(2,1,1,ND,ND)
15	*15(3,0,3,1,1)*, 16(1,0,1,ND,ND)
16	*16(3,0,3,0,1)*, 17(2,0,2,ND,ND)
17	*17(2,0,2,0,0)*, 18(1,0,1,ND,ND), 18(3,1,2,1,0), 18(2,0,2,1,0)
18	*18(2,0,2,1,0)*, *18(3,1,2,1,0)*, 19(2,1,1,ND,ND)
19	*19(3,0,3,1,1)*, 20(1,0,1,ND,ND)
20	*20(3,0,3,0,1)*, 21(2,0,2,ND,ND), 21(3,1,2,ND,ND)

Atoms removed at each sequence are in italics.
Z is designation of atom in Fig. 12(a).
N_1,N_2,n,m are defined in text.
ND indicates that the value was not determined.

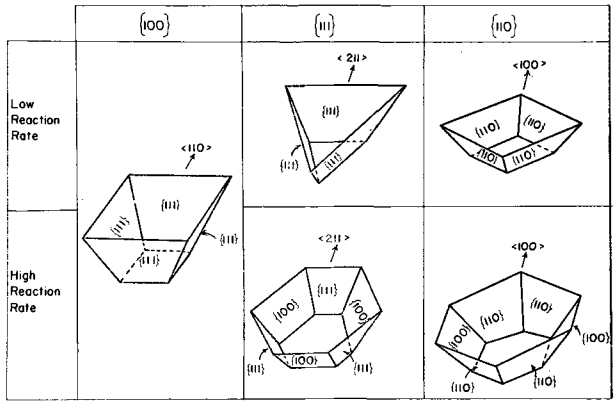

Fig. 12. Summary of pit morphologies obtained by simulation for {100}, {111}, and {110} fcc surfaces at low and high reaction rates. All simulations assume uniform deepening of a pit until it is arrested and a planar base is formed.

Also, at high reaction rates factor (D) is ignored on the assumption that small changes in the effective volume of an array of spaces are insignificant in this case.

Only factors (A), (B), and (E) are therefore considered relevant at high reaction rates and permit the following general rules for removal during the simulations:

H-1: Let N_1 be the number of spaces adjacent to an atom [factor (A)].

H-2: Let N_3 be the number of the adjacent spaces which are overlapped by a space or spaces in an upper layer [factor (E)].

H-3: Remove the atom with the largest ($N_1 - N_3$). If more than one atom has the same ($N_1 - N_3$), proceed as follows:

H-4: Let n be the number of the ($N_1 - N_3$) spaces which are shared amongst other atoms with ($N_1 - N_3$) spaces [factor (B)].

H-5: Remove the atom with the smallest n.

In applying these rules, it was realized that the factor (E) must be interpreted a little differently for less close-packed surfaces ({100} and {110}). In rules H-2 and H-3 spaces overlapped by upper layer spaces are discounted completely. But in the less close-packed surfaces, those spaces are never completely overlapped and could contribute to the ease of removing adjacent atoms on the upper layer. With this modification the correspondence between the morphologies obtained by simulation and in experiment was attained.

Simulations for the three low-index surfaces at high reaction rate are shown in Fig. 9 and the right hand sides (b) of Fig. 10 and 11. In {100} and {110} surfaces, the second layer spaces overlapped by the first layer spaces were considered to contribute to the ease of removing the adjacent first layer atoms, as described above, and so N_3 was always taken as zero for the first layer atoms. For {111} these spaces were completely discounted according to rules H-2 and H-3. Factor (B) was again interpreted differently for {110} as at low reaction rate.

It is seen that the increased reaction rate produces no change in the morphology on {100} surfaces but results in different types of six-sided pits in the other two surfaces, as observed experimentally (Fig. 2 and 4).

Figure 12 summarizes the simulated shapes for the three low-index surfaces at both low and high reaction rates.

Simulation for metal-oxygen bonding stronger than metal-metal bonding.—In all the simulations noted above no account has been taken of the possible effect of the bonding of the oxygen, present in the passivating film, with metal atoms of the first layer. It is possible that such bonding could be sufficiently strong to change the priorities of bond breaking under the influence of aggressive ions. Consequently, additional simulations were carried out in which the rules were modified such that atoms would always be removed from the second layer in preference to the first provided they had a finite number of spaces which are not discounted due to the overlap by any upper layer atoms. First layer atoms were only removed when there was no such second layer atoms available for removal.

The pit on the left hand side (a) of Fig. 13 shows the result of the application of these rules on {110}. It is seen that they develop what is almost a one dimensional pit which increases in length but not in width. But atoms such as 3′ in (a) could reasonably be expected to be removed in due course, although atoms 1,3,5,7---- always keep ahead of them. If it is supposed that the atom 3′ is removed after 6 and before 7, then the resulting shape would be as shown in the pit situated on the right hand side (b) of Fig. 13. One concludes, therefore, that rectangular pits will be developed on {110} surfaces subject to these conditions.

Using the same modified rules on {110} and {111} surfaces did not change the simulations from those obtained earlier. This result may be significant in that the anomalous samples only exhibited different pits on the {110} surfaces and they were, in fact, rectangular.

Application to Body-Centered Cubic Metals

In order to test the aggressive ion accessibility criterion for other crystal structures, the simulation method was used to predict pit morphologies on passivated low-index surfaces of body-centered cubic crystals, although few detailed studies of corrosion pit morphologies on body-centered cubic crystals have been reported.

Janik-Czachor and Szklarska-Smialowska (16) investigated the morphologies of corrosion pits on Fe-16% Cr formed under galvanostatic conditions. On all surfaces studied the pits exhibited regular polyhedral shapes and contained facets composed of {110} and {100} planes.

Taoka *et al.* (17) report similar shapes for corrosion pits produced chemically on the surfaces of Fe-3% Si. The existence of {110} and {100} facets on similar pits produced by the same etch procedure in Ferrovac E iron has also been confirmed by Spink and Ives (18). There is good reason to suppose that the surface condition existing during these chemical etch treatments involves the presence and breakdown of surface films, and the results can presumably be included with those in which the passive state is induced electrochemically.

A summary of the pit morphologies observed experimentally (16-18) in body-centered cubic metals is presented schematically in Fig. 14.

In accord with the experience with fcc surfaces, the accessibility factors (A), (B), (C), and (D) were considered of major importance at low reaction rates (*i.e.* low anodic current). At high reaction rates (or high anodic currents) the factor (E) was adopted in preference to factors (C) and (D).

In applying the rules for removal formulated previously, it was found necessary in bcc to consider both first and second nearest neighbor spaces for factor (A), whereas in fcc only nearest neighbors needed to be

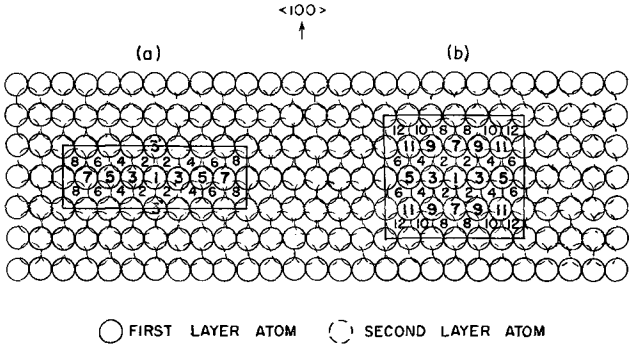

Fig. 13. Consequences of simulation on {110} surface assuming metal-oxygen bond strength to be greater than metal-metal bond strength.

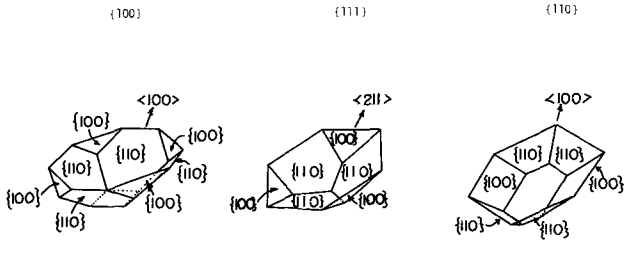

Fig. 14. Summary of pit morphologies in Fe, Fe-16% Cr, and Fe-3% Si, for {100}, {111}, and {110} surfaces, as reported in the literature.

considered. This makes factor (D) unimportant for bcc crystals.

The rules which govern the progress of the simulation for low reaction rate can be stated as follows:

L-1: Let N_1 be the number of the nearest neighbor spaces adjacent to an atom and N_2 be the number of the second nearest neighbor spaces adjacent to that atom [factor (A)].

L-2: Let $N_1°$ be the number of nearest neighbor spaces on the same layer as the atom which are subject to overlap of an atom or atoms remaining in an upper layer, and let $N_2°$ be the number of second nearest neighbor spaces in the same layer which are subject to overlap from above [factor (C)].

L-3: Remove the atom with the largest $(N_1 + N_2 - N_1° - N_2°) \equiv M_L$ (effective space). If more than one atom has the same M_L, proceed as follows:

L-4: Remove the atom with the largest $(N_1 - N_1°)$ (effective nearest neighbor space). If more than one atom has the same $(N_1 - N_1°)$, proceed as follows:

L-5: Let n be the number of the M_L spaces which are shared with other atoms having M_L spaces [factor (B)].

L-6: Remove the atom with the smallest n. L-4 distinguishes between the contribution of first and second nearest neighbor spaces.

At high reaction rates the specific rules for removal during simulation incorporate factors (A), (B), and (E), and are summarized as follows:

H-1: Let N_1 be the number of nearest neighbor spaces adjacent to an atom and N_2 be the number of second nearest neighbor spaces [factor (A)].

H-2: Let N_1^s be the number of nearest neighbor spaces on the same layer as the atom which are subject to overlap by a space or spaces existing on a layer above, and let N_2^s be the equivalent parameter for the second nearest neighbor spaces [factor (E)].

H-3: Remove the atom with the largest $(N_1 + N_2 - N_1^s - N_2^s) \equiv M_H$ (effective space). If more than one atom has the same M_H, proceed as follows:

H-4: Remove the atom with largest $(N_1 - N_1^s)$ (effective nearest neighbor space). If more than one atom has the same $(N_1 - N_1^s)$, proceed as follows:

H-5: Let n be the number of those M_H spaces which are shared with any of the other atoms having M_H spaces [factor (B)].

H-6: Remove the atom with the smallest n.

The above working rules permit the simulation of pit formation by atom-by-atom removal, and as an example the sequence for {110} at low reaction rate is summarized in Table IV. The individual simulations for low index bcc surfaces are shown in Fig. 15-17. The resulting pit morphologies are summarized in Fig. 18.

The agreement between the simulations (Fig. 18) and the experimental observations (Fig. 14) is good. The observed morphologies are predicted for {111} and {110} surfaces, and a combination of the low and high reaction rate is necessary to describe the {110} observations.

Table IV. Simulation 110-L (bcc)

Removal sequence	Atoms Z ($N_1 + N_2, N_1° + N_2°, M_L, N_1 - N_1°, n$) prior to removal
1	*1* (arbitrary)
2	*2(1,0,1,1,1)*, 3(1,0,1,0,ND)
3	*3(4,0,4,3,1)*, 4(5,2,3,ND,ND)
4	*4(5,0,5,5,3)*, 5(2,0,2,ND,ND)
5	*5(3,0,3,3,2)*, *5(4,1,3,3,2)*, 6(2,1,1,ND,ND)
6	*6(4,1,3,3,3)*, 7(3,0,3,2,ND)
7	*7(4,0,4,3,1)*, 8(3,0,3,ND,ND)
8	*8(4,0,4,3,1)*, 9(4,2,2,ND,ND)
9	*9(6,0,6,3,0)*, 10(3,0,3,ND,ND)
10	*10(4,0,4,3,0)*, 11(3,0,3,ND,ND)

Atoms removed at each sequence are in italics.
Z is designation of atom in Fig. 17(a).
$N_1, N_2, N_1°, N_2°, M_L, n$ are defined in text.
ND indicates that the value was not determined.

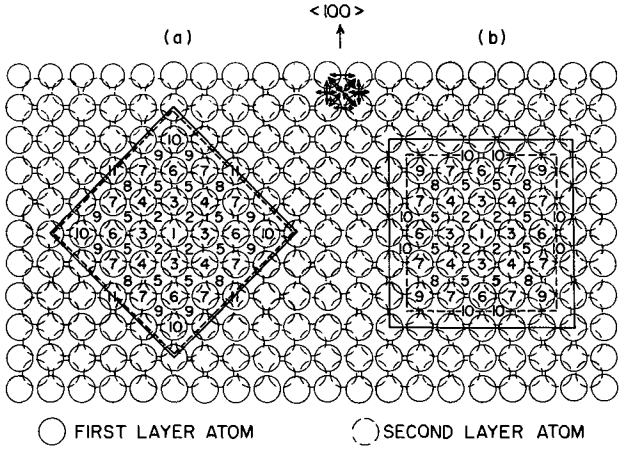

Fig. 15. The simulation of pits on a {100} bcc surface, for (a) low reaction rate (rules L) and (b) high reaction rate (rules H). Nearest neighbor and second nearest neighbor atom relationships are shown at upper center by double and single arrows, respectively, joining atoms.

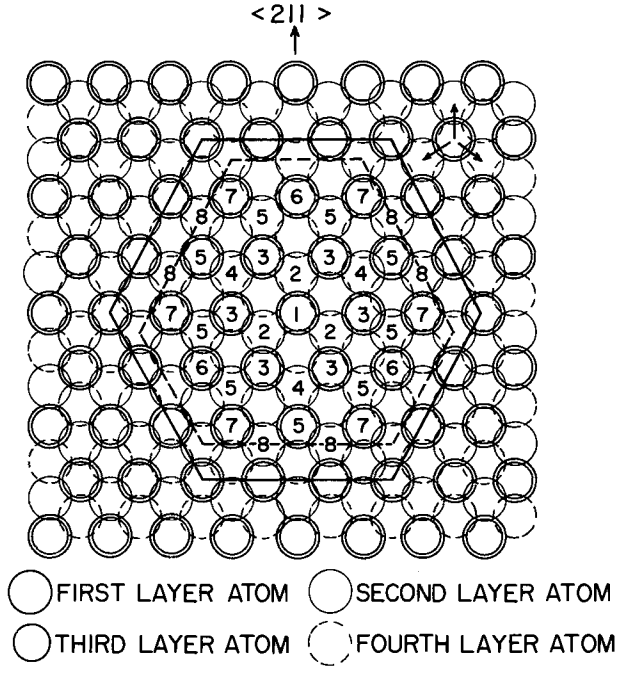

Fig. 16. Pit simulation on a {111} bcc surface for both low and high reaction rates.

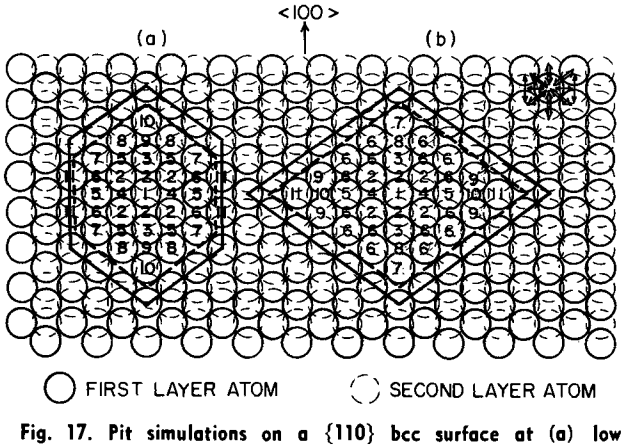

Fig. 17. Pit simulations on a {110} bcc surface at (a) low reaction rate (rules L) and (b) high reaction rate (rules H).

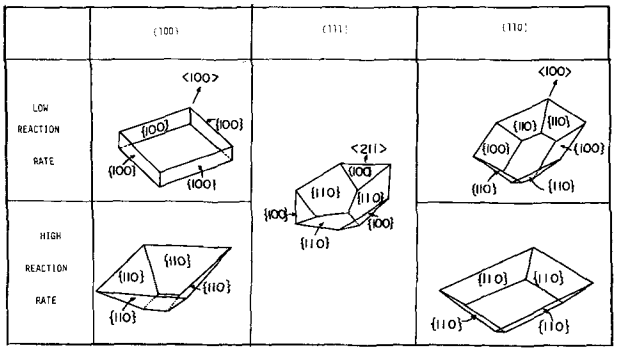

Fig. 18. Summary of pit morphologies predicted by the simulations for {100}, {111}, and {110} bcc surfaces at low and high reaction rates.

These simulations can also be related to the changes with time under galvanostatic conditions reported by Janik-Czachor and Szklarska-Smialowska (16) for Fe-16% Cr. They reported changes in pit morphology with time for pits on {100} and {110} surfaces. In particular, pits on {100} changed in superficial shape from square to octagonal and on {110} the shape of the base of pits changed from rhombohedral to hexagonal. Since the size and number of pits were observed to increase with time, the current density in a given pit must be reduced with time under galvanostatic control. Consequently the reaction rate in the pit is reduced. The morphological changes predicted by the simulations on {100} and {110} in making the transition from high to low reaction rate are therefore consistent with the experimental observations. No changes are either predicted or reported for {111} surfaces.

Discussion

A review of the factors which were necessary in order for the simulations to approximate the experimentally observed pitting morphologies suggests that the important consideration determining atom removal during pit development is the configuration of the spaces adjacent to each atom. When allowance is made for blockage of spaces and the sharing of spaces between equally unbonded atoms, we have seen that the simulations developed the appropriate morphologies if atoms with more adjacent space were removed in preference to those with less. Furthermore, those rules which required modification from one crystallographic surface to another could be related to the differences in the atom-atom configuration in these surfaces.

The realization that the simple "bond-breaking" model does not develop correct morphologies (nor would the equivalent "adjacent space" model) and the success of the simulations which were achieved suggests that the important factor is the accessibility of the aggressive ions in placing themselves close to metal atoms within the pit in order to remove them. This model is consistent with the suggestions of Kolotyrkin (14, 15) and is also supported by independent observations that during pitting corrosion the interior of pits are in the active state, while the remainder of the surface is passivated (19) and the realization that the susceptibility for pitting of nickel single crystal surfaces is directly proportional to the reactivity of that surface during active dissolution (13).

The necessity for introducing the blocking effect of already adsorbed aggressive ions on upper layers when pitting occurs at high reaction rates also substantiates this model. It is difficult to envisage a process involving only the metal substrate that would explain the morphological dependence on reaction rate.

The apparent success of the simulation in which second layer atom removal takes preference over first layer removal in reproducing the pit morphologies observed on the anomalous samples suggests that the effect of metal-oxygen bonding could certainly modify the aggressive ion capability of removing atoms. If these anomalous crystals were more defective (for example, have high impurity content) it is possible that the dissolution rate of the metal substrate would be increased, accentuating the effect of oxygen in bonding the surface layer. In addition, the {110} surface on which pits of different morphology were observed both experimentally and by simulation is far more readily passivated than are the {100} and {111} surfaces (13).

Much of the complication involving the description of the simulation method employed in this study has been due to the need for an effective means of describing the simulation process in written form. It is much simpler to appreciate the relative priorities for atom removal when the simulation is carried out by hand using models of spheres with the appropriate packing and surface orientation. Such a procedure leads the experimenter with no doubt as to the conclusions quoted above.

The prediction of the crystallographic orientation of the facets occurring within the corrosion pits has also been provided by the simulation. Of course, the development of macroscopic facets of these orientations supposes that the third and successive atom layers are removed at the same rate as the first two layers but slightly behind them. However, in the real situation when many atom layers are removed to form a macroscopic pit, delays in the initiation of layer removal can be expected due, for example, to the accumulation of corrosion product in the pit, resulting in a random variation of removal boundary spacing. The subsequent development of the removal boundaries may then be subject to interactions leading to combinations of monatomic steps which coalesce to form macroscopic ledges, in a manner similar to that proposed by Gilman (20) and Ramachandran and Ives (21) for etch pits on lithium fluoride. In this case the risers of such macroscopic ledges will have the crystallographic orientation already suggested by the simulation, and the macroscopic orientation of the pit sides will differ from the crystallographic orientation predicted by an amount dependent on the density of ledges.

Both the simulations for fcc and for bcc surfaces suggest the aggressive ion accessibility criterion to be relevant for determining dissolution morphologies within corrosion pits. A mechanism is thereby provided to explain why various crystallographic facets are stabilized under various corrosion conditions—a fact stated many times before but only rationalized vaguely in terms of the relative close-packing of the various crystal orientations. From the studies reported here it is possible to appreciate how different crystallographic surfaces are stabilized under different conditions and that their degree of close-packing is not the only factor to be considered.

Acknowledgment

This research was supported by the Defence Research Board of Canada.

Manuscript submitted Sept. 9, 1970; revised manuscript received *ca.* May 10, 1971.

Any discussion of this paper will appear in a Discussion Section to be published in the June 1972 JOURNAL.

REFERENCES

1. F. C. Frank, *Discussions Faraday Soc.*, **5**, 48, 67 (1949).
2. N. Cabrera and M. M. Levine, *Phil. Mag.*, **1**, 450 (1956).
3. P. J. Holmes, *Acta Met.*, **7**, 203 (1959).
4. U. Bertocci, L. P. Hulett, and L. H. Jenkins, *This Journal*, **110**, 1190 (1963).
5. B. Sostak and A. A. Urosovkaya, *Kristallografiya*, **4**, 913 (1959).
6. M. B. Ives and D. D. McAusland, *Surface Sci.*, **12**, 189 (1968).

7. B. W. Batterman, *J. Appl. Phys.*, **28**, 1236 (1957).
8. B. A. Irving, *ibid.*, **31**, 109 (1960).
9. F. C. Frank, "Growth and Perfection of Crystals," p. 411, John Wiley & Sons, Inc., New York (1958).
10. F. C. Frank and M. B. Ives, *J. Appl. Phys.*, **31**, 1996 (1960).
11. I. M. Novoselskii, "Crystallization Processes," Sirota *et al.*, Editors, p. 79 (English Translation) Consultants Bureau, New York (1966).
12. I. Garz, H. Worch, and W. Schatt, *Corrosion Sci.*, **9**, 71 (1969).
13. T. Tokuda and M. B. Ives, *ibid.*, **11**, 297 (1971).
14. Y. M. Kolotyrkin, *This Journal*, **108**, 209 (1961).
15. G. M. Florianovich, L. A. Sakolova, and Y. M. Kolotyrkin. *Electrochim. Acta*, **12**, 879 (1967).
16. M. Janik-Czachor and Z. Szklarska-Smialowska, *Corrosion Sci.*, **8**, 215 (1968).
17. T. Taoka, E. Furabayashi, and S. Takeuchi, *Jap. J. Appl. Phys.*, **4**, 120 (1965).
18. G. M. Spink and M. B. Ives, *J. Appl. Phys.*, **42**, 511 (1971).
19. W. Schwenk, *Korrosion*, **13**, 20 (1960).
20. J. J. Gilman, *J. Appl. Phys.*, **31**, 936 (1960).
21. T. R. Ramachandran and M. B. Ives, *ibid.*, **38**, 3675 (1967).

The Effect of Water on Passivity and Pitting of Titanium in Solutions of Methanol and Hydrogen Chloride

F. Mansfeld*

North American Rockwell Science Center, Thousand Oaks, California 91360

ABSTRACT

The effect of water on passivity and breakdown of passivity by pitting of titanium in solutions of methanol and hydrogen chloride has been studied. In anhydrous solutions no passivation occurs. Small additions of water lead to passivation, the region of passivity being limited by the pitting potential to noble values. The critical pitting potential becomes more noble with increasing water content of the electrolyte. Values obtained under steady-state conditions (V_c) seem to level off at higher water contents, while values obtained under nonstationary conditions (V_c') increase linearly with water content. No passivation occurs when 12*N* aqueous HCl was added to pure methanol to produce an aqueous solution of CH_3OH + 0.01*N* HCl, but passivation was observed when an aqueous solution of CH_3OH + 1.0*N* HCl was produced. This is explained by the higher water content of the latter solution, which is sufficient to passivate the surface at potentials below the pitting potential.

In studies of passivity or breakdown of passivity through pitting, the effect of the electrolyte composition has been studied extensively. Since most of these studies have been carried out in aqueous solutions, the effect of water could not be investigated, although there is a general accord that the water molecule plays an important role in passivity of the transition metals and alloys in acid solutions.

One of the few studies of passivity in nonaqueous solutions was carried out by Kolotyrkin and Kossyi (1) who studied the effect of water on the anodic behavior of chromium in methanol solutions of hydrogen chloride. Potentiostatic polarization curves were measured in solutions of methanol which had been saturated with dry gaseous hydrogen chloride, then diluted with methanol to which certain amounts of H_2O were added. It was found that active anodic dissolution in CH_3OH-1*N* HCl-H_2O proceeds without participation of H_2O molecules, while increasing amounts of H_2O lead to a more and more extended region of passivity, which was not observed in the absence of water. The passive film was destroyed at higher anodic potentials by pitting and it was found that the critical potential for pitting was a linear function of the water content of the electrolyte at a constant concentration of HCl. Tsinman *et al.* (2) studied the anodic behavior of Ti in water-methanol solutions containing chloride ions and found that at constant HCl concentration pitting occurred at low H_2O concentration, and not at higher H_2O concentrations. Pitting was also observed during the anodic polarization of titanium in methanol solutions of NaBr (3). Tsinman *et al.* (4) studied the influence of water and the nature of the electrolyte on the anodic activation of a Ti alloy (VT-1) in methanol solutions by a galvanostatic method. They found that the critical pitting potential did not depend on the acidity of the solution, which is in contrast to what was found by Kolotyrkin and Kossyi (1). They also found that the pitting potential became more noble with increasing water content and varied in the series Cl^-, $Br^- < I^- << ClO_4^- << NO_3^-$. Meshcheryakova *et al.* (5) studied the behavior of titanium (VT-1) in ethanol-water solutions of hydrochloric acid. They found that titanium is not passive in anhydrous 20% HCl-ethanol solutions and corrodes with a rate of about 5 mm per year (about 630 mdd). The corrosion rate dropped to half of this value when 1% water was added and became rather small when 6-32% water was added (0.01 mm per year or 1.2 mdd). Corrosion was uniform except in solutions containing 4-6% H_2O where pitting occurred after 300 hr. The pitting potential was found to be proportional to the logarithm of the water concentration.

Levy and Seitz (6) also found that the pitting potential of a Ti-8Al-1Mo-1V alloy in CH_3OH + 0.4% HCl + H_2O became more noble with increasing water content. From their data (linear plot of potential *vs.* current density) no information about the effect of water on the active dissolution of this alloy can be obtained.

Schwabe and Schmidt (7) and Schmidt (8) studied the effect of water content on the anodic behavior of Ni in 2*N* H_2SO_4-dimethyl formamide-water and 2*N* H_2SO_4-acetonitrile-water solutions. It was found that passivation occurred only in the presence of water, the critical concentration of H_2O being $\approx$ 0.1% in dimethyl formamide and $\approx$ 3% in acetonitrile solutions.

Since only a few data concerning the effect of H_2O on passivity of Ti in CH_3OH-HCl solutions exist (2, 4, 6) and this effect is also of practical importance in stress corrosion cracking of Ti alloys (9), a sys-

* Electrochemical Society Active Member.

Key words: anhydrous solutions, aqueous solutions, critical pitting potential, corrosion rates.

tematic study of the anodic behavior of Ti in CH_3OH-HCl-H_2O solutions has been carried out.

Experimental Procedures

Anhydrous solutions of CH_3OH-HCl were prepared by saturating methyl alcohol (nanograde, Mallinckrodt) with HCl gas. These solutions were then diluted by adding more methyl alcohol to give a certain concentration of HCl which was measured by titration. Aqueous solutions of CH_3OH-HCl were prepared by adding water to anhydrous solutions of CH_3OH-HCl or by adding certain amounts of concentrated hydrochloric acid to pure methanol. Commercially pure Ti (Ti-75A containing about 4000 ppm total interstitial impurities) was machined to a cylindrical electrode (about 2 cm^2 geometric surface) and connected to a holder so that only the electrode, Teflon, and glass were in contact with the solution. The electrode was degreased in boiling benzene at 80°C for 5 min, then etched in a solution of 40% HNO_3-2% HF-H_2O for 1 min, washed thoroughly in pure methanol, and then immediately immersed in the test solution, which had been deaerated with argon for 1 hr. The reference electrode was an aqueous saturated calomel electrode (SCE), except for solutions containing 0.01*N* HCl, where a reversible hydrogen electrode was used in a separate compartment and the same solution. All potentials refer to SCE. After the rest potential had become constant the potential was increased in steps of 10 mV/min using a Wenking potentiostat. At higher potentials when no pitting was observed, the rate of potential change was 50 mV/5 min. Since methanol solutions of hydrogen chloride have high electrical conductivity due to the anomalously high mobility of the methoxonium ion $CH_3OH_2^+$, no major experimental problems concerning iR-drops were encountered.

Results

Figure 1 shows potentiostatic polarization curves for Ti-75A in anhydrous CH_3OH + xN HCl for x = 1.0, 0.1, or 0.01.[1] The effect of HCl concentration is clearly seen. The curves are shifted parallel in the noble direction with decreasing HCl concentration, and no active-passive transition is observed up to the highest currents studied. For comparison, Fig. 2 shows polarization curves in methanol to which sufficient concentrated HCl was added to give aqueous solutions of CH_3OH + xN HCl for x = 1.0, 0.1, or 0.01. Again, the rest potential has the most noble value for the lowest HCl concentration, but surprisingly, passivity is observed in the solution with the highest HCl concentration (1.0*N*) but not for the solution with the lowest HCl concentration (0.01*N*). For the solution which contains 0.1*N* HCl, the region of passivity is small due to pitting, the occurrence of which was confirmed by microscopical observation. In these aqueous HCl-CH_3OH solutions the H_2O content increases with increase of the HCl content, because of the water content of concentrated HCl (37% HCl).

[1] Due to the water content of pure methanol (≈0.02%) these "anhydrous solutions" contain a small amount of H_2O.

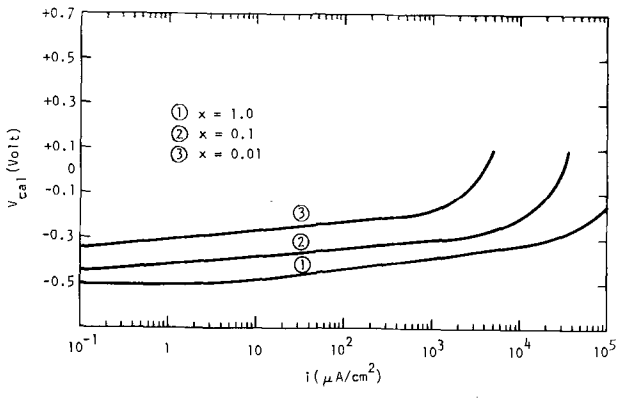

Fig. 1. Potentiostatic anodic polarization curves for Ti 75A in solutions of CH_3OH + xN HCl anhydrous (x = 1.0, 0.1, or 0.01).

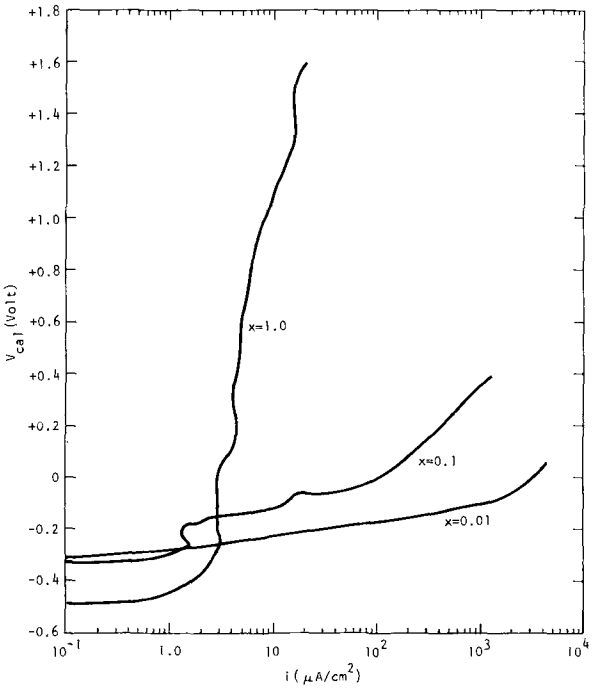

Fig. 2. Potentiostatic anodic polarization curves for Ti 75A in solutions of CH_3OH + xN HCl aqueous (x = 1.0, 0.1, or 0.01).

In the experiments of Fig. 3 increasing amounts of H_2O were added to a solution of anhydrous 1*N* HCl-CH_3OH. In the absence of H_2O no active-passive transition is observed; addition of 0.63% H_2O shifts the polarization curve in the noble direction, a small region of passivity is observed limited by breakdown of passivity through pitting. With increase in H_2O-content the region of passivity is extended, the passive C.D. being about 1.3 μA/cm^2. The passive region is limited by the critical potential for pitting V_c' which becomes more noble as the H_2O content increases. After each run the specimen was investigated under a microscope to make sure that pitting has indeed occurred. At higher water contents, establishment of V_c' from polarization curves was very difficult. In aqueous 1*N* HCl-CH_3OH (about 6.3% H_2O) no precise value of V_c' could be established. For this reason, the following two different experiments were carried out to determine more precisely the steady-state value, V_c, of the

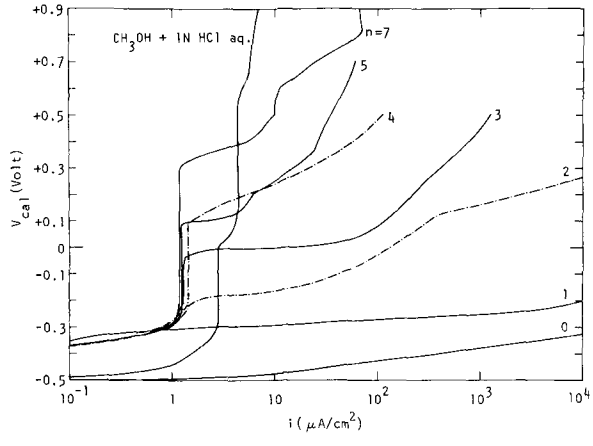

Fig. 3. Potentiostatic anodic polarization curves for Ti 75A in solutions of CH_3OH + 1*N* HCl anhydrous + n × 0.63% H_2O (n = 0-7).

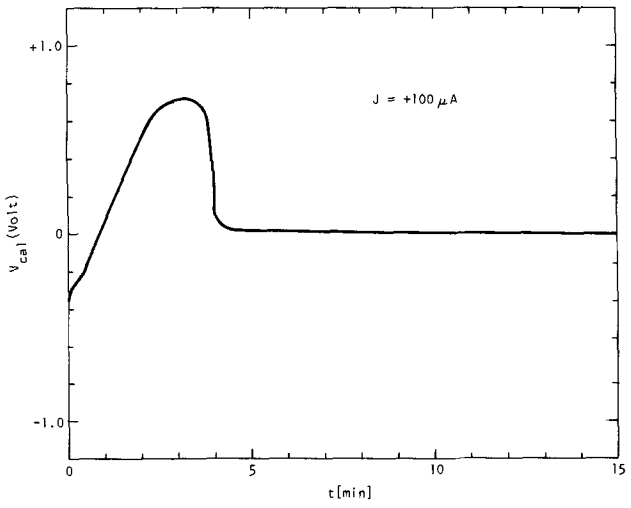

Fig. 4. Changes of potential at a constant anodic current of 100 μA in CH_3OH + 1*N* HCl anhydrous + 4.4% H_2O.

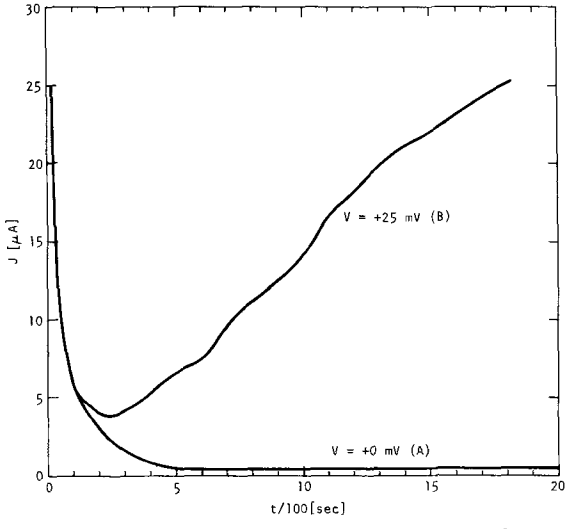

Fig. 5. Changes of current at constant potential in CH_3OH + 1*N* HCl anhydrous + 4.4% H_2O.

critical pitting potential.[2] In the first experiment, a constant C.D. of about 50 μA/cm^2 was applied to the test electrode and the potential *vs.* time curve recorded. This technique has recently been used by Tsinman *et al.* (4). Figure 4 shows the results for CH_3OH + 1*N* HCl + 4.4% H_2O. After application of the constant C.D. the potential increased slowly to more noble values. When the maximum value was reached, small fluctuations of the potential, which were probably due to formation of the first pits, were observed. The potential then decayed fast to a constant value, which has been called the activation potential by Tsinman (4). Microscopic observation of the electrode after the test showed occurrence of a number of pits. In the next experiment this constant potential was applied to a fresh electrode immediately after immersion into a fresh solution and the current *vs.* time curve recorded. If the potentiostatically applied potential was below the critical pitting potential V_c, the current decayed continuously due to passivation of the surface and no pits were observed (curve A, Fig. 5). The potential was then increased by 15 or 25 mV. If V_c was exceeded, the current increased after an initial decrease and pitting was observed (curve B). Critical pitting potentials estimated from polarization curves

[2] The notation by Leckie and Uhlig (10) is used here to distinguish between short-time (V_c') and steady-state (V_c) critical pitting potentials.

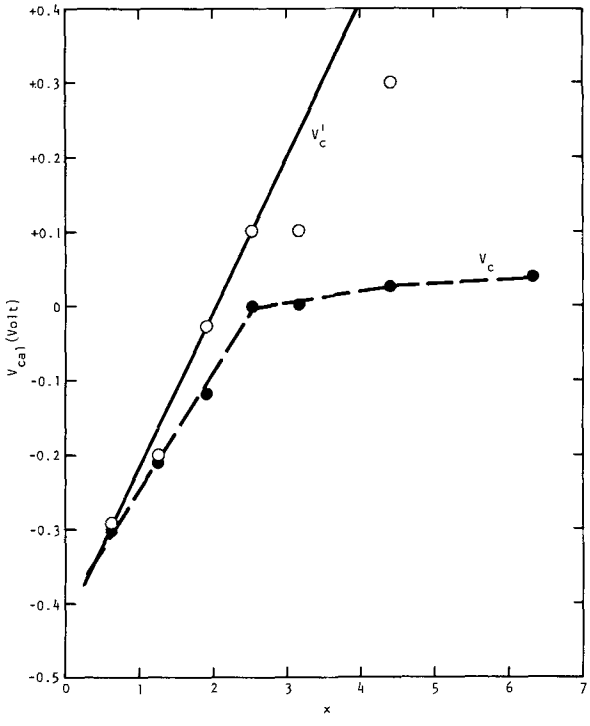

Fig. 6. Dependence of pitting potential on water content of CH_3OH + 1*N* HCl anhydrous + *x*% H_2O.

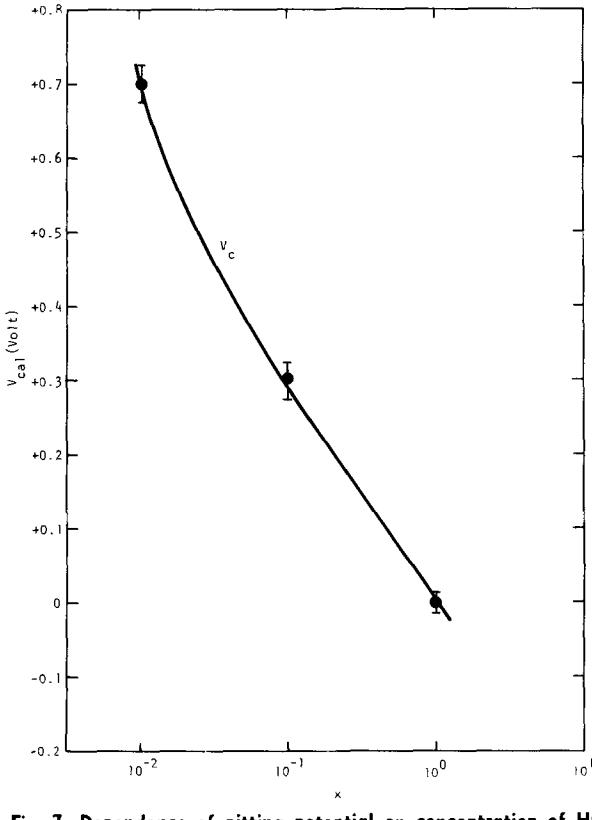

Fig. 7. Dependence of pitting potential on concentration of HCl anhydrous in solutions of CH_3OH + 3.15% H_2O + *x*N HCl (*x* = 1.0, 0.1, or 0.01).

(V_c') and measured more precisely at a constant potential (V_c) are plotted in Fig. 6. While V_c' seems to increase linearly with water content, values for V_c seem to level off after a H_2O content of 2.5% H_2O. Values of V_c in solutions of CH_3OH + 3.15% H_2O + *x*N HCl (x = 0.01, 0.1, 1.0) are shown in Fig. 7, which

shows an increase of about 0.3V when [HCl] is decreased by a factor of 10.

Discussion

The results obtained in this investigation have shown clearly that passivation of Ti cannot occur in CH_3OH-HCl in the absence of water. In "anhydrous" solutions anodic dissolution occurs following Tafel behavior. The polarization curves are shifted parallel in the noble direction as the HCl concentration decreases. Addition of water to the anhydrous electrolyte leads to passivation at a concentration as low as 0.6% water although the extent of the passive region is very small. This results from the fact that the critical pitting potential V_c' is only slightly noble to the corrosion (and passivation) potential. It has to be considered at this point that the surface concentration of water might be different from that in the bulk due to double-layer effects and due to solvation of dissolved metal ions. The latter effect would decrease the amount of water available for passivation. No information is available concerning double-layer effects in the solutions studied. Increasing additions of water lead to a broader region of passivity in which the current is independent of potential. At a certain potential (the critical pitting potential) chloride ions are adsorbed strongly enough to displace the adsorbed water molecules and penetrate the passive film. As more water is added to the electrolyte the passivating species (presumably the oxygen of water) is more strongly adsorbed and V_c is shifted to more positive values. When a sufficient amount of water is added to produce a sufficient concentration of the passivating species at the surface of the metal, the critical pitting potential increases only very slightly. This is seen better in experiments at constant current or potential (Fig. 4 and 5). At a sufficiently high, constant water content, the pitting potential becomes more noble as the chloride ion concentration decreases, as observed for many metals in aqueous electrolytes.

These findings also explain the initially surprising results of Fig. 2, where the electrode was polarized in the anodic direction in solutions prepared from pure methanol and concentrated hydrochloric acid containing a constant ratio of water to chloride ion. In the solution of CH_3OH + 0.01*N* HCl the water content is too small to allow formation of a passive film. In the solution containing 0.1*N* HCl, enough water is present in the bulk to passivate the surface. The passive film is, however, not very stable and therefore penetrated by chloride ions at a relatively low potential. In CH_3OH + 1*N* HCl, enough water is present to protect the surface from pitting up to rather noble values. The film becomes more and more stable when the electrode is polarized slowly in the noble direction. A precise value of V_c' is then difficult to detect. In the experiments of Fig. 4 and 5 an active electrode was used for determination of the pitting potential, values of V_c are therefore considerably more active than those of V_c'. This might also apply to the results of Kolotyrkin and Kossyi (1) who found a linear relationship between the pitting potential and water content from potentiodynamic curves in aqueous CH_3OH-HCl solutions.

The present results might also explain the observation of Meshcheryakova *et al.* (5) that pitting occurs only in a narrow concentration range of H_2O additions (4-6% H_2O) to ethanol-hydrochloric acid solutions. Presumably below 4% H_2O titanium did not become passive and no pitting would occur while above 6% H_2O the passive film was stable enough so that the critical pitting potential as determined by nonstationary methods was outside the range of potentials studied. The effect of water addition on corrosion rates observed by Meshcheryakova *et al.* (5) was also found in the present work where titanium specimens corroded at a rate of 3.1 mdd in anhydrous CH_3OH + 0.01*N* HCl as determined by weight loss after eight days, but only at a rate of 0.12 mdd when 0.3% H_2O was added to the solution.

The fact that the surface of titanium is free of a passivating film in anhydrous solutions of CH_3OH-HCl but covered with a passivating film in aqueous solutions of CH_3OH-HCl is interesting insofar as it will allow ellipsometric investigations and comparison of film-free and filmed surfaces. It is also interesting for studies of the mechanism of stress corrosion cracking (SCC) of Ti and Ti alloys, since SCC in anhydrous solutions, where the walls of a crack and crack tip are not covered by a passive film and are therefore active, can be compared with SCC in solution containing enough water for passivation. Under these latter conditions a potential difference is expected between the passive walls of the crack and the crack tip leading to the establishment of a galvanic couple. Preliminary results (11, 12) concerning SCC of Ti 75A in anhydrous and aqueous CH_3OH-HCl solutions have been obtained, ellipsometric investigations on the same material in the same solutions have been started (13).

Acknowledgment

The author expresses his thanks to Dr. E. P. Parry for many helpful discussions and to D. H. Hern for preparation of the test solutions.

Manuscript submitted Feb. 5, 1971; revised manuscript received April 20, 1971.

Any discussion of this paper will appear in a Discussion Section to be published in the June 1972 JOURNAL.

REFERENCES

1. Ya. M. Kolotyrkin and G. G. Kossyi, *Protection of Metals*, **1**, 237 (1965).
2. A. I. Tsinman, E. P. Kovsman, and V. S. Kuzub, *Ukr. Khim. Zh.*, **31**, 923 (1965); *C. A.*, **64**, 1618g (1966).
3. N. D. Tomashov, R. M. Altovskii, and V. V. Vladimirov, Collection: Corrosion and Protection of Construction Materials, Mashgiz, Moscow (1961), p. 164, quoted in Ref. (1).
4. A. I. Tsinman, V. S. Kuzub, and A. N. Katrevich, *Soviet Electrochemistry*, **2**, 513 (1966).
5. I. D. Meshcheryakova, T. P. Kashcheeva, and M. L. Rutkovskii, *Zashch. Metal.*, **6**, 286 (1970); *Protection of Metals*, **6**, 265 (1970).
6. M. Levy and D. W. Seitz, Jr., *Corrosion Sci.*, **9**, 341 (1969).
7. K. Schwabe and W. Schmidt, *ibid.*, **10**, 143 (1970).
8. K. Schmidt, *Protection of Metals*, **5**, 529 (1969).
9. E. G. Haney and W. R. Wermouth, *Corrosion*, **25**, 87 (1969).
10. H. P. Leckie and H. H. Uhlig, *This Journal*, **113**, 1262 (1966).
11. F. Mansfeld, H. L. Marcus, and P. J. Stocker, In preparation.
12. F. Mansfeld, Proc. Int. Symposium on Stress Corrosion Mechanisms in Ti Alloys, Jan. 27-29, 1971, Atlanta, Ga. To be published.
13. F. Mansfeld and T. Smith, Paper 77 to be presented at Electrochem. Soc. Meeting, Cleveland, Oct. 3-7, 1971.

The Solubility of Meta-Dinitrobenzene in Dimethyl Sulfoxide

John S. Dunning* and Douglas N. Bennion*

Energy and Kinetics Department, School of Engineering and Applied Science, University of California, Los Angeles, California 90024

ABSTRACT

The solubility of meta-dinitrobenzene (m-DNB) in dimethyl sulfoxide (DMSO) was determined as a function of temperature in a dry nitrogen atmosphere glove box. Water content of the solutions was below 100 ppm as measured by Karl Fischer titration. The m-DNB saturation concentrations were determined by absorbance measurements of diluted sample solutions. The solubility was found to vary from 3.51 molal at 24.00°C to 4.64 molal at 49.75°C. From a plot of the logarithm of the saturation molality *vs.* the inverse of the absolute temperature the differential heat of solution was determined to be 2053 cal/mole in the temperature range considered if the activity coefficient correction is neglected.

Meta-dinitrobenzene (m-DNB) has been used as the cathode depolarizer in certain nonaqueous primary cells (1). The activated life of such cells depends upon the cell design and the diffusivity and solubility of the electrode depolarizer. Dimethyl sulfoxide (DMSO) may be useful as a solvent for nonaqueous electrochemical systems (2). The diffusion coefficient of m-DNB in a DMSO solution has previously been reported (3) to be 6.15 x 10^{-6} cm^2/sec. The solubility of m-DNB in DMSO will be considered here.

Experimental

The solubility was determined as a function of temperature at atmospheric pressure. Experiments were carried out in a dry nitrogen atmosphere maintained in a glove box. As received DMSO was purified by vacuum distillation using a packed column. Only DMSO with water content below 100 ppm as determined by Karl Fischer titration was used for the experimental study. The detailed procedure for the purification of m-DNB and DMSO and Karl Fischer titration is described elsewhere (3, 4). The temperature of the solution was controlled by placing it in a double walled vessel through which a fluid of constant temperature was passed. The fluid temperature was controlled by a mercury contact temperature bath to ±0.01°C. Temperatures of the solution were measured with a copper-constantan thermocouple as well as with a calibrated thermometer. Stirring of the solution was accomplished by means of glass-coated magnetic stirring bar.

The temperature of the solution was raised to approximately 50°C to start the experiment. A period of one week was allowed initially for the solution to reach equilibrium before samples were taken. The temperature was lowered after each sample was taken and the system was allowed to equilibrate for at least 24 hr. About half of the samples were taken in this manner. Then the temperature was raised after each sampling and the system was again allowed 24 hr to come to equilibrium. There was no systematic variation of the measured solubilities between the two methods of changing temperature.

Samples were withdrawn using a 10 ml pipet equipped with a glass wool particle filter and maintained at the temperature of the solution. The samples were diluted to either 1/20 or 1/40 of the saturation concentrations for convenient analysis. The concentration was determined using a Beckman Model DU spectrophotometer. Details of the spectrophotometric method used are reported elsewhere (4).

* Electrochemical Society Active Member.

Key words: solubility, meta-dinitrobenzene, dimethyl sulfoxide, density.

Table I. The solubility of m-DNB in DMSO

Temperature (°C)	Saturation concentration (mole/1000g solvent)
49.75	4.640
46.00	4.419
39.50	4.128
37.50	4.045
36.25	3.995
33.88	3.890
31.00	3.796
30.50	3.730
29.25	3.703
28.50	3.679
24.00	3.505

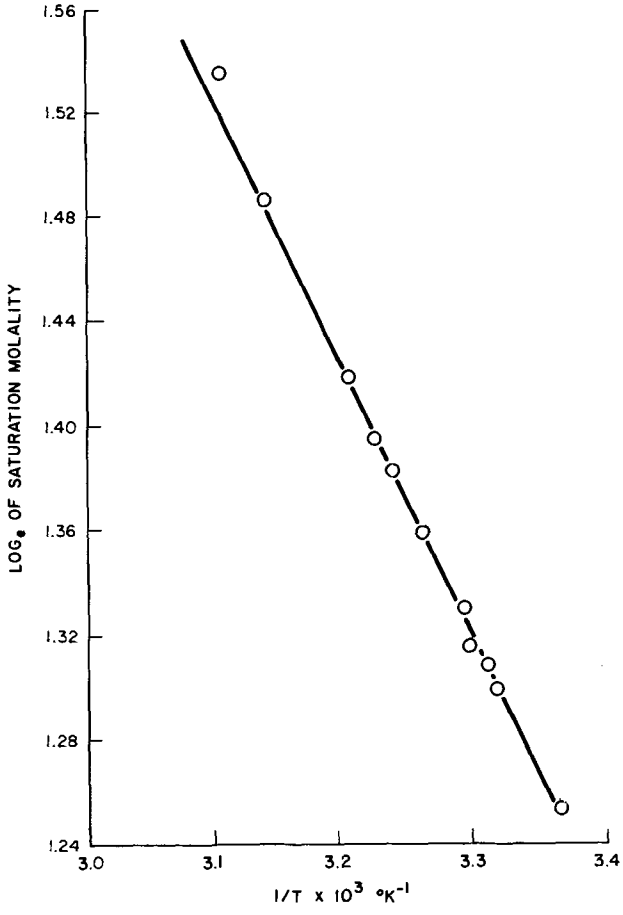

Fig. 1. Differential heat of solution plot for solubility of m-DNB.

Table II. Density of meta-dinitrobenzene/DMSO solutions at 25°C

m-DNB concentration (mg/ml)	Density of solution (g/ml)
0	1.0961
4.316	1.0968
10.204	1.0976
18.938	1.1000
27.229	1.1022
36.532	1.1046
50.610	1.1073

Preliminary solubility measurements of 2,4 dinitroanaline in DMSO indicate a range of solubilities from 1.8 molal at 27.5°C to 2.6 molal at 46.8°C. The value of R $(\partial \ln m/\partial\ 1/T)_{sat}$ is approximately −2770 cal/mole.

The densities of various solutions of m-DNB in DMSO were determined by weighing of the solution contained in a 100 ml volumetric flask at 25°C. Tests of the solubility of 2,4 dinitroaniline (Eastman) in DMSO were also conducted.

Results

It was found that the solubility of m-DNB in DMSO increased from 3.51 molal at 25.00°C to 4.64 molal at 49.75°C. The data are shown in Table I. At saturation, the equality of chemical potentials of the solute in solution and in the solid phase yields the following relation

$$\left(\frac{\partial \ln m_i}{\partial\ 1/T}\right)_{sat} = -\frac{\Delta H_s}{R}\left(1 + \left(\frac{\partial \ln \gamma_i}{\partial \ln m_i}\right)_T\right)$$

where m_i is the saturation concentration, ΔH_s is the differential heat of solution for m-DNB in a saturated solution, and γ_i is the activity coefficient of m-DNB in DMSO.

Figure 1 shows a plot of the experimental values of the logarithm of the molality *vs.* the inverse of the absolute temperature. The slope of the line times R is −2053 cal/mole. An empirical equation for molality $m = 112.8 \exp(-2053/RT)$ fits the data quite well in the temperature range considered.

The densities of various solutions of m-DNB in DMSO are shown in Table II. A plot of the data shows a nearly linear relationship between density and concentration in this dilute region.

Acknowledgment

This work was supported by the U.S. Naval Air Systems Command through Corona Laboratory under Contract No. N00123-70-C-0188.

Manuscript submitted March 10, 1971.

Any discussion of this paper will appear in a Discussion Section to be published in the June 1972 JOURNAL.

REFERENCES

1. W. C. Spindler, *Proc. Advances in Battery Technol. Symposium*, Los Angeles, **1**, 21 (1965).
2. J. N. Butler, *J. Electroanal. Chem.*, **14**, 89 (1967).
3. J. S. Dunning and D. N. Bennion, *This Journal*, **117**, 485 (1970).
4. J. S. Dunning, M.S. Thesis, University of California, Los Angeles, June 1968.

Electrochemical Dissolution of ZnO Single Crystals

D. D. Justice*,[1] and R. M. Hurd*,[2]

Department of Chemistry, North Texas State University, Denton, Texas 76203

ABSTRACT

Dissolution rates for the zinc face of ZnO single crystals were measured as a function of potential in KOH solutions. In the absence of light, there was no potential dependency between −1.2 and +3.0V *vs.* SCE. Upon irradiation with light of sufficient energy to produce electron-hole pairs, a potential dependent dissolution process was superimposed on the continuing potential independent process. The results are interpreted on the basis of a combination of both electrochemical and chemical dissolution processes.

Dissolution of the ionic crystalline state to form solvated ions involves oxidation-reduction reactions for metallic conductors, surface solvation and bond breaking for insulators, and probably some of each for semiconductors. The dissolution mechanism for metals is well known; however, the mechanism by which nonconducting crystals lose ions to the solution has been studied only slightly. The dissolution processes occurring on substances that span the "conductivity gap" between conductors and insulators have also been little studied; however, from the work that has been done, the existence of oxidation-reduction steps has been demonstrated on germanium (1) and silicon (2).

Germanium and silicon can be thought of as forming one type of "bridge" between conductors (metals) and insulators. Compound semiconductors, such as ZnO, can be thought of as forming a second bridge. The potential dependency of the dissolution rates of this first bridge has already been examined (3). The purpose of this investigation was to determine if the dissolution rates of single-crystal ZnO were a function of potential and, if possible, to measure these rates as a function of potential and correlate them with existing theories of electrochemical dissolution.

* Electrochemical Society Active Member.
[1] Present address: Department of Chemistry, Rice University, Houston, Texas 77001.
[2] Present address: Consultant, P. O. Box 5187, West Austin Station, Austin, Texas 78703.
Key words: semiconduction, photopotential, electron-hole pairs, potentiostatic polarization, atomic absorption.

Experimental

A Magna 4700 potentiostat in a typical three-electrode circuit was used to maintain constant potentials over the long periods of time required to obtain the dissolution rates. These rates were measured with a Perkin-Elmer 303 atomic absorption spectrophotometer from accumulations of zinc ions in solution as a function of time. ZnO single crystals were obtained from Electronic Space Products, Inc., and had resistivity values between 2.0 and 10.0 ohm-cm. Etching characteristics (4) were used to identify the faces; only the zinc face was exposed to solution. Apparent surface areas were measured by a microscope and ranged from 0.026 to 0.042 cm^2. Ohmic contacts were obtained by the method used by Dewald (5). Thermostating at 26° ± 1°C was maintained by the air-conditioning in the laboratory; all room lights and other heat producing equipment were continuously operated. All solutions were bubbled with nitrogen for

several hours before the ZnO electrode was inserted in the cell. During measurements bubbling was discontinued and the outlet to the atmosphere was turned off. Currents were small enough so that IR drops between the ZnO electrode and the Luggin capillary could be neglected; IR drops in the semiconductor could be neglected except during high cathodic polarization.

A high-intensity microscope lamp was used to generate electron-hole pairs; glass filters were used to obtain a band of light between 360 and 400 mμ with the transmission maximum at 365 mμ. When a thermometer was placed directly in the solution, no change in temperature was measured in the presence or absence of light. As the intensity of light was increased (either by increasing the voltage to the lamp or by placing the lamp closer to the ZnO electrode), open-circuit potentials shifted in the cathodic direction from −150 mV *vs.* SCE (dark) to as much as −850 mV; thus, open-circuit potentials were an indication of light intensity.

Results

Dark dissolution rates were essentially independent of potential between −1.2 and +3.0V *vs.* SCE. In Fig. 1 dissolution rates for an 8.5 ohm-cm crystal in 1.0*N* KOH in the dark are shown on the same figure with the current-potential relation. The open-circuit dissolution rate is plotted to correspond to zero current, and anodic and cathodic dissolution rates are plotted relative to this point. Even though there was a sharp increase in cathodic currents around −1.2V, the dissolution rate did not measurably change. For an area of 10^{-4} cm², the 0.068 mg/hr cm² measured in this study for 1.0*N* KOH corresponds to the dissolution of about 4 x 10^{-12}g of ZnO in a 2-sec etch compared to about 2 x 10^{-10}g measured by Dewald (5) in 3.0*N* KOH.

From capacity values of ZnO in electrolyte systems (6), the space charge within the crystal is minimum at potentials near 600-700 mV cathodic to SCE (flat band potential). In this work, light intensity could be adjusted to easily attain an open-circuit potential of −650 mV which was chosen as the potential from which to begin measurements. During the first hour the lamp was adjusted slightly in order to maintain a constant open circuit, but then the potential remained essentially constant for 50 hr or longer; thus, light intensity was adjusted for an hour before any external voltage was applied. Open-circuit dissolution rates in light at −650 mV were almost twice those in the dark. Upon anodic polarization these rates increased; upon cathodic polarization they decreased. In Fig. 2 rates for an 8.5 ohm-cm crystal in 1.0*N* KOH are plotted on the same figure with the current-potential relation in order to show the close correlation between the two types of data. Around −1.2V the dark dissolution rates did not change but in light decreased and closely paralleled the polarization curve. Regardless of the polarization, the dissolution rates in light never became smaller than those in the dark.

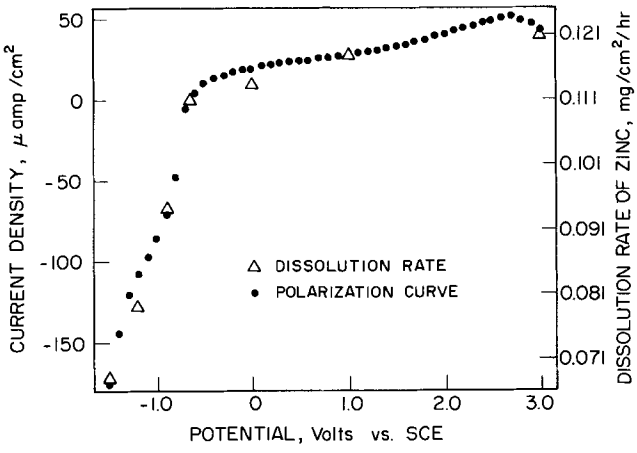

Fig. 2. Correlation of zinc dissolution rates with the current-potential relation for the zinc face of an 8.5 ohm-cm ZnO single crystal in 1.0*N* KOH. For each rate light was used to obtain an open-circuit potential of −650 mV *vs.* SCE.

As the hydroxide ion concentration decreased, larger anodic currents were obtained during polarization measurements. As shown in Fig. 3, the dissolution rates for an 8.5 ohm-cm crystal in 0.5*N* KOH still parallelled the polarization curve. For a given hydroxide ion concentration, the increase in dissolution upon anodic polarization became smaller as the resistivity of the crystal decreased. In Fig. 4 the polarization curve and dissolution rates are shown for a 2.0 ohm-cm crystal in 0.5*N* KOH. These data can be compared to those in Fig. 3 for an 8.5 ohm-cm crystal in 0.5*N* KOH. As shown in Fig. 2, 3, and 4, a passive type of peak was observed in light at approximately +3.0V. This peak was not examined in detail but became more pronounced as the current density of the polarization curves increased. Dissolution rates are summarized in Table I.

Assuming that electrons were released to the conduction band as zinc atoms passed into solution and that these electrons were measured as an external current flow, the weights of zinc expected after 100 hr were calculated, first on the basis of one and then two electrons per atom. In Table II these values are compared to the weights found by analyses. Experimental

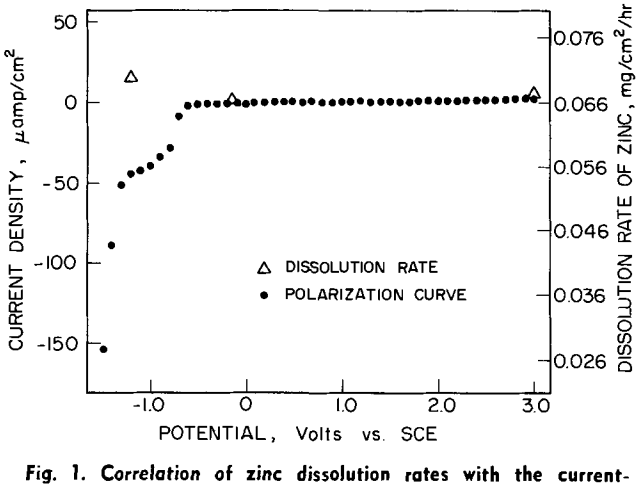

Fig. 1. Correlation of zinc dissolution rates with the current-potential relation for the zinc face of an 8.5 ohm-cm ZnO single crystal in the dark in 1.0*N* KOH.

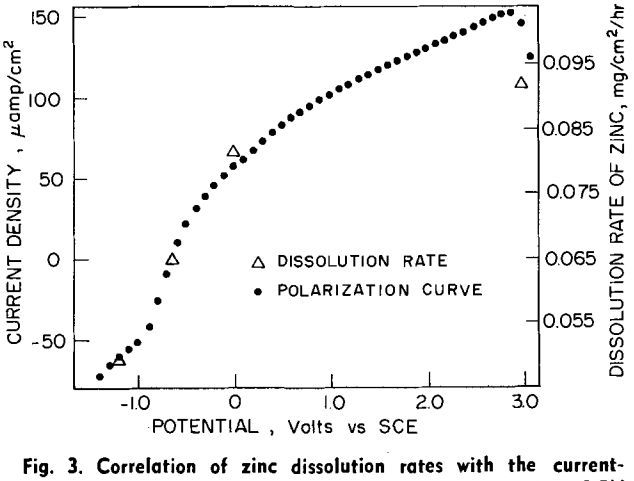

Fig. 3. Correlation of zinc dissolution rates with the current-potential relation for an 8.5 ohm-cm ZnO single crystal in 0.5*N* KOH. For each rate light was used to obtain an open-circuit potential of −650 mV *vs.* SCE.

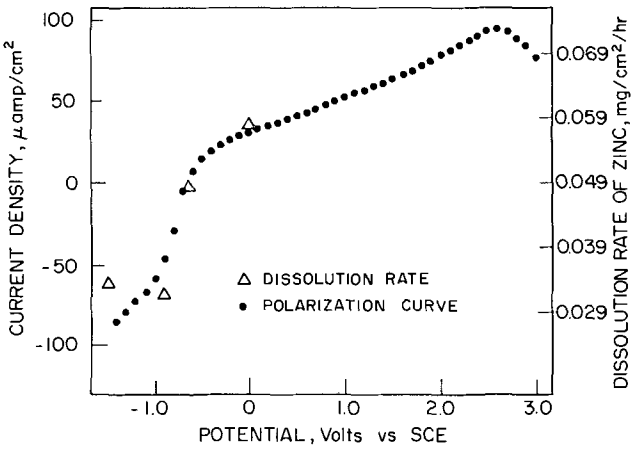

Fig. 4. Correlation of zinc dissolution rates with the current-potential relation for the zinc face of a 2.0 ohm-cm ZnO single crystal in 0.5*N* KOH. For each rate light was used to obtain an open-circuit potential of −650 mV vs. SCE.

amounts were always larger than those expected from current measurements.

In all the figures and more noticeable in Fig. 1, a "plateau" was found at −1.0V. This was most likely due to the slow desorption of hydroxide ions or to the reorientation of water dipoles with the more positive end toward the surface; *i.e.*, surface coverage by hydroxide ions or water dipoles was changing with potential.

Discussion

Dark dissolution rates between −1.2 and +3.0V were independent of potential and thus essentially chemical in nature. Large photovoltages indicated that large numbers of electron-hole pairs were produced; the increase in dissolution indicated that one of the delocalized charge carriers (holes) was involved in the dissolution process.

The open-circuit potential of −650 mV for the 8.5 ohm-cm crystal in 1.0*N* KOH was about 50 mV anodic to flat band potential (6). An anodic space charge existed in the crystal, and the holes produced and separated in this region were forced to the surface even at open circuit (7). Upon anodic polarization the surface hole density was additionally increased by increasing the depth from which holes were separated by the electrical field. The anodic current and dissolution rates parallel the increased surface hole density. Cathodic polarization resulted in a large decrease in surface hole density which paralleled a sharp decrease in the measured cathodic dissolution rates.

Since the flat band potential becomes more anodic as the *p*H decreases (6), a smaller anodic space charge region existed in 0.5*N* KOH, and a higher light intensity was needed to generate the current necessary to obtain the open-circuit potential of −650 mV. As seen from a comparison of Fig. 2 and 3, more holes were available to be forced to the surface by anodic polarization; upon cathodic polarization; a smaller proportion was forced back from the surface. In 0.5*N* KOH total dissolution was smaller, due to a decrease in the chemical rate with a decrease in hydroxide ion concentration, down to a solubility minimum near *p*H 9 (8) for powdered ZnO.

The flat band potential also becomes more anodic as resistivities increase (6). Compared to an 8.5 ohm-cm crystal, a larger proportion of holes was separated and forced to the surface in a 2.0 ohm-cm crystal. The influence of light and anodic polarization was less for the 2.0 ohm-cm crystal, as seen from a comparison of Fig. 3 and 4.

Table I. Summary of dissolution rates

Potential, mV *vs.* SCE	8.5 ohm-cm in 1*N* KOH (light) mg/hr cm²	8.5 ohm-cm in 0.5*N* KOH (light) mg/hr cm²	2.0 ohm-cm in 0.5*N* KOH (light) mg/hr cm²	8.5 ohm-cm in 1*N* KOH (dark) mg/hr cm²
+3000	0.121	0.092	0.063	0.068
+1000	0.118	—	—	—
0	0.113	0.082	0.058	—
−200	—	—	—	0.066
−650	0.111	0.065	0.049	—
−900	0.094	—	0.032	—
−1200	0.080	0.049	—	0.070
−1500	0.068	—	0.034	—

Table II. Comparison of weight of zinc found experimentally to the weight in mg of zinc expected from current measurements

Potential, V *vs.* SCE	(Si dt) (at. wt Zn) / 2F	(Si dt) (at. wt Zn) / 2F	Wt actually found
8.5 ohm-cm in 1.0*N* KOH in light			
Open circuit	—	—	0.45
0.0	0.22	0.11	0.46
+1.0	0.24	0.12	0.49
+3.0	0.26	0.13	0.50
8.5 ohm-cm in 1.0*N* KOH in darkness			
Open circuit	—	—	0.26
+3.0	0.01	0.005	0.26
8.5 ohm-cm in 0.5*N* KOH in light			
Open circuit	—	—	0.25
0.0	0.17	0.09	0.32
+3.0	0.28	0.14	0.36
−1.2	—	—	0.19
2.0 ohm-cm in 0.5*N* KOH in light			
Open circuit	—	—	0.19
0.0	0.10	0.05	0.23
+3.0	0.20	0.10	0.25
−1.2	—	—	0.12

Conclusions

The over-all potential independent process can be described by

$$ZnO + 2\,OH^- + H_2O \rightarrow Zn(OH)_4^{-2} \qquad [1]$$

In this proposed chemical dissolution process, an electron is transferred from zinc to oxygen by a strong localized electrical field established by adsorbed hydroxide ions. This is a direct transfer because most of the electrons do not have enough energy to be delocalized to the higher lying conduction band. The small portion which has enough energy to make the transition can be considered to be electron-hole pair production which causes the mixed potential measured at open circuit even in the dark. Applied potentials cannot add enough energy to measurably increase the portion of electrons that has enough energy to make the transition. In addition applied voltages influence mainly the space charge region of the semiconductor and appear only to a limited extent across the semiconductor-solution interface. The composition of the phase at the semiconductor-solution interface therefore does not change, and thus the localized electrical field established by adsorbed ions is not changed.

Since the weight of zinc actually measured in solution was always greater than the amount expected from current measurements, a chemical dissolution process continues even in light; however, an additional dissolution process involving holes increases the total dissolution process. The following reactions (9) have previously been presented for this potential dependent (electrochemical) process

$$ZnO + 2(e'\sim/e'/) + 4\,OH^- \rightarrow Zn(OH)_4^{-2} + 2e' \qquad [2]$$

$$2H_2O + 2e' \rightarrow H_2 + 2\,OH^- \qquad [3]$$

$$ZnO + 2\,OH^- + 2H_2O + 2(e'\sim/e'/) \rightarrow Zn(OH)_4^{-2} + \tfrac{1}{2}\,O_2 + H_2 \qquad [4]$$

where ($e'\sim/e'/$) represents an electron-hole pair. Electrons are delocalized to the conduction band; the potential dependent step is the arrival of holes at the semiconductor surface.

The proposed electrochemical dissolution process for ZnO actually is analogous to the electrochemical dissolution of germanium (1) and silicon (2) except that in the proposed reactions for ZnO, light energy decomposes a mole of water into its constituent elements for each mole of ZnO that dissolves electrochemically. Electron-hole pairs are necessary for the electrochemical dissolution of all three semiconductors; however, in germanium and silicon the forbidden gap is small enough so that applied potentials can generate electron-hole pairs, whereas in ZnO the forbidden gap is so large that applied potentials of the magnitude used in this study cannot generate electron-hole pairs but can only alter the distribution of those produced by light.

Additional chemical data are needed to establish these proposed chemical and electrochemical reactions; in particular, precise measurements of the rates of evolution of hydrogen and oxygen gases are needed, as it is these data that will establish the fraction of the total dissolution rate which occurs by the electrochemical process.

Acknowledgment

This research was supported by Faculty Research Funds from North Texas State University.

Manuscript submitted Jan. 11, 1971; revised manuscript received *ca.* April 25, 1971.

Any discussion of this paper will appear in a Discussion Section to be published in the June 1972 JOURNAL.

REFERENCES

1. W. Brattain and C. Garrett, *Bell System Tech. J.*, **34**, 129 (1955).
2. R. M. Hurd and P. T. Wrotenbery, *Ann. New York Acad. Sci.*, **101**, 876 (1963).
3. R. M. Hurd and N. Hackerman, *Electrochim. Acta*, **9**, 1633 (1964).
4. A. N. Mariano and R. E. Hanneman, *J. Appl. Phys.*, **34**, 384 (1963).
5. J. F. Dewald, *Bell System Tech. J.*, **39**, 615 (1960).
6. F. Lohmann, *Ber. Bunsenges. Phys. Chem.*, **70**, 428 (1966).
7. H. Gerischer, *This Journal*, **113**, 1174 (1966).
8. L. Blok, Ph.D. Thesis, University of Utrecht, Utrecht, Holland.
9. K. Hauffe and J. Range, *Ber. Bunsenges. Phys. Chem.*, **71**, 690 (1967).

Electrochemistry of Aziridinium Salts–Reduction of Alkyl Radicals to Anions as Function of Solvent

Donald A. Tyssee and Manuel M. Baizer*

Central Research Department, Monsanto Company, St. Louis, Missouri 63166

ABSTRACT

The reductive degradation of aziridinium salts has been shown to follow different pathways depending on whether the solvent is protic (water) or aprotic (acetonitrile). Of prime importance is the variation in potential required for the reduction of an alkyl radical to an anion in the two solvents. The failure to recognize this fact in the electrolysis of compounds whose reduction potentials are subject to similar solvent shifts is discussed.

Mantsavinos and Christian (1) have examined the polarographic behavior of aziridinium salts and report that aziridinium ions of the general structure I undergo a single two electron reduction at approximately -1.2V (SCE) in aqueous solutions to give a trialkylamine, $R_2NCH_2CH_3$. In contrast, Mayell and Bard (2) exam-

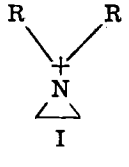

I

$R = CH_2CH_2Cl$

ined the electrochemical behavior of benzyldimethylanilinium bromide and concluded that in either water or acetonitrile there is an initial one electron uptake at -1.6V (SCE) followed or accompanied by cleavage of a C-N bond to give dimethylaniline and the benzyl radical which then abstracts a hydrogen atom from the solvent to give toluene or dimerizes to give bibenzyl. Similarly, a radical pathway has been invoked to account for the observed behavior upon bulk electrolysis of benzyltrialkylammonium salts in water at -2.2V (3). In this case, toluene was formed upon bulk electrolysis in water, whereas in aprotic solvents a mixture of toluene and bibenzyl was formed. The use of active *d*-α-phenylethyltrimethylammonium nitrate demonstrated the presence of radical intermediates in aprotic solvents since upon bulk electrolysis only inactive coupled products were formed. The preparative utility of ammonium salt cleavage has been studied extensively by Horner (4).

Aziridinium salts reduce at easily accessible potentials. This allows one to investigate their electrochemical properties in solvent-electrolyte systems in which phenomena associated with electrolyte discharge are not of consequence. Namely, attention can be directed to the influence of solvent and/or electrolyte on 1 *vs.* 2 electron uptake and the mode of decomposition of intermediates to products. It is the purpose of this paper to report on the electrochemical behavior of aziridinium salts and to compare this behavior under conditions of both micro- and macro-electrolyses.

Experimental

Materials.—Acetonitrile (Matheson, Coleman and Bell-spectro-quality) was passed through Linde Type 3A molecular sieves and stored under nitrogen until used. Tetraethylammonium, tetramethylammonium, and lithium perchlorates were recrystallized from water and dried in a vacuum oven.

Aziridinium salts.—The aziridinium salts were prepared either as described previously (5) using silver

* Electrochemical Society Active Member.
Key words: bond cleavage, radical intermediates, ring opening, isotope effect.

perchlorate or generated *in situ* from the suitable 2-chloroethyldialkylamine liberated by neutralization of the commercially available amine hydrochlorides.

Polarography.—All polarograms were obtained with a Sargent Model XXI polarograph. Standard polarographic H cells were used throughout. The polarograms were recorded against a saturated calomel electrode as the reference using 0.1M supporting electrolyte. The concentration of depolarizer was 5×10^{-4} to 10^{-3}M. No correction was made for *IR* drop. Electrode constants were $m = 1.54$ mg sec^{-1}, $t = 5$ sec and $m^{2/3}t^{1/6} = 1.74$ at an Hg column height of 67 cm.

Cyclic voltammetry.—The cyclic voltammograms were obtained using a Wenking Model 66TA1 potentiostat and an Exact Model 505 function generator. Recording of the current-voltage curves was accomplished with a Tektronix 502-A Dual Beam Oscilloscope and a C-27 camera attachment. A three-compartment cell fitted with a Luggin capillary was used. The working electrode was a mercury drop suspended on a mercury-coated platinum wire. The reference electrode was a saturated calomel electrode and the auxiliary electrode a platinum wire. Solutions were 0.1M in supporting electrolyte and 5×10^{-4} to 10^{-3}M in depolarizer.

Bulk electrolysis.—Electrolyses were done at a mercury pool using a standard H cell with a glass frit divider. The potential was controlled using a saturated calomel electrode positioned at the mercury surface and a suitable potentiostat. Solutions were 0.2M in electrolyte. The aziridinium salt was either added initially in one portion or portion-wise over the duration of the run to keep its concentration in the bulk of the solution low. Electrolyses were carried out on sufficiently small quantities so that pH control was not necessary. The solvent/electrolyte mixture was pre-electrolyzed prior to the coulometric runs and deaerated continuously.

Isolation of amine products.—Typically the aqueous solution was made basic, extracted with ether, and analyzed by gas chromatography (Ucon/KOH). For runs in acetonitrile, the work-up procedure involved acidification, removal of acetonitrile *in vacuo*, and ether extraction after neutralization of the acidic residue.

Product identification.—Products were identified by the combined techniques of NMR, gas chromatographic retention times compared to authentic samples, and mass spectroscopy compared to authentic samples. Ethylene was identified in the off-gas by mass spectroscopy. Mercury was detected using the dithizone test—the samples having previously been oxidatively degraded with fuming nitric acid followed by aqueous bicarbonate neutralization.

Results

Polarography and coulometry.—Polarograms of N,N-diethylaziridinium perchlorate (II) in various solvent-electrolyte

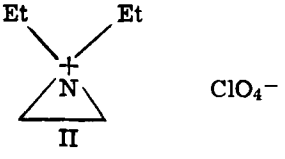

II

systems are shown in Fig. 1. The variation of diffusion current with the height of the mercury column is illustrated in Fig. 2. The influence of phenol on the total diffusion current as well as on the presence of a polarographic maxima is illustrated in the polarograms of Fig. 3.

Because of the ease of removing acetonitrile during work-up, this solvent was used instead of dimethylformamide for coulometric and preparative studies. The aziridinium salts show identical behavior polarographically in either acetonitrile or dimethylformamide.

Coulometry of the aziridinium salt (II) at −1.8 to −1.9V in acetonitrile using tetraethylammonium perchlorate was consistent with a one-electron uptake at this potential. In contrast, coulometry at the same potential in water with tetraethylammonium perchlorate as the supporting electrolyte gave a two-electron uptake as did coulometry at −1.7V in water using lithium perchlorate as the supporting electrolyte.

Cyclic voltammetry.—The cyclic voltammogram of N,N-diethylaziridinium perchlorate in dimethylformamide is shown in Fig. 4. Included for comparison is the polarographic wave shape.

Bulk electrolyses.—Attempts to isolate products from the bulk electrolyses at controlled potential of N,N-diethylaziridinium perchlorate were complicated by the chemical reactivity of the starting material. Although coulometry allowed a distinction to be made between one- and two-electron reductions, increasing the concentration of the depolarizer to a scale (*i.e.* 10^{-1} to 1M) sufficient for product isolation resulted in low current efficiencies (*i.e.* less than 50% in most cases). Secondary products arising from competing chemical reactions included N,N,N',N'-tetraethylethylenediamine, polymeric quaternary ammonium salts, and 2-diethylaminoethanol (from hydrolysis of the original aziridinium salt).

Electrolysis in water (−1.6V to −1.9V).—Data relative to the electrolyses of aziridinium salts in aqueous solutions are given in Table I.

Careful examination by gas chromatography combined with rapid scan mass spectroscopy of the reaction mixture formed upon electrolysis of N,N-diethylaziridinium perchlorate (II) suggested that the peak eluting as triethylamine is actually a mixture of triethylamine and trace amounts of an amine of molecular weight 99.

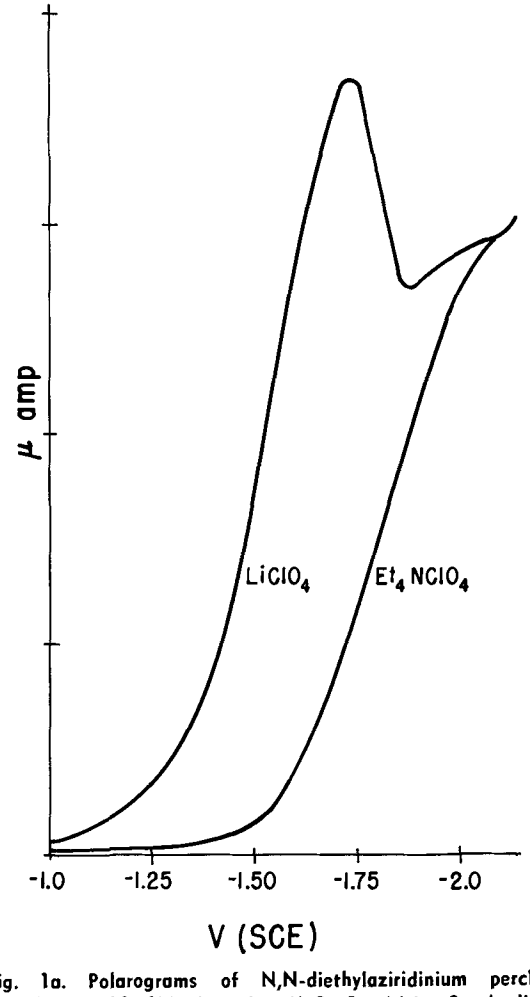

Fig. 1a. Polarograms of N,N-diethylaziridinium perchlorate (6×10^{-4}M) in 10^{-1}M electrolyte-H_2O. Sensitivity 2 μA div^{-1}.

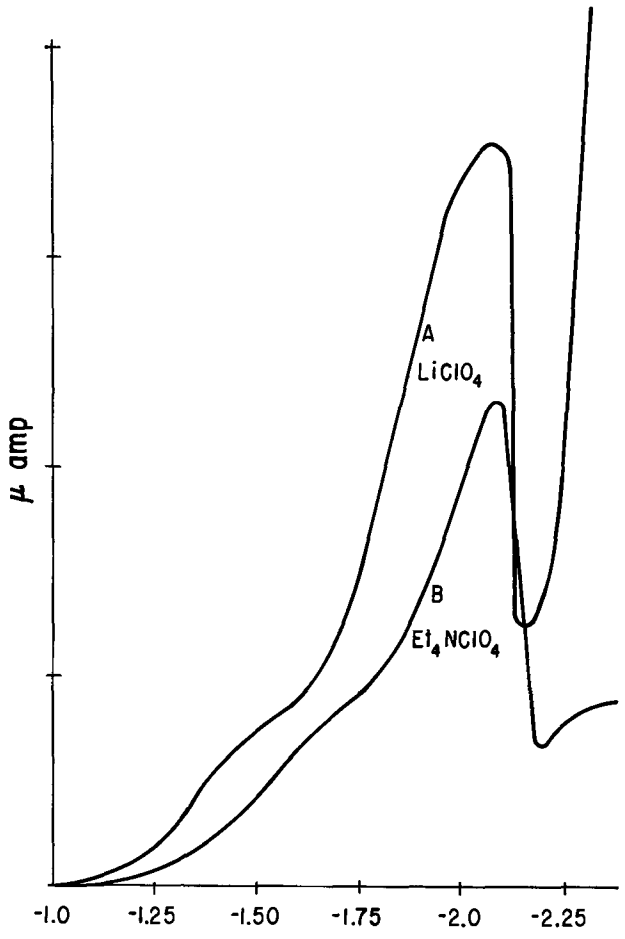

Fig. 1b. Polarograms of N,N-diethylaziridinium perchlorate ($6x10^{-4}M$) in $10^{-1}M$ electrolyte-DMF. Sensitivity 3 μA div^{-1}.

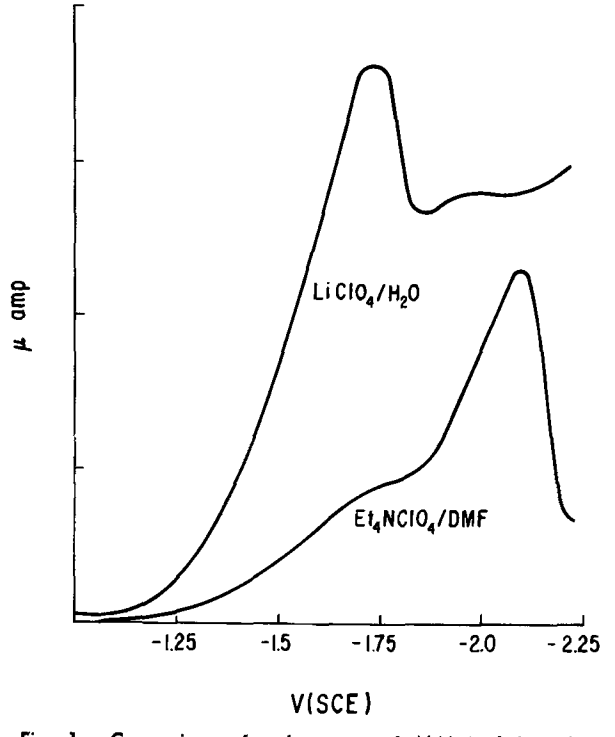

Fig. 1c. Comparison of polarogram of N,N-diethylaziridinium perchlorate ($6x10^{-4}M$) in $LiClO_4$ ($10^{-1}M$)-H_2O at sensitivity of 2 μA div^{-1} and in Et_4NClO_4 ($10^{-1}M$)-DMF at sensitivity of 3 μA div^{-1}.

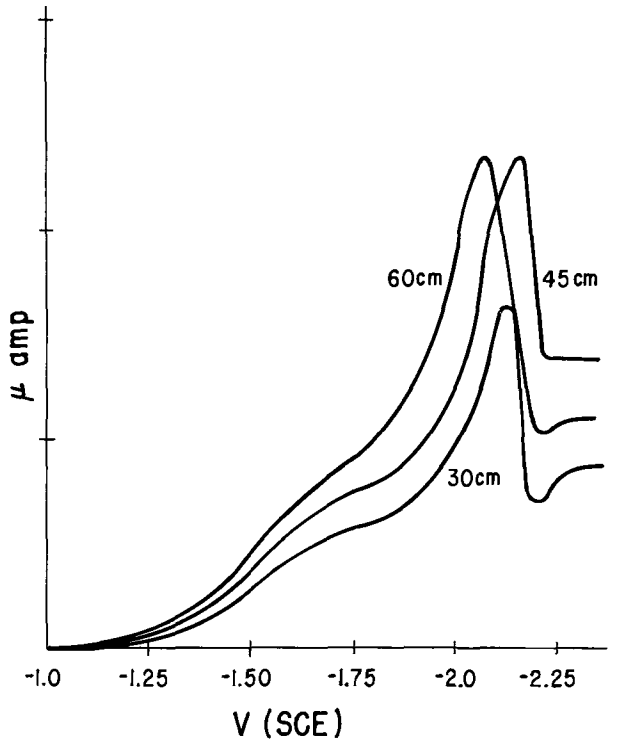

Fig. 2. Variation of diffusion current with Hg column height in polarogram of N,N-diethylaziridinium perchlorate ($6x10^{-4}M$) in DMF ($10^{-1}M$ Et_4NClO_4). Sensitivity 3 μA div^{-1}.

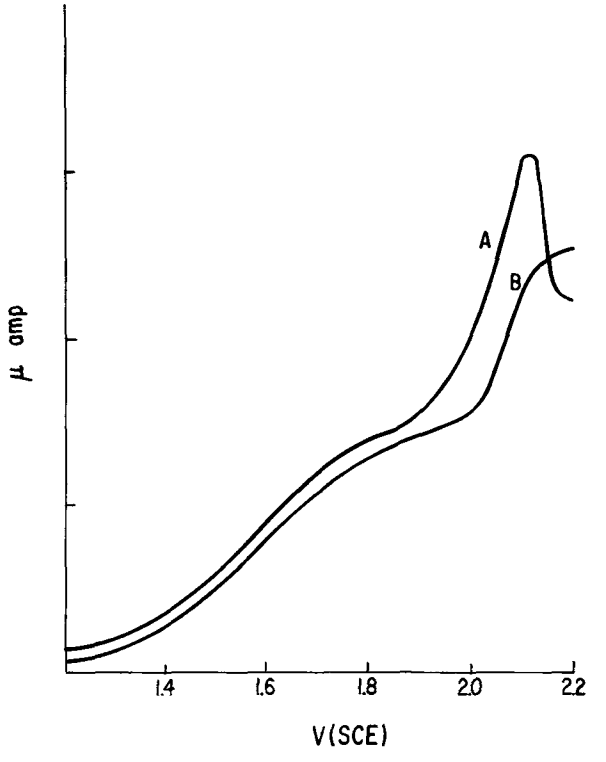

Fig. 3. Influence of phenol on the polarographic reduction of N,N-diethylaziridinium perchlorate ($1.1x10^{-3}M$) in DMF ($10^{-1}M$ Et_4NClO_4). *(A)* in the absence of phenol. *(B)* in the presence of $4x10^{-3}M$ phenol. Sensitivity 4 μA div^{-1}.

Fragmentation patterns are consistent with diethylvinylamine (III).

$$Et_2N\text{-}CH{=}CH_2$$
III

No evidence was obtained for the presence of N-ethyl-

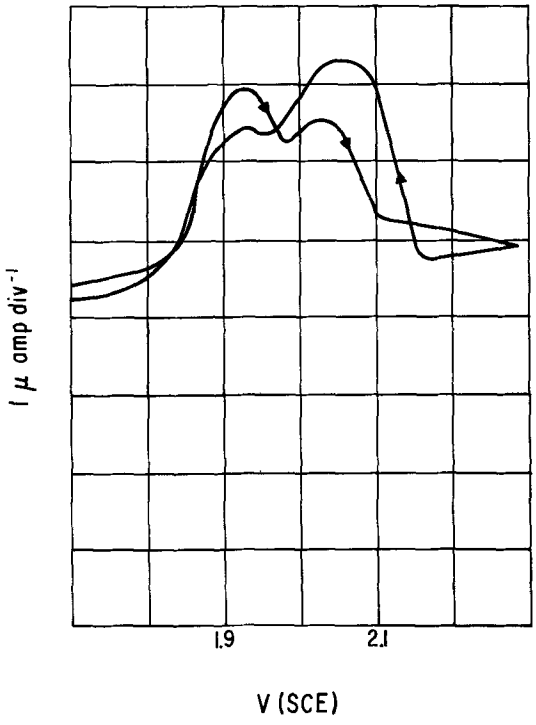

Fig. 4a. Cyclic voltammogram of N,N-diethylaziridinium perchlorate (6×10^{-4}M) in DMF (10^{-1}M Et_4NClO_4). Scan rate 0.32V sec^{-1}.

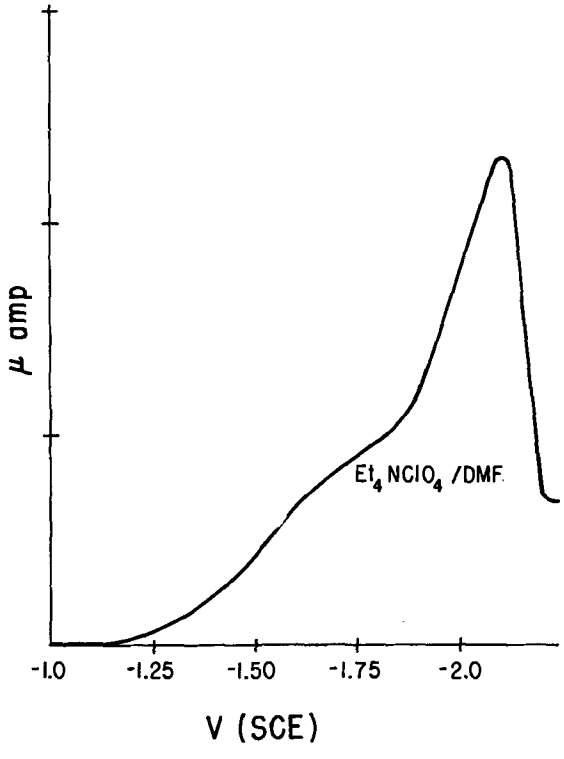

Fig. 4b. Polarogram of N,N-diethylaziridinium perchlorate (6×10^{-4}M) in DMF (10^{-1}M Et_4NClO_4). Sensitivity 3 μA div^{-1}.

aziridine (IV) arising from elimination of the β protons of the ethyl moiety.

IV

During the electrolysis of II, secondary products formed as a result of subsequent chemical reactions included N,N,N',N'-tetraethylethylenediamine and a polymeric ammonium salt (V).

Table I. Preparative electrolysis of aziridinium salts in water

Salt[a]	Solvent/electrolyte	Products (ratio)
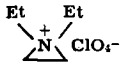	$H_2O/LiClO_4$ H_2O/Et_4NClO_4	Et_2NH[b] Et_3N $Et_2NCH_2CH_2NEt_2$
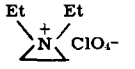	$H_2O(l)/D_2O(l)/Me_4NClO_4$	$Et_2N—CH=CH_2$ polymeric ammonium salts $CH_2=CH_2$ $Et_2NCH_2CH_3$(l) $Et_2NCH_2CH_2D$(l)
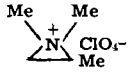	H_2O/Me_4NClO_4	$Me_2NCH_2CH_2CH_3$[c] $Me_2NCH_2CH(Me)NMe_2$

[a] The initial concentration of the aziridinium salt was 1M when all of the salt to be electrolyzed was added at the beginning of the electrolysis. Several electrolyses were done in which the concentration of aziridinium salt was maintained at a lower level (*i.e.* 0.1M) by portion-wise addition to the cell. The same products were obtained regardless of the method of addition.

[b] The mole ratio of products formed was extremely variable. Attempts to establish a trend in product distribution with method of addition of II (*i.e.* portion-wise addition or adding all of II to be electrolyzed initially), current density, or electrolyte used were not successful.

[c] These were major products. No 2-dimethylaminopropane was detected.

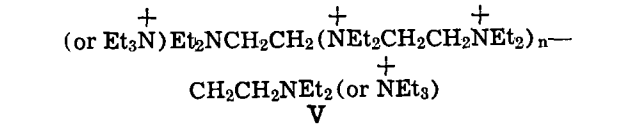

V

The polymeric ammonium salt was characterized by NMR spectroscopy of the aqueous solution remaining after ether extraction of the basic electrolysis mixture. In the case of electrolyses in which $LiClO_4$ was used as the electrolyte, NMR spectra were run directly on the aqueous solution. In the case of electrolyses in which Me_4NClO_4 was used as the electrolyte, the tetramethylammonium cation was precipitated as the hexafluorophosphate salt prior to NMR analysis. Terminal triethylammonium groups were identified by comparing the shift of the methyl triplet relative to water. The salt $Et_3\overset{+}{N}CH_2CH_2NEt_2$ (prepared by the addition of N,N-diethylaziridinium perchlorate to a large excess of triethylamine) was used as a standard. The separations from water for the methyl triplet are 204 and 218 Hz respectively for the ammonium and neutral amine function. The water soluble product obtained upon exhaustive electrolysis of N,N-diethylaziridinium perchlorate showed only a triplet centered at 202 Hz. In addition, the expected quartet was observed (centered at 92 Hz upfield from H_2O) for $\overset{+}{N}CH_2CH_3$ as well as a singlet (85 Hz upfield from H_2O) for the internal methylenes.

Electrolysis in acetonitrile (−1.8V to −1.9V).—Electrolysis at controlled potential of N,N-diethylaziridinium perchlorate using either tetraethyl or tetraethylammonium perchlorate as the supporting electrolyte gave a variety of products. These included products of the primary electrochemical process (*i.e.* triethylamine, diethylamine and organo-mercury compounds) as well as products of subsequent chemical reactions between the aziridinium salt and electrochemically derived compounds. Again, as in the case of water, electrolysis on a preparative scale resulted in diminished current efficiencies as a result of competitive chemical reactions.

Evidence for the presence of radical intermediates in the form of organo-mercury compounds was obtained by the dithizone test (*cf.* Experimental). By analogy with other compounds which have been shown to undergo a one-electron reduction to a radical species which reacts with the mercury electrode (6, 7), it is assumed that a similar organo-mercury product is also

formed here. Attempts to trap the diethylaminoethyl radical with known radical scavengers including styrene, butadiene, or acrylonitrile were without success. This is in contrast to previous work which has shown that alkyl radicals generated electrochemically from alkyltriphenylphosphonium or sulfonium salts add to styrene in addition to reacting with the mercury electrode (6). In addition, gas chromatographic analysis of the amine products showed no evidence of the compound expected from coupling of two diethylaminoethyl radicals [*i.e.* $Et_2N(CH_2)_4NEt_2$].

Gas chromatographic analysis of the total reaction mixture suggested that a product was formed in barely detectable amounts whose retention time was the same as that of succinonitrile possibly formed by the coupling of $\cdot CH_2CN$. Previously it has been shown (6, 7) that reduction of this radical occurs more negatively than −1.7V, and therefore the absence of significant amounts of succinonitrile is expected.

Discussion

Aqueous electrochemistry.—The polarographic and coulometric data are consistent with one two-electron reduction of N,N-diethylaziridinium perchlorate (II) at *ca.* −1.5V in water using a $LiClO_4$ electrolyte. Changing the electrolyte to $Et_4N\ ClO_4$ results in an apparent shift in half-wave of *ca.* −0.32V as well as in removal of the polarographic maximum.

As mentioned previously, the data obtained from bulk electrolyses were complicated by side chemical reactions in which products of the electrochemical reaction react chemically with the aziridinium salt to give nonactive product. The rates of such bimolecular chemical reactions were sufficiently depressed on a microscale so that reliable coulometric data could be obtained.

Several factors point to the conclusion that the first step in the reduction of II is addition of one electron followed by ring opening to a radical intermediate which, in aqueous solutions, is reduced to a carbanion at the applied potential. The diethylaminoethyl carbanion thus formed may abstract a proton from water (or unreduced aziridinium salt) or undergo an elimination to yield the diethylamine anion and ethylene.

The step-wise nature of the reduction is demonstrated by the reduction of N,N-dimethyl-2-methylaziridinium perchlorate (Table I). If a direct two-electron reduction were occurring initially or simultaneous with ring opening, the expected product would be the more stable primary anion (VI). A one-electron reduction followed by ring opening would yield the more stable secondary radical (VII). Reduction of VII followed by protonation would give 1-dimethylaminopropane (Eq. [1]).

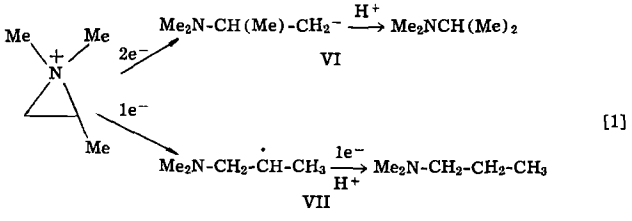

[1]

The exclusive product obtained (Table I) upon electrolysis of N,N-dimethyl-2-methylaziridinium perchlorate was that corresponding to a one electron reduction followed by ring opening to a radical intermediate (*i.e.* 1-dimethylaminopropane).

In order to distinguish between a radical or anionic precursor of triethylamine, an electrolysis of II was conducted in a 1/1 molar mixture of D_2O and H_2O, using tetramethylammonium perchlorate as the supporting electrolyte. Analysis of the isotopic enrichment in triethylamine by mass spectroscopy gave an isotope effect of 1 (*i.e.* $Et_3N/Et_2NCH_2CH_2D$). This is the value expected for anion protonation. Radical abstraction would be expected to give an isotope effect (k_H/k_D) greater than one as a consequence of the greater strength of the O-D bond (8). Although the isotopic enrichment in the electrolysis products of compounds previously reported to lead to products arising from hydrogen radical abstraction from water were not investigated, it is likely that a similar anionic intermediate rather than radical intermediate is involved, as has been reported (2-3). The known inability of water to quench radical polymerization as well as the unfavorable energetics required in the homolytic cleavage of an OH bond relative to forming a CH bond (*i.e.* 118 kcal for H_2O *vs.* 98 kcal for a CH bond) are also consistent with an anionic intermediate and serve to strengthen the argument against a radical intermediate being formed in aqueous solution.

During the electrolysis of II a substantial amount of diethylamine was formed (Table I). This, taken with the observation that ethylene is formed, suggests that in the region of the electrode surface sufficiently anhydrous conditions exist so that prior to diffusion of the diethylaminoethyl anion into the bulk of the solution elimination occurs to give ethylene and the diethylamino anion. The formation of detectable amounts of diethylvinyl amine further supports the argument that a sufficiently basic species exists at or near the electrode surface to abstract a proton from unreduced aziridinium salt. The existence of an anhydrous layer at the electrode surface during aqueous electrolysis using quaternary ammonium electrolytes has been reported previously (9, 10). It thus appears that aziridinium salts behave in a similar fashion (*i.e.* to other ammonium salts) even to the extent that an "anhydrous" electrode layer exists when they are electrolyzed in the presence of a lithium containing electrolyte.

The following scheme is consistent with the aqueous electrolysis of aziridinium salts (Eq. [2]).

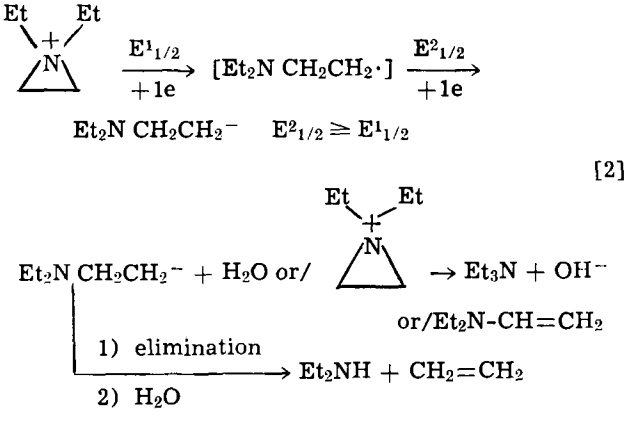

[2]

Because of the chemical reactivity of aziridinium salts, products formed initially *via* an electrochemical pathway accumulate in the cell during a bulk electrolysis and subsequently consume a portion of the aziridinium cation resulting in the observed decrease in current efficiency (Eq. [3]).

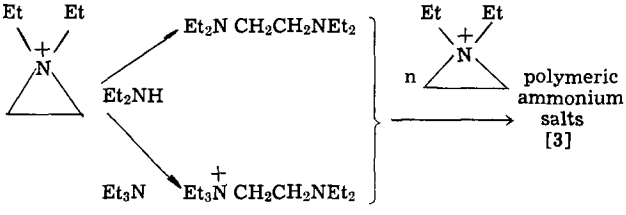

[3]

Nonaqueous electrochemistry.—Polarographic and coulometric results indicate that the reduction of N,N-diethylaziridinium perchlorate occurs in two one-electron steps. The first reduction is diffusion controlled (Fig. 2) and occurs at approximately −1.5 to −1.65V (SCE) depending on the electrolyte whereas the second reduction step occurs in the region *ca.* −1.9 to −2.1V (SCE) and exhibits a large maximum. The total dif-

fusion current constant (after the maximum) of the combined waves appears to be concentration dependent (Fig. 1b and 3) and is sensitive to the presence of proton donors (Fig. 3). It has been shown previously (6) that such an event occurs when an anion formed in the second reduction step reacts with depolarizer diffusing to the dropping electrode and is consistent with the behavior observed in aqueous electrolyses in which diethylvinylamine was detected in the products (Eq. [4]). Addition of phenol protonates the diethylaminoethyl anion so that all of the aziridinium salt diffusing to the electrode is available for reduction. The net result is to increase the total diffusion current.

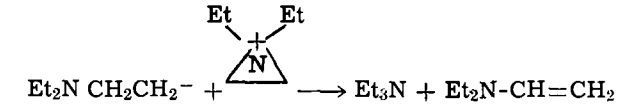

[4]

Numerous attempts to isolate radical products (other than organo-mercury compounds) by electrolyzing II at the first wave in the presence of known radical acceptors (*i.e.* butadiene, styrene, and acrylonitrile) were unsuccessful. However, the qualitative features (Fig. 4) of the cyclic voltammogram (11) as well as the detection of organo-mercury products are evidence for the formation of radical intermediates. The absence of radical coupling to give N,N,N',N'-tetraethylbutanediamine (VIII)

$$Et_2N(CH_2)_4NEt_2$$
VIII

is surprising in view of the reported formation of bibenzyl in the electrolysis of trimethylbenzylammonium salts (3). At present we have no explanation for this other than to note that dibenzylmercury is thermally converted to bibenzyl (12). As in the case of water, the formation of both diethylamine and triethylamine was observed indicating the potential control was not sufficient to prevent partial reduction to the anion followed by elimination or that radical abstraction by the diethylaminoethyl radical from acetonitrile is occurring. As discussed above, possibly trace amounts of succinonitrile were formed.

The following scheme is consistent with aziridinium salt electrolyses in aprotic solvents (Eq. [5])

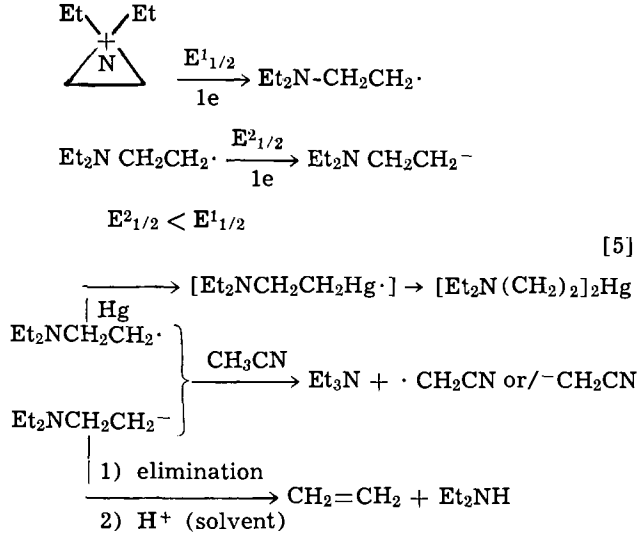

[5]

Conclusions

The shift in half-wave potential of the second reduction step with solvent is of prime importance and resolves the question of the fate of alkyl radicals under varying electrolysis conditions. The extreme shifts observed in this study are shown in Fig. 1c. In water the radical (as R· or RHg·) is reduced at a potential as positive as or more positive than that required to form it initially. Changing to an aprotic solvent (dimethylformamide or acetonitrile) shifts the potential for the reduction of this radical to more negative values so that two distinct electron transfers occur.

The product distribution obtained upon bulk electrolysis of the aziridinium salts in aqueous solution is consistent with an anhydrous region being present at the electrode surface. In view of this, it might be expected that polarographic data obtained in aqueous and nonaqueous solutions would be the same. It is clear that they are not. This apparent contradiction is resolved if one compares the changes occurring at an electrode under conditions of micro- and macro-electrolysis. Polarographic current densities are of a sufficiently small magnitude such that the solution pH is maintained at the electrode whereas under the conditions of a bulk electrolysis in which protons are involved, the higher current densities result in a highly basic electrode region. This is especially true when only a limited amount of water is available initially as a consequence of the presence of the ammonium salt. The observed effect under aqueous conditions is a product distribution indicative of an anhydrous electrode region.

Earlier work (2, 3) postulating reduction to a radical intermediate in protic solvents followed by homolytic cleavage of an OH bond from the solvent to give the observed product is perhaps better described in terms of a direct two electron reduction to an anionic fragment which then reacts with the solvent. In aprotic solvents the reduction apparently proceeds in the stepwise manner previously reported for similar reductive cleavages.

Manuscript submitted Sept. 18, 1970; revised manuscript received *ca.* May 10, 1971.

Any discussion of this paper will appear in a Discussion Section to be published in the June 1972 JOURNAL.

REFERENCES

1. R. Mantsavinos and J. E. Christian, *Anal. Chem.*, **30**, 1071 (1958).
2. J. S. Mayell and A. J. Bard, *J. Am. Chem. Soc.*, **85**, 421 (1963).
3. (a) M. Finkelstein, R. C. Petersen, and S. D. Ross, *J. Am. Chem. Soc.*, **81**, 2361 (1959); (b) S. D. Ross, M. Finkelstein, and R. C. Petersen, *ibid.*, **82**, 1582 (1960); (c) B. C. Southworth, R. Osteryoung, K. D. Fleischer, and F. C. Nachod, *Anal. Chem.*, **33**, 208 (1961).
4. L. Horner and H. Röder, *Chem. Ber.*, **101**, 4179 (1968) and references therein.
5. (a) N. J. Leonard, *Record Chem. Progress (Kresge-Hooker Sci. Lib.)*, **26**, 211 (1965); (b) D. R. Crist and N. J. Leonard, *Angew. Chem., Intern. Ed.*, **8**, 962 (1969).
6. (a) J. H. Wagenknecht and M. M. Baizer, *J. Org. Chem.*, **31**, 3885 (1966); (b) J. H. Wagenknecht and M. M. Baizer, *This Journal*, **114**, 1095 (1967).
7. J. L. Webb, C. K. Mann, and H. M. Walborsky, *J. Am. Chem. Soc.*, **92**, 2042 (1970).
8. K. B. Wiberg, *Chem. Rev.*, **55**, 713 (1955).
9. F. Matsuda, *Tetrahedron Letters*, 6193 (1966) and references therein.
10. J. P. Petrovich, *Electrochim. Acta*, **12**, 1429 (1967) and references therein.
11. D. A. Tyssee, *J. Electroanal. Chem.*, **30**, 14 (1971).
12. (a) K. C. Bass, *J. Organometal. Chem.*, **4**, 1 (1965); (b) K. C. Bass and P. Nababsing, *J. Chem. Soc. (C)*, 1984 (1966).

Adsorption of Thiourea and Derivatives at the In-Hg Electrolyte Interface

R. Narayan[1] and Norman Hackerman*,[2]

Department of Chemistry, The University of Texas at Austin, Austin, Texas 78712

ABSTRACT

The double layer capacitance and interfacial tension of polarized Hg, In, and In-Hg (10 to 60 mole percent [m/o] In) electrodes were measured in 0.1M perchloric acid in a mixture of potassium chloride and hydrochloric acid (pH 1.6) and in the electrolytes containing thiourea and derivatives using the galvanostatic charging technique. Addition of thiourea increases the capacitance of the mercury electrode over the whole range of potentials. With the In-Hg electrodes, thiourea addition depresses the capacitance over a range of anodic potentials and increases the values over a range of cathodic potentials. A pronounced hump in the capacitance curve is observed; the nature of the hump and the depression of the capacitance are markedly influenced by the presence of Cl^-. These results are interpreted in terms of a reorientation of the adsorbed species in the interface. Effects of substituent groups on the above behavior were investigated using S-methyl isothiourea and tetramethyl thiourea.

The adsorption of thiourea from aqueous solutions at a mercury electrode has been investigated recently by capacity measurements (1) and tensammetric studies (2). Double layer capacity measurements with a mercury electrode in aqueous solutions containing thiourea have been very useful in the understanding of metal/solution interfaces. The results have been variously interpreted by Parsons (3) and Devanathan (4); the former investigating the dielectric behavior of the inner layer based on these results. Dutkiewicz and Parsons (5) studied the adsorption of thiourea from formamide at a mercury electrode, and observed that a direct interpretation of the capacity curves is rather difficult. The present investigation was undertaken to study the influence of the material of the electrode on the adsorption behavior of thiourea. Amalgams of compositions varying from 0-60 m/o can be easily prepared and handled. Butler (6,7) obtained electrocapillary curves for indium amalgams in 0.1M $HClO_4$ using the sessile drop method and double layer capacitances for the same system with a fast dropping amalgam electrode and a capacitance bridge. The In-Hg/0.1M $HClO_4$ system behaves like an ideally polarizable system over a range of potentials and the characteristic capacitance "hump" is also seen with amalgams of higher concentration (40%). It was believed worthwhile to obtain evidence by using the alternative charging curve technique and a hanging drop electrode, and to study adsorption characteristics at the interface. The use of a hanging drop electrode would also prove useful to achieve near equilibrium for any slow adsorption processes.

Experimental

All chemicals were analytical grade materials. The solutions were prepared using conductivity water. Supporting electrolyte solutions were treated with purified activated charcoal prior to use. The mercury was double distilled under vacuum and indium was 99.99% pure. The amalgams were prepared by adding the requisite amount of indium to weighed quantities of mercury kept under acidified water. The amalgams were stored in closed glass containers and kept in a vacuum desiccator.

The microelectrode was a hanging drop electrode, supplied by Metroohm Instruments and worked satisfactorily both with mercury and with amalgams. The areas were checked from weight measurements (assuming the small drop to be nearly a sphere) and capacitance measurements for mercury in 0.1M KCl. Agreement between the two methods was satisfactory. The counterelectrode was a large cylindrical platinum gauze. Attempts were also made to use indium rods as microelectrodes but with only partial success.

Cells were designed to accommodate a saturated calomel electrode with an intervening bridge of the experimental solution. A flat surface was incorporated into the main body of the cell for observation of the meniscus in the electrocapillary measurements.

Pure helium was used for degassing in the capacitance measurements and cylinder N_2, after passing through a purification train, was used for degassing and maintenance of pressure in the electrocapillary studies.

Capacitance measurements were made by the method developed earlier in this laboratory by Riney *et al.* (8). Potential time curves were obtained on a Tektronix oscilloscope 535A with a plug-in D type preamplifier and recorded using a Polaroid camera. The initial linear region (the first 5-10 μsec in the potential time trace) was used for calculations.

Results

Capacitance values for indium amalgam electrodes in 0.1M $HClO_4$ show satisfactory agreement with those obtained by Butler (7) who used an a-c bridge for his measurements. Capacitance-potential variations in KCl-HCl are similar to those in 0.1M $HClO_4$ but the capacitance values are generally higher. The hump is also observed in KCl-HCl medium. Capacitance curves with addition of Cl^- ions to $HClO_4$ are similar to those in $HClO_4$ but with larger capacitance values, significantly large with electrodes of higher amalgam concentration (greater than 20% amalgam concentration).

Addition of thiourea results in a depression of the capacitance of the amalgam electrode over a range of potentials (Fig. 1 and 2), the range depending on amalgam concentration. At cathodic potentials the capacitance increases to a value above that in the supporting electrolyte and the transition is marked by a rounded hump in the curves (Fig. 2). A sharp peak is observed when Cl^- ions are present in small quantity (Fig. 3) and the depression in the capacitance at anodic potentials is also greater. This observation is restricted to electrodes with 20% or more of indium in the amalgam.

In a chloride solution, the influence of amalgam concentration is even more marked; sharp peaks being

* Electrochemical Society Active Member.
[1] Present address: Department of Chemistry, Indian Institute of Technology, Madras 36, India.
[2] Present address: Department of Chemistry, Rice University, Houston, Texas 77001.
Key words: double layer capacitance, hanging drop electrode, surface orientation.

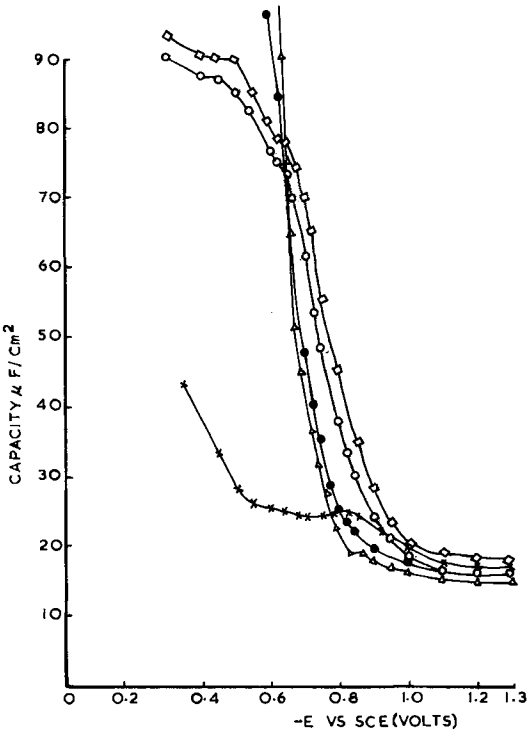

Fig. 1. Capacity potential variations for 10 m/o indium amalgam in 0.1M $HClO_4$ with additions of thiourea and derivatives. ●—0.1M $HClO_4$, ○—0.0052M thiourea, □—0.0105M thiourea, ×—0.0016M tetramethyl thiourea, △—0.0063M S-methyl isothiourea.

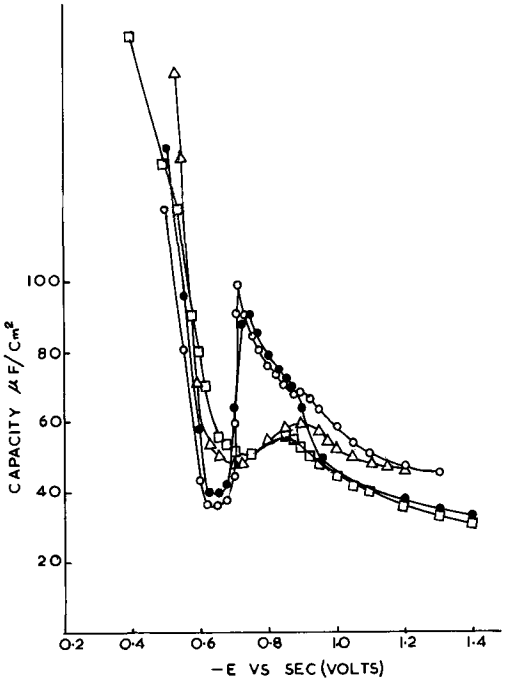

Fig. 3. Effects of additions of thiourea and Cl^- on the double layer capacitance with 60 m/o indium amalgam in 0.1M $HClO_4$. □—0.1M $HClO_4$ + 0.0052M thiourea, ●—0.1M $HClO_4$ + 0.0052M thiourea + 0.01M HCl, △—0.1M $HClO_4$ + 0.0210M thiourea, ○—0.1M $HClO_4$ + 0.0210M thiourea + 0.01M HCl.

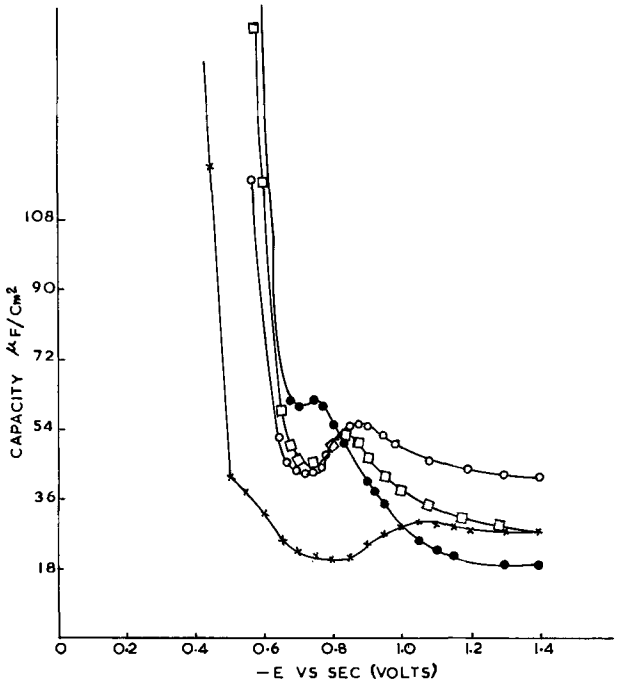

Fig. 2. Capacity potential variations for 50 m/o indium amalgam in 0.1M $HClO_4$ with additions of thiourea and derivatives. ●—0.1M $HClO_4$, □—0.0105M thiourea, ○—0.0210M thiourea, ×—0.0016M tetramethyl thiourea.

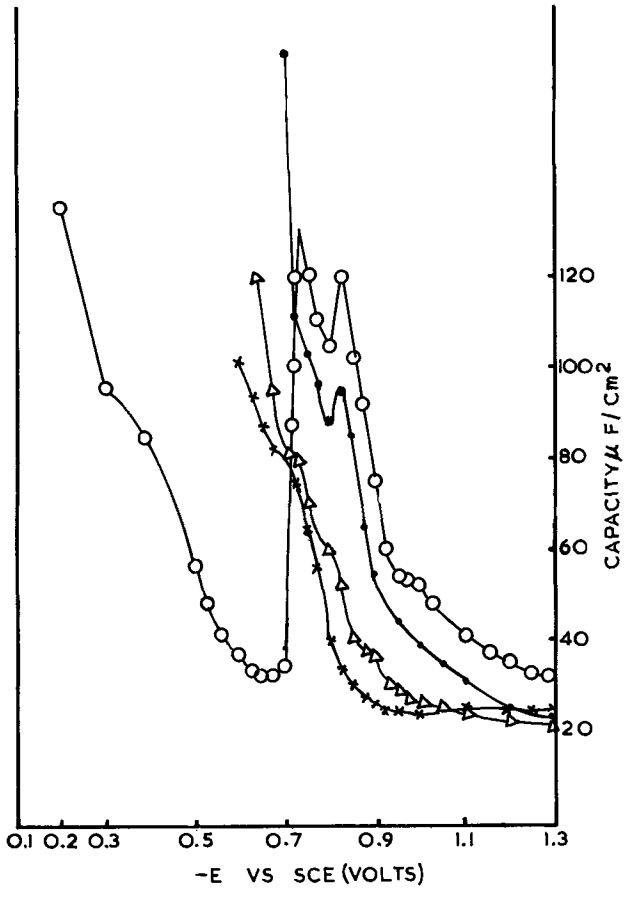

Fig. 4. Effect of additions of thiourea and derivatives on the double layer capacitance with 60 m/o indium amalgam in KCl + HCl. ●—KCl + HCL (pH = 1.6), ○—KCL + HCl + 0.0052M thiourea, △—KCl + HCl + 0.0063M S-methyl derivative, ×—KCl + HCl + 0.0016M tetramethyl derivative.

obtained instead of humps with 25% or higher amalgams (Fig. 4, 5, and 6). Electrocapillary studies (Fig. 7) indicate that thiourea and tetramethyl thiourea are very strongly adsorbed and shift the potential of zero charge (pzc) to more cathodic potentials. The capacitance in the presence of tetramethyl thiourea is decreased over a large range of potentials. No sharp desorption peaks are observed (Fig. 1, 2, 4, and 5). With

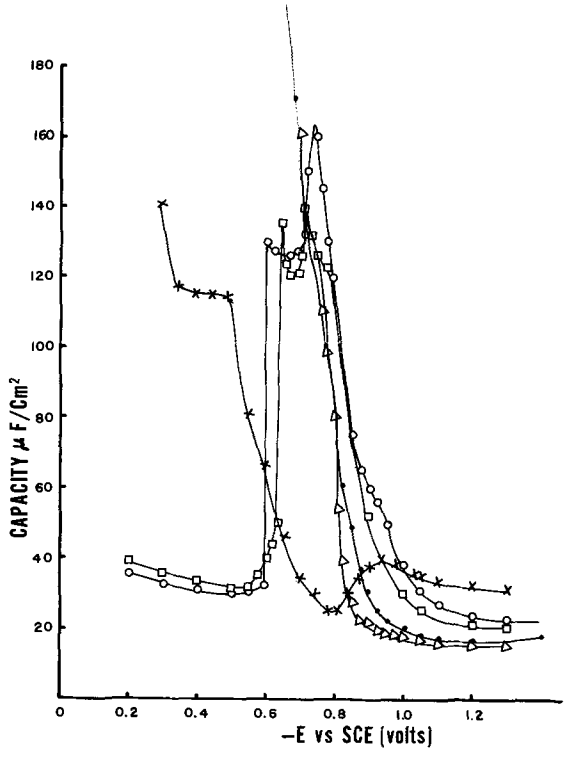

Fig. 5. Double layer capacitance of 25 m/o indium amalgam in a solution of KCl + HCl (pH = 1.6) with additions of thiourea and derivatives. ●—KCl + HCl (pH = 1.6), □—0.0105M thiourea, ○—0.0210M thiourea, ×—0.0016M tetramethyl thiourea, △—0.0063M S-methyl isothiourea.

S-methyl isothiourea both capacitance (Fig. 1, 4, 5, and 7) and interfacial tension values are lowered to a very small extent over the whole range of potentials.

Discussion

The characteristic humps of capacitance curves are evident in the In-Hg/electrolyte system. In 0.1M $HClO_4$ the maximum of the hump occurs at approximately 100 mV more anodic than the potential of zero charge for mercury and amalgams of 50 and 60 m/o respectively. The charge q_m is different for the three electrodes at this potential. Thus the processes causing the humps seem to be potential dependent. The hump is perhaps absent in the case of amalgams of lower concentrations due to dissolution of indium from the amalgam at cathodic potentials. The pzc is known to be close to the potential for reversible dissolution of indium in the concentration range 1 to 20 m/o.

Parsons (3) explained the increased capacitance of mercury electrodes in the presence of thiourea as being due to the constant orientation of this species with the negative end of its dipole toward the mercury. With the amalgam electrodes the capacitance is increased over a range of potentials in the presence of thiourea, probably resulting from a similar orientation of the dipole. However, the capacitance is lowered when the electrode is anodically polarized beyond a certain potential, the transition being marked by a hump in the capacitance curve.

The potential range and height of this hump depend on the concentration of the amalgam and, to a lesser extent, on the concentration of thiourea. Electrocapillary studies by us indicate that the maxima of these humps for the higher concentrations occur at potentials practically coinciding with the respective pzc and that thiourea is strongly adsorbed in this region, as shown by a lowering of the interfacial tension. Thus these humps do not result from a slow desorption of thiourea.

The constant orientation of thiourea can be the result of strong Hg-S interaction. The capacitance

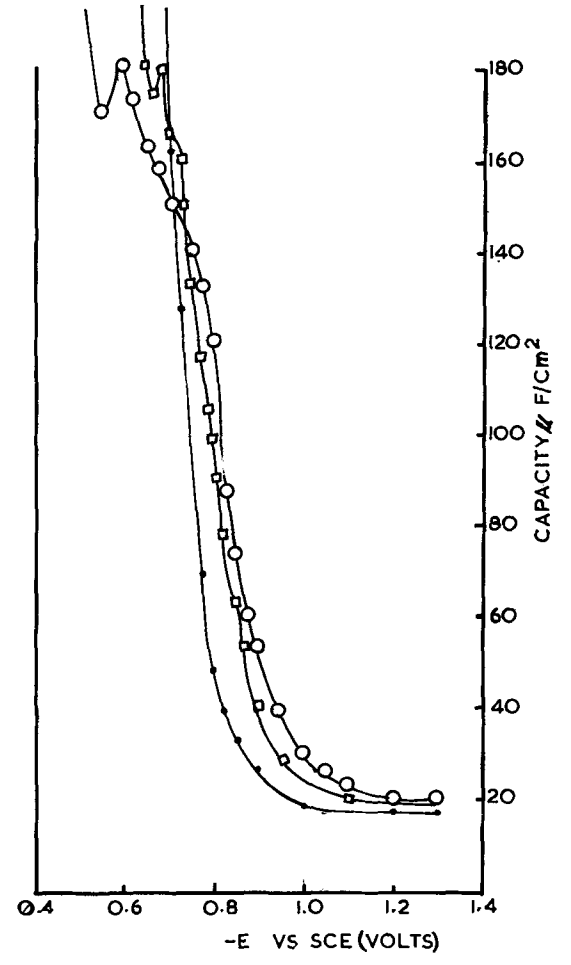

Fig. 6. Double layer capacitance of 20 m/o indium amalgam in a solution of KCl + HCl (pH = 1.6) with additions of thiourea and derivatives. ●—KCl + HCl (pH = 1.6), □—0.0105M thiourea, ○—0.0210M thiourea.

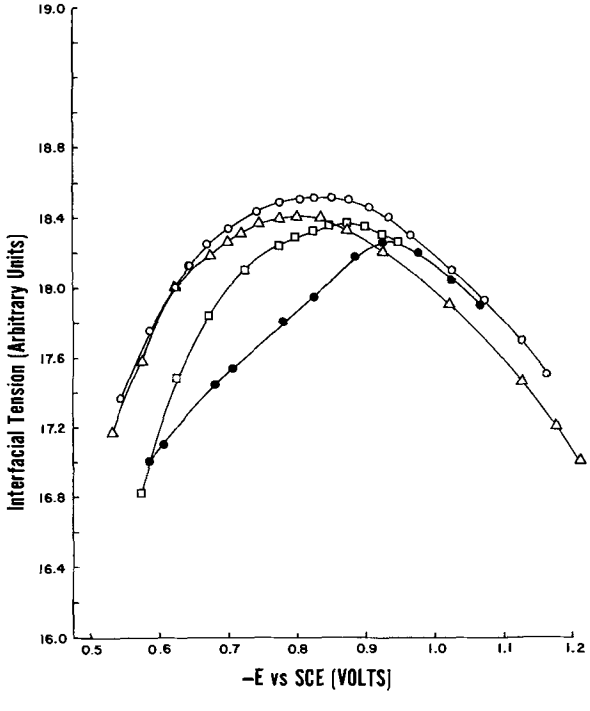

Fig. 7. Electrocapillary curves for 50 m/o indium amalgam in 0.1M $HClO_4$. ○—0.1M $HClO_4$, △—0.1M $HClO_4$ + 0.0063M S-methyl isothiourea, □—0.1M $HClO_4$ + 0.0052M thiourea, ●—0.1M $HClO_4$ + 0.0016M tetramethyl thiourea.

being lowered below the values in the supporting electrolyte at anodic potentials is indicative of a change in the adsorption layer. Electrocapillary studies with indium amalgams (6, 9) show that the interfacial composition of indium increases with anodic polarization. Curves for lower concentrations of amalgams show that indium is even positively adsorbed at potentials anodic to the pzc. Such positive adsorption is observed for higher concentrations of amalgams (<10.3%) in the presence of bromide ions (9). Thiourea with its specific adsorptive character can exert a similar influence, increasing the interfacial concentration of indium. Thus we expect with positive polarization an increased interaction involving indium, possibly as an $In-N^+$ interaction. This in turn should result in reorientation of the adsorbed species and hence a different capacitance. With increasing positive polarization the state where all dipoles were oriented with S toward Hg will change to a state with more and more dipoles oriented with N^+ toward In, the transition being marked by a hump in the capacitance curves. Information, at present lacking, regarding complexes of thiourea will prove useful in this context. We have to also consider relative changes in the electronegativities of Hg and In and any compound formation as the interfacial composition of In is increased.

In the presence of small concentrations of Cl^-, sharp peaks are obtained instead of humps. In a solution with chloride as the only anion, additional peaks at more anodic potentials are seen. Further, the lowering of capacitance due to thiourea becomes greater and a flat region extending over 50 mV is obtained. The capacitance at more cathodic potentials (−1.0V) is not affected. Lastly, the formation of peaks instead of humps in the presence of Cl^- ions is seen only when the concentrations of indium exceed 20 m/o in the amalgam.

The electrocapillary studies showed that Cl^- is adsorbed from a solution of 0.1M $HClO_4$. The pzc is shifted cathodically to a small extent due to this adsorption. To some extent Cl^- also increases the double layer capacitance of amalgam electrodes of composition exceeding 20 m/o of indium.

The calculations of Parsons (3) show that lateral interactions (repulsive) are very strong in the adsorbed layer containing thiourea dipoles. Hence if repulsive forces are considerable, then the adsorbed Cl^- ions act as bridges to reduce these forces, a more likely process with the positive ends of the dipoles oriented toward the metals. Additional dipoles can thus be accommodated and a greater depression in capacitance would result, as observed. The process of reorientation may also take place readily over a short range of potentials leading to the sharp peaks rather than humps.

It is more difficult to understand the critical composition of 20 m/o of indium in the amalgam to bring about the influence of the Cl^- ions. The adsorption of Cl^- ion is obviously the result of specific interaction forces between the metal and Cl^- and hence would depend on the interfacial composition of the amalgam. Upon specific adsorption Cl^- can indeed change the relative surface excess of In and may have an even greater influence in the presence of thiourea. One can further point to a relevant observation of Butler (6). The negative surface excess or surface deficiency of indium passes through a maximum in 0.1M $HClO_4$ for all potentials at approximately 20 m/o indium in the bulk of the amalgam. Frumkin (9), however, has indicated the necessity of keeping in mind possibilities of compound formation, for example, $InHg_3$ at 26 m/o In.

A 10% amalgam electrode obviously behaves like a mercury electrode. The adsorption of thiourea increases the capacitance over the entire ideally polarizable region, and the increase is greater with increased adsorption or concentration of thiourea. The dissolution of indium from this amalgam takes place at potentials more positive than approximately −0.65V and thiourea has some influence on this dissolution. The measurement of the capacitance becomes less accurate at such positive potentials and hence curves extending over the same potential range could not always be obtained. However, we observe from Fig. 2 and 3 that thiourea with its differential effects does not unduly affect the dissolution of indium from the amalgams with higher indium concentrations. Thus all the arguments given are truly restricted to the ideally polarizable region. In a purely chloride medium (Fig. 4, 5, and 6) there is a gross change in the behavior of indium of dissolution in the presence of thiourea, particularly for the lower concentration of amalgam (25% indium). Further studies have to be made before offering any explanation.

Tetramethyl thiourea, even in very small concentrations, adsorbs strongly at the Hg-solution and amalgam-solution interface. From electrocapillary studies, the desorption potential is taken to be about −1.0V. There is a considerable lowering of the interfacial tension and, to a lesser extent, the capacitance. This behavior resembles most surfactants except that a depression peak is absent in the capacitance. Kumler and Fahler (10) report that symmetrical substitution of the four hydrogens in thiourea decreases the dipole moment because steric hindrance prevents occurrence of forms with separation of charges which would make an appreciable contribution to the structure. As compared with thiourea, the decreased dipole moment may be reflected in a lowering of the capacitance. Any increase of the thickness of the double layer due to adsorption will also lead to a lowering. Steric factors appear to prevent N^+ to metal interaction so this derivative is always adsorbed with the S adjacent to the metal, no reorientation being possible. Thus the capacitance curves would be similar with both mercury and amalgam electrodes. Further, in the absence of reorientation, effects due to Cl^- are not expected.

The weak adsorption of the S-methyl derivative, as indicated by the very small lowering of capacitance and interfacial tensions, the nearly symmetrical nature of the electrocapillary curves, and the absence of any effect on the overvoltage for hydrogen discharge (thiourea and tetramethyl thiourea considerably reduce this factor), indicate that the mechanism of adsorption is different from that of the other two. By blocking the $-S$ by a $-CH_3$ group, it is likely that adsorption even at a mercury solution interface is through the nitrogen over the whole range of potentials and as a less dipolar species. Thus reorientation is unlikely and interaction forces are reduced. Hence the presence of Cl^- will not bring about any great changes in the adsorption except as a competing species.

More light can probably be shed on these forces of interaction by similar measurements using other metals for electrodes and also electrochemical polarization techniques. One approach would be to study the corrosion inhibition behavior of thiourea and derivatives. Some such studies have been done (11). It is known that thiourea in small concentrations (1 to 3 mM) inhibits corrosion but that it promotes the process when present in higher concentrations. Further investigations by one of us (RN) have shown that S-methyl and S-benzyl derivatives inhibit the corrosion of iron, the efficiency increasing with the concentration of the inhibitor (CE is 90% at 40 mM concentration).

Acknowledgments

The authors gratefully acknowledge the financial support of this work by The Robert A. Welch Foundation of Houston, Texas and the Office of Naval Research under Contract Nonr-375(15).

Manuscript submitted Oct. 20, 1970; revised manuscript received *ca.* April 13, 1971. This was Paper 73 presented at the Chicago Meeting of the Society, Oct. 15-19, 1967.

Any discussion of this paper will appear in a Discussion Section to be published in the June 1972 JOURNAL.

REFERENCES

1. F. W. Schapink, M. Oudeman, K. W. Leu, and S. N. Helle, *Trans. Faraday Soc.*, **56**, 415 (1960).
2. R. Narayan, *Proc. Nat. Inst. Sci. India*, **32A**, 63, 1966; and *Proc. Indian Acad. Sci.*, **54**, 109 (1961).
3. R. Parsons, *Proc. Roy. Soc.*, **261A**, 79 (1961).
4. M. A. V. Devanathan, *ibid.*, **264**, 133 (1961).
5. E. Dutkiewicz and R. Parsons, *J. Electroanal. Chem.*, **11**, 196 (1966).
6. J. N. Butler, *J. Phys. Chem.*, **69**, 3817 (1965).
7. J. N. Butler, *J. Electroanal. Chem.*, **9**, 237 (1965).
8. J. S. Riney, G. Schmid, and N. Hackerman, *Rev. Sci. Instr.*, **32**, 588 (1961).
9. N. S. Polyanorskaya and A. N. Frumkin, *Elektrokhimiya*, **1**, 538 (1965).
10. W. D. Kumler and J. Fahlen, *J. Am. Chem. Soc.*, **64**, 1942 (1944).
11. I. A. Ammar and J. S. Darwish, *Corrosion Sci.*, **7**, 579 (1967).

The Low-Temperature Activity of Water in Concentrated KOH Solutions

P. Bro* and H. Y. Kang*

P. R. Mallory & Company, Inc., Laboratory for Physical Science, Northwest Industrial Park, Burlington, Massachusetts 01803

ABSTRACT

The vapor pressures of H_2O-KOH solutions were measured manometrically between −40° and 25°C for concentrations between 2*M* KOH and 15*M* KOH. The effect of the temperature on the vapor pressure agreed with that predicted from the Clapeyron equation. An increase in the KOH concentration decreased the vapor pressure. The logarithm of the relative activity of KOH increased almost linearly with the KOH concentration, but it changed little with temperature. The data suggest that KOH hydrates occur as solid phases in the low concentration portion of the phase diagram. Furthermore, the existence of a eutectic point in the system was reflected in the properties of the solutions at temperatures far above the eutectic point.

The thermodynamic properties of concentrated potassium hydroxide solutions are of interest because they affect the operation of alkaline batteries. Water is consumed at metal oxide cathodes with the formation of hydroxyl ions, *e.g.*

$$HgO + 2e^- + H_2O \rightarrow Hg + 2\,OH^-$$

and, at low temperatures in particular, the kinetics of this reaction are affected by the activity of the water. The hydroxide formed at a zinc anode is in equilibrium with water

$$Zn(OH)_2 \rightleftharpoons ZnO + H_2O$$

and the state of the reaction product depends on the activity of the water. The activity of the potassium hydroxide is also of paramount importance, but that is not discussed here. Note that we employ $Zn(OH)_2$ and ZnO to designate the zinc ion species present in the system without implying that they are the species actually present (1). The reduction of water by zinc, with the formation of hydrogen, is also of interest, but it is of less importance at low temperatures.

There is a paucity of thermodynamic data on the H_2O-KOH system at low temperatures. The phase diagram of the H_2O-KOH system has been published (2), and its utility for the analysis of the performance of alkaline batteries is well recognized (3). Data are available on the activity of KOH in aqueous KOH solutions to concentrations of 4.0*M* KOH between 0° and 35°C (4) and to 17.0*M* KOH between 0° and 70°C (5). The activity of the water in KOH-H_2O solutions are available at 0°C (6) and 25°C (7), but no activity data are available for temperatures below 0°C which is a region of great interest for battery applications because of the severe low-temperature limitations on battery performance. The activity of the water in H_2O-KOH solutions is reported in this paper.

* Electrochemical Society Active Member.

Key words: H_2O-KOH system, H_2O-KOH-ZnO system, concentrated electrolytes, thermodynamic properties, low-temperature activity, vapor pressure, heat of vaporization, Gibbs-Duhem equation, phase diagram, eutectic behavior.

Experimental Methods

The activity of the water in the alkaline solutions was determined by measuring the vapor pressure of water above the solutions using the all-glass high-vacuum apparatus shown schematically in Fig. 1. The system was evacuated with S1 closed and S2-S4 open. Then, the sample container was connected to the vacuum line, the sample being located inside the low-temperature chamber (Associated Testing Laboratories, Model No. SW-5101), and the solution was frozen in a liquid nitrogen trap. S4 was then closed and S1 opened. When the pressure had decreased to about 10^{-5} mm Hg, S1 was closed and the sample warmed to room temperature. The same procedure was repeated three times to remove residual gases from the solution. Then, S1 was closed, S4 opened, and the system brought to about 10^{-5} mm Hg. When the sample had reached the desired temperature, as judged from the temperature of an identical sample container located near the

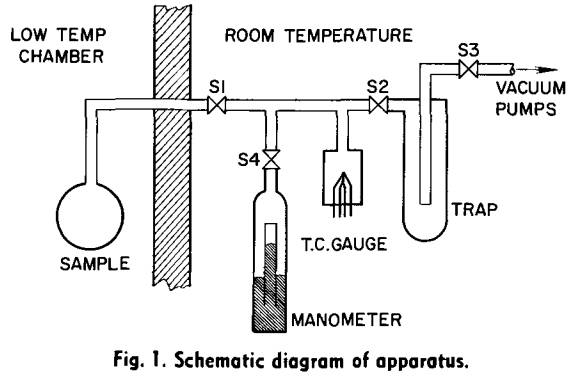

Fig. 1. Schematic diagram of apparatus.

shielded window of the low-temperature chamber, S2 was closed and S1 opened. The system was kept in this state until a constant pressure was observed on the pressure gauges (NRC thermocouple gauge No. 501 and a homemade Dubrovin gauge reading to 0.10 mm Hg). The gauges were calibrated using triply distilled water in the sample container instead of KOH solutions, and literature values (8) were used for the vapor pressure of ice and water.

The low-temperature chamber maintained the desired temperatures within ±0.5°C, and the sample temperatures were read with liquid-filled thermometers from a batch of thermometers having a standard deviation of 1.5°C from an NBS certified temperature over the entire temperature range. Replication of the pressure measurements indicated a precision of ±0.11 mm Hg at 10.0 mm Hg and ±0.0035 mm Hg at 0.300 mm Hg.

The potassium hydroxide solutions were prepared from Fisher Polypac 45.2% KOH solutions by dilution with triply distilled water. All the solutions were stored under argon atmospheres and all the solutions were prepared in argon-filled glove bags to eliminate CO_2 contamination.

Experimental Results

The observed vapor pressures are given in Table I for the KOH-H_2O system. The reported values were obtained on single-phase systems. At low-temperatures phase separations occurred with some of the solutions, but since phase separation gives rise to changes in the composition of the solutions the observed vapor pressures of the two-phase systems is of little interest, except as noted later.

The values reported in Table I were obtained in the chronological sequence shown. There appears to be a good agreement between the values obtained when the measurement temperatures were approached from above and from below and this agreement is taken as evidence that equilibrium prevailed in the system. It may be seen that the vapor pressures decreased markedly with a decrease in the temperature and with an increase in the KOH concentration.

Table I. Observed vapor pressure of H_2O-KOH solutions

T, °C	P, mm Hg	T, °C	P, mm Hg
10.3 w/o KOH 2.04M KOH		14.8 w/o KOH 3.08M KOH	
25	20.8	25	20.5
11	8.40	12	9.00
0	4.08	0	3.75
−11	1.70	−11	1.75
−9	1.78	−10	1.75
1	4.25	1	4.00
12	9.50	14	10.5
25	21.1	25	20.5
23.0 w/o KOH 5.32M KOH		30.3 w/o KOH 7.75M KOH	
25	17.2	25	13.5
11	7.50	10	5.25
0	3.00	−1	2.25
−11	1.25	−11	0.920
−21	0.630	−20	0.476
−31	0.230	−32	0.151
−31	0.230	−41	0.068
−22	0.500	−31	0.195
−10	1.50	−21	0.450
0	3.00	−10	1.05
9	6.00	−1	2.25
27	19.5	10	5.25
		25	13.3
37.0 w/o KOH 10.5M KOH		45.2 w/o KOH 14.7M KOH	
25	9.35	25	4.75
11	3.45	10	1.65
0	1.60	0	0.580
−10	0.740	−10	0.270
−21	0.280	−20	0.110
−31	0.135	−30	0.040
−41	0.050	−30	0.041
−31	0.145	−20	0.105
−20	0.340	−10	0.250
−9	0.740	0	0.640
1	1.70	10	1.70
12	3.80	25	4.75
26	9.84		

Table II. Least square constants and vapor pressures, H_2O-KOH

KOH conc	2.04M	3.08M	5.32M	7.75M	10.5M	14.7M
Log A*	21.67	21.34	21.52	21.29	20.36	22.79
B, °K	5546	5457	5564	5572	5423	6330
T, °C						
25	21.3	20.7	17.3	13.4	8.69	4.70
20	15.5	15.1	12.6	9.71	6.37	3.27
15	11.2	10.9	9.03	6.98	4.62	2.25
10	7.95	7.82	6.42	4.96	3.31	1.53
5	5.59	5.53	4.51	3.48	2.35	1.02
0	3.88	3.86	3.12	2.41	1.64	0.673
−5	2.65	2.66	2.14	1.65	1.13	0.436
−10	1.79	1.81	1.44	1.11	0.771	0.279
−15	—	1.21	0.955	0.736	0.517	0.175
−20	—	—	0.625	0.480	0.341	0.108
−25	—	—	0.400	0.308	0.222	0.065
−30	—	—	0.252	0.194	0.141	0.038
−35	—	—	—	0.120	0.088	—
−40	—	—	—	0.073	0.054	—

* Natural logarithm, mm Hg.

In order to facilitate the comparison of the data, the least square values were computed using the correlation

$$P = A \exp(-B/T) \quad [1]$$

and the smoothed data are given in Table II together with the constants A and B.

Discussion

Our results may be compared with the values reported in the literature for the KOH-H_2O solutions at 25°, 20°, and 0°C; no values were found in the literature for lower temperatures. The comparison is illustrated in Fig. 2. It may be noted that the Kangro and Groeneveld (7) and the Dieterici (6) results were obtained by direct measurements of the vapor pressures and the Kobayashi (9) and the Robinson and Stokes (10) values were obtained by calculation from emf measurements. The latter used the data of Harned and Cook (4) and of Akerlof and Bender (5). All the 25°C values from the literature are in good agreement. It may be seen that our data fall slightly below the literature values at 25°C for the more concentrated KOH solutions, but otherwise they agree reasonably well. The 20°C data of Kangro and Groeneveld lie very close to their 25°C data, but slightly below the 25°C points shown in Fig. 2. Our 20°C data likewise fall slightly below our 25°C data. They are not shown in Fig. 2 to avoid cluttering the graph. At 0°C our data lie a little further below the 25°C data points, as may be seen in Fig. 2, but the 0°C water activity-KOH concentration curve generally follows the course of the 25°C curves. The data reported by Dieterici for 0°C lie considerably above all the other values shown in Fig. 2 and may be considered, at least provisionally, to be in error.

The consistency between the literature values and our results lends support to the belief that our results

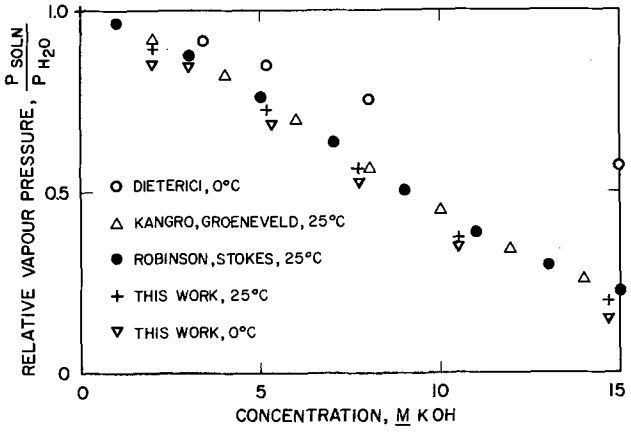

Fig. 2. Comparison of vapor pressure data of H_2O-KOH solutions.

Table III. Comparison of the vapor pressure of ice and of $KOH-H_2O$ solutions at the freezing points

Solution, M KOH	Freezing point,* °C	Vapor pressure, mm Hg Solution	Ice**
2.04	−9.2	1.91	2.093
3.08	−15.6	1.15	1.175
5.32	−34.0	0.172	0.187
7.75	−60.6	—	—
10.5	−43.0	0.040	0.0684
14.7	−34.3	0.024	0.182

* From data of Cohen-Adad and Michaud (2).
** From ref. (8).

at the lower temperatures provide a reliable set of values for the vapor pressure of the KOH solutions.

The $KOH-H_2O$ phase diagram presented by Cohen-Adad and Michaud (2) indicates the formation of ice in solutions containing less than 30.9 w/o (weight per cent) KOH and of $KOH \cdot 5H_2O$ in more concentrated solutions upon cooling. This being the case, it is to be expected that the observed vapor pressure data should extrapolate to values close to but slightly greater than those of pure ice and $KOH \cdot 5H_2O$, respectively, at the temperatures reported to be the freezing points of the solutions. This comparison is made in Table III for the $KOH-H_2O$ solutions. It may be seen that the solution vapor pressures are consistently lower than that of ice. In the case of the 14.7M KOH solution it is known that the solid phase is $KOH \cdot 5H_2O$ and its vapor pressure would be expected to be lower than that of ice at the same temperature. For the less concentrated solutions the experimental data indicate that the solid phase in equilibrium with the solutions, if ice, would have a greater water activity than the solutions and this appears to be unreasonable. The results suggest that the H_2O is more strongly bound in the solutions than in ice at the same temperatures. It follows that the solid phases may not be ice at all but some hydrates of KOH. Although the published $KOH-H_2O$ phase diagram does not indicate any solid phases other than ice for the less concentrated solutions some work of O'Nan (11) indicates that solid KOH hydrates do indeed form in the less concentrated $KOH-H_2O$ solutions. This matter is of some importance for the low-temperature operation of alkaline cells where alkali depletion occurs in the anodes, and their operability depends on whether pure ice forms or a more KOH-rich phase. The relevant considerations have been discussed by Gomis *et al.* (3).

The vapor pressure correlation represented by Eq. [1] is the integrated form of the Clapeyron equation for an ideal vapor with neglect of the liquid volume, and we have

$$\Delta H_{vap} = BR \qquad [2]$$

(R is the gas constant)

The experimental data gave the heats of vaporization shown in Table IV. It was independent of temperature between −40° and 25°C, and changes in the concentration of KOH did not affect it perceptibly. The average heat of vaporization was 11.2 kcal/mole. This value may be compared with the literature values of 10.4 kcal/mole at 30°C and 10.7 kcal/mole at 0°C (12) for the heat of vaporization of pure water. The good agreement between the two sets of values suggests that the water is present in the alkaline solutions in the same thermodynamic state as it is in pure water, except for possible differences in its state of order.

Table IV. Heat of vaporization of water from alkaline solutions

KOH, molal conc	ΔH_{vap}, kcal/mole
2.04	11.0
3.08	10.8
5.32	11.1
7.75	11.1
10.5	10.8
14.7	12.6

The vapor pressure of the H_2O-KOH solutions may be used to calculate the activity coefficient of the KOH by means of the Gibbs-Duhem equation. However, two problems arise which require that the usual integration path be replaced by a more appropriate choice. The Gibbs-Duhem equation is generally integrated by the use of the osmotic coefficient of the solution, and it is necessary to integrate from the state where the osmotic coefficient approaches unity; the standard state. At temperatures below 0°C it is not possible to measure the vapor pressure of very dilute KOH solutions, since a phase change occurs, and the osmotic coefficient cannot be determined. Another problem concerns the accuracy of the osmotic coefficients calculated from solution vapor pressures of dilute solutions. A tremendous error magnification occurs for dilute solutions, and vapor pressure data are not suitable for the calculation of electrolyte activity coefficients for dilute solutions. The dilemma posed by the two problems can be resolved by selecting an experimentally accessible reference state. The choice of reference state is quite arbitrary, but convenience dictates that the same reference state be used for all the temperatures of interest. We selected, therefore, the eutectic composition as the reference state for the H_2O-KOH system, and integration of the Gibbs-Duhem equation gives the activity of the KOH solution of any composition relative to the KOH activity of a solution at the same temperature having the eutectic composition. The relative activities are given in Table V, and the data available from the literature have been included for comparison. No data are available at temperatures other than 25°C, but it may be seen that our results agree well with the published data at 25°C. Some discrepancies occur in the most dilute and the most concentrated solutions where the vapor pressure measurements are recognized to be a poor means for obtaining electrolyte activity data.

Table V. Relative activity* of KOH in H_2O-KOH solutions

KOH M	−40°C	−30°C	−20°C	−10°C	0°C	10°C	20°C	25°C	25°C, literature value**
2	—	—	—	—	0.029	0.036	0.048	0.10	0.059
3	—	—	—	0.080	0.064	0.078	0.082	0.13	0.104
4	—	—	0.14	0.16	0.13	0.14	0.15	0.17	0.179
5	—	0.25	0.25	0.26	0.23	0.24	0.23	0.26	0.275
6	0.41	0.41	0.42	0.43	0.39	0.40	0.37	0.41	0.439
7	0.65	0.66	0.66	0.65	0.64	0.62	0.62	0.64	0.648
8	1.00	1.00	1.00	1.00	1.00	1.00	1.00	1.00	1.00
9	1.5	1.5	1.4	1.5	1.6	1.5	1.5	1.6	1.40
10	2.4	2.3	2.2	2.3	2.7	2.3	2.4	2.5	2.06
11	3.7	3.5	3.4	3.5	4.5	3.6	3.5	3.9	2.85
12	—	5.7	5.3	5.3	7.3	5.5	5.0	5.6	4.18
13	—	9.6	9.0	8.2	11.4	8.3	7.0	7.9	5.50
14	—	19.7	19.3	15.8	18.6	12.6	10.4	10.9	7.35

* Relative mean molal activity with reference to an 8.0M KOH solution.
** Reference (10), recalculated to 8M KOH reference state.

The good agreement between our results and the published values at 25°C suggests that our results at the lower temperatures provide a valid measure of the relative activity of KOH in aqueous solutions at the lower temperatures as well. It may be noted that the KOH activity of the solutions increases very strongly with the KOH concentration. The logarithm of the relative activity increases almost linearly with the KOH concentration at all the temperatures shown. The rate of increase appeared to be nearly independent of temperature.

The Gibbs-Duhem equation was integrated via the term $(M \cdot P)$, *i.e.*, the product of the KOH concentration and the vapor pressure, and it was observed that plots of $(M \cdot P)$ *vs.* M displayed well defined maxima, Table VI. All the maxima occurred at the eutectic composition of the H_2O-KOH system regardless of the solution temperature. The maxima in these curves are equivalent to inflection points in the chemical potentials of KOH at the eutectic composition of the solutions at the various temperatures. Such inflection points are normally associated with stability regions, and it is interesting that the stabilizing influences responsible for the formation of a eutectic point should be discernible at temperatures much above the eutectic temperature.

It is well known (13) that the concentration of zinc oxide in electrolytically generated zincate solutions in H_2O-KOH have zinc oxide concentrations in excess of the reported equilibrium values (14), and it was of interest to examine the effect of the zinc oxide on the vapor pressure of the H_2O-KOH solutions likely to occur in alkaline cells with zinc anodes. We prepared some H_2O-KOH-ZnO solutions with a ZnO concentration exceeding the equilibrium values and measured their vapor pressures with the results shown in Table VII. It may be seen by comparing the results with the data in Table II that the addition of ZnO led to a decrease of the vapor pressure of all the H_2O-KOH solutions at room temperature. At lower temperatures the same effect persisted but only in the dilute KOH solutions. As the temperature decreased the vapor pressure of the H_2O-KOH-ZnO solutions approached that of the H_2O-KOH solutions with the same KOH concentration. In the most concentrated KOH solutions at low temperatures the vapor pressure of the H_2O-KOH-ZnO solutions exceeded that of the H_2O-KOH solutions.

Although the thermodynamic state of the H_2O-KOH-ZnO solutions we used is undefined [see (1)], the solutions are nevertheless of practical interest in battery technology. As a first approximation, the activity of the water in the H_2O-KOH solutions may be used for the analysis of the behavior of both alkaline cells with cadmium anodes and alkaline cells with zinc anodes.

Table VI. Eutectic precursor patterns in H_2O-KOH system*

KOH, *M*	−40°C	−30°C	−20°C	−10°C	0°C	10°C	20°C	25°C
2	—	—	—	—	8.40	16.6	31.6	43.2
4	—	—	2.82	6.44	14.4	28.8	55.6	76.4
6	0.522	1.41	3.49	8.10	17.4	36.0	70.8	97.8
8**	0.560	1.51	3.74	8.72	18.8	38.0	73.6	104.8
10	0.530	1.45	3.64	8.40	17.0	36.0	68.0	94.0
12	—	1.21	3.07	7.20	13.8	31.2	62.4	85.2
14	—	0.81	1.99	5.04	10.5	25.2	51.8	72.8

* Product of KOH molality and solution vapor pressure is tabulated.
** Eutectic composition is 8.0*M* KOH.

Table VII. Least square constants and vapor pressures, H_2O-KOH-ZnO

KOH conc	3.09*M*	5.36*M*	7.83*M*	10.5*M*	14.6*M*
ZnO, w/o	2.78	4.28	5.57	6.69	8.0
Log *A**	21.24	20.65	20.60	19.80	19.29
B, °K	5455	5337	5406	5290	5332
T, °C					
25	18.8	15.5	11.7	7.76	4.04
20	13.8	11.4	8.58	5.73	2.98
15	9.96	8.32	6.23	4.19	2.17
10	7.13	6.00	4.47	3.03	1.57
5	5.04	4.27	3.17	2.16	1.12
0	3.52	3.01	2.22	1.53	0.780
−5	2.42	2.09	1.53	1.06	0.546
−10	1.65	1.43	1.05	0.731	0.374
−15	1.10	0.965	0.702	0.495	0.252
−20	—	0.641	0.464	0.330	0.168
−25	—	0.419	0.302	0.216	0.110
−30	—	0.269	0.193	0.140	0.071
−35	—	—	0.121	0.088	—
−40	—	—	0.074	0.055	—

* Natural logarithm, mm Hg.

Conclusions

Manometric techniques were found to be satisfactory for the measurement of the vapor pressure of potassium hydroxide solutions between −40° and 25°C.

The vapor pressure of the solutions decreased markedly with the temperature in accordance with the Clapeyron equation, and the experimental data led to a heat of vaporization of water of 11.2 kcal/mole for the H_2O-KOH solution between −40° and 25°C. The heat of vaporization was not affected noticeably by the concentration of the alkaline solutions. The vapor pressure decreased markedly with an increase in the KOH concentration, as expected.

The vapor pressures of the solutions at their freezing points were less than those of pure ice. This is inconsistent with the published phase diagrams which show solid ice to form in solutions less concentrated than 8.0*M* KOH. It is thought that hydrates of KOH must be present rather than ice.

The low-temperature activity coefficients of KOH cannot be calculated from the vapor pressure data by the Gibbs-Duhem equation since dilute solutions cannot be prepared at the low temperatures. Instead, the activities of KOH in the various solutions were calculated relative to those of KOH solutions with the eutectic composition. The logarithm of the relative activity increased almost linearly with the KOH concentration at all the temperatures, but it changed very little with temperature at constant composition.

Inflection points were observed in the chemical potentials of the electrolyte expressed as a function of the KOH concentration at a constant temperature. The inflection points occurred at the eutectic composition of the system over the entire temperature range, and their existence indicated the presence of eutectic precursor interactions in the system far above the eutectic temperature.

The addition of ZnO to the aqueous KOH solutions changed their vapor pressures, but the changes were sufficiently small that as a first approximation the vapor pressure of the H_2O-KOH solutions may be used for the analysis of the behavior of alkaline cells with zinc anodes as well as alkaline cells with cadmium anodes.

Manuscript submitted Jan. 27, 1971; revised manuscript received April 26, 1971.

Any discussion of this paper will appear in a Discussion Section to be published in the June 1972 JOURNAL.

REFERENCES

1. P. Pascal, Editor, "Nouveau Traite de Chimie Minerale," Vol. V, Masson & Co., Paris (1962).
2. R. Cohen-Adad and M. Michaud, *Compt. rend.*, **242**, 2569 (1956).
3. J. P. Gomis, Y. Lecoufee, and F. Putois, Abstract No. 8, Electrochemical Soc. Meeting, Detroit, Mich., Oct. 5-9, 1969.
4. H. S. Harned and M. A. Cook, *J. Am. Chem. Soc.*, **59**, 496 (1937).
5. G. C. Akerlof and P. Bender, *ibid.*, **70**, 2366 (1948).
6. C. Dieterici, *Wied. Ann.*, **50**, 47 (1893).
7. W. Kangro and A. Groeneveld, *Z. Phys. Chem. N.F.*, **32**, 110 (1962).
8. C. D. Hodgman, Editor, "Handbook of Chemistry and Physics," 42nd Edition, The Chemical Rubber Publishing Co., Cleveland, Ohio (1961).

9. Y. Kobayashi, *J. Sci. Hiroshima Univ.*, **1932**, 269.
10. R. A. Robinson and R. H. Stokes, *Trans. Faraday Soc.*, **45**, 612 (1949).
11. T. O'Nan, Mallory Battery Co., Tarrytown, New York, Personal communication.
12. N. A. Lange, Editor, "Handbook of Chemistry," 10th Edition, McGraw-Hill Book Co., New York (1967).
13. N. A. Hampson, P. E. Shaw, and R. Taylor, *Brit. Corr. J.*, **4**, 207 (1969).
14. T. P. Dirkse, *This Journal*, **106**, 154 (1959).

Convective Diffusion on a Rotating Spherical Electrode

Der-Tau Chin*

Electrochemistry Department, Research Laboratories, General Motors Corporation, Warren, Michigan 48090

ABSTRACT

The Levich theory of the rotating disk has been extended to the case of rotating spherical electrodes by means of a series expansion method. It is shown that the rate of mass transfer near the pole of rotation is the same as on a rotating disk. It decreases, however, in meridional direction toward the equator. Results for a sphere or hemispherical electrode can be summarized as

$$Sh = 0.474\, Re^{1/2}\, Sc^{1/3}$$

$$I_{lim} = 0.474\, nFC_{\infty} D^{2/3}\, \nu^{-1/6}\, \omega^{1/2}$$

where Sh and Re are the Sherwood and the Reynolds numbers based on the sphere radius, and Sc is the Schmidt number.

Study of the transport process on a rotating spherical cap is of interest to the electrochemist. In the first place it could provide an insight regarding the effect of surface curvature on the rate of ionic transfer to a rotating disk electrode (RDE). Second, such a study would extend the application of RDE to corrosion and high-rate metal dissolution studies. The RDE is generally made of a circular disk electrode mounted concentrically on the surface of an electrically inert rotating disk. Since theoretical considerations require the RDE to have a perfectly flat surface, the RDE made this way is always polished carefully until the central disk electrode becomes flush with the nonconductive surface. For high rate dissolution studies (such as in the case of electrochemical machining), it is, however, extremely difficult to maintain a flat surface during the experimental runs, for the disk electrode made of the metal being dissolved would recede from the surface of the RDE and subsequently cause an irregular feature on the surface of the disk. This surface irregularity would then generate secondary flows, which in turn would interrupt the hydrodynamic boundary layer over the rotating disk. The Levich theory (1, 2) is therefore no longer valid, and access to the quantitative study of reaction kinetics becomes impossible.

One way to overcome the problem is to replace the disk electrode on the RDE with an electrode having a spherical surface as illustrated in Fig. 1. The electrode now has a spherical head fastened on one end of a rotating rod coated with nonconducting material and will be called a rotating spherical electrode (RSE). The advantage of this combination is that the spherical head is less subject to a change of surface geometry due to dissolution of electrode material into the electrolyte; the problem associated with the induced secondary flows as in the case of RDE could therefore be minimized.

Experimental investigation of laminar boundary layer flow induced by a sphere rotating in an infinite fluid has been performed by Kobashi (3), Kreith, Roberts, Sullivan, and Sinha (4), and by Bowden and Lord (5). Using smoke and hot wire techniques, these investigators found that the boundary layer originates at the pole and develops with increasing thickness toward the equator. The fluid is drawn in toward the sphere along the axis of rotation, as shown in Fig. 1, and moves over the spherical surface toward the equator where a radial outflow jet is formed. Bowden and Lord's photographic study revealed that the outflow in the vicinity of the equator is confined to a very narrow zone, and the flow of the radial jet is laminar within a short distance from the sphere surface. For Reynolds numbers, based on the sphere radius, of less than 1.25×10^4, the result of the study by Kreith *et al.* indicates that this outflow zone is less than 2° latitude in width. Theoretical analysis of this flow problem was first considered by Howarth (6), who introduced appropriate boundary layer equations and obtained an approximate solution by means of the Karman-Pohlhausen momentum integral method. Owing to the limitation of the boundary layer assumptions, he was unable to predict the outflow of fluid at the equator. Despite this shortcoming, however, his model has been used successfully to predict the torque required to maintain a constant speed of rotation (5), and to describe the velocity distribution and the thickness of the boundary layer along the surface except in the vicinity of the equator (4). Recently, Banks (7) and Manohar (8) have obtained the exact solution of Howarth's boundary layer equations by means of numerical integrations with the help of digital computers. A second theoretical model is proposed by Nigam (9), who assumes that the boundary layer thickness is uniform over the sphere surface, and that

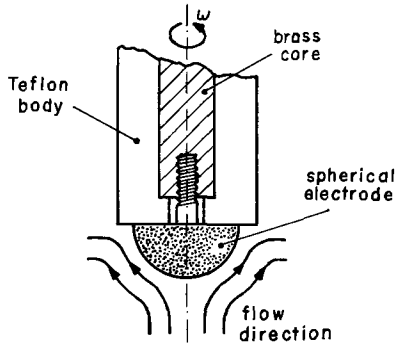

Fig. 1. Rotating spherical electrode

* Electrochemical Society Active Member.
Key words: theory of mass transfer, limiting current distribution, rotating spheres.

9. Y. Kobayashi, *J. Sci. Hiroshima Univ.*, **1932**, 269.
10. R. A. Robinson and R. H. Stokes, *Trans. Faraday Soc.*, **45**, 612 (1949).
11. T. O'Nan, Mallory Battery Co., Tarrytown, New York, Personal communication.
12. N. A. Lange, Editor, "Handbook of Chemistry," 10th Edition, McGraw-Hill Book Co., New York (1967).
13. N. A. Hampson, P. E. Shaw, and R. Taylor, *Brit. Corr. J.*, **4**, 207 (1969).
14. T. P. Dirkse, *This Journal*, **106**, 154 (1959).

Convective Diffusion on a Rotating Spherical Electrode

Der-Tau Chin*

Electrochemistry Department, Research Laboratories, General Motors Corporation, Warren, Michigan 48090

ABSTRACT

The Levich theory of the rotating disk has been extended to the case of rotating spherical electrodes by means of a series expansion method. It is shown that the rate of mass transfer near the pole of rotation is the same as on a rotating disk. It decreases, however, in meridional direction toward the equator. Results for a sphere or hemispherical electrode can be summarized as

$$Sh = 0.474\, Re^{1/2}\, Sc^{1/3}$$

$$I_{lim} = 0.474\, nFC_{\infty} D^{2/3}\, \nu^{-1/6}\, \omega^{1/2}$$

where Sh and Re are the Sherwood and the Reynolds numbers based on the sphere radius, and Sc is the Schmidt number.

Study of the transport process on a rotating spherical cap is of interest to the electrochemist. In the first place it could provide an insight regarding the effect of surface curvature on the rate of ionic transfer to a rotating disk electrode (RDE). Second, such a study would extend the application of RDE to corrosion and high-rate metal dissolution studies. The RDE is generally made of a circular disk electrode mounted concentrically on the surface of an electrically inert rotating disk. Since theoretical considerations require the RDE to have a perfectly flat surface, the RDE made this way is always polished carefully until the central disk electrode becomes flush with the nonconductive surface. For high rate dissolution studies (such as in the case of electrochemical machining), it is, however, extremely difficult to maintain a flat surface during the experimental runs, for the disk electrode made of the metal being dissolved would recede from the surface of the RDE and subsequently cause an irregular feature on the surface of the disk. This surface irregularity would then generate secondary flows, which in turn would interrupt the hydrodynamic boundary layer over the rotating disk. The Levich theory (1, 2) is therefore no longer valid, and access to the quantitative study of reaction kinetics becomes impossible.

One way to overcome the problem is to replace the disk electrode on the RDE with an electrode having a spherical surface as illustrated in Fig. 1. The electrode now has a spherical head fastened on one end of a rotating rod coated with nonconducting material and will be called a rotating spherical electrode (RSE). The advantage of this combination is that the spherical head is less subject to a change of surface geometry due to dissolution of electrode material into the electrolyte; the problem associated with the induced secondary flows as in the case of RDE could therefore be minimized.

Experimental investigation of laminar boundary layer flow induced by a sphere rotating in an infinite fluid has been performed by Kobashi (3), Kreith, Roberts, Sullivan, and Sinha (4), and by Bowden and Lord (5). Using smoke and hot wire techniques, these investigators found that the boundary layer originates at the pole and develops with increasing thickness toward the equator. The fluid is drawn in toward the sphere along the axis of rotation, as shown in Fig. 1, and moves over the spherical surface toward the equator where a radial outflow jet is formed. Bowden and Lord's photographic study revealed that the outflow in the vicinity of the equator is confined to a very narrow zone, and the flow of the radial jet is laminar within a short distance from the sphere surface. For Reynolds numbers, based on the sphere radius, of less than 1.25×10^4, the result of the study by Kreith *et al.* indicates that this outflow zone is less than 2° latitude in width. Theoretical analysis of this flow problem was first considered by Howarth (6), who introduced appropriate boundary layer equations and obtained an approximate solution by means of the Karman-Pohlhausen momentum integral method. Owing to the limitation of the boundary layer assumptions, he was unable to predict the outflow of fluid at the equator. Despite this shortcoming, however, his model has been used successfully to predict the torque required to maintain a constant speed of rotation (5), and to describe the velocity distribution and the thickness of the boundary layer along the surface except in the vicinity of the equator (4). Recently, Banks (7) and Manohar (8) have obtained the exact solution of Howarth's boundary layer equations by means of numerical integrations with the help of digital computers. A second theoretical model is proposed by Nigam (9), who assumes that the boundary layer thickness is uniform over the sphere surface, and that

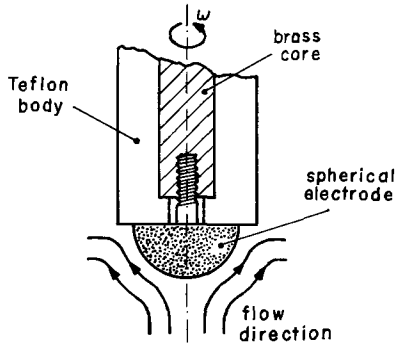

Fig. 1. Rotating spherical electrode

* Electrochemical Society Active Member.
Key words: theory of mass transfer, limiting current distribution, rotating spheres.

the assumption of the boundary layer does not break down at the equator. Though Nigam is able to predict an outflow in the region between latitude 54.75° and the equator, his solutions have been repeatedly proved to be incorrect from both theoretical and phenomenological points of view (4, 5, 8).

The problem of heat transfer from a rotating sphere has been studied experimentally by Kreith *et al.* (4) for Prandtl numbers between 0.024 and 217, and theoretically by Singh (10), Banks (11), and Baxter and Davies (12). Singh's computation is trivial because he employs Nigam's velocity result in the analysis. Banks calculates the thermal boundary layer numerically at Prandtl numbers equal to 0.7 and 1.0. Baxter and Davies' study is confined to high Prandtl numbers; they obtain an implicit approximate solution based on Howarth's approximate momentum solutions.

For the quantitative application of RSE to the study of electrochemical processes, one requires knowledge regarding the nature of ionic transfer on the spherical electrode. The object of this report is to discuss in detail the theoretical background behind such a problem. A mathematical model based on Howarth's and Banks' momentum results will be described. It will be shown that, at high Schmidt numbers, Levich's theory of the rotating disk electrode can be extended to the case of a rotating sphere by means of a series expansion method.

Boundary layer equations.—In the following analysis we shall use spherical polar coordinates, r, θ, ϕ, with r measured radially outward from the center of the sphere, θ measured from the axis of rotation, and ϕ the azimuth. The spherical electrode is assumed to be rotating at a sufficiently high speed to permit application of the boundary layer approximations, and the motion of the fluid is assumed to be symmetrical about the axis of rotation. Also, the physical properties of the fluid will be assumed to be constant. Neglecting the effect of external forces, the equations (4, 6, 11) of fluid motion and convective diffusion on a rotating spherical electrode of radius r_o are given as

Continuity

$$\frac{\partial V_r}{\partial r} + \frac{1}{r_o}\frac{\partial V_\theta}{\partial \theta} + \frac{\cot\theta}{r_o} V_\theta = 0 \qquad [1]$$

θ-momentum

$$V_r \frac{\partial V_\theta}{\partial r} + \frac{V_\theta}{r_o}\frac{\partial V_\theta}{\partial \theta} - \frac{V_\phi^2 \cot\theta}{r_o} = \nu \frac{\partial^2 V_\theta}{\partial r^2} \qquad [2]$$

ϕ-momentum

$$V_r \frac{\partial V_\phi}{\partial r} + \frac{V_\theta}{r_o}\frac{\partial V_\phi}{\partial \theta} + \frac{V_\theta V_\phi}{r_o}\cot\theta = \nu \frac{\partial^2 V_\phi}{\partial r^2} \qquad [3]$$

Convective-diffusion

$$V_r \frac{\partial C}{\partial r} + \frac{V_\theta}{r_o}\frac{\partial C}{\partial \theta} = D \frac{\partial^2 C}{\partial r^2} \qquad [4]$$

Boundary conditions

$$\left.\begin{array}{ll} \text{at } r = r_o, & V_r = V_\theta = 0 \\ & V_\phi = r_o\omega \sin\theta \\ & C = C_o \\ \text{at } r \to \infty, & V_\theta = V_\phi = 0 \\ & C = C_\infty \end{array}\right\} \qquad [5]$$

We may normalize the above equations with the following dimensionless variables and by expanding the dependent variables in a power series of θ

$$Re = \frac{r_o^2 \omega}{\nu}, \quad Sc = \frac{\nu}{D} \qquad [6]$$

$$\eta = \left(\frac{\omega}{\nu}\right)^{1/2} (r - r_o) \qquad [7]$$

$$V_r = (\nu\omega)^{1/2} \{H_1 + \theta^2 H_3 + \theta^4 H_5 + \ldots\} \qquad [8]$$

$$V_\theta = r_o\omega \{\theta F_1 + \theta^3 F_3 + \theta^5 F_5 + \ldots\} \qquad [9]$$

$$V_\phi = r_o\omega \{\theta G_1 + \theta^3 G_3 + \theta^5 G_5 + \ldots\} \qquad [10]$$

$$C = C_\infty + (C_o - C_\infty)\{\Phi_1 + \theta^2\Phi_3 + \theta^4\Phi_5 + \ldots\} \qquad [11]$$

Here the dependent variables F_i, G_i, H_i, and Φ_i with $i = 1, 2, 3, \ldots$, are functions of η only. Details of this lengthy substitution are illustrated in ref. (6) and (11) and will not be discussed here. The results for the first two terms in the series expansions are

Zeroth order equations

$$H_1' + 2F_1 = 0 \qquad [12]$$

$$H_1F_1' + F_1^2 - G_1^2 = F_1'' \qquad [13]$$

$$H_1G_1' + 2F_1G_1 = G_1'' \qquad [14]$$

$$H_1\Phi_1' = \frac{1}{Sc}\Phi_1'' \qquad [15]$$

$$\left.\begin{array}{l} \text{b.c. at } \eta = 0,\ F_1 = H_1 = 0,\ G_1 = \Phi_1 = 1 \\ \text{at } \eta \to \infty,\ F_1 = G_1 = \Phi_1 = 0 \end{array}\right\} \qquad [16]$$

First order equations

$$H_3' + 4F_3 - (1/3)F_1 = 0 \qquad [17]$$

$$H_1F_3' + H_3F_1' + 4F_1F_3 - 2G_1G_3 + (1/3)G_1^2 = F_3'' \qquad [18]$$

$$H_1G_3' + H_3G_1' + 4F_1G_3 + 2F_3G_1 - (1/3)F_1G_1 = G_3'' \qquad [19]$$

$$H_3\Phi_1' + H_1\Phi_3' + 2F_1\Phi_3 = \frac{1}{Sc}\Phi_3'' \qquad [20]$$

$$\left.\begin{array}{l} \text{b.c. at } \eta = 0,\ F_3 = H_3 = \Phi_3 = 0,\ G_3 = -1/6 \\ \text{at } \eta \to \infty,\ F_3 = G_3 = \Phi_3 = 0 \end{array}\right\} \qquad [21]$$

It is seen that the zeroth order equations are the same as the well-known transfer problem on a rotating disk (2, 13). Thus, for small values of η, we may immediately apply Cochran's result (14), and write the zeroth order solutions for the velocity distributions near the spherical surface

$$F_1 = a\eta - (1/2)\eta^2 - (b/3)\eta^3 - (b^2/12)\eta^4 + \ldots \qquad [22]$$

$$G_1 = 1 + b\eta + (a/3)\eta^3 + (1/12)(ab - 1)\eta^4 + \ldots \qquad [23]$$

$$H_1 = -a\eta^2 + (1/3)\eta^3 + (b/6)\eta^4 + \ldots \qquad [24]$$

The values of the constants, a and b, have been computed by a number of investigators (14-17); the most accurate ones, however, are those of Rogers and Lance (17)

$$\left.\begin{array}{l} a = 0.51023 \\ b = -0.61592 \end{array}\right\} \qquad [25]$$

For large Schmidt numbers, the zeroth order diffusion solution is described by Levich's theory of the rotating disk (2, 18). Using the present notation, it can be expressed as

$$\Phi_1 = 1 - 0.62045\, Sc^{1/3} \int_0^\eta \exp\left(-\frac{aSc}{3}\eta^3\right) d\eta \qquad [26]$$

It seems, therefore, that with an additional term characterized by Φ_3, it is possible to extend the Levich theory to the case of a rotating spherical electrode. To find the function, Φ_3, one needs information about the first order velocity distributions. However, no analytical solution has been available in the literature. In the next section our analysis is started with an attempt to develop appropriate expressions for the first order velocity distributions near the electrode surface.

Series solution for the first order momentum equations.—Equations [17-19] describing the first order velocity distributions are a set of linear, second order differential equations. An analytical expression can

be made possible if we expand F_3, G_3, and H_3 in a Taylor series about $\eta = 0$

$$F_3 = f_0 + \eta f_1 + \eta^2 f_2 + \eta^3 f_3 + \dots \quad [27]$$

$$G_3 = g_0 + \eta g_1 + \eta^2 g_2 + \eta^3 g_3 + \dots \quad [28]$$

$$H_3 = h_0 + \eta h_1 + \eta^2 h_2 + \eta^3 h_3 + \dots \quad [29]$$

Inserting these expressions into Eq. [17]-[19], and making use of Eq. [21]-[24], leads to the following expressions for the first order velocity components near the surface

$$F_3 = f_1\eta + (1/3)\eta^2 + (1/6)(b - 2g_1)\eta^3 + \dots \quad [30]$$

$$G_3 = -1/6 + g_1\eta + (1/6)(2f_1 - a)\eta^3 + \dots \quad [31]$$

$$H_3 = (a/6 - 2f_1)\eta^2 - (1/2)\eta^3 + \dots \quad [32]$$

Here, f_1 and g_1 are the values of the radial velocity gradients contributed by the first order velocity components at the sphere surface. These values have been computed numerically by Banks (7). His result is given as

$$\left.\begin{aligned} f_1 &= -0.22129 \\ g_1 &= 0.24765 \end{aligned}\right\} \quad [33]$$

Equations [30]-[33] can be used where required for the appropriate convection terms in the first order diffusion equation.

Method of solution of the first order diffusion equation.—In this section we proceed with an analysis that could lead to simplification of the first order diffusion equation. An analytical solution is then given for the case of high Schmidt numbers. Since, for the transfer process occurring at high Schmidt numbers, the thickness of the concentration boundary is much thinner than that of the momentum boundary layer, we would therefore start with stretching the mass transfer domain by introducing a new variable defined as

$$Z = Sc^{1/3}\eta \quad [34]$$

Substituting the new variable into Eq. [20], and making use of Eq. [22], [24], and [32] for the appropriate convection terms, we have

$$(a/6 - 2f_1)Z^2\frac{d\Phi_1}{dZ} - aZ^2\frac{d\Phi_3}{dZ} + 2aZ\Phi_3 - \frac{d^2\Phi_3}{dZ^2} = Sc^{-1/3}\left\{(1/2)Z^3\frac{d\Phi_1}{dZ} - (1/3)Z^3\frac{d\Phi_3}{dZ} + Z^2\Phi_3\right\} + 0(Sc^{-2/3}) \quad [35]$$

We note that the left hand side of this equation is independent of Sc, while the leading terms on the right vary inversely with the cube root of the Schmidt number. Thus, for the transfer process occurring at large Schmidt numbers, we may neglect the right hand side, and by replacing $d\Phi_1/dZ$ with an expression evaluated from Eq. [26], Eq. [35] can now be simplified to

$$\frac{d^2\Phi_3}{dZ^2} + aZ^2\frac{d\Phi_3}{dZ} - 2aZ\Phi_3 = -0.62045(a/6 - 2f_1)Z^2e^{-(a/3)Z^3} \quad [36]$$

The boundary conditions are

$$\left.\begin{aligned} &\text{at } Z = 0, \Phi_3 = 0 \\ &Z \to \infty, \Phi_3 = 0 \end{aligned}\right\} \quad [37]$$

A solution that satisfies both Eq. [36] and [37] can be found as

$$\Phi_3 = \frac{0.62045}{5a}(a/6 - 2f_1)Ze^{-(a/3)Z^3} \quad [38]$$

Substituting Eq. [26] and [38] into Eq. [11] we arrive at a concentration distribution over the rotating spherical electrode

$$\Phi = \frac{C - C_\infty}{C_0 - C_\infty} = 1 - 0.62045\int_0^Z e^{-(a/3)Z^3}dZ + 0.12833\,\theta^2Ze^{-(a/3)Z^3} + \dots \quad [39]$$

where

$$Z = Sc^{1/3}\eta = Sc^{1/3}(\omega/\nu)^{1/2}(r - r_0)$$

To obtain a generalized expression for the rate of transport process over the electrode, we now define a mass transfer coefficient, K, as

N = average mass flux on the electrode surface

$$= \frac{-\int_0^{2\pi}\int_0^{\theta} r_0^2\sin\theta\, D\left(\frac{\partial C}{\partial r}\right)_{r=r_0}d\theta d\phi}{\int_0^{2\pi}\int_0^{\theta} r_0^2\sin\theta d\theta d\phi} = K(C_0 - C_\infty) \quad [40]$$

Carrying out integration for the denominator and introducing the dimensionless variables, the Sherwood number defined as (Kr_0/D) can be evaluated from the following equation

$$Sh = \left(\frac{Kr_0}{D}\right) = -\frac{Re^{1/2}Sc^{1/3}}{1 - \cos\theta}\int_0^{\theta}\left(\frac{\partial\Phi}{\partial Z}\right)_{Z=0}\sin\theta d\theta \quad [41]$$

Substituting Eq. [39] into Eq. [41] and carrying out the integration, we obtain the dimensionless rate of transfer to a spherical electrode having an active surface specified by the angle θ

$$Sh = Re^{1/2}Sc^{1/3}\left\{0.62045 - 0.12833\frac{2(\cos\theta - 1) + 2\theta\sin\theta - \theta^2\cos\theta}{1 - \cos\theta}\right\} \quad [42]$$

For a hemispherical electrode, or a sphere whose entire surface is subject to the mass transfer, we have $\theta = \pi/2$; thus

$$Sh = 0.474\,Re^{1/2}Sc^{1/3} \quad [43]$$

In an excess supporting electrolyte, the average current density due to flux of mass to the electrode surface is related to the mass transfer coefficient, K, by

$$I = -n\mathbf{F}N = n\mathbf{F}K(C_\infty - C_0) \quad [44]$$

Substituting this relation into Eq. [42], and rearranging the equation in dimensional form, we have

$$I = n\mathbf{F}(C_\infty - C_0)D^{2/3}\nu^{-1/6}\omega^{1/2}\left\{0.62045 - 0.12833\frac{2(\cos\theta - 1) + 2\theta\sin\theta - \theta^2\cos\theta}{1 - \cos\theta}\right\} \quad [45]$$

For a sphere or a hemispherical electrode, $\theta = \pi/2$, and Eq. [45] becomes

$$I = 0.474\,n\mathbf{F}(C_\infty - C_0)D^{2/3}\nu^{-1/6}\omega^{1/2} \quad [46]$$

The limiting current density may be obtained by setting $C_0 = 0$

$$I_{\text{lim}} = 0.474\,n\mathbf{F}C_\infty D^{2/3}\nu^{-1/6}\omega^{1/2}, \text{ (for } \theta = \pi/2) \quad [47]$$

Discussion of Results

The correlations given by Eq. [42]-[43] and [45]-[47] would allow one to estimate the rate of mass flux and the diffusion current density on a rotating spherical electrode. Essentially, these results represent only the asymptotic behavior of a transport process occurring at large Schmidt numbers, and only the main region solution that disregards the boundary layer eruption at the equator. Here we discuss some implications of the theory, particularly as they bear on the various simplifications made in obtaining the solution.

The Sherwood number given by Eq. [42] differs from that of a rotating disk only by a correction func-

tion of θ. This implies that the correlation is actually an extension of Levich's theory. It would, therefore, be of theoretical interest to compare this rate of mass transfer to that of a rotating disk. From such a comparison, one would also be able to gain an insight regarding the effect of surface curvature for the rotating disk experiment. Using the present notation, the Levich theory (1, 2) of transfer on a rotating disk electrode can be expressed as

$$Sh_D = 0.62045\, Re^{1/2}\, Sc^{1/3} \qquad [48]$$

The ratio of average mass flux on a spherical electrode to that on a disk electrode can be obtained by dividing Eq. [42] by Eq. [48]

$$\frac{Sh}{Sh_D} = \frac{I}{I_D} = 1 - 0.207\left\{\frac{2\theta \sin\theta - \theta^2\cos\theta}{1-\cos\theta} - 2\right\} \qquad [49]$$

where the subscript, D, implies the process occurring at the disk electrode. Equation [49] is plotted in Fig. 2 as a solid curve. It is seen that the rate of transfer at the pole ($\theta = 0$) is the same as the disk electrode; however, it decreases with increasing θ toward the equator. In the polar region, the effect of curvature is not significant; for θ less than 0.7 (about 40°) the value of the Sherwood number estimated from Levich's equation is only 5% greater than the value given by Eq. [42]. However, for a sphere or a hemispherical electrode ($\theta = \pi/2$), the average rate is reduced to about 76% of the flux at the disk electrode. Also given in Fig. 2 are the values of approximate calculations made by Baxter and Davies (12); these are represented by the circular dots. Owing to the nature of the equation used, these authors were not able to perform the calculation for $\theta = \pi/2$. In spite of the approximate nature, their values agree reasonably well with the present analysis; the maximum deviation occurring at $\theta = 1.4$ (80°) is only 2.5%.

We now demonstrate that the solution is consistent with the notion that the concentration boundary layer is well within the hydrodynamic boundary layer, and that the application of Taylor's series expansions for the first order velocity distributions is valid for the case of large Schmidt numbers. Using the Nernst diffusion concept (19), the thickness of the concentration boundary layer can be defined as

$$\delta_c = -\frac{D(C_0 - C_\infty)}{D\left(\frac{\partial C}{\partial r}\right)_{r=r_0}} \qquad [50]$$

Substituting Eq. [39] into Eq. [50] we have

$$\delta_c = \frac{1.61}{1 - 0.207\theta^2}\left(\frac{\nu}{\omega}\right)^{1/2} Sc^{-1/3} \qquad [51]$$

Thus the thickness of the concentration boundary layers varies from $1.6(\nu/\omega)^{1/2}Sc^{-1/3}$ at the pole to $3.3(\nu/\omega)^{1/2}Sc^{-1/3}$ near the equator. The analysis of Cochran (13, 14), Banks (7), and Manohar (8) indicates that the thickness of the hydrodynamic boundary layer, δ_m, would vary approximately from $4(\nu/\omega)^{1/2}$ at the pole to $10(\nu/\omega)^{1/2}$ in the vicinity of the equator. Thus

$$\frac{\delta_c}{\delta_m} \sim \frac{0.4}{Sc^{1/3}} \qquad [52]$$

In a liquid system, a typical value for the Schmidt number is on the order of 1000; the concentration boundary layer is therefore about 20 times smaller.

The flux of mass contributed from the equatorial region itself has thus far been neglected. The fluid flow in the region is characterized by eruption of the boundary layer into a swirling, flat radial jet. The velocity distribution in the jet has not been resolved, and there is presently no knowledge of the nature of convective diffusion near the equator. However, the experimental work performed by Kreith and his associates (4) has shown that for Reynolds numbers less than 1.25×10^4, this region occupies less than 2% of the total surface area over the sphere. The extrapolation of the main region solution to the equatorial region would therefore not result in a significant error. The maximum discrepancy would be less than 2%. Another factor that deserves consideration is the effect of the second order term, Φ_5, in the series expansion for the concentration profile, Eq. [11]. Banks (11) has computed numerically the thermal boundary layers for Prandtl numbers between 0.7 and 1.0. His results indicate that the contribution of $\Phi_5'(0)$ to the local flux at the surface is about 0.5%. For practical applications this difference is negligible. Perhaps of greater importance is the effect of neglecting the higher order terms of Sc^{-1} in obtaining the diffusion solution. The Levich theory that has been used as the zeroth order solution for the rotating sphere is subject to an error on the order of $Sc^{-1/3}$ (20). Also, as shown in Eq. [35], the first order solution is made possible only by dropping the leading correction terms that vary inversely with the 1/3 power of the Schmidt number. We would therefore expect that the result given in this analysis is subject to an error on the order of $Sc^{-1/3}$; for a typical liquid system with a Schmidt number of 1000, this would be about 10%.

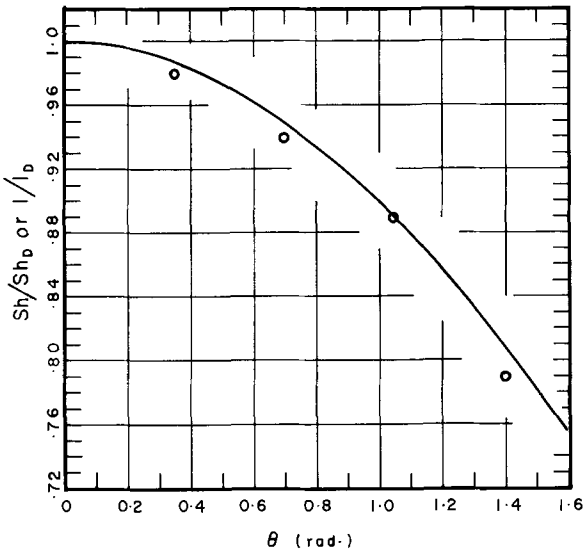

Fig. 2. Comparison with disk electrode. The solid line is the result of this analysis, Eq. [49]. The circular dots are Baxter and Davies' approximate calculations [ref. (12)].

Based on the above discussions, we may conclude that the diffusion solution expressed in the forms of Eq. [42]-[43] and [45]-[47] should give a reasonably accurate estimate of the mass transfer rate to the rotating sphere. For electrochemical applications, these equations should provide access to the quantitative study of diffusion coefficients and reaction kinetics of electrode processes.

Manuscript submitted Nov. 4, 1970; revised manuscript received *ca.* April 28, 1971.

Any discussion of this paper will appear in a Discussion Section to be published in the June 1972 JOURNAL.

LIST OF SYMBOLS

a	dimensionless constant, 0.51023
b	dimensionless constant, −0.61592
C	concentration of diffusion species, g-mole/cm^3
D	diffusivity, cm^2/sec
$\mathbf{F}$	Faraday constant, coulomb/g-equiv
F_i	dimensionless meridional velocity components defined by Eq. [9]
f_1	dimensionless constant, −0.22129
G_i	dimensionless azimuthal velocity components defined by Eq. [10]

g_1 dimensionless constant, 0.24765
H_i dimensionless radial velocity components defined by Eq. [8]
I current density, A/cm^2
i dummy index, 1, 2, 3, . . .
K mass transfer coefficient defined in Eq. [40], cm/sec
N average rate of mass flux at the electrode surface, g-mole/cm^2 sec
n number of electrons transferred in electrochemical reactions, g-equiv/g-mole
r radial coordinate, cm
r_o radius of spherical electrode, cm
Re Reynolds number defined as $r_o^2\omega/\nu$ dimensionless
Sc Schmidt number defined as ν/D, dimensionless
Sh Sherwood number defined as Kr_o/D, dimensionless
V velocity components, cm/sec
Z dimensionless radial distance defined as $Sc^{1/3}\eta$

Greek Symbols

δ boundary layer thickness, cm
η dimensionless radial distance defined as $(\omega/\nu)^{1/2}(r - r_o)$
θ latitude coordinate, rad
ν kinematic viscosity, cm^2/sec
Φ dimensionless concentration defined as $(C - C_\infty)/(C_o - C_\infty)$
Φ_i dimensionless concentration defined by Eq. [11]
ϕ azimuthal coordinate, rad
ω angular velocity, rad/sec

Subscripts

c concentration boundary layer
D transfer process on a rotating disk
lim limiting current process
m momentum boundary layer
o electrode surface
r radial component
θ meridional component
ϕ azimuthal component
∞ bulk of fluid

Superscripts

differentiation with respect to η

REFERENCES

1. V. G. Levich, *Acta Physicochim. URSS*, **17**, 257 (1942).
2. V. G. Levich, "Physicochemical Hydrodynamics," Prentice Hall, Inc., Englewood Cliffs, New Jersey (1962).
3. Y. Kobashi, *J. Sci. Hiroshima Univ.*, **A20**, 149 (1957).
4. F. Kreith, L. G. Roberts, J. A. Sullivan, and S. N. Shina, *Int. J. Heat Mass Transfer*, **6**, 881 (1963).
5. F. P. Bowden and R. G. Lord, *Proc. Roy. Soc.*, **A271**, 143 (1963).
6. L. Howarth, *Phil. Mag., Ser. 7*, **42**, 1308 (1951).
7. W. H. H. Banks, *Quart. J. Mech. and Applied Math.*, **18**, 443 (1965).
8. R. Manohar, *ZAMP*, **18**, 320 (1967).
9. S. D. Nigam, *ibid.*, **5**, 151 (1954).
10. S. N. Singh, *Appl. Sci. Res.*, **A9**, 197 (1960).
11. W. H. H. Banks, *ZAMP*, **16**, 780 (1965).
12. C. B. Baxter and D. R. Davies, *Quart. J. Mech. and Applied Math.*, **13**, 247 (1960).
13. H. Schlichting, "Boundary Layer Theory," McGraw Hill Book Co., New York (1960).
14. W. G. Cochran, *Proc. Cambridge Phil. Soc.*, **30**, 365 (1934).
15. E. M. Sparrow and J. L. Gregg, *J. Heat Transfer, Trans. ASME*, **81c**, 249 (1959).
16. M. Litt and G. Seard, *Chem. Eng. Sci.*, **19**, 867 (1964).
17. M. H. Rogers and G. N. Lance, *J. Fluid Mech.*, **7**, 617 (1960).
18. A. C. Riddiford, "The Rotating Disk System," in "Advances in Electrochemical Engineering," Vol. 4, P. Delahay and C. W. Tobias, Editors, Interscience Publishers, New York (1966).
19. W. Nernst, *Z. Phys. Chem.*, **47**, 52 (1904).
20. J. Newman, *J. Phys. Chem.*, **70**, 1327 (1966).

Technical Note

Induced Osteogenesis by Electrical Stimulation

Didya D. Levy

Bioengineering Division, Polytechnic Institute of Brooklyn, Brooklyn, New York 11201

The ability of bone to act as a transducing element, converting a mechanical deformation into an electrical signal, is probably in part responsible for its remodeling capability. By monitoring the voltage response of cortical bone to a mechanical step deformation, Becker, Bassett, and Bachman (1), and Cochran (2) have provided a means for quantitatively investigating the remodeling system of bone. These response curves can be fitted to an equation containing two exponential terms of the form

$$V_o(t) = V_p(t)[K + (1 - K)\, e^{-t/\tau_2} - e^{-t/\tau_1}]$$

where V_o is the output voltage of the system when loaded by a step deformation, V_p the peak voltage, K a d-c multiplicative factor, and τ_1 and τ_2 the system's two time constants. In order to ascertain the resonant frequency of the system, *i.e.* the frequency at which the system response would be maximal, the fitted response curve must first be transferred to the Laplace domain where it has the form

Key words: bone growth, electrical stimulation, *in vivo* studies.

$$V_o(S) = V_p(S)[K/S + (1 - K)/(S + \tau_2) - 1/(S + \tau_1)]$$

The system's transfer function, defined as

$$H(S) = \frac{V_O(S)}{V_p(S)}$$

has the form

$$H(S) = \frac{AS + B}{S^2 + CS + D}$$

where A, B, C, and D are obtainable from analysis and, for the curve cited in (1), have the values 19.34, 0.677, 20.69, and 13.84 respectively (3). Substituting for S and squaring both sides, one can plot the square of the transfer function *vs.* frequency and arrive at a frequency value for which the system transfer function is a maximum. Figure 1 illustrates this maxima as occurring at a frequency of approximately 4.5 rad/sec (0.7 Hz). Inasmuch as previous investigators have demonstrated an osteogenic response to stimulation by

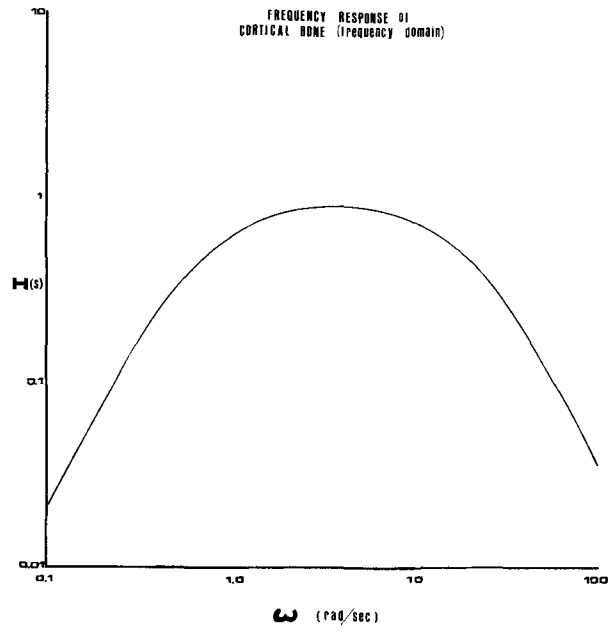

Fig. 1. System transfer function plotted on log-log scales as a function of input frequency. The transfer function is maximum at an input frequency of 4.5 rad/sec (about 0.7 Hz).

a d-c (voltage) source (4-6), an effort was made to determine if this response could be improved upon by use of a pulsed d-c current source operating at this frequency.

Experimental Techniques

Initial attempts at using a unijunction transistor oscillator as a pulsing source proved to be unsatisfactory primarily owing to its relatively large size. An astable multivibrator (AMV) was then designed to meet the size and reliability requirements imposed by surgical considerations. The circuit, shown schematically in Fig. 2, was encapsulated first in a clear epoxy and then in a pharmaceutical grade beeswax to minimize toxicological effects. The driving electrodes were Teflon coated platinum-iridium.

In each instance a pulsing source was used to drive a bone, a control device was implanted in the contralateral bone. Control units, similar to the pulsing units in both shape and weight, were of two basic types: passive and d.c. These control units were fabricated of the same materials as were the pulsing units and, in the

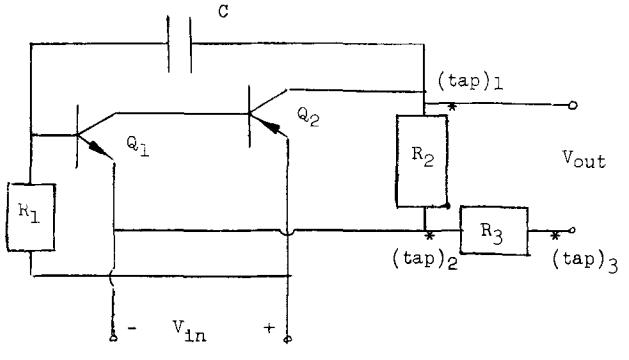

Fig. 2. A schematic representation of an AMV. The three taps were used to note potential drops across two portions of the circuit and, in so doing, provide information on the amount of energy delivered to the bone. The potential drop from points 3 to 1 (through the bone) is the difference between the drop from 1 to 2 and from 2 to 3. The current through the bone is equal to the drop from 2 to 3 divided by the known resistance R_3. The product of these two values is approximately the energy input to the bone; total energy input being this value multiplied by the product of pulsewidth, firing rate, and total time in operation.

case of the d-c control, operated at the same voltage level as was reported in the literature by O'Connor (4), Bassett (6), and Lavine (7), *viz.* 1-1.4V.

Because of their relatively small size, several of these units could be implanted in the rib cage and femurs of a subject dog. Thus 48 devices (12 passive, 6 d.c., and 20 AMV's) were implanted in eight dogs. A typical sterile procedure involved making an incision above the target femur, dissecting away the underlying fascia, and exposing the *biceps femoris*. The surgical plane between it and the underlying *vastus lateralis* was uncovered permitting rapid access to the femur with a minimum of trauma. An incision was made through the periosteum and a high-speed drill with a number 57 bit was used to drill two holes through the cortex. Electrodes, extending midway into the lumen, were seated in these holes and the entire unit was then anchored to the bone with a surgical silk (00). After a four-day recovery period, the dogs were returned to their kennels where they were then free to function normally.

Active stimulators contained Teflon coated cable leads that were extended through the skin of the subject dog and could be connected to an oscilloscope where its operating mode could be continuously monitored. Typically, the output characteristics of a pulsing source, monitored *in vivo*, were such that the unit fired a rectangular d-c pulse at a rate of 0.5 Hz, a pulsewidth of 5 msec, and a delivered peak current of approximately 1 mA. The total potential drop between the two electrodes was on the order of 1.1V and so

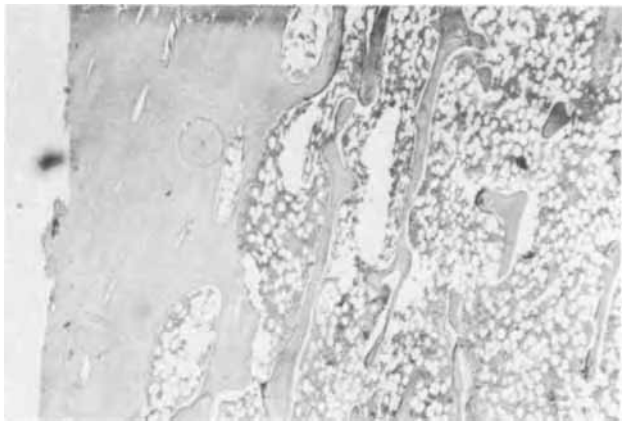

Fig. 3. Photomicrograph, at approximately 40 diameters, of a longitudinal section of a rib 2-10 mm from the point of electrode insertion. This section shows no unusual cellular activity despite the proximity of the passive control.

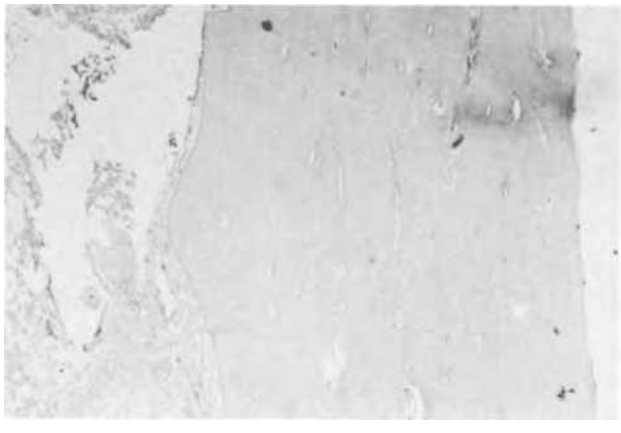

Fig. 4a. A longitudinal section through a rib at X40 showing the cortex and a portion of the lumen. No cellular activity is evident on the periosteal surface. There is, however, some activity along a portion of the endosteal surface.

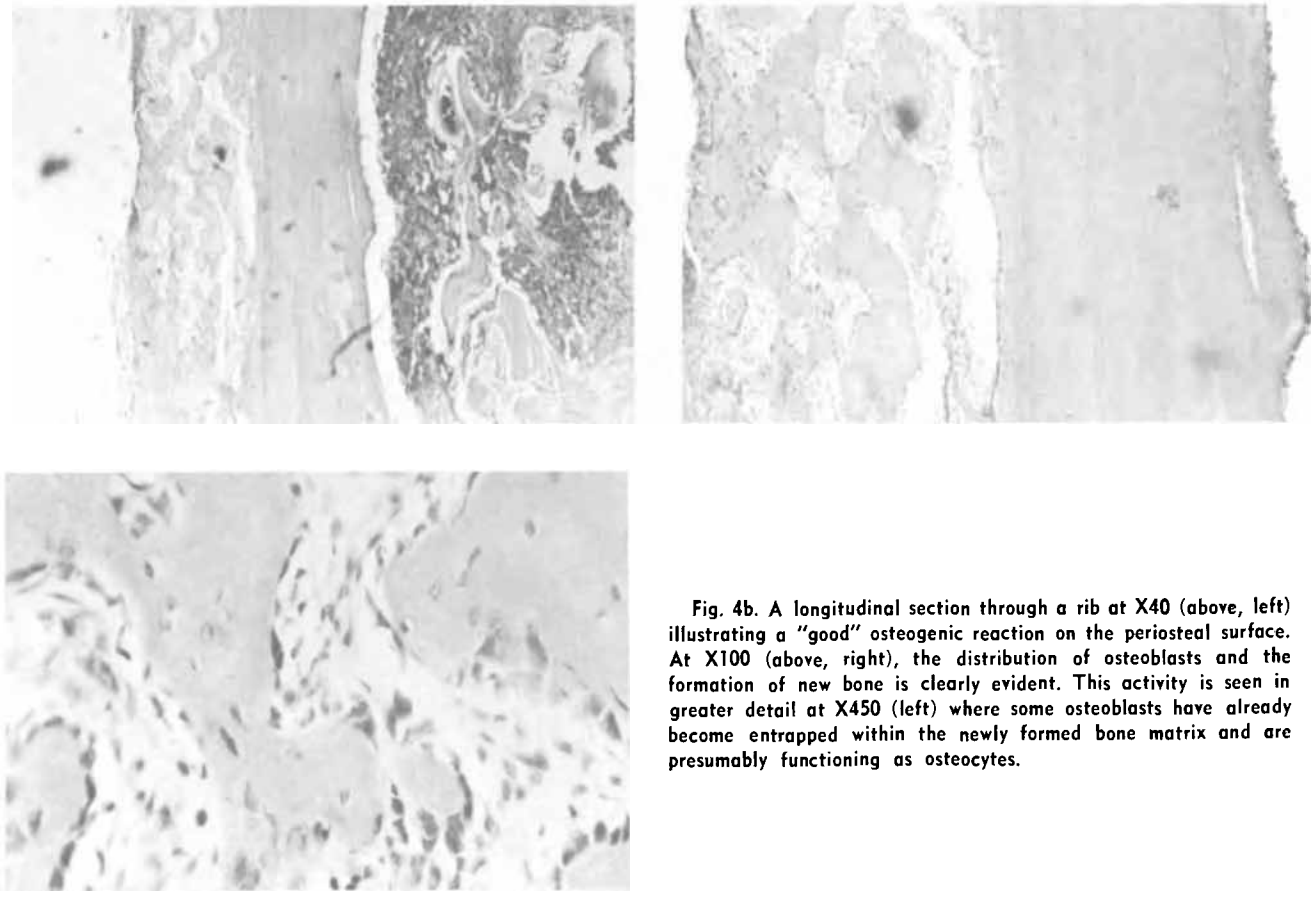

Fig. 4b. A longitudinal section through a rib at X40 (above, left) illustrating a "good" osteogenic reaction on the periosteal surface. At X100 (above, right), the distribution of osteoblasts and the formation of new bone is clearly evident. This activity is seen in greater detail at X450 (left) where some osteoblasts have already become entrapped within the newly formed bone matrix and are presumably functioning as osteocytes.

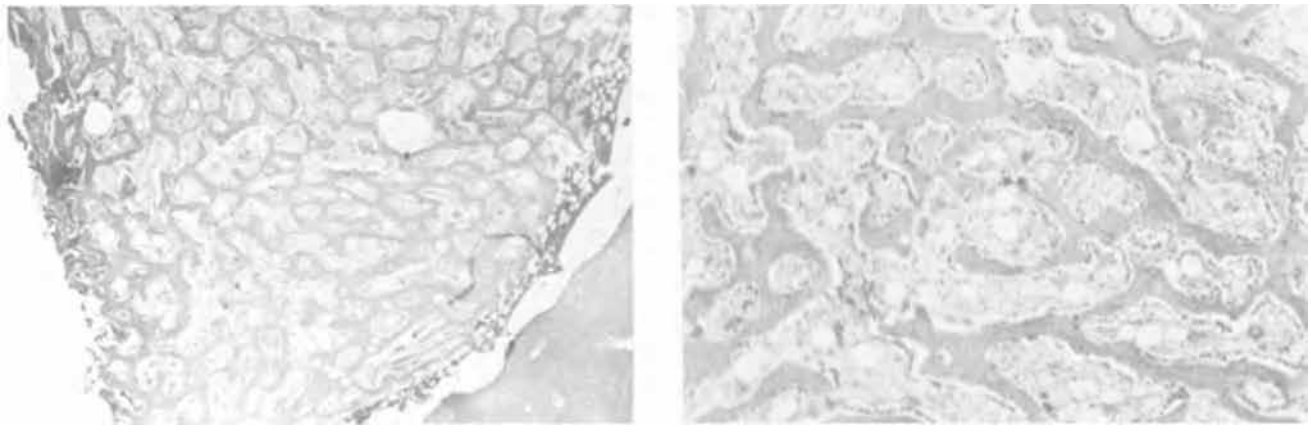

Fig. 5a. Photomicrographs at X40 (left) of a cross section through a femur driven by an AMV. The entire marrow space is filled with a dense mesh-like array of trabecula. This callus extended 5-6 cm in either direction from the point of stimulation. Detail at X100 (right) illustrates the process of laying down more new bone, increasing the trabecula thickness, is proceeding at a rapid pace.

the total energy delivered to the tissue during the two-week duration of an experiment was approximately 3.3W-sec. D-C voltage sources similar to those cited previously delivered approximately 144 W-sec during a like period.

Results and Conclusions

The use of passive control devices established that no significant histological changes were caused by the trauma associated with drilling through the cortices of bones and the subsequent electrode emplacement in these holes (Fig. 3).

In most instances where a d-c device was used to stimulate bone, there were no gross changes visible on the outer surface of the bone. There were, however, some changes in the marrow space that were characterized by variations in color and texture. Microscopic observations indicated that results were not consistent and could not necessarily be correlated with either total energy input or implant location. There was, though, a definite osteogenic response in every *in*stance that a d-c device was used. These responses varied from no apparent response on either the periosteal (outer) or endosteal (inner) cortical surface (Fig. 4a) to a considerable response on the periosteal surface and a good response in the medulla (Fig. 4b).

The response of bone to pulsed stimulation was consistent. Tissue reaction occurred in the central lumen (Fig. 5a) and on both the periosteal and endosteal surfaces (Fig. 5b). Newly formed bone appeared most often as a consequence of direct osteoblastic activity although in several instances new bone was noted as forming from a cartilagenous precursor (Fig. 6).

A summary of the tissue response evoked by a d-c source *vis-a-vis* a non-d-c source in the contralateral

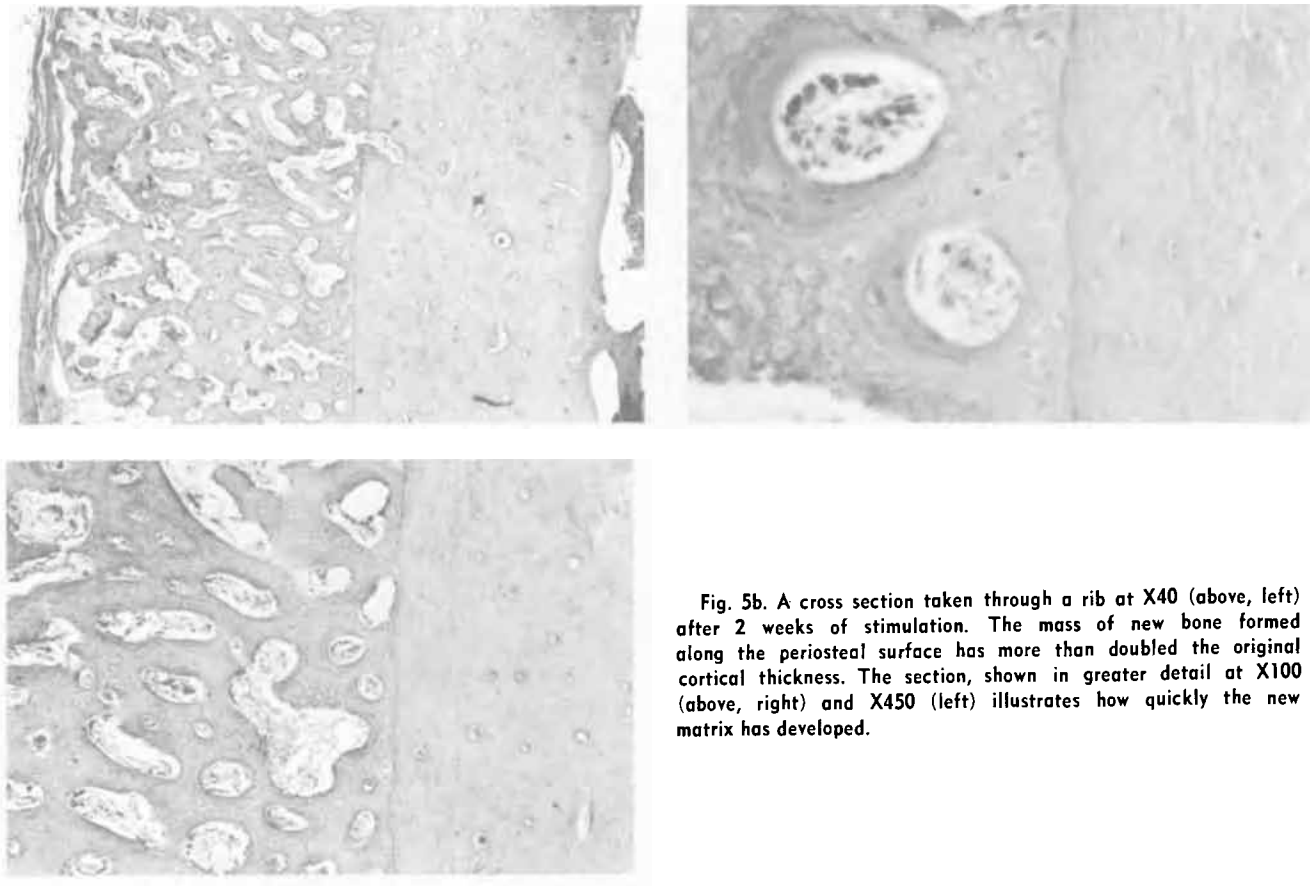

Fig. 5b. A cross section taken through a rib at X40 (above, left) after 2 weeks of stimulation. The mass of new bone formed along the periosteal surface has more than doubled the original cortical thickness. The section, shown in greater detail at X100 (above, right) and X450 (left) illustrates how quickly the new matrix has developed.

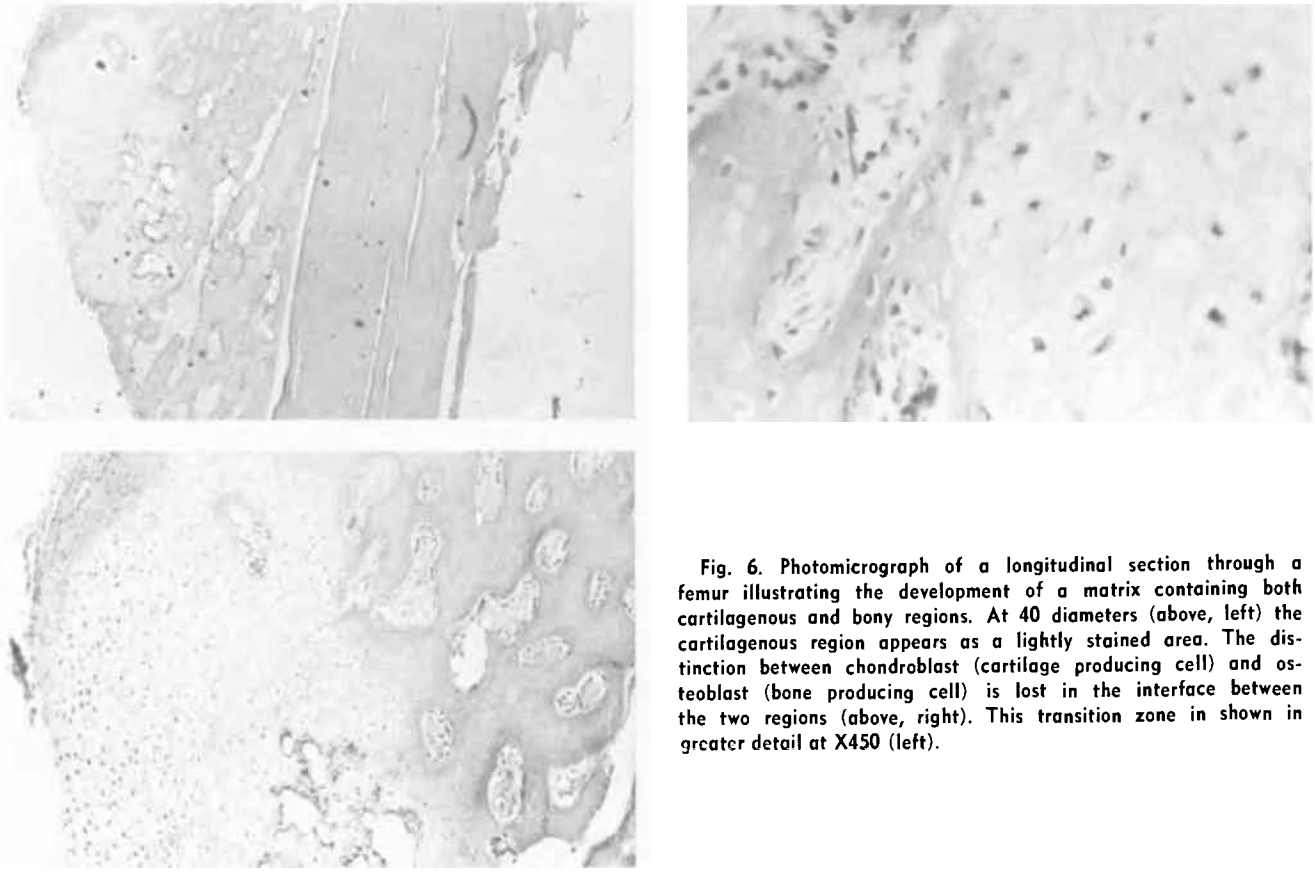

Fig. 6. Photomicrograph of a longitudinal section through a femur illustrating the development of a matrix containing both cartilagenous and bony regions. At 40 diameters (above, left) the cartilagenous region appears as a lightly stained area. The distinction between chondroblast (cartilage producing cell) and osteoblast (bone producing cell) is lost in the interface between the two regions (above, right). This transition zone in shown in greater detail at X450 (left).

bone is offered in Table I. The criterion for judging the qualitative tissue response was based upon the total area of newly formed bone when slide-mounted samples were analyzed. Of the five sets of data presented in the table, there was only one instance of a considerable osteogenic response to d-c stimulation. In almost every instance where contralateral sections were compared, more bone was laid down in response

Table I. Response of contralateral bones to both d-c and pulsed stimulation

Unit location	Oscillator class	Repetition rate (Hz)	Pulse width (msec)	Operating time (days)	Tissue response	Energy input (W-sec)
Rt. 8 rib	d.c.	—	—	14	considerable	180
Lt. 8 rib	AMV	0.5	0.6	3	good	0.16
Rt. 11 rib	d.c.	—	—	14	minimal	144
Lt. 11 rib	AMV	0.48	1.7	7	good	1.1
Lt. 12 rib	d.c.	—	—	17	minimal	2160
Rt. 12 rib	AMV	0.45	1.5	17	considerable	0.57
Rt. 9 rib	d.c.	—	—	17	minimal	2160
Lt. 9 rib	AMV	0.5	1.5	17	considerable	0.64
Lt. femur	d.c.	—	—	10	some	108
Rt. femur	AMV	1.2	5	5	considerable	0.22

to pulsed stimulation than to d-c stimulation despite the fact that the total energy delivered to the bone by a d-c source was as much as 3800 times greater than the energy delivered by a pulsing source. Thus on the basis of data obtained during these experiments, it seems reasonable to conclude that a greater osteogenic response can be elicited by a pulsing source than by a d-c source.

Acknowledgment

This paper is based upon the dissertation submitted to the Faculty of the Polytechnic Institute of Brooklyn in partial fulfillment of the requirements for the degree of Doctor of Philosophy (Bioengineering), June 1971.

Manuscript submitted Nov. 2, 1970; revised manuscript received *ca.* May 10, 1971. This was Paper 77 presented at the Atlantic City Meeting of the Society Oct. 4-8, 1970.

Any discussion of this paper will appear in a Discussion Section to be published in the June 1972 JOURNAL.

REFERENCES

1. R. O. Becker, C. A. L. Bassett, and C. H. Bachman, Bioelectric Factors Controlling Bone Structure, in "Bone Biodynamics," H. M. Frost, Editor, pp. 209-239, Little, Brown & Co., Boston (1964).
2. G. V. B. Cochran, Sc.D. Thesis, University Microfilms Publication #70-3412, Columbia University, New York (1966).
3. D. D. Levy, Masters Thesis, Polytechnic Institute of Brooklyn, New York, p. 13 (1969).
4. B. T. O'Connor, *Nature*, **222**, 249, (1969).
5. L. S. Lavine, *J. Am. Med. Assoc.*, **208**, 1482 (1969).
6. C. A. L. Bassett and R. J. Pawluk, *Nature*, **204**, 653 (1964).
7. L. S. Lavine, I. Lustrin, and M. H. Shamos, *ibid.*, **224**, 1112 (1969).

Correction

In the paper "A New Technique for Investigating the Electrochemical Behavior of Electroless Plating Baths and the Mechanism of Electroless Nickel Plating," by N. Feldstein and T. S. Lancsek which appeared on pp. 869-874 in the June 1971 JOURNAL, Vol. 118, No. 6, on p. 872 the Tafel slope should read:

$$-\frac{n\alpha\mathbf{F}}{RT} = \frac{d\ln i}{dE}$$

In the paper "Concentration Reversion in Potentiostatic Electrode Kinetics," by C. A. Johnson, S. Barnartt, and F. D. Glasser which appeared on pp. 576-580 in the April 1971 JOURNAL, Vol. 118, No. 4, on p. 579 the numerical listings in columns 11 and 12 of Table II were transposed. The table should read:

Table II. Potentiostatic reactions exhibiting concentration reversion. Cylindrical electrodes

Test No.	D_Y cm² sec⁻¹ × 10⁶	D_B	c_Y^o mol cm⁻³ × 10⁵	c_B^o	i_o, mA cm⁻²	β	η, mV	α,mm	$\frac{1}{\alpha\lambda_B}$ *	$\frac{1}{\alpha\lambda_Y}$ **	t_m, sec	At t_m $-u_Y$	At t_m u_B	At t_m $i/i_{t=0}$
Group I: First-order reactions (y = n = b = ν)														
1	4	0.4	5	1	1	0.5	10	0.1356	0.346		35.6	0.01327	0.324	0.278
2	4	0.4	5	1	1	0.5	40	0.2045	0.411		114.	0.0914	2.31	0.268
3	0.4	4	0.5	1	0.1	0.5	10	0.2		0.794	790.	0.210	0.01729	0.313
4	0.4	4	1	1	1	0.5	10	0.0827		0.384	16.	0.206	0.0415	0.273
Group II: Reactions second order in Y (y = n = 2, b = ν = 1)														
5	5	0.5	10	1	1	0.5	30	1.0	0.310		1200.	0.1791	4.27	0.182
6	5	0.5	10	1	3	0.25	20	0.1	0.475		29.6	0.0797	2.08	0.252
7	0.5	5	10	1	0.4	0.5	20	1.0		0.277	2070.	0.317	0.316	0.239
8	0.5	5	5	0.5	3	0.75	30	0.1		0.224	18.3	0.414	0.416	0.229

* Compare $\sqrt{D_Y/D_B} - 1 = 2.16$.

** Compare $\sqrt{D_B/D_Y} - 1 = 2.16$.

JOURNAL OF THE ELECTROCHEMICAL SOCIETY

SOLID STATE SCIENCE

SEPTEMBER 1971

SSS

The Influence of the Complexing Agent Concentration on the Etch Rate of Germanium

Michael F. Ehman*,[1], J. W. Faust, Jr.**,[2], and William B. White[3]

Materials Research Laboratory, The Pennsylvania State University, University Park, Pennsylvania 16802

ABSTRACT

This paper reports the effect of the concentration of the complexing agent in an etching solution on the etch rate and surface morphology. The {100} surface of germanium was etched in a solution of the basic composition $X:H_2O_2:H_2O$ in the volume ratio 1:1:4, where X was tartaric, acetic, citric, oxalic, HCl and HF acids, and mannitol. There was no change in the shape or orientation of the etch figures with variation of the type or orientation of the complexants. It was found that the etch rate was a function of the concentration of the complexant when the concentration of the oxidizing agent was held constant. The variation in etch rates and activation energies with the complexing agent concentration indicated that the reactions are diffusion controlled. A model is proposed for the crystal-solution interface which is consistent with the interdependence of the etch rates and the complexing ratio of the germanium.

The rapid development of the solid-state device industry in the decades of the 1950's and 60's was also accompanied by a multifold increase in the number and types of chemical etchants and polishes available for the resultant modern materials. The etchants and polishes are used not only for defect characterization and removing damaged layers, but also for preparing surfaces for orientation by optical goniometric techniques and thinning for transmission electron microscopy. In the case of elemental semiconductors, almost every etchant consists of two basic components and usually a third: (*a*) an oxidizing agent to place the surface atoms in a state suitable for being taken into solution; (*b*) a complexing agent to take the species into solution; and (c) usually a modifier. On the basis of these functions, two major etching systems have been developed for germanium. One is based on the use of HNO_3 as the oxidizing agent, and the second uses H_2O_2. The system Ge:HNO_3:complexant has been studied by several investigators in order to determine the etching mechanisms (1-4). An example of a polish-etchant in this system is CP-4A [HF:HNO_3: acetic acid (3:5:3)]. In this case both HF and acetic acid are reported to act as complexing agents. This system is characterized by high etch rates and activation energies, and variable induction periods making basic mechanism studies difficult. The system Ge:HF:H_2O_2 has also been studied by numerous approaches in order to determine the effects of various parameters on the etching characteristics. Two separate reaction schemes have been proposed for the oxidation processes in hydrogen peroxide solution. One is based on the oxidation of Ge to the divalent state in the form of GeO and further oxidation to the tetravalent state (5-7), whereas the second involves the formation of $Ge(OH)_2^{++}$ at the surface and dissolution as H_2GeO_3 (8, 9). Neither of these reaction schemes has been able to ascribe a general role to the complexing and oxidizing agents in etching processes. Faust (4) studied the reaction rates and the effect on the surface morphology of several oxidizing and complexing agents common to the HNO_3 and H_2O_2 etching systems. He found that the oxidizing agent controlled the mode of attack, *i.e.* the initial development, shape, and orientation of the etch figures, whereas the rate of attack varied with the type of complexing agent present in the solution. Since the shape and orientation of the pits appeared to be constant for a given oxidizing agent, it was decided to examine the variation of etching behavior with the type and concentration of the complexing agents in the solution.

Sample Preparation and Experimental Procedures

The samples used in this study were cut from an ingot of approximately 40 ohm-cm resistivity with the major crystallographic orientation parallel to the {100} planes. The samples were cut into rectangles measuring approximately 12 mm x 6 mm x 3 mm in order to minimize the effects of etch rates on the side areas with respect to those on the main face area. After being cut on an abrasive string saw using a SiC slurry, the samples were then lapped in a water slurry of 5μ Alundum on a glass flat until the surface was uniformly matted and the damaged material from the cutting processes had been removed. The samples were then pre-etched in the etchant to be studied to remove the damaged layer produced by the mechanical processes discussed above (3).

* Electrochemical Society Active Member.
** Electrochemical Society Student Member.
[1] Present address: Autonetics Division of North American Rockwell Corporation, Anaheim, California.
[2] Present address: College of Engineering, University of South Carolina, Columbia, S.C. 29208.
[3] Also affiliated with the Department of Geochemistry and Mineralogy.
Key words: mechanism, hydrogen peroxide, activation energy, morphology, etch pits.

The base etchant used in this investigation was the Superoxol etch developed by Theurer (10). The etchant has the following composition: 48% HF:30% H_2O_2:H_2O in a volume ratio of 1:1:4. The complexing agents used were oxalic, citric, acetic, tartaric, hydrochloric, and hydrofluoric acids, and mannitol. In each case the oxidizing agent was 30% H_2O_2. The reference state for the concentration of the complexing agents was chosen to be a 0.75 molar solution of oxalic acid. This concentration was selected since oxalic acid is the least soluble of the above reagents in distilled water. A saturated solution at 15°C contains 0.75 moles of the acid per liter. The complexing agents were added in the ratio shown above, *i.e.* 1 part of a 0.75M solution of oxalic: 1 part of 30% H_2O_2: 4 parts of water. The chemicals used in the etchants were reagent grade and were prepared by dilution of saturated solutions at room temperature. Distilled water was used throughout the study for dilutions, etchant components, and washing of samples. The reagents were stored separately in polyethylene bottles until one hour before use. The etchant was then mixed in quantities large enough for a complete run and placed in the temperature bath. Camp (6) found that solutions stored this way are stable for long periods of time; however, in this study they were used within 24 hr of mixing.

The etching was carried out in a constant temperature bath with the temperature controlled to ±0.5°C. The etch rates were measured at five temperatures between room temperature and 70°C. The temperatures were read at the start and finish of each run; in each system the reactions did not change the temperature of the solution more than one degree contigrade. Fresh solutions of the etchants were used for each run and were allowed to equilibrate thermally with the bath before each run. The surface area of the sample to solution-volume ratio was approximately 2 cm^2: 600 ml.

The variation in etch rate with mechanical motion of the sample in the solution was minimized by rapid agitation of the sample in a perforated Teflon basket up and down in the beaker. It was found that the ratio increased with increased movement of the sample, as would be expected, and leveled off at approximately three movements per second over a distance of 3.5 cm. Teflon was used since some metal ions present in other plastics catalytically decompose H_2O_2.

Results and Discussion

The etch rate data for the Ge:complexing agent: H_2O_2:H_2O systems are shown in Fig. 1-6 as a function of the concentration of the following complexing agents: oxalic acid, acetic acid, tartaric acid, citric acid, HCl, HF, and mannitol, respectively. The data shown are for the {100} surface. The reaction rates on the {110} and {111} surfaces were not measured since the relationship between the rates on the major crystallographic surfaces have been thoroughly investi-

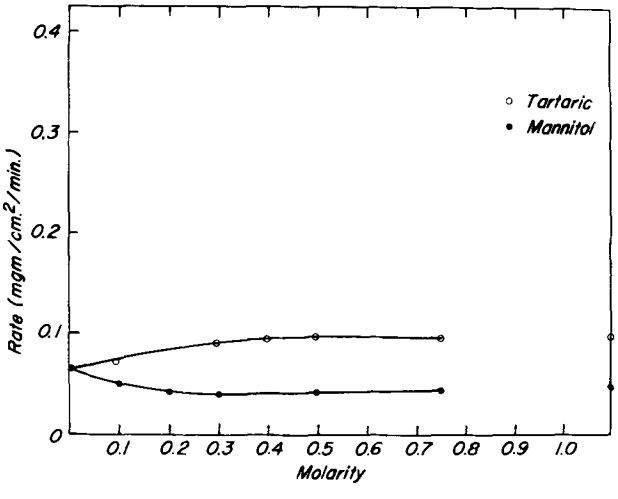

Fig. 1. Plot of the etch rates vs. molarity of tartaric acid and mannitol in the etchant at 20°C. The points on the right hand line are for a saturated solution.

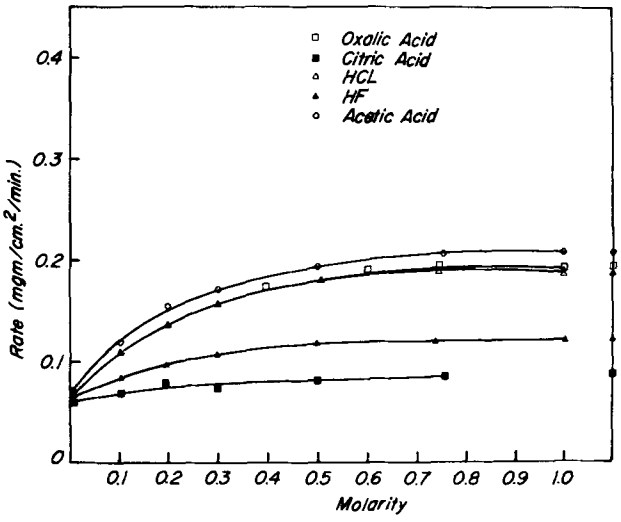

Fig. 2. Plot of the etch rates vs. molarity of oxalic acid, citric acid, HCl, HF, and acetic acid in the etchant at 20°C. The points on the right hand line are for a saturated solution.

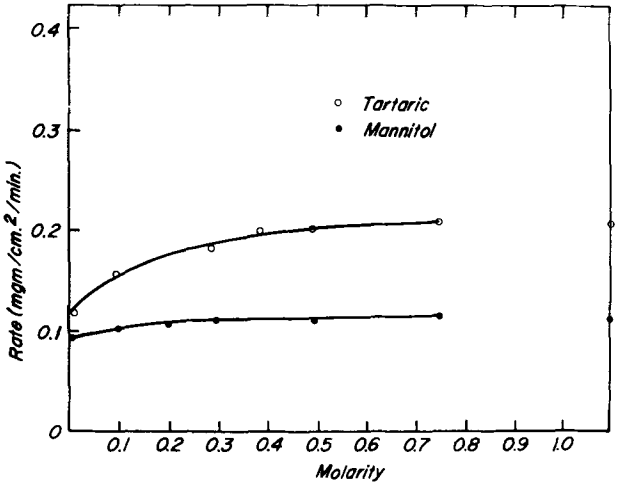

Fig. 3. Plot of the etch rates vs. molarity of tartaric acid and mannitol in the etchant at 40°C. The points on the right hand line are for a saturated solution.

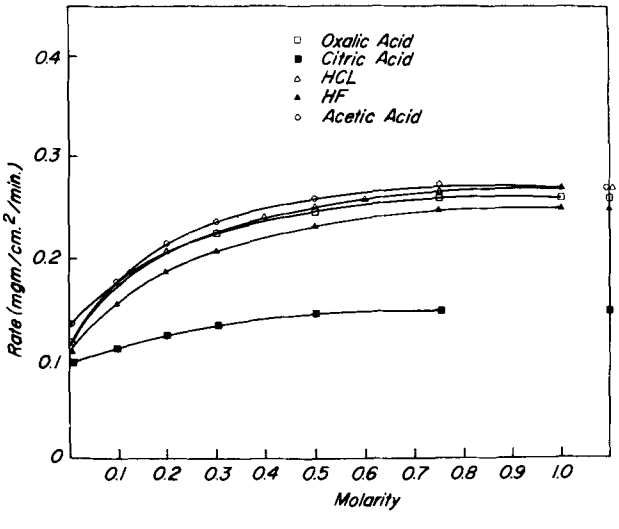

Fig. 4. Plot of the etch rates vs. molarity of oxalic acid, citric acid, HCl, HF, and acetic acid in the etchant at 40°C. The points on the right hand line are for a saturated solution.

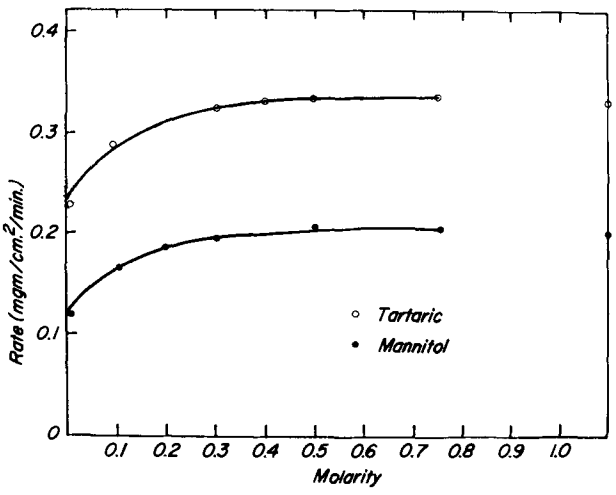

Fig. 5. Plot of the etch rates vs. molarity of tartaric acid and mannitol in the etchant at 60°C. The points on the right hand line are for a saturated solution.

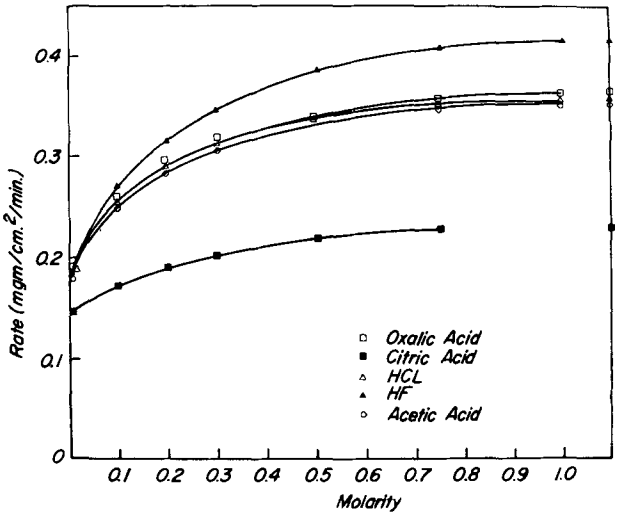

Fig. 6. Plot of the etch rates vs. molarity of oxalic acid, citric acid, HCl, HF, and acetic acid in the etchant of 60°C. The points on the right hand line are for a saturated solution.

gated. Camp (6) has shown that in the system Ge: HF: H_2O_2: H_2O plots of the etch rate as a function of $1/T$ for the three surfaces had similar slopes, but the {110} and {111} surfaces had slightly lower rates. The rates shown in the plots are for 20°, 40°, and 60°C. In general the rates were measured at five temperatures between room temperature and 60°C. However, for simplicity, the complete data are not shown.

Microscopic examination of the surfaces showed that there was no variation in the shape or orientation of the etch figures between the types of complexing agents or over the range in concentrations as was predicted by Faust (4).

The most striking feature of the plots of the etch rate as a function of the concentration of the complexing agent is the leveling off of the rate between 0.3 and 0.4M solutions at a given temperature in the systems containing tartaric acid and mannitol and approximately 0.7M in the oxalate, citrate, HCl, acetate, and HF systems. Several investigators have shown that in aqueous solutions with low pH values, tartaric acid reacts with germanium to form a complex with a tartrate-to-Ge ratio of 1:1. Using potentiometric titrations and conductivity measurements Pflugmacher and Rohrmann (11) were able to show that the complex formed in aqueous GeO_2 solutions in a strong monobasic acid contained one germanium to one hydroxy-acid molecule. In aqueous solutions Gmelin (12) suggests that GeO_2 reacts with water as follows

$$GeO_2 + H_2O \rightleftarrows H_2GeO_3\ (aq) \qquad [1]$$

This suggests that the tartrate radical would then react with metagermanic acid. Using ion-exchange techniques Everest and Salmon (13) were able to confirm the presence of $HGeO_3^-$ in low pH solutions when GeO_2 was dissolved in water. Vartapetian (14) suggested that a complex of the type $GeO[O_2CCH(OH)CH(OH)CO_2H]$ is formed in acid media, and was able to isolate the pyridine salt $GeC_4O_7H_4$ in a crystalline form from the solution. The 1:1 complexing ratio was later verified by Vartapetian and Tchakirian (15) and Mattock (16). In an etching system one would expect that at a given concentration (since there is a 1:1 complexing ratio) when a state is reached where for every germanium atom dissolving there was one tartrate radical present at the crystal-solution interface, the etch rate would approach a constant value. This constant rate should not change if further amounts of tartaric acid were present in the solution. Looking at Fig. 1, 3, and 5, we can see that this behavior is observed. These rates, however, are significantly lower than those reported by Faust (4) even though the activation energies at concentrations in this saturated range compare favorably with those reported in the same study. This apparent increase in rate at the higher concentrations of tartaric acid might be related to the change in complexing ratio with increasing amounts of acid reported by Everest and Harrison (17). They reported that in concentrated solutions the complexes formed were of the type Ge_xTr_{x-1}, where $X \simeq 5$.

The complexing ratio of mannitol to monogermanic acid in very dilute solutions of low pH was reported to be 1:1 (18). Therefore we would expect the etch rate *vs.* concentration curves to be in a form similar to those of tartaric acid. Looking at Fig. 1, 3, and 5, one can see that indeed this behavior is observed.

If the complexing ratio changed to a value of 2:1 (complexant: Ge) then one would expect the rate curves to level out at a higher concentration of the complexant in the solution. The curves for citric, oxalic, hydrochloric, hydrofluoric, and acetic acids all exhibit this behavior as can be seen in Fig. 2, 4, and 6. Citric acid was reported by Clark and Waddams (19) to complex germanium in a ratio of 2 citrates: 1 germanium. Their conclusions were based on conductivity, polarimetric, and pH measurements. The chemistry of germanium in oxalic acid solutions has been studied by several investigators (20-24). The results of these studies show that the complex that is present in the solution is highly dependent on the pH of the solution and the oxalate concentration. Douville *et al.* (23) concluded, from comparison of *IR* spectra of solutions containing germanium and oxalic acid with known oxalate complexes, that in acidic media the complexes are composed of tetravalent Ge. Other authors (20-22) have suggested that when germanium is in solutions containing compounds with two adjacent hydroxyl or carbonyl groups, the complexes take one of the following forms: $H_2Ge(C_2O_4)_3$; $Ge(C_2O_4)_2$ or $GeO(C_2O_4) \cdot xH_2O$. More recent investigations by Everest (24) have indicated that in solutions of oxalate concentrations below a pH of 3, a complex of the type $[GeO(C_2O_4)_2]^{2-}$ forms; whereas in high oxalate concentrations, the complexes were of the type $[Ge(C_2O_2)_4]^{2-}$. Johnson (25) has reported the existence of $GeOCl_2$. The observed rate data shown in Fig. 2, 4, and 6, indicate that this complexing ratio is reasonable for hydrochloric acid when compared to that observed in the 1:1 and 2:1 complexing ratios discussed above. Although it has not been possible to identify the fluoride complex of germanium in aqueous solutions, the etch rate data exhibit the same behavior as the hydrochloric acid curves, suggesting that the fluorine is complexed with the Ge in a ratio of 2:1. If it is completely analogous to the chloride case, one might expect it to be in the form $GeOF_2$.

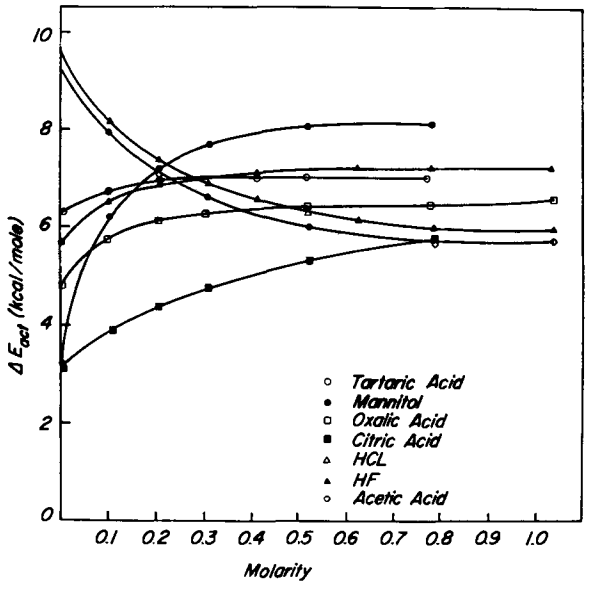

Fig. 7. Plot of the activation energy vs. molarity of the complexing agents in the etchant.

The curves for acetic acid, Fig. 2, 4, and 6, leveled off between 0.7 and 0.8M, suggesting a complex with a ratio of 2:1, although germanium-acetate complexes have not been reported in the literature. Some difficulty was noted in this system in obtaining consistent rate data when using solutions that were not fresh (*i.e.* older than 48 hr).

The etch rates presented in the data above are slightly lower than those presented by other investigators working in similar systems. This variation is normal in etch rate studies due to the numerous factors that can affect the rates such as surface area determination, resistivity, dislocation density, degree of agitation, temperature control and measurement, etc. The germanium crystals used in this study had an impurity content of less than 1 ppm and the dislocation density was less than 50 per cm^2. Both of these are very low and may possibly be a major factor to the lower rates.

The activation energies determined from the etch rates are plotted as a function of concentration in Fig. 7 for the systems discussed above. In each case the plots of the activation energy as a function of the concentration leveled off at approximately the same concentration as the rates did. Laidler (26) has separated the reaction mechanisms on solid surfaces for heterogeneous reactions into five consecutive steps:

1. Volume diffusions of the reacting species to the surface.
2. Adsorption of the species on the surface.
3. Reaction on the surface.
4. Desorption of the reaction products.
5. Volume diffusion of the products from the surface.

The activation energy calculated from comparison of the etch rates at two different temperatures using the Arrhenius equation is that for the slowest step in the reaction sequence above. Abramson and King (27) have suggested that the general limit for the diffusion controlled reactions is 10 kcal/mole or less, between 10 and 20 kcal/mole for the adsorption or desorption steps, and surface reactivity controlled reactions greater than 25 kcal/mole. All of the activation energies calculated in this study are well within the range of diffusion controlled reactions. The sensitivity of the etch rate to the degree of agitation of the solution, along with the observed dependence of the etch rate on concentration support the diffusion-controlled reaction mechanisms.

It would be tempting to relate the variation in activation energy at the lower concentrations of the complexing agents to the nature of the activated complexes; however, the present knowledge about the reacting species and over-all chemistry of the solutions does not permit this. Once the interface is "saturated," *i.e.* for every germanium that is dissolved there is one or more (depending on the complexing ratio) complexing species present at the interface, then the activation energies observed can be used for purposes of comparison between systems and reaction mechanisms determined. It must be remembered, however, that the measured activation energies are "apparent" (*i.e.* they are undoubtedly a sum of several steps rather than the actual activation energy for a single step.)

It is interesting to note that in the system Ge:HF:H_2O_2:H_2O (Fig. 2, 4, and 6), there was no variation in activation energy within temperature ranges as had been noted by Camp (6). Camp found that the activation energy for the (100) surface in this system (using concentrated reagents) was approximately 13.6 kcal/mole below room temperature, whereas above room temperature it was approximately 8.6 kcal/mole. This observation was verified in this study when using 48% HF and 30% H_2O_2; however, when using dilute HF solutions the effect was not present. The activation energies reported by Camp for the upper temperature region are in the same range as those determined in this study, therefore corroborating his suggestion that the reactions are diffusion controlled above 20°C.

Summary and Conclusions

It has been found that under carefully controlled conditions, the etch rate of germanium in etchants composed of *X*:30% H_2O_2:H_2O (1:1:4) (where *X* is HCl, HF, acetic, citric, oxalic, and tartaric acids, and mannitol) is a function of the complexing agent.

The dependence of the etch rate on the stirring rate of the solution, the parabolic behavior of the etch rate as a function of concentration, and the range in values of activation energies for the reactions strongly indicate that the etching processes are diffusion controlled.

Based on the results reported here and those by others, the following sequence for germanium etched in peroxide based solutions is suggested

$$2H_2O_2 \rightarrow H_3O_2^+ + O_2H^- \qquad [3]$$

which provides the peroxide ion for the oxidation step with the holes coming from the valence band of the germanium.

$$Ge + O_2H^- + H_2O + 2e^+ \rightarrow \underset{\text{surface}}{Ge(OH)_2^{++}} + OH^- \qquad [4]$$

The hydroxyl complex formed above then is desorbed from the surface and reacts with water

$$\underset{\text{solution}}{Ge(OH)_2^{++}} + H_2O \rightarrow H_2GeO_3(aq) + 2H^+ \qquad [5]$$

to form metagermanic acid. The metagermanic acid then reacts with the complexant. In the case of hydrochloric acid the reaction would be

$$H_2GeO_3 + 2HCl \rightarrow GeOCl_{2(aq)} + 2H_2O \qquad [6]$$

to form the germanium oxychloride species as the final reaction products.

A model is proposed for the crystal-solution interface whereby the etch rate of the material is a function of the concentration (specifically the number of complexing ions at the interface) of the complexing agent in the solution. The increase in rate of dissolution as the concentration of the complexant is increased is probably due to the increased availability of reactants. The rate continues to increase parabolically until, as in the case of a 1:1 complexing ratio, there is a complexing ion present at the crystal-solution interface for every germanium ion formed at the surface. In the case of a 2:1 complexing ratio, the concentration at which the rate becomes constant is just

twice that observed for a 1:1 complex. This model predicts then that once this constant, or the "saturated" zone is reached, the rate will remain constant no matter how much additional complexant is present in the solution. This behavior was observed in the systems studied.

It is further suggested from the rate data that the rate controlling step is the diffusion of the final reaction products from the interface.

Acknowledgments

This work was supported by the Advanced Research Projects Agency under Contract No. DA-49-043.

Manuscript submitted July 13, 1970; revised manuscript received ca. April 26, 1971.

Any discussion of this paper will appear in a Discussion Section to be published in the June 1972 JOURNAL.

REFERENCES

1. M. C. Cretella and H. C. Gatos, *This Journal*, **105**, 487 (1958).
2. B. Schwartz and H. Robbins, *ibid.*, **111**, 196 (1964).
3. A. F. Bogenschutz, W. Krusemark, K. H. Löcherer, and W. Mussinger, *ibid.*, **114**, 970 (1967).
4. J. W. Faust, Jr., in "Reactivity of Solids," J. W. Mitchell, R. C. DeVries, R. W. Roberts and P. Cannon, Editors, p. 337, John Wiley and Sons, New York (1969).
5. W. W. Harvery and H. C. Gatos, *This Journal*, **105**, 654 (1958).
6. P. R. Camp, *ibid.*, **102**, 586 (1955).
7. S. G. Ellis, *J. Appl. Phys.*, **28**, 1262 (1957).
8. D. R. Turner, *This Journal*, **103**, 252 (1956).
9. N. Cerniglia and P. Wang, *ibid.*, **109**, 508 (1962).
10. H. C. Theurer, U.S. Pat. No. 2,542,727 (1951).
11. A. Pflugmacher and I. Rohrmann, *Angew. Chem.*, **69**, 778 (1957).
12. L. Gmelin, in "Gmelin's Handbuch der anorganishcen chemi," system 45, p. 455, 503, Verlag, Leipzig-Berlin (1958).
13. D. A. Everest and J. E. Salmon, *J. Chem. Soc.*, **1954**, 2438.
14. O. Vartapetian, *Ann. Chim. (Paris)*, (13) **2**, 916 (1957).
15. O. Vartapetian and A. Tchakirian, *Compt. Rend.*, **236**, 81 (1953).
16. G. V. R. Mattock, *J. Chem. Soc.*, **1954**, 989.
17. D. A. Everest and J. C. Harrison, *ibid.*, **1960**, 3752.
18. D. A. Everest and J. C. Harrison, *ibid.*, **1957**, 4319.
19. E. R. Clark and J. A. Waddams, *Nature*, **180**, 904 (1957).
20. P. A. Bardet and A. Tchakarian, *Compt. Rend.*, **189**, 914 (1929).
21. A. Tchakarian, *Compt. Rend.*, **204**, 356 (1937).
22. A. Tchakarian, *Ann. Chim. (France)*, **12**, 415 (1939).
23. A. Douville, B. Duval, and C. Lecompte, *Compt. Rend.*, **212**, 697 (1941).
24. D. A. Everest, *J. Chem. Soc.*, **1953**, 4117.
25. O. H. Johnson, *Chem. Rev.*, **51**, 431 (1952).
26. K. J. Laidler, "Chemical Kinetics," p. 152, McGraw-Hill Book Co., New York (1950).
27. M. B. Abramson and C. B. King, *J. Am. Chem. Soc.*, **61**, 2290 (1939).

Ionic Conduction in Calcium Doped Polycrystalline Lithium Iodide

Carl R. Schlaikjer* and Charles C. Liang*

P. R. Mallory & Company, Inc., Laboratory for Physical Science, Northwest Industrial Park, Burlington, Massachusetts 01803

ABSTRACT

The ionic conductivity of polycrystalline lithium iodide containing 0 to 3% (mole) calcium iodide was studied at temperatures between −30° and 130°C. The conductivity increased linearly with the concentration of calcium iodide, and it was concluded that the introduction of calcium ions to the lithium iodide crystals induced Schottky defects. The activation energy for the ionic conduction process of 9.96 kcal/mole agreed well with the value obtained by other investigators. The electronic conductivity of the calcium doped lithium iodide polycrystals was negligible compared to the ionic conductivity.

In view of the recent developments in high voltage solid-state battery systems (1, 2), lithium iodide has received a great deal of attention as a solid electrolyte material. Its compatibility with the intrinsically high voltage anode material lithium, and the extremely low electronic conductivity of lithium iodide made it possible to develop high voltage solid state battery systems such as Li/LiI/AgI (1, 2). The relatively low ionic conductivity of lithium iodide electrolyte (10^{-7} ohm^{-1} cm^{-1} at 25°C) made necessary the fabrication of thin film, low capacity Li/LiI/AgI cells in order to obtain useful current densities. However, if the conductivity of lithium iodide could be increased substantially, cells with higher capacity and thicker electrolyte layers could be produced by the conventional fabrication techniques rather than the vacuum deposition techniques as reported previously (1, 2).

The formation of crystal defects in lithium halides by the addition of minute quantities of higher valent cations has been shown to increase the ionic conductivity (3). Magnesium doped lithium iodide was examined recently by Jackson and Young (4) who studied the Schottky disorder in lithium iodide single crystals and observed an increase in the ionic conductivity. The present work was undertaken to study the conductivity of polycrystalline lithium iodide with the inclusion of various quantities of calcium iodide in the crystal structure.

Experimental Techniques

The preparation of anhydrous lithium iodide.—Fisher reagent grade chemicals were used in the preparation of lithium iodide. Lithium carbonate was prepared by adding a 20 mole per cent (m/o) excess of ammonium bicarbonate solution to a lithium hydroxide solution. It was filtered and dried at 200° C for several hours.

Hydriodic acid was distilled under an argon atmosphere. After the distillation, the acid was treated with an excess of lithium carbonate through a long tube located at the top of the distillate flask. The carbon dioxide generated from the reaction and the argon gas

* Electrochemical Society Active Member.

Key words: Schottky defects, ionic conductivity, solid electrolytes, lithium iodide, calcium iodide.

present in the flask protected the acid from the atmosphere until an excess of carbonate was added.

Immediately after the excess of lithium carbonate had been filtered, the lithium iodide solution was placed in a vacuum oven and heated to 85°C until solid. The remaining water in the crystals was removed by heating in a vacuum oven at 120°C overnight. The lithium iodide was then transferred under dry carbon dioxide to a Vacuum Atmospheres dry box (less than 15 ppm H_2O). Analyses of the lithium iodide showed that the iodide content was as expected for anhydrous lithium iodide, and no excess of alkali was found in the sample. The lithium iodide so prepared could be fused in the dry box without decomposition or discoloration.

The preparation of calcium doped lithium iodide.—Mallinckrodt $CaI_2 \cdot 2H_2O$ was dehydrated by heating under vacuum in an evacuated flask first at 100°C for several hours then at 300°C for about 3 hr. The calcium iodide was transferred to the dry box in the flask. Analysis of the iodide present showed that it was anhydrous.

A powder mixture of the anhydrous lithium iodide and the anhydrous calcium iodide in a mole ratio of 10 to 1 was blended, fused at 600°C, quenched to ambient temperature, and pulverized. This powder was used to prepare further dilutions with lithium iodide. Samples of lithium iodide containing 0.2 m/o to 3 m/o of calcium iodide were prepared from the 10 to 1 stock by similar fusion and quenching processes.

The conductivity measurements.—The calcium doped lithium iodide samples were pulverized in a Fisher mechanical grinding apparatus for 30 min and annealed at 150°C for 30 min.

Pellet samples were prepared by pressing the powder in a 7/16" diameter steel die under a pressure of 66,500 psi with lithium electrodes incorporated on both sides of the pellet. Samples for the conductivity measurements at different temperatures were hermetically sealed in metal-ceramic cell cases and equilibrated in a Tenney constant temperature chamber until readings changed by no more than 2% over a half-hour period.

Conductivity measurements were made with square wave excitation from 1 to 10 kHz of a bridge constructed from Helipot precision potentiometers. A Tektronix Type E differential preamplifier made possible the application of only 3 mV peak to peak to the sample. The reproducibility of measurements was within ±2.5%.

The determination of the lattice parameter.—Debye-Scherrer powder patterns of lithium iodide containing various amounts of calcium iodide were obtained at room temperature immediately after annealing using conventional techniques with CuK_α radiation.

The lattice parameter of each sample was obtained by the Nelson-Riley extrapolation. The uncertainty in the results was about ±0.003Å. A precision camera was not used to reduce this uncertainty because of the extreme air sensitivity of the samples.

The characteristics of the electrochemical cell.—Mallinckrodt silver iodide was used as the cathode material. It was dried at 160°C for about 16 hr before use. Metz fine silver powder was used to form the cathode current collector. Lithium iodide containing calcium iodide was the electrolyte material and Foote lithium ribbon was used as the anode.

The $Li/LiI(CaI_2)/AgI$ solid electrolyte cells were fabricated by pressing the cathode current collector, the cathode, the electrolyte, and the anode in a 7/16 in. die under a pressure of 66,500 psi.

The cell voltages under open circuit and various discharge current densities were measured by means of a Keithley 610B electrometer and recorded by a Varian 14A strip chart recorder.

Results

The inclusion of calcium iodide caused a substantial increase in the conductivity of the polycrystalline lithium iodide. Figure 1a shows that the conductivity of lithium iodide increased linearly with the concentration of calcium iodide up to 1 m/o. An amount of 0.2 m/o of calcium iodide increased the conductivity at 28° ± 0.5°C from 4.5×10^{-7} ohm^{-1} cm^{-1} to 2.3×10^{-6} ohm^{-1} cm^{-1}. As the concentration of calcium iodide reached 1 m/o, the conductivity of the polycrystalline matrix was as high as 1.2×10^{-5} ohm^{-1} cm^{-1}.

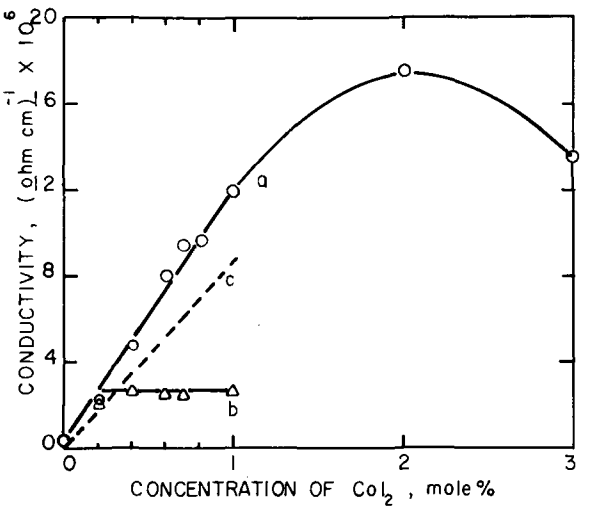

Fig. 1. The conductivity of lithium iodide as a function of the concentration of calcium iodide at 28° ± 0.5°C. (a) Freshly annealed at 150°C for 30 min, (b) 500 hr after annealing, and (c) based on the calculated mobility of the cation vacancy.

It was found that the conductivity of lithium iodide containing 0.4 m/o or more calcium iodide decreased substantially as a function of time after annealing at 150°C for 30 min. It reached a constant value of about 2.6×10^{-6} ohm^{-1} cm^{-1} at 28° ± 0.5°C after about 500 hr regardless of the initial calcium iodide concentration. The data of Fig. 1a represent the conductivity of the samples at 28° ± 0.5°C, measured as soon as possible after quenching from 150°C while those of Fig. 1b represent the conductivity of the samples at 28° ± 0.5°C measured long after quenching (at least 500 hr), when no change in conductivity with time was noted. In each case, the reproducibility of the measurement was ±2.5%. The change in ionic conductivity with doping level was calculated theoretically and the results are shown in Fig. 1c.

The above observation shows that the samples containing 0.4 m/o or more calcium iodide were metastable immediately after the 150°C annealing process. This was also evident from the fact that the conductivity measurements at various temperatures of the metastable sample were not reproducible over the time period required for the measurements over a temperature range of −30° to 130°C after one 30 min annealing treatment. However, the conductivity measurements at various temperatures for samples containing 0.2 m/o or less calcium iodide were reproducible (±2.5%) and independent of time. Nevertheless, it was found that reasonably reproducible conductivity measurements for lithium iodide containing 0.4 m/o or more calcium iodide could be obtained when the sample was annealed at 150°C for 30 min then quenched to the predetermined temperature before each measurement at each temperature. The results of these measurements were used to construct the log σ *vs.* $1/T$ plot shown by Fig. 2c.

The activation energy of the conduction process for the polycrystalline lithium iodide and the calcium doped lithium iodide was determined over the temperature range of −30° to 130°C. Previous investigators (3, 4) have shown that the extrinsic conduction region for lithium iodide occurs at temperatures below 250°C. Therefore, the activation energy of 9.96 kcal/mole, de-

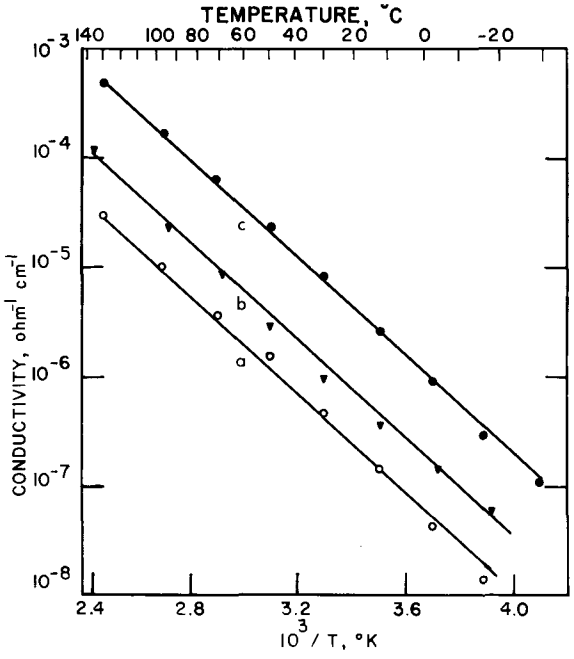

Fig. 2. The conductivity of lithium iodide containing calcium iodide as a function of temperature. Concentration of calcium iodide: (a) 0, (b) 0.2 m/o, (c) 1.0 m/o (the sample was annealed at 150°C for 30 min before each measurement).

termined from the slopes of the log σ *vs.* $1/T$ plots shown in Fig. 2, applied to the extrinsic conduction region. This result is in excellent agreement with the value of 0.43 eV or 9.93 kcal/mole obtained by Jackson and Young (4) for the magnesium doped lithium iodide single crystals.

The lattice parameters of the samples are given in Fig. 3. It was noted that the uncertainty of the measurements made the exact determination of the lattice parameter rather difficult. Nevertheless, the results suggested strongly that within the solubility limits of the calcium iodide in the polycrystalline lithium iodide, the lattice parameter increased with the concentration of calcium iodide.

The conductivity of lithium iodide containing 0.4 m/o or more calcium iodide decreased substantially as a function of time after annealing. It reached a constant value of about 2.6 x 10^{-6} ohm^{-1} cm^{-1} at 28° ± 0.5°C after about 500 hr regardless of the initial calcium iodide concentration. It was found also that the rate of the decrease in conductivity was higher for the sample containing higher concentration of calcium iodide as shown by Fig. 4.

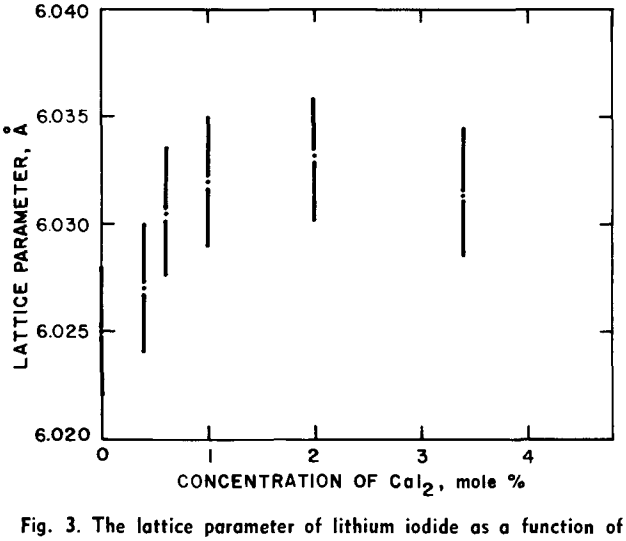

Fig. 3. The lattice parameter of lithium iodide as a function of the calcium iodide concentration (annealed samples).

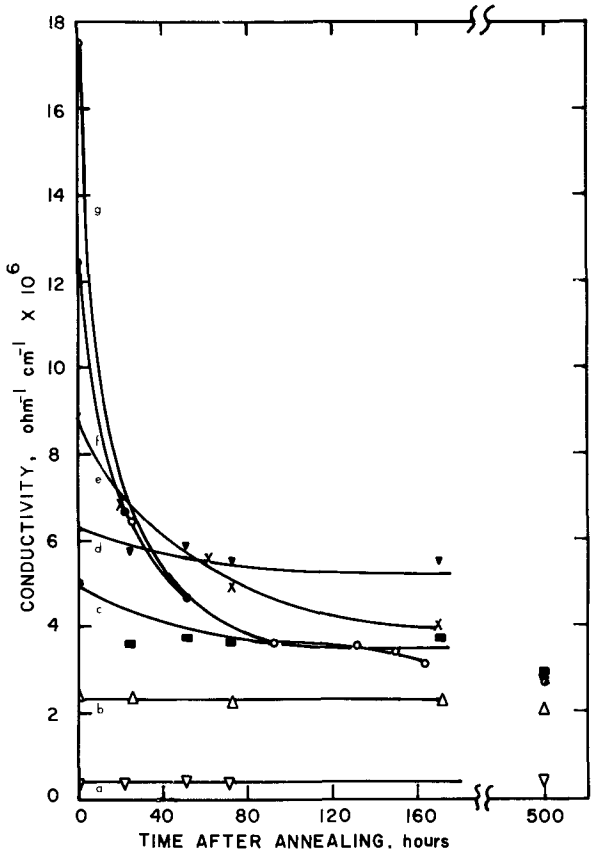

Fig. 4. The conductivity of lithium iodide containing calcium iodide as a function of time after annealing. Temperature: 28° ± 0.5°C. Concentration of calcium iodide: (a) 0, (b) 0.2 m/o, (c) 0.4 m/o, (d) 0.6 m/o, (e) 0.7 m/o, (f) 1.0 m/o, (g) 2.0 m/o.

Lithium-silver iodide solid electrolyte cells with calcium doped lithium iodide electrolytes exhibited an open circuit voltage of 2.1V which was expected from the Gibbs free energy change of the cell reaction (1, 5).

$$Li + AgI \rightarrow LiI + Ag$$

Figure 5 shows the polarization curve of a Li/LiI(0.2%

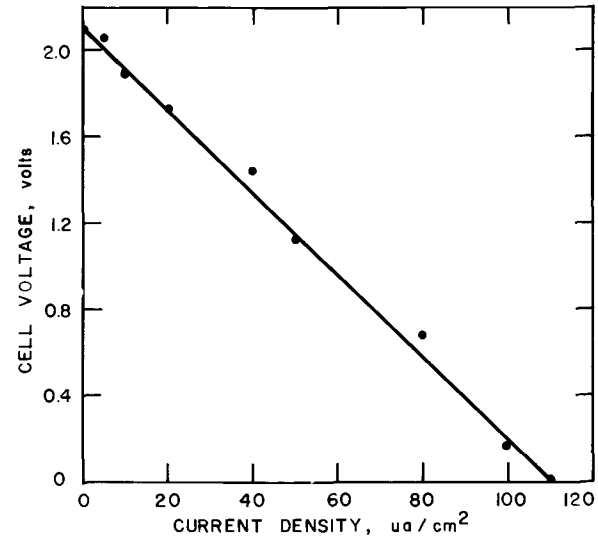

Fig. 5. The polarization curve of a typical Li/LiI (0.2 m/o CaI_2) AgI solid electrolyte cell. Temperature: 28° ± 0.5°C, thickness of the electrolyte: 0.04 cm, geometric surface area of the electrolyte: 0.7 cm^2.

CaI_2)/AgI solid electrolyte cell. The linearity of the polarization curve indicated that the voltage loss was of an ohmic nature and the observed short circuit current of 110 $\mu A/cm^2$ was expected from the resistance of the electrolyte layer with a measured thickness of 0.04 cm.

Discussion

As expected from the fact that the inclusion of divalent calcium ions in the lithium iodide matrix will induce defects (6), the ionic conductivity of lithium iodide increased linearly with the concentration of calcium iodide as shown by Fig. 1a. The fact that the linearity of the conductivity *vs.* concentration plot extended only to 1 m/o of calcium iodide can be explained by the saturation of calcium iodide in the polycrystalline lithium iodide under the experimental conditions.

The uncertainty in the determination of the lattice parameter was ± 0.003Å which makes the exact value uncertain by this amount. Nevertheless, Fig. 3 gives an indication that within the solubility limits of the calcium iodide in the polycrystalline lithium iodide, the lattice parameter increased nearly linearly with the concentration of calcium iodide as predicted by Vegard's law (7).

The formation of a solid solution between calcium iodide and lithium iodide is evident from the above experimental results. However, whether the dissolution of calcium iodide in lithium iodide formed a substitutional solution inducing Schottky defects or an interstitial solution inducing Frenkel defects needs to be discussed. It is known that lithium iodide forms a close packed, face centered cubic structure. Two types of voids exist in the lattice: tetrahedral voids and voids surrouding the lithium ions (8). The radii of the two types of voids are about 0.49Å (*i.e.* 0.225 x 2.2Å) and 0.29Å (*i.e.* 0.13 x 2.2Å), respectively. The empirical ionic radius of a calcium ion is 1.06Å (9) which is too large to squeeze in these voids without seriously distorting the crystal lattice. On the other hand, the space occupied by the lithium ion has a radius of about 0.91Å (8) which may be large enough for a calcium ion to replace the lithium ion resulting in a slight increase in the lattice parameter. Therefore, we believe that the inclusion of calcium ions in lithium iodide induces primarily Schottky defects and accordingly, the ionic conduction is due to the mobility of cation vacancies. This conclusion is in agreement with that of Jackson and Young (4) who observed that the inclusions of the divalent magnesium ions in the lithium iodide single crystals did not alter the ionic conduction behavior in the intrinsic region and concluded that Schottky defects were induced by the incorporated magnesium ions. Furthermore, the agreement between the activation energy of 9.96 kcal/mole with that determined by Jackson and Young (4) leads us to the conclusion that the extrinsic conduction mechanism in the polycrystalline matrix is similar to that in the single crystals, namely, that the conduction is due to the mobility of cation vacancies.

The theoretical mobility of the cation vacancy μ in the lithium iodide crystals can be calculated from the following equation (6)

$$\mu = \frac{4ea^2\nu}{kT} \exp\left(-\frac{E}{kT}\right)$$

where a represents the distance between the nearest neighbor cation and anion, E the activation energy (which is equal to the activation energy of the conduction process in the extrinsic region), ν the lattice frequency while e and kT have the usual significance. The vibrational frequencies for lithium iodide have been calculated by Karo (11) and a single value of 3.32×10^{13} sec^{-1} was selected to represent the vibrational spectra. We have adopted Karo's value of ν for the calculation of μ. The mobility of the cation vacancy in lithium iodide at 28°C calculated according to the above equation was 3×10^{-7} $cm^2/sec\text{-}volt$. Whereas the experimental value of μ at 28°C obtained from the slope of the conductivity *vs.* the concentration of calcium iodide in the lithium iodide plot (Fig. 1a) was 4×10^{-7} $cm^2/sec \cdot volt$. The agreement between the calculated value and the experimental value was quite satisfactory.

The decrease in the conductivity with time, of lithium iodide containing 0.4 m/o or more calcium iodide, shows that the equilibrium solubility of calcium iodide in lithium iodide is probably less than 0.4 m/o at 28° ± 0.5°C. During the 150°C annealing process, as much as 1 m/o of calcium iodide can dissolve in lithium iodide. As the temperature decreases to 28° ± 0.5°C, the excessive amount precipitates to form a separate phase. However, the rate of precipitation is rather slow as may be seen from Fig. 4. Since the conductivity of polycrystalline lithium iodide is directly proportional to the concentration of the calcium iodide in the lattice, we could determine the equilibrium solubility of calcium iodide in lithium iodide from Fig. 1b and a value of 0.23 ± 0.03 m/o at 28° ± 0.5°C was found.

All the Li-AgI test cells with the various lithium iodide-calcium iodide electrolytes exhibited an open circuit voltage of 2.1V, which is expected from relevant thermodynamic data (1, 5), and this leads to the conclusion that the electronic conductivity of the calcium doped lithium iodide is negligible compared to its ionic conductivity (10). The current capability of test cells with 0.04 cm thick electrolyte layers shown in Fig. 5 indicated that the cells had a purely ohmic impedence and that they were capable of delivering short circuit currents of 110 $\mu A/cm^2$ at room temperature.

Acknowledgment

The authors are grateful to Drs. P. Bro, R. Selim, and Y. Shen for helpful discussions concerning this work, and to Mr. S. Fantasia for the Debye-Scherrer photographs.

Manuscript submitted Nov. 4, 1970; revised manuscript received *ca.* April 28, 1971.

Any discussion of this paper will appear in a Discussion Section to be published in the June 1972 JOURNAL.

REFERENCES

1. C. C. Liang and P. Bro, *This Journal*, **116**, 1322 (1969).
2. C. C. Liang, J. Epstein, and G. H. Boyle, *ibid.*, **116**, 1452 (1969).
3. Landolt-Bornstein, "Zahlenwerte und Funktionen," Vol. 2, part 6, pp. 225-242, Springer, Berlin (1959).
4. B. J. H. Jackson and D. A. Young, *J. Phys. Chem. Solids*, **30**, 1973 (1969).
5. W. M. Latimer, "Oxidation Potentials" 2nd ed., pp. 190 and 329, Prentice Hall, Inc., Englewood Cliffs, N. J. (1961).
6. D. W. Dreyfus and A. S. Nowick, *J. Appl. Phys.*, **33**, 473 (1962).
7. L. S. Darken and R. W. Gurry, "Physical Chemistry of Metals," p. 76, McGraw-Hill Book Co., New York (1953).
8. L. V. Azaroff, "Introduction to Solids," pp. 64-68, McGraw-Hill Book Co., New York (1960).
9. N. A. Lange, "Handbook of Chemistry," p. 108, McGraw-Hill Book Co., New York (1956).
10. D. O. Raleigh, Solid State Electrochemistry, "Progress in Solid State Chemistry," H. Reiss, Editor, Vol. 3, pp. 92-94, Pergamon Press, New York (1967).
11. A. M. Karo, *J. Chem. Phys.*, **31**, 1489 (1959).

Diffusion and Solubility of Yb^{3+} in CdS

W. W. Anderson and H. J. Chang

Department of Electrical Engineering, Ohio State University, Columbus, Ohio 43210

ABSTRACT

Diffusion studies were performed to determine the temperature and sulfur partial pressure dependence of Yb diffusion and solubility in CdS. Over the temperature range of 930° to 990°C and pressure range of 3.3-33 atm, the diffusion appears to consist of a saturated surface component and a slow deep diffusing component. The slow diffusing component can be described by the approximate relation

$$D \simeq 4 \times 10^{-4} P_{S_2}^{1/2} e^{-1.85/kT} \text{ cm}^2/\text{sec}$$

where the sulfur partial pressure, P_{S_2}, is measured in atmosphere and the activation energy for the process is $\Delta E = 1.85$ eV. The surface concentration (and hence solid solubility) of Yb^{3+} obeyed the relation

$$[Yb^{3+}]_{sat} \sim P_{S_2}^{1/2}$$

These results suggest that the diffusion and solubility of Yb^{3+} is determined by the cadmium ion vacancy concentration in CdS.

Diffusion studies were performed to determine the temperature and sulfur partial pressure dependence of Yb diffusion and solubility in CdS. From these studies we hoped to obtain information on the incorporation and diffusion mechanisms of the trivalent rare earth ions in the CdS lattice. Sample preparation and measurement techniques were identical to those used in a previous study (1) and are very briefly reviewed here.

Diffusion was from a saturated vapor phase source of Yb metal or Yb_2S_3. Since the crystal surface is a one-phase, three-component system, it is necessary to specify four intensive thermodynamic variables. In these experiments, the variables were partial pressure of Yb(g) or Yb_2S_3(g), partial pressure of S_2, total pressure, and temperature. The pressure, P_{S_2}, was determined by the quantity of sulfur included in the evacuated diffusion ampoule. The total pressure, P_T, is essentially identical to P_{S_2} for our range of sulfur pressures, $3.3 \leq P_{S_2} \leq 33$ atm. The diffusant partial pressure, P_{Yb} or $P_{Yb_2S_3}$ is the saturated vapor pressure of the gas phase over a liquid Yb(l) or solid Yb_2S_3(s) source. From observations of a luminescent flash when a diffusion ampoule containing metallic Yb and S is heated and examination of the solid yellowish residue after a diffusion run, it appears that metallic Yb is completely converted to Yb_2S_3 before significant diffusion begins and the equilibrium vapor over a Yb_2S_3(s) is the source of Yb diffusing into CdS.

The Yb concentration as a function of depth was measured by the intensity of Yb^{3+} photoluminescence as a function of depth from the surface. Hence, only the active Yb^{3+} concentration was measured which may differ from the total Yb^{3+} concentration and certainly differs from the total Yb concentration, especially in regions of high concentration.

The CdS crystals were obtained from Eagle-Picher Industries, Inc. They were undoped, ultrahigh purity grade, dark insulating, and photosensitive. The room temperature free electron concentration was not measurable by standard Hall effect techniques so that $n < 10^{11}$ cm^{-3}. The crystals used in the previous study by Girton and Anderson were characterized by a room temperature free electron concentration of $n = 3.5 \times 10^{15}$ cm^{-3} before diffusion (1). In both this and the previous study, the crystals were diffused without any equilibration process such as firing in Cd or S vapor, *i.e.* the diffusion was carried out on the as received material.

Key words: luminescence, rare earths, compound semiconductors.

Results

In Fig. 1, we show a typical plot of Yb^{3+} emission intensity as a function of depth from the diffused surface. The results of three different diffusion times are normalized and plotted on the one figure. The Yb^{3+} concentration (assumed to be proportional to Yb^{3+} emission intensity) follows neither a complementary error function nor Gaussian distribution. (The departure from ideal behavior near the surface is more evident on a plot of intensity *vs.* $d/\sqrt{t}$ than the intensity *vs.* d^2/t plot shown in Fig. 1. However, the surface saturation is easily seen from the first two plotted points of the 6 hr and 9 hr diffusions.) From the experimental conditions, a complementary error func-

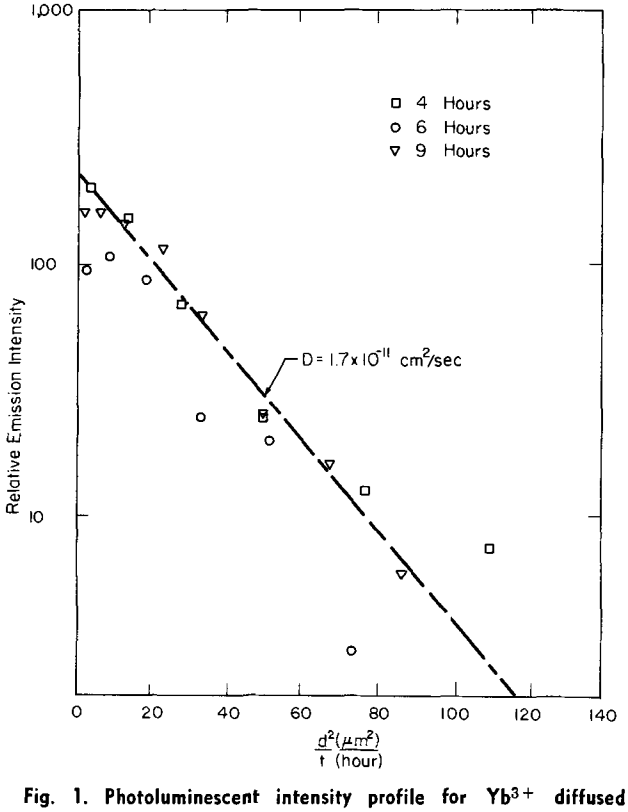

Fig. 1. Photoluminescent intensity profile for Yb^{3+} diffused into CdS at 930°C and 8 atm S_2 pressure.

tion distribution was expected. There are several possible reasons for the apparent saturation of the concentration near the surface including (*a*) concentration quenching of Yb^{3+} fluorescence (2), (*b*) out diffusion of Yb during quenching, (*c*) field-aided diffusion (3), (*d*) formation of diffusion barrier on surface, and (*e*) concentration dependent diffusion (4). The relative merit of some of these possibilities are discussed later.

Diffusion coefficients were obtained from the slope of the deep penetrating part of the log intensity *vs.* d^2/t curves as shown in Fig. 1. For

$$\frac{d^2}{t} > 4D \qquad [1]$$

this gives the correct value of D within 10% for the erfc distribution and is exact for the Gaussian. The straight line drawn in Fig. 1 gives some preferential weight to data points in the central portion of the measured intensity range. The lowest emission intensity points were subject to considerable (±50%) measured error. The highest emission intensity points were in the "non-normal" surface saturation region. However, diffusion coefficients determined from the slopes of lines drawn with maximum and minimum slopes as allowed by the given data points do not vary by more than 40%, *i.e.* the worst case uncertainty in diffusion coefficient is $D = (1.7 \pm 0.7)\ 10^{-11}$ cm²/sec. From our treatment of the data we believe the actual uncertainty of measured values of diffusion coefficient is better than the worst case value by at least a factor of two, *i.e.* $D = D_m \pm 0.2\ D_m$ where D_m is the reported value of diffusion coefficient at a particular temperature and sulfur pressure. Although a limited range of temperatures and pressures were investigated, the dependence of D and $[Yb^{3+}]_{sat}$ on T and P_{S_2} was readily evident as described in the following analysis.

An Arrhenius plot of the measured diffusion coefficients is shown in Fig. 2. The results at each of three different sulfur vapor pressures can be described fairly well by an activation energy of 1.85 eV.

The diffusion coefficient as a function of S_2 vapor pressure is shown in Fig. 3. At the two lower temperatures, 960° and 930°C, a very strong pressure dependence is indicated,

$$D \sim P_{S_2}^{0.67} \qquad [2]$$

The higher temperature data used to determine the two points at 990°C was not too reliable and so it is not possible to say with certainty that there is significant change in S_2 pressure dependence at this higher temperature. A change in the dominant mechanism determining charge neutrality in the crystal at the higher temperature would produce a change in slope (5, 6). However, on the basis of the limited data obtained and experimental uncertainties involved, it is reasonable to approximate all of the data points by

$$D \sim P_{S_2}^{1/2} \qquad [3]$$

and, for the crystals used in these experiments we find that

$$D \simeq 4 \times 10^{-4}\ P_{S_2}^{1/2}\ e^{-1.85/kT}\ \text{cm}^2/\text{sec} \qquad [4]$$

fits all of the data points obtained within 40%. The theoretical origin of proportional relation [3] will be given in the next section.

When the emission intensity is plotted as a linear function of distance from the surface rather than as the distance squared in Fig. 1, the apparent saturation of concentration extends for an appreciable distance. If we take this saturated intensity (concentration) as proportional to the maximum solubility of Yb^{3+} in CdS, we find the results shown in Fig. 4. The solubility is a strong function of sulfur pressure but does not vary significantly with temperature. Again, considering the experimental accuracy involved, the functional dependence of solubility is approximately

$$[Yb^{3+}]_{sat} \sim P_{S_2}^{1/2} \qquad [5]$$

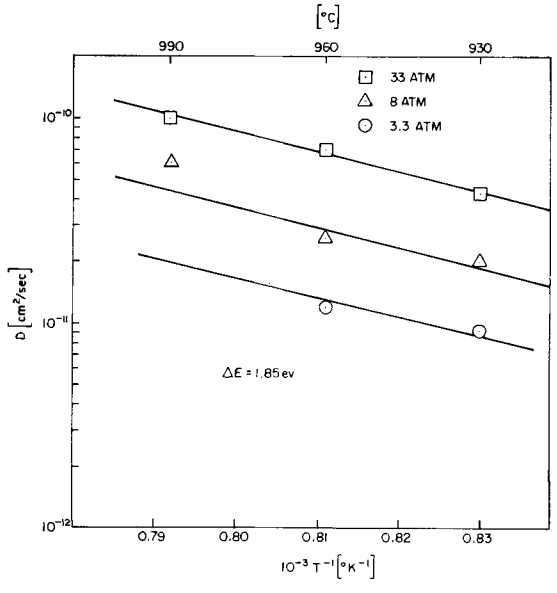

Fig. 2. Temperature dependence of diffusion coefficient of Yb^{3+} into CdS.

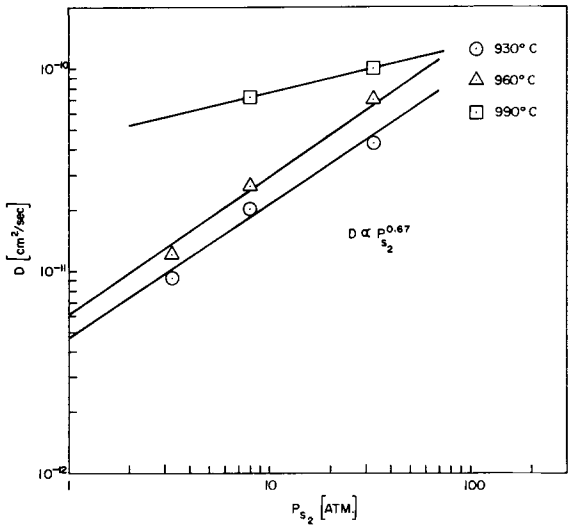

Fig. 3. Sulfur pressure dependence of Yb^{3+} diffusion coefficient in CdS.

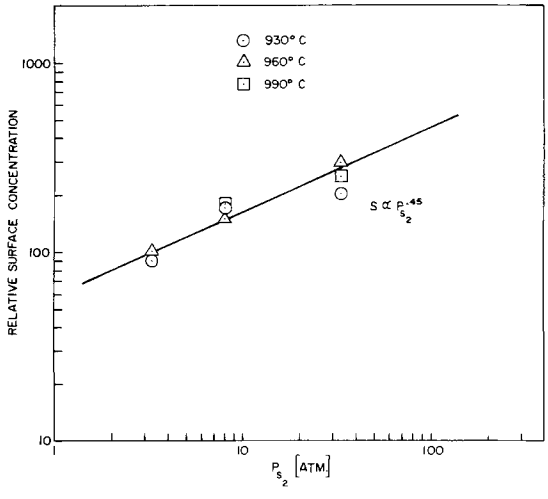

Fig. 4. Sulfur pressure dependence of Yb^{3+} surface concentration in CdS.

Discussion

The strong P_{S_2} dependence of Yb^{3+} diffusion and solubility indicates a native crystal defect dominated incorporation and diffusion mechanism. Of the four simplest native crystal defects, Cd and S vacancies and interstitials, vacancies in the Cd sublattice seem the most likely defect to enhance the solubility and motion of a metal ion with size and electronegativity comparable to the Cd^{2+} ion (7). In addition, there is good evidence for vacancy controlled self-diffusion of Cd in CdS under excess sulfur vapor pressure (8, 9).

It has been suggested that the dominant native defects in CdS are Cd interstitials and vacancies (10). The density of neutral Cd vacancies at the diffusion temperature is completely determined by the S_2 pressure through the relation

$$[V_{Cd}] = \frac{K_F}{K_I K_{CdS}} P_{S_2}^{1/2} \quad [6]$$

where the equilibrium constants involved in Eq. [6] are defined by:

$K_F = [V_{Cd}][Cd_i]$, equilibrium constant for formation of neutral Frenkel pair

$K_I = [Cd_i]/P_{Cd}$, equilibrium constant for introduction of neutral Cd interstitial

$K_{CdS} = P_{Cd}P_{S_2}^{1/2}$, equilibrium constant for sublimation of CdS.

The equilibrium constant for sublimation of CdS is quite well-established by theory and experiment (11) to be

$$K_{CdS} = 2 \times 10^{10}\, e^{-3.38/kT}\ \text{atm}^{3/2} \quad [7]$$

There is one reported determination for K_I (5)

$$K_I \simeq 1.32 \times 10^{19}\, e^{-0.95/kT}\ \text{cm}^{-3}\ \text{atm}^{-1} \quad [8]$$

and an estimate of K_F (5)

$$K_F \simeq 4 \times 10^{44}\, e^{-5.38/kT}\ \text{cm}^{-6} \quad [9]$$

In this estimate, the enthalpy of Frenkel pair formation is only bracketed within a 0.5 eV range and the pre-exponential factor may be in error by a factor of $10^{\pm 8}$ due to neglect of vibrational entropy associated with a vacancy and interstitial (12).

If diffusion is *via* neutral Cd vacancies, V_{Cd}, the functional form of Eq. [6] is adequate to explain the present results. However, this will not account for the order of magnitude difference in the present values of D and those previously obtained on different samples of CdS (1). Normally, the density of singly and doubly charged vacancies exceed the density of neutral vacancies

$$[V'_{Cd}],\ [V''_{Cd}] > [V_{Cd}]$$

and diffusion may proceed *via* these charged vacancies. In fact, diffusion of Cd in CdS has been found to be *via* the doubly charged vacancy, V''_{Cd} (9). If the charge neutrality condition at the temperature of diffusion is determined by a donor impurity through the relation

$$n \simeq N_D >> \text{(other charged species)} \quad [10]$$

then both charged vacancy concentrations will also be proportional to $P_{S_2}^{1/2}$ through the relations

$$[V'_{Cd}] = \frac{2N_D}{N_c} e^{E_g - E_{A1}/kT}\,[V_{Cd}] \quad [11]$$

and

$$[V''_{Cd}] = \left(\frac{N_D}{N_c}\right)^2 e^{2E_g - E_{A1} - E_{A2}/kT}\,[V_{Cd}] \quad [12]$$

where E_g is the semiconductor band gap, E_{A1} and E_{A2} are the first and second ionization energies of the Cd vacancy double acceptor defect and N_c is the conduction band effective density of states (13). Calculations show that for Eq. [10] to be valid under our experimental conditions, $N_D \simeq 10^{18}\ \text{cm}^{-3}$ and K_F must be at least a factor of 10^{-3} smaller than given by Eq. [9]. This is not too surprising since the corresponding pre-exponential factor in CdTe is a factor of 10^{-8} smaller than the simple estimate (12, 13)

$$K_F \simeq N^2\, e^{-E_F/kT} \quad [13]$$

where N is the density of lattice points on the Cd ion sublattice.

A Cd ion vacancy density determined by Eq. [11] or [12] will be quite sensitive to donor impurity concentration. A series of experiments reported by Woodbury (8) on the self-diffusion of Cd in CdS suggest a simple vacancy diffusion process with

$$D_{Cd} \sim [V'_{Cd}] \sim N_D \quad [14]$$

However, the experimental conditions were such that, during diffusion

$$[V'_{Cd}] < [V''_{Cd}] \sim N_D^2 \quad [15]$$

and a functional dependence of the diffusion coefficient of the form

$$D_{Cd} \sim N_D^2 \quad [16]$$

might have been expected.

The important point of the above discussion is that metal ion diffusion, if it proceeds by a simple charged vacancy process, is experimentally and theoretically dependent on chalcogen partial pressure and pre-existing impurity concentration in the crystal. As memtioned in the beginning of the paper, crystals from different sources were characterized by different free electron concentrations at room temperature. Although the impurities and/or defects responsible for the observed electron concentration are unknown, different donor concentrations are to be expected. Thus, the difference in results of the two investigations, carried out under identical laboratory conditions but with crystals from different sources, are readily understandable.

If charge neutrality at the diffusion temperature is determined by some condition other than Eq. [10], charged native defect concentrations will generally be less pressure dependent than indicated by Eq. [11] and [12], *i.e.*

$$[V'_{Cd}] \sim P_{S_2}^{1/4} \quad [17]$$

if

$$[V''_{Cd}] \simeq [Cd_i^{\cdot\cdot}] >> \text{(other charged species)} \quad [18]$$

or alternatively

$$[V'_{Cd}] \sim P_{S_2}^{1/3} \quad [19]$$

and

$$[V''_{Cd}] \sim P_{S_2}^{1/6} \quad [20]$$

if

$$n \simeq 2[Cd_i^{\cdot\cdot}] >> \text{(other charged species)} \quad [21]$$

Numerical calculations indicate that if Eq. [10] describes the charge neutrality condition over a certain temperature and pressure range, then Eq. [21] will describe the charge neutrality condition over the same pressure range but at higher temperatures. Although the limited accuracy of the data from which Fig. 3 is constructed does not warrant firm conclusions, the indicated change in pressure dependence from the 930° and 960°C curves to the 990°C curve is not unexpected.

We now return to the problem of nonideal diffused concentration profiles mentioned in the Results. Since the maximum Yb^{3+} emission intensity at the surface saturates at different levels depending on the sulfur pressure at which the samples were prepared, we do not believe this saturation is a Yb^{3+} ion fluorescence concentration quenching phenomena. Furthermore, a number of experiments on different rare earth ions in a variety of crystals has shown an onset of concentration quenching at the relatively large value of 2×10^{20} rare earths/cm^3 (2). Such a concentration is two orders of magnitude greater than the maximum rare earth concentration it has been possible to introduce into a CdS crystal (14). We therefore eliminate possibility (*a*) of the Results as a cause of the nonideal concentration profiles.

The small values of Yb^{3+} diffusion constants measured eliminate the possibility of significant out diffusion of Yb^{3+} during the rapid quenching of the samples to room temperature from the diffusion temperature. Quench cooling time was typically 90 sec. We thus eliminate possibility (*b*) of the Results as a cause of the nonideal concentration profiles.

Field aided diffusion, (*c*), is significant only when charge neutrality is determined by the diffusing species and electrons or holes. However, the pressure dependence of solubility and diffusivity indicate a dominant concentration of other charged crystal defects. Formation of a diffusion barrier on the crystal surface, (*d*), such as an impermeable oxide can not be ruled out although microscopic examination of the surface showed no indication of a film. A concentration dependent diffusivity, (*e*), such as observed for Zn in GaAs (4) remains an open possibility.

Conclusion

The diffusion and solubility of Yb^{3+} in CdS has been shown to depend on the defect structure of the crystal. This defect structure is determined by impurities in the as grown crystals and vapor pressure of crystal constituents during diffusion annealing. The pressure dependence of diffusion constant and solubility suggest that vacancies in the Cd sublattice are the controlling factor. For a crystal with a fixed (but unknown) impurity concentration, it was possible to write a simple relationship, Eq. [4] for the pressure and temperature dependence of the deep diffusing component of the diffused impurity concentration.

Acknowledgment

Research supported by Army Research Office-Durham under contracts DAHCO4-67-C-0043 and DAHCO4-70-C-0041.

Manuscript submitted Jan. 21, 1971; revised manuscript received *ca.* March 10, 1971.

Any discussion of this paper will appear in a Discussion Section to be published in the June 1972 JOURNAL.

REFERENCES

1. D. G. Girton and W. W. Anderson, *Trans. TMS-AIME*, **245**, 465 (1969).
2. L. G. Van Uitert and L. F. Johnson, *J. Chem. Phys.*, **44**, 3514 (1966).
3. J. W. Allen, *J. Phys. Chem. Solids*, **15**, 134 (1960).
4. H. C. Casey, M. B. Panish, and L. I. Chang, *Phys. Rev.*, **162**, 660 (1967).
5. R. Boyn, O. Goede, and S. Kuschnerus, *Phys. Status Solidi*, **12**, 57 (1965).
6. E. Nebauer, *ibid.*, **29**, 269 (1968).
7. K. A. Gschneidner, Jr., "Rare Earth Alloys," pp. 71-74, D. Van Nostrand Company, New York (1961).
8. H. H. Woodbury, *Phys. Rev.*, **134**, A492 (1964).
9. D. Shaw and R. C. Whelan, *Phys. Status Solidi*, **36**, 705 (1969).
10. R. Boyn, *ibid.*, **29**, 307 (1968).
11. P. Goldfinger and M. Jeunehomme, *Trans. Faraday Soc.*, **59**, 2851 (1963). W. J. Wöster and M. G. Geers, *J. Phys. Chem.*, **66**, 1252 (1962). R. A. Isakova and V. N. Nesterov, *Russ. J. Inorg. Chem.*, **11**, 522 (1966). B. K. Veselovski, *Zh. Prik. Khim*, **15**, 422 (1942).
12. F. A. Kröger, "The Chemistry of Imperfect Crystals," pp. 427-430, North-Holland Publishing Company, Amsterdam (1964).
13. D. de Nobel, *Philips Res. Rept.*, **14**, 430 (1959).
14. W. W. Anderson, *J. Chem. Phys.*, **44**, 3283 (1966).

Time-Dependence of Zinc Diffusion in Gallium Arsenide under a Concentration Gradient

C. H. Ting

IBM Components Division, East Fishkill Facility, Hopewell Junction, New York 12533

and G. L. Pearson

Stanford University, Stanford, California 94305

ABSTRACT

The diffusion profiles of Zn in GaAs under a concentration gradient have been determined as a function of diffusion time for diffusions at 600° and 750°C. Pure radioactive Zn^{65} is used as the diffusion source. It is found that local equilibrium is not reached for these diffusions since the diffusion profiles can not be expressed in terms of a single variable $x/\sqrt{t}$. When the diffusion depth is plotted against the square root of diffusion time, a linear relationship is not obtained. The deviation from linear relationship is found to be quite pronounced at lower diffusion temperatures, and less so at higher diffusion temperatures. These observations indicated that the diffusion process can not be described by Fick's second law (with a concentration-dependent effective diffusion coefficient, $\overline{D}$). Under this condition, the Boltzmann-Matano analysis which has been used quite extensively to obtain values of the effective diffusion coefficient of $\overline{D}$ from the diffusion profiles of Zn in GaAs is not valid. Results are discussed in terms of nonequilibrium in the interstitial-substitutional diffusion. Complications due to the presence of diffusion-induced defects are also described.

Zinc diffusion in GaAs is anomalous in that the zinc concentration profiles obtained under concentration gradient diffusions from a constant vapor source do not obey a complementary error function, but exhibit a rather steep front (1, 2). The steep diffusion front indicates that the effective diffusion coefficient is strongly concentration-dependent. The concentration-dependent diffusion coefficient is generally interpreted

Key words: Boltzmann-Matano analysis, nonequilibrium interstitial-substitutional diffusion, diffusion induced defects.

in terms of the interstitial substitutional diffusion model (3-5) and can be obtained from the diffusion profiles through the Boltzmann-Matano analysis (1, 2, 5) if equilibrium is reached.

In spite of the wide application of the Boltzmann-Matano analysis for zinc diffusions in GaAs, no effort was made to check whether equilibrium is reached for diffusions under a concentration gradient. The possibility of nonequilibrium was discussed by Kendall (7), and also by Shaw and Showan (8). In this work, we demonstrated by measuring zinc profiles over a wide range of annealing time that equilibrium is not reached at lower diffusing temperatures.

Experimental Procedures

High purity (99.9999%) radioactive Zn^{65} was used as a diffusion source. The starting material was single-crystal GaAs wafers oriented in the <111> direction (obtained from Monsanto Company). The diffusions were carried out in evacuated quartz ampoules at 600°, 650°, and 750°C for various lengths of diffusion period. The quartz ampoules were cleaned in aqua regia, pumped down to a 10^{-6} Torr before being sealed off. A quartz plug was used in the ampoule to reduce the total volume to less than 1 cm^3. After diffusion, the samples were washed in dilute HCl for 30 min to remove any excess zinc on the surface, and were then cut into circular disks of 0.5 cm diameter. Diffusion profiles were obtained by measuring the radioactivity of the removed layer, using the standard lapping, weighing, and counting procedure.

For the diffusion temperatures in this study, the Zn_3As_2 phase is present in the Ga-As-Zn ternary system (8). Under this condition, the ternary liquid compositions are not on the pseudobinary line of Zn and GaAs, but lie on the gallium-rich side of the ternary phase diagram (2, 8). The experimental parameters for the 600°, 650°, and 750°C diffusions are summarized in Tables I, II, and III respectively.

Experimental Results

The zinc concentration profiles for the 600°, 650°, and 750°C diffusions are shown in Fig. 1, 2, and 3, respectively. For sample No. 1, the penetration depth is rather small; therefore, two sets of data points obtained from opposite sides of the sample were used to increase the accuracy in constructing the concentration profile.

The effective diffusion coefficient D of Zn in GaAs can be obtained from the concentration profiles through

Table I. Diffusion parameters for Zn in GaAs at 600°C

Sample No.	Weight (mg) GaAs	Weight (mg) Zn^{65}	Ampoule volume (cm^3)	Diffusion time (hr)
1	65.90	0.59	0.8	16
2	45.56	0.40	0.7	64
3	45.74	0.46	0.7	144
4	47.22	0.70	0.8	360

Table II. Diffusion parameters for Zn in GaAs at 650°C

Sample No.	Weight (mg) GaAs	Weight (mg) Zn^{65}	Ampoule volume (cm^3)	Diffusion time (hr)
5	62.44	0.40	0.8	6
6	85.50	0.34	0.6	24
7	88.53	0.47	0.7	64
8	88.89	0.57	0.85	144
9	80.86	0.65	0.65	290

Table III. Diffusion parameters for Zn in GaAs at 750°C

Sample No.	Weight (mg) GaAs	Weight (mg) Zn^{65}	Ampoule volume (cm^3)	Diffusion time (hr)
10	85.60	1.28	0.6	1
11	87.54	1.10	0.75	3
12	87.87	0.87	0.75	6
13	60.39	0.87	0.75	12
14	60.78	0.36	0.6	25

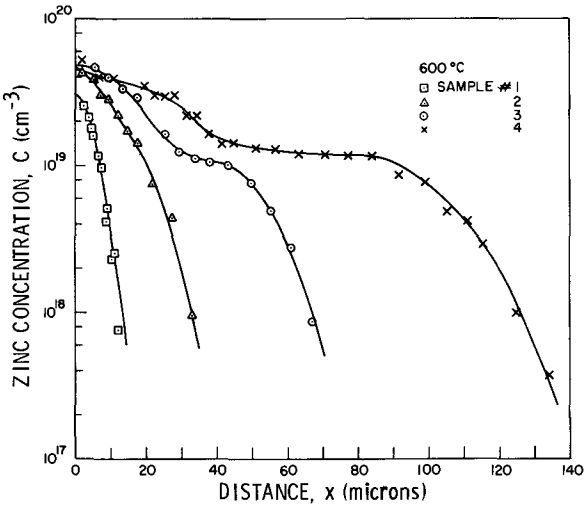

Fig. 1. Diffusion profiles of Zn in GaAs at 600°C. Diffusion time: Sample No. 1 = 16 hr, No. 2 = 64 hr, No. 3 = 144 hr, No. 4 = 360 hr.

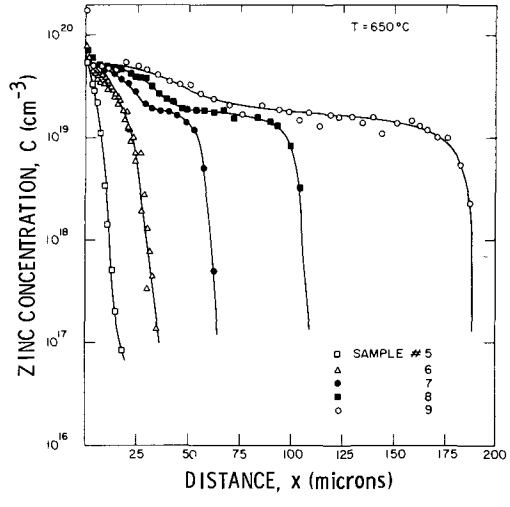

Fig. 2. Diffusion profiles of Zn in GaAs at 650°C. Diffusion time: Sample No. 5 = 6 hr, No. 6 = 24 hr, No. 7 = 64 hr, No. 8 = 144 hr, No. 9 = 290 hr.

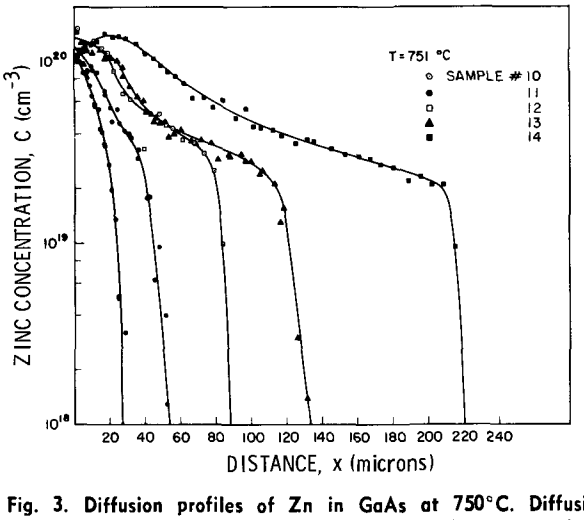

Fig. 3. Diffusion profiles of Zn in GaAs at 750°C. Diffusion time: Sample No. 10 = 1 hr, No. 11 = 3 hr, No. 12 = 6 hr, No. 13 = 12 hr, No. 14 = 25 hr.

the Boltzmann-Matano method. If $\overline{D}$ is only a function of zinc concentration, the diffusion equation in one-dimensional form is given by Fick's second law

$$\frac{\partial c}{\partial t} = \frac{\partial}{\partial x}\left(\overline{D}\frac{\partial c}{\partial x}\right) \quad [1]$$

For diffusion in a semi-infinite media, this equation can be simplified by the Boltzmann transformation $\lambda = x/\sqrt{t}$. In terms of the new variable (λ) Eq. [1] becomes

$$-\frac{\lambda}{2}\frac{dc}{d\lambda} = \frac{d}{d\lambda}\left(\overline{D}\frac{dc}{d\lambda}\right) \quad [2]$$

Equation [2] can be integrated to give

$$\overline{D} = -\frac{1}{2t}\frac{\int_0^{c_x} x\,dc}{\left(\frac{dc}{dx}\right)_{c_x}} \quad [3]$$

Using Eq. [3], the value of D can be obtained from the concentration profiles by evaluating the area under the profile and the concentration gradient at the point of interest. In evaluating $\overline{D}$, large errors are involved in determining the slopes of the profiles, especially near the diffusion front where a large change in concentration occurs in a rather small distance. A method of improving the accuracy of the calculations near the extremes of the concentration range has been developed by Hall (10).

The value of $\overline{D}$ as a function of zinc concentration for the 600°C diffusions is obtained from the profiles shown in Fig. 1, using the technique developed by Hall. The results are shown in Fig. 4. Figure 4 shows that different values of $\overline{D}$, are obtained from profiles with different diffusion time. The values of $\overline{D}$ obtained by this method change not only with zinc concentration but also with diffusion time. Therefore, the Boltzmann-Matano analysis does not give valid values of the effective diffusion coefficient.

As indicated by Eq. [2], the diffusion equation can be expressed in terms of a single variable, $\lambda = x/\sqrt{t}$. The concentration of the diffusant C, therefore, will change only with $x/\sqrt{t}$, but not with respect to x and t separately. This would yield a fixed value of $x/\sqrt{t}$ for a given concentration level, regardless of the length of diffusion time. When the concentration profiles obtained for various diffusion time are plotted against the normalized distance $x/\sqrt{t}$, all profiles should coincide. Another way to express the same condition is to plot the diffusion depth (where concentration is equal to a fixed level C_d) against the square root of diffusion time ($\sqrt{t}$), then a straight line through the origin should be obtained.

The concentration profiles for the 600°C diffusions shown in Fig. 1 are replotted as a function of normalized distance $x/\sqrt{t}$ in Fig. 5. One can see clearly that the profiles do not coincide.This indicates that the diffusion process discussed here cannot be described by Fick's second law, as given by Eq. [1]. The diffusion depth, obtained from the concentration profile shown in Fig. 1 and 2, where zinc concentration is 10^{18} cm^{-3}, is plotted against the square root of diffusion time in Fig. 6. It can be clearly seen that a linear relationship is not obtained.

The X_d *vs.* $\sqrt{t}$ curves in Fig. 6 can roughly be separated into two regions. In the first region (where diffusion time is relatively short), the data points seem to fit a straight line through the origin. For the second region (where diffusion time is relatively long), the data points seem to fit another straight line which does not pass through the origin, *i.e.*

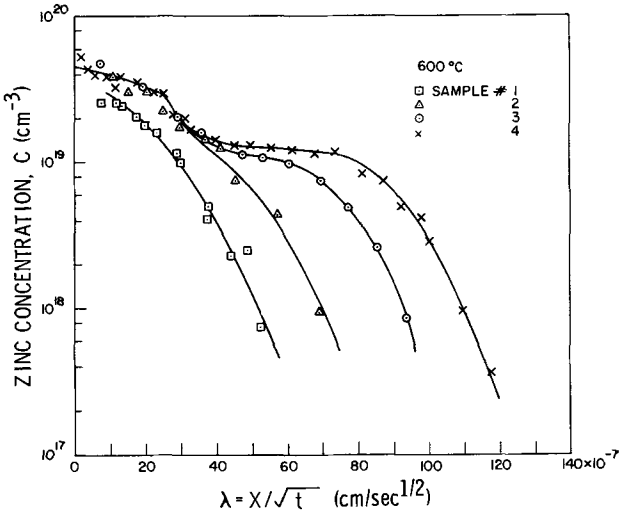

Fig. 5. Diffusion profiles of Zn in GaAs at 600°C as a function of $\frac{X}{\sqrt{t}}$.

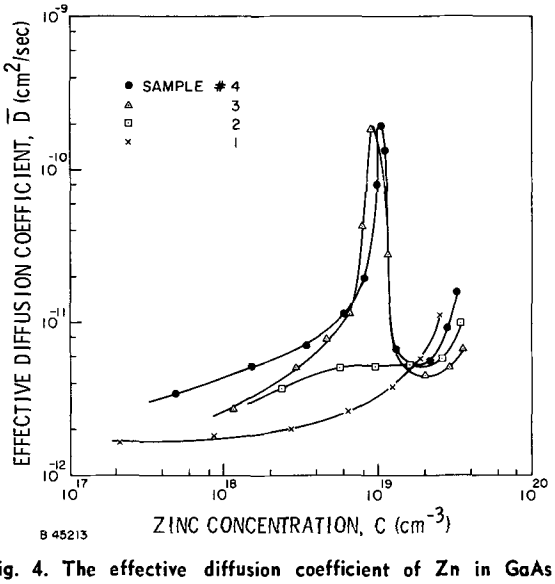

Fig. 4. The effective diffusion coefficient of Zn in GaAs vs. Zn concentration at 600°C as obtained from Boltzmann-Matano analysis.

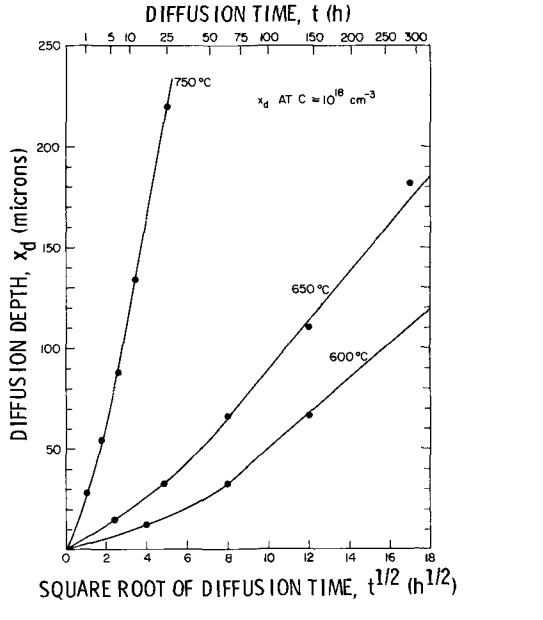

Fig. 6. Diffusion depth vs. square root of diffusion time for Zn in GaAs for diffusions at 600°, 650°, and 750°C.

$$X_d = S_2 (\sqrt{t} - \sqrt{t_o}) \quad [4]$$

where S_2 is the slope of the straight line, and t_o is the intercept of this straight line with the time axis. Figure 6 indicates that the intercept t_o decreases rapidly as the diffusion temperature is raised. At sufficiently high temperature, t_o will be so small that it will be comparable to or less than the necessary warm-up time of the diffusion sample. At this point, t_o can no longer be determined easily from the diffusion experiment and therefore can be ignored. Thus, the linear relationship between x_d and $\sqrt{t}$ will be a limiting case for high-temperature diffusions.

Nonequilibrium in Interstitial-Substitutional Diffusion

The nonlinear relationship in the x_d *vs.* $\sqrt{t}$ diagram, as shown in Fig. 6, cannot be explained by manipulating the concentration-dependent effective diffusion coefficient, $\overline{D}$. It is reasonable, therefore, that some nonequilibrium phenomena are responsible for this nonlinear behavior. The qualitative features of the nonequilibrium diffusion can be understood in terms of the interstitial-substitutional model.

In the literature, the interstitial-substitutional diffusion model has been used extensively to explain various experimental results of zinc diffusion in GaAs. However, local equilibrium between the interstitial and substitutional species is always assumed to be valid whenever this model is used (2, 4, 5, 10, 11). When an equilibrium condition is not reached, one must take the transitions between interstitial and substitutional zinc into consideration. Then Fick's law is no longer adequate to describe the diffusion process. The transitions between interstitial and substitutional zinc can be described by the reaction

$$Zn_i^{+r} + V_{ga} \underset{k_2}{\overset{k_1}{\leftrightarrows}} Zn_s^{-} + (r+1)e^{+} \quad [5]$$

where k_1 and k_2 are rate constant for the reversible reactions. Under this condition, the concentrations of interstitial and substitutional zinc C_i and C_s can be described by the following equations

$$\frac{\partial C_i}{\partial t} = D_i \frac{\partial^2 C_i}{\partial X^2} - k_1 C_v C_i + k_2 p^{(r+1)} C_s \quad [6a]$$

$$\frac{\partial C_s}{\partial t} = D_s \frac{\partial^2 C_s}{\partial X^2} + k_1 C_v C_i - k_2 p^{(r+1)} C_s \quad [6b]$$

where D_i and D_s are the interstitial and substitutional zinc diffusion coefficients, respectively, C_v is the gallium vacancy concentration, and p is the hole concentration. Equation [6a] simply states that the rate of change in interstitial zinc concentration is equal to the diffusion flux minus the amount that changed from interstitial into substitutional positions, plus the amount that changed from substitional into interstitial positions. The constants k_1 and k_2 are the transitional probabilities from interstitial into substitutional positions, and *vice versa*. Equation [6b] gives a similar expression for the rate of change in substitutional zinc.

If the equilibrium between interstitial and substitutional zinc is reached during the diffusion process, then the two transitional terms in Eq. [6] will just cancel each other, *i.e.* $k_1 C_v C_i = k_2 p^{(r+1)} C_s$. Under this condition the two transitional terms would disappear and Eq. [6] can be reduced to the form of Fick's second law, and the concentration will be a function of only $x/\sqrt{t}$. This corresponds to the extreme case that the transitions between interstitial and substitutional zinc can be considered as an instantaneous reaction. The other extreme case is that where the reaction by which the immobilized substitutional zinc is formed proceeds very fast compared with the diffusion process. In this case, local equilibrium can be assumed to exist between the interstitial and substitutional zinc. Here also Eq. [6] can be reduced to the form of Fick's second law. Except for the two extreme cases outlined above, the coupled diffusion Eq. [6] must be used to describe the diffusion process of zinc in GaAs. The diffusion Eq. [6] cannot be reduced to a single variable by using a new variable $\lambda = x/\sqrt{t}$; therefore, a linear relationship between x_d and $\sqrt{t}$ is not expected in this case.

Two time constants, T_i and T_s, can be obtained from Eq. [6]. They are

$$T_i = \frac{1}{k_1 C_v} = \text{the lifetime of interstitial zinc before conversion into substitutional zinc}$$

$$T_s = \frac{1}{k_2 p^{r+1}} = \text{the lifetime of substitutional zinc before conversion into interstitial zinc.}$$

At equilibrium $k_1 C_v C_i = k_2 p^{r+1} C_s$, therefore, the ratio of the interstitial and substitutional lifetime is equal to the ratio of equilibrium concentration of these two species, *i.e.* $T_i/T_s = C_i/C_s$. It has been estimated that the ratio C_i/C_s is very small, usually 10^{-5} or less (12); therefore, T_s is greater than T_i by a factor of 10^{+5} or more. The time constants T_i and T_s, generally, change exponentially with temperature. Since the time constant increases rapidly as temperature is lowered, the assumption that equilibrium between interstitial and substitutional zinc is probably good for a high diffusion temperature, but poor for a relatively low diffusion temperature. The above discussion agrees well with the qualitative feature of the X_d *vs.* $\sqrt{t}$ diagram, in that the deviation from the linear relationship is quite pronounced at lower diffusion temperatures and less so at higher diffusion temperatures.

Figure 6 shows that the diffusion is slower for shallow diffusions and more rapid for deeper diffusions. Two limiting cases can be used to illustrate this point. The first extreme case is for very short diffusion times. If the diffusion time is so short that it is less than the time constant T_2, then the transitions from interstitial to substitutional sites will not be completed. Under this condition, zinc diffuses as two separate streams, *i.e.* the interstitial and substitutional, with negligible interaction between them. The measured concentration profile is essentially the profile of substitutional zinc, since the interstitial concentration is so small. Therefore, this limiting case gives essentially a substitutional diffusion characterized by its low diffusion constant. The other extreme case is for very long diffusion time. If the diffusion time is so long that it is longer than the time constant T_s, then local equilibrium between the interstitial and substitutional is maintained. Under this condition, the diffusion is dominated by the transitions between the two species, which gives an effective diffusion coefficient. The value of $\overline{D}$ in this case is given by $\overline{D} = D_i \dfrac{\partial C_i}{\partial C_s}$ which is rather large. From the above discussion, it is reasonable to expect the effective diffusion coefficient to increase with the diffusion time as the interstitial-substitutional equilibrium is approached.

The discussion presented so far gives the correct qualitative features observed in the X_d *vs.* $\sqrt{t}$ plot; however, no quantitative agreement is available at present. This is because the parameters D_i, D_s, k_1, and k_2 used in Eq. [6] have not been determined by any measurements, and the vacancy concentration C_v may not be a constant. Therefore, without any detailed knowledge on the atomic interaction for zinc in GaAs, quantitative agreement between the nonequilibrium interstitial-substitutional model and the experimental results cannot be obtained at present.

Discussion

The interstitial-substitutional nonequilibrium is not the only possible nonequilibrium mechanism in the diffusion process. Other possible sources should not be

overlooked. The most important complication is the presence of diffusion-induced defects. It has been shown beyond doubt that zinc diffusion under a concentration gradient generates induced defects (12-14) when pure zinc is used as a diffusion source and when the diffusion time is sufficiently long. For a very short diffusion time, usually no induced defects can be detected. It seems possible that the appearance of the induced dislocations is the cause for the nonlinear behavior in the X_d *vs* $\sqrt{t}$ plot.

The induced dislocation represents a rapid diffusion path or a "diffusion pipe" for substitutional zinc; thus, the enhanced diffusion in the diffusion pipes may dominate the diffusion process (14). However, the assumption that zinc diffusion in GaAs is dominated by enhanced substitutional diffusion in the induced defects has many difficulties. A few of these difficulties are:

(*A*) For diffusion runs with relatively short diffusion time (where the diffusion depth is in the first region of the X_d *vs.* $\sqrt{t}$ plot) the effect of enhanced diffusion in the induced dislocations is supposed to be negligible and normal diffusion should result. However, the effective diffusion coefficient obtained from shallow diffusion still shows concentration dependence.

(*B*) The value of the effective diffusion coefficient obtained from shallow diffusions is too large for substitutional diffusions.

(*C*) The effective diffusion coefficient decreases with external arsenic vapor pressure (5). This observation can be explained only in terms of the interstitial-substitutional model.

(*D*) Isoconcentration diffusion for the melt-doped sample generates little or no induced dislocations; yet the value of the effective coefficient is very large (12).

In view of the above-mentioned difficulties and the excellent agreement between the interstitial-substitutional model and various experimental data of zinc diffusion in GaAs, it is reasonable to say that zinc diffusion in GaAs is not dominated by the enhanced substitutional diffusion in the induced dislocations. If the contribution of interstitial diffusion is reduced significantly, such as for diffusion under very high external arsenic pressure, then the contribution due to the enhanced diffusion in dislocations may be important.

Although it is unlikely that the diffusion process is dominated by the enhanced substitutional diffusion in the induced defects, it is possible that the induced defects may produce a significant change in the interstitial diffusion. For instance, the induced defects may increase the values of the interstitial diffusion coefficient or the ratio of interstitial to substitutional zinc. Under this condition, the effective diffusion coefficient, D, given by $\overline{D} = D_i \frac{\partial C_i}{\partial C_s}$, would be increased significantly in the region with induced defects so that the appearance of induced defects is responsible for the nonlinear behavior in the X_d *vs.* $\sqrt{t}$ relationship. This model also has its difficulties:

(*A*) The value of $\overline{D}$ obtained from the samples with fully developed induced defects is not larger than the value of $\overline{D}$ obtained from isoconcentration diffusions in melt-doped samples where no induced defects were observed (12).

(B) The value of $\overline{D}$ obtained from relatively shallow diffusions has a weak concentration dependence, as illustrated in Fig. 4, and also by Chang and Pearson (4). This is quite different from the C^2 dependence of $\overline{D}$ predicted from the equilibrium interstitial-substitutional diffusion model.

Even though it is difficult to explain the nonlinearity between X_d and $\sqrt{t}$ in terms of the induced defects alone, the fact that zinc diffusion does induce defects in GaAs should not be ignored. It is possible that the influence of the induced defects could be combined with the effects on nonequilibrium in interstitial-substitutional diffusion. However, we cannot conjecture about such a complicated diffusion model without additional experimental data.

Conclusions

From the series of diffusions at 600°, 650°, and 750°C, it is found that equilibrium is not reached for zinc in GaAs at these temperatures. This is demonstrated by the fact that the diffusion profiles for various diffusion time at a fixed temperature do not coincide when plotted against $X/\sqrt{t}$ and also by the fact that the diffusion depth X_d does not vary linearly with the square root of diffusion time. Under this condition, the well known Boltzmann-Matano analysis cannot be used to yield meaningful values of effective diffusion coefficient $\overline{D}$. This is illustrated by the fact that different values of $\overline{D}$ are obtained when the Boltzmann-Matano analysis is applied to the diffusion profiles with different diffusion times.

Quantitative verification of nonequilibrium in the interstitial-substitutional diffusion model is impossible since no experimental data are available regarding the time constants involved in the interstitial-substitutional transitions. The fact that the diffusion-induced defects are always observed in the long diffusion runs greatly increases the complications.

Acknowledgment

This work was supported jointly by the U. S. Army Signal Corps., the U. S. Air Force, and U. S. Navy through contract NONR 225 (83).

Manuscript submitted Jan. 25, 1971; revised manuscript received *ca.* April 12, 1971.

Any discussion of this paper will appear in a Discussion Section to be published in the June 1972 JOURNAL.

REFERENCES

1. F. A. Cunnell and C. H. Gooch, *J. Phys. Chem. Solids*, **15**, 127 (1960).
2. H. C. Casey, Jr., M. B. Panish, and L. L. Chang, *Phys. Rev.*, **162**, 660 (1967).
3. R. L. Langini, *Solid-State Electron.*, **5**, 127 (1962).
4. L. L. Chang and G. L. Pearson, *J. Appl. Phys.*, **35**, 1960 (1964).
5. L. R. Weisberg and J. Blanc, *Phys. Rev.*, **131**, 1548 (1963).
6. K. K. Shih, G. W. Allen, and G. L. Pearson, *J. Phys. Chem. Solids*, **29**, 379 (1968).
7. D. L. Kendall in "Semiconductors and Semimetals," Willardson and Beer, Editors, Vol. 4, p. 163, Academic Press, New York (1968).
8. D. Shaw and S. R. Showan, *Phys. Status Solidi*, **32**, 109 (1969).
9. M. B. Panish, *This Journal*, **113**, 861 (1966).
10. L. D. Hall, *J. Chem. Phys.*, **21**, 87 (1953).
11. K. Weiser, *J. Appl. Phys.*, **34**, 3387 (1963).
12. C. H. Ting, Ph.D. Dissertation, Stanford University 1968; SU-SEL-68-069, Stanford Electronics Laboratories, Stanford, California (August 1968).
13. J. F. Black and E. D. Jungbluth, *This Journal*, **114**, 181 (1967).
14. M. Maruyama, *Jap. J. Appl. Phys.*, **7**, 476 (1968).

Vapor Growth of a Semiconductor Superlattice

A. E. Blakeslee*

IBM Thomas J. Watson Research Center, Yorktown Heights, New York 10598

ABSTRACT

It has been predicted that under certain conditions a multilayer sandwich structure consisting of alternating close-spaced layers of two semiconductors of different energy gap will exhibit intriguing transport and optical properties, including a negative resistance. This type of structure has been created with a specially designed vapor growth system, wherein the composition is made to alternate many times between $GaAs_{1-x}P_x$ and $GaAs_{1-y}P_y$ ($0 \leq x < y$) with a period as small as 110Å. The presence of the repetitive structure has been confirmed by electron microscopy on cleaved and etched cross sections and by x-ray diffraction. The uniformity of spacing, as well as the period, is of prime importance. The effects of crystal orientation and reactant gas composition on this property are described.

Esaki and Tsu (1) have proposed the concept of the superlattice negative conductance amplifier. Essential to this concept is a semiconductor structure into which is built a periodic variation of potential. That is, if it is possible to create a structure in a monocrystalline semiconductor where the potential varies a few tenths of an electron volt in a periodic fashion and such that the period of the variation is less than the mean free path of the carriers, novel electrical and optical effects are predicted, the most striking of which is that a negative resistance can be observed at relatively low electric fields. The theoretical basis for this proposal is illustrated in Fig. 1, which is a plot of energy *vs.* electron momentum in *k*-space. The discontinuity in the curve occurs at the edge of the first Brillouin zone, corresponding to the normal lattice periodicity. In the superlattice device the additional periodicity of the superimposed potential subdivides the Brillouin zone into so-called mini-zones with boundaries inversely proportional to the superlattice spacing. The mini-zone boundaries occur at much lower momentum values and the associated forbidden energy gaps occur at lower energies. Just as in the normal Brillouin zone, there is an inflection point in E *vs.* k in the mini-zone, and an electron should decelerate upon increasing the applied potential past this point, resulting in a negative differential conductance.

* Electrochemical Society Active Member.

Key words: gallium arsenide phosphide, crystal growth, multilayers, semiconductor devices.

Figure 2 shows two methods by which the proposed periodic structure might be achieved. In the top diagram the same semiconductor is changed back and forth from n-type to p-type, accompanied by the resultant movement of the band edges, by rapidly changing from an n-type to a p-type dopant. A maximum potential change in each band of close to the bandgap energy, E_g, is possible with this method. In the second method, with which this paper is concerned, the doping is constant or nearly so, but the basic semiconductor material is changed. It alternates between two different semiconductors with different energy gaps, E_{g1} and E_{g2}. The illustration shows the difference in forbidden gap energy, ΔE_g, to be divided equally between the conduction and valence bands, but such does not have to be the case and in general is not. Of the two methods, the second would be more stable against interdiffusion, since impurities have larger diffusion coefficients in general than do alloy constituents.

The structure produced by the alloy method is equivalent metallurgically to a long-period one-dimensional superlattice (Fig. 3). Natural superlattices (2) are thermodynamically stable at some temperature, whereas the artificial ones are not, but this distinction has no bearing on the present problem. Instead of an alternation of lattice planes containing different atoms A B A B A . . . , as in the simplest type of one-dimensional superlattice, in the present case there are n planes of A, m planes of B, n of A etc., where $n + m$ is the number of normal unit cells with spacing a within

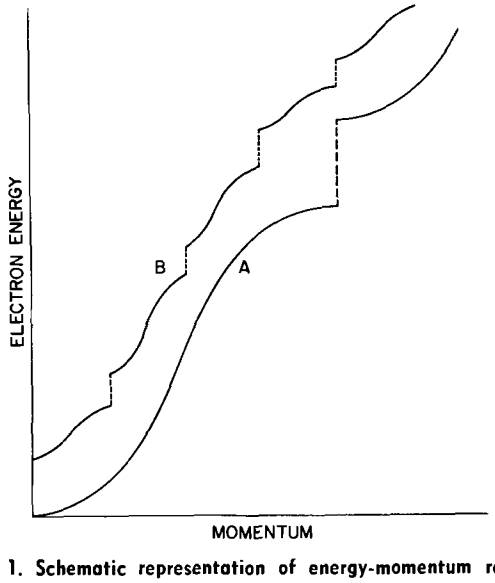

Fig. 1. Schematic representation of energy-momentum relationship in (A) normal crystal; (B) superlattice.

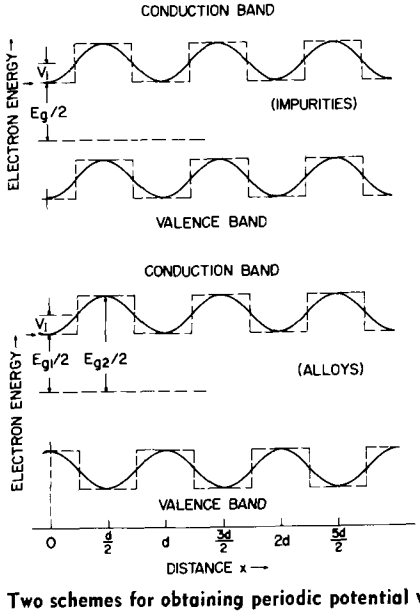

Fig. 2. Two schemes for obtaining periodic potential variation

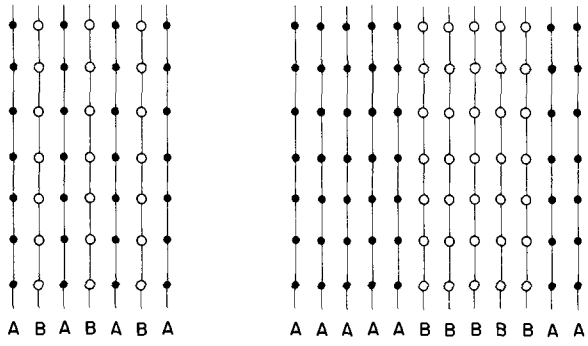

Fig. 3. Schematic illustration of one-dimensional superlattices

a superlattice having period d. This is an idealized description, of course. In any real case the transition from A to B would occur across more than one atom layer, and varying degrees of admixture might exist across the whole period. Calculations (1) show that for most suitable pairs of semiconductors A and B, $n + m$ should be of the order of 30; that is, the superlattice spacing should be about 100-300Å. The amplitude of potential variation within the pertinent band, *e.g.*, the conduction band for n-type material, should be a few tenths of an electron volt. Constancy of the lattice spacing across the superlattice is vital to the exhibiting of the predicted properties. The superlattice period must therefore be uniform to better than 5%, possibly even 1%.

Experimental

We have chosen to attempt to produce such a semiconductor superlattice by the technique of epitaxial vapor growth, using the ternary compound $GaAs_{1-x}P_x$. The value of x, which is the mole fraction of phosphorus on group V sites and is therefore nearly proportional to the potentials of the band edges, is made to oscillate between two values by varying the PH_3 concentration in the epitaxial reactor. The period of alternation is a few hundred angstroms. Thus in the idealized drawing of Fig. 3, material A would be GaAs, where $x = 0$, and B would be $GaAs_{1-x}P_x$ with some maximum value of x, say $x = 0.5$. This could produce a maximum change in bandgap of approximately 0.6 eV at room temperature. The difference between the maximum and minimum values of x that can be realized is directly a measure of the amplitude of the potential variation. The magnitude of this difference, Δx, is of more significance to the electrical behavior than is the steepness of the gradient. Whether a significant Δx can be built into and maintained in the crystal at such close tolerances obviously depends critically on the extent of interdiffusion of the P and As components both in the gas phase and in the solid. Results thus far indicate that neither of these phenomena has occurred to any serious degree.

Figure 4 is a schematic of the epitaxial structure in a form suitable for electrical testing. The substrate is (100)-oriented GaAs which is doped n-type to about 10^{18} carriers/cc. A layer of GaAs doped with sulfur is grown first, followed by the band of thin alternating layers and then by another uniform GaAs layer. The top and bottom GaAs layers provide ohmic contacts to

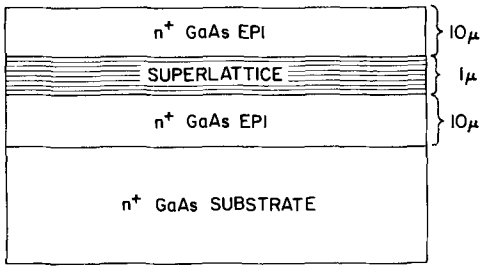

Fig. 4. $GaAs/GaAs_{1-x}P_x$ superlattice sandwich structure

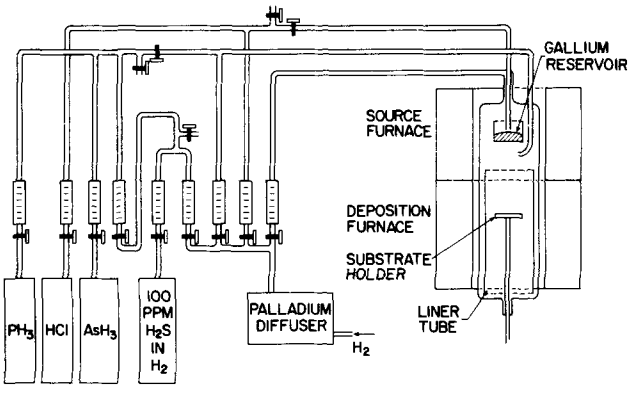

Fig. 5. Vapor deposition system for $GaAs_{1-x}P_x$

the superlattice. The superlattice portion is not intentionally doped. It turns out to be n-type, with between 10^{16} and 10^{17} carriers/cc.

The vapor growth system is illustrated in Fig. 5. It is essentially a modification of the process described by Tietjen and Amick (3). GaAs is obtained by reacting AsH_3 gas with GaCl vapor produced by chlorination of Ga with HCl gas at 900°C. The substrate temperature is usually about 760°C. The system shown is unsatisfactory for producing the thin-layered structures because of the relatively large reaction zone volume in which AsH_3 and PH_3 will mix by interdiffusion, preventing sharp separation in the crystal. To make the superlattice structure possible, a modification shown in Fig. 6 was introduced wherein an electromechanical valve served to send the PH_3 stream alternately into the reaction mixture or to vent it from the system. Also, the diameter of the reactor was constricted. By using narrow ID quartz tubing and relatively high flows of carrier H_2, it has been possible to achieve rapid injection of PH_3 into the growth region. The rate of injection can be as fast as once a second, and gas velocities as high as 5 m/sec are reached in some parts of the system. Typical values of gas flow rates are: HCl, 10 cc/min; AsH_3, 10 cc/min; PH_3, 5 cc/min. The sum total of all carrier H_2 flow rates was originally 1000 cc/min. In a second modification to the system the total carrier gas flow was increased to 2000 cc/min, but more importantly the diameter of the substrate zone was decreased from 45 to 15 mm, the result of the

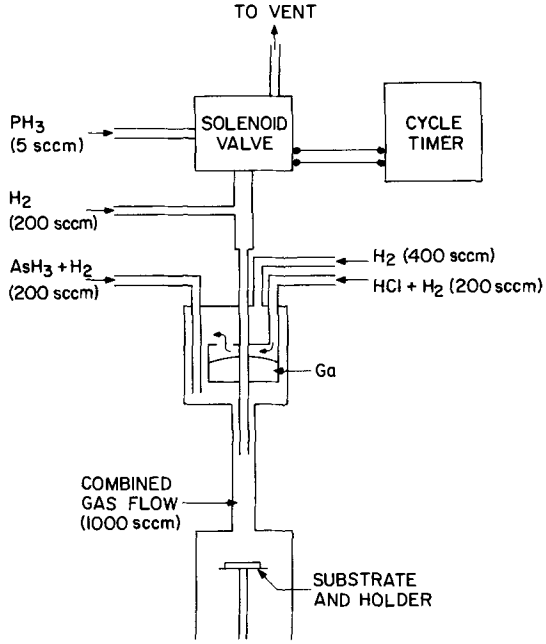

Fig. 6. Injection system for growing alternating layers

Table I. Effect of changes in reactor tube design on flow properties

	I Wide tube	II Constricted upper part	III Constricted upper and lower parts
C_{mid}	0.85 C_0	0.01 C_0	—
T	12 sec	1.9 sec	0.27 sec
τ	—	1.7 sec	0.055 sec

$$C_{mid} = C_0 \operatorname{erfc} \frac{x_{mid}}{2\sqrt{Dt}}$$

$$\tau = \left\langle \frac{4\sqrt{Dt}}{V} \right\rangle$$

two changes being to increase gas velocity in the vicinity of the substrate by a factor of 18.

A rough estimate of the expected effect of the modifications on the flow properties of the system is shown in Table I. The first parameter, C_{mid}, is the result of a simple complementary error function diffusion calculation, assuming two successive PH_3-bearing and PH_3-free pulses of gas are effectively semi-infinite in extent. C_{mid} is the concentration of PH_3 at the point x_{mid}, which is midway between two successive pulses of PH_3. C_0 is the initial maximum PH_3 concentration in the center of a PH_3 pulse. Since complete interdiffusion would result only in increasing C_{mid} from 0 to $1/2C_0$, the value of 0.85 C_0 given in the first column is physically impossible, showing that diffusion would be far too great in the wide tube. T is the residence time of PH_3 in the system between the solenoid valve and the substrate. The third parameter, τ, defined as $4\sqrt{Dt/V}$, is a time constant reflecting the two factors which primarily determine the sharpness of the gaseous interface, namely the diffusion length and the streaming velocity of the gas. From these three criteria it is seen that a large improvement is effected by constricting the upper part of the reaction tube and a somewhat further one by continuing the constriction past the substrate position.

Results

Observation by electron microscopy is the most usual evaluative procedure applied to the grown layers. The wafer is first cleaved across the epitaxial layers on a (110) cleavage face and etched for 15 sec in a 10:1:1 $H_2O:H_2O_2:HF$ solution. This brings out what appears under visual microscopy as a thin line parallel to the substrate. A platinum-shaded carbon replica is then made of the cleaved and etched surface, and this is examined by transmission electron microscopy.

Figure 7 shows the first attempted superlattice. A corrugated band of nearly parallel lines is clearly visible between the uniform GaAs layers at top and bottom. In some places where the edges are not in shadow it is possible to count the exact number of alternations which were attempted, namely 30. The wide layer just above the superlattice is not a part of it but rather an artifact of the growth procedure. The diagonal lines crossing the superlattice represent the intersection of (111) stacking faults with the cleavage plane. It can be seen that the spacing is variable in this picture, and a more detailed study at several points along this band would reveal a slight decrease of the average spacing in the direction of growth. The average spacing here is about 300Å and was produced by injecting the PH_3 for 3 sec and then turning it off for 3 sec, repeating this procedure 30 times. The corrugations themselves are produced by preferential etching, the GaAs layers etching faster than the $GaAs_{1-x}P_x$.

Scanning electron microscopy (SEM) is faster than the replica transmission method and offers the advantage that it is possible to observe the specimen directly while maneuvering it into different positions, but it lacks the high resolution of the replica method. A special adaptation of this type of examination is shown in Fig. 8. This is the double cleave technique, where after cleaving and etching the specimen it is cleaved again perpendicular to the original cleaved surface, and the intersection is then observed by SEM. Figure 8a illustrates clearly that the whole superlattice area is raised above that of the GaAs sandwiching it on both sides because the GaAs etched at a faster rate. The resolution of this microscope was not good enough to bring out the individual striations within this band. However, they are visible in the second photograph, Fig. 8b, which depicts a superlattice with a much larger spacing, in this case about 2000Å. It is not clear whether the deep gouge at the right of the photograph represents a defect in the original growth or whether it is simply a cleavage phenomenon.

Electron microscopic techniques are very useful to demonstrate when a superlattice has been successfully grown and to measure its period. However, they reveal very little about the amplitude of the concentration variation. It is known that relatively small concentration inhomogeneities and other effects such as temperature fluctuations can produce strong etching effects (4). Furthermore, a substantial lattice strain must be present due to the approximately 2% difference in lattice constants, and mismatch dislocations have been reported for this system (5). Strain and distortion of the lattice could be responsible for some of

Fig. 7. Replica transmission electron micrograph of 300Å superlattice structure.

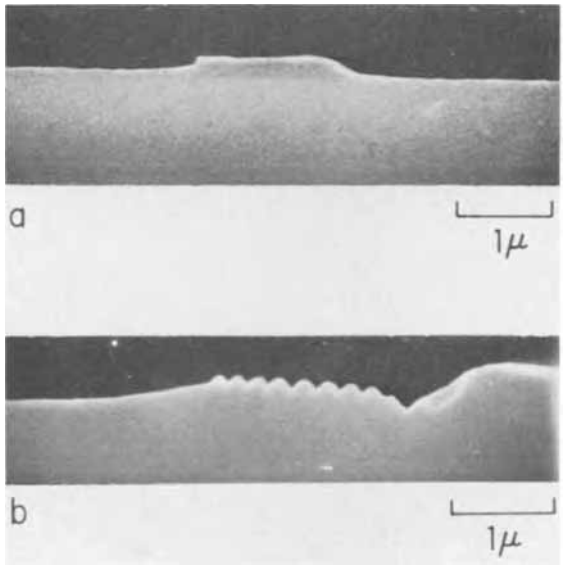

Fig. 8. Scanning electron micrographs of doubly cleaved superlattice structures.

the enhanced etching. Thus it was difficult to know whether the observed variation in etch rate corresponded to a change in phosphorus concentration sufficient to produce the desired effects. Some attempts at measuring the concentration profiles directly by counting neutron-activated layers removed by RF sputter etching and by the ion microprobe resulted in failure, presumably because removal of parallel layers only a few angstroms thick could not be accomplished.

The most conclusive proof that a nontrivial change in the phosphorus mole fraction actually exists within the superlattice has been obtained by an x-ray technique. The x-ray measurements were made by recording the intensity of (400) diffraction peaks from a type of sample that differed from those previously described in that the top layer of GaAs was not grown. This form of specimen, which is more suitable also for certain electrical measurements, allows the x-rays to penetrate directly into the superlattice. When very thin layers of two different crystalline substances are interleaved together and when the successive layers are thin enough that many of them can exhibit simultaneous and coherent x-ray diffraction, the separate peaks characterizing the two individual materials will disappear and be replaced by an average reflection with which are associated satellite peaks, or side bands. Previous work involving detection of satellites has always entailed naturally occurring superlattice crystals (2).

Satellite x-ray peaks have been observed for several of our specimens. Figure 9 shows the sharpest x-ray spectrum that has been seen, indicating that this specimen has the most perfect superlattice that has been grown to date. The peak at 66.2° is the (400) reflection from the GaAs substrate. The peak at 67.5° is the same reflection from the interleaved $GaAs_{1-x}P_x$ layers. The satellite peaks are seen 0.5° above and below this parent peak. Each of the peaks shows a splitting due to the α_1 and α_2 components of the CuKα radiation. Both the presence of the satellites and the α_1-α_2 resolution are indicative of the high degree of coherence of the superlattice. An analysis of this spectrum (6) has predicted that for this degree of sharpness to result, the period within the superlattice must be constant to better than 1% in this case. The high intensity (48% of that of the central peak) of the right hand side peak is strong evidence for the existence of a significant amplitude in the periodic phosphorus profile. The asymmetry in the height of the two side bands and the fact that the central peak position corresponds to a lattice constant smaller than expected for an unstrained combination of 0 and 50% GaP layers are attributed to an anisotropic stress distribution in the superlattice.

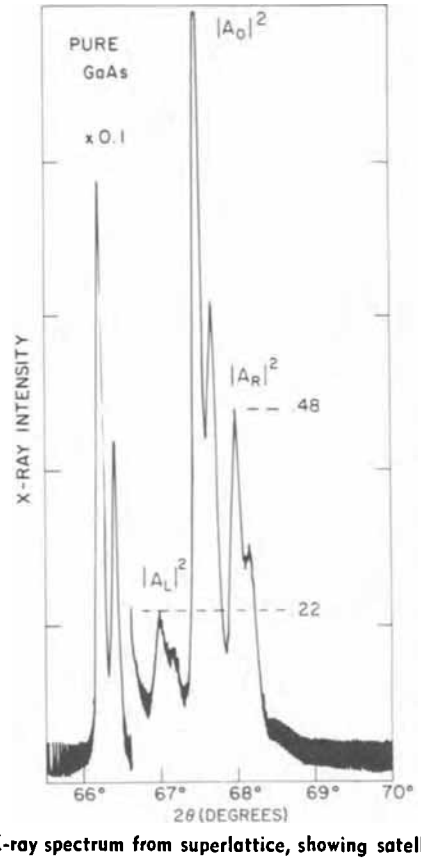

Fig. 9. X-ray spectrum from superlattice, showing satellite peaks

Various alternative hypotheses to account for the x-ray diffraction effects have been considered. One such model is that several discrete layers of material, each of which is homogeneous within itself but distinct in composition from the others, give rise to separate diffraction peaks; another is that the satellite peaks are due to slightly misoriented segments. The experimental observation that the angular spacings between satellite and parent peaks vary regularly and inversely with the layer spacings, in accordance with simple Bragg diffraction theory, supports the assumption of a superlattice as opposed to the fortuitous situations mentioned above as alternative hypotheses.

Having demonstrated the feasibility of making a superlattice, there remains the difficult task of perfecting it to the point where it can meet the stringent requirements imposed by the device theory. This reduces essentially to controlling the growth rate so that the layers are flat, parallel, and equally spaced. Many cases have been seen that are far from the ideal, for example the defective growth shown in Fig. 10, which shows a sample with four successive superlattice bands. Note that these bands are neither straight nor parallel. Since the growing interface obviously became rough before growth of the superlattice was begun, solution of this problem was equivalent to that of avoiding growth pits in epitaxial layers. Effects of temperature and orientation on the phenomenon of surface pitting have been reported (7), but neither of these effects was found to be responsible for the nonplanar epitaxy. The key to the problem turned out to be an unsuspected variable, the flow rate of HCl. A minimum HCl flow rate, and hence a minimum GaCl pressure in the reactor, was found necessary in order to ensure surface planarity. For (100) substrates and 750°-760°C, the minimum HCl flow is 10 cc/min; for higher temperatures and for (111A) substrates the rate must be higher.

Another way to improve the flatness is by suitable choice of the orientation. In looking at the epitaxial growth at the edge of the wafer shown in Fig. 10 it was noted that, although many kinks and jogs existed in the part growing in the <100> direction, there was

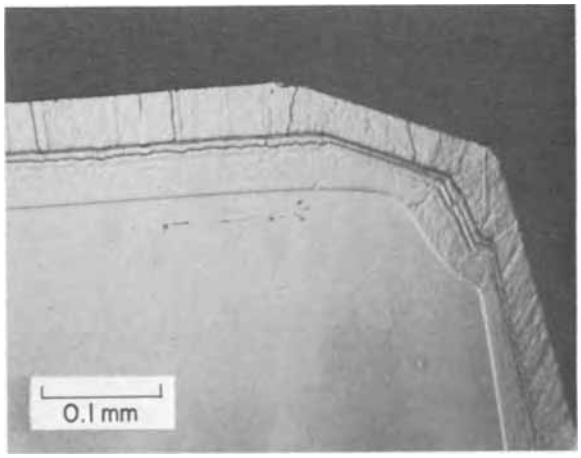

Fip. 10. Nonplanar growth on sample containing four superlattice bands.

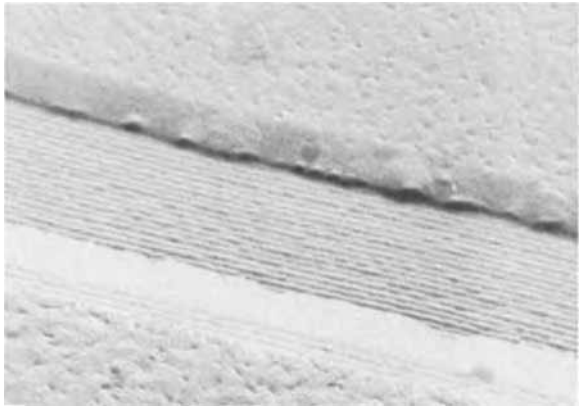

Fig. 11. 200Å superlattice with constant periodicity

another direction in which facets formed and the superlattice layers were flat and parallel. It was determined that this was the <311> direction. Subsequent superlattice growth on a (311A)-oriented substrate verified that the resulting layers were indeed very flat.

By applying some of this knowledge it was possible to greatly improve the morphology of the growth. An example of one of the best layers is given in Fig. 11. The spacing here is about 200Å. The layers are actually more parallel than they look because the corrugated surface is slightly mottled by the etching. The smallest spacing that has been resolved so far is 110Å, but this was not constant across the whole superlattice.

Electrical properties of these layers have been reported elsewhere (6). Very briefly they are the following. Foremost is the fact that the negative resistance has not yet been observed. However, existence of an electrical as well as a metallurgical superlattice, has been tentatively concluded from measurements of cathodoluminescence, capacitance *vs.* voltage at 4°K, and conductance *vs.* temperature. Since a barrier height of only 60 meV, which is only 10% of the maximum possible bandgap change, was detected, it is concluded that most of the potential oscillation exists in the valence band. Thus in order to realize the negative resistance properties it may be necessary to exploit the capability of the system described here with p-type $GaAs_{1-x}P_x$ or with another semiconductor system.

Acknowledgment

Many persons at the IBM Research Center have played a part in this work. The author is particularly indebted to L. Esaki for the original concept of the electronic superlattice, to L. L. Chang and R. Tsu for characterization studies, to C. F. Aliotta and C. G. Bremer for electron microscopy, to H. Cole and colleagues for the x-ray work, and especially to B. K. Bischoff for the meticulous preparation of the crystal layers.

Manuscript submitted Oct. 15, 1970; revised manuscript received *ca.* May 8, 1971. This was Paper 148 presented at the Los Angeles Meeting of the Society, May 10-15, 1970.

Any discussion of this paper will appear in a Discussion Section to be published in the June 1972 JOURNAL.

REFERENCES

1. L. Esaki and R. Tsu, *IBM J. Res. Develop.*, **14**, 61 (1970).
2. C. S. Barrett and T. B. Massalski, "Structure of Metals," Chap. 11, 3rd ed., McGraw-Hill, New York (1966).
3. J. J. Tietjen and J. A. Amick, *This Journal*, **113**, 724 (1966).
4. R. E. Ewing and D. K. Smith, *J. Appl. Phys.*, **39**, 5943 (1968).
5. M. S. Abrahams, L. R. Weisberg, and J. J. Tietjen, *ibid.*, **40**, 3754 (1969).
6. L. Esaki, L. L. Chang, and R. Tsu, Proc. of Int. Conf. on Low Temp. Physics (LT-12), Kyoto, Japan, Sept. 1970.
7. A. E. Blakeslee, *Trans. Met. Soc. AIME*, **245**, 577 (1969).

High-Temperature Annealing of Oxidized Silicon Surfaces

F. Montillo[1] and P. Balk

IBM Thomas J. Watson Research Center, Yorktown Heights, New York 10598

ABSTRACT

The densities of fixed charge (Q_{ox}) and trapping centers (N_{ss}) on thermally oxidized silicon surfaces have been measured by the MOS capacitance technique upon annealing in O_2, N_2, He, and vacuum at various temperatures from 600° to 1100°C. These surface characteristics are always determined by the conditions of the final high-temperature process, except for Q_{ox}, which will never increase in neutral ambients. In all atmospheres, higher annealing temperatures yield lower Q_{ox} values. It was also found that the N_{ss} values are very sensitive toward trace amounts of water in the high-temperature ambient. They decrease for increasing water vapor pressure. Effects of other impurities were not observed in this study. Based on saturation values and kinetic data a discussion is given of some models for both types of centers.

The properties of oxidized silicon surfaces have been studied extensively during the past decade. The interest in this topic was strongly stimulated by the advent of the field effect transistor. Two characteristics are of particular significance for their effects on the performance of this device: the tendency of both n- and p-type silicon substrates to form n-type surfaces upon oxidation, and the presence of trapping states near the semiconductor-oxide interface (1). Accordingly, several workers in this field have investigated the conditions that determine the amount of positive surface or oxide charge (invoked to explain the excess of electrons occurring in n-type space charge layers at silicon surfaces) and the density of surface trapping states.

Notwithstanding the fact that these phenomena are well known, there is no generally accepted physical model to account for the above characteristics. In fact, three different models may be invoked to describe the observations: The first one distinguishes between fixed surface charge centers, located in the oxide, and inter-

[1] Present address: IBM Components Division, East Fishkill, New York 12524.

Key words: surface charge, interface states, CV-measurements.

facial trapping states (2). One must also consider the possibility that both surface charge and trapping states may be related to centers directly at the oxide-silicon interface (3). A third model allows only for centers in the oxide near the interface, and considers trapping states as induced by point charges in the oxide (4). Although many workers assume that the centers are related to vacancies in the oxide or at the interface, it has also been suggested that they are caused (2, 5) or stabilized by (6) impurities, notably Na.

With respect to the phenomenological behavior of the centers there is no complete clarity either. It has been reported that upon oxidation in O_2 to a given thickness, a larger oxide charge results for lower temperatures (7), and that at a given temperature the amount of charge is larger when the rate of oxidation before terminating the process was larger (3, 6). Annealing in neutral ambients, like N_2, will under certain conditions eliminate the charge, but it is not certain whether this will happen for a wide range of temperatures (7) or only for the very highest (6, 8).

The density of trapping states obtained upon oxidation in O_2 is strongly dependent on the partial pressure of water vapor in this ambient (9, 10). For dryer O_2 larger numbers of states have been observed. The situation with regard to nonoxidizing atmospheres is less clear. It has been reported that annealing of clean samples at very high temperatures (*e.g.* 1100°C) in neutral ambients will eliminate interface states (8). On the other hand, vacuum annealing surprisingly results in an increase in the trap density particularly at higher temperatures (10). Low temperature annealing (*e.g.* at 400°C) in H_2 (9, 11) or wet N_2 (11) will completely eliminate these centers.

Both the amount of oxide charge and the density of interface states obtained for O_2 or N_2 and He ambient annealing are dependent on sample orientation (2, 6, 7, 10, 12, 13).

In view of the uncertainties cited above, the present authors have attempted to explore the different annealing processes in a systematic fashion. In addition to a consistent set of data, some interesting similarities and differences in behavior between the centers responsible for oxide charge and those giving rise to interface trapping will be reported. Finally, we will attempt to explain some apparently contradictory observations described in the literature. The convenient MOS capacitance technique made it possible to include a wide variety of conditions in the experimental investigation. However, for establishing detailed models for the studied effects more sophisticated approaches may be necessary.

Experimental

The samples used in this study were 2 ohm-cm (100) and (111) orientated, chemically-mechanically polished Monsanto and Dow-Corning silicon wafers of both conductivity types. They were cleaned by rinsing with organic solvents, HF, and distilled water, and oxidized at 1000° or 1100°C, generally to 1000Å, in a rf heated silica tube (Fig. 1a) or in a silica tube in a resistance heated furnace. The oxidation ambient was either dry O_2 (water content $< 1 \times 10^{-2}$ Torr, as measured at the outlet of the tube) or O_2 into which a predetermined higher amount of water vapor (generally 6×10^{-2} Torr) had been injected. Water vapor pressures were determined using a Panametrics Al_2O_3 conduction cell. Very clean oxide films were obtained by vapor etching in H_2-HCl, followed by *in situ* oxidation in the rf heated tube (Fig. 1a). Some of the films were stabilized by forming a phosphosilicate glass layer approximately 100Å thick, containing 4 mole per cent (m/o) P_2O_5, on their surface (14).

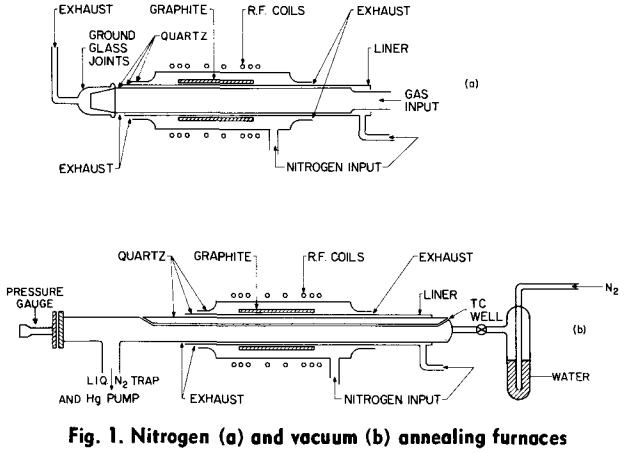

Fig. 1. Nitrogen (a) and vacuum (b) annealing furnaces

Neutral ambient annealing was done in helium or nitrogen in the temperature range of 500° to 1100°C. The helium was dried through a trap filled with Linde 13X molecular sieve at liquid nitrogen temperature, the nitrogen through a molecular sieve trap at room temperature. These treatments and also vacuum annealing (at 10^{-6} Torr and 500° to 1000°C) were carried out in very similar rf heated quartz tubes (Fig. 1b). The vacuum annealing tube was also used for annealing in N_2 ambients below atmospheric pressure. These N_2 ambients, containing various water vapor pressures, were obtained by bleeding dry N_2 or N_2, saturated at room temperature with water vapor, into the tube while pumping, and by adjusting the gas flow such that the desired total pressure was obtained. The samples were allowed to cool rapidly in the annealing ambient.

The samples were evaluated using the MOS capacitance or C-V technique (15) at room temperature and at liquid nitrogen temperature, for a measurement frequency of 1.5 Mc. To this end, aluminum dots were evaporated from a rf heated boron nitride crucible onto the unheated substrates. As a measure of the interface state density their number N_{ss} between the room temperature and liquid nitrogen temperature Fermi levels was used (10)

$$N_{ss} = \frac{C_{ox}}{q} [V_{FB} \text{ (room temp)} - V_{FB} \text{ (liq } N_2 \text{ temp)}] \quad [1]$$

where V_{FB} is the flatband voltage and C_{ox} the oxide capacitance, both obtained from the C-V plots. There is some uncertainty in the room temperature V_{FB} values, and consequently in N_{ss}, since even at 1.5 Mc the interface state capacity may not be completely eliminated. The surface or oxide charge was obtained from the shift of the room temperature C-V curves with respect to the theoretical curve for the proper resistivity and oxide thickness

$$Q_{ox} = C_{ox} [V_{FB} - V_{FB} \text{ (theor.)}] \quad [2]$$

These C-V measurements were made after a 5 min anneal at 500°C, which removes all interface states observable by field effect measurements (16) or by capacitance measurements according to Eq. [1]. It should be noted that the use of these operational definitions (1) and (2) for interface state density and oxide charge allows a direct comparison with results obtained by other workers only for the latter quantity. For interface state densities such comparisons are necessarily qualitative, except for comparisons with the work of Brown and Gray (10), who first introduced the technique adopted in this study.

Results

The experimental results obtained upon annealing of silicon substrates covered with "very clean," "regular" or P_2O_5 stabilized oxide films were always quite similar. It was found from electrothermal stressing tests that the "regular" oxides contained generally not more than 5×10^{10} mobile species (presumably Na ions) per cm^2 whereas the mobile charge level for "very clean" films was typically half this number or less. The mobile Na content in the stabilized films was below 1×10^{10} per cm^2. These numbers were not af-

fected by the different annealing treatments, nor did the outcome of such treatments show any correlation with variations in the low Na content of the samples. For P_2O_5 doped oxides the possibility of phosphorus penetration through the film strongly limited the maximum feasible annealing times at the highest temperatures. The only difference between "regular" and "very clean" films was in an area unrelated to the subject of interest for this paper. The incidence of defect breakdown (17) was considerably lower in the latter type of oxide film.

Although the results obtained on n and p-type substrates always showed the same trends, the N_{ss} values measured on n-type samples tended to be somewhat larger than those for the other resistivity type. A simple explanation for this observation may be that the part of the gap scanned, namely that between the room and liquid nitrogen temperature Fermi levels, is somewhat larger for n-type material because of its lower carrier density at a given resistivity.

The results did depend on the sample orientation: both Q_{ox} and N_{ss} values are generally larger for (111) than for (100) surfaces. Our data here are in agreement with those found in the literature.

When a sample was subjected to a sequence of annealing treatments in different ambients, the final values of Q_{ox} and N_{ss} were those characteristic of the last high temperature process. The behavior of Q_{ox} in neutral ambients forms an exception, which will be discussed later.

Oxygen annealing.—When the annealing is carried out below the oxidation temperature, both Q_{ox} and N_{ss} increase. The kinetics of the process is orientation dependent. It may be seen in Fig. 2 that for (111) oriented samples Q_{ox} passes through a maximum before obtaining its final value, whereas for (100) samples Q_{ox} increases monotonically until it reaches its maximum. Here and in the following figures and tables each set of N_{ss} and Q_{ox} values after a given treatment was obtained on a different sample. N_{ss} exhibits a similar behavior as Q_{ox}, and approximately the same amount of time is required for the change to take place. The rate of these processes depends not only on the annealing temperature, as expected, but also on the thickness of the oxide film. For example, the time required to reach the maximum in the Q_{ox} curve for (111) oriented samples is proportional to the oxide thickness (18). This suggests that the diffusion of oxygen through the layer is the rate-determining step in the process. In the times involved approximately one mono-molecular layer of oxide, and thus a completely new interface, is formed.

The temperature dependence of the saturation or equilibrium values of Q_{ox} and N_{ss} for (100) oriented samples is shown in Fig. 3. These curves can be traversed reversibly. Larger values were obtained for the (111) orientation.

It was reported by Brown and Gray (10) that the interface state density increases for decreasing water

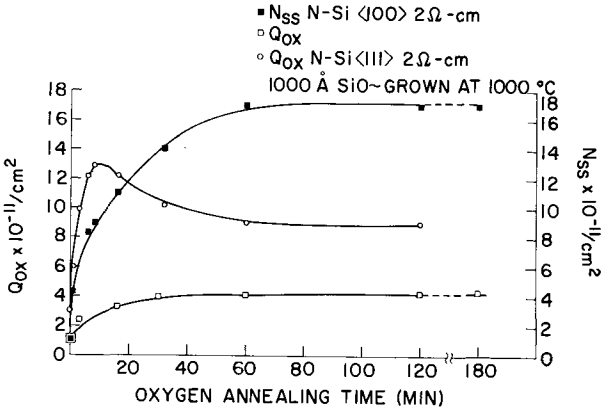

Fig. 2. Dependence of N_{ss} and Q_{ox} on annealing time in O_2 at 600°C.

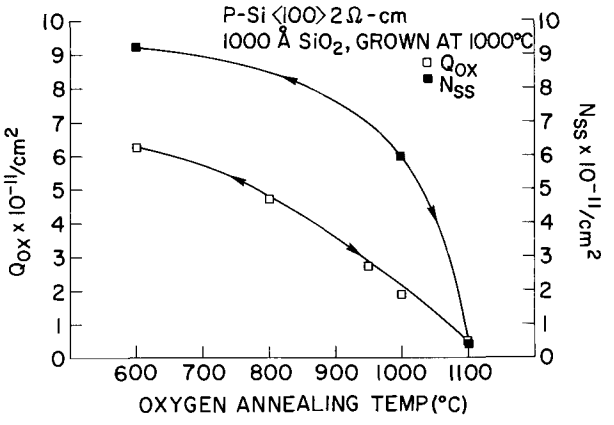

Fig. 3. Saturation values for N_{ss} and Q_{ox}, obtained upon O_2 annealing at various temperatures. The arrows indicate that the curves can be traversed in both directions.

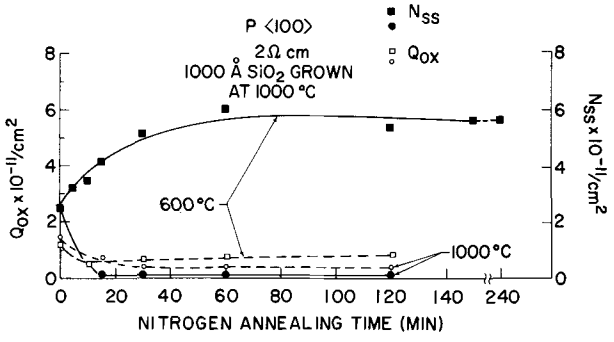

Fig. 4. Dependence of N_{ss} and Q_{ox} on annealing time in N_2 at 600° and 1000°C.

content of the oxygen during the oxidation process down to 80 ppm of water (60 x 10^{-3} Torr). A similar relationship was found for most of the cases studied in the present investigation (Table I) between oxidation at 5 x 10^{-3} and 60 x 10^{-3} Torr. The effect of water vapor on Q_{ox} was very small in the cases investigated, which were all in the low pressure range.

N_2 and He annealing.—Annealing in N_2 and in He leads to the same results. However, in contrast to the results obtained for O_2, it may be seen (Fig. 4) that in neutral ambients N_{ss} and Q_{ox} do not always change in the same direction. Specifically, Q_{ox} will never increase but only remain constant or decrease upon annealing in neutral ambients, whereas N_{ss} may change in both directions. Figure 5 shows the dependence of the decrease of Q_{ox} on time for different temperatures upon annealing of (111) oriented samples in He. A high concentration of oxide charge had first been induced in the surfaces by exposure to O_2 at 600°C. Though the number of data points is rather limited, an exponential decay of the excess charge (towards the new saturation value) with time appears to give a good description of the kinetics. However, the oxide charge approaches a different final value for each temperature. The activation energy for the rate constant is rather low (approximately 0.5 eV). The in-

Table I. Effect of water vapor pressure in oxidation ambient on N_{ss} and Q_{ox}

	Oxide growth at 1000°C in O_2 with H_2O pressure (Torr)	N_{ss} x 10^{-11}	Q_{ox}
p⟨100⟩	5 x 10^{-3}	6	1
	60 x 10^{-3}	3	1
p⟨111⟩	5 x 10^{-3}	25	4
	60 x 10^{-3}	26	5
n⟨100⟩	5 x 10^{-3}	11	1
	60 x 10^{-3}	4	1
n⟨111⟩	5 x 10^{-3}	33	4
	60 x 10^{-3}	20	5

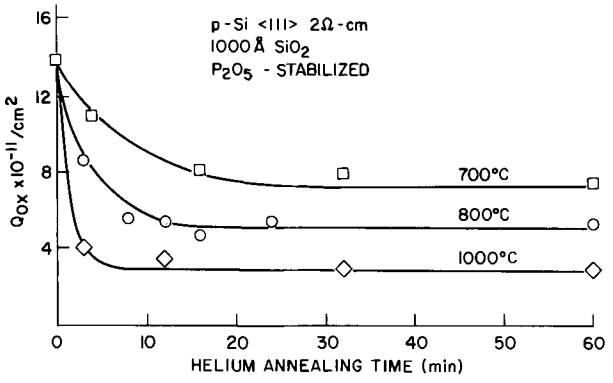

Fig. 5. Dependence of Q_{ox} on annealing time in He at various temperatures.

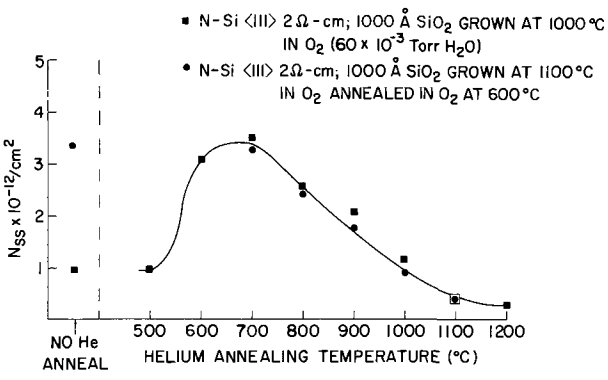

Fig. 7. Saturation values for N_{ss}, obtained upon He annealing at various temperatures. The values before annealing are also indicated.

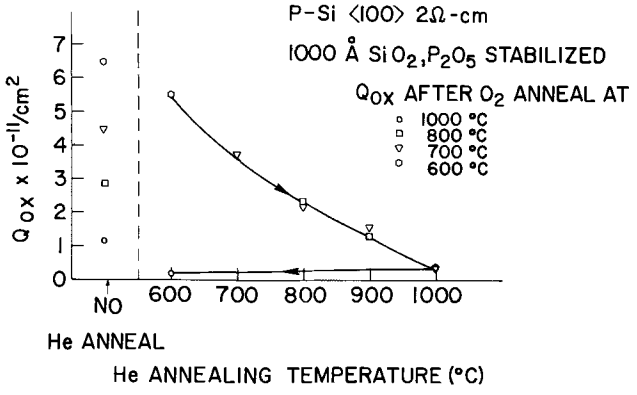

Fig. 6. Saturation values for Q_{ox}, obtained upon He annealing at various temperatures. The arrows indicate that in this case increase in Q_{ox} is not possible. The values before annealing are also indicated.

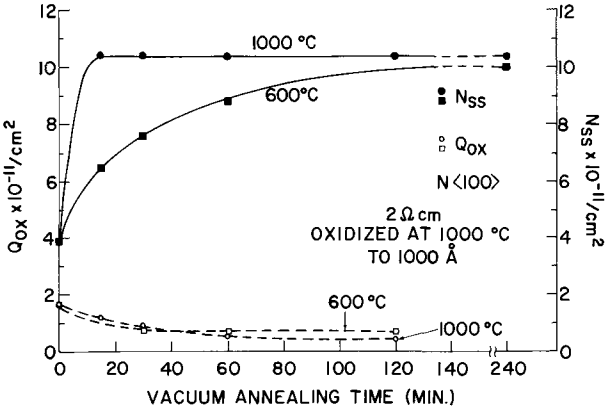

Fig. 8. Dependence of N_{ss} and Q_{ox} on annealing time in vacuum at 600° and 1000°C.

crease in N_{ss} at 600°C in Fig. 4 follows a similar rate law. The Q_{ox} values finally attained in this process are given in Fig. 6 as a function of temperature. They do not depend on the value before annealing, as long as that value was larger than or equal to the quasi-equilibrium value for the annealing temperature (as given by the declining curve in Fig. 6). The time required for the reduction in Q_{ox} is dependent on oxide thickness. An increase in Q_{ox} is never obtained during annealing in neutral ambients.

The N_{ss} data plotted in Fig. 7 demonstrate that the saturation value for this parameter tends to be independent of the value before annealing in the temperature range for which sufficient information is available (700° to 1100°C). The process thus appears to be reversible. At the lowest temperature investigated (500°C) no change at all was observed from the initial value even after many hours.

Vacuum annealing.—Vacuum annealing experiments were carried out only at or below 1000°C. At this temperature oxide shorts would gradually develop, which made electrical measurements more difficult. Our data (Fig. 8) indicate that vacuum annealing in the 600° to 1000°C temperature range always results in an increase in N_{ss} for samples prepared by oxidation in O_2 at 1000°C. On the other hand, such an increase was for N_2 annealing obtained only in the lower part of this temperature range (Fig. 4). The 1000°C vacuum annealing saturation values are in agreement with Brown and Gray's data (10). As in N_2, the approach of the saturation value for N_{ss} during vacuum annealing at 600°C can be satisfactorily described as a first order reaction. However, the process appears to be somewhat slower in vacuum.

These effects are again demonstrated in Table II, which also offers a comparison between the (111) and (100) surfaces. The trends are the same for both orientations, although the Q_{ox} and N_{ss} values are larger for the (111) surface. The data also indicate that the Q_{ox} values for N_2 and vacuum annealing at a given temperature are very similar, and become very small for the (100) orientation at 1000°C.

Water vapor in neutral ambient annealing.—The difference between the N_2 and vacuum annealing results at 1000°C is rather unexpected, since both ambients may be considered as nonreactive towards the SiO_2-Si system. The qualitative reversibility of the N_2 and vacuum annealing effects, shown in Table III, indicates that in each case the system moved toward an equilibrium condition, characteristic for the final ambient to which the sample was exposed. This observation led to the suspicion that some gaseous impurity might be responsible for the "N_2 results."

Measurement of the water content of the N_2 showed that this quantity is temperature dependent (Table

Table II. Effect of annealing ambient and sample orientation at 600° and 1000°C on N_{ss} and Q_{ox}

Sample	After annealing in									
	O_2(60 x 10^{-3} Torr H_2O) at 1000°C		Vacuum at 600°C		N_2 at 600°C		Vacuum at 1000°C		N_2 at 1000°C	
	N_{ss} x 10^{-11}	Q_{ox} x 10^{-11}	N_{ss} x 10^{-11}	Q_{ox} x 10^{-11}	N_{ss} x 10^{-11}	Q_{ox} x 10^{-11}	N_{ss} x 10^{-11}	Q_{ox} x 10^{-11}	N_{ss} x 10^{-11}	Q_{ox} x 10^{-11}
p-<100>	3	1	9	2	6	0.7	11	0.4	0.1	0.3
p-<111>	26	5	48	7	37	6	136	2	9	2

Table III. Effect of sequential N_2 and vacuum annealing on N_{ss} and Q_{ox}

Sample	After annealing in: O_2(60 × 10^{-3} Torr H_2O) at 1000°C		Nitrogen at 1000°C		Vacuum at 1000°C		Vacuum at 1000°C and nitrogen at 1000°C		Nitrogen at 1000°C and vacuum at 1000°C	
	N_{ss} × 10^{-11}	Q_{ox}	N_{ss} × 10^{-11}	Q_{ox}	N_{ss} × 10^{-11}	Q_{ox}	N_{ss} × 10^{-11}	Q_{ox}	N_{ss} × 10^{-11}	Q_{ox}
N <111> 2 ohm-cm	20	5	8	4	135	3	8	3	46	1

Table IV. Observed water vapor pressures in N_2 at various temperatures at exhaust of annealing furnace

Temperature (°C)	N_2 flowrate: 2 liters/min at 1 atm	0.25 liters/min at 1 atm
25	0.1 × 10^{-3} Torr	0.1 × 10^{-3} Torr
600	0.4 × 10^{-3} Torr	5 × 10^{-3} Torr
900	5 × 10^{-3} Torr	36 × 10^{-3} Torr
1000	7 × 10^{-3} Torr	60 × 10^{-3} Torr

IV). At room temperature it is very low. The increase at high temperatures must be caused by diffusion of water through the wall of the quartz tube, since the water content of the N_2 is inversely proportional to the flow rate of the gas. The non-negligible oxidation rates of silicon in "dry Ar" at 850° and 1000°C, observed by Nakayama and Collins (19), were probably also caused by water permeation through their quartz furnace tube. A quantitative comparison of the water vapor pressures estimated from their data (they are in the range from 0.1 to 1 Torr) with those following from the data of Table IV is difficult because of the different geometries of the systems.

Table V shows that indeed the N_{ss} values correlate directly with the water vapor pressure in the ambient, whereas any obvious relationship with the N_2 pressure is lacking. Even at low water content of the ambient the surface characteristics are still very sensitive to the actual value of the vapor pressure. These observations explain at the same time the difference between the N_2 and vacuum annealing results, discussed before. This difference is most pronounced at the highest temperature (1000°C) at which data are available for both cases. At 900°C the dependence of N_{ss} on the water vapor pressure is considerably weaker (Table VI).

Discussion

The implications of the foregoing results for the construction of models for oxide charge and interface state centers is discussed next. All such models are necessarily tentative, but they are useful in stimulating discussion and further experimentation.

Oxide charge centers.—The important findings are: At a given temperature and oxide thickness a distinct value of Q_{ox} is obtained in O_2. This value is generally lowered upon annealing in neutral ambients at the same temperature. At higher temperatures lower values are obtained. In the pressure range investigated (*i.e.* below 10^{-1} Torr) the water content of the ambient is relatively unimportant. The rate at which the new Q_{ox} value is reached decreases with increasing oxide thickness.

These observations are compatible with a model in which the oxide charge centers are defects in the oxide structure near or at the oxide-silicon interface. Such a model has first been proposed by Revesz *et al.* (6). The concentration of these centers would be determined by a dynamic equilibrium between the oxidation reaction, which disturbs the interfacial region and leads to formation of oxide charge centers, and an annealing process, which tends to eliminate them. The orientation dependence of Q_{ox} indicates that the charge must be located at or near the interface, since one does not expect that the entire SiO_2 glass film would exhibit substrate orientation dependent properties. The experimental results do not allow very specific conclusions with regard to the nature of the defects. However, it is possible that they involve hydroxyl groups (2). In this case their formation would require the presence of water or hydroxyl groups, whereas their removal would be determined by the outdiffusion of such species. Such a model would be compatible with the observed thickness dependent rate of decay of Q_{ox} in neutral ambient annealing.

Recently Fowkes and Burgess (5, 20) have proposed that oxide charge may be caused by Na^+ ions, located in positively charged Si-O-Na centers introduced near the interface upon oxidation at intermediate temperatures. During oxidation at very high temperatures, and particularly during neutral ambient annealing, oxygen vacancies would form throughout the oxide. These centers would readily trap electrons and immobilize Na^+ ions. However, from our finding that the mobile

Table V. Effect of water vapor pressure in neutral ambient annealing on N_{ss} and Q_{ox} at 1000°C

Substrate: p (111) 2 ohm-cm,	Annealing ambient (1000°C): H_2O pressure (Torr)	N_2 pressure (Torr)	N_2 flowrate (liters/min @ 1 atm)	Surface characteristics: N_{ss} × 10^{-11}	Q_{ox} × 10^{-11}
Oxidized at 1000°C		Before annealing		25	7
In O_2 with 60 × 10^{-3}	<10^{-6}	Vacuum		107	3
Torr in H_2O	1 × 10^{-3}	80	2	83	2
	2 × 10^{-3}	0.1	—	58	—
	7 × 10^{-3}	760	2	15	2
	60 × 10^{-3}	760	0.25	7	4

Table VI. Effect of temperature and water vapor pressrue on N_{ss} in neutral ambient annealing

Substrate: p (111) 2 ohm-cm,	Annealing ambient: N_2 pressure (Torr)	N_2 flowrate (liters/min @ 1 atm)	900°C: H_2O pressure (Torr)	900°C: N_{ss} × 10^{-11}	1000°C: H_2O pressure (Torr)	1000°C: N_{ss} × 10^{-11}
Oxidized at 1000°C	Before annealing			25		25
In O_2 with 60 × 10^{-3}	Vacuum		<10^{-6}	64	<10^{-6}	107
Torr of H_2O	80	2	0.6 × 10^{-3}	43	1 × 10^{-3}	83
	760	2	5 × 10^{-3}	35	7 × 10^{-3}	15
	760	0.25	36 × 10^{-3}	25	60 × 10^{-3}	7

Na content of the samples was not affected by annealing, and that it was also low on surfaces with high Q_{ox}, it appears unlikely that Na impurities were responsible for the charge in our experiments.

Interface states.—The observation that new equilibrium concentrations of oxide charge centers and interface states form in comparable times during O_2 annealing suggests a similarity in nature between the two types of centers. In addition, their orientation dependence is the same.

Nonetheless, there are also some striking differences in the annealing behavior of the centers. During vacuum annealing Q_{ox} and N_{ss} may change in opposite directions, such that Q_{ox} is virtually eliminated, whereas N_{ss} becomes very large. An outstanding feature of the interface states is their pronounced sensitivity towards water vapor in the annealing ambient, even at very low concentrations.

These observations are satisfactorily described by a simple model (9, 11) of the interface states as caused by chemically unsaturated silicon atoms at the interface. Such centers would be able to react with water at elevated temperatures under formation of silanol groups

$$\begin{array}{c} | \\ -\mathrm{Si}\cdot \\ | \end{array} + \mathrm{H_2O} \rightarrow \begin{array}{c} | \\ -\mathrm{Si}- \\ | \end{array} \mathrm{OH} + \mathrm{H}$$

A somewhat comparable reaction of water with intrinsic defects in SiO_2 was invoked by Weeks and Lell to explain their optical absorption and electron spin resonance data on bulk silica (21). At high temperatures in vacuum one has to assume a breaking of the Si-OH bond, and release of water vapor. The observed first order rate behavior of the vacuum and N_2 annealing processes at 600°C is compatible with this model. On the basis of the assumptions made in the foregoing section, the oxide defects related to Q_{ox} would tend to disappear due to removal of hydroxyl or water vapor under these experimental conditions, which would explain the opposite behavior of the two types of centers.

The model suggests that a set of two states of different energies may be observed for each center as is indeed the case (10). It also explains the high reactivity of interface state centers towards H_2 at low temperatures (200° to 500°C). They are completely eliminated in this ambient in 1 hr at temperatures as low as 300°C, most likely under formation of silane groups (9)

$$\begin{array}{c} | \\ -\mathrm{Si}\cdot \\ | \end{array} + \mathrm{H_2} \rightarrow \begin{array}{c} | \\ -\mathrm{Si}- \\ | \end{array} \mathrm{H} + \mathrm{H}$$

The observed linear pressure dependence of the rate of this reaction, which is not diffusion-limited, and its enhancement in atomic hydrogen (22) would indeed be expected for the above model. Above 500°C H_2 was found less and less effective with increasing temperature in removing interface states. This may reflect a decrease in stability of the Si-H bond at these higher temperatures which has also been suggested by Kooi (2).

As shown earlier, the N_{ss} values upon O_2 annealing are also sensitive toward the water content of this ambient. It is not clear if the decrease in saturation value with temperature requires a similar explanation as the parallel decrease in Q_{ox}. This decrease may also be caused by the increase in the water content of the O_2 with temperature due to the increased permeability of the quartz walls.

Finally, it may be interesting to note that very high interface state densities were observed on oxidized surfaces of germanium-doped silicon samples (23). A substantial fraction of these states could not be eliminated by low temperature reaction with hydrogen. This behavior suggests that in this case interfacial germanium atoms of valency less than four may be responsible for the centers. Such oxygen deficiency is known to occur readily in bulk GeO_2 (24).

Conclusions

The following conclusions may be drawn from the material obtained in the present investigation:

Q_{ox} and N_{ss} are in most cases a unique function of time, temperature and ambient in the last high-temperature annealing step to which the specimen was exposed. A notable exception to this rule is that Q_{ox} never increases during neutral ambient annealing.

N_{ss} is very sensitive towards the water content of O_2 and neutral annealing ambients even at partial pressures well below 10^{-1} Torr.

The amount of mobile Na in samples with a low concentration of this impurity is not affected by heating in clean O_2 or neutral ambients.

Explanation of the present data does not require the assumption that the occurrence of oxide charge and surface states are caused by Na.

The centers correlating with N_{ss} and Q_{ox} are distinctly different.

Acknowledgment

The authors are indebted to Mr. R. Greenland for skillful assistance in the experimental part of this study.

Manuscript submitted Nov. 9, 1970; revised manuscript received *ca.* April 1, 1971. This was Paper 534 presented at the Montreal Meeting of the Society Oct. 6-11, 1968.

Any discussion of this paper will appear in a Discussion Section to be published in the June 1972 JOURNAL.

REFERENCES

1. G. Cheroff, F. Fang, and F. Hochberg, *IBM Journal*, **8**, 416 (1964).
2. E. Kooi, *Philips Res. Rept.* **21**, 477 (1966).
3. A. G. Revesz and K. H. Zaininger, *IEEE Trans. Electron Devices*, **ED13**, 246 (1966).
4. A. Goetzberger, V. Heine, and E. H. Nicollian, *Appl. Phys. Letters*, **9**, 444 (1966).
5. F. M. Fowkes and T. E. Burgess, *Surface Sci.*, **13**, 184 (1969).
6. A. G. Revesz, K. H. Zaininger, and R. J. Evans, *J. Phys. Chem. Solids*, **28**, 197 (1967).
7. B. E. Deal, M. Sklar, A. S. Grove, and E. H. Snow, *This Journal*, **114**, 266 (1967).
8. A. G. Revesz, *Phys. Status Solidi*, **19**, 193 (1967).
9. P. Balk, Paper 109 presented at Electrochem. Soc. Meeting, San Francisco, May 9-13, 1965.
10. D. M. Brown and P. V. Gray, *This Journal*, **115**, 760 (1968).
11. E. Kooi, *Philips Res. Rept.*, **20**, 528 (1965).
12. P. Balk, P. G. Burkhardt, and L. V. Gregor, *Proc. IEEE*, **53**, 2133 (1965).
13. E. Arnold, J. Ladell, and G. Abowitz, *Appl. Phys. Letters*, **13**, 413 (1968).
14. P. Balk and J. M. Eldridge, *Proc. IEEE*, **67**, 1558 (1969).
15. A. S. Grove, B. E. Deal, E. H. Snow, and C. T. Sah, *Solid-State Electron.*, **8**, 145 (1965).
16. P. Balk, Paper 111 presented at Electrochem. Soc. Meeting, Buffalo, Oct. 10-14, 1965.
17. C. Fritzsche, *Z. Angew. Phys.*, **24**, 48 (1967).
18. N. J. Chou, Unpublished work.
19. T. Nakayama and F. C. Collins, *This Journal*, **113**, 706 (1966).
20. F. M. Fowkes and T. E. Burgess, Paper 112 presented at Electrochem. Soc. Meeting, New York, May 4-9, 1969.
21. R. A. Weeks and E. Lell, *J. Appl. Phys.*, **35**, 1932 (1964).
22. P. Balk, Unpublished work.
23. P. Balk, *This Journal*, **118**, 494 (1971).
24. V. Garino Canina and J. Denoncin, *Compt. Rend.*, **250**, 1815 (1960).

Growth of $In_{(1-x)}Ga_xP$ p-n Junctions by Liquid Phase Epitaxy

B. W. Hakki

Bell Telephone Laboratories, Incorporated, Murray Hill, New Jersey 07974

ABSTRACT

Liquid phase epitaxy (LPE) has been used to grow layers of $In_{(1-x)}Ga_xP$, in the range $0.4 < x < 0.8$, on the Ga (111) surface of GaAs. After an n-layer is grown, p-n junctions are made either by Zn diffusion or by LPE growth of a p-layer from a Zn-doped liquid. The rate of deposition and the dependence of layer composition on charge composition are found to be consistent with liquidus and solidus isotherms for the In-Ga-P system obtained by a first-order calculation.

$In_{(1-x)}Ga_xP$ is a material in which a maximum direct bandgap of 2.17 ± 0.02 eV, at 300°K, is obtained when the molar percentage of GaP is 63 ± 2% (1). This makes the material attractive as a potentially efficient electroluminescent source of visible light at wavelengths as short as 5900Å. The ternary material can be grown in bulk form (2), from solution (3), or by liquid phase epitaxy (4, 5). The principal objective of this paper is to relate experimental and theoretical results pertaining to the LPE growth of $In_{(1-x)}Ga_xP$. It also describes fabrication of p-n junctions by initial LPE deposition of an n-layer and subsequent formation of a p-region either by Zn diffusion or by a second LPE deposition from a Zn-doped liquid.

Growth Procedure

The ternary alloy was prepared by liquid phase epitaxial growth from an In-Ga-P solution on a suitable substrate. The growth apparatus is shown schematically in Fig. 1. The pyrolytic graphite growth vessel is contained in an open silica tube under a flow of hydrogen. Weighed amounts of polycrystalline InP and GaP were placed at the bottom of the well containing the indium. The combined weights of InP and GaP were held constant at 0.14 times the weight of indium.

After a preliminary heating of the charge at 900°C for 15 min, a substrate was tipped on the melt at 875°C and the temperature lowered at 2°-3°C/min. The temperature interval over which deposition took place was varied from 25°-75°C, depending on the desired thickness of the LPE layer. At the end of the cooling cycle the substrate was tipped off. Deposition was carried out on <100>, <311>, and <111> oriented crystals of Si, InP, GaP, and GaAs. The crystalline quality of $In_{(1-x)}Ga_xP$ was poor for all substrates except <111> oriented GaAs. For the latter, better results were obtained with the Ga face than with the As face. The lattice constant of GaAs is 5.65Å, which matches that of $In_{0.5}Ga_{0.5}P$ if Végard's law is valid for the ternary lattice constants.

The growth on the GaAs substrate was usually Te-doped. The ionized impurity concentration, as determined by Schottky barrier diode measurements, was typically 5×10^{17} cm^{-3} at 300°K. After growth of the n-layer, p-n junctions were produced either by Zn diffusion or by LPE growth of a p-layer. Zn diffusion was done by enclosing the n-layer, along with about 50 mg of Zn_3P_2, in a sealed quartz ampoule whose volume was 25 cc. The residual atmosphere was hydrogen at 10^{-2} Torr. The ampoule was then heated to 700°C for periods of time ranging from 0.2 to 1.5 hr, depending on the junction depth required.

LPE growth of p-layers was obtained by adding Zn to a charge and tipping on an n-type $In_{1-x}Ga_xP$ layer. The amount of Zn added to the charge varied from 0.03 to 0.3 a/o (atomic per cent). Because of the high partial pressure of Zn and the use of an open-tube system, it was not possible to get an accurate measure of the segregation coefficient of Zn in the quaternary melt. There were, in adddition, several complicating aspects about the double LPE growth of p-n junctions. First, it was necessary to match the ternary composition of the p-layer with that of the n-layer. Failure to accomplish this could lead to a lattice mismatch at the p-n interface. This lattice mismatch can be a potential source of a high concentration of nonradiative recombination centers for the minority carriers. Second, the cooling time during p-growth had to be short, in order to minimize indiffusion of Zn into the n-layer. Finally, the thickness of the p-layer had to be equal to or slightly larger than a minority carrier diffusion length.

Based on these considerations, double LPE p-n junctions were grown as follows: The n-layer was grown by cooling from 875° to 800°C. The p-charge was matched in liquidus composition to the n-charge. The p-charge was tipped at 805°-810°C, *i.e.*, 5°-10°C higher than the minimum growth temperature of the n-layer. This was done to produce some melt back into the n-layer, and thereby improve the composition match between the n- and p-regions. The p-layer was grown by cooling over a certain temperature interval ΔT, which determined the thickness of this layer.

Experimental Results

Liquidus data at 850°C.—To determine experimental liquidus data for In-rich compositions in the In-Ga-P system, mixtures containing known amounts of InP, GaP, and In were equilibrated in a separate apparatus at 850°C for one-half hour, after which the undissolved compound was retracted from the melt and weighed in order to measure by difference the amount

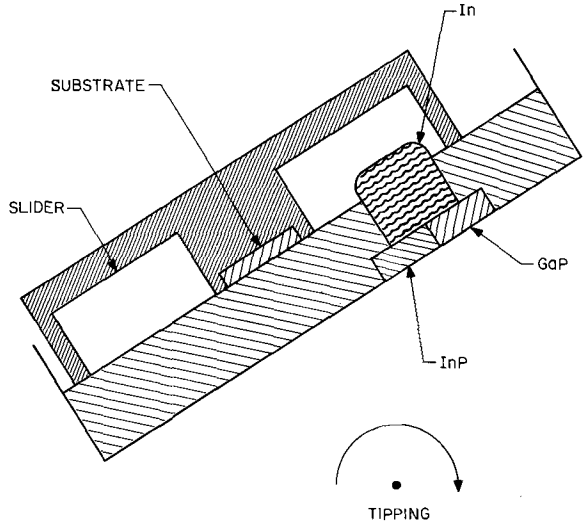

Fig. 1. Liquid phase epitaxial growth vessel

Key words: diffusion, doping, efficiency-electroluminescent, electroluminescence, indium-gallium-phosphide, liquid phase epitaxy, liquidus isotherms, p-n junctions, solidus isotherms, ternary.

that had gone into solution. The liquidus point for the In-P binary system was obtained by using an InP-In mixture containing more than enough InP to saturate the liquid with P. From the weight loss of InP, the atom fraction of P in the binary liquid at 850°C was found to be $X_P = 0.085$.

In determining ternary liquidus points, the amount of InP used was small enough to dissolve completely into the solution, regardless of the initial amount of GaP. (This indicates that the dissolution rate of InP in molten In is so much greater than the rate for GaP that all the InP dissolves before any appreciable amount of GaP does. This kinetic difference, which makes it convenient to use the present method for the liquidus determination, may be due to the lower melting point of InP compared to that of GaP). When the initial amount of GaP exceeded the quantity required to saturate the melt formed by dissolution of the InP, the difference in weight of the GaP before and after equilibration could be used, together with the initial weights of InP and In, to calculate the values of X_{Ga} and X_P for the liquidus composition.

Figure 2 gives the experimental liquidus data at 850°C. For low X_{Ga} and high X_P the error involved in estimating X_{Ga} was large. This was due to the fact that an $In_{(1-x)}Ga_xP$ layer formed on the surface of the GaP source during equilibration. The thickness of such a layer became quite large for high X_P. Since this layer had to be removed in order to obtain the net weight loss of the GaP source, error was introduced by the etching process.

Composition and thickness of the LPE layers.—For the solid ternary deposition it was found that when the total weight of GaP and InP in the source was held constant at 0.14 times the weight of the indium, the mole fraction of InP in the source determined the composition of the epitaxial deposit. An electron beam microprobe was used to measure the K_α and L_α line intensities and thereby deduce the $In_{(1-x)}Ga_xP$ composition in the epitaxial layer (1). Such measurements indicated that the mole fraction x in the deposit was equal, to within 10%, to x_c, the mole fraction of GaP used in the source, for the first and second runs on each charge. This was valid for the range of solid compositions $0.4 < x < 0.8$ investigated. For example, a source with $x = 0.6$ gave rise to a ternary deposit that varied in composition from $x = 0.66$ at 875°C to $x = 0.58$ at 800°C. Figure 3 gives a plot of composition in this deposit as a function of distance away from the substrate. The shift of composition toward InP as the growth temperature decreases is evident. The use of the slider in the growth process allowed the deposition to be terminated at a specific temperature, typically 800°C. This procedure was followed for the example given in Fig. 3. However, if during the tipping-off process a residue of the melt remained on the surface of the substrate, this residue continued to deposit material, of diminishing thickness, down to room temperature. The composition of the ternary that deposited out of the residue varied more rapidly as a function of distance than indicated in Fig. 3 and approached 100% InP.

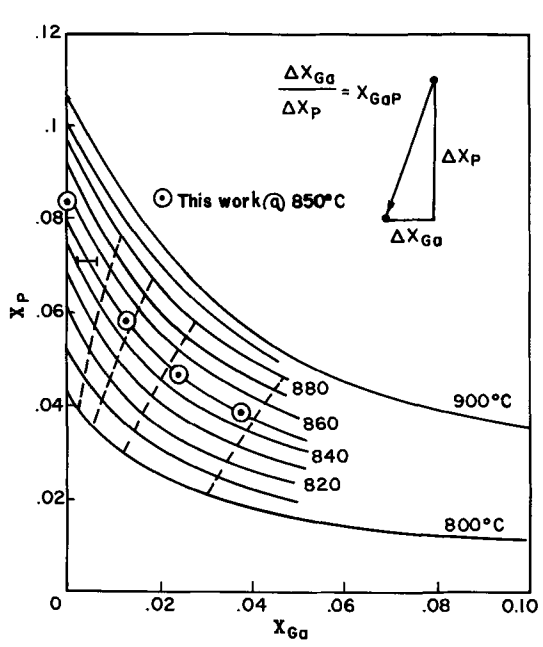

Fig. 2. Liquidus isotherms for the In-Ga-P system, wherein $X_{In} + X_{Ga} + X_P = 1$. The dashed lines give the change in composition of a melt as it is cooled. The experimental error is almost equal to the extent of the circle around each point.

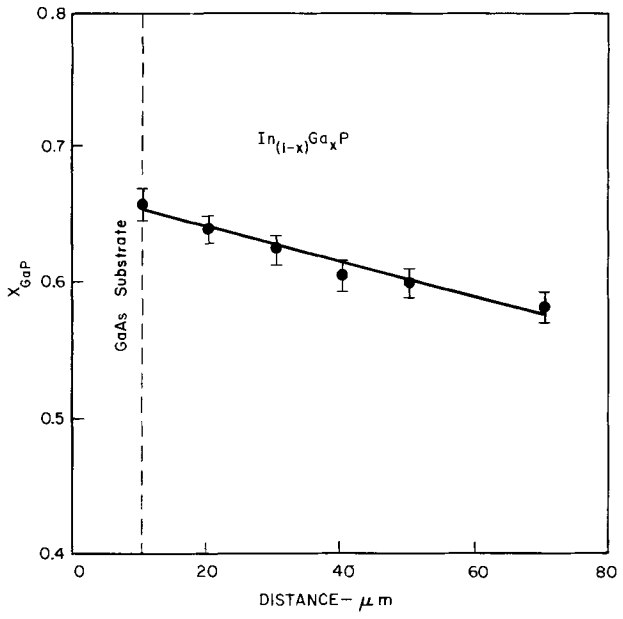

Fig. 3. Composition of LPE deposit as a function of distance away from the substrate.

Subsequent runs on the same charge led to a shift in composition of the LPE layer toward GaP (4). For example, a particular charge resulted in the deposition of $In_{0.47}Ga_{0.53}P$, $In_{0.42}Ga_{0.58}P$, and $In_{0.22}Ga_{0.78}P$ at the completion of the first, second, and third runs, respectively. The final temperature of deposition in each run of the sequence was 850°C.

In the direct bandgap $In_{(1-x)}Ga_xP$, as in any other direct bandgap semiconductor, in order to obtain efficient electroluminescence it is necessary to control accurately the depth of the p-n junction. This involves a compromise between the distance allowed the minority carriers to recombine radiatively, which is of the order of a diffusion length, and the resulting strong optical absorption suffered by the near band-edge emission. In the case of double epitaxial growth of the p-n junction the thickness of the LPE p-layer and thus the junction depth was controlled by adjusting the temperature interval ΔT over which growth took place. Figure 4 shows the thickness of the p-layer, grown in the neighborhood of 800°C, as a function of ΔT. Inspection revealed that deposition took place not only on the substrate but also on all of the external surface of the In-Ga-P melt, thus forming a right circular cylinder whose height and diameter were 0.5 and 0.64 cm, respectively. The weight of the indium charge, resulting in the deposition shown in Fig. 4, was 1.1g. Therefore, if the average thickness of the deposit on the external surface of the melt had the values shown in Fig. 4, then the rate of deposition at 800°C would be 5-7.5 x 10^{-5} cm^3, per gram of charge, per °C. Although a separate study was not made for n-type layers, it was found that in general the rate of deposition of n-doped material was similar to that described above for p-material.

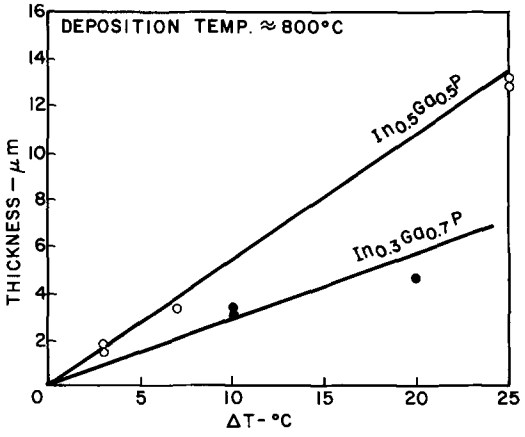

Fig. 4. Thickness of LPE deposit at 800°C as a function of cooling interval for two compositions of $In_{(1-x)}Ga_xP$.

Impurity segregation and diffusion.—For diffused structures, the depth of junction could be controlled by adjusting the diffusion coefficient and the diffusion time. The doping concentration in the host n-LPE layer is $\approx 5 \times 10^{17}$ cm^{-3}. Hence, the p-n junction occurs at a point where $N_{Zn} \approx 5 \times 10^{17}$ cm^{-3}. The junction depth (d) in a number of slices diffused at 700°C for different lengths of time (t) was measured by angle lapping a portion of each slice and etching in a 1:1 mixture of HF and H_2O_2, in the presence of strong light, to reveal the junction. Values of the diffusion coefficient (D) for Zn were then calculated from the relationship $D = d^2/4t$. This expression assumes that D is independent of concentration, so that the diffusing species exhibits an error function distribution. Although the diffusion of Zn in such compounds as GaAs and InSb is known to be strongly concentration dependent, in the absence of more detailed data for the ternary alloys the values of D obtained by using the simple relationship should be useful. These values, measured at 700°C, are shown in Fig. 5 as a function of the ternary composition. As the composition changes from $In_{0.5}Ga_{0.5}P$ to $In_{0.3}Ga_{0.7}P$, the diffusion coefficient of Zn decreases from $\approx 10^{-10}$ cm^2/sec to $\approx 4 \times 10^{-11}$ cm^2/sec. The decrease in diffusion constant as the composition shifts toward GaP is qualitatively consistent with the lower diffusion coefficient of Zn in GaP,

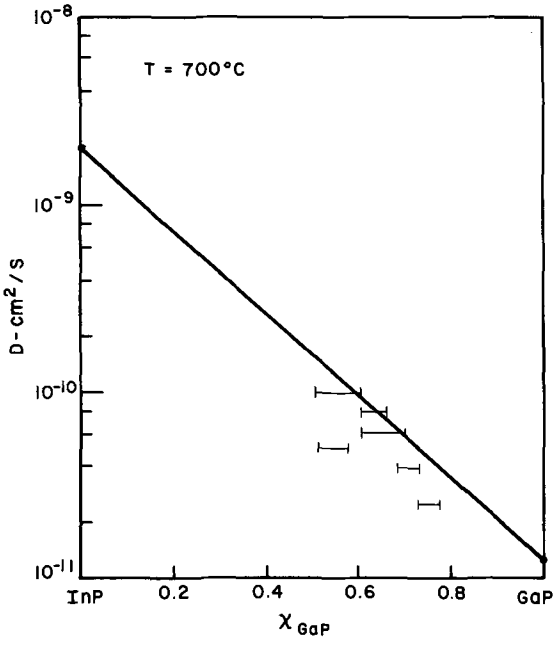

Fig. 5. Diffusion coefficient of Zn into various compositions of $In_{(1-x)}Ga_xP$. The diffusion temperature is 700°C, and the Zn concentration at the p-n junction is $\approx 5 \times 10^{17}$ cm^{-3}.

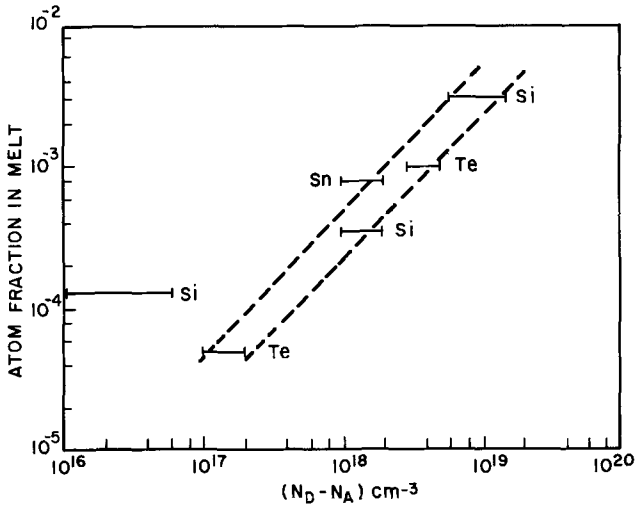

Fig. 6. Net ionized donor concentration ($N_D - N_A$) as a function of doping level in the melt.

$\approx 1.3 \times 10^{-11}$ cm^2/sec, as compared to that in InP, $\approx 2 \times 10^{-9}$ cm^2/sec at 700°C for similar Zn concentrations (6, 7).

Among the n-type dopants investigated, namely Sn, Si, Pb, Se, and Te, the best luminescent efficiencies were obtained by using Se and Te. The net ionized impurity concentration ($N_D - N_A$) in the LPE n-layer is given in Fig. 6 as a function of the atom fraction of dopant, Δ, in the melt. This impurity concentration can be represented by the approximate relation $(N_D - N_A) \approx 3 \times 10^{21}\Delta$ cm^{-3}. However, as seen in Fig. 6, for atom fractions of Si in the melt of about 2×10^{-4}, ($N_D - N_A$) was much smaller than the value indicated by this relation, and varied by over an order of magnitude along the surface of the deposit. This could be explained by a model whereby Si behaves as an amphoteric dopant, introducing a background of $\approx 5 \times 10^{17}$ acceptors per cm^3, for the doping level used. Therefore, for $\Delta < 2 \times 10^{-4}$, critical compensation would result (4). The lowest ionized net impurity concentration of undoped material was in the 5×10^{15} cm^{-3} range.

First-order Calculations

Liquidus and solidus isotherms in the In-Ga-P system.—The equations governing the equilibrium between the liquid and solid in the In-Ga-P system can be written in the simplified and approximate form (3)

$$K_{InP}X_{InP} = \gamma_P X_{In} X_P \quad [1]$$

$$K_{GaP}X_{GaP} = \gamma_P X_{Ga} X_P \quad [2]$$

for the liquid

$$X_{In} + X_{Ga} + X_P = 1 \quad [3]$$

and for the solid

$$X_{InP} + X_{GaP} = 1 \quad [4]$$

where K_{InP} and K_{GaP} are the proportionality constants governing the equilibrium between solid and liquid, γ_P is the activity coefficient for P, X_i is the atom fraction of species i in the liquid, and X_{ij} is the mole fraction of species ij in the solid. The activity coefficients of the various components in [1] and [2] were all set equal to unity, except γ_P.[1]

Equations [1]-[4] can be solved to obtain an equation for the liquidus composition

[1] The assumption that $\gamma_{In} = \gamma_{Ga} = 1$ is not strictly correct. Since $X_{In} \approx 1$, it is probably safe to assume $\gamma_{In} \approx 1$. However, the In-Ga binary data of Macur *et al.* (8) indicate that $\gamma_{Ga} \approx 1.2$, when $X_{Ga} << 1$. The fact that in the present work good agreement between experiment and calculation can be obtained by assuming all activity coefficients to be unity, except γ_P, is somewhat surprising. It is possible that a cancellation process takes place in Eq. [1] and [2] which reduces the error involved in making this assumption.

$$X_{In}^2 + X_{In}\left[-1 + X_{Ga}\left(1 + \frac{K_{InP}}{K_{GaP}}\right)\right] + \frac{K_{InP}}{\gamma_P} - X_{Ga}\frac{K_{InP}}{K_{GaP}}(1 - X_{Ga}) = 0 \quad [5]$$

The activity coefficient of P in the In-Ga-P system at 900°C has been measured by Panish (3) and is given by the empirical relations

$$\gamma_P = \exp(-2.15X_{Ga}^{1/2}) \quad [6]$$

for $0 < X_{Ga} < 0.1$ and

$$\gamma_P = 0.61 \exp(-0.645X_{Ga}^{1/2}) \quad [7]$$

for $0.1 < X_{Ga} < 1.0$.

From the binary data of Panish and Arthur (9), the values of K_{InP} at 900°, 850°, and 800°C are 0.095, 0.07, and 0.04, respectively. From the binary results of Thurmond (10, 7), the values of K_{GaP} at 900°, 850°, and 800°C are 2.16×10^{-3}, 1.25×10^{-3}, and 6.2×10^{-4}, respectively. From these values and (5), liquidus isotherms can be calculated. The calculated isotherms are shown in Fig. 2 for the temperature range 900°-800°C, along with the experimental liquidus points for 850°C. The agreement between the calculated curve at 850°C and the experimental results is adequate.

Once the liquidus composition has been calculated, the corresponding solid composition can be obtained through the use of either [1] or [2], in conjunction with [4]. For the purpose of the present work, the relevant curves are those of X_{GaP} as a function of X_P. These calculated curves are shown in Fig. 7 for 800°-900°C.

Change in composition.—It was observed experimentally (Fig. 3) that there was a shift in composition toward InP as the temperature of deposition decreased (1). This shift in composition can be explained on the basis of the liquidus and solidus isotherms of Fig. 2 and 7. To deduce the shift a graphical method of analysis is used. For example, let the starting temperature be 880°C, with $X_P = 0.067$. From Fig. 2 and 7, respectively, one obtains $X_{Ga} = 0.0185$ and $X_{GaP} = 0.5$. As the temperature is reduced to 870°C, the point in the liquidus curve of Fig. 2 has to move in a direction determined by the relation $X_{GaP} = (\Delta X_{Ga}/\Delta X_P)$. The new liquidus equilibrium point at 870°C is established at $X_P = 0.0635$ and $X_{Ga} = 0.0168$. The new solidus composition in equilibrium with this solution is $X_{GaP} = 0.498$, obtained from Fig. 7. This new GaP concentration establishes the slope in the liquidus diagram when the temperature is lowered from 870° to 860°C. It is seen from Fig. 2 and 7 that as the temperature is progressively lowered, the solidus fraction X_{GaP} gradually decreases. This is due to the depletion of the relatively small Ga content initially found in the solution.

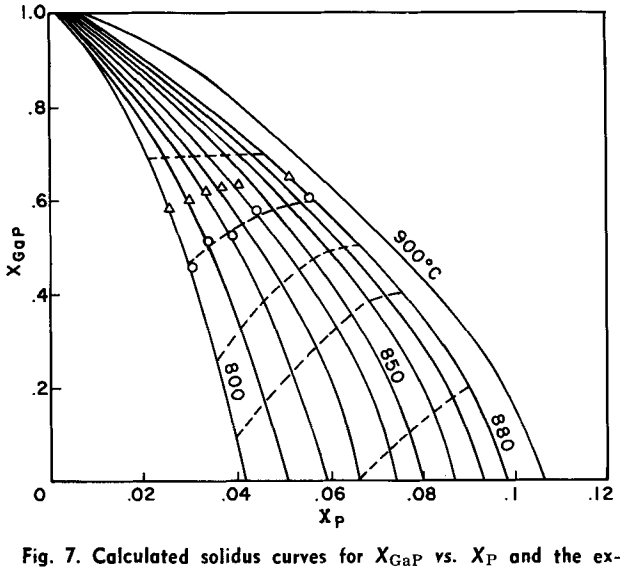

Fig. 7. Calculated solidus curves for X_{GaP} vs. X_P and the experimental curve obtained by cooling at 875°C; the dashed lines give the change in composition of the deposit as the temperature is lowered.

A series of calculated deposition loci are shown on the liquidus and solidus curves of Fig. 2 and 7. It is seen that the compositional variation with temperature is severe at low temperatures and InP-rich compositions. As long as $X_{GaP} > 0.4$, and the minimum deposition temperature is above 820°C, the change in composition with temperature is not very large. To compare the theoretically deduced deposition loci with experiments the liquidus isotherms of Fig. 2 are used in conjunction with Eq. [8] to replot the data of Fig. 3 in terms of X_{GaP} and temperature. These data points are given in Fig. 7 and are in agreement with the graphically deduced curves. For a different charge that gave a slightly higher initial GaP concentration of $x = 0.65$ at 880°C, the experimentally observed variation of x is depicted in Fig. 7 as a function of temperature. Although no theoretically deduced deposition curve is given for this initial composition, it is evident from Fig. 7 that the experimental data are in general qualitative agreement with other deposition loci.

Rate of deposition.—The rate of deposition of $In_{(1-x)}Ga_xP$ as a function of temperature can be determined from the results of Fig. 2 and 7. When the molecular weights are taken into account, the rates of deposition by weight of GaP and InP, as functions of temperature T, can be evaluated in terms of $\partial X_P/\partial T$, the temperature rate of change of the phosphorus fraction in the melt for a particular temperature and composition. For a density of ternary that interpolates linearly between those of InP and GaP, the volume rate of deposition is

$$\frac{\partial V/\partial T}{W_{In}} = 0.266\frac{(1 - 0.31X_{GaP})}{(1 - 0.14X_{GaP})}\frac{\partial X_P}{\partial T}\frac{cm^3}{g°C} \quad [8]$$

From [8] the rate of deposition of $In_{0.3}Ga_{0.7}P$ at 800°C is 6.5×10^{-5} cm³/g-°C and increases to 9×10^{-5} cm³/g-°C for $In_{0.6}Ga_{0.4}P$ at the same temperature. These rates are in fair agreement with the experimentally observed rates of 5-7.5 x 10^{-5} cm³/g-°C at these compositions and temperatures. Similarly, [8] gives rates of deposition of 1.2×10^{-5} and 2.5×10^{-4} cm³/g-°C for GaP and InP, respectively, at 800°C. Obviously, all rates of deposition decrease below 800°C because of the depletion of phosphorus in the melt.

Discussion

The mechanics of the growth process can be understood on the following basis: If the source were all InP, then at 900°C an amount of InP equal to 0.14 times the In weight would be required to saturate the solution with P, corresponding to $X_P = 0.106$ given by the liquidus curve of Fig. 2. The deposit obtained would be InP. As the amount of InP in the source is reduced and GaP is added to keep the total weight constant, the X_P derived from InP is not enough to saturate the liquid. In this case all the InP first dissolves and then enough GaP dissolves to produce a saturated solution of In + Ga + P. Equilibrium is achieved between this solution and a thin layer of $In_{(1-x)}Ga_xP$ which is observed to form on the GaP source. Upon cooling the solution, a ternary is deposited whose composition is predetermined by X_P, and therefore by the mole fraction of InP in the source. Thus, the atom fraction of phosphorus, X_P, acts as the controlling parameter in the growth process. Therefore the layer composition is actually fixed by the ratio of initial weights of InP in the source and the In. The weight of GaP in the source does not affect the layer composition as long as the

GaP available exceeds the amount required to saturate the In-Ga-P liquid.

Additional experimental observations concerning the growth process can now be explained. For instance, the shift in composition toward GaP during successive runs on the same charge is due to a reduction of X_P in the melt, which as seen from Fig. 7 increases X_{GaP} for a fixed temperature of depositions. The X_P reduction is due to two factors: (*i*) the depletion of the phosphorus during the growth process, and (*ii*) loss of phosphorus to the gas stream in the open-tube system.

Conclusion

$In_{(1-x)}Ga_xP$ was grown in the range $0.4 < x < 0.8$ by LPE on the Ga face of <111> oriented GaAs. The p-n junctions were made either by Zn diffusion or by LPE growth of a p-layer on top of the n-layer. The results of first-order calculations of the solidus and liquidus curves are in general agreement with experimental observations. It is also possible to predict the shift in composition of the grown layer as the temperature of deposition is lowered. Finally, the calculated rate of deposition of $In_{(1-x)}Ga_xP$ is in fair agreement with the experimentally observed values.

Acknowledgment

The author is indebted to M. B. Panish for many useful discussions, to C. K. Kim for microprobe analysis of ternary composition, and D. L. Van Haren for experimental assistance in this work. The author is also grateful to A. J. Strauss for many useful suggestions.

Manuscript submitted Sept. 14, 1970; revised manuscript received April 16, 1971.

Any discussion of this paper will appear in a Discussion Section to be published in the June 1972 JOURNAL.

REFERENCES

1. B. W. Hakki, A. Jayaraman, and C. K. Kim, 10th International Conference on Physics of Semiconductors, Cambridge, p. 566 (1970); and *J. Appl. Phys.*, **41**, 5291 (1970).
2. M. R. Lorenz, W. Reuter, W. P. Dumke, R. J. Chicotka, G. D. Pettit, and J. M. Woodall, *Appl. Phys. Letters*, **13**, 421 (1968).
3. M. B. Panish, *J. Chem. Thermodynamics*, **2**, 319 (1970).
4. B. W. Hakki, Paper No. 74 presented at the Los Angeles Meeting of the Electrochemical Society, May 10-15, 1970; *This Journal*, **117**, 94C (1970).
5. A. M. White, E. W. Williams, and P. Porteous, *Phys. Stat. Solidi*, **30**, K125 (1968).
6. H. W. Allison, *J. Appl. Phys.*, **34**, 231 (1963).
7. L. L. Chang and H. C. Casey, Jr., *Solid State Electronics*, **7**, 481 (1964).
8. G. J. Macur, R. K. Edwards, and P. G. Wahlbeck, *J. Phys. Chem.*, **72**, 1047 (1968).
9. M. B. Panish and J. R. Arthur, *J. Chem. Thermodynamics*, **2**, 299 (1970).
10. C. D. Thurmond, *J. Phys. Chem. Solids*, **26**, 785 (1965).

Mass Spectrometric Studies of Vapor Phase Crystal Growth

I. $GaAs_xP_{1-x}$ System ($0 \leq x \leq 1$)

Vladimir S. Ban

RCA Laboratories, Princeton, New Jersey 08540

ABSTRACT

A mass spectrometer has been coupled to an open tube vapor phase crystal growth apparatus in order to study vapor phase processes leading to the deposition of $GaAs_xP_{1-x}$ crystals. Examination of the HCl transport of gallium showed that $GaCl_{(g)}$ was the main transporting species. It was found that vapor resulting from the thermal decomposition of AsH_3, PH_3, and PH_3-AsH_3 mixtures is very complex; dimers and tetramers of As and P, as well as various mixed species of the type As_xP_y ($x + y = 2$ or 4), were present in the vapor phase. The reaction governing the deposition of $GaAs_xP_{1-x}$ crystals was found to be

$$GaCl_{(g)} + \frac{1}{z}M_{z(g)} + \frac{1}{2}H_{2(g)} \rightarrow GaM_{(s)} + HCl_{(g)}$$

where M = As or P. It was established that the mixed As_xP_y species also readily participate in the deposition reaction. Significant deviations from thermochemical equilibrium were detected in the deposition system. The causes of these deviations and their influence on the deposition process are discussed.

Open-tube vapor transport is now a widely used method for the preparation of epitaxial layers of various III-V compounds and alloys. However, despite the significant practical success of this method, understanding of the fundamental chemistry of the growth process is still incomplete. In order to gain such understanding, it is necessary to specifiy the species present in the vapor phase qualitatively and quantitatively (*i.e.* to find the composition of the vapor phase); to determine the dependence of the vapor composition on variables such as temperature, flow rates, and input concentrations of reacting gases; and thereby to identify the chemical reactions occurring in the vapor phase.

Key words: mass spectrometry, vapor phase deposition, $GaAs_xP_{1-x}$ alloys, epitaxial growth, chemical kinetics, thermodynamics.

In recent years several studies have discussed vapor phase processes leading to the deposition of GaAs (1-5). In these articles the vapor phase was treated as a multicomponent system for which the conditions of thermodynamic equilibrium were calculated. Such treatment should, in principle, provide the required information about vapor composition and reactions involving the vapor phase. However, the thermodynamic calculations thus carried out necessarily required several basic assumptions. One had to assume that chemical equilibrium is established throughout the system (*i.e.* various kinetic effects are considered negligible); that all thermochemical data used in the calculations are correct; and that the assumed reactions indeed occur in the system.

The validity of these assumptions can be contested for several reasons. The open-tube growth apparatus is a dynamic system in which steady-state conditions possibly deviating from equilibrium conditions are to be expected. Further, high-temperature thermochemical data are frequently unreliable and contradictory. Finally, reactions have been assumed knowing only the input substances and the final product of the growth process. The experimental evidence which has been offered so far is based on the weight gain or the weight loss of the product and input substances, respectively. Such evidence can yield only indirect information about vapor phase reactions.

In view of the above, we decided to undertake a study which would give more direct information about the processes occurring in the vapor phase. For this purpose we coupled a mass spectrometer to a vapor phase crystal growth apparatus and studied the vapor phase under various experimental conditions. With this experimental setup it was possible to determine the composition of the vapor phase and its dependence on temperature and flow rates in the system, and also to identify reactions occurring in the vapor phase.

The purpose of this paper is to present and discuss the results of these mass spectrometric studies of the vapor phase processes leading to the deposition of $GaAs_xP_{1-x}$ ($0 \leq x \leq 1$) crystals in growth systems using AsH_3 and PH_3 as sources of pnictide elements. In particular, we shall discuss the following topics:

(*a*) HCl transport of gallium;
(*b*) Thermal decomposition of arsine, phosphine, and arsine-phosphine mixtures;
(c) Reactions responsible for the deposition of the $GaAs_xP_{1-x}$ crystals; and
(*d*) Deviations from chemical equilibrium occurring in the system and reasons for these deviations.

Experimental

The essential parts of our experimental set-up, schematically shown in Fig. 1, were a Bendix MA-1 time-of-flight mass spectrometer and an open-tube vapor growth system similar to the one first described by Tietjen and Amick (6).

Sampling of the vapor phase was done by means of a quartz capillary, which was connected to the mass spectrometer by a 20 mm ID quartz tube. In this manner a pressure reduction from 1 atm (the pressure in the growth tube) to 10^{-5} Torr or less (the pressure in the mass spectrometer) was accomplished. The diameter of the capillary was adjusted to give a maximum conductance compatible with the pumping speed of the mass spectrometer pumps.

This adjustment was made by reducing the conductance of a 1 cm long, 0.02 mm ID capillary by the insertion of a quartz fiber of a proper diameter into the capillary. The intake of the capillary was positioned directly in the growth tube. The distance between this intake and the mass spectrometer ion source was about 12 cm. The capillary was maintained at the temperature of the sampled gas.

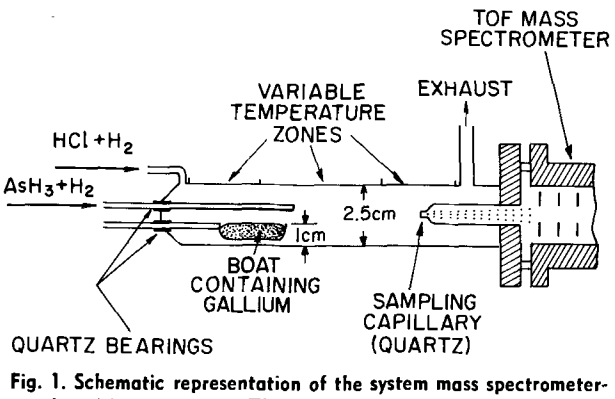

Fig. 1. Schematic representation of the system mass spectrometer-vapor deposition apparatus. The position of the boat and the AsH_3 inlet is variable.

In general, a capillary inlet system can introduce several sampling problems. The conductance of a capillary for a given gas is a function of the molecular weight and temperature of the gas. This can lead to a mass discrimination effect, *i.e.* the ratio of partial pressures of gases with different molecular weights is not the same on both sides of the capillary. The magnitude of this effect differs from system to system. We have calibrated our system by analyzing several gaseous mixtures of known composition (*e.g.* 1:1 AsH_3-PH_3 mixture, air). We found that this effect was generally small (<10%). Nevertheless, the correction factors were determined and applied in the determination of abundances of various gaseous species in the AsH_3-PH_3 mixtures.

Another potential source of trouble is the interaction of a sampled gas with the capillary walls. However, in our case these walls were made of the same material as the growth tube and maintained at the same temperature. Therefore no reaction different from those occurring in the growth tube would occur in the capillary.

The molecular beam, collimated by passing through the capillary, entered the ion source of the mass spectrometer. Since a mean free path at the pressure of 10^{-5} Torr is much longer than the distance between the capillary and the ion source, most molecules arrived at the source region without undergoing any interactions after leaving the capillary. We therefore believe that the sample introduced into the mass spectrometer is representative of the vapor phase in the growth tube.

There are three different zones in the vapor growth system. In the first zone ($T \approx 750$°C) HCl reacts with liquid gallium to form gaseous gallium chloride. In the second zone ($T \approx 850$°C) thermal decomposition of arsine and phosphine takes place. In the third zone ($T \approx 725$°C), gallium chloride reacts with the vapor species containing group V elements, and the deposition of $GaAs_xP_{1-x}$ crystals occurs. The whole process has been described in more detail in Ref. (6).

By varying the temperature profile and by moving the gallium-containing quartz boat or the arsine (or phosphine) inlet tube along the growth tube, we could simulate, in the vicinity of the sampling capillary, conditions characteristic of any of the three zones. This permitted us to study processes occurring in all three zones.

Temperature measurements were made with a thermocouple placed directly into the gas stream. It was found that at flow rates used in our experiments, the gas reached thermal equilibrium in 2 to 3 sec. Also, when varying the temperature profile, the temperature situation was always checked with an internal thermocouple before the mass spectrometric experiments.

By means of flow meters associated with the growth system we could vary the concentrations and flow rates of the input gases and consequently study the vapor phase processes under a variety of conditions. The mass spectrometer reacted almost instantaneously to changes in the growth tube.

We also grew several GaAs crystals in order to demonstrate that the conditions in our growth system were similar to the conditions normally present in open-tube growth systems. The crystallinity and the electrical properties of these crystals were similar to those of crystals prepared in standard systems, thus providing strong evidence that the conditions were also similar.

Results

HCl transport of gallium.—In our vapor growth system 1 liter/min of H_2 mixed with 3 to 5 cm^3/min of HCl is passed over the quartz boat containing liquid gallium at a temperature of about 750°C. The mass spectrometric results show that the following reaction

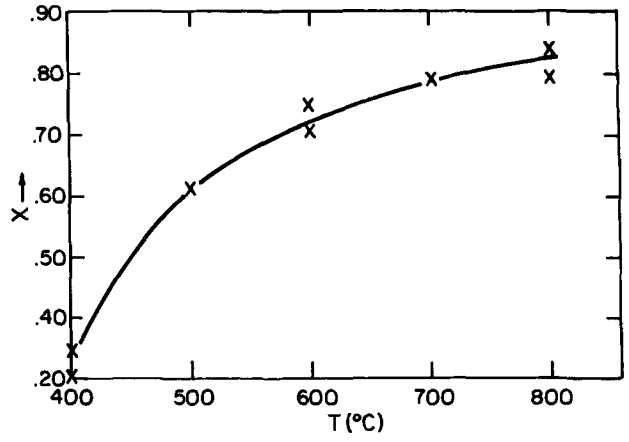

Fig. 2. Mole fraction (x) of HCl converted into GaCl at various temperatures (Reaction [1]). Pertinent parameters: flow rate = 1 liter/min, gas velocity = 5 cm/sec, Ga surface area = 20 cm^2, initial $P_{HCl} = 5.0 \times 10^{-3}$ atm.

occurs under these conditions

$$x\mathrm{Ga}_{(l)} + \mathrm{HCl}_{(g)} \rightarrow x\mathrm{GaCl}_{(g)} + (1 - x)\,\mathrm{HCl}_{(g)} + \frac{x}{2}\mathrm{H}_{2(g)} \quad [1]$$

where x = mole fraction of HCl reacting.

In all experiments, gallium monochloride was the only gallium species observed. The value of x was found by determining the ratio of the HCl signals with and without gallium in the system. Under typical growth conditions the value of x is about 0.80. The temperature dependence of x in the range of 400° to 800°C is shown in Fig. 2. In these experiments the initial partial pressure of HCl, P_{HCl}, was 5.0 x 10^{-3} atm. The flow rate was 1 liter/min, the gas velocity was 5 cm/sec, and about 20 cm^2 of Ga surface was exposed to the gas.

The dependence of x on flow rate of the H_2-HCl mixture over the gallium is shown in Fig. 3. In these experiments, the initial P_{HCl} was kept constant (*i.e.* 5.0 x 10^{-3} atm). A slightly larger gallium boat was used, so that 25 cm^2 of Ga surface was exposed. Gas velocities corresponding to flows of 1, 2, and 3 liters/min are 5, 10, and 15 cm/sec, respectively.

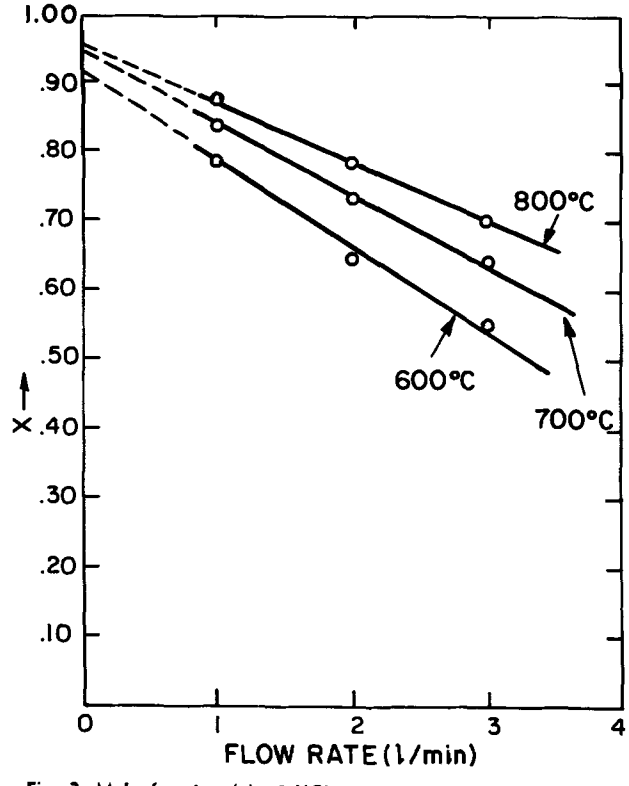

Fig. 3. Mole fraction (x) of HCl converted into GaCl (Reaction [1]) as a function of flow rate. Pertinent parameters: Ga surface area = 25 cm^2, initial $P_{HCl} = 5.0 \times 10^{-3}$ ohm.

Thermal decomposition of AsH_3,PH_3, and AsH_3-PH_3 mixtures.—The second zone in the growth apparatus is normally maintained at 850°C. In this zone 1.2 liter/min of H_2 mixed with 20 cm^3/min of AsH_3 (or PH_3) is introduced ($P_{AsH_3} = 1.6 \times 10^{-2}$ atm), and thermal decomposition of these gases takes place. The thermal decomposition can be described by the following equation

$$\mathrm{MH}_{3(g)} \rightarrow (1 - x)\,\mathrm{MH}_{3(g)} + (1 - \alpha)\frac{x}{4}\mathrm{M}_{4(g)} + \alpha\frac{x}{2}\mathrm{M}_{2(g)} + \frac{3}{2}x\mathrm{H}_{2(g)} \quad [2]$$

where $MH_3 = AsH_3$ or PH_3, $M_4 = As_4$ or P_4, $M_2 = As_2$ or P_2, x = mole fraction of MH_3 decomposing, and α = degree of dissociation of M_4 molecules. At T = 850°C the values of $x = 0.9$ and $\alpha = 0.50$ were obtained for the case of PH_3; in the case of AsH_3 the corresponding numbers were 0.99 and 0.45.

The mole fraction $(1 - x)$ of AsH_3 and PH_3 remaining undecomposed in the temperature interval from 400° to 850°C is graphically shown in Fig. 4.

We also studied the thermal decomposition of various AsH_3-PH_3 mixtures, ranging in composition from 10 to 80 volume per cent AsH_3. The initial total partial pressure of MH_3 gases was kept constant at 1.6 x 10^{-2} atm. A very complex vapor resulted from the decomposition of these mixtures. Besides the normally present As_4, As_2, P_4, and P_2 molecules, various mixed species of the type As_xP_y, where $x + y = 4$ or 2, were also present in amounts comparable to the amounts of nonmixed species. Relative abundances of various nonmixed and mixed species across the whole range of AsH_3-PH_3 mixtures are given in Fig. 5a and 5b, respectively. The trimeric molecules ($x + y = 3$) were also detected but only in relatively small amounts.

Deposition reactions.—Perhaps the most important part of our study was to properly identify the reactions governing the deposition of $GaAs_xP_{1-x}$ crystals. In order to collect the necessary data the temperature profile was adjusted in such a manner that the deposition took place several centimeters upstream from the sampling capillary. Several GaAs substrates normally used in the epitaxial growth process were positioned in the deposition zone, which was maintained at 680° to 720°C. The temperature of the capillary region was

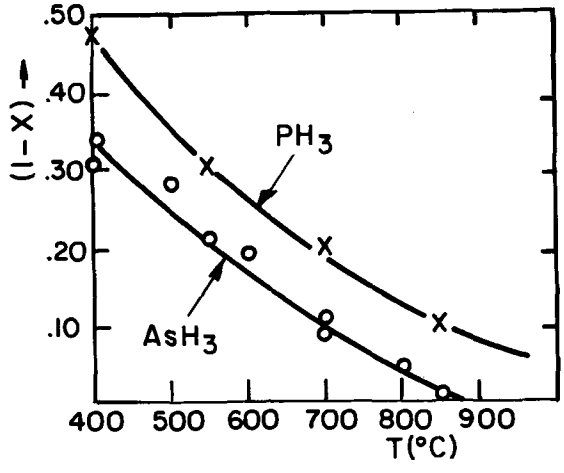

Fig. 4. Mole fraction (1 — x) of AsH_3 and PH_3 remaining undecomposed at various temperatures (Reaction [2]). Initial P_{AsH_3} or $P_{PH_3} = 1.6 \times 10^{-2}$ atm, flow rate = 1.2 liter/min.

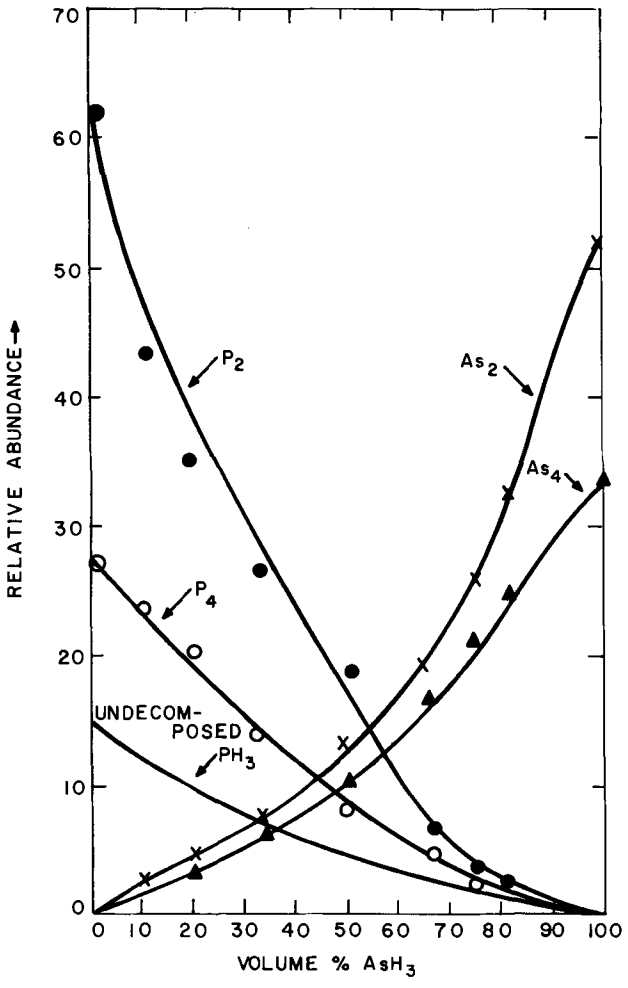

(a) Nonmixed species, *i.e.*, As_x and P_y

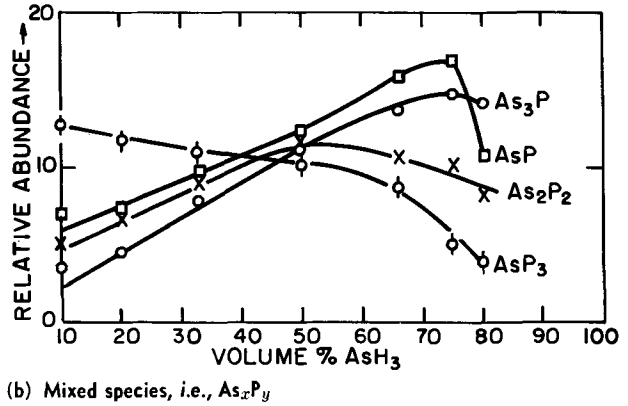

(b) Mixed species, *i.e.*, As_xP_y

Fig. 5. Relative abundances of vapor species resulting from the thermal decomposition of various PH_3-AsH_3 mixtures (initial $P_{AsH_3} + P_{PH_3} = 1.6 \times 10^{-2}$ atm, flow rate = 1.2 liter /min, $T = 850°C$).

somewhat higher in order to prevent clogging of the capillary.

With this arrangement we could identify the gaseous products of the reaction. Since the incoming gaseous reactants were known from our studies of the Ga transport and the thermal decomposition of MH_3 gases, and the solid products were also known, we were able to specify the deposition reaction completely. In the case of GaAs or GaP, the reaction was found to be

$$GaCl_{(g)} + \frac{1}{z}M_{z(g)} + \frac{1}{2}H_{2(g)} \rightleftarrows GaM_{(s)} + HCl_{(g)} \quad [3]$$

where M = As or P, and z = number of M atoms in the reacting molecule. This reaction is different from the one most frequently assumed to regulate the deposition of GaAs, *i.e.*

$$3GaCl_{(g)} + \frac{1}{2}As_{4(g)} \rightleftarrows 2GaAs_{(s)} + GaCl_{3(g)} \quad [4]$$

Gaseous $GaCl_3$ has not been detected in any of our experiments.

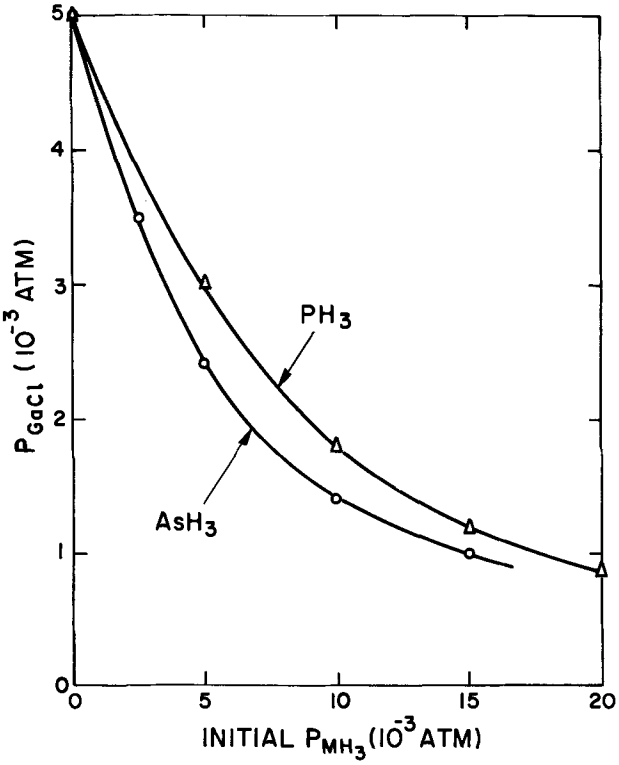

Fig. 6. Reduction of P_{GaCl} in the deposition reaction as a function of the initial P_{MH_3}. Temperature of reacting zone was 680° to 720°C, flow rate = 2.2 liter/min.

The consumption of $GaCl_{(g)}$ in reaction [3] increases as the initial partial pressure of MH_3 gases increases; this is graphically represented in Fig. 6, which shows the value of P_{GaCl} after the deposition at 680° to 720°C, for an initial $P_{GaCl} = 5 \times 10^{-3}$ atm and flow rate of 2.2 liters/min. Table I shows the decrease in percentages of various As_x, P_y, and As_xP_y species remaining after the deposition as a function of initial P_{GaCl}. It is important to note that all M-containing species, including the undecomposed fractions of AsH_3 and PH_3, react with $GaCl_{(g)}$ and thus contribute to the deposition of $GaAs_xP_{1-x}$. (Reaction of the AsP species could not be followed due to the interference of GaCl and AsP mass peaks.) In these experiments the initial values of partial pressures P_{AsH_3} and P_{PH_3} were 0.8×10^{-2} atm. Again, the deposition region was at 680° to 720°C, and the flow rate was 2.2 liters/min.

Table I. Percentages of various As- and P-containing vapor species remaining after $GaAs_xP_{1-x}$ deposition as a function of the initial P_{GaCl} (T = 680°-720°C, initial $P_{AsH_3} = P_{PH_3} = 0.8 \times 10^{-2}$ atm, flow rate = 2.2 liter/min)

Vapor species	Initial P_{GaCl} 10^{-3} atm			
	3.0	5.0	8.0	10.0
PAs_3	68	39	6	2
P_3As	73	44	12	8
As_4	73	44	8	6
P_2As_2	76	48	14	8
As_2	82	51	14	8
AsH_3	83	52	15	8
P_4	86	53	16	9
P_2	82	60	22	11
PH_3	90	70	31	16

Table II. Comparison of the observed partial pressures with the equilibrium partial pressures in the following systems (T = 850°C; P_{H_2} = 1 atm):
(A) Ga-HCl-H_2, (B) AsH_3-H_2, (C) PH_3-H_2, (D) AsH_3-PH_3-H_2

	Vapor species	$P_{(observed)}$ atm	$P_{(equilibrium)}$ atm	Initial pressure, atm
(A)	HCl	1.0×10^{-3}	5.0×10^{-5}	$P_{HCl} = 5.0 \times 10^{-3}$
	GaCl	4.0×10^{-3}	5.0×10^{-3}	
(B)	As_4	2.2×10^{-3}	3.9×10^{-3}	$P_{AsH_3} = 1.6 \times 10^{-2}$
	As_2	3.5×10^{-3}	7.0×10^{-4}	
	AsH_3	1.5×10^{-4}	1.0×10^{-8}	
(C)	P_4	1.8×10^{-3}	3.1×10^{-3}	$P_{PH_3} = 1.6 \times 10^{-2}$
	P_2	3.9×10^{-3}	1.7×10^{-3}	
	PH_3	1.1×10^{-3}	1.0×10^{-7}	
(D)	As_4, As_2	$\Sigma P_{As_x} = 0.7 \times 10^{-3}$	$\Sigma P_{As_x} = 2.0 \times 10^{-3}$	$P_{PH_3} = P_{AsH_3} = 0.8 \times 10^{-2}$
	PH_3, P_4, P_2	$\Sigma P_{P_x} = 0.7 \times 10^{-3}$	$\Sigma P_{P_x} = 2.5 \times 10^{-3}$	
	AsP, As_3P, As_2P_3, AsP_3	$\Sigma P_{As_xP_y} = 2.4 \times 10^{-3}$	Not considered in equilibrium calculations	

Discussion

Studies of Ga transport showed that the GaCl is practically the only gallium chloride present in the vapor phase. Furthermore, it was observed that the conversion of HCl is incomplete. The conversion efficiency drops with increase in flow rate and decrease in temperature. Extrapolating to zero flow rate, one finds that 96% of HCl would be converted at T = 800°C. Using these data one can calculate the equilibrium constant, and therefore the free energy of formation of GaCl at T = 1000°K: $\Delta F_f^\circ{}_{1000} = -30.8$ kcal/mole. This value is in good agreement with the value calculated from Kirwan's data (7): $\Delta F_f^\circ{}_{1000} = -31.7$ kcal/mole. These results suggest that $GaCl_{(g)}$ is the only stable chloride in the presence of liquid Ga at the temperatures maintained in the growth system. $GaCl_3$ could be present in negligible amounts only, since at partial pressures of reactants which exist in our system the following reactions would be shifted strongly to the product side (7)

$$GaCl_{3(g)} + 2Ga_{(l)} \rightarrow 3GaCl_{(g)} \quad [5]$$

$$GaCl_{3(g)} + H_{2(g)} \rightarrow GaCl_{(g)} + 2HCl_{(g)} \quad [6]$$

Reaction [6], however, could not be responsible for the HCl present in our system; the replacement of H_2 by He as the carrier gas did not appreciably change the conversion efficiency of HCl.

In Table II we compare partial pressures of species obtained from our mass spectrometric studies with partial pressures calculated by assuming that chemical equilibrium has been established in the systems considered. The equilibrium partial pressures have been calculated using thermochemical data collected in Ref. (7). The most obvious differences are the significantly higher partial pressures observed for HCl, AsH_3, and PH_3 as compared to values predicted by calculations. Also, the existence of the mixed As_xP_y species could not have been predicted by calculations because no thermochemical data for these species are available. The above results amply illustrate that the actual situation in the vapor phase can be significantly more complex than the models designed on assumptions mentioned in the beginning of this paper.

Our studies have found that the Reaction [3] governs the deposition of $GaAs_xP_{1-x}$ crystals. This is in agreement with the recently published results of Boucher and Hollan (5), who propose a similar reaction for the deposition of GaAs

$$2GaCl_{(g)} + \frac{1}{2}As_{4(g)} + H_{2(g)} \rightleftarrows 2GaAs_{(s)} + 2HCl_{(g)} \quad [7]$$

Our studies have further shown that the dimer molecules (As_2 and P_2), as well as the undecomposed MH_3 gases, react readily with $GaCl_{(g)}$. Thus they also contribute to the deposition of solid phases.

Using data given in Table I and Table II, one can assign the following individual contributions of various arsenic vapor species to GaAs deposition

$$GaCl_{(g)} + \frac{1}{4}As_{4(g)} + \frac{1}{2}H_{2(g)} \rightarrow GaAs_{(s)} + HCl_{(g)}$$

~55% of total GaAs deposited [8]

$$GaCl_{(g)} + \frac{1}{2}As_{2(g)} + \frac{1}{2}H_{2(g)} \rightarrow GaAs_{(s)} + HCl_{(g)}$$

~45% of total GaAs deposited [9]

$$GaCl_{(g)} + AsH_{3(g)} \rightarrow GaAs_{(s)} + H_{2(g)} + HCl_{(g)}$$

<1% of total GaAs deposited [10]

In the case of GaP, reactions equivalent to [9] and [10] play somewhat larger roles.

Table I indicates that all vapor species containing group V elements react readily with $GaCl_{(g)}$. There are, however, some differences in reactivity of these species. The reactivity is here defined as the percentage drop in concentration of any particular species with a given increase in initial P_{GaCl}. According to this definition, the reactivity of the various species follows this order

$$PAs_3 > P_3As \approx As_4 > P_2As_2 > As_2$$
$$\approx AsH_3 \approx P_4 > P_2 > PH_3$$

The difference in reactivity depends on P_{GaCl} and it diminishes at sufficiently high GaCl oversaturation. Under normal growth conditions when $P_{GaCl} = 3\text{-}5 \times 10^{-3}$ atm, the range of differences in reactivity of various species is quite significant (see Table I).

It has been observed previously in preparation of III-V alloys that the P/As ratio in the vapor phase is larger than the P/As ratio in the deposited solid phase (8); the lower reactivity of pure phosphorus species discovered in our experiments is in agreement with these observations.

Deviations from thermodynamic equilibrium in open-tube systems are the next topic of discussion. There are two main reasons for these deviations:

(*a*) Deviations can be caused by the relatively high flow rates which lead to flow patterns where some portion of the reactive gases does not come into contact with the desired surface; the dependence of HCl conversion efficiency on flow rates illustrates this point.

(*b*) Deviations can be caused by various kinetic effects, such as surface reactions and different reactivities of various vapor species; a discusison of these effects follows.

Several recent studies (5, 9, 10, 14) have shown that the growth rate of GaAs does not increase mono-

tonically with the decrease in temperature of the deposition zone, as one might expect from thermodynamic arguments. It was found experimentally that the growth rate peaks at a certain temperature which is dependent on the concentration of input substances, and then the growth rate decreases with the further decrease in temperature. The authors explain the observed effect by postulating the existence of a surface reaction on the substrate with an activation energy of about 40 kcal/mole. Thus the rate of this reaction decreases as the temperature is reduced.

Our data on the reactivity of various vapor species also indicate the importance of kinetics. If thermodynamics were the only factor governing the deposition process, the phosphorus species should have exhibited larger reactivity, since at 700°C GaP should be more readily deposited than GaAs. This follows from the fact that $\Delta F_f°_{900\text{-}1100}$ of GaP is more negative than $\Delta F_f°_{900\text{-}1100}$ of GaAs (7, 11, 12), and consequently, in this temperature range, the free energy change of Reaction [3] is more negative when GaP is deposited.

Our experimental data on reactivity of various vapor species contradict this thermodynamic reasoning, *i.e.* the pure arsenic and the mixed species react more readily than the pure phosphorus species. Following the analogy with the reduction of deposition rate of GaAs discussed elsewhere (5, 9, 10, 14), one might conclude that kinetic effects associated with the surface reaction play a dominant role at the temperature of our experiments (700°C). The consequence is a reduction in the rate of deposition of the phosphide component.

Another possible consequence of different reactivities of various As_xP_y vapor species is the preferential formation of certain solid phases in vapor grown $GaAs_xP_{1-x}$ alloys. It was reported (13) that during the preparation of graded $GaAs_xP_{1-x}$ layers ($x = 0.7\text{-}1.0$) compositions having As/P ratios of 7/1 and 6/2 were more readily formed than others, although the As/P ratio in the vapor phase was varied at a uniform rate. The authors proposed anion ordering as a cause of this phenomenon. Our data suggest that differences in reactivity of vapor species could also influence the composition of deposited layers. In the As-rich vapor the very reactive As_4 and As_3P species are highly abundant. The preferential reaction of $As_4 + As_3P$ (*i.e.* 7 As:1 P) and $As_3P + As_3P$ (*i.e.* 6 As:2 P) combinations would lead to the preferred As/P ratios of 7/1 and 6/2 observed in deposited layers.

The importance of some other kinetic effects in the deposition of III-V compounds has been demonstrated elsewhere, *e.g.* in Shaw's work regarding the influence of the substrate crystallographic orientation on the growth rate of epitaxially deposited GaAs layers (14).

The above discussion indicates that factors other than thermodynamic considerations significantly influence the deposition process, as well as the composition of the vapors in the analyzed systems.

Thermodynamic feasibility of a deposition process is a necessary but not a sufficient condition for successful crystal growth from the vapor phase. A neglect of kinetic factors leads to an oversimplified analysis of growth processes which does not properly describe the actual situation in an open tube crystal growth apparatus.

Conclusions

The main conclusions from this work are:

1. Gallium is transported only as GaCl, but the conversion of HCl into GaCl is incomplete in these growth systems.

2. The vapor resulting from the decomposition of AsH_3, PH_3, and PH_3-AsH_3 mixtures is very complex. Dimers and tetramers as well as various mixed species of the type As_xP_y ($x + y = 4$ or 2) are present in the vapor phase.

3. The reaction governing the deposition of GaAs, GaP, or $GaAs_xP_{1-x}$ crystals is of the type

$$GaCl_{(g)} + \frac{1}{z} M_{z(g)} + \frac{1}{2} H_{2(g)} \rightarrow GaM_{(s)} + HCl_{(g)}$$

4. All vapor species containing the group V elements contribute to the deposition of solid phases, although their reactivities differ somewhat.

5. Significant deviations from thermochemical equilibrium occur in vapor growth systems due to the high flow rates employed in these systems and due to the kinetic effects influencing the rate of deposition. These effects as well as the thermodynamics of the given system should be jointly considered when examining the feasibility of crystal growth from the vapor phase.

Acknowledgments

The author would like to thank A. E. White for excellent technical assistance in the construction and maintenance of the experimental apparatus. Frequent and useful discussions with J. J. Tietjen, D. Richman, R. E. Enstrom, and W. M. Yim are gratefully acknowledged.

Manuscript submitted Dec. 18, 1970; revised manuscript received *ca.* March 31, 1971.

Any discussion of this paper will appear in a Discussion Section to be published in the June 1972 JOURNAL.

REFERENCES

1. V. J. Silvestri and V. Lyons, *This Journal*, **109**, 963 (1962); and D. Richman, *RCA Rev.*, **4**, 596 (1963).
2. R. R. Fergusson and T. Gabor, *This Journal*, **111**, 585 (1964).
3. D. T. J. Hurle and J. B. Mullin, *Proc. Intern. Conf. Cryst. Growth*, p. 241, Birmingham, (1968).
4. H. Seki, K. Moriyama, I. Asakawa, and S. Horie, *Jap. J. Appl. Phys.*, **7**, 1324 (1968).
5. A. Boucher and L. Hollan, *This Journal*, **117**, 932 (1970).
6. J. J. Tietjen and J. A. Amick, *ibid.*, **113**, 724 (1966).
7. D. J. Kirwan, *ibid.*, **117**, 1572 (1970).
8. J. J. Tietjen, H. P. Maruska, and R. B. Clough, *ibid.*, **116**, 492 (1969).
9. D. W. Shaw, *ibid.*, **117**, 683 (1970).
10. W. F. Finch and E. W. Mehal, *ibid.*, **111**, 814 (1964).
11. C. D. Thurmond, *J. Phys. Chem. Solids*, **26**, 785 (1965).
12. L. I. Marina and A. Ya. Nashel'skii, *Russ. J. Phys. Chem.*, **43**, 963 (1969).
13. R. E. Ewing and D. K. Smith, *J. Appl. Phys.*, **39**, 5943 (1968).
14. D. W. Shaw, *This Journal*, **115**, 405 (1968).

Thermodynamic Analysis of the Open-Tube Chemical Vapor Transport of ZnO Using the Zn-H_2O Reaction

A. Reisman* and J. E. Landstein

IBM Thomas J. Watson Research Center, Yorktown Heights, New York 10598

ABSTRACT

A thermodynamic analysis of the open-tube chemical vapor transport of ZnO using the reaction of Zn and H_2O has been attempted, assuming a simple reaction model for Zn and H_2O vapor phase species. Based on this analysis, computer data have been derived to show variation in ZnO vapor phase content as a function of temperature, and reactor Zn and H_2O concentrations. The range of Zn reactor pressures examined was from 0.00260-0.00013 atm with H_2O pressures varying from 10^{-3}-10^{3} of these values over a temperature interval of 723°-1473°K. For the range of Zn pressures examined, H_2O pressures of 10-100X these values lead to vapor phase concentration curves most amenable to precise experimental control. At H_2O pressures 10X those of Zn pressures particularly, high-temperature plateaus develop where vapor phase Zn content is relatively temperature insensitive and which look promising as transient ZnO source sites. Similar plateaus do not exist at lower temperatures where they might have value as temperature insensitive deposition sites.

A variety of methods for the chemical vapor deposition of ZnO have been reported in the recent literature (1-7). A number of these were studied in the present work but were found deficient for a variety of reasons. In some instances deposition rates were too low. When O_2 was admixed with Zn vapor phase species deposition was too abrupt. For some reactions sources of high purity reactants were not available. In others failure to obtain epitaxy was observed. One reaction subsequently abandoned because of an inability on our part to understand and control severe attack of the quartz containers showed some promise, and is worth mentioning, namely the transport of ZnO by H_2, Eq. [1].

$$ZnO(s) + H_2(v) \leftrightarrows Zn(v) + H_2O(v) \qquad [1]$$

This reaction proceeds via a hot to cold process, and in theory can be modulated by transport with H_2-He mixtures and further modulated by injection of H_2O into the reaction zone where deposition is desired. Thus, via use of this injection technique, the normal hot to cold mode can be changed so that deposition may be effected at temperatures greater than that of the ZnO source. Unfortunately, severe attack of the quartz reaction tube and sample holder always occurred in the 600°-700°C region, with or without the use of water injection, necessitating constant equipment replacement. Further, the unavailability of ultra-high purity ZnO and the explosion hazard inherent in H_2 systems coupled with the "corrosion" phenomenon led us to seek another method, despite some limited success in obtaining epitaxy on sapphire basal plane substrates.

The technique to be described below employs a Zn source, He as a carrier gas, and water vapor as a reaction medium. In effect then, the reaction involved is the reverse of the reaction shown in Eq. [1]. Unexplainably, using this approach, Eq. [2], there is no evidence of attack

$$Zn(v) + H_2O(v) \xrightleftharpoons{\text{He carrier}} ZnO(s) + H_2(v) \qquad [2]$$

of the quartz reactor at any temperature or concentration studied, including the range of compositions studied in the H_2 transport experiments. In addition, considerable success (to be discussed in a different publication) in obtaining epitaxial layers of ZnO on insulating substrates has been obtained thus far. The present paper is concerned only with a thermodynamic analysis of the system being studied.

The reaction while basically hot to cold in nature can, if desired, be conducted in the fashion of a pyrolytic reduction with the deposition zone being hundreds of degrees higher than the temperatures of the Zn and H_2O sources.

Experimentally, He is transpired over a Zn bed at a defined temperature at which the vapor pressure of Zn is p'_{Zn}. Simultaneously, He is transpired over a water source where the vapor pressure of H_2O is p'_{H_2O}. The reactants are mixed at a temperature T at which point the reaction depicted in Eq. [2] ensues. Either of two options may then be exercised. The point of mixing may be employed as a transitory ZnO(s) source for a ZnO hot to cold transport down stream, or the substrates may be placed directly in the mixing region for deposition there.

Theoretical Analysis

The symbols to be used in the following discussion are defined in the List of Symbols.

The system contains the four components, Zn, H_2, O, and He coexisting isobarically (at 1 atm nominally) in two phases. Consequently, it possesses three degrees of freedom, *i.e.*, the temperature and two composition variables. Once three such quantities are specified, the system is uniquely defined. We can choose for the concentration variables the component mole ratios of Zn, X, and O, Y, introduced into the reactor portion of the system as defined by Eq. [3] and [4].[1]

$$X = \frac{P_{Zn}}{P_{He^t} + P_{Zn} + P_O} = \frac{p_{Zn} + p_{H_2}}{p_{He} + p_{Zn} + p_{H_2} + p_{H_2O} + p_{H_2}} \qquad [3]$$

$$Y = \frac{P_O}{P_{He^t} + P_{Zn} + P_O} = \frac{p_{H_2O} + p_{H_2}}{p_{He} + p_{Zn} + p_{H_2} + p_{H_2O} + p_{H_2}} \qquad [4]$$

The component partial pressures are of course conserved via the actual species partial pressures, p_x (for each mole of Zn or H_2O reacted, a mole of H_2 species is formed).

Since four vapor phase species are assumed present, solution of their partial pressures requires simul-

* Electrochemical Society Active Member.

Key words: ZnO vapor transport, thermodynamics, vapor transport.

[1] Appendix A presents the rationale for Eq. [3] and [4].

taneous solution of four independent equations. In addition to Eq. [3] and [4] those chosen are

$$K = \frac{p_{Zn}\, p_{H_2O}}{p_{H_2}} \quad [5]$$

and

$$1 = p_{H_2} + p_{He} + p_{Zn} + p_{H_2O} \quad [6]$$

Equation [5] is the equilibrium constant for Eq. [1] (the inverse of that for Eq. [2]), and Eq. [6] represents the nominal constant total pressure constraint in the open-tube system.

As a measure of the equilibrium state in the reactor as a function of T, X, and Y, we may use the quantity Z defined by

$$Z = \left(\frac{p_{Zn}}{p_{He}}\right)_{X,Y,T} \quad [7]$$

Z represents the vapor phase concentration of the component Zn present as the species Zn(v), referenced to the carrier gas and shows as a function of T the variation of Zn vapor phase content, since the He is always confined to the vapor phase. Z can be determined as a function of T for specified constant values of X and Y. For example, if we specify X and plot a family of curves, each curve being at this one value of X and a different value of Y, this family will comprise a set of univariant curves. By knowing the input value of Z, namely Z', we can for each curve determine the ZnO precipitation as a function of temperature by inspection. This matter is pursued further below.

Solutions for Species Partial Pressures

Employing Eq. [3], [4], [5], and [6], values for p_{Zn}, p_{H_2O}, p_{He}, and p_{H_2} at equilibrium can be obtained at specified values of X, Y, and T.[2] The temperature dependency of K referenced to a standard state of 1 atm is given by

$$\log K = \frac{-12{,}300}{T} + 9.179 \quad [8]$$

Specific data for calculating Eq. [8] were obtained from ref. (8) and (9). These are listed in Table I.

Equations [3] and [4] may be rewritten as Eq. [9] and [10] using Eq. [6]

$$X = \frac{p_{Zn} + p_{H_2}}{1 + p_{H_2}} \quad [9]$$

$$Y = \frac{p_{H_2O} + p_{H_2}}{1 + p_{H_2}} \quad [10]$$

Solving Eq. [9] and [10] for p_{H_2}, we obtain

$$p_{H_2} = \frac{p_{Zn} - X}{X - 1} \quad [11]$$

and

$$P_{H_2} = \frac{p_{H_2O} - Y}{Y - 1} \quad [12]$$

Therefore

$$\frac{p_{Zn} - X}{X - 1} = \frac{p_{H_2O} - Y}{Y - 1} \quad [13]$$

and

$$p_{H_2O} = \frac{(p_{Zn} - X)(Y - 1)}{(X - 1)} + Y \quad [14]$$

and

$$p_{Zn} = \frac{(p_{H_2O} - Y)(X - 1)}{(Y - 1)} + X \quad [15]$$

We can substitute Eq. [14] and [11] into Eq. [5] to obtain p_{Zn} as a function of X, Y, and K, Eq. [16]

$$p^2_{Zn}(Y - 1) + p_{Zn}(X - Y - K) + KX = 0 \quad [16]$$

From Eq. [15], [12], and [5], because of symmetry, we can write directly

$$p^2_{H_2O}(X - 1) + p_{H_2O}(Y - X - K) + KY = 0 \quad [17]$$

from which p_{H_2O} may be calculated. Once p_{Zn} and p_{H_2O} are known Eq. [5] may be used to define p_{H_2}, Eq. [18]

$$p_{H_2} = \frac{(\text{solution to Eq. [16]})(\text{solution to Eq. [17]})}{K} \quad [18]$$

Finally, p_{He} may be obtained from Eq. [6].

Species partial pressures were computer calculated as described below using the following values of X, Y, and T: $X = 2.60 \times 10^{-3}$ to $X = 0.13 \times 10^{-3}$ in steps of 0.13×10^{-3} (this coincides to $P_{Zn} = 2$ Torr down to $P_{Zn} = 0.1$ Torr in 0.1 Torr increments); $Y = 10^3X$ to $Y = 10^{-3}X$ in steps of $10X$ (the value $Y = 10^3X$ only provides physically meaningful results for certain values of X to be discussed below; $T = 723$°K to $T = 1473$°K in 50° steps.

Having calculated species partial pressures for all values of the variables, the data were used to machine plot two types of graphs. In the first of these the quantity Z, $(p_{Zn}/p_{He})_R$, which depicts the vapor phase concentration of the component Zn present as Zn species was plotted as a function of T. Thus, for each value of X, the value of Y at a fixed ratio to X was determined. This leads to seven families of curves, each family at constant R, *i.e.*, $R = 0.001$, 0.01, 0.1, 1, 10, 100, 1000. In the second type of graph, Z was calculated as a $f(T)$ for values of X which were kept constant while the seven values of Y relative to X were varied. This data was normalized to the value of Z for each curve at 1473°K, *i.e.*, $Z_T/Z_{1473°}$ was plotted as a $f(T)$ for each of the seven curves (where physically meaningful) in each family.

To obtain computer solutions to Eq. [16], [17], [18], and [6], given the several values of X, Y, and T (the latter being used to define the values of K), and to acquire the data for plotting described above, the program was written in Fortran IV. In the solutions of the quadratic equations for p_{Zn} and p_{H_2O}, one of the roots of each was found to be physically meaningless and was discarded. The values p_{H_2} and p_{He} were then calculated as were the ratios Z and $Z_T/Z_{1473°}$ used for plotting.

Plotting was accomplished using an IBM 1627 Plotter Compatible Software package which was called from the Fortran program. Through the use of the software package, plotter output was obtained concurrently on an IBM 1627 Plotter and on a Stromberg Carlson 4020 Computer Recorder.

The program was run on a System/360 Model 91 under OS taking 47 sec of CPU time which included not only all the calculations, but also the generation of all plots.

[2] Appendix B describes how a useful range of X and Y values can be defined from known experimental parameters.

Table I. Thermodynamic data used for calculating K

Species	Property	Ref. and Page No.	
ZnO(s)	$\Delta H_f°_{(298°K)} = -83.2$ kcal/mole	(8)	280
ZnO(s)	$S°_{298°K} = 10.4$ cal/deg mole	(8)	280
Zn(s)	$\Delta H°_{Sub\,1(298°K)} = 30.9$ kcal/mole	(8)	309
Zn(s)	$S°_{298°K} = 9.9$ cal/deg mole	(8)	280
Zn(v)	$S°_{298°K} = 38.45$ cal/deg mole	(9)	117
H_2O(v)	$\Delta H_f°_{(298°K)} = -57.8$ kcal/mole	(8)	248
H_2O(v)	$S°_{298°K} = 45.1$ cal/deg mole	(8)	248
H_2(v)	$S°_{298°K} = 31.2$ cal/deg mole	(8)	246

Discussion of Results

Figures 1-5 inclusive show the variation in Zn/He vapor phase concentration as a function of T(°K) under conditions of constant R. Because of the manner in which X and Y have been defined (see Appendix), they individually represent atmospheres of the components Zn and H_2O present in the reactor prior to reaction. While 20 curves are possible in each of the families shown in Fig. 1-5, not all of these have physical significance. Thus, in Fig. 1 (where $R = 0.001$)

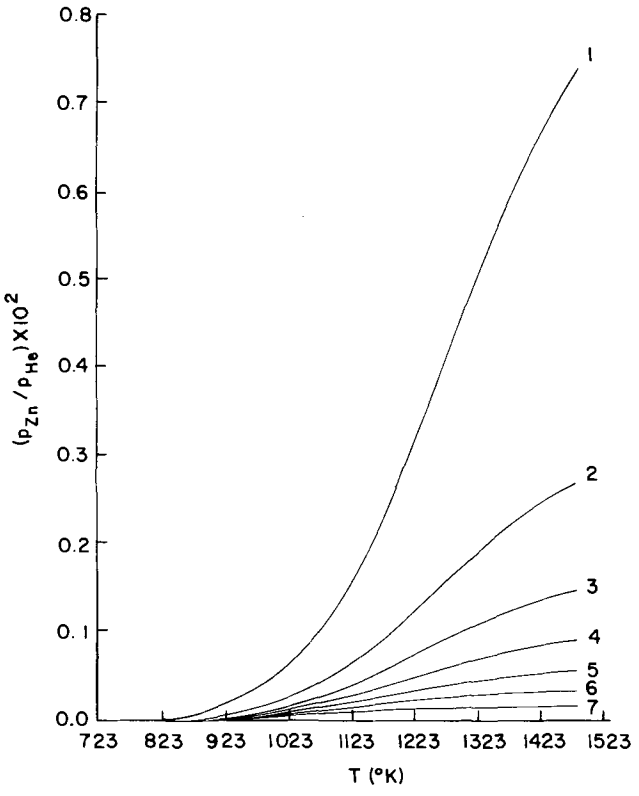

Fig. 1. Vapor phase variation in Zn concentration as a function of T at constant R. $R = 0.001$, $X = 1$, 0.00091; 2, 0.00078; 3, 0.00065; 4, 0.00052; 5, 0.00039; 6, 0.00026; 7, 0.00013.

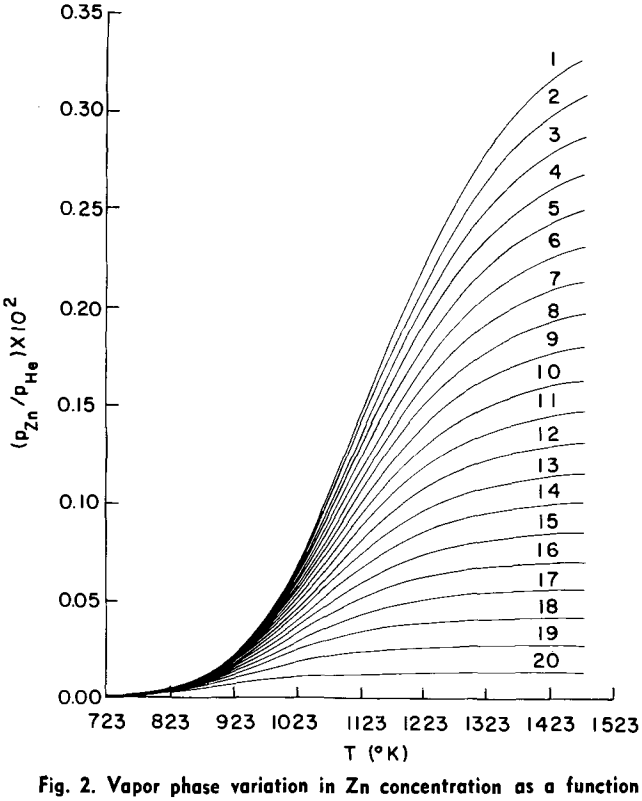

Fig. 2. Vapor phase variation in Zn concentration as a function of T at constant R. $R = 0.01$, $X = 1$, 0.00260; 2, 0.00247; 3, 0.00234; 4, 0.00221; 5, 0.00208; 6, 0.00195; 7, 0.00182; 8, 0.00169; 9, 0.00156; 10, 0.00143; 11, 0.00130; 12, 0.00117; 13, 0.00104; 14, 0.00091; 15. 0.00078; 16, 0.00065; 17, 0.00052; 18, 0.00039; 19, 0.00026; 20, 0.00013.

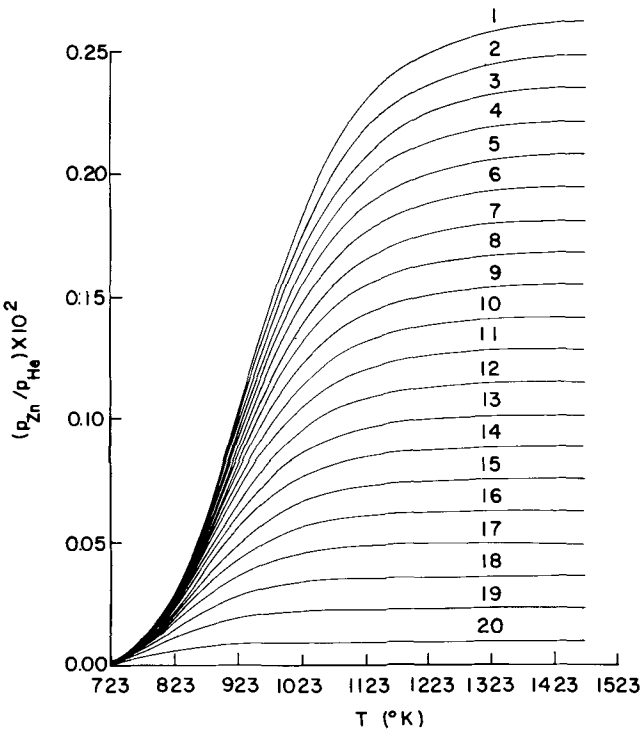

Fig. 3. Vapor phase variation in Zn concentration as a function of T at constant R. $R = 0.1$, $X = 1$, 0.00260; 2, 0.00247; 3, 0.00234; 4, 0.00221; 5, 0.00208; 6, 0.00195; 7, 0.00182; 8, 0.00169; 9, 0.00156; 10, 0.00143; 11, 0.00130; 12, 0.00117; 13, 0.00104; 14, 0.00091; 15, 0.00078; 16, 0.00065; 17, 0.00052; 18, 0.00039; 19, 0.00026; 20, 0.00013.

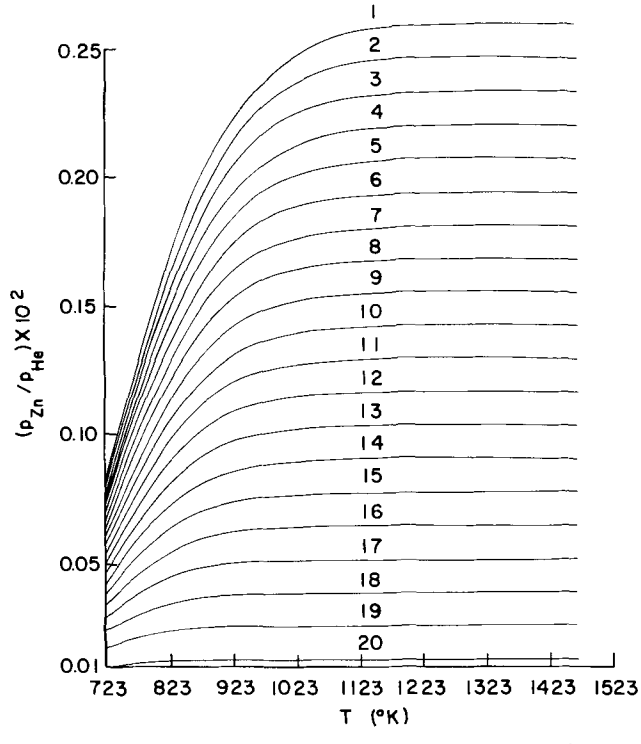

Fig. 4. Vapor phase variation in Zn concentration as a function of T at constant R. $R = 1.0$, $X = 1$, 0.00260; 2, 0.00247; 3, 0.00234; 4, 0.00221; 5, 0.00208; 6, 0.00195; 7, 0.00182; 8, 0.00169; 9, 0.00156; 10, 0.00143; 11, 0.00130; 12, 0.00117; 13, 0.00104; 14, 0.00091; 15, 0.00078; 16, 0.00065; 17, 0.00052; 18, 0.00039; 19, 0.00026; 20, 0.00013.

when the value of X achieves a value of 0.00091, the required value of Y would be 0.91. Since the total pressure cannot exceed 1 atm, the required value of Y for the next higher value of X ($X = 0.00104$) would violate the total pressure constraint. Consequently, only 7 curves appear in Fig. 1. In the remaining families, 20 curves are present in each. Figure 5 representing an R

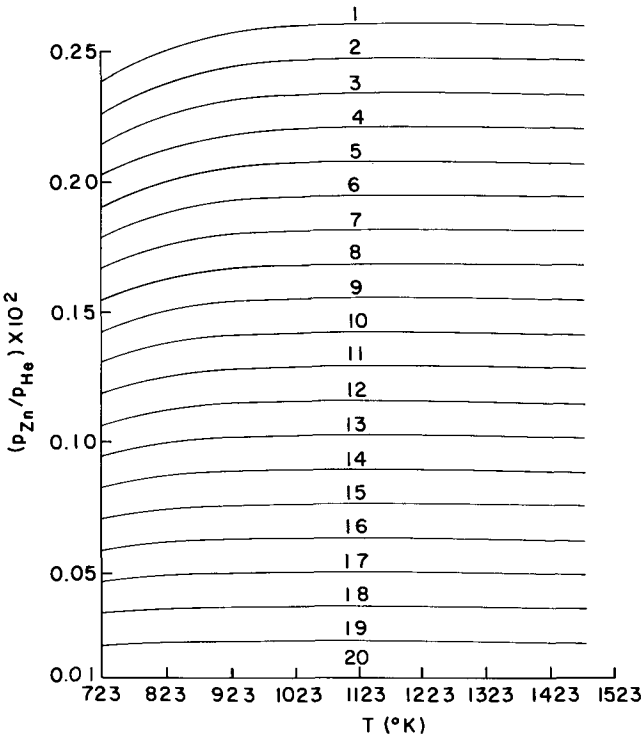

Fig. 5. Vapor phase variation in Zn concentration as a function of T at constant R. $R = 10$, $X = 1$, 0.00260; 2, 0.00247; 3, 0.00234; 4, 0.00221; 5, 0.00208; 6, 0.00195; 7, 0.00182; 8, 0.00169; 9, 0.00156; 10, 0.00143; 11, 0.00130; 12, 0.00117; 13, 0.00104; 14, 0.00091; 15, 0.00078; 16, 0.00065; 17, 0.00052; 18, 0.00039; 19, 0.00026; 20, 0.00013.

value of 10 does not provide experimentally usable information, since as might have been anticipated, the miniscule concentration of water vapor employed, *i.e.*, 0.1 that of Zn introduced leads to only minor variations of Zn vapor phase content as a function of T above the Zn dewpoint at each Zn concentration. At R values of 100 and 1000 no change in Zn vapor phase concentration occurs in the temperature interval surveyed. Figures 1-4 show essentially monotonic variation of Zn/He ratio with T. It might be noted that the greatest variation in Z occurs at the lowest value of R, a not unexpected result. At $R = 0.1$ and 1, the curves exhibit plateaus which are potentially useful for maintaining sources in a nontemperature sensitive environment. Unfortunately, these plateaus, particularly at the lower Zn concentrations, extend to relatively low temperatures and would restrict the range of temperatures over which epitaxial deposition conditions could be sought. Several of the curves for $R = 0.001$ and 0.01, Fig. 1 and 2, respectively, appear to represent a reasonable experimental compromise for utilizing plateau regions for source control, while not sacrificing the temperature range for studying epitaxial phenomena.

Figures 6-10 show normalized data relative to Z at 1473°K for several selected starting Zn component partial presures. From these curves, the fraction of Zn precipitated at each temperature is evident by inspection. These curves enable estimation of the quantity of material deposited, starting with specified concentrations and total flow rates into the reactor.

The predicted occurrence of plateau regions in Fig. 1-10 provides an excellent qualitative tool for testing the validity of the equilibrium transport model in appropriate concentration-temperature regimes. After establishing source bed designs which result in the development of equilibrium partial pressures in the effluents, the reactants can be mixed at elevated temperatures. The drop out of ZnO along a temperature gradient can then be monitored in a liner tube in the reactor to determine the temperature at which deposition first occurs. Qualitatively, the results of such preliminary experiments have shown the analysis to be valid to first order. In addition, utilizing the curves shown in Fig. 6-10, the relative amounts of deposition expected at different temperatures have been monitored in epitaxial growth studies on sapphire and magnesium spinel. These experiments have also lent credence to the validity of the calculated data.

It is evident that Eq. [1] and [2] represent the identical equilibrium. The fused quartz corrosion problem experienced in attempting transport of ZnO powder in an H_2 or H_2-He carrier gas has not been en-

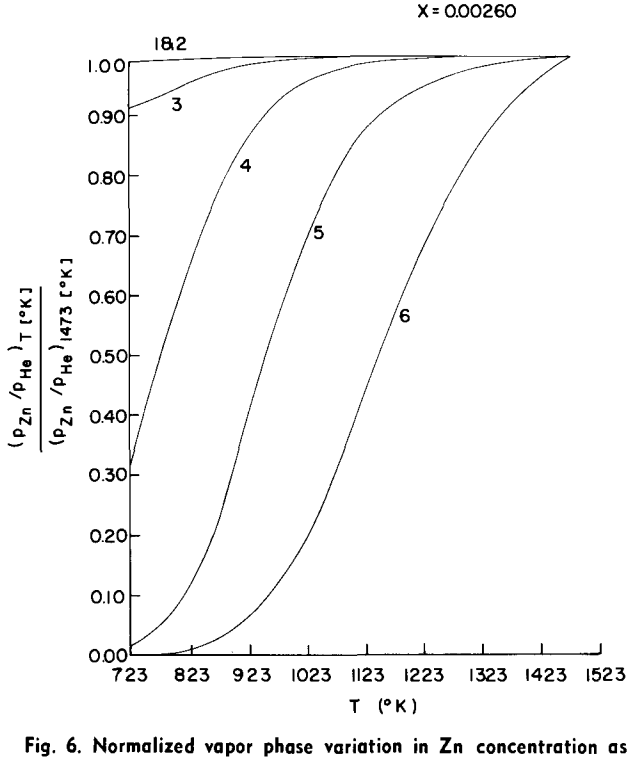

Fig. 6. Normalized vapor phase variation in Zn concentration as a function of T at $X = 0.00260$; $Y = 1$, 0.001X; 2, 0.01X; 3, 0.1X; 4, 1.0X; 5, 10X; 6, 100X.

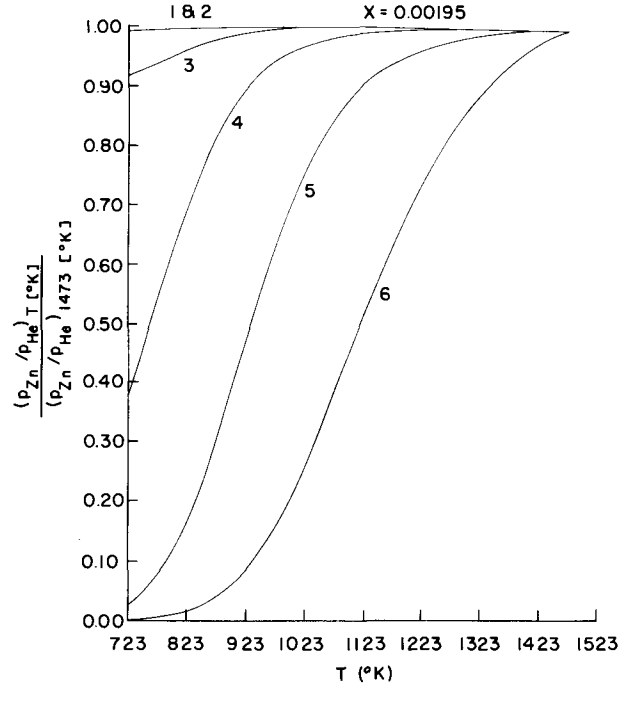

Fig. 7. Normalized vapor phase variation in Zn concentration as a function of T at $X = 0.00195$, $Y = 1$, 0.001X; 2, 0.01X; 3, 0.1X; 4, 1.0X; 5, 10X; 6, 100X.

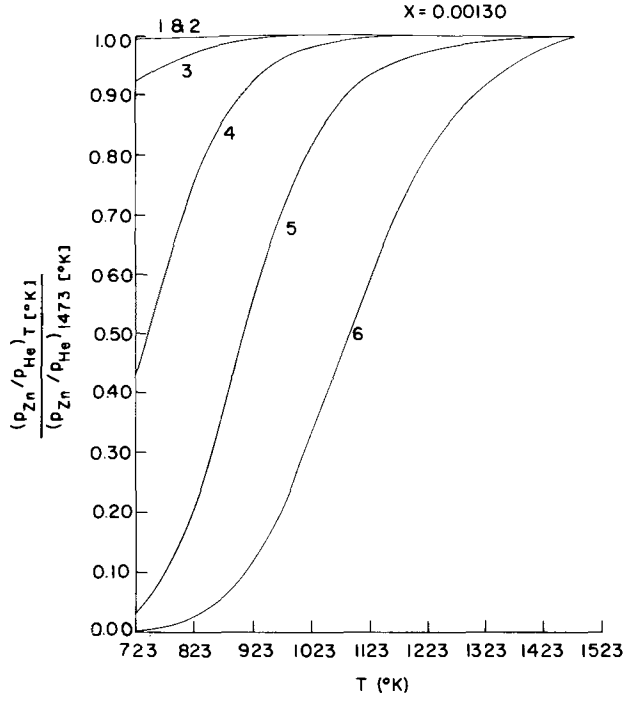

Fig. 8. Normalized vapor phase variation in Zn concentration as a function of T at $X = 0.00130$, $Y = 1$, $0.001X$; 2, $0.01X$; 3, $0.1X$; 4, $1.0X$; 5, $10X$; 6, $100X$.

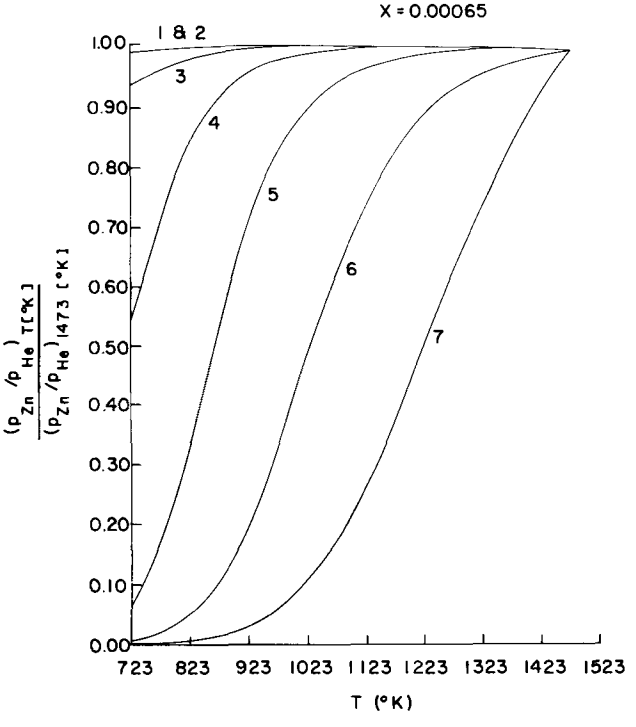

Fig. 9. Normalized vapor phase variation in Zn concentration as a function of T at $X = 0.00065$, $Y = 1$, $0.001X$; 2, $0.01X$; 3, $0.1X$; 4, $1.0X$; 5, $10X$; 6, $100X$; 7, $1000X$.

countered in implementing the experiment via Eq. [2]. Initially it was thought that this might be due to the high hydrogen content of the carrier gas stream employed in transporting the ZnO from a powder source via Eq. [1]. However, in H_2-He mixtures containing equivalent H_2/He ratios to those generated when Zn and H_2O react in a He stream, similar corrosion behavior was observed. The only conclusion that appears to provide a reasonable explanation for the difference in behavior of the two systems is that the "high purity" ZnO sources employed were contaminated by some unknown agent not detected by emission spectroscopic techniques.

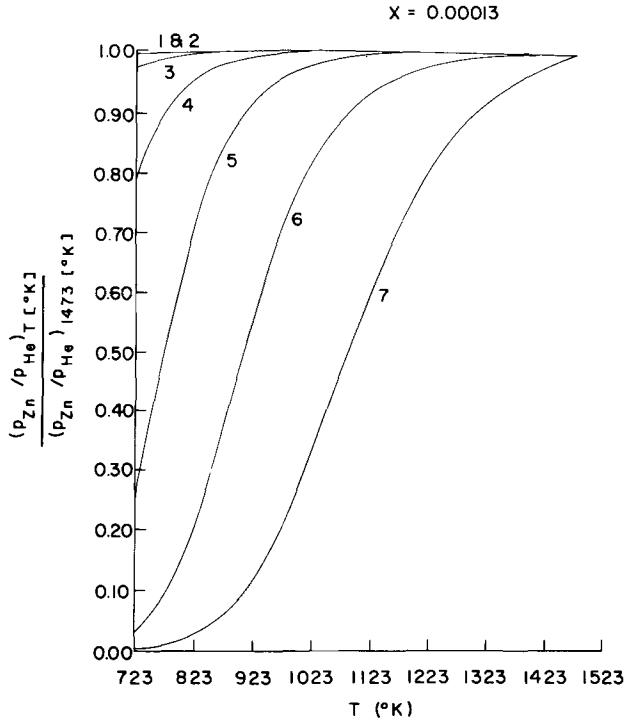

Fig. 10. Normalized vapor phase variation in Zn concentration as a function of T at $X = 0.00013$, $Y = 1$, $0.001X$; 2, $0.01X$; 3, $0.1X$; 4, $1.0X$; 5, $10X$; 6, $100X$; 7, $1000X$.

APPENDIX A

It is most convenient to consider our analysis via the use of pressure values for components, *i.e.*, P_{Zn}, P_O, P_{He}, P_{H_2} and species p_{Zn}, p_{H_2O}, p_{He}, p_{H_2}. We know that for each mole of Zn introduced and subsequently consumed a mole of H_2 is formed. Similarly, for each mole of O introduced (as H_2O) and then consumed, a mole of H_2 is formed. Thus, we can conserve the component moles of Zn and O, m_{Zn} and m_O, respectively, in terms of the species moles present n_{Zn}, n_{H_2O}, n_{H_2}, via

$$m_{Zn} = n_{Zn} + n_{H_2} \qquad [A\text{-}1]$$

$$m_O = n_{H_2O} + n_{H_2} \qquad [A\text{-}2]$$

To convert these terms into pressures, we assume the applicability of the ideal gas equation

$$\text{moles} = \frac{PV}{RT} \qquad [A\text{-}3]$$

Therefore,

$$\frac{P_{Zn}V_{IN}}{RT} = \frac{(p_{Zn} + p_{H_2})V_{OUT}}{RT} \qquad [A\text{-}4]$$

or

$$P_{Zn}V_{IN} = (p_{Zn} + p_{H_2})V_{OUT} \qquad [A\text{-}5]$$

where V_{IN} can be thought of as the total volume prior to reaction which contains the component moles of Zn, m_{Zn} introduced, and in which its component pressure is P_{Zn}, and where V_{OUT} is the total volume after reaction occurs in which the unreacted Zn and its product are contained. Unless we know the term V_{OUT} we cannot rewrite Eq. [A-1] and [A-2] in terms of pressures alone. Suppose, however, we had chosen to define the ratio X where X is given by

$$X = \frac{m_{Zn}}{m_{Zn} + m_O + m_{He^t}} \qquad [A\text{-}6]$$

where m_{He^t} represents the total number of moles of He introduced into the reactor. Conserving the component moles specified, we see that

$$X = \frac{m_{Zn}}{m_{Zn} + m_O + m_{He^t}} = \frac{n_{Zn} + n_{H_2}}{(n_{Zn} + n_{H_2}) + (n_{H_2O} + n_{H_2}) + n_{He^t}} \qquad [A\text{-}7]$$

substituting for the m's and n's the result, Eq. [A-4], we obtain

$$X = \frac{P_{Zn}\, V_{IN}/RT}{(P_{Zn} + P_O + P_{He^t})\, V_{IN}/RT} = \frac{(p_{Zn} + p_{H_2})\, V_{OUT}/RT}{(p_{Zn} + 2p_{H_2} + p_{H_2O} + p_{He})\, V_{OUT}/RT} \quad [A\text{-}8]$$

cancelling terms leads to

$$X = \frac{P_{Zn}}{P_{Zn} + P_O + P_{He^t}} = \frac{p_{Zn} + p_{H_2}}{p_{Zn} + 2p_{H_2} + p_{H_2O} + p_{He}} \quad [A\text{-}9]$$

Note that if the P's are specified in atmospheres, the denominator $P_{Zn} + P_O + P_{He^t} = 1$ in our experiment, since the P_O term is derived exclusively from the H_2O introduced, and the three component pressures, $P_{Zn} + P_O$ (from H_2O) and P_{He^t} account initially for the total pressure.

Therefore,

$$X = P_{Zn}(\text{dimensionless}) = \frac{(p_{Zn} + p_{H_2})\,\text{atm}}{(p_{Zn} + 2p_{H_2} + p_{H_2O} + p_{He})\,\text{atm}} \quad [A\text{-}10]$$

Consequently, from an experimental point of view, both X and an analogous expression for an O ratio, Y, where Y is given by

$$Y = \frac{P_O}{P_{He^t} + P_{Zn} + P_O} = \frac{p_{H_2O} + p_{H_2}}{p_{Zn} + 2p_{H_2} + p_{He} + p_{H_2O}} \quad [A\text{-}11]$$

are simply the partial pressures of Zn and water (in atmospheres) introduced into the reactor prior to reaction, but after dilution has occurred.

APPENDIX B

Selection of X and Y Values

Experimentally, the values of X and Y depend on the vapor pressures of Zn and H_2O at their source sites, and on flow rates of the carrier gas through each source site. We can approach the problem in either of two ways for convenience:

1. We can choose the Zn and H_2O source bed pressures by fixing the source bed temperatures, translate these pressures into a desired ratio of effective Zn/H_2O flow rates, R, and then determine the required carrier gas flows through each source bed (where equilibrium is always assumed to obtain) required to satisfy these boundaries.
2. We can choose the flow rates of carrier gas through each source bed, and determine the vapor pressures of Zn and H_2O required to give specific values of X and Y (therefore of R).

Method 1 (Solving for the required He flow through the Zn source, F_{He}, and through the water source, F'_{He}, given p'_{Zn}, p'_{H_2O}, and R).—At the Zn source, since the total pressure is 1 atm, the partial presures of Zn, p'_{Zn}, and He, p^*_{He} must account for this total pressure. Since the He enters the Zn source at 1 atm and some defined flow rate monitored at a meter located prior to the source, the Zn vaporization must be accompanied by an over-all volume increase proportional to the Zn vapor pressure. The net effect then imposed by the constant pressure constraint is to increase the flow rate (referenced to room temperature, for example), so that the effluent flow out of the Zn source, F_1, is the sum of the input He flow rate, F_{He}, plus an effective Zn flow rate, F_{Zn}, Eq. [B-1]

$$F_1 = F_{Zn} + F_{He} \quad [B\text{-}1]$$

since

$$F_{Zn} = \frac{p'_{Zn}\,(\text{Torr}) \cdot F_1}{760\ \text{Torr/atm}} \quad [B\text{-}2]$$

We see that the relationship between the effluent flow from the Zn bed, F_1, and the He flow measured at a flow meter is

$$F_1 = \frac{F_{He}\, 760}{760 - p'_{Zn}\,(\text{Torr})} \quad [B\text{-}3]$$

Substituting for F_1 in Eq. [B-2], the value shown in Eq. [B-3] yields

$$F_{Zn} = \frac{p'_{Zn}\,(\text{Torr})\, F_{He}}{760 - p'_{Zn}\,(\text{Torr})} \quad [B\text{-}4]$$

At the H_2O source by an exactly analogous argument, we find that

$$F_2 = \frac{F'_{He}\, 760}{760 - p'_{H_2O}\,(\text{Torr})} \quad [B\text{-}5]$$

$$F_O = \frac{p'_{H_2O}\,(\text{Torr})\, F'_{He}}{760 - p'_{H_2O}\,(\text{Torr})} \quad [B\text{-}6]$$

Since effective component flow rates are directly related to the partial pressures of the unreacted components present, we may rewrite Eq. [3] and [4] according to

$$X = \frac{F_{Zn}}{F_{Zn} + F_{He} + F'_{He} + F_O} = \frac{F_{Zn}}{F_3} \quad [B\text{-}7]$$

and

$$Y = \frac{F_O}{F_{Zn} + F_{He} + F'_{He} + F_O} = \frac{F_O}{F_3} \quad [B\text{-}8]$$

where the various flow contributions refer to the unreacted components referenced to effective room temperature flow rates.

Let us now define a new quantity R given by

$$R = \frac{X}{Y} = \frac{F_{Zn}}{F_O} = \frac{p'_{Zn}\, F_{He}\,[760 - p'_{H_2O}\,(\text{Torr})]}{p'_{H_2O}\, F'_{He}\,[760 - p'_{Zn}\,(\text{Torr})]} \quad [B\text{-}9]$$

If we fix values of p'_{Zn} and p'_{H_2O} as well as F_3, the ratio R becomes unique. Since.

$$F_3 = F_1 + F_2 \quad [B\text{-}10]$$

we can write from Eq. [B-3] and its analog for the water bed effluent flow rate Eq. [B-5]

$$F_3 = \frac{F_{He}\, 760}{760 - p'_{Zn}\,(\text{Torr})} + \frac{F'_{He}\, 760}{760 - p'_{H_2O}\,(\text{Torr})} \quad [B\text{-}11]$$

Equations [B-11] and [B-9] may be solved simultaneously for F_{He} and F'_{He} to give Eq [B-12] and [B-13]

$$F_{He} = \frac{F_3 R\,[760 - p'_{Zn}\,(\text{Torr})]}{760\,[R + p'_{Zn}\,(\text{Torr})/p'_{H_2O}\,(\text{Torr})]} \quad [B\text{-}12]$$

$$F'_{He} = \frac{F_3[760 - p'_{H_2O}(\text{Torr})]p'_{Zn}(\text{Torr})/p'_{H_2O}(\text{Torr})}{760[R + p'_{Zn}(\text{Torr})/p'_{H_2O}(\text{Torr})]} \quad [B\text{-}13]$$

Method 2 (Solving for p'_{Zn} and p'_{H_2O} given values for X, R, F_{He}, and F'_{He}.—The output of a computer analysis may be easily specified in terms of fixed values of X at different values of the ratio R. Since the values of p'_{Zn} and p'_{H_2O} needed to give these X and R values depend on what flow rates of carrier gas are employed, the second method more nearly approximates the way an experiment might be performed. It is to be noted that if X and R are both specified along with F_{He} and F'_{He}, the value of Y is uniquely determined, therefore, p'_{Zn} and p'_{H_2O} are also both uniquely determined.

Substituting into Eq. [B-7] the values for F_{Zn} and F_O given by Eq. [B-4] and [B-6] respectively, X may be expressed in terms of p'_{Zn} (Torr), p'_{H_2O} (Torr), F_{He}, and F'_{He}.

Equation [B-9] gives R as a function of these same parameters. Consequently, the expressions for X and R may be solved simultaneously for p'_{Zn} and p'_{H_2O} to give Eq. [B-14] and [B-15], respectively

$$p'_{Zn}\,(\text{Torr}) = \frac{760\, F_{He^t}\, C_O R}{F_{He^t}\, C_O R + F_{He}\,(R - C_O)} \quad [B\text{-}14]$$

$$p'_{H_2O}\ (\text{Torr}) = \frac{760\ F_{He^t}\ C_o}{F_{He^t}\ C_o + F'_{He}\ (R - C_o)} \quad [B\text{-}15]$$

where $C_o = X/(1 - X)$.

Acknowledgments

The authors wish to acknowledge T. O. Sedgwick and M. Berkenblit for their many helpful discussions, and Y. van der Meulen and P. Balk for critically reviewing the manuscript.

Manuscript submitted Dec. 2, 1970; revised manuscript received April 22, 1971.

Any discussion of this paper will appear in a Discussion Section to be published in the June 1972 JOURNAL.

LIST OF SYMBOLS

- p'_{Zn} partial pressure of Zn at a Zn source external to the reactor
- p_{Zn} equilibrium partial pressure of the species Zn after reaction
- P_{Zn} partial pressure of the component Zn in the reactor, prior to reaction having occurred, referenced to room temperature and 1 atm total pressure in the reactor
- F_{Zn} effective flow rate of the component Zn assumed present as the species Zn at the output of the Zn source
- X the ratio of F_{Zn}, as defined above, to the total flow rate in the reactor prior to reaction, referenced to room temperature
- p'_{H_2O}, p_{H_2O}, P_O, F_O: analogs of the Zn terms defined above for the water introduced into the system
- Y analog of the term X for the component O which is derived from the water introduced
- p_{H_2} equilibrium partial pressure of H_2 after reaction has occurred
- R the ratio X/Y ∴ the ratio F_{Zn}/F_O
- F_{He} the flow of He into the Zn source referenced to room temperature
- F'_{He} the flow of He into the water source referenced to room temperature
- F_{He^t} $F_{He} + F'_{He}$
- p_{He} equilbrium partial pressure of He after reaction has occurred
- p_{He^t} total component partial pressure of He introduced into the reactor prior to reaction, referenced to room temperature
- F_1 the flow $F_{Zn} + F_{He}$ emanating from the Zn source
- F_2 the flow $F_O + F'_{He}$ emanating from H_2O source
- F_3 the total flow in the reactor ($F_1 + F_2$) prior to reaction, referenced to room temperature
- Z equilibrium ratio p_{Zn}/p_{He} at specified X, Y, and T following reaction
- Z' the value P_{Zn}/P_{He^t} prior to reaction

REFERENCES

1. G. Galli and J. E. Coker, *Appl. Phys. Letters*, **16**, 439 (1970).
2. H. Schafer and H. Odenbach, *Z. Anorg. Allgem. Chem.*, **346**, (3-4), 127 (1966).
3. Ikumaro Kubo, *Japan. J. Appl. Phys.*, **4**, 225 (1965).
4. E. A. Weaver, *J. Crystal Growth*, **1**, 320 (1967).
5. T. Takahashi, A. Ebina, and A. Kamiyama, *Japan. J. Appl. Phys.*, **5**, 560 (1966).
6. M. Ohnishi, M. Yoshizawa, and S. Ibuki, *ibid.*, **9**, 412 (1970).
7. N. F. Foster, G. A. Coquin, G. A. Rozgonyi, and F. A. Vannatta, *IEEE Trans. on Sonics and Ultrasonics*, **15**, 28 (1968).
8. O. Kubaschewski and E. Evans, "Metallurgical Thermochemistry," Pergamon, London (1958).
9. K. K. Kelley, Bull. No. 584, U.S. Bur. Mines (1960).

Phase Relations and Liquid Structure in the System As-Sb_2Se_3-Se

John S. Berkes and Mark B. Myers

Xerox Corporation, Xerox Square-114, Rochester, New York 14644

ABSTRACT

The phase equilibria for the As-Sb_2Se_3-Se ternary system were determined by sealed system DTA and quench methods. The As_2Se_3-Sb_2Se_3 and As-Sb_2Se_3 ternary sections are true binary systems exhibiting simple eutectic behavior. The general phase relationships are discussed and the liquidus behavior and liquid structure of the selenium rich part of the ternary are treated in detail. A nonregular thermodynamic solution model is used to describe the solution behavior and calculate the size of structural units present in the ternary liquid. A physical interpretation, in terms of these structural units, is given for the observed incipient liquid immiscibility.

The nonoxide glass forming chalcogenides are of great interest because of their photoconductive and semiconductive properties. The preparation of these multicomponent materials in well-controlled and characterized states requires the availability of accurate data concerning their liquidus and subliquidus relationships.

Knowledge of the liquidus relationships can be as important for dealing with noncrystalline solids or glasses as for crystalline solids. A great amount of information concerning the nature of a multicomponent glassy material is available through the knowledge of the phase equilibria of the system. The liquidus temperature is the initial point where supercooling of the melt begins in order to realize the glassy state. Indeed it is the temperature interval between the liquidus and the region initiating glass behavior, conveniently demarked by the glass transition, which must be traversed by supercooling to realize the glassy state. The subliquidus and solidus relationships tell of the metastable and equilibrium states to which a supercooled liquid or glass will try to relax with time. Finally, significant insights concerning variations in the atomic arrangements or molecular associations of the melt and the related glassy state can be realized by a detailed investigation of the behavior of the liquidus as a function of composition. The liquidus often reflects variations in molecular associations or clustering in the liquid or glassy state which are not readily revealed by optical spectroscopy or x-ray radial distribution techniques.

The experimental determination and interpretation of the liquidus behavior in the As-Sb-Se ternary system is the object of this study. A thermodynamic method is employed to estimate the size of liquid species or associations in the melt. The thermodynamic approach is the inverse from the usual method of interpreting discrepancies between experimental

Key words: As-Sb-Se system, phase diagram As-Sb-Se, liquid structure, chalcogenide glasses.

and theoretical liquidus behavior by nonideal solution corrections. Instead, liquid species or groupings of the limiting end member structures are identified which can mix and form ideal solutions. These model mixtures are then considered to reflect the molecular constitution of the real multicomponent liquid.

The As-Sb-Se ternary is a very interesting system for these considerations. A great deal of information exists concerning the crystal and liquid structures of the important element and compounds in the system, namely, Se, As_2Se_3, and Sb_2Se_3. The liquid structure of Se exhibits a well-known temperature dependent ring-linear polymer chain equilibria (1-3), liquid As_2Se_3 is considered (4-6) to consist of aggregates of two dimensional $AsSe_{3/2}$ linked groupings, and liquid Sb_2Se_3 appears to be a loosely associated molecular liquid of low viscosity. The Se-Sb_2Se_3 system as indicated by the liquidus reported in the literature (7) shows a tendency for liquid immiscibility, reflecting marked differences in the liquid structures of Se and Sb_2Se_3. Thus, an investigation of the As-Sb-Se ternary system assures the consideration of the mixing of liquid species which in their pure state exhibit markedly different behavior. A number of different sections through this ternary involves the analyses of solutions of widely different molecular constitution.

Experimental

The mixtures necessary for the phase equilibria investigation were prepared by reaction of Gallard Schlesinger 99.9999% pure elemental components in vacuum sealed silica glass ampoules at 650°C for 16 hr in a rocking furnace. The reacted 50 gram samples were quenched in cold water to assure homogeneity. The quenched products were glasses for compositions with less than 20 atomic per cent (a/o) Sb and more than 35 a/o Se. All other compositions resulted in quenched material which was either partially or completely crystalline.

These prereacted mixtures served as standard starting materials in all subsequent DTA and quench runs. To check for possible inhomogeneities and weighing errors in these reacted mixtures, they were all analyzed by x-ray fluorescence. Calibration standards for these analyses were made by two different techniques. The first method for standards preparation was identical to that used in reacting the original mixtures. This was useful for compositions which quenched to a homogenous glass. The second method involved the mixing of As, Sb, and Se powders and subsequent pressing to theoretical density. These powders had to be sieved to a size smaller than 300 mesh to eliminate errors due to particle size. A check of all the mixtures indicated that they deviated no more than the accuracy of the measuring technique (±1 a/o) from their nominal compositions.

The phase equilibria were determined by DTA and quench methods. Due to the volatility of these materials all the work had to be carried out by sealed system techniques. This required the prereacted mixtures to be crushed and packed into specially designed fused silica ampoules which were subsequently used in DTA and quench experiments. The thermal analyses were carried out using a du Pont Model 900 DTA. This data was checked by static equilibration-quench methods to assure its accuracy and identify the phase fields. In the Sb_2Se_3 poor portion of the As-Sb_2Se_3-Se ternary, it was necessary to rely on quench data exclusively due to the high viscosities and slow reaction rates of these materials. The phase assemblages present in the quench runs were analyzed by x-ray powder diffraction methods. The added sensitivity of the Debye-Scherrer method was employed to aid in the accurate locating of phase boundaries.

Experimental Results

The compilation by Hansen (7) gives three different versions of the phase diagram for the Se-Sb system.

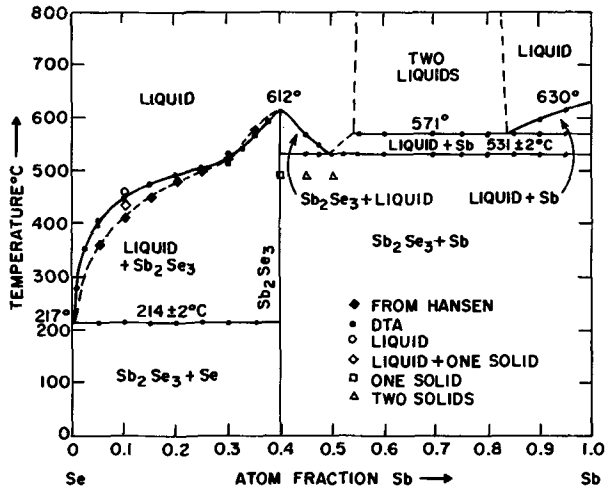

Fig. 1. Phase diagram for the system Se-Sb

In order to determine which of these versions most reliably represents the system, a redetermination has been carried out. Figure 1 contains the results of the present investigation. They are in good agreement with the work of Parravano (8) [from Hansen (7)] except for the detailed shape of the liquidus defining the Sb_2Se_3 + liquid phase field. The present investigation shows a more pronounced flattening of the liquidus indicating a stronger tendency towards liquid immiscibility.

Figures 2 and 3 represent sections in the ternary system which are true binary systems. The information contained in Fig. 1-3 combined with phase equilibria data at compositions distributed on a 5 a/o grid (As-Sb-Se basis) and the phase diagram for the Se-As binary system (5) were used to draw the liquidus for the As-Sb_2Se_3-Se ternary system shown in Fig. 4. A number of additional quench runs were made in the region close to the Se-As binary in order to accurately locate the phase boundaries most of which were located in this region of the ternary system.

Analysis of Ternary Solution Behavior

The experimental liquidus curves will be fitted to thermodynamic model solutions in order to estimate the average size of the liquid species or associations in the As-Sb_2Se_3-Se section of the ternary system. The Se-Sb_2Se_3, As_2Se_3-Sb_2Se_3, and As_4Se_4-Sb_2Se_3 sections are analyzed in detail. All sections have Sb_2Se_3 as one end member, and the liquidus to be analyzed defines the phase field of Sb_2Se_3 + liquid which covers most of this part of the ternary system.

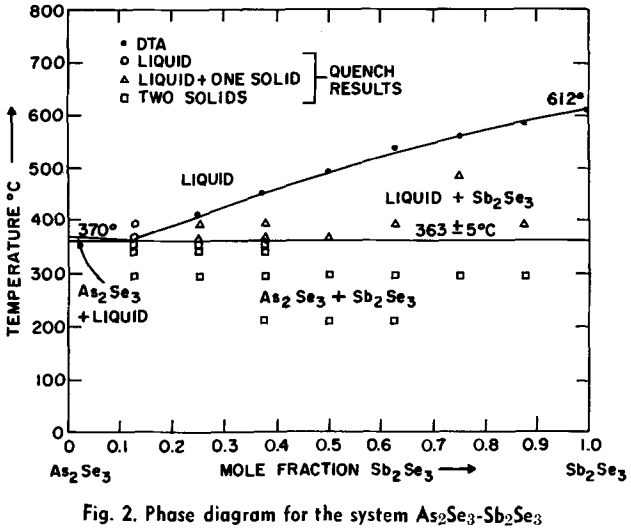

Fig. 2. Phase diagram for the system As_2Se_3-Sb_2Se_3

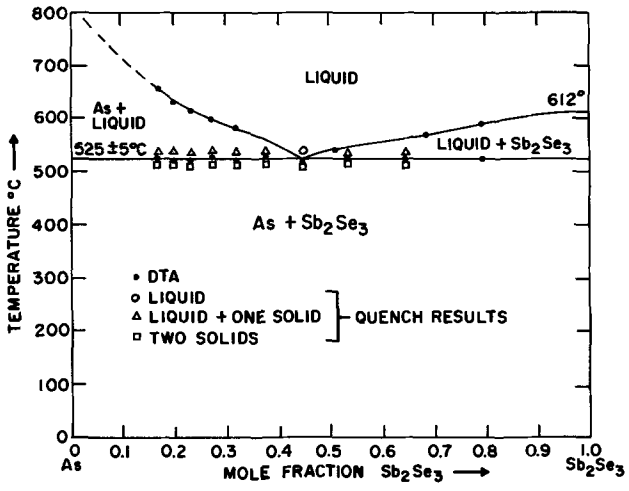

Fig. 3. Phase diagram for the system As-Sb_2Se_3

Thermodynamic considerations.—The basic thermodynamic expressions used in this analysis are discussed in detail in most thermodynamic texts (9, 10). In order to convey the argument employed to analyze the liquidus behavior, the appropriate thermodynamic relationships will be outlined.

The basis for all analyses of multicomponent solution behavior is the Gibbs free energy expression

$$G_l = E_o + \int_o^T Cp\, dT - T\int_o^T \frac{Cp}{T} dT - kT \ln \frac{N!}{\prod_i n_i!} \quad [1]$$

The relationship describes the free energy of a solution, G_l, in terms of the internal energy of the solution at absolute zero, E_o, the temperature integrals of the specific heat, Cp, and the statistical complexions of a system of N particles of i distinct species each present in n_i numbers. In this expression the assumption is made that the pressure volume product is negligible making the enthalpy, H, equal to the internal energy, E_o. In addition it is assumed that a set of ideally interacting liquid species can always be defined.

The Gibbs function expressed in this manner is completely capable of representing the free energy of any solution. However in practice, its application is not possible because of the lack of Cp and E_o data. This difficulty is generally circumvented by making a number of approximations to account for the unknown variables. Indeed, the terminology used to describe the thermodynamic nature of solutions has resulted from the type of approximations applied.

The approximations are made in the following manner. The internal energy of the solution, E_o, can be represented as the sum of two quantities.

$$\mathbf{E}_o = U(X) + \sum_i X_i G^o_{li} \quad [2]$$

The first term is generally a nonlinear function of composition and the second term is the weighted sum of the internal energy of the end members in their liquid states, G^o_{li}. The relative concentration of the ith species is defined by $X_i = n_i/N$.

The same type of approximation is made for the two specific heat integrals the only difference being that the nonlinear term is a function of composition and temperature.

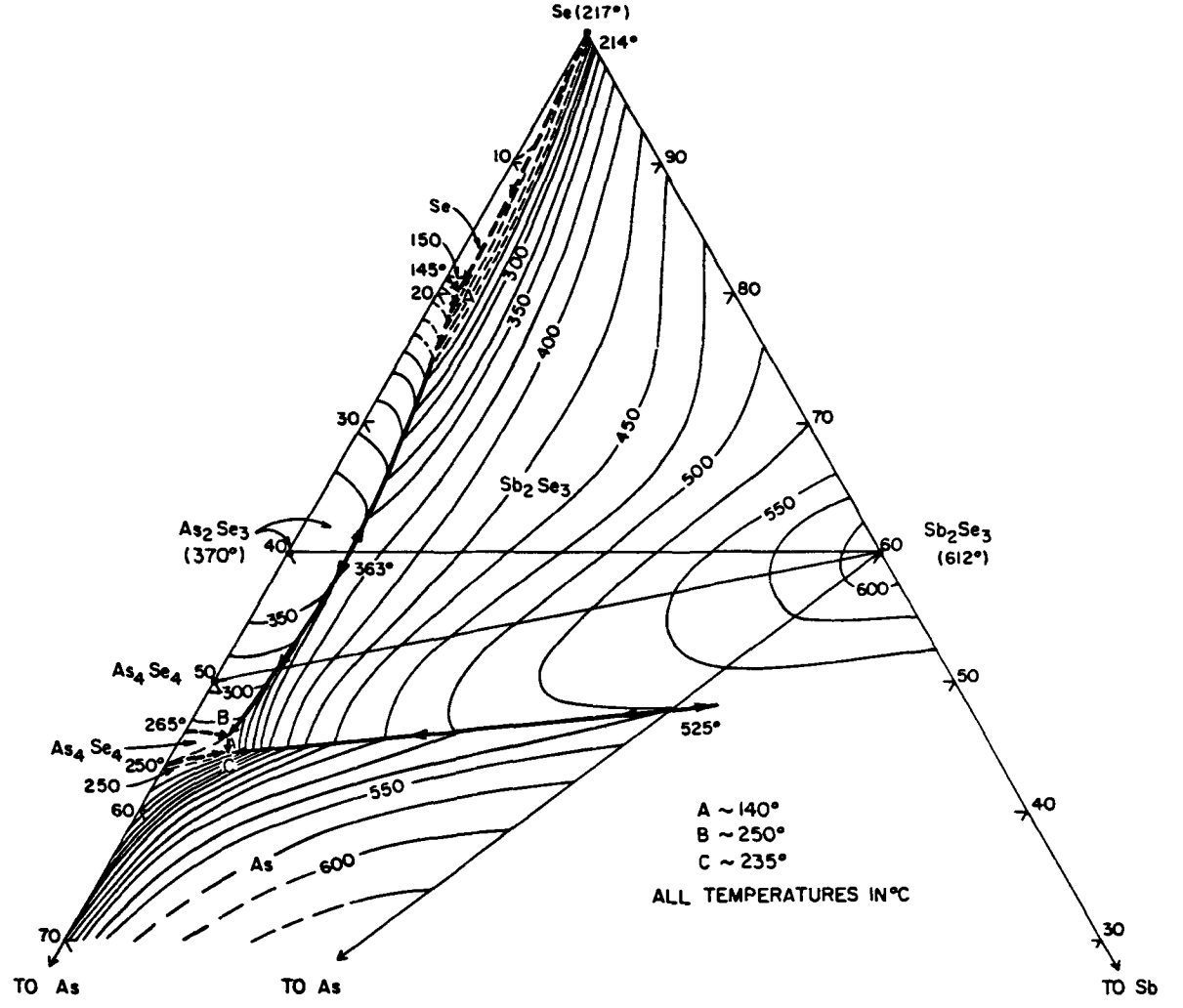

Fig. 4. Phase diagram for the system As-Sb_2Se_3-Se

$$\int_o^T Cp\,dT - T\int_o^T \frac{Cp}{T}\,dT = f(X,T) + \sum_i X_i\,G^T{}_{li} \quad [3]$$

The quantity $G^T{}_{li}$ is the energy of the ith end member obtained from the evaluation of the specific heat integrals. The second terms in Eq. [2] and [3] can be combined so that

$$\sum_i X_i\,G_{li} = \sum_i X_i\,G^o{}_{li} + \sum_i X_i\,G^T{}_{li} \quad [4]$$

Consequently, Eq. [1] can be written as

$$G_l = U(X) + f(X,T) + \sum_i X_i\,G_{li} + RT\sum_{i=1}^{j} X_i \ln X_i \quad [5]$$

The last term in Eq. [1] was transformed to the form in Eq. [5] by making the usual application of Sterling's approximation.

The free energy function expressed by Eq. [5] is the most general form for a solution made up of j distinct components. The equations employed for the various solution types are obtained by making the following approximations:

Ideal solution: $U(X) = 0, f(X,T) = 0$
Regular solution: $U(X) \neq 0, f(X,T) = 0$
Subregular or
nonregular solution: $U(X) \neq 0, f(X,T) \neq 0$

Consequently, for the ideal solution case Eq. [5] reduces to a simple linear combination of the end member parameters. In the regular solution case, this simple form is no longer applicable because the internal energy, $U(X)$, is a nonlinear function of composition. In binary systems, this compositional dependence is approximated (10) by

$$U(X) = \Omega X_1 X_2$$

For $\Omega < 0$, the solution shows a tendency for compound formation and for $\Omega > 0$ there will be a tendency for liquid immiscibility.

The third and most general solution type is the subregular (11) or nonregular (12) solution. In this case both the solution internal energy and specific heat components contribute energies which cannot be represented by a combination of end member quantities. For simplicity the compositional and temperature dependent contributions in Eq. [5] can be combined in the following manner

$$F(X,T) = U(X) + f(X,T)$$

It is noted that except for the $F(X,T)$ term Eq. [5] represents an ideal solution. The question to be asked is, what is the physical significance of $F(X,T)$? The answer has already been given in the name of the term, nonideal. The quantity $F(X,T)$ accounts for the nonideal behavior of the atoms in solution where they exhibit a tendency for the formation of cluster or "molecular" aggregates among like or unlike atoms.

An equally valid way to consider the source of the nonideal term, $F(X,T)$, is that the convenient concentration units employed to describe a solution often do not represent the nature of the molecular constitution of the liquid. In principal, it should be possible to redefine the concentration units of end members in such a way that the actual species present in the liquid are represented as end members and consequently, the property-composition relationships would be that for an ideal solution. For such a solution, composed of complex species, the $F(X,T)$ term will be zero and Eq. [5] will be reduced from the subregular to the ideal case. In choosing these "ideally" interacting species the assumption is made that such a set of species can be defined for any system.

These thermodynamic considerations are applied to the interpretation of the liquidus temperatures by relating free energy ($G_l{}^{X_i}$) of a liquid of composition $X_i{}^l$ to the free energy ($G_s{}^i$) of a coexisting solid end member (i) which has precipitated from the liquid. The condition defining equilibrium for this liquidus composition is

$$G_l{}^{X_i} - G_s{}^i = \left(\frac{\partial G_l}{\partial X_i}\right)_{T_l}(X_i - 1) \quad [6]$$

When Eq. [5] with $F(X,T)$ set to zero is substituted into Eq. [6], the following is obtained (9, 13)

$$(G_l{}^i - G_s{}^i)_{T_l} = -RT\ln X_l \quad [7]$$

where $G_l{}^i$ is the free energy of the end member liquid i. The difference $(G_l{}^i - G_s{}^i)$ is simply the free energy of fusion, ΔG_f, for the pure precipitating end member i at any temperature. The free energy of fusion is given by

$$\Delta G_f = \Delta H_f\left(1 - \frac{T}{T_f}\right) + \int_{T_f}^T \Delta Cp\,dT - T\int_{T_f}^T \frac{\Delta Cp}{T}\,dT \quad [8]$$

where

$$\Delta Cp = Cp\ (\text{liquid}) - Cp\ (\text{solid}) = a + bT + \ldots \quad [9]$$

and ΔH_f is the heat of fusion and T_f is the melting temperature.

The combination of Eq. [7], [8], and [9] provides a general equation for the liquidus of a precipitating end member in a multicomponent solution. The restrictions on its application require the precipitating end member to melt to a liquid specie whose stoichiometry is identical to that of the end member and concentration units are employed so that the liquid displays ideal behavior.

Analyses.—The application of this method to analyze the constitution of the liquid solution is straight forward. An ideal liquidus is calculated for a particular system with Eq. [7], [8], and [9]. Then the experimental liquidus is transformed to a coordinate system whose end members represent the molecular species which may be present in the liquid. If the ideal liquidus and the transformed experimental liquidus coincide, a possible solution has been obtained. It is noted that the ideal liquidus will always be numerically (X *vs.* T) the same independent of the section analyzed in the multicomponent system as long as the precipitating end member is not changed (*i.e.* as long as ΔH_f and ΔCp remain constant and the end member liquid specie does not vary with composition or temperature).

The coordinate or concentration transformation is carried out by a two-step process for the particular ternary system under consideration. The first transformation changes the experimental As-Sb-Se ternary coordinate data into a convenient As_uSe_v-Sb_2Se_3 binary coordinate system employing Eq. [10].

$$y = \frac{u - (u+v)y'}{u + (5 - u - v)y'} \quad [10]$$

The variable y' designates the antimony concentration, y represents the Sb_2Se_3 concentration, and u and v can assume any positive or zero value to define the section of interest. The second transformation involves going from this convenient As_uSe_v-Sb_2Se_3 binary section to a complex coordinate system representing the liquid species. The equation for this transformation will be developed for each specific case.

Three binary sections of the As-Sb-Se ternary will now be analyzed in detail. All of the sections have Sb_2Se_3 as a common end member. Consequently all of the analyses will use a common ideal liquidus for the comparison. The fusion temperature (T_f), the enthalpy of fusion (ΔH_f) and the ΔCp for Sb_2Se_3 used in the calculations are 612°C, 12,970 cal/mole and 18.9 cal/deg mole, respectively (14). The specific heat difference for Sb_2Se_3 was estimated from enthalpy data in the temperature region of the fusion temperature.

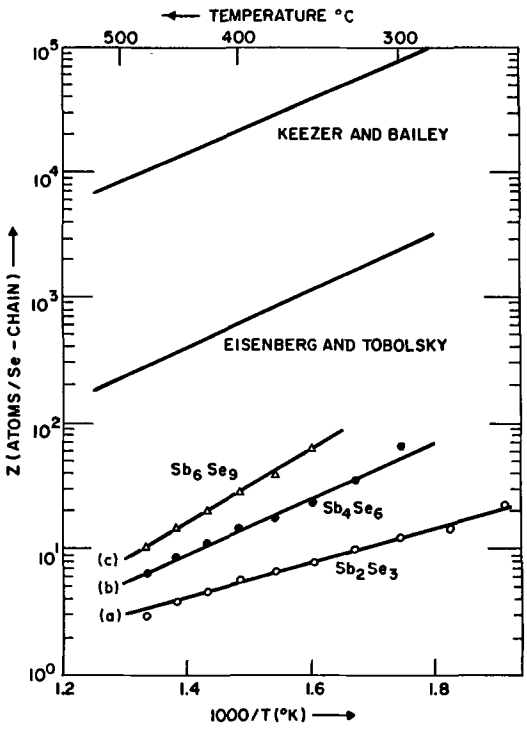

Fig. 5. Temperature dependence of the number average selenium chain length.

The Se-Sb_2Se_3 system.—In order to ascertain possible end member species for the experimental liquidus transformation, evidence for the limiting molecular configurations in this system will be examined. Consideration of the temperature dependence of the viscosity and the specific heat and the solubility or lack of solubility of various forms of Se in CS_2 has lead to the view that liquid selenium consists of a dynamic equilibrium between long polymer chains and eight-membered rings. The results of two different chain length calculations (2, 3) are shown in Fig. 5. The absolute magnitudes for the average chain lengths vary considerably between the two references but the temperature dependences are in good agreement.

The crystal structure for Sb_2Se_3 (15) indicates the presence of well-defined layer like chains with no obvious evidence for distinct $w Sb_2Se_3$ molecules. The melting of these crystals may be envisioned as disordering of the layers and a fragmentation of the chains into smaller $w Sb_2Se_3$ units. Observation of the Sb_2Se_3 melt indicates that it is a highly fluid liquid which cannot be readily quenched into a glass. Based on this observation (w) will probably be small assuming values such as 1, 2, 3, or perhaps 4.

As a first approximation the liquid species present in the Se rich part of the Se-Sb_2Se_3 system will be assumed to consist of Se_8 rings, Se_z chains, and a specie having the Sb_2Se_3 stoichiometry which will be designated by $w Sb_2Se_3$. Figure 6 contains the results of two sets of calculations which transformed the experimental liquidus data for the binary system

$$Se - Sb_2Se_3 \rightarrow (R)Se_8 - (1-R)Se_z - (w)Sb_2Se_3 \quad [11]$$

This transformation was carried out using Eq. [12]

$$X = \frac{y/w}{(1-y)\left[\frac{R}{8} + \left(\frac{1-R}{z}\right)\right] + \frac{y}{w}} \quad [12]$$

In this equation, the variable y designates the Sb_2Se_3 concentration in the Se-Sb_2Se_3 coordinate system and X represents the concentration of $w Sb_2Se_3$ in the ternary system. The quantity designated by X is identical to the ideal liquidus which was calculated using

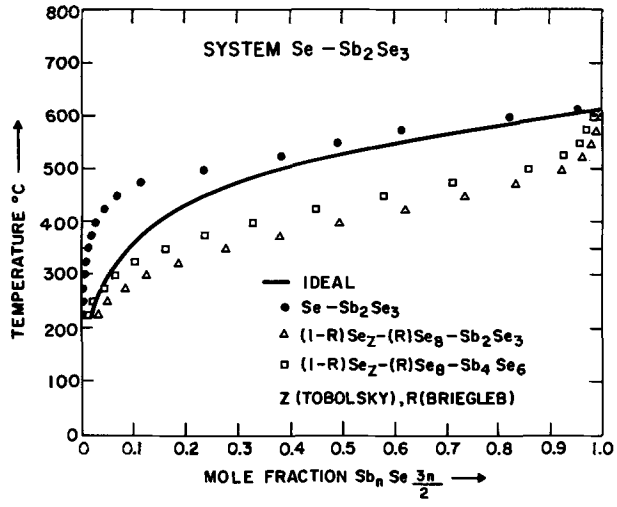

Fig. 6. Liquid structure calculation results for the system Se-Sb_2Se_3.

Eq. [7]-[9]. The variable R represents the fraction of Se in the Se_8 form, and Z is the chain length of the linear polymer molecules. In these transformations the magnitude of R and Z are those of Briegleb (1) and Eisenberg and Tobolsky (2) respectively.

The results of the two transforms designated by open triangles and squares in Fig. 6 were computed for $w = 1$ (Sb_2Se_3) and $w = 2$ (Sb_4Se_6) respectively. These calculations indicate that additional transforms using the same R and Z with other values of w would never result in a resonable fit between the transformed experimental and the ideal liquidus.

A more realistic approach to this problem requires the differentiation between a solution which is concentrated in Sb_2Se_3 and one which is dilute in Sb_2Se_3 (Se rich). If in the dilute solution case it is assumed that the ratio of the rings to chains is the same as for pure selenium but that the chain length as specified by Eisenberg and Tobolsky (2) or Keezer (3) is no longer valid, a magnitude for Z can be calculated using Eq. [12] and the experimental liquidus data. In Fig. 5 the results of these calculations carried out for various values of w are plotted. It is noted that the magnitude of Z for $w = 2$ (Sb_4Se_6) produces a curve whose temperature dependence is the same as the results of the previous workers (2, 3). On the basis of these chain-length temperature dependencies, Sb_4Se_6 is considered to be the best choice for the antimony triselenide specie. These observations suggest that Sb additions are not directly involved in the selenium polymerization reaction; however, they are effective selenium consumers decreasing the amount of selenium available for chain formation and their presence will change the configurational entropy of the solution. A similar but not completely analogous behavior was found for arsenic in arsenic-sulfur solutions (16).

The liquidus curves calculated based on these considerations is shown in Fig. 7. The open triangles show the fit obtained if the transform by Eq. [12] is carried out using the Briegleb (1) ring-chain concentrations (R), the calculated chain length denoted by (b) in Fig. 6, and the molecular unit for $w = 2$ (*i.e.* Sb_4Se_6).

The fit of the transformed data to the ideal liquidus is good, as it should be because the calculations were circular in nature. The experimental liquidus data was used to determine the chain lengths and "Sb_4Se_6" molecule for the transformation. At first it appears that no new information has been obtained, however this is not the case since these calculations have established that Sb_4Se_6 is a reasonable choice for the average molecular unit to which Sb_2Se_3 melts. This specie will be employed for all of the computations involving Sb_2Se_3 in other sections of the ternary system.

The concentrated solution case, near the Sb_2Se_3 end member, is not nearly as complicated as the dilute

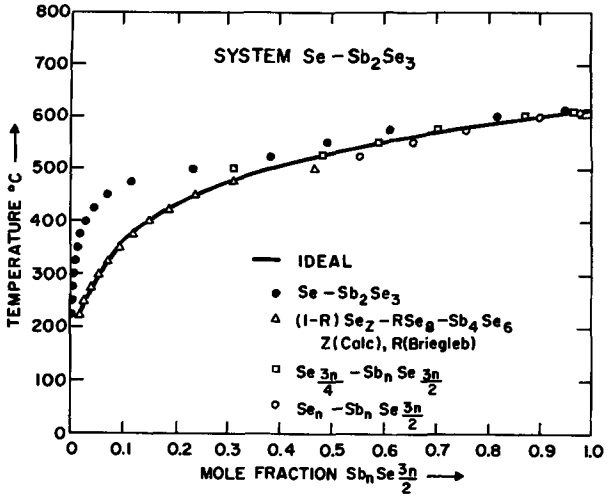

Fig. 7. Liquid structure calculation results for the system Se-Sb_2Se_3.

solution case. As indicated by the solid circles of Fig. 7, the Se-Sb_2Se_3 experimental liquidus almost coincides with the ideal liquidus in the Sb_2Se_3 rich portion. From this starting point, it was assumed that no Se_8 rings remained in these concentrated solutions, and that the liquid was composed of only two species Se_z chains and $w Sb_2Se_3$ aggregates. The open squares and circles of Fig. 7 show that the best fit results in liquid species where the Se chain is either three or four atoms long and the second species is Sb_4Se_6.

The As_2Se_3-Sb_2Se_3 system.—It has been concluded from viscosity (4), glass transition (5), infrared (6), and x-ray (17) studies that As_2Se_3 glasses are composed of $AsSe_{3/2}$ linkages forming $As_mSe_{3m/2}$ aggregates or networks. This conclusion will be applied to the interpretation of this binary system by carrying out the following transformation

$$As_2Se_3 - Sb_2Se_3 \rightarrow As_mSe_{3m/2} - (w)Sb_2Se_3 \quad [13]$$

by

$$X = \frac{y/w}{(1-y)\left(\frac{2}{m}\right) + y/w} \quad [14]$$

The variables X and y were identified in transformation 12 and m is an integer which specifies the size of the arsenic triselenide aggregate.

The transformation specified in Fig. 8 indicates that the best fit is for a liquid solution where the w/m ratio in Eq. [13] is one. Assuming the value of 2 for w the molecular constitution of the As_2Se_3-Sb_2Se_3 system in the 30 to 100 mole per cent (m/o) Sb_2Se_3 range would be a mixture of "average" species, of As_2Se_3 and Sb_4Se_6.

The As_4Se_4-Sb_2Se_3 section.—It is expected that no As_4Se_4 species should exist in the liquid because As_4Se_4 is an incongruently melting compound (5). That is to say, a liquid with an $As_{0.50}Se_{0.50}$ composition will probably be composed of liquid species other than those representative of the crystalline compound. This deduction is supported by x-ray analysis (17) of As_4Se_4 glasses where it appears that $AsSe_{3/2}$ dominates the short range order. Based on this knowledge, the following transformation will be employed

$$As_4Se_4 - Sb_2Se_3 \rightarrow As_\phi Se_p - (w)Sb_2Se_3 - As_{z'} \quad [15]$$

and carried out with Eq. [16]

$$X = \frac{y/w}{(1-y)\left[\frac{4}{p} + \left(4 - \frac{4\phi}{p}\right)\left(\frac{1}{z'}\right)\right] + \frac{y}{w}} \quad [16]$$

A large number of trial solutions determined the best fit to be a coordinate system having $As_3Se_{9/2}$, Sb_4Se_6 and As_4 or As_6 as end members. These results are shown in Fig. 9. Of the three alternate sets of solutions given in Fig. 9, the last one ($As_3Se_{9/2}$-Sb_2Se_3-As) is discarded because the Sb_2Se_3 is not consistent with previous considerations. The other two sets are nearly identical except for a slight difference in the size of the As molecules. In comparison with these results, it is noted that As_4 is the predominant molecular species found in As vapor (18). Particularly for molecular substances, there are often strong similarities between liquid and vapor species hence the above species appear reasonable.

Discussion and Conclusion

The results of the three sets of analyses of the experimental liquidus curves are summarized in Table I. It becomes apparent that the incipient liquid immiscibility in the Se-Sb_2Se_3 system is due to two types of liquid solutions composed of different molecular species. In the selenium rich part of the system, there is the temperature dependent equilibrium mixture of rings and chains in solution with a specie of antimony triselenide. In the selenium poor part of the system, the Se_8 rings are absent, and the liquid solution consists of very short selenium chains (Se_3 or Se_4) and an antimony triselenide liquid species. Within the assumptions made in the calculations, it is concluded that Sb_4Se_6 is the most probable average molecular specie for the antimony triselenide melt for all concentrations analyzed.

The results of the calculations on *in situ* liquids in the As_2Se_3-Sb_2Se_3 system indicate that the average

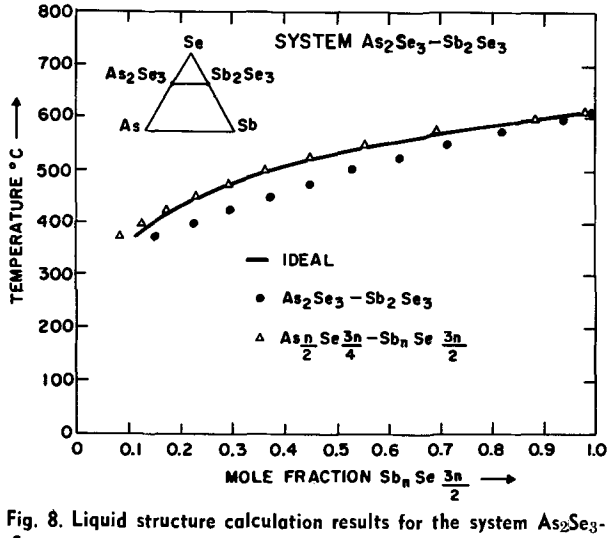

Fig. 8. Liquid structure calculation results for the system As_2Se_3-Sb_2Se_3.

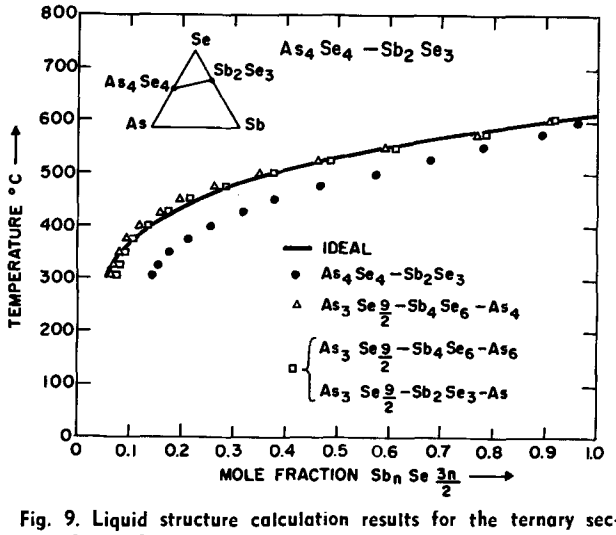

Fig. 9. Liquid structure calculation results for the ternary section As_4Se_4-Sb_2Se_3.

Table I. Possible liquid species from the thermodynamic analyses of the specified systems

System	Liquid species	
	Dilute (Sb_2Se_3 poor)	Concentrated (Sb_2Se_3 rich)
$Se - Sb_2Se_3$	$(1-R)Se_8 - (R)Se_3 - Sb_4Se_6$ $z = 70(280°C) \longleftrightarrow 5(500°C)$	$Se_{3n/4} - Sb_nSe_{3n/2}$ $Se_n - Sb_nSe_{3n/2}$ } $n = 4$
$As_2Se_3 - Sb_2Se_3$		$As_{n/2}Se_{3n/4} - Sb_nSe_{3n/2}$ $n = 4$
$As_4Se_4 - Sb_2Se_3$		$As_8Se_{9/2} - Sb_2Se_3 - As$ $As_8Se_{9/2} - Sb_4Se_6 - As_4$ $As_8Se_{9/2} - Sb_4Se_6 - As_6$

liquid species are As_2Se_3 and Sb_4Se_6. The high viscosity and easy quenchability of the As_2Se_3 liquid has been previously related to a structure consisting of aggregates of $AsSe_{3/2}$ linked networks. It would appear that the As_2Se_3 species found in the As_2Se_3-Sb_2Se_3 system are not consistent with such properties. However, it should be noted that the present analysis is only valid for solutions with appreciable amounts of Sb_2Se_3 present. The phase equilibria work carried out in this investigation has found that the addition of Sb_2Se_3 to As_2Se_3 has a radical effect on the viscosity of the melt and the crystallization kinetics of As_2Se_3 crystals. Pure As_2Se_3 is extremely viscous and crystals grow very slowly, whereas at a composition of 20 m/o Sb_2Se_3, a glass will devitrify quite readily with the relatively rapid formation of As_2Se_3 crystals. These observations support the presence of smaller or less associated As_2Se_3 species calculated for the binary system.

The liquid in the As_2Se_3-Se-Sb_2Se_3 ternary also has a tendency towards immiscibility as can be seen in the flattening of the liquidus in Fig. 4. From the information obtained from the Se-Sb_2Se_3 and the As_2Se_3-Sb_2Se_3 systems, it is possible to estimate the type of liquid species present in the ternary solutions. The properties of the selenium rich liquid are still dominated by the temperature dependent ring-chain equilibrium. This part of the system is made up of Se_z chains, Se_8 rings, Sb_4Se_6 molecules, and $AsSe_{3/2}$ network elements. As the selenium content of the liquid decreases the dominance of the ring-chain equilibrium decreases and finally disappears resulting in a liquid made up of As_2Se_3, Sb_4Se_6, and possibly Se_z (z is small) depending on the composition of the liquid.

The analysis of the As_4Se_4-Sb_2Se_3 section (Table I) indicates that with the exception of compositions near As_4Se_4 the system is composed of $As_8Se_{9/2}$, Sb_4Se_6, and As_4 species. The presence of As_4 is not expected to have a strong influence on the properties of the liquid because it is present as a minor constituent in this particular section. The molecular constitution of this section is quite similar to the As_2Se_3-Sb_2Se_3 system, as indicated by similarities in viscosity and crystallization behavior.

Acknowledgments

The authors wish to express their appreciation for the assistance of J. F. O'Neill during the experimental phases of the investigation and C. V. Bielan for the x-ray fluorescence analyses.

Manuscript submitted Dec. 16, 1970; revised manuscript received *ca.* April 20, 1971.

Any discussion of this paper will appear in a Discussion Section to be published in the June 1972 JOURNAL.

REFERENCES

1. G. Briegleb, *Z. Physik. Chem.*, **A144,** 321 (1929).
2. A. Eisenberg and A. V. Tobolsky, *J. Polymer Sci.*, **46,** 19 (1960).
3. R. C. Keezer and M. W. Bailey, *Mater. Res. Bull.*, **2,** 185 (1967).
4. S. Nemilov and G. Petrovskii, *Izv. An. SSSR Ser.*, **28,** 1283 (1964).
5. M. B. Myers and E. J. Felty, *Mater. Res. Bull.*, **2,** 535 (1967).
6. G. Lucovsky, *ibid.*, **4,** 505 (1969).
7. M. Hansen, "Constitution of Binary Alloys," pp. 1172-1174, McGraw-Hill Book Co., New York (1958).
8. N. Parravano, *Gazz. Chim. Ital.*, **43,** 210 (1913).
9. J. C. Slater, "Introduction to Chemical Physics," Chap. 17, McGraw Hill Book Co., New York (1939).
10. A. H. Cottrell, "Theoretical Structural Metallurgy," Chap. 10 and 11, Edward Arnold, London (1962).
11. H. K. Hardy, *Acta Met.*, **1,** 202 (1953).
12. J. Lumsden, "Thermodynamics of Alloys," p. 335, The Institute of Metals, London (1952).
13. J. S. Berkes and W. B. White, *J. Cryst. Growth*, **6,** 29 (1969).
14. A. C. Glatz and K. E. Cordo, *J. Phys. Chem.*, **70,** 3757 (1966).
15. N. W. Tideswell, F. H. Kruse, and J. D. McCullough, *Acta Cryst.*, **10,** 99 (1957).
16. A. T. Ward and M. B. Myers, *J. Phys. Chem.*, **73,** 1374 (1969).
17. B. Averbach, Personal communication.
18. A. F. Wells, "Structural Inorganic Chemistry," Third ed., p. 662, Oxford University Press, London (1962).

Chemical Vapor Deposited Tungsten–Mechanical Evaluation at High Temperatures

J. S. Chun

Division of Materials Science and Engineering, University of Utah, Salt Lake City, Utah 84112

and P. S. Nicholson

Department of Metallurgy and Materials Science, McMaster University, Hamilton, Ontario, Canada

and A. Sosin and J. G. Byrne

Divsion of Materials Science and Engineering, University of Utah, Salt Lake City, Utah 84112

ABSTRACT

A high-temperature hoop stress measurement apparatus has been developed for ring specimens of CVD tungsten or other refractory metal alloys. This apparatus has the advantage of being adaptable for high-temperature tensile testing. Force is applied to a tapered cone which transmits force to eight equal segments which press uniformly on the inner surface of the ring specimen. The specimen is heated by induction in either vacuum or a protective atmosphere. Equations are developed for stress and strain from hoop stress parameters. Room temperature hoop and tensile tests on aluminum, copper, and brass specimens were compared to ascertain the role of friction in the hoop stress tests. For temperatures up to 1400°C, the effective friction coefficient, μ, of the hoop testing apparatus was determined using CVD tungsten in a similar manner. Design details and the results of the elevated temperature tests on CVD tungsten are discussed.

In recent years there has been wide use of chemical vapor deposition (CVD) techniques to produce refractory metals and alloys. The most common CVD product has been thin-walled tubing. Standard tensile specimens are very difficult to prepare from such tubing.

Holman, Stiles, and Fung (1) have developed an apparatus for room temperature tensile tests of CVD rings. However, the mechanical behavior of tubular CVD materials at elevated temperatures had not been evaluated heretofore. A high temperature hoop stress measurement apparatus was developed for this purpose and is described in this paper. This new apparatus has the additional advantage of being adaptable to high temperature tensile testing.

Apparatus

Figure 1a shows a schematic of the high-temperature hoop stress apparatus. A downward force is applied to a tapered graphite cone which transmits force to eight equal segments that press out uniformly on the inner surface of the ring specimen putting the ring into tension. These components are shown in Fig. 1b. A helium gas atmosphere was used. Figure 2 shows a schematic of the high temperature tensile test apparatus. The transformation from hoop testing to tensile testing requires that only the support block and graphite cone be replaced by pull rods and specimen grips.

For descriptive purposes the apparatus is divided into the following parts: furnace chamber and heating system, load train, and temperature measurement.

Furnace chamber and heating system.—The furnace chamber is basically a 10 in. diameter stainless steel pipe, 13 in. high with ⅜ in. thick stainless steel flanges. A stainless steel plate is sealed with an O-ring to the top flange on the chamber. Motion of the upper pull (or compression) rod is achieved through a stainless steel bellows. The pull rod is a 15/16 in. diameter stainless steel rod, 7 in. long. The bottom flange of the chamber is O-ring sealed to a large stainless steel plate. A 2 in. long, 15/16 diameter stainless steel pull rod is welded to the bottom plate as shown in Fig. 2. Two flanged openings are provided on opposite sides of the heating chamber. A Pyrex window facilitates observation (for temperature measurement with an optical pyrometer) as well as vacuum and/or gas atmosphere introduction. The other flanged opening admits the induction coil. Water cooled copper tubing is wound around the outside and on the top of the furnace chamber.

A tantalum susceptor, heated by induction, radiates heat to the specimen. The power supply is a 20 kW Lepel Induction generator with a frequency of approximately 360,000 Hz. A 12:3 lead coil transformer is placed between the output of the generator and the vacuum seal coaxial lead into the furnace chamber. A 4-turn copper tubing coil with an inner diameter of 3 in. and a length of 1 in. was used for ring specimens. An inner diameter of 1¼ in. and a length of 1 in. was used for tensile specimens. The seamless tantalum susceptor had a ⅛ in. sighting hole to permit temperature measurement by an optical pyrometer.

Load train.—Hoop stress test apparatus.—The entire load train assembly is shown in Fig. 1a. The top of the stainless steel compression rod is threaded to the main compression rod. A ZrO_2 post, 2 in. in diameter and 1 in. high, is placed between the end of the compression rod and the top of the graphite cone to provide thermal insulation. Eight equal split ring graphite segments are set around the tapered cone; the angle of taper is 5°. Eight equal segments of a split ZrO_2 ring are placed between the graphite segments and the CVD ring specimen in order to prevent any possible carburization reaction between the graphite and the CVD tungsten. A ZrO_2 tube serves as a support for the two split rings, the specimen, and the cone. A typical CVD ring specimen is illustrated in Fig. 3b.

Tensile test apparatus.—The entire load train assembly is illustrated in Fig. 2. The top and bottom stainless steel pull rods are threaded into molybdenum alloy couplings. The latter are linked to molybdenum alloy pin grips. A typical flat CVD tungsten tensile specimen is illustrated in Fig. 3a.

Key words: deposition, hoop stress, high-temperature mechanical tests, chemical vapor deposition.

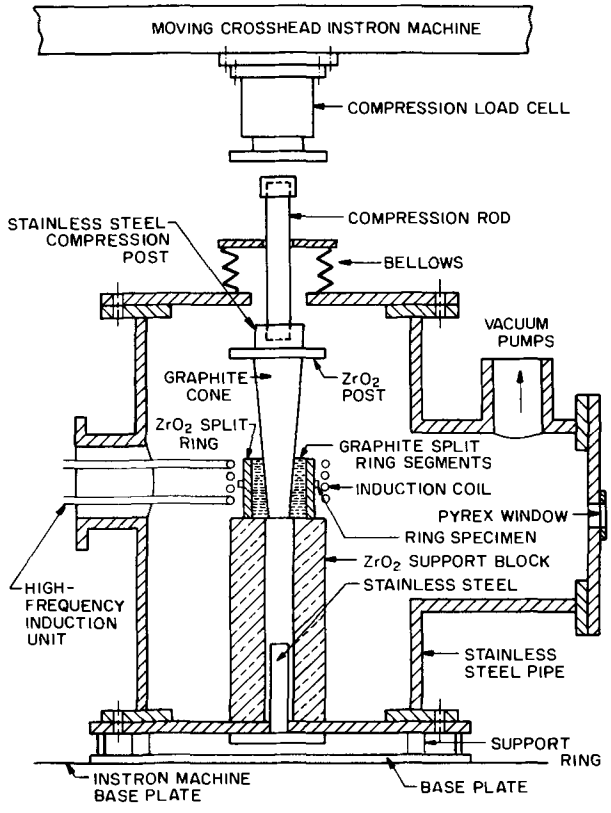

(a) Schematic of complete apparatus.

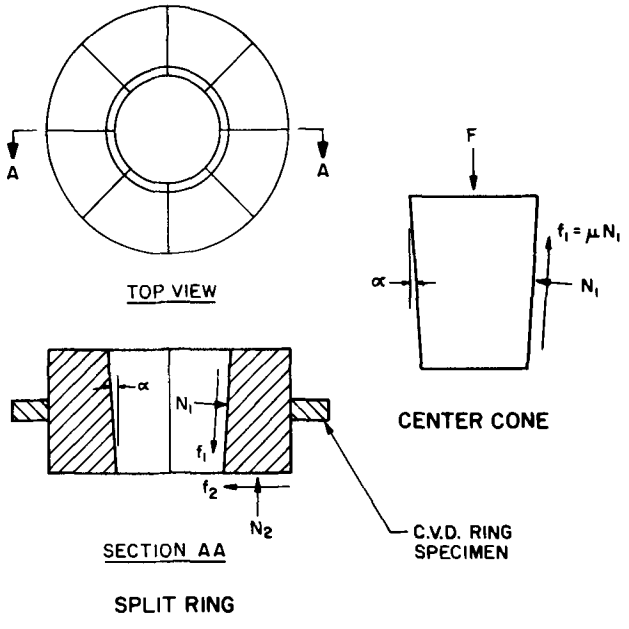

(b) Detail of split ring, cone and ring specimen.

Fig. 1. High-temperature hoop stress measurement apparatus.

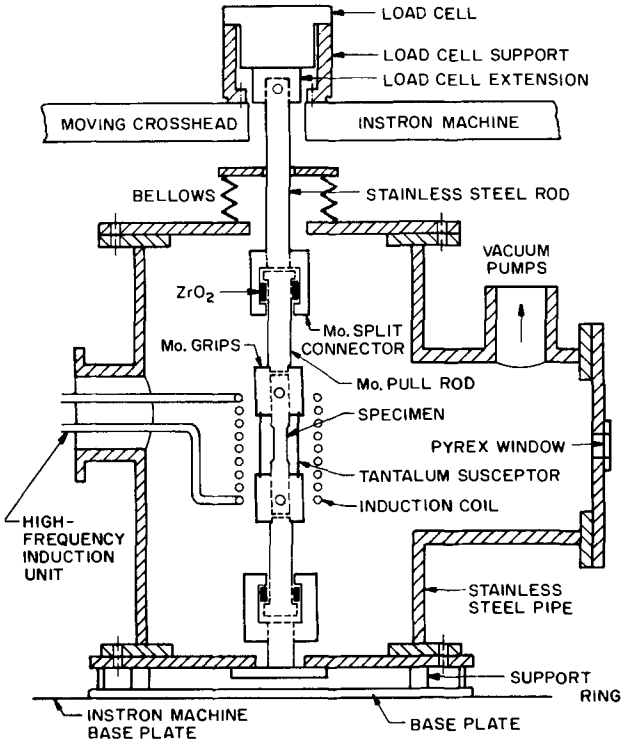

Fig. 2. High-temperature tensile testing apparatus

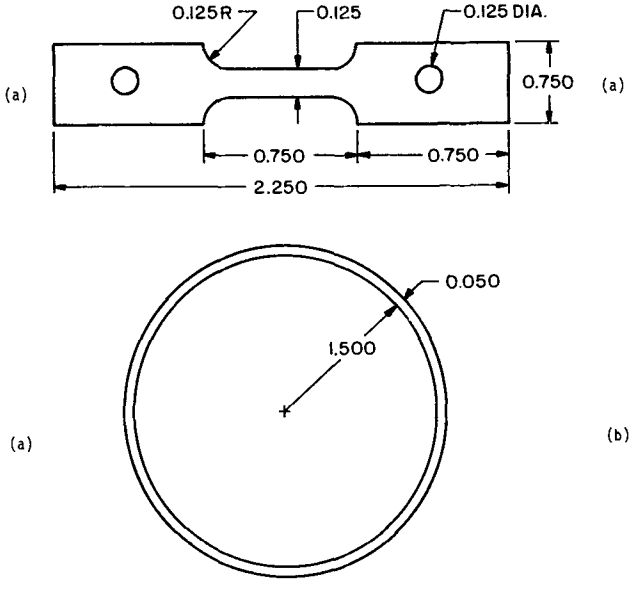

Fig. 3. Diagram of flat tensile (a) and thin-walled (b) specimens.

Temperature measurements.—Temperature measurements were made with an optical pyrometer calibrated by the National Bureau of Standards. An experiment was performed to estimate the temperature difference between an optical pyrometer focused on the specimen and a tungsten 5% rhenium-tungsten 26% rhenium thermocouple placed near the specimen. At 1400°C in a vacuum of 10^{-5} Torr, a temperature difference of 25°C was detected. In all subsequent tensile and hoop tests, the temperature was measured by the optical pyrometer.

Experimental

Sample preparation.—CVD tungsten tubes of 1.5 in. inside diameter and 0.050 in. wall thickness and flat 0.040 in. thick strips of CVD tungsten were purchased from the San Fernando Laboratories of Fansteel Metallurgical Company. The deposition conditions and chemical composition are presented in Tables I and II.

Ring specimens, ¼ in. long, were cut using a lathe tool post grinder with a 0.020 in. thick silicon carbide cutoff wheel operating at approximately 7000 rpm. The CVD tungsten tube was held in a soft collet. Gage

Table I. The deposition conditions of CVD tungsten

Gas flow	cc/min
WF_6	950
H_2	3800
Vacuum	½ atmosphere
Preheated gas temperature	675°C in argon
Deposition time	Approx. 3 hr
Substrate	304 stainless steel

Table II. Chemical analysis of CVD tungsten

Element	ppm
Carbon	6.0
Fluorine	2.0
Hydrogen	0.3
Oxygen	1.0
Nitrogen	<1.0
Aluminum	4.0
Copper	N/D 3.5
Iron	10.0
Nickel	N/D 15.0
Silicon	10.0

N/D means not detected at unit of sensitivity shown.

length and pin holes for flat tensile specimens were spark cut. Any slight damage to the specimen caused by spark cutting (and tool post cutting) was removed by electro-polishing (20g NaOH + 980 cc distilled water). The electropolishing produced a reduction of thickness of approximately 0.002 in.

Determination of texture.—Textures of flat and thin-wall tube CVD tungsten specimens were evaluated by the inverse pole figure x-ray technique (2, 3). A series of composite x-ray specimens were prepared from each of longitudinal, circumferential, outside and inside sections of the tubes, as illustrated in Fig. 4. The specimens were cut in a Servomet Spark Machine and electropolished. A GE X-RD5 diffractometer was used to measure the diffracted intensities. Texture results are expressed in terms of texture coefficients $TC_{(hkl)}$.

Testing procedure.—With the load train and specimen installed, the furnace chamber was evacuated, helium gas was admitted to the chamber, the specimen was slowly heated to the test temperature and left at this temperature for a period of 5 min to establish thermal equilibrium. Hoop stress and tensile tests were performed with an Instron Tensile Machine at a cross-head speed of 0.01 in./min.

Derivation of the Hoop Stress Equation

If a downward force F is applied to the graphite cone, see Fig. 1b, the conditions for equilibrium require

$$F = A_1N_1 (\sin \alpha + \mu_1 \cos \alpha) \quad [1]$$

where A_1 is the area of the tapered surface in contact with the split graphite ring, N_1 is the normal pressure on the tapered surface of the cone, α is the angle of taper, and μ_1 is the friction coefficient between the graphite cone and the graphite split ring.

Considering the split ring, the conditions for equilibrium require

$$A_2N_2 = A_1N_1 (\sin \alpha + \mu_1 \cos \alpha) \quad [2]$$

where A_2 is the total area of the bottom of the split ring and N_2 is the normal pressure on that area. Similarly, equilibrium requires that for the split ring, in the radial direction

$$A_rP + A_2N_2\mu_2 = A_1N_1 \cos \alpha - A_1N_1\mu_1 \sin \alpha \quad [3]$$

where A_r is the inner area of the ring specimen, P is the pressure on the inner surface of the ring, and μ_2 is the friction coefficient between the split ring and the support block.

Dividing Eq. [1] by Eq. [3], using the fact that from Eq. [1] and [2] $F = A_2N_2$, and assuming that μ_1 equals μ_2[1], then P is expressed by

$$P = \frac{F}{A_r}\left[\frac{(1-\mu^2)\cos\alpha - 2\mu\sin\alpha}{\sin\alpha + \mu\cos\alpha}\right] \quad [4]$$

If Eq. [4] is substituted into the hoop stress equation

[1] This assumption will be unnecessary in future work where the support block will also be graphite and the ZrO_2 split ring will not be in contact with the latter.

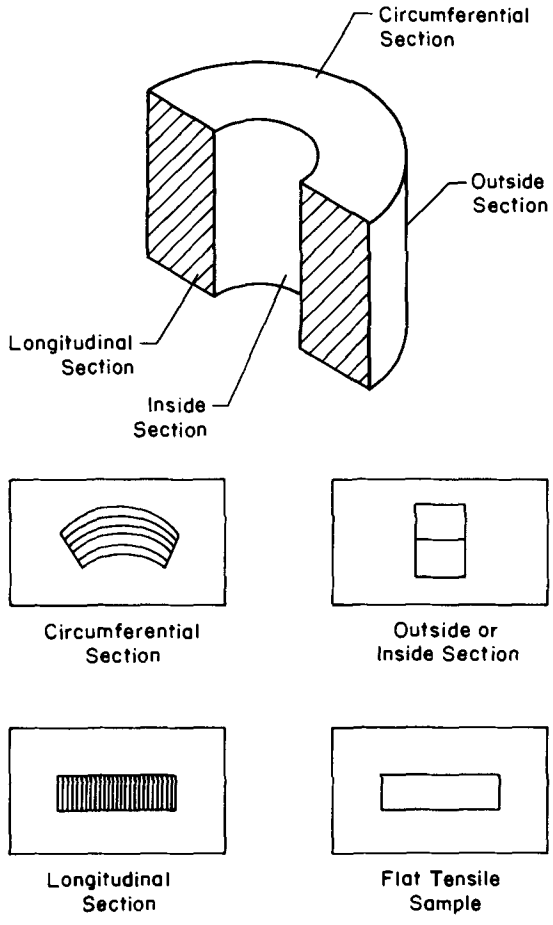

Fig. 4. Section designations for thin-walled CVD tungsten tubes and typical composite samples.

$$\tau_{hoop} = \frac{Pr}{t} \quad [5]$$

where τ is the circumferential stress, r is the internal radius of the ring specimen, and t is the ring thickness, then the hoop stress is expressed by

$$\tau_{hoop} = \frac{F[(1-\mu^2)\cos\alpha - 2\mu\sin\alpha]}{2\pi ht\,[\sin\alpha + \mu\cos\alpha]} \quad [6]$$

h being the height of the ring. Equation [6] has two unknowns, τ_{hoop} and μ the friction coefficient. The friction coefficient can be obtained from the following relation, assuming the tensile yield stress to equal the value of the hoop stress at yielding (See Appendix A).

$$\mu = \frac{-(\sigma/k\cos\alpha + 2\sin\alpha) + [(2\sin\alpha + \sigma/k\cos\alpha)^2 - 4\cos\alpha(\sigma/k\sin\alpha - \cos\alpha)]^{1/2}}{2\cos\alpha} \quad [7]$$

Table III. Tensile data

Material	Specimen number	0.2% yield stress (psi)	Total strain (%)
Brass	1	50,200	26
Brass	2	47,000	28
Brass	3	46,000	28
Brass	4	49,000	30
Brass	5	46,000	28
Brass	6	49,000	18
Brass	7	49,000	32
Brass	8	49,000	30
Al	9	38,000	14
Al	10	39,000	10
Al	11	38,000	13
Al	12	38,000	11
Al	13	38,000	11
Al	14	38,000	10
Al	15	37,000	12
Cu	16	18,000	34
Cu	17	17,000	28
Cu	18	17,000	28
Cu	19	17,000	30

Table IV. Hoop stress data

Specimen number	Material	Specimen height h (inches)	Thickness of specimen t (inches)	$k = \frac{F}{2\pi ht}$	σ(psi)	σ/k	Effective μ
1	Cu	1/16	1/16	4281	17,000	3.97	0.174
2	Cu	1/16	1/16	4586	17,000	3.70	0.193
3	Cu	1/16	1/16	4586	17,000	3.70	0.193
4	Cu	1/16	1/8	4687	17,000	3.62	0.193
5	Cu	1/16	1/8	4484	17,000	3.80	0.184
6	Cu	1/16	1/16	4512	17,000	3.76773	0.180
7	Cu	1/16	1/8	4178	17,000	4.069	0.164
8	Al	1/16	1/16	8356	38,000	4.55	0.145
9	Al	1/16	1/16	7133	38,000	5.33	0.115
10	Al	1/16	1/16	7948	38,000	4.78	0.135
11	Al	1/16	1/8	7745	38,000	4.90	0.131
12	Al	1/16	1/8	7948	38,000	4.78	0.135
13	Al	1/16	1/16	8560	38,000	4.439	0.146
14	Al	1/16	1/8	7745	38,000	4.9064	0.123
15	Brass	1/16	1/16	9172	48,000	5.23	0.119
16	Brass	1/16	1/16	8968	48,000	5.35	0.115
17	Brass	1/16	1/16	8560	48,000	5.607	0.104
18	Brass	1/16	1/16	9375	48,000	5.12	0.120
19	Brass	1/16	1/8	9273	48,000	5.1763	0.117

Here k is $F/2\pi ht$ and σ is the yield stress, separately obtained from a tensile test. It can be shown that the strain is expressed by

$$\epsilon = \frac{C_f - C_i}{C_i} = \Delta r/r_i$$

$$\epsilon = \frac{(\text{vertical distance moved by cone}) \tan \alpha}{r_i} \quad [8]$$

where C_i is the initial circumference, C_f is the final circumference, and r_i is the initial radius of the ring specimen.

Experimental Results and Discussion

Mechanical behavior at room temperature.—The relation between hoop stress and tensile stress has been studied with respect to the influence of friction at room temperature for the metals aluminum, copper,

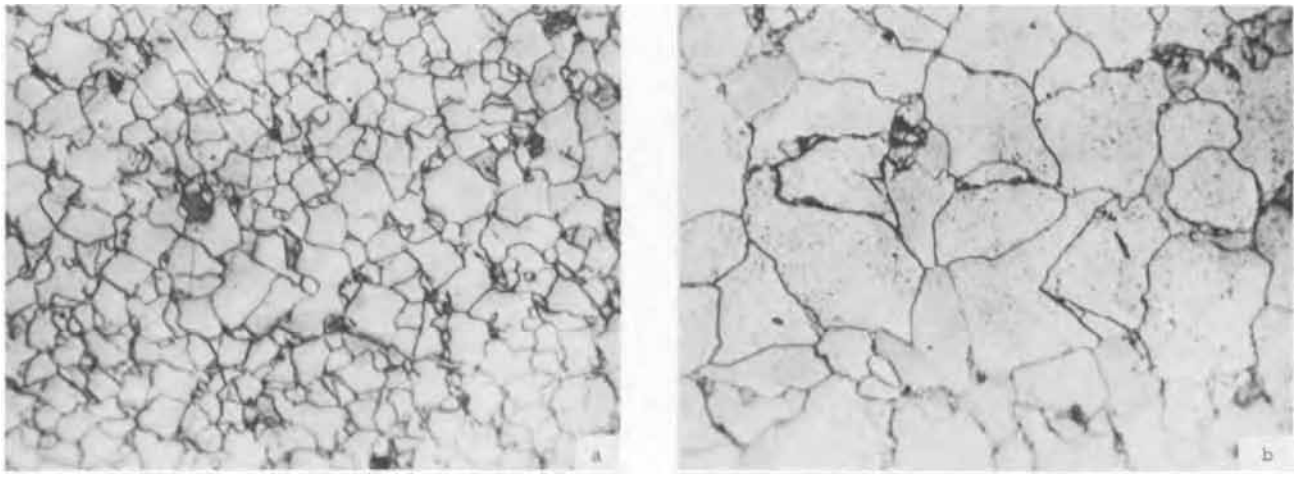

Fig. 5. Typical grain structure of flat specimens (300X). (a) Grain diameter of first deposited surface: 6.8 x 10^{-4} in. (b) Grain diameter 0.040 in. from first deposited surface: 1.1 x 10^{-3} in.

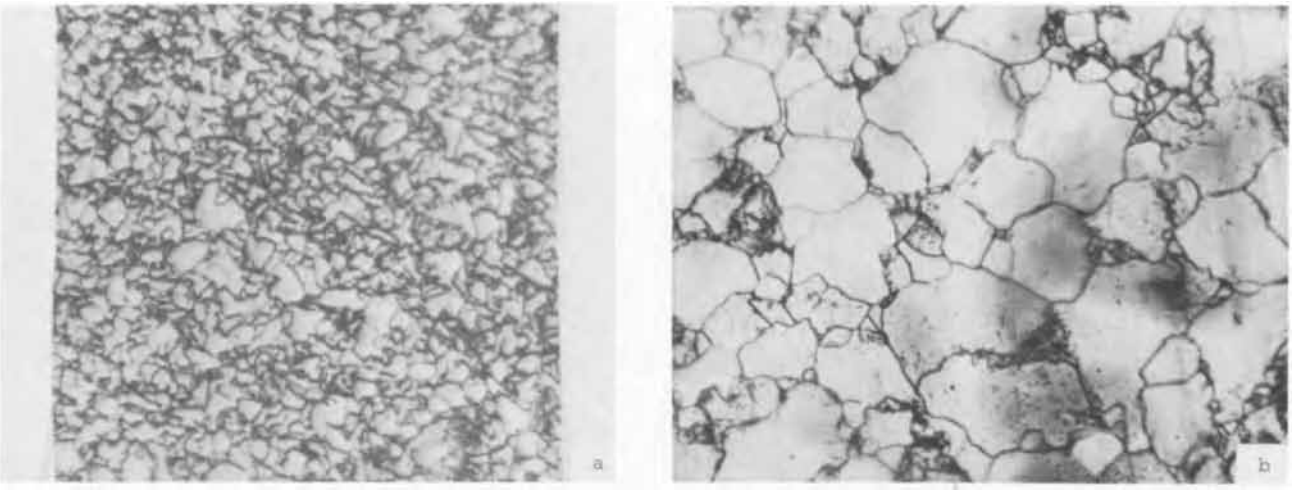

Fig. 6. Typical grain structure of a ring specimen (300X). (a) Grain diameter of first deposited surface: 3.1 x 10^{-4} in. (b) Grain diameter 0.050 in. from first deposited surface: 1.1 x 10^{-3} in.

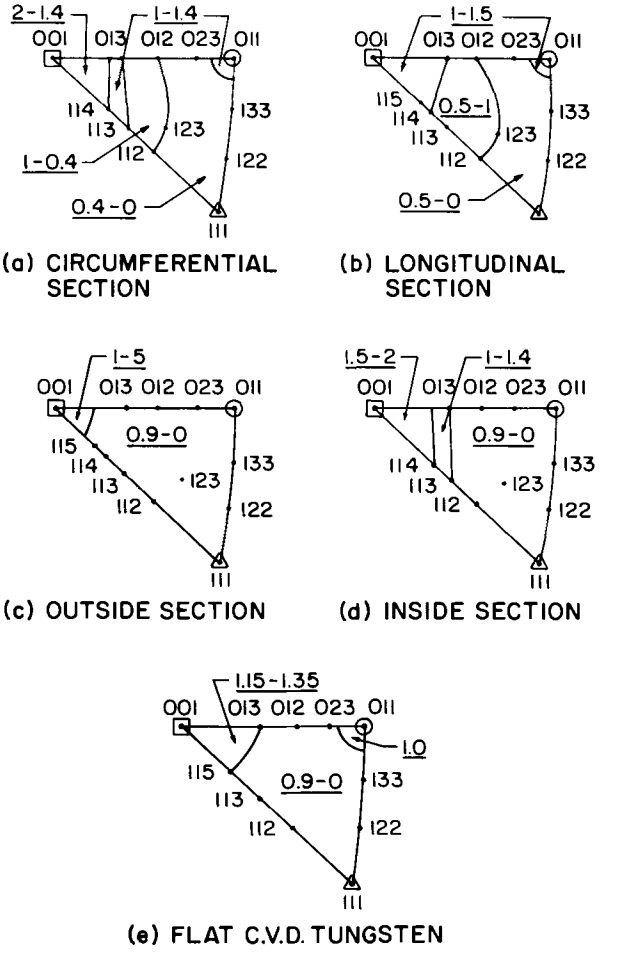

Fig. 7. Inverse pole figures for flat and thin-walled tube. (a) Circumferential section, (b) longitudinal section, (c) outside section, (d) inside section, (e) flat specimen.

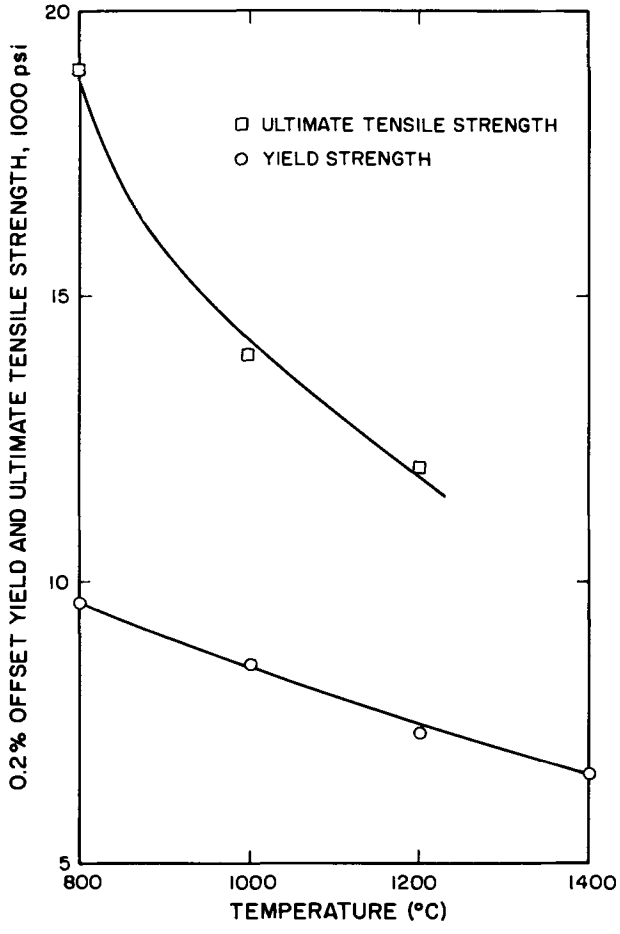

Fig. 8. Temperature dependence of 0.2% yield and tensile strength of flat specimens.

and brass. The tensile and hoop stress specimens were produced from the same plate for each metal.

The cone, split ring, and support block were of stainless steel. The results of tensile tests for these metals are summarized in Table III. The 0.2% yield stress values for each metal are self-consistent and reproducible. From tensile tests enumerated in Table III, the average value of 0.2% offset yield stress for brass is 48,000 psi, for aluminum 38,000 psi, for copper 17,000 psi. These values were substituted into Eq. [7] to obtain the effective friction coefficients for hoop stress measurements at room temperature. The effective friction coefficients for these metals are summarized in Table IV. For copper it varies from 0.17 to 0.19, for aluminum from 0.12 to 0.14, and for brass from 0.11 to 0.12. Thus, each metal has a very consistent and reproducible effective friction coefficient value. Since these results indicated the feasibility of hoop stress measurement at room temperature, the technique was extended to temperatures up to 1400°C for CVD tungsten.

Mechanical behavior at elevated temperatures.— Grain size and texture differences between the flat and thin-wall tube CVD tungsten were carefully noted since these could give mechanical property differences. Figure 5 shows typical flat specimen grain structures. The grain size of the first deposited surface was approximately 6.8 x 10^{-4} in. and 0.040 in. away from the first deposited surface the grain diameter became approximately 1.1 x 10^{-3} in. Figure 6 shows the grain structure of an as deposited CVD ring specimen. The first deposited surface grain diameter is approximately 3.1 x 10^{-4} in. and 0.050 in. away from the first deposited surface, the grain diameter was approximately 1.1 x 10^{-3} in. The tube outside surface grain diameter was almost the same as the last deposited surface of the flat specimens. Texture coefficients, $TC_{(hkl)}$, values for the various diffracting planes are plotted in standard stereographic triangles in Fig. 7. Contour lines include regions of similar TC values.

Circumferential, longitudinal, outside and inside tube sections have {100} as the highest intensity and a <100> fiber axis exists along the length of the tube. These results are similar to earlier findings of others (4, 5).

Figure 8 shows the temperature dependence of the 0.2% offset yield stress and the ultimate tensile stress of flat specimens. The temperature dependence of the elongation is shown in Fig. 9. The yield stress of 6,600 psi at 1400°C and the elongation of 30% at 1400°C are in good agreement with Taylor's (6) results.

The 0.2% yield stress values were substituted into Eq. [7] to obtain the friction coefficient μ for hoop stress tests at each temperature. The results are summarized in Table V. Figure 10 shows that μ decreases linearly with increasing temperature. Table VI shows that the strains calculated by Eq. [8] give very good agreement with the actual measurements. Appendix A presents some background equations and discussion of friction between specimen and segments.

Table V. Hoop stress data

Temperature (°C)	σ(Y.S. psi) from a tensile test	F (lb)	$k = F/2\pi ht$	σ/k	μ
800	6,900	315	4013	2.39	0.28
1000	8,500	240	3058	2.78	0.24
1200	7,300	170	2166	3.37	0.19
1400	6,600	120	1529	4.32	0.14

Table VI. Comparison of measured and calculated values of hoop strain

Temperature (°C)	Total measured strain (%)	Cross-head travel of instron (inches)	Strain calculated from Eq. [8] (%)
800	3.7	0.31	3.6
1000	2.4	0.19	2.2
1200	4.4	0.38	4.4
1400	4.4	0.38	4.4

Conclusions

The mechanical behavior at elevated temperatures of thin-walled CVD refractory metal tubing now can be evaluated directly from hoop stress tests. To do so, the friction coefficient, μ, of the apparatus must first be calibrated *via* tensile tests through the desired temperature range uisng the equation developed in this paper. The yield stress and elongation can then be readily calculated for hoop stress tests. Due to the segmented nature of the pressure on the specimen ring interior, one finds at larger plastic strains that straight chords develop between these segments. This makes the plastic behavior different from that of an ordinary tensile test. We therefore mainly advocate use of this method to determine high temperature yield stress values, although on a relative basis, the ring test is extremely useful in the plastic range as well.

The hoop stress method described here may be well suited to future application in the determination of friction coefficients of high-temperature materials. These would be used in the cone, base, and split ring components during such evaluation.

Acknowledgments

The authors acknowledge the support of ARPA Grant DAHC 15-69-C-0127 which made this work possible. The assistance of Mr. Hong Shim during testing was invaluable. The many helpful discussions with Dr. R. W. Haskell are appreciated.

Manuscript submitted Sept. 23, 1970; revised manuscript received *ca.* March 5, 1971. This was Paper 384 RNP presented at the Los Angeles Meeting of the Society, May 11-15, 1970.

Any discussion of this paper will appear in a Discussion Section to be published in the June 1972 JOURNAL.

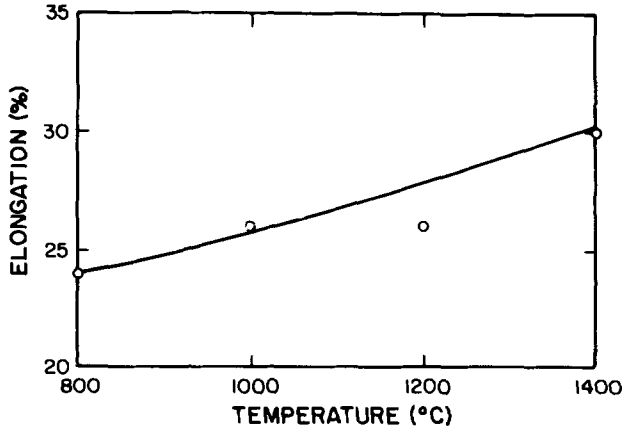

Fig. 9. Temperature dependence of the elongation of flat specimens.

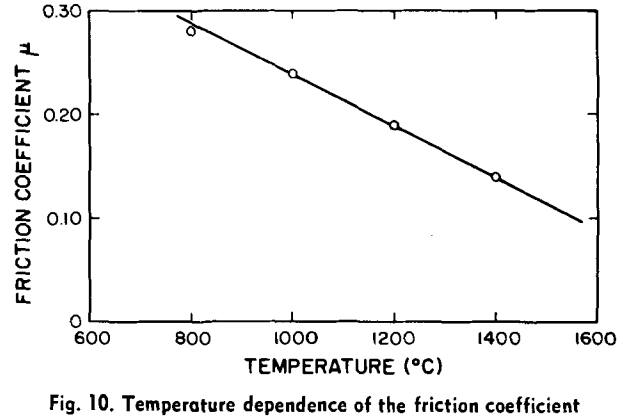

Fig. 10. Temperature dependence of the friction coefficient

APPENDIX A

Clearly the hoop stress test described produces seven straight unsupported chords in a ring specimen, between the eight ZrO_2 segments. This raises several questions: (*A*) Can a 0.2% offset yield stress value from a tensile test be put into Eq. [7] to evaluate μ? (*B*) What influence does friction between the segments and the specimen have? (*C*) How valid is Eq. [8]?

(*A*) If one calculates the change in circumference of a ring of radius 0.75 in. necessary to produce a 0.2% strain, the result is 0.00094 in. If this is distributed over the seven chords the individual chord length or segment separation distance would be 0.000135 in. If some of the 0.2% strain is distributed over supported specimen lengths as well, then clearly the segment separation is even less significant. In either case the tensile stress and strain should be essentially the same at all locations around the circumference of a ring.

(*B*) Frictional stress between the segments and the specimen should act on the inner surface of the specimen in a sense opposite to the tensile stress. Timoshenko (7) showed that the circumferential stress, σ_θ, in a cylinder of inner radius a and outer radius b, subject to internal pressure p_i is

$$\sigma_\theta = \frac{a^2 p_i}{b^2 - a^2}\left(1 - \frac{b^2}{r^2}\right) \qquad [9]$$

This stress is a maximum on the inner surface; however, if $b \leq 1.1a$, then σ_θ max, exceeds σ_θ min by only 10.5%. Thus one can assume a uniform stress equal to $p_i a/(b-a)$ through the wall thickness when $b \leq 1.1a$. This formula is the same as our Eq. [5]. In our case a and t are approximately 0.75 in. and 0.050 in., respectively; so that we are well within this limit. However, if there is some unbalance such that the applied tensile stress is higher at the inner surface, then the direction of any segment-specimen friction should help remove the unbalance. At plastic strains beyond the yield point seven straight chords should develop in the specimen. In the specimen parts in contact with the segments, the circumferential frictional force should be $A_r P \mu_3/16$, in which A_r and P are as defined in the text and μ_3 is the appropriate friction coefficient. The 16 comes from considering each half of each of the eight segments. On the outer specimen surface the friction force is zero, so on the average the stress contribution on the ring cross-section from friction would be $A_r P \mu_3/32$. Thus in the unsupported regions the stress would be the ordinary hoop stress Pr/t, but in the supported sections the stress would be $Pr/t - A_r P \mu_3/32ht$ or

$$\sigma_s = \frac{Pr}{t}\left(1 - \frac{2\pi\mu_3}{32}\right) \qquad [10]$$

where the subscript s on σ represents "supported." Thus beyond the yield point one may expect stress fluctuations from supported to unsupported regions of approximately 6% if $\mu_3 \simeq 0.3$. This consideration need not be considered with regard to Eq. [7] for the reason given in item 1 above but should be considered in the plastic range.

(*C*) Despite the problem raised in item (*B*) above, Eq. [8] does seem to predict the values of elongation at fracture fairly well. Equation [8] should, however, only be regarded as a first approximation to the actual situation.

REFERENCES

1. W. R. Holman, E. B. Stiles, and E. Fung, *J. Sci. Instrum.*, **44**, (1967).
2. G. B. Harris, *Phil Mag.*, **43**, 112 (1952).
3. E. F. Sturcken and W. G. Duke, AEC Research and Development Report DP-607, E. I. du Pont de

Nemours & Company, Savannah River Lab. (November 1961).
4. A. C. Schaffhauser and R. L. Heestand, Thermionic Conversion Specialist Conference of IEEE in Houston, Texas, (1966).
5. J. F. Berkeley, A. Brenner, and W. E. Reid, Jr., *This Journal*, **114**, 561 (1967).
6. J. L. Taylor and D. H. Boone, *J. Less-Common Metals*, **6**, 157 (1964).
7. S. Timoshenko and J. N. Goodier, "Theory of Elasticity," McGraw Hill Book Co., New York (1951).

Thermodynamic Properties of Ternary Refractory Carbides

I. Zirconium-Niobium-Carbon

C. K. Jun and M. Hoch

Department of Materials Science and Metallurgical Engineering, University of Cincinnati, Cincinnati, Ohio 45221

ABSTRACT

The nonstoichiometry of zirconium-niobium-carbide with the sodium-chloride type structure, $Zr_xNb_{1-x}C_y$, was studied by measuring the activities of the components as a function of composition. Equations for the activities of the components as a function of composition were derived from statistical considerations, based on the pairwise interaction energies between various components, E_{ij}.

$$RT \ln a_1 \cdot \frac{1}{x(1-y)} = E_1 + \frac{E_{11}}{2} + (1-x)^2 \left(E_{12} - \frac{E_{11}+E_{22}}{2} \right) + (1-x)y\,(E_{13} - E_{23}) - \frac{1}{2} y^2 E_{33} - RT \ln K_1(T)$$

$$RT \ln a_2 \cdot \frac{1}{(1-x)(1-y)} = E_2 + \frac{E_{22}}{2} + x^2 \left(E_{12} - \frac{E_{11}+E_{22}}{2} \right) + xy\,(E_{23} - E_{13}) - \frac{1}{2} y^2 E_{33} - RT \ln K_2(T)$$

$$RT \ln a_3 \cdot \frac{(1-y)}{y} = E_3 + xE_{13} + (1-x)\,E_{23} + yE_{33} - RT \ln K_3(T)$$

Subscript 1 refers to Zr, 2 to Nb, and 3 to C. The energy terms, $(E_{12} - (E_{11} + E_{22})/2)$, $(E_{13} - E_{23})$, and E_{33} were determined by measuring the variation with composition of the ratio of the activities of the various components. The ratio of activities of the various components at one composition was determined in one experiment; thus, the usual errors in temperature measurement were eliminated. For this study a Bendix Time-of-Flight Mass Spectrometer was used. The samples were prepared by heating the required amounts of oxides and graphite in a high-vacuum induction furnace. The metal-metal interaction energy

$$\left[E_{12} - \left(\frac{E_{11}}{2} + \frac{E_{22}}{2} \right) \right] = 6.54 \pm 0.27 \text{ kcal/mole}$$

is not much different from that in the bcc metallic zirconium-niobium system. The difference between the zirconium-carbon and the niobium-carbon interaction energies $(E_{13} - E_{23})$ is linearly dependent on composition

$$(E_{13} - E_{23}) = (1.08 \pm 0.11) - (6.15 \pm 0.44)\,x \text{ kcal/mole}$$

whereas E_{33}, the carbon-carbon interaction energy, can be expressed as

$$E_{33} = 15.62 + 9.37x - 29.50x(1-x) \text{ kcal/mole.}$$

Space-age requirements for high-temperature materials have created considerable interest in metal-carbon systems primarily because of their high melting temperatures and hardnesses. A number of the resulting investigations have been concerned with the high-temperature phase relationships in binary and ternary systems of refractory transition metals and carbon.

Since the transition metal carbides exist over a wide range of homogeneity, it is necessary to know the activities (or partial molar free energies) of the metal and carbon atoms as a function of composition in order to predict thermodynamic relations and investigate engineering applications.

Key words: carbides, zirconium, niobium, carbon, thermodynamics.

Hoch *et al* (1-5) studied those carbides, nitrides, and oxides of the refractory metals which have a sodium-chloride type structure, and deduced from statistical considerations equations to determine the activities of the components in compounds which deviate from stoichiometry.

The main purpose of the present investigation is to determine the relative activities of the components as a function of composition in the single-phase region of the ternary carbide system, $Zr_xNb_{1-x}C_y$.

Theory

In the single-phase region of the Zr-Nb-C system having a sodium-chloride type structure, the metal sites are randomly filled with zirconium and niobium

atoms, whereas some of the nonmetal sites are empty. Depending on the ratio of zirconium atoms to niobium atoms and the fraction of the nonmetal sites which are empty, the composition of the material can vary. The general formula of this material can be written: $Zr_xNb_{1-x}C_y$ where $0 < x < 1, 0 < y < 1$.

From statistical considerations, the grand partition function for this type of structure is

$$\text{GPF} = \sum \frac{N!}{N_1!(N-N_1)!} \cdot \frac{N!}{N_3!(N-N_3)!} [a_1K_1(T)]^{N_1} [a_2K_2(T)]^{N-N_1} [a_3K_3(T)]^{N_3} \exp\left[-\frac{1}{kT}\left(N_1E_1 + N_2E_2 + N_3E_3 + \frac{N_1^2}{2N}E_{11} + \frac{N_2^2}{2N}E_{22} + \frac{N_3^2}{2N}E_{33} + \frac{N_1N_2}{N}E_{12} + \frac{N_1N_3}{N}E_{13} + \frac{N_2N_3}{N}E_{23}\right)\right] \quad [1]$$

where N is the number of available metal (and carbon) sites and N_i is the number of atoms of element i (subscript 1 refers to Zr, 2 to Nb, 3 to C); a_i is the absolute activity of each component in the crystal phase; $K_i(T)$ is the contribution of an added atom to the partition function for the normal vibrational modes of the crystal; E_i is the energy required to bring an atom from its standard state into the sodium-chloride type lattice; and E_{ij} is the pairwise interaction energy. The small number of Schottky defects and Frenkel disorders present in the metal and nonmetal sublattice can be neglected.

By well-known treatment (6), the following equations are obtained.

$$RT \ln a_1 = RT \ln \frac{(N-N_2)(N-N_3)}{N^2} - RT \ln K_1(T) + \left[E_1 + \frac{N^2-N_2^2}{2N^2}E_{11} - \frac{N_2^2}{2N^2}E_{22} - \frac{N_3^2}{2N^2}E_{33} + \frac{N_2^2}{N^2}E_{12} + \frac{N_2N_3}{N^2}E_{13} - \frac{N_2N_3}{N^2}E_{23}\right] \quad [2]$$

$$RT \ln a_2 = RT \ln \frac{(N-N_1)(N-N_3)}{N^2} - RT \ln K_2(T) + \left[E_2 + \frac{N^2-N_1^2}{2N^2}E_{22} - \frac{N_1^2}{2N^2}E_{11} - \frac{N_3^2}{2N^2}E_{33} + \frac{N_1^2}{N^2}E_{12} + \frac{N_1N_3}{N^2}E_{23} - \frac{N_1N_3}{N^2}E_{13}\right] \quad [3]$$

$$RT \ln a_3 = RT \ln \frac{N_3}{N-N_3} - RT \ln K_3(T) + \left[E_3 + \frac{N_3}{N}E_{33} + \frac{N_1}{N}E_{13} + \frac{N_2}{N}E_{23}\right] \quad [4]$$

Introducing the equations

$$N_1 + N_2 = N$$

$$\frac{N_1}{N} = x$$

$$\frac{N_2}{N} = 1 - x$$

$$\frac{N_3}{N} = y$$

gives

$$RT \ln a_1 \cdot \frac{1}{x(1-y)} = E_1 + (1-x)^2\left[E_{12} - \frac{E_{11}}{2} - \frac{E_{22}}{2}\right] + \frac{E_{11}}{2} + (1-x)yE_{13} - (1-x)yE_{23} - \frac{1}{2}y^2E_{33} - RT \ln K_1(T) \quad [5]$$

$$RT \ln a_2 \cdot \frac{1}{(1-x)(1-y)} = E_2 + x^2\left[E_{12} - \frac{E_{11}}{2} - \frac{E_{22}}{2}\right] + \frac{E_{22}}{2} + xyE_{23} - xyE_{13} - \frac{1}{2}y^2E_{33} - RT \ln K_2(T) \quad [6]$$

$$RT \ln a_3 \cdot \frac{(1-y)}{y} = E_3 + yE_{33} + xE_{13} + (1-x)E_{23} - RT \ln K_3(T) \quad [7]$$

Equations [5], [6], and [7] reduce to the binary equations (1, 7) if either x or y are taken to be 0. By combining Eq. [5], [6], and [7], the following equations are obtained

$$RT \ln \frac{a_1}{a_2} \cdot \frac{(1-x)}{x} = E_1 - E_2 + (1-2x)\left[E_{12} - \frac{E_{11}}{2} - \frac{E_{22}}{2}\right] + \frac{1}{2}[E_{11} - E_{22}] + y[E_{13} - E_{23}] - RT \ln \frac{K_1(T)}{K_2(T)} \quad [8]$$

$$RT \ln \frac{a_1}{a_3} \cdot \frac{y}{x(1-y)^2} = E_1 - E_3 + \frac{E_{11}}{2} - E_{13} + (1-x)(1+y)[E_{13} - E_{23}] + (1-x)^2\left[E_{12} - \frac{E_{11}}{2} - \frac{E_{22}}{2}\right] - \left(y + \frac{y^2}{2}\right)E_{33} - RT \ln \frac{K_1(T)}{K_3(T)} \quad [9]$$

$$RT \ln \frac{a_2}{a_3} \cdot \frac{y}{(1-x)(1-y)^2} = E_2 - E_3 + \frac{E_{22}}{2} - E_{23} + x(1+y)[E_{23} - E_{13}] + x^2\left[E_{12} - \frac{E_{11}}{2} - \frac{E_{22}}{2}\right] - \left(y + \frac{y^2}{2}\right)E_{33} - RT \ln \frac{K_2(T)}{K_3(T)} \quad [10]$$

When a Knudsen cell at temperature T°K is placed in a mass spectrometer, the fundamental equation relating the partial pressure P_i of species i to the measured ion current I_i is

$$K_iP_i = I_iT \quad [11]$$

where K_i is a constant reflecting the physical and electromagnetic dimensions of the apparatus, the probability of formation of ions by electron bombardment, and the sensitivity of the detector to these ions.

A ratio of vapor pressures can thus be related to current intensities as follows

$$\frac{P_i}{P_j} = \frac{K_j}{K_i}\frac{I_i}{I_j} = C\frac{I_i}{I_j} \quad [12]$$

where $C = K_j/K_i$. Since

$$\frac{a_i}{a_j} = \frac{P_i}{P_j} \cdot \frac{P^o_j}{P^o_i} \quad [13]$$

the ratio of activities a_i can be related to the ratio of current intensities I_i

$$RT \ln \frac{a_i}{a_j} = \left(RT \ln \frac{I_i}{I_j} + RT \ln C \right) + RT \ln \frac{P^{o}_{j}}{P^{o}_{i}} \quad [14]$$

or

$$RT \ln \frac{a_i}{a_j} = RT \ln \frac{I_i}{I_j} + Q \quad [15]$$

where

$$Q = RT \ln C + RT \ln \frac{P^{o}_{i}}{P^{o}_{j}} \quad [16]$$

From Eq. [8], [9], [10], and [15], the energy terms in Eq. [5], [6], and [7] can be evaluated by measurements of the intensity ratios I_i/I_j as a function of composition.

In a mass spectrometer, ion intensities of various species can be measured at the same time; thus, the ratio of two activities can be obtained in one experiment. This is the great advantage of the present treatment. In all previous methods of measurement, the activity of a component has been obtained by measuring the pressure (or ion intensity) of the alloy in one experiment and that of the pure element in another. At high temperatures, though, it is difficult to obtain the same temperature in two different experiments because even the temperature determination with an optical pyrometer cannot be done better than ±5°K. As the pressure varies exponentially with temperature, an uncertainty of ±5°K in the temperature measurements can make the value of the derived activity very uncertain.

In the present experimental setup, the two activities are compared at the same temperature, the value of which may be uncertain to ±5°K. However, since the activity of the components does not vary much with temperature, this uncertainty is of no great importance. Moreover, because only the variation of the intensity ratios with composition is required, equilibrium is no longer necessary in the Knudsen cell. If Langmuir conditions are present and the components have vaporization coefficients α_i and α_j, the derived energy terms will be correct even when $\alpha_i \neq \alpha_j$. The only requirement is that α_i/α_j is independent of composition. This makes things much simpler than when equilibrium had to be established in the cell before meaningful activities could be obtained.

In addition, the use of the grand partition function and pairwise interaction energies provides a more detailed description of the activities of the component and the behavior of a solution than the quasichemical model or the more conventional polynomial expression for activities. Equations [5], [6], and [7] can be multiplied out to show that the present representation is equivalent to expressing the activity coefficient as a second order function of composition. The present interpretation also has the advantage that the coefficient can be related to mechanical properties (15).

Previous Investigations

Phase relationships.—The phase relationship in the binary zirconium-carbon system has been reviewed by Storms (8). The ZrC/Zr + ZrC boundary is located at $ZrC_{0.63}$ and is invariant in the temperature region 1900°-3300°C, and the ZrC/ZrC + C boundary is located at $ZrC_{0.96}$.

The phase relationships in the Nb-C system have also been reviewed by Storms (8). The homogeneity limits of the monocarbide are at $NbC_{0.70}$ and $NbC_{0.99}$.

The phase relationship of the Zr-Nb-C system was investigated by Stecher, Benesovsky, Neckel, and Nowotny (9). They found that the monocarbides formed a continuous series of solid solutions. At 1700°C, the lower limit of monocarbide region on the zirconium side was at $ZrC_{0.59}$ and at $NbC_{0.72}$ on the niobium side. The lattice parameter showed a very slight deviation from Vegard's law at the Nb-rich side when the carbon content was $y = 0.67$.

The phase relationship in the binary Zr-Nb metallic system is given by Elliott (10).

Thermodynamic investigations.—Hoch (7) has evaluated the activities of Zr and C and Nb and C in the binary carbides with the NaCl type structure and obtained the following results

For ZrC_y

$$RT \ln a_{Zr} \cdot \frac{1}{1-y} = (1 \pm 1) - (y^2)(14 \pm 1.5) \text{ kcal/mole} \quad [17]$$

$$RT \ln a_C \cdot \frac{1-y}{y} = -(35.2 \pm 4) - (28 \pm 3)(1-y) + 2.7 \times 10^{-3} T \text{ kcal/mole} \quad [18]$$

For NbC_y

$$RT \ln a_{Nb} \cdot \frac{1}{1-y} = -(0.05 \pm 1.0) - (y)^2 (7.6 \pm 1.3) \text{ kcal/mole} \quad [19]$$

$$RT \ln a_C \cdot \frac{1-y}{y} = -(28.6 \pm 2.5) - (15.2 \pm 2.5)(1-y) + 0.4 \times 10^{-3} T \text{ kcal/mole} \quad [20]$$

Though the data were deduced from experimental results obtained at very high temperatures (2500°-2700°K) they give heats of formation comparable to calorimetric measurements which are obtained at room temperature (11).

In the zirconium-niobium binary metallic solution, which is bcc, Hoch (12) has derived from the phase diagram the metal interaction energy in the solid $E_{12} - (E_{11}/2 + E_{22}/2) = 4.9 \pm 0.3$ kcal/mole.

Equipment and Materials

High-temperature, induction-heated, vacuum furnace.—A cylindrical, water-cooled, vacuum chamber, 6¼ in. ID and 12 in. high, was made out of copper. The power leads, copper tubing of ¼ in. diameter, enter the chamber through the rubber glass compression seals and are connected to a copper work coil. The work coil is 12 turns of ¼ in. diameter copper tubing, 3½ in. in length, 1½ in. ID, concentric with the heating chamber.

The vacuum system, connected to the chamber by a 2 in. ID copper pipe, consists of a 2 in. Veeco CT-200 brass cold trap, an N.R.C. H-4-P oil diffusion pump (Type 137), and a Welch Duo-Seal mechanical pump. The pressure is measured by a Veeco DG-2 cold cathode discharge gauge.

A tungsten crucible was placed on a tripod of tungsten rods in the center of the work coil. The power source used to heat material in the crucible is a 20 KW-Thermionic generator (Induction Heating Corporation, Model 1070) with an iron core, R.F. transformer (Taylor-Winfield Corporation, TD-74).

X-ray diffraction unit and mass spectrometer.—A Norelco x-ray diffraction unit and a Debye-Scherrer camera, with effective diameter of 114.6 mm and nickel-filtered copper Kα radiation, was used for taking x-ray diffraction patterns of the samples.

A Bendix Time-of-Flight Mass Spectrometer Model 12-101 was used to analyze the vapors effusing from the Knudsen cell.

Materials.—Carbon powder of 99.9999% purity, zirconium dioxide powder of 99.9% purity, and niobium pentoxide powder of 99.95% purity were obtained from Atomergic Chemetals Company, Division of Gallard Schlesinger Chemical Manufacturing Corporation, Carle Place, New York.

Experimental Procedure

Preparation of samples.—*NbC_y.*—Niobium pentoxide powder and carbon powder of desired compositions for $NbC_{0.95}$, $NbC_{0.9}$, and $NbC_{0.8}$ were mixed well and pressed into cylindrical pellets. Each pellet was then heated in the tungsten crucible at high vacuum for 24

hr at 2260°K. Afterwards Debye-Scherrer x-ray powder diffraction patterns were taken which confirmed the sodium-chloride type structure.

ZrC_y.—Zirconium dioxide powder and carbon powder of desired compositions for $ZrC_{0.95}$, $ZrC_{0.9}$, and $ZrC_{0.8}$ were mixed well and pressed into cylindrical pellets. Each pellet was then heated in the tungsten crucible at high vacuum for 24 hr at 1940°K. As for NbC_y, the fcc structure was subsequently confirmed by x-ray diffraction patterns.

$Zr_xNb_{1-x}C_y$.—ZrC_y powder and NbC_y powder of desired compositions for $Zr_xNb_{1-x}C_y$ were mixed well, pressed into cylindrical pellets, and heated in the tungsten crucible of the high vacuum furnace for 50 hr at a temperature of 2280°K. As with the two binary carbides, ZrC and NbC, the single phase of fcc structure was later confirmed by x-ray diffraction patterns.

One specimen of $Zr_{0.8}Nb_{0.2}C_{0.8}$ was submitted to Ledoux and Company for analysis and 20 ppm of oxygen was reported indicating very little oxygen contamination.

Mass spectrometer operation.—In order to maintain stable temperatures, tungsten Knudsen cells with 0.629 in. OD, 0.441 in. ID, and 0.562 in. height were used. The lids each had a 3/16 in. diam hole drilled into them. The samples were placed in a thin-walled tungsten cup which fitted into the Knudsen cell. Thus, the samples could not contaminate the Knudsen cell body. The relatively large hole in the lid allowed a large fraction of the vapor to escape from the Knudsen cell, and thus made experiments possible at the relatively low temperature of 2340°K.

The Knudsen cell power supply was operated at a constant filament current of 13.6A, and the bombardment voltage was adjusted to get the required temperature. A 15/1000 in. diam tungsten wire was used for the heating filament because it was found to have a much longer life than the 10/1000 in. diam recommended by the manufacturer.

When a new specimen is introduced into the Knudsen cell, it takes about 60-90 min to reach 2340°K. The temperature was measured with an L&N disappearing filament, optical pyrometer through a prism and a glass window, and then corrected for glass absorption and prism absorption.

The intensity of Zr^{90} (natural abundance 51.46%) was measured for zirconium. The intensity of Nb^{93} (natural abundance 100%) and the intensity of C^{12} (98.89%) were measured for niobium and carbon. The measured intensity was corrected for the deviation from electrometer linearity by calibrating with Cu^{63} and Cu^{65}.

Results and Discussion

The nominal composition of the samples is given in Table I, along with the lattice parameter. The lattice parameters were determined using the Nelson-Riley extrapolation method (13) to an accuracy of ±0.001Å.

Table I. Nominal composition and lattice parameter of samples

$Zr_xNb_{1-x}C_y$ x	y	Lattice parameter in Å Before exp.	After exp.	Literature
0.5	0.9	4.578	4.578	
0.141	0.9	4.491	4.490	
0.856	0.9	4.666		
0.5	0.95	4.575	4.576	
0.2	0.95	4.512		
0.7	0.95	4.624		
0.5	0.8	4.572	4.572	
0.2	0.8	4.493	4.491	
0.8	0.8	4.653	4.653	
0	0.9	4.467		
0	0.95	4.469		
0	0.8	4.451		
1	0.9	4.701		
1	0.95	4.699		
1	0.8	4.700		
1	1			4.696 (14)
0	1			4.470 (14)

Table I also contains several lattice parameters which were determined from data obtained after the vapor pressure measurements had been carried out in the Knudsen cell. Within experimental error, these lattice parameters agreed with those measured prior to the vapor pressure runs indicating very small composition change.

The experimental temperature of 2340°K was chosen as the lowest temperature which would give accurately reproducible intensities for the Zr, Nb, and C peaks. At lower temperatures the danger of surface depletion is much less because the activation energy for vaporization is larger than the activation energy for diffusion. As a result of this precaution, the vaporization rate was very low. At 2340°K Sample No. 3 lost only 3.5 mg during 8 hr heating in the Knudsen cell. Less than 2 hr were required to complete the mass spectrometric measurements on each sample.

Intensity rations of Zr^{90} to Nb^{93}, Zr^{90} to C^{12}, and Nb^{93} to C^{12} were measured for all specimens and are given in Table II. For each intensity ratio in Table II, both were measured 10 to 12 times, and the average of the readings was used to calculate the ratio.

Using

$$\frac{I_{Zr}}{I_{Nb}} = \frac{I_{Zr90}}{I_{Nb93}} \cdot C_1 \qquad [21]$$

where C_1 is constant, Eq. [8] and [15] give

$$RT \ln \frac{I_{Zr90}}{I_{Nb93}} \cdot \frac{(1-x)}{x} = (1-2x)\left[E_{12} - \frac{E_{11}+E_{22}}{2}\right] + \frac{1}{2}[E_{11} - E_{22}] + [E_1 - E_2] + y[E_{13} - E_{23}] - RT \ln \frac{K_1(T)}{K_2(T)} - Q - RT \ln C_1 \qquad [22]$$

Plotting $RT \ln I_{Zr90}/I_{Nb93} \cdot (1-x)/x$ *vs.* $(1-2x)$, with y constant, (Fig. 1) shows a straight line relationship. Least squares analysis gives $\left(E_{12} - \frac{E_{11}+E_{22}}{2}\right) = 6.54 \pm 0.27$ kcal/mole, which is included in Table III. $\left(E_{12} - \frac{E_{11}+E_{22}}{2}\right)$ is the interaction parameter between the metal atoms in the fcc metal sublattice, and is of the same order of magnitude as the 4.9 ± 3 kcal/mole reported for the bcc metallic system (12).

By reorganizing Eq. [22] and plotting $\left[RT \ln \frac{I_{Zr90}}{I_{Nb93}} \frac{(1-x)}{x}\right] - \left(E_{12} - \frac{E_{11}+E_{22}}{2}\right)(1-2x)$ *vs.* y with x constant, $(E_{13} - E_{23})$ was calculated at various values of x. The results are presented in Table III, and Fig. 2 shows the linear variation of $E_{13} - E_{23}$

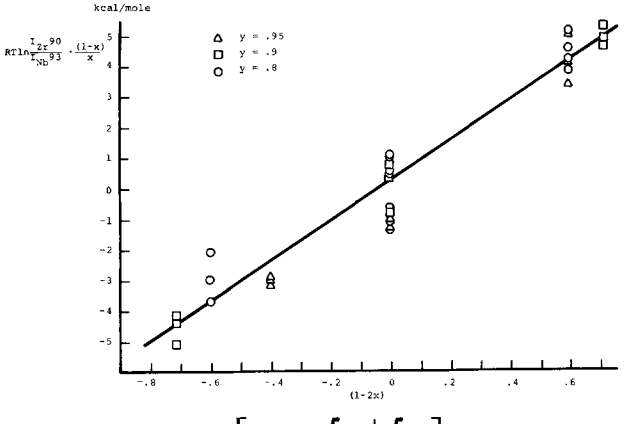

Fig. 1. Evaluation of $\left[E_{12} - \frac{E_{11}+E_{22}}{2}\right]$ in $Zr_xNb_{1-x}C_y$

Table II. Ion intensity ratios

Sample No.	$\frac{I_{Zr^{90}}}{I_{Nb^{93}}}$	$\frac{I_{Zr^{90}}}{I_{C^{12}}}$	$\frac{I_{Nb^{93}}}{I_{C^{12}}}$
1A			0.0154
			0.0243
			0.0232
1B		0.0346	
		0.0329	
		0.0376	
		0.0346	
		0.0376	
		0.0365	
		0.0356	
		0.0343	
1	1.165	0.0295	0.0253
	0.840	0.0280	0.0333
	0.919	0.0318	0.0345
3	0.510		0.0269
	0.463		0.0285
	0.441		0.0260
4	2.006	0.0221	
	2.320	0.0232	
	2.449	0.0189	
3A			0.167
			0.163
			0.156
			0.208
3B			
		0.466	
		0.444	
		0.453	
		0.403	
		0.357	
		0.385	
31	0.846	0.251	0.297
	1.241	0.203	0.164
	1.083	0.241	0.330
	1.116	0.226	0.208
	1.255	0.210	0.188
	1.093	0.226	0.202
	0.937	0.221	
	0.970		0.192
32	0.744		0.208
	0.568		0.249
	0.667		0.199
	0.605		
33	2.585	0.232	
	2.104	0.258	
	1.820	0.236	
		0.216	
21	0.760		
	0.807		
22	0.737		
	0.595		
	0.511		
23	1.260		
	1.247		
	1.188		

with composition. Least squares analysis gives $E_{13} - E_{23} = (1.08 \pm 0.11) - (16.15 \pm 0.44)$ x kcal/mole.

From Eq. [9], [10], [15], [16], Eq. [23] and [24] are derived

$$RT \ln \frac{I_{Zr90}}{I_{C12}} \cdot \frac{y}{x(1-y)^2} = \left[E_1 - E_3 - E_{13} + \frac{E_{11}}{2} \right] + (1-x)(1+y)[E_{13} - E_{23}] + (1-x)^2 \left[E_{12} - \frac{E_{11}+E_{22}}{2} \right] - \left(y + \frac{y^2}{2} \right) E_{33} - RT \ln \frac{K_1(T)}{K_3(T)} - RT \ln C_2 - Q \quad [23]$$

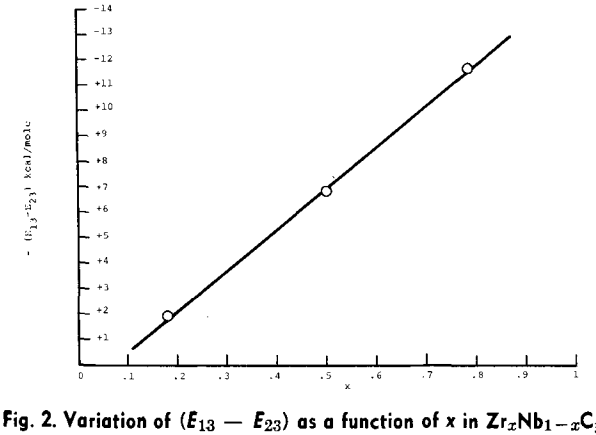

Fig. 2. Variation of $(E_{13} - E_{23})$ as a function of x in $Zr_xNb_{1-x}C_y$

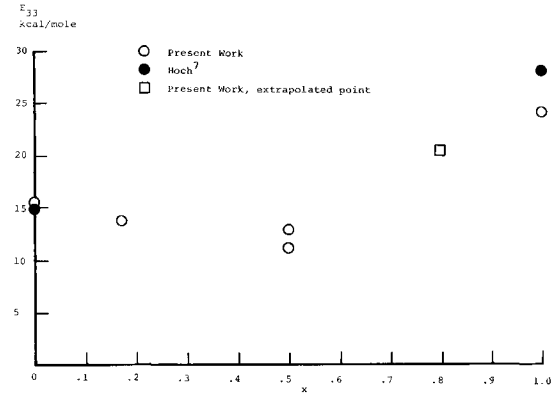

Fig. 3. Variation of E_{33} as a function of component in $Zr_xNb_{1-x}C_y$

$$RT \ln \frac{I_{Nb93}}{I_{C12}} \cdot \frac{y}{(1-x)(1-y)^2} = \left[E_2 - E_3 - E_{23} + \frac{E_{22}}{2} \right] + x(1+y)[E_{23} - E_{13}] + x^2 \left[E_{12} - \frac{E_{11}+E_{22}}{2} \right] - \left[y + \frac{y^2}{2} \right] E_{33} - RT \ln \frac{K_2(T)}{K_3(T)} - RT \ln C_3 - Q \quad [24]$$

Plotting

$$RT \ln \frac{I_{Zr90}}{I_{C12}} \cdot \frac{y}{x(1-y)^2} - (1-x)(1+y)[E_{13} - E_{23}] - (1-x)^2 \left[E_{12} - \frac{E_{11}+E_{22}}{2} \right]$$

vs. $[y + y^2/2]$ gives the carbon-carbon interaction energy, E_{33} varies as the composition of the sample changes. Its measured values are given in Table III. In addition, a value at $x = 0.8$ was obtained by using Sample No. 33 and an interpolated value between Samples No. 4 and 1. This value is therefore less accurate than the others.

In Fig. 3, E_{33} is plotted *vs.* composition. This shows the values for the binary systems, ZrC_y ($x = 1$, $E_{33} = 24.1 \pm 2.1$ kcal/mole) and NbC_y ($x = 0$, $E_{33} = 15.5 \pm 3.6$ kcal/mole), to be in very good agreement with values deduced by Hoch (7) (28 ± 3 kcal/mole and 15.2 ± 2.5 kcal/mole). Starting from niobium carbide on the left, E_{33} remains almost constant until $Zr_{0.5}Nb_{0.5}C_y$ and then rapidly increases to its value for zirconium carbide. This data can be well represented as a function of composition by $E_{33} = 15.62 + 9.37x - 29.50x(1-x)$ kcal/mole.

The carbon interaction energy in the ternary system can be looked upon as the interaction energy of two types of carbon atoms: a carbon atom belonging to niobium carbide and a carbon atom belonging to zirconium carbide. Therefore, there are in the system three

Table III. Calculated pairwise interaction energies in $Zr_xNb_{1-x}C_y$

x	$[E_{13} - E_{23}]$ kcal/mole	E_{33} kcal/mole
1		24.12 ± 2.10
0.8		20.36
0.785	−11.69 ± 2.32	
0.5	−6.83 ± 2.43	11.17 ± 1.47
0.5		12.96 ± 4.12
0.180	−1.91 ± 1.8	
0.171		13.72 ± 1.77
0		15.54 ± 3.60

$(E_{13} - E_{23}) = (1.08 \pm 0.11) - (16.15 \pm 0.44)\,x$ kcal/mole

$E_{33} = 15.62 + 9.37 \times -29.50(1-x)\,x$ kcal/mole

$\left(E_{12} - \frac{E_{11}+E_{22}}{2} \right) = 6.54 \pm 0.27$ kcal/mole independent of composition

types of carbon-carbon interaction energies: (*A*) the energy due to two niobium-carbon atoms, (*B*) the energy due to two zirconium-carbon atoms, and (*C*) the energy due to one zirconium-carbon and one niobium-carbon atom.

Acknowledgment

This research was supported in part by the National Aeronautics and Space Administration under Grant No. NGR 36-004-014.

Manuscript submitted Sept. 29, 1969; revised manuscript received *ca.* March 23, 1971. This was Paper 120 presented at the Detroit, Mich., Meeting of the Society, Oct. 5-9, 1969.

Any discussion of this paper will appear in a Discussion Section to be published in the June 1972 JOURNAL.

REFERENCES

1. M. Hoch, *Trans. AIME*, **230**, 138 (1964).
2. M. Hoch, A. S. Iyer, and J. Nelken, *J. Phys. Chem. Solids*, **23**, 1463 (1962).
3. M. Hoch, *J. Phys. Soc. Japan*, **18**, Suppl. II, 147 (1963).
4. M. Hoch and D. Ramakrishnan, *J. Phys. Chem. Solids*, **25**, 869 (1964).
5. M. Hoch and F. J. Furman, "Thermodynamics," Vol. II, p. 517, International Atomic Energy Agency, Vienna (1966).
6. R. Fowler and E. M. Guggenheim, "Statistical Thermodynamics," University Press, Cambridge (1949).
7. M. Hoch, "Phase Stability in Metals & Alloys," P. S. Rudman, J. Stringer, and R. I. Jaffee, Editors, p. 419, McGraw Hill Book Company, New York (1967).
8. E. K. Storms, Refractory Carbides, in "Refractory Materials," Vol. II, Academic Press, New York (1967).
9. P. Stecher, F. Benesovsky, A. Neckel, and H. Nowotny, *Monatsh. Chem.*, **95**, 1630 (1964).
10. R. P. Elliott, "Constitution of Binary Alloys," First Supplement, McGraw Hill Book Company, New York (1965).
11. M. Hoch, "Anisotropy in Single-Crystal Refractory Compounds," Vol. I, p. 163, Plenum Press, New York (1968).
12. M. Hoch, *Trans. AIME*, **224**, 379 (1962).
13. L. A. Azaroff and M. J. Buerger, "The Powder Method in X-ray Crystallography," McGraw-Hill Book Company, New York (1958).
14. A. Taylor and B. J. Kagle, "Crystallographic Data on Metal and Alloy Structure," Dover Publications, Inc., New York (1963).
15. M. Hoch and S. Yamauchi, *This Journal*, (in press).

Thermodynamic Properties of Ternary Refractory Carbides

II. Zirconium-Uranium-Carbon and Zirconium-Hafnium-Carbon

M. Hoch, M. G. Hapase, S. Yamauchi

Department of Materials Science and Metallurgical Engineering, University of Cincinnati, Cincinnati, Ohio 45221

ABSTRACT

The thermodynamic properties of [ternary] zirconium-uranium-carbide $Zr_xU_{1-x}C_y$ and zirconium-hafnium-carbide $Zr_xHf_{1-x}C_y$ both with a sodium-chloride type structure were studied using the time-of-flight mass spectrometer. The ratio of the activities of the components was measured as a function of composition at 2440°K, and from the variation of the ratio of activities with composition, the pairwise interaction energies were obtained. In the Zr-U-C system, the metal-metal interaction energy, $\left[E_{12} - \frac{E_{11} + E_{22}}{2}\right]$, was found to be 6.7 ± 0.6 kcal/mole, a value close to that obtained in the body-centered cubic, zirconium-uranium [metallic] system. The difference between the zirconium-carbon and uranium-carbon interaction energies, $E_{13} - E_{23}$ can be expressed as a function of composition by the equation

$$E_{13} - E_{23} = 8.5 \pm 0.05 - [23.6 \pm 0.2]x \text{ in kcal/mole}$$

In the Zr-Hf-C system, the metal-metal interaction energy, $\left[E_{12} - \frac{E_{11} + E_{22}}{2}\right]$ was found to be 1.9 ± 0.3 kcal/mole, again a value close to that obtained in the body-centered cubic, zirconium-hafnium [metallic] system. The difference between the zirconium-carbon and hafnium-carbon interaction energies, $E_{13} - E_{23}$, can be expressed as a function of composition by the equation

$$E_{13} - E_{23} = 9.8 \pm 0.05 - [7.5 \pm 0.2]x \text{ in kcal/mole}$$

In earlier papers, Hoch *et al.* (1-7) reported on studies of carbides, nitrides, and oxides of the refractory metals with sodium-chloride type structures. From statistical considerations they deduced equations to determine the activities of the components in these binary compounds which deviate from stoichiometry. This work was later extended to the ternary Zr-Nb-C system (8). The purpose of the present study is to add the single phase regions of Zr-U-C and Zr-Hf-C to the systems investigated. The theory has been described by Jun and Hoch (8).

Key words: carbides, zirconium, uranium, hafnium, carbon, thermodynamics.

Previous Investigations

The phase relationships in the Zr-C and Hf-C systems have been reviewed by Storms (9), and the thermodynamic data by Hoch (1). The phase diagram of the U-C system has also been summarized by Storms (9), and the thermodynamic data by Hoch, Sjodahl, and Juenke (10). A phase diagram for the Zr-U system was developed by Elliott (11), and lattice parameters for $Zr_{0.25}U_{0.75}C$ were given by Adam, Harrison, Riviere, and Thorpe (12).

Following Hoch, the activities of the components as a function of composition can be represented as
In ZrC (1)

$$RT \ln a_{Zr} \cdot \frac{1}{1-y} = (1 \pm 1) - (14 \pm 1.5)y^2 \text{ kcal/mole} \quad [1]$$

$$RT \ln a_C \cdot \frac{1-y}{y} = -(35.2 \pm 4) - (28 \pm 3)(1-y) + 2.7 \times 10^{-3}T \text{ kcal/mole} \quad [2]$$

In UC (10)

$$RT \ln a_C \cdot \frac{1-y}{y} = -28.1 \pm 1.6 \text{ kcal/mole}, \quad 0 < y < 1 \quad [3]$$

In HfC (1)

$$RT \ln a_{Hf} \cdot \frac{1}{1-y} = (1 \pm 1) - (7.5 \pm 4)y^2 \text{ kcal/mole} \quad [4]$$

$$RT \ln a_C \cdot \frac{1-y}{y} = -(47 \pm 10) + (15 \pm 8)(1-y) + 2 \times 10^{-3}T \text{ kcal/mole} \quad [5]$$

While in Zr-C and Nb-C, the high temperature thermodynamic data give heats of formation comparable to calorimetric data (2), this is not the case in Hf-C

Assuming $\Delta H_f = \Delta E_f$, ΔH_f, the heat of formation of HfC_y can be expressed as

$$\Delta H_f = (1 \pm 1) - (62 \pm 18)y + (7.5 \pm 4)y^2 \text{ kcal/mole} \quad [6]$$

This value is compared in Fig. 1 ($\Delta H_f/y$ *vs.* composition) with the values obtained by Mah (13), and Zhelankin and Kutsev (14) using combustion calorimetry. At higher carbon content, the values are in good agreement. At lower carbon content, however, the difference between the values calculated by Hoch (1), and measured by Zhelankin and Kutsev (14) increases. One reason is that Zhelankin and Kutsev's data show a large composition dependence indicating a very large pairwise interaction energy. In fact a straight line through Zhelankin and Kutsev's data in Fig. 1 gives for ΔH_f

$$\Delta H_f \simeq -118y + 64y^2 \text{ kcal/mole}$$

This yield carbon pairwise interaction energy, $E_{33}/2$, of 64 kcal/mole, which seems too high in relationship to the results in the other carbides as does a value of -118 kcal/mole for $(E_3 + E_{23})$.

Equipment and Materials

The same equipment used by Jun and Hoch (8) was employed. Carbon powder of 99.9999%, zirconium oxide of 99.95%, uranium dioxide 99.9% and hafnium oxide of 98.95% purity were obtained from Atomergic Chemetals Company, a division of Gallard-Schlesinger Chemical Manufacturing Corporation, Carle Place, Long Island, New York.

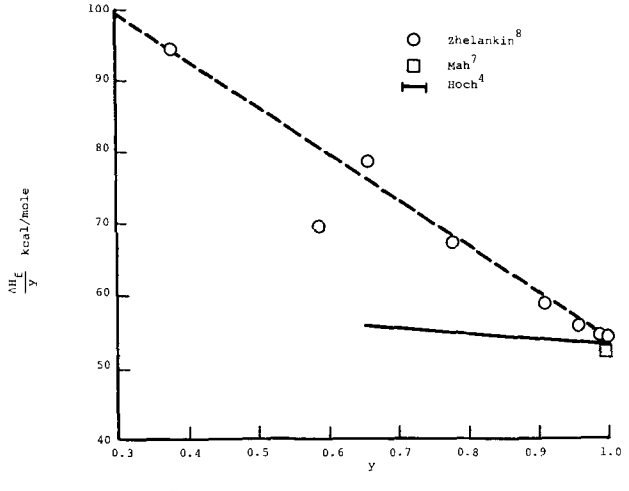

Fig. 1. Heat of formation of HfC_y

Experimental Procedure

Preparation of samples.—ZrC_y, HfC_y, and UC_y were prepared from the dioxide and carbon as described by Jun and Hoch (8). The oxygen to metal ratio in UO_2 was determined gravimetrically by oxidizing the material to U_3O_8, as described by Hoch and Momin (15). The ternary carbides were also prepared as described by Jun and Hoch (8). To avoid any reaction with the atmosphere, the uranium carbides were handled under argon.

Mass spectrometer operation.—Jun and Hoch (8) have described the use of the mass spectrometer. For carbon, the intensity of C^{12} (natural abundance 98.89%) was measured as the carbon peak. For uranium, the intensity of U^{238} (natural abundance, 99.274%) was measured. For zirconium, the intensity of Zr^{90} (natural abundance, 51.46%) was measured.

There are four stable isotopes of hafnium; Hf^{177} (18.5%), Hf^{178} (27.1%), Hf^{179} (13.8%), and Hf^{180} (35.2%). Since none is significantly larger than the others, the intensity of all four isotopes was measured and converted into the values of Hf^{180} using relative abundances. The average of these values was used in the calculations.

Results and Discussion

The nominal compositions of the samples, along with lattice parameters are given in Tables I and II. The lattice parameters were determined using the Nelson-Riley extrapolation method (16), and have an accuracy of ±0.001Å. In UC_y and ZrC_y, these values agree well with the data given by Storms (9).

The intensity ratios of Zr^{90}/U^{238} were measured for all Zr-U-C samples, and are given in Table III. For each intensity ratio reported both peaks were measured four times and the average of the readings used to calculate the ratio. It should also be noted that at

Table I. Nominal composition and lattice parameters of $Zr_xU_{1-x}C_y$ samples

Composition $Zr_xU_{1-x}C_y$ x	y	Lattice parameter, Å
0	0.90	4.955
	0.95	4.956
	1.00	4.961
	1.15	4.960
0.25	0.90	4.894
	0.95	4.843
0.50	0.90	4.825
	0.95	4.819
0.75	0.90	4.761
	0.95	4.748
1	0.85	4.700
	0.90	4.702
	0.95	4.701

Table II. Nominal composition and lattice parameters of $Zr_xHf_{1-x}C_y$ samples

Composition $Zr_xHf_{1-x}C_y$ x	y	Lattice parameter, Å
0	0.82	4.633
	0.87	4.638
	0.96	4.640
0.2	0.82	4.647
	0.87	4.651
	0.96	4.652
0.5	0.82	4.665
	0.87	4.668
	0.96	4.670
0.8	0.82	4.684
	0.87	4.689
	0.96	4.691
1.0	0.82	4.700
	0.87	4.700
	0.96	4.698

Table III. Ion intensity ratios for Zr-U-C

Sample	$\frac{I_{Zr^{90}}}{I_{U^{238}}}$
$Zr_{0.75}U_{0.25}C_{0.95}$	2.160
$Zr_{0.5}U_{0.5}C_{0.95}$	1.887
$Zr_{0.25}U_{0.75}C_{0.95}$	1.364
	1.168
$Zr_{0.75}U_{0.25}C_{0.90}$	3.096
	2.372
$Zr_{0.5}U_{0.5}C_{0.90}$	2.128
	1.949
$Zr_{0.25}U_{0.75}C_{0.90}$	1.136
	1.026

Table IV. Ion intensity ratios for Zr-Hf-C

Sample	$\frac{I^{90}_{Zr}}{I_{Hf^{180}}}$	Sample	$\frac{I^{90}_{Zr}}{I_{Hf^{180}}}$
$Zr_{0.2}Hf_{0.8}C_{0.82}$	0.7092	$Zr_{0.5}Hf_{0.5}C_{0.96}$	2.3674
	0.6494		2.0572
	0.5562		2.3624
	0.5774		2.3975
	0.5322		2.2002
$Zr_{0.2}Hf_{0.8}C_{0.87}$	0.7089		2.0859
	0.7084		
	0.6408	$Zr_{0.8}Hf_{0.2}C_{0.82}$	6.0423
	0.6127		7.3529
	0.5351		6.6756
	0.5399		6.7889
$Zr_{0.2}Hf_{0.8}C_{0.96}$	0.7874		6.7935
	0.9847	$Zr_{0.8}Hf_{0.2}C_{0.87}$	7.5758
	0.8425		5.3999
	0.9211		6.5625
	0.5612		5.5512
	0.6309		4.2668
	0.5800		6.0976
	0.6821		
$Zr_{0.5}Hf_{0.5}C_{0.82}$	1.7705	$Zr_{0.8}Hf_{0.2}C_{0.90}$	5.9524
	1.8829		6.1576
	1.9334		6.9735
	1.7947		7.4349
	1.7039		8.4746
	1.8549		
$Zr_{0.5}Hf_{0.5}C_{0.87}$	2.6420		
	3.1319		
	2.7285		
	2.6344		
	2.4260		
	2.3488		
	2.1943		
	2.9041		

the experimental temperature of 2440°K, the evaporation rate is low in relation to the time needed for measurements so the results were not influenced by any change in composition. The intensity ratios of Zr^{90}/Hf^{180} were likewise measured for all Zr-Hf-C samples, and are given in Table IV. For this system the experiments were carried out at 2570°K.

To obtain the pairwise interaction energies, $RT \ln I_{Zr90}/I_{U238} \cdot (1-x)/x$ and $RT \ln I_{Zr90}/I_{Hf180} \cdot (1-x)/x$ was plotted *vs.* $(1-2x)$ with y constant as shown in Fig. 2 and 3.

Straight lines drawn on the basis of a least squares analysis give $\left[E_{12} - \frac{E_{11}+E_{22}}{2}\right] = 6.7 \pm 0.64$ kcal/mole in the Zr-U-C system, and $\left[E_{12} - \frac{E_{11}+E_{22}}{2}\right] = 1.86$ kcal/mole in the Zr-Hf-C system. These terms represent the interaction energies between the metal atoms in the fcc metal sublattice. They are of the same order of magnitude as those for the bcc metallic systems in U-Zr 4.4 ± 0.2 kcal/mole calculated from

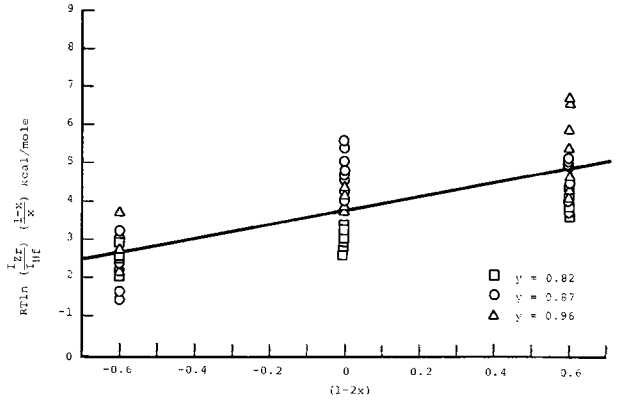

Fig. 2. Evaluation of $\left[E_{12} - \frac{E_{11}+E_{22}}{2}\right]$ in $Zr_xHf_{1-x}C_y$

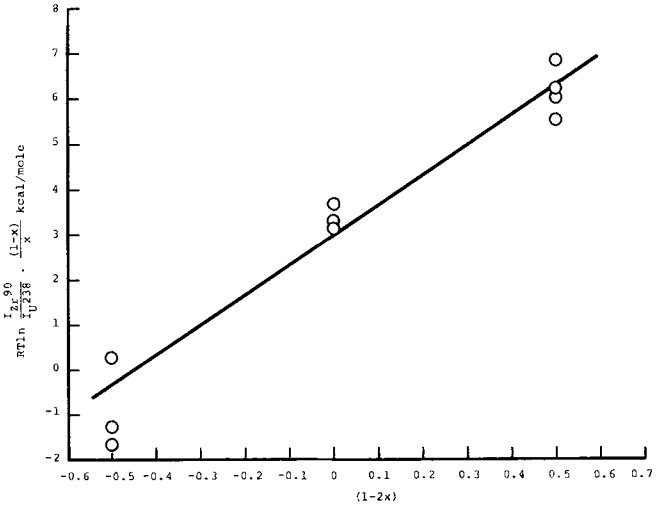

Fig. 3. Evaluation of $\left[E_{12} - \frac{E_{11}+E_{22}}{2}\right]$ in $Zr_xU_{1-x}C_y$

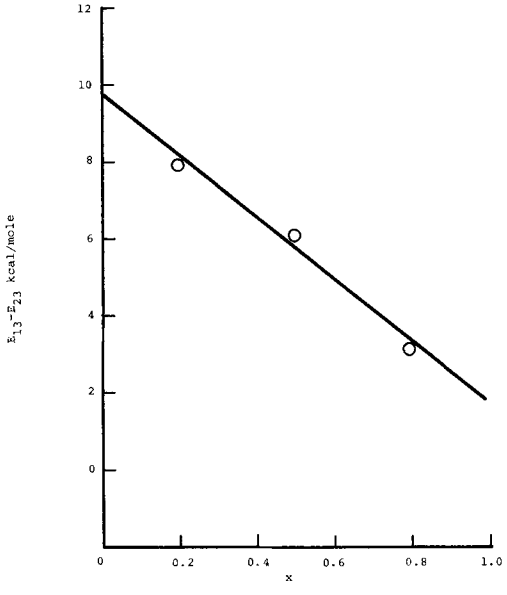

Fig. 4. Variation of $[E_{13} - E_{23}]$ with composition in $Zr_xHf_{1-x}C_y$

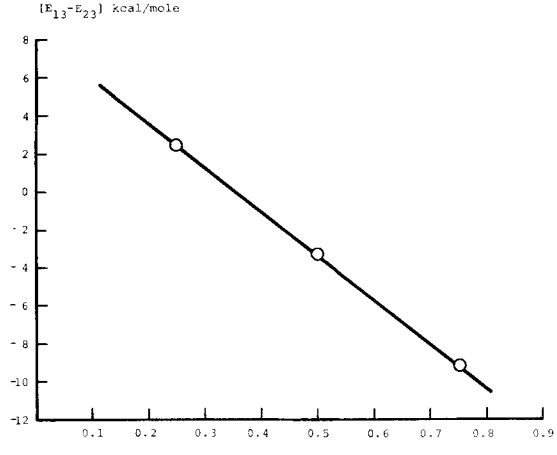

Fig. 5. Variation of $[E_{13} - E_{23}]$ with composition in $Zr_xU_{1-x}C_y$

Table V. Calculated pairwise interaction energies

$Zr_xHf_{1-x}C_y$	Composition x	$[E_{13} - E_{23}]$ kcal/mole
	0.2	7.9 ± 5.8
	0.5	5.9 ± 7.1
	0.8	3.2 ± 2.1
$[E_{12} - \frac{1}{2}(E_{11} + E_{22})] = 1.86 \pm 0.30$ kcal/mole		
$Zr_xU_{1-x}C_y$		
	0.25	+2.6
	0.5	−3.2
	0.75	−9.2
$[E_{12} - \frac{1}{2}(E_{11} + E_{22})] = 6.72 \pm 0.64$ kcal/mole		

the binary phase diagram using a method described elsewhere (17).

Kubaschewski (18, 19), assuming an ideal solution in Zr-Hf binary alloys, calculated the solidus and the liquidus curves for the Zr-Hf phase diagram, and his results showed fairly good agreement with experimentally determined phase relationships. This shows that the Zr-Hf binary alloy is an ideal solution, and therefore, $[E_{12} - \frac{1}{2}(E_{11} + E_{22})] \simeq 0$ for the Zr-Hf bcc metallic solution.

Using the method described earlier, the values of $[E_{13} - E_{23}]$ in both systems were calculated for different values of x, and the results are given in Table III as well as Fig. 4 and 5. Straight lines drawn on the basis of a least squares analysis give $[E_{13} - E_{23}] = 8.5 \pm 0.05 - [23.6 \pm 0.2]\ x$ kcal/mole in the system Zr-U-C, and $[E_{13} - E_{23}] = (9.6 \pm 0.8) - (7.8 \pm 0.2)x$ kcal/mole in Zr-Hf-C. The variation of $[E_{13} - E_{23}]$ with composition, which is the difference between the Zr-C and U-C bonds and the Zr-C and Hf-C bonds, will be discussed in a later paper (20).

Thus, the ternary $Zr_xU_{1-x}C_y$ and $Zr_xHf_{1-x}C_y$ systems behave quite similarly to the $Zr_xNb_{1-x}C_y$ system (8).

Acknowledgment

This research was supported in part by the Air Force Materials Laboratory (MAYA), Wright-Patterson Air Force Base, Ohio 45433, under Contract No. F33615-67-C-1565.

Manuscript submitted Sept. 29, 1969; revised manuscript received ca. March 23, 1971. This was Paper 120 presented at the Detroit, Mich., Meeting of the Society, Oct. 5-9, 1969.

Any discussion of this paper will appear in a Discussion Section to be published in the June 1972 JOURNAL.

REFERENCES

1. M. Hoch, The Role of the Defect Interaction Energy on the Stability of Interstitial Phases in "Phase Stability in Metals and Alloys," P. S. Rudman, J. Stringer and R. I. Jaffe, Editors, pp. 419-429, McGraw Hill Book Co., New York (1967).
2. M. Hoch, Non-Stoichiometry and Bonding in Refractory Monocarbides in "Anisotropy in Single-Crystal Refractory Compounds," Vol. I, pp. 163-175, Plenum Press, New York (1968).
3. M. Hoch, *Trans. AIME*, **230**, 138 (1964).
4. M. Hoch, A. S. Iyer, and J. Nelken, *J. Phys. Chem. Solids*, **23**, 1463 (1962).
5. M. Hoch, *J. Phys. Soc. Japan*, **18**, Suppl. II, 147 (1963).
6. M. Hoch and F. J. Furman, "Thermodynamics," Vol. II, pp. 517-532, International Atomic Energy Agency, Vienna (1966).
7. M. Hoch and D. Ramakrishnan, *J. Phys. Chem. Solids*, **25**, 869 (1964).
8. C. K. Jun and M. Hoch, *This Journal*, **118**, 1498 (1971).
9. E. K. Storms, "Refractory Carbides," Academic Press, New York (1967).
10. M. Hoch, E. F. Juenke, and L. H. Sjohahl, "Thermodynamics of Nuclear Materials, 1967," pp. 497-510, International Atomic Energy Agency, Vienna (1968).
11. R. P. Elliott, "Constitution of Binary Alloys," First Supplement, McGraw Hill Book Co., New York (1965).
12. J. Adam, J. W. Harrison, J. C. Riviere and T. Thorpe, "Carbides in Nuclear Energy," L. E. Russell, Editor, Vol. II, p. 801, Macmillan & Co., New York, (1964).
13. A. D. Mah, *U.S. Bur. Mines Rep.*, **6518**, (9), 8 (1964).
14. V. I. Zhelankin and V. S. Kutsev, *Zh. Fiz. Khim.*, **38**, 562 (1964).
15. M. Hoch and A. C. Momin, *High Temperatures-High Pressures*, **1**, 401 (1969).
16. L. A. Azaroff and M. J. Buerger, "The Powder Method in X-ray Crystallography," McGraw Hill Book Co., New York (1958).
17. M. Hoch, *Trans. AIME*, **224**, 379 (1962).
18. O. Kubaschewski and T. A. Chart, *J. Inst. Metals*, **93**, 329 (1965).
19. O. Kubaschewski, "Thermodynamics of Nuclear Materials," p. 219, International Atomic Energy Agency, Vienna (1962).
20. M. Hoch, and S. Yamauchi, Submitted for publication.

Technical Notes

Etch Rate Characterization of Silane Silicon Dioxide Films

Lou Hall*

Texas Instruments, Inc., Dallas, Texas 75222

In semiconductor manufacturing, it is necessary to process a variety of silicon dioxide films containing different impurities and different impurity concentrations. The etch rate of oxide films is affected by the addition of impurities. If their distribution is such that reverse or vertical slopes are obtained, serious problems such as open metal can result. Impurities can change both chemical and/or the physical nature of the film.

The recent use of chemical vapor deposition has provided a technology which makes it possible to obtain favorable oxide profiles. Studies have been made of the effect of both boron and phosphorus doping on the etch rate of silane silicon dioxide films.

The system used for the deposition of the doped oxide films was the low temperature oxidation of di-

* Electrochemical Society Active Member.
Key words: insulation, chemical vapor deposition, etch rate.

Table I.

% Dopant in gas stream as a function of silane flow	Deposition temperature, °C	E_1 (Å/sec)	E_2 (Å/sec)	E_1/E_2
1% B_2H_6	320	25.6	32.2	0.79
2.5% B_2H_6	320	19.1	22.9	0.84
5% B_2H_6	320	10.8	12.8	0.84
10% B_2H_6	320	5.4	6.4	0.84
0% B_2H_6	320	29.5	32.9	0.90
1% PH_3	320	38.5	45.8	0.84
2.5% PH_3	320	39.2	46.3	0.85
5% PH_3	320	40.9	48.6	0.84
10% PH_3	320	42.8	50.9	0.84

borane and silane, and phosphine and silane. The system was an RF heated production type unit. The chemical reactions involved have been discussed by a number of workers (1-3). The oxide films were deposited on 1½ in. <111> silicon wafers that were cleaned prior to use with H_2O-HNO_3-H_2O.

The etch used consisted of 91.2 weight per cent (w/o) of 40 w/o ammonium fluoride and 8.8 w/o of 49 w/o hydrogen fluoride. The etch temperature was 28°C (room temperature). The etch times were at fixed time increments and the thicknesses of the oxide steps were measured by use of a Talystep I. Photoresist was used as an etch mask. The amount of dopant in the oxide film was not measured but rather the dopant was introduced into the reaction chamber as a percentage of silane flow. The total flow was about 6 liters/min with the O_2 and silane being 1% and 0.25% of the total flow respectively.

The results of the etch studies are given in Table I. Etch rates from 4 positions on each wafer were averaged to obtain the rate given in the table. The use of photoresist masking permitted 4 etchings on the same wafer (Fig. 1). The spread in values was $\leq \pm 2\%$. After E_1 was obtained, oxide remained only in the center portion of the wafer (approximately ¼ of the total oxide area remained). E_2 was obtained by masking the wafer with photoresist so that only the center portion of the remaining oxide could be etched (Fig. 2). The difference in etch rate E_1 and etch rate E_2 is ascribed to an increase in stress in the remaining oxide film.

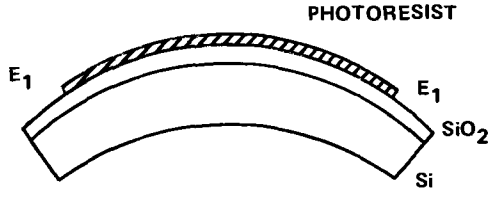

Fig. 1a. Compression

Fig. 1b. Tension

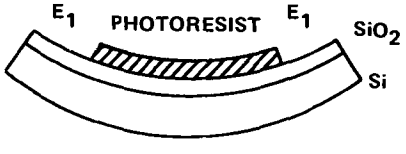

Fig. 2a. Compression

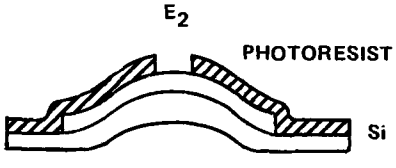

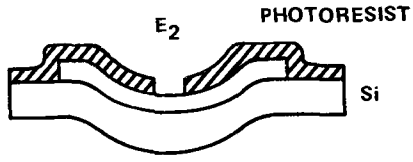

Fig. 2b. Tension

The etch rate of both boron and phosphorous doped silane oxide films are dependent on dopant concentration. The etch rate of the boron doped material decreases with increasing boron concentration while the etch rate of the phosphorous doped material increases with increasing phosphorous content (4). However, the boron doped silane oxides are more sensitive to changes in doping than are the phosphorous-containing films. The decrease in etch rate with increasing boron over the range studied is in agreement with that reported for other boron doped silicon dioxide films (5).

Figure 1 shows the portion of the film etched to obtain E_1. The oxide film and the silicon substrate have different coefficients of thermal expansion. Therefore, the wafer can be in either compression or tension as shown in Fig. 1a and 1b.

Once the outer portion of the oxide film is removed, the stress will be redistributed and the stress in the remaining oxide will increase. Experiments are in progress to determine the effect of stress on the etch rate independent of other parameters.

Figure 2 illustrates the portion of the film etched to obtain E_2. When the oxide films were masked so E_1 and E_2 were obtained simultaneously, E_1 and E_2 were equal. This is the expected result when the chemical composition and stress remains homogeneous across the oxide film.

In Table I the ratio E_1/E_2 is of interest. The boron-doped silane oxide is in compression while the phosphorous doped and undoped silane oxide films are in tension (6). Thus, the increase in etch rate due to stress appears to be independent of the type of stress. Also, the fact that the ratio E_1/E_2 remains constant over the range studied may indicate the stress in the oxide film is influenced more by redistribution of stress in the silicon than by addition of impurities to the oxide.

Two things obtained from Table I are that the etch rate of oxide films are affected both by addition of impurities and/or by stress. Thus, it is possible to have composite oxide films which will provide a controlled etching profile. An important area of application is multilevel fabrication.

Acknowledgment

The author wishes to thank Imogene Killen for doing the etching.

Manuscript received April 7, 1971.

Any discussion of this paper will appear in a Discussion Section to be published in the June 1972 JOURNAL.

REFERENCES

1. N. Goldsmith and W. Kern, *RCA Rev.*, **28**, 153 (1967).
2. T. L. Chu, J. R. Szedon, and G. A. Gruber, *Trans. Met. Soc. AIME*, **242**, 532 (1968).
3. M. L. Hammond and G. M. Bowers, *ibid.*, **242**, 546 (1968).
4. A. Mayer, K. Strater, and D. A. Puotinen, Technical Report AFML-TR-70-191, p. 72, September 1970.
5. R. O. Schwenker, *This Journal*, **118**, 313 (1971).
6. L. H. Hall and W. M. Gosney, To be published.

Effect of Thorium on Ce^{+3} Phosphors

Mary V. Hoffman*

Lighting Research Laboratory, General Electric Company, Cleveland, Ohio 44112

The luminescent properties of Ce^{+3} and Tb^{+3} activation in the monazite structures $LaPO_4$ and $CePO_4$ have been described and the energy transfer from Ce^{+3} to Ce^{+3} and Ce^{+3} to Tb^{+3} in these and other structures have been established (1-3). Energy transfer also has been reported in which Ce^{+3} emission in YPO_4 was sensitized by Th^{+4} (4). The work reported here shows the enhancement of both Ce^{+3} and Tb^{+3} emission in the presence of Th^{+4} in the monazite structure, in which the Th^{+4} does not have a direct role in the energy transfer in the ultraviolet region.

Experimental

Two methods of preparation were used in these tests. Phosphors were prepared from cerium and lanthanum sources of 99.9% purity by co-precipitation of the composition from nitrate solutions with $NaH_2PO_4 \cdot H_2O$. When prepared from oxides of 99.999% purity, the oxides were mixed with $(NH_4)_2HPO_4$ and fired initially at 300°C. Final firing for both methods was 1000°C for several hours.

Spectral distribution curves, excitation data, and decay measurements were obtained by methods which have been described previously (5). Reflectance measurements were made on a Cary 14, using $BaSO_4$ as a reference standard.

Results

The Ce^{+3} emission in $CePO_4$ and $LaPO_4$ matrices is a double band, peaking at 320 and 340 nm, resulting from the splitting of the group state, $^2F_{5/2}$ and $^2F_{7/2}$ (Fig. 1). Green emisison is present when Tb^{+3} is incorporated in $CePO_4$, but is very weak in the $LaPO_4$ matrix unless Ce^{+3} is also present.

* Electrochemical Society Active Member.

Key words: lanthanum phosphate, cerium phosphate, luminescence, energy transfer, thorium, phosphors.

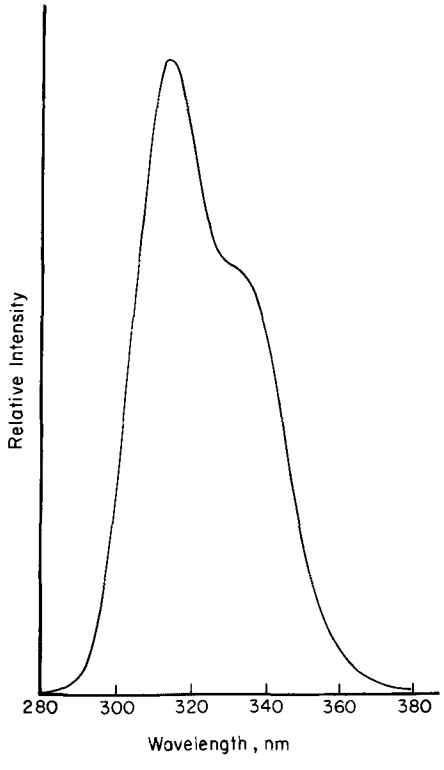

Fig. 1. Emission spectra, $LaPO_4$:Ce, 2537Å excitation

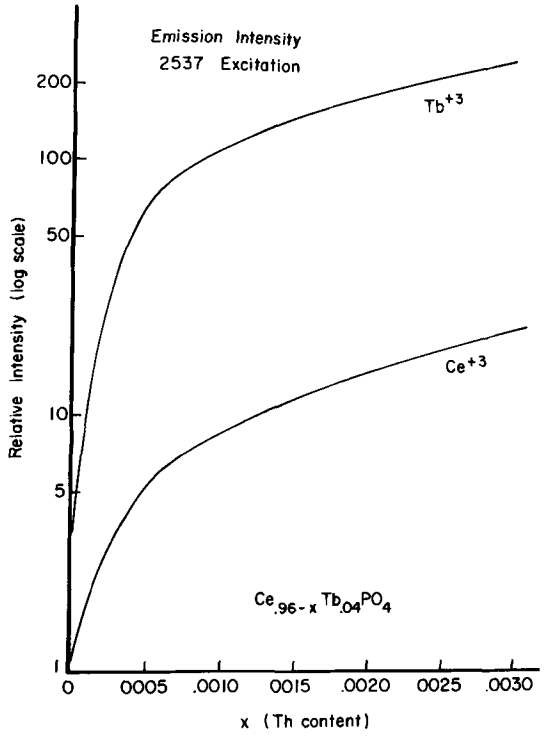

Fig. 2. Intensity of peak height of Tb^{+3} and Ce^{+3} emission in $Ce_{0.96-x}Th_xTb_{0.04}PO_4$ with increasing Th incorporation. 2537Å excitation.

In $CePO_4$ and $CePO_4$:Tb, the incorporation of Th in amounts as low as 0.0005 moles per formula resulted in enhancement of both Ce^{+3} and Tb^{+3} emission, with the maximum enhancement reached at about 0.003 moles of Th. Figure 2 shows the increased intensity of the Ce^{+3} and the Tb^{+3} emission with Th^{+4} incorporation in $Ce_{0.96-x}Th_xTb_{0.04}PO_4$. Figure 3 shows the effect of energy transfer from $Ce^{+3} \rightarrow Tb^{+3}$ in $Ce_{1-x}Tb_xTh_{0.008}PO_4$. Figure 4 shows the effect of Th^{+4} on the intensity of Ce^{+3} emission in $La_{1-x}Ce_xPO_4$, in which a similar enhancement is found.

In order to determine the effect of very low concentrations of Ce and Th, these matrices were prepared from oxides listed as 99.999% purity, but even in these, trace amounts of Ce^{+3} and Tb^{+3} were detected in the unactivated sample. The emission intensities are shown in Table I and are compared to a sodium salicylate standard with a peak height of 50.

Excitation curves were run on the $CePO_4$ and $LaPO_4$ matrices for Ce^{+3} and Tb^{+3} emission, both with and

Table I. Emission intensities

Composition (additions)	Purity	Peak height Ce^{+3} peak	Peak height Tb^{+3} peak
	$LaPO_4$ matrix		
None	5-9's	0.8	0.04
0.01 Th	5-9's	0.9	0.05
0.04 Tb	5-9's	0.8	3.5
0.04 Tb + 0.01 Th	5-9's	0.9	3.9
0.04 Tb	3-9's	1.8	14.5
0.04 Tb + 0.01 Ce	3-9's	5.3	17
0.04 Tb + 0.01 Ce + 0.01 Th	3-9's	3.7	58
	$CePO_4$ matrix		
None	5-9's	1.9	—
0.008 Th	5-9's	11	—
0.04 Tb	5-9's	2	40
0.04 Tb reduced	5-9's	0.9	146
0.04 Tb + 0.008 Th	5-9's	4.7	240

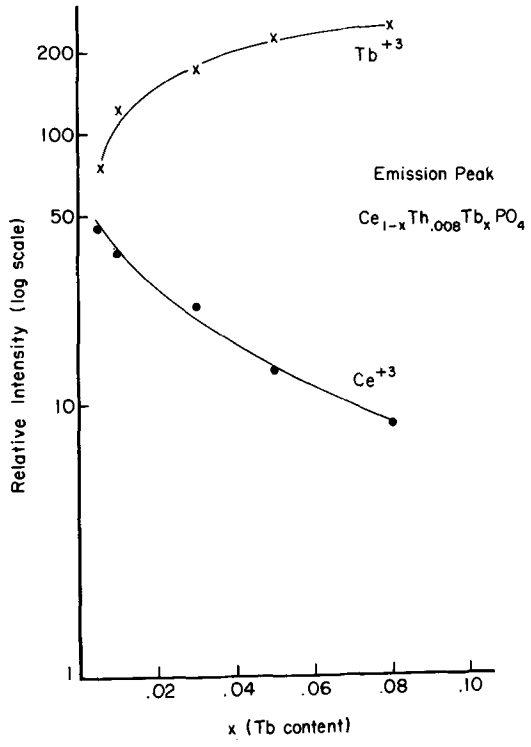

Fig. 3. Intensity of peak height of Tb^{+3} and Ce^{+3} emission in $Ce_{1-x}Tb_xTh_{0.008}PO_4$, showing effect of $Ce^{+3} \rightarrow Tb^{+3}$ energy transfer. 2537Å excitation.

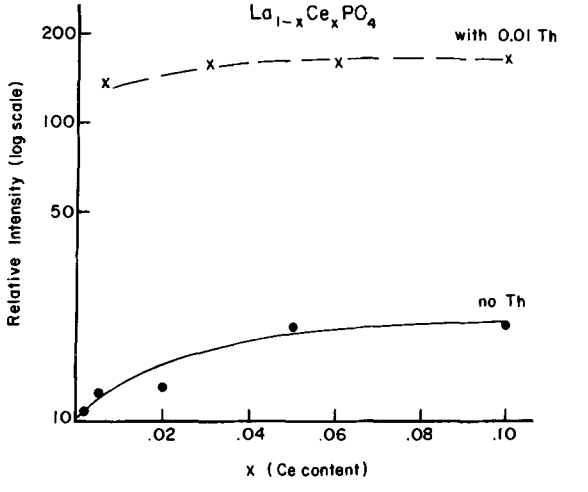

Fig. 4. Effect of Th^{+4} on Ce^{+3} emission in $La_{1-x}Ce_xPO_4$ matrix. 2537Å excitation.

without Th^{+4}. In $CePO_4$:Tb, the excitation is identical for both Ce^{+3} and Tb^{+3} emission, with no change found due to the presence of Th^{+4}. The excitation is that of absorption into the 5d levels of Ce^{+3}.

In the $LaPO_4$ matrix, the lower concentration of Ce permits better resolution of the excitation bands. The excitation of Ce^{+3} (Fig. 5) shows the same transitions, absorbing in the 5d levels. The excitation of Tb^{+3} in $LaPO_4$ (Fig. 6) is into the 5d level of Tb^{+3}, below 215 nm, with very little excitation occurring through the 4f levels. The combination of Ce^{+3} and Tb^{+3} shows an enhancement of the Tb^{+3} emission as a result of the Ce^{+3} absorption and transfer, with the excitation curve showing an additive effect over the range of Ce^{+3} absorption (Fig. 6). The excitation of the Ce^{+3} emission is diminished in the 200-220 nm range due to transfer into the 5d levels of Tb^{+3} (Fig. 5). Excitation curves for both Ce^{+3} and Tb^{+3} emission showed no change with incorporation of Th^{+4} into the lattice. At 205 nm, the incorporation of Ce^{+3} resulted in a two-fold enhancement of the Tb^{+3} emission, and the presence of Th^{+4} increased this to three-fold. The response under cathode-ray excitation showed no visual enhancement of Tb^{+3} emission by the presence of Ce^{+3} or Th^{+4}, but the afterglow of the Tb^{+3} emission was greatly increased with Th^{+4}, indicating that in the very high energy region, Th^{+4} enters into the energy transfer.

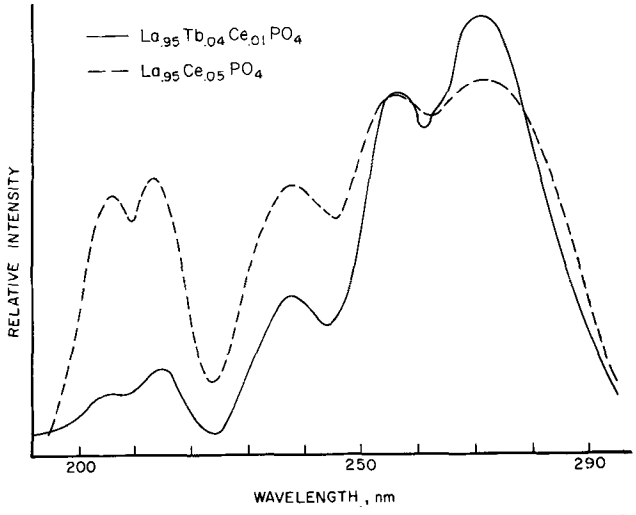

Fig. 5. Excitation spectra of Ce^{+3} emission in $LaPO_4$ matrix with and without Tb^{+3} present.

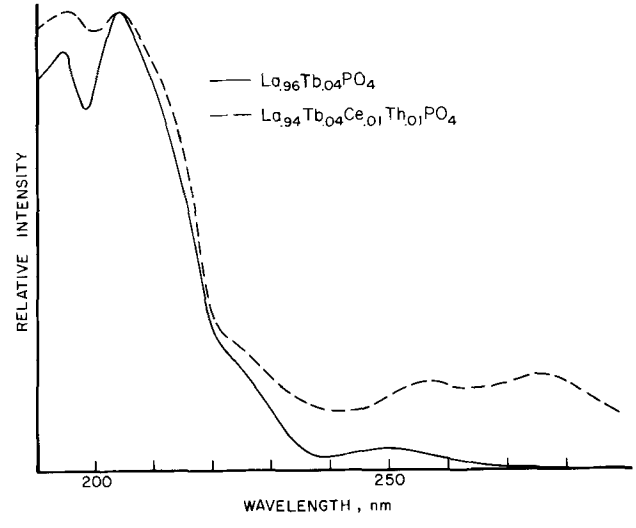

Fig. 6. Excitation spectra of Tb^{+3} emission in $LaPO_4$ matrix with and without presence of Ce^{+3}.

The function of Th^{+4} in the enhancement of both Ce^{+3} and Tb^{+3} emission in the monazite lattice is not one of energy transfer in the wavelength range above 200 nm, but of valence control of the cerium ion. Diffuse reflectance curves run on $CePO_4$ show that in Th^{+4}-free materials, such as those prepared from 5-9's oxides, an absorption edge is present in the region of 450 nm. When fired in a mildly reducing atmosphere (Table I) or when Th^{+4} is incorporated, the absorption edge is shifted to about 370 nm and the emission is increased. Absorption data supplied by the American Potash Company show that ceric ammonium nitrate has an edge at about 440 nm, and that cerous chloride has an edge at 370 nm. In $LaPO_4$, the addition of cerium gives an absorption at 475 nm, which is shifted to 370 nm with Th^{+4} present (Fig. 7). The presence of Tb^{+3} does not result in a change in absorption edge in this region.

The enhancement of emission intensity with the presence of Th^{+4} occurs because of the removal of Ce^{+4} ions in the lattice which provided an absorbing site for energy transferred from Ce^{+3}. Decay measurements on both Ce^{+3} and Tb^{+3} emission show a decrease in the decay time of Tb in the samples which

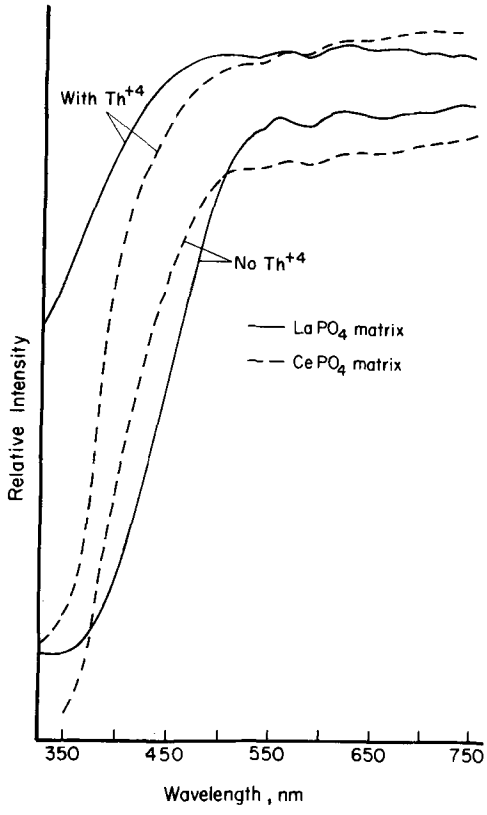

Fig. 7. Diffuse reflectance curves for $LaPO_4$ and $CePO_4$ matrices showing shift in absorption edge with Th^{+4} addition.

contain Ce^{+4} (Table II). The Ce decay times are all less than the 10^{-9}-sec limitation of the instrument, except for $CePO_4$:0.008 Th. This is the only material which does not have a second center accepting energy from the lattice Ce^{+3}, *i.e.*, $Ce^{+3} \rightarrow Ce^{+4}$ or $Ce^{+3} \rightarrow Tb^{+3}$.

These decay measurements show that an absorbing center exists in $CePO_4$ prepared without Th^{+4}, and this center correlates with the diffuse reflectance data indicating the presence of Ce^{+4}. No evidence was found to correlate with the emission and excitation reported by Awazu and Muto for Th^{+4} enhancement of Ce^{+3} in YPO_4. Incorporation of only Th into $LaPO_4$ showed no

Table II. Decay measurements

Composition	Decay time of emission	
	Ce^{+3}, sec	Tb^{+3}, μsec
$CePO_4$	$<10^{-9}$	—
$CePO_4$: 0.008 Th, 0.04 Tb	$<10^{-9}$	2.35
$CePO_4$: 0.04 Tb, air-fired	$<10^{-9}$	0.81
$CePO_4$: 0.04 Tb, reduced	$<10^{-9}$	2.22
$CePO_4$: 0.008 Th	10^{-9}	—

emission, nor was any other reference to Th absorption or emission levels in the ultraviolet region found in the literature.

The incorporation of Th^{+4} in $CePO_4$ (or $LaPO_4$) implies that a defect structure such as $Ce(M^{+4}\square^{-1})PO_4$ exists, with M^{+4} being Ce, Th, or Zr. The absorption data shows that when M is Th and above about 0.001 Th/Ce, all of the cerium is trivalent. There does not appear to be a distribution of Ce^{+4} and Th^{+4} cations. This can possibly be attributed to the size of the ions involved. The ionic radius of Th^{+4} is 1.02Å, closer to Ce^{+3} (1.07Å) than is Ce^{+4} (0.94Å). The effect of Th^{+4} occurs with a very low concentration; incorporation of 0.0005 moles Th per Ce shows a significant change in both the absorption edge and the emission intensity and 0.0030 is sufficient to optimize the intensity effect. This indicates a very limited solid solution of M^{+4} in the structure.

Acknowledgments

The author is pleased to acknowledge the assistance of Miss Jacqueline Holmes for sample preparation and of Dr. Ralph Hewes and Dr. T. F. Soules for optical measurements and helpful discussions.

Manuscript submitted April 1, 1971; revised manuscript received May 3, 1971.

Any discussion of this paper will appear in a Discussion Section to be published in the June 1972 JOURNAL.

REFERENCES

1. P. Denis and J. Loriers, "Les Elements des Terres Rares," International Conference, Paris-Grenoble, 1969, p. 557.
2. R. C. Ropp, *This Journal*, **115**, 841 (1968).
3. G. Blasse and A. Bril, *J. Chem. Phys.*, **51**, 8, 3252 (1969).
4. K. Awazu and K. Muto, *This Journal*, **116**, 282 (1969).
5. M. V. Hoffman, *ibid.*, **117**, 227 (1970).

The Emission Colors of the Strontium Apatite Phosphor System

R. C. Ropp*,[1]

Westinghouse Electric Corporation, Bloomfield, New Jersey 07003

Although published studies of alkaline earth apatite phosphors have been quite numerous in the past, very little has been presented concerning the strontium apatites activated by Sb^{+3} and Mn^{+2}. This situation has perhaps arisen because of the great similarity of the strontium to the calcium system, despite the fact that both have been used commercially for some time, the former for color correction in blends and the latter as the major component in fluorescent lamps. Nevertheless, with the exception of the data given by Rimbach (1), no other information is to be found. Quirk (2) presented data on the color range spanned in the calcium system. The color range spanned by the strontium system is the subject of the present contribution.

* Electrochemical Society Active Member.
[1] Present address: Rutgers, the State University, Chemistry Dept., Newark, N. J. 07102.
Key words: apatites, strontium, colors, emission, phosphors.

Experimental

Phosphors were prepared by firing a mixture of luminescence grade materials, $SrHPO_4$, $SrCO_3$, SrF_2, $SrCl_2$, Sb_2O_3, and $MnCO_3$, for 6 hr at 1150°C. The formulation employed was: $Sr_{4.80}X_{0.96}(PO_4)_{3.00}:Sb_x:Mn_y$. This gives an apatite composition with a minimum of $Sr_2P_2O_7$ and antimonates, the latter not detectable by x-ray powder diffraction analysis. Spectral measurements were made on an energy-corrected instrument; x-y trichromatic color coordinates of the phosphors were calculated employing a suitable program *via* a 360 IBM computer, while those of the lamps were

determined experimentally. The emission monochromator of the instrument was calibrated in microwatts, for a given excitation density, using a standard lamp. A self-contained integrator then gave the integrated band intensity directly in microwatts.

Results

The emission band of Sb^{+3} in $Sr_5F(PO_4)_3$ consists of a blue-green band peaking at 498 nm, whereas that of Sb^{+3} in $Ca_5F(PO_4)_3$ is a blue band peaking at 480 nm (2). The addition of Mn^{+2} introduces a second band at 565 nm in $Sr_5F(PO_4)_3$ (see Fig. 1) whereas the introduction of chloride to form mixed apatites rapidly shifts the color greener. Most of this information is well known to the trade but perhaps less well known is the effect due to optimum activator concentration.

The emission color of the strontium apatites is not antimony dependent above about 3.0 mole per cent (m/o) Sb^{+3} per mole of apatite. Whereas upwards of 16 m/o of Mn^{+2} is required to saturate the emission color in $Sr_5F(PO_4)_3$, *i.e.* to the point where most of the emission lies in the Mn^{+2} emission band, the emission color becomes saturated in $Sr_5Cl(PO_4)_3$ as low as 4 m/o Mn^{+2}. This is illustrated in Fig. 1 and 2 for $Sr_5F(PO_4)_3$ and Fig. 3 for $Sr_5Cl(PO_4)_3$. In Fig. 2, the Sb^{+3} band intensity (integrated as microwatts) decreases almost linearly as the Mn^{+2} band intensity increases. These phenomena place a limitation on the usable formulations available since high chloroapatite compositions can only be employed at low Mn^{+2} concentrations or concentration quenching will be encountered. The upper, practical limit is about 0.75 Cl/0.25 F, although compositions at 0.875 Cl/0.125 F were investigated to fill out the data, despite the very low brightnesses usually encountered.

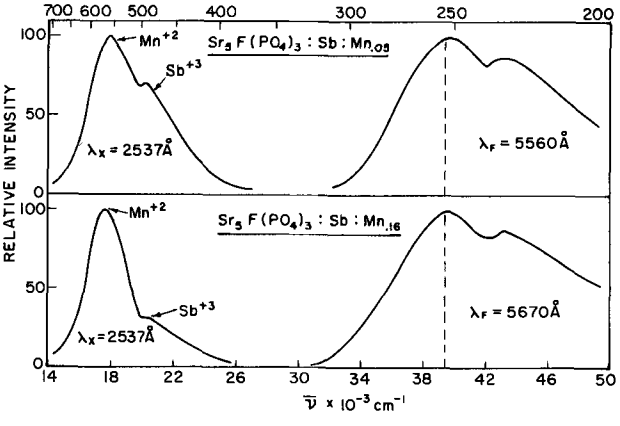

Fig. 1. Spectra of Sb^{+3} activated fluoroapatite phosphors

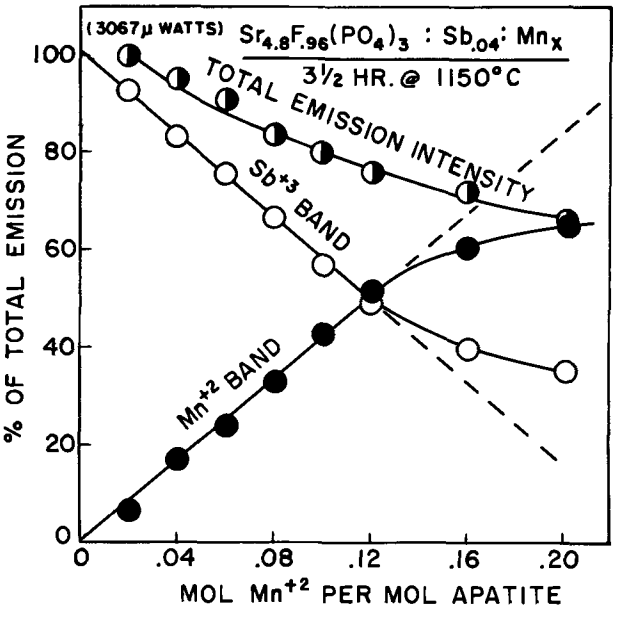

Fig. 2. Comparison of total energy emitted by Sb^{+3} and Mn^{+2} in strontium fluoroapatite.

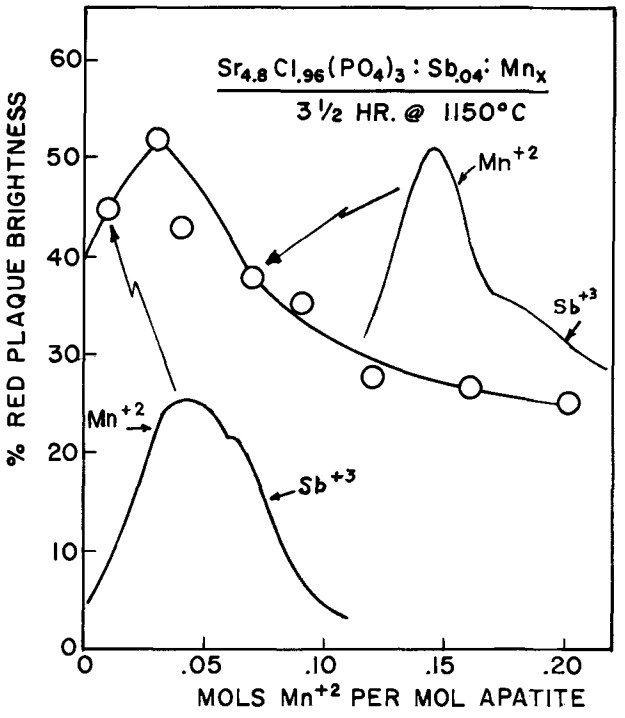

Fig. 3. Output and spectra for Mn^{+2} activation in strontium chloroapatite phosphors.

Figure 4 shows the trichromatic color coordinates calculated for the compositions indicated and were obtained from the emission spectra of the phosphors. In Fig. 5, the actual colors of 40W fluorescent lamps, as determined experimentally, are shown. These colors span the complete range of commercial lamp colors but are, in general, greener than the corresponding calcium halophosphate compositions. The displacement of the phosphor colors (Fig. 4) as compared to the lamp color (Fig. 5) is most certainly due to the mercury arc color contribution, as is well known. For comparison, Table I presents lamp brightnesses observed for 40T12 lamps, for the pure fluoroapatite and a 50/50 F-Cl: $Mn_{0.12}$ composition. Also given are lamp brightnesses for cool-white deluxe (CWX) and warm-white deluxe lamps made from these components. By comparison with known values for lamps made from components in the calcium halophosphate system having equivalent compositions, it may be concluded that the strontium halophosphates are very close in efficien-

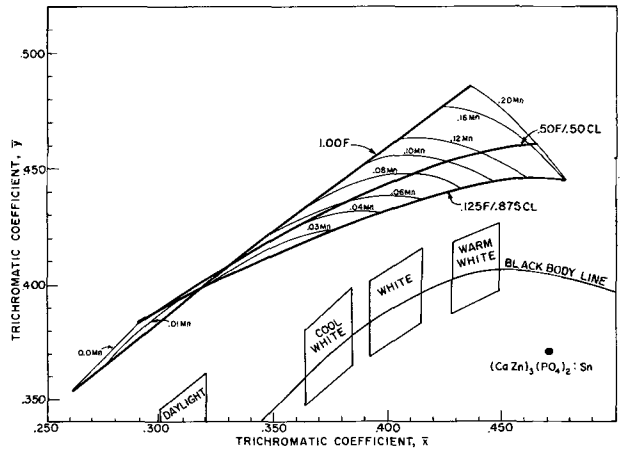

Fig. 4. Effect of composition on phosphor emission color (Sb^{+3} content — 6.0 m/o).

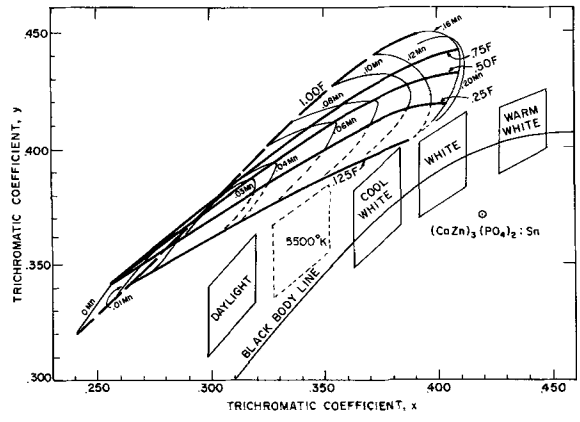

Fig. 5. Strontium halophosphate compositions and lamp color data (Sb^{+3} content — 6.0 m/o).

cy to their calcium counterparts, albeit somewhat greener in emission color.

Conclusions

There are a number of interesting facts which can be deduced from the data presented in the color measurements. First of all, the bluest phosphor is the pure fluorapatite. The addition of even a small amount of chloride serves to shift the color to a point much greener. Thus, it is essential to prevent any contamination by chloride in order to produce the bluest phosphor. It can also be noted that the color of the mixed apatites at zero manganese content is invariant at all F/Cl ratios (see Fig. 4). (Note also that the minimum amount of chloride necessary to cause this shift has not been determined in this work).

A second deduction indicates that the mixed apatites form a different set of loci than the pure fluoroapatite. Although the pure fluoroapatite is bluer than any of the mixed apatites, the addition of Mn^{+2} to the fluoroapatite produces phosphors which are greener than any of the mixed phases.

Table I. Lamp results for strontium halophosphate phosphors (containing 6 m/o Sb^{+3})

Color	Lamp lumens 0 hr	Lamp lumens 100 hr
Blue-green	2651	2558
Yellow	3549	3322
CWX	2471	2395
WWX	2735	2691

The third deduction which can be made shows that the greatest shift in color coordinates occurs at the lowest Mn^{+2} concentrations. Thus, if one should plot the shift in color *vs.* the Mn^{+2} content, *i.e.* $d\bar{x}/d(Mn)$ *vs.* Mn^{+2}, one would obtain a curve peaking at the very low Mn^{+2} contents and tailing out at the higher concentrations.

Perhaps the real value of the data presented in Fig. 4 and 5, lies in being able to choose a composition having suitable emission characteristics for a given application. For example, if one wished to choose phosphors to obtain a lamp close to 5500°K using a $(Ca,Zn)_3(PO_4)_2$:Sn phosphor as one of the components, compositions such as $Sr_5F_{0.75}Cl_{0.25}(PO_4)_3$:Sb:$Mn_{0.01}$ or $Sr_5F_{1.00}(PO_4)_3$:Sb:$Mn_{0.02}$ might be chosen.

Acknowledgment

The author is indebted to E. Chen and G. Grasso for sample preparation, to Dr. C. K. Lui Wei for x-ray measurements, to E. E. Gritz for technical assistance.

Manuscript submitted Jan. 11, 1971; revised manuscript received *ca.* May 21, 1971.

Any discussion of this paper will appear in a Discussion Section to be published in the June 1972 JOURNAL.

REFERENCES

1. H. W. Rimbach, U.S. Pat. 2,976,249 (1961); U.S. Pat. 2,968,626 (1961).
2. R. F. Quirk and M. J. B. Thomas, Paper 31, presented at Electrochem. Soc. Meeting, Toronto, Canada, May 3-7, 1964.

Phosphorescence Decay of Calcium Oxide Activated by Yttrium

L. M. Schwartz, J. M. Voutay-Poncet, and J. Janin

Laboratoire de Spectroscopie et de Luminescence, Université Claude Bernard, Lyon I, 69-Villeurbanne, France

Long Duration Decay Theory

This theory assumes the existence of a continuous trap depth distribution between two limits E_1 and E_2 (1-8). First-order kinetics are involved with negligible retrapping. Under these conditions, with the frequency factor assumed to be constant, the luminescence intensity, at time t, is

$$L = C \int_{E_1}^{E_2} m_E(O)\, P_E \exp(-P_E t)\, dt$$

where P_E is the probability for an electron to escape from a trap

$$P_E = s \exp(-E/kT)$$

$m_E(O)$ is the trap distribution function when the powder is excited until saturation occurs and C is a constant. It is assumed that

$$m_E(O) = A \exp(-\delta E) \quad (8, 9) \qquad (\delta = \text{constant})$$

Key words: phosphorescence, CaO:Y, traps, decay curves, thermoluminescence.

The expression of L then becomes

$$L = AsC \int_{E_1}^{E_2} \exp\left[\left(-\delta - \frac{1}{kT}\right) E\right] \exp[-st \exp(-E/kT)]\, dE$$

Let us set $\epsilon = \delta kT$ and $u = st \exp(-E/kT) = \alpha t$. It follows

$$L = \frac{-ACkT}{s^\epsilon t^{1+\epsilon}} \int_{u_1}^{u_2} u^\epsilon \exp(-u)\, du$$

At fixed temperature, we may write: $ACkT/s^\epsilon = L_O$, then

$$L = -\frac{L_O}{t^{1+\epsilon}} \int_{u_1}^{u_2} u^\epsilon \exp(-u)\, du$$

The integral may be expressed by using the incomplete gamma function

$$\gamma(1 + \epsilon, x) = \int_0^x u^\epsilon \exp(-u)\, du$$

Thus

$$L = \frac{L_0}{t^{1+\epsilon}} [\gamma(1 + \epsilon, u_1) - \gamma(1 + \epsilon, u_2)]$$

That is the intensity expression *vs.* time since $u_i = \alpha_i t$ $(i = 1, 2)$

For such a formula to be verified, four parameters must be evaluated L_0, ϵ, α_1, and α_2. When α_1 and α_2 just as s are known, it is possible to compute the E_1 and E_2 level energies.

Yet, the upper expression generally does not overlap the whole decay interval between 2 and 10^4 sec. It is often necessary to consider the sum of two analogous expressions (9, 10), each of them would correspond to two different groups of traps responsible for the decay. Then it may be written

$$L = (L_0'/t^{1+\epsilon'})\{\gamma(1 + \epsilon'; \alpha_1' t) - \gamma(1 + \epsilon'; \alpha_2' t)\}$$
$$+ (L_0''/t^{1+\epsilon''})\{\gamma(1 + \epsilon''; \alpha_1'' t) - \gamma(1 + \epsilon''; \alpha_2'' t)\}$$

A table of gamma functions was computed for the values

$$-0.99 \leq \epsilon \leq 2 \text{ and } 0.001 \leq x \leq 5$$

Experimental Results

The upper representation was extended to powder samples of yttrium-activated calcium oxide at various temperatures.

For each group of traps, approximative values for the parameters are determined by studying the variations of the product $L \cdot t^{1+\epsilon'}$. That is, a certain value of ϵ' is chosen so that the obtained curve gives the best representation of a gamma function difference (convex curve with a very flat maximum). After an approximative value for ϵ' has been determined, the curves of the functions $L \cdot t^{1+\epsilon'}$ and $\gamma(1 + \epsilon'; \alpha_1' t) - \gamma(1 + \epsilon'; \alpha_2' t)$ are plotted on the same graph for different values of α_1' and α_2' and with a suitable scale so that they superpose each other. The trap distribution is characterized by the values of α_1' and α_2' giving the best superposition, possibly after retouching the precedently determined ϵ' value. The constant L_0' is easily deduced from the curves. Figure 1 shows a logarithmic plot of the decay of CaO(Y) at −78°C. The decay part between 80 and 4800 sec is approximately a straight line; this gives immediately the values ϵ' and L_0': $L_0' = 3.59 \times 10^5$ and $\epsilon' = 0.25$.

As a result of α_2' equals zero whatever t may be and $\gamma(1 + \epsilon', \alpha_1' t)$ must tend to its limit $\Gamma(1 + \epsilon')$ as soon as $t = 80$ sec and this imposes $\alpha_1' t \simeq 0.5$ and $\alpha_1' \simeq 0.06$. The values calculated from the formula

$$L' = (3.59/t^{1.25})\, \gamma(1.25; 0.06t)$$

coincide, with a good precision, with the experimental values until $t = 40$ sec. For $2 < t < 40$ sec, it is necessary that another trap distribution occurs, which is determined by computing for each value of t, the intensity $L'' = L - L'$ and studying the deformations of the curves $L'' \cdot t^{1+\epsilon''}$ for different values of ϵ''. The best coincidence with the experimental results takes place for $\epsilon'' = -0.2$. For this value of ϵ'', the curve system is plotted on Fig. 2 and, last, we carry $\alpha_1'' = 0.5$, $\alpha_2'' = 0.1$. Then it is easy to determine L'' and the formula

$$L = \frac{1.085 \times 10^5}{t^{0.8}} [\gamma(0.8; 0.5t) - \gamma(0.08; 0.1t)]$$
$$+ \frac{3.59 \times 10^5}{t^{1.25}} \gamma(1.25; 0.06t) \quad [1]$$

shows the decay of CaO(Y) at −78°C between 2 and 4800 sec, with an error of less than 8%. On Fig. 1, the points represent the calculated values from this relation.

The value of the frequency factor s is obtained from thermoluminescence curves of CaO(Y) samples irradiated by uv light at −196°C. The curves show several peaks, about −90°C, −50°C, and room temperature. The trap depths and s are determined either by

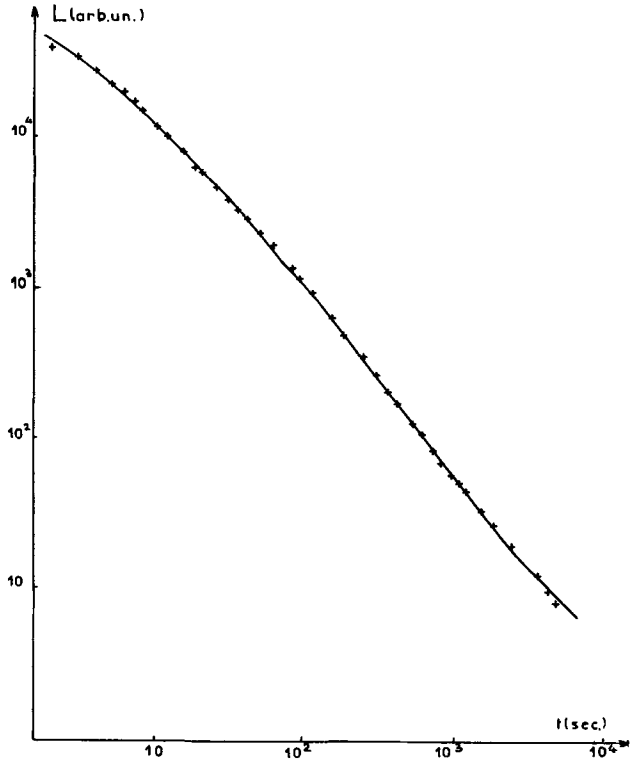

Fig. 1. Phosphorescence decay of CaO(Y) at −78.5°C. ——, Experimental curve; +, calculated values from Eq. [1].

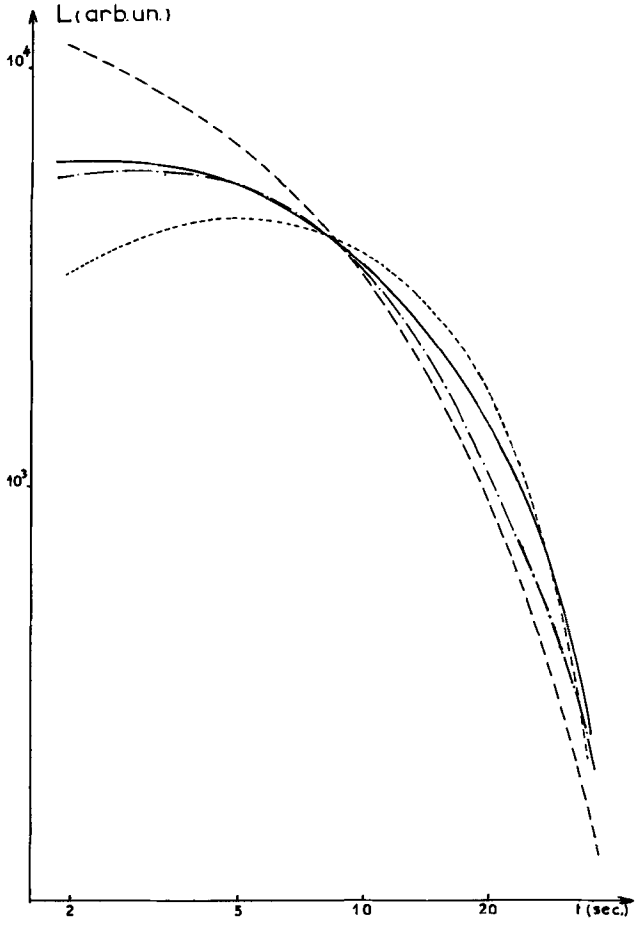

Fig. 2. Curve system for CaO(Y) at −78.5°C. ——, Experimental curve $L'' \cdot t^{0.8}$; — —, curve γ (0.8, $\alpha_1'' t$) − γ (0.8, $\alpha_2'' t$) for $\alpha_1'' = 0.5$, $\alpha_2'' = 0.2$; · — ·, curve γ (0.8, $\alpha_1'' t$) − γ (0.8, $\alpha_2'' t$) for $\alpha_1'' = 0.5$, $\alpha_2'' = 0.1$; - - - -, curve γ (0.8, $\alpha_1'' t$) − γ (0.8, $\alpha_2'' t$) for $\alpha_1'' = 0.2$, $\alpha_2'' = 0.1$.

varying the heating rate (12) or by Grossweiner's or Halperin and Braner's methods (13, 14). The mean value of s is 10^9. Thus we deduce the trap depths corresponding to the α coefficients obtained before. The values found are 0.36 eV for α_1'', 0.386 eV for α_2'', and 0.394 eV for α_1'. These results are consistent with those given by thermoluminescence: 0.32 eV for the peak at −90°C and 0.37 eV for the one at −50°C.

Other experiments were performed at −196°C and 25°C. Thus, at 25°C, an expression similar to the previous one has been found which is valid between 10 and 90,000 sec with an error less than 10% and leads to trap depths falling between 0.55 and 0.64 eV when thermoluminescence gives 0.57 eV

$$L = \frac{2.50 \times 10^5}{t^{1.10}} [\gamma(1.10; 0.5t) - \gamma(1.10; 0.06t)] + \frac{2.32 \times 10^5}{t^{0.835}} \gamma(0.835; 0.0157t)$$

The coefficients at 25°C are not deducible from those of −78°C because the decays correspond to two different thermoluminescence peaks between which there is no correlation.

Likewise, experiments performed with gallium-activated calcium oxide have shown that the above method once again gave results consistent with those set up by the usual thermoluminescence processes (10, 11).

Conclusion

The analysis method of phosphorescence decay curves with the help of the incomplete gamma functions does make it possible, by using one or two (three in certain cases) trap distributions to find an expression of the intensity valid from the early seconds after the excitation until the end of the decay.

Manuscript submitted April 1, 1971; revised manuscript received ca. May 14, 1971. This was Paper 47 presented at the Washington, D. C., Meeting of the Society, May 9-13, 1971.

Any discussion of this paper will appear in a Discussion Section to be published in the June 1972 JOURNAL.

REFERENCES

1. J. T. Randall and M. H. F. Wilkins, *Proc. Royal Soc., London*, **184A**, 366 (1945).
2. R. Urbach, N. R. Neil, and D. Pearlman, *J. Opt. Soc. Am.*, **39**, 675 (1949).
3. D. Curie, *Compt. Rend. Acad. Sci. Paris*, **229**, 193 (1949).
4. J. Saddy, *ibid.*, **228**, 2023 (1949).
5. A. Rose, *Phys. Rev.*, **97**, 322 (1955).
6. J. F. Fowler, *Proc. Royal Soc., London*, **236A**, 464 (1956).
7. W. L. Medlin, *Phys. Rev.*, **123**, 502 (1961).
8. W. L. McCubbin, *J. Chem. Phys.*, **43**, 2451 (1965).
9. L. M. Schwartz and J. Janin, *J. Phys.*, **20**, 311 (1968).
10. L. M. Schwartz and J. M. Poncet, *Compt. Rend. Acad. Sci. Paris*, **270**, 970 (1970).
11. L. M. Schwartz and J. M. Voutay-Poncet, *ibid.*, **271**, 1228 (1970).
12. J. Janin, G. Josseron, J. C. Souillat, and G. Dejardin, *J. Phys. Radium*, **24**, 84 (1963).
13. L. I. Grossweiner, *J. Appl. Phys.*, **24**, 1306 (1953).
14. A. Halperin and A. A. Braner, *Phys. Rev.*, **117**, 409 (1960).

Photometallic Etching of Holograms

P. J. Magill and C. A. Speicher

IBM Systems Development Division, Endicott, New York 13760

In recent years, various techniques have been employed in the construction and replication of holograms. For example, photoresists, bleached emulsions, and thermoplastics (1) have been used for phase-type holograms, whereas thin metallic films (2, 3) have been used for amplitude-type holograms. More recently, the photoanodic engraving of silicon (4) has been demonstrated as a useful technique for producing thin, phase-type holograms. The present note describes another novel method for the fabrication of holograms. This method permits the direct fabrication of holograms on metallic films by use of the photometallic process (5). Conceptually, this process could be used for the fabrication of either phase- or amplitude-type holograms. This would depend on the original film thickness. For example, a 200Å film would be used for an amplitude hologram whereas a film of approximately 5000Å or greater would provide sufficient path differences for a reflective, phase-type hologram. This, of course, assumes that proper control of the photometallic process is possible.

The photometallic process is a method for producing patterns by the preferential etching of surfaces. This process works by the photogeneration of material which subsequently reacts with the surface. The work of Burgess and Schaefer (5) demonstrated etch rates of approximately 100Å/min or greater and resolution capability of about 75 lines/mm. Although this process might be useful for microcircuitry, its application to holography is not readily apparent due to this limited resolution. However, some recent approaches to image formation (6), which use phase-type optical filters, do not require the high carrier frequency that is normally associated with holography. The present work was directed with this in mind and, consequently, only metallic films thick enough for phase-type reflective holograms were utilized.

Key words: holography, photochemistry, thin films, etching.

Two metals (copper and Nichrome) known to have been etched by Burgess and Schaefer, were selected for this study. The Ni-Cr films (≅1000Å thick) were prepared by vacuum deposition and the Cu films (≅3000Å thick) by r-f sputtering. Standard microscope slides were used as substrates which were subjected to a routine cleaning procedure prior to placement in either vacuum chamber. In the case of the r-f sputtered films, the substrates were also cleaned by a sputter-etch bombardment. This was followed by deposition in an argon atmosphere at 10^{-2} Torr at a rate of about 600Å/min. Films prepared in this fashion generally exhibit better adhesion than do similar films prepared by evaporation and, consequently, should permit a better evaluation of the etching process.

The procedure outlined by Burgess and Schaefer for etching was followed; the metal film was coated with a polymer system and subsequently exposed to the desired pattern. Since our primary interest was in producing a phase-type hologram, we were naturally interested in the gray scale patterns that could be obtained, since this would indicate a relationship between light intensity and etch rates.

In the case of Nichrome, the solvent used was methylethylketone (MEK). As previously shown by Burgess and Schaefer, no etching occurred during exposure. Etching did occur during post-irradiation treatment. Some gray scale capability was observed.

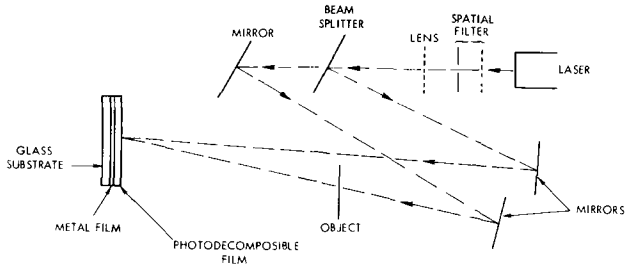

Fig. 1. Arrangement of holographic experiment

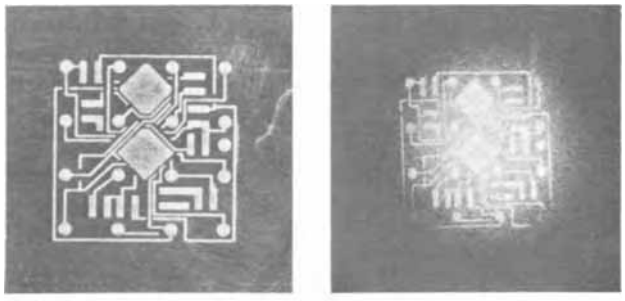

Fig. 2. Construction of a hologram by using the photometallic process. (a) Object, (b) reconstructed image.

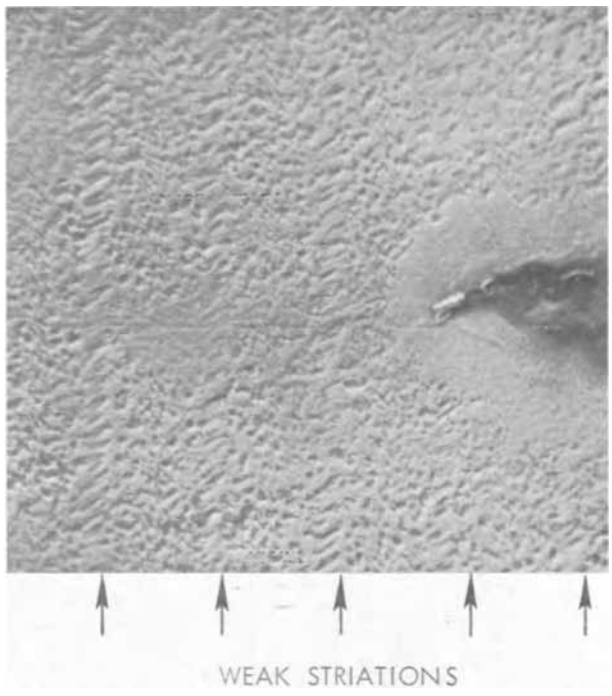

Fig. 3. Scanning electron micrograph (approx. 1700X) of a diffraction pattern etched in copper.

However, the results did not seem to indicate any direct relationship between etch rates and the light intensity. All further work was done using copper films.

For copper films, a 0.1M solution of iodoform in methanol was used as the photoetchant. In addition, 2.5g of alcohol-soluble butyrate (A.S.B.)[1] were dissolved in 50 ml of the 0.1M etchant. The copper films were dipped in the etchant and allowed to dry, leaving a polymer and iodoform film about 0.25 mm thick. Slight etching of the copper occurred during application of this etchant. The multilayer structure of copper and iodoform plus A.S.B. was then exposed to an ultraviolet light source for activation of the photodecomposible iodoform.

The experimental arrangement used to etch and therefore construct holograms in the copper film is shown in Fig. 1. Standard holographic techniques were used for the construction and reconstruction of the hologram. The collimated output of about 30 mW/cm^2 from an argon laser operating at the 3511Å wavelength was used for constructing the holograms. Interference between the reference beam and object beam resulted in intensity variations of the ultraviolet light on the photodecomposable material. The angle between the beams, about one degree, resulted in a spatial frequency of approximately 60 lines/mm. The exposure times were about 60 min.

Figures 2a and 2b show the mask used as the object and the reconstructed image, respectively, from the etched copper film. The reconstruction was obtained by reflecting a collimated beam from a He-Ne (6238Å wavelength) laser from the etched copper surface. The diffraction efficiency of this hologram was approximately 1%. There was also a relatively high level of background noise in the vicinity of the reconstructed image.

Subsequently, a simple hologram (*i.e.*, a diffraction grating) was made. This was done so the etching process could be evaluated. Talysurf[2] measurements of this grating indicated that the etch depth was not greater than 100Å (the resolution of the Talysurf instrument). This seems contrary to the work of Burgess and Schaefer, who demonstrated gray scale capability and relief-height variations that were proportional to the density variations. Holograms observed in reflected light depend on the surface topology. Under normal circumstances, the surface should have relief-height variations that produce the proper phase variations. Since no such surface variations were measured, it is possible that an alternative mechanism would explain the ability to reconstruct an image.

The diffraction grating was examined by a scanning electron microscope (SEM). The results (Fig. 3) show etched lines (evidenced by the faint striations indicated by arrows) resulting from constructive interference at a spatial frequency of about 50 liters/mm. This surface modulation (*i.e.*, the etched lines) produced by the etching process appears to be further modified by noise. This is probably due to a nonuniform etching which results in a relatively nonspecular surface.

The depth of modulation determines the diffraction efficiency. In the case of the present grating, low modulation depth seems apparent when considering the work presented by Jenny (7). He showed an SEM scan of a photopolymer diffracting grating (hologram). The striations that are weak in Fig. 3 are clearly observed in his work. Although his gratings were not metallized surfaces, the similarity of SEM pictures indicates preferential etching of the copper film.

A copper film also was etched using a photographic step tablet as a mask. Evaluation by the SEM appeared to reveal a difference in etch depths from step to step. However, the etching again is nonuniform and, in essence, leads to a different surface roughness for each step rather than to discretely different and uniform steps. Microscopic examination of this etched step tablet did not clarify this point. For the most part, it seemed to indicate localized etching (discrete rather than a continuum), which might be expected from the polymer system. The size of the microscopic etched sites depended on the light intensity; therefore, a variation in surface roughness does exist from step to step.

As a consequence of this variation in surface roughness (dependent on light exposure), light reflected from an etched grating (or hologram) is partially phase retarded and partially scattered. It would seem that the former provides for a reconstructed image as in a phase hologram. The depth of modulation (less than 100Å) would indicate an expected effi-

[1] Eastman Chemical Products, Inc., P.O. Box 431, Kingsport, Tennessee 37662.
[2] Registered trade name, Taylor, Taylor-Hobson Ltd., Stoughton Street, Leicester, England.

ciency of less than 1%. The scattered light arising from the nonspecular surface would seem to produce a noisy and, consequently, an inefficient hologram. It is possible, however, that this scattering, if it were preferential, could contribute to a reconstructed image as in an amplitude hologram. It is therefore conceivable that a compound effect is contributing to the reconstructed image.

The present work has shown that the photometallic process could be used for the fabrication of holograms. It has not, however, demonstrated that a phase hologram may be made distinct from an amplitude hologram. It should be realized that a multitude of materials and, presumably, a multitude of photoetchants are at one's disposal. With the proper combination, it is reasonable to expect that the attainment of either form of hologram is possible.

Acknowledgment

The authors are grateful to R. Lasky for obtaining the SEM information.

Manuscript received Feb. 1, 1971.

Any discussion of this paper will appear in a Discussion Section to be published in the June 1972 JOURNAL.

REFERENCES

1. H. M. Smith, "Principles of Holography," John Wiley & Sons, Inc., New York (1969).
2. J. J. Amodei and R. S. Mezrich, *Appl. Phys. Letters*, **15**, 45 (1969).
3. A. I. Komar, *Opt. Spectroscopy*, **23**, 450 (1967).
4. A. L. Dalisa, *Appl. Phys. Letters*, **17**, 208 (1970).
5. J. F. Burgess and D. L. Schaefer, *J. Vac. Sci. Tech.*, **6**, 134 (1969).
6. L. B. Lesem, P. M. Hirsch, and J. A. Jordon, Jr., *IBM J. Res. Dev.*, **13**, No. 2 (March 1969).
7. J. A. Jenny, *J. Opt. Soc. Am.*, **60**, 1155 (1970).

Orientation Effects on the Electrical Properties of High Purity Epitaxial GaAs

J. V. DiLorenzo* and A. E. Machala

Bell Telephone Laboratories, Incorporated, Murray Hill, New Jersey 07974

Electrical properties, growth rate, and surface morphology of III-V compound semiconductors grown from the vapor phase have a marked dependence on the crystallographic orientation of the substrate (1-8). The effects of substrate orientation on the electrical properties of GaP have been studied most extensively (1-5). These studies are concerned with the incorporation of deliberately added impurities at high concentrations, although some work has been done on the incorporation of background impurities into vapor grown GaP (4, 5). Moest (6) and Williams (7) have reported orientation effects on epitaxial GaAs grown from the vapor phase by transport of bulk GaAs with hydrogen chloride gas. Blakeslee (9) has reported variations in the electrical properties and growth rate of GaAs films grown on substrates misoriented off the {100} and {111} by as much as five degrees.

We have observed that the purity of GaAs epitaxial layers grown from the vapor using the $AsCl_3|Ga$ (saturated with GaAs) $|H_2$ technique (10) depends primarily on three parameters; substrate orientation, substrate temperature (11), and $AsCl_3$ mole fraction (12, 13). It is the purpose of this communication to report substrate orientation effects on the incorporation of low-level background impurities. The remaining growth conditions, $AsCl_3$ mole fraction and substrate temperature, were optimized to yield high purity epitaxial layers. Electron mobilities up to 9820 cm^2/V-sec and 199,000 cm^2/V-sec at 300°K and 77°K, respectively, have been obtained.

The films were grown on {100},[1] {111}A, {211}A and B, and {311}A and B faces of semi-insulating, Cr doped GaAs substrates. For the {211} and {111} orientations, the arsenic (B) or gallium (A) face was revealed by chemical etching with either a 2% Br_2 in CH_3OH solution or a $5H_2SO_4|H_2O|H_2O_2$ solution.

Chemical etching of substrates on the {311} orientation displayed only minor differences in etching behavior. A definite identification of the A and B faces of {311} orientations was achieved from anomalous x-ray scattering measurements at an absorption edge as outlined by Barns *et al.* (14).

Layers were deposited on as many as 4 substrates of different orientations in a single run. Typical growth conditions were as follows: Ga source temperature, 820°C; $AsCl_3$ mole fraction, 0.012-0.016; substrate temperature 702°-707°C.

Hall measurements were made at room temperature and at 77°K on "clover-leaf" samples as described by van der Pauw (15). Carrier concentrations were calculated from the Hall data based on layer thicknesses obtained from measurements of stained angle laps.

In Table I, the thickness and growth rate of epitaxial films are listed along with substrate orientations. For this table as well as the data presented in Tables II and III, all the orientations listed under a given sample number were grown in the same run. These results show that the order of decreasing growth rate is

Table I. Film thickness and growth rate for various substrate orientations

Sample	Orientation	Thickness (microns)	Growth rate (microns/min)
1	{100}[a]	10	0.17
	{211}A	40	0.66
2	{100}	11	0.23
	{211}A	40	0.86
3	{211}A	35	0.69
	{311}B	18	0.34
4	{211}A	36	0.60
	{311}A	17	0.29
	{311}B	15	0.26
5	{100}	41	0.27
	{311}A	54	0.35
6	{100}	47	0.26
	{311}B	35	0.19
7	{100}	20	0.22
	{111}A	107	1.2
	{211}B	41	0.45
	{311}B	29	0.32
8	{100}	69	0.36
	{211}B	117	0.62

[a] All orientations listed as {100} are actually 2° off {100} towards {110}.

* Electrochemical Society Active Member.

Key words: gallium arsenide, vapor phase epitaxy, orientation effects, electron mobility.

[1] Orientations listed as {100} for convenience are actually 2° off {100} toward {110}.

Table II. Electrical properties of samples on various substrate orientations

Sample	Orientation	n(cm^{-3}) × 10^{-14} 300°K	77°K	μ(cm^2/V-sec) 300°K	77°K
1	{100}	2.40	2.44	6440	85,320
	{211}A	6.02	5.94	8270	88,920
2	{100}	0.821	0.806	8690	103,000
	{211}A	4.51	4.71	8800	107,710
3	{211}A	1.3	1.4	8640	125,280
	{311}A	24.5	21.7	7750	45,180
4	{211}A	2.5	2.3	7570	103,770
	{311}A	0.53	0.47	9820	144,000
	{311}B	33.0	27.0	7400	43,040
5	{100}	0.43	0.40	8620	149,000
	{311}A	0.71	0.74	9040	152,000
6	{100}	1.0	0.1	8180	126,750
	{311}B	14.0	13.0	8180	70,920
7	{100}	0.25	0.30	8820	181,030
	{111}A	24.0	17.0	5520	34,220
	{211}B	54.0	22.0	7300	42,500
	{311}B	44.0	26.0	6700	49,330
8	{100}	0.44	0.47	8850	199,000
	{211}B	17.0	15.0	7600	48,300

Table III. Values of the compensation ratio, $\frac{N^+ + N^-}{n}$, for epitaxial films on various orientations

Sample	Orientation	n(cm^{-3}) at 77°K	$\frac{N^+ + N^-}{n}$
1	{100}	2.44×10^{14}	7.0
	{211}A	5.94×10^{14}	3.0
2	{100}	8.1×10^{13}	11.0
	{211}A	4.7×10^{14}	2.5
3	{211}A	1.4×10^{14}	4.7
	{311}B	2.17×10^{15}	3.0
4	{211}A	2.3×10^{14}	4.5
	{311}A	4.7×10^{13}	8.0
	{311}B	2.7×10^{15}	2.8
5	{100}	4.0×10^{13}	9.0
	{311}A	7.4×10^{13}	5.0
6	{100}	1.0×10^{13}	≈30.0
	{311}B	1.3×10^{15}	2.4
7	{100}	3.0×10^{13}	6.5
	{111}A	1.7×10^{15}	5.0
	{211}B	2.2×10^{15}	3.2
	{311}B	2.6×10^{15}	2.2
8	{100}	4.7×10^{13}	3.5
	{211}B	1.5×10^{15}	3.0

{111}A > {211}A > {211}B > {311}B ≃ {311}A > {100}. The growth rates obtained in this work at 705°C are in fair agreement with those of Shaw (8) which were obtained at 750°C.

Table II lists the electrical properties of films grown on various orientations. Table III lists the compensation ratio, that is, the total number of ionized impurities, $N^+ + N^-$, divided by the free-carrier concentration, n, determined from the transport calculations of Rode and Knight (16).

The following is a summary of the major points evident from inspection of Tables II and III:

(*A*) Carrier concentrations as low as 3 x 10^{13} cm^{-3} and mobilities as high as 199,000 cm^2/V-sec at 77°K [Sample 8, {100}] can be achieved. Room temperature mobilities as high as 9820 cm^2/V-sec have been obtained.

(*B*) Carrier concentrations and total ionized-impurities can vary more than two orders of magnitude between samples grown on different orientations [Samples 6 and 7 for example].

(*C*) Growth on a plane 2° off {100} toward {110} produces, in general, more highly compensated films than growth on {211} or {311} planes.

(*D*) The growth rate of films on {311}A and B faces differ very little, even though the free carrier concentrations vary by two orders of magnitude.

(*E*) The arsenic faces of {211} and {311} orientations incorporate more impurities than the gallium faces.

Wolfe *et al.* (17) have recently pointed out that conducting inhomogeneities can cause anomalously high apparent mobilities. To substantiate the present data, the dependence of mobility on magnetic field was investigated for Sample 4 on {311}A, Sample 7 on {100}, and Sample 8 on {100}. The mobility varied from 9820-9400 cm^2/V-sec with a field change from 500-5000 gauss for Sample 4; from 182,200-181,000 cm^2/V-sec with a change of 410-820 gauss for Sample 7; and from 199,000-189,000 cm^2/V-sec with a change from 205-820 gauss for Sample 8. The decrease in mobility with increasing field demonstrates that these mobilities are real and not anomalous.

The influence of substrate orientation on the incorporation of impurities is undergoing detailed study. Further results will be the subject of a forthcoming publication.

Acknowledgments

The authors wish to thank F. Ermanis for performing Hall measurements and R. L. Barns for his x-ray determination of the polarity of the {311} face.

Manuscript received May 9, 1971.

Any discussion of this paper will appear in a Discussion Section to be published in the June 1972 JOURNAL.

REFERENCES

1. R. C. Taylor, *This Journal*, **118**, 364 (1971).
2. A. Mottram, A. R. Peaker, and P. D. Sudlow, *ibid.*, **118**, 318 (1971).
3. R. C. Taylor, *ibid.*, **116**, 383 (1969).
4. Yoshitaka Furukawa, Ganzo Iwane, and Sergo Ando, *Japan J. Appl. Phys.*, **8**, 973 (1969).
5. R. C. Taylor, J. F. Woods, and M. R. Lorenz, *J. Appl. Phys.*, **39**, 5404 (1968).
6. R. R. Moest, *This Journal*, **113**, 141 (1966).
7. F. V. Williams, *ibid.*, **111**, 886 (1964).
8. D. W. Shaw, GaAs: 1968 Symposium Proceedings, p. 50, *Inst. Phys. Phys. Soc.* (1969).
9. A. E. Blakeslee, Paper 32 presented at meeting of Met. Soc. AIME, Chicago, 1968.
10. J. R. Knight, D. Effer, and P. R. Evans, *Solid-State Electron.*, **8**, 178 (1968).
11. J. V. DiLorenzo, To be published.
12. J. V. DiLorenzo, G. E. Moore, and A. E. Machala, *This Journal*, **117**, 102C 1970).
13. B. Cairns and R. Fairman, *ibid.*, **115**, 327C 1968).
14. R. L. Barns, E. T. Keve, and S. C. Abrahams, *J. Appl. Cryst.*, **3**, 27 (1970).
15. L. J. van der Pauw, *Philips Res. Rept.*, **13**, 1 (1958).
16. D. L. Rode and S. Knight, *Phys. Rev.*, **B3**, 2534 (1971) and private communication. The data in Table III were deduced from finite-field Hall mobility calculations.
17. C. M. Wolfe and G. E. Stillman, *Appl. Phys. Letters*, **18**, 205 (1971).

JOURNAL OF THE ELECTROCHEMICAL SOCIETY

ELECTROCHEMICAL TECHNOLOGY

SEPTEMBER 1971

Thermal Conductivity Measurements of Nickel-Cadmium Aerospace Cells

Part I: Cell Conductivities

E. W. Brooman* and J. McCallum*

Battelle Memorial Institute, Columbus Laboratories, Columbus, Ohio 43201

ABSTRACT

Thermal conductivities of four types of sealed, 20 A-hr nickel-cadmium cells have been measured perpendicular to (x-direction) and parallel with (y-direction) the plane of the electrodes. The average conductivities for the discharged cells described are about 0.0030 and 0.0065 (cal/cm^2/sec)/(C/cm) for these x- and y-directions, respectively. Thermal resistance network models give reasonable quantitative agreement with the k_x measurements using conductivity values of 0.0019, 0.0016, and 0.0011 (cal/cm^2/sec)/(C/cm), determined in some preliminary experiments, for the wetted negative and positive electrodes and the separator, respectively. The thermal conductivity of the cells is found to change very little with state of charge.

A paucity of data exists in the published literature concerning experimentally determined values for the thermal conductivity of primary and/or secondary cells (1). Because of the thermal anisotropy of prismatic aerospace cells, reliable data are needed to calculate heat balances and heat dissipation efficiencies for various power system configurations for earth-orbiting and space vehicles. Thermal resistance, capacitance, and conductivity values are also important in evaluating the thermal design of batteries for other than space applications.

A research program to improve sealed, nickel-cadmium cells for the U. S. Air Force included the following thermal conductivity measurements. Because of terminal connections at the top and recessed case bottoms on some cells, measurements were made only in two directions. These two directions are perpendicular to (x-direction) and parallel with (y-direction) the plane of the electrodes, as shown in Fig. 1. The conductivities measured in these directions are referred to as k_x and k_y, respectively. Subsequently, thermal resistance networks were constructed, representative of an external heat source and heat flow through the cells in these directions, in order that the observed conductivities could be correlated with the arrangement and type of components comprising the cells.

Experimental

Sealed nickel-cadmium aerospace cells, having a nominal capacity of 20 A-hr, from four manufacturers were studied.These cells were given the identification of Types I through IV, depending on the manufacturer. All the cells were prismatic in shape, Types I and II cells being taller and thinner than Types III and IV cells. Types I and II cells and Types III and IV cells had similar over-all dimensions. No cell had a third electrode. Types I and II cells had the positive terminal electrically insulated from the cell case; Types III and IV cells had both terminals insulated from the cell case. The Type III cell had the adhesive tape, with which it was supplied, removed for the thermal-conductivity measurements. Typical physical characteristics of the four types of cell are given in Table I.

All the cells had previously been subjected to capacity and voltage matching procedures as part of another investigation (2, 3). Subsequently, the thermal conductivity of the sealed cells was determined after they had been discharged and shorted.

Thermal conductivities of the discharged cells were measured using the comparison technique, whereby, if

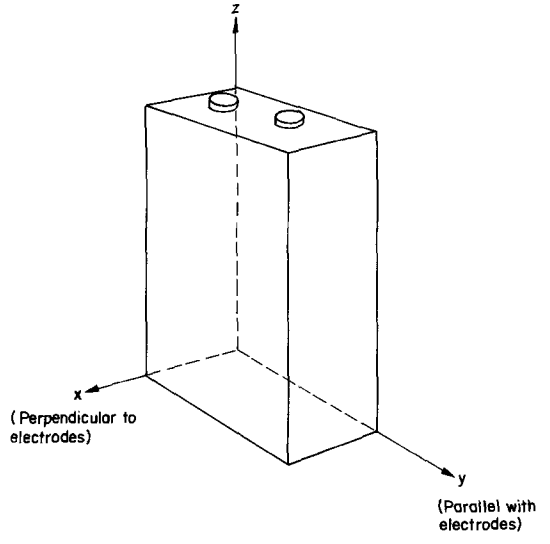

Fig. 1. Directions used to describe the thermal conductivity or resistance of sealed, prismatic cells.

* Electrochemical Society Active Member.
Key words: thermal conductivity, nickel-cadmium cells.

Table I. Average physical characteristics of the four types of 20 A-hr nickel-cadmium cells

Cell type	Side-face dimensions, cm	End-face dimensions, cm	Recessed case bottom	Number of insulated terminals	Number of positive electrodes	Number of negative electrodes
I	7.55 × 16.72	2.25 × 16.72	Yes	1	9	10
II	7.63 × 16.60	2.21 × 16.60	Yes	1	9	10
III	8.15 × 12.10	3.73 × 12.10	No	2	17	18
IV	8.02 × 10.04	3.75 × 10.04	No	2	18	19

the heat flow through the cell in question and a reference material is maintained constant, then the temperature drop across each is inversely proportional to the thermal conductivity of each and directly proportional to the distance the heat flux traverses in each (4). Thus, if k_2 is the thermal conductivity of the cell of cross-sectional area A and thickness d_2, if k_1 is the thermal conductivity of the reference material, also having a cross-sectional area A, but of a thickness d_1, and if the measured temperature drop across the cell is ΔT_2 and that across the reference material is ΔT_1

$$\frac{k_2}{k_1} = \frac{\Delta T_1}{\Delta T_2} \cdot \frac{d_2}{d_1} \quad [1]$$

or

$$k_2 = k_1 \cdot \frac{\Delta T_1}{\Delta T_2} \cdot \frac{d_2}{d_1} \quad [2]$$

The reference material chosen was Plexiglas acrylic sheet about 1.2 cm thick because this gave a reasonable temperature differential, similar to that across the cells. The thermal conductivity of this reference material was taken to be 0.492 x 10^{-3} (cal/cm²/sec)/(C/cm) according to Specification ASTM D702.

The experimental arrangement is shown schematically in Fig. 2. Strip heaters encased in silicone-rubber electrical insulation were held firmly against a copper block, 2.5 cm thick, used to provide a uniformly distributed heat flux. The cell under investigation was placed next to the reference block, and the whole apparatus was clamped between two retaining plates using 2 ft-lb of torque. Plate A was fabricated from Plexiglas and Plate E was fabricated from aluminum to promote a more unidirectional heat flux through the components. The copper block, reference block, and retaining Plate E, all had grooves key-slotted into them which were the exact depth and width of a 30-gauge copper-Constantan thermocouple. When inserted into the slots, the thermocouple's leads and junctions were flush with the surface. The temperature gradients could thus be calculated with precision, and good contact with both surfaces was assured. The junctions were located at the centers of B, C, and E, where the heat flux was assumed most uniform.

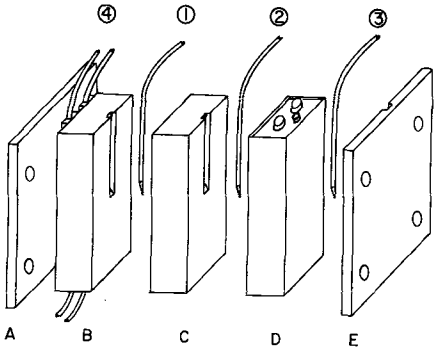

Fig. 2. Major components of the experimental apparatus used to measure thermal conductivities of cells. A, Plexiglas retaining plate; B, copper heating block; C, Plexiglas reference block; D, cell under investigation; E, aluminum heat sink/retaining plate; ① → ③, copper/Constantan thermocouples; ④, silicone-rubber-encased strip heaters.

Because the cells did not have flat faces, good thermal contact with the various components of the apparatus (low contact resistance) could not be assumed. Therefore, silicone vacuum grease, filled with pure aluminum powder to increase the thermal conductivity, was used between components B, C, D, and E before they were bolted together. It should be noted that a separate set of components was fabricated for each cell so that the cross-sectional area of B, C, and D was the same for each particular measurement. Because measurements were taken in directions parallel with and perpendicular to the plane of the electrodes for each of the four types of cells, eight sets of apparatus components were necessary.

The experimental procedure was as follows. The cell was removed from any retaining plates and wrappings and lightly cleaned with a metal polish. Thorough degreasing followed. The copper reference block and the aluminum retaining plate were also polished and degreased, while the Plexiglas components A and C and the thermocouples were just cleaned and degreased. The apparatus was then assembled and bolted together to a 2 ft-lb torque loading, as described previously. Excess, exuded grease was then removed, and the whole apparatus encapsulated with two layers of matted insulation and another of rigid Styrofoam 2.5 cm thick. The heat sink/retaining plate outside surface was left exposed to the laboratory atmosphere but shielded by the projecting Styrofoam to minimize the effects of draughts.

The strip heater(s) used power from the main supply by employing a Variac Autotransformer to reduce the voltage to 10 to 20V. The thermocouples were shielded and the outputs fed to a Sargent M-R recorder. At the beginning of each experiment the thermocouples were calibrated against each other using an ice bath as cold junction. The heater was then switched on and the apparatus allowed to come to the steady state. In the steady state the cell temperatures were about 32° ± 2°C (average of the thermocouple ② and ③ readings).

Steady state was achieved in about 18 hr and was determined from invariant thermal gradients across the cell and reference block. Accuracy of temperature measurement was about ±0.015°C. The error in measuring the lengths of the heat-transfer path was estimated to be ±0.05 cm because of the rounded edges of the cell cases and the small uncertainty of the distribution of the vacuum grease between components. These length measurements therefore probably determine the over-all accuracy of measurement. The reproducibility of the experiments, which were repeated, was about ±5%.

Results and Discussion

The k_x and k_y values obtained for the four types of 20 A-hr cells are summarized in Table II. The ratio k_y/k_x is also given as a measure of the thermal anisotropy of each cell.

In the x-direction, the average conductivity value measured is 0.0044 (cal/cm²/sec)/(C/cm)—hereafter referred to as cgs units. The values for the Types I, II, and III cells are similar and average 0.0030 cgs units, while the k_x value for the Type IV cell is 2 to 3 times higher. The y-direction conductivities for the Types I, II, and III cells are similar to each other, with an average value of 0.0065 cgs units.

Table II. Measured thermal conductivities of four types of nominal 20 A-hr nickel-cadmium cells

Cell type	Direction of heat flow[a]	Thermal conductivity (k), (cal/cm²/sec)/(C/cm)	Ratio k_y/k_x
I	y-direction	$k_y = 0.0070$	2.59
	x-direction	$k_x = 0.0027$	
II	y-direction	$k_y = 0.0067$	1.76
	x-direction	$k_x = 0.0038$	
III	y-direction	$k_y = 0.0056$	2.16
	x-direction	$k_x = 0.0026$	
IV	y-direction	$k_y = —$	—
	x-direction	$k_x = 0.0086$	

[a] See Fig. 1.

Conductivities in the y-direction.—The reported values for k_y for nickel-cadmium cells range from 0.0035 to 0.052 cgs units (5-9, 17), there seemingly being no correlation between the A-hr capacity of the cell and the conductivity value measured. Values obtained in this investigation range from 0.0056 to 0.0070 cgs units, and are higher by a factor of two than the range of values reported with one exception—the value for the Type III cell. Although the value given in Table II for the Type III cell is smaller than the other values obtained, this is the average of measurements on three different cells, the individual results differing by less than ±2%.

Thermal-resistance network models were constructed for the four types of cell (14), and evaluated to predict the k_y values using the relationship

$$R_i = d_i/k_i A_i \qquad [3]$$

where R_i is the thermal resistance of the ith network component. Figure 3 shows a typical network, in this instance for a Type II cell. Table III lists conductivity data used in calculating the R_i's for the various cell components. These individual component resistances were summed in parallel and series to obtain the overall, apparent thermal resistance and conductivity of each cell type. As shown in Fig. 3, the networks consist of the cell case and lining(s), where applicable, in series with the parallel combination of the positive and negative electrodes and separator. This network in turn is in parallel with the cell-case sides and top and bottom. It was difficult to determine the size of the gas gap between the case and the separators/electrodes, so that this network element was neglected. Consequently, only semiquantitative estimates were made (14) for the

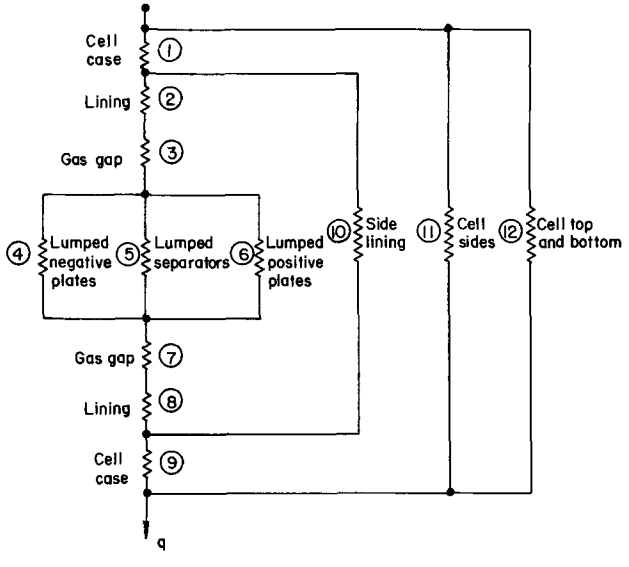

Fig. 3. Thermal resistance network of a Type II cell in a direction parallel with the electrodes (y-direction).

Table III. Selected values for some thermophysical properties of materials commonly used in nickel-cadmium cells and batteries

Material	Specific heat, cal/g/C	Thermal conductivity, cgs units	Specific gravity or density, g/cm³[a]
		Active materials	
Nickel	0.11-0.13	0.152	8.90
NiO	—	0.00225	7.45
NiO·OH	~0.11	—	—
$NiO \cdot xH_2O$	~0.14	0.08	4.10
$Ni(OH)_2$	—	—	4.10
$Ni_2O_3 \cdot xH_2O$	—	—	4.83
Cadmium	0.055	0.23	8.64
CdO	0.081	—	8.15
$Cd(OH)_2$	~0.20	—	4.79
KOH (30%)	~0.82	0.00135	1.30
		Constructional and other materials	
Stainless steel (304)	0.12	0.039	8.03
Magnesium	0.245	0.376	1.74
Aluminum	0.22	0.535	2.70
Copper	0.092	0.940	8.96
Brass	0.09	0.292	8.55
Lead solder	~0.04	~0.060	—
Nylon	~0.40	~0.0006	~1.14
Bakelite	~0.37	~0.001	~1.15
Cellulose films	~0.36	~0.0006	~1.27
Polyester films	~0.43	~0.0005	~1.39
Epoxies	~0.40	~0.003	~1.85
Glass	~0.20	~0.0029	~2.30
Rayon films	~0.35	~0.0005	~1.20
Asbestos	~0.20	~0.0004	~2.50
Alumina	0.175	~0.0044	3.65
Electrical ceramics	~0.20	~0.0051	~2.50
Air (dry)	0.24	~0.00006	~0.0012

[a] Included because it is useful in determining heat capacities in thermal resistance-capacitance models.

thermal networks, and these gave the following order of k_y values: I > II > III, which is in agreement with the measured values given in Table II.

The Type III cell exhibited the lowest measured conductivity, and is the only cell type with trapezoidally shaped electrodes. This electrode configuration leads to the highest thermal resistance value for the electrode pack (network elements ④, ⑤, and ⑥ in Fig. 2) of any cell type. In fact the calculated thermal resistances of the electrode packs were in the order III, IV > I, II. Thus, using Eq. [3], the estimated apparent conductivities of the electrode packs vary in the order I, II > III, IV, which is a similar order to that for the measured conductivities of the complete cells. The average k_y value calculated for the four types of electrode pack is about 0.0234 cgs units, if an average k_y value of 0.030 cgs units is assumed for both electrodes (based upon an 80% porous nickel plaque material). The k_y value calculated for the Type I, 20 A-hr cell electrode pack is about 0.0217 cgs units, which may be compared with a calculated value of 0.0233 cgs units for the electrode pack of an 100 A-hr cell from the same manufacturer (16).

Conductivities in the x-direction.—The reported values for k_x for nickel-cadmium cells range from 0.0016 to 0.0067 cgs units (5-9, 17), with an average value of about 0.0042 cgs units. The measured values for the four types of 20 A-hr cells range from 0.0026 to 0.0086, with an average value of 0.0044 cgs units. Thus, for the direction perpendicular to the plane of the electrodes, there is good quantitative agreement between the values reported here and the values from the literature. A contributing factor to this better correlation could be the fact that it is easier to measure the conductivity of the cell in this direction, because the compression on the cells exerted by the retaining plates in the apparatus forces the cell case and electrode pack together, giving better thermal contact. For the parallel measurements, with compression the thermal contact could have been worsened or improved, depending on whether the cell-case sides are convex or concave, respectively.

Because of differences in cell-case thickness, surface treatment, and possibly composition, it was thought that if measurements were made on the electrode packs alone (cells with the cell cases removed, but not the

Table IV. Measured thermal conductivities, k_x', of four types of 20 A-hr nickel-cadmium cells, with their cell cases removed

Cell type	Thermal conductivity, (cal/cm²/sec)/(C/cm)	Ratio k_x/k_x'
I	$k_x' = 0.0020$	1.38
II	$k_x' = 0.0016$	2.37
III	$k_x' = 0.0021$	1.20
IV	$k_x' = 0.0032$	2.69

Table V. Calculated values for the thermal conductivity of four types of 20 A-hr nickel-cadmium cells

Cell type	Thermal conductivity, (cal/cm²/sec)/(C/cm) k_x (with case)	k_x' (without case)	Ratio k_x/k_x'
I	0.0032	0.0021	1.52
II	0.0025	0.0018	1.39
III	0.0029	0.0019	1.53
IV	0.0028	0.0024	1.17

top containing the terminal fittings, etc.), then less spread in the experimental results for the four types of cells might be observed. The results of these k_x' measurements, made in the same way as for complete cells, are summarized in Table IV.

The spread in thermal conductivity values, k_x', is much smaller, as anticipated, and the average value is 0.0022 cgs units, compared with 0.0044 cgs units for the complete cells. Thus the parallel heat transfer paths afforded by the cell cases effectively double the apparent conductivity of the complete cells.

Thermal resistance network models were also set up to predict the k_x values for the four types of cells. Preliminary measurements made, using a Pyroceram 9606 heat-flow meter apparatus in an evacuable chamber (4), gave values of approximately 0.0019, 0.0016, and 0.0011 cgs units for the discharged, wetted negative and positive electrodes, and wetted separator, respectively, from a Type II cell. Other thermophysical-property data used to evaluate the networks are included in Table III which was compiled from handbooks and manufacturers' literature (13). The resistance networks set up were similar to that shown in Fig. 4 for a Type II cell. For the Type I cell, no element corresponding to the cell lining was interposed between the elements (1) and (3), and (5) and (7) in Fig. 4. Evaluating the networks for the four types of cells gave the calculated values shown in Table V. Both k_x (with cell case) and k_x' (without case) values were calculated, and the ratios k_x/k_x' are given for comparison with the ratios in Table IV. Quantitatively, reasonable agreement exists between the values for k_x' in Table V and in Table IV. The Type IV cell was predicted to have the highest conductivity, and the Type II cell the lowest. This is substantiated by the measurements. Reasonable quantitative agreement also exists between the predicted values for k_x in Table V and the measured values for k_x in Table II, with the exception of the k_x value for the Type IV cell. This Type IV cell conductivity anomaly has not been explained.

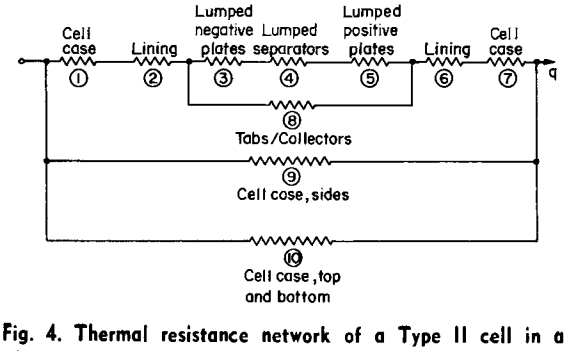

Fig. 4. Thermal resistance network of a Type II cell in a direction perpendicular to the electrodes (x-direction).

General.—When necessary, heat is normally removed from a cell in the x-direction, because the thermal anisotropy of the cell is normally assumed to be small, and the cross-sectional area, A_x, available for heat dissipation is the largest. However, the above results suggest that for some cell types the thermal anisotropy (a large k_y/k_x value) can be significant (see Table II). If the ratio of k_y/k_x far exceeds the ratio of cross-sectional areas A_x/A_y from which the heat is to be extracted, then consideration should be given to extracting heat in the y-direction, and not the x-direction.

In this present study, measurements were not made in the z-direction. Intuitively, if k_y is greater than k_x, then, because of the way in which the cells are constructed, k_z should also exceed k_x. Baker *et al.* (5) also make such an assumption, whereas Shair *et al.* (7) cite earlier experimental work which gave a ratio of about 1:3:6 for $k_x:k_y:k_z$, and Coggi (17) gives a ratio of about 4:9:11 for the $k_x:k_y:k_z$ conductivities. Thus, as discussed above, heat extraction in the z-direction can be more efficient than in the x-direction. However, because of the terminals and other fittings on the top of the cells, and the presence of recessed case bottoms on some cells, the extraction of heat in the z-direction is usually not practical.

In the calculations described above to compute k_y and k_x values for the 20 A-hr cells from thermal resistance networks, values of 0.0019, 0.0016, and 0.0011 cgs units were used for the conductivities of wetted, discharged negative electrodes, positive electrodes, and separator, respectively. These values are derived from some preliminary measurements reported in Ref. (4). If the measured value of the separator, 0.0011 cgs units, is taken in order to calculate the average conductivity of the electrodes from a Type II cell, then a value of 0.0017 cgs units is obtained. This calculated value is close to the average of the measured values of 0.0019 and 0.0016 cgs units for the Type II negative and positive electrodes, respectively. Conversely, if the measured conductivity values of the two types of electrode are substituted into the network shown in Fig. 4, a value of 0.0012 cgs units is obtained for the separator material. Consistency between the thermal resistance network models for the x-direction, and the subsequent conductivity measurements is thus evident.

Effect of state of charge.—The effect of state of charge on the thermal conductivity, k_x, of a Type I and a Type III cell was investigated. The cells were charged at a C/3 rate for 1.5 hr, and the conductivity was then measured, as previously described, while a trickle charge of 0.5A was flowing to maintain that state of charge. The cells were then charged at the C/3 rate for a further 1.5 hr, and put on the same trickle charge, while the conductivity was again measured. These conductivities are referred to as 50% and 100% state of charge conductivities, respectively. After charging, the cells were discharged at a C/2 rate, and the conductivity was measured with the cells shorted. The values obtained were taken as the 0% state of charge conductivities. The cells were taken through two of these charge-discharge cycles and the average increases in conductivity are given in Table VI. The conductivities are seen to increase in approximately a linear manner with increasing state of charge. To a

Table VI. Thermal conductivity, k_x, of a type I and type III cell as a function of state of charge

State of charge per cent	Increase in k_x, per cent[a] Type I Cell	Type III Cell
0	0	0
50	8	6
100	14	12

[a] Taken with reference to the discharged conductivities (0% state of charge).

first approximation, the values given for the discharged state (0% charge) may be used in performing thermal analyses, as these values are experimentally easier to determine and, therefore, are probably more accurate.

For an increase in thermal conductivity for a given cell (constant d and A in Eq. [3]) the thermal resistance must decrease. Intuitively, in a state of full charge, the negative electrode will contain a higher proportion of metallic cadmium than it will in the discharged state; thus, this may effectively lower the thermal resistance of the negative electrodes, and hence the whole cell. Experiments on charged and discharged electrodes are necessary to verify this expectation.

Thermal design.—Based upon the results of this investigation the following observations concerning thermal design of cells and batteries may be made. It is important to strive for the lowest thermal resistance of all cell components. Because the separators and electrodes are primarily chosen for their chemical and electrochemical properties the thermal conductivities of these components in the x-direction are essentially fixed. However, the thermal conductivity of the separator materials may be increased by using the maximum permissible amount of electrolyte consistent with the constraints imposed by the desired oxygen recombination rate within the cells (14).

The variable which may be adjusted to lower the thermal resistance of complete cells is the ratio of thickness to area, d/A. As Eq. [3] shows, R will be minimized when d/A is made as small as possible in the direction of maximum k. This criterion implies that for large k_y/k_x ratios the cells should have as small a y-dimension as possible, and have a maximum cross-sectional area through which the heat flow may traverse.

For complete cells the two thermal resistance network elements which may be influenced directly are the cell liners (electrically insulating the case from the electrodes) and the gas gaps between the edges of the electrodes and the cell case. These two network elements should have the lowest possible thermal resistance in order to lower the over-all cell thermal resistance. This may be achieved by using thin liners of high thermal conductivity, and by minimizing all gas gaps. The other important network element which can be manipulated to reduce the over-all thermal resistance of a cell is the cell case which is the only continuous metallic conduction path in any direction. For other than thermal design considerations (strength, corrosion resistance, and so on) the case is normally made of stainless steel, which is not a high conductivity metal. However, the apparent conductivity of the cell case material can be increased by plating the case with a high conductivity metal such as silver (15), or by using heat extraction fins in conjunction with the case material (4, 15, 17).

If the thermal resistances of all the cell components, hence the over-all cell, are kept to a minimum then temperature gradients within a cell will be minimized. Such small temperature gradients should help to control the diffusion of active materials, and to prolong cell life. Also, lower thermal resistances would result in lower cell operating temperatures, which in most applications would also lead to prolonged life, because of a lower rate of physicochemical degradation of the cell components.

In the design and fabrication of a battery a uniform cell-to-cell temperature is important. Such uniformity enables a more efficient control and balanced operation to be achieved. If all cells do not reach end of charge or discharge at about the same time, excessive heat generation, thermal runaway or cell reversal may occur in the nonuniform cells. In this respect, the efficient stacking of the cells, the choice of heat-dissipating aids (intercell plates, heat pipes, etc.), and the proper choice and control of the heat-sink temperature are important (16). The cell sides (x-direction) are usually the most efficient external surfaces for the extraction of internally generated heat (10), but the present study has shown that the cell end faces (y-direction) should also be considered, when the cell internal configuration is such that no large gas gaps exist in this y-direction, there is a high k_y value, and the cross-sectional area for heat extraction in this y-direction is large compared with the corresponding area for the x-direction.

Conclusions

The thermal conductivities have been measured for four types of 20 A-hr nickel-cadmium cells in the discharged condition, with and without their cell cases intact, and for two representative types of cell as a function of state of charge.

The average conductivity of a complete, discharged 20 A-hr cell in the x-direction (k_x, perpendicular to plane of electrodes) is 0.0030 (cal/cm^2/sec)/(C/cm) which may be compared with previously reported values of 0.0042, 0.0067, and 0.0020 (cal/cm^2/sec)/(C/cm) for 6, 6, and 12 A-hr cells, respectively (5-8). On this basis, thermal conductivity is approximately independent of A-hr capacity of the cells, as indeed, it should be. Through the use of thermal resistance networks, differences in materials and methods of fabrication are used to explain the variations among the measurements reported here. Different materials and details of fabrication should also account for the reported differences for various size cells.

The average conductivity of a complete cell in the y-direction (k_y, parallel with plane of electrodes) is 0.0065 (cal/cm^2/sec)/(C/cm), which may be compared with previously reported values of 0.052, 0.019, and 0.041 (cal/cm^2/sec)/(C/cm) for the 6, 6, and 12 A-hr cells referred to in the preceding paragraph. Once again, on the basis of the present data and the scant data published, the thermal conductivity in this direction appears to be essentially independent of cell size.

The ratios of the two conductivities, (k_y/k_x), taken as a measure of the thermal anisotropy of the cells, are always greater than unity, and are similar to values reported previously for smaller capacity cells. Heat extraction in the y-direction may therefore be more efficient than in the x-direction for certain cell configurations.

Thermal-resistance network models are able to quantitatively predict the k_x values, if the values obtained in some preliminary measurements for the discharged negative and positive electrodes and the separators are used. The values obtained are 0.0019, 0.0016, and 0.0011 (cal/cm^2/sec)/(C/cm), respectively.

Acknowledgments

This work was performed under Wright-Patterson Air Force Base Contracts AF 33(615)-3701, and F33615-69-C-1537 as part of supporting studies to elucidate "Failure Mechanisms in Sealed Batteries." The authors wish to thank Mr. G. H. Miller, Project Monitor, for his continued interest in these studies.

Manuscript submitted Sept. 21, 1970; revised manuscript received April 16, 1971. This was Paper 170 presented at the New York Meeting of the Society, May 4-9, 1969.

Any discussion of this paper will appear in a Discussion Section to be published in the June 1972 JOURNAL.

REFERENCES

1. E. W. Brooman, "An Annotated Bibliography of the Thermal Properties of Primary and Secondary Cells," Technical Report No. AFAPL-TR-70-34 (June, 1970), Wright-Patterson Air Force Base, Contract No. F33615-69-C-1537.
2. J. McCallum and C. L. Faust, "Failure Mechanisms in Sealed Batteries," Technical Report No. AFAPL-TR-67-48, Part 2 (October, 1967), Wright-Patterson Air Force Base, Contract No. AF 33(615)-3701.

3. J. McCallum and C. L. Faust, "Failure Mechanisms in Sealed Batteries," Technical Report No. AFAPL-TR-67-48, Part 3 (February, 1968), Wright-Patterson Air Force Base, Contract No. AF 33(615)-3701.
4. E. W. Brooman and J. McCallum, "Heat Transfer in Sealed Nickel-Cadmium Spacecraft Cells and Batteries," Technical Report No. AFAPL-TR-69-21 (April, 1969), Wright-Patterson Air Force Base, Contract No. AF 33(615)-3701.
5. B. S. Baker, D. Gidaspow *et al.*, "Electrochemical Systems Heat and Mass Transfer," First Quarterly Report (September, 1967), NASA Marshall Space Flight Center, Contract No. NAS 8-21159.
6. K. E. Preusse and R. C. Shair, "Thermal Analysis of Hermetically Sealed Nickel-Cadmium Cells for Space Applications," *Space Power Systems Engineering*, p. 1127, G. C. Szezo and J. E. Taylor, Editors, Academic Press, New York (1966).
7. R. C. Shair, H. N. Seiger *et al.*, "Design, Development, and Manufacture of Storage Batteries for Future Satellites," Final Report (July, 1963), N65-17518, NASA Goddard Space Flight Center, Contract No. NAS 5-809.
8. T. R. Beck and F. S. Kemp, "Heat Generation in Lunar Orbiter Battery," Boeing Document No. D2-23612-1 (October, 1964), NASA Contract No. NAS 1-3800 in part.
9. E. Kantner, P. Tarantino *et al.*, "Investigation of Hermetically Sealed, High Rate, Maintenance Free, Nickel-Cadmium Batteries for Aircraft Application," Technical Report No. AFAPL-TR-66-77 (September, 1966), Wright-Patterson Air Force Base, Contract No. AF-33(615)-2087.
10. S. Gross and H. Oman, "Development and Fabrication of Advanced Battery Energy Storage System," Final Report (November, 1967), NASA Manned Space Flight Center, Contract No. NAS 9-6470.
11. F. E. Betz, "Design and Fabrication of 100 Amp-Hr Nickel-Cadmium Battery Cells," Final Report No. NASA-CR-66300 (March, 1967), NASA Langley Research Center, Contract No. NAS 1-4289.
12. R. E. Thomas, E. W. Brooman *et al.*, "Study of Space Battery Accelerated Testing Techniques, Phase II Report: Ideal Approaches Towards Accelerated Tests and Analysis of Data," (August, 1969), NASA Goddard Space Flight Center, Contract No. NAS 5-11594.
13. E. W. Brooman and J. McCallum, "The Thermal Properties and Behavior of Nickel-Cadmium and Silver-Zinc Cells and Their Components," Technical Report No. AFAPL-TR-68-41 (June, 1968), Wright-Patterson Air Force Base, Contract No. AF 33(615)-3701.
14. E. W. Brooman and J. McCallum, "The Thermal Conductivity of Sealed Nickel-Cadmium Cells," Technical Report in preparation, Wright-Patterson Air Force Base, Contract No. F33615-69-C-1537.
15. T. R. Beck, "Thermal Resistance and Temperature Gradients in Cells of Lunar Orbiter Battery," Boeing Coordination Sheet No. 2-5466-0-788 C/S (February, 1965).
16. W. R. Scott, "Two Kilowatt Long Life Battery," Technical Report No. AFAPL-TR-70-61 (September, 1970), Wright-Patterson Air Force Base, Contract No. F33615-69-C-1291.
17. J. V. Coggi, "Heat Pipe Control of Spacecraft Batteries," McDonnel Douglas Astronautics Co. Paper WD 1216 (June, 1970), Paper presented at the Intersociety Energy Conversion Engineering Conference, Las Vegas, Nevada, September 21-25, 1970.

Fuel Control in Methanol-Air and Formaldehyde-Air Fuel Cell Systems

K. J. Cathro

CSIRO, Division of Mineral Chemistry, P. O. Box 124, Port Melbourne, Victoria, 3207, Australia

ABSTRACT

Two types of fuel control units have been assembled and tested in conjunction with formaldehyde-air and methanol-air fuel cells. One type was based on a continuous fuel analyzer, while the other employed a load sensing technique. Both types gave satisfactory performance, and the advantages and disadvantages of each are discussed.

Fuel cell systems which employ a circulated aqueous electrolyte as a vehicle for bringing fuel to the anodes normally require some form of fuel control. This is necessary because there is usually a lower limit of fuel concentration below which anode performance falls off rapidly, while high concentrations lead to excessive loss of fuel by diffusion to the cathode with a consequent decrease in efficiency. If the cathode catalyst is also effective in promoting fuel oxidation, the oxidation of this diffused fuel could lead to overheating.

The present work describes the development of a fuel control subsystem suitable for low-power (approximately 50W) battery systems using either formaldehyde or methanol as fuel, and a dilute sulfuric acid electrolyte. Since the battery may be used in an application requiring long-term unattended operation (*e.g.* for 1000-3000 hr) reliability and adequate long term stability of the fuel control is essential. A further complication arises when using formaldehyde. Commercial formaldehyde is stabilized against polymerization by the addition of methanol and since formaldehyde is oxidized preferentially, the methanol builds up in the electrolyte, usually to an equilibrium level of about 0.5M. Further, formic acid builds up in solution since it is less rapidly oxidized than formaldehyde and is a partial oxidation product. Therefore, any method used for formaldehyde concentration control must function in the presence of these other constituents. Since the battery output is small, no more than a few watts can be allowed for controller operation.

Several possible methods of fuel control were studied. The first method considered employed a fuel addition rate proportional to battery current plus a constant allowance to cover nonfaradaic losses. This approach was initially dismissed as impractical, since a small error in the addition rate would lead to a cumulative error in fuel concentration. It was later reconsidered and shown to be practical in those cases where there is a concentration-dependent loss of fuel as is described later.

A second possibility was to use cell voltage as a measure of fuel concentration. Unfortunately, cell volt-

Key words: fuel cell, fuel control, formaldehyde, methanol.

age is also affected by such factors as load current, temperature, and the age of the cell. Although most of these other factors could be compensated, the aging effect is unpredictable. Moreover, in the concentration ranges of interest the rate of change of cell voltage with fuel concentration is small. Therefore, this method was discarded as unsatisfactory.

If fuel concentration could be monitored directly by a suitable analyzer, the output of this device could be used to control fuel addition. Since errors are not cumulative, and since the range of fuel concentration over which satisfactory operation of the fuel cell is obtained is relatively wide, the sensing device need not be very precise. It was decided to develop a fuel concentration sensing device. The output of this would be compared to a suitable reference, and fuel added as required to maintain the desired concentration.

Salathe *et al.* (1) in their study of fuel control systems for a hydrazine battery, also describe systems depending on fuel concentration monitoring or load sensing. They point out that a load sensing system (described in their paper as electrolysis pumping) is incapable of allowing for changes in nonelectrolytic consumption of fuel. Thus, the fuel concentration must be biased towards the high side of the usable range to prevent system failure due to low fuel concentration. This causes a high fuel consumption compared to that obtained using the direct concentration monitoring technique. Evans (2), in a paper describing the fuel feed control system for a hydrazine battery, came to similar conclusions.

The only methanol control system described to date (3) used a concentration sensing device. This consisted of a small electrolytic cell, the anode of which was of platinized platinum covered with a membrane. The membrane ensured that the anodic current through the electrode was controlled by the rate of diffusion of methanol through the membrane, thus avoiding errors due to change in activity of the platinum catalyst. A later publication (4) stated that this approach has been changed, with programmed addition of methanol fuel being used, and the detector being used only as an override safety device.

Control by Cyclic Voltammetry

A review of the physical properties of water-fuel-sulfuric acid solutions (*i.e.* such factors as viscosity, density, and surface tension) showed that these would not have sufficient discrimination for use in fuel concentration analysis, even if some suitable low-power method of instrumenting them could be devised. An electrochemical method was then sought. Estimation of the rate of diffusion of fuel through a membrane, measured by the anodic current sustained by an enclosed anode, has been described (3). We were not able to attain any degree of success with this method. In general, it was not possible to get reliable adhesion of available membrane types to the indicator electrode, and response time would have been poor. The simple method of monitoring potential at constant current, as used in hydrazine batteries (1, 2), is not suitable because of the change in the sensing electrode catalytic activity with time.

It was thought that electrode performance would be more stable if its potential were periodically taken to a highly oxidizing value in order to destroy any partially oxidized adsorbed species. This led to the use of cyclic voltammetry. Since the anodic oxidation of both methanol and formaldehyde on platinum is not diffusion controlled (5), there will be little effect of circulation rate on the current peaks observed, and it will be possible to choose the voltage span such that the electrode will be driven to a highly positive potential —and hence cleaned—during each cycle. Although such a system promised to be fairly complex electronically it was decided to test it as described below.

Preliminary experiments.—Preliminary tests were made using a conventional three-electrode cell, the potential of the sensing electrode (the anode) being

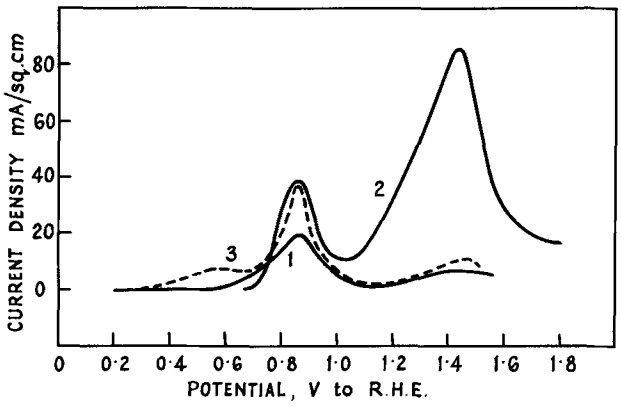

Fig. 1. Current-voltage curves. Curve (1) 0.86M methanol, (2) 0.90M formaldehyde, (3) 1.2M formic acid in 0.5M H_2SO_4 at 60°C on a 1 cm^2 platinum foil electrode. Voltage sweep is positive going at 50 mV/sec.

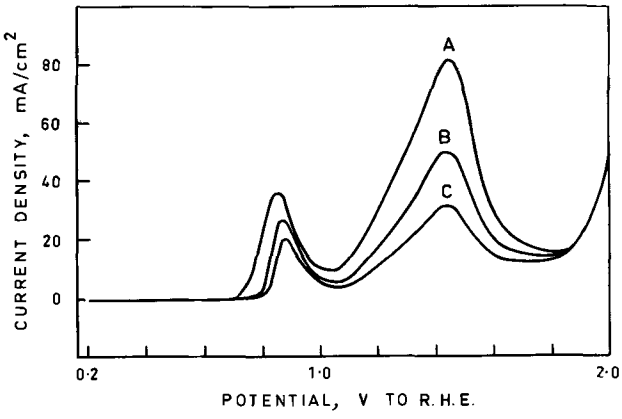

Fig. 2. Current-voltage curve for formaldehyde, methanol, and formic acid. Electrolyte: (A) 0.5M formaldehyde, 0.5M H_2SO_4, 60°C; (B) As for (A), with 0.5 methanol and 0.5M formic acid; (C) As for (A) with 1M methanol and 1M formic acid. Electrode: 0.04 cm^2 platinum bead. Sweep: 50 mV/sec, positive going.

controlled by a potentiostat which was in turn programmed by a waveform generator. Current-voltage curves were recorded using either an *X-Y* recorder or an oscilloscope in the *X-Y* mode. The *X* (potential) axis was driven by a voltage follower, and the *Y* (current) axis measured the potential drop across a suitable resistor. Typical current-voltage curves are shown for the anodic oxidation of methanol, formaldehyde, and formic acid in Fig. 1. The electrolyte in all cases was 0.5M sulfuric acid.

The figure shows oxidation peaks which might be useful for control purposes. The current peak at 0.9V with methanol (which is the only oxidizable component in an operating methanol battery) is sufficiently well-defined for control. For a formaldehyde battery it is necessary to find if the presence of the expected concentrations of methanol and formic acid affect the peak current. Curves 1 and 2 also show that although the peaks would overlap, the peak at +1.5V to R.H.E.[1] in formaldehyde gives a much greater oxidation current than either methanol or formic acid. Thus it might be possible to get an approximate measure of the formaldehyde concentration from the peak current observed at this potential.

To check the possibility of determining formaldehyde in the presence of the other two components current-voltage curves were made on formaldehyde-methanol-formic acid solutions. A typical result is shown in Fig. 2. This shows clearly that the presence of the other components depresses the formaldehyde

[1] All potentials are reported with reference to a hydrogen electrode in the same solution (R.H.E.) unless otherwise stated.

Table I. Relation between formaldehyde concentration and peak current

Temperature: 60°C
Sweep rate: 0.5 V/sec
Other constituents: methanol and formic acid, both 1M

Formaldehyde concentration, M	Peak current at 1.5V, mA/cm²
nil	21.8
0.10	31.3
0.24	42.0
0.48	59.3

Table II. Effect of variation in methanol or formic acid concentration

Temperature: 60°C
Sweep rate: 0.5 V/sec
Formaldehyde concentration: 0.1M

Methanol concentration, M	Formic acid concentration, M	Peak current at 1.5V, mA/sq cm
nil	nil	48.7
1	nil	38.8
nil	1	37.2
1	1	31.3

peak at +1.5V. However, there is still a simple peak current-formaldehyde concentration relationship, as shown in Table I. The effect of change in methanol and formic acid concentrations on the magnitude of the formaldehyde peak current is shown in Table II. Although increasing the concentration of these components depresses the formaldehyde peak current by 20-35%, it seemed likely that their concentration in battery electrolytes would not vary widely, so that their presence would simply require appropriate calibration of the controller setting. It was thought then, that the peak current at +1.5V could be used for formaldehyde concentration control, while for methanol the peak current at +0.9V would be suitable.

The effects of sweep waveform, frequency and electrolyte temperature on the peak currents were examined. Figure 3 shows the effect of temperature, and Fig. 4 that of sweep rate on peak current. Two waveforms were tried also—sawtooth and isosceles triangle. There was little effect of the rate of sweep flyback on peak current in the forward sweep direction, but a triangular sweep was adopted in case the rapid rate of

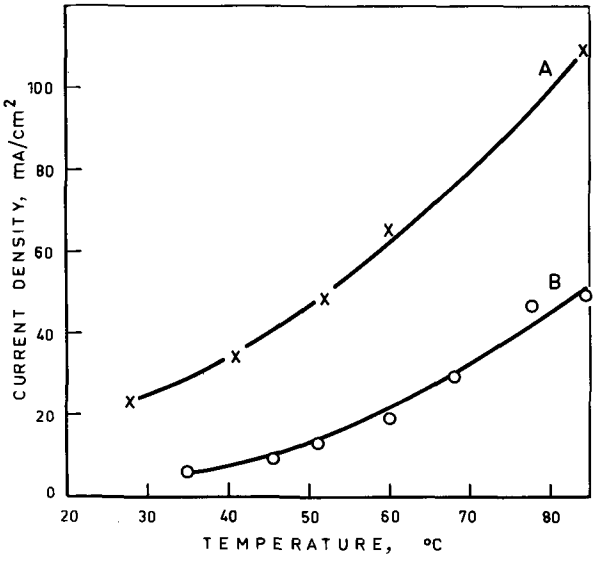

Fig. 3. Curve (A) effect of temperature on peak current for formaldehyde. Electrolyte: 0.50M formaldehyde, 0.5M H_2SO_4; electrode: 1 cm² platinum foil; sweep: 50 mV/sec, 2V triangle; peak measured: at 1.5V. Curve (B) effect of temperature on peak current for methanol. Electrolyte: 0.86M methanol, 0.5M H_2SO_4; electrode: 1 cm² platinum foil; sweep: 50 mV/sec, 2V triangle; peak measured: at 0.9V.

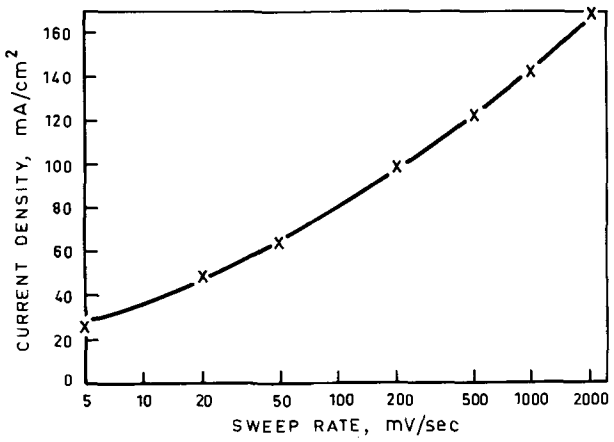

Fig. 4. Effect of sweep rate on peak current for formaldehyde. Electrolyte: 0.50M formaldehyde, 0.5M H_2SO_4; electrode: 1 cm² platinum foil; sweep: variable, 2V triangle; peak measured: at 1.5V.

oxide reduction occurring during a sawtooth flyback led to excessive electrode erosion (6). In fact, such erosion did not prove to be a problem, but the triangular sweep was used throughout the bulk of the work.

In selecting an appropriate sweep rate, it is necessary to note that increase in sweep rate increases peak current and hence sensitivity, and speed of response. Very high rates tend to give a broad peak so a compromise rate of 1 V/sec was chosen. Thus, the operating frequency was 0.25 Hz for triangular and 0.5 Hz for sawtooth waveforms. It is also clear that there is a great variation in peak current with electrolyte temperature. Thus, if the fuel concentration were correct at 70°C, it would be increased 5.3 times at 35°C. While some increase in fuel concentration at low temperature is desirable, this factor is much too high, so some form of temperature compensation is necessary.

For long-term operation the peak currents must be stable with time. During an extended run using methanol the peak current increased for the first few sweeps reaching a fairly steady value after about 20 cycles. Thereafter the value remained constant (±15%) for a further 1200 cycles, or 20 hr at the sweep rate used. A run of similar duration using formaldehyde with formic acid and methanol present showed a steady peak current (±16%) after the first 0.25 hr of operation.

The above tests were made using a 1 cm² platinum foil electrode or a small bead fused onto the end of a short length of platinum wire (area 0.04 cm²) in a conventional three-electrode potentiostatic system. In order to simplify the cell design for use in an actual battery system the reference electrode was omitted and the counterelectrode was made large (3 cm²), and of platinum black-P.T.F.E. hot pressed onto tantalum mesh. This was the cathode and acted as a hydrogen evolution electrode. Because of its large active area, the overpotential was small and did not vary greatly with current density in the range of interest. Thus it took up a potential of approximately 0.08V to R.H.E. when in use. This was further stabilized by passing a small (3 mA) cathodic current through the counterelectrode and a third auxiliary electrode. This reduced the current range to about 5:1 with the result that the potential of the counterelectrode did not vary by more than approximately 30 mV. The sensing electrode consisted of a small platinum sphere fused onto the end of a short platinum wire, as described earlier. This arrangement of a small working electrode and a large depolarized counterelectrode acting as a reference is similar to ordinary polarographic practice, and works well if the ohmic potential drop is small. This will be the case here as the solution resistance is low and the inter-electrode distance short. The wire from the

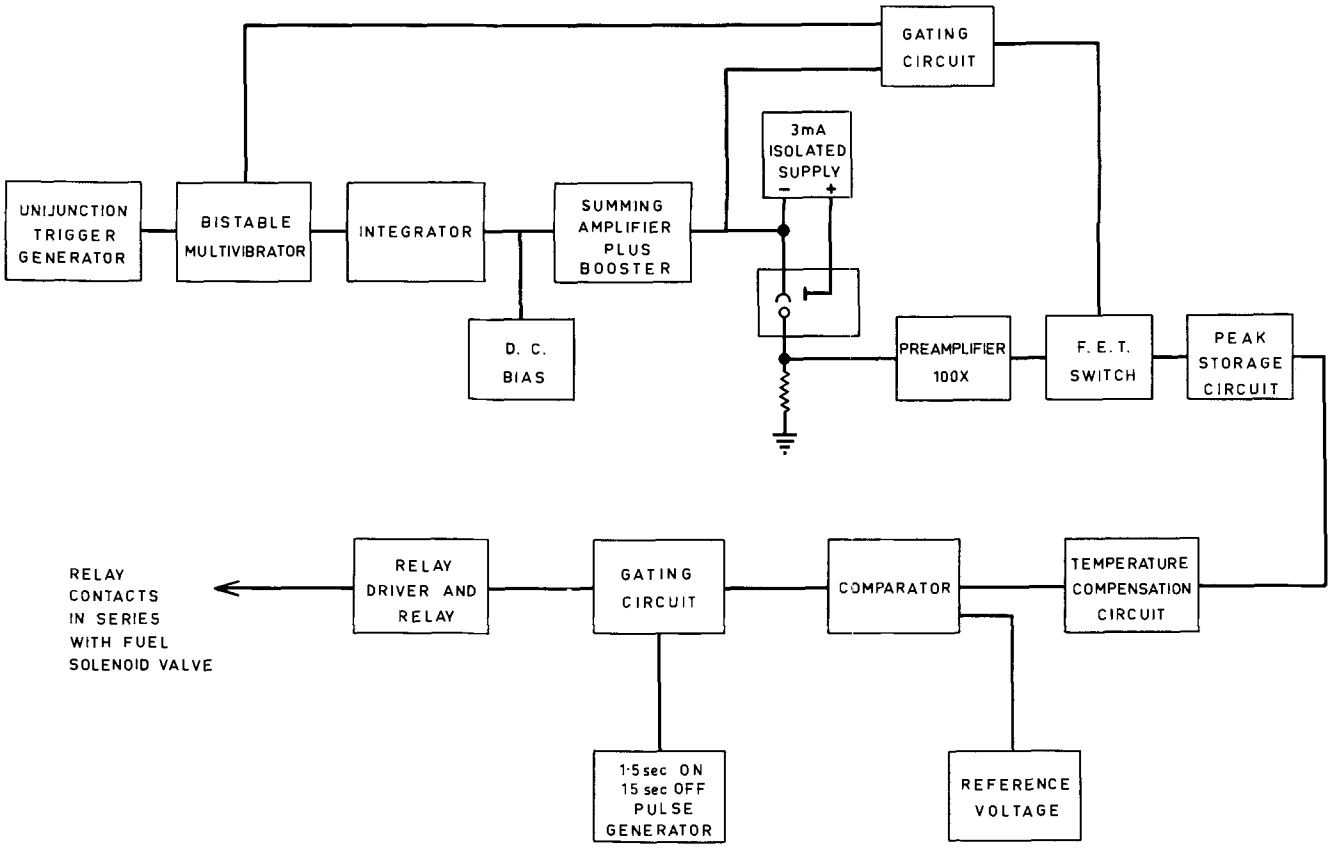

Fig. 5. Block diagram of control circuit for sensing electrode controller

platinum bead electrode was sealed into a glass tube, after a suitable lead-wire had been welded to the platinum wire. The other electrodes were supported by zirconium or niobium rods.

A zero to 2V negative going voltage was impressed on the counterelectrode, and the resulting current through the cell read off as the potential drop across a low value resistor in series with the sensing electrode. This potential drop was amplified, and the peak value in a selected potential range (0.7-1.2V for methanol, 1.3-1.7V for formaldehyde) stored in a reservoir capacitor via a simple field effect transistor switch and gating system. The voltage across the capacitor was read off by a source follower, fed to an electrolyte temperature compensation circuit, and the output of this was compared to a reference voltage. If it fell below the reference level the comparator changed state, turning on the relay which controlled the fuel addition solenoid valve. Fuel was added until the current at the indicator electrode rose above the desired value, when the solenoid would shut off within one cycle. Overshoot was minimized by placing the fuel addition pipe close to the sensing electrode so that the high local concentration of fuel would cause the fuel valve to close earlier than it otherwise would. In an alternative design, it was also arranged, as suggested by Evans (2), for the fuel valve to open on a 1.5 sec on —15 sec off cycle, rather than remaining on continuously. A block diagram of the circuit is shown in Fig. 5.[2] It was energized by a regulated ±6V and unregulated +12V d-c supplies obtained from a d-c/d-c converter. Total power input to the converter was 2.1W, inclusive of power for level and temperature control circuits. Use of a d-c/d-c converter effectively isolated the control circuit from the battery, and prevented difficulties with stray currents in the electrolyte which might have occurred had the system been operated directly from the battery output.

The control system.—Control in a formaldehyde battery.—A sensing electrode was tested for stability by operating it for 2167 hr in a 0.3M formaldehyde, 2M sulfuric acid electrolyte, containing 0.3M formic acid and 0.5M methanol, these concentrations being taken as typical of the steady-state levels achieved in a formaldehyde-air battery. The electrodes were as described above, the sensing electrode had a geometric area of 0.086 cm^2 and a hydrogen adsorption area of 0.11 cm^2 at the beginning of the test.

Using a circuit similar to that shown in Fig. 5, but modified to allow generation of a sawtooth rather than a triangular waveform, a 2V negative-going sweep was applied to the counterelectrode at a rate of 1 V/sec. The output of the peak reading circuit was recorded. From time to time the sensing electrode was withdrawn, the diameter measured, and the surface area determined by hydrogen adsorption. After 1008 hr the electrolyte was made 50 mg/liter in chloride (added as sodium chloride) and at 1296 hr a fresh electrolyte was made 50 mg/liter in ferrous iron (as ferrous sulfate), these being the most likely impurities that would be encountered in an actual system. The sphere diameter and surface area results are shown in Table III, the initial and final outputs of the peak reading circuit are shown as a function of formaldehyde concentration in Fig. 6, while the peak reader output as a function of time is presented in Fig. 7. It is clear that there is some deterioration in performance, particularly after 1000 hr, when the impurities were added. However, bearing in mind that fuel concentration is

Table III. Changes in electrode size with time

Time, hr	Sphere diameter,[a] mm	H_2 ads. area, cm^2
zero	1.15	0.11
114	1.15	0.17
501	1.10	0.38
1000	1.12	0.27
1296	1.12	0.46
2167	1.09	0.45

[2] A full circuit diagram can be obtained by writing to the author.

[a] Uncertainty about 0.02 mm.

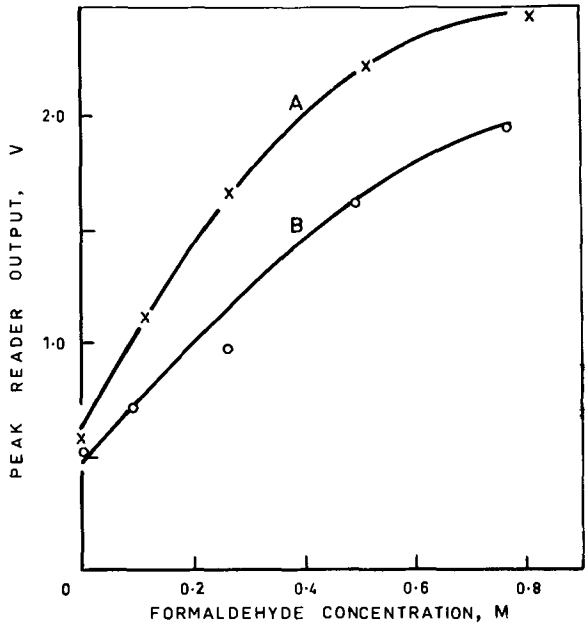

Fig. 6. Variation of peak reader output with formaldehyde concentration. Conditions as given for Fig. 9 except Curve (A)—initial curve, Curve (B)—final curve after 2167 hr. Taken in fresh electrolyte after electrode had been left open circuit overnight.

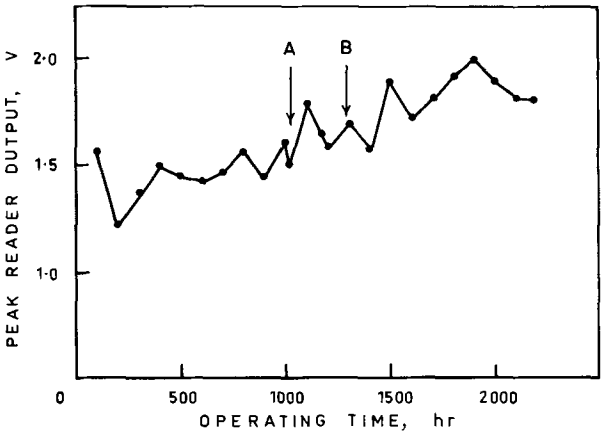

Fig. 7. Variation of peak reader output with time. Electrolyte: 0.3M formaldehyde, 0.5M methanol, 0.5 formic acid, 2M H_2SO_4, 60°C; electrode: platinum bead, initially 0.1 cm^2; sweep: 1.0 V/sec, 2V sawtooth; point (A): 50 mg/l chloride added; point (B): 50 mg/l ferrous iron added.

not critical, the stability attained might well be adequate.

The electrode was not seriously attacked during the run. Reference to Table III shows a decrease in diameter of only about 6%, although there was considerable early surface roughening, as shown by the increased hydrogen adsorption area. This roughening was confirmed by microscopic examination.

The most important test of any fuel control unit is its performance as part of a total battery system. Three formaldehyde-air systems have been tested, the longest run being for 2260 hr. This used a circuit of the type shown in Fig. 5, and electrodes similar to those used in the long-term pot test described above. It is clear from Fig. 8 that fuel concentration was held within acceptable limits for 2200 hr, only failing towards the end of the run, probably due to the electrolyte solution becoming heavily contaminated with corrosion products due to attack on some stainless steel fittings. Figure 9 shows the short-term stability using pulsed addition in one case and continuous addition (until the required concentration is reached) in the other. There

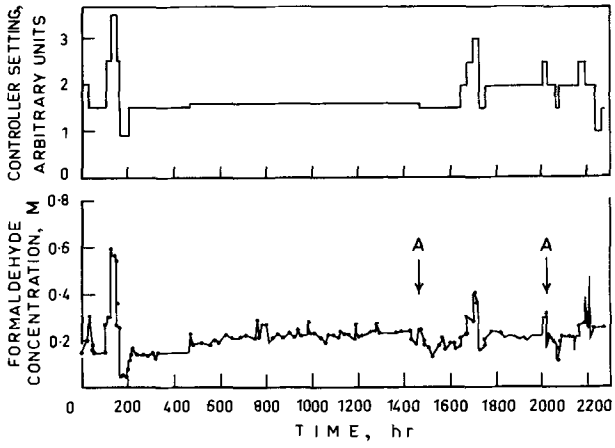

Fig. 8. Variation of formaldehyde concentration with time. Record of fuel concentration in a 40-cell battery system for various control settings. During this test the electrolyte temperature ranged from 45° to 71°C, the total battery load from 42 to 162W, the sulfuric acid concentration from 1 to 2M, the formic acid from 0.3 to 1.2M, and methanol from 0.2 to 0.5M. Electrolyte replaced with fresh at points (A).

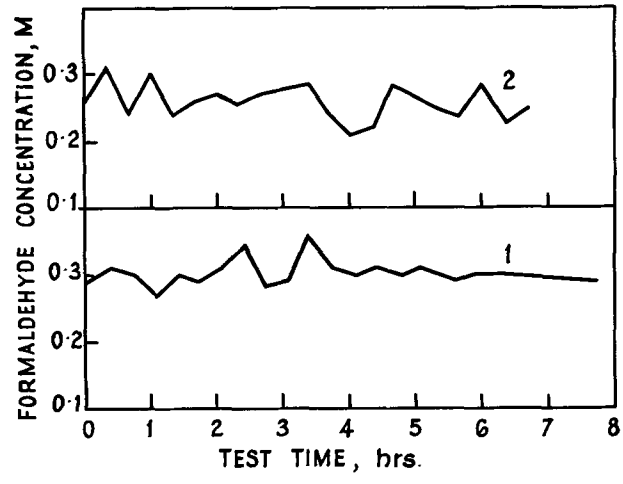

Fig. 9. Short-term stability of fuel controller. Same battery system as for Fig. 8, with controller setting of 2.5 (arbitrary scale). Curve 1: Test begun after 114 hr operation. "Pulsed" (*i.e.* 1.5 sec on, 15 sec off) addition of fuel. Mean concentration 0.30M, relative standard deviation 6.7%. Formic acid 1.04M, H_2SO_4 1.76M. Curve 2: Test begun after 161 hr operation. "Continuous" addition of fuel during addition period. Mean concentration 0.26M, relative standard deviation 10%. Formic acid 0.61M H_2SO_4 1.63M.

is no clear advantage in using pulsed addition. In general the reliability of the control system was good. The formaldehyde concentrations shown in Fig. 8 and 9 were determined volumetrically on a small aliquot of electrolyte.

There were no failures in the electronic section of the system during the whole of the run described, nor were any adjustments of such factors as sweep rate or d-c level required. The fuel addition solenoid valve required adjustment on several occasions, but this may have been due to using a low-powered solenoid.

Methanol battery.—The method described above was used to control methanol concentration in a sulfuric acid electrolyte. The peak current at approximately 0.9V was measured, but there were no other circuit changes from the conditions described for formaldehyde control. Since the absolute value of the peak current density was less than for formaldehyde the sensing electrode was changed to a small strip of platinum of approximately 0.25 cm^2, to give a similar total current. There was no detectable build-up of

partial oxidation products, and since the commercial methanol used contained only a little water as impurity, there was no complication from the presence of other oxidizable substances. Although this system therefore appeared simpler to deal with than that using formaldehyde, in practice control was not always satisfactory. Two long runs were made, one on a small six-cell battery, and the other on a twenty-cell system, auxiliaries being mains-powered in both cases. With both units the methanol concentration would be kept within the desired limits for long periods of time (hundreds of hours), then for no ascertainable reason the sensitivity of the sensing electrode would alter, and the methanol concentration would change rapidly to a new level often causing either fuel starvation or overheating.

The cause of this erratic behavior of the sensing electrode could not be determined. It seemed consistent with an electrode poisoning, as heating the electrode to red heat restored its performance. However, the sudden changes in sensitivity occurred both with reagent-grade and commercial methanol, and even during a test in an all glass pot cell. Since it was not possible to remedy this behavior in the time available an alternative method of fuel control was tested.

Faradaic Control

In principle, if the rate of fuel addition is exactly proportional to the current, then the initial fuel concentration will remain constant. Unfortunately, any errors in the control will be cumulative, so that in practice the fuel concentration would tend to either fall to zero or rise to an excessively high value. In the methanol battery with which the unit was to be used, there were two additional processes utilizing methanol apart from the generation of useful external current. These were the internal shunt current due to electrical leakage between cells via a common electrolyte and the direct oxidation of methanol at the air electrode. Leakage current losses are small and relatively constant, but the loss of methanol by diffusion to the cathode accounts for 25-50% of the fuel fed to the battery. While this is undesirable from the efficiency point of view it does provide a stabilizing influence on the fuel concentration since the diffusion of methanol is proportional to concentration in the electrolyte. Thus, if the control unit overadds slightly, the methanol concentration will rise, but this will be counteracted by an increased diffusion loss to the cathode. Providing that the rate of addition is not too greatly in error, the fuel concentration will equilibrate at some value above the optimum but still within the working range of the battery. To test this possibility a load sensing type of controller (called faradaic hereafter) was assembled and tested as part of a methanol-air system.

Since methanol is completely oxidized to carbon dioxide on the fuel catalyst used (7), the corresponding rate of addition may be calculated using Faraday's laws. The fuel lost to the cathode may be estimated from tests on small single cells. It may be represented by the equation $D = 0.013C\ (1+0.0007I)\ 10^{0.0127T}$, where D is the diffusion rate in mM/cm^2, hr, C is the fuel concentration in moles/liter, I the current density in mA/cm^2, and T the electrolyte temperature in °C. Shunt current losses are difficult to determine, but the presence of carbon dioxide bubbles in the liquid ducts minimizes such losses. In practice they are small and can be assumed constant. Thus the fuel consumption rate, f, can be expressed by Eq. [1]

$$f = a + b + ki \qquad [1]$$

where a and k are true constants, while b is independent of the current i, but is a function of methanol concentration and temperature. For a definite concentration and temperature Eq. [1] can be simulated by a simple analog circuit. The output/voltage of this summing unit is fed to an integrator which in turn causes a comparator to change state when the integrator output voltage exceeds a reference value. The comparator resets the integrator and also operates a three-way solenoid valve via a relay driving circuit. During its "on" time (4 sec) the valve discharges a fixed volume of methanol to the electrolyte reservoir: the metering volume is refilled during the "off" period, which varies with current but is about 10 min at normal load. A block diagram of the circuit is shown in Fig. 10. One point worthy of further discussion relates to the compensation necessary to maintain constant fuel concentration with change in electrolyte temperature. This can be achieved by variation of the voltage which represents the term $(a + b)$ of Eq. [1], and a passive thermistor-controlled circuit is adequate for this purpose. An uncompensated circuit has some advantages however, for as the temperature increases, the fuel concentration will tend to fall because of greater diffusion to the cathode through the separator. This reduction will minimize the possibility of overheating. There will be no significant loss in battery performance as there is a marked increase in fuel electrode activity with temperature. In the opposite case of a decrease in electrolyte temperature the fuel concentration will rise, counteracting the temperature fall, and minimizing loss in fuel electrode performance due to lower temperature.

A faradaic type controller of the type outlined above was constructed and used for fuel control on a 66-cell, 50W methanol system. Since the simpler design, with-

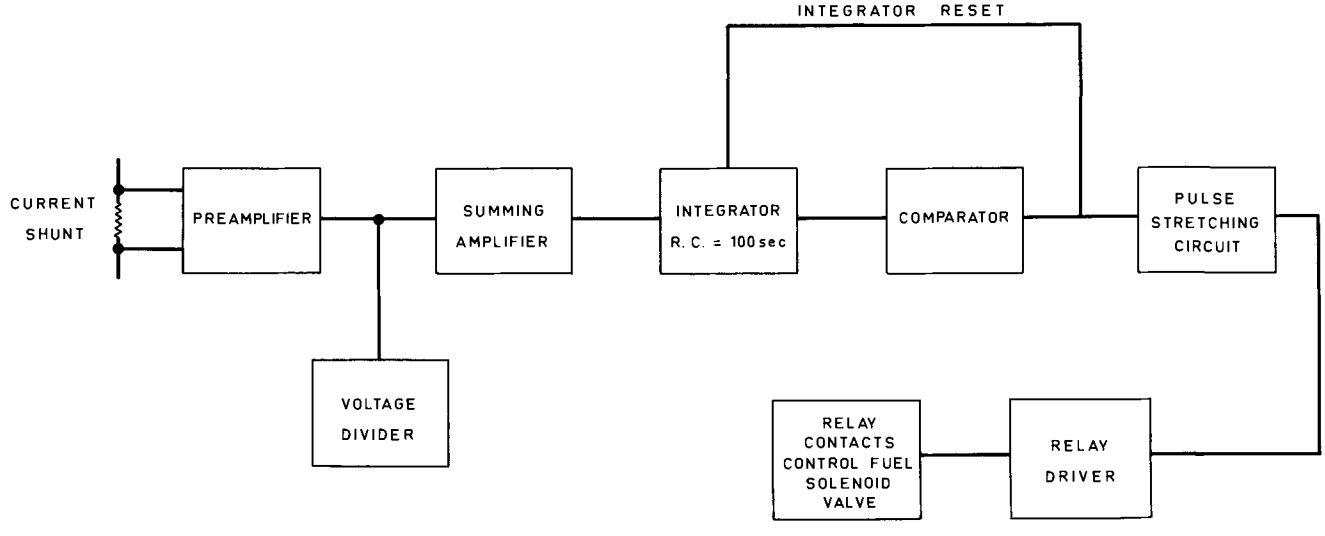

Fig. 10. Block diagram of control circuit for faradaic controller

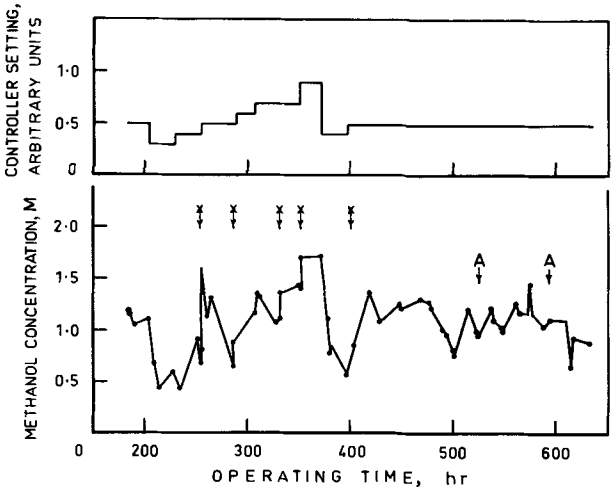

Fig. 11. Variation of methanol concentration with time. Record of fuel concentration in a 66-cell methanol system, for various controller settings, using a faradaic controller. During the period plotted the total battery load was varied from 19 to 110W, causing the temperature to vary between 42° and 76°C. No temperature compensation was used except between the points marked A-A. Points X show times at which fuel was added manually to the reservoir in order to adjust concentration rapidly. H_2SO_4 concentration was between 1.5 and 2M.

out temperature compensation, was likely to be more satisfactory than the temperature-compensated unit, the system assembled could be operated either with or without compensation. This unit was powered via a d-c/d-c converter in order to obtain electrical isolation. The power input to the converter was 1W. The solenoid valve took 10W, but its duty cycle was very low (typically 0.7%), and the over-all drain on the battery was negligible. A plot of fuel concentration (determined by gas chromatography) against time is shown in Fig. 11 for various control settings. It can be seen that the performance of the unit is adequate.

Comparison of the Two Controllers

Both types of controller have worked successfully over sufficient periods of time to prove their usefulness. However, there are some differences in characteristics which are worthy of comment.

Power consumption.—The faradaic type uses far less power which is important for a small battery system. However, the power taken by both types is sufficiently low to be acceptable.

Reliability.—The faradaic type has far fewer components and does not depend on sensing electrode stability. Therefore, in the electronic/electromechanical sense it should be appreciably more reliable. However, when considered in the context of the total system its continued good performance depends on there being no change in the over-all pattern of fuel usage (due for example to electrolyte leakage or a degradation in the cell separators). The direct sensing type is not affected by changes in fuel usage pattern. The tendency is for fuel consumption to increase with the age of a battery system so that a faradaic type controller is normally set to give a higher than optimum concentration early in the battery life. This improves the over-all system reliability, at the cost of reduced fuel efficiency.

Response to load changes.—The response of the sensing electrode system to load changes was dependent mainly upon the time taken by depleted electrolyte to reach the sensor. In the battery system tested this time was approximately 1 min. The faradaic controller is inherently rapid in that the time cycle of fuel addition is adjusted from the instant the load is changed. Due to the considerable amount of reserve fuel present in the electrolyte (at least 30 min at normal load) these response times were quite adequate.

Response to control setting changes.—The sensing electrode type responded rapidly to changes in the concentration control adjustment taking approximately 1 min to complete a concentration increase and 15 min for a concentration decrease. The faradaic type gave a slow approach to the new concentration; typically it took several hours for the new fuel level to stabilize.

Cost.—Absolute cost figures are difficult to prepare, but it is probably worth observing that the faradaic system contains only about 60% of the number of components of the sensing electrode type, and is easier to set up and check. It should therefore be significantly less expensive.

Manuscript submitted Dec. 30, 1970; revised manuscript received *ca.* April 4, 1971.

Any discussion of this paper will appear in a Discussion Section to be published in the June 1972 JOURNAL.

REFERENCES

1. R. E. Salathe, and associates, *Proc. 22nd. Power Sources Conf.*, p. 6, May, 1968.
2. G. E. Evans, *ibid.*, p. 1, May, 1968.
3. G. Ciprios, *Proc. 20th. Power Sources Conf.*, p. 46, May, 1966.
4. G. Ciprios, J. Batzold, and M. Lieberman, "Advances in Energy Conversion Engineering," p. 357, The American Society of Mechanical Engineers, New York (1967).
5. S. Gilman and M. W. Breiter, *This Journal*, **109**, 1099 (1962).
6. T. Biegler, *ibid.*, **116**, 1131 (1969).
7. K. Cathro, *Electrochem. Technol.*, **5**, 441 (1967).

Kinetics of the Thermal Decomposition of Aqueous Manganese(II) Nitrate Solutions on Porous Tantalum

P. K. Gallagher and D. W. Johnson, Jr.

Bell Telephone Laboratories, Incorporated, Murray Hill, New Jersey 07974

ABSTRACT

Porous tantalum electrodes were immersed in aqueous solutions of manganese(II) nitrate and the kinetics of the thermal decomposition of the adhering solution were determined, *in situ*. The rate laws for each of the stages in the decomposition were found to be different from those which best described the decomposition of the bulk solution. However, the activation energies were essentially the same as those for the bulk. The last stage of the decomposition, i.e., the decomposition of the intermediate manganese(III) oxynitrate, exhibited the same dependence on atmospheric moisture content as previously observed for the bulk material. The activation energy was reduced about 12 kcal/mole by the presence of moisture and the pre-exponential term of the Arrhenius equation was lowered by about 10^6 sec^{-1}. Surface area measurements gave smaller values for samples decomposed in moist atmospheres, and scanning electron micrographs indicated such surfaces were also more continuous and homogeneous. The decomposition occurred at lower temperatures for subsequent immersions.

In the manufacture of metal oxide capacitors a layer of semiconducting manganese(IV) oxide is frequently used as the counterelectrode. Such a layer is generally achieved by dipping the anodized metal into an aqueous solution of manganese(II) nitrate and subsequently heating this to decompose the adhering solution to the desired layer of manganese(IV) oxide.

Previous work has determined both the stoichiometry of the various stages (1) and the kinetics of the decomposition of bulk solution (2). The solution initially loses water to form a glassy phase having the approximate composition $Mn(NO_3)_2 \cdot 2H_2O$. This process follows the first-order rate law, $kt = -\ln(1 - \alpha)$, as would be expected. The quantity, α, is the fraction reacted.

At somewhat higher temperatures anhydrous manganese(II) nitrate is formed which decomposes to give the very transient intermediate manganese(III) oxynitrate. The rate law which best described this step for the bulk sample is the Eroffev equation with $n = 4$, $kt = [-\ln(1 - \alpha)]^{1/4}$. The intermediate oxynitrate decomposes to form the desired manganese(IV) oxide according to a contracting area formula, $kt = 1 - (1 - \alpha)^{1/2}$. A number of rate laws fit this portion of the decomposition reasonably well. The contracting area equation given above gave the best general fit to the data.

In this study the kinetics of these decomposition reactions are reinvestigated, *in situ*, rather than using a drop of bulk solution. Isothermal weight loss was followed in both moist and dry air. It was anticipated that the changes in geometry imposed on the solution by its adherence to and occlusion in the porous metal body would certainly change the rates and possibly change the mechanisms of the various steps in the thermal decomposition. In the actual manufacture of these devices it is generally necessary to repeat the process a number of times in order to build up a suitable electrode. Therefore, the possible effects of this change in substrate are also evaluated.

Experimental Procedures and Results

Materials.—Aqueous manganese(II) nitrate manufactured by the Lehigh Valley Chemical Company (capacitor grade, density 1.65) was used. Results of emission spectrographic analysis of the oxide resulting from heating a portion of this solution to 250°C overnight indicated magnesium was present at the tenth of a weight per cent level and calcium, copper, and iron were present in 10-100 ppm amounts. Three different concentrations of this solution were employed in the study. Dilutions were made with triply distilled water. Densities of these solutions were 1.645, 1.528, 1.449 g/cm^3 at 25°C.

Type 601B tantalum electrodes were obtained from the Western Electric Company in both an anodized and unanodized condition. The anodized electrodes were anodized at a constant current of 2A to 30V then held at 30V for 3 hr. The electrolyte was 0.061M HNO_3. The anodized electrodes were stored under deionized water. These particular anodes are cylinders about 4.6 mm in height and 3.3 mm in diameter having about 50% porosity. Attached to each is a tantalum lead wire 0.1 mm in diameter protruding about 13 mm.

Isothermal weight change.—A Perkin-Elmer thermobalance was modified to give weight and temperature as a function of time (2, 3). For these isothermal studies, only the weight portion was operated. The weight was averaged over predetermined constant intervals of time and automatically punched on paper tape. Time intervals ranged from 3-30 sec depending on the rate of weight loss. The temperature of each experiment was determined by measuring the control voltage of the Perkin-Elmer UU-1 controller and comparing it with the calibration equation. This equation was based on the use of magnetic standards as previously described (3). The heating rate for the calibration experiment was 1.25°C/min.

The lead wire was bent to form a convenient hook with which to suspend the sample. The balance was tared to approximately 2 mg less than the basic weight of the anode. Fortunately the control in manufacturing is sufficiently precise that it was not necessary to readjust the tare. Anodized samples were stored under water and consequently they contained about 20 mg of excess water in the porous structure. In the commercial processing they are heated to 135°C for 15 min to dry them. This weight loss represented the first kinetic phase. Both wet and dry air were passed over the sample at about 25 cc/min. The input gas was passed through a column of silica gel, and, if a wet atmosphere was desired, through a bubbler which saturated the gas with water vapor at room temperature.

An initial sample weight was obtained as quickly as possible and then the temperature was raised at a rate of approximately 320°C/min to a temperature in the range of 110°-130°C. The data acquisition unit was

Key words: capacitor technology, moisture catalysis.

started as soon as the UU-1 controller reached the control point. Data was collected at this temperature until essentially constant weight was reached at which time data taking was stopped and the sample cooled to room temperature.

The dried anode was then dipped into the manganese(II) nitrate solution and kept below the surface for 1 min. Care was taken to avoid collection of the solution on the hang down wire from the balance. The temperature was raised rapidly to 150°-200°C. Data collection was again resumed to constant weight. The temperature was then raised to 250°C to obtain a final weight.

The procedure was repeated starting with the dip in the aqueous solution of manganese(II) nitrate. A total of three dips was generally done with each sample, however, this was occasionally repeated as many as six times. On subsequent dips it was usually found that the reaction went nearly to completion in the 110°-130°C range and did not require an intermediate temperature between this and the final 250°C. In this manner there were three types of weight *vs.* time data determined for each anode. These corresponded to the loss of occluded storage water in the anode, 110°-130°C, the initial dehydration step, 110°-130°C, and the decomposition to manganese(IV) oxide, 110°-200°C. A few experiments were performed using unanodized electrodes which had not been stored under water and consequently there was no initial water loss for these samples.

Computer analysis.—The weight data on the tape was transferred to cards using a GE-635 computer. These data cards served as the input for three stages of computer processing. The first stage was to obtain a graphical output of the weight as a function time. Figure 1 is an example of such an output for a sample run in dry air. Figure 1(a) shows the isothermal weight loss at 109°C associated with original drying of the anodized sample; (b) at 110°C corresponds to the dehydration of the manganese(II) nitrate solution from the first dip; (c) gives the weight loss data associated with the decomposition of manganese(II) nitrate to manganese(IV) oxide at 153°C; and (d) shows this combined dehydration and decomposition step for the second dip. Plots of this type gave an over-all view or check on the experiment and served too as the basis for the determination of the initial and final weights for each step.

The second stage of data handling consisted of utilizing the initial and final weights for each step to determine values of α, the fraction reacted. The computer having calculated the values of α for each point then plotted these to conform to the eighteen kinetic equations given in Table I. These equations were selected because of their frequent application to the decomposition of solids. Appropriate equations were determined by visual inspection of the computer output plots for their linearity. As examples, the family of lines resulting from each of the over-all reactions for the initial dip using the solution of density 1.449 g/cm^3 are shown in Fig. 2-5. These data were taken using anodized electrodes in dry air.

It was frequently disconcerting to find that no single equation was obviously best at this point. The choice of equation was then based on the exact degree of fit

Table I. Kinetic equations used in computer analysis

Power law	α^n $n = 1/4, 1/3, 1/2, 1$, and 2
Contracting geometry	$1 - (1 - \alpha)^{1/n}$ $n = 2$ and 3
Erofeev	$[-\ln (1 - \alpha)]^{1/n}$ $n = 1, 3/2, 2, 3$, and 4
2D diffusion controlled	$(1 - \alpha) \ln (1 - \alpha) + \alpha$
3D diffusion controlled	$(1\text{-}2/3\ \alpha) - (1 - \alpha)^{2/3}$
Jander	$[1 - (1 - \alpha)^{1/3}]^2$
Prout Tompkins	$\ln \left(\frac{\alpha}{1 - \alpha} \right)$
Second order	$\frac{1}{1 - \alpha} - 1$
Exponential	$\ln \alpha$

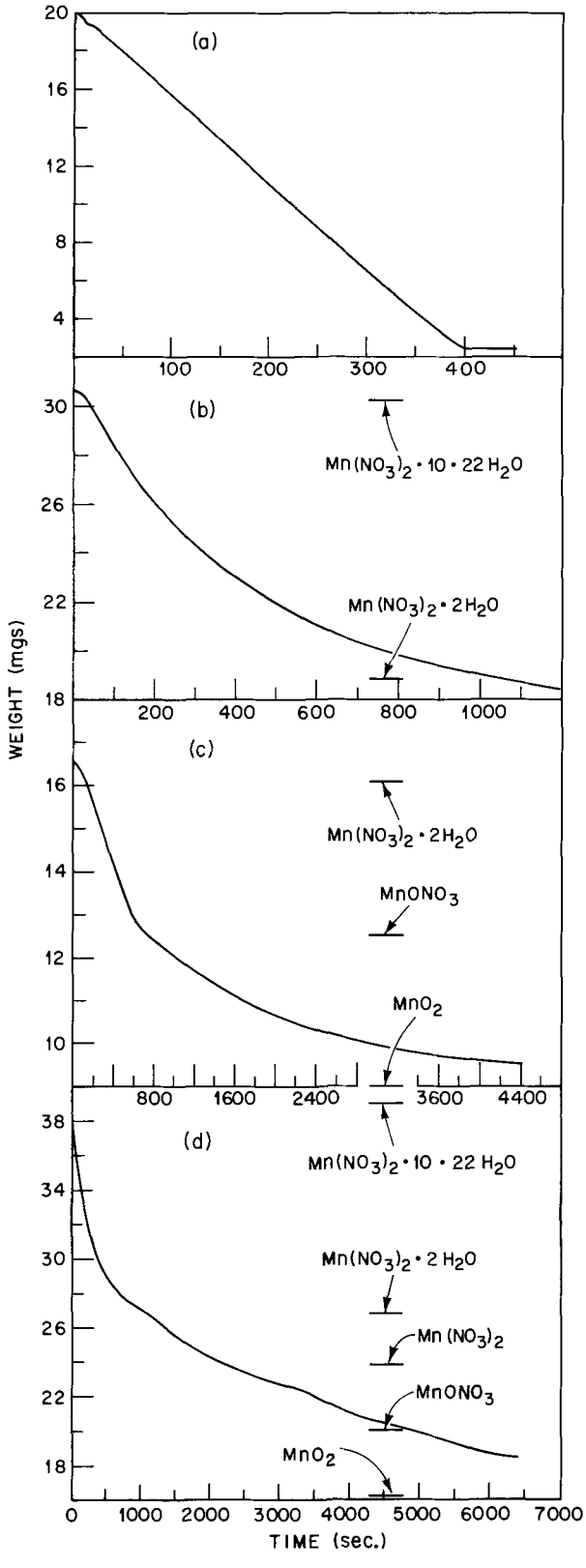

Fig. 1. Weight as a function of time for the thermal decomposition of aqueous manganese(II) nitrate ($d^{25°} = 1.528$ g/cm^3). (a) Loss of occluded water, 109°C; (b) dehydration of solution, 110°C, 1st dip; (c) decomposition of solution, 153°C, 1st dip; (d) combined dehydration and decomposition of solution, 109°C, 2nd dip.

determined by the standard deviation arising from the computed fit of the data to a least squares straight line and calculation of k in the third stage of processing.

The dehydration process shown in Fig. 1 (b) and 3 fit the contracting geometry formula best for the initial dip. Generally the contracting volume equation gave

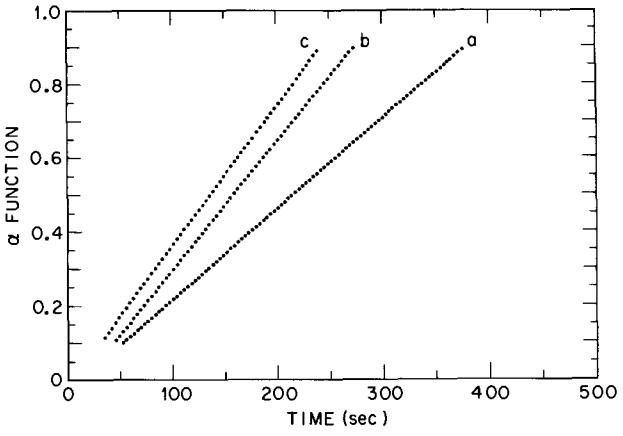

Fig. 2. α vs. time for the loss of occluded water in dry air: a, 109°C; b, 119°C; c, 129°C.

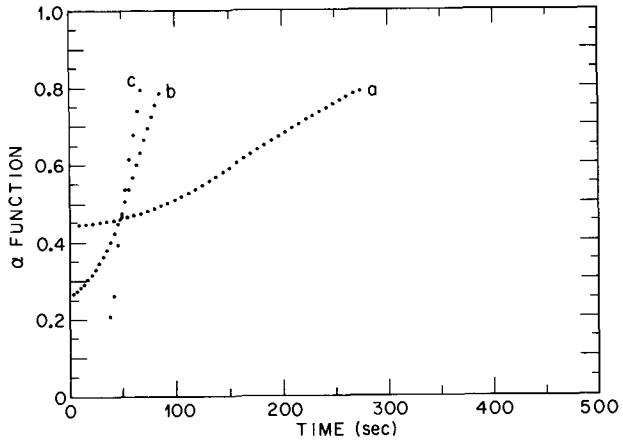

Fig. 4. α vs. time for the first decomposition stage of aqueous manganese(II) nitrate ($d^{25°}$ 1.449 g/cm^3) in dry air, 1st dip: a, 154°C; b, 174°C; c, 193°C.

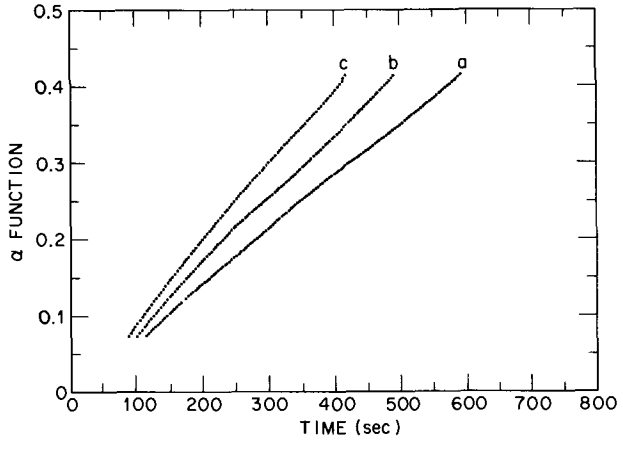

Fig. 3. $1 - (1 - \alpha)^{1/3}$ vs. time for the dehydration of aqueous manganese(II) nitrate ($d^{25°}$ 1.449 g/cm^3) in dry air, 1st dip: a, 110°C; b, 119°C; c, 129°C.

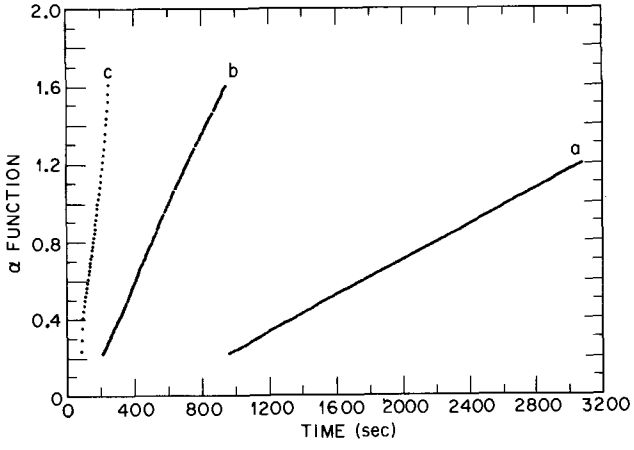

Fig. 5. — Ln $(1 - \alpha)$ vs. time for the second decomposition stage of aqueous manganese(II) nitrate ($d^{25°}$ = 1.449 g/cm^3) in dry air, 1st dip: a, 154°C; b, 174°C; c, 193°C.

better fit than did the contracting area form, however, it appears that the optimum value of n may be between 2 and 3. Similar behavior had been observed in previous work on iron(II) sulfate and the data was processed using a program which plotted the standard deviation as a function of nonintegral values of n in the contracting geometry equation (4). The optimum value in the current study was generally 3.0 but the observed trend was toward 2.0 with increasing temperature, decreasing density of solution, and the use of moist atmospheres.

After the most likely kinetic equation or equations had been selected for each reaction the appropriate experimental data were reprocessed using a third program to fit the best straight lines using a least squares technique. The printed output gave the best value of k and a standard deviation in terms of both $F_{(\alpha)}$ and α. The standard deviation in α is used to determine which equation is most suitable for those cases where several equations were considered.

A final program was devised to plot the values of log k vs. the reciprocal of the absolute temperatures (Arrhenius plot) and a least squares fit was made to determine the best straight line. The resulting activation energies and pre-exponential terms were printed along with the plot. The values are listed in Table II for the solution having a density of 1.449. Figure 6 shows the family of Arrhenius plots for the decomposition series in dry air for this same solution.

As previously mentioned the data can frequently be fitted moderately well by several equations. In all cases the activation energies show very little variation with choice of rate equation. The differences are reflected in the pre-exponential term and the activation energy is virtually independent of the equation in accordance with the results of previous work (2).

Table II. Values* of activation energy and pre-exponential from the Arrhenius equation $k = Ae^{-\frac{\Delta H^\dagger}{RT}}$

	$Mn(NO_3)_2 \cdot 12.72H_2O \rightarrow Mn(NO_3)_2 \cdot 2H_2O + 10.72H_2O$		$Mn(NO_3)_2 \rightarrow MnONO_3 + NO_2$		$MnONO_3 \rightarrow MnO_2 + NO_2$	
	$kt = 1 - (1 - \alpha)^{1/3}$		$kt = \alpha$		$kt = -\ln(1 - \alpha)$	
Atmosphere	$\Delta H\dagger$ kcal/mole	A sec^{-1}	$\Delta H\dagger$ kcal/mole	A sec^{-1}	$\Delta H\dagger$ kcal/mole	A sec^{-1}
Dry air	9.3	0.2×10^0	27.6	1.9×10^{11}	28.7	2.1×10^{11}
Wet N_2 air	11.3	2.9×10^3	30.8	2.2×10^{14}	16.4	7.9×10^5

* This data is for the initial dip in aqueous manganese(II) nitrate solution ($d^{25°}$ = 1.449).

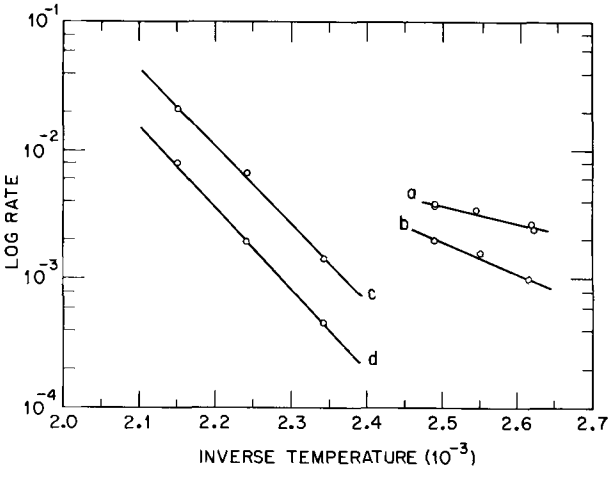

Fig. 6. Arrhenius plots for the reaction of aqueous manganese(II) nitrate ($d^{25°}$ = 1.449) in dry air, 1st dip: a, loss of occluded water; b, dehydration; c, first decomposition stage; d, second decomposition stage.

Surface area and scanning electron micrographs.— The BET technique of nitrogen absorption was used to determine the surface areas and a Perkin-Elmer Sorptometer was employed. The unanodized and anodized tantalum had a surface area of 0.3 and 0.6 m^2/g, respectively, prior to any further treatment. After immersion in the manganese(II) nitrate solution and the completion of kinetic studies, a number of anodes were randomly selected. Their surface areas were found to be 0.8-1.6 and 0.5-0.8 m^2/g for those which had been studied in dry and wet air, respectively.

Figure 7 presents representative scanning electron micrographs showing both unanodized and anodized surfaces before the manganese treatment. The surfaces after three dips and firings show that much of the original void space has been filled. When fired in dry air the surfaces showed cracks and debris and a generally more heterogeneous appearance than those fired in moist air.

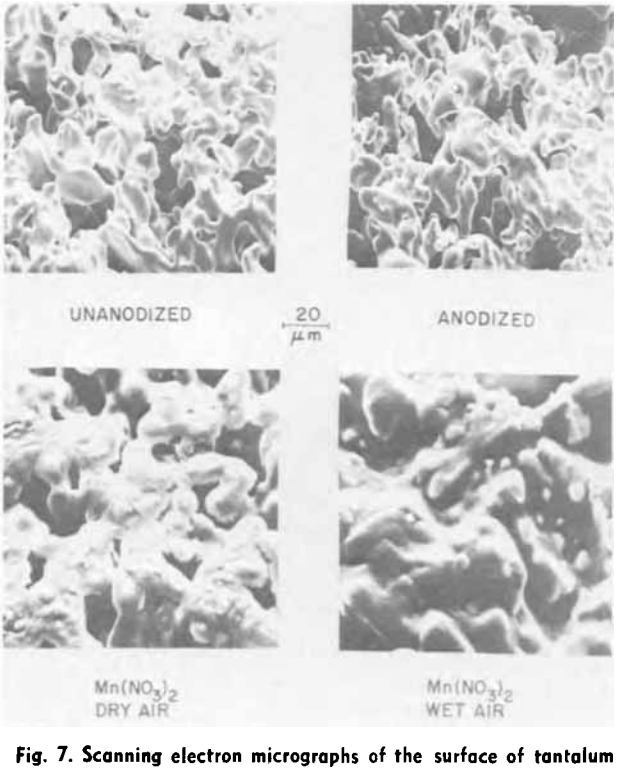

Fig. 7. Scanning electron micrographs of the surface of tantalum anodes at various stages.

Discussion

The evaporation of the water, entrapped in the anode during storage under water, took place in a simple linear fashion. This could be determined directly from the weight loss curves in Fig. 1 (a) and 2. The implication of this behavior is that the area of water exposed to the atmosphere remained constant during the evaporation process. The average amount of water initially held in the porous anode is about 20 mg. This indicates that the pores are essentially filled to capacity. It seems very unlikely that the total surface area, *i.e.*, internal as well as external, would remain constant during the entire weight loss period, therefore, it is concluded that the water escapes only from the external surface of the tantalum mass. The pores are constantly filled with either liquid water or steam but do not significantly effect the rate of weight loss. It is uncertain whether the actual process is simple vapor loss from the pore and thus the pore area at the surface is the critical factor or whether some form of capillary action is active and water evaporates from the entire external anodized surface. The observed activation energy in Fig. 6 is 6.1 kcal/mole and the pre-exponential constant is 8.2 sec^{-1}.

The overlap of the three reactions complicates the treatment of the data and introduces considerable uncertainty to the exact values. The separation of a progression of reactions, by redefining initial and final weights into a series of individual decompositions, has been done in similar studies (2, 4). It, nevertheless, is a highly idealized treatment which assumes that all of the intermediate is formed before any of it begins to react. For this reason, the beginning of the first reaction and the end of the second were stressed in making a determination of the rate law and constant.

Beside the problem of overlapping reactions, there are several other difficulties associated with the interpretation of the kinetics. One of the major ones concerns the nonideal or uncontrolled nature of the sample. There were no nicely sized fractions or pelletized samples to simplify the geometrical considerations. This is an attempt to deal with a real situation and consequently the starting particle size and morphology was restricted to that produced by the preceding evaporation or decomposition. Since several kinetic experiments were performed on the same sample, it meant that there were some variations in the thermal history among the samples, The fact that the data were frequently fitted reasonably well by several kinetic equations also urges caution in the interpretation of the kinetics in terms of a specific geometric mechanism. The individual reaction steps will be discussed with these basic considerations in mind.

Calculations based on the weight gained during the initial dip into the manganese(II) nitrate solution indicate that the pore structure is essentially filled for those samples which have been anodized and dried. The samples which were not anodized gained only 10-30% as much during the initial dip as the anodized samples. Subsequent dips were essentially the same. The anodized surface is apparently wet more readily.

The dehydration of the adhering solution proved very complex. Although the first-order equation was very markedy superior for the description of the weight loss of the bulk material (2) the contracting volume best described the data for the initial dip in this work. The dehydration of subsequent dips reverted to the first-order equation as shown in Table III. This along with the observations regarding the trends in the optimum value of n in the contracting geometry formula and the greatly reduced pickup of solution by the unanodized tantalum, suggest that the wettability of the tantalum by the manganese(II) nitrate solution is a critical factor. The increasing temperature, decreasing concentration of moisture in the

Table III. Selected values of reaction rate constant for dehydration of manganese(II) nitrate solution on tantalum anodes

	$d^{25}MnNO_3$ = 1.528 g/cm³, 129°C, wet air			
	$kt = 1 - (1 - \alpha)^{1/3}$		$kt = -\ln(1 - \alpha)$	
Dip	$k \times 10^4$ sec^{-1}	$\pm\alpha$	$k \times 10^4$ sec^{-1}	$\pm\alpha$
1	10.92	0.006	46.55	0.026
2	11.95	0.021	52.21	0.004
3	12.13	0.024	53.21	0.004

atmosphere, and presence of an oxide layer would intuitively all lead to enhanced spreading of the solution. If the solution remains compacted in a droplet during the process, the volume would be more important leading to a three dimensional dependence of the rate while if it spread over the surface a one dimensional or linear dependence of the rate is reasonable. Finally, if the exposed surface area remained constant as in the studies on the bulk solution (2), then the rate should follow a first-order law. This appears to be true for subsequent dips. For the initial dip, however, geometrical conditions seem to prevail. Actually the dependence should be combined with the first-order dependence which must also be acting, but, in a less significant capacity (6).

Fortunately the activation energy is relatively insensitive to the choice of kinetic equation (2) and the values given in Table II hold well for other concentrations. The values are not significantly different from those obtained for the bulk solution although the optimum kinetic equation is different.

Evaluation of the Arrhenius parameters for other than the first dip is deemed too tenuous to be of value. The surface area and thermal history would vary significantly among the samples and it would be fortuitous if a straight line resulted. The actual rates, in general, went through a maximum as a function of the number of dips for all three stages of the decomposition.

The second stage of the decomposition, *i.e.*, that which forms the very transient oxynitrate species, is best characterized by a simple linear rate law $kt = \alpha$ but the Erofeev equation with values of n from 1-2 fitted almost as well. Again this is different from that observed for the bulk solution which was best described by the Erofeev equation with $n = 4$ (2). The simple power law, however, fitted nearly as well. There does not appear to be any great dependence of the activation energy on moisture content of the atmosphere.

In contrast, the decomposition of manganese(III) oxynitrate shows the same marked and complex dependence on moisture as observed for the bulk solution (2). The effects on the activation energy and pre-exponential are opposed so that there is actually a crossover in the relative rates dependent on temperature. The pre-exponential term is much smaller presumably due to a reduction in surface area arising from improved crystallinity and increased sintering in the presence of moisture. The reduced surface area and smoother surface, see Fig. 7, of the samples decomposed in moist atmospheres are also consistent with this view. This reduces the reaction rate in the presence of moisture. The improved crystallinity means that there is less energy stored in the product phase and consequently the activation energy is lower and approaches the actual thermodynamic enthalpy of the reaction (5). This reduced energy of activation tends to increase the value of the rate constant and thus opposes the effect of the change in surface area.

The selection of the appropriate rate law was least well defined for this reaction. The first-order equation was slightly better than either the contracting volume or area equation although an intermediate value of n might have given the best fit.

Conclusions

There appear to be at least two deductions based on the observed rate which may be of value in the production of tantalum capacitors. First, the moisture content of the atmosphere has a decided effect on the rate and nature of the decomposition, particularly the last stage. Moisture apparently catalyses the decomposition and subsequent ordering of the amorphous oxide. It yields a surface which has a smoother, more homogeneous texture and a better sealed or healed appearance.

Second, the decomposition proceeds more rapidly for subsequent dips than it does for the initial dip. This is presumably the result of the increased surface area available for decomposition rather than an autocatalytic effect. Significant if not total weight loss can occur during what was previously thought to be just a dehydration step. This could allow for substantially reduced firing schedules.

Acknowledgments

The authors would like to thank Mr. F. Schrey for the measurements of the surface areas and Miss B. Cetlin for programming assistance. We are particularly grateful to Messrs. H. M. McKnight and W. M. Baldwin, of the Western Electric Company in Winston-Salem, for providing the tantalum samples, manganese(II) nitrate solution, and processing information.

Manuscript submitted Jan. 11, 1971; revised manuscript received May 6, 1971.

Any discussion of this paper will appear in a Discussion Section to be published in the June 1972 JOURNAL.

REFERENCES

1. P. K. Gallagher, F. Schrey, and B. Prescott, *Thermochimica Acta*, **2**, 405 (1971).
2. P. K. Gallagher and D. W. Johnson, *ibid.*, **2**, 413 (1971).
3. P. K. Gallagher and F. Schrey, *ibid.*, **1**, 465 (1970).
4. D. W. Johnson and P. K. Gallagher, *J. Phys. Chem.*, **75**, 1179 (1971).
5. D. A. Young, "Decomposition of Solids," p. 66, Pergamon Press, New York (1966).
6. P. K. Gallagher and D. W. Johnson, *Thermochimica Acta*, To be published.

Epitaxial Growth of Doped Silicon Using an Iodine Cycle

E. A. Taft*

General Electric Research and Development Center, Schenectady, New York 12301

ABSTRACT

A process for the epitaxial growth of doped silicon using an iodine cycle is described. Advantages in simplicity of equipment and in reproducibility of the deposited silicon layer are attained in a low-pressure closed system with the silicon substrate positioned close to a silicon source. Doping concentrations from 10^{15} to 10^{20} cm^{-3} are readily attained and growth rates exceeding 10 μ/min can be used. The effects of temperature, temperature gradient, and iodine pressure are discussed. The transport efficiency of some dopants is presented.

The reaction of iodine with silicon and works describing the thermal equilibrium conditions have been summarized by Rolsten (1). Chemical transport reactions involving silicon and its volatile iodides has been well referenced to 1966 by Nitsche (2). There appears to be less interest in most of the transport systems today with the ready availability of high-purity silane and of appropriate dopant hydrides which can be decomposed at relatively low temperatures. Decomposition of silane involves the handling of large volumes of hydrogen in the deposition area of a system. Doping of the growing silicon involves other gaseous compounds, and as decomposition proceeds gas ratios change. Thus the regulation and mixing of flowing gases becomes a primary consideration.

In a closed system transport rates were initially quite low (3) but soon rose to quite acceptable values through the use of close-spaced geometries (4). Enhanced deposition rates at low total gas pressures in the system have been recognized by Kurbatov *et al.* (5). Advantages in simplicity of equipment and in fixing of the doping of the deposited silicon layer may be attained in a low-pressure closed system with the silicon substrate positioned close to a silicon source. This paper describes such a system. The effects of temperature, temperature gradient, and iodine pressure on the growth of silicon are discussed. The transport efficiency of some dopants is presented.

Experimental

A typical apparatus, an all-glass demountable vacuum system, is illustrated in Fig. 1. The silicon source and substrate are separated by a quartz spacer, supported on a quartz pedestal, and enclosed by a quartz tube through which optical pyrometer readings can be made. The Viton "O" ring seal requires no grease when used on polished glass surfaces. The iodine reservoir with its thermostated temperature bath is sealed off by a magnetically manipulated polished glass valve. A second glass valve allows the apparatus to be closed to the vacuum system.

Transport studies were first made using ¼ in. thick silicon pieces 1 in. in diameter for both sources and substrates. (Later studies used thin wafers for substrates, this variation is described under Dopant Transfer Ratios.) These pieces allowed uniform temperatures across the diameter to be obtained with induction heating and permitted direct optical pyrometer readings on the sides of the silicon. The use of various quartz spacers and of positions of the rf coil gave all needed adjustments in temperatures and temperature differences. The iodine pressure was controlled by regulating the temperature over the solid or liquid iodine. All other parts of the system were held at a temperature slightly higher than that of the iodine.

In a typical deposition run, the system is evacuated to $<10^{-5}$ Torr with the walls heated. The silicon pieces are then raised to selected temperatures by inductive coupling with the rf coil, and the iodine temperature is adjusted. The valve to the pump is closed, and the one to the iodine is opened. The silicon temperatures are checked as the iodine vapor now in the system changes the heating slightly. After 10 min the valve to the iodine is closed, the one to the pump is opened, and the rf power is turned off. When the silicon pieces are removed, it is found that silicon has been transported from the colder crystal and epitaxially deposited on the hotter crystal.

Results

Growth Rates

The range of silicon temperatures and iodine pressures studied is shown in Fig. 2. The data is presented as observed crystal growth rate as a function of iodine ambient pressure for a series of source and substrate temperatures. The initial studies were made in the low-iodine pressure range of the 1150°-1230°P source-substrate curve. [°P is uncorrected optical pyrometer reading in degrees centigrade measured on the Si surface through a quartz wall. Emissivity corrections for silicon can be made with the aid of Allen (6)]. The transport rate is seen to increase with iodine pressure in this range and is also found to depend strongly on the temperature differences between source and substrate. The rate was found to decrease as the source-substrate spacing increased, up to at least 8 mm spacing.

The effect of spacing was also investigated with silicon temperatures and iodine pressures fixed. Steps were cut on the silicon as shown in Fig. 3, making it possible to determine the rate of deposition at three separation distances in a single run. This procedure tends to cancel effects that are due to adjustments or changes during the run in temperature of the silicon pieces or in iodine pressure. The results are shown in

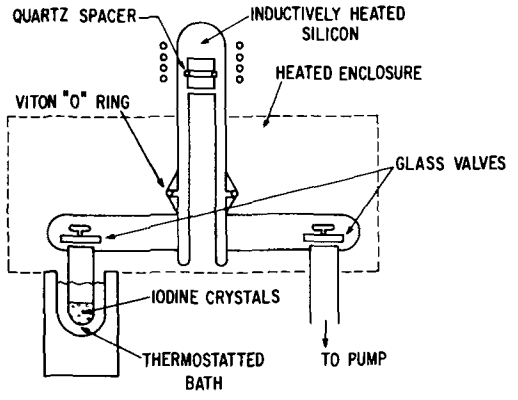

Fig. 1. System for transport of silicon in low-pressure iodine ambient.

* Electrochemical Society Active Member.

Key words: gas transport, thin films, single crystal, closed system, temperature gradient system.

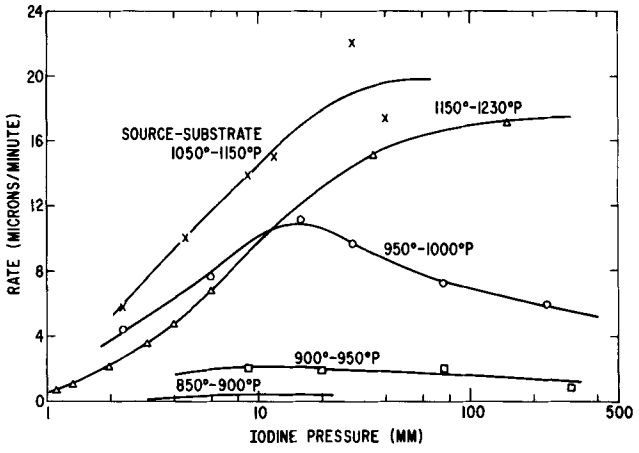

Fig. 2. Transport rates of silicon with 1 mm source-substrate spacing. The temperatures on each curve are for the source silicon and the substrate silicon, respectively, and are the uncorrected pyrometer readings on the centigrade scale.

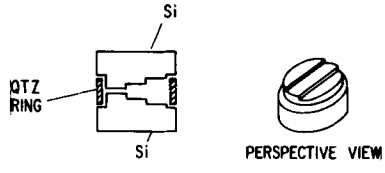

Fig. 3. Silicon configuration for simultaneous transport at several source-substrate spacings.

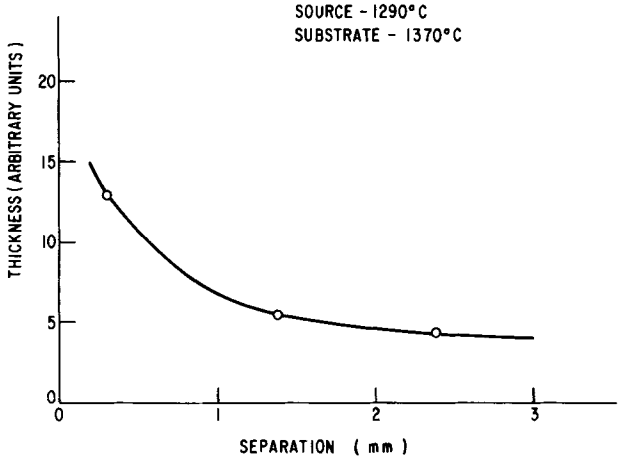

Fig. 4. Thickness of the grown epitaxial silicon layer with changes in source-substrate separation. Similar curves were obtained at iodine pressures of 0.4, 1.0, 2.3, and 5.5 mm.

Fig. 4 as a plot of relative thickness of epitaxial growth, as determined by stacking fault lengths (7), in arbitrary units *vs.* separation of source and substrate. Similar curves were obtained for iodine pressures of 0.4, 1.0, 2.3, or 5.5 mm. If plotted on an inverse spacing abscissa these curves were linear but did not all intersect at zero. The transport is, therefore, substantially diffusion limited at these temperatures with the maximum deposition occurring where the temperature gradient is largest.

These high-temperature, low-iodine pressure conditions readily produced silicon with no polycrystalline growth sites and stacking faults numbering less than 100 cm^{-2}. The good crystal growth was probably aided by the rather obvious thermal cleaning of the silicon if the temperatures were held for a few minutes in vacuum. Evaporated silicon films became visible on the quartz wall adjacent to the substrate within these few minutes at the higher temperatures (>1225°*P*) employed. For the runs at these temperatures, the iodine was introduced before the rf power was raised to the final setting. These runs were then made for times of greater than 10 min so that the initial changes in temperatures over the first minute were not of much consequence. When the growth rates were greater than 10 μ/min, the crystal perfection suffered if the substrate-source temperature differential was not carefully chosen in conjunction with the iodine pressure.

Going to the other curves of Fig. 2, the silicon layer growth rate for iodine pressures below 10 mm shows a definite peak at intermediate temperatures. The deposition rate increases rapidly as the temperature rises above 900°*P* and is greatest in the 1000°-1050°*P* range. At the higher temperatures the transport rate decreases for the same source-substrate temperature difference, as the iodide formation rate decreases with higher source temperatures. At higher iodine pressures the temperatures for maximum transport rates are increased.

Dopant Transfer Ratios

In the initial study of epitaxial growth, using large silicon pieces for temperature measurements, the resistivity of the grown layer appeared to correlate directly with the resistivity of the source silicon: the usual boron dopant was transported in the same ratio as the silicon host material. An extended test of dopant transport in the all-glass system was undertaken with several series of doped crystals used as source silicon. Single-crystal sources were used in these tests to allow accurate dopant evaluations. Substrate heating was accomplished through radiation from silicon susceptors heated by rf induction currents. The substrates could not be observed for pyrometry. Substrates were usually 1 in. diameter etched silicon wafers separated from the susceptor by a polished quartz plate. A 40 mil thick quartz spacer ring supported the source silicon. The susceptor and source diameters were selected to be larger than 1 in. so that the substrate was essentially enclosed by the heated areas. The system initial vacuum was less than 10^{-5} Torr. Total background pressure build-up from outgassing during a reaction period of 15 min with no iodine admitted was less than 10^{-3} Torr. From a given source crystal, a number of films were grown at selected temperatures of the substrate susceptor and of the source; several iodine pressures were utilized; film thicknesses were varied. The resistivities of the grown films were obtained with a four point probe. Normally a "p"-type film would be deposited on an "n"-type substrate and vice versa. The thickness of the epitaxial layers was determined from the observed length of stacking faulits on the (111) wafers (7).

The data has been collected in Fig. 5 where the dopant concentration of the epitaxial deposit is plotted against the source dopant concentration. The concentration was obtained from the room temperature resistivity (8). A large number of the data points are seen to fall on the forty-five degree line which represents a one to one transport of impurity with silicon. Each point is the average of more than three films formed from a given source. In the initial stages of the experiment, each source was run until the deposited film resistivities were shown to be reproducible to at least 10%. Film growth rates of 0.3-5 μ/min were observed as iodine pressures were varied from 0.3 to 10 Torr and source temperatures were varied from 900° to 1100°*P*. Single-crystal layers could be obtained for all growth rates and iodine pressures used. Later in the work fewer substrate wafers for each source were processed as the trend in the impurity transport became apparent. Six dopant elements were tried: B, P, and As appeared to transport reproducibly; Sb was quite variable in transport effectiveness, while Ga and Al seemed to transport very little if at all.

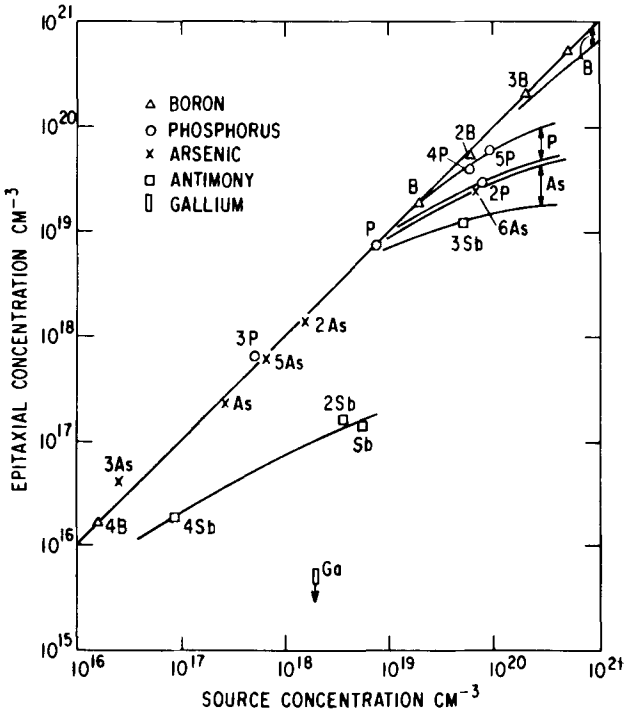

Fig. 5. Concentration of dopant in the epitaxial film vs. the concentration in the source. The upper curves for B, P, and As are for film growth at 3 μ/min; the lower curves obtain for film growth at 1 μ/min.

The data for boron in silicon was obtained for concentrations from 10^{16} to 5 x 10^{20} atoms/cm^3. The indication is for a one to one transport over this full range. However, near the 2 x 10^{20} doping level, a separate study gave a transport efficiency of only 60%. (This data was obtained by A. J. Yerman who used the same experimental system.) Several sources in this high-concentration range, including the one used by Yerman, showed transport efficiencies of 75-100%. The deposition rate of less than 0.2 μ/min selected by Yerman becomes significant and is the end point in a plot of the decrease in transport efficiency with a decrease in silicon film growth rate. This effect is clearly demonstrated in phosphorus or arsenic transport.

Phosphorus shows good transport for source concentrations below 10^{19} atoms/cm^3. At greater concentrations not all of the phosphorus transfers with the silicon from the source to the film. Variation of source or substrate temperature or a change in iodine pressure did not seem to affect the transport efficiency directly. The controlling factor appears to be the growth rate. The upper curve for phosphorus was obtained for growth rates of about 3 μ/min, while the lower curve was obtained for growth at about 1 μ/min.

The data for arsenic at lower concentration levels show the same 100% transport efficiency as do those for phosphorus and boron, but the transport efficiency begins to fall off sooner with increased concentrations. Again, the upper and lower curves were obtained for growth rates of about 3 and 1 μ/min, respectively.

Transport of antimony in doped silicon occurs with low efficiencies. Using the same source under essentially the same test conditions, variations of over 50% in resistivity from film to film, and even across the same film, were observed. With concentrations in the source of 10^{19}/cm^3 only a few per cent of this much antimony could be found in a silicon epitaxial layer. Of interest is the point 3Sb at 5 x 10^{19} cm^{-3} source concentration representing the third source used in the antimony tests. Clearly this silicon crystal was initially mislabeled, and it is arsenic doped, not antimony doped. Of course, this became clear only after the completion of substantiating work with antimony and with arsenic.

Several attempts to form gallium-doped epitaxial layers were unsuccessful. Sources containing greater than 10^{18} cm^{-3} of gallium rendered epitaxial films which generally probed "n" type with resistivities of several ohms-cm. The transport efficiency is thus very small. Considering the lack of control in antimony-doped films where the efficiency of dopant transport is not so small, no effort was expended in determining the actual value of the efficiency. In the case of aluminum, only one lightly doped source at 2 x 10^{16} cm^{-1} was available. But here again, as with gallium, the resulting epitaxial films of silicon were several ohm-cm "n" type. The transport efficiency of aluminum therefore is also small.

Discussion

The transport data for boron, phosphorus, and arsenic in silicon appears to be quite reproducible, although a factor in the transport efficiency for all of these elements at a given source concentration is the growth rate. Points 3As and 3P which are above the line of Fig. 5 by 80 and 30%, respectively, were caused by system contamination. The experiments immediately preceding these runs used sources which were very heavily doped. Acid cleaning of only the quartz parts in the high-temperature zone of the system was effective in removing the residual dopant pickup by the growing layer. While the transport efficiency falls eventually below 100% for all dopants studied, the concentration of dopant at which the decrease begins depends on the particular dopant. It appears that this decrease in antimony, gallium, and aluminum occurs before useful concentrations are obtained.

(It has been assumed that all of the transported dopant is electrically active in the deposited crystal. An actual analysis of the impurity content of the deposits was not made. However the deposits were single crystal and as the source material was also single crystal, the resistivity comparisons seem justified.)

The condition of the initial surface had a large effect on the uniformity and perfection of the deposited layer. The usual surface treatment was a 3:1 HNO_3:HF chemical etch followed by a water rinse. At 600X magnification the surface thus obtained appeared essentially featureless. Square centimeter areas could then be covered by silicon layers 20μ thick with the formation of only very small ripple marks on the surface. Some silicon deposits had large concentrations ($\sim 10^6$ cm^2) of stacking faults and nucleation sites of $\sim 10^4$ cm^2. These nucleation sites were associated with multiple stacking faults but otherwise were similar to widely described tripyramidal faults (9). This type of deposit tended to occur at lower substrate temperatures when combined with higher growth rates. The iodine pressure and the temperature gradient can be adjusted to minimize these crystal defects.

Contamination of the substrate was occasionally troublesome. Carbide film formation especially inhibited silicon growth. At the higher temperatures (>1200°P) used, silicon carbide then becomes, in fact, a useful mask material against epitaxial deposition. At these higher temperatures the residual surface oxide is reduced by the substrate to SiO which vaporizes leaving clean silicon to initiate the epitaxial growth. Added hydrogen gas at these temperatures apeared to be no more effective than the thermal etching in obtaining smooth growth layers. If small amounts of hydrogen were left in the system during the deposition run, the transport rate would decrease. The hydrogen did not appear to enter into the reaction, but only verified the fact that the process rate in this part of the operating range is diffusion limited. Small amounts of argon also reduced the silicon growth rate.

The uniformity in thickness of the deposits was very good as observed stacking fault lengths over the crystal area tended to be constant. The resistivity, in gen-

eral, also was uniform over the wafer. A clean system using reagent grade iodine would regularly produce epitaxial layers with resistivities greater than 50 ohm-cm. Deposits on crystalline surfaces near (111), (100), or (110) orientations did not show any marked variations in growth rate or in the perfection of the epitaxial layer.

A possible advantage of the closed system reaction in forming good crystal at low temperatures occurs with the kinetic exchange of silicon between source and substrate. The deposition or removal of silicon is the net result of partially balanced reactions at the opposed silicon surfaces. Particularly at low temperatures the rate of deposition is limited in part by the rate of decomposition of the iodide. The rate of formation of the volatile iodide remains high as observed through weight losses from both source and substrate silicon. With high chemical reactivity at the substrate surface in addition to the thermal energy, there is greater probability that silicon atoms deposited in positions for poor epitaxial growth will be removed and redeposited in more favorable crystalline positions before they are pinned by subsequently deposited atoms.

May (10) has used equilbrium assumptions to describe the transport for a small region near 1200°C silicon temperatures and 1 mm iodine pressures. For temperatures of 850°-900°C and total pressures near 10 mm the expected action of an equilibrium is toward a reversal in transport direction; that is, from the hotter to the colder silicon. The data of Fig. 2 do not fulfill this expectation, indicating that the iodine ambient atmosphere has modified the reactions to always favor the transport of silicon to the higher temperature substrate. This modifying effect then gives the process a more readily controlled growth parameter in the iodine pressure. The other primary growth parameters are substrate and source temperature. Again these are easily controlled for optimum deposition conditions. With the dopant concentration selected by the choice of source material, the system remains simple in concept, and epitaxial silicon growth factors can be easily adjusted.

Acknowledgments

The initial portions of this study were undertaken in collaboration with the late W. C. Dash. L. J. Keifer assembled the vacuum system and did much of the crystal growth at the higher iodine pressures.

Manuscript submitted Dec. 17, 1970; revised manuscript April 22, 1971.

Any discussion of this paper will appear in a Discussion Section to be published in the June 1972 JOURNAL.

REFERENCES

1. R. F. Rolsten, "Iodide Metals and Metal Iodides," pp. 273-292, John Wiley & Sons, Inc., New York.
2. R. Nitsche, *Fortschr. Mineral.*, **44**, 231 (1967).
3. E. S. Wajda, B. W. Kippenham, and W. H. White, IBM *J. Res. Develop.*, **4**, 288 (1960).
4. E. Sirtl, *J. Phys. Chem. Solids*, **24**, 1285 (1963); F. H. Nicoll, *This Journal*, **110**, 1165 (1963).
5. B. S. Kurbatov, E. V. Rakova, and G. A. Kurov, *Kristallografiya*, **10**, 756 (1965).
6. F. G. Allen, *J. Appl. Phys.*, **28**, 1510 (1957).
7. W. C. Dash, *ibid.*, **33**, 2395 (1962).
8. J. C. Irvin, *Bell System Tech. J.*, **41**, 387 (1962).
9. T. L. Chu and J. R. Gavaler, *Phil. Mag.*, **9**, 993 (1964). (This particular paper shows variations of this growth fault. Their Fig. 2 illustrates the orientation of the accompanying stacking faults usually seen in our deposits.)
10. J. E. May, *This Journal*, **112**, 710 (1965).

Technical Notes

Detection of Metallic Impurities in Acid Zinc Plating Baths

M. Maja and P. Spinelli

Istituto di Elettrochimica e di Chimica Fisica, Politecnico di Torino, Torino, Italy

The electrodeposition of zinc from sulfuric solutions containing impurities has in the past been the object of several investigations (1-8) carried out to determine the best working conditions of industrial cells. In our Institute the general behavior of impurities has been studied for a long time, and researches were developed particularly for nickel, cobalt, and germanium impurities in electrolytic solutions for zinc and manganese electrodeposition.

We found (9) that such impurities have an induction period before causing a reduction in current efficiency. In the case of zinc electrodeposition, for example, we observed that, at the beginning of electrolysis when nickel, cobalt, and germanium impurities are present, current efficiency has a value slightly lower than that found with pure solutions; after a period of induction, this value rapidly decreases to zero while the deposit dissolves into the electrolyte. The dissolution is so complete that the aluminum cathode is brought back to its initial state and a new deposit can start.

The formation and dissolution cycles of the deposit cause oscillations of the cathodic voltage if the electrolysis current is constant, while at constant voltage they cause oscillations of the current.

From analysis of the zinc and impurity deposition and hydrogen evolution characteristic curves, we found that the phenomenon does not depend on the amount of impurity deposited together with zinc, but on extension of the surface-contaminated zones of the cathode, because hydrogen evolution occurs at those zones with a lower overvoltage.

We also observed that zinc dissolution starts in the pores of the deposit which are already present at the beginning of electrolysis. The electrolyte in the pores is renewed with difficulty and the zinc ion concentration decreases so that the impurities are no longer covered with zinc as they are at the exposed surface of the cathode.

During the last few years, the zinc electrodeposition industry has felt the need for a device that could signal with reasonable rapidity when the impurity concentration in the baths exceeded fixed limits in order to effect proper depuration in a short time. Many devices, generally based on the corrosion rate of zinc deposited from impure solutions, have been proposed (11-13).

Key words: electroplating, zinc plating, impurities in zinc plating.

The study of the above-described phenomena suggested (10) a method of controlling the purity grade of the electrolyte, which is based on the determination of the induction time preceding dissolution of the deposit. Since the induction time not only depends on the impurity concentration but also on the temperature and acidity of the electrolyte, it is possible to reduce the time to a few minutes by increasing the temperature and decreasing the pH of the solution.

For example, in the case of an industrial zinc electrodeposition bath, increasing the sulfuric acid concentration up to 350 g/liter and electrolyzing at a current density of 5 A/dm^2, at a temperature of 50°C, by measuring the cathodic voltage it was possible in less than 20 min to detect as little as 2 mg/liter of nickel and cobalt and 20 μg/liter of germanium.

Since the phenomena occurring in the hollows of the deposit greatly affect current efficiency, we thought of improving the bath control method by making electrolysis tests with hollow-shaped cathodes.

Research has been developed for tin, arsenic, bismuth, antimony, cobalt, nickel, iron, copper, germanium, and cadmium in sulfuric solutions containing zinc at various pH's.

Experimental Results

Experiments were carried out depositing zinc at constant current on the internal surface of a hollow drilled into an aluminum electrode and measuring the cathodic voltage variations with time. The hollow, 3 mm wide and 22 mm deep, was drilled into an aluminum disk whose remaining parts were covered with PVC paint 0.25 mm thick.

The electrolytic cell, containing the hollowed cathode, a platinum counterelectrode, and a reference electrode, was fed by a galvanostat.

To define the behavior of the hollowed cathode, some initial electrolysis tests with pure solutions were made. Figure 1 shows how the cathodic voltage varies with time, electrolyzing a sulfuric acid solution (curve a) and a zinc sulfate solution (curve b).

Figure 2 shows the cathodic voltage variations *vs.* time for a zinc sulfate solution containing nickel impurity.

The voltage oscillations are caused by the hydrogen bubbles that are formed in the hollow and periodically released. The frequency of the oscillations depends on the hydrogen partial current, and their amplitude depends on the total characteristic curve for the reactions occurring at the electrode; in fact, the amplitudes are very different according to the electrolyte composition (curves a and b in Fig. 1).

When impurities are present, Fig. 2, there are also oscillations caused by the formation and dissolution cycles of the zinc deposit. These oscillations have a frequency greater than that found for smooth cathodes under the same experimental conditions.

The phenomenon, as shown in Fig. 2, can be divided into three stages:

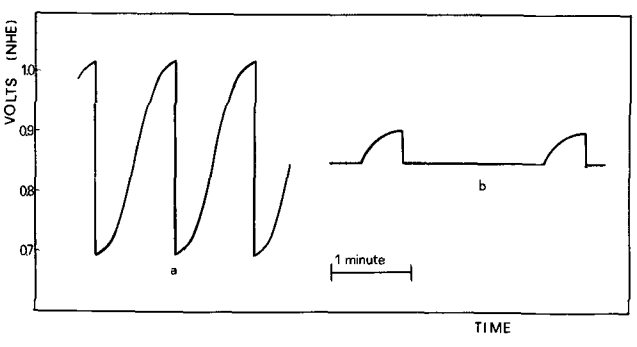

Fig. 1. Cathodic voltage *vs.* time of electrolysis for a hollowed aluminum electrode: (a) H_2SO_4 2*N*, T = 30°C, i = 5 A/dm^2; (b) H_2SO_4 2*N*, Zn^{++} 50 g/liter, T = 30°C, i = 5 A/dm^2.

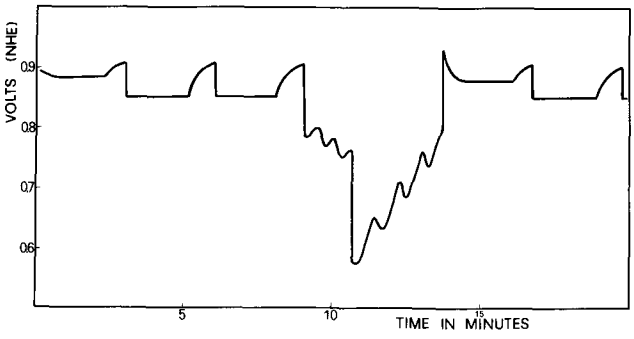

Fig. 2. Cathodic voltage vs. time of electrolysis for a hollowed aluminum electrode: H_2SO_4 2*N*, Zn^{++} 50 g/liter, Ni^{++} 1 mg/liter, T = 50°C, i = 2 A/dm^2.

(*a*) Regular electrolysis with a cathodic voltage greater (in absolute value) than the reversible zinc potential

(*b*) Dissolution of the deposit with a cathodic voltage a little lower (in absolute value) than the reversible zinc potential

(c) Hydrogen evolution on aluminum with a less negative potential and a new polarization of the cathode with respect to zinc.

In the course of the electrolysis (stage *a*), the impurity-contaminated area on the cathodic deposit enlarges and the ion zinc concentration in the hollow decreases. The modifications of the cathodic surface and of the solution composition yield a change in the hydrogen evolution and zinc deposition partial characteristic curves; as the total current is constant, the partial zinc current density decreases and the cathodic voltage becomes less negative until the reversible zinc potential is reached.

Under these conditions, the entire electrolysis current is due to hydrogen evolution and the zinc efficiency is zero. At this point, the corrosion of the deposit begins and continues with an autostimulating mechanism because the impurities previously incorporated into the deposit gradually come to the surface, further increasing the contaminated area on which hydrogen evolves (stage *b*).

When the zinc deposit dissolution has been completed, hydrogen evolves on aluminum and a new polarization of the cathode with respect to zinc begins (stage *c*).

After many formation and dissolution cycles of the zinc deposit, the frequency of the cycles increases, showing that the aluminum cathode is gradually contaminated by the impurities until zinc deposition can no longer occur.

For analytical purposes, it is convenient to consider the first cycle induction period, which is generally well reproducible. Such a period, as indicated before, depends on temperature, electrolyte acidity, and impurity concentration. For a solution containing 50 g/liter of zinc, 10*N* sulfuric acid, it was possible to reproduce the deposit formation and dissolution cycles down to a concentration of 10 μg/liter for germanium, 100 μg/liter for nickel, cobalt, and antimony, 10 mg/liter for bismuth, copper, and arsenic, and 20 mg/liter for iron and tin, Fig. 3.

These results, in agreement with industrial electrolytic cell practice, show the possibility of an impurity classification according to the following dangerous effect decreasing order: Ge, Sb, Ni, Co, Bi, Cu, As, Sn, Fe.

In a semilogarithmic diagram, Fig. 4, plotting the induction time determined for an impurity concentration of 40 mg/liter *vs.* hydrogen overvoltage corresponding to a current density of 10 A/dm^2 (15-16), it can be seen that for many impurities the induction time is a decreasing function of hydrogen overvoltage.

This result does not agree completely with other authors' conclusions (14), but confirms our previous

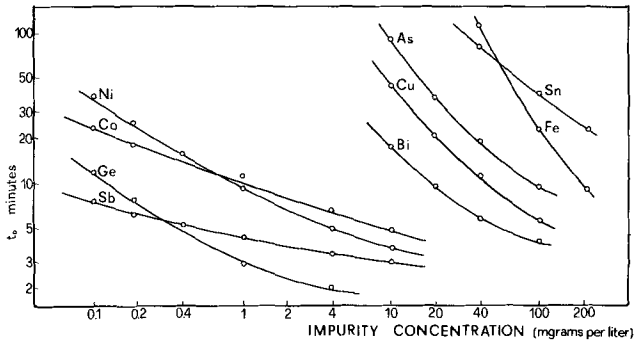

Fig. 3. Effect of impurity concentration on the induction time: H_2SO_4 10N, Zn^{++} 50 g/liter, $T = 50°C$, $i = 2$ A/dm^2.

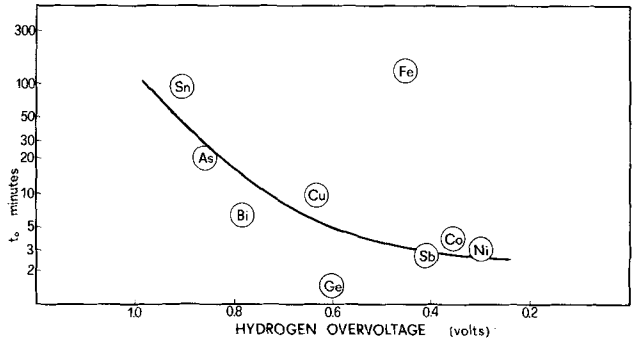

Fig. 4. Relationship between the induction time and hydrogen overvoltage on various impurities: impurity concentration 40 mg/liter, $T = 50°C$, $i = 1$ A/dm^2.

findings (10): the influence of the impurities on the current efficiency is scarcely due to the impurity deposition current and depends almost exclusively on hydrogen overvoltage on the contaminated areas. Anomalies were observed in the case of germanium and iron; such anomalies are probably related to the structure of the impurity in the deposit, because hydrogen overvoltage may have, correspondingly, very different values.

Experiments carried out when more than one impurity (Ge, Co, Ni) contaminates the zinc solution at the same time have shown independent behavior of such impurities, confirming our previous findings (10).

Acknowledgment

The authors wish to thank Professor E. Denina for valuable discussions.

Manuscript submitted Oct. 12, 1970; revised manuscript received *ca.* April 20, 1971.

Any discussion of this paper will appear in a Discussion Section to be published in the June 1972 JOURNAL.

REFERENCES

1. L. Cambi, *Elettrotecnica*, **9**, 189 (1932).
2. R. Piontelli, *Chim. Ind. (Milan)*, **22**, 109 (1940).
3. G. N. Znamenski and V. V. Stender, *Zh. Prikl. Khim.*, **33**, 2728 (1960).
4. G. Scacciati, *Ind. Mineraria (Rome)*, **4**, 511 (1953).
5. U. F. Turonshina and V. V. Stender, *J. Appl. Chem. USSR*, **28**, 151 (1955).
6. U. F. Turonshina and V. V. Stender, *ibid.*, **28**, 347 (1955).
7. U. F. Turonshina and V. V. Stender, *ibid.*, **28**, 447 (1955).
8. D. P. Zosimovich and N. F. Bogatova, *Zh. Prikl. Khim.*, **33**, 1324 (1959).
9. M. Maja, *Elettrochim. Metal.*, **4**, 469 (1967).
10. M. Maja and S. Pozzoli, *Chim. Ind. (Milan)*, **51**, 133 (1969).
11. A. D'Este and R. Guerriero, *Montevecchio*, **16**, 1 (1965).
12. N. A. Fishman, V. L. Klimenko and K. Y. Nevedrov, *Tsvetn. Metal.*, **1**, 30 (1963).
13. S. Tokayev, G. G. Rannev, I. S. Pintchouk, and A. A. Saline, *Teoria i Pratika Metallurgii*, **4**, 184 (1961).
14. G. C. Bratt, *Electrochem. Technol.*, **2**, 323 (1964).
15. K. J. Vetter, "Electrochemical Kinetics," p. 539, Academic Press, New York (1967).
16. C. A. Hampel, "The Encyclopedia of Electrochemistry," p. 869, Reinhold Publishing Corp., New York (1964).

Chemical Vapor Deposition of Arsenosilicate Glass: A One-Liquid-Source System

J. Wong and M. Ghezzo*

General Electric Corporate Research and Development, Schenectady, New York 12301

In this note the chemical vapor deposition of binary arsenosilicate glasses in the range 0-20% As_2O_3 from a one-liquid-source system is described. High deposition rates (500-900 Å/min) at relatively lower substrate temperatures (300°-500°C) are the main advantages of the present system over the so-far reported two-liquid-source systems such as: (*a*) TEOS[1]-$AsCl_3$-O_2-N_2 (1-4); (*b*) TEOS-$AsCl_3$-O_2-Ar (2); (*c*) TEOS-$AsCl_3$-CO_2-H_2 (2); (*d*) $SiCl_4$-$AsCl_3$-CO_2-H_2 (2); and (*e*) TEOS-$AsCl_3$-N_2 (3). Preliminary results indicate definitely that the heat treatment characteristics of these binary glasses on silicon substrates at elevated temperatures are strongly dependent on the As_2O_3 content in the glass.

The system consists of an argon-diluted mixture of silane, oxygen, and arsenic trichloride vapor flowing over a heated silicon substrate supported by a molybdenum pedestal in a quartz vertical reactor similar to the one employed by Brown and Kennicott (5) for depositing binary borosilicate glasses. A schematic representation of the flow system is shown in Fig. 1. The reactant gases and vapor were allowed to premix and/or bypass the reactor while the substrate was being heated to the desired temperature in a pure argon atmosphere or at the end of a deposition run. This procedure assures uniformity of gas composition throughout the deposition and avoids predeposition of pure pyrolytic silica.

The silane tank (from the Matheson Company) contains a calibrated mixture of 1% silane in argon. The use of this diluted silane source eliminates dangers of explosion when mixed with oxygen (6) and measurement of very low flow rates (which is the case if an undiluted silane source is used). The substrates for glass deposition were 1 ohm-cm p-type (100)

* Electrochemical Society Active Member.

Key words: infrared spectrum, composition calibration, n-diffusion source.

[1] TEOS stands for tetraethoxysilane $(C_2H_5O)_4Si$.

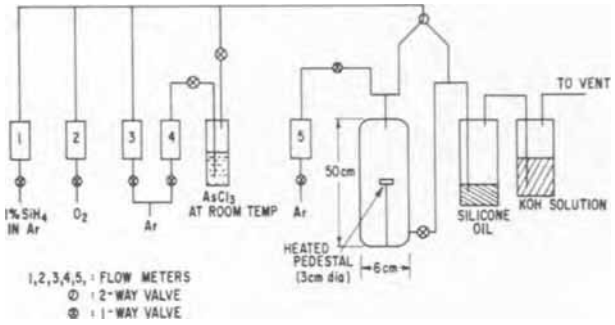

Fig. 1. Schematic representation of the flow system for depositing arsenosilicate glasses.

oriented silicon wafers, 2.5 cm in diameter obtained commercially. Prior to deposition the wafers were treated with an etching solution[2] and rinsed in distilled water. The total argon flow rate was set at 3500 cc/min and the 1% silane mixture flow rate at 230 cc/min, which corresponds to 2.3 cc/min of pure silane. Experiments were performed with oxygen flow rates of 20 cc/min and 95 cc/min. Argon was bubbled through arsenic trichloride at room temperature [24°C, at which $AsCl_3$ has a vapor pressure of 10 mm Hg (7)] with a flow ranging from 5 cc/min to 500 cc/min. With these flow rates, oxygen was always in excess and $AsCl_3$:SiH_4 ratios bracketed the stoichiometric ratio of 1.33 according to the following over-all reaction

$$3SiH_4 + 4AsCl_3 + 6\,O_2 \rightarrow 2As_2O_3 + 3SiO_2 + 12HCl$$

The temperature of deposition varied from 300° to 500°C. The glass deposition rate was found to depend on both the oxygen flow rate and the temperature of the silicon substrate. With an oxygen flow rate of 20 cc/min, the deposition rate varied between 100 and 600 Å/min in the temperature range 300° to 500°C (Fig. 2, curve a). With the oxygen flow rate of 95 cc/min, the deposition rate increased to 550-900 Å/min in the same temperature range (Fig. 2, curve b). Using the TEOS-$AsCl_3$ systems, however, the highest reported (1, 3) deposition rate for binary arsenosilicate glasses was of the order of 1.2 μ/hr, which corresponds to 200 Å/min, even at substrate temperatures up to 700°C.

The infrared spectrum of a film of binary arsenosilicate glass shows a relatively intense absorption band at 930 cm^{-1} which is absent in the corresponding spectrum in vitreous silica (bulk, pyrolytically or thermally grown). This band has been identified as a

[2] Conc. HNO_3:Conc. HF = 3:1 by volume.

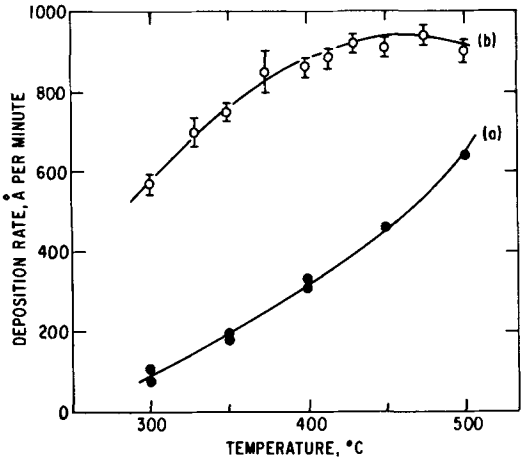

Fig. 2. Deposition rate vs. temperature of silicon substrate at constant flow rates of 1% SiH_4, Ar into $AsCl_3$, and Ar (230, 473, and 3500 respectively), and oxygen flow rate of 20 (curve a) and 95 (curve b). All flow rates in cc/min.

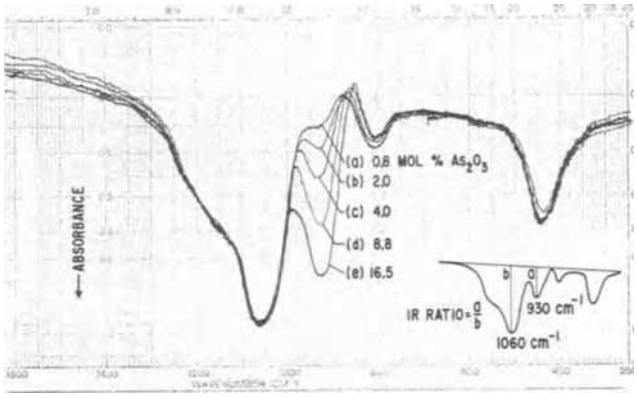

Fig. 3. Infrared spectra of binary arsenosilicate glass deposited at 450°C at constant flow rates of 1% SiH_4, O_2, and Ar (230, 95, and 3500 respectively), and at varying flow rates of Ar into $AsCl_3$: (a) 5; (b) 10; (c) 20; (d) 40; and (e) 100. All flow rates in cc/min. Inset illustrates the base-line method of calculating IR ratios.

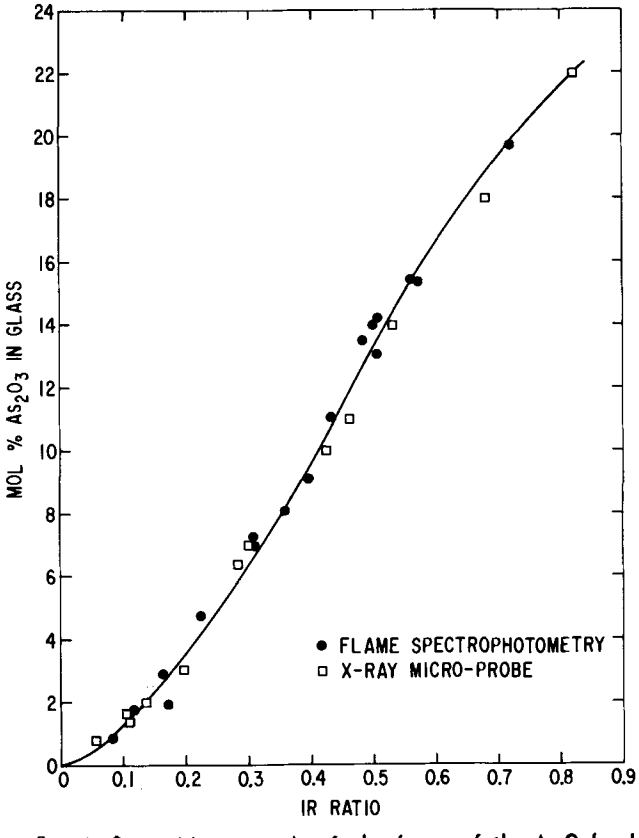

Fig. 4. Composition vs. ratio of absorbance of the As-O band at 930 cm^{-1} to that of Si-O band at 1060 cm^{-1} of as-deposited arsenosilicate glasses.

stretching vibration of arsenic-oxygen quasi-lattices in the binary glass (4). Furthermore, the absorbance of this band increases monotonically with increase in mole per cent (m/o) of arsenic oxide in the glass, as seen from Fig. 3.

A calibration curve has been constructed by measuring the optical density ratio of the As-O absorption peak at 930 cm^{-1} to that of the Si-O peak at 1060 cm^{-1} and plotting against the m/o As_2O_3[3] in the glass calculated from the weight of the film and flame spectrophotometric analysis of silicon in the glass dissolved in a HF solution. The results are shown in Fig. 4. In

[3] Trivalence of the arsenic in all deposited glass was established by the bright yellow precipitate it formed with $AgNO_3$ dissolved in a HF solution (8). Control experiments showed that pure As_2O_3 and pure As_2O_5 gave a similar bright yellow and dirty brown precipitate respectively with $AgNO_3$ in HF solutions.

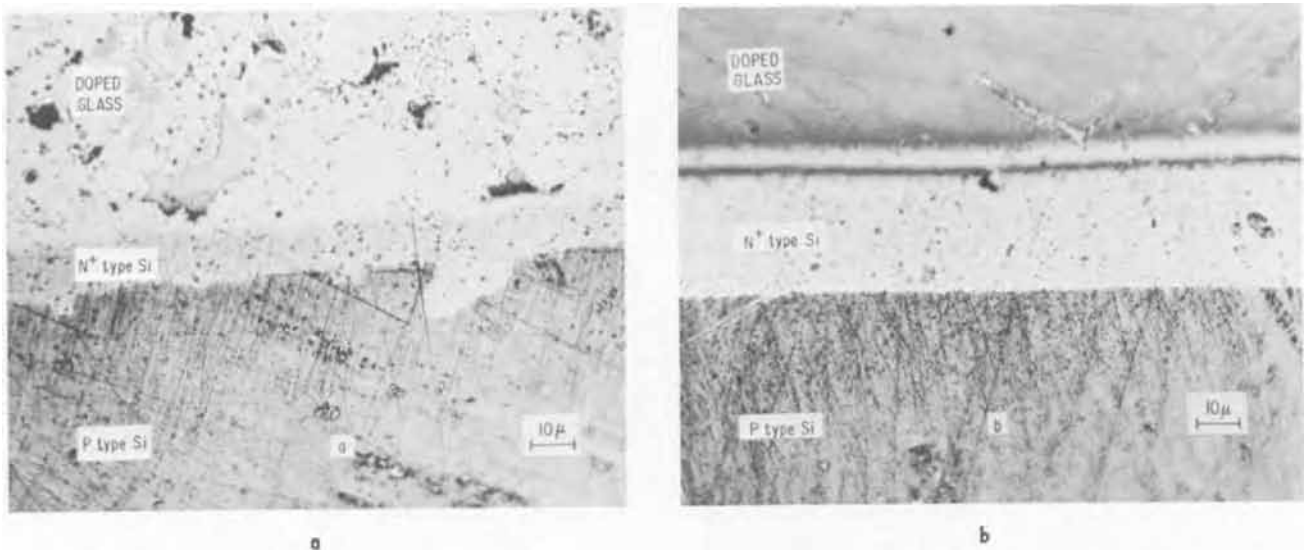

Fig. 5. Angle lapped sections of p-type (100) oriented 1 ohm-cm Si slice after arsenosilicate glass deposition and diffusion in argon at 1100°C. Beveling ratio is 20:1. Mole per cent As_2O_3 in the as-deposited glasses are: (a) 13.5 (IR ratio = 0.50) and (b) 0.5 (IR ratio = 0.05).

addition, composition data obtained for the atomic ratio of As and Si in the glasses by x-ray microprobe analysis using elemental silicon and high purity GaAs as standards, having been converted to m/o As_2O_3 and are plotted in Fig. 4. It can be seen that good agreement is obtained for the two independent sets of chemical analyses within 1 m/o As_2O_3 or better. The infrared spectrum together with the above calibration curve can thus be used as a nondestructive means determining the composition of as-deposited binary arsenosilicate glass films. The IR ratio method of determining composition has been discussed by Kern and Heim (9) for borosilicate glasses (but no calibration curve was given). Such a calibration curve has recently been reported from this laboratory (10) for as-deposited binary borosilicate glass films in the whole composition range obtained by chemical vapor deposition.

After film deposition, the wafers were heated in an argon atmosphere (flow rate: 1 ft^3/hr) at 1100°C for 5 hr. Glass damage was observed in glasses containing more than 1 m/o As_2O_3 (IR ratio = 0.08). Damage to the glass occurs soon after introduction of the wafers into the furnace, as shown by heating small portions of the wafers having various amounts of As_2O_3 in the glass under the above conditions for only 15 min. When the glass is damaged, the diffusion front appears irregular and contains deep spikes, which seem to reflect glass damage on the surface (Fig. 5a). Glasses containing less than 1 m/o As_2O_3 showed no damage during heat treatment; the diffusion front appears uniformly deep under the entire wafer, as determined by angle lapping and staining methods (Fig. 5b).

From the junction depth and the sheet resistivity of the semiconductor surface, measured with the four point probe method, calculations based on Irvin's curves (11) assuming a complementary error function distribution show that surface concentrations of carriers as high as 4×10^{20} per cm^3 can be achieved with undamaged glass samples.

A detailed study on the deposition characteristics of these arsenosilicate glasses, the nature of glass damage at elevated heat treatment temperatures, and the diffusion characteristics of As from the glass into silicon will be published in a subsequent article.

Summary

A one-liquid-source chemical system for depositing binary arsenosilicate glasses is described. Silane, oxygen, and arsenic trichloride are the reagents used. Low deposition temperature (300°-500°C) and high deposition rates (500-900 Å/min) are the main advantages of this system over the corresponding two-liquid-source system based on TEOS so-far reported. Glasses containing 0-20 m/o As_2O_3 and higher have been prepared. After diffusion at high temperature (1100°C) in an argon atmosphere, surface concentrations of carriers as high as 4×10^{20} per cm^3 were obtained.

Acknowledgments

The authors thank D. M. Brown, G. J. Charney, L. F. Cordes, and F. K. Heumann for their assistance in this work, and M. Garfinkel for helpful comments on the manuscript.

Manuscript submitted Jan. 28, 1971; revised manuscript received May 13, 1971.

Any discussion of this paper will appear in a Discussion Section to be published in the June 1972 JOURNAL.

REFERENCES

1. D. B. Lee, *Solid-State Electron.*, **10**, 623 (1967).
2. H. Teshima, Y. Tarui, and O. Takeda, *Bull. Electrotech. Lab. Japan*, **33**, 631 (1969).
3. A. Cuccia, G. Shrank, and G. Queirolo, in "Semiconductor Silicon," R. R. Haberecht and E. L. Kern, Editors, The Electrochemical Society, Inc., (1969).
4. E. Arai and Y. Terunuma, *Jap. J. Appl. Phys.*, **9**, 691 (1970).
5. D. M. Brown and P. R. Kennicott, *This Journal*, **118**, 293 (1971).
6. D. R. Stull, *Ind. Eng. Chem.*, **39**, 540 (1947).
7. R. Bhole and A. Mayer, *RCA Rev.*, **24**, 511 (1963).
8. A. I. Vogel, "A Textbook of MACRO and Semimicro Qualitative Inorganic Analysis", 4th ed., Longman Publishers, (1957).
9. W. Kern and R. C. Heim, *This Journal*, **117**, 568 (1970).
10. A. S. Tenney, *This Journal*, To be published.
11. J. C. Irvin, *Bell System Tech. J.*, **41**, 387 (1962).

Polarization Behavior of Graphite in Sodium Chloride Solutions in the Presence and Absence of Ethylene

A. Belanger, G. Belanger,* and A. K. Vijh*

Hydro-Quebec Institute of Research, Varennes, P.Q., Canada

With the generally projected availability of inexpensive electric power in the near future, electrosynthesis of new organic compounds becomes increasingly more attractive commercially. It has recently been suggested that (1), partial electro-oxidation of low molecular weight hydrocarbons, with an aim to introduce desired functional groups, could provide an interesting avenue for exploitation of the commercial potentialities of the electrosynthetic procedures. In this connection, it has been claimed in the patent literature (2), that ethylene can be partially oxidized to ethylene epoxide by means of a graphite anode in aqueous NaCl solutions (*p*H adjusted to 10.6) through the following over-all reaction

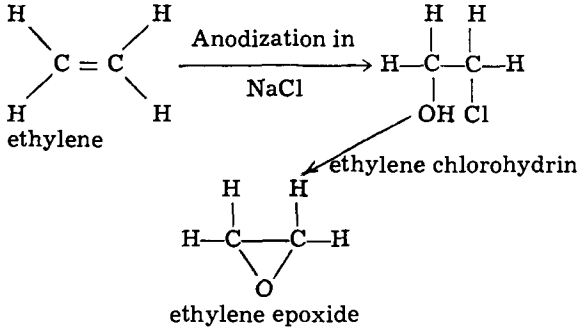

The scope of the work reported here was to examine potentiostatically and potentiodynamically the polarization behavior of graphite in NaCl solutions in the presence and absence of ethylene. The object was to delineate the general electrode kinetic features (3) of the above electrosynthesis. In particular, it was sought to establish whether ethylene is oxidized chemically and homogeneously by the ClO^- produced anodically, as claimed (2), or by a heterogeneous path involving the oxidation of ethylene on the electrode surface. The studies were also extended to explore the cathodic behavior of graphite in the NaCl solution in the presence and absence of ethylene.

Experimental Section

The following instruments were employed in this investigation: Tacussel potentiostat, PRT 20-2B; Tacussel milliammer Type MAL 284; Tacussel digital voltmeter with high input impedance; Honeywell X-Y recorder, Type 550M; Tacussel function generator, Type GSTP 2; General Radio decade resistor box; constant-current d-c power supply (Kepco). Conventional potentiostatic, galvanostatic, and potentiodynamic circuitries were used (3).

Measurements were carried out in 3M sodium chloride solutions ("Baker analyzed") with *p*H adjusted to 10.6 by the addition of sodium hydroxide ("Electrolytic Pellets"—Fisher) solution. Solutions were made in deionized and doubly distilled water, both distillations being over alkaline potassium permanganate. Working electrodes were spectroscopic grade rods (Union Carbide) and were mounted into heat-shrinkable Teflon material as described previously (4). Graphite rod counterelectrodes and hydrogen reference electrodes were employed. The working and the counterelectrodes were thoroughly cleaned and degreased in boiling trichloro-ethylene. The platinized-platinum electrodes for the reference compartment were cleaned before platinization and were rinsed several times in doubly distilled water subsequent to platinization. A three-compartment Pyrex glass cell provided with solution-sealed stopcocks and various gas inlets and outlets (with water bubblers) was used. The working electrodes were carried on the ground-glass sliding tubes generally called "tru-bore" tubing.

Hydrogen gas for the reference electrode was "Electrolytic, Grade A" (Liquid Carbonic) and was deoxygenated by passing over a palladium catalyst ("Deoxo") and further purified by passage through activated charcoal and activated alumina, both at liquid nitrogen temperature. Helium gas for the working and counter compartments was the purest available grade (Grade A provided by Liquid Carbonic) and was deoxygenated over copper at 500°C. Any residual impurities in He were presumably removed by subsequent passage over active charcoal at liquid nitrogen temperature. The ethylene used was obtained from "Liquid Air of Canada" and was 98.5% pure. Ethylene was used without further purification. All connections between the gas lines and the electrolytic cell were made by means of glass-to-glass joints.

Optimum anodic pre-electrolysis, under helium atmosphere, was conducted in solutions in which anodic polarization behavior was subsequently examined; similarly cathodic pre-electrolysis of the solutions was carried out for the investigation of the cathodic polarization behavior. Both anodic and cathodic pre-electrolyses were carried out in solutions in which potentiodynamic scanning over wide ranges of potentials was done.

In the steady-state current-potential relationships, values of the current were read by stopping 1 min at every potential. Generally, quite steady readings of the current were obtained after about 20 sec. All electrode potentials refer to the hydrogen electrode in the same solution.

All experiments were carried out at room temperature in solutions thoroughly stirred by bubbling either helium or ethylene, depending on the type of experiment. Although the previous claims (2) to successful partial oxidation of ethylene refer to the work at 38°C, our experiments carried out at *ca.* 26°C would be expected to yield qualitatively similar results. This is because such moderate difference of temperature (~12°C) would, in general, affect only the rate of the reaction and not the identity of the reaction products themselves.

It may be added that the galvanostatic arrangement was used only during pre-electrolyses in order to pass the high currents (> 50 mA cm^{-2}) needed, with the stopcock between the working and the counter compartments being closed

The electrode kinetic measurements were supplemented by appropriate product analyses. The presence of ClO^- in the anodized solutions in which ethylene was not bubbled was established by means of iodine titration (5) and colorimetric methods (6). The detection of ethylene glycol, formed by hydrolysis of ethylene epoxide, was carried out by V.P. chromatography using a column made of Porapak Q.

Results and Discussion

The sodium chloride solution was first anodized on the graphite electrode by completely isolating the working compartment from the atmosphere and other

* Electrochemical Society Active Member.

Key words: graphite electrode, electrochemical behavior of graphite, electrosynthesis on graphite, anodic and cathodic polarization of graphite.

parts of the cell and in the absence of ethylene for 48 hr at 5 mA. It was observed that the solution became quite yellowish presumably owing to the dissolution of the anodically evolved chlorine gas. The dissolved chlorine gas gives rise to the ClO^- ions by means of the reaction (7)

$$Cl_2 + 2\,OH^- \rightleftharpoons Cl^- + OCl^- + H_2O \qquad [1]$$

The presence of OCl^- was confirmed titrimetrically (5) and colorimetrically (6) as mentioned earlier. When the ethylene was bubbled subsequently through this solution containing ClO^-, without the concomitant passage of current, ethylene glycol was formed thus confirming the previous results (2), namely, chemical homogeneous reaction between ClO^- and C_2H_4 to form epoxide. Essentially the same result, *i.e.* formation of ethylene glycol, was obtained on the anodic polarization of graphite in the NaCl solution in the presence of ethylene bubbling through the working compartment. In order to examine further the possibility of heterogeneous oxidation of ethylene in the latter case, potentiostatic and potentiodynamic studies were carried out. Briefly, it was observed that presence of ethylene does not alter the current potential relations, either potentiostatic or potentiodynamic, corresponding to the anodic polarization of graphite in NaCl solutions. The details on these results follow.

In the anodic polarization studies in the potential range between 1.1V and 2.0V approximately, it was observed that substitution of helium by ethylene in the working compartment did not bring about a significant change in the rate of the electrode reaction at a given steady-state potential. The plots of potentiostatically controlled steady-state potentials against the current density, both in the presence and absence of ethylene, are presented in Fig. 1. Introduction of ethylene does not result in substantial increase or decrease of current at a given potential, keeping in mind the poor reproducibility of the steady-state current-potential relationships probably arising from slow diffusion of chlorine into and out of the graphite electrode (8). The qualitative conclusion drawn from Fig. 1, is confirmed by Fig. 2, in which it is observed that the potentiodynamic profiles are exactly the same in the presence and absence of ethylene. In Fig. 2, the electrode was scanned between −1.2V and +1.9V respectively, and it was observed that ethylene has absolutely no effect on either the anodic or the cathodic portion of the potentiodynamic profile. Thus Fig. 2 would then be consistent with Fig. 1 in which no detectable heterogeneous oxidation of ethylene is indicated. The cathodic, on the potential scale, portion of Fig. 2, is

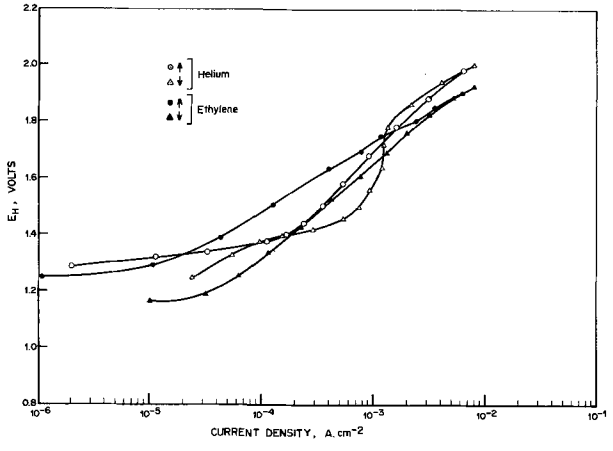

Fig. 1. Steady-state (point-by-point) anodic polarization curves on graphite in 3M NaCl solutions in presence and absence of ethylene. Electrode potentials, E_H, expressed against the hydrogen electrode in the same solution. Within the range of experimental reproducibility, oxidation of ethylene is not indicated (also see Fig. 2).

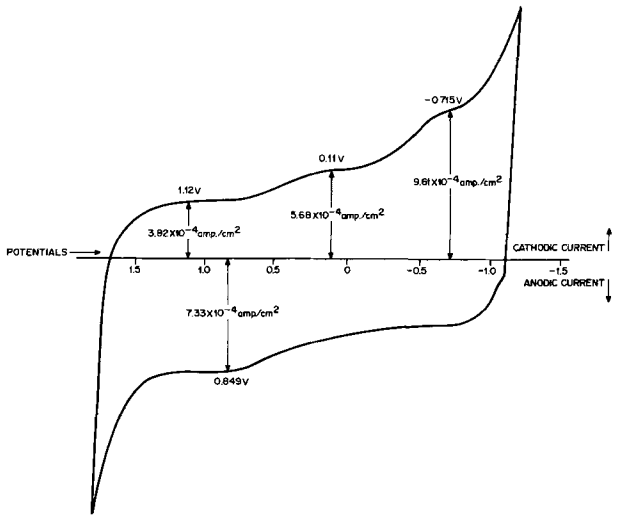

Fig. 2. Repetitive potentiodynamic profiles (sweep rate, dV/dt = 0.3 V sec^{-1}) on graphite in 3M NaCl solutions in presence and absence of ethylene. Essentially same result is obtained in single sweep profiles triggered from a prior steady-state potential. Even though pseudo-faradaic peaks are not observed over a wide range of sweep speeds, high value of (adsorption?) pseudocapacitance, $i \times \frac{dt}{dV}$, ranging between ca. 1000-3000 μF cm^{-2} are observed. There is no evidence of oxidation or reduction of ethylene.

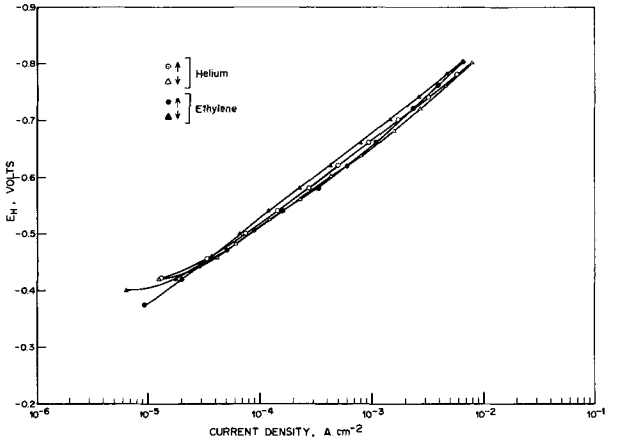

Fig. 3. Steady-state cathodic polarization of graphite in 3M NaCl solutions in presence and absence of ethylene. No reduction of ethylene is observed.

confirmed by Fig. 3, in which steady-state current-potential relationship in the potential range −0.4 and −0.8 are almost identical in the presence and absence of ethylene. It may thus be concluded that the hydrogen evolution reaction on the graphite in NaCl solutions is unaffected by the presence of ethylene, which presumably is neither adsorbed nor reduced (to C_2H_6) of these potentials. It may be added that cathodic reduction of ethylene has been accomplished, however, on platinum (9).

In addition to the negative conclusions, namely, ethylene is neither oxidized nor reduced on the graphite surface in NaCl solutions at room temperature, some positive aspects of Fig. 1-3 may also be discussed here.

In Fig. 2 even though clear-cut peaks indicative of the adsorption and desorption of reaction intermediates are not observed, the pseudocapacitance values estimated from the various portions of the hysteresis range between 1000-3000 μF cm^{-2} approximately with respect to the geometric area of the electrode. Although the real area of the electrode is not known, these capacitance values appear to be higher than the

double layer capacitance even when an appreciable value of the roughness factor is assumed. This would be consistent with the previous evidence on the substantial chemisorption of atomic chlorine on graphite during anodic polarization in solutions containing chloride ions. This information when combined with the generally high (>> 30 mV) Tafel slopes in Fig. 1 would suggest that the evolution Cl_2 on graphite proceeds by the steps

$$Cl^- + C \xrightarrow{\text{"fast"}} C - Cl + e \quad [2]$$

$$C - Cl + Cl^- \xrightarrow{\text{"slow"}} C + Cl_2 + e \quad [3]$$

where C represents a site on the graphite electrode and $C - Cl$ denotes a chlorine atom adsorbed on this site. It is assumed that the electrode coverage by Cl atoms is high, *i.e.* $\theta \to 1$.

Similarly, if it is assumed that the high capacitance values in Fig. 2 at cathodic potentials also indicate some adsorption pseudocapacitance (10) and thence significant steady-state coverage by adsorbed hydrogen, a radical-ion or atomic recombination mechanism for the cathodic hydrogen evolution on graphite would be indicated. The Tafel slope observed (Fig. 3) is near $2.3 \times 2RT/F$ which would tend to eliminate atomic recombination as the possible mechanism. One may thus conclude the following steps for the evolution of hydrogen

$$H_2O + C + e \xrightarrow{\text{"fast"}} C - H + OH^- \quad [4]$$

$$C - H + H_2O + e \xrightarrow{\text{"slow"}} C + H_2 + OH^- \quad [5]$$

The radical-ion step suggested here would be qualitatively consistent with the observed apparent exchange current density (Fig. 3), high heat of sublimation and melting point of graphite, and, good chemisorptive properties of graphite.

It may be added that in the potential range 1.1V to 0V, virtually no current was observed except around 0.95V at which a few microamperes were consistently noticed despite extended pre-electrolysis. This current must be attributed to an impurity redox reaction probably associated with the reduction of traces of oxygen which might have been irreversibly taken up by the graphite electrode before introduction into the solution (11). In any case the origin of this background current (< 8 μA), which did not appear to affect the results in rest of potential regions, could not be established.

Although direct oxidation of ethylene on the electrode surface has not been observed to occur on graphite in this study or previously (2), there has been a report (12) that such a heterogeneous oxidation can proceed on some special catalytic surface prepared by incorporating Ag into a graphite anode.

Acknowledgments

The authors are grateful to Mr. R. Jacques for contributions to the experimental aspects of this work. Thanks are also due to Dr. P. Lenfant for his interest and encouragement. Grateful acknowledgment is also made to the referees of this paper for their suggestions.

Manuscript submitted Dec. 18, 1970; revised manuscript received *ca.* May 17, 1971.

Any discussion of this paper will appear in a Discussion Section to be published in the June 1972 JOURNAL.

REFERENCES

1. T. Dickinson and P. J. Ovenden, Chemistry in Britain, pp. 260 (1969).
2. J. A. M. LeDuc, Fr. Pat. 1,375,298 (1964); also, C.A., 62, 86806 (1965).
3. A. K. Vijh and B. E. Conway, *Chem. Rev.*, **67**, 623 (1967).
4. A. K. Vijh and R. S. Alwitt, *J. Chem. Ed.*, **46**, 121 (1969).
5. G. Charlot, "Les Méthodes de la Chimie Analytique-Analyse Quantitative Minérale," Masson and Cie (1966).
6. D. A. Skoog and D. M. West, "Analytical Chemistry," Holt, Rinehart and Winston (1965).
7. N. Ibl and D. Landolt, *This Journal*, **115**, 713 (1968); *Chem. Ing. Tech.*, **39**, 706 (1967).
8. L. J. J. Janssen and J. G. Hoogland, *Electrochim. Acta.*, **15**, 339 (1970).
9. H. J. Davitt and L. F. Albright, *This Journal*, **118**, 236 (1971).
10. B. E. Conway, "Theory and Principles of Electrode Reaction," Ronald Press, New York (1965).
11. A. Damjanovic in "Modern Aspects of Electrochemistry," Vol. 5, J.O'M. Bockris and B. E. Conway, Editors, Plenum Press (1969).
12. J. A. M. LeDuc, U.S. Pat. 3,427,235 (1969).

JOURNAL OF THE ELECTROCHEMICAL SOCIETY

ELECTROCHEMICAL SCIENCE

OCTOBER 1971

ES

Electrochemical Alloying of Lithium in Organic Electrolytes

A. N. Dey*

P. R. Mallory & Company, Inc., Laboratory for Physical Science, Northwest Industrial Park, Burlington, Massachusetts 01803

ABSTRACT

Lithium metal was found to alloy with the other metals including noble metals in an organic electrolyte electrochemical cell: Li/1M $LiClO_4$ in propylene carbonate/metal at ambient temperature with the evolution of electrical energy. The alloying occurred in many organic electrolytes containing lithium ions. Both the coulombic efficiency and the rate of alloying were found to be high. The alloys were gray to dark gray and brittle. Chemical and x-ray analysis indicated that they were intermetallic compounds.

It was observed (1, 2) earlier in our laboratory that a cathodic chronopotentiogram in the organic electrolyte consisting of 1M $LiClO_4$ in propylene carbonate consisted of several voltage plateaus prior to the lithium deposition. It was postulated that one of these plateaus might be due to the alloying of lithium with the substrate. In this paper, I wish to present some experimental evidence to show that lithium undergoes spontaneous electrochemical alloying (SEA) at ambient temperature with various metals including noble metals at appreciable rates in the organic electrolytes containing lithium salts. The phenomenon results in the dissolution of the lithium anode and the simultaneous deposition and alloying of lithium on the metal cathode, and the evolution of energy in a manner similar to a primary cell.

Experimental

Materials.—Propylene carbonate (PC) (Eastman Kodak) was vacuum distilled at 120°C, 1.2 mm Hg. Anhydrous $LiClO_4$ was used as received from G. Fredrick Smith Company. The water content of the electrolyte consisting of 1M $LiClO_4$ in PC was found to be 0.01% (volume). The other organic solvents such as γ-butyrolacetone, dimethyl sulfoxide, N, N-dimethyl formamide, methyl formate, tetrahydrofuran, and acetonitrile were used as received.

Electrodes.—The lithium anodes were made by pressing a rectangular piece of lithium ribbon (0.02 in. thick, Foote Mineral Company Inc.) on the expanded stainless steel current collector. The cathodes of the various metals such as Sn, Pb, Al, Au, Pt, Zn, Cd, Ag, Mg, Ti, Cu, and Ni were made by cutting out rectangular pieces (2 x 2 cm) of metal foil. The thicknesses of the available metal foils varied from 0.005 to 0.01 in.

Cell.—The cells were constructed by placing two lithium anodes on each side of the metal foil cathode with filter paper separators interposed between the electrodes. Two rectangular Teflon blocks were placed on each side of the anodes and were tied with string to provide stack pressure. The assembly was then placed in a sealed glass jar containing electrolyte (1M $LiClO_4$ in PC). The electrical connections were made either by spot welding stainless steel tabs to the anode current collectors and the cathode metal or by means of alligator clips. Care was taken to ensure that the points of contact were not wetted by the electrolyte. All the above operations were carried out in the dry box filled with dry argon with a moisture content of less than 2 ppm.

The cells were either directly shorted or were discharged through a known resistor. In the latter case, the cell potential was recorded as a function of time.

Spontaneous electrochemical alloying (SEA) and the determination of the alloy composition.—The cathodic alloying of the metal cathodes with lithium started as soon as the external circuit of cell [1] was completed

Li/1M $LiClO_4$-PC/metal [1]

The composition of the lithium metal alloy was determined by dissolving the alloy in water whereby the lithium reacted with water to form LiOH and the metal particles precipitated. The aqueous extract was then titrated with standard acid to determine the amount of lithium present in the metal. The titrations were repeated after various periods of equilibration of the alloy in water to ensure that most of the lithium reacted with water.

X-ray diffraction of the SEA alloys.—The metal foil cathodes (*e.g.*, Al, Sn, Pb, etc.) turned into a gray powder after shorting with the lithium anode in cell [1] for 8-10 hr. These powders (metal lithium alloy) were filtered and thoroughly washed with the PC and then with tetrahydrofuran and dried in the dry box. A portion of the powders which appeared free from any unalloyed metal particles was then packed in a quartz capillary in the dry box and the opening of the capillary was closed with silicone grease. The capillaries were then removed from the dry box and were sealed with a flame. The x-ray diffraction of the alloys were carried out with these capillaries using Debye Scherrer Powder Camera (116.4 mm diameter) with Norelco x-ray system (Cu Kα radiation, Ni filter).

Results and Discussions

The metals such as Sn, Pb, Al, Au, Pt, Zn, Cd, Ag, and Mg form gray or dark gray powder after shorting

* Electrochemical Society Active Member.

Key words: propylene carbonate, cathodic embrittlement, noble metals, lithium-metal alloys, intermetallic compounds.

with the lithium anode in cell [1] within periods of hours to days (at room temperature) depending on the metal. This alloying does not occur in electrolytes containing tetralkyl ammonium salts or salts which do not contain any lithium ions. The phenomenon occurs in many organic solvents such as propylene carbonate, γ-butyrolacetone, dimethyl sulfoxide, N, N-dimethyl formamide, methyl formate, tetrahydrofuran, acetonitrile. The short-circuit (through the ammeter) current densities obtained with several metal cathodes (*e.g.*, Al, Sn, Pb) were of the order of several milliamperes per square centimeter at room temperature. The phenomenon occurs at lower temperatures as long as the electrolyte remains liquid.

The phenomenon is strictly electrochemical. No alloying or any other change on the electrodes were observed as long as the external circuit of cell [1] was open. On closing the circuit, the anodic reaction was determined (weight loss) to be the dissolution of lithium

$$\mathrm{Li} \rightarrow \mathrm{Li}^+ + e \qquad [2]$$

and the cathodic reaction was determined to be the deposition of lithium (weight gain, and chemical analysis), and alloying

$$x\mathrm{Li}^+ + \mathrm{M} + xe \rightarrow \mathrm{Li}_x\mathrm{M} \qquad [3]$$

The initial open-circuit voltages of all the cells were greater than a volt (Table I). The high voltages are due to the presence of metal oxides on the metal cathodes. The shorting of the cells could cause initial electrochemical reduction of the surface oxide of the metals. The open-circuit voltage of the cells after the initial short circuiting varied a great deal from metal to metal. The open-circuit voltages of the cells also decreased as the duration of short circuiting increased.

According to the Nernst equation [4]

$$E = E_0 - 2.303\frac{RT}{\mathbf{F}}\log\frac{a_{\mathrm{Li}+}}{a_{\mathrm{Li}}} \qquad [4]$$

cell [1] is expected to exhibit zero voltage under the following conditions: (*a*) the absence of spurious reactions such as solvent decomposition, and (*b*) the activity of the freshly deposited lithium on the cathode is unity. It was shown earlier (3) that the solvent decomposition reactions did not occur on metal substrates to any measurable extent although it was a dominant reaction on a graphite substrate in a cell similar to [1]. However, the alloying of lithium with the metal caused the activity of Li (a_{Li}) to be less than unity on the metal substrate and hence, the metal electrode assumed a positive potential compared to the lithium anode. The lithium deposition continued as long as the alloying continued. It was found that the alloying continued with the metals such as Sn, Pb, Al, Au, Pt, Cd, Ag, and Mg until the brittle, powdery, dark alloy fell off and lost electronic contact.

Degree of alloying.—The metals examined for the spontaneous electrochemical alloying fell in the following two classes based on the degree of alloying as determined by the drastic change in appearance and the charge transferred through the cell of type [1] due to electrochemical alloying:

Class I: Metals which underwent changes in appearance on alloying: Sn, Pb, Al, Au, Pt, Zn, Cd, Ag, and Mg.

Class II: Metals which did not undergo any significant change in appearance: Ti, steel, stainles steel, Cu, and Ni.

It is apparent that the class I metals will be unsuitable as current collector materials for the lithium anode of the primary and secondary organic electrolyte cells.

Coulombic efficiency.—The apparent coulombic efficiency of the spontaneous electrochemical alloying was investigated by discharging the cells [1] through a 1 kohm resistor and by monitoring the voltage as a function of time. The voltage-time curves of the various cells with the class I metals are shown in Fig. 1. The amount of charge transferred through the external circuit was calculated by integrating the areas under the curves. The theoretical amount of lithium deposited on the cathode was calculated according to reaction [3]. The actual amount of lithium deposited in the metal cathodes was determined by chemical analysis. The coulombic efficiency of alloying of the class I and class II metals is given in the Table I. The open-circuit voltages of the cells and the initial voltages on constant load discharge, which are not obvious from Fig. 1, are also given in Table I.

The coulombic efficiency of the class I metals varied from 70 to 100%. The reasons for low electrochemical alloying efficiency for the metals like Au, Pt, Zn may be: (*a*) the inefficient extraction of Li by water treatment and (*b*) the oxide reduction. Normally, the fraction of the charge required for the oxide reduction is very small compared to the total charge passed for alloying and, therefore, it cannot account for such low efficiency. The efficiency of extraction of lithium by water treatment depends predominantly on the nature of the metal. For example, with soft, low-melting metals like Sn, the exothermic reaction of Li with water disintegrated the alloy into LiOH and finely powdered Sn within a few minutes. With Pb, the exo-

Table I. Determination of coulombic efficiency of spontaneous electrochemical alloying (SEA) of various metals with lithium

Metal	Open circuit voltage	Voltage immediately after shorting through 1 kohm	Coulombs passed through 1 kohm	Moles of Li alloy based on charge passed (theoretical)	Moles of Li in the alloy from chemical analysis	Coulombic efficiency, %*
Sn	1.99	0.605	338.0	3.49×10^{-3}	3.29×10^{-3}	94
Pb	2.45	1.006	447.0	4.64×10^{-3}	4.69×10^{-3}	101
Al	2.44	0.091	506.0	5.25×10^{-3}	4.84×10^{-3}	92
Au	2.77	0.413	249.0	2.58×10^{-3}	1.90×10^{-3}	74
Pt	2.36	0.432	228.0	2.36×10^{-3}	1.90×10^{-3}	80
Zn	2.44	0.732	119.0	1.23×10^{-3}	0.90×10^{-3}	70
Cd	2.47	1.356	94.0	9.70×10^{-4}	9.01×10^{-4}	93
Ag	3.03	0.410	73.0	7.60×10^{-4}	6.92×10^{-4}	91
Mg	1.25	0.026	43.0	4.40×10^{-4}	4.45×10^{-4}	101
Ti	2.78	0.587	2.4	2.50×10^{-5}	0.50×10^{-5}	20
ST-LF8†	2.58	0.678	2.3	2.40×10^{-5}	0.50×10^{-5}	21
ST-AF12†	2.83	0.410	2.2	2.30×10^{-5}	0.50×10^{-5}	22
Cu	2.95	0.659	1.1	1.18×10^{-5}	0.50×10^{-5}	42
Ni	2.47	0.530	0.9	1.00×10^{-5}	0.50×10^{-5}	50

* The coulombic efficiency is defined as the efficiency of lithium deposition on the cathode based on the total charge passed according to reaction [3].

† ST-LF8: stainless steel } Shim assortments from Precision Steel
† ST-AF12: steel } Warehouse Inc.

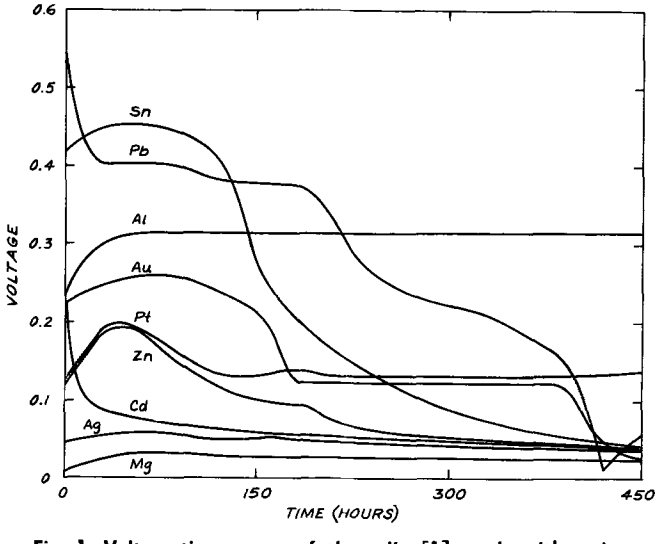

Fig. 1. Voltage-time curves of the cells [1] made with various metal cathodes and discharged with 1 kohm external load.

thermic reaction caused the Pb particles to sinter into porous Pb spheres. Whereas, with high melting metals like Pt and Au, although the initial reaction with water was quite vigorous, the diffusion of Li from the metal matrix to the solution was quite slow and the extraction might be incomplete. The low efficiency for the class II metals may be due to both (*a*) and (*b*), as the extent of alloying is so small that the experimental errors for the extraction and titrations can be very large.

Rate of alloying.—The relative rate of alloying of the various class I metals is directly proportional to the steady-state current flow through the 1 kohm resistor from the cells [1]. These currents are obtainable directly from the discharge curves shown in Fig. 1 by replacing the cell voltage units to milliampere current unit. The apparent voltage plateaus of the discharge curves of Sn, Pb, and Au might not have any significance as the electrodes in the specific cells were very thin and the alloying caused complete disintegration of the electrodes and the consequent loss of electronic contact. The voltage plateaus may be due to a change in the effective surface area of the metal cathodes. Based on the voltage maxima of Fig. 1 (after 60 hr of discharge) the relative alloying rates of the various metals approximately follow their relative hardnesses, *viz.*, the softer the metal, the higher the rate.

It is interesting to note that all the class I metals except Pb and Cd exhibit the initial voltage drop on discharge and the subsequent voltage recovery (Fig. 1). This may be due to the presence of oxide film which acts as a passive film, so to speak, to the electrochemical alloying process.

Lithium-metal alloy composition.—All the class I metals are known (4) to form one or more intermetallic compounds with lithium, whereas the class II metals do not. It appears highly probable that the observed alloying represents simply the electrochemical formation of the metal-lithium intermetallic compounds. Normally, these are formed by heating the metal and lithium at high temperatures, whereas here it is formed at room temperature spontaneously with the evolution of electrical energy.

The composition of the lithium-metal alloys formed electrochemically was determined by chemical analysis and is given in Table II. The known thermally prepared intermetallic compounds with similar compositions are also given in the same table for comparison. It appears that the electrochemically formed alloys are very similar in composition to that of the thermally formed known intermetallic compounds. The available x-ray diffraction data (5) on a specific intermetallic compound LiAl are compared with that of the SEA lithium-aluminum alloy in Table III. It is apparent that the thermally formed LiAl is identical to that of the alloy made by the electrochemical method described in this paper. The x-ray data indicate also the presence of small quantities of Li (dÅ, 2.48) and Al (dÅ, 2.33, 2.03, 0.978) in addition to LiAl in the SEA alloy.

Table II. Composition of the SEA alloys and the thermally prepared known intermetallic compounds

SEA alloy composition				Intermetallic compounds	
Wt %		At. %	Stoichiometry	Stoichiometry	Reference
Li	9	74	$Li_{3.52}Au$	Li_3Au	6
Au	91	26			
Li	5	60	Li_3Pt_2	$LiPt_2$*	6
Pt	95	40			
Li	10.2	77	$Li_{3.31}Pb$	$Li_{10}Pb_3$	4
Pb	89.8	23			
Li	18.8	47	$Li_{0.89}Al$	LiAl	4
Al	81.2	53			
Li	14.6	74	$Li_{2.56}Sn$	Li_7Sn_3	4
Sn	85.4	26			

* The available data on this system is limited. This is the only intermetallic compound reported.

Table III. X-ray diffraction data on the SEA Li-Al alloy and the literature data on the thermally formed LiAl intermetallic compound

SEA Li-Al alloy			LiAl intermetallic compound (5)		
dÅ	Relative intensity*	hkl	dÅ	Relative intensity*	hkl
3.67	S	(111)	3.65	M	(111)
3.38	VVW				
2.48	W+				
2.33	W				
2.24	VS	(220)	2.26	S	(220)
2.03	W				
1.905	M	(311)	1.92	M	(311)
1.586	M-	(400)	1.58	W	(400)
1.452	M-	(331)	1.46	W	(331)
1.433	VVW				
1.294	M	(422)	1.30	S	(422)
1.220	W+	(333) (511)	1.22	M	(333) (511)
1.120	W+	(440)	1.12	M	(440)
1.075	W	(531)	1.07	M	(531)
1.003	W	(620)	1.01	M+	(620)
0.973	VW	(533)	0.969	VW	(533)
0.928	VVW				
0.918	VW	(444)	0.918	VW	(444)
0.897	VW		0.889	M	(553) (711)
0.850	W	(642)	0.849	VS	(642)
0.824	VW	(553) (731)	0.827	S	(553) (731)
			0.796	W	(800)
			0.778	VW	(733)

* VS, very strong; S, strong; M, medium; M+, between S and M; M-, less than M+; W, weak; W+, between W and M-; W-, less than W+; VW, very weak; VVW, very very weak.

Conclusions

1. Lithium metal alloys with various metals such as Sn, Pb, Al, Au, Pt, Zn, Cd, Hg, and Mg electrochemically at ambient temperature in organic electrolytes containing lithium salt producing electrical energy in a cell of the following type

Li/1M $LiClO_4$-PC/metal

2. The coulombic efficiency of the spontaneous electrochemical alloying (SEA) is generally high (80-100%).

3. The alloy compositions are similar to the composition of known thermally prepared intermetallic compounds.

4. The x-ray diffraction data of the Li-Al SEA alloy show this to be identical to the thermally prepared intermetallic compound LiAl.

5. The phenomenon appears to be quite general in nature and can be termed as cathodic embrittlement of metals in contrast to the normally expected cathodic protection of metals.

Manuscript submitted Jan. 8, 1971; revised manuscript received *ca.* April 3, 1971.

Any discussion of this paper will appear in a Discussion Section to be published in the June 1972 JOURNAL.

REFERENCES

1. R. G. Selim, K. R. Hill, and M. L. B. Rao, "Research and Development of a High Capacity Nonaqueous Secondary Battery," Final Report NASA CR-54969, Feb. 1965, P. R. Mallory & Co.
2. A. N. Dey, *This Journal*, **114**, 823 (1967).
3. A. N. Dey and B. P. Sullivan, *ibid.*, **117**, 222 (1970).
4. M. Hansen and K. Anderko, "Constitution of Binary Alloys," McGraw-Hill Book Co. Inc., New York (1958).
5. American Society for Testing and Materials, X-ray Index Cards.
6. R. P. Elliott, "Constitution of Binary Alloys, First Supplement," McGraw-Hill Book Co. Inc., New York (1965).

Electrochemical Reduction of Oxygen in Carbonate and Carbonate-Halide Melts

P. K. Lorenz*,[1] and G. J. Janz*

Rensselaer Polytechnic Institute, Troy, New York 12181

ABSTRACT

The electrochemical reduction of O_2 in molten carbonates occurs through two reactions:

$$\tfrac{1}{2}O_2 + CO_2 + 2e \rightleftarrows CO_3^{-2} \quad [1]$$

and

$$\tfrac{1}{2}O_2 + 2e \rightleftarrows O^{-2} \quad [2]$$

The onset of these two processes has been investigated in molten Li_2CO_3, the ternary eutectic (Li,Na,K)/CO_3, and the two binary eutectics, (LiCl,Li_2CO_3) and (LiF,Li_2CO_3). Reaction [1] is found to start at slightly negative potentials relative to the Au/O_2,CO_2 reference electrode and depends on the supply of CO_2 from the melt. The onset of reaction [2] occurs at more negative polarizations; both are affected by the solubility of O_2 in the melt. The results for reaction [1] correlate well with the thermal dissociation of carbonates as a function of temperature and melt composition. Reaction [2] appears inhibited at lower temperatures but can be obtained reproducibly if the electrode is potentiodynamically cycled several times through the voltage sweep range; at elevated temperatures it occurs readily. The results are examined relative to the differing viewpoints advanced relative to the electrochemical reduction of oxygen in such molten electrolytes.

The electrochemical reduction of molten carbonates has received attention previously, largely by the Russian workers, and differing viewpoints exist as to the over-all reactions and the electrode polarization potentials. The present communication reports the results of potentiodynamic studies on the electrochemical reduction of oxygen and carbon-dioxide-oxygen mixtures in molten Li_2CO_3 (m 618°C) and in the (Li, Na, K/CO_3) ternary eutectic (m 397°C). An extension of these studies to two binary carbonate-halide eutectics, LiCl-Li_2CO_3 (m 500°C) and LiF-Li_2CO_3 (m 608°C), was also undertaken and these results are also reported.

Experimental Results

The electrolysis cell and ancillary apparatus were those used in our studies on the CO and (CO, CO_2) electrodes and have been described elsewhere (1). Potentiodynamic data were gained with the automatic assembly, consisting of a voltage programmer, a potentiostat, and a dual power supply (Duffers Model 600 and 620, respectively). The reference electrode was also described previously (1) [Pt/(CO_2, O_2 in 2:1 ratio)], whereas the working electrode was a gold wire encased in two concentric Pythagoras porcelain tubes. By means of the latter it was possible to suppress the CO_3^{-2} ion dissociation reaction by maintaining an atmosphere of CO_2 (except during the current-voltage scans) above the melt in contact with the working electrode. When the tip of the working electrode contacted the molten electrolyte, measurements were initiated.

Li_2CO_3.—The electrochemical reduction was investigated in the temperature range of 750°-840°C with current-voltage scans and various atmospheres. Illustrative results at 840°C with O_2, CO_2, CO, and Ar atmospheres over the working electrode are in Fig. 1. The shape of the current-potential curve in the presence of O_2 suggests two reduction mechanisms. The initial reduction current under 1 atm of O_2 may be attributed to the reduction of both CO_2 and O_2 to carbonate, as proposed by Stepanov and Trunov (2)

$$CO_2 + \tfrac{1}{2}O_2 + 2e \rightleftarrows CO_3^{-2} \quad [1]$$

whereas, at higher polarization potentials (0.5-0.6V) the reduction of oxygen to oxide sets in (2), *viz.*

$$\tfrac{1}{2}O_2 + 2e \rightleftarrows O^{-2} \quad [2]$$

If there is no O_2 (or little O_2), this O_2 reduction cannot occur. The strong current undoubtedly indicates a high solubility of oxygen in molten Li_2CO_3. In the absence of CO_2 in the mixture, CO_3^{-2} ion formation process disappears. Due to the differences in diffusivities of O_2 and CO_2 in the electrolyte the optimum ratio of the partial pressures of CO_2 to O_2 is about 2.35 for reaction [1] to occur.

(Li, Na, K/CO_3) ternary eutectic.—In Fig. 2 the current-voltage scans in this electrolyte are shown. The increase of O_2 solubility in the melt with increasing temperature is clearly apparent, *i.e.* the currents cor-

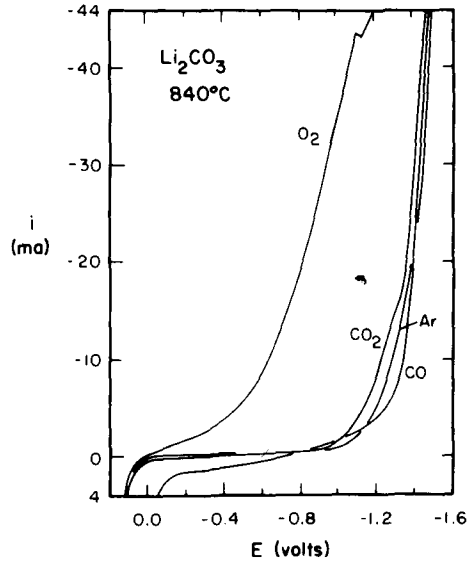

Fig. 1. Illustrative current-voltage scans of the working electrode (W.E.) *vs.* the Pt (CO_2/O_2) reference electrode in Li_2CO_3.

* Electrochemical Society Active Member.
[1] Present address: IBM, Components Division, Essex Junction, Vermont 05452.
Key words: carbonates, carbonate-halide mixtures, electrolyses, electrochemical O_2 reduction, fused salts.

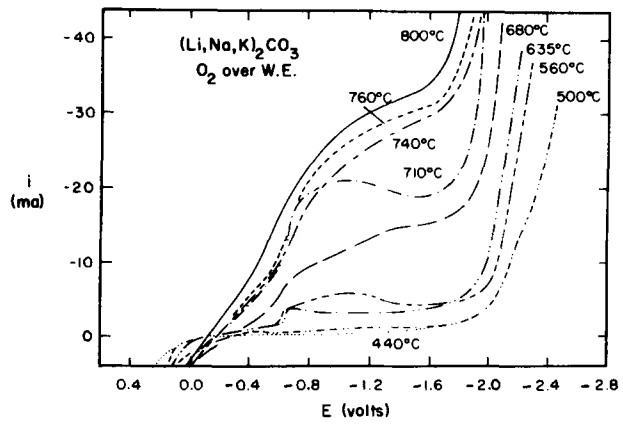

Fig. 2. Illustrative current-voltage scans of the working electrode (W.E.) vs. the Pt (CO_2/O_2) reference electrode in Li,Na,K/CO_3.

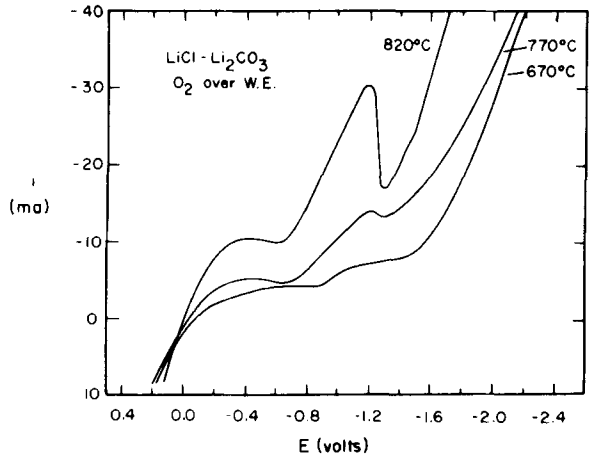

Fig. 3. Illustrative current-voltage scans of the working electrode (W.E.) vs. the Pt (CO_2/O_2) reference electrode in Li/Cl,CO_3.

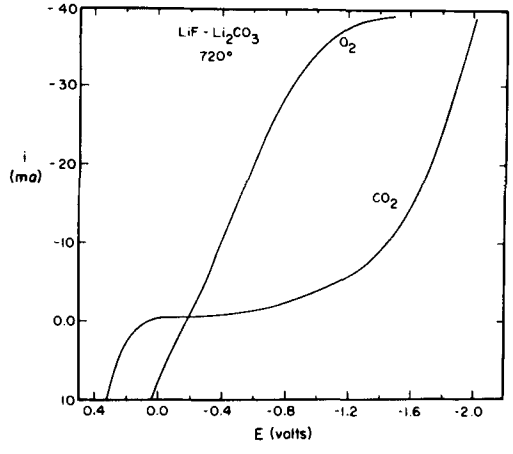

Fig. 4. Illustrative current-voltage scans of the working electrode (W.E.) vs. the Pt (CO_2/O_2) reference electrode in Li/F,CO_3.

responding to oxygen-oxide reduction reaction, Eq. [2]. The results in Fig. 2 are under conditions where the current-voltage scans are reproducible. It was found that above 680°C repeated cycling was not necessary for reproducible results, but at lower temperatures, *e.g.* 560°C, the oxygen reduction process attained reproducible potentials (*e.g.*, −0.6V) only after recycling about three times. At 440°C, it was not possible to induce the oxygen-oxide electroreduction, Eq. [2], even with repeated cycling. When a 2:1 mol ratio of (CO_2, O_2) was used rather than "O_2 only" over the working electrode, the current attributed to the oxygen-oxide electroreduction, Eq. [2], was smaller, while the initial current (attributed to CO_2, O_2, carbonate reduction reaction, *e.g.*, Eq. [1]) was larger.

(Li/Cl, CO_3) eutectic.—The value of the reference electrode potential was found to shift to more positive values (approx. 0.05V, at 800°C) in this electrolyte, compared with its use in molten carbonates. The current-voltage scans at 670°, 770°, and 820°C, in Fig. 3, show that the currents are relatively higher in the 0.0 to −0.6V region, and this correlates directly with a more pronounced thermal dissociation of CO_3^{-2} in this molten mixture, which increases the concentration of CO_2 in reaction [1]. Increased O_2 solubility with increasing temperatures is manifested by the increasing current in the region corresponding to reaction [2].

(Li/F, CO_3) eutectic.—Measurements were attempted at 800°C, but the corrosion of the Pythagoras tubing and baffles was too severe for meaningful results; measurements were limited to 720°C, and the current-voltage scans are illustrated in Fig. 4. The relatively greater thermal dissociation of the carbonate in this molten mixture is evidenced through the higher currents in the 0.0-0.4V region (cf. Eq. [1]). The large currents in the −0.5- −1.0V region indicate that solubility of O_2 is relatively great in such mixtures. Relative to the potential of the reference electrode, a small shift to more positive values was noted (*i.e.*, approx. 0.03V at 720°C).

Discussion

The electrochemical reduction of oxygen in molten carbonates has been investigated primarily by Stepanov and Trunov (2); Klevtsov, Arkhyov, and Stepanov (3); Paskov and Tyurikov (4); and Silakov, Tyurikov, and Vasilistov (5). Some aspects of these are summarized in Table I, and it is seen that there are differing viewpoints on electrochemical reduction of oxygen in carbonate electrolyses, namely Stepanov *et. al.* favoring two processes, the reduction of CO_2 and O_2 at low polarizations, Eq. [1], and the direct reduction of O_2 at higher anodic polarizations Eq. [2], whereas Silakov *et al.* propose peroxide at low anodic polarizations and the onset of a CO_2 reduction at higher polarizations.

Thermodynamically, from the data for Li_2CO_3, one may calculate the reduction potentials; it is thus found that the reduction of O_2 and CO_2 Eq. [1] is predicted

Table I. Electrolysis of molten carbonates

Investigation	Experimental aspects	Comments
Stepanov and Trunov (2)	(Li,Na,K)/CO_3 eutectic, porous Ag electrode	Support the onset of reaction [1] in the low cathodic polarization regions; maximum current when CO_2/O_2 ratio about 2/1.
Klevtsov, Arkhyov, and Stepanov (3)	(Li,Na,K)/CO_3 eutectic, cylindrical Pt electrode	There is a marked increase in i when the top of the electrode cylinder is raised to protrude about 5 mm above the melt; the rate of reaction [1] is thus limited by gaseous diffusion through the melt/electrode meniscus interface.
Paskov and Tyurikov (4)	(Li,Na)/CO_3, (Li,K)/CO_3, Ag wire electrode	Support the work of Klevtsov *et al.* (3), *i.e.*, a sharp increase in i when the meniscus interface is increased.
Silakov, Tyurikov, and Vasilistov (5)	(Li,Na,K)/CO_3, (Li,Na)/CO_3, Li_2CO_3, Pt and Pd electrodes to various degrees of air oxidation prior to electrolysis	The reaction at low potentials could be eliminated by extensive heating of electrode as pretreatment; proposed that anodic polarization of the electrode (without prior heat treatment) produces a metal peroxide ($MO_2 + 2e^- \rightarrow M + O_2^{-2}$), and at polarizations more negative than −0.5, the reduction of CO_2 to C or CO and carbonate was suggested.

feasible at potentials slightly negative to the reference electrode, whereas the reduction of O_2 to oxide Eq. [2] is not feasible until potentials more negative than −0.3V at 840°C are reached. Although the thermodynamic data for the mixtures are insufficient for such exact predictions, one may assume that the predictions for Li_2CO_3 hold in first approximation for the ternary carbonate eutectic, and more qualitatively provide guidelines for the carbonate/halide mixtures. The experimental results for Li_2CO_3 and the ternary eutectic (in Fig. 1 and 2) are in accord with the theoretically predicted potentials and support the viewpoint advanced by Stepanov *et al.*, namely that reaction [1] is the process occurring in the low cathodic polarization region. The current-voltage curves for CO_2 and Ar atm over the working electrode (Fig. 1) indicate that the CO_2 and carbonate reductions occur well outside the polarization range for the oxygen reduction reactions, and that these appear well separated. No changes in these current-voltage traces were observed if the electrode was heated in O_2 prior to the electrolyses; this contrasts with the observations of Silakov *et al.*, namely, that the reaction at low polarizations could be thus eliminated. The test electrodes in the work of Silakov *et al.* (5) were Pt and Pd, and it follows from the present results that Au does not show the same behavior.

It is also apparent at higher temperatures and in an O_2 atm that the CO_2, O_2 reduction Eq. [1] proceeds more readily as evidenced by the higher currents. This is not unexpected since the thermal dissociation of carbonates to CO_2 is enhanced with increasing temperatures; the increased rate is in accord with CO_2 being a limiting reactant. The current-voltage traces for the LiCl, Li_2CO_3 and LiF, Li_2CO_3 electrolysis in Fig. 3 and 4, respectively, provide additional support for this observation. The halide ion is known to influence the thermal dissociation of carbonates, the greatest effect being noted in LiF-Li_2CO_3 mixtures (6), and the observed currents are in relative agreement with the thermal dissociation to CO_2 of the carbonate, in the order LiF,Li_2CO_3 > LiCl,Li_2CO_3 > (Li,NaK)CO_3. Further, during the electrolysis of the ternary eutectic, if a 2/1 mixture of CO_2/O_2 was used over the working electrode, the current at lower polarization potentials was greater, and at higher polarizations, less, than with only oxygen as the atmosphere. The preceding observations, although qualitative, are firm support for the CO_2, O_2 reaction, *i.e.*, Eq. [1]

$$CO_2 + \tfrac{1}{2}O_2 + 2e \rightleftarrows CO_3^{-2} \qquad [1]$$

as the process in the low cathodic polarization region in the electrolysis of molten carbonates, and carbonate halide mixtures.

At the more negative polarizations, the process appears to be the direct reduction to the oxide ion, *i.e.*, Eq. [2]

$$\tfrac{1}{2}O_2 + 2e \rightleftarrows O^{-2} \qquad [2]$$

and at lower temperatures this proceeds reproducibly after the electrode is potentiodynamically cycled several times. As illustrated in Fig. 5, five successive cycles were required to obtain reproducibility at 560°C. The current increase accompanying reaction [2] moves from a potential of −1.3V to the reproducible values of −0.55V (Fig. 5, curves I, IV, and V, respectively). The potentials of about −1.0V (curves II and III, Fig. 5), correspond to the reduction of CO_2 (supplied from the thermal dissociation of the carbonate) to C and CO_3^{-2}, *i.e.*

$$3CO_2 + 4e \rightleftarrows C + 2CO_3^{-2} \qquad [3]$$

and after the onset of this reaction, the reduction of O_2 proceeded readily. If the inhibition of the oxide reduction reaction, Eq. [2], is due to an oxide layer on the Au electrode, the onset of the carbon deposition reaction, Eq. [3], followed by oxide layer attack

$$C + 3O^{-2} - 4e \rightleftarrows CO_3^{-2} \qquad [4]$$

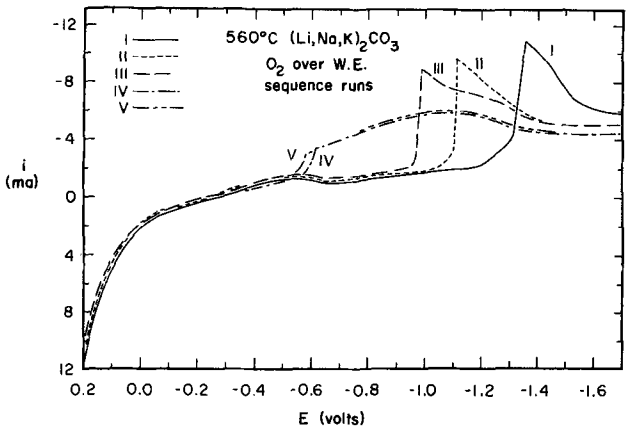

Fig. 5. Voltage-current scans of the working electrode (Au) vs. the Pt (CO_2/O_2) reference electrode during the electrolysis of the (Li,Na,K)/CO_3 ternary eutectic at 560°C, with O_2 over the working electrode. The electrode was cycled five times, and the traces are illustrated as I-V, respectively.

would account for the reproducibility attained in the O_2 reduction reaction (Eq. [2] and Fig. 5, curves IV and V), since the latter proceeds electrochemically apparently uninhibited, on the clean Au surface but not on a gold oxide surface. At 700°C, repetitive potentiodynamic cycling is no longer necessary to obtain reproducibility for the oxygen reduction reaction.

The cathodic deposition of carbon in fused carbonate electrolyses and the role of Li salts in such electrolytes have been discussed elsewhere (7-10). In the present work it is sufficient to note that while the current-voltage curves show clearly that CO_2 is reduced in electrolyses of the various carbonates, visual inspection (9) of the electrode showed C on the electrode at the lower temperatures only. Thermodynamic free energy considerations predict that the stability of C exceeds that of CO below 700°C, and that above this the CO_2 reduction to CO is favored

$$2CO_2 + 2e \rightleftarrows CO + CO_3^{-2} \qquad [5]$$

The difference in the thermodynamically predicted reduction potentials for reactions (Eq.) [3] and [5], respectively, is <0.1V, and separation in this temperature range was not attempted. Although the reduction products were not investigated in detail, it appears that reactions (Eq.) [3] and [5] are possibly the dominant processes contributing to the CO_2 reduction and that thermodynamic control (relative to C or CO end products) was undoubtedly operative for the temperature range investigated (440°-810°C).

Inspection of the results for the LiCl-Li_2CO_3 system shows the suggestion of two limiting currents (Fig. 3, 670° and 770°C, respectively). In light of the preceding considerations, it is significant to note that these two are observed as expected when reaction (Eq.) [1] occurs at slightly less negative potentials than reaction (Eq.) [2], and when reaction (Eq.) [2] is followed by, say, reaction (Eq.) [3]. A further result, namely that for electrolyses under CO_2 or Ar the second limiting current was not found, is additional support for the viewpoints advanced above.

Relative to the two oxygen reductions (reactions [1] and [2], respectively) it was of interest to examine the temperature-dependence of the electrolysis, and the derived enthalpies of activation, summarized in Table II, are from analyses of the log i *vs.* $1/T$ graphs at −0.4 and −0.7V, respectively. The enthalpy of activation for the CO_2, O_2 reduction process (16 kcal) is somewhat less than direct reduction of O_2 (20 kcal). The enthalpies of activation for the direct reduction of O_2 show only minor fluctuations for the different solvents. The hindrance of the O_2 reduction, thus, may be attributed to an electrode property, such as the postulated oxide

Table II. Heats of activation for O_2 reduction reactions

Electrolysis solvent	Slope × 10^{-3}	$\Delta H_{act.}$ kcal/mole
$CO_2 + \frac{1}{2}O_2 + 2e \rightleftarrows CO_3^=$		
$(Li,Na,K)_2CO_3$	4.0	18 ± 1
Li_2CO_3	3.2	15 ± 1
$LiCl\text{-}Li_2CO_3$	3.5	16 ± 1
$\frac{1}{2}O_2 + 2e \rightleftarrows O^=$		
$(Li,Na,K)_2CO_3$	4.6	21 ± 1
Li_2CO_3	4.1	19 ± 1
$LiCl\text{-}Li_2CO_3$	4.4	20 ± 1

layer, rather than a solvent property. By comparison, the enthalpies of activation, corresponding to CO_2 and O_2 reduction to carbonate show variations with the different solvents; the precision of the values probably does not justify conclusions other than that this process is dependent on the supply of CO_2 to the reaction zone.

Acknowledgments

The authors thank Manfred Breiter for helpful discussions during this work. This work was made possible, in large part, by financial support received from the U. S. Office of Naval Research, Division of Chemistry, and the U. S. Department of Defense (Project Themis: High Energy Power Sources).

Manuscript submitted March 1, 1971; revised manuscript received May 19, 1971.

Any discussion of this paper will appear in a Discussion Section to be published in the June 1972 JOURNAL.

REFERENCES

1. P. K. Lorenz and G. J. Janz, *This Journal*, **116**, 1063 (1969).
2. G. K. Stepanov and A. M. Trunov, *Tr. 6, Ural'sk Fil. Akad. Nauk. (SSSR)*, **3**, 73 (1965); English transl., Consultants Bureau, New York (1966).
3. L. P. Klevtsov, G. G. Arkhyov, and G. K. Stepanov, *Soviet Electrochem.*, **3**, 888 (1967).
4. Y. M. Paskov and G. S. Tyurikov, *ibid.*, **3**, 441 (1967).
5. A. V. Silakov, G. S. Tyurikov, and N. P. Vasilistov, *ibid.*, **1**, 541 (1965).
6. M. Schenke, G. H. J. Broers, and J. A. A. Ketelaar, *This Journal*, **113**, 404 (1966).
7. J. Dubois and R. Buvet, *Bull. Soc. Chim. France*, 2522 (1963).
8. N. Busson, S. Palous, R. Buvet, and J. Millet, *Compt. Rend.*, **260**, 6097 (1965).
9. M. D. Ingram, B. Baron, and G. J. Janz, *Electrochim. Acta*, **11**, 1629 (1966).
10. M. V. Smirnov, L. A. Tsiovkina, and V. A. Oleinikova, *Tr. 6 Ural'sk Fil. Akad. Nauk. (SSSR)*, **3**, 61 (1965); English transl., Consultants Bureau, New York (1966).

Corrosion Inhibition Effects of Small-Sized Polymethyleneimine

Kunitsugu Aramaki*

Department of Engineering, Keio University at Hiyoshi, Yokohama, Japan

ABSTRACT

It has been reported that the inhibition effect of medium-sized polymethyleneimines on the corrosion of iron in HCl solution is notably good, and that this effect is closely related to strain in their rings. Inhibition mechanism of small-sized polymethyleneimines containing 2 to 5 methylene groups was studied. Corrosion rates of pure iron in HCl solution were determined by polarization measurement. Inhibition efficiency of these imines decreases with increase in number of methylene groups. Because of decreasing with increase in the methylene number, the strain in the imine ring seems to be related to the inhibition effectiveness of these imines. From discussions of the corrosion inhibition data together with basic strength, relative molecular area, and molecular structure of these imines, and with infrared spectra of reaction products derived from these imines, it is concluded that the inhibition efficiency of these imines does not depend on the π-electron bonding between metal and nitrogen atom, as shown for medium-sized ones. The high inhibition effect of C_2 and C_3 imine is caused by that of polymer molecules formed by the ring-opening reaction of these imines.

Structural effects of polymethyleneimines,[1] $\overbrace{(CH_2)_n NH}$, containing four to fourteen methylene groups on their corrosion inhibition have been studied by Hackerman and his co-workers (1-3). The inhibition efficiency of medium-sized polymethyleneimines with 9 to 12 methylene groups is markedly high, especially with 10, for iron corrosion in 6.1M HCl solution. This high efficiency is closely related to large strain in ring of these cyclic imines. Because of the large strain in the ring, angle of C-N-C bond in the imine ring is near 120°, which means sp^2 hybrid orbital geometry in nitrogen atom. This geometry provides an unshared π-electron pair on nitrogen atom. It has been concluded that the enhanced inhibition effectiveness of medium-sized polymethyleneimines is caused by donation of the π-electron pair on nitrogen atom to metal (3).

There also is a strain in ring of small-sized polymethyleneimines containing 2 to 4 methylene groups, and the strain of C_2 and C_3 imine is undoubtedly stronger than of C_{10} imine (4). The angle of C-N-C bond in the small-sized ring is, however, smaller than in C_5 imine ring which is free from the strain, while that in the medium-sized one is larger.

If this strong strain in C_2 and C_3 imine ring improves corrosion inhibitor performance of polymethyleneimine, the enhanced efficiency of these cyclic imines would be expected as shown in the case of C_{10} imine. In order to confirm effects of the ring strain on the corrosion inhibition, comparative study on the effi-

* Electrochemical Society Active Member.
Key words: polarization study, polymerized inhibitor, ring strain.
[1] The term "cyclic imine" and "secondary amine" are used for polymethyleneimine and symmetric dialkylamine in this paper as are C_n imine and C_n amine; for example, C_3 imine for trimethyleneimine and C_4 amine for diethylamine.

ciency of polymethyleneimines with 2 to 5 methylene groups and of symmetric secondary amines, $(C_{n/2}H_{n+1})_2NH$, with 2 to 6 carbon atoms was carried out. These differ in structure only in the presence of ring closing bond and of two hydrogen atoms. Ammonia was also tested as both cyclic imine and secondary amine without the methylene group. Some compounds which are to be formed by reactions of these cyclic imines in the corrosion environment were used as inhibitors for investigating details of the inhibition mechanism.

Corrosion rates were determined on pure iron wire in 6.1M HCl solution with and without inhibitors at 30°C by polarization measurement, by volumetric measurement of evolved hydrogen, and by weight loss measurement. Approximate area of metal surface covered by each inhibitor molecule in the adsorbed position was determined with arranged molecular models. Basic strength was also measured to compare the adsorption activities of these inhibitors with each others.

Experimental

Corrosion inhibitors.—Trimethyleneimine (C_3 imine) was synthesized by hydrogenolysis of N,N-trimethylene-*p*-toluenesulfonamide(5) which was prepared by the reaction of *p*-toluenesulfonamide with 1,3-dibromopropane(6). Hydrochloride of 2-chloroethylamine and 3-chloropropylamine, triethylenetetramine, heptaethyleneoctamine, and tripropylenetetramine were also synthesized by the usual procedures. These products were repeatedly purified by distillation or by recrystallization. Absence of impurities was confirmed by infrared spectrometry and by gas chromatography.

Ethyleneimine (C_2 imine), pyrrolidine (C_4 imine), piperidine (C_5 imine), ammonium chloride, dimethylamine hydrochloride, diethylamine hydrochloride, and dipropylamine were obtained as high grade commercial reagents and also purified by distillation or by recrystallization before use.

These inhibitors were dissolved in constant boiling (107°C) 6.1M HCl solution which was prepared by diluting analytical reagent grade solution.

Corrosion rate measurements.—Corrosion rates of pure iron wire (99.89%,[2] Mallinckrodt analytical reagent grade, 0.36 mm diameter) were determined in 6.1M HCl solution with and without inhibitor at 30°C by the three kinds of measurements in the same manner as previously given in detail (2).

The galvanostatic polarization was made by supplying current with a coiled platinum wire, a 90V battery and a variable resistor. Potential of iron electrode in the solution deaerated with nitrogen gas was measured by using a saturated calomel electrode and an electrometer.

The hydrogen evolution measurement was carried out with a gas burette for 4 hr together with the weight loss determination.

Effectively covered area was determined by arranging framework molecular models on a plane in an assumed conformation of the inhibitor molecule adsorbed on the metal by the formation of a metal-nitrogen coordinate bond. Chair type conformation was applied to C_5 imine, and half-chair type to C_4 imine. To keep alkyl groups of secondary amine apart from the plane, the models were arranged in gauche conformation for C-N bonds and in a staggered one for C-C bonds. Details of this measurement have also been shown (2).

The *p*Ka value was determined by titration with $HClO_4$ in 50% diethyleneglycol-water solution at 30°C. The pH of the solution was followed with a glass electrode and a pH meter.

Infrared absorption spectrometric analysis of products by the reaction of C_2 or C_3 imine in 6.1M HCl solution was carried out. The solutions of these imines at 0.1M concentration were dried up at 30°C in a vacuum desiccator containing concentrated sulfuric acid and sodium hydroxide pellets separately. Residual white powder was analyzed on an infrared absorption spectrometer with KBr disk.

[2] C, 0.03%; Mn, 0.04%; P, 0.002%; Si, 0.001%; S, 0.02%.

Results

Corrosion current, i_{corr}, was determined by intersection of extrapolated anodic and cathodic Tafel lines. The data were obtained in the several runs at each of the inhibitor concentrations. They were reproducible within less than ±4% except the values of C_3 imine with deviation of about ±30%.

Corrosion currents for the cyclic imines are shown in Fig. 1 as a function of the inhibitor concentration. For small-sized imines, i_{corr} increases with increase in the number of methylene groups. The polarization curves for these cyclic imines showed that they inhibit both cathodic and anodic reaction of pure iron in the

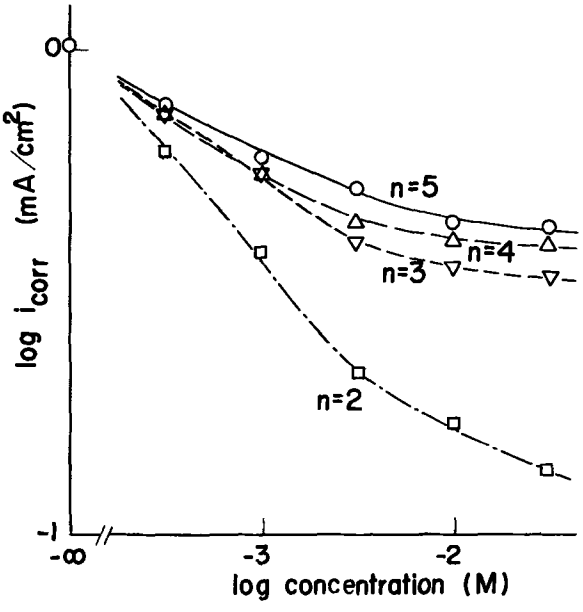

Fig. 1. Effect of cyclic imines on corrosion current; n = number of methylene groups.

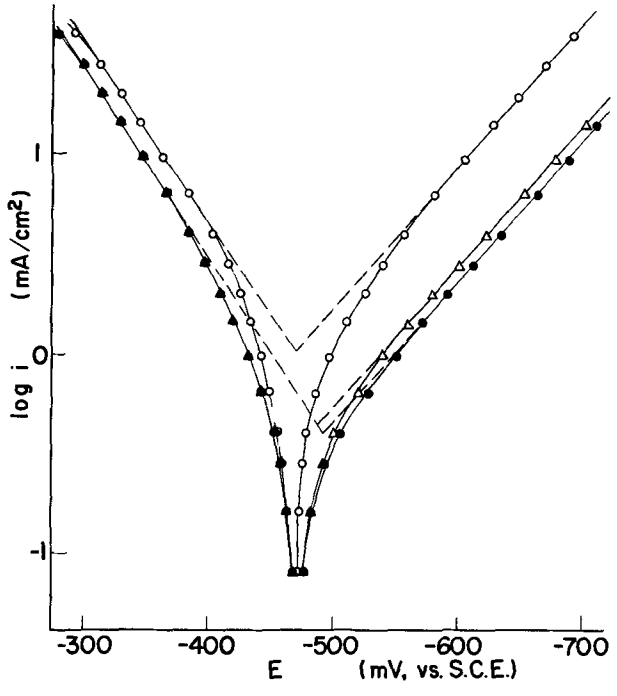

Fig. 2. Polarization curves of pure iron in 6.1M HCl without inhibitors (○), with C_4 imine (●), and with C_5 imine (△) at 0.01M.

acid solution and are more effective on the cathodic reaction than on the anodic one. Some typical curves with and without inhibitors are shown in Fig. 2. Corrosion potential was observed to shift toward less noble potential within 30 mV by the addition of these imines at the concentration given in the experiment.

Corrosion rates of iron wire in 6.1M HCl solution with and without inhibitors at 30°C were also measured by the hydrogen evolution and weight loss technique. Reproducibility of these rates was within ±4% with the exception for C_3 imine. The hydrogen evolution and weight loss data for these inhibitors are not shown here but correspond well to the corrosion rates calculated from the i_{corr} values, as for instance corrosion rates measured by polarization, by hydrogen evolution, and by weight loss are 26,200, 22,800, and 22,000 mdd without inhibitors, and 11,600, 10,700, and 9960 mdd with C_5 imine, respectively.

Corrosion currents for secondary amines are shown in Fig. 3 together with that for ammonia. The data indicate a decrease of i_{corr} with increase of the carbon number.

The i_{corr} values for 2-chloroethylamine, 3-chloropropylamine, triethylenetetramine, heptaethyleneoctamine, and tripropylenetetramine are collectively shown in Fig. 4. The data are plotted *vs.* the concentration of ethyleneimine unit, CH_2CH_2NH for triethylenetetramine and heptaethyleneoctamine, and of propyleneimine unit, $CH_2CH_2CH_2NH$ for tripropylenetetramine. Triethylenetetramine and heptaethyleneoctamine are good inhibitors, being better than 2-chloroethylamine. A high inhibition effectiveness of tripropylenetetramine is also shown in the figure.

The approximate area of metal surface effectively covered per an inhibitor molecule was measured by using molecular models. The ratio of the area of each inhibitor to the C_5 imine area is defined here as the relative molecular area and is shown in Table I. The larger area for C_4 imine than the value for C_5 imine was determined because the ring of C_5 imine in the adsorbed position is perpendicular to metal surface while that of C_4 imine seems to be kept almost parallel to the surface. The values of the relative molecular area for all the other cyclic imines and secondary amines show linear increases with the number of methylene groups.

The basic strengths of these imines and amines are also tabulated in Table I. These values correspond well

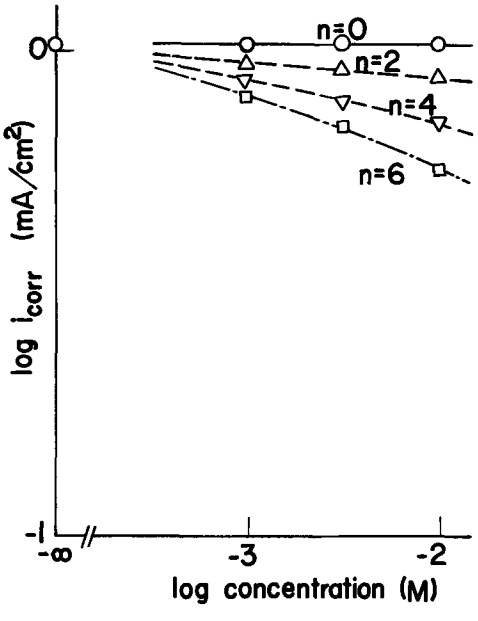

Fig. 3. Effect of secondary amines on corrosion current; n = carbon number.

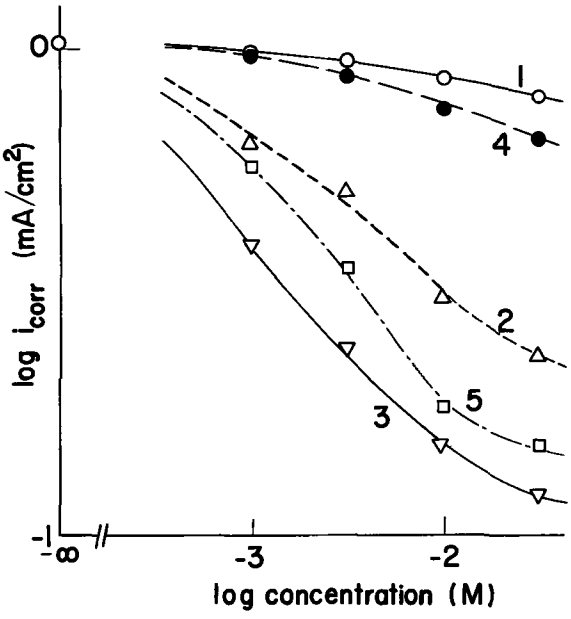

Fig. 4. Effect of C_2 and C_3 imine derivatives on corrosion current; 1: 2-chloroethylamine, 2: triethylenetetramine, 3: heptaethyleneoctamine, 4: 3-chloropropylamine, 5: tripropylenetetramine.

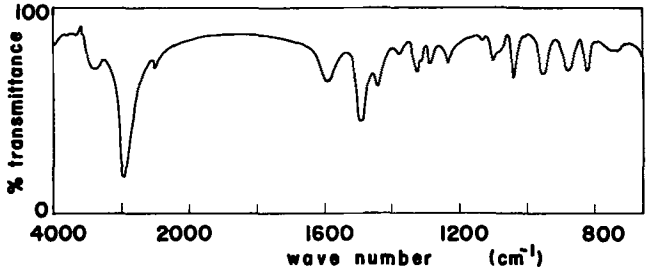

Fig. 5. Infrared spectrum of the reaction product derived from C_2 imine.

to those given previously (7). The pK_a value for the series of cyclic imines decreases with increase in the number of methylene groups with the exception for a notably lower value of C_2 imine. There are little differences in the values for the series of secondary amines.

The infrared absorption spectra of the products derived from C_2 and C_3 imine in the HCl solution are respectively shown in Fig. 5 and Fig. 6. Many frequencies of absorption bands in these spectra were observed to be inconsistent with those of C_2 and C_3 imine.

Discussion

For the series of cyclic imines, the order of inhibition effectiveness is $C_2 > C_3 > C_4 > C_5$, while $C_0 < C_2 < C_4 < C_6$ for the secondary amine series including ammonia as C_0. Because the strain in the small sized imine ring increases with decrease in the carbon number, the inhibition of cyclic imines seems to be related to the

Table I. pK_a value and relative molecular area of cyclic imines and secondary amines

Inhibitor	pKa	Relative molecular area
C_2 imine	8.00	0.74
C_3 imine	11.18	0.94
C_4 imine	11.15	1.06
C_5 imine	10.71	1.00
C_0 amine	9.14	0.37
C_2 amine	10.47	0.68
C_4 amine	10.51	1.01
C_6 amine	10.48	1.43

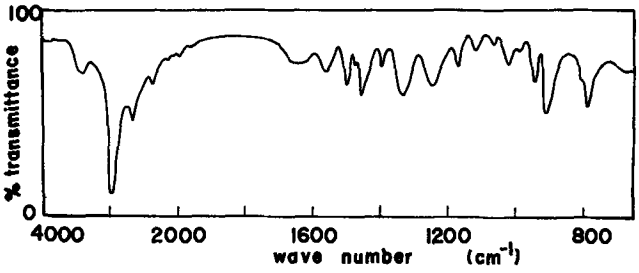

Fig. 6. Infrared spectrum of the reaction product derived from C_3 imine.

strain in their rings. The inhibitor efficiency increases with the ring strain for the series of medium-sized cyclic imines. This relation of the ring strain or the C-N-C bond angle of medium-sized cyclic imines to the inhibition effectiveness has been concluded by discussing i_{corr} data *via* the relative molecular area, the basic strength value, and the molecular structure (2). To elucidate the relation between the inhibitor efficiency and the ring strain of small-sized cyclic imines, discussions in the same manner as reported for medium-sized ones were also tried in this paper.

Figure 7 shows log i_{corr} *vs.* relative molecular area plots for cyclic imines and for secondary amines at 0.01M of the inhibitor concentration. A linear relation is seen in this figure for secondary amines, decreasing log i_{corr} with the increase of relative molecular area. Ammonia is here assumed to be the smallest cyclic imine and to have no strain in the ring. All of secondary amines are also free from the ring strain as well as C_5 imine. A line which is drawn through the points of C_0 imine (ammonia) and C_5 imine is taken to be that for the series of small-sized cyclic imines without the strain in their rings because of the linear relation for secondary amines. Corrosion current deviations of each point for cyclic imines from this line were measured on the figure and plotted against the pK_a value in Fig. 8. The deviation, Δ log i_{corr}, means the decrease of log i_{corr} due to the ring strain. Because of a linear relation of Δ log i_{corr} to the basic strength for medium-sized cyclic imines, as shown in Fig. 8, it has been concluded that the ring strain plays an important role in the imine inhibition (2). As can be seen in the figure, however, this relation for small-

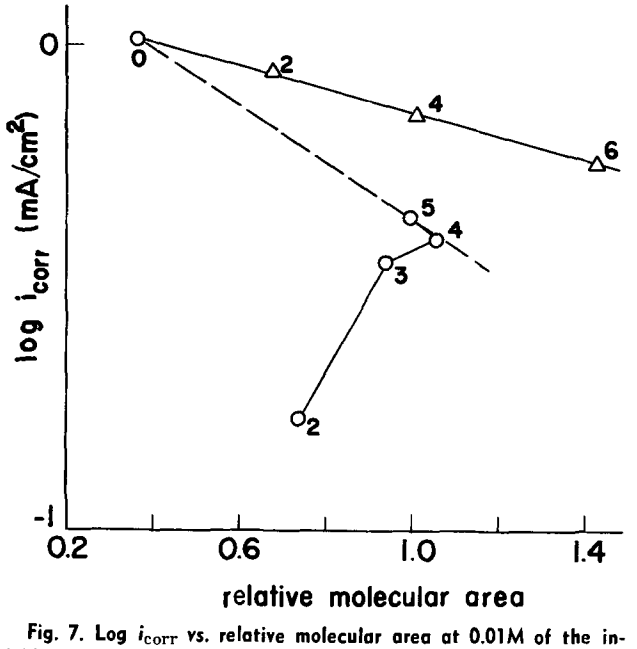

Fig. 7. Log i_{corr} vs. relative molecular area at 0.01M of the inhibitor concentration; cyclic imine ○, secondary amine △. Number indicates the carbon number.

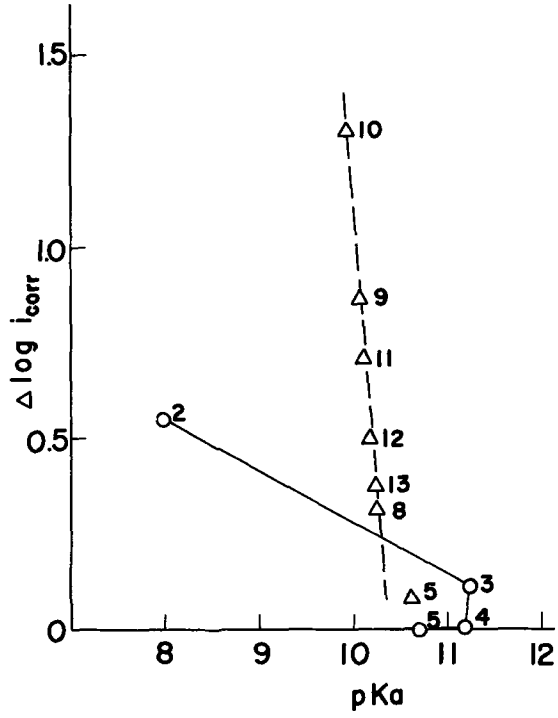

Fig. 8. Relation of pK_a to Δ log i_{corr} for the series of medium-sized cyclic imines △ and of small-sized cyclic imines ○. Number indicates the carbon number.

sized cyclic imines disagrees with that for medium-sized ones. This result suggests that effect of the ring strain or the C-N-C bond angle of small-sized imine on its corrosion inhibition is different from that of medium-sized one.

In consideration of rate constants and equilibrium constants for reactions of cyclic compounds, it is presumed that there is no possibility of unshared π-electrons on nitrogen atom of cyclic imines with less than five methylene groups except C_4 imine (8). In the small rings of C_2 and C_3 imine, bond angle strain is large and has a predominant effect. Since the C-N-C bond angles in C_2 and C_3 imine ring are of orders of 60° and 90°, sp^3 hybrid orbital geometry of nitrogen atom (C-N-C angle 109°28′) is favored over sp^2 geometry (C-N-C angle 120°), which provides unshared π-electrons on the nitrogen atom. Therefore, there can be no π-electron pair on the nitrogen atom in C_2 and C_3 imine ring.

In common rings of C_4 and C_5 imine, bond opposition strain caused by repulsion between hydrogen atoms seems to be of importance. The C_5 imine ring in which hydrogen atoms are of staggered conformation remains sp^3 hybridization of nitrogen atom. However, there seems to be the bond opposition strain in the ring of C_4 imine, because of eclipsed conformation of hydrogen atoms. To release this strain, the sp^3 geometry of nitrogen atom in C_4 imine may change to the sp^2 hybridization, since hydrogen atoms around the nitrogen atom are the stable staggered conformation in the latter hybridization. The effect of unshared π-electrons on the inhibitor performance might thus be observed only for C_4 imine.

According to the above discussion of the bond opposition strain in the imine ring, the sp^3 geometry of the nitrogen atom in pyrrolidinium cation is believed to be less stable than that in piperidinium cation. The presence of the sp^2 nitrogen geometry should, therefore, result in a weaker basic strength of C_4 imine than of C_5 imine. The pK_a value of C_4 imine, however, is larger as shown in Table I. A similar evidence has been indicated in dissociation constant data of C_4 and C_5 imine-trimethylborane complex (9). From these

facts the effect of sp^2 geometry on the C_4 imine inhibition is not taken to be predominant over that of the sp^3 geometry.

The anodic polarization current of iron electrode in HCl solution is not notably decreased by the addition of medium-sized cyclic imines, as has been shown for C_9 imine (1). This can be explained by means of chemical adsorption of these imines through formation of coordinate bond with their π-electrons to the anodic metal surface. If C_4 imine is adsorbed on iron surface via π-electron bonding as well as medium-sized imines, greater effect on anodic reaction than on cathodic reaction should be observed. The experimental results in Fig. 2 show that difference in i_{corr} values between C_4 and C_5 imine rather depends on that in cathodic polarization curves. This difference in cathodic polarization is probably caused by the enhanced basic strength of C_4 imine. Since the inhibition effect of C_4 imine on the anodic reaction is not significant, it is concluded that the π-electron bonding between metal and nitrogen atom of C_4 imine is not important to its inhibition effectiveness.

It cannot be explained in terms of the relative molecular area and pK_a values that C_2 and C_3 imine are better inhibitors than C_4 and C_5 imine. As mentioned above, the C_2 and C_3 imine rings are highly strained but have nothing to do with the π-electron bonding adsorption on metal. Ring-opening reactions of these imines due to the high ring strain are possible in the presence of proton (10). For example, C_3 imine may be decomposed in the presence of hydrochloric acid, forming 3-chloropropylamine

$$\overbrace{(CH_2)_3\,NH}^{\text{C}_3\text{ imine}} + HCl \rightarrow ClCH_2CH_2CH_2NH_2$$

or polypropylenepolyamine

$$m\ \overbrace{(CH_2)_3\,NH}^{\text{C}_3\text{ imine}} \rightarrow (CH_2CH_2CH_2NH)_m$$

The infrared absorption spectrum of the product by the reaction of C_3 imine in 6.1M HCl solution suggested the ring-opening reaction, because C-H bending band of C_3 imine at 1340 cm^{-1} disappeared in the spectrum. As C-Cl stretching band was observed at about 780 cm^{-1}, the formation of 3-chloropropylamine is presumable. Agreement of absorption bands for C_3 imine product with those for hydrochloride of polypropylenepolyamine such as tripropylenetetramine was also found in this spectrum. It can be concluded from these data that C_3 imine is reacted with hydrochloric acid, resulting in forming mixtures of 3-chloropropylamine and polypropylenepolyamine. Although the presence of corroding iron in the acid solution is not taken into account in this experiment, these ring-opened products of C_3 imine are believed to act as inhibitors of iron corrosion.

On the basis of this result, the corrosion inhibition effects of some compounds which are possibly derived from C_3 imine were determined. The i_{corr} value of tripropylenetetramine, one of polypropylenepolyamine is lower than of C_3 imine, while that of 3-chloropropylamine is higher as shown in Fig. 1 and Fig. 4. These data indicate that the inhibition effect of chlorinated amine is not important to the inhibitor performance of C_3 imine. Again, C_3 imine is not adsorbed on iron surface *via* π-electron bonding. In fact, this imine rather decreases the cathodic polarization current, the result being analogous to that of tripropylenetetramine. The inhibition efficiency of C_3 imine is thus concluded to depend on the action of polymer molecules. The large deviation of i_{corr} values for C_3 imine may be related to the selective formation of polymerized or chlorinated product by the reaction of C_3 imine in the HCl solution. The formation of polymer inhibitor gives rise to a good inhibition effectiveness, whereas that of chlorinated amine decreases the effect. No adsorption mechanism of polymer inhibitor together with chlorinated one on iron surface was further amplified.

The C_2 imine ring is also easily opened in the HCl solution, because of the high strain in the ring, resulting in the formation of chloroethylamine or polyethylenepolyamine. For this imine, however, the polymerization reaction may be predominant over the addition reaction of hydrochloride. The infrared spectrum of the product prepared by the reaction of C_2 imine in the HCl solution, shown in Fig. 5, is rather similar to that of polyethylenepolyamine hydrochloride, and no strong absorption band of C-Cl stretching frequency appears at 650-800 cm^{-1} region.

The inhibition efficiency of 2-chloroethylamine is too low to keep the sufficient inhibitor performance of C_2 imine. The polymer molecules are effective inhibitors for iron corrosion in the HCl solution. It is reasonable, therefore, that the high inhibition effectiveness of C_2 imine is caused by the inhibitor action of the polymer molecules formed by the reaction of C_2 imine in the solution.

Many molecular structures of the reaction products can be supposed in such the polymerization of C_2 imine. Two straight-chained polymers were chosen as typical ones in this study. Ring-closing polymerization is possible to result in forming rings containing more than 6 members, as

$$m\ \overbrace{(CH_2)_2\,NH}^{\text{C}_2\text{ imine}} \rightarrow \overbrace{(CH_2CH_2NH)}^{\text{polyethylenepolyamine}}_m$$

The formation of medium sized ring by means of the polymerization of C_2 imine cannot be expected, because large strain in this ring may interfere with the ring-closing reaction. Six-membered polymer is not such a good inhibitor as C_2 imine because i_{corr} obtained in an additional experiment for piperazine (six-membered polymer) at 0.01M is 0.412 mA/cm^2.

Conclusion

From these discussions, it is concluded that the inhibition effectiveness of C_2 and C_3 imine for the iron corrosion in the HCl solution depend on the formation of polymer molecules by the ring-opening reactions due to the high strain in their rings. These polymers probably including straight-chain and large ring compounds act as good corrosion inhibitors. This high effectiveness may arise from a markedly enhanced stability of net total adsorption bonding in the polymer molecules, as interpreted by Annand, Hurd, and Hackerman (11).

C_4 and C_5 imine with little strain in their rings are less effective on the inhibition of iron corrosion. These common-sized cyclic imines seem to be mainly adsorbed on cathodic area of metal surface because of the high stability of their ammonium cations. There seems to be no strong adsorption of these imines on metal by virtue of the π-electron bonding. Further studies on the common-sized cyclic imines including precise discussion of polarization curves, nitrogen conformation, and steric hindrance will be needed for elucidating the inhibitor mechanism.

Acknowledgments

The author wishes to express an appreciation to Dr. N. Hackerman of Rice University for his advice on the discussion of this paper.

Manuscript submitted Jan. 28, 1971; revised manuscript received *ca.* June 7, 1971.

Any discussion of this paper will appear in a Discussion Section to be published in the June 1972 JOURNAL.

REFERENCES

1. N. Hackerman, R. M. Hurd, and R. R. Annand, *Corrosion*, **18**, 37t (1962).
2. K. Aramaki and N. Hackerman, *This Journal*, **115**, 1007 (1968).
3. K. Aramaki and N. Hackerman, *ibid.*, **116**, 568 (1969).
4. S. Kaarsemaker and J. Coops, *Rec. Trav. Chim.*, **71**, 261 (1952); J. Coops, H. van Kamp, W. A. Lam-

bregets, J. Visser, and H. Dekker, *ibid.*, **79**, 1226 (1960).
5. C. C. Howard and W. Marckwald, *Ber.*, **32**, 2031 (1899).
6. O. Manasse, *ibid.*, **31**, 3264 (1898).
7. S. Searles, M. Tamres, F. Block, and L. Quarterman, *J. Am. Chem. Soc.*, **78**, 4917 (1956).
8. E. L. Eliel, "Stereochemistry of Carbon Compounds," p. 256, McGraw-Hill Book Co., New York (1962).
9. H. C. Brown and M. Gerstein, *J. Am. Chem. Soc.*, **72**, 2926 (1950).
10. G. D. Jones, *J. Org. Chem.*, **9**, 484 (1944).
11. R. R. Annand, R. M. Hurd, and N. Hackerman, *This Journal*, **112**, 144 (1965).

An Ellipsometric Study of Chromium Passivation

M. A. Genshaw*,[1] and R. S. Sirohi[2]

The Electrochemistry Laboratory, The University of Pennsylvania, Philadelphia, Pennsylvania 19104

ABSTRACT

In situ ellipsometry has been combined with electrochemical measurements to gain insight into the mechanism of passivation of chromium in pH 1.7 K_2SO_4 solution. At −410 mV *vs.* NHE a region of active dissolution at an apparently oxide-free surface was observed. With an anodic potential step to −360 mV, passivation occurs with growth of less than 1Å of oxide film. This film is thicker at more anodic potentials and probably consists of Cr_2O_3. The mechanism of passivation most consistent with the experimental observations is that of simultaneous oxide formation and metal dissolution, with passivation resulting from formation of a monolayer of film.

Chromium exhibits a very low dissolution current when passive and transmits this property to its alloys. Accordingly, numerous investigations into the cause of passivation of chromium have been undertaken. An excellent survey of this work is given by Gmelin (1) where the differing views are well summarized. A number of recent studies concerned with passivation of chromium as well as chromium alloys have been reported (2-20).

In this work, ellipsometry has been applied in conjunction with electrochemical measurements to give further insight into the nature and thickness of the film formed during the passivation process. In a very early application of ellipsometry, Micheli (21) could not detect any difference between active and passive chromium surfaces and concluded that no film was present. More recently, Andreeva (15) using *in situ* ellipsometry has observed increased thicknesses of the film at chromium with application of either cathodic or anodic polarization.

Experimental

Ellipsometer.—An L119 Gaertner ellipsometer with a horizontal plane of incidence was used in this study. The angle of incidence was 71.7° (65.2° outside the cell). The quarter wave plate was kept fixed at 45° orientation and was positioned between polarizer and electrochemical cell. A 2W tungsten arc lamp (Sylvania TC 2) operated from a well-filtered 90 mA d-c power supply was used as a source of light. The collimation was effected by a projection lens, the deviation from true collimation is expected to be less than 0.003 radian. A 3 mm aperture at the test surface was used. A photo transistor (Motorola MRD 300) with a current to voltage transducer was used as a light detector. The voltage output could either be read on a Keithley electrometer or be fed directly to a recorder. The highly stable (0.1% fluctuation) tungsten lamp along with the phototransistor makes an ideal combination for the study of transients. However, the phototransistor suffers from a disadvantage as its dark current is strongly affected by the variation in the temperature of the surrounding, and thus should not be used for long transients if the temperature is not controlled. An interference filter (50Å band width around 5500Å) was used just before the detector. The ellipsometer rested on a 1 in. thick aluminum plate which was supported by a shock absorber, to minimize the effects of outside vibration.

Cell.—The air-tight cell was made of Teflon. For the passage of light, ⅛ in. thick windows of synthetic quartz ($n = 1.460$ at $\lambda = 5500$Å) were held tightly against Viton o-rings, facing each other and perpendicular to the reflecting surface. Thus, the path of light through the windows was oblique. Connections to the cell were made through Beckman fittings. Solution could be transported to the cell from a reservoir of circulating, pre-electrolyzed nitrogen-saturated solution under nitrogen atmosphere. Electrolyte could be drained and the cell washed with conductivity water or electrolyte without distributing the optical alignment.

Electrodes.—A zone-refined polycrystalline chromium loaf (purchased from Material Research Corporation) was machined to a rod of cross-section 1.63 cm^2. One end of it was ground and polished flat with different grades of emery and γ-alumina. At the other end, a stainless steel screw was used to make connection with the external circuit. The rod was fitted in a tapered threaded Teflon piece with a Viton o-ring seal. This rod could be screwed into the cell so that the reflecting face was in the vertical plane.

A smooth platinum foil electrode sealed in a glass tube and separated from the solution by a fine frit was used as a counterelectrode. A saturated calomel electrode was used as a reference electrode, and all potentials are reported with respect to normal hydrogen electrode. The calomel electrode was positioned several millimeters diagonally above the test electrode. The experimentally determined *IR* drop at the highest current used was less than 10 mV.

Electrolyte.—All the solutions were made from conductivity water. The pH 1.7 H_2SO_4 + 0.5M K_2SO_4 solution was pre-electrolyzed at 1.35V between platinized platinum gauze in an atmosphere of nitrogen for at least 24 hr before using it.

Method of measurement.—Optical measurements were made by the method of equal intensity settings as described by Archer (22) The Δ and ψ values are

* Electrochemical Society Active Member.
[1] Present address: Ames Company, Div. Miles Laboratories, Inc., Elkhart, Indiana 46514.
[2] Present address: Department of Mechanical Engineering, Indian Institute of Technology, Madras 36, India.
Key words: ellipsometry, passivity, chromium, film, thin film.

corrected for the oblique traversal of rays through the quartz windows (23). Details of the ellipsometric technique and method of interpretation are given in the literature (22, 24-28). Transient measurements were made by measurements of intensity using an improved version (29) of the technique described earlier (28, 30) either applying potential steps or switching from a constant potential to constant current. Measurements were also made using linear potential sweep (31). Also measurements were made by potentiostating the electrode at various potentials and measuring Δ and ψ values. The current is also measured simultaneously by a Keithley electrometer.

In steady-state measurements Δ is measurable to 0.02° and ψ to 0.01°. In the transient measurements the changes in Δ and ψ are measurable to better than ±0.05°. The reproducibility of the reference values of Δ and ψ are within a range of 5° in Δ and 7° in ψ observed which are probably due to variations in surface roughness and orientation.

Results and Discussion

Current-potential relation.—Measurements are conducted potentiostatically with a freshly polished surface, which is initially passive as no dissolution occurs if it is potentiostated at −400 mV, by varying the potential in steps toward anodic values beginning at −760 mV. The variation of current with potential is shown in Fig. 1. As the potential is made more anodic, the rate of hydrogen evolution decreases and a region of active dissolution commences at −500 mV. The anodic current decreases sharply at ~ −385 mV, and a cathodic region is then observed. Over the range −160 to +840 mV the current density is less than 1 μA/cm^2.

The cathodic region between −360 and −60 mV is probably due to hydrogen evolution at the passive surface, as has been suggested by other workers (2, 9).

The bare surface parameters.—Since the hydrogen evolution in the experiment described above produced bubbles which prevented ellipsometric measurements, a special procedure was adapted to produce an active, bubble-free surface. The electrode was potentiostated for about 1 sec at −760 mV (19) and then held at −410 mV. Ellipsometric intensity measurements showed an increase in Δ while the electrode was at −760 mV, but no steady value is obtained before bubbles appear (after several seconds). At −410 mV after the brief reduction the dissolution current increased slowly to a constant value while ellipsometrically a large decrease in Δ occurred followed by an increase with a final value which is 3 to 4 degrees higher than that of the freshly polished electrode. During the same treatment ψ decreases 0.1 to 0.2 degrees.

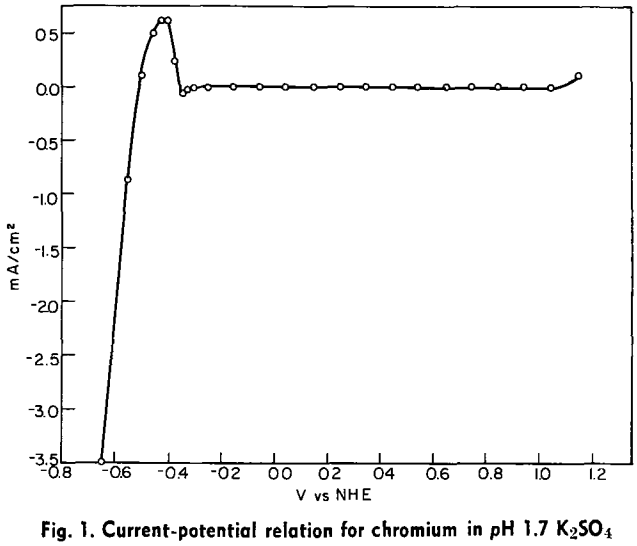

Fig. 1. Current-potential relation for chromium in pH 1.7 K_2SO_4

Table I. Optical parameters reported for chromium

Reference	n	k	Δ	ψ	Comment
Micheli (21)	2.14	2.88	86.90	28.35	
Churchill (32)	3.14	4.17	115.6	28.3	In air with oxide.
Hill and Weaver (33)	0.6	1.32	50.33	39.59	1500Å film
Kostyuk and Shklyareuskii (34)	2.0	2.7	82.56	28.71	λ = 5500, 45°C
	2.5	3.9	103.41	29.96	λ = 5500, 400°C
McCrackin *et al.* (35)	3.235	4.426	114.36	28.87	λ = 5461
	2.95	4.258	110.61	29.28	
This study	4.167	5.186	126.35	29.02	

An increase in Δ is characteristic either of the formation of a film with a refractive index less than that of the medium (solution) or the removal of a film of refractive index higher than that of the medium. Since the formation of a thin stable film of low refractive index, *e.g.* a gas, is unlikely, the increase in Δ was attributed to the removal of the passive film by reduction at −760 mV (19) and dissolution at −410 mV. The surface remained bright during the active dissolution. It should be noted that the increase in Δ (equivalent to 9-12Å as calculated for Cr_2O_3 with $n = 2.55$) corresponds well to the dissolution of the 10-15Å film reported to form on chromium in air (15, 32) and that the experimental value of Δ is higher, indicative of a cleaner surface, than that calculated for our conditions from data reported by other workers (Table I).

A calculation of the effect of the concentration gradient of Cr^{+++} in the solution shows that the change in refractive index near the surface would be about 0.0002 units, which should be insignificant (a gradient of 0.2°C would produce an equal change). In addition, stirring, which would affect the concentration gradient, has no effect on the measured Δ.

The surface state attained at −410 mV was used as an optical and electrochemical reference state for the transient measurements and all optical calculations are based on the assumption that no film is present at −410 mV. It is not possible to prove that the surface is indeed bare at this potential although the relatively free dissolution makes the presence of a film approaching a monolayer coverage unlikely.

The film present.—The transient (potential step, galvanostatic, and potential sweep) measurements give similar linear Δ-ψ plots which have an average slope $d\psi/d\Delta$ of −0.100 ± 0.002. Using the exact ellipsometry calculations for transparent film (*e.g.* imaginary part of refractive index is zero), a value of 2.54 ± 0.04 is obtained for the refractive index. This value is very close to 2.55 reported for Cr_2O_3 (36). Thus, it appears probable that the film is Cr_2O_3, as has been suggested by other workers (8, 9, 15, 37-39). From calculations using the exact ellipsometry equations for nontransparent films, the film must have the real part of its refractive index equal to or lower than 2.54. For refractive indices lower than 2.54 to fit the experimental data, the films must be light-absorbing.

As an approach toward limiting the number of fits to the optical data for nontransparent films, coulometric data is considered (Fig. 2). This data was taken from the anodic transients in the potential region in which, in the steady state, the metal is passive and, in the transients at constant current, a linear change in delta with time was observed. No correction for possible dissolution has been made with the presumption that the species produced does not dissolve at a significant rate. From these measurements, a change of 1.44 degrees in delta was found to correspond to a charge passed of one millicoulomb. By assuming a roughness factor (R) and a bulk density (assumed to be that of the bulk material with no correction for surface effects) one can calculate a relation between thickness and delta and from this, using the ellipsom-

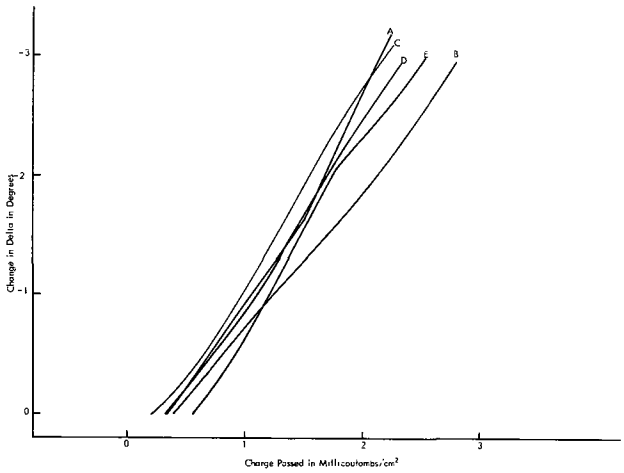

Fig. 2. The change of Δ from tre initial value (δΔ) as a function of change in galvanostatic oxidation transients. Curve A:2; B:4; C:6; D:8; and E:10 mA/cm².

etry equations, the film optical constants. As the roughness factor is an adjustable parameter, fits can be obtained for almost any desired value of the real part of the refractive index (n).

With roughness factor R, $R = 1.7$, and the bulk density of 5.21 g/cc [Ref. (36)] for Cr_2O_3, a refractive index of ~4.2 is required to fit the coulometric thickness and optical thickness (Δ). However, the $d\psi/d\Delta$ slope for this value of n is more positive than −0.01 which is incompatible with the observed −0.10. Thus, a fit is not possible.

A calculation for CrOOH using $R = 1.7$, $d = 4.11$ g/cc [Ref. (40)] requires n to be 2.90 which is again incompatible with the optical measurements [$n = 2.0 \pm 0.1$, Ref. (35)].

A fit for either Cr_2O_3 or CrOOH may be produced by varying the roughness factor taken. For Cr_2O_3 a fit at $n = 2.55$ exists if a roughness factor of 1.1 is taken; for CrOOH fits exist at $n = 2.55$ with $R = 1.5$, and at $n = 2.0 - 0.005\ i$ with $R = 1.15$. Thus, it is apparent that coulometry does not lead to a unique identification of the passive film. However, it is not possible to obtain fits for $Cr(OH)_3$ [$n = 1.620$, Ref. (40)] [$d = 3.12$ g/cc, Ref. (40)] and CrO_2 [$d = 4.88$ g/cc, Ref. (40)] with any value of roughness factor greater than 1.0, so that they cannot be the passive film, a conclusion which is supported by the high solubility of $Cr(OH)_3$, [Ref. (40)] and the reversible potential for formation of CrO_2 being very anodic to the potential of passivation (9, 41).

We conclude that the passive film at chromium is most probably Cr_2O_3, as supported by numerous other workers on passivity and a consistency with the ellipsometric measurements.

The film thickness required for passivation.—To determine the minimum film thickness required for passivation, potential step measurements, starting from −410 mV, were undertaken. The initial current at −410 mV was 1.0×10^{-3} A/cm². With a step to −385 mV the current initially increased, then during a period of 2 min decreased to 2×10^{-4} A/cm². The change in Δ at 2 min was 0.1°. At longer times the current remained constant while the film thickness increased substantially. Similarly, with a step from −410 to −360 mV, the current after 2 min reached a cathodic value of 4×10^{-5} A/cm² with a change in Δ of 0.25°. The onset of the cathodic current requires the virtual cessation of the anodic reaction and that passivation has occurred. The film thickness change (for $n = 2.54$) for a 0.25° change in Δ is 0.8Å. (For n of 2.0 the thickness would be 0.7Å, for $n = 3.0$ 1.0Å). In terms of charge this is equivalent to 170 microcoulomb/cm² (using $R = 1$). Thus, it is apparent that a film of the order of a monolayer is sufficient to cause passivation of chromium.

A very similar result has been obtained by Frankenthal (20) using Fe-24% Cr in 2N H_2SO_4. He reports a film thickness of 360 microcoulomb/cm² determined by coulometry at the potential of maximum cathodic current.

The role of dissolution in passivation.—A mechanism which has been proposed for film formation at several metals is the dissolution-precipitation mechanism (27, 42). This mechanism suggests that dissolution proceeds freely until a saturation concentration of ions is reached at the surface whereupon film formation proceeds. Since the film formed has been shown to probably contain Cr^{+++}, the saturation concentration of Cr^{3+} may readily be calculated from the solubility product data (41, 43) and is 0.3-0.9 moles/liter for the least soluble form of Cr_2O_3. A plot of $i\tau^{1/2}$ *vs.* i, where τ is the time of initial film formation as determined from the time at which the first measurable change in Δ occurred is linear as predicted from theory (44) (Fig. 3). It should be noted that the starting condition with chromium actively dissolving is not that required for the theoretical derivations (no dissolution before the current is applied). Applying the theory and using the slope and intercept of the $i\tau^{1/2}$ *vs.* i plot to calculate the saturation solubility of the precipitating species, a value of $\sim 7 \times 10^{-4}$ moles/liter is obtained. This is substantially lower than the saturation solubility of Cr^{3+} with respect to Cr_2O_3 (41). The presence of the initial concentration gradient of 0.01 M/liter would, as a first approximation, make the precipitation due to a change in concentration of 7×10^{-4} M/liter or about 10%. It seems unlikely that such a small change would be sufficiently reproducible to permit measurements or the attainment of a stable measurement of active dissolution. Thus, we conclude that a dissolution precipitation mechanism is not followed in chromium passivation.

The experimental data is also consistent with a constant value of $i\tau$ of 340 ± 80 microcoulomb/cm² for the amount of chromium dissolved during galvanostatic passivation transients over a current range 1-25 mA/cm² as obtained from the extrapolation of the linear Δ-time region of the transient to Δ equals zero (Fig. 2). This extrapolation presumes that the charge not utilized in film formation corresponds to chromium dissolved in the solution.

A second mechanism of film formation which has been proposed (45-47) is the occurrence of dissolution and film formation in parallel paths. In this type mechanism, the dissolution takes place at the surface not covered by the film. Although numerical relations between dissolution currents and film coverage have

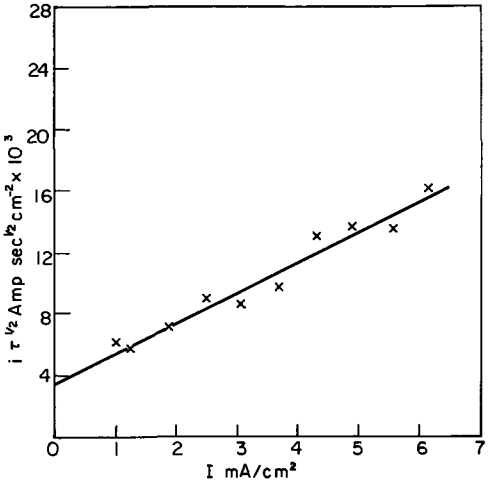

Fig. 3. Plot of $i\tau^{1/2}$ *vs.* i for initial film formation during galvanostatic passivation of chromium.

been proposed for the case of potentiostatic measurements (46), in the case of chromium a quantitative correlation is difficult because the fairly rapid dissolution process can lead to undercutting of the film and consequent exposure of fresh surface.

Qualitatively, this mechanism would predict that a significant amount of dissolution would occur during the passivation. For the case of equal rates of dissolution and oxide formation, somewhat less than a monolayer of chromium would dissolve during the formation of a monolayer of oxide. Since the rate of dissolution is experimentally much faster than the rate of oxide formation, even though less than a monolayer of oxide is sufficient for passivation, it is not unreasonable that the amount of dissolution experimentally observed (340 microcoulomb/cm^2) could take place.

The mechanism suggested by Frankenthal (20) for the passivation of iron-chromium alloys by the blockage of kink sites does not seem plausible as passivation should occur at coverages of the order of 0.01% when all kink sites are blocked. As passivation is observed at about 30% coverage, this mechanism does not seem likely.

Other mechanisms involving film transformation apparently do not occur as no evidence for the formation of more than one film was found.

Thus, we conclude that the most probable mechanism for chromium passivation is that of oxide formation and metal dissolution reactions occurring simultaneously, with passivation resulting when a monolayer (or possibly less) of oxide covers the surface.

The mechanism of film growth.—As apparent from the kinetic plots (Fig. 4 and 5), the kinetics of film growth do not obey either the direct or the inverse logarithmic law at all potentials. Similarly, any power ($t^{1/2}$, *etc.*) law is also not obeyed. This is not surprising when one considers that the film thickness varies from zero to a few layers and most mechanisms proposed apply to continuous films of sufficient thickness so that the interfaces and bulk processes may be differentiated.

When insufficient film is present to cause passivation ($-410 < V < -360$), the film growth continues

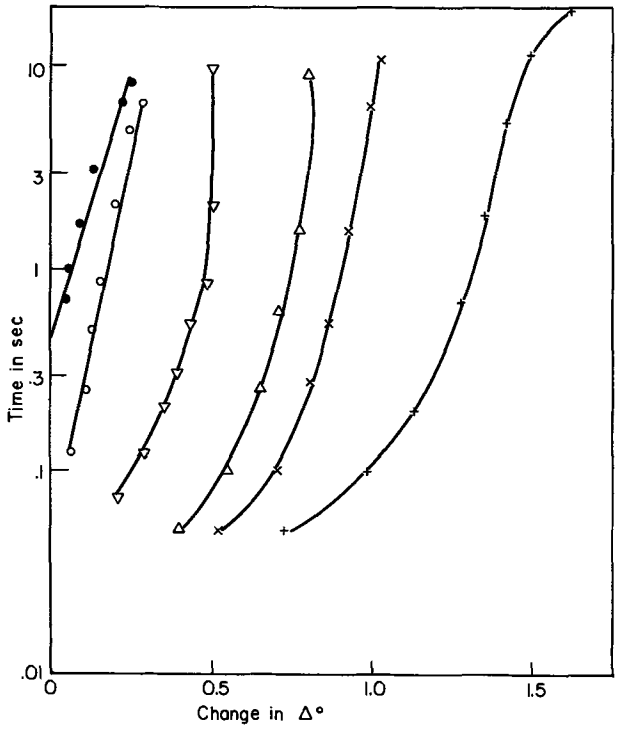

Fig. 4. Δ-log time relation for potentiostatic oxidation from −410 mV to: ● −360, ○ −260, ▽ −160, △ +40, x +140, + +240 mV.

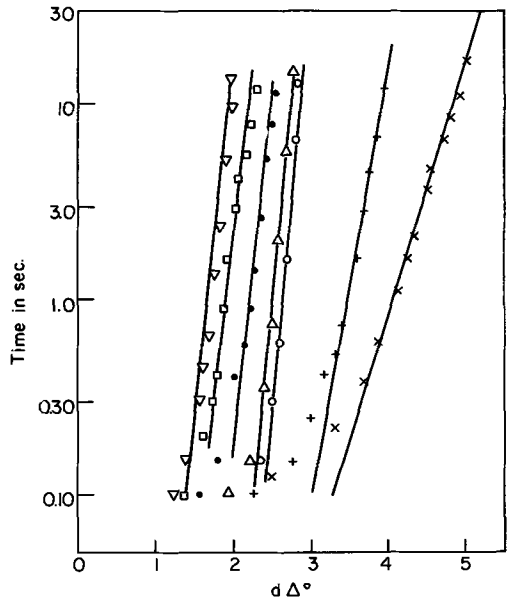

Fig. 5. Δ-log time relation for potentiostatic oxidation from −410 mV to: ▽ 340, □ 440, ●540, △ 740, ○ 840, + 940, X 1040 mV.

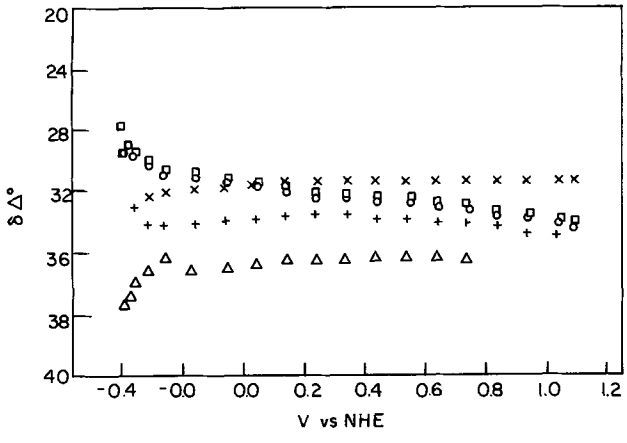

Fig. 6. δΔ (the change in Δ from the initial value) *vs.* potential in potential staircase measurements (5 experiments).

for a relatively long time (at least 15 min) and a thick film is formed which from Fig. 6 may be estimated to be ~100-120Å. Since simultaneous dissolution is occurring, the film present must not be a protective passive film. It would appear likely that it must be a porous film or incomplete monolayer which permits active dissolution of the metal below. At more anodic potentials, passivation occurs with the thick film remaining.

The thicker films present at more anodic potentials show growth kinetics which occur over decades of time but fit neither the direct nor inverse logarithmic laws.

The Difference between Potential Step, Linear Potential Sweep, Galvanostatic and Potential Staircase Results

A comparison between galvanostatic, potential step, and potential sweep measurements of Δ *vs.* potential is made in Fig. 7 and 8. It is apparent that the results are quite similar in trend when the sweep rate, current, or time are chosen to give approximately equivalent conditions.

With slow potential sweep measurements, Fig. 9, the changes in Δ become substantially greater with the major change occurring in the region −400 to −200 mV and nearly parallel curves at more anodic potentials.

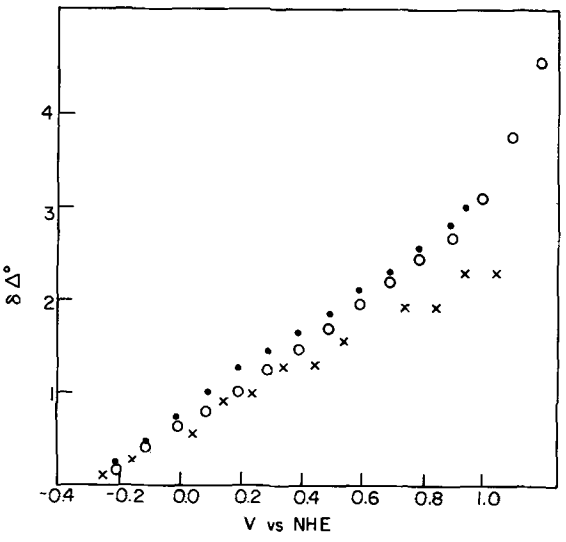

Fig. 7. Dependence of $\delta\Delta$ on potential. ● potential sweep at 2 V/sec, ○ galvanostatic at 2.5 mA/cm^2, X potential step at 0.1 sec.

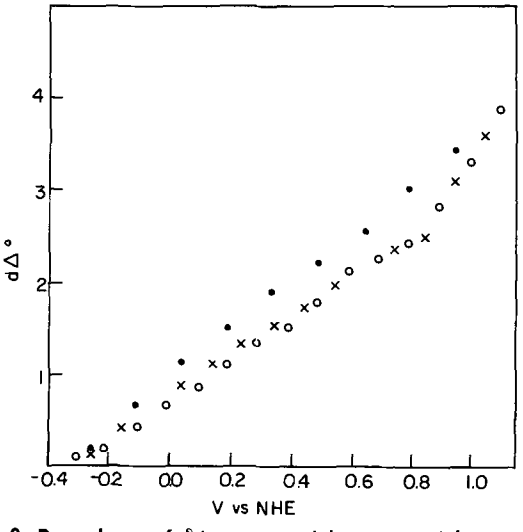

Fig. 8. Dependence of $\delta\Delta$ on potential. ● potential sweep 0.75 V/sec, ○ galvanostatic at 1 mA/cm^2, X potential step at 0.3 sec.

In the potential staircase measurements which are equivalent to a very slow potential sweep, this trend is even more pronounced, Fig. 6, with nearly all the change in Δ occurring in the potential region -410 to -380 mV. The changes in Δ in the potential staircase measurements are quite reproducible. The changes in ψ, Fig. 10, are much less reproducible in magnitude although similar in trend. Such a large variation in ψ would indicate that the film forms vary in their optical properties. Indeed, these films are distinctly different from those formed in the transient measurements in that they are visually apparent as a white appearance of the electrode. As the films should not be visually resolvable since the change in Δ indicates that they are 100-120Å thick, they must manifest themselves through scattering of light. This can occur if the simultaneous dissolution and film formation processes lead to the formation of inclusions of metal in the film as has been suggested for nickel (48). Such heterogenous films have been treated theoretically by Maxwell Garnett (49) and the calculations lead to values of optical constants which are not incompatible with those required to fit the experimental values of Δ and ψ.

Acknowledgment

We wish to thank the Office of Saline Water, U. S. Department of the Interior, for their support of this work under Grant No. 14-01-0001-1320. We also wish to thank Professor J. O'M. Bockris for encouraging us in this work.

Manuscript submitted Dec. 8, 1969; revised manuscript received ca. March 18, 1971. This was Paper 417 presented at the Montreal Meeting of the Society, Oct. 6-11, 1968.

Any discussion of this paper will appear in a Discussion Section to be published in the June 1972 JOURNAL.

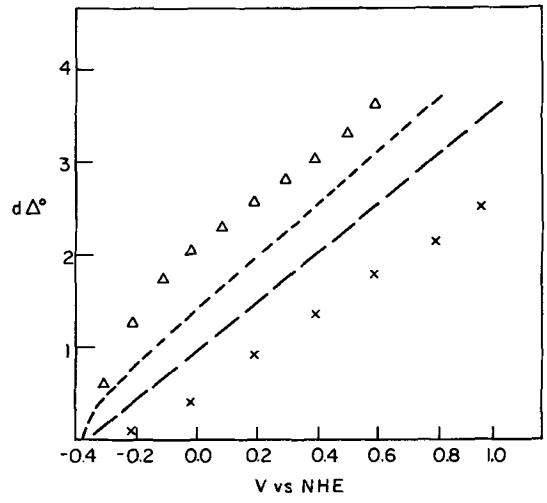

Fig. 9. Dependence of $\delta\Delta$ on potential in potential sweep measurements. △ 0.01, - - - 0.05, — — 0.5, x 5 V/sec.

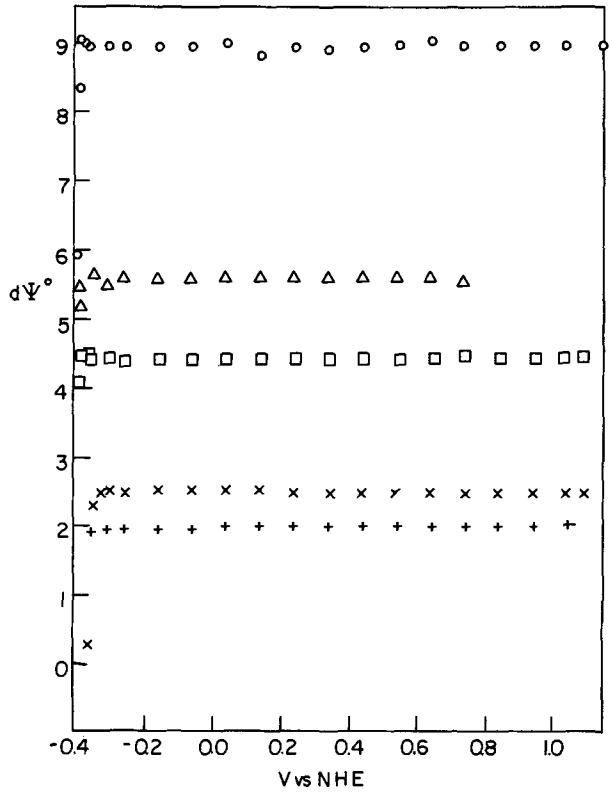

Fig. 10. Dependence of $\delta\psi$ (the change in ψ from the initial value) on potential in potential staircase measurements (5 experiments, symbols match Fig. 6).

REFERENCES

1. "Gmelin's Handbuch der Anorganischem Chemie," Vol. 52, part A, No. 2, p. 456, Verlag Chemie, Weinheiml Bergstrasse (1963).
2. C. Edeleanu, *Nature*, **173**, 739 (1954).
3. V. M. Knyazheva and Y. M. Kolotrykin, *Dokl. Akad. Nauk S.S.S.R.*, **114**, 1265 (1957).

4. P. F. King and H. H. Uhlig, *J. Phys. Chem.*, **63**, 2020 (1959).
5. Y. M. Kolotrykin, Congr. Metallic, Corros., London (1961), p. 10, Butterworths, London (1962).
6. N. D. Greene, C. R. Bishop, and M. Stern, *This Journal*, **108**, 836 (1961).
7. A. M. Sukhotin, E. I. Antonovskaya, and A. A. Pozdeeva, *Russ. J. Phys. Chem.*, **36**, 1284 (1962).
8. V. V. Andreeva and T. P. Stepanova, *Korroziya Metal. i Splavov Sb.* **1963**, 44.
9. T. Heumann and F. W. Diekotter, *Ber. Bunsenges. Physik Chem.*, **67**, 671 (1963).
10. Y. M. Kolotrykin and V. M. Knyazheva, *Russ. J. Phys. Chem.*, **36**, 653 (1962).
11. K. Schawbe, K. Muller, and A. Loge, *Electrochim. Acta*, **8**, 193 (1963).
12. T. Heumann and H. S. Panesor, *This Journal*, **110**, 628 (1963).
13. T. Heumann and F. W. Diekotter, *Z. Elektrochem.*, **62**, 745 (1964).
14. C. C. Seastrom, *Corrosion*, **20**, 179t (1964).
15. V. V. Andreeva, *ibid.*, **20**, 35t (1964).
16. J. R. Myers, F. H. Beck, and M. G. Fontana, *ibid.*, **21**, 277 (1965).
17. H. W. Pickering and R. P. Frankenthal, *This Journal*, **112**, 761 (1965).
18. G. T. Seaman, J. R. Myers, and R. K. Saxen, *Electrochim. Acta*, **12**, 855 (1967).
19. R. P. Frankenthal, *This Journal*, **114**, 542 (1967).
20. R. P. Frankenthal, *ibid.*, **116**, 580 (1969).
21. T. J. Micheli, *Archives des Sciences Physiques et Naturelles* **X**, 122, Geneva (1900).
22. R. J. Archer, *J. Opt. Soc., Am.*, **52**, 970 (1962).
23. R. J. Archer, *This Journal*, **104**, 619 (1957).
24. A. B. Winterbottom, *Kgl. Norske Videnskab. Selskabs Skrifter*, **1955**, 1.
25. J. Kruger and W. J. Ambs, *J. Opt. Soc. Am.*, **49**, 1195 (1959).
26. R. R. Stromberg, E. Passaglia, and D. J. Tutas, Symposium on ellipsometry in the measurement of surfaces and thin films. National Bureau of Standards, Misc. Pub. 256 (1963).
27. J. O'M. Bockris, A. K. N. Reddy, and B. Rao, *This Journal*, **113**, 1133 (1966).
28. J. Kruger and J. P. Calvert, *ibid.*, **114**, 43 (1967).
29. V. Brusic, M. A. Genshaw, and B. D. Cahan, *Appl. Opt.*, **9**, 1634 (1970).
30. A. K. N. Reddy and J. O'M. Bockris, in Ref. (26), p. 229.
31. Sweep Generator designed by B. D. Cahan.
32. E. Churchill, Thesis, Iowa State University of Science and Technology, Ames, Iowa, 1960, p. 20.
33. R. M. Hill and C. Weaver, *Trans. Faraday Soc.*, **54**, 1464 (1958).
34. V. P. Kostyuk and I. N. Shklyareuskii, *Opt. Spectry*, **1963**, 165.
35. F. L. McCrackin, E. Passaglia, R. R. Stromberg, and H. L. Steinberg, *J. Res. Nat. Bur. Std.*, **67A**, 4 (1963).
36. R. C. Weast, Editor, "Handbook of Chemistry and Physics," 49th ed., p. B192, Chemical Rubber Co. Cleveland, Ohio (1968).
37. F. F. Faizullin and V. K. Levina, *Zashch. Metal.*, **2**, 623 (1966).
38. Z. A. Solov'eva and A. T. Vagramyan, *Dokl. Akad. Nauk S.S.S.R.*, **154**, 918 (1964).
39. E. M. Mahla and N. A. Nielson, *This Journal*, **93**, 1 (1958).
40. Ref. (1) Vol. 52, part B, p. 35, (1962).
41. M. Pourbaix, "Atlas D'Equilibres Electrochimiques," p. 260, Gauthier-Villars, Paris (1963).
42. W. J. Muller, *Z. Elektrochem.*, **30**, 401 (1922).
43. L. G. Sillen and A. E. Martell, "Stability Constants of Metal-Ion Complexes," p. 48, The Chemical Society, London, 1964.
44. A. K. N. Reddy, N. A. V. Devanathan, and J. O'M. Brockris, *J. Electroanal. Chem.*, **6**, 61 (1963).
45. K. Schwabe, *Electrochim. Acta*, **3**, 186 (1960).
46. U. Ebersbach, A. Schwabe, and K. Ritter, *Electrochim. Acta*, **12**, 927 (1967).
47. W. A. Muller, *This Journal*, **107**, 157 (1960).
48. S. R. Rajugopalan, K. S. Indira, and K. S. G. Doss, *J. Electroanal. Chem.*, **10**, 465 (1965).
49. J. C. Maxwell Garnett, *Phil. Trans.*, **203**, 385 (1904); **205**, 237 (1906).

Electrodeposition of Chromium and Nickel-Chromium from Amide Solvents

D. J. Levy* and W. R. Momyer*

Lockheed Palo Alto Research Laboratory, Lockheed Missiles & Space Company, Palo Alto, California 94304

ABSTRACT

Chromium was deposited from hexaamminechromium(III) formate in 30 mole per cent acetamide/formamide at cathode current efficiencies up to 50%. The current density range for optimum plating efficiency varied from 25 to 150 mA/cm^2 depending on the chromic ion concentration in the bath. Aquation of this chromic complex during electrolysis takes place at an appreciable rate when the water content exceeds 400 ppm and results in decreased plating efficiency. There was no correlation between the effectiveness of bridging groups for electron transfer between chromous and chromic ion and the electrodeposition of chromium in the amide solvent system. The observed effectiveness of ligands for promoting chromium deposition was: $SCN^- > NH_3 > Cl^-$ and $N_3^- > H_2O$. Sulfamic acid, boric acid, and sodium thiocyanate were effective in increasing plating efficiency at low concentrations; it was also observed that thiocyanate lowered the chromium deposition potential. Chromium-nickel alloys were produced over the entire concentration range of 0-100% chromium by the addition of hexaamminenickel(II) formate to the bath. Alloy composition was influenced more by electrolyte composition and bath temperature than by current density.

Chromic acid baths catalyzed with sulfate ion are generally utilized for electrodepositing chromium. However, these baths deposit chromium only at low plating efficiency, are unsuitable for alloy deposition, and possess many well-known undesirable operating characteristics. In addition, a more stable solvent system than water is desirable in the bath in order to increase chromium plating efficiency.

Deposition of chromium from aqueous trivalent solutions was known as early as 1853. Much of the earlier

* Electrochemical Society Active Member.

Key words: chromium electrodeposition, nonaqueous solvents, amides, nickel-chromium alloys.

work (1) and some later studies with chromic sulfate solutions (2-4) have been reviewed. Chromium deposition has also been reported from chromic chloride dissolved in formamide (5), acetone (6, 7), and a mixed dimethylformamide-water electrolyte (8). It has often been difficult to confirm results reported in the literature because insufficient details were given for preparing the specific chromic complex used.

The present authors recently reported (9) that chromium can be electrodeposited from ammonium reineckate, a $NH_4[Cr(NH_3)_2(SCN)_4]\cdot H_2O$, or thiocyanatopentamminechromium(III) thiocyanate to yield satisfactory chromium deposits at current efficiencies from 25 to 65%. However, the baths are unstable during prolonged electrolysis. The purpose of this investigation was to study the role of water and sulfur-containing ligands in the deposition reaction, to determine the effect on chromium deposition of bridging ligands known to facilitate electron transfer between chromic and chromous ions, to seek a suitable organic solvent with greater electrochemical stability than formamide, and to investigate the feasibility of electrodepositing chromium alloys.

Experimental

Apparatus and procedures.—The apparatus and procedures described previously (9) were used in the present investigation. Plating efficiency (cathode current efficiency) was again obtained from weight determinations and expressed as per cent of theoretical calculated on a trivalent basis. Experiments were performed with 60 ml of 0.2M hexaamminechromium(III) formate in an open electrolysis cell at 23°C and 25 mA/cm^2 unless stated otherwise. Plating experiments at low water levels were performed in a dry box and the water content of the bath monitored by titrating aliquots from the bath with Karl Fischer reagent (10). Alloy plating studies were performed in a sealed, two-compartment electrolysis cell using 100 ml of electrolyte. The electrolyte was transferred from the plating compartment to a storage compartment by means of vacuum and dry nitrogen before the cathodes were removed for weight determinations. This restricted water absorption from the ambient air and improved alloy bath stability. The composition of the alloy films was determined by electron microprobe analysis and, therefore, the per cent chromium and nickel reported are surface values rather than the average content of the bulk film.

Materials—All of the solvents used in the plating baths were either reagent grade or the highest purity available commercially. The solvents were predried for several of the experiments by passing them through a glass column packed with activated molecular sieves. The water content of the standard 30 m/o (mole per cent) acetamide/formamide solvent was easily reduced to less than 100 ppm by this technique.

Hexaamminechromium(III) and hexaammine nickel (II) complexes were prepared by the methods presented in ref. (11). The anhydrous chromic chloride for preparing the chromic complex was purchased from Research Inorganic Chemical Company (Sun Valley, California). Hexaamminechromium(III) chloride was converted to the formate salt by first adding the stoichiometric amount of freshly prepared silver carbonate to an aqueous solution of the complex. An excess of formic acid was added to destroy the carbonate and the mixture was filtered through a medium glass frit to remove the silver chloride precipitate. The filtrate was then added to a large volume of acetone to precipitate the desired complex. This complex was purified by redissolving the material in methyl alcohol, reprecipitating with acetone, and washing with ethyl alcohol and then acetone. The anhydrous hexaamminechromium(III) formate complex was obtained by equilibrating the complex with phosphorous pentoxide in a sealed glass container for several weeks. Chloropentaamminechromium(III) chloride was obtained as a byproduct from the hexaamminechromium(III) synthesis. This compound was used as the starting material for preparation of thiocyanatopentaamminechromium(III) and azidopentaamminechromium(III) complexes by the procedures outlined in Gmelin (12).

Discussion of Plating Studies

Chromium plating from acidopentaamminechromium (III) complexes.—Plating studies with ammonium reineckate and thiocyanatopentaamminechromium(III) thiocyanate indicate that thiocyanate catalyzes reduction of chromic ion in amide solvents (9), but the role of thiocyanate in the plating mechanism was not established. Skala (13) found that the purpeo complex, $[Cr(NH_3)_5Cl]\ Cl_2$, is suitable for electrodeposition of chromium in aqueous media while the luteo complex, $[Cr(NH_3)_6]\ Cl_3$, is not. The data suggest that the more efficient electroreduction of chromic ion to the metal in the presence of thiocyanate may be due to this ligand functioning as a bridging group for electron transfer.

The effectiveness of various bridging groups to facilitate electron transfer between chromous and chromic ions (14) is

$$Br^- \simeq N_3^- > Cl^- > OH^- > F^- > NCS^- > H_2O$$

The effectiveness of halides as bridging groups for electron transfer between chromous ion and pentaamminechromium(III) ion has also been established (15) and is in the order

$$I^- >> Br^- > Cl^- >> F^-$$

Several acidopentaamminechromium(III) complexes were compared to the hexaamminechromium(III) complex in order to determine the influence of the electron bridging group on chromium plating efficiency in the organic solvent system. The hexamminechromium (III) complex provides a good comparison because the coordinated ammonia is a relatively poor bridging group for electron transfer.

The halide salts of the pentaamminechromium(III) and hexaamminechromium(III) complexes are only slightly soluble in 30 m/o acetamide/formamide and it is necessary to convert these complexes to other salts for plating studies. The anion markedly influences the solubility of metallic salts in organic solvents and those salts which are highly solvated and most difficult to prepare in the anhydrous state exhibit the highest solubilities (16). Nitrate and thiocyanate salts are normally quite soluble in organic solvents but nitrate is more easily electroreduced than chromic ion and thiocyanate is of marginal electrochemical stability (17). Perchlorates also yield high solubilities and are desirable because they will not interact with the ammine chromic complexes (18). However, the oxidizing ability of this anion can create a safety hazard, particularly with nitrogen-coordinated complexes (12). Formamide is similar in solvent properties to water (16) and carboxylate salts offer the best possibility for improved solubility without interfering side effects. Acetate and formate yield the required degree of solubility for electroplating studies, but formate is the preferred salt because better quality deposits are obtained at slightly higher plating efficiencies.

The results of the bridging group experiments are presented in Table I. It is apparent that there is no direct correlation between chromium plating efficiency

Table I. Effect of bridging group on chromium plating efficiency

Chromic complex	Bridging group	Initial plating efficiency, %
$[Cr(NH_3)_5\ SCN](SCN)_2$	SCN-	62
$[Cr(NH_3)_5\ SCN](HCO_2)_2$	SCN-	56
$[Cr(NH_3)_6](HCO_2)_3$	NH_3	35
$[Cr(NH_3)_5Cl](C_2H_3O_2)_2$	Cl-	11
$[Cr(NH_3)_5\ N_3](HCO_2)_2$	N_3-	14
$[Cr(NH_3)_5\ N_3](C_2H_3O_2)_2$	N_3-	10

and the effectiveness of the bridging group for electron transfer between chromous and chromic ions. The thermodynamic stability of the chromic complex appears to be a more important consideration in electroplating chromium than kinetic effects introduced by the bridging groups.

The thiocyanatopentaamminechromium(III) complex yields the highest chromium plating efficiency of the four complexes. The formate salt produces better quality deposits than the thiocyanate salt although at slightly lower efficiency. The chloropentaamminechromium(III) complex is too unstable for plating studies. Rapid release of the coordinated chloride during electrolysis produces an insoluble pentaamminechromium(III) chloride. The azidopentaamminechromium(III) complex deposits chromium at the lowest efficiency in spite of the fact that azide is the best electron bridging group. The formate salt of this complex produces better quality deposits at slightly higher efficiency than the acetate salt. The hexaamminechromium(III) complex deposits the best quality chromium films at reasonable (30-35%) plating efficiencies.

Chromium plating from hexaamminechromium(III) formate.—Hexaamminechromium(III) formate (HAF chromium) possesses the following desirable properties as a potential source of chromium in the amide plating bath:

1. Excellent solubility in the organic solvent.
2. The complex is stable to oxygen and moderately stable to water (12).
3. Low thermodynamic stability of the complex permits efficient metal deposition at reasonable potentials.
4. Reaction kinetics for metal deposition appear favorable.
5. Chromous catalyzed decomposition of the complex is low because ammonia is a poor electron bridging group.
6. The ammonia ligand is volatile under the plating conditions which eliminates accumulation of ammonium salts in the electrolyte.
7. The formate anion can be electrolytically oxidized to volatile products which reduce salt accumulation and provide a more desirable anode reaction than solvent oxidation.

The optimum plating parameters and bath composition were established for the HAF chromium bath in order to evaluate more fully the stability and properties of this complex during electrolysis.

The effect of HAF chromium concentration on plating efficiency is illustrated in Fig. 1. A linear dependence is observed up to a concentration of 0.25M (molar) and doubling the concentration in this range roughly doubles the plating efficiency. Chromium plating efficiency does not increase substantially at concentrations above 0.4M and the maximum plating efficiency with this complex is near 50%.

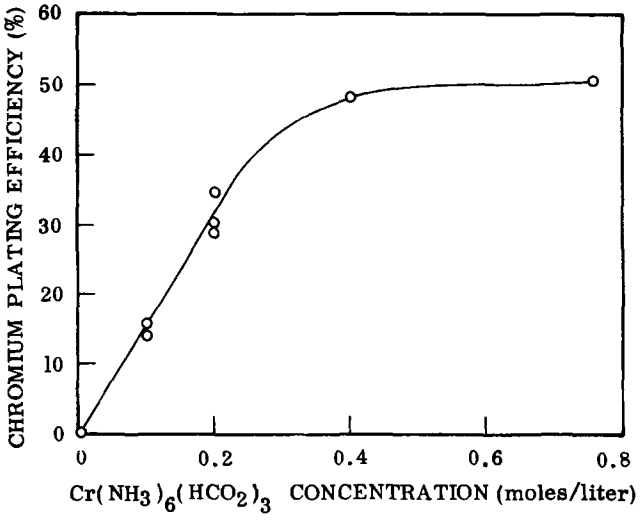

Fig. 1. Chromium plating efficiency as a function of hexaamminechromium(III) formate concentration.

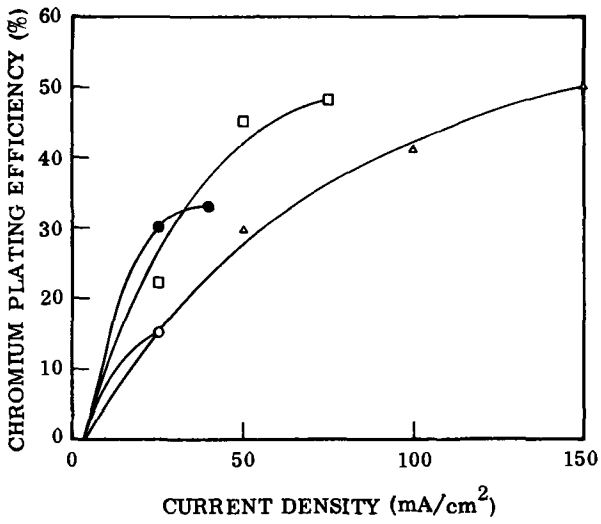

Fig. 2. Effect of current density and Cr(III) concentration on plating efficiency, 0.1M, ○; 0.2M, ●; 0.4M, □; 0.78M, △.

The current density for maximum plating efficiency increases as the HAF chromium concentration is increased (Fig. 2). A broader range of current density for plating is observed at the higher concentrations and the bath exhibits better covering and throwing power. The deposits are also somewhat brighter and smoother under these conditions. The more concentrated baths provide improved performance but the 0.2M HAF chromium bath was primarily investigated in the present study in order to minimize the effort of synthesizing the HAF complex.

The pH of the bath also affects the chromium plating efficiency. The bath normally buffers at a pH between 9 and 10 due to the release of large quantities of ammonia by the plating reaction, *i.e.*, $Cr(NH_3)_6^{+3} + 3e^- \rightarrow Cr^\circ + 6NH_3$. Maximum plating efficiency is obtained in this pH range. Adjusting the pH to 7 or less will drastically reduce plating efficiency because solvent reduction occurs at a lower potential and ammonium salts increase rapidly in the bath. Increasing the bath pH above 10 produces only a slight decrease in plating efficiency.

The chromium plating efficiency decreases as the temperature of the HAF chromium bath is increased. This parameter was not investigated quantitatively for this system, but a temperature dependence similar to the thiocyanatopentaamminechromium(III) bath (9) is expected. Formamide reduction proceeds more readily at higher temperatures and this is the principal reaction occurring at temperatures greater than 50°C. It is estimated from the data presented in Fig. 9 (plating performed at 32°C) that the plating efficiency decreases by 0.7%/°C temperature rise above 23°C.

Plating studies with thiocyanatopentaamminechromium(III) and hexaamminechromium(III) show that thiocyanate catalyzes chromium deposition. However, the increase in plating efficiency is probably not due to an electron bridging effect and coordination of thiocyanate to the chromic ion is not required. Sodium thiocyanate, sulfamic acid, and boric acid additives to the HAF chromium bath all result in a substantial increase in chromium plating efficiency at low concentrations (Fig. 3). The sharp concentration dependence with the sulfamic and boric acid additives is caused by a change in pH and can be eliminated by addition as the alkali metal salts. The lower initial plating efficiency with these two additives reflects a lower purity of HAF chromium. The complex used in these tests was prepared by a methathesis reaction between ammonium formate and hexamminechromium(III) nitrate in liquid ammonia and it is difficult to eliminate ni-

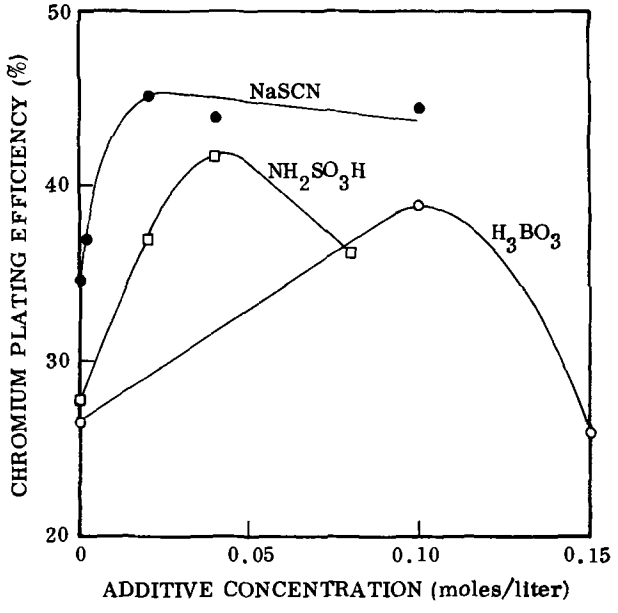

Fig. 3. Influence of various additives on chromium plating efficiency.

trate contamination by this method. The additives are not as effective in increasing plating efficiency when added to more concentrated HAF chromium baths (compare Fig. 1 with Fig. 7).

Current-potential curves were obtained on HAF chromium baths in an effort to establish the role of the thiocyanate additive in the plating mechanism. Figure 4 illustrates that lower potentials are required for chromium plating in the presence of thiocyanate. Chromium deposition first occurs at a potential of −1.16V (*vs.* Ag/AgCl) with thiocyanate while a potential of −1.36V is required to initiate plating without thiocyanate. Thiocyanate also reduces the plating potential by 80 mV at 25 mA/cm² (the current density for maximum plating efficiency).

The data indicate that thiocyanate also may be increasing the overpotential for the solvent reduction reaction. An attempt was made to measure the reduction potential of 30 m/o acetamide/formamide with and without sodium thiocyanate. The reduction potential listed in the literature (19) for pure formamide is −1.6V ($E_{1/2}$ *vs.* saturated calomel electrode). The reduction potential measured in the present study is −1.69V (*vs.* Ag/AgCl) for the solvent and −1.78V for the solvent with sodium thiocyanate (Fig. 5). Considerable error may have been introduced in obtaining the reduction potential from the graphical intercept of the slopes of the two curves because sharp limiting currents for solvent reduction were not obtained. However, the data suggest that thiocyanate does increase the overpotential for the solvent reduction reaction.

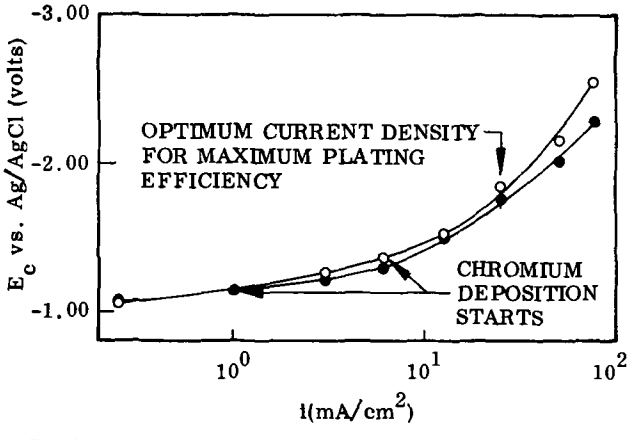

Fig. 4. Current-potential curves for chromium deposition. No additive, ○, and 0.02M NaSCN, ●.

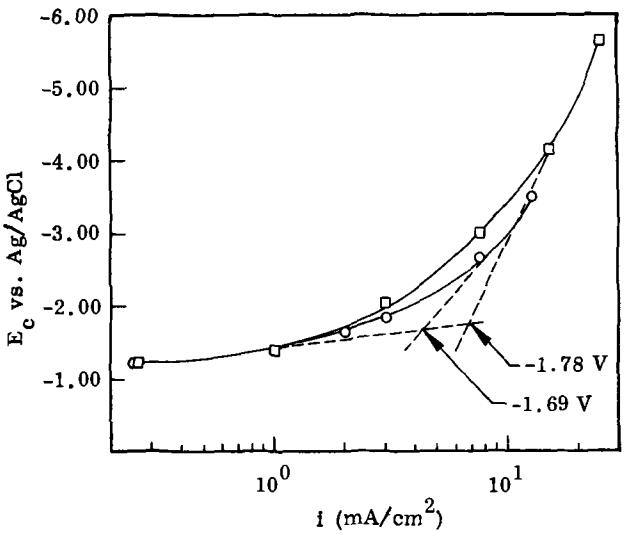

Fig. 5. Current-potential curves for the reduction of 30 m/o acetamide/formamide. No additive, □, and 0.02M NaSCN, ○. Copper cathode.

The performance of the HAF chromium bath was investigated during prolonged electrolysis in order to evaluate bath stability. Tests with the pentaamminechromium(III) complex indicate that bath deterioration occurs as a result of aquation of the chromic complex. The aquation rate of the hexaammine complex is of the same order of magnitude as the thiocyanatopentaammine complex (12) and, therefore, deterioration in the HAF chromium bath was also expected. Figure 6 illustrates the deterioration observed when less than 12% of the available chromium is plated from the bath. Poorer performance is obtained with the more concentrated bath because additional water is added with the HAF chromium complex. The hexamminechromium(III) formate, as synthesized, was not anhydrous but contained from ½ to 1 mole of water, *i.e.*, $Cr(NH_3)_6(HCO_2)_3 \cdot ½\text{-}1\ H_2O$. Spectral analysis of the baths after electrolysis indicated the presence of aquated chromic complexes.

An improvement in performance is observed when thiocyanate is added to the electrolyte (Fig. 7). Bath deterioration is not nearly as rapid, particularly in the case of the more concentrated bath, but the decrease in plating efficiency during electrolysis is still greater than can be accounted for by depletion of the chromic complex due to the plating reaction. The improved bath stability with thiocyanate is largely a

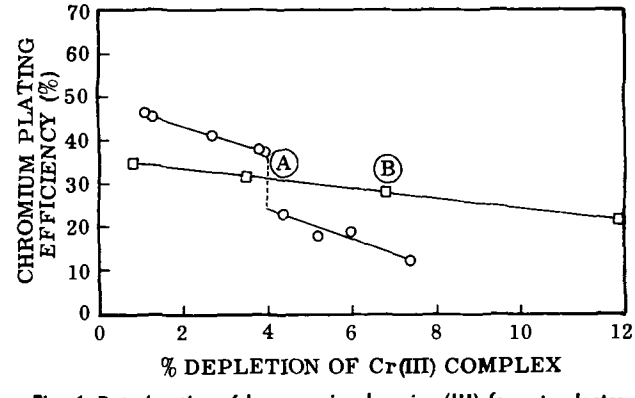

Fig. 6. Deterioration of hexaamminechromium(III) formate electrolyte during electrolysis. A. 24-hr interruption of test. Electrolyte color change from amber to purple. B. 24-hr interruption of test. Initial concentration: 0.4M HAF chromium, ○; 0.2M HAF chromium, □.

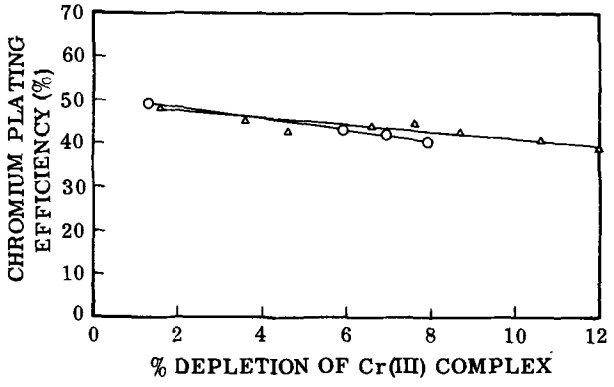

Fig. 7. Deterioration of electrolyte during electrolysis. Initial concentration: 0.2M Cr(III) complex + 0.02M NaSCN, △; 0.4M Cr(III) complex + 0.04M NaSCN, ○.

result of a decrease in the rate of the side reactions during electrolysis.

Thiocyanate reduces the rate of solvent reduction as a result of the increased chromium plating efficiency. However, the reduction products of formamide are probably not too detrimental to the bath because only hydrogen and volatile basic components are produced (19). The anode reactions appear to have more effect on chromium plating efficiency than the cathode reactions. The most desirable anode reaction for the HAF chromium bath is oxidation of formate, *i.e.*, $HCO_2^- \rightarrow CO_2 \uparrow + H^+ + 2e^-$. Sparging carbon dioxide into the bath reduces the plating efficiency slightly and produces a milky cast to the chromium deposit, but insoluble products do not form in the presence of carbon dioxide and the plating characteristics of the bath are not drastically affected unless the sparging rate is sufficient to reduce the pH of the bath. The basic by-products liberated at the cathode also neutralize the acid generated by formate oxidation at the anode. The result is that a pH of 9 to 10 is still maintained during electrolysis with the formate salt of hexaamminechromium(III) ion.

Formate oxidation is not the only anode reaction that occurs in the HAF chromium bath. Plating tests with ammonium reineckate in 30 m/o acetamide/formamide indicate improved bath stability with chromium rather than platinum anodes. Formamide oxidation to cyanuric acid proceeds in good yield on platinum anodes (20) and therefore the poorer performance with platinum anodes probably results from the generation of cyanuric acid. Better HAF chromium bath stability is also observed with chromium rather than platinum anodes, but chromium anodes are not completely inert in the bath. Small quantities of hexavalent (and lesser amounts of trivalent) chromium ions are produced during prolonged electrolysis. Completely insoluble anodes which catalyze formate, but not formamide, oxidation should improve bath stability.

The addition of thiocyanate to the HAF chromium bath provides other possible anode reactions. Oxidation of thiocyanate to sulfate occurs in the thiocyanatopentaamminechromium(III) thiocyanate bath and produces the insoluble, pale orange, chromic sulfate salt (9). An insoluble yellow material forms on the anode during prolonged electrolysis of the HAF chromium bath with the thiocyanate additive. The material is primarily an insoluble sulfate salt of the hexaamminechromium(III) complex but some thiocyanogen may also be produced. The oxidation of thiocyanate is not particularly deleterious to the bath and the net result is that thiocyanate and hexaamminechromium (III) ions are consumed and must be added to the bath periodically.

Thiocyanate addition to the HAF chromium bath is also desirable because anation[1] of the aquochromic

[1] Substitution of an anion for water in the coordination sphere.

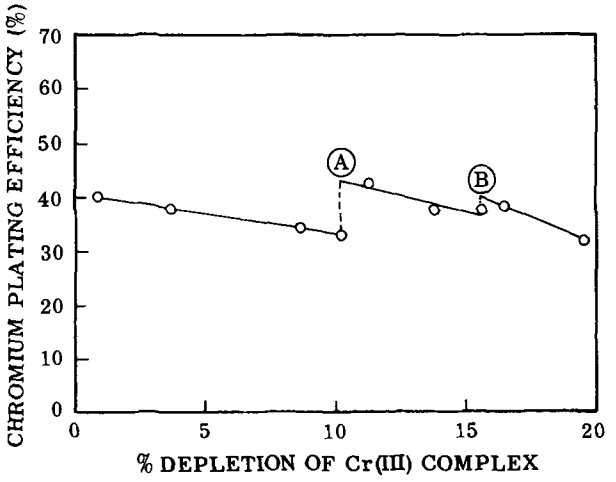

Fig. 8. Replenishment of electrolyte to maintain initial concentration during electrolysis. A. Addition to maintain 0.02M NaSCN. B. Addition to maintain 0.2M Cr $(NH_3)_6(HCO_2)_3 \cdot x\ H_2O$.

complexes is possible. Anation of aquopentaamminechromium(III) ion with thiocyanate occurs readily in acidic aqueous solutions (11). Thus, it is possible to convert the aquochromic complexes, which are not suitable for efficient electroreduction, to the thiocyanato derivatives, which are easily reduced.

The HAF chromium bath with thiocyanate addition is relatively stable during prolonged electrolysis when the concentrations of thiocyanate and hexaamminechromium(III) ion are maintained within rather narrow limits (Fig. 8). However, some deterioration is evident after 15% of the available chromium is plated from the bath. The blue color characteristic of hexaaquochromic ion is observed in the bath at this point.

The primary cause of HAF chromium bath deterioration is aquation of the hexaamminechromium(III) complex. Figure 9 illustrates the effect of water content on chromium plating efficiency. The initial plating efficiencies are lower in these tests because the bath temperature in the dry box is slightly higher than ambient. Operating the bath at 32°C does not noticeably affect bath stability. Test I illustrates the decay in chromium plating efficiency during electrolysis without drying the bath. The initial plating efficiency is near 22% at a water content of 2640 ppm. The decay in plating efficiency during electrolysis is slightly greater than the baths with lower water contents. Reducing the water content to 200 ppm increases the initial plating efficiency to 26% (tests II and III). The decay in plating efficiency during electrolysis is a result of a decrease in the concentration of the chromic complex by the plating reaction (see Fig. 1). The bath is stable when the water content of the bath is less

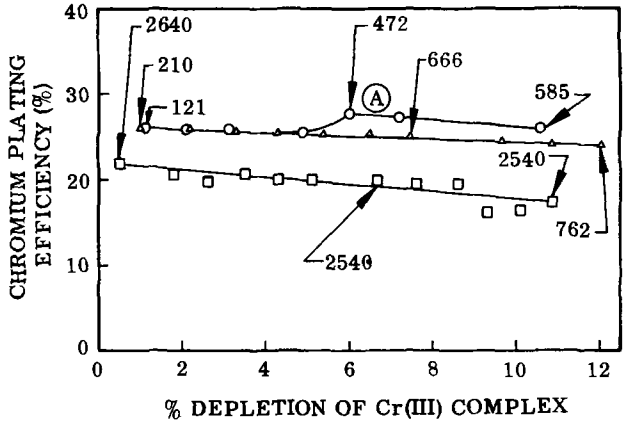

Fig. 9. Chromium plating efficiency at low water concentrations. Test I, □; test II, △; test III, ○. Numbers denote ppm water. 32°C. A=100-hr interruption of test.

than 400 ppm. Water concentrations above 1000 ppm substantially reduce the initial chromium plating efficiency and result in bath deterioration.

An interesting effect is illustrated in test III. The chromium plating efficiency begins to increase after electrolysis of the bath for several hours and the bath color changes from orange to red. Spectral analysis of the bath indicates the presence of the disolvotetraamminechromium(III) ion (21). Replacement of ammonia by the solvent (formamide or acetamide) in the chromic complex is therefore desirable because the weaker complex formed is more easily electroreduced in this solvent system. A hexasolvochromium(III) complex should yield substantially higher chromium plating efficiency than the hexaamminechromium(III) complex and provide a bath with fewer side reactions. Additional solvent would be the only material released into the bath by the plating reaction. However, the hexasolvochromium(III) complex is expected to be even more susceptible to aquation than the hexaamminechromium(III) complex.

Aquation of the chromic complex and deterioration of the HAF chromium bath can be eliminated by operation at low water levels, but it is difficult to maintain concentrations less than 400 ppm. Aquation of chromic complexes proceeds at measurable rates even in the very stable ethylenediamine complexes (12). Therefore, the only practical way to eliminate bath deterioration is by electroreduction of the aquated chromic complexes formed and higher reduction potentials are required to accomplish this efficiently. It is not feasible to investigate potentials much greater than −1.69V (*vs.* Ag/AgCl) in the present solvent system because formamide reduction occurs at potentials greater than this value and decreases the chromium plating efficiency. A solvent system with greater electrochemical stability is required in order to eliminate the aquation problem.

Chromium plating in other organic solvents.—Formate salts are generally of limited solubility in organic solvents and hexaamminechromium(III) formate is insoluble in most of the organic solvents which are more stable than formamide (Table II). Thiocyanatopentaamminechromium(III) thiocyanate is only slightly more soluble in these solvents which indicates that the anion is not the primary factor influencing solubility. Amminechromium(III) complexes are practically insoluble in the electrochemically stable organic solvents.

A hexaformamidochromium(III) complex might yield considerably better solubility in these solvents. Formamide is similar in solvent properties to water and hexaaquochromium(III) chloride and perchlorate are quite soluble in many of the stable solvents (9). The formamide complex would, however, be difficult to prepare because it is not very stable. A mixed formamidoamminechromium(III) complex is easier to synthesize and might provide the required solubility.

Dimethyl sulfoxide and an acetamide melt are the only relatively stable solvents other than formamide in which the HAF chromium complex is sufficiently soluble for electroplating studies (Table III). The dimethyl sulfoxide bath deposits bright chromium at low plating efficiency. Dimethyl sulfoxide is not sufficiently stable during prolonged electrolysis and the odor of sulfur-containing decomposition products is evident. An acetamide melt provides better performance than the dimethyl sulfoxide solvent but the chromium plating efficiency is low as a result of the higher operating temperatures.

Acetamide is quite soluble in DMF at room temperature and the HAF chromium complex readily dissolves in this mixture to yield stable solutions at chromic ion concentrations near 0.2M. Plating studies in this solvent yield metallic deposits at plating efficiencies near 65%. The initial chromium plating efficiency in the DMF mixture is roughly twice as great as that obtained with the standard formamide/acetamide solvent. However, the bath is unstable during prolonged electrolysis and insoluble products form. None of the other solvent systems tested are as satisfactory as the acetamide/formamide structure.

Alloy plating.—One of the principal advantages of a chromium plating bath utilizing trivalent chromium rather than chromic acid is that alloy deposition is possible. A brief experimental program was undertaken in order to demonstrate the feasibility of electrodepositing chromium alloys from the organic solvent system. Nickel-chromium alloy plating was investigated in the present study primarily because it was reported that nickel can be electrodeposited from hexaamminenickel(II) bromide dissolved in both formamide and acetamide (22). Hexaamminenickel(II) formate (HAF nickel) is therefore a convenient source of nickel which can be added to the standard HAF chromium bath without interfering with the chromium plating process. It should be relatively simple to deposit other chromium-metal alloys as long as the alloying metal is more easily electroreduced than hexaamminechromium(III) ion.

A suitable bath composition for plating nickel-chromium films is 0.2M HAF chromium and 0.04M HAF nickel dissolved in 30 m/o acetamide/formamide. The alloy films in the present tests were electrodeposited at a current density of 25 mA/cm^2 and at 23°C unless otherwise indicated. Semibright, metallic deposits are obtained under these conditions with a chromium content near 85%.

The chromium content in the alloy film can be controlled by adjustment of the bath temperature, HAF chromium and nickel concentrations, and cathode current density. Alloy films were plated with the chromium content varying from less than 1 to greater than 99% by adjustment of these three variables. Temperature is the most sensitive and convenient parameter for controlling the composition of the alloy film, but more rapid bath deterioration occurs at higher temperatures unless the water content is low (less than 400 ppm). Operation of the bath at temperatures greater than 100°C would simplify water control but the chromium content of alloy films plated under these conditions is quite low (Table IV). Evidently, there is no synergistic effect on chromium plating efficiency induced by the nickel in the alloy plating bath.

The effect of current density on the composition of the alloy film is illustrated in Fig. 10. The alloy composition does not change substantially in the current

Table II. Solubility of hexaamminechromium(III) formate in electrochemically stable organic solvents

Solvent	Solubility†	Solvent	Solubility†
Dimethylformamide (DMF)	i	Trimethyl phosphate	i
Dimethylacetamide	i	Liquid ammonia	i
n-Methylacetamide	i, reacts	Ether	i
Acetamide*	s	Methyl formate	i
Propylene carbonate	i	Pyridine	sp s
Tetrahydrofuran	i	Acetonitrile	i
Dimethyl sulfoxide	sl s	Nitromethane	i
4-Butyrolactone	sp s	Dimethylmethyl phosphonate	sp s

* Melting point, 81°C.
† i, insoluble; sp s, sparingly soluble; sl s, slightly soluble; s, soluble.

Table III. Electrolysis of hexaamminechromium(III) formate in selected organic solvents

Solvent	Temperature, °C	Chromium plating efficiency, %	Deposit appearance
Acetamide	100	4	Metallic, bright
	80	10.5	Metallic, matte
50 m/o Acetamide/DMF	22	67	Metallic, matte
Dimethyl sulfoxide	22	1	Metallic, bright

Table IV. Influence of electrolyte temperature on composition of alloy films

Temperature, °C	Cathode current density, mA/cm²	Film thickness, μ	Chromium, %	Nickel, %
22	25	2.5	97	3
22	25	4.5	94.6	5.4
100	25	4.5	0.25	99.75
100	12.5	2.4	0.04	99.96

density range from 12 to 37 mA/cm² (80-85% chromium and 15-20% nickel), but the deposit is practically all nickel at current densities less than 6 mA/cm². The relationship between the weight determinations and film thickness is as follows: 1 mg/cm² is equivalent to 1.4μ of chromium or 1.1μ of nickel. It is apparent from Fig. 10 that alloy films are deposited at reasonable plating rates in the current density range yielding nearly constant alloy composition.

The plating rate and chromium content of the alloy film continuously decreases during electrolysis if no attempt is made to control the water content of the bath (see Fig. 11). The bath is no longer effective for alloy plating after removal of approximately 22% of the available metal by plating. Aquation of the metal-ammine complexes is responsible for the bath deterioration.

Better performance is observed if the water intake of the bath is restricted (Fig. 12). The plating rate increases during the initial stages of plating as the metal-ammine complexes are converted to the solvo-ammine complexes. However, the plating rate begins to decrease after approximately 5% of the available metal is removed from the bath by plating. The high initial water content of the bath (near 2500 ppm) results in substantial aquation of the metal complexes even when additional water absorption is restricted.

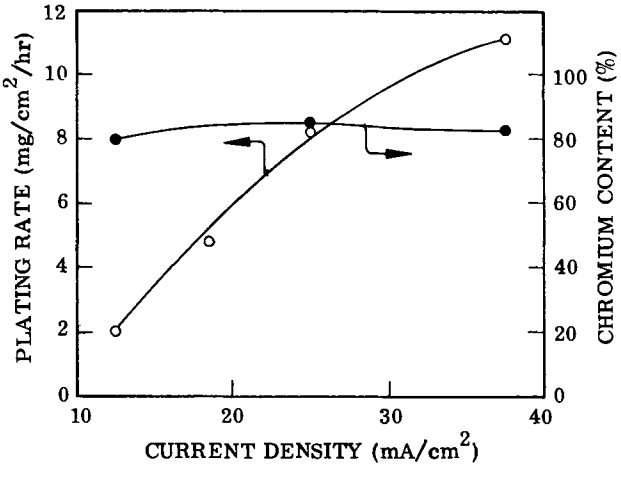

Fig. 10. Influence of current density on nickel-chromium alloy composition and deposition rate.

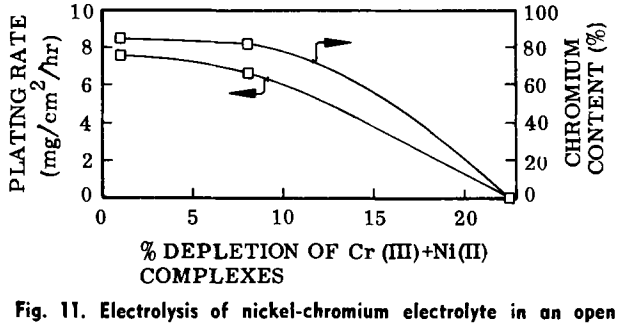

Fig. 11. Electrolysis of nickel-chromium electrolyte in an open cell. Initial water content ca. 2500 ppm.

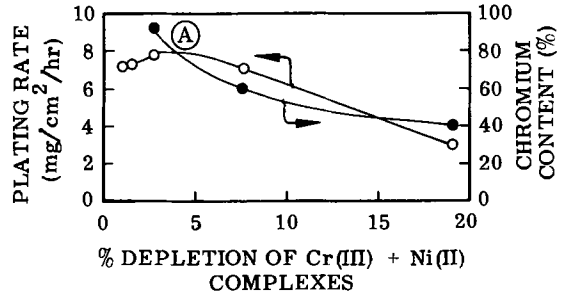

Fig. 12. Electrolysis of nickel-chromium electrolyte in a closed cell. Initial water content ca. 2500 ppm. A. 3-day interruption of test.

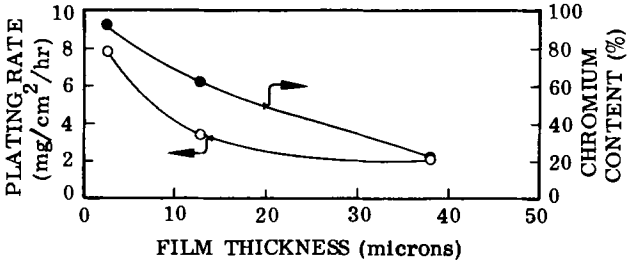

Fig. 13. Thickness effects of the nickel-chromium deposit

The bath is still effective for alloy plating after 19% of the available metal has been plated although the plating rate is considerably lower. The chromium content of the alloy film is stabilizing near 40% under these conditions. The plating rate and chromium content of the alloy films will level off at higher values if the bath is dried before sealing it in the cell.

The average plating rate and chromium content of the alloy film declines as thickness increases (Fig. 13). This effect is not entirely a result of bath deterioration due to aquation of the metal-ammine complexes. For example, a 2μ alloy film was electroplated immediately after plating a 13μ film. The 13μ film plated at a rate of only 3.5 mg/cm²/hr and the surface layer contained 62% chromium while the 2μ film plated at a rate of 7.1 mg/cm²/hr and the surface layer contained 85% chromium. This effect may be due to a decrease in the effective current density as a result of an increase in the surface roughness of the substrate during plating. Alloy plating under potentiostatic conditions rather than at a constant current should eliminate this effect.

The appearance of the alloy films is similar to the chromium films deposited from the thiocyanatopentaamminechromium(III) thiocyanate bath. Thin films have a metallic luster and are semibright. Thicker films, *i.e.*, greater than 10μ, have a matte appearance and some nodule formation is evident. An electron microprobe analysis indicates that nickel and chromium are the only constituents present. However, the analysis was not sufficiently accurate to determine low concentrations of the light elements and there may be small amounts of hydrogen, nitrogen, and oxygen in the electrodeposits (9). Films thicker than 10μ afforded good protection for copper substrates in accelerated corrosion tests (immersion in ammonium polysulfide). This indicates that defects are not continuous through the entire coating thickness and is an indication of good coating integrity. The adherence of the coating to copper is good in that the coating will survive bend tests through angles greater than 90 degrees.

Summary

Chromium can be electrodeposited from organic electrolytes at high cathode current efficiencies (near 50%). The plating baths consist of anhydrous chromic

complexes dissolved in amide solvents. An electrolyte of hexaamminechromium(III) formate in 30 m/o acetamide/formamide yields the most consistent plating results. The optimum hexaamminechromium(III) formate concentration in the bath is 0.2-0.4M and maximum plating efficiency is obtained by operating the bath at ambient temperature (23°C) in the current density range from 25 to 50 mA/cm^2.

The bath is stable only at water concentrations less than 400 ppm although satisfactory plating performance is obtained over a period of several days with water concentrations as high as 2500 ppm (steady-state value under ambient conditions). In the presence of water, aquation occurs and chromium is deposited at lower cathode current efficiency from the resulting complexes. Cathode current efficiency is increased by the addition of small concentrations of sulfur-containing compounds (thiocyanate or sulfamic acid) or boric acid. It was observed that thiocyanate reduces the potential for chromium deposition and may also increase the overpotential for amide solvent reduction.

Ligands known to be effective electron bridging groups for the chromous/chromic redox reaction are

$$N_3^- > Cl^- > SCN^- > H_2O$$

Substitution of these ligands for an ammonia group in the hexaamminechromium(III) complex showed that their effectiveness for promoting chromium deposition was

$$SCN^- > NH_3 > Cl^- \text{ and } N_3^- > H_2O$$

It was concluded that electron bridging groups have very little effect on the electroreduction of chromic ion and that low thermodynamic stability of the chromic complex is of greater importance than kinetic considerations.

It was demonstrated that chromium alloys can be efficiently electrodeposited from organic electrolytes. It is possible to electrodeposit nickel-chromium alloys by addition of hexaamminenickel(II) formate to the standard chromium bath. The composition of the alloy can be varied over the entire range of 0-100% chromium by proper selection of the HAF chromium and nickel concentrations, the bath temperature, and the plating current density. The alloy deposits exhibit good adherence to copper and accelerated corrosion tests indicate good film integrity. Electron microprobe analysis of the film indicates that nickel and chromium are the only metallic elements present.

Hexaamminechromium(III) formate was found to exhibit little or no solubility in a number of organic solvents which have good electrochemical stability. A thiocyanate counterion induced only slightly greater solubility than formate ion and it was concluded that the anion was not the primary factor affecting solubility. The former compound was soluble in dimethyl sulfoxide and in acetamide/dimethylformamide but these electrolytes exhibited low plating efficiency and insoluble reaction products, respectively.

Acknowledgments

The authors gratefully wish to acknowledge the many helpful discussions with Professor James H. Swinehart, University of California (Davis), concerning the chemistry of coordination compounds.

Manuscript submitted Dec. 16, 1970; revised manuscript received *ca.* May 24, 1971.

Any discussion of this paper will appear in a Discussion Section to be published in the June 1972 JOURNAL.

REFERENCES

1. C. J. Kasper, *J. Res. Natl. Bur. Std.*, **40**, 31 (1948).
2. A. Brenner, "Electrodeposition of Alloys," Vol. II, pp. 117-120, Academic Press, New York (1963).
3. L. Domnikov, *Metal Finishing*, **64**, (6), 107 (1966).
4. M. R. Holmes *et al.*, *ibid.*, **65**, (1), 87 (1967).
5. R. D. Blue and F. C. Mathers, *Trans. Electrochem. Soc.*, **63**, 231 (1933).
6. Wolfram Lampen A. G., German Pat. 237,014 (1910).
7. C. U. Chisholm, *Trans. Inst. Metal Finishing*, **47**, 134 (1969).
8. N. R. Bharucha and J. J. Ward, *Products Finishing*, **33**, (4), 64 (1969).
9. D. J. Levy and W. R. Momyer, *Plating*, **57**, 1125 (1970).
10. J. Mitchell, Jr. and D. M. Smith, "Aquametry," pp. 65-102, Interscience Publishers, Inc., New York (1948).
11. L. F. Audrieth, "Inorganic Syntheses," Vol. III, pp. 153-155 and 194-196, McGraw-Hill Book Co., Inc., New York (1950).
12. Gmelins Handbuch der Anorganischen Chemie, Chrom, Tl C, System No. 52, pp. 24-156, (1965).
13. L. W. Skala, U.S. Pat 2,470,378 (1949).
14. D. L. Ball and E. L. King, *J. Am. Chem. Soc.*, **80**, 1091 (1958).
15. A. E. Ogard and H. Taube, *ibid.*, **80**, 1084 (1958).
16. L. F. Audrieth and J. Kleinberg, "Nonaqueous Solvents," pp. 45 and 145, John Wiley & Sons, Inc., New York (1953).
17. A. J. deBethune and N. A. Swendeman Loud, "Standard Aqueous Electrode Potentials and Temperature Coefficients at 25°C," Clifford A. Hampel, Ill. (1964).
18. N. V. Duffy and J. E. Earley, *J. Am. Chem. Soc.*, **89**, 2, 272 (1967).
19. G. H. Brown and H. S. Hsiung, *This Journal*, **107**, 57 (1960).
20. D. E. Couch, *Electrochim. Acta*, **9**, 327 (1964).
21. J. H. Swinehart, University of California (Davis), Private communication.
22. L. F. Yntema and L. F. Audrieth, *J. Am. Chem. Soc.*, **52**, 2693 (1930).

The Structure of the Complexed Copper Species in Electroless Copper Plating Solutions

L. N. Schoenberg*
Bell Telephone Laboratories, Incorporated, Murray Hill, New Jersey 07974

ABSTRACT

The bonding mode of the copper ion in various formulations of a well-known electroless copper bath consisting of copper sulfate, sodium hydroxide, potassium sodium tartrate, and formaldehyde has been determined by electron paramagnetic resonance spectroscopy. Other ligands related to tartrate in structure, but with fewer potential bonding sites, were also studied. It was discovered that 2,3-butane diol, α-hydroxy butyric acid, malic acid, glycolic acid, and mandelic acid could be substituted for tartrate in an electroless copper bath, but that succinic acid, β-hydroxy butyric acid, and salicylic acid could not. The plating rate of copper-tartrate solutions as a function of *p*H was studied, and it was found that the maximum plating rate occurs at about *p*H 12.8. The structure of the copper complex is *p*H dependent and is one factor affecting the deposition rate.

Procedures for the electroless deposition of copper have been known for some time. Solutions suitable for this purpose generally consist of a copper-containing salt, a complexing agent, a reducing agent, and a source of hydroxide ions. Various additional substances, such as brightening agents and stabilizing agents, may also be incorporated. The role of the complexing agent in determining important bath parameters such as stability and plating rate has not yet been well investigated.

The deposition of electroless copper can be considered to consist of two half reactions, namely, the reduction of copper ions to copper metal (cathodic reaction) and the oxidation of the reducing agent, generally formaldehyde to formic acid (anodic reaction). The catalytic surface mainly affects the rate of the anodic half reaction (1). In principle, it is possible to envision an alkaline electroless copper bath, consisting of a copper complex and a reducing agent, that is indefinitely stable in the absence of a catalytic surface and yet that in the presence of a catalytic surface plates very rapidly. To formulate a bath of this type, an understanding of the bonding mode of the copper ion in such solutions is clearly of importance.

Tartrate is the most commonly used complexing agent in electroless copper baths (2) and was chosen for study because of its suitability for investigation using the technique of electron paramagnetic resonance. It further provided the opportunity for gaining information about the nature of copper-tartrate complexes, a field long investigated but in a state of much confusion. The nature of the copper complex both before and after the addition of reducing agent was of concern, as is made clear below.

Copper Tartrate Complexes

A study of the mode of bonding between copper and the tartrate anion is complicated by the many conceivable bonding types that can be envisioned. The several ionizable hydrogen atoms make complex formation very *p*H dependent. Figure 1 indicates several of the copper-tartrate complexes that have been proposed at one time or another, mostly in the early literature (3). Other structures can readily be envisioned. Only two or three of the four positions in the first coordination sphere of copper have been indicated as filled. The other positions may be considered to be occupied by another molecule of tartrate or by hydroxide ions. While the structures in which copper is bonded to two carbonyl oxygens can be rejected tentatively because of the unstable seven-membered ring which would be required, the other structures are sterically possible (4). In addition, dimeric structures containing two copper atoms per molecule have been proposed and spectrophotometric evidence of their existence in 1 to 1 copper-tartrate solutions has been exposited (5).

To determine which of the oxygens might be bonding, it was decided to attempt to form electroless copper baths using as chelating agents various model compounds related to tartaric acid. The structures of these model compounds are depicted in Fig. 2.

The fact that the alcoholic oxygens can indeed participate in bonding if the *p*H is sufficiently high is evidenced by the successful use of 2,3 butane-diol in which coordination can take place only through alcoholic oxygens. Moreover the failure of succinic acid to coordinate indicates that where coordination through carbonyl oxygens would involve a seven-membered ring, the alcoholic oxygens are essential.

The fact that α-hydroxy butyric acid could be used as a chelating agent while β-hydroxy butyric acid under the same conditions could not is in accord with the tendency of copper to prefer a five-membered ring. As a result, certain structures in which an alcoholic oxygen and nonadjacent carbonyl oxygen are bonded to the copper atom may be considered as more remote possibilities.

In accord with the above facts, malic, mandelic, and glycolic acid, all of which have a carbonyl group and an adjacent hydroxide group, can successfully chelate copper. Salicylic acid is unable to form a copper complex under the same conditions. The reason for this is apparent from bond angle considerations. The relevant oxygen atoms are forced to remain too far apart to bond due to the rigidity of the benzene ring.

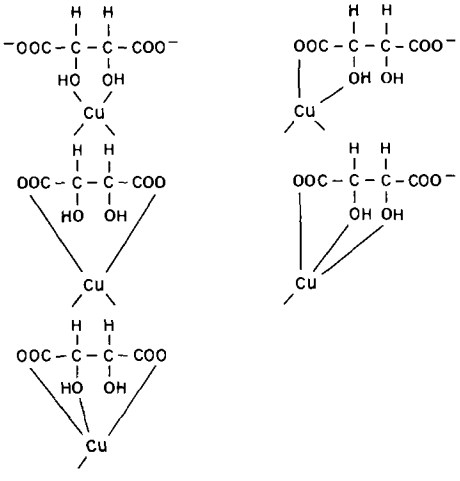

Fig. 1. Several of the possible structures of the copper-tartrate anion. Only two or three of the four positions in the first coordination sphere of copper have been indicated as filled.

* Electrochemical Society Active Member.

Key words: electroless copper plating, copper complex ions, electron paramagnetic resonance.

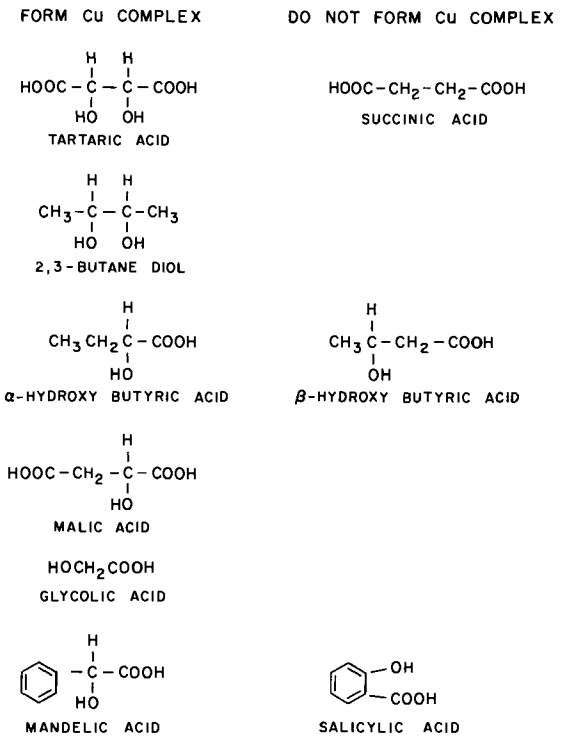

Fig. 2. Structures of the ligands used in the present work

Electron Paramagnetic Resonance

All of the electron paramagnetic resonance (EPR) spectra discussed below were obtained from frozen solutions. Therefore, a brief description of EPR as applied to frozen solutions is desirable. McGarvey (6) provides an understandable and rigorous treatment of the firm quantum mechanical base underlying the interpretation of EPR spectra. He also discusses the interpretation of frozen solution spectra.

Figure 3 depicts the splitting of the spin energy states of an electron, first by a magnetic field and second by interaction with the nuclear magnetic moment of the copper nucleus ($I = 3/2$). Also given is an approximate equation for the energy value of each level. The relevant selection rules are that $\Delta M_I = 0$ and $\Delta M_S = \pm 1$. Thus the four allowed transitions are those indicated by arrows and the energy of the four transitions can be approximated by

$$E = h\nu = g\beta H_0 + Am_I$$

where g = gyromagnetic ratio, β = Bohr magneton, h = Planck's constant, ν = frequency, A = hyperfine coupling constant, and $m_I = \pm 1/2, \pm 3/2$.

The parameters which are characteristic of the species being measured are g and A. In a nonsymmetrical molecule g and A are anisotropic, and in the case of a tetragonal molecule, g and A can be resolved into components parallel and perpendicular to the magnetic field. If θ is the angle between the magnetic field and the Z axis, then (7)

$$g = (g_{||}^2 \cos^2\theta + g_{\perp}^2 \sin^2\theta)^{1/2}$$

and

$$A = g^{-1} (A_{||}^2 g_{||}^2 \cos^2\theta + A_{\perp}^2 g_{\perp}^2 \sin^2\theta)^{1/2}$$

The spectra are obtained by varying the magnetic field strength at a fixed frequency. The spectra are presented as the first derivative of the absorption curves *vs.* the magnetic field, a method which enables greater sensitivity to be obtained. The parameters $g_{||}$, $g_{\perp}$, and $A_{||}$ can readily be extracted from such spectra. A representative spectrum is depicted in Fig. 4 and the procedure for calculating the parameters is indicated. D_1 is the distance in millimeters from the start of the scan to the point midway between the second and third peaks. D_2 is the distance from the start of the scan to the midheight point of the indicated line. Since all of the parameters in the first equation are known except $g_{||}$ and $g_{\perp}$, they can be calculated. $A_{||}$ in gauss is dependent on the distance between the second and third peaks (178 mm = 1000 gauss). The values of the parameters obtained from a frozen solution are average values for all of the bonds in the molecule under study.

The parameter g is affected primarily by the extent of splitting of the 3d energy levels by the ligand field and by the magnitude of spin-orbit coupling. The parameter A is affected primarily by the ratio of the nuclear magnetic moment to the nuclear spin and by the electron spin density in the immediate vicinity of the nucleus, *i.e.*, the closeness of the electron to the nucleus (8). In the present study, possible structures were assigned on the basis of trends in the values of these parameters.

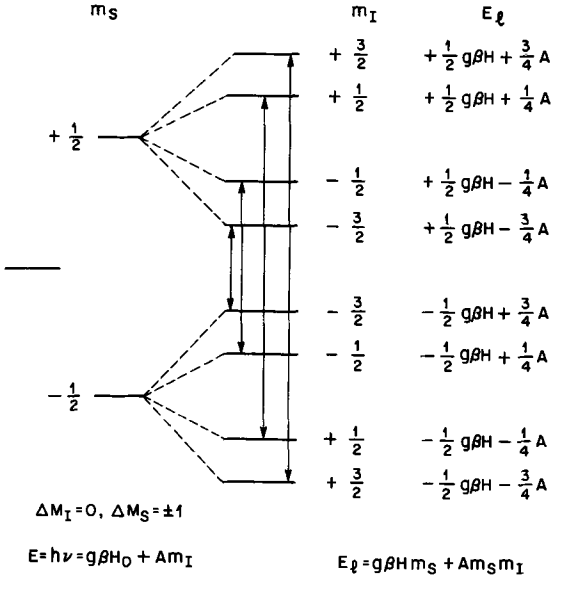

Fig. 3. Splitting of the spin energy states of an electron, first by a magnetic field and second by interaction with the nuclear magnetic moment of the copper nucleus $\left(I = \frac{3}{2}\right)$.

EPR Results and Discussion

Until recently, no information on the EPR spectra of alkaline aqueous solutions of copper-tartrate complexes

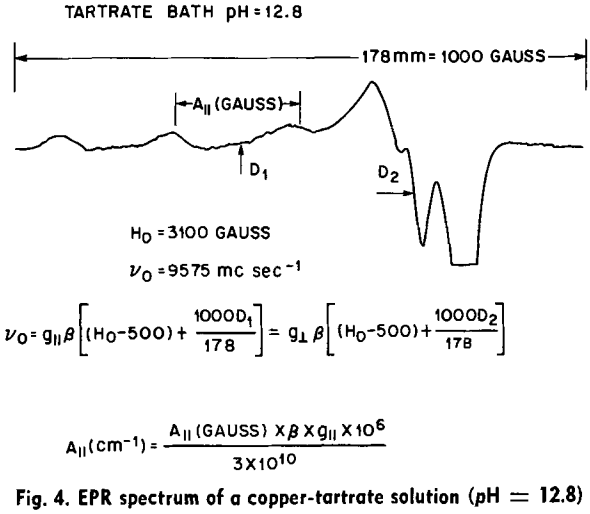

Fig. 4. EPR spectrum of a copper-tartrate solution (pH = 12.8)

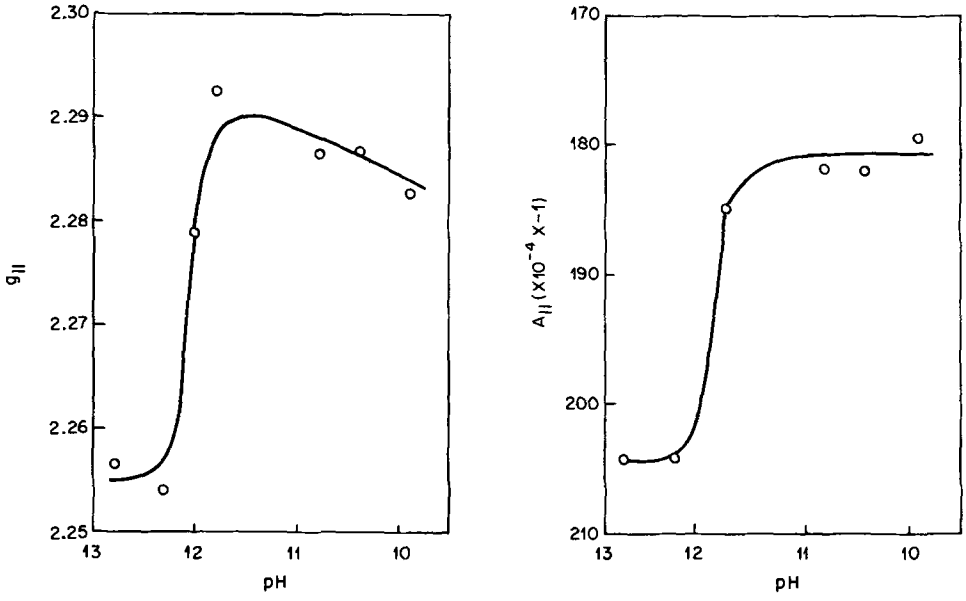

Fig. 5. Values of $g_{||}$ and $A_{||}$ of copper-tartrate solutions as a function of pH.

was available, although single-crystal measurements of the EPR parameters of Cu^{2+} in Rochelle salt had been reported (9). A recent paper, however, presented EPR parameters for 1 to 1 copper-tartaric acid solutions at two pH levels (4.3 and 11.3) (10). The present work has considered the entire range of pH from 5.2 to 13.7 in order to elucidate more fully this complicated system.

The parameters obtained from copper-tartrate solutions as a function of pH are shown in Table I along with the results obtained from a very highly basic solution of copper sulfate in which the complexed copper must be present as the tetrahydroxocuprate anion. The values of $g_{||}$ and $A_{||}$ as a function of pH are plotted in Fig. 5. It can be seen that as the pH decreases, $g_{||}$ increases and $A_{||}$ decreases. There is a jump at pH 12.0 which can be attributed to a change in bonding mode which will be subsequently discussed.

At pH 7.7 a spectrum characteristic of a dimer was obtained (Fig. 6). Its general outline is in accord with the shape that would be theoretically expected. Other examples of dimer spectra may be found in ref. (11). In the acidic pH range, the alcoholic hydrogen atoms are not ionized and different types of species are present which were not considered further due to their inapplicability to electroless copper plating.

No evidence of dimer formation was noted at high values of pH either in the solutions considered in Table I or in a solution ten times as concentrated (the concentration of practical electroless baths). This does not prove conclusively the nonexistence of dimers, but only that if a dimer is present, the copper atoms are far enough apart so as not to interact with each other. It can be shown, however, that for no effect to be noticed the copper atoms must be about six or more Angstroms apart. Molecular models indicate that such a large separation between two copper atoms connected by a tartrate molecule is unlikely, but barely possible.

Table I. EPR parameters of copper-tartrate solutions from pH 5.2 to 13.7

Sample	pH	$g_{||}$	$A_{||}$ †	$g_{\perp}$	α^2
$Cu(OH)_4^{2-}$	≥14	2.264	208	2.066	0.90
Tartrate*	13.7	2.242	206	2.061	0.91
		2.257	ca. 195	—	—
	12.8	2.255	204	2.046	0.88
	12.3	2.253	204	2.045	0.88
	12.0	2.273	199	2.059	0.89
	11.8	2.284	185	2.047	0.86
	10.8	2.279	182	2.050	0.84
	10.4	2.279	182	2.051	0.84
	9.9	2.276	179.5	2.055	0.84
	7.7	—	—	—	—
	5.2	2.321	167	ca. 2.058	0.85

* 0.014M $CuSO_4 \cdot 5H_2O$. 0.06M KNa tartrate. NaOH to indicated pH.
† $cm^{-1} \times 10^4 \times -1$. $g_{||}$, $g_{\perp}$ ± 0.004. $A_{||}$ ± 6, α^2 ± 0.02.

At a pH of 13.7 two species were detected. Possible structural assignments will be discussed later.

The value of the parameter α^2 is a measure of the covalency of the copper-oxygen bond. Its value varies from 0.5 to 1.0. The tabulated values were calculated from the approximation (12)

$$\alpha^2 = \frac{-A}{P} + (g_{||} - 2.0023) + \frac{3}{7}(g_{\perp} - 2.0023) + 0.04$$

where P defines the principal value of A due to interaction between the copper ion nucleus and the unpaired electron. The value of P for $Cu^{2+} = 0.036$ cm^{-1}. The closer α^2 is to unity, the more ionic is the corresponding bond (13). The trend of the tabulated values is in accord with the expected trend, namely that the most ionic bonds are those in which hydroxide ions are bonded to the copper.

The postulated structures for the copper-tartrate complexes as a function of pH are depicted in Fig. 7. It is reasonable to assume increased hydroxide coordination with increasing pH. As mentioned above, the decreasing value of α^2 with decreasing number of coordinated hydroxides is in accord with the expected trend. As indicated in Fig. 7, the discontinuity in the parameters $g_{||}$ and $A_{||}$ is attributed to the coordination of a second tartrate anion.

Support for the theory that the change in bonding mode between pH 13.7 and 12.8 is between all hydroxide coordination at the higher pH and some car-

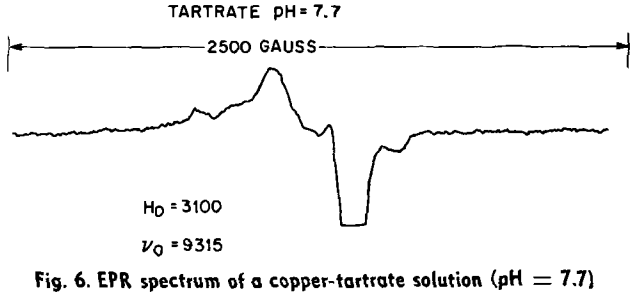

Fig. 6. EPR spectrum of a copper-tartrate solution (pH = 7.7)

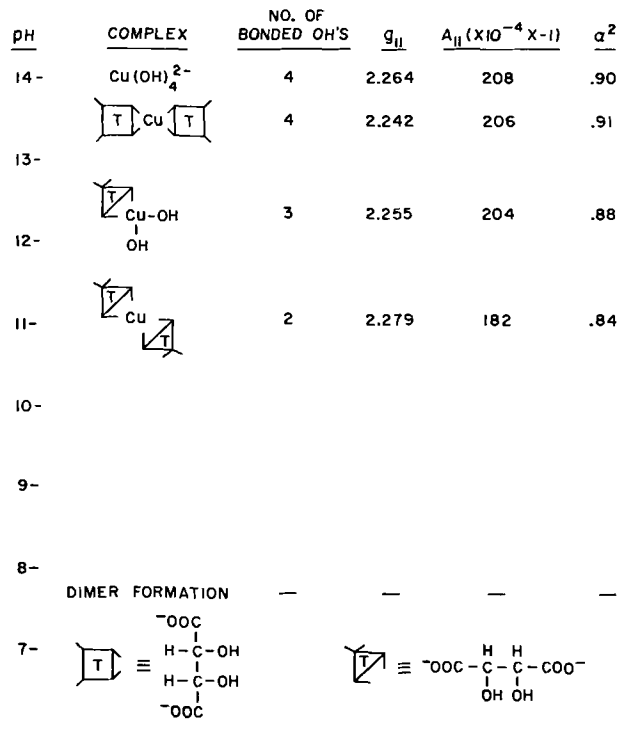

Fig. 7. EPR parameters and the proposed structures of copper-tartrate complexes as a function of pH.

bonyl coordination at the lower pH is found in the change in appearance of the $g_{\perp}$ region of the spectra (Fig. 8). Included for comparison is the spectrum of Cu-2,3 butane-diol in which coordination must be occurring through hydroxide groups. The spectral envelopes of the $g_{\perp}$ regions in all of the species in which four hydroxides are coordinated are similar. All of the Cu-tartrate spectra between pH 9.9 and 12.8 have $g_{\perp}$ regions similar to the right spectrum of Fig. 8 which is attributed to the coordination of three hydroxide groups.

Table II presents the EPR parameters obtained for various solutions using α-hydroxy butyric acid and 2,3 butane-diol as the complexing agents in place of tartrate. In every instance two species were noted in the solutions containing α-hydroxy butyric acid. The species with the lower $g_{||}$ value is the major component. A representative spectrum is shown in Fig. 9.

It has not been possible to assign a structure to these two species with certainty. The $g_{||}$ and $A_{||}$ parameters of the minority species are in agreement with those of the copper-tartrate species in which two molecules of tartrate are bonded through the hydroxyl and carbonyl oxygens. The $g_{||}$ value of the majority species is in accord with the value of the copper-tartrate species with one molecule of tartrate and two hydroxide ions. However, the $A_{||}$ and α^2 values of the α-hydroxy butyric acid species are somewhat low. Also there is no apparent change in the relative concentrations of the two α-hydroxy butyric acid species with pH.

With the thought that one of the species might be due to an impurity, α-hydroxy butyric acid was obtained from another manufacturer. Two species with similar EPR parameters to those mentioned above were formed. In the absence of other evidence, then, the above-discussed assignments are the best that can presently be made.

There is no difficulty with the assignment of structure of the butane-diol solution. Bonding can only occur through hydroxyl oxygens and the EPR parameters and the appearance of the $g_{\perp}$ region of the spectrum are in agreement with this bonding mode. Experiments in varying the pH of the butane-diol bath were not carried out, so the measured species may contain either one or two molecules of 2,3 butane-diol.

In Table III are depicted the parameters obtained before and after the addition of formaldehyde to a pH 12.8 Cu-tartrate solution (Cu^{2+} = 0.014M, tartrate = 0.06M). The formaldehyde was adjusted to pH 12.4 before the addition and one part by volume of formaldehyde to three parts by volume of Cu-tartrate were used. The final pH was approximately 12.7. Three measurements were made at varying elapsed times before freezing of the sample. In all cases there resulted a significant increase in $g_{||}$ and a corresponding decrease in $A_{||}$. This indicates very strongly that the formaldehyde, which in basic solution exists mostly as

Table II. EPR parameters of copper-α-hydroxy butyric acid and copper-butane-diol solutions

Sample	pH	$g_{||}$	$A_{||}$ †	$g_{\perp}$	α^2
α-OH-butyric*	13.0	2.260 2.283	193 180	2.045	0.85
	12.5	2.255 2.289	190 181	2.045	0.84
	11.4	2.258 2.275	192 185	2.049	0.85
	9.4	2.256 2.277	192 188	2.043	0.84
Butane-diol**	13.25	2.244	206	2.069	0.87

* 0.014M $CuSO_4 \cdot 5H_2O$. 0.23M α-hydroxybutyric acid. NaOH to indicated pH.
** 0.014M $CuSO_4 \cdot 5H_2O$. 0.78M 2,3 butanediol. NaOH to indicated pH.
† $cm^{-1} \times 10^4 \times -1$.

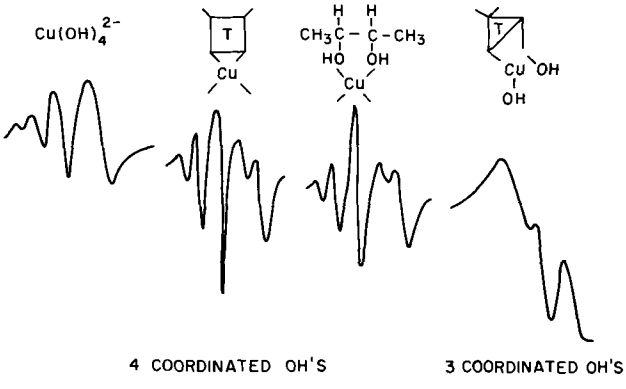

Fig. 8. The $g_{\perp}$ region of the EPR spectra of some of the complexes discussed in the present work.

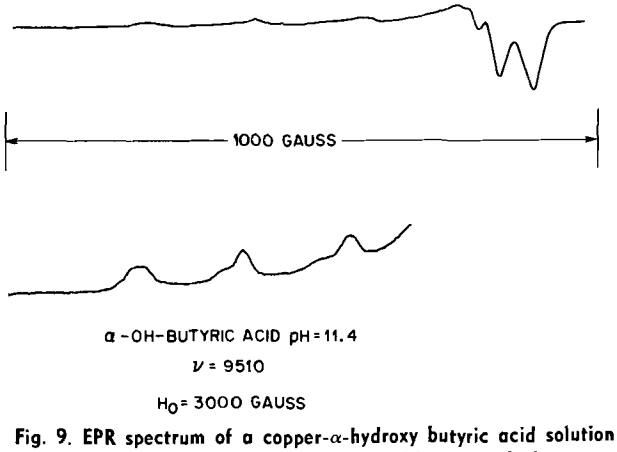

Fig. 9. EPR spectrum of a copper-α-hydroxy butyric acid solution (pH = 11.4). The lower curve is an amplification of the upper curve.

Table III. EPR parameters of various solutions before and after the addition of formaldehyde

Sample	pH	$g_{\parallel}$	$A_{\parallel}$ †	$g_{\perp}$	α^2
Tartrate*	12.8	2.255	204	2.046	0.88
Tartrate + HCHO					
Time after mixing					
1 sec		2.291	189	2.058	0.88
30 sec		2.286	186	2.055	0.86
100 sec		2.288	189	2.056	0.87
$Cu(OH)_4^{2-}$	≧14	2.264	208	2.066	0.90
$Cu(OH)_4^{2-}$ + HCHO	≈13.5	2.267	202	2.060	0.88

* 0.014M $CuSO_4 \cdot 5H_2O$, 0.06M KNa tartrate, NaOH to indicated pH.
† $cm^{-1} \times 10^4 \times -1$.

the methylene glycol anion 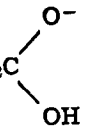 has entered the first coordination sphere of the copper ion.

Moreover the new values of the parameters are very close to those of the species (Fig. 7 and Table I) in which it is proposed that two hydroxyl and two carbonyl oxygens are coordinated. It can be shown that formaldehyde cannot directly compete with hydroxide ions for copper ion since the addition of formaldehyde to a tetrahydroxocuprate solution resulted in no significant change in $g_{\parallel}$ and $A_{\parallel}$ (Table III). Therefore, it is highly likely that the methylene glycol anion is displacing the tartrate anion as one step in the electroless deposition process.

The fact that formaldehyde is indeed bonded to the copper can be substantiated by a consideration of the wavelengths of the maxima of the broad bands in the visible region of the absorption spectra. Upon the addition of 0.4M formaldehyde (pH 12.9) to a solution containing 0.02M copper sulfate and 0.4M potassium sodium tartrate (pH also 12.9), the maximum is shifted from 670 to 660 mμ.

The position of this maximum in complexes of transition metals is commonly related to the stability of the complex; a shift to lower wavelength (higher energy) indicating a more stable complex (14). Since the stability of the tartrate-formaldehyde-hydroxide-copper complex is apparently greater than that of the tartrate-hydroxide-copper complex, it would appear that a solution of the former complex would be indefinitely stable were it not for the tendency of the oxidation of formaldehyde to occur catalyzed by random variables such as dust particles and scratches in the container.

Plating Rate as a Function of pH

It has previously been reported that the pH of an electroless copper plating solution is the variable having the greatest effect on the deposition rate (15). Figures 10 and 11 are plots of the plating rate *vs.* pH obtained in the present work using solutions containing 0.02M $CuSO_4 \cdot 5H_2O$, 0.4M HCHO, and sufficient NaOH to obtain the desired pH. Plating was carried out on platinum substrates. Solutions containing 0.4M (Fig. 10) and 0.1M (Fig. 11) potassium sodium tartrate were studied. In both cases maxima at about pH 12.8 were obtained.

Maxima in plating rate *vs.* pH curves were not observed by Saito (15) but were observed by Okinaka at a somewhat higher pH (16). The electrochemical experiments of Saito indicated that both the anodic and cathodic half reactions are significantly affected by pH.

Methylene glycol is a weak acid with a dissociation constant of 1.62×10^{-13} at 23°C (17). The calculated per cent dissociation as a function of pH is given in Table IV.

When considered alone, the increase in concentration of methylene glycolate with pH would result in an ever-increasing plating rate. However, the concentration of hydroxide ions also increases with pH. At high pH's we have observed (Table III) that copper ion has a greater affinity for hydroxide than for methylene glycolate. Hence the maximum in the plating rate may be due to a competition between the two coordinating species.

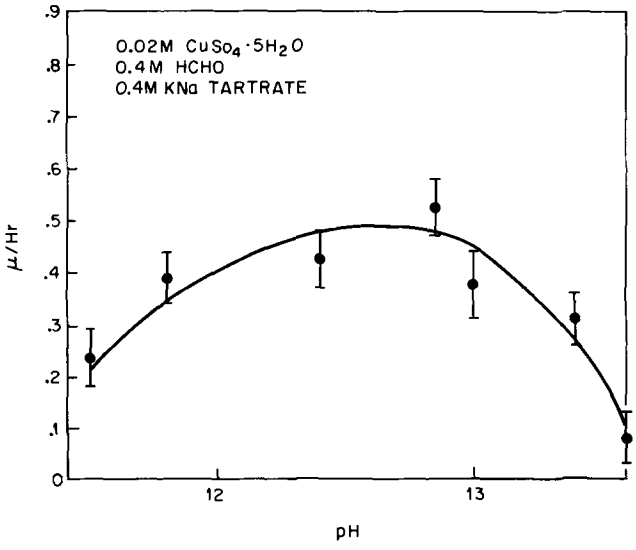

Fig. 10. Plating rate vs. pH in a solution containing 0.02M $CuSO_4 \cdot 5H_2O$, 0.4M HCHO, and 0.4M KNa tartrate.

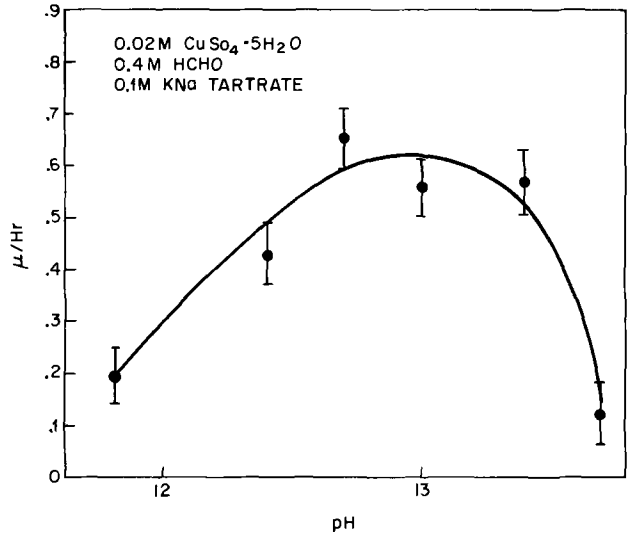

Fig. 11. Plating rate vs. pH in a solution containing 0.02M $CuSO_4 \cdot 5H_2O$, 0.4M HCHO, and 0.1M KNa tartrate.

The calculated concentration of methylene glycolate (from 0.4 moles of formaldehyde) and hydroxide are plotted as a function of pH in Fig. 12. A maximum in the plating rate in the vicinity of pH 12.8 could be predicted since the curves begin to converge rapidly at this point. The effect of this is that the concentration of hydroxide becomes comparable to and finally greater than the concentration of methylene glycolate. Therefore hydroxide bonding to the copper ions becomes predominant.

Table IV. Calculated per cent dissociation as function of pH

pH	% Dissociated
11	1.6
12	13.9
13	61.8
14	94.2

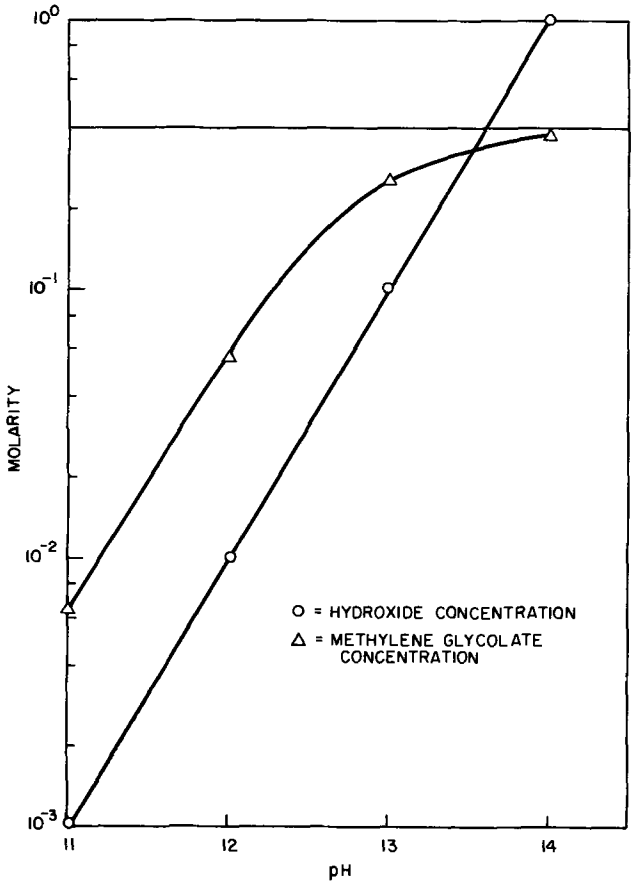

Fig. 12. Calculated concentration of methylene glycolate (from 0.4 moles of formaldehyde) and hydroxide as a function of pH.

A second factor which may cause the maximum is the variation in structure of the copper species. As the structure changes from one containing one tartrate ion and two hydroxide ions per copper ion to one containing two tartrate ions per copper ion (Fig. 7) steric hindrance may make it more difficult for methylene glycolate to enter the primary coordination sphere of the copper ion.

Since the nature of the copper complex and therefore the plating rate of an electroless bath changes with pH and since the pH of the bath changes with storage and during use, it is not surprising that problems in the reproducible use of electroless copper baths are often encountered. We have also found that the appearance of the deposits is pH dependent due to a change in the morphology of the copper deposit. Details of this and of the effect of certain additives are to be reported in a future publication.

Acknowledgment

The author is indebted to W. E. Blumberg for running the EPR spectra and for helpful discussions during the course of this work. D. R. Turner and P. J. Boddy reviewed the manuscript and made helpful comments.

Manuscript received Feb. 10, 1971.

Any discussion of this paper will appear in a Discussion Section to be published in the June 1972 JOURNAL.

REFERENCES

1. Y. Okinaka, Paper 144 presented at the Detroit Meeting of the Society, Oct. 5-9, 1969.
2. W. Goldie, "Metallic Coating of Plastics," Vol. 1, p. 65, Electrochemical Publications Limited, Middlesex, England (1968).
3. S. Kirschner and R. Kiesling, *J. Am. Chem. Soc.*, **82**, 4174 (1959) and references therein.
4. T. D. O'Brien in "Chemistry of the Coordination Compounds," p. 261, J. C. Bailar, Editor, Reinhold Publishing Corp., New York (1956).
5. J. H. Dunlop, D. F. Evans, R. D. Gillard, and G. Wilkinson, *J. Chem. Soc. (A)*, **1966**, 1260.
6. B. R. McGarvey in "Transition Metal Chemistry," Vol. 3, pp. 89-201, R. L. Carlin, Editor, Marcel Dekker, Inc., New York (1966).
7. S. Fujiwara in "Spectroscopy and Structure of Metal Chelate Compounds," p. 289, K. Nakamoto and P. J. McCarthy, Editors, John Wiley & Sons, Inc., New York (1968).
8. R. Drago, "Physical Methods in Inorganic Chemistry," pp. 329-332, Reinhold Publishing Corp., New York (1965).
9. J. Stankowski, *Acta. Phys. Pol.*, **33**, 387 (1968).
10. N. D. Chasteen and R. L. Belford, *Inorg. Chem.*, **9**, 169 (1970).
11. W. E. Blumberg and J. Peisach, *J. Chem. Phys.*, **49**, 1793 (1968).
12. D. Kivelson and R. Neiman, *ibid.*, **35**, 149 (1961).
13. R. Drago, *op. cit.*, p. 355.
14. M. M. Jones, "Elementary Coordination Chemistry," p. 255, Prentice-Hall, Inc., Englewood Cliffs, N. J. (1964).
15. M. Saito, *J. Metal Finish. Soc. Japan*, **17**, (7), 10 (1966).
16. Y. Okinaka, Private communication.
17. M. Wadano, *Ber.*, **67**, 191 (1934).

Mechanism of the Electrocrystallization of Nickel and Cobalt in Acidic Solution

I. Epelboin* and R. Wiart

Groupe de Recherche du C.N.R.S., "Physique des Liquides et Electrochimie," Universite de Paris, Paris 5e, France

ABSTRACT

This mechanism is studied by means of the analysis of the polarization characteristic and of the cathodic impedance. The results, obtained from an acidic solution of the Watts type, strongly support the hypothesis that the cathodic reaction occurs in several steps probably involving an adion $(MeOH)_{ads}$. In the case of nickel, the results can be accounted for by a mechanism implying two successive transfer reactions in which $(NiOH)_{ads}$ acts as an intermediate compound and not as a catalyst. The presence in the electrolyte of either sodium benzenesulfonate or 2-butyne 1,4-diol (two inhibitors commonly used for the electrocrystallization of nickel) specifically modifies the kinetic parameters of transfer reactions and diminishes the capacity of the electrochemical double-layer. This capacity is defined thanks to a least-squares analysis of the cathodic impedance.

It is accepted in recent years that the electrocrystallization of a polyvalent metal Me^{z+} occurs in several steps. More particularly, authors agree (1-6) that an intermediate MeOH adsorbed at the electrode is formed during the cathodic reaction of the electrolytic deposition of nickel and cobalt in acidic medium. However, the electrochemical reactions leading to the metal are still a matter for discussion, and the intermediate $(MeOH)_{ads}$ is considered to be either a catalyst or a compound which is consumed at the electrode (7). In order to settle this problem, we have analyzed the cathodic polarization and the cathodic impedance during the electrocrystallization of nickel and cobalt from an electrolytic solution of the Watts type.

Furthermore, using the two above-mentioned methods, we have been able to study the influence on the reaction mechanism of two compounds commonly employed to inhibit the electrocrystallization of nickel (sodium benzenesulfonate and 2-butyne 1,4-diol). It is well known that the presence, in the electrolyte of one of these organic compounds (which are representative of two types of inhibitors: alkaline sulfonates and acetylenic alcohols) modifies, in a specific way, the state of the surface and the structure of the deposit (8). Moreover, organic compounds are adsorbed at the electrode, and this adsorption gives rise to a decrease of the electrochemical double-layer capacity (9-11). The definition of this capacity is difficult when electrochemical reactions occur at the electrode (12). We tried to define it more accurately by calculating (by a least-squares computer calculation) the elements of the equivalent circuit of the cathodic impedance.

Theoretical

In the present state of knowledge, authors accept the formation of an intermediate species, MeOH adsorbed at the electrode during the electrocrystallization of nickel and cobalt (1-6). The discharge arises from the ion $(MeOH)^+$ formed by the following chemical reaction

$$Me^{2+} + H_2O \rightarrow (MeOH)^+ + H^+$$

This ion adsorbs according to the Transfer Reaction [I]

$$(MeOH)^+ + e^- \underset{K_1'}{\overset{K_1}{\rightleftarrows}} (MeOH)_{ads} \qquad [I]$$

However, interpretations on what occurs after this latter step are divergent. Different reactions leading to the electrocrystallization of the metal are considered (2-5).

$(MeOH)_{ads}$ is a catalyst.—Heusler (2, 3) proposed a mechanism for the cathodic deposition of the iron group metals which is analogous to the catalytic mechanism he put forward for the anodic dissolution. Here, Reaction [I] is reversible, and the compound $(MeOH)_{ads}$ catalyzes the Transfer Reaction [II]

$$(MeOH)_{ads} + (MeOH)^+ + 2e^- \xrightarrow{K_2} (MeOH)_{ads} + Me + OH^- \qquad [II]$$

If MeOH is assumed to adsorb according to the Langmuir isotherm and if the electrolysis current I is not limited by the convective diffusion transport of the metal ions toward the cathode, then current I obeys Expression 1, established in the Appendix

$$I = \frac{2\mathbf{F}K_1K_2\beta[MeOH^+]^2}{K_1[MeOH^+] + K_1'\beta} \qquad [1]$$

where $\mathbf{F}$ is the Faraday and β the maximum number of $(MeOH)_{ads}$ species per surface unit, *i.e.* the maximum superficial density of $(MeOH)_{ads}$ expressed in mole·cm^{-2}. The electrochemical rate constants K_1, K_1', and K_2 are assumed to follow Tafel's law

$$K_i = k_i \exp(-b_iV) \qquad [2]$$

where $b_i = \alpha_i z_i \mathbf{F}/RT$, according to the previously used nomenclature (12); k_i, α_i, and $z_i\mathbf{F}$ denote the pre-exponential rate-constant, the cathodic transfer coefficient, and the number of coulombs per mole involved in the cathodic reaction, respectively.

According to Relation [1], the apparent order of the over-all deposition reaction, with respect to the metal ions, must be 2 near the equilibrium potential ($K_1[MeOH^+] << K_1'\beta$), whereas it must tend toward 1 at high cathodic polarizations ($K_1[MeOH^+] >> K_1'\beta$).

$(MeOH)_{ads}$ is an intermediate consumed at the electrode.—As in the case of the anodic dissolution of iron (12) during which $(FeOH)_{ads}$ desorbs according to the following process

$$(FeOH)_{ads} \rightarrow (FeOH)^+ + e^-$$

it can be considered that the $(MeOH)_{ads}$ species is consumed at the electrode during electrocrystallization. In the case of cobalt, Simonova and Rotinyan (4) proposed a mechanism in which $(MeOH)_{ads}$ is consumed during the Transfer Reaction [III]

$$(MeOH)_{ads} + (MeOH)^+ + 3e^- \xrightarrow{K_3} 2Me + 2\,OH^- \qquad [III]$$

* Electrochemical Society Active Member.

Key words: polarization curve, faradaic impedance, rotating-disk electrode, double-layer capacity, multistep mechanism, coverage relaxation, inhibition.

This reaction, which entails the transfer of 3 electrons, probably is an over-all reaction occurring in several steps which cannot be distinguished. We therefore shall take into account only Reactions [I] and [III] related by MeOH adsorbed according to the Langmuir isotherm.

If θ is the fraction of the cathodic surface covered by $(MeOH)_{ads}$ Reaction [I] will take place on the fraction $(1 - \theta)$, and Reaction [III] on the fraction θ. If Reaction [I] is supposedly irreversible ($K_1 >> K_1'$), and if convective diffusion transport is not the rate-determining step, the current-potential relation can be written (see Appendix)

$$I = \frac{4\mathbf{F}[MeOH^+]K_1K_3\beta}{K_1 + K_3\beta} \quad [3]$$

In this case, the apparent order of the over-all reaction with respect to the metal ions is 1, independent of the overpotential.

If the partial currents I_1 and I_3, which correspond to Reactions [I] and [III]

$$I_1 = 4\mathbf{F}K_1[MeOH^+] \quad [4]$$

$$I_3 = 4\mathbf{F}K_3\beta[MeOH^+] \quad [5]$$

are introduced into Eq. [3], we obtain

$$I = \frac{I_1 I_3}{I_1 + I_3} \quad [6]$$

Analysis of the faradaic impedance.—If we superimpose a sinusoidal variation of low amplitude and frequency f on the continuous polarization of the electrode, we can calculate the faradaic impedance Z_f. According to Heusler's mechanism, Z_f is inductive whatever the potential is, and becomes a mere transfer resistance when the overpotential tends toward an infinite value (13). On the other hand, if $(MeOH)_{ads}$ is an intermediate consumed at the electrode, this impedance can be either inductive or capacitive according to the potential (5).

A detailed calculation of the faradaic impedance of the electrode on which Reactions [I] and [III] evolve is given in the Appendix. This calculation leads to Eq. [7]

$$\frac{1}{Z_f} = \frac{I}{4}\left[b_1 + 3b_3 + \frac{(3I_3 - I_1)(b_1 - b_3)}{4\mathbf{F}j\omega\beta + I_1 + I_3}\right] \quad [7]$$

where $\omega = 2\pi f$

According to this equation, if $b_1 > b_3$, the reactive element is an inductance for $3I_3 > I_1$, and a capacity for $3I_3 < I_1$. It is well known that many faradaic impedances present such an inductance [(12) and references therein]. Equation [7] can be written as

$$\frac{1}{Z_f} = \frac{1}{R_t} + \frac{1}{\rho + jL\omega} = \frac{1}{R_t} + \frac{1}{\rho(1 + j\omega\tau)} \quad [8]$$

with the transfer resistance

$$R_t = \frac{4}{I(b_1 + 3b_3)} \quad [9]$$

the faradaic resistance

$$\rho = \frac{4(I_1 + I_3)}{I(3I_3 - I_1)(b_1 - b_3)} \quad [10]$$

and the faradaic time-constant

$$\tau = \frac{L}{\rho} = \frac{4\beta\mathbf{F}}{I_1 + I_3} \quad [11]$$

Equation [8] shows that the faradaic impedance consists of the transfer resistance R_t, set in parallel with the series connection of a resistance and a reactance.

The representative schema of the electrode over-all impedance, in the case of an inductive faradaic impedance, is given in Fig. 1. The resistance R_e is that of the electrolyte; the capacity C, set in parallel with the faradaic impedance, is that of the electrochemical double-layer. If this capacity is independent of frequency, this schema (Fig. 1) is an equivalent circuit, and the electrode over-all impedance can be written as

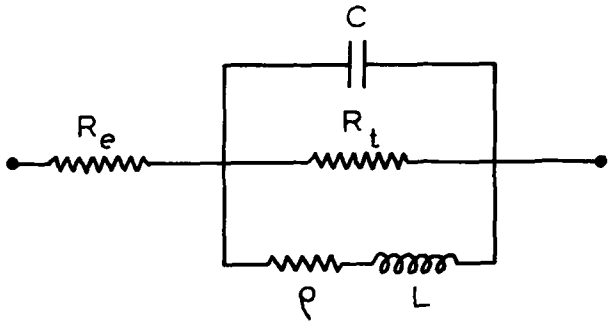

Fig. 1. Representative schema of the electrode impedance. R_e = Resistance of the electrolyte. C = Capacity of the electrochemical double-layer. R_t = Transfer resistance. ρ = Faradaic resistance. L = Self-inductance.

$$Z = R_e + \left[\frac{1}{R_t}(1 + j\omega\tau_{HF}) + \frac{1}{\rho(1 + j\omega\tau)}\right]^{-1} \quad [12]$$

where $\tau_{HF} = R_tC$ = high frequency time-constant.

This theoretical investigation reveals that it is possible to distinguish between the two considered mechanisms by studying the influence of the metal ion concentration and the cathodic potential on the electrolysis current I and the electrode impedance Z.

Experimental

Electrolytic solution and electrolysis cell.—In order to perform such a study, we chose an electrolyte of the Watts type, whose pH was constant. This solution is particularly suitable for it can (*i*) bear high current densities, (*ii*) maintain a cathodic efficiency close to unity for a large range of current densities, and (*iii*) allow the addition of organic compounds at relatively high concentrations. A liter of this solution contained 300g of $MeSO_4$, 7 H_2O, 35g of $MeCl_2$, 6 H_2O, and 40g of H_3BO_3, all these compounds being ultrapure.

The organic compounds added to the electrolyte were two inhibitors of electrocrystallization: sodium benzenesulfonate (C_6H_5-SO_3Na) and 2-butyne 1,4-diol (CH_2OH-$C{\equiv}C$-CH_2OH).[1] It is well known that these two types of compounds have a specific effect on the state of the surface of the nickel deposit, depending on the texture of this deposit (8, 14).

During the electrolysis, the solution was maintained at 50° ± 0.5°C by water circulation. The soluble anode was a nickel (or cobalt) cylinder whose area was close to 1 dm^2. The reference electrode was immersed in the electrolyte, and consisted of two compartments separated by fritted-glass. The compartment where the calomel electrode was immersed was filled with a KCl saturated solution; the other one contained the electrolyte of the cell.

Rotating disk electrode.—The metal deposition occurred on the cross section of a copper cylinder; this section, whose area (0.2 cm^2) was much smaller than that of the counterelectrode, was previously polished by emery paper (600 grade). The disk electrode was driven either by an asynchronous motor or by a compressed air turbine. Its rotation speed was sufficiently high so that the current was independent of the rotation speed, *i.e.* of the convective diffusion transport of

[1] The purity of these two compounds was checked in the "Laboratoire de Chimie Organique I de la Sorbonne," and we want to express here our gratitude to C. Georgoulis, Director of the No. 138 C.N.R.S. Research Team, associated with the Universite de Paris VI, for his help.

chemical species. This rotation speed was measured by an electronic stroboscope (15) and was stable to better than 1%.

Plotting of the polarization curve and measurement of the impedance.—The plotting of the cathodic polarization curve and the measurement of the impedance were carried out under potentiostatic conditions. The current-potential curve was corrected for ohmic drop. This term was determined by an interruptor method (16), and from the high-frequency limit of the impedance.

We can obtain the electrode impedance by superimposing a sinusoidal potential of low amplitude on the continuous polarization potential. Some of the results were achieved by means of an impedance meter and an electronic potentiostat built in our laboratory (17). Joining this method to that of Lissajous, we were able to obtain the electrode impedance up to a frequency of about 0.1 Hz. However, when the pH varies with time during the electrolysis, measurements become more difficult at low frequencies. We performed them, in this case, by means of a digital transfer function analyzer (Solartron, J M 1600 Type) connected to a potentiostat which was built in our laboratory and which allowed measurements of electrochemical impedances in a frequency range between 10^{-5} Hz and 50 kHz (18).

Results and Discussion

Study of the polarization curve.—During the electrocrystallization of nickel, we studied the influences of the electrolyte pH and the metal ion concentration on the polarization curve. Such a study is more difficult in the case of cobalt because the pH varies with time during electrocrystallization. However, in this case, the current-potential curve does not obey Tafel's law at a pH of 4.2 ± 0.2. As a matter of fact, $\partial \log I/\partial V$ varies with the cathodic potential, and this variation is in agreement with a deposition mechanism implying several steps (6).

In the case of nickel, the current-potential curve remains the same when the electrolyte pH varies between 3.5 and 5.6. At a fixed pH (= 4.5), the ion metal concentration has an effect on the reaction rate, which is shown in Fig. 2. The concentrations c of Ni^{2+}, which correspond to curves 1 to 3, are 1.22M, 0.15M, and 0.063M, respectively. When the concentration of Ni^{2+} decreases from 1.22M, Ni^{2+} is progressively substituted in the electrolyte by Na^+, so that the concentrations of SO_4^{2-} and Cl^- remain constant (5). At high current densities, the current-potential curves have been discontinued either at a potential (about −1.2V/SCE) at which hydrogen evolution is no longer negligible, or at a current (about 150 mA) at which electrolysis conditions are no longer those for a steady-state.

Within the potential range studied here, (*i.e.* between −0.7 and −1.12V/SCE), the value of $(\partial \log I/\partial \log c)_V$ is 1 ±8%, which shows that the order of the reaction is one with respect to Ni^{2+}.

Consequently, Heusler's hypothesis (3) concerning an intermediate NiOH acting as a catalyst must be rejected, since, according to Eq. [1], the order of the over-all reaction should decrease from 2 to 1 when the cathodic polarization increases. On the other hand, our experimental results strongly support the mechanism put forward by Simonova and Rotinyan (4).

To conform with Eq. [6], which must be satisfied at each point of the polarization curve, each polarization curve presented in Fig. 2 has two asymptotes, and all these asymptotes form a family of parallel straight lines, at ±10%. When the cathodic polarization is low, the curve tends toward a straight line which represents the variation of current I_1 and whose slope is $b_1 = 23V^{-1}$. When the cathodic polarization is high, the asymptote represents the variation of current I_3 and its slope is $b_3 = 8.5V^{-1}$.

Analysis of the cathodic impedance.—This analysis

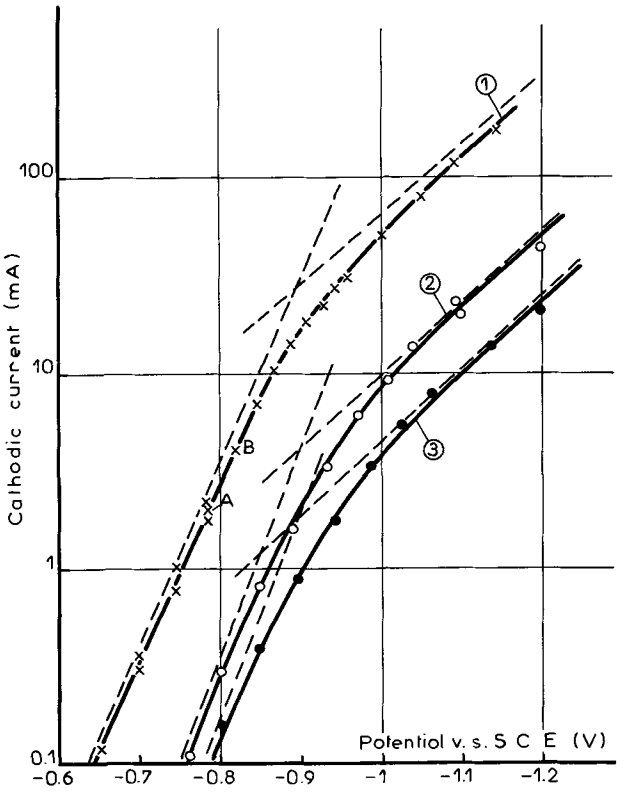

Fig. 2. Influence of the concentration (c) of Ni^{2+} on the steady-state current-potential curves corresponding to the electrocrystallization of nickel at a rotating disk electrode (area = 0.2 cm^2). (pH = 4.50 ± 0.05; temperature = 50° ± 0.5°C). X: Curve 1 where c = 1.22M and rotation speed = 2000 rpm; ○: Curve 2 where c = 0.15M and rotation speed = 9500 rpm; ●: Curve 3 where c = 0.063M and rotation speed = 8000 rpm. The continuous line represents experimental curves and the dotted line represents partial currents deduced from Eq. [4], [5], and [6]. A: I = 2 mA, V = −0.78 V/SCE; B: I = 4 mA, V = −0.82 V/SCE.

corroborates the results obtained from the plotting of the current-potential curve. When the cathodic polarization exceeds a certain value (about −0.96V/SCE, in the case of nickel), the impedance is capacitive at all frequencies. On the contrary, within the range of low cathodic polarizations, the electrode impedance presents an inductive character at low frequencies.

The impedance diagrams relative to the electrocrystallization of nickel, represented in the complex plane ($Z = R - jG$) on Fig. 3, correspond to this last range. They were obtained from the Watts solution under the same polarization conditions as those of points A and B in Fig. 2. We checked on the two diagrams (A) and (B) that the resistance obtained by extrapolating

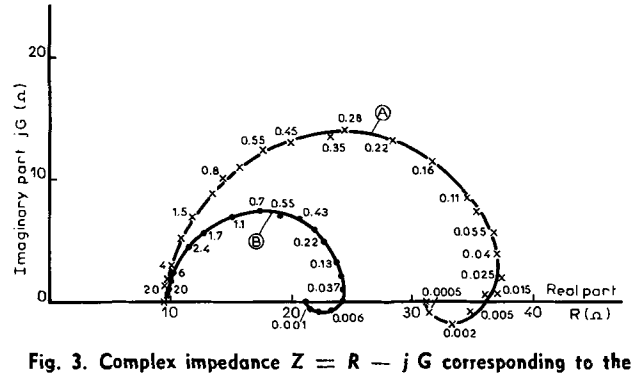

Fig. 3. Complex impedance $Z = R - jG$ corresponding to the electrocrystallization of nickel under the same conditions as for points A and B in Fig. 2. Frequencies are expressed in kHz.

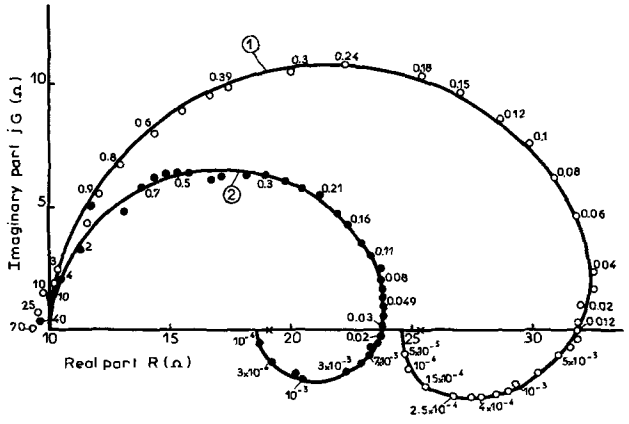

Fig. 4. Complex impedance $Z = R - jG$ corresponding to the electrocrystallization of cobalt, at a rotating-disk electrode (area = 0.2 cm²), from an electrolyte of the Watts type (concentration of Co^{2+} = 1.22M; pH = 4.2 ± 0.2; temperature = 50° ± 0.5°C). ○ Curve 1: I = 3 mA, V = −0.74 V/SCE; ● Curve 2: I = 6 mA, V = −0.81 V/SCE. Frequencies are expressed in kHz.

at zero frequency is equal to the reverse of the slope of the steady-state current-potential curve which corresponds to the points A and B in Fig. 2, respectively. At high frequencies, the faradaic impedance is shunted by the electrochemical double-layer capacity, and the electrode impedance is reduced to the electrolyte resistance R_e. At low frequencies, in conformity with the schema in Fig. 1, the impedance has an inductive character: the imaginary component G of Z becomes negative, while the real component R passes through a maximum.

During the electrocrystallization of cobalt, the same phenomenon is observed at low cathodic polarizations. As an illustration, Fig. 4 shows the diagrams obtained from the Watts solution under the following polarization conditions: I = 3 mA V = −0.74 V/SCE (diagram 1); I = 6 mA, V = −0.81 V/SCE (diagram 2).

Determination of the electrochemical double-layer capacity.—In order to define the concept of electrochemical double-layer capacity when an electrocrystallization process occurs at the electrode, we calculated by a least-squares method (19), the elements of the representative circuit of the impedance from experimental data. The confidence interval of the results was calculated on the 10% level of significance. All calculations were carried out on a 360/75 IBM computer.

A numerical calculation shows that we can account for our experimental results by assuming the faradaic impedance shunted by a constant capacity C. Tables I and II summarize the values of the parameters of Eq. [12] obtained under the same polarization conditions as those in Fig. 3 (for nickel) and in Fig. 4 (for cobalt), respectively. Under these polarization conditions, we

Table I. Electrocrystallization of nickel

Experimental values of the parameters of the electrode impedance under the same polarization conditions as for points A and B in Fig. 2.

R_e = Resistance of the electrolyte
R_t = Transfer resistance
τ_{HF} = High frequency time-constant
ρ = Faradaic resistance
τ = Faradaic time-constant

Parameters	Polarization conditions A	B
R_e (ohm)	9.81 ± 0.18	9.95 ± 0.13
R_t (ohm)	27.0 ± 0.5	14.3 ± 0.3
τ_{HF} (msec)	0.444 ± 0.016	0.200 ± 0.007
ρ (ohm)	112 ± 43	68 ± 22
τ (msec)	79 ± 64	56 ± 34

Table II. Electrocrystallization of cobalt

Experimental values of the parameters of the electrode impedance under the same polarization conditions as for diagrams 1 and 2 in Fig. 4. Notations are the same as for Table I.

Parameters	Polarization conditions 1	2
R_e (ohm)	10.43 ± 0.28	10.36 ± 0.27
R_t (ohm)	22.03 ± 0.39	13.64 ± 0.34
τ_{HF} (msec)	0.584 ± 0.015	0.372 ± 0.011
ρ (ohm)	49.2 ± 3.8	24.7 ± 2.1
τ (msec)	373 ± 49	142 ± 21

verified no frequency dependence of the electrochemical double-layer capacity C at high frequencies. Consequently, the concept of double-layer capacity can be used for the study of the action of organic inhibitors on the cathodic reaction.

Influence of organic inhibitors on the cathodic reaction kinetics.—Analysis of the impedance shows that the presence of either of the two inhibitors studied here causes a decrease, but no frequency dependence of the electrochemical double-layer capacity C. For instance, in the presence of 3.10^{-2}M sodium benzenesulfonate, this capacity changes from 70 to 45 μF/cm² at a current of 4 mA. Similarly at 6 mA, the addition of 8.10^{-3}M 2-butyne 1,4-diol leads to a capacity C of 50 μF/cm². These results are in agreement with those of the literature (9-11).

Not only do these inhibitors decrease the capacity C, but they also have a considerable influence on the kinetic parameters of the two Transfer Reactions [I] and [III] as shown by the current-potential curve (Fig. 5). Curve 1 was obtained from the Watts solution without inhibitor (concentration ç of Ni^{2+} = 1.22M). It can be seen (curve 2) that the addition of 4.10^{-3}M to 3.10^{-2}M sodium benzenesulfonate modifies neither the slopes b_1 and b_3 of the two asymptotes nor the partial current I_3, but diminishes the partial current I_1 at a given cathodic potential.

On the other hand, the presence of 2-butyne 1,4-diol (8.10^{-3}M; curves 3 and 4, Fig. 5) diminishes both I_1 and b_3. This is clearly shown on curve 4. The presence of this inhibitor also modifies the parameters of the impedance. It shifts indeed, toward the cathodic potentials, the limit of the polarization range within which the impedance is inductive, since this inductive character persists when the potential is −1.10 V/SCE (5). Table III gathers together the values of the elements of the equivalent circuit of the impedance obtained under the same polarization conditions as those of points C, D, E, and F in Fig. 5 in the presence of 8.10^{-3}M 2-butyne 1,4-diol in the electrolyte. At these cathodic polarizations, we can assume that reaction [I] is irreversible, and we can compare the experimental values of the impedance parameters with those that are calculated from Eq. [9], [10], [11] and which are shown in the last column of Table III. The value of β is assumed equal to the density of the nickel atoms in the (111) plane ($3.1\ 10^{-9}$ mole cm²) which forms at the metal surface during the growth of crystallites. There is a good agreement between experimental values and calculated values, except for the time-constant τ whose experimental value is systematically higher than the calculated value. These differences might be due to the fact that the hypothesis of an adsorption according to the Langmuir isotherm assumes a uniformly accessible surface for the electrode, but this condition cannot be satisfied with a textured deposit.

Conclusion

The shape of the polarization curves obtained in the absence of any convective diffusion transport, and the inductive character of the impedance at low frequencies lead to the conclusion that the electrocrystallization of nickel and cobalt occurs in several steps. By

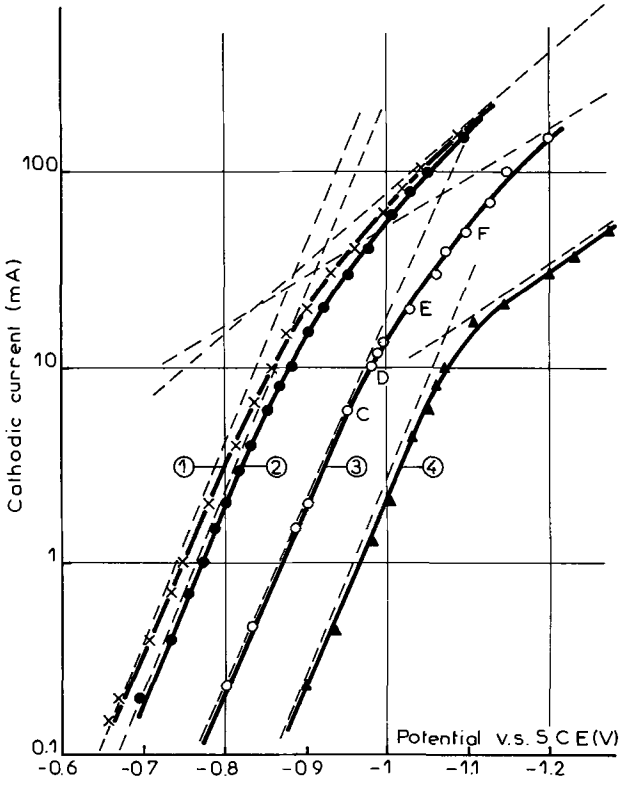

Fig. 5. Influence of organic compounds on the steady-state current-potential curve in the case of the electrocrystallization of nickel (pH = 4.5; temperature = 50° ± 0.5°C) at a rotating-disk electrode (area = 0.2 cm²). Curves 1, 2, and 3 are obtained with an electrolyte of the Watts type (concentration c of Ni^{2+} = 1.22M, rotation speed = 2000 rpm). For Curve 4: c = 0.15M. rotation speed = 9000 rpm. X Curve 1: without organic compound, ● Curve 2: with 3.10^{-2}M sodium benzenesulfonate, ○ Curve 3 and ▲ Curve 4 with 8.10^{-3}M 2-butyne 1,4-diol. The continuous line represents experimental curves and the dotted line represents partial currents deduced from Eq. [4], [5], and [6]. Polarization conditions for points C, D, E, and F are given in Table III.

calculating the elements of the equivalent circuit of the cathodic impedance, we were able to define the capacity of the electrochemical double-layer, which showed no frequency dependence, and to separate this capacity from the faradaic impedance. Unfortunately, in the case of cobalt, we could not further investigate the mechanism of the electrocrystallization, since the current-potential curve varied with the pH. On the other hand, in the case of nickel, the experimental results support a faradaic process implying two successive reactions, during which $(NiOH)_{ads}$ acts as an intermediate consumed at the electrode and not as a catalyst. Furthermore, the presence in the electrolyte of organic inhibitors, such as sodium benzenesulfonate or 2-butyne 1,4-diol, not only diminishes the capacity of the electrochemical double-layer, but also specifically modifies the rates of the two successive transfer reactions.

We hope that these two methods can be generalized for the study of the electrocrystallization of other metals. The two methods described in this article have indeed already been used for the study of the electrocrystallization of copper in an acidic solution (20).

Table III. Electrocrystallization of nickel

Comparison between experimental values and calculated values of the parameters of the electrode impedance. The polarization conditions are the same as for points C, D, E, and F in Fig. 5.

C	:	I = 6 mA	V = −0.95 V/SCE
D	:	I = 10 mA	V = −0.98 V/SCE
E	:	I = 20 mA	V = −1.03 V/SCE
F	:	I = 50 mA	V = −1.10 V/SCE

The values of the parameters are calculated from Eq. [9], [10], and [11].

Polarization conditions	Parameters	Experimental values	Calculated values
C	R_e (ohm)	9.78 ± 0.25	•
	R_t (ohm)	16.4 ± 0.5	16.7
	τ_{HF} (msec)	0.163 ± 0.011	•
	ρ (ohm)	16.4 ± 5.5	15.8
	τ (msec)	340 ± 150	5.4
D	R_e (ohm)	9.67 ± 0.19	•
	R_t (ohm)	9.4 ± 0.3	10
	τ_{HF} (msec)	0.073 ± 0.005	•
	ρ (ohm)	14.5 ± 4	10.6
	τ (msec)	23.5 ± 8	4.1
E	R_e (ohm)	9.45 ± 0.19	•
	R_t (ohm)	4.87 ± 0.24	5
	τ_{HF} (msec)	0.043 ± 0.006	•
	ρ (ohm)	9.1 ± 2.5	6.4
	τ (msec)	6.9 ± 3.4	2.7
F	R_e (ohm)	9.43 ± 0.67	•
	R_t (ohm)	2.12 ± 0.08	2
	τ_{HF} (msec)	0.0203 ± 0.0016	•
	ρ (ohm)	3.7 ± 1.6	4
	τ (msec)	4.4 ± 2.2	1.2

• Not calculated.

We hope that these two methods can be generalized for the study of the electrocrystallization of other metals. The two methods described in this article have indeed already been used for the study of the electrocrystallization of copper in an acidic solution (20).

Manuscript submitted Feb. 10, 1971; revised manuscript received June 2, 1971.

Any discussion of this paper will appear in a Discussion Section to be published in the June 1972 JOURNAL.

APPENDIX

We give here a detailed calculation leading to Eq. [1], [3], and [7].

$(MeOH)_{ads}$ acts as a catalyst.—Supposing that $(MeOH)_{ads}$ species cover a fraction θ of the cathodic surface, the forward reaction [I] will take place on a fraction $(1 - \theta)$, while the reverse reaction [I] and reaction [II] will occur on a fraction θ (21). Under steady-state conditions

$$K_1 (1 - \theta) [MeOH^+] = K_1' \beta\theta \quad [13]$$

Consequently

$$\theta = \frac{K_1 [MeOH^+]}{K_1 [MeOH^+] + K_1'\beta} \quad [14]$$

Reactions [I] and [II] lead to a current I obeying Eq. [15] (see Ref. 21).

$$\frac{I}{F} = K_1 (1 - \theta) [MeOH^+] - K_1'\beta\theta + 2K_2\beta\theta [MeOH^+] \quad [15]$$

Combination of Eq. [14] and [15] leads to Eq. [1]

[1]

$$I = \frac{2F K_1 K_2 \beta [MeOH^+]^2}{K_1 [MeOH^+] + K_1' \beta} \quad [1]$$

$MeOH_{ads}$ is an intermediate consumed at the electrode.—Reaction [I] (supposed here irreversible) takes place on a fraction $(1 - \theta)$ of the cathodic surface, whereas Reaction [III] occurs on a fraction θ. Under steady-state conditions

$$K_1 (1 - \theta) [MeOH^+] = K_3 \beta\theta [MeOH^+] \quad [16]$$

Consequently

$$\theta = \frac{K_1}{K_1 + K_3 \beta} \quad [17]$$

Current I is then given by Eq. [18]

$$\frac{I}{F} = K_1 (1 - \theta) [MeOH^+] + 3 K_3 \beta\theta [MeOH^+] \quad [18]$$

Equation [3] can be deduced from Eq. [17] and [18]

$$I = \frac{4F [MeOH^+] K_1 K_3 \beta}{K_1 + K_3 \beta} \quad [3]$$

According to Eq. [18], I is a function of θ and V; the faradaic impedance Z_f is consequently expressed by

$$-\frac{1}{Z_f} = \left(\frac{\partial I}{\partial V}\right)_\theta + \left(\frac{\partial I}{\partial \theta}\right)_V \frac{\Delta\theta}{\Delta V} \quad [19]$$

These two partial differentials can be calculated by differentiating Eq. [18] and using the value of θ given in Eq. [17]

$$\left(\frac{\partial I}{\partial V}\right)_\theta = -\mathbf{F}\,[\mathrm{MeOH}^+]\,\frac{K_1 K_3 \beta}{K_1 + K_3 \beta}\,(b_1 + 3b_3) \quad [20]$$

(Coefficients b_1 and b_3 are defined in Eq. [2])

and $$\left(\frac{\partial I}{\partial \theta}\right)_V = \mathbf{F}\,[\mathrm{MeOH}^+]\,(3K_3\beta - K_1) \quad [21]$$

The dependence of the superficial density $\beta\theta$ of $(\mathrm{MeOH})_{ads}$ with time is given by Eq. [22]

$$\beta\frac{d\theta}{dt} = K_1\,[\mathrm{MeOH}^+]\,(1-\theta) - K_3\,[\mathrm{MeOH}^+]\,\beta\theta \quad [22]$$

Using the following relation $d(\Delta\theta)/dt = j\omega\,\Delta\theta$ and the total differential of Eq. [22], we can obtain

$$\frac{\Delta\theta}{\Delta V} = \frac{K_1 K_3 \beta}{K_1 + K_3 \beta}\,[\mathrm{MeOH}^+]\,\frac{b_3 - b_1}{j\omega\beta + [\mathrm{MeOH}^+]\,(K_1 + K_3\beta)} \quad [23]$$

Equation [7] is readily obtained by combining Eq. [19], [20], [21], and [23], and introducing the expressions of currents I_1, I_3, and I given by Eq. [4], [5], and [6]

$$\frac{1}{Z_f} = \frac{I}{4}\left[b_1 + 3b_3 + \frac{(3I_3 - I_1)\,(b_1 - b_3)}{4\mathbf{F}j\omega\beta + I_1 + I_3}\right] \quad [7]$$

REFERENCES

1. J. Matulis and R. Slizys, *Electrochim. Acta*, **9**, 1177 (1964).
2. K. E. Heusler, *Ber. Bunsenges. Phys. Chem.*, **71**, 620 (1967).
3. K. E. Heusler and L. Gaiser, *Electrochim. Acta*, **13**, 59 (1968).
4. M. V. Simonova and A. L. Rotinyan, *Zh. Prikl. Khim.*, **37**, 1951, (1964).
5. R. Wiart, Thèse de Doctorat d'Etat, Paris, (1968), No. d'enregistrement C.N.R.S.: A.O. 2605; *Oberfläche-Surface*, **9**, 213, 241, and 275, (1968).
6. F. Lenoir and R. Wiart, *Compt. Rend. Acad. Sci. Paris, Series C*, **269**, 204 (1969).
7. J. O'M. Bockris and A. Damjanovic, "Modern Aspects of Electrochemistry," No. 3, p. 224, Butterworth, London (1964).
8. I. Epelboin, M. Froment, and G. Maurin, *Plating*, **56**, 1356 (1969).
9. O. Volk and H. Fischer, *Electrochim. Acta*, **4**, 251, (1961).
10. E. Raub, N. Baba, and M. Stalzer, *Metalloberfläche*, **18**, 321 (1964).
11. S. S. Kruglikov, N. T. Kudryavtsev, and R. P. Sobolev, *Electrochim. Acta*, **12**, 1263 (1967).
12. I. Epelboin and M. Keddam, *This Journal*, **117**, 1052 (1970).
13. M. Keddam, Thèse de Doctorat d'Etat, Paris, (1968), No. d'enregistrement C.N.R.S.: A.O. 2192.
14. G. Maurin, Thèse de Doctorat d'Etat, Paris (1970), No. d'enregistrement C.N.R.S.: A.O. 4073; *Oberfläche-Surface*, **11**, 297, 309 (1970); **12**, 8, 24, 47, 54 (1971).
15. M. Daguenet, Publications Scientifiques et Techniques du Ministère de l'Air, Paris, No. 453 (1969).
16. P. Morel, *Traitements de Surface*, No. 89, 9 (1969) and No. 91, 37 (1970).
17. M. L. Boyer, I. Epelboin, and M. Keddam, *Electrochim. Acta*, **11**, 221 (1966).
18. I. Epelboin, C. Gabrielli, and J. C. Lestrade, *Rev. Gén. Elec.*, **79**, 669 (1970).
19. J. P. Badiali, H. Cachet, and J. C. Lestrade, *Electrochim. Acta*, **16**, 731 (1971).
20. I. Epelboin, F. Lenoir, and R. Wiart, *Compt. Rend. Acad. Sci., Paris, Series C*, **271**, 338 (1970).
21. K. J. Vetter, "Electrochemical Kinetics," p. 600, Academic Press, New York and London (1967).

Enhancement of Liquid Film Heat Transfer by Electrolytic Gas Evolution

R. B. MacMullin*

R. B. MacMullin Associates, Niagara Falls, New York 14303

and K. L. Mills and F. N. Ruehlen

Phillips Petroleum Company, Bartlesville, Oklahoma 74003

ABSTRACT

A study has been made of heat transfer in three types of internally cooled electrolytic cells employing a common nonaqueous electrolyte. The heat transfer surfaces were in part cathodic and evolved hydrogen gas. The gas evolution was utilized to promote rapid circulation of electrolyte. By varying the relative areas that were gas evolving and nongas evolving, the heat transfer coefficients through the bath side liquid film in contact with these surfaces could be estimated. The film coefficient is greatly enhanced by electrolytic gas evolution and is of the order of 2.5 to 3. Film coefficients appear to follow an exponential law, $h = k \cdot I^n$. Useful application of the effect for purposes of cell design is pointed out.

Most electrolytic processes, as conducted in real cells, evolve surplus heat which must be dissipated in one way or another. The sources of heat are of two kinds: surplus electrical energy and surplus chemical energy.

Surplus electrical energy: The net heat Q_e generated by passage of the current I is

$$Q_e = VI - \Delta H \cdot I/\mathbf{F}$$

If V is the actual cell voltage, which includes the emf E, the electrode overvoltages, and all other internal IR drops; I is the current in kiloamperes; ΔH is the heat absorbed for the over-all electrode reaction in kilojoules per gram equivalent, and 1 kj = 0.239 kcal; and $\mathbf{F}$ = 96.5 kilocoulombs per gram equivalent; then Q_e is in kilowatts, and 1 kW = 860 kcal/hr, or 3413 Btu/hr.

* Electrochemical Society Emeritus Member.

Key words: liquid film heat transfer, electrolytic gas evolution, film coefficients, electrolytic process, gas lift, hydrogen fluoride, potassium fluoride, pilot plant, enhanced heat transfer, scale-up self-cooling.

Surplus chemical energy.—This is the algebraic sum of all the chemical reactions (other than the electrode reactions) that also occur in the cell, *e.g.*: back reactions between anode and cathode products, and reactions between anode and/or cathode products and other materials either existing in or introduced into the cell as feed. This algebraic sum Q_c is usually exothermic.

In order to achieve a steady-state cell temperature, the total excess heat may be dissipated in a number of ways:

1. Positive difference in enthalpy between product streams and feed streams. This includes phase changes, such as partial vaporization of feed streams, including the solvent.
2. Loss of heat from cell to ambient surroundings via convection and radiation.
3. Forced rejection of heat from cell to coolants, generally via internal heat transfer surfaces.

Some large industrial cells require no internal heat transfer surfaces. In a diaphragm type chlor-alkali cell, the excess I^2R heat is balanced principally by the evaporation of water which is evolved with the chlorine and hydrogen. In a mercury type chlor-alkali cell, the excess I^2R is balanced principally by the increased enthalpy of the very large brine throughput.

Some types of cells require indirect cooling means, either internal or external to the cell. If external, the electrolyte is recycled back to the cell. In chlorate electrolysis, the electrode products NaOH and Cl_2 are allowed to react to form $NaClO_3$, and thus a large amount of excess chemical energy is released as heat. Cells of both types (internal and external cooling coils) are in common use.

Less common, but of increasing importance, are cells designed to carry out organic chemical syntheses by introducing organic feed streams which react with either or both of the electrode products as fast as they are formed. Halogenation of hydrocarbons at an anode can be conducted in this way, and even the subsequent hydrolysis of the halocarbons in the catholyte chamber, can also be conducted. The dissipation of heat in such operations can be a problem.

Assuming the cell designer is faced with the problem of providing auxiliary cooling, he has the choice of:

(*a*) Circulating the anolyte, the catholyte, or the common electrolyte if the cell is undivided, through an external heat exchanger and back to the cell. A pump is required. The engineering problems are many, and in some cases this turns out to be a difficult or expensive solution to the problem.

(*b*) Cooling the cell by providing internal heat exchangers. If gas is evolved at an electrode, the gas lift effect can be utilized for creating a strong circulation of the electrolyte. By placing the heat exchanger optimally with respect to the circulation, fairly good heat transfer can be realized. This solution dispenses with the moving parts (the pump) mentioned under (*a*).

Under (*b*), the cell designer has still another option: he might, for example, combine the separate functions of electrode and heat transfer, by cooling the electrode itself. This has two advantages:

1. It cuts cost, since no separate heat exchanger is needed, and this also conserves space.
2. The heat transfer coefficient between bath and a heat conducting surface is greatly enhanced if the surface is a gas-evolving electrode.

The idea is not new. Many patented chlorate cells (4-8) employ water-cooled cathodes, these being hydrogen evolving. In all cases, the gas evolution is utilized to promote electrolyte circulation. The fact that gas evolution promotes heat transfer is not new either and has been reported by several investigators (1, 2). The enhancement factor of the film coefficient may be in the range of 2 to 3 times.

The present authors have designed and operated, on a pilot scale, a variety of cells having cooled cathodes. These cells were built for the purpose of carrying out fluorination of hydrocarbon gases. The excess heat release was sufficiently large to create a major problem in scale-up to industrial size cells. Consequently, the heat transfer problem was studied in depth. The results of this study confirm the high enhancement factor for gas-evolving surfaces and has provided the basis for intelligent scale-up.

Experimental

In the experiments to be described, the common electrolyte approximates the composition KF·2HF (anhydrous) in liquid form at a temperature in the range 93°-110°C. The three cells used were of various shapes, rectangular and cylindrical, and, with the exception of the anodes, were fabricated entirely of carbon steel. Electrolysis of the bath resulted in depletion of its HF content, which was replenished regularly to maintain constant composition and operating bath levels. The electrodes were either parallel or concentric, and the anode-cathode gap was in the range of ½ to 1 in. Vertical height of electrodes ranged from 12 to 24 in. in the active area. The number of electrode pairs per cell ranged from 1 to 5, and these were arranged to take full benefit of the gas lift effect to promote circulation of electrolyte upward in the electrode gap. Return paths for degassed electrolyte were provided, as illustrated in Fig. 1-3.

During electrolysis, hydrogen gas (containing some HF vapor corresponding to the vapor pressure of the bath) was evolved at the cathodes. No gas whatever was discharged at the anode into the gap. The anode processes that did take place are immaterial to this heat transfer study. In some cases the cathodes were water-cooled; in others cooled with boiling methanol. Noncathodic heat transfer surfaces were cooled similarly.

With a power supply of 1000A d.c. total, cathode current density was varied over the range of 80 to 200 A/ft^2. Current efficiency was in all cases substantially 100%.

The cells were provided with numerous thermocouples for temperature measurement of bath, coolant, and metal wall on cathodic heat transfer surfaces. Coolant flow rates were accurately measured. In some cases, fluid bath velocities were measured directly by means of a pitot tube.

By varying the percentage of the total cooling surface that was cathodic, the over-all heat flux through

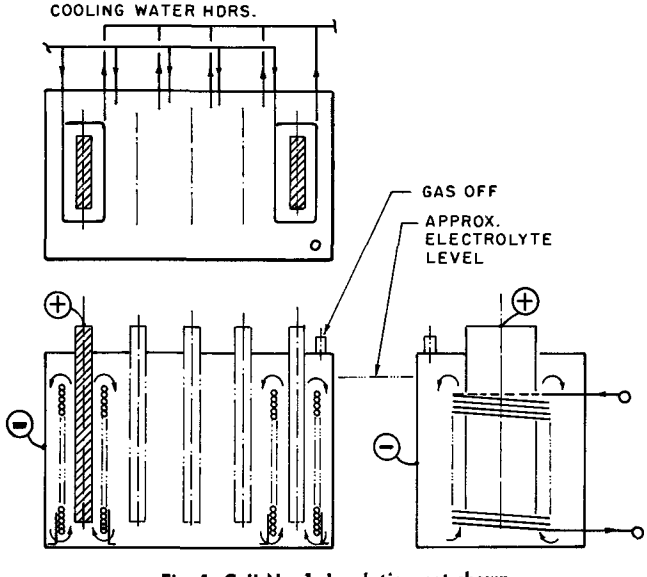

Fig. 1. Cell No. 1. Insulation not shown

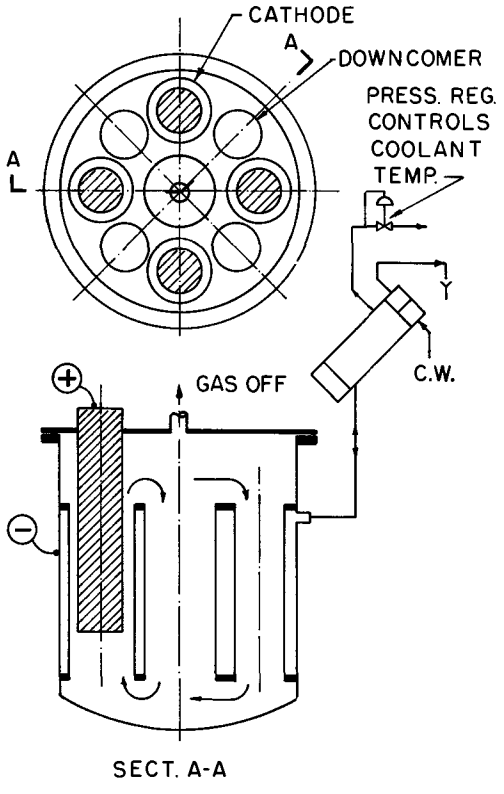

Fig. 2. Cell No. 2. Insulation not shown

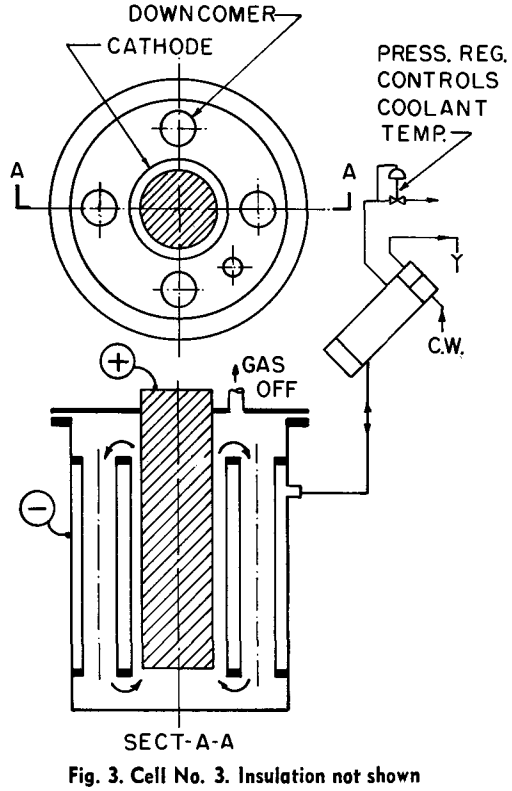

Fig. 3. Cell No. 3. Insulation not shown

cathodic and noncathodic surfaces could be differentiated, although these two paths for heat transfer were in parallel. Although the cell bodies were thermally insulated, some heat was lost to the surroundings, and this could be estimated with sufficient accuracy to permit fairly accurate estimates of the actual heat transferred through the cooling surfaces within the cell. See Appendix.

Film coefficients on the coolant side, and thermal conductivity of the steel walls of the heat transfer surface could be readily estimated. From these, and the over-all coefficient, the film coefficients on the bath side were calculated. Both over-all U's and bath-side film coefficients were found to be a function of cell current. Cell current, of course, determines H_2 gas evolution and indirectly, the bulk fluid velocity past the heat transfer surface. Schematic diagrams of the three types of cell used are shown in Fig. 1-3.

Results

Series I.—Rectangular Cell No. 1 contained five anode-cathode pairs. Cathodes of ⅜ in. OD tubing were wound into rectangular coils, adjacent coils touching. Cathodes were independently water cooled. These coils could serve either as gas evolving or nongas evolving coolers. Results are summarized in Table I.

Discussion.—1. Because these tubes touched, the areas used in calculating the U's are circumferential tube areas. It is possible that the effective area for heat transfer on the bath side is somewhat less, and the effective U's somewhat greater than shown in Table I. Effective current densities could also be somewhat higher for the same reason.

2. In any event, the enhancement ratio $R = h_c/h_{nc}$ is of the order 3.0.

Series II.—Cylindrical Cell No. 2 contained four cylindrical electrode pairs. One central and four surrounding pipe downcomers provided for return circulation and additional nongas evolving cooling surface. The central cathode and the downcomers were cooled with boiling methanol. The cell was operated with all downcomers open.

Series III.—Like Series II, but operated with the central downcomer open, all others closed.

The over-all U's at various current levels are summarized in Tables II and III for Series II and III, respectively.

Table I. Summary, cell No. 1, Series I

Subscript c, cathodic (gas evolving); nc, noncathodic (nongas evolving). All values of U and h refer to bath-side areas (geometric) in Btu/ft², hr, °F. I, amperes. i, A/ft². Average bath temperature, 202°F.

Test No.	% Cathodic	I	i_c	U	U_c	U_{nc}	h_c	h_{nc}	R
3	0	460	79.4	35.10		35.10		42.60	
6	0	450	77.7	36.50		36.50		42.90	
Average		455	78.55	35.80		35.80		42.75	
1	40	810	69.9	44.12	54.50	37.50	67.1	42.75	1.57
2	50	940	81.1	66.20	95.80	36.80	150.0	42.75	3.51
4	50	940	81.1	66.12	87.20	37.24	142.5	42.75	3.33
5	50	740	63.8	59.41	82.60	36.20	126.5	42.75	2.95
7	50	450	77.7	62.15	87.90	36.35	160.0	42.75	3.74
Average			74.72	59.80	81.60	36.82	129.2	42.75	3.02

Table II. Summary, cell No. 2, Series II

Cooling surface is 32.9% cathodic. All downcomers open. Over-all U refers to bath side area in Btu/ft², hr, °F. I, amperes, i_c, A/ft² on cathode. Average bath temperature, 207°F.

Test No.	I	i_c	U	$I^{0.844}$	K
5	950	184.5	62.61	10.56	5.93
8	931	186.7	55.06	10.48	5.25
9	931	186.7	53.75	10.48	5.25
6	917	178.2	55.21	10.44	5.28
4	855	166.0	62.18	10.20	6.09
3	760	147.6	62.06	9.80	6.33
10	760	147.6	56.63	9.80	5.78
7	713	138.4	54.28	9.58	5.67
2	665	129.1	58.68	9.35	6.27
11	665	129.1	51.96	9.35	5.56
11-A	570	110.7	57.86	8.87	6.52
11-B	570	110.7	58.99	8.87	6.65
12	475	92.3	39.49	8.35	4.73
	Average				5.780 ± 0.453

Table III. Summary, cell No. 2, Series III

Cooling surface is 49.4% cathodic. Downcomers: center 1 open; other 4 plugged. Over-all U refers to bath-side area, in Btu/ft², hr, °F. I, amperes. i_c, A/ft² on cathode. Bath temperature T_1, °F as noted.

Test No.	T_1	I	i_c	U	$I^{0.344}$	K
1	205.5	950	184.5	75.40	10.56	7.14
4	206.5	950	184.5	75.55	10.56	7.16
5	206.9	950	184.5	68.49	10.56	6.48
6	228.5	950	184.5	73.61	10.56	6.97
7	229.0	950	184.5	71.27	10.56	6.75
8	228.0	950	184.5	69.38	10.56	6.57
12	230.0	950	184.5	73.04	10.56	6.92
13	230.0	950	184.5	73.70	10.56	6.98
14	229.9	950	184.5	74.13	10.56	7.02
9	230.0	760	147.7	60.35	9.80	6.16
10	230.0	760	147.7	62.04	9.80	6.33
2	205.0	712.5	138.4	64.94	9.58	6.77
11	229.4	570	110.7	73.04	8.88	8.23
3	205.0	475	92.3	64.94	8.33	7.80
	Average					6.945 ± 0.308

Discussion.—1. On the assumption that U is an exponential function of I of the form

$$U = K \cdot I^n \qquad [1]$$

the data for Series II was processed for a least square best fit which gave $K = 8.736 \pm 0.892$ and $n = 0.2808 \pm 0.1379$.

The data for Series III was unsuitable for a meaningful regression analysis, since most of the data was taken at 950A, with insufficient data at low amperage.

In Series IV and V there is ample evidence for the exponential relation, with $n = 0.344$ approximately. We have therefore calculated the K's for Series II and III on this basis, as shown in Tables II and III. The average values of K are as follows:

Series	% Cathodic	K ($n = 0.344$)
II	32.9	5.780
III	49.4	6.945

If C = the fraction cathodic, and K_c and K_{nc} equal the values of K for cathodic and noncathodic conditions, respectively

$$K = C \cdot K_c + (1 - C)\, K_{nc} \qquad [2]$$

Solving the two sets of data gives

$K_c = 10.535$
$K_{nc} = 3.455$
$R_u = K_c/K_{nc} = 2.96$

where R_u is the enhancement ratio of the over-all coefficient U.

2. It is now possible to re-analyze the data, assigning a calculated heat flux through the cathodic and noncathodic areas independently. This results in the following values for the bath-side film coefficients

$$h = k \cdot I^{0.344}$$

Cathodic	k_c av	15.38
Noncathodic	k_{nc} av	5.43
R_h		2.83

Thus, the enhancement ratio for the bath film coefficient, $R_h = 2.83$ as compared to the over-all enhancement ratio $R_u = 2.96$. This confirms the known fact that the bath film is the controlling factor in heat transfer in these cells.

Series IV.—Large cylindrical cell No. 3 contained a single cylindrical electrode assembly and four peripheral pipe downcomers for return circulation and additional nongas evolving cooling surface. The central cathode and the downcomers were cooled with boiling methanol. The cell was operated with all downcomers open.

Table IV. Summary, cell No. 3, Series IV

Cooling surface, 43.15% cathodic. All downcomers open. Over-all U refers to the bath-side area, Btu/ft², hr, °F. I, amperes. i_c, A/ft² on cathode. Bath temperature T, as noted, °F.

Test No.	T_1	I	i_c	U	Log I	Log U	U calc.
7	219.7	900	224.5	68.83	2.9542	1.8378	69.30
6	210.7	800	199.6	66.11	2.9031	1.8203	66.20
8	220.0	800	199.6	71.04	2.9031	1.8515	66.20
2	212.0	700	174.7	60.35	2.8451	1.7807	63.00
5	210.0	700	174.7	63.47	2.8451	1.8026	63.00
9	210.0	700	174.7	62.32	2.8451	1.7946	63.00
10	215.0	700	174.7	62.58	2.8451	1.7964	63.00
11	220.0	700	174.7	60.88	2.8451	1.7845	63.00
12	224.0	700	174.7	65.18	2.8451	1.8141	63.00
33	219.8	700	174.7	62.97	2.8451	1.7991	63.00
1	210.5	600	149.7	57.90	2.7782	1.7627	59.30
32	210.8	600	149.7	57.82	2.7782	1.7921	59.30
3	210.0	500	124.8	54.82	2.6990	1.7389	55.50
31	211.0	500	124.8	53.58	2.6990	1.7290	55.50
35	211.2	500	124.8	54.81	2.6990	1.7389	55.50
4	211.0	400	99.9	51.78	2.6021	1.7142	50.90
34	210.6	400	99.9	51.51	2.6021	1.7119	50.90
Extrap.	210	(300)		(46.2)	2.4771	(1.6646)	45.67

Regression analysis gives log $K_u = 0.72018 \pm 0.01267$.
$K_u = 5.2500 \pm 0.155$, n, $= 0.37933 \pm 0.02462$.
Best fit: $U = 5.250 \cdot I^{0.3793}$.

Table V. Summary, cell No. 3, Series V

Cooling surface, 80.00% cathodic. All downcomers plugged. Circulation in electrode gap only. Over-all U refers to the bath-side area, Btu/ft², hr, °F. I, amperes. i_c, A/ft² on cathode. Bath temperature, T, as noted, °F.

Test No.	T_1	I	i_c	U	Log I	Log U	U calc.
6	217.9	600	149.7	80.3	2.7782	1.9047	80.8
2	211.9	500	124.8	74.1	2.6990	1.8698	73.8
4	210.8	400	99.9	67.4	2.6021	1.8287	66.2
3	211.7	300	74.8	56.8	2.4771	1.7543	57.4

Regression analysis gives log $K_u = 0.52967 \pm 0.00690$.
$K_u = 3.386 \pm 0.054$, $n = 0.49626 \pm 0.03069$.
Best fit: $U = 3.386 \cdot I^{0.4963}$.

Series V.—Similar to Series IV but with downcomers plugged. Restricted circulation both ways in the gap was still possible and confirmed by observation.

The over-all U's at various current levels are summarized in Tables IV and V.

Discussion.—In Fig. 4, log U is plotted against log I, for Series IV and V. Average values of U at each value of I are used. The slopes of these lines give n for the equation

$$U = K \cdot I^n$$

For Series IV, $n = 0.379$; for Series V, $n = 0.496$.

The regression line values of U, as read from Fig. 4, for several currents are given in Table VI.

These data are plotted in Fig. 5. The lines are extrapolated to 100% cathodic current to give values of U_c. With these values of U_c, the heat flux on the cathodic cooling surfaces can be calculated for Series V, and hence the bath side coefficients, as follows:

I, amperes	300	400	500	600
h_c (cathodic)	110.9	124.8	130.8	141.3

A plot of log h_c *vs.* log I in Fig. 6 gives the relation

$$h_c = k_c \cdot I^n$$

Table VI. Regression line values of U

Series % Cathodic		IV 43.15%	V 80.0%	U_c 100.0
I	300	45.67	57.40	63.7
	400	50.90	66.18	74.5
	500	55.50	73.84	83.8
	600	59.30	80.80	93.5
	700	63.00	87.40	100.7

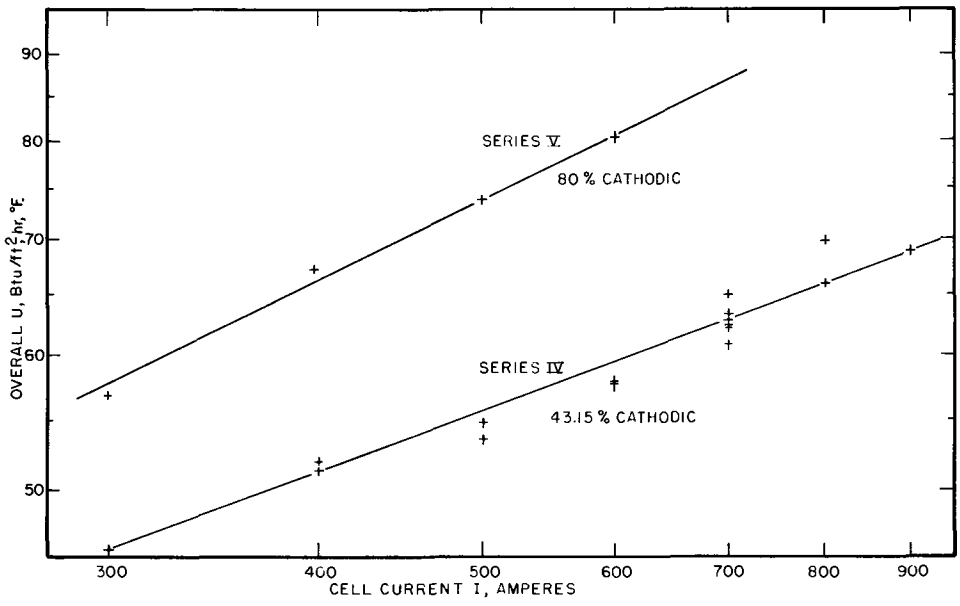

Fig 4. Over-all heat transfer coefficient U vs. current in cell No. 3. Series IV, 43.15% cathodic. Series V, 80.0% cathodic.

and with the best value of $n = 0.344$, the average value of k_c is 15.68.

The data of Series IV were then re-worked making various assumptions as to the value of R. The heat flux through the cathodic cooling surfaces for these values of R then yielded the corresponding values of k_c, the average values of which (for 19 runs) were as follows:

Assumed R	1.5	2.0	2.5	3.0	3.5	4.0
Avg k_c	12.10	13.91	15.31	16.50	17.48	18.30
Avg k_{nc}	8.06	6.95	6.12	5.50	4.99	4.575

A plot of this data is shown in Fig. 7.

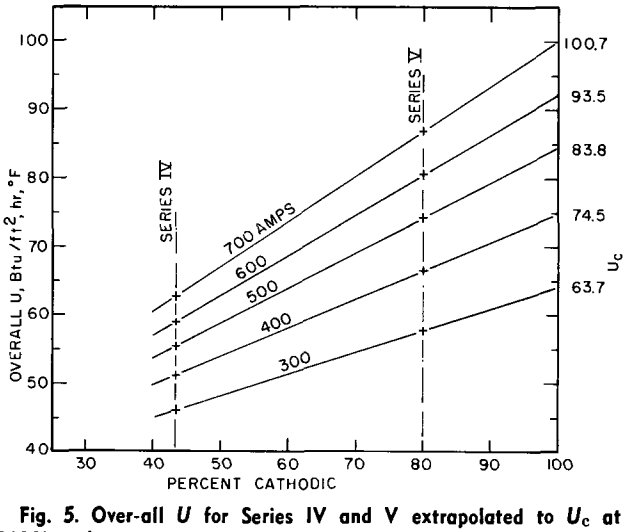

Fig. 5. Over-all U for Series IV and V extrapolated to U_c at 100% cathodic surface.

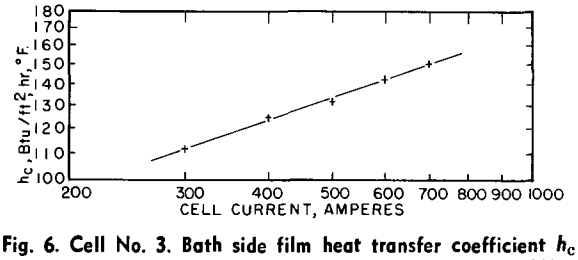

Fig. 6. Cell No. 3. Bath side film heat transfer coefficient h_c in cathodic region. Equation of this line is $h_c = 15.68 \cdot I^{0.344}$.

Assuming that the k_c is the same for Series IV (unrestricted circulation) and Series V (restricted circulation), and dependent only on $I^{0.344}$, then the k_c of 15.68 derived above, corresponds to an R value of 2.68 for Series IV. Since this assumption may not be strictly accurate, we can say that the enhancement ratio for the 19 runs of Series IV was at least 2.68.

Summary

The primary object of this paper was to present evidence that electrolytic gas evolution enhances the liquid film heat transfer coefficient by a factor of the order of 2.5 to 3.5, depending on the rate of gas evolution in the gap.

For purposes of design and scale-up, we have shown that the over-all heat transfer in a cell provided with a means of internal cooling, chiefly depends on two factors: the per cent of the total area that is gas evolving, and the rate of gas evolution, which is proportional to current.

Since the measurements of the bath-side film coefficients were made in several quite different types of cell and electrode geometries, it is worthwhile to see

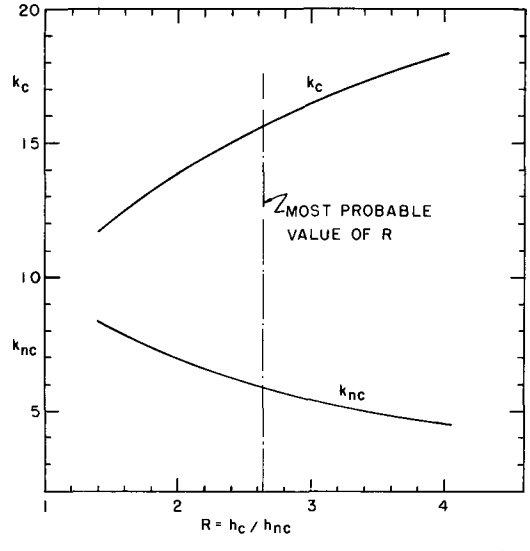

Fig. 7. Series IV runs. Values of k in the equation $h = k \cdot I^{0.344}$ for various assumed values of $R = h_c/h_{nc}$. If $k_c = 15.68$, as in Series V, the most probable value of R for Series IV is 2.64.

Table VII. Comparison of film coefficients in three different types of cell at the same current density, calculated from our data

i_c is cathodic current density, A/ft². h is bath film coefficient, Btu/ft², hr, °F. Subscript c, cathodic, gas evolving; nc, noncathodic, no gas evolved. R is enhancement ratio. h_c/h_{nc}.

Cell No.	Electrodes	Coolant	$i_c = 203$			$i_c = 101.5$		
			h_c	h_{nc}	R	h_c	h_{nc}	R
1	Multiple	Water	181.5	60.0	3.02	143.5	47.3	3.02
2	Multiple	CH_3OH	167.3	59.2	2.83	133.2	47.2	2.83
3	Single	CH_3OH	163.0	61.7	2.64	128.0	48.5	2.64
Average			170.6	60.3	2.83	134.9	47.7	2.83

how these coefficients compare. It is probably best to make the comparison at some arbitrary current densities on the gas-evolving electrode, as shown in Table VII. The concordance is quite good.

Effect of fluid velocity on film coefficient.—A direct measurement of velocity in the nongas evolving downcomers of No. 2 cell, during Series II runs, at a cathode current density of 194 A/ft², indicated a maximum velocity along the center line of a 5.5 in. ID pipe of 1.40 ft/sec, which when corrected for velocity profile, gives an average velocity of about 1.1 ft/sec.

The properties of the fluid were as follows:

ρ = 118 lb/ft³ (known)
μ = 14.2 cp = 0.00955 lb/ft-sec = 34.4 lb/ft-hr (known)
C_p = 0.685 (estimated)
k = 0.14 (estimated)

from which Re = 6230 and Pr = 169.

Using the Dittus-Boelter equation

$$Nu = 0.023\ Re^{0.8}\ Pr^{0.4} \qquad [4]$$

$$hD/k = 194.4 \text{ and } h = 59.5$$

This value of h is consistent with the h_{nc} shown in Table VII, column 1.

When the fluid velocities are not known, as in the case of a proposed cell design, these velocities can usually be calculated with sufficient accuracy. The principle involved (3) is to balance the gas lift head against the algebraic sum of the friction heads in the complete circuit of the circulating electrolyte.

Conclusions

1. Heat transfer from bulk electrolyte to a metal cooling surface is greatly enhanced when the surface is a gas evolving electrode. For the particular system studied, the enhancement ratio of the fluid film heat transfer coefficient is in the range 2.5-3.0.

2. Actual film coefficients, either gas evolving or nongas evolving, are affected by fluid velocity in the usual predictable manner. The gas lift effect can be utilized to promote circulation, hence fluid velocity. Since the gas evolved is proportional to the current, the heat transfer coefficients depend on the current exponentially, that is, $h = k \cdot I^n$. For the particular cells used in this study, $n = 0.344$ approximately.

3. Self-cooling of electrodes appears to be an economical way of cooling cells internally in those cases where cell cooling is necessary.

Manuscript submitted Jan. 25, 1971; revised manuscript received *ca.* May 17, 1971. This was Paper 172 presented at the Washington, D. C., Meeting of the Society, May 9-13, 1971.

Any discussion of this paper will appear in a Discussion Section to be published in the June 1972 JOURNAL.

APPENDIX

For each run, a careful heat balance was made to determine the total heat generated within the cell. Call this Q_1. It involves seven items in all. Let Q_2 be the observed heat removed by the coolant. The difference $Q_3 = Q_1 - Q_2$ is the heat lost to the surroundings. This is a small number, around 10% of Q_1.

Q_3 was then apportioned to Q_4, the loss from cell surfaces at bath temperature to ambient, and Q_5, the loss from cell surfaces at coolant temperature to ambient, in proportion to area and ΔT to ambient. Only Q_5 passes through the internal heat transfer surfaces. It was usually less than 5% of Q_1.

The total heat passed by the total heat transfer surfaces is $Q_6 = Q_2 + Q_5$. The total flux is Q_6 divided by ΣA. The over-all $U = Q_6/\Sigma A \cdot \Delta T$. The method of apportioning the total heat flux through nc and c surfaces is fully explained in the text.

REFERENCES

1. F. O. Mixon, W. Y. Chow, and K. O. Beatty, "Heat Transfer," A.I.Ch.E. Symposium Series No. 30, 1960, Vol. 56, p. 75.
2. U. Magrini, *Calore*, No. 4, p. 125 (1966).
3. R. B. MacMullin, *Electrochem. Technol.*, **1**, 5 (1963).
4. The Schumacher Cell, as operated at Henderson, Nevada. See U.S. Pat. 2,515,614, July 18, 1950 (J. C. Schumacher).
5. West German Pat. 957,937, Feb. 14, 1957 (Krebs & Co., Berlin).
6. U.S. Pat. 1,492,121, April 29, 1924 (Diamond Match Co.).
7. French Pat. 1,457,223, Dec. 10 1965 (Daiki Engr. Co., Japan).
8. U.S. Pat. 3,404,083, Oct. 1, 1968 (M. S. Kircher).

Principles and Applications of A-C and D-C Rapid Polarography with Short Controlled Drop Times

A. M. Bond*

Department of Inorganic Chemistry, University of Melbourne, Parkville 3052, Victoria, Australia

ABSTRACT

The techniques of a-c and d-c rapid polarography employing short controlled drop times and fast scan rates of potential are discussed in detail. Particular emphasis is given to comparing the methods with conventional polarography in electroanalytical applications. The shapes and main characteristics of both a-c and d-c polarograms are essentially the same as in conventional polarography. Any differences encountered generally arise from the different time scales of the two techniques. Reversible, quasi-reversible, and irreversible electrode processes are considered. In analytical applications, the rapid methods are superior to conventional polarography because of the considerable time saving gained from the fast scan rates of potential. The reproducibility is also marginally better. In fundamental studies, such as in the characterization of electrode processes, rapid polarography is also shown to be particularly useful. The analogy of behavior akin to a streaming mercury electrode is considered, as are other phenomena and characteristics introduced by having short controlled drop times. It is concluded that the technique could be given wider usage than presently accorded.

One of the disadvantages of conventional polarography compared with other analytical methods has always been that the natural drop times of the dropping mercury electrode (DME)—usually between 2 and 8 sec—necessitate reasonably slow scan rates of potential, and the time required for recording a polarogram is correspondingly long. Scan rates of potential must be slow for two major reasons: (*A*) to avoid violating the constant potential-current conditions assumed for theoretical purposes, and (*B*) to provide a high degree of precision of measurement. Each drop represents one data point on the current-voltage curve, and especially over the steeply rising portion of a d-c polarogram or around the peak or summit potential of an a-c polarogram, a large number of data points is necessary. Obviously, the faster the scan rate, the fewer data points on the graph and this results in a decrease in precision. Thus, even if the theoretical constant potential-current requirement did not need to be met, there would still be an excellent practical reason why the scan rate cannot be increased beyond well-defined limits when natural drop times are used.

In electroanalytical methods with stationary electrodes, such as the hanging drop mercury electrode, platinum electrode, glassy carbon electrode, *etc.*, fast scan rates of potential are used routinely. The theory for stationary electrode voltammetry includes terms for the scan rate of potential and so restriction given as (*A*) above for polarography does not apply, nor does that given as (*B*), because a continuous current-voltage curve is obtained. Similarly, with streaming (mercury) electrodes, no restriction is placed on current-voltage curves. However, although voltammetric methods may be used with considerable time saving, they have several well-established difficulties and disadvantages compared with the polarographic method (1). Consequently, the dropping mercury electrode technique still remains in widespread use, especially in analytical studies, and in most cases voltammetry is used only when the polarographic method is inapplicable, *e.g.*, when the latter is not sufficiently sensitive, does not cover suitable potential range, *etc.*, or alternatively for theoretical or other reasons, where a stationary or streaming electrode should give different results from a DME, *i.e.*, involve a different product, different electrode mechanism.

If, for the polarographic method, time saving is required through shortening of the scan rate, then the only real possibility is shortening of the drop time. In principle this could be achieved by using suitable glass capillaries and increased lengths of mercury columns; but a much more convenient method is to mechanically knock or remove the mercury drop at selected time intervals to produce a short controlled drop time. This has been the preferred technique, and the one employed here.

In the theoretical or philosophical sense the drop time could be shortened indefinitely until the mercury drops become so close together that a streaming mercury electrode, rather than a dropping mercury electrode is obtained. Thus at some drop time or range of drop times, a transition between a DME and a streaming electrode should be encountered. The nature of electrode processes and the physical characteristics of a short drop time DME itself could also be expected to undergo certain transitions as the drop time is decreased.

Various features of short controlled drop time d-c polarography have been already reported in the literature [see Ref. (1)-(8), for instance]. Relatively little application of the rapid technique to a-c polarography has been made until recently, apart from these laboratories (9), although recent publications (8-11) show growing interest.

In addition to the obvious ones of time saving there are practical advantages in use of controlled drop times, if sufficiently short. Therefore experimental findings on the so-called "rapid" a-c and d-c polarographic methods in the drop time range 0.16 to 0.32 sec are presented critically. In particular, a detailed comparison and discussion of advantages relative to the conventional polarographic method are given. However, the outline of work based on results obtained in these laboratories over a number of years is deliberately comprehensive, and includes an account of the transition towards streaming mercury electrode behavior, the sensitivity of the method in the analytical sense and the changes in electrode processes relative to those obtained with conventional polarography.

Experimental

All chemicals used were of reagent grade purity. All measurements were made at 25°C, unless otherwise stated. Polarograms were obtained using the

* Electrochemical Society Active Member.
Key words: alternating and direct current rapid polarography.

Metrohm Polarecord E 261. A-C polarography was carried out using the Metrohm A-C Modulator E 393 with an applied a-c voltage of 10 mV, rms at 50 Hz. Rapid polarographic techniques with drop times between 0.16 and 0.32 sec for both the a-c and d-c work were obtained using Metrohm Polarographie Stand E 354. The ohmic *IR* drop was compensated for in the d-c polarography, using Metrohm *IR* Compensator E 446 and the three electrode polarographic method. No *IR* compensation was undertaken in the a-c polarography.

Results and Discussion

Recording, damping, and maximum scan rates of potential.—With conventional a-c and d-c polarography scan rates of potential are usually in the range 5-15 min per volt, depending on the drop time and accuracy of measurement required. Because of the large current fluctuations associated with each drop during the considerable period of growth, recorder damping is frequently necessary, particularly with low concentrations of depolarizer, and with a-c polarography (12). The possibility of distortion of the wave shape caused by damping must always be considered; however, with slow scan rates of d-c potential used with conventional d-c and a-c polarography, distortion is usually not significant.

In the case of rapid polarography, with an extremely short drop time, very little time is available for growth of the mercury drop. Hence current fluctuations are small and damping is completely unnecessary even with the lowest detectable concentrations of depolarizer. Figure 1 shows this with respect to a-c and d-c polarography at low concentrations. The removal of the need for damping is an extremely convenient feature of rapid polarography and facilitates ready measurements with minimum possibility of recorder distortion.

The recorder used in this work was an X-Y recorder with a response time of 1 sec for full scale deflection. This is by no means the fastest X-Y recorder available

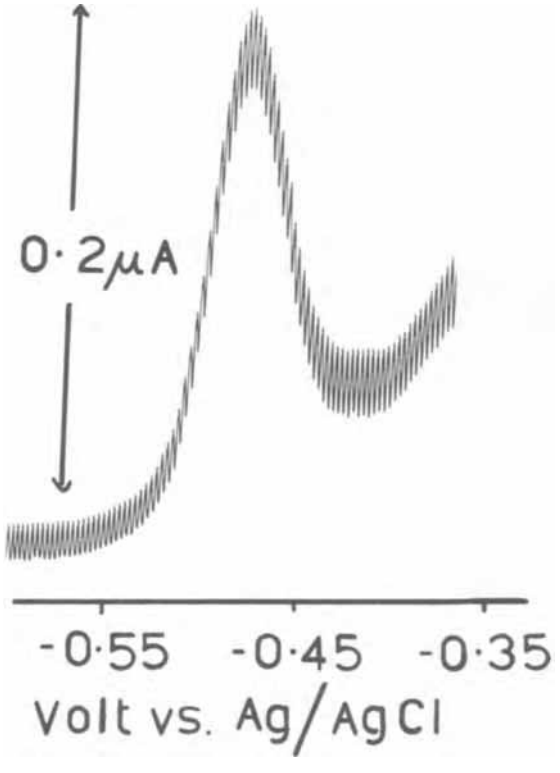

Fig. 1a. Rapid a-c polarogram of 2 x 10^{-5}M rhodium(III) in 0.02M NaBr/4M $HClO_4$. Scan rate of d-c potential is 0.5V per min. Zero damping is applied.

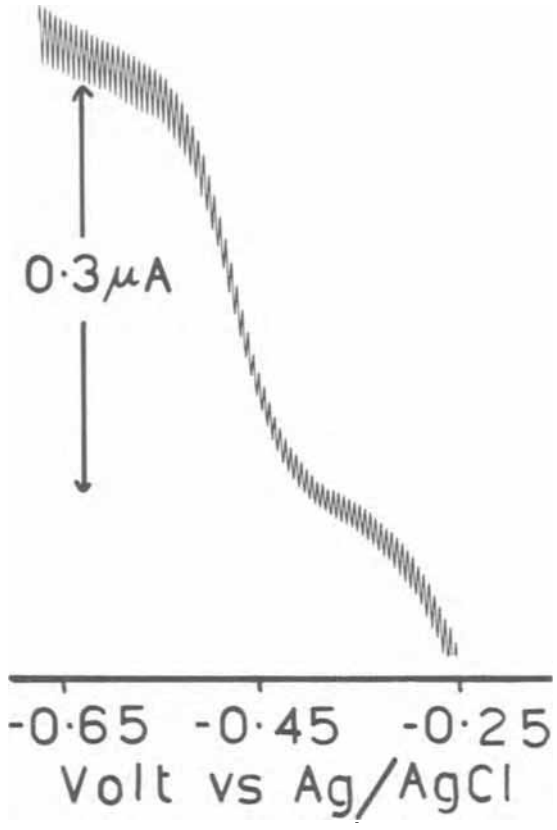

Fig. 1b. Rapid-dc polarogram of same solution as in Fig. (1a). Scan rate of d-c potential is 1.0V per min. Zero damping is applied.

but it is a typical response time for use in polarographic studies and the same as that used previously to consider the influence of scan rate and damping in a-c polarography (12). For rapid polarography, damping other than that inherently present in any recorder, is not used and damping is unlikely to give rise to recorder distortion, but scan rate could. Recorder distortion would certainly be encountered if $di/dt >$ response time of recorder. The equation of a reversible d-c wave is given by

$$E = E_{1/2^r} + \frac{RT}{n\mathbf{F}} \ln\left(\frac{i_d - i}{i}\right) \qquad [1]$$

The equation for a reversible a-c wave, provided the a-c voltage is sufficiently small, can be expressed as

$$E = E_{1/2^r} + \frac{2RT}{n\mathbf{F}} \ln\left\{\left(\frac{I_p}{I}\right)^{1/2} \pm \left(\frac{I_p - I}{I}\right)^{1/2}\right\} \qquad [2]$$

where E = d-c potential of the dropping mercury electrode, $E_{1/2^r}$ = reversible d-c half-wave potential, i and I are the direct and alternating current respectively, and i_d and I_p are the limiting direct current and maximum alternating current respectively. Other symbols are those used conventionally.

The shape of both a-c and d-c polarograms is governed by many variables. However, the gradient of current-voltage curves is in general greatest for reversible electrode processes where the steepness or gradient is directly proportional to the number of electrons involved in the charge transfer. Hence, in considering the maximum possible scan rate attainable without distortion of the wave, only equations for the reversible electrode process need be considered and these are the ones described by Eq. [1] and [2].

The maximum scan rate recordable can therefore be calculated as follows. For d-c polarograms

$$\frac{di}{dt} = \frac{di}{dE} \times \frac{dE}{dt} = \frac{di}{dE} v \qquad [3]$$

where $dE/dt = v$, the scan rate of d-c potential. The maximum value of $di/dE = (di/dE)_{max}$ occurs where $i = i_d/2$. Calculating di/dE from Eq. [1] and substituting $i = i_d/2$ into the expression gives

$$\left(\frac{di}{dt}\right)_{max} = -0.25\, i_d \left(\frac{n\mathbf{F}}{RT}\right) v \qquad [4]$$

Assuming i_d to be equal to the full scale of the recorder, which is close to the condition usually employed in experimental conditions, then at 25°C it follows that $(di/dt)_{max} = -9.74\ nv$ full scale deflections per sec. Consequently $(di/dt)_{max}$ will be less than the response time of recorder with a full scale deflection of 1 sec if $-9.74\ nv \leq 1$. That is, provided the scan rate is less than about $100/n$ mV per sec, no recorder distortion should be encountered in rapid d-c polarography.

With a-c polarography, using the same calculation procedure, it is found as shown previously (12) that

$$\left(\frac{dI}{dt}\right)_{max} \text{ is approximately } 0.4\, I_p \left(\frac{n\mathbf{F}}{RT}\right) v \qquad [5]$$

and therefore at 25°C, $(dI/dt)_{max} = 15.6\ nv$ full scale deflections/sec, which will be less than the response time of a recorder with a full scale deflection of 1 sec, if $15.6\ nv \leq 1$. Again, provided the scan rate is less than about $60/n$ mV per sec, no recorder distortion should be encountered in rapid a-c polarography.

Experimentally, results were found to be in excellent agreement with this theoretical treatment, and for $n = 1$, 2, or 3 it was found that scan rates of up to 30 mV per sec with rapid d-c polarography and 20 mV per sec with a-c polarography, could be used without any distortion. Furthermore, scan rates of 50 mV per sec were tried with $n = 1$ [$Tl(I) + e \rightleftarrows Tl(O)$], and with $n = 3$ [$In(III) + 3e \rightleftarrows In(O)$]; with the case of $n = 3$, distortion was observed as theoretically predicted. Figure 2 shows rapid a-c polarograms for $Tl(I)$ ($n = 1$) in 1M NaCl for various scan rates up to 50 mV per sec, and they can be seen to be of the same height. For comparison, Fig. 3 shows the "apparent" peak height of the $In(III)$ ($n = 3$) electrode process at the same scan rates. The recorder distortion at the highest scan rates can be seen.

In view of the above argument, if a normal X-Y recorder with a full scale deflection of 1 sec is to be used, the maximum scan rate of d-c potential that can be used satisfactorily is 20-30 mV per second if distortion is to be avoided. With a drop time of 0.16 sec this means that approximately 5 to 8 mV is covered per drop, which is about the minimum necessary if

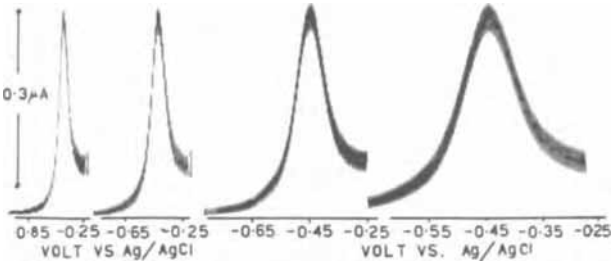

Fig. 2. Recording of a rapid a-c polarogram for the electrode process Tl(I) + e ⇌ Tl(O) in 1M NaCl at various scan rates of d-c potential. *(Right to left)* (a) 0.5 V/min (8.3 mV/sec), (b) 1.0 V/min (16.7 mV/sec), (c) 2.0 V/min (33.3 mV/sec), (d) 3.0 V/min (50.0 mV/sec). Concentration of thallium(I) is 8×10^{-5}M.

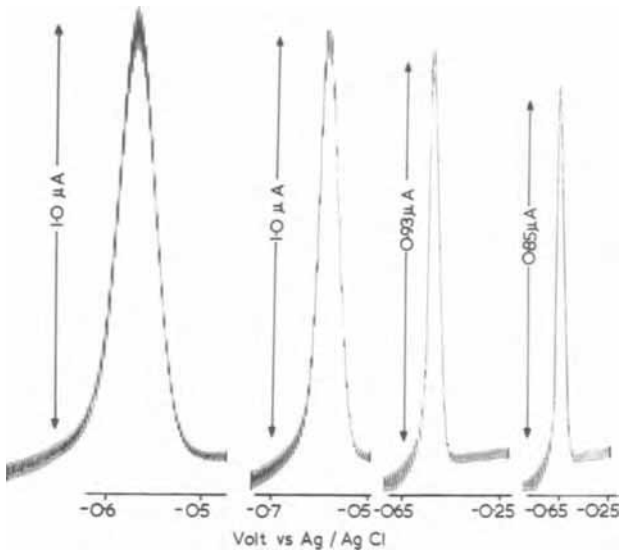

Fig. 3. Recording of a rapid a-c polarogram for the electrode process In(III) + 3e ⇌ In(O) in 1M NaCl at various scan rates of d-c potential. *(Left to right)* (a) 0.5 V/min (8.3 mV/sec), (b) 1.0 V/min (16.7 mV/sec), (c) 2.0 V/min (33.3 mV/sec), (d) 3.0 V/min (50.0 mV/sec).

marked loss in precision, due to lack of data points, is to be avoided in recording a polarogram. Hence, in the practical as well as theoretical sense, there is no advantage in using faster response recorders than the normal X-Y type, unless even shorter drop times than 0.16 sec are used. With a scan rate of 20 to 30 mV per sec, a complete a-c or d-c polarogram can be recorded in about 10 sec. In these laboratories, slower speeds of d-c scan rate are normally used than this maximum value. In routine analysis, where i_d and I_p values are the only parameters of interest, a scan rate of 1V per min is generally used. In electroanalytical applications where potential needs to be measured, the scan rate used is 0.5V per min. These scan rates still allow complete polarograms to be recorded well inside a minute, which is considerably faster than the conventional polarographic method. However, scan rates of up to 3V per min were used successfully when a glass DME was used in relatively concentrated glass corrosive hydrofluoric acid (10).

Reproducibility.—With any technique, reproducibility and precision of results are always of extreme importance. With the experimental arrangement used in these laboratories, working with a scan rate of d-c potential of 0.5V per min, six research workers (including the author) have always found that the reproducibility of the d-c i_d value is better than 0.5%, and that of the a-c I_p value is better than 1%. This reported reproducibility is based on at least six results for each of more than 100 solutions. For a full-scale deflection of 250 mm on the current axis of the X-Y recorder, a range of 2 to 3 mm has been usually encountered with i_d values and 2 to 5 mm with I_p values. Reproducibility of i_d and I_p values has been found to be marginally better than the conventional polarographic method, using a much slower scan rate of d-c potential (0.5V per 12 min), and a natural drop time of between 2 and 5 sec.

Measurements of the d-c $E_{1/2}$ values and a-c summit or peak potentials, E_s, have been carried out on even more systems by the same six workers. Attempting to read potentials to 0.2 mV, mean deviations for $E_{1/2}$ have been found to be in the range 0.9 to 1.1 mV; a-c E_s values on reversible systems have always been considerably superior, showing mean deviations of 0.6 to 0.8 mV. The reproducibility of potential parameters

as with current parameters, has always been found to be marginally better with the rapid method, using controlled drop time, than with the conventional polarographic method.

All results show conclusively that the considerable time saving obtained with the rapid polarographic method is not gained at the expense of reproducibility or precision, as is often the case when an attempt is made to increase the rate of measurement. In fact, an improvement in these vital factors is observed, making the technique highly attractive from two points of view, *viz.*, speed and reproducibility.

Dependence of i_d and I_p on Various Parameters

Dependence upon mercury column height and drop time.—Rapid d-c polarography.—The Ilkovic equation, $i_d = kcnm^{2/3}t^{1/6}D^{1/2}$, where i_d is the limiting or diffusion current, k is a constant, c is the concentration of depolarizer, n is the number of electrons involved in the charge transfer, m is the flow rate of mercury, t is the drop time, and D is the diffusion coefficient of the depolarizer, has been shown to be valid over drop times ranging from those used with the conventional DME down to the millisecond region (3, 7). In the drop time range of 0.16 to 0.32 sec, the predicted dependence of i_d on n, c, m, t, and D was found, and the validity of the Ilkovic equation with short controlled drop times was confirmed. Thus, this equation can be used for discussion purposes in this and subsequent sections.

As the Ilkovic equation is obeyed, it follows that increasing the mercury column height at constant drop time increases the flow rate of mercury and i_d increases accordingly.

The dependence upon $t^{1/6}$ predicted by the Ilkovic equation would indicate that the decrease in i_d, going from a drop time of 3 sec, say, in the conventional method, to $t = 0.16$ sec in the rapid method, would not be particularly large, because with $t = 3$ sec, $t^{1/6} = 1.2$ sec$^{1/6}$, and with $t = 0.16$ sec, $t^{1/6} = 0.74$ sec$^{1/6}$. At the shorter drop time of the rapid method, the value of $m^{2/3}$ is also decreased compared with the natural drop time. Over-all, the value of i_d with the rapid d-c method is therefore predicted to be slightly less for measurements made with the same concentration of depolarizer, and experimentally this has been confirmed on all systems measured. Increase in drop time at constant mercury column height over the drop times 0.16, 0.20, 0.24, 0.28, and 0.32 sec also increases i_d, as would be expected.

Rapid a-c polarography.—The value of I_p in a-c polarography is given by the expression

$$I_p = \frac{n^2 \mathbf{F}^2 AC\ (\omega D)^{1/2}\ \Delta E}{4RT} \sin\left(\omega t' + \frac{\pi}{4}\right)$$

where A = area of electrode, ω = angular frequency, ΔE = amplitude of applied alternating potential, t' = time. Other symbols are as used before.

The area of the electrode, A, is proportional to $m^{2/3}t^{2/3}$ and with natural drop time this is a constant, independent of mercury column height. Thus I_p is dependent only upon the particular capillary used with conventional a-c polarography, and not the mercury column height. However, with rapid a-c polarography, dependence on column height is predicted because t is now a constant, and as the height of mercury increases, $m^{2/3}t^{2/3}$ increases and therefore I_p does also. In fact, with t a constant, a similar dependence to d-c polarography should be found, and this is found experimentally.

The a-c dependence on $t^{2/3}$ rather than on $t^{1/6}$ as in d-c polarography would suggest that a-c currents found with the rapid polarographic method would be substantially less than with conventional a-c polarography. Taking the previous example of a drop time of 3 sec in the conventional method, gives a value for $t^{2/3}$ of 2.1 sec. By comparison, for a value of 0.16 sec in rapid polarography, $t^{2/3} = 0.29$ sec. This calculation illustrates that a marked difference in current magnitudes is expected. Experimentally, in agreement with theory, considerably lower currents are observed with the short drop time of rapid a-c polarography, and this lowers the concentration detection limit of the method compared with that of the conventional a-c method. Further discussion of this is given in the next section.

Increase of drop time at constant mercury column height for the values 0.16, 0.20, 0.24, 0.28, and 0.32 sec increases A, and hence I_p increases with increasing drop time as would be expected.

Dependence on concentration of depolarizer detection limits.—Figure 4 shows plots of i_d and of I_p *vs.* concentration of depolarizer for rapid and conventional polarography with both the a-c and d-c methods. The electrode process considered is

$$Sn(II) + 2e \rightleftarrows Sn \text{ (amalgam)}$$

in 5*M* HCl, and it is reversible (13).

In general, linear a-c and d-c plots are observed with the rapid polarographic method when the corresponding conventional method gives linear plots. However, in certain circumstances where the short drop time of the rapid polarographic method causes alterations to the electrode process (see later), it can be noted that this analogy between the rapid and conventional method does not necessarily follow.

The slightly lower currents obtained with the rapid d-c method and the markedly lower currents of the rapid a-c method, compared with their respective conventional d-c and a-c counterparts, are clearly il-

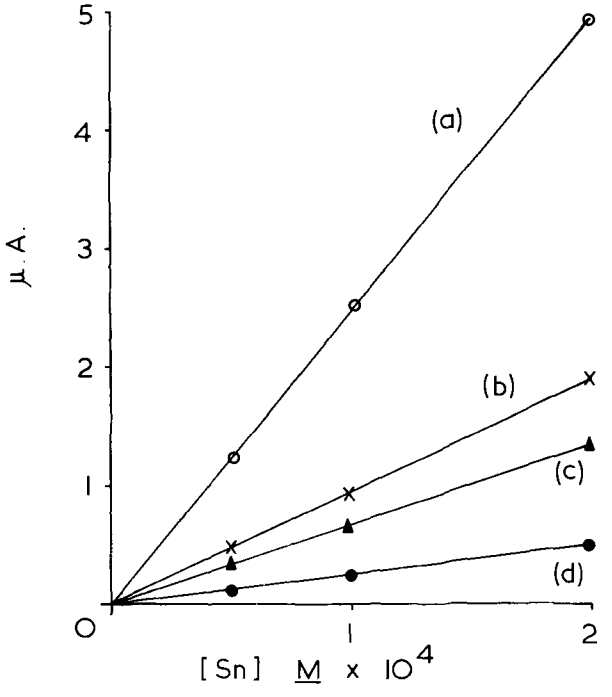

Fig. 4. Comparison of analytically used calibration curves in rapid and conventional a-c and d-c polarography for the electrode process Sn(II) + 2e ⇌ Sn(O) in 5M HCl. (a) I_p *vs.* concentration of tin using conventional a-c polarography, (b) i_d *vs.* concentration of tin using conventional d-c polarography, (c) i_d *vs.* concentration of tin using rapid d-c polarography, (d) I_p *vs.* concentration of tin using rapid a-c polarography.

lustrated in Fig. 4, which also verifies graphically discussion in the previous section on relative current magnitudes.

The limit of concentration detection of rapid d-c polarography in most cases has been found to be about $10^{-5}M$, a level very similar to that for conventional d-c polarography. In rapid a-c polarography, the limit of detection for reversible electrode processes has been found to be in the range 10^{-5} to 5×10^{-6}, somewhat less than the range 5×10^{-6} to $10^{-6}M$ found with a-c polarography. The slightly higher detection limit in rapid a-c polarography is considered to be almost entirely a function of the lower currents associated with the short drop time. The lower detection limit in the a-c polarography was primarily established by the double-layer charging current, rather than by noise, so the use of phase-sensitive a-c polarography, which discriminates against the charging current, should enable an improvement in the detection limit reported above.

Dependence on other variables.—The other variables to be considered in the Ilkovic equation are n and D. Values of D do not vary greatly with inorganic depolarizers, and as i_d is proportional to $D^{1/2}$, little variation from this term is observed from one system to another in conventional polarography. Examination of reduction of Zn(II), Pb(II), Cu(II), and Cd(II) in various electrolytes, with the same capillary at the same mercury column height showed that i_d/C is approximately the same for all systems. Furthermore, the order of magnitude of i_d/C for these systems was identical with that obtained with conventional d-c polarography.

Measurement of i_d/C values for the group Bi(III), Rh(III), Sb(III), In(III) showed i_d/C values to be in general slightly higher than for the group above, and for Tl(I) and U(VI) [$U(VI) + e \rightleftarrows U(V)$] the values were slightly lower. This trend reflects the dependence of i_d on n.

For reversible a-c electrode processes, I_p is proportional to n^2, and with the rapid a-c as well as with the conventional method, values of I_p/C are considerably greater as n increases from 1 to 3.

In summary, it can be seen that the equations describing each of i_d and I_p in terms of the various parameters, can be applied to the rapid polarographic method, with sufficient precision to enable successful predictions concerning the method and the shortened controlled drop time does not invalidate the main features of polarographic theory.

Influence of Rapid A-C and D-C Polarography on Various Electrode Processes

Charge Transfer Rate Determining

Because of the different time scale of the rapid polarographic method, an electrode process may exhibit different behavior from that observed with conventional d-c methods. Here, the simplest case is considered where charge transfer is considered as the rate determining step.

Reversible a-c and d-c electrode processes.—A reversible d-c electrode process should have certain characteristics, including the following: (*i*) The current-voltage curve can be described by the equation

$$E = E_{1/2} + \frac{2.303RT}{n\mathbf{F}} \log \frac{i_d - i}{i}$$

(*ii*) $E_{1/2}$ should be independent of concentration, (*iii*) $E_{1/2}$ should be independent of drop time.

For an electrode process with an extremely large value of the heterogeneous charge transfer rate constant, k_s, (*e.g.* $> 10^{-1}$ sec^{-1}) and for which the conventional d-c electrode process is entirely reversible, meeting all the requirements listed above, then under rapid d-c polarographic conditions the current-voltage curve has always been found to be fitted to a high degree of precision by the Heyrovsky-Ilkovic equation, given as condition (*i*).

The condition, that $E_{1/2}$ is independent of concentration, is also obeyed by reversible d-c electrode processes with rapid polarography.

The third condition that $E_{1/2}$ should be independent of drop time should theoretically mean that $E_{1/2}$ obtained should be the same as with conventional d-c polarography for reversible electrode processes. With extremely short drop times this was observed for cadmium (7). However, with measurements made on a large number of systems, this has in fact not been strictly observed in all cases in this work, although values are usually within several millivolts, and certainly always less than 10 mV. The small discrepancy can be rationalized in several ways by considering some different conditions applying at a rapidly dropping mercury electrode:

(*i*) Depletion at the mercury drop is likely to be encountered when drops are falling in such rapid succession.

(*ii*) Many of the measurements have been made in halide and other solutions where adsorption phenomena are likely to be present. $E_{1/2}$ values reflect in part the state of the solution near the electrode surface (double layer) as well as the bulk, and at shorter drop times it has been shown that adsorption phenomena are likely to be reduced (5-7, 14). Hence, slight differences in $E_{1/2}$ may arise because of the slightly different state of the electrode surface or double layer at the extremely short drop times of the rapid method.

(*iii*) Maxima present in conventional d-c polarography are frequently absent or altered with rapid polarographic conditions (5, 7). Polarograms for reduction of Sn(II) [Ref. (13)] provide an example where the maximum is eliminated. Maxima need not be removed, however, at the drop time used in this work, as is shown by the work of Wolf (2). However, the point to be made is that the measurement of $E_{1/2}$ in the presence of maxima, although reproducible, can be somewhat arbitrary as the value of i_d to be used is somewhat uncertain. Furthermore, comparison of a value of $E_{1/2}$ with that obtained on a rapid polarogram with a different maximum or no maximum may be expected to give slightly different $E_{1/2}$ values.

Delahay (15) has shown that for conventional d-c polarography with normal drop times, electrode processes with k_s values greater than 2×10^{-2} cm sec^{-1}, give rise to reversible electrode processes. Obviously, with the much shorter drop times of the rapid polarographic method, considerably higher k_s values would be needed for the observation of a reversible electrode process. Zinc(II) reduction in various media approaches quite closely to being reversible with very long drop times. However, as the drop time decreases, the departure of the electrode process from reversibility becomes more severe (16). With rapid polarography the electrode process is quasi-reversible (16, 17), and the nonreversibility of the electrode process is accentuated markedly. In fact, any electrode process which shows even a slight departure from d-c reversibility with conventional polarography will be easily recognized as being quasi-reversible on the time scale of rapid polarography. In addition to zinc, cited as an example above, tin(II) reduction in fluoride media (18) illustrates this clearly.

As with d-c polarography, the time scale of rapid a-c polarography is less than that for conventional a-c polarography. For a highly reversible a-c electrode

process the rapid a-c polarogram has exactly the same shape and characteristics as the conventional a-c polarogram (*i.e.* fits Eq. [2]). Furthermore E_s is independent of concentrations of depolarizer, has a value very close to $E_{1/2}$, and is similar in magnitude for both conventional and rapid a-c polarography. Any departure from a-c reversibility in the conventional method is also markedly accentuated at short drop times, as shown with zinc(II) and tin(II) (16-18).

Quasi-reversible and irreversible electrode processes. —As with reversible electrode processes, quasi-reversible and irreversible electrode processes exhibit the same features and are described by the same equations for both rapid and conventional a-c and d-c polarography. The time scale is again different of course, and a quasi-reversible electrode process measured by conventional methods may appear irreversible with short drop times.

The quasi-reversible electrode process in both a-c and d-c polarography is characterized by considerable drop time dependence. Hence, wave shapes and $E_{1/2}$ and E_s can be substantially altered with drop time. This contrast to reversible electrode processes occurs because with nonreversible electrode processes, kinetic terms are involved in determining many polarographic parameters. However, in the main, differences observed in rapid and conventional d-c polarograms, are just those expected because of different drop times.

An irreversible electrode process can often be described in terms of the charge transfer coefficient, α, by the equation

$$E = E_{1/2} + \frac{2.303RT}{\alpha n\mathbf{F}} \log \frac{i_d - i}{i} \qquad [6]$$

where (1)

$$E_{1/2} = E_{1/2}^{r} + \frac{RT}{n\mathbf{F}} \ln \frac{1.349\ k_s t^{1/2}}{D^{1/2}} \qquad [7]$$

If a conventional d-c polarogram fits Eq. [6], then unless the short drop time induces a different electrode mechanism, the rapid d-c polarogram has also been found to closely follow this equation. However, as shown by Eq. [7], a considerable negative shift in $E_{1/2}$ is observed. This feature in fact enables the ready distinction of nonreversible and reversible electrode processes. Furthermore, this feature certainly eliminates any possible ambiguity between, say, an irreversible electrode process with $n = 1$ and $\alpha = 0.5$ fitting Eq. [6], and a reversible electrode process with $n = 2$ being described by Eq. [1], both equations being identical with the set of parameters given. Some typical data to show the comparison of rapid and conventional d-c polarograms for irreversible electrode processes are given in Table I.

For irreversible a-c electrode processes, E_s is more negative than $E_{1/2}$, and as for d-c polarography, the wave shape is independent of k_s (19). The difference between E_s and $E_{1/2}$ depends principally on k_s, n, and α and E_s is also related to drop time in a similar fashion to $E_{1/2}$ (19). Hence with rapid a-c polarography, the behavior on decreasing the drop time gives rise to a more negative E_s value, the wave shape, however, remains essentially unaltered. Because both $E_{1/2}$ and E_s values for irreversible electrode processes are governed by the same drop time dependence, it could be anticipated that the shifts in going from conventional to rapid method would be virtually identical. Table I includes some typical experimental data which verify this and other features of rapid a-c polarography for irreversible a-c electrode processes.

Kinetically Controlled Electrode Processes—Analogy with A Streaming Mercury Electrode

In reduction or oxidation of inorganic complexes (or organic compounds), the electrode process can occur *via* a wide variety of mechanisms. By way of example, rearrangement and/or dissociation of a complex could occur prior to the charge transfer, and if both the initial complex and rearranged or dissociated complex are electroactive, two kinetically controlled pathways may be available for the electrode process.

It has been well established that a streaming mercury electrode can often discriminate between kinetically controlled and slow electrode processes. Thus, certain electrode processes observed with a dropping mercury electrode may not be apparent at a streaming mercury electrode. As mentioned in the introduction, a streaming mercury electrode can be considered as a rapidly dropping mercury electrode of extremely short drop time, and hence, as the drop time is shortened, the transition in behavior to that of a streaming mercury electrode should become apparent.

This phenomenon has been observed recently in the studies of Cover and Connery (5) on the formaldehyde system and in studies by Bond, Heath, and Martin (20, 21) on the polarographic behavior of some dithioacetylacetone complexes. In the latter work, for example it was shown that the palladium complex, $Pd(SacSac)_2$, in acetone, undergoes two reduction steps (21):

$$Pd(II) + e \rightarrow Pd(I)$$

and

$$Pd(I) + e \rightarrow Pd(O)$$

The first reduction step, $Pd(II) \rightarrow Pd(I)$, is reversible and identical using either the rapid or conventional polarographic method. The second reduction step, $Pd(I) \rightarrow Pd(O)$, however, varies substantially with the different techniques.

Figure 5 shows a comparison of rapid and conventional polarograms of $Pd(SacSac)_2$. The d-c polarogram for the complex using conventional techniques shows three distinct waves, the height of the two more negative waves being equal to the first reversible $Pd(II) \rightarrow Pd(I)$ wave. The rapid polarogram, however, shows only two reversible one-electron-reduction waves of equal height, corresponding to the consecutive reduction $Pd(II) \rightarrow Pd(I) \rightarrow Pd(O)$. Both these waves have the same $E_{1/2}$ values and electrode characteristics as the first two waves of the conventional d-c polarogram. The third wave of the conventional d-c

Table I. Some typical data for irreversible electrode processes[a]

Electrode process	Medium	$-E_{1/2}$ rapid V	$(E_{1/4} - E_{3/4})$ rapid mV	$-E_{1/2}$ conv. V	$(E_{1/4} - E_{3/4})$ conv. mV	$-E_s$ rapid V	Half width rapid mV	$-E_s$ conv. V	Half width conv. mV
Ni(II) + $2e \rightleftarrows$ Ni(O)	1*M* $NaClO_4$	1.04	66 ± 4	1.03	66 ± 4	1.04	120 ± 10	1.04	120 ± 10
Ni(II) + $2e \rightleftarrows$ Ni(O)	1*M* NaF	1.05	66 ± 4	1.05	66 ± 4	1.06	120 ± 10	1.06	120 ± 10
Co(II) + $2e \rightleftarrows$ Co(O)	1*M* $NaClO_4$	1.41	100 ± 5	1.35	100 ± 5	1.46	205 ± 20	1.43	195 ± 20
Co(II) + $2e \rightleftarrows$ Co(O)	1*M* NaF	1.46	105 ± 5	1.41	100 ± 5	1.50	220 ± 20	1.48	220 ± 20
Sb(III) + $3e \rightleftarrows$ Sb(O)	0.2*M* $HClO_4$	0.26	68 ± 2	—	—	0.27	110 ± 3	—	—
Mn(II) + $2e \rightleftarrows$ Mn(O)	1*M* $NaClO_4$	1.49	40 ± 2	1.47	35 ± 2	1.49	80 ± 5	1.48	80 ± 5
Mn(II) + $2e \rightleftarrows$ Mn(O)	1*M* NaF	1.54	44 ± 2	1.52	54 ± 3	1.55	110 ± 5	1.53	110 ± 5
Fe(II) + $2e \rightleftarrows$ Fe(O)	1*M* $NaClO_4$	1.47	80 ± 5	1.40	76 ± 5	1.49	190 ± 20	1.47	200 ± 20
Fe(II) + $2e \rightleftarrows$ Fe(O)	1*M* NaF	1.51	100 ± 5	1.45	70 ± 3	1.55	200 ± 20	1.50	210 ± 20

[a] All potentials measured relative to Ag/AgCl (5*M* NaCl) at 25°C.

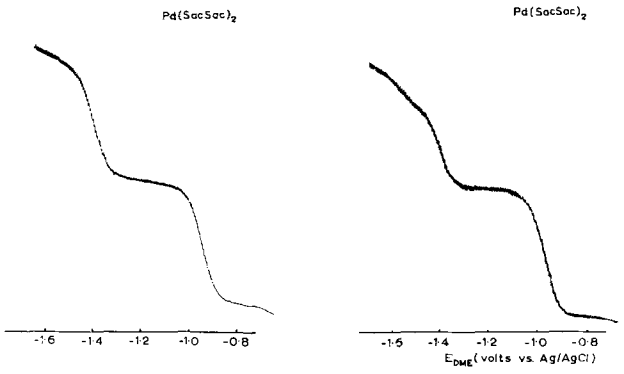

Fig. 5. Comparison of rapid *(left)* and conventional *(right)* polarograms of Pd(SacSac)$_2$ in acetone. Potential is relative to Ag/AgCl (0.1M LiCl in acetone). Supporting electrolyte is 0.1M tetraethyl-ammonium perchlorate.

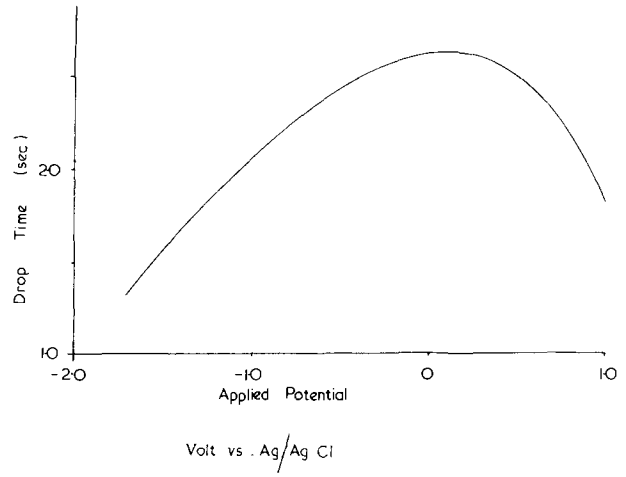

Fig. 6. Drop time *vs.* potential plot in acetone. Supporting electrolyte is 0.1M tetraethyl-ammonium perchlorate.

polarogram, not appearing on the rapid polarogram, is therefore an alternative kinetically controlled reduction process for Pd(I) $\rightarrow$Pd(O), and presumably results from partial dissociation or rearrangement of a Pd(I) complex, the product of the first electrode process. With the much shorter time scale of rapid polarography, insufficient time is available to produce a detectable concentration or the alternative Pd(I) complex, and hence only the two reversible waves are observed.

This example shows how rapid polarography can be used as a powerful tool in electrochemistry for the understanding of electrode processes, although to date it has not been used frequently in this area.

Determination of numbers of electrons in consecutive electrode processes.—In the previous section, it was shown how rapid polarography can be used in the study of electrode mechanisms. However, other electrochemical applications are also possible.

When a number of consecutive electrode processes are observed from the one complex at different potentials, and all are diffusion controlled, then according to the Ilkovic equation, the ratios of the various i_d values should be close to the ratio of the numbers of electrons involved in each electrode process. However, with the conventional method, the drop time is well known to be markedly potential dependent, as may be evidenced by the so-called electrocapillarity curves (1) commonly used to study electrode phenomena. Consequently $m^{2/3}t^{1/6}$ in the Ilkovic equation is potential dependent, and ratios of i_d values of two consecutive electrode processes, separated by a considerable potential dependence, may give a completely false idea of the relative numbers of electrons in the respective electrode processes. By contrast, in the rapid polarographic method, the drop time is controlled and therefore independent of the potential. This eliminates a variable usually encountered in polarography, and this can be useful in studies such as the one now under consideration.

Figure 6 shows a plot of drop time *vs.* potential of the conventional method in acetone, and Fig. 7 shows a conventional d-c polarogram for reduction of the complex RuNOCl(SacSac)$_2$. In acetone, two reduction steps with half-wave potentials of -0.27 and -1.43V *vs.* Ag|AgCl are observed. The i_d values are obviously quite different. Table II shows the ratios of i_d at various drop times. However, with the rapid polarographic method, the i_d values are equal, showing simply and conveniently that the same number of electrons [later shown to be one (21)] are involved in both electrode processes. The difference in i_d values of the two electrode processes resulted solely from the

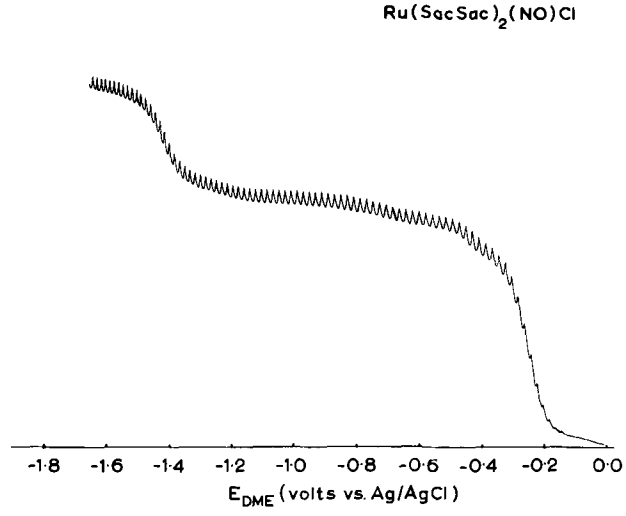

Fig. 7. Conventional d-c polarogram of Ru(SacSac)$_2$(NO)Cl in acetone. Supporting electrolyte is 0.1M tetraethyl-ammonium perchlorate.

considerable variation of $m^{2/3}t^{1/6}$ with potential, as shown by Fig. 6. The rapid polarographic method, however, quickly establishes that variations in i_d arise from this and shows that the same number of electrons is involved.

Figure 8 shows a comparison of rapid and conventional d-c polarograms for reduction of Pt(SacSac)$_2$ in acetone. A considerable difference in i_d values of the two electrode processes Pt(II) $\xrightarrow{e}$ Pt(I) $\xrightarrow{e}$ Pt(I)

Table II. Some polarographic parameters obtained by rapid and conventional d-c polarography for the Ru(SacSac)$_2$(NO)Cl complex

	Wave A		Wave B		
Drop-time[a] sec	$-E_{1/2}$[b] V	$(E_{1/4} - E_{3/4})$ mV	$-E_{1/2}$[b] V	$(E_{1/4} - E_{3/4})$ mV	i_d (A/B)[c]
3.78	0.258	60	1.428	60	0.51
2.48	0.260	60	1.428	56	0.49
2.12	0.260	56	1.432	56	0.56
1.60	0.272	60	1.432	60	0.53
1.18	0.265	60	1.432	56	0.58
0.16[d]	0.276	56	1.424	60	1.00

[a] Measured at $E_{1/2}$.
[b] Potentials are measured relative to Ag/AgCl [0.1*M* LiCl (acetone)].
[c] Ratio of diffusion currents.
[d] Rapid polarographic method.

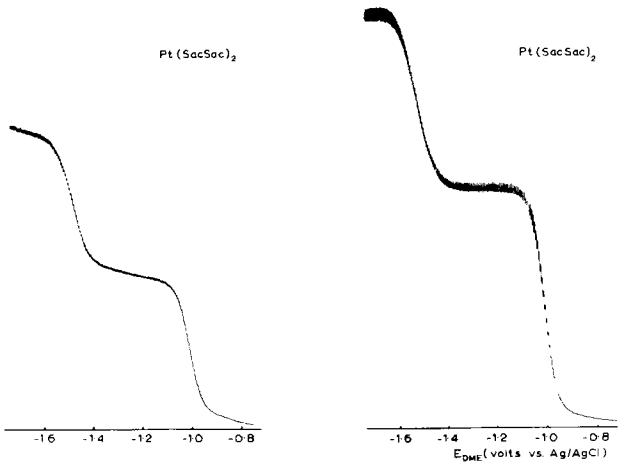

Fig. 8. Comparison of rapid *(left)* and conventional *(right)* d-c polarograms of $Pt(SacSac)_2$ in acetone. Supporting electrolyte is 0.1M tetraethylammonium perchlorate.

is obvious with the conventional method, but as expected, they are almost equal with the rapid polarographic method, confirming simply and conveniently that equal numbers of electrons are involved in both electrode processes.

That this use of the rapid polarographic method is possible, confirms again the earlier findings that the Ilkovic equation can still be successfully used in applications of polarography with drop times as short as 0.16 sec.

Other applications.—The fast scan rates permitted by the rapid polarographic method have allowed other applications of the technique in glass corrosive hydrofluoric acid media (10, 18, 22, 23) and for the study of complexes formed in precipitating systems (24, 25) as described elsewhere.

Conclusion

The above discussion and results have been presented in an endeavor to demonstrate that the rapid polarographic method, with short controlled drop times, is an extremely useful electrochemical technique. In analytical applications it is markedly superior to the conventional polarographic method, because of the considerable time saving gained from the faster potential scan rates. Furthermore, a slight increase in precision and reproducibility is obtained. Thus, while maintaining all the advantages of having a dropping mercury electrode, the technique permits the use of routine and rapid polarographic methods on a time basis which is competitive with other methods.

When used in conjunction with conventional polarographic methods, rapid polarography can also be an extremely powerful tool in electrochemistry, and can often be successfully used to elucidate electrode processes and to provide information not readily accessible by the conventional method.

In the light of the above analytical and electrochemical uses of the method, it is concluded that the rapid polarographic method warrants considerably wider use than presently accorded.

Manuscript submitted Feb. 23, 1971; revised manuscript received *ca.* May 14, 1971.

Any discussion of this paper will appear in a Discussion Section to be published in the June 1972 JOURNAL.

REFERENCES

1. J. Heyrovsky and J. Kuta, "Principles of Polarography," Academic Press, New York (1966).
2. S. Wolf, *Angew. Chem.*, **72**, 449 (1960).
3. D. Wolf, *J. Electroanal. Chem.*, **5**, 186 (1963).
4. V. G. Mairanovskii, *Zavodsk. Lab.*, **31**, 1187 (1965).
5. R. E. Cover and J. G. Connery, *Anal. Chem.*, **41**, 918 (1969).
6. J. G. Connery and R. E. Cover, *ibid.*, **41**, 1191 (1969).
7. R. E. Cover and J. G. Connery, *ibid.*, **41**, 1797 (1969).
8. A. M. Bond, *J. Electroanal. Chem.*, **23**, 277 (1969).
9. A. Zatka, *ibid.*, **27**, 164 (1970).
10. A. M. Bond and T. A. O'Donnell, *Anal. Chem.*, **41**, 1801 (1969).
11. A. Ledieu and J. Bye, *Bull. Soc. Chim. France*, 801 (1970).
12. A. M. Bond and J. H. Canterford, Unpublished work, University of Melbourne, 1970.
13. A. M. Bond, *Anal. Chem.*, **42**, 1165 (1970).
14. J. Heyrovsky and J. Kuta, "Principles of Polarography," pp. 299-329, Academic Press, New York (1966).
15. P. Delahay, *J. Am. Chem. Soc.*, **75**, 1430 (1953).
16. A. M. Bond, *J. Electroanal. Chem.*, **20**, 109 (1969).
17. A. M. Bond, *ibid.*, **28**, 433 (1970).
18. A. M. Bond and R. J. Taylor, *ibid.*, **28**, 207 (1970).
19. D. E. Smith and T. G. McCord, *Anal. Chem.*, **40**, 475 (1968).
20. A. M. Bond, G. A. Heath, and R. L. Martin, *This Journal*, **117**, 1362 (1970).
21. A. M. Bond, G. A. Heath, and R. L. Martin, *Inorg. Chem.*, In press.
22. A. M. Bond, *This Journal*, **117**, 1145 (1970).
23. A. M. Bond, *J. Electroanal. Chem.*, **23**, 269 (1969).
24. A. M. Bond, *Anal. Chim. Acta.*, **53**, 159 (1971).
25. A. M. Bond and G. Hefter, *J. Electroanal. Chem.*, In press.

A Computer Controlled Capillary Electrometer

John Lawrence[1] and David M. Mohilner*

Department of Chemistry, Colorado State University, Fort Collins, Colorado 80521

ABSTRACT

A completely automatic capillary electrometer controlled by an on-line digital minicomputer is described. This instrument is based on the maximum bubble pressure principle and is not subject to the systematic errors of the classical Lippmann electrometer in the presence of dilute solutions of weakly adsorbed electrolytes. Details of the interface hardware and the necessary software are given. The instrument is capable of producing very high quality electrocapillary data comparable to that which can be obtained with a capacitance bridge in the case of simple salt solutions and superior to bridge data in the case of the electrosorption of organic compounds which exhibit very high capacitance desorption peaks.

The interfacial tension (or interfacial free energy), γ, is the most fundamental property characterizing the equilibrium state of the electrical double layer at an electrode-electrolyte interface. Precise knowledge of this property as a function of temperature, pressure, electrode potential, and system composition permits all of the other thermodynamic properties of the double layer such as excess charge density, q^M, and relative surface excesses of system components, Γ's, to be calculated (1). In the case of solid electrodes, no reliable method has yet been devised for the direct measurement of γ, although some recent progress has been reported by Beck (2). In the case of liquid metal electrodes, especially mercury, direct measurements of γ date back to the original work of Lippmann (3) of nearly a century ago. The instrument invented by Lippmann for such measurements, which he named the "capillary electrometer," and to which we shall refer as the "Lippmann electrometer," was based on the capillary rise principle (4). It was the principal instrument used to study the electrical double layer in the first half of this century, and it has continued to be widely used although probably differential capacitance measurements at dropping mercury electrodes based on the principles first described by Grahame (5) have been more often employed for high-precision double-layer studies in recent years.

It is true that differential capacitance measurements, coupled with measurements of the potential of zero charge, can supply essentially all of the information required for a complete thermodynamic description of the electrical double layer in the presence of simple salt solutions. For the case of such solutions, differential capacitance may be said to provide a satisfactory substitute for interfacial tension measurements. However, in the case of the adsorption of organic molecules at electrode surfaces this is not true. In the first place, recent studies have shown (6, 7) that integration of differential capacitance under the very high desorption peaks characteristic of most organic sorbates fails to yield the correct thermodynamic value of the charge density even when the capacitance is extrapolated to zero frequency. Secondly, it appears now that it is the rule, rather than the exception, that the electrosorption of organic compounds is congruent neither with respect to electrode potential, E, nor with respect to charge density, q^M, *i.e.*, that the so-called lateral interaction parameter in the adsorption isotherm is not a constant, but rather is a function either of E or of q^M. When this is the case, there exist no known relationships which permit calculation of fractional surface coverage, θ, from charge density-potential curves. The known equations due to Frumkin (8) and to Parsons (9) which express either q^M at constant E or, alternately, E at constant q^M as linear functions of θ are now known to be both the necessary (9) and the sufficient (7) conditions for congruence of electrosorption with respect to electrode potential or charge density, respectively. Thus, when the electrosorption is noncongruent, neither of these relationships may be used to calculate θ. In such cases it appears that the only valid way to obtain correct electrosorption isotherms is to measure the interfacial tension of the electrode directly.

In the past, nearly all interfacial tension measurements have been made with the Lippmann electrometer. Unfortunately, until quite recently it was not realized that this classical instrument is subject, under certain conditions, to very serious systematic errors (10). As is true in the case of all types of capillary rise measurements (4), the Lippmann electrometer is reliable only when the contact angle at the three-phase boundary (mercury-solution-glass) inside the capillary is constant and preferably zero. When the contact angle is constant as is true, for example, in the case of aqueous 0.1M NaCl, very precise measurements of γ are possible with a Lippmann electrometer (11). In the case of such solutions the only serious drawback of this instrument is the extreme tedium[2] of using it. On the other hand, in the case of dilute solutions of weakly adsorbed electrolytes such as aqueous NaF solutions (10, 13, 14) a systematic negative error appears in the vicinity of and especially at potentials positive to the point of zero charge when the interfacial tension is measured with a Lippmann electrometer. This systematic error is shown to be present by comparison of the shape of the directly measured electrocapillary curve with that of the corresponding electrocapillary curve obtained by double integration of the differential capacitance. Such systematic errors have also been observed in the case of dilute solutions of other electrolytes, including HCl and KCl solution (15, 16). As was first shown by Schiffrin (15) and later verified in this laboratory (14), the replacement of the Lippmann electrometer by a capillary electrometer based on the maximum bubble pressure (MBP) principle entirely eliminates this source of systematic error. Since the maximum bubble pressure method is known to be independent of contact angle (4), these results support the contention (10) that the source of the systematic error in the case of the Lippmann electrometer is the development of a finite and potential-dependent contact angle at the three-phase boundary inside the capillary.

* Electrochemical Society Active Member.

[1] Postdoctoral Fellow, 1969-1971. Present address: Bell-Northern Research, Ottawa, Ontario, Canada.

Key words: electrocapillary, interfacial tension, maximum bubble pressure, interface hardware, software.

[2] Recently Conway and Gordon (12) described a technique to relieve some of the tedium and strain on the operator's eyes by using a television camera focused through a microscope to view the meniscus inside the capillary of the Lippmann electrometer. With this modification, the operator watches a TV monitor instead of having to peer through the microscope.

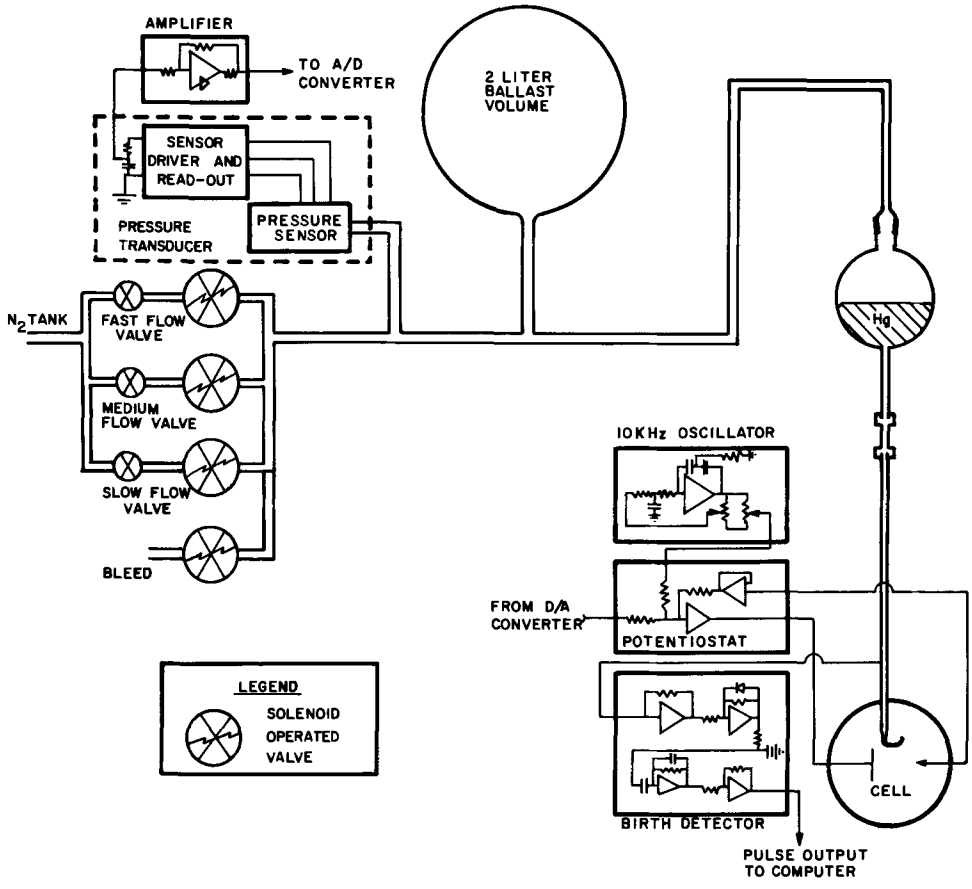

Fig. 1. Maximum bubble pressure apparatus.

Because of the systematic errors which may be present in measurements of γ with the Lippmann electrometer, and because it is not always possible from the Lippmann electrometer measurements themselves to detect whether or not these systematic errors are present in the data, we believe that a capillary electrometer based on the maximum bubble pressure (MBP) method provides the most realistic solution to the problem. Moreover, it is much simpler to automate a capillary electrometer based on the MBP principle than it would be to automate a Lippmann electrometer.

In the present paper we describe in detail the instrumentation which has been developed in this laboratory for a completely automatic capillary electrometer based on the MBP principle. This electrometer is controlled by an on-line digital minicomputer. The results of our experiments with this instrument indicate that the quality of the data it can yield, as determined by the agreement of the charge density-potential data obtained by differentiation of the electrocapillary curve with integrated differential capacitance data, is at least comparable to that which can be obtained with a capacitance bridge.

Experimental

General description of the instrument.—The maximum bubble pressure (MBP) apparatus (Fig. 1) consists of three main components: (*a*) the electrochemical cell with its associated potentiostat, (*b*) a gas pressure control and measurement system, and (*c*) the birth detector circuit (14) which determines when the maximum bubble pressure has been achieved. This apparatus receives control signals from, and transmits information to, the minicomputer[3] in a closed loop configuration.

[3] The minicomputer used in this laboratory is a Digital Equipment Corporation (DEC) Model PDP-8/I. It is equipped with an 8K core (12 bit words), 32K random access magnetic disk (DF-32), a high speed paper tape reader-punch (PC8/I), an ASR-33 teletype, analog-to-digital converter (ADC-1), and additional interface built in this laboratory from DEC digital logic modules (Flip-chips).

The MBP electrode is a fine capillary (10 to 14μ internal radius) which is drawn, after thorough cleaning, from 1 mm. ID borosilicate glass capillary tubing (6 mm OD). The capillary is bent into a U-shape (15) so that its orifice is directed upward. After being bent, the capillary is dewetted by sucking the vapor of dichlorodimethylsilane through it for approximately 3 min.[4] After the capillary is dewetted, its tip is recut as was recommended by Payne (17) for dropping electrodes. Figure 2 is a close-up photograph of an actual MBP capillary used in this study. The MBP capillary is sealed to a length of ¼ in. OD glass tubing. It is connected to a mercury reservoir by means of a stainless steel Swagelok union equipped with Teflon ferrules. The electrode is inserted into one compartment of the two compartment cell via a Teflon 10/30 standard taper thermometer adapter. The cell is provided with an outer jacket through which water from a thermostat is pumped. The auxiliary electrode is a mercury pool at the bottom of the same compartment into which the MBP electrode dips. The reference electrode dips into the other compartment of the cell. Figure 3 is a photograph of the assembled cell.

The potentiostat (Fig. 1) is an operational amplifier circuit with an adder configuration for two voltage input signals (18). The potential controlling amplifier is a Philbrick P-85AU, and the voltage follower is Philbrick P-25AU. The d-c voltage input signal to the potentiostat comes from a 12-bit digital-to-analog (D/A) converter which is a part of the computer interface. The value of the d-c potential is determined by a program command (*cf.* section on software below). The other voltage input signal to the potentiostat comes from a 10 kHz sine wave oscillator (18) which causes a controlled, 5 mV peak-peak a-c potential to be superimposed on the d-c potential of the

[4] An important precaution in the use of dichlorodimethylsilane vapor as a dewetting agent for capillaries is to insure that the inner wall of the capillary is first wet with a monolayer of water. We have found that a convenient way to insure this condition is to draw water vapor from above a beaker of warm water through the capillary for a few minutes immediately before dewetting.

MBP electrode. This signal is required for the operation of the birth detector. The MBP electrode is connected to the summing point of the current amplifier of the birth detector circuit (Fig. 1); it is therefore held at a virtual ground potential.

A detailed description of the birth detector has been published previously (14). It suffices here to say that this circuit detects the instant in time when the mercury, under slowly increasing pressure, has been pushed to the very tip of the up-turned capillary and has formed a protruding semidroplet or "bubble" whose surface has a minimum radius of mean curvature, and which has just started to expand. That is, this circuit detects the instant of "birth" of a mercury droplet at the tip of the capillary. The corresponding difference of pressure across the curved interface at the instant when the mercury droplet begins to expand is the "maximum bubble pressure," *i.e.*, the maximum pressure which can be exerted against the interfacial tension without starting a continual flow of mercury. Except for the fact that the fluid in the capillary is mercury instead of air, the experiment is exactly analogous to the maximum bubble pressure measurement of classical surface chemistry (4, 19), and, hence, the name. The maximum bubble pressure, Δp, is, according to the Laplace equation (4, 19, 20), directly proportional to the interfacial tension, γ. Thus

$$\Delta p = 2\gamma/r \qquad [1]$$

where r is the radius of mean curvature[5] of the surface of the protruding "bubble."

When the maximum bubble pressure has been reached, the birth detector produces a sharp voltage pulse which is transmitted to the computer interface and serves to signal the computer that it is time to record the pressure.

The pressure, Δp, is the sum of two components: one due to the mercury head above the tip of the capillary, the other due to nitrogen gas pressure exerted on the mercury in the reservoir (Fig. 1). The gas pressure is controlled by four solenoid actuated valves[6] which operate under computer control by program command. Three of these solenoid valves control nitrogen flow into the gas pressure system. The flow rate through each solenoid valve and into the system is determined by the setting of a needle valve[7] (Fig. 1). The gas pressure system contains a 2 liter ballast volume to smooth fluctuations during pressure increase. The fourth solenoid valve serves to bleed the gas pressure to atmospheric in order to stop the flow of mercury through the capillary after each measurement of the maximum bubble pressure.

[5] If the orifice of the capillary is perfectly circular, the protruding bubble of mercury will be a true hemisphere, and its radius will be identical with that of the capillary orifice. This would, of course, be the minimum radius which the mercury surface could assume. Therefore, according to Eq. [1], the corresponding pressure difference Δp across the curved interface will be the maximum which can be exerted if the interface is to be in mechanical equilibrium. Any infinitesimal increase of the applied pressure will cause the protruding hemisphere to begin to expand, and hence its radius and surface area will start to grow. The birth detector circuit actually detects the instant when the surface starts to expand.

If the orifice of the capillary is not a true circle, Eq. [1] is still valid but r is no longer the radius of the capillary. Rather r now stands for the radius of mean curvature (20) of the interface, and it is given by the following equation

$$\frac{1}{r} = \tfrac{1}{2}\left(\frac{1}{R_1} + \frac{1}{R_2}\right) \qquad [2]$$

where R_1 and R_2 are the two principal radii of curvature of the surface.

[6] The valves used are Model V52D2100 normally closed, 2-way, "bubble tight" valves equipped with 24V d-c solenoids manufactured by Skinner Electric Valve Division, New Britain, Connecticut. The power for all four solenoids is provided by a single regulated d-c power supply, Model W-740, manufactured by Wescom, Inc., Downers Grove, Illinois. A single power supply is sufficient because only one of the solenoid valves is ever actuated at any given time.

[7] The needle valves for the fast and medium rates of pressure increase are miniature forged needle valves (Model 3212G4B), while the valve for the slow flow rate is a micrometer metering valve (Model 2PY280), all of which are manufactured by Hoke, Inc., Cresskill, New Jersey.

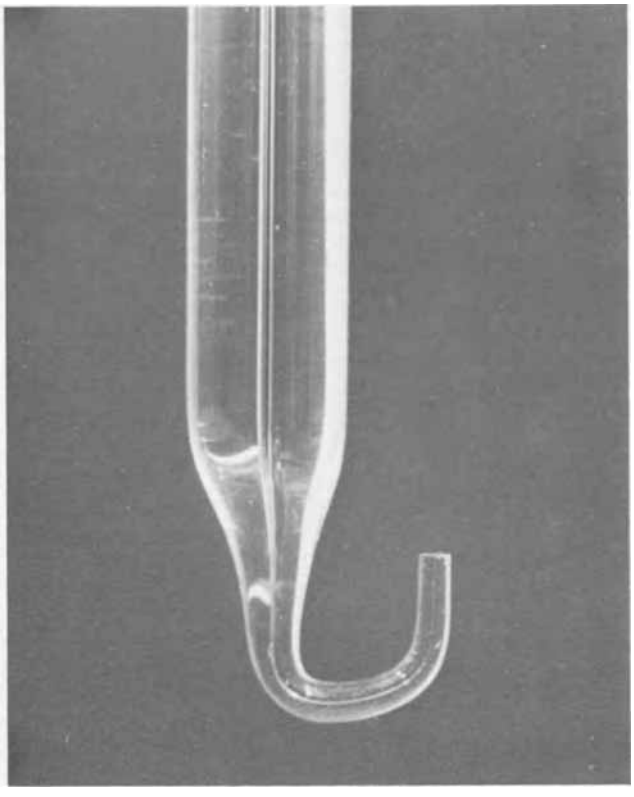

Fig. 2. Close-up photograph of typical MBP electrode. Diameter of capillary at orifice is about 20μ.

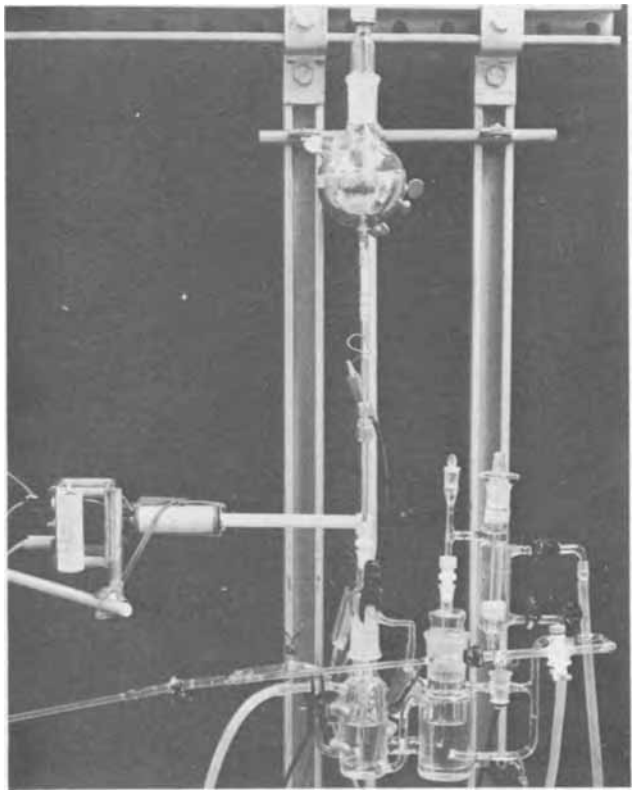

Fig. 3. Assembled MBP cell. Left compartment contains MBP electrode. Right compartment contains salt bridge for reference electrode. Reference electrode is water jacketed calomel. Drop knocker is on left of photograph.

The gas pressure is measured by a pressure transducer (Fig. 1) which consists of a Lion Research Corporation (Newton, Massachusetts) Model DC-303

differential, capacitive pressure sensor coupled to a Model PM-100A sensor driver and readout. The sensor, although originally calibrated over a range of 0-100 mm Hg, is capable of being operated safely over a range of 0-200 mm with no loss of precision. It is over this latter range that the sensor is used in the MBP apparatus. One side of the pressure sensor is connected to the gas pressure system, and the other side is left open to the atmosphere. The PM-100A then outputs an analog voltage which is the measure of the difference of pressure between the gas pressure system and the atmosphere. This analog voltage is then scaled by an operational amplifier (Philbrick Model 1700, chopper stabilized) before being input to the A/D converter. The purpose of the scaling is to insure maximum precision in the digital representation of the analog voltage. The pressure transducer and scaling amplifier combination is calibrated by connecting the pressure sensor to a separate, manually adjustable gas pressure system. The pressure in this latter system is read on a wide bore mercury manometer with the aid of a cathetometer calibrated to 0.01 mm. The scaled analog voltage output of the PM-100A is read to the nearest 0.1 mV with a Fluke Model 8300A digital voltmeter. The table of calibration data (pressure *vs.* voltage) is then fitted to a least squares 4th degree polynomial by digital computer (CDC 6400), and the five coefficients of this best-fitting calibration polynomial are then input to the PDP-8/I computer and stored in its memory. During the measurement of an electrocapillary curve, the digitized, scaled analog voltage from the PM-100A corresponding to each individual measurement of pressure is converted into a pressure by means of this calibration polynomial. Our experience indicates that recalibration of the pressure transducer need not be done more often than once a month.

Figure 4 is a block diagram of the complete, closed loop apparatus. The items on the right hand side of this diagram represent the MBP apparatus, proper (*cf.* Fig. 1). The large double rectangle on the left represents the computer. The items in the center of Fig. 4 represent the interface between the computer and the experimental apparatus. The arrows in the figure indicate the direction of information flow.

Interface hardware.—The interface required for communication between the MBP experiment and the computer consists (Fig. 4) of three digital-to-analog (D/A) converters, four relay drivers, one positive input converter, one bipolar output converter, and an analog-to-digital (A/D) converter. A complete list of all digital logic modules required is given in the Appendix. Every discrete type of operation of each interface device requires one-third of a hardware

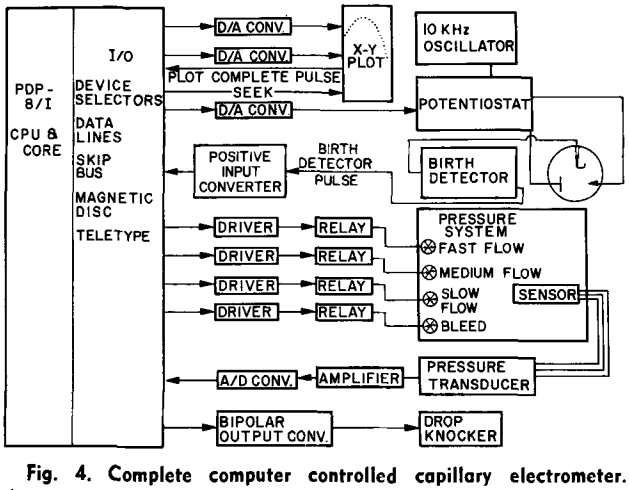

Fig. 4. Complete computer controlled capillary electrometer. Arrows in center section of drawing indicate direction of information flow.

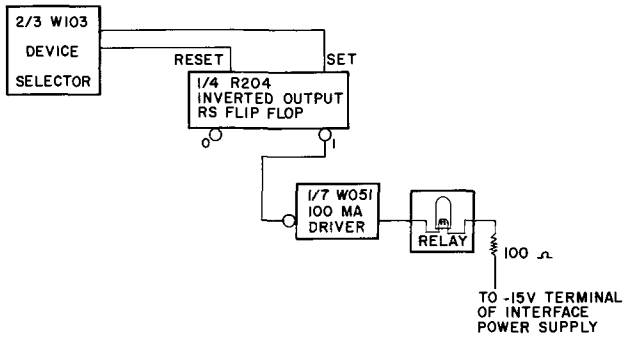

Fig. 5. Logic diagram for relay interface

device selector module (W103) to decode the corresponding program command and translate it into a voltage pulse which initiates the interface device operation (21, 22). D/A converters have only one type of operation, namely, to convert a binary number appearing in the accumulator of the computer into an analog voltage. Therefore, one W103 suffices for all three D/A's. Relay drivers require two device codes, one for energizing, the other for de-energizing the relay coils. Therefore, each relay driver requires two-thirds of a W103. The A/D converter requires three device codes, and, therefore, uses a whole W103 device selector module.

One of the D/A converters is used to provide the d-c voltage input signal to the potentiostat. The resolution of this converter is one part in 4095. This means that the d-c potential of the MBP electrode is controlled to better than 0.5 mV. The other two D/A converters are each 10-bit and are used only to operate an X-Y plotter[8] so that a graphical record of every measurement is produced. The resolution of the plot is one part in 1023. Examples of the plots obtained are shown in Fig. 11 and 13 below.

Each of the four solenoid valves (Fig. 1 and 4) which control the pressure in the gas pressure system is energized or de-energized on program command by the action of a relay (Clare Model RP 3718-G75) through whose contacts the current from the solenoid power supply[6] passes. Figure 5 shows the interface logic diagram for a relay. When the R-S flip-flop is in the "zero" state the relay is de-energized and therefore the current to the solenoid valve is cut off. When the flip-flop is changed to the "one" state the relay and, hence, the solenoid valve are energized. The device selector decodes the two program commands, "energize" or "de-energize" (SET or RESET respectively, *cf.* Fig. 5), and translates them into voltage pulses which cause the flip-flop to go to either the "one" or "zero" state.

When the maximum bubble pressure has been achieved, the birth detector produces a sharp analog voltage pulse (14). This analog pulse must be converted to the proper standard digital voltage level in order to interact with the computer. That conversion is accomplished by a W510 positive input converter. Figure 6 shows the logic diagram of the interface between the birth detector and the computer. When the positive voltage pulse from the birth detector occurs, the W510 switches (in 100 nsec) from ground to −3V. When this happens the R107 inverter applies a corresponding positive voltage level change (−3V to ground) to the "set" input of the R-S flip-flop which has previously been put in the "zero" state by a program command via the W103 device selector. This flip-flop serves the purpose of a "birth detector flag" whose state is continually tested by the computer which operates in a wait loop (duration 60 μsec) as the pressure is building up in the gas pressure system

[8] The plotter is a Hewlett Packard Model 7004A X-Y recorder equipped with two Model 17171A d-c preamplifiers, one Model 17173A null detector, and one Model 17012B point plotter.

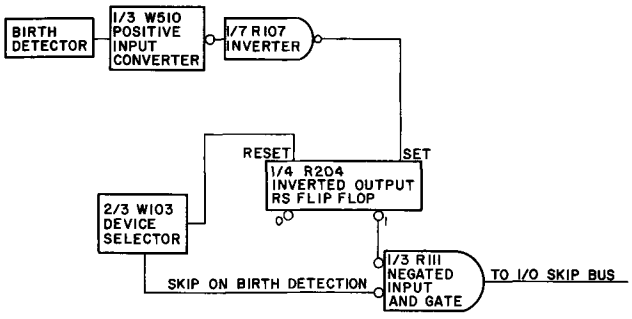

Fig. 6. Logic diagram for birth detector interface

prior to birth detection. When birth is detected by the hardware, the "one" output of this flip-flop enables one of the two inputs of the negated input AND gate (R111); otherwise this input is disabled. A statement in the waiting loop, "skip on birth detection flag," then causes the W103 device selector to enable the other input of this AND gate once each time around the waiting loop. If birth has been detected by the hardware during a pass through the waiting loop, the AND gate is enabled and outputs a voltage level which causes the skip bus of the computer to be driven to ground. When the skip bus is driven to ground, the computer skips the next instruction in the program and enters a routine to store the current value of the gas pressure in memory.

The analog voltage from the pressure transducer is converted by the A/D converter (Fig. 4) to a digital number at the beginning of each occurrence of the birth detection waiting loop. The A/D converter used is a single channel, 12-bit DEC ADC-1 successive approximation type converter which is equipped with a 150 nsec sample-and-hold amplifier (A400). (The analog voltage range of the A/D is ±5.000V.) In order to achieve maximum digital accuracy the analog output of the pressure transducer is scaled to give a maximum output voltage of −5.000V (Fig. 1).

In the early stages of development of this instrument it was observed that occasionally spurious low pressure measurements were produced. The cause of these spurious measurements was traced to the fact that sometimes the mercury droplet produced at the tip of the capillary did not fall off, but rather sat over the orifice of the upturned capillary (*cf.* Fig. 2). In order to preclude the occurrence of such spurious pressure readings, a simple solenoid actuated drop-knocker was interfaced to the computer. After each MBP measurement this drop-knocker twice raps the capillary sharply, thereby insuring that no droplet is left sitting over the orifice to interfere with the next measurement. (The rapping rod of the drop-knocker can be seen in Fig. 3.) The interface used is a DEC W602 bipolar output converter (Fig. 4). The output of the W602 saturates an NPN transistor which, in turn, activates a silicon controlled rectifier. The SCR serves as a switch to discharge a 200 μF capacitor, charged to 50V, through the solenoid coil of the drop-knocker. (Figure 7 is the logic diagram for the drop-knocker.) An alternative method of interfacing a drop-knocker would be to connect a solenoid driver (W040) directly to the drop-knocker solenoid.

Software.—The computer program for the automatic capillary electrometer is designed to operate with a DEC PDP-8/I computer having a single 4K memory core [4096 (decimal) 12-bit words] and one 32K random access magnetic disk (DF-32). The program[9] is written in the disk version, PALD, of the standard PDP-8 assembly language, PAL. This program, in its entirety, is too large to fit within the 4K memory and still to have room for the necessary data buffers. Therefore, in order to conserve the amount of memory actually occupied by the program at any one time, a disk overlay system is used. With this system, the program is divided into four parts: a main (or controlling) program which is resident in core at all times, and three overlay programs which are stored on the magnetic disk as system programs and which are called into core as they are required by the main program. Each overlay occupies the same portion of the memory as its predecessor. The idea of this programming system is illustrated in Fig. 8. In addition

[9] Listings of the assembly language program will be supplied upon request to the authors.

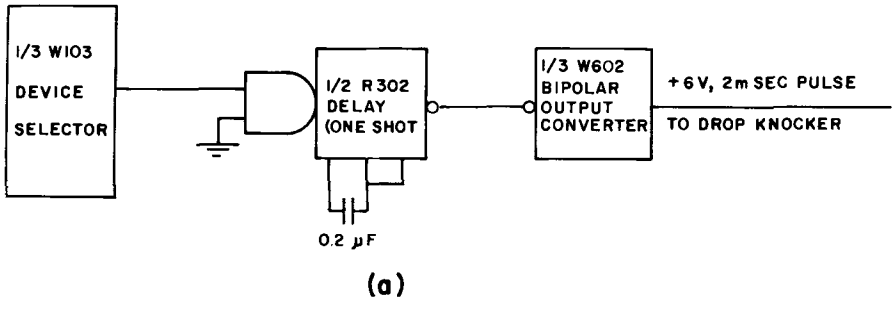

Fig. 7. Drop knocker. (a) Logic diagram for interface. (b) Circuit diagram for drop knocker.

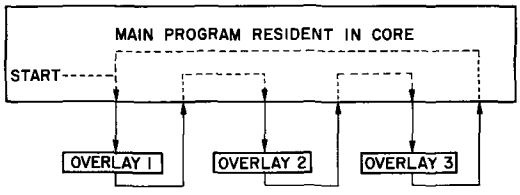

Fig. 8. General programming scheme

to the main program, it is also necessary to have the software floating point package and the disk monitor permanently resident in core. The floating point package contains all of the algorithms necessary for decimal arithmetic operations, and the disk monitor actually accomplishes the transfer of overlay programs from the disk into core after receiving the relevant disk file name from the main program. Figure 9 is a block diagram of the core allocation map. The fractional area of each block in that diagram is equal to the fraction of the memory occupied by the designated entity. The numbers in parenthesis in the block diagram give the range of memory addresses used for each purpose. (These addresses are expressed in octal arithmetic.)

The main program consists of subroutines for message writing on the teletype, plotting the electrocapillary curve on the on-line plotter, and overlay calling.

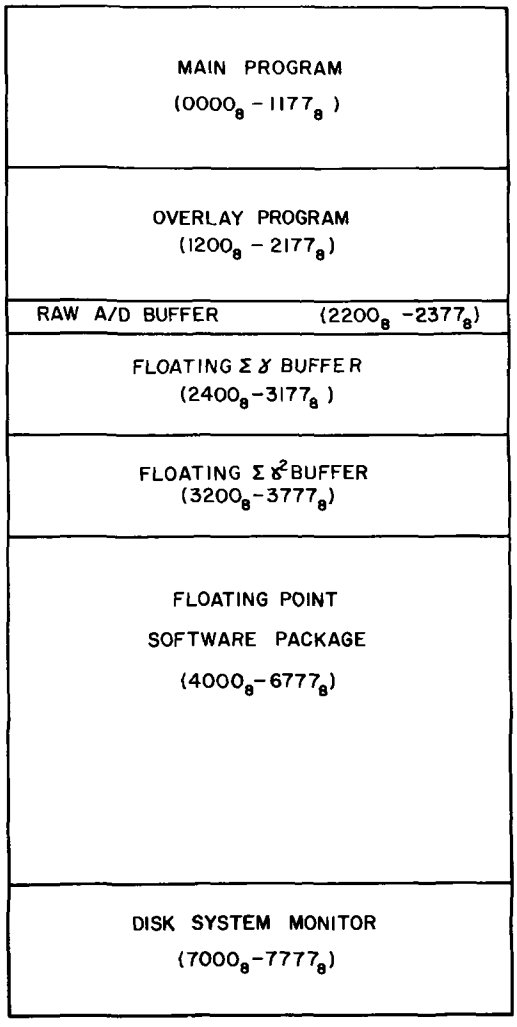

Fig. 9. Core allocation map. The fractional area of each block in this diagram is equal to the fraction of the computer memory used for the designated purpose. Actual address limits of each block of core are given in octal arithmetic.

In addition, it contains storage locations for various constants and variables required by the overlays. The actual control of the experiment is accomplished by the three overlays. As each overlay completes its task it returns control to a predetermined address in the main program (*cf.* Fig. 8). The main program then transmits the disk file name of the next overlay required to the disk monitor, and the disk monitor transfers the new overlay program into the same block of core occupied by the previous overlay (*cf.* Fig. 9).

The purpose of overlay 1 is to accept from the experimenter, via the teletype, the necessary input parameters for the performance of the experiment. These parameters include: the capillary calibration constant used to convert pressure measurements into interfacial tensions; the head of mercury above the capillary tip; the head of solution above the capillary tip (used for back-pressure correction); the number of electrode potentials (E) at which the interfacial tension (γ) is to be measured (maximum of 128 points per curve); the initial electrode potential; the potential increment between points; and the number of times the measurement of the complete electrocapillary curve is to be replicated.

Overlay 2 actually runs the experiment. The flow diagram for this overlay is shown in Fig. 10. The first task of this overlay is to make a rough run through the electrocapillary curve which will serve as a guide for the subsequent high precision measurements. For this purpose, only the medium flow rate of gas into the gas pressure system is used (*cf.* Fig. 1 and 4). The flow diagram for the steps required to make the rough run are given in the left hand part of Fig. 10. At each potential the 12-bit digital equivalent of the analog voltage output of the pressure transducer produced by the A/D at the instant of birth detection (*i.e.*, the maximum bubble pressure) is written in a memory buffer (denoted RAW A/D in Fig. 9). When the rough run through the electrocapillary curve has been completed, the high precision electrocapillary measurements are then made following the logic in the middle and right hand portions of the flow diagram in Fig. 10 starting at the point marked "A." In order to speed the measurements, the gas pressure is first increased rapidly using the fast flow valve (*cf.* Fig. 1 and 4). The A/D reading is checked continuously against the value which was stored at the same electrode potential in the RAW A/D buffer during the rough run. When the pressure is within 3 cm (Hg) of that required for birth detection during the rough run, the fast flow valve is closed and the medium flow valve is opened. The pressure is then increased at the medium flow rate until it is within 1.5 cm of the value stored during the rough run. At this time the medium flow valve is closed and the slow flow valve is opened. The pressure then increases very slowly until birth is detected. (In order to protect the A/D converter from receiving an analog voltage overload, a check is made to insure that the pressure has not exceeded 99% of full scale.) When birth is detected, indicating that the maximum bubble pressure has been achieved, the pressure increase is stopped and the current contents of the A/D register are stored in the same location in the RAW A/D buffer where the previous rough measurement had been stored. (The decision when to switch gas flow rates in the next repetition of the measurement will then be based on the value of the pressure stored in the RAW A/D buffer during the preceding high precision run.) The value of the gas pressure is then floated using the floating point package. Then the head of mercury above the capillary tip is added and head of solution above the capillary tip (expressed in equivalent cm Hg) is subtracted, and the net value of the maximum bubble pressure is multiplied by the capillary calibration constant (*cf.* Eq. [1]) to obtain the interfacial tension γ. The floating point decimal value

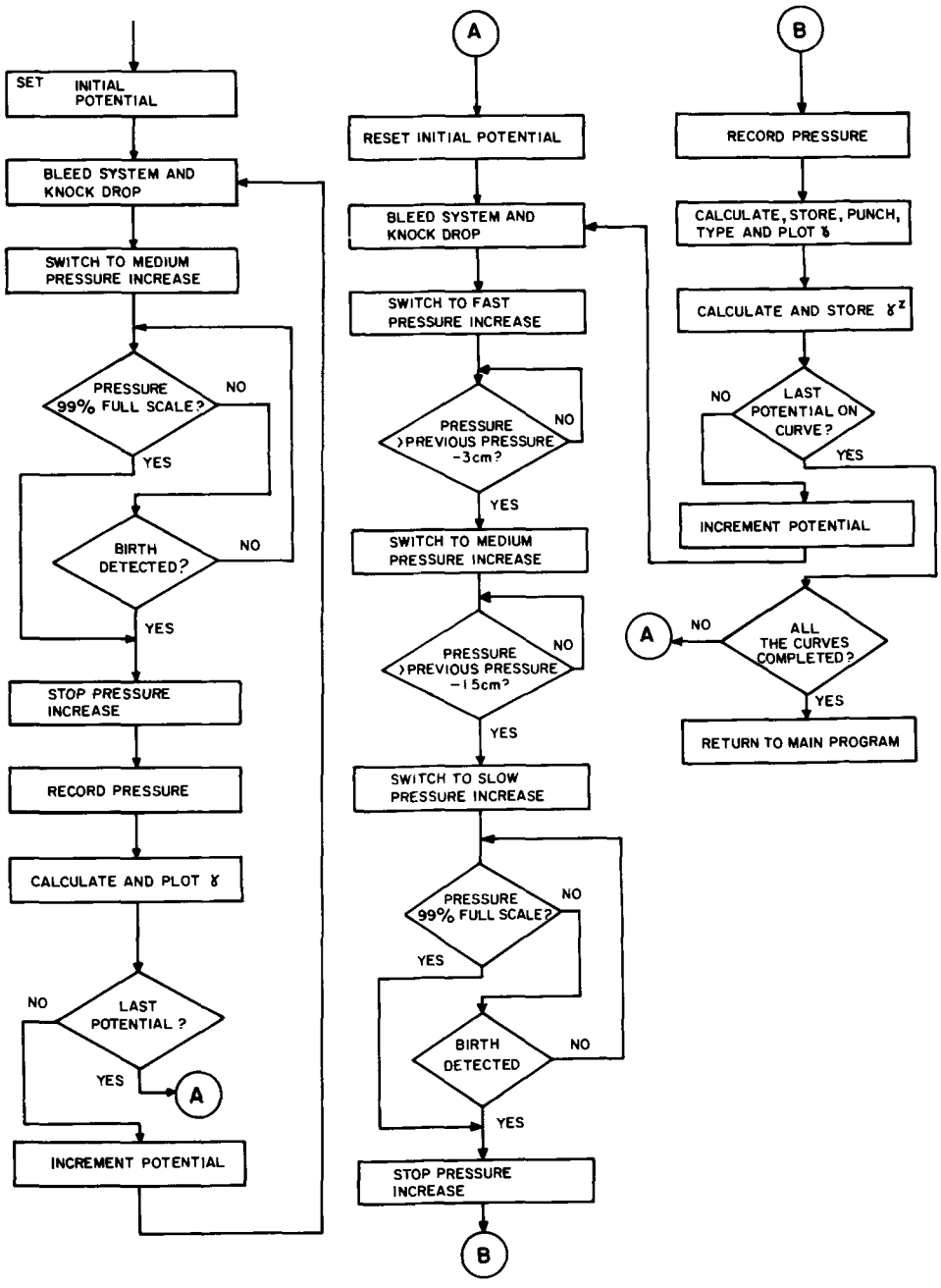

Fig. 10. Flow diagram for overlay program No. 2.

of the interfacial tension is punched on high speed paper tape for a permanent record and also typed by the teletype opposite the value of the electrode potential. The floating binary version of γ (expressed as three 12-bit words) is then stored in the floating buffer (denoted by FLOATING $\Sigma\gamma$ in Fig. 9). This buffer was filled initially with zeros by overlay 1. On each subsequent high precision measurement of γ the new value is added to the sum of the previous ones. This is necessary in order to be able to calculate the average value of γ at the completion of the experiment. Similarly, the sum of the squares of the interfacial tensions are accumulated in the buffer denoted FLOATING $\Sigma\gamma^2$ in Fig. 9 to permit later calculation of the standard deviation of γ at each electrode potential. When the high precision measurement of γ at each E has been repeated the desired number of times (typically, five times), overlay 2 returns control of the system to the main program which then causes overlay 3 to be brought into core.

The purpose of overlay 3 is to calculate the average value of γ at each electrode potential. These values are typed out on the teletype, punched on high speed paper tape, and plotted on a graph. The standard deviation of γ at each potential is also typed on the teletype. If the relative standard deviation exceeds a predetermined amount (*e.g.*, one part per thousand) the teletype also prints the message "EXAMINE!" to alert the experimenter to review the individual values of γ determined at the given potential in order to identify a possible spurious measurement for subsequent discard before proceeding with the thermodynamic analysis of the data.

Results and Discussion

Calibration.—The computer-controlled capillary electrometer is calibrated using an electrolyte solution for which the absolute value of the interfacial tension at the electrocapillary maximum is known from an independent method of measurement, namely: the sessile drop method. After calibration, the performance of the instrument was judged by comparison of the values of the surface charge density, q^M, calculated according to the Lippmann equation (1) by differentiation of the electrocapillary curve with respect to electrode potential with the corresponding values of q^M obtained by integration of the differential capacitance from the point of zero charge.

The calibration is based on the value, 426.2 ± 0.2 dyne cm^{-1}, of the interfacial tension of mercury in

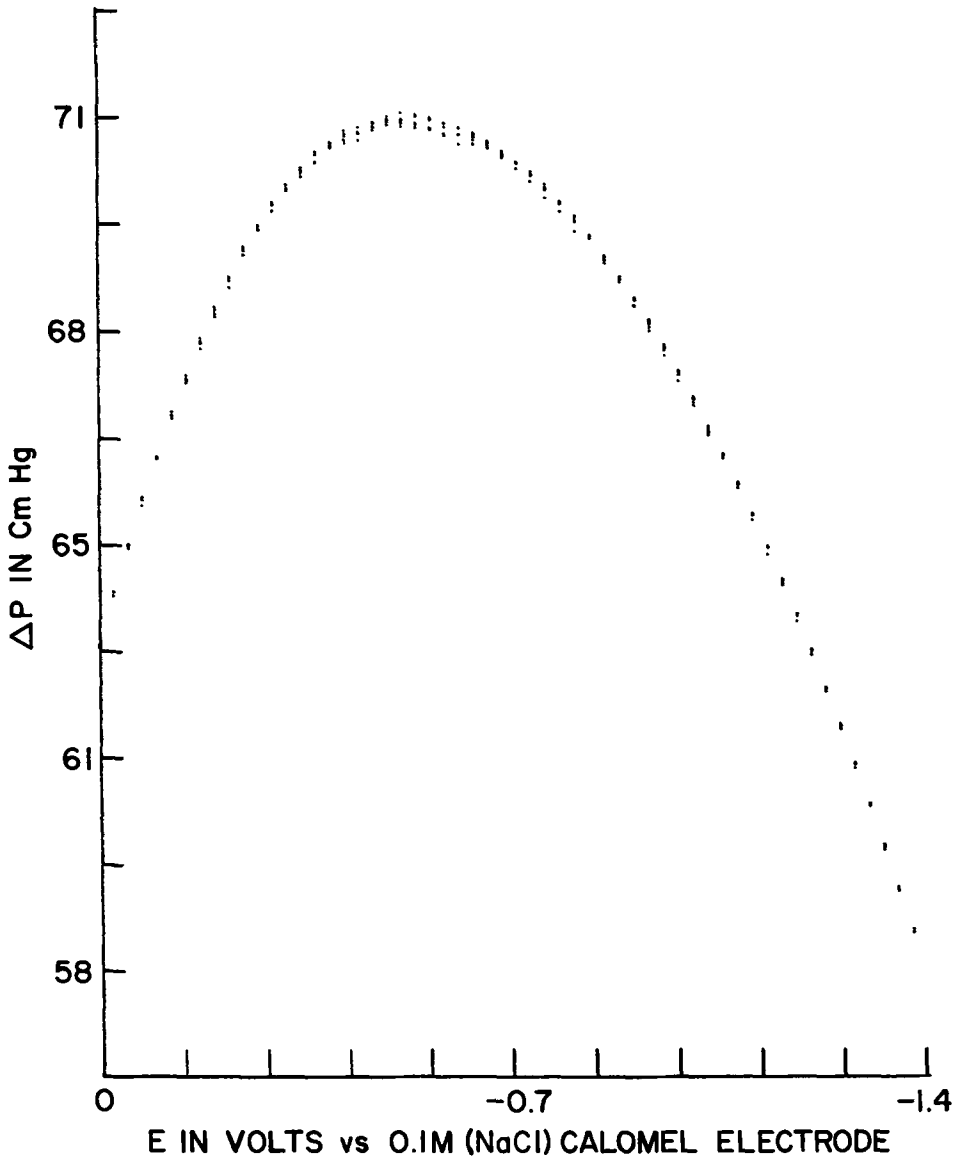

Fig. 11. Typical calibration experiment. Solution is 0.05M Na_2SO_4. Each dot represents an individual determination of the maximum bubble pressure. This experiment was repeated five times.

contact with 0.05M Na_2SO_4 at the electrocapillary maximum at 25°C determined by Smolders and Duyvis (23) by the sessile drop method in 1961. This determination is generally considered to be the most reliable absolute value of the interfacial tension of an ideal polarized mercury electrode which is available. Figure 11 shows the actual plot of the maximum bubble pressure Δp (in cm Hg) *vs.* electrode potential which was produced in a calibration experiment. The measurements were replicated five times (not counting the rough run), and the small scatter of the measurements can be seen from the graph. The average value of Δp at each of the 57 potentials was calculated and the data was smoothed on the CDC 6400 computer using the previously published (24) moving least squares technique with the "runs cutoff criterion." The value of Δp at the potential of zero charge, E_z, was found by computer interpolation. The value, 426.2 dyne cm^{-1}, was then assigned to Δp at E_z, and the calibration constant was calculated. (The calibration constant multiplied by Δp in cm Hg yields interfacial tension γ in dyne cm^{-1}.) All values of Δp were then multiplied by the calibration constant to obtain the γ-E curve which was then differentiated by the moving cubic fit routine (25) to obtain the charge density-potential curve. We measured the differential capacitance of a dropping mercury electrode in the same solution using a General Radio Model 1615-A transformer ratio-arm bridge, and we determined the potential of zero charge by the streaming electrode method of Grahame (26). (The potential of the isolated streaming electrode was measured with a Fluke Model 8300A digital voltmeter as a function of pressure and in accordance with the recommendation of Grahame, the most negative value found was accepted as the value of $E_z \cdot E_z = -0.532$V *vs.* 0.1M NaCl calomel electrode.) The differential capacitance was integrated by digital computer from E_z to obtain q^M. The values of q^M obtained by differentiation of the electrocapillary curve were then compared at each elertrode potential to the values of q^M obtained by integration of the differential capacitance curve. The results are illustrated in Fig. 12. For perfect agreement between the two methods of determining q^M, the points would lie on the solid line of unit slope. It can be seen that the actual agreement is quite good. The points in the centers of the small ovals are the actual experimental points. (In order to make the experimental points clearly visible, the ovals are drawn with their major axes about three times larger than the standard deviation of the experimental error.) The value of the standard deviation of the experimental error in the determination of q^M from the derivative of the electrocapillary curve (taking the values of q^M determined from integration of the differential capacitance as correct) was 0.12 μcoulomb cm^{-2}; the average value of the error was 0.03 μcoulomb cm^{-2}.

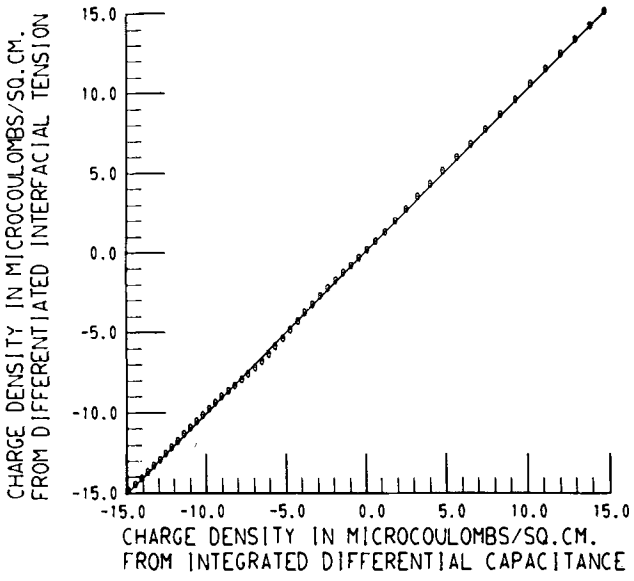

Fig. 12. Typical calibration graph for a capillary. (Results of experiment illustrated in Fig. 13.) Perfect correlation is given by solid line of unit slope.

Applications.—The apparatus has now been tested with a variety of salt solutions, and it is being used routinely in this laboratory for measurements of the electrocapillary curves of organic compounds in aqueous electrolyte solutions. Typical results are shown in Fig. 13 for the electrosorption of 2-butanol on mercury from aqueous 0.01M NaF. The points plotted in this figure are averages of five determinations. The points shown on the curve represent measurements at each of 57 electrode potentials for the 0.01M NaF base electrolyte (top curve) and for 14 different concentrations of 2-butanol ranging from 0.01 to 1.0M. It should be noted that measurements such as these could not have been obtained at all with a classical Lippmann electrometer because of the systematic errors to which that instrument is subject. (In the case of 0.01M NaF, the Lippmann electrometer shows negative errors slightly cathodic of the electrocapillary maximum, and these errors increase to more than 10 dyne cm^{-1} on the anodic branch.) The time and labor required to make this set of measurements was also very much less than would have been needed to make an equal number of measurements with a Lippmann electrometer even if it could have been safely used. The typical rates of pressure increase used with our instrument are (*cf.* Fig. 1 and 4): fast flow, 50 mm Hg/sec; medium flow, 7 mm Hg/sec; slow flow, 0.7 mm Hg/sec. With these flow rates it requires approximately 45 sec for the automatic electrometer to change the electrode potential, make the MBP measurement, and record the measurement on the teletype, paper tape, and plotter. This means that three repetitions of a 60 point electrocapillary curve requires

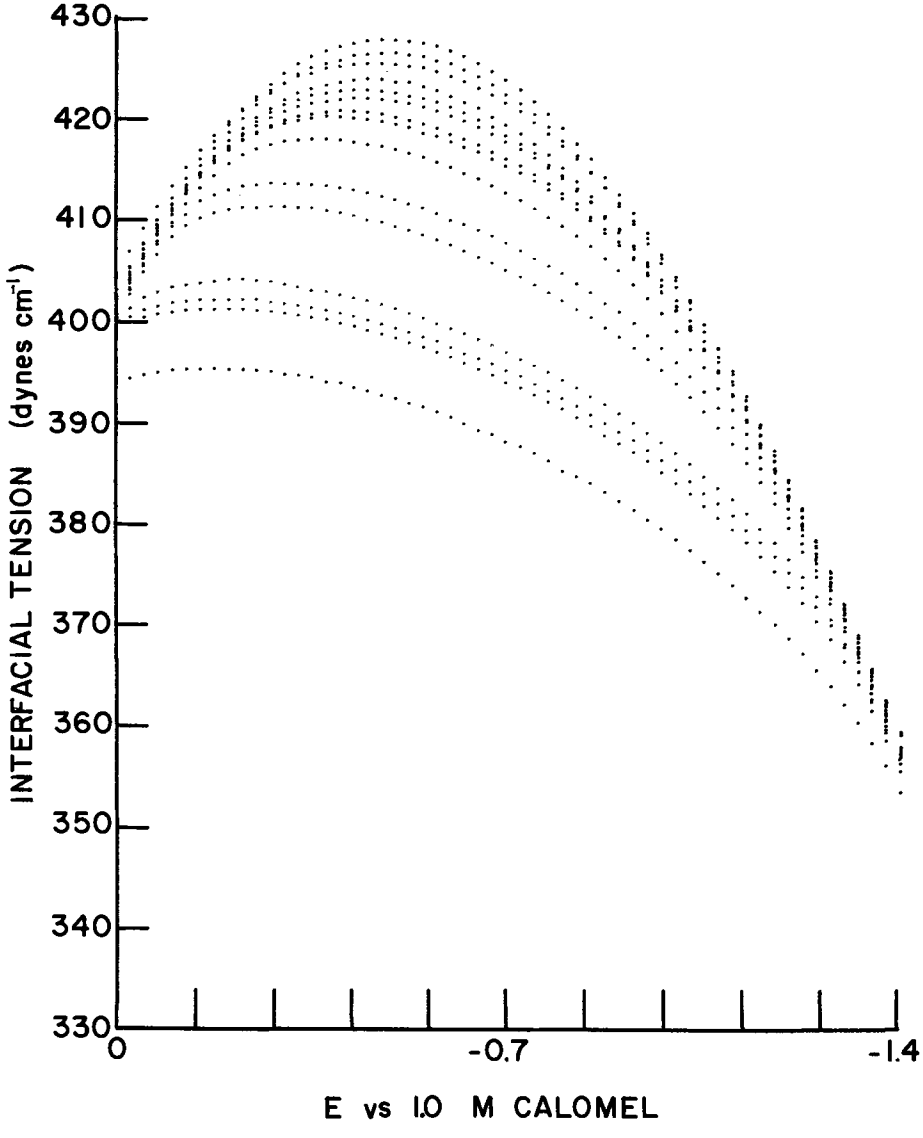

Fig. 13. Electrocapillary curves obtained by the computer controlled capillary electrometer for the electrosorption of 2-butanol on mercury from aqueous 0.01M NaF solution. Each point is the average of five determinations. Concentration 2-butanol (reading from top curve to bottom): 0.0M, 0.01M, 0.04M, 0.05M, 0.06M, 0.07M, 0.09M, 0.10M, 0.15M, 0.19M, 0.30M, 0.50M, 0.60M, 1.00M.

less than 3 hr. Since the operation of the experiment is completely automatic after setting up, the experiment requires no attention from the experimenter. The only work required from the experimenter is to prepare the solution and fill the cell, deaerate the solution, and enter into the memory of the computer via the teletype the necessary input parameters as required by overlay 1. The computer then starts the experiment, runs it the desired number of times, and records the data. When the measurements have been completed the electrocapillary data recorded on high speed paper tape are transferred to magnetic tape and the thermodynamic analysis is accomplished on the large digital computer[10] (CDC 6400) using the previously published methods (24, 25).

Minimal system requirements.—The minicomputer system employed in this laboratory makes the experiments with the computer-controlled capillary electrometer very convenient. However, it should be pointed out that it would be quite feasible to construct a workable instrument using a significantly less expensive minicomputer system having fewer peripherals, for example: a PDP-8/E with 4K core and no magnetic disk or high speed paper tape reader-punch. For a computer system with no magnetic disk, the program could simply be split into three separate programs, each corresponding to one of the overlays described above. Program 1 would accept the input parameters and punch them on low speed paper tape, *i.e.*, on the teletype. Program 2 would read the tape produced by program 1, run the experiment and punch out the results on low speed paper tape. Program 3 would perform the same task as our overlay 3. The only difference in the practical operation of such a system and the one described in this paper would be that the operator would have to load each of the three programs manually using the binary loader. The same interface (*cf.* Fig. 4 and Appendix) would, of course, be required, although one could dispense with the on-line plotter. Obviously, equivalent minicomputers of other manufacturers could also be used to construct this instrument.

Conclusions

The design of a completely automatic capillary electrometer controlled by an on-line digital minicomputer has been described. The performance of this instrument has been evaluated, and it was found that the quality of the electrocapillary data it can produce is comparable to that which can be obtained with a capacitance bridge in the case of simple salt solutions. In the case of solutions of organic neutral compounds the results are superior to those obtained with a capacitance bridge (7). Because this instrument is based on the maximum bubble pressure principle instead of the capillary rise principle it is completely immune from the systematic errors which render a Lippmann electrometer useless for measurements in dilute solutions of weakly adsorbed electrolytes such as 0.01M NaF. The instrument has been tested and is now being used routinely in this laboratory for the studies of the electrosorption of organic molecules at electrodes.

Acknowledgment

We are very grateful for support of this work by the Office of Naval Research under Contract No. N0014-67-0299-0007-AA, Project NR 359-493, and by the Air Force Office of Scientific Research, AFOSR (AFSC), USAF, under Grant No. AF-AFOSR-70-1887. We take pleasure in thanking Mr. Hisamitsu Nakadomari and Dr. Giorgio Papeschi of this laboratory for help with several of the experiments and Dr. Patricia R. Mohilner, Colorado State University Computer Center, for valuable advice on the computer programming.

Manuscript submitted April 13, 1971; revised manuscript received *ca.* May 28, 1971.

Any discussion of this paper will appear in a Discussion Section to be published in the June 1972 JOURNAL.

[10] The reason a large digital computer is used for the thermodynamic analysis is that the computational floating point precision of the PDP-8/I (12 bits, sign and exponent, plus 24 bit mantissa) is not sufficient for the matrix inversion routines used in the smoothing program (24). The CDC 6400 has a 60 bit word length (21 bits, sign and exponent, plus 48 bit mantissa) which means that the analysis programs may be written in single precision FORTRAN. A 60 bit floating point package for the PDP-8/I computer is currently being written in this laboratory which should make it possible to carry out the thermodynamic analysis of the data on the minicomputer also.

APPENDIX

Table I is a list of the digital logic modules (DEC flip chips) used to construct the various interface components on the system described in this paper. The interface for this system is built from DEC "negative logic" (−3V and ground) discrete circuit component modules, *i.e.*, R, A, and W series digital logic modules. In order to aid in the selection of components for an interface based on "positive logic" (+3V and ground) we also give the nearest equivalents to our interface in terms of DEC M and A series integrated circuit digital logic modules. The number in parentheses immediately preceding the logic module model number is the number of modules of the indicated type required. It should be noted that the D/A converters also require a stable analog reference voltage source. We employ two Hewlett Packard Model 6215A power supplies for this purpose. The Model ADC-1 A/D converter is purchased as a single packaged unit installed at the factory.

Table I. List of digital logic modules

Interface device	Number needed	Negative logic modules per device		Positive logic modules per device	
12-bit D/A	1	(1)	A605	(1)	M613
		(2)	A604	(1/3)	M103
		(2)	A601	(2)	M206
		(6)	R202		
		(1/3)	W103		
10-bit D/A	2	(2)	A604	(1)	A618
		(2)	A601	(1/3)	M103
		(5)	R202		
		(1/3)	W103		
Relay driver	4	(1/7)	W051	(1/2)	M040
		(1/4)	R204	(1/8)	M203
		(2/3)	W103	(2/3)	M103
Birth detector interface	1	(1/3)	W510	(1)	M501
		(1/7)	R107	(1/8)	M203
		(1/4)	R204	(1/10)	M133
		(1/3)	R111	(2/3)	M103
		(2/3)	W103		
Drop knocker	1	(1/2)	R302	(1/2)	M302
		(1/3)	W602	(1/12)	M050
		(1/3)	W103	(1/3)	M103
Plot control	1	(1/2)	R302	(1)	M306
		(1/3)	R111	(1/10)	M133
		(1/2)	R202	(1/6)	M207
		(1/3)	W510	(1)	M501
		(1/7)	R107	(2/3)	M103
		(2/3)	W103		

REFERENCES

1. For a recent review *cf.* D. M. Mohilner in "Electroanalytical Chemistry," Vol. 1, pp. 241-409, A. J. Bard, Editor, Marcel Dekker, Inc., New York (1966).
2. T. R. Beck, CITCE Meeting, Detroit, 1968, Extended Abstracts, pp. 214-216; *J. Phys. Chem.*, **73**, 466 (1969).
3. G. Lippmann, *Compt. rend.*, **76**, 1407 (1873); *Pogg. Ann.*, **149**, 561 (1873); *J. Phys.*, **3**, (1), 41 (1874); *Ann. Chim. Phys.*, **5**, (5), 494 (1875); *ibid.*, **12**, (5), 265 (1877).
4. For an excellent recent discussion of the principles of capillarity see: A. W. Adamson, "Physical Chemistry of Surfaces," 2nd edition, Interscience Publishers, Inc., New York (1967).
5. D. C. Grahame, *J. Am. Chem. Soc.*, **63**, 1207 (1941); *ibid.*, **71**, 2975 (1949).
6. C. Cachet, I. Epelboin, J. Lestrade, and P. Ravel, *Compt. rend.*, **C264**, 1524 (1967).
7. K. Doblhofer and D. M. Mohilner, *J. Phys. Chem.*, **75**, 1698 (1971).
8. A. N. Frumkin, *Z. Physik*, **35**, 792 (1926).
9. R. Parsons, *Trans. Faraday Soc.*, **55**, 999 (1959); see also: E. Dutkiewicz, E. Garnish, and R. Parsons, *J. Electroanal. Chem.*, **16**, 505 (1968).

10. J. Lawrence, R. Parsons, and R. Payne, *ibid.*, **16**, 193 (1968).
11. K. Doblhofer, *This Journal*, **116**, 77C (1969).
12. B. E. Conway and L. G. M. Gordon, *J. Phys. Chem.*, **73**, 3609 (1969).
13. R. Parsons, *Rev. Pure Appl. Chem. (Australia)*, **18**, 91 (1968).
14. J. Lawrence and D. M. Mohilner, *This Journal*, **118**, 259 (1971).
15. D. J. Schiffrin, *J. Electroanal. Chem.*, **23**, 168 (1969).
16. J. O'M. Bockris, K. Müller, H. Wroblowa, and Z. Kovac, *ibid.*, **10**, 416 (1965); **15**, 101 (1967).
17. R. Payne, *ibid.*, **7**, 134 (1964).
18. D. E. Smith in "Electroanalytical Chemistry," Vol. 1, pp. 104-132, A. J. Bard, Editor, Marcel Dekker, Inc., New York (1966).
19. N. K. Adam, "The Physics and Chemistry of Surfaces," Dover, New York (1968).
20. R. Defay and I. Prigogine, "Tension Superficielle et Adsorption," Editions Desoer, Liege (1951).
21. "Small Computer Handbook," Digital Equipment Corp., Maynard, Massachusetts (*cf.* 1968 or 1970 editions).
22. "Digital Logic Handbook," Digital Equipment Corp., Maynard, Massachusetts (*cf.* 1968 or 1970 editions).
23. C. A. Smolders and E. M. Duyvis, *Rec. Trav. Chem.*, **80**, 635 (1961).
24. P. R. Mohilner and D. M. Mohilner, "Thermodynamic Analysis of Electrocapillary Data," in "Applications of Computers to Analytical Chemistry," H. B. Mark, Jr., Editor, Marcel Dekker, New York (In press).
25. D. M. Mohilner and P. R. Mohilner, *This Journal*, **115**, 261 (1968).
26. D. C. Grahame, E. M. Coffin, J. I. Cummins, and M. A. Poth, *J. Am. Chem. Soc.*, **74**, 1207 (1952).

Exchange in the Zn, Zincate, ZnO System

T. P. Dirkse,* L. A. Vander Lugt,* and N. A. Hampson[1]

Chemistry Department, Calvin College, Grand Rapids, Michigan 49506

ABSTRACT

The results of a radiochemical study of the system Zn/Zn(II), OH^-/ZnO are presented. It is shown that the exchange of tagged Zn(II) between solid ZnO and zincate ion is slow and appears to be negligible in zincate solutions based on 30% KOH. Commercial implications are discussed. Attempts to study the charge transfer reaction at a solid zinc electrode were unsuccessful due to the high parasitic corrosion rate.

Although considerable progress has been made in understanding the processes which occur at a solid zinc electrode in KOH solutions, some unsettled questions still remain. One of the reasons for this is that the nature of concentrated KOH solutions is not fully understood; the situation is further aggravated when zincate ion is present in the solution.

Zincate solutions may be prepared by dissolving ZnO in aqueous KOH. Two complex ions have been identified in the solution $Zn(OH)_3^-$, and $Zn(OH)_4^{2-}$ (1). It is generally agreed that the most common of these is $Zn(OH)_4^{2-}$ (2). A further complication with these solutions is the readiness with which "supersaturated" zincate solutions can be prepared, *i.e.* solutions in which the concentration of the dissolved Zn(II) species is greater (often by a factor of 2) than that of solutions in equilibrium with solid ZnO. Raman spectra (3, 4) and N.M.R. (5) have been used to study potassium zincate systems based on KOH solutions ranging from 4 to 15 mol l^{-1} and it has been concluded that the only significant anion is the tetrahedral $Zn(OH)_4^{2-}$. In more dilute solutions there were indications of "second coordination sphere" influences and indications of ion pair association.

Of special interest for power source applications and significance to the study of the zinc-alkali electrode process is the electrolytic production of supersaturated zincate electrolytes by the anodic oxidation of zinc in KOH (6). Practically nothing is known about such solutions except that the precipitate that forms extremely slowly appears to be composed mainly of ZnO. Above a certain concentration of zincate the Zn(II) appears to be electrochemically inactive (7). Raman spectra studies of supersaturated solutions indicate that above the equilibrium solubility limit Zn(II) species are not present as $Zn(OH)_4^{2-}$ (4).

* Electrochemical Society Active Member.
[1] Present address: Chemistry Department, Loughborough University of Technology, Leicestershire, England.
Key words: radioactive zinc, zinc exchange, alkaline system, zinc, zinc oxide, zincate.

The process of discharge of zinc electrodes (dissolution of zinc) occurring in energy conversion devices generally involves the ultimate production of ZnO as a solid phase. For the whole process, then, at least two exchange reactions occur involving Zn and Zn(II) species. These are: first, the charge transfer reaction (exchange of electrons and ions between electrode and solution); and second, the exchange between solution Zn(II) and lattice Zn(II) in ZnO.

The charge transfer reaction has been investigated using electrochemical methods and in the case of the zinc amalgam electrode the results have been confirmed using radiochemical techniques (8). Radiochemical techniques appear to offer the only method of studying the solution/oxide exchange equilibrium. Recently in this laboratory the exchange of Zn^{65} between soluble Zn(II) species in 7 mol l^{-1} KOH and solid ZnO has been investigated. It was reported in a preliminary communication (9) that the rate of exchange of Zn was so slow as to be virtually undetectable.

In this paper we present the detailed results of the investigation concerning the exchange of Zn^{65} between soluble Zn(II) species in electrolytes based on various concentrations of KOH and solid ZnO. We note the results of experiments on the electrolytic production of ZnO through the intermediacy of supersaturated potassium zincate solutions and also the results of an attempt to follow the Zn/Zn(II) exchange using the radiochemical technique.

Experimental and Results

Materials and general procedures.—The radioactive form of zinc used was Zn^{65} available as carrier-free $Zn^{65}Cl_2$. Radioactive zinc electrodes (1 cm x 1 cm) were prepared by electrodeposition onto platinum at a rate of 2 mA cm^{-2} from a dilute solution of $Zn^{65}Cl_2$. Zincate concentrations were determined by titration with EDTA, and samples (0.5 ml or 1.5g) were used

for radioactive counting. All work was carried out at room temperature, 23° ± 1°C.

Zincate/solid ZnO exchange.—Each mixture contained about 3g of undissolved ZnO, having a particle size of 0.3μ, suspended in 60 ml of KOH solution (10, 20, 30, and 45%) previously saturated with tagged ZnO. These mixtures were agitated on a mechanical shaker. The results are shown in Fig. 1. The amount of exchange was followed by noting the decrease in count rate of the solution and by measuring the uptake of Zn^{65} by the solid ZnO. The latter procedure was more inconvenient because of the problems associated with the washing of the solid ZnO.

In the case of the 30% KOH solution, no exchange occurred during the experimental time period. In the case of 10% and 20% KOH, a small amount of exchange occurred. This could not be ascertained from Fig. 1, but was determined from the count rate of the solid ZnO at the end of the run. The "time infinity" values on Fig. 1 are calculated values based on the assumption of complete exchange. It is clear that in no case were these values approached on the present time scale.

The system based on 45% KOH did not show a change in radioactivity of solution with time within the uncertainty limits inherent in the radiometric counting. To check this, the amount of undissolved ZnO in the system was increased to 12g. Figure 2 shows the results; a small but significant amount of exchange occurs.

As a check on the results shown in Fig. 1, the solid was removed from each system at the completion of the experiments and counted for radioactivity. The results are shown in Table I. For 30% KOH no exchange has occurred, the solid ZnO being free of tagged Zn. For 10% KOH the ZnO shows pronounced activity but the 20% and 45% KOH systems exhibit only weak activity.

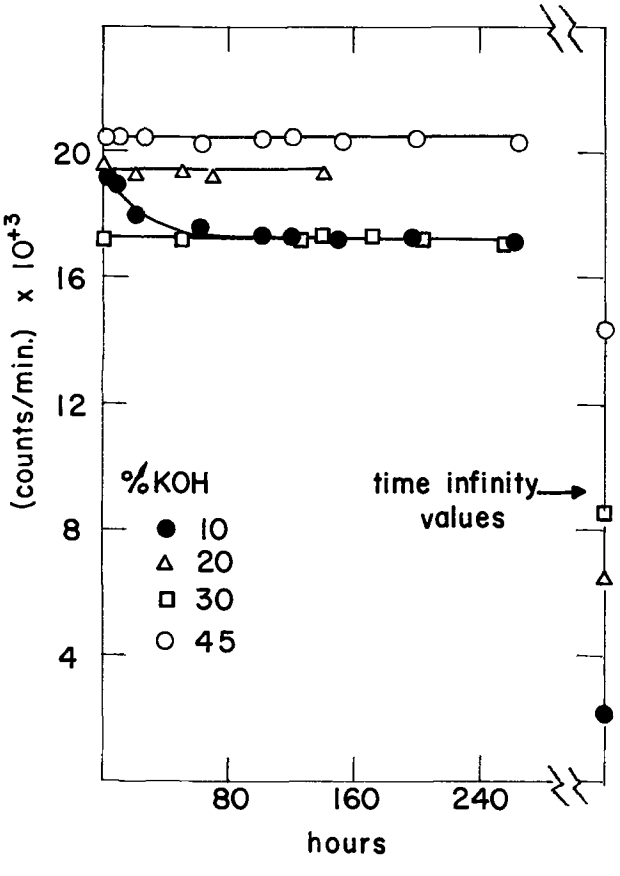

Fig. 1. Change in radioactivity of KOH solutions saturated with ZnO and in equilibrium with 3g excess ZnO. Counting rates in 10^3 counts per min.

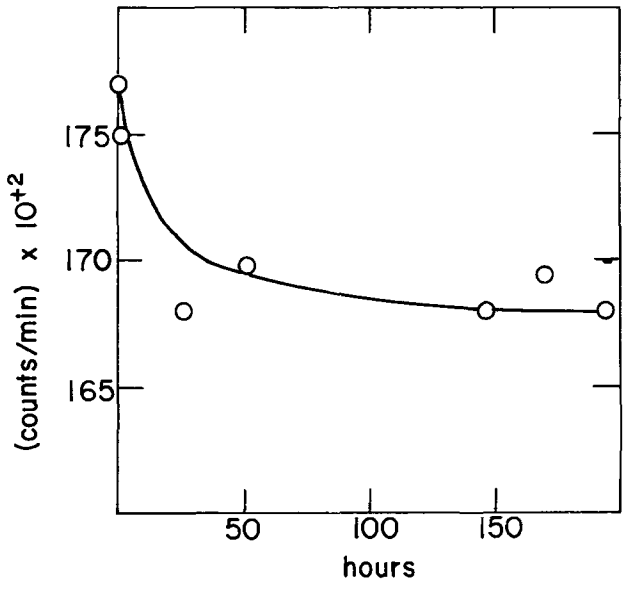

Fig. 2. Change in radioactivity of 45% KOH saturated with ZnO and in equilibrium with 12g excess ZnO. Counting rates in 10^2 counts per min.

Discharge of Zn into KOH saturated with tagged ZnO.—The electrolyte system consisted of KOH solutions saturated with tagged ZnO, zinc anodes, and cadmium oxide cathodes. As current passes through the cell the zinc dissolves and the cathode is reduced to cadmium metal. Charge was passed until a supersaturated solution of potassium zincate [2 to 3 times the equilibrium concentration of Zn(II)] resulted. This was verified by EDTA analysis. The supersaturated solution was stored until a precipitate of ZnO was deposited. This required about 2 days for the first signs of solid deposition to appear. From time to time throughout the precipitation period solution samples were removed, filtered, analyzed, and counted for radioactivity. In the 35% KOH solution, the supersaturated solution contained 0.1 mole Zn(II). At the end of the run, 2.4g of ZnO had precipitated.

The results of these experiments are given in Table II. The solution shows no change in the proportion of the atoms of zinc which are tagged.

Zincate/zinc metal exchange reaction.—Tagged solid zinc electrodes were suspended in untagged potassium

Table I. Radioactivity of solid ZnO that had been in equilibrium with tagged zincate solutions of potassium zincate

% KOH	(counts/min)	% Exchange
10	185,000	~10
20	8,300	~2
30	2,080	0
45	37,000	~3

Table II. Exchange in electrolytic zincate solutions

Time, days	10% KOH (counts/mole zincate)	35% KOH (counts/mole zincate)	45% KOH (counts/mole zincate)
0	22,400	1740	5760
3	21,400	—	—
4	—	—	5790
5	—	1800	—
6	21,400	—	—
8	—	1730	—
11	21,630	—	—
13	—	1780	—

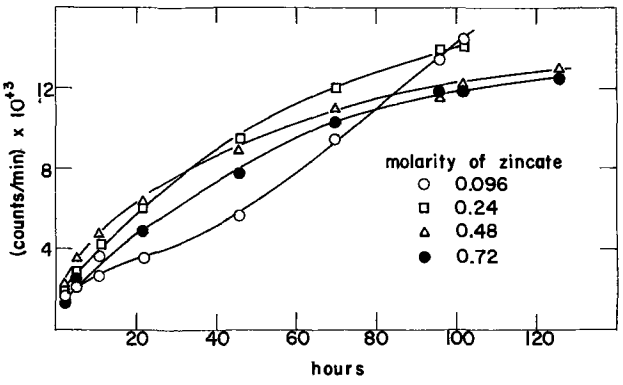

Fig. 3. Change in radioactivity of 45% KOH in contact with tagged zinc electrodes at room temperature. Counting rates in 10^3 counts per min.

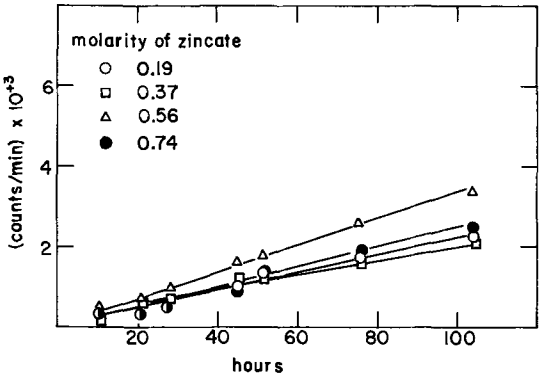

Fig. 4. Change in radioactivity of 35% KOH in contact with tagged zinc electrodes at room temperature. Counting rates in 10^3 counts per min.

zincate solutions. The change in the radioactive count for the solution was measured from time to time. Figure 3 shows the change in radioactivity for a zincate solution based on 45% KOH and Fig. 4 shows similar data for a solution based on 35% KOH. The solution radioactivity increased markedly. Examination of the electrode at this point revealed that the zinc deposit had been corroded to such an extent that the platinum base had become exposed. Data are tabulated in Table III. Calculation of the rate of corrosion by measuring the weight loss indicated a rate of 2×10^{-6} mol hr^{-1} cm^{-2}.

In a further series of experiments with solid electrodes, untagged zinc sheets were placed in tagged zincate solutions. Again no change in the radioactivity of the solution could be detected.

Discussion

The exchange between zincate and solid ZnO.—Saturated zincate electrolytes based on 30% KOH solutions in contact with ZnO exhibit rates of exchange of Zn too small to be measured in the present experiments. This effect may be an extension of the observation (9) that the rate of exchange decreases with increase in the pH of the electrolyte. However, this is not substantiated by the results obtained in 10, 20, and 45% KOH solutions. In the 10% and 20% KOH solution a small exchange rate was noted. In the 45% KOH system exchange was detected and confirmed only when the surface/volume ratio had been considerably increased to enhance the radioactive changes occurring in the electrolyte.

Table III. Zinc-zincate exchange in 35% KOH at room temperature

Run	Start of run: mg Zn	Start of run: (10^7 cts/min) g^{-1}	End of run: mg Zn	End of run: (10^7 cts/min) g^{-1}	For complete exchange: (10^6 cts/min) g^{-1}
1	77	1.45	39	1.33	8.8
2	76	1.52	32	1.31	17.5
3	85	1.24	31	1.39	5.7
4	78	1.39	15	1.35	4.5

No satisfactory theoretical explanation has yet been developed to account for the behavior of the ZnO/zincate system. The detection of a little exchange at the higher KOH concentration is a further perplexing aspect. A possible explanation is that below 30% KOH zincate ion is in some respect different from that in zincate solutions based on KOH of concentration greater than 30%. Further work in this area is urgently required.

The main concomitant of the present work is that in strongly alkaline solutions of zincate, in which energy conversion devices are conventionally operated, the mechanism cannot include any step which assumes a rapid equilibrium between zincate ion and solid zinc oxide. Such mechanisms apply in the case of microporous zinc electrodes operating in low electrolyte volume to active material ratio when electrolyte efficiencies well in excess of 100% are readily achieved. The nonestablishment of an equilibrium between products (ZnO) and the electrolyte may explain why this system is not subject to considerably more concentration polarization than is generally observed. The reduction of a ZnO-rich phase (discharged negative) may well be expected to go by a solid phase "direct" reduction in the absence of a rapid Zn(II) exchange between solution and ZnO. This latter aspect may explain the high microporosity of such zinc negative plates. The absence of a significant solution (or surface) diffusion step hinders the development of compact deposits on cycling (as occurs in the lead-acid battery but is far less marked in the zinc electrode in alkali).

The production of supersaturated zincate solutions.—The experiments indicate that Zn(II) produced electrochemically and zincate ion in solution are in equilibrium. There is evidence that supersaturated solutions produced by dissolving ZnO in KOH contain two solution species (4) in which case it follows from the present experiments that these two are themselves in equilibrium.

The zinc/zincate exchange reaction.—The results of the weight loss *vs.* time correlation, 2×10^{-6} mol hr^{-1} cm^{-2}, agrees very well with the reported rate of corrosion of zinc in alkaline solution in contact with the atmosphere (10). The result of the experiment with the untagged zinc sheets that no change in solution radioactivity occurs, further reinforces the idea that the exchange reaction at the Zn/Zn(II), OH^- interphase cannot be followed by radiochemical experiment due to the spontaneous corrosion of zinc in the electrolyte. The uptake of tagged zinc from solution in any case would be small and the parasitic dissolution of the electrode due to local action is difficult to suppress and has the effect of obscuring any atomic exchange. Carefully purified microelectrodes used in ultrapurified systems are not feasible where it is necessary to measure a significant reduction in radioactivity.

Acknowledgment

The work reported here was supported by Air Force Aero Propulsion Laboratory, Air Force Systems Command, United States Air Force.

Manuscript submitted Dec. 28, 1970; revised manuscript received *ca.* June 10, 1971. This was Paper 3

presented at the Cleveland, Ohio, Meeting of the Society, Oct. 3-7, 1971.

Any discussion of this paper will appear in a Discussion Section to be published in the June 1972 JOURNAL.

REFERENCES

1. T. P. Dirkse, C. Postmus, and R. Vandenbosch, *J. Am. Chem. Soc.*, **76**, 6022 (1954).
2. T. P. Dirkse, *This Journal*, **101**, 328 (1954).
3. J. S. Fordyce and R. L. Baum, *J. Chem. Physics*, **43**, 843 (1965).
4. J. F. Jackovitz and A. Langer, Paper 321, presented at Electrochem. Soc. Meeting, Montreal, Canada, Oct. 6-11, 1968.
5. G. H. Newman and G. E. Blomgren, *J. Chem. Physics*, **43**, 2744 (1965).
6. T. P. Dirkse, *This Journal*, **102**, 497 (1955).
7. N. A. Hampson, G. A. Herdman, and R. Taylor, *J. Electroanal. Chem.*, **25**, 9 (1970).
8. M. Quintin, L. Kervajan, and M. Collier, *Compt. Rend.*, **260**, 4510 (1965).
9. L. A. Vander Lugt and T. P. Dirkse, *This Journal*, **118**, 265 (1971).
10. T. P. Dirkse and R. Timmer, *ibid.*, **116**, 162 (1969).

Energetics of Single Ion Solvation in Nonaqueous Solvents and the Effects on Electrode Kinetics

Mark Salomon

U. S. Department of Transportation, Transportation Systems Center, Cambridge, Massachusetts 02142

ABSTRACT

Individual ionic energies of solvation are estimated for solvation in methanol and in a 20% dioxane-water mixture. As found in a previous paper (1), these solvation energies are about 10 to 15 kcal/mole larger (more positive) than most previous estimates. A detailed discussion is presented on these differences. The medium effect is discussed in relation to the kinetics at electrode surfaces and it is proposed, and demonstrated, that the standard chemical free energy of transfer of the activated complex from water to an organic solvent is, effectively, zero. Based on this assumption, a new method is presented for the calculation of differences in surface potentials between water and an organic solvent.

In a previous paper (1) it was proposed that single ion solvation energies can be estimated from the empirical relation

$$d\,\Delta G^{o}_{conv} = \text{constant}/r - 2\Delta G^{o}_{solv}(RI) \quad [1]$$

In Eq. [1] $\Delta G^{o}_{solv}(RI)$ is the solvation energy of the reference ion and $d\Delta G^{o}_{conv}$ is the difference in conventional energies of solvation between a cation and anion of equal ionic (crystal) radius, r. For monovalent ions, the conventional energies, referred to the solvated proton, are given by

$$\Delta G^{o}_{conv}(M^+) = \Delta G^{o}_{solv}(M^+) - \Delta G^{o}_{solv}(H^+) \quad [2a]$$

$$\Delta G^{o}_{conv}(X^-) = \Delta G^{o}_{solv}(X^-) + \Delta G^{o}_{solv}(H^+) \quad [2b]$$

The constant term in Eq. [1] is therefore

$$\text{constant}/r = \Delta G^{o}_{solv}(M^+) - \Delta G^{o}_{solv}(X^-) \quad [3]$$

Izmailov (2) actually proposed the use of these relations some 10 years prior to the present use. However Izmailov proposed that $\Delta G^{o}_{solv}(M^+)$ and $\Delta G^{o}_{solv}(X^-)$ are accurately described by a function in $1/r$ or $1/n^2$ (n is the principal quantum number of the lowest vacant orbital of the ion) and that plots of $\Delta G^{o}_{conv}(M^+)$ and $\Delta G^{o}_{conv}(X^-)$ *vs.* $1/r$ should extrapolate to the same intercept; *i.e.* at $1/r = 0$, the common intercept is $\Delta G^{o}_{solv}(H^+)$. There are several objections to this assumption. If it is correct, then it follows that the choice of crystal radii will seriously effect the extrapolations as the intercepts will vary depending upon which set of radii are chosen (see below for numerical results). Also, this simple assumption regarding a common intercept is actually an acceptance of the Born equation. It is well established [see discussions in Ref. (1), (3-5)] that the leading electrostatic terms are really those for ion-dipole ($1/r^2$), ion-quadrupole ($1/r^3$) and dipole-dipole interactions ($1/r^3$) in the first solvation sphere. Other electrostatic terms such as ion-induced dipole ($1/r^4$), ion-induced quadrupole ($1/r^5$) and other multipole interactions are difficult to treat analytically and are often neglected as they are probably quite small. Nonelectrostatic terms such as those due to the London dispersion forces, hydrogen bonding, charge transfer and σ- and π-bonding require a quantum mechanical approach for their analytical treatment and it is highly unlikely that a simple $1/r$ plot, even if linear, would yield an intercept equal to $\Delta G^{o}_{solv}(H^+)$. In general (see below), the $1/r$ plots of Eq. [2a] give higher (more positive) intercepts than those of Eq. [2b]. In Izmailov's works (2) Eq. [2b] was used to obtain the intercept since this relation was found to be linear in $1/r$ and the plot for cations (Eq. [2a]), which was not linear, was subjected to a long extrapolation to the intercept obtained from the anion plot. In previous work (1) it was found that $1/r$ plots of Eq. [2a] and [2b] were linear (using more recent thermodynamic data for solvation energies) and that the intercepts were not identical. It was concluded that:

(1) A linear relation for ΔG^{o}_{conv} *vs.* $1/r$ is strictly empirical and that the intercepts contained residual energetic terms due to those forces which have a higher order dependence than $1/r$. The intercept of the $1/r$ plot of Eq. [2a] can be represented by the sum[1]

$$(\text{intercept})_a = -\Delta G^{o}_{solv}(H^+) + \sum_{j=1}^{n-1} a_j/r^n \quad [4a]$$

Similarly, for Eq. [2b], the intercept of the simple $1/r$ plot is

$$(\text{intercept})_b = -\Delta G^{o}_{solv}(H^+) + \sum_{j=1}^{n-1} b_j/r^n \quad [4b]$$

Key words: medium effects, solvent effects, single ion solvation energies, electrode kinetics, surface potentials.

[1] Born charging is omitted from this sum since it is really a function of $\{r(\text{ion}) + 2r(\text{solvent})\}^{-1}$ as discussed elsewhere (4, 5).

where $n = 2, 3, 4, \ldots\ldots$ and a_j and b_j are constants which are not necessarily equal.

(2) With the exception of the Born charging energy, all other electrostatic interactions are highly dependent upon structural properties; *e.g.* the number of solvent molecules in the inner solvation sphere and the alignment of their multipoles with respect to the radial direction of the ion. Both the enthalpy and entropy terms are very sensitive to these structural parameters (3-8) and a simple $1/r$ dependence for these terms could not be considered valid. Free energy relations are, however, considerably simpler since much cancellation occurs between the enthalpy and entropy terms (1, 6, 9) and in this context we have proposed earlier (1) that

$$\lim_{r \to \infty} \{\Sigma\, a_j/r^n - \Sigma\, b_j/r^n\} \to 0 \qquad [5]$$

Since the energies and enthalpies are not exact functions of $1/r$, there are no reasons to believe that the individual intercepts in Eq. [4] are equal to $\Delta G^\circ_{solv}(H^+)$. These intercepts are dependent upon the choice of crystal radii used in the calculation and it is more valid to consider differences in conventional energies (*i.e.* Eq. [1]) since the difference in intercepts is independent of the choice of radii as long as the sum of the cation and anion values equal the observed value. The assumption that the "neutral" part of the solvation energy or enthalpy is simply related to some function of the ionic radius (*e.g.* r^2 or r^4) has proved to be a popular approach in evaluating these single ion contributions (1-3, 8, 10, 11). It should be pointed out that this procedure may be invalid if, as discussed by Noyes (12), these neutral energies for the individual ions are more accurately related (identical) to the neutral energies for an iso-electronic rare gas molecule.

Data and Results

Table I lists conventional free energies for various ions referred to the proton in methanol and in a 20% (by weight) dioxane-water mixture. These data are based on the emf studies of Feakins *et al.* (15-17). Also included in this table are the reciprocals of the crystal radii obtained from Ref. (13) and (14). Figures 1 and 2 are plots of Eq. [1] for the 20% dioxane-water mixture using, respectively, Pauling's radii and Gourary and Adrian's radii. Plots of Eq. [1] for methanol and water have a similar appearance. The results for these three systems are summarized in Table II. For the aqueous system (1) the value of $\Delta G^\circ_{solv}(H^+)$ based on Eq. [1] is identical using either Pauling's or Gourary and Adrian's radii. The fact that $\Delta G^\circ_{solv}(H^+)$ in the nonaqueous solvents are, very slightly, dependent upon which set of radii are used (to within ± 1 kcal/mole) is attributed to the shorter range of linearity using the Gourary and Adrian radii which therefore leads to a greater uncertainty in the extrapolation to $r = \infty$. In the discussions below, the results for the nonaqueous systems based on Pauling's radii are compared with the aqueous data from Ref. (1). Table III summarizes the single ion solvation energies obtained

Table I. Conventional free energies and crystal radii[a,b]

Ion	ΔG°_{conv} (ion) Methanol	Dioxane/water	1/r G & A	P
Li+	135.9	137.2	1.075	1.639
Na+	162.3	162.9	0.855	1.042
K+	180.9	180.4	0.671	0.752
Rb+	183.1	184.6	0.610	0.676
Cs+	188.5	186.6	0.546	0.602
OH-		−365.3	0.885[c]	
Cl-	−329.6	−334.8	0.610	0.553
Br-	−323.9	−328.6	0.556	0.513
I-	−317.5	−320.7	0.490	0.461

[a] ΔG° values are in kcal/mole at 25°C based on molar units and are referred to the solvated proton. r_i values are in A and G & A refers to Gourary and Adrian (13) and P to Pauling (14).
[b] Referred to 1 atm at 25°C. Note that 1 kcal = 4.184 kJ.
[c] r_{OH^-} obtained from Ref. (1).

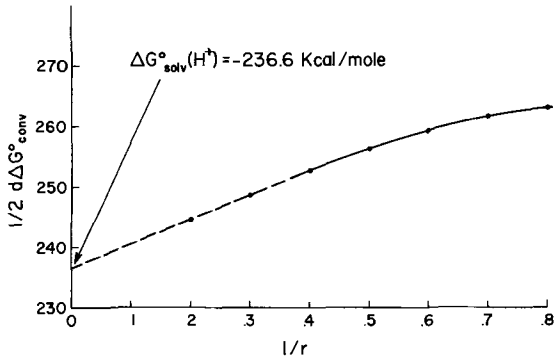

Fig. 1. Plot of Eq. [1] for 20% dioxane-water mixture using the crystal ionic radii of Pauling.

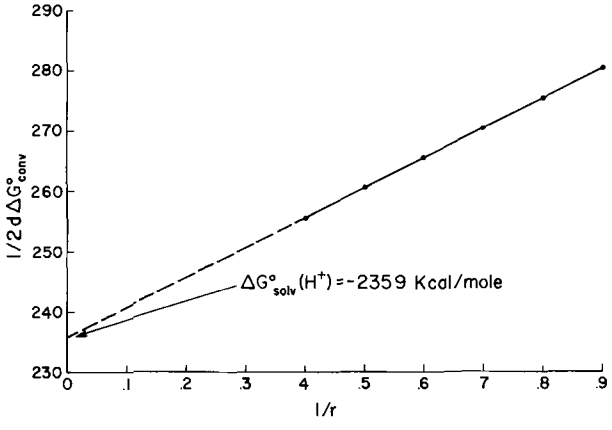

Fig. 2. Plot of Eq. [1] for 20% dioxane-water mixture using the crystal ionic radii of Gourary and Adrian.

Table II. Solvation energies for the proton in several solvents at 25°C (molar units)*

Solvent	Intercepts from Eq. [2] Eq. [2a]	Eq. [2b]	Eq. [2a]	Eq. [2b]	ΔG°_{solv} (H+) from Eq. [1]	
Water	−211.2	−265.9	−219.6	−251.5	−235.0	−235.0
20% dioxane in water	−209.4	−263.9	−222.0	−248.2	−236.6	−235.9
Methanol	−203.3	−268.8	−219.1	−257.9	−236.1	−237.9
Radii from	G & A		P		G & A	P

* All entries in this table are in kcal/mole. The aqueous data are from Ref. (1).

Table III. Single ion free energies of solvation at 25°C*

Solvent ion	$-\Delta G^\circ_{solv}$ (ion) in kcal/mole H_2O^a	H_2O^b	H_2O^c	$MeOH^d$	$MeOH^b$	20% dioxane in water[d]
H+	235.0	258.0	251.1	237.9	253.0	235.9
Li+	97.8	117.0	114.6	102.0	116.0	98.7
Na+	72.4	96.0	89.7	75.6	93.0	73.0
K+	54.9	78.0	73.5	57.0	76.0	55.5
Rb+	50.7	74.4	67.5	54.8	—	51.3
Cs+	46.7	64.0	60.8	49.4	60.5	47.3
OH-	131.1	—	—	—	—	129.4
F-	128.7	—	113.9	—	—	—
Cl-	100.3	74.0	84.2	91.7	71.0	98.9
Br-	94.2	68.0	78.0	86.0	67.0	92.7
I-	85.7	59.4	70.0	79.6	59.5	84.8

* All data are based on Pauling radii and on the molar scale except those of Izmailov (2) which are based on the molal scale. The references are:
[a] (1), [b] (2), [c] (19), [d] present work.

Table IV. Single ion free energies of transfer from water to several organic solvents at 25°C

Solvent ion	ΔG°_t (ion) in kcal/mole* MeOH[a]	MeOH[b]	MeOH[c]	MeOH[d]	MeOH[e]	20% dioxane[a] in water	20% dioxane[f] in water
H^+	−2.9	−2.4	−2.0	−5.8	5.0	−0.9	−0.5
Li^+	−3.8	−3.2	—	−6.7	1.0	−0.9	−0.2
Na^+	−2.8	−2.3	−1.8	−5.9	3.0	−0.6	−0.2
K^+	−1.9	−1.2	−1.2	−5.2	2.0	−0.6	−0.2
Rb^+	−4.1	—	−1.2	−5.4	5.4	−0.6	−0.1
Cs^+	−2.7	—	−1.3	−5.5	3.6	−0.6	−0.1
Cl^-	8.5	7.8	7.8	11.2	3.0	1.4	0.9
Br^-	8.2	2.6	7.3	10.6	1.5	0.7	—
I^-	6.1	0.8	6.2	9.7	−0.2	0.9	0.5

* All data from Ref. (10), (15), (22) and the present work are based on molar units; remaining data are based on molal units. The references are:
[a] Present work, [b] (15), [c] (10), [d] (20), [e] (21), [f] (15) and (22).

by the author and several other investigators. A more complete review is given elsewhere (18). It has been noted in Ref. (18) that if more recent values for ΔG°_{conv}(ion) are used in the original Izmailov method (2), then it is found (for water) that $\Delta G^\circ_{solv}(H^+) = 251.5$ kcal/mole. It has also been observed here and in Ref. (1) that the cation plots of Eq. [2a] are linear [there is curvature for this plot around the point for Li^+ when the Gourary and Adrian radii are used; Pauling's radii lead to completely linear plots (1)]. Latimer, Pitzer, and Slansky (19) added a small constant factor (the δ-factor) of 0.10Å to all anion radii and a large constant factor of 0.85Å to all cation radii to obtain linear plots of Eq. [2a] and [2b] such that they had a common intercept. These δ-factors for water have been reported to be as high as 0.42Å for anions (23) and as low as 0.64Å for cations (24).

The medium effect for single ions is an important factor in studying solvation behavior. King (25) has given an excellent review on this subject and Popovich (21) and Criss and Salomon (18) have reviewed some more recent developments in this field. Feakins *et al.* (15-17, 22) have studied the alkali metal halides and acid halides in great detail and have proposed that the standard chemical free energies of transfer of ions from water to pure methanol or a methanol-water mixture can be obtained from

$$\Delta G^\circ_t = \Delta G^\circ_t(H^+) + k/r_- \qquad [6a]$$

and from

$$\Delta G^\circ_t = \Delta G^\circ_t(X^-) - m/r_+ \qquad [6b]$$

Here ΔG°_t is the measured standard chemical free energy of transfer of the halogen acid HX or the metal halide MX and k and m are constants. It was found that the $\Delta G^\circ_t(H^+)$ values obtained from Eq. [6a] and [6b] were significantly different and average values were used. Popovych (21) has determined ΔG°_t(ion) values for the transfer from water to methanol by assuming that ΔG°_t(large cation) = ΔG°_t(large anion). Alfenaar and DeLigny (10) suggested that the extrapolations based on [6a] and [6b] could be improved by first correcting for the neutral free energy of transfer, $\Delta G^\circ_{t,n}$, which is assumed to be a function of r^2. They assume the applicable relations for the evaluation of $\Delta G^\circ_t(H^+)$ are

$$\Delta G^\circ_t(HX) - \Delta G^\circ_{t,n}(X^-) = \Delta G^\circ_t(H^+) + a/r_- + b/r^2_- + c/r^3_- + \ldots. \qquad [7a]$$

$$\Delta G^\circ_t(H^+) - \Delta G^\circ_t(M^+) + \Delta G^\circ_{t,n}(M^+) = \Delta G^\circ_t(H^+) - a/r_+ + d/r^2_+ + e/r^3_+ + \ldots \qquad [7b]$$

The quantities on the LHS of [7a] and [7b] are known and plotted *vs.* $1/r$. The resulting curves were not linear and a long nonlinear extrapolation was made to a common intercept. The ΔG°_t(ion) values for the transfer from water to methanol and to the 20% dioxane-water mixture obtained from these various methods are given in Table IV. There is fairly good agreement between the present values and those of Feakins *et al.* The data of Alfenaar and DeLigny are in moderate agreement with these two sets of ΔG°_t(ion) values but Popovych's results are markedly different. The standard real free energies of transfer which were measured by Case and Parsons (20) are discussed below. The negative ΔG°_t(cation) values indicate that methanol is a stronger base than is the water molecule in pure aqueous solutions. It has been suggested recently (21) that the reverse situation exists; *i.e.* that the water molecule in pure water is a stronger base than is the methanol molecule in pure methanol. The basis of this conclusion rests in the calculation of positive ΔG°_t(cation) values. There are however several reasons why the positive ΔG°_t(cation) values of Popovych and Izmailov should be questioned (18, 26). Izmailov's results are based on a questionable extrapolation. Popovych has based his results on the assumption that the free energies of transfer of the triisoamylbutylammonium cation (TAB^+) is equal to that for the tetraphenyl boride anion (Ph_4B^-). The experimental free energies of transfer were obtained mainly from solubility data. TAB^+ and Ph_4B^- were chosen as reference ions because of the equality of the Stokes radii of these two ions in water and methanol. Besides the fact that the significance of Stokes radii are unclear (8), it has also been pointed out (18) that solubility measurements for large organic salts are very difficult to perform and are subject to the following possible sources of error:

1. The possible formation of ion pairs.
2. The possible formation of crystal solvates.
3. The possibility of complex ion formation.
4. The possibility of micelle formation.

Coetzee and Sharp (42) have recently found experimental (NMR) evidence showing that there is indeed specific solvation effects with large reference ions and suggest caution in accepting them as ideal solutes. Emf measurements, which can easily be corrected for non-ideal behavior, therefore yield the most accurate ΔG°_t(salt) values [cf. (18), (27)]. Table V illustrates

Table V. Experimental ΔG°_t (salt) values for HCl and KCl for the transfer from water to methanol and the sum $\Delta G^\circ_t(M^+) + \Delta G^\circ_t(X^-)$ at 25°C*

Salt	ΔG°_t (salt) (experimental)	$\Delta G^\circ_t(M^+) + \Delta G^\circ_t(X^-)$	ΔG°_t (ion) calc. from	Reference
HCl	5.36 (15, 16)	5.36	1/r plot	15, 16, p
		5.36	Reference ion	21
		5.59	1/r plot	2
KCl	6.29 (15, 16)	6.29	1/r plot	15, 16, p
		5.29	Ref. ion (solubility)	21
		4.09	1/r plot	2

* ΔG°_t values are in kcal/mole based on molal units; reference p indicates present results.

the accuracies in the reported ΔG°_t(ion) values by comparing the experimental value of ΔG°_t(salt) with the same quantity calculated from the sum of the individual ΔG°_t(ion) values.

Electrode Kinetics and the Medium Effect

The medium effect has been applied to acid base behavior (25), structural properties (15, 16, 18, 20, 21) and to nucleophilic substitution reactions (28). Very few studies are concerned with cation substitution or transfer reactions [cf. ref. (28)] and only one example dealing with the electrochemical proton transfer reaction in H_2O and MeOH-H_2O mixtures has been reported (29). The relative rates of ion substitution or transfer reactions is given by

$$k^{\circ}_w/k^{\circ}_s = \exp\{[\Delta G^{\circ}_t(\neq) - \Sigma\, \Delta G^{\circ}_t(r)]/RT\} \quad [8]$$

In this relation k° is the specific rate constant for water (w) and some organic solvent (s); $\Delta G^{\circ}_t(\neq)$ is the standard chemical free energy of transfer of the activated complex and $\Delta G^{\circ}_t(r)$ is that for a reactant ion or molecule. For anion nucleophilic substitution reactions, the rates in dipolar aprotic solvents are typically 10^6 times greater than they are in water and this has been shown to be due, mainly, to the large positive ΔG°_t(anion) values (28). If on the other hand, ΔG°_t(ion) is negative, as they usually are for the transfer of small cations from water to most organic solvents (18, 28), then one might "predict" that k°_w/k°_s will be greater than unity since the reactant would be in a lower free-energy state in the organic solvent. The fact that the rates of solvent molecule exchange between bulk solution and the inner solvation sphere of transition metal ions are orders of magnitude faster in pure water than they are in methanol or MeOH-H_2O mixtures has been offered as proof of this type of behavior (18). In the present paper, the relative rates of cation transfer at electrodes are considered. A general electrode reaction involving the transfer of cations is

$$M_h^+ + e_M^- \rightleftharpoons X^{\neq} \rightarrow M_M \quad [9]$$

where the subscripts h and M refer, respectively, to a hydrated species and a species located on or in the metal electrode. The ratio of standard exchange currents for reaction [9] in water and some organic solvent is given by (18, 29)

$$i_o(w)/i_o(s) = \exp\{[\Delta G^{\circ}_t(\neq) - \Delta G^{\circ}_t(M^+) + (1-\beta)(\psi_s - \psi_w)\mathbf{F} + \beta\mathbf{F}(\phi_s - \phi_w)]/RT\} \quad [10]$$

In Eq. [10], ψ is the potential at the outer Helmholz plane (specific adsorption is not considered here), ϕ is the absolute single electrode potential, and β is the transfer coefficient. Equation [10] is valid only if β has the same value in the two solvents under consideration. It is also convenient to define the following rate constant ratio (30)

$$i_o(w)/i_o(s) = k^{\circ}_a(w)/k^{\circ}_t(s) = [k^{\circ}_t(w)/k^{\circ}_t(s)]\exp\{(1-\beta)(\psi_s - \psi_w)\mathbf{F}/RT\} \quad [11]$$

where k°_a is the standard rate constant and k°_t is the standard rate constant corrected for double layer effects and is often referred to as the true heterogeneous constant. There are several complicating factors involved in dealing with these relations. One problem is concerned with the potential difference term $\phi_s - \phi_w$. It is not valid to equate this term with the standard chemical free energy of transfer of a single ion or ions as has been done previously (29). This potential difference term is however given exactly in terms of the standard real free energies of transfer (18, 20, 27, 31); *e.g.* for the reversible hydrogen electrode in two solvents we can write

$$\Delta\alpha^{\circ}_t(H^+) = \Delta G^{\circ}_t(H^+) + (\chi_s - \chi_w)\mathbf{F} = [\phi_s(H^+) - \phi_w(H^+)]\mathbf{F} \quad [12]$$

where χ is the surface potential for the indicated solvent. In this context it should be mentioned that methods of arriving at individual ionic contributions to the standard chemical free energies of transfer, ΔG°_t(ion), based on the assumption that an electrode reaction is independent of the nature of the solvent are basically incorrect because of the neglect of these χ terms. The χ terms do not enter into Eq. [8] as they cancel because we are considering differences in free energies between the initial and activated states. Thus in order to be able to "predict" relative rates of electrochemical reactions, the χ-potentials or the standard real free energies must be known. Another critical quantity in Eq. [8] and [10] is the free energy of transfer of the activated complex. In a previous paper (29) this term was adjusted empirically by use of the Born equation. Parker (28) has shown that a reasonable assumption for some S_N2 type reactions is $\Delta G^{\circ}_t(\neq) = 0$ and below it is shown that this assumption is satisfactory for electrochemical reactions. Since the χ-potentials are important quantities in these calculations, it is of interest to present some discussion on their evaluation.

Case and Parsons (20) have used Kenrick's method (32) to measure real free energy differences of ions between water and several organic solvents. Some of their results are included in Table IV. Only one paper (31) reports the measurement of an individual χ value which is based on the assumption that for very large hydrocarbon anions (R^-) and cations (R^+), the following relation holds

$$\lim_{r\to\infty}\ [\alpha_{R^+} - \alpha_{R^-}] \rightarrow 2\chi \quad [13]$$

Here α_R is the real free energy of solvation of a hydrocarbon ion. In this way the value of χ for acetonitrile (AN) was estimated to be -0.10V at 25°C. The negative value of χ corresponds to a surface orientation with the positive end of the solvent dipole (the hydrocarbon part of the molecule) directed towards the gas phase (31). From direct measurements of the standard real free energy of transfer of the Ag^+ ion from water to AN, $\Delta\alpha^{\circ}_t(Ag^+) = -10.1$ kcal/mole (20), one can estimate χ_{H_2O} using the reported values of $\Delta G^{\circ}_t(Ag^+)$ which vary from -3.1 to -7.5 kcal/mole (see 18, 28). From Eq. [12] we have

$$\chi_{AN} - \chi_{H_2O} \approx -0.113 \text{ to } -0.304\text{V at } 25°C \quad [14a]$$

and for $\chi_{AN} = -0.1$V we have

$$\chi_{H_2O} \approx 0.01 \text{ to } 0.20\text{V at } 25°C \quad [14b]$$

There is good evidence to show that the surface potential of water is about 0.1V (33-35) which is in good agreement with the value estimated above and indicates that the water molecules at the solution-air interface are preferentially oriented with the oxygen atom in the gas phase. For methanol the data in Table IV give $\chi_{MeOH} - \chi_{H_2O} = -0.137$V so that χ_{MeOH} is close to zero and is possibly negative indicating that the dipoles are directed with the hydrocarbon part of the molecule directed towards the gas phase.

We now have all the quantities required to predict the relative rates of proton discharge at mercury cathodes in water and in methanol with the exception of $\Delta G^{\circ}_t(\neq)$. This quantity can be empirically estimated by choosing an appropriate model of the activated complex as has been done previously (29). This method is unsatisfactory because by using the activated complex as a variable parameter, we can explain everything but predict nothing (38). In order to be able to predict relative rates of electrochemical reactions, it is proposed here that $\Delta G^{\circ}_t(\neq)$ for the transfer of large cationic activated complexes from water to any organic or mixed organic-water solvent is zero. To show that this approximation at least holds for the proton discharge reaction at Hg cathodes in methanol and water, we can use Eq. [10] to calculate

$\Delta G^o_t(\neq)$ as shown below. For this reaction, we have the following inputs to Eq. [10] at 25°C [see Ref. (29) for references to the original literature]

$$i_o(w)/i_o(s) = 0.56 \qquad \beta = 0.5$$
$$\Delta G^o_t(H^+) = -2.9 \text{ kcal/mole}$$
$$(\phi_{MeOH} - \phi_w)\mathbf{F} = -5.98 \text{ kcal/mole}$$
$$(\psi_{MeOH} - \psi_w)\mathbf{F} = -0.44 \text{ kcal/mole}$$

These data all refer to the molar concentration scale and making the appropriate substitutions into Eq. [10] gives $\Delta G^o_t(\neq) = -33.5$ cal/mole. Considering the uncertainties in the input data, the assumption that $\Delta G^o_t(\neq) = 0$ is certainly a good one. If this is indicative of general behavior, then Eq. [10] simplifies to

$$i_o(w)/i_o(s) = \exp\{[-\Delta G^o_t(M^+) + (1-\beta)(\psi_s - \psi_w)\mathbf{F} + \beta(\phi_s - \phi_w)\mathbf{F}]/RT\} \quad [15]$$

Thus $i_o(w)/i_o(s)$ can be estimated for any reaction providing enough free energy data are available. It is also interesting to note that Eq. [15] offers a new approach to the calculation of the $\chi_s - \chi_w$ term. Consider the electrode reaction

$$Li^+ + e^-_{Hg} \rightleftharpoons X\neq \rightarrow Li(Hg) \quad [16]$$

for which $k^o_t(w) = 0.02$ cm/sec (36) and $k^o_t(DMSO) = 2.9 \cdot 10^{-5}$ cm/sec (37). Taking $\beta = 0.70 \pm 0.05$ (36, 37) and for the transfer of Li^+ from water to dimethylsulfoxide we have $\Delta G^o_t(Li^+) = -6.0$ kcal/mole (molar scale) (28), all data being reported for 25°C. Making the appropriate substitutions into Eq. [11] and [15], it is found that $\alpha^o_{DMSO}(Li^+) - \alpha^o_w(Li^+) \approx -4.34$ kcal/mole and from Eq. [12] it is found that

$$\chi_{DMSO} - \chi_w \approx 0.072V \text{ at } 25°C \quad [17]$$

Thus χ_{DMSO} is about 0.17V which indicates that at the liquid-air interface, the hydrocarbon part of the molecule is directed towards the bulk of solution and the thionyl ($S = O$) group is directed towards the gas phase.

Conclusions

Any method employing a $1/r$ extrapolation for the evaluation of single ion contributions to solvation energies or energies of transfer must be cautiously regarded because of the long extrapolations involved. This is particularly true for nonlinear extrapolations. The use of reference ions is also associated with several difficulties as discussed above. Since detailed electrostatic-quantum mechanical calculations have not as yet given satisfactory results [cf. (18)] for these ion-solvent and solvent-solvent interaction energies, empirical methods still represent an important procedure for the evaluation of ΔG^o(ion) values. The empirical method used here and in Ref. (1) does at least give linear relations and does not make the questionable assumption that the cation and anion $1/r$ plots give identical intercepts at $r = \infty$. Considering single ion solvation, the only quantities known with some degree of confidence are the standard entropy of solvation of the proton in water (4-6, 9, 39, 40); the standard chemical and real free energies of transfer from water to methanol solutions; and possibly the sign of the surface potential of water (positive) and of acetonitrile (negative).

Gurney's aqueous value of -31.3 eu for $\Delta S^o_{solv}(H^+)$ (40) is generally accepted as the most reliable one (4, 5, 9, 39). If we take as an upper limit values of ~ -260 kcal/mole for $\Delta H^o_{solv}(H^+)$ as indicated in several recent works (7, 11), then this requires that $\Delta G^o_{solv}(H^+) \approx -251$ to -258 kcal/mole [cf. Ref. (5)]. Using Randles' elegantly measured value of $\Delta\alpha^o_{solv}(H^+) = -260$ kcal/mole (41), then from

$$\Delta\alpha^o_{solv}(H^+) = \Delta G^o_{solv}(H^+) + \mathbf{F}\chi_{H_2O} \quad [18]$$

we would have to conclude that χ_{H_2O} is negative regardless of the source of $\Delta G^o_{solv}(H^+)$. It is of course possible that our estimates of χ_{H_2O} above are in error and this only serves to indicate the need for additional work in this area.

Acknowledgment

The author is grateful to Professor J. F. Coetzee for sending him data prior to its publication [cf. Ref. (42)].

Manuscript submitted Dec. 29, 1970; revised manuscript received *ca.* June 3, 1971.

Any discussion of this paper will appear in a Discussion Section to be published in the June 1972 JOURNAL.

LIST OF SYMBOLS

ΔG^o_t(ion)	Standard free energy of transfer of an ion from water (w) to some organic solvent (s)
$\Delta G^o_{solv}(X)$	Standard free energy of solvation of species X (X may be an ion or a salt)
$\Delta G^o_t(\neq)$	Standard free energy of transfer of an activated complex from water to an organic solvent
ΔG^o_{conv}	Conventional standard free energy
$i_o(y)$	Standard exchange current density in solvent y
k^o_a	Standard electrochemical rate constant
k^o_t	Standard electrochemical rate constant corrected for double layer effects
$\Delta\alpha^o_t$(ion)	Standard real free energy of transfer of an ion from water to an organic solvent
$\Delta\alpha^o_{solv}(X)$	Standard real free energy of solvation of species X
χ	Surface potential

REFERENCES

1. M. Salomon, *J. Phys. Chem.*, **74**, 2519 (1970).
2. N. A. Izmailov, *Russ. J. Phys. Chem.*, **34**, 1142 (1960); *Dokl. Akad. Nauk. SSSR*, **149**, 884 (1963).
3. A. D. Buckingham, *Discussions Faraday Soc.*, **24**, 151 (1957).
4. B. E. Conway, *Ann. Rev. Phys. Chem.*, **17**, 481 (1966); "Physical Chemistry, An Advanced Treatise," H. Eyring, Editor, Vol. IXA, Academic Press, New York (1970).
5. B. E. Conway and M. Salomon, "Chemical Physics of Ionic Solutions," B. E. Conway and R. G. Barradas, Editors, John Wiley and Sons, New York (1966); see also B. E. Conway, "Modern Aspects of Electrochemistry," B. E. Conway and J. O'M. Bockris, Editors, Vol. 3, Chap. 2, Butterworths, London (1964).
6. D. D. Eley and M. G. Evans, *Trans. Faraday Soc.*, **34**, 1093 (1938).
7. H. F. Halliwell and N. C. Nyburg, *ibid.*, **59**, 1126 (1963).
8. See selected papers in "Chemical Physics of Ionic Solutions," B. E. Conway and R. G. Barradas, Editor, John Wiley and Sons, New York (1966).
9. B. E. Conway and J. O'M. Bockris, "Modern Aspects of Electrochemistry," Vol. 1, Chap. 2, Butterworths, London (1954).
10. M. Alfenaar and C. L. DeLigny, *Recueil*, **84**, 81 (1965); **86**, 929 (1967).
11. D. F. C. Morris, *Struct. Bonding (Berlin)*, **4**, 63 (1968).
12. R. M. Noyes, *J. Am. Chem. Soc.*, **84**, 513 (1962).
13. B. S. Gourary and F. J. Adrian, *Solid State Phys.*, **10**, 128 (1960).
14. L. Pauling, "Nature of The Chemical Bond," Cornell Press, Ithaca, N.Y. (1960).
15. D. Feakins and P. Watson, *J. Chem. Soc.*, 4686 (1963).
16. D. Feakins, "Physico-Chemical Processes in Mixed Aqueous Solvents," F. Franks, Editor, Elsevier, New York (1967).
17. H. P. Bennetto and D. Feakins, "Hydrogen Bonded Solvent Systems," A. K. Covington and P. Jones, Editors, Taylor and Francis, London (1968).
18. C. M. Criss and M. Salomon, "Physical Chemistry of Organic Solvents," A. K. Covington and T. Dickinson, Editors, Chap. 2.4, Plenum Press, London, In press, (1971).
19. W. M. Latimer, K. S. Pitzer, and C. M. Slansky, *J. Chem. Phys.*, **7**, 108 (1939).

20. B. Case and R. Parsons, *Trans. Faraday Soc.*, **63**, 1224 (1967).
21. O. Popovych, *Anal. Chem.*, **38**, 558 (1966): *CRC Critical Reviews in Analytical Chemistry*, **1**, 73 (1970).
22. D. Feakins and D. J. Turner, *J. Chem. Soc.*, 4986 (1965).
23. N. E. Khomutov, *Russ. J. Phys. Chem.*, **39**, 336 (1965).
24. J. M. Simon, PhD Thesis, University of Pittsburgh, 1969 [quoted by Popovych Ref. (21)].
25. E. J. King, "Acid Base Equilibria," Pergamon, London (1965).
26. F. Franks and D. J. G. Ives, *Quart. Rev.*, **20**, 1 (1966).
27. M. Salomon, "Physical Chemistry of Organic Solvents," A. K. Covington and T. Dickinson, Editors, Chap. 2.2, Plenum Press, London, In press, (1971).
28. A. J. Parker, *Chem. Rev.*, **69**, 1 (1969).
29. M. Salomon *J. Phys. Chem.*, **70**, 3853 (1966).
30. P. Delahay, "Double Layer and Electrode Kinetics," John Wiley and Sons, New York (1965).
31. B. Case, N. S. Hush, R. Parsons, and M. E. Peover, *J. Electroanal. Chem.*, **10**, 360 (1965).
32. F. B. Kenrick, *Z. Physik. Chem.*, **19**, 625 (1896).
33. A. N. Frumkin, Z. A. Iofa, and M. A. Gerovich, *Zh. Fiz. Khim.*, **30** 1455 (1956).
34. J. E. B. Randles and D. J. Schiffrin, *J. Electroanal. Chem.*, **10**, 480 (1965).
35. D. J. Schriffrin, *Trans. Faraday Soc.*, **66**, 2464 (1970).
36. H. Imai and P. Delahay, *J. Phys. Chem.*, **66**, 1683 (1962).
37. D. R. Cogley and J. N. Butler, *ibid.*, **72**, 4568 (1968).
38. H. S. Johnston, "Gas Phase Reaction Rate Theory," p. 325, Ronald Press, New York (1966).
39. J. E. Desnoyers and C. Jolicoeur, "Modern Aspects of Electrochemistry," J. O'M. Bockris and B. E. Conway, Editors, Vol. 5, Plenum Press, New York (1969).
40. R. W. Gurney, "Ionic Processes in Solution," Dover New York (1962).
41. J. E. B. Randles, *Trans. Faraday Soc.*, **52**, 1573 (1956).
42. J. F. Coetzee and W. R. Sharp, *J. Am. Chem. Soc.*, In press.

Solvation of Alkali Metal Perchlorates in Water

Mark Salomon[1]

NASA, Electronics Research Center, Cambridge, Massachusetts 02142

ABSTRACT

The crystal lattice energies and the energetics of solvation of the alkali metal perchlorates are calculated from a combination of experimental and empirical (theoretical) data. The results indicate that the crystal radius of the perchlorate ion is 1.85Å. The free energy and enthalpy of formation of gaseous ClO_4^- are also estimated.

Perchlorates constitute an important class of salts for studies in solvation phenomena. Despite the wide use of these salts, little is known about several important properties such as the crystal radius of the ClO_4^- ion, the lattice energies and enthalpies of the salts and the free energy and enthalpy of formation of the gaseous ClO_4^- ion. In this paper, a method is discussed in which these properties may be evaluated. In this work only the alkali metal perchlorates are considered.

Entropies of gaseous ions.—The relation between the lattice free energy and enthalpy is given by

$$\Delta G^\circ_{lat} = \Delta H^\circ_{lat} - T\{\Sigma S^\circ_{i,g} - S^\circ_{cryst}\} \quad [1]$$

where $S^\circ_{i,g}$ is the entropy of the gas phase species i, and S°_{cryst} is the crystal entropy. All thermodynamic properties considered in this paper refer to standard conditions of 298.15°K and 1 atm.

For monatomic gaseous ions only the translational degrees of freedom contribute to the entropy so that

$$S^\circ_{i,g} = R\{5/2 + \ln (g(2\pi mkT)^{3/2}V/Nh^3)\} \quad [2a]$$

If the ground state of the electronic energy level is singly degenerate and there are no significant populations of excited states then $g = 1$ and the above equation reduces to

$$S^\circ_{i,g} = 25.930 + 6.8636 \log_{10}M, \text{ (cal/K.mole)} \quad [2b]$$

In these two equations M is the molecular weight of the gaseous ion in g/atoms and all other terms have their usual significance. For polyatomic molecules or ions, rotational and vibrational contributions to the entropy are evaluated from (1)

$$S_{i,rot} = R\{3/2 \ln T + 3/2 \ln I - \ln \sigma\} + 267.65 \text{ cal/K.mole} \quad [3]$$

$$S_{i,vib} = R \sum_i^n \{x(e^x - 1)^{-1} - \ln (1 - e^{-x})\} \quad [4]$$

Here I is the moment of inertia in g-cm^2; σ is the symmetry factor; $x = h\nu/kT = 1.4387\ \omega/T$ where ω is in cm^{-1}; and n is the number of vibrational degrees of freedom for the polyatomic ion composed of N atoms ($n = 3N - 6$ for a nonlinear molecule). For the gaseous perchlorate ion, $\sigma = 12$ which corresponds to a regular tetrahedron (1, 2) for which all three moments of inertia are identical so that $I = (8/3)\ m\ r^2$ where m is the mass (amu) of the oxygen atom. Taking

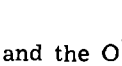

$r = 1.4$Å and the O Cl O angle as 110° (1, 2), then the fundamental frequencies listed in Table I are obtained using the force constants k (stretch) = 8.24 and k (bend) = 0.670 md/Å.

Lattice enthalpies and free energies.—Since lattice enthalpies or free energies cannot be measured for the perchlorates, other methods of estimating these quantities must be sought. Our first attempt involved the use of the empirical equation (in kcal/mole)

$$-\Delta H^\circ_{lat} = [600/(r_+ + r_-)]\ (1 - 0.4/(r_+ + r_-)) \quad [5]$$

which is claimed (3) to be accurate to within 1-2 kcal/mole. In Eq. [5], r_+ and r_- are, respectively, the crystal radii of the cation and anion in Å. The most accurate crystal radii are believed [*e.g.* see Ref. (4)

[1] Present address: 78 Commonwealth Park West, Newton, Massachusetts 02159.

Key words: perchlorate ion, crystal lattice energies, crystal radii, solvation energies, solvation enthalpies, free energy and enthalpy of formation.

Table I. Properties of gaseous ClO_4^- and its (solid) salts*

For gaseous ClO_4^-					
Property	Value	Salt	$-\Delta G°_f$	$-\Delta H°_f$	$S°_{cryst}$
ω_1	935	$LiClO_4$	60.71	91.0	30.0
$\omega_2(2)$	462	$NaClO_4$	60.79	91.48	34.0
$\omega_3(3)$	1102	$KClO_4$	71.79	102.80	36.1
$\omega_4(3)$	628				
$I \times 10^{40}$	138.84				
$S°_{1,\,trans}$	39.64				
$S°_{1,\,rot}$	19.85				
$S°_{1,\,vib}$	3.04				

* Reference state is 298.15°K and 1 atm.
ω units are cm^{-1}; number in parenthesis is the degeneracy.
I units are $g\text{-}cm^2$.
S units are eu (cal/K·mole).
ΔH and ΔG are in kcal/mole; 1 kcal = 4.184 kJ.

and (5)] to be those of Gourary and Adrian (6). However values of r_- must often be estimated from "thermochemical" data, *i.e.* they are based on a theoretical calculation such as the Meyer-Born-Madelung treatment in which r is usually determined from the repulsive potential (7, 8). On this basis the crystal radius of ClO_4^- has been found (9, 10) to equal 2.45Å (average value). According to Pauling (2), this radius has a value of 2.0Å. The use of Eq. [5] for any of the alkali metal perchlorates does not yield consistent results with either of these radii and it is concluded that this relation is not valid for the salts presently under consideration (see below).

Free Energies and Heats of Solvation

In our previous work (11) it was found that the conventional enthalpies of OH^-, F^-, Cl^-, Br^- and I^- could be fit to a power series by the least squares method, *i.e.* (in kcal/mole)

$$\Delta H°_{conv}(\text{anion}) = -223.47 - 1945.8/(r_- + 1.38)^2 + 2304.9/(r_- + 1.38)^3 \quad [6]$$

Conventional enthalpies and energies for monovalent anions are defined by

$$\Delta H°_{conv}(x^-) = \Delta H°_{solv}(x^-, \text{absolute}) + \Delta H°_{solv}(H^+, \text{absolute}) \quad [7]$$

$$\Delta G°_{conv}(x^-) = \Delta G°_{solv}(x^-, \text{absolute}) + \Delta G°_{solv}(H^+, \text{absolute}) \quad [8]$$

In Eq. [6], the constant 1.38Å corresponds to the radius of the water molecule and the relation for $\Delta H°_{conv}$ was fit to a function in $(1/r^2 + 1/r^3)$ since they are the leading energetic terms (11-13). In previous work (11) it was postulated that the leading term in the plot of conventional free energies is that in $1/r$ and this is shown in Fig. 1 (neglect, for the moment, the point corresponding to ClO_4^-). The relation for this straight line, in kcal/mole,[2] is

$$\Delta G°_{conv}(\text{anion}) = -265.9 - 114.07/r_- \ (\pm 0.5) \quad [9]$$

The intercept (−265.9) does not represent the absolute solvation energy of the proton since it still contains major contributions from ion-dipole, quadrupole,

[2] 1 kcal = 4.184 kJ.

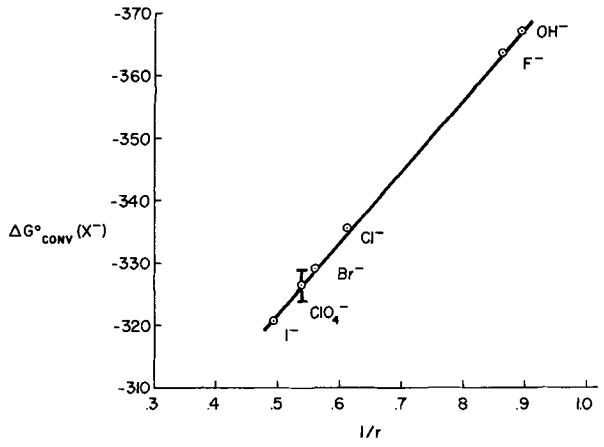

Fig. 1. Plot of convention free energy of solvation for anions vs. the reciprocal of the crystal radius.

etc., interactions (11), and Eq. [9] is therefore strictly empirical. The conventional terms are all (except for the perchlorates) experimentally available. The only experimental data available for alkali metal perchlorates are the heats of solution (14) and the solubilities (15). The free energies of solution for the moderately soluble K, Rb, and Cs perchlorates can be obtained from

$$\Delta G°_{soln} = -2RT \ln(m_\pm \gamma_\pm) \quad [10]$$

where $\ln \gamma_\pm$ is obtained from the Davies equation (16)

$$\ln \gamma_\pm = -Am^{1/2}/(1 + m^{1/2}) + 0.3Am \quad [11]$$

The relations between the heats and energies of solvation and solution are

$$\Delta H°_{solv} = \Delta H°_{lat} + \Delta H°_{soln} \quad [12]$$

$$\Delta G°_{solv} = \Delta G°_{lat} + \Delta G°_{soln} \quad [13]$$

The calculations proceeded as follows. Values of $r_{ClO_4^-}$ were assumed starting from 1.2Å up to 3.0Å and $\Delta H°_{conv}$ (ClO_4^-) was calculated from Eq. [6]. This result was used to obtain the enthalpies of solvation for the K, Rb, and Cs salts from

$$\Delta H°_{solv}(MClO_4) = \Delta H°_{conv}(ClO_4^-) - \Delta H°_{conv}(M^+) \quad [14]$$

Values of $\Delta H°_{conv}$ (M^+) are 180.1, 184.3, and 188.3 kcal/mole, respectively, for $M = K^+$, Rb^+, and Cs^+ (11) (for $M = Li^+$ and Na^+, $\Delta H°_{conv} = 137.2$ and 162.6). From these enthalpies of solvation, the lattice enthalpies were calculated using Eq. [13]. Adding the entropy terms (*cf.* Table I) the lattice free energy is obtained (Eq. [1]) and finally the free energy of solvation is obtained from Eq. [13]. For the three salts (K, Rb, Cs), the value for $r_{ClO_4^-}$ which best fit Eq. [9] is 1.85Å and the point for ClO_4^- shown in Fig. 1 was obtained in this manner. Using this value of −326.08 ± 2.5 kcal/mole for $\Delta G°_{conv}$ (ClO_4^-), the values for the Li and Na salts were obtained by the additivity requirement. The results are shown in Table II. Under

Table II. Thermal Properties (molal units) of alkali metal perchlorates at 25°C

(kcal/mole)

Salt	m_{sat}[b]	$\Delta H°_{soln}$[c]	$\Delta G°_{soln}$[d]	$-\Delta H°_{lat}$	$-\Delta G°_{lat}$	$-\Delta H°_{solv}$	$-\Delta G°_{solv}$
$LiClO_4$	—	−6.35	−9.5	198.7	(179.5)	(205.0 ±0.1)	(189.0 ± 2.5)
$NaClO_4$	—	3.32	−1.80	180.7	(161.7)	(177.4 ± 0.1)	(163.5 ± 2.2)
$KClO_4$	0.1491	12.20	2.40	169.7	150.8	157.5	148.4
$RbClO_4$	0.0849	13.56	3.04	163.9	145.1	150.4	142.0
$CsClO_4$	0.0688	13.25	3.29	156.6	138.4	143.4	135.1

[a] Those values given in parentheses were obtained using the additivity requirement.
[b] Molalities of saturated solutions are from Ref. (15).
[c] Ref. (14).
[d] Calculated from Eq. [10].

no conditions did Eq. [5] yield any consistent relation between $\Delta H°_{conv}$ and $\Delta G°_{conv}$. The free energy and enthalpy of formation of gaseous ClO_4^- is obtained by considering the cycle

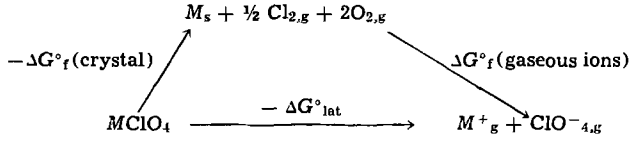

where the subscripts g and s refer to solid and gaseous species, respectively.
Hence

$$\Delta G°_f(ClO^-_{4,g}) = -\Delta G°_{lat} + \Delta G°_f(\text{crystal}) - \Delta G°_f(M^+_g) \quad [15]$$

and

$$\Delta H°_f(ClO^-_{4,g}) = -\Delta H°_{lat} + \Delta H°_f(\text{crystal}) - \Delta H°_f(M^+_g) \quad [16]$$

Using the tabulated values for the heats and energies of formation of the crystals (17) for the three salts (K, Rb, Cs), it is found that $\Delta G°_f(ClO^-_{4,g}) = -36.3 \pm 0.3$ kcal/mole and $\Delta H°_f(ClO^-_{4,g}) = -56.3 \pm 0.2$ kcal/mole.

Conclusions

It should be pointed out that in the estimations of the thermal properties of the perchlorates, the choice of crystal radii for the anions OH^-, F^-, Cl^-, Br^-, I^- appear to be critical. The radii of Gourary and Adrian are chosen because they appear to be the more reasonable ones (4, 5, 19). It might still be argued that a readjustment of the radii back to the original Pauling values might also produce valid results. This does not appear to be the case since those values for $\Delta H°_{lat}$ calculated *via* Eq. [5] based on either Pauling's radii (2) or those quoted by Halliwell and Nyberg (3) still give solvation energies lower by 10-25 kcal/mole than those shown in Table II.

One should also note that the present method assumes that those thermodynamic properties associated with the perchlorate ion follow the same empirical relations (Eq. [6] and [9]) derived for the halide ions. Whether this is a valid procedure or not cannot be determined at present but this assumption is not without precedence (19).

Manuscript submitted Jan. 11, 1971; revised manuscript received *ca.* June 3, 1971.

Any discussion of this paper will appear in a Discussion Section to be published in the June 1972 JOURNAL.

REFERENCES

1. E. A. Moelwyn-Hughes, "Physical Chemistry," Pergamon, London (1964).
2. L. Pauling, "Nature of the Chemical Bond," Cornell, Ithaca, N.Y. (1944).
3. H. F. Halliwell and S. C. Nyberg, *J. Chem. Soc.*, 4603 (1960).
4. D. F. C. Morris, *Struct. Bonding (Berlin)*, **4**, 63 (1968).
5. J. E. Desnoyers and C. Jolicoeur, "Modern Aspects of Electrochemistry," J. O'M. Bockris and B. E. Conway, Editors, Vol. 5, Plenum Press, New York (1969).
6. B. S. Gourary and F. J. Adrian, *Solid State Phys.*, **10**, 128 (1960).
7. M. P. Tosi and F. G. Fumi, *J. Phys. Chem. Solids*, **25**, 45 (1964).
8. M. F. C. Ladd and W. H. Lee, "Progress in Solid State Chemistry," H. Reiss, Editor, Vol. 1, Chap. 2, McMillan New York (1964); see also Vol. 2 (1965) and Vol. 3 (1967).
9. K. B. Yatsimirskii, "Thermochemie von Komplex Verbindungen," Academie-Verlag, Berlin (1956).
10. A. F. Kapustinskii, *Quart. Rev.*, **10**, 283 (1956).
11. M. Salomon, *J. Phys. Chem.*, **74**, 2519 (1970).
12. A. D. Buckingham, *Discussions Faraday Soc.*, **24**, 151 (1957).
13. B. E. Conway, "Modern Aspects of Electrochemistry," J. O'M. Bockris and B. E. Conway, Editors, Vol. 3, Chap. 2, Butterworths, London (1964).
14. V. B. Parker "Thermal Properties of Aqueous Uni-univalent Electrolytes," NBS Reference Data Series NSRDS—NBS2, April 1965.
16. C. W. Davies, "Ion Association," Butterworths, London (1962).
17. JANAF Thermochemical Tables, The Dow Co., Midland, Mich., Aug. 1965 and addenda.
18. M. J. Blandamer and M. C. R. Symons, *J. Phys. Chem.*, **67** 1304 (1963).
19. H. F. Halliwell and N. C. Nyberg, *Trans. Faraday Soc.*, **59**, 1126 (1963).

Technical Note

The Charging of Cu in Organic Electrolytes

Stuart G. Meibuhr*

Electrochemistry Department, Research Laboratories, General Motors Corporation, Warren, Michigan 48090

The advent of high energy density batteries has focused research efforts on metal halide cathodes such as $CuCl_2$. This research has centered principally on the use of Lewis acid solutes in propylene carbonate solvent. Rao found (1) that the oxidation of Cu metal resulted in soluble CuCl rather than the slightly soluble $CuCl_2$. Eisenberg *et al.* obtained (2) an i_o value of 3-6 x 10^{-5} A/cm^2 for the room temperature reduction of $CuCl_2$ to Cu in the same type of Lewis acid electrolytes.

The study of $CuCl_2$ electrodes had been initiated in this laboratory by using two types of organic solvents: one in which the $CuCl_2$ was only slightly soluble (for example, propylene carbonate), and the other extreme in which the $CuCl_2$ was very soluble (for example, triethylene glycol dimethyl ether [TEGDME]). Initial polarization studies on porous $CuCl_2$ electrodes immersed in 1M $NaClO_4$ solutions of TEGDME containing 0.5M $CuCl_2$ showed that the charging polarization was unusually high—in the order of several volts. No such high charging polarization was observed in propylene carbonate. The cause of the high polarization was postulated as due to the forma-

* Electrochemical Society Active Member.
Key words: triethylene glycol dimethyl ether, triethylene glycol, polarization, cupric chloride, cuprous chloride film.

tion of a highly resistive, insoluble film. The verification of that postulate is the subject of this note.

The IR-free and the IR-included charging polarization was measured simultaneously with a Kordesch-Marko bridge as a function of time at a smooth Cu electrode (1 cm^2) immersed into either of two electrolytes made from TEGDME or triethylene glycol (TEG). These electrolytes both contained 1M $NaClO_4$, dried as previously described (3), and anhydrous $CuCl_2$. However, the solubility of CuCl was different in each solution; CuCl would be an intermediate product formed during the charging process (1). In TEGDME, the solubility of CuCl was found to be low whereas in TEG, the solubility was found to be high. A Cu wire reference electrode was located 2 mm from the working Cu electrode. Both solvents were vacuum distilled; Karl Fischer water analysis showed that TEGDME had a water content <20 ppm and TEG had a water content ~100 ppm.

The potential-time plots, which resulted from using the TEGDME solution, are shown in Fig. 1; curve A represents the *IR*-free data and curve B represents the *IR*-included data. Both sets of data were obtained at the low current density of 0.25 mA/cm^2. Higher current densities only served to develop the high polarization more quickly. The large voltage difference between the two curves indicates a large *IR* loss that cannot be attributed simply to solution resistance. The solution resistivity was determined to be 275 ohm-cm; this value corresponds to only 15 mV solution *IR* drop at this current density. Since CuCl was previously found to be insoluble in this solution, it appears highly likely that the high polarization was due to the formation of a highly resistive, insoluble film. Curve B exhibits three branches. The transition times (τ) corresponding to the first two branches are identical in length—85 min. These times each represent the passage of 1.275 coulomb. If one assumes that there exists 1 charge/site for the fcc Cu metal, the number of μcoulomb/cm^2 = 210. If one also assumes a surface roughness factor of 10, then τ_1 corresponds to the buildup of a film of about 600 layers thick. Its composition is postulated as solvated CuCl. Since the value for τ_2 is identical to the value for τ_1, we postulate that

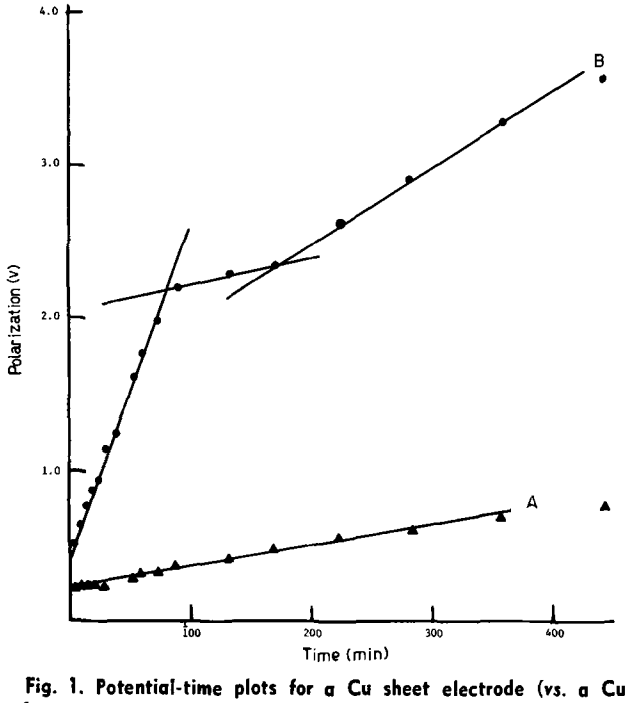

Fig. 1. Potential-time plots for a Cu sheet electrode (vs. a Cu reference electrode) in a TEGDME-1M $NaClO_4$ + 0.5M $CuCl_2$ solution at a constant charging current density of 0.25 mA/cm^2. Curve A, *IR*-free polarization; B, *IR*-included polarization.

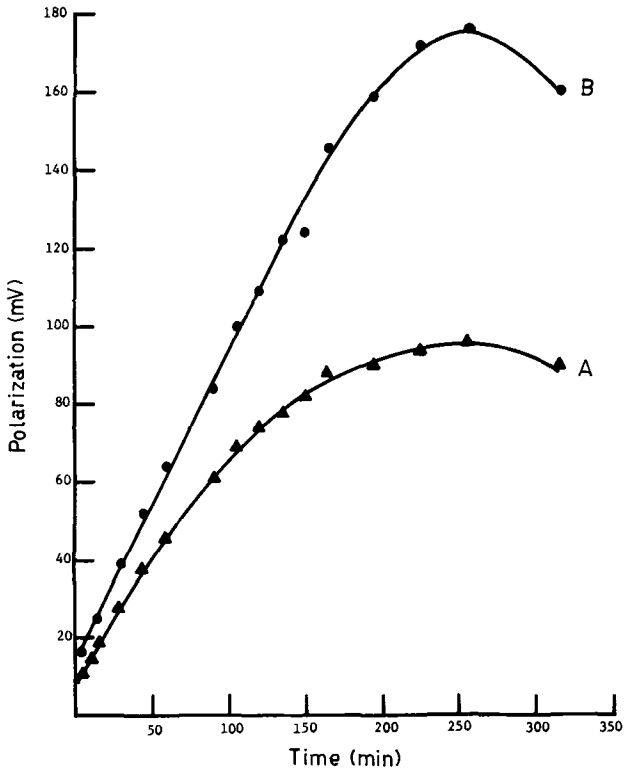

Fig. 2. Potential-time plots for a Cu sheet electrode (vs. a Cu reference electrode) in a TEG-1M $NaClO_4$ + 0.5M $CuCl_2$ solution at a constant charging current density of 0.25 mA/cm^2. Curve A, *IR*-free polarization; B, *IR*-included polarization.

τ_2 corresponds to the conversion of Cu(I) to insoluble Cu(II). The thick film was easily seen with the naked eye when the electrode was removed from the electrolyte.

The potential-time plots, which resulted from using the TEG solution, are shown in Fig. 2. Note the change in the voltage scale from Fig. 1; the two curves carry the same connotation as in Fig. 1. A much lower *IR*-drop occurred during the charging of Cu in this solution than in TEGDME. The *IR*-drop (the difference between curves A and B) can be entirely attributed to the solution resistivity. The low polarization obtained in TEG solutions supported the original hypothesis that a resistive film, probably CuCl was formed in TEGDME, a solution in which CuCl is soluble. Furthermore, no visible film was formed in TEG.

No transition times were observed in the TEG solution, probably because the intermediate product, CuCl, can migrate away from the electrode surface. In TEGDME, no such migration can occur because of its low solubility.

One explanation for the decrease in the potential values (Fig. 2) at times > 250 min could be that the reference potential value was not constant. If Cu(I) is formed in solution, the Cu reference potential would change to reflect this concentration change. The reference potential would no longer be determined exclusively by the Cu(0) $\rightleftarrows$ Cu(II) reaction, but also by the Cu(0) $\rightleftarrows$ Cu(I) and the Cu(I) $\rightleftarrows$ Cu(II) reactions. This potential shift at these long times does not affect the conclusions made regarding the film formation in TEGDME. The reason that no such potential decrease was observed in TEGDME solutions (Fig. 1) can be due to two causes: (*a*) the potential decrease was too small to affect the large observed potential, or (*b*) no such potential shift occurred because Cu(I) is not soluble in TEGDME solution.

These data show that: (*i*) a thick resistive film forms during the anodic charging of Cu in TEGDME

solution; (*ii*) the process of charging a Cu electrode proceeds stepwise in solvents in which the intermediate product, CuCl, is insoluble. Similarly, it may also proceed stepwise in solvents in which CuCl is soluble.

Manuscript submitted May 20, 1971; revised manuscript received July 9, 1971.

Any discussion of this paper will appear in a Discussion Section to be published in the June 1972 JOURNAL.

REFERENCES

1. M. L. B. Rao, *This Journal*, **114**, 13 (1967).
2. M. Eisenberg, R. E. Kuppinger, and K. M. Wong, *ibid.*, **117**, 577 (1970).
3. S. G. Meibuhr, *ibid.*, **118**, 709 (1971).

JOURNAL OF THE ELECTROCHEMICAL SOCIETY

SOLID STATE SCIENCE

OCTOBER 1971

Preparation and Properties of Aluminum Oxide Films Obtained by Glow Discharge Technique

H. Katto and Y. Koga

Central Research Laboratory, Hitachi Ltd., Kokubunji, Tokyo, Japan

ABSTRACT

Amorphous aluminum oxide films have been deposited on silicon substrates by decomposing aluminum trichloride in an rf induced glow discharge of oxygen. Among various deposition parameters, it is shown that the reactant gas pressures affect greatly the deposition rate and the resultant film quality. The properties of these films such as infrared transmission, etch rate, film structure, resistivity, dielectric constant, and dielectric strength are described. Aluminum-aluminum oxide-silicon (MAS) structures were prepared and characterized by the positive values of flat band voltage, distortion of C-V curves, and a large, positive shift in flat band voltage under negative bias at an elevated temperature. The field effect electron mobility was as low as 70 $cm^2/V \cdot sec$, while it could be improved by the annealing at around 700°C, or by putting a thin layer of thermally oxidized silicon dioxide between the aluminum oxide and the silicon.

In the use of MOS transistors and high field devices, some limitations have been recognized in the use of silicon dioxide as a gate insulator or a passivating medium. In particular, attention has been drawn to the inability of the oxide to give positive values of threshold voltage and to stop fast diffusing alkali metals. Aluminum oxide is one of the materials that has been investigated in an attempt to overcome these problems, and the results concerning preparation and properties of aluminum oxide films have been published by several authors using the reaction of an aluminum halide with a hydrogen-carbon dioxide mixture at 900°C (1), thermal decomposition of an aluminum alkoxide at 420°C (2), plasma anodization (3), reactive sputtering (4), reactive vacuum evaporation (5), and r.f. sputtering (6).

In the present study, aluminum oxide films have been deposited by decomposing aluminum trichloride in a radio frequency glow discharge of oxygen. In the glow discharge deposition, adherent films up to several microns can easily be obtained at fairly low deposition temperatures; thus the technique offers the possibility of depositing films on a wide variety of substrate materials. A complete understanding of discharge reactions requires detailed studies. Here, a semi-empirical approach has been taken to optimize growth conditions, and to evaluate the properties of aluminum oxide films deposited by the r.f. glow discharge method for field effect devices.

Experimental

Deposition apparatus.—Figure 1 shows the general arrangement of the apparatus, which is similar to the one presented by Swann *et al.* (7), differing in that the silicon substrate is grounded through a platinum-rhodium (4:1) susceptor in order to obtain a larger deposition rate. A 400 kHz, 10 kW radio frequency generator; Model MA-1003H (Kokusai Electric), is used to supply energy for both the chemical reaction and substrate heating by means of a radio frequency coil surrounding a vertical fused silica tube with a diameter of about 60 mm. The susceptor temperature is measured by an infrared pyrometer: Thermodot Model TD 7B (Infrared Industries). The pressure of oxygen in the reactor chamber is controlled by a leak valve and monitored by a Pirani vacuum gauge. Aluminum trichloride is placed in an oxygen stream and heated up to 70°-120°C to get a pressure necessary for the deposition of aluminum oxide. The vapor pressure of aluminum trichloride was estimated by using the known vapor pressure curve (8).

The glow discharge is sensitive to the shape and arrangement of the metal susceptor and earth line, and is liable to concentrate on the sharpened or irregular points of metals disposed in the reactor tube. There-

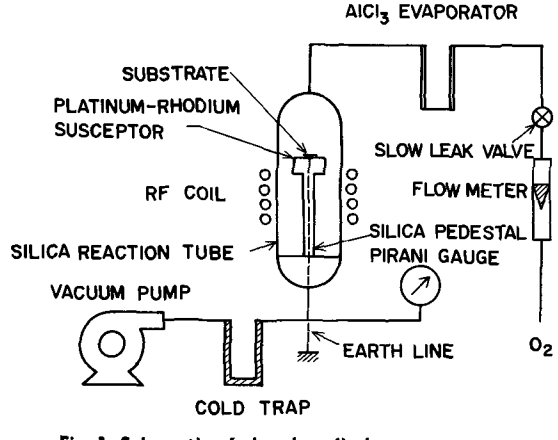

Fig. 1. Schematic of the glow discharge apparatus

Key words: dielectric, passivation.

fore, to get the glow discharge stable on the metal susceptor, the under side of the susceptor and the earth line are carefully shielded by a silica tube.

Fabrication and measurements.—Aluminum oxide films were deposited usually on (100) surfaces of p- or n-type silicon slices of resistivity 30-50 and 3-7 ohm-cm. P-type silicon slices of resistivity 3-7 ohm-cm were used for n-channel MAS or MAOS transistor fabrication. In general, the oxide deposition is independent of the silicon substrate resistivity.

Because of the mobility problem encountered by aluminum oxide-silicon structures (see later), aluminum oxide films were also deposited on silicon dioxide-silicon samples prepared by thermally oxidizing silicon in dry oxygen at 1000°C. The oxide thickness was up to 500Å. Postdeposition heat treatment in N_2, O_2, and H_2 have also been made. For the electric evaluation of the interface properties of aluminum oxide-silicon structure, MIS structures with a diameter of 1 mm were prepared by evaporating aluminum by the filament method using a metal mask.

The film thickness of aluminum oxide deposited on silicon was measured by observing the change in interference colors on the basis of the color chart made by interferometry for the aluminum oxide, similar to the one used for silicon dioxide (9). The infrared transmission curve was taken using a Model EPI-G2 Hitachi infrared spectrophotometer. Film structure was determined by reflection electron diffraction and electron micrography. Electrical and interface properties were studied by the MOS capacitance and conductance methods. Capacitance-voltage (C-V) measurements were made in the dark at 1 MHz using a semiautomatic recording apparatus. The d-c bias sweep speed was controlled manually between about 0.1 and 1 V/sec. The stability of the charge distribution was evaluated by applying positive and negative voltages to the gate electrodes of samples at 250°C. Field effect electron mobility was measured by constructing n-channel MAS and MAOS transistors with ring gates. The field effect electron mobility and the threshold voltage (V_{TH}) were obtained from the square-law characteristic of the transistors in the saturation region.

Results and Discussions

Growth rate.—In the glow discharge method, the deposition is dependent on the vapor pressures of reactants, the temperature of the substrate, the intensity and wave forms of discharge field, and the geometrical configuration inside the reaction chamber. The deposition is sensitive to the configuration of the susceptor and the rf coil, and the deposition rate is very low when the susceptor is set lower than the coil. It is suggested that, in order to obtain efficient deposition, the mixed reactant gases should not be exposed to the glow discharge field before they come close to the substrate. In the present study, therefore, the susceptor is always positioned higher than the coil.

Assuming this configuration and with other parameters fixed, the deposition rate of aluminum oxide films is dependent on the vapor pressure of oxygen and aluminum trichloride as shown in Fig. 2. When the temperature of aluminum trichloride is lower than about 80°C, the deposition rate is strongly dependent on the temperature of aluminum trichloride, that is, nearly proportional to its vapor pressure. If, however, the temperature of aluminum trichloride exceeds 80°C, the deposition rate is almost independent of the pressure of aluminum trichloride. It seems to indicate that, as far as aluminum trichloride is sufficiently supplied, the deposition rate is limited by the ionization of oxygen which is mainly determined by the oxygen pressure.

The deposition rate is largest at the oxygen pressure of about 1 or 2 Torr, when the vapor pressure of aluminum trichloride is held constant. As the oxygen pressure is made either lower or higher than 1-2 Torr,

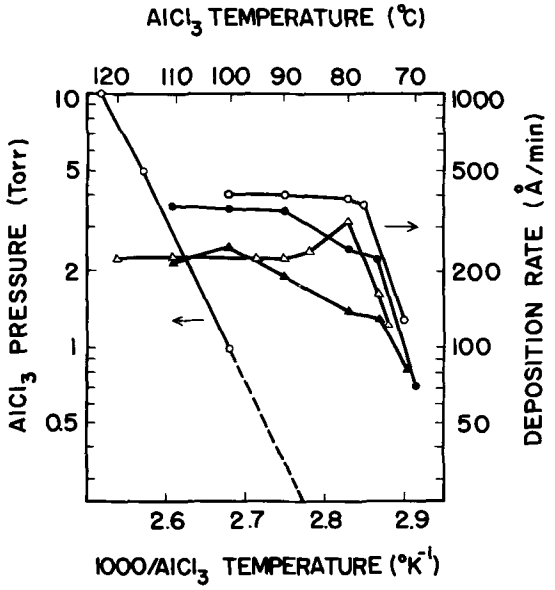

Fig. 2. Deposition rate of Al_2O_3 as a function of pressure of O_2 and temperature of $AlCl_3$. RF voltage, 4 kV; substrate temperature, 480°C. O_2 pressure: ▲ 3 Torr, ● 2 Torr, ○ 1 Torr, △ 0.5 Torr. Vapor pressure of $AlCl_3$ is also shown as a function of temperature.

the deposition rate decreases monotonically. This tendency can probably be interpreted by considering the degree of ionization of oxygen in the glow discharge field as a function of oxygen pressure. When the oxygen pressure exceeds about 3 Torr, the film thickness uniformity becomes poor. The deposition rate is completely independent of the flow rate of oxygen into the reaction chamber between 10 and 200 cc/min.

The dependence of deposition rate on the substrate temperature cannot be evaluated exactly because of the limitation of the deposition apparatus. In our apparatus, the substrate temperature is controlled mainly by the position of the rf coil and partly by the rf voltage. The change of temperature is always accompanied by the change of discharge field in the reaction chamber. In practice, however, the deposition rate does not seem to be strongly dependent on the temperature, and a fairly fast deposition rate can be obtained even at temperatures as low as below 100°C.

The dependence of deposition rate on the intensity of discharge cannot be evaluated exactly for the same reason as mentioned above because the coil supplies energy to both the susceptor and the gaseous reaction. Assuming, however, that the deposition is not so strongly dependent on the temperature, the deposition rate is found nearly linearly dependent on the rf voltage applied to the reaction chamber. This is analogous to the result obtained for the rf sputtering (6).

Film structure and composition.—Examination of the infrared transmission spectrum of the aluminum oxide films shows a broad absorption peak around 15μ, as shown in Fig. 3, very similar to the one for aluminum oxide films obtained by the thermal decomposition of aluminum triethoxide $Al(OC_2H_5)_3$. Electron diffraction patterns show that aluminum oxide films are amorphous unless they are annealed at about 800°C or over. The aluminum oxide films are transparent and visually very smooth, but electron micrographs show, as shown in Fig. 4, that the surface of aluminum oxide films becomes uneven as they are annealed at 700° or 800°C. The crystallization of aluminum oxide as evidenced by the electron diffraction pattern may have some connection with the unevenness of the film surface. But the degree of crystallization is considered low from the diffraction pattern, especially at 700°C, so the phenomenon is mainly attributed to the film structure change due to something like vaporization

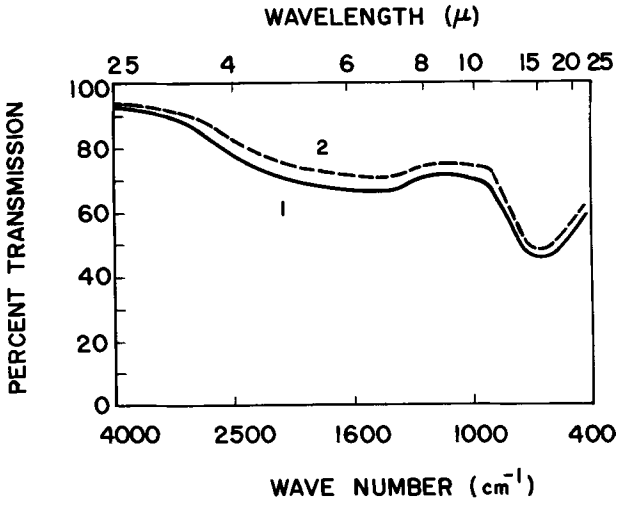

Fig. 3. Infrared absorption spectra of Al_2O_3 films deposited by: curve 1, glow discharge technique; curve 2, thermal decomposition of $Al(OC_2H_5)_3$.

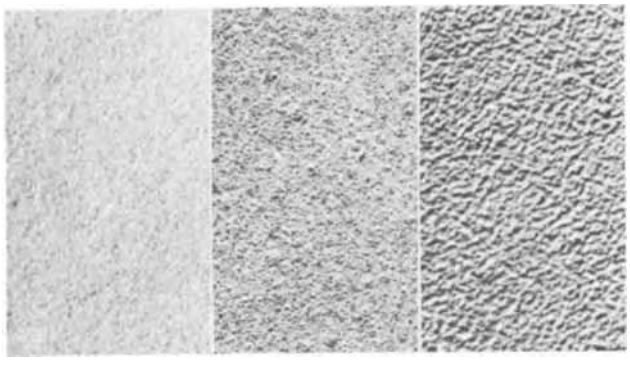

Fig. 4. Electron micrographs for Al_2O_3 films. Al_2O_3 films from left: as deposited at 400°C; annealed at 700°C in N_2 for 1 hr; annealed at 800°C in N_2 for 1 hr. Magnification *ca.* 25,000X.

or chemical reactions of some unknown impurities in the film.

Etch rate.—Etch rate studies have been made for the P-etch solution and for the conc phosphoric acid. As shown in Fig. 5, etch rates for the P-etch solution are normally about 10 Å/sec, and increases to over 100 Å/sec at lower rf voltages supplied during deposition. The discharge becomes unstable when the rf voltage is made a little lower than 2 kV in our apparatus, and the large etch rates of films deposited at lower rf voltages can be attributed to the insufficient intensity of the discharge for obtaining dense films. If the vapor pressure (temperature) of aluminum trichloride is as low as 0.03 Torr (70°C) during deposition, the etch rate of the film is unusually high, *i.e.* over 200 Å/sec by the P-etch solution, though the reason is not clear. Post-deposition heat treatment at 700°C in nitrogen for 1 hr results in the slight reduction of the etch rate. Heat treatment at temperatures over 800°C makes the film almost insoluble in the P-etch solution. For the conc phosphoric acid, the etch rate is dependent on the etch temperature as shown in Fig. 6 for both aluminum oxide films deposited at 400°C and annealed at 700°C in nitrogen for 1 hr. For these films, fine patterns can be etched by the phosphoric acid heated to around 70°C using an ordinary photoresist. Films annealed at 800°C for 20 min are much slower in being etched by the phosphoric acid, *i.e.* at the rate of 10 Å/sec at 85°C and 70 Å/sec at 120°C.

Electrical properties.—Electrical properties of aluminum oxide films deposited by the glow discharge

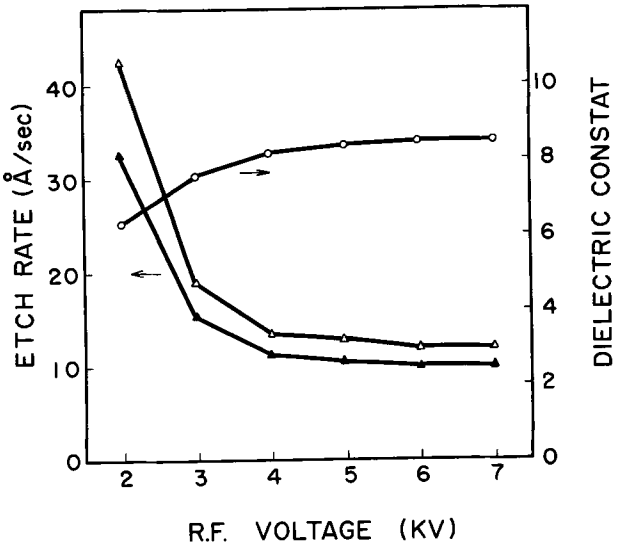

Fig. 5. Etch rate for P-etch solution and dielectric constant as a function of rf voltage during deposition. △ as deposited (480°C); ▲ annealed at 700°C in N_2 for 1 hr.

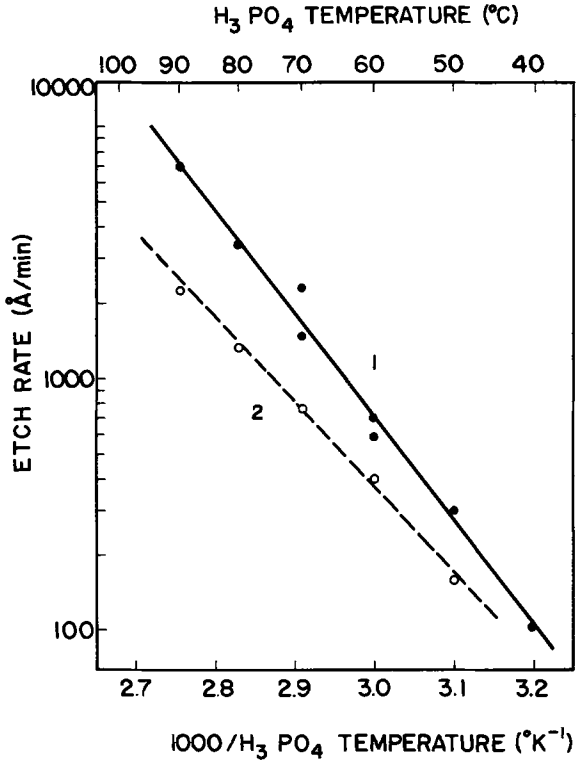

Fig. 6. Etch rate of Al_2O_3 in H_3PO_4 as a function of temperature. Curve 1, as deposited (34 Å/sec in P-etch solution); curve 2, annealed at 700°C in N_2 for 1 hr (18 Å/sec in P-etch solution)

method depend on deposition parameters, especially on the vapor pressures of the reactant gases. When the temperature of aluminum trichloride is as high as 110°C, or the pressure of oxygen is lower than about 0.5 Torr, deposited aluminum oxide films contain grainy spots and are electrically leaky, suggesting the incomplete reaction due to the insufficient oxygen concentration. Vapor pressures of about 2 Torr for oxygen and about 0.3 Torr (90°C) for aluminum trichloride are most conveniently used for obtaining flat and good insulating films with moderate deposition rates. In this condition, the dielectric constant of the deposited film is normally 8.5, with a decrease to about 6 at lower rf voltages, as shown in Fig. 5, prob-

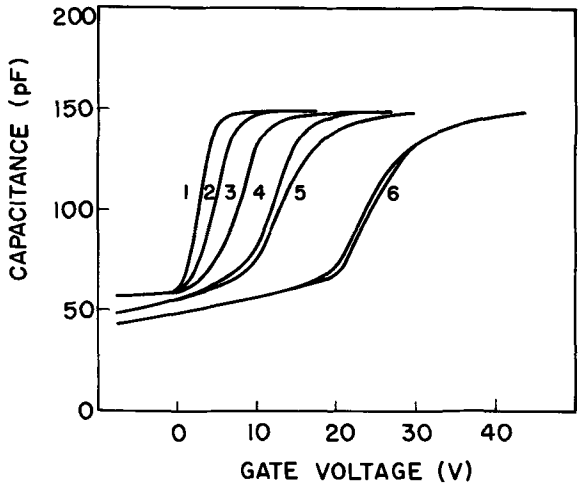

Fig. 7. Typical MAS capacitance curves for 4000Å Al_2O_3 films as a function of deposition rate. Deposition rate: curve 1, 255 Å/sec; curve 2, 350 Å/sec; curve 3, 480 Å/sec; curve 4, 580 Å/sec; curve 5, 605 Å/sec; curve 6, 680 Å/sec.

ably related to the low film density (10), and the tan δ is about 0.01 at 1 MHz. The dielectric strength, as defined by 0.05 μA per a 1 mm diameter spot, is usually over 5 x 10^6 V/cm by film thickness around 4000Å. The dielectric strength is slightly affected by the annealing at 700°C, but serious degradation can be observed when the film is annealed at 800°C or over, probably due partly to the crystallization of aluminum oxide and to the content of some unknown impurities in the film.

MIS Structures

C-V measurements.—Figure 7 shows typical C-V curves for 4000Å aluminum oxide films with the deposition rate as a parameter. The films are deposited at 480°C with an oxygen pressure 2 Torr and an aluminum trichloride temperature 90°C. The deposition rate is in this case controlled mainly by the rf voltage. The position of the rf coil is slightly moved to adjust the deposition temperature to 480°C. The flat band voltage, V_{FB}, is found positive in all cases, increasing with the deposition rate. The oxide charge as determined from the C-V curve is negative and found by the etching experiment to be located at or near the silicon-aluminum oxide interface. The V_{FB} value is affected by the postdeposition annealing, generally increasing by the 700°C annealing process, but reproducible data and interpretation could not be obtained. The distortion in the C-V curves of aluminum oxide films indicates the presence of fast interface states, which increases with the deposition rate, or the rf voltage. The distortion is not eliminated by annealing the films at 700°C under gas atmosphere N_2, O_2, or H_2, and it is suggested that the interface states were produced by the damage due to the glow discharge of oxygen. Hysteresis of the C-V curve is only slightly recognized, generally of the order of 0.1V. Only, the aluminum oxide film deposited very slowly with an aluminum trichloride temperature as low as 70°C is found to show the unusually large hysteresis, though the reason is not yet clear.

Drift of the MAS structures under BT stress.—Figure 8, curve 1 shows the V_{FB} shift of the aluminum oxide film, deposited at 480°C, under bias applied at 250°C. The V_{FB} increases considerably under the BT stress biased negative. Also, there is a tendency that V_{FB} increases (decreases) gradually as the positive (negative) bias is increased. Figure 8, curve 2 shows the V_{FB} shift under BT stress for the aluminum oxide film annealed at 700°C in nitrogen for an hour. It can be seen in the curve that the tendency vanishes for V_{FB} to shift positively (negatively) as the positive (negative) bias is increased. This kind of instability can be attributed to the polarization effect, which was discussed to be the main cause of the instability observed in the aluminum oxide film deposited by the thermal decomposition of aluminum triethoxide (11). From the fact that V_{FB} does not shift in the negative direction under the positive bias, the aluminum oxide film is free from the positive ion instability due to Na^+ ions and the like as observed in silicon dioxide films (12). The large positive increase of V_{FB} under negative bias is observed also in the aluminum oxide film deposited by the thermal decomposition of aluminum isoproxide and annealed in oxygen at 700°C (13). As discussed in (13), this can probably be attributed to some negatively charged particles like OH^- ions, by the analogy of Na^+ ions in the silicon dioxide film, or electrons injected into the aluminum oxide from the gate metal. The instability of these films is irreversible, that is, the V_{FB} value once attained by BT stress under some finite bias remains almost unchanged under another BT stress test with less or zero bias. The authors found this kind of irreversibility in the instability also in the silicon dioxide film deposited by the thermal reaction of silane and oxygen, so it may probably be common to films deposited at low temperatures. The phenomenon resembles the trapping instability found in vapor-deposited silicon nitride or silicon dioxide (14), but the direction of V_{FB} shift under BT stress is opposite. It probably indicates the presence of deep trapping centers for ions at the silicon-dielectric interface.

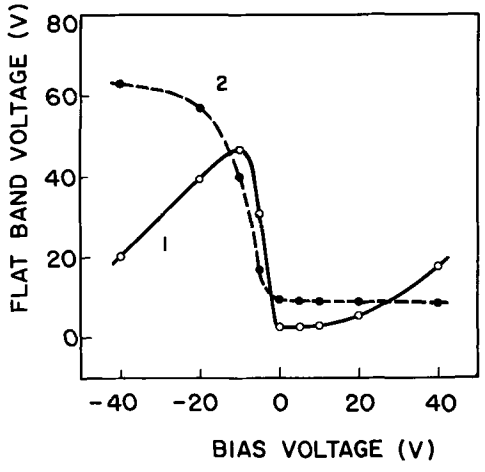

Fig. 8. V_{FB} shift under BT stress at 250°C for 15 min in air. Curve 1, as deposited; curve 2, annealed at 700°C in N_2 for 1 hr.

The instability of V_{FB} under negative bias is detected even at the room temperature. As shown in Fig. 9,

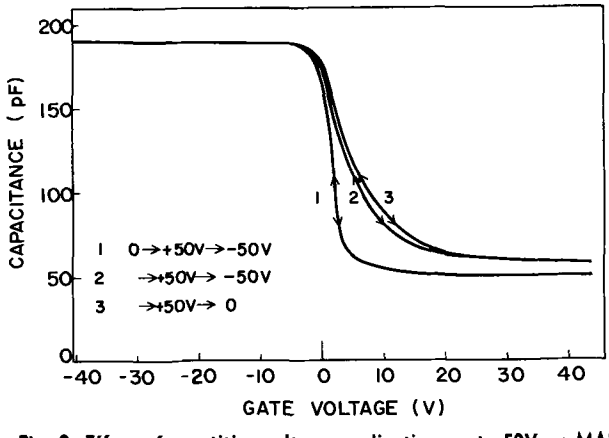

Fig. 9. Effect of repetitive voltage application up to 50V on MAS capacitance of the 3200Å Al_2O_3 film at room temperature.

Table I. Characteristics of MAS and MAOS transistors, using Al_2O_3 films deposited at 480°C
Heat treatment: 700°C, N_2, 1 hr

Al_2O_3 thickness, Å	SiO_2 thickness, Å	Heat treatment, N_2, 700°C, 1 hr	Threshold voltage, V	cm^2 V·sec Electron mobility,
3000	0	No	4.0	70
3000	0	Yes	6.0	140
3000	200	No	1.8	270
3000	200	Yes	0.5	350
3000	500	No	1.0	430
3000	500	Yes	0.1	530

the C-V curve of the aluminum oxide film deposited at 480°C is distorted after a large negative voltage (−50V) is applied to the film. The figure shows that the C-V curve traces quite the same path after +50V is applied, and so the application of positive voltages does not produce such instability effects.

Field effect mobility of electrons.—N-channel MAS and MAOS transistors were fabricated by using aluminum oxide films as a gate insulator to evaluate field effect mobility of electrons in the channel under the gate insulator. The transistors have the following dimensions: channel length, 14μ; channel width (periphery) 540μ. Substrate resistivity is 3 to 7 ohm-cm for (100) surfaces of p-type silicon wafers. The result is summarized in Table I.

The transistor having aluminum oxide as a gate insulator deposited directly onto the silicon surface at 480°C has the electron mobility around 70 $cm^2/V \cdot sec$. Annealing of the film at 700°C for an hour results in the increase of the electron mobility up to about 140 $cm^2/V \cdot sec$. Transistors whose gate insulator are made by depositing aluminum oxide on slightly thermally oxidized (up to 500Å) silicon surface shows larger electron mobilities, up to 530 $cm^2/V \cdot sec$ after the annealing at 700°C.

The authors found the same trend in the electron mobility when silicon dioxide films deposited by the decomposition of tetraethoxysilane $Si(OC_2H_5)_4$ in the glow discharge of oxygen were used as gate insulators of the transistors. The low electron mobility in the surface channel can partly be attributed to the intrinsic nature of the aluminum oxide/silicon interface, but is mainly due to the surface damage caused by the bombardment of charged particles (15). The damage due to the bombardment is evidenced by the fact that the thickness of silicon dioxide has influence on the magnitude of the electron mobility. In the aluminum oxide deposition process, the silicon dioxide/silicon interface can be influenced only by the charged particles' bombardment. It is known that the surface damage caused by electron bombardment is restored by the annealing at 500°C (15). So, in the glow discharge methods, the damage is caused mainly by the bombardment of ionized oxygen so that it cannot be restored completely even by the annealing at 700°C.

Conclusions

Decomposition of aluminum trichloride in the glow discharge of oxygen at moderately low temperatures results in amorphous aluminum oxide films. Among various deposition parameters, the reactant gas pressures affect greatly the film deposition rate and the resultant film quality. At the oxygen presure of about 2 Torr and the aluminum trichloride temperature of about 90°C, coherent, good insulating films are obtained at the deposition rate of a few hundred Å/min or over. The physical and electrical properties of these films compare favorably with those of films obtained by the thermal decomposition of aluminum alkoxides. The MAS capacitance shows the positive value of flat band voltage, V_{FB}, and a large positive shift of V_{FB} under negative bias at 250°C. Distorted C-V curves indicate the presence of fast interface states, which can not be eliminated by the annealing up to 700°C. MAS transistor characteristics show that the field effect electron mobility is as low as 70 $cm^2/V \cdot sec$, while it becomes much higher by the annealing at around 700°C, or when a thin layer of thermally oxidized silicon dioxide is put between aluminum oxide and silicon.

Manuscript submitted Feb. 10, 1971; revised manuscript received May 17, 1971.

Any discussion of this paper will appear in a Discussion Section to be published in the June 1972 JOURNAL.

REFERENCES

1. S. K. Tung and R. E. Caffrey, Paper 24 RNP presented at Electrochem. Soc. Meeting, Chicago, Ill., Oct. 15-19, 1967.
2. J. A. Aboaf, *This Journal*, **114**, 948 (1967).
3. A. Waxman and K. H. Zaininger, *Appl. Phys. Letters*, **12**, 284 (1968).
4. T. Tanaka and S. Iwauchi, *Japan. J. Appl. Phys.*, **7**, 1420 (1968).
5. E. Ferrieu and B. Pruniaux, *This Journal*, **116**, 1008 (1969).
6. C. A. T. Salama, *ibid.*, **117**, 913 (1970).
7. R. C. G. Swann, R. R. Mehta, and T. P. Cauge, *ibid.*, **114**, 713 (1967).
8. D. R. Stull, *Ind. Eng. Chem.*, **39**, 540 (1947).
9. W. A. Pliskin and E. E. Conrad, *IBM J. Res. Dev.*, **8**, 43 (1964).
10. S. M. Hu and L. V. Gregor, *This Journal*, **114**, 826 (1967).
11. S. Nishimatsu, T. Tokuyama, and M. Matsushita, in "Thin Film Dielectrics," F. Vratny, Editor, p. 338, The Electrochemical Society Softbound Symposium Series, New York (1969).
12. E. H. Snow, A. S. Grove, B. E. Deal, and C. T. Sah, *J. Appl. Phys.*, **36**, 1664 (1965).
13. M. T. Duffy and A. G. Revesz, *This Journal*, **117**, 372 (1970).
14. B. E. Deal, P. J. Fleming, and P. L. Castro, *ibid.*, **115**, 300 (1968).
15. E. H. Snow, A. S. Grove, and D. J. Fitzgerald, *Proc. IEEE*, **55**, 1168 (1967).

Properties of Aluminum Oxide Films Obtained from Nitrous Oxide and Aluminum Trimethyl

L. H. Hall* and W. C. Robinette*

Texas Instruments, Inc., Dallas, Texas 75222

ABSTRACT

Aluminum oxide (both amorphous and γ-Al_2O_3) have been deposited from the reaction of aluminum trimethyl and nitrous oxide at 650°C. The refractive index is 1.75 ± 0.02 and the dielectric constant is 8.5 ± 0.3. Films have a resistivity of 10^{14} ohm-cm at 10^6 V/cm. D-C current-voltage characteristics indicate a Poole-Frenkel model of conduction similar to that for Si_3N_4 films. Turn on voltage and MAOS capacitor flat band voltage stability of ±0.03V at 300°C and 10^6 V/cm has been attained.

A number of authors have reported on pyrolytic aluminum oxide films prepared from organoaluminum compounds (1-3). This paper deals with films prepared from the reaction of nitrous oxide and trimethylaluminum. Electrical characteristics, including d-c conduction and complex dielectric constant, and alumina-silicon interface properties have been studied as a function of applied electric field and temperature during measurement. Aluminum oxide was deposited on 4-8 ohm-cm, n- and p-type silicon substrates of several different crystal orientations. The film thickness was varied from 800 to 3800Å. Film thickness was measured using an ellipsometer with either a mercury arc source (λ = 5461Å) or a laser source (λ = 6328Å). Electrical measurements were made on capacitor (MAS, MAOS) structures. Metal (aluminum or gold) was evaporated on the alumina surface and capacitor dots ranging in area from 5 x 10^{-5} to 2 x 10^{-2} cm^2 were photolithographically defined.

Experimental

The deposition systems used were single slice and multislice vertical reactors. The aluminum trimethyl vapor, and nitrous oxide, both diluted with argon, were transported in separate inlet tubes so that the two gases are mixed only after entry into the reactor chamber. Although several different aluminum alkyls can be used, the trimethyl was chosen because it is a liquid at room temperature and has a vapor pressure of 8.4 mm Hg at 20°C. Nitrous oxide was chosen as the source of oxygen since it is not an oxidizing agent and is only appreciably thermally decomposed at temperatures of 600°C and greater. The highest grade purity commercially available for aluminum trimethyl and nitrous oxide was used without further purification. A constant temperature chamber was used to maintain a constant supply of aluminum trimethyl. The deposition rate of the aluminum oxide films was controlled by limiting the amount of reactant gases entering the reaction chamber.

The quality of the aluminum oxide films obtained is highly dependent upon the aluminum trimethyl reacting completely to give aluminum oxide. If a fast deposition rate is used there is generally a residue after etching of the film. Also these films had poor electrical properties. However, an interesting aspect of such a process is that the amount of excess aluminum can be controlled, and this may provide an interesting material.

Only a cursory examination of films which did not have a refractive index between 1.72 and 1.80 was made as the refractive index is a very sensitive measurement of the purity of deposited films. Electrical properties of amorphous and γ-aluminum oxide films showed no difference as long as the refractive index was the same.

Film deposition temperature was kept between 640° and 660°C as this was about the lowest temperature at which good electrical films were obtained with nitrous oxide. It was not desired to have a high-temperature process since aluminum oxide films become crystalline at high temperatures. Also there are a number of good high temperature processes for aluminum oxide. A slow deposition rate, <75 Å/min, gave γ-aluminum oxide films. Good amorphous films which etched at a uniform rate in Bell No. 2 were obtained in the single slice vertical reactor. This is a desirable property of oxide films which are to be used in semiconductor processing.

Results and Discussion

D-C conduction.—Direct current measurements were made using a resistance-programmed Kepco ABC 1000 voltage supply and a Hewlett-Packard 425-A micromicroammeter. Data were taken with samples in slice form on an unilluminated probe stage with a controlled ambient at temperatures between 250° and 575°K. Current measurements were taken after a stabilization period of ~ 5 min after field application. The percentage change in the current values after this time period was small (≤ 1%).

A ln I *vs.* $V^{1/2}$ plot at various temperatures for a representative high-resistivity alumina sample is shown in Fig. 1. From these data the high field conductance in the temperature range 250°-541°K may be expressed as

$$I \sim I_0 \exp\left(\frac{\beta V^{1/2} - \Psi}{kT}\right) \qquad [1]$$

where I is the measured current, V the applied voltage, β and Ψ are constants to be explored, k is Boltz-

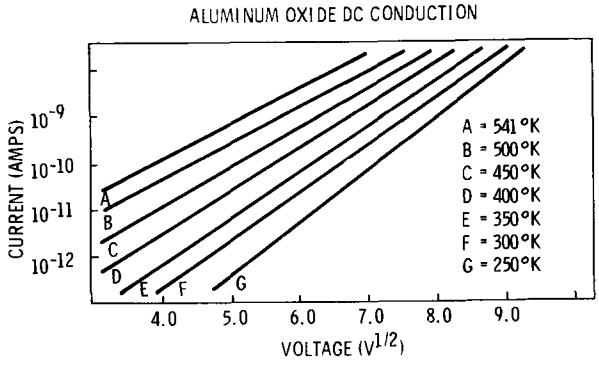

Fig. 1. Al_2O_3 d-c conduction for high resistivity material

* Electrochemical Society Active Member.
Key words: chemical vapor deposition, d-c conduction, insulation.

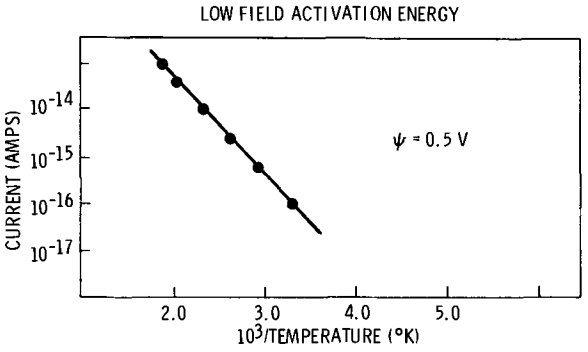

Fig. 2. Zero voltage current intercept (I_i) vs. reciprocal temperature.

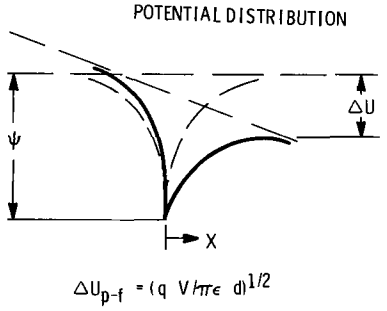

Fig. 3. Potential distribution acting on an electron escaping a donor-like trap.

mann's constant, T is the absolute temperature, and I_o is the extrapolated, zero voltage intercept.

The activation energy at low fields, Ψ, is found to be 0.5 eV in Fig. 2 by extrapolating the curves in Fig. 1 to the zero voltage intercept. This intercept I_o plotted *vs.* reciprocal temperature yields Ψ from the line slope.

Some samples deposited at other than ideal conditions exhibit very high conduction levels indicating very low activation energies. Due to the nonohmic conduction characteristics resistivities will be compared at a fixed field of 10^6 V/cm. Samples exhibiting high conduction levels have resistivities in the 10^6-10^8 ohm-cm range. Samples with activation energies of 0.5 eV have a resistivity of $1.0 \pm 0.1 \times 10^{14}$ ohm-cm.

None of the parameters studied were found to be dependent on electrode materials used.

Model.—The d-c current-voltage characteristics of the alumina films investigated are analyzed in terms of the Poole-Frenkel model of conduction discussed by Brown *et al.* (4) for silicon nitride films. A bulk, electronic conduction mechanism is proposed with the mechanism being field-aided thermal ionization of trapping levels in the film. The mechanism of Poole (5) and Frenkel (6) has been used by many workers including Vermilyea (7) (ZrO_2), Mead (8) (Ta_2O_5), Hartman *et al.* (9) (SiO); for Si_3N_4 in particular Brown *et al.* (4), Sze (10), Hu *et al.* (11), and Frohman-Bentchkowsky and Lenzlinger (12). The reader is referred to reference (4) for a more complete discussion of the model than will be given here. If an electron escapes a donor-like trap at an energy qU below the conduction band it is acted upon by both any external voltage applied and the field produced by the ionized donor. The potential distribution seen by the electron is shown in Fig. 3. The energy barrier is seen to be lowered by an amount $q\Delta U$.

$$\Delta U_{p\text{-}f} = \left(\frac{qV}{\pi \epsilon d}\right)^{1/2}$$

$$\Delta U_s = \left(\frac{qV}{4\pi \epsilon d}\right)^{1/2}$$

where U is the trap depth below the conductor band for Schottky or Poole-Frenkel emission, ϵ is the optical dielectric constant, and d is the film thickness.

The fact that $\Delta U_s = \Delta U_{p\text{-}f}/2$ due to image force effects is compensated for in the total conductivity expression by a factor of 2. This factor arises from a statistical description of electron population above the donor-like centers, assuming that at low temperatures all centers are filled (13).

The conductivity of a film arising from Poole-Frenkel emission was expressed by Frenkel (6) as

$$\sigma = \sigma_o \exp\left[-q(U_{p\text{-}f} - \Delta U_{p\text{-}f})/2kT\right]$$

However, if one assumes the electron deficiency of the donor-like centers to be greater than the excited electron density then

$$\sigma = \sigma_o \exp\left[q(\sqrt{qV/\pi \epsilon d} - U_{p\text{-}f})/kT\right] \quad [2]$$

The slope of a ln I *vs.* $V^{1/2}$ plot for this system would be twice as large as one for Schottky emission or the "normal" Poole-Frenkel effect. Mott and Gurney (14) have outlined the statistical derivation and point out that this electron deficiency might well be expected in a material which has an excess of metallic ions over its stoichiometric requirement. This could easily be the case in the films investigated here. Similar treatments have been reported by Mark and Hartman (15) and Simmons (16).

Application of model.—Equation [2] is of the same form as Eq. [1], with

$$\beta = [q^3/\pi \epsilon d]^{1/2} \text{ and } \Psi = qU_{p\text{-}f}$$

To establish the model proposed here the slope of the current-voltage characteristics is shown *vs.* oxide thickness in Fig. 4 for thicknesses of 850-3800Å. The slope of this plot is $-1/2$ as is predicted by the $(1/d)^{1/2}$ dependence of the theoretical slope value. The dashed line is the line predicted by the Schottky or "normal" Poole-Frenkel effect while the heavy line is calculated using the proposed Poole-Frenkel formulation.

In Fig. 5 the current-voltage slope is plotted *vs.* temperature. The higher temperature points follow a line of slope -1 as is expected for the model. The deviation of the lower temperature points from a line of slope -1 is not understood. A fitting of these data including Fowler-Nordheim conduction characteristics has not been possible. No study was made varying the index of refraction to test the ln I-$V^{1/2}$ slope dependence on this parameter ($\epsilon = n^2$).

Complex dielectric constant.—Dielectric data were obtained using a General Radio 1615A capacitance bridge, G.R. null detector, and a G.R. 1203-B function

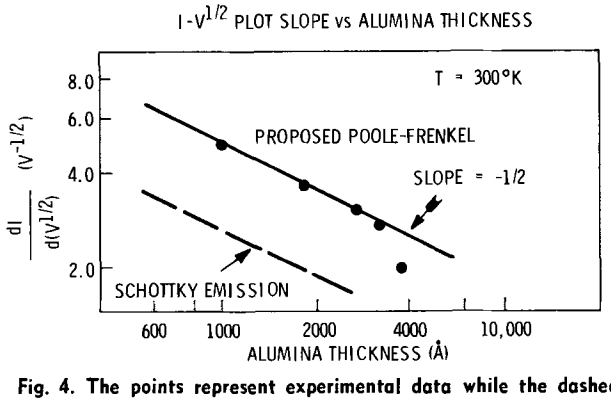

Fig. 4. The points represent experimental data while the dashed line is calculated from Eq. [2].

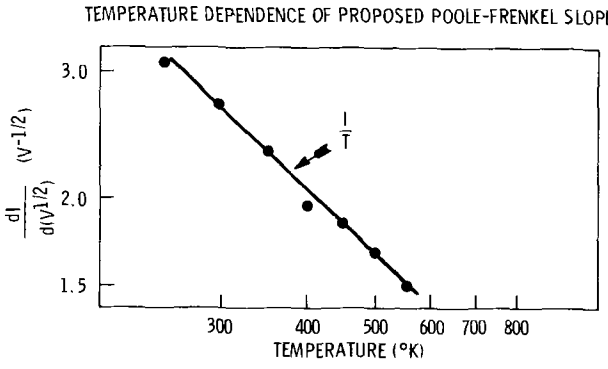

Fig. 5. 1/T dependence of proposed Poole-Frenkel slope

generator. Signal level was maintained at 100 mV and monitored with a Ballentine 861 a-c voltmeter. Capacitance-voltage measurements were made using a Moseley 20-2A x-y recorder, Boonton 71-A capacitance meter, Kepco ABC-1000 power supply, and a Hewlett-Packard 3300A function generator.

The real part, ϵ', of the complex dielectric constant is equal to 8.5 ± 0.3, at 100 kHz, very near the reported value of 8.6 for α crystalline Al_2O_3 (17). A variation of ϵ' between 7.7 and 9.2 was found for samples deposited at other than ideal temperatures and flow conditions.

The dielectric loss, ϵ'', varies from 0.009 to 0.1, at 100 kHz, but these values were found to be extremely dependent on substrate surface preparation. Localized surface imperfections and film imperfections as well as surface impurities prior to deposition might be expected to contribute to the variation in ϵ''. No trend could be seen relating dielectric loss to capacitor area or particular substrate cleanup. The substrates were not vapor etched prior to alumina deposition.

Surface electrical properties.—The silicon wafers were not etched *in situ* prior to silicon oxide growth or Al_2O_3 deposition, and again only films with Al_2O_3 refractive index of 1.75 were investigated. The well-known property of Al_2O_3 to cause a tendency toward a more p-type surface on both n- and p-type silicon was verified with these films. *N* channel enhancement mode field effect devices on 5 ohm-cm silicon were constructed. Turn-on voltage and MAOS capacitor flat band voltage stability of ±0.3V at a threshold voltage of +1V at 300°C and 10^6 V/cm has been attained. MAS capacitors with similar stability were fabricated.

Conclusions

It has been demonstrated that aluminum trimethyl and nitrous oxide can be used to chemically vapor deposit aluminum oxide films at 650°C of electrical quality similar to that of films deposited from the aluminum chloride, carbon dioxide, and water reaction at 900°C. The films prepared by this technique have resistivities in the 10^{14} ohm-cm at 10^6 V/cm. However, they can also have resistivities in the 10^6-10^8 ohm-cm range if the films contain a high impurity content. This is similar to data reported on films prepared by the low-temperature pyrolysis of aluminum alkoxides.

While it is important to accurately control the amount of the aluminum trimethyl vapor and the oxygen/aluminum ratio to obtain high quality electrical films, this method is interesting in that a controllable excess of aluminum in the aluminum oxide film may provide an interesting material for some novel applications in MOS technology.

High-resistivity aluminum oxide films prepared by the reaction of nitrous oxide and trimethylaluminum have been characterized as to d-c conduction, dielectric constant, and stability properties.

Films of 10^{14} ohm-cm resistivity at 10^6 V/cm have been found to exhibit a "special" mechanism of conduction previously reported for Si_3N_4 films (4). The applicability of this model has been demonstrated by detailed study of the variation of the magnitude of the ln I-$V^{1/2}$ slope expressed as

$$S_{p\text{-}f} = (q^3/\pi \epsilon d)^{1/2}/kT$$

This slope value is found to be twice as large as that of the "normal" Poole-Frenkel effect (6), thus implying a low-field thermal activation energy equal to the energy barrier height for electron emission instead of ½ of that height.

Stability of the flat band voltage for MAOS structures and field-effect transistors is ±0.3V at 10^6 V/cm and 300°C. The dielectric constant for high-resistivity films is found to be 8.5 ± 0.3.

Acknowledgment

The authors wish to thank G. Brown and G. Carlson for helpful discussions of the results, W. Tefteller and M. Gosney for critically reading the text, and R. Tucker and S. Sharp for technical assistance.

Manuscript submitted Nov. 25, 1970; revised manuscript received *ca.* May 25, 1971.

Any discussion of this paper will appear in a Discussion Section to be published in the June 1972 JOURNAL.

REFERENCES

1. V. F. Korzo, L. A. Ryabova, and Ya. S. Savitskaya, *Soviet Phys.—Semicond.*, **2**, 705 (1968).
2. L. A. Ryabova and Ya. S. Savitskaya, *Thin Solid Films*, **2**, 141 (1968).
3. J. A. Aboaf, *This Journal*, **114**, 948 (1967).
4. G. A. Brown, W. C. Robinette, Jr., and H. G. Carlson, *ibid.*, **115**, 948 (1968).
5. H. H. Poole, *Phil. Mag.*, S. 6, **32**, 112 (1916), and *ibid.*, 195 (1917).
6. J. Frenkel, *Phys. Rev.*, **54**, 647 (1938).
7. D. A. Vermilyea, *Acta Met.*, **2**, 346 (1954).
8. C. A. Mead, *Phys. Rev.*, **128**, 2088 (1962).
9. T. E. Hartman, J. C. Blair, and R. Bauer, *J. Appl. Phys.*, **37**, 2468 (1966).
10. S. M. Sze, *J. Appl. Phys.*, **38**, 2951 (1967).
11. S. M. Hu, D. R. Kerr, and L. V. Gregor, *Appl. Phys. Letters*, **10**, 97 (1967).
12. D. Frohman-Bentchkowsky and M. Lenzlinger, *J. Appl. Phys.*, **40**, 3308 (1969).
13. N. F. Mott and R. W. Gurney, "Electronic Processes in Ionic Crystals," 158ff, Oxford University Press (1940).
14. N. F. Mott and R. W. Gurney, "Electronic Processes in Ionic Crystals," p. 156, Oxford University Press (1940).
15. P. Mark and T. E. Hartman, *J. Appl. Phys.*, **39**, 2163 (1968).
16. J. G. Simmons, *Phys. Rev.*, **155**, 657 (1967).
17. A. R. von Hippel, "Dielectric Materials and Applications," p. 301, The M.I.T. Press (1954).

Double Epitaxial Isolation Method for the Fabrication of Integrated Circuit Transistors

Kiyoshi Demizu

Mitsubishi Electric Corporation, Kita-Itami Works, Mizuhara 1-Chome Itami, Japan

ABSTRACT

A new fabrication method is proposed which eliminates the isolation process by introducing a p-type epitaxial layer into the I.C. fabrication process. The typical values of BV_{CEO}, BV_{CBO}, and h_{fe} of I.C. transistors made by this new method are 6.5 ~ 10V, 16 ~ 18V, and 20 ~ 60, respectively. This new method is suitable for the fabrication of high-density integrated circuits in view of its simple process and better transistor performance.

In the application of conventional I.C. fabrication methods to L.S.I., laterally spreading areas occupied by the isolation diffusion process are a space limiting factor to the fabrication design. To improve this matter, the C.D.I. (collector-wall diffusion isolation) method was proposed by Murphy and others (1, 2). They used a p-type epitaxial layer as the base, and eliminated the isolation diffusion. However, there are some difficulties in obtaining a high level of transistor breakdown voltage and in controlling the thickness of the epitaxial layer. The D.E.I. (double epitaxial isolation) method, which has some advantages in integrated circuit fabrication, is proposed in this paper.

Fabrication Method

A comparison of manufacturing processes between the D.E.I. method and the conventional method is shown in Fig. 1. The D.E.I. method starts with diffusion of n^+-buried layers into the p-type substrate in those regions that are to hold the finished transistors. This step is identical to the conventional process. Next, a 2-3μ p-type epitaxial layer is grown, and followed by an approximately 2μ n-type epitaxial layer. It should be emphasized that this epitaxial growth is one continuous process. The change from p-type to n-type is achieved by activating valves in the gas feed line at the appropriate times during processing.

During the heat cycles of epitaxial and base diffusion processing, there is an autodiffusion from the n^+-buried layer into the p-type epitaxial layer. This converts the conductivity type of the epitaxial layer above the buried layer from p-type to n-type. This inverted layer acts as the collector of the finished transistor.

The p-type impurity diffusion of 3.0μ in depth is simultaneously applied to the base and isolation regions. The p-type diffused base extends completely through the n-epitaxial layer, and then the actual base-collector junction is in the inverted epitaxial layer where the p-type epitaxial layer has been converted to n-type. The regions of the p-type epitaxial layer not over the n^+-buried layer are unaffected throughout the entire process. During the base diffusion, p-type isolation regions are diffused through the n-type epitaxial layer and into the p-type epitaxial layer, making the transistor's collector an isolated n-type island in a p-type sea. The transistor is completed by simultaneously diffusing the n^+-emitters and the n^+-collector contacts.

The D.E.I. method has many important advantages, because in this method the isolation is performed simultaneously with the base diffusion. The isolation diffusion depth is only as deep as the base. As shown in Fig. 2, both the isolation mask alignment and the isolation diffusion process are eliminated in the D.E.I. method. Since impurity diffusion proceeds about the same distance vertically and laterally, the shallower isolation diffusion yields narrower isolation regions. Thus, each transistor takes up less space.

A comparison of chip sizes of the Quad Nand circuits designed by the D.E.I. method with those utilizing the conventional method is shown in Fig. 3. As is evident from this figure, by using the D.E.I. method the chip size of the circuit is reduced by about 30%.

Transistors made by the D.E.I. method have compensated collector regions as a result of auto diffusing the n-type impurity from the n^+-buried layer into the p-type epitaxial layer. Thus, it was important to investigate how the autodiffusion influences the characteristics of transistors.

At first, the impurity distribution of the autodiffusion layer was studied in detail. As shown in Fig. 4, the p-type epitaxial layer is grown upon an n-type substrate with localized n^+-buried layers, and then the autodiffusion is brought about by heat treatment for 1-8 hr at 1215°C.

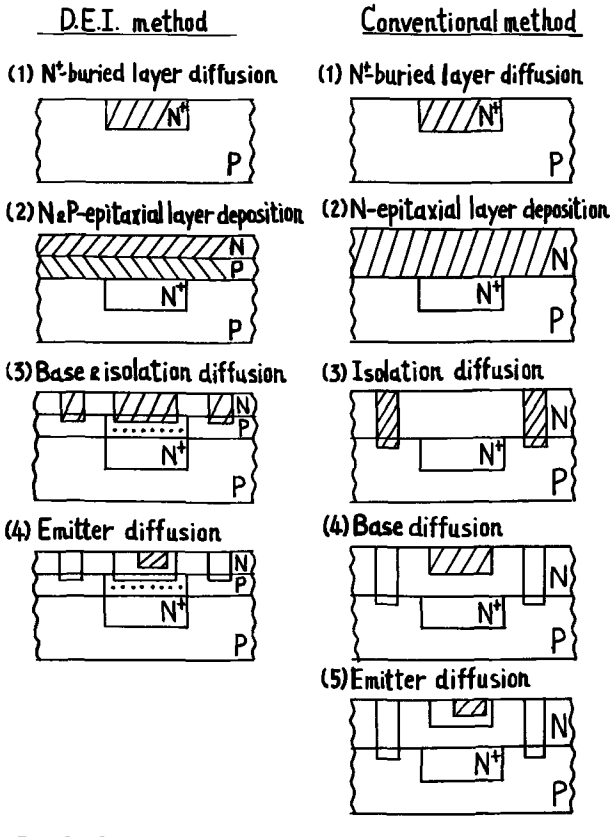

Fig. 1. Comparison of manufacturing processes for the D.E.I. method and the conventional method.

Key words: isolation, I.C. transistor, autodoping, epitaxial.

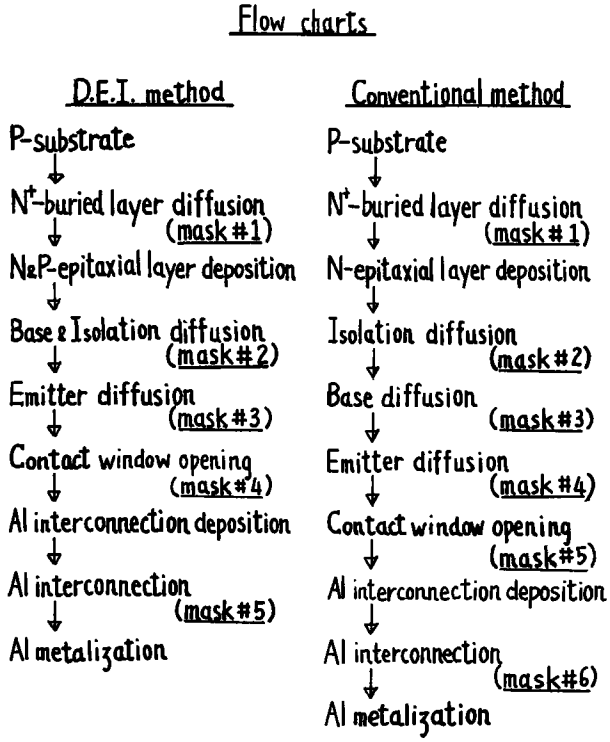

Fig. 2. Flow charts of the D.E.I. and the conventional method

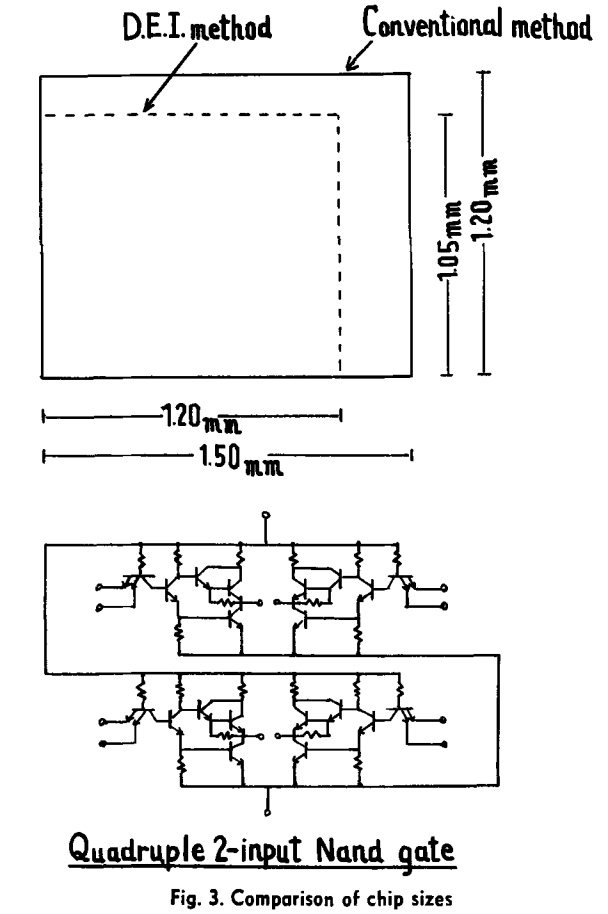

Fig. 3. Comparison of chip sizes

The p-n junction was observed by angle-lapping and stain-etching. Distances between the surface of the p-type epitaxial layer and the p-n$^+$ junction were measured. The experimental results are shown in Fig. 4, where the parameter is the resistivity of p-type epitaxial layer. The gradient of these lines is about

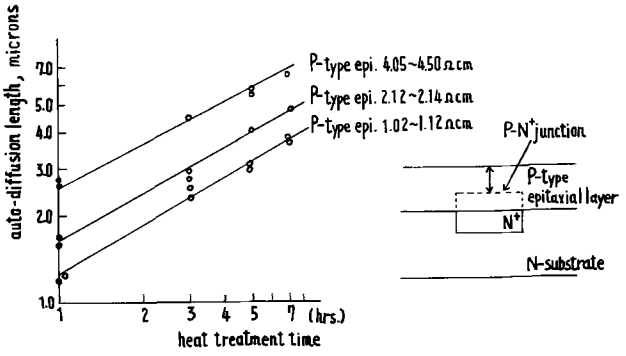

Fig. 4. The relation between heat treatment time and auto-diffusion length.

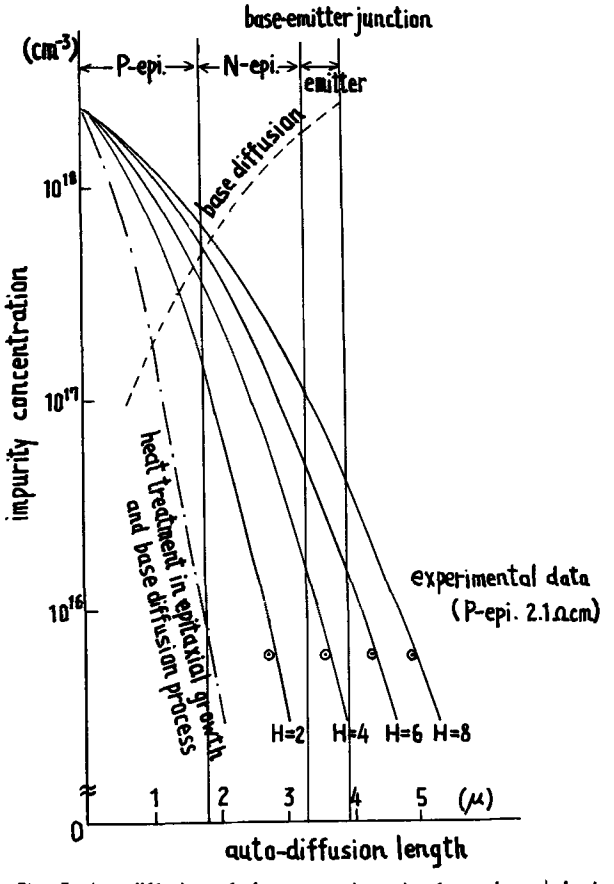

Fig. 5. Autodiffusion of the n-type impurity from the n$^+$-buried layer.

one-half, so these experimental data show that auto-diffusion from the n$^+$-buried layer is approximately given as error function.

Autodiffusion profiles of n-type impurity from the n$^+$-buried layer are shown in Fig. 5, where parameter H is the heat treatment time. In this figure $x = 0$ is the interface between the n$^+$-buried layer and p-type epitaxial layer before any heat treatment. The broken line in this figure is the impurity profile of the base diffusion given as error function. The emitter-base junctions are given as a step junction of 0.6μ in depth from the surface.

As is evident from Fig. 5, with increasing heat treatment time, the position of the base-collector junction is closer to that of the emitter-base junction, that is, the base width decreases. Also the maximum inverse breakdown voltage of the base-collector junction, BV_{CBO}, and the series resistance of the transistor, R_S, decrease. This means that the current gain of transistors becomes higher with increased heat treatment.

Experiments and Results

In the D.E.I. method a high breakdown voltage of the base-collector junction is maintained by controlling the thickness of the p-type epitaxial layer. Conditions for sample fabrication are summarized in Fig. 6.

The relation between BV_{CBO} and the heat treatment time is shown in Fig. 7. A heat treatment time of zero means that autodiffusion from the n^+-buried layer to the p-type epitaxial layer takes place only during heat treatments in the epitaxial growth (D_1t_1) and the base diffusion (D_3t_3). Inversion of the p-type layer into n-type material is essentially completed during epitaxial growth and base diffusion processes for sample TR-6, but requires more than three additional hours of heat treatment for sample TR-5 because of its thick p-type epitaxial layer. The values of BV_{CBO} of TR-6 hardly vary with heat treatment time, since impurity concentrations of base and collector regions are very high (from 10^{17} to 10^{18} cm^{-3}), while those of TR-5 vary considerably, since the impurity concentration density is in the range of 10^{16} to 10^{17} cm^{-3}. The broken lines in this figure give calculated values of BV_{CBO} based on McKay's data (3). The assumptions in this case are that the impurity profile of the autodiffusion layer is given as error function and the impurity distribution at the base-collector junction is step-shaped.

The structure of a transistor in which the p-type epitaxial layer is eliminated from the D.E.I. scheme is shown in Fig. 8. This fabrication method is tentatively named S.E.I. (single epitaxial isolation). Transistors made by the S.E.I. method have lower breakdown voltages, from 11 to 15V in TR-6 and TR-5 substrates. Hence, it is evident that the p-type epitaxial layer in the D.E.I. method plays a very important role in improving transistor breakdown voltage.

Deposition	Sample number	
	TR-5	TR-6
N^+-buried layer	17~23Ω/□, 7~8μ	17~23Ω/□, 7~8μ
P-type epitaxial layer	2.0~3.0Ωcm, 3.0~3.6μ	2.0~3.0Ωcm, 1.8~2.1μ
N-type epitaxial layer	0.7Ωcm, 2.4~2.7μ	0.3Ωcm, 2.1~2.4μ
Heat treatment time	3, 4, 6, 8 hrs.	0, 1, 2, 4, 6, 8 hrs.
Base & isolation diffusion	200Ω/□, 3.0μ	200Ω/□, 3.0μ

Fig. 6. Conditions of fabrication

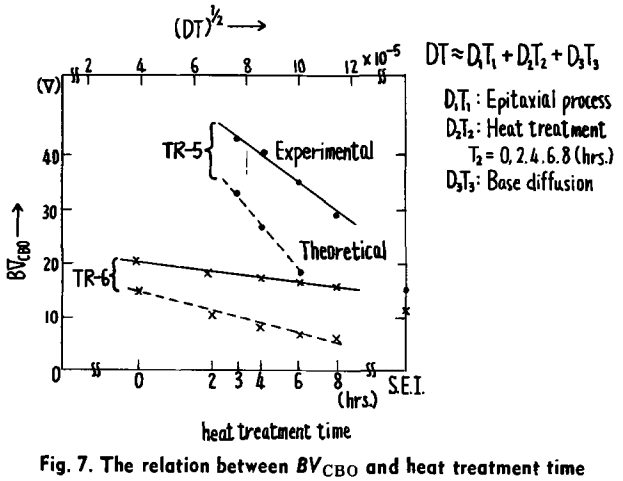

Fig. 7. The relation between BV_{CBO} and heat treatment time

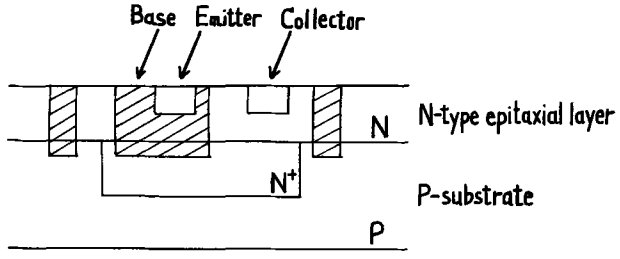

Fig. 8. S.E.I. transistor structure (p-type epitaxial layer is eliminated from D.E.I. structure).

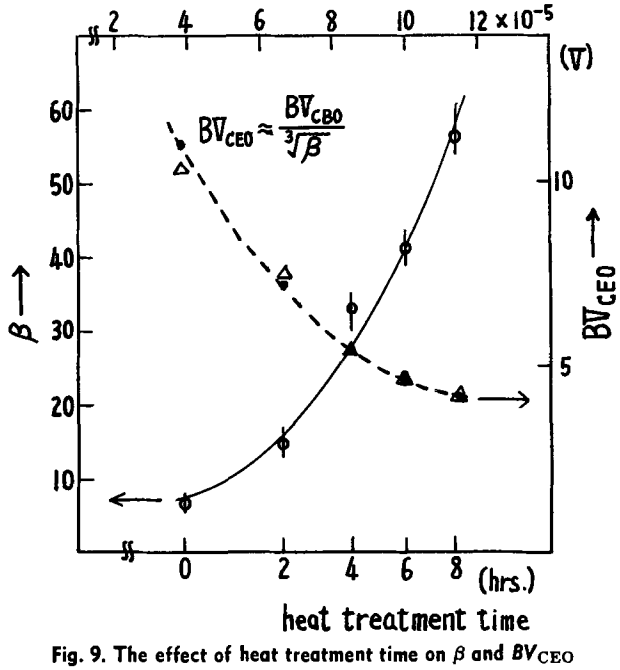

Fig. 9. The effect of heat treatment time on β and BV_{CEO}

The effect of heat treatment time on β and BV_{CEO} is shown in Fig. 9. Fabrication conditions of the samples for these experiments are the same as for TR-6, and emitter diffusion time is kept constant regardless of any heat treatment time. With increased heat treatment time, β increases and BV_{CEO} decreases to about 5V. As mentioned before, these facts mean that with increased heat treatment time, the base width is reduced. Generally speaking, there is a relation between BV_{CEO}, β and BV_{CBO} of transistors as follows

$$BV_{CEO} \approx \frac{BV_{CBO}}{n\sqrt{\beta}} \qquad n = 2 \text{ to } 6 \qquad [1]$$

Th broken lines in Fig. 9 give the values of BV_{CEO} calculated from measured values of β and BV_{CBO} for $n = 3$. These calculated values show good agreement with experiment.

The relation between collector series resistance, R_S, and heat treatment time for the D.E.I. method is represented in Fig. 10. With increased heat treatment time, as autodiffusion proceeds, the values of R_S become lower than those of transistors made by conventional methods. The series resistance, R_S, of I.C. transistors made by the D.E.I. method consists of four components

$$R_S = \eta\,(R_E + R_N + R_{C1} + R_{C2}) \qquad [2]$$

Here, η is a constant coefficient, and R_E and R_{C1} are resistances in the compensated region.

If ρ_S represents the mean value of sheet resistance in the compensated collector region, then the value of ρ_S may be estimated from the measured values of the R_S. The results are summarized in Fig. 11. The mean values of compensated collector region sheet resistance

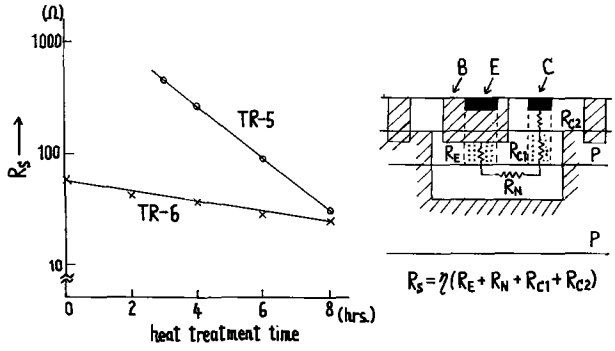

Fig. 10. The relation between heat treatment time and collector series resistance R_S.

Heat treatment time (hrs.)	R_S (Ω) Measurement values	ρ_S (Ω/□) estimated from measurement values	Estimated impurity concentration (cm^{-3}) in inverted layer
0	62.5	5.7×10^3	1.1×10^{16}
2	34.5	3.6×10^3	1.2×10^{16}
4	29.0	2.7×10^3	1.6×10^{16}
6	27.5	2.7×10^3	1.3×10^{16}
8	26.0	2.5×10^3	1.4×10^{16}

Fig. 11. Estimated values of sheet resistance and impurity concentration in the inverted collector layer.

decrease from 5.7 x 10^3 ohm/square to 2.5 x 10^3 ohm/square with increased heat treatment time. If this compensated collector region consisted of only n-type impurity, the impurity concentration in this layer would be from 1 to 2 x 10^{16} cm^{-3}.

Conclusion

A comparison of the fundamental characteristics of transistors made by various methods is shown in Fig. 12. The first and third columns of this figure give a comparison of conventional I.C. transistors and the D.E.I. I.C. transistors. Except for slightly lower values of breakdown voltage, the characteristics of D.E.I. transistors are quite similar to conventional ones. The value of BV_{CEO} given in the top row is sufficient for logic circuits; they are normally operated in the vicinity of 6V.

Storage time of the D.E.I. transistors is lower than that of conventional ones without gold-diffusion, because the impurity distribution in the collector pro-

Description	Conventional method	CDI method	DEI method	SEI method
BV_{CEO} (V)	8~15	<5	6.5~10	2.9~3.4
BV_{CBO} (V)	40~60	10	18	11~12
β normal	30~60	25~35	20~60	20~60
R_S (Ω)	52	10	40	50
β inverse	0.4~0.5	2.0~3.5	0.5~0.8	1.2~1.6
f_T (MC)	200	1500	250	400
Storage time (n.sec.)	27~30	5	18~20	18
C_c (PF)	11.5		16.5	36

Fig. 12. A comparison of the characteristics of transistors made by various methods.

duces a field that sweeps stored charge out of the collector as the transistor comes out of saturation. The fourth column of Fig. 12 shows the characteristics of transistors made by the S.E.I. process. It is simpler, but collector breakdown voltage tends to run too low even for logic circuits.

The second column of Fig. 12 presents characteristics of transistors with collector wall diffusion isolation. Although the breakdown voltage is higher than for a S.E.I. transistor, it is still marginal even for standard logic circuits.

In both the single epitaxial isolation and the collector wall diffusion methods, precise thickness control of an epitaxial layer is an important problem. There is much less of a problem in double epitaxial isolation transistors, because thickness can be adjusted by subsequent heat treatment. The D.E.I. method will be suitable for the fabrication of higher density integrated circuits in view of its simpler processes and better transistor performance.

Acknowledgments

The author wishes to acknowledge helpful discussions with Professor J. Nishizawa, Dr. H. Yamashita, and T. Oukubo. Thanks are due to K. Yukawa for the experimental work.

Manuscript submitted Nov. 10, 1970; revised manuscript received *ca.* May 31, 1971. This was Paper 295 presented at the New York Meeting of the Society, May 4-9, 1969.

Any discussion of this paper will appear in a Discussion Section to be published in the June 1972 JOURNAL.

REFERENCES

1. B. T. Murphy and V. J. Glinksi, International Electron Devices Meeting (October 1968).
2. T. Makimoto and M. Maki, International Electron Devices Meeting (October 1968).
3. K. G. Mckay, *Phys. Rev.*, 94, 877 (1954).

Effect of Partial Dissolution During LPE Growth of $Al_xGa_{1-x}As$ on the Efficiency of Diffused Light-Emitting Diodes

K. K. Shih* and J. M. Blum*

IBM Thomas J. Watson Research Center, Yorktown Heights, New York 10598

ABSTRACT

Light-emitting diodes have been prepared by Zn diffusion to form p-n junctions in Te-doped $Al_xGa_{1-x}As$ layers grown by liquid phase epitaxy. When the growth process is interrupted by a partial dissolution cycle, the external quantum efficiencies for junctions formed in the material grown after dissolution are about five times greater than those obtained without a dissolution cycle. Efficiencies of about 1 x 10^{-3} have been measured at about 6750Å for uncoated diodes. Electron microprobe analysis shows that in the regrown material there is a sharp initial drop in Al concentration, after which the Al concentration gradient becomes considerably less than in layers grown without dissolution. In addition the dislocation density in the regrown layers is about a factor of two lower than in material grown without dissolution.

Efficient visible light emission has been obtained (1) from $Al_xGa_{1-x}As$ p-n junctions grown by the liquid phase epitaxial (LPE) method. It is important to develop a simple diffusion process as an alternative technique for making high efficiency $Al_xGa_{1-x}As$ light-emitting diodes. This would make it possible to prepare planar monolithic structures and therefore enable the economical fabrication of high density monolithic arrays. Linden (2) has made diodes by Zn diffusions into $Al_xGa_{1-x}As$ crystals grown by the LPE method, but these diodes had very low quantum efficiencies (about 10^{-5} at 7000Å).

We have studied the diffusion of Zn into $Al_xGa_{1-x}As$ epitaxial layers grown by the LPE method. By optimizing the diffusion processes and doping levels of the material, slight improvements of quantum efficiency in diffused diodes have been achieved. More important, a substantial improvement in efficiency has been obtained by using a dissolution cycle during the LPE growth of the material into which Zn is subsequently diffused to form the diodes. This cycle dissolves a thin surface layer of the epitaxial overgrowth prior to the regrowth of another thin layer. In order for the improvement in efficiency to be realized, the p-n junction must be formed in the regrown layer near the region where the dissolution takes place.

In order to grow $Al_xGa_{1-x}As$ crystals for diffusion studies the vertical growth method described by Rupprecht *et al.* (1) was employed. N-type GaAs single crystals with (100) orientation were used as substrates. Te was added as the n-dopant. A typical solution composition is 20g Ga, 3g GaAs, 3 mg Te, and a variable amount of Al depending on the desired composition. The cooling cycle I shown in Fig. 1 was used to grow one epitaxial layer. The solution was heated to 955°C and then cooled in contact with the GaAs substrate to about 860°C at a rate of about 0.4°C/min. The AlAs concentration of the epitaxial layer was about 50 mole per cent (m/o) at the interface with the substrate and about 25 m/o at the surface. To prepare diodes, this layer, which was about 60-80 μm thick, was etched into five steps at about 6 μm intervals as depicted in the insert in Fig. 1, and Zn was diffused into the surface of these steps at 700°C for 30 min. The diffusion junction depth is about 3-5 μm. The external quantum efficiencies and wavelengths of the diodes made from each step were measured at 300°K, and the data are plotted as solid circles in Fig. 2.

Cooling cycle II with a dissolution cycle during the growth process, as shown in Fig. 1, was used to grow another $Al_xGa_{1-x}As$ n-type epitaxial layer. In this case, the solution was first cooled at a rate of 0.4°C/min from 955° to 900°C. The temperature was then raised five degrees to 905°C, kept there for 5 min, and finally lowered to 860°C again at a rate of 0.4°C/min. (This cooling cycle is the same as the one which Woodall *et al.* (1, 3) used to grow $Al_xGa_{1-x}As$ p-n junctions with high efficiencies, but they added Zn during the process to form the grown junctions.) As before, the epitaxial layer was etched into five steps, and Zn was diffused into the surfaces of the steps at 700°C for 30 min. The diode results are shown by open circles in Fig. 2. In the region where dissolution had taken place, the diodes are substantially more efficient than those made from the epitaxial layer grown by cooling cycle I.

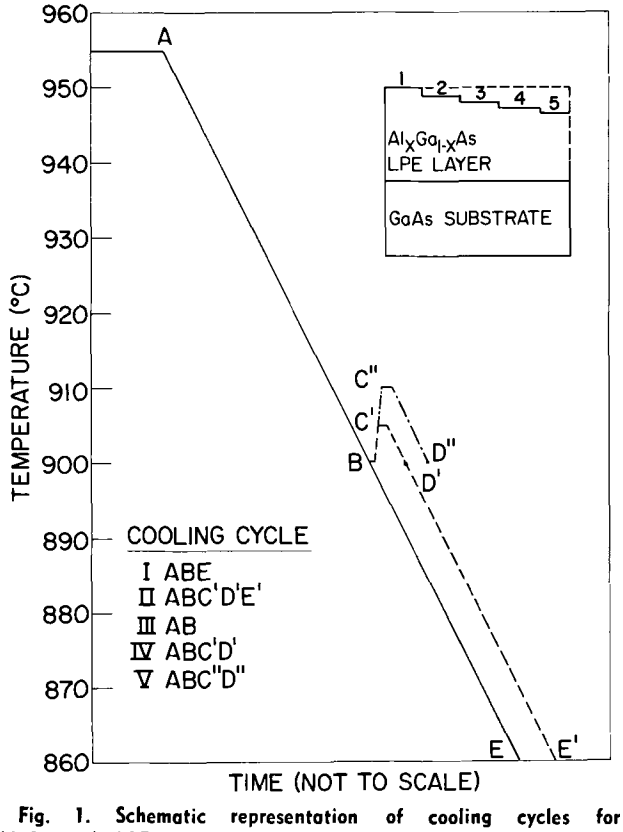

Fig. 1. Schematic representation of cooling cycles for $Al_xGa_{1-x}As$ LPE. Cooling rate 0.4°C/min.

* Electrochemical Society Active Member.

Key words: $Al_xGa_{1-x}As$, liquid phase epitaxy (LPE), dissolution, regrowth, diffusion, light-emitting diodes, III-V alloys.

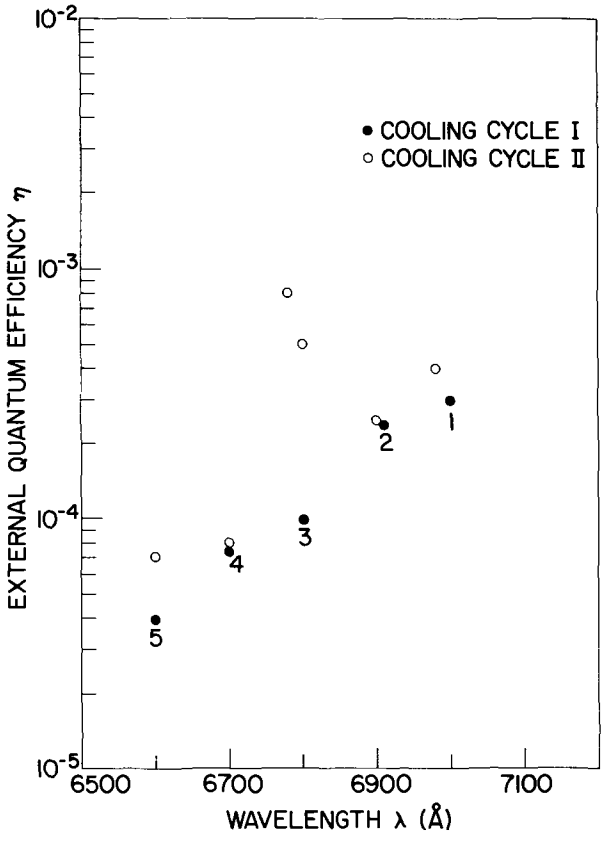

Fig. 2. The external quantum efficiency of $Al_xGa_{1-x}As$ diffused diodes as a function of diode emission energy at 300°K. Solid and open circles correspond to diodes made from epitaxial layers grown with cooling cycles I and II in Fig. 1, respectively.

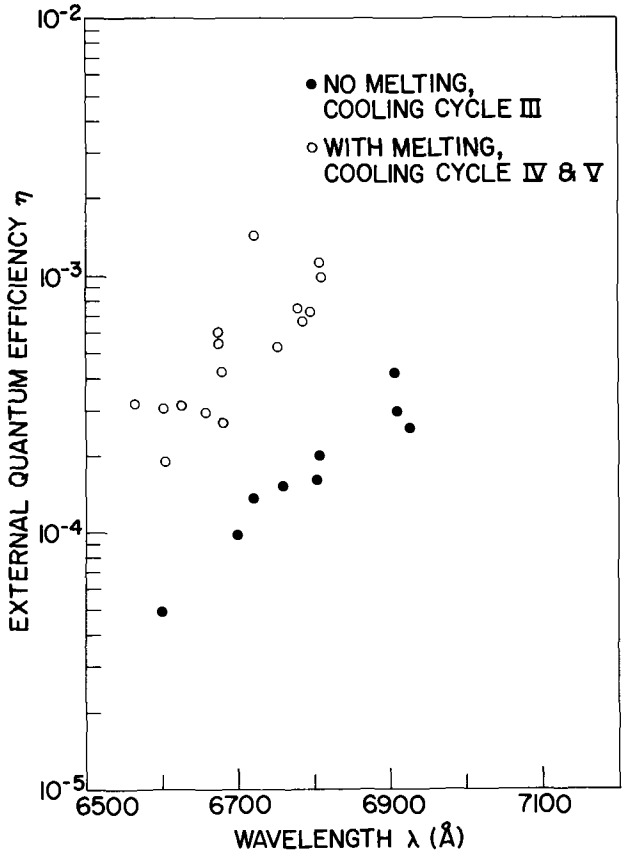

Fig. 3. The external quantum efficiency of $Al_xGa_{1-x}As$ diffused diodes as a function of diode emission energy at 300°K. Solid and open circles correspond to diodes made from epitaxial layers grown without and with a dissolution cycle, respectively.

In order to confirm that the dissolution cycle during the LPE growth of the $Al_xGa_{1-x}As$ is responsible for the improvement in the quantum efficiency of diodes made by subsequent diffusions, many additional layers using the same composition of solution but different amounts of Al have been grown by using the cooling cycles III, IV, or V shown in Fig. 1. In cooling cycle III the solution was heated to 955°C and cooled at a rate of about 0.4°C/min to 900°C. For layers grown with a dissolution cycle, after cooling to 900°C, the temperature was raised 5°C (cycle IV) or 10°C (cycle V). After 5 min at the higher temperature, the solution was cooled again to 900°C. The initial concentration of Al in each of the solutions was different. The AlAs concentration in the epitaxial layers varied between 50-54 m/o at the interface with the substrate and between 32-36 m/o at the surface, and the total thickness of the layers was about 30-50 μm. Zn was subsequently diffused into the surface of these layers at 700°C for 30 min. Figure 3 shows the external quantum efficiencies of the $Al_xGa_{1-x}As$ diffused diodes as a function of the diode emission energy, both measured at 300°K. Solid circles represent the diodes made from layers grown by using cooling cycle III, and open circles represent the diodes made from layers grown by using cooling cycles IV and V. The efficiency decreases as the wavelength decreases because the direct-indirect bandgap composition is approached. The efficiency of diodes made from material grown with a dissolution cycle is improved by a factor of about five, but this value is about a factor two lower than that of the grown junctions (1, 3).

The electron microprobe has been used to measure the composition profiles of epitaxial layers along the growth axis. The mole fraction of AlAs, x in $Al_xGa_{1-x}As$, is plotted in Fig. 4 as a function of dis-

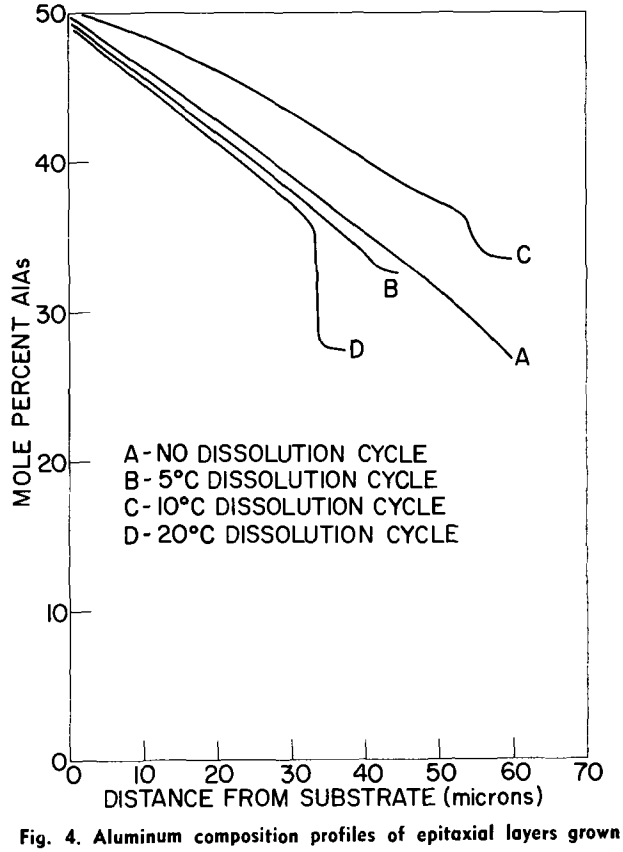

Fig. 4. Aluminum composition profiles of epitaxial layers grown with or without a dissolution cycle.

tance from the substrate for four representative layers. Because of the high segregation constant of Al (3), the concentration of Al decreases with increasing distance from the substrate. Curve A is a typical Al profile of a layer which was grown by using cooling cycle III in Fig. 1. Curves B and C are typical Al profiles of layers grown by using 5° and 10°C dissolution cycles, respectively, corresponding to cooling cycles IV and V in Fig. 1. It is apparent that consequences of dissolution on the material grown after this step are twofold: there is a sharp drop in Al concentration, after which the rate of decrease of the Al concentration with distance is much smaller than the rate of decrease prior to the dissolution cycle. An epitaxial layer with a 20°C dissolution cycle was grown and its profile (curve D) exhibits an even larger initial decrease in Al concentration. A kinetic effect must be responsible for the observed composition profiles, since under equilibrium conditions dissolution and regrowth would not cause any change in the Al concentration profile.

The two changes in the Al concentration profile are probably the major factors which contribute to the large increase in quantum efficiency of diodes made from material grown with a dissolution cycle. The regrown region is about 5 μm thick. The diffused p-n junction, which is about 3-5 μm deep, is normally located in the regrown region after the abrupt drop in Al concentration. Since the radiative recombination occurs on the p-side of the junction, the sudden decrease in bandgap due to the drop in Al concentration, which is about 0.02 eV for a 5°C dissolution step, may increase the radiative recombination by enhancing the injection of electrons and confining the holes in the p-region. The result would be similar to the effect observed in $Al_xGa_{1-x}As$-GaAs heterojunction lasers, where a marked decrease in current threshold is attained using the heterostructure to increase carrier confinement with suppression of the onset of hole injection (4-6).

The diode efficiency may also be increased by the flattening of the Al concentration profile in the regrown region. Because of this change in profile, the Al concentration and therefore the average bandgap are greater in this region (curves B, C, and D in Fig. 4) than in the corresponding region grown without a dissolution step (curve A in Fig. 4). This will reduce the fraction of the light emitted at the junction which is absorbed by the regrown region. In order to determine the degree of improvement one could expect from the flattening effect a rough estimate has been made of the degree to which the absorption is reduced. The photon energy emitted by $Al_xGa_{1-x}As$ diodes is approximately 0.03 eV less than the bandgap at the junction (7), and a 5°C dissolution step causes an increase of about 0.03 eV in the bandgap at the surface of the epitaxial layer. On the basis of these values, together with the slope of the intrinsic absorption edge for direct bandgap material such as GaAs and InP (8, 9), the average absorption coefficient at the emitted wavelength was assumed to be 5×10^2 cm^{-1} for the regrown region and 5×10^3 cm^{-1} for the corresponding region grown without a dissolution step. For a junction depth of 3 μm, the absorption by the regrown region would then be about one-fourth that of the region grown without dissolution. Such a reduction would make a significant contribution to the increase of about a factor of 5 in diode efficiency obtained by using a dissolution cycle.

The effect of the dissolution cycle on the dislocation density of the grown $Al_xGa_{1-x}As$ was also investigated. Dislocations were observed by using the etchant described by Abrahams and Buiocchi (10) to etch 5° angle-lapped surfaces which had been mechanically polished to a mirror finish. The dislocation density of the typical epitaxial layer is of the order of 10^4-10^5 cm^{-2}, and it decreases by about a factor of two in the regrown region. The dislocation density may be reduced in the regrown regions because the dissolution and waiting provides more time for establishing a better liquid-solid interface. This reduction in dislocation density may improve the quality of devices produced by subsequent diffusions.

In conclusion, it was found that the external quantum efficiency of $Al_xGa_{1-x}As$ diodes made by Zn diffusion into layers which were regrown after a 5°-10°C dissolution step is improved by about a factor of approximately five. This may be attributed to the abrupt change of Al concentration so that the injection of electrons into the p-side is enhanced, the leveling effect of the Al concentration gradient in the regrown region so that the absorption of emitted light is reduced, and the reduction in dislocation density.

Acknowledgments

The authors gratefully acknowledge the technical assistance of C. B. Burstell, J. F. DeGelormo, V. Garrison, and K. C. Williams and the helpful discussions with M. R. Lorenz and A. Onton. We appreciate the electron probe analysis done by J. D. Kuptsis and C. F. Aliotta.

Manuscript submitted March 11, 1971; revised manuscript received *ca.* May 24, 1971.

Any discussion of this paper will appear in a Discussion Section to be published in the June 1972 JOURNAL.

REFERENCES

1. H. Rupprecht, J. M. Woodall, and G. D. Pettit, *Appl. Phys. Letters*, **11**, 81 (1967).
2. K. J. Linden, *J. Appl. Phys.*, **40**, 2325 (1969).
3. J. M. Woodall, H. Rupprecht, and W. Reuter, *This Journal*, **116**, 899 (1969).
4. I. Hayashi and M. B. Panish, *J. Appl. Phys.*, **41**, 150 (1970).
5. H. Kressel, H. Nelson, and F. Z. Hawrylo, *ibid.*, **41**, 2019 (1970).
6. Zh. I. Alferov, M. V. Andreev, E. I. Korol'kov, E. L. Portnoi, and D. N. Tret'yakov, *Soviet Phys.—Semicond.*, **2**, 1289 (1969).
7. A. Onton, Private communication.
8. T. S. Moss, *J. Appl. Phys.*, **32**, 2136 (1961).
9. W. J. Turner, W. E. Reese, and G. D. Pettit, *Phys. Rev.*, **136**, A1467 (1964).
10. M. S. Abrahams and C. J. Buiocchi, *J. Appl. Phys.*, **36**, 2855 (1965).

Charge Injection in MAOS Systems

P. Balk[1] and F. Stephany

Institut für Halbleitertechnik, Technical University, Aachen, West Germany

ABSTRACT

A study of charge injection in metal-Al_2O_3-SiO_2-silicon (MAOS) structures has been made using the capacitance-voltage technique. Thin SiO_2 films were grown thermally on the Si substrates, whereas Al_2O_3 layers were obtained by pyrolytic deposition from $AlBr_3$ in a NO-forming gas mixture. Independent of the electrode material, negative charge is introduced into the oxide system when a positive voltage is applied to the metal. With Al electrodes, the oxide also becomes negatively charged under negative bias. Only for large negative voltages will a gradual loss of negative charge occur, leading to a net positive oxide charge. Charge injection under negative bias is not observed on O_2 annealed Al_2O_3 layers, or on samples with Au electrodes. The results are discussed in terms of a qualitative model.

Charge storage in metal-Si_3N_4-SiO_2-silicon (MNOS) structures has attracted considerable interest since the late sixties because of its potential for memory device application. For stressing voltages exceeding a threshold value carriers will, depending on the direction of the electric field, enter or leave traps near the Si_3N_4-SiO_2 interface, thus changing the state of charge of the system, and thereby the threshold voltages of IGFET devices incorporating such double layers as gate insulators (1-7). Particularly for very thin SiO_2 layers (<30Å), when the charging takes place by direct tunneling through this oxide film into the traps, these processes are quite fast. The field and time dependencies of the charging processes are determined by the trap energies and by the spatial distribution of the traps. These characteristics will depend, in turn, on the method by which the layers were prepared. The somewhat different results obtained in Ref. (5) and (6) (logarithmic increase in induced charge with time under electric stress *vs.* relatively rapid saturation of the charging process) must be related to details of the sample preparation process.

The discovery of such charge storage behavior in the MNOS system raises the question of similar effects occurring in sandwich structures with other insulators. Indeed, it has been reported recently that also in MAOS structures (A = Al_2O_3) with Al electrodes the charge can be varied easily in an electric field. However, here both positive and negative voltage stress tends to induce negative oxide charge. The behavior appears to be independent of the method by which the Al_2O_3 film was obtained: reactive evaporation of Al in O_2 (8), pyrolysis of trimethyl-Al in O_2 at 450°C (4) or of Al-isopropoxide in O_2 at 420°C (9), pyrolysis of $AlCl_3$ in CO_2-H_2 at 850°C (10), or of $AlBr_3$ in NO-H_2-N_2 at 900°C (11). Only for rf sputtered Al_2O_3 films does the injection of negative charge under negative bias on the metal appear to be absent (12). Although some authors (8, 10) have not mentioned the occurrence of SiO_2 in their insulator system, it appears likely that in all cases a layer of native oxide was present on the silicon wafers used as substrates for Al_2O_3 deposition.

In the present study we have explored the mechanism of charging in MAOS systems with Al_2O_3 films prepared by high-temperature pyrolysis of $AlBr_3$ in a NO-H_2-N_2 mixture. It is shown that electron injection from the Al electrode into the Al_2O_3 accounts for the introduction of negative charge under negative voltages. The effects of the nature of the metal electrode and of annealing the dielectric are demonstrated. A qualitative model is presented to explain the observations.

[1] Present address: IBM Thomas J. Watson Research Center, P.O. Box 218, Yorktown Heights, New York 10598.

Key words: layered insulators, charge storage, trapping centers, CV measurements.

Experimental

Silicon substrates [1 and 10 ohm-cm p- and 1 ohm-cm n-type, (100) oriented, chemically-mechanically polished Wacker material] were cleaned in organic solvents, HNO_3, and water. Immediately after a final HF dip they were placed under N_2 flow in an rf heated oxidation and deposition apparatus. Very thin SiO_2 films (<30Å) were formed by oxidation at 900°C in forming gas (80% N_2, 20% H_2) with 2% NO (Deutsche l'Air Liquide). Thicker layers were obtained in O_2 at the same temperature. After oxidation, Al_2O_3 films were deposited in the same apparatus and at the same temperature from a 0.03% $AlBr_3$ (Merck)-2% NO-forming gas mixture (13) at a linear flow rate of 400 cm min^{-1}. The deposition rate was about 80 Å min^{-1}. Under these conditions, polycrystalline films of γ-alumina with a grain size of 100-200Å will form (13). Capacitor structures were completed by evaporation of metal (Al or Au) dots through a metal mask, without heating the substrate.

Ellipsometric SiO_2 thickness determinations on a series of samples, oxidized in NO-forming gas by the same procedure as used for our standard thin SiO_2 films, yielded a value of 13 ± 3Å. The layers formed in O_2 were at least 40Å, the thickness depending on oxidation time. Measurements of the capacitance-voltage characteristics of MAOS samples on n-type substrates with 13Å SiO_2 films and Al electrodes indicated that these were converted to p-type after exposing them to a 900°C heat treatment for an extra 15 min period. This suggests that Al readily penetrates the SiO_2 layer, possibly converting it into an aluminosilicate. For this reason one should consider the SiO_2 thickness value measured before Al_2O_3 deposition only as a semiquantitative indication of the thickness of the SiO_2 layer in the composite dielectric film. The Al_2O_3 thickness was obtained from the capacitance of the system, using a value of 9.8 for the dielectric constant (13).

Pulses of various amplitudes and lengths were applied using a HP 214A pulse generator. For pulse lengths ≥ 1 sec the voltages were switched on and off manually. The state of charging of a MAOS system was evaluated from its flatband voltage (V_{FB}), obtained from a capacitance-voltage (CV) measurement (14), generally made at 3 Mc. An attempt was made to estimate the density of interface states from the displacement of the CV curves between room temperature and liquid N_2 temperature (15). If such states occur, one expects a shift in negative direction for p-type substrates at the low temperature, and in positive direction for n-type samples. However, for samples of both conductivity types an increase in V_{FB} (by 0.1V to 1V) was obtained. This displacement did not change upon electrically stressing the samples. We cannot explain this observation at the present time.

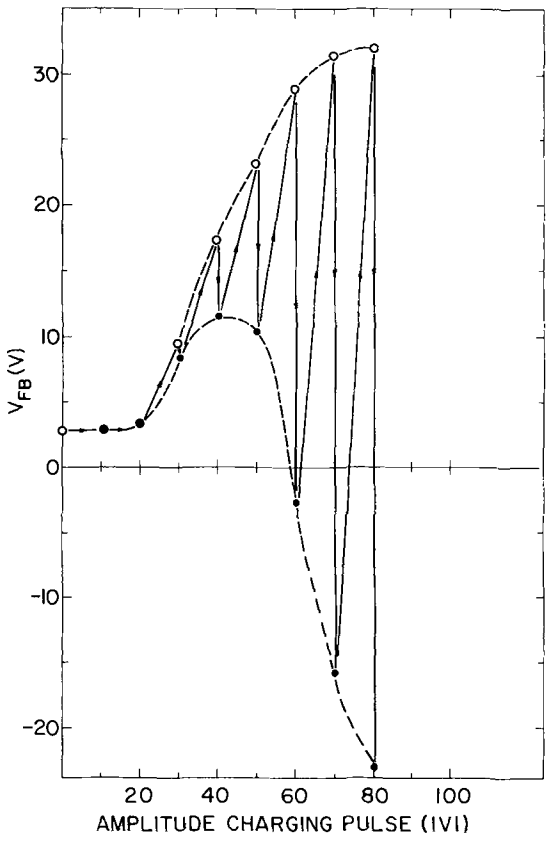

Fig. 1. V_{FB} shift under alternating pos. (○) and neg. (●) 1 sec pulses of increasing amplitude (see arrows). Sample: Al-Al_2O_3(1300Å)-SiO_2 (13Å)-Si [p-type, (100), 1 ohm-cm].

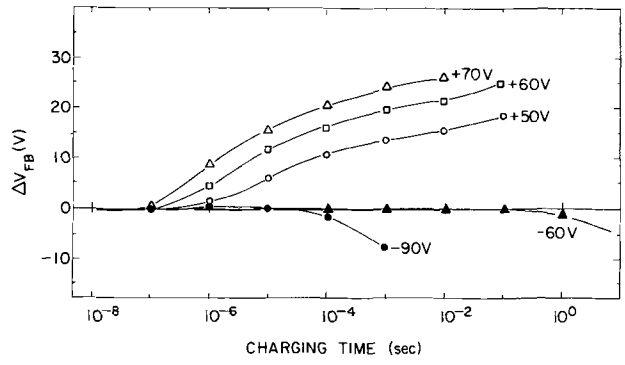

Fig. 2. Time dependence of V_{FB} shift (ΔV_{FB}) for various charging voltages. Sample: Al-Al_2O_3(1100Å)-SiO_2(13Å)-Si [p-type, (100), 1 ohm-cm]

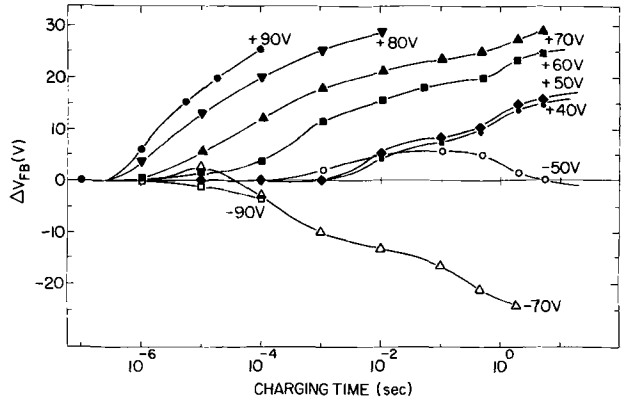

Fig. 3. Time dependence of V_{FB} shift (ΔV_{FB}) for various charging voltages. Sample: Al-Al_2O_3(1300Å)-SiO_2(40Å)-Si [p-type, (100), 1 ohm-cm].

Nevertheless, it appears reasonable to conclude that the interface state densities were always relatively small (approximately 10^{11} cm^{-2} or less), and that the V_{FB} values can thus be directly correlated with the charge in the oxide system.

Results and Discussion

Some characteristic features of the charging behavior of a MAOS system with Al electrode are illustrated in Fig. 1, which shows the effect on V_{FB} of alternating positive and negative pulses (pulse length: 1 sec) applied to the metal electrode. Before stressing, such capacitors exhibit a positive V_{FB} value, which implies the presence of negative charge in the oxide system. Small stressing pulses (<20V) do not change V_{FB}. Increasing the pulse amplitude beyond this threshold value first leads to an increase in V_{FB} both for positive and negative pulses, independent of the order of application. Thus, in both cases the negative charge in the oxide increases. For larger stresses, V_{FB} continues to rise under positive voltages, but decreases under negative voltages. This suggests that in the latter case a different charging process becomes dominant. When applying only voltage pulses of the same sense to the sample, one obtains curves which are qualitatively similar to the dotted lines connecting the positive and negative voltage points. A situation where the positive and negative V_{FB} shifts become of equal magnitude for applied voltages of opposite sign is only approached for very large stresses.

This point is also apparent in Fig. 2 and 3, which show the time dependence of the V_{FB} shift for large positive and negative voltages, obtained on samples with two different SiO_2 thicknesses. The shifts with positive voltage are roughly logarithmic with time, but show a tendency to saturate. Their dependence on oxide thickness is relatively small. Under negative stress two competitive processes appear to determine the shapes of the time dependence curves: first negative charge is introduced into the oxide, but somewhat later the negative charge content of the oxide system appears to decrease, as seen from the reversal of the direction of V_{FB} shift. The balance between these two processes tends to change in favor of the second one for larger voltages and thinner oxides. This complex behavior is only observed for larger negative voltages. As reported earlier (11), for voltages just above the charging threshold, V_{FB} will first increase but then remain constant. Rather similar charging characteristics were observed at liquid nitrogen temperature when stressing such MAOS structures in the enhancement direction.

A comparison of the dependence of V_{FB} on pulse amplitude (pulse length: 1 sec) for two different SiO_2 thicknesses, both obtained by oxidation of the substrate in O_2, is shown in Fig. 4. The data for the thicker composite film have been normalized to 1400Å, the thickness of the thinner one, in order to make a direct comparison of the curves possible. It may be seen that that threshold for V_{FB} change under negative voltage stress is not dependent on the SiO_2 thickness. Such behavior suggests that this initial increase in V_{FB} is determined by charge injection from the metal into the Al_2O_3 film. However, the subsequent decrease for larger negative voltages, and the increase under positive stress are both affected by the thickness of the SiO_2 film. From this, it may be concluded that in the latter two processes charge transport into or across the SiO_2 layer takes place. The weak temperature dependence appears to indicate that in both cases the rate-determining step involves a tunneling process.

From literature data for the bandgap of Si (16), the barrier energy for holes between Si and SiO_2 (17), the bandgap of SiO_2 (18) and the electron affinity of

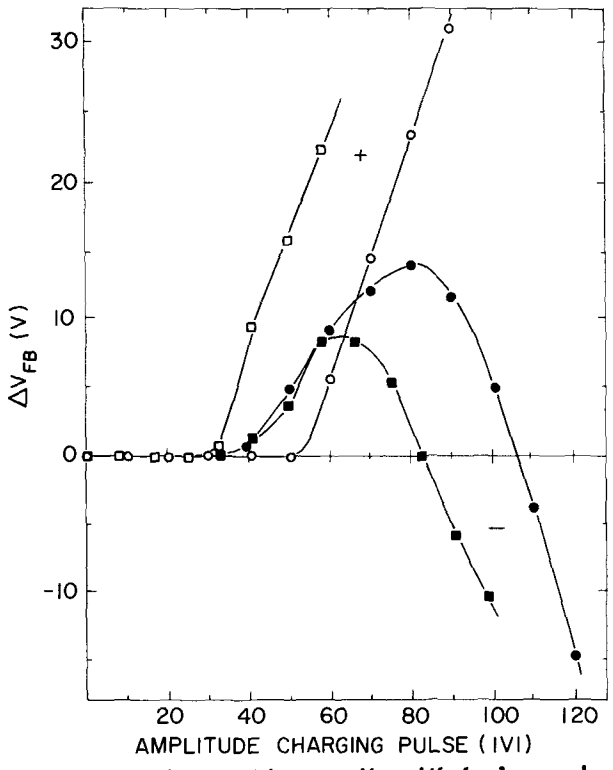

Fig. 4. Effect of SiO_2 thickness on V_{FB} shift for 1 sec pulses. Samples: □: Al-Al_2O_3(1700Å)-SiO_2(40Å)-Si [p-type, (100), 10 ohm-cm], data normalized to 1400Å; O:Al-Al_2O_3(1400Å)-SiO_2(73Å)-Si [p-type, (100), 10 ohm-cm].

this material (19), the bandgap of Al_2O_3 (20), the work function of Al (16), and the barrier energy for electrons between Al and Al_2O_3 (21), the energy band diagram shown in Fig. 5a may be constructed for the Al-Al_2O_3-SiO_2-Si system. Also indicated in this diagram are some trapping states, which occur in this material in relatively high densities compared to SiO_2 (22, 23). It must be stressed that such a diagram is necessarily tentative, since the data on the Al-Al_2O_3 barrier and those on the deeper traps most likely refer to amorphous material.

The relatively low threshold field (approximately 3 x 10^6 V cm^{-1}) suggests that under negative bias electrons tunnel directly from the Al electrode into the traps in the Al_2O_3 (Fig. 5b). In Fig. 5b-d, we made the assumption that the centers at approximately 1 eV below the Al_2O_3 conduction band play a dominant role in the charging effects, but the possibility that deeper traps also participate cannot be excluded. In comparison, Fowler-Nordheim tunneling of 10^{11} electrons cm^{-2} (this charge does not significantly affect the field across the oxide, thus permitting a simple calculation) in 10^{-3} sec would require a field of approximately 8 x 10^6 V cm^{-1}. This may be inferred from literature data on tunneling from a deposited Al electrode into an Al_2O_3 film (24), taking into account the built-in field of the film. One would thus expect that this tunneling mode only occurred for the highest stressing voltages in our MAOS samples. The electrons will drift further into the oxide *via* a field enhanced thermal excitation (Poole-Frenkel effect) or a field ionization mechanism, causing V_{FB} to shift in positive direction. At the same time, the accumulation of charge near the electrode reduces the local field at that interface, which results in a decreasing electron injection rate. Thus, for voltages just above the threshold the V_{FB} shift will saturate. At high voltages electron injection into the silicon, *via* tunneling into the SiO_2 conduction band, will gradually become the dominant process (Fig. 5c). This causes a decrease in the negative oxide charge, and consequently in V_{FB},

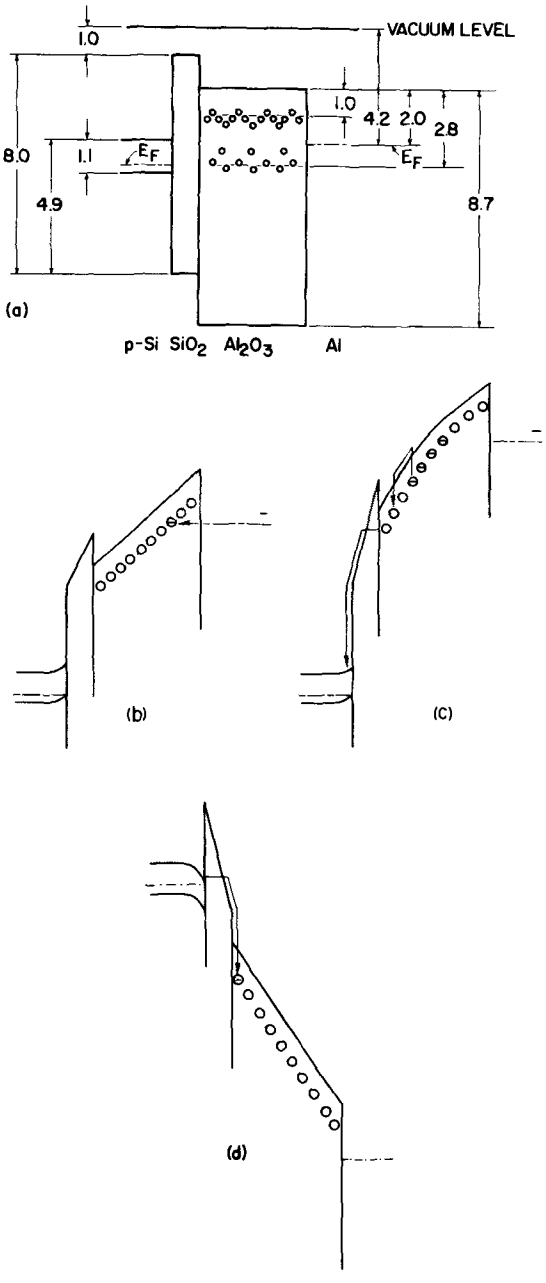

Fig. 5. (a) Energy band diagram for MAOS structure (energies in eV); (b) charge injection under moderate negative bias; (c) charge drift and emission under large negative bias; (d) injection under positive bias.

after the initial rise. The fact that V_{FB} attains negative values implies that the charge in the system has become positive. It is not possible to decide on the basis of the present data whether this means that positively charged centers are being created under application of negative voltages, or that such centers are always present in the films, but compensated by oppositely charged trapping states.

For positive-stressing voltages and thick SiO_2 layers (as exemplified by the capacitor with 73Å SiO_2 film in Fig. 4) Fowler-Nordheim tunneling of electrons into the SiO_2 conduction band (Fig. 5d), followed by drift into the Al_2O_3 conduction band and subsequent trapping, appears the only likely explanation of the data. The observed threshold voltage of approximately 55V is quite compatible with the value of nearly 50V, required for tunneling of 10^{11} electrons in 10^{-3} sec into the SiO_2 conduction band, estimated from Lenzlinger and Snow's work (25). The threshold field for this type of injection should be independent of SiO_2 thick-

ness, unless the SiO_2 films exhibit different internal field distributions, caused by different charge distributions before stressing. Such charge distributions may result from the before-mentioned Al penetration, which will particularly affect the behavior of the thinner SiO_2 layers. It is not clear whether the smaller threshold values, obtained on samples with thinner SiO_2 films, are caused by such a thickness dependence of the charge distribution, or that a new mechanism (direct tunneling into the traps) manifests itself in this case. Tsang *et al.* (26) have recently concluded that in a MAOS structure with Al electrode, very thin (approximately 20Å) SiO_2 film, and Al_2O_3 film prepared from $AlCl_3$ in CO_2-H_2, charge injection at both electrodes takes place by direct tunneling for the appropriate direction of field.

The above model implies that electron injection at the metal electrode can be suppressed by previously filling the traps in the region of the Al_2O_3 film near the electrode. In this case a negative V_{FB} shift should start immediately upon application of negative voltages larger than the threshold value. This conclusion is borne out by the data in Fig. 6, which shows the time dependence of the change in V_{FB} under negative voltage after the Al_2O_3 traps had been partially filled by application of a 1 sec pulse of +50V amplitude. The same effect is apparent in Fig. 7, which shows the hysteresis behavior of a MAOS sample for 1 sec pulses. Starting with the application of negative pulses to the Al electrode, one observes, as before, an initial rise in V_{FB}, followed by a decrease for larger negative voltages. Returning in the opposite direction, V_{FB} remains constant, until at the positive threshold of approximately +20V a steep increase begins. Traversing a complete counterclockwise loop, by varying the stressing voltage from positive to negative to positive again, the negative to positive return trace is again horizontal, and at the same V_{FB} value as before. It will be clear that the shape of such hysteresis loops depends on the pulse length.

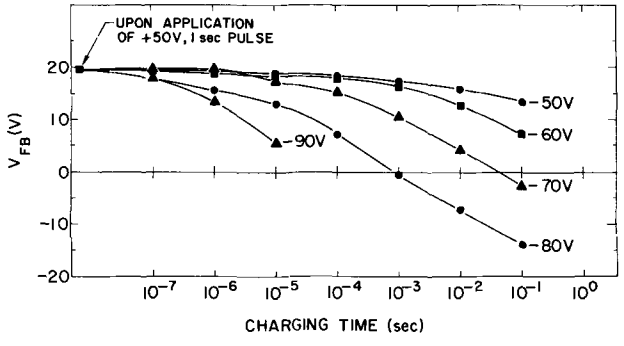

Fig. 6. Time dependence of V_{FB} shift under negative bias after application of 1 sec + 50V pulse. Sample: Al-Al_2O_3(1300Å)-SiO_2(40Å)-Si [p-type, (100), 1 ohm-cm]

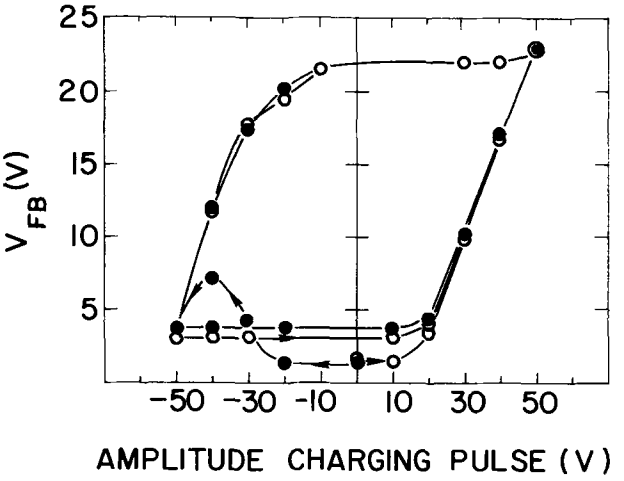

Fig. 7. Hysteresis behavior of MAOS capacitor with Al electrodes. Arrows indicate sign of initial stressing voltage (pulse length: 1 sec). Sample: Al-Al_2O_3(1300Å)-SiO_2(13Å)-Si [p-type, (100), 1 ohm-cm].

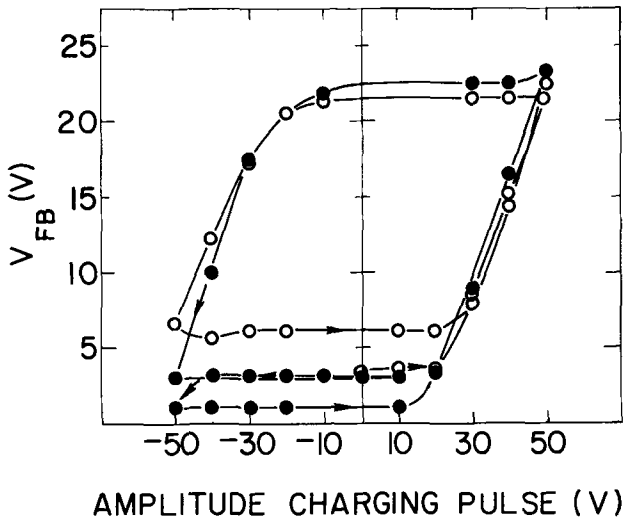

Fig. 8. Hysteresis behavior of MAOS capacitor with Au electrode. Arrows indicate sign of initial stressing voltage (pulse length: 1 sec). Same substrate as used in Fig. 7.

Since tunneling probabilities depend exponentially on barrier heights, the electron injection rate from the metal into the Al_2O_3 layer is only appreciable for electrode materials with a relatively low work function. Figure 8 shows that indeed for MAOS systems with an Au electrode [vacuum work function: 4.7 eV for Au, 4.2 eV for Al (16)] the hysteresis loop does not show the initial increase in V_{FB} for negative pulses as was the case with Al electrodes. In other respects the loop is rather similar to that for Al electrodes.

It is known (22) that annealing alters the trap density in Al_2O_3. Also, Kalter (27) has found that the negative charge in the thermal SiO_2-high temperature pyrolytic Al_2O_3 composite layer system decreases during annealing in O_2 at 900°C. The change saturates in approximately 1 hr. It appears likely that the charge centers are of the same nature as the trapping states discussed above in explaining the memory behavior of MAOS systems. Since high temperature pyrolytic Al_2O_3 films are commonly grown under only marginally oxidizing conditions such centers may be oxygen vacancies. It may be expected that O_2 annealing would reduce their concentration.

For these reasons the effect of such annealing treatment at 900°C on the charging of the oxide films was investigated. It was found that the increase in V_{FB} under negative bias has already been considerably reduced after 15 min annealing, and has disappeared completely in 1 hr. The V_{FB} hystersis loop in Fig. 9, obtained after 1 hr annealing, and measured with 1 sec pulses and Al electrodes, shows this effect. Note also that the magnitude of the positive and negative threshold voltages for V_{FB} shift have become quite comparable. Larger positive or negative pulses of equal magnitude yield V_{FB} shifts of opposite sign, but of comparable magnitude. The data appear to support the contention that O_2 annealing reduces the trap density in Al_2O_3, since the direct tunneling from Al into Al_2O_3 traps seems to be suppressed. In the case of O_2-annealed samples very similar results are obtained with Au electrodes.

Finally, it was observed quite generally on unannealed samples with Al electrodes that the capacitance-voltage characteristic developed a step-like dis-

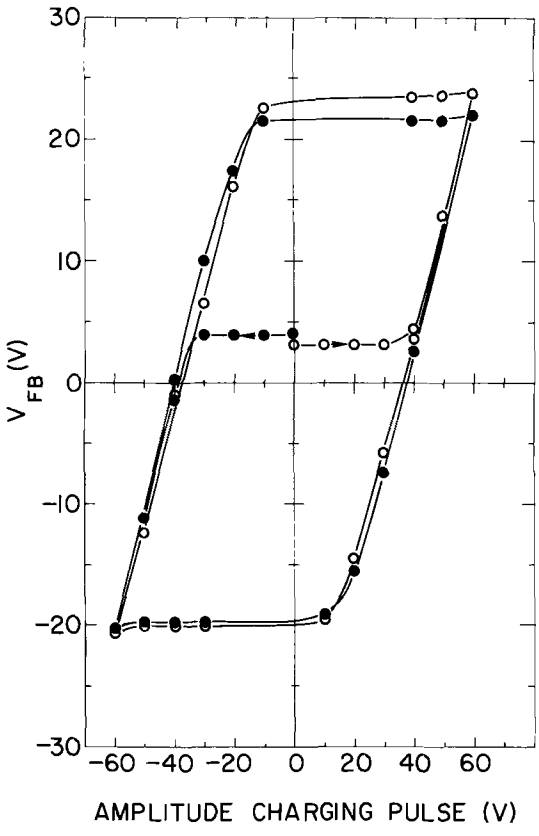

Fig. 9. Hysteresis behavior of MAOS capacitor with Al electrode. Arrows indicate sign of initial stressing voltage (pulse length: 1 sec). Sample: Al-Al_2O_3(1300Å)-SiO_2(13Å)-Si [p-type, (100), 1 ohm-cm], annealed for 1 hr in O_2 at 900°C before metallization.

tortion and a gradual flattening of the steep part in the curve during the increase of V_{FB} under negative voltage stress. This distortion would gradually disappear when the curves moved back (and V_{FB} decreased) at larger stressing times or upon application of positive voltages. Such effects were never observed on samples with Au electrodes, or on O_2-annealed structures. It appears likely that these distortions reflect a nonuniform rate of change of the surface potential under the electrode. This behavior could be caused by a varying electron injection rate under negative bias, which may imply a nonuniform trapping center density across the surface.

Conclusions

The present study confirms that negative charge builds up in MAOS systems with Al electrodes under application of negative voltages exceeding a certain threshold value. This behavior is most likely caused by injection of electrons into traps in the Al_2O_3 film by direct tunneling or possibly, at higher fields, also *via* Fowler-Nordheim tunneling into the Al_2O_3 conduction band. Thus, it can be suppressed by using an electrode material with a larger work function, like Au. Elimination of oxide traps should have a similar effect. Since O_2 annealing probably results in a reduced trap density, the absence of negative charge accumulation for a negatively biased Al electrode in O_2-annealed samples tends to confirm this model. The model also implies that the injected charge will drift across the oxide by a Poole-Frenkel mechanism or through field emission from the traps.

Exchange of charge between the silicon and the composite oxide film takes place *via* Fowler-Nordheim tunneling in the case of thick SiO_2 films. For very thin films our data do not allow us to decide between this mechanism and direct tunneling. In the thin SiO_2 case the situation is complicated by the interdiffusion of the film constituents. The high dielectric constant of Al_2O_3 tends to enhance the field in the SiO_2 layer, and thus yields relatively low threshold fields for charge injection at the silicon.

When operating under conditions where charge injection from the metal electrode is suppressed, the amount of oxide charge changes roughly logarithmically with time for both directions of voltage stress. This lack of distinctive saturation may be undesirable for memory device application.

Acknowledgments

The authors like to acknowledge continued support and interest in this work by Professor Dr. H. Beneking. They are also indebted to Dr. G. Ackermann (IBM Laboratory, Boeblingen) for a number of ellipsometric measurements of oxide film thickness, to Dr. P. J. Tsang (IBM Components Division, East Fishkill) for directing their attention to Ref. (20) and (21), and to Drs. N. J. Chou, P. J. Krick, and T. O. Sedgwick (IBM Thomas J. Watson Research Center, Yorktown Heights, New York) for helpful discussions.

Manuscript submitted Dec. 9, 1970; revised manuscript received May 17, 1971.

Any discussion of this paper will appear in a Discussion Section to be published in the June 1972 JOURNAL.

REFERENCES

1. H. C. Pao and M. O'Connell, *Appl. Phys. Letters*, **12**, 260 (1968).
2. F. A. Sewell, Jr., H.A.R. Wegener, and E. T. Lewis, *ibid.*, **14**, 45 (1969).
3. D. Frohmann-Bentchkowsky and M. Lenzlinger, *J. Appl. Phys.*, **40**, 3307 (1969).
4. J. T. Wallmark and J. H. Scott, *RCA Rev.*, **30**, 335 (1969).
5. E. C. Ross and J. T. Wallmark, *ibid.*, **30**, 366 (1969).
6. M. Pulver and G. Dorda, *Phys. Status Solidi* (a), **1**, 65 (1970).
7. G. Dorda and M. Pulver, *ibid.*, **1**, 71 (1970).
8. E. Ferrieu and B. Pruniaux, *This Journal*, **116**, 1008 (1969).
9. M. T. Duffy and A. G. Revesz, *ibid.*, **117**, 372 (1970).
10. T. Tsujide, S. Nakanuma, and Y. Ikushima, *ibid.*, **117**, 703 (1970).
11. P. Balk and S. Stephany, *NTZ-Nachrtech. Z.*, **23**, 526 (1970).
12. C.A.T. Salama, *This Journal*, **117**, 913 (1970).
13. J. Aboaf, Private communication.
14. A. S. Grove, B. E. Deal, E. H. Snow, and C. T. Sah, *Solid-State Electron.*, **8**, 145 (1965).
15. D. M. Brown and P. V. Gray, *This Journal*, **115**, 760 (1968).
16. A. S. Grove, "Physics and Technology of Semiconductor Devices," John Wiley & Sons, New York (1967).
17. A. M. Goodman, *Phys. Rev.*, **152**, 780 (1966).
18. R. Williams, *ibid.*, **140**, A569 (1965).
19. A. M. Goodman and J. J. O'Neill, Jr., *J. Appl. Phys.*, **37**, 3580 (1966).
20. A. H. Laufer, J. A. Prigog, and J. R. McNesby, *J. Opt. Soc. Am.*, **55**, 64 (1965).
21. A. M. Goodman, *J. Appl. Phys.*, **41**, 2176 (1970).
22. J. P. Mitchell, *IEEE Trans. Nuclear Sci.*, **NS-15**, 154 (Dec. 1968).
23. G. A. Filaretov, V. I. Stafeev, Yu. Z Bubnov, and T. N. Chizhik, *Soviet Phys.-Semicond.*, **1**, 1242 (1968).
24. S. R. Pollack and C. E. Morris, *J. Appl. Phys.*, **35**, 1503 (1964).
25. M. Lenzlinger and E. H. Snow, *ibid.*, **40**, 278 (1969).
26. P. J. Tsang, V. Y. Doo, and N. J. Chou, Paper presented at AIME Technical Conference on Electronic and Magnetic Materials, New York, Aug. 1970.
27. H. Kalter, Private communication.

Preparation and Properties of $In_xGa_{1-x}As$ Single Crystals by Solution Growth Technique

Kiyoshi Takahashi, Toyosaka Moriizumi, and Shinji Shirose[1]

Department of Electronics, Tokyo Institute of Technology, O-okayama, Meguro-ku, Tokyo, Japan

ABSTRACT

Single-crystalline $In_xGa_{1-x}As$ layers were grown epitaxially on GaAs substrates by the solution-growth technique. X-ray microanalyses showed that the value of "x" obtained in $In_xGa_{1-x}As$ was between 0.0 and 0.2. Hall measurements were made for undoped $In_xGa_{1-x}As$ crystals as a function of the composition x. The crystals were n-type and their mobilities varied little as x increased from 0.0 to 0.2. Doping of some impurities, such as Zn and Ge, was tried. Ge was found to be an amphoteric impurity in the $In_xGa_{1-x}As$ crystals, and a pn junction could be made in one solution-growth cycle.

Recently III-V ternary alloys have attracted much attention, because it is possible to change energy gaps or carrier mobilities by controlling the mixing ratio of two terminal compounds. In the case of InAs-GaAs alloys, several attractive properties have been reported; *e.g.*, coherent light emission with wavelengths between 0.84μ and 3.1μ (1) and thermoelectric properties with a high figure of merit (2). Moreover, in the devices for high-frequency and room-temperature operation, an $In_xGa_{1-x}As$ crystal has a great advantage because it is possible to make a semiconductor with a higher electron mobility than GaAs and with a wider energy gap than InAs.

Homogeneous, single-phase $In_xGa_{1-x}As$ alloys have been prepared by many investigators utilizing several kinds of growth techniques; *i.e.*, directional freezing (3), zone-leveling (4), vapor growth (5), Czochralski pulling (6), and solution-growth techniques (7). However, a single-crystal $In_xGa_{1-x}As$ alloy has been grown only within a limited range of x, although the vapor epitaxial experiments (5) were successful throughout the entire composition range.

In the present work, $In_xGa_{1-x}As$ crystals were prepared by Nelson's solution-growth technique (8). The crystalline nature, the composition ratio x, and the electrical properties of the grown crystals deposited on GaAs substrates were studied. Furthermore, the impurities were doped into $In_xGa_{1-x}As$ crystals, and the amphoteric properties of Ge therein were studied.

Crystal Growth

The solution-growth apparatus employed for this study was based on the work of Nelson (8). The crystal growth was carried out in a graphite boat, which was placed in a H_2 gas flow ($\sim$ 2 liter/min) atmosphere. The melt consisted of solvent metals (In + Ga, 500 mg) and of a GaAs polycrystal. The solvent metals, In and Ga, were six-9's pure. The GaAs polycrystal was an undoped n-type crystal with n $\simeq 10^{17}$ cm^{-3}, and its weight was heavy enough for the GaAs polycrystal to become saturated in the solvent: *i.e.*, 110 mg at the maximum growth temperature, T_M = 800°C, and 60 mg at T_M = 700°C. The In was etched in conc HCl, and Ga was etched in conc HBr. The GaAs polycrystal was etched in 2% Br_2-methanol solution. The GaAs substrate was a semi-insulating crystal with $\rho = 10^6$-10^8 ohm-cm at room temperature or an n-type wafer with electron concentration n $\simeq 10^{17}$ cm^{-3}. Its dimension was 5 mm x 5 mm x 0.5 mm, and its surface was usually the (111)B face. It was polished with 0.3μ Linde-Alumina powder and was chemically etched in a $H_2O + 3H_2SO_4 + H_2O_2$ solution.

In the preliminary stage of growth, the solvent and the GaAs polycrystal were mixed by heating to T_M. Then the GaAs substrate was set in a boat after the furnace was cooled to room temperature. For the crystal growth, the temperature program as shown in Fig. 1 was adopted. The substrate was dipped in the melt two minutes after the furnace was heated up to T_M, 700°C or 800°C. One minute later, the temperature was lowered with the constant cooling rate of 1°C/min or 15°C/min, and an $In_xGa_{1-x}As$ crystal began to grow on the substrate. At 400°C, the melt was removed from the grown layer by a quartz slider, and the boat was pulled out of the furnace.

Crystalline Nature

Crystal orientation of the substrate surface affects the crystalline quality of the grown layer. The surface of the grown layer was investigated through a microscope. Figure 2(a) and (b) show the surfaces of the layers grown on (100) or (111)A substrate, respectively. The former surface was rough like corn and was polycrystalline. The interface between the substrate and the grown layer was very rough in this case. The latter surface was terraced and easily broken into flakes. Hence, hereafter these substrates were not used, and only (111)B substrates were used. Figure 3 demonstrates the surface patterns of the layers which were grown on (111)B substrates cooled at the rate of 1°C/min or 15°C/min from T_M (= 700°C), in solutions of various atomic ratios of In to Ga. The atomic ratio of the solvent metals, In to Ga, which hereafter will be designated as AR, determined the surface patterns, the crystalline qualities, and the x values of the grown $In_xGa_{1-x}As$ layers. As shown in Fig. 3, when AR was

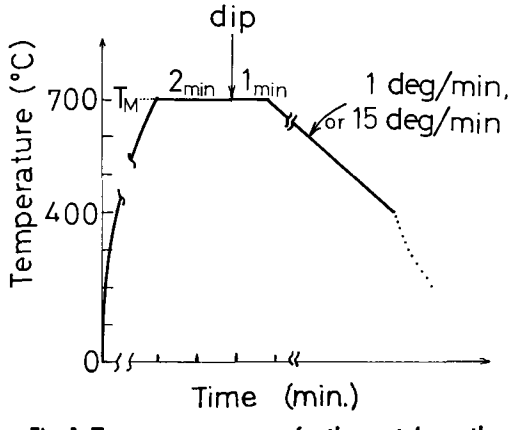

Fig. 1. Temperature program for the crystal growth

[1] Present address: Musashi Works of Hitachi, Ltd., Kodaira-shi, Tokyo, Japan.

Key words: liquid epitaxy, solution growth, indium$_x$ gallium$_{1-x}$ arsenic.

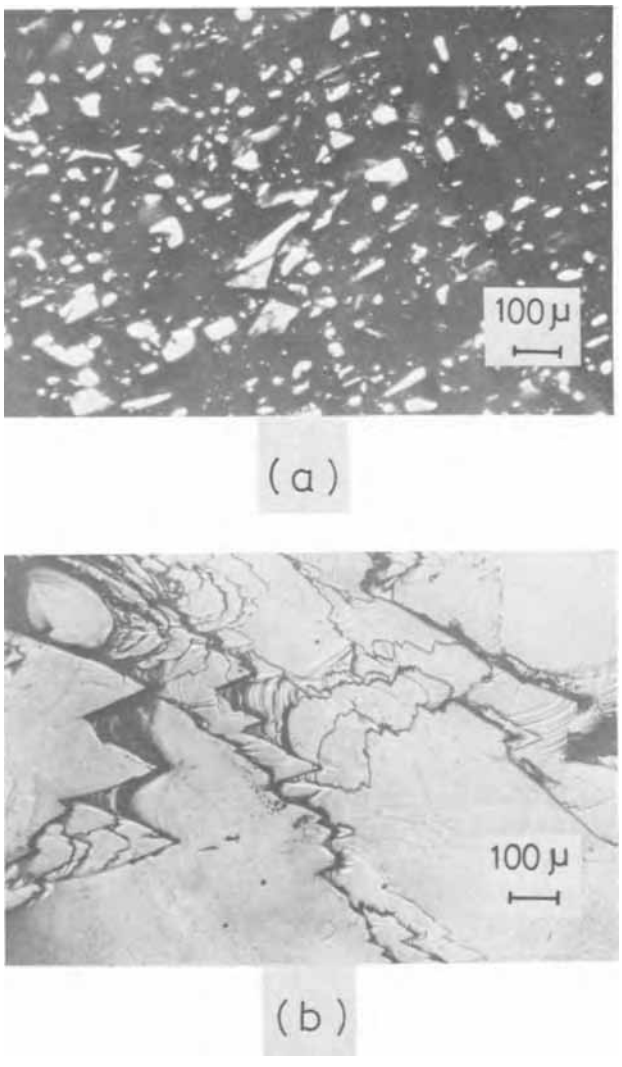

Fig. 2. Surfaces of the layers grown on (a) (100) and (b) (111)A faces of GaAs substrates.

smaller than 1.0, wavy patterns, which are peculiar to solution-grown crystals, were found. When AR was larger than 10, the surfaces were rough and dendritic. Besides the effects of AR, smaller cooling rates and higher maximum growth temperatures resulted in smoother surfaces, although their effects were much weaker than the effects of AR. As for the thickness d of the grown layer, it depended on T_M; *i.e.*, d is $\sim 80\mu$ for $T_M = 800°C$ and $\sim 40\mu$ for $T_M = 700°C$.

In order to clarify the crystalline quality of the grown layer, an electron diffraction study was performed. When AR was smaller than 30, a spot pattern as shown in Fig. 4 was observed, which indicated that the grown layer was a single crystal and had the (111) plane, the same orientation as that of the GaAs substrate. When AR was over 30, a Debye-Scherrer ring was observed, which revealed that the grown layer was polycrystalline.

The composition of the grown $In_xGa_{1-x}As$ layer was studied by two methods; *i.e.*, (a) using an X-ray Micro-Analyzer (X.M.A.) and (b) studying the photocurrent-spectrum of the pn $In_xGa_{1-x}As$ homojunction (9). In the first method, an electron beam microprobe ($\sim 2\ \mu\phi$) scanned the cross section of the grown layer at every 2μ. One example of the X.M.A. data is shown in Fig. 5 for the layer of AR = 10. From the data, the composition x in the grown layer was calculated as shown in Fig. 6, and the growth parameters used were as follows: AR = 10, cooling rate was 1°C/min or 15°C/min, and T_M was 700°C or 800°C. It is observed from Fig. 6 that the transition of the composition at the GaAs-$In_xGa_{1-x}As$ interface is almost abrupt and that x is almost constant in the middle of the layer and decreases toward the surface of the layer. In addition, a faster cooling rate and a lower maximum growth temperature (T_M) give a larger x-value. This is because a long growth time and a higher T_M result in the deficiency of As in the solution which makes the x-value low, as indicated in the phase diagram of $In_xGa_{1-x}As$ by Stringfellow and Greene (10). This is also the reason why the x-value was so small in the grown crystal, even when the AR-value was very large in the solution.

In the second method, a pn $In_xGa_{1-x}As$ homojunction was prepared by diffusing Zn into an undoped $In_xGa_{1-x}As$-grown layer. The Zn diffusion process was performed at 700°C for 0.5-1 hr in a closed quartz ampoule with the As vapor pressure of 1 atm. The photocurrent spectrum of the pn $In_xGa_{1-x}As$ homojunction had a sharp peak, as shown later in this paper. From the wavelength of the peak, the band gap, E_g, of the $In_xGa_{1-x}As$ layer was calculated. Then, x was deduced by assuming the linear relationship between E_g and x, although this assumption is a little inaccurate (2). In Table I, the obtained values of E_g and x were shown as a function of AR. In the table, the x-values for AR = 10 have been derived from the X.M.A. study shown in Fig. 6, while those for AR = 0.1, 1, 20, and 30 (in the brackets) have been deduced approximately from this assumption. When AR was over 30, the grown layer was found to be polycrystalline as mentioned previously. Hence, the upper limit of x in the present growth technique is 0.2 for $In_xGa_{1-x}As$ single crystal.

The 5° angle-lapped section of the interface between the (111)B substrate and the grown $In_xGa_{1-x}As$ layer was investigated after staining it in a HF(50 cm^3) + HNO_3 (1 or 2 drops) solution. As shown in Fig. 7, the interface was flat. The flatness was independent of the cooling rate, T_M, and AR-value. Furthermore, to study the crystalline imperfections at the interface and in the $In_xGa_{1-x}As$ layer, a (111)A bevel-lapped section that was at an angle of 70.5° to the (111)B surface of the grown layer and 35.2° to the (110) cleavage plane was etched in a $HF+3HNO_3+2H_2O$ solution. Figure 8 shows the distribution of etch pits which appeared on the etched (111)A face. There were less etch pits in the grown layer than in the substrate. It is evident, therefore, that the solution-grown $In_xGa_{1-x}As$ layer had a lower dislocation density and a better crystalline quality than the GaAs substrate crystal. However, a great many etch pits were found at the interface. These etch pits may in part result from the misfit dislocations which compensate the lattice mismatch between GaAs and $In_xGa_{1-x}As$, as reported by Grenning for GaAs-$GaAs_xP_{1-x}$ heteroepitaxy (11).

Table I. Energy gaps and "x" values of the grown $In_xGa_{1-x}As$ layers. Cooling rate was 1 deg/min

	AR	0	0.1	1	10	20	30
T_M = 700°C	E_g (eV)	1.40	~1.40	~1.39	1.29	1.25	1.23
	x	0	(~0)	(~0.01)	0.15	(0.18)	(0.20)
T_M = 800°C	E_g (eV)	1.40	/	/	1.30	1.26	1.23
	x	0	/	/	0.11	(0.16)	(0.20)

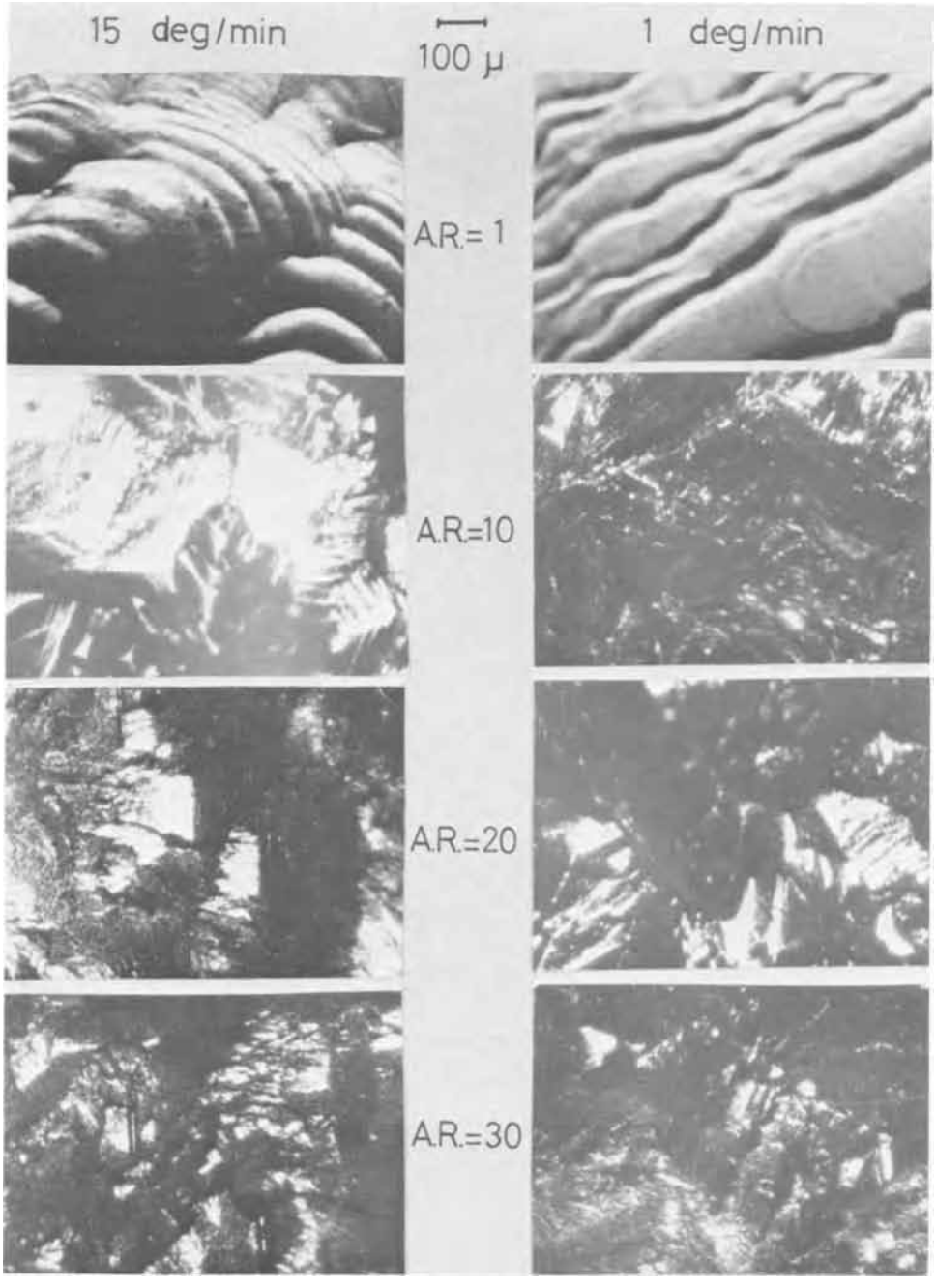

Fig. 3. Variations of the surfaces of the layers grown on (111)B substrates with the various In:Ga atomic ratios in the solution. The maximum growth temperature, T_M, was 700°C and cooling rate was 15 deg/min or 1 deg/min.

Electrical Properties

The electrical parameters of the $In_xGa_{1-x}As$ layer grown on a semi-insulating GaAs substrate—i.e., resistivity ρ, Hall mobility μ_H and carrier concentration n—were obtained from Hall measurements by the van der Pauw method at room temperature (12). The growth conditions were as follows: T_M was 700°C and the cooling rate was 15°C/min or 1°C/min. For accuracy of measurements, some humps on the grown layers were lapped off with No. 4000 abrasive and 0.3μ Linde-Alumina, and then mechanical-chemical polishing was performed. For the lead wires, 50 μ ϕ Au wires were spot-welded at four corners of the grown layer. The conduction type of the grown layers was found to be n-type. Figure 9 shows the results of electron mobility μ_H and electron concentration n which have been plotted as a function of AR. The electron concentration n decreased with the increase of AR, while μ_H remained almost constant. Although AR = 0-30 corresponds to x = 0-0.2, μ_H did not increase in this composition range in spite of the expectation mentioned previously. This is partially due to the impurity compensation effect, as deduced from the decreasing electron concentration with the increase of AR.

Impurity Doping

Attempts were made to dope acceptor impurities, Zn or Ge (10 mg, each), into the solution to obtain a p-type layer. When Zn was doped into the $In_xGa_{1-x}As$ layer which was grown on an n-type GaAs ($n \simeq 10^{17}$ cm^{-3}), a p · $In_xGa_{1-x}As$-n · GaAs heterojunction was formed. Its photoresponse will be taken up later in this report.

It has been reported that Si is an amphoteric impurity in GaAs (13-15) and a pn junction can be made in the solution-grown GaAs layer with Si as the dopant on both p- and n-type sides of the junction (14). On the other hand, although Ge is also an am-

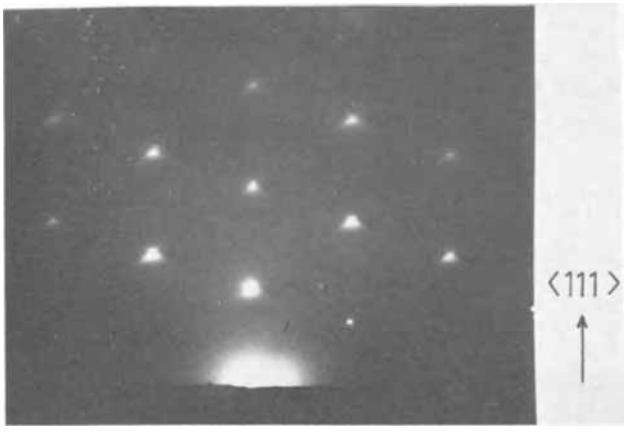

Fig. 4. Electron diffraction pattern of the (111)B surface of $In_xGa_{1-x}As$-grown layer. T_M = 700°C, AR= 10, and cooling rate = 15 deg/min.

photeric impurity, only a p-type layer can be obtained in the solution-grown Ge-doped GaAs (15, 16). However, the present work revealed that when Ge was doped into the $In_xGa_{1-x}As$ crystal, a pn junction appeared in the grown layer. Hence, the same effect as found upon doping Si in GaAs occurred upon doping Ge in $In_xGa_{1-x}As$. It has been suggested that for the solution growth of GaAs the arsenic vapor pressure in the solution determines which of the lattice sites Si atoms or Ge atoms enter (13, 14). If Si atoms or Ge atoms enter a Ga lattice site, an n-type is obtained, and similarly a p-type GaAs is obtained when Si atoms or Ge atoms enter an As lattice site. Moreover, as indicated by the present study, the addition of In to GaAs can also control the behavior of Ge. As In has a larger tetrahedral radius than Ga or As (17), Ge can enter an In site more easily than enter an As or a Ga site. It follows, therefore, that the increase of In atoms in $In_xGa_{1-x}As$ makes Ge enter a III-atom site as a donor, resulting in an n-type $In_xGa_{1-x}As$. However, as the furnace temperature is lowered, the arsenic vapor pressure in the solution is reduced so much that Ge substitutes as an acceptor into the arsenic site. Hence a p-$In_xGa_{1-x}As$ appeared at the end of the growth, and a pn junction was formed in the grown layer.

When T_M was lowered to 600°C, a p-type $In_xGa_{1-x}As$ could be grown directly on the substrate by doping with Ge. Thus, by the proper choice of T_M, a pn $In_xGa_{1-x}As$ homojunction or a p · $In_xGa_{1-x}As$-n · GaAs heterojunction can be made. The photocurrent spectra of both junctions are shown in Fig. 10 together with the spectra of the Zn-doped p · $In_xGa_{1-x}As$-n · GaAs heterojunction and the Zn-diffused pn $In_xGa_{1-x}As$ homojunction. The Ge-doped junctions had larger photoresponses at wavelengths ~ 1μ than Zn-doped junctions. This fact can be attributed to deep Ge acceptor levels, as observed in Si-doped GaAs pn junctions (15).

Conclusion

The epitaxial growth of the $In_xGa_{1-x}As$ layer on a GaAs substrate was achieved by Nelson's solution growth. The solution consisted of In, Ga, and polycrystalline GaAs. When AR (In:Ga atomic ratio) in the solution varied from 0.0 to 30, single-crystalline $In_xGa_{1-x}As$ of the composition x ranging from 0.0 to 0.2 was grown. When x was over 0.2, the grown layer was polycrystalline. The same result has been reported recently by Antypas (7), although the substrates used have (111)A faces of GaAs. In those cases, the x value was very small in the grown crystal in comparison with the value of AR in the solution. This is due to the deficiency of As in the solution.

The crystalline quality of the $In_xGa_{1-x}As$-grown crystal was found to be good from a microscopic ob-

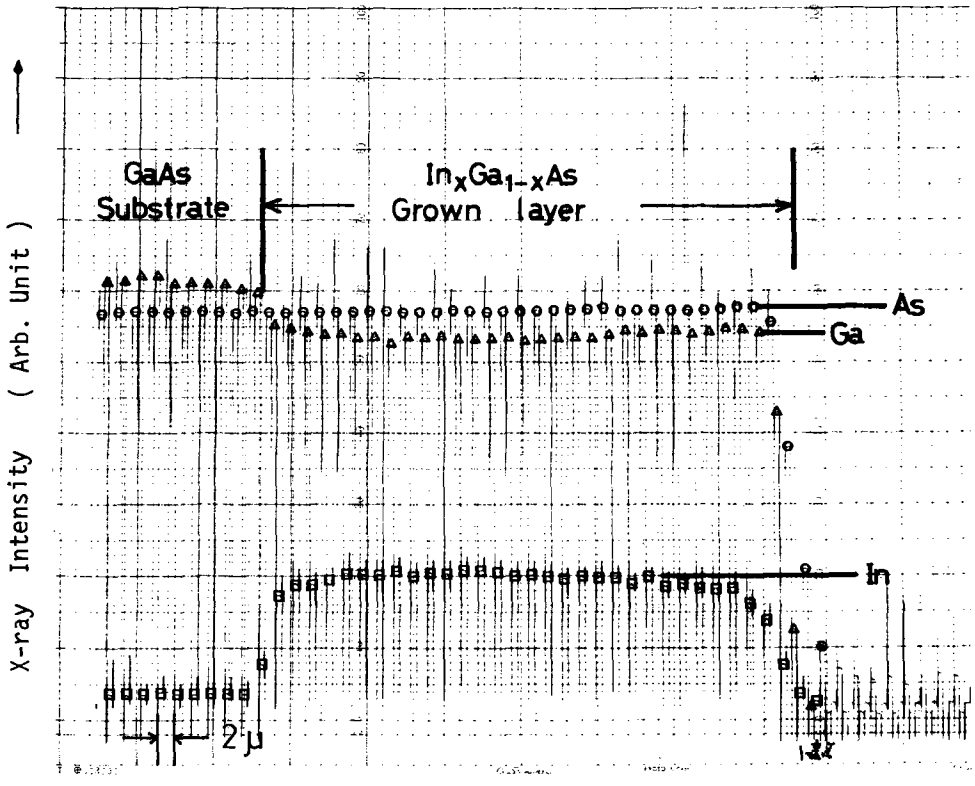

Fig. 5. X.M.A. data of the $In_xGa_{1-x}As$-grown layer when AR = 10, cooling rate was 15 deg/min and T_M = 800°C. Scanning spot: 2 $\mu\phi$. Scanning step: 2μ.

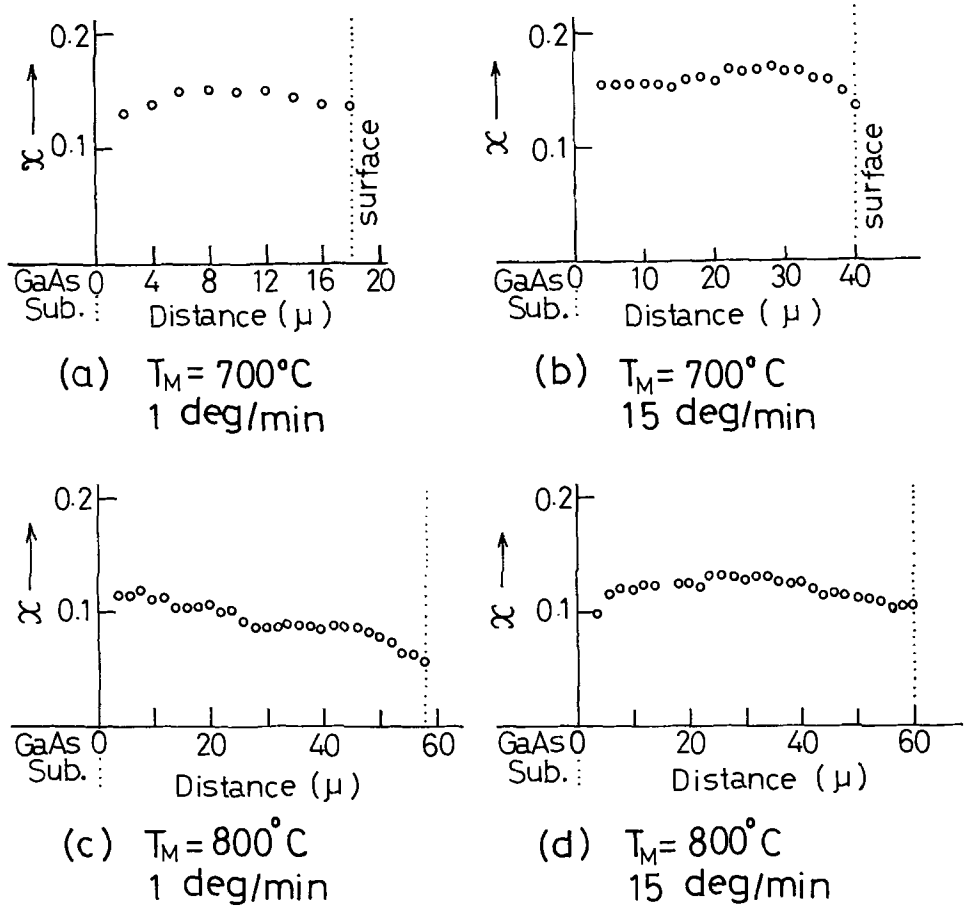

Fig. 6. Composition profiles of the grown layers obtained from X.M.A. data. The growth parameters were: AR = 10, cooling rate = 1 deg/min or 15 deg/min, and T_M = 700°C or 800°C. The In content, x, was shown as a function of the distance from GaAs substrate along the growth direction.

servation and an electron diffraction study. Moreover, etch pits distribution in the bevel-lapped section revealed that the number of defects was smaller in the grown layer than in the substrate. Hence, a good heteroepitaxy was achieved.

Hall measurements of the grown $In_xGa_{1-x}As$ layers were made, and the variations of the electrical parameters, ρ, μ_H, and n, as a function of AR were studied. It was found that an undoped $In_xGa_{1-x}As$ was of n-type, whose electrical parameters were $\rho \simeq 10^{-2}$ ohm-cm, μ_H = 4000-5000 $cm^2/V \cdot sec$, and $n \simeq 10^{17}$ cm^{-3} at room temperature and did not vary much with the increase of AR. To increase the electron mobility, it is necessary to improve the growth technique so that a larger x-value can be achieved.

Ge was found to be an amphoteric impurity in the solution-grown $In_xGa_{1-x}As$ crystal. By the proper choice of T_M, the layer containing a pn junction or a p-type layer was obtained by doping Ge. Moreover, it has been found that by changing x, a p-type or an n-type layer can be grown easily by doping a proper amount of Ge. It seems reasonable to suggest that Ge tends to enter into an In site and hence, x determines into which site more Ge atoms enter, a III-atom site or a V-atom site. The details of Ge-doped $In_xGa_{1-x}As$ will be reported later.

Acknowledgments

The authors wish to express their appreciation to Professor Y. Sakai for his valuable suggestions and en-

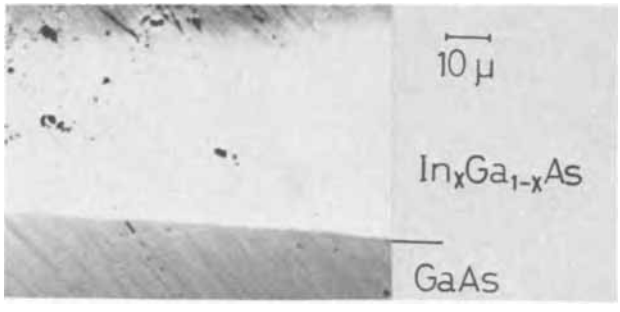

Fig. 7. Stained section with an angle of 5° lapped off. T_M = 700°C and cooling rate = 1 deg/min.

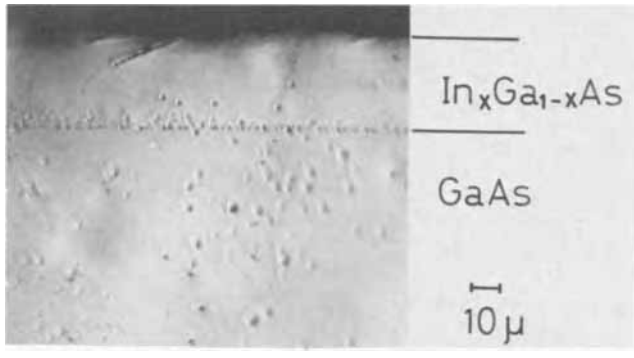

Fig. 8. Distribution of etch pits on the (111)A bevel-lapped section.

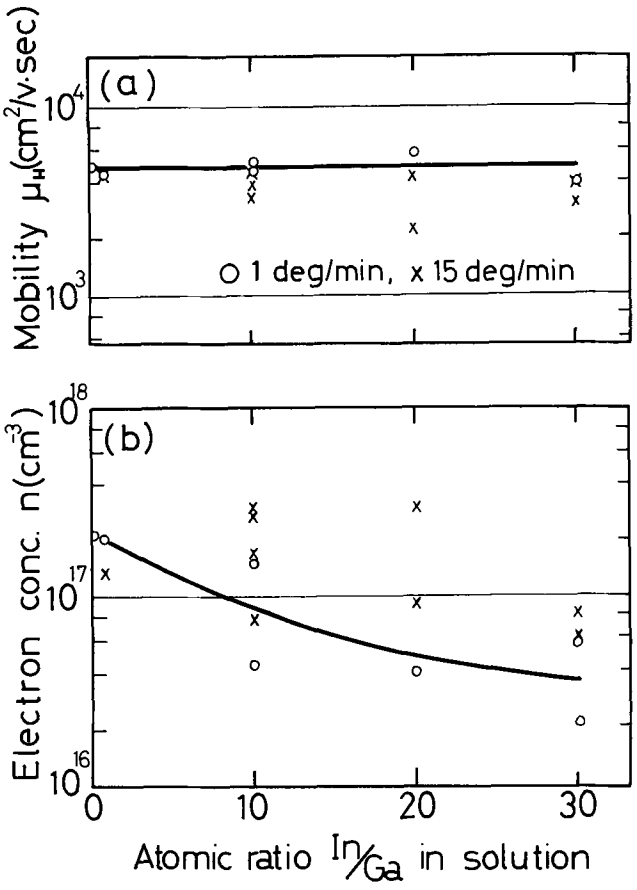

Fig. 9. The variations of electrical parameters, (a) Hall mobility, μ_H, and (b) electron concentration, n, of $In_xGa_{1-x}As$-grown layer as a function of the atomic ratio In/Ga in the solution. The electron concentration was estimated, assuming $n = 1/q\rho\mu_H$ (q is the electronic charge). The range of AR = 0-30 corresponds to that of $x = 0.0$-0.2.

couragement during the course of this work. They also wish to thank M. Kurihara for his assistance in preparing the samples.

Manuscript submitted Feb. 16, 1971; revised manuscript received *ca.* May 12, 1971. This was Paper 85 presented at the Washington, D. C., Meeting of the Society, May 9-13, 1971.

Any discussion of this paper will appear in a Discussion Section to be published in the June 1972 JOURNAL.

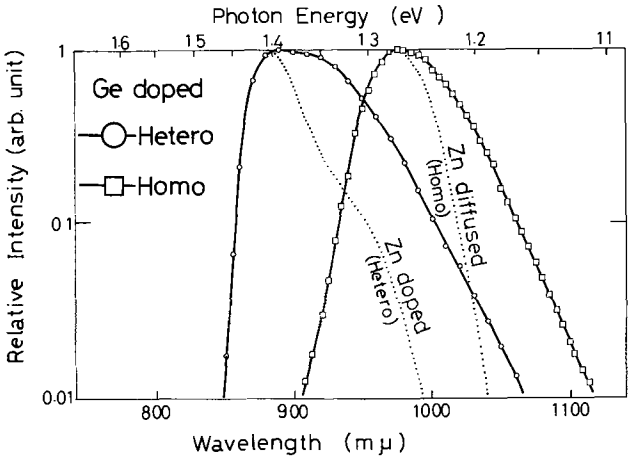

Fig. 10. Photoresponse spectra of the Ge-doped p-$In_xGa_{1-x}As$-n-GaAs heterojunction and the Ge-doped $In_xGa_{1-x}As$ pn homojunction. For the sake of reference, that of a Zn-doped heterojunction and a Zn-diffused homojunction are also shown. AR = 10 and cooling rate = 1 deg/min.

REFERENCES

1. I. Melngailic, A. J. Strauss, and R. H. Rediker, *Proc. IEEE*, **51**, 1154 (1963).
2. E. F. Hockings, I. Kudman, T. E. Seidel, C. M. Schmelz, and E. F. Steigmeier, *J. Appl. Phys.*, **37**, 2879 (1966).
3. J. C. Wooley, C. C. Gillett, and J. A. Evans, *Proc. Phys. Soc. (London)*, **77**, 700 (1961).
4. M. S. Abrahams, R. Braunstein, and F. D. Rosi, *J. Phys. Chem. Solids*, **10**, 204 (1959).
5. R. W. Conrad, P. L. Hoyt, and D. C. Martin, *This Journal*, **114** 164 (1967).
6. J. W. Wagner, *ibid.*, **117**, 1193 (1970).
7. G. A. Antypas, *ibid.*, **117**, 1393 (1970).
8. H. Nelson, *R C A Rev.*, **24**, 603 (1963).
9. S. Shirose, T. Moriizumi, and K. Takahashi, *Proc. Appl. Phys. Meet. of Japan*, No. 2, p. 103 (1969).
10. C. B. Stringfellow and P. E. Greene, *J. Phys. Chem. Solids*, **30**, 1779 (1969).
11. D. A. Grenning, *J. Appl. Phys.*, **39**, 2783 (1968).
12. J. van der Pauw, *Philips Res. Rep.*, **13**, 1 (1958).
13. R. F. Brebrick, *J. Appl. Phys.*, **33**, 422 (1962).
14. H. Rupprecht, J. M. Woodall, K. Konnerth, and D. G. Pettit, *Appl. Phys. Letters*, **9**, 221 (1966).
15. T. Moriizumi and K. Takahashi, *Japan. J. Appl. Phys.*, **8**, 348 (1969).
16. F. E. Rosztoczy, F. Ermanis, I. Hayashi, and B. Schwartz, *J. Appl. Phys.*, **41**, 264 (1970).
17. C. Hilsum and A. G. Rose-Innes, "Semiconducting III-V Compounds," p. 6, Pergamon Press, New York (1961).

Analysis of Impurity Distribution in Homoepitaxial n on n^+ Films of GaAs. II

J. V. DiLorenzo*

Bell Telephone Laboratories, Incorporated, Murray Hill, New Jersey 07974

ABSTRACT

The nature and cause of a high-resistivity region (*i* layer) at the interface of n-type GaAs on bulk n^+ GaAs have received the attention of many workers in the field. Our previous investigations of impurity distributions of n^+ GaAs films on n^+ bulk GaAs substrates by Direct Image Mass Analysis (DIMA) have correlated a high concentration of silicon with a high-resistivity region at the interface. Further analysis of the impurity distribution in epitaxial layers grown on bulk substrates and epitaxial layers grown on buffer layers (epitaxial layers doped to the mid-10^{17} cm^{-3} range) by vapor phase epitaxy and liquid phase epitaxy have been performed. The main conclusions of the present analysis are: (*A*) The buffer layer is effective in isolating the lightly doped n layer from segregated impurities at the buffer-substrate interface. (*B*) Group I and Group II elements have a great affinity for GaAs surfaces. (*C*) Preliminary observations on impurity "clusters" indicate that complicated impurity interactions may be present in GaAs. (*D*) The occurrence of a high concentration of silicon at the interface of epitaxial GaAs is definitely established.

We have recently reported (1) on the analysis of impurity distribution of n on n^+ epitaxial films of GaAs. The analysis was done using a Direct Image Mass Analyzer (DIMA). These films contained high resistivity regions between the epitaxial film and substrate (2-5). This region, called the *i* layer, was found to contain the localized impurities potassium, lithium, chlorine, iron, and silicon. A correlation was obtained between a high localized concentration of silicon at the interface and the appearance of the *i* layer.

In this paper we report on further analysis, using the DIMA, of the impurity distribution of several films of epitaxial GaAs doped in the mid-10^{15} cm^{-3} range grown by either vapor phase epitaxy (VPE) or liquid phase epitaxy (LPE). These films were grown on either bulk GaAs substrates or epitaxial GaAs substrates (buffer layer).

The data obtained confirm the previous conclusions that silicon, as well as other impurities, has a tendency to localize at the interface. In addition, several films showed the appearance of impurity "clusters," i.e. areas of high local concentration of an impurity. Definite correlations are obtained between absence or presence of impurities at the interface and the cleaning history of that wafer.

Experimental

Growth procedures.—The VPE layers of GaAs were grown using the $AsCl_3|Ga$ (saturated with GaAs)$|H_2$ synthesis system (6). Details of the handling and cleaning procedures have been previously given (1). The buffer layers, that is epitaxial layers doped to the 5×10^{17}-10^{18} cm^{-3}, and the lightly doped layers were grown in a continuous fashion. The buffer was doped with sulfur to the mid 10^{17} to 10^{18} cm^{-3} range.

The LPE film, LA039, was grown using a dipping system which has been previously described (7).

Substrates were either silicon, selenium, or tellurium doped boat grown or Czochralski grown ingots.

Analytical technique.—The DIMA technique has been previously described (1). Briefly, it is worth noting the three types of information which are obtained from this technique. Ion images are obtained which show the lateral distribution of a particular impurity and the continuous change in that distribution with depth (see Fig. 3-7). Secondly, in depth changes of the concentration of a particular impurity are read out as current on the y-axis and time, i.e. depth, on the x-axis (see Fig. 1 and 2). Finally, recorded mass spectra of elements from mass 1 through 70 at some depth greater than 1μ into the film were obtained. This is useful as a qualitative chemical analysis for impurities located at that depth.

Results

Film properties.—The properties of the films are listed in Table I. The net donor concentration of the films, n, and of the *i* layer, n_i, listed in Table I, were obtained by the continuous profiling technique described by Copeland (8). Two of the films (D185 and LA039), which were grown directly on bulk substrates, have *i* layers (defined as $[(n - n_i)/n] \times 100$) ranging from 0-13% for D185 to 15-45% for LA039.

Chemical analysis.—A total number of 39 craters (or "burns"), approximately 300μ in diameter were

Table I. Film properties

	Subs. dopant	Buffer thickness (microns)	Epitaxial layer thickness (microns	n carrier conc. in film (cm^{-3})	n_i carrier conc. in *i* layer (cm^{-3})	$[(n - n_i)/n] \times 100$	Film dopant	Buffer dopant
E 532	Si	5.9	6.5	$3\text{-}4 \times 10^{15}$	$3\text{-}4 \times 10^{15}$	0	Undoped	Sulfur
D 185	Si	None	2.7	1.5×10^{15}	$1.5\text{-}0.95 \times 10^{15}$	0-13%	Undoped	—
K 21	Te	10.9	6.5	5×10^{16}	5×10^{16}	0	Undoped	Sulfur
D 203	Se	7.9	6.2	$4\text{-}5 \times 10^{16}$	$4\text{-}5 \times 10^{16}$	0	Undoped	Sulfur
J 70	Si	12.4	5.0	9×10^{14}	9×10^{14}	0	Undoped	Sulfur
BB 273[a]	Unknown	None	39.5	$\approx 10^{16}$	Unknown	—	Undoped	—
LA 039	Sn	None	7.9	2×10^{15}	$1.7\text{-}1.1 \times 10^{15}$	15-45%	Undoped	—

[a] Sample grown using the $HCl/Ga/AsH_3$ system.
Source: A. E. Blakeslee, I.B.M., Yorktown Heights, New York.

* Electrochemical Society Active Member.
Key words: mass analysis, ion image analysis.

Table II. Impurities found in the samples and localized at the interface

Sample	Impurities in film[a] Si	Cr	Fe	Mg	Ca	K	Na	Al	C	H	Cl	Mn	Impurities localized at interface	Comments
K21 VPE	+	+		+	+D	+D	+	+	+D	+D	+		Not looked for	
LA039 LPE	+D	+N	+	+	+	+D	+D	+N	+		+D		Ca, Al, K	Al and Cr clusters, strong i layer localization of Ca
D185 VPE	+D	+D	+D			+D	+D	+D	+		+D		Na, K, Ca, Si	High concentrations of Na, Si at interface chelated and *in situ* etched
J70 VPE	+D	+D	+D	+	+	+	+	+	+			+	Na, Ca, K, Si	High concentrations of Na, K, Ca at interface. Not *in situ* etched
E532 VPE	+	+D	+D	+	+		+	+	+		+		Na	High concentrations of Na in film, *in situ* etched
BB273 VPE (AsH_3)		+D	+D	+	+	+	+	+		+		+	Not looked for	Very high concentrations of Na and K in film
D203 VPE	+	+	+	+	+	+	+	+	−	−	−		Na, Ca, K, Si	Sample chelated and *in situ* etched

[a] = Impurities were either found by a recorded MASS Spectrum (Mass 1—68) or Visual.
For visual observation: +D = found, diffuse in sample; +N = found, nonuniform; − = not found but looked for; blank = not looked for.

made by sputtering with O_2^+. The minimum average number of burns for each sample was four.

A list of impurities found in the samples at the interface between the epitaxial layer and bulk substrate are presented in Table II. The impurities were observed either by recording a mass spectrum at a depth of approximately 2μ below the surface of the film or by observing the impurities visually by ion imaging. In the latter case the impurity is either noted by a *D* for diffuse in the film or by an *N* for nonuniform. In addition, in depth distributions of various elements were made as outlined in Ref. (1). Representative traces of the in depth distribution of various impurities are shown in Fig. 1 and 2. The numerical scale on the *x*-axis of each trace is the scale obtained by dividing the total crater depth by the total time of burn. Errors as large as 20% in the optical determination of the crater depth are possible (1). The vertical line between the words epi and substrate is the position of the interface as determined by angle lap and strain.

Impurities found.—Silicon and sodium.—In Fig. 1c the silicon signal from sample D185 is reproduced. The appearance of a large silicon signal at 4.5μ, in reasonable agreement with the interface, is apparent. As mentioned above, we believe the error in determining the crater depth accounts for the discrepancy between the peak and interface position. Note also the greater signal for silicon in the substrate compared to the epitaxial films. By similar determinations silicon signals for samples D185, D203, and J70 were observed at the interface. For samples D185, D203, E532, and J70, a

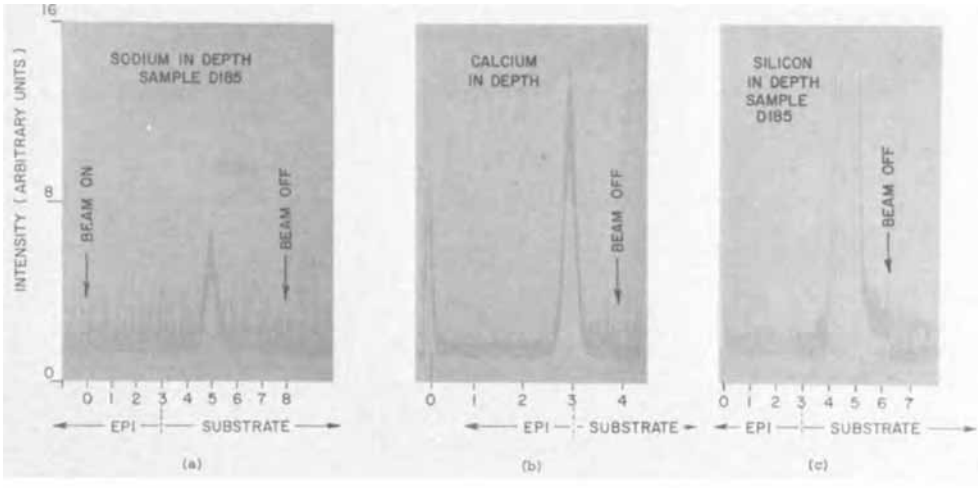

Fig. 1. Profiles of the sodium distribution (a) calcium distribution (b) and silicon distribution (c) in sample D185.

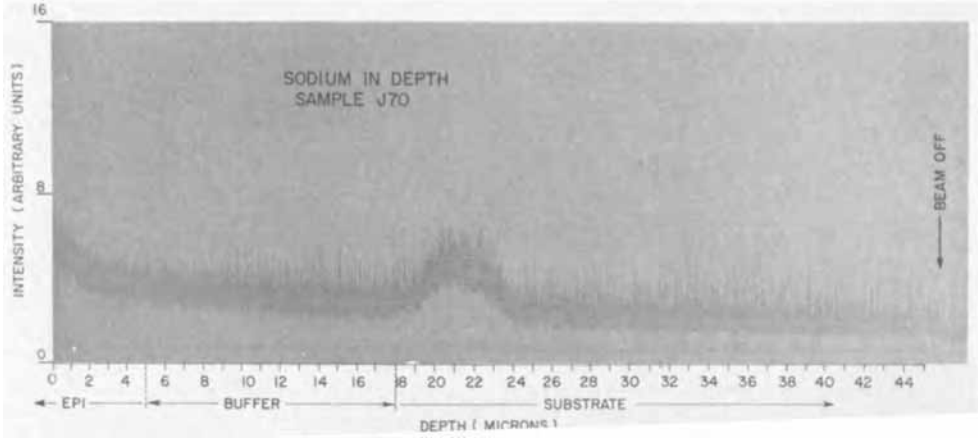

Fig. 2. Profile showing the sodium distribution in sample J70.

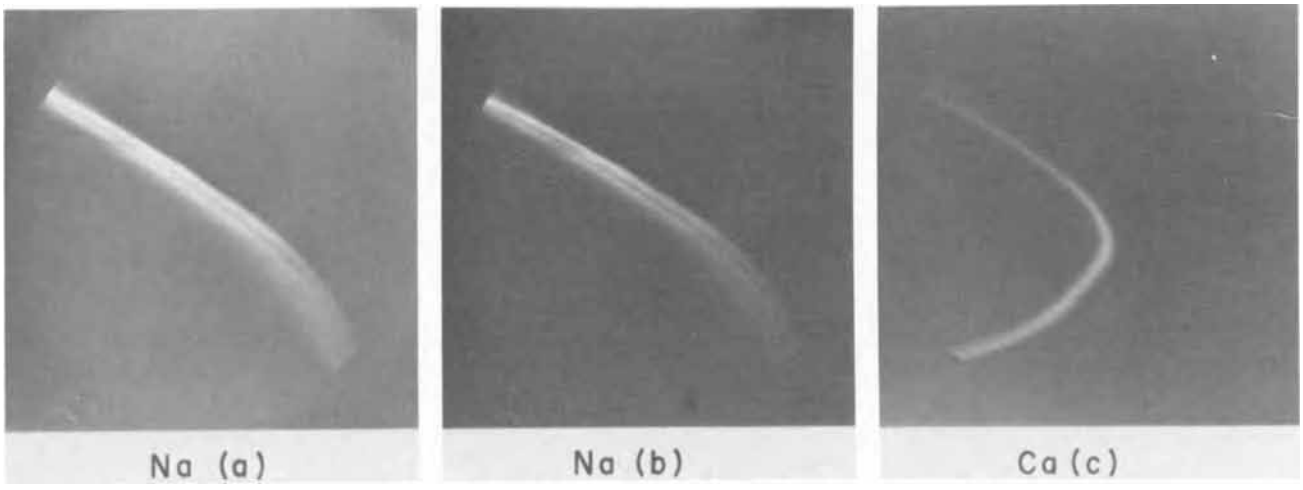

Fig. 3. Ion images from sodium (Na^+) in samples D185 (a) and D203 (b) and calcium (Ca^+) in sample J70 (c).

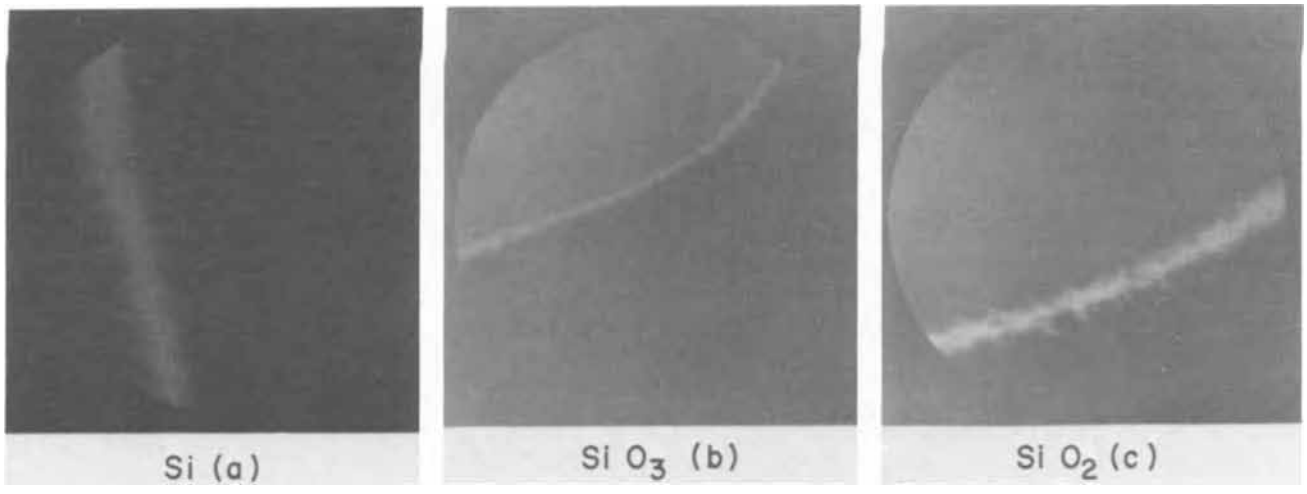

Fig. 4. Ion images from (a) Si^+, (b) SiO_3^-, and (c) SiO_2^- in samples D185.

high concentration of sodium occurs at the epi-substrate or buffer-substrate interface. The sodium concentration at the buffer-substrate interface of sample E532 is lower relative to the other samples.

Calcium.—A representative trace of the signal resulting from a localization of calcium at the interface of sample D185 is shown in Fig. 1b. Sample E532 shows no calcium at the interface both by in depth analysis and ion image analysis (see Table II). Sample LA039 shows the appearance of a high concentration of calcium at the interface ($\simeq 5\mu$) as well as an area rich in calcium ($\approx 1.5\mu$) below the surface.

Ion image analysis.—As discussed previously (1), the ion images appearing from an impurity localized at an interface appear as a white "band" of new moon-like character, defining the interface. Contrast effects on the concave side of the ring are due to the substrate while those on the convex side are due to the film.

In Fig. 3-5 ion images from various species located at the interface are presented. In Fig. 6 the appearance of "impurity clusters" in sample LA039 is shown. Figure 7 shows the aluminum nonuniformity in the substrate of sample J70.

Table III.

Sample	Beaker etch	*In situ* etched	Chelated
D185	Yes	Yes	Yes
D203	Yes	Yes	Yes
E532	Yes	Yes	No
J70	Yes	No	No

Discussion

Our previous observations (1) of a high concentration of silicon at the interface are further substantiated by the data shown in Fig. 1c and Fig. 4 for sample D185. Definite confirmation was obtained that the signal at mass 28 is Si^+ (and not CO^+ for example which has a mass 28). Oxygen sputtering was used and images corresponding to the masses for Si^+, SiO_2^-, and SiO_3^- species were obtained. (The compound negative ions SiO_2^- and SiO_3^- are assumed to arise chemically from a Si + O_2 reaction.) The ion images for these ions from sample D185 are shown in Fig. 4. The data clearly indicate that silicon is the impurity present at the interface.

We have observed a definite correlation between the cleaning history of a sample and impurity localization. The complete cleaning details of the samples D185, D203, J70, and E532 are given in the Appendix. The samples were given either of the treatments listed in Table III. The "chelation" step was performed because of prior work which suggested that this was useful to remove heavy metal surface contamination (4) (copper, iron, etc.).

From the data in Fig. 1-7 and Table II, the following conclusions concerning the contamination of elements at the interface for the samples were reached

D185 (Na,K,Ca) = D203 (Na,K,Ca)
> J70 (Na,K,Ca) > E532 (Na, low)

It seems clear that the introduction of the "chelating" step greatly increased the contamination of Group I and II elements at the interface. This is despite ex-

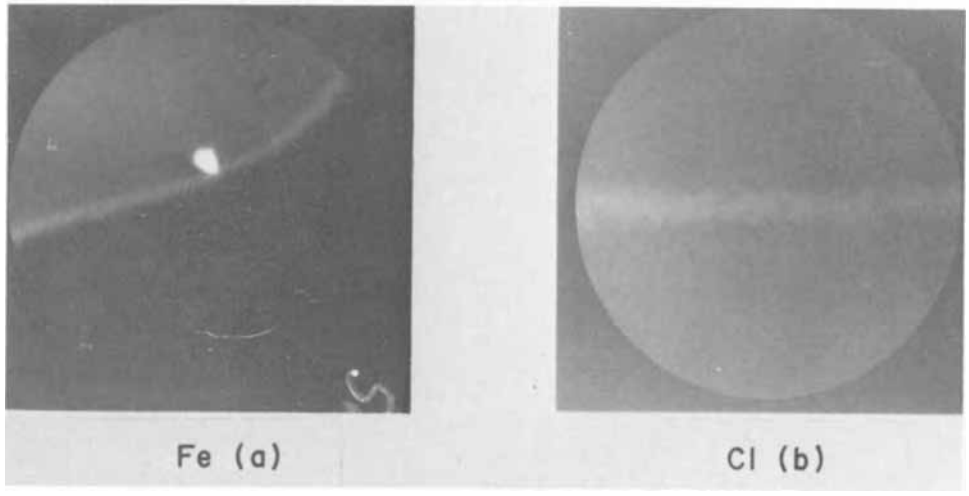

Fig. 5. Ion images from iron (Fe^+) and chlorine (Cl^-) in sample D185.

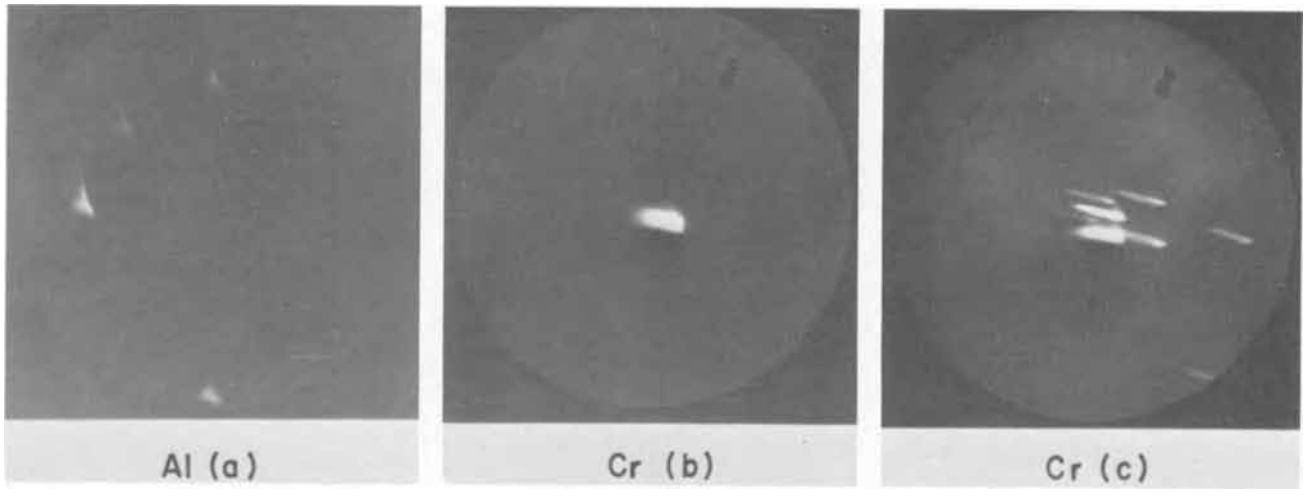

Fig. 6. Ion images from aluminum (Al^+) (a), chromium (Cr^+) (b) (c) in sample LA039.

tensive rinsing in 18 megohm-cm water after treatment. Also *in situ* etching greatly reduces the surface contamination as evidenced by the very clean interface of sample E532 compared to J70 (Table II and Fig. 3).

However, photoluminescence data (9) indicates that the order of copper contamination in these samples is

$$D185 < E532 < J70$$

Therefore, although we removed surface copper contamination by use of the chelation step, Group I and II element contamination was observed.

As assumed, the buffer layer is effective in providing a protective layer between the bulk substrate and lightly doped region for the impurities observed (see Fig. 2 for example).

The iron image shown in Fig. 5 shows three interesting features: (*A*) The high concentration of iron in the substrate contrary to the manufacturer's claim (10). (*B*) The localization of a high contamination of iron (white spot). (*C*) Buildup of iron at the interface. The cause of iron "clump" is not known.

Although preliminary, the data presented in Fig. 6 are quite interesting. Figure 6a shows aluminum ion images from sample LA039, while chromium images are shown in 6b and c. The results indicate that large ($\approx$10-30μ) "clusters" of aluminum or chromium rich

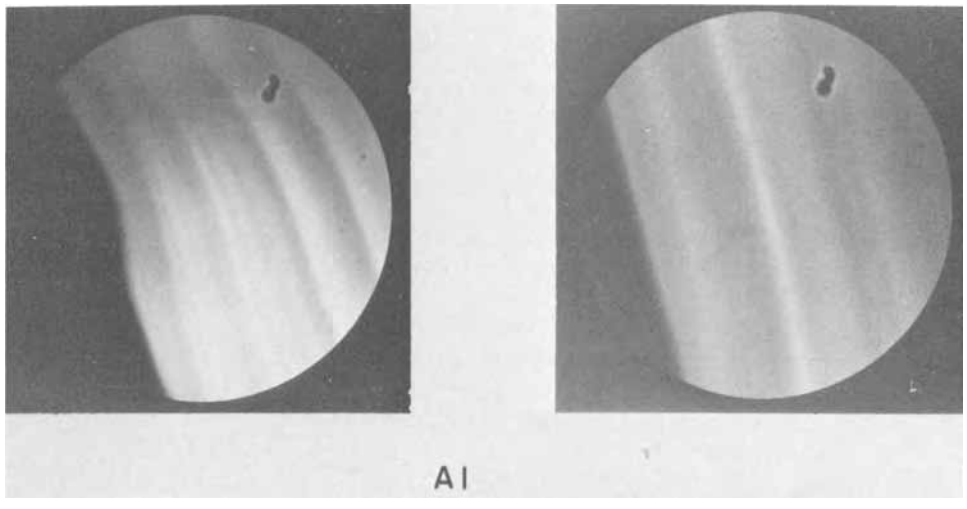

Fig. 7. Ion images from aluminum (Al^+) in substrate of sample J70.

areas are present. Note also the nonuniform distribution of chromium indicated by the nonuniform contrast in Fig. 6c. This data was obtained on only one sample, and the generality of this nonhomogeneous distribution is not known.

Also interesting is the nonuniformity of aluminum in the substrate of sample J70. This substrate was grown by the Czochralski process and was tin-doped. Presumably the impurity striations arise from impurity segregation known to occur in Czochralski crystals. Similar to the observation made on iron above, aluminum was not indicated by the manufacturers (11) as an impurity present in the ingot.

Summary and Conclusions

The continuing analysis of impurity distribution in epitaxial GaAs have led to the following conclusions: (*A*) The occurrence of a high concentration of silicon at the interface of epitaxial GaAs is definitely established. (*B*) The "buffer" layer is effective in isolating the lightly doped layer from segregated impurities at the interface. (*C*) Group I and II elements have a great affinity for GaAs surfaces. (*D*) Preliminary observations on impurity "clusters" suggest that complicated impurity interactions may be present in GaAs.

Acknowledgments

We wish to thank A. Machala for growing some of the epitaxial samples. We wish to especially thank R. Lewis, while at Bell & Howell for performing the analysis on the DIMA. We also wish to thank S. Knight for extensive discussion of these results, and also A. E. Blakeslee, L. R. Dawson, and W. A. Johnson for providing some of the epitaxial wafers.

Manuscript submitted Feb. 22, 1971; revised manuscript received June 1, 1971.

Any discussion of this paper will appear in a Discussion Section to be published in the June 1972 JOURNAL.

APPENDIX

Preepitaxial Cleaning Procedures of Substrates for Samples D185 and D203

1. Boil in acetone 3 times.
2. Boil in trichloroethylene 3 times.
3. Boil in acetone 2 times.
4. Boil in isopropanol 3 times.
5. Rinse in 17-18 $\times$ 10^6 ohm-cm water 5 min.
6. Etch in $5H_2SO_4$: $1H_2O$: $1H_2O_2$ for 2 min.
7. Rinse in 17-18 $\times$ 10^6 ohm-cm water for 15 min.
8. Soak in 10% by weight solution of sodium ethylene-diamine-tetraacetate at (pH = 7) for 45 min.
9. Rinse in rapidly flowing 17-18 $\times$ 10^6 ohm-cm water for 20 min.
10. Immerse in isopropanol.
11. Load into the reactor from isopropanol wet and dry in hydrogen.
12. Etch *in situ* with HCl removing 7-10μ of substrate.

Preepitaxial Cleaning Procedures of Substrates for Samples E532 and J70

1. Acetone soak 5 min (ultrasonic agitation).
2. Cohben[1] boil for 3 min (ultrasonic agitation).
3. Rinse in methanol.
4. Boil in methanol 3 min (ultrasonic agitation).
5. Rinse in methanol 5 times.
6. Soak 1 min in concentrated HCl.
7. Rinse in methanol 10 times.
8. Etch 10 min. in $5H_2SO_4$: $1H_2O$: $1H_2O_2$.
9. Rinse in methanol 10 times.
10. Store in Cohben.
11. Load wet from Cohben.

Sample E532 was then etched *in situ* in the reactor. The amount of material removed was unknown. Sample J70 was not given the *in situ* etch.

[1] Cohben, Inc., Fairfield, New Jersey.

REFERENCES

1. J. V. DiLorenzo, R. B. Marcus, and R. Lewis, *J. Appl. Phys.*, **42** 729 (1971).
2. Fumio Hasegawa and Takishi Saito, *Japan J. Appl. Phys.*, **1**, 1125 (1968).
3. R. H. Cox and T. C. Blocker, Paper 100 presented at Electrochem. Soc. Meeting. Los Angeles, May 10-15, 1970.
4. C. M. Wolfe, A. G. Foyt, and W. T. Lindley, *Electrochem. Technol.*, **6**, 208 (1968).
5. E. Munoz, W. J. Snyder, and J. L. Moll, *Appl. Phys. Letters*, **16**, 262 (1970).
6. J. R. Knight, P. Effer, and P. R. Evans, *Solid-State Electron.*, **8**, 178 (1965).
7. L. R. Dawson and J. M. Whelan, *Bull. Am. Phys. Soc.*, **13**, 375 (1968).
8. J. Copeland, IEEE Trans. Electron Devices, **10**, 445 (1969).
9. W. A. Brantley, Bell Telephone Laboratories, Private communication.
10. Ingot No. G1-450, Monsanto Co., Silicon-doped, boat-grown ingot, n $\simeq$ 10^{18}/cm^3.
11. Ingot No. 1456, Bell & Howell Co., Pasadena, Calif. Silicon-doped, Czochralski-pulled ingot, n $\simeq$ 10^{18}/cm^3.

Phosphosilicate Glass Stabilization of MOS Structures

L. H. Kaplan and M. E. Lowe

IBM Components Division, East Fishkill Facility, Hopewell Junction, New York 12533

ABSTRACT

The flatband voltage and stability of metal-glass-oxide-silicon (MGOS) systems were studied for phosphosilicate glass layers of varying thickness and composition. Thickness from 30 to 200Å and compositions from 1 to 6 mole per cent (m/o) P_2O_5 were used with a total insulator thickness of 500Å. Electrical properties were measured after contamination (before metallization) of 4 different levels of sodium ranging from approximately 10^{11} to 10^{14}/cm^2. The initial flatband voltage was found to be linear with both sodium contamination and PSG thickness. The ΔV_{FB} shift (due to +10V bias at 200°C for 10 min) is a decreasing linear function of the product of thickness and P_2O_5 concentration up to a value of (t_{PSG} x M%) sufficient to trap all sodium. At higher PSG levels, the ΔV_{FB} increases. For a desired level of Na protection, the thickness—mole per cent product needed, can be determined by the figures supplied.

The use of thin phosphosilicate glass (PSG) films to cover thermally grown SiO_2 layers on IGFET devices is well documented (1). Such films prevent the drift of cationic impurities, *e.g.* sodium, and the resultant instability in threshold voltage. The PSG layer acts as a getter for Na^+ ions, removing them from the SiO_2 layer and acting as a barrier to their entrance from the ambient. Although clean processing techniques tend to lower the Na^+ level greatly, the ever increasing performance requirements for microcircuits make

Key words: flatband voltage, flatband shift, sodium protection, MOSFET.

the use of stabilization system such as PSG almost mandatory.

The use of PSG systems has certain inherent limitations. The films, when of sufficient thickness and/or concentration, have exhibited polarization, which can itself increase threshold shifts (2, 3). Additionally, it has been shown (4) that, while PSG prevents migration of Na^+ ions through the oxide (the amount of Na^+ protection being dependent on PSG thickness and phosphorus concentration), the addition of the PSG layer causes an increase in the flatband voltage (V_{FB}), (negative), corresponding to a decreased threshold voltage (positive) for N-channel devices and to an increased negative V_T for P-channel devices.

For these reasons, it seemed appropriate to investigate the PSG system in an attempt to optimize PSG properties such that both a minimum thermal bias shift (ΔV_{FB}) and minimum flatband voltage might be realized.

Similar investigations of PSG thickness and concentration have been performed in the past (5, 6). However, these studies were concerned mainly with P_2O_5 concentrations above 4 m/o. Consideration of the polarization effects mentioned above, as well as of the increased demands for device stability necessitated by thinner gate insulators, make it advisable to extend this range.

Experimental

A matrix of PSG layers with varying thicknesses and P_2O_5 concentrations between 30 and 200Å and 1-6 m/o for a total SiO_2 thickness of 500Å was proposed for this study. Using a $POCl_3$ deposition system, considerable difficulty in obtaining all the desired PSG layers was encountered.

The PSG layers used were deposited on 500Å SiO_2 layers, thermally grown in dry O_2 on 2 ohm-cm, (100), p-type Si wafers. Deposition was performed by bubbling N_2 through $POCl_3$ and subsequent mixing with additional N_2 and O_2 at the furnace entrance. To achieve varying thickness and P_2O_5 concentrations, such variables as bubbler temperature and deposition temperature were altered. A method of diluting the $POCl_3$ saturated N_2 at constant volume was also utilized. Concentrations as low as 4 ppm were obtained by these methods. However, altering the $POCl_3$ concentration did not give predictable or reproducible results. The most reliable method for producing PSG layers of desired arbitrary concentrations was found to be by varying the temperature of the postdeposition anneal, while keeping the deposition parameters constant. Although all desired levels of thickness and P_2O_5 concentration were not achieved, a sufficient number of samples was obtained for a valid study. Properties of the PSG layers in the 17 sets of samples used were obtained by the well-known step etch technique (7) and are shown in Table I.

To determine the effectiveness of the various PSG layers against Na^+ contamination, four different Na^+ contamination levels were used for each PSG condition. The controlled contamination of the wafers was achieved by vacuum evaporation of the residue from measured small volumes of dilute NaCl solutions. The sodium levels were determined by MOS measurements on unstabilized oxides contaminated at the same time as the experimental samples. All samples were metallized with 10,000Å thick Al dots (using an electron-beam heated source), annealed in N_2 at 400°C for 20 min, and tested. V_{FB} and ΔV_{FB} were determined by CV measurements before and after thermal bias stressing for 10 min at 200°C with the Al electrode at +10V with respect to the Si substrate.

Table I. PSG properties of films used

Thickness (Å)	Mole per cent P_2O_5
34	0.9
39	1.5
34	7.8
54	1.8
52	2.6
50	3.9
60	1.1
67	1.5
66	3.1
65	3.8
66	5.3
90	3.2
106	1.8
147	1.3
162	6.5
189	2.4
191	4.2

Results and Discussion

The behavior of the sodium ions in SiO_2/PSG systems is complex (4, 5). It is beyond the scope of this paper to explore most of the effects involved. The purpose here is to present a practical report of the variation of V_{FB} and ΔV_{FB} as functions of the PSG properties thickness and m/o of P_2O_5, as well as of the Na^+ contamination level. To this end, only such theory and only such models as will enable one to recognize trends, as they exist, will be presented.

Flatband voltage.—Assuming that $Q_{ss} = 0$ and that all charge is due to sodium, the expected flatband voltage may be arrived at by starting with the following well-known relationships.

$$Q_{eff} = \frac{-\epsilon_o \epsilon_{ox}}{t_{ox}} (V_{FB} - \Delta W_F) \quad [1]$$

$$Q_{eff} = Q_{ox} + Q_{ss} \quad [2]$$

and

$$Q_{ox} = \int_o^{t_{ox}} \frac{t_{ox} - x}{t_{ox}} q_{ox} dx \quad [3]$$

The final expression for V_{FB} will be determined by the functional dependence of q_{ox} upon x. For the method of contamination used in this work, it might be expected that all Na^+ is initially concentrated near the metal-PSG interface, with essentially zero concentration elsewhere in the oxide. Since, in this case, $X = t_{ox}$, Q_{ox} reduces to zero and $V_{FB} = \Delta W_F$ regardless of sodium level or PSG parameters. However, experimentally this was not found to be true. The flatband voltage before stressing (but after annealing at 400°C) was found in all cases to vary linearly with the concentration of deposited sodium, when plotted on a log-log basis. Figure 1 shows some typical examples for a variety of PSG thicknesses and concentrations. V_{FB} is shown in Fig. 2 to vary linearly with PSG thickness at each contamination level.

It seems clear that the functional dependence of q_{ox} upon x hypothesized is incorrect. If the Na^+ diffuses during the 400°C postmetallization anneal, the distribution may be assumed to consist of two parts. Because of the gettering effect of the PSG, the Na^+ should be localized in this layer to a point at which all available trapping sites are filled. Although the trapping process is recognized to be transient and

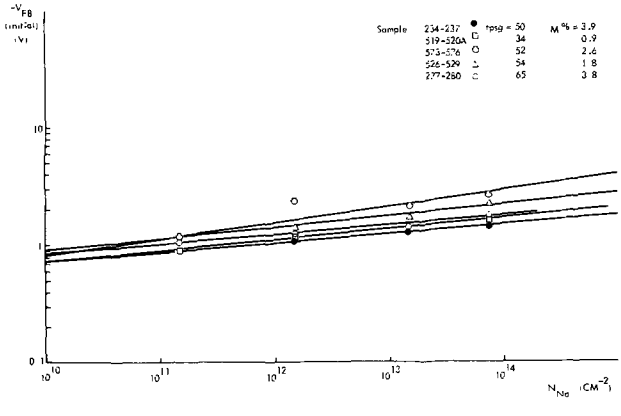

Fig. 1. Typical curves of V_{FB} vs. sodium concentration

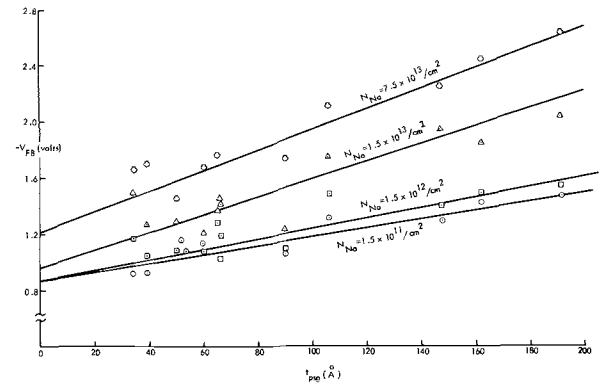

Fig. 2. Initial flatband voltage vs. PSG thickness for four levels of contamination.

merely constitutes a slowing-up of any motion imparted to the ions, at any given point in time, some Na^+ will be in a trapped condition and some in a mobile condition. The data of Fig. 2 strongly imply that the Na^+ distribution in the PSG layer is one of uniform density. The increase of V_{FB} with PSG thickness would rule out any major accumulation of trapped Na^+ at the Al-PSG boundary, since it indicates that thicker PSG layers have their sodium distributed closer to the Si/SiO_2 interface, on the average.

Any sodium ions in excess of those required to fill traps will be distributed in the PSG and SiO_2. The exact nature of this distribution is somewhat in doubt, since the radiochemical and neutron activation work (8, 9) done to establish such distributions has been on much thicker oxide films. The simplest functional dependence which could be assumed is, of course, constancy. As shown below, this assumption leads to fairly good agreement with the experimental data. It might be noted in passing, that a linear distribution ($q_{ox}/q = A + Bx$) was also investigated and found to bear no relation to the experiment.

Prior to any electrochemical stressing, q_{ox} may be considered as being made up of two parts; the charge densities due to trapped and mobile ions, respectively. For the uniform distribution in x indicated above

$$Q_{ox} = \int_o^{t_{ox}} \frac{t_{ox} - x}{t_{ox}^2} qN_{Nam}\,dx + \int_{t_{ox}-t_{PSG}}^{t_{ox}} \frac{t_{ox} - x}{t_{ox}t_{PSG}} qN_{Nat}\,dx \quad [4]$$

where the integration limits for the last term (corresponding to trapped Na^+) were changed to conform to the distribution of trapped sodium in the PSG. Integrating Eq. [4] and combining with Eq. [1] and [2], one obtains

$$V_{FB} = \Delta W_F - \frac{q\,t_{ox}}{2\epsilon_0\epsilon_{ox}}\left(N_{Nam} + \frac{N_{Nat}\,t_{PSG}}{t_{ox}}\right) \quad [5]$$

By definition, $N_{Nam} = N_{Na} - N_{Nat}$. Substituting and rearranging

$$V_{FB} = \Delta W_F - \frac{q\,t_{ox}}{2\epsilon_0\epsilon_{ox}}\left[N_{Na} + \left(\frac{t_{PSG}}{t_{ox}} - 1\right)N_{Nat}\right] \quad [6]$$

The number of Na^+ ions which can be trapped by a PSG layer (N_{Nat}) can be simply calculated, under the assumption that all traps are active, based upon the "nonbridging oxygen" model advanced by Eldridge and Kerr (5). The number of PO^- trapping sites is calculated from the density and m/o, and thickness of the PSG. After evaluating numerical constants, the expression becomes

$$N_{Nat} = 1.33 \times 10^{20}\ t_{PSG}\ m/o$$

Substituting for N_{Nat}, as well as for numerical constants, and assuming an oxide thickness of 500Å, one obtains, for the case where the PSG is insufficient to trap all of the sodium

$$V_{FB} = \Delta W_F - 1.053 \times 10^{-12} N_{Na} - (2.8 \times 10^{13}\,t_{PSG} - 1.4 \times 10^8)\,t_{PSG}\,m/o \quad [7]$$

If all the sodium is trapped, $N_{Nat} = N_{Na}$ and Eq. [6] reduces to

$$V_{FB} = \Delta W_F - \frac{q\,t_{PSG}N_{Na}}{2\epsilon_0\epsilon_{ox}} \quad [8]$$

As previously noted, Fig. 2 shows a linear relationship between V_{FB} and t_{PSG}. This is in direct agreement with Eq. [8], suggesting that, even for the highest levels of contamination, all sodium has become associated with trapping sites in the PSG.

Without offering any further interpretation of the above data, it is quite clear that the V_{FB} for systems containing PSG increases with PSG thickness for any given Na^+ level. This is in good agreement with previously described findings (6). Further, it seems evident from Fig. 3 that higher sodium concentrations produce higher initial flatband voltages with any given thickness of PSG.

Change in V_{FB} with electrothermal stress.—Consideration of the "nonbridging oxygen" model mentioned earlier would seem to indicate a linear relation between ΔV_{FB} and the product of PSG concentration and thickness. Figure 4 shows the variation observed experimentally between these variables. Plots of ΔV_{FB} against PSG concentration or thickness separately produced no clear relationship. The plot of Fig. 4 is in semilog format to allow the wide range of ΔV_{FB} to be shown in a single plot. A linear format, however, shows that each curve (for a given contamination level) has a decreasing linear region at low values of m/o x t_{PSG}, and a flat or increasing region at higher values.

The data described above are in agreement with an extension of the treatment used previously to predict V_{FB}. This treatment assumes that, for a given stress temperature and electric field, some of the sodium associated with the PSG behaves as mobile sodium due to emission from the traps. For all practical purposes, therefore, the total sodium content may then be classified as either mobile or trapped. However, because of the emission process, only a fraction of the available traps will contain "trapped" sodium. Since $\Delta V_{FB} = V_{FB}$ (after stressing) $- V_{FB}$ (before stressing), it is now necessary only to formulate an expression for V_{FB} (after stressing). For this, Eq. [4] must be modified by replacing its first term (corresponding to the mobile Na^+) to account for all mobile Na^+ being located at the interface.

Thus, $Q_{ox} = Q_{eff}$, which is defined as the charge which, if placed at the interface, would have the same effect as that of the distributed charge, q_{ox}. Since the real charge, qN_{Nam}, is now completely at the interface,

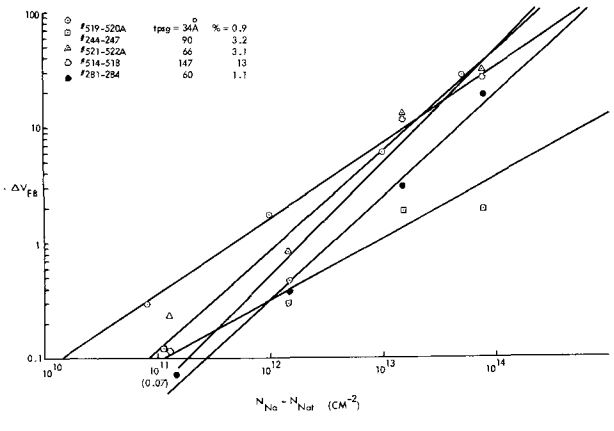

Fig. 3. Typical curves of ΔV_{FB} vs. sodium concentration

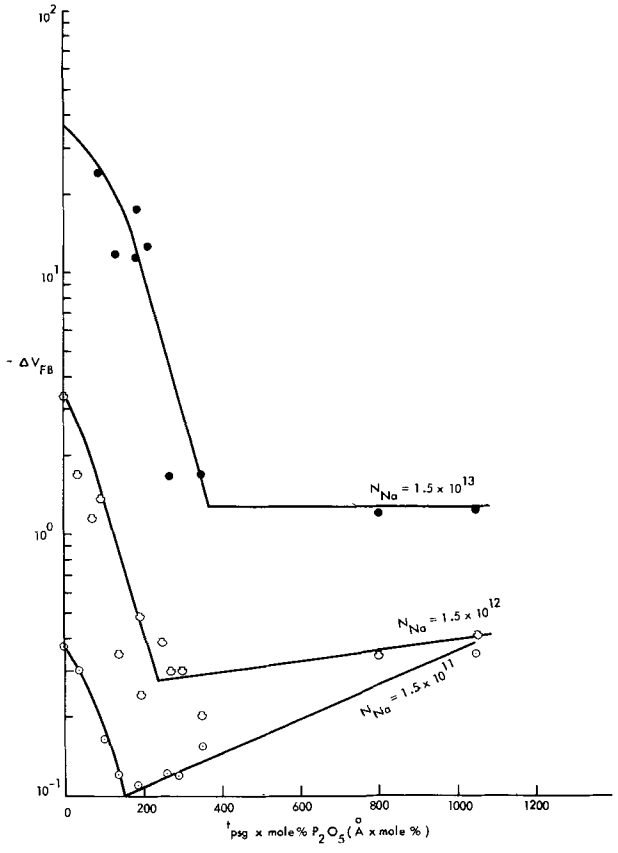

Fig. 4. Variation of thermal bias flatband voltage shift with thickness x m/o P_2O_5. (Thickness measured in Å.)

it is equal to the mobile charge contribution to Q_{ox}. Then, analogous to Eq. [4]

$$Q_{ox} \text{ (after stress)} = q N_{Nam} + \int_{t_{ox}-t_{PSG}}^{t_{ox}} \frac{t_{ox} - x}{t_{ox} t_{PSG}} q N_{Nat} dx \quad [9]$$

Analogous treatment to that of Eq. [5] and [6] gives

$$V_{FB} \text{ (after stress)} = \Delta W_F - \frac{q t_{ox}}{\epsilon_0 \epsilon_{ox}} \left[N_{Na} + \left(\frac{t_{PSG}}{2t_{ox}} - 1 \right) N_{Nat} \right] \quad [10]$$

Subtracting V_{FB} (before stress), as obtained from Eq. [6], one obtains for the saturation shift on thermal bias stress

$$-\Delta V_{FB} = \frac{q t_{ox}}{2\epsilon_0 \epsilon_{ox}} (N_{Na} - N_{Nat}) = 1.053 \times 10^{-12} (N_{Na} - N_{Nat}) \quad [11]$$

When the amount of PSG is insufficient to trap all sodium, $N_{Nat} = 1.33 \times 10^{20}\ t_{PSG} \cdot \text{m/o} \cdot G$ where G is some fraction which accounts for all available traps not being permanent. Therefore

$$-\Delta V_{FB} = 1.05 \times 10^{-12} N_{Na} - 1.40 \times 10^{8} \cdot t_{PSG} \cdot \text{m/o}\, G \quad [12]$$

This predicts the linear decrease in ΔV_{FB} with t_{PSG} m/o shown in the data of Fig. 4. As predicted by Eq. [11], $-\Delta V_{FB}$ was found, in each of the seventeen PSG types studied, to be linear with $(N_{Na} - N_{Nat})$. Figure 3 shows several typical log-log plots of this type for a variety of PSG characteristics.

Conclusion

The data presented allow the estimation of the degree of protection given by PSG films of various thickness/concentration combinations against the deleterious effects of Na^+ contamination levels which might be experienced during device fabrication. However, the sole criterion used here is the flatband voltage shift under bias of +10V (2 x 10^6 V/cm) at 200°C for 10 min. No attempt is made to correlate these shifts with in-use conditions. From Fig. 4, it appears that sodium concentrations higher than approximately 10^{12}/cm^2 create shifts of greater than 0.2V, regardless of the thickness and concentration of the PSG used. For shifts as low as 0.1V, it would seem necessary to maintain the Na^+ contamination at 10^{11}/cm^2.

It is interesting to consider the quantity G, introduced in Eq. [12]. By rearrangement of this equation, G may be expressed as follows

$$G = \frac{\Delta V_{FB} + 1.05 \times 10^{-12} N_{Na}}{1.40 \times 10^{8}\ t_{PSG}\ \text{m/o}} \quad [13]$$

Values for G calculated in this way are plotted in Fig. 5. The factor is evidently a function of PSG parameters as well as the Na^+ level and can have rather low values. The range of G values calculated for PSG films in this work is from 0.0003 to nearly unity. Another independent study in this laboratory shows the same effect (10).

Even if more permanent traps could be made available so that lower shifts could be obtained at high Na^+ density, the practical protection would still be limited by consideration of initial V_{FB} requirements. While the ΔV_{FB} was shown here to depend only on the product of t_{PSG} and m/o, (neglecting polarization effects), the V_{FB} is clearly seen (Fig. 2) to depend upon the thickness of PSG at a given Na^+ level. Figure 2 also demonstrates that the dependence grows more pronounced as the Na^+ concentration is increased. It is very likely, then, that the V_{FB} thickness dependence is actually caused by sodium trapped in the PSG layer. In any event, the optimum configuration of PSG would seem to consist of the minimum thickness consistent with processing considerations and a concentration of P_2O_5 sufficient to yield a (t_{PSG} x m/o) product which will protect against the Na^+ level of interest.

Finally, it should be noted that there are other modes of Na^+ contamination which might not be expected to yield results equivalent to the ones quoted. Sodium contamination during device fabrication may arise from several sources, among which are: incorporation during oxidation, contamination during photoresist processing, and contamination due to handling between all premetal process steps. Clearly, no one controlled contamination process can be expected to simulate all of these mechanisms. The vacuum deposition of NaCl most closely resembles the modes of contamination due to photoresist and handling. Other methods, such as treatment with boiling NaCl solution, would be expected to give somewhat different results. It is believed that the method of contamination used

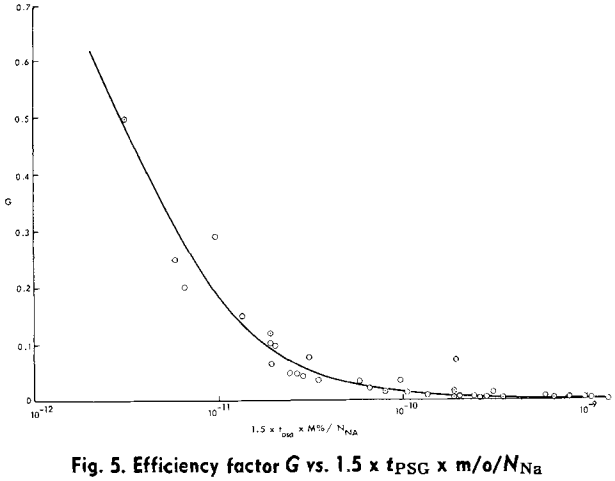

Fig. 5. Efficiency factor G vs. 1.5 x t_{PSG} x m/o/N_{Na}

here yields the most accurately controlled contamination levels and is a good substitute for the total contamination experienced in IGFET processing.

Manuscript submitted March 19, 1971; revised manuscript received May 14, 1971.

Any discussion of this paper will appear in a Discussion Section to be published in the June 1972 JOURNAL.

SYMBOLS

X	distance from the Si/SiO_2 interface in SiO_2
t_{ox}	thickness of SiO_2 + PSG in cm
t_{PSG}	thickness of PSG layer in cm
q	charge of electron in coulombs
q_{ox}	charge density in oxide (both mobile and trapped) (cm^{-3})
q_{oxm}	mobile charge density in oxide (cm^{-3})
Q_{ss}	effective charge due to states and charges other than Na^+ at the interface (cm^{-2})
Q_{ox}	effective charge due to distributed charge in oxide (cm^{-2})
Q_{eff}	$Q_{ox} + Q_{ss}$ (cm^{-2})
ϵ_o	dielectric constant of vacuum
ϵ_{ox}	dielectric constant of SiO_2
ΔW_F	work function difference between Al and Si
V_{FB}	flatband voltage
ΔV_{FB}	change in flatband voltage after stressing 10 min at +10V at 200°C
N_{Na}	area concentration of Na^+ (mobile and trapped) (cm^{-2})
N_{Nam}	area concentration of mobile Na^+ (cm^{-2})
N_{Nat}	area concentration of trapped Na^+ (cm^{-2})
G	fraction of total PSG traps which are permanent at a given T and Field

REFERENCES

1. D. R. Kerr, J. S. Logan, P. J. Burkhart, and W. A. Pliskin, *IBM J. Res. Develop.*, **8**, 377 (1964).
2. E. H. Snow and B. E. Deal, *This Journal*, **113**, 263 (1966).
3. J. M. Eldridge, R. B. Laibowitz, and P. Balk, *J. Appl. Phys.*, **40**, 1922 (1969).
4. S. R. Hofstein, *Solid-State Electron.*, **10**, 657 (1967).
5. J. M. Eldridge and D. R. Kerr, Abs. 532, p. 530, Electrochem. Soc. Extended Abstracts, Fall Meeting, Montreal, Oct. 6-11, 1968.
6. F. J. Montillo, Unpublished work.
7. J. M. Eldridge and P. Balk, *Trans. Met. Soc. AIME*, **242**, 539 (1968).
8. T. M. Buck, F. G. Allen, J. V. Dalton, and J. D. Struthers, *This Journal*, **114**, 862 (1967).
9. E. Yon, W. H. Ko, and A. B. Kuper, *IEEE Trans. Electron Devices*, **13**, 276 (1966).
10. G. O'Rourke, Unpublished works.

The Chemical Polishing of Sapphire and MgAl Spinel

A. Reisman,* M. Berkenblit,* J. Cuomo,* and S. A. Chan

IBM Thomas J. Watson Research Center, Yorktown Heights, New York 10598

ABSTRACT

Based on air annealing studies at 1500°C, it appears that bulk and surface mechanical damage in sapphire and MgAl spinel ($MgAl_2O_4$) may be greatly minimized. Such annealed surfaces can then be effectively polished chemically leaving essentially featureless surfaces. Preannealed sapphire orientations can be polished at 285°C in a 1:1 H_2SO_4:H_3PO_4 mixture for 15 min while MgAl spinel orientations may be treated in a 3:1 H_2SO_4:H_3PO_4 mixture at 250°C for the same length of time. (111) MgAl spinel and $(10\bar{1}4)$ sapphire cannot be chemically polished by the procedures described but are presumably amenable to removal of most surface and mechanical saw and polish induced bulk damage via the high-temperature annealing process.

Sapphire and, more recently, MgAl spinel ($MgAl_2O_4$) have been employed extensively as single-crystal dielectric substrates for the epitaxial growth of a variety of materials. Wafers of these dielectrics are available only in mechanically polished form. Because of the damage introduced during mechanical preparation, a number of liquid- and gas-phase treatments have been applied prior to use to effect nonselective etching (chemical polishing) of the surfaces. Among these are included molten borax (1-4), heated phosphoric acid (2, 5-7), molten V_2O_5 (8), molten lead fluoride (9), heated vaporous sulfur fluorides (10), heated vaporous fluorinated hydrocarbons (11), HCl-H_2 at elevated temperatures (12), and H_2 annealing (2, 4, 5, 13, 14), among others. In fact, none of these approaches has been too satisfactory for a variety of reasons. Molten salt approaches are cumbersome, often are somewhat selective, and in common with others noted above are highly orientation dependent. The vapor-phase etchants are quite orientation dependent and sometimes exhibit low removal rates. Heated phosphoric acid has shown some promise but tends to leave insoluble residues behind. Further, because it dehydrates and polymerizes, its chemical behavior varies continuously with time at temperature. H_3PO_4 is also somewhat orientation selective and frequently results in dense pitting. H_2 annealing exhibits a vanishing low removal rate and was found by us not to eliminate polishing scratch damage when subjected subsequently to the liquid-phase portion of the polishing technique to be described below. Finally, where some modicum of success might be attributed to some of the methods mentioned above for sapphire, their applicability to Mg spinel is an unknown quantity.

* Electrochemical Society Active Member.

Key words: chemical polishing, sapphire chemical polishing, MgAl spinel chemical polishing.

Experimental Procedure

Sapphire and magnesium spinel wafers were obtained from Insaco Corporation (Quakertown, Pennsylvania) and Union Carbide Company (Crystal Products Division, San Diego, California) as 3/4 or 1 in. diameter sawed, lapped, and mechanically polished materials prepared from Czochralski-grown ingots. Several sapphire wafers cut from vapor-grown ingots, obtained from the Lexington Laboratories (Cambridge, Massachusetts), and mechanically polished by Insaco were also examined. The nominal sapphire orientations studied included (0001), $(10\bar{1}4)$, $(11\bar{0}0)$, $(11\bar{0}2)$, $(11\bar{2}6)$, and $(11\bar{2}0)$. X-ray analysis showed these to be within 1°-4.5° of these specified orientations. Spinel orientations examined included (111), (110), and (100) and were within 1°-2° from the specified planes.

Wafers were rinsed ultrasonically in acetone and deionized water, then dried in a filtered nitrogen stream. Microscopic examination prior to further treatment showed the presence of a variable number of random polishing scratches, the density being greatest at the wafer periphery.

The polishing procedures developed are of two kinds, an anneal in air at 1500°C, and a wet chemical polish effected in the temperature range 250°-300°C. The air anneal or the wet chemical technique may be utilized separately but when possible (namely when the wet chemical technique does not exhibit orientation dependence) were found to provide the most useful surfaces for epitaxy when applied in sequence. The high-temperature anneal serves to remove most if not all surface and induced bulk damage while the wet chemical technique removes retained surface debris and contaminants.

Annealing of the samples was conducted in air in a platinum wound resistance furnace using an Alundum furnace tube, Fig. 1. The samples were placed on a slab single-crystal sapphire support and loaded into the furnace at 750°C. The furnace temperature was raised to 1500°C and the samples were held at this temperature for varying periods of time. They were examined microscopically for evidence of residual scratch damage, then subjected to chemical polishing which was useful for revealing remnant bulk scratch damage.

The wet chemical polishing treatment involves nonselective etching of the sapphire or MgAl spinel wafers in sulfuric-phosphoric acid mixtures at 300°C or less. It was found that unlike the behavior of pure phosphoric acid which tends to polymerize when heated to form a practically water insoluble, extremely viscous fluid, H_2SO_4-H_3PO_4 mixtures do not thicken or become water insoluble. The H_2SO_4 appears to prevent degradation of the H_3PO_4. Equally important is the observation that with H_2SO_4-H_3PO_4 mixtures, insoluble residues do not form on the wafer surface nor is surface pitting a problem. While loss of H_2SO_4 does occur during a polishing cycle, the amount of volatilization is not great, due to the vapor pressure reduction resulting from dilution with phosphoric acid. Polishing of sapphire and spinel was studied in the temperature range 200°-300°C using various H_2SO_4/H_3PO_4 ratios contained in a platinum crucible, with and without wafer rotation. The wafers were held in a platinum basket. The apparatus employed is shown schematically in Fig. 2. In all studies, Mallinckrodt 85% H_3PO_4 Analytical Reagent and Mallinckrodt Sulfuric Acid Transist AR grade were employed. Fresh solutions were heated to temperature slowly to allow the H_3PO_4 to lose its absorbed water and highest vapor pressure water of hydration at *ca.* 185°C. Polishing solutions were replaced after two polishing cycles in practice, although regeneration to a given volume with either a 3/1 or stronger H_2SO_4/H_3PO_4 mixture appears to enable additional cycles without adverse effect.

Results and Discussion

Removal rate studies.—Preliminary studies were conducted over the temperature range 200°-450°C, where feasible, using pure sulfuric acid, sulfuric/phosphoric acid volume ratios of 9/1, 3/1, 1/1, 1/3, and

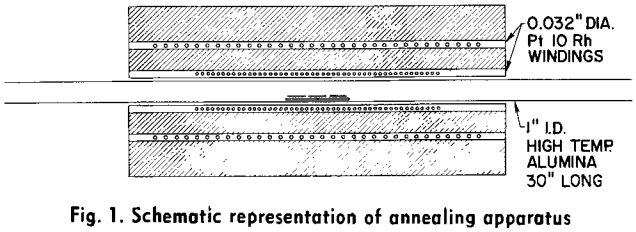

Fig. 1. Schematic representation of annealing apparatus

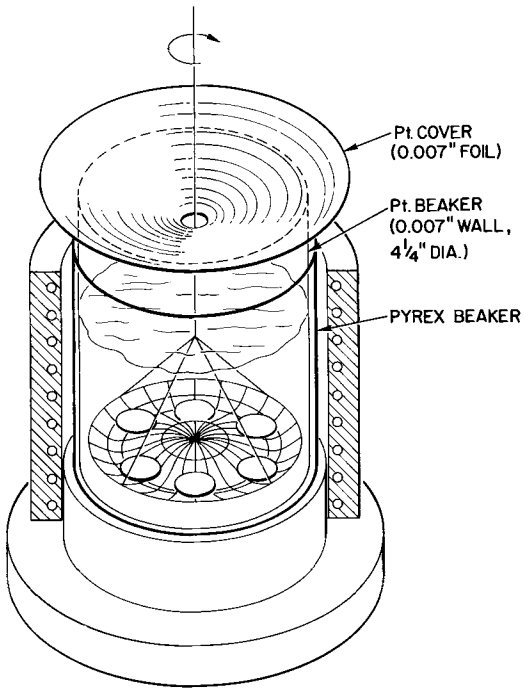

Fig. 2. Schematic representation of wet chemical polishing apparatus.

pure phosphoric acid. Rotation rates of 0, 0.5, 10, and 50 rpm were examined. In general, removal rates were independent of the rotation rates examined. Surface quality was, however, distinctly superior at the lower rotation rates and best when the samples were stationary. Table I tabulates all etching results obtained at 0.5 rpm. Figure 3 shows the variation of log {(0001) sapphire removal rate} as a function of T^{-1} °K^{-1} for pure phosphoric acid in the temperature interval 285°-450°C and for 9:1 H_2SO_4:H_3PO_4 mixtures in the temperature interval 250°-300°C (above 300°C the evaporation rate of the H_2SO_4 became too great in the 9:1 mixture to obtain reproducible results). Figure 4 shows the variation of log {(111), (110), and (100) magnesium spinel removal rate} as a function of T^{-1} °K^{-1} for 3:1 H_2SO_4:H_3PO_4 mixtures

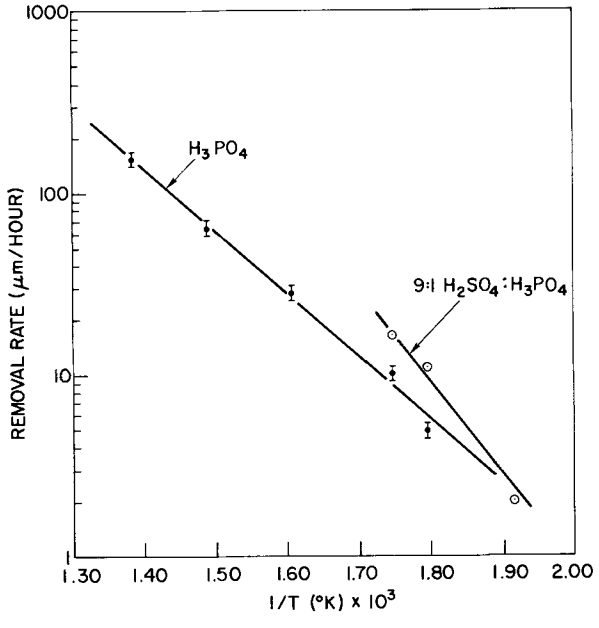

Fig. 3. Variation of log {(0001) sapphire removal rate} as a function of $T^{-1}[°K]^{-1}$ for 9:1 H_2SO_4:H_3PO_4 and H_3PO_4.

Table I. Removal rate, μm/hr

Material	Orientation	Temp, °C	H_2SO_4	H_2SO_4:H_3PO_4 ratio 9:1	3:1	1:1	1:2	1:3	1:9	H_3PO_4
Sapphire	(0001)	450								156.0
		400								63.0
		350								28.2
		300								9.9
		285								4.8
		285						7.8		
		285				9.0				
		285			11.1					
		285		10.8						
		285	Residue							
		250		2.0						
		300		16.2						
		300					13.8			
	$(10\bar{1}4)$	285				0.3				
		300				0.9				
	$(1\bar{1}00)$	325						2.3		
		285				0.4				
	$(11\bar{2}0)$	285				0.4				
	$(11\bar{2}6)$	285				1.7				
	$(11\bar{2}3)$	285				1.3				
	$(01\bar{1}2)$	285				3.0				
	$(11\bar{2}4)$	285				1.2				
Spinel	(100)	285			45.0					
		250			10.8					
		200			1.0					
	(111)	300			28.8					
		285			12.6					
		250			2.0					
	(110)	285			30.3					
		250			6.6					
		250								8.7
		250						7.5		
		250		6.4						
		250	Residue							
		300								51.0

in the temperature interval 200°-300°C. Figure 5 shows the variation in etch rate of (0001) sapphire at 285° and 300°C in different H_2SO_4:H_3PO_4 mixtures and (110) magnesium spinel at 250°C in the same composition interval. Data for other sapphire orientations have not been plotted but can be obtained from Table I.

It is to be noted that removal rate data for pure sulfuric acid are not given. This is because the samples following such treatment were covered with a heavy deposit and weight gains occurred.

From Fig. 3 and 4 it is seen that linear semilog plots were obtained which in general exhibit somewhat different slopes. Such results indicate that the etching behavior observed occurs in a surface limiting regime and is representative of chemical rather than diffusion limiting kinetics. This explains the independence of removal rate on rotation rate. Based on these data, the removal rates of (0001) sapphire in phosphoric acid and in a 9:1 H_2SO_4:H_3PO_4 mixture as a function of temperature are given by Eq. [1] and [2], respectively

$$\log R_{(0001)\text{sapphire}}^{H_3PO_4} = \frac{-3.472 \times 10^3}{T[°K]} + 6.968 \quad [1]$$

$$\log R_{(0001)\text{sapphire}}^{9:1} = \frac{-5.050 \times 10^3}{T[°K]} + 10.037 \quad [2]$$

The removal rates of (111), (110), and (100) MgAl spinel in a 3:1 H_2SO_4:H_3PO_4 mixture as a function of T are given by Eq. [3]-[5], respectively

$$\log R_{(111)\text{spinel}}^{3:1} = \frac{-6.971 \times 10^3}{T[°K]} + 13.658 \quad [3]$$

$$\log R_{(110)\text{spinel}}^{3:1} = \frac{-5.524 \times 10^3}{T[°K]} + 11.350 \quad [4]$$

$$\log R_{(100)\text{spinel}}^{3:1} = \frac{-5.103 \times 10^3}{T[°K]} + 10.787 \quad [5]$$

In all instances R is the removal rate in μm/hr.

From Fig. 5 it is seen that the removal rate of (0001) sapphire increases with increasing H_2SO_4 concentration and tends to level off at high H_2SO_4 concentrations. However, (110) MgAl spinel shows its maximum removal rate in pure H_3PO_4 but does show a leveling off at high H_2SO_4 concentrations. These data indicate that over a rather broad composition range the removal rate is not too concentration dependent.

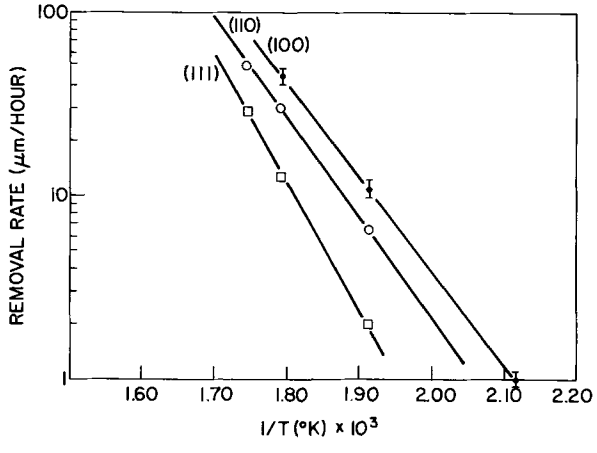

Fig. 4. Variation of log {(111), (110), and (100) MgAl spinel removal rate} as a function of $T^{-1}[°K]^{-1}$ for 3:1 H_2SO_4:H_3PO_4.

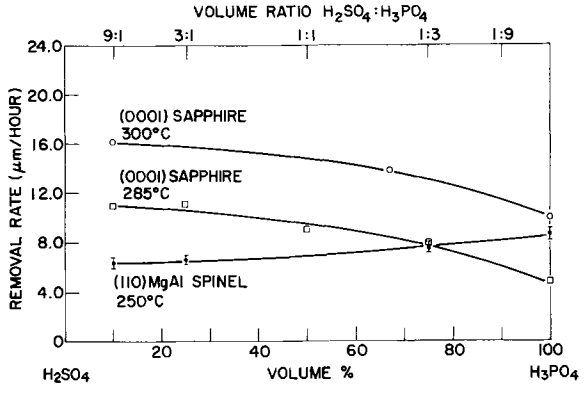

Fig. 5. Variation of removal rate with polishing solution composition for (0001) sapphire and (110) MgAl spinel.

While the polishing of certain sapphire and spinel orientations could be effected reasonably well in pure phosphoric acid, pronounced pitting and residue formation were problems, as were the changes in the properties of the H_3PO_4 with continued heating. For sapphire, the best polishing was achieved at a 1:1, H_2SO_4:H_3PO_4 ratio at a temperature of 285°C. While somewhat higher temperatures can be employed, 285°C provides a good practical working temperature from the point of view of removal rate and relatively low volatility of H_2SO_4 from the mixture. Neither pitting nor residue formation is a problem. In badly damaged wafers, chemical polishing alone requires the removal of a few mils of material which can be accomplished with minimal deterioration of surface planarity. However, a certain degree of etch propagation of scratch damage may occur which necessitates too much removal, from a practical point of view, to completely eliminate all traces of damage. In practice, when the chemical polishing alone was employed, only 0.5 mil was removed which left very faint traces of such scratch damage.

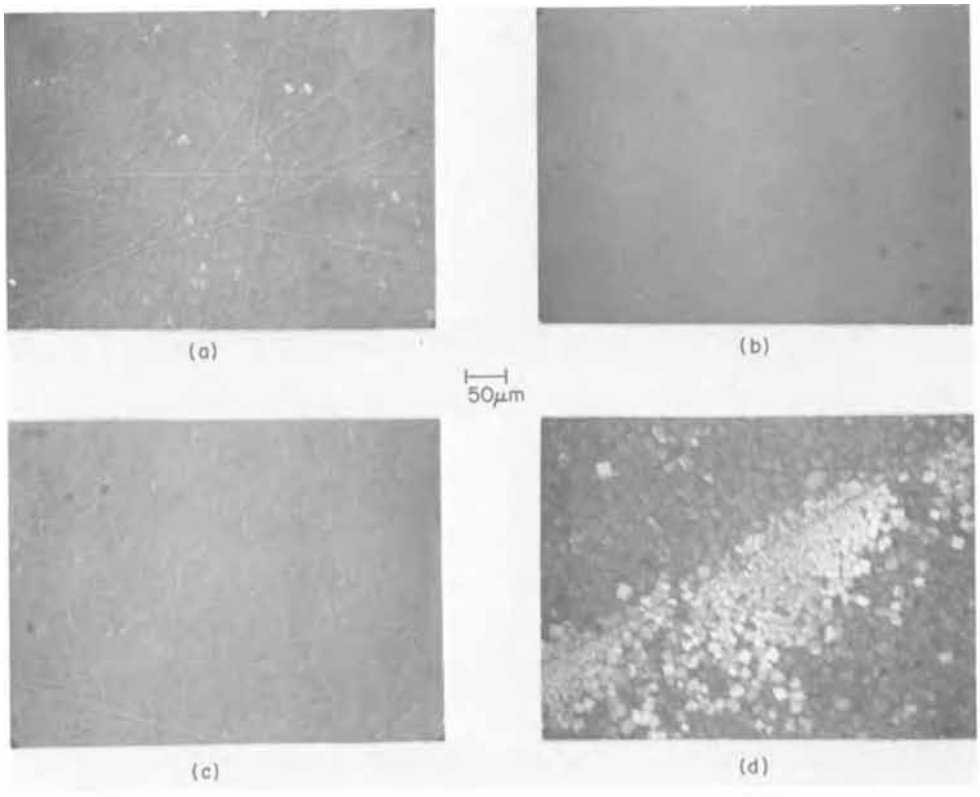

Fig. 6. Polishing behavior of (0001) sapphire, 90 min at 285°C. (a) H_3PO_4, (b) 1:1 H_2SO_4:H_3PO_4, (c) 3:1 H_2SO_4:H_3PO_4, (d) H_2SO_4.

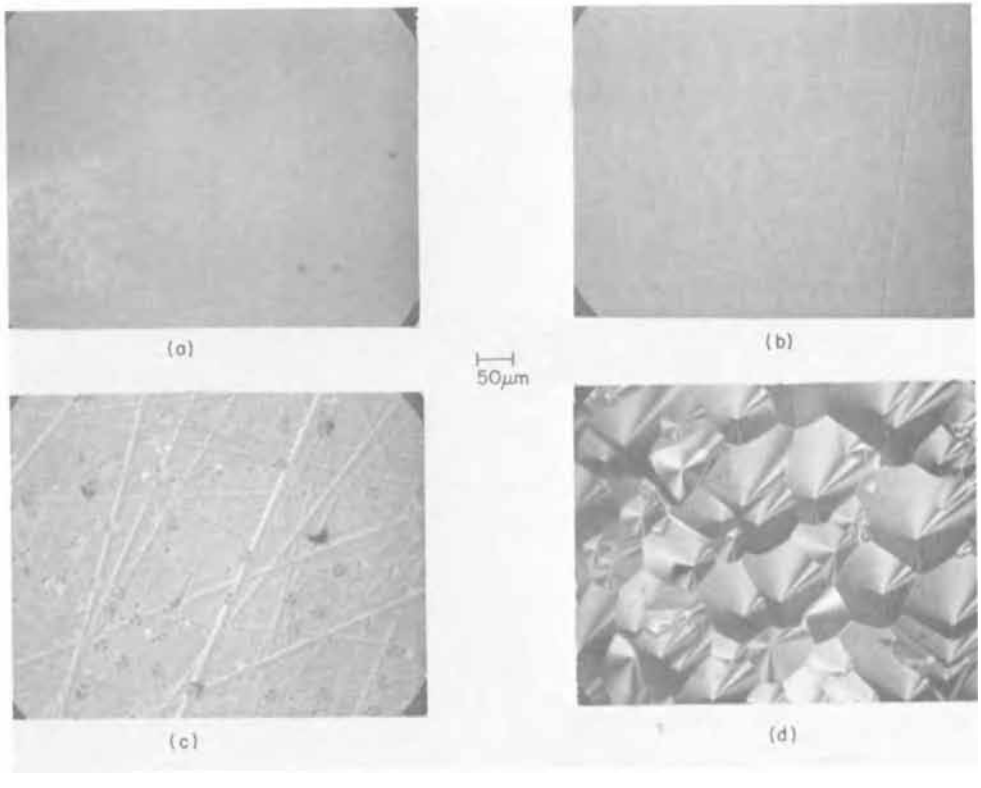

Fig. 7. Polishing behavior of MgAl spinel, 90 min, 3:1 H_2SO_4:H_3PO_4. (a) (100) at 250°C, (b) (110) at 250°C, (c) (111) at 250°C, (d) (111) at 300°C.

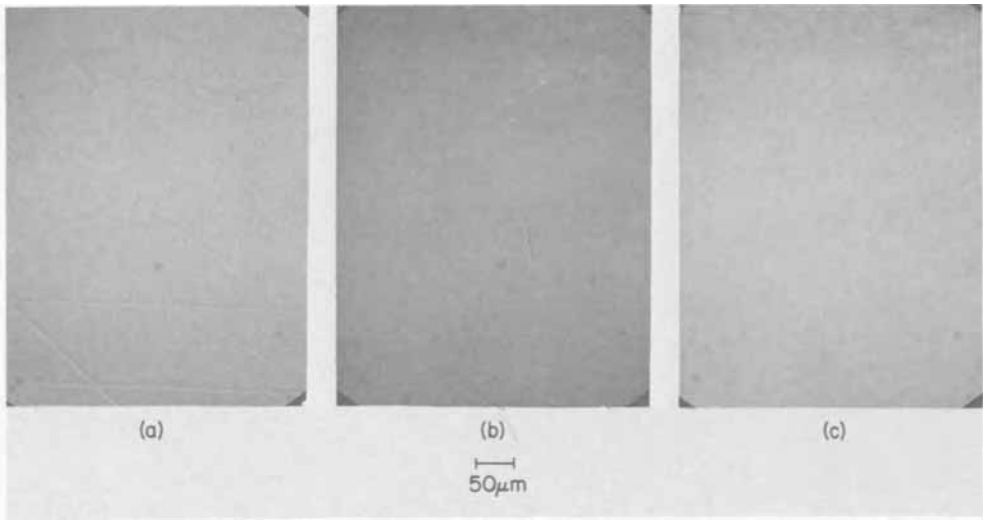

Fig. 8. Effect of preanneal of (110) MgAl spinel at 1500°C on chemical polishing behavior. (a) No anneal, (b) 1 hr anneal, (c) 4 hr anneal.

In Fig. 6a-d is shown the polishing behavior of (0001) sapphire. Figure 6a shows the effect of a 90 min etch in pure phosphoric acid at 285°C. Figure 6b shows a similar time-temperature polish in a 1:1 mixture. Figure 6c shows the behavior under the same conditions in a 3:1 H_2SO_4:H_3PO_4 mixture and Fig. 6d shows the results of a like H_2SO_4 treatment. Figure 6b is representative of a surface polished with the practical constraints mentioned. While visual damage is greatly minimized, as compared to pure phosphoric acid, or other H_2SO_4:H_3PO_4 compositions, the faint residual scratch evidence (real damage or etch propagated damage) mentioned above is present.

Of the other sapphire orientations examined, aside from the variation in removal rate with orientation (see Table I), all but the $(10\bar{1}4)$ could be polished successfully. The latter could not be polished either because the etching was selective or because massive scratch damage was present.

The behavior of MgAl spinel was similar to that of sapphire except in detail. A 3:1 H_2SO_4:H_3PO_4 mixture at 250°C provided the best surfaces although the composition range from 1:1-3:1 was quite adequate. In Fig. 7a-c the surfaces of (100), (110), and (111) spinel following 90 min treatments at 250°C in 3:1 mixtures are shown. Figure 7a shows a (100) surface and Fig. 7b a (110) surface. Figure 7c shows the (111) surface, from which it is evident that polishing could not be effected on this orientation. In Fig. 7d, the behavior of (111) spinel at 300°C in this same mixture shows even greater selectivity.

Annealing studies.—The effects of an annealing at 1500°C in air on damage were studied by heating the wafers for different periods of time, then following this annealing by chemical polishing. The effects were quite dramatic and unexpected. For example, if a mechanically polished (110) spinel wafer is chemically polished (3:1 H_2SO_4:H_3PO_4, 250°C) for only 15 min without a preanneal, the resulting surface, Fig. 8a, exhibits a very dense scratch pattern indicative of the region of heaviest damage. If such a wafer is annealed for 1 hr and then subjected to a 15 min chemical polish, Fig. 8b, surfaces result which exhibit minimal evidence of scratch damage. Finally, if a 4 hr preanneal is applied followed by a 15 min chemical polish, Fig. 8c, essentially featureless surfaces result. To allow for normal variation in the degree of mechanical damage, it was found adequate to anneal for 2-4 hr periods before applying the 15 min chemical polishing treatment. Similarly, a marked improvement was observed for the (100) spinel and the various sapphire orientations examined in this study following a preanneal in air at 1500°C and chemical polishing. Air annealing does not effect the chemical polishing behavior of the different orientations. Both spinel and sapphire wafers prepared by this process have been used successfully for deposition of epitaxial ZnO and Si.

Similar studies were conducted using vacuum annealing at 1500°C. While comparable results were obtained they were not quite as good as those obtained using the air annealing approach.

Acknowledgment

The authors wish to thank J. M. Green for his many helpful discussions.

Manuscript submitted Feb. 11, 1971; revised manuscript received *ca.* May 7, 1971.

Any discussion of this paper will appear in a Discussion Section to be published in the June 1972 JOURNAL.

REFERENCES

1. P. H. Robinson and C. W. Mueller, *Trans. Metal. Soc. AIME*, **236**, 268 (1968).
2. T. A. Zeveke, L. M. Kornev, and V. A. Tolomasov, *Soviet Phys-Cryst. (English Transl.)*, **13**, 493 (1968).
3. T. A. Tomilovskii, *Tr. Inst. Kristallogr., Akad. Nauk-SSSR*, **8**, 309 (1953).
4. C. C. Wang, *J. Appl. Phys.*, **40**, 3433 (1969).
5. I. L. Porter and R. G. Wolfson, *ibid.*, **36**, 9, 2746 (1965).
6. H. M. Manasevit and W. I. Simpson, *ibid.*, **35**, 4, 1349 (1964).
7. R. Aeschlimann, F. Gassmann, and T. P. Woodman, *Mater. Res. Bull.*, **5**, 167 (1970).
8. M. M. Faktor, D. G. Fiddyment, and G. R. Hewns, *This Journal*, **114**, 356 (1967).
9. R. Scheuplein and P. Gibbs, *J. Am. Ceram. Soc.*, **43**, 458 (1960).
10. H. Manasevit and F. L. Morritz, *This Journal*, **114**, 204 (1967).
11. H. Manasevit, *ibid.*, **115**, 434 (1968).
12. T. L. Chu, M. H. Francombe, G. A. Gruber, J. J. Oberly, and R. L. Tallman, Westinghouse Res. Lab. Report No. A.F.C.R.L. 65-574, A.D. 619992 (1965).
13. C. C. Wang, G. E. Gottlieb, G. W. Cullen, S. H. McFarlane, III, and K. H. Zaininger, *Trans. Met. Soc. AIME*, **245**, 441 (1969).
14. G. W. Cullen, G. E. Gottlieb, C. C. Wang, and K. H. Zaininger, *This Journal*, **116**, 1445 (1969).

Nondestructive Determination of the Composition and Thickness of Thin Films of Pyrolytically Deposited Borosilicate Glass by Infrared Absorption

A. S. Tenney

Corporate Research and Development, General Electric Company, Schenectady, New York 12301

ABSTRACT

The compositions of thin films of pyrolytically deposited borosilicate glass were correlated with the infrared spectra of these films over the entire composition range. Although the composition has been related to the ratio, R, of the B-O absorbance maximum at about 1300 cm^{-1} to the Si-O maximum at about 1050 cm^{-1}, the relationship between R and composition was found to be dependent on deposition conditions for glasses of more than about 30 m/o (mole per cent) B_2O_3. Nevertheless, if R' is defined to be the ratio of the areas of the B-O and Si-O bands, respectively, the relationship between R' and mole fraction is independent of temperature and other deposition conditions. The composition dependence of the integrated intensity of these bands as well as of film density and refractive index and the temperature dependence of composition and deposition rate were determined also.

The "IR peak ratio" R, the ratio of the absorbance peak of the B-O vibrational band at about 1300 cm^{-1} ($\sim 7.5\mu$) to that of the Si-O band at about 1050 cm^{-1} ($\sim 9.4\mu$), has been correlated with the composition of thin films of pyrolytically deposited borosilicate glass (1, 2). The aim of the present work was to determine the relationship between R and composition with accuracy greater than had been achieved previously (2), to discover any dependence of this relationship on deposition conditions, and to extend this study to glasses of higher boron concentration.

Experimental

Most glasses were deposited on chemically etched 10 ohm-cm silicon wafers by pyrolytic oxidation of silane and diborane in either of two (geometrically different) vertical reactors as described by Brown and Kennicott (3). The rest were made in a horizontal Silox reactor. To keep glasses of more than about 25 m/o (mole per cent) B_2O_3 from absorbing water from the air, it was necessary to deposit a cover glass of 100-200Å pure SiO_2 on top of the usually about 6000Å of the glass to be studied.

The infrared spectra of these glasses were determined with a Perkin-Elmer Model 457 double-beam recording spectrophotometer on the "fast" scan mode (2000, 1000 cm^{-1}/min) with a slit setting of "N" (6). For samples with cover glass, a wafer of the same type and resistivity covered with 100-200Å pyrolytically deposited SiO_2 was placed in the reference beam; the reference for uncovered samples was a bare wafer. The base line was drawn to correct for oscillations due to interference of the thin films so that the relationships between spectra and composition are general for glasses of different thicknesses.

The thicknesses and refractive indices of these glasses were determined with a Gaertner ellipsometer.

Glasses were deposited on circular wafers approximately 1 in. in diameter, with a deviation of about 0.005 in. for a given wafer, as measured with a micrometer. The area of the film was taken to be the area of the wafer, and the film volume to be the area times the thickness.

Analysis

The film was dissolved in dilute HF solution (50 ml 50% HF/1 H_2O). Boron was determined colorimetrically by extracting methylene blue fluoroborate (4) with 1, 2-dichloroethane. The amount of boron in the glass film could be determined within ±2% except for glasses containing less than 5 μg boron for which the uncertainty was ±0.1 μg boron. The details of the boron analysis are presented elsewhere (5).

Silicon was determined with an Instrumentation Laboratories atomic absorbance spectrophotometer Model 153 in the range 0-40 ± 0.5 μg silicon/ml. This amounted to about a 2% error for most glasses. The silicon found was corrected for that in the cover glass, if present. Excess silicon (presumably etched from the wafer itself) was found if the wafer on which the glass was deposited were left in the dilute HF solution too long (>2 hr). It took a maximum of 5 min to etch the glass from the wafers and no excess silicon could be detected from wafers left in dilute HF for <10 min.

The film weights of several samples were determined by weighing the wafer before and after deposition of the glass (and again, as a check, after removal of the glass) using a Cahn recording electromicrobalance. The films were found to weigh 500-700 ± 15 μg.

The film weight and the B_2O_3 mole fraction $N_{B_2O_3}$ were calculated from the results of the analyses assuming boron and silicon to be present as B_2O_3 and SiO_2, respectively. It was found that within experimental error (2.5%) the weight thus calculated agreed with that found by direct weighing. With the precision of the boron and silicon analyses given above, $N_{B_2O_3}$ was determined in the range 0-1.0 within ± 0.005-0.02, the uncertainty depending somewhat on composition.

Results and Discussion

It was found that the relationship between the IR peak ratio, R, and $N_{B_2O_3}$ was dependent on temperature and other deposition conditions. In Fig. 1, R is shown as a function of $N_{B_2O_3}$ for glasses grown in three different reactors at temperatures from 250° to 500°C. The 300°, 350°, and 375°C lines are drawn to represent results from glasses grown in (vertical) reactor 1 only. The results from reactor 1 and (vertical) reactor 2 (open symbols) indicate that for a given R (or $N_{B_2O_3}$), $R/N_{B_2O_3}$ decreases with increasing deposition temperature in a given reactor. Also, the dependences of R on $N_{B_2O_3}$ for glasses grown in the different reactors at identical temperatures are found to be in disagreement. For instance, the results for R *vs.* $N_{B_2O_3}$ from reactor 1 at 350°C agree with those from (Silox) reactor 3 at 450°C and with those from reactor 2 at

Key words: borosilicate glass composition, IR peak ratio.

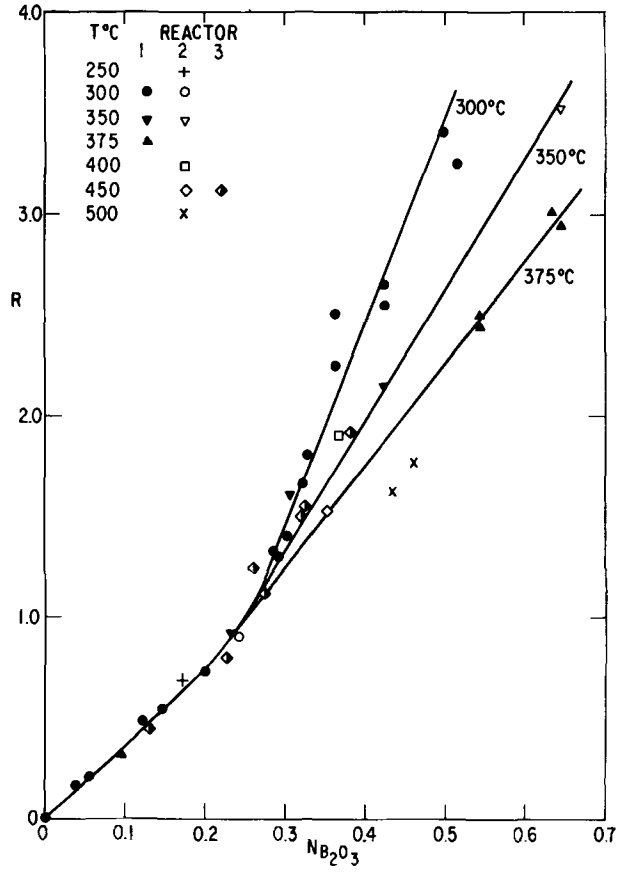

Fig. 1. Infrared peak ratio R vs. B_2O_3 mole fraction $N_{B_2O_3}$ for thin films of borosilicate glass pyrolytically deposited in vertical reactors 1 (closed symbols) and 2 (open symbols) of different geometry, and in horizontal Silox reactor 3 (half-filled symbols) at temperatures from 250° to 500°C.

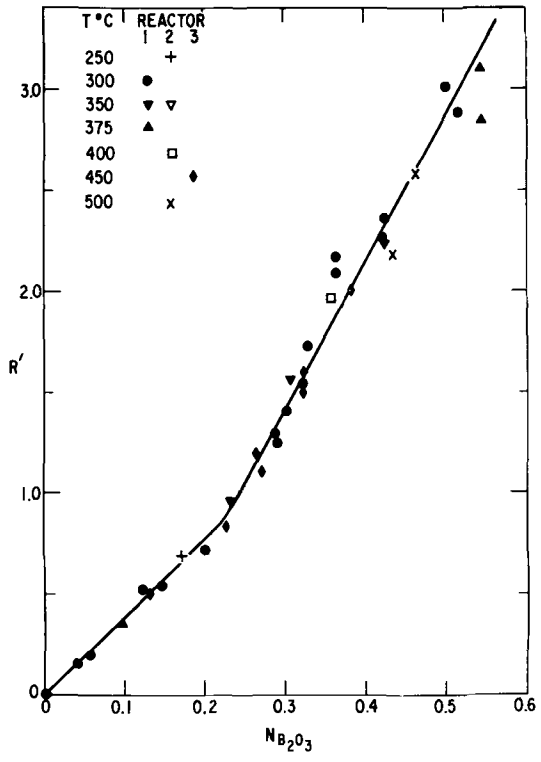

Fig. 2. Infrared band area ratio R' vs. B_2O_3 mole fraction $N_{B_2O_3}$ for thin films of borosilicate glass pyrolytically deposited in vertical reactors 1 (closed symbols) and 2 (open symbols) of different geometry, and in horizontal Silox reactor 3 (half-filled symbols) at temperatures from 250° to 500°C.

450°C > T > 400°C. Thus, the relationship between $N_{B_2O_3}$ and the infrared peak ratio is dependent not only on temperature but also on other deposition conditions (presumably related to reactor geometry). Although this relationship may be employed to determine the composition of borosilicate glasses from the infrared spectra, a calibration curve (of R *vs.* $N_{B_2O_3}$) must be generated for each glass reactor at each temperature (at least for glasses with $N_{B_2O_3} > 0.3$).

However, the relationship between $N_{B_2O_3}$ and R', the ratio of the integrated intensity or area of the B-O band to that of the Si-O band was found to be independent of deposition conditions. For simplicity (since the spectrophotometer employed records absorbance logarithmically) the area of a band is approximated by the product of the peak intensity in absorbance units times the bandwidth in cm^{-1} at half the peak height. In Fig. 2, this area ratio is shown as a function of mole fraction for the glasses whose peak ratios are shown in Fig. 1. The accuracy of the band area approximation should be suspected since neither band is symmetric. Nevertheless, when several spectra were replotted in linear absorbance units and the band areas determined with a planimeter, the results were found to agree with those shown in Fig. 2 with about the same precision. It is concluded that employing this approximation of the integrated intensities introduces little error at least in results involving area ratios. Most of the scatter seen in Fig. 2 probably results from stated imprecision of the chemical analysis.

Although the composition of thin films of borosilicate glass may be determined from their infrared absorbance spectra and the plot of R' *vs.* $N_{B_2O_3}$ shown in Fig. 2, R' must approach infinity as $N_{B_2O_3}$ approaches 1.0. In order to be able to correlate infrared results with $N_{B_2O_3}$ over the whole composition range, a quantity $N_{R'}$ is defined to be the area of the B-O band divided by the area of the B-O band plus the area of the Si-O band. This "area fraction," corresponding in some sense to an "optical mole fraction," approaches 0 and 1.0 as $N_{B_2O_3}$ approaches these values, respectively. Simple algebra shows

$$N_{R'} = \frac{R'}{1 + R'}$$

With an uncertainty of 0.01 absorbance in the peak heights and 5 cm^{-1} in the half-widths, it is found that $N_{R'}$ may be determined over the range 0-1.0 to a precision of better than ±0.03, the uncertainty being largest for glasses near the middle of the concentration range.

The composition of thin films of pyrolytically deposited glass may be determined nondestructively from the infrared spectra of these films and from Fig. 3, where the dependence of the infrared band area fraction $N_{R'}$ is shown as a function of the B_2O_3 mole fraction $N_{B_2O_3}$. This calibration curve is comprised of results on glasses deposited from 250° to 500°C in three different reactors: two vertical and one horizontal, all of different geometries.

A comparison of the results shown in Fig. 2 with those shown in Fig. 1 suggests that, while the integrated intensities of the infrared bands are insensitive to structural differences in glasses formed under various deposition conditions, the peak intensities reflect (and, in fact evidence) these differences. It is well known that the integrated intensity is a more reliable measure of concentration than is the peak intensity. However, the fact that the peak intensities depend on deposition conditions while the integrated intensities do not suggest (as indeed the data show) that the shape of at least one of the bands depends on deposition conditions.

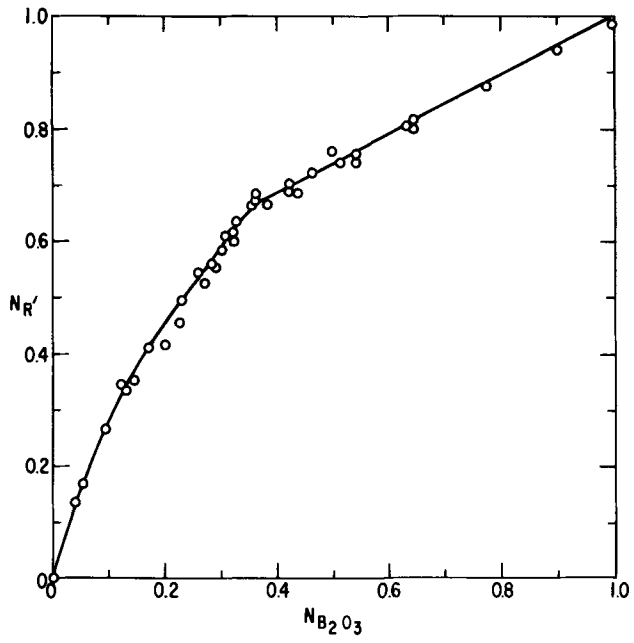

Fig. 3. Infrared band area fraction $N_{R'}$ vs. B_2O_3 mole fraction $N_{B_2O_3}$ for thin films of pyrolytically deposited borosilicate glass.

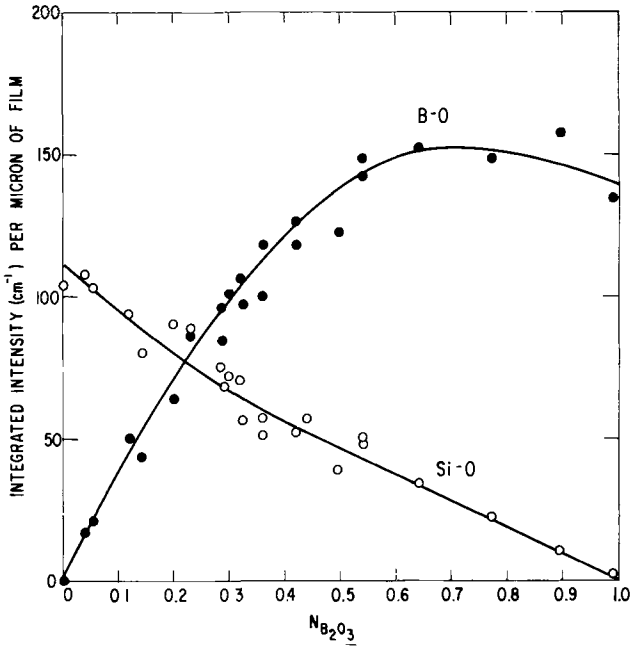

Fig. 4. Integrated intensity normalized to 1μ of film vs. B_2O_3 mole fraction for the major B-O and Si-O absorbance bands (at ~1300 and ~1050 cm^{-1}, respectively) in the borosilicate glass spectrum.

The linear absorption coefficient of a band may be calculated by dividing its peak height by the film thickness. This quantity was found to be temperature dependent for both the B-O and Si-O bands. However, like the area ratio, the integrated intensity is independent of temperature from 300° to 375°C. It should be pointed out that while quantities involving ratios of peak heights or areas such as R and R' are relatively insensitive to differences in spectrophotometer settings, the absolute values of peak heights or integrated intensities do depend on these settings. Thus absorbance coefficients reported here strictly apply only for the settings stated above.

The integrated intensity of each major band normalized to 1μ of film is shown as a function of B_2O_3 mole fraction in Fig. 4. From the glass composition, the band areas and the plots in Fig. 4, the thickness of the film may be determined. Although the area of either band may be used to measure film thickness, that of the larger band—which one this is depends on composition—gives more reliable results. This method is at best precise to ±5% for 6000Å of film making it about as accurate as using the interference colors. Nevertheless, it could be useful if thickness results did not accompany a spectrum or if the order of the color were not known.

Thus, employing Fig. 3 and 4, the composition and thickness of thin films of pyrolytically deposited borosilicate glass may be determined from their spectra alone.

The fact that the composition dependence of the integrated intensities is not linear suggests that the absorbance per mole or atom (of B and Si) is not independent of composition. This effect is particularly striking in the case of the B-O band whose absorbance is apparently greater for a glass of 60-70 m/o B_2O_3 than for pure B_2O_3. This composition dependence as

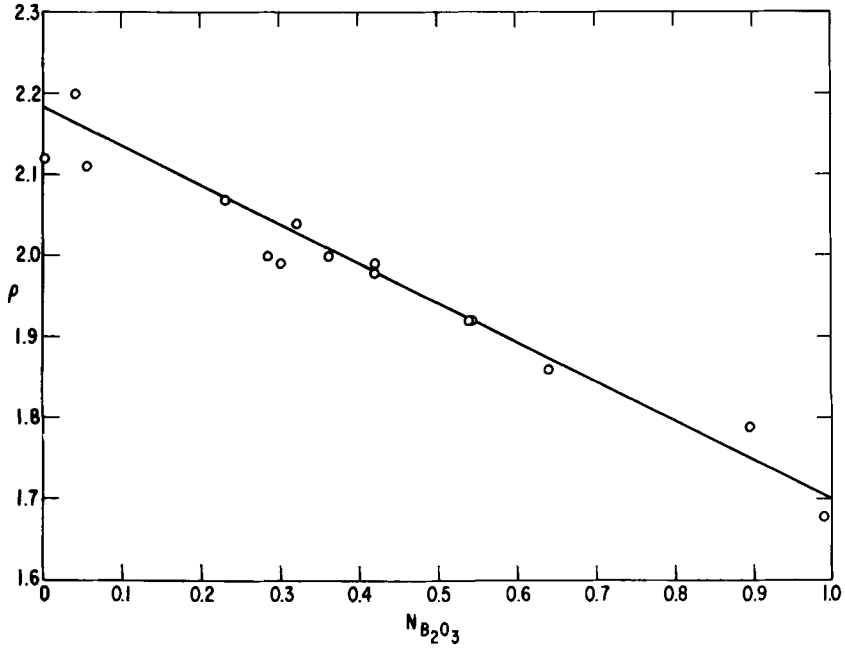

Fig. 5. Density ρ (as deposited) vs. B_2O_3 mole fraction $N_{B_2O_3}$ for thin films of borosilicate glass.

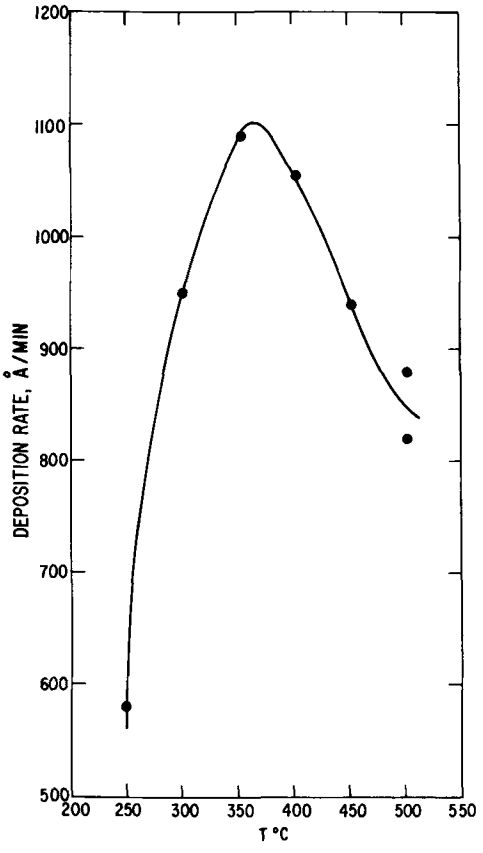

Fig. 6. Borosilicate glass deposition rate, Å/min (under constant reactant flows), vs. temperature.

well as the temperature (and composition) dependence of the band shapes mentioned above and several other characteristics of the IR spectra of these glasses will be considered further in a subsequent publication (6).

From the film volume and weight, the density ρ of the glass, as deposited, may be calculated. The densities found are plotted as a function of $N_{B_2O_3}$ in Fig. 5. It was found that

$$\rho = 2.18 - 0.48\, N_{B_2O_3} \pm 0.1$$

for glasses deposited from 300° to 375°C. The density of 2.18 obtained for pure SiO_2 agrees with those found in the literature for bulk glasses (7), while the value of 1.70 for B_2O_3 is lower than those previously reported (7-9). The scatter in the results shown in Fig. 5 is probably due largely to the uncertainty of the chemical analysis and to the as much as 5% variation in film thickness across a given wafer.

The refractive index was found to be 1.46 ± 0.01 for glasses as deposited from 300° to 375°C and within this experimental uncertainty to be independent of concentration and temperature of deposition. This value agrees with those reported for SiO_2 (7) and for B_2O_3 (9).

The temperature dependence of the glass growth rate and composition (for given gas flows) were found to be in agreement with the results of Kern and Heim (10). While the growth rate increases with temperature, reaches a maximum at 375°C, and then decreases as shown in Fig. 6, $N_{B_2O_3}$ increases continuously with temperature as shown in Fig. 7 for glasses deposited from a B_2H_6 to SiH_4 flow rate ratio of 0.5. Kern and Heim's results indicate a leveling off of $N_{B_2O_3}$ with temperature at about 450°C. The present data are in agreement with this conclusion. However, $N_{B_2O_3}$ apparently increases again for glasses grown from 450° to 500°C.

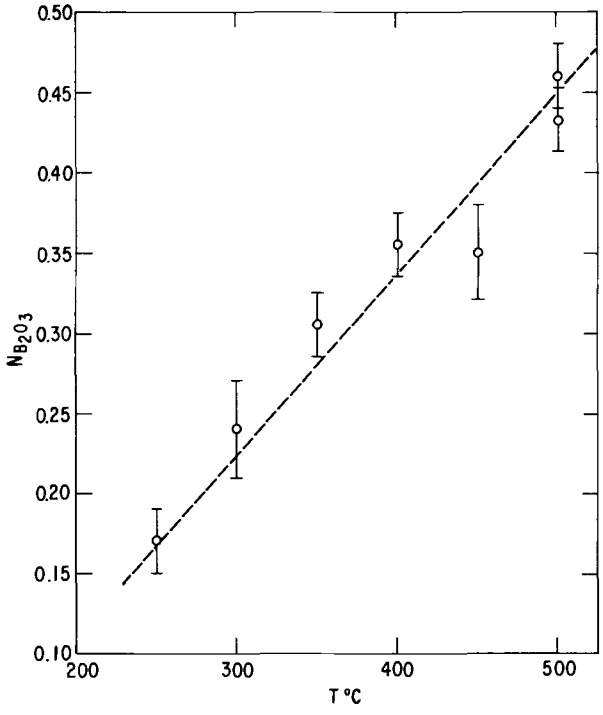

Fig. 7. B_2O_3 mole fraction vs. temperature for borosilicate glass deposited from a B_2H_6 to SiH_4 flow rate ratio of 0.5.

Acknowledgment

We thank E. A. Taft for all ellipsometric results presented here and for many valuable discussions throughout this work.

Manuscript submitted March 19, 1971; revised manuscript received *ca.* June 8, 1971.

Any discussion of this paper will appear in a Discussion Section to be published in the June 1972 JOURNAL.

REFERENCES

1. (a) W. Kern and R. C. Heim, *This Journal*, **117**, 568 (1970); (b) W. Kern, *ibid.*, **116**, 251C RNP 372 (1969).
2. E. A. Taft, To be published.
3. D. M. Brown and P. Kennicott, *This Journal*, **118**, 293 (1971).
4. J. Utsumi and A. Isozaki, *Nippon Kagaku Zasshi*, **88**, 545 (1967).
5. A. S. Tenney, To be published.
6. A. S. Tenney and J. Wong, To be published.
7. R. C. Weast, Editor, "Handbook of Chemistry and Physics," 50th ed., pp. B-94, B-153. The Chemical Rubber Co., Cleveland (1969).
8. P. B. Macdeo, W. Capps, and T. A. Litowitz, *J. Chem. Phys.*, **44**, 3357 (1966).
9. M. Imaoka and T. Yamazaki, *J. Ceram. Assoc. Japan*, **73**, 264 (1965).
10. W. Kern and R. C. Heim, *This Journal*, **117**, 562 (1970).

The Free Energy of Mixing in the Lithium-Germanium Binary System[1]

Gunter H. R. Kegel, Richard J. Laramee,[2] and Brahm D. Bhardwaj[3]

Lowell Technological Institute, Lowell, Massachusetts 01854

ABSTRACT

The free energy of mixing of the solid solution of Li in Ge has been measured for 250°C $\leq T \leq$ 420°C. An equilibrium method is used. Germanium samples are immersed in molten Li-Pb alloys of known lithium activity. After reaching equilibrium the lithium concentration in the samples is measured and the free energy of mixing is obtained from the lithium activity and the concentration. The partial molar heat and entropy of lithium in the solid solution are given.

Various techniques may be used to measure the free energy of mixing in binary systems. These procedures have been described by Lewis and Randall (1) and some of the results obtained by different workers for binary alloys have been collected by Hultgren, Orr, Anderson, and Kelley (2). Few if any, of these procedures are suitable in the case reported in this paper because the Li solubility in Ge is small, about a few parts per million, and the lithium diffusion coefficient is small at the low temperatures under consideration. In view of these restrictions a variant of an existing technique has been applied; lithium is diffused into germanium from an external phase consisting of a liquid alloy with known lithium activity. Once equilibrium is reached the Li activity in the alloy equals that in the germanium.

Ideally Ge should be insoluble in the external phase and vice versa. This requirement is approximated if lead is used as an external phase because the solubility of Ge in Pb is small [see, *e.g.*, Thurmond and Kowalchik (3)] and the diffusion coefficient of Pb in Ge is probably orders of magnitude smaller than that of Li (4). Li-Sn alloys were used by Reiss and Fuller to diffuse Li into silicon (5); they were found unsuitable because the germanium solubility in tin is too large (3).

Once equilibrium is established the lithium concentrations in the germanium and in the alloy have to be determined. The lithium activity in the alloy can be obtained from the Li-Pb phase diagram. These data give the partial molar free energy of Li in Ge and thence heat and entropy of mixing.

Experimental Procedure

Germanium samples were cut from horizontally grown, single-crystal material containing approximately 3 x 10^{14} cm^{-3} of gallium. Samples were about 2.7 cm long, 1.0 cm wide, and 0.13 cm thick. These pieces were ground and etched; tin plating, using an alkaline bath, was found to facilitate wetting with the Li-Pb alloy. For lithium diffusion a germanium sample and an adequate amount of alloy were placed in the diffusion apparatus, under vacuum, and were heated to the desired equilibration temperature. Diffusion times were chosen as follows: The time required to obtain a lithium distribution uniform to within 1% was computed, as outlined in Appendix A. This time interval is denoted by $t_{0.01}$. Actual diffusion times were substantially longer than $t_{0.01}$, assuring that the Li distribution would be uniform to 1% or better in the germanium samples. Diffusion times and temperatures, the parameters $t_{0.01}$, and other pertinent data are listed in Table I.

At the end of the diffusion period the alloy was drained and kept for analysis; the sample was cleaned and mounted in a conductivity measuring device. From the sample conductivity the lithium concentration was computed, as outlined in the next section.

The Li content of the alloy was determined by dissolving the alloy in Hg, extracting Li with water, and titrating the extract with HCl.

Data Reduction

Li dissolves in Ge as a donor (6) hence the conduction electron concentration and the sample conductivity are functions of the lithium concentration. Since our samples also contained gallium, an acceptor, we have to consider the following set of reactions

$$\begin{array}{ccc} Li \rightleftharpoons Li^+ & + & e^- \\ + & & + \\ Ga \rightleftharpoons Ga^- & + & e^+ \\ \Updownarrow & & \Updownarrow \\ Li^+Ga^- & & e^+e^- \end{array} \qquad [1]$$

At the measuring temperature of 60°C Ga and Li are almost fully ionized. The equilibrium constant for the reaction $Li^+ + Ga^- \rightleftharpoons Li^+ Ga^-$ has been evaluated by Reiss, Fuller, and Morin (6) and the constant for the reaction $e^+ + e^- \rightleftharpoons e^+e^-$ has been determined by Morin and Maita (7). These data can be used to obtain concentrations of Li^+, Ga^-, e^+, e^-, and Li^+Ga^-, all as functions of the total lithium concentration.

The conductivity σ is given by

$$\sigma = e\,(n\,\mu_n + p\,\mu_p) \qquad [2]$$

Here e is the electronic charge, n and p are concentrations of electrons and holes, respectively, and μ_n and μ_p are the corresponding mobilities. Mobility data are available in the literature (8) so that σ can be computed as a function of the lithium concentration. This function is shown in Fig. 1.

We should add here the diffusion of lead or tin into the sample can be neglected, as far as the sample conductivity is concerned. Lead and tin are Group IV elements and are not expected to be electrically active

Table I. Diffusion parameters

Sample	Diff. temp, °C	Diff. time, hr	Lithium concentration in sample, cm^{-3}	Lithium concentration in alloy, a/o	$t_{0.01}$, hr (see text)
P1	285	336	3.8×10^{16}	20.7	22.0
P2	250	360	1.02×10^{16}	13.0	45.5
P3	330	65	1.08×10^{17}	13.5	9.96
P4	360	66	8.0×10^{16}	13.3	6.23
P5	390	42	1.12×10^{17}	14.0	4.13
P6	420	44	2.6×10^{17}	13.4	2.73

[1] Work supported by the Germanium Information Center.
[2] Present address: Raytheon Manufacturing Company, Bedford, Massachusetts 01730.
[3] Present address: Rice University, Houston, Texas 77000.
Key words: activity of Li in Ge, Li-Pb system, Li diffusion.

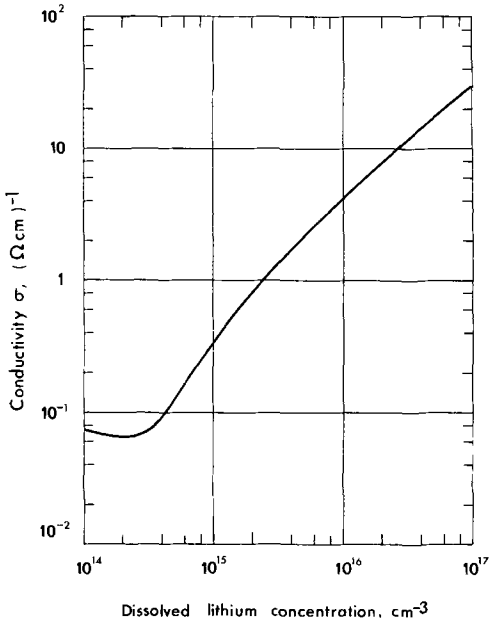

Fig. 1. Sample conductivity σ in function of the total dissolved lithium concentration at 60°C.

in Ge, *i.e.*, they do not supply electrons or holes. As neutral impurities, lead and tin atoms contribute to the scattering of charge carriers so that the carrier mobilities will be attenuated. This effect is negligible because the depth of lead or tin diffusion is likely to be small. This question is examined in more detail in Appendix B.

Activity of Li in Li-Pb Alloys

The phase diagram of the Li-Pb system has been determined by Grube and Klaiber (9). In the range $235°C \leq T \leq 327°C$ both solid and liquid solutions are found at the Pb-rich end of the diagram. We assume that both solutions are regular, see *e.g.* Swalin (10), and we write for the excess free energy of mixing

$$\Delta G_m^{xs,L} = \Omega_{AC}^{L} X_A^{L} X_C^{L} \quad [3]$$

$$\Delta G_m^{xs,S} = \Omega_{AC}^{S} X_A^{S} X_C^{S} \quad [4]$$

Here X are atom fractions; subscripts A, B, and C refer to Li, Ge and Pb, respectively; superscripts L and S refer to liquid and solid phases. The Ω are interaction parameters (10).

From [3] and [4] the partial molar free energies of Li and Pb can be obtained. At a given temperature the partial molar free energy of Li at the liquidus is equal to that at the solidus, an analogous relation holds for Pb. These two conditions are used to obtain Ω_{AC}^{L} and Ω_{AC}^{S}. The result is

$$\Omega_{AC}^{L} = -2.69 \text{ kJ/mole} \quad [5]$$

$$\Omega_{AC}^{S} = \omega_{AC}^{0} + \omega_{AC}^{1} T \quad [6]$$

$$\omega_{AC}^{0} = 33.7 \text{ kJ/mole} \quad [7]$$

$$\omega_{AC}^{1} = -56 \text{ J/mole K°} \quad [8]$$

The liquidus and solidus calculated with these data fit the experimental results by Grube and Klaiber quite well, as shown in Fig. 2. This shows, that our assumption about the regular character of the solutions is consistent with the experimental data.

Results

It is convenient, though not essential, to assume that the solid solution of Li in Ge be regular. In this case the partial molar free energy of Li in Ge is

$$\Delta\bar{G}_A^{S} = (1 - X_A^{S})^2 \Omega_{AB}^{S} + RT \ln X_A^{S} + \Delta G_{fA} \simeq \Omega_{AB}^{S} + RT \ln X_A^{S} + \Delta G_{fA} \quad [9]$$

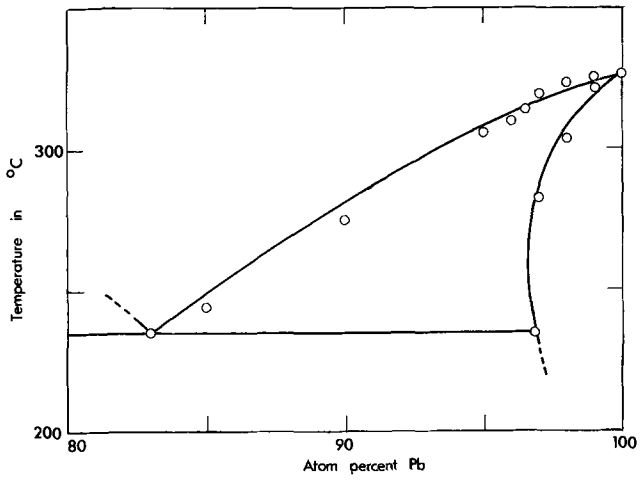

Fig. 2. Lead-rich end of the lithium-lead phase diagram. The points indicate the results by Grube and Klaiber (9). The liquidus and the solidus have been calculated assuming solid and liquid solutions to be regular.

Here we omitted X_A^{S} in the first term because $X_A^{S} \simeq 10^{-5} << 1$. The last term is the free energy of fusion of Li at temperature T. For the Li-Pb alloy we have

$$\Delta\bar{G}_A^{L} = (1 - X_A^{L})^2 \Omega_{AC}^{L} + RT \ln X_A^{L} \quad [10]$$

Equating $\Delta\bar{G}_A^{L}$ and $\Delta\bar{G}_A^{S}$ we obtain Ω_{AB}^{S}. These data are shown in Fig. 3.

A note should be added concerning the data at 285° and 330°C. The lithium concentration in these samples has reached the saturation value as measured by Morin and Reiss (11). In this case

$$\Delta\bar{G}_A^{L} > \Delta\bar{G}_A^{S} \quad [11]$$

and only an upper limit for Ω_{AB}^{S} is obtained.

It is interesting to compare our results with those obtained from the Li-Ge phase diagram. Pell (12) has calculated the liquidus assuming the liquid solution to be regular. The solidus has been determined by Reiss, Fuller, and Morin (6) and by Pell (12). These data may be analyzed in the same fashion as those for the Li-Pb phase diagram and Ω_{AB}^{S} can be obtained. The result is also shown in Fig. 3, it is consistent with our measurements.

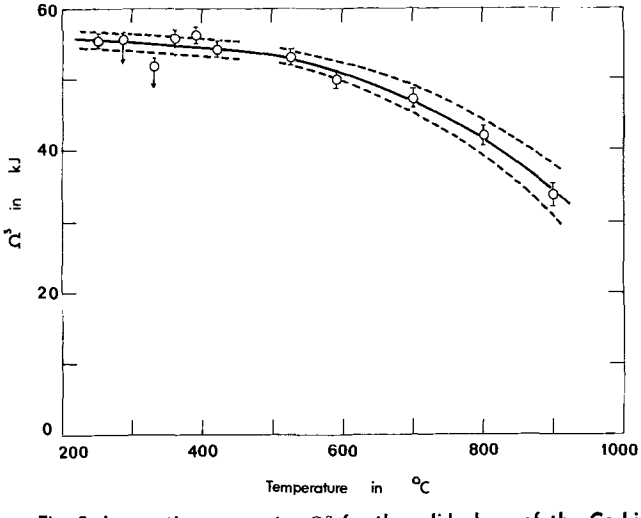

Fig. 3. Interaction parameter Ω^{S} for the solid phase of the Ge-Li system. Points with $T < 500°C$ were obtained from measurements reported in this paper; points with $T > 500°C$ were computed from data by Pell (12). Dashed lines indicate the range of systematic errors; random errors are shown by error flags.

In the temperature range covered by our measurements $\Omega_{AB}{}^{S}$ can be written as

$$\Omega_{AB}{}^{S} = 59.6 \text{ kJ/mole} - 7.7 \text{ J/(mole °K)}\ T \quad [12]$$

Equation [9] shows that

$$\Omega_{AB}{}^{S} = \Delta\overline{G}_{A}{}^{xs,L} \quad [13]$$

Hence the partial molar heat of lithium is

$$\Delta\overline{H}_{A} = 59.6 \text{ kJ/mole} \quad [14]$$

and the excess partial molar entropy

$$\Delta\overline{S}_{A}{}^{xs} = 7.7 \text{ J/(mole °K)} \quad [15]$$

Manuscript submitted Oct. 19, 1970; revised manuscript received April 2, 1971.

Any discussion of this paper will appear in a Discussion Section to be published in the June 1972 JOURNAL.

APPENDIX A

Lithium Distribution

The lithium distribution in the samples can be calculated by solving the diffusion equation with appropriate initial and boundary conditions (13). In our case the sample thickness a ($a = 0.13$ cm) is much less than its width b ($b = 1.0$ cm) or length c ($c = 2.7$ cm), so that most of the lithium reaches the sample interior by diffusion in the x-direction. (See Fig. 4). If we neglect diffusion in y- or z-direction we have

$$\frac{\partial C}{\partial t} = D\frac{\partial^2 C}{\partial x^2} \quad [16]$$

Here $C(x, t)$ is the lithium concentration and D is the lithium diffusion coefficient. The initial and boundary conditions are $C(x, 0) = 0$; $C(0, t) = C(a, t) = C_0$.

It is apparent, that at all times during the diffusion cycle the lowest lithium concentration will be found in the sample center, $x = a/2$. Solving the diffusion equation, we find for $C(a/2, t)$

$$C(a/2, t) = C_0 - \frac{4}{\pi} C_0 \sum_{n=0}^{\infty} \frac{(-1)^n}{2n+1} \exp\left\{ - (2n+1)^2 \frac{t}{\tau} \right\} \quad [17]$$

where

$$\tau = \frac{a^2}{\pi^2 D} \quad [18]$$

The parameter $t_{0.01}$ is defined as the time required to obtain a lithium distribution which is uniform to within 1%. Thus.

$$C(a/2, t_{0.01}) = 0.99\ C_0 \quad [19]$$

Substituting [19] into [17] and solving for $t_{0.01}$ we get

$$t_{0.01} = 4.85\ \tau \quad [20]$$

Numerical values of $t_{0.01}$ are given in Table I; they were obtained using the lithium diffusion coefficients determined by Fuller and Severiens (14).

APPENDIX B

Tin and Lead Impurities

In this appendix we examine the influence of lead and tin impurities upon the sample conductivity. We consider tin first.

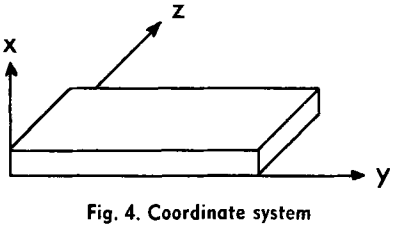

Fig. 4. Coordinate system

Table II. Tin diffusion

Sample	u_0, Eq. [21], cm	A, Eq. [28]	δ, Eq. [27], cm
P1	1.80×10^{-7}	5062	4.69×10^{-7}
P2	4.02×10^{-8}	5816	1.06×10^{-7}
P3	4.40×10^{-7}	4201	1.13×10^{-6}
P4	1.21×10^{-6}	4459	3.13×10^{-6}
P5	2.42×10^{-6}	4136	6.22×10^{-6}
P6	5.72×10^{-6}	3339	1.45×10^{-5}

The solubility of tin in germanium is large at the temperatures of interest: $X_{Sn} \simeq 5 \times 10^{20}$ cm^{-3} (15). The Sn diffusion coefficient in Ge, D_{Sn}, does not seem to be known. It is unlikely, however, that this diffusion coefficient differs substantially from that of the adjacent elements, Sb and In.

At the end of the diffusion cycle, the tin concentration in the sample, $C_{Sn}(u)$, at a depth u below the surface, is given by (13)

$$C_{Sn}(u) = C_{Sn}(0) \text{ erfc } \frac{u}{u_0} \quad [21]$$

$$u_0 = 2\sqrt{D_{Sn}\, t}$$

Here $C_{Sn}(0)$ is the Sn concentration at the sample surface and t is the diffusion time. If we assume that the Sb diffusion coefficients reported by Fuller (16) hold for Sn too, then we can compute u_0; the result is given in Table II.

Tin and lead act as neutral impurity scatterers in Ge; their action is accounted by introducing a neutral impurity mobility μ_N (8). For Sn and for electrons we have

$$\mu_N = \frac{1}{20} \frac{m^* e^3}{4\pi\epsilon\hbar^3} \frac{1}{C_{Sn}(u)} = \frac{\lambda}{C_{Sn}(u)} \quad [22]$$

where

$$\lambda = 2.32 \times 10^{22} \text{ (V sec m)}^{-1} \quad [23]$$

If we denote by μ_0 the electron mobility in the absence of tin, then the total mobility μ is given by (8)

$$\frac{1}{\mu(u)} = \frac{1}{\mu_N} + \frac{1}{\mu_0} \quad [24]$$

Our measurements depend on the average mobility, μ_{av}, which is essentially equal to $\mu(u)$ averaged over the interval $0 \leq u \leq a/2$

$$\mu_{av} \simeq \frac{2}{a} \int_0^{a/2} \mu(u)\ du \quad [25]$$

It is convenient to write

$$\mu_{av} = \mu_0 \left(1 - \frac{2\delta}{a}\right) \quad [26]$$

Here the parameter δ may be considered as the thickness of an equivalent layer with zero mobility. Combining Eq. [21] to [26] we obtain

$$\delta = u_0 \int_0^{\frac{a}{2u_0}} \frac{dv}{1 + (A \text{ erfc } v)^{-1}} \quad [27]$$

where

$$A = \frac{\mu_0}{\lambda} C_{Sn}(0) \quad [28]$$

The parameters δ have been computed assuming $C_{Sn}(0) = X_{Sn} = 5 \times 10^{20}$ cm^{-3}; the results are given in Table II. It is apparent that $2\delta/a$ is negligibly small, so that in very good approximation $\mu_{av} = \mu_0$. Similar results apply to the hole mobilities.

The solubility of Pb in Ge is much smaller than that of Sn, $X_{Pb} \leq 6 \times 10^{17}$ cm^{-3}, so that the role of this impurity is negligible too.

REFERENCES

1. G. N. Lewis and M. Randall, "Thermodynamics," revised by K. S. Pitzer and L. Brewer, McGraw-Hill Book Co., New York (1961).
2. R. Hultgren, R. L. Orr, P. D. Anderson, and K. K. Kelley, "Selected Values of Thermodynamic

Properties of Metals and Alloys," John Wiley & Sons, Inc., New York (1963).
3. C. D. Thurmond and M. Kowalchik, *Bell Syst. Tech. J.*, **39**, 169 (1960).
4. U. Gürs and K. Gürs in "Landolt-Bornstein, Zahlenwerte und Funktionen," Vol. IV, part 2c, p. 734, H. Borchers and E. Schmidt, Editors, Springer, New York (1965).
5. H. Reiss and C. S. Fuller, *J. Metals*, **8**, 276 (1956).
6. H. Reiss, C. S. Fuller, and F. J. Morin, *Bell Syst. Tech. J.*, **35**, 536 (1956).
7. F. J. Morin and J. P. Maita, *Phys. Rev.*, **94**, 1525 (1954).
8. P. P. Debye and E. M. Conwell, *ibid.*, **93**, 693 (1954).
9. G. Grube and H. Klaiber, *Z. Elektrochem.*, **40** 754 (1934).
10. R. A. Swalin, "Thermodynamics of Solids," John Wiley & Sons, Inc., New York (1964).
11. F. J. Morin and H. Reiss, *J. Phys. Chem. Solids*, **3**, 196 (1957).
12. E. M. Pell, *ibid.*, **3**, 74 (1957).
13. H. Reiss and C. S. Fuller in "Semiconductors," p. 224, N. B. Hannay, Editor, Reinhold Publishing Corp., New York (1960).
14. C. S. Fuller and J. C. Severiens, *Phys. Rev.*, **92**, 1322 (1953); **96**, 21 (1954).
15. F. A. Trumbore, *Bell Syst. Tech. J.*, **39**, 205 (1960).
16. C. S. Fuller, *Phys. Rev.*, **86**, 137 (1952).

Nonstoichiometric Disorder in Single Crystalline MnO

N. G. Eror[1] and J. B. Wagner, Jr.*

Department of Materials Science and Materials Research Center, The Technological Institute, Northwestern University, Evanston, Illinois 60201

ABSTRACT

The electrical conductivity of single crystalline manganous oxide was investigated over the temperature range of 900°-1150°C while in thermodynamic equilibrium with oxygen partial pressures of 10^{-6}-10^{-21} atm. Results indicated that MnO may be either p- or n-type. Slopes of 1/6 and −1/6 are obtained from the log σ *vs.* log p_{O_2} data for the p- and n-type regions, respectively. Thermogravimetric measurements at thermodynamic equilibrium support the evidence of the electron mobility being much greater than that for electron holes in MnO. The enthalpies of formation of nonstoichiometric disorder and activated enthalpy of movement of electron holes in p-type MnO were determined to be −18 and 12 kcal/mole, respectively. The bandgap of MnO was calculated from the minima of the log σ *vs.* log p_{O_2} data to be 52.8 kcal/mole (2.3 eV).

Davies and Richardson (1) investigated the nonstoichiometry of manganous oxide at 1500°, 1575°, and 1650°C as a function of oxygen partial pressure. The concentration of excess oxygen was determined by chemical analysis for trivalent manganese. Calculations from the data of Davies and Richardson indicate that for large deviations from stoichiometry the manganese vacancy concentration is proportional to $P_{O_2}^{1/6}$. For this oxygen pressure range the nonstoichiometric disorder may be described by

$$\tfrac{1}{2}\,O_2 \rightleftarrows O_O + V_{Mn}'' + 2p \qquad [1]$$

where V_{Mn}'' and p refer, respectively, to doubly ionized manganese vacancies and electron holes.

Marion and co-workers (2) found that polycrystalline MnO may be either p- or n-type on the basis of electrical conductivity measurements as a function of oxygen partial pressure over the temperature range 900°-1200°C. Later measurements (3) at 1000°C of the electrical conductivity and Seebeck coefficient have been interpreted on the basis of ± 1/6 oxygen partial pressure dependence due to doubly ionized manganese vacancies (Eq. [1]) for the p-type region and Mn^{+2} interstitials for the n-type data. The metal excess disorder could be expressed by

$$Mn_{Mn} + O_O \rightleftarrows Mn_i^{\cdot\cdot} + 2n + \tfrac{1}{2}\,O_2 \qquad [2]$$

where $Mn_i^{\cdot\cdot}$ denotes a manganese interstitial. Tannhauser and co-workers (4) have also determined that MnO may be either p- or n-type at elevated temperatures. Electrical conductance, Seebeck effect, and thermogravimetric measurements on polycrystalline and single-crystal samples over the temperature range 1100°-1557°C have been interpreted on the basis of a predominantly metal deficit compound with the mobility of electrons much greater than that for electron holes. This mobility ratio was later calculated to be approximately 50 at 943°C on the basis of Hall effect measurements on a MnO single crystal (5). DeWit and Crevecoer (6, 7) have confirmed that the mobility of electrons is much greater than that for electron holes at elevated temperatures and report a ratio of approximately 1000 at 1100°C for polycrystalline MnO. Lacombe *et al.* (8) have measured the electrical conductivity and Mn diffusion in MnO and conclude that the atomic defects associated with the p- and n-type regions are doubly ionized manganese vacancies and triply ionized manganese interstitials, respectively. Price and Wagner (9), however, have reported Mn tracer diffusion data in single crystalline MnO that are in agreement with a model of doubly ionized cation vacancies for describing nonstoichiometric MnO.

Experimental

The experimental technique has been described previously (10) except that an Ainsworth semimicro vacuum recording balance for a 4g single crystal was also used for the thermogravimetric measurements. See Table I for chemical analysis of the single crystals.

Experimental Results and Discussion

The electrical conductivity of single crystalline MnO as a function of oxygen partial pressure derived from CO-CO_2 mixtures is shown in Fig. 1. As can be clearly seen the electrical conductivity of single crystalline MnO can be either n- or p-type over the temperature range 900°-1150°C. The n- to p-type transitions or minima in the isothermal log σ *vs.* log p_{O_2} plot are near the center of the log p_{O_2} *vs.* $1/T$ single-phase region and lie near a constant CO/CO_2 ratio of unity. Hed and Tannhauser (4) found the same type of behavior at higher temperatures and Marion and co-workers (2) report similar behavior for polycrystalline MnO.

* Electrochemical Society Active Member.
[1] Present address: Oregon Graduate Center, Portland, Oregon 97225.
Key words: lattice defects, electronic conductivity, thermogravimetry.

Table I. Analyses of MnO crystals (as-received boule)

Analytical Laboratory "A" Impurity	Weight per cent
Aluminum	0.005
Iron	0.001
Molybdenum	0.001
Nickel	0.001
Vanadium	0.001
Chromium	0.0005
Copper	0.0005
Lead	0.0005
Silicon	0.0005
Silver	0.0001

As, Bi, Ca, Nb, Co, Cs, K, Li, Na, Hf, P, Rb, Sb, Sn, Ti, W, and Zr were not detected.

Analytical Laboratory "B"

Ca, Co, Fe, Si, V, Al, Cr, Cu, Mo, Ni, Ag, and Pb all < 1 ppm weight (Ti = 0.001 weight per cent).

The linear p-type log σ *vs.* log p_{O_2} data are limited to approximately two decades of oxygen partial pressure for each of the temperatures investigated. A slope of approximately 1/6 is found at the lower temperatures and nearly 1/5 for the higher temperatures. These data are given in Table II together with the probable error. This oxygen partial pressure dependence suggests that the disorder may be described by an expression of the form of Eq. [1] for the lower temperatures and by a transition to an expression of the form

$$\tfrac{1}{2}\,O_2 \rightleftarrows O_O + V_{Mn}' + p \qquad [3]$$

for the higher temperatures and oxygen partial pressures.

The electronic conductivity, σ, may be expressed by (10, 11)

$$\sigma = \text{const.}\ p_{O_2}^{1/2\,m} \exp\left[-\frac{\Delta H_f}{mRT} - \frac{\Delta H_p}{RT}\right] \qquad [4]$$

where ΔH_f denotes the enthalpy of dissolution of oxygen, m denotes the degree of ionization of the lattice defects, ΔH_p is the enthalpy of motion of the electronic carriers, and the other terms have their usual significance. Arrhenius plots for the electrical conductivity of p-type manganous oxide at constant oxygen partial pressures may be constructed from the data in Fig. 1. It is clear that only three temperatures correspond to any single oxygen partial pressure for which the p-type conductivity is linear in Fig. 1. For this reason the linear regions were extrapolated in order to provide additional data points in constructing the Arrhenius plots at constant oxygen partial pressure. The log σ *vs.* $1/T$ relationship for p-type manganous oxide at fixed oxygen partial pressures is given in Fig. 2 where the data obtained by extrapolation of the linear log σ *vs.* log p_{O_2} data has been denoted. The slopes of the Arrhenius data in Fig. 2 result in a value of 8 kcal/mole for the sum, $\Delta H_f°/m + \Delta H_p$. These data are given in Table III. The oxygen partial pressures were obtained from CO/CO_2 ratios and precise values for the oxygen partial pressure could only be obtained at temperatures above 900°C. It was not possible to obtain a constant concentration of disorder by quenching (10, 11) manganous oxide since even at 900°C the specimen was found to have equilibrated as rapidly as a homogeneous CO/CO_2 ratio could be established in the furnace reaction tube assembly.

Table II. Oxygen partial pressure dependence of the electrical conductivity

Temperature, °C	Oxygen partial pressure dependence of the electrical conductivity (with probable error) p-type	n-type
900	1/5.9 ± 0.3	−1/5.40 ± 0.05
950	1/5.9 ± 0.2	−1/6.14 ± 0.07
1000	1/5.7 ± 0.1	−1/5.92 ± 0.05
1050	1/5.4 ± 0.2	−1/6.23 ± 0.05
1100	1/5.2 ± 0.1	−1/6.42 ± 0.02
1150	1/5.4 ± 0.2	−1/6.42 ± 0.14

There was a departure from the linearity of the log σ *vs.* log p_{O_2} data for CO_2/CO ratios greater than approximately 200. Since the increase in electrical conductivity was identified with a specific CO_2/CO ratio rather than a particular oxygen partial pressure, it was possible to have a higher value of the electrical conductivity at temperature T_1, than at temperature T_2, where $T_1 < T_2$. Similar behavior at more elevated temperatures can be interpreted from the data of Hed and Tannhauser (4) for CO_2/CO ratios greater than 50. This behavior is not readily apparent since the published data (4) are reported on the basis of CO_2/CO values rather than oxygen partial pressure. Hed and Tannhauser (12) have interpreted our data on the basis of the decrease in concentration of cation vacancies with increasing temperature at constant oxygen pressure for the high oxygen compositions of MnO. The same behavior is also true for lower concentrations of nonstoichiometric disorder where the log σ *vs.* log p_{O_2} data are linear. Bransky (13), on the other hand, has made thermogravimetric measurements and has found

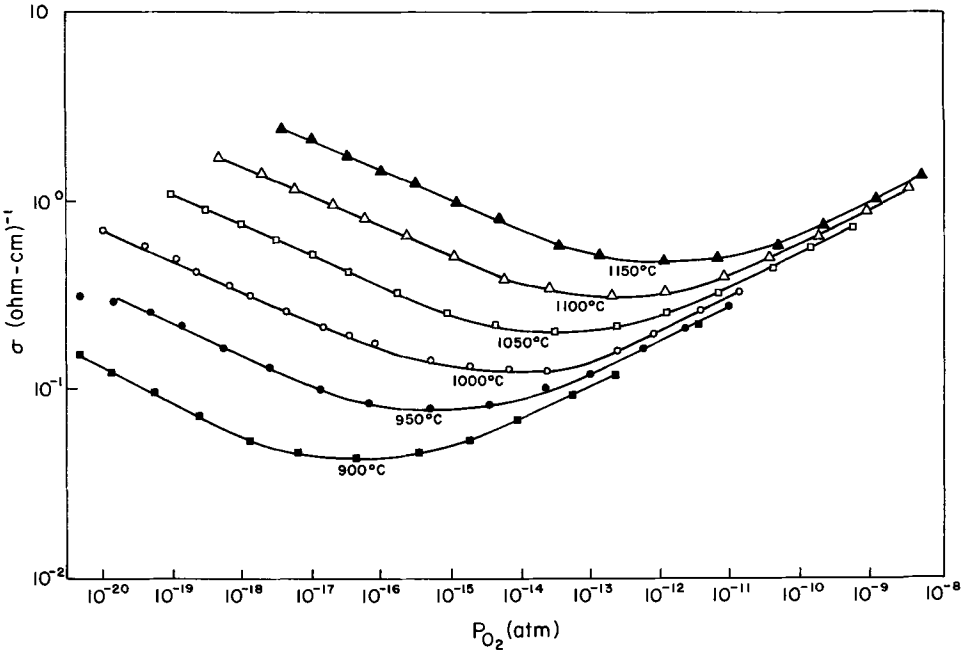

Fig. 1. Oxygen partial pressure dependence of the electrical conductivity of MnO showing the minimum in conductivity.

Table III. Sum of the activation energies for defect formation and electrical conduction for MnO

p_{O_2}	$\frac{\Delta H_f^\circ}{3} + \Delta H_p$ (kcal) (p-type) (probable error)	$\frac{\Delta H_f^\circ}{3}$ (kcal) (p-type) (probable error)	ΔH_p (kcal) (p-type) (probable error)	[(Measured activation energy sum)/D]† (kcal) (n-type) (95% confidence level)
10^{-9}	7.0 ± 0.3			
7×10^{-10}	6.0 ± 0.2	−5.9 ± 0.6	11.9 ± 0.8*	
			11.8 ± 0.5**	
10^{-11}	8.0 ± 0.4			
2.5×10^{-13}	8.0 ± 0.7			
10^{-17}				53.7 ± 1.1
10^{-18}				52.4 ± 1.3
10^{-19}				51.7 ± 0.8
		Bandgap 52.8 ± 0.6 kcal/mole (2.3 eV)		

† See text.
* Calculated by difference.
** Mobility data, see Fig. 5.

a ¼ power oxygen partial pressure dependence with no break in the weight charge data for p-type MnO. Bransky's data do not extend to CO_2/CO ratios of 200, however.

In the present study it was found that there were but small weight changes near the p- to n-type transition and at 1000°C one had to increase the oxygen partial pressure by four decades before significant weight changes were apparent (*e.g.*, $> 10^{-3}$ mole fraction). The isothermal weight change data were fitted to the integer, $2m$, that produced the best straight line as a function of $p_{O_2}^{1/2m}$ and extrapolated to $p_{O_2}^{1/2m} = 0$ for an estimate of the "stoichiometric weight" (10). The weight of the crystal at 1000°C as a function of $p_{O_2}^{1/6}$ is shown in Fig. 3. The similarity of Fig. 3 and Fig. 1 for the p-type electrical conductivity at 1000°C should be noted: both are linear over the same oxygen partial pressure range.

An oxygen partial pressure of 7×10^{-10} atm was selected for weight change measurements as a function of temperature because of the necessity of an oxygen partial pressure to produce significant weight changes and also intersect linear electrical conductivity-oxygen partial pressure dependence data as shown in Fig. 1. The log $[V_{Mn}'']$ *vs.* $1/T$ plot at an oxygen partial pressure of 7×10^{-10} atm is shown in Fig. 4. The slope of Fig. 4 yields a value of −5.9 kcal/mole for ΔH_f°. The activated enthalpy of movement of an electron hole, ΔH_p, is, therefore, 11.9 kcal/mole. These data are given in Table III.

The very small deviations from stoichiometry reported here are in agreement with the lower temperature results of Hed and Tannhauser (4). The immeasurably small deviations found for the n-type region, even when the sample was equilibrated with essentially pure CO, lends further support to the higher mobility electrons as the source of the n-type electrical conductivity. It is interesting to note that the parabolic oxidation of manganese to manganese oxide is independent of the oxygen partial pressure when the CO_2/CO ratio is less than one (14) (n-type region). Price and Wagner (9) on the other hand have measured the tracer diffusion coefficient of Mn^{54} in single crystalline MnO and did not observe any inflection in the diffusion data near the p- to n-type transition. This result (9) would indicate that the concentration of manganese vacancies is monotonically decreasing as the oxygen partial pressure is lowered and remains as the predominant nonstoichiometric atomic disorder.

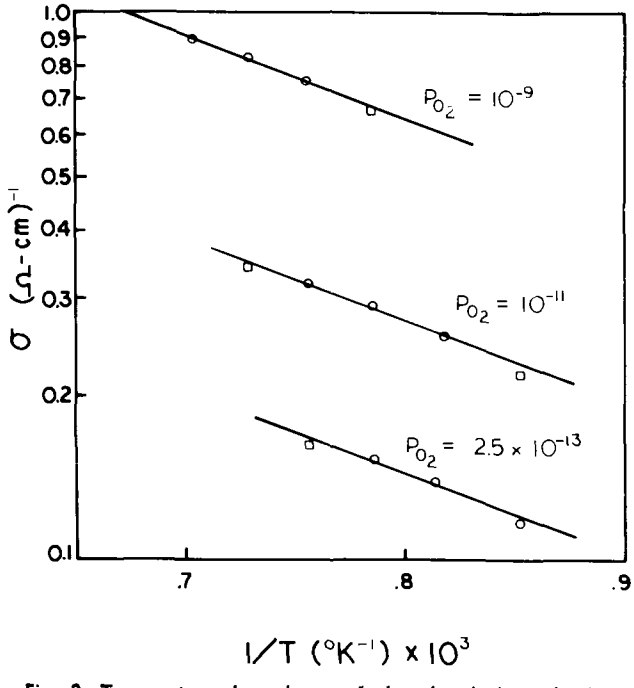

Fig. 2. Temperature dependence of the electrical conductivity of p-type MnO. The symbol, □, denotes data obtained by extrapolation as explained in the text.

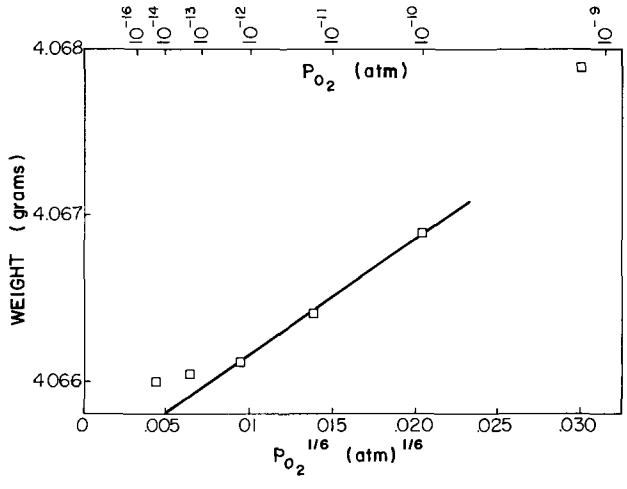

Fig. 3. Oxygen partial pressure dependence of the weight of p-type MnO at 1000°C. The values of the individual oxygen pressures are 7×10^{-10}, 7×10^{-11}, 7×10^{-12}, 7×10^{-13}, 7×10^{-14}, and 7×10^{-15} atm.

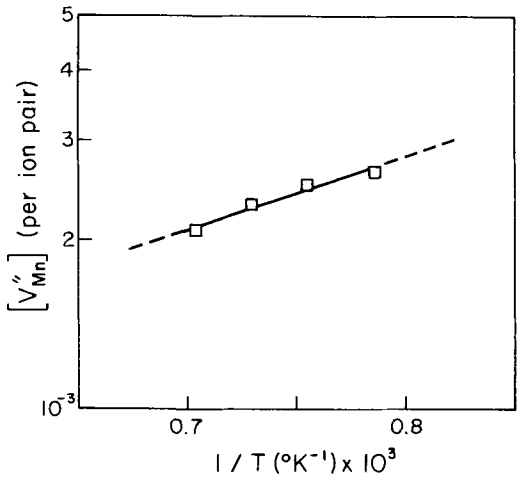

Fig. 4. Temperature dependence of the manganese vacancy concentration in MnO at constant oxygen partial pressure of 7 x 10^{-10} atm.

The thermogravimetric data may be combined with the electrical conductivity data in order to calculate the mobility of the electron holes. The mobility data may then be used to determine the activation energy of motion of an electron hole. The mobilities of the electron holes at an oxygen partial pressure of 7 x 10^{-10} atm have been calculated on the basis of two electron holes for each cation vacancy ($\sigma_p \propto p_{O_2}{}^{1/6}$) and are given in Table III. The temperature dependence of the mobility of the electron holes is shown in Fig. 5 and the resultant activation energy for motion of an electron hole is calculated to be 11.8 kcal/mole (see Table III).

The minima of the log σ *vs.* log p_{O_2} data may be used to determine the bandgap of MnO (15, 16). The log $\sigma_{min.}$ data as a fuction of $1/T$ are shown in Fig. 6. The data in Fig. 6 yield an activation energy of 63.4 kcal/mole (2.8 eV). Others (15, 16) have approximated this to be the bandgap at 0°K but it is actually given by

$$\frac{\partial \ln \sigma_{min.}}{\partial (RT)^{-1}} = \frac{-E_g}{2} + \frac{1}{2}\frac{\partial \ln \mu_p}{\partial (RT)^{-1}} + \frac{1}{2}\frac{\partial \ln \mu_n}{\partial (RT)^{-1}} \quad [5]$$

Since the p-type conductivity has a significant energy term associated with the mobility, the correction is an important one. For a calculated value of $[\partial \ln \mu_n]/[\partial (RT)^{-1}]$ of -1.3 kcal/mole at 1000°C based on $\mu_n \propto (kT)^{-1/2}$ and the measured value of $[\partial \ln \mu_p]/[\partial (RT)^{-1}]$ of 11.9 kcal/mole, the bandgap for single crystalline MnO at 0°K is calculated to be 52.8 kcal/mole (2.3 eV).

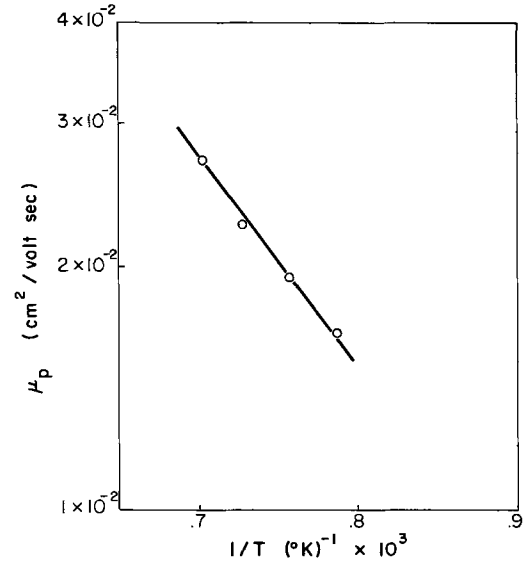

Fig. 5. Temperature dependence of the mobility of electron holes in MnO.

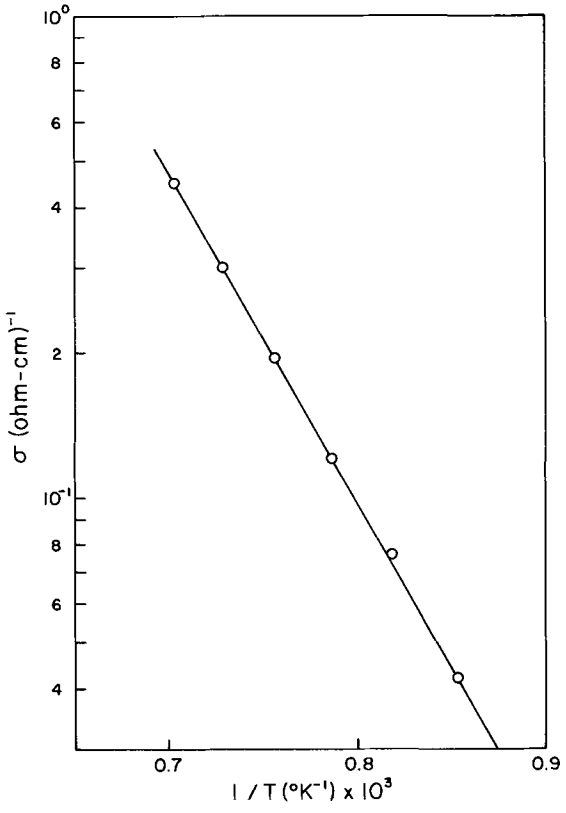

Fig. 6. Temperature dependence of the minima in conductivity obtained from the log σ *vs.* log p_{O_2}. See Fig. 1.

The electrical conductivity of n-type manganous oxide was found to be proportional to the $-1/6$ power of the oxygen partial pressure derived from CO/CO_2 mixtures over the temperature range of 900°-1150°C. These data are given in Table II.

For temperatures above 1000°C it was possible to employ CO/CO_2 ratios of 10^3 but at temperatures below 1000°C such large ratios resulted in values of the electrical conductivity that were insensitive to the calculated oxygen partial pressure. When the temperature was kept constant and the CO/CO_2 ratio was decreased after the electrical conductivity had been measured in the region which was insensitive to the oxygen partial pressure, it was found that the electrical conductivity tended to remain somewhat insensitive to changes in oxygen partial pressure. If, however, the temperature were raised to 1000°C the electrical conductivity values were found to correspond to the previous data measured at 1000°C. This behavior suggests the possibility of a phase change so the nonlinear, n-type electrical conductivity has been deleted.

It has been shown that the mobility of the electron is much greater than that for electron holes in MnO (5-7). This means that the predominant type of nonstoichiometric disorder is metal deficit at the p- to n-type transition and for at least some range of the n-type MnO. Simkovich (17) reports that carbon is a dopant in the ppm range in n-type MnO that has been equilibrated in CO/CO_2 atmospheres and may, therefore, contribute to the n-type electrical conductivity.

If the electrons responsible for the electronic conductivity result from the intrinsic electronic equilibria because of the decrease in electron holes, due to a decreasing cation vacancy concentration, then

$$\sigma = ne\mu_n = \text{const.}\ p_{O_2}^{-1/2m} \exp\left\{\left[\frac{\Delta H_{f_p}^\circ}{m} - \left(E_g + \frac{\partial \ln \mu_n}{\partial (RT)^{-1}}\right)\right] \Big/ RT\right\} \quad [6]$$

where $\Delta H_{f_p}^\circ$ is the enthalpy of formation of an ionized cation vacancy, E_g the intrinsic energy gap, and μ_n the mobility of an electron. The log σ *vs.* $1/T$ data for n-type MnO are shown in Fig. 7. The sum, $[(\Delta H_{f_p}^\circ/m) - E_g - (\partial \ln \mu_n)/(\partial (RT)^{-1})]$, is 52.6 ± 3.2 kcal/mole (see Table III) while the sum, $[E_g + (\partial \ln \mu_n)/(\mu (RT)^{-1})]$ is 51.5 ± 0.6 kcal/mole. $\Delta H_{f_p}^\circ/m$ is then calculated to be zero, within the experimental error.

If, on the other hand, the electrons that are responsible for the n-type electronic conductivity are due to doubly ionized cation interstitials then the measured activation energy for n-type electronic conduction may be represented by the sum, $[(\Delta H_{f_n}^\circ/m) + (E_1/m) + (E_2/m)]$, where $\Delta H_{f_n}^\circ$ is the enthalpy of formation of a cation interstitial and E_1 and E_2 are the first and second ionization energies, respectively, of the quasi-free electrons. The measured activation energy sum is 52.6 ± 3.2 kcal/mole (see Table III) and since m is equal to 3 the sum, $(\Delta H_{f_n}^\circ + E_1 + E_2)$, is found to be 158 kcal/mole (6.9 eV).

Stoichiometric compensation (18) of an acceptor dopant such as Li^+ may result in the creation of metal excess lattice disorder in MnO (the electronic disorder could still be p-type, however). This effect has probably been observed for the case of Li-doped CoO (19). Similar thermogravimetric and conductivity measurements are needed on Li-doped MnO as a function of p_{O_2} and temperature in order to estimate the concentration of interstitial manganese relative to the majority lattice defects, cation vacancies, in undoped MnO.

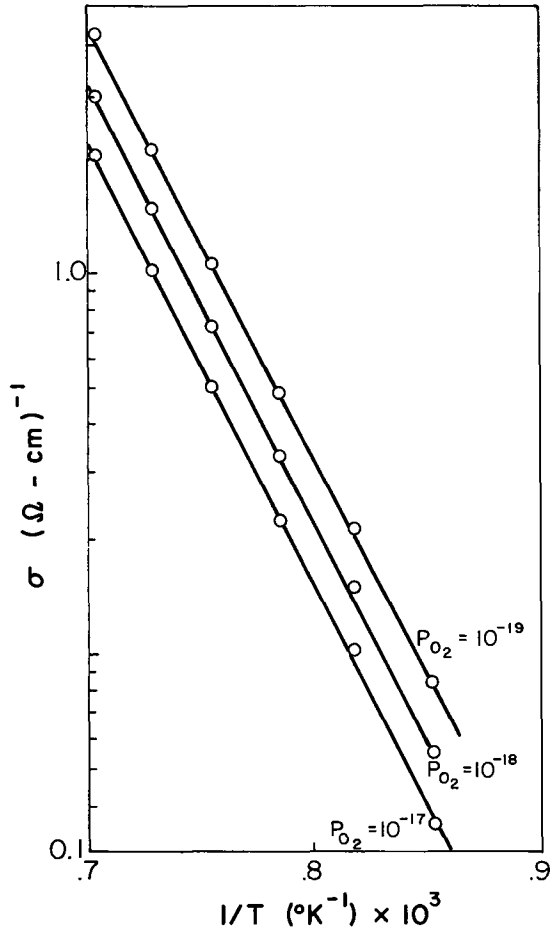

Fig. 7. Temperature dependence of the electrical conductivity of n-type MnO.

We have assumed that the electrical conductivity of manganous oxide is primarily electronic. Employing the value of approximately 1.0 x 10^{-9} cm^2/sec for D^* of the more mobile ion Mn, from the diffusion data of Price and Wagner (9) at 1032°C and an oxygen partial pressure of 10^{-11}, an appropriate electrical conductivity of 0.31 $(ohm\text{-}cm)^{-1}$, and p of 4.6 x 10^{22}, the transference number of the more mobile ion may be calculated from the Nernst-Einstein relation. The transference number of the more mobile ion at 1032°C and an oxygen partial pressure of 10^{-11} atm is found to be 8.3 x 10^{-4} which indicates that the electrical conductivity is primarily electronic.

Conclusions

1. Manganous oxide was found to exist as either p- or n-type from electrical conductivity measurements.
2. The p-type electrical conductivity was found to be proportional to the 1/6 power of the oxygen partial pressure. This oxygen partial pressure dependence suggests that the nonstoichiometric disorder in p-type manganous oxide may be described by

$$\tfrac{1}{2}O_2 \rightleftarrows O_O + V_{Mn}'' + 2p \quad [7]$$

3. The n-type electrical conductivity was determined to be proportional to the −1/6 power of the oxygen partial pressure. The n-type electrical conductivity was found to be consistent with high mobility electrons and metal deficit atomic disorder. If a portion of the n-type electrical conductivity is due to metal excess atomic disorder then

$$Mn_m + O_O \rightleftarrows Mn_i^{\cdot\cdot} + 2n + \tfrac{1}{2}O_2 \quad [8]$$

could describe the nonstoichiometry.

4. The sum of the enthalpy of formation of nonstoichiometric disorder and enthalpy of movement of the electronic defect was determined for both p- and n-type manganous oxide. The enthalpy of formation of p-type disorder and hence the enthalpy of movement of the electron holes were also determined. See Table III.
5. The bandgap of MnO was determined from the electrical conductivity minima at the p- to n-type transition to be 52.8 kcal/mole (2.3 eV).
6. Thermogravimetric measurements indicated that the departure from stoichiometry was small, ~3 x 10^{-3}, at 1000°C and 7 x 10^{-10} atm oxygen partial pressure for p-type manganous oxide and not detectable for n-type manganous oxide.
7. Mobilities of the electron holes were calculated from the thermogravimetric and electrical conductivity data at 7 x 10^{-10} atm oxygen partial pressure.
8. The transference number of the manganese ion at 1032°C and 10^{-11} atm oxygen partial pressure was calculated to be 8.3 x 10^{-4}.

Acknowledgments

This paper was supported by a grant from the Advanced Research Projects Agency through the Materials Research Center of Northwestern University. It is based in part on a Ph.D. thesis submitted by N. G. Eror to the Graduate School, Northwestern University, 1965.

Manuscript submitted Aug. 17, 1970; revised manuscript received *ca.* May 5, 1971. This was Paper 107 presented at the San Francisco Meeting of the Society, May 9-13, 1965.

Any discussion of this paper will appear in a Discussion Section to be published in the June 1972 JOURNAL.

REFERENCES

1. M. W. Davies and F. D. Richardson, *Trans. Faraday Soc.*, **55**, 604 (1959).
2. A. Duquesnoy and F. Marion, *Compt. Rend.*, **256**, 2862 (1963).

3. H. Le Brusq, J. J. Oehlig, and F. Marion, *ibid.*, **266C**, 965 (1968).
4. A. Z. Hed and D. S. Tannhauser, *J. Chem. Phys.*, **47**, 2090 (1967).
5. M. Gvishi, N. M. Tallan, and D. S. Tannhauser, *Solid State Commun.*, **6**, 135 (1968).
6. H. J. deWit and C. Crevecoer, *Phys. Letters*, **25A**, 393 (1967).
7. C. Crevecoer and H. J. deWit, *Solid State Commun.*, **6**, 295 (1968).
8. J. P. Bocquet, M. Kawahara, and P. Lacombe, *Compt. Rend.*, **265C**, 1318 (1967).
9. J. B. Price and J. B. Wagner, Jr., *This Journal*, **117**, 242 (1970).
10. N. G. Eror and J. B. Wagner, Jr., *J. Phys. Chem. Solids*, **29**, 1597 (1968).
11. N. G. Eror and J. B. Wagner, Jr., *Phys. Status Solidi*, **35**, 641 (1969).
12. A. Z. Hed and D. S. Tannhauser, *This Journal*, **114**, 314 (1967).
13. I. Bransky, Private communication to N. Eror, 1969.
14. K. Fueki and J. B. Wagner, Jr., *This Journal*, **112**, 384 (1965).
15. J. Rudolf, *Z. Naturforsch.*, **14a**, 727 (1954).
16. J. H. Becker and H. P. R. Frederikse, *J. Appl. Phys. Suppl.*, **33**, 447 (1962).
17. G. Simkovich, Private communication to N. Eror, 1969.
18. N. G. Eror and D. M. Smyth, "The Chemistry of Extended Defects in Non-Metallic Solids," Proc. of the Inst. for Advanced Study on the Chem. of Extended Defects in Non-Metallic Solids, Casa Blanca Inn, Scottsdale, Arizona, April 16-26, 1969, North Holland Publishing Co., Amsterdam.
19. B. Fisher and J. B. Wagner, Jr., *J. Appl. Phys.*, **38**, 3838 (1967).

Preparation of Beta-Rhombohedral Boron Whiskers[1]

Iqbal Ahmad and W. J. Heffernan

Benet Research and Engineering Laboratories, U. S. Army Watervliet Arsenal, Watervliet, New York 12189

ABSTRACT

Whiskers of beta-rhombohedral boron have been prepared by the reduction of BBr_3 and BCl_3 with hydrogen, involving a vapor-liquid-solid mechanism. The liquid forming impurities used were Au, Pt, Cu, and Ag. Gold was found to be the best. Optimum conditions for the whisker growth were: for BBr_3-1200°C, 25:1 H_2/BBr_3 molar ratio, and 100 cc/min flow rate; for BCl_3-1300°C, 1000:1 H_2/BCl_3 molar ratio, and 1000 cc/min flow rate. Whiskers from BBr_3 reduction were mostly circular in cross section, while those with BCl_3 were predominantly faceted.

In view of the current interest in beta-rhombohedral boron as an advanced structural material, it was considered of interest to prepare it in the form of high-strength filamentary single crystal whiskers. Two techniques were investigated: (*A*) Vaporization of elemental boron at high temperatures (1800°-1900°C) from BN crucibles, (*B*) Chemical vapor deposition (CVD) by the reduction of boron trihalides with hydrogen. With the first technique, whiskers 5-15μ in diam and up to 1 cm long with tensile strengths as high as 1.3 x 10^6 psi were obtained. The details of this work have already been published (1). Results obtained with the second technique are discussed in the present paper.

The formation of tetragonal boron whiskers, 2-3 mm long and 0.1 mm wide, as a result of the reduction of BCl_3 with H_2 (H_2/BCl_3, molar ratio of 100:1) over an inductively heated (1300°-1800°C) boron rod have been described by Olempska *et al.* (2). Sitarik and Ellis (3) have reported growth of alpha-rhombohedral boron whiskers by the reduction of BCl_3 with H_2 (1000°C, H_2/BCl_3 molar ratio of 1500:1.4, and flow rate 1.5 liter/min) on an amorphous boron substrate by a vapor-liquid-solid (VLS) mechanism (4). Platinum was used as the liquid-forming impurity. Some of the whiskers were 2 mm long and 25μ in diam.

To the best of the authors' knowledge, whiskers of beta-rhombohedral boron prepared by CVD have not been reported in the literature.

Experimental Details

CVD-H_2/BBr_3.—In the initial studies, formation of boron whiskers by simple chemical vapor deposition was investigated. BBr_3 was selected as a source of boron. As compared with BCl_3, it is relatively easier to purify (5). Prior to attempting whisker growth, rates of deposition of boron on resistively heated Ta strips at various molar ratios (H_2/BBr_3) and flow rates were determined. The apparatus is schematically illustrated in Fig. 1. Most of the runs were made at 1200°C, as below this temperature, alpha and tetragonal boron can also form. However, a number of runs were also made at higher temperatures. The temperature dependence of deposition rate at 12:1 molar ratio and 0.008 moles of BBr_3/cm^2 hour (total flow 100 cc/min) flow rate is shown in Fig. 2.

It is not proposed to give the details of the morphology of the deposits as a function of various variables. The major conclusions, however, were that higher temperature, higher molar ratio (H_2/BBr_3), and higher flow rate encouraged needle growth. Reproducible acicular growth of beta-rhombohedral boron was observed under the following conditions: temperature, 1200°C; H_2/BBr_3, 98:1, flow rate, 400 cc/min.

CVD-VLS:H_2/BBr_3 (Au, Pt, Cu, Ag).—From the above series of experiments it became obvious that, to promote whisker growth, a catalytic mechanism such as that provided by vapor-liquid-solid (4) was necessary. For the selection of liquid-forming impurities, the available phase diagrams were examined. Bates *et al.* (6), have studied the phase equilibria of Au-B, Pt-B, and Cu-B. Apparently none of these systems showed solid solubility of these elements in boron. Therefore, all of them were considered to be promising as liquid-forming impurities.

A tantalum strip was first coated with boron at a relatively low temperature (900°-1000°C). Particles of gold (−100 mesh) were then sprinkled over the boron deposits, the temperature of the strip was raised to 1200°C, and a gas mixture of H_2/BBr_3 (12:1) was allowed to flow at 200 cc/min. Whiskers were found to grow within a minute as shown in Fig. 3. Because of the low molar ratio, in some areas there was excessive

[1] The views of the authors do not purport to reflect the position of the Department of the Army or Department of Defense.

Key words: whiskers, beta-rhombohedral boron, vapor-liquid-solid, chemical vapor deposition.

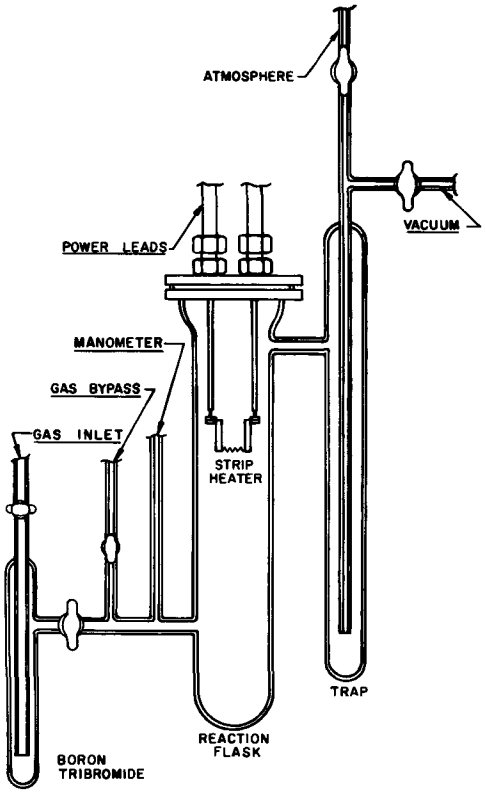

Fig. 1. Apparatus for the deposition of boron from $BBr_3 + H_2$

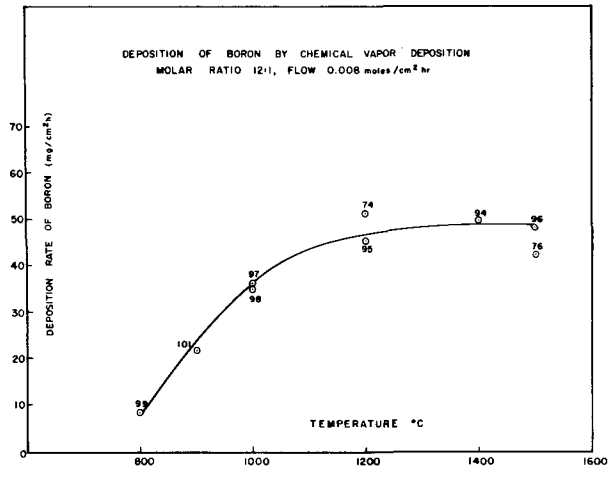

Fig. 2. Dependence of boron deposition rate with temperature. Molar ratio 25:1 and 0.008 mol/cm² hr flow rate.

nucleation resulting in an "explosion" or "flower" effect (Fig. 4). Sometimes there was a secondary Au deposition on whiskers from which more whiskers nucleated giving a Christmas-tree-like growth. All of these whiskers were identified by x-ray diffraction as beta-rhombohedral boron.

In some runs, Pt, Cu, and Ag particles (−100 mesh) were used. Platinum gave encouraging results. However, with Cu and Ag, curly-type whiskers appeared and the growth was rough. Au was found to be the best.

The steep temperature gradient normal to the strip severely limited the length of these whiskers. To grow longer whiskers it was necessary to provide a better temperature gradient. Consequently, the apparatus was redesigned as shown in Fig. 5. In this apparatus, a graphite stick heater was used as a substrate. A Hoskin clamshell-type furnace was placed around the

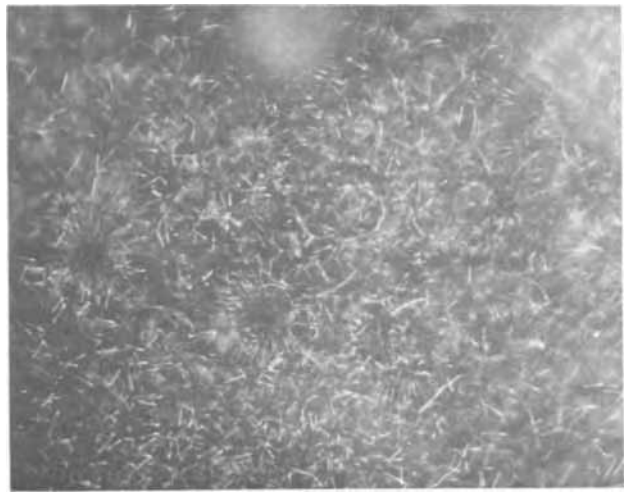

Fig. 3. Whiskers of beta-rhombohedral boron by VLS, Au, 1200°C (X120).

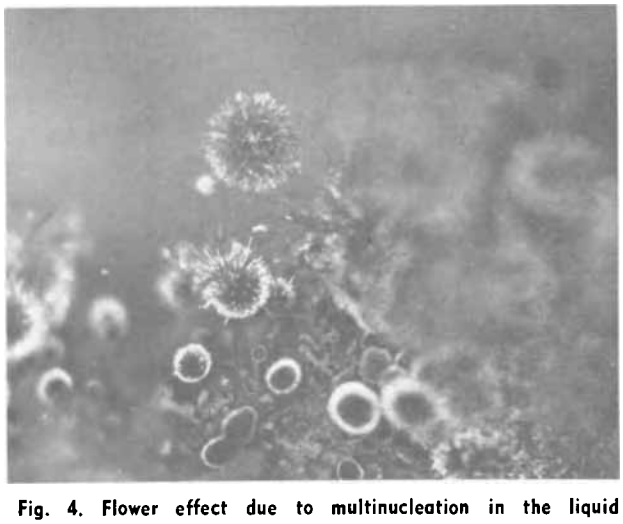

Fig. 4. Flower effect due to multinucleation in the liquid globule (X120).

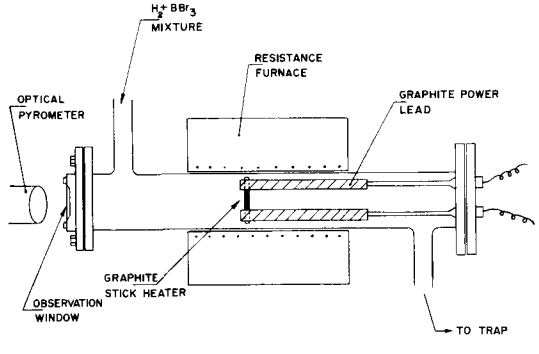

Fig. 5. Resistively heated graphite stick heater with clamshell furnace to provide shallow temperature gradient.

tube containing the substrate assembly. Unfortunately, because of the radiation losses, this furnace did not reach temperatures high enough to give the desired temperature gradient at 1200°C. Although whiskers of beta-rhombohedral boron with Au, Pt, and also Cu were obtained (Fig. 6a) in most cases they were not well-formed. At lower temperature regions (950°-1000°C), especially on the graphite leads, whiskers of tetragonal boron formed with both Au and Cu (Fig.

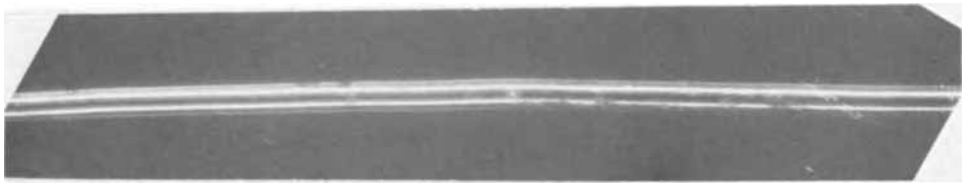

Fig. 6. Morphology of boron whiskers formed in graphite stick heater apparatus. (a, left) A beta-rhombohedral boron whisker (X385).

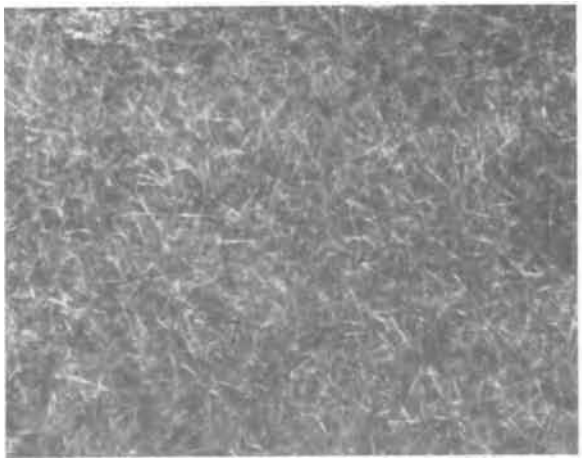

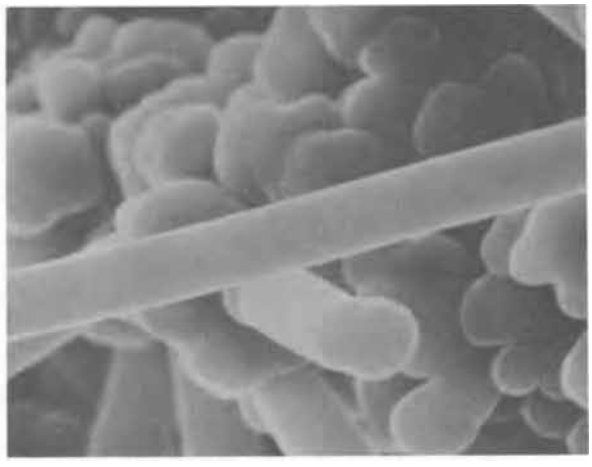

Fig. 6. Morphology of boron whiskers formed in graphite stick heater apparatus. (b, above left) A view of tetragonal boron whiskers formed on graphite leads (X120). (c, above right) Magnified view of (b). (d, left) Thread-like fibrous growth (X200).

6b). These whiskers were round in cross section (Fig. 6c) and had very smooth surfaces. Sometimes, very long thread-like fibers were also observed (Fig. 6d). In these experiments, even though a graphite heater was used, no evidence of the formation of B_4C was noted.

Finally, an apparatus shown in Fig. 7 was set up. In this apparatus a boron disk with metal particles sprinkled on it was positioned on a graphite base which, in turn, was placed in a graphite susceptor. In a few experiments, particles were also placed on the graphite base. Due to the geometry of the apparatus there was a preferential deposition of boron at the gas entrance side; however, at the middle of the substrate the deposition was less. The boron disk was positioned between these two regions to avoid excessive nucleation. With this setup, whiskers approaching 5 mm in length were obtained. The major observations were as follows:

(*A*) X-ray diffraction analysis showed that the majority of the black whiskers were beta-rhombohedral boron. However, sometimes minor amounts of tetragonal boron were also detected.

(*B*) At 1100°C, whiskers were observed only below 100:1 molar ratio. As the molar ratio was decreased, the time of growth reduced. At 25:1, the whiskers grew within 1 min.

(*C*) The best whisker growth was at 1200°C and a molar ratio of 25:1 (Fig. 8). They were predominantly round in cross section. At lower temperatures they were generally ill-formed. Occasionally, very fine straw-colored, apparently transparent whiskers, were also observed. X-ray diffraction analysis showed them to be predominantly B_4C.

Figure 9 is a trace of the microprobe analysis of the boron whisker grown from platinum, showing the concentration of platinum at the tip. Frequently, overgrowth was detected under high magnification, even on the apparently smooth surface of the boron whisker (Fig. 10). In one case a fractured whisker also showed a hollow core. The diameter of the whisker was 35μ while the core diameter was 25μ.

CVD-VLS:H_2/BCl_3 (Au, Pt).—In spite of considerable variation of the parameters such as flow rates, molar ratios, and the temperatures, the problem of the formation of nonfaceted whiskers could not be suc-

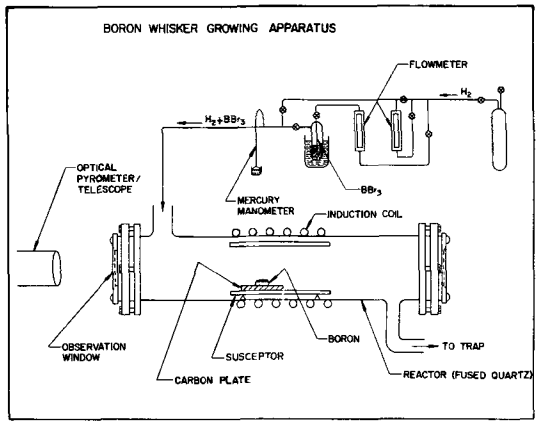

Fig. 7. Apparatus for the growth of whiskers involving induction heating.

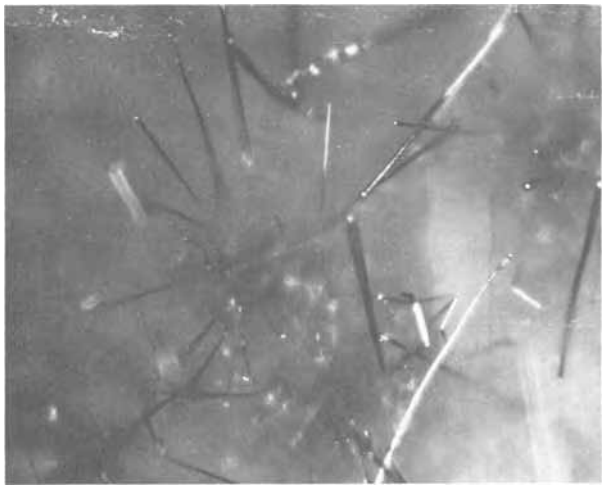

Fig. 8. A view of whiskers formed at 1200°C. Molar ratio 25:1 and flow rate 1000 cc/min (X120).

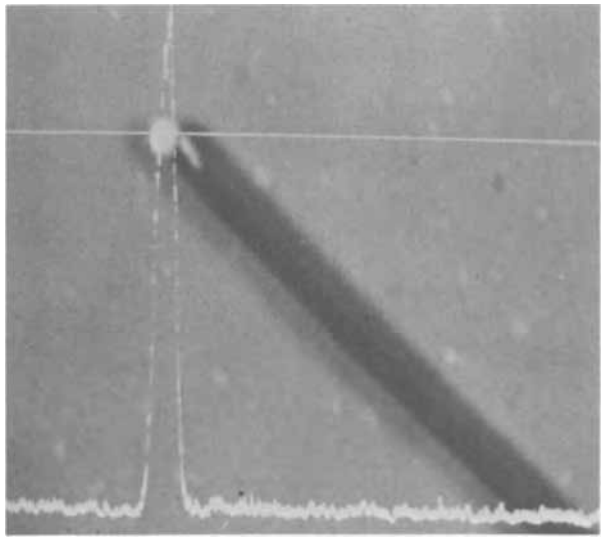

Fig. 9. Platinum distribution over tip of a whisker

cessfully solved. It was felt that circular cross section could have been due to the instability of the liquid-solid interface, caused by the fast reduction of BBr_3 under the conditions used. Thermodynamic considerations indicated that BCl_3 should be less easily reducible than BBr_3 at these temperatures from which a better control of the growth of whiskers could be expected. Therefore, in another series of experiments, BCl_3 instead of BBr_3 was used. In these runs a relative predominance of faceted whiskers was achieved. Whiskers of good quality (Fig. 11) were obtained at 1300°C at a molar ratio of 1000:1.

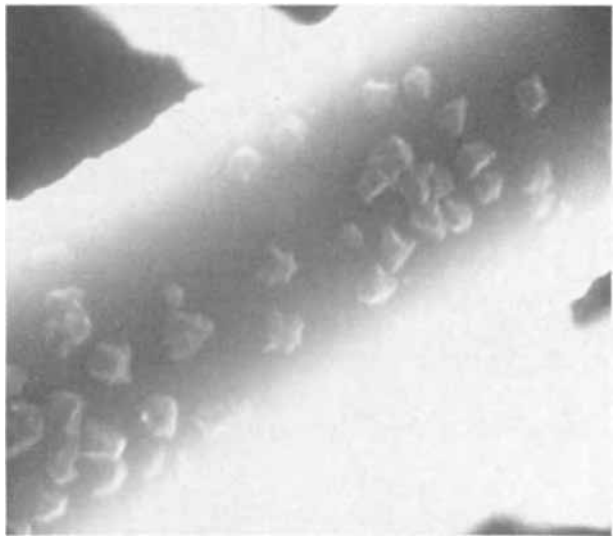

Fig. 10. Overgrowth on an apparently smooth surface of a whisker (X10,000).

Some runs were made without a boron disk. A graphite plate was used as a growth substrate. In these runs there was an evidence of very fine and long, apparently transparent, leader whiskers with liquid balls on their heads. They formed within a few minutes. When extended times were used, such whiskers, when on the gas entrance side of the substrate, either thickened or developed an overgrowth of polyfaceted, well-formed crystals as shown in Fig. 12. This overgrowth sometimes looked like beads on a thin string. Bushes of such whiskers without overgrowth were also observed at the exit end of the carbon substrate, as shown in Fig. 13. On x-ray diffraction they were found to be B_7C.

In one experiment, platinum was used in the form of a thin wire as a liquid-forming impurity. While only a very few whiskers of boron were obtained, in the region where the wire was positioned, golden-

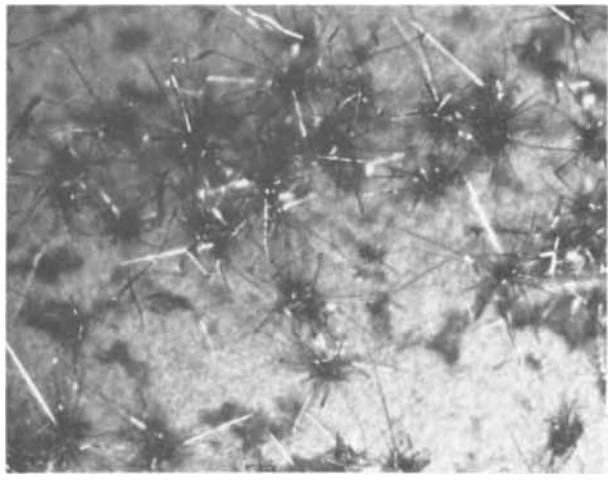

Fig. 11. Boron whiskers grown at 1300°C, 1000:1 ratio, 400 cc/min (X1200).

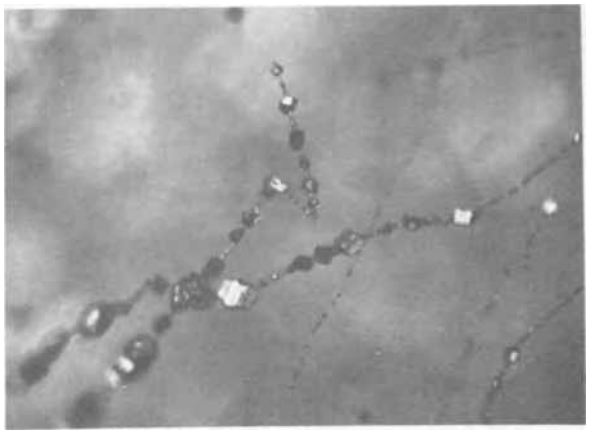

Fig. 12. Polyfaceted overgrowth on a leader whisker at 1200°C. (X120).

Fig. 13. Bushes of leader whiskers grown at 1300°C, 500 cc/min, 500:1 ratio (X275).

colored whiskers were formed (Fig. 14). Under high magnification they appeared to be platelets and were identified as platinum boride.

Discussion

The main objective of this study was to produce beta-rhombohedral boron whiskers and characterize their physical and mechanical properties. The work reported here has shown the feasibility of the preparation of these whiskers by CVD involving VLS mechanism. However, the quality and size of the whiskers achieved so far are not suitable for the purpose of characterization.

It has already been mentioned that, although acicular growth of boron was achieved from simple CVD, it was found necessary to employ a VLS mechanism for the promotion of proper whisker growth. However, with BBr_3, apparently because of the considerably negative free energy of reaction of H_2 with BBr_3 in the temperature range of interest, it was not possible to establish a controlled whisker growth from the metal particles. This is apparent from the bushy growth obtained. Toward the gas entrance side there was invariably multinucleation from these particles.

It is also clear that, under the process conditions used, it was very difficult to control the temperature- and chemical-potential gradients in the substrate region. Some improvement was achieved by the use of BCl_3 in that more faceted whiskers formed. However, the growth and quality of whiskers were still unsatisfactory.

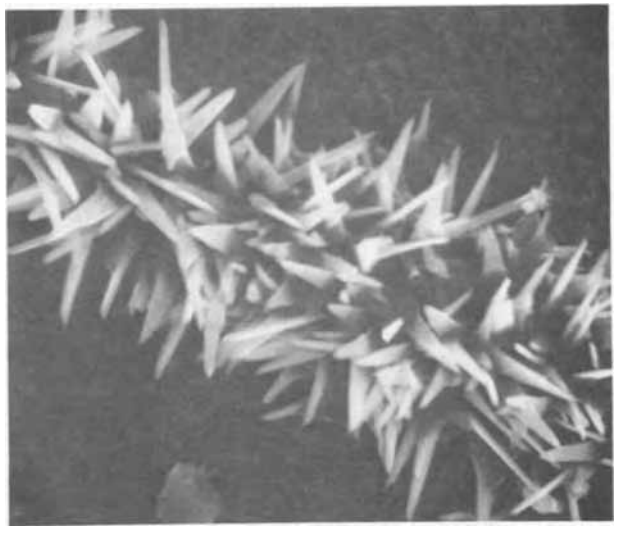

Fig. 14. Golden-colored whiskers of platinum boride (X1000)

This study, nevertheless, confirmed that alpha-rhombohedral and tetragonal whiskers can be obtained at temperatures below 1000°C. At temperatures of 1100°C or higher, this technique yielded essentially beta-rhombohedral boron. However, traces of tetragonal were also observed.

The formation of straw-colored boron carbide whiskers is noteworthy. The authors did not find any reference in the literature to a straw or orange-colored boron carbide phase. It appears that this phase in very fine size is not opaque. Analogous to this is the example of SiC, which in thick section is opaque black, while its whiskers are transparent and light green in color.

The formation of the leader whiskers can possibly be explained as follows. In the initial stages of heating, the molten metal particles pick up some carbon from the carbon substrate. When the $BCl_3 + H_2$ mixture is introduced, the dissolved carbon reacts with boron formed on the surface of the molten metal, resulting in the nucleation of fine boron carbide whiskers. Such whiskers in the gas inlet side then act as nucleation sites for the overgrowth of B, as structurally beta-rhombohedral boron is very similar to B_4C. In the exit-end side, boron in the reactants is depleted and therefore no boron overgrowth occurs. In the middle zone, boron whiskers form together with some B_4C whiskers.

Acknowledgments

This paper was presented at the Second International Conference on Chemical Vapor Deposition held at Los Angeles, California May 10-15, 1970.

Manuscript submitted Aug. 26, 1970; revised manuscript received April 6, 1971.

Any discussion of this paper will appear in a Discussion Section to be published in the June 1972 JOURNAL.

REFERENCES

1. I. Ahmad, and G. P. Capsimalis, "Reactivity of Solids," pp. 477-486, John Wiley and Sons, Inc., New York (1969).
2. Z. Olempska, A. Badzian, K. Pietrzak, and T. Niemyski, *J. Less-Common Metals*, **11**, 351 (1966).
3. J. P. Sitarik and W. C. Ellis, *J. Appl. Phys.*, **37**, 2399 (1966).

4. R. S. Wagner and W. C. Ellis, *Trans. AIME*, **233**, 1053 (1965).
5. C. F. Powell, C. J. Ish, and J. M. Blocher, Jr., "Boron Synthesis, Structure, and Properties," Conference Proceedings, p. 8, Plenum Press, Inc., New York (1960).
6. H. E. Bates, F. Wald, and M. Weinstein, "Advanced Fibrous Reinforced Composites," *SAMPE Proceedings*, **10**, E-43 (1966).

Technical Notes

Magnetoelectret Effect in Shellac Wax

P. K. C. Pillai, Kamlesh Jain, and V. K. Jain

Department of Physics, Indian Institute of Technology, New Delhi-29, India

Eguchi (1) made the first thermoelectret from a mixture of carnauba wax, shellac wax, and beeswax. Many other workers studied the electret properties in different materials. Recently Bhatnagar (2) has developed a magnetoelectret by applying a magnetic field instead of an electric field. This new class of electrets also retains the surface charge for a very long time.

Experimental

In the present investigations, the powder of shellac wax was put into a cavity of mica sheet 1 mm thick and 4 cm^2 in area. A solid slab of the material was obtained in the mica holder by using the technique developed by Jain and Pillai (3) without the application of the field. The sample was kept in a desiccator for some time, until it lost all the surface charges due to stripping. A heating system was also made to heat both faces of the sample, when it was kept between the two pole pieces of an electromagnet. A thermocouple of copper constantan was fixed near the face of the sample for recording the temperature. The sample with the holder was mounted vertically between the pole pieces of the magnet, and the temperature of the sample was maintained at 70°C (softening point).

The distance of the poles was reduced to 1 in. to get the maximum magnetic field. The sample was polarized by heating and cooling under the same magnetic field strength. The magnetoelectret that was formed was taken out from the jig, and surface charge on both the surfaces was measured daily for about 28 days. The measurements were taken with the help of a d-c amplifier and electrometer (Type 1230A, Serial No. 1200) using a special measuring device (4, 5). The sample was short circuited with metallic foil after measurements and was kept under desiccated conditions for further studies.

Key words: Electret, magnetoelectret, polarization.

Results

In order to study this effect in detail, three series of samples were made with variation of polarizing time, temperature, and field.

In the first case, a series of the magnetoelectrets was made by applying a field of 4.75 kilo Gauss (kG) to 12 kG at a fixed temperature of 70°C for 75 min. From the surface charge decay characteristics (Fig. 1-3), it can be seen that both north and south faces of the electret show a permanent positive surface charge,

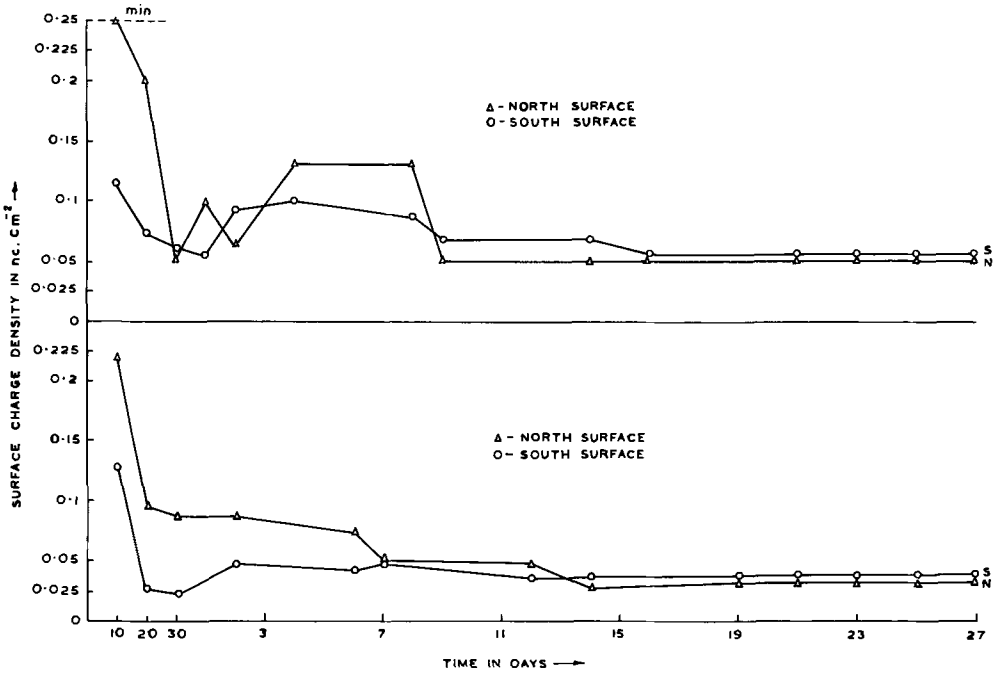

Fig. 1. (top) Variation of surface charge density vs. time for shellac wax electret formed at 12 kG/mm in 75 min polarizing time.

Fig. 2. (bottom) Variation of surface charge density vs. time for shellac wax electret formed at 8.75 kG/mm in 75 min polarizing time.

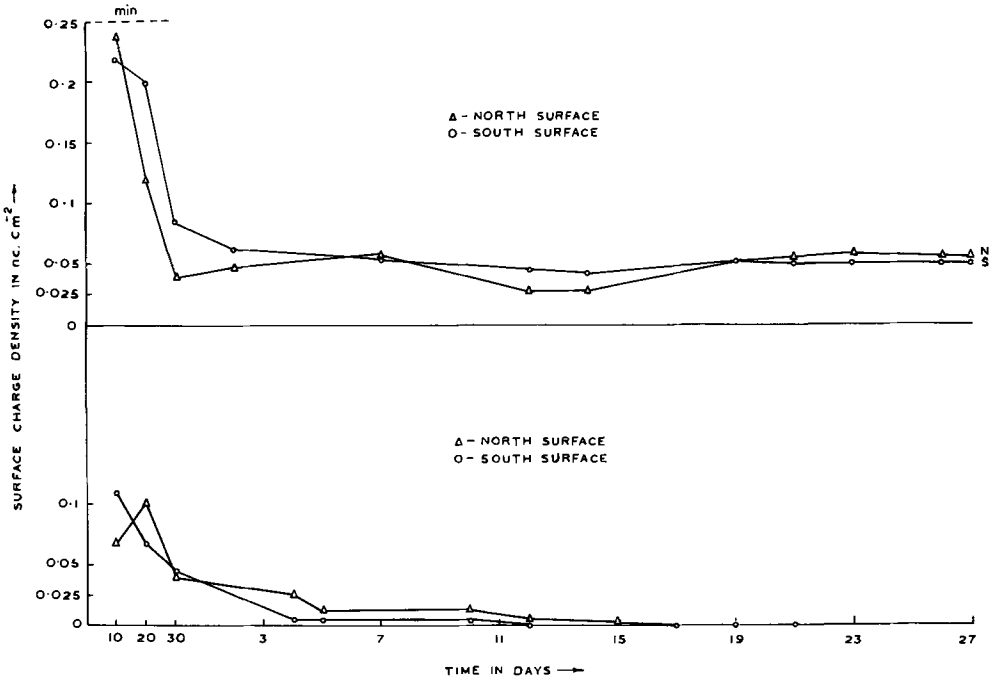

Fig. 3. (top) Variation of surface charge density vs. time for shellac wax electret formed at 4.75 kG/mm in 75 min polarizing time.

Fig. 4. (bottom) Variation of surface charge density vs. time for shellac wax electret formed at zero field in 75 min polarizing time.

which decreases very quickly in the initial stage and then becomes constant. The final surface charges on the samples of this series increase with an increase of the polarizing field.

To confirm the presence of a magnetoelectret effect, a sample was also made without the application of a magnetic field under the same conditions. It was found that the sample showed some charges of low value due to the stripping and molding (6, 7). But the charges were not permanent and decayed to zero (Fig. 4) within a few days time.

Secondly, the effect of polarizing time was studied. The samples were made by applying 10.5 kG at 70°C and the heating time was varied from 15-60 min. Each sample was allowed to cool down to room temperature in 30 min under the magnetic field. It can be seen from the graphs (Fig. 5 and 6) that the surface charge increased with the increase of polarizing time. An increase in the final value of the surface charge was also found with an increase of polarizing time.

In the next case, the studies were made with the change of polarizing temperature from 70°C to room temperature (22°C). The samples were made at 55°C and at 22°C and the characteristics are shown in Fig. 6 and 7. It can be seen that at 55°C the final surface charge obtained is very low in comparison with the sample made at 70°C. The sample prepared at room temperature did not show any surface charge from the very beginning.

Discussion

The formation of the thermoelectret (8) can be explained on the basis of the contributions from different mechanisms such as (*A*) spray charge, (*B*) ionic displacement, (*C*) dipolar orientation, and (*D*) molding and stripping charges. But these phenomena are inadequate to explain the formation of a magnetoelectret state in solid materials.

In the present investigations, the effect of spray charge is completely ruled out as the dielectric is not

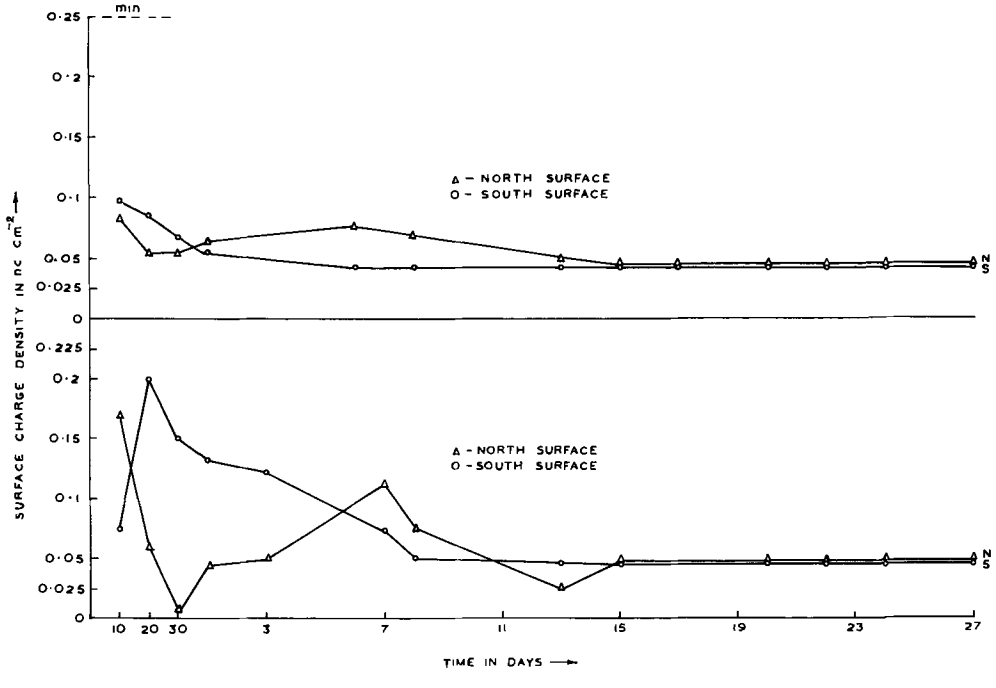

Fig. 5. (top) Variation of surface charge density vs. time for shellac wax electret formed at 10.5 kG/mm in 45 min polarizing time.

Fig. 6. (bottom) Variation of surface charge density vs. time for shellac wax electret formed at 10.5 kG/mm in 75 min polarizing time.

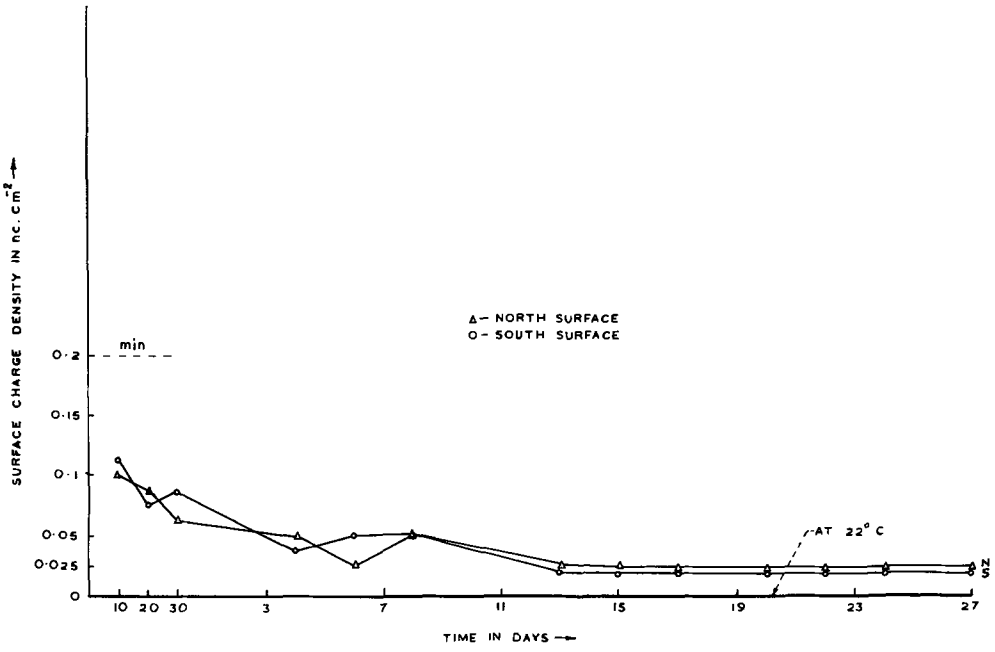

Fig. 7. Variation of surface charge density vs. time for shellac wax electret formed at 10.5 kG/mm in 75 min polarizing time at 55°C polarizing temperature.

being solidified under an electric field. The formation of magnetoelectrets may be due to the orientation of ionic charges or dipolar molecules or both which get frozen in the dielectric during its solidification.

The existence of polar molecules itself is insufficient to explain the development of charge on the magnetoelectret sample. But how a magnetic field causes dipoles to orient in their own direction is difficult to visualize.

The possibility of forming the magnetoelectret is confirmed by the results obtained by McMahon (9). He found that when certain organic compounds solidified in an electric field, the dielectric constant of these compounds in the solid state becomes higher than normal. The increase in the constant is isotropic and bears no relation to the direction of the field applied during the solidification. But in the case of a magnetic field, an anisotropic change takes place in the value of the dielectric constant, causing it to be greater than normal in the direction of the applied field and lower at right angles to this direction. McMahon postulated this mechanism of orientation of the molecules through diamagnetic coupling with the field. Diamagnetic anisotropy is observed in many aromatic ring compounds and according to Selwood (10), the principal susceptibility is generally perpendicular to the plane of the ring. Hence, in a magnetic field such molecules should tend to orient themselves so that the plane of the rings is parallel to the field and when the wax is solidified in a magnetic field, the molecules tend to orient with an axis of highest polarization in the direction of magnetic field.

Bhatnagar (11) has also mentioned that this explanation cannot directly be applied to the present case because the substance has an open chain structure; but according to Selwood, ring structure is not a necessary prerequisite for diamagnetic anisotropy, and chain compounds might also possess this property. Selwood says in open chain compounds "containing few or no multiple bonds, the maximum diamagnetic susceptibility corresponds to the greatest dimensions of the molecule." Thus it appears that McMahon's ideas may as well be extended to substances containing open chain compounds.

Although the above theory explains the nature and magnitude of the initial and final charges which appear on the electret surface, it fails to give a proper explanation for the appearance of a positive surface charge on the surface of the sample facing the north pole of the magnet. It can be due to the following two reasons (5, 6). First, due to the stripping after heating of the sample, positive charges were obtained on both the surfaces. Second, the dipoles oriented in the direction of the field in turn attract the excessive positive ions which are stuck on the surface when the sample is solidified from the bulk of the material. These ions are bound due to the attractive force of dipoles. The observed surface charge on an electret may therefore be written as

$$\sigma_{\text{eff}} = \sigma_D + \sigma_i + \sigma_m$$

where σ_{eff} = effective surface charge, σ_D = contribution of charge due to polar orientation, σ_i = component due to ionic polarization, and σ_m = contribution due to the molding and stripping.

The magnitude and nature of the effective charge depends of course, on the relative contributions of each one of these quantities and that varies from material to material and also depends on the polarizing conditions under which an electret is fabricated.

Acknowledgments

The authors wish to thank Professor S. C. Jain and Professor K. L. Chopra for the encouragement given to them during the course of this investigation. They are also grateful to Dr. A. K. Sreedhar, Dr. R. K. Jain, Dr. N. Chaudhri, and Dr. S. C. Gupta and their colleagues for the help given during the investigations.

Manuscript submitted April 5, 1971; revised manuscript received June 10, 1971.

Any discussion of this paper will appear in a Discussion Section to be published in the June 1972 JOURNAL.

REFERENCES

1. M. Eguchi, *Phil. Mag.*, **49**, 178 (1925).
2. C. S. Bhatnagar, *Indian J. Pure Appl. Phys.*, **2**, 331 (1964).
3. V. K. Jain and P. K. C. Pillai, *Phys. Status Solidi*, **28**, 415 (1968).
4. P. K. C. Pillai and V. K. Jain, *J. Sci. Ind. Res. (India)*, **29**, 270 (1970).
5. P. K. C. Pillai and V. K. Jain, *J. Phys. D.*, **3** 829 (1970).
6. P. K. C. Pillai, V. K. Jain, and G. K. Vij, *This Journal*, **116**, 836 (1969).
7. P. K. C. Pillai and V. K. Jain, *J. Appl. Phys.*, **40**, 3487 (1969).
8. B. Gross, *J. Chem. Phys.*, **17**, 866 (1949).
9. W. McMahon, *J. Amer. Chem. Soc.*, **78**, 3290 (1956).
10. P. W. Selwood, "Magneto-Chemistry," Chap. VII, Interscience Publishers Inc., New York (1956).
11. M.L. Khare and C. S. Bhatnagar, *Indian J. Pure Appl. Phys.*, **7**, 160 (1969).

The Mechanism of the Emission Color Shift with Activator Concentration in Eu^{+3} Activated Phosphors

Lyuji Ozawa and Philip M. Jaffe

Zenith Radio Corporation, Chicago, Illinois 60639

The emission of Eu^{+3} activated phosphors usually results from three excited states, namely $^5D_2$ (blue-green), $^5D_1$ (green-orange), $^5D_0$ (red) and the emission color shifts from yellow to red with an increase in activator concentration (1-3) and/or in the phosphor temperature (4-6).

In the case where the phosphor temperature is held constant, the emission color shift as a function of activator concentration is due to the difference in concentration dependence curves of the $^5D_2$, $^5D_1$, and $^5D_0$ emissions in the Eu^{+3} spectrum. However, only the concentration quenching mechanism of the $^5D_0$ emission is understood. The $^5D_0$ emission intensity depends on the concentration of isolated single activator ions which in turn depend on the crystal structure of the host and the mole fraction of activator (7). For weakly absorbed direct photoexcitation, the $^5D_0$ emission intensity per activator ion follows the equation

$$\frac{I_{ob}}{x} = (1 - x)^z \qquad [1]$$

where x is the activator concentration and z the weighted number of nearest neighbor cation sites.

Since the optimum activator concentration of the $^5D_1$ and $^5D_2$ emissions from many phosphors is around 0.01 mole fraction, electrostatic multipolar interaction may be involved in the concentration quenching. The quenching by multipolar interaction between rare earth ions has been studied by the change of decay time (8, 9). Van Uitert (8) indicates that the intensity of multipolar interaction can be also determined from the change of the emission intensity from the emitting level which has multipolar interaction. The emission intensity per one activator ion follows the equation

$$I_{ob}/x = (1 + \beta'(x)^{\theta/3})^{-1} \qquad [2]$$

where $\theta = 6$, 8, or 10 for dipole-dipole, dipole-quadrupole, quadrupole-quadrupole interactions, respectively, and β' is a constant for each interaction for a given host crystal.

For strongly absorbed exciting radiation, however, the observed concentration dependence curve, (I_{ob}/x) *vs.* x, deviates from the curves calculated by Eq. [1] and [2]. Equations [1] and [2] apply only to weakly absorbed exciting radiation used here (10).

Experimental

The Eu^{3+} activated phosphors studied in this paper are $(Y_{1-x}Eu_x)_2O_3$, $(Y_{1-x}Eu_x)_2O_2S$, and $Li(Y_{1-x}Eu_x)O_2$. The yttrium oxide and the europium oxide used were 6*N* and 3*N*, respectively. The preparation of the phosphors are reported in a previous publication (10).

The optical measurements were made on 2 mm thick powder samples, which were packed in planchettes. The concentration dependence of selected emission lines was determined by measuring their intensities as a function of activator concentration. The emission spectra of $(Y_{1-x}Eu_x)_2O_3$ and $Li(Y_{1-x}Eu_x)O_2$ phosphors were obtained with the 365 nm radiation from a mercury discharge lamp plus a Corning filter No. 7-54; for $(Y_{1-x}Eu_x)_2O_2S$, however, 395 nm radiation was used.

Results and Discussion

The concentration dependence curves studied were classified according to the ^5D_J emitting level. The emission lines quenched in the order $^5D_2$, $^5D_1$, and finally $^5D_0$ as the activator concentration increased. This order was independent of a change in either the exciting wavelengths or in the host. The relative intensities of the $^5D_2$, $^5D_1$, and $^5D_0$ emissions, however, were markedly different for a given host.

The I_{ob}/x *vs.* x curves of the $^5D_{0\text{-}2}$ emissions from $(Y_{1-x}Eu_x)_2O_3$ are shown in Fig. 1. The magnitude of the absorption coefficient was obtained by monitoring the $^5D_0$ emission because if the exchange interaction only was involved the I_{ob}/x *vs.* x curve of the $^5D_0$ emission would have followed Eq. [1] which applies for weakly absorbed exciting radiation. The data of the $^5D_0$ emission below $x = 0.1$ in $(Y_{1-x}Eu_x)_2O_3$ fitted on the calculated curves as shown in Fig. 1. These results indicate that below these activator concentrations Eq. [1] and [2] can apply to analysis of the experimental data. The I_{ob}/x data of the $^5D_1$ and $^5D_2$ emissions, over the activator concentration range of 0.01 to 0.1 mole fraction, fit on straight lines whose slopes are respectively 6/3 and 8/3 which indicate that dipole-dipole and dipole-quadrupole interactions are involved in the concentration quenching mechanism of the $^5D_1$ and $^5D_2$ emissions, respectively. The same results were obtained with $Li(Y_{1-x}Eu_x)O_2$ (10). The possible transitions involving the electrostatic multipolar interaction of Eu^{+3} are

Eu^{+3} (Excited)	Eu^{+3} (Relaxed)	
$^5D_2 \rightarrow {}^5D_1$;	$^7F_1 \rightarrow {}^7F_4$	(Q – D)
$^5D_1 \rightarrow {}^5D_0$:	$^7F_0 \rightarrow {}^7F_3$	(D – D)

The dependence of the quenching, I_q, upon the rate of transfer by electrostatic multipolar interaction is represented by the following equation (11)

$$I_q = A/(1 + r^{-\theta}) \qquad [3]$$

where r is the distance between activator ions and A is a constant.

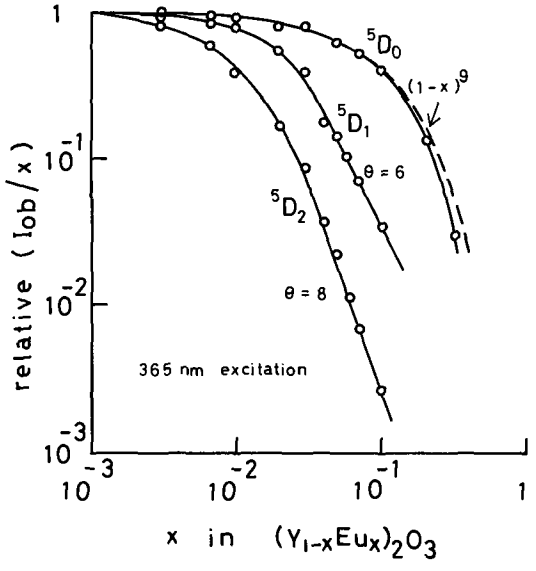

Fig. 1. Concentration dependence curves (I_{ob}/x *vs.* x) for $^5D_0$, $^5D_1$, and $^5D_2$ emissions from $(Y_{1-x}Eu_x)_2O_3$ under 365 nm ($4f^6$) excitation.

Key words: luminescence, phosphors, Eu^{+3} activation, concentration dependence.

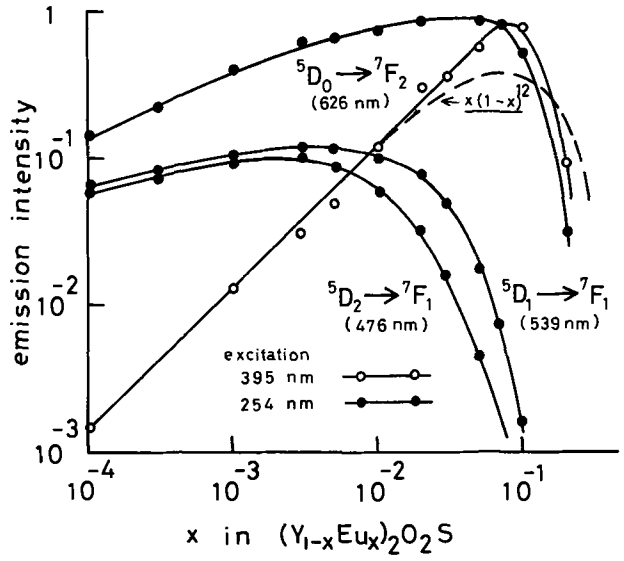

Fig. 2. Concentration dependence curves (I_{ob} vs. x) for $^5D_0$, $^5D_1$, and $^5D_2$ emissions from $(Y_{1-x}Eu_x)_2O_2S$ under 254 nm (host excitation ●) and 395 nm ($4f^6$ ○) excitations.

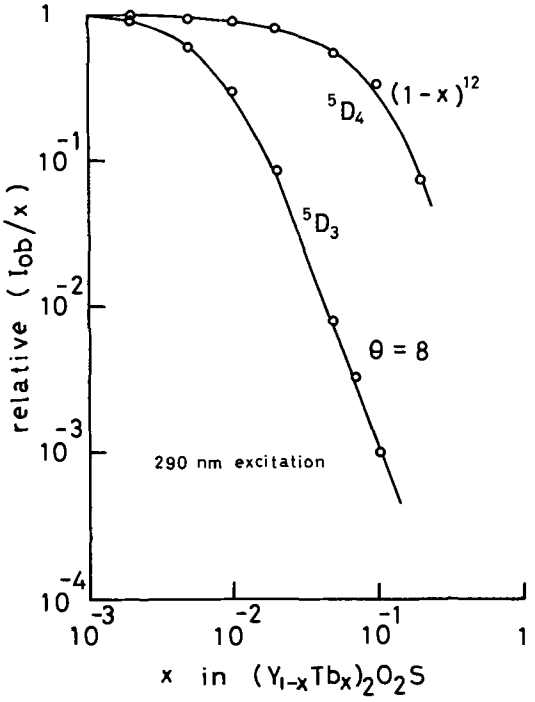

Fig. 3. Concentration dependence curves (I_{ob}/x vs. x) for $^5D_4$ and $^5D_3$ emissions from $(Y_{1-x}Tb_x)_2O_2S$ under 290 (f-d) excitation.

The concentration dependence curve of the $^5D_0$ emission from $(Y_{1-x}Eu_x)_2O_2S$ phosphor under the 395 nm exciting radiation ($4f^6$) had a positive deviation from the calculated curve, $x(1-x)^{12}$, as shown in Fig. 2. Therefore the concentration quenching mechanism of $(Y_{1-x}Eu_x)_2O_2S$ phosphor could not be exactly determined from the experimental data. Eu^{+3} seems to be a special case, however, since the I_{ob}/x *vs.* x curve of the $^5D_4$ Tb^{+3} in $(Y_{1-x}Tb_x)_2O_2S$ phosphor under the 290 (f-d) exciting radiation fitted on the calculated curve $(1-x)^{12}$ and the slope of the I_{ob}/x curve of the $^5D_3$ Tb^{+3} emission was 8/3 (see Fig. 3). Dipole-quadrupole interaction was estimated as the concentration quenching mechanism of the $^5D_3$ Tb^{+3} emission. These results agreed with the results of the other Tb^{+3} activated phosphors (12). From the results of $(Y_{1-x}Tb_x)_2O_2S$ phosphor, it is believed that in $(Y_{1-x}Eu_x)_2O_2S$ phosphor other quenching mechanisms may also be involved. However, the behavior of the concentration dependence curves of $(Y_{1-x}Eu_x)_2O_2S$ phosphor was qualitatively similar to those of $(Y_{1-x}Eu_x)_2O_3$ and $Li(Y_{1-x}Eu_x)O_2$ phosphors; *i.e.* the Eu^{+3} emission lines in the spectrum quenched in the order of $^5D_2$, $^5D_1$, and finally $^5D_0$ when the activator concentration increased. Therefore, the dominant mechanism of the concentration quenching of $(Y_{1-x}Eu_x)_2O_2S$ phosphor may be similar to those of $(Y_{1-x}Eu_x)_2O_3$ and $Li(Y_{1-x}Eu_x)O_2$ phosphors.

It is noted that the degree of the color shift over the same concentration range markedly depends on the phosphor host; well-known examples are white to orange to red with $(Y_{1-x}Eu_x)_2O_2S$, yellow to red with $(Y_{1-x}Eu_x)_2O_3$, and very little change with $(Y_{1-x}Eu_x)VO_4$. These color shift differences originate from the relative amounts of the $^5D_2$, $^5D_1$, and $^5D_0$ emissions at low activator concentrations. At low activator concentrations, where Eu^{+3} — Eu^{+3} interactions are unimportant, the $^5D_2$ to $^5D_1$, $^5D_1$ to $^5D_0$ relaxations and consequently the color shift are determined by host interactions. A phosphor which has a large amount of $^5D_2$ or $^5D_1$ emission at low concentration will show a large color shift as the activator concentration increases. Naturally, in order to study the color shift due to temperature effects the activator concentration should be very low, say, below 3×10^{-4} mole fraction.

Acknowledgment

The authors wish to thank Mrs. H. Stanczyk for her assistance in preparation of samples and in measurements and Dr. H. Forest for helpful discussion.

Manuscript submitted March 22, 1971; revised manuscript received June 29, 1971.

Any discussion of this paper will appear in a Discussion Section to be published in the June 1972 JOURNAL.

REFERENCES

1. L. G. Van Uitert and R. R. Soden, *J. Chem. Phys.*, **32**, 1687 (1960).
2. R. C. Ropp *et al.*, *Electrochem. Technol.*, **4**, 24 (1966).
3. P. M. Jaffe and J. D. Konitzer, *This Journal*, **116**, 633 (1969).
4. C. W. Struck and W. H. Fonger, *J. Chem. Phys.*, **52**, 6364 (1970).
5. K. A. Wickersheim, R. A. Buchanan, and E. E. Anderson, Abs. 40, p. 122, Electrochem. Soc. Extended Abstracts, Spring Meeting, Los Angeles. Calif., May 10-15, 1970.
6. O. J. Sovers and T. Yoshioka, *J. Chem. Phys.*, **49**, 4945 (1970).
7. L. G. Van Uitert and S. Iida, *ibid.*, **37**, 986 (1962).
8. L. G. Van Uitert, *This Journal*, **114**, 1048 (1967).
9. E. Nakazawa and S. Shionoya, *J. Chem. Phys.*, **47**, 3211 (1967).
10. L. Ozawa, H. Forest, P. M. Jaffe, and G. Ban, *This Journal*, **118**, 482 (1971).
11. L. G. Van Uitert, *Appl. Phys. Letters*, **9**, 225 (1966).
12. T. Hoshina, *Japan. J. Appl. Phys.*, **6**, 1203 (1967).

JOURNAL OF THE ELECTROCHEMICAL SOCIETY

ELECTROCHEMICAL TECHNOLOGY

OCTOBER 1971

An Improved Calcium Anode for Thermal Batteries

Robert P. Clark and Kenneth R. Grothaus

Sandia Laboratories, Albuquerque, New Mexico 87115

ABSTRACT

A technique is described for preventing electrical shorting resulting from the formation of $CaLi_2$ alloy in thermal cells employing a Ca anode and LiCl-KCl electrolyte. The cell employed in this work was Ca/LiCl-KCl-$CaCrO_4$/Fe. The method consists of immersing the Ca anode in an acetic acid solution, thereby forming a layer of $3Ca(CH_3COO)_2 \cdot 2CH_3COOH$ on the anode surface. This double salt decomposes to $CaCO_3$ either prior to or at the beginning of the cell discharge. The resulting high concentration of Ca^{++} at the anode-electrolyte interface retards the displacement by Ca of Li from the LiCl in the electrolyte. Cell and battery test results are given which demonstrate the improvement in performance resulting from application of this technique.

A thermal battery is a primary battery whose cells contain an electrolyte which is solid and virtually nonconductive at ambient temperatures, but which becomes highly conductive when heated to temperatures above its melting point. Because of its relatively low melting point, good thermal stability, and high electrical conductivity, the lithium chloride-potassium chloride eutectic is the most commonly used thermal battery electrolyte. The anode most often selected, calcium, is chosen for its large negative reduction potential, low equivalent weight, high melting point, low polarization and ready availability. Unfortunately, calcium displaces lithium from the molten electrolyte as shown in Reaction [1] (1).

$$Ca(s) + 2Li^+ \xrightarrow{352°C} Ca^{++} + 2Li(l) \qquad [1]$$

The molten lithium in turn reacts with additional calcium according to Reaction [2] to form a calcium-lithium alloy of composition $CaLi_2$ with a melting point of 230°C (2)

$$Ca(s) + 2Li(l) \xrightarrow{352°C} CaLi_2(l) \qquad [2]$$

The presence of an excess of a molten metal in a voltaic cell is obviously an undesirable situation because of the possibility of shorting. Electrical noise and cell degradation due to the $CaLi_2$ alloy have long been major problems in thermal batteries (3). Although thermal batteries can be overdesigned so as to be highly reliable, the unpredictable nature of this alloy results in poor reproducibility of performance especially with regard to activated battery life. Possible solutions to this problem are elimination of the Ca anode and/or the LiCl electrolyte. Unfortunately, the alternative materials often create more problems than they solve. Replacement of a Ca anode with Mg, for example, usually results in a reduced output voltage for a given thermal cell (1, 4). Unpublished results from this laboratory show that between 450° and 600°C, the output voltage for the cell M/LiCl-KCl-$CaCrO_4$/Fe is approximately 0.8V less for M = Mg than for M = Ca at current densities ranging from 0.11 to 120 mA/cm^2. Substitutes for the LiCl-KCl eutectic which possess the desirable combination of electrolyte properties previously mentioned for LiCl-KCl have not been found.

Key words: thermal batteries, anodes, calcium, batteries.

In the present paper, a technique is described for chemically treating the Ca anode such that $CaLi_2$ alloy formation is no longer a significant problem. The process involves the production of a high concentration of Ca^{++} ions at the anode-electrolyte interface, thereby greatly reducing the formation of Li (Reaction [1]). This is accomplished by depositing a layer of $3Ca(CH_3COO)_2 \cdot 2CH_3COOH$ on the Ca anode through the reaction between Ca and acetic acid. The double salt ultimately thermally decomposes to form $CaCO_3$. The existence of these salts has been shown with the aid of x-ray diffraction and thermogravimetric analysis.

Experimental

Materials.—All materials used were of a grade equivalent to that used in production thermal batteries. Anodes were: rolled sheet Ca pressed on an iron backing, or Ca vapor deposited on the backing.

The electrolyte consisted of reagent grade LiCl and KCl vacuum dried for 16 hr at 120°C, mixed in the eutectic ratio (5), fused at 400°C, cooled, and ground to a powder.

Baker and Adamson (Allied Chemical) technical grade $CaCrO_4$ was used as the cathodic depolarizer. Glacial acetic acid and acetone were both reagent grade. The cathode consisted of sheet iron.

Procedures

Calcium anodes used in the evaluation were of three types: control samples which had been cleaned with 5 volume per cent (v/o) HNO_3 in acetone, anodes which were cleaned and then immersed for 180 sec in 20 v/o CH_3COOH in acetone and anodes which were cleaned and immersed for 60 sec in 25 v/o CH_3COOH in acetone. All three anode types were tested in single thermal cell configurations and in five-cell thermal batteries.

Anodes treated with other acetic acid concentration-immersion time combinations, with acetic acid vapor and with acetic acid in Freon 113 (1,1,2 trichloro - 1,2,2 trifluoroethane), were evaluated but are not discussed here since these experiments lead to results equivalent to those reported in this paper.

Single cell tests.—The thermal cell was of the type Ca/LiCl-KCl-$CaCrO_4$/Fe. The over-all cell reaction is quite complex but may be written in simplified form as

$$3Ca + 2CaCrO_4 \rightarrow 5CaO + Cr_2O_3 \quad [3]$$

The LiCl-KCl eutectic electrolyte, the $CaCrO_4$ cathodic depolarizer, and an inert silica binder material were mixed and pressed into a homogeneous pellet configuration. The binder served to maintain the pellet dimensions even at temperatures above the electrolyte melting point. This depolarizer-electrolyte-binder (DEB) pellet was placed between a Ca anode and an Fe cathode to form a single cell. The cell was discharged by heating it between two electrically heated nickel platens from which the cell was electrically insulated. Constant platen temperatures of 450°, 500°, 550°, and 600°C were used in these investigations. These values are representative of actual temperatures experienced by cells inside an activated thermal battery during its operation (6). Cells were discharged through constant resistance loads ranging in value from 2800 to 2 ohms, corresponding to approximate current densities of 0.11 to 120 mA/cm². DEB pellets of various depolarizer, electrolyte, and binder concentrations were used in the tests. The single cell testing arrangement is shown in Fig. 1.

Dependent variables measured included peak cell voltage under load, cell capacity in amp · sec, the occurrence of electrical noise and weight of $CaLi_2$ alloy extruded from the Ca-DEB pellet interface.

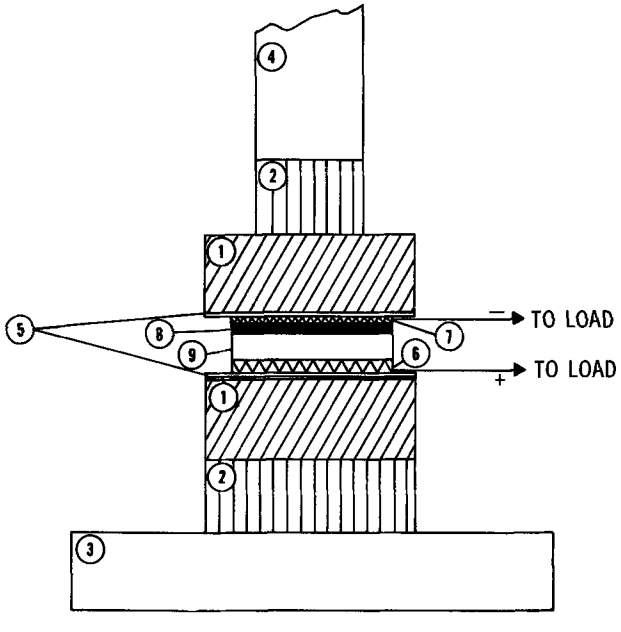

(1) ELECTRICALLY HEATED PLATENS
(2) CERAMIC THERMAL INSULATOR
(3) TESTER BASE
(4) RAM
(5) MICA ELECTRICAL INSULATOR
(6) IRON CATHODE
(7) IRON BACKING ON ANODE
(8) CALCIUM ANODE
(9) DEPOLARIZER-ELECTROLYTE-BINDER PELLET

Fig. 1. Single cell test arrangement

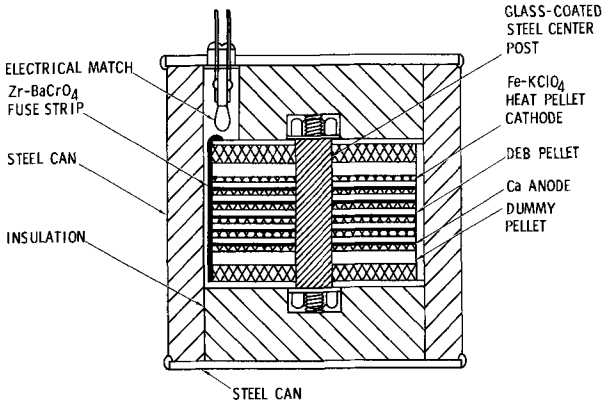

Fig. 2. Cutaway of thermal battery configuration

Battery tests.—Calcium electrodes of each of the three types were also evaluated in five-cell thermal batteries. The five cells were stacked in series with the anode of one cell in contact with the cathode of the next as shown in Fig. 2. Batteries were activated by means of an electrical match which ignited a zirconium-barium chromate fuze strip which in turn ignited iron-potassium perchlorate heat-generating pellets. The heat-generating pellets contained an amount of iron in excess of the stoichiometric mixture so that they also served as the cathodes. The cell stack was surrounded with insulation and hermetically sealed in a thin steel case. Batteries of this general type have been successfully used in the past to evaluate the effect of variables on performance (6).

Batteries were tested at seven ambient temperatures ranging from −54° to 71°C. Performance over this ambient temperature range is a common thermal battery requirement. Batteries were activated and discharged with a high impedance load (approximately 4 mA/cm²) for 120 sec followed by a heavier load for the remainder of the discharge. Approximate current densities after the first 120 sec ranged from 16 to 155 mA/cm². This type of discharge (high impedance load followed by a heavy load) is typical for thermal battery applications (3). If discharge rates are sufficiently high, much of the $CaLi_2$ which forms will be utilized electrochemically at the anode according to Reaction [4]

$$CaLi_2 \rightarrow Ca^{+2} + 2Li^+ + 4e^- \quad [4]$$

Consequently, under very light loads (as employed during the first 120 sec), the rate of $CaLi_2$ formation will be larger than the rate of electrochemical utilization, causing the shorting effects to be more pronounced. Voltage *vs.* time was monitored for each battery; electrical noise was noted and batteries were disassembled after testing to allow measurement of visible $CaLi_2$ alloy.

Results and Discussion

Cell tests.—Typical cell test results are shown in Table I. Data at each condition represent the average for at least three separate single cell discharges. These data show that cells with treated anodes exhibit reduced amounts of extruded $CaLi_2$ alloy and a corresponding absence of electrical noise. Within experimental error capacities of treated cells are equal to or greater than capacities of cells with untreated anodes. This is particularly significant at 450°C where any effect of increased cell *IR* which might be caused by the $CaCO_3$ layer on the anode surface would be most severe. This effect probably accounts for the differences in peak voltages observed at 450°C. No significant variation in peak voltage is observed at any other one temperature.

Some discussion of the relationship between $CaLi_2$ alloy weight and electrical noise is in order. The fact

Table I. Discharge data for single thermal cells with acetic acid treated calcium anodes
Cell description: Ca/LiCl-KCl-$CaCrO_4$/Fe

Temp. (°C)	Ca treatment (v/o acetic acid)	Ca treatment (Reaction time, sec)	Approximate current density (mA/cm²)	Peak voltage (V)	Capacity to 2.0 V/cell (A-sec)	Weight $CaLi_2$ extruded (mg)	Electrical noise
450	0	0	120	2.43	74	57	No
450	20	180	120	2.33	140	2	No
450	25	60	120	2.23	71	0	No
500	0	0	0.11	2.88	>0.6	43	Yes
500	20	180	0.11	2.88	>0.6	15	No
500	25	60	0.11	2.87	>0.6	10	No
550	0	0	60	2.60	278	60	No
550	20	180	60	2.60	296	0	No
600	0	0	0.11	2.91	0.06	85	Shorted
600	20	180	0.11	2.89	0.47	55	No
600	25	60	0.11	2.87	0.87	49	No

that such a relationship does exist has been previously established (3). Also, in the present work it was possible to visually observe intermittent and/or permanent shorting caused by the bridging of molten $CaLi_2$ between anode and cathode. An inspection of discharged thermal batteries further verified $CaLi_2$ alloy as the cause of electrical noise. However, a quantitative correlation between alloy weight and electrical noise is not possible for two major reasons. First, the weight of extruded $CaLi_2$ alloy can be determined only semiquantitatively at best. The complete separation of the alloy from impurities (*e.g.* electrolyte, depolarizer, reaction products, etc.) is virtually impossible. Furthermore, in cases of prolonged cell shorting, the alloy often ignites, becoming partially or completely oxidized. Secondly, the nature of the extruded alloy is a function of the anode treatment. With untreated anodes, the $CaLi_2$ tends to form in a few very large globules. However, for anodes treated with acetic acid the alloy is extruded as many very small droplets. Consequently, the likelihood of resulting shorting is far greater for the larger globules even though the total weight of extruded alloy could be less.

Battery tests.—One of the difficulties associated with thermal batteries has been the inability to make accurate estimates of battery performance based on single cell data. Consequently, it has been the practice in thermal battery technology to use single cell tests primarily for rough screening evaluations. Any materials or processes selected on this basis must then be thoroughly tested in actual batteries. Because the present work has as its goal an anode for practical use in thermal batteries, an extensive evaluation of anodes in batteries was undertaken. Representative data for batteries are shown in Tables II and III. Each set of data represents the average of results for at least two separate batteries.

Table II shows discharge data as a function of temperature for batteries with each of the three Ca types. Comparison of untreated anodes with Ca anodes immersed for 180 sec in 20 v/o acetic acid and showed the following: treated anodes resulted in decreased weight of extruded alloy; a corresponding decrease in electrical noise was observed except at 71°C where both treated batteries were noisy while 7 of 10 untreated batteries exhibited noise; cell capacities were not significantly affected by the treatment. The results for batteries with anodes treated for 60 sec in 25 v/o acetic acid show that: alloy weight was further decreased; noise was eliminated and cell capacity was decreased markedly only at −54°C. This loss of capacity is due to *IR* at the anode-DEB pellet interface caused by the $CaCO_3$ layer on the Ca. The *IR* drop becomes significant for high-current densities at low temperature.

In order to determine the maximum current density which the treated anodes can sustain without large capacity losses, a comparison was made of test results at −54° and 71°C for untreated and treated Ca at a variety of current densities. The data are shown in Table III.

From this table it can be noted that the treated anodes result in less $CaLi_2$ extrusion with a corresponding decrease or, in these cases, absence of noise. For treated anodes peak voltages are low at −54°C for the higher current densities (147 and 155 mA/cm²) due to resistance of the deposited $CaCO_3$ layer. Battery capacity at 71°C is generally improved by the acetic acid treatment. Untreated anodes suffer losses due to intermittent or permanent shorting and also

Table II. Discharge data as a function of temperature and treatment conditions for thermal batteries with acetic acid treated calcium anodes
Cell description: Ca/LiCl-KCl-$CaCrO_4$/Fe
Current density: First 120 sec—4 mA/cm²
After 120 sec—155 mA/cm²

Ca treatment (v/o acetic acid)	Ca treatment (Reaction time, sec)	Ambient temp. (°C)	Capacity to 1.0 V/cell (A · sec)	Weight $CaLi_2$ extruded (mg)	Per cent of batteries with electrical noise
0	0	−54	207	27	20
20	180	−54	195	0	0
25	60	−54	95	0	0
0	0	−40	238	18	0
20	180	−40	198	0	0
25	60	−40	181	0	0
0	0	−18	253	16	0
20	180	−18	201	0	0
25	60	−18	199	0	0
0	0	7	260	35	0
20	180	7	242	13	0
25	60	7	226	3	0
0	0	52	257	52	50
20	180	52	226	30	0
25	60	52	226	13	0
0	0	60	275	60	50
20	180	60	298	21	0
25	60	60	318	9	0
0	0	71	150	62	70
20	180	71	114	29	100
25	60	71	147	13	0

Table III. Discharge data as a function of current density for thermal batteries with acetic acid treated calcium anodes
Cell description: Ca/LiCl-KCl-$CaCrO_4$/Fe
Current density: First 120 sec—4 mA/cm²
After 120 sec—As shown

Ca treatment (v/o acetic acid)	Ca treatment (Reaction time-sec)	Approximate current density after 120 sec (mA/cm²)	Capacity to 1.0 V/cell (A · sec) @ −54°C	Capacity to 1.0 V/cell (A · sec) @ 71°C	Weight $CaLi_2$ extruded (mg) @ −54°C	Weight $CaLi_2$ extruded (mg) @ 71°C	Per cent of batteries with electrical noise @ −54°C	Per cent of batteries with electrical noise @ 71°C	Peak voltage under load @ −54°C	Peak voltage under load @ 71°C
0	0	155	207	150	27	62	20	70	11.90	12.35
25	60	155	95	147	0	13	0	0	11.10	12.35
0	0	147	267	0	25	106	0	100	11.90	—
25	60	147	210	236	0	56	0	0	11.30	12.10
0	0	140	230	115	48	51	0	0	11.75	11.50
25	60	140	206	199	3	4	0	0	11.60	12.00
0	0	116	277	201	32	62	0	50	12.55	12.40
25	60	116	255	222	0	30	0	0	12.30	12.55
0	0	53	178	83	18	67	0	100	12.95	12.20
25	60	53	140	177	0	32	0	0	13.00	12.83
0	0	16	76	71	16	35	0	50	13.25	13.48
25	60	16	72	94	0	24	0	0	13.40	13.50

because of loss of active anode material due to extrusion of $CaLi_2$. Capacity for treated cells at −54°C is only slightly less than for untreated, except at 155 mA/cm² where the decrease becomes very significant. Thus, treated anodes can be utilized over the complete temperature range −54° to 71°C without significant loss of capacity or peak voltage for current densities less than ~150 mA/cm².

Chemical reactions.—The chemistry of this treatment is explained with the help of thermogravimetric analyses and x-ray diffraction identification of compounds. The calcium anode and acetic acid react according to Reaction [5]

$$3Ca + 8CH_3COOH \rightarrow 3Ca(CH_3COO)_2 \cdot 2CH_3COOH + 3H_2\uparrow \quad [5]$$

The double salt was identified by x-ray diffraction. The existence of this compound ($3Ca(CH_3COO)_2 \cdot 2CH_3COOH$) has been previously established (7). This material decomposes very slowly at room temperature and very rapidly above 170°C to form calcium acetate.

Calcium acetate undergoes thermal decomposition at 400°-430°C to calcium carbonate (8) which is stable at the internal battery operating temperatures. Batteries may be assembled containing anodes coated with $3Ca(CH_3COO)_2 \cdot 2CH_3COOH$ or the anodes may be heated prior to assembly so that either a $Ca(CH_3COO)_2$ or a $CaCO_3$ coating exists.

The first compound adheres well to the calcium; however, the pressure generated within the battery due to the decomposition of the double salt during battery activation may be undesirable. In this case, the $Ca(CH_3COO)_2$ or the $CaCO_3$ coated anodes could be employed, although adherence to the anode is only fair with $Ca(CH_3COO)_2$ and poor with $CaCO_3$. In any event, once the cell is activated thereby reaching temperatures in excess of 450°C, the coating will consist of $CaCO_3$ which is moderately soluble in the LiCl-KCl eutectic electrolyte. (Rough measurements in this laboratory show that this solubility is approximately 5g $CaCO_3$/100g LiCl-KCl eutectic at 550°C.) Thus, a relatively high concentration of Ca^{++} ions will exist at the anode-electrolyte interface. This will cause the equilibrium in Reaction [1] to be shifted to the left, thereby retarding the formation of $CaLi_2$ alloy (Reaction [2]). Attempts to accomplish this same effect by adding Ca^{++} ion (as $CaCl_2$ or $CaCO_3$) to the electrolyte itself successfully reduced the rate of $CaLi_2$ formation; however, the melting point of the electrolyte was increased by this addition such that the conductivity of the electrolyte and output of the cell were severely degraded.

Conclusion

This work demonstrates the practical improvements in thermal batteries which resulted from reacting calcium anodes with acetic acid in a prescribed manner. The quantity of extruded $CaLi_2$ alloy was decreased, and the resulting electrical noise and shorting were virtually eliminated. No significant detrimental effect on cell capacity or voltage was noted except for discharges at 155 mA/cm² and −54°C. The particular acetic acid concentration and reaction time necessary for application of the technique are dependent upon the specific battery requirements. The method has been successfully applied to several commercial thermal batteries (9) and should find application to future thermal battery requirements.

Acknowledgment

The authors are indebted to R. L. Blucher and W. Jones, both of Catalyst Research Corporation, Baltimore, Md., for testing of batteries and to Dr. B. H. Van Domelen of Sandia Laboratories for his valuable suggestions during preparation of the manuscript.

This work was supported by the U. S. Atomic Energy Commission.

Manuscript submitted Jan. 14, 1971; revised manuscript received *ca.* May 14, 1971.

Any discussion of this paper will appear in a Discussion Section to be published in the June 1972 JOURNAL.

REFERENCES

1. S. M. Selis and L. P. McGinnis, *This Journal*, **108**, 191 (1961).
2. D. G. Carfagno, Ph.D. Thesis, Syracuse University, Syracuse, N. Y. (1966).
3. P. T. Boling, Sandia Laboratory Report, SC-DR-66-655, April 1967.
4. W. J. Hamer, M. S. Malmberg, and B. Rubin, *This Journal*, **103**, 8 (1956).
5. H. A. Laitinen, W. S. Ferguson, and R. A. Osteryoung, *ibid.*, **104**, 516 (1957).
6. D. M. Bush, Sandia Laboratory Report, SC-RR-69-497, Nov. 1969.
7. L. Walter-Levy and J. Perrier, *Compt. Rend.*, **246**, 1553 (1958).
8. J. Panzer, *J. Chem. Eng. Data*, **7**, 140 (1962).
9. R. L. Blucher, Private communication.

The Corrosion Behavior of Zn-22Al Alloy Sheet

D. N. Williams, B. G. Koehl, W. E. Berry,* and E. S. Bartlett

Battelle Memorial Institute, Columbus, Ohio 43201

ABSTRACT

The corrosion behavior of three lots of annealed Zn-22Al sheet material was compared with that of 380 aluminum die-casting alloy using four accelerated corrosion test environments: 100% relative humidity at 120°F, 100% relative humidity at 120°F plus a trace of ammonia, 100% relative humidity at 120°F plus 100 ppm sulfur dioxide, and alternate immersion in 3½% sodium chloride solution at room temperature. Corrosion rates of the Zn-22Al materials as measured by weight change and metallographic evidence of subsurface attack were considerably less than observed in the 380 aluminum die-casting alloy. Intergranular attack was observed extending 2-4 mils beneath the surface in the Zn-22Al material exposed to high-humidity environments except when sulfur dioxide was present. Intergranular attack appeared related to the presence of a zinc-rich grain-boundary phase. Although the corrosion behavior of Zn-22Al material was not affected in most cases by exposure under stress, one material which was relatively free of intergranular attack when exposed without stress developed cracks when exposed under stress.

Zn-22Al alloy sheet is presently being considered for use in applications where extensive forming is required. When properly processed, this alloy shows superplastic behavior and is readily formed into complex shapes (1, 2). After forming, the alloy can be heat-treated to a nonsuperplastic condition having attractive strength and creep resistance. The postforming heat-treatment is designed to produce a lamellar eutectoid microstructure composed of the two terminal solid-solution phases. [See ref. (3) for a recent discussion of the phase diagram of the aluminum-zinc system.]

The present study was designed to examine the corrosion behavior of Zn-22Al alloy sheet in this final heat-treated condition. Since the alloy is expected to compete with aluminum die-cast components, at least in initial applications, the corrosion behavior was compared to that of the 380 die-casting alloy (Al-8.5Si-3.5Cu). All corrosion studies were conducted with accelerated-corrosion-test procedures.

Materials

Sheet material at about 50 mil thickness was used in this investigation. Three lots of material were evaluated, each of which had been processed somewhat differently.

One lot of sheet material was processed by a commercial supplier. This sheet, referred to as direct-chill material, was cast as a 14-in.-thick direct-chill ingot, scalped heavily to remove high-zinc surface segregates, and rolled to sheet on a commercial mill.

The other two lots of sheet materials were cast and fabricated to sheet in the laboratory. One lot, designated as tilt-mold material, was cast into a 1¼-in.-thick preheated tilt mold and scalped to remove 62 mils per side prior to rolling. The other lot, referred to as chill-mold material, was cast into a 1½-in.-diameter copper ingot mold and processed to sheet without scalping.

All three materials were hot rolled in the high-temperature single-phase field at about 650°F to an intermediate thickness. A final cold reduction of about 50% was used following quenching from the high-temperature phase field. This treatment placed the materials in a superplastic state. Following this treatment, all materials were heated to 650°F, held approximately 1 hr, and slow cooled at less than 30°F/min to below 450°F to place the material in an optimum use condition.

The direct-chill material showed evidence of alloy segregation in the central region as shown in Fig. 1. Electron-probe studies showed this region to be high in zinc. Noticeable grain-size differences were apparent among the three materials, the direct-chill material showing the largest grain size and the tilt-mold material the finest. The coarseness of the lamellar eutectoid structure also varied among the three materials. The direct-chill material appeared to have a coarser eutectoid structure than the other two materials. The eutectoid structure in this material is shown in Fig. 2. The differences in eutectoid coarseness were attributed to differences in the cooling rate following the 650°F anneal.

The chemical composition of the three materials is shown in Table I. The direct-chill material was of somewhat higher purity than the other two materials, and the chill-mold material was much lower in aluminum than desired: the intended range was 21.5 to 22.5. Tensile properties of the three materials shown in Table II indicated that processing and compositional differences among these three materials had a significant effect on strength and ductility.

The 380 aluminum alloy samples exposed in the corrosion study for comparison purposes were obtained

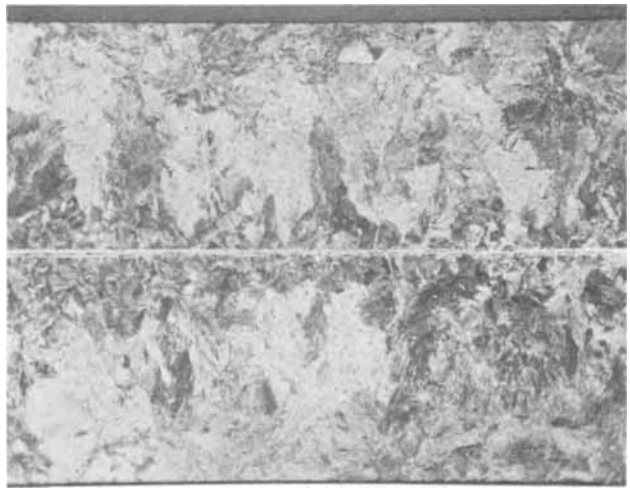

Fig. 1. Microstructure of direct-chill Zn-22Al alloy sheet showing zinc-rich alloy segregation at the center of the sheet. 45×.

* Electrochemical Society Active Member.

Key words: superplasticity, intergranular attack, pitting, alternate immersion, humidity tests.

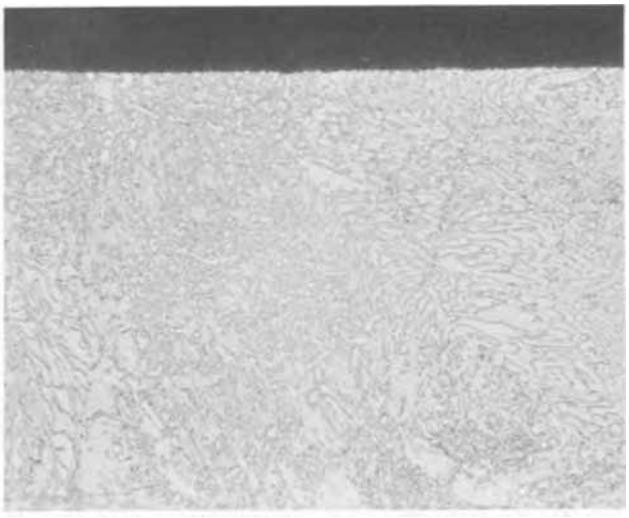

Fig. 2. Eutectoid structure in direct-chill alloy sheet adjacent to rolling surface. 540×.

from a thin-wall commercial die casting. Samples were cut from positions of the casting showing approximately 50-mil thickness and exposed with the as-cast surface intact. The 380 alloy has a nominal composition of Al-8.5Si-3.5Cu and typical tension properties as die cast of:

0.2% offset yield strength	24,000 psi
ultimate tensile strength	48,000 psi
elongation in 2 in.	3 %

Corrosion-Test Procedures

Four accelerated-corrosion test procedures were used to compare these materials:

1. Continuous exposure to 100% relative humidity at 120°F.
2. Continuous exposure to 100% relative humidity at 120°F with a trace of ammonia (1 ppm).
3. Continuous exposure to 100% relative humidity at 120°F with 100 ppm sulfur dioxide.
4. Alternate immersion in 3½% sodium chloride solution (10 min immersion followed by 50 min drying in ambient air).

Humidity tests were conducted in cabinets meeting Army-Navy-Aeronautical Specification AN-H-31. Duplicate samples measuring 1 x 2 in. were continuously exposed for 100, 250, 500, and 1000 hr in each environment and examined for weight change, visual appearance, and microstructural evidence of corrosion attack. Previous experience had shown that an adherent film formed on those specimens exposed to 100% relative humidity at 120°F. However, as will be noted later, some spalling occurred in humid air containing SO_2 and in 3½% NaCl solution. Because of the limited amount of material, replicate samples could not be removed at intermediate exposure periods for descaling to determine weight loss. Nevertheless, the weight changes for spalling specimens did show trends and the data are reported for this purpose.

Table I. Composition of three Zn-22Al materials

Material identification	Per cent by weight				
	Al	Fe	Si	Cu	Mg
Direct-chill	22.7	0.007	<0.005	0.001	<0.001
Tilt-mold	22.1	0.049	0.04	0.005	<0.001
Chill-mold	18.9	0.02	0.02	0.002	<0.001

Table II. Tensile properties of three Zn-22Al materials

Material identification	Tensile properties of 50-mil-thick sheet			
	0.2% Offset yield strength, psi	Ultimate strength, psi	Elongation, % in 2 in.	Reduction in area, %
Direct-chill	28,900	31,500	13	18
Tilt-mold	36,200	38,000	18	28
Chill-mold	29,200	30,300	16	16

The main criterion for evaluating corrosion performance was a metallographic examination of transverse cross sections (across the rolling direction). The entire periphery of the cross section was examined. Maximum depth of pitting or intergranular attack was recorded. If selective attack was observed, it was quite extensive. Only an occasional specimen exhibited an isolated area of selective attack.

Some corrosion studies were performed under stress. Cantilever-loaded bend samples measuring 6 x 1 x 0.05 in. were loaded so as to produce measurable creep during the test and were exposed to selected high-humidity environments. U-bend samples measuring 4 x 0.5 x 0.05 in. were bent over a ¾-in.-diameter mandrel and were exposed to alternate immersion in sodium chloride. The legs of the U-bend specimens were pulled up parallel using stainless steel nuts and bolts inserted through holes at either end of the specimen. Teflon washers were used to insulate the nuts and bolts from the specimens. The long axis of both types of specimens was parallel to the rolling direction of the sheet. Both types of bent beam specimens produced yield-strength stress levels in the outer fibers on the tensile side of the specimens.

Results

The corrosion behavior of the Zn-22Al material in 100% relative humidity at 120°F was not greatly affected by the presence of ammonia as shown by the results after exposure in both environments in Table III. Exposure to these environments resulted in the formation of an adherent gray film mottled with spots of white corrosion product. There was little tendency for spalling in these materials. A log-log plot of the weight-gain measurements for the tilt-mold material suggested that corrosion was following a cubic-rate law. Based on the weight-gain data, there did not ap-

Table III. Corrosion behavior of Zn-22Al material in 100% relative humidity at 120°F

Material identification	Ammonia present	Weight gain, mg/dm², in				Maximum depth of corrosion, mils, in 1000 hr	
		100 hr	250 hr	500 hr	1000 hr	Surface pitting	Intergranular attack
Direct-chill	No	30	46	59	58	2	0[a]
Direct-chill	Yes	25	42	52	54	1	0
Tilt-mold	No	34	44	65	74	1.4	3
Tilt-mold	Yes	37	53	59	77	2	4.2
Chill-mold	Yes	30	41	44	50	0	2.8
380 Al alloy	No	131	105	97	110	0	3
380 Al alloy	Yes	100	116	124	125	0	3

[a] One area showing some intergranular attack was noted, but it was obviously an isolated occurrence.

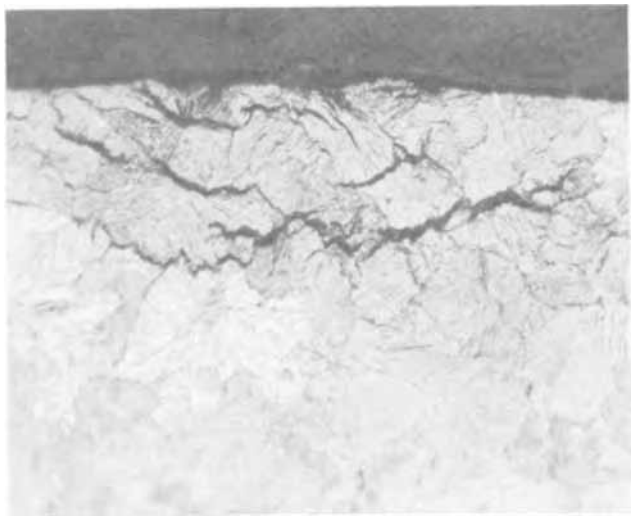

Fig. 3. Intergranular attack in the Zn-22Al sheet (tilt-mold material) after exposure to 100% relative humidity for 1000 hr. 345×.

pear to be a large difference in the rate of corrosion among the three Zn-22Al materials. All three were corroded to a lesser extent than the 380 aluminum alloy.

Metallographic examination of the corrosion samples after exposure showed two distinct types of attack, surface pitting and intergranular attack. The appearance of intergranular attack in a Zn-22Al material is shown in Fig. 3. Both types of attack were localized and were found under areas showing obvious corrosion product buildup. Measurements of the maximum depth of pitting and of intergranular attack after 1000 hr of corrosion are presented in Table III. The tilt-mold and chill-mold materials showed severe intergranular attack, but there was little evidence of this type of attack in the direct-chill material at the conclusion of 1000 hr of exposure. The aluminum alloy also showed intergranular attack. Pitting was about equally severe in the direct-chill and tilt-mold materials, but was not observed in either the chill-mold material or in the 380 aluminum alloy.

Backscatter scanning electron microscope studies suggested that intergranular attack in the Zn-22Al material was related to the presence of a zinc-rich grain-boundary phase. This technique readily distinguishes between zinc-rich and aluminum-rich phases. The zinc-rich phase fluoresces, appearing light in the micrographs, while the aluminum-rich phase remains dark. The appearance of the grain-boundary phase in the tilt-mold material is compared with that in the direct-chill material in Fig. 4. The chill-mold material also was found to contain a zinc-rich grain-boundary phase in the material adjacent to the surface. Zinc segregation in surface regions of these materials apparently occurred during casting and was not completely removed by scalping prior to rolling to sheet. Low aluminum, such as present in the chill-mold material, should have magnified this problem. The lesser depth of intergranular attack in chill-mold material was attributed to the form of the zinc-rich grain-boundary phase which, as shown in Fig. 5, was less continuous than that observed in the tilt-mold material.

After detection of intergranular attack in these materials, samples of the direct-chill and the tilt-mold materials previously exposed for 1000 hr in the 100% humidity environment containing ammonia were returned to the corrosive environment for an additional 500 hr to provide a total exposure of 1500 hr to determine if the depth of intergranular penetration would increase. Weight gains after 1500 hr were 62 and 80 mg/dm^2, respectively. Metallographic examination of these samples showed intergranular attack to a maximum depth of 4.4 mils in the tilt-mold material, not greatly different than the 4.2-mil depth of pitting observed after 1000 hr. A few intergranular penetrations were noticed after 1500 hr, up to 3.2 mils deep, in one side of the direct-chill material. Because of their localized nature, it is suspected that they resulted from a random high-zinc region rather than from the increased exposure time.

Cantilever-loaded bend samples of the Zn-22Al materials were stressed so as to produce measurable creep during exposure and were examined after 1000 hr of exposure to determine if stress accelerated intergranular penetration. Both the depth of pitting and the maximum depth of intergranular attack tended to be lower on the compression surface than on the tension surface, as shown in Table IV. Comparison with the data in Table III shows that stress did not increase the depth of intergranular attack in either the chill-mold or the tilt-mold material, but did result in intergranular attack in the direct-chill material which, in unstressed exposure, was relatively free of intergranular attack. Measurements of depth of pitting under stress did not compare well with those made on unstressed

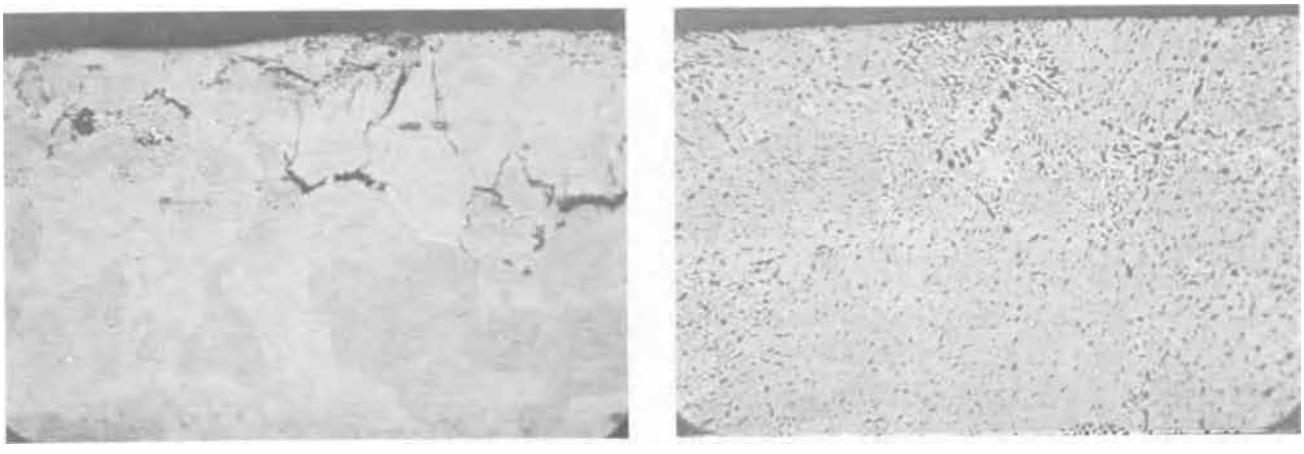

Fig. 4. Back-scatter scanning electron micrographs showing grain-boundary phases near the surface of Zn-22Al material. Both samples exposed for 100 hr to a 100% relative humidity environment containing ammonia. (a, left) Zinc-rich (light) phase in tilt-mold material (note intergranular attack). 695×. (b, right) Aluminum-rich (dark) phase in direct-chill material. 695×.

Table IV. Effect of stress on the corrosion behavior of Zn-22Al material exposed to 100% relative humidity at 120°F

Material identification	Ammonia present	Deflection, in., in 1000 hr[a]	Maximum depth of corrosion penetration in 1000 hr, mils			
			Surface pitting		Intergranular attack	
			Tension side	Compression side	Tension side	Compression side
Direct-chill	No	0.43	1.0	0.8	1.1	0.5
	Yes	0.46	0.8	1.0	3.0	0
Tilt-mold	Air test[b]	0.86	—	—	—	—
	No	0.81	0	0	3.5	2.4
	Yes	0.94	0.4	0	4.2	2.4
Chill-mold	Yes	0.36	2.0	0	3.0	1.6

[a] Maximum calculated (elastic) fiber stress in bending was 2000 psi. Deflection was measured at the tip of a 5-in.-long cantilever beam.
[b] Exposed at 120°F in normal laboratory air.

samples. Based on one comparison, that for tilt-mold material, corrosion did not appear to affect the creep rate.

The corrosion product developed on zinc-base materials in a high-humidity environment containing sulfur dioxide is water soluble. As a result, as shown in Table V, the Zn-22Al material exposed to this environment exhibited a loss in weight. Pitting was more severe in this environment than observed in high-humidity environments free of sulfur dioxide. Based on depth of pitting, and on the weight gain measured for the 380 aluminum alloy, the sulfur dioxide-containing environment was more corrosive than the other high-humidity environments. However, no intergranular attack was observed.

The most corrosive environment examined was alternate immersion in a 3½% sodium chloride solution at room temperature as shown in Table VI. Heavy corrosion deposits were rapidly developed, and spalling occurred early in the test series. The weight gain exhibited by the 380 aluminum die-casting alloy was much greater than that observed in the two Zn-22Al materials. Although the difference was not large, the corrosion rate appeared somewhat greater in the tilt-mold than in the direct-chill material. Metallographic measurements suggested from 1 to 3 mils of general surface reaction occurred in the Zn-22Al materials during 1000-hr alternate-immersion exposure. Neither Zn-22Al material showed intergranular attack in alternate immersion, but deep surface pitting was observed. Metallographic examination of pits formed in Zn-22Al material showed some evidence of intergranular penetrations along the periphery of the corrosion pit. As shown in Table VI, severe intergranular attack was observed in the 380 aluminum alloy in this environment.

U-bend samples of the direct-chill and tilt-mold Zn-22Al materials were also exposed to alternate immersion in the 3½% sodium-chloride solution. The depth of surface pitting was less in the stressed condition, and no evidence of intergranular attack was observed as a result of exposure under stress.

Sheet material from the direct-chill ingot was also exposed to accelerated corrosion test environments in the superplastic condition, that is, prior to the final annealing treatment. In all cases, the amount of corrosion was less than that observed with annealed material as indicated both by weight gain and by visual appearance.

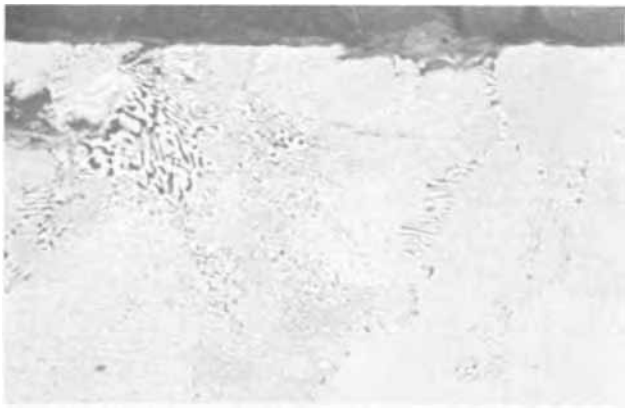

Fig. 5. Back-scatter scanning electron micrograph of the chill-mold material before corrosion exposure. 575×.

Conclusions

The conclusions resulting from these studies are as follows:

1. Zn-22Al sheet material in the nonsuperplastic use condition showed considerably less corrosion in several accelerated corrosion tests than did 380 aluminum die-casting alloy. The corrosion environments were 100% humidity at 120°F, including selected contaminants in two exposures, and alternate immersion in 3½% sodium-chloride solution. Alternate immersion was the most severe corrosion environment of those studied.

2. Surface pitting and intergranular attack accompanied corrosion. Intergranular attack was encountered in two of the three high-humidity environments studied, but not in alternate immersion. Intergranular attack appeared to be related to the presence of a continuous zinc-rich grain-boundary phase.

3. Stress did not increase the depth of intergranular attack in those materials showing this type of corrosion in unstressed tests, but did result in some intergranular attack in one Zn-22Al material which was relatively free of this attack in unstressed tests.

Table V. Corrosion behavior of Zn-22Al material in a 100% relative humidity environment containing 100 ppm sulfur dioxide

Material identification	Weight gain, mg/dm², in				Maximum depth of corrosion, mils, in 1000 hr	
	100 hr	250 hr	500 hr	1000 hr	Surface pitting	Intergranular attack
Direct-chill	−21	−22	−23	−40	3.2	0
Tilt-mold	−11	−8.4	−5.7	−5.7	4.0	0
380 Al alloy	87	118	177	176	10.0	0

Table VI. Corrosion behavior of Zn-22Al material in alternate immersion in 3½% sodium chloride solution

Material identification	Weight gain, mg/dm², in				Maximum depth of corrosion, mils, in 1000 hr	
	100 hr	250 hr	500 hr	1000 hr	Surface pitting	Intergranular attack
Direct-chill	73	51	251	957	12	0
Tilt-mold	75	80	271	1700	8	0
380 Al alloy	754	2250	3500	3510	10	>25[a]

[a] Intergranular attack traversed the sample thickness in same areas.

Acknowledgment

This work was supported by the International Business Machines Corporation, Endicott, New York.

Manuscript submitted Dec. 23, 1970; revised manuscript received June 1, 1971.

Any discussion of this paper will appear in a Discussion Section to be published in the June 1972 JOURNAL.

REFERENCES

1. T. H. Thomsen, D. L. Holt, and W. A. Backofen, *Metals Eng. Quart.*, **10**, (5), 1 (1970).
2. R. Whitehead, *Steel*, **165**, 25 (Dec. 15, 1969).
3. G. R. Goldak and J. G. Parr, *J. Inst. Met.*, **92**, 230 (1963-1964).

Electrodeposition of Aluminum from Alkyl Benzene Electrolytes

G. A. Capuano*

Department of Chemistry, University of Quebec in Montreal, Montreal, Quebec, Canada

and W. G. Davenport

Department of Metallurgical Engineering, McGill University, Montreal, Quebec, Canada

ABSTRACT

Aluminum was electrodeposited onto metallic substrates from a number of electrolytes consisting essentially of an $AlBr_3$ solute of commercial purity and technical grade alkyl benzene solvents or solvent mixtures.[1] Bright, fine-grained, adherent aluminum coatings were obtained at cathode efficiencies of the order of 70-85% and at anode efficiencies approaching 100%. Specific conductance of the electrolytes was 1-3 x 10^{-3} ohm^{-1} cm^{-1} while applied potentials of 3-6V provided current densities of 10 mA/cm^2. The most effective solvents were those of the ethylbenzene family. Ethylbenzene solvents are also effective in promoting plating with other solvents particularly benzene, toluene, and xylene. Technical grade solvents in equilibrium with atmospheric moisture were successfully employed throughout the tests.

Aluminum is in many ways almost ideal as a coating metal. While its coherent oxide film makes it highly corrosion resistant, it can be made even more resistant by anodizing it with coatings which may be dyed to attractive shades of color. Aluminum is a ductile metal with good electrical and thermal conductivities yet, by anodizing, a coating of higher insulating characteristics can be applied. It is not surprising, therefore, that many attempts have been made to deposit it onto other metals.

The electrodeposition of aluminum has proven to be extremely difficult and only limited commerical success has been attained. The principal reason is that aluminum, because of its high position in the electromotive series, is not easily deposited from aqueous solutions. Hydrogen gas is evolved before the applied potential is sufficiently high to deposit aluminum.

The well-known Hall process for the production of metallic aluminum avoids this problem by utilizing alumina dissolved in molten cryolite as the electrolyte. Similar fused-salt procedures have been devised for electroplating aluminum by which molten aluminum salts, usually the chloride or the bromide, are dissolved in various inorganic and organic salts such as potassium chloride, sodium chloride, and ethyl pyridinium bromide. Molten salt electroplating has not, however, found any large scale application due, most likely, to the complexity of the procedures and to uneven plating quality.

Some early investigators claimed that aluminum could be deposited from aqueous solutions (1-3). None of their findings could be verified, however, and no aqueous process has ever been successful. The analogy between ammonia and water led other workers (4) to attempt to electrodeposit aluminum from liquid ammonia. Again, no success was recorded from these systems.

It was soon recognized that moisture should be absent for the successful electrodeposition of aluminum. It was natural, then, to turn to organic solvents to provide a suitable room temperature electrolyte.

Investigations into aluminum electrodeposition from organic electrolytes up to 1967 have been comprehensively reviewed by Brenner (5, 6). In brief, the solvents and solutes employed to date can be classified as:

Solutes: (*a*) Aluminum halides.
(*b*) Aluminum organo compounds.

Solvents: (*a*) Ethyl bromide with or without an aromatic (7-14).
(*b*) Amino-aromatic (15-17).
(*c*) Ether (18-27).
(*d*) Amino or amide with or without ether (28-31).
(*e*) Aromatic (32-36).

The most successful electrolytes of each of these solvent groups are shown in Table I. All solvents and solutes used in the electrolytes, with the exception of the technical grade xylene used by Simanavicius were anhydrous and reagent grade.

As is indicated in Table I the electrolytes have been extremely reactive (ethyl bromide electrolytes), inflammable (ether and ethereal electrolytes), extremely sensitive to moisture or oxygen, or the plating quality has been rather poor. These drawbacks have prevented practical acceptance of the organic electrolytes.

It has been the object of the present work to continue the search for practical room temperature electrolytes for the deposition of aluminum.

* Electrochemical Society Active Member.

Key words: aluminum, deposition, organic electrolyte, electrodeposition.

[1] Patent application filed (1970).

Table I. Summary of the most successful electrolytes based on previous solvent types

Type	Investigators	Solvent	Solute	Results and comments
Ethyl bromide	Blue and Mathers (10, 12)	Benzene Xylene Ethyl bromide	$AlBr_3$ $AlCl_3$	Gray aluminum deposits. Violent reaction during preparation. HBr evolution during electrolysis (18).
Amino-aromatic	Wier and Hurley (15)	Ethyl pyridinium Bromide + toluene	$AlCl_3$	Very conductive electrolyte but very sensitive to moisture and oxygen. Undergoes electrolytic decomposition (22). Deposits dark and brittle (18), solvent expensive.
Ether	Couch and Brenner (22)	Diethyl ether	$AlCl_3$ LiH	Excellent aluminum deposits. Electrolyte undergoes electrolytic decomposition (5) at the anode. Too inflammable for industrial uses.
Amino-ether	Menzies and Salt (31)	Butyl amino ether	$AlCl_3$	Bath difficult to prepare. Sublimation of the solute and complete exclusion of moisture from the solvent was required (31).
Aromatic	Simanavicius and Levinskiene (35, 36)	O-m-and P xylene	$AlBr_3$	Deposits were dark gray (36). Hydrogen evolution at the cathode.

Criteria for Potential Electrolytes

In choosing solvents potentially useful for plating aluminum, the two main criteria considered were: the ability of the solvent to dissolve an aluminum salt; and the ability of the electrolyte to release aluminum from its ion during electrolysis.

The dissolution of an aluminum salt into an organic solvent will take place through the formation of a mutual coordination bond between solvent and solute, *i.e.* the solute will act as a Lewis acid and the solvent as a Lewis base. Successful solvents will likely, therefore, be of this Lewis base type.

On the other hand, the electrolyte must be able to release aluminum from its ion during electrolysis and thus, solvents which can be used successfully to plate aluminum will be those containing relatively weak coordination centers (5), for example, the oxygen atom of an ether or the double bond of an aromatic hydrocarbon. Solvents with more unsaturated and hence stronger coordination centers such as nitrogen or carbonyl groups, will form too stable an aluminum complex, and aluminum will not be released from the complex upon electrolysis.

Solvents which have no coordination ability, *e.g.* aliphatic hydrocarbons, will not, however, form suitably conductive solutions.

The fact that aromatic hydrocarbons have suitably weak coordination centers and the evidence that some initial success had been obtained with xylene indicated that an investigation into alkyl benezene solvents would be in a logical direction. The most suitable solutes appeared to be the simplest, *i.e.* aluminum halides.

The investigation was centered upon finding practical electrolytes, and for this reason technical grade solvents and solutes were employed throughout the work.

Experimental

The experimental investigation was divided into two sections: (*a*) An exploratory program in which the suitability of a number of types of electrolytes for aluminum electrodeposition was investigated. (*b*) A more detailed study of two of the more effective electrolyte systems.

Exploratory Investigation

The exploratory investigation focused upon binary electrolytes consisting of an aromatic hydrocarbon and an aluminum halide, usually aluminum bromide. If the binary electrolyte appeared to be promising, a more common and less expensive solvent, *e.g.* benzene or toluene was added to the electrolytes and its behavior was tested.

In brief, the study consisted of a series of experiments in which aluminum was plated onto a copper cathode from an aluminum anode via the various experimental electrolytes. All experiments were carried out under near identical conditions so that the behavior of the electrolytes could be directly compared.

Apparatus.—The electrolytic cell consisted of a 180 ml electrolytic Pyrex beaker and a cover of transparent acrylic plastic (Fig. 1). The cover was machined and an "O" ring provided complete sealing of the cell.

The anode was 1 mm sheet aluminum in the form of a hollow cylinder 2 in. long and 1.27 in. ID, provided with regularly spaced 0.2 in. holes at ¼ in. intervals. An aluminum stem 5 in. long and ¼ in. wide held the anode in the beaker cover. A copper cathode 7 in. long, ½ in. wide, and 0.5 mm thick was placed centrally inside the anode.

Potentials applied during electrolysis were measured by a high impedence "Tacussel" (Solea, Lyon, France) electronic millivoltmeter Type 570AS, and currents

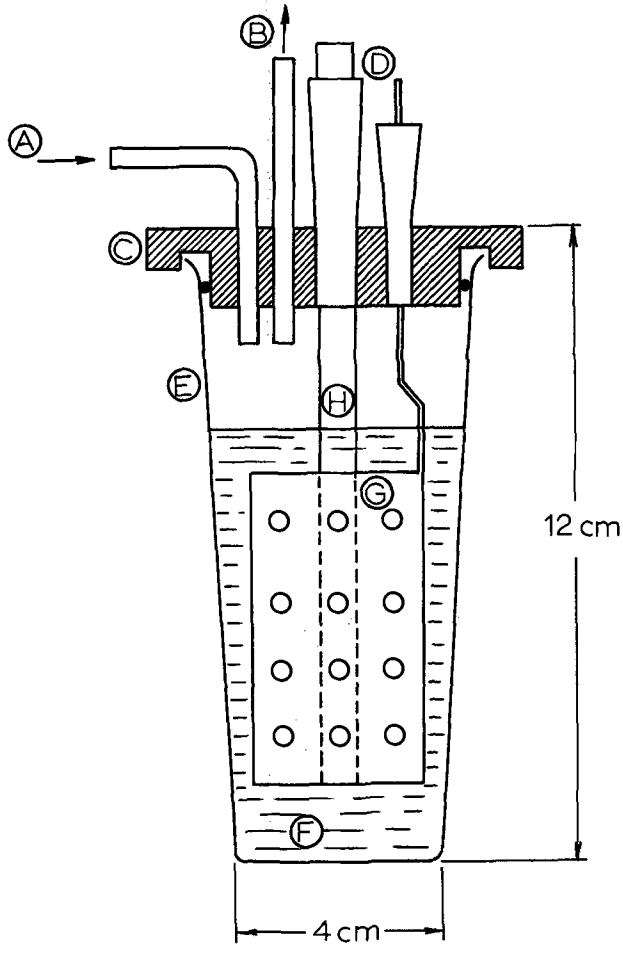

Fig. 1. Electrolytic cell. A, dry argon inlet; B. argon outlet; C, acrylic plastic cover; D, electrical contacts; E, 180 ml electrolytic beaker; F, electrolyte; G, aluminum anode; H, copper cathode.

Table II. Summary of results of the exploratory investigation

Solvents	Gas evolution	Plating quality	Results and comments
Benzene	—	Nonmetallic	Only asphalt like material plated.
Bromobenzene	—	Nonmetallic	Only asphalt like material plated.
Toluene	None	Poor	Black deposits.
Xylene	H_2	Fair	Dark gray coatings.
Ethylbenzene	None	Very good	Cathode efficiency up to 80%.
Ethylbenzene-toluene (1:1)	None	Excellent	Improved electrolyte performance over ethylbenzene alone.
Ethylbenzene-benzene (1:1)	None	Good	
Ethylbenzene-xylene (1:1)	H_2	Good	
Ethylbenzene-cymene (1:1)	None	Good	
Ethylbenzene-bromobenzene (1:1)	None	Good	
Diethylbenzene	None	Very good	Cathode efficiency up to 75%.
Diethylbenzene-toluene (1:1)	None	Excellent	Improved electrolyte performance over diethylbenzene alone.
Diethylbenzene-benzene (1:1)	None	Good	
Triethylbenzene	None	Fair	Low cathode efficiency (20%).
Triethylbenzene-benzene (1:1)	—	Poor	Black coating.
Trimethylbenzene (mesitylene)	H_2	Good	Cathode efficiency up to 75%.
Trimethylbenzene-benzene (1:1)	H_2	Fair	
Tetramethylbenzene (durene)			
20% in toluene	H_2	Good	Durene is solid at room temperature.
20% in benzene	—	No plating	
Isopropylbenzene	None	Good	
Isopropylbenzene-benzene (1:1)	None	Good	
Isopropylbenzene-toluene (1:1)	None	Good	
Methylisopropylbenzene (cymene)	—	Poor	Black coating.
Cymene-benzene	—	No plating	

were recorded on a calibrated "Tacussel" milliammeter, Type MAR298.

Materials.—Copper cathode: Cold rolled copper sheet, manufactured to SAE71 (99.9+% copper). Aluminum Anode: Alcan aluminum sheet 2S grade (99+% aluminum). Aluminum Bromide: Anhydrous, technical grade. Alfa Inorganics Inc., Beverly, Massachusetts. Ethylbenzene: Technical grade. Matheson, Coleman and Bell, Norwood (Cincinnati), Ohio. Toluene: Commercial grade. Chemical division of the Esso Imperial Oil Company, Montreal. Benzene: Reagent grade. Fisher Scientific, Montreal. Diethylbenzene, Triethylbenzene, Trimethylbenzene, Cumene, Durene, Cymene, Xylene: Technical or practical grade. The Eastman Organic Chemicals, Rochester, New York. Argon: Technical grade, 99.99% Ar, 20 ppm N_2, 20 ppm O_2, 10 ppm H_2, L'Air Liquide Canada Ltée., Montreal.

Procedure.—The electrolyte was prepared by placing 50g of $AlBr_3$ in a dried electrolysis beaker followed immediately by the addition of 70 ml of solvent to give a solution of approximately 25 mole per cent (m/o) or 45 weight per cent (w/o) $AlBr_3$ for most electrolytes. A Teflon-covered magnetic bar was placed into the beaker, the cover and electrodes were fitted, and a flow of dry argon through the beaker was started. The solution was stirred until the $AlBr_3$ dissolved.

Contrary to the experience with the preparation of a number of previous electrolytes (18), no violent reactions occurred during preparation and no cooling was required.

The electrodeposition was carried out at 10 mA/cm^2 with 3-6V usually required to produce this current density. The plating was performed for 1½ hr while the solution was gently stirred. After electrolysis the cover was removed and the electrodes were immersed in a water and then an acetone bath. The electrodes were weighed before and after each experiment.

Operating conditions.—Conditions kept constant during the exploratory tests were: (*A*) Electrodes: Identical electrodes were used in all tests, immersed to the same depth in the electrolyte. The copper cathodes were cleaned in 1/3 HNO_3; 1/3 H_3PO_4; 1/3 CH_3COOH before all tests. (*B*) The electrolyte in each test was composed of 45 w/o $AlBr_3$ and 55 w/o solvent. Approximately 90 ml of electrolyte were used in each test. (*C*) Operating temperature: 25° ± 5°C. (*D*) Copper cathode immersion area: 10 ± 0.5 cm^2. (*E*) Current density: cathode current density was the operating parameter held constant in all exploratory tests. The current density was 10.0 ± 0.1 mA/cm^2 based upon the immersion area of the copper cathode at the beginning of each test.

Results.—The results of the exploratory tests are summarized in Table II. The appearance of the aluminum coatings from selected electrolytes is shown in Fig. 2. The thickness of the aluminum deposit on the ethylbenzene specimen is 0.5 mil.

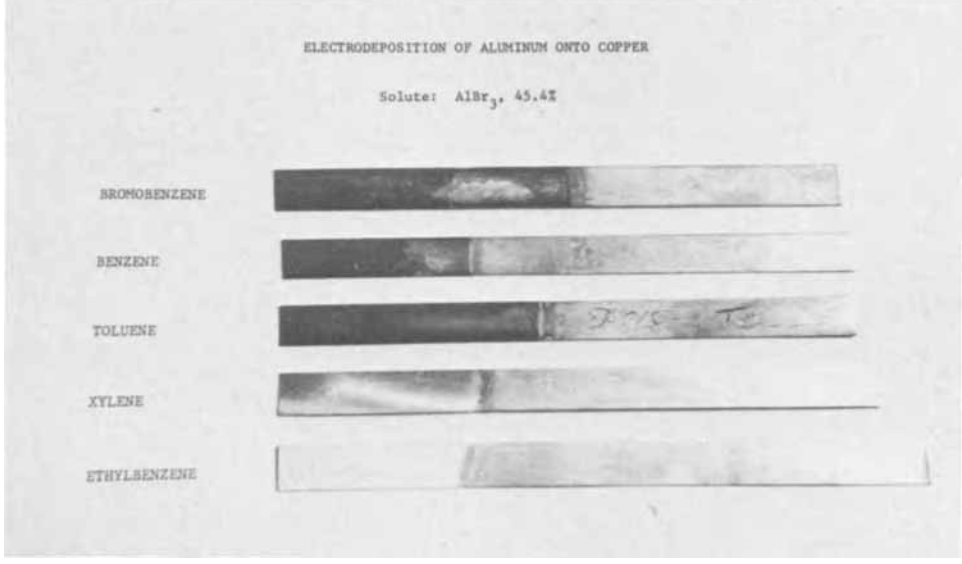

Fig. 2. Appearance of aluminum coatings from selected exploratory electrolytes.

The plating performance recorded in Table II is qualitative, and it has been estimated on the basis of appearance of the coating, its adherence to the substrate, and the consistency of performance of the electrolyte.

The tests clearly indicated that solvents in the ethylbenzene family are the most promising for aluminum plating. Plating quality has been the best with electrolytes based upon ethylbenzene and diethylbenzene, and a majority of electrolytes based on these solvents avoid gas evolution. Tests using alternative metal substrates (mild steel, brass, platinum, aluminum) were equally successful with these electrolytes.

Aluminum chloride and aluminum iodide were also tested in the exploratory program but both resulted in black deposits and cathode current efficiencies of less than 20%.

Detailed Study of Systems: Ethylbenzene-Xylene-$AlBr_3$ and Ethylbenzene-Toluene-$AlBr_3$

The ethylbenzene family of solvents was the most promising found during the exploratory experiments and thus a detailed study of ethylbenzene electrolytes was made. The main factors considered were plating quality, electrode efficiencies, and electrolyte conductivity, while the principal variables were electrolyte usage time, $AlBr_3$ concentration, and the effect of adding less costly solvents to ethylbenzene based electrolytes.

Apparatus.—The apparatus in the detailed study was similar to that in Fig. 1 with the exception that two flat aluminum anodes (1½ cm wide, 1 mm thick, and 18 cm long) were placed on either side of the copper cathode (1 cm wide, 0.5 mm thick, 18 cm long) through a Teflon cover. A 400 ml electrolysis beaker was employed, the usual electrolyte volume being 300 ml.

Conductivity determinations were made with a "Tacussel" direct reading conductimeter Type CD7A (Solea, Lyon, France) at a frequency of 5000 Hz using "Tacussel" conductivity cell CM .01/G. A silver coulometer was placed in series with the aluminum cell for determinations of electrode efficiencies.

Operating conditions.—The standard conditions in the detailed study were: (*A*) Electrodes: identical electrodes were used in all the tests. (*B*) Operating temperature: 25° ± 5°C. (*C*) Current density: cathode current density was the operating parameter held constant in all tests at 10 ± 0.1 mA/cm² based upon the immersion area of the cathode at the beginning of each test. (*D*) Plating time: 1½ hr starting with a new copper cathode. A plating time of 1½ hr at 10 mA/cm² with an anticipated 80% cathode efficiency would give an aluminum thickness of approximately 0.0005 in. United States Military Specification MIL-C-23217A (ASG) 1963 indicates that this thickness is the minimum coverage necessary for good corrosion protection.

The standard current density of 10 mA/cm² was chosen on the basis of a study (electrolyte: ethylbenzene-xylene 1:1; 53.4 w/o $AlBr_3$) of cathode efficiency *vs.* current density (Fig. 3). Each point in Fig. 3 represents a separate test in which 0.15 A-hr were passed starting with a new copper cathode. As shown in Fig. 3, cathode efficiency maximizes at a current density of about 10 mA/cm².

Results

An example result of the plating experiments is shown in Fig. 4 for the system ethylbenzene-$AlBr_3$. A graph of this type was obtained for each experimental electrolyte. Each point on the electrode efficiency curves represents an experiment of 1½ hr at 10 mA/cm² starting with a new cathode, and thus the graphs illustrate the performance of the electrolyte (under standard plating conditions) for considerable times of usage. The tests in Fig. 4 for example represent 42 hr total electrolysis time.

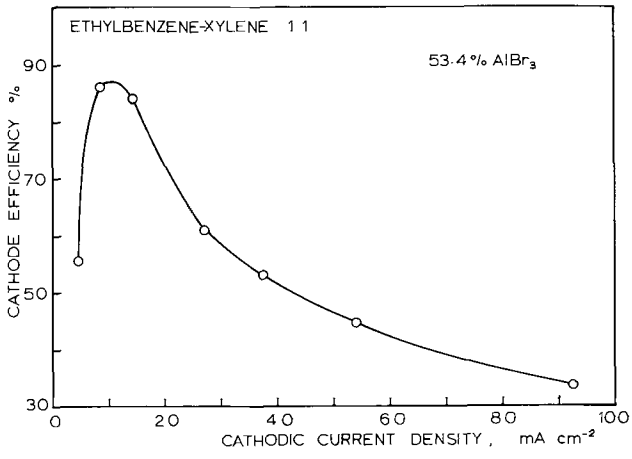

Fig. 3. Cathode efficiency as a function of current density; ethylbenzene xylene 1:1, $AlBr_3$ 53.4%.

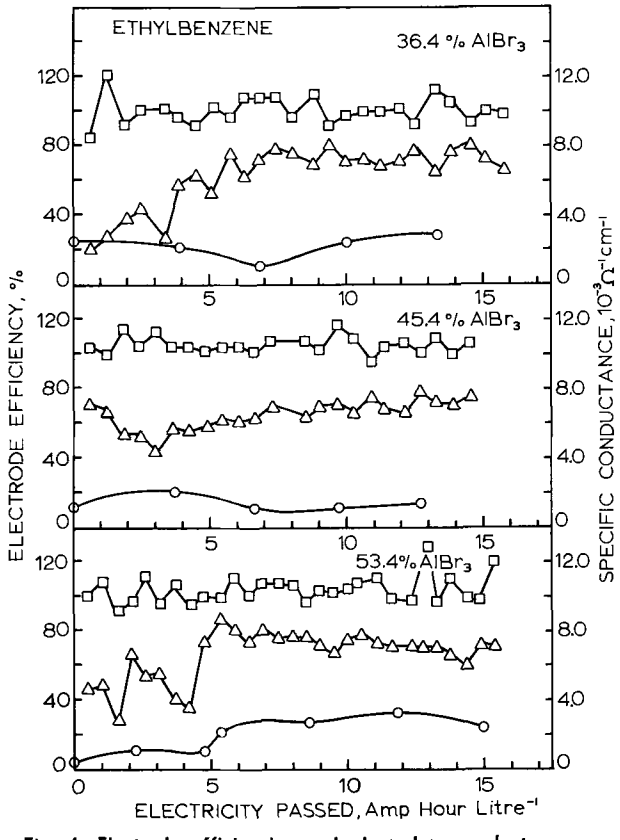

Fig. 4. Electrode efficiencies and electrolyte conductance as a function of electricity passed through electrolyte; ethylbenzene-$AlBr_3$ system. □ Anode efficiency, △ cathode efficiency, ○ specific conductance.

In common with all the electrolytes studied in detail, the anode efficiency is very nearly 100% with some scatter around this value. Cathode efficiency is much more variable, however, and a "working up" period of 3-4 hr is required before the cathode efficiency stabilizes, in this system, for example, at about 80% cathode efficiency. This "working up" period was not encountered in the case of the ethylbenzene-toluene electrolytes. The specific conductance of the electrolytes also required an initial period for stabilization. The performance of the electrolytes is summarized in Fig. 5-8.

It is clear that in terms of cathode efficiency the addition of ethylbenzene to toluene electrolytes markedly improves performance. Similar, though less pro-

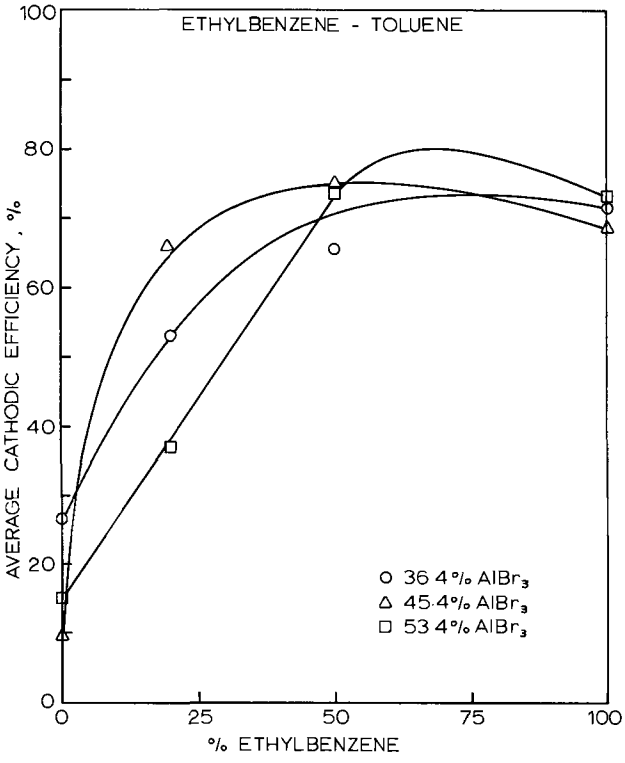

Fig. 5. Cathode efficiencies; ethylbenzene-toluene system

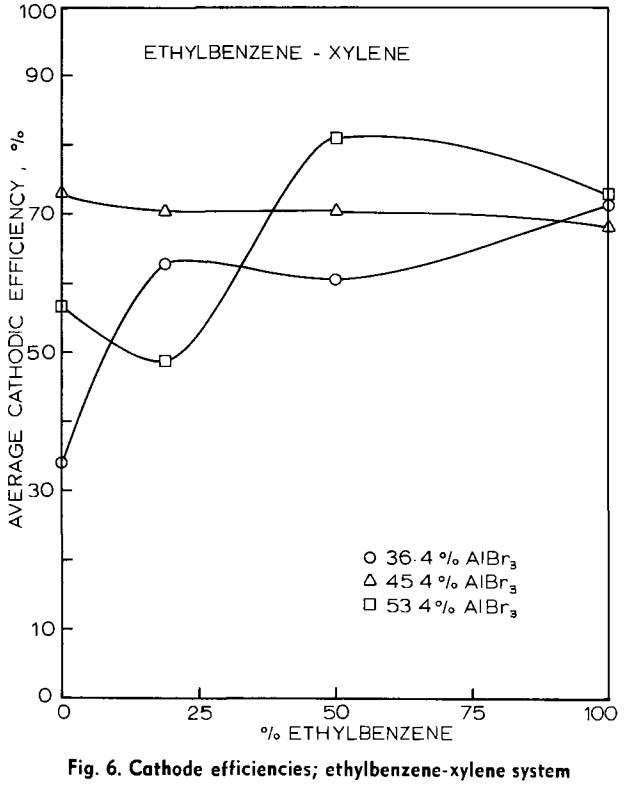

Fig. 6. Cathode efficiencies; ethylbenzene-xylene system

nounced behavior is obtained for the xylene electrolytes. Figure 7 shows, however, that there is some loss of electrolyte conductivity with the addition of ethylbenzene to toluene electrolytes. This means that the applied potential must be increased to maintain current density at a specific value.

The most marked indication of the effect of ethylbenzene was in plating quality from toluene electrolytes. Figure 9 shows that with toluene alone a very thin black deposit is obtained. On the other hand, an ethylbenzene-toluene electrolyte produces an attrac-

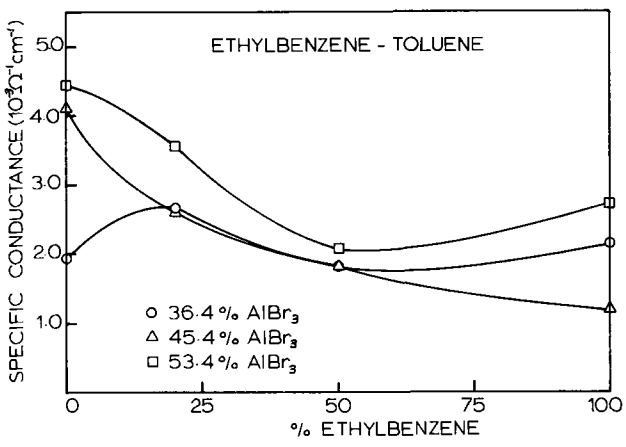

Fig. 7. Electrolyte conductance; ethylbenzene-toluene system

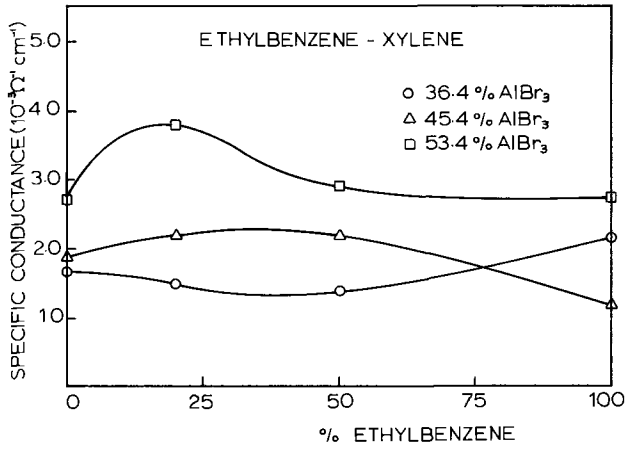

Fig. 8. Electrolyte conductance; ethylbenzene-xylene system

tive whitish gray aluminum deposit at 75% cathode efficiency. Figure 10 shows a similar though less pronounced situation for xylene electrolytes.

Comparison of the two systems indicates that the ethylbenzene-toluene electrolytes are preferable on the basis of quality of plating and the observation that hydrogen was evolved from each of the ethylbenzene-xylene electrolytes. Hydrogen evolution, though not as serious a problem as the evolution of HBr which had been obtained using ethyl bromide electrolytes, indicates a decomposition of the solvent, and places an upper limit on possible cathode efficiencies.

Plating quality.—The coherency of the aluminum coatings was tested by subjecting a number of aluminum plated samples to a bend test in which the aluminum plated samples were bent 90°, usually about 20 times, until failure. In all cases of plating from electrolytes containing ethylbenzene, the copper cathode broke before the aluminum layer became detached. The photomicrograph in Fig. 11 further indicates the excellent adhesion between the aluminum coating and the copper cathode (electrolyte: ethylbenzene-toluene 1:1, 45% $AlBr_3$). The thickness of the deposit in Fig. 11 is 0.5 mil. Other experiments at somewhat lower current efficiencies produced sound aluminum deposits of 2 mil thickness.

The grain size of the deposited aluminum (electrolyte: ethylbenzene-toluene 1:1, 45% $AlBr_3$) was analyzed by examining transmission-type x-ray diffraction spectra. The target aluminum coating was separated from the copper cathode by sanding off one side of the electrode to expose the copper base, and by then dissolving the copper in concentrated nitric acid. The resulting aluminum slice 1 cm wide, 5 cm long,

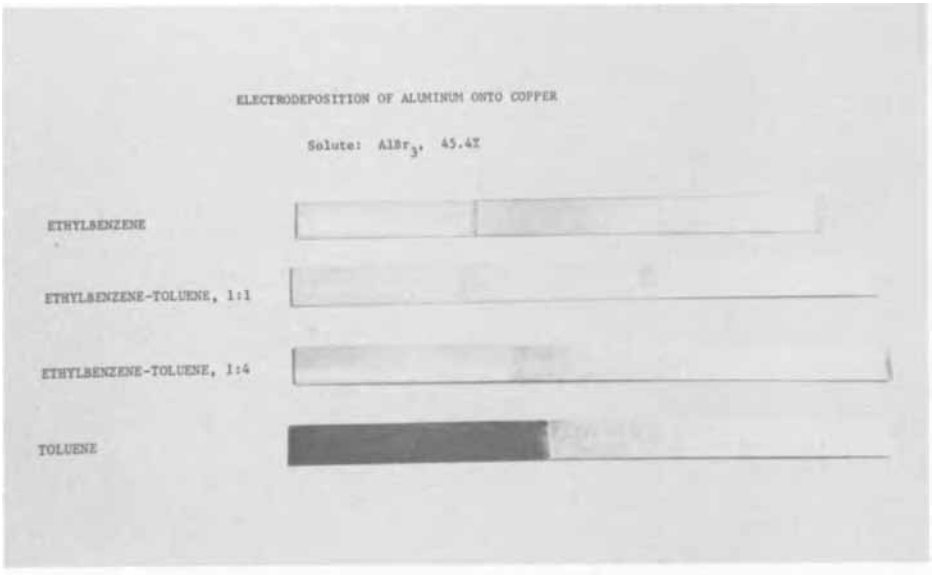

Fig. 9. Appearance of aluminum coatings; ethylbenzene-toluene system.

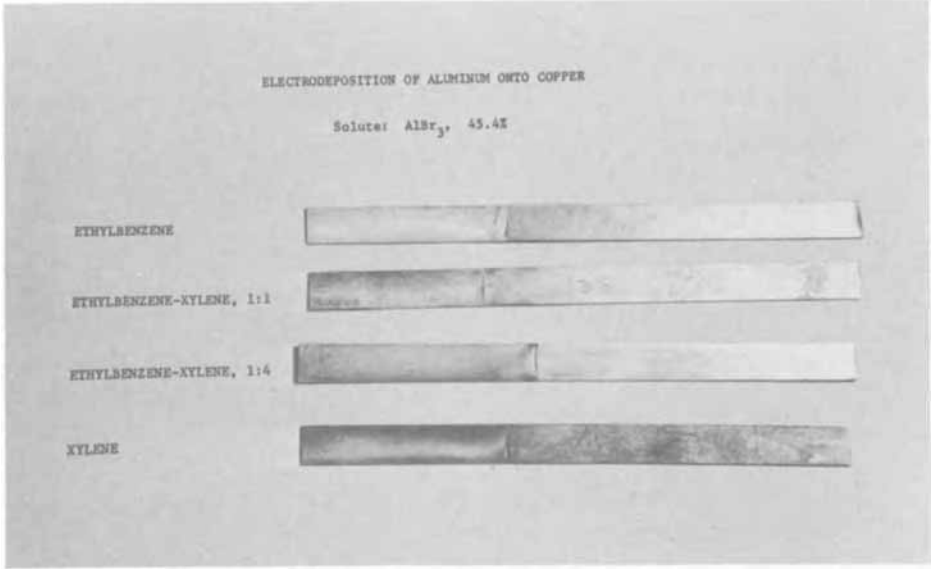

Fig. 10. Appearance of aluminum coatings; ethylbenzene-xylene system.

and 0.013 mm thick was exposed in a flat Phillips x-ray camera.

Figure 12 illustrates the resultant diffraction pattern in which the aluminum lines are clearly shown. The partially continuous nature of the lines indicates that the aluminum coatings are relatively fine-grained, *i.e.* in the order of 10^{-3} to 10^{-4} cm grain diameter. A spectrographic analysis of some aluminum deposits (electrolyte: ethylbenzene-toluene 1:1, 45% $AlBr_3$) showed that traces of metals more noble than aluminum present in the electrolyte were plated out on the first 2 or 3 cathodes. Subsequent coatings were of equal or higher purity than the anode material.

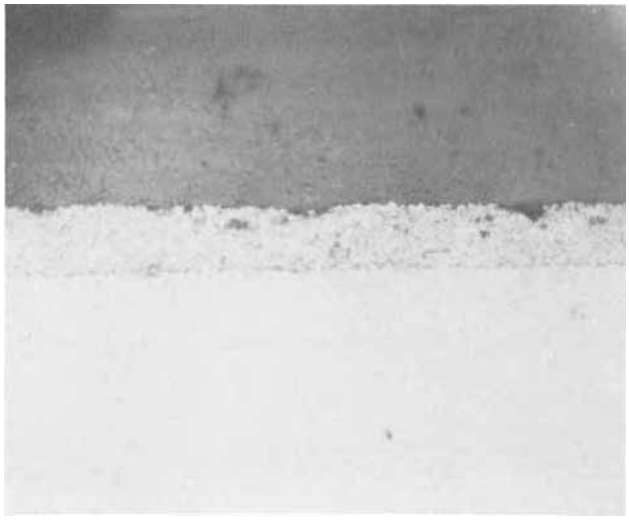

Fig. 11. Photomicrograph of aluminum coating on copper. Magnification 500X.

Discussion

Perhaps the most interesting result of the investigation has been that solvents which contain moisture can be successfully used in the electrolytes. There is some evidence which indicates that water is a beneficial component of the electrolyte as was demonstrated by a study of the system ethylbenzene-xylene 1:4 (45.4% $AlBr_3$) with the solvent in both anhydrous and hydrous form.

In the hydrous case (technical grade in equilibrium with the atmosphere) a good aluminum deposit was obtained at 5 applied volts. Attempts to plate aluminum from the same solvent, after drying overnight with P_2O_5 and redistillation, were not at all successful even after passing an electrical current for 20 hr. A reactive gas (presumably HBr) was evolved during the anhydrous experiment.

The electrolyte was a dark brown in the case of the moist solvent, while in the case of the dried solvent

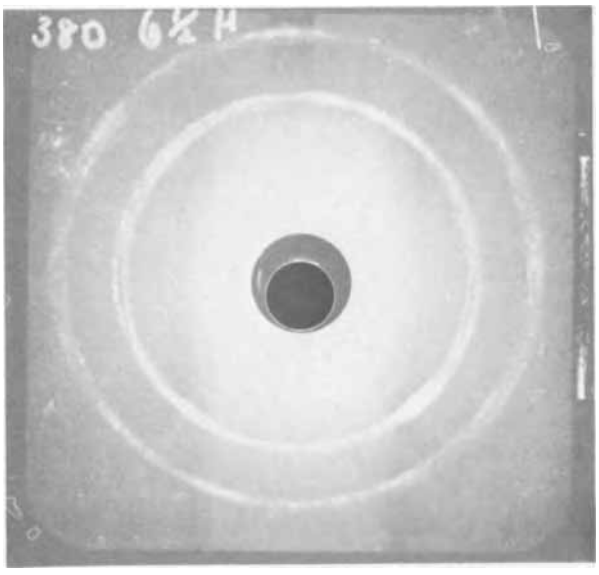

Fig. 12. Transmission x-ray diffraction spectrum from aluminum coating.

the complex was a scarlet color similar to that reported by Blue and Mathers (12) for the benzene-ethylbromide $AlBr_3$ system.

In addition the conductivity of the electrolyte from the hydrous solvent was considerably higher (some 5 times) than that of the anhydrous electrolyte, indicating that the presence of moisture improves electrolyte conductivity.

Mechanism of electrolysis.—Brown and Wallace (37) performed a series of vapor-pressure-composition-phase studies for the systems benzene-$AlBr_3$ and toluene-$AlBr_3$ from which they determined the existence of compounds of the type $Al_2Br_6 \cdot nArH$, where ArH represents an aromatic hydrocarbon. These authors attributed the conductivity of anhydrous organic solutions of these compounds to the formation of π complexes

$$Al_2Br_6 \cdot nArH \rightarrow \underset{(\pi \text{ complex})}{(Al_2Br_5 \cdot nArH)^+} + Br^-$$

Simanavicius and Levinskiene proposed a complex similar to the π type (36) and suggested that the mechanism of reduction of aluminum from solution for the system xylene-$AlBr_3$ involves the reaction

$$AlBr_2 \cdot nC_6H_4(CH_3)_2^+ + 3e^- \rightarrow Al^o + nC_6H_4(CH_3)_2 + 2Br^-$$

(π-type complex)

The equivalent anode reaction would be the reverse of the above equation.

In the present work, the presence of moisture in the solutions resulted in good aluminum plating and solutions of relatively high conductivity. It can be postulated that moisture in the system tends to displace bromine from the aluminum halide-aromatic compound due to the high affinity of OH^- for aluminum. For the case of ethylbenzene the complex formation would be of the type

$$2(Al_2Br_6 \cdot C_6H_5C_2H_5) + H_2O \rightarrow \underset{(\text{Hydroxy } \pi \text{ complex})}{(Al_2Br_4OH \cdot C_6H_5C_2H_5)^+} + Br^- + Al_2Br_7^- + \underset{(\sigma \text{ complex})}{(C_6H_5C_2H_5H^+)}$$

Thus, by this mechanism, the water would also act to form the σ complex previously reported (38, 39) to result from the reaction of HBr with aromatic hydrocarbon-$AlBr_3$ systems.

It is clear, however, that the quantity of moisture present in the solvent is insufficient to produce more than a limited concentration of hydroxy π complexes and σ complexes in the electrolytes.

Faced with the experimental result that anhydrous solutions of ethylbenzene-xylene (45.4% $AlBr_3$) failed to plate aluminum while hydrous electrolytes were successful, it appears that hydroxy π and σ complexes are essential to initiate the aluminum deposition even though they are present at low concentration.

The electrodeposition in the presence of moisture would be

$$C_6H_5C_2H_5H^+ + (Al_2Br_4OH \cdot C_6H_5C_2H_5)^+ + 6e^- \text{ ——— } 2Al^o + 4Br^- + H_2O + \underset{(\text{Ethylbenzene})}{2C_6H_5C_2H_5}$$

The anode reaction would be the reverse of this process.

The belief that the complexes formed from hydrous solvents are different from the anhydrous π complexes is reinforced by the fact that the color of complexes in the present work varied from brown to black as opposed to the red complexes previously reported for anhydrous electrolytes (12, 37). Further work has to be carried out to confirm this view.

It must be emphasized, however, that although water is a desirable ingredient in the electrolytes to a certain level, an excess of water will result in precipitation of the aluminum from the solution as $Al(OH)_3$, thus completely destroying the capability of the electrolyte.

Value of the electrolytes.—It would seem that the electrolytes presented in this paper are very promising, and that they warrant further investigation on a larger scale. The principal advantages are simplicity of preparation and cheapness of the solvents (technical-grade) along with good plating characteristics. In addition, the best electrolytes (for example ethylbenzene-toluene 1:1, 50% $AlBr_3$) give a uniform operation which is largely unaffected by changes in electrolyte composition or operating conditions.

Future work.—Experimental work to determine the most useful types of electrolytes is continuing and studies of mechanism and electrode potential have been initiated. Application of the electrolytes to the electrowinning of aluminum is also under investigation.

Conclusions

(*A*) A number of electrolytes, consisting essentially of an $AlBr_3$ solute and alkylbenzene solvents or solvent mixtures were developed for the electrodeposition of aluminum onto metallic substrates. Solvents of the ethylbenzene family appear to be the most useful for the electrolytes.

(*B*) Technical grade solvents and aluminum bromide of commercial purity are suitable for the electrolytes.

(*C*) Water up to a certain level is a desirable ingredient in the electrolytes as it improves electrolyte conductivity. Technical grade solvents in equilibrium with atmospheric moisture are good starting materials for the electrolytes.

(*D*) Extensive studies of ethylbenzene-toluene-$AlBr_3$ electrolytes and ethylbenzene-xylene-$AlBr_3$ electrolytes have shown that in both systems ethylbenzene improves electrolyte stability and plating performance.

Acknowledgments

The authors wish to thank the National Research Council of Canada for financial support of this work and to Mr. Guy Robidoux of The Esso Imperial Oil Company for supplying a number of experimental solvents. The authors also wish to thank Mr. P. Capuano for his technical assistance.

Manuscript submitted Oct. 28, 1970; revised manuscript received *ca.* May 24, 1971. This was Paper 207 presented at the Atlantic City Meeting of the Society, Oct. 4-8, 1970.

Any discussion of this paper will appear in a Discussion Section to be published in the June 1972 JOURNAL.

REFERENCES

1. S. A. Tucker and E. G. Thomssen, *Trans. Electrochem. Soc.*, **15**, 497 (1909).
2. P. Marino, *Brit. Pat.* 10133 (1915).
3. G. L. Williams, *U.S. Pat.* 1,351,144 (1920).
4. R. Taft and H. Barham, *J. Phys. Chem.*, **34**, 929 (1930).
5. A. Brenner, *This Journal*, **106**, 148 (1959).
6. A. Brenner, *Advan. Electrochem. Electrochem. Eng.*, **5**, 205 (1967).
7. V. A. Plotnikov, *J. Russian Phys. Chem. Soc.*, **3**, 466 (1902).
8. H. E. Patten, *Trans. Electrochem. Soc.*, **6**, 9 (1904).
9. E. Wertyporoch and B. Adamus, *Z. Physik. Chem.*, **A168**, 31 (1934).
10. R. D. Blue and F. C. Mathers, *Trans. Electrochem. Soc.*, **65**, 339 (1934).
11. R. D. Blue and F. C. Mathers, *ibid.*, **69**, 519 (1936).
12. R. D. Blue and F. C. Mathers, *Metal Cleaning and Finishing*, **10**, 114 (1938).
13. C. C. Downie, *Metallurgia*, **18**, 134 (1938).
14. N. I. Ternovaya and O. K. Kudra, *Tz. Kievst Politek. Inst.*, **38**, 13 (1962).
15. L. H. Hurley and T. P. Wier, *This Journal*, **98**, 207 (1951).
16. W. H. Safranek, W. C. Schickner, and C. L. Faust, *ibid.*, **99**, 53 (1952).
17. M. A. Miller and C. D. Baker, *U.S. Pat.* 2,763,605 (1956).
18. R. J. Heritage, *Bull. Inst. Metal Finishing*, **5**, 106 (1955).
19. V. A. Plotnikov, *J. Russ. Phys. Chem. Soc.*, **39**, 163 (1907).
20. D. B. Keyes and S. Swann, *Ind. Eng. Chem.*, **20** 1068 (1928).
21. D. B. Keyes and S. Swann, *University of Illinois Bull. No. 206*, May 20, 1930.
22. D. E. Couch and A. Brenner, *This Journal*, **39**, 163 (1952).
23. K. Ziegler and H. Lehmkuhl, *Fed. Rep. of Germ. Pat.* 1,056,377 (1962).
24. E. J. Smith and L. D. McGraw, *U.S. Pat.* 3,355,368 (1967).
25. F. J. Schmidt and I. J. Hess, *Plating*, **53** (2), 229 (1966).
26. J. G. Beach, L. D. McGraw, and C. L. Faust, *ibid.*, **55** (9) 936 (1968).
27. F. A. Clay, W. B. Harding, and C. J. Stimetz, *ibid.*, **56**, (9), 1027 (1969).
28. R. D. Blue and F. C. Mathers, *Trans. Electrochem. Soc.*, **63**, 231 (1933).
29. N. F. Murphy and A. C. Dumas, *Electroplaters Soc.*, **43**, 162 (1956).
30. B. O. Holland, *J. Australian Inst. Metals*, **6**, 212 (1961).
31. I. A. Menzies and D. B. Salt, *Trans. Inst. Metal Finishing*, **43**, 186 (1965).
32. E. L. Lalbin, *Brit. Pat.* 106, 400 (1916).
33. W. Menzel: *German Pat.* 694,738 (1940).
34. P. F. Kalynzhuaya, *Kim. Zur.*, **18**, 661 (1952).
35. L. Simanavicius and A. Levinskiene, *Chem. Chem. Technol.*, **7**, 143 (1965) and *Elektroklimya*, **2**(3), 353 (1966).
36. L. Simanavicius and A. Levinskiene, *Trans. Acad. Sci. Lithuanian SSR*, **B4** (47), 39 (1966).
37. H. C. Brown and W. J. Wallace, *J. Am. Chem. Soc.*, **75**, 6265 (1953).
38. H. C. Brown and H. W. Pearsall, *ibid.*, **74**, 191 (1952).
39. H. C. Brown and W. J. Wallace, *ibid.*, **75**, 6268 (1953).

Selective Electroless Metal Deposition Using Patterned Photo-Oxidation of Sn(II) Sensitized Substrates

J. F. D'Amico, M. A. De Angelo, J. F. Henrickson, J. T. Kenney, and D. J. Sharp

Western Electric Company, Engineering Research Center, Princeton, New Jersey 08540

ABSTRACT

Surface deposits containing hydrated Sn(II) species are generated when substrates are immersed in stannous chloride solutions, and then rinsed in water. These deposits, after a later immersion in an aqueous solution of $PdCl_2$, are capable of activating electroless plating baths to produce a metal deposit on the substrate. The Sn(II) species, however, can readily be photo-oxidized by exposure to ultraviolet light in air, yielding Sn(IV) and thereby destroying the latent catalytic surface. Thus, selective electroless metal deposits on a variety of substrates may be generated by exposure through an appropriate mask.

The generation of electroless metal photopatterns on dielectric substrates using an additive process called photoselective metal deposition (PSMD) was described in several earlier papers (1-4). Here we wish to present a more detailed explanation of the process chemistry, especially as it relates to the imaging capability.

PSMD combines conventional electroless (chemical) plating techniques (5, 6) with a photochemical imaging step; the substrate, sensitized with a divalent tin species and consequently catalytic to a chemical plating bath, can be rendered noncatalytic by exposure to ultraviolet radiation. Thus, positive images of a photomask can be generated on the substrate. The patterning capability extends to any metal for which a useful electroless plating bath is available; the present list would include Cu, Co, Pd, Ni, and Au.

Metal-patterned dielectrics have a variety of current uses, the most important of which, in terms of economic value, is the manufacture of printed wiring on a variety of both flexible and rigid substrates. In the current production, printed wiring is produced on Mylar, epoxy-composites, phenolics, or Kapton, with copper as the most widely used conductor. The present printed wiring technology is, by and large, based on a "subtractive" process; in its simplest form, a metal foil is laminated to the substrate, then selectively removed by an etchant to generate the desired pattern. The metal regions to be retained are protected by an etch resistant photo or printed mask.

Key words: pattern generation, photo-imaging, ultraviolet photochemistry.

An additive process such as PSMD can provide an alternative approach, useful in a variety of applications previously requiring resist and etch procedures. Moreover, in many applications a significant cost saving is possible since the cost of fabricating the initial metal-substrate laminate can be replaced by a less expensive plating of the PSMD pattern to build up the conductor. The PSMD process is applicable to a wide variety of flexible and rigid substrates and a broad range of metal deposition systems.

The Imaging Sequence

Substrates patterned by PSMD undergo the following basic steps, depicted schematically in Fig. 1:

(1) Substrate Preparation—The substrate is cleaned or etched as required to produce a clean and wettable surface.

(2) Sensitization—A light-sensitive layer containing Sn(II) species is deposited on the surface.

(3) Photo-Oxidation (Latent Image Formation)—Substrate is uv-light exposed in air through a mask. Exposed regions of the sensitizer are rendered inactive by photo-oxidation, while the unexposed regions retain their potential for subsequent activation of electroless metal deposition.

(4) Activation—On immersion into a solution of dilute $PdCl_2$, the unexposed regions of the sensitizer chemically reduce palladium ions to the metal, thus covering the active sensitizer sites with a micro-thin, discontinuous palladium deposit. Later this deposit will act to catalyze metal deposition. In the exposed regions, no Sn(II) sites remain, no palladium metal deposits, and thus no metallization can occur.

(5) Metallization—The surface is metallized by immersion in an appropriate electroless plating bath. When very thick deposits are required, an electroplating step may be added to increase the deposit thickness.

The PSMD process chemistry, as we reported earlier (1-4), follows the current technology for the blanket coating of plastics (5, 6). Thus, we will not elaborate on this aspect of the process, but will instead focus on how the light active deposits are formed (sensitization) and discuss various aspects of the photo-imaging reaction. Experimental details related to the sensitization and image formation are given in the Appendix.

Sensitization

The metallization of dielectrics requires the presence of catalytic sites at which the reduction of metal ions from solution may be readily initiated. Moreover, in useful electroless plating systems, the deposition, once begun, must be autocatalytic so that the metallization may continue after overcoating of the catalyst.

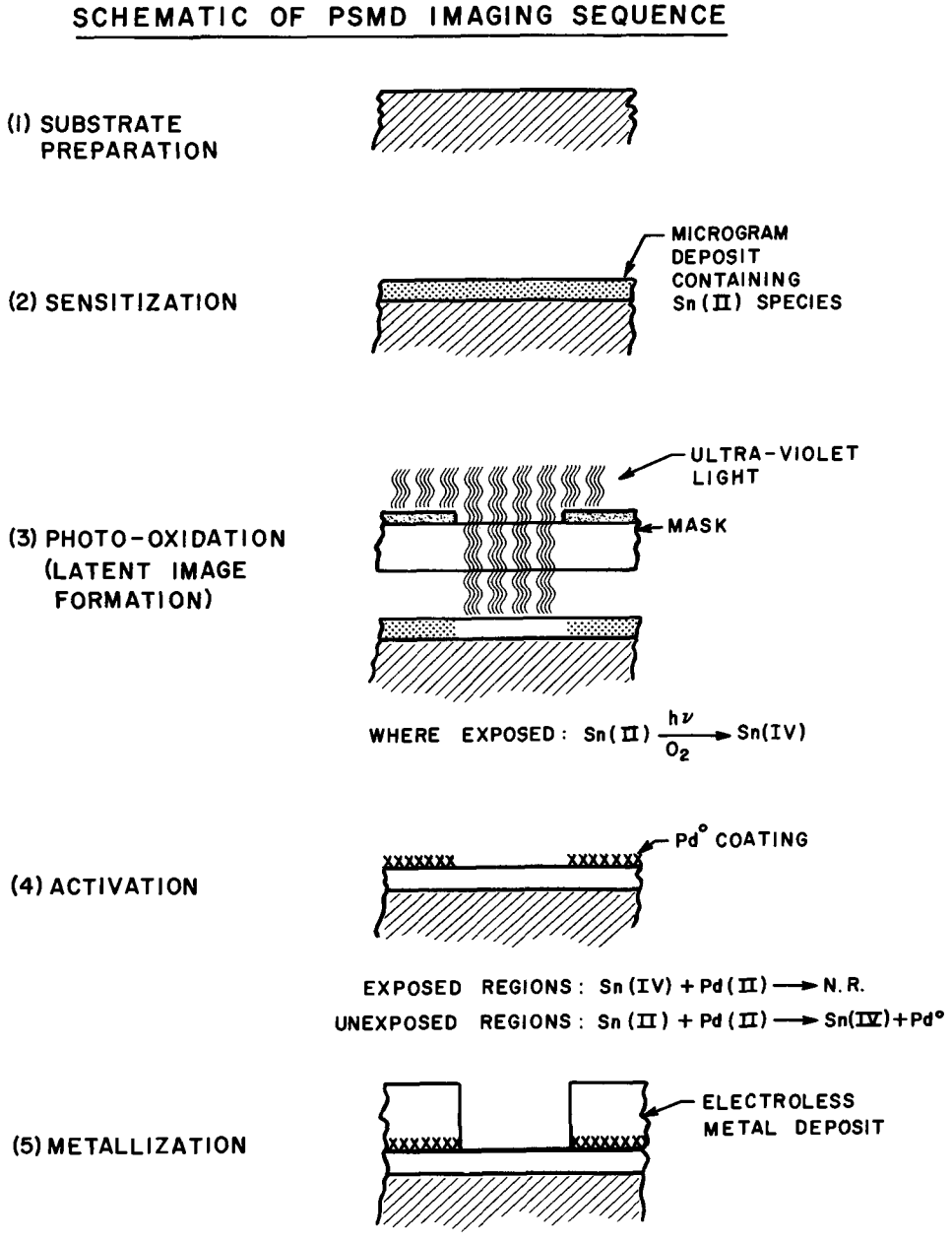

Fig. 1. Schematic of PSMD imaging sequence

The catalytic sites are usually provided by pre-application of a micro-deposit of a suitable metal referred to as the "activator." Palladium, gold, silver, and platinum have proved useful as activators for electroless baths (5), palladium being by far the most widely used.

The morphology of sensitizer deposits from solutions similar to those used in PSMD (we cite a typical formulation below) has been reported by several investigators, *e.g.* Marton and Schlesinger (7), Sard (8), and Sewall (9). Electron microscopy studies (8) show a typical sensitizer deposit to be composed of a particulate matter with the smallest resolvable particles 10-20Å in diameter and a tendency for these particles to agglomerate into clumps on the order of 50-100Å in diameter. The surface coverage of the deposits is found to be on the order of 50% to 70%. The activator deposits were found (7, 8) to replicate the sensitizer, and in turn, the depositing metal replicates the activator. The metal deposit then grows outward to cover the substrate and build up the conductor.

The generation of useful conductor deposits can be accomplished using a very wide variety of chemical formulations and process conditions, as is evident in reviewing the literature (10). This latitude becomes somewhat narrowed, however, if the generation of images rather than a blanket substrate metallization is desired. In PSMD, for example, the sensitizer deposit uniformity, and likewise its optical properties become important. The result is that somewhat more careful attention must be given to the process chemistry and associated preparative procedures than is customary in the current technology.

A typical sensitizer solution (10g of reagent grade $SnCl_2 \cdot 2H_2O$ and 10 ml conc HCl in a liter of water) is 0.044M in Sn(II) and 0.1M in HCl. The sensitizer deposit is formed by a brief immersion of the substrate into this solution followed by a gentle rinse in deionized water. This procedure generates an adherent deposit containing microgram/cm^2 quantities[1] of both divalent and tetravalent tin species. The tetravalent tin is the result of air oxidation of the reagent $SnCl_2 \cdot 2H_2O$ plus oxidation of divalent tin in both the solution and in the sensitizer deposit. The structure of the sensitizer deposit has not yet been fully determined; on polyimide (du Pont Kapton), however, it appears quite similar (11) to colloids formed in the sensitizer solution on standing. For our purpose, we will consider the active sensitizer species as consisting of a hydrated stannous oxide.

Our studies on the mechanics of the sensitization show that the deposit is the result of two distinct processes: (*a*) colloid formation in solution which is a consequence of air oxidation and hydrolysis of the divalent tin chloride, and (*b*) precipitation of soluble tin species from the liquid layer adhering to the substrate due to the rapid *p*H increase during the subsequent water rinse (1, 2). The interrelation of factors (*a*) and (*b*) and likewise the structural and chemical details of the generated sensitizer films depend very greatly on such solution factors as *p*H, concentration, and age. They also depend upon the substrate and its preparation, and finally on how the immersion and rinsing process is executed.

In generating the tin deposits, it is important that the aqueous sensitizer solution wets the substrate, otherwise a uniform sensitizer film will not be produced. When the substrates are hydrophobic, special pretreatments such as chemical etching may be available to render the surface hydrophilic and produce the desired wetting. An alternative is the use of a new class of wetting promoters (12) which permit the photosensitizer to be uniformly deposited on virtually any surface.

[1] Analytical determinations of total tin weight were made using x-ray fluorescence. This method was also used to determine palladium.

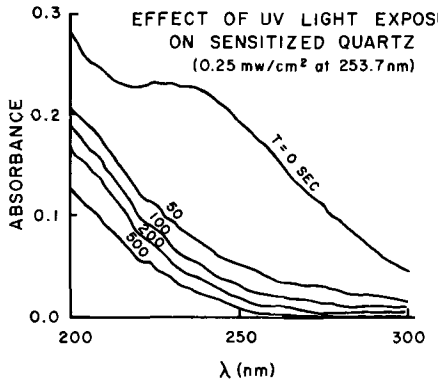

Fig. 2. Effect of uv light exposure on sensitized quartz (0.25 mW/cm^2 at 253.7 nm).

Photo-Oxidation (Latent Image Formation)

The image generation involves photo-oxidation of the divalent tin components of the sensitizer to their tetravalent state, thus rendering the substrate "noncatalytic" for metallization in those areas not shadowed by the photomask. The model which we proposed in the preceding section, namely, a photo-oxidation of Sn(II) plus galvanic reduction of palladium ions to the metal by the remaining Sn(II) is supported by considerable experimental evidence which is presented as follows:

(*A*) Early observations of the uv absorption spectrum of the sensitizer deposits on quartz (see Fig. 2) showed a systematic reduction in absorbance upon exposure. A similar behavior had been observed for dilute stannous chloride solutions in ~0.1M HCl. For these solutions, the uv absorption spectrum upon irradiation was found to approach that of an equally concentrated stannic chloride-HCl solution, indicating that the effect of the light was a conversion of the Sn(II) species to Sn(IV). A similar conversion of Sn(II) in the sensitizer deposit was assumed, despite likely differences in the exact species involved.

(*B*) More recent analytical determinations for Sn(II) in the sensitizer deposits on Kapton have been made using microcoulometry (13) and Mössbauer spectroscopy (11). Upon uv exposure in air, the fraction of Sn(II) was found to be systematically diminished or even reduced to zero depending upon the extent of exposure. A corresponding decrease in the palladium deposit[1] after activation of the exposed specimens was also observed.

(*C*) Solutions found to be active for catalyzing metallization were also found to contain a detectable concentration of Sn(II) (14). When solutions in which Sn(II) was no longer detectable were used for sensitization, no metal deposits could be generated. At the same time, the total tin weight[1] in the deposit remained undiminished.

(*D*) The Mössbauer spectra (11) show an essentially quantitative conversion of Sn(II) to Sn(IV) after the sensitized substrate is immersed for 30 sec in the palladium chloride activator solution. Thus, the palladium is reduced by the Sn(II) rather than merely adsorbed, as has been suggested as an alternative mechanism (15).

(*E*) The presence of oxygen is required for imaging. Light exposure in argon, in wet and dry nitrogen, and in vacuum did not deactivate the sensitizer (on Kapton). The extent of reaction (based on extent of image development at constant light exposure), on the other hand, was found to be quite sensitive to the partial pressure of the ambient oxygen.

We expect that the basic imaging characteristics for a given weight and type of sensitizer deposit should be independent of the substrate used. However, as we have already stated, the type and condition of the

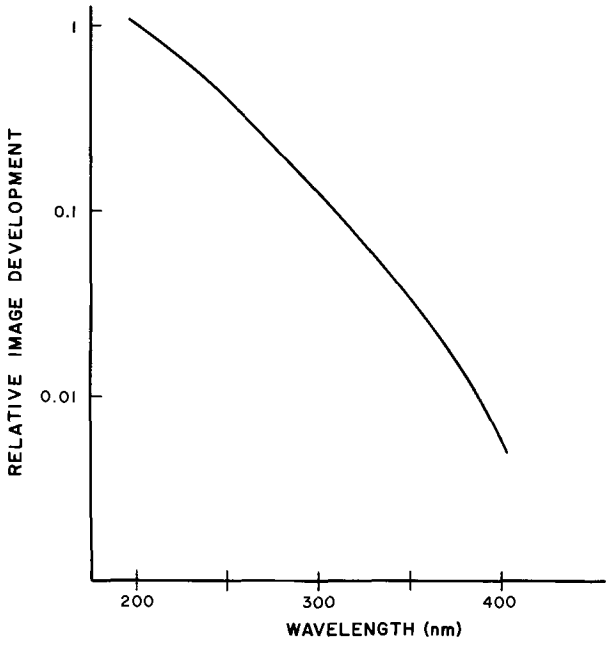

Fig. 3. Relative image development vs. wavelength. Light intensity constant at 0.2 mW/cm^2.

substrate surface can affect the nature of the tin deposit; thus potential substrate effects must be taken into account in the discussion and evaluation of the imaging.

Thus far, we have made PSMD images in copper on several substrates: Kapton, quartz, Mylar, glass, and several epoxy materials. Our most extensive evaluation of the imaging has been carried out on 2 and 3 mil Kapton which was processed as described in the Appendix. For this system, representative optical properties were found as follows:

(*A*) Relative Spectral Response, Fig. 3—These results are based on measurements of the light energy required at each wavelength to produce (approximately) complete image development.

(*B*) Incident Light for Image Development—22 millijoules/cm^2 at 254 nm, light intensity at 0.2 mW/cm^2. This energy is comparable to that required by KPR photoresist.

(*C*) Light Intensity Dependence—Over the useful wavelength range, the extent of image development was found to be nonlinear with respect to the incident light intensity (*i.e.* the reaction does not follow a photographic reciprocity law). The image development was found proportional to the nth power of light intensity, where $1/2 < n < 1$, implying that the photoactivated species participate not only in the tin oxidation, but also in one or more side reactions which do not contribute to the image development (16).

Conclusion

We have shown that dielectric substrates sensitized with Sn(II) species can be photo-oxidized by uv light exposure, and that this reaction can be used for generating electroless metal images. The process can be applied to produce a variety of components such as printed wiring, electroformed metal piece parts, fine metallic grids, photomasks. The method of fabrication and the process chemistry can be selected and adjusted to optimize each application. Both batch and continuous processing applications of this process have been successfully produced in our laboratory (1-4).

At present, the PSMD process technology is being rapidly expanded for use with a wide variety of substrates and pattern configurations, devoted mainly to the topic of printed wiring applications. In addition, basic studies of the important process steps are being carried out and will be reported in the near future.

Acknowledgments

The authors gratefully acknowledge the support and encouragement of many of our co-workers throughout the initial PSMD process development. Special acknowledgments are due to D. M. Lando and F. A. Litt for invaluable technical discussions, and to A. M. Ferrara, R. V. Dafter, R. M. Higgins, and B. R. Bell for technical assistance. We would also like to acknowledge the valuable services of D. A. Green who developed and calibrated the x-ray fluorescence methods for the tin and palladium analyses and performed many of the early determinations.

Manuscript received April 7, 1971; revised manuscript received June 3, 1971. This is a condensation and updating of Paper 136 presented at the Detroit Meeting of the Society, Oct. 5-9, 1969; and Paper 262 presented at the New York Meeting of the Society, May 4-9, 1969.

Any discussion of this paper will appear in a Discussion Section to be published in the June 1972 JOURNAL.

APPENDIX

Experimental Procedures for Sensitization and Copper Imaging of Polyimide (Kapton) Substrates

Sensitizer Solution: 10g $SnCl_2 \cdot 2H_2O$ (Reagent Grade), 10 ml conc HCl/liter of deionized water.

Activator Solution: 0.5g $PdCl_2$, 5 ml conc HCl/liter of deionized water.

Substrate Preparation: Substrate etch in 10*N* NaOH, 10 min. Deionized water rinse, 10 min.

Sensitization: Immerse in Sensitizer Solution, 3 min. Deionized water-rinse, 5 min. Dry in nitrogen jet.

Exposure: Useful uv light sources: Low pressure Hg lamp (essentially monochromatic at 254 nm), high pressure xenon arc for continuum uv source. Photomasks: nichrome on quartz.

Activation: Immerse in activator solution, 30 sec. Water rinse, one min.

Metallization: Immerse in proprietary electroless copper 1.5 to 15 min as desired. We have found a number of proprietary solutions to be satisfactory, among them are solutions marketed by Enthone, Photocircuits and Shipley.

REFERENCES

1. D. J. Sharp, Abs. 262, p. 651, Electrochem. Soc. Extended Abstracts, Spring Meeting, New York, May 4-9, 1969.
2. D. J. Sharp, J. F. Henrickson, J. F. D'Amico, and J. T. Kenney, Abs. 136, p. 367, Electrochem. Soc. Fall Meeting, Detroit, Mich., Oct. 5-9, 1969.
3. D. J. Sharp, J. F. Henrickson, J. F. D'Amico, and J. T. Kenney, 23rd Annual Conference, Photographic Science and Engineering, New York, N. Y., May 1970.
4. D. J. Sharp, *Plating*, **58**, 786 (1971).
5. W. Goldie, "Metallic Coating of Plastics," Vol. I and II, Electrochemical Publications Ltd., Middlesex, England (1968).
6. E. B. Saubestre, Series: "Electroless Plating Today," *Metal Finishing*, **60**, Nos. 6-9, 1962.
7. J. P. Marton and M. Schlesinger, *This Journal*, **115**, 16 (1968).
8. R. Sard, *ibid.*, **117**, 864 (1970).
9. P. Sewall, Masters thesis, Lehigh University, June 1969.
10. See for example, W. Goldie, "Metallic Coating of Plastics," Vol. I., Chap. 5, Electrochemical Publications Ltd., Middlesex, England (1968).
11. R. L. Cohen, J. F. D'Amico, and K. West, *This Journal*, In press.
12. J. T. Kenney, W. P. Townsend, and J. A. Emerson, To be published.

13. D. J. Lando, To be published.
14. Sn(II) detection was made using an ammonium phosphomolybdate indicator paper, as outlined in F. Feigl, "Spot Tests In Inorganic Analysis," Elsevier, New York, 5th ed., p. 108 (1958). The detection limit for this test is given as 1.5 mg tin weight/liter, which corresponds to about 0.003% of the initial stannous tin in solution.
15. W. Goldie, "Metallic Coating of Plastics," Vol. I, Electrochemical Publications Ltd., Middlesex, England (1968). This alternative explanation is examined in Chap. 5.
16. J. F. D'Amico F. A. Litt, and M. A. De Angelo, To be published.

Electrochemical Delineation of Tungsten Films for Microelectronic Devices

Werner Kern* and J. M. Shaw

RCA Corporation, David Sarnoff Research Center, Princeton, New Jersey 08540

ABSTRACT

A process is described for delineating high resolution patterns in tungsten films on semiconductor device wafers. The process is based on high-speed anodic dissolution in alkaline ferricyanide electrolyte of exposed tungsten on a photoresist masked wafer. Slow chemical etching in the same solution occurs simultaneously with the electroetching to remove isolated residual areas of tungsten. The effects of important process variables are discussed, and optimized conditions are presented. The process is capable of accurately defining patterns in several-micrometer thick tungsten suitable for metallization and intraconnection patterns on transistor and integrated circuit wafers The technique is also suitable for patterning tungsten and molybdenum foils. The capability and applicability of the process is illustrated with photomicrographs of representative devices.

One of the steps in the fabrication of silicon integrated circuits is the formation of the metal patterns which serve to contact and intraconnect both the active and passive elements of the circuits. Aluminum is used most frequently for this purpose, but tungsten offers several significant advantages. Chemical vapor deposition of tungsten films from tungsten hexafluoride for microelectronic device applications has been described recently by Shaw and Amick (1). The present paper is concerned with delineating the high resolution patterns required to make these films useful as a metallization system for modern microelectronic device technology.

Tungsten can be etched with solutions of alkaline potassium ferricyanide, ammonium persulfate, hot hydrogen peroxide, or mixtures of nitric acid and hydrofluoric acid (2-4). Anodic dissolution of tungsten in strong sodium hydroxide solution is used to etch tungsten wire and to sharpen tungsten probes (2). However, etching simply to remove material or to polish the surface, and etching to delineate high precision patterns in films, are quite different problems.

Originally, we delineated device metallization patterns in tungsten films by chemical etching techniques. Severe problems were encountered with photoresist undercutting, poor pattern definition, and nonreproducibility of the etching. In the search for a better solution, we found that the anodic etching of tungsten films in caustic solutions can yield much better results than chemical etching. Development and optimization of this approach led to the present process which meets all normal requirements for pattern delineation in device metallizing. Transistor and integrated circuit metallization patterns in tungsten films now compare favorably with the best patterns of standard aluminum films produced in factory processing.

* Electrochemical Society Active Member.

Key words: etching, metallization, transistors, integrated circuits, sealing.

Description of the Process

Figure 1 shows a schematic diagram of the electrolysis circuit of the etching system. A photograph of the assembled laboratory apparatus with its associated equipment is presented in Fig. 2. The etch solution, prepared by combining separate stock solutions of appropriate concentrations, consists of the following mixture dissolved in deionized and distilled water:

5 w/o (weight per cent) potassium hydroxide (KOH pellets, 85%, cp)
5 w/o potassium ferricyanide ($K_3Fe(CN)_6$ crystals, cp)
1 w/o Tergitol[1] nonionic XD surface active agent.

The solution is vigorously agitated with a magnetic stirring rod during etching. A platinum sheet serves as the cathode. The tungsten-coated device wafer is first patterned with a suitable photoresist, such as KTFR (Kodak Thin Film Resist) by standard techniques. It is held in the reverse action tweezers shown in Fig. 3 so that the exposed anode contact touches the tungsten film on the wafer. Before applying a potential, the wafer is introduced into the electrolyte solution until it is completely submerged. Immediately following introduction in the bath the current density is adjusted to about 200 mA cm^{-2}. The progress of etching is monitored with a milliammeter as indicated in Fig. 1. The dual-channel current and voltage chart recorder[2] shown in Fig. 2 is a useful optional accessory. When the electrolysis current has dropped to 20-30% of its initial value, the wafer is pulled out of the bath and rinsed in water. The wafer is released from the holder, dried by centrifuging at low speed, and examined under the microscope for completeness of pattern etching. Additional etching is sometimes required to remove incompletely etched spots of tungsten or to sharpen up the definition of some parts in

[1] Registered Trademark, Union Carbide Chemical Company.
[2] *e.g.*, Rectigraph®, Esterline Angus Instrument Company, Inc.

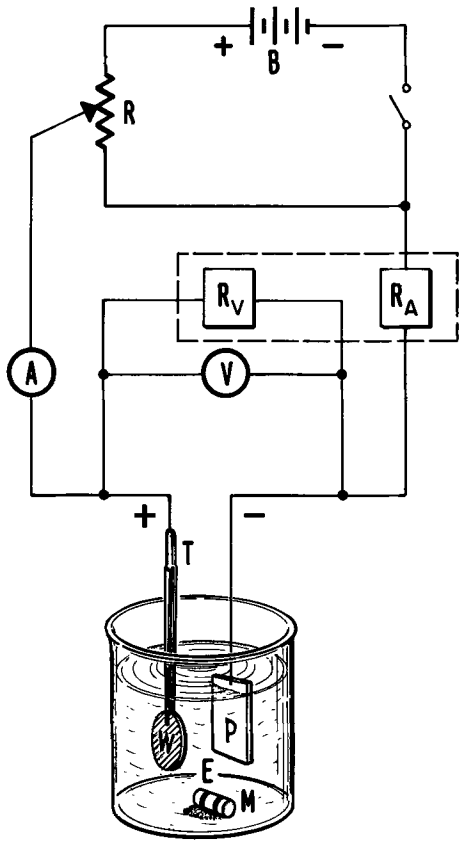

Fig. 1. Schematic of electrolysis circuit

B—D-C supply (22.5V battery)
R—Variable resistor (500 ohms, 0.16A)
A—Milliammeter
V—Voltmeter
T—Insulated tweezer sample holder
R_A—Current recorder (optional)
W—Tungsten sample (anode)
P—Platinum sheet (cathode)
M—Magnetic stirring bar
E—Electrolyte solution
R_V—Voltage recorder (optional)

the pattern. This is readily accomplished by immersing the wafer in the electrolyte, which now serves as a slow chemical etch, for an additional brief period of typically 5-10 sec with no potential applied. The photoresist mask is next stripped away with a suitable agent.[3] The wafer is rinsed in 6*N* HCl for several minutes and finally in deionized and distilled water.

Discussion

Shortcomings of chemical etch techniques.—The pattern delineation of tungsten films is based on selective masking with photoresist followed by removal of the exposed film regions. Removal by chemical etching is possible, but the definition of the resulting pattern is not sufficient for microelectronic circuit fabrication. The reason for this shortcoming lies mainly in the relatively poor adherence of the photopolymer resist films to the tungsten surface, resulting in undercutting with consequent degradation of the metal pattern. This situation is aggravated during prolonged exposure to etchants, or by the high temperatures required with chemical etchants that attack tungsten slowly. Attempts to improve the resist adhesion by changing the photoresist and etch processes, or by modifying the tungsten surface prior to etching were unsatisfactory. For best results, etching time must be minimized. Increases in the temperature and concentration of the chemical etchants minimized this exposure time by

[3] Hot chromic-sulfuric acid mixture is excellent for this purpose and does not attack the tungsten. Alternatively, less dangerous hot organic photoresist removing agents can be used, such as A-20 stripping solution, Electronic Grade, No. 2695 Baker & Adamson.

Fig. 2. Electroetching apparatus

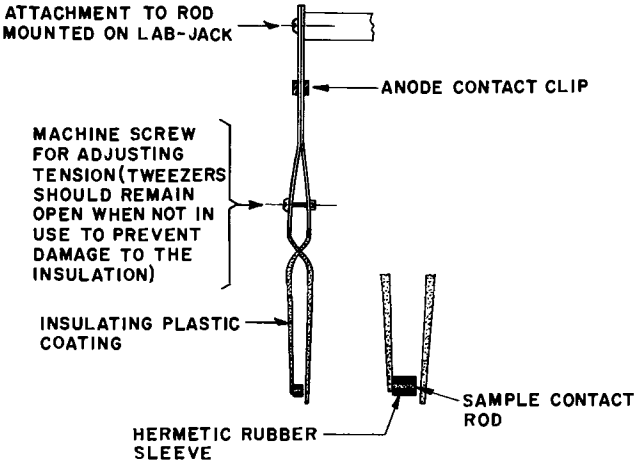

Fig. 3. Wafer holder and anode contact

speeding up the dissolution rate as expected, but also increased the rate of attack at the tungsten/polymer interface and made it difficult to stop the reaction precisely on completion of the etching.

Principle of electrolytic etch process.—For these reasons electrolytic etch methods with alkaline and acid electrolytes were investigated as a means of increasing the etch rate and to make the etching process self-limiting. However, a purely electrochemical process would be difficult to use because completion of the pattern delineation would have to coincide with beginning film discontinuity. Etching with a solution of a composition that effects both electrochemical etching at a high rate and chemical etching at a low rate was therefore chosen as the basis of tungsten removal.

Composition of the etch solution.—Strong caustic solutions containing ferricyanide were found best for this dual etching process. They are effective both as electrolytes for the anodic oxidation and for the direct chemical dissolution of the tungsten. Alkaline solutions are preferred over acids because of the greater solubility of tungsten salts at high *p*H, and because tungsten surfaces become passivated less easily in

alkaline media. Potassium hydroxide is preferable to sodium hydroxide from a standpoint of device contamination. Potassium ferricyanide also acts as an effective electrode depolarizer.

The addition of a suitable surface active agent was found beneficial. A low foaming, nonionic, water soluble, and alkali resistant surfactant compound which meets these requirements was selected from the polyalkylene glycol-ether types. The presence of this agent was found to improve the uniformity of the etching, to prevent the formation of tungsten islands, and to aid the electrolyte solution in wetting and penetrating into the smallest recesses of the photoresist patterns. Concentrations of mixture components were adjusted to yield a composite electrolytic plus chemical etch rate for optimum pattern etching.

Apparatus.—The special holding fixture shown in Fig. 3 was designed to allow submerging the entire device wafer in the electrolytic etch bath while making a sealed, insulated electrical contact between the tungsten film and the anode. The tungsten area that is covered by the tweezer contact, and that consequently will not be pattern etched, is typically a circular area of less than ⅛ in. diameter. For complete wafers this represents a very small loss in device yield, especially since the contact can be located near a wafer edge.

The electroetching apparatus was designed to afford simple, fast and accurate control over the process. A dual-channel current and voltage recorder with a chart speed of 6 in. min^{-1} was used for accurately following and recording the progress of the etching during development of the process, but the instrument is not required for routine etching applications. A dry cell or commercial d-c regulated power supply can be used as an external source of electromotive force.

Etch rate as a function of current density and type of tungsten.—Initial etching parameters were studied using smooth tungsten foils whose edges and backsides were masked, leaving exposed an area of 2.00 cm^2 on one surface. A minimum etch time of 100 sec was used and a minimum quantity of 25 mg of tungsten was removed per test to obtain reliable data. A fresh etch solution was used for each experiment. The uniformity of tungsten removal over the sample was monitored by thickness gauging, and the exact quantity of tungsten removed was determined by weighing on an analytical microbalance. A plot of typical data showing the etch rate at 25°C as a function of current density is presented in Fig. 4. The intersection of the linear curve with the abscissa at zero current density represents the chemical etch rate in the same etch bath for the same stirring conditions. The total etch rate at 25°C and at a current density of 200 mA cm^{-2} (of exposed tungsten area) is 380 Å-sec^{-1} of which 50 Å-sec^{-1} is by chemical dissolution. Electrochemical etching at this current density is thus approximately 87% by electrolytic action and 13% by chemical dissolution. The current efficiency of oxidizing the tungsten metal to hexavalent tungsten under these conditions is practically 100%. It is also seen from Fig. 4 that the tungsten foil and the tungsten deposited by chemical vapor reaction (1) etched at the same rate.

Smooth voltage and current curves were obtained up to 250 mA cm^{-2}. Higher current densities led to instabilities which appear to be caused by electrode polarization that, for the potassium ferricyanide concentrations used, becomes important at this threshold value. A value of 200 mA cm^{-2} was therefore chosen as a practical and controllable current density for the process.

Etch rate as a function of stirring, temperature, electrode spacing, and electrolyte composition.—Vigorous stirring is required to obtain reproducible etching. The positioning and spacing of the electrodes in the bath did not appreciably affect the electrolysis current, nor

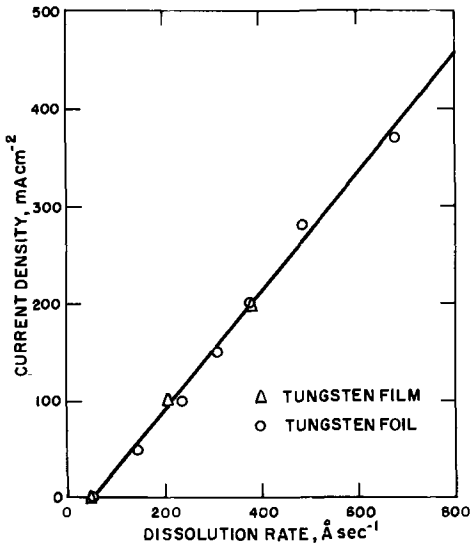

Fig. 4. Dissolution rate of tungsten foil and CVD film as a function of current density. Point at 0 mA cm^{-2} is the chemical etch rate; the line shown represents the total of the chemical and the electrolytic etch rates.

did changes of ± 5°C from the normal 25° bath temperature.

The effects of bath concentration on the electrolysis current and voltage stability were studied with concentrations of double, one-half and one-third of the concentration normally used. Increasing the concentration increased mainly the chemical etch rate, whereas dilution by two-fold or more caused electrolysis instability.

Termination of electroetching.—The approaching endpoint of electrolytic etching is manifest by the following changes: (*a*) an abrupt drop in current flow, (*b*) an abrupt rise of voltage, (*c*) a visually observable clearing of the metallization pattern, and (*d*) formation of oxygen bubbles on the device wafer. The most readily monitored criterion is the decrease of the current flow as measured with the ammeter. With the use of a strip chart recorder the etching process can

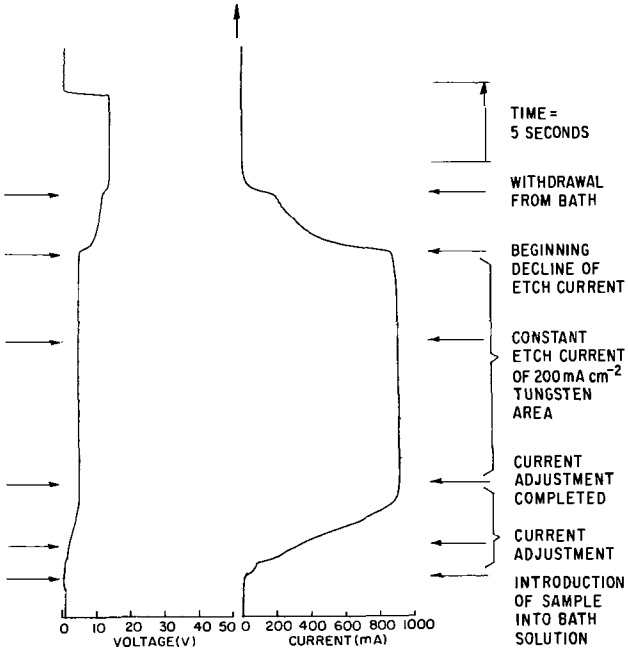

Fig. 5. Voltage and current recording obtained during electroetching a typical tungsten metallized device wafer.

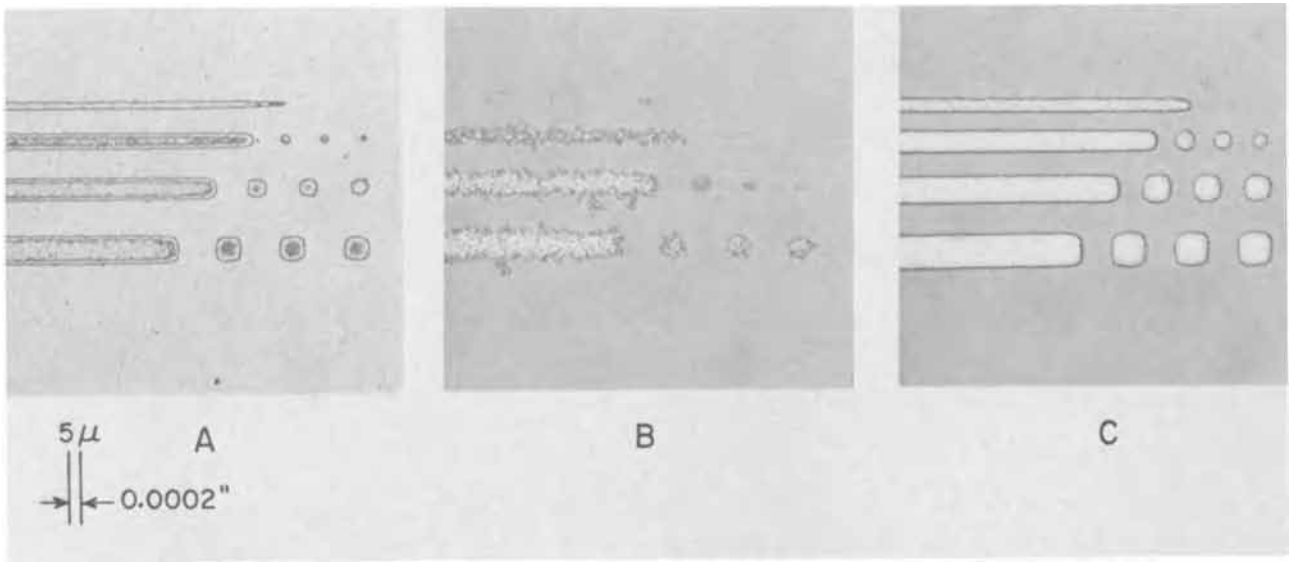

Fig. 6. Test patterns for tungsten etching resolution. A. Original photoresist pattern on tungsten film; B. Chemically etched pattern; C. Electroetched pattern.

be conveniently followed and traced for later reference or analysis. A typical current and voltage recording as a function of etching time obtained during the patterning of a 6000Å thick tungsten film is presented in Fig. 5. Etching proceeded at a uniform current density for 15 sec. The beginning decline of the current flow indicates that the continuity of the tungsten film is just becoming disrupted, meaning that the etching of the individual pattern parts is nearly completed. It can be seen from the curve that the steep decline in the current flow becomes less steep at about 50% of the full etch current. For optimum pattern resolution the best time to remove the wafer from the etch bath is at a value of 20-30% of the full electrolysis current. However, very accurate timing of the process is not necessary, since the "high-speed" electroetching stops automatically when the pattern becomes discontinuous.

Pattern resolution as a function of etching parameters.—The resolution of tungsten patterns obtained under various process conditions was tested with tungsten films of 5000Å thickness deposited on oxidized silicon wafers by chemical vapor phase reaction (1). Precision test patterns having lines and squares two, three, four, and five ten-thousandths of one inch width were used with standard KTFR processing. The surfactant in the etch solution was found to yield considerably cleaner patterns, free of grainy, residual tungsten islands observed without it. Photomicrographs of test patterns processed by the electroetching process *vs.* samples processed by chemical etching in the same solution at 40°C are presented in Fig. 6 for comparison.

Chemical surface cleaning of etched device wafers.—Following removal from the alkaline etch bath, the device wafer should be subjected to a thorough surface decontamination treatment designed to strip the photoresist layer and to remove adsorbed impurity ions. The resist layer is removed by a suitable stripping agent as described previously. Adsorbed ionic impurities are removed by desorption in 6*N* HCl for several minutes. It was shown previously by radiochemical tracer analysis that treatment with 6*N* HCl effectively desorbs alkali ions (5) and iron deposits (6) that are present after etching. Handling, rinsing, drying, storing, etc. of the wafers is best carried out by the techniques described in a separate paper on wafer cleaning (7). These treatments leave the surface in a state suitable for sealing with chemically vapor deposited silicon dioxide (8, 9), silicate glasses (9, 11), silicon nitride (12), or any desirable combination of these layers (12, 13).

Applications

The process has been applied for the delineation of tungsten films deposited on oxide-coated silicon device wafers, including discrete planar transistors, power transistors, integrated circuits, and multilayer crossover structures. The thickness of the tungsten films was usually in the 0.5-2 μm range, but films up to 5 μm have been patterned with excellent resolution.[4] Photographs of several representative devices are presented to illustrate the capability of the patterning process.

Figure 7 shows a 1¼ in. diameter silicon wafer with about 5000 tungsten-metallized planar NPN transistors on 0.015 in. centers patterned uniformly over the entire wafer area by electroetching. An enlargement of

[4] 12 μm thick films have been delineated by a two-step photoresist etch technique.

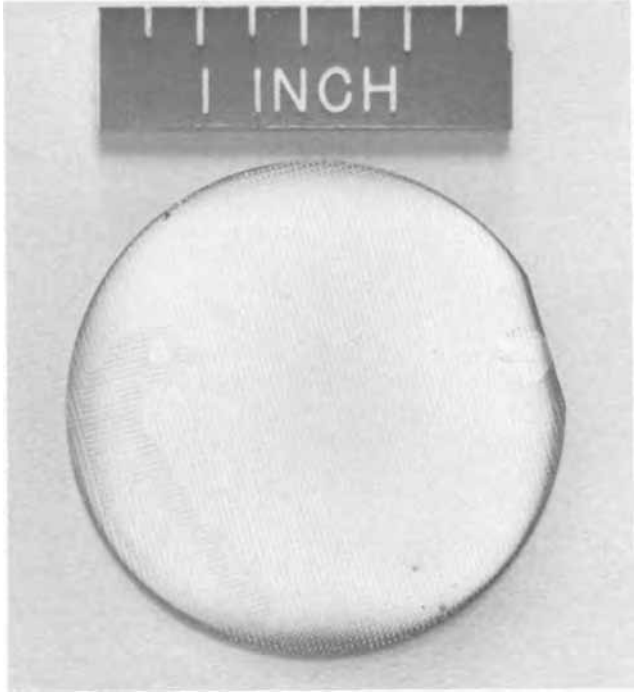

Fig. 7. Electroetched wafer with tungsten metallized planar transistor. Small area scribed "R" shows unetched portion masked by sample holder; (area on left is a nonuniformity in the oxide); wafer contains about 5000 flip-chip transistors.

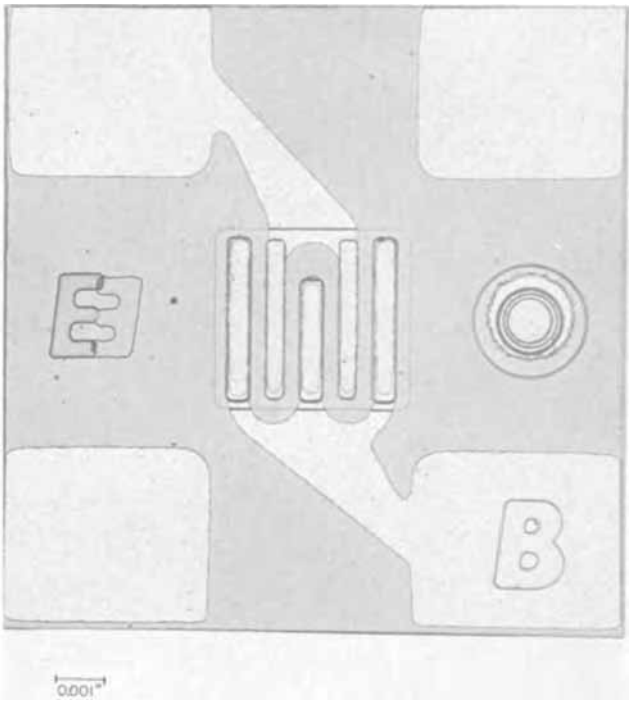

Fig. 8. Photomicrograph of flip-chip test transistor from wafer shown in Fig. 7.

one transistor from this wafer is presented in Fig. 8. The width of the emitter contact stripes of this experimental flip-chip transistor is 0.0004 in.

Figure 9 shows a photomicrograph of a high frequency power transistor taken with a scanning electron microscope at an angle of 65° at 1000-fold magnification. The 2.5-μm thick tungsten stripes exhibit excellent definition and follow the relief contour of the device surface with uniform thickness.

Details within an area of an integrated circuit chip metallized with 6000Å of tungsten are shown in Fig. 10. The width of the narrowest intraconnection leads is 0.0005 in.

Figure 11 finally shows a finished array of typical flip-chip integrated circuits metallized with tungsten

Fig. 9. Portion of a multiple contact power transistor examined by scanning electron microscopy at 1000X. The tungsten stripes are 2½ μm thick.

Fig. 10. Photomicrograph of central area of an integrated circuit chip. The narrow intraconnection tungsten stripes are 0.0005 in. wide.

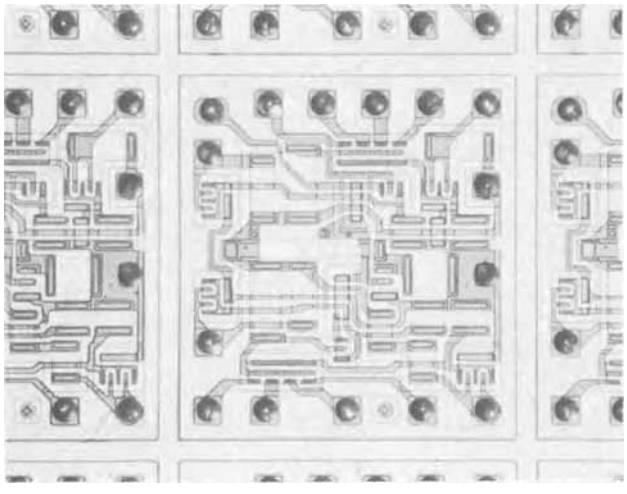

Fig. 11. Array of finished integrated circuits metallized with tungsten. Patterned by electroetching, sealed with silicon nitride, and provided with solder bumps for face-down bonding. The dimension of each IC is 0.050 by 0.055 in.

and patterned by electroetching. A high-temperature silicon nitride film seals the device surface. Openings were etched through the silicon nitride film to expose a circular area of the tungsten terminal pads which were provided with a solderable interface metal layer (14) and solder bumps.

Photographs of a tungsten-metallized and nitride/glass sealed integrated circuit chip (12), of a crossover pattern prepared using tungsten and vapor deposited SiO_2 (1), and of several "Decal" dielectric air isolated integrated circuits (15), all processed by the methods described, were presented in earlier publications.

In addition to the primary objective of delineating metallization patterns for semiconductor microcircuits, the process has been applied to the patterning of tungsten films of up to 12μ thickness on glass and ceramic

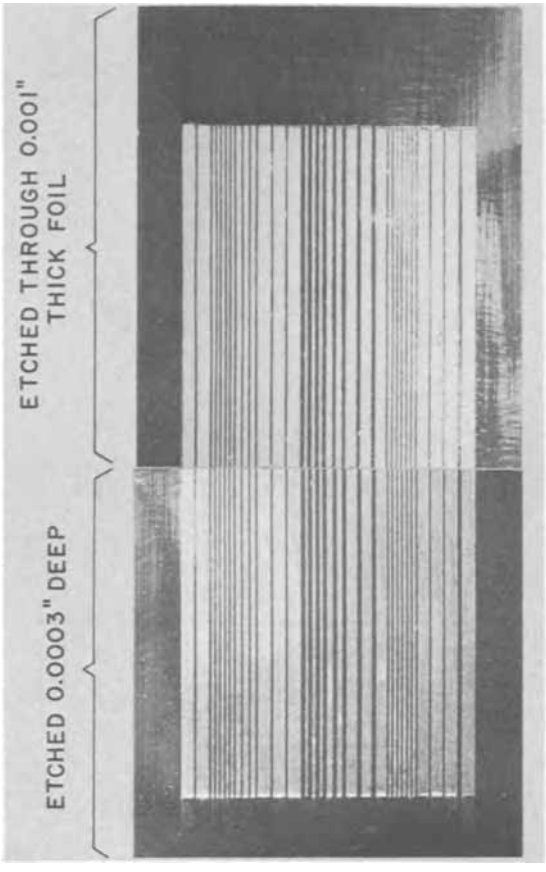

Fig. 12. Line pattern etched in tungsten foil masked by offset printing. Dark lines are elevated metal of 0.005, 0.010, and 0.020 in. width. White areas are etched tungsten (top picture) or background seen through the openings (bottom picture).

substrates. It has also been applied to creating patterns in tungsten foil. If the patterns are relatively large, the photoresist masking techniques can be replaced by more economic offset printing methods (16) with etch-resistant printing inks. Using this technique, lines down to 0.005 in. width and 0.0003 in. height were delineated with good resolution and with an etch factor of 1.0. These patterns were also completely etched through 0.001 in. foil as shown in the photographs in Fig. 12.

The same process of masking and electroetching is applicable also to molybdenum foil. The dissolution rate of molybdenum electroetched at 200 mA cm^{-2} is 392 Å-sec^{-1}.

Summary and Conclusions

A process has been devised for accurately delineating patterns in tungsten films for microelectronic device applications. It is based on combined chemical etching and electrolytic dissolution which proceeds rapidly at room temperature, allowing the photoresist mask to remain intact during etching. The composition of the etchant was designed to yield reproducible and smooth etching characteristics free of tungsten island formation. A special wafer holder was designed to allow the device wafer to be contacted to the anode and submerged during the electroetching. The process has been standardized to yield a chemical etch rate of 50 Å/sec, plus an electrolytic etch rate of 330 Å/sec at an optimum current density of 200 mA cm^{-2} exposed tungsten area. The high-speed electrolytic etching stops automatically when the pattern becomes discontinuous.

Resolution of the tungsten patterns in films up to 1μ thickness are limited essentially by the resolution that can be achieved in photoresist masking. Lines of 5μ width can easily be produced with resist films of 5000Å thickness. Films as thick as 12μ have been patterned successfully.

A post-etch chemical treatment effectively removes alkali ions and trace impurities from the device wafer surface, leaving the device surface in a condition suitable for the subsequent high-temperature sealing operations employing vapor deposited silicon nitride, oxides, or silicate glass layers.

The process has been demonstrated to be applicable also for delineating patterns in thick tungsten films deposited on glass and ceramic substrates, and for patterning foils of tungsten and molybdenum utilizing offset printing techniques for masking.

The principle of accelerating the dissolution of selectively masked films by electrolytic action superimposed on chemical etching appears to be generally applicable for a variety of metals.

Manuscript submitted Dec. 28, 1970; revised manuscript received May 28, 1971. This was Paper 71 presented at the Washington, D.C., Meeting of the Society, May 9-13, 1971.

Any discussion of this paper will appear in a Discussion Section to be published in the June 1972 JOURNAL.

REFERENCES

1. J. M. Shaw and J. A. Amick, *RCA Rev.*, **31**, 306 (1970); also *This Journal*, **116**, 376C (1969).
2. C. J. Smithells, "Tungsten," 3rd ed., p. 121, Chapman and Hall Ltd., London (1952).
3. K. C. Li, "Tungsten", in "Rare Metals Handbook," 2nd ed., p. 589, C. A. Hampel, Editor, Reinhold Publishing Corp. (1961).
4. C. J. Smithells, "Metals Reference Book," 4th ed., Vol. 1, p. 363, Plenum Press, New York (1967).
5. W. Kern, *RCA Rev.*, **31**, 207 (1970).
6. W. Kern, *ibid.*, **31**, 234 (1970).
7. W. Kern and D. Puotinen, *ibid.*, **31**, 187 (1970).
8. N. Goldsmith and W. Kern, *ibid.*, **28** 153 (1967).
9. W. Kern and A. W. Fisher, *ibid.*, **31**, 715 (1970).
10. W. Kern and R. C. Heim, *This Journal*, **117**, 562 (1970).
11. W. Kern and R. C. Heim, *ibid.*, **117**, 568 (1970).
12. M. T. Duffy and W. Kern, *RCA Rev.*, **31**, 742 (1970).
13. J. A. Amick and W. Kern, in "Chemical Vapor Deposition," Second Internatl. Conf., p. 551, J. M. Blocher, Jr. and J. C. Withers, Editors, The Electrochem. Soc., Inc., New York (1970).
14. W. Kern and J. M. Shaw, To be published.
15. A. I. Stoller and W. H. Schilp, Jr., *RCA Rev.*, **29**, 507 (1968).
16. R. J. Ryan, T. E. McCurdy, and N. E. Wolff, *ibid.*, **29**, 582 (1968).

Technical Notes

Effects of Various Additives in the Electrolyte on Oxygen Reduction at Ferric Phthalocyanine-Catalyzed Graphite Electrode

A. Kozawa,* V. E. Zilionis,* and R. J. Brodd*

Union Carbide Corporation, Consumer Products Division, Research Laboratory, Cleveland, Ohio 44101

Hemin and ferric phthalocyanine (FePc) were found to be good catalysts for oxygen reduction in saline solution and in blood (1-4), when a graphite or carbon was used as substrate (2). The activity of FePc-catalyzed graphite for oxygen reduction approached that of platinized Pt in 1M KOH (3). Platinum catalyst or a platinum electrode is known to be sensitive to various impurities. It has been shown that simple cations (Ca^{++}, Sr^{++}, Ba^{++}) and anions (Cl^-, Br^-) at a concentration of $10^{-4} \sim 10^{-2}$M significantly influence oxygen reduction at a platinum electrode (5). In this work, the influence of various additives in the electrolyte on oxygen reduction at FePc-catalyzed graphite electrodes was investigated. It is desirable to accumulate knowledge about what kind of impurities would deactivate the FePc catalyst for oxygen reduction especially during long-term operation in blood. Another reason is a basic interest in the interrelation of adsorption and electrode reaction rates. Unlike platinum catalysts (platinum black or platinized platinum on an electrode surface), FePc catalyst has a well-defined chemical structure, and the active center for oxygen reduction seems to be the iron atom in the molecule (2). Systematic data on the effect of various additives (anions, cations, complexing agents, etc.) would be meaningful in order to clarify some aspects of the electrode reaction in relation to adsorption.

Experimental

In our early work (1-4) isotonic saline solution (0.15M NaCl + 0.05M potassium sodium phosphate buffer, pH 7.15) or 0.05M sodium acetate solution (NaAc) was used. Here, 0.5M NaAc (pH 7.0) was primarily used as a base solution to provide a more desirable buffer action and to eliminate $PO_4^{\equiv}$ and Cl^- which would be strongly adsorbed on the Fe atom of FePc. The 0.5M NaAc (pH 7.0) base solution was prepared by adding concentrated acetic acid to 0.5M NaAc. Whenever 0.05M or 2M NaAc solutions were used; the pH was adjusted to desired values by adding HAc or NaOH.

Concentrated stock solutions of various additives (if possible 2M) were prepared and added to the base solution in concentrations of 0.01 to $\sim$ 0.1M. Since the $i-E$ curve was relatively sensitive to the pH of the solution, pH values of the solution after addition of the additives were measured. Unless otherwise noted, the pH remained 7.0 $\pm$ 0.1. Reagent grade chemicals and conductivity water were used throughout the studies.

A rotating disk-ring electrode technique was used in these studies (1). The disk electrode was made of a pyrolytic graphite and had an exposed surface of 0.196 cm^2. The disk radius was 0.25 cm and the platinum ring electrode had an inside radius of 0.277 cm and an outside radius of 0.360 cm. The collection efficiency measured experimentally ($N = i_r/i_d$, i_r = ring current, i_d = disk current) was approximately 0.39. FePc catalyst was applied on the surface of the pyrolytic graphite disk electrode. The electrode was always rotated at 120 rpm while taking the $i-E$ curves. The $i-E$ curves were taken in oxygen (1 atm) saturated solutions at 23°C $\pm$ 1°C at a sweep rate of 0.12 V/min. While sweeping the disk electrode potential toward the negative direction, the current at the ring electrode was measured at +0.62V *vs.* SCE. At this potential the H_2O_2 reaching the ring electrode is oxidized to O_2. Knowing the collection efficiency, N, of the ring electrode it is possible to calculate the fraction of the reaction current producing the hydrogen peroxide intermediate. The portion of the disk current which produces hydrogen peroxide is given approximately by $i_{H_2O_2} = i_r/N$ where i_r is the measured ring current. This calculation neglects the electrochemical reduction of H_2O_2 on the disk electrode as well as the possible self-decomposition of H_2O_2 in transit between the disk and ring electrode.

Results and Discussion

The main purpose of this note is to present various experimental facts and point out the behavior of various types of additives on oxygen reduction at a FePc catalyst graphite electrode. Current potential ($i-E$) curves presented in this paper were selected from a large number of experiments as representing significant behavior. Most of the effects caused by the various additives on the $i-E$ curve could be explained on the basis of adsorption on the catalyst surface.

A tentative model for adsorption of various types of additives on the FePc catalyst is useful when interpreting the results. FePc is essentially a large hydrocarbon molecule except for the Fe and nitrogen sites in the molecule. The hydrocarbon portion (pyrols) would adsorb $CH_3-\overset{\overset{O}{\parallel}}{C}-O^-$ or CH_3-CO_2H, since it may attract a methyl group. Nitrogen atoms would preferentially adsorb any metal ions since nitrogen can be an electron donor. Although in the FePc molecule, all the electrons of the nitrogen atom are used to bond with Fe, some attraction for other metal ions can be expected. The central Fe atom does have two free orbitals to accept any ligand, such as H_2O, Cl^-, Br^-, OH^-: O_2^-—R (oxyacid), etc. The FePc molecule requires one monovalent anion to balance the formal charge. This may contribute to the anion adsorption on the molecule. These three types of adsorption sites in FePc are shown pictorially in Fig. 1.

* Electrochemical Society Active Member.

Key words: oxygen reduction, ferric phthalocyanine-graphite, additives.

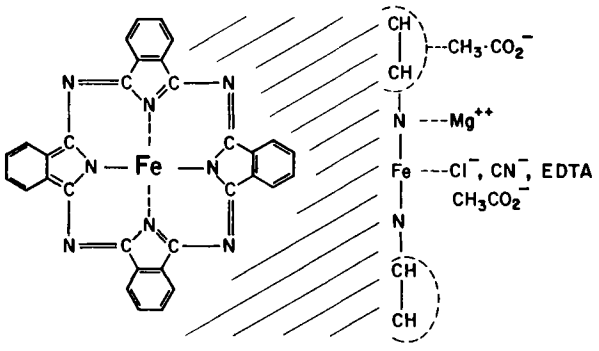

Fig. 1. Adsorption on ferric phthalocyanine

The nature of the oxygen reduction process at the electrode must also be considered. Oxygen is reduced by at least two kinds of electrochemical reactions, one produces H_2O_2 in a two-electron process and the other produces H_2O in a four-electron process

$$O_2 + 2H^+ + 2e^- \rightarrow H_2O_2 \quad [1]$$

$$O_2 + 4H^+ + 4e^- \rightarrow 2H_2O \quad [2]$$

Figure 2 shows the $i-E$ curves taken at a FePc-catalyzed graphite (FePc-Gr) electrode and also at an uncatalyzed pyrolytic graphite electrode in O_2-saturated 0.05M NaAc solutions (pH 6, 7, and 8). It should be noted that the FePc-Gr electrode is far better for oxygen reduction than is the uncatalyzed electrode. Practically no H_2O_2 is produced at the FePc-Gr electrode over the pH range studied, while at the uncatalyzed graphite electrode most of the disk current is due to an electrochemical reaction producing H_2O_2 (Reaction [1]). At the FePc-Gr electrode, the oxygen reduction reaction approximated a four-electron process (Reaction [2]). In fact the current value in the plateau ($-0.3 \sim -0.6$) region of the $i-E$ curve corresponds to the diffusion limited current for a four-electron reduction of dissolved O_2 under these rotational conditions. With the rotating disk ring electrode, approximate values for the current associated with each reaction path can be obtained as well as identification of a mechanism change. If the oxygen reduction current decreases at a certain potential with certain additives there are two possibilities. (*A*) The four-electron process changes to a two-electron process due to the influence of the nature of the adsorption on the various reaction paths. (*B*) The same four-electron process is taking place but a portion of the electrode (or catalyst) surface is simply blocked by the adsorbed material. If the first is the case, we should see an increase in the ring current and therefore, an increase in the fraction of current producing hydrogen peroxide. If the second is the case, the ring current should not increase.

Two-step $i-E$ curves for oxygen reduction are very frequently reported at various electrodes as the dropping mercury (6), graphite (2), gold and other electrodes. The first step is attributed to the reduction of O_2 to H_2O_2 and the second step to the reduction of O_2 to H_2O. At the FePc-Gr electrode, two-step $i-E$ curves of this type are obtained under certain conditions. The $i-E$ curve at pH 6 (curve 1, Fig. 2) has two steps, but the first step disappears as the pH value is increased (curves 2 and 3, Fig. 2).

The pH effect shown in Fig. 2 can be explained by the dissociation of HAc and its adsorption. Let us assume that undissociated HAc does not have the ability to complex or to be adsorbed on the Fe sites of the FePc catalyst as do Ac^- ions formed by dissociation. In acetate solution having low pH values there are more HAc molecules than dissociated Ac^- ions. Therefore, Ac^- adsorption is less; and the Fe sites of FePc have decreased blockage. But at high pH values, the Ac^- ion concentration is high and the Fe sites may be blocked by adsorption. Because of this situation at low pH, some oxygen reduction starts at more positive potentials and produces the first step in the curve. At more negative potentials all the Ac^- ions adsorbed on the Fe sites will be detached because of the charge repulsion, and the Fe sites then become available to catalyze oxygen reduction.

Figure 3 shows $i-E$ curves at FePc-Gr and uncatalyzed graphite electrodes in 0.05, 0.5, and 1.0M NaAc solutions. The height of the first step (see curves 1, 2, and 3) increases with increasing acetate concentration from 0.05 to 1.0M. The current value in the plateau region ($-0.2 \sim -0.7$ *vs.* SCE) of curves 1, 2, and 3

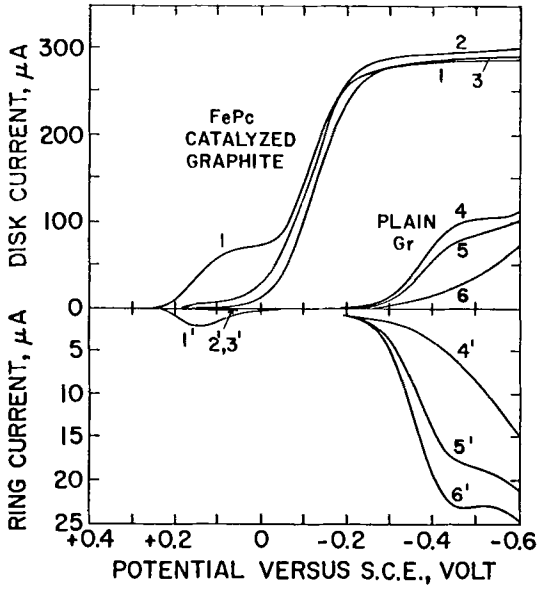

Fig. 2. Current-potential curves for FePc-graphite, curves 1-3, and graphite, curves 4-6, electrodes in the following solutions: Curves 1,4—0.05M sodium acetate pH 6; Curves 2,5—0.05M sodium acetate pH 7; Curves 3,6—0.05M sodium acetate pH 8.

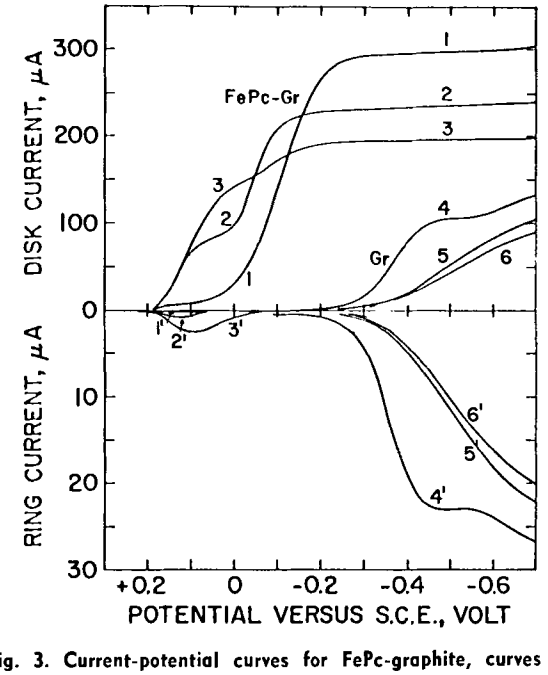

Fig. 3. Current-potential curves for FePc-graphite, curves 1-3, and graphite, curves 4-6, electrodes in solutions with increasing acetate concentration: Curves 1,4—0.05M sodium acetate pH 7; Curves 2,5—0.5M sodium acetate pH 7; Curves 3,6—1.0M sodium acetate pH 7.

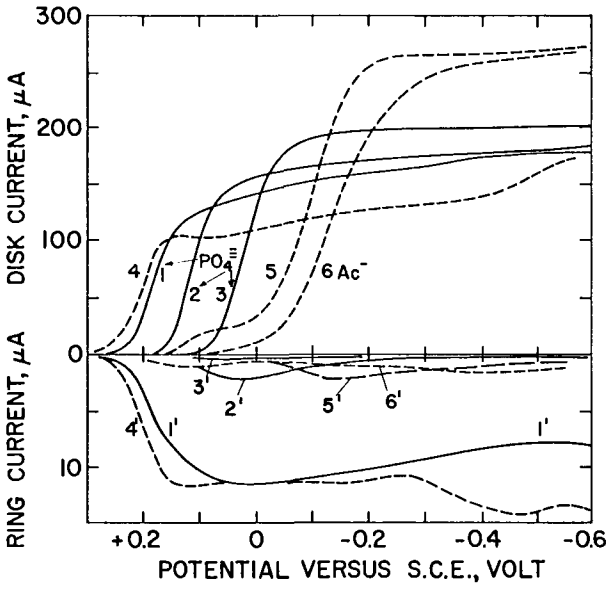

Fig. 4. Current-potential curves for FePc-graphite electrodes in 0.2M sodium phosphate, curves 1-3, and 0.2M sodium acetate solutions, curves 4-6: Curves 1,4—pH 5; Curves 2,5—pH 7; Curves 3,6—pH 9.

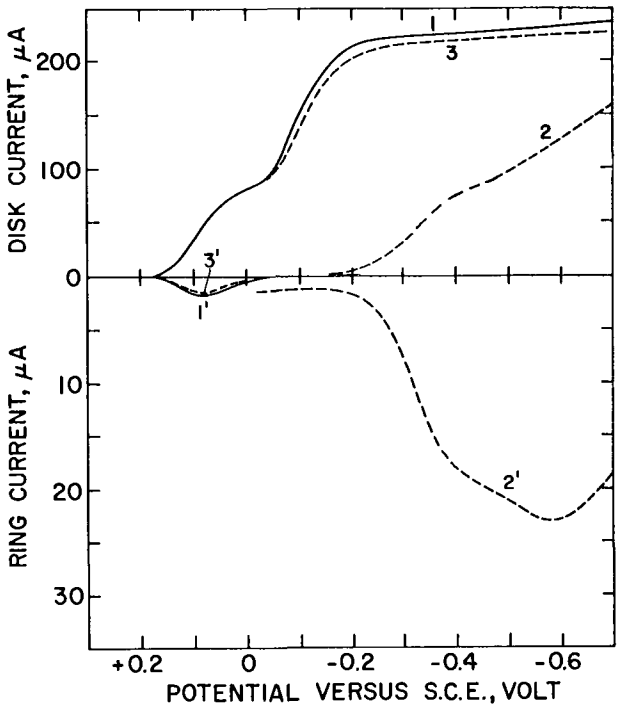

Fig. 5. Current-potential curves for FePc-graphite electrode in sodium acetate solution with and without cyanide additive. Curve 3 was taken after rinsing the electrode in Curve 2 with water: Curves 1,3—0.5M sodium acetate pH 7.0; Curves 2—0.5M sodium acetate + 0.01M sodium cyanide pH 9.25.

decreases with increasing acetate concentration, presumably due to a decrease in oxygen solubility.

Figure 4 shows $i-E$ curves taken in 0.2M Na_3PO_4 (pH 5, 7, and 9) and 0.2M NaAc (pH 5, 7, and 9) solutions at FePc-Gr electrodes. It is interesting to note that the curves in the phosphate solution shift toward the negative direction by approximately 33 mV/pH as the pH value increases, but in the acetate solution some unusual distortions are seen at pH 7 and 9 (see curves 4, 5, and 6). This may indicate that at pH 7 and 9 the acetate ion (0.2M) is adsorbed at the FePc electrode and hinders the O_2 reduction in this region (+0.2 ~ 0V). Another point to be noted is that the plateau current in the acetate solution decreases with decreasing pH from 7 or 9 to 5 (see curves 4, 5, and 6). It was shown previously (3) that in 0.1N H_2SO_4 solution, the plateau current of the $i-E$ curve is approximately half the value associated with the four-electron process. At pH 5, the behavior of the FePc-Gr electrode is approximately the same as that in 0.1N H_2SO_4. In acid solution (0.1N or 1.0N H_2SO_4), the activity of FePc for oxygen reduction deteriorated rapidly (3).

When $i-E$ curves were taken repeatedly at FePc-Gr electrodes, they were reproducible in most solutions indicating that the catalyst activity remains the same. In some solutions having pH values of 6 or less or in solutions containing certain anions *e.g.*, $PO_4^{\equiv}$ the shape of the curve changed rapidly because of deactivation of the FePc-catalyst. In 0.2M Na_3PO_4 solution, the repeated $i-E$ curves are reproducible at pH 9, but at pH 5 and 7, the electrode activity deteriorated rapidly on repeated sweeps.

Cyanide ions added to the acetate base solution greatly hinder the activity of the FePc catalyst for oxygen reduction as shown in Fig. 5. The $i-E$ curve for oxygen reduction in CN^--containing solution (curve 2) is very similar to that at a plain graphite electrode.

It is well known that the O_2-carrying ability of hemin is lost when cyanide ions are introduced in blood, since the CN^- ion is strongly adsorbed on the Fe atom of hemin. The results obtained here (Fig. 5) are analogous to the physiological effect of cyanide. However, the poisoning of FePc catalyst by CN^- is not permanent since, when the electrode which had been operated in CN^--containing solution was washed with water and operated in a CN^--free solution, the poisoning effect disappeared almost completely (see curve 3, Fig. 5). The inhibitive effect of EDTA (0.01M) is considerable and quite similar to that of CN^-. However, in this case the poison was more permanent. The electrode which was washed with water and tested in an EDTA-free solution did not recover its activity completely as in the case of CN^-. The activity of electrodes exposed to EDTA could be restored only after repeated rinsing with water. One explanation may be that the EDTA may remove the Fe from the FePc complex causing an irreversible loss of activity.

Cyanide ion and EDTA must be attached to the iron atom of the FePc catalyst. Their ability to form stable complexes with iron is well known. Therefore these additives are expected to hinder the oxygen reduction reaction. It is almost certain that iron in the FePc is the site for the electrochemical oxygen reduction, since among the various metal phthalocyanines tested, the catalytic activity is highly dependent on the kind of central metal ion; the active order among the active metal Pc's were Fe(III) > Fe(II) > Co > Cu, etc., (1). Increased peroxide formation was noted for CN^- and EDTA additives. Evidently they block the active sites of the iron for oxygen reduction.

Figure 6 shows the effects of adding small amounts of "Triton X-100" (a nonionic surface active agent-alkylaryl polyether alcohol), pyridine, and quinoline. These additives are typical materials which inhibit oxygen reduction at the FePc-Gr electrode. It should be noted that, although the disk current is greatly reduced in the presence of 0.002% quinoline (curve 4), the fraction of the current producing hydrogen peroxide is not greatly increased. This indicates that the inhibition effect does not necessarily change the oxygen reduction reaction from the four-electron process to the two-electron process.

In contrast to the behavior of $PO_4^{\equiv}$ and CN^- the effect of $SO_4^=$ addition to 0.5M NaAc is only slight. Also the addition of Cl^- and Br^- to 0.5M NaAc solution had little effect on the over-all behavior. The slight decrease in the plateau current was observed

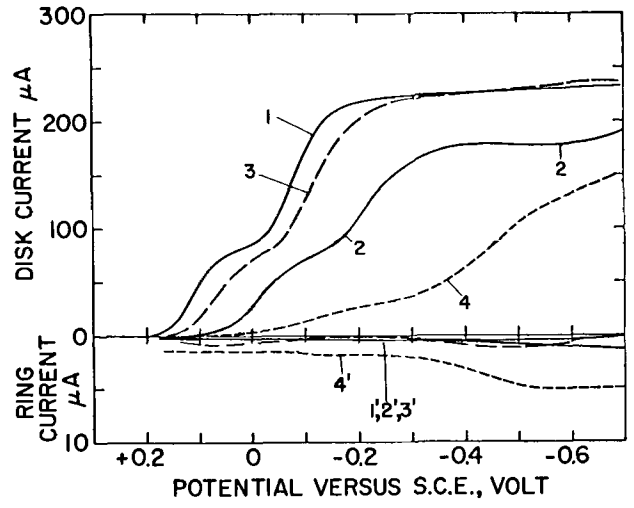

Fig. 6. Current potential curves for FePc-graphite electrode in sodium acetate solution plus the following additives: Curve 1—0.5M sodium acetate pH 7.0; Curve 2—0.5M sodium acetate + 0.01% "Triton X-100" pH 6.97; Curve 3—0.5M sodium acetate + 0.01% pyridine pH 7.1; Curve 4—0.5M sodium acetate + 0.002% quinoline pH 7.1.

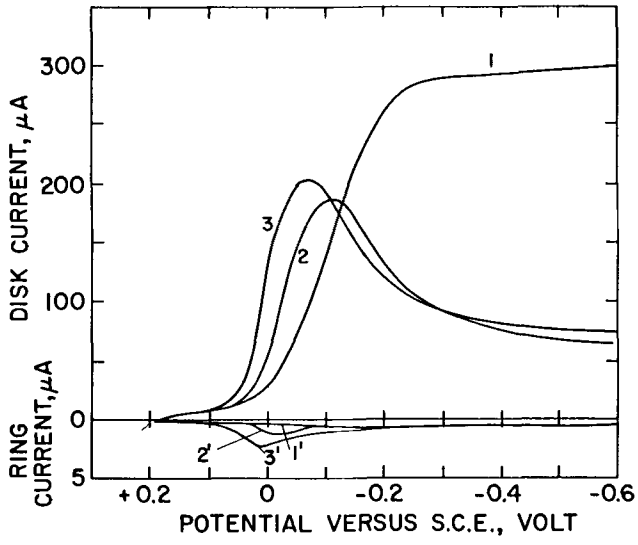

Fig. 7. Current-potential curves for FePc-graphite electrode in sodium acetate solution with and without magnesium additive: Curve 1—0.05M sodium acetate pH 7.0; Curve 2—0.05M sodium acetate + 0.1M magnesium nitrate pH 7.0; Curve 3—0.05M sodium acetate + 0.2M magnesium nitrate pH 7.0.

perhaps due to decreasing oxygen solubility. The following additives were found to have practically no effect on the $i-E$ curves: Na oxalate (0.01M, 0.02M), Na tartrate (0.01M, 0.1M), urea (0.01M, 0.1M), KNO_3 (0.01M, 1M).

In solution containing only bromide ion there was little effect of pH on the $i-E$ curves. Br^- ions must be strongly adsorbed on Fe sites, since the Fe(III)-halide complex is very stable. Such a Br^- adsorption should be influenced very little by a pH change in the solution. However, when a certain negative potential is imposed, the adsorbed Br^- on the Fe of FePc should be desorbed and consequently, oxygen reduction should take place when the potential becomes sufficiently negative.

When a Br^- solution containing no acetate ion was used, the Br^- effect was considerably different from the effect of Br^- added to the 0.5M NaAc solution. In the bromide solution the pH effect is very small in the pH range of 5-9, although in acetate solution the $i-E$ curve develops a pronounced second step at lower pH values.

The effect of divalent positive ions is not clear. Adding $Ca(NO_3)_2$ (0.01M, 0.1M), and $Sr(NO_3)_2$ (0.01M, 0.1M) has no notable influence on the $i-E$ curves. As shown in Fig. 7, addition of Mg^{++} produces a somewhat beneficial effect around $+0.1 \sim -0.1$V, since the current is larger with Mg^{++} additions than that in 0.05N NaAc solution. However, the current decreases considerably as the potential becomes more negative. At higher Ac^- concentration the plateau current is not depressed as much as in lower Ac^- solutions.

The only possible site for Mg^{++} adsorption is the nitrogen atom of FePc. Let us assume Mg^{++} ions are adsorbed on some N-sites. This adsorbed Mg^{++} would somehow promote oxygen reduction at the Fe-site of FePc. When a more negative potential is applied (or the electrode is swept toward more negative potential) Mg^{++} adsorption should be increased since the Mg^{++} is positively charged. If hydrated Mg^{++} ions would be adsorbed on two N-sites of FePc, oxygen reduction may be hindered physically since it is difficult for the O_2 molecule to approach the Fe site because of steric hindrance. This would account for the current decrease shown in Fig. 7 (curves 2 and 3).

The effect of Pb^{++} addition shown in Fig. 8 is quite similar to that of Mg^{++} in the potential range of $+0.2 \sim 0.1$V, but the plateau current remains steady at

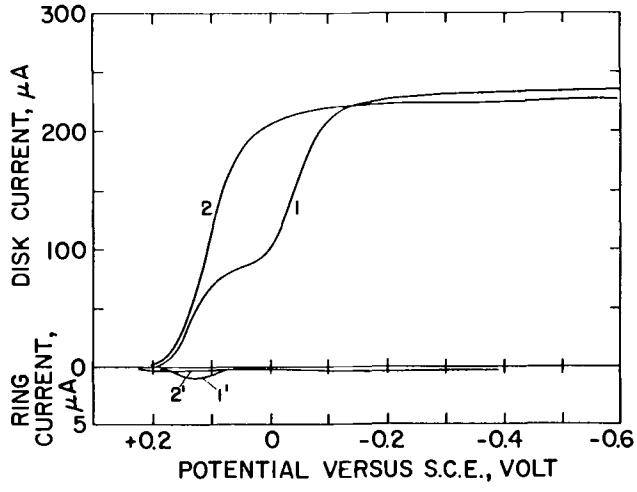

Fig. 8. Current-potential curves for FePc-graphite electrode in sodium acetate solution with and without lead additive: Curve 1—0.5M sodium acetate pH 7.0; Curve 2—0.5M sodium acetate + 0.01M lead nitrate pH 6.9.

negative potentials. This kind of beneficial action of Pb^{++} for oxygen reduction has been reported previously using dropping mercury electrode (6, 7) as well as various solid electrodes (8).

Acknowledgment

A portion of the research on which this report is based was performed pursuant to Contract No. PH-43-68-1391 with the Artificial Heart Program, National Heart and Lung Institute, Department of Health Education and Welfare.

Manuscript submitted Oct. 29, 1970; revised manuscript received May 28, 1971. This was Paper 9 presented at the Atlantic City Meeting of the Society, Oct. 4-8, 1970.

Any Discussion of this paper will appear in a Discussion Section to be published in the June 1972 JOURNAL.

REFERENCES

1. A. Kozawa, V. E. Zilionis, R. J. Brodd, and R. A. Powers, "Artificial Heart Program Conference Proceedings," National Heart Institute, June 9-13, Washington, D.C., Chap. 71, p. 849.

2. A. Kozawa, V. E. Zilionis, and R. J. Brodd, *This Journal*, **117**, 1470 (1970).
3. A. Kozawa, V. E. Zilionis, and R. J. Brodd, *ibid.*, **117**, 1474 (1970).
4. A. Kozawa, Abs. 321, p. 840, Electrochem. Soc. Extended Abstracts, Spring Meeting, Los Angeles, May 10-15, 1970.
5. A. Kozawa, *J. Electroanal. Chem.*, **8**, 20 (1964).
6. F. Strand, *Collection Czech. Chem. Commun.*, **11**, 391-402 (1939).
7. D. C. Grahame, *Anal. Chem.* **30**, 1738 (1958).
8. Y. Okinaka, Paper presented at the Annual Meeting of the Chemical Society of Japan (April 1961).

Electrical Resistivity of Magnetite Anodes

R. Itai, M. Shibuya, T. Matsumura, and G. Ishi*

The Japan Carlit Company, Limited, Shibukawa-shi, Gunma-ken, Japan

Considerable progress has been made in quality and economy of magnetite anodes, and they are now used not only in traditional chlorate cells, but also in such new fields as cathodic protection and electrodialysis.

Electrolytic manufacture of sodium chlorate with magnetite anodes has been described in a previous paper (1). Since they have relatively high electrical resistance compared with graphite, this should be kept as low as possible through quality control. Much work has been done with regard to factors which govern electrical resistance of commercial magnetite anodes. In the present paper, effects of composition, temperature, and some additives on resistivity of cast magnetite samples prepared from relatively pure mill scale, are described.

Experimental

Composition of magnetite and its raw materials may be expressed in terms of Fe(III)/Fe(II) atomic ratios (*AR*). Pure magnetite corresponds to an *AR* of 2.00.

Determination of AR.—Dissolve a weighed portion of a sample in 12*N* H_2SO_4, titrate it with 0.1*N* $KMnO_4$ which gives Fe(II). Dissolve another portion in 8*N* HCl, add $SnCl_2$ to reduce any Fe^{3+}, oxidize the excess $SnCl_2$ with a saturated solution of $HgCl_2$, add $MnSO_4$ and finally titrate it with 0.1*N* $KMnO_4$ to obtain the total iron which gives Fe(III) by difference.

Preparation of magnetite samples.—Mill scale of as high quality as was available was melted under conditions similar to the practical ones. Composition of the mill scale used throughout is shown in Table I. Purity was much better than that of hematite ore, a common raw material for commercial magnetite anodes. The feed was a mixture of unoxidized and partly oxidized mill scales in such a ratio as to give any target *AR* value in the final product.

Melting was carried out in a 15 kW resistor furnace. The melt was poured into a red-hot cast iron mold and was left cooling overnight in an annealing furnace preheated above 800°C. Samples, 15 mm wide, 75 mm long, and 8 mm thick, were ground out of ingots.

Electrical measurements.—A constant d-c current (10 to 200 mA) was led through a sample plated with Cu on both ends, and the voltage drop across a pair of silver knife edges on which it rested was measured by a potentiometer. For measurements at temperatures higher than 150°C, a thin silica tube, on which a pair of Cu wires were wound 30 mm apart, pressed tightly against a sample, provided potentiometric contacts. The unit was placed in a silica tube, 30 mm inner diam, inserted in a horizontal tube furnace with Ni-Cr resistors and swept by a stream of CO_2.

* Electrochemical Society Active Member.

Key words: magnetite anodes, electrical resistivity, activation energy, atomic ratio.

Table I. Composition of mill scale used for casting magnetite

SiO_2	Al_2O_3	CaO	MgO	FeO	Fe_2O_3
1.09%	0.93%	0.50%	0.13%	44.2%	53.5%

Results and Discussion

Effect of AR on resistivity.—Direct-current resistivity, ρ, at 25°C of cast magnetite as a function of *AR*, is shown in Fig. 1. The curve has a jump at $AR = 2.0$, corresponding to stoichiometric magnetite. As *AR* passed the stoichiometric point from the lower to the higher *AR* region, ρ increased 10^2-fold. The observed value of ρ at $AR = 2$ was about five times as high as that reported for pure single crystals of Fe_3O_4 (2, 3). The difference might be explained by the fact (4) that conductivity of polycrystalline magnetite is 10-20% of that of single crystals, and partly by the presence of small amounts of impurities in our samples.

From the practical point of view, it is obviously advantageous to keep *AR* of the anode products as close to the value of 2 as possible but never in excess of it.

Effect of temperature.—Resistivity of samples with different *AR*'s was measured between 2° and 900°C and log ρ was plotted against $1/T$ as shown in Fig. 2, where T is absolute temperature. Curves formed two groups, an upper and a lower. The curves for $AR \gtrless 2.0$ belonged to the latter. Below 300°C they roughly coincided with a curve reported for $FeO_{1.07}$ (4). The discrepancy at $AR = 2$ of the observed from the reported

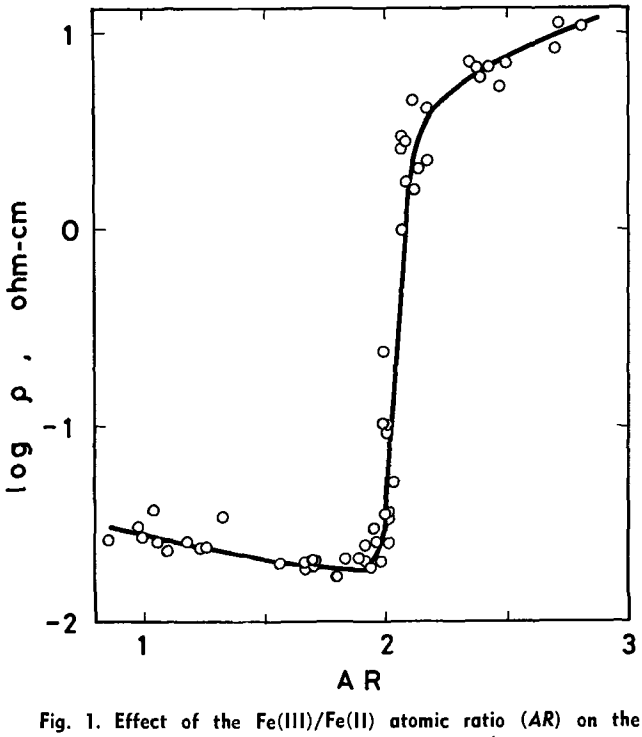

Fig. 1. Effect of the Fe(III)/Fe(II) atomic ratio (*AR*) on the electrical resistivity at 25°C of cast magnetite samples.

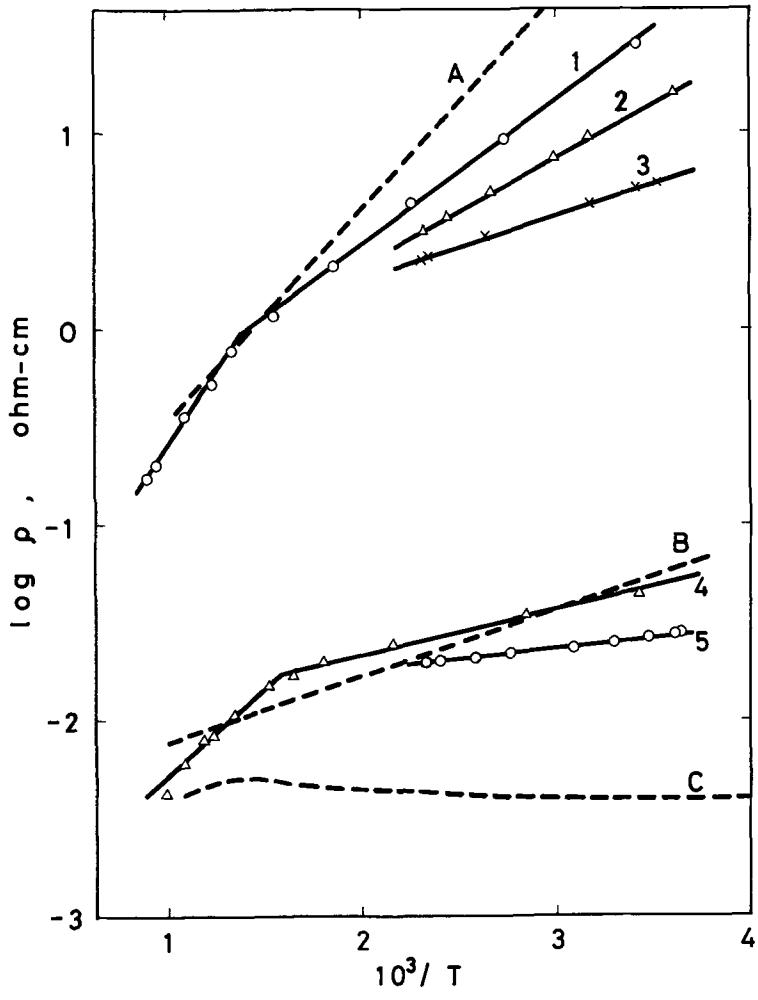

Fig. 2. Temperature dependence of the electrical resistivity of cast magnetite with various *AR*'s, compared with that of γ-Fe_2O_3, Fe_3O_4, and FeO: 1) *AR* = 2.72, 2) 2.44, 3) 2.11, 4) 1.03, 5) 1.97, (A) γ-Fe_2O_3, (B) $FeO_{1.07}$, (C) Fe_3O_4 (see text).

curve (3) could be attributed to the same reason as given above. The curves for $AR > 2$ formed the upper group. A curve for a preparation of epitaxially grown γ-Fe_2O_3 (5) is also shown. Curves for α-Fe_2O_3 presumably lie higher than those for γ-Fe_2O_3 (6). Curves for those samples with which the measurements extended up to 900°C had a kink at about 430°C.

Activation energy, *E*, for the low-temperature part, showed a minimum at the stoichiometric magnetite composition (Fig. 3). At this point, the temperature coefficient of resistivity at 25°C was about −0.2% per degree. The increase in *E* was much steeper towards the higher *AR* region than towards the opposite.

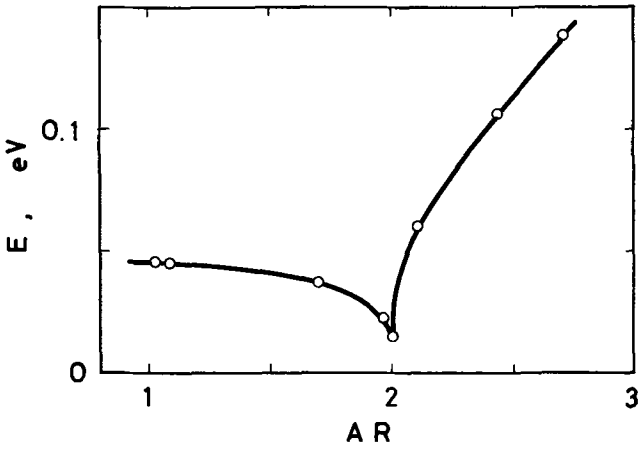

Fig. 3. Activation energy for the low-temperature part of the resistivity curves as a function of *AR*.

Microscopic observations.—Five samples with *AR*'s from 1.04 up to 2.70 were inspected microscopically (Fig. 4 a-e). The samples with $AR = 1.04$ and 2.70 showed two distinct phases, whereas those with $AR = 1.35$, 2.00, and 2.29 showed a single phase. In the $AR = 1.04$ sample, either wuestite or metallic iron appears as a separate phase, while in the $AR = 2.70$ sample, maybe α-Fe_2O_3 has segregated. In view of the poor solubility of wuestite or iron in magnetite (7), it is surprising that those samples having *AR*'s well below the stoichiometric value were found to be uniform, even though they had been anealed during preparation.

Effect of additives.—The commercial magnetite anodes contain certain amounts of impurities, such as silica, alumina, and lime (1). In order to study the

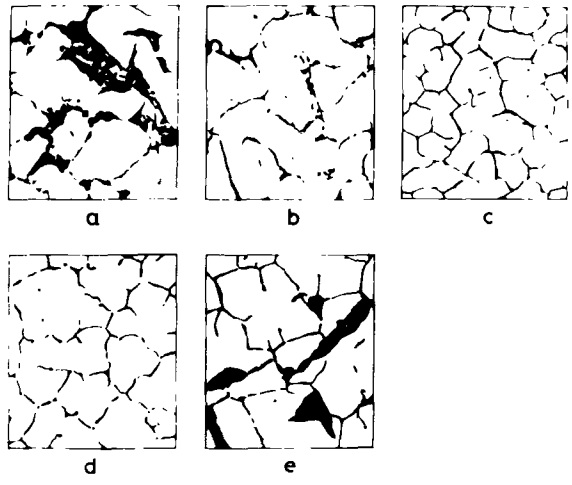

Fig. 4. Schematic representation of microscopic structures at various *AR*'s (X269): (a) $AR = 1.04$, (b) 1.35, (c) 2.00, (d) 2.29, (e) 2.70.

Table II. Effect of additives on electrical resistivity of cast magnetite

Group	Additive: Compound	Additive: % added	Critical AR	Corresponding resistivity, ohm-cm	No. of phases
—	None	—	2.0	0.020	1
I	KNO_3	2	2.0	0.035	2
II	MgO	1	2.1	0.026	1
		3	2.2	0.033	1
II	CaO	1*	2.1	0.027	1
II	ZnO	5	2.2	0.035	1
III	Al_2O_3	1	1.9	0.025	1
		3	1.8	0.042	1
		5	1.7	0.075	1
IV	SiO_2	1	2.0	0.030	2
		3	2.0	0.039	2
		5	2.0	0.045	2
IV	TiO_2	2	1.8	0.028	2
V	P_2O_5	2	2.0	0.091	2

* Preparation was so difficult that only a few samples were available for measurements.

roles played by such impurities, certain elements of Group I and V were added to the mill scale as the corresponding oxides, except for potassium where the nitrate was used. Electrical measurements and microscopic observations were made on samples prepared as before. The critical *AR* at which the jump occurred, the associated value of ρ, and the number of phases observed near the critical value of *AR* are summarized in Table II. Typical examples of microscopic structures where the number of phases is one and two, respectively, are shown in Fig. 5a and b.

Potassium gave little effect except that it brought about a second phase. Elements of Group II caused more or less rises of the critical *AR*, that is, some shifts towards the higher *AR* region, but the corresponding changes in ρ were not substantial. CaO made cast magnetite so fragile that only a few pieces were available for measurements.

With Al_2O_3, only one phase formed in samples, and the critical *AR* lowered. The increase in the corresponding ρ was a little more enhanced than those observed with the Group II oxides.

Such changes in the critical values of *AR* may be postulated, at least qualitatively, as follows. Group II oxides might form corresponding spinels by joining with excess Fe_2O_3 within the lattice of $AR = 2$, causing rises of the critical *AR*. Similarly, alumina could combine with the interstitial Fe^{2+} to form $FeAlO_4$, lowering the critical *AR*.

This was no longer the case with SiO_2, for it went into a separate phase, having little influence on the

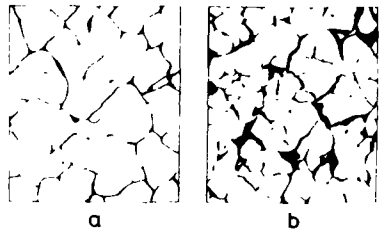

Fig. 5. Schematic representation of microscopic structures of magnetite containing additives (X269): (a) 5% Al_2O_3, $AR = 2.0$, (b) 5% SiO_2, $AR = 1.9$.

conduction process. The gradual increase in ρ as the addition level increased may be taken as being caused by the increasingly silica-rich matrix. P_2O_5 behaved quite like SiO_2.

Addition of TiO_2 was an intermediate case. It caused two separate phases to exist, while a lowering of the critical *AR* cannot be neglected. Partial solubility of TiO_2 in magnetite might be a possible answer, but no further discussion will be attempted here.

Generally, rises in the critical *AR* are favorable on account of conductivity, but other factors, such as thermal and mechanical properties as well as electrochemical performance, should also be considered.

Thus our resistivity measurements made on cast mill scale magnetite provided useful guidelines for the manufacture of commercially acceptable magnetite anodes.

Manuscript submitted Dec. 28, 1970; revised manuscript received *ca.* March 26, 1971. This was Paper 166 presented at the Washington, D.C., Meeting of the Society, May 9-13, 1971.

Any discussion of this paper will appear in a Discussion Section to be published in the June 1972 JOURNAL.

REFERENCES

1. T. Matsumura, R. Itai, M. Shibuya, and G. Ishi, *Electrochem. Technol.*, **6**, 402 (1968).
2. J. M. Lavine, *Phys. Rev.*, **123**, 1273 (1961).
3. P. A. Miles, W. B. Westphal, and A. van Hippel, *Rev. Mod. Phys.*, **29**, 279 (1967).
4. D. S. Tannhauser, *Phys. Chem. Solids*, **23**, 25 (1962).
5. H. Takei and S. Chiba, *J. Phys. Soc. Japan*, **21**, 1255 (1966).
6. R. Matejec, *Mitt. Forschungslab. Agfa Leverkusen-Munchen*, **3**, 273 (1961).
7. L. S. Darken and R. W. Gurry, *J. Am. Chem. Soc.*, **68**, 798 (1946).

Brief Communication

Electric Conductivity of Carbon Black Suspensions in Molten Sulfur

T. K. Wiewiorowski

Freeport Sulphur Company, A Division of Freeport Minerals Company, Belle Chasse, Louisiana 70037

Molten sulfur is a very poor electrical conductor. In certain applications it would be desirable to increase its electrical conductivity. For example, molten sulfur is being considered as the cathode reactant in sodium-sulfur and lithium-sulfur batteries, but its low electrical conductivity in these rechargeable batteries makes current collection at the cathode a very difficult task. The poor electric conductivity of molten sulfur

Key words: batteries, carbon black, conductivity—electric, sulfur, suspensions.

is undoubtedly one of the major technological barriers in the successful commercial developments of lithium-sulfur and sodium-sulfur batteries. In an effort to overcome this problem, the electrical current collection system at the cathode in one prototype lithium-sulfur cell consisted of an elaborate metal mesh to maximize its surface area and increase the current output of the cell (1). Although somewhat improved, this current output did not reach a sufficiently high level to render the system suitable for practical applications. Furthermore, the use of an extended metal mesh in the current collection system of a battery significantly increases the weight of the battery and consequently decreases its specific energy (energy per unit weight).

The performance of sodium-sulfur and lithium-sulfur batteries can be greatly enhanced by increasing the electric conductivity of the molten sulfur contained in the cathode compartments of these batteries. It has been found that compositions of matter consisting of molten sulfur and powderized carbon have electric conductivities substantially higher than that of pure molten sulfur.

The concentration of carbon used in preparing a particular composition depends primarily on the desired electrical conductivity of the melt and on the physical properties of the specific carbon employed, such as density, crystallinity, particle size, and porosity. The carbon content of the suspension may vary between 0.1% and 15% by weight.

The preparation of carbon-in-sulfur suspensions can be accomplished by blending carbon powder into molten sulfur, while providing sufficient agitation to achieve uniform distribution of the solid in the liquid phase. Carbons consisting of small porous particles form quite stable suspensions in molten sulfur and show little or no tendency to settle even after extended periods of time. This is important in applications where a uniform suspension is desired and where it is impractical to provide mechanical agitation in order to maintain such uniformity of suspension. It was quite surprising to observe that such suspensions have conductivities several orders of magnitude higher than that of pure molten sulfur, even though the carbon content of these compositions was only in the order of 0.1%-15%.

The physical properties of the suspension are strongly affected by the type and amount of carbon it contains. For example, suspensions of powderized carbon in molten sulfur in which the carbon content is below about 2% by weight have a fluidity similar to that of molten sulfur. In the case of finely divided carbons, these compositions gradually acquire the consistency of a paste as the carbon content is raised above about 2%.

A series of carbon black suspensions in molten sulfur was prepared and their electrical conductivities determined at 130°C using a direct current conductivity measuring circuit with a sensitivity of about 10^{-7} ohm^{-1} cm^{-1}. The results obtained are shown in Table I. In all cases tested, the electrical conductivity of the suspensions was at least three orders of magnitude higher than the conductivity of molten sulfur, which is reported to be in the order of 5×10^{-11} ohm^{-1} cm^{-1}. Note that the suspension containing 2.0% of Vulcan XC-72R carbon black, manufactured by the Cabot Corporation, had a conductivity in the order of 10^{-1} ohm^{-1} cm^{-1}. In this case, the enhancement in electrical conductivity resulting from the presence of the carbon black in the molten sulfur is about ten orders of magnitude.

In another experiment, a 5% by weight suspension of Vulcan XC-72R carbon black in molten sulfur was prepared by thoroughly mixing 25g of carbon black into 475g of molten sulfur. The mixture, contained in a glass beaker, was placed in a thermostatically controlled oven and maintained at 142°C without agitation. In order to evaluate the stability of the molten sulfur-carbon black suspension, conductivity readings were obtained over a period of ten days by immersing an electrical conductivity probe near the bottom, in the center, and near the surface of the suspension. The conductivity reading was not affected by the location of the conductivity probe, indicating that no settling of the carbon black occurred. The results shown in Table II demonstrate the excellent stability of this suspension. Throughout the entire testing period the electrical conductivity of the suspension remained about ten orders of magnitude higher than the reported conductivity of pure molten sulfur.

Preliminary tests intended to compare the performance of carbon-in-sulfur suspensions with pure molten sulfur in a lithium-sulfur cell indicate that the conductive suspensions will facilitate considerable simplification of the current collection system in lithium-sulfur and sodium-sulfur batteries.

Table I. Electrical conductivity of carbon black suspensions in molten sulfur

Trade name of carbon black manufactured by the Cabot Corp.	Weight per cent of carbon black	Electrical conductivity of suspension ohm^{-1} cm^{-1}
Vulcan XC-72R	0.10	2×10^{-7}
Vulcan XC-72R	0.20	1.4×10^{-5}
Vulcan XC-72R	0.30	3.2×10^{-4}
Vulcan XC-72R	0.40	1.1×10^{-3}
Vulcan XC-72R	0.50	2.4×10^{-2}
Vulcan XC-72R	0.75	1.0×10^{-2}
Vulcan XC-72R	1.00	2.1×10^{-2}
Vulcan XC-72R	1.25	3.2×10^{-2}
Vulcan XC-72R	1.50	5.2×10^{-2}
Vulcan XC-72R	2.00	1.1×10^{-1}
Carbolac 1	0.58	5.6×10^{-6}
Carbolac 1	1.15	7.5×10^{-5}
Carbolac 1	2.28	1.2×10^{-3}
Carbolac 1	3.38	1.0×10^{-2}
Vulcan 9	3.22	1.2×10^{-6}
Vulcan 9	4.25	2.4×10^{-5}
Vulcan 9	5.26	1.4×10^{-4}
Vulcan 9	6.25	5.2×10^{-4}
Vulcan 9	9.90	5.9×10^{-3}
Vulcan 9	20.00	3.6×10^{-1}

Table II. Electrical conductivity of 5% Vulcan XC-72R carbon black suspended in molten sulfur as a function of time

Time elapsed from commencement of test (days)	Electrical conductivity of suspension (ohm^{-1} cm^{-1})
0.2	2.9
1.0	3.0
2.0	3.1
3.0	3.1
6.0	3.9
8.0	4.1
10.0	4.1

Acknowledgment

The author wishes to acknowledge the assistance of Dr. C. G. Collins, Jr., and W. L. Thornsberry, Jr., in conducting the experimental work reported in this paper.

Manuscript received May 27, 1971.

Any discussion of this paper will appear in a Discussion Section to be published in the June 1972 JOURNAL.

REFERENCES

1. H. Shimotake and E. J. Cairns, "Lithium/Chalcogen Secondary Cells," Fourth Advances in Battery Technology Symposium, Los Angeles (December 1968).

JOURNAL OF THE ELECTROCHEMICAL SOCIETY

ELECTROCHEMICAL SCIENCE

NOVEMBER 1971

The Adsorption and Reaction of Cyclic Olefins on a Fuel Cell Electrode

H. J. Barger, Jr., G. W. Walker, and R. J. York

Electrochemical Division, U. S. Army Mobility Equipment Research & Development Center, Fort Belvoir, Virginia 22060

ABSTRACT

The adsorption and reaction during cathodic pulse of 1,2- and 2,3-dimethylcyclopentene and 1,2- and 2,3-dimethylcyclohexene were studied. The *cis* to *trans* ratios of the reduced hydrocarbon products were analyzed by gas chromatography. In view of the large difference in reduced isomer ratios obtained for the different size ring systems, different modes of adsorption are postulated for each ring system. A π-bonded, aromatic, adsorbed intermediate is proposed for the dimethylcyclohexene system, since the *cis/trans* ratio is the same as that obtained upon pulsing an electrode which has been in contact with *ortho*-xylene. The cyclopentyl results are explained in terms of a less restricted adsorption geometry, with the relative thermodynamic stabilities of the reduced isomers contributing extensively to the *cis/trans* ratio observed.

The primary purpose of this investigation is the study of hydrocarbon adsorption at a fuel cell electrode in order to elucidate the electrooxidation process.

Brummer (1) has shown that the oxidation process involves adsorption on the electrocatalyst, followed by the rapid formation of the intermediates CH-α and O-type, with the subsequent slow oxidation of O-type to CO_2

$$\text{Adsorption} \xrightarrow{\text{Fast}} \text{CH-}\alpha \xrightarrow{\text{Fast}} \text{O-type} \xrightarrow{\text{Slow}} CO_2$$

It has also been shown that the reaction must occur by adsorption and that all intermediates are adsorbed on the electrocatalyst (2). A method of studying the adsorption process was adopted whereby an evolved product would retain the essential geometrical features of the reactant hydrocarbon. This method involved adsorption at fixed potential followed by a galvanostatic cathodic pulse (3) with subsequent trapping of the reduced hydrocarbons.

By proper choice of reactant, one can conceivably obtain some insight into the adsorption geometry on the electrocatalyst. Dimethylcycloolefins, for example, may yield both *cis*- and *trans*-dimethylcycloalkanes upon cathodic pulse, and the cycloalkane isomer ratio allows speculation as to the mode of adsorption. The olefins, 1,2-dimethylcyclopentene, and 2,3-dimethylcyclopentene were chosen for this study for several reasons: (*a*) this type, or quite similar types, of molecule occurs in substantial concentrations in hydrocarbon fuels which fuel cells may ultimately be able to utilize; (*b*) the molecules have been extensively studied under normal heterogeneous catalysis conditions (4-6) so the effect of electrocatalyst potential could be determined; and (c) the reduction products, *cis*- and *trans*-1,2-dimethylcycloalkanes, are readily separable by gas chromatography.

Key words: fuel cell, hydrocarbon adsorption, hydrogenation, aromatization, π complex, cycloolefin, isomerization, electroreduction.

Experimental

The electrochemical cell and circuitry used in this study have been previously described (7). The circular working electrode was an LAA25 American Cyanamid type consisting of 25 mg/cm^2 platinum black bonded with 25% Teflon on a tantalum screen, and having a geometrical area of 20.2 cm^2. The counterelectrode was of the same material but with an area approximately three times that of the working electrode. Potentials were measured against the dynamic hydrogen electrode (8) which was typically 40 mV cathodic to the normal hydrogen electrode in the same electrolyte. The electrolyte, 85% H_3PO_4, was maintained at 120°C and contact to the reference electrode compartment was effected through a Luggin capillary. Water vapor losses from the electrolyte, due to the elevated working temperature, were replenished by passing humidified inert gas into the cell. Reactants were introduced into the working electrode gas cavity in an argon stream by passing the inert gas at a known flow rate through a heated saturator containing the hydrocarbon of interest. The inert gas was first passed through copper turnings heated to 425°C to remove traces of oxygen.

Reactants[1] 1,2-dimethylcyclohexene (12DMCH), 2,3-dimethylcyclohexene (23DMCH), 1,2-dimethylcyclopentene (12DMCP), and 2,3-dimethylcyclopentene (23DMCP) were used as received from K & K Laboratories Inc. Baker spectroquality *ortho*-xylene was also used as received. Gas chromatographic analysis of each reactant showed them to be of 99% purity, with no impurity found in greater than 0.2% abundance.

[1] Reactants and products will be hereafter referred to by the abbreviations in parentheses.

Retention times of and instrument sensitivities to the above reactants were determined before each run. Calibration of the instruments for the product hydrocarbons was accomplished on known samples of *cis*-1,2-dimethylcyclohexane (*cis*-DMCH), *trans*-1,2-dimethylcyclohexane (*trans*-DMCH), *cis*-1,2-dimethylcyclopentane (*cis*-DMCP), and *trans*-1,2-dimethylcyclopentane (*trans*-DMCP) obtained from K & K Laboratories Inc. Separation and identification of the cyclohexyl derivatives were effected on three six-foot columns connected in series with a helium flow of 32 cc/min at 110°C using a Hewlett-Packard 5750 gas chromatograph. The column series consisted of a UCON LB-550X on Sil-O-Cel firebrick column between two squalane on diatomite columns. Separation and identification of the cyclopentyl compounds were accomplished with a Perkin Elmer 154D Vapor Fractometer on a six-foot squalane on diatomite column at 62°C with a carrier flow of 100 cc/min. All reported ratios and percentages have been normalized according to the instrument sensitivity measurements.

A potential step technique (9) was used to prepare a reproducible electrocatalyst surface.[2] In order to oxidize the catalyst surface and any adsorbed impurities, the working electrode was held at 1.35V until the observed current had decreased to 10 mA. Next the potential was stepped cathodically to 0.05V for 20 min to reduce the catalyst oxide film formed at 1.35V. The potential was then stepped to the adsorption potential and the hydrocarbon reactant was passed over the working electrode in the inert gas stream for approximately 1 hr. Flows of 4.8×10^{-6} moles/min for 12DMCH, 8.8×10^{-6} moles/min for *ortho*-xylene, and 1.4×10^{-6} moles/min for 12DMCP were used. These flows derive from the equilibrium vapor pressures of the hydrocarbons in the inert gas stream which had passed over the reactants at 8 cc/min and 40°C. The varying flows were offset by allowing the electrocatalyst sufficient reactant contact time to achieve steady state. The contact time necessary to achieve steady state was determined by measuring the charge accumulation with anodic, galvanostatic, charging curves. Steady-state conditions were assumed when the electrocatalyst surface coverage became constant. The 60 min contact time allowed more than enough time for each reactant to achieve steady-state coverage. The long equilibration time, although necessary to achieve steady state, does present some complications. As the time of electrosorption increases, the possibility of competing reactions and adsorption site migrations also increases. Such effects might tend to obscure the specific mechanism involved in the electrode reaction. However, the requirement to achieve reproducible electrode coverage before pulse necessitates the acceptance of the above factors. The lines and working electrode gas cavity were then swept with inert gas for 30 min. After this time, gas chromatographic analysis revealed only trace amounts of reactant remained in the gas cavity. The working electrode was then galvanostatically cathodically pulsed at 1.0A and the resulting evolved hydrocarbons were trapped in 2,2-dimethylbutane, octane, or passed directly into the gas chromatograph.

Results

Dimethylcyclopentenes.—Table I shows the *cis/trans* (hereafter designated C/T) ratios obtained with 12DMCP and 23DMCP as reactants. The close correspondence of results, independent of cyclopentyl reactant, was not surprising since it was observed that an equilibrium was established between 12DMCP and 23DMCP upon passing one or the other over the electrocatalyst surface (Table I). The attainment of an equilibrium condition occurred with or without a potential applied to the working electrode. Isomerization, however, only occurred when the cycloolefin contacted the working electrode, and was not a consequence of the elevated temperature. The mean C/T ratio obtained upon cathodically desorbing the cyclopentyl compounds from an electrode which had been held at a 0.30V adsorption potential was 0.52 ($cis = 1.25 \times 10^{-8}$ moles).[3] Cyclopentane and methylcyclopentane were obtained along with *cis*- and *trans*-DMCP upon cathodic pulse and accounted for approximately 15% of the total pulse products. Passage of either 12DMCP or 23DMCP over the working electrode under potentiostatic conditions of 0.05V resulted in a mean C/T ratio of 0.47 ($cis = 2.5 \times 10^{-8}$ moles). The apparently rather small potential dependence of the C/T ratio was supported by a mean ratio of 0.51 ($cis = 9.5 \times 10^{-9}$ moles) at an adsorption potential of 0.20V.

Table I. Isomer ratios for 1,2- and 2,3-dimethylcyclopentene reactants

Reactants	0.05V (C/T)[a]	0.20V (C/T)[a]	0.30V (C/T)[a]	During adsorp. at 0.30V[b]
12DMCP	0.46	0.51	0.53	7.78
23DMCP	0.48	0.49	0.51	7.53

[a] Ratio of *cis*-1,2-dimethylcyclopentane to *trans*-1,2-dimethylcyclopentane.
[b] Ratio of 1,2-dimethylcyclopentene to 2,3-dimethylcyclopentene during reactant adsorption and before pulse.

Table II. Isomer ratios for dimethylcyclohexene and *ortho*-xylene

Reactants	0.05V (C/T)[a]	0.30V (C/T)[a]	0.50V (C/T)[a]	During adsorp. at 0.30V[b]
12DMCH	1.12	2.21	2.47	2.48
23DMCH	1.17	2.18	2.53	2.44
Ortho-xylene	1.51	2.20	2.54	—

[a] Ratio of *cis*-1,2-dimethylcyclohexane to *trans*-1,2-dimethylcyclohexane.
[b] Ratio of 1,2-dimethylcyclohexene to 2,3-dimethylcyclohexene during reactant adsorption and before pulse.

Although the study was continued at 0.50V, a competing reaction occurred at this more anodic adsorption potential which interfered with the accuracy of the C/T data, therefore these results are not reported here. This reaction involved a one carbon expansion of the cyclopentyl ring and is under further investigation (10).

Dimethylcyclohexenes.—Table II lists the isomer ratios obtained with 12DMCH and 23DMCH as reactants. As with the cyclopentyl reactants, an equilibrium was established between the 1,2- and 2,3-dimethylcycloolefin isomers upon passage of either isomer over the electrocatalyst surface. The isomerization required contact of the cycloolefins with the working electrode, with or without an applied potential. As a consequence of the equilibrium, the C/T ratios obtained at the three potentials of interest (0.05V, 0.30V, and 0.50V) were independent of cyclohexyl reactant.

In contrast to the cyclopentyl olefins, the C/T ratios obtained with 12DMCH and 23DMCH showed a high percentage of *cis* isomer upon cathodic desorption. Similar results, low C/T from cyclopentyl reactants and high C/T from cyclohexyl reactants, have been previously observed during studies of the dimethylcyclohexene isomers and the dimethylcyclopentene isomers under conditions of normal heterogeneous catalysis (4, 11). At adsorption potentials of 0.30V and 0.50V, the mean isomer ratio obtained was 2.2 ($cis = 2.9 \times 10^{-7}$ moles), respectively; whereas pass-

[2] The cell gas cavity was swept with an inert gas at a flow rate of 8-10 cc/min throughout the potential step sequence.

[3] Reported quantities are included to give orders of magnitude only, since the total amount of products varied as the electrode aged and underwent changes in surface area. However, the relative amounts of one product to another are reasonably constant. The estimated error for all reported C/T ratios is 5%.

Table III. Products occurring during adsorption and cathodic pulse of the 1,2- and 2,3-dimethylcyclohenes

0.05V	During adsorption at 0.30V and 0.50V[a]	After cathodic pulse from 0.30V and 0.50V[b]
Cis-DMCH	12DMCH	*Cis*-DMCH
Trans-DMCH	23DMCH	*Trans*-DMCH
Methylcyclohexane	*Ortho*-xylene	Methylcyclohexane
Cyclohexane		Cyclohexane
Ortho-xylene		*Ortho*-xylene

[a] Traces of *cis*- and *trans*-1,2-dimethylcyclohexane.
[b] Trace of toluene.

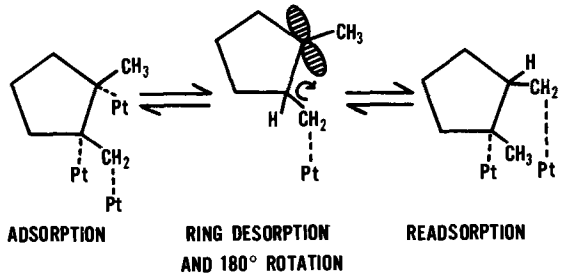

Fig. 1. Surface motion of intermediate

ing either dimethylcyclohexene isomer over the electrocatalyst potentiostated at 0.05V resulted in a C/T ratio of 1.12. The hydrocarbon products obtained during adsorption and after cathodic pulse are listed in Table III. As with the cyclopentyl reactants, monosubstituted cycloalkane and cycloalkane were obtained as pulse products and substantial quantities (2-10%) of the aromatic compound, *ortho*-xylene, were observed both during adsorption and after cathodic pulse at all potentials studied. The formation of *ortho*-xylene from 1,2-dimethylcyclohexene has also been observed during normal catalytic hydrogenation on reduced platinum oxide (11).

Ortho-xylene.—*Ortho*-xylene was studied under the same conditions as 12DMCH and 23DMCH to determine the effect of its hydrogenation on the reduced isomer ratios obtained with cyclohexyl reactants. At 0.05V, a potential at which the electrocatalyst sites should be covered by a monolayer of hydrogen or be actively evolving hydrogen, the aromatic reactant gave a higher C/T ratio than that obtained with cyclohexyl reactants. However, at 0.30V and 0.50V, the C/T ratios obtained with *ortho*-xylene as reactant were in good agreement with those obtained after reaction of the dimethylcyclohexenes.

Discussion

Although unactivated olefins and aromatic hydrocarbons are known to be difficult to reduce electrochemically (12), several investigators have reported reductions of these compounds at platinum electrodes by a variety of electrochemical methods (13-15). Little is known, however, about the nature of the adsorption process and adsorption geometry. The reduction of 12DMCP, 23DMCP, 12DMCH, and 23DMCH to their respective *cis*- or *trans*-dimethylcycloalkane seemed at first glance a simple means of studying the stereochemical aspects of electroreduction. The products and reduced isomer ratios obtained indicate that the processes occurring at the electrode are considerably more complicated than first imagined.

Dimethylcyclopentenes.—The C/T ratios obtained with 12DMCP or 23DMCP as reactants are not those expected if simple *cis* addition is to account for the mechanism of hydrogenation during cathodic desorption. By *cis* addition 12DMCP should give only *cis* product while 23DMCP should give both *cis*- and *trans*-DMCP. If the unlikely assumption is made that 23DMCP gives only the *trans* product upon pulsing, then from the 12DMCP/23DMCP equilibrium value a C/T ratio of approximately seven would be expected. Apparently the C/T ratio is not solely determined by the cycloolefin equilibrium, but is probably also a consequence of the adsorption geometry of the intermediate, and the thermodynamic stabilities of the reduced isomers (16).

To account for the high *trans* isomer percentage, the adsorption geometry must be such that the molecular motions of the adsorbed intermediate are not too severely hindered. A mechanism such as that shown in Fig. 1 could account for the *trans* isomer percentage. Adsorption of the dimethylcyclopentene reactant at the double bond and at one of the methyl groups would be the first step of this mechanism. The observation of the demethylated[4] compounds, methylcyclopentane and cyclopentane, supports the importance of electrocatalyst-methyl group interactions during the adsorption process. Such an interaction is not unexpected since the allylic positions in olefins, which the methyl groups occupy, are known to possess a high degree of reactivity. It has been postulated that olefins are capable of reversibly adsorbing by loss of a hydrogen atom at an allylic position as a mechanism for catalytic deuterium exchange (17). The next step of the mechanism would involve the addition of hydrogen to one end of the double bond followed by partial desorption, involving only the ring, and subsequent rotation of the ring 180° about the single bond between the ring and the platinum bound methyl group. Finally, readsorption of the ring would result in the plane of the molecule originally facing the electrocatalyst now facing away. Hydrogenation at this time would result in the *trans* isomer due to the two hydrogen additions occurring from opposite sides of the molecule.

Siegel and Smith (18) have proposed a mechanism for heterogeneous catalytic hydrogenation of dimethylcycloolefins whereby the migration of the double bond from the 1,2 to the 2,3 position followed by complete desorption and rotation of the molecule would yield the *trans* product. This process could not account for the high percentage of *trans* isomer obtained in this study. Since their mechanism is dependent on the cycloolefin equilibrium, a reasonable degree of correlation between the C/T and 12DMCP/23DMCP ratios would be expected. The mechanism proposed in this paper does not require any dependence of the C/T ratio on the dimethylcyclopentene equilibrium. Siegel and Smith's mechanism also differs from that proposed here in that their mechanism invokes complete molecular desorption whereas the proposed mechanism involves only partial desorption with retention of a methyl-platinum bond.

An alternate explanation of the observed results is that the C/T ratio is controlled only by the difference in activation energies between the reaction paths to the respective reduced isomers upon cathodic hydrogenation of a common adsorbed intermediate. As previously stated, olefins are believed to be capable of reversibly adsorbing by loss of a hydrogen atom at a reactive allyl carbon with direct formation of a 3-carbon π-bonded species (17). Formation of such an allylic π-bonded intermediate, as shown in Fig. 2, would not only provide a facile pathway for the observed cycloolefin isomerization, but also provides the common intermediate necessary to explain the C/T ratios on the basis of the thermodynamic stabilities of the reduced isomers. At present both alternatives

[4] The demethylation process, although not of major concern herein, might proceed via mechanisms similar to those which have been postulated to account for fragmentation in normal alkanes (3, 7). However, mechanistic interpretations based on demethylation fragments would have no significance, since it has been shown that C_1-C_6 fragments occur during the cathodic desorption of cyclohexane and benzene (23). Thus it would be impossible (unless isotopic labelling were used) to state whether any observed fragments were a result of the dimethylcycloolefin ring degradation or from demethylation of the intact ring.

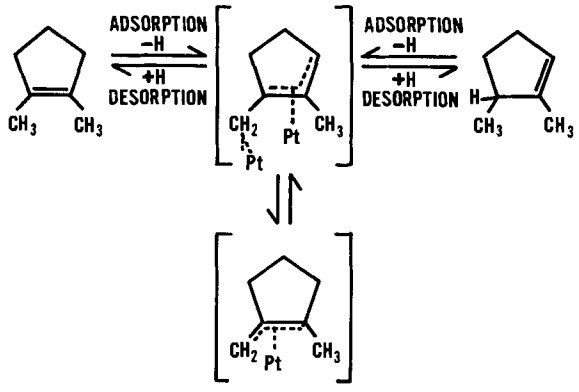

Fig. 2. Allylic cyclopentyl intermediate

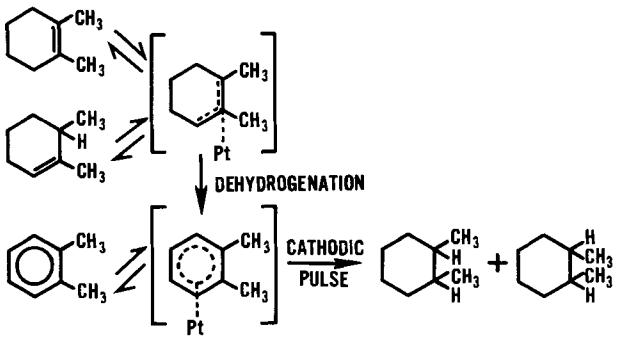

Fig. 3. Aromatic intermediate

appear equally plausible. A study of the temperature dependence of the C/T ratio now underway may ultimately determine the proper mechanism.

Dimethylcyclohexenes.—The C/T ratios obtained with 12DMCH and 23DMCH as reactants again do not appear to correspond to those expected if *cis* addition is to account for the mechanism of hydrogenation. Only in the extreme case of 23DMCH giving all *trans*-DMCH isomer could the C/T ratio be explained on the basis of the 12DMCH/23DMCH equilibrium observed during adsorption. It seems unlikely, however, that the 23DMCH adsorption geometry would be such as to make the cathodic hydrogenation stereospecific for the production of the *trans* isomer.

The presence of methylcyclohexane and cyclohexane (Table III) suggests the importance of platinum-methyl interactions and that the initial adsorption processes may be similar for both cyclopentyl and cyclohexyl reactants. If the proposed mechanism is to be applicable to both DMCP and DMCH reactants, the dimethylcyclohexene adsorption geometry must be able to be modified from the cyclopentyl adsorption geometry in such a way that desorption and rotation from the electrocatalyst surface is restricted. An increased interaction of the ring itself with the electrocatalyst could restrict its motion by effecting a stronger bond between the ring and the active surface. Such restricted ring motion could account for the higher *cis* percentages observed. In contrast to the DMCP results, the dimethylcyclohexene reactants give a C/T ratio which is markedly dependent on potential. The increase in the C/T ratio with more anodic potentials suggests that as the catalyst becomes more "electron deficient," the ring motion becomes more restricted. To account for this behavior the ring would have to possess some nucleophilic, or "electron rich," character.

The marked similarity in results obtained for 12DMCH, 23DMCH, and *ortho*-xylene suggests the existence of a common reaction path for both olefin and aromatic. It would then be required that both systems pass through a common intermediate while absorbed on the electrocatalyst. The formation of six individual carbon-platinum sigma bonds from each ring carbon to electrocatalyst sites hardly seems likely due to the steric requirements imposed on such a bond scheme. It also would seem doubtful that an energetically favored system, such as the aromatic *ortho*-xylene, could find such a surface reaction thermodynamically favorable. However an aromatic π-orbital interaction with the catalyst constitutes a distinct possibility. π complexes have been postulated for the interaction of olefinic and aromatic hydrocarbons with a platinum surface by other investigators (17, 19, 20) for deuterium exchange reactions. If the dimethylcyclohexenes adsorb by loss of a hydrogen atom from an allylic ring carbon with direct formation of a π-bonded species (16), the achievement of an energetically favored state, such as an aromatic system, could provide the impetus to dehydrogenate the cyclohexyl species. Figure 3 is a representation of the DMCH isomers and *ortho*-xylene reacting through a common π adsorbed aromatic intermediate to form *cis*- and *trans*-1,2-dimethylcyclohexane isomers. Evidence that such an aromatization is possible electrochemically can be found in the work of Luksha and Weissman (21) on anodic oxidation of various hydrocarbons at a porous platinum black, Teflon electrode. They observed that overpotential data obtained for cyclohexyl olefins were not consistent with that obtained for other olefins. Instead the cyclohexyl olefin results were close to those obtained for aromatic species. Such a similarity can be explained by dehydrogenation of the cyclohexyl compounds under anodic conditions to aromatics, with a resultant behavior more like aromatics than olefins (21). It might then be expected that under more cathodic conditions aromatization might not occur. This would explain the noncorrespondence of the C/T ratios of *ortho*-xylene, 12DMCH, and 23DMCH at 0.05V. Since the electrocatalyst would be "electron rich" at this potential, there would be no driving force to form a π-electron cloud within the adsorbed species. The increased C/T ratio with increased anodic potential might be expected for this type of intermediate, since the electrocatalyst would show increased electrophilicity as the potential becomes more anodic. Thus a stronger interaction would result between the "electron deficient" catalyst and the electron rich π-cloud of the aromatic intermediate.

Summary and Conclusions

The following similarities between the dimethylcyclohexene isomers and *ortho*-xylene have been observed upon adsorption and reaction at a fuel cell electrode. With 12DMCH or 23DMCH as reactant, *ortho*-xylene was observed both during adsorption and after cathodic pulse, suggesting a common reaction path for both species, and that the conversion from DMCH to the aromatic compound readily occurs. The C/T data obtained on cathodic pulse are virtually identical for both cycloolefin and aromatic reactants, again suggesting a common reaction path.

The differences in the data obtained for the DMCP isomers and the DMCH isomers clearly point to different processes occurring for the two ring sizes. With cyclopentyl olefins as reactants, the C/T ratio appears to be highly dependent on the ability of the adsorbed intermediate to partially desorb and rotate about the bond connecting the ring to the platinum bound methyl group. The apparent driving force is suggested to be the greater thermodynamic stability of the *trans*-1,2-dimethylcyclopentane over the *cis*-isomer (16).

The reduced product ratio obtained with the cyclohexyl reactants on the other hand appears to be controlled by a more complex interaction of the hydrocarbon with the electrocatalyst. Based on the similarities observed between the dimethylcyclohexene and

ortho-xylene reduction products, the interaction is postulated to be the formation of an aromatic π-bonded intermediate with little dependence on the thermodynamic stability of the *trans* reduced isomer over the *cis* (22).

Acknowledgment

The support of Dr. J. R. Huff is gratefully acknowledged.

Manuscript submitted March 1, 1971; revised manuscript received July 13, 1971. This was Paper 2 presented at the Atlantic City Meeting of the Society, Oct. 4-8, 1970.

Any discussion of this paper will appear in a Discussion Section to be published in the June 1972 JOURNAL.

REFERENCES

1. S. Brummer, J. Ford, and M. Turner, *J. Phys. Chem.*, **69**, 3424 (1965).
2. S. Brummer and M. Turner, *ibid.*, **71**, 2825 (1967); *ibid.*, 3494 (1967); *ibid.*, 3902 (1967).
3. L. Niedrach, *This Journal*, **111**, 1309 (1964).
4. S. Siegel and B. Dmuchovsky, *J. Am. Chem. Soc.*, **86**, 2194 (1964) and references therein.
5. F. Hartog and P. Zwietering, *J. Catalysis*, **2**, 79 (1963).
6. A. Hussey, R. Baker, and G. Keulks, *ibid.*, **10**, 258 (1968) and references therein.
7. H. Barger, Jr. and M. Savitz, *This Journal*, **115**, 686 (1968).
8. J. Giner, *ibid.*, **111**, 376 (1964).
9. S. Gilman, *J. Phys. Chem.*, **67**, 78 (1963).
10. H. Barger, Jr., G. Walker, and R. York, *J. Am. Chem. Soc.*, **93**, 2800 (1971).
11. S. Siegel, P. Thomas, and J. Holt, *J. Catalysis*, **4**, 73 (1965).
12. F. Popp and H. Schultz, *Chem. Rev.*, **62**, 19 (1962).
13. S. Langer and S. Yurchak, *This Journal*, **116**, 1228 (1969).
14. L. Burke, C. Kemball, and F. Lewis, *Trans. Faraday Soc.*, **60**, 918 (1964).
15. T. M. Beloslyudova and D. V. Sokolskii, *Elektrokhimiya*, **2**, 704 (1966).
16. M. Epstein and G. Barrow, *J. Res. Nat. Bureau Std.*, **43**, 245 (1949).
17. F. Gault, J. Rooney, and C. Kemball, *J. Catalysis*, **1**, 225 (1962).
18. S. Siegel and G. Smith, *J. Am. Chem. Soc.*, **82**, 6082 (1960).
19. J. Rooney, *J. Catalysis*, **2**, 52 (1963) and references therein.
20. J. Rooney, *Chem. Brit.*, **2**, 242 (1966).
21. E. Luksha and E. Weissmann, *This Journal*, **116**, 118 (1969).
22. E. Eliel, "Stereochemistry of Carbon Compounds," 1st ed., p. 214, McGraw-Hill Book Co., New York (1962).
23. M. Savitz and A. Hubbard, *This Journal*, **116**, 714 (1969).

The Role of Passivity in the Mechanism of Stress-Corrosion Cracking and Metal Dissolution of 18Cr-8Ni Stainless Steels in Boiling Magnesium and Lithium Chlorides

B. E. Wilde*

U. S. Steel Corporation, Applied Research Laboratory, Monroeville, Pennsylvania 15146

ABSTRACT

Electrochemical polarization measurements conducted on AISI Type 304 stainless steel in boiling lithium chloride have shown that the alloy exists in a stable state of passivity. Similar investigations in boiling magnesium chloride indicated a stable passive state, but the data were more ambiguous than the lithium chloride data because of the effect of pitting corrosion. Controlled potential corrosion studies and microchemical analysis in boiling magnesium and lithium chloride have indicated that Type 304 stainless steel is in a passive state at the potential where the alloy cracks under freely corroding conditions. Further, cation partial current density curves have shown clearly that nickel enrichment does not take place in either corrodent at the corrosion potential. The data presented strongly support the film-rupture model (slip-step dissolution) of crack initiation.

Much effort has been expended over the last 25 years to elucidate the mechanism of stress corrosion cracking (SCC) of austenitic stainless steels in chloride-containing environments (1-5). These efforts have resulted in several models proposed to explain the initiation and propagation stages of cracking and have been the subject of several recent reviews (6, 7). Two of the models rely on the presence of a film on the surface of the corroding steel and in the advancing crack tip, which subsequently affects the anodic dissolution of the metal.

Champion (8) and Logan (1) suggest that localization takes place by a rupture of a film on the surface where slip-step emergence occurs because of dislocation movement under plastic flow. Rapid anodic dissolution then occurs on the bare metal, followed by a refilming process that stifles the dissolution reaction. The propagation stage is envisaged as a repetitive repassivation and rupture process at the crack tip. This model has been criticized by various workers who believe that passivating films are not likely to form on austenitic steels in magnesium chloride (9, 10).

To overcome this criticism, Latanision and Staehle (6) have suggested that nickel enrichment may occur and result in a thin film of the relative noble nickel, which would decelerate anodic dissolution. They propose that initiation and propagation then take place by a similar film rupture and formation mechanism as proposed by Champion (8) and Logan (1). The nickel enrichment concept, although not proven, finds support from the experiments of Pickering (11), who demonstrated that such noble metal enrichment can take place in certain SCC environments on Cu/Au alloys, as a result of preferential copper dissolution.

Clearly, from the viewpoint of these two models, it is essential to establish whether or not a passive

* Electrochemical Society Active Member.
Keywords: electrode kinetics, anodic dissolution, cation partial current density, polarization and corrosion product films.

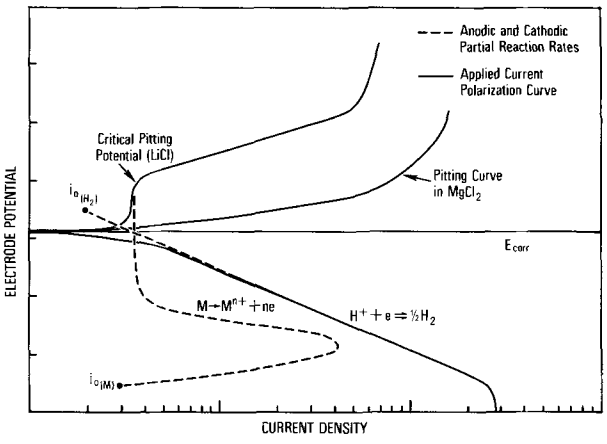

Fig. 1. Schematic representation of the partial current and applied current relationships possible for Type 304 stainless steel in $MgCl_2$ and LiCl.

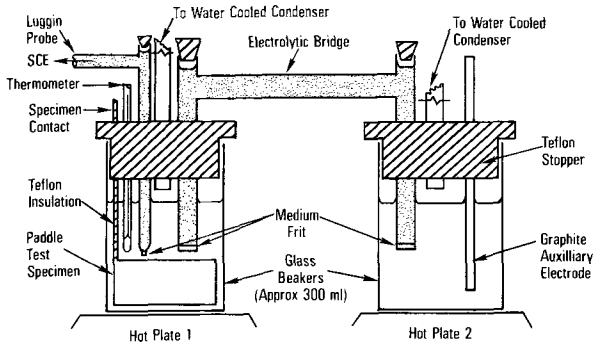

Fig. 2. Schematic representation of controlled potential corrosion apparatus.

film or nickel-rich film forms on austenitic steels exposed to concentrated chloride solutions. In an attempt to clarify these questions, Davis and Wilde (12) conducted electrochemical measurements on austenitic steels in boiling magnesium chloride and from transient polarization studies concluded that the electrode kinetic behavior of Type 304 stainless steel was consistent with the presence of a passivating film at steady state. These authors demonstrated that the shapes of cyclic polarization curves for this alloy in boiling $MgCl_2$ were identical to those obtained with the alloy in an unambiguous state of passivity; namely when exposed to oxygenated $1\overline{M}$ Na_2SO_4 acidified to *p*H 2 with H_2SO_4 at 25°C.

If the above interpretation is correct, the anodic and cathodic partial reaction rates should be similar to those depicted by the dotted lines in Fig. 1. Further, the applied current polarization behavior should be, and indeed is, as that represented by the solid lines in Fig. 1. Additional circumstantial support for this interpretation comes from the shape of the potential transients following immersion (9, 12), which are very similar to those reported elsewhere (13) for this alloy passivating in aerated dilute acid media.

A possible method to unambiguously establish the validity of this interpretation is the use of chemical analysis following corrosion at a controlled potential active to the corrosion potential, to demonstrate an active to passive transition in terms of the cation partial currents as suggested by Pickering and Byrne (14). These authors along with Condit *et al.* (15) have successfully employed this technique to construct cation partial rate curves for alloy dissolution in room-temperature electrolytes. The present communication describes the results of an attempt to extend this technique to higher temperatures and more complex electrolytes along with conventional polarization studies to establish the electrode kinetic nature of the surface of Type 304 stainless steel in boiling $MgCl_2$ (150°C) and boiling LiCl (146°C).

Materials and Experimental Work

The Type 304 stainless steel used in this study had the chemical composition shown in Table I. Specimens for electrochemical polarization studies were machined from bar stock after annealing at 1000°C for

Table I. Chemical composition of the steel used in this investigation

Composition (weight per cent)									
C	Mn	P	S	Si	Cu	Ni	Cr	Mo	N
0.052	1.25	0.023	0.018	0.52	0.08	9.75	18.8	0.36	0.036

30 min and water quenching. Cylinders (2 cm long by 0.625 cm diameter) were drilled and tapped to fit a Stern-Makrides type electrode holder (16), and were abraded down to 600 grit silicon carbide finish, ultrasonically cleaned in a detergent, washed in distilled water (7.63 megohm cm at 25°C), and hot-air-dried prior to use.

Polarization experiments were conducted with the procedures and equipment described elsewhere (17). All electrode potentials are expressed against the saturated calomel half-cell (SCE), and measured via a Luggin-Haber probe (filled with liquid and/or solid corrodent) which extended from the boiling flask to a beaker at room temperature containing a SCE in either 35% $MgCl_2$ or saturated LiCl at 25°C. No attempt was made to correct for Soret thermal potential errors (8) or those arising from liquid junctions (18, 19).

Specimens for controlled potential studies were cut out of 2 mm thick sheet stock having been heat-treated and surface-prepared as above. For maximum analytical sensitivity, the paddle specimens had a nominal surface area of 20 to 30 cm^2.

The magnesium and lithium chlorides used in this study were of reagent grade quality and were prepared as follows: (*A*) 850g $MgCl_2 \cdot 6H_2O$ were added to 70 ml water, resulting in a solution boiling at 150°C. (*B*) A saturated solution of LiCl was prepared with distilled water at 25°C. This solution boiled at 146°C.

Controlled potential corrosion tests were conducted in an apparatus shown schematically in Fig. 2. The apparatus was divided into two compartments, separated by an electrolytic bridge containing frits at both ends. By this facility the catholyte could be isolated conveniently to eliminate the effects of the chlorine liberated in the anolyte while maintaining electrolytic conductance. The porosity of the frits was such that approximately 300 mA could be passed through the bridge at 140° to 150°C. Samples were exposed for a suitable period of time to reach steady state, and approximately 100 ml of catholyte were removed by rapid pouring into a convenient beaker for analysis.

The precise analytical procedure employed is described in Appendix 1, but the following will be given in the interests of clarity. The hot catholyte sample was carefully poured into distilled water[1] to a final volume of 500 ml and cooled to room temperature. The cooled solution was transferred to the main part of the cyclic extraction vessel shown in Fig. 3. After addition of ammonium pyrolidine dithio carbamate, the complexes of iron, chromium, and nickel were precipitated by adjustment of the *p*H to 3.0, leaving the salts of magnesium and lithium in solution. The transition metal complexes were then extracted on a continuous 12 hr recycle basis into

[1] Note it is essential to pour the sample into water to avoid sputtering.

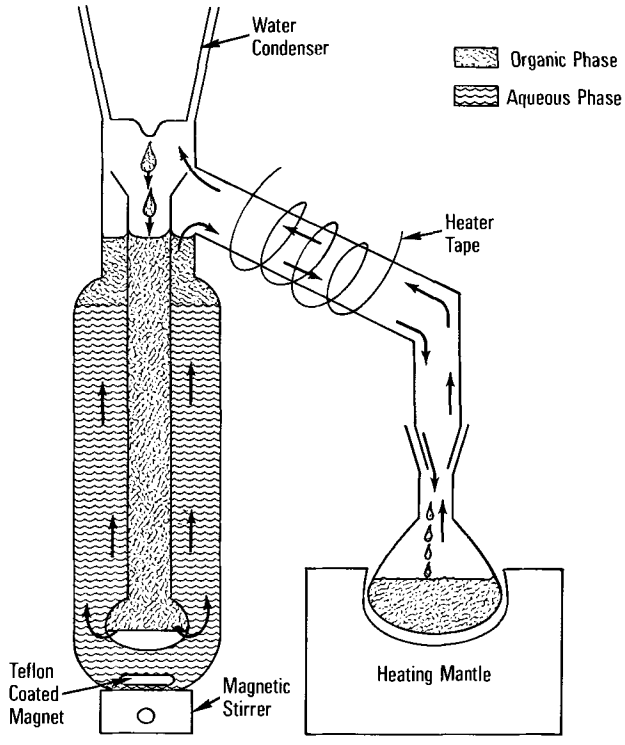

Fig. 3. Schematic representation of the continuous two-phase liquid extraction assembly used to extract Fe^{2+}, Ni^{2+}, and Cr^{3+} from $MgCl_2$ and LiCl.

methyl-isobutyl ketone. The organic extract was evaporated down to almost dryness on a hot plate, then finally to dryness in a room temperature circulating air cabinet.[2] The residue was oxidized with concentrated nitric acid three times, and evaporated to dryness to leave the nitrate salts of iron, chromium and nickel. These residues were dissolved in 5 ml concentration HNO_3 and diluted to a standard volume of 10 ml, thus effecting a concentration factor of 10.

The absorbance of the residue solutions was determined by atomic absorption spectrometric techniques (20) and compared with a standard graph to obtain the concentration of Fe, Cr, and Ni in the 10 ml aliquot. This latter figure was equal to that in the original 100 ml sample, which was converted to cation partial current densities as described in Appendix 2.

Results and Discussion

For simplicity of presentation the data will be developed and discussed in three sections: (*A*) polarization and analytical experiments in boiling $MgCl_2$, (*B*) polarization and analytical experiments in boiling LiCl, and (*C*) a brief review of how the present data fit into current mechanistic thinking.

$MgCl_2$—polarization studies.—Potentiodynamic anodic polarization curves obtained for Type 304 stainless steel in this corrodent evidenced an acceleration of the pitting observed at E_{corr}. Potentiodynamic cathodic polarization curves are shown in Fig. 4 at various sweep speeds. In all except the fastest sweep, an arrest or inflection was observed around −0.750 V_{SCE}. Recently Staehle *et al.* (21) have described the cathodic polarization behavior of some Fe-Cr-Ni alloys in boiling $MgCl_2$, where inflections and applied current minima were noted during potentiodynamic polarization. These authors have suggested that this behavior is consistent with what one would expect by cathodic polarization of a stable passive electrode, since i_{app} should decrease at the passivation potential because of the dictates of the mixed potential theory (22)

[a] It was found essential to adopt this procedure to avoid loss of the chromium chelate by distillation.

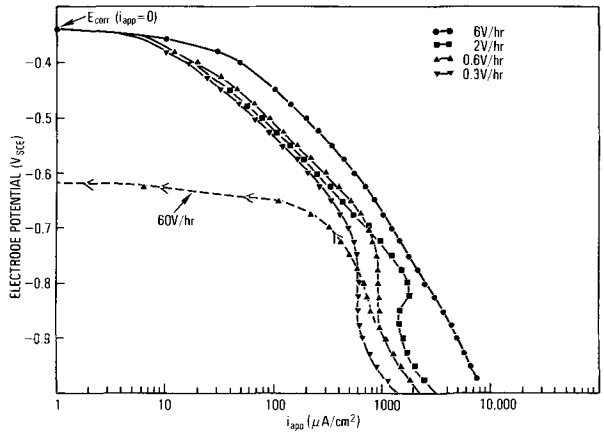

Fig. 4. Potentiodynamic cathodic polarization curves for Type 304 stainless steel in boiling $MgCl_2$.

$$i_{app} = \Sigma i_{red} - \Sigma i_{ox} \qquad [1]$$

where Σi_{red} represents the sum of all the operative cathodic partial processes and similarly Σi_{ox} represents the sum of the anodic reactions.

Since no significant minima were observed, and a wide range of potential independent applied current was found at −0.750 V_{SCE}, it must be assumed that the cathodic process has differing kinetics on the passive surface as compared with those on an active or nonpassive surface, and is not in fact represented by the one reduction process as depicted in Fig. 1.

A similar situation has been reported for the reduction of protons on an active and passive chromium surface. In this latter case Wilde and Hodge (23) have shown that one reduction curve (see Fig. 1) cannot be used to describe the electrode kinetic behavior of chromium. Significant differences were reported in exchange current density, Tafel slope, stoichiometric number and activation energy for the hydrogen evolution reaction. A typical galvanostatic cathodic polarization curve on passive chromium is shown in Fig. 5, which is similar to that obtained on Type 304 stainless steel in boiling $MgCl_2$ as shown in Fig. 6.

A possible reason for this behavior could be the changes in the transmission coefficient α_c, and exchange current density $i_{o(H_2)}$ when polarizing an initially passivated surface (which can support a limited rate of proton reduction) to a situation where the passive film becomes unstable and the surface shifts to an active state having a different α_c and $i_{o(H_2)}$.

To emphasize the existence of a passive state in $MgCl_2$, the 0.6 V/hr sweep was reversed after prolonged exposure at −1.0 V_{SCE}. As reported previously

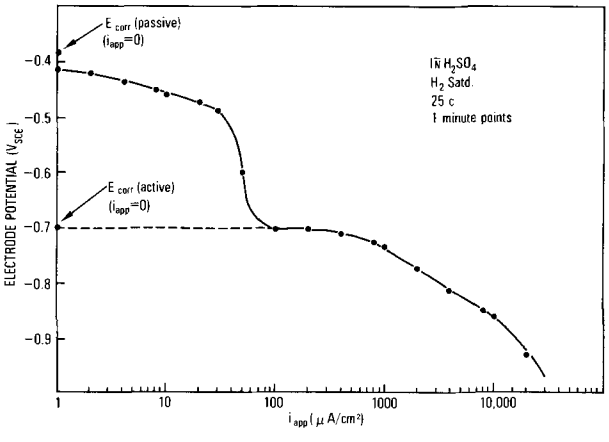

Fig. 5. Galvanostatic cathodic polarization curve on passive chromium in 1N sulfuric acid.

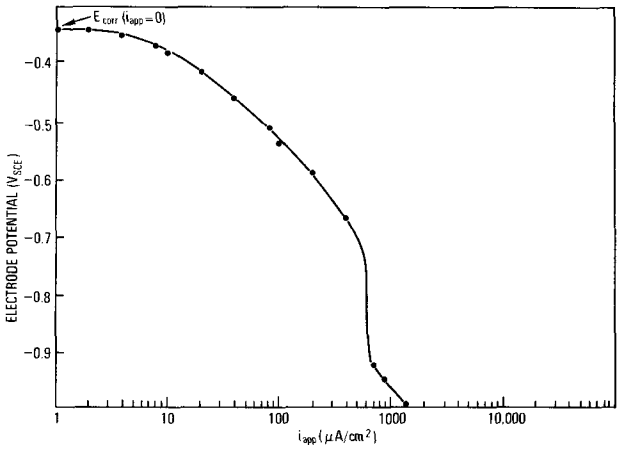

Fig. 6. Galvanostatic cathodic polarization curve for Type 304 stainless steel in boiling $MgCl_2$.

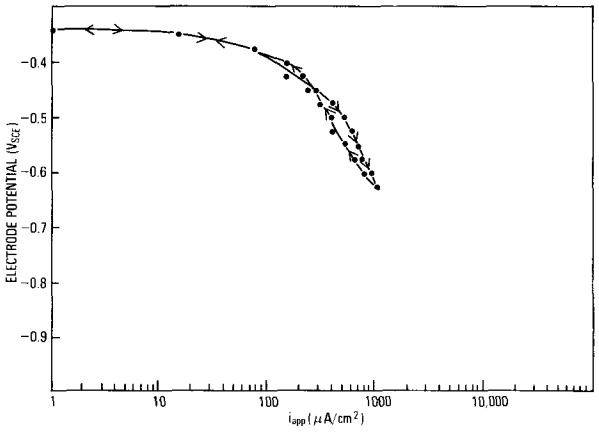

Fig. 7. Cyclic potentiodynamic cathodic polarization curve for Pt in boiling $MgCl_2$.

(12) a second more active mixed potential was noted at −0.715 V_{SCE}. Since the reverse sweep was conducted at 60 V/hr (a speed assumed to be faster than the repassivation kinetics), it is thought that this latter potential represents the corrosion potential of a film free surface. To verify that this behavior was not an experimental artifact, a cyclic cathodic-polarization experiment was conducted on a bright platinum electrode. These data are shown in Fig. 7, where virtual complete reversibility was observed with both sweeps going through the same mixed potential in contrast to the behavior of stainless steel.

Controlled potential corrosion studies.—Before the controlled potential corrosion tests, a series of synthetic standards was put through the analytical procedure to assess the efficiency of the Fe, Cr, and Ni extraction from $MgCl_2$. The results are shown in Table II along with equivalent data for LiCl. The standard solutions were prepared by suitable dilution of a stock solution containing 1.000g of pure Fe, Cr, and Ni metal dissolved in dilute HNO_3. Two significant facts are evident from Table II: first, the efficiency of recovery of pure standards was excellent for all three elements; and second, the impurity content of the $MgCl_2$ was rather high, being equivalent to the anticipated level of Fe, Cr, and Ni resulting from corrosion. This factor, although decreasing the inherent sensitivity of the measurement, did not affect the excellent recovery efficiency of standards added to $MgCl_2$ at the 50 μg level.

Table II. Check on analytical separation technique with synthetic standards

Sample	Concentration added, μg/10 ml Fe	Cr	Ni	Concentration found, μg/10 ml Fe	Cr	Ni
Reagent blank	0	0	0	<0.1	0	<0.1
Synthetic standard	10	10	10	11.3	11	10
100 ml $MgCl_2$	0	0	0	146*	4*	24*
100 ml $MgCl_2$	50	50	50	206	50	90
100 ml LiCl	0	0	0	9*	6*	6*
100 ml LiCl	10	10	10	20	16	17

* Residue analyzed after extracting 100 ml of $MgCl_2$ and LiCl and expressed as total Fe, Cr, and Ni in final 10 ml volume.

The rate of dissolution of Type 304 stainless steel in boiling $MgCl_2$ at the steady-state corrosion potential was determined every 24 hr to steady state. These data are summarized in Fig. 8, from which it is clear that a steady state dissolution rate was attained after 72 hr. Since it was essential that a steady state be reached prior to analysis so as not to encounter effects resulting from one or more components being involved in film formation, all subsequent analyses were conducted as follows. The specimen was exposed at a fixed potential for 72 hr, after which the corrodent was discarded and replaced by a fresh batch for 24 hr, the latter being analyzed for Fe, Cr, and Ni.

During experiments conducted at potentials more negative than −0.600 V_{SCE}, precipitation of magnesium hydroxide occurred as a result of the local increase in pH at the metal/electrolyte interface during prolonged hydrogen ion reduction. Typical examples of this phenomenon are shown in Fig. 9. Also of interest in Fig. 9 is the pronounced stress-corrosion cracking that took place at the sheared edges of the specimen exposed at E_{corr}. However, although not clear from Fig. 9, the majority of the attack at E_{corr} took the form of elongated pits in the midst of apparently untouched shiny bright metal. This behavior strongly resembles the breakdown of passivity observed on similar steels in chloride media at lower temperatures (24). The nature of the deposits shown in Fig. 9 varied, with the applied potential being loose and gelatinous at −0.700 V_{SCE} and becoming hard and brittle at −0.800 V_{SCE} and −0.900 V_{SCE}. Although not clear from the figure, the covered area increased markedly as the applied potential became more negative.

The results of the controlled potential tests are given in Table III and summarized as cation partial current density polarization curves in Fig. 10.

At the steady-state corrosion potential, it is evident that although the partial current density for Ni^{2+} is less than that for Fe^{2+}, it is nevertheless greater by a factor of three than the partial current density for

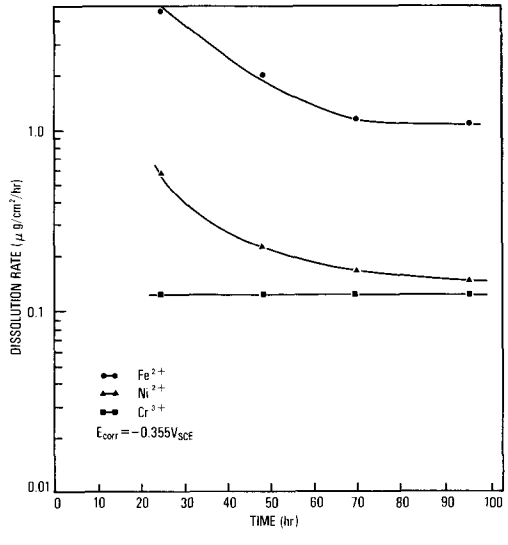

Fig. 8. The change in dissolution rate with time for Type 304 stainless steel at E_{corr} in boiling $MgCl_2$.

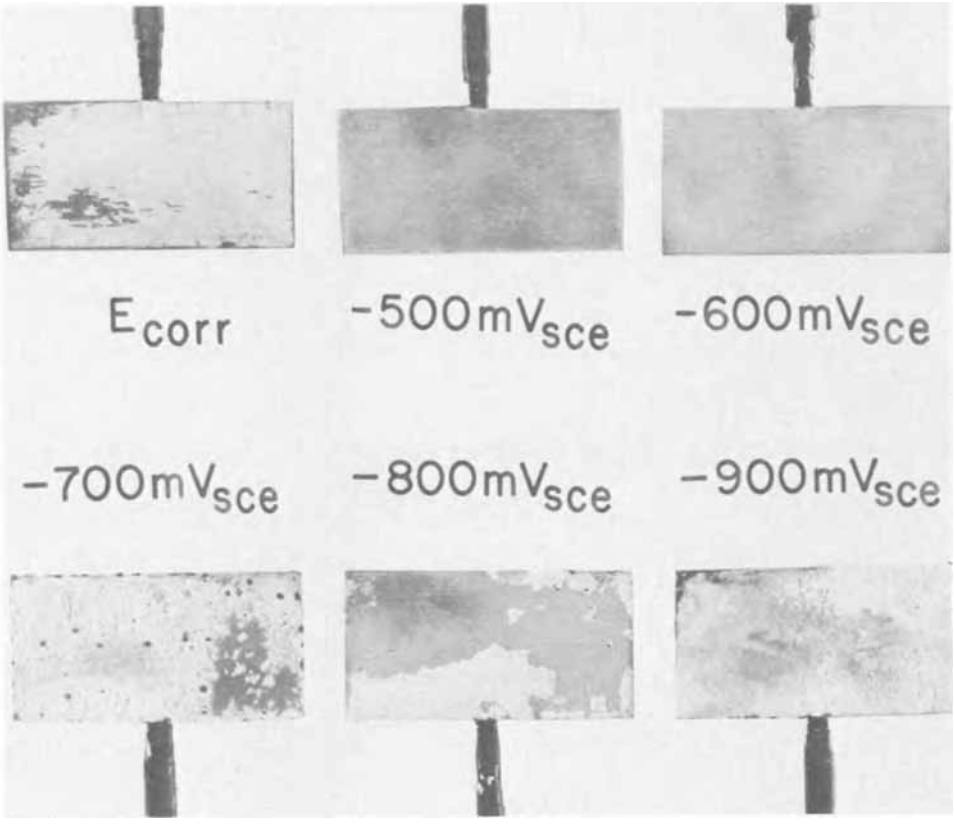

Fig. 9. Photograph of paddle specimens after exposure to boiling $MgCl_2$. Note cracks and pits at E_{corr} and $Mg(OH)_2$ deposit at potentials more active than -0.600 V_{SCE}.

Cr^{3+}. These findings are in conflict with the nickel-enrichment theory (6). Inspection of Fig. 10 indicates that a small, active-passive transition occurs at -0.700 V_{SCE}, which is shown better in Fig. 11 where the sum of the cation partial current densities is plotted. This value of the passivation potential is qualitatively very close to the potential where inflections were observed in the cathodic polarization curves (Fig. 4). In Fig. 11 a 200 mV wide passive range is shown at potential active to E_{corr}, which translates into a pitting situation at E_{corr} presumably due to the critical pitting potential E_c being more active than -0.355 V_{SCE}.

It is also of interest from the point of view of the mechanism of alloy dissolution to note the ratio at which the various components enter solution. A general summary is given in Fig. 12, where the dissolution fraction is calculated as the ratio of the cation partial current density to the total dissolution current density. Two points of interest emerge. First, during the process of passivation the dissolution fraction of Cr reaches a maximum at the passivation potential (-0.700 V_{SCE}) after which it progressively decreases as the passive film is formed to a value well below the stoichiometric level for Cr. This behavior strongly suggests that the Cr dissolution products are being incorporated into a passive film. Second, the dissolution fraction for nickel increases from the stoichiometric value at E_{corr}, passes through a maximum at -0.420 V_{SCE} and then decreases to a potential independent value (-0.600 to -0.900 V_{SCE}) of approximately 4%. It is clear from this behavior that although nickel enrichment occurs at active potentials, it does not at the steady-state corrosion potential. Therefore, it must be concluded that during stress-corrosion cracking under freely corroding conditions, nickel enrichment plays no role in the initiation of cracks.

The dissolution fraction for Fe evidenced a minimum at the passivation potential, after which Fe entered the corrodent in a manner close to the stoichiometric factor in the alloy. At the corrosion potential, however, (where pitting corrosion was observed) iron dissolves preferentially while nickel dissolves at the stoichiometric rate and chromium appears to be tied up in the passive film.

It must be pointed out that the above data should be considered as semiquantitative, in view of the experimental problems caused by magnesium hydroxide precipitation and the relative high Fe, Cr, and Ni impurity content of the $MgCl_2$. In the former case it was necessary to assume that the measured corrosion products resulted from the unfilmed area as measured with a planimeter. Implicit in this latter assumption

Table III. Results of controlled potential corrosion tests in boiling $MgCl_2$

Control potential, V_{SCE}	Partial current density, $\mu A/cm^2$ Fe	Cr	Ni	$\Sigma M \rightarrow M^+ + e$ $\mu A/cm^2$
-0.355 (E_{corr})	0.71	0.034	0.083	0.827
-0.400	0.32	0.056	0.093	0.469
-0.500	0.33	0.07	0.06	0.460
-0.600	0.37	0.12	0.02	0.510
-0.700	1.02	0.600	0.07	1.69
-0.800	0.51	0.081	0.028	0.619
-0.900	0.28	0.039	0.017	0.336

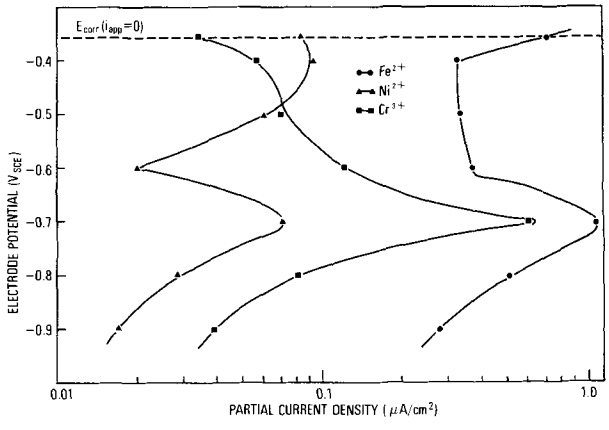

Fig. 10. Partial current dissolution curves for Fe^{2+}, Ni^{2+}, and Cr^{3+} from Type 304 stainless steel in boiling $MgCl_2$.

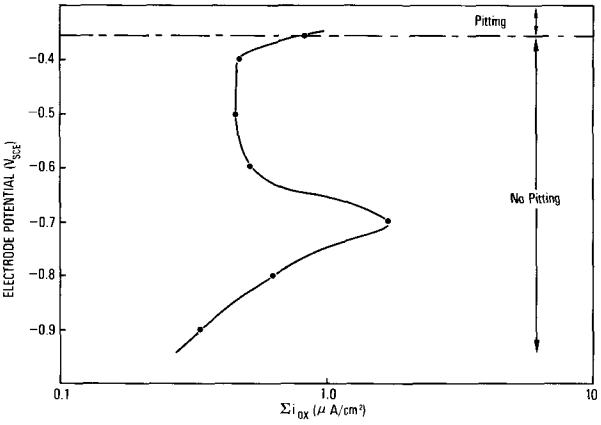

Fig. 11. Total cation partial current density plot showing active-passive type behavior of Type 304 stainless steel in boiling $MgCl_2$.

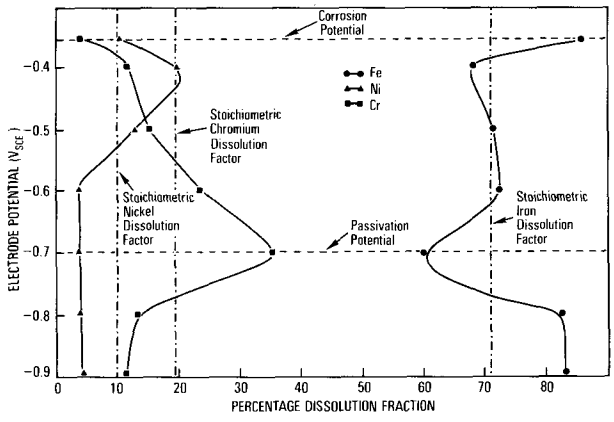

Fig. 12. Component dissolution relationships for Type 304 stainless steel in boiling magnesium chloride.

is the fact that the $Mg(OH)_2$ was an effective barrier through which dissolution could not take place.

LiCl-polarization studies.—Essentially the same experiments that were conducted in boiling $MgCl_2$ were conducted in boiling LiCl. It was felt that since this latter solution: (*i*) had a soluble hydroxide, (*ii*) was inherently of better chemical purity than $MgCl_2$, and (*iii*) caused cracking of Type 304 stainless steel in a manner identical to $MgCl_2$ and in times almost as short, experiments in this media would be less subject to the ambiguity encountered in $MgCl_2$. A summary of the stress corrosion behavior in both LiCl and $MgCl_2$ is given in Table IV along with typical cross-section metallography of cracks from both solutions in Fig. 13. Potentiostatic anodic polarization curves were constructed by using 25 mV steps every 3 min after an unstressed specimen had reached a steady-state corrosion potential. A typical curve is shown in Fig. 14, from which two points of interest emerge. First, unlike Type 304 stainless steel in $MgCl_2$, a wide range of passivity was observed. Second, at -0.360 V_{SCE} a distinct critical pitting potential (E_c) was noted. At a more noble potential than E_c rapid pitting of the specimen took place, as shown in Fig. 15.

These latter observations were of interest from the viewpoint of recent proposals which suggest that the stress-corrosion cracking of austenitic stainless steels in chloride media results from hydrogen embrittlement caused by absorption of hydrogen into the metal via proton discharge in pits (25). Although it is not possible to discount the above mechanism during crack propagation, it is clear from Fig. 14 that cracking initiated at potentials well active to E_c [where no pit-initiation was possible (26)] and it must be con-

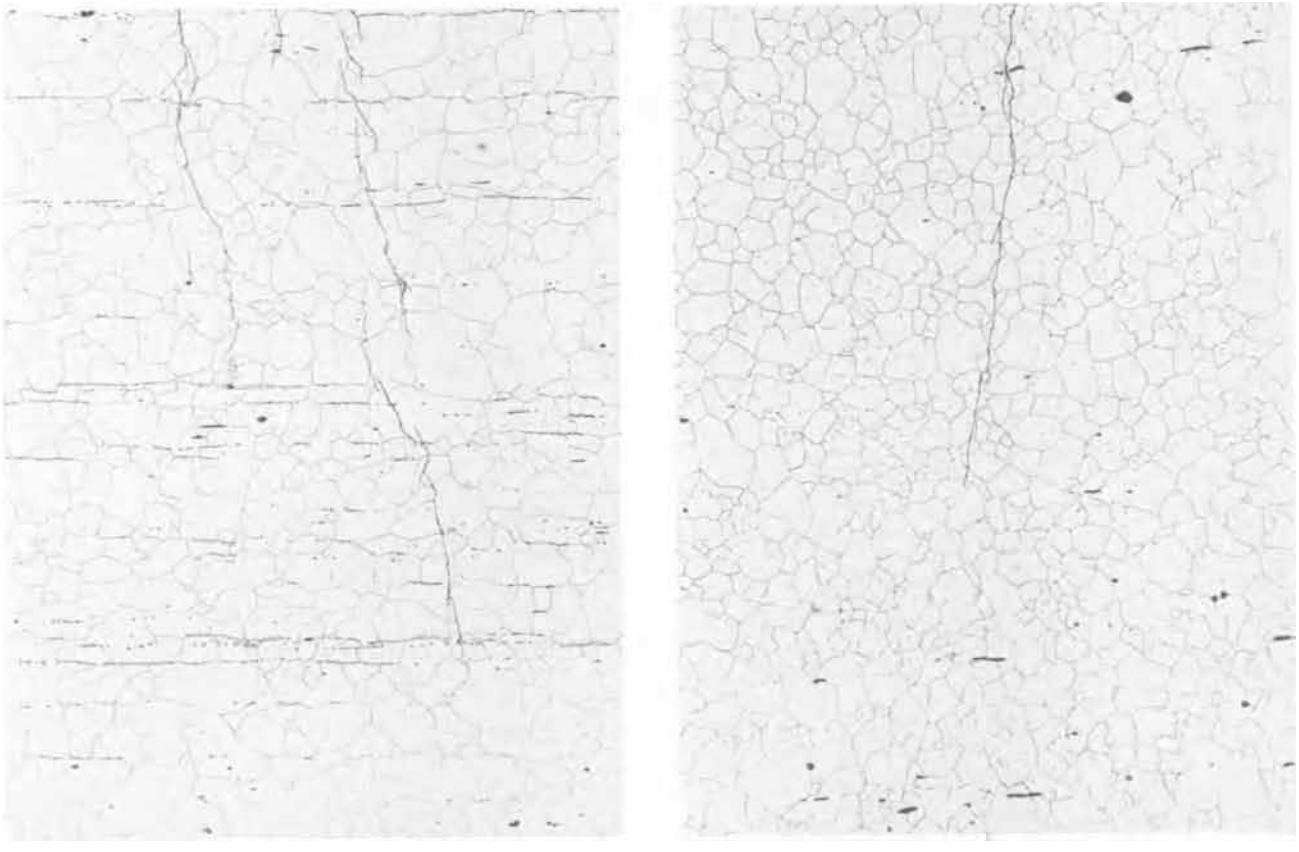

Fig. 13. Photomicrograph indicating similar nature of stress-corrosion cracks obtained on Type 304 stainless steel in $MgCl_2$ (left) and LiCl (right).

Table IV. Stress corrosion cracking data in Type 304 stainless steel in boiling $MgCl_2$ and LiCl

Corrodent	Time to failure* (hr) 1	2	3	Mean
$MgCl_2$ (BP 150°C)	3.34	4.36	5.62	4.4
LiCl (BP 146°C)	11.55	15.36	21.3	16.1

* Specimens stressed to 75% of the room temperature engineering yield strength after immersion in the hot corrodent.

cluded that pitting corrosion is not a precursor of crack initiation, at least in boiling LiCl.

A typical galvanostatic cathodic polarization curve is shown in Fig. 16, where each point represents less than 1 mV change in 15 min. It is of interest to note the influence of immersion time. Although the steady-state corrosion potential was −0.495 V_{SCE} (a condition where one would expect film formation to be complete), the kinetics of the cathodic partial process were decreased by increasing the immersion time from 20 to 48 hr. Values of the Tafel constant increased from −0.087 V/decade to −0.095 V/decade.

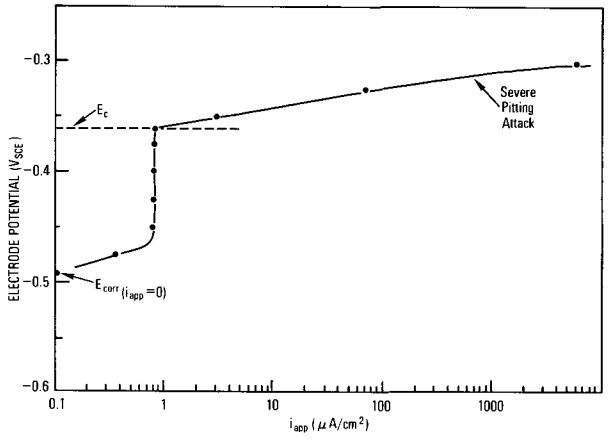

Fig. 14. Potentiostatic anodic polarization curve for Type 304 stainless steel in lithium chloride solution boiling at 146°C.

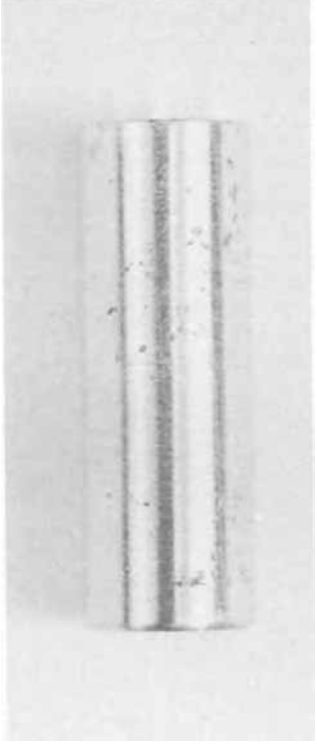

Fig. 15. Macrophotograph of anodic polarization specimen showing passivity breakdown and pit-initiation.

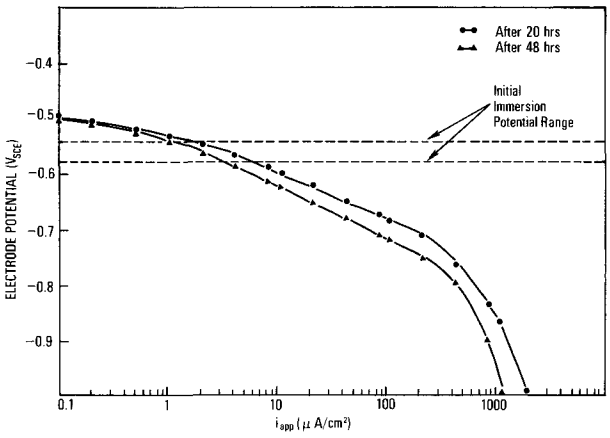

Fig. 16. Galvanostatic cathodic polarization curves for Type 304 stainless steel in boiling LiCl solution.

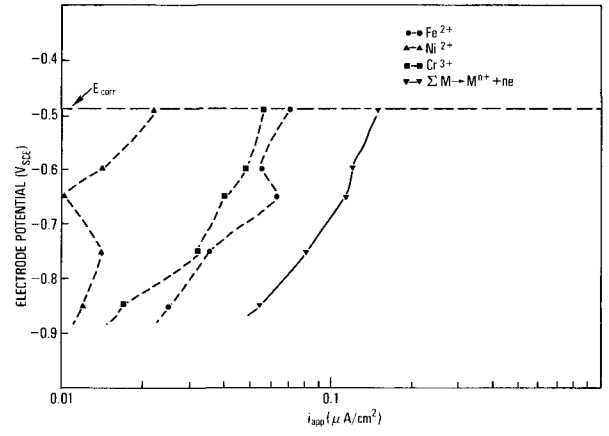

Fig. 17. Partial current dissolution curves for Fe^{2+}, Ni^{2+}, and Cr^{3+} from Type 304 stainless steel in boiling LiCl.

Potentiodynamic polarization measurements on Type 304 stainless steel in boiling LiCl at 1.5 V/hr sweep speed did not reveal any applied current minima nor the inflections noted with $MgCl_2$, and essentially duplicated the curves shown in Fig. 16. In view of the obvious state of passivity (Fig. 14) it must be concluded that the cathodic process is entirely supported on the passive film, and in this respect the electronic conductivity of the passive film formed in LiCl must be considerably different from that formed in $MgCl_2$ [possibly because of the incorporation of the cation into the film (12)].

Controlled potential corrosion studies.—The results of the controlled potential corrosion tests in boiling LiCl are summarized in Table V and Fig. 17. Unlike the situation with $MgCl_2$ no evidence of an active-passive transition was observed, indicating that Type 304 stainless steel in LiCl is in a stable passive state even at potentials as active as −0.900 V_{SCE}. By use of the data shown in Fig. 17, the component dissolution ratios were calculated as for $MgCl_2$ and are presented in Table VI.

Table V. Results of controlled potential corrosion tests in boiling LiCl

Control potential, V_{SCE}	Partial current density, μA/cm^2 Fe	Cr	Ni	$\Sigma M \rightarrow M^{n+} + ne$, μA/cm^2
−0.490 (E_{corr})	0.07	0.056	0.022	0.146
−0.600	0.055	0.048	0.014	0.117
−0.650	0.063	0.040	0.010	0.113
−0.750	0.035	0.032	0.014	0.018
−0.850	0.025	0.017	0.012	0.054

Table VI. Summary of cation dissolution fractions observed in boiling LiCl

Control potential, V_{SCE}	Percentage dissolution fraction Fe	Cr	Ni
−0.490	46.2	31.5	22.2
−0.600	47	41	12
−0.650	56	35.5	8.5
−0.750	43	39.5	17.5
−0.850	47.4	37.9	14.2
Mean	47.9	31.1	14.9

In contrast to the trends observed in $MgCl_2$, the percentage dissolution fractions for each cation were essentially constant over the potential range −0.400 to −0.850 V_{SCE}. Referring to the mean values, it appears that both Cr and Ni are dissolving at a rate higher than the stoichiometric level for the alloy. In addition, it would seem that Fe in this case is involved in film formation, in contrast to the chromium in the case of $MgCl_2$.

Mechanistic considerations.—The data presented indicate that Type 304 stainless steel in boiling $MgCl_2$ and LiCl exists in a stable state of electrochemical passivity. Furthermore, no evidence has been obtained to indicate that nickel enrichment occurs on the steel surface under freely corroding conditions. In view of these facts it appears that the initiation of stress corrosion cracks evolves from a passive film breakdown process. Although in boiling $MgCl_2$ pitting corrosion occurs in addition to cracking, it should not be concluded that the film breakdown process that leads to pitting is responsible for crack initiation. Evidence to support this point of view is presented in the boiling LiCl experiments where no pitting took place since E_c was more noble than E_{corr}.

The model recently proposed by Staehle *et al.* (21) for crack initiation involving slip-step dissolution is consistent with the experimental data obtained in this study. The picture regarding the propagation mechanism is less clear; consequently, only a limited review of the more important observations will be made.

It is becoming well established that the evolution of hydrogen from a growing crack is a common observation (27, 28). This observation indicates that at least a part of the cathodic partial process supporting crack growth occurs within the confines of the crack. These data can be understood on the basis of the observations of Marek and Hochman (29) who have reported considerable acidification of the corrodent in the crack tip when Type 304 stainless steel was cracked in boiling $MgCl_2$. This acidification process presumably occurs by a similar hydrolysis reaction to that described by Brown *et al.* (30) during crack propagation in high strength steels in sodium chloride, and allows proton reduction and hydrogen evolution to occur.

On the basis of the above evidence, it is not considered likely that the film-rupture model proposed for crack propagation by Champion (8) and Logan (1) is applicable because acid conditions at the crack tip would tend to destroy the passive film which has been shown to be stable on the surface at a bulk *p*H of 3 to 4.

Other authors have suggested that crack propagation occurs as a result of hydrogen absorption into the steel at the crack tip. Troiano and his school (31, 32) suggest that crack growth occurs because of a triaxial decohesion phenomenon essentially identical to that proposed for crack growth in high-strength steels. Unfortunately, this thesis as yet is not amenable to direct proof. However, although the absorption of hydrogen into Type 304 stainless steel under cathodic polarization in LiCl at lower temperatures has been demonstrated by electrochemical permeation experiments (33), and also during pitting corrosion of a number of stainless steels (34), it has not been established beyond doubt that a similar absorption process occurs at 146° to 150°C under freely corroding conditions. The answer to this latter question rests in the relative magnitude of the temperature coefficients of the absorption-rate constant (35) and the Tafel recombination rate constant (36), which to the best of the author's knowledge have not been determined. Another hydrogen absorption model has been proposed by Vaughan and Phalen (37) who suggest that crack propagation involves the formation of an unstable "hydride" phase under strain, which subsequently dissolves. However, there are several reported facts that are difficult to rationalize on the basis of a "hydrogen embrittlement" model.

First, Davis (38) has conducted experiments on stressed roll-bonded specimens consisting of a susceptible and a nonsusceptible steel in boiling $MgCl_2$. He demonstrated that crack propagation arrested at the interface, and changed to a lateral dissolution mode of attack along with severe crack blunting. The only difference between the two steels was 0.177% Mo and 0.014% P; the hydrogen diffusivity, corrosion rate, and corrosion potential[3] were identical when tested individually in boiling $MgCl_2$. It does not seem reasonable in view of the very similar mechanical properties and hydrogen diffusivities of the two steels that total crack arrest should occur if a bulk controlled crack propagation mechanism were operative.

Second, the fact that crack propagation can be arrested immediately on application of a cathodic current (a condition that may be expected to enhance hydrogen absorption) seems to preclude the applicability of crack growth by a "hydrogen embrittlement" mechanism. It seems more likely that although hydrogen evolution and possibly absorption does occur during crack propagation, the basic mechanism of crack growth must involve an electrochemical stage, to which hydrogen contributes little, if anything, in the case of austenitic stainless steels.

The author believes that the mechano-chemical model proposed by Hoar and Hines (9) for crack propagation remains the one most generally applicable. The acidification discussed previously would favor this latter model since it is based on the concept that deforming film-free metal (at the crack tip) dissolves more rapidly than nondeforming metal because of the effective increase in the metal exchange-current density resulting from surface disarray caused by dislocation emergence (39, 40).

Conclusion

The following conclusions may be drawn from the data presented.

1. Electrochemical polarization measurements on Type 304 stainless steel in boiling LiCl have shown that the alloy exists in a stable state of passivity.
2. Controlled potential corrosion studies and chemical analyses in boiling $MgCl_2$ and LiCl have confirmed that Type 304 stainless steel is in a passive condition.
3. Construction of cation partial current density curves has shown that nickel enrichment does not occur in the cracking or corrosion potential in either $MgCl_2$ or LiCl.
4. The data presented suggest that the probable mechanism of stress corrosion cracking of Type 304 stainless steel in boiling $MgCl_2$ and LiCl is as follows: (*a*) passive film rupture by a process of slip-step emergence. (*b*) crack propagation by a strain assisted anodic dissolution process. The basic crack propagation mechanism may be assisted by corrodent acidification with crack tip and the presence of a pre-existing susceptible path caused by metallurgical factors such as dislocation structure.

Acknowledgments

The author would like to thank Dr. H. W. Pickering (U. S. Steel Corporation) for his suggestion on the

[3] These steels were so similar galvanically speaking, that extreme difficulty was encountered during etching to find the interface.

need for this study and Dr. J. A. Davis (Bell Aerospace Inc.) who obtained some of the preliminary data in $MgCl_2$. In addition, thanks are also due to Mr. J. Finkenbine (McGill University) for assistance in developing the analytical procedures and apparatus.

Manuscript received March 23, 1971.

This paper was presented at the NACE "Research in Progress Symposium," Chicago, Illinois, March 22-26, 1971.

Any discussion of this paper will appear in a Discussion Section to be published in the June 1972 JOURNAL.

APPENDIX 1

1. Transfer 100 ml of the hot corrodent to a beaker containing 300 ml of distilled water, taking great care to avoid sputtering. Mix the solution thoroughly and cool to room temperature. Carefully transfer the contents by means of a funnel to the extraction unit through the center tube. Rinse the beaker with a further 100 ml of water and add to the extractor.
2. Accurately weigh 1g of ammonium pyrolidine dithiocarbamate (APDC), stir with 10 ml water, and add to the extractor via the funnel. Rinse out beaker and add to extractor.
3. Stir extractor slowly with magnet and carefully adjust pH to 3.0 with 10% HCl.
4. Add 185 ml methyl isobutyl ketone (MIBK) carefully down center tube. About 100 ml should overflow into boiling flask.
5. Attach condenser and extract for 12 hr.
6. Cool down and evaporate off MIBK out of boiling flask down to approximately 25 ml. Evaporate the remaining 25 ml in a room temperature forced-air cabinet.
7. Add 10 ml concentrated HNO_3 to residue and evaporate to dryness. Repeat with two more portions of HNO_3.
8. Add 5 ml conc. HNO_3, warm and cool. Transfer quantitatively to a 10 ml volumetric flask, using distilled water for the transfer.
9. Read absorption for Fe, Cr, and Ni using an atomic absorption spectrometer and read off concentration from a standard curve.

APPENDIX 2

For simplicity we shall consider the translation of M micrograms Fe obtained by analysis into an equivalent partial current on the assumption that the dissolution reaction proceeds with the formation of Fe^{2+}. Now

$$96{,}500 \text{ coulombs} \equiv 27.93 \times 10^6 \ \mu\text{gFe} \qquad [i]$$

thus M μgFe are equivalent to

$$\frac{M \times 9.65 \times 10^4}{27.93 \times 10^6} \text{ coulombs} \qquad [ii]$$

Since 1 coulomb $\equiv 10^6$ μA $\times$ 1 sec, and since M μgFe resulted from dissolution over a 24 hr period (8.65×10^4 sec), the partial current required to give the above number of coulombs is

$$\frac{M \times 9.65 \times 10^4 \times 10^6}{27.93 \times 10^{-6} \times 8.65 \times 10^{-4}} = M \times 0.0399 \ \mu\text{A} \qquad [iii]$$

Since M μgFe occurred by dissolution from a specimen of surface area Acm^2, then the Fe partial current density is simply

$$\frac{M \times 0.0399}{A} \ \mu\text{A/cm}^2 \qquad [iv]$$

In the case of the conversion of Cr and Ni analyses into partial currents, it was assumed that the dissolution products were Cr^{3+} and Ni^{2+}, thus requiring the use of 17.3 and 29.35, respectively, in the right hand portion of Eq. [i]. The factors to be used in Eq. [iv] are 0.0646 for Cr and 0.0381 for Ni.

REFERENCES

1. H. L. Logan, *J. Res. Nat. Bur. Std.*, **48**, 99 (1952).
2. T. P. Hoar and J. G. Hines, *J. Iron Steel Inst., (London)* **177**, 248 (1954).
3. C. Edeleanu, *ibid.*, **173**, 248 (1954).
4. R. B. Mears, R. H. Brown, and E. H. Dix, "Symposium on Stress Corrosion Cracking of Metals," p. 323, ASTM-AIME (1945).
5. J. C. Hodge and J. L. Miller, *Trans. Am. Soc. Metals*, **28**, 25 (1940).
6. R. M. Latanision and R. W. Staehle, "Stress Corrosion Cracking of Iron-Nickel-Chromium Alloys," in "Proceedings of Conference on Fundamental Aspects of Stress Corrosion Cracking," R. W. Staehle, A. J. Forty, and D. Van Rooyen, Editors, NACE, Houston, Texas (1969).
7. E. N. Pugh, J. A. S. Green, and A. J. Sedricks, RIAS Technical Report 69-3, March (1969).
8. F. A. Champion, "International Symposium on Stresses in Metals and Alloys," p. 468, Institute of Metals, London (1948).
9. T. P. Hoar and J. G. Hines, "Stress Corrosion Cracking and Embrittlement," W. D. Robertson, Editor, p. 107, John Wiley and Sons, New York (1956).
10. S. Barnartt and D. Van Rooyan, *This Journal*, **108**, 222 (1961).
11. H. W. Pickering, "Proceedings of Conference on Fundamental Aspects of Stress Corrosion Cracking," R. W. Staehle, A. J. Forty, and D. Van Rooyen, Editors, p. 159, NACE, Houston, Texas (1969).
12. J. A. Davis and B. E. Wilde, *This Journal*, **117**, 1348 (1970).
13. B. E. Wilde and N. D. Greene, *Corrosion*, **25**, 300 (1969).
14. H. W. Pickering and P. J. Byrne, *This Journal*, **116**, 1492 (1969).
15. D. O. Condit, R. L. Beauchamp, and R. W. Staehle, in "Proceedings of Conference on Fundamental Aspects of Stress Corrosion Cracking," R. W. Staehle, A. J. Forty, and D. Van Rooyen, Editors NACE, Houston, Texas (1969).
16. M. Stern and A. C. Makrides, *This Journal*, **107**, 782 (1960).
17. W. D. Henry and B. E. Wilde, *Corrosion*, **25**, 515 (1969).
18. P. G. Shewmon, "Diffusion in Solids," p. 189, McGraw-Hill Book Co., New York (1963).
19. E. C. Potter, "Electrochemistry Principles and Applications," p. 96, Cleaner-Hume Press Ltd., London (1961).
20. A. W. Morris, *Analytica Chimica Acta*, **42**, 397 (1968).
21. R. W. Staehle *et al.*, *Corrosion*, **26**, 451 (1970).
22. C. Wagner and W. Traud, *Z. Elektrochem.*, **44**, 391 (1938).
23. B. E. Wilde and F. G. Hodge, *Electrochim. Acta*, **14**, 619 (1969).
24. B. E. Wilde and E. Williams, To be published.
25. J. H. Shively, R. F. Hehemann, and A. R. Troiano, *Corrosion*, **23**, 215 (1967).
26. B. E. Wilde and E. Williams, *This Journal*, **117**, 775 (1970).
27. N. A. Nielsen, *J. Mater.*, **5**, 794 (1970).
28. D. A. Vaughan, D. I. Phalen, C. L. Peterson, and W. K. Boyde, *Corrosion*, **19**, 315t (1963).
29. M. Marek and R. F. Hochman, *Corrosion*, **26**, 55 (1970).
30. J. A. Smith, M. H. Peterson, and B. F. Brown, *ibid.*, **26**, 539 (1970).
31. M. B. Whiteman and A. R. Troiano, *ibid.*, **21**, 53 (1965).
32. A. R. Troiano, *Trans. ASM*, **52**, 54 (1969).
33. B. E. Wilde, In preparation.
34. B. E. Wilde, In preparation.
35. C. D. Kim and B. E. Wilde, *This Journal*, **118**, 202 (1971).
36. K. J. Vetter, "Electrochemical Kinetics, Theoretical and Experimental Aspects," p. 520, Academic Press, New York (1967).
37. D. A. Vaughan and D. I. Phalen, *Materials Eng. Quart.*, ASM, p. 39, August (1965).
38. J. A. Davis, *Corrosion*, **26**, 95 (1970).
39. T. P. Hoar, J. C. Scully, *This Journal*, **11**, 348 (1964).
40. T. P. Hoar, in "Proceedings of Conference on Fundamental Aspects of Stress Corrosion Cracking," R. W. Staehle, A. J. Forty, and D. Van Rooyen, Editors, NACE, Houston, Texas (1969).

Sectioning of Sputtered Tantalum Films by Anodic Oxide Growth in Fluoride Solutions

P. S. Wilcox

Bell-Northern Research Laboratories, Ottawa, Ontario, Canada

ABSTRACT

The growth of anodic oxides in fluoride solutions and the subsequent stripping away of this oxide has been used to section thin Ta films. The mass of tantalum removed can be controlled either by the total charge passed during anodization or by the anodization voltage. Control by the charge passed is limited by the presence of oxygen in the sputtered tantalum. This effectively makes the anodization current efficiency greater than 100%. Control using the anodization voltage method is limited by a possible difference in oxide growth field for different tantalum samples and the fact that there is an upper limit to the usable voltage. This upper limit to the anodization voltage depends on the electrolyte concentration. More concentrated solutions give a linear relation between anodization voltage and the mass of tantalum removed over a larger voltage range and is, therefore, more useful for sectioning films. However, the film thickness which can be removed is limited because the oxide growth becomes very nonuniform at higher voltages.

Anodic oxidation of tantalum in electrolytes containing fluoride ions results in an oxide film which does not adhere well to the tantalum and can be stripped easily from the metal. This property has been used to investigate diffusion near the surface in bulk Ta (1). It can also be used to section sputtered Ta so that the film properties may be determined as a function of depth into the film. The variation of resistivity, temperature coefficient of resistance, and oxygen content of sputtered Ta films has been obtained by anodization in citric acid (2). However, this technique is restricted to films up to 2000Å thick. The method of oxide stripping is a simple and rapid technique and, subject to certain limitations, is an accurate method of removing specific amounts of tantalum from the surface of a film of any thickness. The purpose of this paper is to describe the technique of oxide stripping and to discuss the limitations on the method.

Experimental

Tantalum films were sputtered onto cleaned glass (Corning 7059) substrates in a d-c diode sputtering system. The films were deposited at 3.5-4.5 kV. and 0.5 mA/cm^2 in a dynamic argon atmosphere at a pressure of approximately 30 mTorr, the deposition rate being about 200 Å/min. The films were 4000-5000Å thick with a resistivity of 170 to 250 μohm cm, consistent with their tetragonal β-Ta structure.

Film areas of approximately 16 cm^2 were anodized in solutions of HF, BaF_2, and NH_4F with concentrations ranging from 0.01 to 1.0% by weight using a platinum foil cathode approximately 1 in.^{2} in area. Unless otherwise specified the oxides were grown at a constant current density of 1 mA/cm^2 in unstirred solutions at room temperature.

The samples were weighed before anodizing (m_1), after anodizing (m_2), and after removal of the oxide (m_3) by sticking "scotch" tape to the oxide and stripping. Weights were obtained to an accuracy of 5 μg using a Mettler microbalance. Before each weight measurement the sample was rinsed in trichlorethylene and dried in a nitrogen jet.

Before the initial anodization, the samples were cleaned by ultrasonic agitation in a detergent solution followed by a deionized water rinse. Sample areas were defined on three sides by the substrate edge and on the fourth by a thick oxide stop-off grown in dilute citric acid using a Q-dope[1] mask.

Key words: tantalum, anodic oxide, oxide stripping, fluoride electrolyte.

[1] Manufactured by G. C. Electronics.

For each anodization step, the mass of tantalum stripped is given by the weight difference $m_1 - m_3$. The anodic film mass is $m_2 - m_3$ while the contribution of elements incorporated from the electrolyte during anodizing is $m_2 - m_1$. The oxide thickness was determined by stripping only part of the oxide from the tantalum and measuring the height of the resultant step using a Talysurf (Taylor Hobson Model 4). The oxide growth field was then calculated from the thickness and the voltage.

In addition to the sputtered Ta films, metallurgical grade Ta foil was sectioned in order to serve as a comparison to the sputtered films.

Results

Figure 1 shows the variation in the mass of tantalum $(m_1 - m_3)/Q$ removed per unit charge with the charge per unit area (Q/A) passed through the anodization cell. Curve b is the average of values obtained for ap-

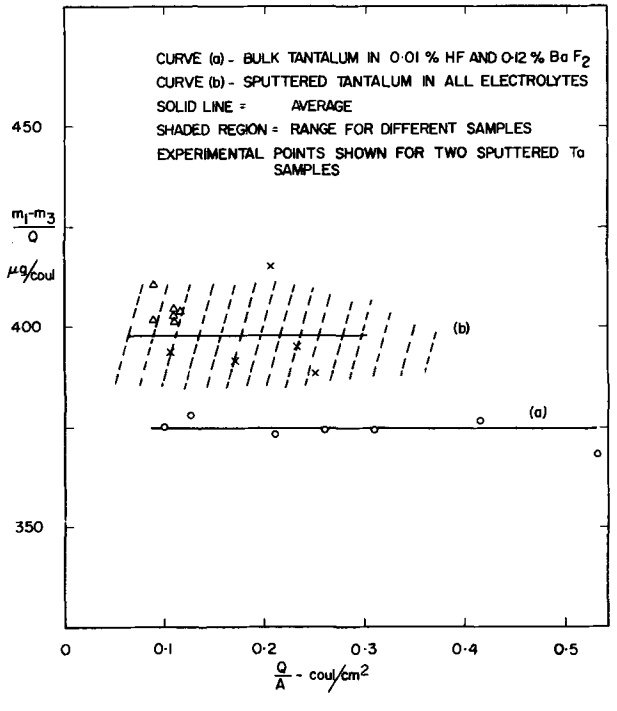

Fig. 1. Mass of tantalum removed per unit charge vs. charge density.

proximately five anodization steps on each of ten different samples. Samples were anodized in 0.01, 0.10, and 0.50% solutions of NH_4F and 0.01 and 0.12% solutions of BaF_2 (0.12% is the solubility limit of BaF_2). In some cases different solutions were used with the same sample. Experimental values are shown in Fig. 1 for two samples; the shaded region represents the mean range of values for all the different samples. No differences due to either the type or concentration of the electrolyte were observed. Curve a is the average of the experimental points obtained for anodization of tantalum foil in 0.01% HF and 0.12% BaF_2. The former electrolyte could not be used with the sputtered films because it etched the glass substrate.

For the tantalum foil, $(m_1 - m_3)/Q$ is constant at 375 μg/coulomb; whereas, the average value for sputtered films is 398 μg/coulomb.

Figure 2 shows the mass of tantalum removed per unit area per volt of anodization, $(m_1 - m_3)/AV$, plotted against the anodization voltage V. The anodization voltage is the anode-cathode potential less the ohmic voltage drop in the circuit, with no account being taken of the potential differences across the various interfaces. Curve a is the average of the values obtained for the tantalum foil which was anodized in 0.12% BaF_2. Curve b is the average of the values obtained for sputtered films anodized in all electrolytes except the 0.01% solutions of NH_4F and BaF_2. The results for the 0.01% solutions of NH_4F and BaF_2 are shown by curve c. Experimental points are shown for the same samples as in Fig. 1; the shaded region indicates the range of values for sputtered film samples anodized in all electrolytes except those of 0.01% concentration. The value of $(m_1 - m_3)AV$ for bulk tantalum is 0.98 μg/cm^2 volt. For sputtered films in stronger electrolytes the average value is 0.95 μg/cm^2 volt. The value for the sputtered films in the 0.01% electrolytes is 0.95 at $V < 60$ volts, but it decreases rapidly with increasing V.

Figure 3 shows the variation in weight gain per unit charge, $(m_2 - m_1)/Q$, on anodizing with the charge per unit area passed through the anodization cell. Curve a is the average of values for the tantalum foil anodized in 0.12% BaF_2. Curve b is the average of the values for sputtered films anodized in all electrolytes except the 0.1 and 0.5% NH_4F solutions; the average of the values for these two electrolytes is shown by curve c. Experimental points are shown for the same samples as in Fig. 1; but because of the small weights being measured, there is considerably more scatter here. The shaded regions represent the range of values for all the sputtered film samples. For all cases, no dependence of $(m_2 - m_1)/Q$ on Q/A was observed; but the values given by curves a, b, and c were 92, 83, and 60 μg/coulomb, respectively.

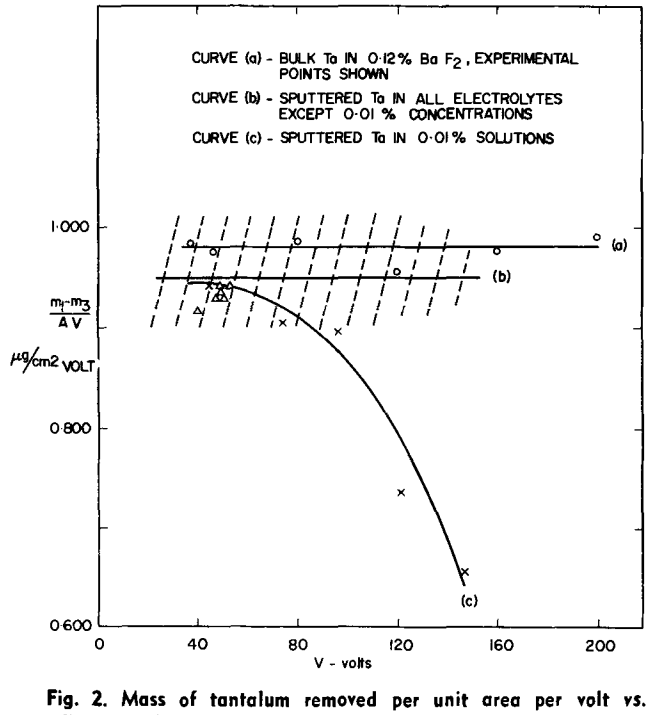

Fig. 2. Mass of tantalum removed per unit area per volt vs. anodization voltage.

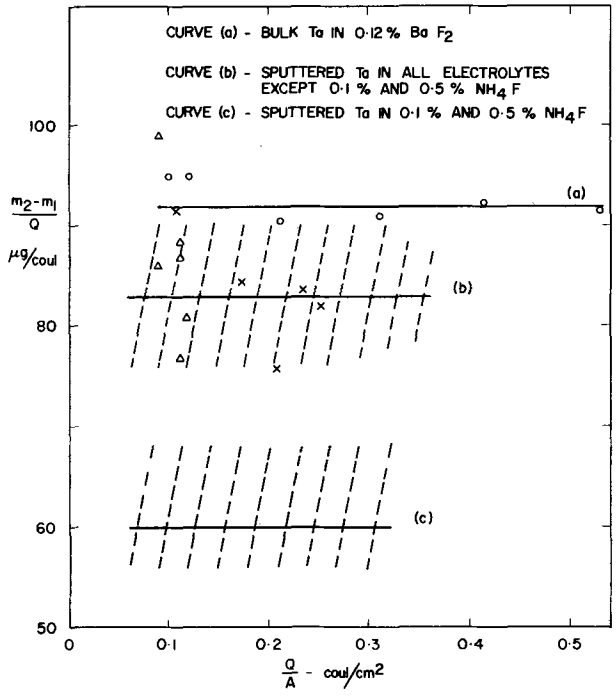

Fig. 3. Weight gain on anodizing per unit charge vs. charge density passed.

Discussion

Current efficiency.—If 100% current efficiency is assumed, then the tantalum removal rate calculated from Faraday's law is 375 μg/coulomb for the Ta foil. Since β-Ta contains about 7-15% oxygen (3) then the calculated tantalum removal rate is between 388 and 410 μg/coulomb for the sputtered films. These values agree with those shown in Fig. 1, thus the different values for bulk and sputtered Ta is due to the difference in their oxygen content. The differences between sputtered films is also probably due to differences in oxygen content.

There is a greater variation between samples when the mass of tantalum removed per unit area per anodization volt, $(m_1 - m_3)/AV$, is considered rather than the mass removed per unit charge. The maximum variation in $(m_1 - m_3)/AV$ is $\pm 6\%$, whereas the maximum variation in $(m_1 - m_3)/Q$ is $\pm 3\%$. Some of the variation in $(m_1 - m_3)/AV$ might be attributed to different oxide growth fields for the different samples. It has been observed that the field can range from 6.33 to 6.58 x 10^6 V/cm for growth in dilute citric acid (3). The higher value for bulk tantalum shown in Fig. 2 is consistent with the lower oxide growth field observed for tantalum foil. The oxide thickness measurements made with the Talysurf were accurate to only $\pm 5\%$; therefore, it could not be determined conclusively if the observed variations in the oxide growth field for anodization in dilute citric acid were carried over to oxide growth in fluoride solutions. Some of the variation between samples might also be attributed to the nonlinear growth effects and discoloration effects which are discussed in subsequent sections.

Assuming 100% current efficiency and that the weight gain on anodizing is due solely to the uptake of oxygen, then the value of $(m_2 - m_1)/Q$ should be 83 μg/coulomb. Since fluoride is incorporated in the film the actual value of $(m_2 - m_1)/Q$ should be higher.

The value of 92 μg/coulomb for bulk tantalum (Fig. 3) can be explained on the basis of part of the charge transfer being caused by fluoride ions. The average value of 83 μg/coulomb for the sputtered films, represented by curve b in Fig. 3, indicates that very little fluorine is incorporated during oxide growth on these films. It is not clear why more fluorine should be incorporated in oxides grown on bulk tantalum than on sputtered films.

The very low value of $(m_2 - m_1)/Q$, shown by curve c in Fig. 3, is peculiar to the 0.5 and 0.1% concentrations of NH_4F (but not to the 0.01% concentration). This low value cannot be attributed to a low current efficiency, because then the same effect would be observed in the value of $(m_1 - m_3)/Q$ (curve b in Fig. 1). Also, the solutions do not dissolve the substrate or tantalum under conditions of no applied voltage. One possibility is that, on anodizing, some of the tantalum or the oxide passes into the electrolyte. This would result in a low value of $(m_2 - m_1)/Q$ but would not affect the value of $(m_1 - m_3)/Q$. It is perhaps significant that the values of $(m_1 - m_3)/AV$ for 0.5% NH_4F were about 5% higher than for 0.1% NH_4F and 0.12% BaF_2. If part of the oxide is being dissolved, the anodization voltage will be reduced causing a higher value of $(m_1 - m_3)/AV$. A mechanism for the dissolution of the oxide is possible if it is assumed that some tantalum fluoride is formed, since tantalum fluoride is soluble in water. A similar effect might also occur in the other electrolytes. This possibly accounts for the difference between curve b in Fig. 3, and the value for bulk tantalum in curve a. However, it still cannot be explained why the values of $(m_2 - m_1)/Q$ should be higher for bulk tantalum nor why more concentrated solutions of NH_4F are more effective in lowering $(m_2 - m_1)/Q$.

Nonlinear anodization characteristics.—Some information on the anodization behavior can be obtained from the voltage-time (V-t) curves during the constant current anodization. For all 0.01% fluoride solutions and current densities between 0.1 and 5.0 mA/cm^2, the V-t plots for sputtered tantalum are linear to about 60V and then the voltage starts to increase faster with time. The sharply decreasing curve in Fig. 2 is a result of this. Since the amount of tantalum removed is more closely proportional to the total charged passed, $(m_1 - m_3)/AV$ will decrease when the voltage is increasing nonlinearly with time. The nonlinear V-t plots are a peculiarity of the sputtered tantalum; when tested as high as 200V, bulk tantalum does not show this effect.

Step height measurements indicated that the oxide growth field in the region of the linear V-t plots is close to that for oxide growth in dilute citric acid (*i.e.*, about 6.4 x 10^6 V/cm at 1 mA/cm^2). The nonlinear increase of voltage with time is not associated with a rapidly increasing oxide thickness but is due to an increasing average oxide growth field.

In more concentrated fluoride solutions the linearity of the V-t plots is extended to higher voltages. At the higher voltages there is, however, a tendency for the voltage to increase at a slightly lower rate with time. This is possibly indicative of increased electronic leakage. In some of the samples, it was observed that values of $(m_1 - m_3)/Q$ decreased slightly at higher voltages. This would be expected for a lowered current efficiency. In solutions of 0.12% BaF_2 and 0.1 and 0.5% NH_4F, the V-t plots for sputtered films are linear to between 130 and 140V.

The region of linearity in the V-t plots was sensitive to the properties of the sputtered material. For example, tantalum which did not adhere well to the glass substrate exhibited nonlinear V-t plots at much lower voltages. The V-t plots were also sensitive to sample history. This will be discussed under Discoloration effects.

The V-t curves are repeatable, even in the nonlinear region. For example, if an oxide is grown, stripped away, regrown, etc., several consecutive times, the V-t plots are identical for each growth stage. This repeatability was unaffected by the absence or presence of a cleaning step after each oxide stripping step. Thus, any fluoride left on the tantalum surface after stripping of the oxide seems to have no effect on the subsequent anodization. However, there is evidence that some fluoride remains on the tantalum surface. Two samples which had been anodized in 0.12 and 0.01% BaF_2, respectively, and the oxide stripped away were then anodized in dilute citric acid. The sample which had been previously anodized in 0.01% BaF_2 produced a clear colored adherent oxide, and the V-t plot was linear to at least 200V. This is what is observed when a freshly sputtered film is anodized in citric acid. For the sample which had been previously anodized in 0.12% BaF_2, the oxide was nonadherent and discolored. The V-t plot was nonlinear above 80V. When a sample was given a simple swabbing with trichlorethylene, after stripping of an oxide grown in 0.12% BaF_2, then the subsequent oxide growth in dilute citric acid exhibited V-t plots linear to a slightly higher voltage. The oxide was now more adherent (although still strippable). It was generally observed that oxides grown in the 0.01% fluoride solutions were more adherent than those grown in the concentrated solutions.

Discoloration effects.—The aforementioned repeatability of the V-t plots holds true only if no discoloration of the tantalum occurs. The type and degree of this discoloration depends on electrolyte concentration and the formation voltage. It is also associated with the discoloration of the oxide.

In all fluoride solutions with concentration of 0.1% or higher, and at voltages usually about 150V, the oxide becomes covered with circular patterns of different colored spots. It also takes on a generally splotchy and mottled appearance. In spite of this, the V-t plots are linear for the HF electrolytes. The stains left on the tantalum after removal of the oxide have a brownish appearance, and they are of a permanent nature as subsequent anodizations and strippings do not remove the stains. The V-t plots become nonlinear, for all electrolytes except HF, at lower voltages when the tantalum becomes discolored. Figure 4 is an electron micrograph of the tantalum surface, and it shows that discoloration is associated with a pitting of the surface. As indicated by the Talysurf, the top surface of the oxide is covered with bumps. This suggests accelerated oxide growth in localized regions resulting in pits in the tantalum due to excessive tantalum consumption. Vermilyea (4), on anodizing bulk Ta in a solution containing HF, found that after a time the oxide tended to separate from the metal. This may be the cause of some of the discoloration noted here.

Oxides grown in 0.01% fluoride solutions to high voltages develop a characteristic discoloration different from that of the more concentrated solutions. The oxide is smooth and uniform in appearance but has a "milky" color. The sharpness of the interference colors is reduced. This type of discoloration does not leave any stains on the tantalum surface, but examination with an optical microscope in the dark field mode indicated a very fine surface roughness on both the tantalum and the oxide. Figure 5 is an electron micrograph of the tantalum surface and it shows a uniform distribution of very small bumps. These bumps are probably associated with the fine oxide roughness which scatter the light and give the oxide its milky color. The causes of these surface roughness and discoloration effects are not known.

There is one other factor which can affect the V-t plots and that is the presence of a thick thermal oxide or an oxide formed in dilute citric acid. The effect of this initial oxide layer is to extend the linearity of the V-t plots to higher voltages and to prevent oxide stripping below a certain voltage. For example, with an initial 50V oxide (formed in dilute citric acid) it is

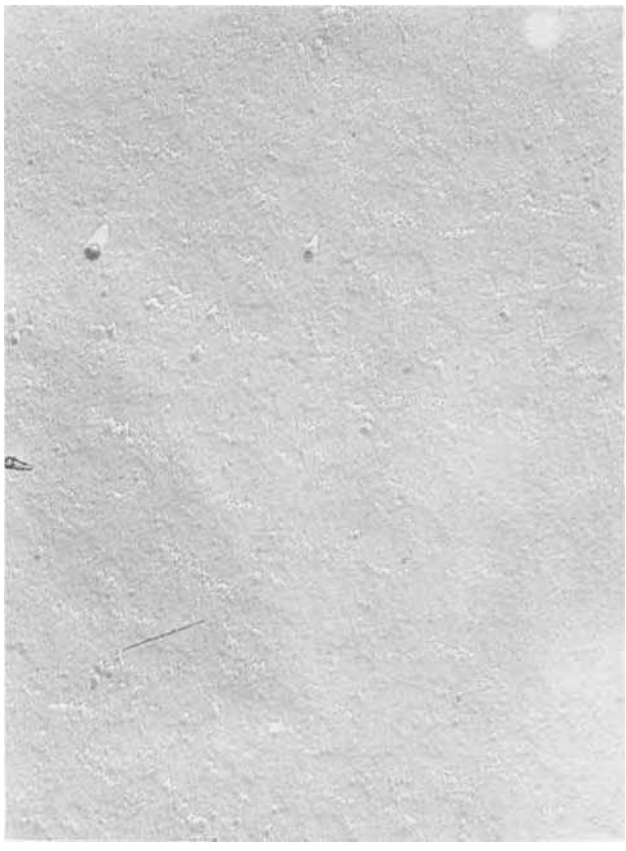

Fig. 4. Electron micrograph of a two-stage carbon replica showing pitting of a Ta surface after anodizing to >150 in 0.1% or stronger electrolytes. Latex sphere diameter, 880Å.

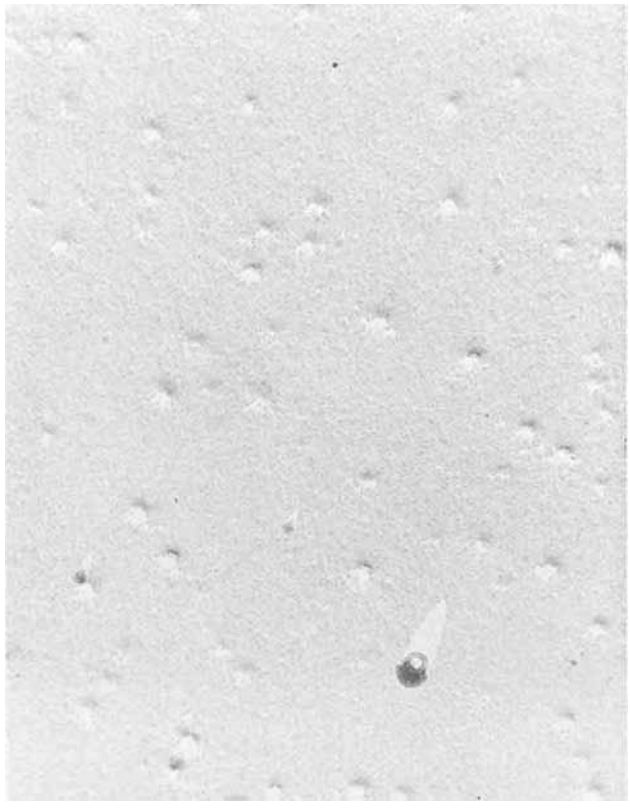

Fig. 5. Electron micrograph of a two-stage carbon replica showing bumps on a Ta surface after anodizing to high voltages in 0.01% electrolytes. Latex sphere diameter, 880Å.

necessary to anodize to about 180V in 0.1% HF before the oxide can be stripped. This upper voltage is lower for lower anodization current densities. This phenomenon might be useful in sectioning films in larger increments than is feasible by using only a fluoride solution. When using a straight fluoride solution, the largest feasible increment is about 100V. Higher voltages can result in discoloration and pitting of the tantalum. The increment could be doubled by growing an initial adherent oxide layer and subsequently anodizing it in a fluoride solution.

Conclusions

Sputtered tantalum films can be sectioned by anodizing in fluoride solutions and stripping of the anodic oxide. The mass per unit area of tantalum removed can be controlled by either the formation voltage or the total charge passed during anodization. The formation voltage is the more convenient method to control; the total charge passed method requires that the sample area be carefully defined. However, the total charge passed method, in comparison to the voltage method, is a more precise measure of the mass of tantalum removed. Also the charge passed method is less dependent on experimental conditions. The presence of oxygen in the tantalum affects the amount of tantalum removed as determined by the total charge passed.

A suitable electrolyte is a saturated (0.12%) BaF_2 solution. The electrolyte concentration is a major factor in the stripping technique. Solutions which are too dilute (<0.1%) result in nonlinear relations between the mass of tantalum removed and the formation voltage, while solutions which are too concentrated (≥0.1%) can result in excessive discoloration and pitting of the tantalum surface at higher voltages. The anodization voltage should not exceed 100V as higher voltages result in pitting of the tantalum surface which can effect subsequent anodizations.

Acknowledgments

The author would like to thank W. D. Westwood and F. C. Livermore for reviewing the manuscript and offering many helpful suggestions, and also L. E. Brosselard for preparation of the electron micrographs. This work was carried out under contract to and on behalf of Microsystems International Ltd.

Manuscript submitted March 15, 1971; revised manuscript received June 10, 1971.

Any discussion of this paper will appear in a Discussion Section to be published in the June 1972 JOURNAL.

REFERENCES

1. R. E. Pawel and T. S. Lundy, *J. Appl. Phys.*, **35**, 435 (1964).
2. F. C. Livermore, P. S. Wilcox, and W. D. Westwood, *J. Vacuum Sci. Technol.*, 17th National Symposium, Washington (1970).
3. P. S. Wilcox and W. D. Westwood, *Can. J. Phys.*, **49**, 1543 (1971).
4. D. A. Vermilyea, *This Journal*, **102**, 207 (1955).

Some Physical and Dielectric Properties of Hydrous Alumina Films

Robert S. Alwitt*

Research and Development Laboratories, Sprague Electric Company, North Adams, Massachusetts 01247

ABSTRACT

Properties of pseudoboehmite films, produced by the reaction of aluminum foil with boiling water, were studied by a variety of techniques. For reaction times of 1-30 min the average film porosity decreased linearly with increasing film weight. The surface area of freshly prepared films was similar to that of alumina gel, but decreased on aging in air. Aging in 1*N* $NaNO_3$ inhibited the area decrease. The series capacitance decreased on aging in air or nitrate electrolyte. It was determined that with the sample immersed in electrolyte the measured dielectric properties were those of an inner region impermeable to electrolyte. This layer was not the same as a typical barrier oxide. The films exhibited a low frequency dielectric dispersion. From the temperature dependence of the loss maxima the activation energy and relaxation time for the process were found to be 13.4 kcal/mole and 6.2×10^{-15} sec. These are in the range found for other systems containing hydroxyl chains or bound water.

Films produced by the reaction of aluminum or aluminum oxide with water are of importance in corrosion (1), the sealing of porous anodic oxides (2), and the manufacture of electrolytic capacitors (3). A recent paper by Vedder and Vermilyea (4) has greatly extended our knowledge of the formation and physical properties of these porous hydrous films. They identified the film produced by reaction with boiling water as pseudoboehmite, a poorly crystallized oxide with a structure close to that of boehmite but containing more hydroxyl than corresponds to the formula AlOOH. The composition of the film will vary, but reaction at 100°C has always been found to result in an average water content of 27% (3, 5, 6).

Some new data on film thickness and surface area are presented here, but the primary purpose of this paper is to report on the dielectric properties of films produced by the reaction of aluminum with boiling water. This was of interest to us because these films are often incorporated into the dielectric layer of electrolytic capacitors (3). There may be more general interest in the comparison of the dielectric properties of this film with those of other materials such as boehmite, ice, and silica gel.

Procedure

The hydrous films were grown on 99.99% Al foil specimens that had been cleaned by chemical polishing in a mixture of 15 parts 70% HNO_3 + 85 parts 85% H_3PO_4 for 2 min at 85°C, followed by a 10 min etch in 1*N* NaOH at room temperature. The reaction with boiling, distilled deionized water was in Pyrex beakers for times up to 30 min. For reaction times of 3 min or less, two samples were prepared consecutively and then the water discarded. For longer reaction times fresh water was used with each sample.

Series capacitance and RC were measured with a resistance ratio arm bridge. The maximum amplitude of the a-c signal was 0.2V rms. A large capacitance (1300 μf) was in series with the signal generator to block the passage of d-c current through the measuring cell. Two measuring cell designs were used. For measurements at a frequency of 120 Hz the foil sample was held equidistant between two platinized electrodes spaced 7 mm apart and the gap was filled with electrolyte. With this cell, small deviations in sample alignment produced some measurement errors at higher frequencies (5-10 kHz). To eliminate these errors, measurements over a range of frequencies were made with the foil sample separated from platinized electrodes by single sheets of 0.001 in. thick Benares paper. This is a paper commonly used in electrolytic capacitors. The assembly was held between glass slides and impregnated with electrolyte. A comparison of measurements in the two cells showed that no unique effects were introduced by the paper (7). For both cells the measuring electrolyte was 5.9*N* $NaNO_3$. Preliminary experiments indicated no effect from dissolved CO_2 on dielectric properties, so all solutions were in equilibrium with ambient atmosphere.

The weight of aluminum reacted at several immersion times was determined directly from the weight loss of metal substrate. The hydrous film was stripped in CrO_3-H_3PO_4 solution at 85°C for 10 min (5).

Film thickness measurements were made using aluminum evaporated on glass slides. After evaporation, the slide was immersed in boiling water for the required time, dried, and then warmed sufficiently to melt Apiezon wax rubbed across the surface at several places. After the wax hardened, the slide was immersed in the CrO_3-H_3PO_4 solution at 60°C for 30 min to dissolve the exposed hydrous film. At these conditions no undercutting of the wax took place. The wax was then dissolved in warm toluene. The height of the oxide steps so produced was measured by interferometry using the method of fringes of equal chromatic order.

Surface areas were determined from the amount of N_2 adsorbed from a 10% N_2-90% He stream at liquid N_2 temperatures. The change in N_2 content of the gas stream passing over the sample was detected by the change in thermal conductivity. Areas were calculated from the linear region of a standard BET plot over the range of N_2 relative pressures 0.13-0.33. Prior to measurement, samples were outgassed in the N_2-He stream at 85°C for 2 hr. To increase the total sample surface area the hydrous film was developed on heavily etched foil normally used in electrolytic capacitors.

Results and Discussion

Physical properties.—The weight of aluminum reacted at several immersion times is shown in Fig. 1. The crosses were calculated from the results reported by Vedder and Vermilyea (4) assuming 27% water in the films. These authors report significant inhibition of film formation by impurities leached from Pyrex. Apparently no such effects were encountered at the short reaction times used in our experiments, except perhaps with a 30 min boil.

* Electrochemical Society Active Member.

Key words: hydrous alumina film, pseudoboehmite, aluminum oxide, physical properties, dielectric properties.

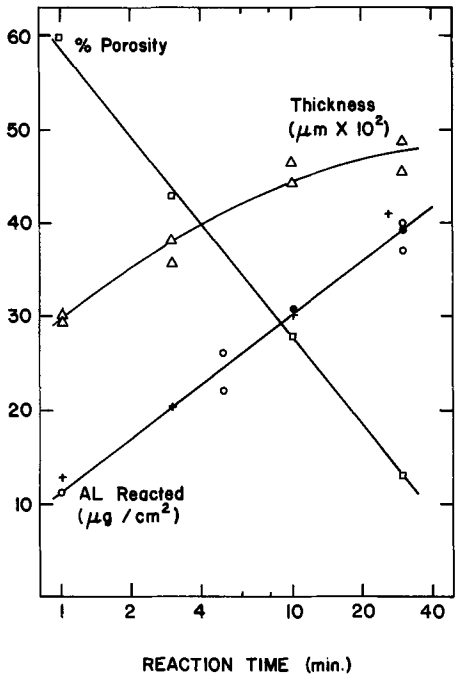

Fig. 1. Weight of Al reacted, film thickness (△), and porosity (□) of hydrous films from reaction of Al with boiling water. Weights determined with cleaned foil (○), evaporated Al on foil (●), and calculated from Fig. 18 of ref. 4 (+).

Measured film thicknesses are also recorded in Fig. 1. Vedder and Vermilyea (4) reported thicknesses of 0.3 and 0.5μ for films produced by reacting aluminum with boiling water for 9 and 40 min, respectively. They also found inhibiting effects from material leached from glass slides from some suppliers. A comparison of their values with the thicknesses in Fig. 1 suggests the absence of strong inhibiting effects in this work.

The porosity of the film was calculated from the thicknesses, weights, and specific film density of 2.4 g/cc (5). The decrease in porosity with increasing reaction time is shown in Fig. 1. The porosity decreased linearly with increasing film weight over the range covered. It would be risky to extrapolate this relationship to shorter or longer reaction times.

The surface areas of three freshly prepared oxide films (3 min reaction time) were in the range 133-154 m^2/g. This is about one-third of the values reported for pseudoboehmite precipitates (8), but within the range found for alumina gel and silica gel. Measurements on one of these samples showed the area decreased, on standing in air at 25°C and 30% RH, to 109 m^2/g after 17 hr and 78 m^2/g after 11 days. The surface area of hydrous alumina precipitate has been found to decrease similarly (9). In that case, vacuum storage prevented the area decrease but admission of water vapor produced a rapid reduction.

Because of changes in dielectric properties observed after aging in aqueous nitrate solutions, it was of interest to see what effect this treatment had on surface area. Three samples, prepared as above, were immersed in 1*N* $NaNO_3$ for 40 hr at 25°C. The surface areas were in the range 119-149 m^2/g. Thus, immersion in this electrolyte inhibited the aging process responsible for the area decrease. It might be noted that nitrate anion is not specifically adsorbed onto aluminum oxides.

Dielectric properties.—The series capacitance and resistance of a film grown during a 3-min immersion in boiling water and then aged in air at 25°C and 30% RH for about 4 hr are shown in Fig. 2. Measurements were made in 0.044*N* $NaNO_3$ (230 ohm-cm resistivity) and 5.9*N* $NaNO_3$ (10 ohm-cm). Also shown are the properties of a film grown during the aging period on a substrate that had not been exposed to

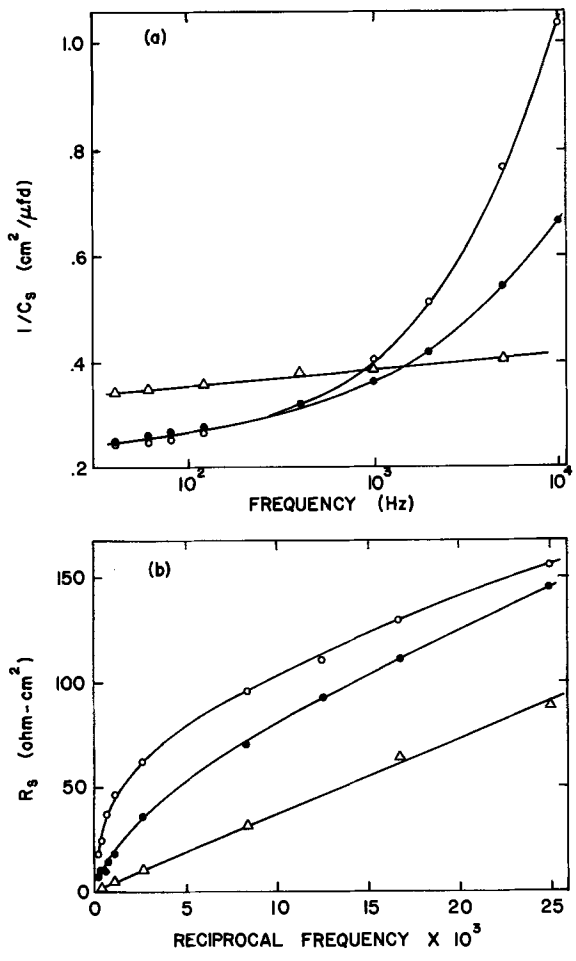

Fig. 2. Dielectric properties of oxide films in $NaNO_3$ electrolyte. Hydrous film grown during 3-min boil measured in 230 ohm-cm (○) and 10 ohm-cm (●) solutions. Air-formed oxide measured in 10 ohm-cm solution (△).

boiling water. The air-grown film exhibits the linear relationships usually found with amorphous oxide dielectric films (10) but the hydrous film does not.

The complex structure of the hydrous oxide made it necessary to establish what features of the film were reflected in the dielectric properties. First, it can be noted that for these electrolyte concentrations the smallest diffuse double layer capacitance would be about 10 $\mu f/cm^2$ (11). This is much greater than any values measured in this study. Thus, the observed capacitance is a property of the solid hydrous oxide.

The portion of the hydrous film that is permeable to electrolyte could contribute to C_s and R_s because of its colloidal properties (12), or it could contribute to R_s alone because of the tortuous electrolyte paths through the film. In both cases, R_s would be almost proportional to electrolyte resistivity at low frequencies. This was not found to be so. Instead of a 20:1 ratio, about the largest effect seen was a 15% difference (Fig. 2b). In some experiments no difference was found in R_s measured in the two solutions. This indicates that dielectric properties of the porous outer portion were not measured. The observed properties are those of a less permeable inner region. Vedder and Vermilyea (4) showed the existence of such a region but its thickness has not been established.

This compact region is obviously not the same as a typical barrier oxide, nor does it contain a layer that is the same as the air-formed oxide. The evidence for the latter point is the higher capacitance of the hydrous film at low frequencies. The only similarity noted between the hydrous and air-formed films was in the frequency dependence of R_s and C_s at low frequencies.

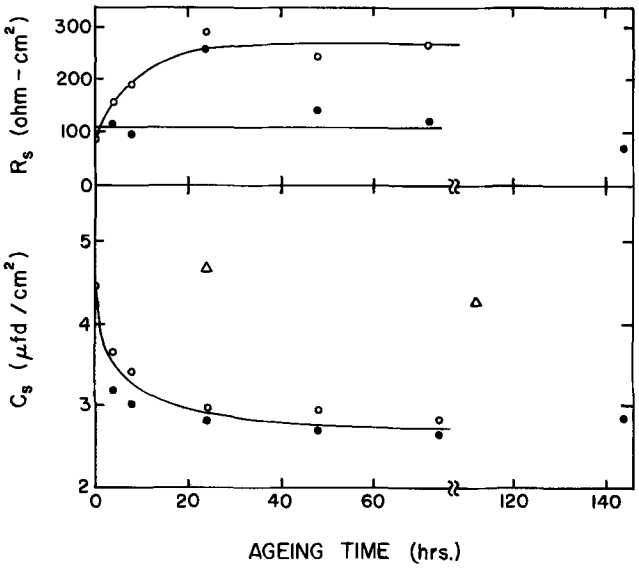

Fig. 3. Effect of aging on dielectric properties (120 Hz) of films produced in 3-min boil. Aged in air (○), 0.044*N* $NaNO_3$ (●), and vacuum (△).

The capacitance of hydrous films decreased on aging in air and in aqueous solutions (Fig. 3). Vacuum storage prevented this change. The series resistance was unchanged in the electrolyte but increased on aging in air.

The changes in the air-aged sample could be explained by a thickening of the inner compact region, although we have no knowledge that this occurred. Although there are some similarities between the changes of capacitance and surface area during aging, there is no exact parallel. This is not surprising since capacitance and surface area are properties of different portions of the hydrous oxide film. It might be noted that no changes in dielectric properties occurred on aging of anodic barrier films or air-formed oxides.

Specimens were aged for 40 hr at 25°C in nitrate electrolytes of different composition. Any changes in dielectric properties were independent of solute concentration (0.044-1.0*N* $NaNO_3$), small changes in *p*H (5.1-7.2), or cation species (Na^+, NH_4^+, R_3NH^+, R_4N^+).

The effect of a change of anion is shown in Table I. The ranges represent fifteen samples (1*N* $NaNO_3$), six samples (0.044*N* $NaNO_3$), and five samples (salicylate). The other results are the average for two specimens. The first six solutions listed had about the same effect on aging. Without more extensive tests it is not possible to say whether acetate and formate were significantly different. Borate exerted a profound effect on dielectric properties and this will be the subject of another report.

Dielectric dispersion curves were generated by calculating values for the parallel capacitance, C_p, and $C_p \tan \delta$ from the relations

$$C_p = C_s/[1 + (\tan \delta)^2] \quad [1]$$

$$\tan \delta = 2\pi f R_s C_s \quad [2]$$

Table I. Effect of anion on capacitance of aged films

Films produced by 3-min immersion in boiling water. Aged 40-48 hr at 25°C. Capacitance at 120 Hz.

Aging electrolyte	pH	C_s, μf/cm^2
1*N* sodium nitrate	6.0-6.2	2.3-3.6
0.044*N* sodium nitrate	6.0-6.2	2.3-3.7
0.1*N* sodium salicylate	6.3	2.6-3.8
0.1*N* sodium benzoate	6.3	3.0
0.1*N* ammonium tartrate	6.0	2.4
0.1*N* ammonium phosphate	6.5	2.3
0.1*N* sodium acetate	6.2	2.1
0.1*N* ammonium formate	6.4	2.0
0.2*N* ammonium borate	7.0	0.91

The real part (ϵ') and imaginary part (ϵ'') of the complex dielectric constant are

$$\epsilon' = (d/A\epsilon_r)\, C_p \quad [3]$$

$$\epsilon'' = (d/A\epsilon_r)\, C_p \tan \delta \quad [4]$$

where d and A are the dielectric thickness and area and ϵ_r is the permittivity of free space. Plots of C_p *vs.* log f and $C_p \tan \delta$ *vs.* log f are the usual dispersion curves with the ordinate multiplied by a constant.

Dispersion curves of films produced during 3- and 30-min immersions in boiling water and then aged for 40 hr in 1*N* $NaNO_3$ at 25°C are shown in Fig. 4. The lower capacitance for the 30-min film is probably the result of a thicker compact region. According to Fig. 1 the porosity of this film is only 13% compared with 44% for the 3-min film. An interesting feature of these results is the shift in the frequency of the maximum of $C_p \tan \delta$ (loss maximum).

Dielectric properties of films produced in a 3-min boil and then aged 40 hr in 1*N* $NaNO_3$ at 25°C were measured at temperatures down to −20°C in 5.9*N* $NaNO_3$. The activation energy (E_a) of the relaxation process responsible for the dielectric dispersion was obtained from the slope of a plot of log f_{max} *vs.* $1/T$ (Fig. 5), where f_{max} is the frequency of the loss maxi-

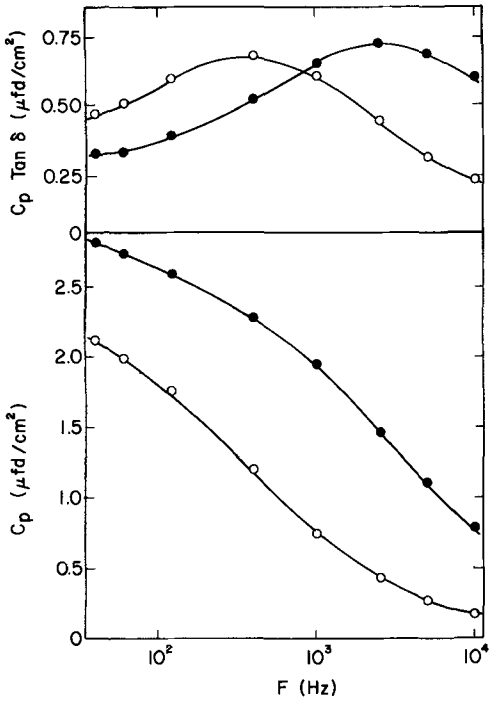

Fig. 4. Dielectric dispersion of well-aged films produced by immersion in boiling water for 3 min (●) and 30 min (○).

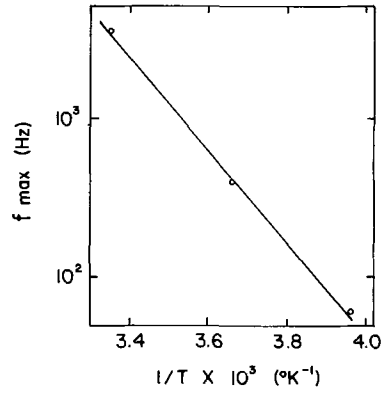

Fig. 5. Arrhenius plot for dielectric dispersion of well-aged films produced by immersion in boiling water for 3 min.

Table II. Dielectric dispersion constants for several systems

System	E_a (kcal/mole)	τ_0 (sec)	Ref.
Pseudoboehmite film	13.4	6.2×10^{-15}	This work
Boehmite	15.6	1.5×10^{-13}	14
Ice	13.2	5.3×10^{-16}	15
~2 monolayers H_2O on γ-alumina	12.6	1.9×10^{-12}	16
~4 monolayers H_2O on alumina	14.7*	4.8×10^{-16}	17
~½ monolayer H_2O on silica gel	14.2	2.5×10^{-16}	18
~1 monolayer H_2O on silica gel	11.3	5.9×10^{-15}	18

* Calculated from maxima in Fig. 1b. of ref. (17).

mum at each temperature (13). The value of E_a was 13.4 kcal/mole. The relaxation time (τ) is given by the expression

$$\tau = \tau_0 \exp (E_a/RT) \quad [5]$$

where τ_0 is a constant and $\tau \equiv (2 \pi f_{max})^{-1}$. The value of τ_0 was found to be 6.2×10^{-15} sec.

These values are close to those found for systems containing hydroxyl chains or an ordered water structure. Some examples are listed in Table II.

Mata Arjona and Fripiat (14) found that the low frequency dielectric absorption in boehmite was probably due to ion pair defects propagating along the OH chains. It is generally accepted that the low frequency relaxation process in ice is due to the movement through the lattice of orientational defects (Bjerrum defects) arising from the rotation of a proton about an oxygen position (13). There is no general agreement on the nature of the relaxation process responsible for the dielectric dispersion of ordered water layers on alumina and silica. Hasted (19) has suggested that the process may be similar to that in ice.

On the basis of E_a and τ_0 values it is not possible to choose between the above two mechanisms to account for the relaxation process in pseudoboehmite. Since pseudoboehmite has a high concentration of OH groups not constrained to the boehmite lattice, the structural factors that inhibit the propagation of Bjerrum defects in boehmite (14) may not be limiting in pseudoboehmite.

There is also a third possibility. The poor crystallinity of pseudoboehmite and its platelet structure probably result in a high density of grain boundaries in the compact inner region of the film. These could act as surfaces for termination of defect propagation. A higher charge density in these regions would produce a Maxwell-Wagner effect (13). The value of E_a would still be governed by the process for defect propagation, but τ_0 would depend on the properties and spatial distribution of grain boundaries.

Conclusions

1. Pseudoboehmite films undergo aging processes like those experienced by alumina gels.
2. The films have an impermeable inner region which determines the dielectric properties measured in aqueous electrolytes. This region does not contain a layer with the same properties as the barrier portion of an air-formed oxide.
3. The dielectric properties of the film are characteristic of systems containing hydroxyl chains or bound water.

Acknowledgment

The author is grateful to Mrs. E. Vigna for obtaining many of the laboratory results reported here.

Manuscript submitted May 17, 1971, revised manuscript received *ca.* July 3, 1971.

Any discussion of this paper will appear in a Discussion Section to be published in the June 1972 JOURNAL.

REFERENCES

1. A. J. Breen, Ph.D. Thesis, Dept. of Metallurgy, Imperial College of Science and Technology, London (1967).
2. J. P. O'Sullivan, J. A. Hockey, and G. C. Wood, *Trans. Faraday Soc.*, **65**, 535 (1969).
3. R. S. Alwitt, *This Journal*, **114**, 843 (1967).
4. W. Vedder and D. A. Vermilyea, *Trans. Faraday Soc.*, **65**, 561 (1969).
5. W. J. Bernard and J. J. Randall, Jr., *This Journal*, **107**, 483 (1960).
6. F. J. Burger and D. M. Cheseldine, *ibid.*, **107**, 1025 (1960).
7. R. S. Alwitt, *J. Phys. Chem.*, **73**, 1056 (1969); *This Journal*, **116**, 1024 (1969).
8. G. C. Bye, J. G. Robinson, and K. S. W. Sing, *J. Appl. Chem.*, **17**, 138 (1967).
9. M. R. Harris and K. S. W. Sing, *ibid.*, **7**, 397 (1957).
10. L. Young, "Anodic Oxide Films," Academic Press, New York (1961).
11. D. C. Grahame, *Chem. Rev.*, **41**, 441 (1947).
12. G. Schwarz, *J. Phys. Chem.*, **66**, 2636 (1962); R. S. Alwitt, *ibid.*, **73**, 1052 (1969).
13. V. V. Daniel, "Dielectrc Relaxation," Academic Press, New York (1967).
14. A. Mata Arjona and J. J. Fripiat, *Trans. Faraday Soc.*, **63**, 2936 (1967).
15. R. P. Auty and R. H. Cole, *J. Chem. Phys.*, **20**, 1309 (1952).
16. M. G. Baldwin and J. C. Morrow, *ibid.*, **36**, 1591 (1962).
17. J. L. Wood, *Brit. J. Appl. Phys.*, **10**, 404 (1959).
18. S. Kondo and M. Muroya, *Bull. Chem. Soc. Japan*, **42**, 1165 (1969).
19. J. B. Hasted in "Progress in Dielectrics," Vol. 3, J. B. Birks, Editor, John Wiley & Sons, Inc., New York (1961).

The Effect of Boric Acid on the Dielectric Properties of Hydrous Alumina Films

Robert S. Alwitt*

Research and Development Laboratories, Sprague Electric Company, North Adams, Massachusetts 01247

ABSTRACT

Aging hydrous aluminum oxide films in boric acid solutions accelerated the surface area decrease and markedly changed the dielectric properties of the films. The effect on dielectric properties could be removed by immersion in a borate-free electrolyte. The observations were accounted for by a model in which adsorbed borate anions increased the relaxation time of a Maxwell-Wagner process occurring within a compact inner region of the films. It was postulated that borate anions penetrated to the interior of the oxide by diffusion along platelet surfaces. Borate was the only anion found to exert this particular effect on the hydrous oxide films.

In a previous paper we presented some information on the properties of pseudoboehmite films grown on aluminum in boiling water (1). It was noted that these hydrous oxide films attained a much lower capacitance when immersed in a borate electrolyte than when immersed in other salt solutions. In this paper we present the results of an investigation of the effect of borate species on some physical and dielectric properties of pseudoboehmite films. We think these results are of intrinsic interest. In addition, they are of practical importance because borate electrolytes are widely used for forming barrier anodic oxides on aluminum and as electrical contact in the measurement of dielectric properties.

Experimental Procedure

The general procedures and materials were the same as used previously (1). All hydrous oxide films were produced by reacting aluminum foil with boiling water for 3 min. Initial work was done in solutions of 50 g/liter H_3BO_3 with NH_4OH added to give a resistivity of 230 ohm-cm and a pH about 6.5. Subsequently, solutions of H_3BO_3 were used containing 1*N* $NaNO_3$ as supporting electrolyte and adjusted to pH 6.1 ± 0.1 with NaOH and HNO_3.

Results

Surface area and weight changes.—Hydrous oxide films aged in borate electrolytes for 40 hr at 25°C had about one-half the specific surface area of films aged in nitrate electrolytes. For example, samples aged in 1*N* $NaNO_3$ + 0.2M H_3BO_3 had a specific area of 61 m^2/g, and a specimen aged in 50 g/liter H_3BO_3 had an area of 66 m^2/g. This compares with 119-149 m^2/g for films aged in 1*N* $NaNO_3$ (1). On subsequent aging in a nitrate solution there was some increase in area of borate-aged samples. For example, the area of one of the above samples increased from 66 to 83 m^2/g after immersion for 40 hr in 0.04*N* $NaNO_3$.

A sample aged in air for 11 days had a specific area of 78 m^2/g (1). This is about the same as the specific area of films aged in borate for 40 hr. This suggests that the role of borate may have been to accelerate aging to some final state.

The weight change of samples aged for several days at 25°C was measured. Each foil specimen was coated with about 900 μg of hydrous oxide. Samples aged in nitrate electrolyte gained 12-42 μg and those aged in borate gained 7-60 μg. The weight gain did not appear to be affected by the composition of the electrolyte. The reason for the gain is probably the incorporation of water as pseudoboehmite aged to bayerite and gibbsite (2).

Dielectric properties.—With samples aged in nitrate solutions it was found that the dielectric properties measured were essentially those of a compact inner portion of the film (1). With borate-aged samples this was also found to be the case, as indicated by a series resistance that was little dependent on measuring electrolyte resistivity. For example, $NaNO_3$ was added to 25 g/liter H_3BO_3 to give solutions with resistivities of 17 and 230 ohm-cm; the series resistance of samples in these solutions differed by only 25%.

The changes in series capacitance and resistance on aging in a borate solution at 25°C are illustrated in Fig. 1. After 144 hr the sample was immersed in a nitrate electrolyte. There was a rapid recovery of capacitance and resistance to values typical of "normal" aging. The reversible nature of this property is in contrast to the essentially irreversible change in surface area. This is another indication that dielectric behavior is determined in a portion of the film that does not contribute to specific surface area.

Dispersion curves are shown in Fig. 2 for samples aged for 40 hr at 25°C in solutions containing different concentrations of boric acid. The effect of increasing boric acid concentration appeared to be to shift the curves to a lower frequency range.

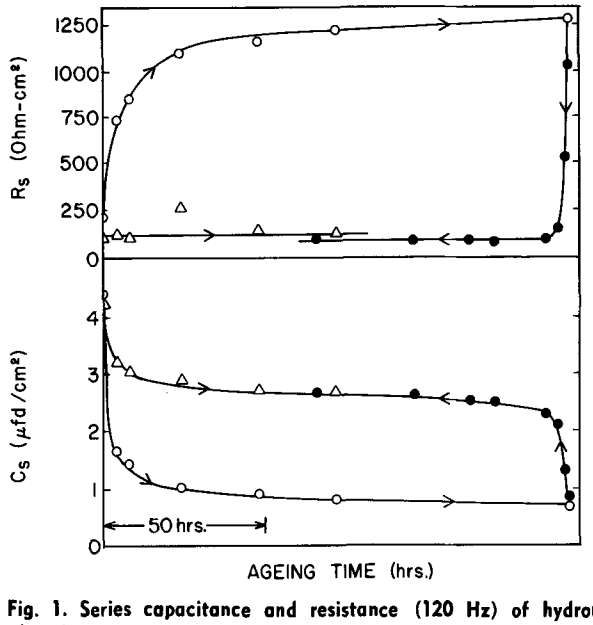

Fig. 1. Series capacitance and resistance (120 Hz) of hydrous oxide films during aging in 50 g/liter H_3BO_3 (○), followed by aging in 4.4 x $10^{-2}N$ $NaNO_3$ (●). Typical results upon direct aging in 4.4 x $10^{-2}N$ $NaNO_3$ (△) also shown.

* Electrochemical Society Active Member.

Key words: borate anions, boric acid, hydrous alumina film, pseudoboehmite, aluminum oxide, dielectric properties.

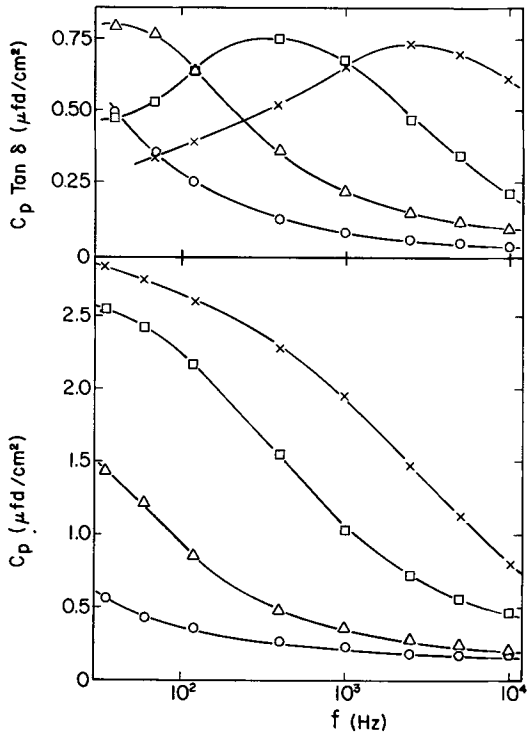

Fig. 2. Dielectric dispersion of hydrous oxide films after aging in 1*N* $NaNO_3$ containing 0.8M H_3BO_3 (○), 0.1M H_3BO_3 (△), 0.025M H_3BO_3 (□), and no H_3BO_3 (X).

It is sometimes possible to extract information about the dielectric dispersion process from a Cole-Cole diagram, which is a plot of real part *vs.* imaginary part of the complex dielectric constant, each point obtained at a different frequency (3). The data obtained at different boric acid concentrations were treated in this fashion. The results are illustrated in Fig. 3 for the data of Fig. 2. The locus of these points did not fit a simple curve, such as a semicircle or circular arc. But Fig. 3 does relate the important information that the data obtained at all boric acid concentrations, and in the absence of borate, fall on the same curve. This means that a single dispersion equation describes the dielectric behavior of these films, with the relaxation time (τ) a function of boric acid concentration. The presence of boric acid did not alter the nature of the relaxation process responsible for dielectric dispersion, but only increased the relaxation time for the process. The frequency at which maximum dielectric absorption occurs is proportional to $1/\tau$ ($2\pi f_{max} = 1/\tau$). The dependence of f_{max} on boric acid concentration is shown in Fig. 4.

Further evidence was obtained that boric acid had no effect on the nature of the relaxation process. The activation energy for the dielectric relaxation process was determined from the temperature dependence of f_{max}. Samples were aged 40 hr at 25°C in 1*N* $NaNO_3$ containing 1.25 x 10^{-2}M and 5.0 x 10^{-2}M H_3BO_3, pH 6.1. Dielectric properties were measured at several temperatures in 5.9*N* $NaNO_3$ adjusted to the same boric

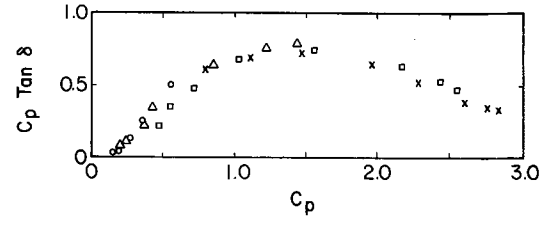

Fig. 3. Cole-Cole plot of dielectric dispersion of films aged in 1*N* $NaNO_3$ containing boric acid. Same data and symbols as in Fig. 2.

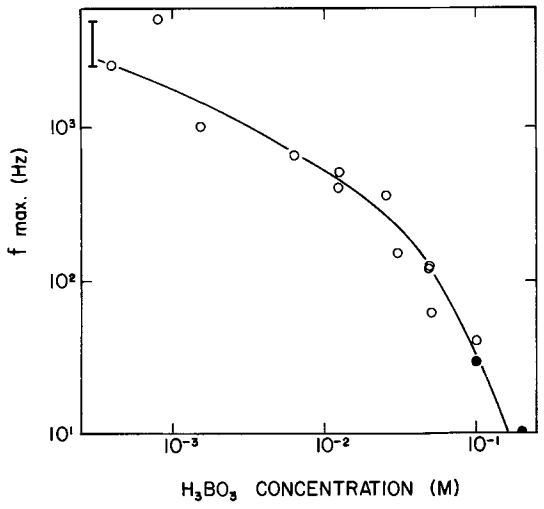

Fig. 4. Effect of boric acid concentration on f_{max}. Filled circles at lowest f_{max} represent extrapolated estimates. Vertical line to the left gives range obtained in the absence of boric acid.

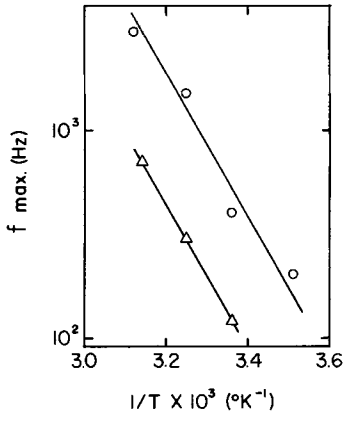

Fig. 5. Arrhenius plot for dielectric dispersion of films aged in 1*N* $NaNO_3$ containing 1.25 x 10^{-2}M H_3BO_3 (○) and 5.0 x 10^{-2}M H_3BO_3 (△).

acid concentration and *p*H as the aging solution. The results are shown in Fig. 5. At both boric acid concentrations the data could be fit by lines with a slope equivalent to an activation energy of 13.8 kcal/mole. This is not significantly different from the value of 13.4 kcal/mole obtained in 1*N* $NaNO_3$ (1). Thus, boric acid had no effect on the activation energy of the relaxation process.

In 1*N* $NaNO_3$ the *p*H of the aging solution, over the narrow range *p*H 5-7, had no effect on the dielectric properties (1). This was not the case in borate electrolytes. Samples were aged for 40 hr at 25°C in 1*N* $NaNO_3$ + 0.03M H_3BO_3 adjusted to several *p*H values. The value of f_{max} decreased with increasing *p*H as shown in Table I. A similar shift in f_{max} with *p*H was observed in 0.1M H_3BO_3.

Discussion

In a study of the point of zero charge (pzc) of pseudoboehmite (4) it was found that in the presence of borate species the pzc was shifted to more acid values. The data were interpreted as evidence for the

Table I. Effect of *p*H on f_{max}

*p*H	f_{max} (Hz)
5.5	640
6.0	150
7.1	100

specific adsorption of borate anions, both the monomer $B(OH)_4^-$ and the cyclic trimer $B_3O_3(OH)_4^-$.

It is very likely that adsorption of borate species was the cause of the marked change of dielectric properties in boric acid solutions. The species was desorbed readily in nonborate electrolytes, as judged by the reversible nature of the dielectric change (Fig. 1). If the effective adsorbed species was undissociated boric acid it would be expected that the surface would have become saturated at some concentration less than, say, 0.1M. No saturation behavior was observed, but rather there was an increased dependence of f_{max} on boric acid concentration at the highest concentrations. This suggests that adsorbed borate anions caused the observed behavior. Boric acid is only weakly dissociated; for example, at 0.2M H_3BO_3 and *p*H 6 there is less than 3% ionization. The effect of *p*H on f_{max} also supports the idea of anion adsorption controlling the dielectric behavior. With increasing *p*H the anion concentration increased and f_{max} decreased.

There is no evidence that surface charge had any effect on the measured dielectric properties. In the earlier study with nitrate solutions (1) it was found that varying *p*H and ionic strength, both of which alter surface charge, had no effect. It might be noted that the electric field induced in the oxide by a layer of adsorbed charge would be expected to be too weak to account for more than a small fraction of the observed effect [for example, see ref. (5)].

There was no general response to adsorbed anions. Phosphate and salicylate had no more effect than nitrate (1). Yet salicylate is adsorbed to about the same extent as $B(OH)_4^-$, as judged by its effect on pzc (4).

The premise that adsorbed borate anions increase the relaxation time of a process occurring within an oxide layer many atoms thick leads to interesting consequences. First, there must be some penetration of the oxide by anions. Borate anions are not particularly small so any regions open to these ions must also be penetrated by other species, ions such as nitrate which do not affect dielectric properties. Thus, the action of borate is not to affect some internal electric field but must be a localized structural effect.

Pseudoboehmite films consist of thin platelets, less than 300Å thick, extending from the metal surface (2). The platelet boundaries in the compact inner region can probably act as paths for easy diffusion into the oxide and are likely surfaces for anion penetration. It was previously suggested that increased charge density on these surfaces could give rise to a Maxwell-Wagner effect (1). Taking this into account leads to a model in which borate adsorbed on platelet surfaces increases the relaxation time of the Maxwell-Wagner effect.

For a heterogeneous dielectric consisting of a nonconducting matrix containing conductive inclusions, the relaxation time will increase if the dielectric constant of the inclusions is increased or if the conductivity of the inclusions is decreased (6). The relaxation time of the alumina/borate system varied over two orders of magnitude, so it seems more reasonable to assign the effect to a change in conductivity.

Progress falters at this point since the mechanism for conduction on the platelet surfaces is not known. Two structural features that may be important can be stated: First, the surfaces of pseudoboehmite platelets probably have the fundamental structure of the plane of OH groups in boehmite (2, 7). Second, the B-O bond distance in $B(OH)_4^-$ is given as 1.47Å by Pauling (8), so the OH-OH distance in this tetrahedral ion is about 2.42Å. This compares with 2.47 ± 0.07Å for the OHO distance in boehmite (7). Thus, it is possible for $B(OH)_4^-$ to adsorb onto two adjacent OH groups, possibly by hydrogen bonding. Other tetrahedral $>B<^{OH}_{OH}$ structures might also be bound in this fashion.

Borate solutions are widely used as electrolytes for the formation of anodic barrier oxide films on aluminum. They are unsurpassed in their ability to form to high voltages without breakdown occurring. Perhaps this is related to some unique surface properties provided by borate adsorption.

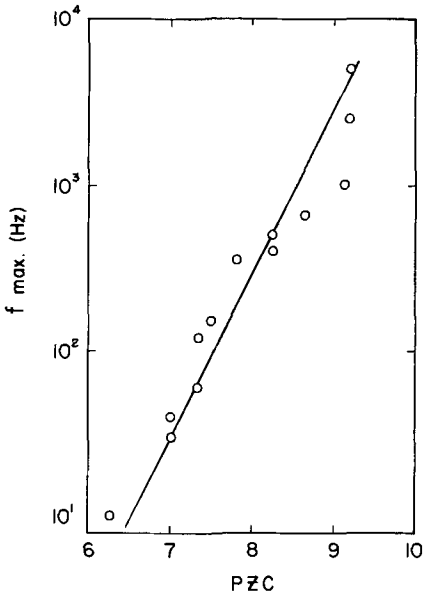

Fig. 6. Correlation between f_{max} of pseudoboehmite films and pzc of pseudoboehmite suspensions. Each point obtained at a different H_3BO_3 concentration.

Based on results at 10^{-3}M concentration, it is reported that boric acid does not inhibit the reaction of aluminum with water (9). It is our experience, corroborated by studies of Randall and Bernard (10), that at higher concentrations of boric acid this reaction is inhibited, although to a lesser extent than with phosphate. It is significant that at 10^{-3}M, boric acid does not yet affect the pzc (4) and has only a slight effect on f_{max}. This is too low a concentration for judging the interaction of boric acid with aluminum oxide.

There is a striking correlation between f_{max} of pseudoboehmite films and the pzc of pseudoboehmite suspensions. This is shown in Fig. 6. The data points are from Fig. 4 and the pzc corresponding to each boric acid concentration is from Fig. 2 in ref. 4. The line is drawn with a slope of one decade change in f_{max} per unit change in pzc. We interpret this as indicating that the dielectric relaxation time and pzc have the same functional dependence on the concentration of adsorbed borate anions.

Summary

Adsorption of borate anions onto hydrous oxide films accelerated the surface area decrease during aging and increased the relaxation time of the dielectric process in the compact inner region. It was inferred that the dielectric properties of pseudoboehmite films were governed by a Maxwell-Wagner effect and the adsorbed borate decreased the conductivity of oxide platelet surfaces.

Acknowledgment

The author is grateful to Mrs. E. Vigna for obtaining many of the laboratory results reported here.

Manuscript received May 17, 1971.

Any discussion of this paper will appear in a Discussion Section to be published in the June 1972 JOURNAL.

REFERENCES

1. R. S. Alwitt, *This Journal*, **118**, 1730 (1971).
2. W. Vedder and D. A. Vermilyea, *Trans. Faraday Soc.*, **65**, 561 (1969).
3. K. S. Cole and R. H. Cole, *J. Chem. Phys.*, **9**, 341 (1941); R. H. Cole in "Progress in Dielectrics," Vol. 3, J. B. Birks, Editor, John Wiley & Sons, Inc., New York (1961).

4. R. S. Alwitt, *J. Colloid. Sci.*, To be published.
5. V. Daniel and P. R. Vein, *Trans. Faraday Soc.*, **60**, 1310 (1964).
6. V. V. Daniel, "Dielectric Relaxation," Academic Press, New York (1967).
7. P. P. Reichertz and W. J. Yost, *J. Chem. Phys.*, **14**, 495 (1946).
8. L. Pauling, "The Nature of the Chemical Bond," 3rd ed., Cornell Univ. Press, Ithaca, New York (1960).
9. D. A. Vermilyea and W. Vedder, *Trans. Faraday Soc.*, **66**, 2644 (1970).
10. J. J. Randall, Jr. and W. J. Bernard, Private communication.

Electrochemical and Structural Aspects of Gold Electrodeposition from Dilute Solutions by Direct Current

H. Y. Cheh[1] and R. Sard*

Bell Telephone Laboratories, Incorporated, Murray Hill, New Jersey 07974

ABSTRACT

The electrochemical and structural aspects of gold deposition from dilute cyanide, citrate, and phosphate-buffered plating solutions were studied using rotating disk electrodes. Current-potential curves were recorded galvanostatically for 0.005M Au solutions at 60°C, and the morphology of deposits approximately 1μ thick, which corresponded to different regions of the i-V curves, was determined by scanning electron microscopy. Transmission electron microscopy was used to elucidate the early stages of growth (~0.1μ).

The cyanide system, which has an exchange current density of 0.82 mA/cm^2 and a transfer coefficient of 0.7, showed the greatest tendency to form an outward growth morphology consisting of fine features termed spikes. These features are responsible for the characteristic brown appearance of deposits plated under certain conditions. Increasing current density and decreasing rotation speed, in general, both favor the formation of spikes which occurs over a given range of potential (150 mV $< |\eta| <$ 300 mV) and not at a particular concentration of gold at the interface. The spikes, which are typically 0.1-1.0μ in size and $>10^8$/cm^2 in density, were also observed for deposits from the citrate system and to a much lesser extent in the phosphate system. At low overpotentials, a smooth, layer type of growth is formed.

The formation of the various morphological features is governed by the electrode potential below the limiting current density and by mass transport near or above limiting current.

The electrodeposition of gold is an extremely important aspect of electronics technology. Among the factors responsible for this development are the following beneficial properties of electrodeposited gold: high purity and conductivity, low porosity, high corrosion resistance, and the ability to form excellent thermocompression bonds. It is noteworthy that the successful device applications that utilize such properties have resulted primarily from empirical studies that were aimed at optimizing specific systems to meet certain engineering requirements (1). Consequently, there is relatively little available information regarding the electrochemical and mass transport phenomena that govern gold deposition. Moreover, the relationships between these phenomena and the structure of the resulting gold deposits have yet to be established. Such relationships are obviously important because of the well-known fact that film properties are, in general, structure sensitive (2).

The purpose of the present investigation is, therefore, to elucidate both the electrochemical and structural aspects of electrodeposited gold. The approach taken differs somewhat from previous studies of electrocrystallization (3-5) in several respects. First, all experiments were conducted on rotating disk electrodes in order to control the mass transfer characteristics of the system. Although the advantages of the RDE are well established in many fields of electrochemical research (6, 7) and some structural data were reported concerning the effects of addition agents in Ni (8) and Cu (9) deposition, it appears that this method has yet to be applied to a detailed structural study of electrocrystallization. Second, steady-state experiments under galvanostatic conditions were carried out in order to more closely approximate the type of plating carried out in device applications. Another reason for taking this approach is that the scale on which relevant physical changes occurred in the gold systems studied was on the order of 1μ or less. This precluded the use of *in situ* optical methods (10) for studying structure.

Unlike the more frequently studied systems for Cu and Ag deposition, relatively little is known about the mechanism of gold plating in various plating solutions. Maja (11) studied both the thermodynamic and electrochemical kinetic behavior of gold in cyanide gold solutions. Adsorbed $Au(CN)_2^-$ was suggested as a reaction intermediate for cathodic deposition. However, based on a recent study employing fast scan techniques, MacArthur (12) has postulated that the adsorbed intermediate species is AuCN. Polarization curves of citrate gold solutions containing $KAu(CN)_2$, citric acid, and KOH to control the pH were obtained by Taran *et al.* (13). No limiting current was observed in acid medium. This was attributed to the onset of hydrogen evolution before reaching mass transport limitations for gold deposition. Similar behavior was observed by Cheh (14) and by Visco (15).

In the present study, polarization measurements were obtained for three gold-plating systems: cyanide,

* Electrochemical Society Active Member.
[1] Present address: Department of Chemical Engineering and Applied Chemistry, Columbia University, New York, New York 10027.
Key words: electrodeposition, gold, structure.

Table I. Composition and properties* of plating solutions

	g/liter	M	pH	Kinematic viscosity ν, cm²/sec	Diffusivity of $Au(CN)_2^-$ D, cm²/sec
1. Cyanide gold solution**					
$KAu(CN)_2$	1.5	0.0052	10.8	0.00469	1.68×10^{-5}
KCN	35	0.54			
2. Citrate gold solution					
$KAu(CN)_2$	1.3	0.0045	5.0	0.00518	1.67×10^{-5}
$(NH_4)_2HC_6H_5O_7$	50	0.22			
3. Phosphate gold solution					
$KAu(CN)_2$	1.3	0.0045			
K_2HPO_4	120	0.69	7.5	0.00604	1.63×10^{-5}
KH_2PO_4	30	0.22			

* Properties measured at 60°C as reported in Ref. (16).
** This solution was the one normally used for gold plating experiments in the cyanide system. However, in the structural study one set of experiments was carried out in a solution with twice the gold concentration (0.01M).

citrate, and phosphate. These data were used as a guide to study the structural aspects of electrodeposited gold which was accomplished by scanning and transmission electron microscopy.

Experimental

Electrochemical measurements.—Three dilute gold-plating solutions, of the type normally used in a strike process (16), were used for these experiments. The compositions of these solutions are given in Table I. Solutions were purged with nitrogen gas in order to minimize oxygen concentration. The *p*H, kinematic viscosity, and diffusion coefficient of $Au(CN)_2^-$ for these solutions, which were reported previously by Cheh (16), are also included in Table I.

Polarization curves were obtained galvanostatically on a gold RDE at 60°C. A copper cylinder of 0.635 cm diam was imbedded in an epoxy sleeve and gold-plated. A high-speed rotator[2] was used to drive the electrode at known constant speeds. A coil of platinum was used as the counterelectrode. A saturated calomel electrode was placed in the reference compartment of the cell, which is illustrated in Fig. 1. Constant currents were applied by connecting a decade resistance box and a 45V battery in series with the plating cell. The potential between the cathode and the reference electrode was measured and recorded on a Varian Model G 22A recorder with an input impedance of 1 megohm at 10V span.

Physical measurements.—A necessary requirement of any structural study involving metal deposition under a wide variety of conditions is that the substrate surfaces must be well defined, reproducible, and relatively easy to prepare. These considerations led to the adoption of the following procedure for preparing thin Cu or Au disks with mirror-bright surfaces. First, films approximately 2000Å thick of Cu (or Au) were thermally evaporated onto clean glass slides (1 × 3 in.) at about 1000 Å/min in a Varian PS10E vacuum system at ~ 1×10^{-5} Torr. The metallized slides were then masked with Teflon tape (*e.g.*, 3M Company No. 549) having 10 punched holes of 8 mm diam. Copper disks, approximately 20μ thick, were then plated in an electrolyte consisting of 0.5M $CuSO_4$ and H_2SO_4 at 6 mA/cm² at room temperature. After rinsing in distilled water and removing the tape, the disks were readily removed from the glass, dried in N_2, and stored in a vacuum desiccator. Immediately prior to use, the substrates were immersed in a 20% HNO_3 solution for a few seconds, rinsed, then placed on the electrode and secured with a Teflon screw cap as shown in Fig. 1. The mirror-bright surface of the disk was wet at all times to minimize the probability of trapping a gas bubble at the surface when the cell was raised to immerse the rotating electrode. No attempt was made to exclude oxygen from the system in these experiments. Current densities were preset to give the desired value as soon as the substrate entered the electrolyte.

In addition to the type of plating system used (Table I), the other variables considered were current density and rotation speed. Under most sets of conditions, two Cu substrates were plated for times which differed by an order of magnitude in order to yield deposits with calculated thicknesses in the vicinity of 0.1 and 1.0μ. The purpose of this was to determine whether any structural changes occurred over this interval and to facilitate direct observations of the microstructure formed at the early stages (~0.1μ) by transmission electron microscopy. Also, some experiments were carried out on Au surfaces to determine whether substrate effects could be detected on thicker films.

Scanning electron microscopy (SEM, Cambridge Stereoscan) was used to characterize the surface morphology of all the deposits generated in this study. Small, pie-shaped specimens were cut from each disk and mounted, usually 6-8 on a holder, for observation at 45° to the beam (21 kV, secondary electrons). The magnification range from 20 to 20,000 was surveyed and representative micrographs were taken, usually at 10,000X and at least one other magnification, using the *Y*-direction correction accessory. Suitable specimens for transmission microscopy were prepared by slowly dissolving the Cu substrate in a chromic-sulfuric acid solution (17). After rinsing the thin gold deposits in distilled water and absolute ethyl alcohol, these were examined at 100 kV by transmission electron microscopy (TEM, Siemens Elmiskop) and selected-area electron diffraction.

Thickness measurements were carried out with a Betascope, DZ800 instrument using a Promethium radioisotope that was calibrated with NBS thickness standards. The precision of the readings was estimated to be within ± 7%.

Reflectivity spectra over the range 4300-7500Å were recorded with a Perkin Elmer Model 402 Spectrophotometer using the specular reflectance attachment with a 2-mm mask. These measurements were carried out to determine whether this relatively simple macroscopic method, which was shown to be an effective means of characterizing electroless gold deposits (18), can be correlated with the microscopic structural information in a meaningful way.

[2] Supplied by Pine Instruments Company, Grove City, Pennsylvania.

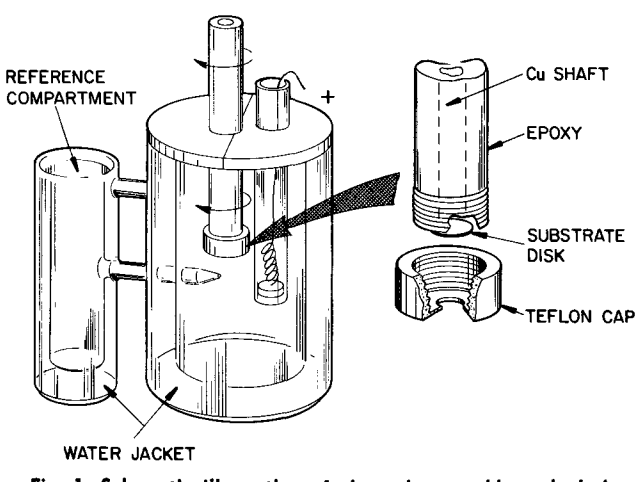

Fig. 1. Schematic illustration of electrode assembly and plating cell. Inlet and outlet connections are not shown.

Results and Discussion

Electrochemical behavior.—Alkaline cyanide gold solution.—Polarization curves for the alkaline cyanide gold solution at various rotational speeds are shown in Fig. 2. Due to the large excess of CN^- in the solu-

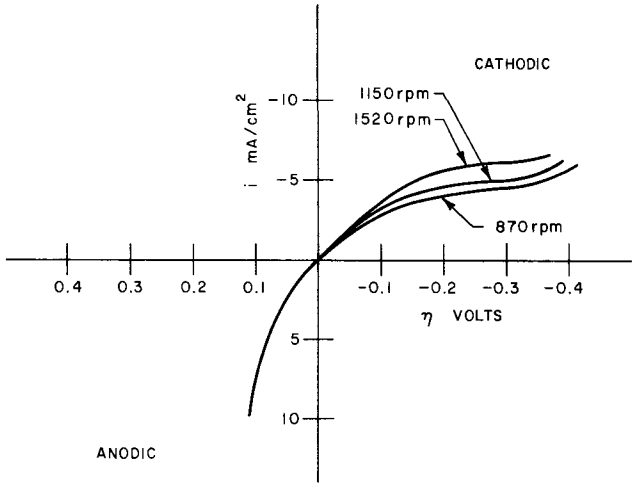

Fig. 2. Polarization curves for cyanide gold solution

tion, no anodic limiting current density is observed. Within the experimental uncertainty, the cathodic limiting current density varies linearly with the square root of rotational speed. The Volmer-Tafel equation for the present system can be expressed as

$$i = i_o \left[\exp\left(\frac{\alpha n\mathbf{F}}{RT}\eta\right) - \left(\frac{i_l - i}{i_l}\right) \exp\left(-\frac{(1-\alpha)\, n\mathbf{F}}{RT}\eta\right)\right] \quad [1]$$

where i is the applied current density, i_o is the exchange current density for the deposition process, i_l is the limiting current density for gold deposition, α is the transfer coefficient, η is the overpotential which is defined as the difference between the electrode potential (E_c) and the equilibrium potential (E^o), and n, $\mathbf{F}$, R, and T have their usual meaning. By differentiating Eq. [1] with respect to η and letting both i and η approach zero, an expression for i_o can be obtained

$$i_o = \frac{\left(\frac{di}{d\eta}\right)_{i,\,\eta\to 0}}{\frac{n\mathbf{F}}{RT} + \frac{\left(\frac{di}{d\eta}\right)_{i,\,\eta\to 0}}{i_l}} \quad [2]$$

The exchange current density is found from the experimental value of $\left(\frac{di}{d\eta}\right)_{i,\,\eta\to 0}$ and Eq. [2] to be 0.82 mA/cm². Based on the anodic portion of Fig. 2, the transfer coefficient is found to be 0.7, which is in agreement with the value obtained from the data given in Ref. (11). According to Maja, the cathodic rate is proportional to the square root of $Au(CN)_2^-$ concentration. This dependence would lead to an i_o value of 0.89 mA/cm² for this system.

The over-all reaction for gold deposition in the alkaline cyanide system is

$$Au(CN)_2^- + e^- \rightleftarrows Au + 2CN^- \quad [3]$$

The standard heterogeneous rate constant, k_s is calculated from the following equation

$$i_o = n\mathbf{F}k_s\, C_o^{\alpha} C_R^{2(1-\alpha)} \quad [4]$$

where C_o and C_R are the concentrations of $Au(CN)_2^-$ and CN^-, respectively. From Eq. [4], k_s was found to be 3.9×10^{-3} cm/sec.

Citrate gold solution.—Reproducibility of polarization measurements in the citrate gold solution was in general poor. Typical results are shown in Fig. 3. It is

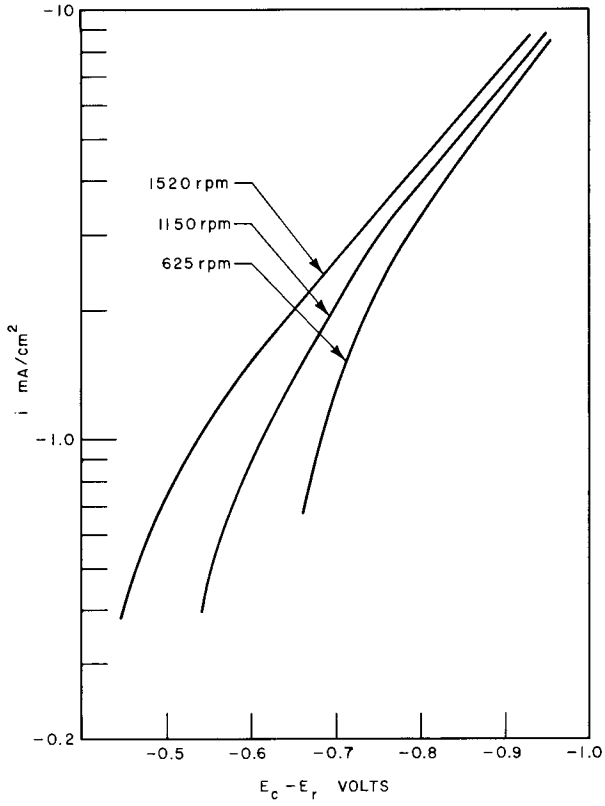

Fig. 3. Polarization curves for citrate gold solution

evident that no limiting step for gold deposition can be seen here due to the gradual onset of the H_2 evolution reaction. However, the limiting current density for deposition can be calculated from the transport properties of the system (16) and the following equation (19)

$$i_l = -\frac{0.554\, n\mathbf{F} D^{2/3}\, \nu^{-1/6}\, \omega^{1/2}\, C_o}{0.8934 + 0.316\,(D/\nu)^{0.36}} \quad [5]$$

where D is the diffusion coefficient of $Au(CN)_2^-$, ν is the kinematic viscosity of the solution and ω is the rotation speed. The values[3] were found to be 5.2 mA/cm² at a rotation speed of 1520 rpm and 4.1 mA/cm² at 870 rpm. It was not possible to extract kinetic parameters in this system.

Phosphate gold solution.—The results for the phosphate gold solution are shown in Fig. 4. Well-defined limiting current density is observed here. The values at various rotation speeds agree well with those obtained in an independent study based on current efficiency measurements (14). It was not possible to measure the equilibrium potential, presumably due to the small amount of free CN^- existing in the solution. Hence, no direct experimental information on the magnitude of i_o for this system can be obtained. However, if the anodic portion of Eq. [1] is neglected then the transfer coefficient can be calculated from the cathodic portion of the Volmer-Tafel equation

$$E_c - E_r = \frac{-RT}{(1-\alpha)n\mathbf{F}} \ln\left[\frac{-i}{i_o\left(1 - \frac{i}{i_l}\right)}\right] + (E^o - E_r) \quad [6]$$

[3] All current densities appearing in the text are cathodic; therefore the negative sign will be omitted.

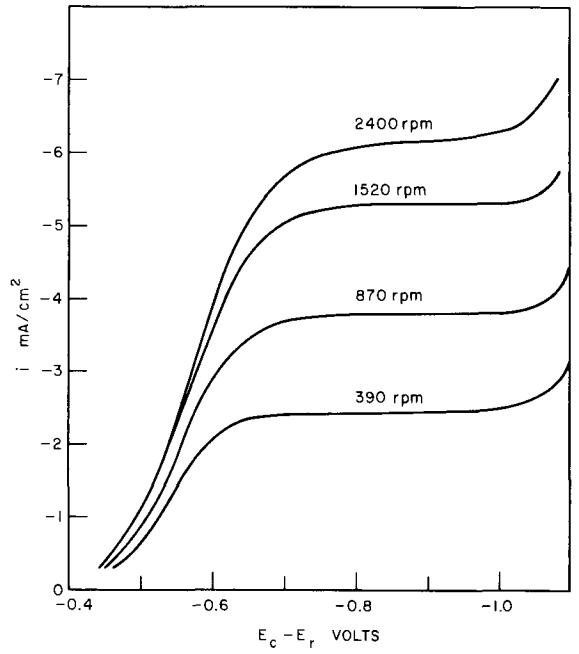

Fig. 4. Polarization curves for phosphate gold solution

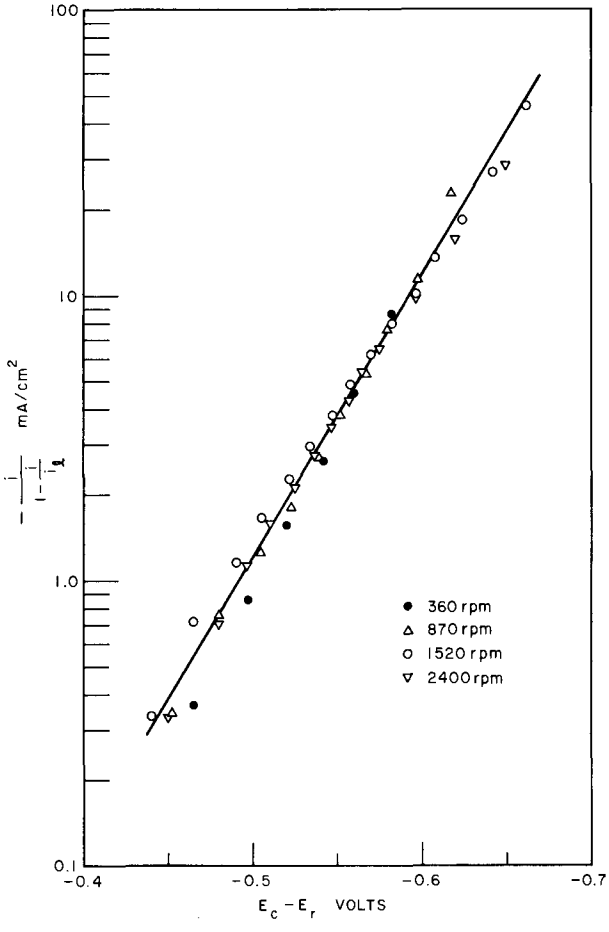

Fig. 5. Plot of ln $[-i/(1 - i/i_l)]$ vs. $E_c - E_r$ for phosphate system.

where $E_c - E_r$ is the potential difference between the cathode and the reference electrode. A plot of $\ln[-i/(1 - i/i_l)]$ *vs.* $E_c - E_r$ is presented in Fig. 5. The Tafel slope is measured to be 0.101V and this provides a value of 0.35 for the transfer coefficient.

In contrast to the cyanide system, the *p*H of the phosphate buffered solution is such that nearly all free cyanide is present as HCN. Hence, the electrode reaction can be written as

$$Au(CN)_2^- + 2H^+ + e^- \rightleftarrows Au + 2HCN \qquad [7]$$

The standard potential for this reaction is calculated to be 0.268V (*vs.* SCE) at room temperature based on the known values (20) of the dissociation constant for HCN and E^o for Eq. [3]. Following Delahay's treatment for irreversible i-V characteristics (21), Eq. [6] can be rearranged to give

$$E_c = \frac{RT}{(1-\alpha)n\mathbf{F}} \ln\left[\frac{i_l - i}{i}\right] + E_{1/2} \qquad [8]$$

where the half-wave potential is given by

$$E_{1/2} = E^o + \frac{RT}{(1-\alpha)n\mathbf{F}} \ln\left[\frac{k_s n\mathbf{F}C_o}{-i_l}\right] \qquad [9]$$

This treatment yields the heterogeneous rate constant $k_s = 6 \times 10^{-11}$ cm/sec based on the data in Fig. 4 and 5 and the room temperature value of $E^o = 0.268$V. Since the value of E^o for Eq. [7] at 60°C is unknown, the rate constant must be considered as an approximate result.

Physical behavior.—Alkaline cyanide solution.—This system yielded the greatest variation in deposit appearance, as surfaces ranged from bright yellow to dark brown depending on plating conditions. Tables II and III list the actual conditions studied together with thickness data obtained by calculation (μ_c) based on 100% current efficiency and by beta backscatter measurement (μ_β). A brief discussion of these data is given in the Appendix. Also listed in Tables II and III are reflectivity data (R_s) for these deposits. However, as discussed in the Appendix, this type of measurement is of limited usefulness in the cyanide system.

The SEM results in Fig. 6 illustrate the changes in morphology due to increasing current density at 760 rpm. The relatively smooth-faceted deposit formed at 0.63 mA/cm² (Fig. 6a) is yellow-gold in color and has a matte appearance. Increasing C.D. leads to the formation of outward growing features termed "spikes"; when these become sufficiently large and dense (Fig. 6c and 6d), the deposits are dark brown. In between the regions where these two types of deposits are formed is a transitional structure (Fig. 6b) which occurs at about 1.6 mA/cm² for these conditions. Similar structural features were also noted for thin deposits ($\sim 0.1\mu$); however, at this stage there was an increased tendency to form spikes, *e.g.*, they are evident at 1.6 mA/cm² for these conditions.

The same general behavior, *i.e.*, the transition to spikes, occurred at all rotation speeds. For example, at

Table II. Results for cyanide gold (0.005M) system*

i, mA/cm²	ω, rpm	t, min	μ_c	μ_β	R_s	Structure**
2.52	1520	6.5	1.0	0.44	0.49	I → II
4.41	1520	4.1	1.1	0.85	0.19	II → III
6.30	1520	3.3	1.3	0.95	0	III
2.52	1430	7.0, 0.67	1.1, 0.11	0.67, 0.09	0.42, 0.75	I → II, (E) III
3.78	1430	5.0, 0.50	1.2, 0.12	0.92, 0.08	0.65, 0.48	II, (E) III
5.67	1430	3.33, 0.33	1.2, 0.12	0.86, 0.08	0, 0.70	III
0.63	760	60, 5.0	2.4, 0.20	2.0, 0.20	0, 0.93	Type I, Fig. 6a
1.58	760	19.3, 2.0	1.9, 0.20	1.31, 0.12	0.16, 0.70	Type II, Fig. 6b
2.52	760	6.67, 0.67	1.1, 0.11	0.80, 0.06	0, 0.51	Type III, Fig. 6c
3.78	760	5.0, 0.50	1.2, 0.12	0.92, 0.10	0, 0.67	Type III, Fig. 6d
0.63	230	45, 4.5	1.8, 0.18	1.62, 0.15	0, 0.34	I
1.26	230	25, 2.5	2.0, 0.20	1.86, 0.19	0.21, 0.64	I, (E) II
2.52	230	15, 1.5	2.4, 0.24	2.30, 0.23	0, 0.24	I → II, (E) III

* All experiments with Cu substrates.
** Structure type classified according to morphology of thick deposits; E signifies early stage: Type I = flat, faceted surfaces; Type II = transition, mixed character; Type III = outward growing spikes.

Table III. Results for cyanide gold (0.01M) system*

i, mA/cm²	ω, rpm	t, min	μ_c	μ_β	R_s	Structure**
2.52	1520	7.5, 0.67	1.2, 0.11	1.3, 0.06	0.17, 0.81	III
5.67	1520	3.33, 0.3	1.2, 0.11	1.2, 0.04	0, 0.57	III
5.67 A	1520	3.33	1.2	1.04	0	III
6.93 A	1520	2.73	1.2	1.14	0	Type III, Fig. 7a
8.69	1520	2.17	1.2	1.12	0	Type III, Fig. 7b
9.99	1520	1.70	1.2	1.2	0	III → IV, Fig. 7c
11.91	1520	1.58, 0.14	1.2, 0.15	1.2, 0.13	0.80, 0.89	Type IV, Fig. 7d
13.23 A	1520	1.58, 0.14	1.2, 0.15	12	0	V
1.26 A	870	15.0	1.2	1.18	0.77	I
2.52 A	870	7.5	1.2	1.17	0	II
3.78 A	870	5.0	1.2	1.13	0	III

* Experiments with Au substrates denoted by A in column 1.
** Structure Types I, II, III as defined in Table II; Type IV = smooth, very-fine grained deposit; Type V = particle growth, powder formation.

higher rpm (1430-1520 rpm), the transition to spikes takes place at 3-4 mA/cm²; and at about 1.3 mA/cm², for thin deposits plated at 230 rpm. Under these last conditions, however, the thicker deposits did not exhibit spikes.

Experiments were carried out in a more concentrated cyanide solution (0.01M) to determine the effect of surface concentration. Applied C.D. values were chosen such that the surface concentration of $Au(CN)_2^-$ was identical to that in the dilute solution. To achieve these conditions, the surface concentration (C_e) was calculated from (19)

$$i = -\frac{0.554\, nFD^{2/3}\, \nu^{-1/6}\, \omega^{1/2}\, (C_0 - C_e)}{0.8934 + 0.316\, (D/\nu)^{0.36}} \qquad [10]$$

for C.D. values used with the dilute solution. Corresponding C.D. values for the concentrated solution (2 C_0) were then obtained using Eq. [10] with the appropriate ω values for each C_0.

It was found that different structures were formed at equivalent values of C_e in the two solutions. The experimental evidence for this statement is presented in Fig. 7 and the results are listed in Table III. Each micrograph in Fig. 7 should be compared with the corresponding one in Fig. 6 in order to see the different structures formed at equivalent C_e values (0.0044M, 0.003M, 0.0021M, and 0.0002M, respectively for a-d).

As indicated in Table III, the transition from a smooth-faceted type of growth to spiked was observed for deposits plated at 870 rpm. The C_e values for these conditions are 0.009M for the smooth deposit formed at 1.26 mA/cm², 0.0075M for the transitional structure at 2.52 mA/cm², and 0.006M for the spikes formed at 3.78 mA/cm². These data together with the results obtained at 1520 rpm provide additional evidence that the surface concentration of gold is not what determines which structure forms. At 1520 rpm, deposition at 2.52 mA/cm² (C_e = 0.0082M) yields well-defined spikes (similar to Fig. 7a) and increasng C.D. to 8.7 mA/cm²

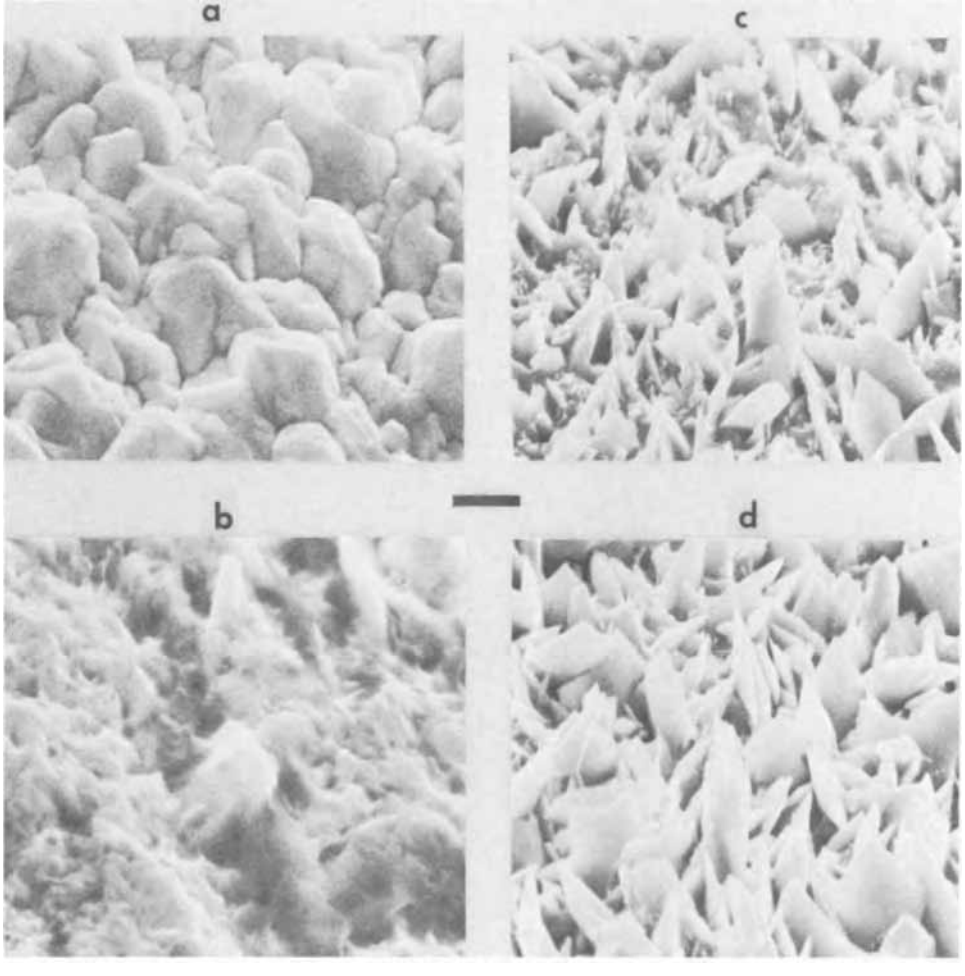

Fig. 6. Morphology of deposits plated in cyanide system (0.005M) at 760 rpm. a, 0.63 mA/cm²; b, 1.6 mA/cm²; c, 2.5 mA/cm²; d, 3.8 mA/cm². Scanning electron micrographs, magnification bar represents 1 μ in this and subsequent figures. 10,000X originally.

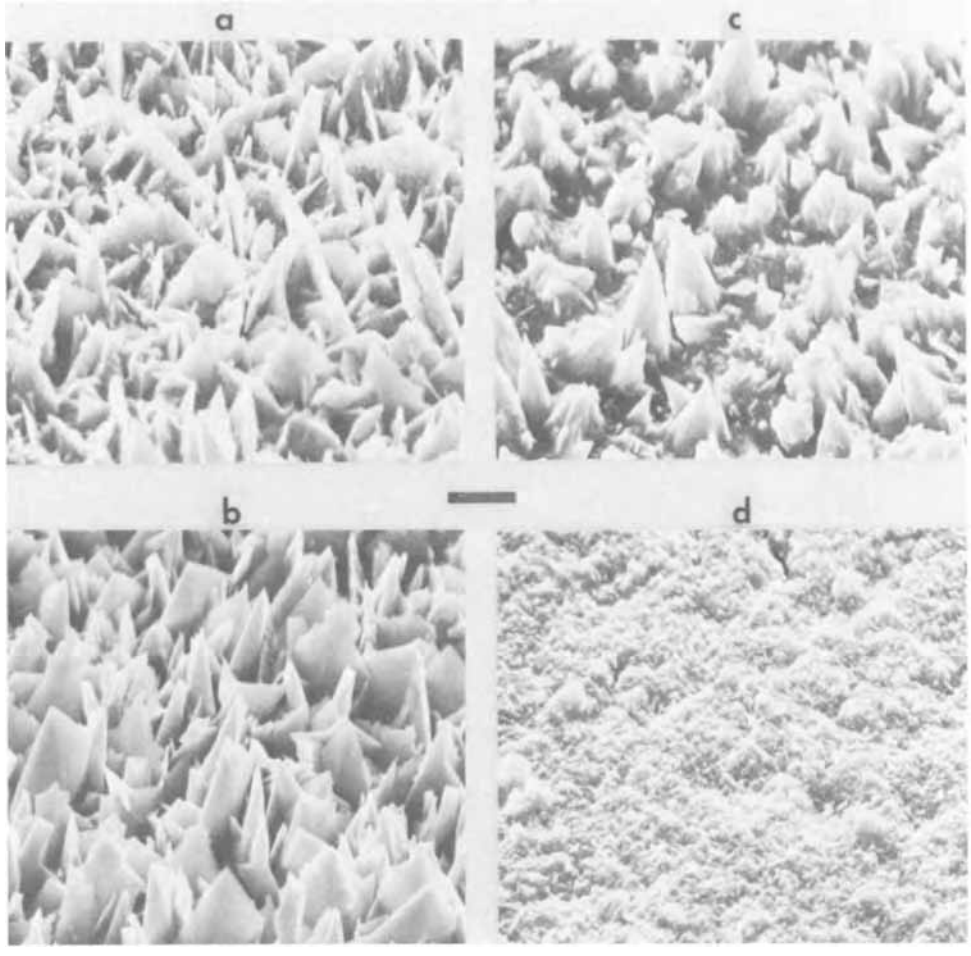

Fig. 7. Morphology of deposits plated in 0.01M $Au(CN)_2^-$ solution at 1520 rpm. Surface concentrations are equivalent to corresponding deposits in Fig. 6. a, 6.9 mA/cm^2; b, 8.7 mA/cm^2; c, 10.0 mA/cm^2; d, 11.9 mA/cm^2. Scanning electron micrographs, 10,000X originally.

causes very little change as the density of spikes increases approximately twofold to 2 x 10^8/cm^2 (Fig. 7b). Further increases in C.D. result in another transition (Fig. 7c) back to yellow-appearing deposits with a very fine grain size at about 12 mA/cm^2 (Fig. 7d), which is in the vicinity of the limiting C.D. (C_e = 0.0002M). Above this C.D. the formation of powderlike structures of the type discussed by Ibl (22) was observed, but no systematic study of the structures formed above i_l was carried out.

It appears on the basis of these results that morphology is not determined primarily by either the surface concentration or C.D. Hence, it is instructive to consider whether overpotential is controlling the formation of the various structures. The smooth, faceted surfaces which formed at 0.63 mA/cm^2 in the dilute solution (Fig. 6a) and at 1.26 mA/cm^2 in the more concentrated one correspond to overpotentials of less than ~50 mV in magnitude (Fig. 2). The transitional structures (*e.g.* Fig. 6b) were formed in the region from −50 to −100 mV. Spikes (Fig. 6c, d and 7a, b) appeared over the potential range from −150 to −300 mV. The previously mentioned transition to a fine-grained type of deposit (Fig. 7d) occurred at higher potential in the concentrated solution.

The results obtained from the alkaline cyanide system indicate that below i_l the formation of the different structures is governed by the potential[4] rather than by mass transport.

Citrate solution.—The deposits plated in the citrate solution were in many respects similar to those obtained in the cyanide system at low gold concentration. Results are given in Table IV and the transition from flat, faceted growth to the outward growing spikes is illustrated in Fig. 8 for deposits plated on gold substrates at 870 rpm. On Cu substrates similar results were obtained except that the transition region, which occurs at 2.5 mA/cm^2 on Au (which corresponds to ~ −0.75V according to Fig. 3), is displaced towards a lower value as these conditions yield a spiked structure like that in Fig. 8c. When the rotation speed is increased to 1520 rpm at 2.5 mA/cm^2, a smooth, flat, fine-grained surface similar to that in Fig. 8a (1.26 mA/cm^2) is formed. It is significant that either way, *i.e.* increasing ω (from 870 to 1520 rpm)

[4] Previous studies (23, 24) of Cu deposition onto stationary single crystal electrodes have also shown that different types of growth habit are associated with specific ranges of overpotential.

Table IV. Results for citrate gold system*

i, mA/cm^2	ω, rpm	t, min	μ_c	μ_β	R_s	Structure**
2.52	1520	7.5, 0.67	1.2, 0.1	0.8, —	0.75, 0.99	I, (E) Fig. 9c, d
5.04	1520	3.75, 0.33	1.2, 0.1	0.9, 0.06	0.27, 0.69	III
1.26	870	15, 1.25	1.2, 0.1	0.6, 0.04	0.65, 0.85	I
1.26 A	870	15	1.2	0.9	0.87	Type I, Fig. 8a
2.52	870	7.5, 0.67	1.2, 0.1	0.8, 0.07	0, 0.76	II → III (E) Fig. 9a, b
2.52 A	870	7.5	1.2	0.93	0.85	Type II, Fig. 8b
3.78	870	5.0, 0.5	1.2, 0.1	0.9, 0.08	0, 0.65	III
3.78 A	870	0.5	1.2	1.0	0	Type III, Fig. 8c

* Experiments with Au substrates denoted by A in column 1.
** Structure Types I, II, III as defined in Table II; E signifies early stage.

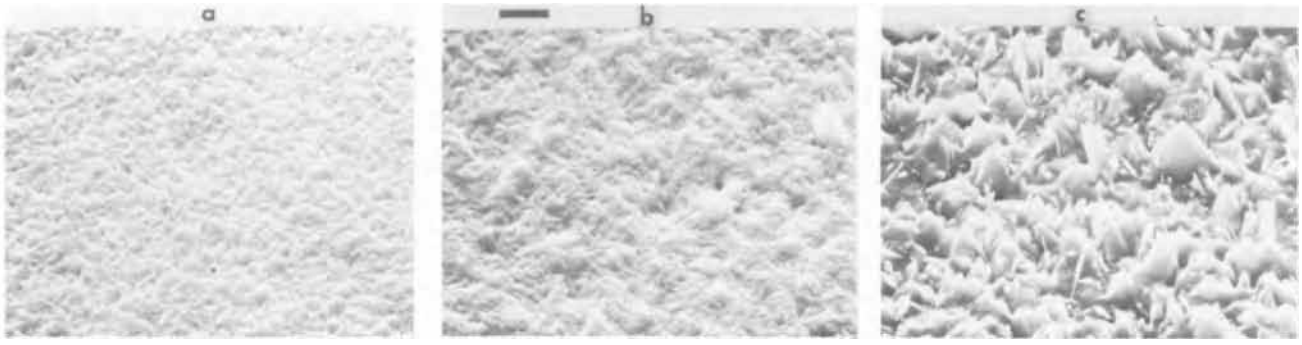

Fig. 8. Morphology of deposits plated in citrate system at 870 rpm. (Thickness, approximately 1μ). a, 1.3 mA/cm^2; b, 2.5 mA/cm^2; c, 3.8 mA/cm^2. Scanning electron micrographs 10,000X originally.

at constant i (2.5 mA/cm^2), or decreasing i (from 2.5 to 1.3 mA/cm^2) at constant ω (870 rpm), which both correspond to a potential decrease of about 60 mV in magnitude, the same structure is obtained. This result is in agreement with the previous discussion concerning the cyanide system. However, it must be recognized that increasing ω or decreasing C.D. have similar qualitative effects on mass transport. Specifically, at 1520 rpm 2.5 mA/cm^2 corresponds to $i_l/2$, whereas at 870 rpm 1.3 mA/cm^2 corresponds to $i_l/3$. Therefore, the available data do not permit a completely unambiguous determination of whether potential or mass transport is the controlling factor regarding the structures formed in this system.

The same general behavior was also noted for the thinner citrate deposits, except that the scale of structural features is significantly reduced. Thus, for example, the thin sample plated at 1.3 mA/cm^2 and 870 rpm exhibited an extremely fine grained microstructure consisting of crystallites approximately 300-500Å in size (as determined by TEM using dark-field images) and other particles about twice as large which were present on the surface. A two-fold increase in i led to the formation of spikes (Fig. 9a). The results obtained by TEM (Fig. 9b) indicate that the spikes protrude from a fine-grained, thin, continuous layer of gold. The spikes, which appear dark in transmission due to absorption, are seen to range from about 1000

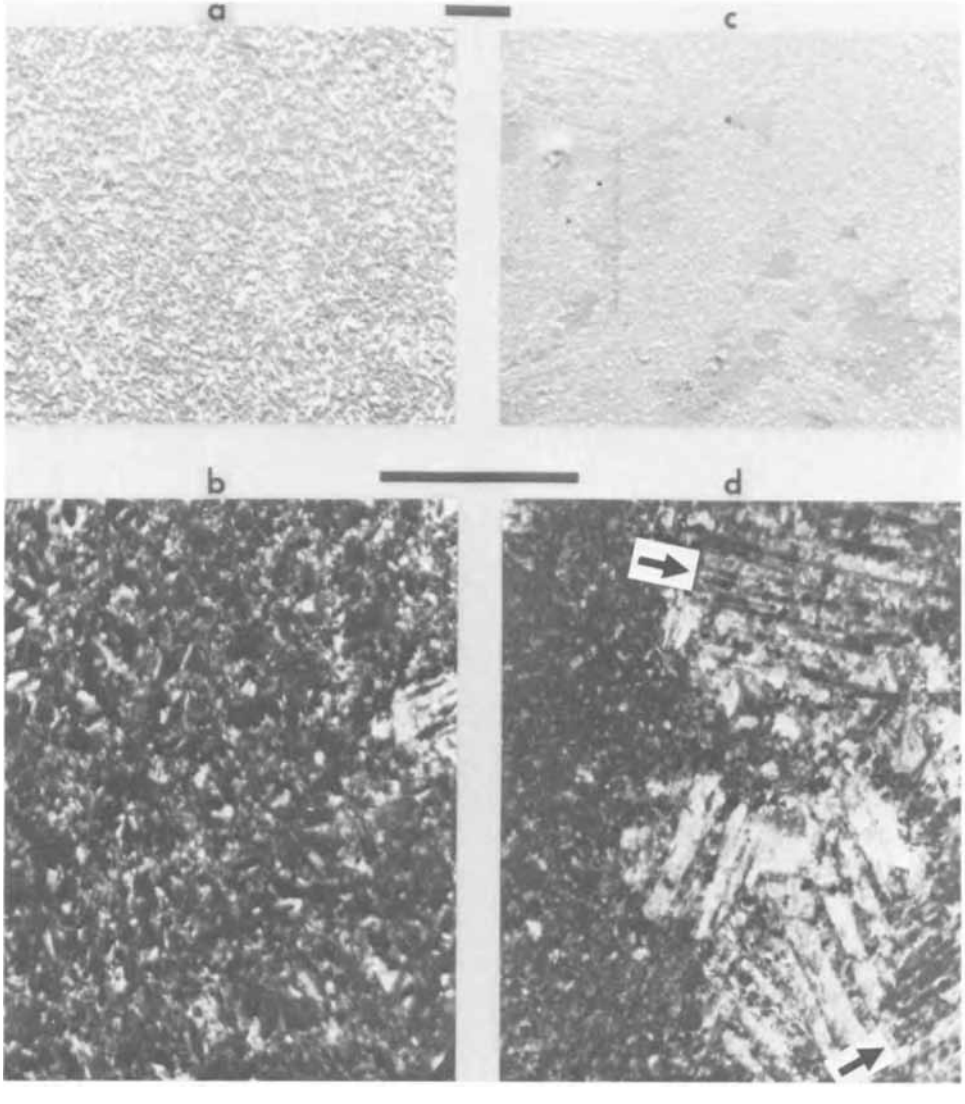

Fig. 9. Structure of thin deposits ($\sim$ 0.1μ thick) plated in citrate system at 2.5 mA/cm^2. a, 870 rpm. SEM: 10,000X; b, Same as a, TEM: 30,000X; c, 1520 rpm, SEM: 10,000X; d, Same as c, TEM: 30,000X.

Table V. Results for phosphate gold system*

i, mA/cm²	ω, rpm	t, min	μ_c	μ_β	R_s	Structure**
2.52 A	1520	6.5	1.0	0.33	0.99	I
4.41 A	1520	3.75	1.0	0.63	0.89	I
6.30 A	1520	3.33	1.3	0.99	0.57	I
2.52	1480	6.5, 0.67	1.0, 0.1	0.7, 0.06	0.67, 0.99	I
4.72	1480	5.0, 0.50	1.5, 0.15	—	0.84, 0.99	I
0.63	760	2.5	0.10	0.04	0.99	I, Fig. 11a
1.26	760	40.0, 1.25	3.2, 0.1	1.7, 0.05	0.33, 0.96	I, Fig. 10a, (E) Fig. 11b
2.52	760	20.0, 0.67	3.2, 0.1	2.1, 0.06	0.23, 0.99	I
3.62	760	5.0, 0.5	1.1, 0.1	0.9, 0.06	0.59, 0.73	I, (E) Fig. 11c
4.41	760	5.0	1.4	1.1	0.49	II, Fig. 10b
4.41	760	0.67	0.2	0.14	0.71	III, Fig. 10c, 11d

* Experiments with Au substrates denoted by A in column 1.
** Structure Types I, II, III as defined in Table II; E signifies early stage.

to 2500Å in length and number about $2 \times 10^9/cm^2$. Increasing i to 3.8 mA/cm² yielded a similar structure with about 1.6×10^9 spikes per cm² and these range from 1000 to 4000Å in length.

The effect of increasing rotation speed to 1520 rpm at 2.5 mA/cm² is shown in Fig. 9c. No spikes are formed; instead there exists a heterogeneous surface consisting of relatively large ($\sim 1\mu$) regions of different contrast and an overgrowth of small particles (< 1000Å). TEM results (Fig. 9d) show that these large regions are, in fact, Au crystallites which apparently copied the surface structure of the Cu substrate and preceded the particle nucleation. At higher C.D. (5 mA/cm²), the transition to spikes was observed, but the large-grained, initial layer was quite similar to Fig. 9d. It is also evident from Fig. 9d (*e.g.* the regions denoted by arrows) that the particles nucleated preferentially at structural defects such as twin faults and grain boundaries. These results indicate that the initial deposition onto Cu is rather complex and consists of a substrate-dominated stage which results in an epitaxial[5] layer several hundred angstroms thick, followed by another stage where the type of growth is controlled by the deposition conditions. This latter stage is of primary concern here; the epitaxial stage will be the subject of a future paper.

The changes in reflectivity (R_s) correlate reasonably well with microscopic observations and show, in addition to the expected decreases with increasing i, t, and decreasing ω, that at lower current densities (1.3 and 2.5 mA/cm²) thick deposits plated on Au (Fig. 8a, b) are even more reflective than the thin ones plated on Cu. This effect is apparently a consequence of an increased surface roughness which results in the latter case. It appears that the change in reflectivity is a very sensitive indicator of morphological changes as the features protruding from the surfaces in Fig. 9 are on the order of 10% of the wavelength. In general, for a given set of plating conditions the reflectivity is greater for samples from the citrate system than for corresponding cyanide samples.

[5] The fact that the initial stage of Au electrodeposition onto Cu substrates is epitaxial (i.e. in parallel orientation) has been reported previously (25, 26) for other plating systems.

Phosphate solution.—Deposits from the phosphate system showed the least variation over the range of conditions studied and tended to be more reflective and yellow than the samples from the other systems. Results are given in Table V. Thicker deposits (1-2μ) are matte yellow in appearance due to the smooth, faceted features present on their surfaces (Fig. 10a). As discussed in the Appendix, such surfaces show reduced specular reflectivity; however, the R_s values, in general, were much higher for deposits from the phosphate bath than corresponding ones plated in the citrate system.

Increasing C.D. appears to cause a refinement in the size of surface features and a slight tendency towards outward growth (Fig. 10b, 4.4 mA/cm², 760 rpm). The thin deposit plated under these same conditions was the only nonyellow appearing one observed in this system and Fig. 10c clearly shows the formation of spikes on the surface.

The factors responsible for the greater tendency for spikes to form at shorter times, which was also noted previously for the other systems, have not been established conclusively. One observation which appears to be related to this phenomenon is that the potential-time curves (14) showed a maximum (of approximately 200 mV in magnitude above the steady-state value) at about 0.5 to 1 min, which corresponds to the conditions used for preparing the thin deposits. While it seems probable that this rise in potential is associated with the energy required for the initial stage of three-dimensional gold nucleation, no detailed study of this effect was carried out.

Additional information on the structure of thin deposits was obtained by TEM. Some bright-field micrographs showing the effect of C.D. at 760 rpm are shown in Fig. 11. At low C.D. (0.63 mA/cm², Fig. 11a), the structure is seen to be essentially a replica of the Cu substrate as the relatively large crystallites ($\sim 1\mu$) with numerous twin faults were also present in evaporated Cu films. As C.D. is increased to 1.3 mA/cm² the growth centers become more apparent due to the formation of thicker, three-dimensional nuclei. These appear as dark gray and black blotches about 0.5μ across in Fig. 11b. A similar structure was also

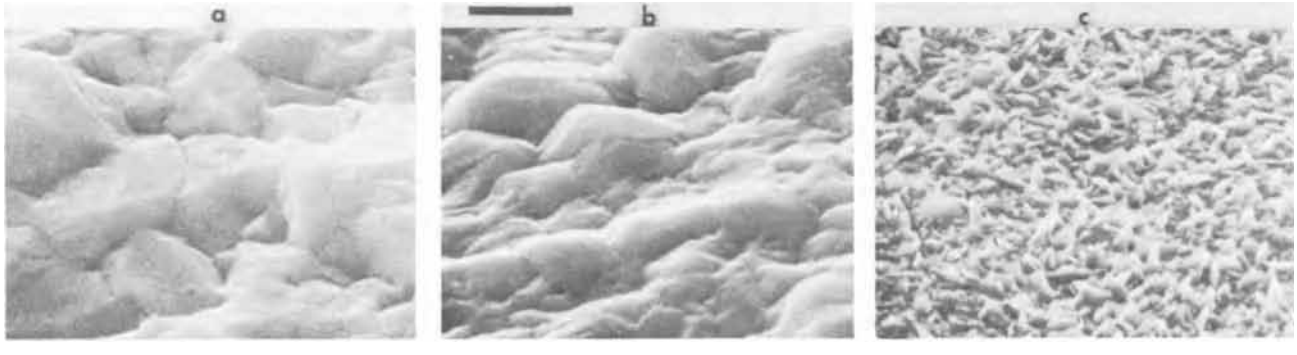

Fig. 10. Morphology of deposits plated in phosphate system at 760 rpm. a, 1.3 mA/cm²; 1.7μ thick. b, 4.4 mA/cm²; 1.1μ thick. c, 4.4 mA/cm²; 0.14μ thick. Scanning electron micrographs, 20,000X originally.

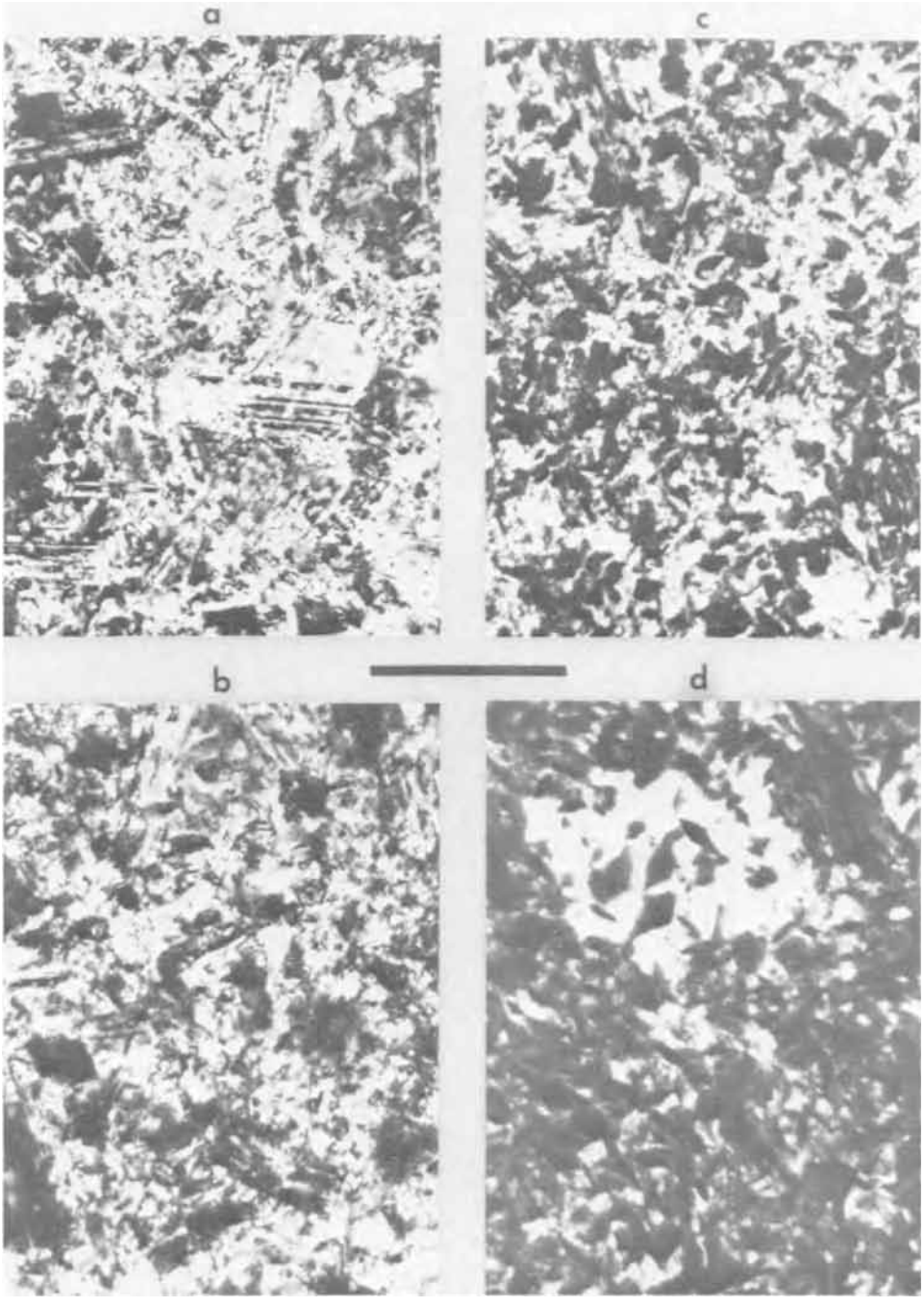

Fig. 11. Structure of thin deposits (~ 0.1μ thick) plated in phosphate system at 760 rpm. a, 0.63 mA/cm^2; b, 1.3 mA/cm^2; c, 3.6 mA/cm^2; d, 4.4 mA/cm^2. Transmission electron micrographs, 30,000X originally.

formed at 2.5 mA/cm^2. Dark-field images were used to aid interpretation of these structures, *i.e.* to differentiate between absorption contrast due to the thicker regions and diffraction contrast effects. In the vicinity of i_l, at 3.6 mA/cm^2 (Fig. 11c) spikes are present, and these become more numerous and regular at 4.4 mA/cm^2 (Fig. 11d). Apparently the spikes do not form directly on the Cu substrates but are supported by thin (few hundred angstroms) epitaxial Au layers which are white in Fig. 11c, d as the primary contrast here is due to absorption. Inspection of these and other similar micrographs indicates that the spikes are generally thin parallelograms in cross section. Although they appear in some cases to have a particular crystallographic orientation, and lie with their long axes parallel to <110> directions in the epitaxial Au layer, it was not possible to establish whether such behavior is general. Spikes were not formed when the rotation speed was increased by a factor of two at approximately this same deposition rate (4.7 mA/cm^2), which is consistent with the previous discussion regarding the citrate and cyanide systems.

Summary

This study of the electrochemical and physical aspects of gold deposition onto rotating disk electrodes has provided the following information.

Polarization data for the alkaline cyanide system (0.005M) yield an exchange current density of 0.82 mA/cm^2 and a transfer coefficient of 0.7. From these data k_s was calculated to be 3.9×10^{-3} cm/sec. This system showed the greatest tendency to form an outward growth morphology consisting of fine features termed spikes that are responsible for the characteristic brown appearance of deposits plated under a wide variety of conditions. By electron microscopy it was observed that the spikes are typically 0.1-1.0μ in size and $> 10^8$/cm^2 in density. Increasing C.D. and decreasing ω, in general, both favor the formation of spikes which occurs over a given potential range and not at a particular concentration of gold at the interface. At low overpotentials, a smooth, layer type of growth is formed.

The citrate system gave the most irreproducible polarization results and did not show a well-defined limiting step for gold deposition due to the gradual

nature of the hydrogen evolution reaction. Deposits showed the same general structural characteristics as for the cyanide system, and the formation of spikes also appears most likely to be governed by the potential of the reaction.

Polarization data for the phosphate system showed well-defined limiting current density and gave a Tafel slope of 0.101V; however, the insufficient quantity of CN^- in solution precluded determination of i_o. Following Delahay's treatment for irreversible electrode reactions, the k_s value for this system was calculated to be 6×10^{-11} cm/sec. These deposits were more reflective and yellow than corresponding ones from the other systems due to the decreased tendency to form spikes which occurred only in the vicinity of i_l for thin deposits (0.1μ). The transition from spikes in thin deposits to smoother surfaces at steady state, which was observed for all three systems in the potential region where the transitional structures formed, is associated with the maximum in the potential-time curves.

Finally, by transmission electron microscopy it was established that the initial stage of deposition is rather complex and consists of a substrate-dominated stage which results in an epitaxial layer several hundred angstroms thick, followed by another stage where three dimensional growth occurs. At the beginning of this stage, which is controlled by the deposition conditions, structural defects such as twin faults and grain boundaries in the epitaxial layer act as preferential sites for nucleation.

Acknowledgment

Thanks are due to Y. Okinaka for his critical review of the manuscript and to R. D. Heidenreich and G. W. Kammlott for making the electron microscope facilities available.

Manuscript received June 18, 1971; revised manuscript received *ca.* July 22, 1971.

Any discussion of this paper will appear in a Discussion Section to be published in the June 1972 JOURNAL.

APPENDIX

Characterization of gold deposits by spectrophotometry.—The purpose of making reflectivity measurements on the gold deposits generated in this study was to determine whether this approach would facilitate more quantitative comparisons of the different morphologies. Spectra were recorded with the Perkin Elmer Model 402 Spectrophotometer which was used previously to study electroless gold deposits (18). Because of the small sample size, a 2-mm circular mask was inserted in the specular reflectance attachment. The instrument yields plots of relative absorbance *vs.* wavelength as illustrated in Fig. 12. These curves correspond to the deposits whose SEM results are given in Fig. 6-10. The method used to compare spectra of this type was to determine the relative separation of each curve from the specular gold reference at the arbitrarily selected value of $\lambda = 6500$Å. From this separation, the R_s values quoted in Tables II-V were computed as fractions of the value for the specular gold reference surface. Although the R_s values appear to correlate reasonably well with deposit morphology in most cases, they should be considered as semiquantitative data for the following reasons. First, while a single parameter is suitable for describing the separation of similarly shaped curves, it is evident that the spectra obtained from the gold deposits (Fig. 12) show both a displacement and change in slope at a given wavelength. Second, a relatively large number of surfaces (*e.g.* particularly those from the cyanide system) had a nonspecular or matte appearance, either orange or brown in color, and could not be measured as they gave no detectable signal. Finally, the R_s values are sensitive not only to the type of structure formed, but are significantly affected by subtle features like grain size and the amount of faceting both of which vary with thickness. Recent evidence obtained with electroless gold deposits (27) suggests that most of these difficulties can be overcome by measuring the total light reflected, *i.e.* diffuse plus specular, using an integrating sphere (28). It appears that this approach can be applied to a more quantitative study of gold deposits provided that larger area (> 1 cm^2) samples of equivalent thickness are compared.,

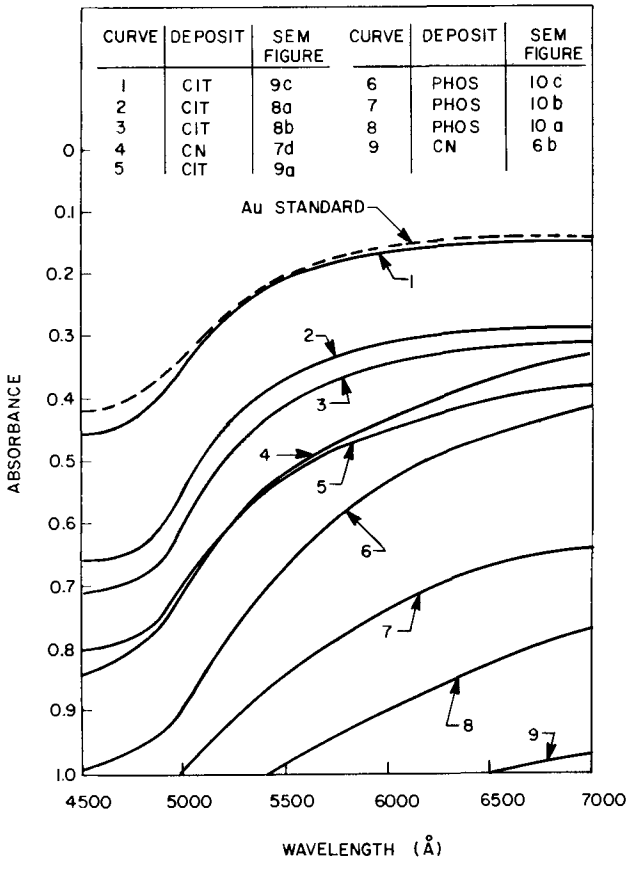

Fig. 12. Optical spectra of representative electrodeposited gold surfaces. Numbered curves correspond to deposits whose SEM results are given in Fig. 6-10.

Some comments regarding thickness data.—The efficiency of gold plating was not of major interest in this work. However, the thickness data (μ_c and μ_β values) presented in Tables II-V provide support for the following generalizations regarding efficiency: (*A*) For all three gold plating systems (0.005M), efficiency increases from less than 50% at low C.D. to more than 80% in the region below i_l. (*B*) The more concentrated cyanide system (0.01M) showed a significant increase in efficiency with most μ_β/μ_c values in the range from 0.95 to 1.0.

Both of these results appear to be related to the effects of oxygen which, as mentioned previously, was not excluded from the solution during these experiments. This interpretation is based on the excellent agreement between the present results and a recently completed quantitative electrochemical study (14) of the current efficiency of gold deposition in phosphate and citrate systems which were identical to those used in this work. The increased efficiencies noted for the more concentrated cyanide system probably result from a salting out effect which, in addition to the higher current densities used, acts to further diminish the oxygen reduction current.

LIST OF SYMBOLS

C_e	surface concentration of $Au(CN)_2^-$
C_o	bulk concentration of $Au(CN)_2^-$
C_R	concentration of $(CN)^-$
D	diffusion coefficient of $Au(CN)_2^-$
E^o	equilibrium potential
E_c	potential of working electrode
E_r	potential of reference electrode
F	Faraday's constant
i	applied current density
i_l	limiting current density for gold deposition

i_o exchange current density
k_s standard heterogeneous rate constant
n number of electrons transferred
R gas constant
R_s index of reflectivity
T temperature
t plating time
α transfer coefficient
η overpotential
ω rotation speed
ν kinematic viscosity of solution
μ_c calculated gold thickness in microns
μ_β measured gold thickness by beta backscatter

REFERENCES

1. R. G. Baker and T. A. Palumbo, Paper presented at AES Symposium, Palo Alto, Feb. 1971; *Plating*, **58**, 791 (1971).
2. K. L. Chopra, "Thin Film Phenomena," McGraw-Hill Book Co., New York (1969).
3. J. O'M. Bockris and G. A. Razumney, "Fundamental Aspects of Electrocrystallization," Plenum Publishing Corp., New York (1967).
4. J. O'M. Bockris and A. Damjanovic, Modern Aspects of Electrochemistry, *3*, Butterworths, 1964, Ch. 4.
5. M. Fleischman and H. R. Thirsk, *Advan. Electrochem. Electrochem. Eng.*, **3**, Chap. 3 (1963).
6. R. N. Adams, "Electrochemistry at Solid Electrodes," Chap. 4 Marcel Dekker, Inc., New York (1969).
7. A. C. Riddiford, *Advan. Electrochem. Electrochem. Eng.*, **4**, 47 (1966).
8. R. Wiart, Thesis, "Contribution ã l'étude cinétique de l'électrocristallization du nickel," Paris (1968).
9. P. Javet, Thesis, "Contribution ã la connaissance de la cinètique de transport et de l'action de la thiouree lors de la deposition electrolytique," Univ. Neuchâtel (1966).
10. A. Damjanovic, M. Paunovic, and J. O'M. Bockris, *J. Electroanal. Chem.*, **9**, 93 (1965).
11. M. Maja, *Atti. Accad. Sci. Torino: Classe Sci. Fis. Mat. Nat.*, **99**, 1111 (1965).
12. D. M. MacArthur, *This Journal*, Submitted for publication.
13. L. A. Taran, S. I. Berezina, and G. S. Vozdvizhenskii, *Tr. Kazan. Khim. Tekh. Inst.*, **36**, 591 (1967).
14. H. Y. Cheh, Unpublished results.
15. R. E. Visco and R. H. Sonner, Unpublished results.
16. H. Y. Cheh, *This Journal*, **118**, 551 (1971).
17. R. Weil and R. Paquin, *ibid.*, **107**, 87 (1960).
18. R. Sard, Y. Okinaka, and J. R. Rushton, *Plating*, **58**, 893 (1971).
19. D. P. Gregory and A. C. Riddiford, *J. Chem. Soc.*, 3756 (1956).
20. W. M. Latimer, "Oxidation Potentials," 2nd ed., pp. 137, 195, Prentice-Hall, New York (1952).
21. P. Delahay, "New Instrumental Methods in Electrochemistry," Chap. 9, Interscience, New York (1954).
22. N. Ibl, *Advan. Electrochem. Electrochem. Eng.*, **2**, Chap. 2 (1962).
23. S. C. Barnes, *Electrochim. Acta*, **5**, 79 (1961).
24. S. C. Barnes, G. G. Storey, and H. J. Pick, *ibid.*, **2**, 195 (1960).
25. E. W. Dickson, M. H. Jacobs, and D. W. Pashley, *Phil. Mag.*, **11**, 575 (1965).
26. E. R. Thompson and K. R. Lawless, *Electrochim. Acta.*, **14**, 269 (1969).
27. R. Sard, Unpublished results.
28. M. Froment and J. C. Lestrade, *Electrochim. Acta*, **11**, 21 (1966).

Electrochemistry of Alloxan and Its N-Methyl Derivatives in Aqueous Solution

Barbara H. Hansen[1] and Glenn Dryhurst

Department of Chemistry, University of Oklahoma, Norman, Oklahoma 73069

ABSTRACT

Alloxan, methyl- and dimethyl alloxan in aqueous solutions are reduced by way of three processes. The first cathodic wave (wave I_a), appears between *p*H 0-8 and is a kinetically controlled two-electron, one-proton reduction to the respective dialuric acid anion. Dehydration of the reducible carbonyl site is the kinetic factor. A second *p*H independent kinetically controlled reduction wave (wave I_b) is observed for 1.0 mM solutions of methyl- and dimethyl alloxan and for 10.0 mM solutions of alloxan between *p*H 0-3. The process involved is the transfer of two electrons to protonated alloxan molecules, again producing the dialuric acid anion. Wave II, detected only in the limited *p*H range of *ca.* 4.7-5.9, is a virtually *p*H independent, two-electron reduction of the hydrated form of alloxan to the dialuric acid dianion as the potential controlling process. This study indicates that wave II is not due to the further reduction of dialuric acid. Evidence is also given which refutes the view that alloxantin exists to a large degree in aqueous solutions.

Alloxan is produced upon electrochemical (1) and enzymatic (2, 3) oxidation of uric acid in weakly acidic solution. Dimethyl alloxan is an electrochemical oxidation product of theophylline (4) and caffeine (5). Methyl alloxan is an electrooxidation product of theobromine (5). Only alloxan itself has been studied electrochemically (6, 7) and is reported to show only two cathodic waves at the dropping mercury electrode (DME). The first wave (occurring at most positive potentials) has been shown to be a two-electron, one-proton reduction of alloxan to the anionic form of dialuric acid in a kinetically controlled electrode reaction (7). The reaction responsible for the other wave (wave II) that occurs at much more negative potentials over a very limited *p*H range has not been properly characterized, although it has been suggested that it is due to further reduction of the wave I product, dialuric acid, to barbituric acid or to other more highly reduced species (7).

Consideration of the structures of alloxan (I), alloxantin (II), and dialuric acid (III) suggests that alloxantin would be the most probable primary reduction product. The literature, however, contains conflicting

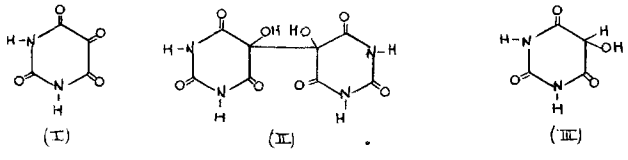

(I) (II) (III)

[1] Present address: Department of Chemistry, Aquinas College, Grand Rapids, Michigan 49506.

Key words: 2,4,5,6-trioxypyrimidine, alloxantin, dialuric acid.

reports on the stability of alloxantin (8-10). Struck and Elving (7) claim that alloxantin is not appreciably dissociated in solution (to alloxan and dialuric acid) and that it is polarographically active and gives rise to an anodic wave at the same $E_{1/2}$ as that of dialuric acid, and a small kinetically controlled cathodic wave at the same $E_{1/2}$ as that of alloxan. It was also claimed to give only a very small cathodic wave at potentials corresponding to alloxan wave II (7). In some recent work in this laboratory (4, 5) it become necessary to understand the details of the electrochemistry of alloxan and its N-methyl derivatives. It became clear that more study was necessary, first to clarify the involvement of the methylated alloxantins in the polarographic reduction of the alloxans, second to ascertain the nature of the wave II process, and third to explain the process responsible for a further small wave which was observed at low pH.

Experimental

Chemicals.—Dimethyl and methyl alloxan were prepared according to the method of Fischer (11). Alloxan was obtained from Nutritional Biochemicals, alloxantin from Eastman, and dialuric acid from Calbiochem. Buffer solutions had an ionic strength of 0.5. Argon used for deoxygenation was equilibrated with water.

Apparatus.—Equipment employed for polarography, voltammetry, and coulometry has been described elsewhere (4, 5, 12-14, 16, 19), with the exception that salt bridges in the electrochemical cells were composed of agar-potassium sulfate. The reference electrode was a saturated mercurous sulfate [0.40V *vs.* SCE (15)] and the counterelectrode was a cylindrical platinum gauze dipping in saturated potassium sulfate solution. All potentials are referred to the SCE at 25°C.

The DME had an M value of 1.375 mg sec^{-1} and $t = 5.08$ sec^{-1}, at open circuit with $h = 70$ cm.

The cell used for macroscale coulometric and preparative electrolysis contained three compartments and was adapted from that described previously (16), with the reference and counterelectrodes described above. All compartments were equipped with stoppers and bubblers to ensure complete deoxygenation.

Solutions.—Solutions of the alloxans were not stable so each test solution was made up in the desired buffer immediately prior to use. Solutions used for the pH study were normally about 1 mM in concentration.

Determination of coulometric n-values.—General procedures employed for the determination of coulometric n-values are described elsewhere. In most cases the electrolysis was considered complete when the quantity of acid added into a titration coulometer (15) per unit time matched that required for identical electrolysis of background solution. However, at the pH values where wave II is observed alloxan is very unstable. Electrolysis time was therefore limited to 30 min. The concentration of the remaining alloxan was determined polarographically by comparison with a calibration curve prepared as described below.

Polarographic i_l — C curves at pH 4.9 to 5.1.—Two consecutive concentration-decomposition studies were performed on each alloxan. Solutions of the respective alloxan were prepared (1.0 mM) in pH 4.9 or pH 5.1 McIlvaine buffer and 1, 2, 3, 4, and 5 ml aliquots immediately transferred into volumetric flasks containing the background solution giving a total 10 ml volume. The solutions were allowed to stand for 30 min. Immediately after this period polarograms from −1.2 to −1.6V were obtained. The solutions were scanned in the order 0.1, 0.5, 0.2, 0.4, and 0.3 mM. Background current at the potential of the limiting current of wave II was obtained as the average from several background polarograms and was subtracted from the average limiting current at each concentration.

UV spectrophotometric procedures.—Samples studied spectrally had to be maintained in an oxygen-free environment. All flasks, cells, and pipettes were flushed with nitrogen prior to use. Positive nitrogen pressure was used to transfer solutions from pipettes. Solutions used for dilution of the reduction product solution or for dissolution of alloxantin and dialuric acid were also thoroughly deoxygenated.

Alloxantin dissociation study.—A solution, 0.2 mM in alloxantin, was prepared in pH 4.7 acetate buffer as follows: a weighed quantity of alloxantin was placed in a volumetric flask which had been flushed with nitrogen and a deoxygenated solution of buffer added. Dissolution was accomplished by heating in a water bath (*ca.* 5 min) while a steady stream of nitrogen was passed through the solution. After cooling, an air-free transfer was made to the nitrogen-filled polarographic cell, and polarograms from −1.2 to −1.6V and then from +0.4 to −0.2V were recorded.

Results and Discussion

Aqueous solutions of methyl and dimethyl alloxan exhibit three cathodic waves at the DME. Wave I_a (the most positive wave) occurs between pH 0-8 and 0-7.1 for methyl and dimethyl alloxan respectively. Wave I_b appears between pH 0-3 and wave II between about pH 4.7-5.9 for both compounds. Above pH 4-5 alloxan and its N-methyl derivatives begin to decompose into the appropriate nonelectroactive alloxanic acids (Eq. [1]); this reaction becomes rapid at pH 7-8 (18).

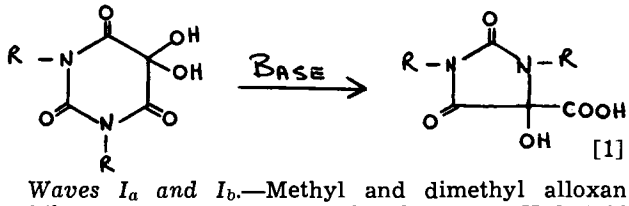

[1]

Waves I_a and I_b.—Methyl and dimethyl alloxan exhibit waves I_a and I_b together between pH 0 (1M H_2SO_4, Fig. 1A) and pH 3. Above pH 3 wave I_b disappears (Fig. 1B). Wave I_a for both compounds shifts linearly more negative with increasing pH, $E_{1/2}$

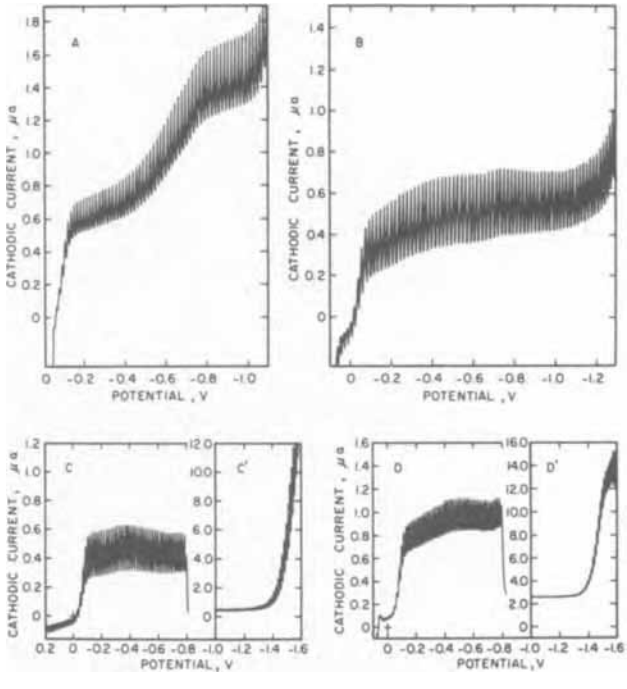

Fig. 1. Polarograms of dimethyl alloxan in A, 2M H_2SO_4; B, McIlvaine buffer pH 3.7; C, Acetate buffer pH 4.3; D, McIlvaine buffer pH 4.9. Concentration dimethyl alloxan A, 1.3 mM; B, 1.1 mM; C, 1.1 mM; D, 1.5 mM.

$= 0.10\text{-}0.033$ pH for methyl alloxan, and $E_{1/2} = 0.10\text{-}0.036$ pH for dimethyl alloxan. These equations compare favorably with that for the first wave of alloxan where $E_{1/2} = 0.060\text{-}0.031$ pH (7), and are in accord with that expected for a reversible process involving two electrons and one proton. The diffusion current constants ($I = i_l/Cm^{2/3}t^{1/6}$) for wave I_a of methyl and dimethyl alloxan are very small. Between pH 0-5.9 the mean diffusion current constant for methyl alloxan was 0.23 and for dimethyl alloxan was 0.30. The limiting current for wave I_a for both compounds was independent of the corrected mercury column height indicating that the electrode reaction was kinetically controlled. A temperature coefficient of 4.3% per °C (methyl alloxan) and 5.2% per °C (dimethyl alloxan) further confirmed the kinetic nature of the wave I_a process.

Wave I_b is essentially pH independent and occurs at -0.27 ± 0.03V for methyl alloxan and -0.34 ± 0.07V for dimethyl alloxan. The limiting current for wave I_b decreases significantly as the pH approaches 3. Above pH 3 wave I_b is not observed indicating that the species reduced exists only at low pH. The diffusion current constant for wave I_b of methyl alloxan (0.10 between pH 0-2) is considerably smaller than for wave I_b of dimethyl alloxan (0.17 between pH 0-2). The temperature coefficient of the limiting current for wave I_b of dimethyl alloxan, 1.2% per °C in chloride buffer pH 1.9, is smaller than that expected for a kinetically controlled process.

Polarograms of dimethyl alloxan in McIlvaine buffers above pH 2.2 (Fig. 1B, D) and in acetate buffers pH 3.4-5.3 (Fig. 1C) indicate that the shape of the current-potential curve for wave I_a at potentials immediately more negative than the half-wave potential differs between the two buffers. In McIlvaine buffers this region is more drawn out and the limiting current is reached at potentials approximately 0.3V more negative than with acetate buffers. This effect does not constitute a second distinguishable reduction wave. A similar phenomenon, *i.e.* a wave more drawn out than is generally expected, was reported (19) for parabanic acid and its N-methylated derivatives in McIlvaine buffers over a limited pH range. This was explained as the reduction of phosphate complexes, the structures of which were also proposed, of the respective parabanic acid. The arrangement of carbonyl groups in dimethyl alloxan is similar to those of the parabanic acids and, therefore, analogous complexes are plausible for a dimethyl alloxan phosphate interaction. The wave I_a reduction in McIlvaine buffer, pH $\geq$ 2.9, may represent, therefore, the reduction of both dehydrated dimethyl alloxan and the dimethyl alloxan-phosphate complex.

Wave II.—Wave II of methyl and dimethyl alloxan can be observed between pH 4.7-5.9 and is comparable to wave II of alloxan (7). Accurate measurement of the limiting current is complicated by the decomposition of the alloxans to the appropriate alloxanic acid. However, the limiting current appeared to be diffusion controlled as evidenced by its dependence on the corrected mercury column height. The diffusion current constant for wave II of methyl alloxan ranged from 3.8 at pH 4.7 to 1.7 at pH 5.9. For dimethyl alloxan over the same pH range the value changed from 2.8-1.6. The systematic decrease of the diffusion current constant with increasing pH reflects the increasing rate of decomposition of the alloxans to the alloxanic acids. Over approximately the same pH range alloxan itself gives an average diffusion current constant for wave II of about 3.6 (7).

The half-wave potential for wave II of methyl alloxan (-1.46 ± 0.01V) and dimethyl alloxan (-1.41 ± 0.01V) between pH 4.7-5.9 are pH independent. Between pH 4.6-6.6 wave II of alloxan is also virtually pH independent (-1.51 ± 0.02V) (7).

Table I. Coulometric determination of the number of electrons involved in the reduction of alloxan and n-methylated derivatives

Supporting electrolyte	pH	Controlled potential	n
		Dimethyl alloxan	
		Wave I	
1*M* HOAc	2.3	−0.4	1.9[a]
		Wave II	
McIlvaine	4.9	−1.4	1.9[c]
		Methyl alloxan	
		Wave I	
1*M* HOAc	2.3	−0.4	1.9[c]
		Wave II	
McIlvaine	4.8	−1.50	1.6[c]
		Alloxan	
		Wave I[b]	
Acetate	4.0	—	1.9
		Wave II	
McIlvaine	4.8	−1.50	2.3[c]

[a] Mean of at least three determinations usually. Reproducibility of data ±5%.
[b] Values from work of Struck and Elving (7).
[c] At pH values of about 5 the decomposition of the alloxans was quite rapid and the reproducibility of data was ±10-15%.

Coulometry

Data from coulometric determinations of the number of electrons involved in the reduction of alloxan, methyl alloxan, and dimethyl alloxan at controlled potentials corresponding to waves I (includes I_a plus I_b in the case of the methylated compounds) and II respectively are summarized in Table I. Clearly, electrolysis of all alloxans at potentials corresponding to the crest of wave I results in the transfer of close to 2 electrons per molecule reduced. Complete electrolysis was not attempted at potentials corresponding to wave II because the alloxan solutions were not sufficiently stable at the required pH. The period of the electrolysis was therefore limited to 30 min. The concentration of the remaining parent compound was determined polarographically (see Experimental). Average coulometric n values of 2.3, 1.6, and 1.9 were obtained for alloxan, methyl and dimethyl alloxan respectively.

Identification of Reduction Products

It is clear that both waves I and II of alloxan species involve 2*e*. Because of our greater interest in dimethyl alloxan, product identification was limited to this compound; analogous products were assumed from the other alloxans.

Wave I.—Polarography of a 1*M* HOAc solution of reduced dimethyl alloxan revealed the presence of a single large anodic wave, $E_{1/2} = 0.01$V (Fig 2). Dialuric acid shows analogous polarographic behavior to this product (attempts to prepare dimethyl dialuric acid in this laboratory were unsuccessful).

Dialuric acid was isolated as a solid upon macroscale reduction of alloxan (7); dimethyl dialuric acid was not observed as a solid product under similar conditions upon reduction of dimethyl alloxan.

When aliquots of the electrolyzing solution were taken at intervals and examined spectrophotometrically a highly oxygen-sensitive species absorbing at $\lambda_{max} = 274$ mμ was observed which increased in concentration as the electrolysis proceeded; upon exposure to air the absorbing species disappeared. Under the same solution conditions alloxantin and dialuric acid show similar behavior, except that the absorption of the nonmethylated species occurs at $\lambda_{max} = 271$ mμ; only dialuric acid absorbs in these regions (20). Alloxantin does not itself absorb; its apparent absorbing properties therefore arise as a result of its disproportionation to alloxan and dialuric acid. The slight shift in the λ_{max} value for the methylated dialuric acid is readily understood by consideration of the spectra of methylated and nonmethylated ureido species such as the uracils which show shifts of similar magnitudes and direction (21).

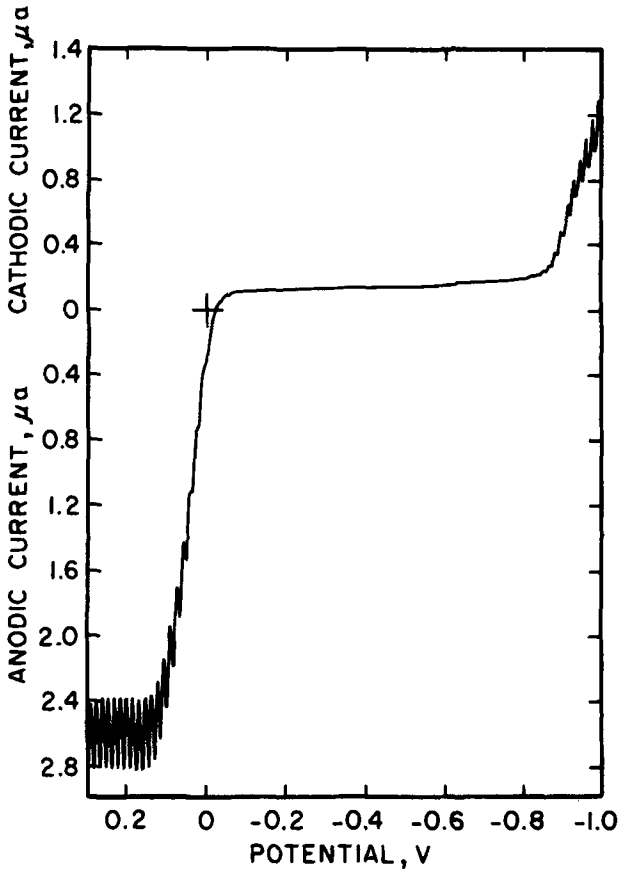

Fig. 2. Polarogram of reduction product of dimethyl alloxan electrolyzed at −0.4V (wave I) in 1M HOAc. Initial concentration dimethyl alloxan 1.0 mM.

Polarographic dissociation studies (7) have been reported to show that alloxantin does not exhibit wave II in a height comparable to that observed with alloxan itself, hence supporting the view that alloxantin is not highly dissociated. In our studies it was found that in acetate buffer pH 4.7 alloxantin does show wave II and that it is at least ten times the height of wave I. In order to obtain sufficiently accurate measurements of the current for waves I and II of alloxantin it was necessary to employ a concentration of at least 0.2 mM, which required warming of the solution (under air-free conditions) to achieve dissolution. These polarographic and spectrophotometric studies therefore support the view that alloxantin is rapidly dissociated in solution to give an equimolar mixture of alloxan and dialuric acid.

Wave II.—Polarography of the product of electrolysis of dimethyl alloxan in pH 5.1 McIlvaine buffer at potentials on the crest of wave II showed a well-formed anodic wave ($E_{1/2} = -0.09$V) (Fig. 3) which grew in height as the electrolysis proceeded; the height for cathodic wave II correspondingly decreased. The two-electron nature of the wave II process and the fact that the $E_{1/2}$ for its reduction product is identical with that from the wave I reduction and for wave I_a itself ($E_{1/2} = -0.09$V in both cases) (Fig. 3) suggests that the product for wave II is identical to that from wave I, *i.e.* dimethyl dialuric acid. That this is so is further confirmed by the susceptibility of the wave II product to air oxidation back to dimethyl alloxan and its uv absorption spectra ($\lambda_{max} = 276$ mμ), which is in the region expected for dimethyl dialuric acid (for dialuric acid at the same pH $\lambda_{max} = 273$ mμ).

Mechanism

The over-all electrochemical reduction of alloxan, methyl and dimethyl alloxan indicates the same number of electrons for their polarographic waves I and II, with similar current controlling factors and $E_{1/2}$ — pH equations; the basic polarographic processes are hence essentially identical for all compounds.

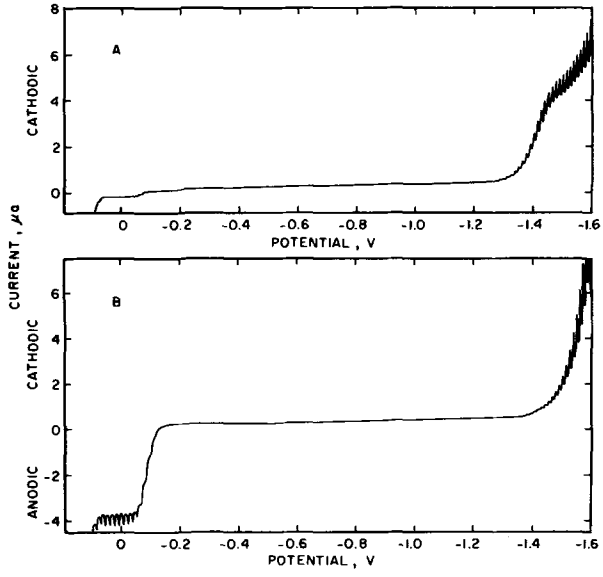

Fig. 3. Polarograms of A, 1.0 mM dimethyl alloxan and B, reduction product of 1.0 mM dimethyl alloxan after electrolysis at −1.40V (wave II). Background, McIlvaine buffer pH 5.1.

Wave I_a.—The kinetic step involved in wave I_a is undoubtedly dehydration of the carbonyl group at C-5, a process well characterized for several related systems (6, 22) (Fig. 4) and for alloxan itself (6, 7). The $E_{1/2}$ — pH relationships for all compounds (shift of *ca.* 30 mV per pH unit) is in accord with a two-electron, one-proton reversible process. Polarography and cyclic voltammetry of alloxan at a pyrolytic graphite electrode support the view that the process is virtually reversible (Fig. 5). In order to observe the anodic peak at *ca.* −0.1V in Fig. 5 it is only necessary to scan the first cathodic peak at $E_p = -0.2$V. A two-electron reduction process is indicated by coulometry, and the product is the respective dialuric acid. Accordingly, in support of the mechanism of Struck and Elving (7) wave I_a is a two-electron, one-proton reduction of the alloxan (II, Fig. 4) to the appropriate dialuric acid anion (III, Fig. 4). At this stage it is not possible to decide whether alloxantin is the primary product of the electrochemical reduction of alloxan because of the rapid dissociation of alloxantin in aqueous solution. These findings on the extent of dissociation are in accord with those of Hill and Michaelis (9).

Wave I_b.—Wave I_b is observed most distinctly for dimethyl alloxan; it is considerably smaller for methyl alloxan and, except at very high alloxan concentrations and very low pH, is not normally observed for alloxan itself. Wave I_b for methyl and dimethyl alloxan is under kinetic control and occurs at a more negative potential than wave I_a; its $E_{1/2}$ is essentially pH independent, and the height of the wave decreases with increasing pH and disappears above pH *ca.* 3. It is known that alloxans form protonated species at very low pH (10, 20) and reduction of this species no doubt results in wave I_b. Since both waves I_a and I_b below pH 3 occur to the positive side of the electrocapillary maximum (*i.e.*, the electrode is positively charged), then approach of a cationic species towards the electrode would be energetically more difficult than approach of a neutral species, hence wave I_b occurs at more negative potentials than wave I_a (23). The kinetic nature of wave I_b would normally be expected to result in a temperature coefficient of >5% per °C; however, that for wave I_b of dimethyl alloxan

is much lower (1.2% per °C at pH 1.9). Previous studies of other cationic acids (24, 25) has indicated that cationic acid dissociation constants increase with increasing temperature, *i.e.* the concentration of the cationic species is lower at 40°C than at 25°C (the temperatures employed in this work to evaluate temperature coefficients). Thus, although the temperature coefficient of wave I_b is of a magnitude normally associated with a diffusion-controlled process, it actually represents a kinetically controlled process modified by appreciable changes in the solution concentration of the electroactive species, *i.e.* the dimethyl or methyl alloxan cation.

Thus, in other words alloxan at low pH exists primarily in the hydrated form which is not electroactive at the wave I_a, I_b potentials. It is probable that an equilibrium mixture of protonated and nonprotonated hydrated alloxan exists (10, 20). Some alloxan however exists in the dehydrated form and again no doubt an equilibrium mixture of protonated and nonprotonated dehydrated alloxan exists. The nonprotonated dehydrated alloxan (II, Fig. 4) gives rise to wave I_a which at low pH is primarily kinetically controlled by the dehydration reaction (I → II, Fig. 4) but also no doubt to a much lesser extent by the deprotonation reaction (IV → II, Fig. 4). Wave I_b corresponds to reduction of protonated dehydrated alloxan which again is primarily kinetically controlled by the dehydration reaction but also possibly by the protonation reaction (II → IV, Fig. 4). The behavior of the dehydrated alloxan and its conjugate acid is polarographically analogous to the well-documented behavior of polarographically reducible weak acids (26), except that as a result of the electrode reaction occurring at a positively charged electrode and the positive charge of the acid the relative potentials of the acid and its conjugate base are reversed. Thus normally with a neutral weak acid (HA) and its conjugate base (A^-) reduction occurs at a negatively charged electrode so that the conjugate base (A^-) is reduced at more negative potential than the acidic species. The mechanism for wave I_b is presented in Fig. 4 where the structure of the cationic form of alloxan (IV, Fig. 4) is written in a general form.

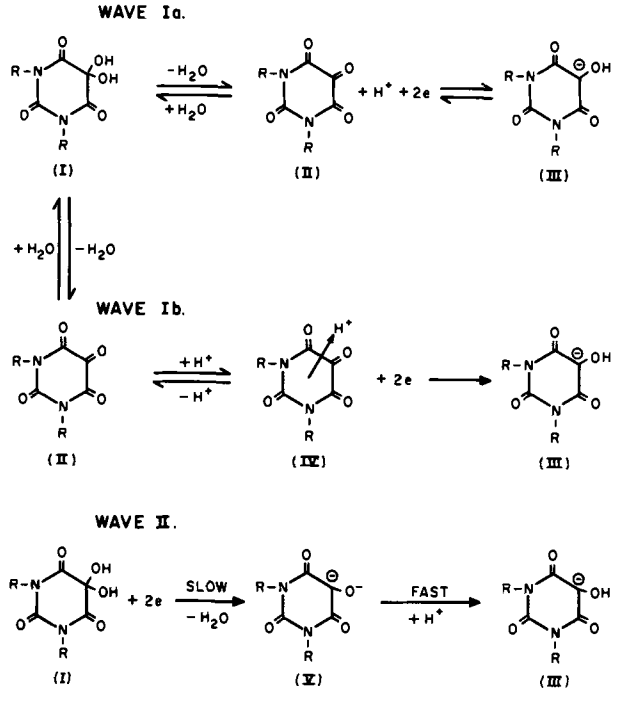

Fig. 4. Proposed reaction pathways for the polarographic reduction of the alloxans. I, hydrated alloxan; II, dehydrated alloxan; III, dialuric acid monoanion; IV, alloxan cation; V, dialuric acid dianion.

The current for wave I_b of methyl alloxan is much smaller than that for dimethyl alloxan. However, the inductive effect of an electron-releasing substituent, such as $-CH_3$, is similar, although less pronounced, to a negative charge on nitrogen (21). Thus, a methylated amide carbonyl is expected to be a more favored proton acceptor than a nonmethylated amide carbonyl. It is thus expected that dimethyl alloxan would be a better proton acceptor, or more readily form an alloxan cation than methyl alloxan. This is reflected in the magnitude of the wave I_b limiting currents. In the case of unsubstituted alloxan, the proton acceptor properties are the least of all three compounds so that even in 1*M* H_2SO_4 solution a 10 mM solution of alloxan is required before wave I_b can be observed.

Wave II.—The magnitude of the polarographic diffusion current constant and coulometry indicate that wave II is a 2*e* process for all alloxan species. Polarography and spectra indicate that the electrolysis product from dimethyl alloxan is identical to that produced from wave I, *i.e.*, dimethyl dialuric acid. Cyclic voltammetry indicates that the wave II process is not reversible. The computed αn_a values (26) for all three alloxans (1.07 ± 0.01) and the virtual pH independence of wave II supports the view that it involves a two-electron potential-controlling and over-all transfer of electrons to give the dianion of dialuric acid (V, Fig. 4). The only possible route by which this mechanism can proceed is by reduction of the hydrated form of alloxan (I, Fig. 4), the predominant solution species. In the case of all three compounds it is very unlikely that wave II is due to reduction of the dialuric acid as suggested by Struck and Elving (7). This is so because not only is dialuric acid not reduced at the wave II potential (or any

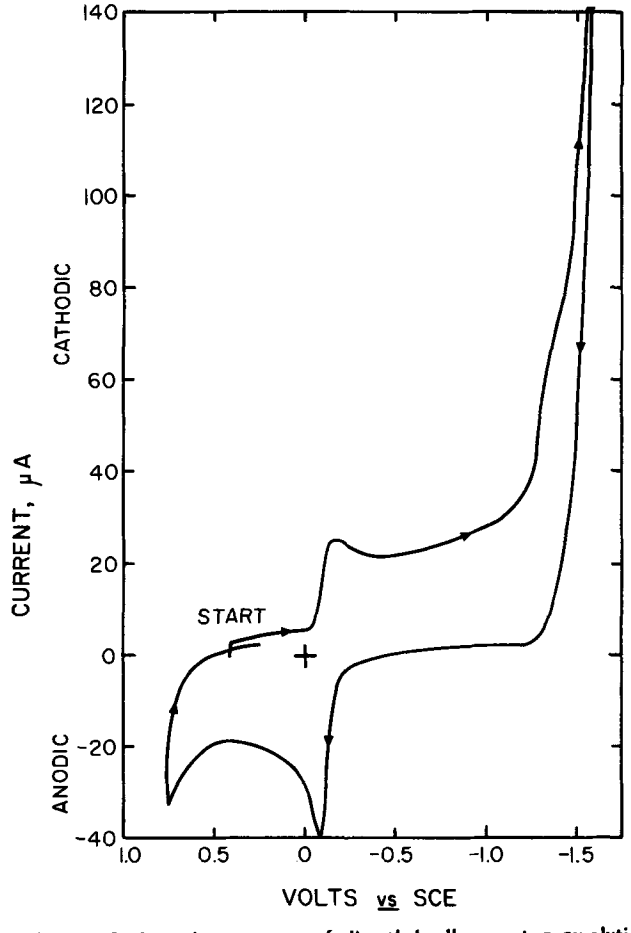

Fig. 5. Cyclic voltammogram of dimethyl alloxan at a pyrolytic graphite electrode in McIlvaine buffer pH 4.7. Scan rate, 200 mV/sec; electrode area, 10 mm².

other potential), but even if it was wave II should also be at least partly under kinetic control.

Dissociation of alloxantins in solution.— In view of the distinct contradiction between our study of alloxantin and that of earlier workers (7) a further discussion of their data and ours is presented.

The former workers indicate [Fig. 7, Ref. (7)] that a 0.25 mM solution of alloxantin in pH 4.0 acetate buffer gives almost exactly one-half the anodic current observed for a 0.5 mM solution of dialuric acid and about half the cathodic current (wave I) observed for a 0.5 mM solution of alloxan; the half-wave potentials for all waves being essentially identical. The cathodic currents for alloxantin and alloxan (wave I) are under kinetic control. This immediately suggests that alloxantin is completely dissociated in aqueous solution, especially so since it is very difficult to see an obvious way that the alloxantin process could be under kinetic control. The fact that we detect dialuric acid spectrally and via its anodic polarographic wave in solutions prepared from alloxantin, and also that alloxan wave II can be observed polarographically in such solutions at the appropriate pH, further supports the view that alloxantin is completely dissociated. Struck and Elving (7) further attempted to confirm the nondissociation of alloxantin by adding large excesses of alloxan to the polarographic solutions. If alloxantin were partially dissociated or the association constant were not too large, then the excess alloxan should have decreased the anodic wave if it was due to dialuric acid. The fact that it did not was taken to infer that alloxantin was not dissociated at all to dialuric acid. However, it is equally plausible to explain the effect if the dissociation constant for alloxantin is very large as our data suggest.

Acknowledgment

The authors would like to thank the National Science Foundation which supported the work described.

Manuscript submitted April 20, 1971; revised manuscript received *ca.* July 6, 1971.

Any discussion of this paper will appear in a Discussion Section to be published in the June 1972 JOURNAL.

REFERENCES

1. W. A. Struck and P. J. Elving, *Biochemistry*, **4**, 1343 (1965).
2. G. Soberon and P. P. Cohen, *Arch. Biochem. Biophys.*, **103**, 331 (1963).
3. K. G. Paul and Y. Avi-Dor, *Acta Chem. Scand.*, **8**, 637 (1954).
4. B. H. Hansen and G. Dryhurst, *J. Electroanal. Chem.*, Submitted for publication.
5. B. H. Hansen and G. Dryhurst, *ibid.*, In press.
6. S. Ono, M. Takagi, and T. Wasa, *Bull. Chem. Soc. Japan*, **31**, 364 (1958).
7. W. A. Struck and P. J. Elving, *J. Am. Chem. Soc.*, **86**, 1229 (1964).
8. E. Biilman and N. Berg, *Chem. Ber.*, **63 B**, 2188 (1930).
9. E. S. Hill and L. Michaelis, *Science*, **78**, 485 (1933).
10. G. M. Richardson and R. R. Cannan, *Biochem. J.*, **23**, 68 (1929).
11. E. Fischer, *Chem. Ber.*, **14**, 1912 (1881).
12. G. Dryhurst, M. Rosen, and P. J. Elving, *Anal. Chim. Acta*, **42**, 143 (1968).
13. G. Dryhurst and P. J. Elving, *This Journal*, **115**, 1014 (1968).
14. G. Dryhurst, *ibid.*, **116**, 1411 (1969).
15. J. J. Lingane, "Electroanalytical Chemistry," 2nd ed., p. 363, Interscience Publishers, New York (1958).
16. G. Dryhurst, *This Journal*, **116**, 1357 (1969).
17. J. J. Lingane, "Electroanalytical Chemistry," 2nd ed., p. 457, Interscience Publishers, New York (1958).
18. E. D. Korn, "Methods in Enzymology," Vol. IV, p. 634, E. P. Colowick and N. O. Kaplan, Editors, Academic Press, New York (1957).
19. G. Dryhurst, B. H. Hansen, and E. B. Harkins, *J. Electroanal. Chem.*, **27**, 375 (1970).
20. J. Patterson, A. Lazarow, and S. Levey, *J. Biol. Chem.*, **177**, 187 (1949).
21. F. Bergmann and S. Dikstein, *J. Am. Chem. Soc.*, **77**, 691 (1955).
22. S. G. Mairanovskii, "Catalytic and Kinetic Waves in Polarography," p. 37, Plenum Press, New York (1968).
23. P. J. Elving and J. S. Leone, *J. Am. Chem. Soc.*, **80**, 1021 (1958).
24. H. A. Laitinen, "Chemical Analysis," p. 46, McGraw Hill, New York (1960).
25. D. H. Everett and W. F. K. Wynne-Jones, *Proc. Royal Soc. (London) Ser. A*, **169**, 190 (1938).
26. L. Meites, "Polarographic Techniques," 2nd ed., John Wiley and Sons, New York (1965).

The Electrochemical Behavior of Technetium and Iron Containing Technetium

G. H. Cartledge

Chemistry Division, Oak Ridge National Laboratory, Oak Ridge, Tennessee 37830

ABSTRACT

The electrochemical behavior of pure technetium and iron containing 0.1 weight per cent (w/o) technetium has been determined by polarization in sulfuric acid. Evolution of hydrogen on technetium has a Tafel slope approximating −40 mV/decade. At overvoltages noble to the hydrogen-evolution potential, oxidation of technetium or its surface oxides has a rate of *ca.* 10^{-6} A/cm^2 until the potential becomes high enough to form soluble pertechnic acid. The current density then rises rapidly. The presence of technetium in iron modifies the electrochemical behavior because dissolution of iron leads to enrichment of the surface in residual technetium. This causes the open-circuit potential to ennoble, with lowering of the overvoltage for evolution of hydrogen. Passivation is also rendered more difficult and much less effective in lowering the passive corrosion current density.

Recent studies showed that technetium forms hydrous oxides as surface films in which the element exhibits valencies of 1+, 2+, 3+, and 4+, as well as two hybrid oxides Tc_3O_4 and Tc_4O_7. The compounds were identified in both anodic polarization of the metal and cathodic reduction of $Tc(OH)_4$ deposited electrolytically on the metal. The measurements led to free energies of formation for all the compounds (1). The present paper gives the results of studies of the po-

Key words: technetium, hydrogen evolution, polarization, passivity, iron-technetium, electrode potential, technetium oxides, "unpolarizability."

larization of technetium and of an iron alloy containing 0.1% technetium. It was found that the contrasting electrochemical properties of iron and technetium give rise to some unusual behavior in polarization; the radioactivity of technetium permits a correlation of this behavior with the concentration of technetium in the surface during anodic polarization.

Experimental

Materials.—The technetium electrodes were similar to those described in connection with the thermodynamic measurements (1), namely, a 0.72g rf-melted pellet and technetium plated over platinum or gold substrates. In addition, a swaged rod of pure technetium was used as a check on the polarization. An iron master alloy was made by addition of 1 w/o of technetium powder to pure iron; this was then diluted to 0.1 w/o. The product was machined down to rods of 0.25 in. diameter, cut into 1 cm lengths, and these were tapped and threaded for attachment to the insulated stainless steel electrode assembly. The electrodes were then encapsulated in quartz tubes *in vacuo* and heat treated for 30 min at 700°C, with air cooling. The specimens remained in the capsules until the beginning of the measurements. (The author is indebted to the Metals and Ceramics Division for preparation of the alloy electrodes, and especially to Mr. Carl Koch for loan of a rod of pure technetium.)

Procedure.—Just prior to their first use, technetium electrodes were either reduced in H_2 at 425°C or cathodically polarized in 1*N* NaOH for 10 min at *ca.* 0.5 A/cm^2. They were then dipped into 12*N* HCl for a few seconds, rinsed, and at once put into the cell. In certain experiments a second cathodic polarization followed a complete cathodic and anodic series of measurements without intervening treatment of the electrode. The iron alloy electrodes were first electropolished in H_3PO_4:HNO_3:CrO_3 (80:20:excess) at *ca.* 80°C, treated with 6*N* NH_4OH containing H_2O_2 to convert superficial technetium or its oxides to soluble ammonium pertechnetate, then etched in 6*N* HCl containing a little H_2O_2, rinsed and at once transferred to the cell. This was an H cell holding 125 ml of electrolyte in each side. Hydrogen or helium purified by passage over copper at 425°C was aspirated through the solution, and the electrolyte could be renewed without access of air. Polarization was effected both galvanostatically from batteries and potentiostatically, as in (1). Potentials are expressed in mV referred to SCE. Measurements were made at 24°C.

Results

Technetium electrodes: cathodic polarization.—The anodic oxidation of hydrogen on a technetium surface is so rapid that cathodic polarization curves rarely indicate Tafel behavior until the current density is great enough to be significantly affected by both *IR* and concentration polarization. A fortunate circumstance, however, was the discovery that this anodic process has a rate which is approximately independent of the potential over a considerable range of overvoltage on both sides of the $\eta = 0$ axis. This behavior is shown in Fig. 1. Here, a platinum spiral was plated first with gold and then with technetium. The electrode was heated in hydrogen at 425°C to reduce any oxide in the film. The resultant electrode had a bright, silvery appearance. It was then polarized in 1*N* H_2SO_4 in an atmosphere of hydrogen. Polarization covered the range of overvoltage from −100 to +50 mV. It was found that application of an *IR* correction in the 10^{-3} decade (X's on the curve) indicated a probable Tafel line which crossed the $\eta = 0$ axis at about 9 x 10^{-5} A/cm^2. Such a Tafel was then tested on the positive side to evaluate the anodic current density. The X's on the anodic side of Fig. 1 show that this is between 9 x 10^{-5} and 1 x 10^{-4} A/cm^2 and that it varies little, if any, with overvoltage. An average value of 9.5 x 10^{-5} A/cm^2 was found to bring the measured cathodic current densities precisely up to the Tafel line indicated at higher current densities. The points denoted by X's in the 10^{-4} decade are calculated by application of this anodic correction. Concentration polarization is seen to begin at the highest negative potentials. This approximate constancy of the anodic oxidation of hydrogen made it possible to utilize polarization data in other experiments with equal success. It may be noted that Joncich, Stewart, and Posey observed a similar constancy in the polarization of rhenium (2).

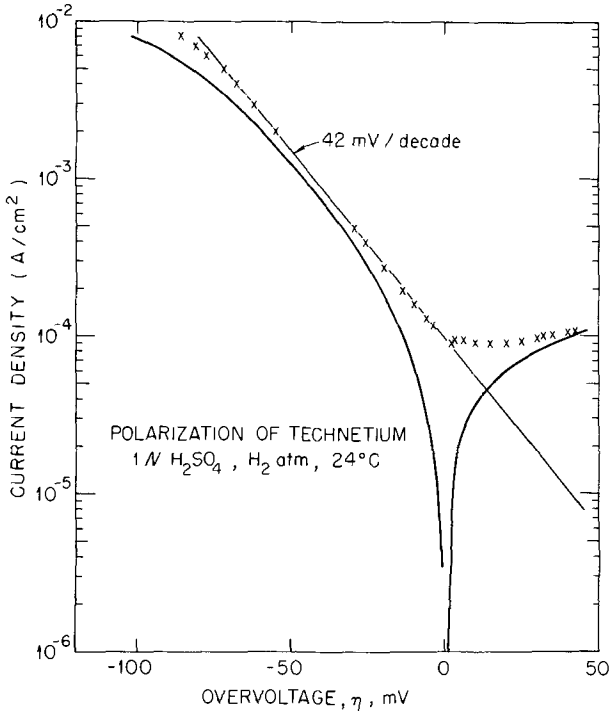

Fig. 1. Cathodic and anodic polarization of technetium in 1*N* H_2SO_4 in hydrogen. Curves show the consistency of the cathodic Tafel line with the assumption of a constant anodic current density of 9.5 x 10^{-5} A/cm^2.

The assumption of a constant anodic current density at overvoltages between 0 and −50 mV proved to be legitimate even in experiments in which helium was used as the purging gas. This circumstance arose from the further discovery that hydrogen, liberated at high negative overvoltages, is only slowly lost as the overvoltage is decreased. (This will be illustrated later.) For analyzing cathodic polarization curves, therefore, the procedure was to look for a possible Tafel line which would (*A*) parallel the polarization curve in the middle of the 10^{-3} decade and (*B*) cut the $\eta = 0$ axis at such a current density as would correct the cathodic data in the lower current densities up to a Tafel line consistent with the higher current densities when applied as a constant anodic current density. As a first approximation, the sum of the *IR* and concentration polarization corrections may be assumed to be proportional to the current density in the upper 10^{-3} and lower 10^{-2} decades. Then both the polarization correction, $j\,x$, and Tafel slope may be estimated algebraically from two equations of the form $(\eta_3 - j_3 x) - (\eta_1 - j_1 x) = -0.48T$, in which the subscript 3 refers to the overvoltage at a current density j_3 that is 3 times as large as that at j_1. T is the Tafel slope in mV/decade, x is the correction factor in mV/mA-cm^{-2}, and η is in mV. The estimate obviously becomes more exact when applied in the region in which the corrections for both anodic current and concentration polarization are as small as possible, that is, from the middle of the 10^{-3} decade to that of the 10^{-2} decade. The approximated Tafel line will usually have a slope that is numerically too small, but from its intersection on the $\eta = 0$ axis

it may be determined by trial what small shift in j_+ is needed to satisfy criterion (*B*) above.

Sixteen cathodic polarizations were conducted with the pellet or rod of technetium and with technetium plated over gold or platinum. In two instances, a film of corrosion product was deliberately formed by leaving the electrode in the cell overnight in an atmosphere of helium. The resulting open-circuit potential was very close to the reversible potential of the Tc-TcOH couple (1) when polarization was started. The curve in Fig. 1 is representative of 10 experiments with fully reduced electrodes, the average Tafel slope being -41.2 ± 1.8 mV/decade (37 to 44). The two coated electrodes agreed in having a Tafel slope of -80 mV/decade. When a cathodic polarization followed an anodic polarization to some 100 mV noble to the H.E.V., the cathodic Tafel slope was intermediate between these values (-47, -47, -48 mV/decade). By polarizing a given electrode both when fully reduced and, afterwards, when some anodic film had been formed, it was found that the correction for anodic current is considerably reduced by formation of film.

It is noteworthy that the j_+ value for the pellet electrode and for those in which technetium was plated over platinum was considerably larger than it was when a thin layer of technetium was plated over gold (*ca.* 10^{-3} *vs.* 10^{-4} A/cm²). For this reason, measurements with the different types of electrodes gave Tafel lines which span about 70 mV in their position on the axis of overvoltage. Although the absolute surface areas undoubtedly differed somewhat from the estimated areas, this variation could not be sufficient to account for the observed span. A possible factor may be the fact that platinum absorbs more hydrogen than does gold. Such an explanation would be consistent with other experiments in an atmosphere of helium. In these, it was observed that the current density at a given negative overvoltage decreases if the electrode is left on open circuit for some time and then polarized again at the same potential. The current density at this potential can be raised by holding the electrode at a higher negative potential to recharge the electrode fully with hydrogen and then restoring the original potential. It thus appears that the rate of the cathodic process is related to the concentration of hydrogen in the electrode. (The necessity to use helium in polarizations near or noble to the H.E.V. arises from the fact that oxidation of technetium begins in this region, although the current density is much lower than that for oxidation of hydrogen.)

Technetium electrodes: anodic polarization.—As was shown before (1), technetium forms a series of hydrous oxides as surface films when subjected to anodic polarization, or when $Tc(OH)_4$ precipitated upon the metal is reduced cathodically. The numerous couples between the metal and one of these oxides, or between two of the oxides, have normal potentials, V_H^o, covering the span between 0.031 and 0.768V. Anodic polarization therefore oxidizes both hydrogen, if present, and technetium or its oxides. A further complication in anodic polarization is the slowness of the transitions between the several couples formed by the insoluble oxidation products, hence the results of an anodic polarization are highly dependent upon the state of the electrode when polarization is started.

In discussing the analysis of cathodic polarization curves above, Fig. 1 was used to illustrate the constant rate of oxidation of hydrogen from the technetium surface on both sides of η_0. This behavior is further examined in experiments represented by Fig. 2. Curves 1 and 2 pertain to anodic scans at the rate of 48.3 mV/min, following cathodic polarization of the pellet electrode in 1*N* H_2SO_4 in hydrogen. After this initial polarization, the open-circuit potential was -263 mV, or within 3 mV of the calculated H.E.V. Helium then replaced hydrogen before beginning the scan at -400 mV. Curve 1 shows that the current density fluctuated somewhat during the first part of the experiment, but

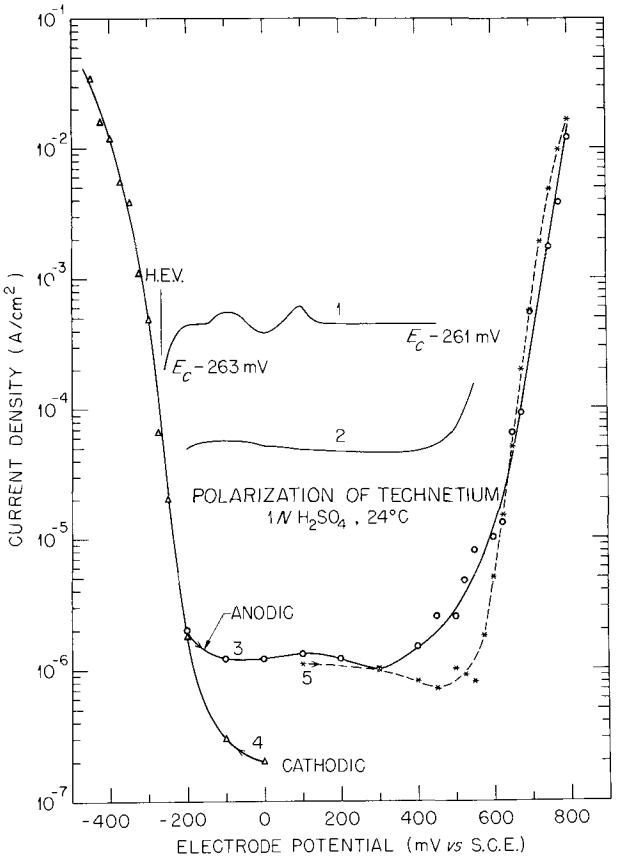

Fig. 2. Polarization of technetium electrodes in 1*N* H_2SO_4. Curve 1: Scan at 48.3 mV/min in helium after cathodic polarization. Curve 2: Second scan after 20 min on open circuit. Curve 3: Potentiostatic anodic polarization after holding potentials of -200 to 0 mV for 48 min to oxidize hydrogen. Curve 4: Cathodic polarization of electrode bearing film from curve 3. Curve 5: Anodic polarization following curve 4 and elimination of hydrogen at -100 and 0 mV (61 min).

then remained at 4.5×10^{-4} A/cm² until the scan was discontinued at +450 mV. During this interval (17.6 min), the open-circuit potential ennobled only 2 mV, thus indicating that the electrode still contained hydrogen.

The electrode was then left on open circuit for 20 min, during which time the potential rose and was still rising at -235 mV, when the scan was repeated, beginning at -200 mV. The result is shown in curve 2. The oxidation rate is an order of magnitude lower, but as the succeeding experiments showed, more drastic treatment is required to suppress the hydrogen reaction completely.

In the measurements represented by curve 3, the pellet electrode was given a rapid cathodic polarization (in helium), and when the current became anodic each potential was maintained potentiostatically until an approximately constant current density was realized. These times were 23 min at -200 mV, 17 min at -100 mV, and 8 min at 0 mV. Polarization was then continued to 800 mV. The valley in the curve then fell at around 10^{-6} A/cm². The great increase in the current density beginning at 400 mV corresponds to conversion of the oxide film into soluble $HTcO_4$; it was observed in several similar experiments always to begin in the vicinity of 400 mV. (The normal potential of the $Tc(OH)_4$-TcO_4^- couple, V_H^o, is 0.738V, or 0.493V SCE.) The electrode was left in the cell overnight on open circuit with helium passing. Upon renewing the solution, the electrode potential was found to be 249 mV, or within 3 mV of the reversible potential of the Tc(II-IV) couple (1).

The electrolyte from the anodic half cell was analyzed for pertechnic acid, $HTcO_4$. For this purpose, an aliquot was treated with excess of $BaCO_3$ to remove all solutes but $Ba(TcO_4)_2$. A small aliquot of this solution

was evaporated on a counting plate for measurement of the beta activity. The total solution contained 0.6 mg of technetium as a result of the oxidation.

The filmed electrode was next polarized cathodically from 0 mV to −450 mV and back to −300 mV, the results being shown in curve 4. This curve, when corrected, gives a Tafel slope of −80 mV/decade, in agreement with the result for another electrode bearing a corrosion film. The low rate of reduction of the film at 0 mV is clearly seen, although the thermodynamic data indicate that $Tc(OH)_4$ should be reduced at this potential.

Following this cathodic polarization, the same electrode was held at 0 mV and −100 mV until the current density indicated substantial elimination of excess hydrogen (13 min at 0 mV, 40 min at −100 mV, and 8 min again at 0 mV). Anodic polarization from 100 mV now gave results (curve 5) in close agreement with those of curve 3 for higher potentials.

The results, taken together, show that technetium and its surface films are oxidized with a rate approximating 10^{-6} A/cm² over a range of potentials from −200 to +400 mV; at higher potentials, oxidation to $HTcO_4$ occurs rapidly. The tenacity with which hydrogen is retained in the metal is also shown, together with the fact that oxidation of hydrogen is essentially independent of the potential over a wide range.

The iron-technetium electrode.—The alloy electrodes were polarized in 1*N* H_2SO_4 (*p*H 0.35) and a 1*N* mixture of H_2SO_4 and Na_2SO_4 at a *p*H of 2.7. The indicated pretreatment gave as nearly reproducible a surface as it seemed possible to obtain, since the initial cathodic polarization of different specimens gave closely agreeing results. Figure 3, curve 1 shows the results for two potentiostatic cathodic polarizations (○,□). Concentration polarization becomes important at the higher current densities, but a Tafel line with a slope of −110 mV/decade is apparently indicated, this being only slightly less, numerically, than that normally observed on pure iron. The corrosion potential, *ca.* −500 mV (SCE), is approximately normal, but the indicated corrosion current density appears to be slightly higher than that for pure iron. Curve 1 is representative of numerous measurements.

When potentiostatic polarization was carried to potentials noble to the corrosion potential, an anomalous anodic curve was always obtained. At overvoltages up to perhaps +50 mV, a maximum current was observed quickly when the potential was shifted to a more noble value; it then decreased slowly. Intermittent measurement of the open-circuit potential showed that this was shifting in the noble direction as anodic corrosion proceeded, hence, at a fixed applied potential, the overvoltage decreased with passage of current. Curve 2 in Fig. 3 shows the results for a typical electrode, the approximately stabilized current densities being plotted against the applied potential. It is seen that the electrode is almost unpolarizable at *ca.* −440 mV until the current density has risen to the order of 10^{-2} A/cm². After anodic polarization was terminated at 4.6×10^{-2} A/cm², cathodic polarization in renewed electrolyte gave curve 3. The open-circuit potential had shifted to −470 mV, as shown at E'_c, in Fig. 3. It may be seen that the cathodic Tafel slope is not significantly diminished in this instance, but that the overvoltage for a given rate of evolution of hydrogen is about 70 mV lower than it was for the freshly prepared electrode.

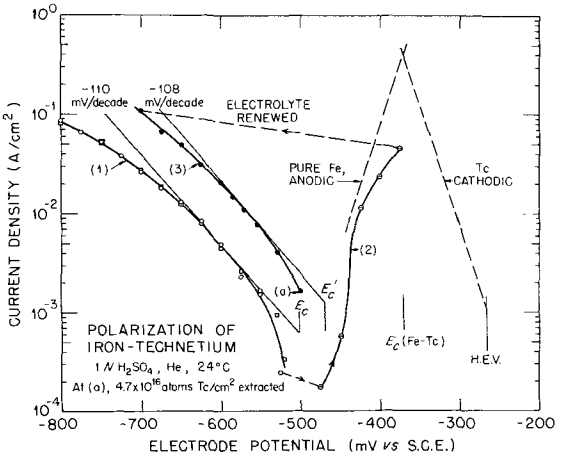

Fig. 3. Polarization of iron-technetium electrodes in 1*N* H_2SO_4 under He at 24°C. Curve 1: Two cathodic polarizations, ○, □, E_c, corrosion potential. Curve 2: Anodic polarization with shifting corrosion potential, $E_c \rightarrow E'_c$. Curve 3: Cathodic polarization after anodic polarization to 4.6×10^{-2} A/cm². The dashed curves represent Tafel lines for evolution of hydrogen on the technetium pellet and a typical anodic curve for pure iron, also in 1*N* H_2SO_4 (for subsequent consideration).

Examination of the electrolyte after similar anodic polarizations showed that little, if any, technetium passed into solution (beta count too small to be statistically significant), although at considerably more noble potentials surface technetium can be oxidized to soluble pertechnic acid, as was noted previously. That dissolution of iron during anodic polarization left technetium to accumulate on the surface was demonstrated analytically. It was found that a 10-min extraction of the electrode with 6*N* NH_4OH containing H_2O_2 oxidized the superficial technetium to TcO_4^-, the beta activity of which could be determined after evaporation of a small aliquot on a counting plate. Similar treatment of electrodes was employed to remove extractable technetium before their first use.

At the conclusion of the successive polarizations represented by curves 1-3 in Fig. 3 (point a), such an analysis showed the presence of 2.4 μg of extractable technetium from 0.306 cm², which corresponds to 4.7×10^{16} atoms per cm². In the original alloy, uniform distribution of technetium would correspond to the order of 10^{12} atoms per cm², hence the shift in the corrosion potential during anodic polarization is associated with an enrichment of the surface layer in the alloying element. Since the highest potential reached in the anodic polarization of Fig. 3 was 140 mV negative to the reversible potential of the Tc-TcOH couple in 1*N* H_2SO_4 (1), it must be presumed that the metal remained in elemental form. In numerous experiments, it was observed that residual technetium rose to the order of 10^{16}-10^{17} atoms/cm² during typical anodic polarizations.

In view of the early discovery of this constant change in the surface state, in later experiments, such as those represented by Fig. 3, the open-circuit potential was measured, in anodic polarizations, just prior to each change of the potential. In this way, ambient overvoltages were obtained and used for the curves in Fig. 4. The current densities plotted are those read just before taking the open-circuit potential and raising the potential. Curve (2η), in Fig. 4, represents the same data as those for curve 2 in Fig. 3. Comparison of the two curves shows that, while the current density rose from 10^{-3} to 10^{-2} A/cm², the potential was raised by 16 mV, but the overvoltage increased by only 4 mV. The "unpolarizability" depends upon the rate at which the potential is raised.

For further study of this anodic effect, a freshly cleaned electrode was polarized cathodically in 1*N* H_2SO_4, the first part of the curve being shown as 4 in Fig. 4. The entire curve was in close agreement with curve 1 in Fig. 3. Upon completion of the cathodic polarization, the electrode was left to corrode spontaneously in the cell, with helium passing. After *ca.* 16 hr, the cell solution was renewed and it was found that the open-circuit potential had shifted from −504 to −452 mV. An electrode of pure iron in the same solution was at −500 mV. The alloy electrode was then polarized anodically to a maximum current density of 16.3 mA/cm², during which time the open-circuit potential remained essentially constant (−452 to −450

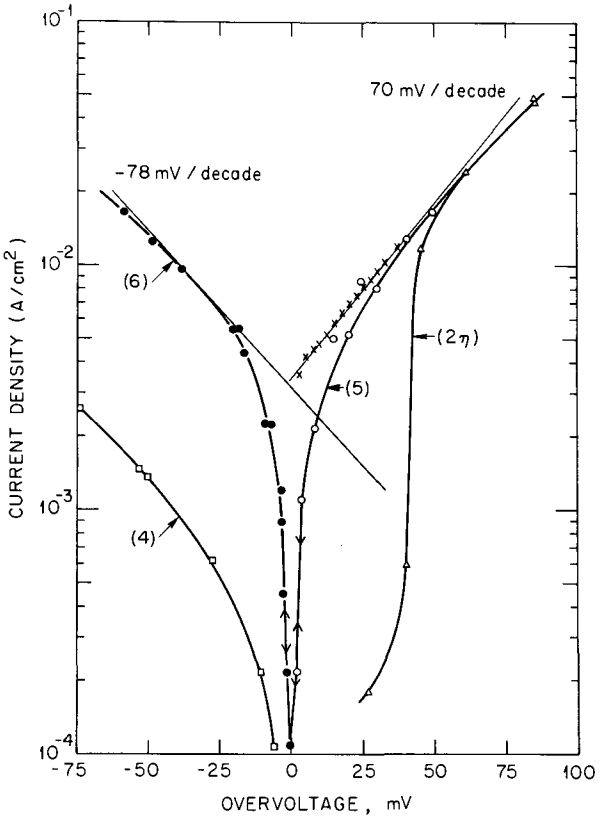

Fig. 4. Polarization of iron-technetium electrodes in 1N H_2SO_4 under He, plotted as overvoltages. Curve 2η: Data of curve 2 in Fig. 3 plotted as overvoltages against the measured ambient open-circuit potential. Curve 4: Portion of cathodic curve of a fresh electrode. Curve 5: Anodic curve for the same electrode after spontaneous corrosion for ca. 16 hr under He; x's calculated from subsequent cathodic curve 6. Curve 6: Repetition of cathodic polarization after anodic curve 5. Points on curves 5 and 6 were taken with both rising and falling potentials.

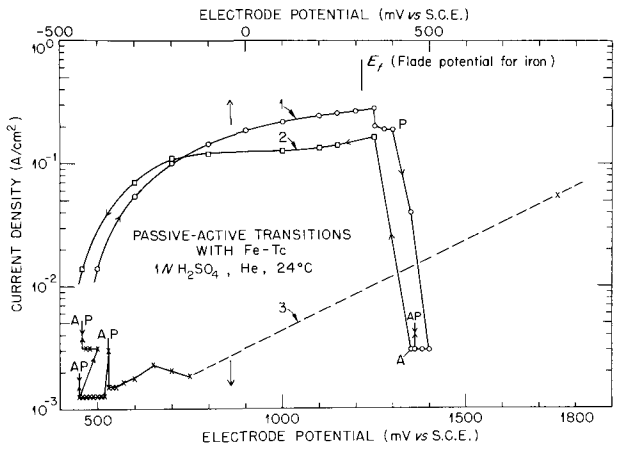

Fig. 5. Passivation (P) and activation (A) of iron-technetium electrodes in 1N H_2SO_4, 24°C, He. Curve 1: Anodic passivation at 400-500 mV; (upper scale). Curve 2: Activation at 450 mV; (upper scale) Curve 3: Fast passivation at 2V and activation at ca. 450 mV; (lower scale).

mV). The calculated overvoltages are therefore significant for a surface state already enriched in technetium to somewhat less than 4.6 x 10^{16} atoms/cm^2. (This was the value found after an additional anodic polarization in which a further slight ennobling of the corrosion potential occurred.)

The data for the initial anodic polarization of this electrode are given in curve 5 of Fig. 4. It is seen that there is no region of unpolarizability in this case, and that the curve merges smoothly into the linear part of curve (2η) obtained after the open-circuit potential had virtually stabilized at the more noble value in the previous experiment.

Polarization was next continued into the region of cathodic potentials and back to the open-circuit potential, with the results shown in curve 6 of Fig. 4. The apparent Tafel slope is distinctly less than that for the fresh electrode and indicates a substantial increase in the corrosion current density at the ennobled corrosion potential. On the anodic side, the curve represented by x's is calculated from the extrapolated cathodic Tafel and shows that the electrode, after overnight corrosion, is more polarizable than pure iron, which normally has a Tafel slope of +40 mV/decade. In repeated experiments, it was found that extraction of an anodically polarized electrode with ammoniacal peroxide caused a subsequently measured cathodic polarization curve to revert to that of a freshly prepared electrode. Hence this treatment effectively removes excess technetium from the surface.

On the right side of Fig. 3 the dashed curves represent the Tafel lines for anodic polarization of pure iron and cathodic polarization of the pellet of technetium, respectively, in 1N H_2SO_4. It is seen that, ideally, a couple between the two electrodes should have a potential of about −375 mV, if their areas were equal and there were no concentration polarization. Actually, concentration polarization causes the curves to bend over considerably (Fig. 5, curve 1 and Fig. 1). Hence their intersection would come at a lower local current density than that indicated by the dashed Tafel lines, but in the same region of potentials. This was verified experimentally. An electrode of Armco magnetic iron was directly shorted to the pellet in 1N H_2SO_4. The area of the iron electrode was 1.6 times that estimated for the pellet, but the potential of the couple came quickly to −372 mV. This figure is of interest in connection with the observation that the usual anodic polarizations caused the open-circuit potential to shift only to the region of −440 to −460 mV, although subsequent extraction of the superficial technetium indicated amounts sufficient to form a complete layer 10-100 atoms or more in thickness. It is therefore apparent that the thin layer of technetium on iron, if, indeed, the 10^{16}-10^{17} atoms/cm^2 are coalesced into a true layer, is quite unlike the surface of bulk technetium with respect to evolution of hydrogen. As was indicated previously for the technetium electrodes plated over gold, the solubility of hydrogen in the metal may be playing a role.

Passivation.—When the iron-technetium alloy was dipped into concentrated HNO_3, the results were visually the same as those observed with pure iron. Decided differences were found, however, in experiments on anodic polarization to high current densities. Polarization was effected potentiostatically at 24°C in 1N sulfate solutions at pH 0.35 (1N H_2SO_4) and 2.70, with helium passing through the solution. To obtain high current densities, the 0.25 in. electrodes were completely encased in "shrinkable vinyl" tubing and then a small hole was drilled through the tubing to expose the metal. For the two sets of measurements represented by Fig. 5, the holes had areas of 0.08 and 0.1 cm^2, respectively. Before being polarized, the metal was prepared by successive treatment with 6N NH_4OH plus H_2O_2, 6N HCl plus H_2O_2, and, finally, 12N HCl.

In none of several experiments did the decrease in current density indicative of passivation begin at the Flade potential of iron at either pH value. Figure 5 shows the results of two representative experiments in 1N H_2SO_4. For curve 1, the active electrode was polarized in steps from −400 mV. The current density decreased slightly at 350 mV, fell sharply at 400 mV, and further to a steady value at 500 mV. The current density, 3 mA/cm^2, however, was much greater than the 7 μA/cm^2 observed with pure iron (3). The current density just before passivation was approximately the

same as that for iron. When the potential was lowered slightly, the electrode remained "passive" down to 460 mV, when activation and repassivation ocurred. At 450 mV, the electrode activated sharply; the further polarization to lower potentials is shown in curve 2. The electrode was darkened, presumably by formation of oxidation products of technetium.

To minimize effects arising from insoluble oxidation products, a freshly cleaned electrode was polarized at once to a potential of 2V (not allowing for the *IR* drop). For 1.2 min, the electrode drew the maximum anodic output of the potentiostat (490 mA/cm^2). Passivation was then indicated visually by evolution of oxygen and a drop of the current density to 250 mA/cm^2. Also, excess technetium on the surface was presumably oxidized to $HTcO_4$. As shown in Fig. 5, curve 3, the current density at 1.75V was 56 mA/cm^2. The potential was then lowered to 750 mV in one step and the curve gives the subsequent results. Instability at 530 mV was followed by repassivation, which persisted to 450 mV. The two types of experiments agree in showing that active-passive transitions occurred between 450 and 500 mV, although the current densities of 1-3 mA/cm^2 are too large to be considered as truly passive in the usual sense of the term.

Discussion

The electrochemistry of technetium is chiefly characterized by the broad span of potentials over which it is almost inactive. In Fig. 2, it is seen that elimination of hydrogen reduces the anodic current density to the order of 10^{-6} A/cm^2, based on the estimated geometrical area. Consideration of roughness would certainly reduce this number by a factor of 3 or, perhaps, more. The exchange current for liberation of hydrogen on the pellet electrode is similar to that on platinum (*ca.* 10^{-3} A/cm^2) in 1*N* H_2SO_4, so that the minimal activity of the technetium itself does not measurably polarize the hydrogen electrode potential in an atmosphere of hydrogen. In cathodic polarization, the hydrogen overvoltage is less than it is on platinum, the Tafel slope being *ca.* −40 mV/decade, rather than −119 mV/decade. In Ref. (2), a low value for the Tafel slope was reported also for rhenium, though it would seem that the exchange current is considerably larger on technetium than it is on rhenium.

Figure 2 illustrated also the tenacity with which hydrogen is retained by technetium. The assumption that anodic oxidation of hydrogen proceeds at an essentially constant rate over an appreciable range of potentials is shown both in Fig. 2 and also in the analysis of polarization curves, such as that given in Fig. 1. This shows that the rate is at least partly controlled by a slow diffusion process within this region of potentials.

As shown previously (1), technetium forms couples with its hydrous oxides as films for which reversible potentials can be determined. For the lowest valence state, we have: $Tc + H_2O \rightarrow TcOH + H^+ + e^-$; $V_H^o = 0.031V$. This potential was observed repeatedly in an atmosphere of helium, the compound TcOH with a free energy of formation of −56.0 kcal mole^{-1} being identified in couples both with the metal itself and with the hydrous oxides formed at higher potentials. Potentials in the range of $V_H^o = 0.01$ to 0.02V were several times observed as brief halts in potential-time curves on open circuit when hydrogen was being displaced by helium. Since the lowest couple potential for technetium and its corrosion product is noble to the H.E.V., these cannot be considered as corrosion potentials. In the light of Fig. 2, they represent pseudostationary potentials of a hydrogen electrode on technetium at a diminished activity of adsorbed hydrogen. As shown in (1), spontaneous ennobling of the potential occurs slowly, presumably as a radiolytic effect (4), and often with an easily recognizable halt when the potential of the Tc(0-I) couple is reached.

Figure 2 shows that the rate of oxidation of TcOH and the other film components is less than 10^{-6} A/cm^2 until the potential is high enough to produce soluble pertechnic acid. It was observed further that the metal remains black at the most noble potentials shown in Fig. 2. It must therefore be presumed that under these conditions metal is oxidized more rapidly than the oxide film.

The polarization measurements show that the 0.1% addition of technetium to iron alters its cathodic behavior and initial corrosion rate very little. Under spontaneous corrosion or anodic polarization, however, irreversible accumulation of excess technetium on the surface reduces the overvoltage for liberation of hydrogen, with the consequent ennobling of the open-circuit potential. The apparent "unpolarizability" during an initial anodic polarization is thus of different origin from that observed in the presence of iodide ions and some other anions, in which a reversible change in the extent of adsorption of an inhibiting species occurs.

It may be significant that, in the experiments represented by Fig. 3 and curve 6 of Fig. 4, determination of extractable technetium gave essentially equal amounts. The cathodic polarization curves had different slopes, however, and the open-circuit potential had shifted in the noble direction by different amounts before cathodic polarization. The larger shift in the open-circuit potential coincided with the decrease in the numerical value of the Tafel slope. Both observations indicate that the surface of the electrode was more like that of pure technetium in the experiment of Fig. 4. It may be inferred that the difference arose from the fact that the technetium accumulated in a slow spontaneous corrosion in this case, whereas it was built up rapidly at a polarized potential in the other experiment. This difference might well cause the anodic attack to be of different type or distribution in the two cases.

That the presence of even low concentrations of technetium interferes with the complete passivation of iron need not be surprising, if it is noted that formation and oxidation of technetium surface compounds are shown by Fig. 2 to increase rapidly just above the potential at which passivation of iron might be expected to occur. Previous work has shown that even a considerable deposit of $Tc(OH)_4$ on an iron surface is not, in itself, protective in the absence of inhibiting pertechnetate ions in solution (5), although a very small amount, in combination with the film of passive iron, facilitates the processes leading to passivation in the presence of the inhibitor (6). Thus, the fact that the current density is decreased by 4.5 orders of magnitude in the passivation of iron but by only 2 orders when 0.1% of technetium is present may well be attributable to continuous rupturing of the film by formation and further oxidation of technetium components in the surface. These processes, in effect, would introduce porosity into the film. Alternatively, the oxidation of technetium components in the film may provide a mechanism by which electrons may be removed from the film more readily than by creation of electron holes in the fully oxidized film of iron, which was postulated to be the origin of real passivity (7).

Acknowledgment

It is a pleasure to acknowledge helpful discussions with Drs. E. J. Kelly, Robert E. Meyer and F. A. Posey.

Research was sponsored by the U.S. Atomic Energy Commission under contract with Union Carbide Corporation.

Manuscript submitted April 19, 1971; revised manuscript received *ca.* July 6, 1971.

Any discussion of this paper will appear in a Discussion Section to be published in the June 1972 JOURNAL.

REFERENCES
1. G. H. Cartledge, *This Journal*, **118**, 231 (1971).
2. M. J. Joncich, L. S. Stewart, and F. A. Posey, *ibid.*, **112**, 717 (1965).
3. U. F. Franck, *Z. Physik. Chem.*, N. F., **3**, 183 (1955).
4. G. H. Cartledge, *Nature*, **186**, 370 (1960).
5. G. H. Cartledge, *J. Phys. Chem.*, **59**, 979 (1955).
6. G. H. Cartledge, *This Journal*, **113**, 328 (1966).
7. G. H. Cartledge, *Chimia*, **23**, 450 (1969).

Nonaqueous Electrochemistry of 1-Hydroxy-9,10-Anthraquinone and Its Conjugate Base

Ivan Piljac[1] and Royce W. Murray*[2,3]

Department of Chemistry, University of North Carolina, Chapel Hill, North Carolina 27514

ABSTRACT

The electrochemical behaviors of 1-hydroxy-9,10-anthraquinone (HOAQ) and its conjugate base (OAQ^-) have been compared in DMF and acetonitrile solvents. HOAQ is reduced in two one-electron steps to stable anion radical and dianion, while OAQ^- reduces in a single two-electron wave accompanied by a monoprotonation reaction. Addition of phenol as proton source to DMF solutions of OAQ^- forms a heteroconjugate acid-base dimer, $\text{Ø}OH \cdots OAQ^-$. This complex is reduced at a potential intermediate between that of HOAQ and OAQ^-, and interpretation of its reaction includes consideration of concomitant formation of $\text{Ø}OH \cdots O\text{Ø}^-$ homoconjugate dimer. The conjugate base OAQ^- is oxidizable by a one-electron reaction which is followed by rapid hydrogen atom abstraction to yield HOAQ as product. Combined thin-layer spectroelectrochemical and coulometric measurements form an important supplement to the conventional electroanalytical methods used in this study.

Among the extensive literature dealing with the electrochemistry of quinones, there are several reports (1-5) which give data, in aprotic media, on compounds bearing hydroxyl groups in positions conducive to hydrogen-bonding to quinone oxygen. This hydrogen-bonding is expected to stabilize the quinone against reduction. A greater hydrogen-bonding stabilization ensues, however, in the negatively charged semiquinone product of the charge transfer (2, 4). The net experimental result observed for such quinones is a polarographic $E_{1/2}$ for the first electron transfer step which is considerably more positive than the $E_{1/2}$ for the analogous reduction step for the parent (unsubstituted) quinone.

The present study was undertaken to compare the cathodic electrochemistry of one such hydroxyquinone, 1-hydroxy-9,10-anthraquinone, denoted HOAQ, with that of its conjugate base, denoted as OAQ^-, in N,N-dimethylformamide and other aprotic solvents. The intramolecular hydrogen-bonding effect is absent in the OAQ^- conjugate base. It was also of interest to examine the relative effects of added proton donors on the HOAQ and OAQ^- electrochemistries and to utilize in particular the advantages of combined thin layer coulometric and spectroelectrochemical experiments (6) to acquire a detailed picture of the protonation steps which might accompany charge transfer in the aprotic and added-proton situations. Several interesting effects came to light under this detailed scrutiny, a novel one of which is a demonstration of participation of homoconjugate and heteroconjugate acid-base dimers in an electrochemical reaction.

In addition to these cathodic studies, some data on an oxidation reaction of the phenolate OAQ^- species are presented.

Experimental

Chemicals.—Dimethylformamide (Baker and Adamson, reagent grade) was purified according to Brummer (7) and was kept under nitrogen. All solution preparations and manipulations were carried out in a dry nitrogen atmosphere. Acetonitrile (Eastman Spectrograde) was used as received. Propylene carbonate (Eastman Practical Grade) was purified and stored as described earlier (8).

1-Hydroxyanthraquinone (Aldrich Chemical Company, Red Label) was purified by vacuum sublimation; its solutions were yellow in color. The tetraethylammonium salt of HOAQ was prepared by adding a small excess of tetraethylammonium hydroxide to a solution of HOAQ in ethyl alcohol. The solution was boiled for several minutes and filtered through a medium sintered glass frit. The filtrate was evaporated almost to dryness, and the crystals formed were collected and washed by Soxhlet extraction with 3% ethyl alcohol in diethyl ether to remove any traces of parent HOAQ. The washed crystals were collected by filtration, dried *in vacuo* at 60°C for several hours, and stored in a dry atmosphere. Elemental analysis of the black-purple tetraethylammonium salt showed that it was a monohydrate: $(Et)_4N^+OAQ^- \cdot H_2O$: carbon, determ. 70.19 ± 0.10%, theor. 71.1%; hydrogen, determ. 7.96 ± 0.05%, theor. 7.81%; nitrogen, determ. 3.90%, theor. 3.77%; oxygen, determ. 17.51 ± 0.27%, theor. 17.25%. Potentiometric titration of this salt, carried out in glacial acetic acid (9), indicated an equivalent weight of 371 (theoretical 371.22). The potentiometric titration involved addition of an excess of standard $HClO_4$ and backtitration with sodium acetate. The tetramethylammonium salt of HOAQ could be prepared by the same procedure, but elemental analysis of the product showed that it was of unsatisfactory purity.

Tetraethylammonium hydroxide (Eastman Organic Chemicals; 50% solution in water), phenol (Baker Reagent Grade), and benzoic acid (Allied Reagent Grade) were used as received. Tetraethylammonium perchlorate (Eastman Organic) was recrystallized twice from water and dried at 110°C.

Gas-liquid chromatographic analysis of the water concentration in the DMF solvent gave a value of 0.040 molar as the probable worst case. The procedure

* Electrochemical Society Active Member.
[1] Present address: Laboratory of Inorganic Chemistry, Faculty of Technology, University of Zagreb, Zagreb, Yugoslavia.
[2] Alfred P. Sloan Research Fellow 1969-1972.
[3] Present address: Chemistry Section, National Science Foundation, Washington, D.C. 20550.
Key words: hydroxyanthraquinone, acid-base dimers, optically transparent electrodes, spectroelectrochemistry, polarography.

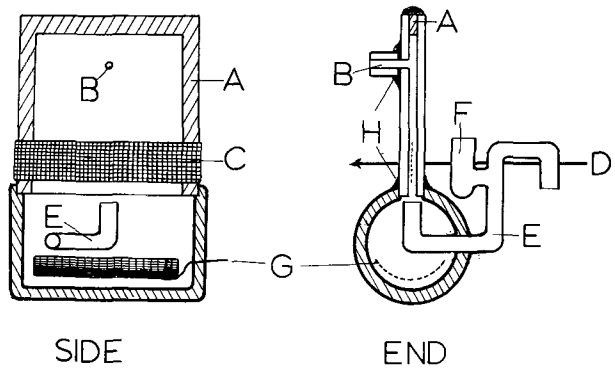

Fig. 1. Optically transparent thin layer electrode assembly. A, 50μ Teflon spacer each side of minigrid; B, Solution inlet; C, 500 lines/in. gold minigrid (area clear of spacer 1.58x0.9 cm); D, Light path; E, Bridge to reference electrode; F, Reference electrode compartment; G, Pt gauze auxiliary electrode; H, Epoxy cement.

used was similar to one reported for analysis of propylene carbonate (10).

Solutions were prepared under nitrogen fresh for each experiment. Solutions of HOAQ are stable; those of OAQ^- are stable (violet color) if stored under nitrogen but tend to decompose (to HOAQ) when exposed to air.

Apparatus and procedure.—Figure 1 shows the optically transparent thin layer cell assembly, an elaboration of an earlier arrangement (6), employed in measurements of coulometric electrolysis charges and product spectra. A gold minigrid (500 lines/in.) was used in the all-glass cell, which had an electrode area of 1.58 x 0.9 cm and thin-solution layer thickness of 114 ± 1μ as measured by comparison to absorbances of both HOAQ and OAQ^- in a standard 500μ spectrophotometer cell. Correction of the spectral thickness, for the minigrid electrode volume, gives a solution thickness of 112μ to be used for calculations with coulometric data. The electrode was optically masked down to a window of 1.5 x 4 mm with black tape, slightly smaller than the optical beam dimension of the Cary Model 14 spectrophotometer employed for spectral measurements. The sample solution was transferred with nitrogen pressure from the 10 ml volumetric flask (in which it had been prepared and degassed with presaturated nitrogen) through glass tubing (with shrinkable Teflon joints at breakage-prone points) into the thin layer cell mounted in the Cary compartment. The cell was preflushed with nitrogen before the initial filling. It was found necessary, especially for extended spectral observations, to insert a Teflon stopcock immediately adjacent to the inlet tube of the thin layer cell. This stopcock was closed after filling the cell with fresh solution to prevent any slight solution flow through the cell caused by temperature gradients in the closed solution system. Such gradients, in the absence of this precaution, could cause slow and artifactual changes in the thin layer solution spectrum. The reference beam of the spectrophotometer was passed through an identical but empty thin layer cell made with 500 lines/in. gold minigrid. The same thin layer cell survived an extended series of spectroelectrochemical measurements.

For polarographic and cyclic voltammetric experiments, a previous cell (8) was modified so that the salt bridge compartment between the working and reference electrodes extended as a capillary tip terminating within 1 mm of the working electrode. This bridge compartment could be filled with degassed solution; this solution and that used in the reference electrode compartment was identical to the sample solution under study. An SCE with NaCl filler electrolyte was employed as reference electrode.

The hanging mercury drop electrode employed for cyclic voltammetry was prepared according to Shain *et al.* (11). Rotated Pt wire and stationary Pt or Au foil or wire electrodes were pretreated as recommended by Adams (12). A Pt mesh served as auxiliary electrode in all experiments.

The electrochemical instrumentation was based on a Philbrick Researches Model K7-A10 operational amplifier manifold using conventional passive circuitry. Data recording was by a Tektronix Model 564 oscilloscope, a Model 1005 Beckman 10" Recorder, and a Hewlett-Packard Model 7004A X-Y recorder. The maximum current was measured in polarographic experiments and was multiplied by the factor 6/7 for calculations of polarographic constants I_d (13).

Results and Discussion

Electrochemistry of 1-hydroxy-9,10-anthraquinone.—The results of a variety of electrochemical experiments on 1-hydroxy-9,10-anthraquinone (HOAQ) are summarized in Table I. The two reduction steps in DMF, CH_3CN, and propylene carbonate solvents, exemplified by the polarographic curve G of Fig. 2, are diffusion controlled by polarographic and chronoamperometric criteria. Both the values of $E_{1/2}$ for the two waves and their potential separation agree with earlier polarographic results in DMF (2, 4). Cyclic voltammetry of HOAQ in DMF at Pt and Au electrodes (Fig. 3, Curve 1) demonstrates chemical reversibility of both cathodic reactions through sweep-rate-independent unity peak current ratios. Similar results are obtained in CH_3CN and propylene carbonate solvents. On a mercury electrode in DMF, the two cathodic waves are well behaved, but the anodic cyclic voltammetric waves are "noisy" in a manner highly reminiscent of behavior ascribed in another system to streaming effects (14).

Table I. Summary of electrochemical characteristics of 1-hydroxy-9,10-anthraquinone
0.1*M* Et_4NClO_4 electrolyte

		1st wave	2nd wave	Solvent
Polarography	$E_{1/2}$, *vs.* SCE	−0.64$_5$V	−1.26V	DMF
	I_d[a]	2.11	1.99	
	0.059/n	59 mV	62 mV	
	$E_{1/2}$, *vs.* SCE	−0.77V	−1.20V	CH_3CN
	0.059/n	59 mV	62 mV	
	$E_{1/2}$, *vs.* SCE	−0.74V	−1.20V	Propylene carbonate
	0.059/n	59 mV	61 mV	
Cyclic voltammetry	$i_{p(c)}/i_{p(a)}$	1.00 ± 0.05[b]	1.00 ± 0.5[b]	DMF
	$i_{p(c)}/i_{p(a)}$	1.0[c]	1.1-1.4[c]	
Chronoamperometry[d]	$it^{1/2}$, μA sec$^{1/2}$	4.58 ± 0.12	9.4 ± 0.13	DMF
Thin layer coulometry[e]	Q_{cath}/Q_{anod}	0.97	0.99	DMF
		$Q_{cath(1)}/Q_{cath(2)}$ = 0.91		

[a] From (6/7) $i_{d(max)}/td^{1/6}m^{2/3}C$[b].
[b] On Pt or Au electrodes; V = 0.1 to 1.0 V/sec.
[c] On Hg electrode; anodic wave of first wave is "noisy," possible streaming effect, properties of neither anodic wave reproducibly correlatable with potential sweep rate. V = 0.1 to 1.0 V/sec.
[d] Potential steps on Hg electrode to −0.9V and −1.6V respectively; time scale 0.025-1.0 sec. [HOAQ] = 1.20 millimolar.
[e] Q_{cath}/Q_{anod} ratios for forward-reverse potential stepping 0 to −0.9V and −0.9V to −1.6V, respectively.

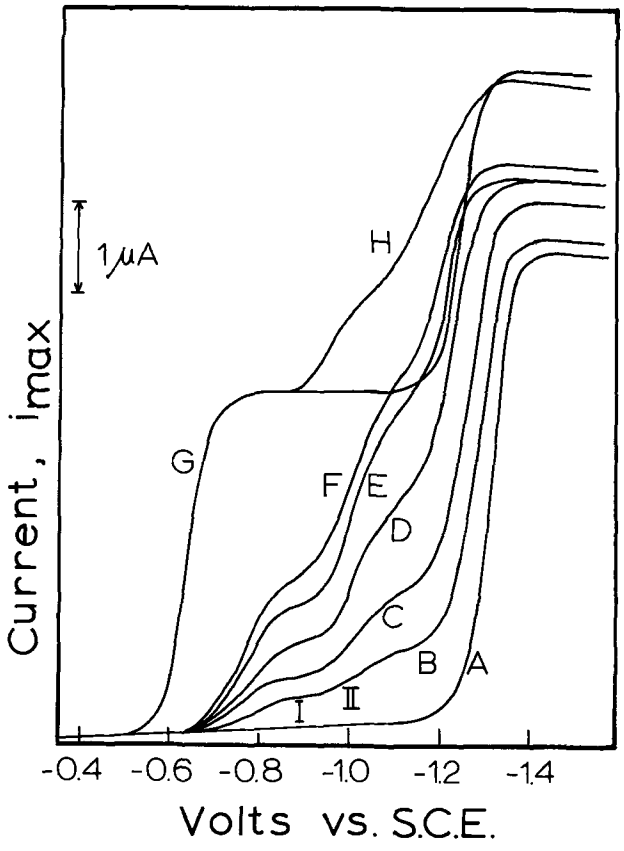

Fig. 2. Polarograms of 0.835 mM $Et_4N^+OAQ^-$ in 0.1M TEAP-DMF. Curve A, OAQ^- only; curve B, added [ØOH] = 0.26 mM; curve C, [ØOH] = 0.38 mM; curve D, [ØOH] = 0.67 mM; curve E, [ØOH] = 0.96 mM; curve F, [ØOH] = 1.20 mM; curve G, 1.02 mM HOAQ only; curve H, 1.02 mM HOAQ with added [ØOH] = 0.78 mM.

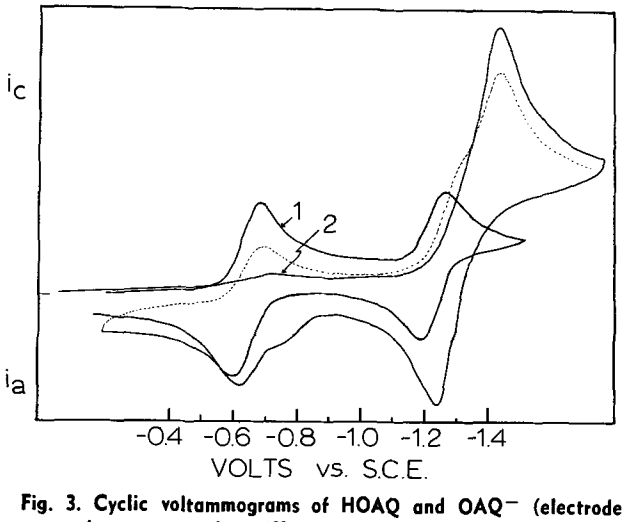

Fig. 3. Cyclic voltammograms of HOAQ and OAQ^- (electrode areas and current scales differ for curves 1 and 2). Curve 1, HOAQ on Pt in DMF; curve 2, OAQ^- on Pt in DMF, —— first cycle, . . . second cycle.

Thin layer potential step coulometry in DMF solvent (Au minigrid electrode) demonstrates that both HOAQ reduction steps involve single electrons. Spectra of both one- and two-electron products are stable in DMF over a one-hour observation period, and both charge and reactant spectra could be quantitatively recovered upon reverse potential stepping in the optically transparent thin layer cell.

Thus, reduction of HOAQ in DMF solvent on Au and Pt electrodes yields stable one- and two-electron products

$$HOAQ + e \rightarrow HOAQ^{\cdot-} \quad [1]$$

$$HOAQ^{\cdot-} + e \rightarrow HOAQ^{2-} \quad [2]$$

The absence of significant protonation accompanying the second reduction step, indicated by its chemical reversibility, is confirmed by other spectral results presented later. The apparent slight polarographic irreversibility of Reaction [2] is probably then a charge transfer rate effect (15).

Spectra of HOAQ, $HOAQ^{\cdot-}$, and $HOAQ^{2-}$ are presented in Fig. 4; band positions and intensities are: HOAQ, 400 nm ($\epsilon = 5.28 \times 10^3$); $HOAQ^{\cdot-}$, 388 nm ($\epsilon = 5.18 \times 10^3$), 462 nm ($\epsilon = 5.19 \times 10^3$), 540 nm ($\epsilon = 9.40 \times 10^3$); and $HOAQ^{2-}$, 462 nm ($\epsilon = 1.58 \times 10^4$), 544 nm ($\epsilon = 2.97 \times 10^3$).

Spectra of HOAQ and its one- and two-electron thin layer electrolysis products in CH_3CN solvent are blue-shifted from those in DMF by 5-10 nm but are otherwise similar. The spectra of the cathodic products decay in intensity (shape unchanged) with a half-life of about one-half hour, and charge recovery is incomplete upon reverse potential stepping in the thin solution cell. In propylene carbonate solvent, fairly rapid changes in spectral intensity and shape are observed for both reaction products. Thus, while the one- and two-electron products of the quinone reduction are stable in all three solvents on the time scale of cyclic voltammetry, on the slower thin layer electrolysis time scale, stability is observed only in DMF solvent. This solvent is accordingly emphasized in subsequent experiments in this report.

Cathodic electrochemistry of the conjugate base of HOAQ.—Solutions of the tetraethylammonium salt, $Et_4N^+OAQ^-$, of 1-hydroxy-9,10-anthraquinone exhibit a single cathodic wave at a potential somewhat more negative than the second of the two one-electron reactions of HOAQ. Figure 2, curve A, illustrates this wave in DMF solvent. Table II summarizes some data; the reaction is rather irreversible. The polarographic I_d for the quinone salt reduction is 84% of the sum of I_d's for the two one-electron steps for HOAQ; that n equals two for OAQ^- reduction is confirmed by potential step thin layer coulometry.

The reduction of OAQ^- is accompanied by a quantitative monoprotonation step; the stable product spectrum observed in the transparent thin layer cell is identical in band positions and intensities (±4%) to that of the two-electron product of HOAQ, itself, curve A, Fig. 4. The reaction is, thus, written

$$OAQ^- + HS + 2e \rightarrow HOAQ^{2-} + S^- \quad [3]$$

where HS is the medium proton source. If Reaction [3]

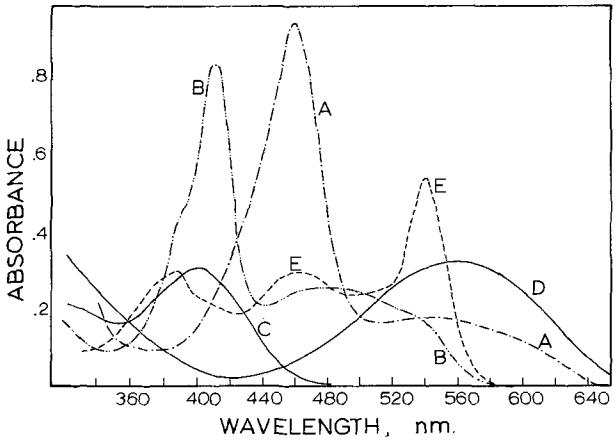

Fig. 4. Thin layer cell spectra in 0.1M TEAP-DMF. l = 114μ. Curve A, 5.25 mM HOAQ at −1.4V ($HOAQ^{2-}$); curve B, 5.08 mM HOAQ plus 5.08 mM benzoic acid at −0.8 or −1.4V (H_2OAQ^-); curve C, 5.08 mM HOAQ; curve D, 5.25 mM OAQ^-; curve E, 5.08 mM HOAQ at −0.8V ($HOAQ^{\cdot-}$).

Table II. Summary of cathodic electrochemistry of conjugate base of 1-hydroxy-9,10-anthraquinone
0.1*M* Et_4NClO_4 electrolyte

		DMF	CH_3CN	Propylene carbonate
Polarography	$E_{1/2}$	−1.36V	−1.27V	−1.20V
	$0.059/n$	50 mV	56 mV	55 mV
	I_d	3.46		
R.P.E. voltammetry	$E_{1/2}$	−1.36V		
	$0.059/n$	62 mV		
Chronoamperometry[a]	$it^{1/2}$, μA $sec^{1/2}$	17.47		

[a] Potential step −0.4V to −1.42V on Hg electrode; time scale 0.02 to 1.6 sec. [OAQ⁻] = 1.83 millimolar. Electrode area is larger than that of analogous experiment in Table I.

occurs through an ECE sequence, the protonation rate must be high, inasmuch as no deviation from diffusion control could be detected by either polarographic or chronoamperometric criteria.

Protonation also accompanies the two-electron reduction of OAQ^- in CH_3CN solvent, and the $HOAQ^{2-}$ product spectrum undergoes the same slow decay of intensity as that of $HOAQ^{2-}$ resulting from reduction of HOAQ in this solvent.

It is evident that the effect on the quinone reduction of removing the phenolic hydrogen is considerable; the $E_{1/2}$ for the first electron step for OAQ^- in DMF lies at least −0.72V negative of that of HOAQ. Several factors can contribute to this interesting difference; they are the differences in electronic substituent effects of the −OH and $-O^-$ groups, the intramolecular hydrogen-bonding present in HOAQ and $HOAQ^-$, and the negative charge of OAQ^-. Brodsky *et al.* (16) in a study of substituent effects for a series of 1-substituted anthraquinones in DMF, found a reasonable correlation of the polarographic $E_{1/2}$ of the first wave with Hammett σ_m substituent constants. The −OH and $-O^-$ substituents were not included in their study. Using σ_m values of +0.12 and −0.71 (17) for the −OH and $-O^-$ substituents, and taking account of apparent differences in junction potentials (by difference-referencing to our $E_{1/2}$ of −0.84V for anthraquinone as compared to theirs of −0.97V), approximate $E_{1/2}$ values of −0.83 and −1.15V, respectively, are predicted for HOAQ and OAQ^- from this earlier correlation line. Our measured $E_{1/2}$ for HOAQ (−0.64V) is more positive than this substituent-based prediction. The difference is attributable, from discussions by Peover (2) and Jones and Spotswood (4), to hydrogen-bonding, the negatively charged semiquinone ($HOAQ^-$) being stabilized to a greater extent than is the parent HOAQ. The measured $E_{1/2}$ of OAQ^- (−1.36V) is more negative than predicted from the Hammett approach. This latter difference can be regarded as having the same origin as the difference in reduction potentials of any sequence of one-electron reductions of a neutral quinone or aromatic hydrocarbon. The additional energy required for the second electron transfer can be attributed mainly to the repulsion energy of two electrons in the dinegative product (18). In the sense that the OAQ^- reactant already bears a negative charge at the quinone reaction center, an additional energy requirement is imposed on its reduction.

A second difference between the HOAQ and OAQ^- electrochemistries is the stability of the mono- and dinegative charge transfer products of HOAQ as compared to the immediate protonation of the charge transfer product of OAQ^-. Assuming that reduction of OAQ^- involves an ECE process, this means that the OAQ^{2-} species exhibits a higher basicity than $HOAQ^-$ or $HOAQ^{2-}$. This difference probably arises through the intramolecular hydrogen bonding stabilization of oxygen sites in the latter two species.

A number of reoxidation experiments were carried out on the $HOAQ^{2-}$ solutions resulting from OAQ^- reduction in DMF. It would be supposed that these solutions would exhibit the same two-wave oxidation pattern as that of a $HOAQ^{2-}$ solution derived from HOAQ reduction. This expectation is realized only in part. A cyclic voltammogram of OAQ^- on Pt (Fig. 3, curve 2) or Au in DMF displays, following the cathodic peak, anodic waves at −1.25, −0.76 (small), and −0.63V *vs.* SCE. The anodic wave at −1.25V bears neither 1:1 nor 1:2 peak current relation to its cathodic wave [$i_{p(a)}/i_{p(c)} = 0.70$]. If the $HOAQ^{2-}$ product of OAQ^- reduction in DMF is reoxidized at −0.8V in the thin solution cell, the spectrum resulting is mainly that of $HOAQ^-$ (bands at 388, 467, and 540 nm), but absorption at 568 nm clearly shows the presence of some OAQ^-. ($Et_4N^+OAQ^-$ absorbs at 568 nm with $\epsilon = 5.6 \times 10^3$). An increasing proportion of OAQ^- is observed upon prolonged electrolysis at this potential. Stepping further to 0V converts the spectrum to mainly that of OAQ^-, with a small amount of HOAQ evident by absorption at 400 nm. A potential step directly to 0V following OAQ^- reduction at −1.5V initially yields mainly HOAQ, but this spectrum is slowly converted to that of OAQ^- upon extended electrolysis.

These thin layer spectral results make it clear that Reaction [3] and the protonation step it involves can be reversed and provide inspiration for the following interpretation of the anodic cyclic voltammetric waves. The anodic wave at −1.25V (Fig. 3, curve 2) must be composed of two overlapping reactions: a direct one-electron oxidation of $HOAQ^{2-}$ to $HOAQ^-$ (reverse of Reaction [2]) and an oxidation of $HOAQ^{2-}$ accompanied by deprotonation and, consequently, transfer of a second electron to yield OAQ^- (reverse of Reaction [3]). Hence, $1.00 > i_{p(a)}/i_{p(c)} > 0.50$. The subsequent anodic waves at −0.76 and −0.63V are those of $HOAQ^-$ oxidation accompanied and not accompanied, respectively, by a rapid subsequent deprotonation step.

This pattern of anodic events is also observed in CH_3CN solvent, but the deprotonation step permitting the reversal of Reaction [3] is more quantitative than in DMF solvent. Thus, the cyclic voltammetric $i_{p(a)}/i_{p(c)}$ for the second wave is nearly unity in this solvent, and the two waves due to $HOAQ^-$ oxidation (−0.9 and −0.7V) are barely perceptible. The thin layer oxidation (at 0V) of $HOAQ^{2-}$ obtained from OAQ^- reduction yields a spectrum only of OAQ^-.

It is evident that the experimental data for $HOAQ^{2-}$ oxidation in both DMF and CH_3CN solvents require that the base S^- resulting from Reaction [3] either be a stable species or decompose to another stable strong base. Existence and reaction participation of such residual base products has been generally disregarded in organic electrochemical studies in nonaqueous, unbuffered media. The identity of the proton source HS in these experiments could not be established with certainty; from the general similarity of behavior in two solvent systems, it seems likely that it is either residual water impurity or the Et_4N^+ cation, with the Reaction [3] reversal then being caused by hydroxide ion or triethylamine.

Anodic electrochemistry of OAQ^-.—A well-defined anodic wave is observed for the $Et_4N^+OAQ^-$ quinone salt on Au or Pt electrodes in a variety of solvent media (Table III). Assignment of $n = 1$ to this reaction is made clear by thin layer coulometry and by comparison of anodic and cathodic limiting currents at the rotated Pt electrode. Quantitative matching (intensity and wavelength) of thin layer spectra clearly show that the reaction product is the parent acid species HOAQ. The reaction is formulated as a one-electron production of a neutral phenoxyl radical with subsequent hydrogen atom abstraction

$$OAQ^- - e \rightarrow [OAQ\cdot] \xrightarrow{HD} HOAQ + [D\cdot] \quad [4]$$

The rotated Pt electrode current-potential curves

Table III. Summary of anodic electrochemistry of conjugate base of 1-hydroxyanthraquinone
All results refer to rotated Pt electrode voltammetry

Solvent medium	$E_{1/2}$ vs. SCE	0.059/n	$i_{l(a)}/i_{l(c)}$[a]
DMF; 0.1M Et_4NClO_4	+0.57$_5$V	60 mV	0.46
Propylene carbonate; 0.1M Et_4NClO_4	+0.51V	59 mV	0.50
Methylene chloride; 0.2M Bu_4NClO_4	+0.54V	60 mV	
Dimethoxyethane (DME); 0.2M Bu_4NClO_4	+0.60V	64 mV	

[a] Ratio of limiting R.P.E. current for OAQ- oxidation to limiting current for two-electron reduction of OAQ- on same R.P.E.

for OAQ^- oxidation have a reversible shape (Table III); a similar result has been given by Vermillion and Pearl (19) for oxidation of other phenoxides. This is clearly a pseudoreversibility, however. Cyclic voltammetry of the anodic OAQ^- wave reveals no corresponding cathodic peak in any solvent at any potential sweep rate examined; the cathodic potential sweep cycle shows only waves for anodically generated HOAQ and fresh OAQ^-. Reconciliation of the voltammetry and cyclic voltammetry results requires that the rate of the hydrogen atom abstraction reaction be fast compared to the cyclic voltammetry time scale but slow in comparison to the rate of the primary charge transfer step (20).

The $Et_4N^+OAQ^-$ quinone salt also exhibits an anodic wave at a mercury electrode; this was briefly examined. In propylene carbonate solvent, the anodic polarographic wave has $E_{1/2} = -0.12V$ *vs.* SCE, $0.059/n = 60$ mV, and a diffusion current of magnitude 0.46 as compared to the cathodic OAQ^- reaction. In cyclic voltammetry, the anodic wave has a cathodic counterpart of approximately equal magnitude. These data indicate a fairly reversible one-electron/OAQ^- formation of a mercury complex.

Effects of proton donors on cathodic electrochemistry of OAQ^-: Heteroconjugate acid-base dimers in electrochemistry.—The influence of two proton sources, benzoic acid and phenol, on the reduction of the $Et_4N^+OAQ^-$ quinone salt was studied in DMF solvent. Addition of benzoic acid gave the trivial result of immediate, quantitative protonation to yield HOAQ. Addition of the weaker acid phenol gave, on the other hand, a rather interesting and novel result.

As shown by curves B-F of Fig. 2, addition of phenol to OAQ^- solutions generates two new cathodic waves, designated I and II, lying at potentials between those of the two cathodic waves of the parent acid HOAQ. These are polarographically diffusion controlled reactions (constant $i_d/h^{1/2}$); diffusion control in wave I was also ascertained by potential sweep chronoamperometry (constant $i_p^I/v^{1/2}$). Although the poorly defined plateau of wave II makes accurate measurements difficult, waves I and II appear to be of equal magnitude. The diffusion current of wave I is proportional to [ØOH]; for [ØOH]/[OAQ^-] = 0.31, 0.46, 0.63, 0.80, 0.98, and 1.15, i_d^I/[ØOH] = 1.06, 1.23, 1.15, 1.32, 1.08, and 1.25 $\mu A \cdot mM^{-1}$, respectively.

The basis for understanding of these electrochemical results is found in spectra of phenol-OAQ^- mixtures in DMF, examples of which are shown in Fig. 5. A small change in absorbance at 400 nm occurs upon phenol addition, and, for [ØOH]/[OAQ^-] $\geq$ 2, it appears that a small amount of proton transfer (to yield HOAQ) has probably taken place. At [ØOH]/[OAQ^-] $\leq$ 1, however, the spectral changes are inconsistent with a simple proton transfer. The original OAQ^- band at 568 nm undergoes a pronounced blue shift and a lowering of absorbance which is much larger than the absorbance change at 400 nm, and an isosbestic point becomes obvious at 523 nm. These effects demonstrate that in the presence of phenol an equilibrium between OAQ^- and another species is

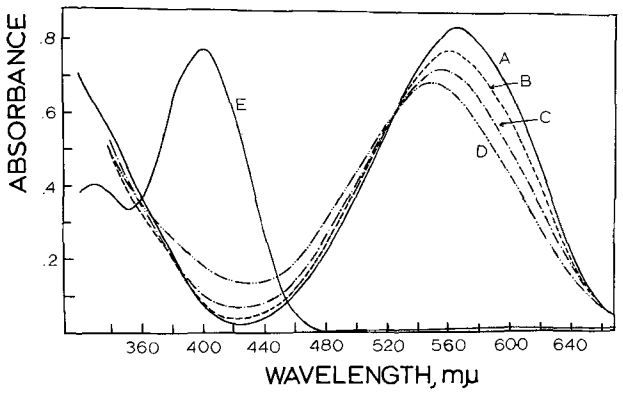

Fig. 5. Spectra in 0.1M TEAP-DMF. $l = 500\mu$. Curve A, 2.94 mM OAQ^-; curve B, 2.94 mM OAQ^- plus 1.5 mM ØOH; curve C, 2.94 mM OAQ^- plus 3.4 mM ØOH; curve D, 2.94 mM OAQ^- plus 5.7 mM ØOH; curve E, 2.93 mM HOAQ.

established. The new species in the phenol-OAQ^- mixtures must be their heteroconjugate acid-base dimer

$$\text{ØOH} + OAQ^- \rightleftharpoons \text{ØOH} \cdots OAQ^- \qquad [6]$$

An extensive literature has been developed by Kolthoff and co-workers and Coetzee (21-28) on interactions of weak acids with their conjugate bases and with other bases in nonaqueous solvents (homoconjugate and heteroconjugate acid-base dimers). Formation constants have been obtained in both CH_3CN and dimethylsulfoxide solvents; they are larger in the former solvent where, for instance, the ØOH $\cdots$ ØO^- homoconjugate has $K^f_{HA_2^-} = 11 \times 10^3$. While quantitative dimer studies do not appear to have been made in DMF solvent, the properties of this solvent are sufficiently similar to those of CH_3CN and DMSO that formation of acid-base dimers in DMF can be anticipated. By analogy with the data in CH_3CN solvent, it can also be anticipated that an order of dimer stability ØOH $\cdots$ ØO^- > ØOH $\cdots$ OAQ^- > QAOH $\cdots$ OAQ^- should occur. Consistent with this ordering is the fact that, in contrast to ØOH,OAQ^- mixtures, spectra and polarograms of HOAQ,OAQ^- mixtures in DMF show strictly additive relations between HOAQ and OAQ^- spectral bands and polarographic waves, respectively.

Recognizing that the phenol-OAQ^- mixtures in DMF actually constitute mixtures of OAQ^- and the dimer ØOH . . . OAQ^-, wave I in the polarograms of Fig. 2 must correspond to the reaction

$$\text{ØOH} \cdots OAQ^- + e \rightarrow [\text{Ø}O \cdots HOAQ]^{2-} \rightarrow HOAQ^{\cdot -} + \text{Ø}O^- \qquad [7]$$

Dissociation of the dimer charge transfer product $[\text{Ø}O \ldots HOAQ]^{2-}$ (OAQ^{2-} should be a much stronger base than ØO^-) yields phenolate ion, which can interact with unreduced ØOH $\cdots$ OAQ^- dimer to produce the more stable ØOH . . . ØO^- dimer

$$\text{ØOH} \cdots OAQ^- + \text{Ø}O^- \rightarrow \text{ØOH} \cdots \text{Ø}O^- + OAQ^- \qquad [8]$$

These reactions predict that for [ØOH]/[OAQ^-] $\leq$ 1, two phenol species are required to effect a one-electron reduction of one OAQ^- species at the potential of wave I. The i_d^I — [ØOH] proportionality is, thus, explained, as is the fact that for [ØOH]/[OAQ^-] = 1.0, the current for wave I is approximately one-fourth (0.20) of that of the original two-electron wave for OAQ^-. This interpretation of wave I is confirmed with certainty by thin layer electrolysis of an equimolar mixture of phenol and OAQ^- at −0.8V; the product spectrum is that of an equimolar mixture of $HOAQ^{\cdot -}$ and OAQ^-.

The second polarographic wave (wave II) caused by the addition of phenol to OAQ^- solutions in DMF corresponds to one-electron reduction of the one-half of the original OAQ^- remaining after Reactions [7]-[8].

(Recall that $i_d^{I} \simeq i_d^{II}$). The potential for this reaction is less negative than that for normal OAQ^- reduction owing to the presence of the proton source $\phi OH \cdots O\phi^-$

$$OAQ^- + e \rightarrow [OAQ^{2-}] \xrightarrow{\phi OH \cdots O\phi^-} HOAQ^{\cdot-} + \phi O^- \quad [9]$$

Reaction ceases at the one-electron stage since Reaction [9] occurs at a potential positive of that required to reduce $HOAQ^{\cdot-}$. In confirmation, thin-layer electrolysis of an equimolar mixture of phenol and OAQ^- at -1.0V gives a product spectrum quantitatively identical to that of the $HOAQ^{\cdot-}$ species obtained from one-electron reduction of HOAQ (Fig. 4).

The third wave in the phenol-OAQ^- mixture polarograms of Fig. 2 can be ascribed to overlapping reduction of OAQ^- and $HOAQ^{\cdot-}$. (A partial splitting is visible in curve D.) When $[\phi OH]/[OAQ^-] = 1.0$, this wave has $E_{1/2}$ equal to that of the second wave of HOAQ, as expected, and thin-layer electrolysis at -1.4V gives the spectrum of $HOAQ^{2-}$.

Thin-layer reoxidation, at 0V, of phenol-OAQ^- mixtures following reduction at -1.4V gives unity Q_{cath}/Q_{anod} charge ratios. A deprotonation similar to that discussed above for OAQ^- occurs (reverse of Reaction [3]), with ϕO^- in this case serving as the base $\underline{S}^-$. The OAQ^- spectrum reappears during the thin-solution oxidation much more rapidly than was the case in the absence of phenol.

The reduction of OAQ^- in DMF was also examined for further protonation of the two-electron reduction product ($HOAQ^{2-}$). The thin-solution spectrum following electrolysis at -1.4V for $[\phi OH]/[OAQ^-] = 2.0$ corresponds to a new species with bands at 412 nm ($\epsilon = 1.54 \times 10^3$) and 490 nm ($\epsilon = 4.48 \times 10^3$). This spectrum is identical to that observed for reduction of a 1:1 mixture of HOAQ and benzoic acid at -1.4V (Fig. 4) and must correspond to the diprotonated species H_2OAQ^-. Little further spectral change could be discerned in phenol-OAQ^- mixtures reduced at $[\phi OH]/[OAQ^-] = 3.0$.

A series of experiments on phenol-OAQ^- mixtures paralleling those above was carried out in acetonitrile solvent. Spectral changes similar to those of Fig. 5 were noted, but the spectra show that in these mixtures significant direct protonation to form HOAQ accompanies heteroconjugate dimer formation even at $[\phi OH]/[OAQ^-] < 1$. Polarograms of phenol-OAQ^- mixtures have split waves like those of Fig. 2, but the wave separations are small, precluding quantitative studies. Thus, Reactions [6]-[9] can only be qualitatively surmised to occur in acetonitrile solvent.

The wave splittings caused by acid-base dimer formations in these experiments are, in a sense, entirely analogous to nonaqueous titration curve splittings such as those reported by Harlow and Bruss (29). The possibilities for dimer participation in the numerous electrochemical experiments in which proton sources have been added to nonaqueous solutions of organic compounds appear, however, to have gone unrecognized in the electrochemical literature. The sole exception is a report by Fujinaga, Izutsu, and Takaoka (30) who explain a wave splitting of quinoline reduction in DMF by phenol in terms of a "hydrogen bonded phenol-quinoline complex." Neither coulometry nor spectral data are given to support the interpretation, which may, unfortunately, contain some error in its details owing to neglect of $\phi OH \cdots O\phi^-$ formation.

Although much further experimentation will be required to completely characterize the role of acid-base dimer formation in electrochemical processes, several generalities appear probable at this point. First, dimer formation upon proton source addition will be most common with basic samples and with proton sources whose conjugate bases have strength comparable to that of the sample. Second, the reduction potential for a sample involved in dimerization will lie between the reduction potentials of the completely protonated and nonprotonated forms of the sample. (From recent studies on phenols (31), a similar statement may also apply to oxidations.) Third, even though a sample may not itself participate in dimer formation, formation of species such as $\phi OH \cdots O\phi^-$ can complicate kinetic studies of anion radical protonation reactions. Last, the dimer formation event may provide a mechanistically useful perturbation in the study of organic electrode reactions; conversely, the electrochemical properties of dimers may provide further insight into the chemistry of the dimers themselves.

Effects of proton donors on cathodic electrochemistry of HOAQ.—The effects of added proton donors on sequential one-electron reductions of aromatic hydrocarbons and other substances have been reviewed by Peover (15). Mixtures of benzoic acid and 1-hydroxyanthraquinone in DMF exhibit a classical Hoijtink (32) pattern of polarograms; the first reduction wave for HOAQ grows at the expense of the second as benzoic acid is added in increasing concentrations. The chemical step of the ECE reaction occurring in the first reduction wave (protonation of $HOAQ^{\cdot-}$ by benzoic acid) appears to be essentially quantitative, as $[\phi COOH]/[HOAQ] = 1.0$ is sufficient to replace completely the two one-electron waves with a single two-electron wave. [A similar alteration of anthraquinone polarography in DMF by benzoic acid (15) has been reported to require a threefold excess of the acid.]

Spectra of thin layer electrolysis products parallel the polarographic results for benzoic acid-HOAQ mixtures. The bands of $HOAQ^{\cdot-}$ resulting from reduction at -0.8V are, as benzoic acid is added, proportionately replaced with those of the protonated two-electron product, H_2OAQ^- (whose spectrum at a $[\phi COOH]/[HOAQ] = 1.0$ ratio is shown by curve B of Fig. 4). As noted earlier, an identical spectrum results from reduction of a $[\phi OH]/[OAQ^-] \geq 2$ mixture.

Proton donors too weak to cause the ECE (Hoijtink) reaction for a substance polarographically reduced in two one-electron steps are without effect on the first one-electron wave but often produce a shifting of the second wave to less negative potentials. This effect is usually interpreted as a post-electron transfer protonation of the product of the second reduction step. Such behavior is observed upon addition of phenol to HOAQ solutions in DMF solvent but with the added feature that the second wave is not only shifted positively but is also split into two waves. Figure 2, curve H shows the polarogram obtained for a somewhat less than equimolar mixture of phenol and HOAQ; the more positive of the two new waves can be clearly seen here, and the second is poorly resolved from the second wave of the residual excess of HOAQ. The poor definition of both new waves preclude accurate wave height measurements, but they appear to be of equal height and to be proportional to the added phenol at less than equimolar ratios. These results are again interpretable by reactions involving formation of the $\phi OH \cdots O\phi^-$ homoconjugate dimer. Thus, in a 1/1 mixture of phenol and HOAQ, the wave at ~ -0.95V occurs from transfer of the second electron, the wave being shifted by subsequent protonation by ϕOH

$$HOAQ^{2-} + \phi OH \rightarrow H_2OAQ^- + \phi O^- \quad [10]$$

The ensuing formation of the homoconjugate $\phi OH \cdots O\phi^-$ means that only one-half of the phenol is available as such for Reaction [10], and, in the 1/1 mixture, the wave at -0.95V is approximately one-half of the height of the original second-electron wave. The second of the new waves caused by phenol is the same as Reaction [10] but with the less acidic $\phi OH \cdots O\phi^-$ acting as proton source, producing a smaller positive shift of reduction potential. We note finally that formation of a heteroconjugate $\phi OH \cdots HOAQ^{\cdot-}$ following the first charge transfer could provide an alternative interpretation of these results.

Acknowledgment

This work was supported by the UNC Materials Research Center under Contract SD-100 with the Advanced Research Projects Agency and by the National Science Foundation under Grant GP-8669.

Manuscript submitted March 31, 1971; revised manuscript received *ca.* July 2, 1971.

Any discussion of this paper will appear in a Discussion Section to be published in the June 1972 JOURNAL.

REFERENCES

1. P. H. Given, M. E. Peover, and J. Schoen, *J. Chem. Soc.*, **1958**, 2674.
2. M. E. Peover, *ibid.*, **1962**, 4540.
3. A. S. Lindsay, M. E. Peover, and N. G. Savill, *ibid.*, **1962**, 4558.
4. R. Jones and T. McL. Spotswood, *Australian J. Chem.*, **15**, 492 (1962).
5. L. Ya. Kheifets and V. D. Bezuglyi, *Elektrokhim.*, **2**, 800 (1966).
6. R. W. Murray, W. R. Heineman, and G. W. O'Dom, *Anal. Chem.* **39**, 1666 (1967).
7. S. B. Brummer, *J. Chem. Phys.*, **42**, 1636 (1965).
8. I. Piljac and R. T. Iwamoto, *Inorg. Chim. Acta*, **3** 49 (1969).
9. M. J. Blake, *J. Am. Pharm. Assoc. Sci. Ed.*, **46**, 163 (1957).
10. R. J. Jasinski and S. Kirkland, *Anal. Chem.*, **39**, 1663 (1967).
11. J. W. Ross, R. D. DeMars, and I. Shain, *ibid.*, **28**, 1768 (1956).
12. R. N. Adams, "Electrochemistry at Solid Electrodes," Dekker, 1969.
13. L. Meites, "Polarographic Techniques," 2nd ed., p. 121, Interscience Publishers, New York (1965).
14. K. S. Santhanam and A. J. Bard, *J. Am. Chem. Soc.*, **88**, 2669 (1966).
15. M. E. Peover Electrochemistry of Aromatic Hydrocarbons and Related Substances, in "Electroanalytical Chemistry," Vol. 2, M. Dekker, Inc., New York (1967).
16. A. E. Brodsky, L. L. Gordienko, and L. S. Degtiarev, *Electrochim. Acta*, **13**, 1095 (1966).
17. H. H. Jaffe, *Chem. Rev.*, **53**, 191 (1953).
18. N. S. Hush and J. Blackledge, *J. Chem. Phys.*, **23**, 514 (1955).
19. F. J. Vermillion, Jr., and I. A. Pearl, *This Journal*, **111**, 1392 (1964).
20. T. L. Perrin, Mechanisms of Organic Polarography, in "Progress in Physical Organic Chemistry," Vol. 3, p. 182.
21. I. M. Kolthoff, M. K. Chantooni, and S. Bruckenstein, *J. Am. Chem. Soc.*, **83**, 3927 (1961).
22. J. F. Coetzee and G. Padmanabhan, *J. Phys. Chem.*, **69**, 3193 (1965).
23. I. M. Kolthoff and M. K. Chantooni, *J. Am. Chem. Soc.*, **87**, 1004 (1965).
24. I. M. Kolthoff, M. K. Chantooni, and S. Bhowmik, *ibid.*, **88**, 5430 (1966).
25. I. M. Kolthoff, M. K. Chantooni, and S. Bhowmik, *ibid.*, **90**, 23 (1968).
26. I. M. Kolthoff and M. K. Chantooni, *ibid.*, **91**, 25 (1969).
27. I. M. Kolthoff and M. K. Chantooni, *ibid.*, **91**, 2875 (1969).
28. I. M. Kolthoff and M. K. Chantooni, *ibid.*, **91**, 4621 (1969).
29. G. A. Harlow and D. B. Bruss, *Anal. Chem.*, **30**, 1833 (1958).
30. T. Fujinaga, K. Izutsu, and K. Takaota, *J. Electroanal. Chem.*, **12**, 203 (1966).
31. T. E. Neal, Ph.D. Thesis, University of North Carolina, Chapel Hill, 1970.
32. G. J. Hoijtink, J. van Schooten, E. de Boer, and W. Y. Aalbersberg, *Rec. Trav. Chim.*, **73**, 355 (1954).

An Experimental Study of Mass Transfer on a Rotating Spherical Electrode

Der-Tau Chin*

Electrochemistry Department, Research Laboratories, General Motors Corporation, Warren, Michigan 48090

ABSTRACT

Convective diffusion of electrolytic ions to a rotating spherical electrode has been investigated experimentally over the range of Reynolds numbers from 200 to 40,000, and Schmidt numbers between 920 and 37,000. The study was carried out by measuring the limiting currents for the reductions of ferricyanide and tri-iodide ions with a platinum hemispherical electrode. The results confirm the validity of a mass transfer theory reported previously for Reynolds numbers within the range 200-15,000. At Reynolds numbers above 15,000, the flow becomes turbulent, and the rate of mass transfer varies with $Re^{0.67}$. The characteristics of fluid flow around the spherical electrode were observed by generating dyes electrochemically near the pole of rotation.

In a previous paper (1), the rationale for the use of a rotating spherical electrode (RSE) was described. A mathematical model was formulated for the rate of ionic transfer to the spherical electrode in the laminar flow region.

An inherent limitation of a rotating disk electrode (RDE), used in metal dissolution studies, is that the disk would recede into the support and upset the fluid flow characteristics. Consequently, high rate dissolution reactions cannot be studied precisely with a RDE. The concept of a RSE is to replace the central disk electrode on the RDE with a spherical head electrode. The spherical head merely reduces in size during metal dissolution, and does not alter the flow characteristics. Owing to this geometrical advantage, the RSE has been proposed in this laboratory as an analytical tool for our investigations into the mechanism of electrochemical machining. For other applications, the new technique could also be used to study corrosion and high-rate electrodeposition reactions.

The present study was designed to check the transfer theory. Reductions of ferricyanide and tri-iodide ions in the presence of excess supporting electrolytes were used for the investigations. Details of these electrochemical reactions and their applications to the mass transfer studies have been reported elsewhere (2, 3). This paper describes an experimental setup for the use of such an electrode as well as the results of

* Electrochemical Society Active Member.
Key words: convective diffusion, limiting current.

limiting current measurements over an extended range of experimental conditions.

Experimental

Spherical electrode.—The electrode used was a RSE having a replaceable platinum hemispherical electrode. It was composed of three separate sections: a brass holder, an acrylic support, and a hemispherical head electrode. Figure 1 shows the construction details.

The acrylic support was a cylindrical rod, 2.5 cm diam and 8.2 cm long, having a 0.6 cm hole through the center. The lower end of the support was threaded to accommodate the electrode. Its upper end was machined to fit tightly into the brass holder. A neoprene gasket, 0.08 cm thick and 2.5 cm diam, was cemented to the lower end to prevent leakage of electrolytes into the interior of the RSE.

The brass holder was made from a 2.5 cm diam rod. It also had a central through hole to accommodate a copper wire used as the electrical connection to the head electrode. Its upper portion was precision machined to a No. 1 Morse taper to fit snugly into the spindle shaft of a rotating assembly (Fig. 2).

The electrode was electroplated with a layer of smooth platinum, 0.003 cm thick. Three such electrodes were prepared for the study; the radii of their hemispherical heads were 0.478, 0.645, and 0.772 cm. The electrical connection was made by soldering a copper wire to the tail end of each electrode. After the electrode was screwed into the acrylic support, the wire would extend to the top portion of the brass holder and was secured there with a set screw. The assembled RSE was approximately 16.5 cm long.

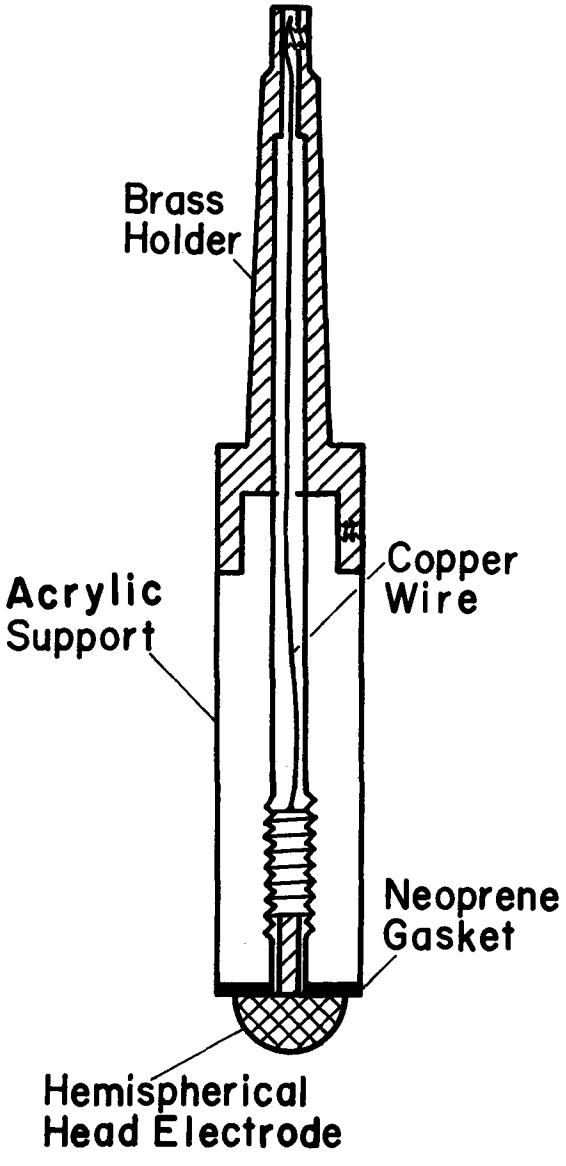

Fig. 1. Rotating spherical electrode

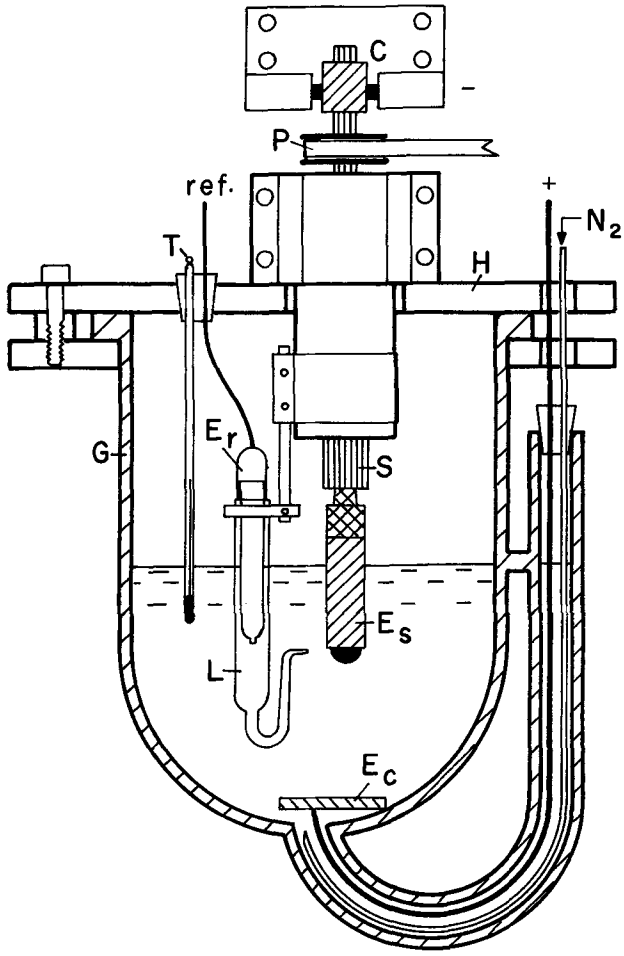

Fig. 2. Schematic diagram of cell arrangement. C, slip-ring contacts; E_c, counterelectrode; E_r, reference electrode; E_s, rotating spherical electrode; G, glass jar; H, cell cover; L, Luggin capillary tube; P, pulley and belt; S, spindle shaft; T, thermometer.

Solutions.—The ferricyanide electrolyte was composed of 0.01M potassium ferricyanide, 0.01M potassium ferrocyanide, and 2M sodium hydroxide. For the tri-iodide system, a solution containing 0.002M iodine and 0.1M potassium iodide was used. All the solutions were prepared by dissolving Baker analyzed chemicals in distilled water without further purification. Iodometric titrations were used to determine the concentrations of ferricyanide and tri-iodide ions. During some of the experimental runs, sucrose was added to the tri-iodide electrolyte to increase the solution viscosity and to decrease the diffusivity of tri-iodide ion; this allowed a variation in Schmidt numbers ranging from 920 to 37,000. The solution viscosity was measured with a falling ball viscosimeter. To determine the diffusivities for ferricyanide and tri-iodide ions, a platinum rotating disk electrode (0.635 cm diam) was employed, and the diffusivity computation was performed according to Levich's disk equation (4).

Cell arrangement.—Figure 2 is a schematic diagram of the cell arrangement. The cell was a Pyrex bell jar, 21.5 cm ID x 28 cm high. It had a ground glass flange to fit against the underside of an aluminum cell cover mounted on an aluminum frame. Connected to the bottom of the cell was a glass U-tube, which allowed insertion of an electric lead for the counterelectrode as well as a polyethylene tube for bubbling of nitrogen through the electrolyte.

A Gilman spindle assembly was attached directly to the aluminum frame and extended down into the cell. The spindle shaft had a tapered hole on the lower end to accommodate the RSE as shown in the figure. Electrical contact to the RSE was made by two carbon brushes which were spring loaded to ride on the rhodium-plated surface of a brass slip-ring mounted on the top of the spindle shaft. The whole spindle assembly was mounted eccentric to the center of the cell. This arrangement was necessary in order to avoid inducing swirling of the electrolyte at high rotational speeds.

A d-c motor secured on a separate frame was used to drive the rotating assembly. The connection between the pulleys on the motor and the spindle shaft was provided by a rubber timing belt. A Cole-Parmer 4420 electronic speed controller was used to control the speed of rotation.

A platinum-plated copper sheet, 4 × 4 cm, embedded in an epoxy block was used as the counterelectrode. It was located at the bottom of the cell. The reference electrode was a saturated calomel electrode placed in a Luggin tube. The tube was immersed in the electrolyte. To avoid disturbing the flow characteristics, the capillary tip was positioned at the downstream side of the spherical head as shown in Fig. 2.

Limiting current measurements.—Diffusion-limited currents were measured for the reduction of ferricyanide and tri-iodide ions over a speed range of 100-6000 rpm. All the experiments were performed at 24° ± 1°C. For each run, the RSE was first cleaned with methanol, and was cathodically treated at −1.5V for 2 min in a 2M NaOH solution followed by rinsing in distilled water. The clean electrode was then transferred quickly into the cell, and installed on the spindle of the rotating assembly.

The potential of the RSE was controlled by a Magna 4700M potentiostat. The current was measured using a standard resistor and the voltage drop was measured with a Keithley 610C electrometer. A Magna 4510 linear scan unit and a Honeywell 540 XYY′ recorder were used in conjunction with the potentiostat. For each run, current/potential curves over the entire anticipated potential range of interest were first plotted on the recorder to determine the limiting current range. A proper potential setting was then chosen for the potentiostat, and the limiting current readings were made with the electrometer at various rotational speeds. Normally, a potential of −0.3V *vs.* SCE was used for the reduction of ferricyanide ion. For the tri-iodide system, the potential setting varied from 0 to −0.2V *vs.* SCE, depending upon the sucrose concentrations.

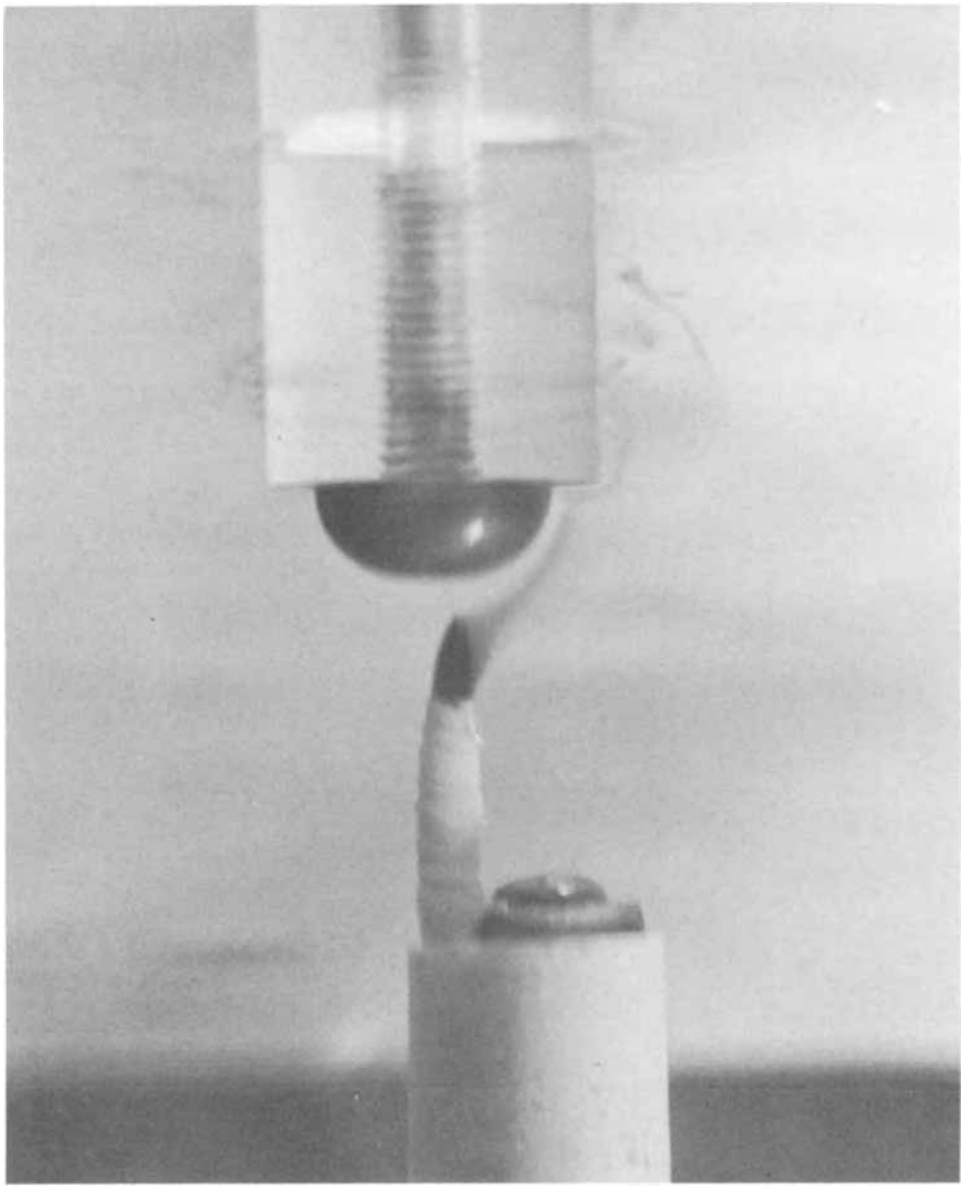

Fig. 3. Photograph of the flow pattern around a hemispherical electrode rotating at a Reynolds number of 1300.

The reproducibility of the measurements was within ± 5%.

To avoid a possible secondary reaction due to reduction of dissolved oxygen, high purity nitrogen was passed through the electrolyte before the start of each experiment. The gas was presaturated with water vapor and iodine vapor by passing it through a solution of the same composition as the test electrolyte. During the run, a nitrogen atmosphere was maintained by passing the gas over the electrolyte.

Flow observations.—The fluid flow around the spherical head was visually examined by generating dyes electrochemically near the pole of rotation. The dye generator was a small conical electrode, 0.026 cm diameter and 0.6 cm long, made from an AWG No. 10 copper wire, and was positioned about 0.3 cm below the RSE. The electrolyte used was a 2M sodium nitrate solution containing 0.01% thymol blue. When the conical electrode was made cathodic with respect to the counter-electrode located at the bottom of the cell, a blue stream was produced in the yellow electrolyte due to the increase in pH in the vicinity of the conical electrode. In this way, the flow induced by the RSE was made visible, and motion pictures of the flow pattern were taken with the aid of light sources behind the cell.

Results

Flow of electrolytes.—Figure 3 is a photograph showing the dye movement around the spherical electrode rotating at a Reynolds number of 1300. It was observed that under the laminar condition, the fluid was drawn in toward the spherical surface along the axis of rotation. From there, it was carried by the swirling motion toward the equator. In the neighborhood of the equator, the flow bent smoothly 90° toward the radial direction, and then moved along the support surface to the bulk of the electrolyte.

Limiting currents.—For the ferricyanide system, the limiting currents were measured with three different sizes of hemispherical heads. The results are given in Fig. 4, where the current is plotted against the square root of angular velocity. The electrolytic concentrations as well as the associated electrolyte properties are shown in the accompanying table. In the low speed region, the data points for each electrode fall on a straight line passing through the origin as predicted by the transfer theory (1). In the high-speed region, a break point occurs for the large electrodes, beyond which there is another linear portion with a larger slope. Presumably the break point signifies the beginning of the turbulent flow. The rotational speed at which the break point occurs increases with decreasing electrode size. For the 0.478 cm radius electrode, no break point was observed within the speed range investigated.

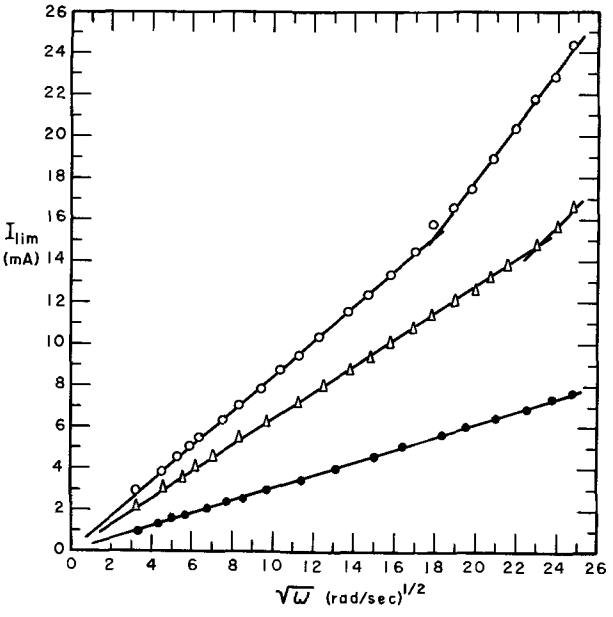

Fig. 4. Limiting currents for reduction of ferricyanide

	r_o (cm)	$C_\infty \times 10^3$ (mole/liter)	$\nu \times 10^2$ (cm^2/sec)	$D \times 10^6$ (cm^2/sec)
○	0.772	8.53	1.20	4.86
△	0.645	9.61	1.28	4.98
●	0.478	8.53	1.20	4.86

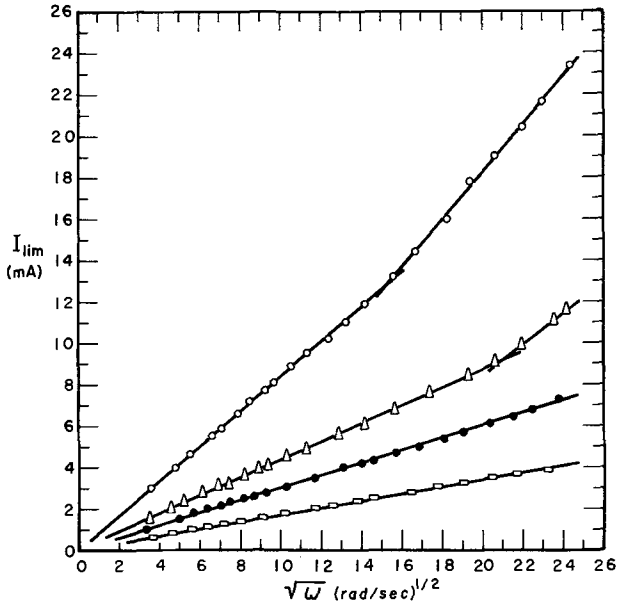

Fig. 5. Effect of sucrose content on the limiting current for reduction of tri-iodide. A hemispherical electrode with a radius of 0.772 cm was used for the measurements.

	Sucrose concentration (mole/liter)	$C_\infty \times 10^3$ (mole/liter)	$\nu \times 10^2$ (cm^2/sec)	$D \times 10^6$ (cm^2/sec)
○	0	2.38	0.91	9.91
△	0.84	2.34	1.65	4.47
●	1.06	2.13	2.82	3.43
□	1.58	2.22	6.20	1.69

The tri-iodide electrolyte was used primarily for showing the effect of Schmidt numbers on the transfer measurement. The solution viscosity was increased by adding sucrose to the electrolyte. Figure 5 shows the results of limiting current measurements with a 0.772 cm radius electrode for various sucrose concentrations. The accompanying table in the figure gives the electrolyte concentrations as well as the solution viscosities and the diffusivities of tri-iodide ion. Again, a linear portion passing through the origin is obtained for all the electrolytes. The effect of viscosity is: (*A*) to increase the speed at which the break point occurs, and (*B*) to decrease the diffusivity and, hence, the limiting current.

Discussion

As shown in a previous paper (1), the theory for mass transfer to the hemispherical electrode in the laminar flow region is given by the following expression

$$\mathrm{Sh} = 0.474\,\mathrm{Re}^{1/2}\,\mathrm{Sc}^{1/3} \qquad [1]$$

Here Sh is the Sherwood number defined as Kr_o/D, Re is the Reynolds number based upon the electrode radius, and Sc is the Schmidt number. The mass transfer coefficient, K, is related to the limiting current, I_{lim}, by

$$K = \frac{I_{lim}}{A\,n\,\mathbf{F}\,C_\infty} \qquad [2]$$

where A is the surface area of the electrode, and C_∞

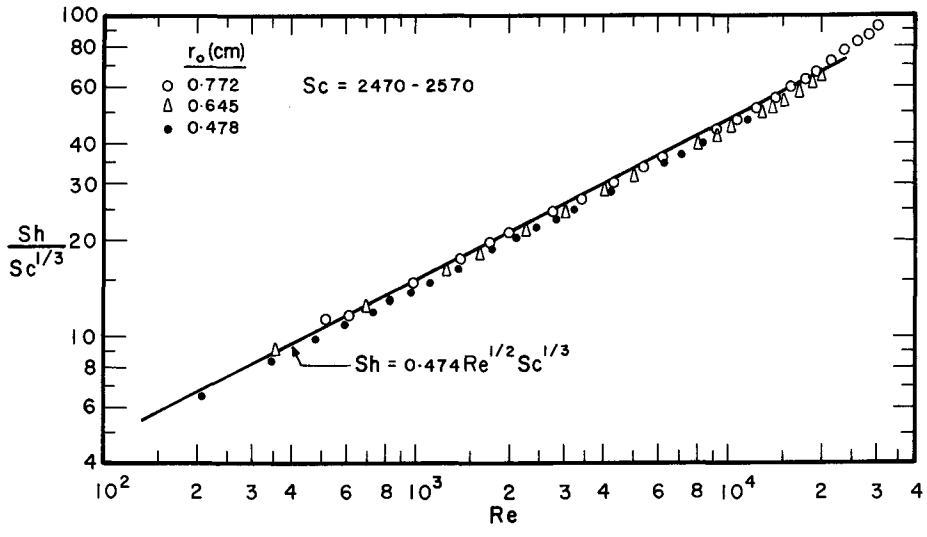

Fig. 6. Comparison with mass transfer theory for the ferricyanide data.

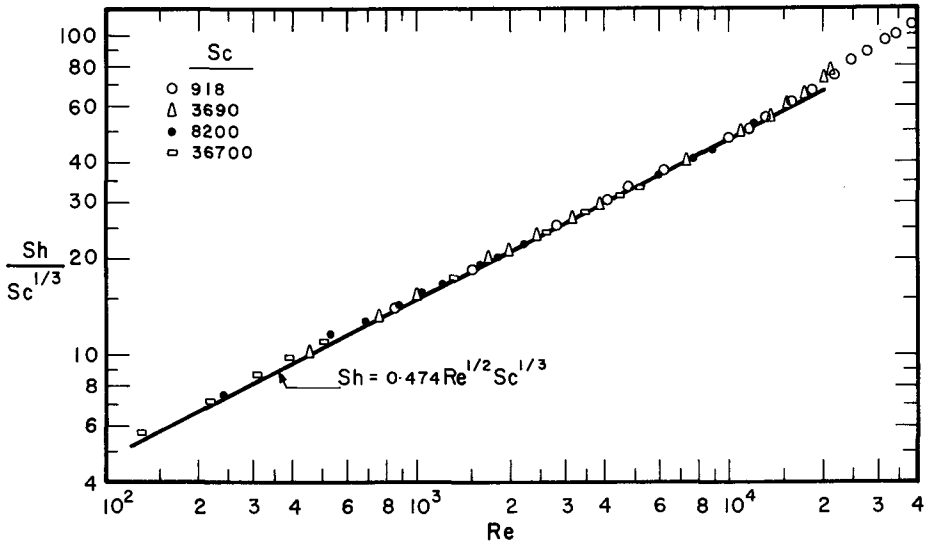

Fig. 7. Comparison with mass transfer theory for the tri-iodide data.

is the bulk concentration of the diffusing ion. Accordingly, a log-log plot of $Sh/Sc^{1/3}$ *vs.* Re would be expected to be linear with a slope equal to ½ for the limiting current results obtained in the laminar region.

Such plots are shown in Fig. 6 for the ferricyanide data, and in Fig. 7 for reduction of tri-iodide ion. The experimental points are indicated by the symbols ○, ●, △, and □. The solid line is the theoretical prediction given by Eq. [1]. The data replotted this way merge together into a single curve over the range of Reynolds numbers from 200 to 40,000. For Reynolds numbers less than 15,000, the data vary with the one-half power of Re, and the agreement with theory is apparent. An analysis of the laminar data gives an empirical proportional constant of 0.47 ± 0.02, as compared to the theoretical value of 0.474.

Poorer agreement is found for smaller size electrodes as shown in Fig. 6, where the results with the 0.478 and 0.645 cm electrodes lie about 7% below the theoretical line. This discrepancy can probably be attributed to an experimental uncertainty due to an edge effect imposed by the underside wall of the acrylic support. A close examination of Fig. 3 reveals that the flow beyond the equator of the hemispherical electrode is not a free stream as in the case of a rotating sphere (5, 6). The flow characteristics near the electrode edge would therefore deviate from the case considered in the theory. Ideally, a support having a radius equal to that of the spherical head should be used. For practical purposes, this situation is difficult to maintain, especially during dissolution reactions. It can be expected that the smaller the electrode size as compared to the support, the more apparent will be the edge effect. Presently, the exact nature of this edge effect is not known; further study on this aspect seems to be necessary.

Apart from the above considerations, the agreement between the theory and the experimental results is reasonably good, judging from the 5% reproducibility for the measurements. There is little doubt that the theory is valid in the laminar flow region over the range of Schmidt numbers reported in the present paper.

Figures 6 and 7 show that for Reynolds numbers larger than 15,000, the flow becomes turbulent, and the mass transfer characteristics deviate from the laminar theory. An analysis of the data within the range of Reynolds numbers from 15,000 to 40,000 reveals that the Sherwood number is proportional to $Re^{0.67}$. Interestingly, this 0.67 power coincides with the result of an earlier heat transfer measurement from a rotating sphere (5). Since there are fewer data points available in this region, no definite conclusion can be made regarding the Schmidt number dependence for turbulent flow.

An experimental investigation of heat transfer from a rotating sphere has been reported by Kreith, Robert, Sullivan, and Sinha (5) over the range of Prandtl numbers from 0.024 to 217. These authors also supplemented their experiments with a theory (5, 7) derived from Nigam's (8) incorrect velocity analysis. More elaborate thermal boundary layer computations have been performed by Banks (9) for Prandtl numbers equal to 0.7 and 1.0. Baxter and Davies (10) re-

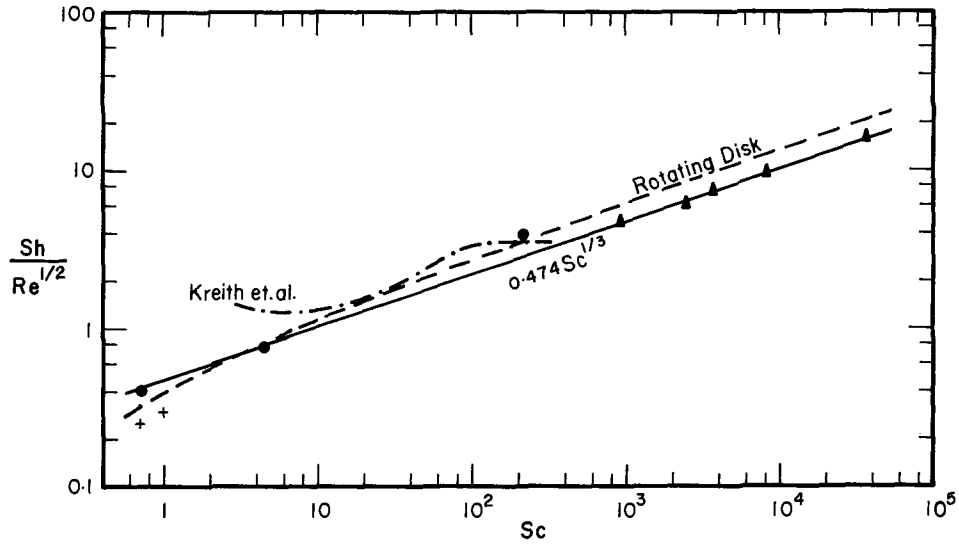

Fig. 8. Comparison with heat transfer results. The triangles are the limiting current data obtained in the laminar region (200 < Re < 15,000). The dots are the results of Kreith *et al.*'s heat transfer measurements. Banks' numerical computations are represented by the crosses.

ported an approximate theory for transfer to a rotating spherical cap at large Prandtl numbers; however, owing to the nature of the equations used, these authors were not able to carry out computations for the cases of a hemispherical cap or a sphere. Since the Prandtl and the Nusselt numbers of heat transfer are analogous to the Schmidt and the Sherwood numbers, respectively, used for the mass transfer studies, it seems desirable to compare the results of the present study with those reported previously. Such a comparison is given in Fig. 8, where $Sh/Re^{1/2}$ is plotted in a log-log fashion *vs.* the Schmidt number. The solid triangles are the present limiting current results obtained in the laminar region. The solid line is the theoretical prediction from Eq. [1]. Kreith *et al.*'s laminar data are indicated by the dots, and their theoretical analysis is shown as the dash-dot curve. Banks' results are indicated by the crosses. Also given in the figure is the rotating disk theory over the range of Schmidt numbers as calculated by Litt and Serad (11) with an analog computer.

It is seen that Kreith *et al.*'s theory does not correlate the data at all; Banks' computation, on the other hand, falls short of the heat transfer measurement. The rotating disk theory predicts a $Sc^{1/3}$ variation at large Schmidt numbers; it gives a transfer rate 32% too high for the case of a sphere or a hemispherical electrode. Only the solid line representing a $0.474\ Sc^{1/3}$ dependence is capable of following the experimental points over the extended range of Schmidt numbers. However, Eq. [1] represents only the asymptotic behavior of the transport process occurring at large Schmidt numbers; the agreement with the heat transfer data at small Sc may simply be fortuitous.

Conclusions

In summary, convective diffusion on a rotating hemispherical electrode has been studied experimentally over the range of Reynolds numbers from 200 to 40,000, and Schmidt numbers between 920 and 37,000. At Reynolds numbers below 15,000, the theory reported previously (1) appears to give a satisfactory correlation with the experimental data. For Reynolds numbers larger than 15,000, the flow becomes turbulent, and the rate of mass transfer varies with $Re^{0.67}$.

Acknowledgment

The author is indebted to Dr. J. L. Griffin, also of the Electrochemistry Department, General Motors Research Laboratories, for his invaluable assistance in the construction of the experimental apparatus.

Manuscript submitted March 24, 1971; revised manuscript received *ca.* July 16, 1971. This was Paper 188 presented at the Washington, D.C. Meeting of the Society, May 9-13, 1971.

Any discussion of this paper will appear in a Discussion Section to be published in the June 1972 JOURNAL.

LIST OF SYMBOLS

A	surface area of spherical electrode, cm^2
C_∞	bulk concentration of diffusing species, g-mole/cm^3
D	diffusivity, cm^2/sec
$\mathbf{F}$	Faraday constant, coulomb/g-equiv
I_{lim}	limiting current, A
K	mass transfer coefficient, cm/sec
n	number of electrons transferred in electrochemical reaction, g-equiv/g-mole
r_0	radius of spherical electrode, cm
Re	Reynolds number, defined as $r_0^2\omega/\nu$, dimensionless
Sc	Schmidt number, defined as ν/D, dimensionless
Sh	Sherwood number, defined as Kr_0/D, dimensionless
ν	kinematic viscosity, cm^2/sec
ω	angular velocity, rad/sec

REFERENCES

1. D. T. Chin, *This Journal*, **118**, 1434 (1971).
2. L. P. Reiss and T. J. Hanratty, *A.I.Ch.E. J.*, **9**, 154 (1963).
3. J. D. Newson and A. C. Riddiford, *This Journal*, **108**, 695, 699 (1961).
4. V. G. Levich, *Acta Physicochim. U.R.S.S.*, **17**, 257 (1942); also "Physicochemical Hydrodynamics," Prentice-Hall, Englewood Cliffs, New Jersey (1962).
5. F. Kreith, L. G. Roberts, J. A. Sullivan, and S. N. Sinha, *Intern. J. Heat Mass Transfer*, **6**, 881 (1963).
6. F. P. Bowden and R. G. Lord, *Proc. Roy. Soc. (London) Ser. A*, **271**, 143 (1963).
7. S. N. Singh, *Appl. Sci. Res.*, **A9**, 197 (1960).
8. S. D. Nigam, *ZAMP*, **5**, 151 (1954).
9. W. H. H. Banks, *ibid.*, **16**, 780 (1965).
10. C. B. Baxter and D. R. Davies, *Quart. J. Mech. and Applied Math.*, **13**, 247 (1960).
11. M. Litt and G. Serad, *Chem. Eng. Sci.*, **19**, 867 (1964).

Technical Note

Interface Equilibrium Concentrations During Diffusion

S. M. Hu*

IBM Components Division, East Fishkill Facility, Hopewell Junction, New York 12533

In the literature (1) it has been shown that, during the diffusion of a solute from a semi-infinite source into a semi-infinite sink, the interface concentrations of the solute in both phases are invariant with time. This was proved under the conditions that the diffusivities D_1 and D_2 in both phases are constant, and that the segregation of the solute between the two phases is described by $C_{2,0} = kC_{1,0}$ (where k is the segregation coefficient; C_1 and C_2 are the solute concentrations in the two phases, and the subscript 0 denotes the interface $x = 0$), provided that equilibrium is established at the interface and that the interface is not moving during diffusion. The latter condition means that there is no Kirkendall effect. This assumption is generally reasonable for diffusions in semiconductors in which highest concentrations seldom exceed a few atomic per cent, and in which the vacancy pump effect is negligible (2). The purpose of this note is to point out that the time-invariance of interface concentrations is still valid under the more general conditions that D_1 and D_2 are respectively functions of C_1 and C_2, and that the equilibrium between the two phases is described by $C_{2,0} = f(C_{1,0})$, where f is an arbitrary function.

This aspect is of practical importance in, for example, the diffusion of a solute from a doped oxide into a semiconductor at high concentrations. For generality, we assume the ratio between the surface areas of the two phases to be r, which is not necessarily unity except for the case of direct physical contact.

In the present case the concentrations at the interface in the two phases are nonarbitrary and must be determined as a condition of self-consistency, although in cases of diffusion in one semi-infinite medium the surface concentration is an arbitrary constant (or an arbitrary function of time). Hence, one may start by assuming that the surface concentrations are time-invariant, and then prove that the resulting solution is consistent with the boundary conditions including this assumption. Under this assumption, one can express the concentrations as functions of a single Boltzmann variable $u = x/2\sqrt{t}$. The continuity equations can be written

$$-2u\frac{dC_2}{du} = \frac{d}{du}\left(D_2\frac{dC_2}{du}\right) \qquad [1]$$

$$-2u\frac{d(C_s - C_1)}{du} = \frac{d}{du}\left[D_1\frac{d(C_s - C_1)}{du}\right] \qquad [2]$$

where C_s is the initial bulk concentration in the source, and D_1 is a function of $(C_s - C_1)$. The initial conditions are

$$(C_s - C_1) = C_s - C_{1,0}, \text{ at } u = 0$$
$$= 0, \text{ as } u \to -\infty \qquad [3]$$

and

$$C_2 = C_{2,0}, \text{ at } u = 0$$
$$= 0, \text{ as } u \to -\infty \qquad [4]$$

A solution to [1] is then obtainable from an iterative scheme (3) as

$$C_2 = C_{2,0}\left[1 - \frac{\int_0^u D_2^{-1}\exp\left(-\int_0^u 2uD_2^{-1}\,du\right)du}{\int_0^\infty D_2^{-1}\exp\left(-\int_0^u 2uD_2^{-1}\,du\right)du}\right] \qquad [5]$$

One obtains a similar expression for C_1, or equivalently $(C_s - C_1)$. At the interface, one has

$$C_{2,0} = f(C_{1,0}) \qquad [6]$$

$$C_{2,0}\left[\int_0^\infty D_2^{-1}\exp\left(-\int_0^u 2uD_2^{-1}\,du\right)du\right]^{-1} =$$
$$r(C_s - C_{1,0})\left[\int_0^\infty D_1^{-1}\exp\left(-\int_0^u 2uD_1^{-1}\,du\right)du\right]^{-1} \qquad [7]$$

The mass flows at the surfaces of the source and the sink are given by Eq. [7] since, from Eq. [5]

$$-\left(D_2\frac{\partial C_2}{\partial X}\right)_{X=0} = -\frac{1}{2\sqrt{t}}\left(D_2\frac{dC_2}{du}\right)_{X=0}$$
$$= -\frac{C_{2,0}}{2\sqrt{t}}\left[\int_0^\infty D_2^{-1}\exp\left(-\int_0^u 2uD_2^{-1}\,du\right)du\right]^{-1} \qquad [8]$$

and similarly for $-\left(D_1\frac{\partial C_1}{\partial X}\right)_{X=0}$

The definite integrals in Eq. [7] are independent of u, and hence, invariant with time. Since both Eq. [6] and [7], which together determine $C_{1,0}$ and $C_{2,0}$, do not contain u, $C_{1,0}$ and $C_{2,0}$ must be invariant with time. This in turn upholds the original assumption of $C_{1,0}$ and $C_{2,0}$ being time-invariant on which is based the application of Boltzmann transformation.

The solution of Eq. [6] and [7] requires the solution of [5] and its companion expression for $(C_s - C_1)$, and *vice-versa*. Hence, the actual numerical scheme involves a two-level iteration. For example, the first-level iteration involves searching $C_{1,0}$; then one obtains $C_{2,0}$ with Eq. [6]. This is followed by the second-level iteration, solving Eq. [5]. Fulfillment of Eq. [7] is the criterion for the first-level iteration. If the diffusivities in both media are constant, Eq. [7] reduces to

$$C_{2,0}/\sqrt{D_2} = r(C_s - C_{1,0})\sqrt{D_1} \qquad [9]$$

$C_{1,0}$ and $C_{2,0}$ are then obtainable from a straightforward algebraic solution of Eq. [6] and [9]. In the special case in which Eq. [6] reduces to $C_{2,0} = kC_{1,0}$ which, in combination with Eq. [9]

$$C_{1,0} = rC_s/(k\sqrt{D_1/D_2} + r) \qquad [10]$$

Manuscript submitted March 10, 1971; revised manuscript received *ca.* July 28, 1971.

Any discussion of this paper will appear in a Discussion Section to be published in the June 1972 JOURNAL.

* Electrochemical Society Active Member.

Key words: diffusion, interface concentrations, segregation coefficient, variable diffusivity.

REFERENCES
1. For example, see J. Crank, "The Mathematics of Diffusion," p. 37, Oxford Univ. Press, Clarendon, England (1956).
2. S. M. Hu and M. S. Mock, *Phys. Rev.*, **B1** 2582 (1970).
3. J. Crank, "The Mathematics of Diffusion," p. 148 ff., Oxford Univ. Press, Clarendon, England (1956).

Correction

In the paper "Reduction Mechanism of Thin-Film CuF_2 Electrodes in Propylene Carbonate Electrolyte," by Brian Burrows which appeared on pp. 1130-1132 in the July 1971 JOURNAL, Vol. 118, No. 7, the expression MHz cm^{-2} should read:

$$mc\ cm^{-2}$$

for millicoulomb per square centimeter. This substitution applies to both the text and the table headings on pp. 1130 and 1131.

JOURNAL OF THE ELECTROCHEMICAL SOCIETY

SOLID STATE SCIENCE

NOVEMBER 1971

A Study of the Dissolution of SiO_2 in Acidic Fluoride Solutions

John S. Judge*,[1]

IBM, Components Division, Hopewell Junction, New York

ABSTRACT

Data are presented on the dissolution rates of SiO_2 films in a variety of acidic fluoride solutions. It is shown that the rate of dissolution is linearly dependent on the concentration of HF_2^- and HF in relatively dilute fluoride solutions. Both reactions have a similar temperature dependence characterized by an activation energy of 9.1 and 8.1 kcal/mole, respectively. The reaction with HF_2^- is about four to five times as fast as that with HF. Extrapolation to more concentrated solutions suggests that higher polymeric species of the type $H_xF_{x+1}^-$ may also be active in the dissolution process. Raman data indicates that no single product species is formed although the product spectrum is consistent with the presence of some SiF_6^{2-}.

The dissolution of glasses by acidic fluoride solutions is probably one of the most familiar of chemical reactions. Nevertheless, the chemistry of this process has received very little study. In recent years, this reaction has taken on new technological importance through its use in the manufacture of micro-miniature electronic devices. Many different fluoride solutions, from concentrated HF to solutions highly buffered with NH_4F, are being used for SiO_2 dissolution through photoresist masks. Recently, Dey, Lundgren, and Harrell (1) reported on the temperature and agitation dependence of the rate of SiO_2 dissolution in one of the buffered HF solutions whose composition they failed to specify. It is the purpose of this study to determine what species in solution may be responsible for the dissolution and how these depend on the formulation of the solution, *i.e.*, to begin to elucidate the chemistry involved in the dissolution of SiO_2 in acidic fluoride solutions.

Experimental

The SiO_2 used in this study was in the form of thin films, ~5000Å thick, produced by the thermal oxidation of single-crystal silicon wafers. These were Monsanto wafers (111) orientation, p-type, ~15 ohm cm. They were oxidized in an oxygen, water vapor atmosphere (mole fraction $H_2O = 0.373$) at 1100°C. (These conditions are mentioned here although the etch rate data does not appear to be particularly sensitive to the conditions of oxide formation.)

The thickness of the oxide film was measured by an interference technique (2). The dissolution rates were calculated from the thickness changes which were found to be linear with time in all cases. The dissolution rates were, in general, measured under quiescent conditions although mild agitation has no measurable effect on the rates.

Reagent grade chemicals were used in all cases. It was necessary to standardize the NH_4F stock solutions utilizing an Orion fluoride electrode and Orion standard fluoride solutions. A hydrogen electrode was used for pH measurements in these acidic fluoride solutions. Jarrel-Ash kindly furnished the Raman spectrum of several solutions run on their Laser-Raman Spectrophotometer.

Results and Discussion

In relatively dilute fluoride solutions, the only significant species present are related by Eq. [1] and [2].

$$K_1[HF] = [H^+][F^-] \quad [1]$$

$$K_2[HF_2^-] = [HF][F^-] \quad [2]$$

Farrer and Rossotti (3) conclude that these are the only species present up to at least one molar fluoride. The constants, K_1 and K_2, have been determined many times [summarized in ref. (4)]. The most recent values for 1M ionic strength solutions and chloride media were reported by Mesmer and Baes (5) to be:

	25°C	60°C
$K_1 =$	1.30×10^{-3}	6.57×10^{-4}
$K_2 =$	0.104	3.66×10^{-2}

Of course, these values will be a function of ionic strength and, therefore, cannot be used quantitatively in more concentrated media such as buffered fluoride etches, which are commonly 10 → 15M in fluoride. Nevertheless, it is instructive to consider how the concentrations of the various species will depend on pH.

Figure 1 is a plot of the calculated concentrations of HF and HF_2^- for solutions of 15F total F^- as a function of pH (or more precisely $-\log_{10}[H^+]$), assuming the noted values of K_1 and K_2 (6). The values on the ordinate are normalized to add up to 1.00, such that the fraction of free fluoride is the difference between 1.00 and the sum of the two plotted values. It is apparent that in the region of pH > 7 all of the fluoride exists as uncombined fluoride ion. As the pH is lowered, the $[HF_2^-]$ begins to increase and reaches a maximum in the region of pH 3. At the same time, HF becomes a significant species below a pH of 4 and increases monotonically as the pH is further lowered.

* Electrochemical Society Active Member.
[1] Present address: Micro-Bit Corporation, Lexington, Massachusetts 02173.
Key words: etching, buffered HF, photoetching.

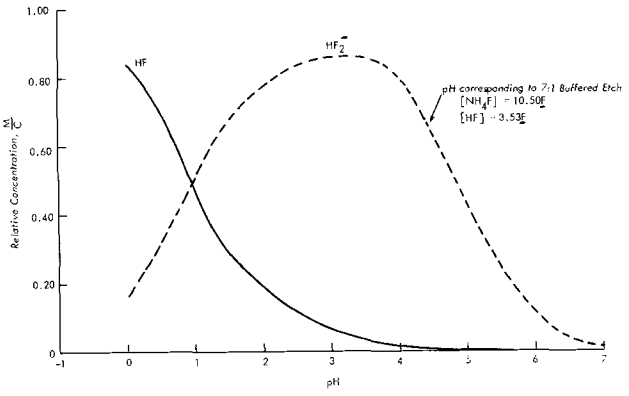

Fig. 1. Mole fraction of fluoride as HF and HF_2^-, calculated for 15M total F^-, and using the constants of Ref. (5). (——— mole fraction of fluoride as HF; - - - - - - - mole fraction of fluoride as HF_2^-).

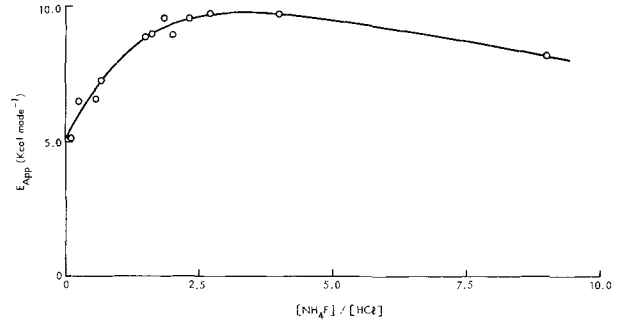

Fig. 2. Dependence of apparent activation energy on the ratio of NH_4F to HCl.

The pH of one commonly used buffered HF etchant composition is indicated on this figure. It is apparent that this composition would contain only HF_2^- and F^- and very little HF if higher polymeric species are not significant at these high concentrations.

In Table I, the etch rates and apparent activation energies in the temperature range 30°-60°C are listed for a selection of solutions made up of various amounts of NH_4F and HF. The ΔEapp values are calculated from relationship [3]

$$\text{Rate} = A \exp(\Delta E\text{app}/RT) \qquad [3]$$

assuming no change in the pre-exponential factor which includes concentration terms. It is apparent that ΔEapp tends to increase as the ratio of NH_4F to HF is increased. This suggests several parallel reaction paths of different activation energy.

In order to be able to treat the rate data more quantitatively, a series of solutions were prepared at a constant value of 1M ionic strength. The acidity of these solutions was varied using HCl and the fluoride

Table I. Effect of varying the concentration of NH_4F and HF on the apparent activation energy for the dissolution of SiO_2

Solution composition (F)				
NH_4F	HF	$[NH_4F]/[HF]$	ΔEapp. (kcal/mole)	Etch rate at 30°C (A/sec)
0	10.0	0	6.7	36.2
2.00	10.0	0.2	8.1	60.5
1.00	2.50	0.4	8.2	15.0
8.00	10.0	0.8	8.8	112
8.00	2.50	3.2	10.3	19.4
10.5	3.53	3.0 (7:1 buffered HF)	11.0	22.0
Dey *et al.* (1)	?	?	8.2	20

content, by including various amounts of NH_4F or NH_4Cl. Thus, the conditions of ref. (4) are met for these solutions and their values of K_1 and K_2 can be used to calculate the various concentrations. The composition and the calculated values of the concentrations of the various species are shown in Table II.

Again, the apparent activation energy for these solutions exhibited a similar dependence on the ratio of NH_4F to H^+ (or the pH). This relationship is shown in Fig. 2. It is apparent that the solutions with the greatest temperature sensitive rates have a composition with a ratio of NH_4F to HCl near three.

Although the solutions of Table II do not include one without added acid, such solutions have been investigated. They have a pH of ~7, and as can be seen from Fig. 1, contain essentially all fluoride in the unprotonated state. Such solutions exhibit essentially zero rate of SiO_2 dissolution, immediately allowing one to exclude free fluoride as one of the species responsible for the dissolution.

For these solutions then, the rate equation will have the general form

$$R = A[HF] + B[HF_2^-] + C \qquad [4]$$

where any of the values A, B, or C may become zero if the data so requires.

A least squares fit of the dissolution rate data to Eq. [4] yielded the following values for A, B, and C (with R in Å/sec and concentrations in molarity).

Temperature, °C	A	B	C
25	2.50	9.66	−0.14
60	10.4	48.6	−1.02

The linear fit of the rate data to relationship [4] with these values of the constants is shown in Fig. 3 and 4 where the experimental rates are plotted *vs.* $A[HF] + B[HF_2^-]$.

In general, these terms A and B will contain an exponential temperature dependence and a pre-exponential term. The temperature dependence is somewhat different for each term so that the over-all concentration dependent part of the rate equation for dilute fluoride solutions becomes as shown in Eq. [5].

$$R(\text{Å/sec}) = 5.0 \times 10^7 [HF_2^-]\, e^{-\Delta E_1/RT} + 2.2 \times 10^6 [HF]\, e^{\Delta E_2/RT} + C(T) \qquad [5]$$

Table II. Composition and calculated concentrations of various species in 1M ionic strength fluoride solutions

Composition (F)			Calculated concentrations (M) × 10^3 T = 25°C				Calculated concentrations (M) × 10^3 T = 60°C				SiO_2 dissolution rate (A/sec^{-1})	
[HCl]	[NH_4F]	[NH_4Cl]	[HF]	[HF_2^-]	[F^-]	[H^+]	[HF]	[HF_2^-]	[F^-]	[H^+]	T = 25°C	T = 60°C
0.100	0.864	0.100	13	87	677	0.0255	5	95	669	0.00508	0.739	3.00
0.200	0.768	0.200	41	159	409	0.129	16	183	385	0.0296	1.452	7.34
0.270	0.701	0.270	81	189	242	0.435	41	228	202	0.134	1.871	10.30
0.300	0.672	0.300	109	191	182	0.778	63	236	136	0.306	2.068	10.60
0.350	0.624	0.350	175	173	102	2.24	136	215	58.9	1.49	2.232	11.00
0.400	0.576	0.400	266	128	49.4	7.01	240	155	23.2	6.81	1.971	10.55
0.600	0.384	0.400	369	8	2.14	224	363	10	1.05	227	0.768	2.97
0.800	0.192	0.200	190	0.74	0.405	609	189	1.05	0.204	610	0.266	0.820
0.900	0.096	0.100	95	0.14	0.154	805	95	0.201	0.0775	805	0.088	0.240
0.450	0.240	0.550	234	3.2	1.42	213	231	4.47	0.708	214	0.451	1.57
0.150	0.288	0.700	86	63	75.5	1.48	62	87	51.1	0.80	0.901	4.58
0.250	0.384	0.600	164	83	52	4.10	140	107	27.6	3.34	1.339	6.46

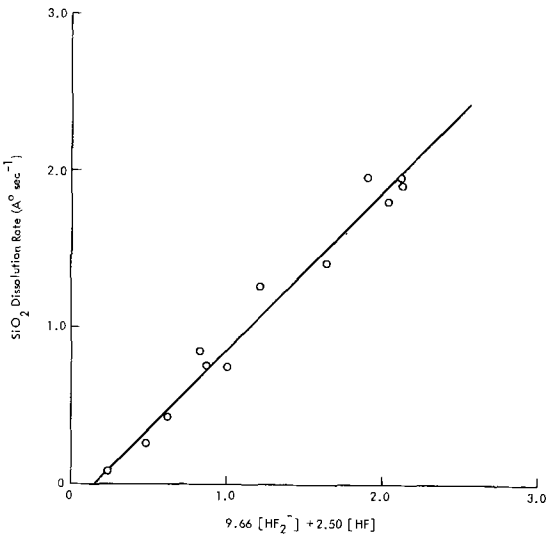

Fig. 3. Linear dependence of the dissolution rate of SiO_2 at 23°C on the plotted function of [HF_2^-] and [HF].

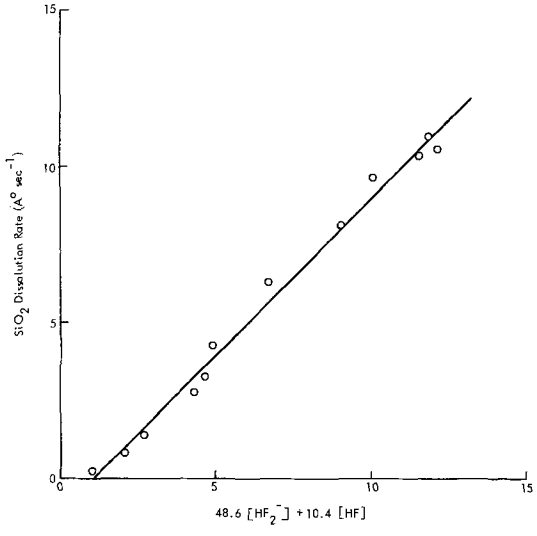

Fig. 4. Linear dependence of the dissolution rate of SiO_2 at 60°C on the plotted function of [HF_2^-] and [HF].

where

$$C(T) \sim 0.025\ (T\text{-}292)$$
$$\Delta E_1 = -9.1 \times 10^3$$
$$\Delta E_2 = -8.1 \times 10^3$$

It is now clear that the change in apparent activation energy with solution composition is in part a reflection of the change in the constants K_1 and K_2 with temperature which results in significant changes in [HF_2^-] and [HF] as can be seen from Table II. In all cases, the [HF_2^-] increases with temperature, whereas [HF] decreases for solutions containing relatively large amounts of HF_2^- and remains nearly constant for the more highly acidic solutions.

The fact that the value of C is not zero is at first surprising, but a much better fit of the data is obtained with these small but nonzero values. It might be expected that as the concentration is lowered, the concentration at the surface will become significantly lower than bulk concentration, *i.e.*, diffusion control becomes the case. This would result in the extrapolation of high concentration rates intersecting the zero rate point at some small but nonzero concentration, as is observed. In addition, as the temperature is raised, the value of this intercept should increase, as it does.

A test of the validity of this relationship can be made by comparing calculated rates from it to measured

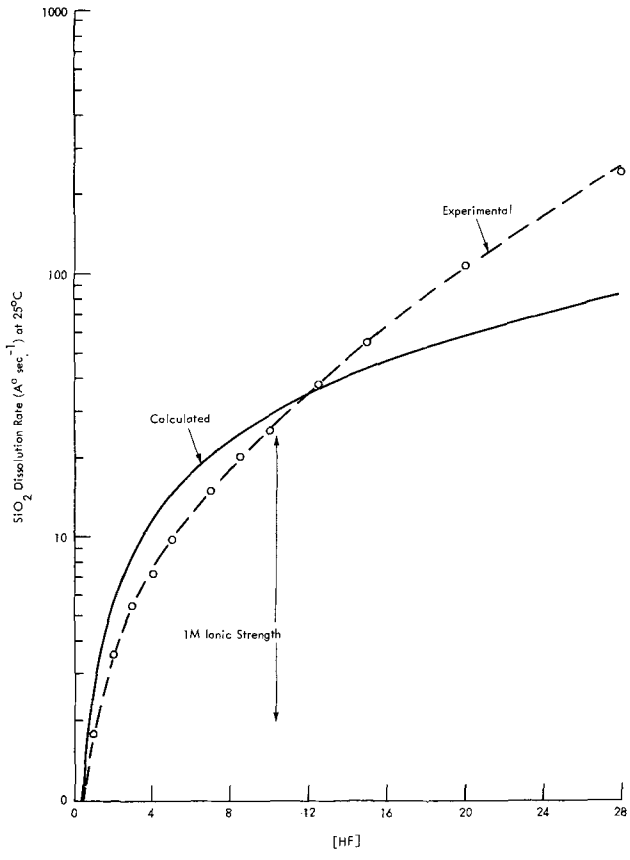

Fig. 5. Dependence of the dissolution rate of SiO_2 on the concentration of HF (——— calculated from Eq. [4], using K_1 and K_2 for 1M ionic strength; - - - - experimental).

rates in a slightly different system, namely, solutions of various concentrations of HF. The same one molar ionic strength values of K_1 and K_2 have been used to calculate the concentrations of HF and HF_2^- from which the rates in Fig. 5 are derived.

It is apparent that for the more dilute solutions, *i.e.*, solutions <10M, the measured and calculated rates are at least qualitatively in agreement. At high concentrations of HF, however, the rate of SiO_2 dissolution is significantly higher than would be predicted on this model. This suggests that other polymeric species may become of importance in chemically attacking the SiO_2 surface in these concentrated solutions, although the change in the nature of the media and the concomitant changes to be expected in the values of K_1 and K_2 could, perhaps, be sufficient to account for this deviation. In this connection, it is important to note that the agreement between the measured and calculated values is best near 1M ionic strength where the constants used will have the correct values. Evidence for higher polymeric species in more concentrated HF has been provided by Jones and Penneman (7). They found an infrared absorption at 1820 cm^{-1} in solutions greater than 6F in HF which is not due to HF_2^- or HF and is not shifted in D_2O. The ion $H_2F_3^-$ has been identified crystallographically in the solid state (8), and some phase rule studies (9) have indicated the presence of $H_3F_4^-$ and $H_4F_5^-$. The large positive deviation of the experimental rates from those calculated on the basis of dilute solution measurements may indicate that these higher polymeric species have a high activity in the dissolution of SiO_2.

The over-all reaction is often assumed to involve the formation of hexafluorosilicate ion in solution. It is most likely a gross over-simplification to assume that this is the exclusive product since aqueous H_2SiF_6 will itself dissolve up to 20 m/o (mole per cent) more SiO_2 (10). It has been proposed (11) that a series of products of the form $SiF_i(OH_2)_k$, where $i + j + k \leq 6$,

Table III. Raman spectrum of product species in 7:1 buffered HF (10.5F in NH_4F, 3.5F in HF), 0-2500 cm^{-1}

$\Delta\nu$ (cm^{-1})	Relative intensity
183	Medium
195	Shoulder
288	Weak
435	Weak
656	Medium Weak
832	Medium
915	Weak
1375	Medium
1569	Medium
1587	Medium
1640	Very Strong
1700	Very Weak
1733	Very Weak
1865	Medium
2010	Strong
2073	Very Strong
2115	Medium
2363	Weak
2422	Weak
2452	Medium

may form in the reaction of SiO_2 with H_2SiF_6. This would also probably apply to the solution of SiO_2 in HF.

A solution 10.5F in NH_4F and 3.5F in HF (commonly referred to as 7:1 buffered HF) was examined by Raman spectroscopy before and after dissolving SiO_2 in it by exposing a one inch quartz disk in a 500 cc volume of solution for two days. The solution which had no SiO_2 dissolved in it, exhibited no detectable absorptions in agreement with the work of Woodward and Tyrrell (12). The spectrum of the solution with the SiO_2 dissolved in it is reported in Table III. A very large number of peaks are observed, indicating the presence of multiple product species. The medium intensity peak at 656 cm^{-1} coincides with the Raman absorption reported previously for hexafluorosilicate ion in aqueous solution (13) and may indicate its presence as one of the product species.

Conclusions

It has been shown that the dissolution rate of SiO_2 in dilute acidic fluoride solutions depends on the concentration of HF_2^- and HF, but not free fluoride. The rate of attack of HF_2^- is about four to five times that of HF. The temperature dependence of the rate is similar for both species and is characterized by an activation energy of 9.1 and 8.1 kcal/mole, respectively. Quantitative characterization of the dissolution of SiO_2 in concentrated fluoride solutions must await the determination of the concentration dependence of the dissociation constants, K_1 and K_2, and identification of the role of higher polymeric species which are present in these solutions.

Acknowledgments

It is a pleasure to acknowledge the valuable assistance of Mr. M. J. Galindo in performing most of the experimental work and the Jarrel-Ash Company, Waltham, Massachusetts, for running the Raman spectra.

Manuscript submitted Feb. 20, 1970; revised manuscript received *ca.* June 4, 1971.

Any discussion of this paper will appear in a Discussion Section to be published in the June 1972 JOURNAL.

REFERENCES

1. J. Dey, M. Lundgren, and S. Harrell, *Proc. Kodak Photoresist Seminar*, II, 4 (1968).
2. A. J. Warnecke, Paper presented at the Kodak Photoresist Seminar, Philadelphia, May 1969.
3. H. N. Farrer and F. J. C. Rossotti, *J. Inorg. Nucl. Chem.*, **26**, 1959 (1964).
4. V. A. Buslaeu and M. P. Gustyakoya, *Zh. Neorgan. Khim.*, **10**, 1524 (1965).
5. R. E. Mesmer and C. F. Baes, Jr., *Inorg. Chem.*, **8**, 618 (1969).
6. K. Srinivasan and G. A. Rechnitz, *Anal. Chem.*, **40**, 509 (1968).
7. L. Jones and R. Penneman, *J. Chem. Phys.*, **22**, 781 (1954).
8. J. D. Forrester, M. E. Senko, A. Zalkin, and D. H. Templeton, *Acta Cryst.*, **16**, 58 (1963).
9. J. P. Buettner and A. W. Jache, *Inorg. Chem.*, **2**, 19 (1963).
10. S. M. Thomsen, *J. Am. Chem. Soc.*, **74**, 1690 (1952).
11. K. K. Kleboth, *Monatsh. Chem.*, **99**, 1177 (1968).
12. L. A. Woodward and J. V. Tyrrell, *Trans. Faraday Soc.*, **38**, 517 (1942).
13. R. B. Badachhape, G. Hunter, L. D. McCory, and J. L. Margrave, *Inorg. Chem.*, **5**, 929 (1966).

Flexure Measurements on a U-Nb-Zr Alloy During Oxidation and Temperature Cycling

R. E. Pawel* and J. V. Cathcart*

Metals and Ceramics Division, Oak Ridge National Laboratory, Oak Ridge, Tennessee 37830

ABSTRACT

As part of a general program to study the fundamental oxidation characteristics of a uranium-7.5 weight per cent (w/o) niobium-2.5 w/o zirconium alloy, measurements of the flexure of thin specimens reacting on one side were utilized to assess the extent of stress generation during oxidation. During the early stages of the reaction at 700°C, rapid flexing of the specimens was observed. Because the depth or thickness of the layer involved in this reaction was quite small, the stress within this zone must have been large to account for the observed bending stresses. The model relating flexure to a uniform stress in the growing oxide film appeared to be applicable and led to film stress values of the order of 10^6 psi. When the oxidation process was interrupted, the high stresses then dissipated rapidly as the reaction slowed. This behavior was analyzed in terms of a balance between stress generation and relief in both the oxide film and the substrate metal. We also used flexure measurements during thermal cycling of these specimens to study the kinetics of some of the structural transformations exhibited by this alloy. The presence of an elastic stress gradient was found necessary to promote significant flexure during the transformation period in these specimens, suggesting that shear forces play an important role in the transformations, particularly those involving the α'' structure.

The importance of mechanical effects on the over-all process of gaseous oxidation is generally acknowledged to be large for a number of metals. Many manifestations of these effects have been observed and their influence upon the over-all oxidation behavior discussed. Thus, stress buildup and the response of both the film and substrate metal to the stresses are regarded as important features in most oxidation processes and may be primary factors in determining whether or not an oxide film will be "protective."

The techniques which have been used to obtain quantitative data on stress development during oxidation have so far been limited to x-ray methods (1), optical methods (2), and methods which involve measurements of the macroscopic strain of the oxide film and/or the substrate. The latter category includes the "flexure" technique, in which the curvature of a specimen reacting on one side is measured. The first application of this procedure to an oxidation reaction was made by Dankov and Churaev (3) in 1950; variations of this method have since been utilized in high temperature gaseous oxidation studies of several pure metals (4-7) but few alloy systems (4c, 8, 9). In addition, some investigators have employed different types of measurements of the strain which occurred as a result of oxidation in order to obtain data from which to infer a stress distribution (10, 11). These results all indicate that significant, and in many cases dominant, stress systems and responses may arise during oxidation.

In the present paper we will consider the flexure behavior of a U-7.5 w/o Nb-2.5 w/o Zr alloy during oxidation at 700°C. During the course of this work we also found that the alloy exhibited some unusual flexure sequences upon temperature cycling. We will discuss these in terms of the structure of the alloy and the possibility of extending the uses of the flexure technique to the study of stress-sensitive transformations.

Background Information

The details of the oxidation characteristics of the alloy are being published elsewhere (12) and will not be presented here. However, it is useful to furnish a brief description of the alloy and its oxidation behavior in order to provide suitable background for our interpretation of the flexure data. A more complete picture is available in the literature (12-16.)

At 700°C, this ternary alloy has a single phase, body-centered-cubic structure (γ) which may be retained with minor modification by quenching. Aging of the quenched material at temperatures less than 400°C yields several transition structures; at temperatures between 400°C and the critical temperature, about 650°C, the equilibrium phases $\alpha + \gamma_3$ appear (α is the uranium-rich solid solution, γ_3 is niobium-rich). The time-temperature-transformation diagram determined by Dean (13) for this material is shown in Fig. 1. The metastable phases, γ^s, γ^o and α'' all have structures closely related to the parent γ, and have essentially the same density. Yakel (14) has discussed these structures and described the atomic displacements necessary for their formation. The observed changes for γ^s and γ^o did not involve a chemical ordering.

At 700°C with oxygen pressures of a few microns, the oxide films which form on the surface of electropolished specimens during the early stages of oxidation are generally very uniform in thickness. They consist mainly of a compact, columnar UO_2 matrix in which stringers of a metallic niobium-rich phase ex-

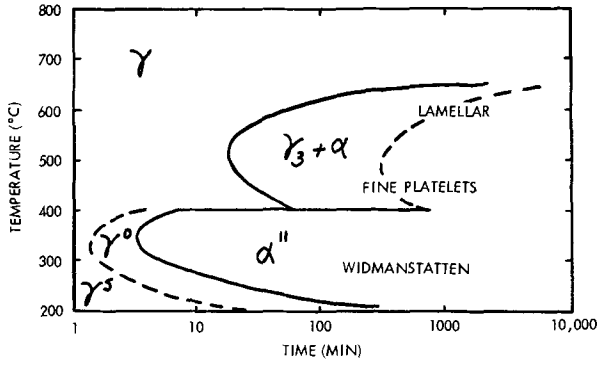

Fig. 1. Time-temperature-transformation diagram for a uranium alloy containing 7.5 w/o Nb and 2.5 w/o Zr. [After Dean, Ref. (13)].

* Electrochemical Society Active Member.

Key words: alloy oxidation, stresses in oxide film, uranium alloy oxidation.

tend normal to the metal surface into the oxide. The solubility of oxygen in the alloy is thought to be quite low, as is the case for pure uranium (15). Similarly, growth of the oxide layer is thought to take place primarily by anion diffusion, probably aided by the presence of a high density of short circuit paths.

Experimental Procedure

Specimens in the shape of 1 cm x 4 cm coupons were cut from 0.05 cm and 0.075 cm sheets of arc-cast, hot-rolled alloy. They were then annealed in vacuum for 2 hr at 800°C and quenched into ice water to retain the γ-bcc structure. The specimens were prepared by standard metallurgical grinding techniques, electropolished in a 5% perchloric acid-methanol solution, then vapor-coated on one side with a thin (~4000Å) layer of 3 Au-1 Al (by weight). This mixture has proved very effective in protecting this alloy from oxidation at temperatures of at least 700°C; it was also used with appropriate caution for a few experiments at 800°C and above. Specimens were mounted vertically in the apparatus, shown schematically in Fig. 2, by a small stainless-steel vise so that the bottom of a quartz fiber "transducer" could be viewed with a cathetometer. The deflection of the fiber is directly related to the curvature of the specimen. These deflection measurements could be obtained during the various oxidation, annealing, and temperature cycling experiments performed in the apparatus. The details of the apparatus, the flexure measurements, and procedures necessary for their interpretation have been discussed previously (7).

Results and Discussion

Stresses Generated During Oxidation

The fact that a significant stress system arises during the oxidation of this alloy was noted early in the investigation when it was observed that thin specimens increased dramatically in area during oxidation. In these experiments the metal was undergoing plastic deformation most probably as a result of compressive forces generated in the growing oxide and the associated tensile forces created in the metal. Lateral extensions of 40% were not unusual.

In order to ascertain the conditions under which it would be possible to obtain flexure measurements and to test the efficiency of the protective layer, we oxidized a series of 1 x 4 x 0.05 cm alloy specimens at 700° and 800°C at oxygen pressures up to 300μ. Several

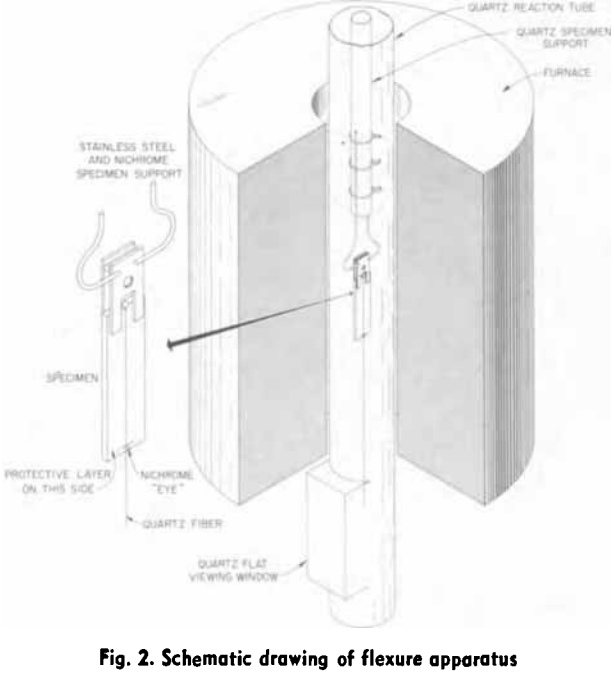

Fig. 2. Schematic drawing of flexure apparatus

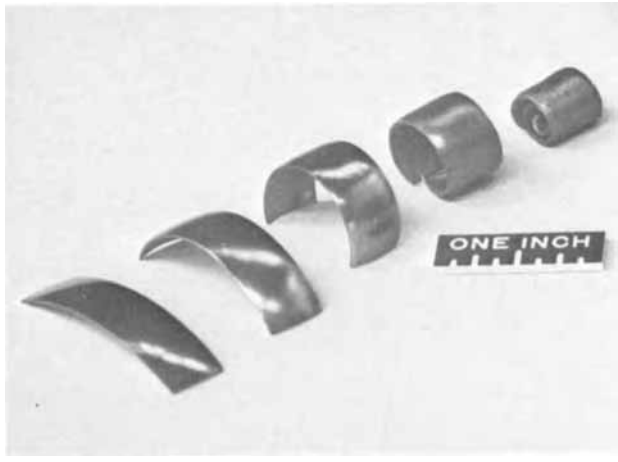

Fig. 3. U-7.5 w/o Nb-2.5 w/o Zr alloy specimens oxidized on top side at 800°C for the following times and oxygen pressures: 5 min at 100μ, 15 min at 100μ, 1 hr at 100μ, 2 hr at 150μ, and 3 hr at 200μ. (Exposures of 8, 25, 100, 300, and 600μ hr, respectively.)

materials were tried as protective layers (combinations of Al, Au, and Ag) before choosing the Au-Al mixture mentioned above. At these temperatures, oxidation invariably resulted in bending of the specimens, the bending becoming quite severe as oxidation continued. Fig. 3 shows a series of such specimens oxidized at 800°C. The degree of bending of these specimens is, of course, much more than that measured in a typical flexure measurement and is obviously associated with considerable plastic deformation of the metal. Similar behavior has been reported for extended oxidation of niobium (7b).

Flexure experiments.—Some of the typical characteristics of specimen flexure during the early stages of oxidation are illustrated in Fig. 4, which is a plot of fiber deflection as a function of time for a sequence of oxidation/anneal periods at 700°C. The deflection was quite rapid as the oxygen pressure was increased up to about 20μ during the first oxygen cycle. The bending occurred such that the oxidizing side was convex.[1] After only 2.3 min, the specimen curvature reached the limit measurable in our apparatus, and the oxygen leak valve was closed. As the pressure decreased, the degree of bending was observed to decrease quite rapidly. This cycle was repeated several times and each time less oxygen pressure was required to initiate comparable bending rates.

For ideal cylindrical bending, the fiber deflection measured in our apparatus (7) is directly related to the degree of curvature of the specimen (for small curvatures) by

$$\rho_x = \frac{LQ}{2Z} \qquad [1]$$

where ρ_x = radius of curvature in the long dimension. L = specimen length, Q = fiber length, and Z = lateral deflection of the end of the fiber. For all experiments reported in the present paper, L = 4 cm and Q = 25 cm. If the specimen deforms entirely elastically, the maximum stress level in the metal can be approximated[2] by the ideal maximum bending stress

$$\sigma_s = \pm \frac{hE}{2\rho_x} \qquad [2]$$

where h = specimen thickness and E = Young's modulus which, for this alloy, is thought to be at least 5 x 10^6 psi at 700°C (16). Thus, the largest maximum

[1] For convenience, we define "positive" (+) flexure as that bending which increases the convexity of the oxidized or nonprotected side of the specimen.

[2] A correction is necessary because of the fact that the neutral axis is not the specimen midplane for these oxidation experiments.

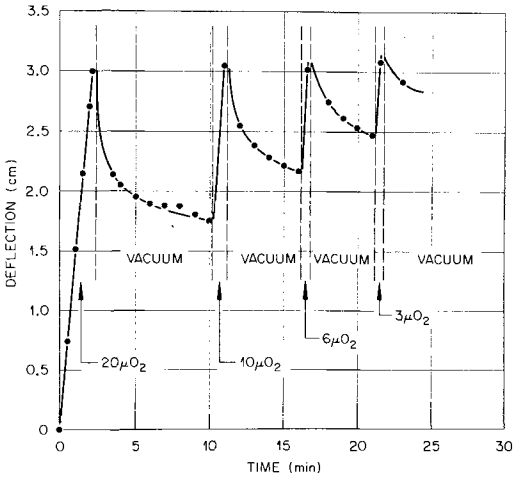

Fig. 4. Flexure characteristics during oxidation/annealing experiment at 700°C. Pressures listed above are maximum pressures reached during that part of cycle. Specimen thickness 0.041 cm; fiber length 25 cm.

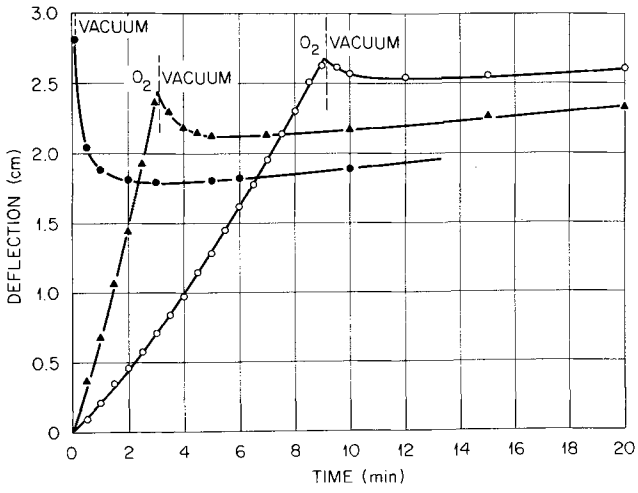

Fig. 5. Flexure of U-Nb-Zr alloy during oxidation/annealing cycles at 700°C. ● Specimen thickness 0.052 cm, oxygen pressure 100-200μ for about 20 sec; ▲ specimen thickness 0.061 cm, nominal oxygen pressure 5μ; ○ specimen thickness 0.061 cm, nominal oxygen pressure 2.5μ.

elastic bending stress obtained from the data of Fig. 4 is about 6000 psi. Tensile data (16b) indicate a yield stress for the alloy of about 5000 to 6000 psi at 700°C. However, the poor creep resistance of this alloy at this temperature, plus the very efficient stress generation mechanism operative during oxidation, leads to nonelastic behavior on the part of the alloy at a very early stage of oxidation. Caution must therefore be exercised in using the flexure data in calculations based on ideal elastic behavior.

For these reasons we confine our attention to the first minute of oxidation for the flexure curves shown in Fig. 4. The largest bending stress encountered is then only ~3000 psi, and the assumption that elastic behavior predominated in the metal seems more reasonable. In this region of the flexure curve, the average stress in the oxide may then be calculated from the simple film stress equation (3, 7b, 9)

$$\sigma_f = \frac{1}{3}\sigma_s \frac{h}{w} \qquad [3]$$

where σ_f is the average stress in an oxide film of thickness w, σ_s is the maximum bending stress given in Eq. [2], and h is the specimen thickness. The equation is accurate for $h>>w$. The oxide film formed in 1 min at 700°C at a pressure of 20μ is approximately 0.5μ thick; Equation [3] then shows that an average stress of about 800,000 psi compression must exist in the film. Comparable results were obtained from several similar experiments.

The very rapid unbending of the specimen during the subsequent vacuum annealing periods came as something of a surprise. Indeed, the unbending generally commenced as the pressure was falling—well before it could reach its limiting value. While this deflection-time behavior was reminiscent of that for tantalum and niobium under similar conditions (7a) in which the redistribution of oxygen in the metal was controlling the unbending, the possibility that the mechanisms are the same is remote. The low solubility of oxygen in this case, as well as the very high diffusivity necessary to account for the rate of unbending (greater than 10^{-6} cm²/sec), strongly suggests a different reason for the observed behavior.

An alternate mechanism is suggested by the deflection data presented in Fig. 5. In these experiments, the specimens were oxidized to about the same total flexure at different rates by changing the oxygen pressure. The degree of unflexing upon subsequent removal of the oxygen was found to depend very much upon the original flexing rate. These characteristics, coupled with the very high film stresses and maximum bending stresses which existed, pointed strongly to an interaction of elastic and plastic effects in both the oxide film and the metal as a basis for a model which may be proposed as follows: (*a*) During the early stages of oxidation, the total strain energy remains small, and elastic behavior predominates in the metal. However, stresses in the oxide film quickly reach values in the range of 10^6 psi and some forms of stress-relief become operative. During this part of the process, a "steady state" exists between the stress-generating and the stress-relieving mechanisms in the oxide film. (*b*) As the film thickness and, therefore, the total strain energy of the system increase, the maximum bending stress in the specimen becomes sufficiently high for stress relief in the form of plastic flow or creep to begin in the metal. As oxidation continues, bending will likewise continue, perhaps even at an increasing rate because of the relatively decreased resistance. (*c*) When the oxygen pressure is suddenly reduced, the means of stress-renewal in the oxide film is withdrawn (or becomes slower), the dynamic balance is broken, and the result is a rapid decrease in the stress level in the oxide. The remaining elastic components of the bending stresses in the metal react to the decreased stress level by partially "unbending" the specimen. This will take place rapidly as the effective stress in the oxide drops to a level where its rate of creep is negligible. (*d*) At 700°C creep in the metal is expected to continue even at comparatively low stress levels. Thus, for longer annealing times the remaining elastic stress in the oxide might be expected to exert its influence, resulting in additional flexure of the specimen at a rate governed essentially by creep of the metal. An example of this behavior is shown in Fig. 6 which shows some additional, but very slow, flexure for long annealing times.

The flexure behavior of this alloy during oxidation is therefore explained on two premises: first, there is a highly efficient stress-generation mechanism available in the form of anion diffusion in the oxide coupled with a large oxide/metal volume ratio. Second, we surmise that for a given rate of stress generation, the relative rates of stress relief in both oxide and metal play an important role in determining the details of flexure in a given experiment.

Flexure During Transformation

While the flexure of the alloy specimens during the isothermal oxidation and annealing experiments was reasonably self-consistent and reproducible, abnormally large changes in the final specimen curvature were generally observed after the specimens were

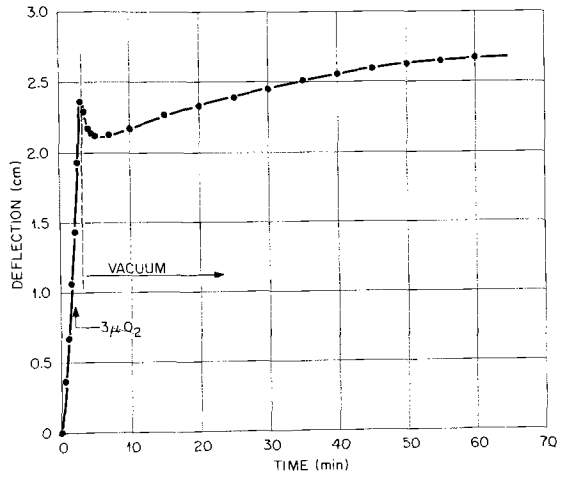

Fig. 6. Flexure of alloy specimen during oxidation/annealing experiment at 700°C. Specimen thickness 0.061 cm.

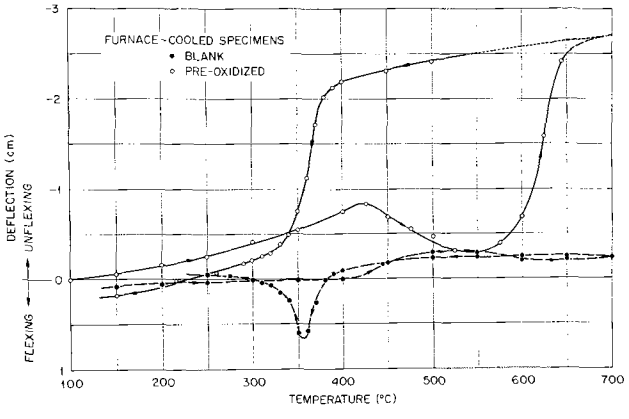

Fig. 7. Flexure during thermal-cycling in vacuum for unoxidized (●) and preoxidized (○) specimens. Initial radius of curvature for oxidized specimen was approx. 10 cm. Both specimens originally furnace-cooled from 700°C.

cooled and removed from the flexure apparatus. These anomalous changes were larger than those to be anticipated as a result of differential thermal contraction and/or differential transformation strain effects between the metal and the thin oxide film. We therefore conducted a series of temperature-cycling experiments in which these flexure effects were documented in detail.

Temperature cycling.—Specimens were prepared for these experiments as previously described, and several unoxidized ("blank") specimens were temperature-cycled from 30° to 700°C in vacuum (10^{-6} Torr) in the flexure apparatus. These specimens exhibited only minor bending effects over the complete temperature cycle regardless of the initial structural state of the specimen. Such behavior is shown in the "blank" run of Fig. 7 where a small deflection was observed on heating at about 450°C; a larger hump occurred on cooling starting at about 400°C. Undoubtedly such minor effects could be attributed to inhomogeneities in the specimen resulting in slightly different transformation rates from one side to the other; if the transformation were influenced by a free surface, the protective Au-Al coating on one side might also exert an effect.

When a specimen was lightly oxidized on one side at some stage of the experiment, however, the subsequent flexure characteristics during temperature cycling in vacuum were very much different. Typical behavior for a furnace-cooled preoxidized specimen is shown in Fig. 7 for direct comparison with the unoxidized sample. (In this case the oxidation treatment

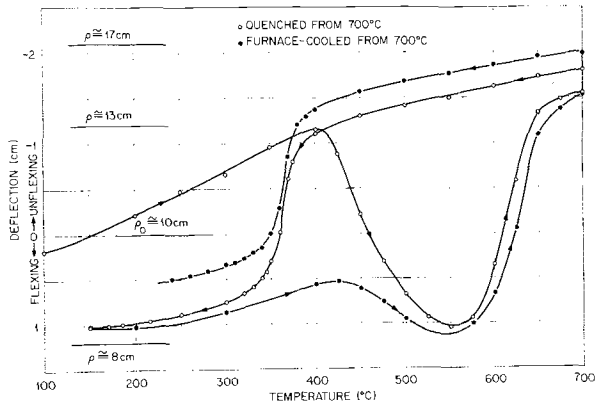

Fig. 8. Flexure during thermal cycling of oxidized and quenched alloy specimen. Initial radius of curvature, ρ_0, after quench from 700°C was approx. 10 cm. ○ First cycle (quenched condition). ● Second cycle (slow-cooled condition). Approximate specimen curvatures corresponding to the deflection values are shown in the figure.

consisted of 2.5 min at 5μ O_2 pressure at 700°C. The radius of curvature after oxidation, computed from the fiber deflection, was about 21 cm. After slow cooling it was measured directly as about 10 cm). Upon heating at a rate of about 10°/min, the specimen unflexed as the temperature was increased to 425°, flexed from 425° to 550°, and finally very rapidly unflexed from 550° to 650° to approach a radius of curvature of 21.7 cm. As the specimen was cooled, flexing occurred slowly until 400°C was reached; between 400° and 300°C the large increase in flexure returned the specimen virtually to its original shape. From the phase diagram and TTT curves (13) for this alloy, it appeared that a good correlation existed between this flexure behavior and the structural transformation of the alloy.[3] For instance, referring to Dean's transformation curves in Fig. 1, it is apparent that the large flexure which occurred during the cooling cycle shown in Fig. 7 parallels the formation of α'' from the matrix γ. (In our apparatus, cooling rates were sufficiently fast so that only the α'' transformation was involved.) On the other hand, the exact sequence of events during heating as the $\gamma^{s,o}$ and α'' phases revert eventually to the high-temperature γ phase is not so clear.

Information which helped to correlate further the flexure and structure data was obtained by making temperature-cycle flexure experiments on specimens heat-treated to yield different starting structures. For example, Fig. 8 and 9 illustrate the flexure behavior of specimens oxidized on one side, then heat treated to yield γ^s (quenched) and $\gamma_3 + \alpha$ (isothermally transformed) structures. While virtually identical cooling curves were obtained in both cases, the flexure during heating obviously depended upon the starting structures. In Fig. 8, the quenched specimen unflexed at a rapid rate during heating to 400°C, then exhibited a comparatively large dip—bending then unbending—as the temperature was increased to 700°C. On the other hand, (in Fig. 9) the isothermally transformed specimen consisting of essentially equilibrium $\gamma_3 + \alpha$ did not show either the initial rapid rate of unbending or the abrupt reversal at 400°C; it did however, show the large degree of unbending starting at about 600°. It is significant that quenched or transformed speci-

[3] These curvature changes were thought to be larger than those which would occur as a result of a uniform relative dilation between the alloy and the very thin oxide during transformation. Thus, in order for a transformation to influence significantly the curvature of such a specimen, it must occur "differently" on one side of the specimen compared to the other. If the flexure change is permanent, the difference must be one which involves "texture" or "extent" of the transformation rather than "rate" which would result in flexing, then unflexing, as the reaction went to completion. Also, a volume or shape change must be involved in the transformation to produce the necessary strain. Since the effect was not observed on annealed, unoxidized specimens, something connected with the oxidation of the specimens on one side created the condition which leads to this difference.

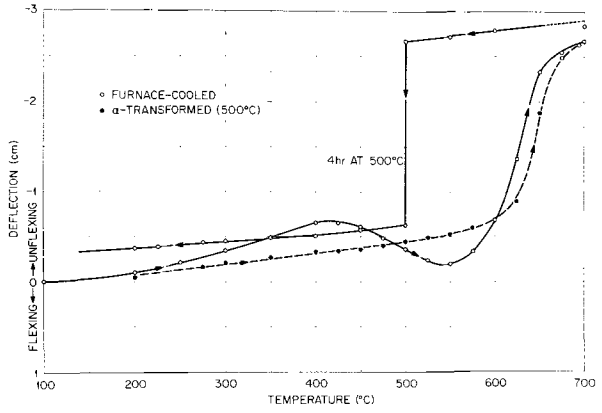

Fig. 9. Flexure during thermal cycling of oxidized specimen isothermally transformed 4 hr at 500°C. Initial curvature after cooling oxidized specimen was 8 cm. ○ Isothermal transformation cycle. ● Isothermally transformed specimen.

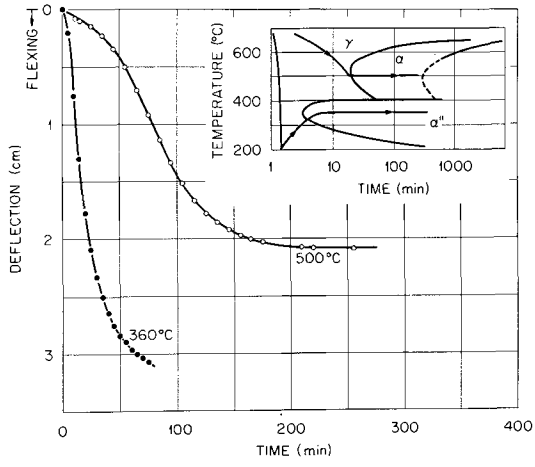

Fig. 10. Flexure during isothermal transformation at 360°C and 500°C for preoxidized specimens. Temperature schedule and time-temperature-transformation curves (13) shown in inset.

mens that had not been preoxidized did not react in this manner but rather behaved in the same way as the "blank run" of Fig. 7.

Summarizing these data, the fewest flexure variations on heating occurred with the specimen with the fewest expected variations in structure. The structure of the isothermally transformed specimen appeared to remain stable upon heating (Fig. 9) to about 600°C where we can associate this part of the flexure curve with the production of γ. Specimens having initial structures consisting of the metastable γ^s (Fig. 7) or $\gamma^{s,o}$ plus α'' (all furnace-cooled specimens) exhibited some intermediate transformations which depended heavily upon the heating rate. Reactions producing α'' or $\gamma_3 + \alpha$ from either γ or $\gamma^{s,o}$ phases resulted in further bending of an oxidized specimen, and vice versa. The increased rate of unflexing at low temperatures in the quenched specimen, for example, may have been associated with some intermediate stage of the reaction, perhaps the formation of additional γ^o.

Superimposed on all these possible transformation effects is the differential thermal contraction between the oxide film and the metal. For these specimens, the additional flexure from this source was small because the oxide layer was generally quite thin compared to the metal. However, the effect was measurable during heating and cooling in temperature ranges where transformations did not interfere. This permitted us to obtain estimates of both film and bending stress values which might result. According to the bimetal thermostat analysis of Timoshenko (17), a specimen oxidized on one side and typical of those under consideration here might be expected to exhibit maximum elastic bending stresses of 1500 psi or more, solely as a result of cooling or heating a few hundred degrees. Stresses in the oxide film due to this source could approach 35,000 psi.

Isothermal transformations.—With only slight modifications of the experimental procedures described above, we were able to use the flexure technique on preoxidized specimens to follow the isothermal transformation kinetics of this alloy. Examples of the flexure at constant temperature due to the $\gamma \rightarrow \gamma_3 + \alpha$ and $\gamma_s \rightarrow \alpha''$ transformations are shown in Fig. 10. The temperature schedule is superposed on Dean's TTT curves in the inset, and reasonable agreement is seen to exist between our data and those obtained by more conventional techniques. Long-time isothermal transformation experiments of this sort did not result in significant unbending of the specimen, which indicated that a differential texture or extent of the transformation is involved in this flexure.

Stress effects.—The item which is primarily responsible for the difference in the transformation behavior is thought to be the elastic stress gradient which exists in the specimens at the time of transformation. In specimens which have been oxidized on one side, the resulting stress system includes substantial bending stresses; even if these are reduced to some degree by annealing periods in vacuum, the action of the forces of differential thermal contraction alone could reestablish a significant stress gradient across the specimen during cooling.

The belief that elastic stress effects, rather than some other aspect of the oxidation treatment, were responsible for the observed transformation-flexure behavior was enforced by additional flexure measurements on specimens in which elastic stress gradients were imparted by strictly physical means. Unoxidized, unprotected specimens quenched from 800°C were deformed in bending at room temperature using an adjustable metal hose clamp to produce a uniform radius of curvature in the desired range. Sufficient uniform plastic deformation was induced into these specimens so that when they were released from the clamp, springback increased the radius of curvature only to about that value which had been observed in the oxidation experiments. Of course, the residual elastic stress distribution here is not a completely linear entity such as a pure bending stress. However, elastic stress gradients do exist in these specimens which might be expected to influence a stress-sensitive transformation.

The results of such an experiment with respect to the α'' transformation are shown in Fig. 11. A mechanically deformed γ-quenched specimen was heated in vacuum to 350°C, flexing only slightly during the 25 min heating period. Held at this temperature, flexure now occurred, decreasing the radius of curvature of the specimen from 12 cm to about 7 cm in a short period of time. The behavior was practically the same as that observed on specimens in which the original deformation was accomplished by oxidation and/or by differential thermal contraction. This specimen was then reheated to 800°C for 90 min to reform the γ phase and to anneal out the stresses left by the original room-temperature deformation. After quenching the specimen, the radius of curvature was found to be identical to that observed before the initial heating, 12 cm. Thus, the strain, in this case differential strain, caused by the formation or removal of the α'' was completely reversible. The curve shown by the open circles in Fig. 11 shows the flexure behavior observed when the annealed specimen was reheated to 350° and held for an extended period of time. No changes in flexure were found. The absence of flexure changes for a specimen in a condition completely identical to that in the first cycle—except for the presence of residual elastic stress gradients—is significant. This behavior indicates that

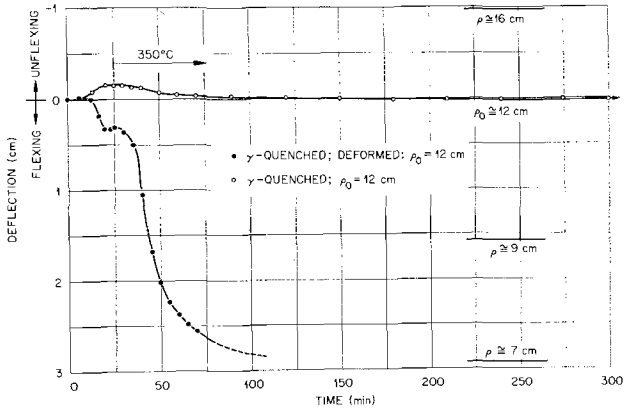

Fig. 11. Flexure of mechanically deformed specimen with initial radius of curvature of 12 cm. ● γ-quenched, deformed. ○ Same specimen, annealed 90 min at 800°C to relieve elastic stresses, γ-quenched; radius of curvature after quenching was 12 cm. Approximate specimen curvatures corresponding to the deflection values are shown in the figure.

the transformation is indeed affected by the presence of a stress gradient and strongly suggests that it takes place by a mechanism in which martensitic or shear processes play an important role. This is in accord with previous investigators (18) who have also concluded that shear transformation mechanisms are important in several uranium alloy systems.

Conclusions

The flexure technique was used to observe stress buildup during the oxidation of a uranium-7.5 w/o niobium-2.5 w/o zirconium alloy. These measurements indicated that the effective stress in the oxide film approaches 10^6 psi and were instrumental in the establishment of a mechanism accounting for the stress generation and relief behavior. This model furnishes an important facet in the complete description of the oxidation process.

The application of the flexure technique to the study of oxidation phenomena in an alloy system must be made with the realization that extraneous sources of flexure may be operative under certain conditions. Conversely, one may sometimes make use of flexure methods to investigate the nature of these "extraneous sources." For example, in this investigation we used such measurements to observe the kinetics of certain phase transformations in this alloy. The transformations were subject to a flexure measurement because they proved to be sensitive to the elastic stress gradients which could be imposed by either oxidation or mechanical means.

Acknowledgment

The authors express their appreciation to J. J. Campbell for his contribution to the experimental phases of this investigation. Discussions with H. L. Yakel and T. G. Kollie concerning the structure of the various alloy phases were very helpful.

Research was sponsored by the U.S. Atomic Energy Commission under contract with the Union Carbide Corporation.

Manuscript submitted Dec. 18, 1970; revised manuscript received *ca.* June 22, 1971. This was Paper 126 presented at the Atlantic City Meeting of the Society, Oct. 4-8, 1970.

Any discussion of this paper will appear in a Discussion Section to be published in the June 1972 JOURNAL.

REFERENCES

1. B. Borie, C. J. Sparks, and J. V. Cathcart, *Acta Met.*, **10**, 691 (1962).
2. J. V. Cathcart, J. E. Epperson, and G. F. Petersen, *ibid.*, **10**, 699 (1962).
3. P. D. Dankov and P. V. Churaev, *Dokl. Akad. Nauk SSSR*, **73**, 1221 (1950).
4. (a) W. Jaenicke and S. Leistikow, *Z. Phys. Chem.*, **15**, 175 (1958); (b) (with A. Stadler), *This Journal*, **111**, 1031 (1964); and (c) (with A. Stadler and L. Albert), *Mem. Sci. Rev. Met.*, **LXII**, 231 (May 15, 1965).
5. D. H. Bradhurst and P. M. Heuer, MAT/TN 8, Aust. Atomic Energy Commission Res. Establishment, Lucas Heights, January 1968.
6. (a) R. F. Tylecote, *Mem. Sci. Rev. Met.*, **LXII**, 241 (May 15, 1965); and (b) (with W. K. Appleby), *Corrosion Sci.*, **10**, 325 (1970).
7. (a) R. E. Pawel and J. J. Campbell, *This Journal*, **116**, 828 (1969); and (b) *Acta Met.*, **14**, 1827 (1966); (c) (with J. V. Cathcart), *This Journal*, **110**, 551 (1963); and (d) *This Journal*, **116**, 1144 (1969).
8. V. R. Howes and C. M. Richardson, *Corrosion Sci.*, **9**, 385 (1969).
9. C. Roy and B. Burgess, *Oxidation of Metals*, **2**, 235 (1970).
10. P. Poole and L. L. Shreir, *Electrochem. Acta.*, **13**, 269 (1968).
11. F. M. Rhines and J. S. Wolf, *Met. Trans. AIME*, **1**, 1701 (1970).
12. J. V. Cathcart, R. E. Pawel, and G. F. Petersen, *Oxidation of Metals*, In press.
13. C. W. Dean, "A Study of the Time-Temperature-Transformation Behavior of a Uranium—7.5 Weight Percent Niobium—2.5 Weight Percent Zirconium Alloy" M. S. Thesis, Dept. of Met. Engr., University of Tennessee (Oct. 24, 1969) (USAEC Y-1694, 1969).
14. Harry L. Yakel, *J. Nucl. Mater.*, **33**, 286 (1969).
15. J. H. Gittus, "Uranium," Butterworths, Washington (1963).
16. See for example: (a) H. D. Weiss, UCID—15170, Lawrence Radiation Laboratory, Univ. of Calif., July 28, 1967; and (b) V. A. Bugrov, V. K. Grigorovich, and O. S. Ivanov, "Physical Chemistry of Alloys and Refractory Compounds of Thorium and Uranium," pp. 62-69, Bykov Met. Inst., USSR Acad. Sci., Moscow (1968) (UCRL-Trans. 10454).
17. S. Timoshenko, *J. Opt. Soc. Am.*, **11**, 233 (1925).
18. See for example: (a) M. Anagnostidis, M. Colombie, and H. Monti, *J. Nucl. Mater.*, **11/1**, 67 (1964); and (b) K. Tangri and D. K. Chaudhuri, *ibid.*, **15/4**, 278 (1965).

Oxidation of Ni-Cr-Al Alloys Between 1000° and 1200°C

C. S. Giggins and F. S. Pettit

Pratt & Whitney Aircraft, Materials Engineering and Research Laboratory, Middletown, Connecticut 06457

ABSTRACT

The oxidation of Ni-Cr-Al alloys in 0.1 atm of oxygen has been studied at temperatures of 1000°, 1100°, and 1200°C. Twenty-one alloys with varying chromium [2-30 weight per cent (w/o)] and aluminum (1-9 w/o) contents were examined. It was found that all of the alloys initially underwent a period of transient oxidation before steady-state conditions were established. The transient period of oxidation usually did not exceed 1 hr and was characterized by rapid conversion of thin surface layers of the alloys to oxides with the subsequent formation of continuous layers of one of the following oxides: NiO, Cr_2O_3, or Al_2O_3. Steady-state conditions were established with the formation of these continuous oxide layers, and oxidation occurred by three different mechanisms which were characterized by the growth of an external layer of NiO over a subscale of Cr_2O_3 and Al_2O_3, the growth of an external layer of Cr_2O_3 over an Al_2O_3 subscale or the growth of a continuous, external layer of Al_2O_3.

Nickel-base superalloys are currently used in numerous high-temperature applications which require both mechanical strength and oxidation resistance. Virtually all such alloys in use today were developed empirically through a judicious selection of strengthening elements and elements required for oxidation resistance. Elements usually added to improve mechanical properties include Mo, W, Ta, and Nb through solid solution hardening and Al and Ti via formation of a γ' precipitate in a γ-nickel matrix. Carbon is used to improve grain boundary properties while Al and Cr are included to develop oxidation resistance. Finally, elements such as yttrium (1) as well as inert dispersoids (1, 2) have also been found to improve the oxidation resistance of alloys. In order to develop high strength nickel-base alloys with improved oxidation resistance, it is necessary to determine the influence of these types of elements upon oxidation properties. However, before it is possible to examine the effect of different elements on the oxidation behavior of nickel-base superalloys, it is essential to define the oxidation mechanisms for simpler but related alloys such as Ni-Cr-Al alloys.

Thermodynamic considerations have shown that Cr_2O_3 and Al_2O_3 are the stable oxide phases formed on Ni-Cr and Ni-Al alloys, respectively, whenever these alloys contain more than one part per million of chromium (3) or aluminum (4). In view of these conditions, Cr_2O_3 and Al_2O_3 should be the principal products formed on virtually all oxidized Ni-Cr-Al alloys. Furthermore, since the equilibrium constant for the following reaction is very small (*e.g.* 3×10^{-18} at 1100°C[1])

$$Al_2O_3 + 2Cr(\text{alloy}) = Cr_2O_3 + 2Al(\text{alloy}) \quad [1]$$

Al_2O_3 should be the stable oxide phase formed on Ni-Cr-Al alloys that contain more than 1 ppm aluminum. For example, when the activity of chromium and aluminum in the alloy is taken as 1 and 10^{-7} respectively, the mole fraction of Al_2O_3 in the Al_2O_3-Cr_2O_3 solid solution is 0.9997. Previous studies (6-9) on the oxidation of Ni-Cr-Al alloys show that much more than 1 ppm aluminum is required to form an external Al_2O_3 scale on these alloys and it is apparent that other parameters in addition to thermodynamic conditions must be considered when discussing the oxidation of such alloys. Although some experimental work (6-9) has been accomplished, a mechanistic description for the oxidation of Ni-Cr-Al alloys is not available. The purpose of the present study was to determine the oxidation mechanisms of Ni-Cr-Al alloys at temperatures between 1000° and 1200°C.

Key words: oxidation, Ni-Cr-Al alloys, mechanisms.

[1] Thermodynamic data obtained from Ref. (5).

Experimental

The alloys listed in Table I were prepared from high-purity metals by nonconsumably arc melting and casting as 100g buttons. These alloys were then given a preliminary annealing treatment in vacuum at 1000°C for 48 hr to promote homogeneity. Each button was cut into approximately 0.250 in. thick sections that were subsequently cold-rolled to 0.050 in. thicknesses and annealed in vacuum at 1000°C for 48 hr to provide a twinned, equiaxed γ matrix. Two of the alloys, Ni-10Cr-9Al and Ni-30Cr-6Al, were studied in the cast-annealed condition due to difficulties encountered during cold-rolling. Most of the alloys were single phase γ and the remainder exhibited either two phase, $\gamma + \gamma'$ or three phase $\gamma + \gamma' + \alpha$Cr structures in agreement with the Ni-Cr-Al phase diagram (10). Rectangular specimens were cut from the sheet and buttons to provide surface areas of approximately 2.5 cm^2. All specimens were polished through 600-grit SiC abrasive paper, ultrasonically agitated in ethylene trichloride and rinsed with ethyl alcohol.

The alloys were isothermally oxidized at temperatures of 1000°, 1100°, and 1200°C in static oxygen at 0.1 atm. Oxidation kinetics were determined by the weight-gain method using an automatic vacuum microbalance. The specimens were raised from the cold zone to the hot zone of the furnace after oxygen had been admitted to the system. The experimental apparatus and procedure have been described in a previous paper (4) and will not be included here.

Table I. Composition of alloys

Alloy designation	w/o chromium	w/o aluminum	Phases present
Ni-5Cr	4.9	—	γ
Ni-3Al	—	3.1	γ
Ni-2Cr-4Al	2.0	4.0	γ
Ni-2Cr-6Al	2.0	6.0	γ
Ni-3Cr-6Al	3.0	6.0	γ
Ni-5Cr-1Al	5.1	1.0	γ
Ni-5Cr-3Al	5.0	3.0	γ
Ni-5Cr-4Al	5.0	4.0	γ
Ni-5Cr-6Al	5.0	6.2	$\gamma + \gamma'$
Ni-5Cr-9Al	5.0	8.9	$\gamma + \gamma'$
Ni-10Cr-1Al	10.0	1.0	γ
Ni-10Cr-2Al	10.0	2.0	γ
Ni-10Cr-3Al	10.0	3.1	γ
Ni-10Cr-6Al	9.9	6.0	$\gamma + \gamma'$
Ni-10Cr-9Al	10.0	8.9	$\gamma + \gamma'$
Ni-15Cr-6Al	14.8	5.9	$\gamma + \gamma'$
Ni-20Cr-2Al	19.9	2.0	γ
Ni-20Cr-3Al	19.9	3.0	γ
Ni-20Cr-4Al	19.9	4.0	γ
Ni-20Cr-6Al	19.8	5.9	$\gamma + \gamma'$
Ni-30Cr-2Al	30.0	2.0	γ
Ni-30Cr-4Al	30.0	4.0	$\gamma + \alpha$Cr
Ni-30Cr-6Al	29.9	6.0	$\gamma + \gamma' + \alpha$Cr

Note: The impurity level of all alloys was less than 0.4 w/o.

Upon completion of the kinetic measurements, the oxidized specimens were examined optically to evaluate their surface topography. Transverse sections of representative specimens were subsequently prepared by standard metallographic techniques and examined optically at high magnifications. Some of the oxidized specimens were studied with a Cambridge Microscan electron probe-microanalyzer to determine the distributions of nickel, chromium and aluminum in the oxides and substrates in the same manner as described for nickel and chromium in a previous paper (3).

Standard x-ray diffraction techniques were employed for phase identification of the oxidation products. Oxides that did not spall during cooling were examined *in situ*. Spalled and extracted (10% Br-methanol) oxides were studied by the Debye-Scherrer method. Oxides formed during the initial period of oxidation, *i.e.* < 1 hr, were also extracted from selected specimens and examined by transmission electron microscopy with a Philips EM200 electron microscope.

Results and Discussion

The experimental results obtained for the oxidation of Ni-Cr-Al alloys in 0.1 atm of oxygen for 20 hr or more were found to fall into three distinct groups which correspond to three different oxidation mechanisms. The diagrams presented in Fig. 1 show the proposed compositional limits for these three oxidation mechanisms at 1000°, 1100°, and 1200°C. Construction of these diagrams was accomplished by evaluation of the kinetic data and characterization of the oxides formed via optical and electron metallography, x-ray and electron diffraction and electron probe microanalysis. Most of the surfaces of the alloys studied oxidized uniformly but a few alloys, with compositions close to the boundaries of the diagrams shown in Fig. 1, oxidized nonuniformly and appeared to be oxidizing by different mechanisms on different portions of their surfaces. These latter alloys will be referred to as transition alloys in the subsequent discussion.

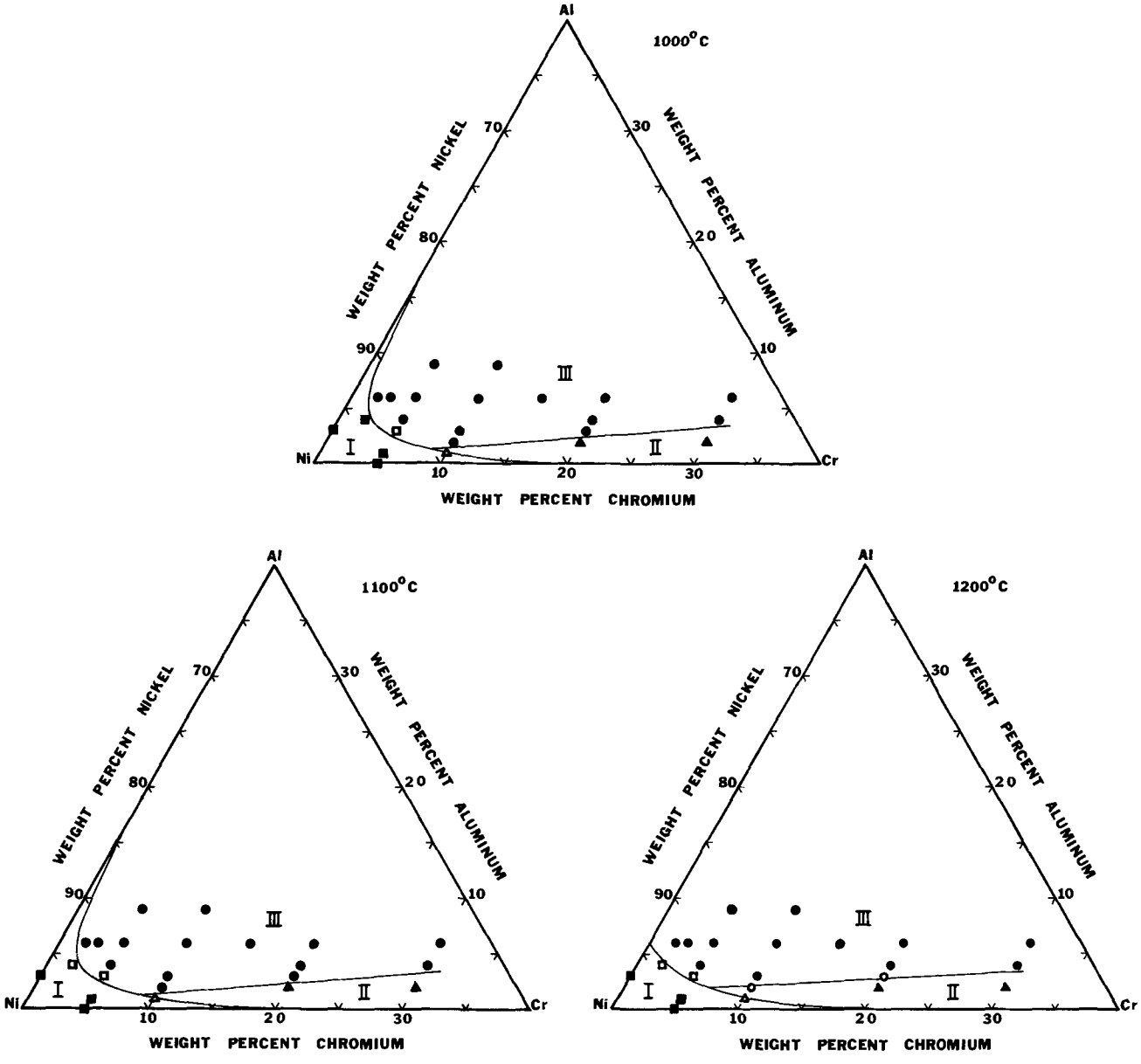

Fig. 1. Isothermal diagrams showing the compositional limits for the three oxidation mechanisms of Ni-Cr-Al alloys in 0.1 atm of oxygen at 1000°, 1100°, and 1200°C. (I) An external scale of NiO and a subscale of chromium and/or aluminum oxides is formed. (II) An external layer of Cr_2O_3 and a subscale of Al_2O_3 is formed. (III) Only an external layer of Al_2O_3 is formed. The data points in this diagram correspond to the compositions of the alloys studied. Solid squares, triangles and circles indicate alloys that conform to mechanisms I, II, and III respectively. Open symbols represent alloy compositions where evidence for mechanisms on both sides of the boundaries were observed.

Group I alloys.—The oxidation kinetics for all alloys with compositions corresponding to region I of Fig. 1 eventually obeyed the parabolic rate law. Usually this rate law was followed virtually from the beginning of the weight-increase measurements although in some cases conformance was not evident for up to 10 hr of oxidation. Typical results are presented in Fig. 2. The parabolic rate constants for alloys in this group were always about an order of magnitude greater than that for pure nickel oxidized under the same conditions, Fig. 3.

A photomicrograph of a transverse section through an oxidized specimen, typical of Group I, is shown in Fig. 4. A dense external scale is evident above a zone of internal oxide precipitates. X-ray analysis of *in situ* and extracted oxides showed that the outer scale was NiO while the subscale precipitate was composed of a mixture of Cr_2O_3, Al_2O_3, and $Ni(Cr,Al)_2O_4$.

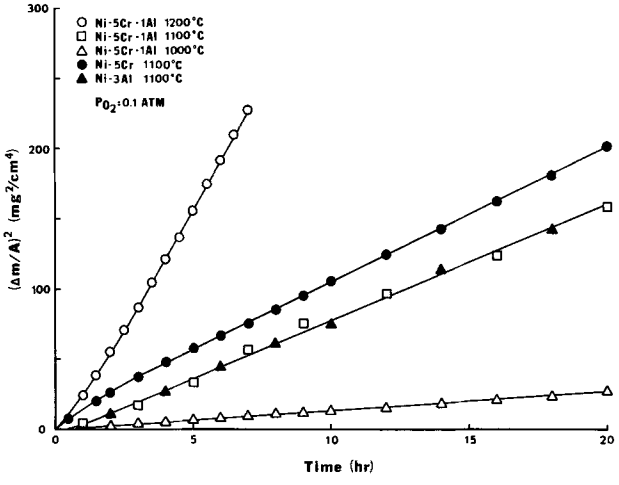

Fig. 2. Typical oxidation data for Group I alloys.

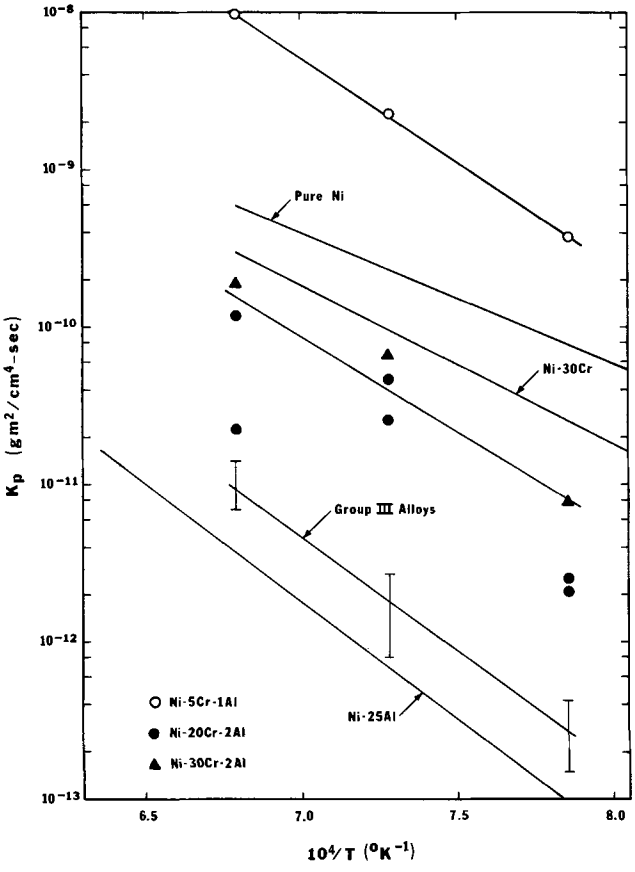

Fig. 3. Temperature dependence of the parabolic rate constants obtained for the oxidation of a typical Group I alloy (Ni-5Cr-1Al), Group II alloys (Ni-20Cr-2Al, Ni-30Cr-2Al), and Group III alloys. Parabolic rate constants for the growth of NiO on pure nickel (3), Cr_2O_3 on Ni-30Cr (3), and Al_2O_3 on Ni-25Al (4) are included for comparison.

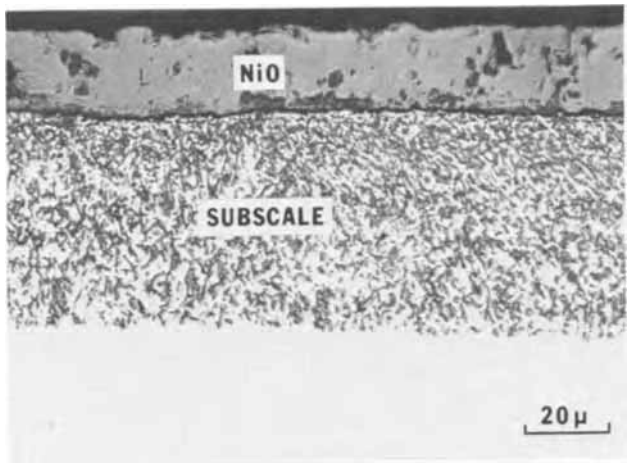

Fig. 4. Microstructure of Ni-2Cr-4Al after 20 hr of oxidation in 0.1 atm of oxygen at 1000°C. This structure is representative of oxidized Group I alloys.

The results show that nickel is oxidized externally to form a continuous scale whereas a discontinuous subscale of Al_2O_3 and Cr_2O_3 is developed by the internal oxidation of both chromium and aluminum. The oxidation rates of these alloys must therefore be controlled by transport through the NiO scale. The oxidation rates are greater than that for pure nickel probably because solution of chromium and aluminum from the alloy increases the cation vacancy concentration in the NiO scale (11). Furthermore, the apparent activation energy obtained from the parabolic rate constants for these alloys is greater than that for pure nickel since the solubility of chromium (12) and probably aluminum in NiO increases with temperature.

Group II alloys.—Typical weight-gain *vs.* time curves for alloys with compositions in region II of Fig. 1 are presented in Fig. 5. The oxidation kinetics for these alloys usually obeyed the parabolic rate law and the parabolic rate constants were close to those for the growth of Cr_2O_3 on nickel-chromium alloys (3) as shown in Fig. 3. In some experiments with alloys in this group the oxidation kinetics did deviate from the parabolic rate law. Occasionally the external oxide scale would crack during isothermal oxidation and

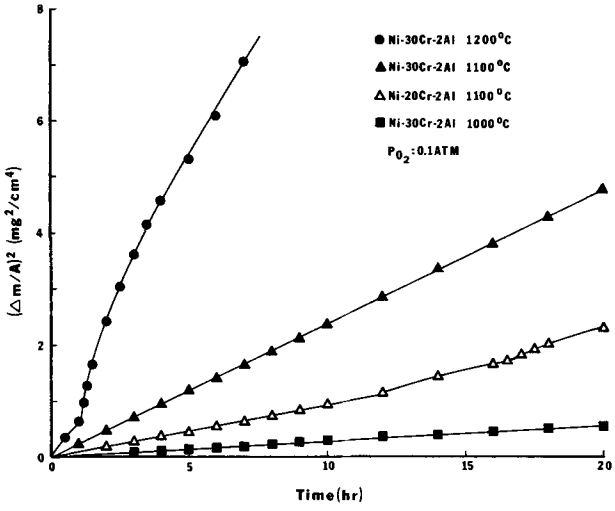

Fig. 5. Typical oxidation data for Group II alloys

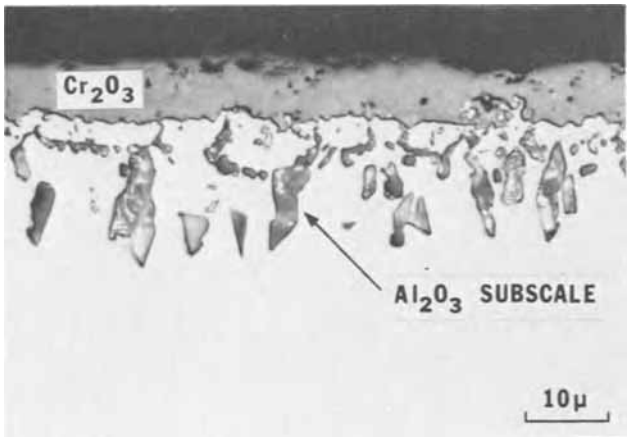

Fig. 6. Microstructure of Ni-20Cr-2Al after 21 hr of oxidation in 0.1 atm of oxygen at 1100°C. This structure is representative of oxidized Group II alloys.

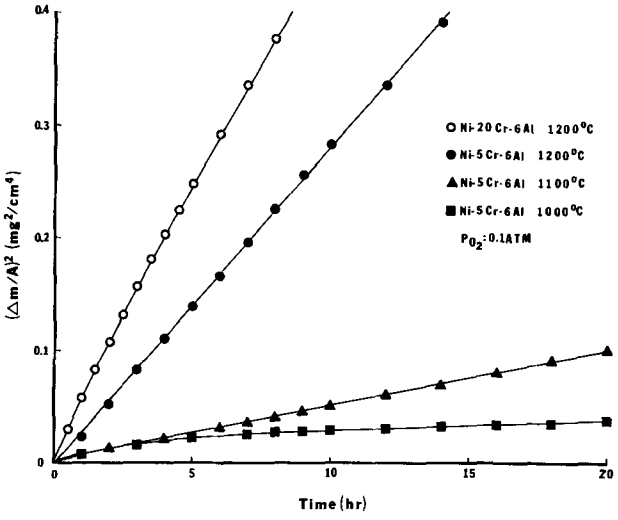

Fig. 7. Typical oxidation data for Group III alloys

the cracks would heal upon subsequent oxidation as shown for two of the curves presented in Fig. 5. In other cases, the instantaneous parabolic rate constant decreased gradually with the oxidation time and final values were found to be close to those for Group III alloys as can be seen in Fig. 3 for the Ni-20Cr-2Al alloy.

A cross-sectional view of the microstructure for a typical specimen from this group is presented in Fig. 6. X-ray analysis of spalled, *in situ*, and extracted oxides showed that the dense outer scale was Cr_2O_3 and the subscale precipitate was exclusively Al_2O_3. Quantitative compositional data obtained from an examination of this specimen with the electron probe-microanalyzer (EPM) further substantiated the preceding oxide characterization. For this group of alloys, the chromium and aluminum are selectively oxidized to form an external scale of Cr_2O_3 and an internal subscale of Al_2O_3. The oxidation rate is controlled by diffusion through the aluminum-doped Cr_2O_3 scale. The specimens, whose oxidation kinetics did not exactly obey the parabolic rate law but had a gradually decreasing parabolic rate constant, were found to have semicontinuous Al_2O_3 scales beneath the external Cr_2O_3 layers which probably caused the slower oxidation rates of these alloys.

The oxidation kinetics for this group of alloys can be influenced by formation of CrO_3 gas via the following reaction

$$Cr_2O_3(s) + \frac{3}{2}O_2(g) = 2CrO_3(g) \qquad [2]$$

However, even at 1200°C, the effect of CrO_3 formation is negligible compared to the weight changes produced by growth of the Cr_2O_3 scale for the oxidation times used in the present experiments which was usually 20 hr. In the case of alloys in this group where the oxygen pick up is decreased due to the formation of a semicontinuous Al_2O_3 scale, as occurred during oxidation of some of the Ni-20Cr-2Al specimens, weight losses caused by the formation of CrO_3 are not negligible and probably did affect the oxidation kinetics for these specimens.

Group III alloys.—Typical weight-gain *vs.* time curves for alloys with compositions corresponding to region III are presented in Fig. 7. The oxidation kinetics for alloys in this group obeyed the parabolic rate law virtually from the beginning of the weight-increase measurements. The rate constants were substantially smaller than those of the previous two groups and similar to those for the growth of Al_2O_3 on Ni-25Al alloys as shown in Fig. 3. A transverse section through an oxidized specimen, typical of this group, is shown in Fig. 8 where only an external scale

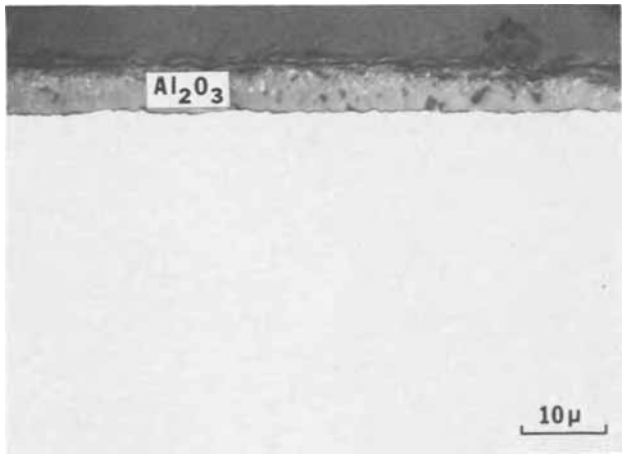

Fig. 8. Microstructure of Ni-20Cr-4Al after 20 hr of oxidation in 0.1 atm of oxygen at 1200°C. This structure is representative of oxidized Group III alloys.

is evident. This dense, continuous external scale did spall from localized areas during cooling. X-ray analysis of spalled, *in situ*, and extracted oxides indicated that the scales formed on the surfaces of this group of alloys consisted of only Al_2O_3. Quantitative EPM examination of this specimen also confirmed that the external scale was Al_2O_3 which contained a small amount of chromium in solution. The results obtained for this group of alloys show that the aluminum is selectively oxidized and the oxidation rate is controlled by diffusion through the external Al_2O_3 scale.

Transient oxidation.—The oxidation data presented thus far have been for the oxidation of alloys under steady-state conditions where virtually all features of the oxidation reactions are independent of time except for the thicknesses of the oxide layers which increased with time. It was found that before steady-state conditions were established, all of these alloys had a period of oxidation where the morphology and composition of the oxide layers changed with time. In addition the oxidation kinetics did not conform to any simple rate law. Chattopadhyay and Wood (13) have obtained similar results from studies on the oxidation of Fe-Cr and Ni-Cr alloys and have referred to this type of oxidation as transient oxidation to differentiate it from steady-state oxidation, *i.e.* oxidation under steady-state conditions. In the present study the duration of the transient oxidation period for most alloys was less than 1 hr from the beginning of weight-increase measurements and transmission elec-

tron microscopy was used to examine the thin extracted films that were formed. The transition alloys, which were defined previously, were the exception since localized transient oxidation occurred on these alloys for as long as 20 hr and these types of oxidation structures could be studied with conventional thick film techniques. The results obtained from examination of the microstructures of oxidized transition alloys were extremely useful in deciphering the latter stages of the transient oxidation process, in particular, the factors interrelating the three mechanisms observed for the oxidation of Ni-Cr-Al alloys under steady-state conditions.

To avoid confusion, it is important to emphasize the difference between use of the terms transient oxidation and oxidized transition alloys. Transient oxidation was observed on all of the alloys that were studied, however, in the case of the transition alloys localized transient oxidation persisted for extremely long periods of time. Finally, it should also be mentioned that since transient oxidation is nonuniform and involves the development of continuous layers of certain oxides as steady-state conditions are approached, it is not possible to determine oxide thicknesses at which transient oxidation ceases and oxidation under steady-state conditions begins.

Transition alloys.—The oxidation kinetics for the transition alloys did not obey any simple rate law since the surfaces of these alloys did not oxidize uniformly as shown in Fig. 9 and 10 and the structure of the oxide scales changed with the time of oxidation. In view of this condition meaningful data was obtained principally from examination of the microstructures of oxidized specimens.

A photomicrograph of a transverse section through an oxidized specimen with a composition near the boundary between regions I and II of Fig. 1 is shown in Fig. 9. The nonuniformity of the oxidation is obvious. In this photomicrograph one part of the alloy has developed an external layer of Cr_2O_3 with internal Al_2O_3 particles (*i.e.* mechanism II) whereas the other has formed an external scale of NiO with internal particles of both Cr_2O_3 and Al_2O_3 (*i.e.* mechanism I). At the boundary between these structures the internal precipitates of Cr_2O_3 and Al_2O_3 particles are observed to be continuous but aluminum is still oxidized internally beneath this duplex scale. This shows that the transition from mechanism I to II occurs when the volume fraction of internal Al_2O_3 and Cr_2O_3 particles is sufficient to establish a continuous, duplex oxide layer beneath the NiO scale which still allows sufficient diffusion of oxygen into the alloy to oxidize the aluminum internally.

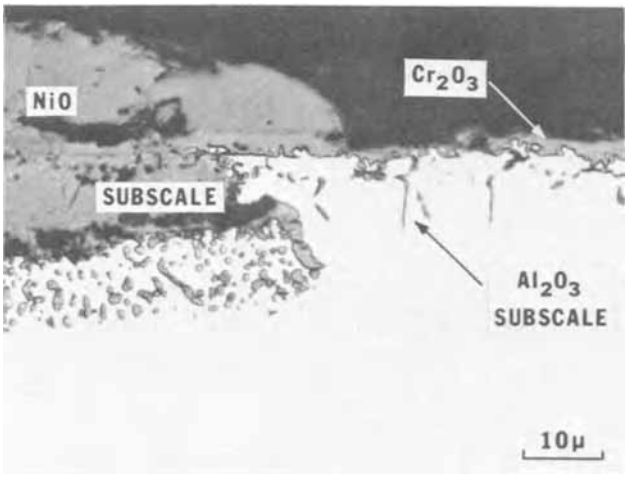

Fig. 9. Nonuniform oxidation morphology of Ni-10Cr-1Al after 20 hr of oxidation in 0.1 atm of oxygen at 1000°C. A portion of the alloy has oxidized as a Group I alloy whereas the remainder has oxidized as a Group II alloy.

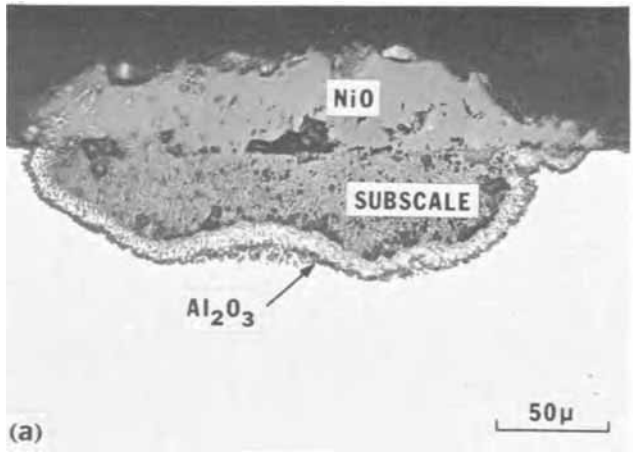

Fig. 10 (a). Nonuniform oxidation morphology of Ni-5Cr-3Al after 20 hr of oxidation in 0.1 atm of oxygen at 1100°C. A portion of the alloy has oxidized as a Group I alloy whereas the remainder has oxidized as a Group III alloy.

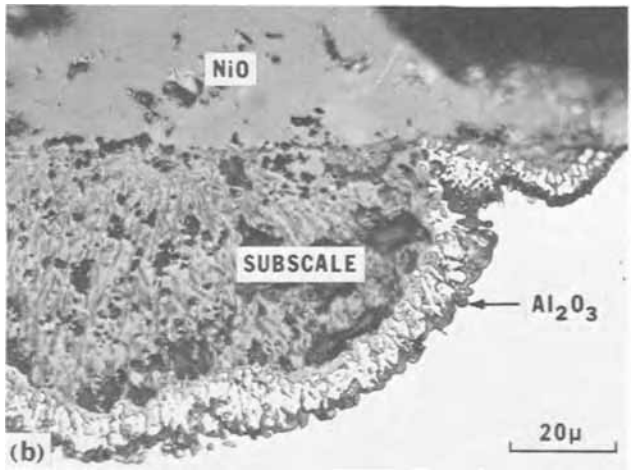

Fig. 10 (b). This high magnification photomicrograph shows that a continuous layer of Al_2O_3 has formed beneath a duplex layer containing both Cr_2O_3 and Al_2O_3 in the region where the alloy has oxidized as a Group I alloy.

A transverse section of an oxidized specimen with a composition near the boundary between regions I and III of Fig. 1 is shown in Fig. 10. Most of the surface of this specimen was covered with a thin, external Al_2O_3 scale, however, numerous mounds of NiO were also evident on the specimen surface. Figure 10(a) shows a typical nickel mound with the external Al_2O_3 scale at the edges. In Fig. 10(b) a continuous layer of Al_2O_3 is seen to have formed beneath the NiO mound at the subscale front. EPM results for this specimen have shown that the continuous layer of oxide immediately above the Al_2O_3 layer in Fig. 10(b) contained both Al_2O_3 and Cr_2O_3. These results show that the transition from mechanism I to III occurs by the formation of a continuous, duplex layer of Cr_2O_3 and Al_2O_3 beneath the NiO scale which inhibits the diffusion of oxygen into the alloy and thereby permits the development of the continuous Al_2O_3 layer.

Representative areas of a transverse section through an oxidized specimen typical of alloy compositions at the boundary between regions II and III of Fig. 1 are presented in Fig. 11. It is evident that a continuous, external layer of Cr_2O_3 is present on all of the sections, however, the morphology of the internal zone of Al_2O_3 is seen to vary from coarse particles to a con-

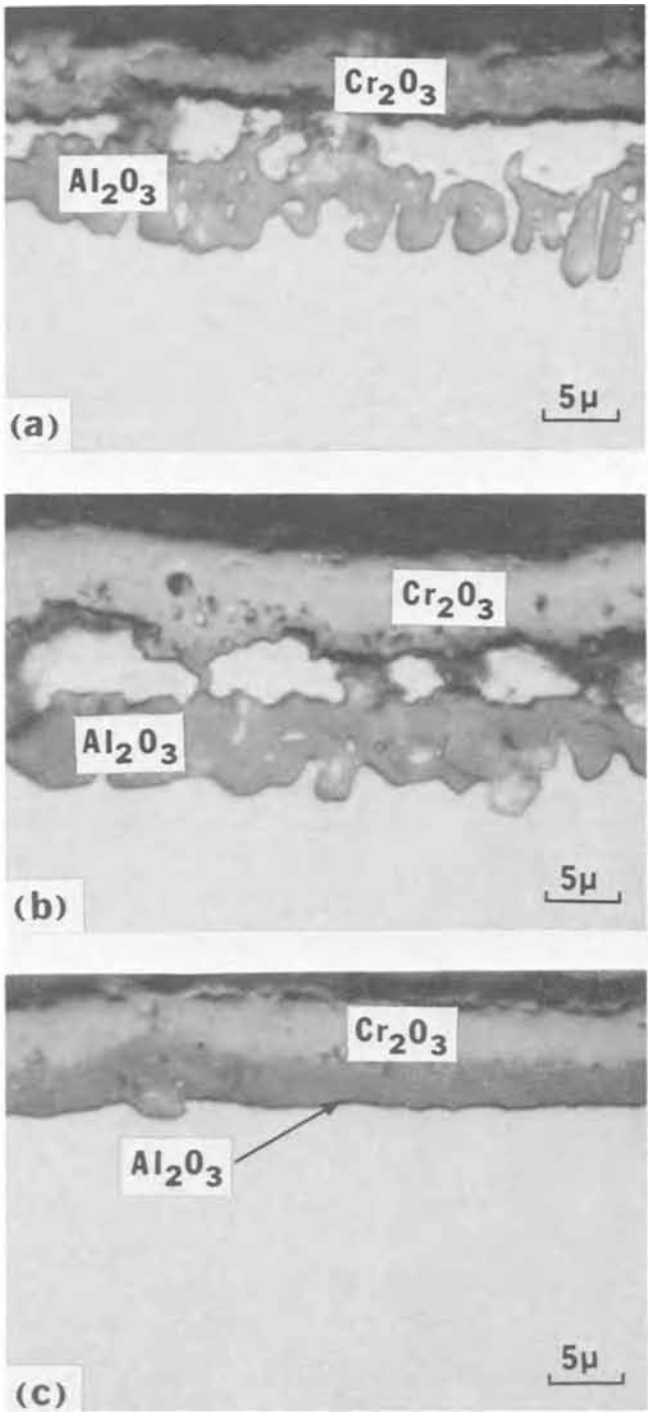

Fig. 11. Oxidation morphology for three different areas of Ni-20Cr-3Al after 20 hr of oxidation in 0.1 atm of oxygen at 1200°C. These microstructures show the different stages for the transition from Group II to Group III. (a) Formation of coarse, discontinuous Al_2O_3 particles beneath an external Cr_2O_3 scale. (b) The Al_2O_3 particles beneath the Cr_2O_3 scale are continuous. (c) No internal oxide particles are evident. The external layer is Cr_2O_3 at the oxide-gas interface and the internal layer is Al_2O_3 at the alloy-oxide interface.

tinuous layer. This shows that Al_2O_3 particles beneath an external Cr_2O_3 layer can coarsen and grow laterally to form a continuous Al_2O_3 layer.

Thin film studies.—In order to examine the transient oxidation of the alloys in which steady-state conditions were established after short periods of oxidation (*i.e.* Group I, Group II, and Group III alloys), the thin oxide films formed on a Ni-15Cr-6Al alloy after 1 min, 5 min, and 40 min of oxidation at 1000°C in 0.1 atm of oxygen were extracted by dissolving the alloy in 10% Br-methanol solution and examined with the electron microscope. Electron and x-ray diffraction indicated that after 1 min of oxidation $Ni(Cr,Al)_2O_4$, NiO, and Cr_2O_3 were present on the surface of this alloy. The spinel phase was the major phase. As the oxidation time was increased, the same oxide phases as well as α-Al_2O_3 were detected but evidence for the formation of layers in the film was observed, as shown in Fig. 12 where an inner layer of oxide is visible below a crack in the outer oxide layer. During preparation of one specimen for examination, this outer layer became delaminated as shown in Fig. 13. Comparison of the electron diffraction patterns for the total oxide and the exposed inner layer showed that the inner layer was Cr_2O_3 containing small particles of spinel whereas the outer layer was composed predominantly of NiO and spinel. It was not possible to examine the thin films which developed on this alloy for oxidation times greater than 40 min since the thicknesses of these films were too large for transmission electron microscopy. However, the oxide layer that was present on this alloy under steady-state conditions was predominantly Al_2O_3, (*i.e.* similar to that shown in Fig. 8) and therefore, in view of the results obtained from studies with the transition alloys, it can be concluded that an Al_2O_3 layer forms beneath the inner Cr_2O_3 layer during the latter stages of transient oxidation.

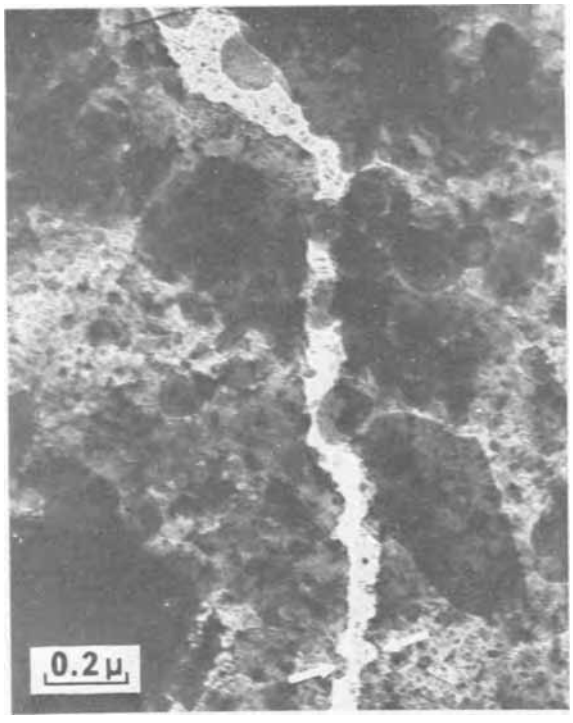

Fig. 12. Transmission micrograph of oxide scale formed on Ni-15Cr-6Al after 40 min in 0.1 atm of oxygen at 1000°C. This scale appears to be composed of two layers of oxide. The outer layer has cracked and exposed the inner layer. (Arrows indicate matching surfaces of cracked outer layer.)

The thin films formed on Ni-5Cr-6Al, Ni-10Cr-6Al, Ni-20Cr-6Al, and Ni-30Cr-6Al alloys after 1 min of oxidation at 1000°C in 0.1 atm of oxygen were also examined with the electron microscope. The oxide films obtained from these alloys were similar to those described for the Ni-15Cr-6Al alloy except that the proportions of the different oxide phases in these films varied with the compositions of the alloys. For example, the films from the Ni-30Cr-6Al alloy contained much more Cr_2O_3 than those extracted from the Ni-5Cr-6Al alloy.

Oxidation mechanisms for Ni-Cr-Al alloys.—The results obtained from the oxidation of Ni-Cr-Al alloys show that these alloys are oxidized under steady-state conditions by one of three different mechanisms and that the particular mechanism which prevails for a specific alloy is determined by the composition of the alloy. These oxidation mechanisms are always preceded by a transient oxidation period where a thin surface layer of the alloy is converted to oxide with little diffusion occurring in the alloy due to the rapid uptake of oxygen by the alloy. The latter stage of the transient oxidation period is characterized by the development of layers of certain oxide phases in the scale. The transient period of oxidation is usually completed after about 1 hr for most Ni-Cr-Al alloys. In the case of alloys with compositions where a transition in oxidation mechanisms occurs (*i.e.* boundaries in Fig. 1) localized transient oxidation has been observed after more than 20 hr of oxidation.

Considering all of the results that have been obtained in the present study, the following model can be constructed to describe the oxidation of Ni-Cr-Al alloys. At the beginning of oxidation of any Ni-Cr-Al alloy, the rapid uptake of oxygen converts the surface layer of the alloy to oxide. As illustrated in Fig. 14(a), this layer is predominantly $Ni(Cr,Al)_2O_4$ and NiO, however, the composition of this layer is determined by the composition of the alloy, since little diffusion takes place in the alloy and therefore significant amounts of Cr_2O_3 or Al_2O_3 would be present on alloys with sufficiently high chromium or aluminum contents.

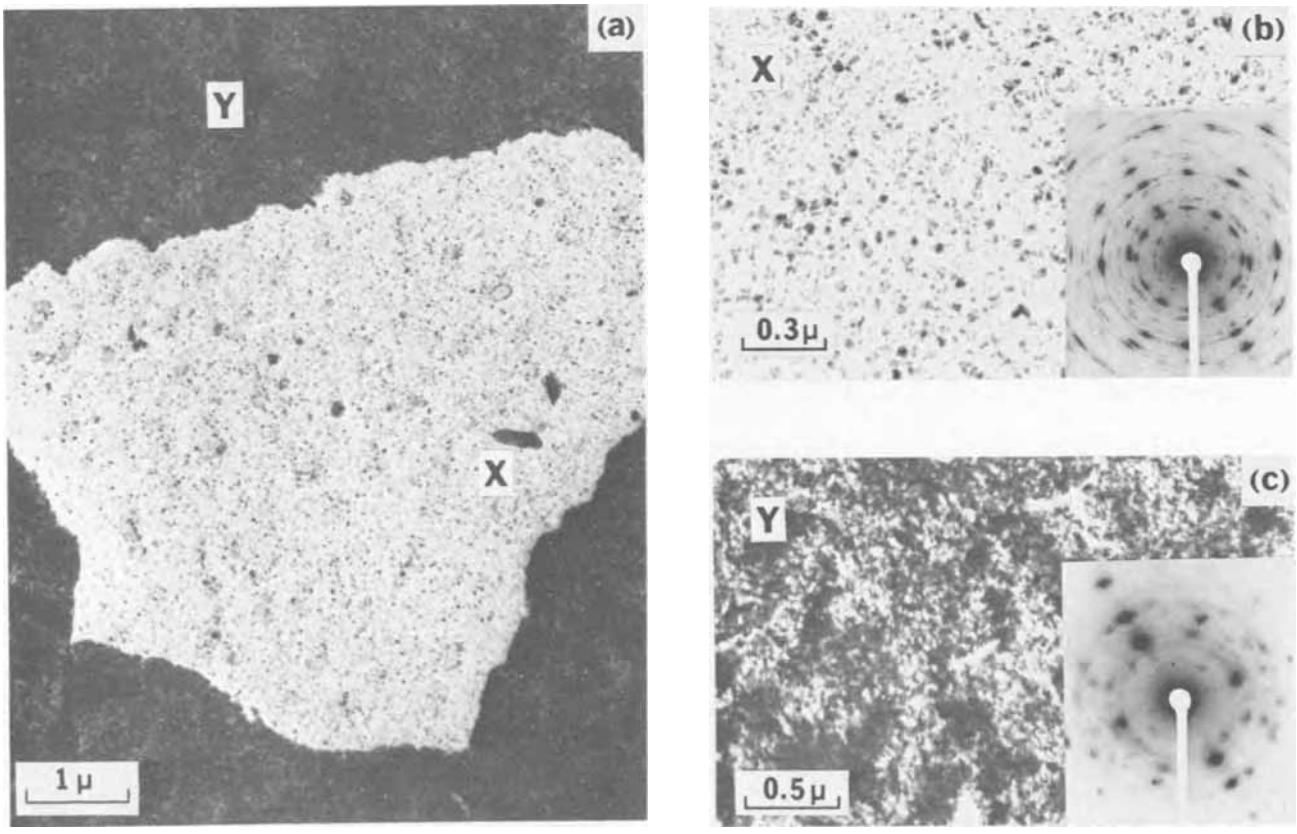

Fig. 13. Transmission micrographs and diffraction patterns of a different area of the oxide scale shown in Fig. 12. The area denoted by X is the inner oxide since the outer layer was delaminated. The diffraction patterns show that the inner layer is Cr_2O_3 with small particles of $Ni(Cr,Al)_2O_4$ while the outer layer, Y, contains substantial amounts of NiO and $Ni(Cr,Al)_2O_4$ in addition to a small amount of Cr_2O_3. In view of the compositions of the two layers, the inner layer must have been in contact with the alloy substrate.

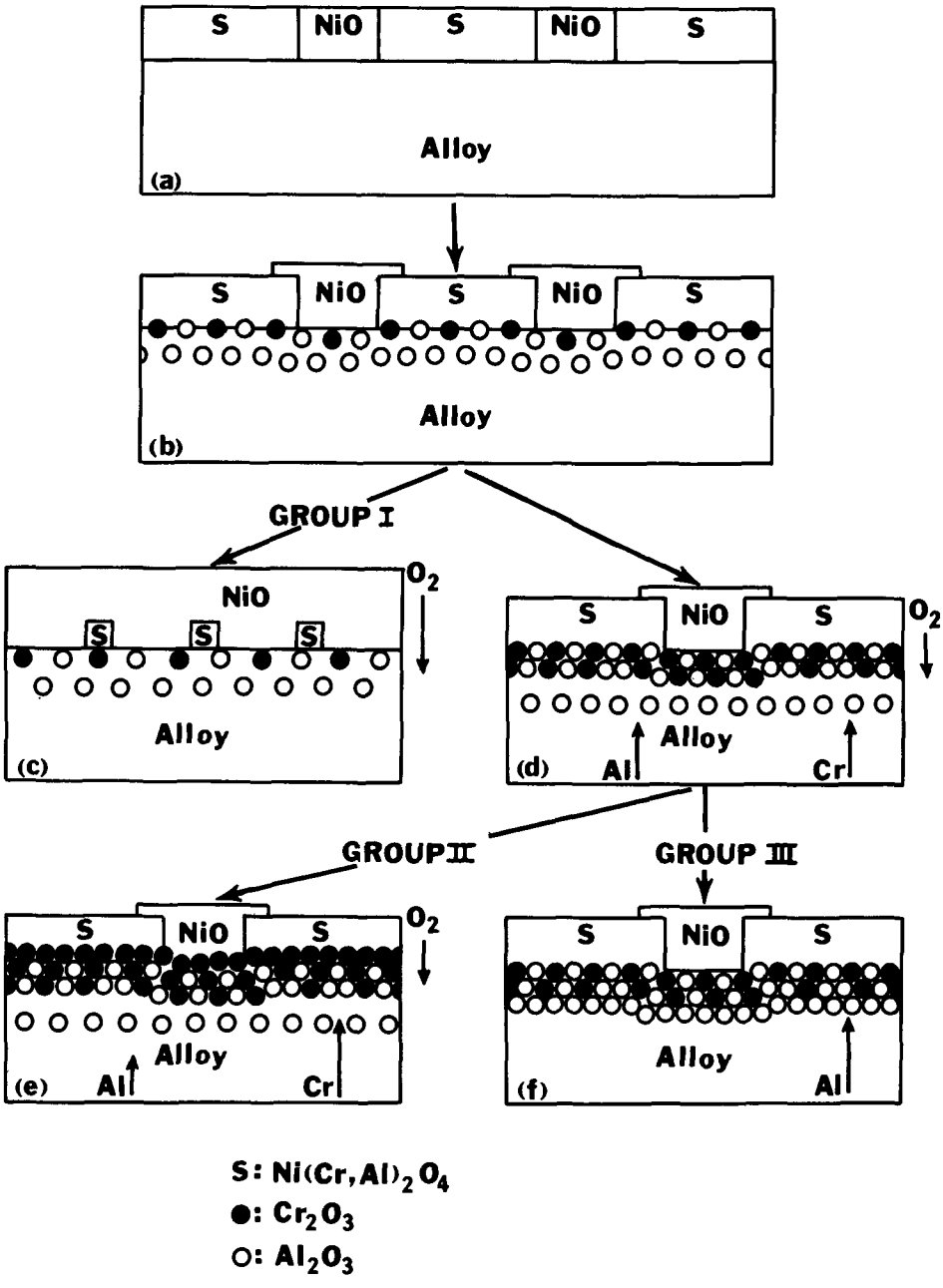

Fig. 14. Schematic diagram illustrating the oxidation mechanisms for Ni-Cr-Al alloys. (a) Conversion of a thin alloy surface layer to oxide by rapid uptake of oxygen. The oxide phases formed are determined by the composition of the alloy. (b) Diffusion within the alloy results in the formation of a Cr_2O_3 and Al_2O_3 subscale beneath the external scale. (c) For alloys with low chromium and aluminum concentrations, the subscale cannot become continuous and NiO in the external scale predominates (Group I). (d) For alloys with higher chromium and aluminum concentrations, the subscale becomes continuous but aluminum is still oxidized internally beneath this duplex internal oxide layer. (e) For alloys with smaller aluminum concentrations, the aluminum continues to be oxidized internally and the continuous duplex layer is enriched in chromium (Group II). (f) For alloys with larger aluminum concentrations, the Al_2O_3 subscale zone becomes continuous beneath the duplex oxide layer (Group III).

As the oxidation reaction continues, diffusional processes in the alloy begin to affect the oxidation reaction. Since the oxygen activity required to oxidize chromium and aluminum in the alloy is less than that established over the alloy by the NiO or spinel in the external scale, oxygen moves into the alloy and precipitates Cr_2O_3 and Al_2O_3 as illustrated in Fig. 14(b). The activity of oxygen required to oxidize the aluminum in the alloy is smaller than that required to oxidize the chromium and the particles of Al_2O_3 therefore extend deeper into the alloy than the particles of Cr_2O_3. If the combined volume fraction[2] of precipitated Cr_2O_3 and Al_2O_3 particles is not sufficient to restrict the movement of oxygen into the alloy, as is the case for Group I alloys, chromium and aluminum continue to be oxidized internally and form a discontinuous subscale of particles beneath the external scale. In the external scale the growth of NiO is much faster than that of any other oxide phase that can be present and NiO completely envelopes the other phases in the external scale as indicated in Fig. 14(c). When the NiO layer becomes virtually continuous, the oxidation reaction proceeds under steady-state conditions and is controlled by transport through the NiO layer (*i.e.* mechanism I). The oxidation rates of alloys that are oxidized by this mechanism are greater than that for pure nickel probably because some chromium and aluminum are dissolved in the NiO which increases the cation vacancy concentration of this oxide.

For alloys where the combined volume fraction of precipitated Al_2O_3 and Cr_2O_3 is sufficient to inhibit the movement of oxygen from the external scale into the alloy, as is the case for Group II and Group III alloys, diffusion of chromium and aluminum from the interior of the alloy results in the precipitation of additional Cr_2O_3 and Al_2O_3 in the subscale zone and a continuous layer of Cr_2O_3 and Al_2O_3 particles is formed beneath the external oxide layer as shown in Fig. 14(d). The formation of this continuous, duplex layer of oxides further reduces the flux of oxygen into the alloy since it establishes a lower oxygen activity over the alloy than that established by the nickel-rich external scale. Consequently, the volume fractions of precipitated Cr_2O_3 and Al_2O_3 are increased to still larger values. For the Group II alloys the flux of oxygen from the duplex scale into the alloy is still sufficient to oxidize the aluminum internally but not the

[2] Use of the volume fraction of precipitated oxides in oxidation processes as developed by Wagner (14) and by Rapp (15) has been discussed in a previous paper by the authors (3).

chromium. Chromium therefore diffuses from the alloy through the duplex scale to form Cr_2O_3 above the duplex scale as illustrated in Fig. 14(e). When the Cr_2O_3 scale becomes continuous, steady-state conditions have been achieved and the oxidation reaction is controlled by transport of chromium through the layer of Cr_2O_3 (*i.e.* mechanism II). In the case of the Group III alloys, the volume fraction of precipitated Al_2O_3 is sufficient to form a continuous layer beneath the duplex zone as shown in Fig. 14(f). Steady-state conditions are reached when the Al_2O_3 layer becomes continuous and the oxidation reaction is controlled by transport through the Al_2O_3 scale (*i.e.* mechanism III).

It is important to emphasize that the transient oxidation period for most Ni-Cr-Al alloys exists for less than 1 hr and the oxides that are formed prior to the formation of continuous Cr_2O_3 or Al_2O_3 layers on the Group II and Group III alloys are usually not evident after 20 hr of oxidation. Frequently the oxide phases formed during the transient period of oxidation could not be detected after 20 hr and it appears that these oxides have been dissolved in the continuous Cr_2O_3 or Al_2O_3 layers or their amounts were too small to be detected. Finally, the nonuniform oxidation of the surfaces of the transition alloys indicates that when the volume fractions of precipitated Cr_2O_3 and Al_2O_3 achieve values where a transition from one mechanism to another is imminent, local differences in surface preparation or impurity content may affect the amount of precipitated oxides whereby different portions of the alloy surface are oxdized by different mechanisms. When such conditions exist, localized transient oxidation will continue until one of the two oxidation mechanisms prevails.

Summary and Concluding Remarks

The particular oxidation mechanism by which a specific Ni-Cr-Al alloy is oxidized is determined by the combined volume fraction of Cr_2O_3 and Al_2O_3 precipitated within the alloy. Chromium allows a continuous, external layer of Al_2O_3 to be formed on Ni-Cr-Al alloys at lower aluminum concentrations than would be necessary if the chromium were not present in the alloy (see Fig. 1) by contributing to the volume fraction of precipitated oxide which reduces the movement of oxygen into the alloy. C. Wagner has proposed such an effect for chromium on the selective oxidation of aluminum in Fe-Cr-Al alloys (16). It is interesting to note that aluminum promotes the formation of continuous Cr_2O_3 layers on some Ni-Cr-Al alloys for similar reasons.

Acknowledgments

The authors wish to express their sincere appreciation to P. A. Scott, V. Nevins, and K. P. Gumz for technical assistance. They also wish to acknowledge that the electron microscopy studies were done with B. H. Kear, L. P. Lemaire, and D. E. Fornwalt. Finally, the authors wish to thank G. W. Goward for many helpful discussions.

Manuscript submitted April 30, 1971; revised manuscript received *ca.* June 18, 1971. This was Paper 114 presented at the Atlantic City Meeting of the Society, Oct. 4-8, 1970.

Any discussion of this paper will appear in a Discussion Section to be published in the June 1972 JOURNAL.

REFERENCES

1. C. S. Wukusick and J. F. Collins, *Mater. Res. Std.*, **4**, 637 (1964).
2. C. S. Giggins and F. S. Pettit, *Met. Trans.*, **2**, 1071 (1971).
3. C. S. Giggins and F. S. Pettit, *Trans. TMS-AIME*, **245**, 2495 (1969).
4. F. S. Pettit, *ibid.*, **239**, 1296 (1967).
5. J. F. Elliott and M. Gleiser, "Thermochemistry for Steelmaking," Vol. I, Addison-Wesley Publishing Co., Reading, Mass. (1960).
6. O. S. Tumarev and L. A. Panushin, *Izv. Vysshik Uchebn. Zavedenii, Chernaya Met.*, p. 125 (1959).
7. D. V. Ignatov and R. D. Shamgunova, "Mechanism of the Oxidation of Nickel and Chromium Alloys," book published in Moscow in 1960, NASA TT F-59 (1961).
8. I. Kvernes and P. Kofstad, Studies on the Behavior of Nickel-Base Superalloys at High Temperatures, Technical Report AFML-TR-70-103 (1970).
9. R. Kosak, Jr. Ph.D. Thesis, Ohio State University (1969).
10. A. Taylor and R. W. Floyd, *J. Inst. Metals*, **81**, 451 (1952-53).
11. O. Kubaschewski and B. E. Hopkins, "Oxidation of Metals and Alloys," 2nd ed., p. 90, Butterworth and Co., Ltd., London (1962).
12. G. H. Meier and R. A. Rapp, Ohio State University, Private communication.
13. B. Chattopadhyay and G. C. Wood, *This Journal*, **117**, 1163 (1970).
14. C. Wagner, *Z. Electrochem.*, **63**, 772 (1959).
15. R. A. Rapp, Acta Met., **9**, 730 (1961).
16. C. Wagner, *Corrosion Sci.*, **5**, 751 (1965).

Growth of Semi-Insulating Cadmium Telluride

Nanse R. Kyle

Hughes Research Laboratories, Malibu, California 90265

ABSTRACT

A modified Bridgman method for growing cadmium telluride is described. This method controls the composition of the melt, and thus the solid, by controlling the pressure of one of the components of cadmium telluride (CdTe) over the melt. The theory of equilibrium between solid-liquid-gas for this system indicates that the liquid acts only as a transferring medium between gas and solid. Thus the system may be treated as a gas-solid system with respect to defect chemistry. The synthesis and purification of CdTe is described in detail, and empirical results for producing large single crystals are given. Crystals grown by this system are compared with the defect chemistry presented by de Nobel.

D. de Nobel (1) has shown that cadmium telluride (CdTe) can undergo stoichiometric deviations, and that such changes in composition are caused mainly by lattice defects which determine the conductivity and type of conduction. Since cadmium telluride does show a deviation from stoichiometry, the constituents of the crystal itself can act as impurities. Figure 1 is a schematic phase diagram for a two-component system A-B, with one compound AB showing deviation from stoichiometry. For each point of the liquidus there is a corresponding pressure of the volatile component. If a

Key words: crystal growth, cadmium telluride, semi-insulating cadmium telluride, II-VI compound, radiation detector material, modified Bridgman crystal growth, optical modulator material.

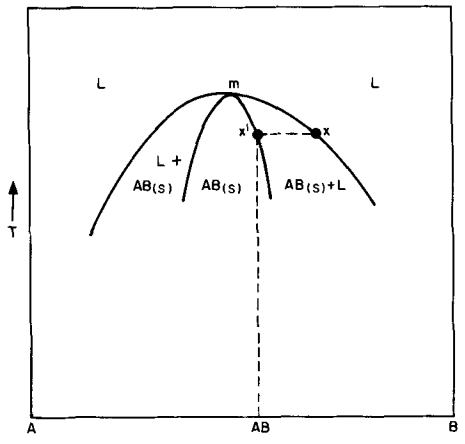

Fig. 1. T-X diagram of the system A-B where compound near AB can solidify at other than exact stoichiometric ratio.

specific vapor pressure of the component is maintained over the melt, the system has a tendency to remain at the composition corresponding to the vapor pressure applied. As solidification takes place, the segregation process tends to make the melt more and more concentrated relative to the excess component present. However, at this point, the liquid is no longer in equilibrium with the vapor, and a reaction between the vapor and melt sets in until equilibrium is again reached. The end result depends on the rate at which the composition changes as a consequence of the segregation, as compared with the rate at which atoms are transferred between the melt and the vapor. Eventually, a stationary state will be reached in which the crystals attain a composition between x' and m.

Because the composition of CdTe is a function of the chemical potential of one of the components when grown from the melt, it is desirab e to grow the crystals under conditions which control the chemical potential of one of the components. This is accomplished utilizing the Bridgman technique. By elongating the tube so that cadmium or tellurium can be placed high in the tube where its vapor pressure is controlled by a second furnace operating significantly below the crystal furnace temperature, the properties of the compound can be determined by the pressure of one of the components above the melt. Use of the elongated tube is referred to as the modified Bridgman system or technique. This system (*i*) controls the composition of the melt, and consequently the solid, by controlling the pressure of one of the components of CdTe over the melt; (*ii*) stops decomposition of the melt; and (*iii*) fixes the distribution coefficients of the dopants.

The theory of equilibrium between solid-liquid-gas for this system indicates that the liquid acts only as a transferring medium between gas and solid; thus the system may be treated as a gas-solid system with respect to defect chemistry. Cadmium telluride synthesis and purification are also described in detail, and empirical results for producing the large single crystals are given. Crystals grown by this system are compared with the defect chemistry presented by de Nobel (1).

Experimental

Equipment.—The equipment used for growing CdTe crystals by the modified Bridgman technique consists of a Marshall multitapped platinum-wound furnace and a Marshall multitapped Kanthal-wound furnace, plus a power supply and a digital temperature control unit for each furnace. The crystal is lowered out of the furnace on a metal support by a screw-driven apparatus whose speed can be varied. The temperature profile of the furnace is adjusted by controlling the power to each tap on the furnace by a series of variable autotransformers and stepdown transformers. Each autotransformer is adjusted individually until the desired profile is obtained. A large autotransformer than can handle the power of the system is used to raise or lower the temperature profile.

Purification.—Cadmium telluride has been synthesized by many processes, including the reaction of cadmium and tellurium previously purified by zone melting or sublimation, followed by crystal growth, as well as purification of the compound CdTe by zone melting. Some controversy exists regarding the purification of tellurium:

1. Weidel (2) determined that distillation and zone refining were unsatisfactory. He used thermal decomposition of H_2Te to obtain pure tellurium.
2. Shvartsenau (3) found that zone melting of tellurium in quartz under hydrogen at 6 cm/hr gave greater than 99.999% purity, although magnesium and silicon were not removed.
3. Blakemore (4) used several hundred zone passes through tellurium to attain extreme purity.

Multiple distillation has been used by several investigators (3-7) with and without zone refining:

1. Silvey *et al.* (8) found that distillation is very effective for purification of cadmium.
2. Aleksandrov and Verkin (9) used 15 zone passes at 15 mm/hr in agron.

Based on the above information and because the segregation coefficients (1, 10-12) of most impurities for solid-liquid purification (such as zone melting) of CdTe are of approximately 0.5 (magnesium = 1, aluminum > 1), purification by sublimation of CdTe was chosen. Zone refining would require that the material be subjected to a very large number of passes to remove the impurities. This would intensify the contamination problem because the melt would be in contact with the container at high temperatures for extended periods of time. Purification by sublimation is rapid, and less chance of container contamination exists; no melt is involved and sublimation temperatures are low. In addition, the compound recombines stoichiometrically according to the equation

$$CdTe_{(s)} \rightleftarrows Cd_{(g)} + \frac{1}{2} Te_{2(g)}$$

Therefore, any excess cadmium or tellurium is effectively segregated because the vapor pressure of both cadmium and tellurium is much higher than that of CdTe.

Purification by sublimation is based on a distribution equilibrium between the solid and gas phase. Impurities which are nonvolatile will be effectively segregated, and those which are volatile will be in equilibrium with the sublimate and condensate. Starting with the purest cadmium and tellurium available (99.9999% pure from Cominco), the components are reacted to form the compound CdTe and then sublimed to purify it. This is a one-step process which takes place in a closed evacuated tube (Fig. 2). When this technique is used, the starting material may consist of the compound CdTe or the pure elements cadmium and tellurium. In either case the material is placed in a long quartz tube which has been cleaned in electronic grade $HF-HNO_3$, washed in continuously deionized water in a closed system, and coated with pyrolytic carbon. The acid cleaned tubes, as well as the pyrolytic carbon coated tubes are continuously washed in this system until needed.

Once the tube is loaded, it is sealed off under a vacuum of 10^{-8} Torr. When using CdTe as the starting material, the pyrolytically coated tube is placed directly in the furnace so that the CdTe is in the flat zone of the temperature profile. The tube is withdrawn from the furnace at approximately 0.6 cm/hr. Excess cadmium or tellurium (which has a higher vapor pressure than CdTe) collects in the cool end of the tube, while CdTe collects in a much hotter sec-

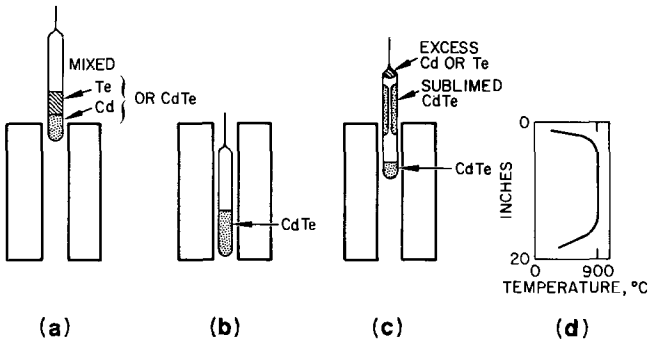

Fig. 2. Synthesis of CdTe and its purification by sublimation. (a) Cadmium and tellurium (or CdTe) are sealed in a pyrolytic carbon coated quartz tube and allowed to react. (b) The tube is lowered into the furnace. (c) The tube is slowly withdrawn from the furnace. (d) Temperature profile.

tion. Normally, two sublimations are sufficient for purification of the material.

When starting materials are cadmium and tellurium, near stoichiometric amounts are sealed at 10^{-8} Torr in a pyrolytically coated quartz tube. Initially, the tube is partially lowered into the furnace until the heat is sufficient to start the reaction between cadmium and tellurium. The reaction is exothermic and very rapid. When it stops, the tube is then lowered completely into the furnace and withdrawn at approximately 0.6 cm/hr, as mentioned.

For a series of sublimations, the tube sizes are graduated so that the coalesced material travels directly from one tube to another. No attempt is made to clean the material mechanically or chemically. This method also reduces the possibility of contamination by minimizing handling. In addition, the CdTe sublimate is heated in the sublimation tube under a hydrogen atmosphere to remove any oxides before the tube is sealed under vacuum. Removing the oxides prevents removal of the pyrolytic coating through reaction of the carbon with the oxides. If oxides are present, the quartz reacts with them, weakening the walls. (This has caused an implosion.) In addition, the CdTe is prevented from sticking to the quartz tube. It is important that molten material in crystal growth does not come into contact with the quartz container, since quartz has been found to be very soluble in CdTe and consequently a source of contamination. It has also been found that in spite of a heavy coating of pyrolytic carbon on the usual commercial quartz used for crystal growing, this coating did not stop impurities from coming through from the quartz although it was considerably reduced to approximately 20 ppma (parts per million atomic). Consequently, synthetic quartz, which has the lowest impurity content of any available quartz, is used to grow the crystals.

Mass spectrographic analysis (13) of crystals grown in synthetic quartz is tabulated in Table I. This is a typical impurity concentration in parts per million atomic for CdTe grown in synthetic quartz by the modified Bridgman technique. Impurities not shown were not detected, and thus have concentrations less than 0.1 ppma. Silicon, phosphorus, manganese, iron, nickel, copper, cesium, thorium, and uranium cannot be detected because they are interfered with by background lines of tellurium and cadmium. Emission spectrographic analysis was used to determine the concentrations of some of these elements, although giving only an upper limit.

The results of varying the cadmium pressure above the melt in commercial quartz containers in order to change the electrical properties of crystals grown by the modified Bridgman process were masked by the impurities from the quartz. Since beginning the use of synthetic quartz, the change in electrical properties has been observed as a function of cadmium pressure and the results have become reproducible.

Table I. Mass spectrographic analysis of a recently grown CdTe crystal

Element	Detection limit	Concentration[b]
H	0.1	1.0
Li	0.002	N.D.
C	0.01	0.67
N	0.02	0.03
O	0.02	0.20
Na	0.003	1.6
Mg	0.01	N.D.
Al	0.02	0.02
Cl	0.03	0.24
Si	2.0	N.D.
Zn	0.1	0.1
S	0.3	N.D.
Cl	0.03	N.D.
K	0.003	0.029
Ca	0.05	N.D.
V	0.01	0.02
Cr	0.01	0.073
Rb	0.005	N.D.
In	0.05	N.D.
Cs	0.007	N.D.
Pb	0.1	N.D.
Fe[a]	0.1	N.D.
Ch	0.01	N.D.
Se	0.05	N.D.
In	0.05	N.D.
Cu[a]	1.00	<1.0
Si[a]	0.5	<0.5
P	0.2	<0.2

[a] Emission analysis.
[b] N.D. = not detected.

Modified Bridgman system.—The Bridgman technique for growing CdTe has the advantages of producing uniform ingot size and more uniform distribution of impurities in the direction transverse to the direction of growth. The main disadvantage of the original Bridgman technique is that if the melt is not stoichiometric the composition of the melt changes continuously as solidification takes place, changing the composition of the solid as it grows. The change in composition of the melt affects the electrical properties of the crystal and causes the segregation coefficient of any dopants to change accordingly (10).

CdTe readily dissociates at high temperatures according to the equation

$$CdTe_{(l)} \rightleftarrows CdTe_{(g)} + \frac{1}{2} Te_{2(g)}$$

Therefore, growth of CdTe from the melt requires a closed system because of the dissociation and mass transport which occurs constantly through the vapor phase to lower temperature regions. The Bridgman method can be used to grow CdTe; however, the modified Bridgman method permits control over the composition of the crystal and consequently the electrical parameters.

In the modified Bridgman technique, the tube is elongated (Fig. 3) so that cadmium or tellurium can be placed in a reservoir high in the tube, where the

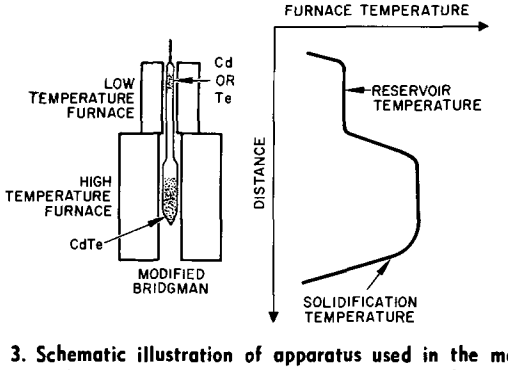

Fig. 3. Schematic illustration of apparatus used in the modified Bridgman technique for growth of single crystals, together with the temperature profile.

vapor pressure can be controlled by a second furnace operating significantly below the temperature of the crystal furnace. The pressure of one of the components above the melt effectively stops, or at least minimizes, vaporization of CdTe. Since this pressure is held constant, the composition of the melt and consequently that of the crystal is held constant. (In practice, the composition of the solid is determined by the composition of the solid-melt interface, which can be appreciably different from the average melt composition. However, in this system the solid-melt interface is also theoretically held constant, and thus the results are reproducible.) In addition, because the distribution coefficient of dopants is a function of the component pressure (10), it is also fixed. In theory, therefore, crystals of CdTe can be grown stoichiometrically, cadmium-rich or tellurium-rich, simply by changing the pressure of one of the components.

Equilibrium between vapor and liquid.—In the modified Bridgman technique, the vapor phase is in equilibrium with the liquid phase, which in turn, is in equilibrium with the solid phase. It is necessary to assume a model for the liquid which is equivalent to the normal crystalline model of the solid. Two types of models are used. One may be called the gas-like and the other the crystal-like model. In the gas-like model, the perfect liquid is assumed to consist of molecules and dissociation products of the molecules. Ionization may occur, which leads to additional imperfections. In the crystal-like model, the liquid is regarded as a crystal with an exceptionally large concentration of Schottky-Wagner or Frenkel-type defects. Intrinsic excitation and ionization are assumed to take place exactly as in a solid. Statistically, both models are equivalent and give the same results.

If α is defined as a defect in the liquid caused by addition of Cd_x (x indicates an uncharged atom in the liquid) and β is a defect in the liquid caused by the removal of Cd_x from the liquid, then

$$Cd_{(g)} \rightleftarrows Cd_{(l)} + \alpha$$

for small concentrations of α

$$K_1 = \frac{[\alpha]}{P_{Cd}} \qquad [1]$$

In addition

$$Cd_{(l)} \rightleftarrows Cd_{(g)} + \beta$$

for small concentrations of β

$$K_2 = [\beta][P_{Cd}] \qquad [2]$$

Under these conditions

$$K = P_{Cd}\, P_{Te}{}^{1/2} \qquad [3]$$

since

$$CdTe \rightleftarrows Cd_{(g)} + \frac{1}{2} Te_{2(g)}$$

Accordingly

$$[\alpha][\beta] = K_{\alpha\beta} \qquad [4]$$

or the composition of the liquid is a function of P_{Cd}.

Equilibrium between liquid and solid.—In the equilibrium between liquid and solid, reactions are needed to describe the transfer of atoms from one phase to another, as well as imperfections within each phase. Transfer of electrons or ions need not be considered because both phases remain neutral. If such particles are transferred, electrons and ions are transferred in equal concentrations, so that the final reactions may be expressed in terms of the transfer of neutral atoms and vacancies.

If a is a defect caused by removal of a tellurium atom from the solid and b is a defect caused by removal of a cadmium atom from the solid, then

$$M^x_{(s)} + \beta \rightleftarrows M^x_{(l)} + b$$

where M^x_s and M^x_l are un-ionized atoms in the solid and the liquid, respectively. For small concentrations of β and b

$$K_3 = \frac{b}{\beta} \qquad [5]$$

In addition

$$Te^x_{(s)} + \alpha \rightleftarrows Te^x_{(l)} + a$$

$$K_4 = \frac{[a]}{[\alpha]} \qquad [6]$$

and

$$[a][b] = K_{ab} \qquad [7]$$

Using [4], [5], and [6]

$$[a][b] = K_3 K_4 K_{\alpha\beta} = K_{ab}$$

The above theory was simplified by assuming that: (*i*) the liquid is always homogeneous; (*ii*) diffusion in the solid is slow, and thus the composition of the solid does not change after it has grown from the liquid; (*iii*) the gas phase equilibrium $CdTe_{(g)} \rightleftarrows Cd_{(g)} + (1/2)\ Te_{2(g)}$ is reached quickly, with CdTe molecules not present in any significant amounts; (*iv*) the distribution coefficients are constants which are independent of composition; and (*v*) the solid-liquid distribution is adjusted quickly. In the modified Bridgman system, the gas and solid phases are physically separated so that the liquid phase essentially acts as a communication medium, since the liquid phase composition is determined by the pressure of one of the CdTe components.

Optimum growth conditions.—Optimum growth conditions for producing large single crystals of CdTe (Fig. 4) were determined empirically by evaluating growth rate, crystal rotation, temperature gradients, and crystal size. Radioactive isotopes were especially useful in this evaluation because they revealed the shape of the solid-liquid interface during growth.

A primary problem in growing crystals from the melt is that of maintaining a shape convex (pointing in the direction of growth) or at least flat at the solid-liquid interface. This convex shape is obtained when the heat flows axially from the melt (*i.e.*, along the axis of growth) instead of radially. The convex isotherm formed under these conditions is considered ideal for single-crystal synthesis from the melt. If the solid-liquid interface becomes concave because of radial heat flow, the resultant cooling causes spurious nucleation. Radiotracer experiments indicate that our crystals are grown with a flat solid-liquid interface. In these experiments the melt was doped with radioactive indium (which was determined to have a segregation coefficient of 0.51 ± 0.04 under 1 atm cadmium). Under normal conditions an impurity is segre-

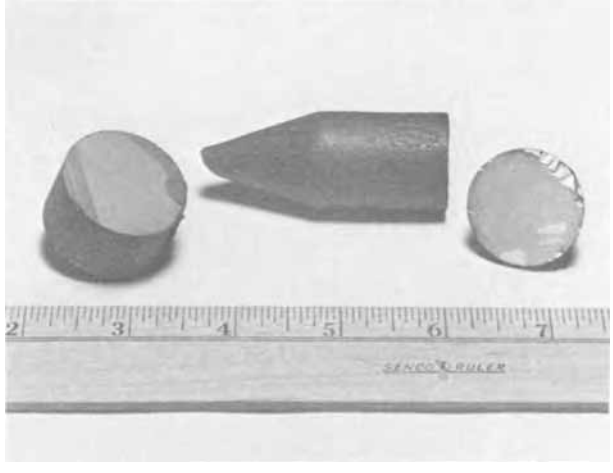

Fig. 4. Cadmium telluride crystals grown by the modified Bridgman technique, showing crystallinity.

gated uniformly from the growing crystal; by freezing in the indium at the solid-liquid interface at several points along the growth axis of the crystal, the shape of the interface could be determined by autoradiography.

As a result of these experiments, the following conditions for single-crystal growth are specified:

1. A sharp temperature gradient in the growth zone is necessary for an axial flow of heat. Crystals grown through a shallow gradient were invariably polycrystalline. We use a minimum gradient at the melting point of 20°C/cm.

2. A flat profile is required to minimize the radial flow of heat and thermal convection in the melt.

3. Slow growth is necessary to avoid rapid cooling of the surface, which would result in a concave solid-liquid interface. Thermal conductivity is the dominant factor determining growth rate. Therefore, for low thermal conductivity material, the growth must be slow. For CdTe, a concave shape was obtained for growth speeds much greater than 0.50 cm/hr. At speeds greater than 0.50 cm/hr the dislocation density [determined using the method of Inoue *et al.* (14) except that a 10% volume solution of bromine in methanol was used to chemically polish the material] rapidly goes into the thousands (Fig. 5). However, the rate which produces the least number of dislocations (in the order of 100/cm^2) is not the best rate for producing large single crystals for the seeds that form initially propagate linearly through the crystal along the growth axis, producing many crystals. The speed is too slow for one of the growing planes to dominate, so that large areas of a single-crystal material are produced. As a compromise, a speed of 0.25 to 0.50 cm/hr is used.

4. Large crystals of approximately 2.5 cm diameter minimize radial temperature fluctuations across the ingot by incorporating the properties of a large mass.

5. A large metal heat sink on the nose of the crystal assists in the axial flow of heat with subsequent statistical improvement in the number of single crystals, as compared with crystals grown without the heat sink.

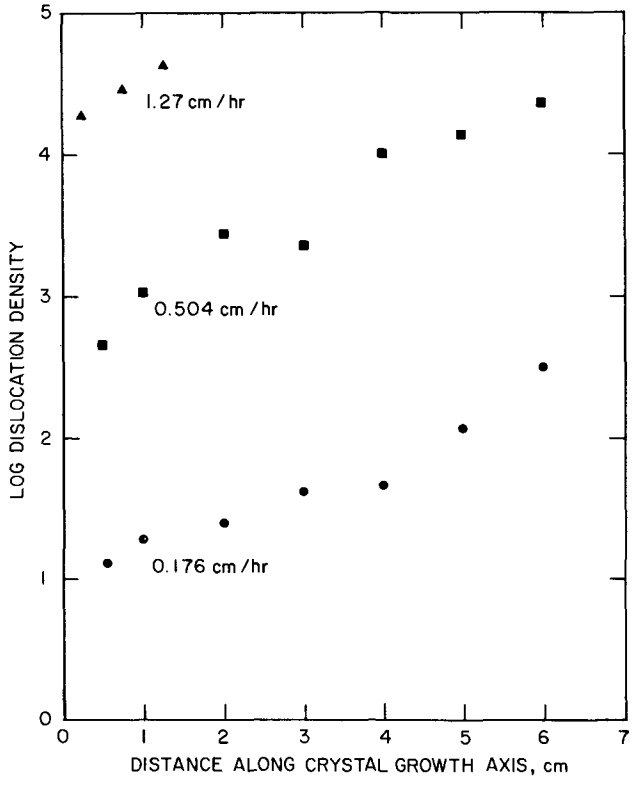

Fig. 5. Dislocation density with respect to growth rate

Table II. Nondoped CdTe crystals grown under component atmosphere

Crystal number	Atmosphere	Pressure, atm	Resistivity, ohm-cm	Type	Electron mobility, M	Carrier concentration, N_h
12	Cd	1	10^7-10^9	—	—	—
14	Cd	1	10^5	—	—	—
16	Cd	1	10^7	—	—	—
17	Cd	1	10^6-10^8	—	—	—
11	Te	0.32	75-1300	p	—	—
5	Cd	2.6	4.6-1.7	n	957 997	1.4×10^{15} 3.8×10^{15}

6. The crystal must be rotated in asymmetrical furnaces. Rotation will smooth out the asymmetry of the furnace and also minimize radial fluctuations.

7. The solid-liquid interface can become concave if the melt temperature is well above the melting point of the material. A temperature of 5°-10°C above the melting point is ideal but not rigid.

8. The pressure of one of the components above the melt affects the crystallinity. In particular, when the cadmium pressure was much above or below 1 atm, the crystallinity degenerated. This may be related to Lorenz's work (15), which shows that for every set of fixed component pressures there are two points in phase-space where solid, liquid, and vapor are *in* equilibrium.

Relationship of crucible geometry to crystallinity.—In the Bridgman method the material is initially in the liquid state. As the material moves through the temperature gradient, chance nucleation takes place in the tip of the tube. There is no guarantee that nucleation will take place such that a 100% single crystal is formed each time. Seven different configurations of quartz crucibles were tested to determine whether the different methods of crystal nucleation and slopes of growth had any effect on the crystallinity of the material. Only one of the configurations offered any advantage in getting a single crystal start. This shape was a ball which grew into a neck constriction then expanded gradually into the big tube.

Defect chemistry of cadmium telluride.—The equations describing the reactions involving the various imperfections and the mass action relations resulting from it are given by de Nobel (1); they are used as a basis for the following discussion. The types of imperfections which appear in the solid and the manner in which their concentration varies with the preparation conditions depend on the energy levels of the imperfections and the values of the constants governing the reactions involving the various imperfections.

Pure cadmium telluride.—When CdTe is prepared under high cadmium pressure, cadmium is introduced into the crystal at interstitial sites (Cd_i), which ionize and give rise to an equal concentration of Cd_i^+ (cadmium atom which has lost an electron) and free electrons (n).[1] Decreasing the pressure lowers the electron concentration, until a transition point is reached in which the material changes from n- to p-type. This occurs when $(V_{Cd}') = (Cd_i^{\cdot})$ where (V_{Cd}') is a cadmium vacancy with a negative effective charge. Upon further reduction of the pressure, cadmium vacancies (V_{Cd}') dominate and the material becomes p-type.[2] The area of interest for high-resistivity material is where $(V_{Cd}') = (Cd_i^{\cdot})$. This transition range between n- and p-type is theoretically very narrow and thus is very sensitive to pressure changes.

Ingots No. 12, 14, 16, and 17 (Table II) were grown under a cadmium pressure of 1 atm, which corresponds empirically to the transition region discussed above. For comparison, ingots No. 5 and 11 were grown under

[1] High temperature measurements by Whelan and Shaw (16), Smith (17) and Zanio (18) indicate that the material is n-type due to the presence of a doubly ionized native donor (Cd^{++}).

[2] High-temperature measurements by F. T. J. Smith indicate that for compositions close to tellurium saturation the electrical properties are dominated by foreign impurities rather than by native defects.

Table III. Indium-doped CdTe crystals grown under component atmosphere and quenched or slow-cooled

Crystal number	Resistivity, ohm-cm	Indium, atoms/cm³	Cadmium atmosphere pressure, atm	Carrier concentration, N_h	Electron mobility, μ	Quench temperature, °C
21	10^7	2.4×10^{17}	1.0	—	—	>1000
22	10^8	2.5×10^{17}	1.0	—	—	>1000
24	10^7	2.5×10^{17}	1.0	—	—	>1000
25	10^5	5×10^{17}	1.0	—	—	>1000
01	10^5	1.9×10^{18}	2.1	—	—	>1000
23	0.93	2.5×10^{17}	1.0	—	—	<1000
02	0.63	2×10^{18}	2.1	1.64×10^{17}	603	Slow-cooled

a cadmium pressure of 2.6 atm and a tellurium atmosphere of 0.3 atm, respectively. All crystals were slow-cooled to room temperature during the growth process.

Cadmium telluride-indium.—When CdTe is doped with indium (a donor) and slowly cooled following solidification, the electrical properties of the crystal are determined predominantly by the amount of indium put in the crystal and the pressure of one of the components of the compound. If CdTe is doped with indium and rapidly cooled (quenched) from high temperatures, the electrical properties are no longer dominated by the indium content.

In the quenching process under an atmosphere of one of the components, it is assumed that all atomic positions of vacancies and foreign atoms remain unchanged, while only the electrons and holes are free to redistribute themselves over the crystal. Consequently, quenching under a high cadmium pressure would introduce cadmium interstitials as the dominant donor. As the pressure is lowered, the donor impurity (indium) becomes the dominant electron supplier. This n-type region ends at the cadmium pressure in which all electrons either recombine with holes or are trapped at deep-lying levels during the quenching process. The imperfections which trap electrons are thought to be V_{Cd}' centers.

As the cadmium pressure is lowered further, the V_{Cd}'' (cadmium vacancy with effective charge of -2) functions as a trap for the holes during the quenching process. The ionization energy of these V_{Cd}'' levels is too large to give appreciable conduction at room temperature. It is not clear whether these deep-lying energy levels consist of a double-negative charged cadmium vacancy or associates of cadmium vacancies with donors (1, 19, 20). However, the result is that the transition from n- to p-type material takes place over a wide range of atmospheres in which the crystal has an extremely high resistivity (Table III). The range showing low resistivity p-type conductivity is never reached. Consequently, high-resistivity material is obtained by this process without extremely critical limits on cadmium pressure, temperature of quench, rate of quench, or donor (indium) concentration. It is obvious that the high-temperature equilibrium state cannot be completely quenched, especially in our crystals with diameters on the order of 2.5 cm. However, the high-temperature disorder is maintained well enough that room-temperature resistivities are reasonably reproducible. If the cooling takes place slowly or if the quench occurs at a temperature that is too low, vacancies and foreign atoms are able to move to energetically more favorable positions; thus the Fermi level is no longer near the center of the forbidden energy zone, and something less than high-resistivity material is formed. This is evident in crystal 23, which was quenched at a lower temperature than the earlier ones.

A quantitative evaluation of quench temperature *vs.* electrical properties was made on crystal 25 (Fig. 6) in order to show more precisely the effect of quenching on large ingots. This crystal weighed 139g and had a diameter of 2.54 cm. The temperatures indicated in Fig. 6 are those along the ingot before it was removed rapidly from the furnace and allowed to air quench. The "distance, cm" gives the distance from the nose of the crystal that rods were taken from slices at that point and of the thickness indicated. This is in good agreement with the phase diagram (1), which indicates that indium-doped CdTe grown at a pressure of 1 atm should have high resistivity if it is quenched rapidly from 1000°C to room temperature.

According to the phase diagram, if the pressure of cadmium is lowered sufficiently, the indium-doped CdTe can be slow-cooled to room temperature and the result will still be high-resistivity material. It naturally followed that high-resistivity CdTe could be grown using the Bridgman process by adding an excess of tellurium to the melt with the indium. However, by this method the composition of the liquid is constantly changing as solidification takes place. Ingots 32, 35, and 39 (Table IV) grown by this method were slow-cooled or quenched. Ingots 37 and 38, grown by the modified Bridgman method, yielded similar results, as did ingot 34 which was solution grown (4:1 Te to Cd by weight).

Resistivity of rods taken transverse to ingots.—The resistivity of single-crystal rods from ingots grown under various conditions (Table V) was measured as a function of distance along the rods (Fig. 7). These rods were cut perpendicular to the growth axis of the crystal and had a cross-sectional area approximately

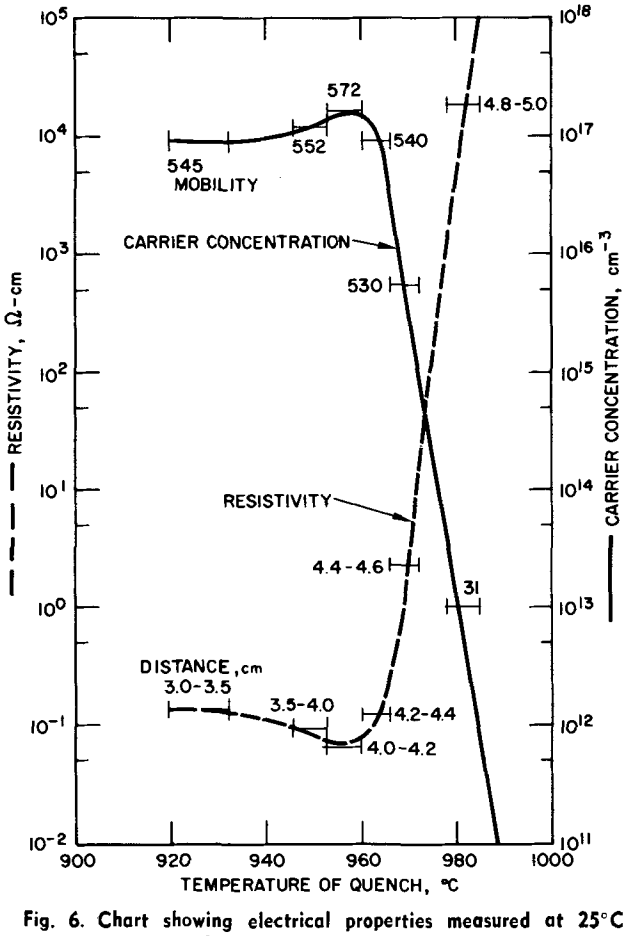

Fig. 6. Chart showing electrical properties measured at 25°C as a function of quench temperature.

Table IV. Indium-doped CdTe crystals grown with an excess of Te or under a Te atmopshere, slow-cooled or quenched

Crystal number	Indium, atoms/cm³	Weight CdTe, g	Weight Te (added), g	Resistivity, ohm-cm	Method of growth
39	3.6×10^{17}	174.41	3.41	10^5	Slow-cooled, Bridgman
35	1.7×10^{17}	135.54	2.68	10^8	Slow-cooled, Bridgman
32	2.6×10^{17}	122.68	2.39	10^8	Quenched, Bridgman
37	2.5×10^{17}	307.6	Te atm = 0.84 atm	10^8-10^9	Slow-cooled, Bridgman
38	2.5×10^{17}	294.2	Te atm = 0.84 atm	10^6-10^7	Slow-cooled, Bridgman
34	7.8×10^{18}	58.4	91.3	10^5	Slow-cooled, solution

0.1 cm². They were cut from the ingots with a wire saw, polished in a 12% solution of bromine in methyl alcohol, and indium-silver electrical contacts made. CdTe polished in bromine-methyl alcohol does not show any of the surface conduction that has been observed with other polishing etchants. All resistivity measurements were made at room temperature in the absence of light and are precise to ±20%.

In Fig. 7, the rods show a wide variation in resistivity which at first glance may indicate great inhomogeneity. But at this level, the change in carrier concentration is extremely small. That is, a small change in carrier concentration can change the resistivity greatly. However, it is certain that this variation is due to different cooling rates between crystals as well as along a crystal. No two crystals were exactly the same size in dimension; *e.g.*, the weights varied from 150 to 300g. Also, the thickness of the quartz walls has a significant effect on the cooling rates. A more uniform distribution was achieved by growing very small, pencil-like crystals, or by heat-treating small volume pieces. However, since small crystals could not meet the requirements of the optical modulator, the emphasis has been on large crystals.

Discussion

The high-temperature quenching results for CdTe doped with indium are in good agreement with de Nobel's theory, especially considering that the ingots had diameters on the order of 2.5 cm and weighed approximately 300g. For the undoped crystals if they were pure, n-type material should be obtained at $P_{Cd} \sim 1$ atm according to the phase diagram. Since high-resistivity material is obtained at this pressure, it is obvious that the material is not really pure but that impurities are playing a role in obtaining the high-resistivity material.

Even if the material was pure, it is nearly impossible to grow a stoichiometric crystal with control of pressure since the pressure must be adjusted with temperature in order to stay on the stoichiometric line, if such conditions could be obtained in growing a crystal which must pass through a temperature gradient. For example, initially it would be easy to be in the high-resistivity range for the cadmium pressure range is 1.1 atm wide at 1000°C. As the temperature decreases to 700°C the stoichiometric line is only 1.28×10^{-3} atm wide. Thus a change in pressure of ±0.003 atm at 700°C would change the resistivity by a factor of 10^5. Even for solution growth in excess tellurium at 700°C high-resistivity pure cadmium telluride would be difficult to grow as the P_{Te_2} range is only 5×10^{-6} atm wide. On the other hand, a small amount of donor extends this range considerably. For example, at 1000°C the high-resistivity range is P_{Cd} 0.36 to 4.3 atm and at 700°C any cadmium pressure between 1.9×10^{-3} to 4.1×10^{-5} atm will give high-resistivity material. However, it would sublime before reaching 10^{-5} atm. Thus, for pure cadmium telluride there is no appreciable pressure range that will produce a small number of charge carriers. Whereas, for donor-doped CdTe there is a wide range in which the carrier concentration is extremely low. For acceptor-doped material, there occurs a change in conductivity from p- to n-type, but it also occurs without an appreciable width in which the charge carriers are very low.

Table V. Conditions of growth for crystals in Fig. 7

Crystal number	Indium, atoms/cm³	Atmosphere and pressure, atm	Method of cooling
22	2.5×10^{17}	Cd 1	Quenched
16	None	Cd 1	Slow-cooled
17 Nose	None	Cd 1	Slow-cooled
17 Tail	None	Cd 1	Slow-cooled
30	2.5×10^{17}	Cd 1	Quenched
32	2.5×10^{17}	Te 1	Quenched
29	2.5×10^{17}	Cd 1	Quenched

The modified Bridgman method was developed primarily to grow high-resistivity material for gamma detectors and optical modulators. It has been useful for growing material for the study of impact ionization (21) and superradiance (22) in CdTe where reproducibility is important. An example of this is in Fig. 8 in which $P_{Cd} = 0.8$ is plotted on a T-X diagram of the existence region. At this pressure the defect concentration as a function of temperature is given. If a donor is added to the melt, then the entire excess Te side becomes high resistivity. Reference to Fig. 8 also shows that if solution growth takes place on the excess cadmium side or excess tellurium side, retrograde solubility takes place. Thus as the crystal cools after growth, cadmium or tellurium atoms will have to precipitate out in the material. We have noticed that CdTe grown from cadmium solutions, tellurium solutions, and from the melt at 1 atm of cadmium pressure differ in the cell constant. For cadmium solution grown crystals a value of $a = 6.4794$Å was obtained. For tellurium solution, $a = 6.4823$Å and for melt growth at $P_{Cd} = 1$ atm, $a = 6.4805$Å.

Borsenberger *et al.* (23) and Woodbury *et al.* (24) suggest that the dominant Te defect is an electrical neutral interstitial defect which correlates with our increase in lattice size. An electrically neutral Te atom could fit in an interstitial site, causing an increase in cell size, easier than a negatively charged Te atom which is much larger. An antistructure configuration does not seem very logical in view of the difference in the atom sizes. Neither does the I-A or S-A structure seem possible. For the cadmium-rich side it is generally agreed by many authors that the dominant defect is a cadmium interstitial. A method currently

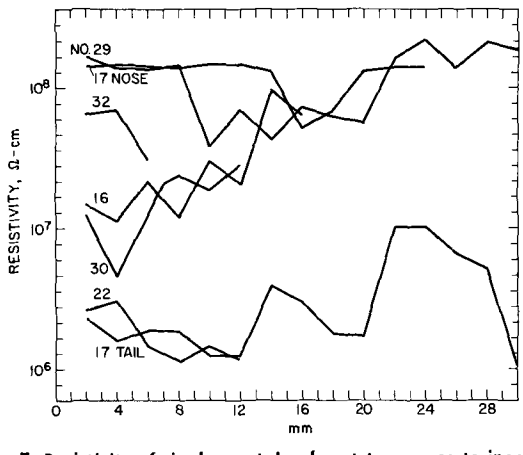

Fig. 7. Resistivity of single-crystal rods cut transverse to ingots

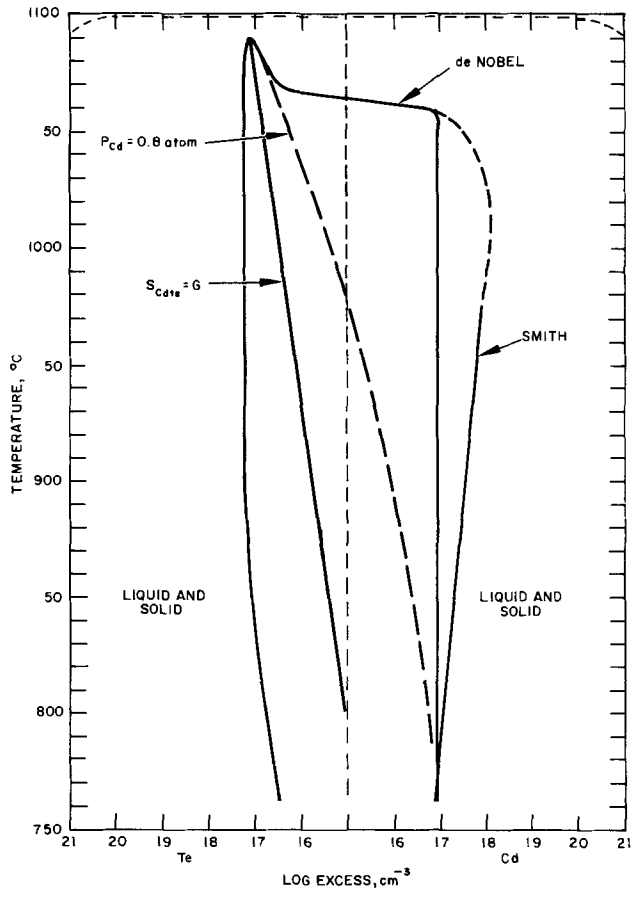

Fig. 8. Expanded phase diagram of CdTe

being investigated is vapor growth. The $S_{CdTe} = G$ line (Fig. 8) indicates that vapor growth takes place entirely in the existence region and depending on the temperature will approach stoichiometry. This method eliminates the high-temperature liquid phase, and bypasses the retrograde solubility curve with the added bonus of being low-temperature operational and self-purifying. As with any vapor growth, the greatest problem will be to make large single crystals. For gamma detector use the problem is not too severe, but for the optical modulator there is much to be done.

Acknowledgments

The author wishes to acknowledge the support of this work by the Atomic Energy Commission, the Office of Naval Research, The Air Force Flight Dynamics Laboratory, and particularly by the Hughes Research Laboratories. In addition, the assistance of Robert A. Walker in the preparation of the crystals is greatly appreciated.

Manuscript submitted Dec. 18, 1970; revised manuscript received *ca.* May 26, 1971.

Any discussion of this paper will appear in a Discussion Section to be published in the June 1972 JOURNAL.

REFERENCES

1. D. de Nobel, *Philips Res. Rept.*, **14**, 361 (1959).
2. J. Weidel, *Z. Naturforsch.*, **9a**, 697 (1954).
3. N. F. Shvartsenau, *Soviet Phys.-Solid-State (English Transl.)*, **2**, 797 (1960).
4. J. S. Blakemore, K. C. Nomura, and J. W. Schultz, *J. Appl. Phys.*, **31**, 2226 (1960).
5. V. E. Bottom, *Science*, **115**, 570 (1952).
6. T. J. Davis, *J. Appl. Phys.*, **28**, 1217 (1957).
7. S. A. Semendovich and N. N. Astashev, *Zh. Techn. Fiz.*, **28**, 725 (1958).
8. G. A. Silvey, V. J. Lyons, and V. J. Silvestri, *This Journal*, **108**, 653 (1961).
9. B. N. Aleksandrov and B. I. Yerkin, *Fiz. Metal. i Metalloved.*, **9**, 362 (1960).
10. M. R. Lorenz and S. E. Blum, *This Journal*, **113**, 559 (1966).
11. Masami Yokozawa, S. Otsuka, and S. Takayanagi, *J. Appl. Phys.*, **4**, 1080 (1965).
12. H. H. Woodbury and D. T. F. Marple, AFFDL-TR-70-3 (Air Force Flight Dynamics Laboratory, January 1970).
13. Bell and Howell Research Center, Pasadena, California.
14. M. Inoue, I. Termato, and S. Takayanagi, *J. Appl. Phys.*, **33**, 2578 (1962).
15. M. R. Lorenz, *J. Phys. Chem. Solids*, **23**, 939 (1962).
16. R. C. Whelan and D. Shaw, *Phys. Status Solidi*, **29**, 145 (1968).
17. F. T. J. Smith, *Trans.* AIME, **1**, 617 (1970).
18. R. K. Zanio, *Appl. Phys. Letters*, **15**, 8 (1969).
19. M. R. Lorenz and B. Segall, *Phys. Letters*, **7**, 18 (1963).
20. G. Mandel, *Phys. Rev.*, **134**, A1073 (1964).
21. Gerald S. Picus, Donald F. DuBois, and Lynette B. Van Atta, *Appl. Phys. Letters*, **12**, (3), 81 (1968).
22. Lynette B. Van Atta, Gerald S. Picus, and Amnon Yariv, *ibid.*, **12**, (3), 84 (1968).
23. P. M. Borsenberger and D. A. Stevenson, *J. Phys. Chem. Solids*, **29**, 1277 (1968).
24. H. H. Woodbury and R. B. Hall, *Phys. Rev.*, **157**, (3), 641 (1967).

Electrical Breakdown in Anodic Oxide Films on Zircaloy-2

N. Ramasubramanian* and T. Trottier

Chalk River Nuclear Laboratories, Atomic Energy of Canada Limited, Chalk River, Ontario, Canada

ABSTRACT

In Zircaloy-2/anodic oxide, 250 to 2500Å thick/gold structures, three types of electrical breakdown characteristics have been observed. By comparing the breakdown characteristics of oxide films grown on the alloy in the as-received condition and vacuum-cooled or quenched from the β phase conditions (Widmanstätten and martensitic type structures, respectively) it was possible to identify the location of a majority of the initial breakdown spots with that of a few of the second-phase particles.

A study of electrical breakdown in metal-insulator-metal structures is complimentary to electrical conductivity measurements. By suitable experimental procedures distinction can be made between the properties of weak spots in the insulator and those of the bulk (1). We have observed electrical switching in zirconia films, grown by thermal and anodic means on zirconium and a number of its alloys. Areas of impurity and intermetallic precipitates have been identified as

* Electrochemical Society Active Member.
Key words: Zircaloy-2, anodic oxide, second-phase particles, electrical breakdown.

localized paths for electron conduction in these oxide films (2). A study of the electrical breakdown characteristics of these films was undertaken to locate the weak spots present and to understand processes involved in the destruction and possible variations in behavior with changes in the oxide thickness. The results obtained on Zircaloy-2 are presented here.

Experimental

The hot-rolled Zircaloy-2 (Zr-1.5% Sn-0.1% Fe-0.1% Cr-0.05% Ni), *i.e.* as-received material was supplied by Wah Chang Corporation. Specimens 2 x 2 cm carrying a short stem were cut from 0.1 cm thick sheets, mechanically polished, pickled in a hydrofluoric-nitric acid mixture and washed in water. Some samples were given a heat treatment to produce different metallographic structures. These were either vacuum-cooled or water-quenched from the β phase to give Widmanstätten and martensitic type structures, respectively. Details of the technique can be found in a paper by Holt (3). Following the heat treatment the above procedure for surface preparation was followed.

Anodic oxide films were grown in saturated solutions of sodium nitrite and ammonium borate, 0.1% potassium hydroxide and 1*N* potassium nitrate solutions by fixed voltage anodization to various thicknesses. The maximum current density during a step was 1 mA/cm^2 and the current was allowed to decay to ~0.05 mA/cm^2. Oxygen evolution during the various anodizing steps was more vigorous (visual observation) on the heat-treated samples than on the as-received material. A growth constant of 28 Å/V was used for estimating the thicknesses (4). Gold counterelectrodes 3 and 6 mm in diameter and 1000-1500Å thick were evaporated through masks; in a single operation on four specimens at a time using a specimen to source distance of ~10 cm. Each specimen carried a minimum of four diodes. The diodes were tested in an evacuated, helium-filled tube and also in air on the stage of an optical microscope. The series resistance for measuring the current varied in the 10^2 to 10^4 ohm range. Conventional electronic equipment (Keithley electrometers and a Moseley x-y recorder) was used to trace the $i \times V$ curves and a Tektronix oscilloscope, Type 564 to trace $i \times t$ characteristics. The breakdown areas were examined on a scanning electron microscope.

Results

As-received Zircaloy-2.—Oxide films 250-2500Å thick were tested. The d-c resistivities of these films were $\geq 10^{12}$ ohm-cm. Their behavior could be broadly classified into three categories.

"Single-hole" breakdowns.—All the specimens tested (anodized to various voltages in the range 25-80V) showed "single-hole" breakdowns of the self-healing type (1), the first ones occurring at and above about 15V. In Fig. 1, $i \times V$ curves obtained is a typical case are shown; for the sake of clarity only a few of the tracings are included. The diode carrying a 50V (~1400Å) film was set up on the stage of an optical microscope. When the d-c voltage across the diode was gradually increased, a sudden current burst was observed at 37V and, simultaneously, light emission spots were seen on the gold surface. Microscopic examination showed the spots to be "single-hole" breakdowns where gold, oxide, and some of the alloy had been evaporated. The average frequency of the first spots to appear was 10/cm^2.

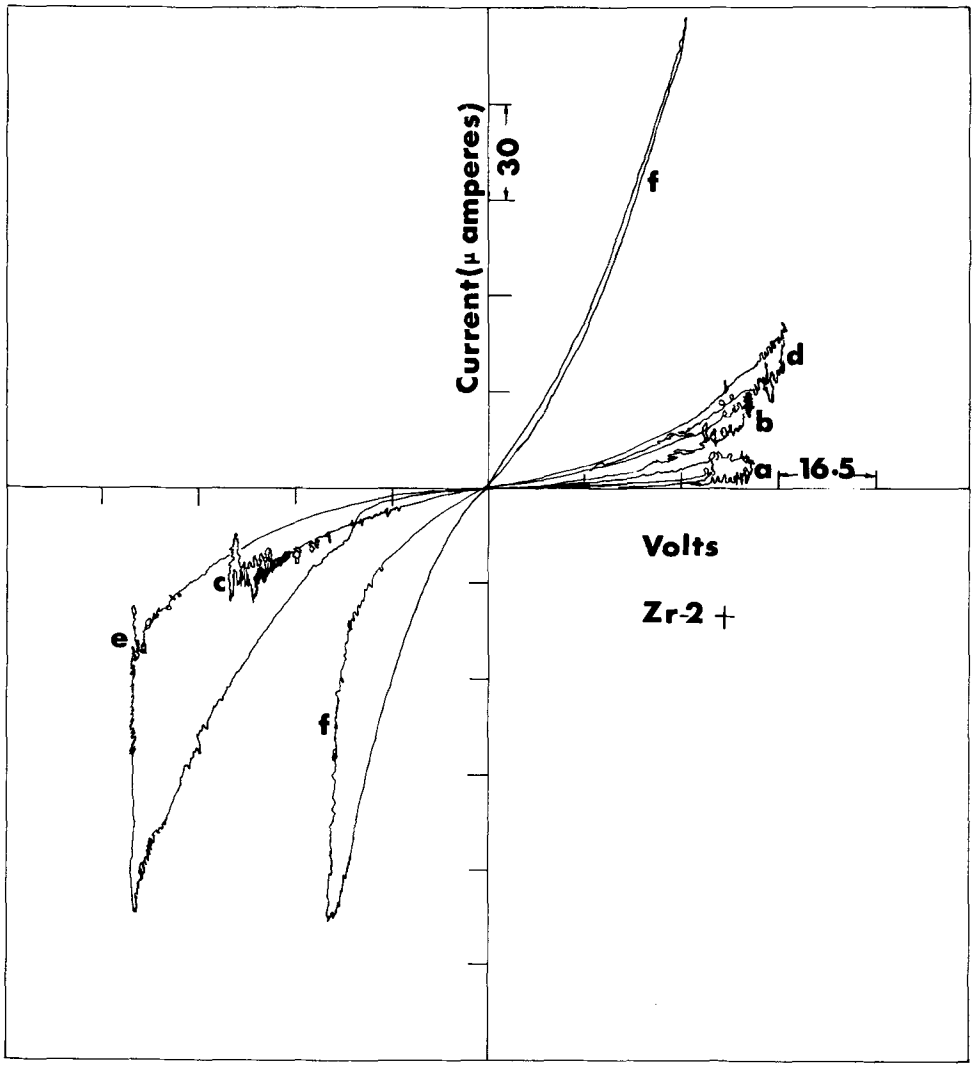

Fig. 1. Current bursts and increase in conductivity associated with "single-hole" breakdowns in Zircaloy-2/1400Å anodic oxide film, grown in KNO_3/gold (0.27 cm^2); tracing of x-y recorder plots: a, atmospheric conditions; b and c, in vacuum at room temperature: d, in helium at 190°K; and e and f, in helium at 80°K.

As the applied voltage was increased additional current bursts associated with light emission spots were observed and the current through the diode increased with the increasing number of breakdowns. The diode was then placed in the sample cell, evacuated and tested under vacuum at room temperature, then filled with helium and tested at 190 and 80°K. More breakdowns occurred over the range of 15-45V. The following characteristics were observed, in general, regarding the breakdowns and current bursts: (*i*) during a period when the applied voltage was being reduced current bursts and light emission still occurred, *i.e.* at lower voltages than during the preceding period of increasing applied voltage; (*ii*) similarly, during cathodic bias, breakdowns occurred at lower voltages than in the previous anodic step and vice versa and; (*iii*) the freshly produced breakdown spots spread in a radial fashion around a previously formed one.

The breakdown characteristics were all similar whether the test was carried out in atmospheric conditions, in vacuum at room temperature, or in helium at 80°-300°K. No effects of polarity on the Zircaloy was found. The impedance of the diode was checked on a GR 1680A automatic capacitance bridge at various stages during the testing. There were only small decreases in the capacitance readings, changing in the same fashion as the decrease in area of the gold electrode. The breakdowns were thus the self-healing "single-hole" type.

The micrographs of the breakdown areas and oscilloscope traces of the current rise during the breakdown are shown in Fig. 2. The breakdowns were mostly of the same size, 25 μm in diameter, and the density after a cycle similar to that in Fig. 1 was around $10^4/cm^2$. That a considerable amount of Zircaloy is evaporated during a breakdown is clearly evident from the scanning electron micrograph showing the ruffled structure of a light emission spot. The oscillogram was traced using a 560 ohm series resistance to measure the current. It is readily seen that the current bursts in the recorder tracings in Fig. 1 do not indicate the true current rises during breakdowns. The poor response of the electrometer to the speed of the process responsible for the current transients results in a mere jitter in recorder tracings. From the oscillogram a current density of 10^3 A/cm^2 during light emission, can be estimated assuming the area of current flow to be that of the whole breakdown region, and that the evaporated gold in that region was not destroyed (thus enabling the maximum current to be traced). The current rise and the fall to nearly half the maximum value occurred in a microsecond; a gradual fall to 5% of maximum occurred over 100 μsec.

Delayed breakdown.—With some diodes, carrying a 40-80V anodic oxide film, only the leakage current flow was detected at 80 and 190°K when applied potentials of both polarities were increased to near the forming voltage. Similarly at room temperature a positive bias on the alloy to near the forming voltage was without any influence on the current flow. Varying the time of holding at various applied voltages also did not result in any changes. But when the alloy was made negative to about 15V and held at that potential for ½ to 2 min current bursts associated with the appearance of a few light emission spots on the diode surface were noticed. The diode simultaneously became highly conducting. Breakdown areas had the same appearance as those shown in Fig. 2.

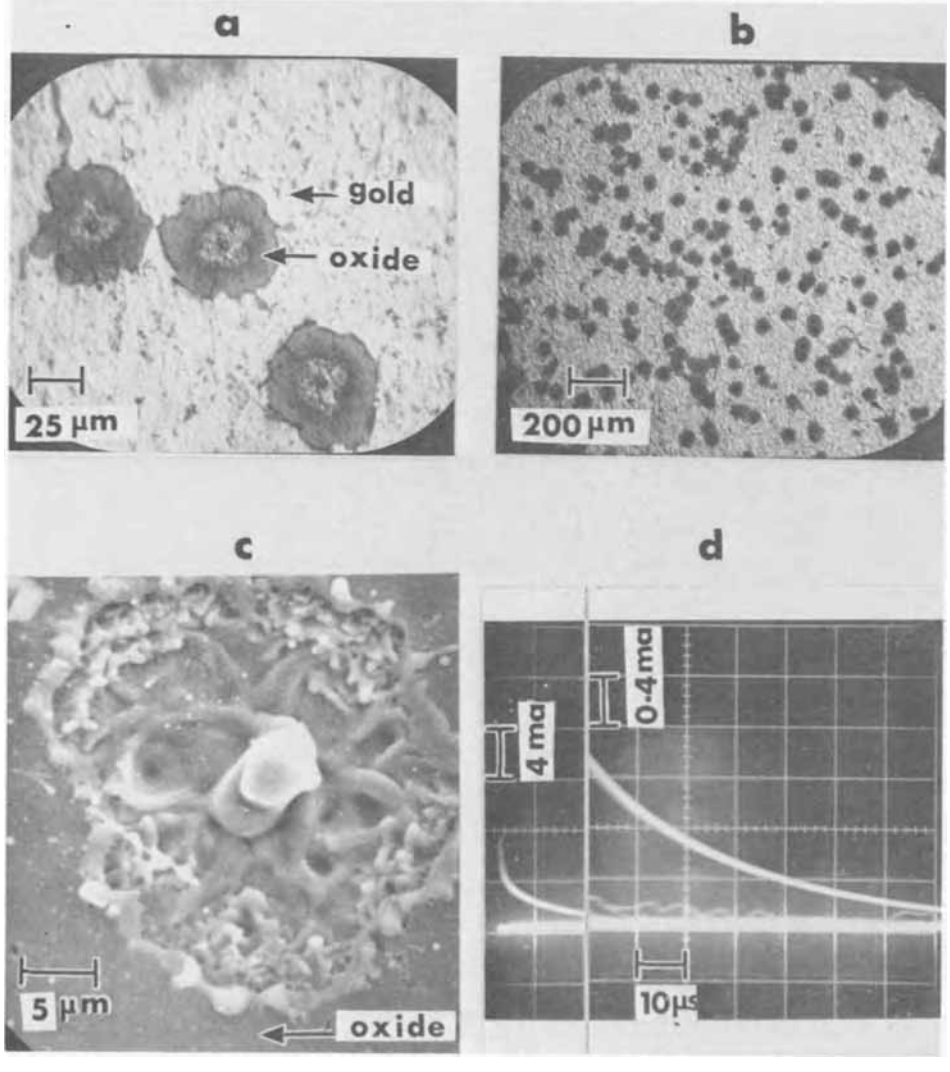

Fig. 2. Optical and scanning electron micrographs and current-time oscillograms of the single-hole breakdowns associated with the current bursts in Fig. 1. (a) First breakdown spots, (b) after tracing curve f in Fig. 1, (c) scanning electron micrograph of a breakdown and, (d) current transients during a breakdown.

Nondestructive breakdown.—This term is used to distinguish the current bursts which were not associated with any detectable microscopic changes on the gold surface from those involving "single-hole" breakdowns. The nondestructive breakdown was a chance occurrence and was detected only with a few diodes. In the temperature range of 80°-300°K these current bursts were observed at applied potentials of ±5 to 10V. With oxide films <750Å thick, the diodes invariably were highly conducting subsequently. The oscillograms of current rise were similar to that in Fig. 2 but the currents were two orders of magnitude less.

A total of 150 diodes distributed among 30 specimens were tested. The delayed type "single-hole" breakdowns were the most common; about 70% of the diodes exhibited this type. The nondestructive type of breakdown was a chance occurrence and was observed on ~10% of the diodes.

Heat-treated specimens.—Almost all the tin in the alloy is in solid solution in α zirconium in the as-received material. The alloying additions Fe, Cr, and Ni are precipitated as intermetallics of zirconium and are distributed uniformly through the alloy matrix in sizes ranging from ~0.5-2.5 μm in diameter. When the alloy is cooled in vacuum from the β phase (a nominal rate of 11°/sec from 1050°C), Widmanstätten morphology, with a parallel plate structure of α zirconium containing mostly tin in solid solution, is obtained. There is microsegregation of alloying additions; these are precipitated as intermetallics in between the α platelets. On quenching from the β phase a martensitic type structure results in which tin as well as the other alloying additions are in solution with no detectable microsegregation. An indication of a slight enrichment of iron at the grain boundaries was noticed in the electron microprobe analysis (3, 5).

In the as-received material carbon, phosphorus, and silicon are present in ppm quantities. These elements have very low solubilities in both the α and β phases of zirconium and probably exist as second-phase precipitates. These impurity precipitates, numbering about $10^3/mm^3$, are considered as the likely sites for nucleation of the α platelets (3).

Vacuum-cooled specimens.—A total of 30 diodes, the oxide thickness varying in the 1200-2500Å range, were tested. They all exhibited the delayed type of breakdown described previously. A typical set of data, $i \times V$ curves and scanning electron micrograph of one of the first breakdowns associated with the current bursts, is shown in Fig. 3. The potential across the diode was measured by direct connection to the oscilloscope's input; sample impedance was obviously higher than that of the scope's amplifier input and hence the larger current flow. The diode was first tested at 80° and 190°K; the Zircaloy was held for over 2 min at various potentials up to ±25V. Only the leakage current was measured. Then tracings in Fig. 3 were made at room temperature, the anodic bias being the first step. In the 13-19V region of negative bias on the alloy current bursts were observed following a waiting period of ~½ min at 13V. The gold surface showed two types of changes subsequent to the current bursts in the $i \times V$ tracing; a few darkened circular areas ~5 μm in diameter and a number of isolated "single-hole" breakdowns. The "single-hole" breakdowns were all centered on the boundaries between the α platelets.

The optical and scanning electron micrographs of the initial breakdowns in films of different thicknesses grown in 0.1% KOH solution are shown in Fig. 4. No variation of the breakdown voltage was found with changes in the anodizing voltage; all the initial breakdowns occurred when the alloy was biased negative to 18 ± 2V. The frequency of occurrence of these was on the average $10/cm^2$, same as that obtained with the as-received material. Isolated breakdowns were of the ordinary kind to be observed. The occurrence of a group of four or more breakdowns as shown in Fig. 4

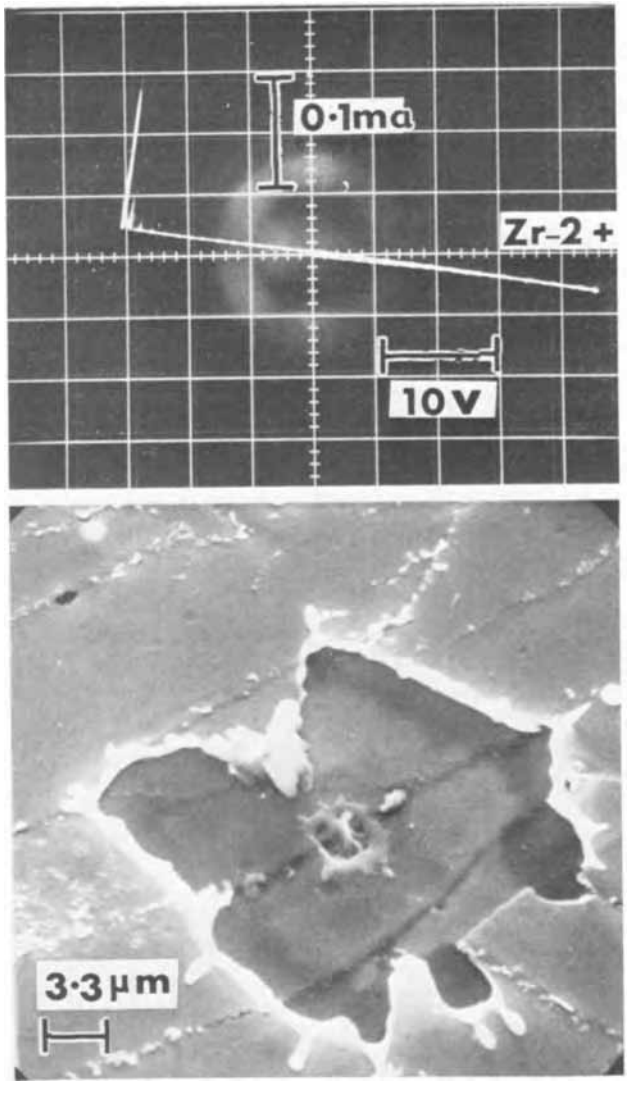

Fig. 3. Zircaloy-2 was vacuum cooled from the β phase (Widmanstätten morphology) and anodized to 80V in ammonium borate; current-voltage curves and scanning electron micrograph of one of the initial breakdowns when tested at atmospheric conditions.

(a) was uncommon and these forming any regular patterns was just accidental.

All these initial breakdowns (excepting a few which were located at the intersections of two or more boundaries) were centered on the boundaries between the α platelets.

The series resistance in the circuit influenced the occurrence or not of a breakdown. When this was of the order of a few hundred ohms, breakdowns occurred. However, when the resistance was ≥2K ohm the diodes invariably switched to a high conductivity ON state without resulting in any detectable changes on the gold surface. On turning the diodes OFF (high-impedance state) using a current pulse, breakdown spots were seen, centered on the boundaries between the α platelets.

In Fig. 5 scanning electron micrographs of vacuum-cooled samples in the pickled and anodized conditions are shown. Electrolytic anodization has resulted in the growth of porous oxide ridges along the α platelet boundaries. Films grown in nitrite solution showed extensive cracking along these oxide growths. However, the entire area along a boundary was not covered by these porous oxide growths; there were some portions where the anodic oxide growth had a similar appearance to that on the α platelet. The α platelet boundaries housing the segregated material are sites

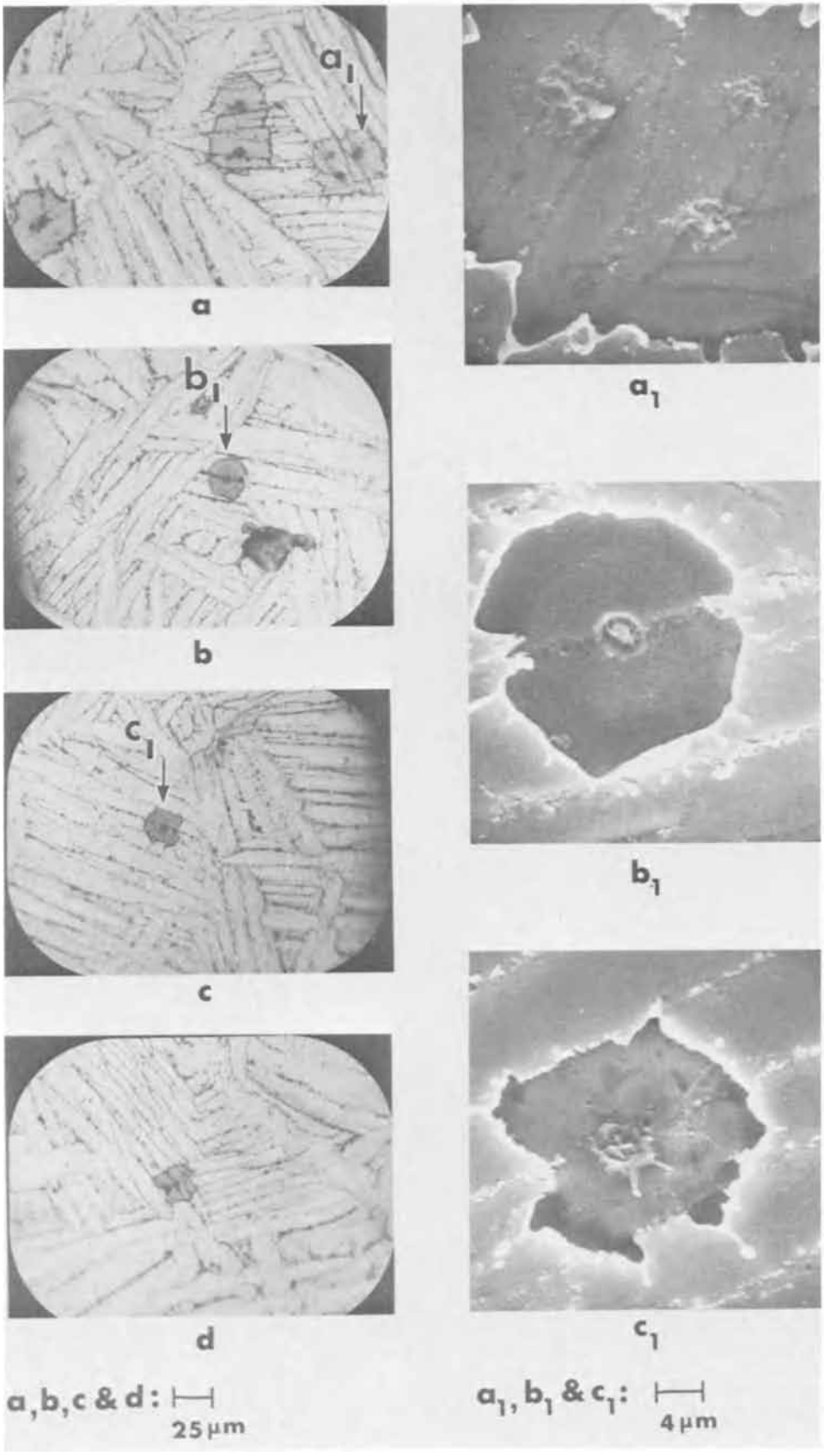

Fig. 4. Optical and scanning electron micrographs of initial electrical breakdowns in Zircaloy-2 (vacuum-cooled from the β phase)—anodic oxide grown in 0.1% KOH solution—gold structures; a, b, c and d—40, 50, 60, and 70V oxide films.

of heterogeneous oxide growth at lower anodizing voltages also is evident from Fig. 4.

Water-quenched specimens.—A typical set of data for a β-quenched sample tested at room temperature is shown in Fig. 6. After a holding time of 15 sec at −14V on the alloy current bursts were observed. Microscopic examination showed "single-hole" breakdowns with three out of a total of four located at the prior β grain boundaries.

With quenched samples a sensitivity towards nitrite and nitrate ions was noticed. The oxide films grown in $NaNO_2$ and KNO_3 solutions on these samples were highly heterogeneous with ridges of porous oxide growth. However, as in the case of as-received and vacuum-cooled samples, no specific correlation was

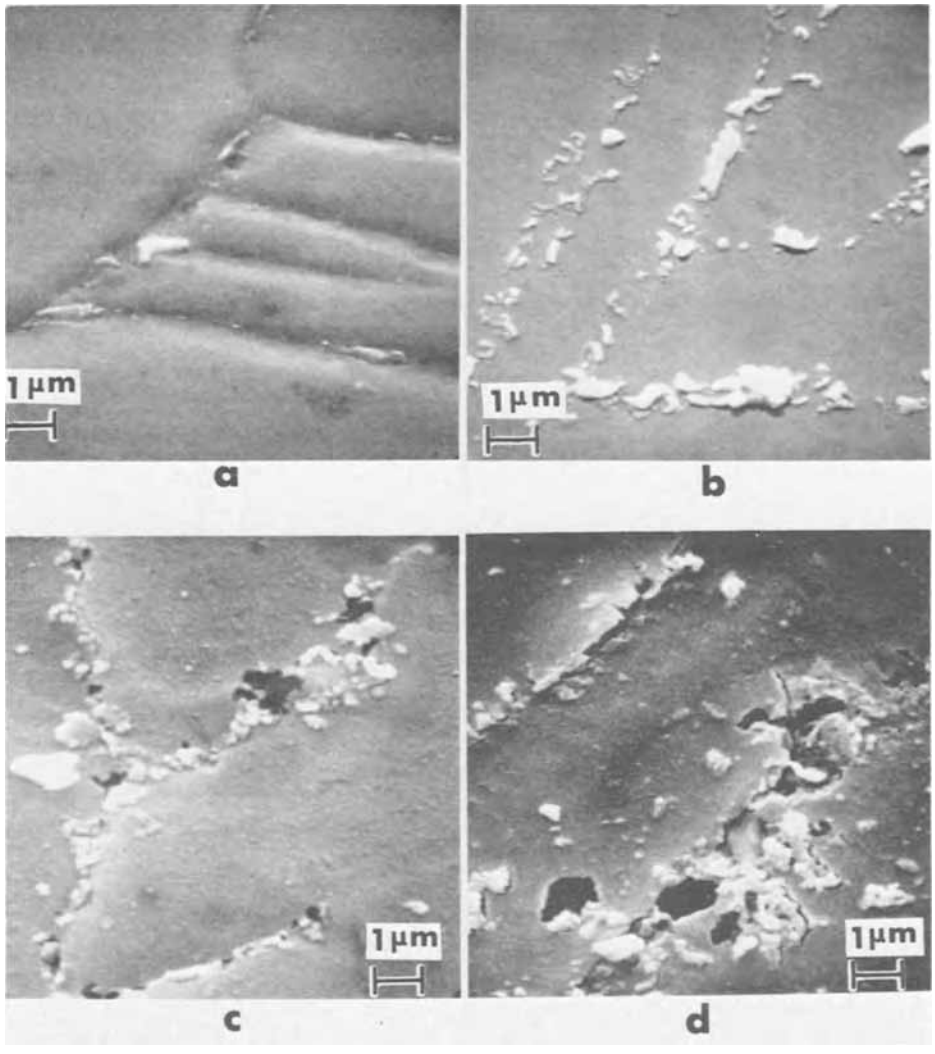

Fig. 5. Scanning electron micrographs of Zircaloy-2 vacuum-cooled from the β phase in (a) pickled and (b, c and d) anodized conditions; 80V films grown in (b) potassium hydroxide, (c) ammonium borate and, (d) sodium nitrite solutions.

found between the type of breakdown and the anodizing electrolyte used.

Discussion

Location of weak spots.—When the results obtained on the as-received and heat-treated materials are compared the advantages of using the Widmanstätten and martensitic type of structures for locating breakdown spots are obvious. In the as-received samples, because the second phase intermetallic and/or impurity precipitates are uniformly distributed and the breakdown areas are an order of magnitude larger in size (Fig. 7), it is difficult to identify the centers of the light emission and breakdown spots. In the case of oxide films on vacuum-cooled samples, there is a clear and definite indication that the boundaries between the α platelets are the location of first breakdowns. These boundaries house the second phase precipitates segregated during the nucleation and growth of the α platelets.

The composition and behavior towards anodization of the second phase particles in vacuum-cooled samples are likely to be different from those of the precipitates in the as-received material. However, the experimental observations, that the majority of the breakdowns in as-received material is the same delayed type as in the vacuum-cooled samples; that though the oxide films grown in nitrite and nitrate solutions are porous their breakdown characteristics are the same as those of the films grown in ammonium borate and potassium hydroxide; and that no systematic variation of breakdown voltage with oxide thickness is found, indicate the existence of a common source of weak spots in all cases. Moreover, in the case of anodic oxide films grown on the as-received material it has been shown that second phase precipitates are sites of localized electrochemical activity (2). Therefore, it is reasonable to assume that the conclusion reached in the case of vacuum-cooled samples regarding the delayed type of breakdown would be applicable to that of the as-received material also.

Areas of breakdown.—The intermetallic particles in Zircaloy-2 are either Zr-Fe-Ni or Zr-Fe-Cr phases. Information on the solid solubility of Fe, Ni, and Cr in zirconium oxide is not available and often the solubility in α zirconium is assumed to be applicable to the oxide case (6). In a detailed study on the growth of anodic oxide films on zirconium and Zircaloy-2, the importance of the oxide formed on the intermetallic particles in determining the current decay and leakage rate was pointed out by Cox (7). However, details regarding the nature of the oxide films formed on these particles and the mechanism of their growth are still largely in the speculative stage.

It is evident from Fig. 5 that thick porous oxide grows on the second phase particles in the α platelet boundaries during wet anodization. These boundaries for the most part are covered by such heterogeneous oxide growth. However, the average frequency of occurrence of the initial breakdowns is found to be only $\sim 10/cm^2$. Therefore it is unlikely that these porous oxides are the sites of first breakdowns. Moreover, in some experiments when the applied voltage was gradually increased the breakdowns occurring subsequent to the first ones were still isolated and their propagation along a boundary was not observed. Other than eliminating the possibility that the initial breakdowns occur in the pores of these oxide films, it is difficult at this stage, however, to correlate them with a specific type of oxide grown on the second-phase particles.

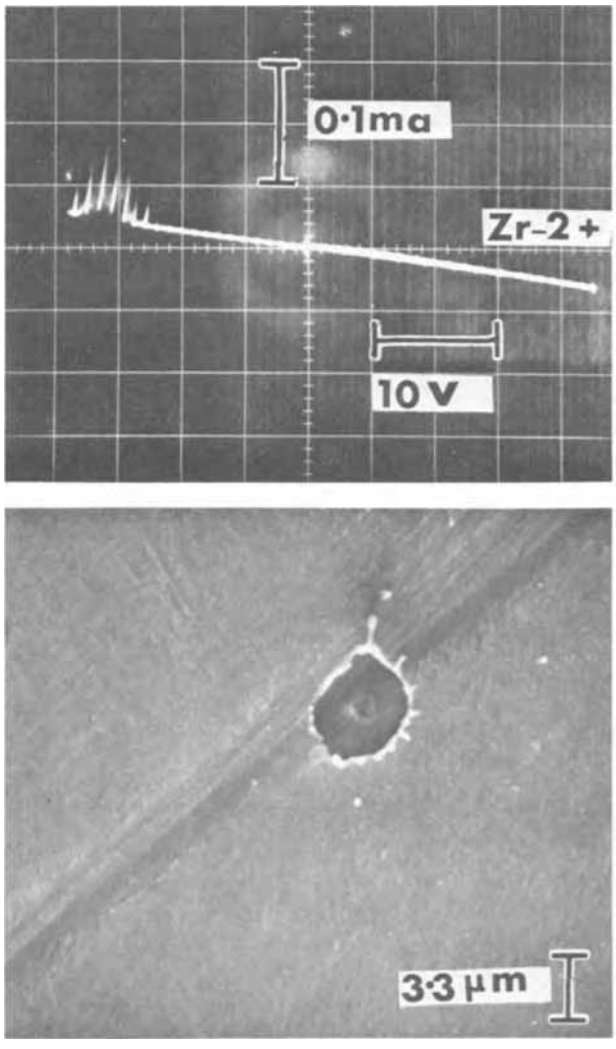

Fig. 6. β quenched Zircaloy-2 anodized in ammonium borate to 80V and tested at room temperature; current-voltage curves and scanning electron micrograph of one of the breakdowns.

Mechanism of breakdown.—The breakdown of these oxide films on the second phase precipitates is then considered to occur in two stages following the model suggested by Klein (1). A conducting channel is formed, which becomes thermally unstable, and triggers the breakdown by the discharge of the stored electrostatic energy. The "single-hole" and the nondestructive types of breakdown are obviously electronic in origin because they occur at liquid nitrogen and higher temperatures. The delayed breakdown does not occur at temperatures $<<300°K$ and is facilitated by a negative bias on the alloy. These characteristics and the necessity of a holding time indicate that an additional step of ionic migration is involved prior to the conducting channel formation. It is not clear at present, where the former two types of breakdowns occur in the as-received material.

During "single-hole" breakdowns in silicon dioxide breakdown spot current densities up to 10^{10} A/cm^2 have been estimated by Klein (1). Therefore the low current density of 10^3 A/cm^2 obtained in the present study might be due to two causes, *viz.* (*a*) gold at the breakdown site has partly evaporated and only part of the maximum current attained was recorded on the oscillogram and (*b*) the area of current flow at the instant of breakdown was smaller than the area observed subsequently. However, the conductivity change observed here agrees with that of Budenstein and Hayes (8) who reported in the case of silicon monoxide a change by a factor of 10^{10}. In this investigation a factor of 10^{11} is calculated for the rise in conductivity at the breakdown spot.

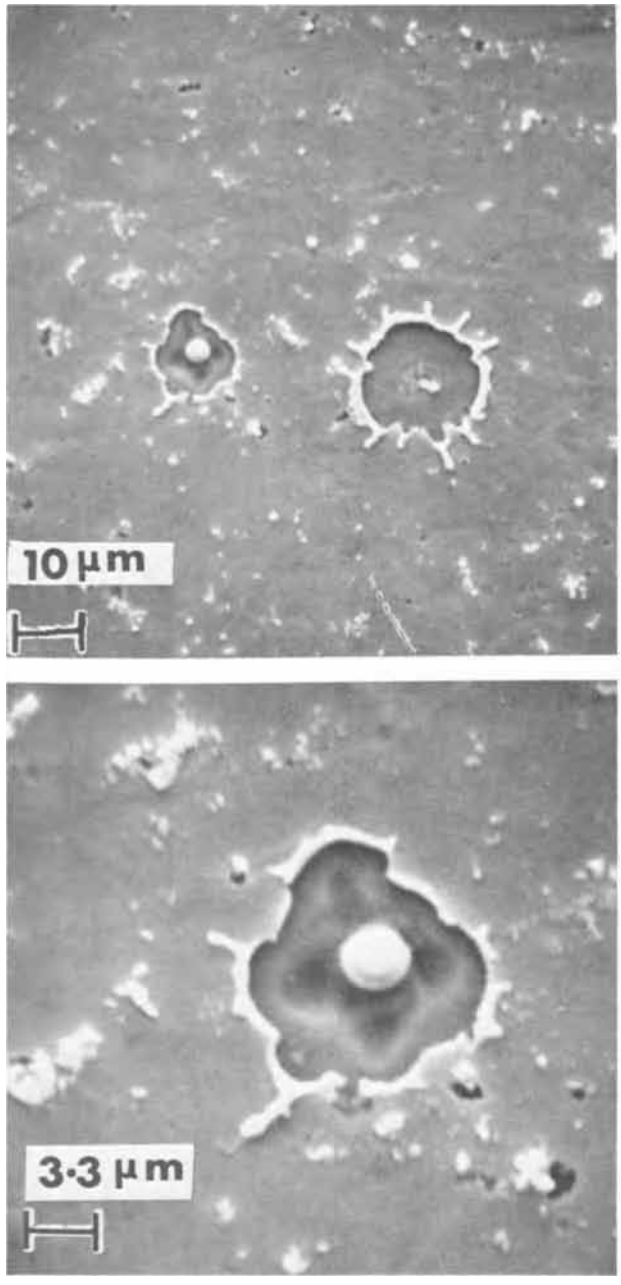

Fig. 7. Scanning electron micrographs of breakdowns in Zircaloy-2 (as-received material)—50V anodic oxide film grown in ammonium borate—gold structures.

Conclusions

Three different types of electrical breakdown are observed in anodic oxide films on Zircaloy-2: "single-hole" type at 80°-300°K associated with light emission and evaporation of the gold electrode, oxide and alloy material; delayed type at 300°K, the easy direction is with the alloy negative; nondestructive type at 80°-300°K and low voltages, without any evaporation of materials.

In oxide films grown on the as-received Zircaloy-2, more than 70% of the initial breakdowns is of the delayed type; these spots are identified with the location of a few of the second-phase precipitates in the alloy.

Acknowledgments

The authors wish to express their thanks to Mr. H. J. Arnal for his assistance with the scanning electron microscope and Dr. B. Cox for his encouragement and discussions.

Manuscript submitted Feb. 8, 1971; revised manuscript received ca. July 19, 1971.

Any discussion of this paper will appear in a Discussion Section to be published in the June 1972 JOURNAL.

REFERENCES

1. N. Klein, *This Journal*, **116**, 963 (1969).
2. N. Ramasubramanian, *ibid.*, **116**, 1237 (1969); AECL-3082, March, 1968.
3. R. A. Holt, *J. Nucl. Mater.*, **35**, 322 (1970).
4. N. Ramasubramanian, *This Journal*, **117**, 947 (1970).
5. R. A. Holt, Private communication.
6. S. Nomura and C. Akutsu, "Zirconium and Its Alloys", J. P. Pemsler, E. C. W. Perryman, and W. W. Smeltzer, Editors, p. 98 The Electrochemical Society Softbound Symposium Series, New York (1966).
7. B. Cox, *This Journal*, **117**, 654 (1970).
8. P. P. Budenstein and P. J. Hayes, *J. Appl. Phys.*, **38**, 2837 (1967).

The Chemical Polishing and Etch Pitting of Sapphire

R. G. Vardiman

Metallurgy Division, U. S. Naval Research Laboratory, Washington, D. C. 20390

ABSTRACT

Three dislocation etchants, H_3PO_4, KOH, and $KHSO_4$, and two chemical polishes, H_3PO_4 and $Na_2B_4O_7$ have been investigated as to their effective temperature and orientation ranges on sapphire. In addition the etchants are compared for effectiveness of dislocation pitting. It is found that the best pitting is obtained with $KHSO_4$ on the $\{2\bar{1}\bar{1}0\}$ plane, and KOH on the (0001) plane.

Sapphire (single crystal α-aluminum oxide) is an important and widely used material in modern technology. Characterization of its crystalline defects—in particular determination of the dislocation structure—is increasingly important in electronic, as well as mechanical applications. For those interested in observing the dislocation structure of sapphire by etch pitting, its high resistance to chemical attack creates some difficulties. Only a few etchants have been found which develop pits at dislocation sites, and these function only at rather high temperatures. They are further restricted as to their effective orientation range, although this has been defined in only one case (1).

The best known etchant for sapphire is phosphoric acid (H_3PO_4). Scheuplein and Gibbs (1) found dislocation pits for two types of sapphire surface orientations: within a few degrees of the basal plane (0001) at 320°C, and in the region of the $\{1\bar{1}01\}$ to $\{1\bar{1}02\}$ planes[1] at 375°C. Barber and Tighe (2) found that polishing and etching in phosphoric acid were highly temperature dependent; polishing for various planes occurred about 50°C above the etching temperature. They also used hot concentrated potassium hydroxide (KOH) for etching the basal plane. They observed that with both etchants the dislocation structure was often incompletely developed in subgrain boundaries. Alford and Stephens (3) used potassium bisulfate ($KHSO_4$) at 675°C to develop etch pits on the basal (0001) and prismatic $\{2\bar{1}\bar{1}0\}$ planes.

A number of chemical polishes have been reported. Besides the above mentioned phosphoric acid (2, 3), they include borax (4, 5) vanadium pentoxide (6), and potassium aluminum fluoride (3). Again, applicable orientation ranges are not well defined.

The present work compares the utility of the above three etches (H_3PO_4, $KHSO_4$, and KOH) in examining the dislocation structure of sapphire, as well as determining their effective orientation and temperature ranges. In addition, the polishing ranges of phosphoric acid and borax have been investigated.

Experimental Methods

Etching and polishing effects for specific planes were examined on sectioned rods or oriented disks obtained from Union Carbide or Hugo Keller Company. Orientation boundaries of etched or polished regions were determined by comparison of optical observations with Laue back-reflection x-rays on ⅜ in. diam spheres (obtained from Insaco). Although this method permits boundary positions to be defined to ±1°, there are two possible sources of variation. First, the distinction between adequate and inadequate etching or polishing represents a subjective judgment. Second, the boundary position may be a function of etching time and the procedure employed. To minimize this latter problem, all boundaries shown in this study define areas which appear adequately etched or polished after preheating the specimen in air and immersing it in the reagent for 3 min. Temperatures were measured with a chromel-alumel thermocouple, and were controlled to ±5°C. The handling of the various reagents is discussed in later sections.

With regard to the crystallography of sapphire, the hexagonal structural unit cell (7) ($c/a=2.73$) is used in this paper. Since the sapphire lattice has only threefold symmetry (Laue class $\bar{3}$m), some confusion is possible with the use of hexagonal indices. Therefore, orientation effects will be shown on stereographic triangles with strong x-ray reflections marked and indexed. This will distinguish between planes, such as $(10\bar{1}2)$ and $(1\bar{1}02)$, which have similar indices but are not identical as in the hexagonal system. As a guide to the stereographic triangles, some useful interplanar angles, as calculated from a computer program (8), are given in Table I.

X-ray topography was used as a check on the dislocation etching. Good resolution was obtained on the (0001) surface with the Berg-Barrett technique as described by Newkirk (9). With Cr radiation, the operative reflection on this case is $\{2\bar{1}\bar{1}6\}$.

Table I. Selected interplanar angles for sapphire ($c/a=2.73$)

	(0001)	$(2\bar{1}\bar{1}0)$	$(10\bar{1}2)$
$(1\bar{1}01)$	72.4°	34.4°	55.6°
$(1\bar{1}04)$	38.2°	—	47.0°
$(10\bar{1}2)$	57.6°	43.0°	—
$(2\bar{1}\bar{1}3)$	61.2°	28.8°	—

Key words: aluminum oxide, sapphire, dislocation, etch pits.

[1] Hexagonal structural unit cell, as used in this paper.

Surface Preparation

Mechanical polish.—All specimens obtained for this investigation had been initially mechanically polished in fine diamond paste to a scratch-free appearance. However, after treatment with one of the etchants (none of which dissolve sapphire at an appreciable rate at etching temperatures) the surface showed a highly scratched appearance. This effect has been noted by others (6). Hockey (10) has shown that after fine polishing, the surface is highly distorted and has a high dislocation density. Apparently this layer, less than 1μ thick, can be dissolved by the hot etchants to expose a surface which shows the effects of previous coarse grinding and polishing.

The simplest way to eliminate this effect is to vacuum anneal the specimen at about 1700°C for 2-3 hr. Some evaporation occurs during this treatment, and the resulting surface is sufficiently strain free that no scratch marks develop during etching. Only surfaces near the basal orientation are inappropriate for this treatment, as they tend to develop pits during evaporation.

Chemical polish.—The high temperature anneal described above is inappropriate for experiments involving nonequilibrium dislocation distribution. In this case, and also when the initial surface is not smooth, it is necessary to use a chemical polish which re-

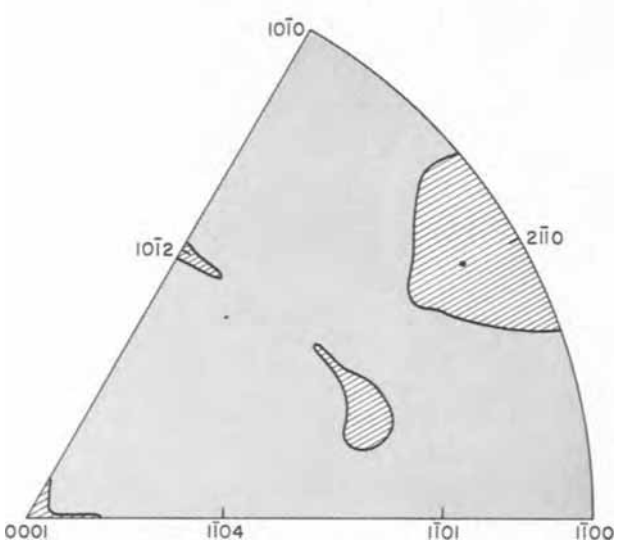

Fig. 1. Areas polished by borax at 850°C (stippled). Hatched regions develop pits.

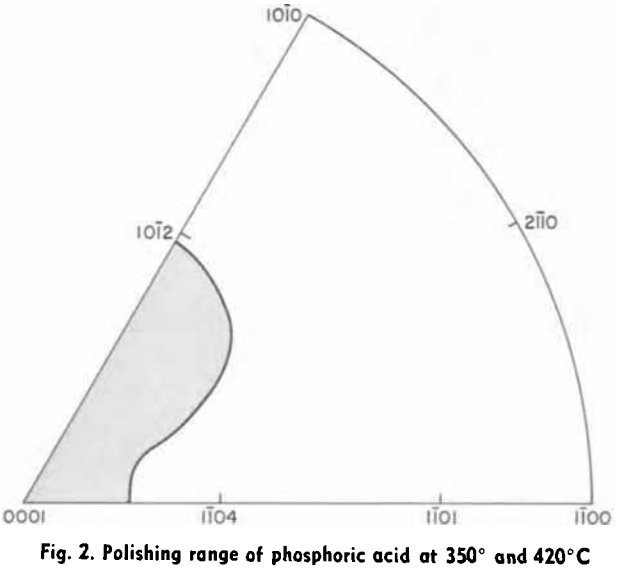

Fig. 2. Polishing range of phosphoric acid at 350° and 420°C

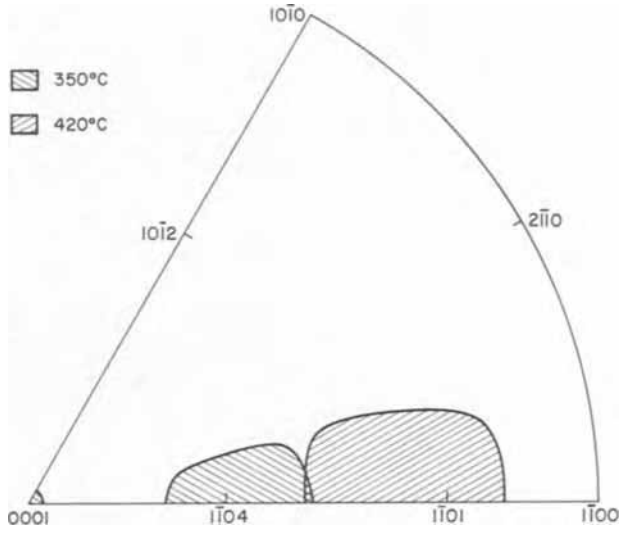

Fig. 3. Orientations adequately etched by phosphoric acid in 3 min at 350° and 420°C.

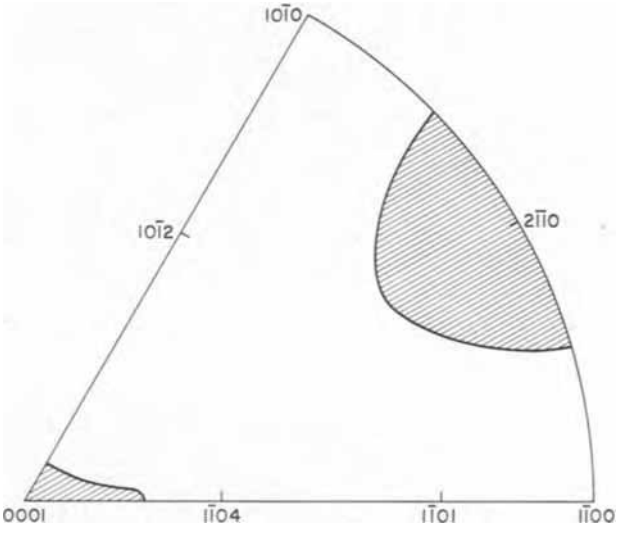

Fig. 4. Etch pitting range for potassium bisulfate for 3 min at 550°C (shaded).

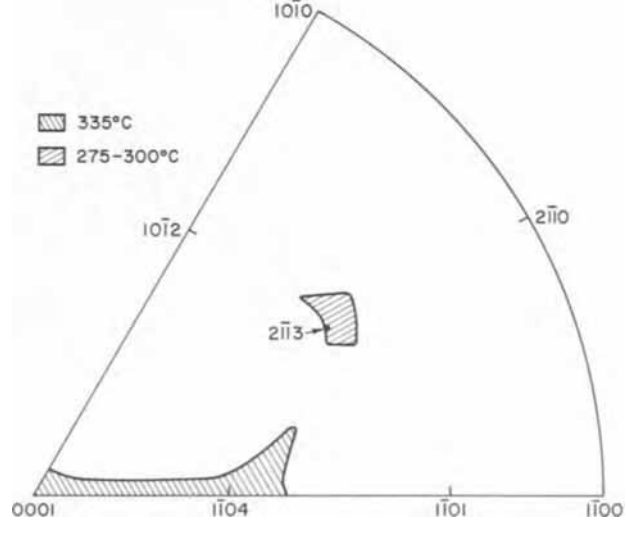

Fig. 5. Areas satisfactorily etch pitted by potassium hydroxide in 3 min at indicated temperatures.

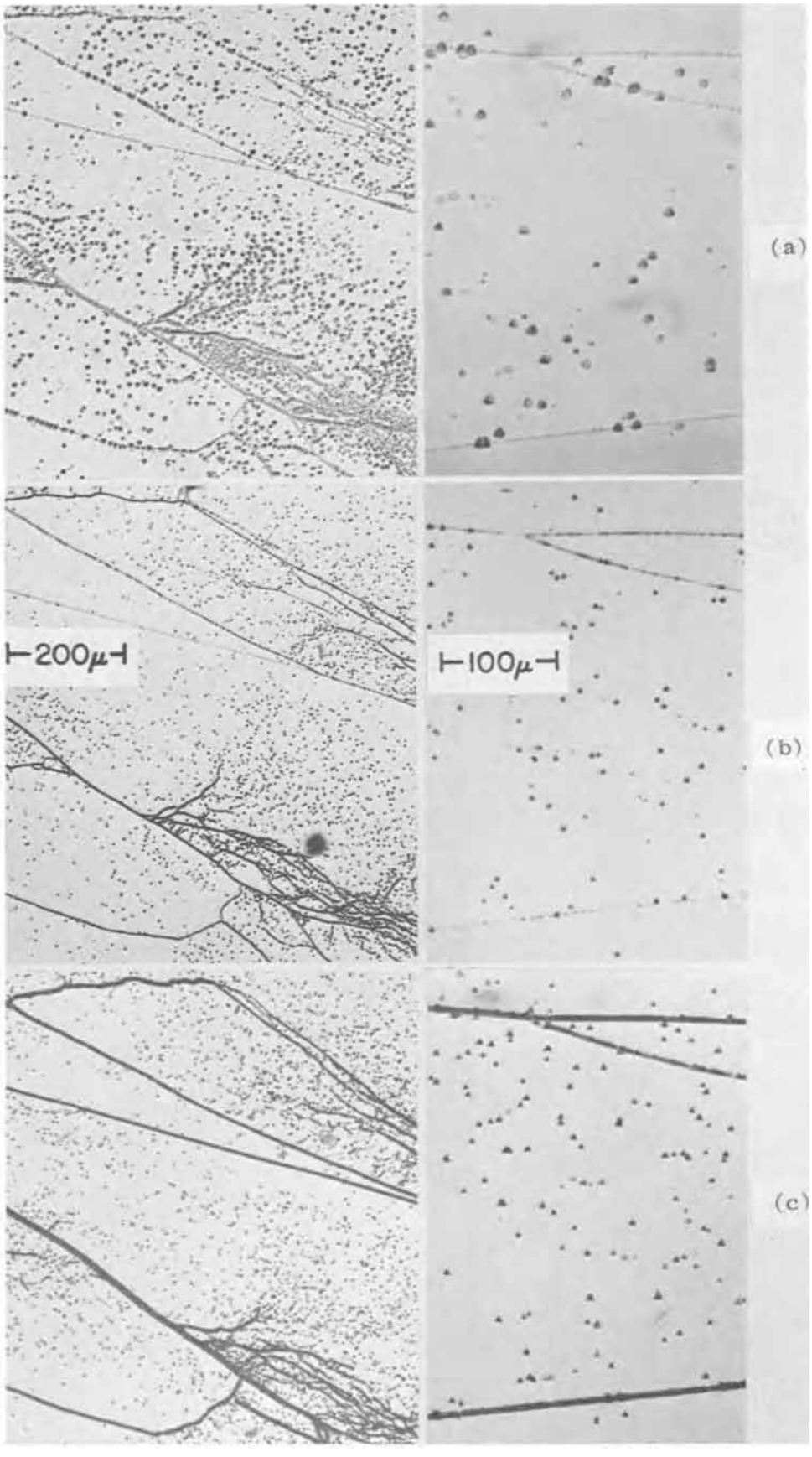

Fig. 6. (0001) surface of sapphire, etched 3 min in (a) phosphoric acid at 325°C; (b) potassium bisulfate at 500°C; and (c) potassium hydroxide at 350°C. Polished in phosphoric acid between etches.

moves material at a moderate rate. For most orientations (Fig. 1) good results can be obtained with molten sodium tetraborate, $Na_2B_4O_7$ (borax), above 800°C (5). The borax is melted in a platinum crucible. Material adhering to the specimen after polishing is then dissolved in boiling water, and any remaining surface film can be removed in dilute HCl. The dissolution rate of sapphire in borax varies little with orien-

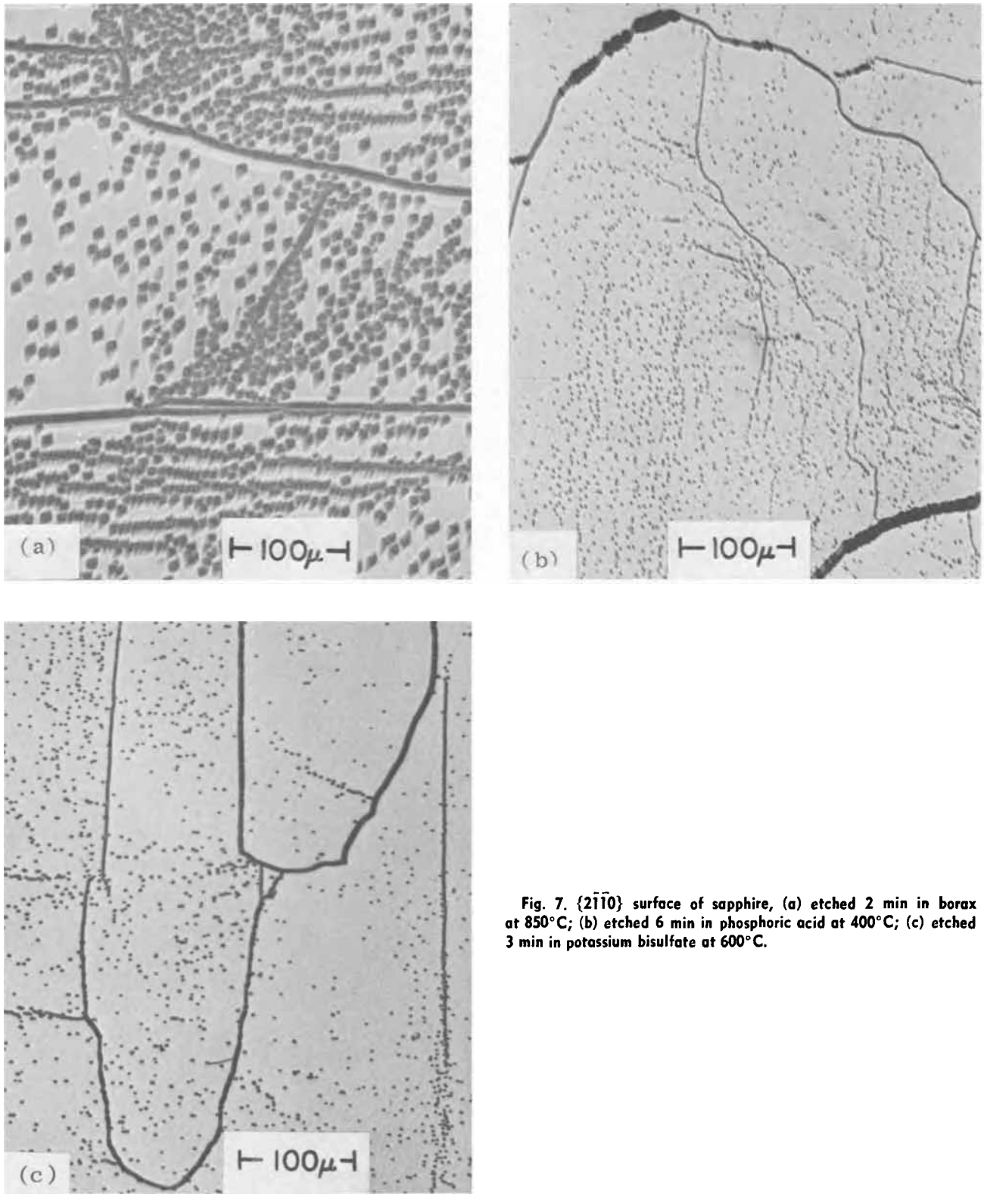

Fig. 7. $\{2\bar{1}\bar{1}0\}$ surface of sapphire, (a) etched 2 min in borax at 850°C; (b) etched 6 min in phosphoric acid at 400°C; (c) etched 3 min in potassium bisulfate at 600°C.

tation, and the resulting surface is microscopically smooth, except for orientations where pitting or roughness develops. These are principally the area near the (0001) plane and a larger area around the $\{2\bar{1}\bar{1}0\}$ plane, as shown in Fig. 1.

For polishing (0001) surfaces, one may use concentrated phosphoric acid (85%) at 420°C (3). The rate of attack of this acid is highly orientation dependent. Figure 2 shows the orientation range of polished surfaces at 420°C. Remaining orientations show little evidence of attack (except for pitting). Because reaction products may adhere strongly to the surface at this temperature, the specimen must be vigorously agitated. Using a large volume of acid (200-300 cc) for polishing is also helpful in this respect. Because of chemical changes, fresh acid should be used for each treatment. At these temperatures a Pyrex beaker may be used, but must be changed frequently due to the slow attack of the acid. Higher temperatures might extend the orientation range of polishing (2), but would require a forced-flow apparatus such as that described in Ref. (11).

Dislocation Etchants

We will describe here the orientation and temperature effects of the three etchants, and the manner of their use. In the next section we will discuss the quality of pitting at various orientations, and the utility of each etchant for determining the dislocation structure.

Phosphoric acid.—Pitting with this etch is highly temperature dependent. The basal plane etches at 320°C. Etching in an area near $(1\bar{1}04)$ begins at about 335°C, and as the temperature is increased, the etched region extends towards $(1\bar{1}01)$. The extent of the well-etched areas at 350°C and 420°C are shown in Fig. 3. At 420°C, the basal plane polishes (see preceding section) whereas the region around $(1\bar{1}04)$ is simply overetched. Longer times or higher temperatures extend the 420°C area toward $(2\bar{1}\bar{1}0)$ (see Fig. 7b). The precautions given in the remarks on polishing apply in using phosphoric acid as an etch above 400°C.

Potassium bisulfate.—A relatively easy etch to use, a small amount may be melted in a platinum crucible, and renewed when necessary with additions of sulfuric acid and $KHSO_4$ while cool. Little general dissolution of the sapphire is found with this reagent. The extent of the etched regions around the basal and prismatic planes at 550°C is shown in Fig. 4. Adequate etching can be obtained at this temperature for both orientations, but the basal plane pitting is more easily controlled at 500°C, while it is helpful to go to 600°C for the prismatic area. Boundaries of the etched regions are not particularly temperature dependent.

Potassium hydroxide.—This etch was prepared by adding KOH crystals to a concentrated aqueous solution until boiling no longer occurred at 350°C. Etched regions observed with this concentration of reagent are shown in Fig. 5. Little etching is observed below 320°C. However, the small area near $(2\bar{1}\bar{1}3)$ which etches below 300°C, can be very useful, since the axes of many Verneuil-grown boules fall in this region. Large areas suddenly develop pits around 325°C, but in most of these the pits cannot be identified with the dislocation structure. The exception is the area along (0001)-$(1\bar{1}04)$, where sharp triangular pits develop well around 335°C (see Fig. 6c), although they are weakly developed even below 320°C. There are two centers to this region where the pits are equilateral, at (0001) and near $(1\bar{1}04)$.

Etching-Comparison

Although dislocation etchants have not been found for a substantial portion of the orientations as shown by the stereographic triangles of Fig. 3-5, the areas which can be etched allow a determination of the complete dislocation structure of most crystals, and the examination of any potential slip plane. Not all of the etchants are equally good, however, and a comparison of the pitting on the basal and prismatic planes, where more than one etchant may be employed, is instructive.

(0001).—All three etchants develop dislocation pits on the basal plane. In Fig. 6, the same areas have been etched with each reagent after repolishing. Both H_3PO_4 6(a) and $KHSO_4$ 6(b) show areas of incomplete etching. This is particularly noticeable in certain sub-boundaries, as has been observed previously (2) for H_3PO_4. A substantial improvement is seen for KOH, Fig. 6(c). Here, pit size is much more uniform, and most sub-boundaries are completely pitted. Incomplete etching is also found in the $\{1\bar{1}01\}$-$\{1\bar{1}04\}$ area for phosphoric acid. It is possible that this is partly an impurity effect, and might not be observed in sapphire of different origin. Nevertheless, these data indicate that KOH would be the etchant of choice for the (0001)-$(1\bar{1}04)$ orientation range.

$\{2\bar{1}\bar{1}0\}$.—Although borax and phosphoric acid pit this plane, the results are not entirely satisfactory, as may be seen in Fig. 7. The borax pits 7(a) are shallow and poorly defined, while the phosphoric acid pits 7(b) are elongated and uneven in size. The clear superiority of potassium bisulfate is shown in Fig. 7(c). No gaps show in the sub-boundaries, and pit size is even more uniform than for KOH on the basal plane (Fig. 6c). Since a $\{2\bar{1}\bar{1}0\}$ plane may be found to intersect basal, pyramidal, and prismatic slip planes, this combination of plane and etchant is recommended where only one surface is to be examined.

Discussion and Conclusion

The similarity of the etching patterns in Fig. 6 indicates that these etchants produce pits only at dislocation sites. Repeated etching by H_3PO_4 on the basal plane and $KHSO_4$ on the prismatic plane show no change in the pit pattern or increase in the number of pits. Finally, a comparison of an x-ray topograph of the basal surface with the etch pit pattern produced by KOH on the same area in Fig. 8 shows a satisfactory correspondence. Whether all dislocation sites pit is

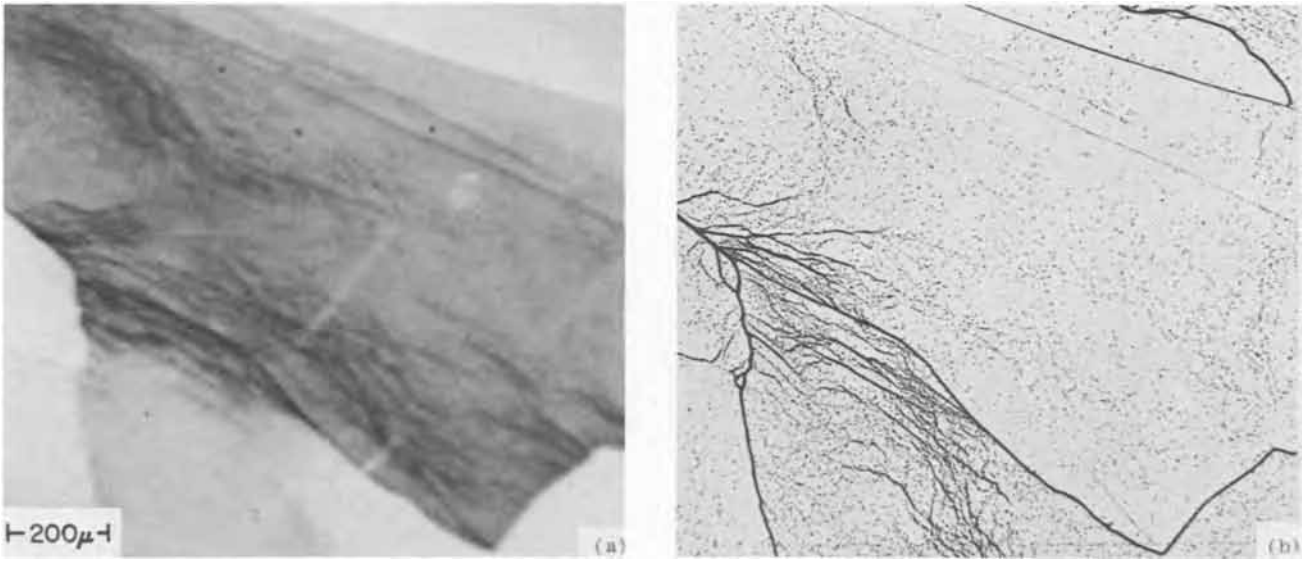

Fig. 8. (0001) surface of sapphire; (a) Berg-Barret x-ray micrograph, $\{2\bar{1}\bar{1}6\}$ reflection; (b) optical micrograph, etched 3 min in KOH at 350°C.

more difficult to determine. However, comparing Fig. 6 and 7, it would seem that uniformity of pit size and continuity in the sub-boundaries are good guides to an etchant's reliability. From this point of view, the dislocation structure of sapphire may be accurately determined by etch pitting with potassium hydroxide on planes in the range (0001)-{$1\bar{1}04$}, and by potassium bisulfate on planes in the vicinity of {$2\bar{1}\bar{1}0$}.

Acknowledgments

I wish to thank C. L. Vold, who made a number of x-ray topographs for these studies, and Dr. R. A. Meussner, who gave a very helpful critique of the manuscript. This work was supported by the Office of Naval Research and the Naval Air Systems Command.

Manuscript submitted April 16, 1971; revised manuscript received *ca.* July 9, 1971. This was Paper 2 presented at the Washington, D.C., Meeting of the Society, May 9-13, 1971.

Any discussion of this paper will appear in a Discussion Section to be published in the June 1972 JOURNAL.

REFERENCES

1. R. Scheuplein and P. Gibbs, *J. Am. Ceram. Soc.*, **43**, 458 (1960).
2. D. J. Barber and N. J. Tighe, *J. Res. Nat. Bur. Stds.*, **69A**, 271 (1965).
3. W. J. Alford and D. L. Stephens, *J. Am. Ceram. Soc.*, **46**, 193 (1963).
4. P. H. Robinson and C. W. Meuller, *Trans. Met. Soc. AIME*, **236**, 268 (1965).
5. A. G. King, *Materials Science Research*, Vol. 3, p. 529, W. W. Kriegel and H. Palmour III, Editors, Plenum Press, New York (1966).
6. M. M. Faktor, D. G. Fiddyment, and G. R. Newns, *This Journal*, **114**, 356 (1967).
7. M. L. Kronberg, *Acta Met.*, **5**, 507 (1957).
8. E. A. Metzbower, *N.R.L. Rpt.* 6919 (1970).
9. J. B. Newkirk, *Trans. Met. Soc. AIME*, **215**, 483 (1959).
10. B. J. Hockey, *J. Am. Ceram. Soc.*, **54**, 233 (1971).
11. N. J. Tighe, *Rev. Sci. Instr.*, **35**, 520 (1964).

The Morphology of Electrolytic Breakdown Products in Anodic Films on Silicon

J. Zahavi,[1] I. A. Blech, and J. Yahalom

Department of Materials Engineering, Technion—Israel Institute of Technology, Haifa, Israel

ABSTRACT

The local electrolytic breakdown regions in p-type Si were investigated. Large amounts of brittle material in the form of hills were seen to form during the breakdown. The material is amorphous, probably $SiO_2 \cdot (H_2O)_x$. The hills are severely cracked and have a residual tensile stress.

The morphology and crystallization of anodic oxide films under electrolytic breakdown voltage were previously reported for aluminum, tantalum, and titanium (1,2). It was found that the electrolytic breakdown of anodic films of aluminum and tantalum was associated with crystallization, whereas in titanium a crater-like morphology with a polycrystalline structure was revealed (1, 2). Vermilyea (3, 4) has found that some crystallization of tantalum anodic oxide films is observable after certain periods, depending on the anodizing conditions.

The structure and the effect of electrolytic breakdown of anodic oxide films on silicon were considered by some authors (5, 6). Schmidt and Owen (5) found that anodic films grown on silicon in phosphoric acid were of three types: completely structureless nonporous films, films with round spots of increased film thickness and films with round holes. Schmidt and Michel (6) found that electrolytic breakdown of anodic oxide films in p-type silicon was associated with severe damage to the oxides, when the voltage started to oscillate without rising any further. The present work is concerned with the morphology and structure of anodic films on silicon under electrolytic breakdown.

[1] Present address: Department of Metallurgy and Mining Engineering, University of Illinois, Urbana, Illinois, 61801.

Key words: electrolytic breakdown, breakdown, silicon, silicon oxide.

Experimental Results

A (111) oriented p-type silicon wafer (~0.015 ohm-cm) was anodized in 0.8% and 80% wt H_2SO_4 without stirring at a constant current density of 20 mA/cm^2. The anodizing circuit has been described previously (7). In the concentrated solution, the cell emf increased with time, reached a value of 52V in about 10 sec, then dropped to 36V in another 10 sec, climbed slowly (24 sec) to 38V, after which it remained substantially constant (Fig. 1).

The cell emf in the dilute solution can also be seen in Fig. 1. The forming emf increased quickly (~2 sec) to 22V and more gradually to 70V in 8 min. During the next 12 min it dropped to 45V and then remained almost constant with a very slight decrease. No distinct breakdown voltage could be defined.

Anodizing for shorter periods than the first breaking point of the curve in Fig. 1 caused no apparent change

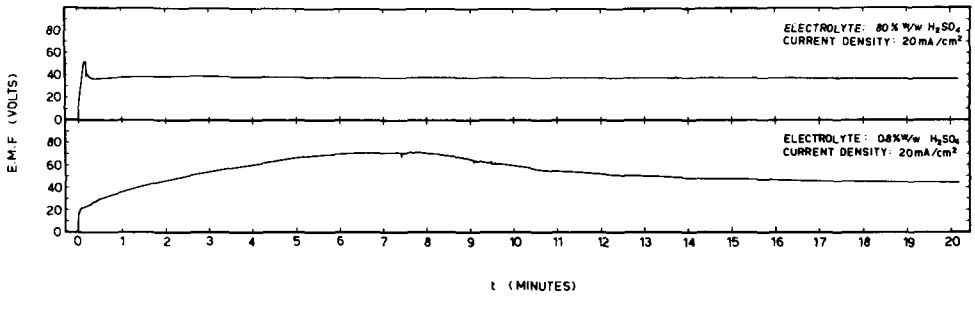

Fig. 1. Cell voltage transients during anodizing.

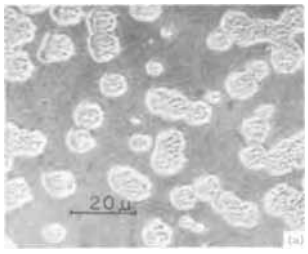

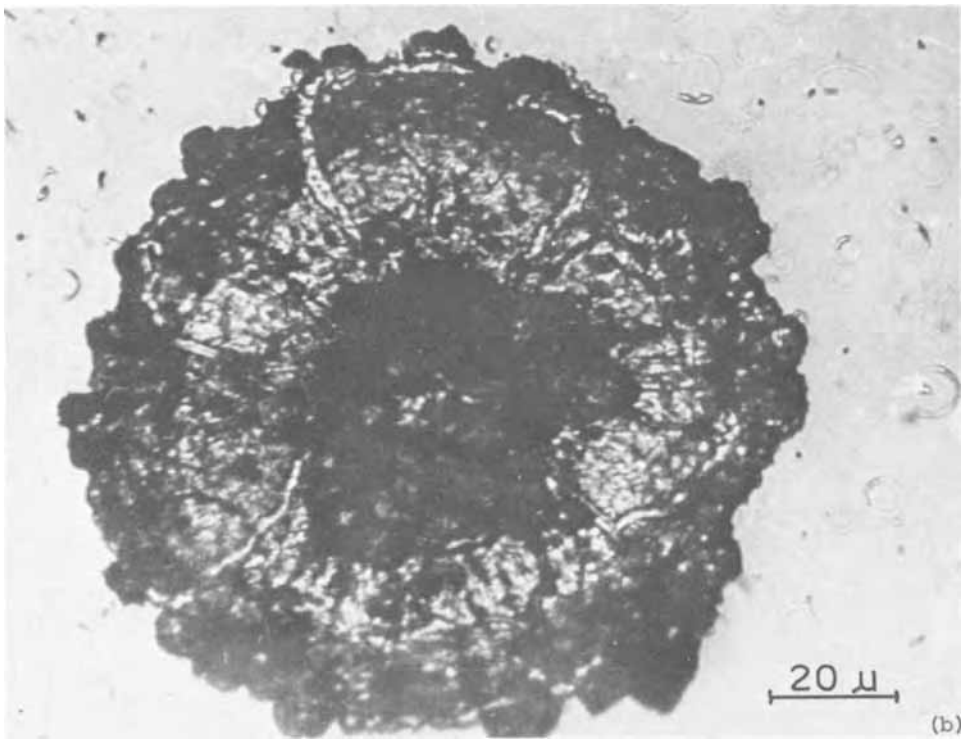

Fig. 2. Optical micrograph of breakdown regions after 15 min anodization. (a) 0.8% H_2SO_4, (b) 80% H_2SO_4.

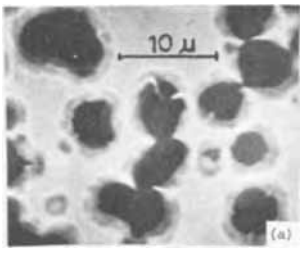

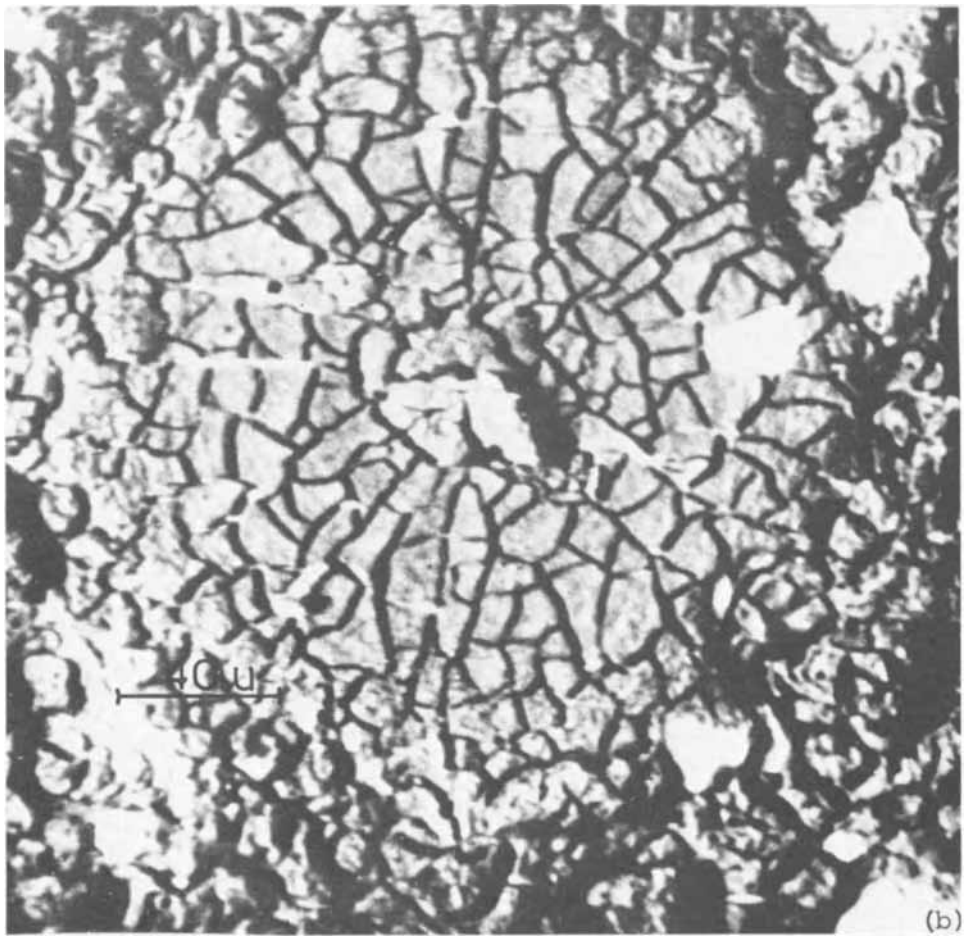

Fig. 3. Backscattered electron image of breakdown regions after 15 min anodization. (a) 0.8% H_2SO_4, (b) 80% H_2SO_4.

in the smooth nature of the film surface. However, anodizing for longer periods produced many areas of breakdown.

Photomicrographs of anodic films formed for about 15 min in dilute and concentrated solutions are seen in Fig 2a and 2b respectively. The effect of breakdown in these films was the creation of hills, the size of which depended on the solution concentration. The typical diameter of hills formed in the dilute solution was about 10μ, while that for the concentrated solution was about 100μ. The heights, measured by adjusting the focus of the objective lens, were 6μ and 10μ respectively. The anodic film thickness in the field was of the order of 0.1μ.

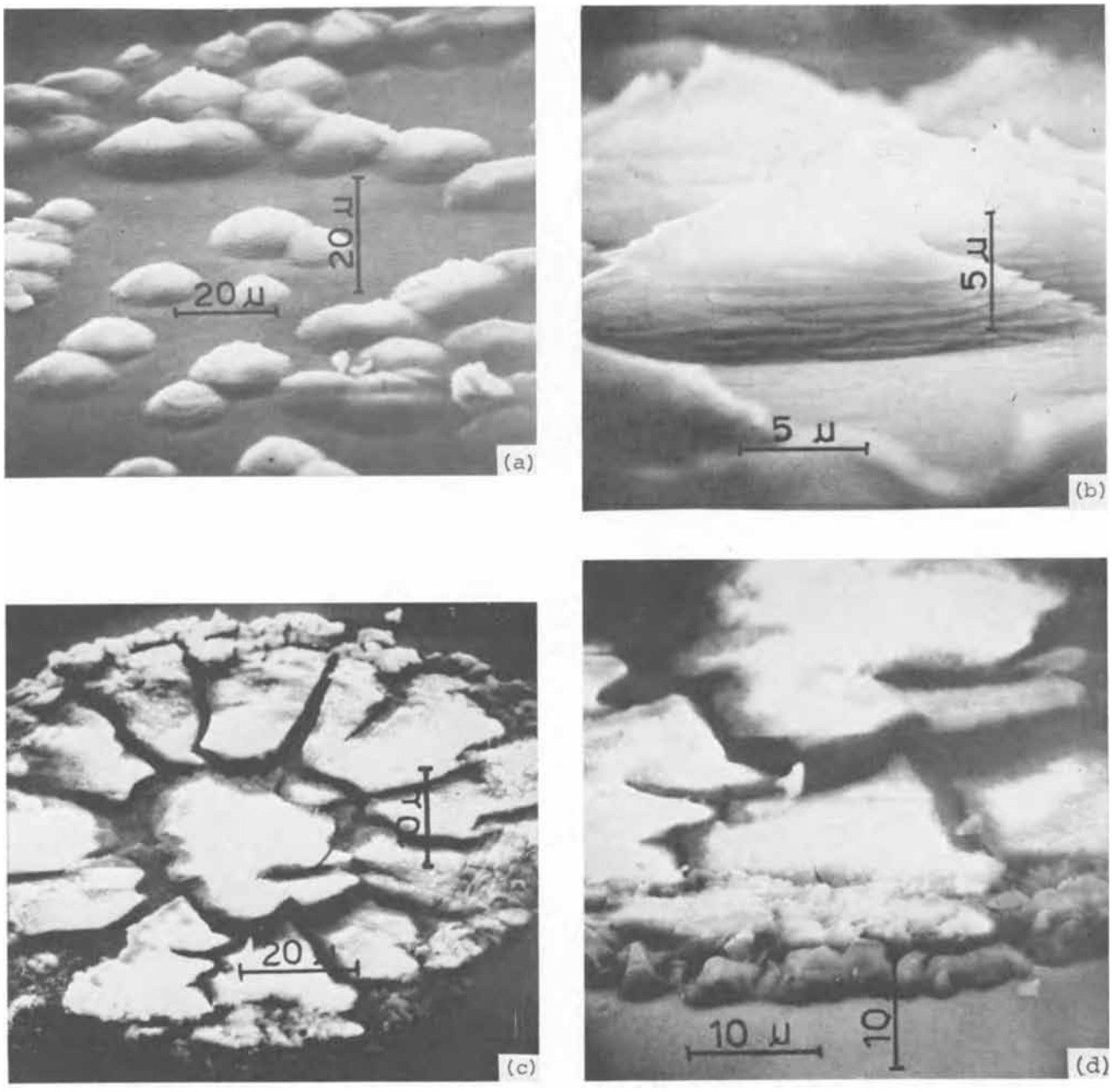

Fig. 4. Scanning electron micrographs of region of breakdown after 15 min anodization. (a) 0.8% H_2SO_4, (b) 0.8% H_2SO_4, (c) 80% H_2SO_4, (d) 80% H_2SO_4

The hills are typically round and their height decreases gradually from a central summit. The shape of the hills, formed in the dilute solution, can be seen in Fig. 3a, the backscattered electron image, obtained in the JEOL JXA-5 Microprobe. A better view of the breakdown regions is provided by scanning electron micrographs, Fig. 4a and 4b. Figures 3 and 4 reveal severe cracks in the hills, branching mainly from the hill's summit. A layered structure is also observed at the base of the hills. The shape of the hills, formed in the concentrated solution, is seen in the backscattered electron image, Fig. 3b, and in the scanning electron micrographs, Fig. 4c and 4d. The hills formed in the concentrated solution had severe cracks which have the appearance of "mud cracks." The white areas in Fig. 3b are due to flaking of the breakdown product. Craters, typically 1-2μ deep, remain in the underlying Si when the hills are chemically etched.

The hill material is probably thicker in the center of the hill, since most of the material remained attached to the Si in spite of the severe cracking around it (Fig. 3b). This conclusion is confirmed by the absorbed electron image of the breakdown regions in dilute and concentrated solutions, Fig. 5a and 5b respectively. The thicker breakdown regions absorb more electrons than the surrounding film. The hill material exhibits poor adhesion to the underlying Si, since it could be easily removed by scraping it with a sharp tool.

X-ray transmission topography furnishes further evidence for the existence of material in intimate contact with the Si inside the breakdown regions (Fig. 6). Diffraction contrast is seen inside the breakdown regions. Such contrast can be brought about if there is intimate contact between the hills and the substrate inside the breakdown region. The stresses in the hill are of a tensile nature as can be judged from the stronger x-ray intensity diffracted from the hill edge whose strain vector $\overline{H}$ is opposite to that of the diffraction vector $\overline{g}$ ($\overline{g}\cdot\overline{H}<0$) (8, 9) (Fig. 6). Since the material in the hills could be easily attacked by 1:20 HF, x-ray topographs were also taken of the surface after the dissolution of the film. This revealed that there are no residual stresses after removal of the hills, which implies that the stresses in the Si in the regions of breakdown are essentially elastic within the sensitiv-

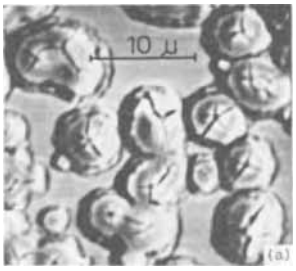

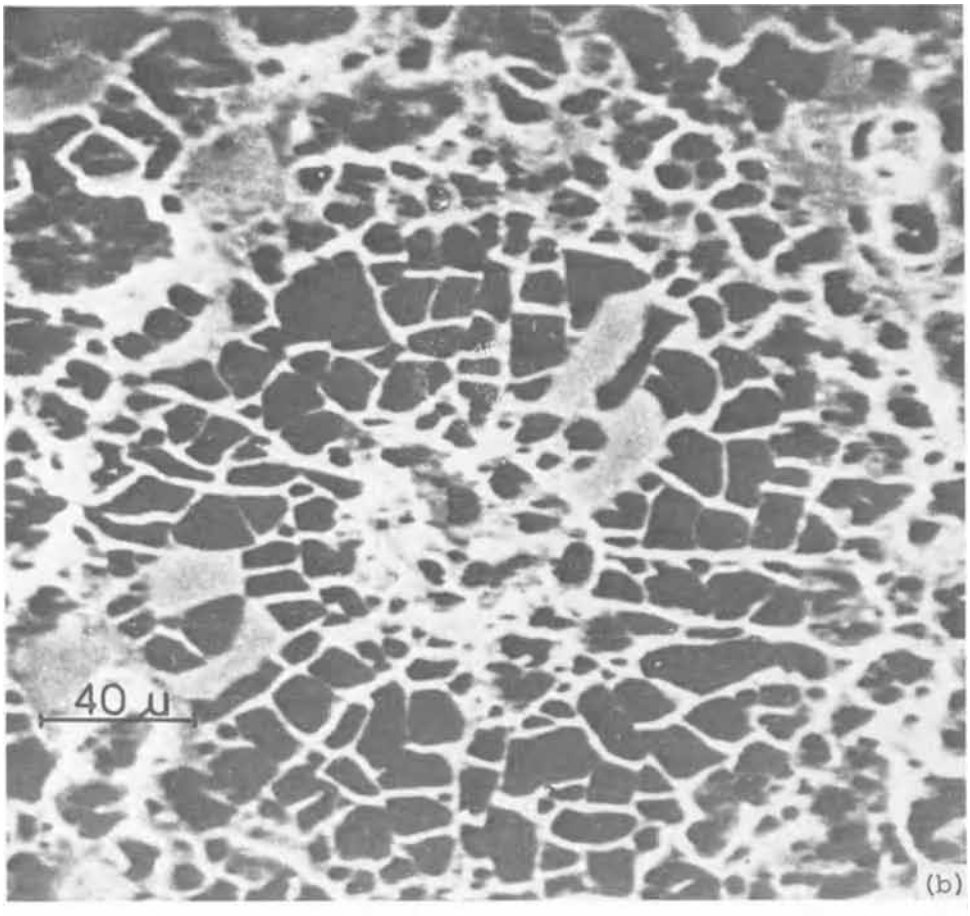

Fig. 5. Absorbed electron image of breakdown regions after 15 min anodization. (a) 0.8% H_2SO_4, (b) 80% H_2SO_4.

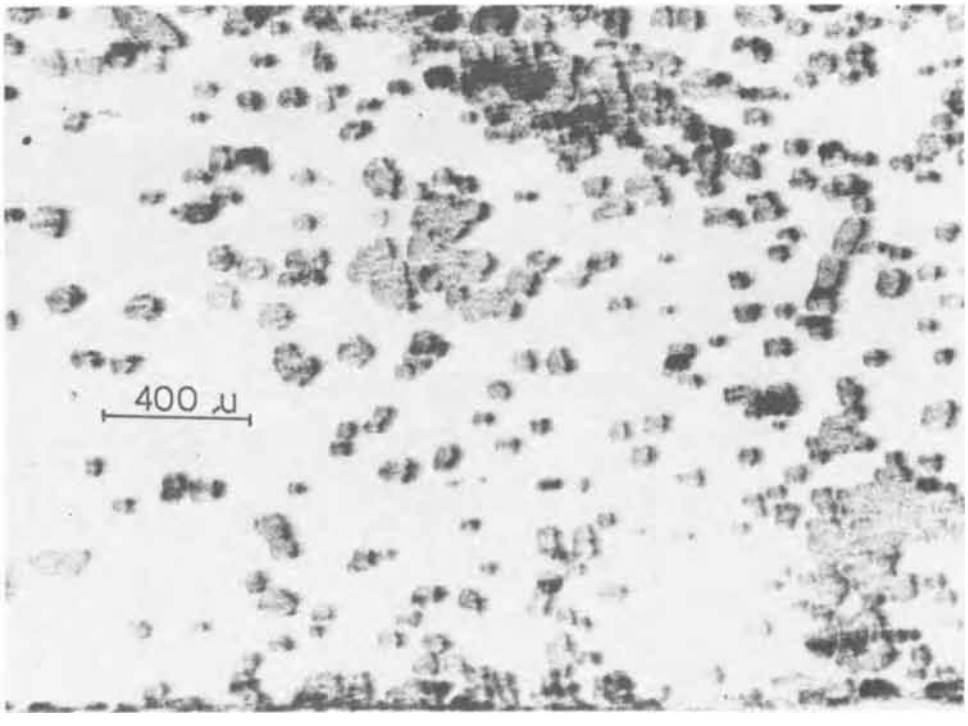

Fig. 6. Transmission x-ray topograph of film after breakdown in 80% H_2SO_4 (15 min anodizing). MoKα radiation, $\bar{g}$ = [220] pointing from right to left.

ity range of the technique. X-ray topography of films before breakdown showed no local stresses.

Attempts to detect a crystalline structure were done both by x-ray diffractometry of the film after breakdown and by the powder method using the scrapings of the breakdown products. No sharp diffraction lines could be detected. Also, electron diffraction patterns taken by grazing the summit and the edge of the hills, were typical of an amorphous material.

X-ray microprobe analysis was done along the bright line shown in the backscattered electron image of the breakdown region in the concentrated solution (Fig. 7). In this image the region of breakdown is on the upper left side. The x-ray intensity records are shown in Fig.

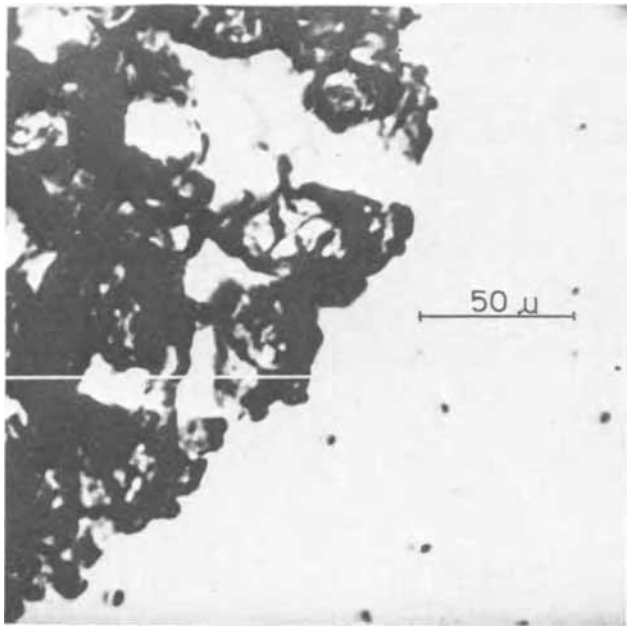

Fig. 7. Backscattered electron image of a breakdown zone and the adjacent intact anodic film 80% H_2SO_4 (15 min anodizing).

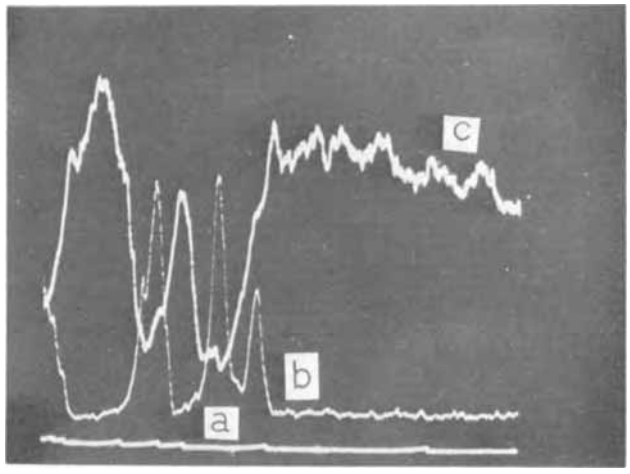

Fig. 8. Electron probe x-ray microanalysis along bright line in Fig. 7.

(a) background

(b) oxygen Kα

(c) silicon Kα

8. Above the background curve (a), the x-ray Kα intensities are seen for oxygen, curve (b), and silicon, curve (c).

The x-ray images for oxygen and silicon for the area shown in Fig. 8 are given in Fig. 9a and 9b respectively. The fractured regions are characterized by a higher silicon content (due to the underlying substrate wafer) while the breakdown product contains less silicon.

An excess of oxygen was detected in the breakdown region over the normal oxygen concentration in SiO_2. This excess may be explained by the formation of the amorphous hydrated oxides $SiO_2 \cdot (H_2O)_x$ in the regions of breakdown.

Conclusions

The morphology and composition of electrolytic breakdown products of anodic films was investigated. It is concluded that the breakdown region is comprised of a brittle material, probably amorphous $SiO_2 \cdot (H_2O)_x$. While previous evidence for the existence of water in anodic oxide films was obtained in infrared absorption studies (10), the present assumption about the composition can only be regarded as a hypothesis. The material is severely cracked and does not adhere well to the Si. This material is under residual tensile stress. The thickness of the breakdown regions is very large compared to the normal anodic film volume. It is proposed that the breakdown products form by a very rapid growth during the local heating produced by the breakdown (11).

Acknowledgment

The authors wish to thank Drs. W. Pliskin and V. Vromen for critically reviewing the manuscript.

Manuscript submitted April 13, 1971; revised manuscript received *ca.* June 17, 1971.

Any discussion of this paper will appear in a Discussion Section to be published in the June 1972 JOURNAL.

REFERENCES

1. J. Yahalom and J. Zahavi, *Electrochim. Acta*, **15**, 1429 (1970).
2. J. Yahalom and J. Zahavi, *ibid.*, **6**, 603 (1971).
3. D. A. Vermilyea, *This Journal*, **102**, 207 (1955).
4. D. A. Vermilyea, *ibid.*, **104**, 542 (1957).
5. P. F. Schmidt and A. E. Owen, *ibid.*, **111**, 682 (1964).

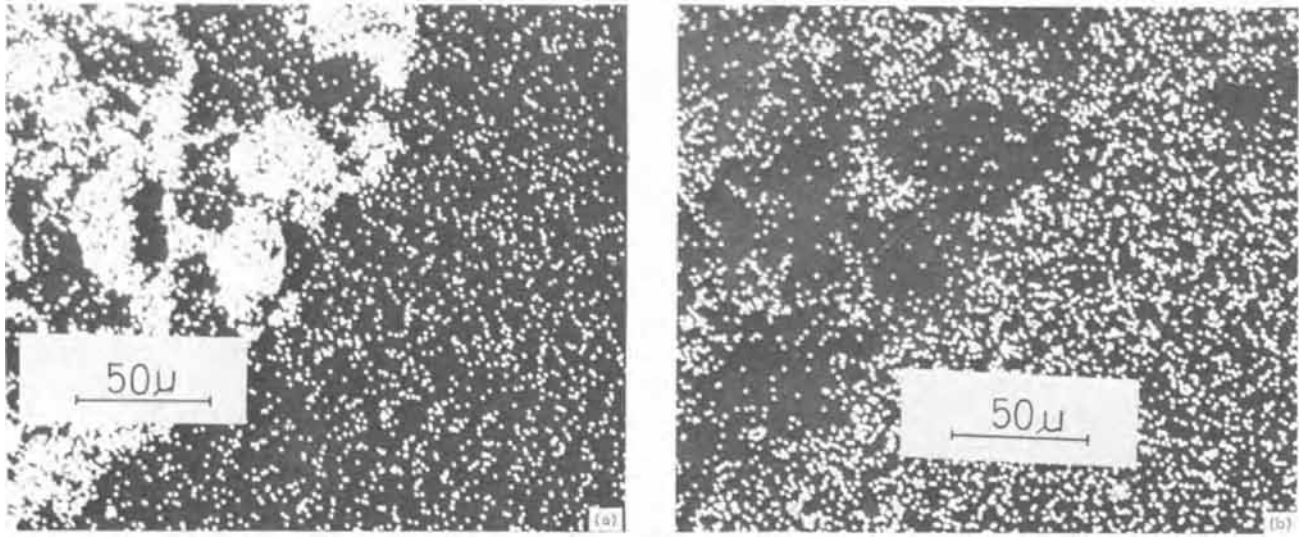

Fig. 9. Electron microprobe x-ray image for the region shown in Fig. 8 (a) Oxygen Kα, (b) silicon Kα

6. P. F. Schmidt and W. Michel, *ibid.*, **104**, 4, 230 (1960).
7. J. Zahavi and J. Yahalom, *Electrochim. Acta*, **16**, 89 (1971).
8. E. S. Meieran and I. A. Blech, *Phys. Status. Solidi*, **29**, 653 (1968).
9. E. S. Meieran and I. A. Blech, *J. Appl. Phys.*, **36**, 3162 (1965).
10. W. A. Pliskin and H. S. Lehman, *This Journal*, **112**, 1013 (1965).
11. N. Klein, Private communication.

The Optical Properties of Mn^{+2} in Calcium Halophosphate Phosphors

F. M. Ryan

Westinghouse Research Laboratories, Pittsburgh, Pennsylvania 15235

and F. M. Vodoklys*

Westinghouse Lamp Division, Bloomfield, New Jersey 07003

ABSTRACT

A study of the optical properties of Mn^{+2} in commercial halophosphate phosphors has revealed that the Mn^{+2} is located on four distinguishable sites: on the simple Ca(I) site, on the simple Ca(II) site, on a Ca(II) site adjacent to an antimony-oxygen pair, and on a Ca(II) site adjacent to a chlorine ion in those phosphors containing chlorine. The Mn^{+2} fluorescence that results when the excitation is via energy transfer from antimony ions is primarily due to Mn^{+2} situated on a Ca(I) site, with smaller components due to Mn^{+2} located on the other sites observed.

During the twenty years that halophosphate phosphors have been utilized in fluorescent lamps many improvements have been made in their performance. These improvements have resulted in better maintenance, higher efficiency, and an increased selection of different spectral distributions. The technique used in improving the phosphors has been essentially trial and error guided by a sense of chemical intuition. It cannot be contested that this approach has been very successful in improving the phosphor. However, a basic understanding of many of the details of the operation of the phosphor has been lacking.

The difficulties in understanding the operation of the halophosphate phosphors have been due to the complexity of the halophosphate system. The commercial halophosphate phosphors form into the fluorapatite structure which has the hexagonal space group $P6_3/m(C_{6h}^2)$. This is a complicated crystal structure with 42 atoms in the unit cell. In pure calcium fluorophosphate there are two molecules of $Ca_5(PO_4)_3F$ per unit cell, with two inequivalent sites for the Ca^{+2} ions. The Ca(I) site has C_3 point group symmetry with each calcium ion having six oxygen nearest neighbors which form a twisted triangular prism about it. The Ca(II) site has C_{1h} point group symmetry. The Ca^{+2} ions on Ca(II) sites are situated at the corners of equilateral triangles with an F^- ion in the center. In "cool white" (CW), a typical commercial halophosphate phosphor, various additives are introduced which complicate matters even further. A CW phosphor may be viewed as being calcium fluorophosphate with about 10% of the fluorine ions replaced by chlorine, 2% of the calcium ions by manganese, and an additional 1% by cadmium. Antimony is believed to be incorporated as an antimony-oxygen pair replacing a calcium(II) ion and its adjoining fluorine ion (1-3). If this model is correct, an additional ½% of the calcium ions are replaced with antimony and an additional 2½% of the fluorine ions by oxygen.

In the operation of this phosphor in a fluorescent lamp the antimony absorbs the ultraviolet radiation present in the mercury discharge. The antimony either fluoresces in the blue region of the visible spectrum or transfers energy to the manganese ions. The manganese ions then fluoresce in the yellow. These gross features of the operation of the phosphor have been known for a long time. There have remained many mysteries, however, such as the mechanisms by which various phosphor additives cause wavelength shifts in the manganese fluorescence. For example, the incorporation of chlorine into calcium fluorophosphate shifts the manganese fluorescence emission to longer wavelengths (4). Several explanations have been proposed to explain this shift. Butler and Jerome (5) suggested that in halophosphate phosphors the manganese is located on the calcium(II) site which is adjacent to the halogens. Replacing some fluorines with chlorine might therefore shift the manganese fluorescence. Nagy, Wollentin, and Lui (6) ascribed the shift to a lattice distortion due to chlorine since the ionic size of chlorine is larger than the fluorine it replaces. Johnson (7) proposed that the manganese emission shift with addition of chlorine is due to a shift in preferred location of manganese from the calcium(I) position in pure fluorapatite to calcium(II) in the chloro-fluorapatite. There has been no way to choose between models such as these since no information on the precise locations and environments of manganese in halophosphate phosphors was available. This information could not be obtained because, in addition to the complicated apatite structure and the incorporation of relatively large amounts of antimony, manganese, cadmium, and chlorine, only powders were available for study.

After Johnson (8) succeeded in growing single crystals of calcium fluorophosphate it became possible to perform electron spin resonance measurements of the Mn^{+2} to compare with the optical properties of the Mn^{+2}. One could therefore identify specific environmental symmetries for Mn^{+2}. These could then be correlated with the optical spectra of Mn^{+2} at the various sites in the crystals. In a previous paper (9) we found that in fluorapatite, manganese is associated with at least four inequivalent environments; the Ca(I) site, the Ca(II) site, and two similar to the (I) and (II) sites but with "modified" environments. We labeled

* Electrochemical Society Active Member.
Key words: luminescence sites, energy transfer, excitation spectra.

Table I. Composition of samples

Sample	Wt % Mn	Wt % Sb	Wt % Cl	Wt % Cd	Mn(I)/ΣMn	Mn(II)/ΣMn	Mn(Sb)/ΣMn	Mn(Cl)/ΣMn
"10% Mn" FAP	1.95	0	0	0	0.63	<0.37	0	0
"Yellow halo"	1.67	0.87	<0.05	1.15	>0.8	<0.2	<0.05	0
"Cool white"	0.75	0.63	0.59	0.99	>0.6	<0.1	<0.05	~0.25

these sites the Mn(I), Mn(II), Mn(Im), and Mn(IIm). The Mn(I), Mn(II), and Mn(IIm) all possessed different optical properties that could be distinguished readily from one another by means of their characteristic excitation and fluorescence spectra, and decay times.

In this work we have used the techniques and results of our single-crystal experiments as a guide to understanding the sites of manganese and their related optical properties in the more complicated system of the real phosphor. We find this approach to be very successful in explaining many of the phenomena of manganese in commercial halophosphate phosphors.

Samples

While many different types of halophosphate phosphors were studied, three particular samples illustrated all of the phenomena observed and form the nucleus of this paper. The first is a single crystal of calcium fluorophosphate, fluorapatite, doped with manganese by pulling from a melt containing 10% manganese. The optical properties of this crystal have been previously reported (9). The other two samples are commercial phosphors, a "yellow halo" (YH) and a "cool white" (CW), produced by the Westinghouse Lamp Division at Bloomfield, New Jersey. They were prepared by firing raw mixes of luminescent grade calcium dibasic phosphate, calcium carbonate, calcium fluoride, ammonium chloride, cadmium carbonate, antimony trioxide, and manganous carbonate in an atmosphere of nitrogen. The YH was fired at 1130°C and the CW at 1180°C. The principal differences between YH and CW are that the former contains no chlorine and has a higher manganese concentration than CW. Analyses were done by x-ray fluorescence spectroscopy using a Norelco x-ray fluorescence spectrometer. The tungsten target x-ray tube was powered at 50 kV-20 mA. For manganese, a vacuum was pulled in the sample and dispersing chambers to increase sensitivity. For chlorine determinations, a PET crystal and flow counter were used to disperse and detect the radiation. Chemical analyses of the samples are listed in Table I.

Experimental Techniques

The optical excitation and fluorescence measurements were performed at 1.8°K with the samples immersed in liquid helium below the λ point to eliminate bubbling. The optical excitation and fluorescence envelopes were narrowed slightly at 1.8°K compared to 300°K. This made it easier to separate the contributions to the excitation and fluorescence spectra from the various types of Mn^{+2} present in the samples. Measurements performed at 77° and 300°K showed optical phenomena similar to those occurring at 1.8°K so that the conclusions we arrive at concerning the behavior of Mn^{+2} in our samples at 1.8°K apply to 77° and 300°K as well.

The powder phosphor samples presented an unusually difficult problem in measurement technique, particularly in the measurement of their excitation spectra. In measuring the excitation spectra of powders the strong diffuse reflectance of the excitation light into the fluorescence detector requires good rejection of the excitation wavelengths by the detector. Since the absorption of Mn^{+2} is due to a forbidden transition with an oscillator strength of less than 10^{-6} in calcium fluorophosphate (9), the ratio of excitation light intensity to fluorescence intensity was much higher than one commonly attempts to measure in powders. In addition, due to the presence of several types of manganese centers, we found it necessary at times to excite and view at the same, or nearly the same wavelength. This required a discrimination of the excitation light compared to the fluorescence light that could only be achieved by utilizing time resolved spectroscopy and sampling only the slowly decaying after-glow of the Mn^{+2} ions ($\tau \sim 8$ msec for all species) and not the excitation light.

Our time resolved spectra were obtained by using synchronous mechanical choppers for exciting and viewing. A block diagram of the system we developed is shown on Fig. 1. Here the coupling between the reference chopper and the synchronous chopper is electrical rather than the conventional mechanical coupling. This allows a greater flexibility in the arrangement of components. Under our experimental conditions this arrangement allowed no detectable excitation light to reach the fluorescence detector. This apparatus was used to obtain both the fluorescence and excitation spectra reported here.

The precise identification of the wavelengths of several of the sharp excitation peaks shown on the figures (such as the peaks at 4009 and 4037Å) was obtained by scanning a narrow wavelength range about these peaks at a much higher resolution than was used for obtaining the figures.

Optical Properties of Mn^{+2} in a Commercial "Yellow Halo" (YH) Phosphor

While we have studied the optical properties of manganese in a wide selection of commercial halophosphate phosphors two particular phosphors, the "YH" and the "CW," illustrate all of the phenomena observed. The major difference between the YH and CW phosphors is that the YH contains no chlorine and therefore is a somewhat simpler system to study, even though YH contains more manganese than CW.

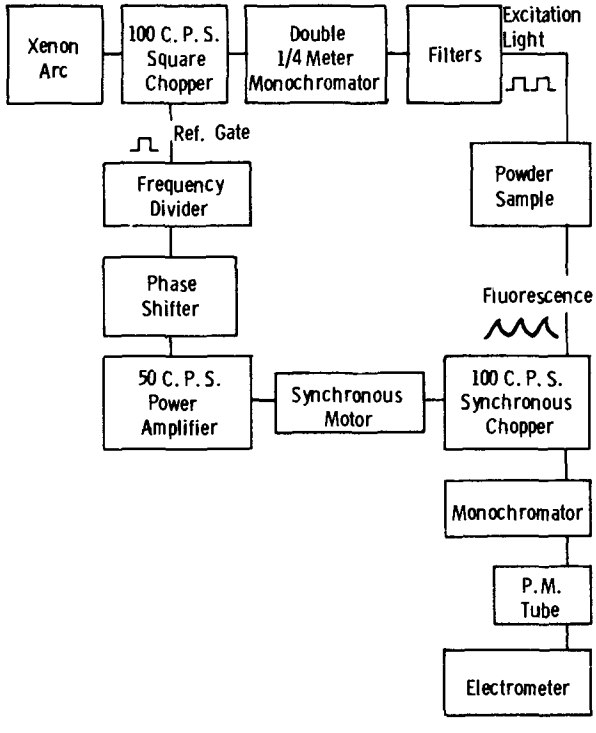

Fig. 1. Experimental arrangement for measuring the time resolved excitation and fluorescence spectra.

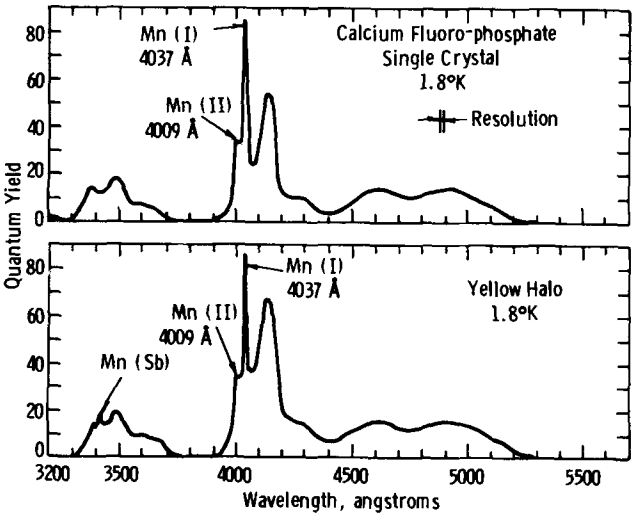

Fig. 2. 1.8°K excitation spectra of a calcium fluorophosphate single crystal and a "yellow-halo" phosphor.

Figure 2 shows the excitation spectrum of Mn^{+2} in YH along with the unpolarized excitation spectrum of Mn^{+2} in a single crystal of calcium fluorophosphate to which it is compared. In the calcium fluorophosphate crystal all of the resolved peaks shown are due to Mn(I) except for the peak at 4009Å which is due to Mn(II). The remainder of the Mn(II) excitation lines are lost in the Mn(I) envelopes. To obtain these excitation spectra all slowly decaying luminescence (in the order of milliseconds) emitted between 5000 and 8000Å was monitored. This wavelength range contains the fluorescences of all of the various Mn^{+2} types present in these samples. The Mn(I) and Mn(II) identifications are based on our previous single-crystal work (9). This crystal contains a concentration of 1.95 w/o (weight per cent) manganese which is in the same range of concentration as the phosphors measured which contained 1.67 and 0.75 w/o for the YH and CW phosphors, respectively. It is therefore considered to be a good crystal for comparing excitation and fluorescence spectra with the phosphors as the line widths due to concentration broadening would be similar.

The YH phosphor contains cadmium and antimony in addition to the manganese that the calcium fluorophosphate crystal contains. It can be seen that the crystal and YH possess essentially identical excitation spectra, the only difference being the appearance of a new minor excitation peak near 3425Å which has been labeled Mn(Sb). The Mn^{+2} in the YH phosphor is therefore behaving almost exactly like the Mn^{+2} in the crystal. In analogy to the crystal we therefore come to the following conclusions about the sites of Mn^{+2} in YH: most of the Mn^{+2} is situated on the Mn(I) site, with a small contribution on the Mn(II) site. An additional Mn^{+2} center is observed in a relatively small amount, Mn(Sb), which is associated with the presence of antimony in the phosphor. We term this center the "antimony associated" manganese center. It is not due to the presence of cadmium as we have prepared YH phosphors without cadmium that still show the presence of this center. We feel that it is due to manganese situated on a Mn(II) site with an antimony ion located on an adjacent Ca(II) site. Arguments supporting this assignment are presented later in the paper. An estimate of the relative occurrence of the various Mn^{+2} species in YH is given in Table I. In our previous single-crystal work such estimates were obtained from electron spin resonance measurements. Electron spin resonance measurements were of little value in studying the Mn^{+2} in our powders since at these high manganese concentrations the resonance lines are very broad (10). The powder estimates were

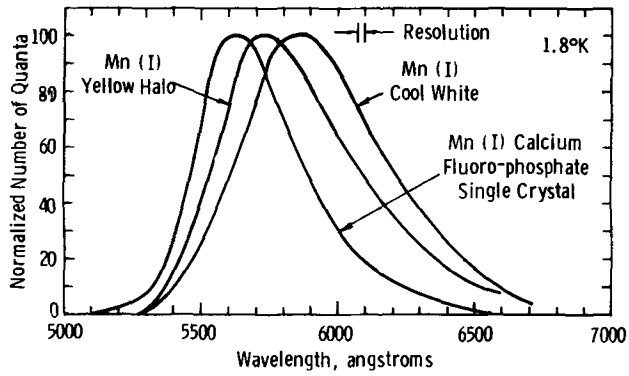

Fig. 3. 1.8°K fluorescence envelopes of the Mn(I) center in a calcium fluorophosphate single crystal, a "yellow halo," and a "cool white" phosphor.

therefore obtained by a comparison of the relative strengths of the excitation peaks of the various species of Mn^{+2} in our powders with the relative strengths of the excitation peaks of the various species of Mn^{+2} in single crystals of calcium fluorophosphate on which electron spin resonance measurements had been made. The assumptions must be made that all species have identical quantum efficiencies and that the oscillator strength of a given Mn^{+2} center in the fluorapatite crystals is the same as the comparable Mn^{+2} center in the phosphor. These assumptions introduce some uncertainty in the relative occurrence numbers stated in Table I for the powders.

The fluorescence envelopes of the Mn(I) centers in the calcium fluorophosphate crystal and the YH phosphor are shown in Fig. 3. They were obtained by pumping at 4037Å where only the Mn(I) species is strongly excited (9). The addition of cadmium and antimony to calcium fluorophosphate has shifted the 1.8°K Mn(I) fluorescence envelope about 100Å to longer wavelengths (the shift at 300°K is somewhat less). The Mn(Sb) fluorescence envelope was too weak to measure accurately, although it was determined that it fluoresces with an envelope that is shifted slightly to longer wavelengths than the Mn(I) envelope.

Optical Properties of Mn^{+2} in a Commercial CW Phosphor

Commercial CW phosphors contain chlorine in addition to all of the additives present in the YH phosphor. The presence of the chlorine (which represents about 10% of the total halogens) is found to create a new Mn^{+2} center associated with the presence of chlorine which we term the Mn(Cl) center. Its excitation spectrum is shown on Fig. 4 and its fluorescence envelope on Fig. 5. This fluorescence was obtained by exciting at 5450Å which pumps Mn(Cl) but not the other manganese types. The CW phosphor contains four easily identifiable types of Mn^{+2} centers. As they result in somewhat different fluorescence envelopes it is possible to accentuate the excitation spectra of the various centers by selectively viewing at certain fluorescence wavelengths. In Fig. 4 two excitation spectra are shown. The first excitation spectrum is that which results when viewing the fluorescence occurring at 5500Å. Viewing at 5500Å accentuates the Mn(I) and Mn(II) excitation peaks and so this excitation spectrum selectively displays the Mn(I) and Mn(II) components. It may be seen that this excitation spectrum is identical to that observed in the fluorapatite crystal in Fig. 2. The second excitation spectrum of Fig. 4 was obtained by viewing the fluorescence occurring at 6000Å which accentuates the Mn(Cl) and Mn(Sb) components. Some Mn(I) component is still visible, however, as there is still a sizable 6000Å component to the Mn(I) fluorescence.

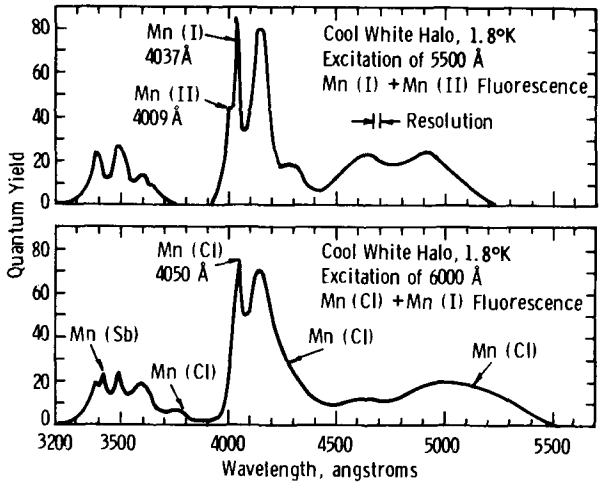

Fig. 4. 1.8°K excitation spectra of the Mn(I), Mn(II), Mn(Cl), and Mn(Sb) centers in a "cool white" phosphor.

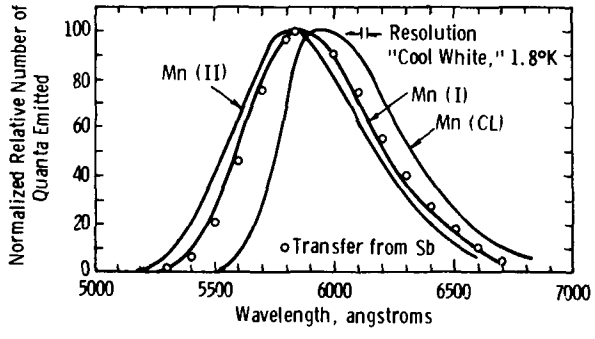

Fig. 5. 1.8°K fluorescence envelopes of the Mn(I), Mn(II), and Mn(Cl) centers in a "cool white" phosphor along with the Mn^{+2} fluorescence envelope that results when the excitation is due to transfer from antimony ions.

On Fig. 5 the normalized fluorescence envelopes of the Mn(I), Mn(II), and Mn(Cl) centers in CW are shown along with the fluorescence envelope that results when the antimony ions are pumped by 2537Å radiation and the Mn^{+2} is excited by energy transfer from the antimony. From Fig. 5 it is seen that the Mn^{+2} fluorescence envelope that results when energy is transferred from the antimony ions may be made up by a suitable combination of the various Mn^{+2} types present in the CW phosphor. On Fig. 6 we present the linear combination of the three major Mn^{+2} components that yields a composite envelope giving a "best fit" to the envelope resulting when excitation is via antimony. It occurs for approximately 70% Mn(I), 20% Mn, and 10% Mn(II). These component percentages lie within the probable error limits of the relative absorption (excitation) strengths of the various species. This implies that the various Mn^{+2} types receive relative amounts of energy from the antimony ions that do not differ greatly from their relative absorption strengths during excitation by external light. All three species therefore are active in the functioning of the CW phosphor in a fluorescent light and contribute to its composite manganese fluorescence envelope.

Discussion

The assignment of components in the optical spectra of our phosphor samples to Mn(I) and Mn(II) was relatively simple, as the Mn(I) and Mn(II) excitation and fluorescence spectra in the phosphors closely resembled their counterparts in single crystals of calcium fluorophosphate. No Mn(Sb) or Mn(Cl) centers were present in the calcium fluorophosphate crystals that we studied previously so that models for these

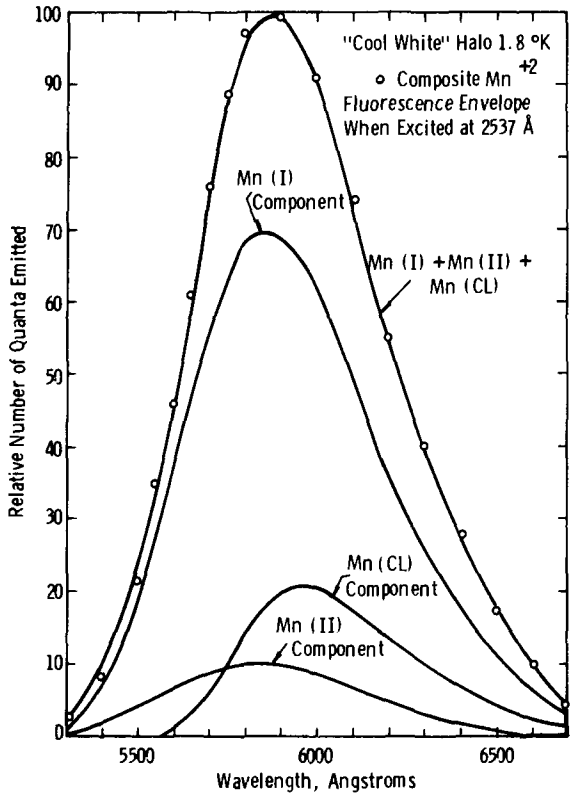

Fig. 6. Linear combination of the Mn(I), Mn(II), and Mn(Cl) centers that gives a best fit to the composite Mn^{+2} envelope that results when the excitation is due to transfer from antimony ions at 1.8°K. The combination is 70% Mn(I), 20% Mn(Cl), and 10% Mn(II).

centers must be derived from more indirect arguments. The models that we propose for these two centers are therefore somewhat speculative and represent what we believe the centers to look like, rather than what we can prove them to be.

In our previous single-crystal work we found that if our crystals were grown under certain conditions (a deficiency of fluorine and/or an excess of oxygen), defect centers would be formed along the halogen chains (9). These centers consisted of clusters of fluorine vacancies and oxygen ions substitutional for fluorine. They exhibited an attractive force on substitutional manganese ions which caused nonrandom pairing, forming centers such as the one we termed the Mn(II) "modified," or Mn(IIm) center. Our model for this center is that it consists of a manganese ion located on a Ca(II) site immediately adjacent to an oxygen vacancy complex. No corresponding center due to pairing of manganese ions located on Ca(I) sites with the defect centers was observed to occur. This is undoubtedly because the Ca(I) site is much farther away from the halogen chain than the Ca(II) site, and that an attractive force between the manganese ions and the defect centers would cause them to be located as closely together as possible, *i.e.*, with the Mn on the Ca(II) site.

Another observation we can make from the single-crystal data is that the Mn(I) and Mn(II) centers exhibit no observable modifications in their ESR or optical spectra due to the presence of the defects on the fluorine chains. Thus it appears that the excitation spectra of manganese ions are practically unaffected by the presence of defects unless they occur at a nearest neighbor position. We are therefore led to expect that the Mn(Cl) and Mn(Sb) centers, which exhibit characteristic excitation spectra that differ significantly from the Mn(I) and Mn(II) spectra, are formed by having a manganese ion located adjacent to the

chlorine ions and the antimony-oxygen complexes, respectively.

Since the chlorine atoms would most probably enter the lattice substitutionally for fluorine, one expects that in the Mn(Cl) center the manganese ion is located on a Ca(II) site adjacent to a chlorine ion. The presence of a manganese-chlorine attraction analogous to that found for the Mn(IIm) center may be seen from the distribution of the various types of manganese that occurs in CW. In the CW phosphor about 70% of those Mn^{+2} ions located on Ca(II) sites are Mn(Cl) centers. Since only 10% of the fluorine ions are replaced by chlorine, a random distribution of manganese and chlorine would predict that only 10% of the manganese ions on Ca(II) positions would be adjacent to chlorine ions and form Mn(Cl) centers, not 70%.

Piper has reported on ESR measurements of manganese in single crystals of calcium fluorophosphate, chlorophosphate, and mixed fluorochlorophosphates that lend support to our assignment of the Mn(Cl) center to manganese on a Ca(II) position adjacent to a chlorine. In his pure fluorophosphate crystals Piper observed only Mn(I) centers and no Mn(II) centers. In mixed crystals containing small amounts of chlorine he detected, in addition to Mn(I), a single type of Mn(II) associated with the presence of chlorine in the structure. This observation is consistent with our model of the strong interaction between manganese and chlorine ions that gives rise to the formation of the Mn(Cl) center. His failure to observe the Mn(II) center in calcium fluorophosphate is consistent with our observation that at low manganese it is incorporated as Mn(I).

Strong evidence suggests that antimony ions enter the apatite structure as antimony-oxygen pairs, with the oxygen located on a halogen site and the antimony on one of the three adjacent Ca(II) positions (1-3). We conclude that the Mn(Sb) center consists of a manganese ion located on a Ca(II) site adjacent to a antimony-oxygen complex. The Mn(Sb) center is such a minor center in CW that we are unable to determine whether the number of Mn(Sb) centers is greater than a random distribution of manganese and antimony would predict or not.

The shift in the emission envelope of the Mn(I) fluorescence to longer wavelengths as cadmium, antimony, or chlorine are added to calcium fluorophosphate is probably because these ions cause dimensional changes to the fluorapatite lattice. Norita (12) has suggested that the resultant change in the crystal field strength acting on the Mn^{+2} ions due to these dimensional changes would be expected to shift the Mn^{+2} emission envelope. While this effect is certainly present we do not feel that it is primarily responsible for the emission shifts observed. We observe no corresponding shift in the excitation spectra of Mn(I) in our phosphors when cadmium, antimony, or chlorine are added: only a shift in the emission, Norita's model would predict a shift in the excitation levels also due to the change in crystal field strength, particularly the broad excitation peak which corresponds to excitation to the fluorescence state. All of the shift appears after the Mn^{+2} ions are in their excited state, although a slight shift in the lowest lying excitation envelope with additives could easily be missed as the envelope is quite broad. That is, a larger Stoke's shift occurs to the Mn^{+2} ions when the various additives are present. We thus prefer to view the functioning of the additives as "softening" the lattice and allowing larger Stoke's shifts to occur. How this can happen may be seen from the following simple model. Figure 7 shows how a Stoke's shift is commonly pictured as occurring on an energy configuration-coordinate diagram. The ground and excited states of the ion are assumed to be parabolic, $E \sim \frac{1}{2} k Q^2$ where k is the lattice force constant, and to couple to the lattice modes with terms V_1 for the ground state and V_2 for the excited state.

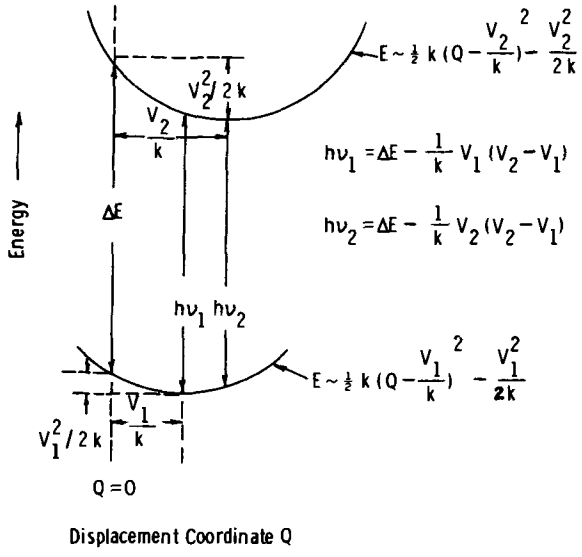

Fig. 7. Energy configuration-coordinate diagram for the Stoke's shift observed in the phosphors. The symbols are defined in the text.

The coupling to the lattice modes is assumed to yield an energy term that is linear in the lattice distortion so that coupling terms in Q^2 or higher are negligible. Adding this term to the parabolic term we have

$$E \sim \frac{1}{2} k Q^2 - QV$$

The Stoke's shift is then observed as the difference between the absorption and emission energies

absorption

$$h V_1 = \Delta E - \frac{1}{k} V_1 (V_2 - V_1)$$

emission

$$h V_2 = \Delta E - \frac{1}{k} (V_2 - V_1)^2 - \frac{1}{k} V_1 (V_2 - V_1)$$

where ΔE is the separation of the levels in the absence of coupling to the lattice modes. The difference in energy between the absorption and emission is thus the term, $\frac{1}{k} [V_2 - V_1]^2$. If k is reduced (the lattice gets softer), hV_2 shifts more than hV_1 by an amount approximately equal to

$$\left[\frac{V_2 - V_1}{k} \right]^2 \Delta k$$

where Δk is the change in the lattice force constant. If Δk is negative then the shift is toward longer wavelengths. In order for the absorption line to shift very little (the location of the center of the lowest energy excitation envelope in this case) while the emission line shifts a much greater amount, one requires that V_1 is small and that V_2/V_1 is large. It is a reasonable assumption that the excited state of the manganese ions would couple more strongly with many of the lattice modes than does the ground state. The observation of a Stoke's shift and the absence of a zero phonon line (9) already informs one that the coupling terms V_1 and V_2 are considerably different. While admittedly crude, this model does qualitatively explain the increased Stoke's shift observed as additives such as chlorine are incorporated into calcium fluorophosphate.

Conclusions

In commercial halophosphate phosphors, Mn^{+2} can find itself in four distinct environments: on the simple Ca(I) site, on the simple Ca(II) site, on a Ca(II) site

adjacent to an antimony-oxygen pair, and on a Ca(II) site adjacent to a chlorine ion in those phosphors containing chlorine. In the most commercially important phosphor of the group, CW, we find that between 60 and 70% of the manganese is present as Mn(I), between 5 and 10% as Mn(II), between 1 and 5% as Mn(Sb), and between 20 and 30% as Mn(Cl). The phosphor functions in the following manner in the fluorescent lamp. The antimony ions absorb the 2537Å radiation and either fluoresce or transfer energy to Mn^{+2} ions. Most of the Mn^{+2} fluorescence that results is due to Mn(I), with smaller components due to Mn(Cl) and Mn(II), and a very small component due to Mn(Sb). The fluorescence envelope of Mn(I) in CW is at longer wavelengths than Mn(I) in calcium fluorophosphate. This Mn(I) envelope shift is primarily responsible for the color shift observed in the CW phosphor relative to calcium fluorophosphate. The shift is not due to a redistribution between the Ca(I) and Ca(II) sites due to the introduction of Sb, Cd, and Cl as Johnson proposed (7), nor due to the formation of new Mn(Cl) centers as Butler and Jerome (5) proposed, although the formation of Mn(Cl) centers does occur to some degree and does cause a slight additional wavelength shift to the composite Mn^{+2} fluorescence envelope.

Acknowledgments

We would like to thank Drs. J. Murphy, R. W. Warren, and R. C. Miller for many valuable discussions.

Manuscript submitted April 5, 1971; revised manuscript received ca. June 13, 1971. This was Paper 38 presented at the Washington, D.C., Meeting of the Society, May 9-13, 1971.

Any discussion of this paper will appear in a Discussion Section to be published in the June 1972 JOURNAL.

REFERENCES

1. J. L. Ouweltjes, *Philips Tech. Rev.*, **13**, 346 (1952).
2. J. S. Prener and F. E. Williams, Electrochem. Soc. Extended Abstracts, May 1-4, p. 31 (1955).
3. J. G. Rabatin, G. R. Gilleoly, and J. W. Hunter, *This Journal*, **114**, 956 (1967).
4. A. H. McKeag and P. W. Ranby, *Ind. Chem.*, p. 3, (August-September, 1947).
5. K. H. Butler and C. W. Jerome, *This Journal*, **97**, 265 (1950).
6. Rudolph Nagy, R. W. Wollentin, and C. K. Lui, *Trans. Electrochem. Soc.*, **95**, 187 (1949).
7. P. D. Johnson, "Proceedings of Luminescence of Organic and Inorganic Materials," p. 563, John Wiley & Sons, Inc., New York (1962).
8. P. D. Johnson, *This Journal*, **108**, 159 (1961).
9. F. M. Ryan, R. C. Ohlmann, J. Murphy, R. Mazelsky, G. R. Wagner and R. W. Warren, *Phys. Rev.*, **B2**, 2341 (1970).
10. R. W. Warren, Private communication.
11. W. W. Piper, *J. Luminescence*, **1, 2**, 2669 (1970).
12. Koziro Norita, *J. Phys. Soc., Japan*, **16**, 99 (1961).

The Effect of Rapid Cooling on Divalent Manganese Ions in Calcium Fluoro-Chlorophosphate Phosphors

F. M. Ryan

Westinghouse Research Laboratories, Pittsburgh, Pennsylvania 15235

and F. M. Vodoklys*

Westinghouse Lamp Division, Bloomfield, New Jersey 07003

ABSTRACT

Quenching experiments were performed on manganese-activated calcium fluoro-chlorophosphate phosphors. Changes in the optical properties of the manganese ions due to quenching were studied in order to explain the manganese fluorescent envelope shift in quenched phosphors reported by other workers. We find that quenching causes a change in the nearest halogen neighbors of manganese ions located on the so-called "Ca(II)" positions. In slowly cooled phosphors these ions have mostly chlorine ions as nearest neighbors while in the quenched phosphors many of the chlorine ions are replaced with fluorine. It is shown that this redistribution will produce a shift in the manganese fluorescence envelope equal in magnitude to that experimentally observed.

Apple and Ishler (1) have observed that if chlorine-containing calcium halophosphate phosphors, activated by antimony and manganese, are cooled very rapidly (from 600°-1200°C) to room temperature, that the spectral distribution of the manganese fluorescent emission shifts to slightly shorter wavelengths while the antimony emission is unchanged. This effect was found to be reversible upon annealing and did not occur in calcium fluorophosphate. They proposed two alternative models to explain this effect. One explanation involved a redistribution of manganese among the various sites it may occupy in these phosphors, due to the quenching. Since one would expect somewhat different emission wavelengths for manganese located on different sites a shift in the composite emission envelope could result from such a redistribution.

Their second model involved changes in the location of the chlorine atoms in the crystal structure of the phosphors due to quenching. It was proposed that a rapid cooling could freeze the chlorine atoms into a more random arrangement than the equilibrium configuration at low temperatures.

At the time they published their paper, progress in understanding the structural and optical properties of the calcium halophosphate phosphors had not yet reached the point where these models could be tested. Since then, some progress has been achieved in characterizing the structural modifications that exist, the nature of the sites that manganese ions occupy in the calcium halophosphate phosphors, and the optical properties of the manganese ions on those sites. This

* Electrochemical Society Active Member.
Key words: quenching, luminescence, fluorescence, optical properties, centers.

information has enabled us to conduct experiments which have clearly revealed the origin of the quenching effect.

Background

The pseudobinary system calcium fluorophosphate: calcium chlorophosphate includes almost all of the commercially important halophosphate lamp phosphors. There are two structures known to exist in this system. Calcium fluorophosphate forms in the hexagonal fluorapatite structure, space group $P\ 6_3/m$ (C_{6h}^2), with two molecules of $Ca_5(PO_4)_3F$ per unit cell. There are two inequivalent calcium ion sites in this structure. The Ca(I) site has C_3 point group symmetry with each calcium ion having six oxygen nearest neighbors which form a twisted triangular prism about it. The Ca(II) site has C_{1h} point group symmetry with each calcium ion situated at the corners of equilateral triangles with a fluorine ion in the center. These triangles and hence the fluorine ions are located on reflection planes. The fluorine ions are at (0,0,1/4; 0,0,3/4) positions in the unit cell as determined from precision x-ray structure measurements.

Calcium chlorophosphate has two known crystallographic modifications (2, 3). Above 200°C it exhibits the x-ray pattern expected for a hexagonal chlorapatite structure with the same space group as the fluorapatite. It has been proposed (4) that the structure of chlorapatite and fluorapatite differ, however; in particular that in chlorapatite the larger size of the chlorine ions relative to the fluorine ions causes them to be displaced from the reflection planes where they are located in the fluorapatite structure to positions midway between the reflection planes at (0,0,0; 0,0,1/2) positions. These positions also satisfy the symmetry requirements of the hexagonal apatite space group. A precise structure determination has not been reported on the chlorapatite structure, which would yield more precise information on the positions of the chlorine ions. One can therefore only state from the type of x-ray measurements that have been performed, that the positions of the chlorine atoms on the average satisfy the symmetry of the hexagonal apatite space group. Random displacements about either the (0,0,1/4; 0,0,3/4) or (0,0,0; 0,0,1/2) positions cannot be ruled out.

Below 200°C calcium chlorophosphate exists in a monoclinic form which appears to differ only slightly from a hexagonal structure. The monoclinic unit cell can be derived from a hexagonal unit cell by doubling the length of one hexagonal "a" axis. Viewing down the monoclinic "a" axis the chlorine atoms are thought to be displaced alternately up and down along the "c" axis, although the magnitude of the displacement has not been determined (3). It is the ordering of these displacements that distinguishes the monoclinic phase from the hypothetical disordered chlorapatite. Prener (3) has pointed out that the monoclinic to hexagonal phase transition observed by x-ray technique could be accomplished either by a simple disordering of the alternate chlorine displacements that exist in the monoclinic form or by a rearrangement in which all chlorine positions are equivalent.

This uncertainty in the positions of the chlorine atoms on a microscopic scale persists into the pseudobinary system. It is known that compounds with a fluorine to total halogen ratio of over 36% are "hexagonal apatites" with no low temperature transition to the monoclinic phase (3), but the exact positions of the chlorine atoms are not yet known.

More pertinent to this paper than structural considerations is information on the manganese ions which are located in these structures. We have previously reported on electron spin resonance (ESR) measurements of manganese in single crystals of calcium fluorophosphate (5). These measurements were compared with optical measurements, and we were able to identify the optical excitation and fluorescence spectra of manganese located on the Ca(I) site, termed Mn(I), on the Ca(II) site, termed Mn(II), and on a Ca(II) site adjacent to an oxygen-vacancy complex, termed Mn(IIm). In a later paper (6) we extended these investigations to calcium fluoro-chlorophosphate phosphors containing manganese. No single crystals of the mixed fluoro-chlorophosphates were available to us so that ESR measurements could not be used to aid in the identification of the manganese sites. The identification of the Mn(I) and Mn(II) optical excitation and fluorescence spectra in the mixed halophosphates was accomplished through their great similarity to the optical excitation and fluorescence spectra of the corresponding centers in calcium fluorophosphate. Two additional types of manganese centers were observed to occur in the mixed fluoro-chlorophosphates; a Mn(Cl) center which we identify as a manganese ion located on a Ca(II) site immediately adjacent to a chlorine ion, and a Mn(Sb) center which we identify as a manganese ion located on a Ca(II) site adjacent to a substitutional antimony-oxygen ion pair. The identification of these centers was accomplished through analogy to the Mn(IIm) center in the fluorophosphates and by use of other indirect evidence. We found that in the mixed fluoro-chlorophosphates almost all of the manganese located on Ca(II) sites was immediately adjacent to chlorine [forming the Mn(Cl) center] evidence of a strong manganese-chlorine attraction.

A typical commercial apatite phosphor is one called "cool white." It is a calcium fluoro-chlorophosphor activated with both antimony and manganese. It was found that all of these manganese centers could receive energy which was transferred from antimony ions when the "cool white" phosphor was excited with 2537Å radiation, and that the manganese emission envelope that resulted was a composite of the various manganese types present.

In view of the additional information about the types of manganese sites in "cool white" it appeared worthwhile to repeat some of Apple and Ishler's quenching experiments to determine what changes might be induced in the various types of manganese centers, due to rapid cooling. A report on the results of these investigations is the purpose of this paper.

Experimental

The "cool white" phosphor that was used in our quenching experiments was a commercial phosphor produced at the Westinghouse Lamp Division at Bloomfield, New Jersey. It was prepared by firing a raw mix of luminescent grade calcium dibasic phosphate, calcium carbonate, calcium fluoride, ammonium chloride, cadmium carbonate, antimony trioxide, and manganous carbonate in an atmosphere of nitrogen at 1180°C. A chemical analysis of the minor constituents in the fired material showed it to contain by weight 0.75% manganese, 0.63% antimony, 0.59% chlorine, and 0.99% cadmium.

We found that in order to obtain quenching effects comparable in magnitude to those reported by Apple and Ishler it was necessary to cool our samples in times considerably shorter than 20 sec and from the highest temperatures they reported. Our best results were obtained for samples contained in thin-walled quartz tubes with a bore size of 3 mm and a wall thickness of 0.5 mm. To obtain an adequate sample volume these tubes were made as long as our furnace could accommodate. The samples were sealed in one third atmosphere of argon at room temperature and heated to 1150°C in 1 hr and kept at temperature for 1 hr. The tubes were quenched by quickly dumping them into a container of water. No measurements of temperatures inside the tubes as a function of time after immersion were performed, but the incandescent glow from the samples disappeared almost instantly after immersion and all boiling ceased within about 2 sec. We feel that the material at the center of the tubes reached a temperature below 100°C in at most 5 sec. Even at this fast quenching rate the portion of the phosphor immediately adjacent to the quartz wall

showed a measurably greater quenching effect than the phosphor portion located at the very center of the tube where the cooling rate was lowest.

Every attempt to quench unencapsulated phosphors directly into water resulted in some pink body coloration of our phosphors which reduced their efficiency measurably. This pink color has been ascribed by Rabatin and Gillooly to Mn^{+3} in calcium orthophosphate, a second phase component often present in halophosphate phosphors (7). Since no such difficulty was reported by Apple and Ishler with their phosphors we surmise that their phosphors contained a smaller amount of calcium orthophosphate than ours. Possibly our unencapsulated phosphors lost enough chlorine during heating to induce the formation of the orthophosphate phase.

All of the excitation and most of the fluorescence measurements reported in this paper were obtained by directly exciting the manganese ions with external light rather than via transfer from antimony ions. These spectra were obtained through the use of time-resolved spectroscopy, a technique which has been described in detail in a previous paper (6). The fluorescence decay times of all manganese species reported here are essentially identical so that the relative strengths of their fluorescence and excitation spectra, obtained by time-resolved techniques, are equivalent to those obtained by the more standard d-c techniques. All spectra plotted on the figures are manganese concentration limited in their resolution.

UV-induced depreciation of the quenched samples was studied by exposing powder plaques of the phosphors to the radiation emitted by a mercury discharge lamp with a Suprasil quartz envelope, operated under discharge conditions identical to those in a 40W fluorescent lamp. The use of a Suprasil envelope for a mercury discharge lamp results in a much higher transmission of the 1849Å mercury line than ordinary quartz so that the radiation emitted from such a lamp closely resembled the energy distribution of radiation incident on the phosphor inside an actual fluorescent lamp. The lamp and phosphor samples were located inside a sealed chamber provided with a constant flow of nitrogen gas to eliminate absorption of the uv radiation by oxygen. The phosphor samples were positioned so that the uv flux incident upon them was closely equal to the flux incident upon the phosphors in a 40W fluorescent lamp. The temperature of the phosphors during the irradiation was approximately 30°C.

The samples were removed and their quantum efficiency measured under 2537Å excitation at various times during the depreciation exposure of 100 hr. These measurements were accurate to within ±2%.

Results

We will discuss now the changes which occurred in the types of Mn^{+2} centers present in a sample of "cool white" phosphor after a quenching of the type described in the experimental section of this paper. Figure 1 shows the fluorescence envelopes of the sample before and after the quenching. These envelopes were obtained by exciting the sample, kept at 300°K, with 2537Å radiation. Time resolved spectroscopy was not used for obtaining these envelopes as a time resolved fluorescence spectrum would reject the antimony emission component, since the antimony ions decay with a much faster decay time than the manganese ions (10 μsec *vs.* 7 msec). The shift in the manganese fluorescence envelope after quenching of approximately 40Å to shorter wavelengths may be seen in Fig. 1. This shift is similar to that reported by Apple and Ishler in their experiments on "cool white." We found this shift to be reversible upon annealing as they also reported.

The excitation spectra of the sample before and after quenching are shown in Fig. 2. Only selected regions of the excitation spectra are shown here in order to demonstrate the changes occurring due to the

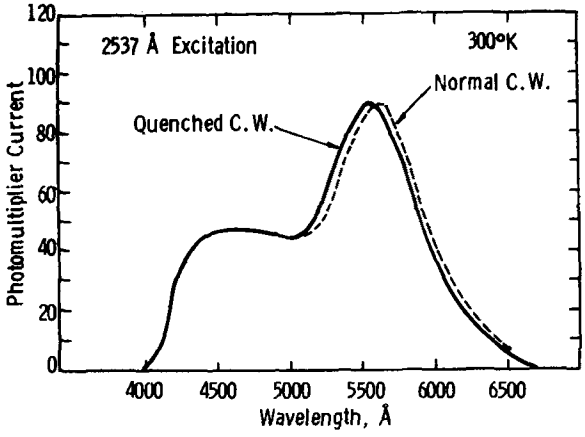

Fig. 1. Fluorescence envelopes of quenched and normal "cool white" phosphors at 300°K. Excitation is at 2537Å.

quenching. The two excitation spectra on the left hand side of the drawing show on an expanded wavelength scale the changes induced by quenching in the relative strengths of two important excitation peaks. The peak located at 4037Å is the dominant sharp line in the excitation spectrum of manganese ions located on the Ca(I) site, *i.e.* Mn(I). The peak located at 4009Å is the dominant sharp line in the excitation spectrum of manganese ions located on a Ca(II) site adjacent to a fluorine ion, *i.e.* Mn(II). These two peaks are made to be of comparable height in these two spectra by monitoring the fluorescence at a selected wavelength (5350Å) where both emissions are equally strong. This allows small changes in the ratio on Mn(II) to Mn(I) due to quenching to be seen more readily than would be possible if nonselective fluorescence viewing were employed for obtaining the excitation spectra. Normally the Mn(II) excitation peak is much weaker

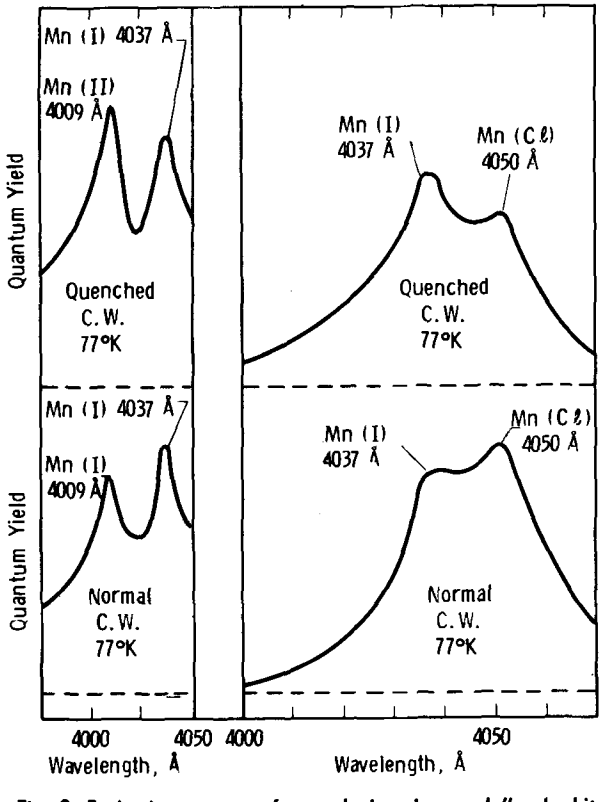

Fig. 2. Excitation spectra of quenched and normal "cool white" phosphors at 77°K. The growth in the number of Mn(II) centers following quenching may be seen on the left hand side of Fig. 2 and the decrease in the number of Mn(CI) centers on the right.

than the Mn(I) peak. It may be seen in Fig. 2 that quenching has increased the ratio of the Mn(II) to Mn(I) but that the strength of the Mn(I) excitation spectrum is unchanged. This means that the number of Mn(II) ions in the phosphor has increased upon quenching.

The two excitation spectra shown on the right hand side of Fig. 2 were obtained by selectively viewing the fluorescence emitted at 6000Å. This choice of wavelength accentuates the fluorescence due to manganese ions located on Ca(II) sites adjacent to chlorine [the Mn(Cl) center]. The dominant sharp line of the Mn(Cl) center is located at 4050Å compared to the Mn(I) line at 4037Å. It can be seen from the curves on the right hand side of Fig. 2 that the Mn(Cl) center has decreased upon quenching relative to the Mn(I) center. We thus find that quenching both reduces the number of manganese ions adjacent to chlorine and increases the number adjacent to fluorine. The decrease in the number of Mn(Cl) centers is numerically equal to the increase in the number of the Mn(II) centers to within our estimated experimental accuracy of 10%. The Mn(Sb) center is such a minor center that little can be said about the changes in its concentration that might occur due to quenching.

By comparing the relative areas under the excitation spectra of the three major species of manganese we find that prior to quenching the manganese is distributed as about 7.5% Mn(II), 65% Mn(I), and 25% Mn(Cl). After quenching, the distribution is changed to about 20% Mn(II), 65% Mn(I), and 12.5% Mn(Cl). From the known fluorescence spectra of each component and these percentages we can calculate the shapes of the composite envelopes to be expected both before and after quenching. They, and the individual components are shown in Fig. 3. The calculated composite Mn^{+2} envelope shifts by approximately 40Å to higher energy due to quenching. This is in good agreement with the shift of the manganese envelope observed for this sample shown in Fig. 1 and is an important confirmation of the validity of this treatment. The small Mn(Sb) components for both the quenched and normal samples were ignored in preparing Fig. 3.

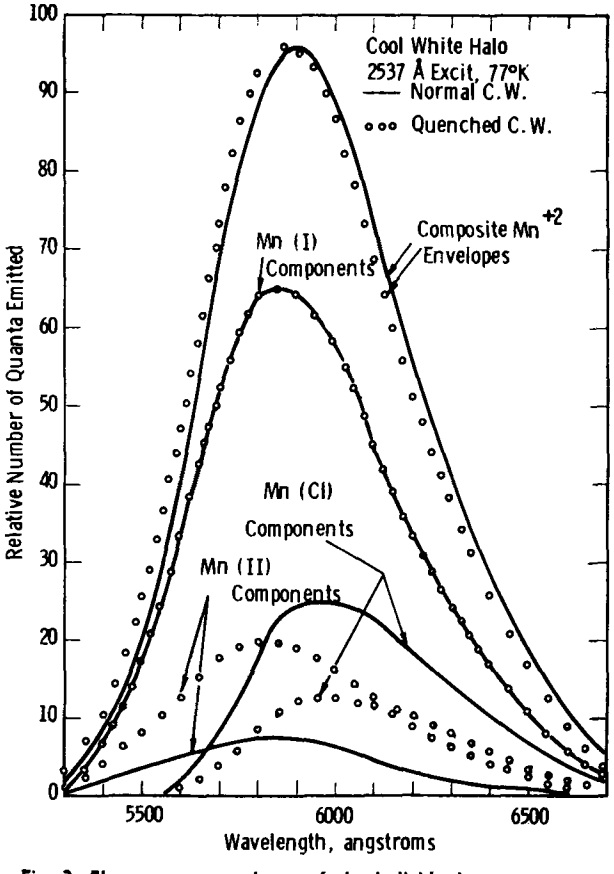

Fig. 3. Fluorescence envelopes of the individual components and the composite envelopes for a "cool white" phosphor before and after quenching.

Depreciation Results

Apple and Ishler reported that their quenched calcium fluorochlorophosphate phosphors were more resistant to depreciation by 1850Å irradiation than their unquenched phosphors. We have studied the depreciation of several samples of "cool white" quenched phosphor and compared the results with those obtained from normal "cool white" phosphor to determine if our phosphors showed the same effect. We found that, within our experimental accuracy of ±2%, quenching had no measurable effect on the depreciation rates of our phosphors up to our maximum depreciation time of 100 hr. The quantum efficiencies of our quenched and unquenched phosphors were identical before depreciation (although the luminous efficiencies of the quenched phosphors were slightly higher due to the manganese envelope shift). We conclude that the enhancement in irradiation resistance that Apple and Ishler observed in their quenched samples was due to a different mechanism than that responsible for the manganese fluorescence shift, and that the effect does not generally occur in quenched calcium halophosphate phosphors.

Discussion and Conclusions

The quenching induced shift in the composite manganese fluorescence envelope can be explained by a redistribution of the manganese ions over the various types of manganese centers present before quenching. In particular, quenching has the net effect of converting some of the Mn(Cl) centers into Mn(II) centers. Since the decrease in the number of Mn(Cl) centers after quenching is numerically matched by the growth of the Mn(II) centers, and no new manganese center appears, one must rule out the formation of new types of manganese centers due to quenching such as a center where the chlorine ion is frozen into an intermediate position in the lattice as was proposed by Apple and Ishler. In slowly cooled (normal) "cool white" most of the manganese ions situated on a Ca(II) position are adjacent to a chlorine ion. This is due to a pairing attraction between the manganese and chlorine ions. At high temperatures these pairs are broken up and the chlorine distribution is randomized. A rapid quench freezes in a more random distribution of chlorine than occurs if the phosphor is allowed to cool slowly.

Some details of this conversion from Mn(Cl) to Mn(II) deserve further comment. The center that we call Mn(Cl) consists of a manganese ion next to a chlorine ion which has replaced a fluorine, but we have not specified the next nearest halide. We have assumed that this center has optical properties that are not measurably altered by the type of halogens located immediately above and below the chlorine ion. Because this is not strictly true, the dominant sharp line in the excitation spectra of the Mn(Cl) center, located at 4050Å, is actually a very narrow envelope containing the sharp lines of all of the varieties of these Mn(Cl) centers corresponding to the different arrangements of halogen next nearest neighbors. An analogous situation occurs for the Mn(II) center.

A Mn(Cl) center with a fluorine ion located directly above or below it along the "c" axis transforms into a Mn(II) center by simply shifting the halogens by one position up or down along the "c" axis. This model does not require any movement or diffusion of the manganese ions and the presence of halogen vacancies would allow such arrangements to occur at relatively low temperatures.

In addition to the shift in the manganese emission envelope in the mixed chloro-fluorophosphates upon quenching, Apple and Ishler reported upon a similar shift after quenching calcium chlorophosphate phos-

phors doped with antimony and manganese. A different mechanism must be responsible for this shift as these phosphors contain no fluorine. In order to investigate this effect, we prepared and quenched some calcium chlorophosphate phosphors, and did observe the wavelength shift in the manganese fluorescence envelope that Apple and Ishler reported for this phosphor upon quenching. On the other hand, excitation spectra taken before and after the quenching revealed little change except that the dominant sharp line in the manganese excitation spectrum of the unquenched chlorophosphate phosphor was located at 4055Å while in the quenched phosphor it was located at 4060.

No analysis of this effect was possible because we had no background information on the optical properties of the various types of manganese present in calcium chlorophosphate phosphors. Such information should prove to be much more difficult to obtain in the chlorophosphate system than in the fluorophosphate system due to its greater structural complexity and the larger number of possible types of manganese sites.

Acknowledgments

The authors would like to express their appreciation to Drs. R. C. Miller and R. W. Warren for many valuable discussions. P. C. Handke provided technical assistance.

Manuscript submitted May 10, 1971; revised manuscript received *ca.* July 2, 1971.

Any discussion of this paper will appear in a Discussion Section to be published in the June 1972 JOURNAL.

REFERENCES

1. E. F. Apple and W. E. Ishler, "Luminescence of Organic and Inorganic Materials," p. 576, John Wiley & Sons, Inc., New York (1962).
2. R. A. Young and J. C. Elliott, *Arch. Oral Biol.*, **II**, 699 (1966).
3. J. S. Prener, *This Journal*, **114**, 77 (1967).
4. S. B. Hendricks, M. E. Jefferson, and V. M. Mosely, *Z. Krist.*, **81**, 3S2 (1932).
5. F. M. Ryan, R. C. Ohlmann, J. Murphy, R. Mazelsky, G. R. Wagner, and R. W. Warren *Phys. Rev.*, **B2**, 2341 (1970).
6. F. M. Ryan and F. M. Vodoklys, *This Journal*, **118**, 1814 (1971).
7. J. G. Rabatin and G. R. Gillooly, *This Journal*, **111**, 542 (1964).

Effects of the $AsCl_3$ Mole Fraction on the Incorporation of Germanium, Silicon, Selenium, and Sulfur into Vapor Grown Epitaxial Layers of GaAs

J. V. DiLorenzo* and G. E. Moore, Jr.

Bell Telephone Laboratories, Incorporated, Murray Hill, New Jersey 07974

ABSTRACT

The effect of the $AsCl_3$ mole fraction on the incorporation of germanium, silicon, selenium, and sulfur in GaAs epitaxial layers has been studied. The layers were grown by vapor phase epitaxy (VPE) using the $AsCl_3|Ga|H_2$ synthesis system. Both room- and low-temperature Hall data as well as photoluminescence spectra were used to examine the incorporation of the impurities into grown layers. The results of these studies indicate that the incorporation of silicon and germanium decreases with increasing $AsCl_3$ mole fraction, and that the incorporation of sulfur and selenium is largely unaffected by changes in the $AsCl_3$ mole fraction. The results are interpreted using a model which proposes that the major background dopant in this system is silicon and that the mole fraction effect is due to the interaction of stable chlorides of silicon with hydrogen chloride in the reactor. A calculation of the activity of silicon as a function of the hydrogen chloride pressure is presented. The results compare reasonably well with the experimental data.

We have recently reported the variation of carrier concentration with the $AsCl_3$ mole fraction (1) of undoped, p-type vapor phase epitaxial (VPE) layers of GaAs. The layers were grown by the $AsCl_3 \mid Ga \mid H_2$ chemical vapor deposition system. The effect was originally reported by Cairns and Fairman (2) for n-type epitaxial layers with residual background doping present in the epitaxial reactor. The effect observed by Cairns and Fairman has now been observed by various other workers as well (3, 4). Cairns and Fairman (5) have also observed a variation in carrier density with $AsCl_3$ mole fraction for epitaxial crystals doped with silicon by transport of silicon from the gallium source.

In this paper, we report on the dependence of the incorporation of germanium, silicon, selenium, and sulfur into VPE GaAs on the $AsCl_3$ mole fraction. The carrier concentration and mobility of the doped layers were determined as well as the low-temperature photoluminescence spectra. In addition, the photoluminescence spectra of several silicon doped VPE GaAs samples were investigated.[1]

An analysis of these data has led to the conclusion that the incorporation of the Group IV dopants, silicon and germanium, into the epitaxial layers depends strongly on the $AsCl_3$ mole fraction. On the other hand, the dependence of the incorporation of sulfur and selenium on the $AsCl_3$ mole fraction was substantially different in that at the higher doping levels the concentration of sulfur and selenium (10^{16} cm^{-3}) is largely unaffected by the $AsCl_3$ mole fraction.

The results are interpreted using a model which suggests that the Group IV elements silicon and germanium, having stable chlorides, can chemically interact with HCl present in the reactor. On the other hand, the incorporation of sulfur and selenium, which do

* Electrochemical Society Active Member.

Key words: gallium arsenide vapor epitaxy, impurity incorporation, electron mobility, photoluminescence.

[1] These samples were kindly furnished by B. Cairns, Fairchild Semiconductor, Research and Development Laboratory.

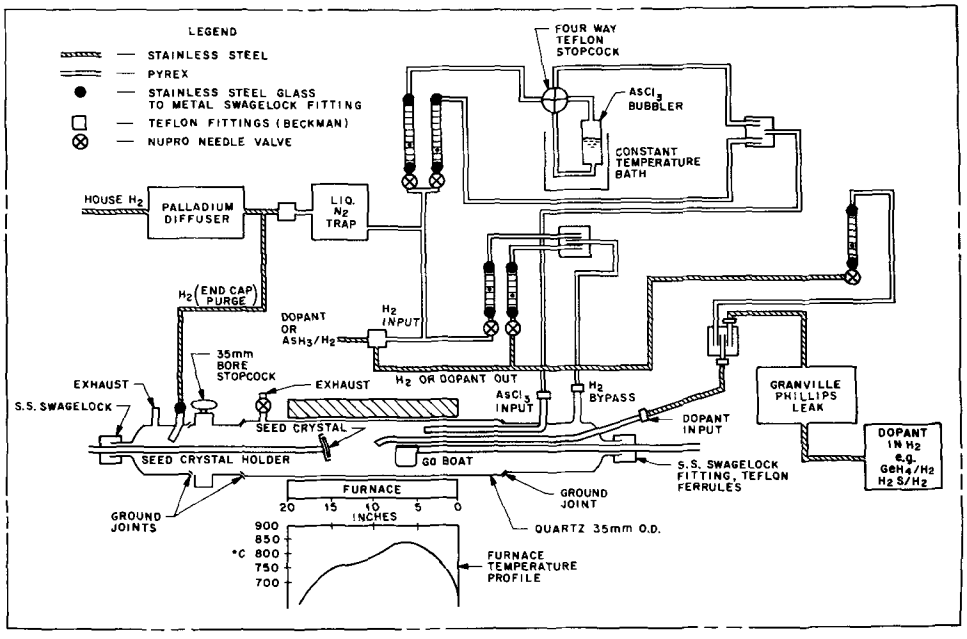

Fig. 1. Schematic diagram of the epitaxial deposition system.

not have stable chlorides at the epitaxial growth temperatures, is unaffected by the HCl concentration in the reactor.

Growth System and Procedures

Epitaxial reactor.—A standard $AsCl_3$ | Ga | H_2 synthesis system (6) was used to grow epitaxial crystals of GaAs substrates. A schematic diagram of the epitaxial reactor is shown in Fig. 1.

The materials used for the construction of the system are indicated in the legend in Fig. 1. The reactor tube, gallium boat, seed crystal holder, $AsCl_3$ input, and hydrogen bypass lines were constructed of high purity synthetic quartz. Epitaxial layers were doped in the 10^{15} to 10^{17} cm^{-3} range reproducibly by introduction of a mixture of either GeH_4, H_2Se, or H_2S in hydrogen through a variable leak, diluting the mixture further with hydrogen and passing it into the reaction zone. The concentrations of dopant gas relative to hydrogen present in the supply tanks were 5 ppm for GeH_4 | H_2, 5 ppm H_2Se | H_2, and 1000 ppm for H_2S | H_2.

The main reactor tube, boat, input glassware, substrate holder and output glassware were cleaned with aqua regia and given multiple rinses in 1.5 x 10^7 ohm-cm deionized water prior to assembly. The ground joints were greased with a minimum amount of a fluorocarbon grease to ensure a leak-free seal.

Starting materials and growth procedures.—Starting materials used were Ga (99.99999%, Eagle Picher Company); $AsCl_3$ (99.99999%, Mitsubishi Metal Mining Company) and Pd-diffused hydrogen. The O_2 contamination of the hydrogen was measured at all inputs to the main reaction tube by gas chromatography. The following results were obtained:

Output of Pd-diffuser: 0.6 ± 0.1 ppm O_2.
Input to liquid N_2 cold trap: 0.6 ± 0.1 ppm O_2.
$AsCl_3$ input to furnace: (0.9 to 2.0) ± 0.2 ppm O_2.
H_2 bypass input: (0.8 to 4.0) ± 0.2 ppm O_2.
Dopant input: 1.0 ± 0.2 ppm O_2.

Substrate materials were either chromium doped, boat-grown, semi-insulating ($\rho > 10^8$ ohm-cm at 300°K) GaAs, or tellurium-, selenium-, or silicon-doped, boat-grown, N^+ ($\rho \simeq 0.003$ ohm-cm at 300°K) GaAs. The substrates were cut as 30 mil thick slices orientated 2° off {100} towards {110}. After cutting, the substrates were chemically cleaned with a $5H_2SO_4$: H_2O: H_2O_2 etch, mechanically lapped, and finally chemically polished using Br_2/CH_3OH.

Prior to epitaxial growth the substrates were degreased in boiling trichlorethylene, rinsed in acetone and given multiple rinses in hot isopropanol. After degreasing, the substrates were etched for 2 min in $5H_2SO_4/H_2O_2/H_2O$ at room temperature and rinsed in deionized water. Following the etch, the substrates were soaked from 30 to 90 min in sodium ethylenediaminetetracetate, a complexing agent for metals, and rinsed for approximately 10 min in running deionized water.

The mole fraction of $AsCl_3$ was varied by changing the relative amounts of flow through the bubbler and H_2 dilutent, maintaining the total flow constant as closely as possible ($\approx$ 130 cm^3/min).

Measurements and Results

Growth parameters.—Ga/As ratio.—The marked dependence of the electrical properties of the epitaxial layers on the $AsCl_3$ mole fraction discussed below could be due to a varying ratio of Ga to As in the gas stream. Thus it was necessary to determine whether the concentration of Ga relative to As in the gas phase was constant as the concentration of $AsCl_3$ was increased.

A boat with a removable liner containing Ga saturated with GaAs was inserted into the furnace and positioned at the normal boat position. $AsCl_3$ was passed into the reactor under flow conditions similar to those of the growth experiments, and the weight loss of the material from the liner was measured to the nearest 0.1 mg to determine the transport of Ga from the boat.

The transport of $AsCl_3$ was determined by trapping the $H_2/AsCl_3$ stream at 77°K and measuring the volume of the liquid obtained in a specified period of time. The flow through the bubbler was 175 cm^3/min, approximately the highest flow used in epitaxial growth (equivalent to an $AsCl_3$ mole fraction of 6 x 10^{-3}). It was found that the bubbler completely saturated the H_2 gas with $AsCl_3$ (to within experimental error of measurement) at these conditions. Therefore, it was assumed that complete saturation of the H_2 with $AsCl_3$ occurred at lower flow rates through the bubbler.

The data obtained on the weight loss of material from the boat and the calculated transport ratio of Ga to As are listed in Table I. The data clearly indicate that the ratio of Ga to As, that is, the ratio of the number of moles of gallium relative to the number of moles of arsenic transported to the deposition zone, is

Table I. Experimentally determined ratio of Ga to As for $AsCl_3$ mole fractions from 1.52×10^{-3} to 5.82×10^{-3}

$AsCl_3$ Mole fraction $\times10^3$	Moles $AsCl_3$/min $\times10^5$	Temp (°C) Ga	Wt. Ga transported (g)	Ga/As ratio
1.52	2.08	858	0.0820	1.88
2.50	3.98	858	0.1513	1.82
4.78	8.58	858	0.3471	1.93
5.82	10.2	858	0.4223	1.84

not changing significantly over the range of $AsCl_3$ mole fractions used in these experiments.

Since, in an epitaxial growth system, the $AsCl_3$ mole fraction is the independent variable, all data have been analyzed in terms of the $AsCl_3$ mole fraction.

Characteristics of the epitaxial layers.—The thickness, the carrier concentration, and Hall mobility, at room temperature and at 77°K, and the photoluminescence of selected layers were measured in an effort to correlate characteristics of the grown layers with various growth parameters.

Electrical measurements.—Germanium doped layers.—In Table II the carrier concentration and Hall mobility at room temperature and at 77°K, the $AsCl_3$ mole fraction, and thickness of germanium-doped layers are listed. The variation in the thicknesses of these layers resulted mainly from different growth periods. We have observed (1) that the growth rate varies only by about 20-30% as the $AsCl_3$ mole fraction changes by as much as a factor of 6. This is consistent with the data of Cairns and Fairman (2).

The layers are divided into three groups. Group A was grown with a GeH_4 mole fraction of 10^{-10} in the vapor. Groups B and C were grown by introducing GeH_4 at mole fractions of 5×10^{-10} and 10^{-9}, respectively. The factor of ten change in the GeH_4 mole fraction produced a change in the carrier concentration of approximately a factor of ten as well. Sample D 225 was undoped and is characteristic of the background level present in the reactor at an $AsCl_3$ mole fraction of 2×10^{-3} prior to the growth of Group C.[2]

The carrier concentration of the germanium-doped layers decreases as the $AsCl_3$ mole fraction increases. This is shown graphically in Fig. 2 where n as a function of the $AsCl_3$ mole fraction for germanium-doped layers is plotted. The rate of decrease for the most lightly doped of the germanium layers, Group A, is greater than for Group B or C.

[2] The room temperature and liquid nitrogen mobilities of sample D225 are typical of the values obtained for undoped samples with $n \simeq 0.6 - 2\times10^{15}$ cm^{-3}.

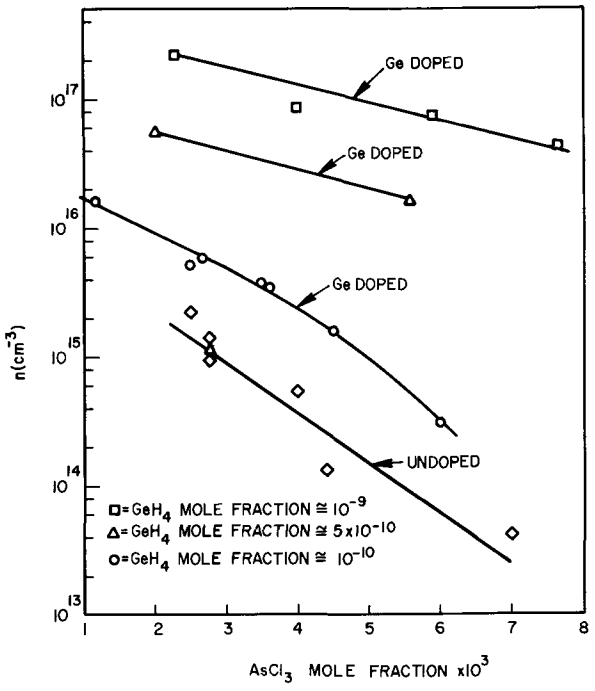

Fig. 2. The carrier concentration, n, of germanium-doped and updoped epitaxial layers plotted against the $AsCl_3$ mole fraction.

Included also in Fig. 2 is the dependence of the carrier concentration of undoped layers on the $AsCl_3$ mole fraction. This plot is representative of the type of variation we have observed although the curve can be displaced vertically from reactor to reactor.

Sulfur and selenium doped layers.—In Table III the thickness, $AsCl_3$ mole fraction, carrier concentration, and Hall mobility at 300°K and at 77°K, are listed for sulfur-doped layers while the same quantities for selenium-doped layers are contained in Table IV. The layers are divided into Groups D, E and F. Group D was grown at an H_2S mole fraction of approximately 10^{-9} while Group E was grown at a mole fraction of

Table II. Carrier concentration and mobility at 300°K and 77°K for Ge-doped layers

[Mole fraction GeH_4 constant at $\cong 10^{-10}$ for Group A, 5×10^{-10} for Group B, and 10^{-9} for Group C]

Sample	Thickness (microns)	Mole fraction $\times10^3$	n (300°K) (cm^{-3})	n (77°K) (cm^{-3})	μ(300°K) (cm^2/V-sec)	μ(77°K) (cm^2/V-sec)
Group A						
D129	8.3	2.7	$5\text{-}6^{15}$	—	[N+ substrate]	—
D133	5.9	3.6	$3\text{-}4^{15}$	—	[N+ substrate]	—
D134	5.0	1.2	1.67×10^{16}	1.16×10^{16}	5060	12,700
D135	6.2	1.5	5.0×10^{15}	4.5×10^{15}	7160	26,400
D136	6.5	2.5	5.38×10^{15}	4.54×10^{15}	6911	28,782
D137	5.9	3.5	(1)4.63×10^{15} (2)4.2×10^{15}	(1)3.80×10^{15} (2)3.38×10^{15}	6220 6600	26,906
D138	5.0	4.5	1.59×10^{15}	1.57×10^{15}	7062	34,024
D139	4.7	6.0	3.2×10^{14}	3.2×10^{14}	7600	55,817
Group B						
D217	3.0	2.0	5.56×10^{16}	4.08×10^{16}	4164	6,925
D218	3.3	5.6	1.66×10^{16}	9.60×10^{15}	4764	17,372
Group C						
D225*	2.0	2.0	6.1×10^{14}	7.2×10^{14}	7630	55,185
D227	(1)3.8 (2)4.1	2.35	(1)2.4×10^{17} (2)2.1×10^{17}	(1)2.0×10^{17} (2) —	(1)2727 (2)3011	(1)3,011 (2) —
D228	7.8	4.00	8.82×10^{16}	6.93×10^{16}	3433	5,209
D229	9.2	5.9	7.4×10^{16}	5.54×10^{16}	3273	5,375
D230	8.3	7.7	4.4×10^{16}	3.3×10^{16}	4841	8,070

(1) Two separate areas of sample.
(2) Two separate areas of sample.
* Undoped.

Table III. Carrier concentration and mobility at 300°K and 77°K for S-doped layers

Sample	Thickness (microns)	Mole fraction $\times 10^3$	n (300°K) (cm^{-3})	n (77°K) (cm^{-3})	μ(300°K) (cm^2/V-sec)	μ(77°K) (cm^2/V-sec)
Group D[a]						
D181	5.3	2.5	4.10×10^{16}	3.13×10^{16}	5075	8,910
D182	5.5	5.6	2.71×10^{16}	1.98×10^{16}	5429	11,782
D191	2.9	6.8	5.78×10^{16}	4.51×10^{16}	3411	5,322
D208	3.8	2.1	2.62×10^{16}	2.07×10^{16}	4982	10,741
D209	7.7	6.8	3.68×10^{16}	2.56×10^{16}	3880	10,206
Group E[b]						
D183	4.4	2.5	1.5×10^{16}	—	N+ substrate	—
D184	6.0	5.6	5×10^{15}	—	N+ substrate	—
D189	2.3	4.0	4×10^{15}	—	N+ substrate	—
D190	5.0	7.0	3×10^{15}	—	N+ substrate	—
D193	6.2	3.0	1.02×10^{16}	8.24×10^{15}	5133	16,343

[a] = H_2S input $\cong 10^{-9}$ mole fraction.
[b] = H_2S input $\cong 5 \times 10^{-10}$ mole fraction.

Table IV. Carrier concentration and mobility at 300°K and 77°K for Se-doped and undoped layers

Sample	Thickness (microns)	Mole fraction $\times 10^3$	n (300°K) (cm^{-3})	n (77°K) (cm^{-3})	μ(300°K (cm^2/V-sec)	μ(77°K) (cm^2/V-sec)
Group F [Se-doped]						
D165	5.9	2.5	$2.5\text{-}4 \times 10^{15}$	—	[N+ substrate]	—
166	5.9	2.5	$5.0\text{-}9 \times 10^{15}$	—	[N+ substrate]	—
167	5.6	2.5	$4.5\text{-}7 \times 10^{15}$	—	[N+ substrate]	—
168	5.9	2.5	1×10^{16}	—	[N+ substrate]	—
169	2.6	2.5	5.75×10^{15}	5.50×10^{15}	7165	33,800
170	3.3	1.5	3.6×10^{15}	3.2×10^{16}	6265	26,139
171	2.9	3.5	1.14×10^{15}	1.17×10^{15}	6503	24,215
172	3.5	4.5	7.48×10^{15}	6.24×10^{15}	6732	22,381
173	6.5	2.5	1×10^{16}	—	[N+ substrate]	—
174	3.5	5.7	1.6×10^{16}	1.1×10^{16}	5000	10,137
Group G [undoped]						
(1) D185	2.5	2.5	$2.0\text{-}2.5 \times 10^{15}$	—	[N+ substrate]	—
(6) D210	6.8	2.8	$0.99\text{-}1.1 \times 10^{15}$	—	[N+ substrate]	—
(7) D211	11.3	2.8	1.3×10^{15}	—	[N+ substrate]	—
(3) D188	4.8	4.0	$5\text{-}6 \times 10^{14}$	—	[N+ substrate]	—
(5) D207	7.4	4.4		1.35×10^{14}		43,393
(4) D194	19.0	2.8	$1.1\text{-}1.5 \times 10^{15}$	1.10^{15}	7525* 7700	44,000
(2) D187	5.0	7.0		$5.3^{13} \times 10^{13}$		64,783

* Mobility obtained by magnetoresistance of microwave devices from two separate areas of sample.

approximately 5×10^{-10}. Group F was grown at an H_2Se mole fraction of approximately 5×10^{-8}.

In Fig. 3 the variation of n with $AsCl_3$ mole fraction for both groups of sulfur-doped layers and for selenium-doped layers is presented. From an analysis of the data in Tables III and IV and Fig. 3, it is apparent that the incorporation of sulfur and selenium is markedly different from that of germanium. There is litle variation in the doping level with $AsCl_3$ mole fraction for sulfur-doped layers having $n \simeq$ (2 to 5) $\times 10^{16}$ cm^{-3} over an $AsCl_3$ mole fraction range of (2 to 7) $\times 10^{-3}$. (Group D). Only a slight decrease in doping level with $AsCl_3$ mole fraction was observed for Group E.

For the layers doped with selenium, we have observed scatter in the value of n at a given mole fraction [see Fig. 3, n at a mole fraction of 2.5×10^{-3}]. This is due to the instability of a 5 ppm H_2Se/H_2 source for doping. For example, the carrier concentration observed at a mole fraction of 2.5×10^{-3} ranged over a factor of three (see Table IV and Fig. 2). We present the data for selenium-doped layers in order to indicate the trend of the variation of selenium incorporation with $AsCl_3$ mole fraction. The carrier concentration of these layers increases slightly with increasing $AsCl_3$ mole fraction. Like sulfur, the dependence of the incorporation of selenium on the $AsCl_3$ mole fraction is different from that of silicon or germanium.

In Fig. 4 the carrier mobilities at 77°K *vs.* $AsCl_3$ mole fraction for germanium-doped samples of Groups A and C, for sulfur-doped samples of Group D and for selenium-doped samples are presented. The increase in carrier mobility of the germanium-doped samples correlates with a decrease in the carrier concentration as the $AsCl_3$ mole fraction increases. The mobility of sulfur-doped samples is invarient with the $AsCl_3$ mole

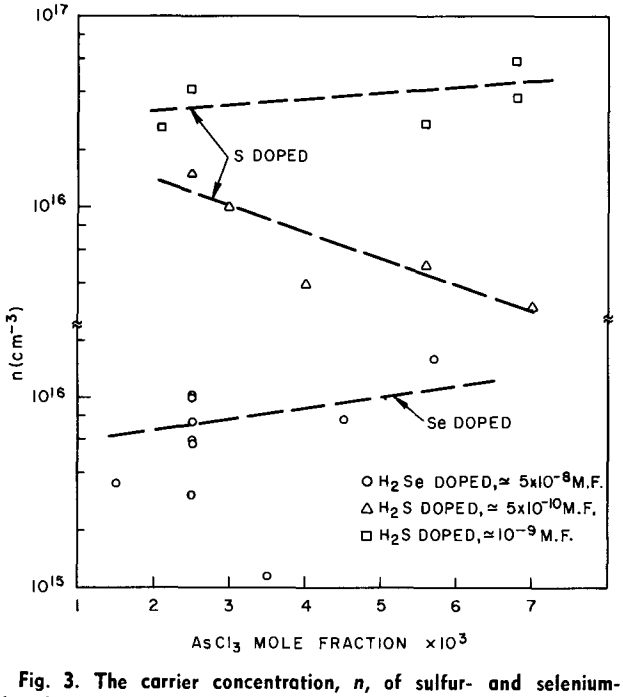

Fig. 3. The carrier concentration, n, of sulfur- and selenium-doped epitaxial layers plotted against the $AsCl_3$ mole fraction.

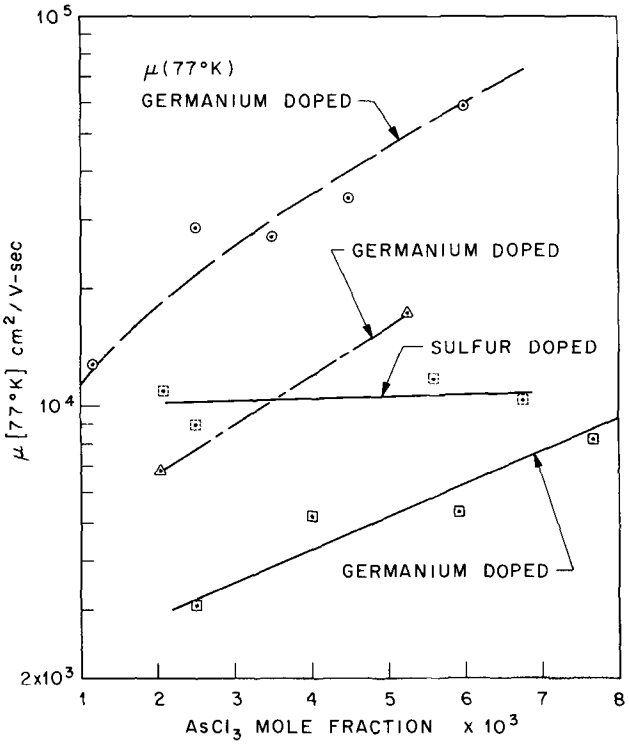

Fig. 4. The carrier mobility, μ, at 77°K of germanium- and sulfur-doped layers plotted against the $AsCl_3$ mole fraction.

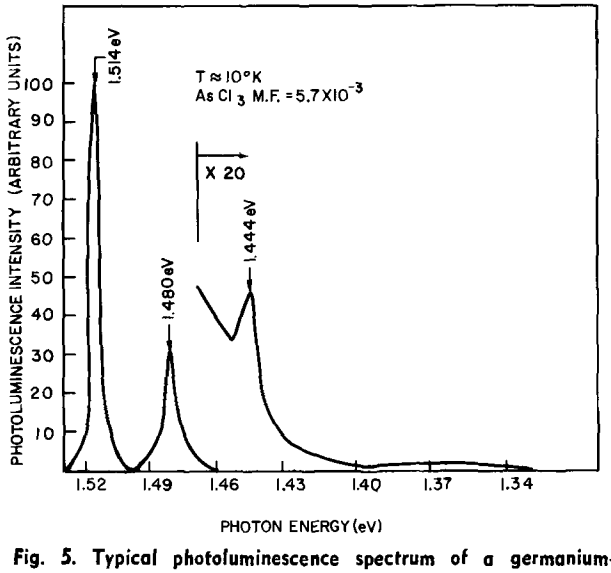

Fig. 5. Typical photoluminescence spectrum of a germanium-doped layer at ~10°K.

fraction, while the mobility of selenium-doped samples decreases with increasing $AsCl_3$ mole fraction.

Photoluminescence

The electrical measurements indicate that increasing the $AsCl_3$ mole fraction inhibits the incorporation of electrically active centers in the Ge- and Si-doped samples but has little effect in the Se- and S-doped crystals. Photoluminescence was used to identify the optically active impurities in the crystals in an attempt to compare their behavior as a function of the $AsCl_3$ mole fraction with that of the electrically active impurities.

A typical low-temperature photoluminescence spectrum of germanium-doped epitaxial GaAs is shown in Fig. 5. Three peaks, occurring at 1.514, 1.480, and 1.444 eV, are readily identifiable. The small rise centered at about 1.356 eV is due to copper, which is a common contaminant in GaAs (1). This peak was noted in only two of the samples studied, and the copper contamination is thought to be insignificant.

The 1.480 eV peak arises from transitions between the conduction band and the Ge acceptors (7, 8) (B-A transitions). Since the energy gap (E_G) for GaAs at 10°K is 1.520 eV (9), the Ge acceptor level lies 40 meV above the valence band. The 1.444 eV peak is the first LO phonon replica of the Ge acceptor peak and occurs 35 meV below the Ge acceptor peak [*i.e.* 76 meV from the valence band], in good agreement with the energy of the LO phonon in GaAs (10).

The higher energy peak at 1.514 eV may be due to a variety of processes. Since the luminescent energy is less than E_G by 6 meV, the recombination does not involve band-to-band transitions. There are two alternative explanations for the nature of the 1.514 eV peak: the recombination may be due to (*I*) donor-to-valence band transitions (D-B) or (*II*) annihilation of excitons bound to neutral or ionized donors (11).

Thus the photoluminescence spectrum consists of a high-energy peak assumed to be due to silicon or germanium donors (depending on the dopant), an acceptor peak (also associated with the germanium dopant), and its phonon replica. No other impurities, aside from slight amounts of copper in two of the crystals, appear in significant amounts. The silicon-doped samples exhibit identical spectra except that the germanium acceptor peak at 1.480 eV is replaced by a peak at 1.490 eV associated with silicon acceptors (12).

The above results indicate that Ge and Si are the only optically active impurities in the samples. The next step is to relate the intensities of the photoluminescence peaks to the concentrations of Si and Ge. To do this we will assume that these recombination paths exist: (*I*) donor-to-valence band (D-B) radiative recombination (the high energy peak in Fig. 5); (*II*) conduction band to acceptor (B-A) radiative recombination (the 1.480 eV peak in Fig. 5); (*III*) all other nonradiative (NR) recombinations.

The rate equation for the valence band then becomes

$$\dot{P} = G - \frac{P}{\tau_{DB}} - \frac{P}{\tau_c} - \frac{P}{\tau_{NR}} = G - \frac{P}{\tau_T} \qquad [1]$$

where P = free hole concentration, G = generation rate of free holes, τ_{DB} and τ_{NR} are the lifetimes for D-B and NR transitions, τ_c is the capture time for the acceptors, and τ_T is the total lifetime for the minority carriers (holes). Assuming equilibrium, we have $P = \tau_T G$.

For D-B transitions we can write (13, 14)

$$I_D = \frac{P}{\tau_{DB}} = \frac{\tau_T G}{\tau_{DB}} = \tau_T G B N^\circ_D \qquad [2]$$

where B is the mean capture coefficient and N°_D represents the number of neutral donors. B depends upon the effective mass, index of refraction, activation energy, recombination energy, and temperature (14). By holding the intensity of the exciting radiation and the temperature constant, we can hold G and B constant. Further, since (15)

$$N^\circ_D \simeq N_D - N_A \qquad [3]$$

for these temperatures, where N_D = the total number of donors and N_A = total number of acceptors, we can write

$$I_D = A\tau_T(N_D - N_A) \qquad [4]$$

Similarly, the rate equation for the acceptors will be

$$N^+_A = \frac{P}{\tau_c} - \frac{N^+_A}{\tau_{BA}} \qquad [5]$$

where N^+_A is the number of neutral acceptors and τ_{BA} is the lifetime of B-A transitions. At equilibrium we have

$$\frac{P}{\tau_c} = \frac{N^+_A}{\tau_{BA}} = I_{BA} \quad [6]$$

τ_c can be written as (16)

$$\tau_c^{-1} = \theta v_{th} N_A \quad [7]$$

where θ is the capture cross section for the center and v_{th} its thermal velocity. Both θ and v_{th} are constants under the experimental conditions and we have, combining Eq. [2], [6], and [7]

$$I_{BA} = C\tau_T N_A \quad [8]$$

Equations [4] and [8] indicate that if the experimental conditions, *i.e.* temperature, intensity of exciting radiation, *etc.*, are held constant for a series of crystals, I_D and I_{BA} will be proportional to $\tau_T(N_D - N_A)$ and $\tau_T N_A$, respectively. If we make the further assumption that τ_T is constant for these crystals, we arrive at the desired correspondence between the intensities of the photoluminescence peaks and the concentration of the various impurities. This last assumption implies that the limiting recombination process is unaffected by changes in the $AsCl_3$ mole fraction. This would be true if the limiting process were band-to-band recombination, for example.

Figure 6 illustrates the dependence of the integrated intensities of the donor (I_D) and acceptor ($I_{Ge} = I_{BA}$) peaks in Ge-doped GaAs on the $AsCl_3$ mole fraction. The data were taken under identical optical and thermal (10°K) conditions. On the same graph the values for N_A and N_D for the same crystals are plotted, using the results of Table II (17). The close correlation of the electrical and optical data leads to several conclusions: (*A*) the assumption that τ_T is a constant for this series appears to be valid; (*B*) the Ge_{donor} to $Ge_{acceptor}$ ratio is independent of the $AsCl_3$ mole fraction; and (*C*) the total number of Ge atoms incorporated decreases sharply as the $AsCl_3$ mole fraction is increased.

Figure 7 shows the same data for the Si-doped samples. The Si-doped samples were grown on N^+ substrates and Hall data could not be taken. Thus

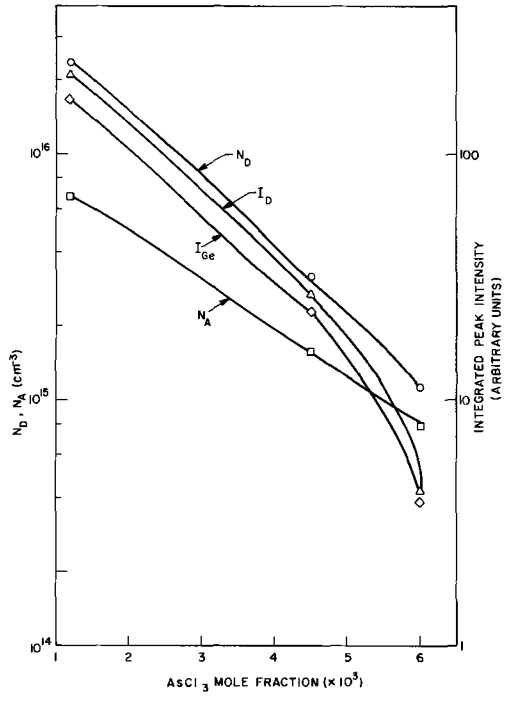

Fig. 6. The impurity concentrations, N_A and N_D, and integrated photoluminescence peak intensities, I_D and I_{Ge}, of Ge-doped GaAs plotted against the $AsCl_3$ mole fraction.

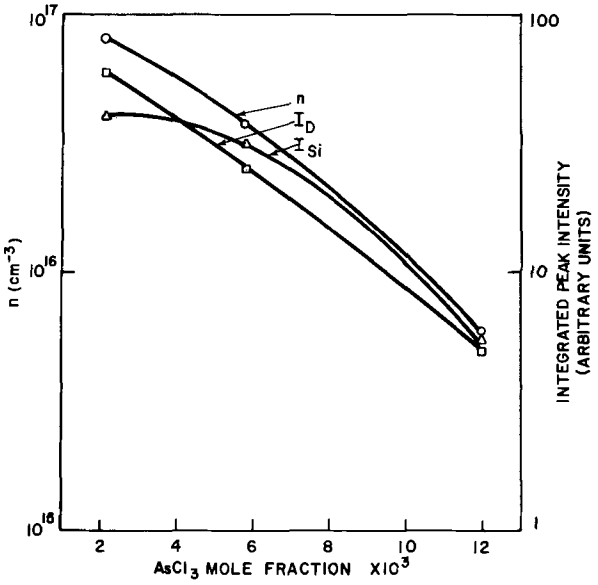

Fig. 7. The carrier concentration and integrated peak intensity of the near bandgap peak and silicon acceptor peak plotted against $AsCl_3$ mole fraction.

$n = N_D - N_A$ is plotted with I_D and I_{Si}. The conclusions are identical to those for Ga-doped crystals.

Discussion

In the discussion of these results it is most useful to keep in mind the data presented in Fig. 2-7. The conclusions which are reached concerning the incorporation of germanium, silicon, sulfur, and selenium are summarized as follows:

1. The incorporation of germanium decreases as the $AsCl_3$ mole fraction increases. This is based on the decrease of n with $AsCl_3$ mole fraction [Fig. 2], the increase in mobility with increasing mole fraction [Fig. 4], and the decrease in integrated peak intensities of germanium donors and acceptors in layers grown with increasing mole fraction [Fig. 6].

2. The incorporation of silicon decreases with increasing $AsCl_3$ mole fraction [Fig. 7].

3. The dependence of the incorporation of sulfur and selenium on the $AsCl_3$ mole fraction is substantially different from that of germanium or silicon. The carrier concentration of sulfur- and selenium-doped layers remains relatively constant as the $AsCl_3$ mole fraction increases [Fig. 3]. In addition, the mobility of these layers does not increase with $AsCl_3$ mole fraction [Fig. 4].

The significance of the above statements, we feel, is that they indicate the mechanism for the mole fraction effect observed in undoped $AsCl_3$/Ga/H_2 systems. The specific mechanism involves the interaction of the various impurities with HCl present in the system. Group IV elements, silicon and germanium, have stable chlorides at temperatures in the vicinity of 800°C. Group VI elements, sulfur and selenium, have only stable hydrides under reactor conditions. We can represent a general reaction between a Group IV element, *M*, and HCl in the presence of H_2 as follows

$$(n-2)H_2(g) + MCl_nH_{4-n}(g) \leftrightarrow M(s) + n\,HCl(g)$$

$$\text{at } P_{H_2} = 1 \text{ atm}$$

$$K = \frac{a_M P^n_{HCl}}{P_{MCl_nH_{4-n}}}$$

$$a_M = \frac{K P_{MCl_nH_{4-n}}}{P^n_{HCl}}$$

where n is an integer, K is the equilibrium constant and a_M is the activity of $M(s)$. The effects of $SiCl_2$,

$GeCl_2$, *etc.* have been neglected. Qualitatively we see that the activity of $M(s)$ varies inversely as P_{HCl} to P^4_{HCl} for the $MClH_3$ to MCl_4 compounds.

This model proposes that in an undoped $AsCl_3/Ga/H_2$ system exhibiting an $AsCl_3$ effect, the major background dopant is silicon, and that the degree of silicon incorporation depends strongly on the HCl pressure, which is proportional to the input $AsCl_3$ mole fraction X_{AsCl_3} [*i.e.* $P_{HCl} \propto P_{AsCl_3} = X_{AsCl_3} P_{total}$]. Using direct image mass analysis (18), we have identified silicon as a major contaminant of layers exhibiting high-resistivity regions (19-21) at the substrate-epitaxial interface. Silicon has been identified as an impurity in VPE films using photoluminescence (1, 12). Doping levels in undoped reactors have been reported as high as 2 to 3 $\times$ $10^{16}/cm^3$ at an $AsCl_3$ mole fraction of $\approx 2 \times 10^{-3}$. We have observed levels as high as 5 $\times$ 10^{17} cm^3 at the same $AsCl_3$ mole fraction. Therefore, it is necessary to determine whether sufficient concentrations of silicon halides are present to explain doping levels of 10^{16} to 10^{17} cm^{-3}.

The major chemical components of the growth system are: $HCl(g)/ H_2(g)/Ga(l)$ saturated with $GaAs/ H_2O(g)/AsCl_3(g)/SiO_2(s)$. The reactions leading to the formation and transport of GaAs in this system are as follows:

[1] $AsCl_3(g) + 3/2\, H_2(g) \rightleftarrows 1/4\, As_4(g) + 3HCl(g)$

[2] $Ga(l) + 1/4\, As_4(g) \rightleftarrows GaAs(s)$

[3] $GaAs(s) + HCl(g) \rightleftarrows GaCl(g) + 1/2\, H_2(g) + 1/4\, As_4(g)$

[4] $Ga(l) + HCl(g) \rightleftarrows GaCl(g) + 1/2\, H_2\,(g)$

therefore for $P^o_{AsCl_3} = P_{AsCl_3}$ (input)

$$P^o_{HCl} \simeq 3P^o_{AsCl_3} \text{ (before boat)}$$

$$P_{As_4} = 1/4\ P^o_{AsCl_3}$$

$$P_{HCl} = 1/3\ P^o_{HCl} \text{ (i.e. downstream of boat)}$$

Reaction [1] goes essentially to completion while reaction [2] produces a skin of GaAs over the gallium source when the saturation concentration of arsenic in gallium at 850°C is reached. Reaction [3] represents the over-all reaction for both transport of the GaAs skin at 850°C and the deposition reaction at the seed. Both of the reactions [2] and [3] are sensitive to the coupling of the influent gas stream containing $AsCl_3$ with the gallium boat. If the coupling is poor, the skin of GaAs will not be uniform and reaction [4] easily takes place. Assuming a well-saturated boat and

$$P^o_{AsCl_3} = 5 \times 10^{-3} \text{ atm}$$

then

$$P_{HCl(equilibrium)} \simeq 5 \times 10^{-3} \text{ atm}$$

downstream of the boat.

In the Appendix we have listed reactions between hydrogen, quartz, and HCl which lead to the formation of the volatile silicon compounds SiO, $SiClH_3$, $SiCl_2H_2$, $SiCl_3H$, and $SiCl_4$. The equations which are solved to obtain the pressures of these compounds are listed also. With the assumption that the hydrogen carrier gas is dry [$P^o_{H_2O} \leq 5 \times 10^{-7}$ atm] we calculate the following pressures of volatile silicon compounds and water for $P^o_{AsCl_3} = 5 \times 10^{-3}$ atm

$$P_{H_2O} = 1.3 \times 10^{-6} \text{ atm}; \quad P_{SiCl_4} = 3.8 \times 10^{-9} \text{ atm}$$

$$P_{SiCl_3H} = 1.2 \times 10^{-9} \text{ atm}; \quad P_{SiCl_2H_2} = 5.0 \times 10^{-9} \text{ atm}$$

$$P_{SiClH_3} = 6.3 \times 10^{-7} \text{ atm}$$

and the pressure of all chlorosilanes

$$\Sigma P_{SiClH_3} \rightarrow P_{SiCl_4} = 6.4 \times 10^{-7} \text{ atm}$$

Our calculations, which neglect $P^o_{H_2O}$ and P_{H_2O} resulting from reaction [A-1] listed in the Appendix, agree well with the more exact calculations of Weiner (22).

The calculated level of volatile silicon in the gas is approximately 0.6 ppm. Since P_{GaCl} and P_{As_4} is approximately 1000 ppm, the ratio of $P_{volatile\ silicon}$ to $P_{Ga,As}$ is approximately 10^{-3}. This level of silicon is sufficient to explain a doping level in an undoped system of 10^{16} to 10^{17} cm^{-3}. It can be seen from Eq. [A-7] and [A-8] in the Appendix that

$$P_{chlorosilanes} \propto \frac{1}{P^2_{H_2O}}$$

A calculation of this dependence by Weiner (22) shows that an input H_2 stream with $P^o_{H_2O} \simeq 5$ ppm reduces the silicon concentration by a factor of 10 relative to our assumption of $P^o_{H_2O} \leq 0.5$ ppm atm. This dependence on the $P^o_{H_2O}$ can explain why we have observed in different systems at the same mole fraction of $\simeq 1.5 \times 10^{-3}$ doping levels from (2 to 5) $\times$ 10^{17} cm^{-3} to as low as 5 $\times$ 10^{14} cm^{-3} (23). Cairns and Fairman's data show $n \simeq$ (2 to 5) $\times$ 10^{16} cm^{-3} for an $AsCl_3$ mole fraction of 1.5×10^{-3}.

In Fig. 8 we have plotted the activity of silicon, a_{Si}, at 750°C as a function of P_{HCl} downstream of the boat. This curve was obtained in the following manner: We assume that the pressure of all chlorosilanes, $\Sigma P_{chlorosilanes}$, by wall reactions at 850°C equals the pressure of chlorosilanes in equilibrium at 750°C with H_2, HCl, and Si at the substrate interface.

$$\Sigma P_{chlorosilanes}\text{, from wall reactions, 850°C} = P_{chlorosilanes}\text{, in equilibrium with HCl, } H_2\text{, Si}$$

$$\Sigma P_{chlorosilanes}\text{, wall} = (P_{SiCl_4} + P_{SiCl_3H} + P_{SiCl_2H_2} + P_{SiClH_3})$$

$$\Sigma P_{chlorosilanes} = \frac{a_{Si}P^4_{HCl}}{K_{SiCl_4}} + \frac{a_{Si}P^3_{HCl}}{K_{SiCl_3H}} + \frac{a_{Si}P^2_{HCl}}{K_{SiCl_2H_2}} + \frac{a_{Si}P_{HCl}}{K_{SiClH_3}}$$

$$\frac{\Sigma P_{chlorosilanes}}{\left[\frac{P^4_{HCl}}{K_{SiCl_4}} + \frac{P^3_{HCl}}{K_{SiCl_3H}} + \frac{P^2_{HCl}}{K_{SiCl_2H_2}} + \frac{P_{HCl}}{K_{SiClH_3}}\right]} = a_{Si}$$

For the curve plotted in Fig. 8, the HCl pressure is taken to be P_{HCl}, neglecting the production of HCl during the deposition according to reaction [3]. The

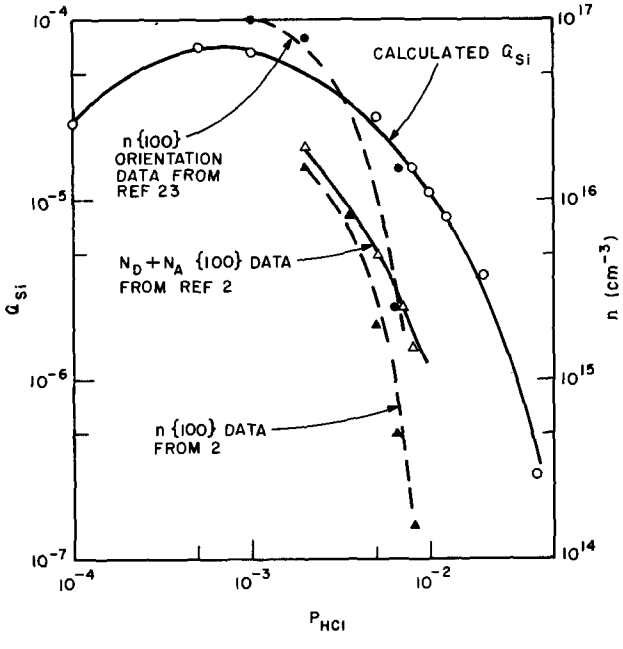

Fig. 8. The calculated activity of silicon, a_{Si}, and selected experimental carrier concentrations plotted against the pressure of HCl.

calculation indicates that the activity of silicon decreases with increasing P_{HCl}.

Also plotted in Fig. 8 are the experimental carrier concentrations, due to residual background doping, for samples grown on the {100} orientation. These curves were prepared from our own unpublished experimental results and from Cairns and Fairman's original data (2). Cairns and Fairman have calculated the total ionized-impurity concentration, $N_D + N_A$, from 77°K Hall mobilities. In Fig. 8 we have plotted their calculated values of $N_D + N_A$ as a function of the $AsCl_3$ mole fraction (note that $P_{AsCl_3} \simeq P_{HCl}$ for this plot). The slope of n *vs.* P_{HCl} is steeper than the calculated activity of silicon as a function of P_{HCl}. The slope of $N_D + N_A$ is in better agreement with the calculated curve. Since the actual silicon incorporation is characterized by $N_D + N_A$ and not $N_D - N_A$ (*i.e.* n), the better correlation is not surprising.

The model we have presented is based entirely on equilibrium thermodynamic calculations. Clearly, there may be kinetic effects operative as well as orientation dependences and growth-rate dependences (24). These effects are presently being investigated.

Conclusions

The investigation of the dependence of the incorporation of dopants into GaAs on the $AsCl_3$ mole fraction has lead to the following conclusions:

(*A*) The incorporation of silicon and germanium decreases as the $AsCl_3$ mole fraction increases.

(*B*) The incorporation of sulfur and selenium is largely unaffected by the $AsCl_3$ mole fraction.

(*C*) The behavior of n with $AsCl_3$ mole fraction for background doping can be explained by assuming that silicon is the major background dopant present in the reactor.

(*D*) The calculated vapor pressure of volatile silicon compounds generated by reactions between HCl(g), H_2(g), and SiO_2(s) is sufficient to explain the doping levels observed in undoped $AsCl_3/Ga/H_2$ systems.

(*E*) The calculated activity of silicon in equilibrium with HCl, H_2, and chlorosilanes at the substrate temperature decreases with increasing HCl pressure. This decrease is in reasonable agreement with the observed experimental decrease in n and $N_D + N_A$ with $AsCl_3$ mole fraction.

Acknowledgments

We wish to thank M. Weiner for extensive discussions concerning this work and his unpublished work. We also wish to thank S. Knight and W. A. Johnson for helpful comments on this work and to A. Machala for growing the epitaxial layers and for general help in all phases of the experimental work.

Manuscript submitted Jan. 28, 1971 revised manuscript received *ca.* June 20, 1971.

Any discussion of this paper will appear in a Discussion Section to be published in the June 1972 JOURNAL.

APPENDIX

Reactions leading to the formation of volatile silicon compounds.—Wall reactions leading to the production of volatile chlorosilanes in the $AsCl_3/Ga/H_2$ system are:

		ΔF° (Kcal/mole) 850°C	K(eq.) 850°C
[A-1]	$H_2(g) + SiO_2(s) \rightarrow SiO(g) + H_2O(g)$	+80.2	3.9×10^{-16}
[A-2]	$3H_2(g) + HCl(g) + SiO_2(s) \rightarrow SiClH_3(g) + 2H_2O(g)$	+80.5	2.0×10^{-16}
[A-3]	$2H_2(g) + 2HCl(g) + SiO_2(s) \rightarrow SiCl_2H_2(g) + 2H_2O(g)$	+79.5	4.1×10^{-16}
[A-4]	$H_2(g) + 3HCl(g) + SiO_2(s) \rightarrow SiCl_3H(g) + 2H_2O(g)$	+70.8	1.5×10^{-14}
[A-5]	$4HCl(g) + SiO_2(s) \rightarrow SiCl_4(g) + 2H_2O(g)$	+56.5	9.8×10^{-12}
and at the boat are			
[A-6]	$4Ga(l) + SiO_2(s) \rightarrow Si(s) + 2Ga_2O(g)$	+87.4	9.2×10^{-18}

The generated pressures of H_2O and chlorosilanes, P_{H_2O} and $P_{chlorosilanes}$, can be obtained by solving the following equations

$$[A\text{-}7] \quad P_{H_2O} = 2[P_{SiClH_3} + P_{SiCl_2H_2} + P_{SiCl_3H} + P_{SiCl_4}]$$

$$[A\text{-}8] \quad P_{H_2O} = 2\left[\frac{K(2)P_{HCl}}{P^2_{H_2O}} + \frac{K(3)P^2_{HCl}}{P^2_{H_2O}} + \frac{K(4)P^3_{HCl}}{P^2_{H_2O}} + \frac{K(5)P^4_{HCl}}{P^2_{H_2O}}\right]$$

The above equations assume: (*i*) P_{SiO} and P_{H_2O} from reaction [A-1] are small, (*ii*) that the contribution of silicon from the boat reaction [A-6] is small, and (*iii*) the vapor pressure of water in the input hydrogen, $P^o_{H_2O}$, is less than or equal to 5×10^{-7} atm.

REFERENCES

1. J. V. DiLorenzo, G. E. Moore, and A. E. Machala, *This Journal*, **117**, 102C (1970).
2. B. Cairns and R. Fairman, *ibid.*, **115**, 327C (1968).
3. W. A. Johnson, Bell Telephone Laboratories, Private communication.
4. K. Lawley, Private communication.
5. B. Cairns and R. Fairman, *This Journal*, **117**, 197C (1970).
6. J. R. Knight, D. Effer, and P. R. Evans, *Solid-State Electron.*, **8**, 178 (1965).
7. G. E. Moore and J. V. DiLorenzo, (ACCG Conference on Crystal Growth Program and Abstracts, 1969) p. 75.
8. F. E. Rosztoczy, F. Ermanis, I. Hayashi, and B. Schwartz, *J. Appl. Phys.*, **41**, 264 (1970).
9. H. C. Casey, *ibid.*, **40**, 163 (1969).
10. S. M. Sze, "Physics of Semiconductor Devices," p. 51, Wiley-Interscience, New York (1969).
11. E. H. Bogardus and H. B. Bebb, *Phys. Rev.*, **176**, 993 (1968).
12. E. W. Williams and E. H. Bebb, *J. Phys. Chem. Solids*, **30**, 1289 (1968).
13. W. P. Dumke, *Phys. Rev.*, **132**, 1998 (1963).
14. E. W. Williams and R. A. Chapman, *J. Appl. Phys.*, **38**, 2547 (1967).
15. R. A. Smith, "Semiconductors," First ed., p. 90, Cambridge University Press, London (1961).
16. J. S. Blakemore, "Semiconductor Statistics," First ed., pp. 188-189, Pergamon Press, New York (1962).
17. D. L. Rode and S. Knight, *Phys. Rev.*, **B3**, 2534 (1971).
18. J. V. DiLorenzo, R. B. Marcus and R. Lewis, *J. Appl. Phys.*, **42**, 729 (1971).
19. Fumio Hasegawa and Takishi Saito, *Japan. J. Appl. Phys.*, **1**, 1125 (1968).
20. R. H. Cox and T. C. Blocker, Paper 100 presented at the Electrochem. Soc. Meeting, Los Angeles, May 10-15, 1970.
21. C. M. Wolfe, A. G. Foyt, and W. T. Lindley, *Electrochem. Technol.*, **6**, 208 (1968).
22. M. Weiner, Private communication.
23. J. V. DiLorenzo, Unpublished work.
24. C. M. Wolfe, G. E. Stillman, and W. T. Lindley, GaAs: 1968 Symposium Proceedings, the Institute of Physics and the Physical Society, (1969) p. 43.

The In-Ga-Sb Ternary Phase Diagram

G. M. Blom*,[1] and T. S. Plaskett*

IBM Thomas J. Watson Research Center, Yorktown Heights, New York 10598

ABSTRACT

The ternary phase diagram for In-Ga-Sb has been determined experimentally and has been verified by calculation. Liquidus compositions are measured along several isotherms together with several solidus compositions on the pseudobinary phase diagram. For the calculation both liquid and solid are assumed to be nonideal. The activity coefficients are calculated using a model with temperature dependent interaction parameters.

Several mixed III-V semiconductor compounds have, because of their band structures, certain advantages over the pure binary compounds. For example, the electronic properties of $In_xGa_{1-x}Sb$ are such that Gunn microwave oscillations can be observed in this material (1), while InSb and GaSb do not show this effect. $In_xGa_{1-x}Sb$ has been grown by liquid phase epitaxy from a nonstoichiometric melt, where the Sb fraction in the liquid does not equal 0.5. The desired solid composition can be grown from either an In-Ga-rich or an Sb-rich melt. Therefore, an understanding of the In-Ga-Sb ternary phase diagram is of major importance in devising crystal growth procedures.

We measured the compositions along isotherms in the In-Ga-Sb liquid and also calculated these isotherms from thermodynamic considerations. The computed isotherms turn out to predict the liquidus lines very well and also give the solidus isotherms. The model for the calculations is based on the known data for the binaries In-Sb, Ga-Sb, and InSb-GaSb. Both liquid and solid are assumed to be nonideal solutions, where an interaction parameter, α, is a measure for the departure from ideality. Similar calculations have been made for other III-V ternary alloys by Stringfellow and Green (2, 3), with a slightly different model and by Blom (4).

Calculation

The model for the calculation of the liquidus and solidus isotherms, for which a detailed description is given in ref. (2, 3, 6), is based on the assumption that equilibrium exists in the system; hence the chemical potentials in the liquid (μ^l) and solid (μ^s) phase are equal for both InSb and GaSb. For InSb, for example

$$\mu^s{}_{InSb}(T) = \mu^l{}_{InSb}(T) = \mu^l{}_{In}(T) + \mu^l{}_{Sb}(T)$$

The chemical potential for each element in the liquid phase can be related to its atomic fraction (N_i) and activity coefficient (γ_i). The chemical potential for the solid is related (5) to the changes in free energy which occur when heating the solid to its melting point, melting it, and cooling it down to the original temperature T, resulting in a supercooled stoichiometric liquid. The final expression for InSb which has to be solved is (2, 3, 6)

$$\gamma_{InSb}N_{InSb} = 4\frac{\gamma_{In}\gamma_{Sb}}{\gamma_{In}{}^{st}\gamma_{Sb}{}^{st}}N_{In}N_{Sb} \exp\left[\Delta S^f{}_{InSb}\left(T^f{}_{InSb} - T\right)/RT\right] \quad [2]$$

where N_{In}, N_{Sb}, and N_{InSb} are the atomic (molecular) fractions of In, Sb, and InSb, and γ_{In}, γ_{Sb}, and γ_{InSb} their respective activity coefficients, $\gamma_{In}{}^{st}$ and $\gamma_{Sb}{}^{st}$ the activity coefficients for In and Sb in a stoichiometric In-Sb melt, $\Delta S^f{}_{InSb}$ the entropy of fusion for InSb and $T^f{}_{InSb}$ its melting point. A similar relation can be written for GaSb. Letting the sum of the atomic fractions in the liquid and of the molecular fractions in the solid both be equal to unity, the equations describing the solid and liquid compositions as a function of temperature can be solved numerically provided that the melting points, entropies of fusion, and activity coefficients are known parameters.

It is the way in which the activity coefficients are determined that can give rise to discrepancies between different models. Obviously, neither the liquid nor the solid in the ternary system are *a priori* ideal ($\gamma_i = 1$) because they generally are not ideal in the binary compounds. Guggenheim (7) describes a lattice model wherein the interaction between nearest neighboring atoms is expressed in terms of the energy per atom and an interaction energy (E_{AB}), which is defined as the energy increase when interchanging two unlike neighboring atoms. An interaction energy equal to zero leads to an ideal solution ($\gamma_i = 1$).

For our calculations we assume a "zero order" approximation in the Guggenheim (7) approach, which means that the atoms in the liquid and the molecules in the solid are randomly distributed in spite of a nonzero energy of mixing. Little would be gained in using a higher order approximation, where no randomness in the distribution of the constituents is assumed, or taking also next nearest neighboring atoms or molecules into account, because the errors introduced in obtaining the interaction parameter α_{AB} are relatively large and of the same order of magnitude as the errors in the heat of fusion (ΔH^f). The interaction parameter α_{AB} is the sum of all the interaction energies E_{AB}. The interaction parameter is composition independent but is assumed, according to measurements on many binary systems, to be linearly dependent on temperature.

The activity coefficient for a binary system is given in terms of the interaction parameter as

$$RT \ln \gamma_{InSb} = \alpha_{InSb\text{-}GaSb} N_{GaSb}{}^2 \quad [3]$$

where $\alpha_{InSb\text{-}GaSb}$ is the parameter describing the interaction between InSb and GaSb molecules in the solid. For the ternary liquid the equivalent expression for the In activity coefficient, for example, is

$$RT \ln \gamma_{In} = \alpha_{In\text{-}Sb}N_{Sb}{}^2 + \alpha_{In\text{-}Ga}N_{Ga}{}^2 + (\alpha_{In\text{-}Sb} - \alpha_{Ga\text{-}Sb} + \alpha_{In\text{-}Ga})N_{Ga}N_{Sb} \quad [4]$$

where $\alpha_{i\text{-}j}$ represents the interaction parameter between unlike atoms i and j. Again when $E_{AB} = 0$ this results in an ideal solution ($\gamma = 1$). Values for $\alpha_{In\text{-}Sb}$ and $\alpha_{Ga\text{-}Sb}$ can be obtained from the binary phase diagrams of In-Sb (8) and Ga-Sb (9) and are assumed to be linear functions of temperature (5, 16). The interaction parameter $\alpha_{In\text{-}Ga}$ has been measured by Macur *et al.* (13).

The phase diagram for liquid and solid, which can now be calculated, does not give any information about the binary eutectic in the ternary system which is known from experimental data to exist. The eutectic composition at a certain temperature is obtained from the crossover point of the liquidus line, described by Eq. [2], and the liquidus line in the Sb region for

* Electrochemical Society Active Member.
[1] Present address: Philips Laboratories, 345 Scarborough Road, Briarcliff Manor, New York 10510.
Key words: semiconductors, pseudobinary phase diagrams, liquid phase epitaxy.

Table I. Parameters used in the calculations for the In-Ga-Sb ternary phase diagram

	T^f (°K)	ΔS^f (eu)	α (cal/mole)
In-Sb } (Liquid)	796 (12)	14.34 (12)	8000-16.68T (°K)
Ga-Sb } (Liquid)	985 (12)	15.81 (12)	6220-8.11T
In-Ga			1066 (13)
InSb-GaSb (Solid)			1500 (14)
Sb	903	5.72	

the same temperature. In the Sb region the isotherm can be written as

$$\gamma_{Sb}N_{Sb} = \exp\left[-\Delta S^f_{Sb}(T^f_{Sb} - T)/RT\right] \quad [5]$$

where ΔS^f_{Sb} and T^f_{Sb} are the entropy of fusion and melting temperature, respectively, for Sb. The activity coefficient γ_{Sb} can be calculated as described in Eq. [4].

Experimental

The liquidus isotherms were determined by a technique similar to that described by Hall (10). Essentially, the method consisted of submerging the end of a weighed bar of GaSb into a melt of Ga:In:Sb of known composition and at a constant temperature until saturation of the melt was obtained (about 3-4 hr). The bar was then lifted from the melt and from its weight loss the composition of the liquid was determined for that temperature.

The solidus line for the pseudobinary GaSb-InSb was also determined for two temperatures by the technique described by Foster and Scardefield (11). In this method crushed samples of GaSb and InSb are equilibrated in the two phase region, *i.e.*, between the solidus and liquidus curves for 2-3 weeks and then quenched in water. The samples were then sectioned and analyzed with an electron microprobe to determine the composition of the solid which was in equilibrium with the liquid prior to quenching.

Results and Discussion

The parameters needed for the calculation of the phase diagram for In-Ga-Sb are the entropies of fusion of InSb and GaSb, their melting points, and the interaction parameters between the constituents in the liquid and in the solid. They can all be obtained from the literature and are given in Table I. The interaction parameter for the solid (14) is obtained by fitting the experimental data for the pseudobinary from Woolley and Lees (15). The value for $\alpha_{InSb\text{-}GaSb}$ is affected by the choice for the interaction parameter for the pseudobinary liquid (B^l) (14) or by $\alpha_{In\text{-}Ga}$ (the connection between these parameters is described below). Because we use a different number for $\alpha_{In\text{-}Ga}$ than Foster and Woods for their interaction parameter in the pseudobinary liquid, their value for $\alpha_{InSb\text{-}GaSb}$ cannot be entirely applicable for our calculation. However, it is the only one available and, more important, the fit we find in the ternary phase diagram is such, as is pointed out later, that we are confident that $\alpha_{InSb\text{-}GaSb} = 1500$ gives a good description of the interaction in the solid.

The isotherms are calculated between 300° and 675°C and are plotted, together with the experimental data, in Fig. 1. The dashed line represents the binary eutectic valley in the phase diagram and the calculated isotherms for higher Sb concentrations are plotted as well; in this latter region only Sb solidifies on cooling. At any point along the binary eutectic line there is immiscibility in the solid, and thus $In_xGa_{1-x}Sb$ and Sb solidify simultaneously.

The endpoints of the binary eutectic line in Fig. 1 can be compared to composition and temperature with the eutectic points in the In-Sb and Ga-Sb binary phase diagrams. The agreement for Ga-Sb is very good: 88% Sb at 590°C as experimental data (9) *vs.* 89% Sb and 592°C for the calculated composition and eutectic temperature. On the In-Sb side of the phase

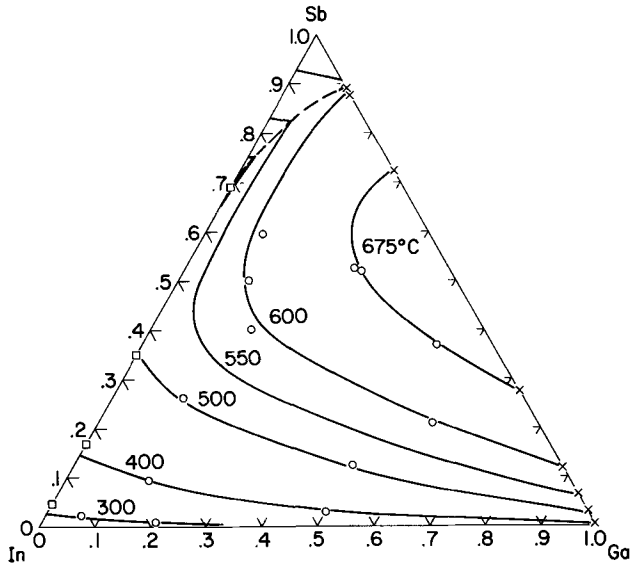

Fig. 1. Liquidus isotherms for the In-Ga-Sb ternary phase diagram. Solid lines: calculated curves; circles: our experimental data; □: ref. (8); x: ref. (9).

diagram again the composition agreement is good: 69% Sb experimental (8) and 71% Sb as calculated concentration. There is in this case, however, a discrepancy in the eutectic temperature of nearly 20°C with the published data; 476°C instead of 494°C (8).

The agreement in the entire phase diagram between the calculated and experimental isotherms is significant and shows that there is no need to adjust any of the parameters. This means that the lattice model seems well able to describe the interaction between atoms and molecules in liquid and solid and that the zero order approximation where only nearest neighbors are involved and a random distribution of the constituents is assumed, is adequate. We have to remember that, while the agreement between experiment and the model is sufficient, the calculation is still an approximation. The temperature dependence of the interaction parameters can be interpreted as due to an entropy contribution of the excess free energy of mixing. For the case that the whole temperature dependence of α contributes to the entropy term, it can be shown that $T\,\Delta S^M_{ex} > \Delta H^M_{ex}$, in contradiction with the model, which assumes only an enthalpy contribution to the excess free energy of mixing. The apparent contradiction between experiment and the predictions by regular or quasi-chemical theories leads to the conclusion that the present theories do not give an accurate chemical description for the III-V semiconductor systems, despite the significant agreement with experimental data.

Figure 2 shows the calculated solidus isotherms, where the GaSb concentrations in the solid are plotted as a function of the Ga concentrations in the liquid. As might be expected, the GaSb concentration in the solid decreases at a fixed Ga fraction in the liquid when the temperature increases, however, at high enough temperatures this trend reverses. We also notice a minimum in the GaSb fraction at $T > T^f_{InSb}$ which represents a point along the pseudobinary. The fact that there exists no Ga fraction smaller than 0.08 at 600°C can be understood from Fig. 1.

The InSb-GaSb pseudobinary phase diagram can be calculated as a special case from the ternary system, where the Sb fraction in the liquid remains constant at 0.5 and therefore in the solid also. The calculated pseudobinary is shown in Fig. 3 and is compared with experimental data. The two experimental liquidus points we determined are excellent fits to the calculated compositions, but they differ from the data of

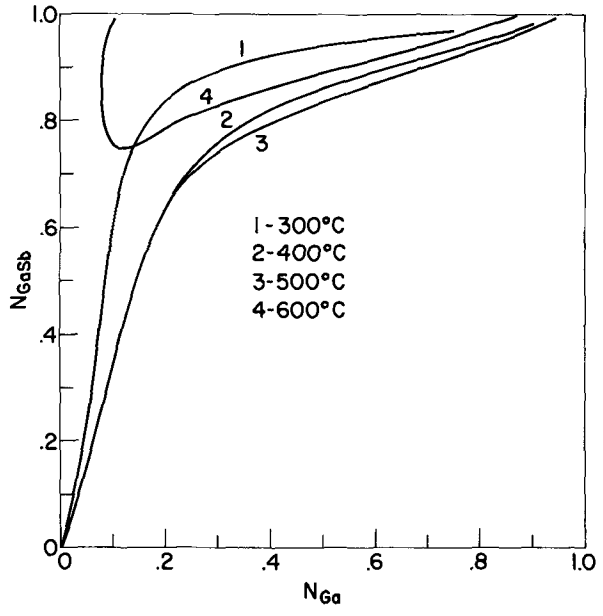

Fig. 2. Calculated solidus isotherms for the In-Ga-Sb system. The GaSb fraction in the solid is plotted as a function of the Ga fraction in the liquid for four different temperatures.

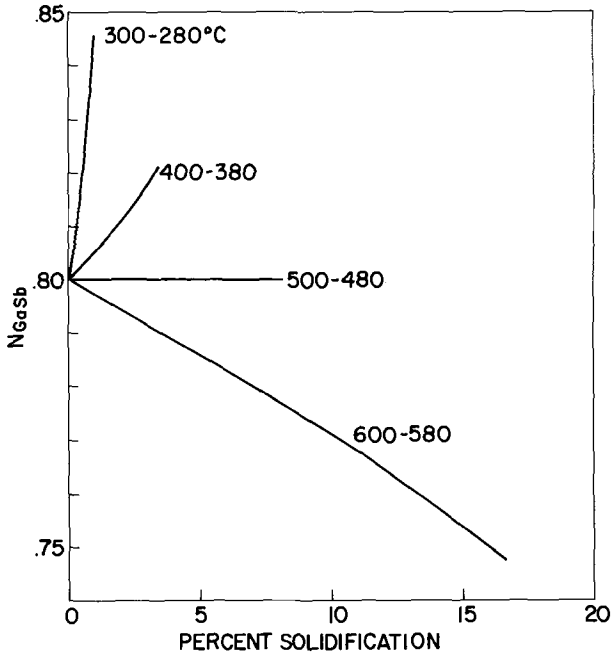

Fig. 4. GaSb fraction in the solid as a function of amount of solidification, thus proportional to the thickness of a liquid phase epitaxial layer, for several temperature ranges of growth.

Woolley and Lees (15) by 0-5% in absolute composition or 0-15°C in temperature. Calculating the ternary and the pseudobinary with the parameters from Table I, it appears that the ternary liquidus isotherms (Fig. 1) give a much better fit with our experimental data than with the pseudobinary liquid as determined by Woolley and Lees (Fig. 3). On the other hand, a shift in the α's such that the calculated curve fits the pseudobinary results in a poor fit in the ternary. The conclusion from these contradictory experimental results appears to be that the thermal analysis data (15) are not accurate enough.

Substituting in Eq. [2] for the pseudobinary case the expressions for the γ's derived from Eq. [3]-[4] gives the following expressions, where $N_{Sb} = 0.5$

$$N_{InSb} \exp[\alpha_{InSb\text{-}GaSb} N^2_{GaSb}/RT] = 2 N_{In} \exp[\Delta S^f_{InSb}(T^f_{InSb} - T)/RT] \exp[2 \alpha_{In\text{-}Ga} N^2_{Ga}/RT] \quad [6]$$

and

$$N_{GaSb} \exp[\alpha_{InSb\text{-}GaSb} N^2_{InSb}/RT] = 2 N_{Ga} \exp[\Delta S^f_{GaSb}(T^f_{GaSb} - T)/RT] \exp[2 \alpha_{In\text{-}Ga} N^2_{In}/RT] \quad [7]$$

It seems that, according to these equations, the only interaction parameters necessary to establish the pseudobinary are those for the solid and $\alpha_{In\text{-}Ga}$. This means that the pseudobinary liquid is independent of the interaction between In and Sb and Ga and Sb. In general, the pseudobinary liquid can in first order be described by the interaction between the two metals and is independent of the group V element. Hence, the InSb-GaSb, InAs-GaAs, and InP-GaP pseudobinary liquids are all determined by one and the same interaction parameter. The InP-GaP pseudobinary has been calculated this way (4) and shows good agreement with experimental data, while the InAs-GaAs system shows an agreement for the liquid within 15°C or 5% GaAs in absolute composition, while the solid fit is excellent.

An important application of the knowledge of the In-Ga-Sb ternary phase diagram is in predicting conditions for liquid phase epitaxial (LPE) growth. In general, $In_xGa_{1-x}Sb$ can be grown from an In-Ga-rich or Sb-rich solution. Growth from a metal-rich solution, however, will result in a smaller variation of the solid composition per unit thickness of the LPE layer. A calculation also shows that, when growing from an In-Ga solution, there is for each solid composition one temperature range where the composition of the solid is practically invariant along the growth axis. For a composition $In_{0.2}Ga_{0.8}Sb$ the variation of the solid composition as a function of the amount of solidification, which is directly proportional to the thickness of the overgrowth layer, is plotted in Fig. 4 for several temperature ranges. This shows that for greatest homogeneity $In_{0.2}Ga_{0.8}Sb$ should be grown in a temperature range of 500°-480°C.

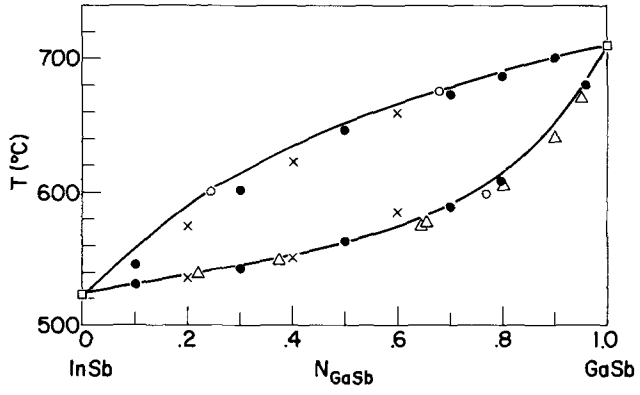

Fig. 3. The InSb-GaSb pseudobinary phase diagram, ○: our data; ●: differential thermal analysis [ref. (15)]; x: ordinary thermal analysis [ref. (15)]; △: x-ray measurements [ref. (15)]; □: [ref. (12)].

Acknowledgment

The authors wish to thank Dr. J. F. Woods for assisting with the computer calculations and Mr. A. H. Parsons for assisting with the experimental work.

Manuscript received March 22, 1971.

Any discussion of this paper will appear in a Discussion Section to be published in the June 1972 JOURNAL.

REFERENCES

1. J. C. McGroddy, M. R. Lorenz, and T. S. Plaskett, *Solid State Commun.*, **7**, 901 (1969).

2. G. B. Stringfellow and P. E. Greene, *J. Phys. Chem. Solids*, **30**, 1779 (1969).
3. G. B. Stringfellow, *This Journal*, **117**, 1301 (1970).
4. G. M. Blom, *This Journal*, **118**, 1834 (1971).
5. L. J. Vieland, *Acta Met.*, **11**, 137 (1963).
6. M. Ilegems and G. L. Pearson, "Symposium on GaAs," p. 3, Dallas (1968).
7. E. G. Guggenheim, "Mixtures," Oxford (1952).
8. T. S. Liu and E. A. Peretti, *Trans. ASM*, **44**, 539 (1952).
9. I. G. Greenfield and R. L. Smith, *Trans AIME*, **203**, 351 (1955).
10. R. N. Hall, *This Journal*, **110**, 385 (1963).
11. L. M. Foster and J. E. Scardefield, *ibid.*, **117**, 534 (1970).
12. B. D. Lichter and P. Sommelet, *Trans. Met. Soc. AIME*, **245**, 99 (1969).
13. G. J. Macur, R. K. Edwards, and P. G. Wahlbeck, *J. Phys. Chem.*, **72**, 1047 (1968).
14. L. M. Foster and J. F. Woods, *This Journal*, **118**, 1175 (1971).
15. J. C. Woolley and D. G. Lees, *J. Less Common Metals*, **1**, 192 (1959).
16. C. D. Thurmond, *J. Phys. Chem. Solids*, **26**, 785 (1965).

The In-Ga-P Ternary Phase Diagram and Its Application to Liquid Phase Epitaxial Growth

G. M. Blom*[1]

IBM T. J. Watson Research Center, Yorktown Heights, New York 10598

ABSTRACT

From the procedure developed for computing the In-Ga-P ternary phase diagram the InP-GaP pseudobinary phase diagram is generated. The free energies for the ternary liquid and pseudobinary solid are calculated as a function of composition, which establishes the stability of the solid *vs.* the liquid and shows on what substrate liquid-phase epitaxial growth is possible. The composition variation of an $In_xGa_{1-x}P$ solid that is deposited during cooling in liquid phase epitaxial growth under various conditions is calculated.

The growth of III-V mixed alloy systems (1-5) is considered to be important because of possible advantages they have over the pure binary compounds. For example, $In_xGa_{1-x}P$ alloys offer the potential of direct recombination ($\Delta k = 0$) luminescence throughout the visible spectrum almost to the green. The understanding of the phase equilibria in the metal-rich ternary systems is of particular interest because the most efficient III-V alloy devices have been grown by liquid phase epitaxy (LPE) from such solutions.

Using the model which is described by Guggenheim (6) as the zero order approximation, and introducing temperature dependent interaction parameters, the ternary liquidus and binary solidus phase diagrams are calculated. The applications for LPE which can be derived from the knowledge of the phase diagrams are emphasized. An analysis of the free energies of liquid and solid as a function of composition is given, which gives insight into the stability and the behavior of a substrate in the ternary In-Ga-P liquid. Assuming equilibrium, the composition of the liquid and solid are calculated as a function of temperature and predictions are given for the composition variation as a function of the thickness of an $In_xGa_{1-x}P$ LPE layer.

Calculation of the Phase Diagram

Several calculations for deriving ternary III-V semiconductor phase diagrams are given in the literature (3, 7-10). They are, as far as the nonideal behavior is concerned, essentially based on the description given by Guggenheim (6). Ilegems and Pearson (7) and Mabbitt (10) determine the liquidus activity coefficient by introducing temperature dependent interaction parameters, but they assume the solid to be ideal, while it can be expected that the departure from ideality in the solid, due to strain, is larger than in the liquid. Stringfellow (9), in applying the quasi-chemical equilibrium (QCE) model, adopted a nonideal liquid and solid.

We use essentially the same model and mathematical description as Ilegems and Pearson (7) with the exception that the solid is assumed to be nonideal also. The linear temperature dependent interaction parameters are obtained from the binary systems (11-14). The entropies of fusion and melting points of InP and GaP are well known from the literature (12, 15, 16). All parameters are listed in Table I. The agreement with experiment for the calculated liquidus and solidus phase diagrams is just as good as Stringfellow (9) obtains with the more complicated QCE model. Thus the QCE treatment does not give a more accurate description of the chemical behavior of the constituents.

The InP-GaP pseudobinary phase diagram can be calculated from the ternary system as a special case, where the phosphorus fraction in the liquid equals 0.5. The equations which describe the concentration in liquid and solid as a function of temperature are

$$N_{InP} \exp[\alpha_{InP\text{-}GaP} N^2_{GaP}/RT] = 2N_{In} \exp[\Delta S^f_{InP}(T^f_{InP} - T)/RT] \exp[2\alpha_{In\text{-}Ga} N^2_{Ga}/RT] \quad [1]$$

and an equivalent one where In and Ga are permutated. N_i denotes the respective fractions in liquid and solid, ΔS^f_{InP} and T^f_{InP} the entropy of fusion and melting point, and $\alpha_{i\text{-}j}$ represents the interaction parameter between the constituents i and j. According to Eq. [1] the interaction parameters for the binary systems In-P and Ga-P do not affect the pseudobinary phase diagram.

Table I. Parameters used in the calculations of the In-Ga-P ternary phase diagram

	T^f (°K)	ΔS^f (eu)	α (cal/mole)
In-P }	1341 (12)	14.7 (15)	0 (12)
Ga-P } (liquid)	1758 (16)	16.0	(7900-7T) (11)
In-Ga }			1066 (14)
InP-GaP (solid)			(−681 + 2.79T) (13)

* Electrochemical Society Active Member.
[1] Present address: Philips Laboratories, 345 Scarborough Road, Briarcliff Manor, New York 10510.
Key words: thermodynamics, electroluminescence, pseudobinary.

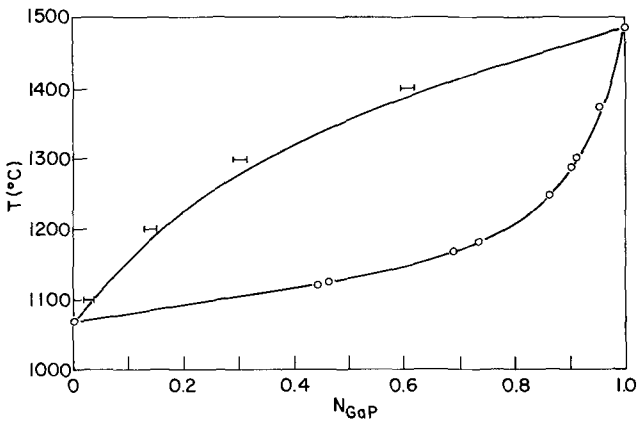

Fig. 1. InP-GaP calculated pseudobinary phase diagram. ○, Foster and Scardefield (17); —, Panish (3).

The calculated InP-GaP pseudobinary is shown in Fig. 1 and is compared with the experimental solidus curve from Foster and Scardefield (17) and values obtained from extrapolated In-Ga-P ternary data (3) for the liquid. The computed solidus gives a perfect fit with the experimental compositions, while the calculated liquid line indicates GaP fractions which are 5 m/o (mole per cent) too high or a temperature 20°C too low. Adjusting $\alpha_{\text{In-Ga}}$ to 2000 cal/mole and increasing the interaction parameter for the solid slightly by 80 cal/mole results in an agreement with the experimental data within the experimental accuracy. It is felt that it is not the uncertainty in $\alpha_{\text{In-Ga}}$ obtained by Macur *et al.* (14) which gives rise to the discrepancy between the experimental liquidus line and the one as calculated and shown in Fig. 1, because the fit is within 2 a/o (atomic per cent) for the rest of the ternary system and becomes worse in varying the respective α's. It might be the application of the lattice model as described by Guggenheim (6), which is questionable for III-V semiconductors. This model was originally derived and applied to organic mixtures where the temperature variations are much smaller than for the In-Ga-P system.

Foster and Woods (13) compared the predictions given by the QCE or zero order approximation treatments for several III-V pseudobinaries with the experimental results. They indicated that the relative magnitude of the enthalpy (ΔH^{M}_{ex}) and entropy (ΔS^{M}_{ex}) term in the excess free energy of mixing (ΔF^{M}_{ex}) are such that in theory $\Delta H^{M}_{ex} > T\Delta S^{M}_{ex}$. This should mean for the interaction parameter $\alpha = a - bT$, which is directly related to ΔF^{M}_{ex} that $a > bT$. Experimentally, however, the ternary and pseudobinary can only be described with an interaction parameter with $a < bT$. Hence there exists a serious contradiction, for the experimentally determined excess free energy is nearly entirely an entropy term ($T\Delta S^{M}_{ex}$), while theory predicts it should be mainly an enthalpy (ΔH^{M}_{ex}).

Application to Liquid Phase Epitaxy

A major application from the knowledge of the In-Ga-P phase diagrams for liquid and solid is in predicting conditions for LPE growth. Only phosphorus fractions smaller than 0.5 are considered because only they have any current application because of the otherwise very high vapor pressures involved.

The criteria for LPE growth under equilibrium conditions are the absence of miscibility gaps in solid and liquid and the stability of the solid in the presence of the liquid. The existence of miscibility gaps comes straightforwardly from the calculations of the isotherms in the In-Ga-P system, when no solution of the equations describing solid and liquid is possible. The stability of a solid, for example a substrate, in a ternary liquid can be expressed in terms of their respective free energies. The free energy for the liquid phase can be written as

$$F^{l} = \mu^{l}_{In}N_{In} + \mu^{l}_{Ga}N_{Ga} + \mu^{l}_{P}N_{P} \quad [2]$$

and for the solid as

$$F^{s} = \mu^{s}_{InP}N_{InP} + \mu^{s}_{GaP}N_{GaP} \quad [3]$$

The atomic and molecular fractions (N_i) in liquid and solid are obtained from the calculation of the phase diagram. The chemical potentials are obtained from the equivalent equations derived by Ilegems and Pearson (7). The entropies of fusion for the pure elements, needed to calculate the chemical potential for the pure elements are $\Delta S^{f}_{P} = 1.9$ eu, $\Delta S^{f}_{In} = 1.8$ eu, and $\Delta S^{f}_{Ga} = 4.4$ eu (18).

Equilibrium is established when the free energy-composition curves of a solid and liquid phase have a common tangent line. Figure 2 is a schematic diagram of the free energies of the ternary In-Ga-P liquid and binary $In_xGa_{1-x}P$ solid phases as a function of composition. Any solid in this system with a higher free energy than for that solid which is in equilibrium with a specific liquid composition will, when brought into contact with that liquid, dissolve isothermally in order to minimize the free energy of the total system from this nonequilibrium situation. For the same reason, isothermal crystal growth will occur if a solid with a lower free energy is introduced into the liquid. The difference in free energy between the equilibrated solid and new introduced one is the driving force for isothermal dissolving or crystal growth.

The free energies for liquid and solid which establish equilibrium at 900°C, calculated according to Eq. [2] and [3], are plotted in Fig. 3, both as a function of the Ga fraction in the liquid; similar curves exist for other temperatures. As expected for equilibrium conditions the free energy for the solid is smaller than that for the liquid at each composition. As is observed in Fig. 3 the free energy of pure InP is always higher than the solid which is in equilibrium with an In-Ga-P ternary melt. Accordingly an InP substrate will tend to decompose in any In-Ga-P melt, while a GaP substrate is stable. Approaching equilibrium dissolving is indeed experimentally observed after exposure of InP to an In-Ga-P melt while LPE of $In_xGa_{1-x}P$ on GaP substrates has been done in many laboratories. When growing under highly dynamic conditions, hence when equilibrium conditions may be disregarded, it might

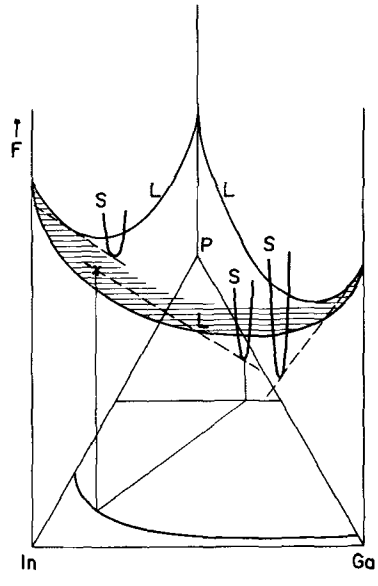

Fig. 2. Schematic diagram of the free energies for liquid and solid as a function of their compositions. The dashed lines represent lowest common tangent lines. L = liquidus lines, S = solidus lines.

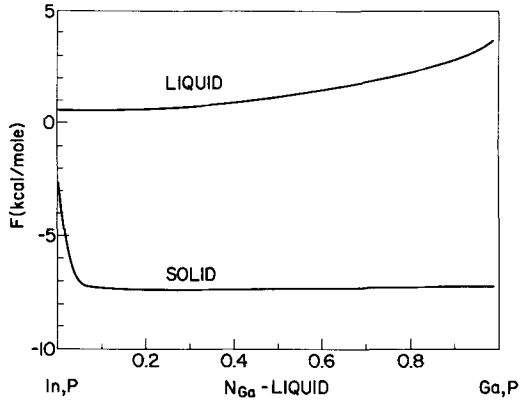

Fig. 3. Calculated free energies which establish equilibrium at 900°C for the liquid and the solid phase both as a function of the Ga fraction in the liquid. Note that the free energy in the solid is not plotted as a function of the composition of the solid, but as a function of the composition of the liquid with which it is in equilibrium.

be possible that heterojunction structures on "wrong" substrates, as for example $In_xGa_{1-x}P$ on an InP substrate, can be grown despite the fact that the difference in free energy is large, as is therefore the driving force for dissolving the substrate.

After establishing the potential possibilities for LPE of $In_xGa_{1-x}P$, from the knowledge of the phase diagrams, the predicted composition variation of a deposited LPE layer is described as a function of the growth temperature, assuming equilibrium. For a melt containing 50 a/o phosphorus, this is known from the pseudobinary phase diagram. When we grow from the In-rich corner of the ternary system the P as well as the Ga atomic fraction in the liquid will decrease upon cooling because the distribution coefficient (C_s/C_l) is for both elements larger than unity. From a numerical calculation on the phase diagram one can determine how, under thermodynamical equilibrium conditions, the composition in liquid and solid vary upon cooling and also how much of the liquid will solidify. Using as an example, a first-to-freeze composition of $In_{0.3}Ga_{0.7}P$, which is nearly the highest Ga content where direct bandgap electroluminescence is possible, we can compare the changes in composition and the amount of solidification (*i.e.*, weight percentage) for various temperature ranges of crystal growth. The results are summarized in Table II. It is shown that in equal temperature changes (ΔT) the highest starting growth temperature, for which we choose the pseudobinary, provides the largest amount of crystallization and also the largest change in solid composition. It is also shown that for equal percentages of solidification, hence for equal thicknesses of a liquid phase epitaxial layer, the composition variation in the solid for various starting growth temperatures is very small and can be neglected for practical LPE purposes. This means that the ratio of the amount of crystallization and composition variation in the solid is nearly independent of temperature. For practical applications under equilibrium conditions there are certain advantages in growing at relatively low temperatures, where the same solid can be achieved in a larger cooling cycle and at lower phosphorus partial vapor pressures.

Table II. Summary of the composition variation and temperature conditions to achieve an $In_{0.3}Ga_{0.7}P$ crystal

T (°C) (starting growth temp)	ΔT (°C)	$1-x$ (after cooling ΔT°C)	Weight % solidification	Ga at. fraction in starting liquid
1168	20	0.62	3.2	0.058
	5	0.68	0.8	
1000	20	0.66	1.4	0.053
	11	0.68	0.8	
900	20	0.68	0.8	0.045

In Table II are also shown the Ga atomic fractions in the liquid prior to growth. It turns out that the Ga concentration is nearly the same in all three cases to achieve a first-to-freeze GaP concentration of 70% in the solid. Hence when we replace P by In it means we can work at lower temperature and grow equally homogeneous $In_xGa_{1-x}P$ crystals. This characterization of a nearly temperature independent Ga concentration in the liquid to achieve a certain GaP fraction in the solid is not restricted to the 70% solid but holds over a wide region in the phase diagram.

Acknowledgment

The author wishes to thank Dr. J. F. Woods for his time and effort to apply the computer programming.

Manuscript submitted March 29, 1971; revised manuscript received *ca.* June 22, 1971.

Any discussion of this paper will appear in a Discussion Section to be published in the June 1972 JOURNAL.

REFERENCES

1. M. B. Panish, R. T. Lynch, and S. Sumski, *Trans. Met. Soc., AIME*, **245**, 559 (1969).
2. M. B. Panish, *J. Phys. Chem. Solids*, **30**, 1083 (1969).
3. M. B. Panish, *J. Chem. Thermodynamics*, **2**, 319 (1970).
4. H. Rupprecht, J. M. Woodall, and G. D. Pettit, *Appl. Phys. Letters*, **11**, 81 (1967).
5. M. R. Lorenz, W. Reuter, W. P. Dumke, R. J. Chicotka, G. D. Pettit, and J. M. Woodall, *ibid.*, **13**, 421 (1968).
6. E. G. Guggenheim "Mixtures," Oxford (1952).
7. M. Ilegems and G. L. Pearson, "Symposium on GaAs," p. 3 (1968).
8. G. B. Stringfellow and P. E. Greene, *J. Phys. Chem. Solids*, **30**, 1779 (1969).
9. G. B. Stringfellow, *This Journal*, **117**, 1301 (1970).
10. A. W. Mabbitt, *J. Mat. Sci.*, **5**, 1043 (1970).
11. C. D. Thurmond, *J. Phys. Chem. Solids*, **26**, 785 (1965).
12. M. B. Panish and J. R. Arthur, *J. Chem. Thermodynamics*, **2**, 299 (1970).
13. L. M. Foster and J. F. Woods, *This Journal*, **118**, 1175 (1971).
14. G. J. Macur, R. K. Edwards, and P. G. Wahlbeck, *J. Phys. Chem.*, **72**, 1047 (1968).
15. B. D. Lichter and P. Sommelet, *Trans. Met. Soc., AIME*, **245**, 99 (1969).
16. R. J. Chicotka, Private communication.
17. L. M. Foster and J. E. Scardefield, *This Journal*, **117**, 534 (1970).
18. K. K. Kelley, Contributions to the Data on Theoretical Metallurgy, Washington (1949).

The Effect of Trace Amounts of Water Vapor on Boron Doping in Epitaxially Grown Silicon

J. Bloem*

Semiconductor Development Laboratory, N. V. Philips Gloeilampenfabrieken, Nijmegen, Holland

ABSTRACT

It was found that silicon epitaxy from silane (SiH_4) can tolerate unexpectedly high water concentrations in the gas phase before deterioration of the growing layer sets in. The extent of boron doping from B_2H_6, however, is shown to be strongly influenced by water vapor concentrations in the ppm region. It is shown that HCl gas at partial pressures greater than 10^{-3} atm has a similar influence on the extent of boron doping and that it makes the system less susceptible to small variations in water vapor concentrations. The results can be explained by consideration of the various gas phase equilibria at or near the silicon-gas interface.

In the epitaxial growth of silicon layers it was discovered early that the presence of oxygen or water vapor has a detrimental effect on the quality of the epitaxial layers (1). In doping the silicon layers, boron doping (using B_2H_6 as the doping agent) appeared to be a more difficult operation than doping with P, As, or Sb compounds. The water content of a well-purified gas was seen to lie in the order of 1 ppm or less (10^{-6} atm in the 1 atm open-tube system used); this value is orders of magnitude higher than the B_2H_6 concentration of 10^{-10} atm used in doping. Because the varying results in boron doping were thought to be explained by small differences in the efficiency of the gas purification, by small leaks in the gas-handling system, or by residual moisture on the surface of the quartz reactor, it seemed appropriate to study the effect of trace amounts of water vapor on boron incorporation.

Experimental Procedure

The horizontal, air-cooled epitaxial reactor consisted of a quartz tube 80 cm in length, of rectangular cross section (10 × 2.5 cm^2) into which a SiC-coated graphite susceptor (9.5 × 24 × 1.0 cm^3) was placed. The susceptor was loaded with 10 silicon slices of 38 mm diam in two parallel rows and was R.F.-heated. The main gas stream for all runs was 75 liters hydrogen per min. The silicon substrates were (111)-oriented, mechanically and chemically polished, with dislocation densities less than 500 dislocations per cm^2. The surface quality of the slices was such that under normal conditions a heat treatment prior to epitaxial growth of the slices in hydrogen at 1250°C for 15 min was sufficient to obtain layers free of spikes and stacking faults. The resistivities of the epitaxial layers were measured both by the four-point probe technique (2) on reference slices of opposite resistivity types and by spreading resistance measurements (3). When p-type doping was studied, higher resistivity (about 2 ohm-cm) n-type substrates were placed on the susceptor along with the low-resistivity (0.007 ohm-cm) n-type substrates. It appeared that lower resistivities were the same on both types of substrates within the experimental error (±15%). By tilting the susceptor (1°30′) and slightly adjusting the temperature over the susceptor (leading edge about 20° cooler than end section), depletion of the gas phase was counteracted in such a way that both thickness and resistivity variations were minimized (±5% for thickness, ±15% for resistivity). Thickness and resistivity values on slices 4 and 10 cm from the leading edge were taken to be representative for the run.

The thickness of the grown layers was measured by the infrared interference technique (4). For the thickness measurements layers grown on Sb-doped substrates (resistivity 0.007 ohm-cm) were used. The thickness of the epitaxial layers was monitored from 10 to 20 μm. Unless otherwise stated, the silicon growth rate was kept at about 1 μ/min ($p_{SiH_4} = 10^{-3}$ atm). The values from the *IR* interference technique were in accord with those obtained by the bevel and stain method. The temperature of the substrates was measured with an optical pyrometer, and the readings were corrected for the emissivity of silicon (5).

The starting silane and diborane (4% SiH_4 in H_2, 1% B_2H_6 in H_2) were diluted with hydrogen to the wanted partial pressures using calibrated flowmeters. The water vapor was obtained from an evaporation cell filled with water at constant temperature (20°C). By passing a small hydrogen stream (0-100 cm^3) over the surface of the liquid and mixing this with the main gas stream (75 liters/min) the water vapor concentration in H_2 was varied from 0 to 50 ppm (0-50 × 10^{-6} atm). In separate runs analysis with a Beckmann moisture meter showed the measured water content of the gas to be in good agreement with the amount calculated from the vapor pressure of water. Epitaxial runs without diborane doping were performed, and silicon layer resistivities higher than 20 ohm-cm, n-type, were consistently obtained. On the addition of water vapor the resistivity remained on this level. Prolonged annealing of the layers at 500°C shows the donor activity expected from the oxygen content (6). The addition of HCl showed the resistivity to decrease; for the highest HCl concentration (2 × 10^{-2} atm) the resistivity dropped to 3 ohm-cm (1.6 × 10^{15} donors/cm^3). Where necessary, corrections for this additional doping effect were applied.

Experimental Results

Influence of water vapor on silicon epitaxy.—Epitaxial runs at 1150°C with increasing amounts of water vapor showed that up to 40 × 10^{-6} atm of water vapor in the gas did not cause stacking faults in the layers, provided that the slices were preheated for 15 min in hydrogen at 1250°C before the introduction of silane. For $p_{H_2O} \approx 10 \times 10^{-6}$ atm small pits become visible on the Si surface. This is an aftergrowth effect: when the silane flow is terminated the freshly grown layer is etched slightly by the water vapor present in the hydrogen. On further cooling, the formation of SiO_2 could be expected; this is not observed presumably because the cooling period is too short. For values of p_{H_2O} greater than 10 × 10^{-6} atm the onset of gas phase reactions gave a brown deposit on the relatively cold upper wall of the reactor. This deposit was accompanied by a decrease in epitaxial layer thickness; the farther the substrate from the leading edge of the susceptor, the greater the decrease. With $p_{H_2O} = 40 \times$

* Electrochemical Society Active Member.
Key words: chemical vapor deposition, silicon thin films, gas phase doping, surface reactions.

10^{-6} atm, deposition of silicon was present only on the first row of silicon slices.

Influence of water vapor on boron doping.—In order to examine the boron content of the grown layers as a function of the silicon growth rate, the partial pressure of diborane ($p_{B_2H_6}$) was kept constant whereas p_{SiH_4} and consequently the growth rate was varied. The variation of growth rate with p_{SiH_4} is shown in Fig. 1, and the boron concentration as a function of growth rate is depicted in Fig. 2. The scatter in the results shown in Fig. 2 decreased considerably after checking the apparatus for minor leaks and careful drying of the quartz tube used. Subsequent experiments then showed the same behavior, *i.e.* no distinct increase or decrease of the concentration of boron incorporated in the layers as long as $p_{B_2H_6}$ is kept constant; only for the highest growth rates a slight decrease in boron concentration is found.

The boron concentration in the layers varies linearly with $p_{B_2H_6}$ (Fig. 3). If the water vapor pressure is increased for a fixed value of $p_{B_2H_6}$ and p_{SiH_4}, a decreasing boron concentration is found; this effect occurs for various diborane concentrations (Fig. 4). For higher values of p_{H_2O} the decrease is proportional to $(p_{H_2O})^2$ (Fig. 4).

The boron concentration in the epitaxial layers is temperature dependent; contrary to the findings for n-type dopants (7) the concentration increases with increasing temperature (Fig. 5). There is some indication of a decreasing influence of water with increasing temperature.

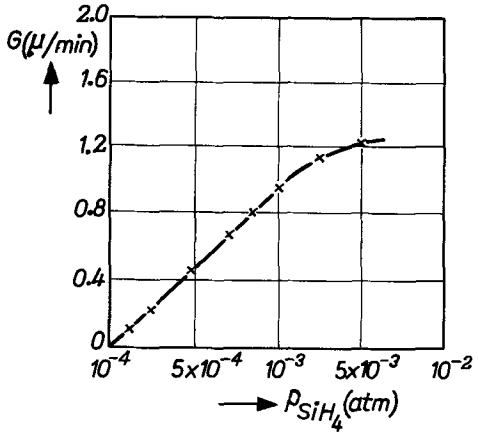

Fig. 1. Growth rate of silicon as a function of the partial pressure of silane in the gas phase.

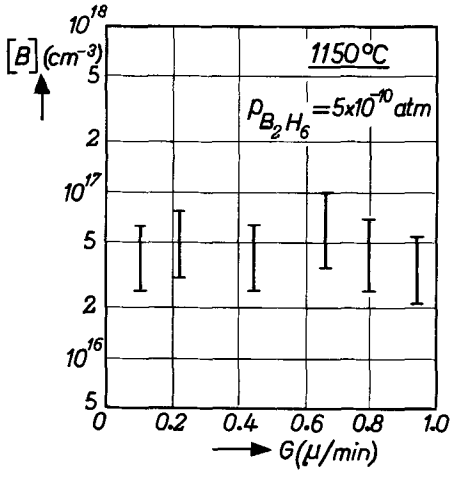

Fig. 2. Boron concentration in the epitaxial layers as a function of silicon growth rate (constant partial pressure of diborane in the system).

Influence of HCl on boron doping.—The introduction of HCl in the epitaxial reactor shows only a small influence on silicon growth rate (8): a ratio p_{HCl}/p_{SiH_4} of 1 reduces the silicon growth rate by 0.4% and a ratio of 4 gives a reduction of 6%. The presence of HCl also counteracts the incorporation of boron in the growing silicon (9).[1] The influence of the introduction of HCl on the acceptor concentration is pronounced if no water vapor is added (Fig. 6, curve $p_{H_2O} = 0$). For an HCl concentration greater than 10^{-3} atm (p_{HCl}/

[1] This effect is used in obtaining pure polycrystalline silicon by the pyrolysis of chlorosilanes.

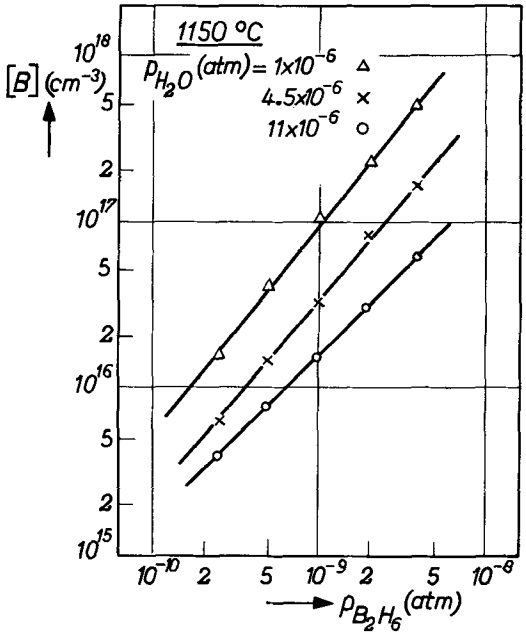

Fig. 3. Boron concentration in epitaxially grown layers vs. the diborane partial pressure introduced into the reactor.

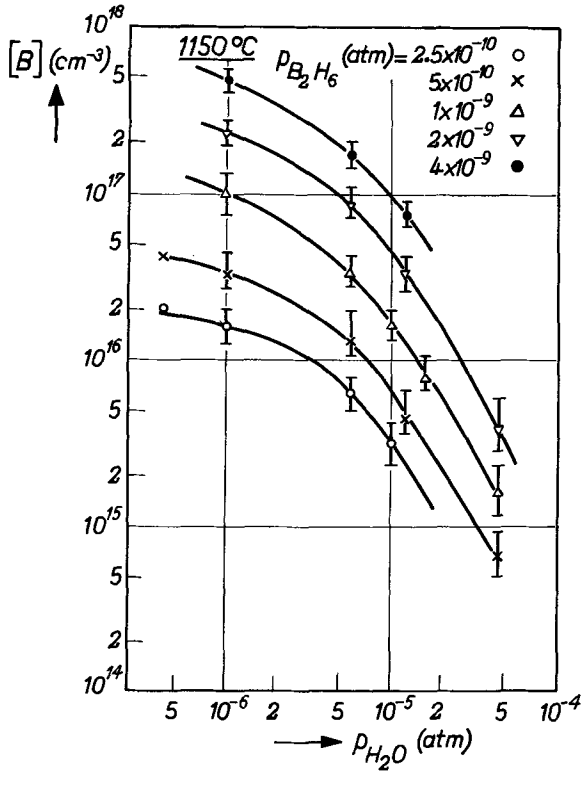

Fig. 4. Variation of boron concentration in the epitaxial silicon layers with water vapor pressure in the gas.

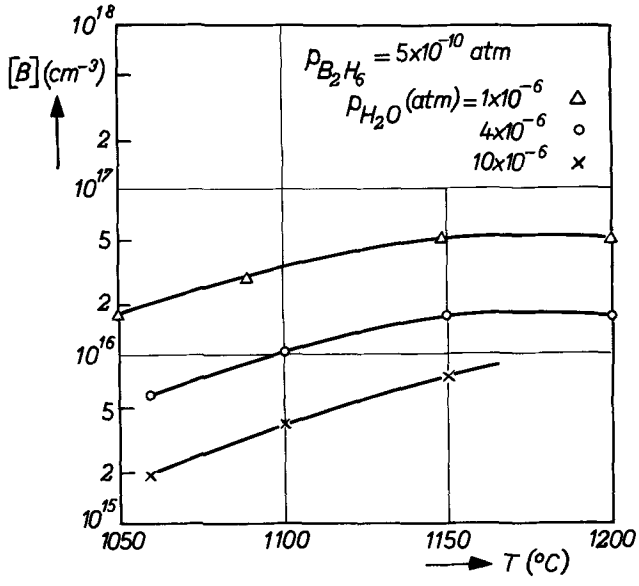

Fig. 5. Temperature dependence of the boron concentration in epitaxial layers for a constant diborane concentration and various water vapor partial pressure in the gas.

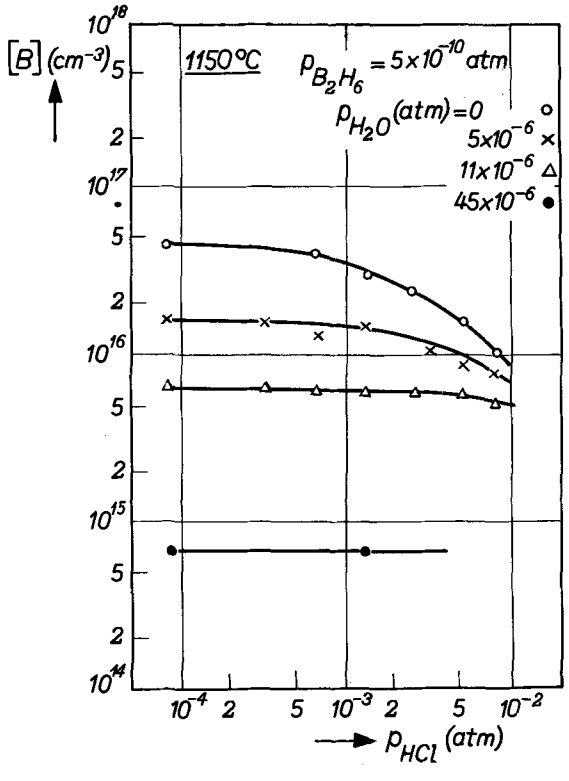

Fig. 6. Boron concentration in epitaxial silicon as a function of the amount of hydrochloric acid added in the gas phase, with the water vapor content as parameter.

$p_{SiH_4} = 1$) the boron concentration in the grown layers is seen to decrease with p_{HCl}.

For gas mixtures containing H_2O, HCl, B_2H_6, and SiH_4 in hydrogen the result is depicted in Fig. 6 and 7. At low values of p_{HCl} the influence of water vapor is more pronounced than at higher values of p_{HCl}.

Discussion

In this section the influence of water and hydrochloric acid vapor on the silicon growth rate and on the boron doping will be treated, starting from possible

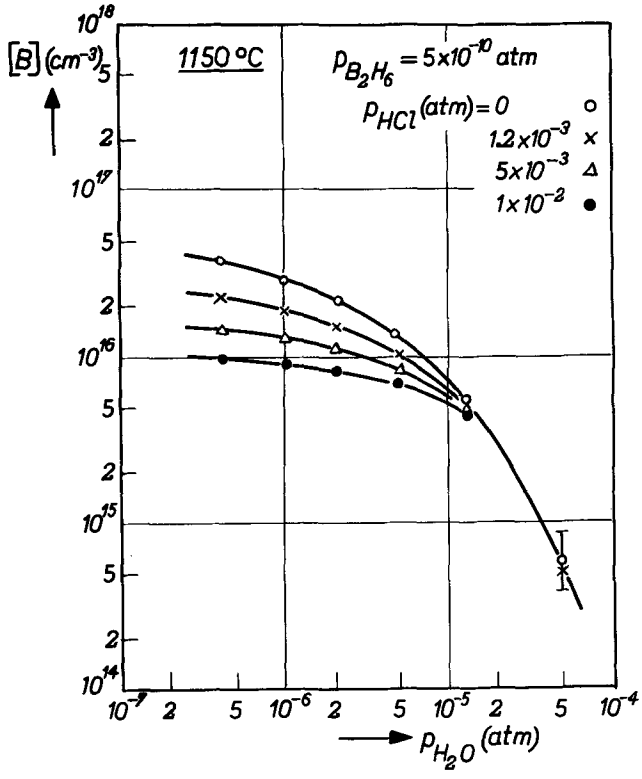

Fig. 7. Boron concentration in epitaxial silicon for a constant vapor pressure of diborane vs. the water vapor pressure, with the hydrochloric acid content as parameter.

reactions in the gas-phase and at the gas-silicon interface. From existing thermochemical data the predominant reaction products can be inferred, the main object being to relate the variation of the boron concentration in silicon to the variations in the gas phase composition. It will be assumed that the reactions are surface catalyzed, *i.e.* the reactions are thought to proceed to equilibrium, the equilibrium constants not being altered by the presence of the surface.

Influence of water vapor on silicon epitaxy.—Two reactions on the silicon surface are of importance, *viz.*

$$Si_{(s)} + 2H_2O_{(g)} = SiO_{2(s)} + 2H_{2(g)}$$
$$K_1 = (p_{H_2O})^{-2} \text{ for } p_{H_2} = 1 \quad [1]$$

$$Si_{(s)} + SiO_{2(s)} = 2\,SiO_{(g)}$$
$$K_2 = (p_{SiO})^2 \quad [2]$$

and the combination of [1] and [2]

$$Si_{(s)} + H_2O_{(g)} = SiO_{(g)} + H_{2(g)}$$
$$K_3 = p_{SiO}/p_{H_2O} \quad [3]$$

If equilibrium [3] at the silicon surface is reached sufficiently rapidly, the value of K_3 being about 30 at 1400°K (10), then the equilibrium vapor pressure of water near the surface will be lower than in the main gas phase. For a diffusion-controlled reaction rate the water vapor pressure at the surface is reduced by a factor K_3, assuming the diffusion coefficients of H_2O and SiO to be the same. In Fig. 8 water and SiO vapor pressures according to Eq [1] and [2] are given (10), *i.e.* values of $K_1^{-1/2}$ and $K_2^{1/2}$ as a function of temperature for $p_{H_2} = 1$. In the regions II and III, formation of SiO_2 is expected (Eq. [1]); whereas in region I the silicon surface will be free from surface oxides. In region II, however, the SiO_2 formed on the surface reacts with silicon to form volatile SiO (Eq. [2]) and the value of p_{H_2O} at the surface is reduced below the value corresponding to the lower curve in Fig. 8 at the temperature studied. It is only for water vapor pressures higher than the value on the upper curve ($K_2^{1/2}$) that the whole surface will be covered by SiO_2, that

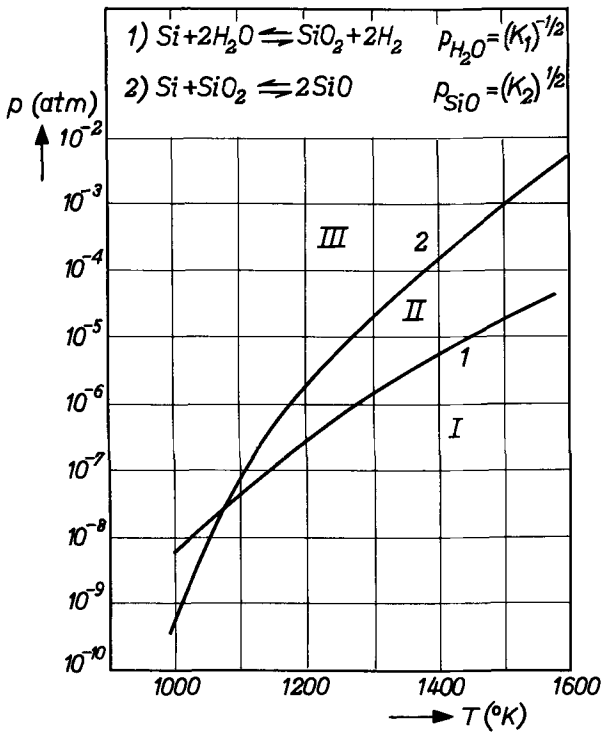

Fig. 8. Water vapor pressures that can be allowed in the gas phase growing epitaxial silicon layers. Curve 1 gives the water vapor pressures at the silicon surface in equilibrium with solid silicon dioxide as a function of temperature. Curve 2 gives the vapor pressure of silicon monoxide in equilibrium with solid silicon and silicon dioxide. For water vapor pressures in region II the formation of volatile SiO prevents the formation of solid SiO_2 on the silicon surface.

is, the actual water vapor pressure at the surface then has reached the critical value indicated by the lower curve. From reaction [1] it would be expected that at 1400°K water vapor pressures greater than 4 ppm would cause the formation of SiO_2. In practice, with up to 50 ppm no deterioration of the layers was observed because of reaction [2]. Epitaxy becomes impossible, however, because of another reason, *i.e.* excessive gas phase reactions.

Water vapor can react with silane in the gas phase or etch the silicon surface. In both cases gaseous SiO is formed. It is postulated that this SiO diffuses into colder parts of the gas stream and decomposes according to

$$2SiO = Si + SiO_2$$

As the vapor pressures of Si and SiO_2 are low, the gas phase is easily supersaturated giving rise to gas phase nucleation of the corresponding compounds. Subsequently decomposition of SiH_4 occurs on the solid nuclei leading to a serious depletion of silane in the gas phase.

Boron doping.—In Fig. 2 it is shown that the boron concentration in the epitaxial layers does not depend on the silicon growth rate under the prevailing conditions.

The silicon growth rate is diffusion-controlled in the range of temperatures studied (8), but for the incorporation of boron in the growing layer diffusion control is not indicated, because otherwise increasing growth rates due to increasing concentrations of SiH_4 would give a decreasing boron concentration. The same number of boron atoms has to be incorporated in increasingly thicker silicon layers.

B_2H_6 is reported to decompose rapidly at elevated temperatures into BH_2 (11) and BH_3 (12). This explains the slope of the curve in Fig. 3, which is about unity. If B_2H_6 were stable, a slope of 0.5 would be expected. The incorporation of boron in silicon can be given as

$$B_2H_6 = 2BH_3(g) \qquad K_4 = 7.0 \quad \text{at } 1400°K \text{ (13)} \qquad [4]$$

$$BH_3(g) = B(g) + 3/2\ H_2(g) \qquad K_5 = 3.2 \times 10^{-8} \quad \text{at } 1400°K \text{ (13)} \qquad [5]$$

$$B(g) = B_{Si} \qquad K_6 \qquad [6]$$

$$B_{Si} = B^-_{Si} + p \qquad K_7 \qquad [7]$$

The gas phase segregation coefficient of boron is best defined as the equilibrium constant of the reaction describing the incorporation of elemental boron in silicon giving ionized acceptor centers.[2]

$$\gamma_B = \frac{p_B}{[B^-]_{Si}} = \frac{p}{K_6K_7} = \frac{n_i}{K_6K_7} \qquad [8]$$

As the acceptor may be assumed to be fully ionized, and the value of p is equal to the intrinsic carrier concentration, n_i at the temperature of the experiment, for B concentrations well below n_i (approximately 10^{20} cm^{-3} at 1400°K or $2 \cdot 10^{-3}$ acceptors per Si atom), K_7 is a constant giving the number density of states in the valence band of silicon. As the ambient pressure is unity, p_B in Eq. [8] is equal to the mole ratio of boron in the gas phase close to the silicon surface. The concentration of acceptor centers in silicon will further be denoted by the symbol [B].

A practical segregation coefficient relates the concentration of dopant in the system ($p_{B_2H_6} = p_o$) to the resulting acceptor concentration in the grown layer. With Eq. [4]-[7] we find, in the absence of water or HCl

$$\gamma_{B_2H_6} = \frac{p_o}{[B]} = \frac{1}{2}\gamma_{BH_3} = \frac{1}{2K_5}\gamma_B \qquad [9]$$

In the gas phase B_2H_6 is dissociated completely into BH_3, and therefore $p_{BH_3} = 2\,p_o$.

Influence of water and HCl concentration on doping.—If water vapor and HCl are present in the gas phase, then reactions with the highly reactive boron hydrides can be expected. According to thermodynamic data (13), the most probable reaction products are BHO_2, BCl, and BClO.

$$BH_3 + 2H_2O = BHO_2 + 3H_2 \qquad K_{10} = 2 \times 10^{11} \quad \text{at } 1400°K \qquad [10]$$

$$BH_3 + HCl = BCl + 2H_2 \qquad K_{11} = 20 \quad \text{at } 1400°K \qquad [11]$$

$$BCl + H_2O = BClO + H_2 \qquad K_{12} = 1.5 \times 10^6 \quad \text{at } 1400°K \qquad [12]$$

from [10] and [11] we obtain

$$H_2 + HBO_2 + HCl = BCl + 2H_2O \qquad K_{13} = 10^{-10} \qquad [13]$$

moreover

$$2\,p_o = p_{BH_3} + p_B + p_{BHO_2} + p_{BClO} + p_{BCl} \qquad [14]$$

With Eq. [1]-[14] the resulting equilibrium can be estimated for any initial gas composition. As all equilibria are coupled it is sufficient to take one boron compound as the source of elemental boron in order to obtain the amount of boron incorporated in the growing layers. It is convenient to select BH_3. According to Brouwer (14), simple linear relations are obtained by splitting Eq. [14] into a number of limiting cases; *e.g.*

[2] The segregation coefficient is often defined as $\alpha = \left(\frac{B}{Si}\right)_{gas} / \left(\frac{B}{Si}\right)_{solid}$. This definition is only meaningful if B and Si are incorporated in the same manner; otherwise α depends on the value of p_{SiH_4} and thus on the silicon growth rate.

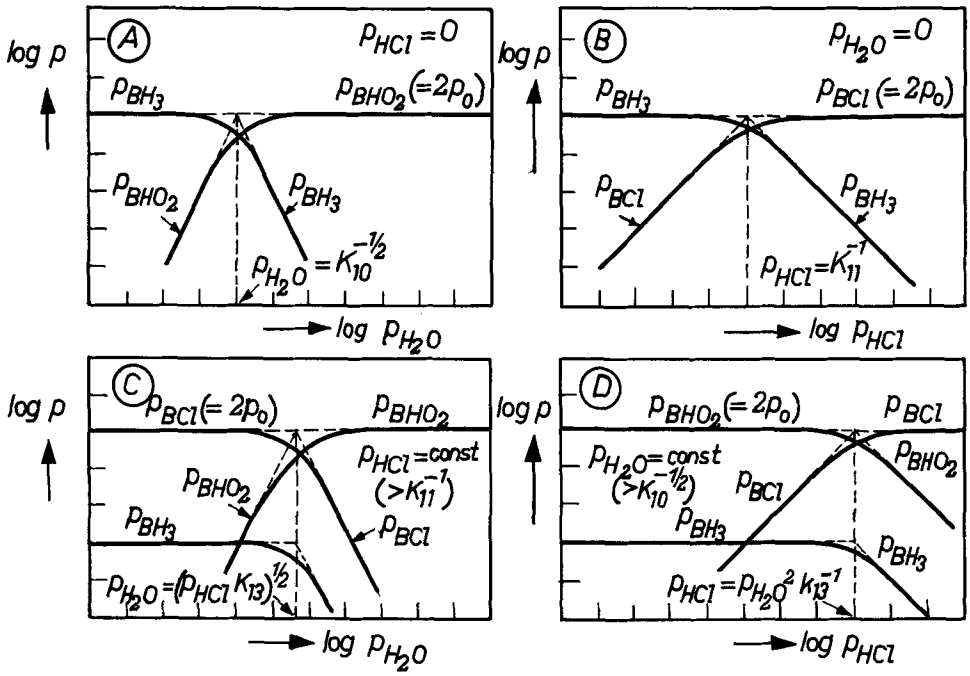

Fig. 9. Schematic representation of the variation of the partial pressures of boron compounds in the gas phase as a function of the water and/or hydrochloric acid content of the gas: A = variation with p_{H_2O} for p_{HCl} = 0, B = variation with p_{HCl} for p_{H_2O} = 0, C = variation with p_{H_2O} for p_{HCl} = constant ($> K_{11}^{-1}$), and D = variation with p_{HCl} for p_{H_2O} = constant ($> K_{10}^{-1/2}$).

$2p_o = p_{BH_3}$; $2p_o = p_{BHO_2}$ in the presence of water or $2p_o = p_{BCl}$ if sufficient HCl is present. In doing this and introducing the values in Eq. [10]-[13] the interrelations can be depicted as in Fig. 9. The acceptor concentration in silicon is proportional to the value of p_{BH_3}. In Fig. 9c and 9d it is seen that p_{BH_3} is constant for not too great values of p_{H_2O} or p_{HCl}. If BClO would be present in greater concentrations and a region $2p_o = p_{BClO}$ would appear, then in Fig. 9c the value of p_{BH_3} would be decreasing with p_{H_2O} even in the low-water vapor concentration range. As this is not apparent in Fig. 7, it is expected that the value of K_{12} has to be lower than calculated. In order to bring the calculated and experimental results into accord, the value of K_{10} and K_{11} have to be taken higher than given with Eq. [10] and [11] together with a lower value of K_{12}. These corrections are well within the accuracy of the thermochemical data (*e.g.* heat of formation of BH_3 given as 25.5 ± 10 kcal mole^{-1} (12) for BH_2 as 48 ± 15 kcal mole^{-1} (13).) In total we expect

$$p_{BH_3} = \frac{2p_o}{1 + K_{10}p_{H_2O}^2 + K_{11}p_{HCl}} \qquad [15]$$

By definition, $\gamma_{BH_3} = p_{BH_3}/[B]$; also, the actual water vapor pressure at the interface is lower than in the main gas by a factor K_3. p_{HCl}, however, will have the same value at the interface and in the main gas (8). Therefore

$$[B] = \frac{2p_o}{\gamma_{BH_3}\left\{1 + K_{10}\left(\frac{p_{H_2O}}{K_3}\right)^2 + K_{11}p_{HCl}\right\}} \qquad [16]$$

The value of [B] can be transformed into a concentration per cm^3 by multiplication with 5×10^{22}, the number of atoms per cm^3 of silicon. The experiments at 1150°C can then be explained with $\gamma_{BH_3} = 10^{-3}$, $K_{10} = 2 \times 10^{13}$, $K_3 = 30$, $K_{11} = 10^3$; with Eq. [9] we find $\gamma_{B_2H_6} = 5 \times 10^{-4}$.

In conclusion it can be stated that the influence of varying amounts of water vapor and HCl in the gas phase on the boron concentration in the silicon can be explained semiquantitatively by assuming the gas phase reactions to come to equilibrium at the silicon interface. The main features of the experimental results are in accord with the predictions given in Fig. 9.

Manuscript submitted Nov. 20, 1970; revised manuscript received April 12, 1971. This was Paper 374 RNP presented at the Los Angeles Meeting of the Society, May 10-15, 1970.

Any discussion of this paper will appear in a Discussion Section to be published in the June 1972 JOURNAL.

REFERENCES

1. B. A. Joyce, *J. Cryst. Growth*, **3, 4,** 43 (1968).
2. L. B. Valdes, *Proc. I.R.E.*, **42,** 420 (1954).
3. R. G. Mazur and D. H. Dickey, *This Journal*, **113,** 255 (1966).
4. W. G. Spitzer and M. Tanenbaum, *J. Appl. Phys.*, **32,** 744 (1961).
5. F. G. Allen, *ibid.*, **28,** 1510 (1957).
6. S. M. Kroon, Private communication.
7. W. H. Shepherd, *This Journal*, **115,** 541 (1968).
8. J. Bloem, *ibid.*, **117,** 1397 (1970).
9. German Pat. 573980 IV C/12C, (Siemens) (1961).
10. O. Kubashewski and E. LI. Evans, "Metallurgical Thermochemistry," Pergamon Press Ltd., London (1956).
11. E. J. Sinke, G. A. Pressley, A. B. Baylis, and F. E. Stafford, *J. Chem. Phys.*, **41,** 2207 (1964).
12. T. P. Fehlner and W. S. Koski, *J. Am. Chem. Soc.*, **86,** 2733 (1964).
13. JANAF Thermochemical tables, Dow Chemical Co., Midland, Mich. (Aug. 1965).
14. G. Brouwer, *Philips Res. Rept.*, **9,** 366 (1954).

Thick Epitaxial Films of Cubic ZnSe and ZnS by Vapor Phase Transport

P. Vohl, W. R. Buchan, and J. E. Genthe

Itek Corporation, Lexington, Massachusetts 02173

ABSTRACT

Films of cubic ZnSe and ZnS have been grown epitaxially on [100] oriented GaAs substrates by vapor phase transport in flowing hydrogen. Thicknesses up to 200 μm over areas up to 5 cm^2 have been obtained. The ZnSe films are superior in crystalline quality to the ZnS films. The films exhibit low birefringent strain, good optical transmission, high resistivity, and near-bulk electro-optic constants. These properties make them suitable for use in information storage devices utilizing the longitudinal linear electro-optic effect.

The objective of this work was to produce cubic ZnSe and ZnS of quality suitable for use in electro-optic information storage devices. These devices are designed to have a laminar structure for utilization of the longitudinal linear electro-optic effect in the spectral range of visible and near ultraviolet light (1). For this mode of operation their geometrical specification calls for an area at least 1 cm^2 oriented in the [100] direction and a film thickness sufficient to prevent excessive current flow at the required operating voltage. The operating requirements for these devices impose quite stringent conditions on the properties of the film. The material must be free of optical defects and birefringent strain. The intrinsic absorption edge must be sharp and the resistivity high. Bulk ZnSe and ZnS do not have the required properties. High resistivity bulk ZnSe is generally strained and contains an undesirable number of twins and low angle grain boundaries. The crystal quality of bulk ZnS is even worse. This material is characterized by stacking faults for a wide range of growth temperatures, probably because of a hexagonal to cubic phase transition which is reported to occur around 1020°C (2). Such structures constitute optical defects and would degrade the electro-optic performance of the device. Thus the requirement for unstrained cubic phase material imposes the condition of low temperature growth for these compounds. This and the plate-like form of the device make epitaxial film growth an attractive approach. Vapor phase growth methods for preparing epitaxial films of ZnSe and ZnS have been reported in the literature (3-7).

After considering possible substrates it was decided to try Si, Ge, and GaAs. In a few preliminary experiments on growing ZnSe and ZnS, the best indications of epitaxy were obtained for films grown on GaAs. It was then concluded that GaAs was more suitable for use as a substrate than either Si or Ge.

In this paper the procedure used for the growth of epitaxial films of ZnSe and ZnS on GaAs by vapor transport are outlined. The effects of different film growth parameters on epitaxial quality are described. The methods used to evaluate the crystalline properties of the films are listed along with the results obtained. Finally, the results of optical absorption, electrical and electro-optic measurements on these films are presented. Concurrently with using vapor phase growth methods, vacuum deposition of epitaxial ZnS films was accomplished by M. E. Behrndt and S. C. Moreno of these laboratories, with the same device objectives. Their results are reported separately (8).

Growth of Epitaxial Films

Method.—The vapor transport method used in this work is simple and highly efficient. Approximately 1/3 to 1/2 of the source material lost by vaporization is deposited on the substrate. A schematic design of the transport chamber incorporated into a modified Pensak furnace is shown in Fig. 1. A vertical quartz cylinder ~2 cm in diameter by ~1 cm high is positioned on a flat source heater. The heater consists of a notched ceramic disk wound with 0.018 in. platinum heater wire. The source is placed on the heater within the quartz cylinder. The cylinder has three supports upon which the substrate is placed, partially enclosing the transport chamber.

There is no separate substrate heater. The substrate is heated by convection from the source heater, and its temperature is substantially uniform because of the excellent thermal convection of the hydrogen carrier gas. The amount of gas-vapor exchange between the ambient environment and the inner chamber is varied by changing the length of the quartz supports. This spacing is generally varied between 0.1 and 2.0 mm. A shelf in the cylinder acts as a baffle to deflect the direct vapor flow away from the outer edge of the substrate, so that in this region the vapor flow is parallel to the substrate, while at the center the flow remains nearly perpendicular to the substrate. A thermocouple is pressed against the back of the substrate. The transport chamber of Fig. 1 is placed inside a Pyrex enclosure on a metal base containing all the gas and electrical feedthroughs. Provisions exist for evacuating the chamber in order to operate at reduced pressure. The ambient gas is normally high-purity hydrogen although a dilute mixture of H_2S in hydrogen has been tried. The hydrogen flows continuously.

The ZnSe source is a wafer cut from a crystal grown in these laboratories (9). The ZnS source is Kodak Irtran II, a hot-pressed ZnS plate. It is believed to contain some halide and metal impurities. To remove any apparent dirt, the surface is cleaned by a dilute nitric acid etch and rinsed with distilled water.

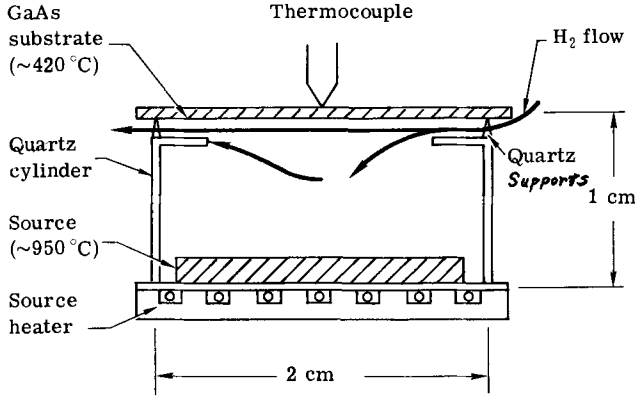

Fig. 1. Schematic drawing of the vapor transport chamber for epitaxial growth of ZnSe and ZnS.

Key words: epitaxy, electro-optic effect, birefringent strain, film growth, II-VI semiconductors, single crystal.

The substrates are [100] oriented single-crystal wafers of n- or p-type, commercially obtained, GaAs. This is the orientation which exhibits the longitudinal linear electro-optic effect. The wafers are either mechanically polished and then etched in methanol-bromine solution or chemically polished. They are between 0.010 and 0.020 in. thick. An optically reflecting scatter-free surface is desirable, although generally some dust particles, scratches, and pits remain after processing.

The source and substrate are dried and installed in the furnace. Prior to film deposition the furnace is evacuated and flushed with hydrogen. The desired hydrogen pressure and flow rates are then established. Films have been grown at hydrogen pressures ranging from 50 Torr to 1 atm, but the best results were achieved at pressures between 100 and 300 Torr, and hydrogen flow rates around 10 cm^3/min. The source heater is raised to a temperature of about 950°C. The substrate temperature is between 400° and 500°C. Under these conditions the films grow at a rate which ranges between 3 and 5 μm/hr. Growth times are between 25 and 40 hr to yield films between 75 and 200 μm thick. The reaction is believed to be $ZnX + H_2 \rightleftarrows Zn + H_2X$ (where X = Se or S). The presence of the hydrogen is probably not important except possibly for serving as a reducing agent or as a carrier gas because vapor transport occurred at about the same rate in the presence of an inert gas.

Effect of growth conditions on epitaxial quality.—Five ZnSe films followed by 30 ZnS films have been grown on (100) GaAs substrates. Both types of film have been grown to thicknesses of 200 μm over areas up to 5 cm^2. The epitaxial quality of the individual films was evaluated primarily by means of microscopic studies of the film surfaces and of cleavage sections. These studies were initially checked against x-ray and electron diffraction results.

Of the ZnSe films, the first was partly epitaxial, and the fourth and fifth were completely epitaxial. The initial deposit of pratically all the ZnS films is epitaxial, but as the thickness increases beyond about 10 μm the tendency toward polycrystalline growth increases. Good reproducibility of thick (>25 μm) ZnS films of high crystalline perfection has not yet been achieved. Of the 30 ZnS films, about five were completely epitaxial. About 20 were partly epitaxial, with epitaxy always occurring in a ring at the outer edge of the substrate, where the vapor flows fast and parallel to the substrate. The centers of these films contained polycrystalline pockets amid the epitaxial material. About five ZnS films were mainly polycrystalline.

During the experiments on ZnS film deposition, a number of growth parameters were varied to determine their effect, if any, on the epitaxial quality of the films. The observations made are summarized in Table I. Of the parameters listed, it was found that hydrogen pressure (c) hydrogen flow rate (d), and especially chamber geometry (g) could be varied to improve the quality of the films. These results imply that the partial pressure and concentration of the vapor species have a pronounced effect on epitaxy, and therefore that the degree of supersaturation is important. Low supersaturation is generally the desired condition for avoiding fast nucleation on the substrate of many misaligned nuclei. The vapor pressure over the source material, for a given temperature distribution, H_2 pressure, and flow rate, is controlled mainly by the pressure drop across the chamber opening. This in turn depends on the spacing as determined by the length of the quartz supports. With "large" spacing, enough vapor is carried out of the chamber to make thick film growth very inefficient. With virtually no spacing, *i.e.*, a closed chamber, the vapor pressure is apparently sufficient to cause enough supersaturation at the substrate to prevent epitaxial growth. At some optimum spacing (with the chamber geometry described this was about 1.0 mm) the vapor pressure established a low enough supersaturation to provide for epitaxy at a reasonably high growth rate. This might be the explanation for epitaxy occurring preferentially at the outer edge of the substrate where the degree of supersaturation is likely to be low because of the pressure drop in this region. Polycrystalline defects increase with film thickness instead of "growing out," suggesting that the amount of supersaturation tends to increase with film thickness. However, no satisfactory explanation for this result has been found.

Table I. Effects observed with variation of ZnS film growth parameters

Parameter	Condition or setting	Effect on epitaxial quality
(a) Substrate preparation	Etching Chemical polishing Outgassing	No marked effect
(b) Substrate temperature	400°-500°C	For a given thickness, film surfaces are rougher with increase in substrate temperature
(c) Hydrogen pressure	100-760 Torr	Lower pressure enhances epitaxy
(d) Hydrogen flow rate	1-10 cm^3/min	Higher flow rate enhances epitaxy
(e) Growth rate	3-5 μm/hr	No marked effect
(f) Cool down time	1-4 hr	No marked effect
(g) Chamber geometry	The spacing for vapor flow out of the transport chamber was varied by changing the length of the quartz supports	Discussed in test

Evaluation of Crystalline Properties

X-ray and electron diffraction.—X-ray diffractometer traces showed strong reflections only from (100) planes. Laue back-reflection photographs were taken on films at least 75 μm thick. These revealed the fourfold symmetry as shown in Fig. 2 and 3 for ZnSe and ZnS, respectively. Electron diffraction patterns of the as-grown surface of a 70 μm thick ZnS film are shown in Fig. 4a and 4b.

Surface morphology.—Figures 5a and 5b are photomicrographs of the as-grown surfaces of a ZnSe and ZnS film, respectively.

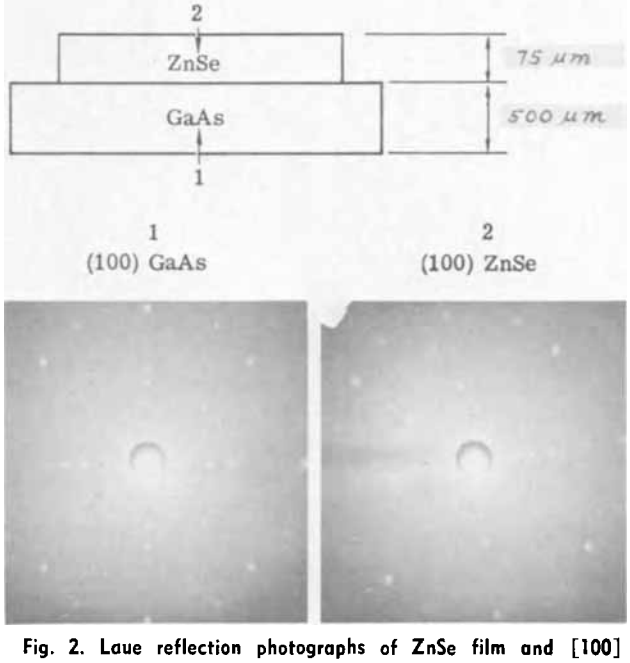

Fig. 2. Laue reflection photographs of ZnSe film and [100] oriented GaAs substrate. The apparent rotation of the ZnSe was caused inadvertently by sample rotation.

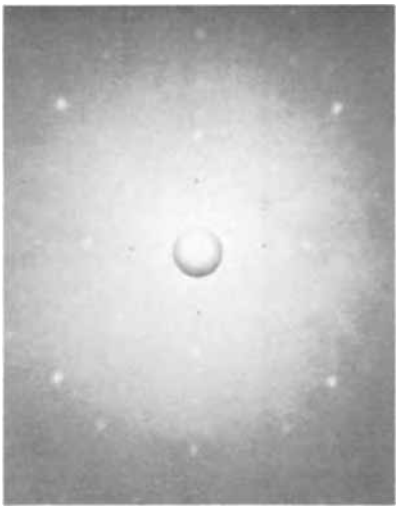

Fig. 3. Laue reflection photograph of ZnS film on [100] oriented GaAs substrate. Film thickness, 100 μm.

Fig. 4. Reflection electron diffraction of as-grown ZnS film on (100) GaAs. a) [100] direction. b) [110] direction at 45°.

ZnSe.—The film is 75 μm thick and was deposited at a substrate temperature of 450°C. The surface is characterized by growth pyramids. The four-fold symmetry of the (100) plane is quite apparent, although a slight elongation of some of the growth pyramids has occurred. On other pyramids, extra planes of higher order are visible. The pyramids are formed by (110) planes which intersect the surface at (100) planes. Steps are

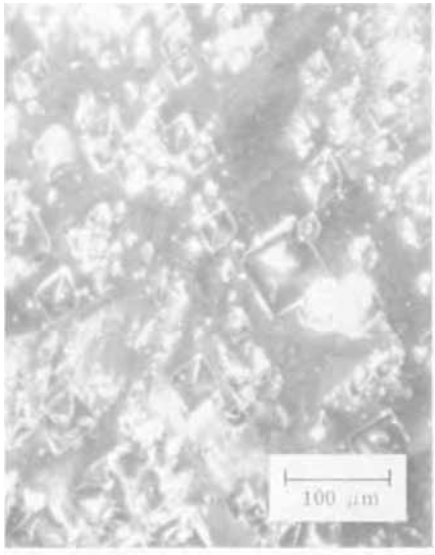

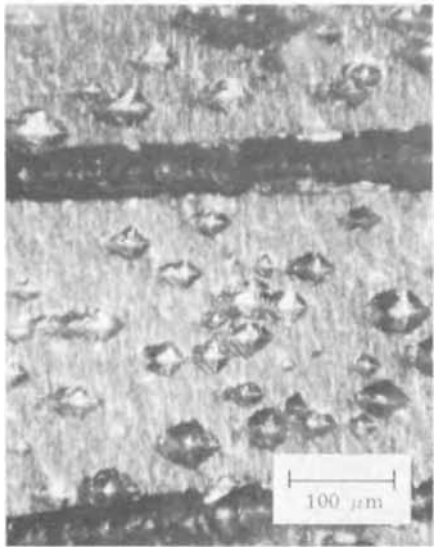

Fig. 5. As-grown surfaces of epitaxial films. (a) 75 μm thick ZnSe film characterized by four-fold growth pyramids. (b) 80 μm thick ZnS film characterized by four-fold pits.

visible on some of the sides; however, it could not be determined whether or not they are spirals. The surface between the pyramids is fairly smooth; the main features are very slight ripples which run parallel to the [110] direction.

ZnS.—The film is 80 μm thick and was deposited at a substrate temperature of 430°C. The surface is characterized by pits of predominately tetragonal shape. Ideally, the pits are inverted growth pyramids and exhibit the four-fold symmetry of the (100) plane observable in the photomicrographs, but actually many of them are elongated and some are even rhombohedral in shape. The two dark horizontal bands are "troughs" which grew from scratches in the surface of the GaAs substrate. The surfaces of ZnS films between the pits are rougher than those of the ZnSe films. In general, the surfaces of ZnSe were smoother and the growth features more nearly four-fold symmetric than those of ZnS for films of similar thickness grown under similar conditions.

Cleavage.—The epitaxial films and the GaAs substrates can be cleaved along (110) planes. A photomicrograph of an epitaxial ZnS/GaAs edge cleaved along a (110) plane is shown in Fig. 6. The film thickness of 80 μm was measured by means of the calibrated eyepiece of the microscope. The junction is directly observable, since the epitaxial film transmits visible

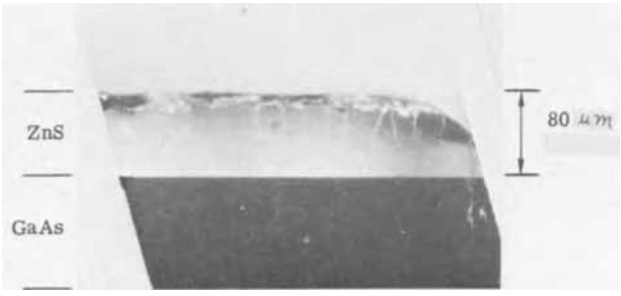

Fig. 6. (110) Cleavage edge of ZnS/GaAs. The ZnS film is brightened by microscope light transmitted through it.

light. Cleavage lines and "broken out" positions of the edge are visible in the photomicrograph. The cleavage lines change direction as they cross the interface. Cleavage defects appear to be more numerous in the top 40 μm of the film. Beyond about 30 μm from the substrate, tiny polycrystalline boundaries become apparent. These seem to flare with increasing thickness, and eventually form the pits which are characteristic of the surface morphology. It is speculated that the defects originate at the surface of the GaAs, are propagated through the film, flare with thickness, and eventually tend to dominate the structure. Beyond 80 μm the epitaxial quality of such films can be substantially degraded. The 4% lattice mismatch at the interface could subsequently induce fiber growth to account for such defects.

Cleavage surfaces of nonepitaxial films are rough. The edges are jagged and not along (110) planes. They scatter light in contrast to the edges of smooth epitaxial films, which reflect light specularly. This effect provides a convenient test for epitaxy because of its good correlation with x-ray and electron diffraction results. Cleaved (110) planes of epitaxial films of ZnSe/GaAs are generally smoother and contain fewer cleavage lines than those of ZnS/GaAs.

Birefringent strain.—The films were further evaluated with a beam splitting Glan-Thompson prism by viewing the reflected light from the GaAs/ZnS or GaAs/ZnSe interface after the top surface of the film was polished to an optical finish. This gives the optical equivalent of viewing between crossed polarizers. Low birefringent strain was readily observed in this manner, together with light scattered from point defects at the top surface of the films. The birefringent strain in the films was compared with that in a number of naturally occurring cubic ZnS crystals in the form of ~125 μm thick wafers, most of which exhibited considerable strain. Almost all of the films showed less strain than even the best natural crystals. Strain was lower in the ZnSe films than in the ZnS films. The light scattering point defects are believed to be polycrystalline "columns" growing up through the film from the GaAs to the surface.

Other Measurements on Epitaxial Films

Optical absorption of a ZnS film.—For this measurement a ZnS film was separated from the GaAs substrate. This was accomplished by first polishing the top surface of the film and then etching away the GaAs with a solution of 2 ml H_2O, 8 mg $AgNO_3$, 1g CrO_3, and 1 ml HF (10), which leaves the ZnS intact. An optical absorption spectrum of the ZnS film at room temperature is shown in Fig. 7. It compares quite well in the steepness of the absorption edge and in the transmission at wavelengths beyond the edge with a spectrum obtained on high-purity, hexagonal single-crystal ZnS.

Current-voltage characteristics of a ZnS film.—Current-voltage characteristics were measured on an unpolished 50 μm thick film of ZnS on a p-type GaAs substrate. A Ga-In "point" contact was made to the ZnS, such that the area to thickness ratio was about 1 at the Ga-In contact and much greater than 1 at the GaAs substrate. Positive and negative polarities were applied to the GaAs. Because of the small contact area at one electrode compared to the ZnS film area, surface leakage is considered to be negligible. The current was recorded with a Cary electrometer. A large transient current flows through the sample upon application of the voltage. It increases with increasing applied voltage and consists of a polarization current and an injected electron current. Some of the injected electrons are subsequently trapped. The transient component of the electron current is about an order of magnitude higher than the final steady-state current. The measurement was made when the transient current was negligible, *i.e.*, about half an hour after the voltage was applied.

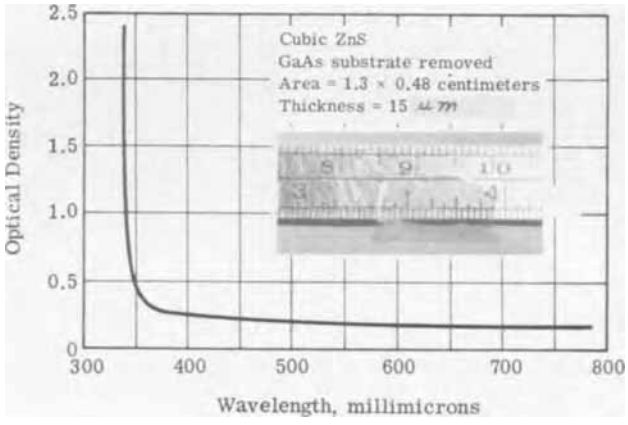

Fig. 7. Optical absorption spectrum of ZnS film at room temperature. Inset shows ZnS film removed from the substrate.

Figure 8 is a plot of ln I *vs.* ln V. Below 400V the slope gradually changes from about 1 to about 9. The observed I-V characteristics may be due to space

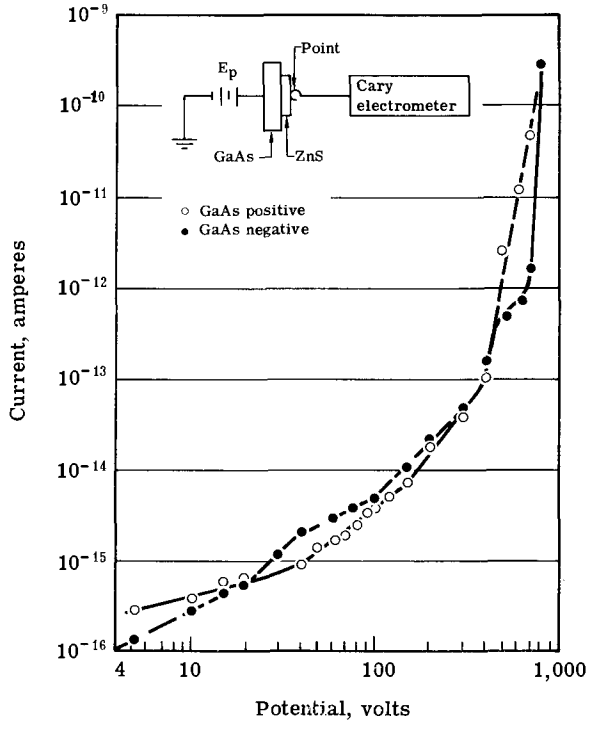

Fig. 8. I-V characteristic of 50 μm thick ZnS film on p-type GaAs substrate. A 3 x 10^{-3} cm^2 area Ga-In contact is made to ZnS top surface.

charge limited currents or field-induced breakdown through hot carrier effects.

Electro-optic measurements.—The ZnS and ZnSe epitaxial films both showed the linear electro-optic effect (Pockels effect) characteristic of materials with $\bar{4}3$ m symmetry.

The electro-optic constants (r_{41}) of one ZnSe and two ZnS films were determined by first measuring the Pockels constant $k = \frac{n_o^3 r_{41}}{\lambda}$ and then measuring the refractive index, n_o, at the same wavelength, λ. The Pockels constant was found by using a calibrated electro-optic light modulator (EOLM) between polarizers in the same optical path as the film being measured. The arrangement is shown in Fig. 9. The films were oriented so that the plane of reflection coincided with the plane defined by two of the cube ($\bar{4}$) axes, and the incident light was linearly polarized perpendicular to the plane of reflection [*i.e.*, parallel to one of the cube ($\bar{4}$) axes]. The retardation introduced by applying a known voltage across the film was balanced by applying a voltage to the EOLM to introduce an equal but opposite retardation. The light intensity transmitted by the system is then

$$I = I_o \sin^2 \pi (\Gamma_1 + \Gamma_2) \quad [1]$$
$$= 0, \text{ when } \Gamma_1 + \Gamma_2 = 0, 1, 2 \ldots$$

where I_o is the incident light intensity and Γ_1 and Γ_2 are the retardations in the film and the EOLM, respectively. Thus, the photomultiplier provided a signal for detecting the null when

$$\Gamma_1 = \Gamma_2$$

i.e.

$$2k_1 V_1 \cos \phi = -k_2 V_2$$

$$k_1 = \frac{|V_2|}{2|V_1|(V_2)_\lambda \cos \phi} \quad [2]$$

where k_1, and V_1 and k_2, and V_2 are the Pockels constants of and voltages applied to the film and the EOLM, respectively, $(V_2)_\lambda$ is the full wave voltage of the EOLM, and ϕ is the angle of refraction in the film. The angle of incidence was 11° for all the measurements so that the angle ϕ was about 4½°; the approximation $\cos \phi \approx 1$ was therefore made. The factor, 2, in the denominator arises from the double pass of light through the film.

The refractive index, n_o, of each film was found by measuring Brewster's angle. The measurements of the Pockels constants and the refractive indices were all made at 633 nm using a 1 mW He/Ne laser source. Voltages of either polarity were applied. The current through the ZnSe film at 40V was 10^{-7}A. For the ZnS samples the currents were always less than 10^{-10}A.

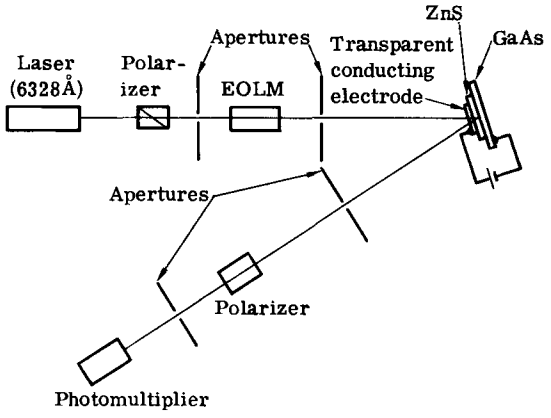

Fig. 9. Schematic of optical arrangement for measuring phase retardation in epitaxial films.

Since the maximum value of V_1 was limited to about 100V by the thickness of the films, the maximum value of Γ_1 was of the order of 10^2. The optical system therefore had an extinction ratio of 10^5 which gave distinct nulls when balancing Γ_1 and Γ_2.

Voltage across the film was applied between the GaAs substrate and a 2 mm diameter transparent conducting platinum electrode evaporated onto the polished surface of the II-VI film. The GaAs/ZnS or GaAs/ZnSe interface acted as a reflector of about 5% efficiency which gave two light passes through the film and double the birefringence. A natural crystal of cubic ZnS was also measured in the same way by using a layer of evaporated Al as the reflecting electrode. The polished surfaces of the films and of the natural ZnS wafer were slightly nonparallel so that the relatively strong reflection from the platinized top surface was excluded by the apertures used.

The results of the measurements along with values for bulk crystals reported in the literature are listed in Table II. The figures for k_1 in column 4 are the average values obtained from Eq. [2] over the range of applied voltage given in column 3. There was no consistent difference between the values obtained with opposite polarities at the same voltage or with different voltages. For the samples studied, the refractive indices in column 5 were used to derive the values for r_{41} in column 6. The accuracy of the Pockels constants is ±2% and that of the refractive indices ±0.4%. The accuracy of r_{41} is therefore about ±3%.

The value of r_{41} obtained for the natural ZnS crystal agrees quite well with that given by Namba (12). The epitaxial films all gave values for r_{41} slightly lower than the values for the bulk crystals although the value for the ZnSe film is very close to the bulk value. The values of r_{41} obtained for the ZnS films are respectively 92% and 83% of the value obtained for the natural crystal. The refractive indices of the films are about 98% of the values for the bulk crystals.

The half-wave voltages calculated from the Pockels constants are 13-14 kV for the epitaxial ZnS films, 10 kV for the epitaxial ZnSe film, and 11.3 kV for the natural ZnS crystal.

Conclusions

GaAs was found to be the most suitable substrate for vapor deposition of [100] oriented cubic ZnSe and ZnS films. Epitaxial films have been grown to thicknesses of 200 μm over areas up to 5 cm². With the ambient hydrogen flow method employed, it was found that the ambient pressure and flow rates affect the epitaxy of the deposited films. The greatest effect on epitaxial quality of the ZnS films was produced by the geometrical arrangement of the transport chamber, which is apparently important in controlling the degree of supersaturation of the vapor species. The best epitaxy is in the initially deposited layers. With increasing thickness, polycrystalline pockets tend to form. The 4% lattice mismatch at the interface could be the origin of subsequent fiber growth. The surfaces of the films are characterized by four-fold growth pyramids in the case of ZnSe and four-fold pits in the case of ZnS. It has been concluded that epitaxial ZnSe films on GaAs are superior in crystalline quality to the ZnS films.

Table II. Measured values of Pockels constant, refractive index, and electro-optic coefficient at 633 nm

Sample	Thickness (μm)	Voltage range (V)	Pockels constant, k_1 ($V^{-1} \cdot 10^{-5}$)	Refractive index, n_o	Electro-optic coefficient, $r_{41} = \frac{\lambda k_1}{n_o^3}$ (10^{-12} m/V)
ZnS/GaAs	40	20-100	3.85	2.30	2.00
ZnS/GaAs	20	20-100	3.63	2.33	1.82
ZnS (natural)	400	20-200	4.44	2.35	2.16
ZnS (bulk)	—	—	—	2.354 (11)	2.1 (12)
ZnSe/GaAs	20	10-40	5.00	2.52	1.98
ZnSe (bulk)	—	—	—	2.580 (13)	2.0 (14) [546 nm]

The optical absorption spectrum of epitaxial ZnS films is similar to that of bulk ZnS. Birefringent strain is far less in these films than in naturally occurring cubic ZnS. The resistivity of ZnSe films is around 10^{11} ohm-cm and that of ZnS is greater than 10^{14} ohm-cm. The Pockels constant of the ZnS films is approximately 85% of the value for natural ZnS crystals. For the ZnSe films it is very close to that reported for bulk ZnSe crystals.

Acknowledgments

We wish to thank W. F. Bolza for his help with the film growth and R. G. Dykeman for the film polishing. We would like to acknowledge J. R. Howley and J. F. Washeba for the x-ray and electron diffraction data and W. A. Simmons for his help with the electro-optic measurements. We also thank R. R. Addiss, who read and criticized the manuscript.

Manuscript submitted Feb. 11, 1971; revised manuscript received May 12, 1971.

Any discussion of this paper will appear in a Discussion Section to be published in the June 1972 JOURNAL.

REFERENCES

1. D. S. Oliver, P. Vohl, R. E. Aldrich, M. E. Behrndt, W. R. Buchan, R. C. Ellis, J. E. Genthe, J. R. Goff, S. L. Hou, and G. McDaniel, *Appl. Phys. Letters*, **17**, 416 (1970).
2. W. L. Roth, in "Physics and Chemistry of II-VI Compounds," p. 117, M. Aven and J. S. Prener, Editors, North Holland Publishing Co., Amsterdam, Holland (1967).
3. A. Baczewski, *This Journal*, **112**, 577 (1965).
4. G. Galli and F. L. Morritz, *ibid.*, **113**, 62C (1966).
5. T. Arizumi, T. Mishinaya, and M. Kakelu, *Japan. J. Appl. Phys.*, **5**, 588 (1966).
6. H. J. Hovel and A. G. Milnes, *This Journal*, **116**, 843 (1969).
7. G. Galli and R. E. Holmes, *Electrochem. Technol.*, **6**, 358 (1968).
8. M. E. Behrndt and S. C. Moreno, *J. Vacuum Sci. and Tech.*, (May/June 1971).
9. P. Vohl, *Mater. Res. Bull.*, **4**, 689 (1969).
10. M. S. Abrahams and C. J. Buiocchi, *J. Appl. Phys.*, **36**, 2855 (1965).
11. W. L. Bond, *ibid.*, **36**, 1674 (1965).
12. S. Namba, *J. Opt. Soc. Am.*, **51**, 76 (1961).
13. D. T. F. Marple, *J. Appl. Phys.*, **35**, 539 (1964).
14. R. W. McQuaid, *Proc. IRE*, **50**, 2848 (1962); *ibid.*, **51**, 470 (1963).

Anneal Behavior of Cd Ion Implanted GaAs

R. G. Hunsperger and E. D. Wolf

Hughes Research Laboratories, Malibu, California 90265

ABSTRACT

The high temperature anneal behavior of lattice damage produced by 60 keV Cd^+ ion implantation of GaAs has been measured for <111> substrates implanted at 77° and 300°K. Measurements of relative lattice disorder were made by the Coates-Kikuchi pattern technique, which employs a scanning electron microscope. Damage produced by ion doses $\geq 10^{14}/cm^2$ was observed to anneal gradually in the temperature range from about 400°-700°C. There was no significant difference in the anneal behavior of samples implanted with the substrate at 77°K and those implanted at room temperature. Hall measurements of surface carrier concentration, average mobility, and sheet resistivity in the implanted layers showed that the electrical properties follow essentially the same trends as the damage anneal curves. Annealing at approximately 800°C or higher was required to obtain maximum electrical activity of the implanted ions and maximum carrier mobility, although a p-type layer could be produced by annealing at temperatures as low as 600°C. Samples implanted with relatively low ion dose ($\sim 10^{13}/cm^2$) exhibited damage anneal stages at temperatures below 500°C, but still required annealing at 700°C or greater to produce a measurable p-type layer.

Ion implantation has been used to dope gallium arsenide with both p- and n-type dopants. The electrical properties of p-type layers have been reported for Zn (1-4), Cd (2, 4), and C (5) implantations, while Se (6), Te (1), S (4, 5), and Si (5) have been shown to form n-type layers. In general, implantation must be performed at temperatures greater than 400°C or must be followed by annealing at such temperatures to eliminate implantation-caused lattice damage and to cause implanted dopant atoms to move to electrically active lattice positions. The relation between lattice damage annealing and the electrical properties of implanted layers depends on a number of variables including ion type, ion energy, substrate temperature during implantation, ion dose, and dose rate. This paper is concerned with the high temperature (>500°C) anneal behavior of lattice disorder produced by 60 keV Cd ion implantation of GaAs at room temperature and its correlation with the electrical properties of the implanted layers, as previously reported (4). The anneal behavior of doped layers produced by implantation of 60 keV Cd ions into GaAs substrates held at 77°K is also described, with respect to both lattice damage and electrical properties of the layers.

Key words: Coates-Kikuchi analysis, lattice disorder, ion-implantation doping.

Experimental

The samples were prepared from gallium arsenide <111> oriented (±3°) wafers approximately 15 mils thick, with the "B" face etch polished in a solution of methyl alcohol and bromine to remove sawing and lapping damage prior to ion-implantation. Ion-implantation was performed, with the substrates either at room temperature, or at 77°K, using a 60 kV magnetically-mass-separated Cd^+ ion beam. The substrates were tilted ~8° off axis to minimize ion channeling effects. Ion dose rate was $\sim 10^{-7}$ A/cm^2. Prior to annealing the samples were coated with a sputtered layer of SiO_2 about 2000Å thick to prevent outdiffusion of dopant atoms and decomposition of the GaAs. Annealing was performed in a nitrogen atmosphere.

The p-type dopant Cd was implanted into n-type substrates so that the resulting p-n junction would provide electrical isolation of the implanted layer during measurement. Substrate background impurity concentration was approximately 1 x $10^{16}/cm^3$. The electrical characteristics of the implanted layers (sheet

resistivity ρ_s, effective surface carrier concentration N_s, and effective mobility μ) were determined using the van der Pauw-Hall measurement technique (7). Square-shaped Hall samples (approx. 4 mm on a side) were diced from the ion-implanted substrate wafers prior to annealing. All Hall measurements were made at room temperature, after the samples were quenched in air from whatever temperature at which they were annealed. The maximum possible error in the Hall measurements is estimated to be approximately 10%. This maximum error could occur only in cases in which the sheet resistivity is large ($>10^4$ ohm/□) and hence the Hall voltage is difficult to measure because of background noise voltage. Otherwise the error is limited to the accumulative instrument error of approximately 3%.

The measurements of implantation-caused lattice disorder were made by the "Coates-Kikuchi" pattern technique, which employs a scanning electron microscope as the measuring instrument. This method is relatively new, and hence a brief description of it is provided even though it has been described elsewhere (8-10).

When a collimated, monochromatic beam of electrons enters a crystal at a well-defined angle with respect to the surface and the lattice, certain Bloch waves are excited in the crystal. The anisotropic backscattering of these coherent waves through single and multiple events can be displayed as a function of the incident beam angle by utilizing a collimated scanning electron beam and a sensitive detector to collect the high energy backscattered electrons (11). Figure 1 (top) is a schematic representation of the experimental method and Fig. 1 (bottom) is an idealized one-dimensional line scan orthogonal to the (110) lattice planes.

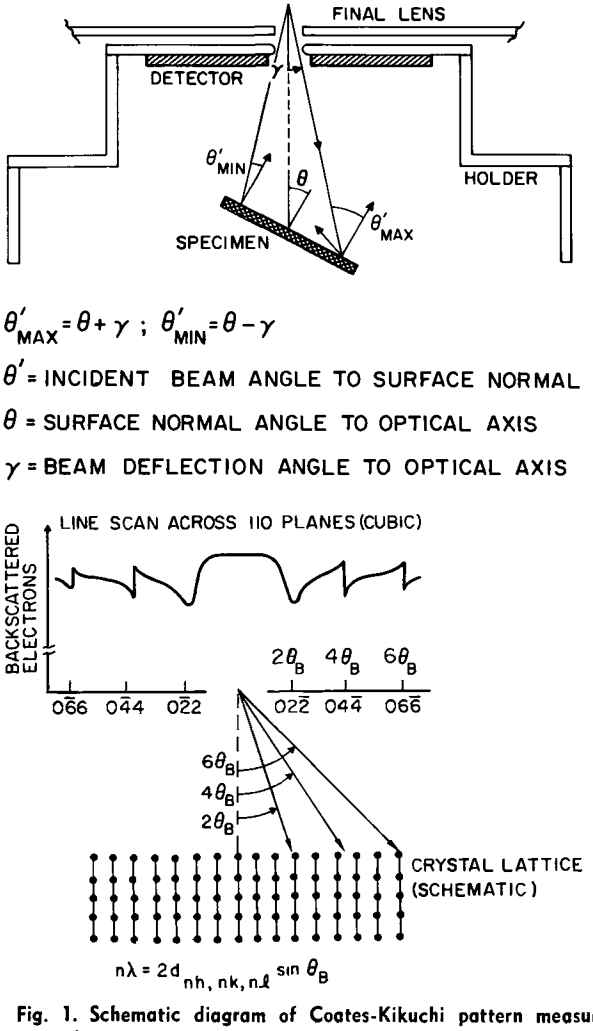

Fig. 1. Schematic diagram of Coates-Kikuchi pattern measurement technique.

The ion-implanted specimens were cleaned in HF to remove the surface oxide and were placed in the scanning electron microscope along with a clean nonimplanted GaAs wafer which served as a reference standard. It should be noted that regions of the samples that were masked from the ion beam during implantation (by the spring clips that held them in place in the apparatus) also served as nonimplanted reference areas. These areas were, of course, SiO_2 coated and annealed along with the rest of the sample. Since the Coates-Kikuchi patterns for these areas were the same as that for the nonimplanted, nonannealed reference standard, the heat treatment can be ruled out as a possible source of lattice disorder. The relative backscattered electron intensities were recorded as illustrated in Fig. 2 [from Ref. (9)] using an annular semiconductor diode detector. The fractional change in intensity ($\Delta I/\Delta I_{ref}$) across the $0\bar{4}\bar{4}$ band edge (line) was determined by dividing the change observed for an ion-implanted sample ΔI by the intensity change for the reference sample ΔI_{ref}. A Faraday cup was used to measure the beam current. The beam current was typically 1×10^{-8} A and did not change between measurements of the unknown and the standard, nor were any other conditions allowed to vary during the measurements. This fractional intensity change ($\Delta I/\Delta I_{ref}$) has been defined earlier (8) as the normalized pattern quality I^*, and is a measure of the lattice perfection (or lack of).

Results and Discussion

The data shown in Fig. 3 give the anneal behavior of implantation-caused lattice disorder, as indicated by the parameter I^*, for implantation performed with the substrate held at either room temperature or 77°K. (The data corresponding to samples implanted at room temperature and annealed at 450°C or below have been previously published (9), but are included for completeness and to allow comparison with the data for samples implanted at 77°K.) For samples implanted with ion dose greater than 1×10^{14}/cm² a gradual annealing of lattice disorder was observed in the temperature range from about 400°-700°C, with relatively little additional improvement after heat treatment at higher temperatures. This same trend was evident in the electrical characteristics of the implanted layers, as shown by the resistivity data of Fig. 4. Hall measurements could not be made for samples annealed below 600°C because there was not sufficient electrical activity to produce a p-type region and resultant p-n junction to isolate the implanted layer from the substrate. There was no significant difference in the anneal behavior of samples implanted with the substrate at 77°K and those implanted at room temperature; in this respect GaAs behaves differently from silicon. For example, a 60 keV Cd ion dose $\geq 10^{14}$/cm² exceeds the level required to form a region of saturated damage in the GaAs, as determined by Rutherford backscattering measurements (13). Davies (14) has found that silicon <111> oriented samples, implanted at 77°K with greater than the saturation dose of 200 keV boron, exhibit an abrupt anneal stage at a temperature several hundred degrees below that required to cause the same change in resistivity in samples implanted at room temperature with the same ion dose. Other authors (15, 16) have also reported what appears to be damage-enhanced annealing in silicon. The difference between the anneal behavior in these particular cases of ion-implanted layers in GaAs and Si indicates that reordering of the lattice depends not just on the over-all degree of lattice damage but also on the particular lattice defects involved. Very little is known about the detailed nature of lattice defects created in either GaAs or Si by ion implantation. However, the different lattice structures of the two materials can reasonably be expected to yield different defect types. For example, di-vacancies have

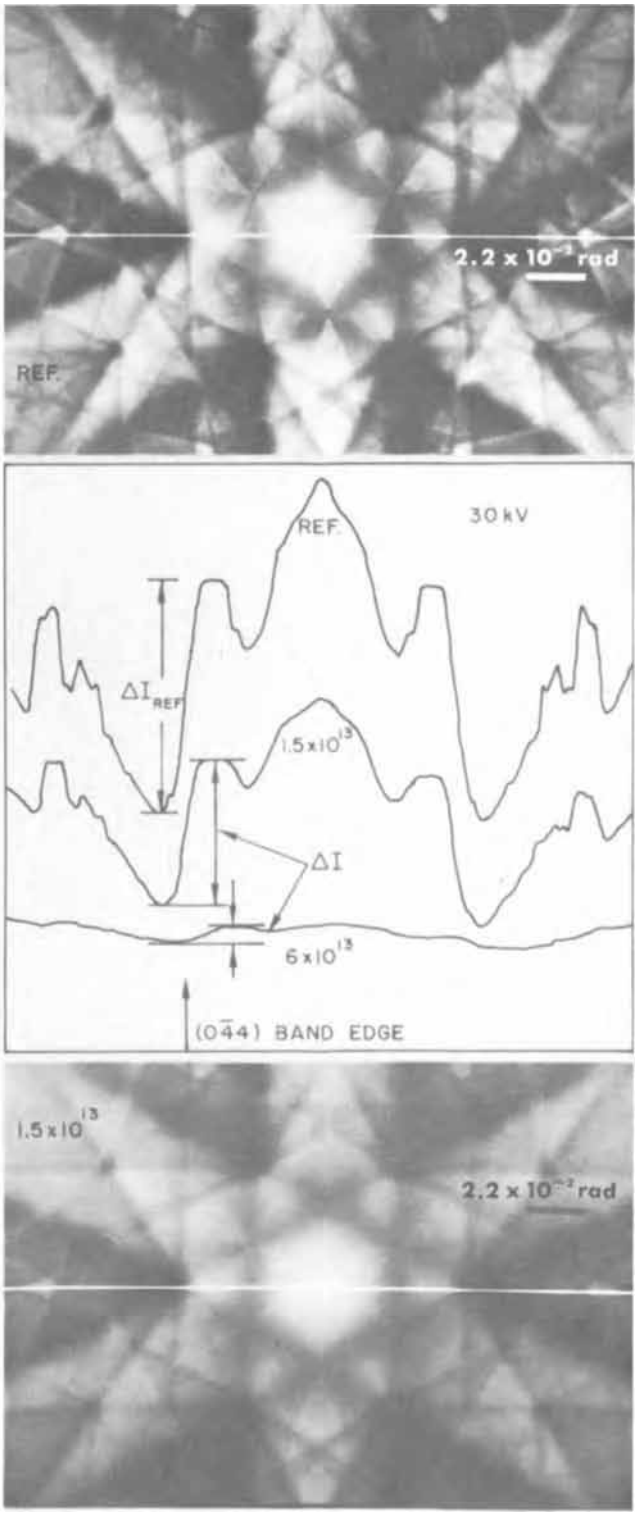

Fig. 2. Coates-Kikuchi patterns for Cd^+ ion implanted GaAs

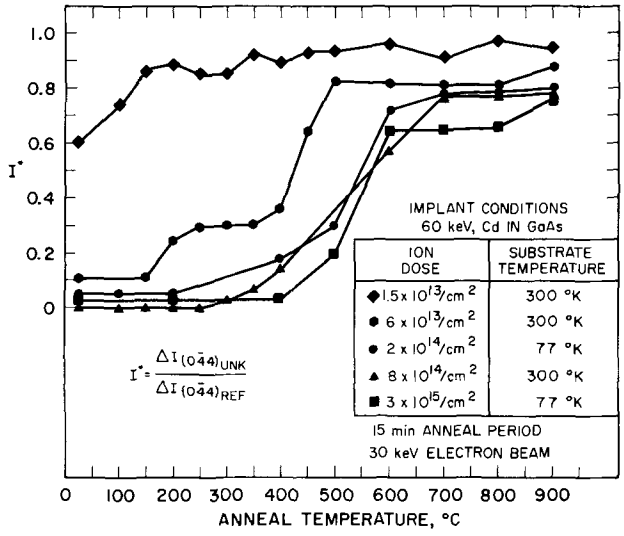

Fig. 3. Normalized pattern quality I^* for implanted and annealed GaAs.

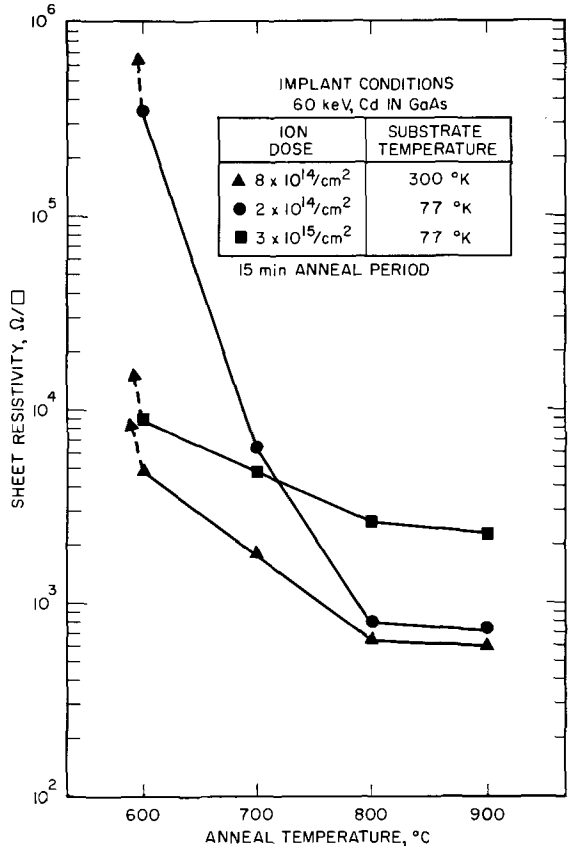

Fig. 4. Dependence of sheet resistivity on anneal temperature

been identified in ion-implanted Si (17), while vacancy-dopant atom complexes appear to form in GaAs (18, 19).

It is interesting to note from the data of Fig. 3 that even after annealing at 900°C, complete recovery was not observed in any sample. There was always a residual disorder, which was greater for the samples implanted with larger ion dose. From a practical viewpoint it is thus desirable to avoid very large doses, for the largest surface carrier concentration that could be produced in any sample after annealing at temperatures up to 900°C was approximately 1-2 x 10^{14}/cm², even in samples with implanted ion doses as high as 3 x 10^{15}/cm². Implantation of more than 2 x 10^{14} ions/cm² served only to reduce carrier mobility and did not result in increased carrier concentration, as shown by the data of Fig. 5 for the samples implanted at 77°K. Similar results were obtained for samples implanted at room temperature (4). For ion doses $\leq 10^{14}$/cm² 100% electrical activity of the implanted ions was observed after annealing at 800°C or higher. The upper limit to the carrier concentration seems to result merely from reaching the solubility limit of Cd in GaAs, which Goldstein (20) has reported to be 2 x 10^{19}/cm³ for the case of diffusion at 900°C from a vapor source. Angle section and stain measurements have shown that the p-type, Cd implanted layer is approximately 0.1μ thick; thus the peak Cd ion concentration per cm³ is $\sim 10^{19}$/cm³ for a sample implanted with 1 x 10^{14} ions/cm².

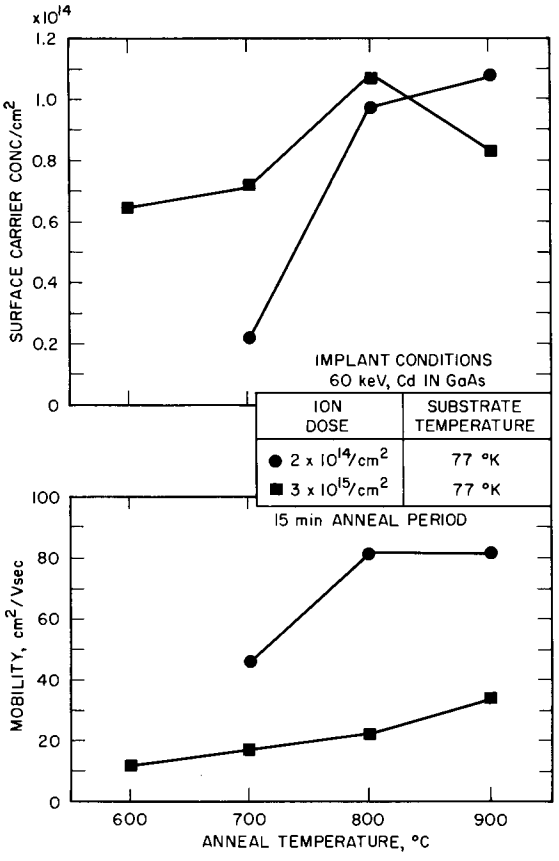

Fig. 5. Dependence of carrier concentration and mobility on anneal temperature.

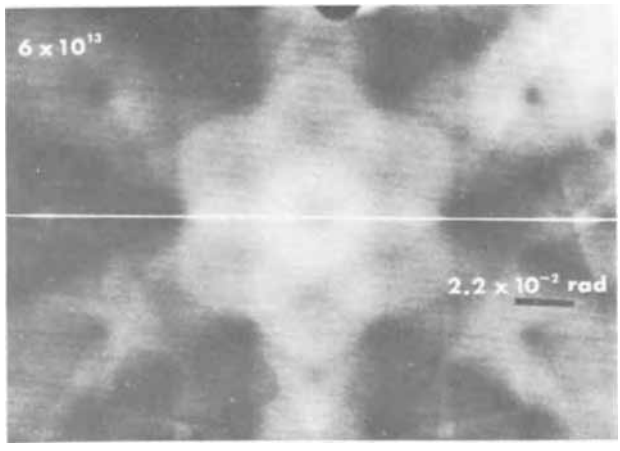

Fig. 6. Coates-Kikuchi pattern for 6 x $10^{13}Cd^+/cm^2$ implanted GaAs after 300°C anneal.

(The concentration *vs.* depth profile for the implanted ions is roughly Gaussian, rather than being uniform.) The exact nature of the residual lattice disorder cannot be determined from the Coates-Kikuchi pattern analysis. However, transmission electron microscopy applied to 40-100 keV Ne implanted GaAs by Mazey and Nelson (21) has shown that networks of small dislocation loops remain following annealing at 700°C. It should be emphasized that the effect of residual lattice damage on the electrical properties (carrier concentration and mobility) of samples implanted with $\leq$ 1 x $10^{14}Cd^+/cm^2$ and annealed at $\geq$800°C is negligible (4).

The anneal behavior of lattice damage in samples implanted with smaller ion dose than that required to produce a layer of saturated disorder is different from that considered thus far for saturation doses. For example, referring again to the data of Fig. 3, the samples implanted with 1.5 x 10^{13} Cd^+/cm^2 exhibited almost complete recovery after annealing at only 150°C. Similar results have been obtained by Weisenberger, Picraux, and Vook (22), who observed that the lattice damage produced by implanting GaAs with low doses of either 140 keV Zn or 150 keV Xe (at 99° and 93°K respectively) was almost completely eliminated by annealing at 125°C for 15 min. It must be emphasized, however, that recovery of the lattice does not necessarily imply that the implanted ions will assume substitutional positions and become electrically active. In the case of the samples implanted with 1.5 x 10^{13} Cd^+/cm^2 it was necessary to perform annealing at 700°C before a p-type layer was observed, and at 800°C before 100% of the implanted ions were electrically active (4).

The samples implanted with 6 x 10^{13} Cd^+/cm^2 (which is approximately the threshold for damage saturation in the case of room temperature implantation of 60 KeV Cd ions) exhibited a small anneal stage between 150° and 250°C and a large anneal stage between 400° and 500°C, separated by a range of anneal temperature within which lattice disorder apparently remained unchanged (Fig. 3, 6 x $10^{13}/cm^2$ dose anneal curve). The Coates-Kikuchi pattern characteristic of this anneal state (shown in Fig. 6) is unusual in that it shows high contrast for the (220) bands but very little fine detail, whereas heavily damaged unannealed crystals or very thin amorphous films exhibit more general over-all diffuseness with no enhanced principal direction scattering. This suggests partial anneal with preferred order in the (110) directions, but with slight random misalignment of the microscopic-damaged zones in other directions which destroys the long range order or fine detail in the reciprocal lattice displays. A similar effect has been observed in certain instances for ion-implanted silicon (23).

Summary

Measurement of the lattice disorder in annealed, 60 keV Cd^+ ion implanted GaAs by the Coates-Kikuchi pattern technique has shown that damage produced by ion doses $\geq$ $10^{14}/cm^2$ anneals gradually in the temperature range from about 400°-700°C. There is no significant difference in the anneal behavior of samples implanted with the substrate at 77°K and those implanted at room temperature. The damage in samples implanted with smaller ion doses anneals at lower temperatures. However, complete recovery was not observed in any sample, even after annealing at 900°C. Hall measurements indicate that ρ_s, N_s, and μ follow essentially the same trends as the damage anneal curves. Annealing at approximately 800°C or higher is required in order to obtain maximum electrical activity of the implanted ions, as well as high mobility, although a p-type layer can be produced by annealing at temperatures as low as 600°C.

Acknowledgments

The authors are grateful to R. Wilson, D. Jamba, and their associates for performing the ion implantations. They would also like to thank P. Coane for making the scanning electron microscope measurements.

Manuscript submitted May 13, 1971; revised manuscript received *ca.* July 19, 1971.

Any discussion of this paper will appear in a Discussion Section to be published in the June 1972 JOURNAL.

REFERENCES

1. J. Mayer, O. Marsh, R. Mankarious, and R. Bower, *J. Appl. Phys.*, **38**, 1975 (1967).
2. R. Hunsperger and O. Marsh, *This Journal*, **116**, 488 (1969).
3. P. Roughan and M. Manchester, *ibid.*, **116**, 278 (1969).
4. R. G. Hunsperger and O. J. Marsh, *Radiation Effects*, **6**, 263 (1970).
5. J. D. Sansbury and J. T. Gibbons, *ibid.*, **6**, 269 (1970).

6. A. Foyt, J. Donnelly, and W. Lindley, *Appl. Phys. Letters*, **14**, 372 (1969).
7. L. van der Pauw, *Philips Res. Rept.*, **13**, 1 (1958).
8. E. D. Wolf, M. Braunstein, and A. I. Braunstein, *Appl. Phys. Letters*, **15**, 389 (1969).
9. E. D. Wolf and R. G. Hunsperger, *ibid.*, **16**, 526 (1970).
10. I. A. Abroyan and A. I. Titoo, *Soviet Phys.-Solid State*, **10**, 2716 (1969).
11. D. G. Coates, *Phil. Mag.*, **16**, 1179 (1967).
12. E. D. Wolf and T. E. Eberhart, *Appl. Phys. Letters*, **14**, *299 (1969)*.
13. J. E. Westmoreland, O. J. Marsh, and R. G. Hunsperger, *Radiation Effects*, **5**, 245 (1970).
14. D. Eirug Davies, *Appl. Phys. Letters*, **14**, 227 (1969).
15. J. W. Mayer, O. J. Marsh, G. A. Shifrin, and R. Baron, *Can. J. Phys.*, **45**, 4073 (1967).
16. W. M. Gibson, F. W. Martin, R. Stensgaard, F. P. Jensen, N. I. Meyer, and G. Galster, *ibid.*, **46**, 675 (1968).
17. H. J. Stein and W. Beezhold, *Appl. Phys. Letters*, **17**, 442 (1970).
18. R. G. Hunsperger and O. J. Marsh, *Metallurgical Transactions*, **1**, 603 (1970).
19. T. Itoh and Y. Kushiro, To be published
20. B. Goldstein, *Phys. Rev.*, **118**, 1024 (1959).
21. D. J. Mazey and R. S. Nelson, *Radiation Effects*, **1**, 229 (1969).
22. W. H. Weisenberger, S. T. Picraux, and F. L. Vook presented at Int. Conf. on Radiation Effects in Semicond., Albany, N. Y., August 1970 (to be published in *Radiation Effects*).
23. D. J. Mazey, R. S. Nelson, and R. S. Barnes, *Phil. Mag.*, **17**, 223 (1968).

The Elimination of Vacancy-Cluster Formation in Dislocation-Free Silicon Crystals

A. J. R. de Kock

Philips Research Laboratories, N. V. Philips' Gloeilampenfabrieken, Eindhoven, Netherlands

ABSTRACT

In dislocation-free silicon crystals grown by the floating-zone technique vacancy clusters are formed. The influence of crystal growth conditions on the cluster formation is studied. Methods for the prevention of vacancy cluster formation during growth, based on a nucleation model, are discussed. In crystals grown by one of these methods vacancy clusters could not be detected.

Up to now relatively little attention has been paid to the influence of point defects on the crystal perfection of as-grown silicon crystals. The main emphasis has been on the prevention of the formation of dislocations and impurity precipitates. For some time now it has been possible to grow silicon single crystals by floating-zone techniques in which no planar or line defects are present. Furthermore, because of the high purity of this material, impurity precipitation will not take place.

However, it has been reported (1, 2) that in dislocation-free floating-zone silicon crystals clustering of vacancies occurred, leading to a poor lattice perfection. Plaskett (1) investigated such crystals, grown in helium, by copper decoration and infrared microscopy. The precipitates present after copper diffusion were attributed to vacancy clusters decorated with copper. Abe and Maruyama (3) investigated similar microdefects in dislocation-free vacuum floating-zone silicon. They attributed these defects to oxygen precipitation. However an explanation for oxygen precipitation in dislocation-free low oxygen-content silicon could not be given. De Kock (2) obtained further evidence that these defects are vacancy clusters. He determined the distribution and concentration of the vacancy clusters in commercial silicon crystals. Two types of vacancy clusters, differing in size, were found to be present. A model was presented which elucidates both the formation and nature of these defects. In this model it is assumed that during cooling of the as-grown dislocation-free crystal vacancy-oxygen complexes are formed acting as nucleation sites for the supersaturated amount of vacancies. Corbett, Watkins, and McDonald (4) have found with their E.P.R. and infrared spectrometric studies of electron-irradiated silicon that complexes of oxygen atoms and a vacancy are readily formed. The temperature T_c below which these complexes are stable depends on the number (n) of oxygen atoms per complex. The A-center ($n = 1$) was found to be stable below 300°C. The complex with $n = 2$ anneals at about 450°C, whereas the complex with $n = 3$ is probably stable below 600°C. It is known (5) that large oxygen complexes taking the form of precipitates are stable up to a temperature of 1350°C. Applying the results of Corbett *et al.* (4) to crystal growth conditions, the formation of stable vacancy-oxygen complexes in different stages of the cooling procedure can be expected. The first stable complexes containing n_1 oxygen atoms will begin to form at about $T = T_{c1}$. This leads to the formation of large clusters, whereas the formation below T_{c2} ($< T_{c1}$) of complexes containing n_2 ($< n_1$) oxygen atoms gives rise to the nucleation of smaller vacancy clusters. Henceforth the large clusters will be called A-clusters, the small ones B-clusters.

In the present paper the vacancy cluster distribution as related to the crystal growth conditions is studied. In particular it will be shown that vacancy cluster formation can be prevented by crystal-growth methods which apparently retard the formation of vacancy-oxygen complexes.

Key words: silicon crystal growth, vacancy clusters in Si, nucleation in Si, nucleation of point defects in Si.

Detection Methods

Vacancy clusters in silicon can be detected by several techniques. The preferential etching of polished surfaces, using *e.g.* HF (50%) : CrO_3 (33% aqueous solution) = 1 : 2 reveals vacancy clusters in the form of etch pits. These etch pits are clearly visible under a normal light microscope (2, 3, 6). In x-ray transmission topographs using the normal Lang technique, the relatively small strain fields around the vacancy clusters cause no detectable contrast for most of the crystals investigated. In some cases only an extremely weak contrast pattern was detected.

A very sensitive detection method (2) has been recently developed. In this method the vacancy clusters are decorated with copper. This is done by heating the sample up to a temperature of about 950°C for 30 min in an argon stream in which copper is evaporated, fol-

lowed by rapid cooling in a nitrogen-argon flow. Subsequently the sample is etched in order to remove possible copper precipitation on the surface. X-ray transmission topographs of the decorated sample are then made. The strain field around the decorated clusters is large enough to cause strong direct image contrast.

Experimental Results of Normal Dislocation-Free Silicon Crystals

Dislocation-free silicon crystals were grown in purified argon (pressure of 1 atm) using the pedestal-pulling technique (7). The crystal growth rates were between 1 and 3 mm/min. Dislocations were eliminated by growing a thin neck at the beginning of the crystal (7, 8). Polycrystalline high-resistive starting material was used. Phosphorus was added up to a concentration of 10^{16} at. cm^{-3}. Figure 1 shows a detail of a preferentially etched longitudinal section of such a crystal. The A-clusters give rise to the formation of etch pits located in a striated pattern. The shape of the pattern indicates that the vacancy-cluster formation mainly occurs in thin layers, being closely related to the solid-liquid interface present during growth. However investigation in the transmission electron microscope of carbon replicas made of preferentially etched surfaces proved a similar distribution of very small vacancy clusters (B-clusters) to be present, which could not be seen in the light microscope. These small ones are also located in a striated pattern and are present in a higher concentration than the larger clusters.

The concentration and actual distribution were determined by x-ray topographs of copper-decorated slices. Figures 2, 3, and 4 show such topographs of longitudinal and cross-sectional slices, cut from crystals with diameters between 23 and 25 mm. In all topographs shown, $MoK\alpha_1$ radiation was used. The direct images of the decorated clusters, black on the original nuclear plate, are visible on these photographs as white dots. The over-all bulk concentration of the A-clusters in our crystals, as determined from these topographs, varied between $5 \cdot 10^5$ cm^{-3} and $5 \cdot 10^6$ cm^{-3}. The concentration in the layers containing the clusters is about one order higher. In crystals grown in the <111> and <100> direction under identical conditions equal cluster concentrations were found. The previously reported (2) dependence of cluster concentration on orientation of the crystals grown by other manufacturers probably originated from differences in growth conditions. The dope concentration and the crystal growth rate had no influence on the defect density.

In contrast with crystals grown in the <100> direction, dislocation-free crystals grown in the <111> direction have a noncircular cross section (Fig. 3). This effect, which is related to the shape of the solid-liquid interface during growth, was reported by Ciszek (9).

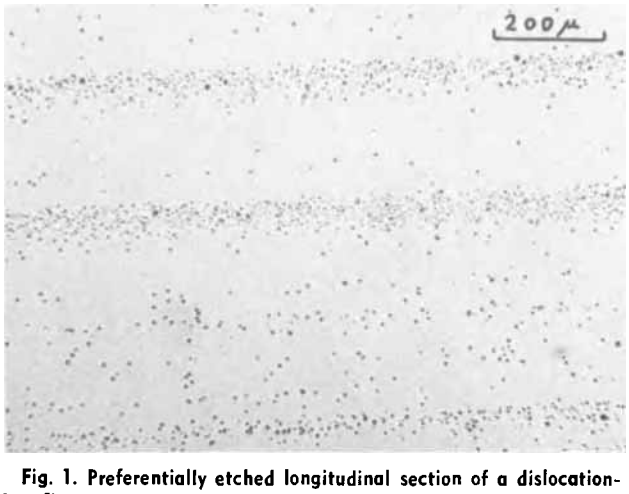

Fig. 1. Preferentially etched longitudinal section of a dislocation-free floating-zone silicon crystal.

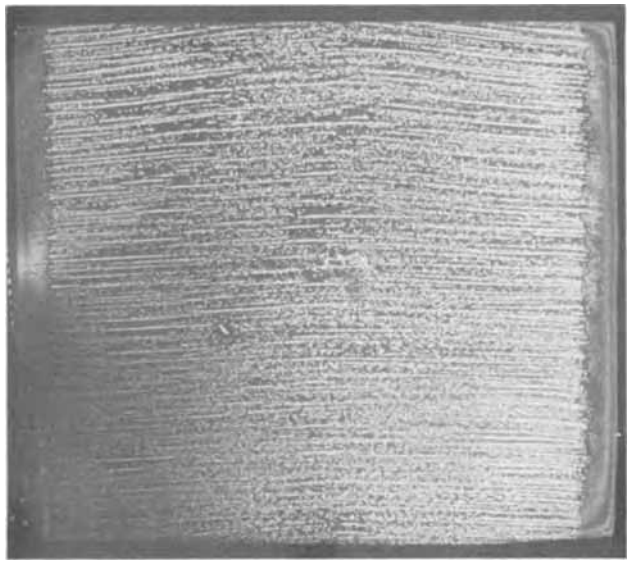

Fig. 2. (111) x-ray transmission topograph of a decorated longitudinal slice. Slice thickness: 2.4×10^{-2} cm. Crystal growth rate: 1 mm/min. Growth direction: <111>.

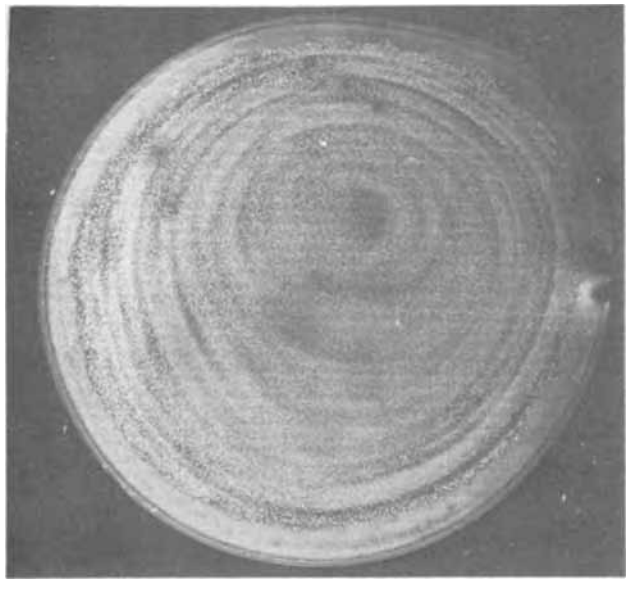

Fig. 3. ($2\bar{2}0$) x-ray transmission topograph of a decorated cross-sectional slice. Slice thickness: 2.0×10^{-2} cm. Growth rate: 3 mm/min. Growth direction: <111>. A-cluster concentration: 1.6×10^6 cm^{-3}.

The distribution of decorated clusters as present in a longitudinal section of a crystal grown in argon is schematically drawn in Fig. 5. The cluster concentration generally exhibits a minimum in the central area of the crystal. No A-clusters are found in a crystal surface layer about 2 mm thick. In some vacuum-grown crystals, received from other manufacturers, this surface layer was completely cluster-free.

Discussion

The striated cluster distribution can be explained with the aid of the described nucleation model. A periodic variation in oxygen concentration (rotational striations) caused by growth rate variations results in a very pronounced variation in complex concentration [see (2)]. For crystals grown in argon A-clusters were absent in a surface layer of about 2 mm (see Fig. 5). This is probably due to the vacancy sink action of

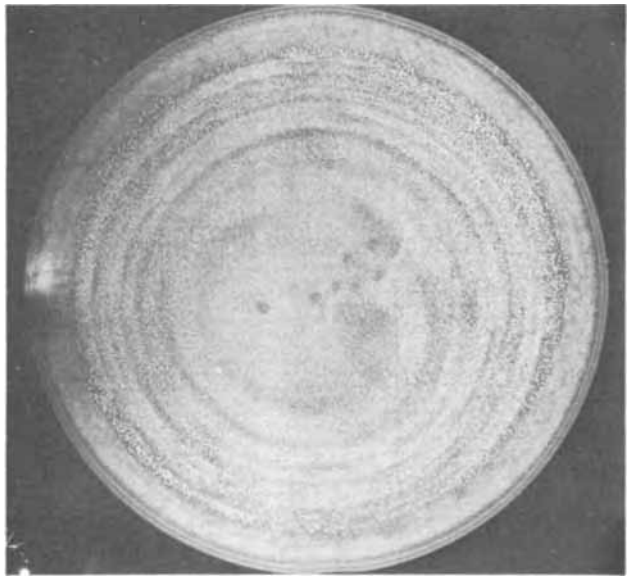

Fig. 4. ($\bar{2}20$) x-ray transmission topograph of a decorated cross-sectional slice. Slice thickness: 2.1×10^{-2} cm. Growth rate: 1 mm/min. Growth direction: <100>. A-cluster concentration: 2.2×10^{6} cm^{-3}.

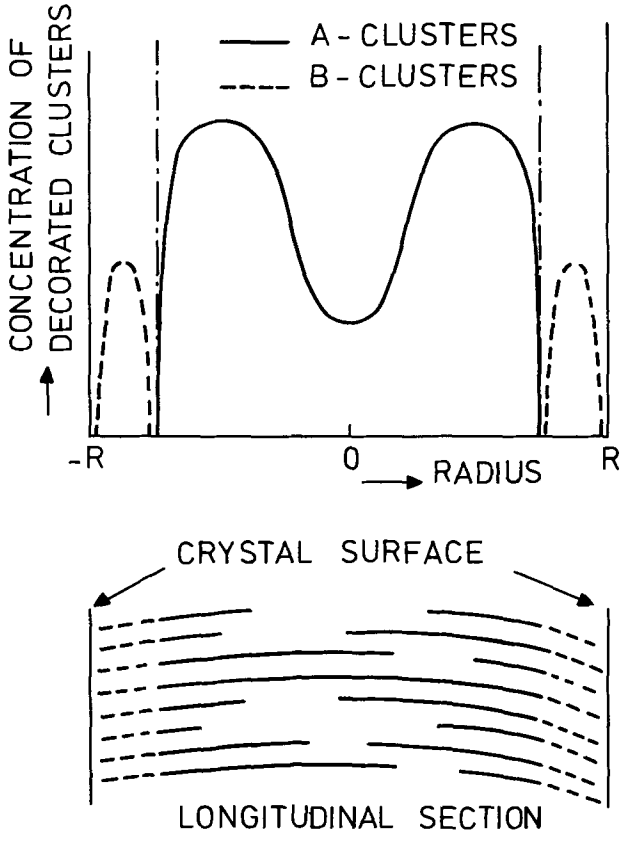

Fig. 5. Distribution and concentration profile of decorated vacancy clusters.

the crystal surface. B-clusters are still present in this layer indicating that they form more readily than the A-defect. This is in agreement with the fact that the over-all concentration of B-clusters is several orders higher than that of the A-type defect. The occasional absence of B-clusters in this region in vacuum-grown material may be caused by a lower oxygen concentration in this area as a result of evaporation of oxygen from the melt in the form of SiO. This effect was found by Kaiser and Keck (10) for crucible-grown material.

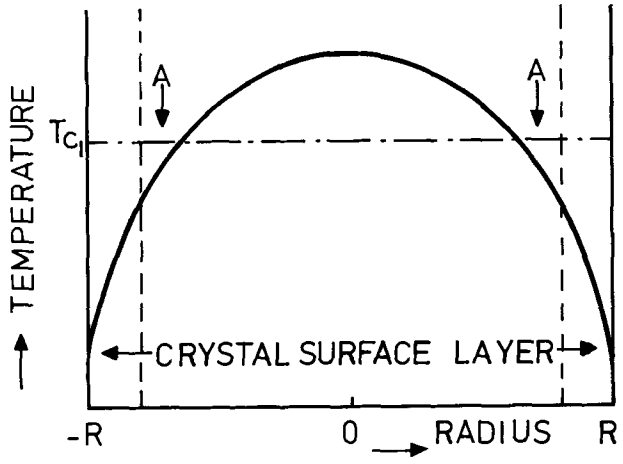

Fig. 6. Temperature distribution in the crystal area where the formation of vacancy-oxygen complexes begins (region A).

Two different processes combine to cause the minimum in the vacancy cluster concentration in the central part of the crystal (Fig. 5). First, the rotational striations decrease in passing from the periphery to the interior of the crystal (11). Furthermore, during cooling of the as-grown crystal the first vacancy-oxygen complexes and consequently the first clusters will be formed in region A (Fig. 6), where T drops below T_{c_1} first. On their way to the surface the excess vacancies from the crystal interior will nucleate here on clusters already formed or contribute to the formation of new nucleation sites. Finally, the temperature over the entire cross section will be below T_{c_1} and the resulting vacancy-cluster distribution will show a minimum in the crystal center.

Prevention of Vacancy Clustering During Growth

Vacancies in silicon are mobile below 150°K with migration energies between 0.18 and 0.33 eV (12, 13). This means that the excess vacancies present during cooling of the as-grown crystal should be able to diffuse out to the surface under normal growth conditions if no nucleation sites (vacancy-oxygen complexes) were formed. Therefore, the growth of vacancy cluster-free silicon should be possible as soon as complex formation is prevented. In principle, this can be achieved in several ways. One method could be based on reduction of the oxygen concentration (C_{ox}). This will lead to a decrease in the probability of complex formation. In floating-zone silicon crystals C_{ox} is generally low (10^{15}-10^{16} at. cm^{-3}) (14, 15). A further reduction will require the use of extremely pure starting material combined with very clean crystal growth conditions (*e.g.* high vacuum). In some crystals having slightly different values of C_{ox}, as measured by infrared absorption at 9μ wavelength at low temperatures, the lowest vacancy cluster concentration was indeed found in crystals having the lowest C_{ox}. However, in addition to the average C_{ox}, the probability of formation also depends greatly on the periodic variation in C_{ox} (2). A reduction of this periodic variation will decrease the probability of formation. The growth rate should therefore be kept as constant as possible.

In the case of very high oxygen concentration the vacancy clustering becomes more complicated. In dislocation-free crystals grown by the Czochralski method, usually containing large amounts of oxygen and carbon, the formation of vacancy-oxygen complexes can also be expected. During cooling of the as-grown crystal, however, the material becomes supersaturated not only with vacancies but also with oxygen and carbon. This will lead to simultaneous precipitation of vacancies, oxygen, and carbon. Besides homogeneous nucleation of the impurities, precipitation of oxygen and carbon

on the vacancy clusters is likely to occur. Indeed it is found that in dislocation-free crucible-grown silicon crystals after annealing at 900°-1300°C oxygen and carbon precipitate in a striated distribution similar to that found for vacancy clusters in floating zone material (16, 17). Batavin (17) in particular presented evidence that vacancy clusters might act as nucleation sites for oxygen and carbon. The precipitates of oxygen and carbon in crystals containing dislocations were found on the dislocations and randomly distributed in the crystal (16).

Another method for preventing vacancy clustering during growth is based on a reduction of the complex formation rate. This can in principle be achieved by adding to the crystal an impurity, which reacts with the oxygen atoms present. The oxygen-impurity bonds formed may lower the effective oxygen mobility in the silicon lattice and therefore the vacancy-oxygen complex formation rate. If this effect is combined with a sufficiently fast growth rate (cooling rate), not enough time will be available for complex formation, giving the extremely mobile vacancies the opportunity to diffuse out to the crystal surface. To be bound to oxygen atoms this impurity should have a strong affinity to oxygen, while it should also possess a high diffusion coefficient in silicon in order to make a fast reaction with oxygen possible. An impurity matching these conditions is hydrogen, which can be added to the crystal by growing the latter in an atmosphere containing hydrogen.

Some evidence for an interaction between oxygen and hydrogen in the silicon lattice was reported by Yukimoto, Hirano, and Sugioka (18, 19). Crystals pulled from the crucible in hydrogen atmosphere exhibited a lower infrared absorption at 9μ compared with crystals pulled in argon. This was thought to be due to the formation of oxygen-hydrogen complexes resulting in a reduction of the total number of Si-O bonds.

Furthermore the diffusion coefficient of hydrogen in silicon is high (*e.g.* $D = 1.70 \times 10^{-4}$ cm^2 sec^{-1} at 1092°C) as measured by van Wieringen and Warmoltz (20).

The two methods described above for eliminating vacancy clusters can, of course, be combined for optimum results.

Experimental Results and Discussion of Vacancy Cluster Elimination

A series of dislocation-free crystals were grown in the <111> direction by the pedestal pulling method in an atmosphere of purified argon to which 10% hydrogen had been added. The total pressure was 1 atm. High-resistivity starting material was used with an oxygen concentration below 10^{16} at. cm^{-3}. The diameter of the crystals varied between 23 and 25 mm. Increasing the growth rate and consequently the cooling rate of the crystal resulted in a continuous decrease in vacancy cluster concentration. This is demonstrated with a series of x-ray topographs of decorated cross-sectional slices (Fig. 7-10). With a growth rate of 1 mm/min (Fig. 8), the cooling rate of a crystal surface layer is already high enough to prevent cluster formation in this area. In the crystal grown at 2 mm/min (Fig. 9) the B-clusters, usually detectable with carbon replica techniques only (2), now become detectable by copper decoration as well. The reason for this is threefold. Firstly, because of the low concentration of A-clusters (7×10^4 cm^{-3}), more copper is available for decoration of the B-type defects. Secondly, the average B-cluster concentration is also reduced (3×10^6 cm^{-3}) by several orders of magnitude compared with material grown in argon. Finally, the B-clusters are probably larger in this case because, as a result of the low cluster concentration, they will capture more excess vacancies per defect. In the slice shown in Fig. 10, which has been cut from a crystal grown at 3 mm/min, no A-clusters were found whereas in the entire sample 107 B-clusters were counted. In all the crystals grown at this rate the A-clusters were totally eliminated. This result indicates that hydrogen not only decreases the formation rate of vacancy-oxygen complexes but apparently also causes an incubation time for complex formation. A reproducible elimination of the B-clusters was found to be more difficult. This again proved that B-defects are formed more readily than A-defects. In some experiments the temperature gradients in a limited region near the solid-liquid interface were reduced by application of a special rf coil construction, resulting in a decrease of the interface curvature. Generally this will cause a decrease of the periodic variation in growth rate. In crystals grown in Ar + 10% H_2 at 3 mm/min using such a coil, zero concentrations of both A- and B-clusters were obtained. In Fig. 11 the cluster concentration as a function of crystal growth rate is plotted. The formation of A- and B-clusters is prevented by growing at a rate of 3 mm/min. This indicates that the incubation time for formation is of the same order for both defects.

Fig. 7. ($\bar{2}20$) x-ray transmission topograph. Growth rate: 0.6 mm/min. A-cluster concentration: 5x10^6 cm^{-3}.

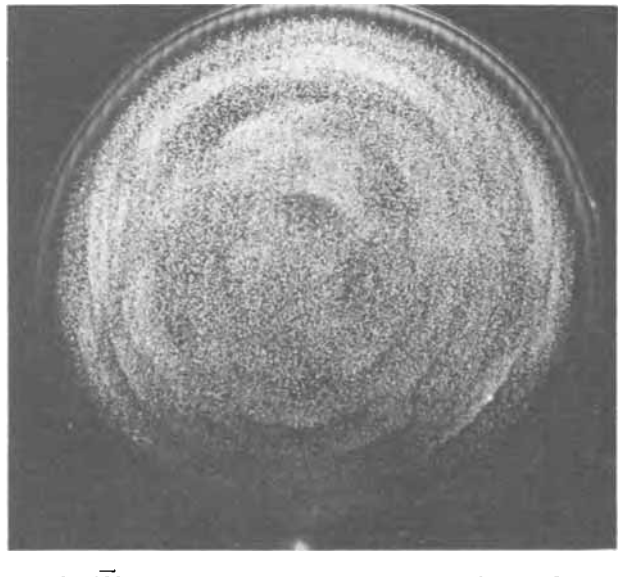

Fig. 8. ($\bar{2}20$) x-ray transmission topograph. Growth rate: 1 mm/min. A-cluster concentration: 8x10^5 cm^{-3}.

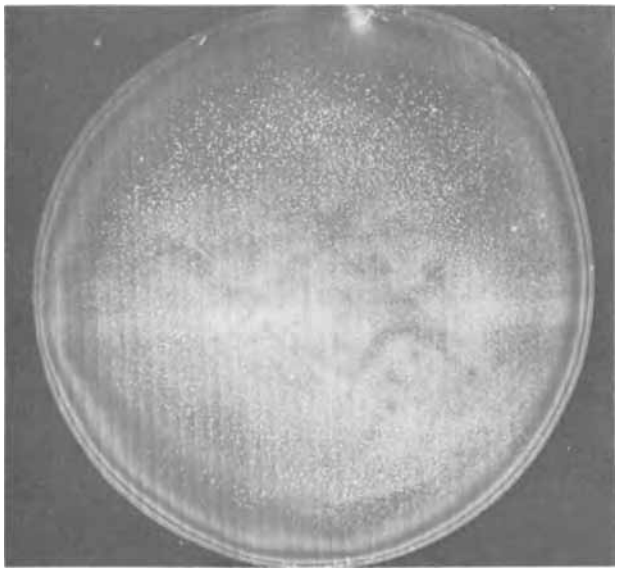

Fig. 9. ($2\bar{2}0$) x-ray transmission topograph. Growth rate: 2 mm/min. A-cluster concentration: 7×10^4 cm^{-3}.

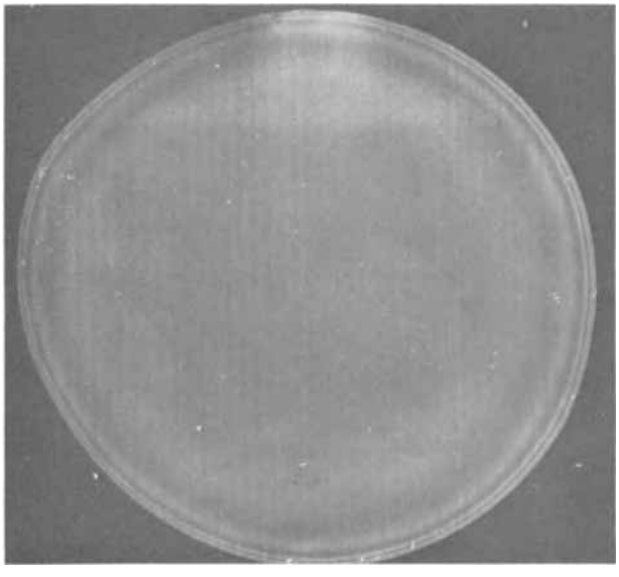

Fig. 10. ($2\bar{2}0$) x-ray transmission topograph. Growth rate. 3 mm/min. A-cluster concentration: 0.

Crystals with various phosphorus dope concentrations (up to 10^{16} at. cm^{-3}) were grown. No influence of the dope on the elimination of clusters was found.

As reported by Yoshimatsu, Sugita, and Yukimoto (21, 22, 19, 20), hydrogen in silicon can give rise to the formation of crystal defects. These defects caused anomalous etching effects and were often detectable in x-ray topographs. Sugita (22) found that in his floating-zone apparatus at least 25% hydrogen in the argon flow was necessary to introduce these defects. We, however, found that in our set-up precipitation of hydrogen in the interior of the crystal occurred with as little as 10% hydrogen. This caused anomalous etching effects. During nonpreferential etching, *e.g.* using HF-HNO_3 etchants, holes were formed at the sample surface. The hydrogen precipitation greatly depends on the crystal perfection and the radial temperature gradient. In a crystal in which the radial temperature gradient was enlarged by an Ar-H_2 flow against the growing crystal, the hydrogen precipitates, formed in the central part of the crystal were large

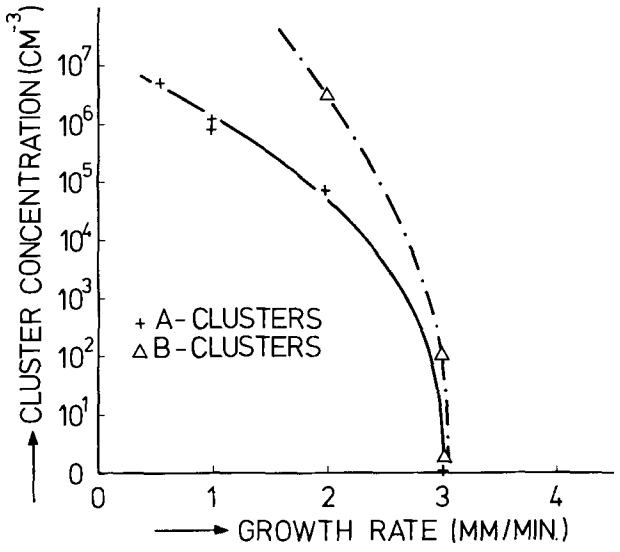

Fig. 11. Vacancy-cluster concentration as function of crystal growth rate. Atmosphere: argon + 10% hydrogen.

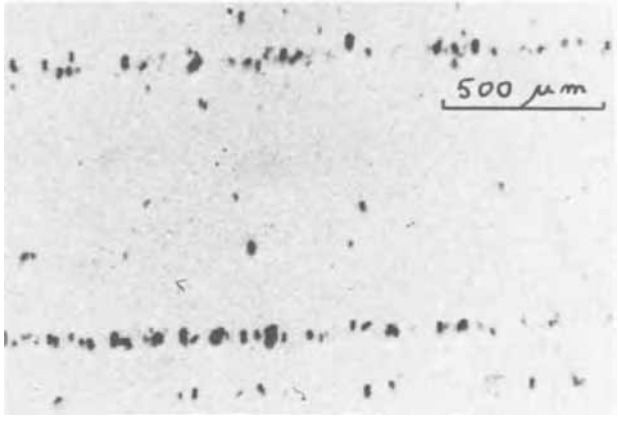

Fig. 12. (111) x-ray transmission topograph of a longitudinal crystal section (dislocation-free). Hydrogen precipitation on the vacancy clusters.

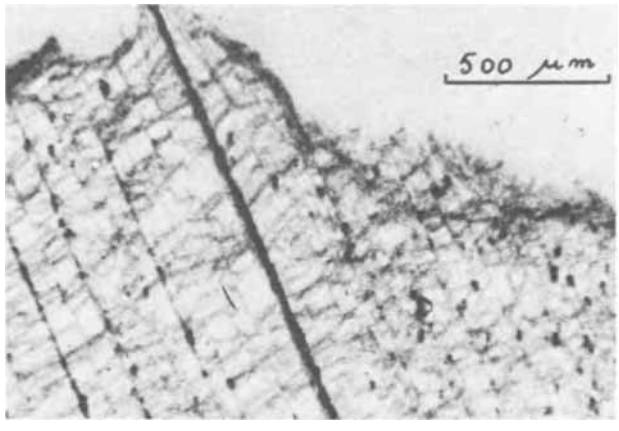

Fig. 13. (111) x-ray transmission topograph of a longitudinal crystal section. Hydrogen precipitation on the disclocation lines.

enough to give contrast in x-ray topographs. The upper part of the crystal was dislocation-free and contained vacancy clusters (growth rate 1 mm/min) (Fig. 12), while dislocations were introduced in the lower part (Fig. 13). The hydrogen was found to precipitate on

the vacancy clusters or on the dislocation lines. The strain fields around these precipitates were up to 100μ in diameter in this case. It proved possible to dissolve these precipitates again by annealing at 550°C for about 3 hr. However, in dislocation-free crystals grown under such conditions that vacancy clusters are not present, hydrogen precipitation could not be detected either by etching or by x-ray transmission topography. Obviously, if no crystal defects acting as nucleation sites for hydrogen are present, hydrogen diffuses out to the crystal surface.

Acknowledgments

The author wishes to express his gratitude to Mr. P. J. Roksnoer for growing the crystals and Mr. P. G. T. Boonen for his active assistance with the crystal characterization.

Manuscript submitted Feb. 22, 1971; revised manuscript received *ca.* June 15, 1971. This was Paper 233 RNP presented at the Atlantic City Meeting of the Society, Oct. 4-8, 1970.

Any discussion of this paper will appear in a Discussion Section to be published in the June 1972 JOURNAL.

REFERENCES

1. T. S. Plaskett, *Trans. AIME*, **233**, 809 (1965).
2. A. J. R. de Kock, *Appl. Phys. Letters*, **16**, 100 (1970).
3. T. Abe and S. Maruyama, *Denki Kagaku*, **35**, 149 (1967).
4. J. W. Corbett, G. D. Watkins, and R. S. McDonald, *Phys. Rev.*, **135**, A1381 (1964).
5. W. Kaiser, *Phys. Rev.*, **105**, 1751 (1957).
6. T. Abe, T. Samizo, and S. Maruyama, *Japan. J. Appl. Phys.*, **5**, 458 (1966).
7. W. C. Dash, *J. Appl. Phys.*, **29**, 736 (1958).
8. W. C. Dash, *ibid.*, **30**, 459 (1959).
9. T. F. Ciszek, A. C. C. G. Conference on Crystal Growth, Gaithersburg, 1969. (To be published).
10. W. Kaiser and P. H. Keck, *J. Appl. Phys.*, **28**, 882 (1957).
11. K. Morizane, A. Witt, and H. C. Gatos, *This Journal*, **114**, 738 (1967).
12. G. D. Watkins, Symposium on Radiation Effects in Semiconductor Components, Toulouse, 1967. (To be published.)
13. G. D. Watkins, *J. Phys. Soc. Japan*, **18**, 22 (1963). Suppl. II.
14. B. Pajot, *Solid-State Electron.*, **12**, 923 (1969).
15. C. Gross, G. Gaetano, T. N. Tucker, and J. A. Baker, First International Symposium on Silicon Materials Science and Technology, New York, 1969 (unpublished).
16. I. L. Shul'pina, L. V. Lainer, M. G. Mil'vidskii, and E. P. Rashevskaya, *Soviet Physics-Solid State*, **9**, 1291 (1967).
17. V. V. Batavin, *Soviet Phys.-Cryst.*, **15**, 100 (1970).
18. Y. Yukimoto, A. Hirano, and Y. Sugioka, *Japan. J. Appl. Phys.*, **6**, 420 (1967).
19. Y. Yukimoto, *ibid.*, **7**, 348 (1968).
20. A. van Wieringen and N. Warmoltz, *Physica*, **22**, 849 (1956).
21. M. Yoshimatsu, *J. Phys. Soc. Japan*, **18**, 335 (1963). Suppl. II.
22. Y. Sugita, *Japan. J. Appl. Phys.*, **4**, 962 (1965).

Preparation of Hafnium-Tantalum Nitride Films by Reactive Alloy Sputtering

L. D. Locker,* C. L. Naegele,[1] and F. Vratny*

Bell Telephone Laboratories, Incorporated, Murray Hill, New Jersey 07974

ABSTRACT

Thin films of hafnium nitride and tantalum nitride with resistivities of 10^{10} and 10^{4} ohm-cm, respectively, have been deposited by rf + d-c reactive sputtering. By sputtering hafnium-tantalum mixtures in pure nitrogen at 7.0×10^{-2} Torr, the complete range of resistivities is obtained, with a linear increase between 10^{5}-10^{9} ohm-cm, corresponding to a relative hafnium content of 40-70%. For a fixed Hf:Ta ratio, the resistivity, deposition rate, and nitrogen content of the films depend on the pressure and substrate temperature. For pure tantalum a dinitride (TaN_2) is deposited, but for pure hafnium the dinitride has not been obtained. An alloy nitride containing 60% Hf can be represented by the formula $Hf_{0.6}Ta_{0.4}N_x$, where x increases from 1.2 to 1.4 as the substrate temperature increases from 225° to 400°C. A sequence of reaction steps on the substrate surface is proposed to explain the deposition rates observed in reactive sputtering.

In the d-c reactive sputtering of tantalum in nitrogen, the transition from tantalum to tantalum nitride occurs as the nitrogen pressure is increased from 10^{-5} to 10^{-2} Torr. The phases Ta_2N, TaN, and TaN_2 have been reported previously (1-4). Corresponding increases in the resistivity of the films occur, with a maximum of 10^{4} ohm-cm. Some of the same compositional and electrical changes are known to occur with reactively sputtered hafnium (5). High-resistivity (*i.e.* 10^{4} ohm-cm) hafnium nitride films have been produced at 3.0×10^{-2} Torr by d-c reactive sputtering onto substrates heated to 350°C. Table I shows that increases in resistivity by more than a factor of 10^{7} are possible as the nitrogen content of the films increases.

* Electrochemical Society Active Member.
[1] Present address: Weston Components, Scranton, Pennsylvania 18501.
Key words: sputtering, thin films, hafnium nitride, tantalum nitride.

Our initial measurements on hafnium nitride films, produced at 7.0×10^{-2} Torr by rf + d-c reactive sputtering onto water-cooled substrates, revealed that the films have a resistivity greater than 10^{10} ohm-cm. Tantalum nitride films produced under the latter conditions show no change from the previously observed value of 10^{4} ohm-cm. These results suggest the possibility of depositing stable thin films with a resistivity that can be controlled over many orders of magnitude by simply varying the tantalum to hafnium ratio. The method to prepare these alloy nitrides in a reproducible manner, and the measurement of their properties are reported below.

Experimental

Film deposition was done by rf + d-c reactive sputtering (6) in an oil diffusion pumped system, with a liquid nitrogen baffle, routinely capable of a pressure of

Table I. Properties of tantalum and hafnium nitrides formed by d-c reactive sputtering

Chemical formula	Nitrogen pressure (Torr)	Resistivity (ohm-cm)	Crystal structure	Density (g/cm³)	Reference
Hf	$<2 \times 10^{-4}$	$(75\text{-}290) \times 10^{-6}$	hcp $a = 3.20$ $c = 5.06$	13.1	(5)
HfN	3×10^{-4}-3×10^{-3}	$(95\text{-}520) \times 10^{-6}$	fcc $a = 4.52$	10.5-11.9	(5)
HfN_x	3×10^{-2}	10^4	fcc $a = 4.96$	6.6	(5)
Ta	$<10^{-5}$	100×10^{-6}	hcp $a = 3.3$	15.6	(1)
Ta_2N	$1\text{-}5 \times 10^{-5}$	200×10^{-6}	hcp $a = 3.05$ $c = 4.95$		(3)
TaN	10^{-4}-10^{-3}	250×10^{-6}	fcc $a = 4.28\text{-}4.48$		(3)
TaN_x	3.6×10^{-2}		fcc $a = 5.02$		(4)
	$1.4\text{-}4.5 \times 10^{-2}$	10^4	fcc $a = 4.98\text{-}5.09$	7-9	(2)

2×10^{-6} Torr prior to the start of each experiment. The simultaneous application of rf and d-c power to the cathode is an advantage in reactive sputtering. The rf increases the degree of ionization in the plasma, and prevents the accumulation of an insulating layer on the cathode. The d-c component is the major source of the negative field at the cathode that extracts ions from the plasma. The combined rf + d-c produces higher deposition rates, and enables a wider range of sputtering parameters to be investigated.

The cathode potential was −3.5 kV d-c with rf power supplied at approximately 3W/in.² of cathode area. The 6 in. × 6 in. sputtering cathode and the substrates were held vertically at a separation of 3 in., as shown schematically in Fig. 1. The sputtering system accommodated square cathodes most easily. No difficulties were encountered due to power loss at the corners. In addition to the rf matching network, a filter consisting basically of an inductor and capacitor separates the rf from the d-c component.

A tantalum wire grid was placed approximately 1 in. from the substrates and held at ground potential. The functions of the grid are to improve the uniformity of electric fields near the substrate, and to reduce the bombardment of the substrate surface by ions and electrons generated in the glow discharge. In the experiments reported here at nitrogen pressures of up to 7.0×10^{-2} Torr the use of the grid improves the uniformity of the films. When the grid becomes coated with a resistive film it is no longer at ground potential, but charges toward the potential of a floating probe. The pattern of such a coated grid has often been observed in the film deposited on the substrate. Thus, frequent cleaning of the grid is required, or for small area substrates a hole may be cut in the grid without loss of uniformity in the film.

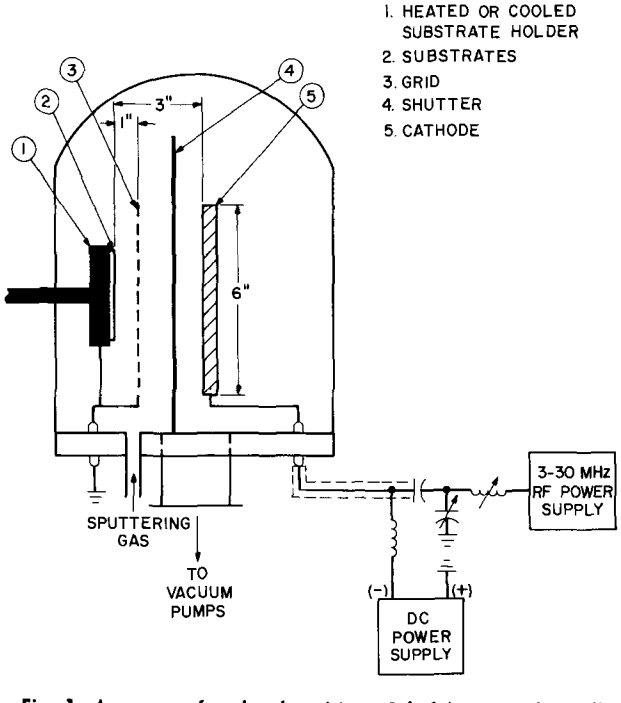

Fig. 1. Apparatus for the deposition of hafnium-tantalum alloy nitrides by rf + d-c reactive sputtering.

Table II lists the types of substrates that were used during the course of the experiments, the quantities measured on each substrate, and the technique that was used. The substrate temperature was regulated by either a water-cooled or resistance-heated substrate holder. Temperature measurements were made with a platinum/platinum-10% rhodium thin-film thermocouple on a sapphire substrate mounted in the center of the substrate holder. Since the presence of the nitrogen discharge affected the thin-film thermocouple emf, both the d-c and rf power were turned off for a short interval while the readings were taken. The thin-film thermocouple measurements were not affected by the nitride film that was being deposited over it.

Preparation of Hf-Ta sputtering sources.—An important factor in the deposition of uniform hafnium-tantalum nitride films with reproducible properties is the preparation of the sputtering cathodes. In previous investigations multicomponent films have been prepared by simultaneous sputtering of the constituents from independent sources, from bulk alloys, with composites formed by inlaying or overlaying ribbons or wires of one component on a plate of the other, or with small particles made self-supporting by powder metallurgical techniques. The first two methods have the advantage that separate sources are not needed for each change in film composition. In all previous reports d-c diode sputtering or pressures much lower than 7.0×10^{-2} Torr have been used. Therefore, previous results do not necessarily apply to rf + d-c reactive sputtering. Preferential sputtering of one component, preferential accommodation on the substrate, or selective formation of a reaction product on the cathode, may lead to poor reproducibility and poor uniformity in reactive sputtering, but may be no problem for d-c sputtering in argon.

Table II. Experimental measurements

Material	Quantity measured	Technique
Sapphire	Film thickness	Taylor-Hobson Talysurf & Talystep
Platinum foil	Density	Weight gain
	Nitrogen content	Micro Kjeldahl
Corning 7059 glass	Hf and Ta content	X-ray fluorescence
		Electron microprobe
	Nitrogen content	Electron microprobe
	Resistivity	Probes
	Structure	X-ray diffraction
Oxidized silicon	Resistivity	Electron beam charging (8)
SiO_2 coated Mo grid	Structure	Electron diffraction
Pt/Pt-10% Rh	Surface temperature	Thin film thermocouple

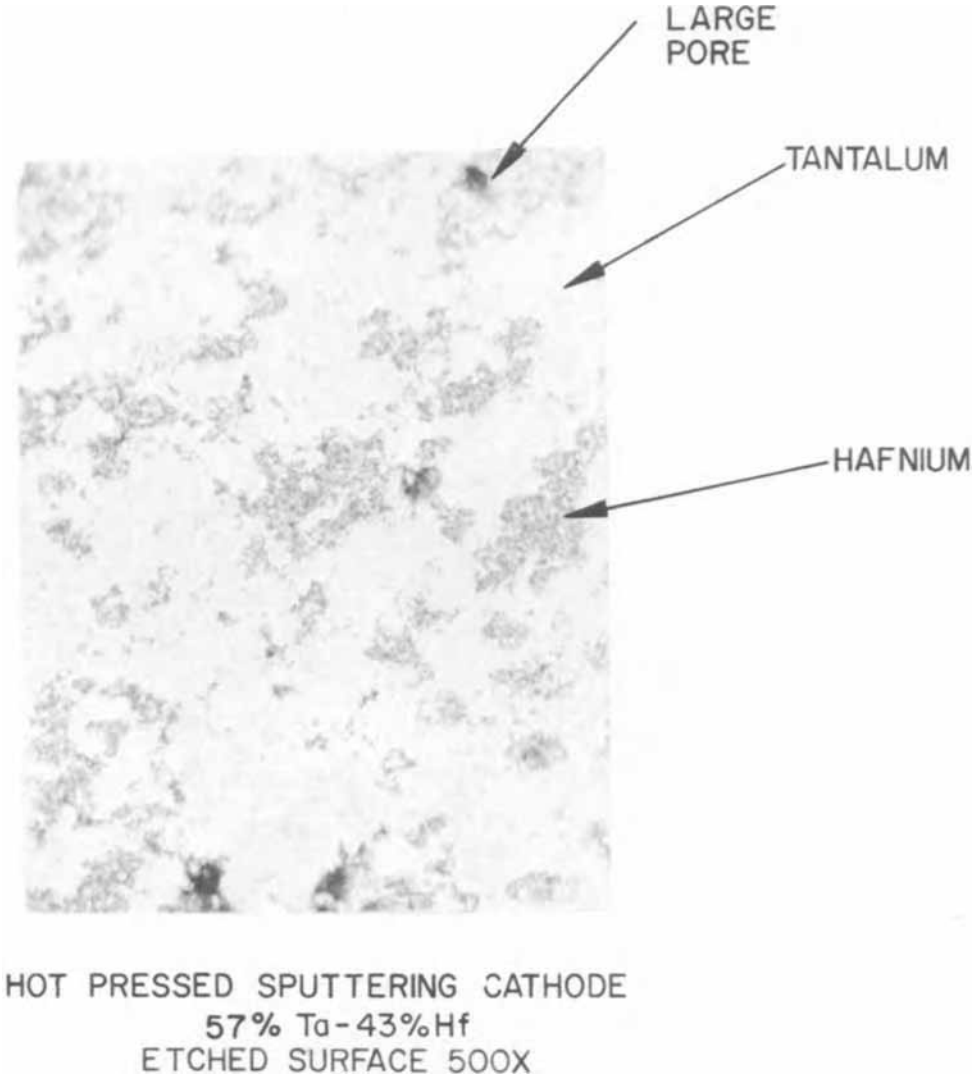

Fig. 2. Optical micrograph of hot-pressed sputtering cathode 500 X. Composition: 57% Ta-43% Hf.

For example, overlays have been used successfully for the deposition of Hf-Ta metal alloys in argon at 2.0×10^{-2} Torr. The compositions of the films are proportional to the relative area of each component exposed to the discharge. However, deviations from the relative area ratio, and lack of reproducibility are characteristics of the same Hf-Ta cathode when it is used in nitrogen at 7.0×10^{-2} Torr. In the latter case a nitride film deposits on both the strips and on the plate. The composition of the layer deposited on the substrate changes with time. The requirement for reproducible composition is rather critical in the hafnium-tantalum nitride system, since the results presented below show that a change of 5% in the relative metal content can change the resistivity by one order of magnitude in the range between 30-65% Hf.

Hot-pressed sputtering sources fabricated from Ta and Hf (2.5% Zr) powders require a new cathode for each composition, but provide reproducibility at least to within the limits of the experimental measurements of the resistivity and composition. The 0.2 in. thick as-pressed disks are cut into 6 in. $\times$ 6 in. squares, and thinned by 0.05 in. by surface grinding with a diamond abrasive. The cathodes have approximately 75% of the theoretical density. A metallograph of the surface of a typical Hf-Ta cathode after etching in an HCl-HNO_3-HF solution is shown in Fig. 2. The distribution of hafnium (dark) and tantalum (light) is evident. Regions of high porosity are also shown in Fig 2. Due to this topography it was necessary to sputter a new target in argon in order to outgas it sufficiently to pump the chamber to 2×10^{-6} Torr. Subsequent experiments could be done without this argon presputter, but a short sputtering period was adopted as standard procedure in all experiments. In addition, a minimum presputter period of 60 min in nitrogen under the actual conditions of each experiment was used before opening the shutter between the cathode and the substrate.

Hot-pressed cathodes have been used to obtain all of the results described below, except of course for pure Ta and Hf. The reproducibility for two sets of consecutive experiments with the substrate at 250° or 400°C, respectively, is shown in Fig. 3 for the source composition 60% Hf-40% Ta. The data show that for rf + d-c reactive sputtering at a nitrogen pressure of 7.0×10^{-2} Torr the resistivity can be reproduced to one-half an order of magnitude, with a confidence limit of 90%. Above approximately 65 weight per cent (w/o) hafnium in the Hf-Ta mixture the pressed plates are extremely brittle, and 6 in. $\times$ 6 in. cathodes have not been successfully fabricated by this method. Plasma spraying techniques are being evaluated and will be reported on in the future.

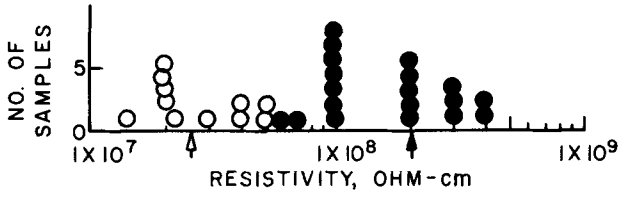

Fig. 3. Reproducibility of resistivity for 60% Hf-40% Ta films ●, substrate at 250°C; ○, substrate at 400°C; arrows indicate mean values.

Results

In all of the experiments the power input to the target has been intentionally kept constant, and the film properties measured as a function of target composition, gas mixture, pressure, and substrate temperature. The temperature is shown below to be extremely important in the deposition process. Since power input has a large affect on substrate temperature (7) the power was fixed.

Resistivity Measurements

Effects of composition.—The resistivity of the hafnium-tantalum nitride films is shown in Fig. 4 as a function of the hafnium content. These results are obtained using a water-cooled substrate holder, with a measured substrate temperature of 250°C. The shape of the resistivity *vs.* composition curve is similar with heated substrates, although the values are lower for corresponding compositions. Changes that occur with increasing amounts of hafnium are further emphasized by the increase in optical energy gap from 2.1 eV (100% Ta) to 3.8 eV (100% Hf). These values were obtained by the same method used previously for highly nitrided tantalum films. (2)

Effects of nitrogen pressure.—Figure 5 shows the effect of nitrogen pressure on the resistivity of the films. The figure consists of three parts; two with nitrogen-argon mixtures and the third with pure nitrogen. In pure nitrogen the resistivity decreases as the pressure increases. However, in the argon-nitrogen mixtures the resistivity increases as the nitrogen partial pressure increases.

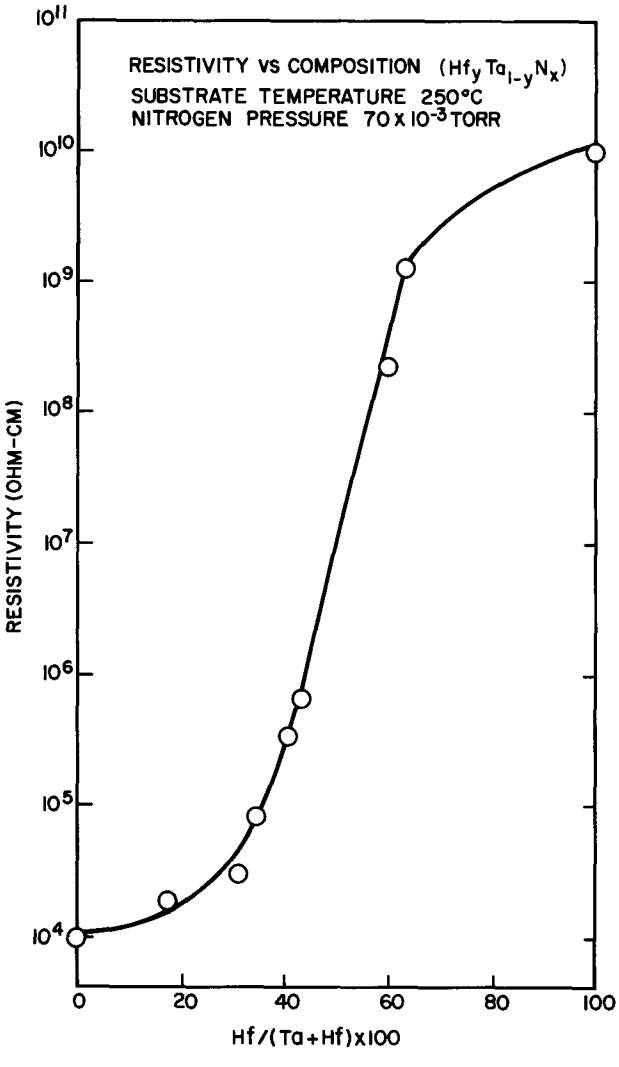

Fig. 4. Changes in resistivity with hafnium content

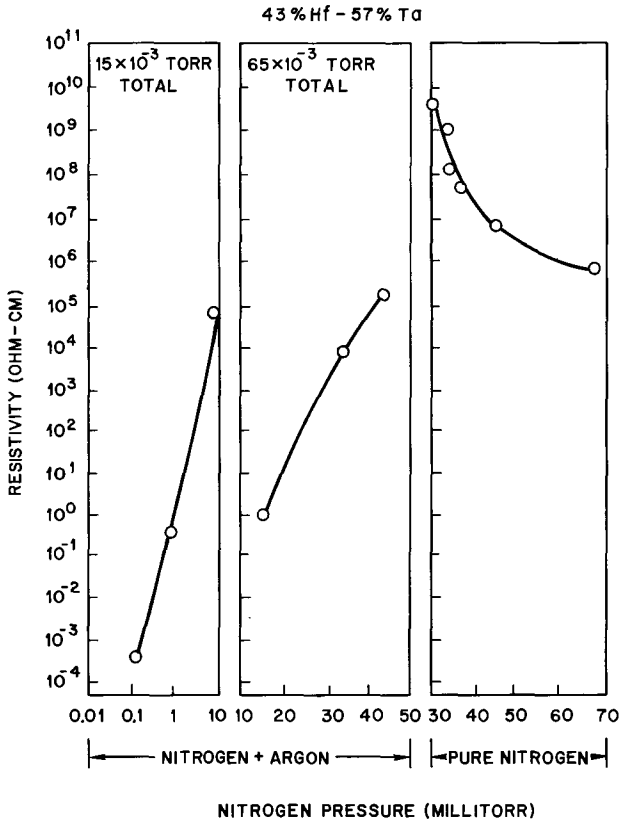

Fig. 5. Resistivity *vs.* nitrogen pressure 43% Hf-57% Ta. Substrate temperature 250°C.

At a total pressure of 1.5×10^{-2} Torr the increase in resistivity with increasing nitrogen partial pressure is in contrast to the plateau of constant resistivity (approx. 1.2×10^{-3} ohm-cm) for reactively sputtered tantalum in the corresponding partial pressure range. For pure tantalum cathodes the product is TaN. For pure hafnium cathodes sputtered in this pressure range there is a change from metallic Hf to HfN. At 1×10^{-4} Torr the hafnium-tantalum alloy nitride films have a metallic appearance. At 10×10^{-3} Torr the films are green and transparent. The resistivity of the films is higher than the values for either TaN or HfN.

At a total pressure of 6.5×10^{-2} Torr and a nitrogen partial pressure of 1.5×10^{-2} Torr the film has the same appearance as the latter one described above, but the resistivity is lower. This resistivity decrease may be attributed to the higher substrate temperature at 6.5×10^{-2} Torr than at a total pressure of 1.5×10^{-2} Torr. The partial pressure range between 1.5×10^{-2}-4.5×10^{-2} Torr is marked by a color change in the film from green to gold. Also, the dissolution rate in hydrofluoric acid is reduced sufficiently, relative to the material prepared at lower pressures, that the films can be removed from glass substrates by etching the glass away in hydrofluoric-nitric acid mixtures.

In pure nitrogen between 3.0×10^{-2}-7.0×10^{-2} Torr the resistivity decreases as the pressure is increased. Again, a pertinent factor is that as the nitrogen pressure is increased, the substrate temperature also increases, undoubtedly due to increased current in the discharge. At 3.5×10^{-2} Torr the substrate temperature is 150°C, and increases by approximately 100°C when the nitrogen pressure is increased to 7.0×10^{-2} Torr.

Effects of substrate temperature.—When the pressure is fixed at 7.0×10^{-2} Torr and the substrate temperature is varied, the resistivity decreases with increasing temperature. The reproducibility of the results shown in Fig. 6 is poorer for the temperature of 125°C than for the higher temperatures, since with a

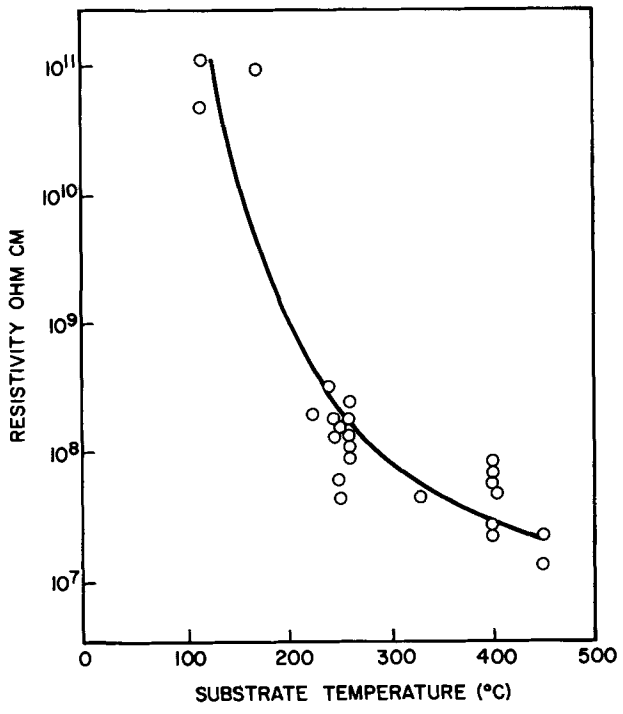

Fig. 6. Resistivity vs. substrate temperature. 60% Hf-40% Ta. Nitrogen pressure 70×10^{-3} Torr.

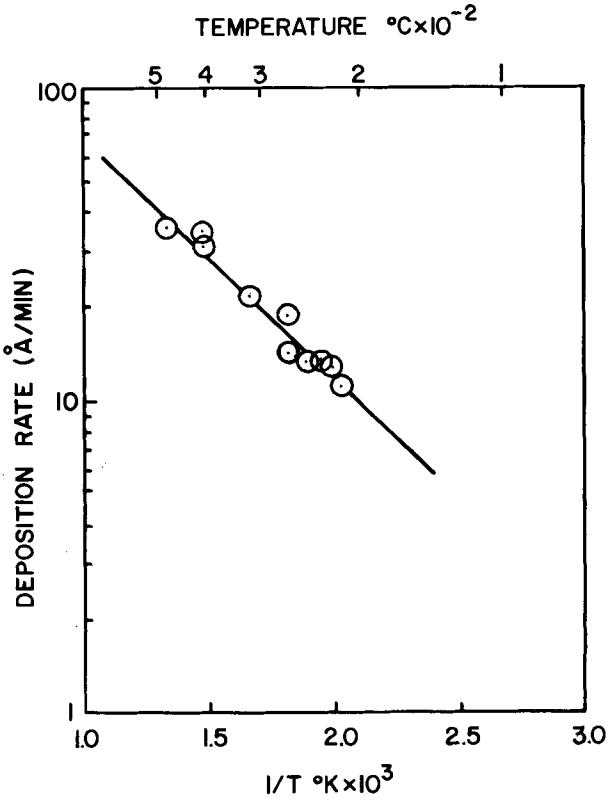

Fig. 7. Effect of substrate temperature on deposition rate. 60% Hf-40% Ta. Nitrogen pressure: 70×10^{-3} Torr.

water-cooled substrate holder it is difficult to control the substrate temperature at 125°C during sputtering. On several samples resistivities of up to 10^{11} ohm-cm have been measured by the electron beam method (8) for films containing 60% Hf, sputtered onto substrates at 125°C.

Deposition Rate vs. Substrate Temperature

The deposition rate increases as the substrate temperature increases from 125° to 450°C. In this temperature range the density decreases by approximately 15%, and the cathode current is constant to within 10%. This is an indication that the films are not porous, and that the plasma density and cathode sputtering rate are not changed by increasing the substrate temperature. If the rate of deposition (Å/min) is plotted in the form of the Arrhenius equation, as in Fig. 7, the slope gives an apparent activation energy of approximately 2 kcal/mole (0.09 eV/molecule). The increase in deposition rate with substrate temperature suggests that the nitride formation occurs at the substrate surface. The relatively low activation energy may be associated with a sequence of reaction processes that affect the over-all deposition rate. This is considered in more detail in the Discussion.

Table III. Structure of Hf-Ta alloy nitrides 43% Hf-57% Ta to 60% Hf-40% Ta

Sputtering nitrogen	Pressure (Torr) argon	Crystal lattice	Similar structure
0.1×10^{-3}	15×10^{-3}	bcc Ta $a = 3.43$Å	bcc Ta
1.0×10^{-3}	15×10^{-3}	fcc $a = 4.40$Å	TaN, HfN
30×10^{-3} to 70×10^{-3}	0	Not assigned	May be mixture of TaN_2 and HfN

d_{hkl} (Å)	Relative intensity
3.93	mw
2.85	s
2.47	w
2.30	vw
2.03	mw
1.92	mw
1.74	ms
1.48	vw
1.42	m
1.33	vw
1.20	vw
1.08	vw
0.978	w
0.943	vw

Structure and Chemical Composition

The results given in Table III may be compared to those summarized in Table I for the unalloyed nitrides prepared in previous studies by d-c reactive sputtering.

Unalloyed Hf and Ta nitrides.—Tantalum nitride films containing no hafnium, prepared at 7.0×10^{-2} Torr have a Ta:N atom ratio of 1:2. This TaN_2 phase has the fcc structure reported previously (2, 4) and listed in Table I. Hafnium nitride films, containing no tantalum, have the same fcc diffraction pattern, with a lattice parameter slightly larger than the tantalum dinitride. In the hafnium nitride case the x-ray diffraction pattern contains additional features attributed to the HfN rocksalt structure. It has not been possible to produce a reactively sputtered hafnium dinitride with the experimental conditions used thus far.

Hf-Ta alloy nitrides.—At a nitrogen partial pressure of 1×10^{-4} Torr the alloy nitride is metallic, but the unit cell dimension is larger than for bcc tantalum. At 1×10^{-3} Torr an fcc structure is obtained, which is similar to the TaN and HfN shown in Table I. Above 1×10^{-2} Torr there is no crystalline x-ray diffraction pattern. The metal to nitrogen atom ratio is still 1:1.

Transmission electron diffraction patterns have been obtained from samples deposited in pure nitrogen. The diffraction results show differences between the Hf-Ta nitride ($Hf_yTa_{1-y}N_x$ [$1 < x \leq 2$]), and the unalloyed nitrides. However, there are no significant changes for compositions between 43% Hf-60% Hf when the substrate temperature is varied between 225°-400°C, and the pressure is varied between 3.5×10^{-2}-7.0×10^{-2} Torr.

The diffraction data are summarized in Table III. The lattice spacings cannot be indexed by the single fcc lattice used for the unalloyed nitrides. Extra lines appear at several positions of primary extinctions. It is

interesting that the extra lines can be indexed as HfN. However, until additional experiments are completed no definite conclusions can be made about the structure.

The density of films containing 60% Hf, deposited at 7.0×10^{-2} Torr onto substrates at 225°C is 6.5 ± 0.9 g/cm³. The theoretical density of the fcc TaN_2 ($a \cong 5.0$Å) lattice, with all of the tetrahedral voids filled with nitrogen atoms is 6.66 g/cm³.

The alloy nitride films prepared with the substrate at 225°C contain 8.2 ± 1.4 w/o nitrogen, and approximately 1 w/o oxygen. This corresponds to $x = 1.2 \pm 0.2$ in a compound with the formula $Hf_yTa_{1-y}N_x$. As the substrate temperature is increased, the Hf:Ta ratio remains unchanged, but the nitrogen content of the films increases. At 400°C the films contain approximately 10 w/o N, corresponding to $x = 1.4$. Thus, the alloy dinitride has not been produced.

Discussion

The wide range of properties, structures, and compositions obtained by sputtering hafnium-tantalum cathodes in nitrogen is one example of the general usefulness of reactive sputtering of alloys. For some systems it may be difficult to obtain sputtering sources that produce films with the same metal composition as the starting material. Assuming that suitable sources can be fabricated by one of the methods described previously, some general conclusions can be made from the results obtained in this study in regard to chemical processes in reactive sputtering and the factors that most significantly affect the ability to control the film properties.

Substrate temperature and film quality.—The deposition rate (Fig. 7), chemical composition, and resistivity (Fig. 6) of the hafnium-tantalum alloy nitride films are functions of substrate temperature. Other variables in the sputtering process, such as power input and nitrogen pressure are not independent variables since they affect the substrate temperature. Thus, reproducibility of film properties requires adequate surface temperature control. In addition, thickness uniformity requires uniform thermal contact between the substrate and the heat sink.

The minimum reproducibility of one-half an order of magnitude in the resistivity (Fig. 3) is attributed primarily to the precision of the substrate temperature control. The thin-film thermocouple measurements indicate that with conventional substrate cooling the substrate temperature cannot be satisfactorily maintained below approximately 200°C, under the conditions of nitrogen pressure (7.0×10^{-2} Torr) and rf + d-c power used. Local temperatures may be even higher. The minimum temperature is limited by the thermal contact to the heat sink. Even when the silicon substrates are held with gallium-indium paste, the measured temperature of 125°C plotted in Fig. 6 is at best a low estimate of the local surface temperature. At 125°C the film thickness uniformity is poor.

Until improved methods are designed to control substrate temperature during sputtering, the values reported in published literature must be viewed critically.

Rate processes in reactive sputtering.—At a nitrogen pressure of 7.0×10^{-2} Torr a nitride film forms on the sputtering cathode. However, to interpret the increase in film growth rate with increasing temperature, found in the hafnium-tantalum-nitrogen system and also in other studies of reactive sputtering (9, 10), it must be concluded that the transfer of a nitride through the glow discharge and direct nucleation and growth of the compound on the substrate does not occur. Rather, a sequence of steps including diffusion to the substrate, adsorption, dissociation, and surface reaction on the substrate are the important processes that control the deposition rate. Although low activation energies are characteristic of diffusion-controlled processes, a rate-limiting surface reaction could also explain the observed value of 2 kcal/mole.

For example, if the surface reaction is

$$(Hf, Ta)_s + yN_s \rightarrow (Hf, Ta)N_y \quad [1]$$

where $(Hf, Ta)_s$ represents the hafnium and tantalum on the surface considered here in combination, N_s is the reactive nitrogen species on the surface, and $(Hf, Ta)N_y$ is the hafnium-tantalum nitride product containing y atoms of nitrogen per metal atom, then the deposition rate can be represented by the equation

$$R = k[N]_s[Ta, Hf]_s \quad [2]$$

where s signifies a surface concentration, and k is the reaction rate constant. A first order process is assumed for simplicity.

If the steps such as adsorption and dissociation, which precede the surface reaction, occur rapidly then the surface species are in equilibrium with the vapor phase (g).

$$\frac{[N]_s}{[N]_g} = K_I \quad [3]$$

$$\frac{[Hf, Ta]_s}{[Hf, Ta]_g} = K_{II} \quad [4]$$

A form of Eq. [2] suitable for evaluation of the activation energy of reaction [1] from the Arrhenius plot (Fig. 7) is

$$R = k(T)[N]_g[Hf, Ta]_g K_I(T) K_{II}(T) \quad [5]$$

and

$$\frac{\partial \ln R}{\partial(1/T)} = \frac{\partial \ln k}{\partial(1/T)} + \frac{\partial \ln K_I}{\partial(1/T)} + \frac{\partial \ln K_{II}}{\partial(1/T)} \quad [6]$$

Therefore, the measured activation energy E is related to the activation energy for the surface reaction (E_s), and to the heats of adsorption (H_I and H_{II}) of the reactant species

$$\frac{E}{R} = \frac{E_s + H_I + H_{II}}{R} \quad [7]$$

Since the chemisorption reaction is exothermic the measured value of $E = 2$ kcal/mole is less than E_s. Values of H_I and H_{II} are difficult to estimate since they depend on the surface coverage, $[N]_s$ and $[Hf, Ta]_s$. As the surface temperature increases, the concentration of the reactants decreases. The relative changes in $[N]_s$ and $[Hf, Ta]_s$ may account for the fact that y increases with temperature. This is found experimentally but neglected in the formulation of the rate equations. Alternatively, the adsorption of one of the reactants may be the rate limiting step, and reaction [1] may be rapid. This also could explain the observed value of E and the temperature dependency of y. In either case a more detailed mechanism would require a calculation of the concentration of reactants on the surface. However, the data do verify that it is a process at the substrate surface that is important in reactive sputtering.

Conclusions

Reactive sputtering of hafnium-tantalum alloys in nitrogen can produce nitride films with a resistivity between 10^4-10^{10} ohm-cm. The control of the properties of these films depends on control of the variables (gas mixture, pressure, substrate temperature, *etc.*) in the sputtering process. Reproducibility of the resistivity to within one-half an order of magnitude between 10^4-10^{10} ohm-cm is easily obtained.

The substrate temperature is especially important in reactive sputtering but is difficult to control below 200°C. The effect of substrate temperature on the composition of the films and on the deposition rate is evidence that the substrate surface is the location of the rate determining processes in thin film deposition by reactive sputtering.

Manuscript submitted Dec. 17, 1970; revised manuscript received July 8, 1971. This was Paper 89 presented at the Detroit Meeting of the Society, October 5-9, 1969.

Any discussion of this paper will appear in a Discussion Section to be published in the June 1972 JOURNAL.

REFERENCES

1. R. W. Berry *et al.*, "Thin Film Technology," D. Van Nostrand, New York (1968).
2. H. J. Coyne, Jr. and R. N. Tauber, *J. Appl. Phys.*, **39**, 5585 (1968).
3. D. Gerstenberg and C. J. Calbick, *ibid.*, **35**, 402 (1964).
4. E. A. Buvinger, *Appl. Phys. Letters*, **7**, 14 (1965).
5. F. T. J. Smith, Private communication.
6. F. Vratny, in "Thin Film Dielectrics," F. Vratny, Editor, p. 143, The Electrochemical Society, Softbound Symposium Series, New York (1969).
7. L. D. Locker, R. W. Landorf, C. L. Naegele, and F. Vratny, *This Journal*, **118**, 65C, (1971).
8. A. N. Chester and B. B. Kosicki, *Rev. Sci. Instr.*, **41**, 1817 (1970).
9. E. Hollands and D. S. Campbell, *J. Mater. Sci.*, **3**, 544 (1968).
10. E. Krikorian, Trans. 12th Nat. Vacuum Symposium, p. 175 (1966).

Technical Notes

Cathodoluminescence of Alkaline Earth Thiosilicate Phosphors

Frank J. Avella*

Bayside Research Center, GTE Laboratories, Incorporated, Bayside, New York 11360

In 1967 Kaldis *et al.* (1) reported that cadmium thiosilicate Cd_4SiS_6 was capable of intrinsic and sensitized host luminescence but it was not an effective host for activation by Eu. This paper deals with a group of thiosilicates which are effective as hosts for luminescent Eu^{2+} and, in part, for Ce^{3+}. These are the alkaline earth orthothiosilicates having the formula M_2SiS_4, where M = Mg, Ca, Sr, and Ba. Information is presented on the synthesis and some of the physical, chemical, and cathodoluminescence properties of these phosphors.

Experimental

Synthesis.—The alkaline earth thiosilicate phosphors were synthesized by firing powder blends of the alkaline earth sulfide, lanthanide sulfide, silicon, and sulfur in evacuated fused silica capsules. The blends were heated at 50°C/hr to a maximum temperature between 800°-1000°C and were held at such temperatures for 24 hr. Inertial cooling proceeded (approximately 100°C in the first hour, then 50°C/hr) to 300°C or lower before the capsules were removed from the furnace. In some cases improved reactions resulted if the fired charge was mortared, re-encapsulated and refired using the same procedure. Compound formation was verified by comparison of x-ray derived lattice parameters with published values (2-4).

The starting materials were luminescent or reagent grade and were reacted in amounts calculated to yield the formula $M_{2-x}Ln_xSiS_4$, where x = 0.005 or 0.01. Ordinarily no charge compensator was included with Ce^{3+}. Considerable difficulty was encountered with synthesis reproducibility and good chemical reactions were no guarantee of good phosphor performance. After experiments with the firing program, various formulations, capsule pressures, alkali fluoride fluxes, use of an iodine transport agent, pelletizing, argon backfill, and inclusion or exclusion of water vapor, the only significant improvement resulted when certain lots of alkaline earth sulfides were used as starting materials. The cause of their efficacy could not be attributed to their chemical purity and has not yet been determined. Samples of the Mg, Sr, and Ba compounds were prepared without crystalline secondary phases, but Ca_2SiS_4 was always accompanied by a small amount of CaS.

Measurements.—Cathodoluminescence measurements were made with a demountable CRT operated at 12 kV with a beam current of 1 mA on a standard TV raster compressed to 4 x 4 in. The phosphors were coated on 1 x 1 in. conductive glass slides using normal settling techniques; however, water sensitive phosphors were settled in a nonaqueous medium. Each coated slide was baked in air at 400°C for 20 min. The emission spectra were recorded in terms of relative energy *vs.* wavelength by known methods. A 0.30 μsec square pulse was used in measuring the decay times.

Results and Discussion

Physical and chemical properties.—Mg_2SiS_4 and Ca_2SiS_4 were reported by Rocktaschel *et al.* (2) to have the orthorhombic olivine type crystal structure with space group D_{2h}^{16}-Pnma. Ribes *et al.* (3) assign the same space group to Ba_2SiS_4 and compare its structure to that of β-K_2SO_4. Dumail *et al.* (4) place Sr_2SiS_4 in the monoclinic system with space group C_{2h}^2-$P2_1/m$. Unlike their oxygen-dominated homologs the Mg, Ca, and Sr orthothiosilicates are hygroscopic; in moist air Mg_2SiS_4 is the least stable and Sr_2SiS_4 the most stable. On the other hand, Ba_2SiS_4 is not hygroscopic nor does it appear to hydrolyze in water. X-ray examination of the phosphor-coated cathode ray test slides after the 400°C heat treatment showed no evidence of decomposition of the Sr and Ba thiosilicates, although Dumail *et al.* (2) had observed that Ba_2SiS_4 begins to oxidize at 280°C. However, it was found that the bake-out did partially decompose the Mg and Ca compounds so that some MgS and additional CaS were present on their respective test slides. When activated with Eu^{2+}, the phosphors have the following body colors: Mg, orange; Ca, grayish yellow; Sr, greenish yellow; and Ba, light brown. With Ce^{3+} as the activator the Sr and Ba phosphors are gray and tan respectively.

Luminescence.—All four thiosilicates were activated by Eu^{2+}, but activation with Ce^{3+} was confirmed only for the Sr and Ba compounds. All six phosphors respond to excitation by ultraviolet and cathode rays. The cathodoluminescence spectra for the Eu-activated phosphors are reproduced in Fig. 1, and the data are

* Electrochemical Society Active Member.

Key words: cathodoluminescence, luminescence, phosphor, alkaline earth thiosilicate, cerium, europium.

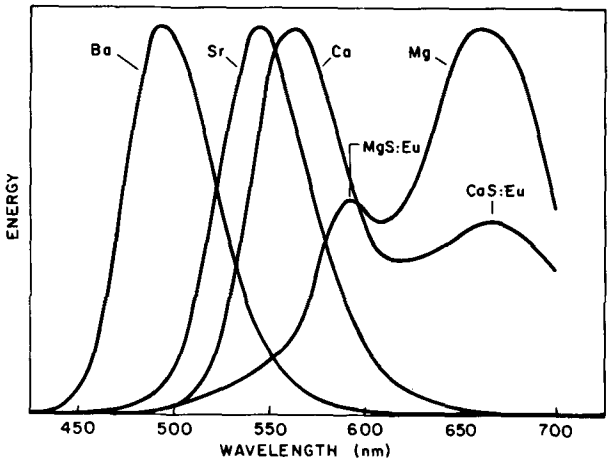

Fig. 1. Cathodoluminescence spectra from M_2SiS_4:Eu (intensities not comparable).

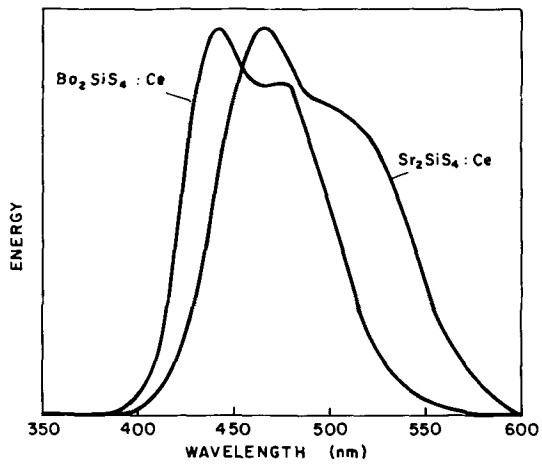

Fig. 2. Cathodoluminescence spectra from M_2SiS_4:Ce (intensities not comparable).

summarized in Table I. The emission bands are characteristic of 5d → 4f Eu^{2+} transitions. Their shift toward shorter wavelength with increasing cation size would be consistent with expansion of the crystal lattice in an homologous isostructural series, but since only the Mg and Ca compounds form such a series, the correlation between spectral band position and cation size cannot be extended to the Sr and Ba compounds. The weaker bands peaking at 592 and 668 nm correspond to Eu^{2+} emissions from the MgS and CaS impurity phases respectively as reported by Jaffe and Banks (5). The Sr and Ba thiosilicates are fairly effective hosts for Eu^{2+}. The emissions from the Mg and Ca compounds are much weaker and, since they also have impurity components, their intensities are not given.

Ce^{3+} activation of the Sr and Ba thiosilicates produces greenish blue and blue cathodoluminescence, respectively, having the spectra shown in Fig. 2. Both emissions have the two overlapping bands attributed to 5d → 4f transitions in the Ce^{3+} ion. The secondary band peaks at about 476 nm in Ba_2SiS_4:Ce, but it is not easily resolvable in Sr_2SiS_4:Ce. In Table II the cathodoluminescence performance of these two phosphors is compared with that of $Ca_2Al_2SiO_7$:Ce, a P-16 type phosphor used as the blue component in some flying-spot scanner tubes. The Sr_2SiS_4:Ce emission is very weak. The emissions from Ba_2SiS_4:Ce and $Ca_2Al_2SiO_7$:Ce have similar values of luminance; the latter is actually more efficient but it emits in a region of lower eye sensitivity. The Sr and Ba thiosilicates have similar nonexponential decay characteristics. The decay times are longer than those recorded for $Ca_2Al_2SiO_7$:Ce by a factor of 2 at $e^{-1}I_0$ and of 5 at 0.1 I_0. This indicates not only a slower initial decay process but also a longer low-level persistence in the thiosilicates; 0.01 I_0 is reached in tens of microseconds. This is not unlike the situation with CaS:Ce where Lehmann and Ryan (6) attribute the relatively slow Ce^{3+} decay to host trapping levels.

In summary, M_2SiS_4 compounds are particularly effective as hosts for Eu^{2+} when M^{II} = Sr and Ba and for Ce^{3+} where M = Ba. The Ce^{3+} decay was found to be slow relative to a P-16 phosphor.

Table I. Cathodoluminescence data for M_2SiS_4:Eu^{2+}

M^{II}	Emission band λ_{max}(nm)	Width at half height (nm)	Chromaticity coordinates (x,y)	Luminance relative to P-1 (%)
Mg	660	87	—	—
Ca	563	63	—	—
Sr	545	56	0.337, 0.626	53
Ba	493	56	0.119, 0.439	20

Table II. Cathodoluminescence data for M_2SiS_4:Ce^{3+}

Phosphor	λ_{max}(nm)	Chromaticity coordinates (x,y)	Relative luminance	Decay (μsec) $e^{-1}I_0$	Decay (μsec) $0.1I_0$
Sr_2SiS_4:Ce	466	0.170, 0.259	Weak	0.08	0.5
Ba_2SiS_4:Ce	442	0.161, 0.152	110	0.10	0.6
$Ca_2Al_2SiO_7$:Ce	400	0.163, 0.042	100	0.05	0.11

Acknowledgments

The author is indebted to J. Menella and M. G. Festa for assistance with the syntheses, to J. A. Baglio for x-ray diffraction analysis, to T. E. Sisneros for cathodoluminescence measurements, to T. E. Peters for many helpful discussions, and to F. C. Palilla for reviewing the manuscript.

Manuscript submitted May 21, 1971; revised manuscript received July 12, 1971. This was Paper 42 presented at the Washington, D.C., Meeting of the Society, May 9-13, 1971.

Any discussion of this paper will appear in a Discussion Section to be published in the June 1972 JOURNAL.

REFERENCES

1. E. Kaldis, L. Krausbauer, and R. Widmer, *This Journal*, **114**, 1074 (1967).
2. G. Rocktaschel, W. Ritter, and A. Weiss, *Z. Naturforsch.*, **19b**, 958 (1964).
3. M. Ribes, E. Philippot, and M. Maurin, *Compt. Rend.*, **268C**, 710 (1969).
4. R. Dumail, M. Ribes, and E. Philippot, *ibid.*, **271C**, 1456 (1970).
5. P. M. Jaffe and E. Banks, *This Journal*, **102**, 518 (1955).
6. W. Lehmann and F. M. Ryan, *ibid.*, **118**, 477 (1971).

The Use of Metalorganics in the Preparation of Semiconductor Materials

IV. The Nitrides of Aluminum and Gallium

H. M. Manasevit, F. M. Erdmann, and W. I. Simpson*

Autonetics Division of North American Rockwell Corporation, Anaheim, California 92803

The use of metalorganic compounds in the preparation of III-V (1-7) and II-VI (8) semiconductor compounds has prompted additional studies in our laboratories to extend the scope of the process to include nitrides of aluminum and gallium, wide bandgap materials in which considerable interest has been generated recently. As wide-bandgap semiconductors, the nitrides can be considered, for example, for the fabrication of semiconductor devices that display high-temperature stability; and in combination with other piezoelectric materials and insulators they are acoustically useful in wide-band high-capacity signal and data processing (9). Aluminum nitride (AlN) is also a refractory electrically insulating material that can be used as both insulating layer and diffusion mask for other semiconductor materials and devices. Gallium nitride (GaN) is transparent to visible radiation; and because of its bandgap, it has potential use for optical devices which will operate in the visible region.

Various methods have been reported for preparing single-crystal films of these nitride materials. These include reactive sputtering (10), gaseous discharge (11-13), and chemical vapor deposition (CVD) (14-19). The latter method has been used more extensively for film preparation and has produced single-crystal AlN films on a number of single-crystal substrates such as Si (14), α-SiC (16, 17), and α-Al_2O_3 (13). Single-crystal GaN growth has also been reported on α-Al_2O_3 substrates (12, 15, 18), (111)-oriented GaAs (12), and (0001)α-SiC (18, 19).

Most CVD processes for the formation of single-crystal nitrides use a hydrogen halide to provide transport of reactants (15) and/or the halide is a major byproduct of the reaction that produces the particular nitride (14, 16, 18, 19). The presence of a halide may set a definite limitation on the purity of the film, for the substrate on which the film is formed may be chemically reactive with the hydrogen halides. This could introduce impurities into the gaseous atmosphere which may be incorporated into the growing film.

Ideally, therefore, one would prefer a process for nitride formation that (*a*) is free of any halide; (*b*) uses an apparatus for growth that is compatible with existing commercial-type apparatus for elemental semiconductor formation; and (c) requires only one hot temperature zone for deposition. The apparatus and techniques meeting these criteria and used for the nitride film formation described here are similar to those which have been previously described (2, 8).

GaN and AlN were formed by mixing the appropriate methyl derivatives of the elements, namely trimethylgallium (TMG) and trimethylaluminum (TMA), respectively, with excess ammonia (NH_3) and decomposing the mixture or the addition product at the substrate which was heated to a sufficiently high temperature to form the corresponding nitride. Pd-purified H_2 was used as the carrier gas in both instances.

Temperature readings, obtained using an optical pyrometer, were made directly on the SiC-covered C pedestal, and are uncorrected for emissivity. The α-Al_2O_3 and Czochralski spinel ($MgAl_2O_4$) substrates were mechanically polished to provide a relatively scratch-free surface as viewed with an optical microscope at 400X magnification, and were treated in H_2 (~1150°C for $MgAl_2O_4$ or ~1250°C for α-Al_2O_3) for about 15 min before film growth. Mechanically polished Si was given a light etch in a mixture of 2 parts of HF, 9 parts of HNO_3, and 4 parts of HAc, rinsed with deionized H_2O and methanol, and heated for 15 min in H_2 at 1250°C to remove surface oxides. The α-SiC substrate used was a flux-grown basal-plane platelet.

Back-reflection Laue x-ray patterns, reflection electron diffraction techniques, and/or full-circle x-ray diffraction analysis were used to establish the reported orientation relationships between the epitaxial film and the substrate.

AlN growth.—Stoichiometric amounts of trimethylaluminum (TMA) and NH_3 react at room temperature (r.t.) to form the solid addition compound $(CH_3)_3Al{:}NH_3$. The reaction has been studied by Wiberg and Bolz (20). Our studies demonstrate that at high temperatures complete dealkylation of the addition compound occurs to form AlN. The over-all reactions may be expressed as in Eq. [1] and [2]

$$(CH_3)_6Al_{2(g)} + 2NH_{3(g)} \xrightarrow[\text{r.t.}]{} 2(CH_3)_3Al{:}NH_{3(s)} \quad [1]$$

$$(CH_3)_3Al{:}NH_{3(s)} \xrightarrow[\sim 1200°C]{} AlN_{(s)} + 3CH_{4(g)} \quad [2]$$

However, the formation of AlN occurs by a stepwise process, with a mole of CH_4 being released at about 60°C, a second mole at ~160°C (20), and the final mole of CH_4 at some higher temperature. Because thermal radiation from the rf heated pedestal at the deposition temperature could cause the formation of AlN powder at a finite distance from the substrate, experimental conditions must be carefully controlled to avoid such formation; otherwise, the powder could impede epitaxy and/or contaminate the film. Therefore, it was found preferable to use a vertical reactor containing a coaxial center tube, mixing the reactants in the upper neck of the center tube, and then directing the addition compound plus NH_3 to the heated substrate with a relatively high total H_2-carrier flow rate.

After a 15 min high-temperature H_2 etch of the substrate surface, the substrate temperature was stabilized for epitaxial growth (~1200°C) and NH_3 flow (~1750 ccpm) was started. A few minutes later TMA vapor was transported to the reactor by bubbling H_2 at 25-100 ccpm through the liquid TMA (stored at ~30°C), and an additional 6-8 lpm of H_2 were then added to "push" the addition compound to the substrate. Growth rates were typically 1-7 μm/hr. These conditions were found sufficient for the growth of epitaxial films on Si, α-SiC, α-Al_2O_3, and $MgAl_2O_4$. The growth of AlN on $MgAl_2O_4[(11\bar{2}0)AlN//(110)MgAl_2O_4]$ was not as reproducible as growth on α-Al_2O_3, probably due to the instability of $MgAl_2O_4$ to H_2 at the growth temperature employed. Crystallographic orientation relationships for growth on α-Al_2O_3 are summarized in Table I.

Film thickness uniformity and growth rate were directly related to reactor geometry; a center tube resulted in films with a concentric ring configuration, with thicker growth occurring at the center of the

* Electrochemical Society Active Member.

Key words: crystal growth, heteroepitaxy, films, insulating substrates, chemical vapor deposition.

Table I. AlN/Al_2O_3 crystallographic orientation relationships

$(0001)AlN//(0001)Al_2O_3$; $[\bar{1}2\bar{1}0]AlN//[\bar{1}100]Al_2O_3$
$(11\bar{2}0)AlN//(01\bar{1}2)Al_2O_3$; $[0001]AlN//[0\bar{1}11]Al_2O_3$
$(0001)AlN//(11\bar{2}0)Al_2O_3$; $[\bar{1}2\bar{1}0]AlN//[\bar{1}100]Al_2O_3$
$(0001)AlN//(111)Si$; $[\bar{1}2\bar{1}0]AlN//[\bar{1}10]Si$

ring. Crazing of the AlN film was observed to begin at about the third fringe of growth (*i.e.* at a thickness of ~0.4 μm) on Si and to extend into the thicker areas of growth. A typical "crazing pattern" structure is depicted in Fig. 1.

In the thinner growth areas it was sometimes possible to find evidence of the early stages of AlN growth. The triangular structure depicted in Fig. 2 was obtained on (111)Si.

The as-grown AlN films have invariably demonstrated insulating properties. Resistivities appear to be on the order of 10^5 ohm-cm or above. Reflection electron diffraction patterns for the single crystal film have been very well defined. The film quality was further substantiated by the excellent results obtained during surface acoustic wave studies using some of the films on α-Al_2O_3 (21).

GaN growth.—By substituting trimethylgallium (TMG) for TMA and pyrolyzing TMG-NH_3 mixtures on wafers of α-Al_2O_3 and α-SiC heated to 925°-975°C, single-crystal films of GaN were formed. The surface structures of (0001)GaN obtained on basal-plane α-SiC and α-Al_2O_3 are depicted in Fig. 3. The orientation relationships which have been determined for α-Al_2O_3 are indicated in Table II. Growth rates approaching 0.1 μm/min were adequate for the growth of epitaxial films. Total flow rates of ~3 lpm were used in these experiments.

An undoped 6 μm-thick white film grown at 930°C was n-type with a carrier concentration above 10^{19} cm^{-3} and a mobility ~60 cm^2/V-sec, as measured with the Van der Pauw technique (22). Further studies are necessary to determine if the low mobility is a characteristic of the process.

Films grown at 910°C possessed a yellow cast; and at 700°C, reddish-brown high-resistivity films were obtained. These films were extremely resistant to acids and bases but could be destroyed by heating in H_2 to 1050°C and above, which left a residue of what seemed to be Ga metal droplets on the surface of the substrate. The films formed at 700°C presumably contained intermediate unpyrolyzed [C-H-Ga-N] polymers, formed in the reaction between TMG and NH_3.

Some rather interesting crystallographic structures have been observed during these studies of GaN growth

Fig. 1. AlN growth features on (111)silicon

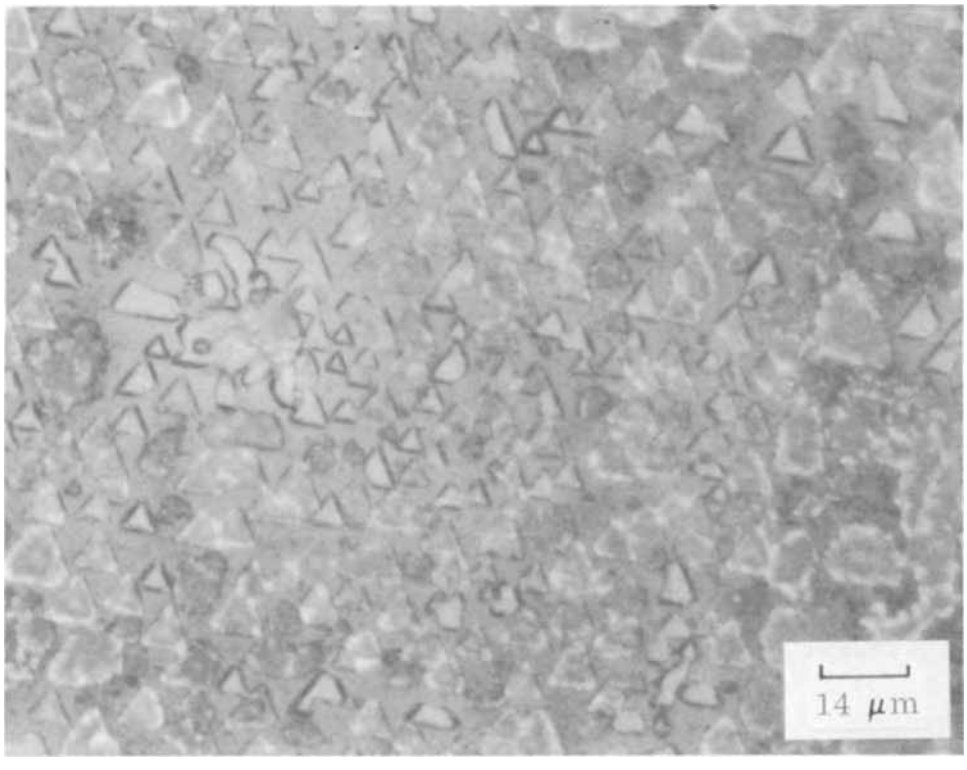

Fig. 2. An early stage for AlN growth on (111)silicon.

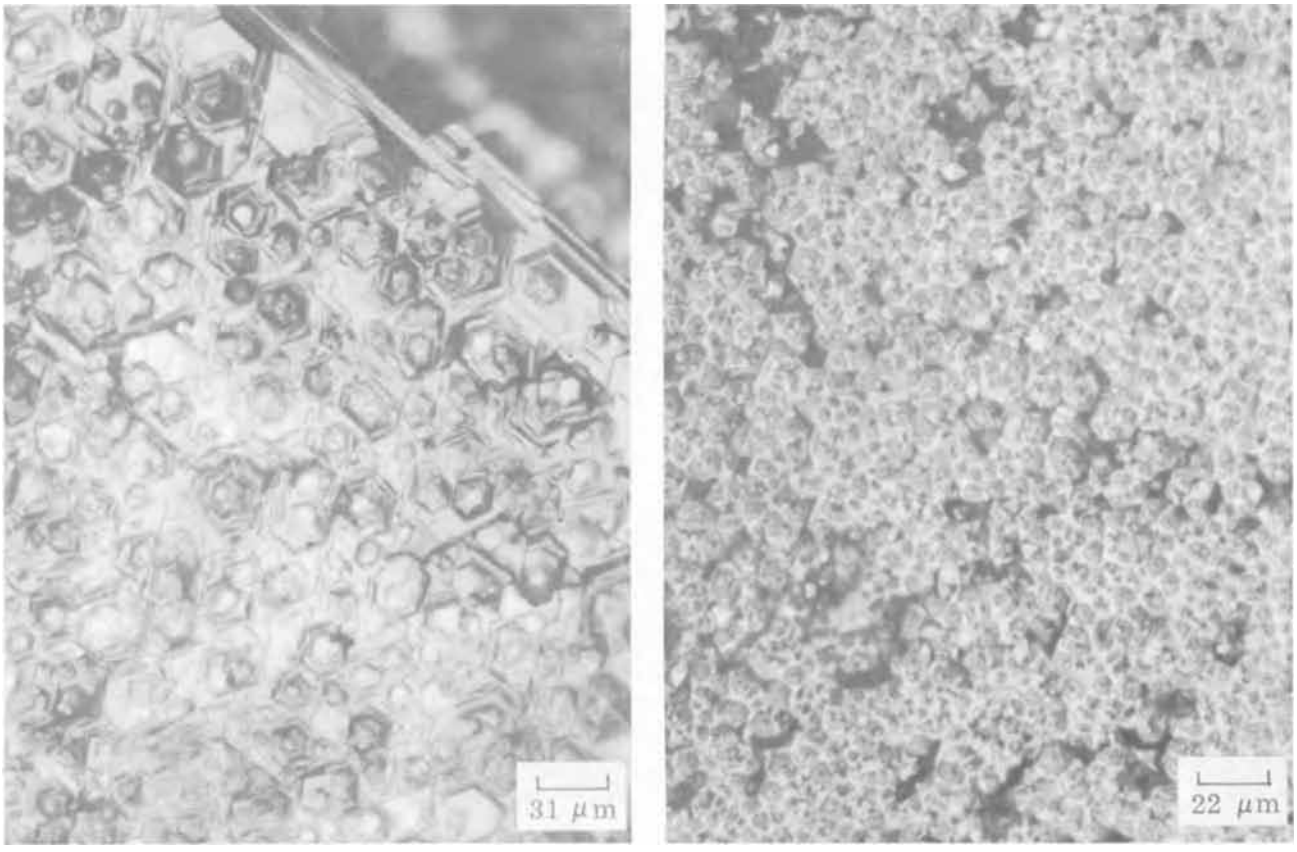

Fig. 3. GaN growth features on basal plane; (a, left) α-SIC; (b, right) α-Al_2O_3

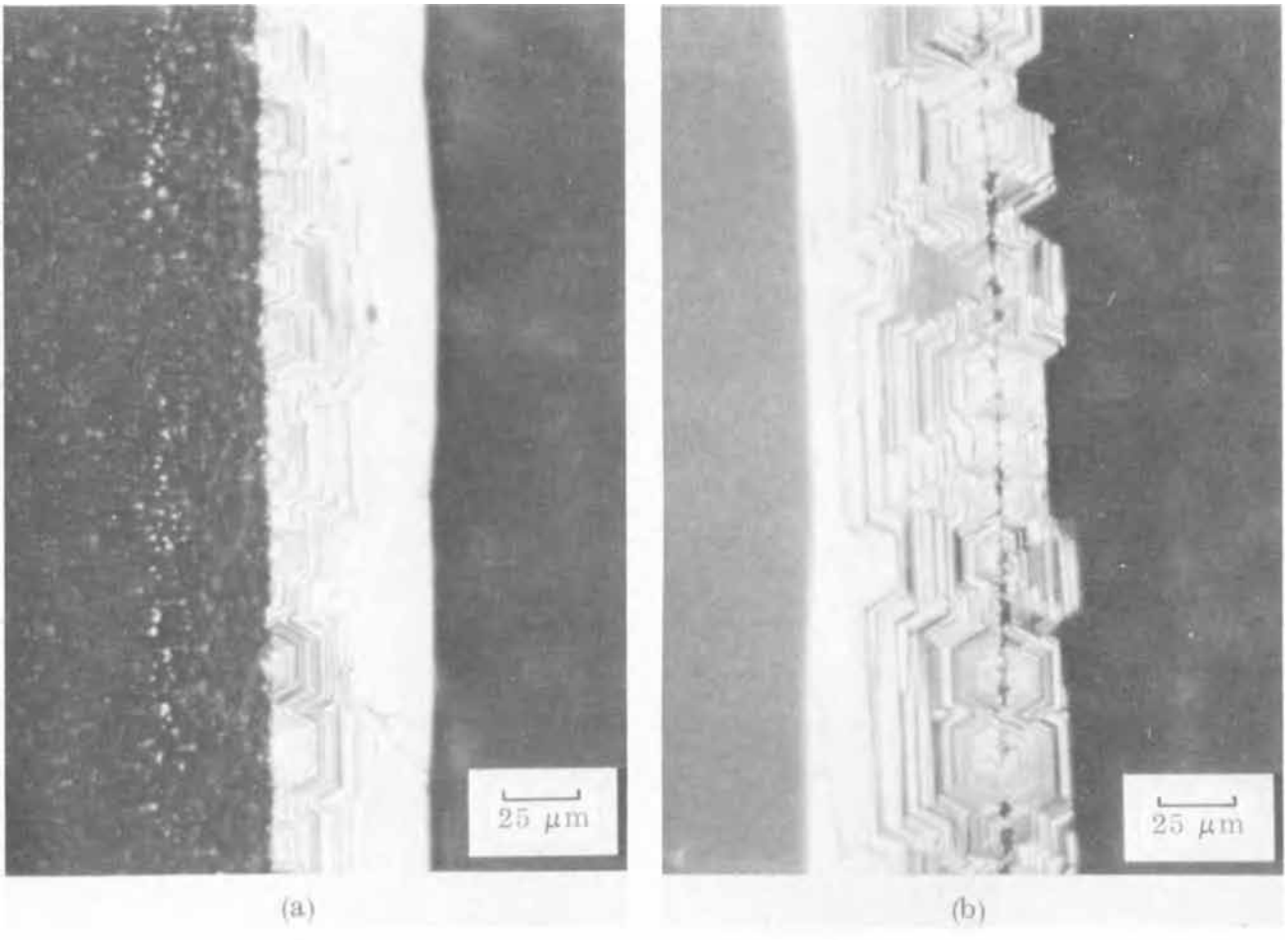

Fig. 4. GaN growth at substrate edges; (a) (0001)Al_2O_3; (b) (111)$MgAl_2O_4$

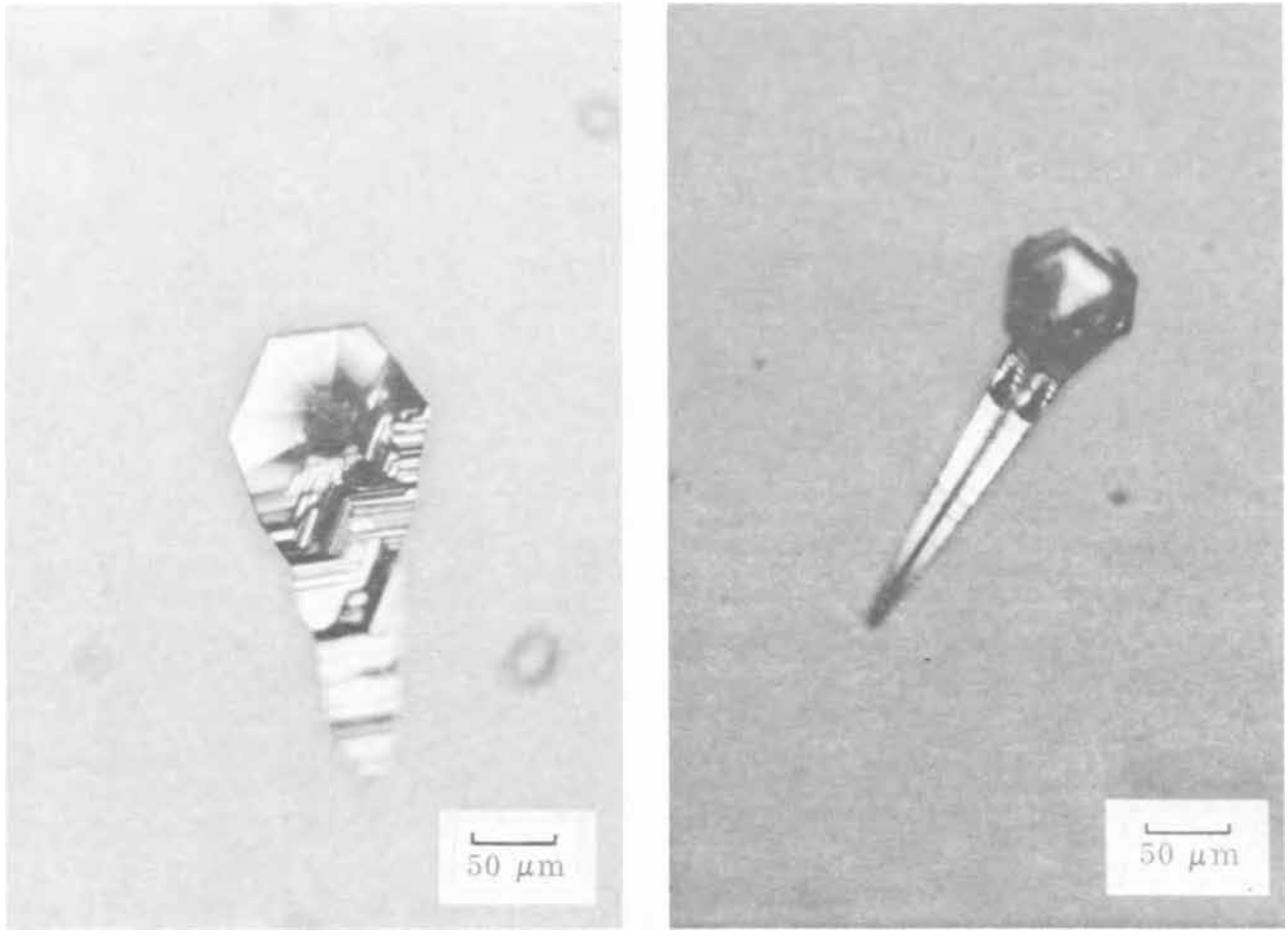

Fig. 5. Two kinds of needle growth of GaN observed during studies

on insulators. GaN displayed a strong tendency to grow at the edges of substrate wafers and to produce well-defined crystallographic growth steps. The growths at the edges of (0001) Al_2O_3 and (111) $MgAl_2O_4$ are recorded in Fig. 4. A slight break in the step-like growth morphology of the crystal can be observed at the edge (center black line) of the $MgAl_2O_4$ wafer.

Step-wise growth could also be observed in random needle-type crystals which sometimes grew very rapidly at the insulator surfaces. Two such structures are shown in Fig. 5. Such crystal growth may have occurred at a Ga droplet which acted as a nucleation site for vapor-liquid-solid (VLS) growth.

In summary, these feasibility experiments have indicated that the scope of the metal-organic process for semiconductor film formation can be extended to include the nitrides of Al and Ga. The relative ease with which these compounds can be formed indicates that further experimentation could produce additional important results in these and related cases.

Acknowledgments

The authors wish to thank Dr. A. C. Thorsen for the electrical measurements, L. A. Moudy for her analysis of the x-ray data, and Dr. R. P. Ruth for his most helpful review of this paper.

This research was supported in part by the U. S. Army Advanced Ballistic Missile Defense Agency (ABMDA), Arlington, Virginia and monitored by the U.S. Army Electronics Command, Fort Monmouth, New Jersey (ECOM) under Contract No. DAAB07-69-C-0452.

Manuscript submitted April 22, 1971; revised manuscript received *ca.* Aug. 10, 1971.

Any discussion of this paper will appear in a Discussion Section to be published in the June 1972 JOURNAL.

Table II. GaN/Al_2O_3 crystallographic orientation relationships

(0001)GaN//(0001)Al_2O_3; $[\bar{1}2\bar{1}0]$GaN//$[\bar{1}100]Al_2O_3$
$(11\bar{2}0)$GaN//$(01\bar{1}2)Al_2O_3$; [0001]GaN//$[01\bar{1}\bar{1}]Al_2O_3$
(0001)GaN//$(10\bar{1}4)Al_2O_3$; $[\bar{1}2\bar{1}0]$GaN 10 deg from $[20\bar{2}1]Al_2O_3$

REFERENCES

1. H. M. Manasevit, *Appl. Phys. Letters,* **12,** 156 (1968).
2. H. M. Manasevit and W. I. Simpson, *This Journal,* **116,** 1725 (1969).
3. H. M. Manasevit and A. C. Thorsen, *Met. Trans.,* **1,** 623 (1970).
4. P. Rai-Choudhury, *This Journal,* **116,** 1745 (1969).
5. K. Lindeke, W. Sack, and J. J. Nickl, *ibid.,* **117,** 1316 (1970).
6. R. W. Thomas, *ibid.,* **116,** 1449 (1969).
7. H. M. Manasevit, *ibid.,* **116,** 250C (1969); **118,** 647 (1971).
8. H. M. Manasevit and W. I. Simpson, *ibid.,* **117,** 196C (1970); **118,** 644 (1971).
9. M. T. Wauk and D. K. Winslow, *Appl. Phys. Letters,* **13,** 286 (1968).
10. A. J. Noreika, N. H. Francombe, and S. A. Zeitman, *J. Vacuum Sci. Technol.,* **6,** 194 (1969).
11. J. Pasternak and L. Roskovcova, *Phys. Status Solidi,* **7,** 331 (1964).
12. B. B. Kosicki and D. Kahng, *J. Vacuum Sci. Technol.,* **6,** 593 (1969).
13. G. A. Cox, D. O. Cummins, K. Kawabe, and R. H. Tredgold, *J. Phys. Chem. Solids,* **28,** 543 (1967).
14. A. J. Noreika and D. W. Ing, *J. Appl. Phys.,* **39,** 5578 (1968).
15. H. P. Maruska and J. J. Tietjen, *Appl. Phys. Letters,* **15,** 327 (1969).
16. T. L. Chu, D. W. Ing, and A. J. Noreika, *Solid-State Electron.,* **10,** 1023 (1967).
17. K. R. Faulkner, D. K. Wickenden, B. J. Isherwood, B. P. Richards, and I. H. Scobey, *J. Mater. Sci.,* **5,** 308 (1970).

18. D. K. Wickenden, K. R. Faulkner, R. W. Brander, and B. J. Isherwood, *J. Crystal Growth*, **9**, 158 (1971).
19. T. L. Chu, *This Journal*, **118**, 1200 (1971).
20. E. Wiberg and A. Bolz, *FIAT-Rev.*, **24**, 160 (1950).
21. J. H. Collins, P. J. Hagon, and G. R. Pulliam, *Ultrasonics*, **8**, 218 (1970).
22. J. L. Van der Pauw, *Philips Tech. Rev.*, **20**, 220 (1959).

Brief Communication

Revelation of Dislocations in (Hg, Cd)Te by an Etch Technique

Sidney G. Parker* and Jack E. Pinnell

Texas Instruments, Incorporated, Dallas, Texas 75222

Etch techniques are frequently used to show the presence of dislocations and their number (1). The (111) planes of material such as (Hg,Cd)Te, which crystallizes in the cubic structure, readily reveal the presence of dislocations as triangular pits or hillocks when etched with a suitable solution (2). Such an etch for $Hg_xCd_{1-x}Te$ has been discovered for values of x ranging from 0.85 to 0.60.

The etch solution consisted of 15 parts of concentrated HNO_3, 15 parts of H_2O, 1 part of concentrated HCl and 1 part of a 5% solution of Br_2 in methanol. The surface to be etched was lapped to a moderately smooth finish with 3200 grit although more polished surfaces were also used. The etching was performed at 25°C for 5-10 min with a dark film forming on the surface. This film was removed by a 1-2 sec treatment with a 5% Br_2-methanol solution followed by a methanol rinse.

Typical etch patterns are shown in Fig. 1 for opposite (111) planes. Because of the difficulty in obtaining large single crystals of $Hg_xCd_{1-x}Te$ we were unable to determine which of the faces was the "A" or metal rich face. However, it can be seen that upon etching, one face developed triangular hillocks or pits while the opposite face gave an irregular pattern. Pits or hillocks denoting dislocations were found for orientations up to 30° off the {111}, although the greater the deviation from the (111) the less regular was the shape of the etch pits. The number of dislocations in $Hg_{0.80}Cd_{0.20}Te$ grown by various techniques varied from 1×10^4 to 5×10^6 per cm^2.

As the Cd content increased it was necessary to dilute the etch solution with H_2O to obtain well defined etch patterns. Longer etch periods were also required

* Electrochemical Society Active Member.

Key words: II-VI materials, pseudobinary compounds, low band-gap materials, crystalline imperfections, preferential etching.

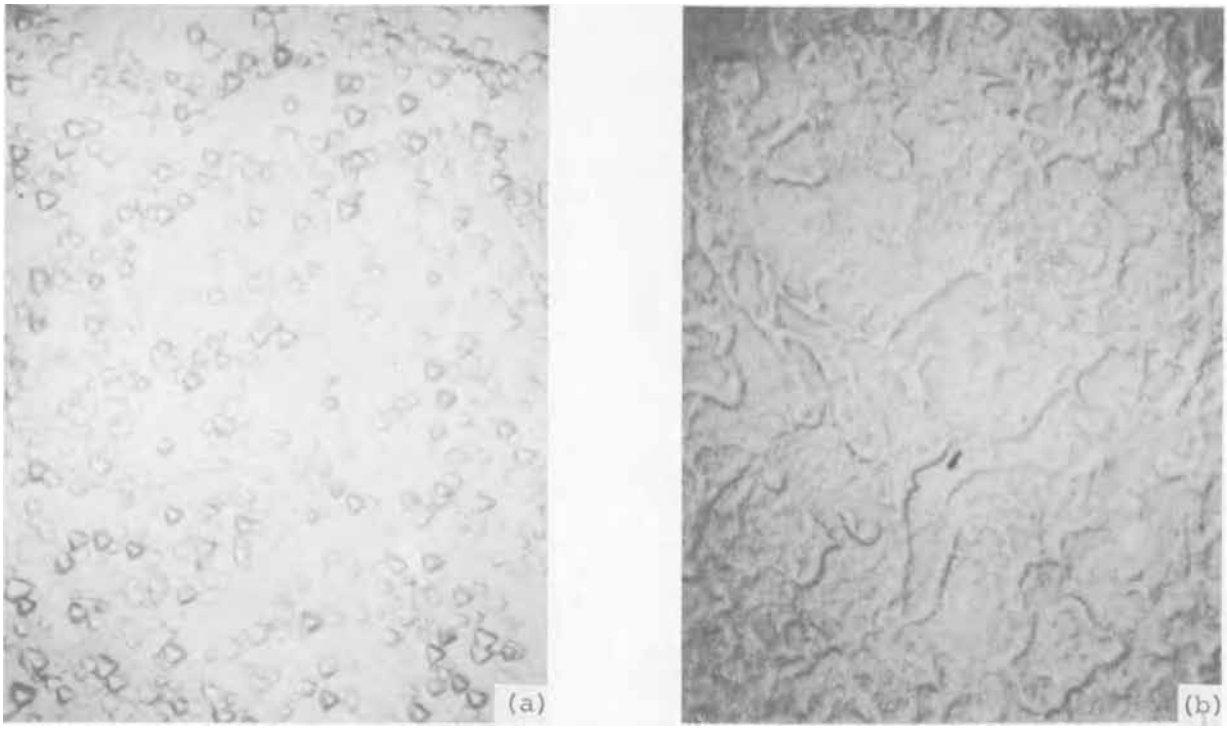

Fig. 1. Etch patterns developed on (111) faces of $Hg_{0.8}Cd_{0.2}Te$. (a) Triangular pattern on one face. (b) Irregular pattern on the opposite face. Magnification 350X.

with increasing Cd concentrations. The etch was not evaluated for compositions other than for the range stated above. Care was necessary not to etch too long with Br_2-methanol or else the etch figures developed by the HNO_3-HCl-Br_2 etch would be obliterated. If the amount of HCl in the etch solution was too great only irregular, over-all etching occurred.

Manuscript submitted June 24, 1971.

Any discussion of this paper will appear in a Discussion Section to be published in the June 1972 JOURNAL.

REFERENCES

1. D. Hull, "Introduction to Dislocations," p. 25, Pergamon Press, New York (1965).
2. H. C. Gatos and M. C. Lavine, "Chemical Behavior of Semiconductors," Technical Report No. 293, Lincoln Laboratory (1963).

JOURNAL OF THE ELECTROCHEMICAL SOCIETY

ELECTROCHEMICAL TECHNOLOGY

NOVEMBER 1971

ECM Study in a Closed-Cell System

I. $NaClO_3$

Kao-Wen Mao*

Electrochemistry Department, Research Laboratories, General Motors Corporation, Warren, Michigan 48090

ABSTRACT

The electrode reactions involved in electrochemical machining (ECM) of mild steel in $NaClO_3$ were studied in a closed cell system at constant current. The cathodic reaction is found to be essentially hydrogen evolution. At the anode, in addition to the metal removal, significant amounts of oxygen are produced and the total anodic current efficiency for Fe^{++} plus O_2 formation is about 100%. Reduction of $NaClO_3$ to NaCl during ECM is caused by the chemical reaction between $NaClO_3$ and Fe^{++}. The experimental results concerning the anodic process are qualitatively explained by the presence of porous anodic oxide films.

Because of its unique method of removing metal, electrochemical machining (ECM) has found increasing industrial application in the last decade (1). For simplicity, ECM may be described as a controlled rapid anodic corrosion process. In the process, metal is removed anodically at current densities of the order of 10 to 100 A/cm^2, and the reaction products precipitate in the electrolyte as sludge. The sludge is carried away by a rapidly flowing stream of electrolyte. The electrolyte gap between the two electrodes often is very small (usually less than 1 mm) to reduce both wild cutting and ohmic heating.

Recently a considerable amount of effort has been expended in studying this process; however, many basic questions concerning ECM electrode mechanisms remain unanswered. Perhaps this can be attributed to (1) the lack of general basic knowledge concerning high current density processes in the field of electrochemistry and (2) the experimental difficulty in measuring *IR*-free potentials of a high current density process in which the electrolyte, mixed with sludge and gas, flows through a very narrow gap.

In the present work, ECM experiments were carried out in a closed-cell system in order to obtain some general knowledge concerning the anodic and cathodic reactions of this high current density process. The possible reactions were determined by studying the changes of compositions of the electrolyte and the amounts of hydrogen and oxygen generated and metal removed. The first system investigated was ECM of mild steel in $NaClO_3$ solutions because of the excellent ECM properties provided by $NaClO_3$ (2). Further, it was hoped that this study could provide information about the reduction of $NaClO_3$ to NaCl during ECM (3). All experiments were conducted at current densities up to 47 A/cm^2 (or 300 A/in.^{2}), because it is this range of current density in which we are mainly interested.

Experimental Procedure

Closed ECM Cell

Figure 1 shows the arrangement of the closed-cell unit. The cell was made mainly of glass. A 25 cm mild steel (1020) tube (0.645 cm OD and 0.462 cm ID) was used as the anode (workpiece) with one end facing a brass or platinum disk (0.953 cm diameter) which served as the cathode (tool). The steel tube passed through the wall of the cell through a hydraulically sealing rubber O-ring. Outside the cell, the tube was attached to a threaded collet driving system actuated by a revolving nut in a sprocket. This arrangement provided different constant feed rates controlled by means of a constant speed motor and sprockets of different sizes.

The electrolyte was circulated by a polyethylene centrifugal pump at a flow rate of about 2 liters/min. After flowing through the steel tube, the electrolyte directly impinged upon the cathode and then drained to the electrolyte reservoir through two channels. The electrolyte reservoir had a capacity of 800 cm^3. The temperature of the electrolyte in the reservoir was maintained at 27° ± 2°C by a water jacket.

Experiments were conducted at different constant currents. The apparent current densities given in this report were based on the cross-sectional area of the tube wall (0.159 cm^2). The gap between the two electrodes was maintained approximately constant at 0.08 cm by using a proper feed rate which was determined by trial and error. The change of the electrolyte gap was followed by the variation of the applied cell voltage. The electrical current, controlled manually, was drawn from a Mallory, Model VA400, power supply. The current and the applied potential were measured by a Weston ammeter (Model 901) and a Sensitive voltmeter (Model C), respectively. A General Motors Research-made coulometer was used to measure the total applied charge. The electrical circuit of the cell, the anode driving system, and an electrical timer were all controlled by one switch. Experiments were terminated when the total charge reached 2500 or 7000 coulombs.

Preparation and Sampling

For each experiment, the steel tube was degreased with detergent, polished with a 600-grit wet grinding paper, rinsed with distilled water, and dried with acetone. After the experiment, the tube was washed in distilled water and dried. The loss in weight of the tube

* Electrochemical Society Active Member.

Key words: electrochemical machining (ECM), $NaClO_3$, current efficiency, oxide films.

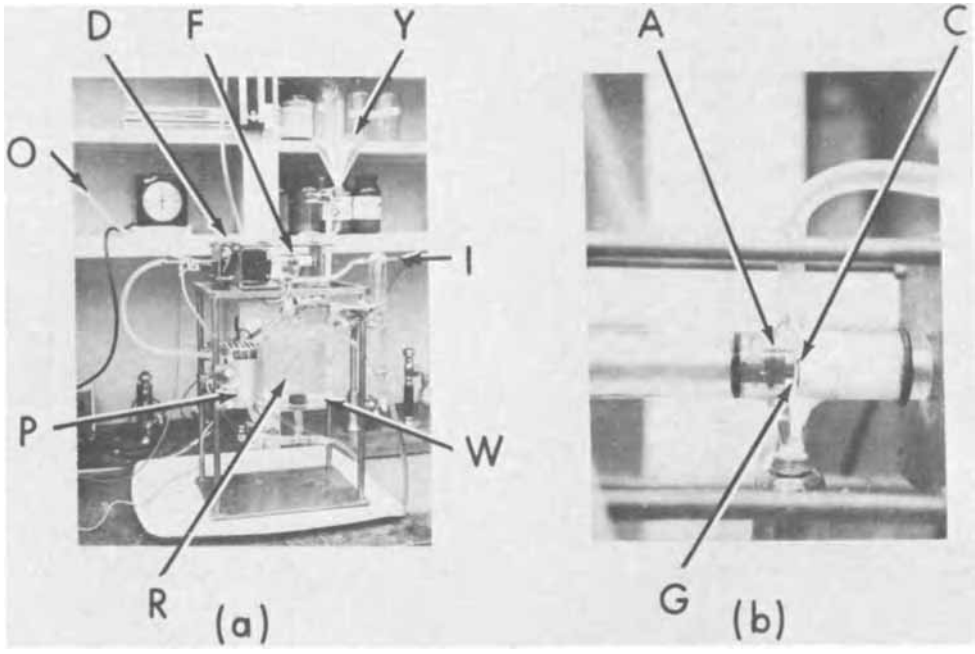

Fig. 1. (a) The closed ECM cell unit and (b) cell fixture. A, tube anode; C, potted cathode; D, anode driving system; F, cell fixture; G, electrolyte gap; I, air or nitrogen inlet; O, gas outlet to the analysis system; P, pump; R, electrolyte reservoir; W, water jacket; Y, electrolyte fill.

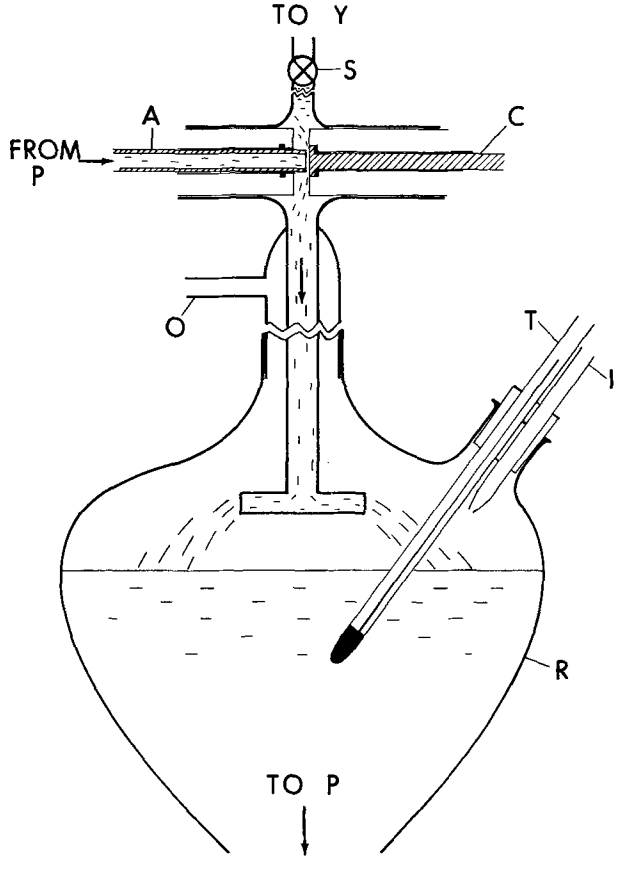

Fig. 1c. Schematic diagram of the closed cell. S, stopcock; T, thermometer; other designations as in Fig. 1(a) and (b).

due to ECM was measured to determine the amount of metal removed. The cathode was also washed in distilled water for each run. The original surface was polished with a 600-grit wet grinding paper.

The electrolyte for each run was freshly prepared. Distilled water was used for making the solution. The $NaClO_3$ used analyzed 99.5% with NaCl content about 0.02%. All other chemicals employed were of reagent grade. A sample of each new electrolyte was taken for chemical analysis. After a run, the mixture of sludge and electrolyte was collected and filtered through Whatman No. 50 filter paper. The sludge was further washed with distilled water (about 900 cc) which had been previously used to wash the cell. The volumes of the electrolyte filtrate and the washing solution were measured before the chemical analyses were made. The concentrations of iron and sodium in the sludge were determined after the sludge was dried overnight in an oven at 100°C. Since the average amount of sodium in the sludge was found to be less than 1%, the washing process used in this work is believed to be adequate. All chemical analyses were carried out by the Chemistry Department of General Motors Research.

Cell Atmospheres and Gaseous Products

Experiments were conducted in two different cell atmospheres: air or nitrogen. The reason for using a nitrogen atmosphere is the capability of detecting, in addition to hydrogen, any possible oxygen generated at the anode during ECM. The inlet flow rate of air or nitrogen to the cell system was about 4 liters/hr. Before entering the cell, the gas was at least partially saturated with water vapor by bubbling through a distilled water column. The pressure of the cell atmosphere was maintained at about 25 cm H_2O below 1 atm for air[1] and 25 cm H_2O above 1 atm for nitrogen. After leaving the cell, the gas was bubbled through a column of 500 g/liter KI solution to remove any chlorine.[2] The gas then further passed through columns of concentrated H_2SO_4 solution, CO_2 absorbent, anhydrous $CaSO_4$ and anhydrous $Ba(ClO_4)_2$ for removing any H_2O and CO_2 before it entered the apparatus for quantitative determination of hydrogen and oxygen.

For experiments in air atmospheres, only the hydrogen was determined. A Sargent-Welch gas purifying furnace, operated at 450°C, was used to collect the hydrogen by reacting with copper oxide (CuO) turnings in a Vycor high silica glass tube. The water produced by the reaction was then collected by anhydrous $Ba(ClO_4)_2$, and the amount of the hydrogen formed during ECM was determined by the weight change of the anhydrous $Ba(ClO_4)_2$.

When using a nitrogen atmosphere, two Sargent-Welch gas purifying furnaces at 450°C were employed. The first was filled with pure copper turnings,[3] and the second, with copper oxide turnings. In the first furnace, oxygen oxidized copper to copper oxide, which was then immediately reduced by the hydrogen

[1] Because air was introduced into the cell by connecting the outlet of the gas analysis system to a vacuum line.

[2] The amount of chlorine in the gas stream was determined by the change of I_2 concentration in the KI solution.

[3] The pure copper turnings were obtained by passing hydrogen through the furnace at 450°C for about 30 min before the ECM experiment.

present. The remaining hydrogen in the gas stream was removed in the second furnace by copper oxide. The water formed in the two furnaces was collected by two different anhydrous $Ba(ClO_4)_2$ columns. The water collected from the first furnace was used to calculate the amount of oxygen generated at the anode, and the total water from the two furnaces was used to determine the amount of hydrogen formed. Before an experiment was started, the cell system was purged with nitrogen for about 3 to 4 hr, with electrolyte circulating, to remove any possible oxygen in the system.

After ECM, the cell system was always purged with the appropriate gas for about 2 to 3 hr to collect any gaseous products dissolved in the electrolyte.

The accuracy of the above method for the determination of oxygen was checked by electrolyzing water in a 15% NaOH solution in the closed-cell system. A platinum disk was used as the cathode, and the anode was made of a palladium tube. Experiments were conducted at a current density of less than 0.3 A/cm^2 for a total applied charge of 350 coulombs. For experiments in a nitrogen atmosphere (the inlet flow rate also at 4 liters/hr), only about 92% of the oxygen was recovered. This may be due to incomplete mixing between oxygen and hydrogen in the gas stream since, after experiments, a small amount of copper oxide (gray color) was found in the glass tube. However, when a small additional amount of hydrogen (less than 10%) was added to the nitrogen stream, such a phenomenon was not observed and almost 100% of the oxygen was accounted for. Since an excess amount of hydrogen was always present in the gas stream during ECM in $NaClO_3$ solutions (see Tables I and II) and also since no copper oxide was observed after the ECM experiments, it is believed that the method used in this work for determining oxygen should be quite accurate.

Results

The results of studying ECM of mild steel in $NaClO_3$ are shown in Tables I and II for experiments in air and nitrogen, respectively. The amount of iron removal was determined by the weight loss of the anode assuming 100% iron in the 1020 mild steel. The amount of iron in the sludge was about 5% lower than the anode weight loss since there was a loss of sludge during the process of collection. The current efficiency for iron removal was calculated on the basis of the reaction

$$Fe \rightarrow Fe^{++} + 2e^- \qquad [1]$$

Because of low concentrations of sodium chloride, the average error for the values of sodium chloride formation, shown in Tables I and II, was estimated to be about 5%. The error was larger when the value was 0.002 mole or less. The amount of $NaClO_3$ reduced after ECM could not be determined due to the limitation of accuracy in chemical analysis (impossible to determine accurately a small difference between two large numbers).

$NaClO_4$ was not observed in the electrolyte after ECM (infrared spectrophotometry). No experiment in 2M $NaClO_3$ at 26 A/cm^2 was performed because no comparable feed rate could be achieved.

For convenience in discussion, the relationship between the current efficiency for iron removal and current density at different $NaClO_3$ concentrations is given

Table I. Results of studying ECM in $NaClO_3$ electrolyte and air atmosphere

Run	$NaClO_3$* concentration (M)	Cathode	Apparent current density (A/cm^2)	Coulombs passed	Current efficiency for H_2 generation (%)	Iron removal: Amount (mole)	Iron removal: Current efficiency (%)	Chlorine formation (10^{-5} mole)	NaCl formation (mole)	Fe/NaCl**	pH change: From	pH change: To
A1	4.5	Brass	47	2500	98.2	0.009687	74.8	—	—	—	7.7	7.4
A2	4.5	Pt	47	2500	98.1	0.01045	80.7	3	0.00180	5.8	—	—
A3	4.5	Brass	47	7000	96.7	0.03006	82.9	5	0.00610	4.9	—	—
A4	4.5	Pt	47	7000	99.3	0.02850	78.6	8	0.00547	5.2	8.1	6.1
A5	4.5	Brass	26	2500	99.0	0.00759	58.6	—	—	—	7.9	6.5
A6	4.5	Pt	26	2500	99.0	0.00786	60.7	3	0.00167	4.7	7.3	6.3
A7	4.5	Brass	26	7000	99.8	0.02273	62.7	6	0.00415	5.5	8.5	6.3
A8	4.5	Pt	26	7000	98.6	0.02496	68.8	9	0.00459	5.4	8.1	5.7
A9	2.0	Brass	47	2500	98.7	0.00782	60.4	1	0.00149	5.3	7.9	6.4
A10	2.0	Brass	47	7000	99.9	0.02432	67.1	3	0.00451	5.4	7.5	5.2
A11	2.0	Brass	37	2500	98.3	0.00600	46.3	1	0.00102	5.9	7.0	6.0
A12	2.0	Brass	37	7000	100.9	0.02167	59.7	1	0.00392	5.5	7.4	6.8

* No $NaClO_4$ was detected after ECM.
** Molar ratio of Fe removed to NaCl formed.

Table II. Results of studying ECM in $NaClO_3$ electrolyte and nitrogen atmosphere (brass cathode)

Run	$NaClO_3$* concentration (M)	Apparent current density (A/cm^2)	Coulombs passed	Current efficiency for H_2 generation (%)	Current efficiency for O_2 generation (%)	Iron removal: Amount (mole)	Iron removal: Current efficiency (%)	Total current efficiency for O_2 and Fe^{++} (%)	Chlorine formation (10^{-5} mole)	NaCl formation (mole)	Fe/NaCl**	pH change: From	pH change: To
N1	4.5	47	7000	98.6	24.8	0.02850	78.6	103.4	10	0.00548	5.2	8.4	5.7
N2	4.5	37	7000	97.2	27.4	0.02632	72.6	100.0	11	0.00480	5.5	8.2	6.7
N3	4.5	26	7000	98.8	35.3	0.02332	64.3	99.6	8	0.00403	5.8	7.8	6.8
N4	4.5	12	7000	100.1	57.9	0.01513	41.7	99.6	3	0.00265	5.7	8.2	7.2
N5	2.0	47	7000	98.7	37.5	0.02299	63.4	100.9	4	0.00415	5.5	6.2	5.8
N6	2.0	37	7000	98.1	39.5	0.02212	61.0	100.5	3	0.00381	5.8	6.4	6.2
N7	2.0	12	7000	101.2	80.8	0.00694	19.1	99.9	0	0.00118	5.9	6.5	6.2
			Average:	98.9† ± 0.5††				100.6 ± 1.0††			5.5† ± 0.3††		

* No $NaClO_4$ was detected after ECM.
** Molar ratio of Fe removed to NaCl formed.
† Including the results given in Table I.
†† Standard deviation.

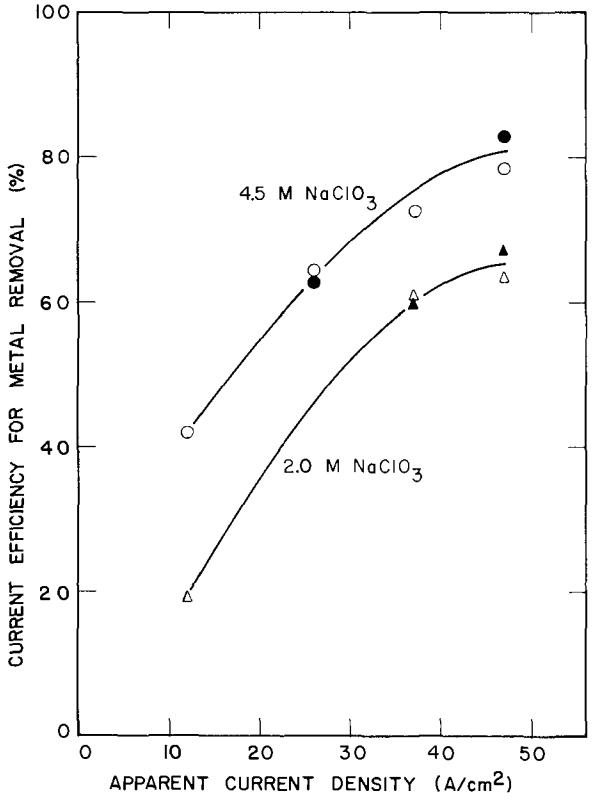

Fig. 2. Relationship between current efficiency for iron removal and current density (brass cathode, 7000 coulomb). ○, ● = 4.5M $NaClO_3$; △, ▲ = 2.0M $NaClO_3$; open symbols for nitrogen atmosphere; filled symbols for air atmosphere.

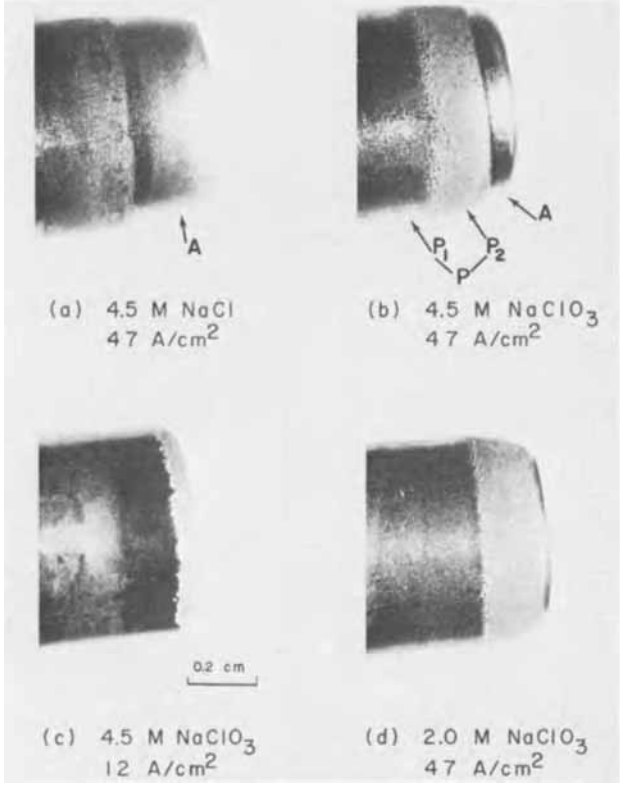

Fig. 3. The tube end finishes obtained by ECM. A, active-cutting region; P, film-protected region, P_1, well-film-protected region; P_2, less-film-protected region.

in Fig. 2. The data used are from the experiments using a brass cathode with a total applied charge of 7000 coulombs.

Tube end finishes obtained with $NaClO_3$ solutions are shown in Fig. 3 in which the finish obtained with

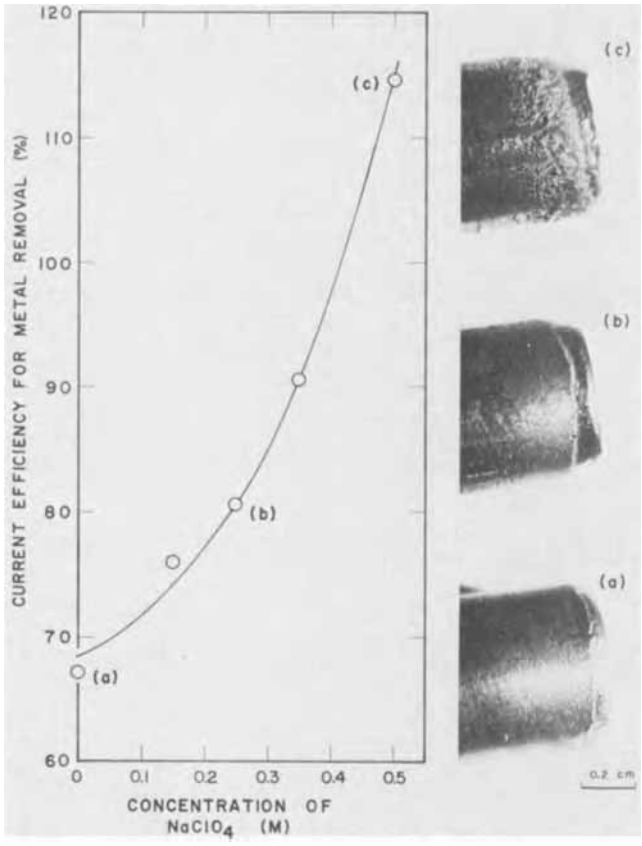

Fig. 4. The effect of ClO_4^- ions on ECM in a 3M $NaClO_3$ solution. (37 A/cm², 2500 coulomb).

NaCl solution (4) is also included for comparison. The results of introducing $NaClO_4$ into a 3M $NaClO_3$ solution at 37 A/cm² are summarized in Fig. 4.

Discussion

ECM Reactions in $NaClO_3$

By comparing the data in Tables I and II (some of them are plotted in Fig. 2), no apparent difference is observed between the results obtained in air and nitrogen atmospheres. Also, it is seen that the cathodic reaction of ECM in $NaClO_3$ solutions is essentially hydrogen evolution. The amount of hydrogen formed, as shown in Table I, is not altered by using different metals such as brass and platinum as the cathode. The results given in Table II indicate that, in addition to the metal dissolution, oxygen is also produced at the anode during ECM in $NaClO_3$. Since the total anodic current efficiency for O_2 and Fe^{++} formations is so close to 100%, it seems that iron is mainly dissolved as ferrous ion at the anode.

The formation of NaCl (or the reduction of $NaClO_3$) during ECM is probably caused by the following chemical reaction

$$6Fe^{++} + NaClO_3 + 3H_2O \rightarrow 6Fe^{+++} + NaCl + 6OH^- \quad [2]$$

A small portion of chlorate is also reduced to chlorine but the amount is very small compared to chloride.

Having in mind the error in determination of the chloride concentration, the results of the present work may not show any definite influence of various operating conditions on the value of the molar ratio of iron removed to NaCl formed. However, the average value of 5.5 given in Table II is certainly lower than the value of 6 according to Eq. [2]. At present no satisfactory explanation can be given. Nevertheless, based on the average current efficiencies given in Table II, one might speculate about the following "possible" reasons for the excess chloride generation. The average efficiency of 98.9% for hydrogen generation in $NaClO_3$ is slightly lower than the 100.2% efficiency for both the

NaCl and $NaClO_4$ systems (4). It is possible that a very small amount of chlorate is reduced at the cathode. On the other hand, the average total current efficiency for O_2 and Fe^{++} formations is slightly higher than 100%. Some iron may be chemically oxidized by chlorate. Since both current efficiencies mentioned above are very close to 100%, a solid conclusion cannot be drawn.

Tables I and II show that the pH of the electrolyte decreases to a neutral value after ECM. This should result from a saturated $Fe(OH)_3$ solution. During ECM in $NaClO_3$ a red-brown sludge was always observed even when the cell was operated in a nitrogen atmosphere. The sludge in solution was nonmagnetic.

Effect of Passivity on ECM

Before discussing the results further one may take a look at the typical tube end finishes obtained with NaCl and $NaClO_3$ solutions in Fig. 3a and 3b. The difference between the finishes obtained with NaCl and $NaClO_3$ is apparent. $NaClO_3$ gives not only better dimensional control (less wild cutting which is indicated by the distance from the tube end over which a reduction of the tube OD has occurred) but also a brighter surface at the tip of the tube. For the sake of convenience, names are given to the various regions of the finishes in Fig. 3a and 3b. The active-cutting region is represented by A, and P represents the film[4]-protected (from wild cutting) region in which P_1 and P_2 stand for the well- and the less-film-protected regions, respectively. [It should be noted that region P_2 sometimes becomes less apparent at a certain site of the finish (see Fig. 4a for example). This is believed to be caused by the nonuniform electrolyte flow and the presence of gases in the solution.]

Hoare and his co-workers (3, 5, 6) have suggested that the good dimensional control obtained with ECM is associated with the presence of a protective and relatively thick iron oxide film at the outside of the active-cutting region. In the case of $NaClO_3$, an even better control is obtained because of the sharp change of the polarization curve from the passive to the transpassive state. In NaCl, since no such film is present (6), the active-cutting region is considerably larger than that in $NaClO_3$ (see Fig. 3a and 3b). The main constituent of the iron oxide film is probably a cubic oxide which is either γ-Fe_2O_3 or Fe_3O_4 or both (3, 7, 8). In a recent study of current transient on a rotating electrode, Chin (9) suggested that the iron oxide film in $NaClO_3$ is porous and its thickness at the passive state is of the order of 1000Å.

Recently, Hoare, Mao, and Wallace (10) reported that the bright surface finish at the active-cutting region in $NaClO_3$ is related to the effect of electropolishing. A thin, uniform, and porous oxide film is present even in the active-cutting region, and the polishing effect is achieved because ferrous ions have to pass through the randomly distributed pores. The thickness of the film for polishing is of the order of 10 to 100Å (11).

The phenomena of the passivity of copper in KNO_3 and K_2SO_4 have been observed by Landolt, Muller, and Tobias (13) at actual ECM conditions. They found that the onset of passivation occurs at the maximum possible mass transfer rate (convective diffusion) of dissolution products, so it depends on electrolyte flow rate and current density. As for conventional low current density processes, they also report that etched surfaces result from active dissolution and pitted or bright surfaces from transpassive dissolution.

Porous Film Model

In this report, the results concerning the anodic process for ECM of steel in $NaClO_3$ will be qualitatively explained by the presence of oxide films. The film is assumed to be porous. The pores are relatively small and randomly distributed. The oxide film is considered as a barrier layer for the transport of the reaction product, ferrous ion, thus slowing down the rate of iron dissolution. The degree of the slowing-down (or polarization) depends on the thickness of the film.[5]

Perhaps it should be noted that the concept of small "pores" mentioned above is somewhat parallel to that of "contaminated oxides" proposed by Hoar and his co-workers (12). In that work the thin, compact films for polishing are suggested to be not pure oxides but oxides contaminated with significant amounts of the anions from the solution, because oxides themselves have very low ionic conductivity at room temperature. During ECM, iron is dissolved at a very high rate, hence the film has to be porous (or highly "contaminated" with not only the anions of the electrolyte but also water molecules) in order to allow the cations to pass through it rapidly.

During ECM of steel in $NaClO_3$ solutions, because of the slowing-down of the metal dissolution by the presence of the film, a part of the current is used for oxygen generation instead of for metal removal (Table II). The reaction of oxygen generation may be written as

$$2H_2O \rightarrow O_2 + 4H^+ + 4e^- \qquad [3]$$

In the case of NaCl, since the protective film is not present during ECM, oxygen generation is not observed and the current efficiency for iron removal is significantly higher (about 94 to 99%) (4).

In Table II, it is seen that the current used for oxygen generation increases as the current density decreases. At 12 A/cm^2, the major anodic reaction becomes oxygen generation. From these results it is reasonable to suggest that at the beginning of the transpassive state the current is mainly consumed in oxygen evolution. According to reported data (6, 9), the transition from the passive to the transpassive state in $NaClO_3$ occurs at a current density of the order of 1 mA/cm^2 and at a potential of about 1.4 to 1.6V *vs.* NHE (which is also the potential range where it is possible for Eq. [3] to take place). Hoare (6) also found by using a constant current stripping pulse technique that a large amount of anodic oxide is removed when the potential is increased to the transpassive state. If this film removal is assumed to be mainly caused by the oxygen generation (because films are pushed away by the oxygen gas), then the oxygen should not all be formed at the exterior surface of the film. Therefore, the oxide films in $NaClO_3$ are likely to be porous and not very electronically conductive.

Effect of Potential on Passivity

The results in Fig. 2 show that current efficiency for iron removal increases with current density. This implies that the oxide films are reduced in thickness as the potential increases, since the degree of the slowing-down of iron dissolution is assumed to depend on the film thickness. The effect of potential on the reduction or breakdown of anodic film has been discussed in the literature (12, 14) although the reason for such an effect is still not clear. Hoar (15) recently proposed, in addition to the anion penetration model,[6] a new "mechanical" mechanism wherein the film breakdown is caused by the repulsive forces between the adsorbed anions at the film/solution interface. According to this model, the film could be more easily dissolved as the potential increases because more ClO_3^- ions are adsorbed. Perhaps, at actual ECM conditions, the influence of pH should also be considered. From a thermodynamic viewpoint, Pourbaix (16) has shown that the passivation properties strongly depend on pH and potential. Iron oxide generally becomes more soluble at low pH. During ECM in $NaClO_3$, be-

[4] The anodic oxide film will be discussed later.

[5] For simplicity, the effect of changing film structure by the influence of potential is not discussed in this report.

[6] The breakdown of passivity is caused by anion penetration which makes the film highly "contaminated" and ionically conductive (12).

cause of the rapid formation of oxygen (and ferrous or ferric hydroxide) at (and near) the anode, the pH of the solution near the anode should be lower than that of the bulk solution. The pH further decreases as the current increases if the electrolyte flow rate is not changed. Hence, the film could be more easily dissolved at a higher current density. The reduction of film thickness may also be attributed to the force exerted on the film by the rapid metal removal and by the formation of gaseous oxygen as well.

The effect of potential on the film thickness may become more evident by comparing the finishes shown in Fig. 3b and 3c. It is clear that the degrees of both brightness of the cutting surface and wild cutting for 12 A/cm^2 are less than those for 47 A/cm^2. This is believed to be caused by the presence of relatively thicker films at a lower potential. The films are gradually reduced in thickness when the potential increases. Therefore, a brighter active-cutting surface and larger wild cutting are observed at a higher potential. Such phenomena have previously been observed at General Motors Research (17).

Since the surface finish of the less-film-protected region (P_2) in Fig. 3b is very similar to that of the cutting region in Fig. 3c, the P_2 region should also be in the transpassive state. The well-film-protected region (P_1) is in the passive state due to the further decrease of potential caused by a longer solution path to the cathode. (5, 6). Because of the sharp change from the passive to the transpassive state in $NaClO_3$, the passivity of iron at the boundary between the two states is very sensitive to the flow pattern of the electrolyte; especially when significant amounts of gases are present in the solution. Relatively small changes in the *IR* of the solution path by any nonuniform flow can lead to an uneven metal removal at the boundary (see Fig. 3b, 3c, and 3d).

It should be noted that the current efficiencies for oxygen generation as well as for iron removal given in this report represent only the average values; the actual current efficiency for oxygen generation (or iron removal) should be higher (or lower) in the less-film-protected region because the film there is supposed to be thicker than at the active-cutting region. One also should recognize that the true average current density in this work is lower than the apparent current density due to the wild cutting.

Effect of Electrolyte on Passivity

The ECM properties of various oxidizing electrolytes have been discussed in the literature (5, 6, 10). In the case of $NaClO_3$, Chin (9) and LaBoda and Hoare (18) found that passivity of iron increases with the concentration of $NaClO_3$. In order to study the effect of the $NaClO_3$ concentration on ECM, experiments were carried out in 3M $NaClO_3$ solution with various additional amounts of $NaClO_4$ (0 to 0.5M). The purpose of introducing $NaClO_4$, a relatively stable compound, is to reduce the effective concentration of $NaClO_3$ (or the oxidizing power of $NaClO_3$), although ClO_4^- has also been found to possess certain film-rupturing power (19). If the film-rupturing power of ClO_4^- is assumed to be negligible at low concentrations of $NaClO_4$ (say less than 0.25M),[7] then the results shown in Fig. 4 indicate that the oxide films are indeed affected by the effective concentration of $NaClO_3$. Because of the decrease of passivity, the current efficiency, wild cutting, and brightness increase with the $NaClO_4$ concentration. However, when the $NaClO_4$ concentration further increases (higher than 0.25M), pitted surfaces in both film-protected and active-cutting regions are observed. Apparently, this is caused by nonuniform oxide films resulting from the "mechanical" film breakdown by ClO_4^- ions (15). Severe grain boundary attacks at high concentration of $NaClO_4$ at point (c) lead to the current efficiency for iron removal higher than 100%.

According to the above argument, the passivity of iron during ECM in $NaClO_3$ would be expected to be proportional to the concentration of the electrolyte. However, the results summarized in Fig. 2 show just the opposite effect, where the current efficiency for iron removal increases with the $NaClO_3$ concentration. This may be attributed to the following reasons:

1. The reaction $2H_2O \rightarrow 4H^+ + O_2 + 4e^-$ (Eq. [3]) has to be preceded by the adsorption of water molecules on the anode surface. The increase in electrolyte concentration is expected to hinder the process of oxygen evolution due to the replacement of adsorbed water by adsorbed anions.[8]

2. Because of the increase of $NaClO_3$ concentration, more ClO_3^- is present in the film. Hence, the film is more ionically conductive at a higher concentration of $NaClO_3$ (12).

At low concentrations of $NaClO_3$, since the current is mainly consumed in oxygen evolution, bright surface finishes and large wild cutting are generally not obtained (17) (see Fig. 3d).

As shown in Table I, the current efficiencies for iron removal are not affected by the amount of the applied charge at 4.5M $NaClO_3$ (although there is a slight difference at 26 A/cm^2), but there is quite a difference between the efficiencies for 2500 and 7000 coulombs at 2M $NaClO_3$. This may be caused by the increase in Cl^- ion concentration. The effect of Cl^- ion on the oxide film breakdown (12, 15) is more apparent at low concentrations of $NaClO_3$.

Conclusions

In view of the results of the present work, it is apparent that the anodic process of ECM of steel in $NaClO_3$ is very complicated due to the presence of porous oxide films. Unlike the copper system (13), the iron oxide film is present on the anode over a wide range of operating conditions and the film is probably reduced in thickness as the potential increases. Significant amounts of oxygen are observed during ECM. The oxygen formation increases with the decreases of potential and electrolyte concentration, and it finally becomes the main anodic reaction when the current density is lower than 12 A/cm^2. The cathodic reaction is essentially hydrogen generation. Reduction of $NaClO_3$ to NaCl during ECM is due to the chemical reaction between $NaClO_3$ and Fe^{++}, the anodic product of iron removal.

Acknowledgment

The author wishes to thank Dr. J. L. Griffin of the Electrochemistry Department, General Motors Research Laboratories, for his initiation of this project and his construction of the initial cell system. Thanks are also due to Drs. J. P. Hoare, D. T. Chin, and W. S. Wong, also of the Electrochemistry Department, for their valuable discussions. The efforts made by R. B. Loranger, H. E. Vergosen, Dr. J. L. Johnson, and other members of the Chemistry Department to carry out the chemical analyses are especially appreciated.

Manuscript submitted April 5, 1971; revised manuscript received *ca.* June 28, 1971.

Any discussion of this paper will appear in a Discussion Section to be published in the June 1972 JOURNAL.

REFERENCES

1. A. E. Debarr and D. A. Oliver, "Electrochemical Machining," American Elsevier, New York (1968).
2. M. A. LaBoda and M. L. McMillan, *Electrochem. Technol.*, **5**, 340 (1967).
3. J. P. Hoare, M. A. LaBoda, M. L. McMillan, and A. J. Wallace, Jr., *This Journal*, **116**, 199 (1969).
4. K. W. Mao, *This Journal*, **118**, 1876 (1971).
5. J. P. Hoare, *Nature*, **219**, 1034 (1968).
6. J. P. Hoare, *This Journal*, **117**, 142 (1970).
7. U. R. Evans, "The Corrosion and Oxidation of Metals," St. Martin's Press, New York (1960).

[7] There is no real argument to support this assumption except that a pitted surface was not observed when the $NaClO_4$ concentration was less than 0.25M.

[8] This also can increase the chance of dissolving the film "mechanically."

8. K. J. Vetter, "Electrochemical Kinetics," Academic Press, New York (1967).
9. D. T. Chin, *This Journal*, **118**, 174 (1971).
10. J. P. Hoare, K. W. Mao, and A. J. Wallace, Jr., *Corrosion*, **27**, 211 (1971).
11. T. P. Hoar, in "Modern Aspects of Electrochemistry," J. O'M. Bockris, Editor, Vol. II, p. 262, Academic Press, New York (1959).
12. T. P. Hoar, D. C. Mears, and G. P. Rothwell, *Corrosion Sci.*, **5**, 279 (1965).
13. D. Landolt, R. H. Muller, and C. W. Tobias, *This Journal*, **116**, 1384 (1969).
14. D. A. Vermilyea, in "Advances in Electrochemistry and Electrochemical Engineering," P. Delahay and C. W. Tobias, Editors, Vol. 3, p. 211, Interscience Publishers, New York (1963).
15. T. P. Hoar, *Corrosion Sci.*, **7**, 341 (1967).
16. M. Pourbaix, "Thermodynamics of Dilute Aqueous Solutions," Arnode, London (1949).
17. M. A. LaBoda, Private communication.
18. M. A. LaBoda and J. P. Hoare, in "Fundamentals of Electrochemical Machining," C. L. Faust, Editor, p. 227, The Electrochemical Society Softbound Symposium Series, New York (1971).
19. T. P. Hoar, *Trans. Faraday Soc.*, **45**, 683 (1949).

ECM Study in a Closed-Cell System

II. NaCl, $NaClO_4$, and $NaNO_3$

Kao-Wen Mao*

Electrochemistry Department, Research Laboratories, General Motors Corporation, Warren, Michigan 48090

ABSTRACT

Electrochemical machining (ECM) of mild steel in NaCl, $NaClO_4$, and $NaNO_3$ solutions was studied in a closed-cell system. The anodic processes are found to be different in the various solutions. In NaCl, the anodic reaction is essentially iron dissolution. In $NaNO_3$, however, most of the current is expended for oxygen generation due to the presence of an electronically conductive oxide film. A small amount of oxygen (less than approximately 10% of the current) is observed in the $NaClO_4$ system. The cathodic reaction in both NaCl and $NaClO_4$ solutions is hydrogen evolution. In the case of $NaNO_3$, little or no hydrogen is observed—the current is mainly consumed in reducing NO_3^- ions.

In previous work, the electrochemical machining (ECM) of mild steel in $NaClO_3$ has been studied in a closed-cell system (1). From the results of that work, it is believed that more general knowledge concerning ECM electrode mechanisms can be obtained by extending the study to other electrolyte systems with different oxidizing powers. Hence, NaCl, $NaClO_4$, and $NaNO_3$ were selected for this work. It was expected that the results would provide a better understanding of the effect of the electrolyte on the ECM process.

Experimental Procedure

The closed-cell system, experimental procedures and conditions, and sampling techniques are identical to those described in the previous paper (1). Reagent grade chemicals were used for all experiments. Chemical analyses were carried out by the Chemistry Department of General Motors Research.

The methods of collecting hydrogen and oxygen for the NaCl and $NaClO_4$ systems are the same as those used for $NaClO_3$ (1). Minor changes were made in the case of $NaNO_3$ since little or no hydrogen was formed during ECM in $NaNO_3$.

The experiments using $NaNO_3$ were conducted in a nitrogen atmosphere only in order to concentrate on the study of oxygen generation. However, the procedure of collecting any hydrogen present was still carried out for each run. Thus, the gas, after leaving the ECM cell unit, was first bubbled through a 20% sulfuric acid solution for removing any ammonia as well as water vapor from the gas stream. Then the gas was further dried by passing it through anhydrous $CaSO_4$ and anhydrous $Ba(ClO_4)_2$ before entering two serially connected Sargent-Welch gas purifying furnaces. The Vycor glass tubes used in these furnaces were filled with pure copper and copper oxide (CuO) turnings, respectively. Any water collected by anhydrous $Ba(ClO_4)_2$ as effluent from the two furnaces was used in the determination of the amount of hydrogen formed.[1] Then, after the experiment, hydrogen was introduced into the first furnace to reduce the copper oxide which was formed by the reaction between the oxygen and the copper turnings. The amount of oxygen generation was then determined by the sum of the water collected after the first furnace (including the water used in determining the amount of hydrogen formed).

Results

The experimental results obtained by ECM of mild steel in NaCl, $NaClO_4$, and $NaNO_3$ are summarized in Tables I, II, and III, respectively. Figure 1 shows the tube end finish obtained with 4.5M $NaNO_3$ at 47 A/cm^2.

The amount of iron removed was determined by the weight loss of the mild steel tube, which was used as the anode, assuming 100% iron in 1020 mild steel, and the current efficiency for iron removal was calculated by the assumption that iron was dissolved as ferrous ion at the anode. The apparent current densities were based on the cross-sectional area (0.159 cm^2) of the tube wall.

In the $NaNO_3$ system, little or no hydrogen was collected. However, significant amounts of ammonia, hydroxylamine, and nitrite were found in the $NaNO_3$ solutions after ECM. At present, the concentration of these reaction products cannot be determined accurately due to the complicated interactions among the various species present. Hence, no quantitative result is given in this report concerning the cathodic reaction species formed in $NaNO_3$.

Discussion

ECM in NaCl Electrolytes

The results in Table I show that during ECM in NaCl solutions the current is mainly consumed in iron dissolution. Further, the current efficiency for iron removal is not affected greatly by the applied current density or the electrolyte concentration. These results certainly indicate that the anodic process in NaCl is much simpler than in oxidizing electrolytes such as $NaClO_3$ (1) for example. Because the protective oxide film is not present in NaCl solutions during ECM (2), the current is not consumed in oxygen generation at relatively low current densities, and good dimensional control and bright surface finish are not able to be

* Electrochemical Society Active Member.

Key words: electrochemical machining (ECM), NaCl, $NaClO_4$, $NaNO_3$, current efficiency, oxide films.

[1] Actual results showed that the second furnace was not necessary because all hydrogen was removed by reacting with oxygen in the first furnace.

8. K. J. Vetter, "Electrochemical Kinetics," Academic Press, New York (1967).
9. D. T. Chin, *This Journal*, **118**, 174 (1971).
10. J. P. Hoare, K. W. Mao, and A. J. Wallace, Jr., *Corrosion*, **27**, 211 (1971).
11. T. P. Hoar, in "Modern Aspects of Electrochemistry," J. O'M. Bockris, Editor, Vol. II, p. 262, Academic Press, New York (1959).
12. T. P. Hoar, D. C. Mears, and G. P. Rothwell, *Corrosion Sci.*, **5**, 279 (1965).
13. D. Landolt, R. H. Muller, and C. W. Tobias, *This Journal*, **116**, 1384 (1969).
14. D. A. Vermilyea, in "Advances in Electrochemistry and Electrochemical Engineering," P. Delahay and C. W. Tobias, Editors, Vol. 3, p. 211, Interscience Publishers, New York (1963).
15. T. P. Hoar, *Corrosion Sci.*, **7**, 341 (1967).
16. M. Pourbaix, "Thermodynamics of Dilute Aqueous Solutions," Arnode, London (1949).
17. M. A. LaBoda, Private communication.
18. M. A. LaBoda and J. P. Hoare, in "Fundamentals of Electrochemical Machining," C. L. Faust, Editor, p. 227, The Electrochemical Society Softbound Symposium Series, New York (1971).
19. T. P. Hoar, *Trans. Faraday Soc.*, **45**, 683 (1949).

ECM Study in a Closed-Cell System

II. NaCl, $NaClO_4$, and $NaNO_3$

Kao-Wen Mao*

Electrochemistry Department, Research Laboratories, General Motors Corporation, Warren, Michigan 48090

ABSTRACT

Electrochemical machining (ECM) of mild steel in NaCl, $NaClO_4$, and $NaNO_3$ solutions was studied in a closed-cell system. The anodic processes are found to be different in the various solutions. In NaCl, the anodic reaction is essentially iron dissolution. In $NaNO_3$, however, most of the current is expended for oxygen generation due to the presence of an electronically conductive oxide film. A small amount of oxygen (less than approximately 10% of the current) is observed in the $NaClO_4$ system. The cathodic reaction in both NaCl and $NaClO_4$ solutions is hydrogen evolution. In the case of $NaNO_3$, little or no hydrogen is observed—the current is mainly consumed in reducing NO_3^- ions.

In previous work, the electrochemical machining (ECM) of mild steel in $NaClO_3$ has been studied in a closed-cell system (1). From the results of that work, it is believed that more general knowledge concerning ECM electrode mechanisms can be obtained by extending the study to other electrolyte systems with different oxidizing powers. Hence, NaCl, $NaClO_4$, and $NaNO_3$ were selected for this work. It was expected that the results would provide a better understanding of the effect of the electrolyte on the ECM process.

Experimental Procedure

The closed-cell system, experimental procedures and conditions, and sampling techniques are identical to those described in the previous paper (1). Reagent grade chemicals were used for all experiments. Chemical analyses were carried out by the Chemistry Department of General Motors Research.

The methods of collecting hydrogen and oxygen for the NaCl and $NaClO_4$ systems are the same as those used for $NaClO_3$ (1). Minor changes were made in the case of $NaNO_3$ since little or no hydrogen was formed during ECM in $NaNO_3$.

The experiments using $NaNO_3$ were conducted in a nitrogen atmosphere only in order to concentrate on the study of oxygen generation. However, the procedure of collecting any hydrogen present was still carried out for each run. Thus, the gas, after leaving the ECM cell unit, was first bubbled through a 20% sulfuric acid solution for removing any ammonia as well as water vapor from the gas stream. Then the gas was further dried by passing it through anhydrous $CaSO_4$ and anhydrous $Ba(ClO_4)_2$ before entering two serially connected Sargent-Welch gas purifying furnaces. The Vycor glass tubes used in these furnaces were filled with pure copper and copper oxide (CuO) turnings, respectively. Any water collected by anhydrous $Ba(ClO_4)_2$ as effluent from the two furnaces was used in the determination of the amount of hydrogen formed.[1] Then, after the experiment, hydrogen was introduced into the first furnace to reduce the copper oxide which was formed by the reaction between the oxygen and the copper turnings. The amount of oxygen generation was then determined by the sum of the water collected after the first furnace (including the water used in determining the amount of hydrogen formed).

Results

The experimental results obtained by ECM of mild steel in NaCl, $NaClO_4$, and $NaNO_3$ are summarized in Tables I, II, and III, respectively. Figure 1 shows the tube end finish obtained with 4.5M $NaNO_3$ at 47 A/cm^2.

The amount of iron removed was determined by the weight loss of the mild steel tube, which was used as the anode, assuming 100% iron in 1020 mild steel, and the current efficiency for iron removal was calculated by the assumption that iron was dissolved as ferrous ion at the anode. The apparent current densities were based on the cross-sectional area (0.159 cm^2) of the tube wall.

In the $NaNO_3$ system, little or no hydrogen was collected. However, significant amounts of ammonia, hydroxylamine, and nitrite were found in the $NaNO_3$ solutions after ECM. At present, the concentration of these reaction products cannot be determined accurately due to the complicated interactions among the various species present. Hence, no quantitative result is given in this report concerning the cathodic reaction species formed in $NaNO_3$.

Discussion

ECM in NaCl Electrolytes

The results in Table I show that during ECM in NaCl solutions the current is mainly consumed in iron dissolution. Further, the current efficiency for iron removal is not affected greatly by the applied current density or the electrolyte concentration. These results certainly indicate that the anodic process in NaCl is much simpler than in oxidizing electrolytes such as $NaClO_3$ (1) for example. Because the protective oxide film is not present in NaCl solutions during ECM (2), the current is not consumed in oxygen generation at relatively low current densities, and good dimensional control and bright surface finish are not able to be

* Electrochemical Society Active Member.

Key words: electrochemical machining (ECM), NaCl, $NaClO_4$, $NaNO_3$, current efficiency, oxide films.

[1] Actual results showed that the second furnace was not necessary because all hydrogen was removed by reacting with oxygen in the first furnace.

Table I. Results of studying ECM in NaCl electrolyte (brass cathode)

Run	Cell atmosphere	NaCl concentration (M)	Apparent current density (A/cm²)	Coulombs passed	Current efficiency for H_2 generation (%)	Iron removal: Amount (mole)	Iron removal: Current efficiency (%)	pH change: From	pH change: To
CL1*	Air	4.5	47	7000	100.8	0.03425	94.4	5.6	9.8
CL2*	Air	4.5	37	7000	100.6	0.03464	95.5	—	—
CL3*	Air	4.5	26	7000	101.2	0.03590	99.0	5.6	9.7
CL4**	Nitrogen	4.5	62	7000	98.3	0.03405	93.9	6.1	10.0
CL5**	Nitrogen	4.5	47	7000	101.2	0.03444	95.0	6.2	10.0
CL6**	Nitrogen	4.5	26	7000	100.1	0.03556	98.0	5.7	10.0
CL7**	Nitrogen	2.0	62	7000	98.7	0.03518	97.0	6.7	10.0
CL8**	Nitrogen	2.0	47	7000	100.5	0.03569	98.4	6.0	10.0
				Average:	100.2 ± 1.0†				

* No chlorine was observed during ECM.
** No oxygen or chlorine was observed during ECM.
† Standard deviation.

Table II. Results of studying ECM in $NaClO_4$ electrolyte (brass cathode)

Run*	Cell atmosphere	$NaClO_4$ concentration (M)	Apparent current density (A/cm²)	Coulombs passed	Current efficiency for H_2 generation (%)	Current efficiency for O_2 generation (%)	Iron removal: Amount (mole)	Iron removal: Current efficiency (%)	Total current efficiency for O_2 and Fe^{++} (%)	NaCl formation (mole)	Fe/NaCl**	pH change: From	pH change: To
PC1	Air	4.5	47	7000	99.1	—	0.03232	89.1	—	0.00132	24.5	5.7	9.9
PC2	Air	4.5	26	7000	100.4	—	0.03288	90.7	—	0.00110	29.9	5.9	9.6
PC3	Nitrogen	4.5	47	7000	99.9	5.8	0.03270	90.2	96.0	0.00214	15.1	5.4	8.4
PC4	Nitrogen	4.5	26	7000	100.4	3.8	0.03319	91.5	95.3	0.00200	16.6	5.3	8.4
PC5	Nitrogen	2.0	47	7000	100.5	8.0	0.03162	87.2	95.2	0.00141	22.6	5.6	9.2
PC6	Nitrogen	2.0	26	7000	100.6	4.9	0.03317	91.5	96.4	0.00143	23.2	5.9	9.3
				Average:	100.2 ± 0.6†								

* No chlorine was observed during ECM.
** Molar ratio of Fe removed to NaCl formed.
† Standard deviation.

Table III. Results of studying ECM in $NaNO_3$ electrolyte and nitrogen atmosphere

Run	$NaNO_3$ concentration (M)	Cathode	Apparent current density (A/cm²)	Coulombs passed	Current efficiency for H_2 generation (%)	Current efficiency for O_2 generation (%)	Iron removal: Amount (mole)	Iron removal: Current efficiency (%)	Total current efficiency for O_2 and Fe^{++} (%)	pH change: From	pH change: To
NA1*	4.5	Pt	47	7000	1.1	54.7	0.01205	33.2	87.9	5.3	11.4
NA2**	4.5	Brass	47	7000	0	55.9	0.01198	33.0	88.9	6.3	11.3
NA3**	4.5	Brass	26	7000	0	50.6	0.01334	36.8	87.4	6.2	11.2
NA4**	4.5	Brass	12	7000	0	96.4	0.00070	1.9	98.3	5.7	11.3
NA5*	2.0	Pt	47	7000	11.6	83.7	0.00424	11.7	95.4	6.0	11.4
NA6**	2.0	Brass	47	7000	0	84.5	0.00418	11.5	96.0	6.1	11.4
NA7**	2.0	Brass	26	7000	0	96.9	0.00097	2.7	99.6	6.1	11.5

* Ammonia, nitrite, and relatively small amount of hydroxylamine were observed after ECM.
** Ammonia, hydroxylamine, and nitrite were observed after ECM.

obtained [see Fig. 3 of Ref. (1)]. In order to have proper dimensional control with NaCl, ECM has to be conducted in a dilute solution at quite a low current density (4).

The slight decrease in the current efficiency for iron removal with the increase in current density (Table I) may result from the generation of oxygen due to the increase of polarization of the metal dissolution process. In this study oxygen was not observed, but it might have been consumed in oxidizing some of the ferrous product.

Although the current efficiency for iron removal in 2M NaCl is slightly higher than that in 4.5M NaCl,[2] the results certainly indicate that the current efficiency is not seriously affected by the concentration of chloride ion.

At the cathode, hydrogen evolution is likely to be the only reaction taking place during ECM since the average current efficiency for hydrogen generation is so close to 100%.

[2] This may be due to the effect of polarization caused by the adsorption of anions (5).

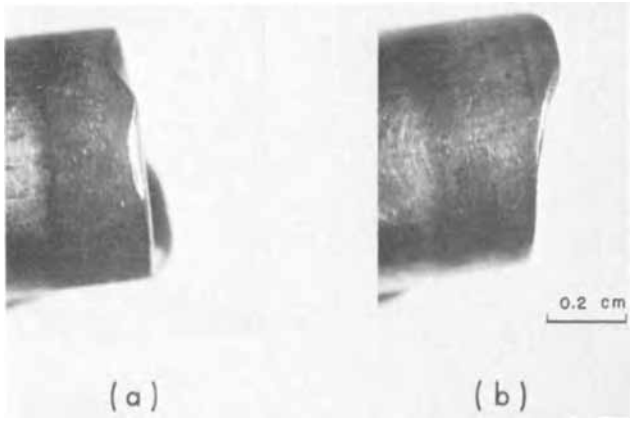

Fig. 1. The tube end finish obtained with 4.5M $NaNO_3$ at 47 A/cm². (a) and (b) are opposite sides of the same tube end.

The final pH of 10 of the NaCl solutions indicates that the solutions are saturated with $Fe(OH)_2$ after ECM. The color of the sludge was greenish-black. The wet sludge from a cell operated in an air atmosphere was found to be partly magnetic, while the sludge obtained under a nitrogen atmosphere appeared to be nonmagnetic. Apparently, in the former system a significant amount of Fe_3O_4 was formed by the reaction between the ferrous hydroxide and dissolved oxygen from the air.

ECM in $NaClO_4$ Electrolytes

Since the average current efficiencies for hydrogen generation in $NaClO_4$ and NaCl solutions are the same (see Tables I and II), it is likely that hydrogen evolution is also the only cathodic reaction for ECM in $NaClO_4$.

According to the results in Table II, some ClO_4^- ions are reduced to chloride, but the amount of chloride formed is significantly lower than that in $NaClO_3$ (1). The chloride formation is probably due to the reaction between ferrous hydroxide and perchlorate. However, since the color of the sludge was always found to be greenish-black and, furthermore, since the final pH of the electrolytes remained in the range for a saturated solution of $Fe(OH)_2$, it is not likely that ferric hydroxide is formed. Because the wet sludge for both air and nitrogen atmospheres was found to be magnetic, it is believed that Fe_3O_4 is the product of the reaction.

From the above discussion, $NaClO_4$ apparently is a more stable species than $NaClO_3$. Because the perchlorate ion is relatively stable and also possesses certain film-rupturing powers (6), one would expect that the oxide film in $NaClO_4$ should be weaker and less uniform than that in $NaClO_3$. Indeed, this was shown by Hoare, Mao and Wallace (3). They found that in $NaClO_4$ the oxide film is almost completely removed at the beginning of the transpassive state. Hence, a bright, polished surface is not observed in the cutting-region, and, furthermore, the surface of the film-protected area is pitted due to the nonuniformity of the films. However, because of the sharp transition from the passive to the transpassive state, the dimensional control obtained with $NaClO_4$ is found to be similar to that observed in $NaClO_3$.

In Table II, it is also seen that a small amount of oxygen is produced during ECM in $NaClO_4$. This may indicate that some residual oxide films are still present in the transpassive state. Perhaps because of these residual films the surface finish with $NaClO_4$ is significantly different from that with NaCl [see Fig. 4 of Ref. (3)]. The presence of such films apparently is not affected by the potential and the $NaClO_4$ concentration since the current efficiency for iron removal is almost constant (about 90%) in the range used in this study.

That the total anodic current efficiency for Fe^{++} and O_2 formations is lower than 100% may indicate that some oxygen is used in oxidizing the ferrous product.

ECM in $NaNO_3$ Electrolytes

In Table III it is seen that hydrogen is not formed at a brass cathode during ECM in $NaNO_3$. The small amount of hydrogen formed at platinum in the same electrolyte is attributed to the relatively low hydrogen overvoltage on platinum. The hydrogen evolution at a copper cathode in KNO_3 has been studied by Landolt and his co-workers (7) at higher current densities (in the range of 50 to 150 A/cm²),[3] and the amount of hydrogen evolved was found to be much less than in KCl. Since, in this work, ammonia, hydroxylamine, and nitrite were detected in $NaNO_3$ electrolytes after ECM, nitrate is apparently reduced at the cathode. The current efficiency for the reduction of nitrate is likely to be affected not only by the cathode material but by the potential as well. (The electrolytic reduction of nitrate at various metals has been investigated by Tafel and others (8) at conventional low current densities.) Because of the formation of ammonia, the final pH of the electrolyte is significantly higher than it is in other systems.

In comparison with $NaClO_3$ (1), the current efficiency for iron removal in $NaNO_3$ is significantly low. This may indicate that the oxide film in $NaNO_3$ is less porous than in $NaClO_3$. During ECM in $NaNO_3$ most of the current is actually consumed in oxygen generation. The current efficiency for oxygen generation is nearly 100% at current densities below 12 A/cm². According to Hoare's study (2), only a relatively small amount of oxide film is removed at the beginning of the transpassive state (at 1.5V *vs.* NHE and 10 mA/cm²). Since the film is not removed to any considerable extent by the oxygen evolution, it is likely that the oxide film in $NaNO_3$ is electronically conductive—thus, oxygen can be formed at the film/solution interface. The electronic resistance of the iron oxide film formed in HNO_3 has been studied by Vetter (9) and was found to be very low.

Figure 1 shows that the tube end is not uniformly machined with 4.5M $NaNO_3$ at 47 A/cm². This nonuniform cutting is believed to be caused by the massive oxygen generation which could lead to a nonuniform coverage of the anode surface with the oxygen gas if the electrolyte flow is not sufficiently fast and uniform. More uniform cutting was observed as current decreased. Because of the low metal removal rate in $NaNO_3$ solutions, it is not possible to give any meaningful comparison about the dimensional control between $NaNO_3$ and $NaClO_3$. The surface finishes obtained with $NaNO_3$ generally are less bright than those machined in $NaClO_3$.

The results in Table III show that the current efficiency for iron removal in $NaNO_3$ increases with the electrolyte concentration and with the current density[4] similar to the results found for the $NaClO_3$ system. Probably these phenomena also can be explained by the arguments given in the previous report (1).

The total anodic current efficiency for Fe^{++} and O_2 formations given in Table III is lower than 100% (especially at high current densities). This may indicate that either some iron is dissolved as ferric ion or that some oxygen is consumed in oxidizing the ferrous product. During ECM, a red-brown sludge of ferric hydroxide was always observed and the wet sludge was nonmagnetic.[5]

Conclusions

From the results of this work [including the previous study of ECM in $NaClO_3$ (1)], it is apparent that the ECM anodic process varies with the electrolyte. In oxidizing electrolytes, the ECM performance is closely

[3] It should be noted that in this work the apparent cathodic current densities are actually lower than the values given in Tables I, II, or III due to the larger cathode area (0.713 cm² compared with 0.159 cm² for anode).

[4] The slight decrease of the efficiency in 4.5M $NaNO_3$ solutions when current density varies from 26 to 47 A/cm² presumably is caused by the nonuniform cutting due to a higher rate of oxygen evolution.

[5] It should be noted that nitrate also can oxidize ferrous hydroxide but the product is Fe_3O_4 (10).

related to the structure of the oxide film formed on the anode. For good ECM performance, the oxide film probably has to be compact, uniform, porous, and preferably thin at the cutting surface; *i.e.*, the film in $NaClO_3$ solutions. Oxygen formation is generally observed when the oxide film is present. In $NaNO_3$ most of the current is consumed in oxygen generation instead of iron removal. This seems to be caused by the presence of an electronically conductive film. The anodic reaction in NaCl is mainly iron dissolution due to the absence of the oxide film.

The cathodic reaction in NaCl, $NaClO_4$ as well as $NaClO_3$ (1) is essentially hydrogen evolution. In $NaNO_3$, however, nitrate is reduced to ammonia, hydroxylamine, and nitrite at the cathode, and little or no hydrogen is formed.

Acknowledgment

The author wishes to thank Dr. J. P. Hoare of the Electrochemistry Department, General Motors Research Laboratories, for helpful discussions and is also grateful to R. B. Loranger, H. E. Vergosen, Dr. J. L. Johnson, and the other members of the Chemistry Department who carried out the chemical analyses.

Manuscript submitted April 5, 1971; revised manuscript received *ca.* June 28, 1971.

Any discussion of this paper will appear in a Discussion Section to be published in the June 1972 JOURNAL.

REFERENCES

1. K. W. Mao, *This Journal*, **118**, 1870 (1971).
2. J. P. Hoare, *ibid.*, **117**, 142 (1970).
3. J. P. Hoare, K. W. Mao, and A. J. Wallace, Jr., *Corrosion*, **27**, 211 (1971).
4. A. E. Debarr and D. A. Oliver, "Electrochemical Machining," American Elsevier, New York (1968).
5. N. D. Tomashov and L. P. Vershinina, *Electrochim. Acta*, **15**, 501 (1970).
6. T. P. Hoar, *Trans. Faraday Soc.*, **45**, 683 (1949).
7. D. Landolt, R. Acosta, R. H. Muller, and C. W. Tobias, *This Journal*, **117**, 839 (1970).
8. J. W. Mellor, "A Comprehensive Treatise on Inorganic and Theoretical Chemistry," Vol. VIII, Longmans, Green and Co., New York (1928); S. Glasstone, "An Introduction to Electrochemistry," D. Van Nostrand, Princeton, N. J. (1962); W. M. Latimer, "Oxidation Potentials," Prentice-Hall, New York (1952).
9. K. J. Vetter, "Electrochemical Kinetics," Academic Press, New York (1967).
10. S. H. Carsley, *J. Phys. Chem.*, **34**, 178 (1930).

JOURNAL OF THE ELECTROCHEMICAL SOCIETY

ELECTROCHEMICAL SCIENCE

DECEMBER 1971

The Effect of Liquid Configuration in Porous Gas Electrodes

T. Katan* and E. A. Grens II*,[1]

Lockheed Palo Alto Research Laboratory, Palo Alto, California 94304

ABSTRACT

The influence of differential pressure on electrode activity was measured for oxygen cathodes made up of beds of uniform silver spheres (156 μm diameter). The extent and nature of this dependence could be explained through use of the concept of pendular and funicular liquid configuration in the pore space of the electrode.

The performance of a porous gas electrode is dependent not only on its pore structure but also on the configuration of the gas-liquid interfaces within the pores. Thus the differential pressure established across an electrode has been found by many investigations to be an important influence (1-7). Explanations presented for differential pressure effects have been based almost entirely on the distribution between gas and liquid filled pores that is found in electrodes with wide ranges of pore size distribution (2, 8, 9). Such theories cannot explain the behavior of electrodes whose pores are all much the same size, although very significant differential pressure effects are also observed for these electrodes.

In gas electrodes with a narrow pore size range (single porosity electrode) the electrochemical reaction must occur primarily under a thin film of electrolyte on the pore walls, the so-called supermeniscus film (10-13). In addition ionic current transport must proceed along electrolyte paths on these walls. For conditions where little or no electrolyte is present in the gas electrode except in the form of thin films it has been found that the performance is scarcely affected by changes in differential pressure and that predictions of overpotential behavior based on a simple film mechanism are quite adequate (6, 14). However, when considerable additional electrolyte is present in the pores, performance deviates considerably from such predictions, and the influence of liquid configuration assumes great importance.

Several investigators have reported strong dependence in the performance of single porosity gas electrodes on differential pressure. Some of the electrodes used by Burshtein *et al.* (their electrode numbers 13-15) in their early studies of structural effects in porous gas electrodes had essentially a uniform pore size (2). The current density produced by these electrodes at constant overpotential showed a distinct maximum at differential pressures on the order of 100 mm Hg for pores with effective radii in the range of 5-10 μm. Ksenzhek later reported additional observations of such behavior for electrodes with apparently narrow pore size distributions (4).

In 1968 Lindstrom made a revealing study of single porosity gas electrodes in which he not only observed maxima in electrochemical activity at particular differential pressures but also correlated this effect with measured changes in the resistance of the electrolyte "film network" in the pores of the electrode (5). He further related this behavior to independent measurements of effective[2] electrode parameters including mean pore diameter, film thickness, and pore and film tortuosity factors. Lindstrom also noted, and qualitatively explained, marked hysteresis effects in the response of electrode activity, liquid penetration, and film network resistance to changes in differential pressure. The work elucidated many aspects of the influence of differential pressure on electrode activity for single porosity electrodes, in terms of measured response of "film network" resistance to differential pressure changes.

Lindholm and Edwardsson also observed drastic changes in "film" conductivity in the region of differential pressure coinciding approximately to maximum electrode activity in a porous oxygen electrode composed of silver electrocatalyst particles (16). The mechanism by which changes in differential pressure across a porous body affect the conductivity of liquid electrolyte paths in the pore space is thus of considerable interest; it can serve as a basis for the understanding of many features in the behavior of single porosity gas electrodes. Earlier work on other porous systems can provide valuable insight into this mechanism.

Over forty years ago Haines observed a variation of the conductivity in damp soils with moisture content very similar to that found in porous electrodes with differential pressure (17). The soils he studied were porous materials quite similar to many electrodes with a single scale of porosity. Therefore the models that he used relating liquid content, liquid configuration in the pores, conductivity, and gas-liquid differential pressure can be considered for the interpretation of gas electrode behavior.

Haines, and other investigators in his field, based their theories upon an "ideal" soil composed of a regular packing of uniform spherical particles (17-21). They discussed two essentially different states of liquid configuration in these porous beds: a "pendular" state at low moisture contents in which the liquid exists as isolated annular rings, or "disks," around the contact points between spheres; and a "funicular" state at higher moisture contents in which these disks have reached such size that they contact each other and form continuous paths through the bed. Haines an-

* Electrochemical Society Active Member.
[1] Department of Chemical Engineering, University of California, Berkeley, California 95720.
Key words: porous gas electrodes, differential pressure, oxygen cathodes, funicular, pendular.

[2] Determined from exterior measurements.

alyzed the relation between gas-liquid differential pressure and moisture content of the bed, at least in the pendular state, and calculated pressures at which liquid content should be sufficient for transition to the funicular state in regular beds of uniform spheres (21). More recently Harris and Morrow have shown that the pendular moisture contents of random packings of uniform spheres are close to those expected in regular packings at the same gas-liquid differential pressures (22).

These concepts are potentially very useful in description of the functioning of all single porosity gas electrodes. However, their validity in this use can only be confirmed on the basis of situations where they yield quantitative predictions that can be compared with experimental observations. The logical choice for such comparison is the porous gas electrode composed of a bed of uniform spherical particles. We have studied the performance of well-characterized oxygen cathodes of this type over ranges of differential pressure including the expected pendular-funicular state transition.

Experimental

In these studies oxygen was reduced at porous silver cathodes in 13.5M KOH at 95.0°C. The arrangement of the test electrode and the reference cell in the electrolyte resembles that employed in a previous investigation (14). It is shown in Fig. 1 and is described in more detail elsewhere (15). The test electrode, 1.3 cm in diameter, consists of a bed of silver spheres of uniform size which rests on a relatively thin silver mesh (4.2 μm thick) sealed across the end of a Pyrex tube. This silver mesh at the lower side of the bed is in contact with the electrolyte while the upper surface of the bed is exposed to the gas phase. Electrical contact to the spheres is established through the mesh. The bed of spheres has uniform thickness and acts as the cathode for electrochemical reduction of oxygen. A differential pressure of oxygen is applied across the electrode at preselected values to change the extent of electrolyte infiltration into the bed.

Three sizes of silver spheres were used, having average diameters of 156, 54, and 14 μm. Before use, these spheres were thoroughly washed in concentrated aqueous ammonia to remove traces of silver oxides. The spheres were then washed with water and with methanol before drying in air at 110°C for 1 hr. This treatment assured reproducible electrode kinetics and minimized electrical resistance at contacts between spheres. Specific resistivity was always less than 0.74 ohm-cm in electrodes composed of loosely packed sphere beds that were treated in this manner.

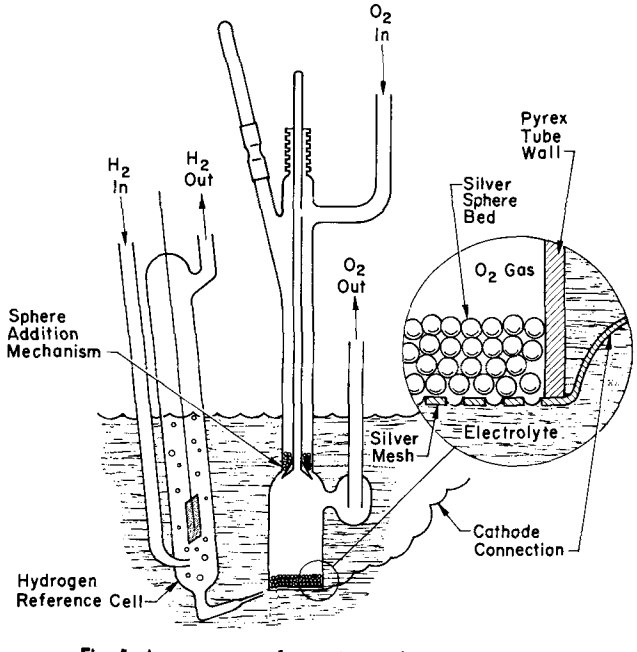

Fig. 1. Arrangement of experimental oxygen cathode

The test electrodes were built up to their final thickness by repeated addition of spheres. The spheres were brought to the temperature of the electrode and then were added to the top of the bed. Thickness of the electrodes was determined from the known density of the sphere packing, the cross sectional area of the bed, and the mass of the spheres added. In a few cases direct observations could be made of the thickness with a microscope; these showed that the actual thickness was within 10% of that calculated and that thickness was quite uniform across the electrode, deviating by less than ±2% from the average value.

Studies of the test electrodes were conducted under galvanostatic conditions. These electrodes were connected, by means of the silver mesh, as cathodes, and current was supplied from a constant current source, an Electronics Measurement, Inc., Model C612 power supply. The circuit was completed through a counter-electrode of smooth platinum foil placed below the test electrode. Electrode current was measured by a Greibach Model 500 ammeter placed in series with the cathode. Electrode potential was determined with respect to a hydrogen (on platinized platinum) electrode operating in cell electrolyte. This reference electrode was located in a separate cell with a Luggin capillary tube leading from this reference cell to a point about 1.5 mm from the edge of the silver mesh of the test electrode. Potential of the test electrode *vs.* this reference cell was recorded with a Sargent MR potentiometer. All electrode potentials in this paper are referred to this hydrogen reference electrode (HRE).

Electrodes were formed under a differential oxygen pressure of 25 cm of water by successive additions of spheres. After each incremental addition of spheres, the current-potential relationships were determined over the cathodic range from the open-circuit potential of about 1035 mV down to 600 mV (*vs.* HRE). The system was allowed to reach steady state at each of the several current values before potential measurements were recorded. When an electrode thickness of 1700 μm had been obtained, the differential oxygen pressure was lowered by increments of approximately 2.5 cm of water to 5 cm of water and then similarly raised to about 80 cm of water; at none of these differential pressures did gas bubbling through the electrode occur. After each differential pressure change, a current-potential curve was again determined. The series of current-potential curves obtained in this manner constituted the basic data used in this study.

Results and Discussion

For this investigation the effect of differential pressure across the electrode on the activity of the electrode has been of primary concern. Thus, it was desirable that other effects on electrode performance be minimized so that those attributable to differential pressure variation could be studied. The effect of temperature was eliminated by careful thermostating and that of oxygen flow past the electrode by maintaining a constant flow of 15 $cm^3\ min^{-1}$. However, no effect caused by changes in oxygen flow rate was observed when the rate was varied from 2 to 50 $cm^3\ min^{-1}$. Electrode thickness was also held constant, and moreover was established at a large enough value so that any further increases in thickness had very little effect on electrode performance. The observable effects of differential pressure variations are enhanced by use of an electrode thickness somewhat greater than the maximum for which the whole electrode can effectively contribute to the electrochemical reaction.

The attainment of sufficient electrode thickness was assessed by comparisons of electrode performances after incremental increases in the thickness of an electrode with spheres having a 156 μm diameter, at a differential pressure of 25 cm of water. Typically, it was found that beyond a thickness of 1000 μm relatively little or no change resulted for further increases up to 4000 μm, as indicated in Fig. 2. This ob-

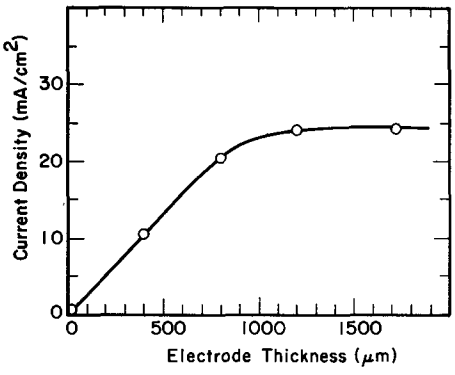

Fig. 2. Effect of electrode thickness on activity of oxygen cathode (156 μm silver spheres). Potential 500 mV (vs. HRE). Differential pressure 25 cm of water.

servation, similar to results reported earlier (14), indicated that the selected constant electrode thickness of 1700 μm for this study was sufficiently large to allow meaningful observations of the effects of differential pressure variation.

Under the conditions described above it was possible to isolate the effects of differential pressure variation on electrode performance. The effects were investigated for an electrode composed of 156 μm silver spheres in a bed 1700 μm thick. The activity of this electrode, expressed as current density at several fixed potentials *vs.* the HRE, is shown as a function of differential pressure in Fig. 3 The upper curves (Fig. 3a) represent the performance at decreasing differential pressure while the lower curves (Fig. 3b) are for increasing differential pressure. A pronounced hysteresis effect is present, as is shown more clearly for the case of 500 mV in Fig. 4. This curve would be retraced, except for some change in the decreasing pressure branch above 15 cm of water, on repeated cycling of differential pressure. For either increasing or decreasing differential pressure electrode activity

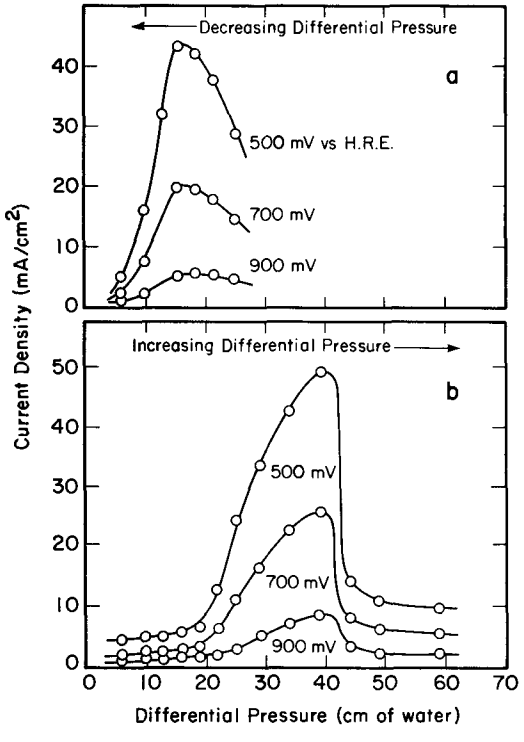

Fig. 3. Effect of differential pressure on activity of oxygen cathode (156 μm silver spheres). Electrode thickness 1700 μm. (a) Behavior for decreasing differential pressure. (b) Behavior for increasing differential pressure.

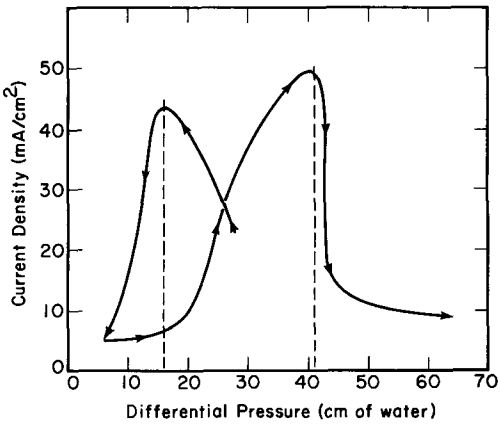

Fig. 4. Hysteresis in effect of differential pressure on activity of oxygen cathode (156 μm silver spheres). Potential 500 mV (vs. HRE). Electrode thickness 1700 μm.

attains a pronounced maximum at a certain characteristic differential pressure that is independent of electrode potential. No matter which way the pressure is being changed, the drop in activity after passing the maximum is steeper than the rise in activity on approach to the maximum. This type of behavior has been previously reported for porous hydrogen electrodes (2), and, more recently, for porous oxygen electrodes (5, 6, 16).

The nature of the response of electrode activity to changes in differential pressure clearly indicates that it is associated with the penetration of liquid into pores and its expulsion from them. Characteristically, as differential pressure decreases liquid enters the pores, and as differential pressure increases it is displaced. However, not all of the infiltrated liquid can be expelled; there is a certain amount retained because of the configuration of the pore space. A meaningful description of the mechanism of this liquid infiltration and expulsion is not possible with the complex porous media usually employed as fuel cell electrodes. However considerable simplification in configuration results with these sphere-bed electrodes. An analysis of the liquid penetration cycle for the relatively simple geometry represented by sphere packings can be made on the basis of the concept of pendular and funicular liquid configurations cited earlier.

When an electrode is initially formed at a relatively high differential pressure, the only liquid that can be present in the bed is in thin supermeniscus films, which have been previously observed and described (10-13), and in the isolated bodies or disks of liquid that collect at the sphere-to-sphere contacts as shown in Fig. 5a. This is the pendular state described by Haines. For this state electrochemical reaction beneath the film on the metal is limited to regions near the bulk electrolyte side of the electrode, because ionic transport must occur through the thin film, which presents a very high resistance.

As differential pressure is decreased more liquid enters the bed by capillary action. Then the liquid disks, which were initially isolated from each other, are enlarged by the entering liquid and eventually come into contact with each other so that paths of liquid much thicker than the previously existing film paths are formed throughout the sphere bed. This is the funicular state. It is characterized by an interconnected network of liquid "filaments" formed by coalescence of the liquid disks at sphere-to-sphere contacts. When liquid disks first come into contact considerable areas of thin film on the spheres still remain. The system of liquid filaments provides low resistance paths for ionic current to these areas of supermeniscus film still covering a large part of each sphere Since these films are in contact with a connected gas phase this is a situation where large regions within the

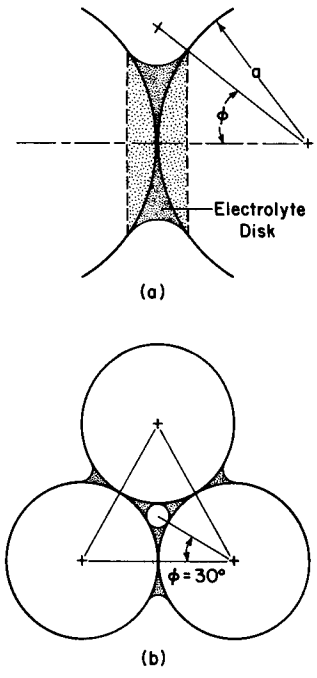

Fig. 5. (a) Configuration of electrolyte disk at the contact of two spheres. (b) Triad sphere arrangement with electrolyte disks at the condition of pendular to funicular transition.

porous electrode are subject to conditions favorable to the electrochemical reaction. Decreasing differential pressure thus leads to increasing electrode activity as the network of liquid filaments is formed. This can be observed down to 16 cm of water in Fig. 3a.

With further reduction in differential pressure more liquid enters the electrode and the areas of sphere surface that are covered only with thin film become reduced in size. Diffusion of oxygen gas to reaction sites on the sphere surfaces must then be through increasingly thicker electrolyte layers, and this process eventually becomes rate limiting. Performance then decreases as seen for lower differential pressures in Fig. 3a. With still further reductions in differential pressure, the pores of the sphere bed would become completely flooded, supermeniscus film areas would be lost, and, eventually, the continuous network of gas channels in the sphere bed would be disrupted and replaced by bubbles of gas entrapped by liquid. A saturation state would be formed (19, 21). This state would result in a drastic suppression of electrode activity.

When differential pressure is increased from the saturation state a continuous interconnected network of gas channels is again established. Improvement in electrode activity occurs as areas on the spheres become again covered only with films and thus readily accessible to the gas phase Further increases in differential pressure cause more liquid to be expelled from the porous structure until the continuous funicular liquid network is ruptured, whereupon ionic transport through thin film to sites of electrochemical reaction inside and throughout the sphere bed is severely restricted, and performance decreases as shown in Fig. 3b. After rupture of the funicular liquid paths, isolated pendular bodies of liquid remain as enlarged disks of liquid around sphere-to-sphere contacts in varying amounts depending on the differential pressure. It would appear that such pendular liquid may be expelled at sufficiently high differential pressures via bulk liquid transport through the supermeniscus film. Once the funicular paths are severed, however, further increases in pressure do not appreciably affect the thickness or the ionic resistance of the supermeniscus film, and the increasing supermeniscus film area cannot be effectively utilized since gas transport is no longer limiting. Performance then remains relatively unchanged, leveling off as shown in Fig. 3 and 4 for the highest pressures.

This interpretation of electrolyte configuration based on the pendular-funicular models leads to an explanation of the observed effects of differential pressure in electrodes with a single scale of porosity. For too high a differential presure, funicular paths are not formed and ionic transport within the supermeniscus film is limiting. For too low a differential pressure insufficient film area remains and diffusive transport of dissolved gas to the site of electrochemical reaction at the solid surface limits electrode activity. These observations are in agreement with experimental results obtained in this study. It can be concluded that the most favorable liquid configuration for obtaining high electrochemical performance for any electrode similar to the sphere bed electrodes considered here is the funicular state that exists just before a funicular to pendular transition or just after a pendular to funicular transition, that is, at a differential pressure which sustains a funicular state but which is not far removed from that for the pendular state. In this condition the supermeniscus film area, and its boundary with meniscus regions, are at a maximum consistent with the existence of low resistance paths for ionic transport, and a connected gas phase system exists throughout the electrode.

When the nature of the hysteresis effect in electrode activity is examined, it is found that the peak in electrode performance, shown in Fig. 3 and 4, is higher and displaced toward higher pressures for the case of increasing differential pressure. This effect is attributed to the typical differences in liquid holdup that occur for decreasing and increasing differential pressure in these systems (21). The liquid disks at sphere-to-sphere contacts can grow, on decreasing differential pressure, only by liquid transport through the supermeniscus film (or through the gas phase) until filaments are formed. This liquid transport is difficult, and what would be stable or equilibrium liquid configurations may not be obtained in any reasonable time. In effect a metastable liquid configuration, containing less liquid than the stable configuration, is established at any differential pressure, and the pressure for transition to the funicular state is shifted to a lower value. Moreover, the funicular configuration that is achieved may be expected to be deficient in connections to some film areas and thus have a relatively low activity maximum. Once liquid paths in the bed are established at low differential pressures, increasing the differential pressure encounters difficulty in reducing all liquid regions to their equilibrium state. Again a metastable condition exists which now shifts the transition to the pendular state to higher differential pressures. In addition a more extensive network of filaments will exist than did for decreasing pressure, and a higher peak is observed in accord with the preceding discussion. The differential pressure for obtaining maximum performance is thus different for decreasing and increasing differential pressure, being shifted to higher values for increasing pressure, as shown in Fig. 4.

The pendular-funicular interpretation just described yields a quantitative prediction for the differential pressure at which a maximum in activity occurs, as in Fig. 3b, when liquid is being displaced from a sphere bed electrode (increasing differential pressure). In the pendular state, a local pressure difference exists across the gas-liquid surface of the liquid disks at the points of contact of the spheres because of the two radii of curvature which define the surface of the liquid. These disks have a well-defined geometry that is simple enough to allow a determination of the local pressure difference across the gas-liquid interface. The liquid disks are just large enough to touch each other at the pendular to funicular state transition. Then the liquid in all disks is connected to the bulk liquid electrolyte at the electrolyte side of the bed and will be at liquid side pressure. The local pressure difference across the

surface of the liquid disks must then be very nearly equal to the gross pressure difference across the bed at pendular to funicular transition. According to the preceding discussions, this differential pressure should correspond to that which yields a maximum in electrode performance on increasing differential pressures.

From the treatments of Haines and Fisher (19-21) the differential pressure for funicular-pendular transition in a sphere bed from which liquid is being expelled can be found in terms of the surface tension of the liquid and the radius of the spheres. Essentially, it is assumed that liquid films exist on the spheres. The pressure difference across the meniscus of liquid held at the contact between two spheres has an equilibrium value which depends on the angle, ϕ, subtended at the sphere center by the radii to the point of contact between spheres and to the (ideal) contact point of the meniscus with the sphere. An expression for this dependence can be derived from the equation of Laplace and Young and the given geometry (18).

$$P = \frac{\sigma}{a} \frac{(1 + \tan \phi/2)(1 - 2\tan \phi/2)}{2 \tan^2 \phi/2} \qquad [1]$$

Here, σ is the surface tension of the liquid and a is the sphere radius. For a sphere bed containing a large fraction of spheres that are in contact with at least two other spheres that are also in mutual contact, that is, forming a triad of three spheres as shown in Fig. 5b, a pendular to funicular transition takes place when $\phi = 30°$. Then local pressure difference across the meniscus is

$$P = 4.1 \frac{\sigma}{a} \qquad [2]$$

Each sphere has approximately eight nearest neighbors in contact in the randomly packed sphere bed of this study, as estimated from the measured fractional void volume of 0.41 with a correspondence method suggested by Smith (23). For such a packing arrangement most spheres must be involved in several "triad" arrangements, which in turn form a network of touching triads throughout the sphere bed; this network serves as the basis for the paths of filaments of liquid in the funicular state. Thus, the differential pressure for a pendular to funicular or a funicular to pendular transition can be calculated for the bed of 156 μm spheres. This requires a value for the surface tension of the electrolyte, which was determined by comparisons of the bubble pressure for a fritted glass disk in water at 25.0°C and in 13.5M KOH at 95.0°C; the surface tension of the 13.5M KOH at 95.0°C was found to be 90 $\pm$1 dyne cm^{-1}.

For a 156 μm sphere bed, Eq. [2] gives a funicular to pendular differential pressure of 48 cm of water. This can be compared with the differential pressures of 40 to 43 cm of water that were observed for maximum electrode activity on increasing differential pressure in Fig. 3 and 4. The increasing pressure branch is the proper one for comparison because electrolyte transport is not inhibited on this branch until after the transition. In view of the imperfections in the packing model for the sphere bed, this is a good agreement indeed. The result not only serves to support the validity of a theory for electrode performance based on the concept of pendular and funicular configurations, but it also substantiates the interpretations we have offered above for the observed dependence of electrode activity on differential pressure. Furthermore, from Eq. [1] it can be seen that a change of only 5° in the angle ϕ causes a change in the calculated differential pressure for pendular-funicular transition by almost a factor of two. This indicates that the liquid configuration at sphere contacts and the arrangement in "triads" must be very close to what we supposed. This quantitative agreement thus confirms both the existence and nature of the pendular and funicular states and the continuous network of triads of spheres in mutual contact which maintains the latter state. It further confirms that peak electrochemical activity in a porous electrode with pores in a single size range occurs at the pendular-funicular transition of liquid configuration in the pores.

A further verification of this interpretation was obtained from additional experiments conducted with electrodes composed of silver spheres 54 μm in diameter. In these electrodes a thin layer of spheres 14 μm in diameter was first placed on the mesh to allow the attainment of significantly higher gas pressures without bubbling through the electrode. The fine and coarse layers were 400 and 1300 μm thick, respectively. The effect of differential pressure on the performance of this 54 μm sphere bed electrode is shown in Fig. 6. As differential pressure is increased, little improvement in performance occurs until 60 cm of water is attained. Then a sharp improvement is noted, with the performance eventually attaining 125 mA cm^{-2} for 0.5V *vs.* HRE at 90 cm of water. Higher differential pressures could not be examined because of limitations of the apparatus. No peak was observed in the pressure range studied; it clearly lies at a higher differential pressure than 90 cm of water. Equation [2] would indicate that the funicular to pendular transition should be expected at 139 cm of water. These results are very limited in scope but they nevertheless demonstrate the shift of the electrode activity maximum to higher differential pressures for the smaller spheres that would be expected from the interpretation offered here, as well as the improved activity associated with the higher specific surface area of the smaller spheres.

Indirect evidence for the importance of the pendular to funicular transition in fuel cell electrodes can also be obtained by comparison of the work of Lindholm and Edwardsson (16) with that of Haines (17), with respect to the effective conductivity of liquid paths in porous media under partially flooded conditions. Haines studied the relationship of conductivity changes to the transition between the pendular and funicular regimes, while Lindholm and Edwardsson related the conductivity to electrode performance. In both cases examination of the conductivity as a function of differential pressure reveals a near linear decrease in conductivity with increasing differential pressure (or decreasing liquid content) until a fairly pronounced change (decrease) in the slope of the relationship is encountered; Haines ascribes this change in slope to the transition between the funicular and pendular regimes. From Lindholm and Edwardsson's work it

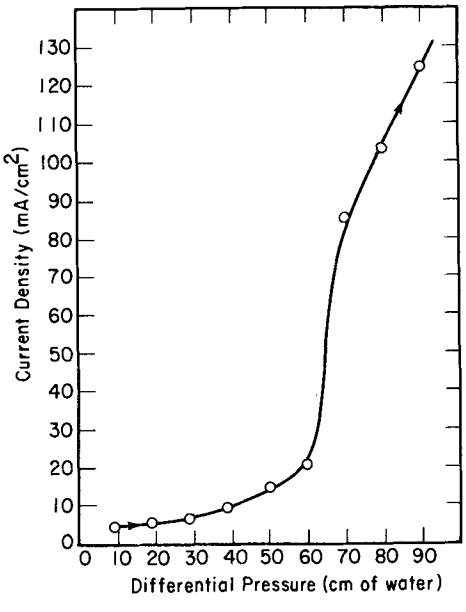

Fig. 6. Effect of increasing differential pressure on activity of oxygen cathode (54 μm silver spheres). Potential 500 mV (*vs.* HRE). Electrode thickness 1700 μm.

can be seen that the same slope change corresponds very nearly to the differential pressure at which maximum electrode activity (current density) is observed.

Local maxima in electrode activity were also seen in the work of Golovkin *et al.* for electrodes composed of spherical particles at differential pressures consistent with the pendular-funicular transition for the sphere sizes involved (7). However these workers found further increases in activity at much higher differential pressures (perhaps because of the activity of a significant "sealing layer" of much finer particles); they offer a theory based on liquid hold-up in systematic distortions of regular packing configurations.

Additional evidence for the pendular and funicular type of liquid configuration may be found in the data reported by Lindstrom (5). Although his electrodes were from particles of irregular shape, at least these particles had a reasonably uniform size. A comparison of Lindstrom's liquid path resistance and electrode activity curves given as functions of differential pressure again shows a maximum in activity closely associated with a change in slope in the resistance (and thus conductivity) relationship. These results also demonstrate a marked hysteresis in both the electrode activity and resistance behavior with increase and subsequent decrease in the differential pressure. These results of Lindstrom not only corroborate the interpretation offered here but also indicate a possibly more general application of the pendular-funicular model to sintered electrode structures of particles of irregular shape.

Conclusions

The present studies have shown that the concept of pendular and funicular liquid configurations in simple porous media can be very useful in explaining the behavior of gas electrodes with a narrow range of pore size. This concept was developed much earlier in the studies of properties of soils, but has not been heretofore applied to electrode systems. The existence of these two states, and the transition between them, accounts for the dependence of electrode activity on differential pressure across the electrode for oxygen cathodes composed of beds of uniform small spheres. Thus this concept can provide an improved understanding of the transport phenomena operative in these electrodes, which can be of value in development of more effective structures.

Acknowledgment

This work has been supported by the National Aeronautics and Space Administration, under Contract No. NAS 3-11833.

Manuscript submitted March 22, 1971; revised manuscript received *ca.* Aug. 9, 1971.

Any discussion of this paper will appear in a Discussion Section to be published in the June 1972 JOURNAL.

REFERENCES

1. R. Burshtein, A. G. Pshenichnikov, and N. S. Shumilova, *Dokl. Akad. Nauk SSSR*, **143**, 1409 (1962).
2. R. Burshtein, V. S. Markin, A. G. Pshenichnikov, Yu. A. Chizmadzhev, and Y. G. Chirkov, *Electrochim. Acta*, **9**, 773 (1964).
3. E. Justi and A. Winsel, "Kalte Verbrennung," F. Steiner, Wiesbaden (1962).
4. O. S. Ksenzhek in, "Fuel Cells," V. S. Bagotskii and Yu. B. Vasil'ev, Editors, Consultants Bureau, New York (1966).
5. O. Lindstrom, *Energy Conversion*, **8**, 33 (1968).
6. I. Lindholm and I. Jonsson, *This Journal*, **116**, 1150 (1969).
7. Yu I. Golovkin, N. P. Vasilitov, E. M. Kuchinskii, and N. A. Fedotov, *Elektrokhimiya*, **5**, 166 (1969).
8. A. G. Pshenichnikov, *Dokl. Akad. Nauk SSSR*, **148**, 1121 (1963).
9. V. S. Markin, Yu. A. Chizmadzhev, and Yu. A. Chirkov, *ibid.*, **150**, 596 (1963).
10. C. Wagner, Unpublished (1957).
11. F. G. Will, *This Journal*, **110**, 145 (1963).
12. E. A. Grens, R. M. Turner, and T. Katan, *Advan. Energy Conversion*, **4**, 109 (1964).
13. D. N. Bennion and C. W. Tobias, *This Journal*, **113**, 589 (1966).
14. T. Katan, S. Szpak, and E. A. Grens, *ibid.*, **112**, 1166 (1965).
15. T. Katan, Final Report (June 1970), NASA Contract No. NAS 3-11833.
16. I. Lindholm and I. Edwardsson, First Quarterly Report (June 1967) and Third Quarterly Report (January 1968), NASA Contract No. NASW-1536.
17. W. B. Haines, *J. Agr. Sci.*, **15**, 529, 536 (1925).
18. R. A. Fisher, *ibid.*, **16**, 492 (1926).
19. W. B. Haines, *ibid.*, **17**, 264 (1927).
20. R. A. Fisher, *ibid.*, **18**, 406 (1928).
21. W. B. Haines, *ibid.*, **20**, 97 (1930).
22. C. C. Harris and N. R. Morrow, *Nature*, **203**, 706 (1964).
23. W. O. Smith, *Physics*, **4**, 425 (1933).

A Secondary, Nonaqueous Solvent Battery

John S. Dunning,* William H. Tiedemann,* Limin Hsueh, and Douglas N. Bennion****

Energy and Kinetics Department, School of Engineering and Applied Science, University of California, Los Angeles, California 90024

ABSTRACT

The feasibility of a room-temperature, nonaqueous organic solvent, electrochemical cell that can deliver 10 mA/cm^2 at 4V has been demonstrated. The cell consists of a lithium negative, a graphite compound positive electrode, and a lithium perchlorate-dimethyl sulfite electrolyte solution. The cell develops an open-circuit potential of approximately 4.5V. Apparently the lithium perchlorate-dimethyl sulfite electrolyte undergoes no or least slow oxidation or reduction within a 4.5V range.

To date, the maximum charge storage has been 90 coulombs/g of graphite. Cycles of 1 hr charge and 1 hr discharge at about 3 mA/cm^2 have been repeated up to 33 times. Failure was apparently due to overcharging and graphite disintegration. On wet stand, from 25 to 50% of the cell capacity is lost over one day.

Dimethyl sulfite, $(CH_3O)_2SO$, has been shown to be a potentially useful solvent for application to batteries (1). While using graphite as a positive electrode in lithium trifluoromethanesulfonate-dimethyl sulfite solutions, a 4.3-4.8V open-circuit potential *vs.* lithium metal was repeatedly observed (2). Brenner (3) has recently reported similar observations and suggests a fluorine-containing compound as the active oxidizing agent. Observations on cells of the type Li/$(CH_3O)_2SO$,

* Electrochemical Society Student Associate Member.
** Electrochemical Society Active Member.
Key words: batteries, nonaqueous solvents, lithium perchlorate, dimethyl sulfite, graphite, lamellar compounds of graphite.

$LiClO_4$/graphite are reported here and observed changes in performance after substituting different salts, solvent, and graphites are described.

Experimental

Materials.—Dimethyl sulfite was purchased from Eastman Kodak Company. It was further purified by agitation with Linde A molecular sieves and subsequent vacuum distillation in a packed column at 53°C and 5.7 mm Hg pressure. The water content was 50 ± 10 ppm as determined by Karl Fischer titration.

Anhydrous $LiClO_4$ was purchased from G. F. Smith Chemical Company. It was heated in a vacuum at 105°C or used without further treatment. Performance of the experiments seemed independent of the heating step. Karl Fischer titration of solutions of dimethyl sulfite and $LiClO_4$ indicated the as-received "anhydrous" $LiClO_4$ contained 1 H_2O per 10 $LiClO_4$ molecules. The heating step, as performed on as-received material, only reduced the water by a factor of one-half to one-third.

The $LiCF_3SO_3$ salt was prepared by reacting $BaCF_3SO_3$ (provided by 3M Company) with H_2SO_4 and by neutralizing the resulting aqueous solution with LiOH. The $LiCF_3SO_3$ was twice recrystallized from acetone and vacuum dried at 110°C for 48 hr. Resulting solutions with dimethyl sulfite did not show appreciable increase in water content above 50 ppm.

The $LiBF_4$ was purchased from Foote Mineral Company. It was vacuum dried at 110°C for 48 hr. Resulting solutions with dimethyl sulfite showed high (order of 1000 ppm) water content.

Lithium ribbon packed in argon was purchased from Foote Mineral Company and used as received.

Five types of graphite were used: Great Lakes Carbon Company grade R-1 nuclear reactor grade graphite of density 1.68 g/cm^3, Union Carbide pyrolytic graphite carbon paper (PGCP) of density 0.471 g/cm^3, Union Carbide graphite foil (GRAFOIL) of density 0.836 g/cm^3, Super Temp Company (Santa Fe Springs, California) reinforced pyrolytic graphite (RPG) of density 1.62 g/cm^3, and Super Temp Company annealed pyrolytic graphite of density 2.24 g/cm^3. The RPG was most extensively tested. It is a porous, carbon matrix throughout on which small crystallites of pyrolytic graphite are deposited. The Super Temp Handbook (4) indicates that 80% of the pores are 18-35μ in diameter. The available internal surface area is estimated as 500 cm^{-1}. The weight of the material is about 94% pyrolytic graphite. Further information is available in the Super Temp Engineering Handbook (4).

Apparatus.—Experiments were performed in an argon-filled Vacuum Atmosphere Corporation glove box Model HE-243-2 DRI-LAB equipped with an HE-493 DRI-TRAIN containing molecular sieves for water removal and Dow Q1 (supported copper) for oxygen removal and an HE-593 titanium sponge furnace operating at 800°C for nitrogen removal. Impurity levels of O_2, N_2, and H_2O were between 1 and 10 ppm as estimated from observation of a tungsten light bulb filament life of one day or more and the rate of formation of an oxide or nitride film on molten sodium or lithium. The temperature in the glove box was maintained at 30° ± 1°C.

The test cell is shown in Fig. 1. The lower, test section of the cell is 3.5 x 4.0 x 0.3 cm. The separator was nonwoven polypropylene cloth (The Kendall Company). Contact to the graphite electrode was by a platinum wire wrapped tightly through a hole in the graphite.

Galvanostatic charging and discharging was accomplished by means of a Heathkit Model IP-32 Regulated Power Supply in series with a Clarostat Model 240-C power decade resistance box. Cell voltages were measured by a Keithley 610B electrometer coupled with a Sargent Model SR chart recorder. Cell current was measured with a Simpson Model 267 volt-ohm-milliammeter.

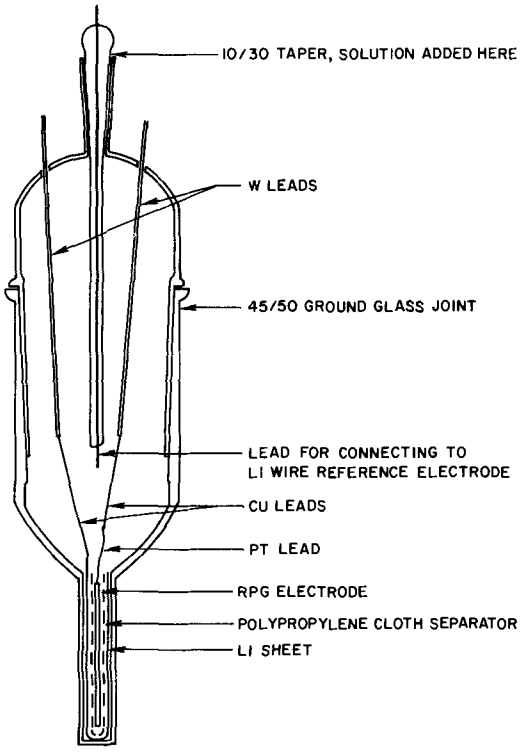

Fig. 1. Test cell

The cells were assembled in the dry box in the discharged state. The electrolyte solution was dimethyl sulfite saturated with lithium perchlorate. The saturation concentration of lithium perchlorate in dimethyl sulfite has not yet been precisely determined. However, a tentative value of 1.73 mole/kg of solution at 23°C was measured. Excess lithium perchlorate was in the bottom of the cell. Constant current was passed through the cell with the graphite electrode attached to the positive terminal of the power supply. Various time periods and rates of charging were used. The open-circuit potential was observed, and the cell potential *vs.* time was recorded during discharge with the electrodes connected across various size resistances. Once the approximate coulombic capacity was established, a timing circuit was used which switched the cell automatically from the charging circuit to the discharging circuit at fixed intervals, generally 1 or 2 hr charge followed by 1 or 2 hr discharge through constant resistance at 2 or 3 mA/cm^2. The cell potential was recorded during the cycling. Cycling was terminated when shorting across the cell electrodes began to occur. Generally the substrate for lithium deposition was a sheet of lithium metal. However, copper, aluminum, and RPG were also tested as possible negative electrode substrates. The solvent was generally dimethyl sulfite, but propylenecarbonate and dimethyl sulfoxide were also tested. Lithium perchlorate was generally used as the electrolyte, but lithium trifluoromethanesulfonate, lithium tetrafluoroborate, lithium nitrate, and lithium thiocyanate were substituted for the lithium perchlorate in a series of tests. Various graphites as mentioned above were used as positive electrodes in addition to some amorphous carbons.

Results

Cell tests.—Using an RPG positive electrode of 5 cm^2 geometric area, a series of 20 min galvanostatic charge-discharge runs were made. Cell voltage was recorded as a function of time for currents of 2 mA/cm^2. A typical result is shown in Fig. 2. Both charge and discharge curves are quite flat. A sharp break downward in the discharge curve occurs at 3.8V. Open-circuit potential is approximately 4.4V with the majority of the discharge above 4.0V. Coulombic efficiencies

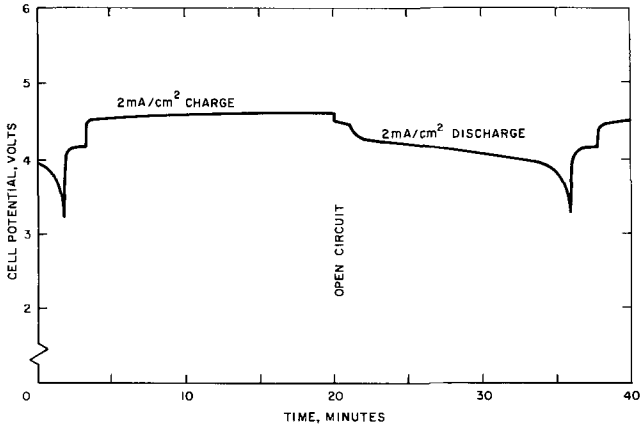

Fig. 2. Typical charge-discharge cycle Li/DMSU, $LiClO_4$/RPG

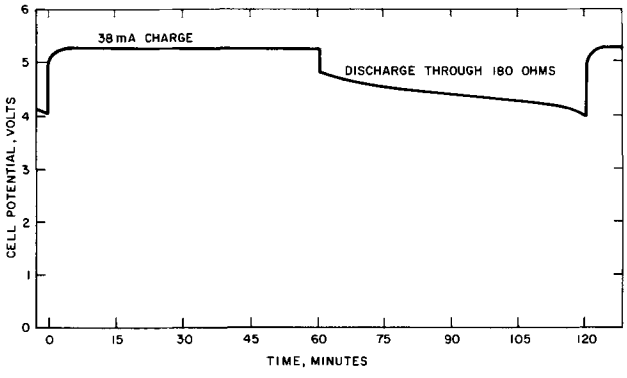

Fig. 3. Typical charge-discharge cycle, Li/DMSU, $LiClO_4$/RPG 23rd cycle. Geometric area ≈ 17 cm² (~62 coulombs/g of RPG).

increased during the first seven cycles as follows: 56%, 73%, 87%, 87%, 89%, 95%, and 90%.

After a 17.5 hr charge at 1 mA/cm², the open-circuit potential was 4.55V and stable during a waiting period of about an hour. A discharge of 2 mA/cm² was carried out for 10 min. Then a 10 mA/cm² (based on geometric area of RPG electrode) discharge was carried out for 30 min to a cutoff potential of 2.5V. Open-circuit cell potential quickly (within a second or so) returned to 4.3V and remained stable for 3 hr. This was followed by a 30 min discharge at 2 mA/cm² with cell potential above 3.5V. A brief short circuit through the ammeter gave 70 mA/cm² for 1 or 2 sec.

The electrolyte solution remained clear during this test. No bubbling was observed at the graphite electrode. A few small bubbles were observed at the lithium electrode.

The RPG electrode had swollen about 30% during charging. The swelling did not diminish on discharge.

In a later charge-discharge cycle (after 26 days of storage out of the electrolyte solution) the RPG electrode was charged for 11 hr at 5 mA (~ 1 mA/cm²). A short circuit through the ammeter gave 620 mA (~ 120 mA/cm²) for 2 or 3 sec. It was next discharged for 4 hr at 10 mA (~ 2 mA/cm²) to a 3.5V cutoff potential. Following this test, a long plateau (several hours) was observed at 2.5-2.0V cell potential at about 2 mA/cm². This low voltage plateau was not investigated further.

Using a lithium wire reference electrode it was determined that the decrease in cell potential at the end of a discharge (see Fig. 2) occurs almost entirely at the graphite electrode. This is expected since there is excess lithium at the negative electrode.

No lithium dendrites were observed except when the lithium perchlorate concentration was below saturation.

Cycle tests.—Two long-term cycle tests were run, each lasting several days. For the first test, an RPG electrode 4.67 x 1.82 x 0.106 cm weighing 1.4535g was used. The cycles were a 1 hr charge followed by 1 hr discharge. A typical cycle is shown in Fig. 3. The size of resistance in the discharge circuit was such as to prevent a rapid fall in the cell potential at the end of an hour. An arbitrary cutoff potential of 4.0V was used. As shown in Fig. 2, very little additional capacity is realized by using a 3.2V cutoff potential. For the first 12 cycles, charging took place at about 0.6 mA/cm² followed by discharge at approximately 0.48 mA/cm². Cycles 13-16 were at about 1.2 mA/cm² on charge and discharge. Cycles 17-26 were at about 2.2 mA/cm² charge and 1.5 mA/cm² discharge. The 27th cycle was increased to a 2 hr charge followed by a 2 hr discharge. However, on the 24th cycle minor jumps in potential began to occur, apparently caused by temporary or intermittent shorts. After 30 min of discharge on the 27th cycle the "shorting" became so severe that the test was terminated. Coulombic efficiency, coulombs in divided by coulombs out, generally varied between 0.66 and 0.9 for these cycles. No charge seemed to be building up on the positive electrode as shown by rapid decrease in cell potential if discharge time was lengthened.

At the end of the run it was observed that the electrolyte solution was a cloudy green color caused by a jellylike suspension. About half of the solid lithium perchlorate initially at the bottom of the cell was still there. On top of the lithium perchlorate was a thick (~ 1 cm) layer of carbon powder which apparently caused the shorting. The RPG electrode was "intact" but had a leached appearance. The lithium reference electrode was discolored black, particularly near the solution-argon interface. A few bubbles were trapped in the cell. There were no salt crystals on or near the graphite electrode. The lithium electrode was still pliable but black in color on the side facing the RPG electrode. The lithium was covered with what appeared to be salt crystals as was the nonwoven polypropylene cloth separator on the side toward the lithium. No lithium dendrites were observed. The polypropylene separator showed no degradation.

A second, similar cycle test yielded 33 cycles and was generally run at about 3 mA/cm². No significant performance differences were noted.

Coulombic capacity.—Various graphite positives were tested and effective charge storage capacity evaluated. The results are shown in Fig. 4. In these tests the discharge took place immediately after the charge. For the three types of graphite tested, the amount of charge recovered was independent of the amount of charge inserted after the charging passes about 90 coulombs/g.

If a cell is charged and then allowed to stand wet for one day, 25-50% of the charge originally inserted can no longer be recovered on discharge.

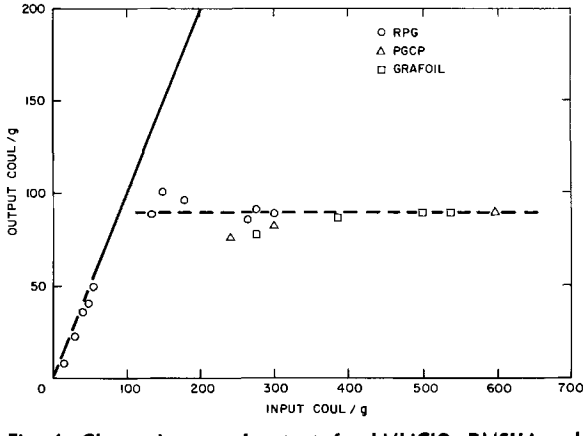

Fig. 4. Charge input and output for Li/$LiClO_4$:DMSU/graphite cell.

Swelling direction.—Tests on pyrolytic graphite chips have shown that swelling takes place along the "c" direction of the graphite. This swelling was not reversible on discharge.

Substitution of materials.—Lithium trifluoromethane sulfonate gave approximately the same performance as lithium perchlorate. Lithium tetrafluoroborate gave a stable open-circuit potential, about 4.6V, but the capacity of the RPG electrode using this salt was only about 10-15 coulombs/g. The charging potential when using lithium tetrafluoroborate was about 0.1-0.2V higher than when using lithium perchlorate as the electrolyte. Tests using lithium nitrate and lithium thiocyanate did not show stable, high open-circuit potentials and no significant coulombic capacity was observed when discharge was attempted. The following salts were too insoluble in dimethyl sulfite to yield any meaningful results: $LiBO_2$, Li_2CO_3, LiCl, Li_2SiO_3, $LiPO_3$, Li_2SO_4, Li_2O, and Li_2O_2.

In addition to the graphites already described, Great Lakes nuclear reactor grade R-1 graphite was tested. These were essentially blocks of material about the same size as the RPG electrodes. The R-1 gave stable cell potentials of about 4.5V. However, the graphite tended to slough off at the surface and crack if charged for more than 1 hr at 10 mA/cm^2. Various types of carbons were also tested, for example, Union Carbide gas fuel cell electrodes. None of the amorphous carbons gave stable open-circuit potentials or appreciable discharge capacities.

Various substrates were used for lithium deposition at the negative electrode. In general, the graphite electrodes were being studied. Thus, using lithium as the negative electrode substrate provided excess lithium capacity and insured that the lithium electrode was not capacity limiting. However, copper seems to work well as a substrate. Aluminum forms an alloy or compound with lithium and lowers the cell potential about 0.3V. Initial rates of charge and discharge using aluminum substrates indicated that the negative electrode overpotentials were small compared with the positive electrode. However, the negative electrode became capacity limiting and the aluminum became brittle, warped, and broke up after a few cycles. When RPG was used as the negative electrode substrate, it performed as a lithium electrode. There was no appreciable under- or overpotential on charging as determined using a lithium wire reference electrode. The cell was capacity limited on discharge by the negative electrode. The RPG did not change dimension. Based on these rather simple tests it did not appear that any lithium intercalation compound was being formed with the graphite.

Wood fiber paper battery separators and nylon cloth were tried as separator materials. They both disintegrated after a day or so in the dimethyl sulfite solutions. The nylon was very poor.

Propylene carbonate was substituted for dimethyl sulfite in a test and essentially the same results were achieved with regard to charge and discharge curves and open-circuit potential. When dimethyl sulfoxide was tried, however, the cell performance was not good. A stable open-circuit potential was not established and no appreciable discharge capacity was realized. Similarly, n-nitrosodimethylamine was not a successful solvent.

Lithium electrolyte solution stability.—Only preliminary tests of the stability of lithium in dimethyl sulfite have been made to date. A white precipitate is observed to form on lithium when immersed in lithium perchlorate-dimethyl sulfoxide solutions. The amount of precipitate produced is proportional to the amount of water in the solution. The reaction apparently ceases when water content is below 5 ppm. The precipitate, when washed and dissolved in water, gives a near neutral pH.

Discussion

The phenomenon of an expanding graphite anode has been known since 1841 (5). This has been explained as the formation of an electrochemical lamellar compound of graphite. That is, anions are incorporated into the interplanar spaces in the graphite structure to provide electroneutrality as the graphite is oxidized to a "macrocation" by the application of an anodic current. Such compounds have been studied in some depth since the mid-1930's (6-9). The similarities in the formation procedure and dimensional changes suggest that a lamellar compound of graphite may be involved in the positive electrode reaction in the Li/$(CH_3O)_2SO$, $LiClO_4$/graphite system. However, there are some differences between the behavior of the nonaqueous, aprotic system reported here and the acid systems. They are:

I) Absence of color change. Graphite compounds prepared in this laboratory by electrochemical oxidation of pyrolytic graphite in $HClO_4$ and H_2SO_4 have a metallic blue color, as reported by other investigators (9). The lithium perchlorate-dimethyl sulfite solutions do not yield a blue-colored graphite product. The graphite remains black.

II) Unlimited expansion of graphite. Lamellar compounds of graphite prepared from pure acid media expand along the "c" direction to an extent limited by the formation of the final stage (most concentrated in anionic species). The tests conducted in lithium perchlorate-dimethyl sulfite show unlimited expansion as the charging process proceeds. No clearly observable final stage was found.

III) Absence of detectable stage formation. Previous workers in acid media have observed stepwise changes in the potential of a graphite anode at constant current (10). Presumably, these correspond to various stages of compound formation as different combinations of interplaner spaces in the graphite are occupied. No such changes in the potential of a graphite anode in nonaqueous media *vs.* either a lithium electrode or a silver-silver perchlorate reference electrode have been observed.

If a simple lamellar compound of graphite is formed in the dimethyl sulfite-lithium perchlorate solutions, one possible reaction characterization would be

$$nC + ClO_4^- = C_nClO_4 + e^-$$

The results shown in Fig. 4 indicate a maximum charge storage capacity of about 90 coulombs/g of graphite. This corresponds to 89 carbon atoms, on the average, per anion using the above relationship. Ratios as low as 6-24 carbon atoms per anion have been observed for some acid media (9). The possible specific energy for such a system is critically dependent upon the value of n in the above relationship. Present results project to a specific energy of 20-45 Whr/kg of battery with n equal to 89.

Using nongraphitic carbons, the cell characterized by a 4.5V stable open-circuit potential does not form. Other workers have found (10, 11) that well-ordered graphites (characterized by negative temperature coefficients of electrical conductivity) are necessary for proper compound formation. The graphites used in this study were not of such perfect crystalline nature but were commercial grades.

The similar performances for the three anions—perchlorate, trifluoromethanesulfonate, and tetrafluoroborate—in addition to similar performances between dimethyl sulfite and propylenecarbonate solvents suggest that the positive electrode reaction is not specific to the particular anion or solvent. This suggests that the simple lamellar compound of graphite formation or a similar reaction gives the correct over-all stoichiometry. Comparing anions that work with those that do not work suggests that the lithium salt of the anion must be soluble in the solvent to be used and the acid of the anion should be a very strong acid. The fact that stable open-circuit potentials of 4.5V, loss of only

50% capacity on storage for one day, and cycle life of up to 33 2-hr cycles are observed suggests that the dimethyl sulfite-lithium perchlorate solution is at least marginally stable to oxidation and reduction over a 4.5V range relative to lithium.

Acknowledgment

This work was supported by the U. S. Naval Air Systems Command through the Corona Laboratories under Contract No. N00123-70-C-0188.

Manuscript submitted March 17, 1971; revised manuscript received Aug. 13, 1971.

Any discussion of this paper will appear in a Discussion Section to be published in the June 1972 JOURNAL.

REFERENCES

1. N. P. Yao, E. D'Orsay, and D. N. Bennion, *This Journal*, **115**, 999 (1968).
2. D. N. Bennion, "Nonaqueous Electrolyte Studies for High Energy Batteries," Final Report to U.S. Naval Weapons Center, Corona, Calif., Contract N123 (62738)-57439A (September 1969).
3. Abner Brenner, *This Journal*, **118**, 461 (1971).
4. "Super Temp Engineering Handbook of Pyrolytic Materials," Super Temp Co., Santa Fe Springs, Calif., 1968.
5. H. L. Riley, *Fuel*, **24**, 8, 43 (1945).
6. W. Rudorff and U. Hoffman, *Z. Anorg. Allgem. Chem.*, **238**, 1 (1938).
7. W. Rudorff, *Z. Physik. Chem.*, **B45**, 42 (1939).
8. G. Henning, *J. Chem. Phys.*, **19**, 922 (1951).
9. G. Henning, *Prog. Inorg. Chem.*, **1**, 125 (1959).
10. M. J. Bottomley, G. S. Parry, A. R. Ubbelohde, and D. A. Young, *J. Chem. Soc.*, **1963**, 5674.
11. I. L. Spain, A. R. Ubbelohde, and D. A. Young, *ibid.*, **1964**, 920.

Overpotential Behavior of Stabilized Zirconia Solid Electrolyte Fuel Cells

T. H. Etsell*,[1] and S. N. Flengas**

Department of Metallurgy and Materials Science, University of Toronto, Toronto, Ontario, Canada

ABSTRACT

The nature and characteristics of the overpotential in cells of the type

$Ar\text{-}O_2$, $H_2\text{-}H_2O$, or $CO\text{-}CO_2/ZrO_2\text{-}CaO/O_2$

were determined from 700° to 1100°C over a wide range of oxygen pressures. Porous Pt black electrodes were deposited on impervious ZrO_2 + 10 m/o (mole per cent) CaO tubes. Almost pure resistance polarization is observed when $Ar\text{-}O_2$ or $H_2\text{-}H_2O$ mixtures are present at the anode. However, for $Ar\text{-}O_2$ mixtures dilute in O_2 at the cathode, diffusion overpotential readily appears and limiting currents are eventually reached. Limiting currents, proportional to P_{O_2}, are controlled by the diffusion of gaseous oxygen in the pores of the Pt electrode. Based on the present results and adsorption data, a mechanism is proposed for the cathode reaction. For $CO\text{-}CO_2$ mixtures, transition overpotential associated with the reaction $CO_2 + 2e \rightleftharpoons CO + O^=$ is observed. The transition factor is about 0.5 and exchange current densities are in the vicinity of 1 mA/cm^2. Equations relating exchange current density to P_{CO}, P_{CO_2}, and the amount of CO adsorbed on the electrolyte are derived and compared with the experimental results. It is concluded that either gaseous or adsorbed CO and gaseous CO_2 are directly involved in the electrochemical step of the reaction.

Solid oxide electrolytes can be used in the construction of high-temperature fuel cells. Only ZrO_2-based electrolytes are suitable since they possess relatively high ionic conductivities and exhibit virtually pure oxygen-ion conduction between oxygen pressures of 1 and 10^{-20} atm at 1000°C (1).

The overpotential behavior of such cells is of interest from both theoretical and practical viewpoints. Nevertheless, only a limited amount of research has been done in this area and there is considerable disagreement among the available results on the overpotential at metal or oxide electrodes in contact with ZrO_2-based electrolytes and either O_2-inert gas (2-11), $H_2\text{-}H_2O$ (12-19), or $CO\text{-}CO_2$ (2, 6, 13, 14, 17, 20-23) mixtures.

Diffusion overpotential is generally observed with O_2-inert gas mixtures at the cathode, but the rate-determining step of the over-all cathode reaction has been concluded to be the diffusion of oxygen atoms in the adsorbed phase at 810°C (3) and through the Pt electrode at 560°C (9, 10), mass transport in the gas phase at 1000°C (6, 7), and either the dissociation of oxygen molecules or the electron transfer step at 400°-800°C (8). At high applied potentials, either oxygen transfer into the electrolyte (9, 10) or electronic conduction in the electrolyte (10) can be rate-limiting. Unspecified overpotential has been reported at the anode (3-5).

Even in atmospheres of oxygen (6, 8, 18, 24-26) and air (4, 6, 9), overpotential has been detected at the electrodes and attributed to slow diffusion processes at 560°-1000°C (4, 6, 9), Pt-O interactions at 600°-1000°C (24), a slow electrochemical step at 900°-1000°C (25), and a constriction resistance at 650°-800°C (26). In the latter case, the Ag cathode was only active at discrete spots which necessitated regions of high current density in the electrolyte. However, in other investigations, significant overpotential at high oxygen pressures has not been observed (2, 5, 11, 15). Impedance measurements have both supported (8, 25, 27, 28) and refuted (29) the existence of overpotential in oxygen and air. Likewise, for $H_2\text{-}H_2O$ mixtures, the possibility of overpotential at the anode from 600°-1100°C has been both confirmed (15, 18, 19) and denied (12-14, 16, 17).

In the case of $CO\text{-}CO_2$ mixtures, diffusion overpotential (6, 13, 20, 21, 23), transition overpotential (20, 21),

* Electrochemical Society Student Associate Member.

** Electrochemical Society Active Member.

[1] Present address: Max-Planck-Institut für Chemie, 65 Mainz, Saarstrasse 23, West Germany.

Key words: zirconia, solid electrolyte, oxide, overpotential, fuel cell.

and reaction overpotential (20) at 800°-1000°C have all been reported. Tafel behavior is often followed (2, 6, 14, 20, 21) although, except in two studies (20, 22), mechanisms have not been given to account for the results. There is serious disagreement concerning the value of the transition factor (2, 14, 20) and the influence of gas composition on overpotential (13, 14, 20, 21). Nickel anodes complicate the analysis due to the formation of NiO (30-32).

The above inconsistencies reflect, in part, the important influence of the electrode on overpotential when gas mixtures are in contact with solid electrolytes. Its composition, structure, and porosity must often be carefully controlled to obtain reproducible results. Electrode structure has recently been shown to be a highly significant variable (10).

To help resolve these discrepancies, current-potential characteristics of porous Pt electrodes in contact with ZrO_2-CaO electrolytes were determined at 700°-1100°C over a wide range of oxygen pressures which were controlled by Ar-O_2 (1 to 10^{-6} atm), CO-CO_2 (10^{-5} to 10^{-21} atm), and H_2-H_2O (10^{-20} to 10^{-23} atm) mixtures. The curves were analyzed to separate the contributions from various types of overpotential. Mechanisms are proposed for the electrode reactions in Ar-O_2 and CO-CO_2 mixtures.

Experimental

The solid electrolytes were impervious ZrO_2 + 10 m/o CaO tubes, closed flat at one end. They exhibited excellent stability when cycled between 700° and 1100°C for two months since their resistances remained unchanged. The closed ends of the tubes were platinized on both sides by applying drops of a 1:1 mixture of a 3-5% chloroplatinic acid solution and formaldehyde solution to the faces which were then heated to 600°-700°C. This procedure, repeated twice for each face, resulted in adherent, porous, fine-grained Pt black deposits.

As illustrated in Fig. 1, a 24-in. long electrolyte tube with an ID of 9.5 mm and OD of 13.5 mm was placed inside a quartz tube with an ID of 15.5 mm and OD of 19 mm which had been made as flat as possible on the bottom. The 6.5-mm alumina rod inside the electrolyte tube contained two 1.5-mm holes which served to hold a 20-mil Pt lead wire and transport gas into the cell. Small slits were cut into the bottom of this rod to facilitate the gas flow. To minimize contact resistance, three springs located at 120° intervals around the top of the cell held the circles of 45-mesh Pt gauze (18 mils thick) firmly against the platinized surfaces of the electrolyte. Irregularities in these surfaces and the inside of the bottom of the quartz tube rendered complete elimination of contact resistance difficult. The lower two Tygon tubing seals kept the pressure approximately constant despite expansion and contraction of the ceramic components during temperature cycling.

Generally, the purified and preanalyzed gas mixtures were passed into the outer compartment. The 6-in. long quartz preheating chamber with an ID of 10 mm, which contained pieces of 1-mil Pt foil, enabled high flow rates to be used without cooling the cell. The constriction at the top of the preheating chamber was made to give the quartz tube added mechanical strength. Oxygen flowed through the inner Pt gauze to form the reference electrode. All of the gases were passed at 1 atm total pressure. Temperature measurements were taken with a Pt-Pt+13% Rh thermocouple welded to the outer Pt gauze.

Potentials were applied to the cell using a circuit consisting of a rectifier and several variable resistors. Potential and current readings were taken with a Weston d-c voltmeter and milliammeter. Upon interrupting the circuit, the cell potential could be recorded quickly and accurately with a Radiometer Universal pH meter. Alternating-current resistance measurements were made with a conductivity bridge equipped with an oscilloscope detector which was supplied by Industrial Instruments (Model RC-18).

Initially, the cells were heated to 1100°C for several hours to reduce contact resistance and partially sinter the Pt black deposits. Reproducible overpotential and resistance results upon temperature cycling could then be obtained.

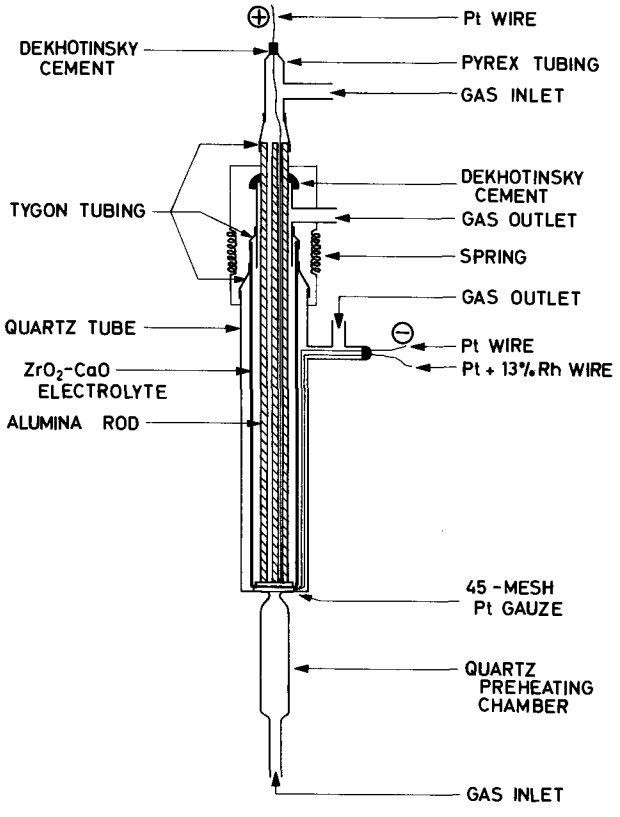

Fig. 1. Cell design for overpotential measurements

Results and Discussion

Close agreement between measured and theoretical emf values (±0.5%) verified the pure ionic conductivity of the electrolyte tubes and the reversibility of the electrodes. Usually, the electrolytes had a-c resistances measured at 3000 Hz of about 1000, 180, 40, and 20 ohms at 700°, 850°, 1000°, and 1100°C, respectively. Occasionally, values which were 15-20% lower than these were found.

Gas flow rates are reported as room-temperature linear speeds based on an approximate area of 0.5 cm^2 for the inlet tube immediately below the outer Pt electrode. High flow rates were used to minimize both concentration effects and the influence of oxygen reaching the outer electrode from the reference electrode because of slight porosity and electronic conductivity in the solid electrolyte. Current densities are based on the geometric area of the outer electrode (1.0 cm^2).

Overpotential measurements were not influenced by the previous history of the cell. The electrodes were sufficiently porous to resist any significant changes in their structure even when treated anodically at high current densities.

Ar-O_2 mixtures.—Current-potential characteristics for O_2 and Ar-O_2 mixtures at 1000°C are shown in Fig. 2. For the Ar-O_2 mixtures, each curve was shifted to pass through the origin by subtracting the appropriate emf from the applied potential.

An important feature of Fig. 2 is that, when pure oxygen is present at both electrodes, only resistance polarization is observed. The slope of the O_2 line, corresponding to the d-c resistance, is virtually identical to the a-c resistance of the electrolyte. This agreement was checked to 250 mA/cm^2 at 1000°C and to 400 mA/

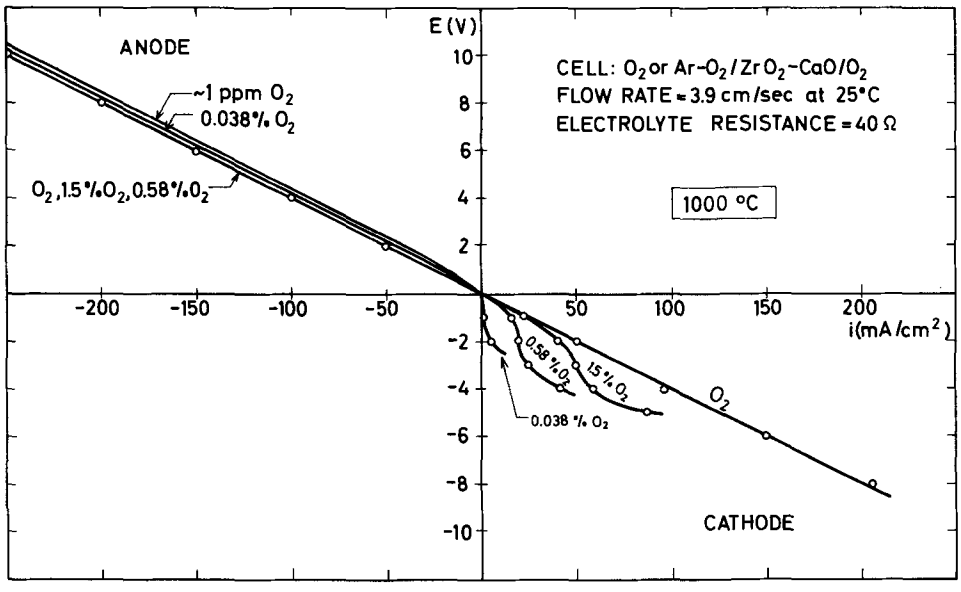

Fig. 2. Anode and cathode characteristics for O_2 and Ar-O_2 mixtures at 1000°C.

cm^2 at 1100°C. Therefore, the reference Pt,O_2 electrode is nonpolarizable and any overpotential can be attributed to the gas mixtures at the outer Pt electrode.

Anodic overpotenial is quite low even for Ar-O_2 mixtures dilute in O_2. At high current densities, the slopes of the lines approximate the a-c resistance of the electrolyte since resistance polarization predominates.

However, cathodic overpotential in the presence of Ar-O_2 mixtures is very high and increases markedly as the oxygen concentration decreases. A tendency towards limiting currents followed by breakdown of the oxide electrolyte at high applied potentials is apparent in Fig. 2. These features are also evident at 700° and 850°C from the curves in Fig. 3 which again have been shifted, when necessary, to pass through the origin. Only resistance polarization was detected with pure oxygen at the cathode. In the breakdown region, the currents increased slowly with time and were recorded after the applied potential had been held constant for 5 min. If sufficient time was allowed, these currents became constant. Breakdown generally occurred when the overpotential exceeded 1.9, 1.7, 1.6, and 1.5V at 700°, 850°, 1000°, and 1100°C, respectively. It did not

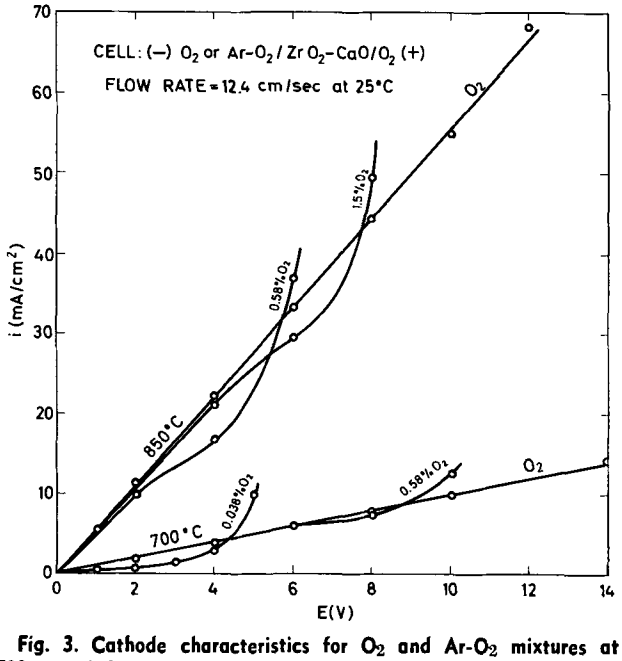

Fig. 3. Cathode characteristics for O_2 and Ar-O_2 mixtures at 700° and 850°C.

lead to any irreversible changes in the electrolyte tubes. Larger currents can cause destabilization of cubic zirconia leading to cracking (11, 33) and an increase in the resistance of the ceramic electrolytes (33).

The over-all cathode reaction which involves three phases is

$$O_{2,g} + 4e \rightarrow 2\,O^{=} \qquad [1]$$

whereby oxygen gas combines with electrons in the electrode to form oxygen ions in the electrolyte. If insufficient oxygen is available due to slow diffusion, adsorption, or dissociation processes near the electrode-electrolyte interface, concentration overpotential will be observed and limiting currents should be realized when the oxygen activity at the surface of the electrolyte becomes negligible with respect to the oxygen activity in the bulk of the gas phase. At high applied potentials, the surface oxygen activity becomes low enough to partially reduce the electrolyte resulting in n-type conductivity. The current increases since a direct electron exchange between the electrode and electrolyte can now occur (3, 9, 10, 34). While the reduced zone slowly spreads towards the anode (34, 35) during which time more $O^{=}$ ions migrate from the cathode side of the electrolyte than are produced via reaction [1], the current continues to increase. Accordingly, the apparent breakdown voltage will be somewhat dependent upon the loading rate, particularly when the electrolyte resistance is high. Conditions favoring breakdown of an oxide electrolyte are low oxygen pressures at the cathode, high current densities, and high temperatures.

A more detailed study of the limiting currents was carried out (smaller applied potential increments) as indicated by the results in Fig. 4. The combination of limiting currents and electrolyte breakdown makes the curves similar in appearance to polarographic waves. Plateaus were not reached when applied potentials exceeding 2V were required, *i.e.*, at low temperatures because of the high resistance of the electrolyte. This is, perhaps, an indication of the inhomogeneous nature of the cathode-electrolyte interface. In regions where the Pt black deposit is very porous, the oxygen activity at the surface of the electrolyte could still be appreciable whereas, in regions where dense Pt particles shield the electrolyte from oxygen, it could be low enough to cause some reduction of the electrolyte.

Regarding the nature of the overpotential, it should be noted that the initial slopes of the curves in Fig. 2-4 for Ar-O_2 mixtures $[(dE/di)_{i=0}]$ were higher than the corresponding a-c resistance, *e.g.*, about 5 and 50% higher at 1000°C for 0.58% and 0.038% O_2, respectively. This difference can be explained by an analysis of Fig.

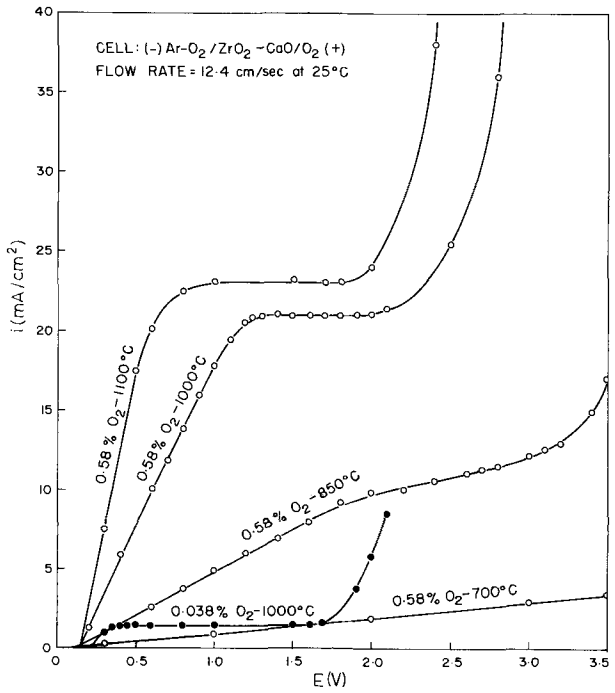

Fig. 4. Current density vs. applied potential with Ar-O_2 mixtures dilute in O_2 at the cathode.

5 which is considered to represent the equivalent circuit for a polycrystalline ionic conductor in either a conductivity or electrochemical cell (see the caption

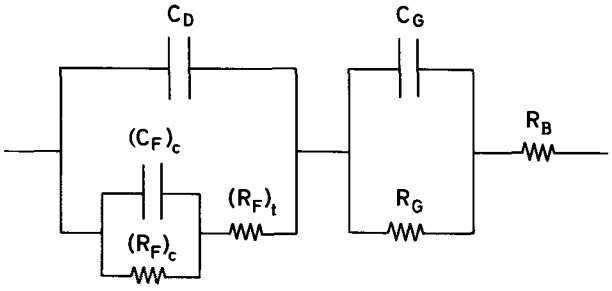

(a) at low frequencies

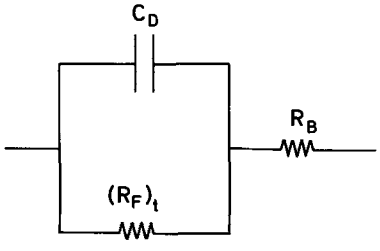

(b) at high frequencies

Fig. 5. Equivalent circuit diagram for a polycrystalline ionic conductor in a conductivity or electrochemical cell. Only one electrode-electrolyte interface is shown: C_D, double-layer capacitance; $(C_F)_c$ and $(R_F)_c$, Faraday capacitance and resistance, respectively, resulting from concentration overpotential (slow mass transport or chemical reaction); $(R_F)_t$, Faraday resistance resulting from transition overpotential (slow electrochemical reaction); C_G and R_G, grain boundary capacitance and resistance, respectively, due to grain boundaries, inter-particle contacts, and free surfaces within the sintered polycrystalline electrolyte; R_B, bulk electrolyte resistance (includes contact resistance between the electrode and electrolyte).

for meaning of symbols). Both $(C_F)_c$ and $(R_F)_c$ decrease as the frequency increases whereas $(R_F)_t$ is independent of frequency. At high frequencies, $(R_F)_c$ is "shorted-out" by $(C_F)_c$ which, in turn, has a negligible reactance compared to the resistance of $(R_F)_t$. A similar situation exists for C_G, R_G, and R_B. The value of $(R_F)_t$ can be determined by extrapolating a plot of the total Faraday resistance *vs.* $f^{-1/2}$ where f is the measuring frequency to $f^{-1/2} = 0$ (29). At very high frequencies, the current through $(R_F)_t$ is shunted through C_D. Hence, three possibilities for the total resistance, R_T, can be distinguished:

1. $R_T = (R_F)_c + (R_F)_t + R_G + R_B$ $(f \geqq 0)$
2. $R_T = (R_F)_t + R_B$ $(f >> 0)$
3. $R_T = R_B$ $(f \to \infty)$

From the present results, $R_{d\text{-}c} = R_{a\text{-}c}$ in pure oxygen where $R_{d\text{-}c}$ is the d-c resistance (R_T at $f = 0$ and $i = 0$) and $R_{a\text{-}c}$ is the a-c resistance (R_T at $f = 3000$ Hz). The measuring frequency of 3000 Hz was high enough for case 3 to apply because $R_{a\text{-}c}$ was independent of oxygen pressure contrary to the expected behavior of $(R_F)_c$ and $(R_F)_t$, $R_{a\text{-}c}$ was unaffected by increasing the frequency to 10,000 Hz, and, assuming $C_D = 100$ μF/cm² (8), its reactance at 3000 Hz is only 0.5 ohm meaning that C_D would serve as an effective current shunt for $(R_F)_t$ if $(R_F)_t$ were appreciable. Therefore, in pure oxygen, $(R_F)_c$, $(R_F)_t$, and $R_G \sim 0$.

As mentioned, however, $R_{d\text{-}c} > R_{a\text{-}c}$ in Ar-O_2 mixtures. Since R_G is independent of oxygen pressure, $R_G \sim 0$. Consider $(R_F)_t$. For an electrochemical reaction involving only oxygen species

$$i_o \propto \theta_O^{1-\alpha} (1 - \theta_O)^{\alpha} \qquad [2]$$

where i_o is the exchange current density, α is the transition factor or transfer coefficient, and θ_O and $1 - \theta_O$ are the fractions of electrochemically active sites which are occupied by adsorbed oxygen atoms and which are free, respectively (see Eq. [19]). Consequently, for $\alpha = 0.5$, i_o is a maximum at $\theta_O = 0.5$. Oxygen atoms are strongly chemisorbed on Pt and ZrO_2. For the reaction

$$O_{2,g} \to 2\ O_{ad} \qquad [3]$$

at 25°C, $\Delta H°_{ad}$ on Pt black $= -60$ kcal/mole (36) where the standard states are $O_{2,g}$ at 1 atm and O_{ad} at $\theta_O = 0.5$. Chemisorption ceases after one monolayer is formed (36, 37) and the adsorbed atoms are mobile (36). Desorption was not observed when Pt was heated to 840°C at $P_{O_2} = 10^{-10}$ atm (38). At 400°-900°C, ΔH_{ad} (integral heat) on ZrO_2 powder ~ -80 kcal/mole (39). It was not determined whether the adsorbed atoms are mobile or localized. Adsorption proceeds with activation energies of zero for Pt (38, 40) and 58 kcal/mole for ZrO_2 (39). To estimate the amount of adsorption at high temperatures, consider $\Delta G°_{ad}$ at 1000°C for reaction [3]. At 1000°C, $S°_{O_{2,g}} = 60.2$ cal/mole-°K (41). If the adsorbed species is very mobile, it can be roughly approximated to be a two-dimensional gas. Since the adsorbed oxygen concentration $\sim 5 \times 10^{14}$ atoms/cm² ($\theta_O = 0.5$), an expression for the translational entropy of a two-dimensional ideal gas (42) gives $S°_{O_{ad}} = 18.3$ cal/g atom-°K at 1000°C. The vibrational contribution, which is small (42), and any change in the entropy of the adsorbent will be neglected. Thus, $\Delta S°_{ad} = -23.6$ cal/mole-°K for reaction [3]. Assuming $\Delta H°_{ad} = -60$ kcal/mole yields $\Delta G°_{ad} = -30$ kcal/mole at 1000°C. Therefore, $\theta_O \sim 1$ at $P_{O_2} = 1$ atm and $\theta_O = 0.5$ at $P_{O_2} \sim 10^{-5}$ atm. Referring to Eq. [2], it is now evident that i_o will increase and, therefore, $(R_F)_t$ will decrease as the oxygen pressure decreases at high oxygen pressures. Accordingly, in Ar-O_2 mixtures, $(R_F)_t \sim 0$ and

$$R_{d\text{-}c} = (R_F)_c + R_{a\text{-}c} \qquad [4]$$

Low transition overpotential in stabilized zirconia cells is supported by investigators who have reported

that, at 1000°C, i_0 = 100 to >1000 mA/cm² at solid electrodes (43) and 600 mA/cm² at liquid electrodes (44). Bauerle (8) recently suggested the possibility of a slow electron transfer step at 400°-800°C. As the resistance to the electrode reaction had a high activation energy (2-2.5 eV), it could be negligible at high temperatures. The activation energy for the resistance of the electrolytes used here was determined to be 1.1 eV.

From Eq. [4], concentration overpotential is solely responsible for the deviations from ideal behavior ($R_{d\text{-}c} = R_{a\text{-}c}$) in Fig. 2-4. Assuming for the moment that this overpotential arises from a slow diffusion process, the diffusion overpotential, η_d, can be simply calculated from the relationship

$$\eta_d = E - E_{rev} - IR_{a\text{-}c} \quad [5]$$

where E is the applied potential, E_{rev} is the reversible potential ($I = 0$), and I is the current. Equation [5] was verified by noting that, upon opening the circuit, the overpotential did not decay rapidly and was initially equal to the total overpotential. Based on Fick's first law, diffusion overpotential can be expressed as

$$\eta_d = \frac{RT}{nF} \ln \frac{i_l}{i_l - 1} \quad [6]$$

where n is the number of electrons associated with the slow diffusing species that are involved in the electrode reaction and i_l is the limiting current density. The plot in Fig. 6, based on the data in Fig. 4 at 1000°C, indicates that $n = 4$. The points are less accurate when $\eta_d > 0.1$V (the theoretical slope for $n = 4$ is 0.063V). Thus oxygen molecules, rather than atoms, are involved in the rate-determining step. Further verification comes from Fig. 7 which shows that the limiting current density is directly proportional to the oxygen pressure. These results support the possibility of a "polarographic-like" technique to analyze gas mixtures for oxygen (45). However, limiting currents were not very reproducible from run to run since they are quite sensitive to the porosity and structure of the cathode. They increased somewhat with increasing flow rate.

Since $i_l \propto P_{O_2}$, substituting Eq. [6] into Eq. [5] gives

$$R_{d\text{-}c} = \left(\frac{\partial E}{\partial I}\right)_{I=0} = kP_{O_2}{}^{-1} + R_{a\text{-}c} \quad [7]$$

where k is a constant. Comparing Eq. [4] and [7] results in

$$(R_F)_c = kP_{O_2}{}^{-1} \quad [8]$$

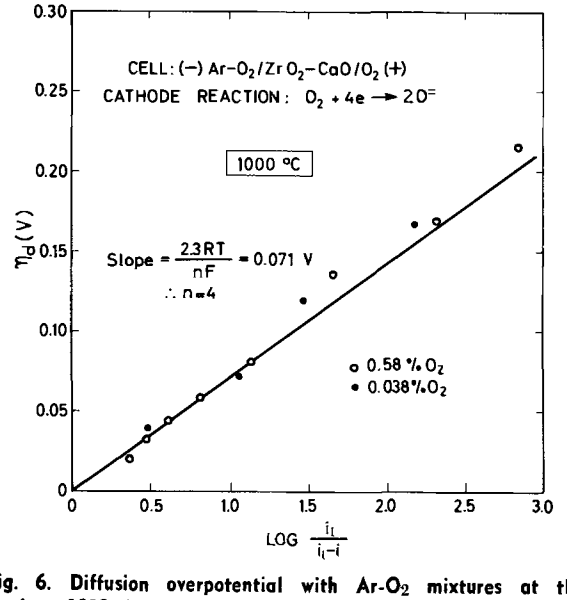

Fig. 6. Diffusion overpotential with Ar-O_2 mixtures at the cathode at 1000°C.

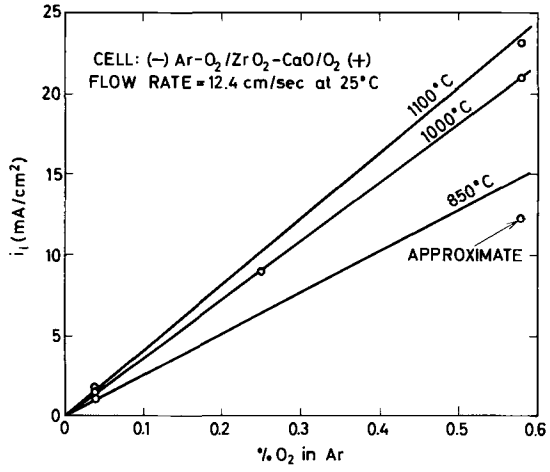

Fig. 7. Limiting current densities with Ar-O_2 mixtures at the cathode.

The quantity $(R_F)_c$ obeyed Eq. [8] and decreased slightly with increasing temperature.

Steps in the cathode reaction involving oxygen molecules include gas diffusion in the electrode pores and surface diffusion along the electrode and electrolyte. Also, the possibility of either slow adsorption or dissociation of oxygen molecules leading to reaction overpotential has not been eliminated. The fact that the limiting currents depended on the gas flow rate supports diffusion and convection in the gas phase as the slow step. Limiting currents increase with temperature (Fig. 7) in accordance with faster diffusion of oxygen molecules.

An earlier study on electrode processes in stabilized zirconia cells indicated that $i_l \propto P_{O_2}{}^{1/2}$ at 810°C (3). Such behavior could be attributed to slow diffusion of oxygen atoms through the electrode or along the electrode and electrolyte. The advantage of porous electrodes in providing oxygen with easier access to the electrolyte is apparent. Contrary to the present results, the plot did not pass through the origin (3). This was attributed to a competing direct electron exchange reaction, necessitating n-type conductivity in the electrolyte. However, the limiting currents appeared at $E <$ 1V corresponding to $P_{O_2} > 10^{-19}$ atm at 810°C. Even at $P_{O_2} = 10^{-19}$ atm, $t_e < 10^{-4}$ where t_e is the electronic transport number (1).

In conclusion, reaction [1] is considered to occur via the following mechanism:

$$O_{2,g}(\text{in bulk}) \rightarrow O_{2,g}(\text{in Pt pores}) \quad [1a]$$

$$O_{2,g}(\text{in Pt pores}) \rightleftharpoons O_{2,ad}(\text{on Pt}) \quad [1b]$$

$$O_{2,ad}(\text{on Pt}) \rightleftharpoons O_{2,ad}(\text{near tpb}) \quad [1c]$$

$$O_{2,ad}(\text{near tpb}) \rightleftharpoons 2\,O_{ad}(\text{near tpb}) \quad [1d]$$

$$2\,O_{ad}(\text{near tpb}) \rightleftharpoons 2\,O_{ad}(\text{at ers}) \quad [1e]$$

$$2\,O_{ad}(\text{at ers}) + 2V_O{}^{\cdot\cdot} \rightleftharpoons 2\,O_O + 4h^{\cdot} \quad [1f]$$

$$4h^{\cdot} + 4e' \rightleftharpoons 0 \quad [1g]$$

In this sequence, tpb means three-phase boundary (lines of contact where the electrode, electrolyte, and gas phases meet), ers means electrochemical reaction site, $V_O{}^{\cdot\cdot}$ is a doubly-ionized oxygen vacancy, O_O is an oxygen ion on a normal lattice site, $h^{\cdot}$ is an electron hole in the electrolyte, and e' is an excess electron in the electrode. Step [1a] is rate-controlling and involves the interdiffusion of oxygen and argon in the pores of the electrode deposited on the solid electrolyte. If simply the collision rate of oxygen gas with the electrode was rate-limiting, kinetic theory predicts that $i_l \sim 10^5$ mA/cm² at $P_{O_2} = 10^{-3}$ atm and 1000°C for an adsorption efficiency of unity. Also, the gas flow rate would have a negligible effect.

Oxygen molecules are then physically adsorbed onto a layer of chemisorbed oxygen atoms covering the electrode (step [1b]). Some direct access of the gas to the electrolyte via Pt channels is certainly possible in which case it reversibly adsorbs as mobile O_2^- ions which can later dissociate to atomic oxygen (46). Since oxygen molecules are not as strongly adsorbed as oxygen atoms [ΔH_{ad} of O_2 on Pt ~ -17 kcal/mole at 200°-400°C (40)], surface diffusion of oxygen molecules to the vicinity of a three-phase boundary (step [1c]) undoubtedly precedes dissociation (step [1d]). Subsequently, oxygen atoms diffuse relatively short distances along the surface of the electrode and electrolyte and through the electrode to electrochemical reaction sites at the surface of the electrolyte (step [1e]). Adsorbed atoms must enter the electrolyte (step [1f]) near a Pt particle so that electron holes can be neutralized quickly (step [1g]). Stabilized zirconia electrolytes will not support high concentrations of electron holes, even at oxygen pressures near 1 atm (1). Consequently, three-phase boundaries are required to minimize diffusion path lengths for oxygen atoms and to maximize the electrochemically active area at the electrolyte surface. The electrochemical step could also occur as follows:

$$2V_O^{\cdot\cdot} + 4e' \rightleftharpoons 2V_O \qquad [1f']$$

$$2\,O_{ad}(\text{at ers}) + 2V_O \rightleftharpoons 2\,O_O \qquad [1g']$$

Electrons are transferred across the electrode-electrolyte interface (step [1f']). If step [1g'] occurs at the gas-electrolyte interface, neutral oxygen vacancies, V_O, are obliged to migrate through the electrolyte. Since ionic migration is relatively slow, the importance of three-phase boundaries is again evident. Several authors have emphasized the necessity of maintaining as much three-phase contact as possible in cells with solid electrodes and oxide electrolytes (3, 4, 9, 47).

Overpotential at the anode (Fig. 2) was most likely observed because either step [1d] or [1a] is slow going to the left resulting in reaction or diffusion overpotential, respectively. An activation energy of about 90 kcal/mole is required to combine oxygen atoms adsorbed on ZrO_2 (39).

Some open-circuit irreversibility of the electrode was noted for Ar-O_2 mixtures very dilute in O_2 (~1 ppm), *i.e.*, the thermodynamic emf was established very slowly upon passing such mixtures into the system. At low oxygen contents, equilibrium between the gas and strongly adsorbed oxygen atoms (<1 monolayer) must be achieved. Step [1d] is probably slow to the left and the gas has a low capacity to chemically remove previously adsorbed species. Overpotential might be expected since the concentration of adsorbed oxygen molecules is very low (8). Accordingly, more oxygen atom diffusion (step [1e]) will be required.

H_2-H_2O mixtures.—Included in the discharge curves presented in Fig. 8 are results for two H_2-H_2O mixtures at the anode at 1000°C. The more dilute mixture contained less than 50 ppm H_2O, but emf measurements indicated that this was the concentration at the electrode-electrolyte interface. Oxygen arrives from the reference electrode compartment due to slight permeability of the electrolyte caused by electronic conductivity. Its influence was minimized by using a high flow rate at the anode. Also, as the cell potential decreases, electronic current in the electrolyte decreases (48). With H_2 as fuel, the cell discharges reversibly. The slopes of the curves ($E < 1.0$V) approximate the a-c resistance of the electrolyte. Overpotential decay characteristics revealed the presence of a small amount of concentration overpotential which was especially significant at low current densities and arose because of a buildup of H_2O at the anode.

CO-CO_2 mixtures.—Marked overpotential is evident in Fig. 8 with CO-CO_2 mixtures at the anode. It was particularly significant (with respect to resistance polarization) at low current densities and limiting currents were not approached, even when 200 mA/cm² at 1000°C and 300 mA/cm² at 1100°C were passed through the cell with the fuel electrode positive—characteristics of transition overpotential. Diffusion overpotential complicates the behavior of the 0.016% and 0.77% CO compositions. Enough CO was not available to maintain the anode reaction. For these gases, a weak dependence of current on flow rate was noted.

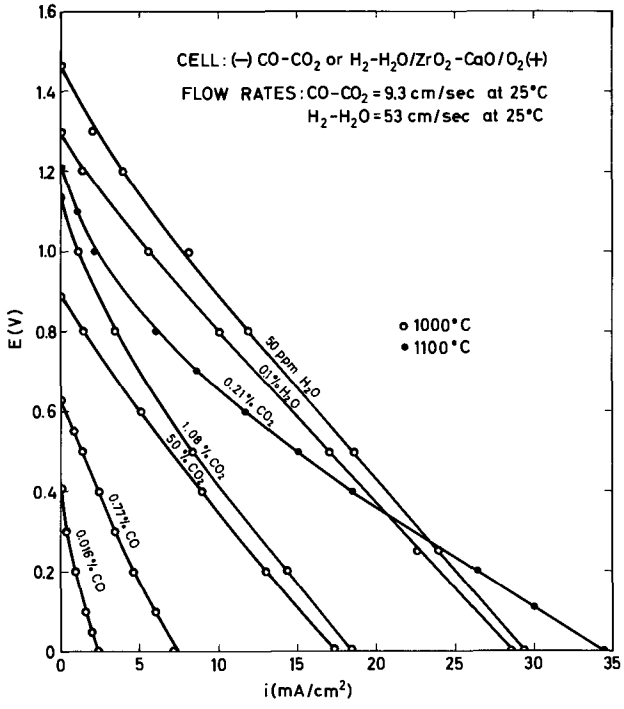

Fig. 8. Fuel cell discharge curves at 1000° and 1100°C

Transition or charge-transfer overpotential, η_t, was calculated from the equation

$$\eta_t = E_{rev} - E - IR_{a\text{-}c} - \eta_d \qquad [9]$$

where E is the cell potential. Small η_d contributions (<0.05V) were determined from cell potential measurements immediately after interrupting the current (η_d decayed much slower than η_t).

Transition overpotential can be expressed by the Tafel equation

$$\eta_t = -\frac{RT}{\alpha n\mathbf{F}} \ln i_o + \frac{RT}{\alpha n\mathbf{F}} \ln i \qquad [10]$$

where n is the number of electrons involved in the slow transition step. This equation applies when the rate of the reverse reaction is negligible compared to that of the forward reaction. A Tafel plot for the 0.21% CO_2 mixture at 1100°C is shown in Fig. 9. No carbon deposition at the anode was observed with this mixture [carbon is thermodynamically stable below 1112°C (41)]. From the slope, $\alpha n \sim 1$, *i.e.*, $\alpha \sim 0.5$ and $n = 2$ (the theoretical slope for $\alpha n = 1$ at 1100°C is 0.272V). From an extrapolation to $\eta_t = 0$, $i_o = 0.6$ mA/cm².

To study the cathode reaction and enable the behavior of CO-CO_2 mixtures dilute in CO to be more readily analyzed, the curves in Fig. 10 were obtained. Reversible potentials have been subtracted from applied potentials so that all the curves pass through the origin. Points below 3V at 700°C have been omitted. Breakdown of the electrolyte is evident at 700° and 850°C and appears at lower applied potentials as the CO_2 concentration decreases. Transition overpotential was determined with an expression similar to Eq. [5]. Again, small η_d contributions (<0.1V) were subtracted. Tafel plots for six curves in Fig. 10 are presented in Fig. 11. When $\eta_t < 0.2$V, the points deviate to the left of the lines since the rate of the reverse reaction cannot be neglected. In every case, $\alpha n \sim 1$

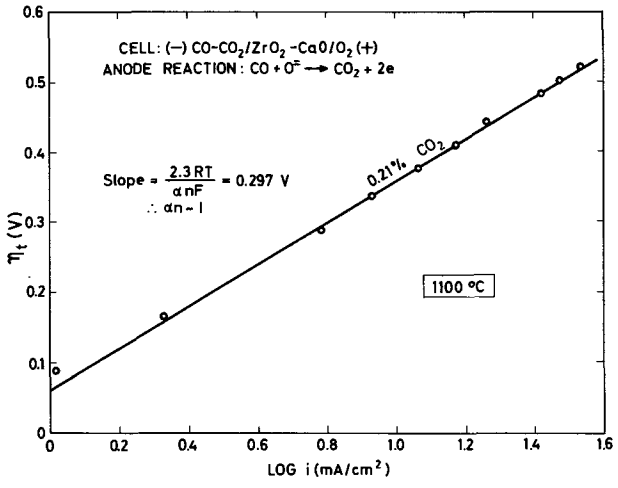

Fig. 9. Tafel plot for a CO + 0.21% CO_2 mixture at the anode at 1100°C.

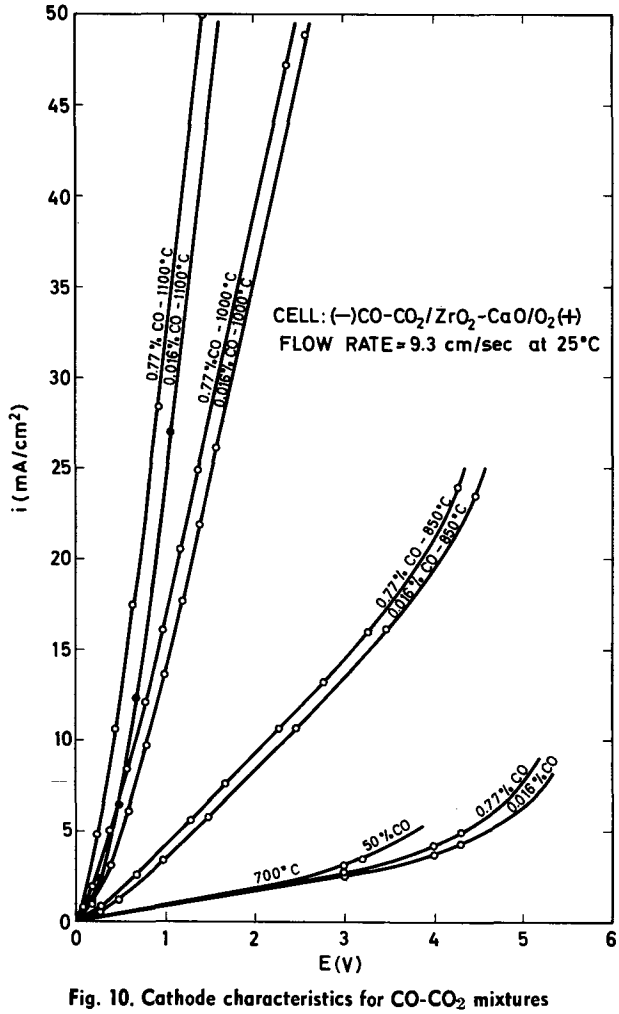

Fig. 10. Cathode characteristics for CO-CO_2 mixtures

(α = 0.46-0.52). Exchange current densities range between 0.1 and 1.6 mA/cm^2. They increase as either temperature or the CO concentration increases. Because of the large $IR_{a\text{-}c}$ drop at 700°C, accurate determination of η_t was difficult. Tafel plots indicated that $i_o \sim 0.05$ and 0.15 mA/cm^2 for the 0.016% and 0.77% CO compositions, respectively. Nevertheless, the a-c resistance of the electrolyte did not influence the Tafel parameters, *e.g.*, values for i_o at 1000°C of 1.1 mA/cm^2 for 0.77% CO and 1.3 mA/cm^2 for 0.89% CO were determined with a-c resistances of 40 and 95 ohms, respectively.

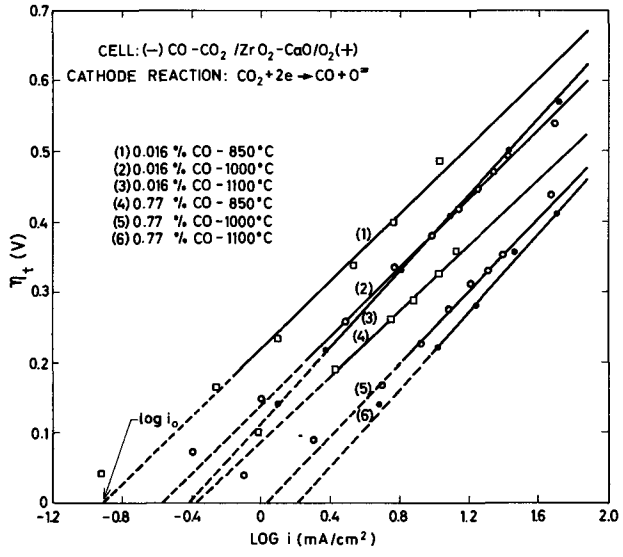

Fig. 11. Tafel plots for CO-CO_2 mixtures dilute in CO at the cathode.

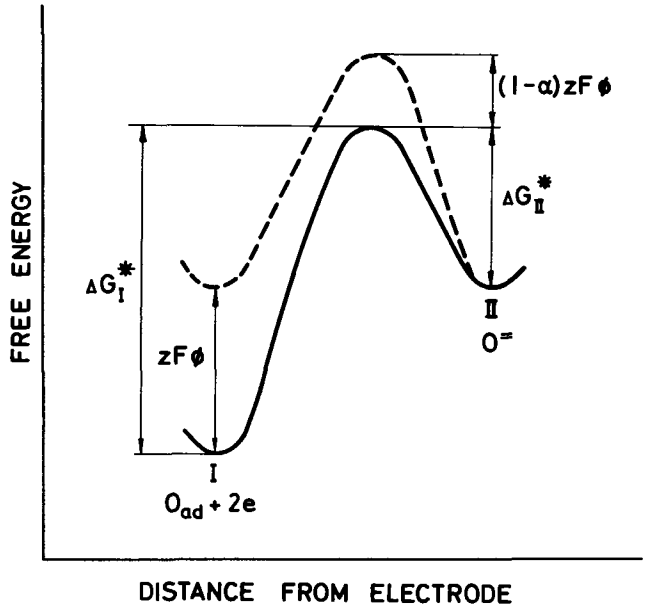

Fig. 12. Free energy profiles at the surface of an oxide electrolyte: ——— chemical free energy before any charge is transferred across the energy barrier, - - - - - electrochemical free energy at equilibrium; α, transition factor, *i.e.*, the fraction of the distance across the Helmholtz double layer where the transition state is located; z, valence of the ions crossing the barrier; ϕ, electrode potential with respect to the bulk of the oxide electrolyte; ΔG_I^* and ΔG_{II}^*, chemical free energies of activation from the initial state (I) and the final state (II) to the transition state, respectively. The pre-electrode state and state II (ϕ = 0) are often equivalent if the potential drop in the diffuse double layer can be neglected—a reasonable assumption for solid ionic conductors.

Regarding the mechanism of the electrode reaction in CO-CO_2 mixtures, the electrochemical equilibria in an oxide electrolyte cell involve the transfer of oxygen across the gas-electrolyte or electrode-electrolyte interface according to

$$O_{ad} + 2e \rightleftharpoons O^= \qquad [11]$$

Oxygen passes through an energy barrier or transition state as schematically drawn in Fig. 12 (symbols are explained in the caption). In this example, electrochemical equilibrium is established after a sufficient number of $O^=$ ions have left the electrolyte to equalize

the free energies of states I and II. Consequently, the double layer consists of electrons in the electrode facing doubly ionized oxygen vacancies at the surface of the electrolyte, ϕ is negative, and $z = -2$. Naturally, for the thermodynamic electrode potential to be established, adsorbed oxygen atoms must be in equilibrium with the gas phase.

The equilibrium given by Eq. [11] and depicted in Fig. 12 (dashed curve) is more fully expressed as

$$O_{ad} + V_O^{\cdot\cdot} + 2e' \rightleftharpoons O_O \qquad [12]$$

which represents the over-all electrochemical equilibrium when only oxygen species participate. The reversible electrode potential, ϕ_{rev}, is

$$\phi_{rev} = \phi^o + \frac{RT}{2F} \ln \frac{\theta_O[V_O^{\cdot\cdot}]}{[O_O](1 - \theta_O)} \qquad [13]$$

where ϕ^o is the standard electrode potential. It includes activity coefficients which are assumed to be constant, *i.e.*, adsorption is assumed to follow a Langmuir isotherm. Adsorbed species other than oxygen atoms occupying electrochemically active sites would simply make the fraction of free sites $1 - \theta_O - \theta_t$ where θ_t is the total fraction of the sites occupied by the additional species. Based on absolute reaction-rate theory, the current in the forward (cathodic) direction, $\vec{i}$, is

$$\vec{i} = k_1\theta_O[V_O^{\cdot\cdot}] \exp [-(\Delta G_I^{o*} - \alpha z\mathbf{F}\phi)/RT] \qquad [14]$$

where k_1 includes $n\mathbf{F}$, a transmission coefficient, and the vibration frequency of the activated species (kT/h), and ΔG_I^{o*} is the standard chemical free energy of activation from state I to the transition state. Similarly

$$\overleftarrow{i} = k_2[O_O](1 - \theta_O) \exp [-(\Delta G_{II}^{o*} + (1 - \alpha)z\mathbf{F}\phi)/RT] \qquad [15]$$

When the reversible potential is established ($\phi = \phi_{rev}$)

$$\vec{i} = \overleftarrow{i} = i_o \qquad [16]$$

Substituting Eq. [13] and [16] into Eq. [14] and recalling that $z = -2$ gives

$$i_o = k_1\theta_O[V_O^{\cdot\cdot}] \exp [-(\Delta G_I^{o*} - \alpha z\mathbf{F}\phi^o)/RT] \left(\frac{[O_O]^\alpha(1 - \theta_O)^\alpha}{\theta_O{}^\alpha[V_O^{\cdot\cdot}]^\alpha}\right) \qquad [17]$$

Therefore

$$i_o = k_3[V_O^{\cdot\cdot}]^{1-\alpha}[O_O]^\alpha\theta_O{}^{1-\alpha}(1 - \theta_O)^\alpha \qquad [18]$$

An identical equation is derived upon substituting Eq. [13] and [16] into Eq. [15]. For $\alpha \sim 0.5$, i_o increases as the electrolyte vacancy concentration increases (the fraction of vacant sites is always less than 0.5). For a given electrolyte composition

$$i_o = k_4\theta_O{}^{1-\alpha}(1 - \theta_O)^\alpha \qquad [19]$$

Equation [19] semiquantitatively describes the relationship between i_o and θ_O. Because of the simplifying assumption that adsorption obeys a Langmuir isotherm, k_4 cannot be regarded as constant over the entire range $0 < \theta_O < 1$, but may be approximately constant if $\theta_O < 0.1$ or $\theta_O > 0.9$.

At the Pt,CO-CO_2 electrode, the over-all equilibrium is

$$CO_{2,g} + 2e \rightleftharpoons CO_g + O^= \qquad [20]$$

Excluding diffusion processes which were found to be relatively rapid, a possible mechanism for the electrode reaction is

$$CO_{2,g} \rightleftharpoons CO_g + O_{ad} \qquad [20a]$$

$$O_{ad} + 2e \rightleftharpoons O^= \qquad [20b]$$

whereby atomic oxygen is adsorbed on either the electrode or electrolyte in step [20a] and diffuses, if necessary, to electrochemically active sites to participate in step [20b]. Nevertheless, step [20a] must occur near three-phase boundaries since the flux of adsorbed oxygen will be very low at the low oxygen pressures under consideration. Studies of the oxidation of CO on Pt (40, 49, 50) have shown that step [20a] is quite rapid. A similar reaction involving CO_{ad} on Pt (50) or ThO_2 (51), a fluorite-type oxide similar to stabilized ZrO_2, is less probable since CO is strongly chemisorbed. For the reaction

$$CO_g \rightarrow CO_{ad} \qquad [21]$$

at 25°C, ΔH_{ad} on Pt $= -48$ kcal/mole (38, 52) and on $ThO_2 = -17$ kcal/mole (51) at low coverage. On both Pt (38, 50) and ThO_2 (51), the process is virtually nonactivated. Consequently, chemisorbed CO might only serve to block reaction sites. This argument does not preclude the possibility of CO physically adsorbing onto chemisorbed oxygen atoms. Carbon dioxide is not adsorbed on Pt at 25°-1400°C (53, 54) or on ThO_2 above 600°C (55).

In the preceding sequence, if step [20b] is slow, transition overpotential will be observed and the discussion based on Fig. 12 will apply. Equation [19] simply becomes

$$i_o = k_4\theta_O{}^{1-\alpha}(1 - \theta_{CO})^\alpha \qquad [22]$$

In CO-CO_2 mixtures, $\theta_{CO} >> \theta_O$ and, therefore, the fraction of free sites $\sim 1 - \theta_{CO}$. Step [20a] will be in equilibrium and its equilibrium constant is

$$K = \frac{P_{CO}\theta_O}{P_{CO_2}(1 - \theta_{CO})} \qquad [23]$$

Rearranging Eq. [23] and substituting into Eq. [22] yields

$$i_o = k_5(1 - \theta_{CO}) \left(\frac{P_{CO_2}}{P_{CO}}\right)^{1-\alpha} \qquad [24]$$

Contrary to the results of this investigation and two other studies (14, 21), Eq. [24] predicts that i_o continuously decreases as the CO/CO_2 ratio increases. From Fig. 9 and 11, $i_o \sim 0.5$ mA/cm^2 for 0.02% and 99.79% CO at 1100°C.

Step [20a] has been suggested as the rate-determining process (20). Reaction overpotential, η_r, would appear due to an accumulation or depletion of adsorbed oxygen at the electrolyte surface. Since step [20b] will be in equilibrium, then, from Eq. [13]

$$\eta_r = \frac{RT}{2F} \ln \frac{\theta_O(1 - \theta_{O,rev})}{\theta_{O,rev}(1 - \theta_O)} \qquad [25]$$

where $\theta_{O,rev}$ and $1 - \theta_{O,rev}$ are the fractions of available active sites occupied by adsorbed oxygen atoms and free, respectively, at the reversible potential ($i = 0$) and θ_O and $1 - \theta_O$ are the corresponding fractions at current density i. A relationship between η_r and i for a given CO-CO_2 mixture is required and, therefore, θ_{CO} is constant (reaction [21] is in equilibrium). Any dependence of adsorption on potential is assumed to be negligible. Adsorbed CO serves only to block a constant number of chemically active sites and, consequently, θ_O is based here on the number of available active sites, rather than the total number of active sites.

The net current density resulting from step [20a] is

$$i = k_6(1 - \theta_O) - k_7\theta_O \qquad [26]$$

In Eq. [26], $i = 2\mathbf{F}v$ where v is the net velocity of reaction [20a]. Cathodic current is positive. Conditions are chosen so that P_{CO} and P_{CO_2} are unaffected by current. At equilibrium, $i = 0$ meaning that

$$i_o = k_6(1 - \theta_{O,rev}) = k_7\theta_{O,rev} \qquad [27]$$

In this sense, $i_o = 2\mathbf{F}v_o$ where v_o is the reaction exchange velocity. Inserting Eq. [27] into Eq. [26] gives

$$i = i_o \left(\frac{1 - \theta_O}{1 - \theta_{O,rev}}\right) - i_o \left(\frac{\theta_O}{\theta_{O,rev}}\right) \qquad [28]$$

Rearranging Eq. [28] and substituting into Eq. [25] leads to

$$\eta_r = \frac{RT}{2F} \ln \left[1 - \frac{i}{i_o \left(\frac{1-\theta_O}{1-\theta_{O,rev}} \right)} \right] \quad [29]$$

or, alternatively

$$\eta_r = -\frac{RT}{2F} \ln \left[1 + \frac{i}{i_o \left(\frac{\theta_O}{\theta_{O,rev}} \right)} \right] \quad [30]$$

Regarding anodic overpotential, if oxygen atoms are weakly adsorbed ($\theta_{O,rev} << 1$), Eq. [29] predicts that, at current densities low enough so that $\theta_O << 1$ but high enough so that $|i| >> i_o$

$$\eta_r = \frac{RT}{2F} \ln \left(-\frac{i}{i_o} \right) \quad [31]$$

That is, Tafel behavior will be observed. The reaction overpotential will be characterized by the appearance of a limiting current when $\theta_O = 1$. From Eq. [26] and [27]

$$i_l = -\frac{i_o}{\theta_{O,rev}} \quad [32]$$

For strong adsorption ($\theta_O, \theta_{O,rev} \sim 1$), Eq. [30] and [32] give

$$\eta_r = \frac{RT}{2F} \ln \frac{i_l}{i_l - i} \quad [33]$$

Cathodic overpotential and weak adsorption ($\theta_O, \theta_{O,rev} << 1$) lead to an expression opposite in sign to Eq. [33] from a consideration of Eq. [26], [27], and [29]. According to Eq. [30], conditions of strong adsorption ($\theta_{O,rev} \sim 1$) and current densities such that $\theta_O \sim 1$ but $i >> i_o$ produce

$$\eta_r = -\frac{RT}{2F} \ln \frac{i}{i_o} \quad [34]$$

From Eq. [26] and [27], a limiting current density given by

$$i_l = \frac{i_o}{1 - \theta_{O,rev}} \quad [35]$$

will be observed when $\theta_O = 0$.

Consequently, reaction overpotential resulting from step [20a] being slow (20) exhibits Tafel behavior for anodic currents if oxygen adsorption is weak and for cathodic currents if oxygen adsorption is strong. Nevertheless, the present results rule out this possibility. In the first place, Eq. [31] and [34] indicate that the Tafel slopes would be half those observed (Fig. 9 and 11). Secondly, as already mentioned, no evidence of limiting currents could be advanced.

Both reactions [20a] and [20b] have now been eliminated as rate-limiting steps and, necessarily, the mechanism they represent must be discarded.

Consider reaction [20] to occur as a single step, *i.e.*, [20a] and [20b] are not independent. It can be fully expressed as

$$CO_{2,g} + V_O^{\cdot\cdot} + 2e' \rightleftharpoons CO_g + O_O \quad [36]$$

In this mechanism, CO and CO_2 participate directly in the electrochemical step of the reaction at the gas-electrolyte interface. Naturally, free active sites at the electrolyte surface are required to effect this reaction. As three phases are involved, reaction [36] must actually occur as follows

$$V_O^{\cdot\cdot} + 2e' \rightleftharpoons V_O \quad [36a]$$

$$CO_{2,g} + V_O \rightleftharpoons CO_g + O_o \quad [36b]$$

At the low oxygen pressures imposed by CO-CO_2 mixtures, excess electrons could migrate through the electrolyte from the electrode-electrolyte interface to the gas-electrolyte interface prior to step [36a]. Alternatively, step [36a] could take place at the electrode-electrolyte interface making neutral oxygen vacancies the migrating species. Since the excess electron concentration in the electrolyte is low ($t_e < 10^{-3}$ at $P_{O_2} = 10^{-16}$ atm and 1000°C) and the ionic conductivity is also low (3.8×10^{-2} ohm^{-1} cm^{-1} at 1000°C), it is advantageous for the steps to proceed near three-phase boundaries.

For reaction [36]

$$\phi_{rev} = \phi^\circ + \frac{RT}{2F} \ln \frac{P_{CO_2}}{P_{CO}} \quad [37]$$

where $[V_O^{\cdot\cdot}]$ and $[O_O]$, which are virtually constant, have been included in ϕ°. Consideration of Fig. 12 and rate theory gives

$$\vec{i} = k_8 P_{CO_2} (1 - \theta_{CO}) \exp [-(\Delta G_1^{o*} - \alpha z F \phi)/RT] \quad [38]$$

A similar expression can be written for $\overleftarrow{i}$. At equilibrium, $\vec{i} = i_o$ and $\phi = \phi_{rev}$. Substituting Eq. [37] into Eq. [38] yields

$$i_o = k_9 (1 - \theta_{CO}) P_{CO_2}^{1-\alpha} P_{CO}^{\alpha} \quad [39]$$

This relationship successfully explains the overpotential behavior in CO-CO_2 mixtures. Since θ_{CO} is undoubtedly quite large (except when P_{CO} is very low) and, therefore, relatively insensitive to gas composition, the $P_{CO_2}^{1-\alpha} P_{CO}^{\alpha}$ factor will predominate. Accordingly, because $\alpha \sim 0.5$, i_o should be a maximum near 50% CO. From the data in Fig. 8 and 11 at 1000°C, i_o is 0.25, 1.1, ~3, and ~0.6 mA/cm^2 for 0.016%, 0.77%, 50%, and 98.9% CO, respectively. In partial support of these data, minimum overpotential was recently observed at 50-70% CO (21), while Zahradnik (22) has shown that earlier results (14) exhibited a trend towards maximum exchange current densities at 50% CO. However, Eq. [39] indicates that the maximum should occur below 50% CO. This is consistent with the finding that exchange current densities are somewhat higher for mixtures dilute in CO than for those dilute in CO_2, *e.g.*, by using Eq. [39] when necessary to interpolate the data in Fig. 8, 9, and 11 (assuming $\theta_{CO} \sim$ constant over narrow gas composition ranges), $i_o = 1.2$ mA/cm^2 for 1% CO and 0.6 mA/cm^2 for 1% CO_2 at 1000°C, and $i_o = 1.0$ mA/cm^2 for 0.2% CO and 0.6 mA/cm^2 for 0.2% CO_2 at 1100°C.

Physically, the mechanism described by reaction [20] or [36] involves direct impingement of gas molecules on the surface of the oxide electrolyte (any CO_{ad} will undoubtedly block the otherwise most active sites). Porous electrodes permitting a considerable amount of gas-electrolyte contact are desirable. For instance, in the anode reaction, carbon atoms in CO collide with $O^=$ ions at the electrolyte surface to form gaseous CO_2 and neutral oxygen vacancies in the electrolyte. In ZrO_2, $O^=$ ions are about one and a half times as large (1) and twice as numerous as Zr^{4+} ions and, therefore, occupy most of the surface area.

The possibility of direct involvement of CO_{ad} in the electrochemical reaction cannot be overlooked, *i.e.*, reactions [20] and [21] could occur in series rather than in parallel. Accordingly

$$CO_{2,g} + 2e \rightleftharpoons CO_{ad} + O^= \quad [40]$$

Since an expression for i_o identical to Eq. [39] can be derived for reaction [40], a distinction cannot be made as to whether CO_g or CO_{ad} participates in the electrochemical step. If ZrO_2 adsorbs CO via carbon atoms linking to $O^=$ ions as reported for ThO_2 (55), CO_{ad} will be favorably located to effect reaction [40].

Equation [39] indicates that the exchange current density depends on the number of free sites. One reason for lower exchange current densities (higher overpotential) in CO-CO_2 mixtures than in H_2-H_2O mixtures (Fig. 8) is that, generally, $\theta_{CO} > \theta_H$. For example, at low coverage and 25°C, ΔH_{ad} of H atoms on Pt ~ −15 kcal/mole H_2 (36, 56) compared to −48 kcal/mole for CO (38, 52) and Pt preferentially adsorbs CO from CO-H_2 mixtures (57). Another reason is the presence of higher energy barriers (Fig. 12) to impede the electrochemical reaction.

Conclusions

To study overpotential in oxide electrolyte fuel cells, the Pt,O_2 electrode serves as an excellent reference electrode over a wide range of temperature and current density. Sufficiently porous electrodes enable the cathode reaction in $Ar-O_2$ mixtures to be solely limited by the diffusion of gaseous oxygen in the electrode pores from 850° to 1100°C. Limiting current densities are directly proportional to oxygen pressure. Although overpotential is essentially absent for H_2-H_2O mixtures, $CO-CO_2$ mixtures cause the appearance of marked transition overpotential at 700° to 1100°C. The transition factor is about 0.5 and exchange current densities, which increase with increasing temperature, vary between about 0.05 and 3 mA/cm². The maximum exchange current density is expected for a gas mixture containing somewhat less than 50% CO. Gaseous or adsorbed CO and gaseous CO_2 participate directly in the electrochemical step of the electrode reaction.

Acknowledgment

The authors wish to thank the National Research Council of Canada for financial support of this investigation.

Manuscript received April 21, 1971. This was Paper 329 presented at the Los Angeles Meeting of the Society, May 10-15, 1970.

Any discussion of this paper will appear in a Discussion Section to be published in the June 1972 JOURNAL.

LIST OF SYMBOLS

C_D	double-layer capacitance
$(C_F)_c$	Faraday capacitance resulting from concentration overpotential
C_G	grain boundary capacitance
CO_{ad}	chemisorbed CO molecule
E	applied potential or cell potential
E_{rev}	reversible potential (emf)
e'	excess electron
f	frequency
ΔG^*	chemical free energy of activation
ΔG_{ad}	free energy of adsorption
ΔH_{ad}	enthalpy of adsorption
$h^{\cdot}$	electron hole
I	current
i	current density
i_l	limiting current density
i_o	exchange current density
k	constant
n	number of electrons associated with the rate-limiting step of an electrode reaction
O_O	$O^=$ ion on a normal lattice site
O_{ad}	chemisorbed oxygen atom
$O_{2,ad}$	physically adsorbed oxygen molecule
R_B	bulk electrolyte resistance
$(R_F)_c$	Faraday resistance resulting from concentration overpotential
$(R_F)_t$	Faraday resistance resulting from transition overpotential
R_G	grain boundary resistance
R_T	total resistance
R_{a-c}	a-c resistance at 3000 Hz
R_{d-c}	d-c resistance at zero current
ΔS_{ad}	entropy of adsorption
t_e	electronic transport number
V_O	neutral oxygen vacancy
$V_O^{\cdot\cdot}$	doubly-ionized oxygen vacancy
z	valence
α	transition factor or transfer coefficient
η_d	diffusion overpotential
η_r	reaction overpotential
η_t	transition overpotential
θ_j	fraction of active sites occupied by adsorbed species j
$\theta_{j,rev}$	fraction of active sites occupied by adsorbed species j at the reversible potential
ϕ	electrode potential with respect to the bulk of the oxide electrolyte
ϕ_{rev}	reversible electrode potential
ϕ^o	standard electrode potential

REFERENCES

1. T. H. Etsell and S. N. Flengas, *Chem. Rev.*, **70**, 339 (1970).
2. A. D. Neuimin, S. V. Karpachev, and S. F. Pal'guev, *Dokl. Phys. Chem.*, **141**, 875 (1961).
3. M. Kleitz, J. Besson, and C. Deportes, *Rev. Energ. Primaire*, **2**, 35 (1966).
4. S. V. Karpachev and A. T. Filyaev, *Sov. Electrochem.*, **2**, 1215 (1966); *Z. Phys. Chem.*, **238**, 284 (1968).
5. M. Guillou, J. Millet, and S. Palous, *Electrochim. Acta*, **13**, 1411 (1968). M. Guillou, A. Lecante, and J. Millet, *Rev. Gen. Elec.*, **77**, 1051 (1968).
6. S. V. Karpachev and Yu. M. Ovchinnikov, *Sov. Electrochem.*, **5**, 181 (1969).
7. C. S. Tedmon, Jr., H. S. Spacil, and S. P. Mitoff, *This Journal*, **116**, 1170 (1969).
8. J. E. Bauerle, *J. Phys. Chem. Solids*, **30**, 2657 (1969).
9. H. Yanagida, R. J. Brook, and F. A. Kröger, *This Journal*, **117**, 593 (1970).
10. R. J. Brook, W. L. Pelzmann, and F. A. Kröger, *ibid.*, **118**, 185 (1971).
11. R. E. W. Casselton, J. S. Thorp, and D. A. Wright, *Proc. Brit. Ceram. Soc.*, **19**, 265 (1971). R. E. W. Casselton, *Elec. MHD, Proc. Symp.*, Vol. V, p. 2951, International Atomic Energy Agency, Vienna (1968).
12. J. Weissbart and R. Ruka, *This Journal*, **109**, 723 (1962); "Fuel Cells," Vol. 2, p. 37, G. J. Young, Editor, Reinhold Publishing Corp., New York (1963).
13. H. Binder, A. Köhling, H. Krupp, K. Richter, and G. Sandstede, *Electrochim. Acta*, **8**, 781 (1963).
14. D. H. Archer, L. Elikan, and R. L. Zahradnik, "Hydrocarbon Fuel Cell Technology," p. 51, B. S. Baker, Editor, Academic Press, New York (1965).
15. E. F. Sverdrup, D. H. Archer, J. J. Alles, and A. D. Glasser, *ibid.*, p. 311.
16. D. H. Archer, J. J. Alles, W. A. English, L. Elikan, E. F. Sverdrup, and R. L. Zahradnik, *Advan. Ceram. Ser.*, **47**, 332 (1965).
17. H.-H. Möbius and B. Rohland, *Rev. Energ. Primaire*, **2**, 27 (1966).
18. T. Takahashi, K. Ito, and H. Iwahara, *ibid.*, **2**, 42 (1966).
19. V. N. Chebotin, M. V. Glumov, A. D. Neuimin, and S. F. Pal'guev, *Sov. Electrochem.*, **7**, 55 (1971).
20. S. V. Karpachev, A. T. Filyaev, and S. F. Pal'guev, *Electrochim. Acta*, **9**, 1681 (1964).
21. S. V. Karpachev, A. E. Zupnik, and M. V. Perfil'ev, *Sov. Electrochem.*, **6**, 564 (1970).
22. R. L. Zahradnik, *This Journal*, **117**, 1443 (1970).
23. V. N. Chebotin, M. V. Glumov, S. F. Pal'guev, and A. D. Neuimin *Sov. Electrochem.*, **7**, 179 (1971).
24. M. V. Perfil'ev and S. F. Pal'guev, "Electrochemistry of Molten and Solid Electrolytes," Vol. 4, p. 147, A. N. Baraboshkin and S. F. Pal'guev, Editors, Consultants Bureau, New York (1967).
25. A. T. Filyaev, S. V. Karpachev, and S. F. Pal'guev, *ibid.*, p. 161.
26. H. Tannenberger and H. Siegert, *Am. Chem. Soc., Div. Fuel Chem., Prepr.*, **11**, 197 (1967).
27. M. V. Perfil'ev, S. F. Pal'guev, and S. V. Karpachev, *Sov. Electrochem.*, **1**, 74 (1965).
28. A. L. L'vov, E. P. Lomova, and E. N. Gushchina, *ibid.*, **5**, 965 (1969).
29. R. Hartung and H.-H. Möbius, *Z. Chem.*, **7**, 325 (1967).
30. H. Schachner and H. Tannenberger, *Rev. Energ. Primaire*, **2**, 49 (1966).
31. M. V. Glumov, A. D. Neuimin, and S. F. Pal'guev, *Sov. Electrochem.*, **4**, 1114 (1968).
32. M. V. Glumov, V. N. Chebotin, S. F. Pal'guev, and A. D. Neuimin, *ibid.*, **6**, 386 (1970).
33. Ya. P. Gokhshtein and A. A. Safonov, *Dokl. Phys. Chem.*, **195**, 829 (1970); *High Temp.*, **8**, 368 (1970).
34. C. Deportes, *Rev. Gen. Elec.*, **76**, 50 (1967).
35. Ya. P. Gokhshtein, *Dokl. Phys. Chem.*, **190**, 10 (1970).
36. J. G. Aston, E. S. J. Tomezsko, and R. A. Fisher, Jr., *J. Am. Chem. Soc.*, **86**, 2097 (1964).
37. Y. L. Sandler and D. D. Durigon, *J. Phys. Chem.*, **72**, 1051 (1968).
38. B. J. Wood, N. Endow, and H. Wise, *J. Catalysis*, **18**, 70 (1970).
39. T. Smith, *This Journal*, **111**, 1027 (1964).
40. A. V. Sklyarov, I. I. Tret'yakov, B. R. Shub, and S. Z. Roginskii, *Dokl. Phys. Chem.*, **189**, 829 (1969).

41. O. Kubaschewski, E. Ll. Evans, and C. B. Alcock, "Metallurgical Thermochemistry," 4th ed., Pergamon Press, London (1967).
42. D. O. Hayward and B. M. W. Trapnell, "Chemisorption," 2nd ed., pp. 298-99. Butterworths, London (1964).
43. R. E. Carter, "Electromotive Force Measurements in High-temperature Systems," p. 103, C. B. Alcock, Editor, Institution of Mining and Metallurgy, London (1968).
44. A. T. Filyaev, S. V. Karpachev, and I. D. Remez, *Sov. Electrochem.*, **6**, 274 (1970).
45. R. J. Ruka and A. J. Panson, Ger. Offen. 1,954,663, May 6, 1970, 12 pp.
46. T. Smith, *This Journal*, **111**, 1020 (1964).
47. M. V. Perfil'ev and S. F. Pal'guev, "Electrochemistry of Molten and Solid Electrolytes," Vol. 3, pp. 97 and 105, A. N. Baraboshkin, Editor, Consultants Bureau, New York (1966).
48. T. Takahashi, K. Ito, and H. Iwahara, *Electrochim. Acta*, **12**, 21 (1967).
49. I. Langmuir, *Trans. Faraday Soc.*, **17**, 621 (1922).
50. H. Heyne and F. C. Tompkins, *Proc. Roy. Soc.*, **A292**, 460 (1966).
51. M. Breysse, *Ann. Chim. (Paris)*, **2**, 367 (1967).
52. D. Brennan and F. H. Hayes, *Phil. Trans. Roy. Soc.*, **A258**, 347 (1965).
53. R. Vanselow and W. A. Schmidt, *Z. Naturforsch.*, **22a**, 717 (1967).
54. A. E. Morgan and G. A. Somorjai, *Surface Sci.*, **12**, 405 (1968)
55. P. Pichat, J. Véron, B. Claudel, and M. V. Mathieu, *J. Chim. Phys.*, **63**, 1026 (1966).
56. E. S. J. Tomezsko and G. T. Furukawa, *J. Catalysis*, **8**, 386 (1967).
57. D. W. McKee, *ibid.*, **8**, 240 (1967).

A Practical Assessment of Recent Transition-State Theories for the Electrical Conductance of Molten Salts

F. W. Dampier*,[1] and G. J. Janz*

Rensselaer Polytechnic Institute, Department of Chemistry, Troy, New York 12181

ABSTRACT

The modification of the Cohen-Turnbull and Adams-Gibbs theories by Angell for equivalent conductance in molten salts is briefly reviewed. The equivalent conductance data for some halide and nitrate melts is examined to determine the degree to which the non-Arrhenius behavior predicted by the Cohen-Turnbull theory occurs. The application of these transition-state theories for the description of the transport properties of molten salts is evaluated. The possibility of using the glass transition temperature as the basis for a corresponding temperature scale for crystallizing salts appears remote.

The present discussion is limited to pure stoichiometric ionic compounds in the molten state. Since a molten salt may be regarded as a highly disordered lattice, with a large number of temperature-independent defects, it has been proposed by various investigators, notably Bloom and Heyman (1), that the variation of electrical conductance with T is governed entirely by an activation energy, E, much as for these compounds in the crystalline state where the ionic conductance is attributed to lattice defects and the migration of ions via vacant sites in the crystal lattice. In another approach, Bockris, Crook, Bloom, and Richards (2) derive an expression for the electrical conductance using the hole model for ionic salts in the molten state and the transition-state theory of reaction rates; the expression shows reasonable accord with experimental results, especially from the Group IA compounds. More recently two additional expressions have been advanced by Angell (3, 4), both based on transition-state models, one starting with the liquid-state theory of Cohen and Turnbull (5), and the other, with that of Adams and Gibbs (6). The approaches by Bloom (1), Bockris (3), Stillinger (7), and others are adequately considered elsewhere (8-10); in this communication the results of an evaluation of the two more recent transition-state based expressions, as advanced by Angell, are reported.

The Free-Volume (Cohen-Turnbull) Model

Angell (3) had interpreted transport properties in ionic liquids using a model based on the concepts of the free-volume theory for transport in liquids, as derived by Cohen and Turnbull (4). Although diffusion was the transport property considered by Cohen and Turnbull, the model can be generalized to include electrical conductance or viscosity.

According to this model a particle of a liquid may undergo diffusive displacement when a void above a certain critical size appears adjacent to it. The voids are considered to arise from the random thermal redistribution of free volume in the liquid structure. The probability of occurrence of such a void adjacent to a given particle was shown to be an exponential function of the ratio of the critical void volume to the total free volume, and an expression for the diffusion coefficient was derived.

$$D = gau\,(-\gamma v^*/v_f) \qquad [1]$$

where g is a geometric factor given the value of 1/6; a, the jump distance; u, the gas kinetic velocity of the particle; γ, an overlap factor for free volume; v^*, the critical void volume; and v_f, the total free volume.

This expression, using known molecular constants and assumptions regarding the free volume and its relation to T_0, reduces to

$$D = AT^{1/2} \exp\,(-k/T - T_0) \qquad [2]$$

where A and k are constants. Differentiating, one obtains

$$\frac{d \ln D}{d(1/T)} = -T/2 - k(T/T - T_0)^2 \qquad [3]$$

The conventional Arrhenius activation energy for diffusion is given by

$$D = A \exp\,(-E_D/RT) \qquad [4]$$

* Electrochemical Society Active Member.
[1] Present address: ESB Incorporated, Research Center, Yardley, Pennsylvania 19067.

Key words: molten electrolytes, glass transition temperature, electrical conductance, Cohen-Turnbull theory, Adams-Gibbs theory.

A similar differentiation with respect to $1/T$ gives

$$\frac{d \ln D}{d(1/T)} = -E_D/R \quad [5]$$

Combining Eq. [3] and [5], one obtains

$$\frac{d \ln D}{d(1/T)} = -E_D/R = -\tfrac{1}{2}T - k\,(T/T - T_0)^2 \quad [6]$$

Equation [6] predicts that if the Cohen and Turnbull model is valid, $(E_D - \frac{1}{2}RT)$ should be a linear function of $(T/T - T_0)^2$, which passes through the origin. A test could also be made of the linearity of a plot of $\ln D/T^{1/2}$ *vs.* $1/(T - T_0)$; this, however, is a less stringent test of the temperature dependence.

In order to test the temperature dependence using Eq. [6], accurate diffusion data are needed. Since electrical conductance can be measured more accurately than diffusion, the temperature dependence of conductance was corrected to correspond to that for a diffusion process by the relation $E_D = E_A + RT$. The latter expression follows from the Nernst-Einstein relation, if one assumes very nearly equal or markedly differing values for the conductance activation energies of the anionic and cationic species in the melt. Thus, according to the free-volume (Cohen-Turnbull) model the corrected activation energy for equivalent conductance $(E_A + \frac{1}{2}RT)$ should be a linear function of $(T/T - T_0)^2$.

The Configurational-Entropy (Adams-Gibbs) Theory

The Adams-Gibbs theory (6) has been developed from a successful statistical mechanical theory of chain polymer liquids at high particle densities (11), which has been generalized to include nonpolymeric liquids. According to this theory, the translational motion of a given molecule occurs by a mechanism in which the cooperative rearrangement of a group of molecules need not be specified. Rather it is the minimum size of the cooperatively rearranging groups which determines the temperature dependence of the translational process. The minimum size of the cooperatively rearranging group can be obtained in terms of the macroscopic configurational entropy if the assumption is made that the cooperatively rearranging groups do not interact significantly. On this basis Angell (4) has shown that the electrical conductance is proportional to the transition probability

$$\Lambda T \propto \omega(T) = A \exp\left[\frac{-C}{\Delta C_p (T - T_0)}\right] = A \exp\left(-\frac{k}{T - T_0}\right) \quad [7]$$

where

$$C = \frac{\Delta\mu s_0^*}{R/N} \quad [8]$$

and ΔC_p is the difference in glassy and liquid state specific heats; $\Delta\mu$, the potential energy hindering the cooperative rearrangement; s_0^*, the configurational entropy of the critical-size cooperative region; and R/N the Boltzmann constant.

A comparison of the expressions for the temperature dependence of diffusion from the Cohen and Turnbull (Eq. [2]) and Adams-Gibbs (Eq. [7]) theories shows the same exponential temperature dependence on $(1/T - T_0)$. But in the development of the Adams-Gibbs theory (6) the frequency factor A was assumed to be negligibly dependent on the temperature and was not completely evaluated. Since the temperature dependence of the Adams-Gibbs expression has not been completely developed it is customary (4) to test the validity of the temperature dependence of this theory using the technique developed for the free-volume model, that is, from a test of the linearity of a plot of $(E + \frac{1}{2}RT)$ as a function of $(T/T - T_0)^2$.

The Physical Significance of the Temperature T_0

According to the Cohen and Turnbull theory, the temperature T_0 (Eq. [2]) is the temperature at which "free volume" begins to appear. Some evidence has been advanced for using values of the glass transition temperature for T_0. Thus, Angell (3) has reported a value of T_0 of 316°K for the 38.1% $Ca(NO_3)_2$ composition of the mixture of $(Ca(NO_3)_2, KNO_3)$ and this compares favorably with the value of 329°K, found by Dietzel and Poegel (12) for the glass transition temperature.

The Adams-Gibbs theory considers T_0 as the temperature at which the configurational entropy of the liquid becomes zero. This interpretation of T_0 derives from the statistical mechanical analysis rather than as the assumption introduced by Cohen and Turnbull. Regardless of the differing interpretations of the physical meaning of T_0, it is numericaly evaluated by an empirical approach, namely it is the value which gives a linear slope when $(E + \frac{1}{2}RT)$ is plotted as a function of $(T/T - T_0)^2$.

The frequent designation of T_0 as the glass transition temperature tends to imply that theories employing this parameter can only be applied to noncrystallizing liquids. This is not the case since the Adams-Gibbs theory is quite general; also the success of Eq. [2] for a variety of ionic liquids (*e.g.* KNO_3; LiCl-KCl, eut.; $PbCl_2$-AgCl) is further support for the general nature of the equations based on this approach.

The Temperature Dependence of Equivalent Conductance

The degree to which the Adams-Gibbs theory can be applied to molten salts will depend on the size of the deviations of equivalent conductance from classical "Arrhenius behavior." The deviations from a linear dependence of $\ln \Lambda$ *vs.* $1/T$ are dependent on how far the experimental temperature range is removed from T_0. For example, if the temperatures are in the range of $3T_0$ to $4T_0$ (*i.e.* 650°-950°K, if T_0 is about room temperature) the apparent Arrhenius activation energy would change only by 15%, whereas for temperatures in the range $1.5T_0$ to $2.0T_0$, the variation would be 130%.

Angell has successfully applied the Cohen-Turnbull theory to a number of glass-forming nitrate melts (3); for these melts the experimental temperature range is sufficiently close to T_0 so that the deviations from Arrhenius temperature dependence are large enough for T_0 to be calculated with reasonable precision. But for melts which crystallize [*e.g.* the majority of the 174 single-salt melts considered in the NSRDS critical compilation (13)], Angell predicted (3) that T_0 cannot be established precisely due to the present experimental uncertainty. Since the application of the Cohen-Turnbull and Adams-Gibbs concepts to crystallizing melts is of considerable interest, it was decided to test the precision of the Arrhenius equation for electrical conductance for a number of halide and nitrate single-salt melts. For this purpose, the NSRDS critical compilation of equivalent conductance data (13) provided a unique source of experimental values and statistical information. The calculations and results of this study are as follows.

Calculations and results.—One measure of the deviation of equivalent conductance from Arrhenius behavior is the precision of the exponential least squares equation. The precisions for a limited selection of halides and nitrates obtained from the NSRDS compilation (13) are in Table I. From a comparison of these precisions with the estimated accuracies for the conductance of these salts (KCl, 0.6%; RbCl, 3.5%) it could be concluded that the equivalent conductance is adequately and precisely represented by the Arrhenius relation. However, a more detailed consideration of the conductance data reveals that the precision of the experimental measurements as a function of temperature

Table I. Precisions for the recommended* exponential equations for equivalent conductance

Salt	% Precision	Salt	% Precision
LiCl	0.048	LiI	0.68
NaCl	0.057	NaI	0.0085
KCl	0.092	KI	0.68
RbCl	0.19	RbI	0.45
CsCl	0.26	CsI	0.48
AgCl	0.21	$LiNO_3$	0.095
TlCl	0.43	$NaNO_3$	0.028
LiBr	0.17	KNO_3	0.14
NaBr	0.12	$RbNO_3$	0.57
KBr	0.53	$CsNO_3$	0.019
RbBr	0.91	$AgNO_3$	0.45
CsBr	0.42	$TlNO_3$	0.35

* Table 177 (Ref. 13).

is considerably smaller than the estimated accuracy; further, systematic deviations from exponential behavior exist for most molten salts. Although several studies of the same salt [cf. KCl, Ref. (13)] often differ in the absolute amount of the values found for the specific conductance, the temperature dependence of the various investigations often tend to agree more closely.

An inspection of the residuals ($\Lambda_{calc} - \Lambda_{exp}$), gives a better indication of the nature of the deviations from Arrhenius behavior than the precision. Partial lists of the residuals for CsCl and $NaNO_3$ are given in Table II. It should be noted that the residuals are not of random size and sign as would be expected if an adequate fit to an exponential equation had been obtained; the residuals are large and positive near the melting point, and as the temperature increases, the residuals decrease and become negative, pass through a negative maxima, then increase and become positive again. Such systematic behavior of the residuals is characteristic of the exponential least squares equations for the majority of some 174 single-salt melts (13). This uniform departure from exponential behavior also indicates that some function other than the customary Arrhenius equation would probably give a more exact fit for equivalent conductance. There is, thus, good evidence to suggest that the temperature dependence of equivalent conductance can be expressed as a function of $(T/T - T_0)^2$ as has been suggested by Angell.

In a number of cases the experimental data selected as the basis for the NSRDS equivalent conductance equation is not entirely satisfactory for an analysis of the deviations from Arrhenius behavior. Often the specific conductance data from two investigators has been combined (*e.g.* as for salts such as LiCl, $NaNO_3$, and KNO_3) in order to have an equation which is valid over as large a temperature range as possible. For some salts the specific conductance has only been measured at temperatures far above the melting point (*e.g.* $LiNO_3$ mp 527°K; the lowest conductance measurement is 558°K). In other cases (*e.g.* CsCl) the specific conductance has only been measured every 20 or 30 degrees, and this makes a precise study of temperature dependence difficult. Conductance measurements near the melting point are frequently erratic (*e.g.* LiCl) and owing to a variety of experimental problems, it is frequently difficult to distinguish genuine irregularities in conductance behavior and "experimental" irregularities.

Table II. Deviations of equivalent conductance from the NSRDS recommended exponential least squares equation

	T°K	Λ	$r = (\Lambda_{calc} - \Lambda_{exp})$	$r\%$
CsCl				
	940	71.0	0.434	0.61
	950	73.2	0.29	0.40
	960	75.45	0.17	0.26
	970	77.7	0.065	0.084
	980	79.95	−0.024	−0.030
	990	82.15	0.099	0.12
	1000	84.4	−0.16	−0.19
	1020	88.8	−0.24	−0.27
	1050	95.5	−0.27	−0.28
	1080	100.2	−0.19	−0.19
	1110	108.7	−0.030	−0.027
	1140	115.3	0.20	0.17
	1160	119.8	0.39	0.33
	1170	122.0	0.50	0.41
$NaNO_3$				
	580	43.3	0.032	0.074
	590	45.4	0.0053	0.011
	600	47.6	−0.011	−0.023
	610	49.7	−0.019	−0.038
	620	51.9	−0.020	−0.038
	630	54.1	−0.016	−0.030
	640	56.3	−0.010	−0.018
	690	67.6	0.17	0.025*

* Λ value is an extrapolated value.

To obtain an estimate of the degree to which the deviations from Arrhenius behavior affect the activation energy for equivalent conductance, an exponential least squares analysis of the first three tabulated values near the melting point was carried out. A comparison of these activation energies (low temperature region) with those for the complete temperature range is in Table III. The values of equivalent conductance used for the least squares calculations in both cases were the values tabulated in the NSRDS compilation (13). Inspection of Table III shows that not only does the activation energy change the greatest amount for the heavier alkali metal chlorides but the activation energies for lithium and sodium chloride decrease near the melting point rather than increase as is the case for the other chlorides, KNO_3 and $AgNO_3$ (Tables IV and V). This decrease in the activation energy raises a further problem; a positive value for T_0, the glass transition temperature, can be obtained only if the activation energy increases as the melting point is approached.

The activation energies in Table III should be accepted with some reservations; slight variations of the activation energy are likely to result when limited temperature ranges are considered due to the experimental scatter of the points. The difference between the activation energies for the two temperature ranges is also influenced by the nearness of the lowest experimental conductance value to the melting point, and the over-all span of the complete range of the measurements (LiCl, 140°; NaCl, 310°).

An alternate approach to gain the change of the activation energy with temperature is the solution of two simultaneous exponential equations, using the values of adjacent points. The equivalent conductance values, for this purpose, were calculated from the specific conductance values at the experimental temperatures without employing the least squares equations for specific conductance.[2] The density values employed in these calculations were obtained from the linear temperature density equations (13). The values of the activation energy obtained from the solution of the simultaneous equations, the exponential least squares equation for the tabulated equivalent conductance values and the residuals for LiCl, CsCl, KNO_3, and $AgNO_3$ are in Tables IV and V.

The activation energies for LiCl, in Table IV, are seen to increase; this is in contrast to Table III where a

[2] The direct calculation of equivalent conductance from the experimental specific conductance values is necessary in order to avoid the averaging effect of the least squares equation.

Table III. A comparison of the activation energy E_Λ for the complete experimental temperature range with E_Λ calculated from the three lowest temperatures

Salt	E_Λ complete T range*	E_Λ first three points*	% change
LiCl	2015 (910-1050°K)	1968 (910-930°K)	−2.3
NaCl	2990 (1080-1290°K)	2927 (1080-1100°K)	−2.1
KCl	3415 (1060-1200°K)	3519 (1060-1080°K)	3.0
RbCl	4401 (990-1200°K)	4599 (990-1010°K)	4.3
CsCl	5110 (940-1170°K)	5450 (940-960°K)	6.3

* The equivalent conductance values employed were calculated using the NSRDS best equations for specific conductance and density [see Ref. (13)].

Table IV. The activation energy for equivalent conductance for some alkali chlorides and nitrates*

T°K	Λ	Residual (Λcalc − Λexp) r	r%	Activation energy
LiCl	Λ = 632.939 exp (−2425.0/RT)			
896.0	161.28	0.833	0.52	
907.6	165.64	−0.676	−0.41	3643.6
917.1	167.97	−0.696	−0.41	2075.9
941.0	172.49	0.534	0.31	1907.7
CsCl	Λ = 1147.06 exp (−5192.68/RT)			
926.5	68.29	0.0389	0.055	
962.2	75.98	−0.113	−0.15	5293.8
985.6	80.84	0.0747	0.092	4998.3
KNO3†	Λ = 809.19 exp (−3849.23/RT)			
609.2	33.57	0.0866	0.26	
626.1	39.70	−0.0342	−0.093	4006.5
636.3	38.58	−0.0496	−0.13	3880.3
644.5	41.12	−0.0657	−0.16	3889.0
658.6	42.75	−0.0293	−0.069	3792.2
667.8	44.50	−0.0137	−0.031	3816.0
683.9	47.52	0.108	0.23	3701.0

* Calculated directly from the experimental κ values without using the least squares equation for specific conductance.
† The specific conductance results of Angell (14) were used to calculate Λ [see Ref. (13)].

Table V. The activation energy for the equivalent conductance of silver nitrate*,†

T°K	Λ	(Λcalc − Λexp) r	r%	Arrhenius activation energy
483.2	28.34	0.374	1.32	
493.2	30.39	1.140	0.46	3250
503.2	32.41	−0.0282	−0.087	3150
513.2	34.44	−0.172	−0.50	3070
523.2	36.44	−0.256	−0.71	2950
533.2	38.40	−0.270	−0.71	2890
543.2	40.37	−0.266	−0.66	2840
553.2	42.31	−0.208	−0.49	2760
563.2	44.26	−0.135	−0.31	2710
573.2	46.18	−0.0120	−0.026	2710
583.2	48.10	0.131	0.27	2690
593.2	50.04	0.272	0.54	2690
603.2	51.94	0.470	0.91	

* The residuals are from the least squares equation Λ = 591.10 exp (−2904.0/RT), s = 0.265 (0.65%).
† The activation energies and equivalent conductances are those of Spooner and Wetmore [see Ref. (13), Table 121, p. 90].

decrease of −2.3% was observed near the melting point. The increase of the activation energy for the lowest equivalent conductance value for LiCl (896.0°K) is quite dramatic (80%) and most certainly is the result of an experimental error. The largest deviations from Arrhenius temperature dependence are those noted for silver nitrate (Table V). The deviations for silver nitrate are more than double the deviations for potassium nitrate and cesium chloride.

The Glass Transition Temperature for Molten Salts

An assessment of the theoretical value of the glass transition temperature, T_0, for crystallizing molten salts requires a quantative evaluation of the precision of the calculation of T_0 from experimental equivalent conductance data. Precise values of T_0 are especially necessary if T_0 is to be considered as the basis of a Corresponding Temperature Scale for molten salts. Since the glass transition temperature can be determined most accurately for systems where the deviations from Arrhenius behavior for equivalent conductance are large, silver nitrate and potassium nitrate were selected for further consideration.

In Table VI the linearity of the corrected activation energy ($E_{corr} = E_A + \frac{1}{2}RT$) as a function of $(T/T - T_0)^2$ has been evaluated using a linear least squares analysis. The precisions of the linear equations are given for various values of T_0 for KNO_3 and $AgNO_3$. The values of the activation energy in these calculations are from Tables IV and V. The temperature given in the first column of Table VI is the average temperature of the two equivalent conductance values used to calculate the activation energy.

Table VI. Values of $\left(\frac{T}{T-T_0}\right)^2$ obtained for several values of T_0 for KNO_3 and $AgNO_3$

T°K	Ecorr cal	$\left(\frac{T}{T-T_0}\right)^2$		$\left(\frac{T}{T-T_0}\right)^2$	
KNO3:		$T_0 = 237$		$T_0 = 250$	
675.8	4372.5	2.3719		2.5189	
663.2	4475.0	2.4213		2.5770	
651.5	4439.6	2.4702		2.6462	
640.9	4525.8	2.5178		2.6881	
631.2	4507.8	2.5639		2.7417	
617.6	4620.2	2.6331		2.8227	
Precision:		36.5 (0.81%)		38.3 (0.85%)	
AgNO3:		$T_0 = 220$	$T_0 = 250$	$T_0 = 270$	$T_0 = 300$
488.2	3735	3.3134	4.2006	5.0060	6.7291
498.2	3645	3.2069	4.0291	4.7662	6.3183
508.2	3575	3.1094	3.8740	4.5518	5.9581
518.2	3465	3.0199	3.7332	4.3590	5.6397
528.2	3415	2.9372	3.6048	4.1850	5.3575
538.2	3375	2.8608	3.4873	4.0269	5.1051
548.2	3345	2.7900	3.3797	3.8829	4.8783
558.2	3315	2.7241	3.2803	3.5040	4.6737
Precision:		24.5 (0.71%)	22.9 (0.66%)	41.7 (1.2%)	19.8 (0.57%)

The equivalent conductance data employed for the KNO_3 calculations are from the measurements by Angell (14). Using this data Angell (3) computed a glass transition temperature $T_0 = 237$°K. In order to test the effect of a change in T_0 on the linearity of the relationship, the value $T_0 = 250$°K was selected for KNO_3 and the precision of the best fit was found to change from 0.81 to 0.85%.

A value for the glass transition temperature for $AgNO_3$ was selected by initially testing the values at 220°, 250°, 270°, and 300°K, in order to determine the best linear relationship between the E_{corr} and $(T/T - T_0)^2$. The value of 300°K (the best fit), thus, could not be found without such a least squares calculation. A visual inspection of the graphs of E_{corr} as a function of $(T/T - T_0)^2$ for 220° 250°, and 300°K reveals very little difference in linearity among the three temperatures. It appears that the actual value of T_0 is not a critical consideration for $AgNO_3$; a variation of about 30 degrees in the value of T_0 is possible without significantly affecting the graphical analysis.

In order to determine values of T_0 to within ±1°, a computer program for an iterative procedure together with a linear least squares analysis would be one approach for the selection of T_0. Although a value of T_0 could be found which would minimize the precision, the selection of such a glass transition temperature would be the result of an arbitrary interpolation since the convergence is rather gradual (*e.g.* $AgNO_3$).

In Fig. 1 and 2, the variation of E_{corr} as a function of $(T/T - T_0)^2$ is illustrated for KNO_3 ($T_0 = 237$°K) and $AgNO_3$ ($T_0 = 300$°K). The deviations for KNO_3 seem relatively greater than for $AgNO_3$ (even though the precisions indicate otherwise) as a result of the smaller total change in the activation energy.

An Evaluation of the Cohen-Turnbull and Adams-Gibbs Based Transition-State Theories

The major achievement of the Cohen-Turnbull theory is the precise description it gives for the temperature dependence of equivalent conductance. Whereas the Arrhenius expression is in error by about 8% for the activation energy of $AgNO_3$, the Cohen-Turnbull theory predicts the variation of the activation energy with a precision of about 0.5%. The glass transition temperature, although difficult to determine exactly, is physically more meaningful than a fitting parameter. The T_0 parameter gained theoretical support through the Adams-Gibbs theory, and this model has been substantiated by experimental results for glass-forming melts.

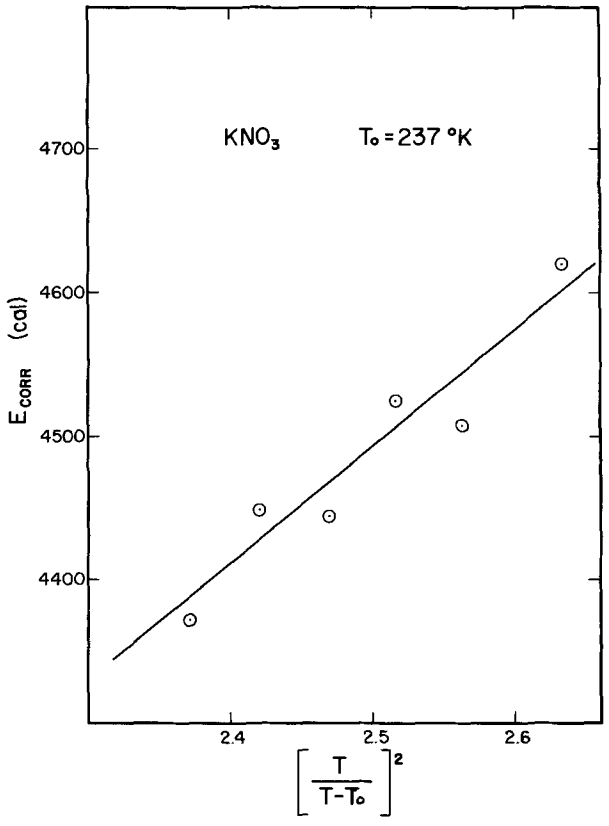

Fig. 1. The temperature dependence of E_{corr} of KNO_3. (The value of 273°K was used for T_o.)

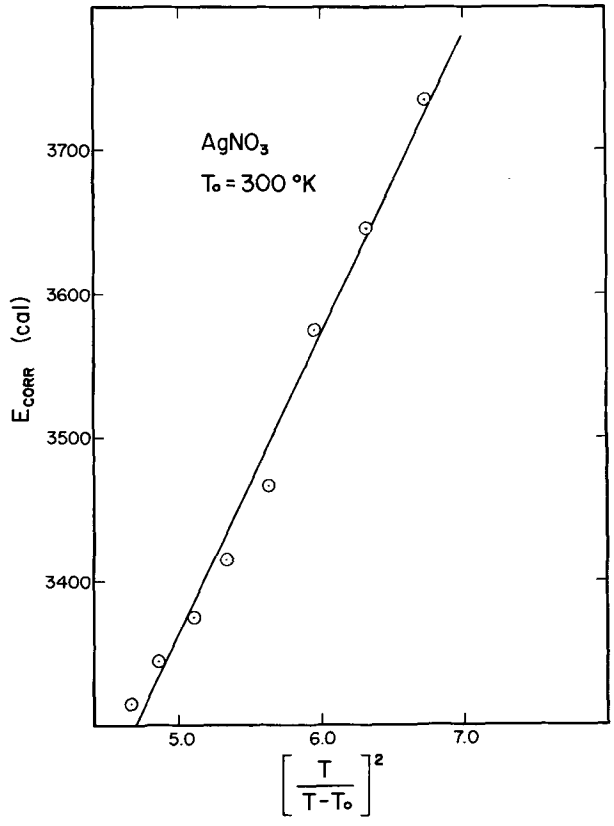

Fig. 2. The temperature dependence of E_{corr} of $AgNO_3$. (The value of 300°K was used for T_o.)

Considering the difficulties encountered in the calculation of precise values of T_o for $AgNO_3$ and KNO_3 the possibilities of using the glass transition temperature as the basis for a Corresponding Temperature Scale for crystallizing molten salts appear to be remote. It will be much more difficult to obtain precise values of T_o for the alkali halides than for $AgNO_3$ and KNO_3 because the halides exhibit significantly smaller departures from Arrhenius behavior than do the nitrates. There seems to be little possibility that an improvement in the accuracy and the precision of the measurement of equivalent conductance by several orders of magnitude would produce any improvement.

Although values of the activation energy, E, and the frequency factor, A, can be calculated (3) from known molecular constants for molten salts by the Cohen-Turnbull theory, close agreement between the theoretical and experimental values has not been obtained. Further developments of transition-state models can be expected to give more precise values for the absolute magnitude of the activation energy for equivalent conductance. It is evident that additional measurements of the transport properties for glassy molten salt systems and binary molten salt systems exhibiting deep eutectics are needed to advance the transition-state models. Accurate equivalent conductance measurements in the molten state but near the melting points of a variety of ionic compounds is another area in need of much attention for this purpose.

Acknowledgments

The support of programs at Rensselaer for studies of fused salts and for the critical evaluation of molten salt data respectively, by the U.S. Department of the Navy, Office of Naval Research, Chemistry Division, and the U.S. National Bureau of Standards, Office of Standard Reference Data, is gratefully acknowledged.

Manuscript submitted May 17, 1971; revised manuscript received *ca.* Aug. 20, 1971.

Any discussion of this paper will appear in a Discussion Section to be published in the June 1972 JOURNAL.

REFERENCES

1. H. Bloom and E. Heymann, *Proc. Roy. Soc. (London)*, **A188**, 392 (1947).
2. J. O'M. Bockris, E. H. Crook, H. Bloom, and N. E. Richards, *ibid.*, **A255**, 558 (1960).
3. C. A. Angell, *J. Phys. Chem.*, **68**, 1919 (1964).
4. C. A. Angell, *ibid.*, **70**, 2793 (1966).
5. M. H. Cohen and D. Turnbull, *ibid.*, **31**, 1164 (1959).
6. G. Adams and J. H. Gibbs, *ibid.*, **43**, 139 (1965).
7. G. J. Janz, C. Solomons, and H. J. Gardner, *Chem. Rev.*, **58**, 461 (1958).
8. F. H. Stillinger, J. G. Kirkwood, and P. J. Wojtowicz, *J. Chem. Phys.*, **32**, 1837 (1960).
9. B. R. Sundheim, Editor, "Fused Salts," McGraw-Hill Book Co., New York (1964).
10. M. Blander, Editor, "Molten Salt Chemistry," John Wiley & Sons, Inc., (Interscience), New York (1964).
11. J. H. Gibbs and E. A. DiMarzio, *J. Chem. Phys.*, **28**, 373 (1958).
12. A. Dietzel and H. J. Poegel, Proceedings of the Third International Glass Congress, Venice, Italy, 1953, p. 219.
13. G. J. Janz, F. W. Dampier, G. R. Lakshminarayanan, P. K. Lorenz, and R. P. T. Tomkins, Molten Salts Vol. 1, Electrical Conductance, Density, and Viscosity Data; National Standard Reference Data Series—National Bureau Standards Publ. No. 15 (1968); U.S. Gov't. Printing Office, Washington, D. C. 20402.
14. C. A. Angell, *This Journal*, **112**, 956 (1965).

MoO_3: A New Electrode Material for Nonaqueous Secondary Battery Applications

Luigi Campanella

Istituto di Chimica Analitica,[1] Università di Roma, Rome, Italy

and Gianfranco Pistoia

Istituto di Chimica Fisica, Università di Roma, Rome, Italy

ABSTRACT

The behavior of MoO_3 as positive electrode material in organic solvent batteries has been investigated. This oxide in $LiAlCl_4$-BL solutions shows low solubility and satisfactory polarization behavior. Micropolarization tests showed the reversibility of the redox process of MoO_3 in the considered electrolyte. From the voltage sweep curve a charge-discharge efficiency of about 100% could be deduced. Discharges at 0.5, 1.0, and 2.0 mA/cm^2 of cells Li/$LiAlCl_4$-BL/MoO_3,C indicated a good cathodic efficiency if a two-electron process is hypothesized. MoO_3 positive electrodes, showing a lower polarization and supplying more practical specific energy, behave better than analogous AgO electrodes in $LiAlCl_4$-BL.

The latest researches in the field of high-energy nonaqueous batteries have been mainly directed to the study of electrochemically active cathode materials characterized by redox reversibility and low solubility. Some new electrode materials have been recently proposed in place of the ones used most so far, *i.e.* the Cu, Ni, and Ag halides. A number of these materials, the performances of which are often not well known, have been reported in a series of patents. These patents have been recently reviewed by Jasinski (1), with attention mainly focused on some oxides (Bi_2O_3, CuO, CrO_3, and AgO) which have been claimed to be useful for the development of secondary cells.

The use of oxides as positive electrodes could be particularly convenient because of their generally low solubility. According to Braeuer (2), however, only AgO seems to behave satisfactorily as a cathode in organic electrolytes. The good behavior of AgO for secondary battery applications has been confirmed by the studies performed by Shaw on several electrode-nonaqueous electrolyte systems (3). In particular, this author recommended the system AgO in butyrolactone (BL) – LiCl + $AlCl_3$.

On the other hand, AgO is not characterized by high values of the utilization coefficient (2) and is quite an expensive substance. In this work, the electrochemical behavior of MoO_3, a naturally occurring and inexpensive oxide, has been considered with the aim of finding a positive material of better electrochemical and practical characteristics than AgO. It has to be noted that so far MoO_3 has never been studied electrochemically in nonaqueous electrolytes; it has only been investigated as a cathode material in KOH aqueous solutions (4).

The low solubility of MoO_3 in organic solvents and its ability to be electrochemically reduced at the usual current densities employed in nonaqueous batteries were first ascertained. The results encouraged a detailed study of the electrochemical properties of MoO_3 in organic solvents and of its use as an electrode in a nonaqueous battery. Considering that AgO behaves reversibly in $LiAlCl_4$-BL (3), this organic electrolyte was also chosen for the present investigation.

Experimental

Materials.—High purity BL (Merck LAB product) was shaken and stored in the presence of Li in order to eliminate hydroxilate impurities. After this treatment, the water content in BL, determined by dead stop end point titration with the Karl Fischer solution, was less than 20 ppm.

$LiAlCl_4$ was prepared by melting equimolar amounts of anhydrous LiCl and $AlCl_3$ at 200°C under dry N_2, according to the method described by Rao (5). Solutions in BL of the salt prepared with this method are completely stable in the absence of moisture showing no change of their pale yellow color with time. When left in the air, these solutions tend instead slowly to gel.

MoO_3 (Carlo Erba RP product), AgO (BDH product) and graphite (Southwestern 1651) were used as received (after drying).

The Li ribbon used for the negative electrodes (99.9%, 15 mil, Alfa Inorganics product) was used as received.

All the chemical manipulations were performed in a dry box under argon atmosphere, the only exception being the preparation of the positive electrode.

Apparatus and technique and specific conductivity.—The specific conductivity, χ, of $LiAlCl_4$-BL solutions was measured, at 25°±0.02°C with a PR 9501 Philips bridge employing a conductivity cell having a constant of 0.5027 cm^{-1}. A starting solution of 25g of $LiAlCl_4$ in 100g of BL was progressively diluted and the corresponding specific conductivities were measured after thermal equilibration. The χ values are reported in Table I.

Solubilities.—MoO_3 was equilibrated at 18°C for six days in a stirred solution of $LiAlCl_1$ in BL (0.92*M*). An aliquot of the supernatant solution was then collected and the MoO_3 solubility calculated by determining the Mo^{VI} content spectrophotometrically with a Bausch-Lomb apparatus, operating at 475 mμ. The color was previously developed by reaction of Mo^{VI} with NH_4CNS and $SnCl_2$. The solubility in the same solution of a MoO_3-graphite electrode, submitted to six charge-discharge cycles, was determined with the same technique.

Table I. Specific conductivity at 25°C of $LiAlCl_4$ in BL

c (g/100g solvent)	$\chi \cdot 10^3$ (ohm^{-1} cm^{-1})
4.31	5.40
7.50	7.70
11.2	9.82
12.8	10.1
16.8	10.6
25.6	9.92

[1] Gruppo "Elettroliti e Processi Elettrochimici" del C.N.R.

Key words: nonaqueous batteries, MoO_3, lithium.

Preparation of the positive electrode.—Because of the nonconductive nature of MoO_3, a sufficient amount of graphite was added to the cathodic mixture in order to avoid excessive polarization and low values of the cathodic efficiency. As the amount of graphite was increased from 10 to 30% a corresponding improvement of the cell performance was observed. For content higher than 30%, no further variation was observed. The electrode performance was negatively influenced by the addition of a binder (such as polyethylene) and by the dissolution of the cathodic mixture in toluene and successive spreading of it on the metal support.

The dry cathodic mixture (70% MoO_3 and 30% graphite) was pressed on a Cu net at 3000 kg/cm^2 in order to obtain satisfactory adherence. After discharge (1-2 days) the above-described electrodes showed a good appearance. Nevertheless, after an activated storage of 40 days (cycling test) the electrodes revealed some deterioration.

The AgO electrode was prepared in a similar way, employing a Cu net, electrolytically silver-plated, as support.

X-ray analysis.—The x-ray powder patterns were obtained using CuKα radiation filtered by nickel. The samples were analyzed under vacuum for 5 hr with the Debye-Scherrer method.

Macro- and micropolarizations.—These experiments were performed in a Type 494 AMEL cell, uisng a Li sheet as counterelectrode and a Li rod as reference electrode, the latter being separated from the working electrode by a Luggin capillary. The oxide working electrode, prepared as described above, and the Li counterelectrode had the same dimensions (1.8 x 2.3 cm). Macropolarization tests were also performed on the AgO electrode for comparison purposes.

Cyclic voltammetry.—The same cell and electrodes employed for the polarization measurements were also used for cyclic voltammetry, which was carried out by the Electroscan Beckman 30, at a potential scanning rate of 20 mV/sec.

Cell assembly and discharge curves.—The positive electrode, consisting of about 0.4g of the MoO_3-graphite mixture (46 mg/cm^2), was sandwiched between two lithium electrodes. Anodes and cathode had the same dimensions (4.3 cm^2 for each side). A double layer of 0.38 mm thick glass fiber [type Paper-Hurlbult 934 AH, described by Boden (6)] was used as electrode separators. An excess of $LiAlCl_4$-BL solution (12-14% by weight, that is 0.9-1.0*M*) was employed.

The discharge curves at current densities 0.5, 1.0, and 2.0 mA/cm^2, respectively, were performed at 25°C, usually without interruption, to 1.0V cutoff (90% discharge depth). No appreciable change in the performances was detected even when the discharge was interrupted overnight.

Cycling test.—It was performed on the cell that had been previously submitted to an initial discharge at 2.0 mA/cm^2 (see Fig. 4). Thirty cycles over 40 days were carried out at 25°C; the charge current density varied between 0.5 and 2.0 mA/cm^2; the discharge current density was 1 mA/cm^2. The voltage varied between 1.0V at the end of the discharge and 3.6V at the end of the charge.

Potentiometric titration of Cl^-.—Variations in the Cl^- content of the solutions were determined by potentiometric titrations. The apparatus employed was the Electroscan Beckman 30 and the electrodes were silver as indicator and saturated calomel as reference. Direct and analytical (derivative) methods for locating the end point of the titration were employed.

Results and Discussion

MoO_3 preliminary test.—The maximum in the specific conductivity for $LiAlCl_4$-BL solutions was 10.6×10^{-3} ohm^{-1} cm^{-1} (see Table I). This value is greater than that observed for solutions of the same salt in propylene carbonate which is 6.6×10^{-3} ohm^{-1} cm^{-1} (7).

The capability of MoO_3 to be electrochemically reduced in a $LiAlCl_4$-BL solution, without excessive polarization, is shown in Fig. 1. The comparison with the AgO behavior shows the better performances of MoO_3.

The solubility of MoO_3 in $LiAlCl_4$-BL (0.92*M*) was 5×10^{-4}*M*, a value which should ensure a satisfactory shelf-life to batteries using MoO_3 as the positive electrode.

On the basis of these promising results, the reversibility of MoO_3 electrodes was then investigated by the micropolarization test (Fig. 2). The cathodic straight line lies on the prolongation of the anodic one, and no appreciable hysteresis can be observed, showing that the electrode can be considered to be reversible. The possibility of cycling the copper grid was excluded by replacing it with a gold grid and observing that the micropolarization curve remained unchanged.

Further investigation by cyclic voltammetry evidenced a cathodic and an anodic peak in the potential range from 1.0 to 3.8V, as shown in Fig. 3. This result seems to indicate a unistep nature for the redox process of MoO_3. A comparison between the anodic and cathodic peak areas shows that the charge-discharge efficiency can be postulated to be nearly 100% in optimum operating conditions.

Discharge behavior.—Since the above-described results indicated MoO_3 as a feasible electrode material in nonaqueous solvents, it formed the cell

$$Li/LiAlCl_4\text{-BL}/MoO_3,C \qquad [1]$$

The open circuit voltage (OCV) of cell [1] is initially 2.8-2.9V and slowly stabilizes at about 2.7V. This is probably due to the deactivation of certain impurities and/or to the reaction between the copper grid and the cathodic mixture. Using a gold grid, the OCV tended to be more stable.

The background activity of the graphite employed in the preparation of the cathode was evaluated separately in a cell containing only graphite as the cathode material and discharged at 1 mA/cm^2. Its results were quite low, being only the 2% of the total delivered capacity.

The discharge curves for cell [1] are reported at various current densities in Fig. 4.

The discharge process of cell [1] is not completely clear, and it seems to be more complicated than the simple formation of lower Mo oxides (MoO_2, Mo_2O_5)

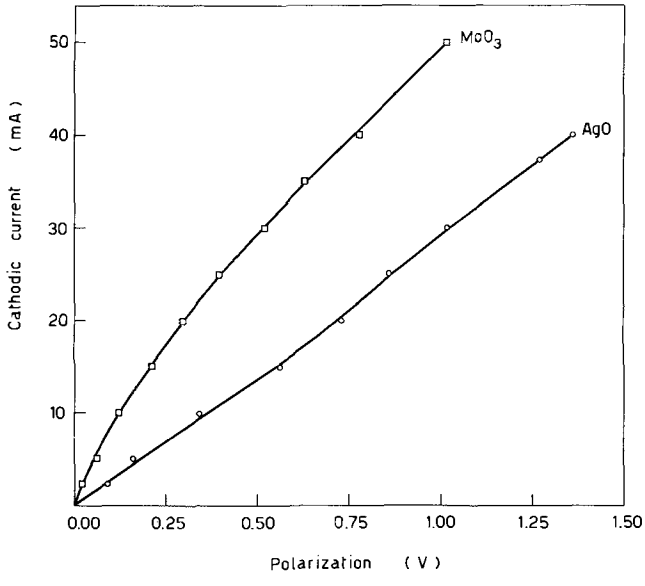

Fig. 1. MoO_3 and AgO polarization in 0.9M $LiAlCl_4$-BL. Electrode surface, 1.8 cm × 2.3 cm.

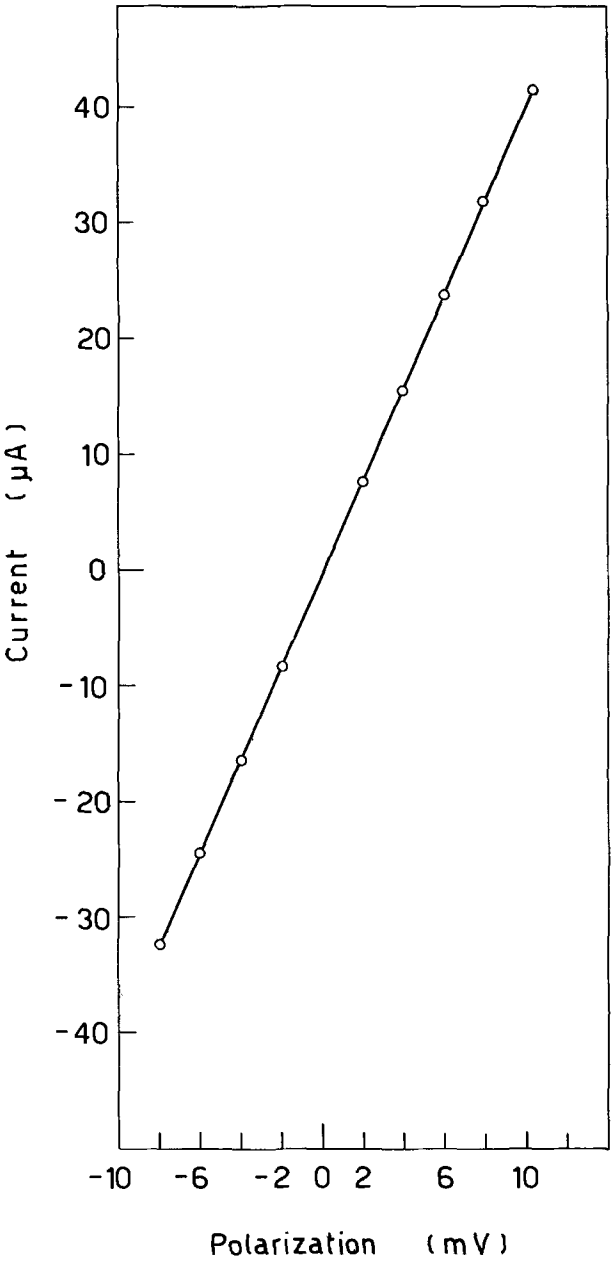

Fig. 2. Micropolarization of a MoO_3 electrode in $LiAlCl_4$-BL 0.9M. Electrode surface, 1.8 cm × 2.3 cm.

and Li_2O. In fact, from the known values of ΔG for Li_2O (−133.8 kcal/mol), MoO_2 (−121.6 kcal/mol), and MoO_3 (−161.9 kcal/mol) and that one estimated

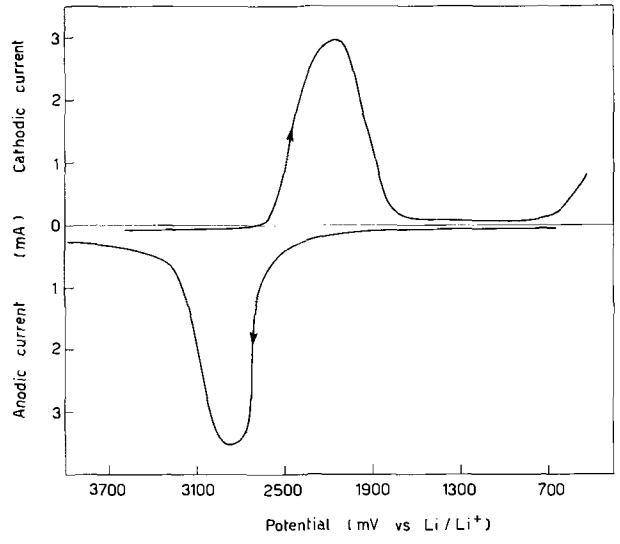

Fig 3. Cyclic voltammetry of a MoO_3 electrode in $LiAlCl_4$-BL 0.9M. Electrode surface 1.8 cm × 2.3 cm. Scanning rate 20 mV/sec.

for Mo_2O_5 (−284 kcal/mol) (8), it is possible to obtain for the formation of these lower Mo oxides E_0 values of about 2.0V. These values are definitely lower than those experimentally observed for cell [1], and the difference can be ascribed only to a minimum extent to impurities contained in the positive electrode mixtures. In fact, the load voltage remains above the value corresponding to the formation of Mo^{IV} or Mo^{V} oxides for a long time, and a large percentage of the total cell capacity is furnished during this time.

It is worthwhile to note that similar behavior has been shown by other oxides in organic electrolytes. In fact, batteries having as cathode: (*a*) AgO in $KAsF_6$-propylencarbonate (PC) (9), $LiClO_4$-methyl formate and $LiClO_4$-PC (2); (*b*) MnO_2 in $KAsF_6$-PC (9); (c) CuO in $LiClO_4$-tetrahydrofurane and $LiClO_4$-PC (10), show both OCV and load voltages higher than those obtainable from thermodynamic data. Therefore, careful study of the mechanism of the oxides' reduction is necessary.

The participation of the electrolyte in positive electrode processes seems to be possible, especially for electrolytes containing PF_6^- or $AlCl_4^-$ or BF_4^- anions, for which the acceptance and release of halide ions has been hypothesized (3, 7). For instance, the cycling behavior of AgO in $LiAlCl_4$-BL (3) is probably due to the reduction of the starting material to Ag, followed by anodic oxidation of Ag to AgCl which is then cycled.

The participation of chloride ions in the processes occurring at the MoO_3 electrode in $LiAlCl_4$-BL has also been investigated. An attempt to identify by x-ray

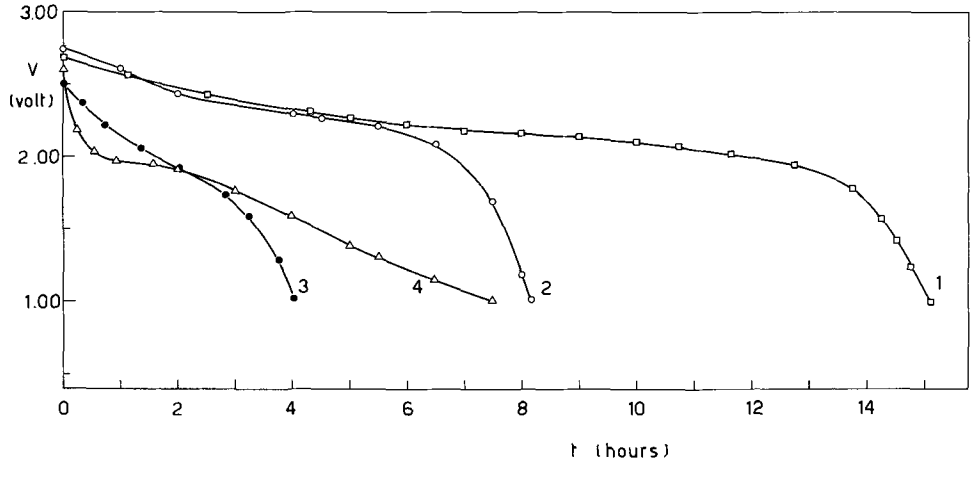

Fig. 4. Discharge curves at 25°C and at various current densities. For curves 1, 2, and 3 (MoO_3) C.D. are 0.5, 1.0 and 2.0 mA/cm^2 respectively; for curve 4 (AgO) C.D. is 1.0 mA/cm^2. Cells of curves 1, 2, and 3 contain 0.27, 0.28, and 0.32g MoO_3 respectively. Cell of curve 4 contains 0.26g AgO.

analysis the formation of compounds involving Cl^- ions on the electrode has not been successful, since the difference between the spectra of a blank formed by MoO_3 + graphite and those of the electrode material after discharge and cycling was not so marked as to make a reliable identification of formed compounds possible.

On the other hand, a variation in the Cl^- content of the solution after discharge was detected. This variation (~5%) was of the order expected on the basis of the amount of current passed through the cell. Thus, the participation of Cl^- ions in the electrode discharge reaction, probably through the formation of Mo oxychlorides, seems to be possible. No further Cl^- decrease was detected, however, in the solution of a charged cell which had been submitted to six cycles. Furthermore, the solubility of the positive electrode in $LiAlCl_4$-BL (0.92*M*), checked after six cycles (with the cell in the charged state), was equal to that of the MoO_3 powder. These results seem to prove the restoration, on charging, of the oxide on the positive electrode.

Whatever the reaction mechanism is, a monoelectron cell reaction has to be excluded, because it would lead to MoO_3 coulombic efficiency higher than 100%. A two-electron total process, to which a theoretical capacity of 0.37 Ahr/g corresponds, seems to be more probable. On the basis of this assumption the cathodic efficiency is quite satisfactory for the different discharge rates (see Table II).

The cell containing MoO_3 is characterized by higher values of voltage and of energy for weight of the cathode material than the cell operating with AgO under the same discharge conditions as expected by the trend of the polarization curves.

The AgO discharge also seems to occur in one step as indicated by the discharge curve of Fig. 4. The single step reduction of AgO has been also observed, for example, in $KAsF_6$-PC (9) and in aqueous KOH at a similar current density (11).

Cycling behavior.—A cell submitted to an initial discharge at 2 mA/cm² was charged and discharged for 30 cycles, during which the cycling efficiency was almost constant with time at the mean value of 61% (C/14 rate, 1.0V cutoff, 90% depth of discharge). During this test a continuous increase of the internal resistance of the cell was observed, probably due to a certain deterioration of the cathode. Consequently the ampere-hours accepted by the cell up to the maximum voltage (3.6V) and then supplied during the discharge were decreasing accordingly.

When a cell was left charged overnight, its charge-discharge efficiency was somewhat reduced due to the lowering of both OCV and voltage on load. In very few cases, however, was the efficiency lower than 50%.

By visual examination of the cell after the cycling test, an appreciable decomposition of the electrolyte could be excluded, while the expected formation of dendrites on the Li electrode and a certain physical deterioration of the MoO_3 electrode were noticed. Using gold instead of copper as the grid, the electrode showed a better appearance after cycling. Furthermore, the charge-discharge efficiency was higher, especially after overnight standing. This confirms the evidence of a certain reactivity of the copper grid with the cathode material.

The term of 40 days adopted for the cycling test is the first evidence of the activated storage capability of the cells containing MoO_3 as cathode. However, one cannot exclude the possibility that a solubility value of $5 \times 10^{-4}M$ can create some problems on longer activated stand periods.

Table II. Cell characteristics

Current density (mA/cm²)	Whr/g oxide	Rate[a]	Cathodic efficiency[a]
0.5	0.52	C/23	66
1.0	0.55	C/12	66
2.0	0.38	C/7	55
1.0 (AgO)	0.40	C/12	56

[a] Based on a two-electron reduction.

Conclusions

The relatively low value of solubility and of polarization make MoO_3 suitable as cathode material for high-energy nonaqueous batteries. Furthermore, since the MoO_3 reduction process is reversible, the construction of secondary cells is possible. Satisfactory charge-discharge efficiency and storage capability are other favorable features of these cells.

The electrochemical properties of MoO_3 are better in comparison with those of AgO considered so far the most efficient oxide for nonaqueous batteries. This stimulates a detailed research on the performances of other insoluble oxides suitable for high-energy nonaqueous batteries.

Acknowledgments

The authors wish to thank Dr. Pierluigi Cignini for the x-ray experimental work and Dr. Bruno Scrosati for his helpful discussion.

This work was partly sponsored by the Consiglio Nazionale delle Ricerche (C.N.R.).

Manuscript submitted March 2, 1971; revised manuscript received *ca.* May 24, 1971.

Any discussion of this paper will appear in a Discussion Section to be published in the June 1972 JOURNAL.

REFERENCES

1. R. Jasinski, *J. Electroanal. Chem.*, **26**, 189 (1970).
2. K. Braeuer and J. Harvey, Tech. Report AD 654813 (May 1967).
3. M. Shaw, O. Paez, and F. Ludvig, Contract NASA-CR-1434 (1969).
4. C. Morehouse and R. Glicksman, *This Journal*, **107**, 361 (1960).
5. M. Bhaskara Rao, *ibid.*, **114**, 13 (1967).
6. D. Boden, H. Buhner, and V. Spera, Final Report, Contract DA-028-043-AMC-01394 (E) (July 1966).
7. R. Jasinski, *Electrochem. Technol.*, **6**, 28 (1968).
8. "Handbook of Chemistry and Physics," 47th edition, p. D-22, The Chemical Rubber Co., Cleveland, Ohio (1966).
9. S. Abens, W. Merz, and C. Walk, Contract NASA-CR-72535. (April 1968).
10. C. Le Sergent and C. Lasne, Brevet d'Invention No. 1,534,811 (France) (June 1968).
11. R. Glicksman and C. Morehouse, *This Journal*, **104**, 589 (1957).

The Anodic Dissolution of Tungsten

J. W. Johnson* and C. L. Wu

Department of Chemical Engineering and Graduate Center for Materials Research, University of Missouri-Rolla, Rolla, Missouri 65401

ABSTRACT

The anodic dissolution of tungsten was studied in H_2SO_4-K_2SO_4 solutions ($pH = -2$ to 2.5) and K_2SO_4-K_2CO_3-KOH solutions ($pH = 11.5$ to 14.5) at 25°C. Faradaic efficiency studies in basic solutions showed the metal to be oxidized to the +6 state. In acid solutions, a thick protective film of yellow WO_3 was formed. Polarization curves possessed linear Tafel regions (slope $\simeq 2.3\ RT/F$) at potentials slightly more positive than the rest potentials. An anodic dissolution mechanism is proposed which involves a surface film of W_2O_5 that is further oxidized to WO_3 and dissolves by hydrolyzation.

Tungsten (1) is one of the so-called "valve metals" which are distinguished by their ability to form highly protective oxide films upon anodic polarization in many aqueous media. Studies of its electrochemical behavior have appeared infrequently in the literature for over 100 years. A bibliography and brief review of much of the early work appears in a paper by Koerner (2). Koerner also reported extensive open-circuit potential measurements of the W electrode and observations of its anodic behavior in various acids and bases. The potentials were dependent on the type of W used, the electrolyte pH, and also showed some variation with the nature of the electrolyte. The former dependence was attributed to the presence of appreciable oxides in the metal and the latter to the effect of specific ions on the solubility of the dissolved W species, primarily $W(OH)_6$. This compound was believed to break down to tungstic cations in acidic electrolytes and anions in basic. Upon commencing polarization in acid electrolytes, films were formed on the W surface whose color changed through a definite sequence. These colors were associated with tungsten oxides of progressively higher oxygen content, *i.e.*

$$W \rightarrow \underset{\text{(brown)}}{WO_2} \rightarrow \underset{\text{(blue)}}{W_2O_5} \rightarrow \underset{\text{(blue)}}{W_4O_{11}} \rightarrow \underset{\text{(green)}}{W_5O_{14}} \rightarrow \cdots \rightarrow \underset{\text{(yellow)}}{WO_3} \quad [1]$$

The passiveness of W in acids was attributed to low solubilities of the oxides in this media and the activeness in bases to high solubilities. A valence of +6 was determined for W dissolving in NH_4OH-NH_4Cl solutions.

Pitman and Hamby (3) noted intense interference colors on W resulting from anodic polishing. They subsequently studied the growth of the oxide, and among other properties, reported it to have a density and dielectric constant of 6.8 g/cm² and 41.7, respectively. A steady-state growth relation between current and thickness was given for 0.1*N* H_2SO_4 at 25°C. It is interesting to note the sequence of colors reported by Koerner for the formation of the various oxides (Eq. [1]) is similar to the sequence of interference colors caused by thickening of transparent oxide films (4).

Thompson and Rice (5) studied the anodic and cathodic behavior of W in KOH solutions. During anodic dissolution, near 100% current efficiencies were found for the oxidation to the W-VI state, even though extremely high polarization (20-100V) occurred in many cases. The break in the polarization curves where the overvoltage rapidly increased was dependent on both C.D. and C_{OH^-}.

El Wakkad *et al.* (6), studied the behavior of W in various buffer solutions. They found the potentials of massive W and powdered W-WO_3 electrodes to correspond closely. A discontinuity in the *E*-pH relation was noted at pH's 4-6. It was proposed that the potentials in neutral and basic solutions were controlled by the reaction

$$W_2O_5 + 2H_2O = WO_3 + WO_4^{-2} + 4H^+ + 2e \quad [2]$$

The discontinuity was attributed to an incompleteness of the reduction portion of the reaction (Eq. [2]) in acid solution with tungsten blue (W_3O_8 or W_4O_{11}) being the product rather than W_2O_5. The effect of pH on potential ($\partial E/\partial pH$) as shown in various plots was *ca.* 50 mV. It was proposed that W dissolves as WO_4^{-2} in strong bases and WO_2^{+2} in strong acids.

Besson and Drautzburg (7) have also reported a study of the anodic dissolution of W in various electrolytes. The oxidation of W was found to proceed quantitatively to the +6 state. Agitation of the electrolyte displaced the Tafel curves. Tafel slopes were reported for both acidic and basic electrolytes that ranged from 55 to 150 mV.

The present study was undertaken in an attempt to establish a more detailed anodic dissolution mechanism for W. It was also of interest to see if a mechanism recently proposed for Mo[8], a chemically similar metal, would be applicable.

Experimental

The tungsten anodes were prepared from cylindrical specimens cut from a rod of 0.75 in. diameter.[1] They were polished on grinding paper down to 600 grit, cleaned in distilled water with ultrasonic agitation, rinsed with distilled water and acetone, dried, and then mounted in a Teflon holder. All solutions employed analytical grade chemicals and distilled water. The electrolyses were carried out in an H-cell containing approximately 300 ml of electrolyte at 25.0° ± 0.1°C. Prepurified nitrogen was bubbled through the electrolyte to purge air from the system and for stirring. The reference electrodes were Hg/Hg_2SO_4 (1*N* H_2SO_4) for acidic and Hg/Hg_2Cl_2 (1*N* KCl) for basic electrolytes. A salt bridge of the same electrolyte as in the electrolysis cell was used to prevent contamination by the reference electrode. All potentials are reported *vs.* the standard hydrogen electrode (SHE) at 25°C.

Results

Self-dissolution experiments were carried out initially with the W anodes kept in the cell at open-circuit for 24 hr. No detectable weight gains or losses were noted except for 1*N* and 3*N* KOH. In these latter electrolytes, an anode with an exposed area of 2.84 cm² lost approximately 5 mg during the 24-hr period.

* Electrochemical Society Active Member.
Key words: tungsten, anodic dissolution, corrosion.

[1] Electronic Space Products, Inc., 4*N* grade (99.99% purity). Typical analysis (ppm): Ca 10, Cu <10, Mg <10, Mo <50, Si <50, Cb <10, Fe <20, Mn 10, Ni <30, Ti <10.

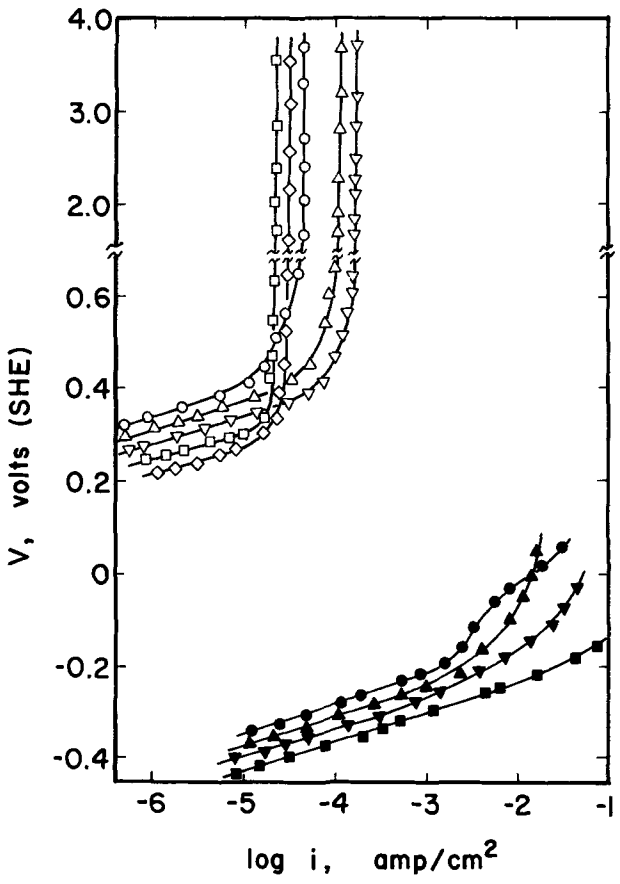

Fig. 1. Anodic polarization of tungsten in aqueous solutions at 25°C. ○, pH = −2.0; △, pH = −0.5; ▽, pH = 0.38; □, pH = 1.5; ◇, pH = 2.5; ●, pH = 11.5; ▲, pH = 12.7; ▼, pH = 13.6, ■, pH = 14.5.

Polarization measurements.—The anodic polarization behavior (steady state) for W was determined potentiostatically in acidic and basic electrolytes and is illustrated in Fig. 1. The curves contain linear (Tafel) sections in the potential region just above the rest potentials. Both the Tafel slopes and the rest potentials are tabulated in Table I. In the acid electrolytes, the active dissolution regions were quite small and limiting currents of 10^{-5}-10^{-4} A·cm² were reached at relatively low overpotentials. Visible oxygen evolution commenced from the anode at potentials of 1.3-2.0V. A lemon-yellow film was formed on the electrode during polarization and was identified by x-ray analysis as WO_3. A high-voltage power supply in a galvanostatic arrangement was used to polarize the W anode in 3*N* H_2SO_4 at C.D.'s greater than the limiting values mentioned above. The results are shown in Fig. 2. The yellow surface film thickened visibly and oxygen was evolved vigorously. At the higher C.D.'s, the potential continually fluctuated by 5-10V.

Table I. Rest potentials and Tafel slopes for the anodic dissolution of tungsten at 25°C

Electrolyte	pH	Rest potential, volts (SHE)	Tafel slope, volts
10.0*N* H_2SO_4	−2	0.29	0.060
3.0*N* H_2SO_4	−0.5	0.28	0.060
1.0*N* H_2SO_4	0.38	0.27	0.058
0.24*N* H_2SO_4 + 0.76*N* K_2SO_4	1.5	0.235	0.065
0.1*N* H_2SO_4 + 0.9*N* K_2SO_4	2.5	0.22	0.058
1.0*N* K_2CO_3	11.5	−0.38	0.072
0.1*N* KOH + 0.9*N* K_2SO_4	12.7	−0.41	0.060
1.0*N* KOH	13.6	−0.42	0.060
3.0*N* KOH	14.5	−0.47	0.058

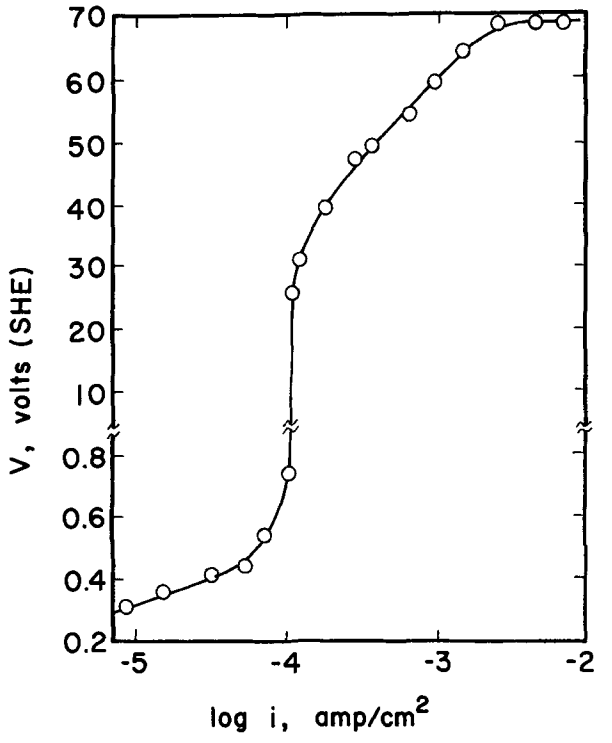

Fig. 2. Anodic polarization (galvanostatic) of tungsten in 3*N* H_2SO_4 at 25°C.

Valence measurements.—The results of the valence determinations in both acidic and basic media are shown in Table II. In the acidic media, oxygen could be seen evolving at all but the lowest current densities. The smallness of the limiting currents precluded an accurate determination of the oxidation state of the dissolving W ions in the active dissolution region. The weight loss for a C.D. of 10^{-4} A·cm² (which occurred over a period of several days) corresponded to a W valence (oxidation state) of 22. Apparently oxygen was also being produced at this C.D., but at such a low rate that it dissolved without bubble formation. It should be noted, though, that significant weight losses of the metal occurred even during visible oxygen evolution at high C.D.'s. (For example, at 0.050 A·cm^{-2}, Table II shows that *ca.* 14% of the anodic current is accounted for by W dissolution.) This and the absence of a decrease in C.D. with increasing potential above the active dissolution region indicates the absence of true anodic passivation.

Table II. Coulombic data for the anodic dissolution of tungsten at 25°C

Electrolyte	Time, sec	Current density,* A·cm⁻²	Weight-loss Expt., g	Weight-loss Cal., g	Apparent valence	Efficiency, %
1*N* H_2SO_4	554,400	0.0001	0.01334	0.0500		26.6†
	554,400	0.001	0.01278	0.0500		25.4
	18,480	0.003	0.01014	0.0500		20.3
	18,480	0.003	0.01060	0.0500		21.2
	5,543	0.010	0.00974	0.0500		19.5
	11,086	0.010	0.01870	0.1000		18.7
	1,664	0.050	0.01143	0.0750		15.2
	1,109	0.050	0.00688	0.0500		13.8
0.1*N* KOH + 0.9*N* K_2SO_4	27,720	0.002	0.04995	0.0500	6.00	
1*N* KOH	27,720	0.002	0.05025	0.0500	5.97	
	27,720	0.002	0.05134	0.0500	5.86	
	55,440	0.002	0.10224	0.1000	5.85	
	5,543	0.010	0.04963	0.0500	6.04	
	5,543	0.010	0.04929	0.0500	6.07	
	1,109	0.050	0.05033	0.0500	5.97	
	2,218	0.050	0.10182	0.1000	5.89	
3*N* KOH	5,543	0.010	0.05042	0.0500	5.95	
	11,086	0.010	0.10160	0.1000	5.91	

* Area of the electrode = 2.84 cm².
† Coulombic efficiency based on W-VI oxidation state.

The oxidation state of W species entering into solution in basic electrolytes is very close to +6 within experimental error. It appears to be independent of both *p*H and C.D., and is in agreement with values reported by other investigators.

Discussion

In alkaline media, the apparent valence data indicate that tungsten goes into solution according to the overall reaction

$$W \rightarrow W\text{-}VI + 6e \qquad [3]$$

Qualitative tests of the anolytes showed the presence of WO_4^{-2} as expected from the absence of color and in accord with thermodynamic data indicating it to be a stable ion at these conditions (9-11). In acid media, the yellow film formed on the electrode surface and identified as WO_3 also indicated that oxidation resulted in the +6 state. The formation of this oxide, which is both relatively insoluble and nonconductive, explains the small potential-independent currents that were observed. The fact that W dissolved over the entire potential region (Tafel, limiting current, and oxygen evolution) is evidence of a slight solubility of the oxide. Also, the absence of pitting indicated the film to be nonporous. Thus, the dissolution is probably accomplished through a hydration reaction to form $WO_3 \cdot H_2O$ (or tungstic acid H_2WO_4). These observations (as well as the simultaneous o.e. at relatively low overpotentials) would appear to preclude interpreting the behavior of W in this media simply in terms of valve-action. In the rigorous sense, valve-action "is the tendency to form a protective high-resistance oxide film on anodic polarization to the exclusion of all other electrode processes" (1).

The open-circuit "rest" potentials of the W electrode (shown in Fig. 3) are a function of *p*H. The value $\partial V_{rest}/\partial pH \simeq 0.059V = 2.3\ RT/F$, indicates a 1:1 ratio of H^+ to electrons in the electrochemical step that is controlling the rest potential. As also seen in Fig. 3, the measured values do not correspond to any of the relations for various W-H_2O equilibria that are available from the literature (12, 13). They agree reasonably well with the values reported by El Wakkad *et al.* (6), but not with the *p*H effect from his proposed reaction (Eq. [2]). The slight solubility of WO_3 as well as previous findings regarding Mo[8], a chemically similar metal, suggest an equilibrium between W_2O_5 and $WO_3 \cdot H_2O$ as a possibility, *i.e.*

$$W_2O_5(s) + 3H_2O(aq) \rightarrow 2WO_3 \cdot H_2O(s) + 2H^+(aq) + 2e \qquad [4]$$

Data are not available pertaining to the standard free energy of formation of $WO_3 \cdot H_2O$, but an approximate value can be obtained by estimating the free energy change, *i.e.* ΔG°_{hyd}, for the following reaction

$$WO_3(s) + H_2O(aq) \rightarrow WO_3 \cdot H_2O(s) \qquad [5]$$

An examination of the data for a large number of monohydrated compounds of compositions $MO_x \cdot H_2O$, H_2MO_y, and $M(OH)_2$ shows that the free energy changes for the reactions of the oxides with water are usually within the limits of ± 10 kcal. For compounds normally found in the hydrated form (*e.g.* CrO_3, MgO, MnO), $-10 < \Delta G^\circ_{hyd} < 0$ kcal, while for compounds normally found in the anhydrous form (*e.g.* TeO_2, GeO_2, SiO_2), $0 < \Delta G^\circ_{hyd} < 10$ kcal. Since anhydrous WO_3 is reported to be the normally stable form, its free energy of hydration should be positive and can be estimated to be 5-10 kcal. For the following calculations, 7.5 ± 2.5 kcal will be used. Thus

$$\begin{aligned}\Delta G^\circ_{f,WO_3 \cdot H_2O} &= \Delta G^\circ_{f,WO_3} + \Delta G^\circ_{f,H_2O} + \Delta G^\circ_{hyd} \qquad [6]\\ &= -182{,}740 + (-56{,}690) + (7{,}500 \pm 2{,}500)\\ &= -231{,}930 \pm 2{,}500 \text{ cal}\end{aligned}$$

The corresponding ΔG° for Eq. [4] is

$$\begin{aligned}\Delta G^\circ &= 2\,\Delta G^\circ_{f,WO_3 \cdot H_2O} - \Delta G^\circ_{f,W_2O_5} - 3\,\Delta G^\circ_{f,H_2O} \qquad [7]\\ &= 2(-231{,}930 \pm 2{,}500) - (-306{,}900) - 3\,(-56{,}690)\\ &= 13{,}100 \pm 5{,}000 \text{ cal}\end{aligned}$$

The Nernst relationship for this reaction is[2]

$$\begin{aligned}E &= (0.3 \pm 0.1) - (2.3\ RT/F) \log (1/a_{H^+}) \qquad [8]\\ &= (0.3 \pm 0.1) - 0.059\ pH\end{aligned}$$

The band (area between long dashed lines) representing Eq. [8] on Fig. 3 includes all the experimental rest potentials. A best-fit line through the points yields a free energy change for Eq. [5] of +8 kcal.

With the above information, the anodic dissolution of W can be described qualitatively as follows:

(*A*) When placed in solution, the W electrode very rapidly forms a film of approximate composition W_2O_5 that completely covers the metal surface. Further spontaneous reaction (corrosion or self-dissolution) ceases except at relatively high *p*H's where W_2O_5 is soluble.

(*B*) Upon polarization, the appreciable conductivity of W_2O_5 allows further electrochemical oxidation to WO_3.

(*C*) The solvation of WO_3 is accomplished by hydration to $WO_3 \cdot H_2O$ (or H_2WO_4) which has a very low conductivity, is only slightly soluble in acids, and is appreciably soluble in bases.

(*D*) The limiting (potential independent) curves in acidic electrolytes can be attributed to an insulating layer of WO_3 which accumulates due to its low solubility. The absence of a limiting current in basic electrolytes is due to the solubility of WO_3 in these media.

(*E*) The rapid complete coverage of the metal surface by W_2O_5 indicates the experimental kinetic parameters are associated with its further oxidation (8). The Tafel slope of ~60 mV is thus associated with a chemi-

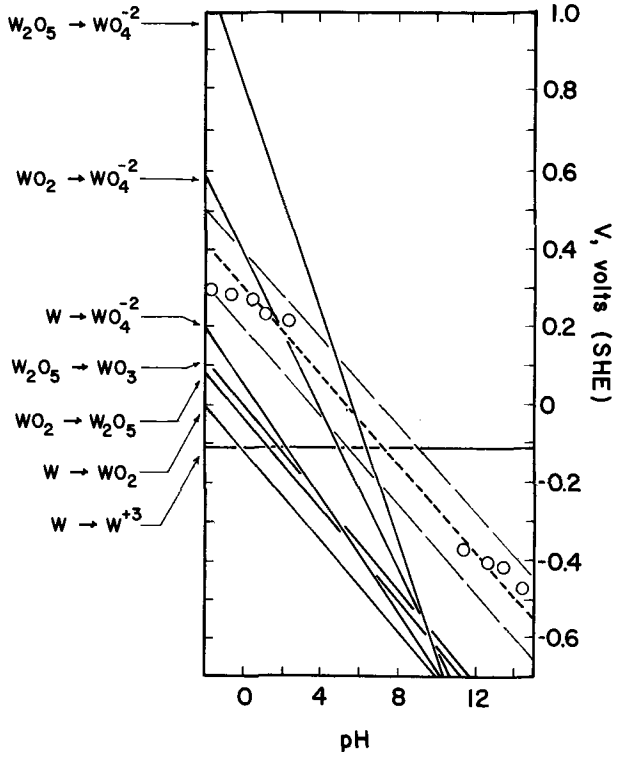

Fig. 3. Comparison of the measured "open-circuit" potentials of the tungsten electrode with the thermodynamic values for various tungsten-water reactions at 25°C. (○, experimental data; ——, Eq. [8]).

[2] For reduction potential.

cal rate-determining step subsequent to the first electron transfer from W_2O_5. The pH effect indicates the production of hydrogen ions (or their equivalent) prior to the r.d.s.

Expressing the above in equation form gives

$$2\,W(s) + 5\,H_2O(aq) \rightarrow W_2O_5(s) + 10\,H^+(aq) + 10e \quad [9]$$

$$W_2O_5(s) + H_2O(aq) = W_2O_5OH(s) + H^+(aq) + e \quad [10a]$$

and/or

$$W_2O_5(s) + OH^-(aq) = W_2O_5OH(s) + e \quad [10b]$$

$$W_2O_5OH(s) + W_2O_5(s) \xrightarrow{\text{r.d.s.}} W_2O_5\text{-}OH\text{-}W_2O_5(s) \quad [11]$$

$$W_2O_5\text{-}OH\text{-}W_2O_5(s) \rightarrow W_2O_5\text{-}O\text{-}W_2O_5(s) + H^+(aq) + e \quad [12]$$

$$W_2O_5\text{-}O\text{-}W_2O_5(s) \rightarrow \cdots \rightarrow 2\,WO_3(s) + W_2O_5(s) \quad [13]$$

$$WO_3(s) + H_2O(aq) \rightarrow H_2WO_4(s) \quad [14]$$

$$H_2WO_4(s) \rightarrow H^+(aq) + HWO_4^-(aq) \quad [15a]^3$$

and/or

$$H_2WO_4(s) + 2\,OH^-(aq) \rightarrow 2\,H_2O(aq) + WO_4^{-2}(aq) \quad [15b]$$

This scheme is similar to the one proposed previously for Mo[8] which also incorporated oxygen-bridged compounds. Such W compounds (W_2O_5, W_4O_{11}, etc.) are known to exist (11). It thus appears that the chemically similar metals Mo and W dissolve anodically in a similar manner.

Acknowledgments

The authors wish to thank Dr. Gary L. Bertrand, Associate Professor of Chemistry, for helpful discussions. This paper is based on a thesis submitted by one of us (C.L.W.) for the M.S. degree in Chemical Engineering at the University of Missouri-Rolla. It is contribution No. 126 from the Graduate Center for Materials Research, University of Missouri-Rolla.

Manuscript submitted June 18, 1971; revised manuscript received ca. Aug. 20, 1971.

Any discussion of this paper will appear in a Discussion Section to be published in the June 1972 JOURNAL.

[3] Or possibly $H_2WO_4 + 2H^+ \rightarrow WO_2^{+2} + 2H_2O$.

REFERENCES

1. L. Young, "Anodic Oxide Films," pp. 2-5, Academic Press, New York (1961).
2. W. E. Koerner, *Trans. Electrochem. Soc.*, **31**, 221 (1917).
3. H. W. Pitman and D. C. Hamby, Report of Linfield Res. Inst., Oregon (1959); [Quoted from Ref. (1), pp. 272-273].
4. U. R. Evans, "The Corrosion and Oxidation of Metals: Scientific Principles and Practical Applications," pp. 55-56, Edward Arnold Ltd. (1961).
5. M. de Kays Thompson and C. W. Rice, *Trans. Electrochem. Soc.*, **67**, 71 (1935).
6. S. E. S. El Wakkad, H. A. Rizk, and I. G. Ebaid, *J. Phys. Chem.*, **59**, 1004 (1955).
7. J. Besson and G. Drautzburg, *Electrochimica*, **3**, 158 (1960).
8. J. W. Johnson, C. H. Chi, C. K. Chen, and W. J. James, *Corrosion*, **26**, 238 (1970).
9. H. Remy and J. Kleinberg, "Treatise on Inorganic Chemistry," pp. 177-178, Elsevier Publishing Co., New York, 1956.
10. Handbook of Chemistry and Physics, 48th ed., p. B-236, Chemical Rubber Co. (1967-1968).
11. F. Albert Cotton and G. Wilkinson, "Advanced Inorganic Chemistry," p. 776, Interscience Publishers, New York (1962).
12. Wendell M. Latimer, "Oxidation Potentials," p. 254, Prentice-Hall, Inc., New York, 1952.
13. M. Pourbaix, "Atlas of Electrochemical Equilibria," p. 280, Pergamon Press (1966).

The Anodic Oxidation of Titanium Carbide

R. D. Cowling and H. E. Hintermann*

Laboratoire Suisse de Recherches Horlogères, Neuchâtel, Switzerland

ABSTRACT

The anodic dissolution of titanium carbide in 2*N* H_2SO_4 has been examined by coulometric experiments and by the application of a rotating ring-disk electrode. The latter technique has shown that the dissolution proceeds through the intermediate formation of Ti(III) ions, which undergo immediate oxidation to Ti(IV) at the electrode surface.

The anodic behavior of titanium carbide in sulfuric acid solution has been described in a previous paper (1). Dissolution begins at about 0.8V(SHE),[1] and produces Ti(IV) ions, CO, and CO_2. Unsuccessful attempts were made to detect trivalent titanium in the nitrogen-saturated solution. The formation of Ti(III) in the dissolution reaction cannot be ruled out, however, since once formed it would be rapidly oxidized to Ti(IV) at the potential of the corroding electrode. The aim of the present study was to investigate the anodic oxidation of TiC more fully than had been previously possible. Pure, single crystal carbide was used instead of the vapor-deposited material on which earlier work (1) had been based. In particular, the occurrence of Ti(III) was examined. Two techniques were employed. First, the dissolution was studied coulometrically.

Assuming that the net reaction is one of the following

$$TiC + H_2O = Ti^{3+} + CO + 2H^+ + 5e^- \quad [1]$$

$$TiC + 2H_2O = Ti^{3+} + CO_2 + 4H^+ + 7e^- \quad [2]$$

$$TiC + 2H_2O = TiO^{2+} + CO + 4H^+ + 6e^- \quad [3]$$

$$TiC + 3H_2O = TiO^{2+} + CO_2 + 6H^+ + 8e^- \quad [4]$$

which account for the fact that both CO and CO_2, but no other gases, are produced during anodic dissolution, the number of electrons, z, associated with the stoichiometric equation is then $5 \leq z \leq 8$, and is unique for each equation. The value of z may be obtained

* Electrochemical Society Active Member.

Key words: corrosion, dissolution, coulometry, rotating ring-disk electrode.

[1] All potentials reported in this paper are referred to the standard hydrogen electrode.

experimentally. Assuming 100% anodic current efficiency, and that the carbide is stoichiometric, z is given by

$$z = \frac{47.9}{F} \cdot \frac{q}{\omega} \qquad [5]$$

where q coulombs results in ω grams of titanium passing into the solution.

The second technique was to construct a rotating ring-disk electrode whose disk was a single crystal of TiC. A platinum ring was used to detect any Ti^{3+} produced during anodic dissolution of the disk.

Experimental

Small single crystals of titanium carbide were kindly donated by Dr. G. E. Hollox, Brown Boveri Research Center, Baden, Switzerland. These were chips from larger crystals which had been grown from sintered carbide, and whose stoichiometry was given as $TiC_{0.97\pm0.01}$. They contained no free carbon.

In making an electrode from such a crystal, the solderability problem was first overcome by vacuum depositing a layer of chromium onto the surface, followed by a layer of copper, each about 1000Å thick. The copper was then built up galvanically to form a solderable contact to a copper wire, and the area comprising the joint was then embedded in a hard setting resin, stable in dilute acid solutions. An electrode thus produced had roughly the same form as a conventional wire electrode fused in glass, *i.e.* the solution was in contact with different crystal surfaces of the carbide at the same time. This was a simpler arrangement than mounting an electrode such that only a given plane contacted the solution, and was justified by the observation that the [100] and [110] faces of titanium carbide showed the same dissolution kinetics. Before use, the electrode was cleaned of any copper and chromium on the surface by anodic stripping in sulfuric acid.

For certain potentiostatic experiments, the quantity of electricity passed was measured directly with an electronic coulometer. This was designed to integrate small currents, of the order of 100 μA, where the conventional silver coulometer is time consuming and can function with less than 100% current efficiency. The voltage drop across a 100 ohm resistance, placed in the counterelectrode lead of the potentiostat, was amplified and then converted into a pulse signal whose frequency was proportional to the current which was being measured. The pulses were then summed with a frequency counter over any desired period of time, and the total count, with the introduction of a single calibration factor, gave a direct value for the number of coulombs which had passed. The instrument was calibrated to give 1000 Hz at 500 μA. At this current, a precision of about 0.1% was obtained, falling to 1% ($\pm$1 count) at 50 μA. A second range gave a precision of about 0.1% at 1.5 mA. Between 50 μA and 1.5 mA, the precision was better than 1%.

Because of the impossibility of machining single crystals of TiC, the construction of the RRDE posed some problems. Eventually it was made in three separate parts, the ring, disk, and body sections (Fig. 1), which were then press-fitted together as shown in the figure. The disk section was constructed by first grinding a crystal into the form of a regular cylinder, diameter 6.7 mm and thickness about 2 mm. A stainless steel cylinder, diameter 6.7 mm and thickness 5 mm, was then stuck onto the back of this, using Araldite resin. The piece was then mounted in Plexiglas, using a standard metallurgical press, and the outside diameter turned to 7.4 mm. A hole of diameter 3 mm was then drilled through to the back surface of the carbide, and the Araldite at the bottom of the hole scraped away. For the ring section, a cylinder of brass was machined to an external diameter of 8.4 mm and an internal diameter of 7.4 mm. To this was brazed a disk of

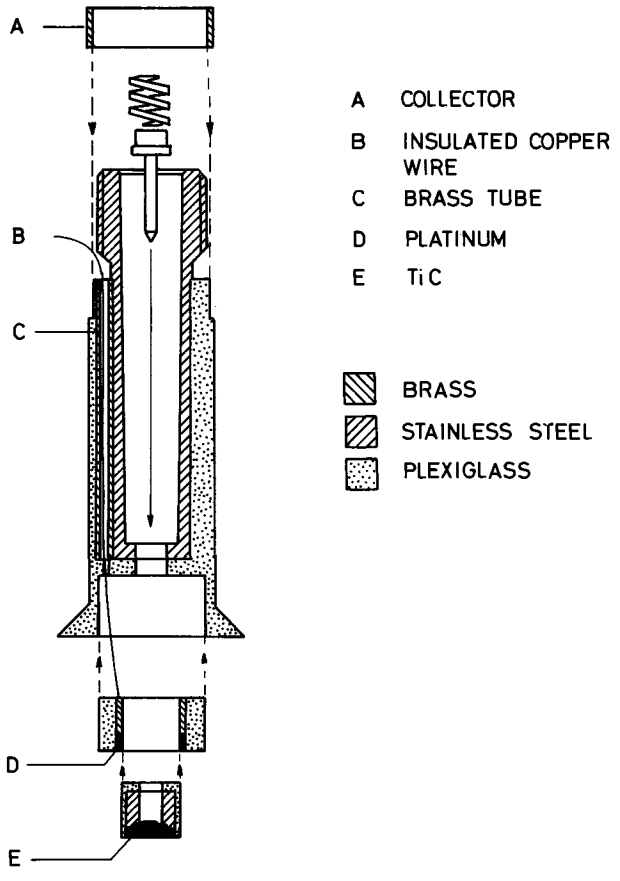

Fig. 1. Rotating ring-disk electrode

platinum, which was then machined to the same internal and external diameter as the cylinder. The brass tube was then cut to a length of 7 mm, and the piece mounted in Plexiglas and the OD turned to 13.5 mm. A fine insulated copper wire, soldered to the top edge of the cylinder, served as the eventual contact for the ring electrode. This passed through a small brass tube attached to, but insulated from, the main body of the electrode, and was fixed to a stainless steel collector ring. The steel body of the electrode was also mounted in Plexiglas, and the three sections were fitted together as shown. Contact to the disk was made by a pin, pressed against the back surface by a spring which was in turn connected through the drive shaft to the potentiostat. The disk diameter was 6.70 mm and the internal and external diameters of the ring were 7.40 and 8.40 mm respectively. The complete rotating disk assembly has been described elsewhere (2). Other experimental details have been described in an earlier paper (1).

Results

Coulometric experiments.—In order to determine whether the dissolution of titanium carbide can be represented by any one of Eq. [1]-[4], a known anodic charge was passed through the electrode, under both galvanostatic and potentiostatic conditions, and the solution subsequently analyzed for titanium by spectrophotometry. z was then calculated by Eq. [5].

A constant anodic current of 1 mA was passed through an electrode of area approximately 0.5 cm^2 in 2N H_2SO_4 saturated with nitrogen During dissolution, the potential of the electrode was 1.01V. The mean value of z, obtained from several experiments on the same electrode, was 6.5 $\pm$ 0.1. However, other electrodes gave different results, suggesting that z varied with current density or, more precisely, with the potential of the corroding electrode. This was investigated by repeating the experiments under

potentiostatic conditions. The current was then integrated with the electronic coulometer described above. At the end of each experiment the solution was analyzed for titanium. By repeating at different potentials, the value of z was obtained as a function of E. The results are shown in Fig. 3A. Below 0.97V, $z \approx 7$ but above this potential, z steadily decreases.

During dissolution of TiC both CO and CO_2 are produced. Potentiostatic experiments showed that as E increases the corrosion produces progressively more CO and less CO_2.

The spectrophotometric analysis of titanium is based on the yellow complex which is formed between titanium ions and H_2O_2. When titanium carbide undergoes anodic dissolution in $2N$ H_2SO_4 containing H_2O_2, the solution becomes progressively more yellow as the concentration of titanium increases. By monitoring the absorbance of the solution, z can be calculated coulometrically. This provides a convenient method for checking the values of z reported above. A constant anodic current was passed through a TiC electrode in a solution containing 50 ml of $2N$ H_2SO_4 and 10 ml of 3% H_2O_2. The absorbance of the solution was measured at half-hourly intervals and plotted as a function of time. A linear relationship was obtained, from the slope of which z was calculated. This was repeated at different currents. The results are shown in Fig. 2. From seven such experiments a value of $z = 4.98 \pm 0.05$ was obtained, which suggests that in the presence of H_2O_2 the anodic dissolution of TiC proceeds by Eq. [1] only. However, analysis of the gaseous corrosion products showed that both CO and CO_2 are formed. An explanation of this, and of the constancy of z in this solution, is proposed below.

As a confirmation of the effect of H_2O_2, the dissolution of TiC was studied in a solution of the same composition under potentiostatic conditions; z was measured as a function of potential. The results shown in Fig. 3B confirm the value of $z = 5$ for potentials less than about 1V. Above this, simultaneous oxidation of the H_2O_2 begins, with a consequent lowering of the current efficiency for carbide dissolution. Calculated values of z therefore become greater.

Rotating ring-disk electrode.—The electrode described above was used to determine whether Ti^{3+} is produced as an unstable intermediate in the anodic oxidation of TiC. The electrode was rotated at 50 rpm in $2N$ H_2SO_4 saturated with nitrogen. A constant potential of 1.15V was applied to the ring, and the ring current i_R was recorded while the disk current i_D was zero. When i_R was steady, a constant anodic current of 200 μA was passed through the disk, which adopted a potential of about 1V. The instant that the disk current was switched on, the ring current rose. When i_D was switched off, i_R fell back to its original value. The absolute value of i_R was very small, less than 0.1 μA (corresponding to 1 $\mu A\ cm^{-2}$). A potential of 1.10V was then applied to the ring with i_D still zero, to establish a new residual ring current. When this was stable, the disk current was switched on and i_R immediately rose. This sequence was repeated at several potentials. Figure 4 shows the effect of i_D on i_R at three ring potentials. Values of i_R were so small that it was not possible to correlate them with values of i_D and with the rotation speed of the electrode. When the residual ring current and the increase, δi_R, which occurred when the disk was switched on were plotted against ring potential, the relationships shown in Fig. 5 were found. These two figures are discussed below.

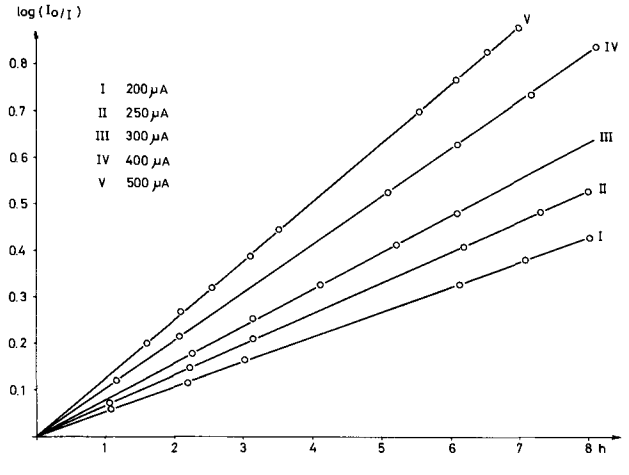

Fig. 2. Spectrophotometric analysis of titanium during constant current charging of TiC in 50 ml of $2N$ H_2SO_4 + 10 ml of 3% H_2O_2.

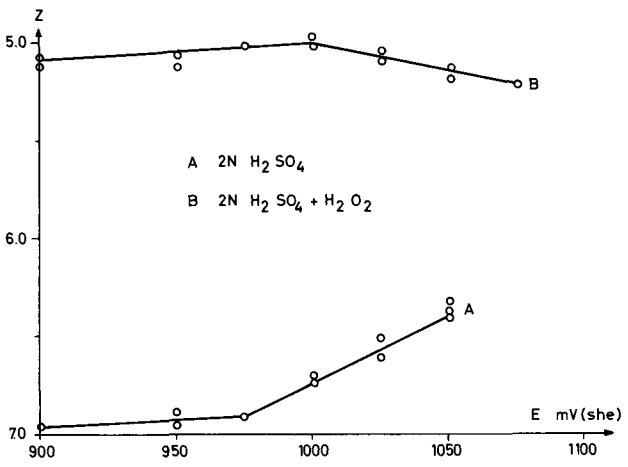

Fig. 3. Dependence of z on potential, where z is the number of electrons required to put one titanium ion in solution.

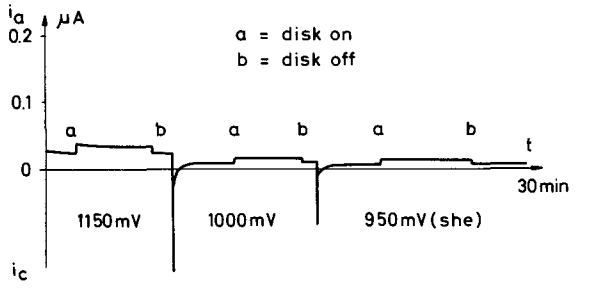

Fig. 4. Effect of disk current on ring current at three ring potentials.

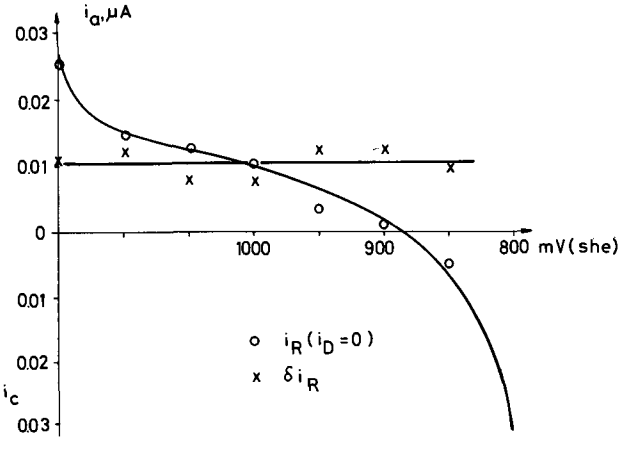

Fig. 5. Dependence of residual anodic ring current, and of δi_R, on potential.

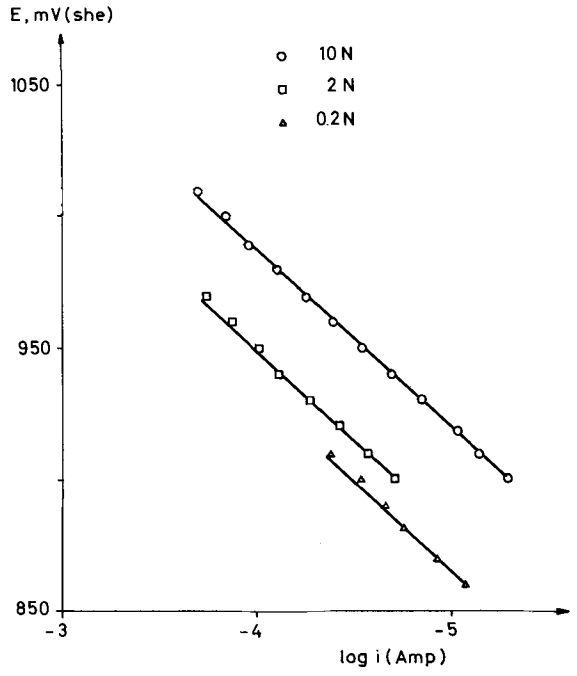

Fig. 6. Tafel curves for the dissolution of TiC in H_2SO_4 solutions.

Tafel curves for the dissolution reaction.—Figure 6 shows Tafel curves obtained in various concentrations of H_2SO_4. A high degree of reproducibility was obtained, and the slope of 0.073V/decade was the same in each solution.

Discussion

The results obtained with the RRDE clearly show (Fig. 4) that dissolution of the TiC disk produces a species which is then oxidized at the ring. When these results are plotted in the form shown in Fig. 5, two interesting features appear. First, the residual ring current (i_R when $i_D = 0$) plotted against ring potential passes through zero at 0.89V. This potential is in close agreement with the equilibrium potential for the Pt/PtO system reported by Hoare (3), who gave a value of 0.88V in the same solution as that used in the present work. When $i_D \neq 0$, the total ring current therefore contains a contribution due to platinum oxidation, plus an additional part due to an oxidizable species produced by the dissolution of the disk. The second feature is that values of δi_R are independent of potential. Absolute values are only about 0.01 μA. This is, however, precisely the order of magnitude which would be expected for the oxidation of an unstable Ti(III) intermediate. From Pourbaix (4), the equilibrium potential for the redox couple Ti^{3+}/TiO^{2+} at pH = 0 and at $TiO^{2+}/Ti^{3+} = 1$ is about 0.16V. Since the potential of the TiC disk is above 0.8V during its dissolution, Ti(III) would undergo immediate oxidation at the disk, and only a very small fraction would be expected to reach the ring. This can be evaluated from the present results. The collection efficiency for the electrode used here is 0.27, from the tabulated values of Albery and Bruckenstein (5). If the dissolution of the disk initially produces Ti^{3+}, for which the stoichiometric reaction may involve 5 electrons (which will be discussed below), a current of 200 μA at the disk should give rise to a ring current of 10.8 μA. Since the observed values of δi_R were about 0.01 μA, only about 0.1% of the Ti(III) produced at the disk was able to leave the surface before being oxidized to Ti(IV). The Ti(III) which reaches the ring is oxidized at the limiting current. This is in good agreement with recent work on the corrosion of titanium (6), in which a similar limiting current was found for the oxidation of Ti^{3+} to Ti^{4+}.

The results of the coulometric experiments can be explained as follows. In the absence of H_2O_2, the effect of which will be discussed below, $z \approx 7$ at potentials below 0.97V (Fig. 3A). Both CO and CO_2 are produced in approximately equal quantities. The reaction therefore clearly follows two paths simultaneously, those represented by Eq. [3] and [4], with Ti(III) occurring as an unstable intermediate. The mean value of z for these two reactions is thus about 7, as observed. At higher potentials, z decreases and a progressive increase in the amount of CO produced was observed. That is, the reaction favors Eq. [3]. It would appear to be contradictory, that as the potential is made more anodic the lower oxide of carbon is favored. This can only be so if CO_2 is formed by the oxidation of CO adsorbed on the electrode surface, and which undergoes progressive desorption above 0.97V. The work of Gilman (7) in fact shows that this is quite possible. He studied the adsorption of CO on a platinum electrode in 1*N* $HClO_4$, and observed that it was adsorbed up to 0.90V (against a hydrogen electrode in the same solution) but that above this potential the surface coverage of CO decreased rapidly. Therefore the dissolution of TiC produces Ti^{3+} and CO as initial products, the Ti^{3+} undergoing immediate oxidation at the electrode surface while the CO may either desorb or be oxidized to CO_2. As the potential increases, the desorption reaction is favored.

This explanation for the potential dependence of z also accounts for the fact that constant current experiments gave values of z which were generally noninteger and which apparently depended on the current density. Thus there is good agreement between the observed potential (1.01V) during the galvanostatic experiment reported above, and that expected from Fig. 3A for $z = 6.5$ (1.02V).

In the presence of H_2O_2 the dissolution of TiC produces both CO and CO_2, but z is constant at 5. This in fact affords further evidence for the intermediate formation of Ti(III). The initial reaction may be represented by Eq. [1], for which $z = 5$, producing Ti(III) and CO as discussed above. The oxidation potential of H_2O_2 is, however, higher than the electrode potential. Therefore oxidation of Ti(III), and of adsorbed CO to CO_2, by H_2O_2 in the double layer occurs at a greater rate than electrochemical oxidation. This may be represented by

$$TiC + H_2O = Ti^{3+} + CO_{ads} + 2H^+ + 5e^-$$

$$CO_{ads} = CO$$

$$CO_{ads} + H_2O_2 = CO_2 + H_2O$$

$$Ti^{3+} + H_2O_2 = \text{yellow complex.}$$

Thus both CO and CO_2 are formed while z remains constant at 5.

The Tafel slope of 0.073V/decade gives $n\beta = 0.81$, where n is the number of electrons involved in the rate-determining step and β is the anodic transfer coefficient. Since the dissolution is a completely irreversible reaction, the absolute value of the overvoltage, η, is not known and the lines of Fig. 6 cannot be extrapolated to $\eta = 0$ to obtain an exchange current density. Whether the R.D. step is a one-electron reaction with $\beta = 0.81$, or a two-electron transfer with $\beta = 0.40$, cannot be determined from the present work, and consequently this step cannot be identified.

Manuscript submitted Nov. 20, 1970; revised manuscript received *ca.* July 7, 1971.

Any discussion of this paper will appear in a Discussion Section to be published in the June 1972 JOURNAL.

REFERENCES

1. R. D. Cowling and H. E. Hintermann, *This Journal*, **117**, 1447 (1970).

2. H. E. Hintermann and E. Suter, *Rev. Sci. Inst.*, **36**, 1610 (1965).
3. J. P. Hoare, *This Journal*, **109**, 858 (1962).
4. M. Pourbaix, "Atlas d'Équilibres Electrochimiques à 25°C," Gauthier-Villars, Paris (1963).
5. W. J. Albery and S. Bruckenstein, *Trans. Faraday Soc.*, **62**, 1920 (1966).
6. R. D. Armstrong, J. A. Harrison, H. R. Thirsk, and R. Whitfield, *This Journal*, **117**, 1003 (1970).
7. S. Gilman, *J. Phys. Chem.*, **66**, 2657 (1962).

Electrodeposition of Resins at Soluble Metal Anodes

Sidney L. Phillips*,[1] and Eugene P. Damm, Jr.

Systems Development Division, International Business Machines Corporation, Poughkeepsie, New York 12602

ABSTRACT

The electrodeposition of dispersed organic polymers onto soluble metal anodes is treated in terms of the diffusion of metal ions through the film as the rate-determining step. Diffusion control of the current was shown by the linearity of plots of current *vs.* $t^{-1/2}$. Equations were derived which relate the instantaneous film thickness and rate of film growth as functions of time. Experiments carried out in an aqueous dispersion gave results in agreement with theoretical predictions. The experimental results do not support the ohmic equation which has been proposed to account for the falloff in current with time.

Electrodeposition of resins from aqueous dispersions has application to coating of metallic objects by organic films (1-6). The deposition process consists of a number of steps, which may include diffusion and migration of cations, anions, and water, flocculation and compaction of the dispersed resin onto the anode, and oxidation of a functional group on the resin. It is generally agreed that flocculation of the resin is caused by metallic ions generated at the anode (2, 5).

In the present work, we report the results of a study focused primarily on deriving equations which can be used to predict deposition rates and the dependence of film thickness on plating time. Included also is a study of the effect of applied voltage on the current and film thickness, and an alternate explanation for the fall off in plating current with time, which has been observed by others (8-10).

Theory

In agreement with other workers, we assume that deposition of resins at soluble metal anodes proceeds via a mechanism involving electrochemical flocculation. After formation of the initial film (5), metal ions formed at the electrode-film interface must pass through the growing organic layer to the film-dispersion interface so that flocculation may continue. One mode of mass transfer of metal ions from the anode through the film is by diffusion.

If the mode of mass transfer of metal ions through the film is by Fickian diffusion, current-time curves will show a typical shape such that a plot of faradaic current *vs.* the reciprocal of the square root of time yields a straight line (14). Plots were constructed according to this relationship using published data for three different dispersion-electrode systems (8-10), and are shown in Fig. 1. As can be seen, straight lines are obtained in each case, showing diffusion control over these time ranges. On this basis, we will assume that the limiting step in the deposition of a concentrated suspension at soluble metal anodes is diffusion of the metal ion through the organic film to derive an equation relating the film thickness as a function of time.

Film thickness controlled by metal diffusion.—The organic film initially formed is assumed free of metal ions (5) so that at the start of the experiment we write

$$t = 0, \quad 0 > x \geqq l: \quad C_O = 0 \qquad [1]$$

Here, t is the time, x is the linear distance within the film, l is the film thickness, and C_O is the concentration of metal ion within the film.

As boundary conditions, we prescribe

$$t > 0, \quad x = 0: \quad C_O = C^*_O \qquad [2]$$

$$x = l: \quad C_O = 0 \qquad [3]$$

$$D_O \left(\frac{\partial C_O}{\partial x} \right) = M \frac{dl}{dt} \qquad [4]$$

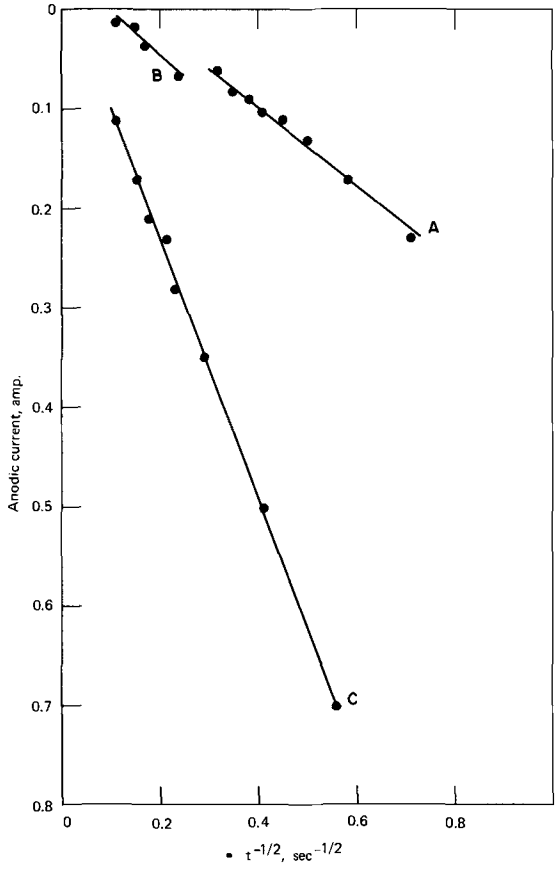

Fig. 1. Current *vs.* $t^{-1/2}$: Curve A. Sumner, tin anode, oleoresinous lacquer emulsion. Curve B. Finn and Mell, iron anode, acrylic copolymer emulsion. Curve C. LeBras, iron anode, polycarboxylic acid polymer.

* Electrochemical Society Active Member.
[1] Present address: Systems Development Division, International Business Machines Corporation, Monterey and Cottle Roads, San Jose, California 59114.
Key words: electrophoretic deposition, electroplating, dispersions, diffusion, growing films.

In Eq. [2], C^*_O is the concentration of metal ion at the electrode-film interface, with the value of C^*_O determined by the solubility of the metal ion in the medium (7). In Eq. [3], the concentration of metal ions at the film-dispersion interface is set equal to zero (4, 8), while in Eq. [4], the flux of metal ions at this interface is equated to the rate of growth of the film. In this last equation, M represents the concentration of metal within the film, and D_O is the diffusion coefficient of the metal ion within the wet film. Deposition occurs as metal ions arrive at the film-dispersion interface by a diffusional process, so that Fick's second law may be applied. For a planar electrode

$$\frac{\partial C_O}{\partial t} = D_O \frac{\partial^2 C_O}{\partial x^2} \qquad [5]$$

Equations [1]-[5], representing diffusion with a moving boundary, may be solved by methods analogous to those used in the comparable cases of the freezing of water (11) or metal-tarnishing reaction (12, 13).

In terms of the measured parameters, the solution is

$$C^*_O/M = \sqrt{\pi}\ \alpha\ \exp(\alpha^2)\ \mathrm{erf}(\alpha) \qquad [6]$$

where

$$\alpha = \frac{l}{2\sqrt{D_O t}} \quad \text{and} \quad \mathrm{erf}(\alpha) = \frac{2}{\sqrt{\pi}} \int_0^{\alpha} e^{-y^2}\, dy \qquad [7]$$

For small values of the argument, $\mathrm{erf}(\alpha)$ is expanded in the series

$$\frac{2}{\sqrt{\pi}} \left[\alpha - \frac{\alpha^3}{3} + \frac{\alpha^5}{5.2!} - \frac{\alpha^7}{7.3!} + \cdots \right]$$

so that for thin films or long times, $C^*_O/M = 2\alpha^2$. In this case, the relation between film thickness and coating time may be written in the form

$$l = \sqrt{2\, D_O\, C^*_O\, t/M} \qquad [8]$$

and the film thickness increases as the square root of time.

The comparable expression for the rate of increase in film thickness with time is

$$\frac{dl}{dt} = \frac{2\, C^*_O\, D_O}{M\sqrt{\pi l}} \left\{ \frac{\alpha \exp(-\alpha^2)}{\mathrm{erf}(\alpha)} \right\} \qquad [9]$$

For small α

$$\frac{dl}{dt} = \frac{C^*_O\, D_O}{Ml} \qquad [10]$$

where integration of Eq. [10] yields Eq. [8]. As can be seen in Eq. [9] or [10], the rate of film growth falls off with increasing film thickness.

In the present work, Eq. [8] was applied to deposition of mixtures of polytetrafluoroethylene and acrylonitrile/butadiene copolymer at copper anodes (3).

Experiment

A programmable transistor power supply[2] was used as the voltage source. In practice, the voltage output was applied directly to the two electrodes so that the experiments were conducted under conditions of constant applied voltage. The cathode was a 250 ml capacity stainless steel beaker, while the anodes were prepared from 1 × 2 in. copper strips. Prior to use, the strips were covered with an insoluble polymeric coating using photoengraving techniques so that only a 0.218 × 0.312 in. rectangle of copper was exposed. For experiments where the current was monitored, a decade-box load resistor was placed in the current-carrying loop and the resulting voltage drop was followed using a Sargent Model SR recorder.[3]

[2] Electronic Measurements Company, Model 214 AM, Eatontown, New Jersey.

[3] E. H. Sargent Company, Chicago, Illinois.

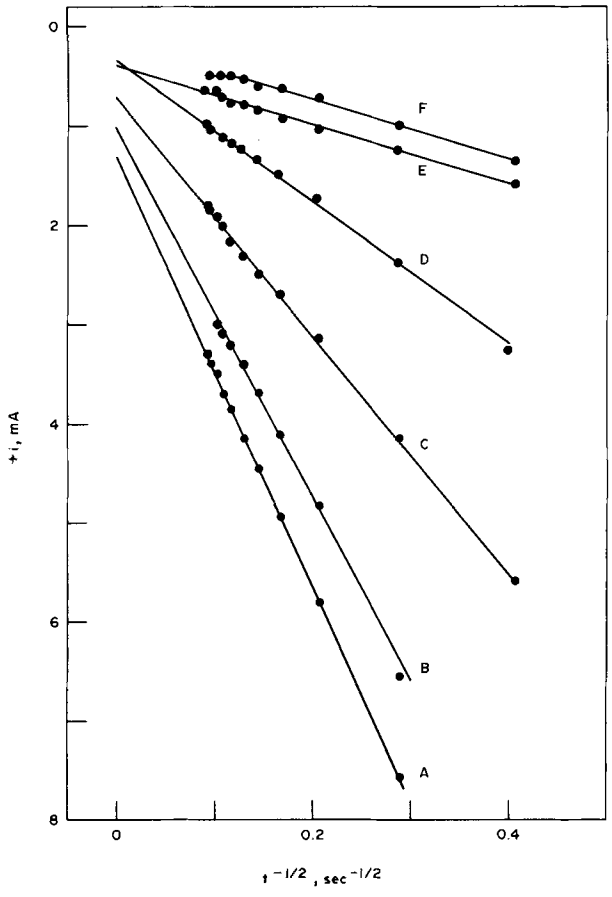

Fig. 2. Plots of faradaic current obtained on anodic dissolution of copper vs. $t^{-1/2}$. Electrode area 0.37 cm². Weight per cent ratio of polytetrafluoroethylene to acrylonitrile/butadiene copolymer: A, 51.1/0; B, 36.6/16.4; C, 24.4/24.6; D, 18.3/28.0; E, 12.2/32.0; F, 0/41.1.

Both of the dispersions were proprietary and were used as received. The polytetrafluoroethylene was E. I. du Pont Teflon 30B containing 61.1 weight per cent (w/o) solids; the acrylonitrile/butadiene copolymer was B. F. Goodrich Hycar 1561, containing 41.1 w/o solids. The dispersions were not stirred during the deposition process.

The electrodes were cleaned with trichloroethylene, followed by detergent and water rinsing before immersion in the dispersion. The two electrodes were then connected to the power supply, and the desired voltage applied for a specific length of time. Usually, the time was measured with a stop watch, but for experiments of less than ten seconds duration a repeat cycle timer[4] was used to apply the voltage.

After completion of deposition, the coated anode was removed from the dispersion and rinsed in distilled water to remove any material which clung to the organic film. The coated anode was then dried under ambient conditions for 2 hr and placed in a forced-flow air oven at 105°C for 10-15 hr. Measurements of the film thickness were made with either a micrometer or under magnification using a Nikon Model C Shadowgraph.

Results and Discussion

Typical plots of the faradaic current *vs.* $t^{-1/2}$ for various weight ratios of the two dispersed substances are shown in Fig. 2. As can be seen, the expected linear plots are obtained in all the experiments where polytetrafluoroethylene is present.

For the acrylonitrile/butadiene copolymer, the current fell rapidly to a constant value, and this behavior is reflected by a change in slope of the linear plot. The

[4] G. C. Wilson & Company, Chatham, New Jersey.

plots shown in Fig. 2 have not been corrected for charging current or residual current effects such as evolution of oxygen (2, 8). Assuming that evolution of oxygen contributes a constant faradaic component to the over-all current at a soluble electrode such as copper, plots such as those shown in Fig. 2 should be obtained; that is, the plots should be linear, but with a positive intercept.

On the basis of these plots, we conclude that passage of copper ions through the polymer film is primarily controlled by a diffusional process describable in terms of Eq. [6] and [8]. Superposed on the anodic copper dissolution current is a contribution from oxidation of the medium, as well as a smaller flow of nonfaradaic charging current caused by a change in the capacitance of the growing organic film.

Variation in film thickness with time.—According to Eq. [8], the instantaneous film thickness is proportional to the square root of time. This relationship was tested for several dispersions, and a typical linear plot obtained from a mixture of polytetrafluoroethylene and acrylonitrile/butadiene is shown in Fig. 3. The data for the plot shown in Fig. 3 were obtained at an applied voltage of 20V, but, as discussed below, higher or lower voltages did not necessarily affect the film thickness significantly.

Effect of applied voltage.—Other workers (4, 8) have accounted for the fall off in faradaic current during an electrophoretic deposition process by noting that the resistance of the growing organic film increases, and therefore the current must decrease according to the ohmic relation, $I = V/(R_F + R)$. In this equation, I is the current, V is the applied voltage, R_F is the time-dependent film resistance, and R is the constant resistance of the dispersed phase. Note that this relation also predicts an increase in current with increasing applied voltage.

In the present work, the applicability of the ohmic equation was tested by depositing Teflon-Hycar organic films onto planar copper electrodes at various applied voltages. The current-time behavior was recorded for those experiments, and typical curves are shown in Fig.

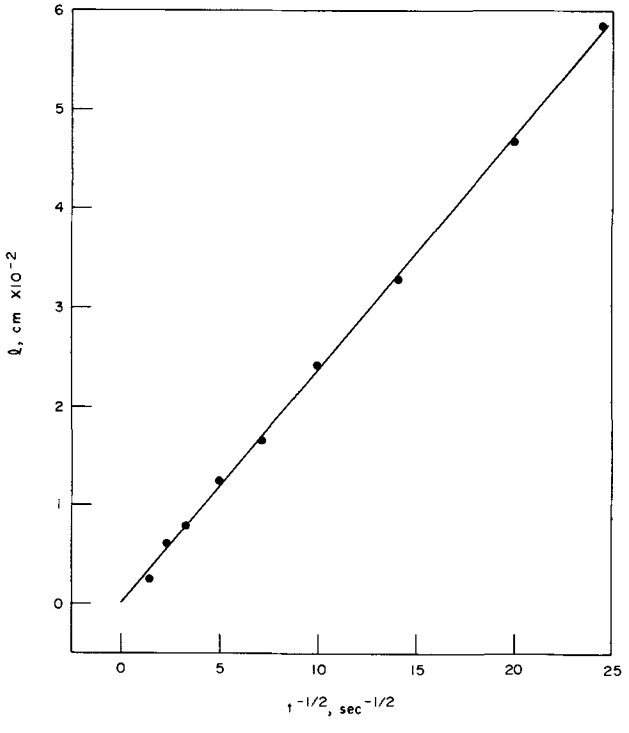

Fig. 3. Plot of film thickness vs. square root of time. Dispersion composed of 36.6 w/o polytetrafluoroethylene and 16.4 w/o acrylonitrile/butadiene copolymer.

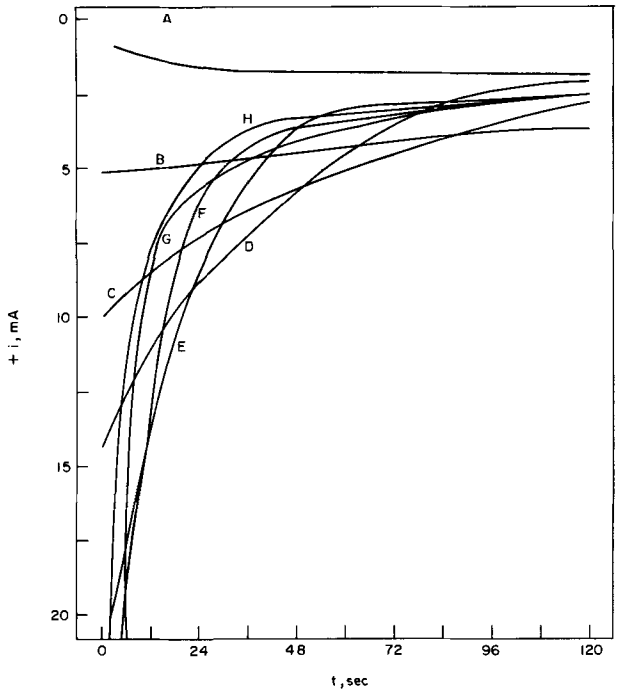

Fig. 4. Current-time curves obtained at various applied voltages for same dispersion composition as in Fig. 2. Applied voltages: A, 1.5; B, 2.0; C, 2.5; D, 3.0; E, 3.5; F, 4.0; G, 5.0; H, 10-100V.

4. Only curves obtained at applied voltages in the range 10-100V gave straight lines over the entire time interval when the current was plotted as a function of $t^{-1/2}$, so that the dissolution of copper is diffusion-limited at all times only over this range. However, the faradaic currents for curves C-G are higher at long times than the corresponding curves obtained at voltages exceeding 10V, indicating that thick films may still be obtained. This is because the film thickness depends on the quantity of metal ions which flowed through the film, so that the important factor to consider is the integral of the current over the time of the experiment which yields the number of coulombs.

Data relating film thickness to the applied voltage are given in Table I and, as can be seen, there is no appreciable change in film thickness over the range 3-100V. Thus, the data in this table and the identical current-time curves obtained at voltages between 10 and 100V do not support the ohmic relation for this dispersion system.

Conclusion

We conclude that the rate-determining step in the deposition of the polymers investigated here is satis-

Table I. Effect of voltage on film thickness

Dispersions composed of 60 w/o Teflon 30B and 40 w/o Hycar 1561. Coating time, 48 sec; planar copper electrode area, 0.44 cm²; dispersed medium resistance, 300 ohms.

Applied voltage, (V)	Film thickness,* (cm)
2.0	0.010**
2.5	0.014**
3.0	0.018
4.0	0.020
5.0	0.019
6.25	0.017
12.5	0.020
25.0	0.017
50.0	0.016
75.0	0.017
100.0	0.019

* Dried in a forced-flow air oven for 2-4 hr prior to measurement.
** Nonuniform thickness. Nominal value given.

factorily described by Eq. [6] and [8]. However, these equations apply when the metal ion is free to diffuse through the organic film. When the dispersion has a high resistance, as in the case of a nonaqueous medium, Eq. [6] and [8] do not hold and the film buildup may follow the relationships derived by Hamaker (12), and Hill, Lovering, and Rees (13). The important characteristic which deposited resins must have to follow Fick's law is probably inclusion of a substantial amount of water in the deposit, so that metal ions can diffuse through the film.

Manuscript submitted Jan. 11, 1971; revised manuscript received *ca.* Aug. 10, 1971. This was Paper 206 presented at the Atlantic City Meeting of the Society, Oct. 4-8, 1970.

Any discussion of this paper will appear in a Discussion Section to be published in the June 1972 JOURNAL.

REFERENCES

1. S. E. Sheppard and L. W. Eberlin, *Ind. Eng. Chem.*, **17**, 711 (1925).
2. C. G. Fink and M. Feinleib, *J. (and Trans.) Electrochem. Soc.*, **94**, 309 (1948).
3. R. W. Logan, "Production of Thin Polytetrafluoroethylene Resin (Teflon) Coatings by Electrodeposition Methods," Contract No. Now 62-0600-C, Department of the Navy, Bureau of Naval Weapons, Final Report, March 19, 1962 to March 19, 1963.
4. D. A. Olsen, *Official Digest/J. Paint Tech.*, **38**, 429 (1966).
5. J. P. Giboz and J. Lahaye, *J. Paint Tech.*, **43**, 79 (1971).
6. S. Mercouris and W. F. Graydon, *This Journal*, **117**, 717 (1970).
7. A. Hickling, *Trans. Inst. Metal Finishing*, **29**, 274 (1953).
8. L. R. LeBras, *Official Digest/J. Paint Tech.*, **38**, 85 (1966).
9. C. G. Sumner, *Trans. Faraday Soc.*, **36**, 272 (1940).
10. S. R. Finn and C. C. Mell, *J. Oil and Colour Chemists' Assoc.*, **42**, 219 (1964).
11. H. S. Carslaw and J. C. Jaeger, "Conduction of Heat in Solids," 2nd ed., Oxford University Press, New York (1959).
12. F. Booth, *Trans. Faraday Soc.*, **44**, 796 (1948).
13. P. V. Danckwerts, *ibid.*, **46**, 701 (1950).
14. P. Delahay, "New Instrumental Methods in Electrochemistry," p. 51, Interscience, New York (1954).
15. H. C. Hamaker, *Trans. Faraday Soc.*, **36**, 279 (1940).
16. C. G. A. Hill, P. E. Lovering, and A. L. G. Rees, *ibid.*, **43**, 407 (1947).

Correlations between the Kinetics of Electrolytic Dissolution and Deposition of Iron

I. The Anodic Dissolution of Iron

F. Hilbert,[1] Y. Miyoshi,[2] G. Eichkorn, and W. J. Lorenz[†]

Department of Electrochemistry, University of Karlsruhe, Karlsruhe, Germany

ABSTRACT

A synopsis of experimental results on the anodic dissolution of iron is given. From these data the existence of two different reaction mechanisms is proved, of the noncatalyzed (Bockris) mechanism and of the catalyzed (Heusler) mechanism. The current density-potential relations under steady-state and nonsteady-state conditions are given. An atomistic model of the two dissolution mechanisms is confirmed by electron micrography. It is shown that a change between reaction mechanisms can be brought about at will. Which one of the two mechanisms is predominant depends on the surface activity of the iron sample, which is determined by the crystallographic substructure. This is shown by x-ray measurements, electrochemical experiments, and electron micrographs. The exchange current densities of the Fe/Fe^{++} electrode are calculated and discussed.

With regard to the industrial use the importance of a detailed knowledge about the electrochemical and corrosion behavior of the metals of the iron group is obvious. However, investigations of the mechanisms of these metal/metal-ion electrodes are difficult, due to the great number of parameters determining the electrochemical behavior: charge transfer overvoltage, crystallization overvoltage, adsorption and desorption of gases and other surface active substances, the formation of intermediate reaction compounds, complexation of the metal ions with components of the solution, passivation phenomena, the occurrence of two or more electrode reactions at the same time (on corroding metals), etc.

For solid metals an important influence of the surface activity on the phase boundary reaction itself is to be expected. However, until now the experimental results regarding this dependence are rather scarce. For thermodynamic equilibria the activity of pure condensed phases is equal to one by definition. For kinetic phenomena this approximation is not valid. This has been known for a long time from investigations of catalytic reactions. Especially in the case of heterogeneous reactions of the catalytic active metals of the iron group an influence of the surface activity should be evident.

Thorough investigations into the mechanisms of complicated metal/metal ion electrodes are possible only if a great number of determining parameters can be eliminated or held constant. For this reason, in many experiments the following model system was used:

High purity metal[3]/acid solution; free of oxygen, surface active substances, and complex forming compounds.

[3] In our experiments the purity was better than 99.95% (1).

[†] Electrochemical Society Active Member through Deutsche Bunsen.

[1] Present address: Institute of Anorganic Chemical Technology, Technical University, Graz, Austria.

[2] Present address: Nippon Steel Corporation, Central Research Laboratories, Fuchinobe, Sagamihara-shi, Kanagawa, Japan.

Key words: corrosion; charge transfer mechanism of iron; crystallographic substructure, influence on charge transfer; iron electrode, exchange current density of.

By using high-purity metal, one eliminates the influence of atomic disorder caused by impurity atoms and the absorption of hydrogen into the metal is made negligible. The kinetics of cathodic hydrogen evolution are relatively well known. Other reactions, *e.g.*, cathodic reduction of oxygen or the formation of surface covering compounds, cannot occur in this medium. The necessary purity grade of all reagents, including water, is very high, owing to the sensitivity of the transition metals to surface active substances. To maintain a high enough electrical conductance of the solution and to simplify somewhat the structure of the electrical double layer a relatively high concentration of an inert electrolyte is necessary. It has been shown (1, 2), that sulfate and perchlorate ions are not surface active on metals of the iron group; for this reason most of the experiments are done in acid solutions of the sodium salts of these anions.

Part I represents mainly a review of the present knowledge about the anodic dissolution of iron, although some as yet unpublished results and interpretations are included. For the first time in print appear the experimental data of the section on Cold working of inactive samples and some of the theoretical interpretations in the sections on Reaction Mechanisms of Anodic Dissolution, Kinetic Equations, Atomistic Model, and Exchange Current Density of the Fe/Fe^{++} Electrode.

General Results

Many papers dealing with the anodic dissolution of iron have been published in the last few years (1-58). All authors agree that the over-all dissolution reaction

$$Fe \rightleftharpoons Fe^{++} + 2e^-$$

shows no dependence on the ferrous iron concentration, but that the reaction is stimulated by hydroxyl ions, even in highly acidic solutions. This is shown by a positive electrochemical reaction order relating to the pH of the solution. At first, a catalytic effect of the hydroxyl ions in acid solutions seems very unlikely. Because at pH = 1 the OH^- concentration is about 10^{-13} moles/liter and one finds one OH^- ion/cm^2, calculated for a distance of 50Å. This concentration is evidently too low to influence the reaction. However, there is the possibility of generation of OH^- ions from water molecules by deprotonation. A positive surface charge and the tendency of the transition metals to form complexes is assumed to be the cause of this reaction. A water dipole will adsorb on the surface with the negative oxygen directed against the positive metal. The energy for deprotonation is supplied by the resulting electrical energy and by the energy of the specific adsorption bond between metal and hydroxyl ions.

The great number of experimental results led mainly to two theories about the anodic dissolution mechanism of pure iron, worked out by Heusler (17-22) and Bockris (24-26). Both authors also investigated the cathodic deposition reaction in order to prove their theories. For some time it seemed impossible to find an explanation for the different results. So the workers seemed to fall into two groups proving either the one or the other theory. Recently it could be shown that both the proposed mechanisms can occur (1, 28, 49-52). They depend on the substructure of the solid. This means that different surface activities lead to different reaction paths for the electrolytic dissolution of iron. The influence of crystal imperfections on the reaction kinetics was quantitatively measured in the model system described above.

Kinetic Parameters of Anodic Dissolution

High-purity iron with very low surface activity is dissolved by a noncatalyzed mechanism, which agrees with the results of Bockris (24-26), Kelly (27), and others. Such a material is produced by zone melting or recrystallization under high vacuum. Evidently single crystals follow the same mechanism.

Highly active material, that is iron with a high density of multidimensional crystal imperfections, dissolves by a catalyzed mechanism, which agrees with results of Heusler (17-22) and others. Such a material with high density of crystal dislocations and strong deformations of the crystal lattice can be produced by cold-working processes.

The two different sets of experimental data obtained in dissolution experiments with these two materials are shown in Table I (1, 28, 49-52). The reproducibility is very good. The density of crystal imperfections was determined by x-ray measurements (1, 28, 49-52). The theoretical values are found from the kinetic equations for the two reaction paths (see below, section on Kinetic Equations). The terminus nonsteady-state means that the results are obtained by galvanostatic or potentiostatic pulse measurements. As can be seen, the agreement between experimental and theoretical results is rather good. The two mechanisms give different Tafel slopes under steady-state conditions and different reaction orders related to the pH. Under steady-state conditions the difference of 10 mV between Tafel slopes is rather small. But precision measurements show this difference beyond doubt. The difference between the reaction orders is big enough and can be exactly determined.

Reaction Mechanisms of Anodic Dissolution

Table II shows the two proposed mechanisms of the anodic iron dissolution (1, 17-28, 49-52). The main difference is in the rate-determining charge transfer reaction. These mechanisms and their dependence on the metal-substructure are discussed in the following section. At the beginning in both cases a potential dependent reaction sequence leads to the formation of adsorbed $(FeOH)_{ads}$. It is assumed, that this sequence is at equilibrium (Eq. [1]).

In the case of the noncatalyzed mechanism this sequence is followed by the charge transfer step. In this rate-determining part of the reaction $FeOH^+$ ions are

Table I. Kinetic data of the iron dissolution at $T = 298°K$

$b_{+,Fe}$ = anodic Tafel slope for the iron dissolution reaction.
$n_{+,pH}$ = electrochemical reaction order related to pH.
$n_{+,Fe^{++}}$ = electrochemical reaction order related to $c_{Fe^{++}}$.

	Steady-state			Nonsteady-state	
	Calculated	Experimental		Calculated	Experimental
		Noncatalyzed mechanism			
$b_{+,Fe}$	+39.4 mV	+40 ± 2 mV	$b'_{+,Fe}$	+40 mV	+60 ± 7 mV
$n_{+,pH}$	+1	+1 ± 0.1	$n'_{+,pH}$	+0.5	+0.5 ± 0.1
$n_{+,Fe^{++}}$	0	0	$n'_{+,Fe^{++}}$	0	0
		Catalyzed mechanism			
$b_{+,Fe}$	+29.6 mV	+30 ± 2 mV	$b'_{+,Fe}$	+59.2 mV	+60 ± 7 mV
$n_{+,pH}$	+2	+2 ± 0.3	$n'_{+,pH}$	+1	+1 ± 0.1
$n_{+,Fe^{++}}$	0	0	$n'_{+,Fe^{++}}$	0	0

Table II. Mechanisms of iron dissolution

$$\begin{array}{lll} Fe + H_2O \rightleftharpoons & Fe(H_2O)_{ads} & [1a] \\ Fe(H_2O)_{ads} \rightleftharpoons & Fe(OH^-)_{ads} + H^+ & [1b] \\ Fe(OH^-)_{ads} \rightleftharpoons & (FeOH)_{ads} + e^- & [1c] \\ \hline Fe + H_2O \rightleftharpoons & (FeOH)_{ads} + H^+ + e^- & [1] \end{array}$$

Noncatalyzed mechanism

$$(FeOH)_{ads} \not\rightleftharpoons FeOH^+ + e^- \quad [2]$$

Catalyzed mechanism

$$Fe + (FeOH)_{ads} \rightleftharpoons [Fe(FeOH)] \quad [3]$$

$$[Fe(FeOH)] + OH^- \not\rightleftharpoons FeOH^+ + (FeOH)_{ads} + 2e^- \quad [4]$$

$$FeOH^+ + H^+ \rightleftharpoons Fe^{++}\text{-aq} + H_2O \quad [5]$$

formed and pass the electrochemical double layer (Eq. [2]).

In the case of the catalyzed mechanism the first sequence is followed by a second surface reaction (Eq. [3]). In this step a catalytic active surface compound is formed. We believe that the formula [Fe(FeOH)] is a possible schematic hypothesis for this compound. The formation of this surface catalyst is dependent on the surface activity of the metal. Plausibly the formation will take place at kinks of the metal crystal or at adatoms in their vicinity. From these surface complexes the reaction products of the charge transfer step (Eq. [4]) are formed. In this rate-determining step Fe^{++} ions pass the electrochemical double layer and form $FeOH^+$ complexes with OH^- ions. In the course of this mechanism, the sequence Eq. [1] is a parallel electrochemical reaction. The over-all reaction after the start consists only of the steps Eq. [3], Eq. [4], and Eq. [5].

The noncatalyzed mechanism takes place if the equilibrium of Eq. [3] is shifted to the left by a very low surface activity of the metal. If the surface activity is high, this equilibrium is shifted to the right. Large amounts of the surface catalyst are formed and the reaction follows the catalyzed mechanism.

The succeeding reaction is the fast hydrolysis step (Eq. [5]), which is the same for both mechanisms.

The noncatalyzed mechanism shows two consecutive charge transfer reactions of one elementary charge unit. On the other hand, the catalyzed mechanism has only one charge transfer reaction, in which two elementary charge units are transported across the double layer. A reaction of this last type is energetically rather improbable. However, the experimental results of the second type cannot be explained in any other way. Another explanation of the different Tafel slopes could be the superposition of crystallization overvoltage. But in this case there exists no explanation for the large difference in reaction orders. For this reason we beleive that the catalyzed mechanism is possible under certain conditions: (*i*) a high density of crystal imperfections and therefore a high catalytic activity of the metal, and (*ii*) dissolution within a limited range of the anodic polarization curve (compare with section on Exchange Current Density of the Fe/Fe^{++} Electrode).

Two things have to be pointed out at this stage: For the first, the scheme of the catalyzed mechanism is only hypothetical. However, the reaction sequence corresponds to the experimental results. For the second, we think, the terms "catalyzed mechanism" and "noncatalyzed mechanism" are not very suitable, although their use is common in the literature. It would be better to term the charge transfer reaction "catalyzed" and "noncatalyzed."

Kinetic Equations

Steady-state conditions.—For the mechanism with noncatalyzed charge transfer one obtains from Eq. [1], [2], and [5] of Table II the following current-potential relations (the zeta-potential is assumed negligible)

$$i_1 = k_1 \cdot a_{Fe} \cdot a_{H_2O} \cdot \exp\left(\frac{\alpha_1 F \epsilon}{RT}\right) - k_{-1} \cdot a_{(FeOH)_{ads}} \cdot a_{H^+} \cdot \exp\left(-\frac{(1-\alpha_1) F \epsilon}{RT}\right) \quad [6]$$

$$i_{o,1} = k_1 \cdot \bar{a}_{Fe} \cdot \bar{a}_{H_2O} \cdot \exp\left(\frac{\alpha_1 F \epsilon_o}{RT}\right) = k_{-1} \cdot \bar{a}_{(FeOH)_{ads}} \cdot \bar{a}_{H^+} \cdot \exp\left(-\frac{(1-\alpha_1) F \epsilon_o}{RT}\right) \quad [7]$$

$$i_1 = i_{o,1}\left[A \cdot \exp\left(\frac{\alpha_1 F \eta}{RT}\right) - B \cdot \frac{a_{(FeOH)_{ads}}}{\bar{a}_{(FeOH)_{ads}}} \cdot \exp\left(-\frac{(1-\alpha_1) F \eta}{RT}\right)\right] \quad [8]$$

with

$$A = \frac{a_{Fe}}{\bar{a}_{Fe}} \cdot \frac{a_{H_2O}}{\bar{a}_{H_2O}}, \quad B = \frac{a_{H^+}}{\bar{a}_{H^+}}, \quad \eta = \epsilon - \epsilon_o$$

$\bar{a}_i$ = equilibrium activity of the species i at $\epsilon = \epsilon_o$

and

$$i_2 = i_{o,2}\left[\frac{a_{(FeOH)_{ads}}}{\bar{a}_{(FeOH)_{ads}}} \cdot \exp\left(\frac{\alpha_2 F \eta}{RT}\right) - C \cdot \exp\left(-\frac{(1-\alpha_2) F \eta}{RT}\right)\right] \quad [9]$$

with

$$C = \frac{a_{FeOH^+}}{\bar{a}_{FeOH^+}}$$

For a consecutive charge transfer mechanism

$$i = i_1 + i_2 \quad [10]$$

is always valid. Herewith one gets from [8], [9], and [10]

$$\frac{a_{(FeOH)_{ads}}}{\bar{a}_{(FeOH)_{ads}}} = \frac{i - i_{o,1} \cdot A \cdot \exp\left(\frac{\alpha_1 F \eta}{RT}\right) + i_{o,2} \cdot C \cdot \exp\left(-\frac{(1-\alpha_2) F \eta}{RT}\right)}{i_{o,2} \cdot \exp\left(\frac{\alpha_2 F \eta}{RT}\right) - i_{o,1} \cdot B \cdot \exp\left(-\frac{(1-\alpha_1) F \eta}{RT}\right)} \quad [11]$$

Under steady-state conditions

$$\frac{d\, a_{(FeOH)_{ads}}}{d\, t} = \frac{i_1}{z_1 F} - \frac{i_2}{z_2 F} = 0 \quad [12]$$

That means $i_1 = i_2$ and $i = 2\, i_2$ for $z_1 = z_2 = 1$. Therefore [8] = [9] and using [11] it follows that

$$i = 2 \cdot i_{o,1} \cdot i_{o,2} \frac{A \cdot \exp\left(\frac{(\alpha_1+\alpha_2) F \eta}{RT}\right) - B \cdot C \cdot \exp\left(-\frac{(2-\alpha_1-\alpha_2) F \eta}{RT}\right)}{i_{o,2} \cdot \exp\left(\frac{\alpha_2 F \eta}{RT}\right) + i_{o,1} \cdot B \cdot \exp\left(-\frac{(1-\alpha_1) F \eta}{RT}\right)} \quad [13]$$

As shown above, sequence [1] is assumed to be fast, while reaction [2] is rate determining. That means that

$$i_{o,1} >> i_{o,2}$$

and simplifying [13]

$$i = 2 \cdot i_{o,2} \left[\frac{A}{B} \cdot \exp\left(\frac{(1+\alpha_2)\mathbf{F}\eta}{RT} \right) - C \cdot \exp\left(-\frac{(1-\alpha_2)\mathbf{F}\eta}{RT} \right) \right] \quad [14]$$

Equation [14] represents the current density-overvoltage relation for the mechanism with noncatalyzed charge transfer. From [14] the following kinetic data can be obtained under anodic polarization ($\eta >> 0$)

$$b_{+,\mathrm{Fe}} = \left(\frac{\partial \eta}{\partial \log i_+} \right)_{a_i, \bar{a}_i} = \frac{2.303\,RT}{(1+\alpha_2)\mathbf{F}} = +39.4 \text{ mV} \quad [15]$$

(with $\alpha_2 = 0.5$; $T = 298°\mathrm{K}$).

$$n_{+,\mathrm{pH}} = \left(\frac{\partial \log i_+}{\partial \mathrm{pH}} \right)_{a_j, \epsilon} = +1 \quad [16]$$

In the case of the mechanism with catalyzed charge transfer from [1], [3], [4], and [5] one gets the following current density-overvoltage relationships using the symbol K for [Fe(FeOH)]

$$i = k_4 \cdot a_{\mathrm{K}} \cdot a_{\mathrm{OH}^-} \cdot \exp\left(\frac{2\alpha_4 \mathbf{F}\epsilon}{RT} \right) - k_{-4} \cdot a_{(\mathrm{FeOH})_{\mathrm{ads}}} \cdot a_{\mathrm{FeOH}^+} \cdot \exp\left(-\frac{2(1-\alpha_4)\mathbf{F}\epsilon}{RT} \right) \quad [17]$$

$$i_{o,4} = k_4 \cdot \bar{a}_{\mathrm{K}} \cdot \bar{a}_{\mathrm{OH}^-} \cdot \exp\left(\frac{2\alpha_4 \mathbf{F}\epsilon_o}{RT} \right) = k_{-4} \cdot \bar{a}_{(\mathrm{FeOH})_{\mathrm{ads}}} \cdot \bar{a}_{\mathrm{FeOH}^+} \cdot \exp\left(-\frac{2(1-\alpha_4)\mathbf{F}\epsilon_o}{RT} \right) \quad [18]$$

$$i = i_{o,4} \left[\frac{a_{\mathrm{K}}}{\bar{a}_{\mathrm{K}}} \cdot \frac{a_{\mathrm{OH}^-}}{\bar{a}_{\mathrm{OH}^-}} \cdot \exp\left(\frac{2\alpha_4 \mathbf{F}\eta}{RT} \right) - C \cdot \frac{a_{(\mathrm{FeOH})_{\mathrm{ads}}}}{\bar{a}_{(\mathrm{FeOH})_{\mathrm{ads}}}} \cdot \exp\left(-\frac{2(1-\alpha_4)\mathbf{F}\eta}{RT} \right) \right] \quad [19]$$

$$i_+ \simeq i_{o,4} \cdot \frac{a_{\mathrm{K}} \cdot a_{\mathrm{OH}^-}}{\bar{a}_{\mathrm{K}} \cdot \bar{a}_{\mathrm{OH}^-}} \cdot \exp\left(\frac{2\alpha_4 \mathbf{F}\eta}{RT} \right) \quad [20]$$

The activities of the catalytic surface complex are given from Eq. [3]

$$\frac{a_{\mathrm{K}}}{\bar{a}_{\mathrm{K}}} = \frac{a_{\mathrm{Fe}}}{\bar{a}_{\mathrm{Fe}}} \cdot \frac{a_{(\mathrm{FeOH})_{\mathrm{ads}}}}{\bar{a}_{(\mathrm{FeOH})_{\mathrm{ads}}}} \quad [21]$$

In this case under steady-state conditions it follows that

$$\frac{d\, a_{(\mathrm{FeOH})_{\mathrm{ads}}}}{d\, t} = \frac{i_1}{z_1 \mathbf{F}} = 0, \quad z_1 = 1 \quad [22]$$

The combination of [22] and [8] leads to

$$\frac{a_{(\mathrm{FeOH})_{\mathrm{ads}}}}{\bar{a}_{(\mathrm{FeOH})_{\mathrm{ads}}}} = \frac{A}{B} \cdot \exp\left(\frac{\mathbf{F}\eta}{RT} \right) \quad [23]$$

The steady-state current density-overvoltage relation for the mechanism with catalyzed charge transfer reaction is written, using [20], [21], and [23] and $K_w \cdot a_{\mathrm{H_2O}} = a_{\mathrm{H}^+} \cdot a_{\mathrm{OH}^-}$

$$i_+ \simeq i_{o,4} \cdot \left(\frac{A}{B} \right)^2 \cdot \exp\left(\frac{(1+2\alpha_4)\mathbf{F}\eta}{RT} \right) \quad [24]$$

From Eq. [24] one obtains the kinetic data

$$b_{+,\mathrm{Fe}} = \left(\frac{\partial \eta}{\partial \log i_+} \right)_{a_i, \bar{a}_i} = \frac{2.303\,RT}{(1+2\alpha_4)\mathbf{F}} = +29.6 \text{ mV} \quad [25]$$

(with $\alpha_4 = 0.5$ and $T = 298°\mathrm{K}$).

$$n_{+,\mathrm{pH}} = \left(\frac{\partial \log i_+}{\partial \mathrm{pH}} \right)_{a_j, \epsilon} = +2 \quad [26]$$

Nonsteady-state conditions.—Under nonsteady-state conditions the anodic pulse measurements show a decrease of the overvoltage or an increase of the current density with time. The oscillographic curves are illustrated schematically in Fig. 1. The values after charging of the double layer give a Tafel slope of about $b'_+ = +60 \pm 7$ mV at 25°C for both dissolution mechanisms.

These anodic transients and the nonsteady-state Tafel slopes can be explained by an increase of the intermediate ion concentration $(\mathrm{FeOH})_{\mathrm{ads}}$ in the case of the uncatalyzed mechanism or by an increase of the catalyst [Fe(FeOH)] in the case of the catalyzed mechanism. In other words, after the charging of the double layer the steady state of Eq. [12] or [22] is not immediately reached.

The quantitative explanation of the nonsteady-state results is difficult in the case of a consecutive charge transfer mechanism (noncatalyzed charge transfer). Plonski (59-61) has studied the galvanostatic transients by a mathematical treatment. The theoretical results, obtained by computer calculations for a model system, indicate the appearance of "superpolarization" under certain conditions. But the experimental steady-state and nonsteady-state Tafel slopes in a wide overpotential range are not predicted by Plonski's model. Losev (62) has measured the intermediate ion concentration at steady state and found a good agreement between theory of consecutive charge transfer mechanism and experimental results. Recently we have given a very raw mathematical approximation to explain the nonsteady-state Tafel slope (63). But it is evident, that computer calculations based on the theory of Plonski should be studied more exactly.

The measurable electrochemical reaction order in the case of the uncatalyzed mechanism

$$n'_{+,\mathrm{pH}} = \left(\frac{\partial \log i_+}{\partial \mathrm{pH}} \right)_{a(\mathrm{FeOH})_{\mathrm{ads}}, a_i, \epsilon} = +0.5 \quad [27]$$

is only a virtual value. It is dependent on the chosen

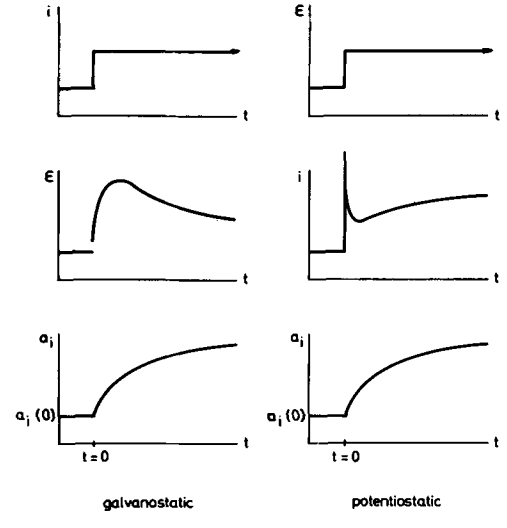

Fig. 1. Pulse measurements (schematic), a_i = intermediate ion activity.

stationary starting conditions, which determine the activity of $(FeOH)_{ads}$ (1, 50).

Now considering the mechanism with catalyzed charge transfer under nonsteady-state conditions, one gets from Eq. [19] with $a_K = \bar{a}_K = \text{const.}$

$$i_+ \simeq i_{0,4} \cdot \frac{a_{OH^-}}{\bar{a}_{OH^-}} \cdot \exp\left(\frac{2\alpha_4 F\eta}{RT}\right) \qquad [28]$$

The current density-overvoltage relation yields the kinetic data

$$b'_{+,Fe} = \left(\frac{\partial\eta}{\partial \log i_+}\right)_{a_{OH^-},\bar{a}_{OH^-}} = \frac{2.303\,RT}{2\,\alpha_4 F} = + 59.2 \text{ mV} \qquad [29]$$

(with $\alpha_4 = 0.5$; $T = 298°K$).

$$n'_{+,pH} = \left(\frac{\partial \log i_+}{\partial \text{ pH}}\right)_{a_k,\epsilon} = +1 \qquad [30]$$

Atomistic Model

It was shown by x-ray investigations of the materials, that the catalyzed mechanism only takes place in the case of high density of multidimensional crystal imperfections (1, 28, 49-52). Owing to the strong deformations of the crystal lattice, the concentration of active centers on the surface is high, as well as the degree of their activity.

If the density of multidimensional disorder is low, the dissolution takes place by the noncatalyzed mechanism. The surface of crystal grains consists of planes of different orientation. These planes are separated by subgrain boundaries that are built up by crystal dislocations. Those dislocations are active centers for the interesting phase boundary reaction. The activation energy for the formation of dissolution nuclei on the nondisturbed crystal planes is relatively high. Therefore the rate of dissolution due to nucleation from crystal planes will be low compared with the over-all dissolution rate, which is preferentially given by successive dissolution of whole monolayers of the subgrains. On account of the high separation energy of metal atoms from the lattice the concentration of adatoms will be low. All this means that the formation of the surface catalyst complex, which needs adatoms or kinks, will be very slow, and the catalyzed charge transfer reaction will supply only a very small part of the current. Substantial proof for this atomistic model was found by electron microscopy of electrolytically etched iron surfaces (51).

The catalyzed mechanism should produce a very rough surface, on account of a high dissolution rate at a great number of active centers. This model for the dissolution of high active metal is shown in Fig. 2. The electron micrograph of Fig. 3 shows the experimental result in good agreement with the model.

The surface produced by the noncatalyzed mechanism should be smooth, because on the slightly disordered planes one can expect the dissolution of more or less a whole monolayer before the next nucleus is formed. This is schematically displayed in Fig. 4.

The micrograph of a recrystallized, anodically etched iron sample is shown in Fig. 5. It seems to prove the theory.

The mean diameter of coherent regions was estimated from electron micrographs and compared with x-ray measurements. For high active material it is less than 1000Å, whereas for low activity metal it is more than 10,000Å.

Changing the Dissolution Mechanism

There are several ways to change the anodic dissolution mechanism by changing the surface activity of the sample (1, 28, 49-52).

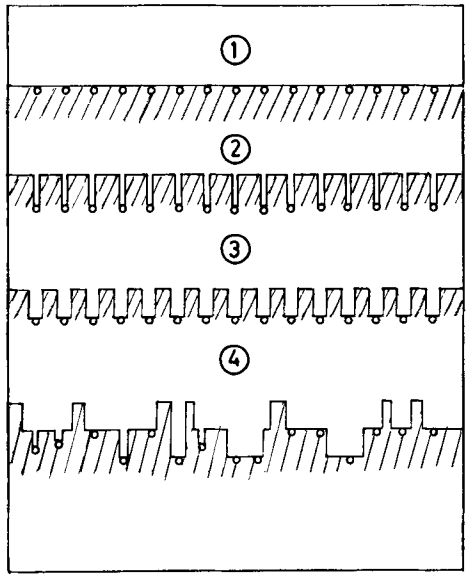

Fig. 2. Development of the surface profile during anodic dissolution of a highly active iron (starting from an electropolished sample). ○ = dislocations; 1,2,3,4 = dependence on time.

Fig. 3. Electron micrograph of an anodically etched iron with high surface activity, $i_+ = 50 \cdot 10^{-3}$ A · cm^{-2}, $t \triangleq 300$ sec, $V = 9600$ (9.6 mm $\triangleq 1\mu$).

Recrystallization of active samples.—The density of crystal imperfections decreases by recrystallization under high vacuum. Table III shows the dependence of the lattice deformations of a highly active sample on the annealing temperature. The data are calculated from the line broadening of x-ray measurements. Above a temperature of about 700°C the lattice deformations practically disappear, and the density of coherent lattice regions is diminished more than two orders of magnitude. This means that the number of subgrains and the density of subgrain boundaries decreases.

Table IV shows the change of the electrochemical kinetic data that is caused by recrystallization of the iron sample at different temperatures. The highly active starting sample gives the data of the catalyzed mechanism. At higher annealing temperatures recrystallized samples give the data of the noncatalyzed mechanism. If the samples are recrystallized at middle temperatures, there is a superposition of both reaction mechanisms.

Cold working of inactive samples.—Unpublished results show that a change from the noncatalyzed to the

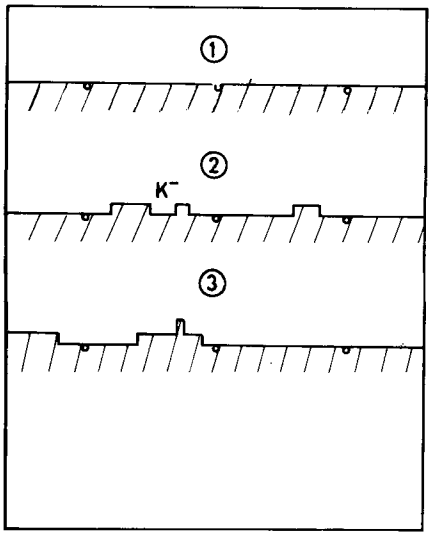

Fig. 4. Development of the surface profile during anodic dissolution of a low activity iron (starting from an electropolished sample). ○ = dislocations; k^- = negative nuclei; 1,2,3 = dependence on time.

Fig. 5. Electron micrograph of an anodically etched iron with low surface activity. $i_+ = 50 \cdot 10^{-3}$ A · cm^{-2}, $t = 300$ sec, $V = 9600$ (9.6 mm ≙ 1μ).

catalyzed mechanism can be brought about by heavy cold working (64). Figure 6 shows current density-potential curves of recrystallized material and of the same iron after heavy mechanical deformation. The change of mechanism is shown by different slopes of the Tafel lines under steady-state conditions, and by the correspondingly different electrochemical reaction orders related to the pH.

Blocking of active surfaces by inhibitors.—In principle it should be possible to change the catalyzed to the uncatalyzed mechanism in this way. Practically, this possibility cannot be realized. A blocking effect is only possible if relatively small inhibitor particles are used that geometrically fit into the semicrystal sites, steps,

Table III. Data of the iron substructure depending on the annealing temperature, obtained by x-ray measurements

Annealing temperature, °C	Mean size of coherent scattering lattice regions, G[Å]	Relative distortions of the lattice regions, ϵ	Density of coherent scattering lattice regions, N[cm^{-2}]
—	1,340	$7.5 \cdot 10^{-4}$	$5.6 \cdot 10^{9}$
350	1,070	$4.8 \cdot 10^{-4}$	$8.7 \cdot 10^{9}$
550	1,800	$3.7 \cdot 10^{-4}$	$3.1 \cdot 10^{9}$
750	18,000	—	$3 \cdot 10^{7}$

Table IV. Kinetic data of the iron dissolution depending on the annealing temperature

Annealing temperature, °C	$b_{+,Fe}$ [mV]	$b'_{+,Fe}$ [mV]	$n_{+,pH}$	$n'_{+,pH}$
—	+30	+60	+1.7 ... 1.9	+1
300	+30	+55	+1.6	+0.97
600	+34 ... 35	+55	+1.43	+0.75
750	+40	+74	+1.05	+0.41
900	+40	+63	+0.93 ... 1.08	+0.45

etc. Organic inhibitors have too large molecular sizes, but the surface active halogenide ions would be suitable. Unfortunately, halogenides change both dissolution mechanisms to a third mechanism (1, 20-22, 37, 42, 47, 48, 51). Experimentally it is impossible to decide if the catalyzed mechanism is first changed to the non-catalyzed and only after that to the halogenide-inhibited mechanism, or if the inhibited mechanism is directly reached.

Blocking of low-activity surfaces by inhibitors.—The noncatalyzed mechanism is changed to the catalyzed mechanism if slightly disordered crystal planes are covered with inhibitors (51). In these areas large inhibitor particles fit in much better than at the crystal imperfections (dislocations, semicrystal sites). The blocking causes the dissolution to take place preferentially at the relatively few regions of heavy disarray, following the reaction path of catalyzed charge transfer, while the noncatalyzed mechanism is suppressed.

The experimental results with the inhibitors β-naphthochinoline and o-phenanthroline are shown in Fig. 7. The change of mechanism causes a change of the Tafel slopes under steady-state conditions.

Further proof for the theory is found by electron microscopy (51). The atomistic model leads to the dissolution scheme of Fig. 8, which is in agreement with the real surface profile after anodic etching, as can be seen in Fig. 9. The micrograph shows the dissolution to take place at the relatively few grain boundaries and dislocations.

Exchange Current Density of the Fe/Fe^{++} Electrode

In the present paper we have tried to calculate exchange current densities for the Fe/Fe$^{++}{}_{aq.}$ electrode from literature data and our own results. In order to make comparisons possible, all data were standardized

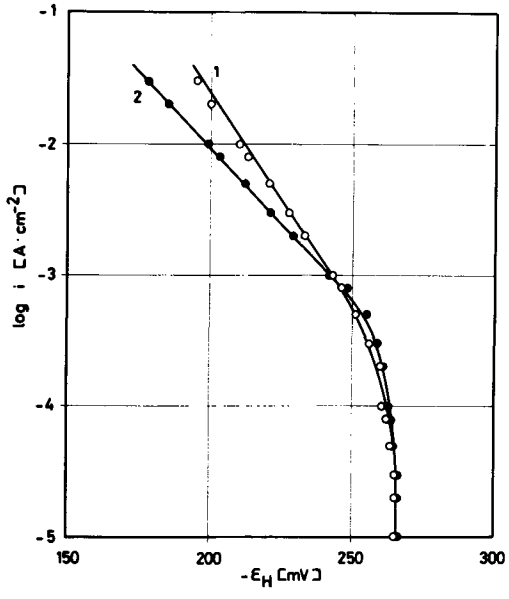

Fig. 6. Steady-state current density-potential curves of recrystallized (2) and cold-worked (1) iron.

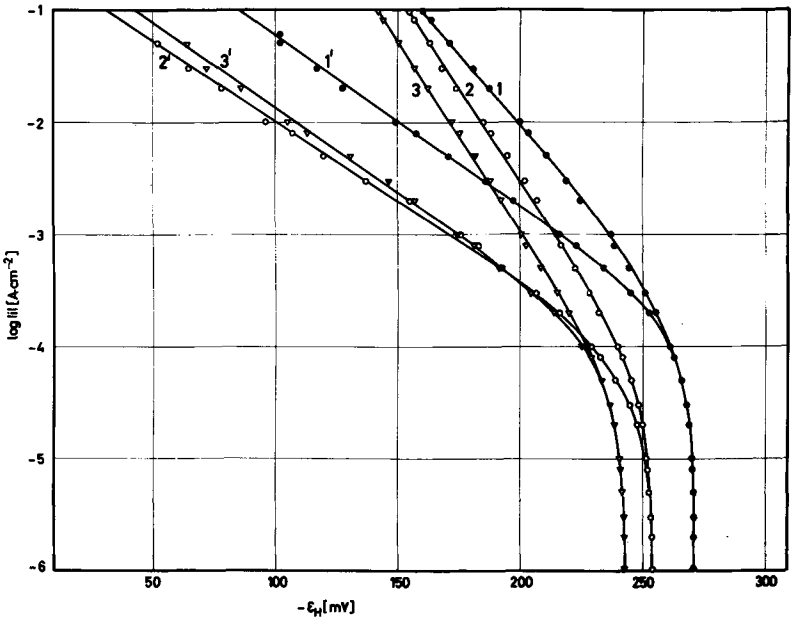

Fig. 7. Steady-state and nonsteady-state current density-potential curves. Electrode: Ommet-iron, annealed at 900°C. Electrolytes: 1 (●), 0.5M H_2SO_4; 2 (○), 0.5M H_2SO_4 + 10^{-2}M o-phenanthroline; 3 (▽), 0.5M H_2SO_4 + 10^{-2}M β-naphthochinoline. Nonsteady-state measurements are marked by primes.

to the conditions: pH = 0, $a_{Fe^{++}} = 1$. The second condition relates all exchange current densities to the standard potential of the iron electrode ($E_{o,H} = -441$ mV). The calculated data are given in Table V. The agreement for each mechanism is good. However, it seems remarkable that the exchange current densities for catalyzed charge transfer are lower than those for noncatalyzed charge transfer. Our explanation is the following one: the noncatalyzed mechanism is energetically favored. Only at elevated anodic potentials and at highly active surfaces the catalyzed charge transfer will be predominant. The activation energy of this process depends much more on the potential. Therefore it becomes predominant at high anodic polarization. The over-all current density is always the sum of two terms

$$i = i_{\text{noncatalyzed}} + i_{\text{catalyzed}} \qquad [31]$$

The polarization curve consists of two regions: at negative potentials the noncatalyzed charge transfer has

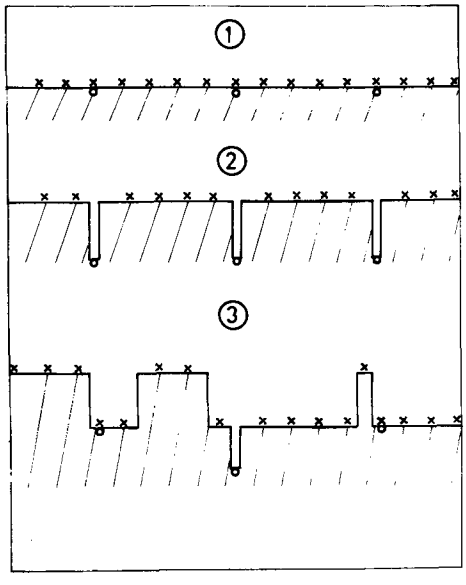

Fig. 8. Development of the surface profile during anodic dissolution of a low activity metal, covered with adsorbed inhibitor molecules. ○ = dislocations; × = adsorbed inhibitor molecules; 1,2,3 = dependence on time.

Fig. 9. Electron micrograph of an anodically etched iron with low surface activity, covered by β-naphthochinoline molecules. $i_+ = 50 \cdot 10^{-3}$ A · cm^{-2}, $t = 300$ sec, $V = 9600$ (9.6 mm ≙ 1μ).

the greater reaction rate and the curve is determined by this process. At more positive potentials the rate of the catalyzed charge transfer is greater and the curve is determined by it. The intersection point of the two parts of the curve depends on the surface activity of the material. The higher the activity, the greater the shifting of this potential to the negative side. In the case of highly active material, we only observe the second part of the curve, because the intersection potential is on the negative side of the corrosion potential.

Table V. Exchange current densities of the Fe/Fe^{++} electrode
$\log i_o^o = \log i_o$ at pH = 0 and $a_{Fe^{++}} = +1$

Noncatalyzed mechanism		Catalyzed mechanism	
$\log i_o^o$	Ref.	$\log i_o^o$	Ref.
−8.11	(24)	−10.28	(1)
−8.57	(24)	−12.50	(18)
−8.48	(1)	−12.70	(15)
−8.40	(27)	−12.05	(41)
		−12.28	(39)
		−11.80	(39)
		−11.31	(40)

Conclusions

The experimental results show that the kinetics of anodic phase boundary reactions depend on the surface activity of the solid. For the iron electrode we hope to have proved, beyond doubt, that the anodic dissolution in aqueous solutions can follow two different mechanisms.

In the meantime our results about the iron electrode (1, 28, 49-52, 63, 64) have been confirmed by measurements of Nobe (65). Moreover, the same two mechanisms seem to be valid for the anodic dissolution of cobalt and nickel (22, 39, 40, 66-70).

Manuscript submitted March 19, 1971; revised manuscript received July 27, 1971.

Any discussion of this paper will appear in a Discussion Section to be published in the June 1972 JOURNAL.

REFERENCES

1. W. J. Lorenz, "Das elektrochemische Verhalten des aktiven Reineisens in sauren Lösungen," Habilitationsschrift Universität Karlsruhe, 1968. Publication in "Advances in Corrosion Science and Technology" in preparation.
2. W. J. Lorenz, G. Eichkorn, and C. Mayer, *Corrosion Sci.*, **7**, 357 (1967).
3. W. A. Roiter, W. A. Juza, and E. S. Poluyan, *Acta Physicochim. USSR*, **10**, 389 (1939).
4. B. Kabanov, R. Burstein, and A. N. Frumkin, *Discussions Faraday Soc.*, **1**, 259 (1947).
5. B. Kabanov and D. Leikis, *Acta Physicochim. USSR*, **21**, 769 (1946).
6. B. Kabanov and D. Leikis, *Ber. Akad. Wiss. USSR*, **58**, 1685 (1947).
7. A. N. Frumkin, *Z. Elektrochem., Ber. Bunsenges. Phys. Chem.*, **59**, 807 (1955).
8. J. J. Kusnezow, *Phys. Chim. USSR*, **21**, 201 (1947).
9. A. C. Makrides, N. M. Komodromos, and N. Hackerman, *This Journal*, **103**, 363 (1955).
10. A. C. Makrides, *ibid.*, **107**, 869 (1960).
11. M. Stern and R. M. Roth, *ibid.*, **104**, 390 (1957).
12. T. P. Hoar and J. Holliday, *J. Appl. Chem.*, **3**, 502 (1953).
13. T. P. Hoar and T. W. Farrer, *Corrosion Sci.*, **1**, 49 (1961).
14. G. Okamoto, M. Nagayama, and N. Sato, CITCE VIII, Butterworth, London (1958) S. 445.
15. H. Kaesche, *Z. Elektrochem., Ber. Bunsenges. Phys. Chem.*, **63**, 492 (1959).
16. H. Kaesche, "Die Korrosion der Metalle," Springer-Verlag, Berlin-Heidelberg-New York (1966).
17. K. F. Bonhoeffer and K. E. Heusler, *Z. Elektrochem., Ber. Bunsenges. Phys. Chem.*, **61**, 122 (1957).
18. K. F. Bonhoeffer and K. E. Heusler, *Z. Phys. Chem. NF*, **8**, 390 (1956).
19. K. E. Heusler, *Z. Elektrochem., Ber. Bunsenges. Phys. Chem.*, **62**, 582 (1958).
20. K. E. Heusler and G. H. Cartledge, *This Journal*, **108**, 732 (1961).
21. K. E. Heusler, "Über den Einfluss von Halogenidionen auf das elektrochemische Verhalten des Kobalts," Vortrag 14. CITCE Meeting, Moskau, 1963.
22. K. E. Heusler, "Elektrochemische Auflösung und Abscheidung von Metallen der Eisengruppe," Habilitationsschrift, TH Stuttgart (1966).
23. H. Gerischer, *Electrochim. Acta*, **2**, 1 (1960).
24. J. O'M. Bockris, D. Drazic, and A. Despic, *ibid.*, **4**, 325 (1961).
25. J. O'M. Bockris and D. Drazic, *ibid.*, **7**, 293 (1962).
26. J. O'M. Bockris and H. Kita, *This Journal*, **108**, 676 (1961).
27. E. J. Kelly, *ibid.*, **112**, 124 (1965).
28. W. J. Lorenz and G. Eichkorn, *ibid.*, **112**, 1255 (1965).
29. F. M. Donahue and Ken Nobe, "Aqueous Oxygen Corrosion of Iron. Transient and Steady State Galvanostatic Phenomena in H_2SO_4." 2nd International Congress on Metallic Corrosion, New York, 1963.
30. T. Hurlen, *Acta Chem. Scand.*, **14**, 1533, 1555, 1564 (1960).
31. T. Hurlen, *Electrochim. Acta*, **7**, 653 (1962).
32. T. Hurlen, *ibid.*, **11**, 1205 (1966).
33. K. A. Christensen, H. Høeg, K. Michelsen, G. B. Nielsen, and H. Nord, *Acta Chem. Scand.*, **15**, 300 (1961).
34. H. H. Uhlig and Z. A. Foroulis, *This Journal*, **111**, 522 (1964).
35. Z. A. Foroulis and H. H. Uhlig, *ibid.*, **112**, 1177 (1965).
36. H. E. Bühler and W. Schwenk, *Z. Metallk.*, **56**, 24 (1965).
37. L. Cavallaro, L. Felloni, G. Trabanelli, and F. Pulidori, *Electrochim. Acta*, **9**, 485 (1964).
38. J. J. Podesta and A. J. Arvia, *ibid.*, **10**, 159, 171 (1965).
39. K. Schwabe and C. Voigt, *Werkstoffe Korrosion*, **16**, 125 (1965).
40. K. Schwabe and C. Voigt, *This Journal*, **113**, 886 (1966).
41. C. Voigt, *Electrochim. Acta*, **13**, 2037 (1968).
42. K. Schwabe and C. Voigt, *ibid.*, **14**, 853 (1969).
43. J. Sedzimir, Z. Zembura, and W. Ziolkowska, *Werkstoffe Korrosion*, **17**, 556 (1966).
44. K. H. Lieser, O. Kalvenes, and S. Compostella, *Corrosion Sci.*, **4**, 51 (1964).
45. H. Fischer and H. Yamaoka, *Chem. Ber.*, **94**, 1477 (1961).
46. H. Yamaoka and H. Fischer, *Electrochim. Acta*, **10**, 679 (1965).
47. W. J. Lorenz, H. Yamaoka, and H. Fischer, *Ber. Bunsenges. Phys. Chem.*, **67**, 932 (1963).
48. W. J. Lorenz, *Corrosion Sci.*, **5**, 121 (1965).
49. G. Eichkorn and W. J. Lorenz, *Naturwissenschaften*, **52**, 618 (1965).
50. W. J. Lorenz and G. Eichkorn, *Ber. Bunsenges. Phys. Chem.*, **70**, 99 (1966).
51. G. Eichkorn, W. J. Lorenz, L. Albert, and H. Fischer, *Electrochim. Acta*, **13**, 183 (1968).
52. G. Eichkorn and W. J. Lorenz, *Z. Metalloberfläche*, **22**, 102 (1968).
53. G. M. Florianovich, L. A. Sokolova, and Ya. M. Kolotyrkin, *Electrochim. Acta*, **12**, 880 (1967).
54. Ya. D. Zytner and A. L. Rotinyan, *Elektrokhimiya*, **2**, 1371 (1966).
55. P. H. Morel, "Contribution à l'étude des méchanismes de dissolution du fer, du nickel et du chrome, par l'analyse des courbes de polarisation anodique," Thèse, Paris, 1968, No. C.N.R.S. AO 2346.
56. M. Keddam, "Contribution à l'étude du méchanisme de la dissolution anodique par analyse de l'impédance faradique," Thèse, Paris, 1968, No. C.N.R.S. AO 2192.
57. I. Epelboin and M. Keddam, *This Journal*, **117**, 1052 (1970).
58. G. P. Cammarota, L. Felloni, G. Palombarini, and S. Sostero Traverso, *Corrosion*, **26**, 129 (1970).
59. I. H. Plonski, *This Journal*, **116**, 944 (1969).
60. I. H. Plonski, *ibid.*, **116**, 1688 (1969).
61. I. H. Plonski, *ibid.*, **117**, 1048 (1970).
62. A. I. Molodov, G. N. Markosyan, and V. V. Losev, "Regularities of Low-Valency Intermediates Accumulation and Their Use for Evaluating Kinetik Parameters of an Electrode Process," 21st CITCE Meeting, Prague/CSSR, 1970.
63. W. J. Lorenz, "The Mechanism of Consecutive Charge Transfer Electrode Reactions," 21st CITCE Meeting, Prague/CSSR, 1970.
64. H. Rosswag, K. Sarropoulos, and W. J. Lorenz, To be published.
65. A. Akiyama, R. E. Patterson, and Ken Nobe, *Corrosion*, **26**, 51 (1970).
66. V. I. Kravtsov and O. G. Lokshtanova, *J. Phys. Chem. USSR*, **36**, 2362 (1962).
67. M. H. Tikkanen and T. Tuominen, "On the Anodic Behaviour of Cobalt," Vortrag 3rd International Congress on Metallic Corrosion, Moskau, 1966.
68. K. E. Heusler, *Z. Elektrochem., Ber. Bunsenges. Phys. Chem.*, **66**, 177 (1962).
69. Z. A. Iofa and Wei Pao-ming, *J. Phys. Chem., USSR*, **36**, 1395 (1962).
70. K. E. Heusler and L. Gaiser, *Electrochim. Acta*, **13**, 59 (1968).

Correlations between the Kinetics of Electrolytic Dissolution and Deposition of Iron

II. The Cathodic Deposition of Iron

F. Hilbert,[1] Y. Miyoshi,[2] G. Eichkorn, and W. J. Lorenz[†]

Department of Electrochemistry, University of Karlsruhe, Karlsruhe, Germany

ABSTRACT

The cathodic iron deposition reaction from acid solutions was studied. The partial current density-potential curves of the iron deposition were calculated by current efficiency measurements. The experiments were carried out under steady-state and nonsteady-state conditions at 25°C under hydrogen atmosphere. Under steady-state conditions a rotating gold disk electrode was used in order to eliminate the rise of pH in the vicinity of the electrode surface. The results show two different reaction mechanisms depending on the pH at the electrode surface. At pH < 2.8 the kinetic data correspond to a noncatalyzed mechanism, while at pH > 2.8 a catalyzed mechanism takes place. The influence of the surface pH on the mechanism is due to the different electrochemical reaction orders related to the pH and the formation of hydrolysis products, which may be incorporated in the deposit. The calculated exchange current densities of the Fe/Fe^{++} electrode show that the noncatalyzed mechanism is the normal one.

In Part I we have shown that results of iron dissolution experiments lead to the hypothesis of two different reaction mechanisms.

It is to be expected that a correlation exists between the mechanisms of anodic dissolution and cathodic deposition of iron. The probable form of such a correlation is a reversal of the reaction sequences while the rate-determining step for each mechanism remains the same. This being the case, we have a more pronounced difference between the electrochemical kinetic data of the two reaction mechanisms. We investigated the kinetics of the cathodic iron deposition in order to confirm this hypothesis.

The cathodic deposition of metals with negative standard potentials from aqueous solutions is relatively difficult. This is due to the fact that the reaction rate of the reduction of hydrogen ions as well as that of oxygen is higher than that of the metal ion reduction.

Under such condition a nonnoble metal dissolves with hydrogen evolution, if the electrolyte is an acidic, oxygen-free, and nonoxidizing one. In this case the reversible equilibrium potential of the metal/metal-ion electrode cannot be adjusted without external current. The corrosion potential will then be obtained and lies between the equilibrium potential of hydrogen and that of the metal/metal-ion electrode.

The value of the corrosion potential is determined by the partial current density-potential curves of the cathodic and the anodic processes. The reaction rate and sometimes the type of mechanism depend on the surface activity of the metal, which will then consequently influence the corrosion potential.

Further complications are caused by mass transport phenomena. For example, with increasing pH of the electrolyte the limiting diffusion current density of hydrogen evolution is reached at relatively low values.

The cathodic polarization of such a mixed electrode in acidic, oxygen-free, and nonoxidizing solution leads at first only to hydrogen evolution. The cathodic metal deposition takes place at potentials that are more negative than the equilibrium potential of the metal/metal-ion electrode. Now the total cathodic current is the sum of the metal deposition current and of the hydrogen evolution current

$$i_{-,\text{total}} = i_{-,H^+} + i_{-,Me^{z+}} \qquad [1]$$

In this potential range it is possible to study the kinetics of metal deposition.

Sometimes the complication due to mixed potentials can be avoided. This can be done by increasing the pH of the solution and thereby shifting the equilibrium potential of the hydrogen electrode in the negative direction. Under the conditions

$$\epsilon_{o,H_2/H^+} \leq \epsilon_{o,Me/Me^{z+}}$$

and

$$i_{o,H_2/H^+} < i_{o,Me/Me^{z+}}$$

the hydrogen evolution reaction may be neglected and the system can be considered practically as a simple metal/metal-ion electrode. However, for a number of mixed electrodes these conditions cannot be fulfilled, because (*i*) the equilibrium potentials are too different, (*ii*) the exchange current density of the metal/metal-ion electrode is too low, or (*iii*) the metal ions hydrolyze or precipitate before the necessary pH is reached. In the case of the Fe/Fe^{++} electrode all these points are valid.

The simultaneous evolution of hydrogen has a pronounced influence on the properties of the deposited metal. Such a metal shows higher hardness and brittleness (1, 2). If the limiting diffusion current density of the hydrogen ions is reached, the pH of the cathode film rises. This rise may lead to the formation of hydrolysis products or even precipitates of the metal hydroxides, which can be incorporated in the metal deposit.

To carry out accurate measurements on iron deposition the following requirements should be taken into consideration.

(*I*) The current efficiency of metal deposition has to be known.

(*II*) The hydrogen ion concentration in the cathode film has to be the same as in the bulk of the solution.

(*III*) The metal ion must not hydrolyze neither in solution nor in the cathode film, forming precipitates.

These requirements were not fully taken into account in the previous literature concerning the iron

* Electrochemical Society Active Member through Deutsche Bunsenges.

[1] Present address: Institute of Anorganic Chemical Technology, Technical University, Graz, Austria.

[2] Present address: Nippon Steel Corporation, Central Research Laboratories, Fuchinobe, Sagamihara-shi, Kanagawa, Japan.

Key words: corrosion; charge transfer mechanism of iron; crystallographic substructure, influence on charge transfer; iron electrode, exchange current density of; rotating disk electrode.

deposition (3-13). Therefore the given results are not comparable. Especially the investigations of Dahms *et al.* (13) show that precipitation of hydrolysis products of Fe^{2+} ions at the electrode surface has a pronounced influence on the charge transfer process of iron deposition. Such a precipitation takes place, if the surface pH increases up to a value of about pH $\simeq$ 5. Consequently, we examined the kinetics of iron deposition from acid solutions under more exact conditions.

Experimental

Steady-state measurements.—For kinetic studies an exact knowledge of diffusion phenomena is necessary. This was taken into account by using a rotating disk electrode for the steady-state measurements. With increasing rotation rate the limiting diffusion current for hydrogen evolution will rise. This leads to a larger potential range, in which the cathodic hydrogen evolution is controlled by charge transfer. In this Tafel range, the pH is the same both in the double layer as well as in the bulk of the electrolyte. Therefore, exact measurements of cathodic iron deposition are only possible in this potential range.

Experiments dealing with hydrogen evolution under steady-state conditions were carried out in system I

$$\text{rotating gold disk/1M } Na_2SO_4 + x \cdot H_2SO_4$$

at pH values from 1.8 to 4.3. The results of these experiments enabled us to make some statements about mass transport of protons in solutions of this type (14).

The simultaneous cathodic hydrogen evolution and iron deposition was studied in system II

$$\text{rotating gold disk/0.875M } Na_2SO_4 + \text{0.1M } FeSO_4 + x \cdot H_2SO_4$$

at pH values from 1.8 to 3.8.

The ionic strength is the same in both systems. For the determination of the electrochemical reaction order

$$(\partial \log | i_{-,Fe^{++}} | / \partial \log a_{Fe^{++}})_{pH,\epsilon} = n_{-,Fe^{++}}$$

the concentration of both $FeSO_4$ and Na_2SO_4 was varied in such a way that the ionic strength was held constant (at constant pH of the solution).

The limiting diffusion current densities for the hydrogen evolution reaction were assumed to be the same for both systems, because the ionic strength is constant and the supporting electrolyte concentration is only slightly different. This assumption was proved experimentally as is shown later.

The steady-state total current density-potential curves were measured potentiostatically. The measured curves correspond to the simultaneous reduction of Fe^{++} and H^+. Using current efficiency measurements it was possible to calculate the partial current density-potential curves for iron deposition. The current efficiency for iron deposition was determined by potentiostatic anodic stripping (Fig. 1). At time $t = 0$ the potential of the rotating gold disk was stepped up from the basis potential (no hydrogen evolution, no iron deposition) to the wanted cathodic one. After the charging of the electrochemical double layer (the sharp current peak in Fig. 1) the reduction of ferrous ions and protons sets in. The decrease of the current to a minimum at time t_{min} and the increase up to time t_1 is believed to be due to the following facts: (*i*) the gold electrode will be covered gradually with iron, (*ii*) the exchange current density of the hydrogen electrode is higher on gold than on iron, and (*iii*) crystallization overvoltage.

The current efficiency is therefore not constant in the range $t = 0$ to t_1. The steady state is then reached at time t_1. At time t_2 the potential is changed to the stripping potential, which is 100-150 mV more positive than the corrosion potential. In this range practically the whole current is used for the anodic dissolution

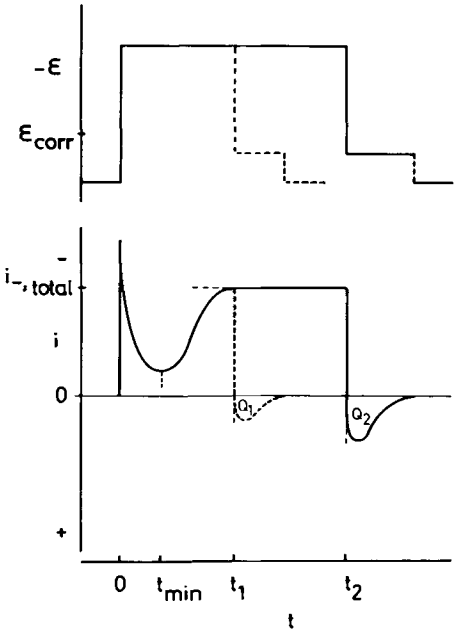

Fig. 1. Electrode potential ϵ and the total current density $i_{-,total}$ as a function of time t (schematic).

of iron. Integration of the current-time curves from t_2 up to t, when the anodic current falls to zero, gives the number of coulombs Q_2 corresponding to the amount of iron deposited. Under the same experimental conditions the amount of iron deposited between $t = 0$ and t_1 was measured and is denoted as Q_1 (dashed lines in Fig. 1). This allows the elimination of the nonsteady-state at the beginning of the pulse.

The partial current density for steady-state cathodic iron deposition is given by

$$| i_{-,Fe^{++}} | = \frac{Q_2 - Q_1}{t_2 - t_1} \qquad [2]$$

The partial current density for hydrogen evolution, i_{-,H^+}, can be calculated using [1]. At time t_1 the rotating disk is already covered with iron, and so the steady-state data refer to iron deposition on an iron substrate. The thickness of the iron deposits did not exceed 1 μm. This ensured undisturbed hydrodynamic conditions at the rotating disk.

Nonsteady-state measurements.—For nonsteady-state experiments a stationary Armco-iron electrode was used. The electrolyte solutions were identical. In these experiments galvanostatic pulse technique was applied. The potential-time curves were recorded by oscilloscope.

In solutions of pH > 2.8 a diffusion overvoltage is superimposed on the charge transfer overvoltage of hydrogen evolution (Fig. 2). The first plateau (curve 1, Fig. 2) relates to charge transfer overvoltage of hydrogen ion reduction on Armco iron. The second plateau (curve 2, Fig. 2) corresponds to simultaneous reduction of hydrogen and ferrous ions with relatively high current efficiency. Evaluation of cathodic transients was done in the following way: for total current density-potential curves the potential values of the second plateau were taken. Current efficiency was calculated from the $i \cdot t$ value of the whole cathodic pulse without correction for the first plateau. Separate measurement of current efficiency for the first plateau is not possible, because the flowing charge is too small. The coulomb value of the first plateau was relatively small compared to the total coulomb value and was neglected. In most cases the calculated current efficiency values were independent of the pulse

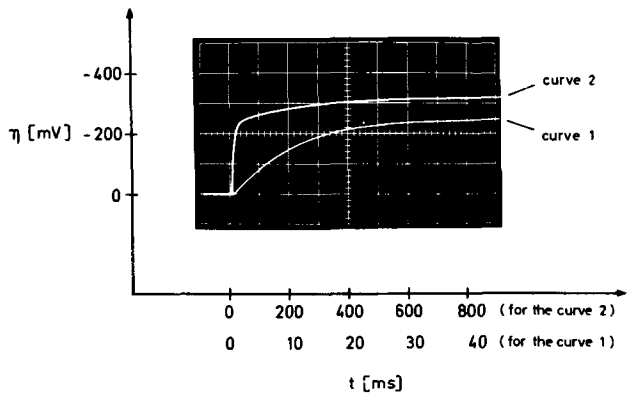

Fig. 2. Electrode potential-time curve under nonsteady-state galvanostatic conditions at pH > 2.8. Electrolyte: 0.1M $FeSO_4$ + 0.875M Na_2SO_4, pH = 3.80 (T = 298°K). $i_{-,total}$ = − 1 mA · cm^{-2}. Curve 1 = the first plateau, curve 2 = the first and the second plateau.

duration except for very short pulses. It was assumed that the pH values in the cathode film were constant after reaching the second plateau.

In solutions of pH < 2.8 no superimposed diffusion overvoltage was detected.

The potentiostatic stripping method is not suitable for determination of the current efficiency of iron under nonsteady-state conditions. Therefore a galvanostatic method was developed (15).

Apparatus.—The electrolytic cell was made from Pyrex glass and contained about 300 cm^3 solution. All solutions were prepared from A.R. grade chemicals, conductance water, and high-purity sulfuric acid. The solutions were deaerated by the bubbling of high purity hydrogen gas for several hours. They were pre-electrolyzed at a platinum cathode kept at potentials not sufficiently negative to reduce ferrous ions. The bubbling of hydrogen was continued during the experiment.

The counterelectrode was separated from the bulk of the solution by a glass frit (Schott, G4). The counterelectrode compartment was bubbled during the experiment with high-purity hydrogen gas to remove anodically formed oxygen.

Ag/AgCl, KCl (saturated) or Hg/Hg_2Cl_2, KCl (saturated) electrodes were used as reference electrodes. The measured potentials were transformed afterward to the standard hydrogen scale.

The rotating disk electrode used for steady-state measurements consisted of gold and had a diameter of 0.80 cm. The rotating speed was always 145 rps. Before each experiment the gold disk was mechanically polished, electrolytically degreased, treated with concentrated acid, and carefully washed with conductance water. The stationary Armco-iron electrodes used for nonsteady-state measurements were electrolytically polished and cleaned, following the procedure described elsewhere (16).

For potentiostatic experiments two Wenking potentiostats 61 RS were used. Galvanostatic pulses were produced by a multichannel pulse generator (17). This instrument was used together with a Tektronix oscilloscope 549 with Type W plug-in unit. Stationary potentials and pH were measured with a Knick-pH-mV-voltmeter 34/1. Glass electrodes for pH determination were of the Type 9255/12 from Schott, Mainz. Calibration of the glass electrodes was done with buffer solutions according to NBS data. Exact adjustment of pH was made with sulfuric acid immediately before beginning the measurements. Current-time curves of the steady-state experiments were recorded with a Beckman 10-in. recorder.

All given potential values are corrected for ohmic overvoltage. Measurement of ohmic drop was made by the galvanostatic pulse technique.

Results and Discussion

Steady-state experiments.—The total current density-potential curves and the current efficiency of iron deposition were measured potentiostatically.

The partial current density-potential curves were calculated according to Eq. [1] and [2] for cathodic iron deposition ($i_{-,Fe++}$) and for hydrogen evolution ($i_{-,H+}$). The results are shown in Fig. 3 and 4 as a function of the pH of the solution. At pH < 2.8 one gets a steady-state Tafel line for iron deposition with a slope of $b_{-,Fe++} = -115 \pm 5$ mV (Fig. 3), while the slope at pH > 2.8 is $b_{-,Fe++} = -39 \pm 5$ mV (Fig. 4).

The horizontal lines ($i_{d,H+}$) in Fig. 3 and 4 represent limiting diffusion current densities of the hydrogen evolution reaction, measured in system I (iron-free, see above). The curves of $i_{-,H+}$, measured in system II, become identical to these lines at high cathodic overvoltages. This shows that the diffusion limiting current density $i_{d,H+}$ for the hydrogen evolution reaction is the same in both systems.

The curves for iron deposition $i_{-,Fe++}$ deviate from the Tafel lines at high cathodic overvoltage as $i_{-,H+}$

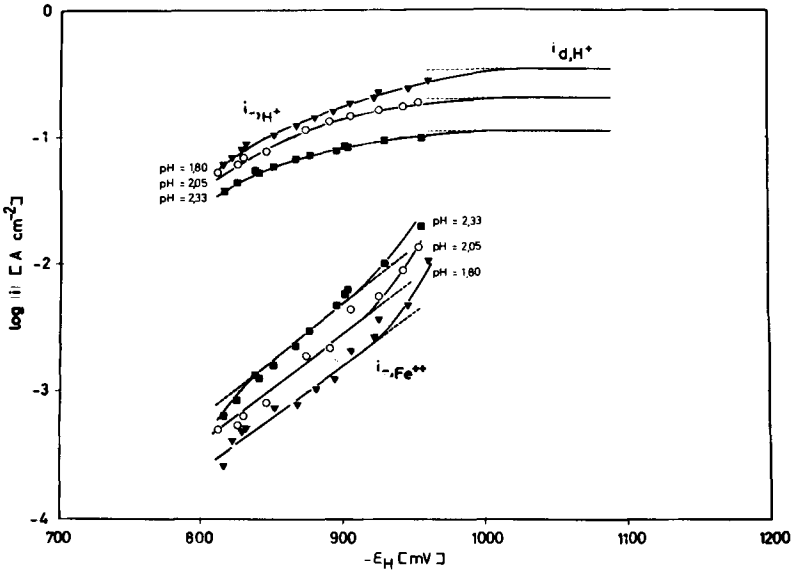

Fig. 3. Partial current density-potential curves under potentiostatic steady-state conditions depending on the pH. Electrolyte: 0.1M $FeSO_4$ + 0.875M Na_2SO_4, pH = 1.80, 2.05, 2.33 (T = 298°K).

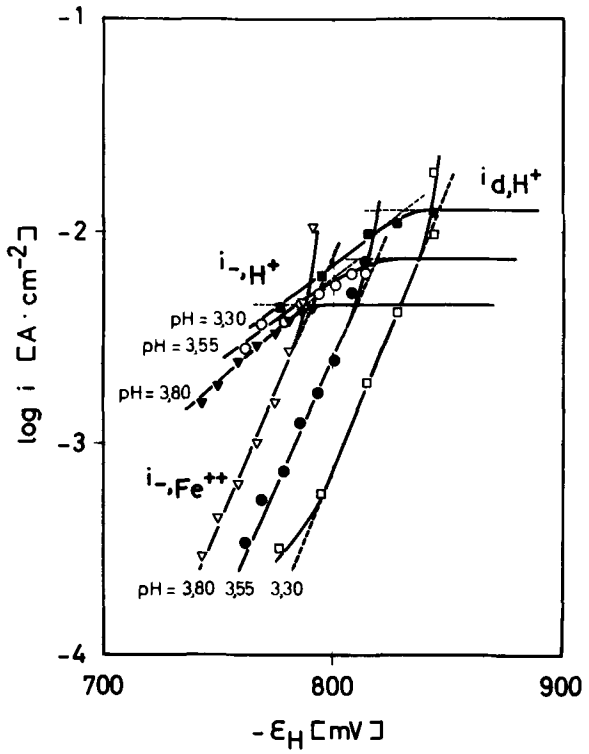

Fig. 4. Partial current density-potential curves under potentiostatic steady-state conditions depending on the pH. Electrolyte: 0.1M $FeSO_4$ + 0.875M Na_2SO_4; pH = 3.30, 3.55, 3.80 (T = 298°K).

→ i_{d,H^+}. This can be seen in Fig. 3 and 4. Here the pH of the cathode film is no longer the same as in the bulk of the solution. A rise of pH causes a rise of $i_{-,Fe^{++}}$ on account of its pH dependence.

Electrochemical reaction orders, relating to the pH of the solution, are shown in Fig. 5. In solutions of pH < 2.8 one gets $n_{-,pH} = +0.9 \pm 0.1$, whereas in solutions of pH > 2.8 the value $n_{-,pH} = +2.0 \pm 0.1$ is found.

The partial current density-potential curves of hydrogen evolution and iron deposition at different ferrous ion concentrations are shown in Fig. 6 and 7. Comparison to the curves of Fig. 3 and 4 shows that the Tafel slopes of iron deposition are independent of the ferrous ion concentration. In the range where i_{-,H^+} becomes of the same magnitude as i_{d,H^+}, the curve of iron deposition again deviates from the Tafel line.

Electrochemical reaction orders, relating to the ferrous ion concentration, are shown in Fig. 8 and 9 for solutions of pH 2.33 and pH 3.80. At pH < 2.8 the reaction order is $n_{-,Fe^{++}} = 1.0 \pm 0.1$, whereas at pH > 2.8 the value is $n_{-,Fe^{++}} = 1.6 \pm 0.2$.

From the curves of Fig. 3, 4, 6, and 7 one can see that the hydrogen evolution reaction is not independent of the iron deposition. First, the electrochemical reaction order of the hydrogen evolution reaction is higher than −1, which is the theoretical value at constant zeta-potential. And second, the partial current density i_{-,H^+} depends on the iron concentration.

Nonsteady-state experiments.—The total current density-potential curves and the current efficiency of iron deposition were measured by the galvanostatic pulse technique. Partial current density-potential curves of iron deposition were calculated from these data.

The experimental results at pH = 1.80 and pH = 2.33 are shown in Fig. 10. The Tafel slope for iron deposition is $b'_{-,Fe^{++}} = -120 \pm 10$ mV. The electrochemical reaction order $n'_{-,pH} = 0.85 \pm 0.1$ is determined from the relation between pH and $i_{-,Fe^{++}}$.

Figure 11 demonstrates the data from measurements in solutions of pH = 3.30 and pH = 3.80. In this pH range the slope of the nonsteady-state Tafel lines is $b'_{-,Fe^{++}} = -65 \pm 5$ mV, in spite of the difference of pH between the cathodic film and the bulk of the solution (cf. section on Nonsteady-state measurements). The constant slope of the Tafel line shows that the pH at the electrode surface is more or less independent of current density over a certain range for a given electrolyte. The value of this surface pH seems to be influenced by the pH of the bulk solution, as can be seen from the different partial current density-potential curves $i_{-,Fe^{++}}$. Therefore an accurate determination of the electrochemical reaction order $n'_{-,pH}$ in this pH range is not possible.

Polarization curves at different ferrous ion concentrations and at pH = 2.33 are presented in Fig. 12. From these data one can estimate the electrochemical reaction order $n'_{-,Fe^{++}} = 0.7 \pm 0.1$. For solutions of pH > 2.8 the determination of $n'_{-,Fe^{++}}$ is not possible for the reasons given above.

Kinetic Data of Iron Deposition

The experimental results show the existence of two different mechanisms. Which kind of mechanism takes place depends on the pH value at the electrode sur-

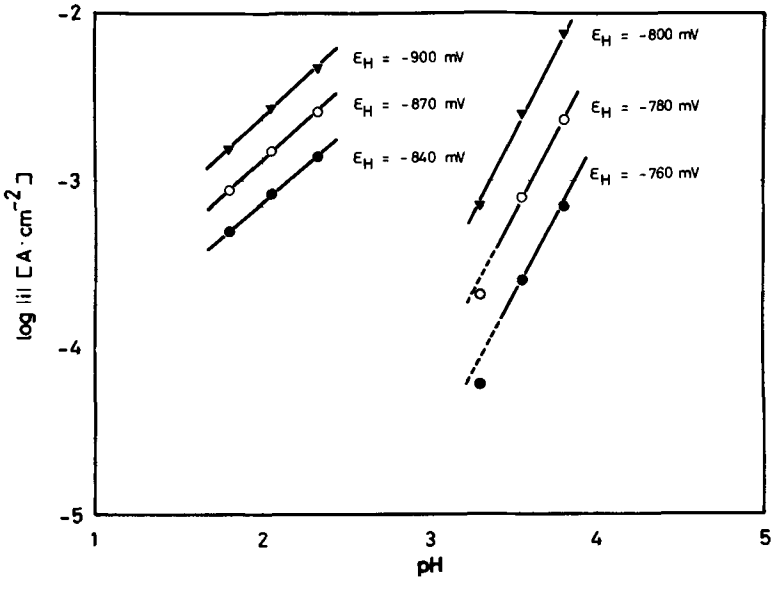

Fig. 5. Electrochemical reaction orders of iron deposition related to the pH. Electrolyte: 0.1M $FeSO_4$ + 0.875M Na_2SO_4 (T = 298°K).

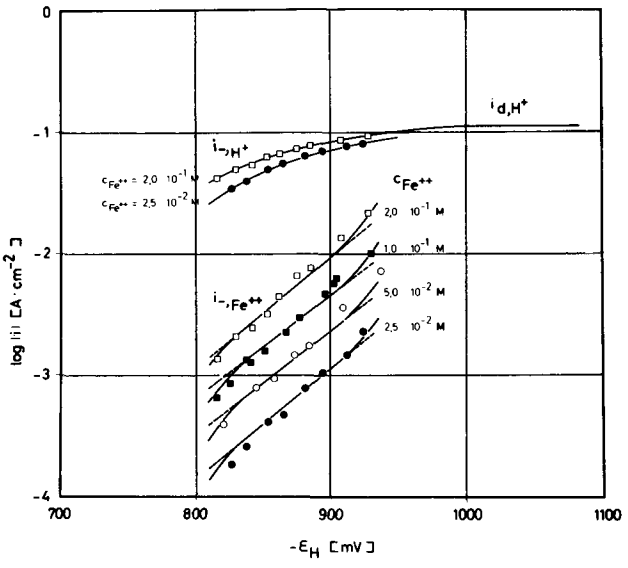

Fig. 6. Partial current density-potential curves under potentiostatic steady-state conditions depending on $c_{Fe}++$. Electrolyte: 0.025M . . . 0.2M $FeSO_4$ + x · Na_2SO_4 (constant ionic strength), pH = 2.33 (T = 298°K).

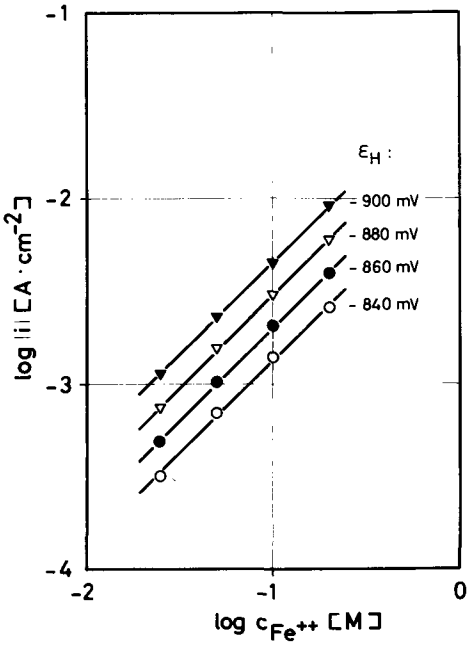

Fig. 8. Electrochemical reaction order of iron deposition related to $c_{Fe}++$ at pH = 2.33 (T = 298°K).

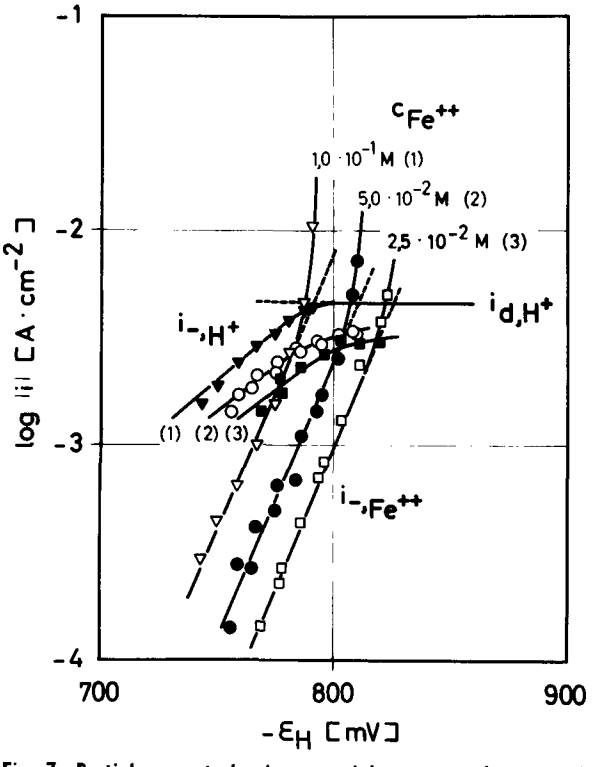

Fig. 7. Partial current density-potential curves under potentiostatic steady-state conditions depending on $c_{Fe}++$. Electrolyte: 0.025M . . . 0.1M $FeSO_4$ + x · Na_2SO_4 (constant ionic strength), pH = 3.80 (T = 298°K).

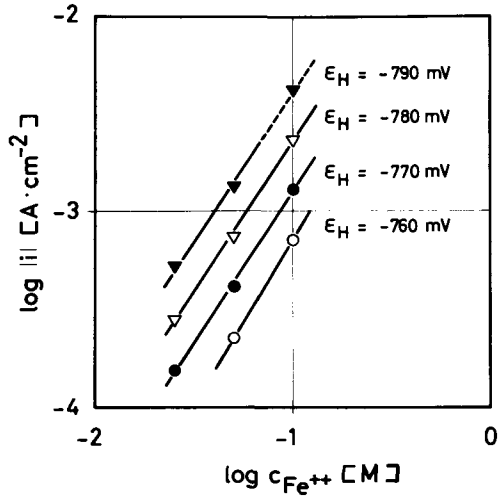

Fig. 9. Electrochemical reaction order of iron deposition related to $c_{Fe}++$ at pH = 3.80 (T = 298°K).

faces. Calculated and experimental values of the kinetic data are shown in Table I. The calculated values are deduced from kinetic relations as will be shown below (*cf.* section on Kinetic Equations).

At pH < 2.8 the experimental data fit to a simple reversal of the noncatalyzed mechanism of the anodic reaction (18). At pH > 2.8 a different mechanism is dominating, which is very probably a reversal of the catalyzed mechanism (18).

In the case of cathodic iron deposition there is a considerable difference between the kinetic data of the two reaction mechanisms. The influence of the surface pH on the type of mechanism is related to the different electrochemical reaction orders. Furthermore, hydrolysis products of $Fe^{++}{}_{aq}$ are formed and incorporated in the deposit at higher pH values of the cathode film. Consequently, the number of multidimensional crystal imperfections and lattice deformations increase. Therefore the surface activity increases too, and the catalyzed mechanism is favored over the noncatalyzed one.

Dahms *et al.* have shown that precipitation of insoluble hydrolysis products on the electrode surface (surface coverage near 1) leads to a sharp change of the deposition process (13). Such precipitation cannot take place under our experimental conditions, because we have evaluated the data of the steady-state measurements only up to current density values: $/ i_{-,total} / < / i_{d,H+} /$. Under this condition the surface pH is practically the same as in the bulk of the solution. Furthermore the formation of insoluble hydrolysis products in solution does not occur at the highest pH value (pH = 3.8) in this study. The con-

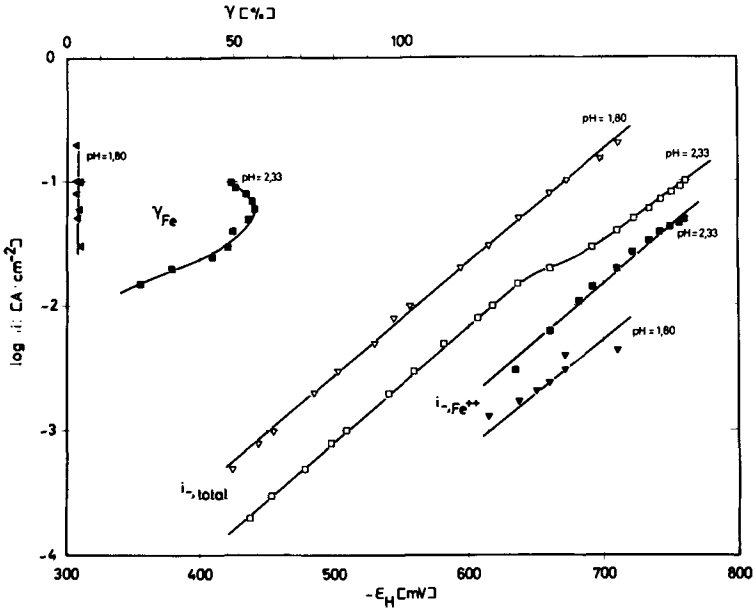

Fig. 10. Total current density-potential curves of simultaneous deposition of iron and hydrogen and partial curves of iron deposition depending on the pH. On the upper left side current efficiency curves of iron deposition. Galvanostatic nonsteady-state conditions. Electrolyte: 0.1M $FeSO_4$ + 0.875M Na_2SO_4; pH = 1.80, 2.33 (T = 298°K).

centration of soluble hydrolysis products (*e.g.* $FeOH^+$) at the electrode surface is at equilibrium with the bulk concentration. This was taken into account in the following kinetic considerations.

The crystallographic substructure of the metal deposits is under investigation.

Mechanisms of the Cathodic Iron Deposition[3]

The noncatalyzed mechanism is a simple reversal of the corresponding anodic process, whereby the rate-determining step (*i.e.*, Eq. [4]) is the same

$$Fe^{++}_{aq} + H_2O \rightleftharpoons FeOH^+ + H^+ \qquad [3]$$

$$FeOH^+ + e^- \rightleftharpoons (FeOH)_{ads} \qquad [4]$$

$$(FeOH)_{ads} + H^+ + e^- \rightleftharpoons Fe + H_2O \qquad [5]$$

Equation [3] is a fast chemical equilibrium reaction,

[3] *Cf.* Part I (18), Table I.

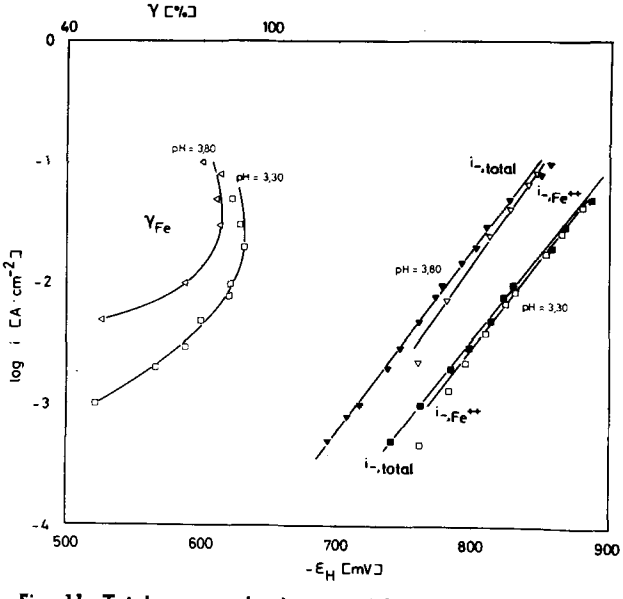

Fig. 11. Total current density-potential curves of simultaneous deposition of iron and hydrogen and partial curves of iron deposition depending on the pH. On the upper left side current efficiency curves of iron deposition. Galvanostatic nonsteady-state conditions. Electrolyte: 0.1M $FeSO_4$ + 0.875M Na_2SO_4; pH = 3.30, 3.80 (T = 298°K).

preceding the rate-determining charge transfer, Eq. [4]. The following electrochemical reaction step, Eq. [5], is also fast compared to [4].

The catalyzed mechanism seems also to be a reversal of the corresponding anodic process. However, the formulation of the kinetics is only hypothetical, as we have pointed out earlier (18). The formation of the catalytic surface complex (possible formula [Fe(FeOH)]) is believed to take place in a parallel reaction according Eq. [7]. The whole sequence may be written as follows

$$Fe^{++}_{aq} + H_2O \rightleftharpoons FeOH^+ + H^+ \qquad [3]$$

$$[Fe(FeOH)] + FeOH^+ + 2e^- \rightleftharpoons [Fe(FeOH)] + Fe + OH^- \qquad [6]$$

Parallel reaction

$$Fe + FeOH^+ + e^- \rightleftharpoons [Fe(FeOH)] \qquad [7]$$

The first step, Eq. [3], is the same as in the noncatalyzed mechanism. The rate-determining charge transfer is described by Eq. [6]. The formation of the catalytic surface complex Eq. [7], goes on parallel to the other steps and is considered to be relatively fast compared to [6].

Kinetic Equations

Steady-state conditions.—The noncatalyzed mechanism according to Eq. [3], [4], and [5] has the following current density-overvoltage relation

$$i = 2i_{o,4}\left[\frac{A}{B}\cdot\exp\left(\frac{(1+\alpha_4)F\eta}{RT}\right) - C\cdot\exp\left(-\frac{(1-\alpha_4)F\eta}{RT}\right)\right] \qquad [8]$$

Equation [8] already has been derived in Part I, (18), Eq. [14], under the condition $i_{o,4} << i_{o,5}$. The expressions for A, B, and C are

$$A = \frac{a_{Fe}}{\bar{a}_{Fe}}\cdot\frac{a_{H_2O}}{\bar{a}_{H_2O}},\quad B = \frac{a_{H^+}}{\bar{a}_{H^+}},\quad C = \frac{a_{FeOH^+}}{\bar{a}_{FeOH^+}}$$

The expression C can be replaced by the following terms according to the chemical equilibrium [3]

$$C = \frac{a_{Fe^{++}}}{\bar{a}_{Fe^{++}}}\cdot\frac{a_{H_2O}}{\bar{a}_{H_2O}}\cdot\frac{\bar{a}_{H^+}}{a_{H^+}} = D\cdot\frac{1}{B} \qquad [9]$$

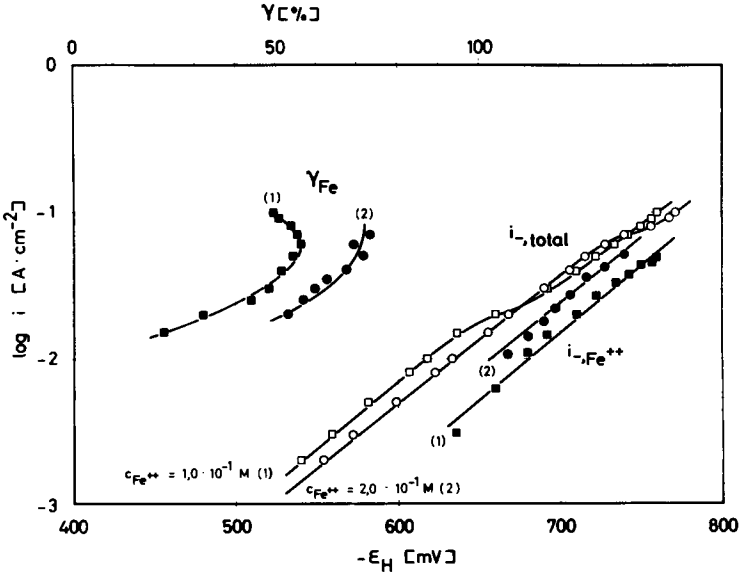

Fig. 12. Total current density-potential curves of simultaneous deposition of iron and hydrogen and partial curves of iron deposition depending on c_{Fe++}. On the upper left side current efficiency curves of iron deposition. Galvanostatic nonsteady-state conditions. Electrolyte: 0.1M $FeSO_4$ and 0.2M $FeSO_4$ + x · M · Na_2SO_4 (constant ionic strength), pH = 2.33 (T = 298°K).

From Eq. [8] and [9] the following kinetic data for the cathodic process ($\eta << 0$) are obtained

$$b_{-,Fe++} = \left(\frac{\partial \eta}{\partial \log |i_{-,Fe++}|}\right)_{a_{FeOH+},\bar{a}_{FeOH+}} = \frac{2.303\,RT}{(1-\alpha_4)\mathbf{F}} = -118.3 \text{ mV} \quad [10]$$

with $\alpha_4 = 0.5$ and $T = 298°K$.

$$n_{-,pH} = \left(\frac{\partial \log |i_{-,Fe++}|}{\partial pH}\right)_{a_i,\epsilon} = +1 \quad [11]$$

$$n_{-,Fe++} = \left(\frac{\partial \log |i_{-,Fe++}|}{\partial \log a_{Fe++}}\right)_{a_i,\epsilon} = +1 \quad [12]$$

For the catalyzed mechanism according to Eq. [3], [6], and [7] the following current density-overvoltage relation is derived (K = [Fe(FeOH)])

$$i = k_6 \cdot a_K \cdot a_{Fe} \cdot a_{OH^-} \cdot \exp\left(\frac{2\alpha_6 \mathbf{F}\epsilon}{RT}\right) - k_{-6} \cdot a_K \cdot a_{FeOH+} \cdot \exp\left(-\frac{2(1-\alpha_6)\mathbf{F}\epsilon}{RT}\right) \quad [13]$$

$$i = i_{o,6}\left[\frac{a_K}{\bar{a}_K}\cdot\frac{A}{B}\cdot\exp\left(\frac{2\alpha_6\mathbf{F}\eta}{RT}\right) - \frac{a_K}{\bar{a}_K}\cdot C\cdot\exp\left(-\frac{2(1-\alpha_6)\mathbf{F}\eta}{RT}\right)\right] \quad [14]$$

For $\eta << 0$ one can write

$$i_{-,Fe++} \cong -i_{o,6}\cdot\frac{a_K}{\bar{a}_K}\cdot C\cdot\exp\left(-\frac{2(1-\alpha_6)\mathbf{F}\eta}{RT}\right) \quad [15]$$

Equation [14] is similar to Eq. [19] in Part I (18). The difference is due to the formulation of the catalytic action of the surface complex [Fe(FeOH)]. Anodically the complex breaks up during the rate-determining charge transfer step and is formed again by a relatively fast topochemical reaction (Part I (18), Eq. [3] and [4]). By summation of these two reaction steps one gets the cathodic charge transfer step, Eq. [6] of this paper.

For the catalyzed mechanism one has under steady-state conditions

$$\frac{d\,a_K}{dt} = -\frac{i_7}{z_7\cdot\mathbf{F}} = 0 \quad [16]$$

The expression for i_7 is

$$i_7 = i_{o,7}\left[\frac{a_K}{\bar{a}_K}\cdot\exp\left(\frac{\alpha_7\mathbf{F}\eta}{RT}\right) - \frac{a_{Fe}}{\bar{a}_{Fe}}\cdot C\cdot\exp\left(-\frac{(1-\alpha_7)\mathbf{F}\eta}{RT}\right)\right] \quad [17]$$

From Eq. [16] and [17] using [9] one can write

$$\frac{a_K}{\bar{a}_K} = \frac{D}{B}\cdot\frac{a_{Fe}}{\bar{a}_{Fe}}\cdot\exp\left(-\frac{\mathbf{F}\eta}{RT}\right) \quad [18]$$

Table I. Kinetic data of the iron deposition at T = 298°K

$b_{-,Fe++}$ = cathodic Tafel slope for the iron deposition reaction
$n_{-,pH}$ = electrochemical reaction order related to pH
$n_{-,Fe++}$ = electrochemical reaction order related to c_{Fe++}

	Steady-state			Nonsteady-state	
	Calculated	Experimental		Calculated	Experimental
		Noncatalyzed mechanism			
$b_{-,Fe++}$	−118.3 mV	−115 ± 5 mV	$b'_{-,Fe++}$	−118.3 mV	−120 ± 10 mV
$n_{-,pH}$	+1	0.9 ± 0.1	$n'_{-,pH}$	+1	+0.85 ± 0.1
$n_{-,Fe++}$	+1	1.0 ± 0.1	$n'_{-,Fe++}$	+1	+0.7 ± 0.1
		Catalyzed mechanism			
$b_{-,Fe++}$	−29.6 mV	−39 ± 5 mV	$b'_{-,Fe++}$	−59.2 mV	−65 ± 5 mV
$n_{-,pH}$	+2	2.0 ± 0.1	$n'_{-,pH}$	+1	?
$n_{-,Fe++}$	+2	1.6 ± 0.2	$n'_{-,Fe++}$	+1	?

By substituting [18] into [15] one gets

$$i_{-,Fe^{++}} \cong -i_{o,6} \cdot \frac{a_{Fe}}{\bar{a}_{Fe}} \cdot \left(\frac{D}{B}\right)^2 \cdot \exp\left(-\frac{[1+2(1-\alpha_6)]F\eta}{RT}\right) \quad [19]$$

Equation [19] is the cathodic steady-state current density-overvoltage relation of the catalyzed mechanism. From [19] one derives the following kinetic data

$$b_{-,Fe^{++}} = \left(\frac{\partial\eta}{\partial \log |i_{-,Fe^{++}}|}\right)_{a_i,\bar{a}_i} = \frac{2.303\,RT}{[1+2\,(1-\alpha_6)]\,F} = -29.6\ \text{mV} \quad [20]$$

with $\alpha_6 = 0.5$ and $T = 298°K$.

$$n_{-,pH} = \left(\frac{\partial \log |i_{-,Fe^{++}}|}{\partial\, pH}\right)_{a_i,\epsilon} = +2 \quad [21]$$

$$n_{-,Fe^{++}} = \left(\frac{\partial \log |i_{-,Fe^{++}}|}{\partial \log a_{Fe^{++}}}\right)_{a_i,\epsilon} = +2 \quad [22]$$

Nonsteady-state conditions.—The noncatalyzed mechanism has identical current density-overvoltage relations and kinetic data under steady-state and under nonsteady-state conditions. The fast reaction step, Eq. [5], is at equilibrium.

For the catalyzed mechanism one derives from Eq. [15] with $a_K = \bar{a}_K = \text{const.}$ and $\eta << 0$

$$i_{-,Fe^{++}} \cong -i_{o,6} \cdot C \cdot \exp\left(-\frac{2(1-\alpha_6)\,F\eta}{RT}\right) \quad [23]$$

The nonsteady-state current density-overvoltage relation, Eq. [23], gives the following kinetic data

$$b_{-,Fe^{++}} = \left(\frac{\partial\eta}{\partial \log |i_{-,Fe^{++}}|}\right)_{a_i,\bar{a}_i} = -\frac{2.303\,RT}{2(1-\alpha_6)\,F} = -59.2\ \text{mV} \quad [24]$$

with $\alpha_6 = 0.5$ and $T = 298°K$.

$$n'_{-,pH} = \left(\frac{\partial \log |i_{-,Fe^{++}}|}{\partial\, pH}\right)_{a_i,\epsilon} = +1 \quad [25]$$

$$n'_{-,Fe^{++}} = \left(\frac{\partial \log |i_{-,Fe^{++}}|}{\partial \log a_{Fe^{++}}}\right)_{a_i,\epsilon} = +1 \quad [26]$$

Exchange Current Density of the $Fe/Fe^{++}{}_{aq}$ Electrode

Exchange current densities were calculated using steady-state experimental data. As in Part I (18) it was necessary to standardize to the following conditions

$pH = 0$

$a_{Fe^{++}} = 1$, which is equivalent to $\epsilon_o = E_o$ (standard potential).

The standardized exchange current density is written as i_o^o.

The cathodic current density of iron deposition $i_{-,Fe^{++}}$ depends on the activity of ferrous ions $a_{Fe^{++}}$. Therefore the exchange current density i_o is also dependent on $a_{Fe^{++}}$.

The exchange current density is found graphically or numerically using the following equation

$$\log i_o = \frac{\epsilon_o - \epsilon}{b_{-,Fe^{++}}} + \log |i_{-,Fe^{++}}| \quad [27]$$

The equilibrium potential ϵ_o is expressed by the Nernst equation

$$\epsilon_o = E_o + \frac{RT}{2F} \ln \bar{a}_{Fe^{++}} \quad [28]$$

The relations between i_o and pH, respectively i_o and $\bar{a}_{Fe^{++}}$, are derived from the kinetic relations.

In the case of the noncatalyzed mechanism Eq. [8] and [9] lead to

$$i_o = 2\,k_{-,4} \cdot \bar{a}_{Fe^{++}} \cdot \bar{a}_{H_2O} \cdot \bar{a}_{H^+}{}^{-1} \cdot \exp\left(-\frac{(1-\alpha_4)\,F\,\epsilon_o}{RT}\right) \quad [29]$$

Using Eq. [28] one gets

$$\left(\frac{\partial \log i_o}{\partial\, pH}\right)_{a_i,\epsilon_o} = +1 \quad [30]$$

and

$$\left(\frac{\partial \log i_o}{\partial \log \bar{a}_{Fe^{++}}}\right)_{a_i} = +0.75 \quad [31]$$

The resulting exchange current density relation of the noncatalyzed mechanism is

$$\log i_o = \log i_o^o + pH + 0.75 \log \bar{a}_{Fe^{++}} \quad [32]$$

The identical derivation gives for the catalyzed mechanism

$$\log i_o = \log i_o^o + 2\,pH + \log \bar{a}_{Fe^{++}} \quad [33]$$

Calculation of ϵ_o, i_o, and i_o^o requires knowledge of $\bar{a}_{Fe^{++}}$. Single ion activity coefficients of Fe^{++} are not available in the literature. Therefore the following calculations are rather doubtful. Nevertheless, following Bockris *et al.* (6) we set

$$f_{Fe^{++}} = f_{Ni^{++}} = f_{\pm,NiSO_4}$$

Tabulated values of $f_{\pm,NiSO_4}$ give a mean activity coefficient of Fe^{++} in 0.875M Na_2SO_4 + 0.1M $FeSO_4$ solution of 0.05.

Using the above value, $\log i_o^o$ was calculated as -6.2 ± 0.5 for the noncatalyzed mechanism and -14 ± 2 for the catalyzed mechanism, respectively. The agreement with data from the anodic dissolution process is not satisfactory [*cf.* Part I (18)]. One of the reasons is probably the assumption $a_{Fe} = 1$ in Eq. [28], which is only a rough approximation in the case of cathodically deposited metal. Nevertheless, it can be seen that the exchange current density of the noncatalyzed mechanism is several orders of magnitude higher than that of the catalyzed mechanism. This conclusion is not influenced by the approximation for $f_{Fe^{++}}$. A detailed discussion was given in Part I (18).

As in the anodic process the current density of the iron deposition reaction consists of two parts

$$i_{-,Fe^{++}} = i_{\text{noncatalyzed}} + i_{\text{catalyzed}} \quad [34]$$

In the vicinity of the equilibrium potential the first term will always dominate. Only at high pH of the cathode film and at high overvoltage the second term may become dominating.

Conclusions

From the experimental data it is shown that the cathodic iron deposition takes place by two different reaction mechanisms, depending on the experimental conditions. These two mechanisms are shown to be most probably a simple reversal of the two mechanisms of the anodic iron dissolution.

Acknowledgments

The authors feel obliged to thank Mrs. Rosswag and Mrs. Burger for helping in the experimental work.

They also acknowledge gratefully the discussions of Prof. Dr. Dr.h.c. H. Fischer. Substantial financial support was granted by the Deutsche Foschungsgemeinschaft and the Bundeswirtschaftsministerium, BRD, for which the authors express their gratitude.

Manuscript submitted March 19, 1971; revised manuscript received July 27, 1971.

Any discussion of this paper will appear in a Discussion Section to be published in the June 1972 JOURNAL.

REFERENCES

1. H. Fischer, "Elektrolytische Abscheidung und Elektrokristallisation von Metallen," Springer-Verlag, Berlin-Göttingen-Heidelberg (1954).
2. M. Smialowski, "Hydrogen in Steel," Pergamon Press, London (1962).
3. T. P. Hoar and T. Hurlen, CITCE VIII, p. 445, Butterworth Scientific Publications, London (1958).
4. T. Hurlen, *Acta Chem. Scand.*, **14**, 1533 (1960).
5. T. Hurlen, *ibid.*, **14**, 1564 (1960).
6. J. O'M. Bockris, D. Drazic, and A. Despic, *Electrochim. Acta*, **4**, 325 (1961).
7. J. O'M. Bockris and D. Drazic, *ibid.*, **7**, 293 (1962).
8. K. E. Heusler, "Elektrochemische Auflösung und Abscheidung von Metallen der Eisengruppe," p. 34, Habilitationsschrift TH Stuttgart (1966).
9. W. J. Lorenz, "Das elektrochemische Verhalten des aktiven Reineisens in sauren Lösungen," p. 67, Habilitationsschrift Universität Karlsruhe (1968).
10. Ya. D. Zytner and A. L. Rotinyan, *Elektrokhimiya (USSR)*, **2**, 1371 (1966).
11. D. M. Drazic, S. Djordjevic, and M. Vojnovic, "The Influence of Diffusion Controlled Hydrogen Evolution Reaction on the Kinetics of Codeposition of Cobalt," 20th CITCE Meeting, Strasbourg, France, 1969.
12. K. E. Heusler and R. Knoedler, *Electrochim. Acta*, **15**, 243 (1970).
13. H. Dahms, *J. Electroanal. Chem.*, **8**, 5 (1964); H. Dahms and I. M. Croll, *This Journal*, **112**, 771 (1965).
14. Y. Miyoshi and W. J. Lorenz, *Ber. Bunsenges. Phys. Chem.*, **74**, 412 (1970).
15. K. Taube and W. J. Lorenz, *J. Electroanal. Chem.*, **25**, 95 (1970).
16. W. J. Lorenz and G. Eichkorn, *Ber. Bunsenges. Phys. Chem.*, **70**, 99 (1966).
17. W. J. Lorenz, H. Meyer, and E. Schmitt, *Z. Instrumentenkunde*, **74**, 56 (1966).
18. F. Hilbert, Y. Miyoshi, G. Eichkorn, and W. J. Lorenz, Part I, *This Journal*, **118**, 1919 (1971).

Transient Behavior during Electrodeposition onto a Metal Strip of High Ohmic Resistance

Richard Alkire*

Department of Chemical Engineering, University of Illinois, Urbana, Illinois 61801

ABSTRACT

Electrochemical deposition onto a thin metal strip of high resistance can result in a deposit of varying thickness along the strip if the electrode resistance is sufficiently large to cause a nonuniform reaction rate distribution. As deposition proceeds, the ohmic resistance of the strip decreases and thus transient behavior is observed. The transient thickening process is modeled by a one-dimensional pseudo steady-state method. The results illustrate how transient behavior during deposit growth depends upon the mass transfer, charge transfer, ohmic resistance, and geometric characteristics of the system. Conditions are discussed under which nonuniform deposits may be anticipated.

In the fabrication of printed circuit boards, the deposition of the metal circuit onto an insulating substrate is accomplished by electroless deposition of a thin metal coating which is subsequently thickened by cathodic electrodeposition. The final deposit is usually not of uniform thickness, being somewhat thicker near the region of electrical contact employed during the cathodic thickening operation. In many cases the nonuniform reaction rate distribution which evidently prevails during growth may be primarily attributed to the high ohmic resistance of the thin electroless deposit. As the metal film becomes thicker, its ohmic resistance decreases; eventually the deposition reaction takes place along the electrode surface at a rate which is essentially independent of the electrode thickness. The transient behavior of high resistance electrodes observed during thickening can be quite complicated since several competing effects come into play. Owing to the industrial importance of the problem, the present study has been conducted in order to demonstrate some of the features which are characteristic of the process. The method of solution is not specifically restricted to the circuit board example; the results may be applied to other situations where the thickness of a resistive metal strip is altered by electrochemical deposition or dissolution.

Several previous investigations have evaluated the current distribution along electrodes of high resistance under specific cases of operation, all in the steady state (1-7). These analyses have shown that the current and potential distributions along a resistive electrode can depend on ohmic resistance of the electrolytic solution and on the rate of sluggish charge-transfer reaction. Calculations were carried out by treating the electrode as a one-dimensional region along which electrochemical reaction takes place. To date, no theoretical analyses are known to be reported either on the effect of mass transport restrictions on the current distribution, or on transient behavior observed during thickening of deposits on electrodes of high resistance. In the present study, conditions are ascertained under which a high electrode resistance may be anticipated to affect the reaction rate distribution along its surface. The theoretical model permits calculation of the transient current, potential, and surface concentration distributions along the electrode, from which the deposit thickness distribution may be determined as a function of the extent of reaction. The study illustrates how the deposit thickness distribution depends on mass transfer, charge transfer, and ohmic effects.

Before proceeding, consideration should be given to the events which take place upon application of a cathodic potential to an electrode. Essentially three

* Electrochemical Society Active Member.
Key words: deposit, growth, nonuniform, distribution.

electrochemical phenomena take place on time scales which are distinctly different. First, the electrical double layer will become charged very rapidly so that Faradaic current will pass through the electrode. Second, concentration gradients will become established in the electrolytic solution near the cathodic surface. Finally, cathodic reaction will cause gradual thickening which will reduce the ohmic resistance of the electrode and thus cause the reaction rate distribution to become more uniform. In principle, the entire system will not achieve a steady state until the cathode becomes sufficiently thick that its ohmic resistance is negligible and the current distribution is uniform. In view of the different time constants that characterize the three processes, however, it is a very good approximation to claim that the double layer and the diffusion layer attain a pseudo steady state rapidly with respect to the time during which thickening takes place. In the theory that follows, it will be assumed that the current distribution changes during deposition at a rate that is determined solely by the rate at which the thickening process occurs.

Typically, electrodeposition will involve a number of effects which are not taken into account in the treatment that follows. For example, the primary current distribution may not be uniform, the mass transfer process may be nonuniform, the deposit roughness may vary during growth, or the ohmic resistance of the electrolytic solution may be appreciable. The predictions made below may thus be applicable in some systems, but certainly not in all. The principal point, however, is that the model presented below contains the essential features of many practical problems and thus serves to refine one's intuition as well as provide the foundation for a detailed pursuit of more complicated situations.

Formulation of the Mathematical Model

Prior to the thickening treatment, the electrode consists of a thin metal strip of uniform thickness and of length l. Electrical contact is made to the thin strip along one edge ($z = l$) while the far edge ($z = 0$) is insulated. A reference electrode is placed in the solution near the edge of the strip at which electrical contact is made. A constant potential power supply provides electrons to the thin cathode at such a rate that the potential difference between the electrical contact point and the reference electrode is maintained at a constant value during electrolysis.

Owing to the simple geometry and uniform stirring conditions which characterize the model electrolysis cell, the deposition reaction will proceed at different rates along the electrode surface only if the potential within the thin metal cathode varies along its length because of ohmic resistance. As deposition proceeds, the ohmic resistance of the electrode decreases, owing to thickening, and the current distribution eventually becomes uniform.

Because rigorous calculations are not necessary for a useful analysis of the system, several simplifying assumptions have been introduced: (I) The resistive electrode is a straight strip of unit width, having length l and an initially uniform thickness a_0. The counterelectrode configuration is such that the primary current distribution along the cathode strip is uniform. (II) The electrical double layer and the mass transfer diffusion layer attain steady-state conditions rapidly with respect to the rate at which the electrode thickness increases. (III) During the growth process, the cathode remains thin with respect to distances over which significant variation in potential takes place in the metal phase, so that a one-dimensional specification of the potential in the electrode is sufficient. (IV) Only one electrode reaction occurs and the (reversible) reaction rate expression has the form given by Eq [3]. (V) The surface of the cathode deposit remains smooth during the course of thickening. (VI) The ohmic resistance of the electrolytic solution is negligible with respect to other resistances within the cell. That is, the inequality

$$\frac{J\beta}{\Phi_a}\frac{a_0\sigma y}{l^2\kappa} << 1$$

must be satisfied, where the symbols are as defined at the end of the text. (VII) The reactive cations arrive at the electrode surface by diffusion but not by migration. The solution is sufficiently dilute that concentrations may be used. (VIII) The electrolytic solution is stirred in such a way that the cations are uniformly accessible to the surface at all points; the mass transfer rate is characterized by a mass transfer coefficient.

The resistance to passage of electrons through the electrode is governed by Ohm's law

$$i(z,t) = -\sigma\frac{d\phi_m(z,t)}{dz} \qquad [1]$$

The electronic current in the metal phase, $i(z,t)$, varies with position owing to the electrode reaction which acts as a sink for the electrons in the electrode

$$\frac{di(z,t)}{dz} = -\frac{1}{a(z,t)}j(z,t) \qquad [2]$$

The deposition reaction rate, $j(z,t)$, varies along the electrode and is related to the metal ion concentration at the surface and to the potentials in both electrode and solution phases by the kinetic expression which characterizes the deposition reaction, assumed here to be of the Volmer form

$$j(z,t) = i_o\left\{e^{\frac{\alpha nF}{RT}\eta(z,t)} - \frac{c^s(z,t)}{c^b}e^{\frac{(\alpha-1)nF}{RT}\eta(z,t)}\right\} \qquad [3]$$

For cathodic reactions, both $\eta(z,t)$ and $j(z,t)$ are negative. The exchange current density in Eq. [3] corresponds to the bulk concentration of reactant cation. The overpotential $\eta(z,t)$ is the difference in potential between the electrode and the solution, outside the diffusion layer, during reaction, minus the difference in potential which exists under equilibrium conditions (8). Therefore the overpotential $\eta(z,t)$ is the sum of charge transfer overpotential plus concentration overpotential. Since resistance effects in the solution phase are negligible by assumption (VI), the potential in the solution outside the diffusion layer is uniform and is denoted $\phi_s{}^\bullet$. Thus the overpotential $\eta(z,t)$ is defined as

$$\eta(z,t) = [\phi_m(z,t) - \phi_s{}^\bullet] - [\phi_m{}^e - \phi_s{}^e] \qquad [4]$$

where the equilibrium condition is denoted by superscript e. It is seen that the overpotential $\eta(z,t)$ varies with position along the electrode strip because the potential in the metal phase is not uniform. At this point it is convenient to introduce the potential at the current-feeder end of the strip, $\phi_m{}^\bullet$. Provided that the reference electrode is positioned in the bulk electrolyte, that is, beyond the diffusion layer, the applied potential which is held constant during electrolysis may be related to the overpotential $\eta(z,t)$ by

$$[(\phi_m{}^\bullet - \phi_s{}^\bullet) - (\phi_m{}^e - \phi_s{}^e)] = [\phi_m{}^\bullet - \phi_m(z,t)] + [\phi_s{}^s(z,t) - \phi_s{}^\bullet] + \{[\phi_m(z,t) - \phi_s{}^s(z,t)] - [\phi_m{}^e - \phi_s{}^e]\} \qquad [5]$$

where $\phi_s{}^s(z,t)$ is the potential in the solution "just outside" the electrical double layer. The quantity on the left side of Eq. [5] is the applied potential which is held constant during electrolysis. The right side of Eq. [5] illustrates that the applied potential is counterbalanced by several overpotentials which develop within the electrolysis cell owing to (a) ohmic losses (η_Ω) in the electrode, $[\phi_m{}^\bullet - \phi_m(z,t)]$; (b) concentration overpotential (η_c) in the solution $[\phi_s{}^s(z,t) - \phi_s{}^\bullet]$; (c) charge transfer overpotential (η_s) at the elec-

trode-solution interface, $\{[\phi_m(z,t) - \phi_s{}^s(z,t)] - [\phi_m{}^e - \phi_s{}^e]\}$. The concentration overpotential is related to the concentration difference across the diffusion layer by

$$\phi_s{}^s(z,t) - \phi_s{}^\bullet = \frac{RT}{n\mathbf{F}} \ln \frac{c^s(z,t)}{c^b} \qquad [6]$$

It may be recognized that the concentration dependence of the exchange current density has been extracted and placed in the exponential terms within the brackets of Eq. [3]. Thus, as noted previously, the exchange current density has the value which corresponds to the bulk concentration of reactant, and the overpotential $\eta(z,t)$ includes both charge-transfer and concentration overpotentials. It may be seen that the ohmic, concentration, and charge transfer overpotentials all vary with distance along the electrode and with time during deposition. The sum of the three overpotentials, however, is constant in accord with Eq. [5].

The local deposition rate, $j(z,t)$, is also related to the concentration difference across the diffusion layer through the mass transfer coefficient which has a uniform value along the entire electrode

$$j(z,t) = -n\mathbf{F}k[c^b - c^s(z,t)] \qquad [7]$$

Equations [1] through [7] may be combined in order to eliminate all variables except $\phi_m(z,t)$ and $a(z,t)$. Before reporting the result, it is convenient to rewrite the problem in terms of dimensionless quantities based on the following definitions:

$$Z = \frac{z}{l}$$

$$\tau = \frac{M\sigma RT}{\rho l^2 n^2 \mathbf{F}^2} t$$

$$C^s(Z,\tau) = \frac{c^s(z,t)}{c^b}$$

$$\Phi_m(Z,\tau) = \frac{n\mathbf{F}}{RT}[\phi_m(z,t) - \phi_m{}^\bullet] \qquad [8]$$

$$\Phi_a = \frac{n\mathbf{F}}{RT}[(\phi_m{}^\bullet - \phi_s{}^\bullet) - (\phi_m{}^e - \phi_s{}^e)]$$

$$J(Z,\tau) = \frac{j(z,t)l}{a^\bullet i^\bullet}$$

$$A(Z,\tau) = \frac{a(z,t)}{a_o}$$

When the variables defined in Eq. [8] are introduced into the set of equations which describes the model, several dimensionless groupings of the system parameters arise

$$\xi = \frac{i_o l^2 n\mathbf{F}}{a_o \sigma RT}$$

$$\Gamma = \frac{kc_b l^2 n^2 \mathbf{F}^2}{a_o \sigma RT} \qquad [9]$$

$$\beta(\tau) = \frac{a^\bullet i^\bullet l n\mathbf{F}}{a_o \sigma RT}$$

The parameter ξ corresponds to the ratio of ohmic resistance to charge-transfer resistance insofar as it contains the ratio of exchange current density to electrode conductivity. Similarly, the dimensionless parameter Γ denotes the ratio of ohmic resistance to mass transfer resistance.

Equations [1] through [7], which describe the model, may now be combined and written in dimensionless form; the result has the somewhat compact form

$$(A\Phi'_m)' = \xi \left\{ e^{\alpha(\Phi_m + \Phi_a)} - \left[\frac{1 + \frac{\xi}{\Gamma} e^{\alpha(\Phi_m + \Phi_a)}}{1 + \frac{\xi}{\Gamma} e^{(\alpha-1)(\Phi_m + \Phi_a)}} \right] e^{(\alpha-1)(\Phi_m + \Phi_a)} \right\} \qquad [10]$$

The symbol prime (') is used to denote differentiation with respect to the spatial variable Z. The left side of Eq. [10] represents the divergence of the potential gradient in the electrode phase. The right side is a net species generation term which is given by the pseudohomogeneous electrochemical reaction rate. The rate expression has both anodic and cathodic terms, the concentration dependence of the cathodic term having been reformulated by combination of Eq. [3] and [7] in view of Eq. [4]-[6]. The Appendix provides details.

Equation [10] has two unknown quantities, $\Phi_m(Z,\tau)$ and $A(Z,\tau)$, and four independent parameters (Φ_a, ξ, Γ, and α). Provided that the deposit thickness distribution is known, Eq. [10] may be integrated with use of two boundary conditions. The conditions that correspond to the present model are (A) Current does not pass through the insulated end of the electrode

$$\Phi'_m(0,\tau) = 0 \qquad [11]$$

(B) The potential at the contact end of the electrode, in the metal, is constant during electrolysis

$$\Phi_m(1,\tau) = 0 \qquad [12]$$

Once the potential and concentration distributions along the wire surface are known, the current distribution may be calculated by

$$J(Z,\tau) = \frac{\xi}{\beta}[e^{\alpha(\Phi_m + \Phi_a)} - C^s e^{(\alpha-1)(\Phi_m + \Phi_a)}] \qquad [13]$$

The deposit thickness distribution may be obtained by integration of the prevailing current distribution over the period of electrolysis

$$A(Z,\tau) = 1 + \int_0^\tau J\beta d\tau \qquad [14]$$

The mathematical model described above has extended previously available treatments by accounting simultaneously for both mass transfer and charge transfer overpotentials in addition to the ohmic losses associated with deposition onto electrodes of high resistance. Further, the model includes transient effects owing to pseudo steady-state thickening of the electrode.

Method of Solution

The solution of Eq. [10] was carried out on a digital computer with use of finite difference numerical methods. The timewise variation of the current distribution was determined by alternate solution of Eq. [10] and [14] at specified time steps. First Eq. [10] was integrated with the deposit thickness distribution set equal to the initial value ($A = 1.0$). Calculations were then carried out at specified time intervals during the pseudo steady-state thickening process. After one time interval the "initial" current distribution, already in hand, was used to evaluate the thickness distribution via Eq. [14]. With use of these results, Eq. [10] was solved again and the sequence was repeated for as many time intervals as required. For the calculations reported in this study it was found that time intervals that were less than the value ($0.05/\beta$) yielded results which were essentially independent of the choice of time step.

The numerical integration of Eq. [10], which is nonlinear and of second order, was accomplished by

first linearizing the equation and placing the results into finite difference form. The tridiagonal matrix was inverted (9) on an IBM 360 computer. The solution of the nonlinear equation was obtained by iteration on the approximate linear solution.

Results and Discussion

Calculations based on the preceding theoretical model have been conducted in order to illuminate several salient features of the process. All calculations have been carried out for cathodic deposition (negative applied potentials) with use of a symmetric transfer coefficient ($\alpha = 0.5$). The dimensionless parameters used in the following presentation should permit evaluation of a wide variety of actual systems.

Consider first the situation which is attained shortly after application of potential. Both the double layer and the diffusion layer have developed to a pseudo steady-state condition, but the deposit thickness has not changed appreciably from its initially uniform value. This state is termed the "initial state" in the subsequent discussion. Figure 1 illustrates the values of the three overpotentials along the length of the electrode for a typical choice of parameters. It is seen that, at any point along the surface, the total of values of the three overpotentials equals the applied potential. At the electrical contact end of the electrode, ohmic losses in the metal phase are zero and the applied potential is "partitioned" between concentration and charge-transfer effects. Further along the electrode, the ohmic resistance consumes an increased fraction of the total applied potential so that both charge-transfer and concentration overpotentials are thereby reduced. Clearly the surface concentration of reactants is lowest near the electrical contact, where concentration overpotential is greatest, and increases along the electrode. In addition, the variation of charge-transfer overpotential clearly indicates that the reaction rate will be greatest near the electrical contact and will decrease along the electrode. Figure 2 shows some typical reaction rate distributions along the cathode for several values of the parameter Γ. It may be seen that when the mass transfer coefficient is large (large Γ), the reaction distribution depends on the parameter ξ: a small value of ξ indicates high electrode conductivity and thus a uniform current distribution, whereas large values of ξ correspond to a nonuniform current distribution. As the mass transfer coefficient is reduced (decreased Γ), the concentration overpotential will be increased relative to the other overpotentials and the reaction rate distribution will be forced to become more uniform along the electrode. For a sufficiently small mass transfer coefficient, the reaction distribution is seen to be essentially uniform even though ξ has a large value. Thus the effect of mass transport limitations is to suppress the large reaction rate near the electrical contact point and thereby render the reaction distribution more uniform.

The variation of total current with applied potential is depicted in Fig. 3 for several values of ξ and Γ. In the absence of mass transfer resistance (large Γ), the "polarization" curves assume a Tafel-like shape. The effect of lowering Γ (increasing the mass transfer resistance) is to reduce the upper value of current which may be passed through the electrode. It may be seen that at sufficiently small values of Γ, the curves in Fig. 3 exhibit a current plateau which corresponds to the limiting current.

Continuing with discussion of the "initial state" (before appreciable thickening occurs), consider how the overpotential distributions depend on the parameters ξ and Γ. Since the total of the three overpotentials equals the applied potential, which is held constant during electrolysis, the relative magnitude of each may be illustrated on an equilateral-triangle graph as shown in Fig. 4. Each different point within the triangle, designated as a partition point, corresponds to a different partitioning of the applied potential among concentration, charge-transfer, and ohmic overpotentials. For example, the partition point which corresponds to the insulated end of the electrode already depicted

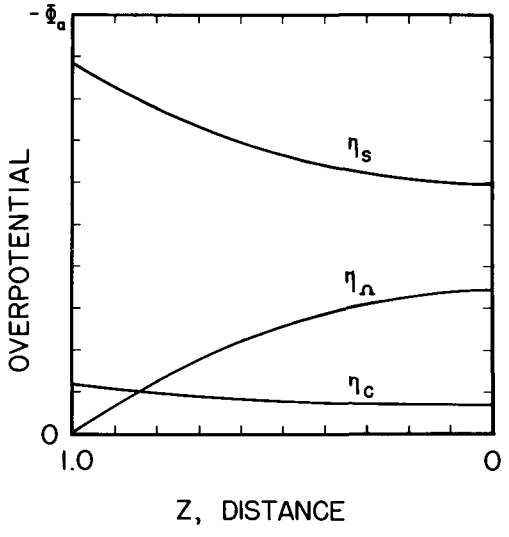

Fig. 1. Overpotential partition distribution along a typical resistive electrode of uniform thickness ($\xi = 1$, $\Gamma = 10$, $\Phi_a = -3.0$).

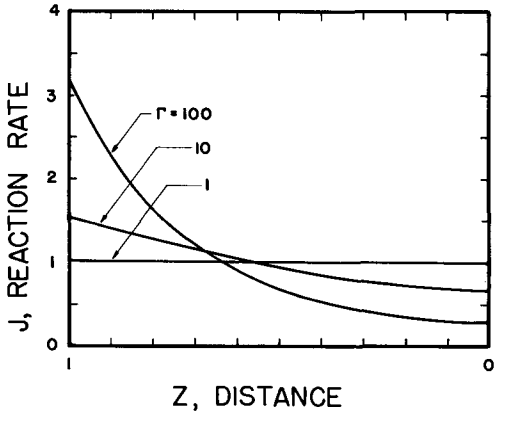

Fig. 2. The effect of mass transport limitations on the current density distribution along a resistive electrode of uniform thickness ($\xi = 10$, $\Phi_a = -3.0$).

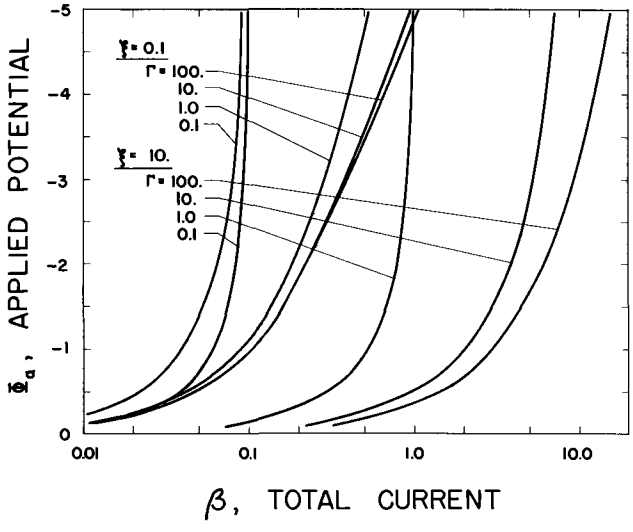

Fig. 3. Current-voltage curves for resistive electrodes of uniform thickness under various conditions of charge- and mass-transport restrictions.

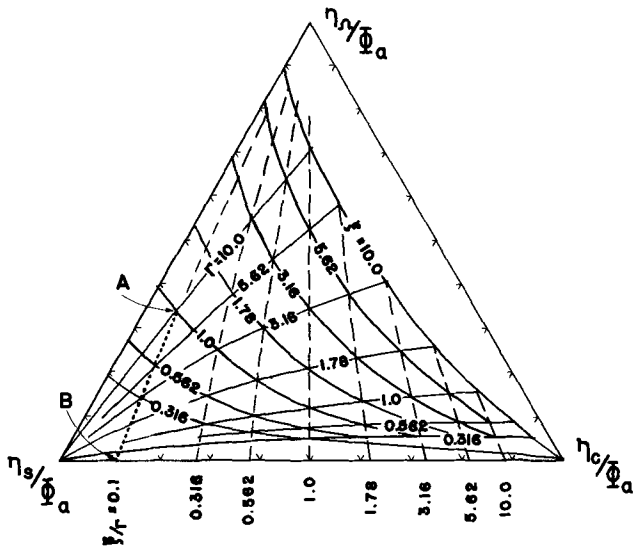

Fig. 4. Overpotential partition at insulated end of a resistive electrode of uniform thickness under various operating conditions ($\Phi_a = -3.0$).

in Fig. 1 ($\xi = 1$, $\Gamma = 10$) is located at point A in Fig. 4. The "partition points" at the insulated end of other systems may also be found in Fig. 4 from the solid grid lines which are drawn at various values of ξ and Γ. Similarly, the partition point in Fig. 4 which corresponds to the electrical contact end of the electrode of Fig. 1 is shown at point B. It may be realized that ohmic effects are always absent at the current feeder so that the partition point falls on the charge transfer-mass transfer "binary" base line at a position which is determined solely by the value of the ratio ξ/Γ. The overpotential partition distribution given in Fig. 1 corresponds to the heavy dotted line which connects points A and B in Fig. 4. By comparing the dotted line with the corresponding intersection of grid points it is seen that the dotted line passes through the locus of points for which the ratio ξ/Γ is constant. That is, the applied potential at any point along an electrode surface is partitioned between charge-transfer and concentration overpotentials in accord with the value of ξ/Γ, independent of ohmic effects. The dashed lines in Fig. 4 correspond to various lines of constant ξ/Γ, as noted beneath the triangle. In accord with the above observations, the overpotential partition distribution along an electrode, prior to significant thickening, may be obtained by locating the end point at the grid location which corresponds to the values of ξ and Γ, and then by following the dashed line of constant ξ/Γ to the $\eta_s - \eta_c$ base line. Although spatial distributions cannot be obtained, the method provides sufficient information to estimate both the extent to which ohmic effects will be appreciable during thickening and the extent to which concentration polarization will become significant once the ohmic resistance is relieved by thickening. Alternatively, Fig. 4 may be used to choose deposition conditions under which deposits of acceptable uniformity and appearance may be obtained. Although the axes of Fig. 4 are normalized by the applied potential, the location of the grid lines depends on the value chosen for the applied potential; an increase in applied potential will usually enhance partitioning into ohmic and concentration overpotentials at the expense of charge transfer overpotential.

At this point, a numerical example should be helpful in establishing some feeling for the matter. Consider copper deposition from an acidified sulfate bath for which approximate values of system parameters would be $n = 2$, $i_o = 10^{-3}$ A/cm^2, $c_b = 5 \times 10^{-4}$ mole/cm^3, $\sigma = 5 \times 10^5$ (ohm-cm)$^{-1}$, and $T = 300$°K. A typical electroless deposit thickness is $a_o = 5 \times 10^{-5}$ cm, and a typical circuit board dimension is $l = 15$ cm. The parameter ξ thus has the value 0.7. In the absence of mass transfer effects, Fig. 4 indicates that for $\Phi_a = -3$ (42 mV applied potential), up to 32% of the applied potential will be consumed by ohmic losses in the electrode phase, so that the current distribution may be expected to be moderately nonuniform. For this system, the diffusion coefficient is about 7×10^{-6} cm^2/sec; if the diffusion layer is of thickness 5×10^{-2} cm, the mass transfer coefficient would be on the order of $k = 7 \times 10^{-6}/5 \times 10^{-2} = 1.4 \times 10^{-4}$, so that Γ would have the value of ten. Referring once again to Fig. 4, it is seen that for $\Gamma = 10$, concentration overpotential consumes only a small portion of the applied potential. As a counterexample, consider a circuit board of length $l = 1$ cm but with the same system parameters as above, so that $\xi = 3 \times 10^{-3}$ and $\Gamma = 4 \times 10^{-2}$. One concludes that ohmic resistance effects in the electrode phase are negligible and will not contribute to a nonuniform deposit.

Now consider the transient behavior which occurs during the thickening process. Figure 5 illustrates, for one set of parameters, how cathodic deposition reduces the ohmic resistance of the electrode and thus renders the reaction rate distribution more uniform during the course of electrolysis. Current distributions are shown for various average deposit thicknesses (A.D.T.) during a tenfold thickening treatment. The initial current distribution (A.D.T. = 1.0) indicates that the deposition rate at the contact end of the electrode is 2.2 times greater than that at the far end of the electrode. After tenfold thickening, however, the current distribution is essentially uniform for the conditions indicated. As the ohmic restriction is thus relieved by thickening, both the concentration and charge transfer overpotentials increase, in relative proportion to the ratio ξ/Γ. Thus, during thickening, the partition point which characterizes the insulated end of the electrode (such as Point A in Fig. 4) moves along a line of constant ξ/Γ toward the $\eta_c - \eta_s$ base line. At a given applied potential, the period of electrolysis during which the current distribution remains nonuniform clearly depends on the initial current distribution, *i.e.*, on the values of ξ and Γ.

During deposition the thickness of the cathodic deposit increases at different rates along the electrode when the "initial" current distribution is not uniform. Figure 6 illustrates several specific cases of transient behavior which are observed during a tenfold thickening operation (that is, the final average deposit thickness is ten times the initial thickness). The ordinate is the deposit thickness distribution which has been normalized by the average prevailing deposit thickness

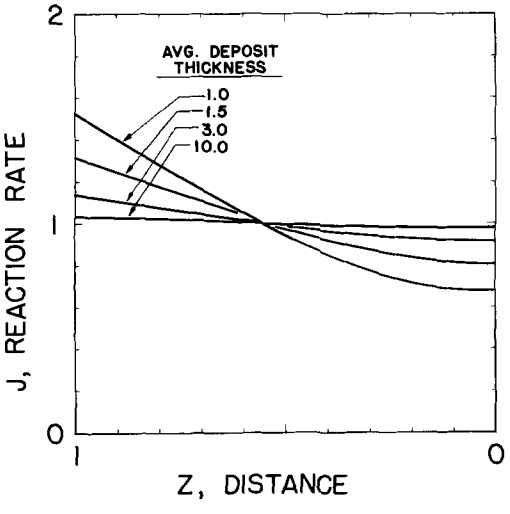

Fig. 5. Current density distributions along a resistive electrode during tenfold thickening by cathodic deposition ($\xi = 10$, $\Gamma = 10$, $\Phi_a = -3.0$).

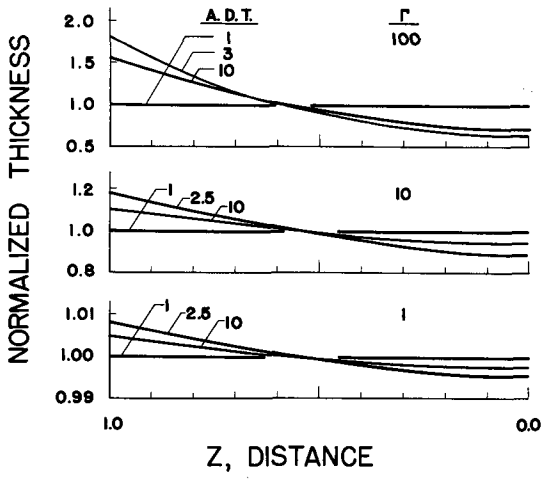

Fig. 6. The effect of mass transport limitations on the deposit thickness distribution during tenfold thickening ($\xi = 10$, $\Phi_a = -3.0$).

$$\frac{1 + \int_0^\tau J\beta d\tau}{1 + \int_0^\tau \beta d\tau} \qquad [15]$$

Normalized distributions are shown at several intermediate stages during the over-all process. As a general observation, the calculations illustrate that the initial deposit thickness distribution (A.D.T. = 1) is uniform and that the thickness becomes more or less nonuniform during the first moments of deposition. Eventually, in accord with Fig. 5, the current distribution becomes uniform so that thickening takes place uniformly along the electrode. Thus the normalized deposit thickness distribution attains a maximum degree of nonuniformity; additional electrolysis renders the deposit more uniform. As shown in Fig. 6, the details of the deposit thickness distributions and the times at which the maximum nonuniformity is attained depend on the value of Γ. When concentration overpotential prevails along the entire electrode (ξ/Γ large), then the current distribution is essentially uniform at the onset of electrolysis and remains so during deposition. The bottom graph of Fig. 6 ($\xi = 10$, $\Gamma = 1$, $\Phi_a = -3$) indicates that a deposit ten times the original layer will be of uniform thickness within ±0.5%. On the other hand, if the ohmic resistance effect is large and not masked by severe mass transport limitations, then the deposit thickness distribution will pass through a highly nonuniform configuration during deposition. The middle graph of Fig. 6 ($\Gamma = 10$) shows that the final deposit thickness will vary by about ±10%. For $\Gamma = 100$ (upper graph of Fig. 6), the final deposit at the contact end will be over twice as thick as at the far end.

Conclusions

The theoretical model presented above is based on assumptions that naturally affect the applicability of the calculated results. Thus while the foregoing predictions may be applicable to many deposition systems, they cannot be expected to apply to all such systems. For example, if a given system is characterized by a value of ξ that is small with respect to unity, one may conclude that ohmic resistance effects in the electrode phase are negligible. However, it would be unwise to claim that it thus follows that the current distribution is therefore uniform for every system having a low value of ξ. The theoretical model focuses on the role of electrode resistance effects and is not intended to provide detailed information in the absence of such effects. On the other hand, it may be recognized that several of the assumptions, such as (I), (IV), (VI), and (VIII), may be altered to suit special circumstances without appreciable complication of the general calculational procedures.

The results presented above find application in the thickening of deposits on insulating substrates as, for example, during the manufacture of printed circuit boards. Although reversible plating baths permit high current densities and rapid device throughput, deposits will be nonuniform if the electroless undercoat is not sufficiently thick. Since the electroless deposition process is slow, an optimum production rate may be anticipated which counterbalances the electroless deposition rate against the uniformity of the cathodically thickened product. If the concentration of reacting ions is low, or if the bath is stirred but slowly, mass transport limitations may set in which render the current density distribution uniform regardless of kinetic or ohmic effects. However, deposition under severe mass transfer limitations can lead to "burned" deposits which are powdery and loosely adherent. If ohmic resistance effects are appreciable and are not masked by mass transport limitations, highly nonuniform deposits may be obtained during the initial period of deposition. In all cases of operation, essentially uniform deposits will be obtained upon extended deposition after the ohmic resistance of the electrode is relieved by thickening. The common usage of a high current density "strike" plating on the electroless deposit may not necessarily achieve the intended goal of coating the basis metal with the plating metal and, indeed, may involve a highly nonuniform deposition. The interplay of the various phenomena that determine the over-all transient thickening process thus provides insight which is useful toward improvement of the over-all production process.

Acknowledgment

The author is indebted to R. Visco and A. Tvarusko, Western Electric Engineering Research Center, for providing financial support for computer calculations.

Manuscript submitted April 19, 1971; revised manuscript received Aug. 16, 1971.

Any discussion of this paper will appear in a Discussion Section to be published in the June 1972 JOURNAL.

APPENDIX

Combination of Eq. [1], [2], and [3] gives

$$\sigma \frac{d}{dz}\left(a \frac{d\phi_m}{dz}\right) = i_o \left\{ e^{\frac{\alpha n F}{RT}\eta} - \frac{c^s}{c^b} e^{\frac{(\alpha-1)nF}{RT}\eta} \right\} \qquad [16]$$

In view of Eq. [4] and [5], and the definitions in Eq. [8], one may rearrange Eq. [16] to the form

$$(A\Phi'_m)' = \xi\{e^{\alpha(\Phi_m+\Phi_a)} - C^s e^{(\alpha-1)(\Phi_m+\Phi_a)}\} \qquad [17]$$

The dimensionless surface concentration, C^s, may be found by eliminating J from Eq. [7] and [13]

$$J = \frac{\Gamma}{\beta}(C^s - 1) = \frac{\xi}{\beta}\{e^{\alpha(\Phi_m+\Phi_a)} - C^s e^{(\alpha-1)(\Phi_m+\Phi_a)}\} \qquad [18]$$

whence

$$C^s = \frac{1 + \frac{\xi}{\Gamma} e^{\alpha(\Phi_m+\Phi_a)}}{1 + \frac{\xi}{\Gamma} e^{(\alpha-1)(\Phi_m+\Phi_a)}} \qquad [19]$$

Substitution of Eq. [19] into Eq. [17] yields Eq. [10].

NOMENCLATURE

English Characters

a	Thickness of electrode, cm
$a^\bullet$	Thickness of electrode at electrical contact point, cm
a_o	Thickness of electrode prior to thickening, cm
A	Thickness of electrode, a/a_o, dimensionless
c^s	Reactant concentration at electrode surface, g-mole/cm³

C^s Reactant concentration at electrode surface, c^s/c^b, dimensionless
$\mathbf{F}$ Faraday's constant, 96,500 coulomb/g-eq
i Current density in the electrode, A/cm^2
$i^\bullet$ Current density in the electrode at the electrical contact point, A/cm^2
i_o Exchange current density of the electrode reaction at bulk concentrations, A/cm^2
j Local reaction rate (current density) along the electrode surface, A/cm^2
J Local reaction rate (current density) along the electrode, $jl/a^\bullet i^\bullet$, dimensionless
k Mass transfer coefficient, cm/sec
l Length of electrode, cm
M Atomic weight of electrode metal, g/g-atom
n Number of electrons taking part in electrode reaction, g-eq/g-mole
R Gas constant, 8.31 joule/g-mole °K
t Time, sec
T Temperature, °K
y Distance between reference electrode capillary and surface of the resistive cathode, cm
z Spatial variable along electrode, cm
Z Spatial variable along electrode, z/Z, dimensionless

Greek Characters

α Transfer coefficient in reaction rate expression, Eq. [3]
β Current density in the electrode at the electrical contact end, $a^\bullet i^\bullet ln\mathbf{F}/a_o\sigma RT$, dimensionless
Γ Ratio of ohmic resistance to mass transfer resistance, $kc_b l^2 n^2\mathbf{F}^2/a_o\sigma RT$, dimensionless
η Overpotential as defined by Eq. [4]
η_c Concentration overpotential in the solution, $[\phi_s{}^s(z,t) - \phi_s{}^\bullet]$, V
η_s Charge-transfer overpotential at the electrode-solution interface, $\{[\phi_m(z,t) - \phi_s{}^s(z,t)] - [\phi_m{}^e - \phi_s{}^e]\}$, V
η_Ω Ohmic overpotential in the electrode phase, $[\phi_m{}^\bullet - \phi_m(z,t)]$, V
κ Conductivity of electrolyte, $ohm^{-1}\text{-}cm^{-1}$
ξ Ratio of ohmic resistance to charge transfer resistance, $i_o l^2 n\mathbf{F}/a_o\sigma RT$, dimensionless
ρ Density of electrode metal, g/g-mole
σ Conductivity of metal electrode, $ohm^{-1}\text{-}cm^{-1}$
τ Time, $M\sigma RTt/\rho l^2 n^2\mathbf{F}^2$, dimensionless
ϕ_m Potential in the electrode, V
$\phi_m{}^\bullet$ Potential in the electrode at the electrical contact end, V
$\phi_m{}^e$ Potential in the electrode at equilibrium, V
ϕ_s Potential in the solution, V
$\phi_s{}^\bullet$ Potential in the solution at the electrical contact end of the cell, V
$\phi_s{}^e$ Potential in the solution at equilibrium, V
$\phi_s{}^s$ Potential in the solution at electrode surface, V
Φ_a Applied potential, $n\mathbf{F}[(\phi_m{}^\bullet - \phi_s{}^\bullet) - (\phi_m{}^e - \phi_s{}^e)]/RT$, dimensionless
Φ_m Potential in the electrode, $n\mathbf{F}(\phi_m - \phi_m{}^\bullet)/RT$, dimensionless

REFERENCES

1. A. Weisselberg, *Trans. Electrochem. Soc.*, **90**, 235 (1946).
2. C. Tobias and R. Wijsman, *This Journal*, **100**, 459 (1953).
3. S. Ishizaka, H. Matsuda, and Y. Wada, *J. Electrochem. Soc. Japan*, **22**, 420 (1954).
4. W. Harvey, *This Journal*, **109**, 638 (1962).
5. J. Wojtowicz, L. Laliberte, and B. Conway, *Electrochim. Acta*, **13**, 361 (1968).
6. V. Fomichev, *Soviet Electrochem.*, **4**, 708 (1968).
7. A. Böhnlein, *Metalloberfläche*, **6**, 210 (1970).
8. P. Delahay, "Double Layer and Electrode Kinetics," p. 168, Interscience Publishers, New York (1965).
9. J. Newman, *I. & E. C. Fund.*, **7**, 514 (1968).

Phase Equilibria in Lithium-Chalcogen Systems

I. Lithium-Selenium

P. T. Cunningham, S. A. Johnson, and E. J. Cairns*

Argonne National Laboratory, Chemical Engineering Division, Argonne, Illinois 60439

ABSTRACT

The equilibrium phase diagram of the lithium-selenium system has been investigated. A miscibility gap extends from 0.5 to 30.5 a/o (atom per cent) lithium above a monotectic temperature of 350.1°C; the critical temperature is greater than 800°C. The only intermediate phase found is Li_2Se which melts at 1302°C.

During the last several years there has been an increasing interest in the development of high-specific-power, high-specific-energy secondary cells based on alkali metal-chalcogen couples (1, 2). To optimize the cell design (especially the cathode configuration) and to evaluate cell performance, it is necessary to understand the phase equilibria involved in these systems. The work reported here was undertaken to determine the phase diagram for the condensed lithium-selenium system.

The study of the phase equilibria in lithium-chalcogen systems has heretofore been very limited. The lithium-selenium phase diagram has not been previously reported. The only information available is that lithium monoselenide, Li_2Se, has been prepared both in liquid ammonia (3, 4) and by the reaction of selenium vapor with molten lithium (5). It has been reported to have an antifluorite structure (4, 5) with a lattice parameter of 6.002Å (5).

* Electrochemical Society Active Member.

Key words: lithium, selenium, lithium selenide, cathode, phase equilibria.

Experimental

Materials.—The selenium used was a special high-purity (99.999 + %) grade obtained from American Smelting and Refining Company, South Plainfield, New Jersey. The lithium was high-purity reactor grade (99.98%) obtained from the Foote Mineral Company, Philadelphia, Pennsylvania. Both elements were used without further purification. The Li_2Se was prepared in 5-10g batches by the reaction of selenium vapor with molten lithium in an apparatus similar to that described by Johnston and Heikes (5). Lithium was contained in a molybdenum boat which was placed in an evacuated quartz vessel together with excess selenium and heated at 300°C for two days. The Li_2Se thus prepared had a light salmon color and produced very sharp x-ray powder patterns corresponding to an antifluorite structure with a lattice parameter of

Table I. Summary of thermal analysis data on the lithium-selenium system

Over-all composition (a/o Li in Se)	Method[a]	Container material	Max temp (°C)	Temperature of thermal effects (°C)[a]			
100.0 (Li)	TA	Ta	220	180.5			
99.3	TA	Ta	210	180.5			
99.0	TA	Ta	220	180.6			
85.0	TA	347 S.S.[b]	1000	180.5			
66.7 (Li_2Se)	DTA	Nb[b]	1350				1302 ± 2
66.7 (Li_2Se)	Visual	Nb	1350				1303 ± 5
55.0	TA	Quartz	400		219.8	349.3	
50.0	TA	Quartz	400		220.0	351.7	
40.0	TA	Quartz	400		220.0	351.8	
40.0	DTA	Al[b]	575		218.0	352.0	
35.0	TA	Quartz[b]	615		220.3	347.0	
35.0	DTA	Al[b]	500		218.0	352.0	
31.9	DTA	Al[b]	415		219.0	354.0	
31.5	DTA	Al[b]	480		219.0	352.0	
20.0	TA	Quartz	430		220.0	349.4	
10.0	TA	Quartz	400		221.0	334.0[c]	
10.0	TA	Quartz	385		220.0	349.8	
10.0	TA	Quartz	410		220.0	350.0	
10.0	TA	Quartz[b]	706		196.0[c]	342.0[c]	
10.0	DTA	Al[b]	400		219.0	352.0	
7.5	TA	Quartz	410		219.8	350.5	
5.0	TA	Quartz	380		210.0[c]	343.0[c]	
5.0	TA	Quartz	370			350.7	
4.0	TA	Quartz	390		220.0	347.0[c]	
3.0	TA	Quartz	420		219.8	341.5[c]	
3.0	TA	Quartz	400		220.3	346.6[c]	
0.0 (Se)	TA	Quartz	400		220.2		

[a] The methods used were heating or cooling curves (TA), where reported temperatures are those of thermal arrests, and differential thermal analysis (DTA), where reported temperatures are those of the intersection.
[b] Sealed container.
[c] Temperature taken from a cooling curve that had clearly undercooled.

6.0014 ± 0.0004Å, which is in good agreement with the value previously reported (5). There was no indication of unreacted lithium. Chemical analysis of portions of several Li_2Se batches indicated an empirical formula of $Li_{2.05\pm0.1}Se$. Li_2Se was mixed with the appropriate terminal phase in a purified-helium-atmosphere glove box (6) to obtain the desired over-all composition for subsequent experiments. The samples were contained in quartz, aluminum, niobium, tantalum, and Type 347 stainless steel, depending on the sample composition and the temperature range covered.

Apparatus and procedures.—The methods used included thermal analysis (heating and cooling curves), differential thermal analysis (DTA), chemical analysis, microscopy, and x-ray diffraction. The DTA samples weighed about 80 mg and were contained in aluminum or niobium capsules with press-fit caps of the same material. Data were obtained with a du Pont Model 900 Differential Thermal Analyzer using a 5°C/min rate of temperature change with powdered alumina as a reference material and a dynamic helium atmosphere. The over-all accuracy of the apparatus, which was checked with NBS standard quartz and KNO_3,[1] was found to be ± 1°C.

Heating and cooling curves were obtained for samples weighing from 10 to 20g using a furnace well which was attached to the floor of a helium-atmosphere glove box (7). Lithium-rich samples were contained in either tantalum or Type 347 stainless steel, whereas selenium-rich samples were contained in quartz. Variation of sample composition because of selenium vaporization was negligible. The selenium-rich samples required vigorous stirring to prevent severe undercooling. Temperatures were measured with platinum *vs.* platinum-10% rhodium thermocouples for both types of thermal analysis. The thermocouples were all fabricated of wire which had been calibrated against NBS pure tin (mp 231.88°C), zinc (mp 419.58°C), and aluminum (mp 660.0°C).

A molybdenum-wound resistance furnace was employed to observe the fusion of Li_2Se. The samples, each about 0.2g, were placed in a niobium crucible, which contained a black-body cavity, and were heated in an argon atmosphere. Temperature was measured with a calibrated optical pyrometer, and the occurrence of fusion was visually determined.

[1] The quartz and KNO_3 are SRM 755 and SRM 756, respectively. They are available from the Office of Standard Reference Materials, National Bureau of Standards, Washington, D. C. 20234.

The samples used for microscopic examination or chemical analysis were placed in quartz ampules, evacuated, and sealed. The ampules were heated to 600-800°C for about 1 hr and cooled to the desired temperature and held at that temperature for periods varying from several hours to several weeks. The samples were then quenched in liquid nitrogen and returned to the helium-atmosphere glove box where the ampules were carefully broken open and the samples examined. Because Li_2Se reacts rapidly with moisture in the air, care was necessary in polishing samples for microscopic examination outside the glove box. The samples were mounted in Polylite (or in some cases Wood's metal) and polished under silicone oil. The polished surface was flooded with silicone oil and a cover glass was placed over the sample. The polished surface could then be examined and photographed at leisure since the surface showed no sign of deterioration for several hours. Information on the number of phases present, their distribution within the sample, and their relative amounts is obtained by microscopy. Chemical analysis was performed on samples that were mechanically separated in the glove box. In most cases, lithium was analyzed by flame photometry, and selenium was obtained by difference. Several checks in which selenium was also determined by the standard potassium iodide method (8) confirmed the accuracy of this procedure (± 5% of the lithium weight).

X-ray diffraction powder photographs were obtained for a large number of samples of various composition and thermal history using a 114.6 mm Debye-Scherrer camera with CuKα radiation.

Results and Discussion

All experimental results are summarized in Fig. 1. The thermal analysis results are listed in Table I. Four thermal effects were observed. On the lithium-rich side of Li_2Se, the only effect noted below 1000°C (the highest temperature attained for this composition range) was at 180.5° ± 0.1°C, which is also the melting point of lithium. The presence of Li_2Se did not affect the lithium melting point within the accuracy of these measurements. The melting point of Li_2Se was observed to be 1302° ± 2°C using DTA and 1303° ± 5°C in the resistance furnace with optical observation. The excellent agreement between these values is considered to be fortuitous considering the difficulty of accurate high-temperature measurements. The melting point of Li_2Se is taken to be 1302° ± 5°C.

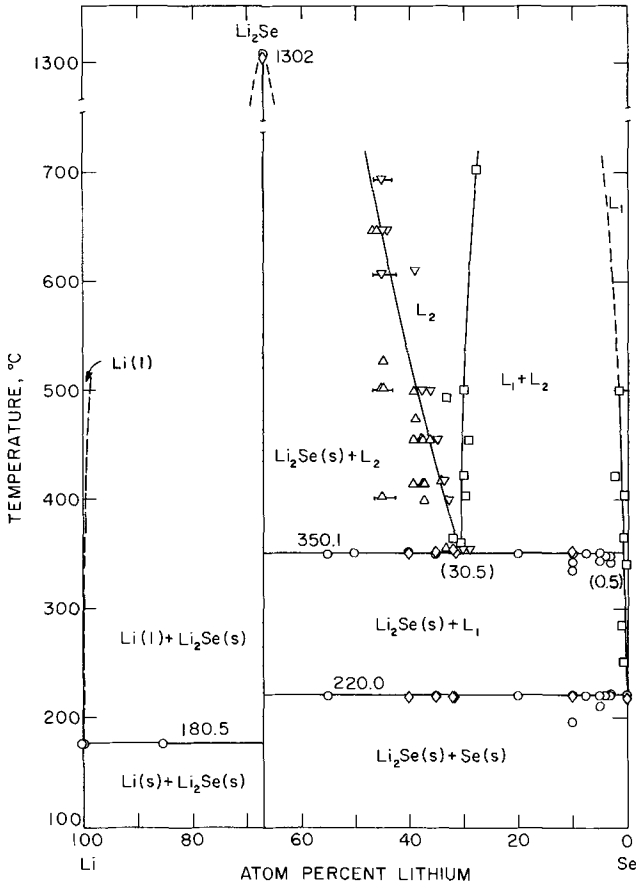

Fig. 1. Partial phase diagram of the lithium-selenium system. ○, Thermal analysis; ◇, differential thermal analysis; □, chemical analysis; ▽, microscopic analysis: sample quenched from above the liquidus; △, microscopic analysis: sample quenched from below the liquidus.

Thermal effects in samples with over-all compositions on the selenium-rich side of Li_2Se were observed at 220.0° ± 0.4°C and 350.1° ± 2.0°C. These temperatures are weighted averages where the weighting used is somewhat subjective. The indicated uncertainties show the variance of the data. The strong tendency for samples containing less than 20 a/o (atom per cent) lithium to undercool led to considerable scatter in the data. The 220°C effect is presumably associated with the eutectic reaction $L_1 \rightarrow Li_2Se(s)$ + selenium. The melting point of selenium is frequently reported to be 217°C, a value which appears to be in error. Our measured value of 220.2° for the selenium melting point is slightly higher than the average eutectic temperature but agrees within experimental uncertainty. The 350.1°C effect is associated with a monotectic type of reaction [$L_2 \rightarrow L_1 + Li_2Se(s)$, see Fig. 1].

The existence of a miscibility gap was confirmed by quenching samples having an over-all composition in the range from 5 to 25 a/o lithium from temperatures above 350.1°C. The quenched samples contained two easily distinguishable zones. One of these was indistinguishable from selenium, whereas the other was black, dull, and granular, distinctly salt-like. These two zones are associated with the separated liquid phases L_1 and L_2, respectively (see Fig. 1). Samples quenched from 800°C still clearly contained these two zones. At temperatures up to about 500°C, the two liquid phases separated easily under gravity within a few hours, with the selenium-like phase being more dense. Separation of the phases was also rapid above 650°C, but the salt-like phase was more dense. Between 550° and 650°C, satisfactory separation was not achieved, even after many days. The extent of the miscibility gap was determined by chemical analysis of the two zones. Results of the analyses are presented in Table II. Considerable care was taken in separating the two zones to prevent cross-contamination which would have led to an apparent narrowing of the miscibility gap. The results certainly represent a lower limit on the extent of immiscibility and are probably accurate to 1 a/o. Chemical analysis of the selenium-like zone in quenched samples was also used to determine the lower liquidus (see Table II and Fig. 1).

Table II. Summary of chemical analyses

Temperature prior to quenching (°C)	Component analyzed	Sample weight (g)	Lithium weight (g)[a]	Lithium (a/o)
700.0	L_2	0.4006	1.30×10^{-2}	27.6
499.5	L_1	0.2926	3.45×10^{-4}	1.32
499.5	L_2	0.5726	2.10×10^{-2}	30.2
492.0	L_2	1.7303	7.27×10^{-2}	33.3
453.2	L_2	0.5053	1.77×10^{-2}	29.2
422.0	L_1	0.7995	1.60×10^{-3}	2.23
422.0	L_2	0.8230	3.00×10^{-2}	30.1
403.5	L_1	0.4836	1.92×10^{-4}	0.45
403.5	L_2	0.5812	2.10×10^{-2}	29.9
364.0	L_1	0.4213	2.00×10^{-4}	0.54
364.0	L_2	0.4550	1.80×10^{-2}	31.9
360.5	L_2	0.7429	2.80×10^{-2}	30.8
340.5	L_1	0.6342	1.00×10^{-4}	0.18
283.0	L_1	0.5431	2.40×10^{-4}	0.50
249.8	L_1	0.4785	3.40×10^{-4}	0.80

[a] Analytical uncertainty is ±5% of the lithium weight.

Thermal effects associated with liquidus crossings could not be observed. The upper liquidus was therefore determined by microscopic examination of quenched samples. Several samples, each differing in over-all composition by about 1 a/o lithium, were prepared and equilibrated at the same temperature prior to quenching (see preceding section). The uncertainty in the absolute composition of these samples was 1 a/o lithium. Examination of samples held at temperature for various time periods indicated that equilibration was complete after about 12 hr. In those samples for which the composition was below the liquidus at the equilibration temperature, there were dendritic crystals as well as large, well-developed primary crystals of Li_2Se, whereas samples above the liquidus prior to quenching contained only fine dendritic crystals. In this way the upper liquidus composition was closely bracketed at a number of temperatures. The results are shown by the triangular symbols in Fig. 1, with the apex-up orientation indicating that the sample was below the liquidus prior to quenching and the apex-down orientation indicating that it was above the liquidus prior to quenching.

X-ray powder patterns were taken on a large number of samples of different over-all composition and thermal history. In all cases, the observed lines were accounted for by the terminal phases and Li_2Se. The lattice constant for Li_2Se was 6.0014 ± 0.0004Å if selenium was in excess and 6.0001 ± 0.0004Å if lithium was in excess. This difference suggests a narrow range of solid solution for the Li_2Se intermediate phase.

The simple monotectic phase diagram which we have found for the region between Li_2Se and selenium indicates a positive deviation from Raoult's law. This can be contrasted with other known alkali metal-selenium systems (9) (Na-Se and K-Se), in which several other selenium-rich intermediate phases have been reported. Indeed, in the sodium-selenium system, in which the most selenium-rich phase is Na_2Se_6, there is no miscibility gap. In the potassium-selenium system a miscibility gap does appear between K_2Se_5 (the most selenium-rich intermediate phase) and selenium. It is of interest to note that the lithium-selenium system bears strong resemblance to the copper-selenium (10) and silver-selenium (9) systems.

Several aspects of the lithium-selenium phase diagram bear directly on the design and operation of lithium-selenium secondary cells. It is clear that for

practical operating temperatures the cell product will be Li_2Se and that complete conversion of the cathode material (selenium) to this phase represents the maximum cell capacity. At temperatures below the monotectic (350.1°C), solid Li_2Se will form in the cathode after only slight discharge and its presence must be carefully considered in cells designed to operate in this temperature region. At temperatures above the monotectic, solid Li_2Se will not form (under equilibrium conditions) until the cathode contains at least 30.5 a/o lithium, and cell potential will be constant throughout most of the discharge up to this point. In actual cell operation, consideration must of course be given to nonequilibrium phenomena, reaction kinetics, and possible interaction with the electrolyte (11). Further study of these areas is in progress.

Additional investigation of the lithium-selenium system is needed, particularly at higher temperatures, to determine the critical temperature of the miscibility gap, and at high lithium contents to determine the liquidus in the region between Li_2Se and lithium.

Acknowledgments

The authors wish to thank Dr. R. C. Vogel and Dr. A. D. Tevebaugh for their encouragement and support, Mr. R. Schablaske for his assistance with x-ray analyses, and Mr. Z. Tomczuk and Mrs. R. Hanna for assistance with chemical analyses. This work was performed under the auspices of the United States Atomic Energy Commission.

Manuscript submitted March 1, 1971; revised manuscript received July 16, 1971.

Any discussion of this paper will appear in a Discussion Section to be published in the June 1972 JOURNAL.

REFERENCES

1. N. Weber and J. T. Kummer, *Proc. 21st Ann. Power Sources Conf., 21,* 37 (1967); N. K. Gupta and R. P. Tischer, Paper 344 presented at Los Angeles Meeting of the Society, May 10-15, 1970, see *Extended Abstracts Theor. Electrochem. Div.*, p. 769 (1970); N. P. Yao, L. A. Heredy, and R. C. Saunders, Paper 60 presented at Atlantic City Meeting of the Society, Oct. 4-8, 1970, see *Extended Abstracts Battery Div.*, p. 148 (1970).
2. E. J. Cairns and H. Shimotake, *Science,* **164,** 1347 (1969). This article reviews work on lithium-chalcogen cells as well as several other high-temperature systems.
3. F. W. Bergstrom, *J. Am. Chem. Soc.,* **48,** 146 (1926).
4. E. Zintl, A. Harder, and B. Dauth, *Z. Elektrochem.,* **40,** 588 (1934).
5. W. D. Johnston and R. R. Heikes, *J. Am. Chem. Soc.,* **80,** 5904 (1958).
6. C. E. Johnson, M. S. Foster, and M. L. Kyle, *Nucl. Applications,* **3,** 563 (1967).
7. C. E. Johnson, S. E. Wood, and C. E. Crouthamel, *J. Inorg. Chem.,* **3,** 1487 (1964).
8. W. W. Scott, "Standard Methods of Chemical Analysis," fifth ed., D. Van Nostrand Co., Inc., Princeton, N. J. (1939).
9. M. Hansen and K. Anderko, "Constitution of Binary Alloys," second ed., McGraw-Hill Book Co., Inc., New York (1958).
10. G. P. Bernardini and A. Catani, *Mineral. Deposita* (Berl.), **3,** 375 (1968).
11. E. J. Cairns, G. H. Kucera, and P. T. Cunningham, Presented at the CITCE Meeting, Prague, Sept. 27-Oct. 2, 1970, Extended Abstracts, p. 95.

Experimental Measurements of the Hall Effect in Very Dilute Solutions

Marie-Claire Bellissent, Paul Gerard, Christian Longevialle, Maurice Meton, Michel Pich, and Geneviève Morand

Laboratoire de Physique Générale, Tour 12, Faculte des Sciences, 9 Quai St Bernard, Paris Vè, France

ABSTRACT

A brief historical account of the Hall effect in very dilute solutions is given in which the interest in Hall effect measurements for the knowledge of electrolytes is shown. Then a systematic examination is presented of the different parasitic voltages which are likely to appear in a Hall cell. The criteria to which the experimental setup must conform to allow detection of the Hall voltage are defined. (This voltage is from 0.1 to 1 μV in our experiments.) Results of measurements in hydrochloric and nitric acid solutions are given confirming the theoretical predictions.

When an electric field is applied in the X direction of a conductor and in the Z direction of a magnetic field, an electric current I_y flows in the Y direction of the Cartesian system of coordinates. The galvanomagnetic measurements are commonly carried out under the condition that $I_y = 0$. To satisfy this, a transverse field E_H must exist. This Hall field takes a value such that the force on charge carriers having a certain "average" velocity is zero in the crossed electric and magnetic fields. Let J_X be the control current density, B the magnetic field, and E_H the Hall field. The Hall coefficient R_H is then defined by the relation

$$E_H = R_H \cdot J_X \cdot B \qquad [1]$$

It is usually most convenient to use parallelepiped-shaped specimens as shown in Fig. 1. If the length of the specimen is 1, the width b, and the thickness e, the Hall voltage produced by the carriers between the two sides perpendicular to OY is simply

$$V_H = E_H \cdot b \qquad [2]$$

Since 1879, when Hall discovered the effect, many scientists have tried to observe it in electrolytes. The attempts were unsuccessful (1) until 1896 when Bagard (2) reported a Hall effect of about 10^{-3}V in SO_4Cu solutions. Bagard's work was strongly criticized by Florio (3), Chiavassa (4), Moretto (5), Heilbrun (6), Delvalez (7), and Voigt (8), who explained the difference between the measured value of the voltage and the theoretical values calculated by Donnan (9), Wind (10), and Larmor (11) by deformation and corrosion of the electrodes, their lack of parallelism, convective motion of the fluid, and by a concentration emf. These two last factors are strongly dependent on

Key words: Hall effect, alternative current, alternative field, very dilute electrolyte solutions, HCl, HNO_3.

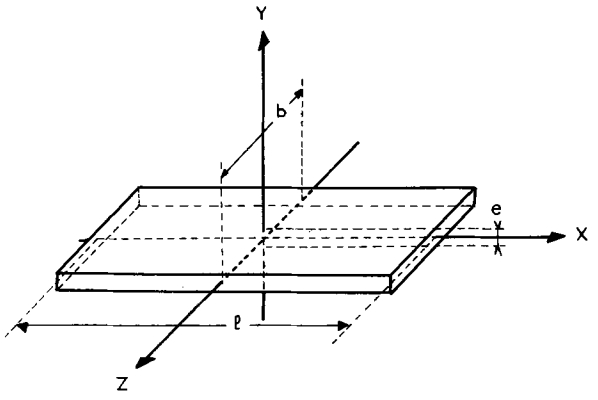

Fig. 1. Hall effect in a parallelepiped-shaped sample

the width of the cell placed in an insufficiently homogeneous magnetic field.

Measurements taking these factors into account gave no reproducible results (12), as the signal was too weak (from 10^{-1} to 1 μV) to be detected by the measuring devices available at that time, and the experimental work on the Hall effect in electrolytes was abandoned until 1950. With better experimental means Evseev (13), Laforgue-Kantzer (14), Muller (15), and Mergault Pages-Nelson (16), working with d.c. found Hall voltages in the tens of millivolt range. However, Trancong Khan (17), Wendhausen (18), and Holzapfel (19) showed that these values are 10^4 to 10^5 times greater than the expected Hall effect. Picard (20) and Naiditch *et al.* (21), using an a-c technique, were able to obtain very encouraging results.

The theoretical work of Friedman and his collaborators renewed interest in measuring the Hall effect. As a matter of fact, by comparing Hall effect measurements with those of electrical conductance in dilute solutions, Friedman (22-24) proposes that it is possible to determine whether the fluctuating motions of the carriers intervene in the transport properties on the macroscopic scale (such as electrical and Hall mobilities and conductances). Friedman (22) calculated first the electrical Hall mobilities of a carrier, whose dynamics obey the Langevin equation. Such a carrier is called a brownon and is characterized by a friction coefficient ζ_i and a mass m_i. Later, in collaboration with Ben-Naim (23) and Harris (24), he tried to describe the nonbrownon case. In view of the difficulty in describing the dynamics of a carrier not obeying Langevin's equation, Friedman and Ben-Naim supposed that the motion still obeyed the Langevin law for short intervals, but that the friction coefficient ζ_i and the mass m_i change in a random way between two sets of values, for instance, due to two different hydration states of the brownon. With this model, they obtained relative values of electrical and Hall mobilities different than those in the first case. This seems to prove that the Hall effect can be used to study fluctuations in the motion of the carrier. Pages-Nelson (25) reached the same conclusion by studying a model in which the cross-section of the ion-solvent collisions takes two well-defined values corresponding to two different hydration states of the ion.

In the present paper we present measurements, with improved a-c technique, of the Hall effect in very dilute solutions.

Calculation of R_H and V_H

Several authors (26, 21, 19) used simplified theories of the Hall effect applied to dilute electrolytes: all led to similar expressions of R_H and V_H, *i.e.*

$$R_H = (1/n_1 e z_1) \cdot [(\mu_1 - \mu_2)/(\mu_1 + \mu_2)] \qquad [3]$$

and

$$V_H = (\mu_1 - \mu_2)\, E\, B\, b$$

where n_1 is the number of ions of the carrier per cubic meter; e is the charge (1,6 · 10^{-19} A-sec); μ_1 is the mobility of the carrier i expressed in m^2-sec^{-1} · V^{-1}; E the electric field in V · m^{-1}; B the magnetic field in Weber · m^{-2}; and b the width of the cell in m. R_H is thus expressed in m^3-sec^{-1} · A^{-1} and V_H in volts.

Holtzapfel (19) showed that when using d-c current, R_H must be corrected by two terms, one from diffusion and the other from polarization voltages due to volume charge and chemical reactions in the neighborhood of the electrodes. This last term is difficult to evaluate. Therefore a-c techniques are preferable. The values of R_H and V_H are very small (about 10^{-1} to 1 μV) in the case of dilute electrolytes, as the carrier mobilities are small. However, it is important to note that the effect is greater if the difference between the mobilities is greater. This is why we began to work with HCl and HNO_3. The experimental device used to detect such a small voltage must satisfy several criteria. We show that the use of an alternating current of frequency ω_1 and of a magnetic field of frequency ω_2 eliminates several problems due to stray voltages.

Stray EMF's

EMF's due to temperature gradients.—Such a gradient gives rise to three galvanomagnetic and thermodynamic effects:

a. The Ettinghausen effect: $V_E = P\, I\, B\, \epsilon/e$

where P is the Ettinghausen coefficient, and ϵ the thermoelectrical power of the couple connecting the Hall probes to a galvanometer.

b. The Nernst effect: $V_N = Q\, B\, b\, (dT/dl)$

where Q is the Nernst coefficient and (dT/dl) the temperature gradient of the specimen.

c. The Righi-Leduc effect: $V_{RL} = S\epsilon\, B\, b\, (dT/dl)$

where S is the Righi-Leduc coefficient.

The Nernst and Righi-Leduc emf depend only on ω_2, the frequency of the magnetic field, whereas the Hall and Ettinghausen emf depend on $(\omega_1 + \omega_2)$ and $(\omega_1 - \omega_2)$. One can thus eliminate the Nernst and Righi-Leduc effects by using frequency filtering making the measurements at $(\omega_1 + \omega_2)$ and $(\omega_1 - \omega_2)$.

Lindbergh (27) calculated the Ettinghausen emf as

$$V_E = \{PI_0H_0/2b\}\{\exp[-(\omega_1 - \omega_2)/\omega_0]\cos(\omega_1 - \omega_2)t - \exp[-(\omega_1 + \omega_2)/\omega_0]\cos(\omega_1 + \omega_2)t\}$$

ω_0 being a constant inversely proportional to the specific heat of the specimen. In order to render the Ettinghausen effect negligible, it is sufficient to use frequencies ω_1 and ω_2 such that $(\omega_1 + \omega_2)$ and $(\omega_1 - \omega_2) >> \omega_0$. In fact, the effect is negligible for frequencies above 5 Hz.

EMF's due to permanent and convective motions in the specimen.—At every point of the specimen, the mechanical force per unit volume in the case of two charge carriers is

$$F = (n_1\, e\, z_1\, v_1 + n_2\, e\, z_2\, v_2) \times B = J \times B$$

Any inhomogeneity of magnetic field or of current density, or of both, gives rise at each point to different densities of force which are not, as it is in solid specimens, balanced by internal stress. The fluid is set into motion. The boundary conditions imposed by the walls give rise to permanent or convection motions. The energy per unit volume and time dissipated in the fluid is equal to the product of F and the local fluid velocity v, *i.e.*, $v \cdot (J \times B)$. Even if the current density is not strictly uniform in the cell, one can suppose that, at each point, it is proportional to the total current passing through the cell, so that v at each point is proportional to I.

a. v has a constant direction (permanent motion). The power dissipated in the cell is proportional to I. These potential differences vary, in this case, linearly with I and B.

b. v varies from one point to another (convective motion). Williams (28) showed that the stray potential differences follow a law which is no longer linear, but a related one.

It is not easy to separate the Hall effect from the stray phenomena due to the liquid motions. Thus it becomes important to minimize these motions. In order to do so, one has to have the current density and magnetic field uniform across the whole cell and reduce the cell thickness to tens or, at most, hundreds of microns. Finally, using alternating current methods, one can reduce considerably the effects of the remaining causes of inhomogeneity.

EMF's due to the Hall probes.—When a current I_X passes through a sample and when there is no magnetic field, a potential difference appears due to the actual impossibility of placing the two probes on the same equipotential. For the cell in Fig. 1, the nonalignment voltage is

$$V_{NA} = I_X \, dl/\sigma \, b \, e$$

where dl is the lateral displacement of the probes, and σ the conductance of the cell. This voltage may be quite important (ranging about 1V in the less favorable cases) with regard to V_H; it is thus necessary to eliminate it. The method of the two frequencies eliminates this parasitic voltage, which depends only on ω_1. One must point out that, using alternating current and field, we can determine the sign of the Hall voltage by comparing its phase to that of a well-known sample. The method of the two frequencies eliminates the stray emf's that we have mentioned. However it produces at least two parasitic effects:

a. The voltage due to the existence of eddy currents in the cell. This is reduced by using a cell 10-100μ thick.

b. The voltage induced by the magnetic induction in the Hall probes

$$V_I = n \, (d\phi/dt)$$

where n is the number of loops (equal to one in this case), and

$$\phi = S \, B_0 \sin \omega_2 t$$

so that

$$V_1 = S \, B_0 \omega_2 \cos \omega_2 t$$

(S is the area of the wires in the direction of B). This voltage is great, as it may be equal to 1.2 volts, when $B = 1$ tesla, $S = 1$ cm^2, and $F = 74$ Hz. It can be considerably reduced by the introduction of another loop in which the flux creates a voltage opposite in phase to that of the probe loop. Residual voltage is compensated by a filtering device that is described later.

Hall Cell

The Hall cell should be parallelepiped-shaped so that the effect is theoretically interpretable and, as was shown by Isenberg, Russel, and Greene (29), five to six times longer than wide. As a matter of fact, let us suppose that the distribution of the electric current density is uniform in the X direction. If the sample is homogeneous, and if the magnetic induction is constant, the Hall field is uniform. But if the length cannot be regarded as great, the current distribution depends on the relative dimensions of the three sides, and on those of the electrodes, with regard to those of the parallelepiped. If the electrode has almost the same direction as the side, it short-circuits the Hall effect. This disadvantage can be reduced by using a sample four, five, or six times longer than wide or thick, and placing the Hall electrodes in the middle of the sample (see Fig. 2). On the other hand, in order to eliminate eddy currents, one must use a cell ten to hundreds microns thick.

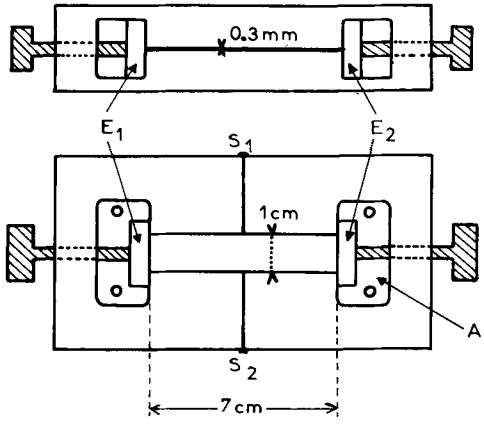

Fig. 2. Hall cell. S_1 and S_2 are Hall probes, E_1 and E_2 are current input electrodes, and A is the filling vessel.

Experimental Device

Measurement circuit.—The measurement circuit shown in Fig. 3 is made of four devices: (*a*) current generating device, (*b*) magnetic induction generating device, (c) device for separation and detection of the Hall voltage, and (*d*) device for measurement and exploitation of the various parameters.

Let us briefly recall the criteria they must obey:

(*i*) Current and magnetic induction are both alternating, with different frequencies, higher than 5 Hz, in order to eliminate the Nernst, Ettinghausen, Righi-Leduc, and nonalignment parasitic emf's.

(*ii*) Magnetic induction must be rigorously homogeneous, and the dimension of the air gap must be great with regard to those of the cell in order to avoid permanent and convective motions of the liquid.

(*iii*) The measurement must be made as quickly as possible in order to prevent the creation of concentration gradients and convective motions of the liquid.

(*iv*) Any vibrations must be carefully avoided.

(*v*) The installation should be placed in a room air conditioned at 20°C.

Current generating device.—The current sent into the cell is emitted by a function generator, as an undamped sine-wave or as a sine-wave-train, parallel or not to the magnetic induction. The characteristics of this device are:

band width ± 1% from 1 to 10,000 Hz
± 3% from 10 to 100 kHz
stability ± 0.5% of p-p amplitude
distortion: less than 0.02 for 1 kHz
amplifier gain: varying from 0 to 10
amplifier output: 40V p-p
0.05A for $0 \leq Z_s \leq 38$ ohms

Magnetic induction generating device.—The magnetic induction is produced by an alternating electromagnet whose poles are 14 cm long. The length of the air gap varies from 0.5 to 2.5 cm. It is placed in a resonant series circuit made of a power supply and a battery of condensers, and produces a maximum field of 12,000 gauss at 74.8 Hz and 17,000 gauss at 50 Hz, when the air gap is 2.5 cm long. More details about the design are to be found in Pich's thesis (30). The field is homogeneous to 10^{-4} on a surface greater than 100 cm^2 and in the whole air gap so that the electrolyte blade is entirely located in a homogeneous field.

Separation and detection device.—The problem is the extraction of a very small signal (about 10^{-7}V) of well-defined frequency drowned in a background noise and mixed with a set of parasitic signals of 10^7 times greater amplitude and of different frequencies. The filtering device is made of four different filters: rejection filter, band filter, high-pass filter, and low-pass

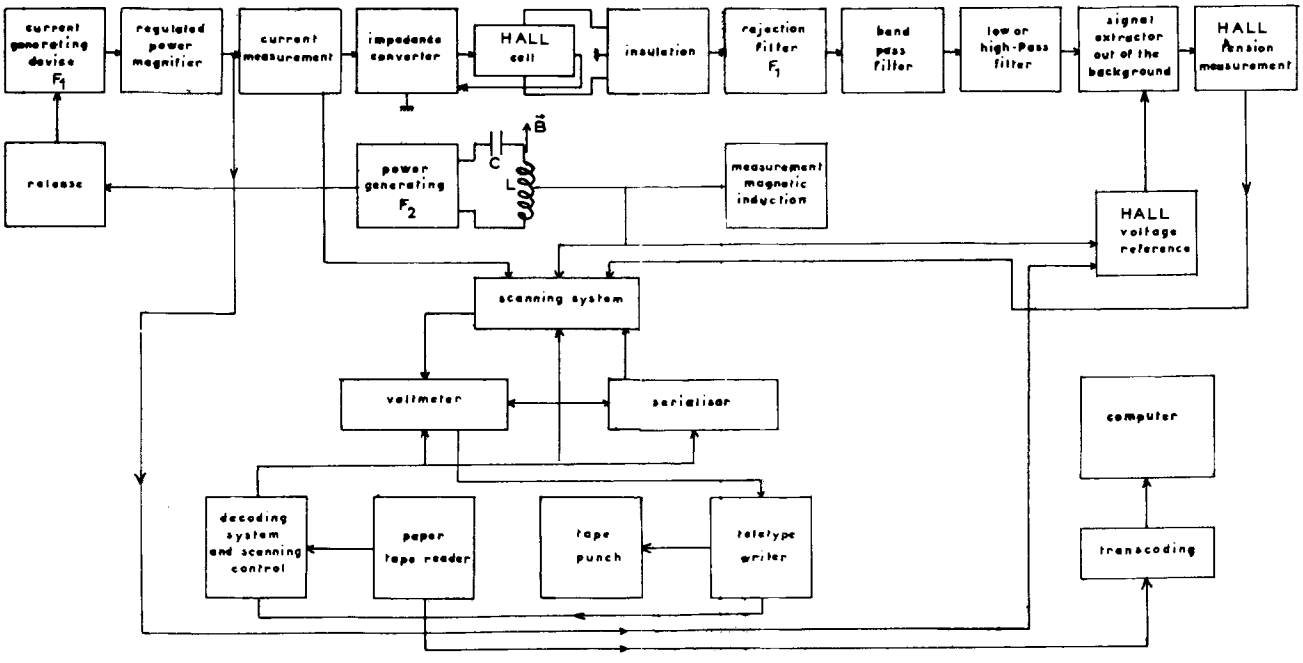

Fig. 3. General organizational chart

filter. This device has an almost instantaneous response time (31). The signal is amplified by a straight band amplifier whose gain varies from 10 to 10^4 with increments of 10. It is then sent to a waveform analyzer which uses an efficient sampling and averaging technique to extract repetitive waveforms from noise. The analyzer has a gain of 10, a time constant varying from 1 to 100 sec, and a band width at 1 db, varying from 1 to 12 Hz. The reference voltage controlling the analyzer is the same as the Hall voltage. The extracted signal is converted and entered into a data acquisition system in order to have a computer (IBM 1620) do the necessary computations. For a more detailed theory of the waveform analyzer, see Longevialle's thesis (32). To control the analyzer, one has to apply a reference voltage with the same frequency as the Hall voltage, the phase and amplitude having any values. It is produced by a Hall effect in a semiconductor submitted to the same magnetic induction and to the same current as the sample. This voltage is much greater than that in the electrolytes, and it is detected merely by a selective amplifier.

Device for measurement and evaluation of the various parameters.—Parameters to measure are: (*a*) electric current, (*b*) magnetic induction, (*c*) gain of the measurement circuit and (*d*) Hall voltage. A first measuring device supplies a constant reading of these values, while a second device records them in the computer.

Measuring device.—(*a*) Current.—As there is no ground in the circuit, measurement is made through an adaptation transformer with unity ratio whose secondary is closed by a resistance R.

$$I = U_R/R$$

U_R is the voltage at the terminals.

(*b*) Magnetic field.—It is measured in the vicinity of the cell with an extra flat coil of very small dimensions

$$B = 10^2\, U/f_2$$

where U is the voltage at the terminals of the coil, and f_2 is the magnetic induction frequency.

(*c*) Gain of the measuring circuit.—The reference voltage mentioned in the section on Separation and detection device is used for this measurement. This voltage is sent into a band filter and measured as U_E. Then it passes through a voltage divider reducing it to value U_S close to that of the Hall voltage. The gain is

$$G = U_S/U_E$$

(*d*) Hall tension.—The Hall signal from the detector is recorded by the first beam of a dual beam oscilloscope. The waveform analyzer ramp is represented by the second beam and both are synchronized by the reference frequency. The voltage is measured by a digital voltmeter after stopping the signal scanning and reading the value recorded in the detector memory.

Data input system.—It is performed with: (*a*) an analogue detector which scans the different beams; (*b*) a digital voltmeter which sequences the beams; (*c*) a serial recorder, which converts the digital voltmeter data in ASCII serial data; and (*d*) a teletypewriter, which includes a typewriter, a tape-reader, and a tape-punch. The reader controls data recording by means of a program tape. They appear in a format which is compatible with the computer.

Operating Technique and Experimental Results

Let us briefly describe the Hall cell.

Cell.—The cells are made of epoxy that can be tooled or moulded with very great precision. Measurement electrodes are platinum wires moulded in the epoxy so that only a small part of the wire is in contact with the electrolyte. The current input electrodes are plates of stainless steel; they cover the whole section of the measurement vessel (in order to assure a uniform current distribution); they can be moved and immersed in the vessel. They are connected to the opening so that the parallelepiped is perfectly defined. Another advantage of the vessel is that losses are prevented and that the electrolyte is isolated (Fig. 2).

Operation.—Choice of frequencies.—We used a current frequency of 303.4 Hz, which is high enough to avoid electrolysis and low enough to produce, together with the magnetic induction frequency of 74.4 Hz, a Hall voltage of 229 and 377.8 Hz which are the values of the Hall voltage frequency that make detection easier.

As a matter of fact, in the detection circuit, right after the impedance adapter, the Hall signal enters several active and passive filters. It is then necessary to have a maximum difference between the frequency of the Hall voltage and that of the nonalignment voltage (which is the same as the current's) in order to weaken as much as possible this parasitic voltage which is the most important one. Besides, by searching this maximum weakening, one eliminates the voltage induced by the induction in the Hall probes loop, as the induction frequency is more than two octaves higher than that of the current.

Electrolytes.—We used hydrochloric and nitric acid solutions whose concentrations c vary from 10^{-3} to 10^{-4} moles · liter^{-1}. The reproducibility of the results depends on the careful preparation of the solutions and on the filling of the cell. The solutions are prepared in a dust-free enclosure, air conditioned at 20°C, by volumetric titration from pure products dissolved in demineralized water whose resistivity is higher than 20 megohms/cm. The cells are cleaned by usual methods, carefully rinsed, and filled very slowly with a polyethylene syringe in order to avoid bubbles.

Adjustments on the measurement circuit.—Measurements are made at the 229 Hz frequency as the rejection rate of parasites is higher. One must set the rejection rate (remaining nonalignment tension must be higher than 100 mV), the magnetic induction (adjusting the no-load current conditions of the output tubes and various parameters of the power supply during the experiment in order to prevent any oscillation of the a-c electronic source), and the Hall frequency (by checking and, if necessary, adjusting the Hall frequency with respect to the reference frequency).

Experimental procedure.—For a given concentration, it is the following: the rinsed and filled cell is put on its stand and the gain is measured. Then the stand is put in the electromagnet air gap so that the cell is in the central area of magnetic induction. When the current and the induction are set to the desired value, the values of each of the parameters are recorded on tape.

Error calculations.—As $R_H = V_H \cdot d/IB$, the relative error is

$$\Delta R_H/R_H = \Delta V_H/V_H + \Delta d/d + \Delta I/I + \Delta B/B$$

The relative errors on V_H and I are of two kinds: errors of reading and of testing. For V_H both are equal to $2 \cdot 10^{-3}$. For I the testing error is negligible with respect to reading error (10^{-2}). The relative error of B is less than 10^{-2}, and that of d is 4/60, so that $\Delta R_H/R_H$ 13.10^{-2} for a given concentration.

Results

The analysis is made by two programs: one puts the experimental values in the requested format and units, and computes R_H for each measurement; the other calculates mean values and root mean squares for a given concentration, current, and induction.

The results are represented in Fig. 4 to 10 giving values of R_H (or V_H) as functions of B, I, c, and e after

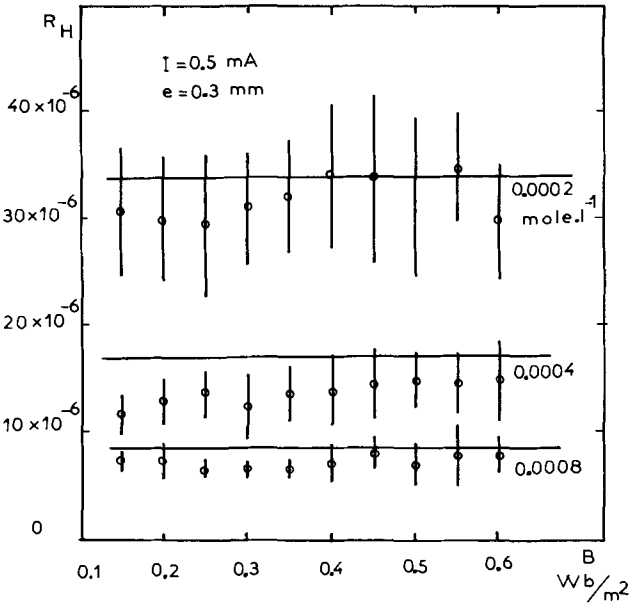

Fig. 5. Variation of R_H as a function of the magnetic field in HNO_3 solutions of various concentrations. Each point represents the mean value of R_H (obtained with 15 measurements). Each vertical bar is the root mean square. The horizontal line is obtained by Eq. [1], [2], and [3].

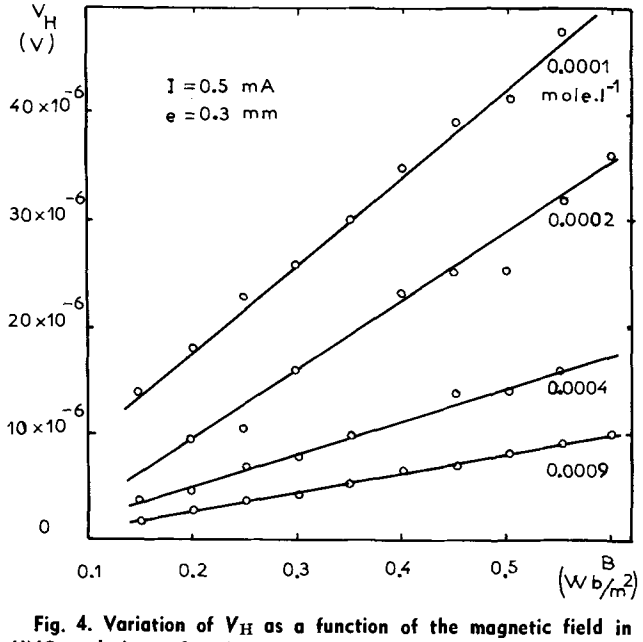

Fig. 4. Variation of V_H as a function of the magnetic field in HNO_3 solutions of various concentrations. Each point is a mean value. The line is best fit for the experimental results.

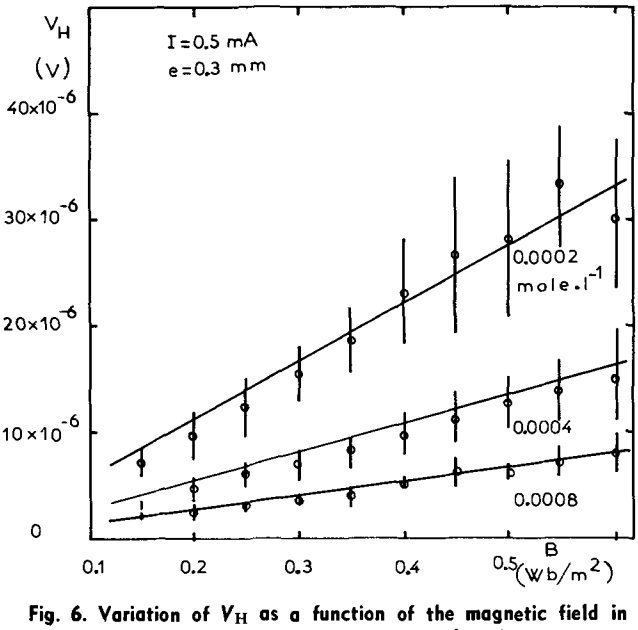

Fig. 6. Variation of V_H as a function of the magnetic field in HNO_3 solutions of various concentrations. Each point represents the mean value of V_H (obtained with 15 measurements). Each vertical bar is the root mean square. The lines are obtained from Eq. [1], [2], and [3].

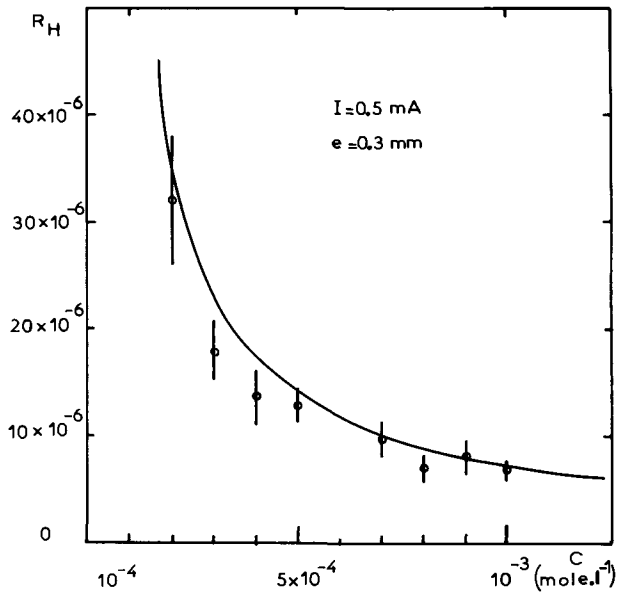

Fig. 7. Variation of R_H as a function of concentration in HNO_3 solutions, for a given d-c current intensity. Each point represents the mean value of R_H (obtained with 15 measurements). Each vertical bar is the root mean square. The curve is drawn according to Eq. [3].

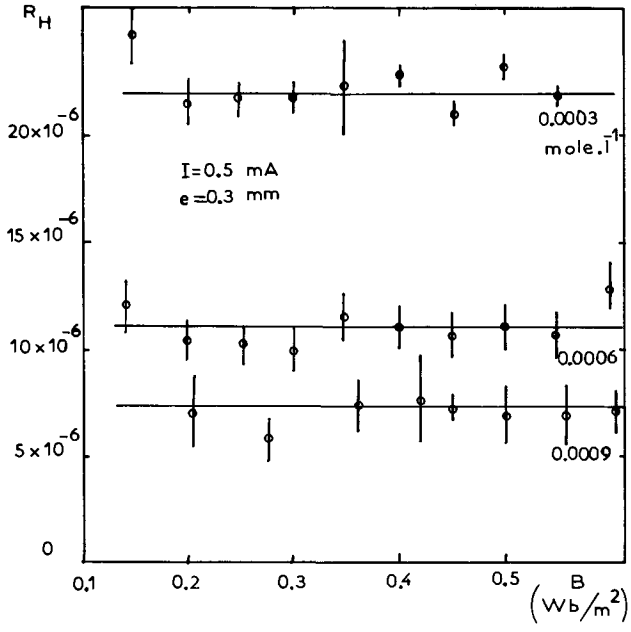

Fig. 9. Variation of R_H as a function of the magnetic field in HCl solutions of various concentrations. Each point represents the mean value of R_H (obtained with 15 measurements). Each vertical bar is the root mean square. The horizontal line is obtained from the relations [1], [2], and [3].

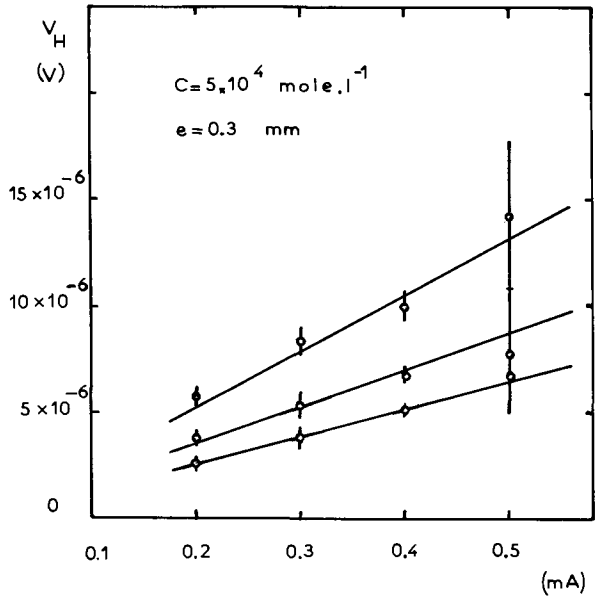

Fig. 8. Variation of V_H in terms of d-c current in HNO_3 solutions of constant concentration; magnetic field has different values. Each point represents the mean value of V_H. Each bar is the root mean square. Measurements were very difficult when the current was less than 0.5 mA, as it proved difficult to keep it constant. That is the reason why the measurements are less numerous than for $I = 0.5$ mA.

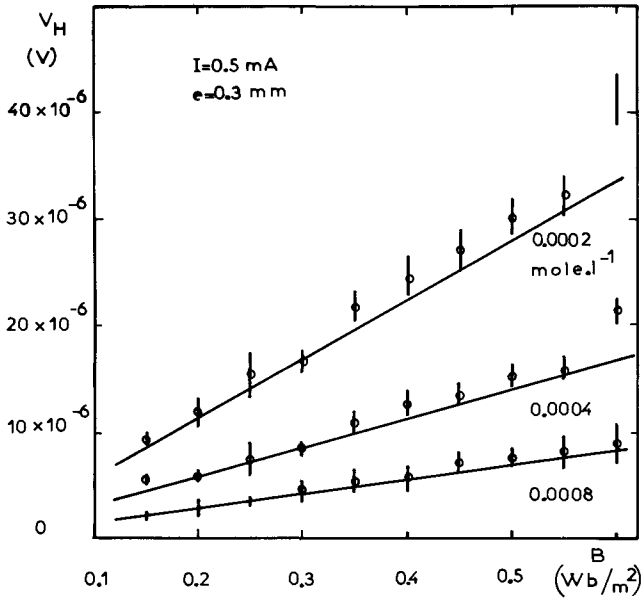

Fig. 10. Variation of V_H as a function of the magnetic field in HCl solutions of various concentrations. Each point represents the mean value of V_H (obtained with 15 measurements). Each vertical bar is the root mean square. The lines are drawn according to Eq. [1], [2], and [3].

about 3000 measurements. One can notice that, on the one hand, V_H is proportional to B and I to $1/c$. On the other hand, R_H has a constant value, as B varies, for fixed I and c. Despite the experimental difficulties, these results confirm that the device does measure the Hall effect in dilute electrolytic solutions, since as shown in Fig. 4-10, the theoretical lines are within the error limits calculated from experimental results.

We are now improving the device by increasing the gain and by using more sophisticated cells and a better filling system. We cannot yet interpret the results obtained because of the restricted concentration range of the limited number of electrolytes. However, the measurements that we are carrying out in acid, base, and neutral solutions, with concentrations between 10^{-4} and 10^{-2} mole · liter^{-1}, should allow us to increase our knowledge of the transport properties of dilute electrolytic solutions.

Manuscript submitted Oct, 7, 1970; revised manuscript received July 7, 1971.

Any discussion of this paper will appear in a Discussion Section to be published in the June 1972 JOURNAL.

REFERENCES
1. A. Roiti, *Rend. Accad. Linc.*, **12**, 397 (1882); *J. de Phys.*, **2**, 513 (1883).
2. H. Bagard, *Compt Rend de l'Acad. des Sci. Paris*, **122**, 77 (1896); *J. de Phys.*, **5**, 499 (1896), **7**, 426 (1898); *Eclair. Elect.*, **15**, 988 (1898).
3. F. Florio, *Nuov. Cim.*, **4**, 106 (1896), **6**, 108 (1897).
4. F. Chiavassa, *Nuov. Cim.*, **6**, 296 (1897).
5. P. Moretto, *ibid.*, **3**, 80 (1902).
6. R. Heilbrun, *Ann. der Phys.*, **15**, 988 (1904).
7. G. Delvalez, *J. de Phys.*, **8**, 360 (1909).
8. W. Voigt, *Gott. Nachr.*, 545 (1910).
9. F. G. Donnan, *Proc. Phys. Soc. London*, **16**, 244 (1898); *Phil. Mag.*, **46**, 465 (1898); *Nature*, **58**, 215 (1898).
10. C. H. Wind, *Versl. Kon. Akad. Amst.*, **3**, 82 (1894), **4**, 210 (1895).
11 J. Larmor, "Hall Effect in Electrolytes" Aether and Matter (1900).
12. A. E. Oxley, *Proc. Roy. Soc. London*, **A88**, 588 (1913).
13. A. M. Evseev, *Russ. J. Phys. Chem.*, **36** (7), 869 (1962).
14. Mme. Laforgue-Kantzer, *Electrochim. Acta*, **10**, 585 (1965).
15. E. Muller, *Trav. Mec. Ondul. Appl. Villeurbanne*, **2**, 1 (1967).
16. P. Mergault and J. Pages-Nelson, *Compt. Rend. Acad. Sci. Paris*, **269C**, 12 (1964).
17. Trancong Khan, *Trav. Mec. Ondul. Appl. Villeurbanne*, **3**, 1 (1967).
18. H. Wendhausen, *Z. Phys. Chemie N.F.*, **583**, 325 (1968).
19. W. Holzapfel, *ibid.*, **59**, 166 (1968).
20. E. Picard, Thesis, Paris (1965).
21. S. Naiditch *et al.*, Research and Development Progress Report No. 223 (1966), Office of Saline Water, U.S.A.
22. H. L. Friedman, *J. Chem. Phys.*, **69**, 462 (1965).
23. H. L. Friedman and A. Ben-Naim, *ibid.*, **48**, 120 (1968).
24. S. Harris and H. L. Friedman, *ibid.*, **50**, 765 (1969).
25. J. Pages-Nelson, *Ann. Phys.*, **4**, 447 (1969).
26. G. Morand *et al.*, *Compt. Rend. Acad. Sci. Paris*, **268**, 888 (1969).
27. O. Lindbergh, *Proc. I.R.E.*, **40**, 1414 (1952).
28. E. J. Williams, *Phil. Mag.*, **50**, 27 (1925).
29. I. Isenberg, B. R. Russel, and R. F. Greene, *Rev. Sci. Inst.*, **19**, 685 (1948).
30. M. Pich, Thesis, Paris (1970).
31. G. Morand *et al.*, *Compt. Rend. Acad. Sci. Paris*, **271**, 121 (1970).
32. C. Longevialle, Thesis, Paris (1970).

Technical Notes

Quinones as Rechargeable and Regenerable Battery Cathode Materials

H. Alt,[1] H. Binder, A. Köhling, and G. Sandstede

Battelle-Institut e.V., Frankfurt (Main), Germany

Organic cathode materials investigated in the past as depolarizers in batteries are reduced irreversibly and, therefore, can only be used in primary cells (1). Quinones and hydroquinones are, however, known to act as completely reversible redox couples, but most of the quinones are slightly soluble and partly unstable in electrolyte solutions (2). In order to test their stability electrochemically, we mixed the quinones with graphitized carbon in a weight ratio of 1:1. The powder was put between two graphite felt disks 1 cm^2 in surface area held together by two tantalum gauze strips in a Plexiglas holder. The open-circuit voltages measured in 2*N* H_2SO_4 are very close to the values of the redox potentials measured in alcoholic solutions. Diphenoquinones, which have a potential of about 950 mV (*vs.* NHE) do not have the required stability in aqueous electrolyte. Only tetrachloro-p-benzoquinone (Chloranil) and tetramethyl-p-benzochinone (Duroquinone) have been found to be sufficiently insoluble and completely stable. In 2*N* H_2SO_4 we measured open circuit potentials of 668 mV and 478 mV, respectively, whereas in 50% aqueous alcoholic solution equilibrium potentials of 664 mV and 480 mV have been found (2).[2]

In order to investigate the reversibility of the electrochemical reduction and oxidation a cyclic potentiodynamic current voltage curve was measured (Fig. 1), using chloranil as test substance. As the voltage decreases, the quinone is reduced to hydroquinone, and if the voltage increases the hydroquinone is oxidized. The two curves are symmetrical with respect to the open-circuit potential. The oxidation peak and the reduction peak are both very narrow, indicating that polarization is low. In addition the areas enclosed by the two curves and consequently the charges are equal, indicating that the reaction is completely reversible. The amount of charge transferred is consistent with that calculated from the quinone content, which points to a 100% utilization of the quinone. The cyclic potentiodynamic curve can be reproduced periodically; this suggests that there is no decrease in capacity, at least up to the, say, 50 cycles measured.

The galvanostatic discharge curve (Fig. 2) at a current density of 60 mA/cm^2 is almost horizontal up to a discharge depth of 80%, the polarization being as low as 40 mV. Even at a current density of 600 mA/cm^2 which corresponds to the extremely unusual discharge rate of 10C[3] there is no breakdown of the voltage. The chloranil cathode can also be heavily loaded at low temperatures (Fig. 3) without polarization increasing drastically.

High currents can also be drained in salt solutions. The open-circuit potential in zinc chloride solution is about 400 mV (*vs.* NHE) according to the pH of 4.8. In the case of ammonium chloride solution it is only 340 mV and thus is about 100 mV lower than the redox

[1] Present address: Farbwerke Hoechst, Frankfurt/Main-Höchst, Germany.

[2] The measured open circuit potentials are the equilibrium redox potentials of solid electrodes and do not change when the ratio quinone/hydroquinone changes as long as a small amount of the second phase is present.

Key words: cyclic voltammetry, rechargeable cathodes, regenerable cathodes, air cathodes, hydrogen peroxide cathodes, quinones.

[3] 1C corresponds to a 1 hr discharge rate (galvanostatic discharge of the theoretical Ahr-capacity in 1 hr). The unit of C is reciprocal with time so that 10C corresponds to 1/10 hr discharge rate.

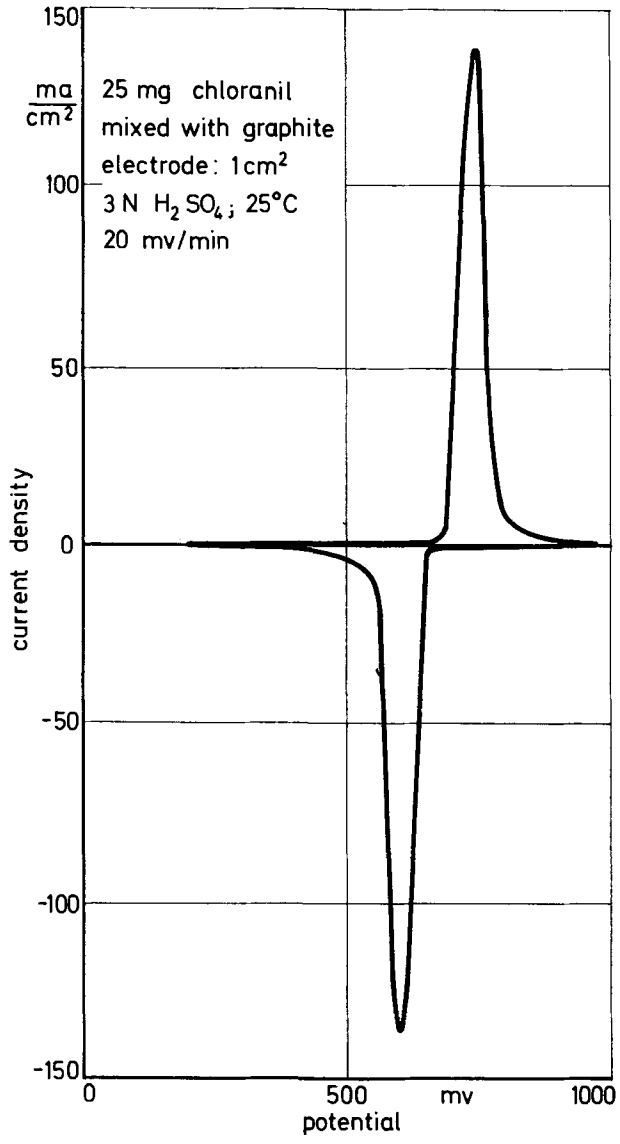

Fig. 1. Cyclic potentiodynamic curve of a chloranil electrode in dilute sulfuric acid.

potential (3) expected from the theoretical pH dependence.

Chloranil cannot only be recharged electrically but also regenerated chemically by means of hydrogen peroxide. Figure 4 shows the discharge curves of chloranil in dilute sulfuric acid after different regeneration times. After 5 min more than half of the capacity is regained. Regeneration with oxygen (air) may even be of greater importance. Normally, hydroquinone is not oxidized by oxygen, but if in contact with a catalytically active material it should be possible to oxidize hydroquinone to quinone with air or oxygen because the oxidation potential of oxygen is higher than that of benzoquinones. As active carbon is known to be capable of activating oxygen, we mixed chloranil and—in another investigation, duroquinone—with Norit BRX active carbon which is electrically conductive.

A hydrophobic electrode has to be produced from a mixture of this type because otherwise the air does not reach the hydroquinone. In order to carry out a simple test we used a hydrophobic fuel cell cathode as a support for the active mass. This cathode is made of BRX carbon and PTFE with a PTFE backing. The quinone/active carbon mixture was put on the electrolyte side of the electrode, which was then covered with a graphite felt disk. The discharge curve is as close to horizontal as for chloranil, polarization being very low (Fig. 5). The capacity is somewhat higher than expected from the amount of duroquinone used. This is due to the fact that the active carbon has a certain capacity because its surface can be partly oxidized. Of course, during the discharge measurements air was replaced by nitrogen.

With chloranil the recovery time was greater than in the case of duroquinone. These results suggest that the regeneration is governed by an electrochemical mechanism. As the active mass was not hydrophobic, the hydroquinone was oxidized anodically, the electrons flowing to the carbon of the supporting electrode where oxygen was cathodically reduced.[4] It seems possible to decrease the recovery time for air regeneration by developing suitable electrodes. Regeneration with air is also possible in salt solutions.

Besides their use as redox material in air cathodes for intermittent operation, quinones can also be used as active mass in secondary batteries. The theoretical energy density of two duroquinone/zinc couples (pH = 3) has been calculated:

duroquinone/SO_4^{2-}/Zn	175 Wh/kg
duroquinone/Cl^-/Zn	190 Wh/kg

These values compare favorably with the theoretical value of 165 Wh/kg for the lead battery. Moreover, relatively light materials can be selected for the construction of the organic active mass.

[4] According to the lower oxidation potential of duroquinone the potential difference between the "oxygen electrode" and the "quinone electrode" is higher than in the case of chloranil; therefore, the current flowing from the durohydroquinone to the carbon of the supporting electrode is higher and the recovery time is shorter than with chloranil.

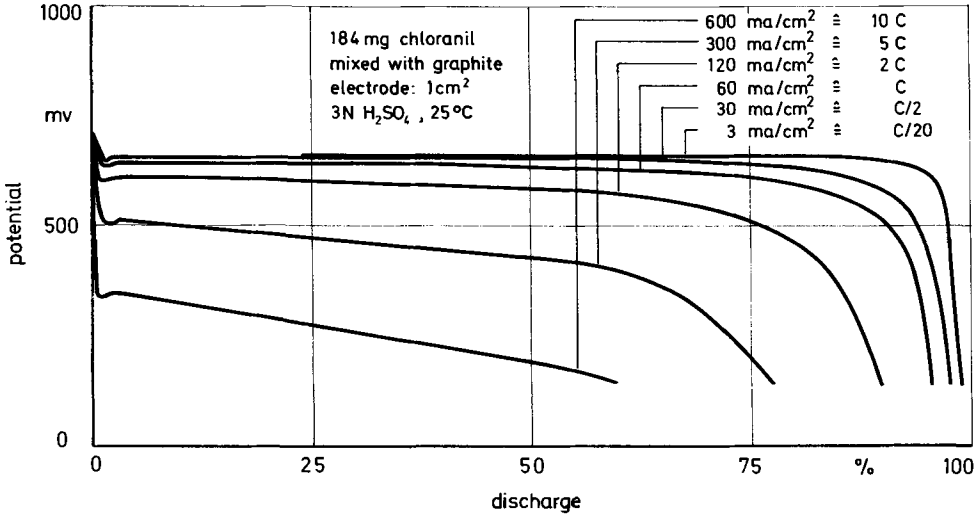

Fig. 2. Discharge curves of a chloranil cathode at different rates in dilute sulfuric acid.

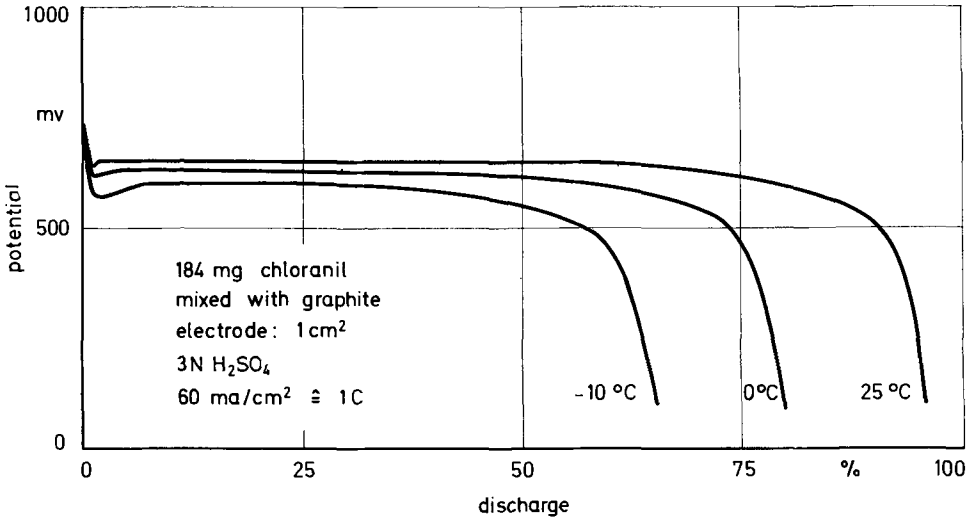

Fig. 3. Discharge curves of a chloranil cathode at different temperatures in dilute sulfuric acid.

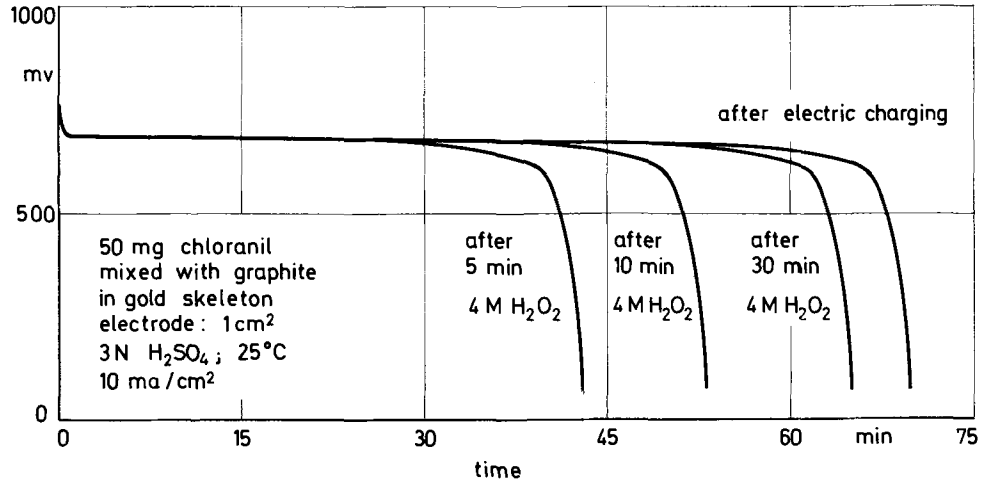

Fig. 4. Discharge curves of a chloranil cathode in dilute sulfuric acid after regeneration with H_2O_2.

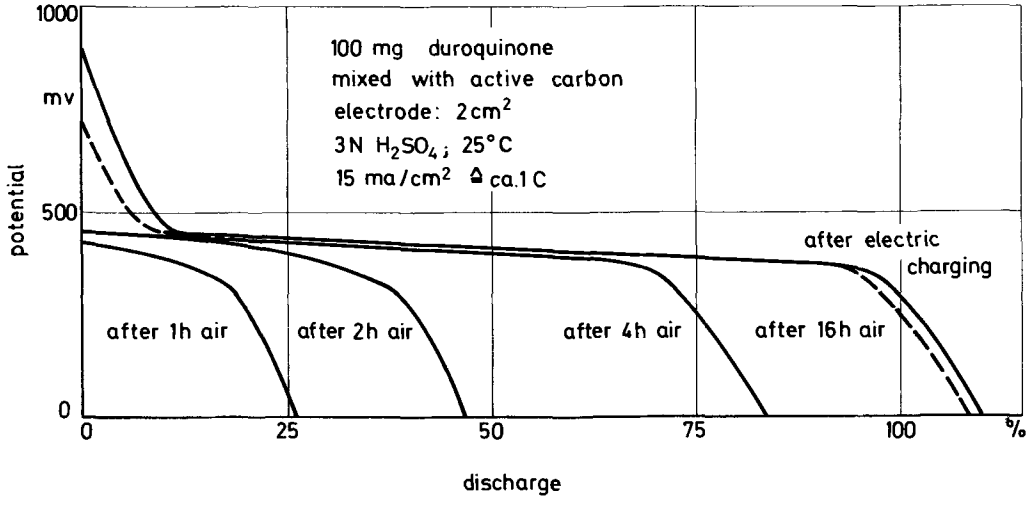

Fig. 5. Discharge curves of a duroquinone cathode in dilute sulfuric acid after regeneration with air.

It should also be noted that quinones are suitable materials for use as cathodes in high energy secondary batteries with organic electrolytes. Their performance is at least the same as that of heavy metal halides; some representatives are still superior because of their insolubility. With the lithium/chloranil couple in propylen carbonate we measured an open-circuit voltage of 3.3V which dropped to 2.6V after 85% discharge. Complete recharge was possible (3). Polymeric quinones should even be better suited because of their higher capacity and complete insolubility.

Manuscript submitted May 17, 1971; revised manuscript received *ca.* Aug. 20, 1971.

Any discussion of this paper will appear in a Discussion Section to be published in the June 1972 JOURNAL.

REFERENCES

1. E. Voss, *Chem. Ing. Tech.*, **42**, 199 (1970).

2. W. M. Clark, "Oxidation-Reduction Potentials of Organic Systems," Williams & Wilkens Co., Baltimore (1960).
3. H. Alt, H. Binder, A. Köhling, and G. Sandstede, Paper presented at the meeting of the Comité International de Thermodynamique et de Cinétique Electrochemiques (CITCE), Prague, Sept. 1970; Extended Abstracts, p. 319.

Adsorption of Cadmium Ions from KOH Solution at a Platinum Electrode[1]

S. Gilman*

Power Sources Division, Electronic Components Laboratory, U. S. Army Electronics Command, Fort Monmouth, New Jersey 07703

and L. D. Sangermano

General Electric Company, Schenectady, New York 12300

Wagner (1) noted the degradation of the platinum-catalyzed oxygen electrode in an experimental cadmium-air battery cell and suggested that the effect might be due to the adsorption of cadmium ions. In this study we verified the degradation effect and made some evaluation of the nature and extent of the adsorption process responsible for the degradation.

Experimental

Voltammetric measurements were made using the electronic equipment described previously (2). Measurements were made in either Cell I or II. Cell I was fabricated of Pyrex glass and was preferred for convenience of use and provision for controlled mechanical stirring. It comprised a main compartment holding 200 cc of solution in which was immersed electrode A or B, and a glass stirrer. The main compartment was separated from the counterelectrode compartment by means of a porous glass disk and from the reference electrode compartment by means of a Luggin capillary and a closed glass stopcock. The counter and reference electrodes were platinized platinum foils and a stream of pure hydrogen gas was allowed to impinge upon the reference electrode surface. Test electrodes A and B were prepared by annealing lengths of 0.030 in. diameter C.P. grade platinum wire and sealing into glass tubing. The geometric areas of electrodes A and B were 0.43 and 0.16 cm^2, respectively.

Cell II was designed so that the electrolyte would not be contacted by any material other than platinum (and less than 0.1 cm^2 of PTFE insulation for the test electrode). A small smooth platinum crucible served as both the counterelectrode and the container for the electrolyte. The test electrode was a length of 0.030 in. C.P. grade platinum wire annealed in a hydrogen flame and encased in heat-shrinkable PTFE tubing, exposing 0.21 cm^2 of geometric area. The reference electrode was a length of 0.1 in. ID platinum tubing platinized at the end immersed in the electrolyte and through which was passed a slow stream of a 1% hydrogen, 99% argon gas mixture. Gas flow was discontinued before making a measurement if a quiescent solution was desired, or continued if stirring was desired. The reference electrode potential (as measured against a conventional hydrogen electrode was found to be highly reproducible and stable. Calculations revealed that the charge associated with the oxidation of hydrogen from the approximately 10^{-5}M solution of hydrogen gas (resulting from use of the dilute hydrogen reference electrode) was negligible and could contribute no significant error to the measured adsorption charges. The platinum crucible was enclosed in a gas-tight quartz vessel provided with a tapered ground quartz cap which served as the electrode support. A second interchangeable cap held a reference electrode and a large platinized gettering electrode (2). For cleanup purposes, the getter electrode was alternatively driven to oxygen evolution, hydrogen evolution and back to oxygen evolution potentials in a portion of electrolyte, and then quickly transferred to the test vessel with the protection of the anodic film (2). The potential was then adjusted to 0.06V and stirring was provided by the reference gas jet.

The 1*N* KOH electrolyte was prepared using A.R. grade KOH pellets and triply-distilled water degassed by sparging with a steam of pure helium for over an hour. The solution was prepared in a platinum evaporating dish under a helium atmosphere in a glove box. Cell II was opened (for electrolyte transfers and gettering) only in the glove box. When required, cadmium ions were added to the KOH solutions by introducing sufficient 0.01M cadmium perchlorate to make the solution 10^{-4}M and then allowing at least several hours for excess cadmium perchlorate to precipitate out.

Both Cells I and II were thermostated at 30°C in an air bath. All potentials are referenced to that of a reversible hydrogen electrode in equilibrium with 1 atm of hydrogen in 1*N* KOH.

Results and Discussion

Polarization curves for oxygen reduction.—These experiments were performed in Cell I using electrode A. The electrode potential was programmed as previously (2) to regenerate a clean and reproducible surface. In the experiment of Fig. 1, after the anodic pretreatment at 1.8 and 1.2V, the surface was reduced and exposed to possible adsorption of cadmium ions at potential U for a time τ. The polarization curves were measured by applying a positive-going potential sweep (speed, 0.1 V/sec) and measuring the resulting current. Pure oxygen was kept bubbling through the electrolyte with additional vigorous stirring by means of the glass stirrer.

In the absence of dissolved cadmium, a single polarization curve was obtained for values of U between 0.1 and 0.5V and for values of τ between 0.1 and 1000 sec (*viz.*, 10 sec trace on rhs of Fig. 1a). That curve exhibits strong dependence of current upon potential in the fractional milliampere current density range. A diffusional influence (curvature toward the voltage axis) is apparent at higher current densities. An oscillatory limiting current dependent on the rotational speed of the stirrer (the average limiting current for the conditions of Fig. 1 is given by the horizontal dashed lines) is assumed to be diffusion-limited. In the presence of

* Electrochemical Society Active Member.
[1] The experimental portion of this work was performed at the NASA Electronics Research Center, Cambridge, Massachusetts.
Key words: ion adsorption, cadmium, platinum.

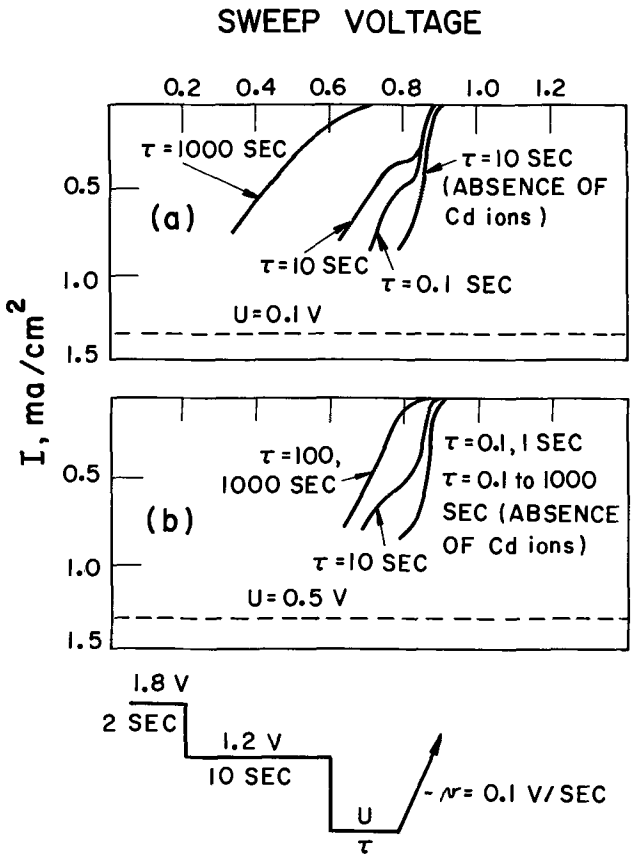

Fig. 1. Polarization curves for electroreduction of oxygen in 1N KOH solution. The polarization curves were measured by applying a linear-potential-time sweep after the indicated electrode pretreatment. The dashed curve was obtained in the absence of cadmium ions for $U = 0.1$ to 0.5V and $\tau = 0.1$ to 1000 sec. The solid curves were obtained after the solution was saturated with cadmium ions. Electrode A was used in Cell 1. The oxygen-saturated solution was mechanically stirred.

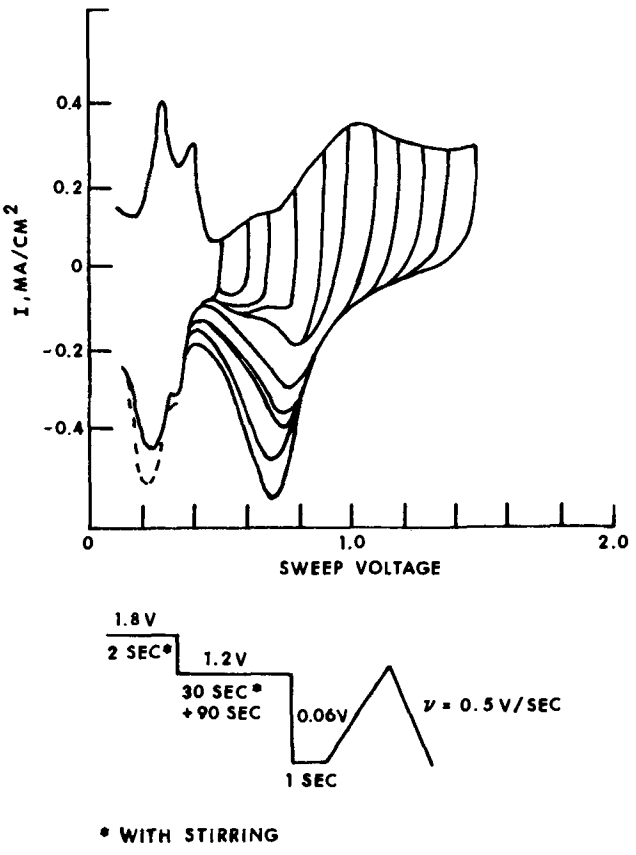

Fig. 2. Current-voltage curves measured during application of a linear potential-time sweep. The 1N KOH solution was degassed with argon and the traces measured by applying triangular sweeps (different amplitudes) after the indicated pretreatment.

dissolved cadmium, polarization increased with decreasing U and increasing τ. Intermediate curves exhibit an inflection at current densities well below the diffusion limit. The inflection may mark a transition between reduction of oxygen to peroxide and to water, as observed on some catalysts other than Pt [*e.g.*, Au, Ref. (3)]. Retardation of oxygen reduction kinetics by metal ions, notably the alkaline ions in acid solution, has been observed by several investigators (4-6).

Reference surface state of a platinum electrode.—The surface state of a Pt electrode in KOH solution may be probed conveniently through application of a linear potential-time sweep. In the experiment of Fig. 2, the potential sweep was applied after anodic treatment of the electrode followed by reduction for 1 sec at 0.06V. Stirring was discontinued during the latter part of the pretreatment to minimize convective diffusion of impurities to the electrode. A complete discussion of the pretreatment scheme appears in Ref. (2). The trace obtained during the sweep of 1.5V is rather similar to that obtained in acid electrolytes (7). Two closely spaced maxima appear during the anodic sweep to approximately 0.4V. Virtually the mirror image of this portion of the trace was obtained during the cathodic sweep to complete the similarity to the hydrogen adsorption region observed in acid electrolytes (7). Above approximately 0.8V, as in acid solutions, there is a very broad oxidation wave terminating in oxygen gas evolution above approximately 1.6V. The corresponding reduction process occurs at markedly lower potentials (peak at 0.7V) and by analogy to the acid electrolyte system, may be assigned to reduction of a film (adsorbed oxygen or oxide precursor) formed during the anodic sweep. Unlike the situation in acid electrolytes, there is no double layer region at potentials intermediate between hydrogen and oxygen adsorption during the positive going sweep. Approximately symmetrical cathodic currents (above the hydrogen adsorption region) may be obtained if the sweep is interrupted at potentials below 0.8V. These currents may correspond to those occurring to a much smaller extent (between approximately 0.6 and 0.8V) in acid solutions and ascribed by Böld and Breiter (8) to hydroxyl radical adsorption.

The effect of electrode pretreatment on the anodic sweep trace, was explored in the experiments of Fig. 3. The potential sequence used was based on the principles previously (2) formulated for acid electrolytes. Employing that sequence, it was found that any particular trace usually could be reproduced to better than 1% on the current axis. From Fig. 3 it is evident that the traces stabilize sometime between 10 and 100 sec. Two mechanisms could account for the time variations: adsorption of impurities from solution; and slow reduction of the surface. To test for the first possibility, the experiments were repeated with stirring and no effect was observed. This would seem to rule out a transport-limited impurity adsorption. In a second test, an attempt was made to getter impurities on a large area platinized platinum gauze electrode held at 0.06V overnight. No effect of gettering was observed, arguing against the possibility of activation-controlled adsorption of impurities.

In support of the second possibility for time-dependence of the electrode surface state, an exponentially decaying reduction current could be measured, where the current remained greater than 0.01 mA/cm² for several seconds. Additional evidence that the variations of Fig. 3 correspond to slow reduction of the sur-

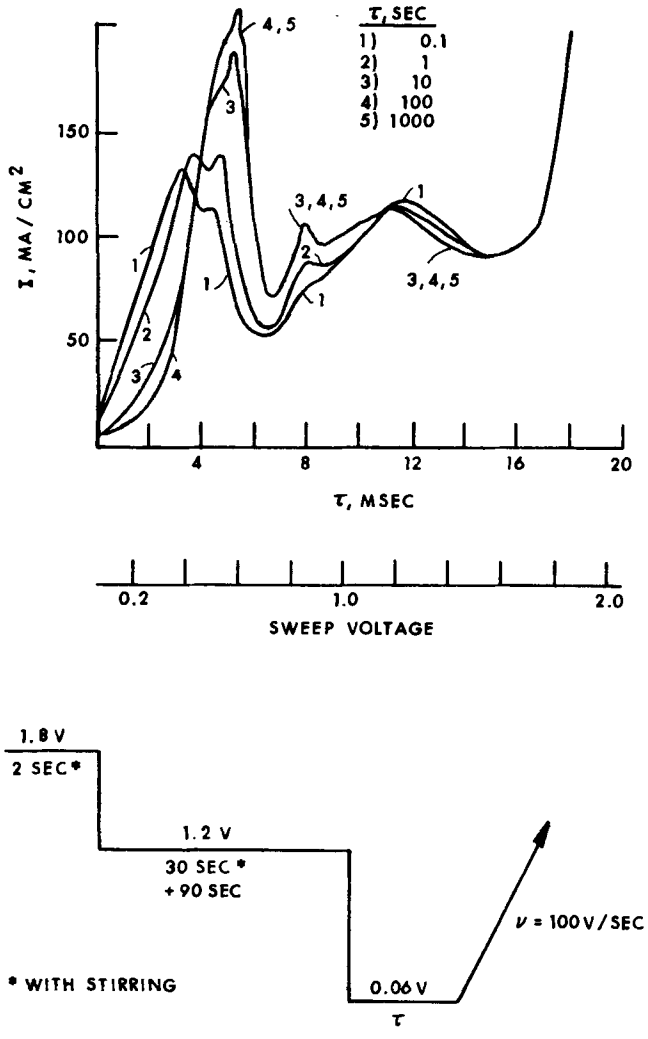

Fig. 3. Time-dependence of the trace obtained during application of a linear anodic sweep. The experiment was performed in Cell II with the solution degassed with an argon-H_2 mixture.

face, was obtained through measurement of the anodic and cathodic charges in the hydrogen adsorption region. The traces were measured as in Fig. 2 with the potential sweep extending from 0.06 to 0.5V. The time, τ, at 0.06V was the variable and the charges, Q, were obtained by integrating the total area under the traces, using a planimeter. The anodic and cathodic charges (corresponding mainly to hydrogen dissolution and deposition, respectively) are plotted against τ in Fig. 4. It can be seen that after approximately 10 sec, Q reaches a value that is (within a few per cent average deviation) independent of the direction of the potential sweep and of stirring. At shorter times, the anodic charge decreases and the cathodic charge increases, as would be expected if there were a concomitant reduction (of the surface) process during τ. If the time effect were due instead to adsorption of an impurity, it would be expected that both the anodic and cathodic values of Q would decrease with increasing τ. It may be noted that the time effects of Fig. 3 are most striking in the hydrogen region where there is a tendency for the waves to shift to more anodic potentials with increasing τ. The effect is less marked at lower values of the sweep speed, indicating that the effect on hydrogen adsorption is partly a kinetic one.

Although impurity effects are not indicated by the experiments of Fig. 3, such effects were encountered in some of our other experiments. Stirring-dependent decreases of currents in the hydrogen region and increases of currents in the oxygen region similar to those encountered in unpurified acid solutions (2) were observed when experiments were performed with some exposure of the electrolyte to the atmosphere. If carbon dioxide (or carbonate) does not adsorb from alkaline solutions as reported by Podlovchenko *et al.* (9) then it appears likely that other organic substances in the air may be troublesome.

The effect of glass as a contaminant was tested by adding crushed Pyrex glass to the Pt crucible of Cell II. A small but noticeable effect of glass was evident after only 10 sec.

Hydrogen adsorption:—Assuming that the anodic and cathodic waves (Fig. 2) obtained below 0.5V correspond to dissolution and deposition of hydrogen atoms, we may estimate the charge ${}_sQ_H$, corresponding to monolayer coverage of the surface with hydrogen atoms, as in acid electrolytes (2), from the cathodic sweep trace. For electrode B, ${}_sQ_H = 0.28$ millicoulomb/cm² suggesting a roughness factor of 1.3 if we assume (2) ${}_sQ_H = 0.21$ millicoulomb/cm² corresponds to R.F. = 1.

Adsorption of cadmium ions:—Our solutions of cadmium ions were obtained by allowing the hydrolysis of an excess of neutral cadmium perchlorate solution to come to equilibrium in 1N KOH at 30°C. Under

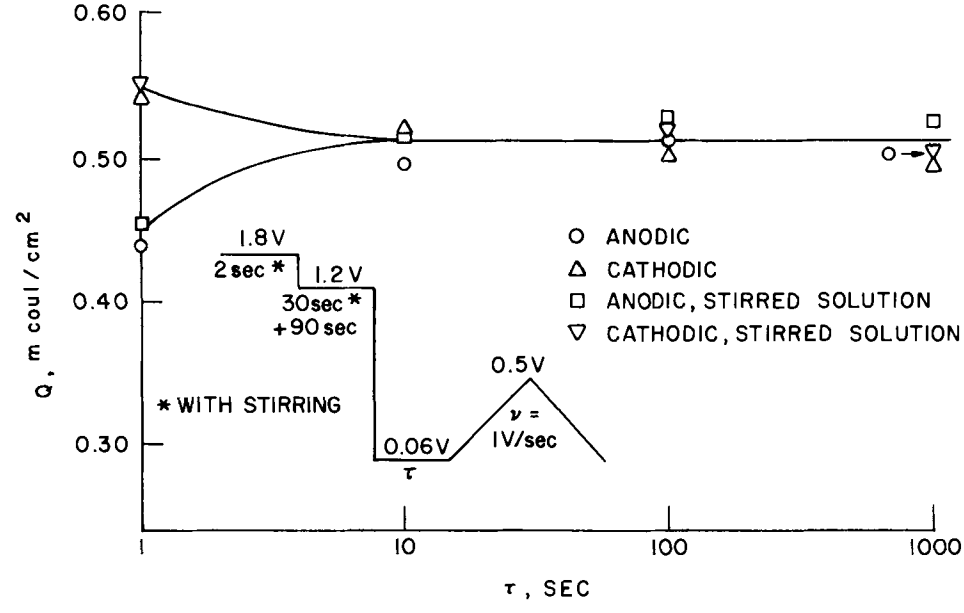

Fig. 4. Dependence of the anodic and cathodic charges in the hydrogen adsorption region upon the reduction time interval.

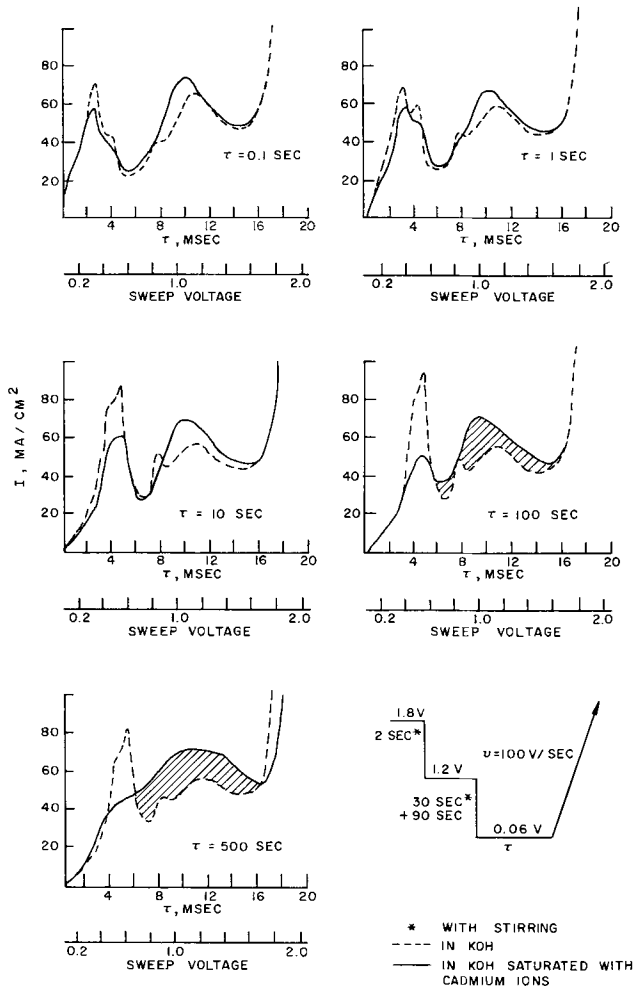

Fig. 5. Time-dependence of the trace obtained during application of a linear anodic sweep in the presence and absence of dissolved cadmium ions.

these conditions (but 5° lower in temperature) the total concentration of bivalent cadmium should be 8 x 10^{-6}M according to Visco and Sonner (10) or 5 x 10^{-6}M according to Ryan *et al.* (11).

The potential sequence of Fig. 5 was selected to determine the effect of cadmium ions on the anodic sweep trace. As shown above, a highly reproducible surface is generated during reduction of the surface at 0.06V, although complete reduction of the surface is not accomplished for $\tau > \sim 10$ sec. Adsorption of cadmium occurs on the freshly (or partially) reduced surface before application of the potential sweep. A high (v = 100 V/sec) value of the sweep speed was chosen so that the adsorption of cadmium ions during the sweep was negligible. The dashed traces were obtained in 1*N* KOH in the absence of cadmium and the solid traces were obtained after addition of cadmium. It is apparent that cadmium ions cause a decrease in hydrogen adsorption and an increase in the charge flowing in the "oxygen adsorption" region. Similar observations were made by Breiter (12) and by Bowles (13) for acid solutions containing copper and thallium ions, respectively. The decrease in hydrogen adsorption may be attributed to blockage of hydrogen adsorption sites by adsorbed cadmium. The increase, Q_{Cd}, of charge at more anodic potentials must correspond to the oxidation of zero (adsorbed cadmium atoms) or monovalent (adsorbed cadmous ions) cadmium to dissolved bivalent cadmium. The present experiments cannot distinguish between these two possibilities, but there is evidence in support of the corresponding adatom adsorption for copper (12) and thallium (13). For adsorption at 0.06V, it is apparent from Fig. 5 that separation of Q_H (charge corresponding to hydrogen adsorption) from Q_{Cd} becomes difficult at large values of τ. This introduces uncertainty only for adsorption potentials $< \sim$ 0.4V where hydrogen coverages are appreciable. Values of Q_{Cd} were approximated at the lower adsorption potentials by integrating from the point at which the traces intersected for the cadmium-containing and cadmium-free solutions (shaded area in Fig. 5).

Values of Q_{Cd} obtained over a wide range of adsorption potentials and apparent steady state at τ = 1000 sec, appear in Fig. 6. For $U > 0.45$V, it was necessary to prereduce the surface briefly at 0.3V as shown. If we make the tentative assumption that cadmium adsorbs as the adatom and that one cadmium adatom occupies one hydrogen adsorption site, then a monolayer of cadmium adatoms would correspond to $Q_{Cd} = 2\ sQ_H$ or 2 x 0.28 = 0.56 millicoulomb/cm². By that criterion, fractional surface coverage, θ_{Cd}, ranges from 0.25 to 0.2 over the range U = 0.1 to 0.7. At the low potential end, the coverage rises steeply as we approach the reversible potential [approximately —0.05V, according to Ref. (14)] for cadmium metal deposition. At the high potential end, θ_{Cd} drops gradually to 0 as we approach 1.2V.

Interpretation of the Q_{Cd} *vs.* U plot of Fig. 6 is difficult because of the complexity of the equilibria between the dissolved ions and because of the interactions of the Pt electrode with the electrolyte in the absence of cadmium ions. Bivalent cadmium might be present as $Cd(OH)_2$, $Cd(OH)_{3-}$, and $Cd(OH)_{4--}$ in alkaline solutions. Ryan *et al.* (11) have suggested that

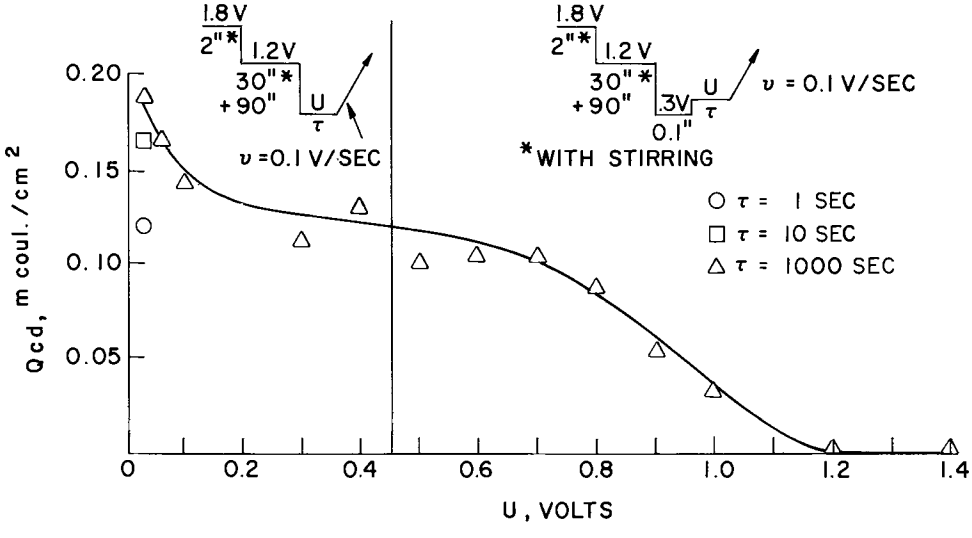

Fig. 6. Dependence of the charge equivalent of adsorbed cadmium upon the potential.

$Cd(OH)_3^-$ and $Cd(OH)_4^{--}$ predominate for OH^- concentrations greater than 0.5*N* while Visco and Sonner (10) argue that $Cd(OH)_4^{--}$ is not encountered even in 15*N* KOH. Adsorption of either negative ion at the original valence would be expected to start near the zpc (zero point of charge) here estimated at 0.72V [based on zpc = −0.11 *vs.* N.H.E. at pH 11.2, Ref. (15)] and to increase with increasing potential. The reverse dependence of Q_{Cd} upon U was actually found. Adsorption as the neutral atom might be expected to yield a semilogarithmic or linear (if heat of adsorption decreases with coverage) dependence of Q_{Cd} upon U. This may be reflected at the low and high potential ends of Fig. 6. The arrest at intermediate potentials may be due to a tendency to form a surface alloy of fixed composition. The decline of Q_{Cd} at high potentials may alternatively reflect a competition with anodic film formation.

Cadmium ion adsorption and electroreduction of oxygen.—From Fig. 6 we see that $Q_{Cd} = 0$ for $U > 1.2$V and hence Cd ion adsorption ought not to affect a platinum-catalyzed oxygen electrode operating near the reversible potential (1.23V). However, practical oxygen electrodes tend to operate at 0.9V or less, as in Wagner's experiment (1). Beginning at 0.9V, in the presence of dissolved cadmium, θ_{Cd} would tend to rise toward the intermediate value reflected by Q_{Cd} in Fig. 6. That coverage would cause a drop in voltage (increase in oxygen overvoltage) and an increased tendency to adsorb cadmium ions until the highest values of Q_{Cd} and the potential of the counterelectrode is reached. This was actually observed in a laboratory cadmium-oxygen battery cell (1).

Manuscript submitted April 22, 1971; revised manuscript received Aug. 17, 1971.

Any discussion of this paper will appear in a Discussion Section to be published in the June 1972 JOURNAL.

REFERENCES

1. O. C. Wagner, *This Journal*, **116**, 693 (1969).
2. S. Gilman, *J. Phys. Chem.*, **67**, 78 (1963).
3. R. Jasinski, *Advan. Chem.*, **47**, 95 (1965).
4. A. Kozawa, *J. Electroanal. Chem.*, **8**, 20 (1964).
5. L. Myuller and V. V. Sobol, *Elektrokhimiya*, **1**, 111 (1965).
6. N. A. Balashova and M. I. Kulezneva, *ibid.*, **1**, 155 (1965).
7. S. Gilman, Chapter in "Advances in Electroanalytical Chemistry," Vol. II, A. Bard, Editor, Marcel Dekker, Inc., New York (1967).
8. W. Böld and M. W. Breiter, *Electrochim. Acta*, **5**, 145 (1961).
9. B. I. Podlovchenko, V. F. Stennin, and A. A. Ekibaeva, *Soviet Electrochem.*, **4**, 1237 (1968).
10. R. F. Visco and R. H. Sonner, Abs. 7, p. 18, Electrochem. Soc. Extended Abstracts, Detroit, Oct. 5-9, 1969.
11. D. E. Ryan, J. R. Dean, and R. M. Cassidy, *Can. J. Chem.*, **43**, 999 (1965).
12. M. W. Breiter, *This Journal*, **114**, 1125 (1967).
13. B. J. Bowles, *Electrochim. Acta*, **10**, 717, 731 (1965).
14. Marcel Pourbaix, "Atlas of Electrochemical Equilibria," p. 417, Pergamon Press, New York (1966).
15. E. Gileadi, S. D. Argade, and J. O'M. Bockris, *J. Phys. Chem.*, **70**, 2044 (1966).

Mass Transfer to a Rough Rotating Cylinder

R. Kappesser, I. Cornet,* and R. Greif

Department of Mechanical Engineering, University of California, Berkeley, California 94720

There have been numerous studies of mass transfer to rotating cylinders. In particular, Eisenberg, Tobias, and Wilke (1, 2) reported that the experimental results for mass transfer in turbulent flow may be correlated by

$$Sh = 0.079\,Re^{0.70}\,Sc^{0.356} \qquad [1]$$

This result is in agreement with other studies of heat and mass transfer to rotating cylinders (3-12). Note that the mass transfer to smooth rotating cylinders is proportional to the angular velocity raised to the 0.7 power.

Theodorsen and Regier determined the friction factor for a smooth rotating cylinder in turbulent flow and the results were given by (13)

$$1/\sqrt{f/2} = -17.5 + 5.75\log_{10}(Re\sqrt{f/2}) \qquad [2]$$

This may be accurately approximated over a range of Reynolds numbers between 200 and 200,000 by the relation (1, 2)

$$f/2 = 0.079\,Re^{-0.30} \qquad [3]$$

which, when used with Eq. [1], results in a modified Chilton-Colburn relation of the form

$$Sh = (f/2)\,Re\,Sc^{0.356} \qquad [4]$$

Makrides, Hackerman, King, and others (14-16) report that the mass transfer varies linearly with the angular velocity in certain cases of cylinder dissolution. Makrides and Hackerman (14) consider this result to be due to the cylinders becoming rough during dissolution. This results in a friction factor which is independent of the angular velocity for values of the Reynolds number greater than a "critical Reynolds number," Re_{crit} (13). This value is obtained from the following approximate relation

$$Re_{crit} = (11.8\,d/\epsilon)^{1.18} \qquad [5]$$

where d is the cylinder diameter and ϵ is the characteristic roughness dimension. For Reynolds numbers greater than this Re_{crit}, the friction factor was estimated to be given by

$$f/2 = (1.25 + 5.76\log_{10} d/\epsilon)^{-2} \qquad [6]$$

Thus, from Eq. [4] and [6], Makrides and Hackerman obtained (14), for the case of dissolving cylinders at Reynolds numbers greater than Re_{crit}

$$Sh/Re\,Sc^{0.356} = f/2 = (1.25 + 5.76\log_{10} d/\epsilon)^{-2} \qquad [7]$$

Their experimental data was in agreement with Eq. [7].

Makrides and Hackerman (14) were the first to recognize and explain the important phenomena discussed above. However, we note that their use of a dissolving surface does introduce time variations in the surface roughness. This, coupled with the nonuniformity of the surface, makes it difficult to characterize the scale of the surface roughness.

Because of these considerations as well as the desire to extend the applicability of their results to a wide range of Reynolds numbers and roughnesses, we utilized another mass transfer system to study this prob-

* Electrochemical Society Active Member.

Key words: friction factor, surface roughness, oxygen reduction, turbulent flow.

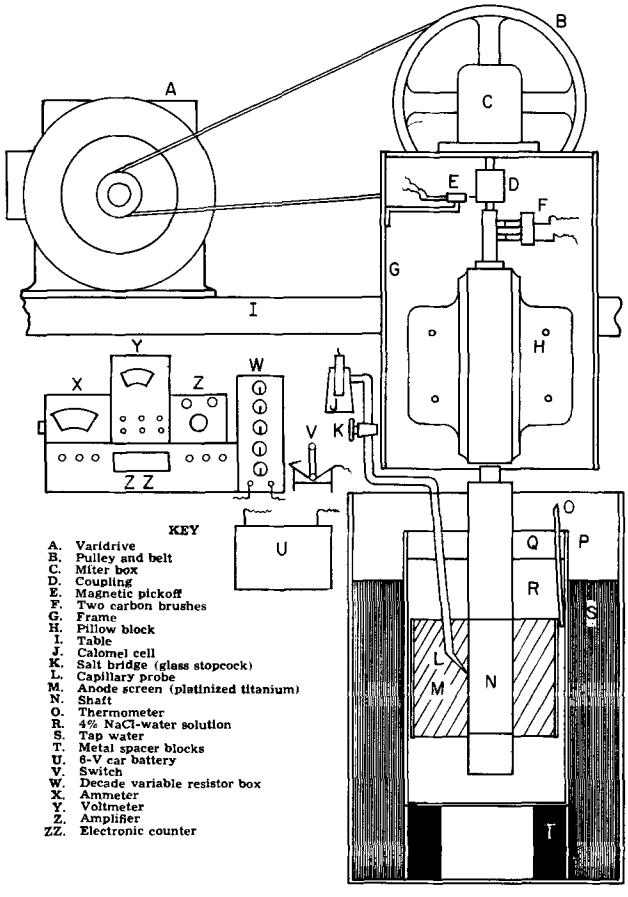

Fig. 1. Apparatus schematic

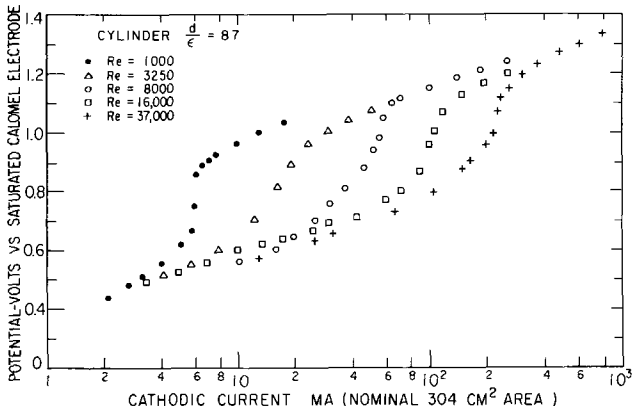

Fig. 2. Representative polarization curves

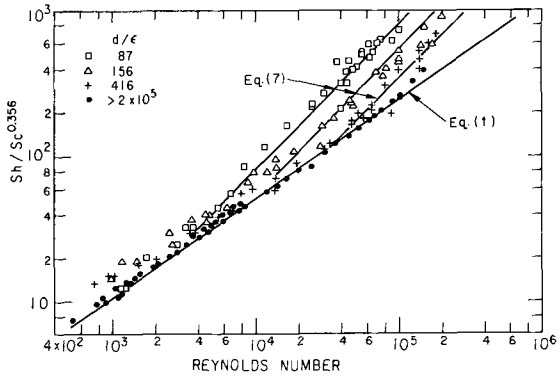

Fig. 3. Mass transfer vs. Re

lem. Briefly, the apparatus (Fig. 1) consisted of an instrumented vertically mounted nondissolving cylinder that was rotated in an oxygenated 4% NaCl-H_2O solution. The mass flux of the oxygen to the cathodic cylinder surface was obtained from the mass transfer limiting current for the reaction

$$O_2 + 2\,H_2O + 4e^- \rightarrow 4\,OH^- \qquad [8]$$

The anode was a platinized titanium cylindrical screen 20 cm in diameter and 15 cm tall, concentric with the rotating cylinder and at the same elevation as the metal portion of the cylinder. Potentials were measured with respect to a saturated calomel cell by means of a capillary probe and a high impedance voltmeter. Cathodic currents were measured by means of a milliammeter. Rotational speeds were measured by a magnetic pickup and electronic counter. The oxygen content was measured by Winkler analysis. Additional information is available in Ref. (11) and (12).

The test cylinders were made of Monel with plastic end pieces. The cylinders were 6.35 cm in diameter, 35 cm long, with a central Monel portion 15.3 cm long. This resulted in a nominal mass transfer surface area of 304 cm², based on the 6.35 cm diameter for a smooth cylinder. Four cylinders were made. The first was a highly polished cylinder with a surface roughness less than 3×10^{-5} cm rms height. The remaining cylinders had staggered diamond knurls machined on their surfaces.[1] The knurls had peak to valley heights, ϵ, of 7.3×10^{-2} cm (cylinder 2), 4.1×10^{-2} cm (cylinder 3) and 1.52×10^{-2} cm (cylinder 4) giving d/ϵ ratios of 87, 156, and 416, respectively.

Cathodic polarization curves were obtained at several rotational speeds for the different cylinders. A typical set of these is shown in Fig. 2. No major difference was observed in the shapes of these curves in comparison with those resulting for the smooth cylinders.

The resulting mass transfer data is presented in Fig. 3. The temperature of the system was 25° ± 1°C. Values of the mass diffusivity, D, and the kinematic viscosity, ν, were obtained by interpolation from the International Critical Tables (17). The values were $D = 2.33 \times 10^{-5}$ cm²/sec and $\nu = 9.3 \times 10^{-3}$ cm²/sec giving a Schmidt number of 400. Operating conditions are shown in Table I.

To check the system a series of runs was carried out on a smooth cylinder and the resulting data is seen to be in excellent agreement with the theoretical expression, Eq. [1], (*cf.* Fig. 3). For the rough cylinders the area used to evaluate current density is based on a diameter of 6.35 cm, as previously noted. This is consistent with Makrides and Hackerman (14), and with Theodorsen and Regier (13) in the presentation of their friction factor data.

From Fig. 3, it is seen that for rough cylinders the mass transfer varies linearly with Reynolds numbers for $Re > Re_{crit}$. Furthermore, there is very good agreement between the data and Eq. [7] for the different roughnesses tested. It should be noted that the friction experiments of Theodorsen and Regier (13) were carried out for sand-roughened surfaces while for the present mass transfer system the surface of the cyl-

Table I. Operating conditions

Cylinder	d/ϵ	Period, sec	RPM	O_2 content, ppm
Smooth	$>2 \times 10^5$	0.08 to 26	750 to 2.3	5 to 6
Fine knurl	416	0.08 to 18.5	750 to 3.23	4 to 6.16
Medium knurl	156	0.071 to 13.4	844 to 4.5	3.68 to 6.64
Coarse knurl	87	0.086 to 12.9	698 to 4.65	2.25 to 6.2

[1] Monel cylinders, 6.35 cm diameter, were knurled with Diamond Pattern Knurls of pitch: coarse, 14; medium, 21; fine, 33 lines per inch. Depth of knurl was regulated by pressure on the tool holder. Depth was measured by averaging several peak top to valley depth diameters.

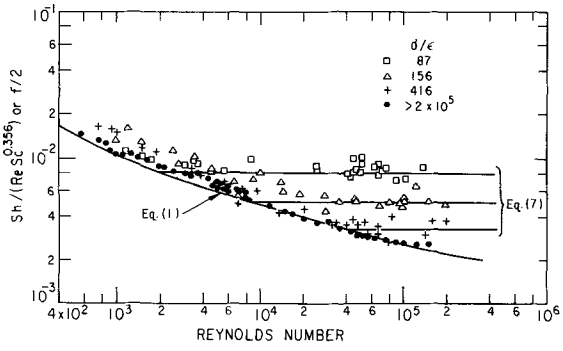

Fig. 4. Mass transfer or friction factor vs. Re

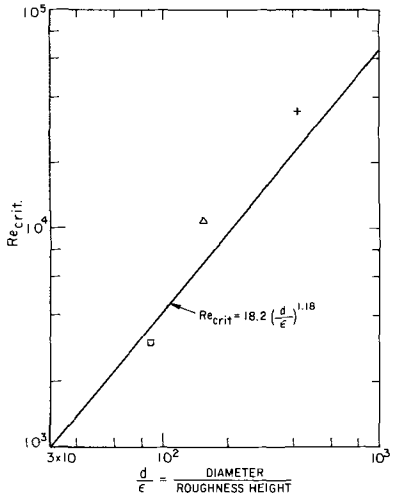

Fig. 5. $Re_{critical}$ vs. relative roughness d/ϵ

inder was covered with diamond-shaped knurls corresponding to a saturated sand roughness condition. Makrides and Hackerman state that the saturated condition also exists for surfaces undergoing dissolution.

For completeness, the experimental results have also been presented in Fig. 4 with an ordinate of $Sh/(Re\ Sc^{0.356})$ or $f/2$ and the results are again compared with Eq. [7]. Note that in this form the results for $Re > Re_{crit}$ are independent of the Reynolds number. Values of Re_{crit} may be obtained from the experimental data for the three roughnesses tested. The three points are presented in Fig. 5 along with the approximate relation, Eq. [5].

In conclusion, the mass transfer to rotating cylinders has been measured over a range of Reynolds numbers from 600 to 250,000 for surface roughnesses varying from d/ϵ equal to 87 to a smooth surface. The results were correlated with

$$Sh = (f/2)\ Re\ Sc^{0.356}$$

where f is the friction factor for the appropriate smooth or rough cylinder.

Acknowledgments

The authors acknowledge with appreciation the support of this research by the Office of Saline Water, U. S. Department of the Interior, Grant No. 14-30-2545 and the Sea Water Conversion Laboratory, University of California, Berkeley. We acknowledge the technical assistance of M. Singh and R. Madahar.

Manuscript submitted May 3, 1971; revised manuscript received Aug. 11, 1971.

Any discussion of this paper will appear in a Discussion Section to be published in the June 1972 JOURNAL.

NOMENCLATURE

ΔC	difference in concentration of oxygen between bulk of solution and metal-fluid interface, g equiv/cm³
d	diameter, cm
f	friction factor, dimensionless
q	mass flux at wall, g equiv/cm²/sec
D	diffusion coefficient, cm²/sec
ϵ	characteristic roughness, cm
ω	angular velocity, radians/sec
ν	kinematic viscosity, cm²/sec

Dimensionless Groups

Sh	Sherwood number, $qd/(D\Delta C)$
Re	Reynolds number, $\omega d^2/2\nu$
Sc	Schmidt number, ν/D
Re_{crit}	critical Reynolds number, $(11.8\ d/\epsilon)^{1.18}$

REFERENCES

1. M. Eisenberg, C. W. Tobias, and C. R. Wilke, *Chem. Eng. Progr. Symp. Ser.*, **15**, 1 (1953).
2. M. Eisenberg, C. W. Tobias, and C. R. Wilke, *This Journal*, **101**, 306 (1954).
3. J. T. Anderson and O. A. Saunders, *Proc. Roy. Soc. (London), Ser. A*, **217**, 555 (1953).
4. G. A. Etemad, *Trans. ASME (Am. Soc. Mech. Engrs.)*, **77**, 1283 (1955).
5. D. Dropkin and A. Carmi, *ibid.*, **79**, 741 (1957).
6. W. M. Kays and I. S. Bjorklund, *ibid.*, **80**, 70 (1958).
7. R. A. Seban and H. A. Johnson, "Heat Transfer from a Horizontal Cylinder Rotating in Oil," *NASA (Nat. Aeron. Space Admin.) Memo.*, 4-22-59w (1959).
8. C. V. King and S. S. Brodie, *J. Am. Chem. Soc.*, **59**, 1375 (1937).
9. J. Postlethwaite and J. Sephton, "Effects of Mass Transport and Oxide Films on the Cathodic Reduction of O_2 on Ni," *Corrosion Sci.*, **10**, 775 (1970).
10. T. K. Sherwood and J. M. Ryan, *Chem. Eng. Sci.*, **11**, 81 (1959).
11. R. R. Kappesser, "Cathodic Protection of a Rotating Cylinder," M.S. thesis, University of California, Berkeley (1967).
12. I. I. Cornet and R. R. Kappesser, *Trans. Inst. Chem. Engrs. (London)*, **47**, T194 (1969).
13. T. Theodorsen and A. Regier, "Experiments on Drag of Revolving Disks, Cylinders, and Streamlined Rods at High Speeds," *NACA Ann. Reports*, **793**, 367 (1945).
14. A. C. Makrides and N. Hackerman, *This Journal*, **105**, 156 (1958).
15. C. V. King and S. S. Brodie, *J. Am. Chem. Soc.*, **59**, 1375 (1937).
16. C. V. King and P. L. Howard, *Ind. Eng. Chem.*, **29**, 75 (1937).
17. National Research Council, "International Critical Tables," **5**, p. 64, McGraw-Hill, New York (1929).

DISCUSSION SECTION

This Discussion Section includes discussion of papers appearing in the *Journal of The Electrochemical Society*, Vol. 118, No. 1, 2, 3, 4, and 6; January, February, March, April, and June 1971.

Electrochemical Studies in Liquid and Solid AgBr

D. O. Raleigh and H. R. Crowe
(pp. 79-86, Vol. 118, No. 1)

R. D. Armstrong and T. Dickinson[1]: It is difficult to understand why Raleigh and Crowe attribute the measured capacitance of the interface Pt/AgBr to an inner layer effect whilst continuing to attribute the capacitance of the C/AgBr interface to a diffuse layer effect. The inner layer capacitance, which arises from the finite size of ions, is always in series with the diffuse layer, so that it is the smallest capacitance of the combination which is dominant. Thus, if a diffuse layer capacity is important in one case (C/AgBr), it is also likely to be important in another (Pt/AgBr). Our own opinion is that in both cases the capacitance arises from an inner layer effect, the differences in magnitude reflecting different true contact areas; and we think that in fitting the measured C-E curve to the theoretical one for C/AgBr, Raleigh[2] is unjustified in placing the theoretical C-E curve at a particular point on the E axis since this point was determined by a calculation of the absolute (*sic*) potential difference between Ag and AgBr.

D. O. Raleigh: We did not attribute the measured Pt/AgBr interface capacitance to an ideal inner layer, but to a layer of adsorbed Ag^+ and/or Br^- ions (depending on potential) on the Pt surface. In this instance, the simple series model for the diffuse and compact layer capacitances is invalid and large over-all capacitances may result[3]. Armstrong and Dickinson are of course entitled to their own interpretation of such data, and the simplicity of a purely inner layer model is admittedly attractive. It seems necessary, however, to deal with diffuse layer capacitance in some manner, and the Grimley-Mott model[4,5] seems reasonable. I have discussed this model for ionic solids at some length in a recent publication[6].

To be sure, the Grimley-Mott estimate of the Ag/AgBr absolute electrode potential may be considerably in error, but the C/AgBr capacitance data[7] match the theoretical curve both in general magnitude and in relative invariance to the potential. Dominance by an ideal inner layer capacitance would require the diffuse layer capacitance to be comparatively large. The theory does not predict this large a diffuse layer capacitance anywhere in the voltage range, regardless of the assignment of the absolute electrode potential. Our way out of the dilemma has been to suggest specific ion adsorption in the Pt/AgBr case.

At this point, it seems useful to state that we are indeed open to alternative explanations and also to point out the dangers in carrying over interface concepts developed for aqueous systems (a practice in which we share some guilt). The solid electrode-solid electrolyte interface is physically unique in a number of respects. Interface models based on a detailed consideration of the microscopic situation would seem to be needed in developing appropriate theoretical treatments.

[1] Electrochemistry Research Laboratories, Department of Physical Chemistry, University of Newcastle-upon-Tyne, Newcastle-upon-Tyne, England.
[2] D. O. Raleigh, *J. Phys. Chem.*, 70, 689 (1966).
[3] R. Parsons, Electrode Double Layer, in "The Encyclopedia of Electrochemistry," C. A. Hampel, Editor, Reinhold Publishing Co., New York (1964).
[4] T. B. Grimley and N. F. Mott, *Discussions Faraday Soc.*, 1, 3 (1947).
[5] T. B. Grimley, *Proc. Roy. Soc. (London)*, A201, 40 (1950).
[6] D. O. Raleigh, *Phys. Stat. Sol. (a)*, 4, 215 (1971).
[7] D. O. Raleigh, *J. Phys. Chem.*, 71, 1785 (1967).

Anodic Dissolution of Beryllium in Anhydrous Media

H. Aida, I. Epelboin, and M. Garreau
(pp. 243-248, Vol. 118, No. 2)

W. J. James and M. E. Straumanis[8]: The recent article regarding the anodic dissolution of Be in anhydrous media by Aida *et al.*, is most interesting in that it appears to provide further proof that the two concepts of "anomalous" dissolution, namely the presence of transitory species of uncommon valence or the "chunk effect" (film and/or metal spalling) are not incompatible.

The authors approach in attributing greater stability to Be^+ in a water solvent-poor interface as opposed to the greater stability of Be^{+2} in a water solvent-rich, appears to us to be a reasonable one. Our disagreements with proponents of unusual transitory ionic states as being responsible for the anomalous dissolution behavior of metals have been based on the fact that these studies were carried out in dilute aqueous media. Thermodynamic considerations of the stability of ions such as Be^+, Al^+, Zn^+, Mg^+, *etc.* in aqueous solutions virtually rules out the possibility of their existence at any measurable distance from the anodic surface. This is not to say, of course, that the anodic expulsion of, *e.g.* Be, does not occur in two consecutive electron discharges to form Be^{2+}.

Consequently, it is not surprising that the attempts by several investigators to detect directly the existence of such unstable species at considerable distances from the electrodes were doomed to failure.

Furthermore, the undisputable detection of such comparatively stable ions (for references see the article under discussion here) as Cu^+ and In^+ can hardly be considered as verification that anomalous dissolution of considerably more active metals occurs as a consequence of formation of uncommon transitory species.

In their discussion of the nature of the Be surfaces, the authors state that the appearance of a gray coloration on the surface or actual identification of metallic particles in the anode region cannot be taken as indisputable evidence of the chunk effect because the formation of metallic particles may always be attributed to the reaction $2\,Be^+ \rightarrow Be^{++} + Be\downarrow$

Whereas the concept of such a disproportionate reaction is supported by knowledge of other more noble metals which undergo this reaction, *e.g.* Cu, there is absolutely no evidence of direct nature that Be undergoes this reaction either in aqueous or anhydrous media.

On the contrary, experimental evidence suggests that this reaction is very unlikely, taking into account the failure to detect Be^+ in aqueous solutions, the inability to plate Be out of such solutions, the presence of deformation twins on the comparatively large Be-chunks and on the etched Be surfaces, indicating that the former initially belonged to the solid Be piece. In fact, the process of detachment of Be platelets from the Be substrate, dissolving in acids, could be observed optically[9].

[8] Graduate Center for Materials Research, University of Missouri-Rolla, Rolla, Missouri 65401.
[9] M. E. Straumanis and D. L. Mathis, *J. Less-Common Metals*, 4, 213 (1962).

Similar behavior has been observed for Al, Mg, Zn, Cd, and Sn in acidic or aqueous salt solutions[10-17]. If the same reasoning were applied to Zn to explain the presence of the gray to black coloration on its surface and the x-ray evidence of metallic particles in the anolyte, how can one explain why, when the Zn surface is amalgamated, no gray coloration is observed together with no metallic particles, and that a valence state of two is obtained in the same electrolytes[18]? Clearly, whereas in the first case Zn particles were detached from the bulk during the dissolution, which resulted in a calculated ionic state less than two, no such process could occur when the metal was amalgamated, since the Zn particles could not penetrate the Hg-surface layer and a valence of two, therefore, resulted.

Furthermore, we have also examined recently by SEM techniques Zn and Mg electrodes exhibiting surface films after anodic dissolution in aqueous media and can state that in all cases the microscopy confirms the source of the metal-like particles as arising from the electrode surface.

The foregoing discussion is not meant to detract from this excellent paper by Aida *et al.* The authors have presented strong evidence for the existence of Be^+ in anhydrous media. Further studies of this nature should go far in accounting on a more quantitative and general basis for the apparently anomalous behavior of many metals in both aqueous and anhydrous media.

H. Aida, I. Epelboin, and M. Garreau: We are pleased to see that W. J. James and M. E. Straumanis agree that anomalous anodic dissolution can be interpreted in terms of the two different basic concepts which have long been opposed in the literature. The protracted discussion on this topic, in which the editors of this Journal allowed us to take part (Discussion Section of June 1957 and June 1959), has been fruitful since it led to a better though still partial understanding of this difficult problem.

We think it necessary, however, to give further information about certain points of our paper that seemed disputable to W. J. James and M. E. Straumanis.

1.—First, we do not think that the transitory species of uncommon valency can only exist in anhydrous solutions. In our experiments, the absence of water in the electrolyte (O, 1 g/liter) highly favors the formation, near the anode, of a layer which is permeable to monovalent ions and almost impermeable to electrons. However, in certain cases, this layer can be partially formed in solutions richer in water. Thus, aluminum dissolves with an apparent valency of about two in an alcoholic solution of $LiClO_4$ containing 100g of water per liter, and this at anodic potentials sufficiently high to cause electrolytic polishing, which is incompatible with the "chunk effect."

2.—Concerning the chunk effect more particularly, the main point seems no longer to be whether the different methods, either those cited by Straumanis and James or ours, may reveal unambiguously its existence. We agree with Straumanis and James and admit that this effect can occur under various conditions; and we think that efforts should henceforth focus on its interpretation rather than on its identification. This is what we are doing at the present time, using the following new approaches: (a) study of the influence of changes in the crystal structure of the dissolved sample, caused either by various thermal treatments or by replacement of polycrystals by very pure single crystals; (b) kinetic study by modern electrochemical methods.

(a) The first results on crystal structure effects show that the disintegration of the metal occurs at the level of the subgrains of the lattice. This might be due to a phenomenon which would start under the influence of the very small differences in the reticular energy which exist between the sites constituting the boundaries of dislocation of the crystal substructure and the unperturbed parts of this crystal.

(b) By improving the analysis of the polarization curves (which have been roughly described in our paper) using a current interruption method completed by electrochemical impedance measurements, we recently showed that the anodic potential necessary to create the layer in which Be^+ is stable was actually much lower than the one predicted by curve c' in Fig. 2. The current-potential curve, corrected for ohmic drop, shows a marked change in the slope at an anodic potential of 1V as measured relative to an Ag/Ag^+ (0.2M) reference electrode. This change corresponds to the border separating the potential range within which Ne equals unity, and the surface is bright, from the range within which Ne differs from unity, and the dissolution is heterogeneous. Consequently, the electric energy actually available at the anode within the field where the chunk effect is observed is not very high. Dissolution can occur rapidly only at the weakest parts of the metallic lattice constituted by the boundaries of dislocation. The surface of the anode is thus divided in two zones: the first one has a small area (emergence of the dislocation boundaries) where the current density is high; the second has a larger area but scarcely contributes to dissolution. The relative importance of the contributions of these zones depends on the potential. Faradaic impedance diagrams obtained at these low potentials provide support for this interpretation since they show, at very low frequencies, more than one time constant.

3.—The fact that beryllium cannot be plated out from the solutions we used is not in disagreement with the formation of stable Be^+ ions moving sufficiently far from the electrode to modify the faradaic yield of the dissolution. In fact, this formation needs a minimal anodic potential which is incompatible with the cathodic reaction $Be^+ + e \rightarrow Be\downarrow$ in the cases considered here.

4.—As for the results obtained with amalgams, we think that the canceling of the anomaly may be related to an easier adsorption of anions on solid surfaces than on liquid surfaces. This might be the reason why the quasi-crystalline anhydrous layer cannot be formed. This interpretation is strongly supported by our results on the anodic dissolution of gallium in $LiClO_4$ solutions in ethanol: with solid Ga ($t = 25°C$) Ne = 1, whereas with liquid Ga ($t = 35°C$) Ne = 3[19].

[10] H. H. Uhlig and R. Krutenat, *This Journal*, **111**, 1303 (1964).
[11] M. E. Straumanis and D. L. Mathis, *This Journal*, **109**, 434 (1962).
[12] M. E. Straumanis, J. L. Reed, and W. J. James, *This Journal*, **114**, 885 (1967).
[13] J. W. Johnson, E. Deng, S. C. Lai, and W. J. James, *This Journal*, **114**, 424 (1967).
[14] W. J. James, M. E. Straumanis, D. K. Bhatia, and J. W. Johnson, *This Journal*, **109**, 1996 (1962).
[15] M. E. Straumanis and D. K. Bhatia, *This Journal*, **110**, 357 (1963).
[16] M. E. Straumanis and K. Poush, *This Journal*, **112**, 1185 (1965).
[17] M. E. Straumanis and M. Dutta, *J. Inorgan. Chem.*, **5**, 992 (1966).
[18] W. J. James and G. Stoner, *J. Am. Chem. Soc.*, **85**, 1354 (1963).

Crystal Structures of the Elements of the Periodic Table and the Mechanisms of Electrolytic Hydrogen Evolution Reaction

A. K. Vijh (pp. 263-264, Vol. 118, No. 2)

S. Trasatti[20]: Some points of Vijh's reasoning seem to be questionable. First of all, Vijh divides the metals into two main classes according to whether or not the hydrogen evolution reaction (h.e.r.) proceeds with significant steady-state chemisorption of hydrogen. However, copper, silver, and gold are included by Vijh into the class of metals adsorbing hydrogen (Vijh's class II), and in fact, this does not seem to be the case.

[19] See M. Garreau, *Métaux*, 544, 425 (1970).
[20] Laboratory of Electrochemistry, University of Milan, Milan, Italy.

Similar behavior has been observed for Al, Mg, Zn, Cd, and Sn in acidic or aqueous salt solutions[10-17]. If the same reasoning were applied to Zn to explain the presence of the gray to black coloration on its surface and the x-ray evidence of metallic particles in the anolyte, how can one explain why, when the Zn surface is amalgamated, no gray coloration is observed together with no metallic particles, and that a valence state of two is obtained in the same electrolytes[18]? Clearly, whereas in the first case Zn particles were detached from the bulk during the dissolution, which resulted in a calculated ionic state less than two, no such process could occur when the metal was amalgamated, since the Zn particles could not penetrate the Hg-surface layer and a valence of two, therefore, resulted.

Furthermore, we have also examined recently by SEM techniques Zn and Mg electrodes exhibiting surface films after anodic dissolution in aqueous media and can state that in all cases the microscopy confirms the source of the metal-like particles as arising from the electrode surface.

The foregoing discussion is not meant to detract from this excellent paper by Aida *et al.* The authors have presented strong evidence for the existence of Be^+ in anhydrous media. Further studies of this nature should go far in accounting on a more quantitative and general basis for the apparently anomalous behavior of many metals in both aqueous and anhydrous media.

H. Aida, I. Epelboin, and M. Garreau: We are pleased to see that W. J. James and M. E. Straumanis agree that anomalous anodic dissolution can be interpreted in terms of the two different basic concepts which have long been opposed in the literature. The protracted discussion on this topic, in which the editors of this Journal allowed us to take part (Discussion Section of June 1957 and June 1959), has been fruitful since it led to a better though still partial understanding of this difficult problem.

We think it necessary, however, to give further information about certain points of our paper that seemed disputable to W. J. James and M. E. Straumanis.

1.—First, we do not think that the transitory species of uncommon valency can only exist in anhydrous solutions. In our experiments, the absence of water in the electrolyte (O, 1 g/liter) highly favors the formation, near the anode, of a layer which is permeable to monovalent ions and almost impermeable to electrons. However, in certain cases, this layer can be partially formed in solutions richer in water. Thus, aluminum dissolves with an apparent valency of about two in an alcoholic solution of $LiClO_4$ containing 100g of water per liter, and this at anodic potentials sufficiently high to cause electrolytic polishing, which is incompatible with the "chunk effect."

2.—Concerning the chunk effect more particularly, the main point seems no longer to be whether the different methods, either those cited by Straumanis and James or ours, may reveal unambiguously its existence. We agree with Straumanis and James and admit that this effect can occur under various conditions; and we think that efforts should henceforth focus on its interpretation rather than on its identification. This is what we are doing at the present time, using the following new approaches: (a) study of the influence of changes in the crystal structure of the dissolved sample, caused either by various thermal treatments or by replacement of polycrystals by very pure single crystals; (b) kinetic study by modern electrochemical methods.

(a) The first results on crystal structure effects show that the disintegration of the metal occurs at the level of the subgrains of the lattice. This might be due to a phenomenon which would start under the influence of the very small differences in the reticular energy which exist between the sites constituting the boundaries of dislocation of the crystal substructure and the unperturbed parts of this crystal.

(b) By improving the analysis of the polarization curves (which have been roughly described in our paper) using a current interruption method completed by electrochemical impedance measurements, we recently showed that the anodic potential necessary to create the layer in which Be^+ is stable was actually much lower than the one predicted by curve c' in Fig. 2. The current-potential curve, corrected for ohmic drop, shows a marked change in the slope at an anodic potential of 1V as measured relative to an Ag/Ag^+ (0.2M) reference electrode. This change corresponds to the border separating the potential range within which Ne equals unity, and the surface is bright, from the range within which Ne differs from unity, and the dissolution is heterogeneous. Consequently, the electric energy actually available at the anode within the field where the chunk effect is observed is not very high. Dissolution can occur rapidly only at the weakest parts of the metallic lattice constituted by the boundaries of dislocation. The surface of the anode is thus divided in two zones: the first one has a small area (emergence of the dislocation boundaries) where the current density is high; the second has a larger area but scarcely contributes to dissolution. The relative importance of the contributions of these zones depends on the potential. Faradaic impedance diagrams obtained at these low potentials provide support for this interpretation since they show, at very low frequencies, more than one time constant.

3.—The fact that beryllium cannot be plated out from the solutions we used is not in disagreement with the formation of stable Be^+ ions moving sufficiently far from the electrode to modify the faradaic yield of the dissolution. In fact, this formation needs a minimal anodic potential which is incompatible with the cathodic reaction $Be^+ + e \rightarrow Be\downarrow$ in the cases considered here.

4.—As for the results obtained with amalgams, we think that the canceling of the anomaly may be related to an easier adsorption of anions on solid surfaces than on liquid surfaces. This might be the reason why the quasi-crystalline anhydrous layer cannot be formed. This interpretation is strongly supported by our results on the anodic dissolution of gallium in $LiClO_4$ solutions in ethanol: with solid Ga ($t = 25°C$) Ne = 1, whereas with liquid Ga ($t = 35°C$) Ne = 3[19].

[10] H. H. Uhlig and R. Krutenat, *This Journal*, **111**, 1303 (1964).
[11] M. E. Straumanis and D. L. Mathis, *This Journal*, **109**, 434 (1962).
[12] M. E. Straumanis, J. L. Reed, and W. J. James, *This Journal*, **114**, 885 (1967).
[13] J. W. Johnson, E. Deng, S. C. Lai, and W. J. James, *This Journal*, **114**, 424 (1967).
[14] W. J. James, M. E. Straumanis, D. K. Bhatia, and J. W. Johnson, *This Journal*, **109**, 1996 (1962).
[15] M. E. Straumanis and D. K. Bhatia, *This Journal*, **110**, 357 (1963).
[16] M. E. Straumanis and K. Poush, *This Journal*, **112**, 1185 (1965).
[17] M. E. Straumanis and M. Dutta, *J. Inorgan. Chem.*, **5**, 992 (1966).
[18] W. J. James and G. Stoner, *J. Am. Chem. Soc.*, **85**, 1354 (1963).

Crystal Structures of the Elements of the Periodic Table and the Mechanisms of Electrolytic Hydrogen Evolution Reaction

A. K. Vijh (pp. 263-264, Vol. 118, No. 2)

S. Trasatti[20]: Some points of Vijh's reasoning seem to be questionable. First of all, Vijh divides the metals into two main classes according to whether or not the hydrogen evolution reaction (h.e.r.) proceeds with significant steady-state chemisorption of hydrogen. However, copper, silver, and gold are included by Vijh into the class of metals adsorbing hydrogen (Vijh's class II), and in fact, this does not seem to be the case.

[19] See M. Garreau, *Métaux*, 544, 425 (1970).
[20] Laboratory of Electrochemistry, University of Milan, Milan, Italy.

It is well known[21] that Cu adsorbs hydrogen from the gas phase only if its purity is unsatisfactory. No adsorption of hydrogen from the gas phase is known to occur also on Ag and Au. Electrochemically, copper[22], silver[23], and gold[24] do not present detectable amounts of hydrogen adsorbed on the surface during the h.e.r. However, if the metals are not especially pure, or are subjected to anodic-cathodic treatments[22,24] (particularly Ag and Au) the exchange current for h.e.r. may become even two orders of magnitude higher, and atomic hydrogen usually appears on the metal surface. Thus, Cu, Ag, and Au belong, in fact, to the group of metals not adsorbing hydrogen (Vijh's class I).

Manganese has been included by Vijh into class I. This metal is atypical in many respects, but not in respect to liability to adsorb hydrogen. Mn chemisorbs hydrogen from the gas phase, though the experimental heat of the process seems to be comparatively low[21]. This fact probably makes the detection of steady-state coverage during h.e.r. very difficult. On the other hand, data on h.e.r. are very scanty for Mn, so that an accurate location of this metal may appear difficult; but other data[25] show that manganese chemisorbs gases like all other transition metals. Thus, I would suggest that Mn be included in class II, though additional evidence may be needed for that. At any rate, this point is not as determinant as that regarding Cu, Ag, and Au.

If we now examine the new situation, we can realize that the analysis of the mechanism of the h.e.r. on the basis of the crystalline structure of metals does not seem to be relevant. In fact, typical metals cannot be separated from atypical metals (in Vijh's sense). On the other hand, the crystalline structure is a consequence of the intimate electronic structure of elements. If we pay attention to the electronic structure, we see that the division of metals into two groups is now clear. Metals in class I are sp metals, while metals adsorbing hydrogen (class II) are transition metals. No exception to this rule does exist. I would like to stress again that the starting point for the understanding of the h.e.r. on metals is not the analysis of the crystalline structure, but rather the electronic theory of metals. It is surprising that Vijh does not make any specific reference to this point. He, for example, explains a high strength for the M-H bond with a high sublimation heat of the metal in question. This is an observation but not an explanation. In fact, a high sublimation heat is a consequence of a strong cohesion which in turn can be explained on the basis of the electronic theory[26].

The lack of any attention to the band theory of metals is apparently due somewhat to Vijh's complicated reasoning about the origin of the hydrogen chemisorption heat. I agree that the adsorption of atomic hydrogen can occur also on sp metals. In fact, from the band theory of metals[26] it is shown that chemisorption is possible whenever the solid possesses unfilled bands and when the atom to be adsorbed has electrons to shear, or *vice versa*; but for the extent of adsorption to be detectable, factors are needed which undoubtedly only transition metals possess. Thus, gold and copper adsorb CO but not hydrogen, though in any case the surface bond is weak[21] simply because in hydrogen adsorption there is a parallel path (atomic recombination) which does not exist in the adsorption of CO. At any rate, the heat of adsorption of CO on Cu and Au is 9 kcal/mole, while on transition metals it goes from 153 on Ti to 42 on Ni[21].

Using band-theory concepts, we can attempt to understand, at least qualitatively, the scale of M-H interaction strength. From the discussion above, the outstanding factor is presumably to be sought in the density of electronic states in the energy bands of the solid near the Fermi level. Almost all properties of transition metals are governed by this factor, *i.e.* conductivity, electronic specific heat, para- and ferromagnetism, *etc.* The average density of states is of the order of twenty times greater in the d-band than in the s-band[27]. In principle, every process involving exchange interaction of electrons should thus be easier on d than sp metals. This is a quantum-mechanical problem, and calculations by Horiuti and Toya[28] seem to corroborate this fact. Qualitatively, we can easily correlate the M-H energy to the density of states. In transition metals the density is high and the strength of the M-H bond is high. In Cu, Ag, and Au, the d-bands are completely filled while the s-band is half-filled. The density of states is here lower than in d-bands, but still rather high because the Fermi surface is presumably just below the limit of the Brillouin zone, in a position of maximum density of states for this type of band. For these metals the strength of the M-H bond is thus relatively high, but no chemisorption can occur from H_2 molecules because the energy of M-H is below 50 kcal/mole, half the energy of dissociation of hydrogen molecules. Some trace of chemisorbed hydrogen can presumably appear on these metals at very high current density during h.e.r. due to kinetic reasons, but this fact is of secondary importance and does not alter the terms of the problem. It is readily realized that these metals can be very sensitive to impurities which can introduce holes in the d-bands so modifying deeply the electronic properties of the solid. In fact, the top of the d-band is not too far from the Fermi level.

With one more electron added to the s-band we go to Zn, Cd, and Hg. In these metals the s-bands are completely filled and they are metallic conductors only because of an overlap of s and p-bands. However, the Fermi level is here presumably close to both the top of the s-band and the bottom of the p-band. Thus, the density of states is in this case very low, and the M-H bond is expected to be very weak, as is in fact the case. If we go on to fill the p-band, we expect the strength of the M-H bond to increase with increasing number of electrons until the band is half filled. However, in this case it is difficult to apply the simple concepts of the band theory of metals for p-elements are not typical metals probably because of the strong orientation of their atomic orbitals. Calculated adsorption heats strongly differ from experimental values of interaction energy but, at any rate, the strength of the M-H bond appears to increase in the series Tl < Pb < Bi, and In < Sn < Sb[22].

Many simple correlations between electronic and electrochemical properties[29] indicate that the scale of general chemical reactivity is the same as in electrochemistry and catalysis, so that in any case the electronic structure is the outstanding factor which determines the behavior of a solid. For the h.e.r. the present author has recently found[29] that all metals fall closely on a same straight line in a log i_o *vs.* work function plot, provided the i_o, exchange currents for sp metals be that relative to the positively charged surface. The i_o values for a negatively charged surface fall on another straight line parallel to the former. Since the M-H strength changes almost linearly with work function, this indicates that the ultimate effect is a "volcano" curve, for the dependence of log i_o on the heat of adsorption of hydrogen as predicted by Parsons[30] and found by Krishtalik[22]. It seems to me that the picture for the h.e.r. would be clearly depicted by this result. A higher strength of the M-H bond de-

[21] D. O. Hayward and B. M. W. Trapnell, "Chemisorption," Butterworths, London (1964).
[22] L. I. Krishtalik, "Advances in Electrochemistry and Electrochemical Engineering," Vol. 7, p. 283, P. Delahay and C. W. Tobias, Editors, Interscience Publishers, New York (1970).
[23] V. I. Bystrov and L. I. Krishtalik, *Elektrokhimiya*, 3, 1345 (1967).
[24] G. M. Schmid, *Electrochim. Acta*, 12, 449 (1967).
[25] S. Cerny and V. Ponec, *Catal. Rev.*, 2, 249 (1968).
[26] A. J. Dekker, "Solid State Physics," Macmillan, London (1965).
[27] C. Kittel, "Elementary Solid State Physics," Wiley, New York (1962).
[28] J. Horiuti and T. Toya, "Solid State Surface Science," Vol. 1, M. Green, Editor, Marcel Dekker, New York (1969). See also T. B. Grimley, *Proc. Phys. Soc., (London)*, 92, 776 (1967).
[29] S. Trasatti, *Chim. Ind. (Milan)*, 53, 364 (1971).
[30] R. Parsons, *Trans. Faraday Soc.*, 54, 1053 (1958).

creases the activation energy for discharge and increases that for the removal of atomic hydrogen. This fact is readily understood if use is made of the potential energy curves[31,32]. Since the M-H energy depends on the electronic structure, this ultimately governs the mechanism of h.e.r. The crystalline structure, as such, does not appear to have a primary effect. I would like to emphasize the fact that volcano-shaped curves have been obtained also in the field of catalysis[33], and the rationale behind them is well known as Sabatier's principle[34].

It is of interest to note that the writer has also found[29] that different relationships between potential of zero charge and work function exist for sp and transition metals, and the difference is to be sought in a restricted possibility of rotation of water on the latter due to chemisorption phenomena. The electronic structure is again the outstanding factor. Close relationships can be also found[29] between electronegativity in Pauling's scale and work function, so that if proper attention is paid to the electronic structure of metals, the picture of their electrochemical properties is less obscure than would appear at first sight, though much still needs to be known. At any rate, it must be stressed that progress in electrochemistry is at this point possible only if the electronic structure of the electrode material is correctly and relevantly taken into account.

A. K. Vijh: We appreciate Dr. Trasatti's keen interest in our paper. The various points he raises are, of course, very pertinent to the fundamental understanding of the mechanisms of the hydrogen evolution reaction (h.e.r.) on metals, a subject which constitutes the very foundations of modern electrode kinetic theory and electrocatalysis, in addition to its involvement in all sorts of applied electrochemical problems. Professor Trasatti has presented a rather detailed dissection of our paper and raised many points which need much further discussion since the arguments formulated in his analysis are not entirely sustained by a further study of the issues he touches upon. For the sake of a systematic treatment of the various matters contained in his critique, it is best to classify them in some logical sequence first. Towards this goal, it is perhaps convenient to classify his points into two broad classes, namely, (A), and (B).

(A) Facts, Pseudo-Facts, Experimental Observations—Direct or Deduced

This category mainly concerns deduced or direct experimental observations with regard to the mechanisms of h.e.r. on Cu, Ag, Au, and Mn and the related vital problem of steady-state coverage by adsorbed hydrogen on these metals during the h.e.r. The three of these metals, namely, Cu, Ag, and Au are no doubt borderline cases as regards the strength of the M-H binding, as determined (or estimated) from the gas phase experimental data. The critically evaluated estimates of this M-H interaction energy, as given by Ehrlich[35] are: Cu-H, 56 kcal/mole^{-1}; Ag, 53 kcal/mole^{-1}; Au-H, ~50 kcal/mole^{-1}. It is clear, therefore, that chemisorption of hydrogen from the gas phase on these metals, at least on Cu and Ag, can give rise to a reckonable steady-state coverage although these metals can by no means be regarded as good adsorbents of hydrogen from the gas phase. However, during the electrochemical evolution of hydrogen, a crucial factor is the presence of overpotential which can give rise to a situation comparable to the presence of astronomically high gas pressures with the result that direct application of the gas phase adsorption data (obtained under ordinary pressures) is misleading. For example, as pointed out by Kita[36] in response to objections raised by Breiter[37] on lines similar to those contained in Trasatti's criticism, a cathodic overpotential of 0.4V corresponds to a very high pressure of *ca.* 10^{15} mm Hg. Under such conditions of applied overvoltage (which are equivalent to enormously high pressures), borderline cases like Cu, Ag, Au, *etc.*, are undoubtedly bound to be covered significantly by adsorbed hydrogen—hence their inclusion in our class II is justified. That moderate values of overvoltage can indeed be equivalent to enormously high gas pressures, with the resultant formation of surface phases on electrode surfaces which cannot be ordinarily formed or predicted thermodynamically, has been plausibly argued in detail by Vermilyea[38] in connection with the oxygen evolution reaction. Other previous calculations on these lines but for the case of hydrogen evolution reaction have been given by Van Rysselberghe[39].

As regards the case of Mn, Ehrlich claims, in agreement with Trasatti, that it chemisorbs molecular hydrogen from the gas phase. Some recent preliminary electrochemical work in our laboratory involving transient studies such as potentiodynamic profiles, open circuit decays and charging curves, *etc.*, gives no evidence, however, to support steady-state coverage on Mn during the h.e.r. This electrochemical evidence, yet to be corroborated, by itself would not appear to be sufficient, however, to justify inclusion of Mn along with "soft" metals in our class I. This is because we have concluded the presence of gold in class II (*i.e.* with the transition metals and with radical-ion or atomic recombination as the mechanism), despite the fact that Schmid's[40] work indicates an absence of significant surface coverage by adsorbed hydrogen on gold during h.e.r. It is fair to add that no exact measurements, on the surface coverage on gold during h.e.r., covering an extended potential range, exist, as has been pointed out by Kuhn and Byrne[41]. Even Schmid's work, which covered only the potential range,—0.3 to 0.4V (h.e.) indicated *ca.* 8% coverage (20 μC cm^{-2}). Furthermore, Will and Knorr[42] reported 3% coverage at the reversible potential. One is perhaps safe in concluding that at high cathodic potentials, gold is covered appreciably by adsorbed hydrogen.

The foregoing evidence and comments show that Trasatti's criticism was derived, unfortunately, from the convenient choice of data and from faulty reasoning, especially, with regard to the effect of overpotential. It is conceded, however, that the case of Mn, Cu, Ag, and Au is not completely clear-cut, as far as direct experimental evidence is concerned, with regard to coverage by chemisorbed hydrogen during steady-state h.e.r.

There is a wide spectrum of indirect evidence, however, which is based on the mechanistic analysis of a large variety of experimentally obtained electrochemical criteria diagnostic of electrode reaction mechanisms, which tends to support our original classification, *i.e.*, Mn with the soft metals (class I) and sustaining h.e.r. by an initial discharge mechanism; Au, Cu, and Ag with the transition metals (class II) on which either a radical-ion or an atomic recombination mechanism is involved. This deduced evidence on these metals is summarized as follows:

1. Copper—A complete consideration of the available experimental evidence has led Matthews[43] and Kita[36] to conclude that the h.e.r. proceeds on copper with a radical-ion mechanism. The electrocatalytic plots reported by the workers[36,43] place copper with the medium overpotential metals. A radical-ion

[31] B. E. Conway and J. O'M. Bockris, *Can. J. Chem.*, 35, 1124 (1957).
[32] R. Parsons and J. O'M. Bockris, *Trans. Faraday Soc.*, 47, 914 (1951).
[33] A. A. Baladin, *Advan. Catalysis*, 10, 120 (1958).
[34] M. Boudart, *Chem. Eng. Progr.*, 57, 33 (1961).
[35] G. Ehrlich in "Proc. Third Congress on Catalysis," W. M. H. Sachtler, C. G. A. Schuit, and P. Zwietering, Editors, North-Holland (1965).
[36] H. Kita, *This Journal*, 113, 1095 (1966).
[37] M. W. Breiter, *This Journal*, 113, 1107 (1966).
[38] D. A. Vermilyea, in "Advances in Electrochemistry and Electrochemical Engineering," Vol. 3, P. Delahay, Editor, Interscience (1963).
[39] P. Van Rysselberghe, *J. Chem. Phys.*, 20, 1522 (1952).
[40] G. M. Schmid, *Electrochim. Acta*, 12, 449 (1967).
[41] A. T. Kuhn and M. Byrne, *Electrochim. Acta*, 16, 391 (1971).
[42] F. G. Will and C. A. Knorr, *Z. Elektrochem.*, 64, 270 (1960).
[43] D. B. Matthews, Ph.D. Thesis, Univ. of Pennsylvania, Philadelphia (1965).

creases the activation energy for discharge and increases that for the removal of atomic hydrogen. This fact is readily understood if use is made of the potential energy curves[31,32]. Since the M-H energy depends on the electronic structure, this ultimately governs the mechanism of h.e.r. The crystalline structure, as such, does not appear to have a primary effect. I would like to emphasize the fact that volcano-shaped curves have been obtained also in the field of catalysis[33], and the rationale behind them is well known as Sabatier's principle[34].

It is of interest to note that the writer has also found[29] that different relationships between potential of zero charge and work function exist for sp and transition metals, and the difference is to be sought in a restricted possibility of rotation of water on the latter due to chemisorption phenomena. The electronic structure is again the outstanding factor. Close relationships can be also found[29] between electronegativity in Pauling's scale and work function, so that if proper attention is paid to the electronic structure of metals, the picture of their electrochemical properties is less obscure than would appear at first sight, though much still needs to be known. At any rate, it must be stressed that progress in electrochemistry is at this point possible only if the electronic structure of the electrode material is correctly and relevantly taken into account.

A. K. Vijh: We appreciate Dr. Trasatti's keen interest in our paper. The various points he raises are, of course, very pertinent to the fundamental understanding of the mechanisms of the hydrogen evolution reaction (h.e.r.) on metals, a subject which constitutes the very foundations of modern electrode kinetic theory and electrocatalysis, in addition to its involvement in all sorts of applied electrochemical problems. Professor Trasatti has presented a rather detailed dissection of our paper and raised many points which need much further discussion since the arguments formulated in his analysis are not entirely sustained by a further study of the issues he touches upon. For the sake of a systematic treatment of the various matters contained in his critique, it is best to classify them in some logical sequence first. Towards this goal, it is perhaps convenient to classify his points into two broad classes, namely, (A), and (B).

(A) Facts, Pseudo-Facts, Experimental Observations—Direct or Deduced

This category mainly concerns deduced or direct experimental observations with regard to the mechanisms of h.e.r. on Cu, Ag, Au, and Mn and the related vital problem of steady-state coverage by adsorbed hydrogen on these metals during the h.e.r. The three of these metals, namely, Cu, Ag, and Au are no doubt borderline cases as regards the strength of the M-H binding, as determined (or estimated) from the gas phase experimental data. The critically evaluated estimates of this M-H interaction energy, as given by Ehrlich[35] are: Cu-H, 56 kcal/mole^{-1}; Ag, 53 kcal/mole^{-1}; Au-H, ~50 kcal/mole^{-1}. It is clear, therefore, that chemisorption of hydrogen from the gas phase on these metals, at least on Cu and Ag, can give rise to a reckonable steady-state coverage although these metals can by no means be regarded as good adsorbents of hydrogen from the gas phase. However, during the electrochemical evolution of hydrogen, a crucial factor is the presence of overpotential which can give rise to a situation comparable to the presence of astronomically high gas pressures with the result that direct application of the gas phase adsorption data (obtained under ordinary pressures) is misleading. For example, as pointed out by Kita[36] in response to objections raised by Breiter[37] on lines similar to those contained in Trasatti's criticism, a cathodic overpotential of 0.4V corresponds to a very high pressure of *ca.* 10^{15} mm Hg. Under such conditions of applied overvoltage (which are equivalent to enormously high pressures), borderline cases like Cu, Ag, Au, *etc.*, are undoubtedly bound to be covered significantly by adsorbed hydrogen—hence their inclusion in our class II is justified. That moderate values of overvoltage can indeed be equivalent to enormously high gas pressures, with the resultant formation of surface phases on electrode surfaces which cannot be ordinarily formed or predicted thermodynamically, has been plausibly argued in detail by Vermilyea[38] in connection with the oxygen evolution reaction. Other previous calculations on these lines but for the case of hydrogen evolution reaction have been given by Van Rysselberghe[39].

As regards the case of Mn, Ehrlich claims, in agreement with Trasatti, that it chemisorbs molecular hydrogen from the gas phase. Some recent preliminary electrochemical work in our laboratory involving transient studies such as potentiodynamic profiles, open circuit decays and charging curves, *etc.*, gives no evidence, however, to support steady-state coverage on Mn during the h.e.r. This electrochemical evidence, yet to be corroborated, by itself would not appear to be sufficient, however, to justify inclusion of Mn along with "soft" metals in our class I. This is because we have concluded the presence of gold in class II (*i.e.* with the transition metals and with radical-ion or atomic recombination as the mechanism), despite the fact that Schmid's[40] work indicates an absence of significant surface coverage by adsorbed hydrogen on gold during h.e.r. It is fair to add that no exact measurements, on the surface coverage on gold during h.e.r., covering an extended potential range, exist, as has been pointed out by Kuhn and Byrne[41]. Even Schmid's work, which covered only the potential range,—0.3 to 0.4V (h.e.) indicated *ca.* 8% coverage (20 μC cm^{-2}). Furthermore, Will and Knorr[42] reported 3% coverage at the reversible potential. One is perhaps safe in concluding that at high cathodic potentials, gold is covered appreciably by adsorbed hydrogen.

The foregoing evidence and comments show that Trasatti's criticism was derived, unfortunately, from the convenient choice of data and from faulty reasoning, especially, with regard to the effect of overpotential. It is conceded, however, that the case of Mn, Cu, Ag, and Au is not completely clear-cut, as far as direct experimental evidence is concerned, with regard to coverage by chemisorbed hydrogen during steady-state h.e.r.

There is a wide spectrum of indirect evidence, however, which is based on the mechanistic analysis of a large variety of experimentally obtained electrochemical criteria diagnostic of electrode reaction mechanisms, which tends to support our original classification, *i.e.*, Mn with the soft metals (class I) and sustaining h.e.r. by an initial discharge mechanism; Au, Cu, and Ag with the transition metals (class II) on which either a radical-ion or an atomic recombination mechanism is involved. This deduced evidence on these metals is summarized as follows:

1. Copper—A complete consideration of the available experimental evidence has led Matthews[43] and Kita[36] to conclude that the h.e.r. proceeds on copper with a radical-ion mechanism. The electrocatalytic plots reported by the workers[36,43] place copper with the medium overpotential metals. A radical-ion

[31] B. E. Conway and J. O'M. Bockris, *Can. J. Chem.*, 35, 1124 (1957).
[32] R. Parsons and J. O'M. Bockris, *Trans. Faraday Soc.*, 47, 914 (1951).
[33] A. A. Baladin, *Advan. Catalysis*, 10, 120 (1958).
[34] M. Boudart, *Chem. Eng. Progr.*, 57, 33 (1961).
[35] G. Ehrlich in "Proc. Third Congress on Catalysis," W. M. H. Sachtler, C. G. A. Schuit, and P. Zwietering, Editors, North-Holland (1965).
[36] H. Kita, *This Journal*, 113, 1095 (1966).
[37] M. W. Breiter, *This Journal*, 113, 1107 (1966).
[38] D. A. Vermilyea, in "Advances in Electrochemistry and Electrochemical Engineering," Vol. 3, P. Delahay, Editor, Interscience (1963).
[39] P. Van Rysselberghe, *J. Chem. Phys.*, 20, 1522 (1952).
[40] G. M. Schmid, *Electrochim. Acta*, 12, 449 (1967).
[41] A. T. Kuhn and M. Byrne, *Electrochim. Acta*, 16, 391 (1971).
[42] F. G. Will and C. A. Knorr, *Z. Elektrochem.*, 64, 270 (1960).
[43] D. B. Matthews, Ph.D. Thesis, Univ. of Pennsylvania, Philadelphia (1965).

mechanism means, of course, a significant steady-state coverage by adsorbed hydrogen during the h.e.r. Recent work of Bockris and Srinivasan[44] involving H/D and H/T isotope effects supports our contentions conclusively.

Dr. Trasatti quotes Krishtalik[45] on this point in order to deduce mechanism for copper. Well, this is somewhat dangerous because Krishtalik failed to quote and discuss several key papers on the subject in his review, as we have pointed out elsewhere[46]. If one is trying to deduce mechanism on the basis of all the significant and relevant information, Krishtalik's review (which is outstanding in several other aspects) is not very helpful since the coverage of literature and viewpoints is quite incomplete in that review.

2. *Gold*—The most recent work[41] and the critical analysis of the previous literature therein indicates that h.e.r. proceeds on gold with atomic recombination as the rate-determining step (r.d.s.) at low overpotentials and radical-ion as the r.d.s. at high overpotentials. Thus significant steady-state coverage by adsorbed hydrogen during the h.e.r. must again be inevitably deduced, although it must be conceded, in all fairness to the viewpoint of Professor Trasatti, that direct evidence on the chemisorption of hydrogen on Au during the h.e.r. was not presented. Various electrocatalytic plots[36,43] again place gold with medium overpotential metals thus indicating a radical-ion mechanism.

3. *Silver*—The electrocatalytic plots of Matthews[43] and Kita[36], based on the review of a lot of previous work, especially of Bockris, Conway, Delahay, Horiuti, and their co-workers, assign a radical-ion mechanism to silver indicating thereby that significant steady-state coverage by chemisorbed hydrogen during steady-state h.e.r. on Ag is most likely. Also, clearly detectable amounts of hydrogen coverage, although far from appreciable, have been reported in several electrochemical studies[45]. This metal would thus again be a borderline and a vexing case.

4. *Manganese*—In the electrocatalytic plots of Matthews[43], Mn is grouped with the soft metals which would be consistent with the placement of this metal in our class I. Some preliminary work, yet to be corroborated, in our laboratory[47] indicates that the h.e.r. proceeds on Mn with initial discharge as the r.d.s. This would again indicate that h.e.r. occurs on this metal without a significant coverage by chemisorbed hydrogen in the steady state, as deduced previously[48] in the paper under discussion.

We have made no attempt to present all the available experimental evidence on Mn, Ag, Au, and Cu in support of our opinions expressed here since that would make the present note unnecessarily lengthy. We have quoted, however, some of the key references on the subject in which all the relevant information is cited and discussed.

One may therefore conclude that the original placement[48] of Cu, Ag, and Au in our class II and of Mn in our class I does not merit a revision at this time. It is conceded, however, that these cases are not completely clear-cut. It is further stressed that our classification of atypical (class I) and typical (class II) metals, in addition to involving some tentative aspects as regards the actual placement of some metals, is also only empirical in nature at present.

(B) Theoretical Interpretations

The second aspect of Dr. Trasatti's criticism involves several matters of a theoretical nature which pertain to the following broad points:

1. *Electronic Effects in Chemisorption*—Dr. Trasatti states that we have not considered electronic effects in chemisorption. In fact, a major point of our paper[48] was to stress, after Ehrlich's analysis[35], that the preeminent position of d-bands in chemisorption originally suggested by Dowden[49], and Dilke, Maxted, and Eley[50] and uncritically accepted by many workers in the field of heterogeneous catalysis[51] and electrocatalysis[52], is not always justified. The main point of these workers[49-59] was that since transition metals readily adsorb gases in general whereas sp metals do not, the chemisorption requires specific interactions involving holes in the d-band. This main thesis is easily demolished when one considers that this viewpoint was based on experimental evidence on the adsorption of molecular gases and that we now know that sp metals do not readily adsorb H_2 from the gas phase because of thermodynamic reasons: the chemical potential of hydrogen atoms bound as molecules in the gas phase is less than that of atoms bound to the solid surface of a sp metal. Chemisorption directly from the atomic gas can occur on nontransition metals as pointed out previously[35, 48] showing thereby that holes in d-bands are not necessarily needed for atoms to be chemisorbed on metals, for which one has only to create conditions in which the metals are not required to break the H—H bond in the H_2.

As regards the second point of Professor Trasatti in this context, one needs to know whether there is any correlation between % d-band character of metals (*i.e.*, in those metals, of course, which show any d-band character at all because of sp hybridization) and the experimentally evaluated best possible estimates of M—H binding energy. As Ehrlich[35] has indicated, there is no particularly strong dependence of M—H interaction energy on % d-band character. The detailed results and related calculations on this matter in relation to the mechanism of the h.e.r. cannot be presented here since they constitute the subject of a thesis[53] and a publication[47] which will not be ready for submission for some time yet. In general, our results support Ehrlich's viewpoint, as was also mentioned in a previous publication.

2. *Electrode Processes in Relation to Band Theory of Solids*—As has been pointed out by Boddy[54], a detailed analysis of electrode reaction experimental data on metals in terms of band theory of solids, as is frequently done for the case of electrode processes on semiconductors and insulators, does not appear to be possible because of two fundamental reasons. As a result of rapid interband transitions in metals, features characteristic of an electrode reaction involving exchange of charge carriers with only one of the bands will not be observed on a given metal. Secondly, there is always a fairly high density of states near the Fermi level in metals so that the rate of the electrode reaction can never be limited by the sluggish or insufficient availability of charge carriers from the solid side of the interface, as is observed in case of semiconductors where saturation effects can be observed. Although detailed, quantitative discussion of electrode processes in terms of band theory of solids cannot be carried out for the aforementioned reasons, some interesting qualitative effects can, however, be pointed out as has been done by Dr. Trasatti. He is right, of course, in stating that in general, a high density of states, as in transition metals will herald higher rates of (or easier) exchange of charge carriers in all processes including chemisorption and electrode reactions. This is an obvious point

[44] J. O'M. Bockris and S. Srinivasan, *Electrochim. Acta*, 9, 31 (1964).
[45] L. I. Krishtalik, in "Advances in Electrochemistry and Electrochemical Engineering," Vol. 7, P. Delahay, Editor, Interscience (1970).
[46] A. K. Vijh, *This Journal*, 117, 367C (1970).
[47] A. Belanger and A. K. Vijh, In preparation.
[48] A. K. Vijh, *This Journal*, 118, 263 (1971).
[49] D. A. Dowden, *Research (London)*, 1, 239 (1948); *J. Chem. Soc.*, 242 (1950).
[50] M. H. Dilke, E. D. Maxted, and D. D. Eley, *Nature*, 161, 804 (1948).
[51] B. M. W. Trapnell, "Chemisorption," Academic Press, New York (1955).
[52] B. E. Conway and J. O'M. Bockris, *J. Chem. Phys.*, 26, 532 (1956).
[53] A. Belanger, Thesis in preparation for the Energy Centre of the National Institute of Scientific Research, University of Quebec at Varennes, P.Q., Canada.
[54] P. J. Boddy in "Progress in Solid State Chemistry," Vol. 4, H. Reiss, Editor, Pergamon Press (1967).

and is frequently discussed in connection with exchange of charge carriers across solid surfaces in general. For example, this is the reason why exchange current densities, for a given electrode reaction, are generally higher on metals than on semiconductors (the case of injection-type electrode reactions on nonmetallic surfaces, which can attain exchange current densities comparable to those of metals under certain suitable conditions are excluded from this argument) or metals covered by semiconducting films, *e.g.* oxides. This point has been discussed by Boddy and will be further elaborated upon in our forthcoming book[55]. The aspect of these matters which is relevant here is whether such generalizations are applicable to the particular case at hand, *i.e.* the h.e.r. To explore this matter further, we note that in terms of Gerischer's formulation[56, 57] of Gurney's quantum mechanical treatment of electrode reactions, the rate of a cathodic reaction may be written as[53-58]

$$i^- = e \int_{-\infty}^{+\infty} \nu^- (E) \cdot D_{el} (E) \cdot f (E - E_{F,el}) \cdot D_{\text{redox}} f (E_{F\text{redox}} - E) dE \quad [1]$$

where i^- is the cathodic rate (*i.e.* the current) of a reduction of, *e.g.* a redox-type reaction; e is the electronic charge; D_{el} and D_{redox} are the density of state functions for the electrode and the electrolyte, respectively; and, $f(E - E_{F,el})$ and $f(E_{F\text{redox}} - E)$ are the Fermi distribution functions for the electrode and the electrolyte, respectively; the term $\nu^-(E)$ is the proportionality factor which contains two terms: the frequency with which electrons arrive at the electrode/solution interface and the probability of tunneling through the potential barrier at the interface. Now when the metal electrode is covered by adsorbed intermediates, as during the h.e.r. on class II metals[48], D_{el} assumes smaller magnitudes and the magnitude of this diminution cannot be readily evaluated. The presence of chemisorbed films can also lead to a decrease in the magnitude of $\nu^-(E)$ again in a manner which is not readily evaluated. It is clear, therefore, that a simple qualitative picture in terms of density of states, as mentioned by Dr. Trasatti, is not very helpful for the case of bonding reactions such as the h.e.r. Even for the nonbonding electrode reactions, problems associated with the solvent adsorption can complicate the picture. That this approach in terms of density of states in metals does not lead one very far is also emphasized by the fact that a calculation of exchange current densities for the h.e.r. for various metals, from a consideration of basic parameters such as in Eq. [1], has not been attempted, not to our knowledge in any case since we have never encountered a table of exchange current densities thus calculated. It is clear therefore that Professor Trasatti's repeated reference to the quantum mechanical treatment in terms of band theory of metals as being preferable for the basic interpretations of the h.e.r., does not help the reader unless he can come forward with a table of exchange current densities calculated from an equation such as Eq. [1].

In this context, it is vital to point out that the approximate quantum mechanical calculations for the estimation of M—H binding energies, as have been done by Eyring *et al.*[59], give results which are hopelessly out of agreement with the experimental values. For a further elaboration of this matter, the reader is referred to Bond[60]. It appears to be a waste of time to attempt exact quantum mechanical calculations of M—H interaction energies since, as has been concluded by Ehrlich[61], such a calculation "from first principles is out of the question."

3. Analogies Between Chemical Heterogeneous Catalysis and Electrocatalysis—Such analogies, which Dr. Trasatti seems to emphasize rather strongly have been well recognized for several years and no doubt are helpful aids to interpretations. If one must refer to these analogies, however, one must also immediately point out the dangers and limitations involved in the loose and unqualified use of these analogies. Some of the serious qualifications which must accompany such analogies and, again, are well known are briefly as follows: direct transfer of information from chemical catalysis to electrocatalysis must take into account an additional factor, namely, the stability of the electrode surface under conditions of electrochemical charge transfer[62]; high fields correspond to extremely high pressures of gases—hence any discussion of chemisorption must be considered in this context as pointed out earlier; what is the relevance of "clean" surface in the gas phase to electrode surface in solution?

4. Relationship Between P.Z.C. and Work Functions of Metals—The correlation given by Professor Trasatti between potentials of zero charge of metals and their work functions which suggests different behavior for sp and d-metals and which he attributes to different orientation of the water molecule on these two types of metals, does not appear to be consistent with previous work of Frumkin, Antropov, Parsons and Bockris. Bockris and Argarde[64] have derived a linear correlation between work functions and p.z.c. for all metals[62, 65]. Previously a similar relationship was noted by Parsons[66] following earlier suggestion by Frumkin[67] that the orientation of water molecules is similar on a number of metals. Detailed discussions of the qualitative aspects of these matters have been recently given by Bockris and Reddy[68]. Although we are not aware of the current unpublished opinions of the various leading workers on this subject, it does appear that Dr. Trasatti's views are not consistent with the published work of the most authoritative investigators in this area of electrochemistry.

It may be added parenthetically that this particular point raised by Professor Trasatti is not really central to the contents of our paper under discussion here. As regards his plea in his closing remarks that more attention should be devoted to the role of properties of the solid in electrode reactions, we are in complete agreement with him. In fact the point made by him is the main theme and thesis of our forthcoming publication[55].

In closing, it may be stated that the points raised by Dr. Trasatti and discussed here need much further investigation and discussion in order to resolve some important issues on which only tentative conclusions can be made at present. There is no doubt about one question, however: the further understanding of electrode processes must involve application of solid-state science in the interpretation of electrochemical reactions. This has been frequently stressed by Bockris[62, 68] and others[55].

[55] A. K. Vijh, "Electrochemistry of Solid Materials," Marcel Dekker, In press (1972).
[56] H. Gerischer in "Advances in Electrochemistry and Electrochemical Engineering," Vol. 1, P. Delahay, Editor, Interscience (1961).
[57] H. Gerischer in "Physical Chemistry: An Advanced Treatise," Vol. 1XA, H. Eyring, Editor, Academic Press (1970).
[58] B. E. Conway, "Theory and Principles of Electrode Processes," Ronald Press (1965).
[59] I. Higuchi, T. Ree, and H. Eyring, *J. Am. Chem. Soc.*, 79, 1330 (1957).
[60] G. C. Bond, "Catalysis by Metals," Academic Press (1962).
[61] G. Ehrlich, *J. Chem. Phys.*, 31, 1111 (1959).
[62] J. O'M. Bockris and S. Srinivasan, "Fuel Cells," McGraw Hill (1969).
[63] S. Trasatti, *Chim. Ind. (Milan)*, 53, 364 (1971).
[64] J. O'M. Bockris and S. D. Argarde, *J. Chem. Phys.*, 49, 5133 (1968).
[65] S. D. Argarde and E. Gileadi in "Electrosorption," E. Gileadi, Editor, Plenum Press (1968).
[66] R. Parsons in "Modern Aspects of Electrochemistry," Vol. 1, J. O'M. Bockris and B. E. Conway, Editors, Butterworths, London (1954).
[67] A. N. Frumkin, *J. Colloid Sci.*, 1, 290 (1946).
[68] J. O'M. Bockris and A. K. N. Reddy, "Modern Electrochemistry," Vols. 1 and 2, Plenum Press (1970).

Electrochemical Behavior of the Aluminum Electrode in Molten Salt Electrolytes

B. S. Del Duca
(pp. 405-411, Vol. 118, No. 3)

R. Piontelli and U. Ducati[69]: The suitability of the solid Al electrodes as "sacrificial anodes" in the molten halides appeared already evident from previous work[70]. The practical want of "electrode" contributions[71] to the measurable overvoltages on carefully prepared electrodes was also stated[72].

A confirmation of the last result is given also by Trémillon and Letisse[73]; in molten $NaAlCl_4$ (even mixed with NaCl or $AlCl_3$) the currents at rotating Al microelectrodes are controlled only by the diffusion of the reacting species in the bath.

Del Duca denounces, on the contrary, considerable contributions ascribed to the surface diffusion of adatoms and to the charge transfer[74], and seems to underestimate the importance of the concentration-polarization effects[75] and the difficulty in eliminating them radically.

As a matter of fact, in the molten salt electrochemistry the concentration-polarization is often responsible for a much more significant contribution to the measurable overvoltages than what is usually granted. It is important particularly in those melts, such as the Al halides, in which the source of the ions exchanged with the electrodes are complexes[76].

These effects are quite analogous for solid (active) or liquid electrodes and their dependence laws *vs.* temperature, convection, and other influences are peculiar[77].

Considering now the experimental technique followed by Del Duca, it does not appear suitable for improving the knowledge actually existing in this field. The relevant points upholding this opinion are the following:

(a.) The surface preparation system is quite inadequate. Under these conditions the unavoidable permanence of oxide layers on the electrode surface[78], also when porous and by consequence not involving passivity, leads to substantial increments of the concentration-polarization.

Moreover this occurs much sooner and it becomes important at a much lower apparent c.d., simulating an electrode overvoltage and an apparent electrode capacitance.

(b.) Under these conditions the stirring system adopted by Del Duca, and which can be considered just a palliative even if the electrode surfaces are active, becomes inefficient. Therefore the potentiostatic currents are insensitive with respect to this kind of stirring.

The above conclusions are upheld also by the quite exceptional rise-times to the steady condition, observed by Del Duca in the so called "transients." They could also explain the data collected in the Table III, whose interpretation, given by Del Duca, appears to be hardly acceptable when the influence of temperature, bath composition, and electrode polarity on the so-called exchange current density is considered.

(c.) The hanging electrode arrangement does not grant the required distribution uniformity of the c.d. on the electrode surface, in spite of the spiral shape of the counterelectrode. This distribution varies, moreover, according to the values of the circulating current intensity and also to the time.

(d.) To fully exploit the galvanostatic current-pulse technique, also the overvoltage *vs.* the time data, after the current break, constitutes an essential source of information and control, apparently ignored in this research.

(e.) The utilization of the solid Al as the reference electrode, although in practice it is admissible, would appear rather questionable if accepting the conclusions of the discussed research.

In conclusion, more recent or modern systems do not necessarily mean more reliable systems and we suspect the description of the Al electrode behavior in molten halides, given by previous works, is much more convincing than the one arising from the paper under discussion here.

[69] Institute of Physical Chemistry, Milan Polytechnic, Milan, Italy.

[70] a) R. Piontelli, G. Sternheim, and M. Francini, *Compt. Rend. Acad. Sci. (Paris)*, 242, 1301 (1956); *J. Chem. Phys.*, 24, 1113 (1956); b) R. Piontelli, *Ann. N. Y. Acad. Sci.*, 79, 1025 (1960); c) R. Piontelli, *Electrochim. Metal.*, 1, 191 (1966).

[71] Defined, from the operational point of view, as the voltage given by a tensiometric cell formed by coupling the working electrode with a reference one of the same kind in the presence of the same electrolyte and in equilibrium for the electrode reaction, in respect of which the contribution is defined.

[72] See also L. A. King, *et al.*, quoted by Del Duca [Ref. (9) in the paper under discussion].

[73] *J. Electroanal. Chem.*, 17, 371 (1968).

[74] Both of them to be included in the electrode-reaction contribution as defined above.

[75] Defined, from the operational point of view, as the voltage just after the current break, given by a tensiometric cell formed by the reference electrode utilized to define the electrode reaction contribution and a second one of the same kind in equilibrium with a bath region having the reference composition (See 2b)

[76] Interesting observations about this point are ascribed to Grube-Hantelmann, *Z. Elektrochem.*, 48, 399, 469 (1942).

[77] Of course all changes in the chemical bath composition involve, as a rule, also changes in the ohmic drop contributions to the measured overvoltages.

[78] See Footnote 70 and: R. Piontelli, G. Sternheim, M. Francini, and R. Manocha, *Rend. Ist. Lombardo Sci. Lettere*, 90, 3 (1956).

Engineering Applications of Current and Potential Distributions in Disk Electrode Systems

L. Nanis and W. Kesselman
(pp. 454-461, Vol. 118, No. 3)

J. Newman[79]: Nanis and Kesselman have recently raised the question of the definition of the resistance in electrode configurations where the primary potential distribution does not prevail and where, instead, surface and concentration overpotentials must exist. They have given a valid justification for defining the resistance as an average potential over the surface of the disk, divided by the total current to the disk.

As Wagner[80] has stated, the term "electrical resistance" is confusing in situations where the potential varies along the boundary of the electrolytic solution. The potential of the electrode is uniform. The ohmic potential drop, the surface overpotential, and the concentration overpotential vary with position on the electrode in such a way that their sum is uniform. There should be no ambiguity if these variations are described in detail.

In such a situation, Newman[81] emphasized the ohmic potential drop and the current density to the center of a disk electrode. Thus, the current-potential curve was calculated by adding the ohmic potential drop, and concentration and surface overpotentials at this point. The same over-all curve would be obtained by performing the addition at the edge of the disk or at any point between the center and the edge. Emphasis was placed on the center of the disk in part because the concentration and surface overpotentials at that point are easily computed from the local current density.

This ohmic potential drop is not, of course, directly comparable to the average resistance. In order to use the average resistance, one would first need to know at what point on the electrode the ohmic potential drop is given by the average resistance. At this point, he would then need to know the local current density and the local surface concentration in order to calculate the concentration and surface overpotentials.

Newman[82] has used a simple equivalent circuit to describe the impedance of a disk electrode system in

[79] Inorganic Materials Research Division, Lawrence Radiation Laboratory and the Department of Chemical Engineering, University of California, Berkeley, California.

[80] C. Wagner, *This Journal*, 99, 1-12 (1952). See especially p. 8.

[81] J. Newman, *This Journal*, 113, 1235-1241 (1966).

[82] J. Newman, *This Journal*, 117, 198-203 (1970).

frequency dispersion in capacity measurements. The low-frequency limit, when the interfacial impedance is purely capacitive, coincides with Nanis and Kesselman's result for uniform current density, $4r_0\kappa R_{eff} = 1.08076$. When faradaic reactions are involved, the value of the effective resistance in the equivalent circuit is different because it includes the impedance of the interface. Thus, the entire electrode system is used to define the effective impedance in this case.

In a later paper[83], Newman points out that, for the secondary distribution on a disk electrode, one can estimate the ohmic potential drop from the total current and the resistance for the primary potential distribution. The surface overpotential obtained by subtracting this ohmic potential from the electrode potential can be associated, with little error, with the average current density.

L. Nanis and W. Kesselman: Newman's comments are helpful in clearing the way for the resolution of electrochemical concepts derived from field theory where confusion has unfortunately arisen. Rather than further compound already prevailing misconceptions, some fundamental concepts require restatement. The Laplace equation

$$\nabla^2\phi = 0 \qquad [1]$$

is more properly stated as (for one dimension)

$$\frac{\partial}{\partial x}\left(\kappa\frac{\partial\phi}{\partial x}\right) = 0 \qquad [2]$$

which emphasizes that the smoothly varying functions which satisfy Eq. [1] possess no discontinuities. In particular, Eq. [1] is intended to apply within a domain. It is customary to assume that conductivity, κ, is independent of position, thus considerably simplifying the mathematical treatment. In view of the confusion generated by the (proper) omission of κ in going from Eq. [2] to the more specialized version in Eq. [1], it is worth re-emphasizing the fact that Eq. [1] applies only within a domain and up to its boundaries. Thus, it is correct to speak of an average potential over the layer of electrolyte immediately adjacent to the metal electrode. Once Eq. [1] is solved, the current density may be determined for any cross-section but the layer next to the metal electrode is particularly convenient for evaluating the total current.

The considerations by Wagner[80] of the definition of electrolyte resistance are at best incomplete. To be precise, he indicated that definition of resistance required terminal faces to have uniform electrical potential, since otherwise the concept of voltage across a conductor (electrolyte) is "meaningless." From this statement and subsequent discussion, it is clear that Wagner was considering a boundary condition outside the domain (electrolyte). As Newman correctly indicates above, the potential may vary along the boundary of the electrolyte while the electrode is at uniform potential. As more attention has been devoted to field problems of electrochemical interest, the analytic difficulties have become more apparent, particularly since so-called "boundary conditions of the third kind" of an unusual nature are involved. In retrospect, however, it seems reasonable that a finite cell resistance associated with a constant potential boundary must remain finite when constant current density conditions are achieved. The concept of domain of applicability is stressed in our paper (p. 456) and the Appendix which deals with the resistance of the non-isopotential disk.

In view of the complexity of analytic methods for the solution of field problems, machine computation methods have proved useful. The relative magnitude of ohmic drop compared with overpotential is a concept basic to electrochemical engineering. When combined as a comparative ratio, the importance of each type of potential drop in determining cell current is readily estimated. This ratio or dimensionless group is the familiar "throwing-power" parameter derived from electroplating methods. For a disk electrode of radius a, the ohmic resistance associated with primary current distribution is given in our Eq. [27] as

$$R_{ohm} = \frac{1}{4\kappa a}$$

Considered as a circuit element, the possibly non-ohmic character of the electrode kinetics at the electrode-electrolyte interface may be represented by the variation of overpotential with respect to current density, $|\partial\eta/\partial J|$. The differential notation is, in fact, a more general definition of resistance. For the area of the disk, a virtual interfacial resistance, R_{int}, may be determined in ohm units as $|\partial\eta/\partial J|\,\frac{1}{\pi a^2}$. The ratio of interface resistance

$$\frac{R_{int}}{R_{ohm}} = \left|\frac{\partial\eta}{\partial J}\right|\frac{4\kappa a}{\pi a^2} = \frac{\kappa}{a}\left|\frac{\partial\eta}{\partial J}\right|\frac{4}{\pi} \qquad [3]$$

to electrolyte ohmic resistance contains the familiar terms with a multiplicative constant close to unity, *i.e.* $4/\pi$. In balancing the various potential drops in point-by-point computation, the relative magnitude of each type may be anticipated by the magnitude of the group in Eq. [3]. (The shift to higher resistance for constant current density conditions may be ignored for the purposes of order of magnitude estimation.) In order to prevent further misunderstanding, the following considerations are in order. When secondary current distribution prevails, the electrode is considered to have a uniform current density. However, there is, likewise, a uniform overpotential as a boundary condition. This condition (actually external to the electrolyte domain) closely resembles the constant potential case. At this point, the true meaning of the comparison of ohmic effects in Eq. [3] is of importance. The sum of the individual potential terms is indeed constant, as indicated above by Newman, but as nearly constant current density conditions are approached, the slight differences in the nearly similar but large overpotentials represents the radial variation of the ohmic potential term. This variation is quite mild and is given in the paper as Eq. [30a] and is shown in Fig. 1 for $0 < r/a < 1$. The entire deviation of local ohmic potential from the average value is totally overshadowed by the overpotential associated with the constant J condition. In going from primary distribution, with its theoretical infinity of J near the edge of the disk, to uniform J, the ohmic drop may be considered to be rearranged slightly as a function of position. Our paper has treated these extreme limiting cases and has bounded the variation which occurs. The combination of mixed features of true electrode resistance and local ohmic potential drop (*i.e.* center of disk) can serve no useful purpose since they are not directly comparable, as pointed out above. When used in conjunction with the recommendation of our paper, *i.e.* large remote reversible counterelectrode rather than remote probe, the average resistance is directly measurable and does not require knowledge of local parameters. The association of the notion of resistance with a point is unfortunate. Clearly from Eq. [27] or [34], the resistance becomes infinite as radius decreases. Resistance has meaning only for a finite size current aperture in the conducting domain. One does not need to know the point on the electrode where the drop matches the average, nor is the local concentration and J neces-

[83] J. Newman, *This Journal*, 117, 507-508 (1970).

sary. One simply no longer needs the temporary concept of local ohmic potential drop. One simply measures the resistance as a matter of course, *i.e.* as the rapid drop (oscilloscope) of the voltage-time trace following current interruption.

The agreement with our result found by Newman[82] in his impedance calculations is gratifying. The low-frequency limit for so-called capacitive impedance corresponds to a large value for the group in Eq. [3]. Since the charging of the double layer is just the establishment of overpotential, the interface potential drop predominates.

In his subsequent paper, Newman[83] has approximated the total disk resistance by the lower resistance limit for primary current density. However, Eq. [5] of that paper may equally well be represented within the limits bounded by our Eq. [27] and the upper limit in Eq. [34]. The maximum error caused by following Newman's procedure is to underestimate the true ohmic resistance drop by 8%. Of course, the error, while possibly small, is at variance with statements in Newman's approach which maintain that, independent of the J distribution prevailing before interruption, the ohmic drop measured by interruption corresponds to the primary distribution. In terms of experimental practice, since overpotential requires some finite time to be established, the ohmic drop at the switching on of constant current should be given by the primary current distribution value. As the overpotential builds, the same constant current exists in the circuit, but the J distribution adjusts to some steady value between the primary limit and the uniform secondary distribution limit. The finally large overpotential is greater than the ohmic drop, in accord with Eq. [3]. However, the rearrangement of the field affects the average domain potential in the electrode plane and the corresponding resistance increases. Thus, the interruption IR drop may be as much as 8% greater than the initial switch-on IR drop. The reshaping of the field, particularly close to the electrode, drastically affects the local current density, which varies as $\infty > \frac{J}{J_{avg}} > 1$ at the edge $r = a$ and as $\frac{1}{2} < \frac{J}{J_{avg}} < 1$ at the center, $r = 0$. Finally, it should be mentioned that there is an aspect of practical importance which deserves attention. The concept of "transient current distribution" may be introduced for electrode systems where nonsteady-state boundary conditions prevail. For a simple constant current circuit, at switch-on, current is used principally for double layer charging, with redistribution to the faradaic process as time elapses. The important point is that current distribution computed on the basis of the steady-state overpotential-current relation is inappropriate at the start of the current passage. It is thus implicit that all systems respond initially with a primary current distribution, although the distribution may smooth to be more uniform in a matter of, *e.g.* milliseconds. The importance of this concept to areas such as pulse charging of batteries and reverse cycle plating is clear but requires both further theoretical and experimental effort.

The Thermodynamics and Electrode Kinetic Behavior of Nickel in Acid Solution in the Temperature Range 25° to 300°C

R. L. Cowan and R. W. Staehle

(pp. 557-568, Vol. 118, No. 4)

D. Lewis[84]: Cowan and Staehle, in the paper under discussion, have referred to some of my early work on the thermodynamics of corrosion processes in aqueous systems at elevated temperatures, and have attributed to me some very inaccurate data on the hydrogen-silver chloride, silver cell. However, nowhere in the report they cite is this cell mentioned, let alone any calculated or experimental values given for its emf; and I have not obtained the results they give in their Table I.

[84] Department of Inorganic Chemistry, The Royal Institute of Technology, Stockholm 70, Sweden; and Materials and Fuels Department, AB Atomenergi, Stockholm 43, Sweden.

Table I. Errors in estimates of the equilibrium constants of typical reactions due to neglecting heat capacity terms

Number of "uncompensated" ions	Reaction	$\log {}_T k$ Estimate 1	$\log {}_T k$ Estimate 2
0	$\frac{1}{2}O_2(g) + H_2(g) = H_2O(l)$	0.17	0.0
0	$NH_4^+ = H^+ + NH_3(aq)$	0.34	0.0
1	$AgCl(s) + e^- = Ag(s) + Cl^-$	1.50	3.21
2	$H_2O = H^+ + OH^-$	2.40	1.48

In later work, described in a report[85] communicated to Staehle shortly after its publication, I have taken results for the reduction of silver chloride (and for some other reactions) to illustrate observations on methods that might be used for estimating equilibrium constants (or electrical parameters) for reactions in aqueous systems up to 374°C. It may be useful to summarize these observations here.

Figure 1 shows values for the equilibrium constant of the reaction

$$AgCl(s) + \frac{1}{2}H_2(g) \rightleftharpoons Ag(s) + H^+ + Cl^- \quad (Ag\ 1)$$

calculated using: (a) the Van't Hoff isobar, *i.e.* neglecting all heat capacities; (b) the assumption that the heat capacities of the aqueous ions are negligible; (c) estimates of the heat capacities of the aqueous ions obtained on the basis of the correspondence relations discovered by Criss and Cobble[86,87]. It is seen that the somewhat modified form of the correspondence relations used in my work leads to results that are in excellent agreement with the corresponding values obtained from the experimental study reported

[85] D. Lewis, Studies of Redox Equilibria at Elevated Temperatures. 1. The Estimation of Equilibrium Constants and Standard Potentials for Aqueous Systems up to 374°C, AB Atomenergi, Studsvik, Sweden. AE-377 (1969).

[86] C. M. Criss and J. W. Cobble, *J. Am. Chem. Soc.*, **86**, 5385 (1964).

[87] C. M. Criss and J. W. Cobble, *J. Am. Chem. Soc.*, **86**, 5390 (1964).

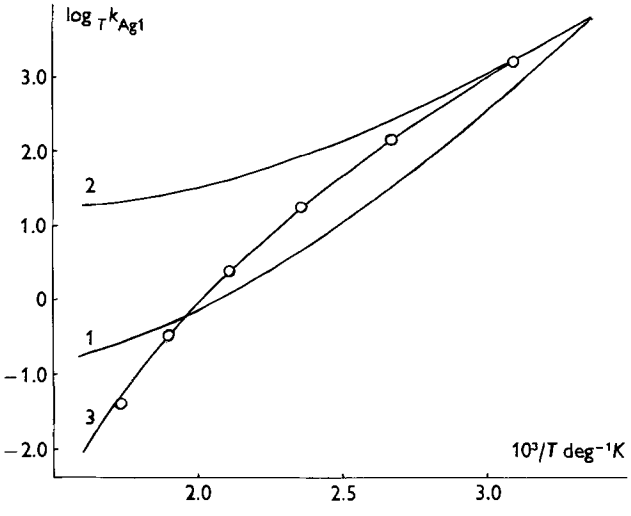

Fig. 1. The variation with temperature of the equilibrium constant for the electrochemical reduction of silver chloride. Values obtained from the experimental study by Greeley *et al.*[88] are indicated by open circles.

by Greeley, Smith, Stoughton, and Lietzke[88]. On the other hand, at the highest temperatures assumption (b) leads to very inaccurate results, like those calculated by Cowan and Staehle, while the Van't Hoff isobar leads to estimates that would be more useful.

Although several other approaches to the problem[89,90] have been shown to give good results in specific cases, I, like many others working in the field, am convinced that at present the Criss and Cobble correspondence relations lead to the most widely useful method for estimating the equilibrium constants for reactions in aqueous systems at elevated temperatures. However, in some cases it may still not be possible to estimate the ionic contributions to the heat capacity of reaction and it is useful to consider the errors that may arise from neglecting them.

Table I of this discussion gives some examples of the errors (log units) that can be expected in estimates of the equilibrium constants for some typical reactions at 350°C, obtained in two ways. First, Estimate 1, $\log_T k$ has been calculated using the Van't Hoff isobar. Secondly, Estimate 2, $\log_T k$ has been calculated with only the heat capacities of ionic constituents set equal to zero. The results obtained on the basis of the Criss and Cobble relations have been taken to be the correct values of the constants and the errors shown in the table are the differences from these results.

Generally, the error introduced by neglecting the heat capacities of ions can be expected to increase with the number of "uncompensated" ions, *i.e.* when there are more cations or anions among the reactants than among the products, or conversely. The error will, of course, be considerable when an electrode (half-cell) reaction is being considered, as illustrated by the results for the silver chloride, silver electrode: thermodynamic parameters for the electron being assimilated into those for the hydrogen-ion. However, when data for conjugate electrode reactions are combined in the estimation of equilibrium constants for complete cell reactions there will be some cancellation of errors.

The errors due to neglecting the heat capacities of cations are opposite in sign to those due to anions and so there will also be some cancellation of errors in the case of reactions like the acid-base dissociation of water. However, in many such cases the resultant may still be large because the errors due to cations may differ considerably in magnitude from those due to anions. Very large errors can be expected when highly charged cations or sulfate-, carbonate- or phosphate-ions are involved.

Finally, without in any way detracting from the work of Townsend[91], one may note that Cowan and Staehle are also mistaken in attributing to him priority in the adoption of the Criss and Cobble method in connection with potential-pH diagrams. In fact, Garrels and Christ[92] drew attention to the method in this connection and Robins and his co-workers were the first to publish equilibrium diagrams based on it[93,94], although there have probably long been many who have independently used it in similar work[95,96].

R. L. Cowan and R. W. Staehle: D. Lewis is mistaken in assuming that we have attributed to him inaccurate data on the H_2-Ag/AgCl cell in Table I of our paper. In fact, we have attributed to him an inaccurate method for calculating the standard electrode potential of half-cell reactions on the standard hydrogen scale at temperatures other than 25°C. As the general heading on our Table I clearly states, the values for the cell reaction were calculated by the method reported in the Lewis reference[97]; *i.e.* by applying Eq. [2] in our paper to the H_2-Ag/AgCl cell reaction with the assumption that the heat capacities of the ionic species (H^+ and Cl^-) are zero. The second column heading in this table might imply that the data were calculated by Lewis because the word "method" was left off immediately after "Lewis." That this is a proof reading or typographical error can be ascertained by noting Table II in R. L. Cowan's dissertation[98]. As a matter of record, R. L. Cowan wrote to D. Lewis[101] in October, 1967 pointing out that the method referred to in Footnote No. 85 did not accurately predict the experimental results of Greeley *et al.*[99,100] for the H_2-Ag/AgCl cell and that any potential-pH diagrams calculated for elevated temperatures by that method (such as those reported in Footnote No. 85 for the Fe-H_2O system) were probably in error. Lewis, in a return letter[102] acknowledged this point.

In regard to the discussion's initial comments concerning his Footnote No. 88, he has reiterated precisely the point we make in our Table I. (We had not received this reference until R. L. Cowan's dissertation[98] was complete and the first draft of our JOURNAL manuscript was complete.)

It should be noted that in Criss and Cobble's original papers[104-106] dealing with ionic entropies and heat capacities above 200°C, the values assigned to the parameters *a* and *b* (Eq. [5] is in our manuscript) used to calculate the entropy and the heat capacity of ions are based on the linear extrapolation of the 25°-200°C values. In fact they do not even give parameters for 350°C. Thus, one should be very careful in assuming that calculated free energy values based on the Criss and Cobble method are absolutely correct, as Lewis implies, at temperatures above 200°C. This is especially true for the 350°C case. As more experimental data are generated in the area of thermodynamic properties of aqueous electrolytes at temperatures above 200°C, the Criss and Cobble parameters should become more well known.

Finally, when we attributed to Townsend[107] the first use of the Criss and Cobble method for calculating *E*-pH diagrams, we did so on the basis that we had a preprint of his article in early 1968, although its eventual publication was delayed to 1970.

A New Technique for Investigating the Electrochemical Behavior of Electroless Plating Baths and the Mechanism of Electroless Nickel Plating

N. Feldstein and T. S. Lancsek (pp. 869-874, Vol. 118, No. 6)

J. P. Randin[108]: The chemical ("electroless") deposition of nickel may be considered as a mixed polyelectrode process wherein the anodic partial process is the

[88] R. S. Greeley, W. T. Smith, Jr., R. W. Stoughton, and M. H. Lietzke, *J. Phys. Chem.*, 64, 652 (1960).
[89] G. B. Naumov and I. L. Khodakovskii, *Dokl. Akad. Nauk SSSR*, 170, 886 (1966).
[90] H. C. Helgeson, *J. Phys. Chem.*, 71, 3121 (1967).
[91] H. E. Townsend, Jr., *Corrosion Sci.*, 10, 343 (1970).
[92] R. M. Garrels and C. L. Christ, "Solutions, Minerals, and Equilibria," Harper and Row, New York (1965).
[93] R. G. Biernat and R. G. Robins, *Electrochim. Acta*, 14, 801 (1969).
[94] B. W. Edenborough and R. G. Robins, *Electrochim, Acta*, 14, 1285 (1969).
[95] I. L. Khodakovskii, *Geokhimiya*, 6, 57 (1969).
[96] V. Ashworth and P. J. Boden, *Corrosion Sci.*, 10, 709 (1970).
[97] D. Lewis, First Annual Report: The Thermodynamics of Corrosion Processes, AB Atomenergi, Stockholm (1966).
[98] R. L. Cowan, Ph.D. dissertation, The Ohio State University (1959).
[99] R. S. Greeley, W. T. Smith Jr., R. W. Stoughton, and M. H. Lietzke, *J. Phys. Chem.*, 64, 652 (1960).
[100] R. S. Greeley, Ph.D. dissertation, The University of Tennessee (1959).
[101] Personal communication, R. L. Cowan to D. Lewis, October, 1967.
[102] Personal communication, D. Lewis to R. L. Cowan, November, 1967.
[103] D. Lewis, Studies of Redox Equilibria at Elevated Temperatures. 1. The Estimation of Equilibrium Constants and Standard Potentials for Aqueous Systems up to 374°C, A.B. Atomenergi, Sweden, AE-377 (1969).
[104] C. M. Criss and J. W. Cobble, *J. Am. Chem. Soc.*, 86, 5390 (1964).
[105] C. M. Criss and J. W. Cobble, *J. Am. Chem. Soc.*, 86, 5387 (1964).
[106] C. M. Criss and J. W. Cobble, *J. Am. Chem. Soc.*, 86, 5394 (1964).
[107] H. E. Townsend Jr., *Corrosion Sci.*, 10, 343 (1970).
[108] Hydro-Quebec Institute of Research, Varennes, Quebec, Canada.

oxidation of hypophosphite and the cathodic partial processes are: the nickel deposition; the phosphorus deposition; and the hydrogen evolution. This concept has been verified experimentally for the copper-formaldehyde system[109]. Each process may involve several steps among which one, at least, is a charge transfer reaction. Coupled chemical reactions may precede or follow the charge transfer step.

If each of the partial cathodic current densities (or deposition rates) can be calculated from experimental data, the steady-state potential measured, which is the algebraic sum of each partial process, cannot be derived from the data presented in the paper under discussion. If a significant interpretation is to be extracted from Fig. 5 and 6 in Feldstein and Lancsek's paper, the correct relationship between potential and current densities should be used.

For a simplified system with only two distinct partial processes under pure activation control, each process having one rate-determining charge transfer step, the measurable mixed potential in the absence of externally applied current is given by[110]

$$V_m = \frac{RT}{(\alpha_a n_a + \alpha_c n_c)\,\mathbf{F}} \left\{ \ln\left(\frac{Q_c}{Q_a}\right) + \ln\left(\frac{I_c}{I_a}\right) \right\} \qquad [1]$$

where:

V_m = mixed potential measured
α_a, α_c = symmetry factors of anodic and cathodic charge transfer step
n_a, n_c = number of charges transferred across the interphase during the anodic or cathodic charge transfer step
Q_a, Q_c = factor containing decomposition frequency of activated complexes, concentrations of reactants, *etc.* as defined in Footnote No. 110
I_a, I_c = exponential integrals containing chemical potentials, as defined in Footnote No. 110.

The general case can be simplified by neglecting reverse reactions in comparison with forward reactions, which are the oxidation of the reducing agent and reduction of the metallic ion. By noting that the anodic and cathodic partial current densities are equal at the mixed potential, and assuming a Tafel relation for both partial reactions, one obtains

$$\ln\left(\frac{i_{o,c}}{i_{o,a}}\right) \cong \frac{\alpha_a n_a \mathbf{F}}{RT}(V_m - V_{e,a}) + \frac{\alpha_c n_c \mathbf{F}}{RT}(V_m - V_{e,c}) \qquad [2]$$

where:

$i_{o,a}; i_{o,c}$ = anodic and cathodic exchange current densities
$V_{e,a}; V_{e,c}$ = equilibrium potential for the anodic and cathodic reactions.

To simplify further Eq. [2], it may be assumed that one of the partial reactions, for example the anodic oxidation of hypophosphite, determines predominantly the rate of deposition (for example, nickel); this means that the anodic Tafel line for this reaction has a much higher slope than the conjugate cathodic Tafel line. In this particular case, the following relation should be observed

$$V_m \cong \frac{RT}{\alpha_c n_c \mathbf{F}} \ln\left(\frac{i_{o,c}}{i_{o,a}}\right) + V_{e,c} \qquad [3]$$

For a given concentration of oxidizing agent (nickel ion), $V_{e,c}$ and $RT/\alpha_c n_c \mathbf{F}$ are constant, so that Eq. [3] may be written as

$$V_m \cong K_1 \ln\left(\frac{i_{o,c}}{i_{o,a}}\right) + K_2 \qquad [4]$$

where K_1 and K_2 are constants. It is worthwhile to note that Eq. [4], describing an approximation for a particular case for two partial processes, is not a usual Tafel-like relation. To rigorously treat the process of chemical deposition of nickel, which includes several partial cathodic processes of comparable rates, a more general relationship should be used.

Consequently, the interpretation of results contained in Fig. 5 and 6 of the paper under discussion does not seem adequate and the complete treatment of the polyelectrode system should be taken into account to reach significant conclusions. The literature gives several treatments of polyelectrode systems[110-113]. Stern[113] describes ideal systems with two and three oxidation-reduction reactions occurring simultaneously. The analysis, while containing several simplifying assumptions, shows the complexity of polarization measurements and indicates the care which must be taken if such measurements are to be interpreted quantitatively. The chemistry of the system must be understood, and the number and magnitude of the rates of each individual oxidation or reduction occurring during polarization should be known. Stern's treatment shows that even ideal polyelectrode systems can produce polarization data which may be difficult to interpret. Complicating factors such as heterogeneity of the electrode surface, changes of electrode area with time-film formation giving rise to a time effect, *etc.* would result in a system which is beyond quantitative description with the present knowledge of the electroless nickel process.

Wagner's treatment[114] predicts experimental methods that are promising for deciding whether a chemical or an electrochemical mechanism prevails for a particular process.

Furthermore, no mention is made in the paper under discussion of an eventual diffusion controlled process which was claimed to occur by several authors[115-117]. Moreover, if any Tafel relation applies to the study under discussion, the correct equation (for example for a cathodic process)

$$\frac{dE}{d(\ln i)} = \frac{-RT}{\alpha n \mathbf{F}} \qquad [5]$$

has to be used and not that reported by the authors. The symbols in Eq. [5] have the same meaning as those used by Feldstein and Lancsek.

The above discussion shows that Fig. 5 and 6 of the paper under discussion cannot be interpreted correctly by using the usual Tafel relation. A relation taking into account the complexity of the system under investigation should be used.

The following discussion will not take into account the restrictions concerning the interpretation of the deposition rate *vs.* the steady-state potentials described above. The disadvantages or advantages of the mechanism proposed by the authors with respect to other mechanisms will not be discussed either.

The modified hydride transfer mechanism proposed by Feldstein and Lancsek for the electroless nickel plating predicts that the oxidation of hypophosphite produces an hydride intermediate reacting with nickel (II) ion to give metallic nickel; with metaphosphite ion to give elementary phosphorus; and with a water molecule (or a proton in acidic media) to give molecular hydrogen. The three reactions are competitive, the first two give rise to the useful metallic deposit,

[109] M. Paunovic, *Plating*, 55, 1161 (1968).
[110] F. A. Posey, *This Journal*, 106, 571 (1959).
[111] J. O'M. Bockris, "Modern Aspects of Electrochemistry," p. 253, Academic Press, New York (1954).
[112] M. Stern and A. L. Geary, *This Journal*, 104, 56 (1957).
[113] M. Stern, *This Journal*, 104, 645 (1957).
[114] C. Wagner, *Electrochim. Acta*, 15, 987 (1970).
[115] J. S. Sallo, J. I. Swenson, and J. M. Carr, *This Journal*, 109, 389 (1962).
[116] G. Gutzeit, *This Journal*, 109, 1219 (1962).
[117] C. H. de Minjer and A. Brenner, *Plating*, 44, 1297 (1957).

whereas the third one corresponds to the oxidation of hypophosphite without simultaneous reduction of any useful element. The main characteristics of the process do not belong only to the mechanism proposed by Feldstein and Lancsek, but also stand for the other mechanisms previously advanced, namely the atomic hydrogen mechanism[118,119], the electrochemical mechanism[119], the hydride transfer mechanism[120], the mechanism involving hydrolyzed nickel with hydroxyl ions[121], and others. By not taking into account reactions [1], [2], and [5] together (see Fig. 7), the authors neglect one of the three competitive reactions, *i.e.* the hydrogen evolution accompanying the oxidation of hypophosphite without simultaneous reduction of any useful element.

The authors state that the relation

$$\frac{d}{dt}[H_2] = \frac{d}{dt}[Ni] + 1.5\frac{d}{dt}[P] \qquad [6]$$

was found to be in "excellent agreement between the hydrogen measured and that expected, based on the composition of the deposit." Equation [6] is valid only if all the hypophosphite oxidized is used to reduce either Ni^{2+} or metaphosphite ion and none is lost through reactions [1], [2], and [5] together (see Fig. 7), which is very unlikely to be found with ordinary bath compositions.

Experimental data reported by Feldstein and Lancsek in Fig. 3 and Table III for nickel deposition were used to calculate the efficiency defined as the molar ratio of the useful product formed to the hypophosphite oxidized =

$$\frac{2\,Ni + 3\,P}{Ni + 1.5\,P + H_{2\ total}},$$

for the modified hydride transfer mechanism, which was found to be between 0.89 and 0.94. Data in Fig. 4 and Table IV (of the paper under discussion) for the cobalt deposition give ratio between 0.63 and 0.79. Thus, reaction [5] in Fig. 7 can hardly be neglected since in the above examples taken from Feldstein and Lancsek's data it represents between 6% and 37% of the hypophosphite consumed. (As the hypophosphite consumed has not been determined, it has been calculated from the mechanism described in Fig. 7. It can be seen that: $H_2PO_2^-$ oxidized = 2 Ni + 3 P + H_2 from reaction [5] (Fig. 7) and H_2 from reaction [5] = H_2 total − Ni − 1.5 P; hence, $H_2PO_2^-$ oxidized = Ni + 1.5 P + H_2 total, where Ni, P and H_2 represent the molar amounts).

Typical hypophosphite utilization reported for a normal industrial plant gives molar ratio of Ni plated to $H_2PO_2^-$ consumed of 0.33[122], which corresponds to a ratio of useful products formed to oxidized hypophosphite of 0.82, assuming a phosphorus content of 8% and also for the modified hydride transfer mechanism. Laboratory experiments usually also fall into the same range of efficiencies, *i.e.* 0.76 to 0.92 in Footnote No. 122.

Reaction [5] in Fig. 7 is valid only in alkaline media. The corresponding reaction in the acidic media becomes

$$(X.....H)^- + H^+ \rightarrow H_2 + X \qquad [7]$$

The proton concentration increases as the pH decreases and, therefore, causes the hydride-proton combination reaction to occur more readily, which leaves a smaller portion of hydride ion to participate in the nickel (reaction [3], Fig. 7) or metaphosphite (reaction [6], Fig. 7) reduction reactions. This assumption has been verified experimentally[123]. Results taken from Footnote No. 123 and calculated according to the modified hydride transfer mechanism are summarized in Table I of this discussion.

Table I. Effect of pH on the hypophosphite efficiency (from Footnote No. 123).

Average pH	$H_2PO_2^-$ efficiency $= \frac{2\,Ni + 3P}{H_2PO_2^-}$
5.6	0.94
5.0	0.78
4.4	0.62
3.9	0.57
2.9	0.15

Modified hydride transfer mechanism proposed by Feldstein and Lancsek gives higher efficiencies than the other mechanisms since the molar ratio $H_2PO_2^-/P$ for the reaction giving rise to phosphorus is three for the modified hydride mechanism as compared to two for either the hydride transfer mechanism[120] or the mechanism involving hydrolyzed nickel[121], and 1.5 for the atomic hydrogen and the electrochemical mechanisms[118,119]. In hydride transfer mechanisms and in the mechanism involving hydrolyzed nickel, every mole of nickel reduced corresponds to two moles of hypophosphite oxidized whereas the ratio $Ni/H_2PO_2^-$ is one for both the atomic hydrogen and electrochemical mechanisms. It follows that the modified hydride transfer mechanism is the one which gives the higher hypophosphite efficiencies and, consequently, the lower ratio of hypophosphite oxidized according to reaction [5] (Fig. 7), *i.e.* without simultaneous reduction of any useful element.

Nevertheless, the aforementioned hypophosphite efficiencies of which some have been calculated from Feldstein and Lancsek's results, prove that the hydride-proton combination reaction cannot be neglected as proposed by the authors since it has been shown that this reaction can be the most important in this system. Consequently, Eq. [6] is incorrect and should be replaced by

$$\frac{d}{dt}[H_{2\ total}] = \frac{d}{dt}[Ni] + 1.5\frac{d}{dt}[P] + \frac{d}{dt}[H_{2\ from\ reaction\ [5]}] \qquad [8]$$

Equation [6] proposed by Feldstein and Lancsek is very unfortunate since it could lead to misinterpretations of the mechanism and to a false estimation of the efficiency of the process.

Acknowledgment

The author thanks Dr. A. K. Vijh and G. Bélanger for valuable discussions.

N. Feldstein and T. S. Lancsek: We wish to thank Dr. J. P. Randin for his interest and comments on our paper. In the paper under discussion, it has been demonstrated that a Tafel-like behavior is obeyed for nickel (or cobalt) and phosphorus deposited from electroless plating baths. In most of the cases, identical slopes have resulted in the log *i vs. E* plots. The latter results were especially of significance and practical use since an *a priori* knowledge of such behavior provides a quick way for the estimation of the deposit composition under varied conditions. As demonstrated in Fig. 7 of the text, and as referred to by Randin, the deposition of nickel from hypophosphite-based solutions may be considered as a mixed polyelectrode process. In such a process, the anodic process is the oxidation of hypophosphite (Fig. 7, reaction [1]) and

[118] A. Brenner and G. E. Riddell, *J. Res. Nat. Bur. Std.*, 37, 1 (1946); *Proc. Am. Electroplaters' Soc.*, 33, 16 (1946).
[119] A. Brenner and G. E. Riddell, *J. Res. Nat. Bur. Std.*, 39, 385 (1947), *Proc. Am. Electroplaters' Soc.*, 34, 156 (1947).
[120] R. M. Lukes, *Plating*, 51, 969 (1964).
[121] P. Cavallotti and G. Salvago, *Electrochim. Metal.*, 3, 239 (1968).
[122] G. Gutzeit, *Plating*, 46, 1158, 1275, 1377 (1959); 47, 63 (1960).
[123] J. P. Randin and H. E. Hintermann, *Plating*, 54, 523 (1967).

the cathodic processes yield the nickel and phosphorus deposited and hydrogen evolved (Fig. 7, reactions [3], [5], and [6], respectively). The authors are not aware of any existing publications to date in which the Ni-P deposition was completely treated as a polyelectrode system; probably due to the complex nature of the reaction. Randin has suggested and outlined in his discussion that a complete treatment of a polyelectrode system is in order to further interpret Fig. 5 and 6. The authors are in agreement with Randin's suggestion; such an investigation is in order since it may provide a better correlation between the reported results (Fig. 5 and 6) and a fundamental model. However, caution should be exercised in the final interpretation since the analysis proposed by Randin is not rigorous and is generally simplified with several assumptions made.

As mentioned in the text, for the various nickel baths used in the study (and not for cobalt), a simplified expression was found correlating the hydrogen to the compositional makeup of the deposit (Ni and P). Specifically, the following correlation was found to apply

$$\frac{d}{dt}[H_2] = \frac{d}{dt}[Ni] + 1.5\frac{d}{dt}[P] \qquad [1]$$

and this result leads to the suggestion that reaction [5] (Fig. 7) does not play a major role for the nickel baths examined. In testing the above correlation it should be emphasized that for the case of the glycine bath, analysis of the deposit was carried out in this laboratory; however, the hydrogen evolution data was taken from the work of Holbrook and Twist. In this case, excellent agreement in demonstrating the above correlation was achieved. In the case of electroless Co-P deposition, as indicated in the text, the molar ratio of hydrogen evolved to deposited cobalt was found to be about 3:1; this ratio is considerably greater than corresponding values found for Ni-P-type systems. Due to this trend, our Eq. [1] was specified by the author to apply only in the nickel cases. The attempt by Randin to extend the meaning of this correlation beyond its initial intent shows that great care must be exercised in comparing baths employing different metals. Nevertheless, it is believed that the basic reactions described in Fig. 7 do apply for cobalt as well as for nickel (despite the obviously different rate ratios).

From the modified hydride mechanism proposed by the authors (Fig. 7) the authors and Randin realized that the following correlation may apply

$$-\frac{d[H_2PO_2^-]}{dt} = 2\frac{d[Ni]}{dt} + 3\frac{d[P]}{dt} + \frac{d[H_2]^*}{dt} \qquad [2a]$$

where $\frac{d[H_2]^*}{dt}$ refers to the hydrogen evolved from reaction [5]. If indeed the contribution of reaction [5] is minor, the following simplified expression will result

Table II

Molar concentration of glycine	Weight reclaimed[a] (mg)		Hypophosphite consumed (mmole)	
	Ni	P	Experimental[b]	Predicted[c]
0	15.61	0.66	0.6	0.6
0.01	34.02	2.55	1.5	1.4
0.04	55.27	2.29	2.4	2.1
0.10	42.55	0.54	1.5	1.5
0.30	33.65	0.52	1.4	1.2

[a] Data taken from the text.
[b] Determined from fresh baths of identical compositions to those used in text.
[c] Based upon Eq. [2b].

$$-\frac{d[H_2PO_2^-]}{dt} = 2\frac{d[Ni]}{dt} + 3\frac{d[P]}{dt} \qquad [2b]$$

In order to test the applicability of Eq. [2a] *vs.* [2b], plating solutions were analyzed for the hypophosphite consumption. This work is in progress and details will be published at a later date. However, Table II is provided showing some preliminary results.

Examination of these results shows that Eq. [2b] does apply and thus the contributions of reaction [5] (Fig. 7) may be considered negligible to a first approximation for the nickel bath examined. This trend is consistent with the simplified form of our Eq. [1] and thus further supports the mechanism proposed in Fig. 7.

The plating solutions chosen for the present investigation were, in most cases, taken from the literature. Whether the results of the published paper are unique to these solutions or not, is not obvious and will require further investigation. However, some of the conditions suggested by Randin (Table I) with bath's pH below 4, are not conditions commonly used in commercial practice. It should be pointed out that it is the interfacial pH which is the important parameter rather than bulk pH. In all cases, the interfacial pH values are below bulk values. Furthermore, operating at bulk pH values below 4, it is reasonable to anticipate the occurrence of a new reaction which etches some of the deposited nickel, thereby decreasing the apparent efficiency of plating and increasing the phosphorus content in the deposit. Thus, the efficiency results in Randin's Table I may be misleading with respect to the basic mechanism taking place.

With respect to the choice of reaction [6] (Fig. 7), it should be noted that several other reactions for the phosphorus formation were proposed, in the literature, some of which require more than one mole of hypophosphite oxidized per mole of phosphorus deposited. In this respect it may be helpful to establish the mechanism and stoichiometry for the phosphorus formation in electrolytic plating. The knowledge of phosphorus codeposition in electrolytic plating may provide a better insight to assist in the screening of the various proposed reactions for the phosphorus deposition in electroless plating.

JOURNAL OF THE ELECTROCHEMICAL SOCIETY

SOLID STATE SCIENCE

DECEMBER 1971

Mechanism of the Oxidation of Titanium Disilicide

F. N. Schwettmann,*,[1] R. A. Graff, and M. Kolodney*

Chemical Engineering Department, The City College of the City University of New York, New York, New York 10031

ABSTRACT

The oxidation of $TiSi_2$ was studied at temperatures of 300°-1300°C. Wafers prepared using the techniques of powder metallurgy had densities of 95 to 98% of the theoretical value. On oxidation at temperatures up to 600°C, the polished wafers formed a protective, titania-silica glass. The rate data indicate a complex surface and diffusion-limited mechanism. Above 600°C, the oxide consisted of an amorphous SiO_2 film with crystalline islands of TiO_2 (rutile). From 1000°-1300°C, parabolic kinetics with an activation energy of 21.3 kcal/mole were observed. These data are consistent with a model in which the rate-determining step is the diffusion of oxygen through the silica film with the simultaneous diffusion of titanium from the substrate to the islands of rutile growing on top of the amorphous silica. The protective nature of the oxide appears to be due in part to the ability of titanium to assume fourfold coordination and replace silicon in the growing silica film without disrupting the tetrahedral network.

In recent years, there has been an increasing demand for structural materials which can be used at temperatures as high as 1300°C. At the present time, tantalum or columbium with a mixed silicide coating provide suitable structural and oxidation resistance for certain applications (1, 2). It has been found that a simple coating of $TaSi_2$ or $CbSi_2$ does not provide sufficient oxidation protection (3). In order to obtain a satisfactory coating, it is necessary to incorporate modifiers such as chromium, titanium, molybdenum, or vanadium silicides into the coating layer (4). In some of the more promising systems, the resulting protective layer consists mainly of $TiSi_2$ (5).

Little work has been done on the oxidation behavior of bulk $TiSi_2$. Samsonov (6) describes the results of an experiment in which $TiSi_2$ was heated to 1200°C over a 4 hr period. An adherent oxide film was formed with a weight gain of only 0.3 mg/cm^2. The author speculates that the protective nature of this film is due to the formation of an eutectic mixture of titanium silicates. No indication was given of the sample quality. The present study was undertaken to provide data and a mechanism for the oxidation of bulk $TiSi_2$.

Experimental

The $TiSi_2$ wafers used in this study were prepared using the techniques of powder metallurgy. The disilicide was formed by the reaction of titanium (99.9%) powder or sponge and silicon (99.99%) powder at 1000°C at a pressure of 10^{-4} Torr. The reaction is quite exothermic and careful control is required to prevent melting of the reaction mass. Microscopic examination and x-ray diffraction showed that no oxide is formed during this process. The spongy product was ground in a hardened steel vial, screened, and the −325 mesh material removed, washed with dilute HCl, and dried. Binder was added and 1 in. diam wafers pressed in a hardened steel die at 5-10 tsi. Sample thickness was approximately 0.1 in. (0.25 cm).

Densification of the compacted wafer was carried out in two stages. In the presinter, the binder was removed by heating slowly to 900°C in vacuum. Final sintering was carried out in a separate furnace at 1375°-1400°C and 5 x 10^{-5} Torr for 15 min. The faces of the sintered disks were ground successively on diamond disks of medium, 30μ, and 6μ coarseness. The ground wafers were lapped with 6μ and then 3μ diamond paste followed by a brief polish with 0.25μ alumina. Prior to oxidation, the lapped wafers were cleaned in boiling organic solvents and water, followed by a quick dip in 10% HF in water.

The oxidation experiments were carried out in a vertical tube furnace. Temperature variation over a 4 in. region in the center of the tube was less than 5°C. The oxidizing atmosphere was a mixture of oxygen and argon flowing at 100 cc/min. The $TiSi_2$ samples were supported on a fused quartz holder and suspended from the top of the furnace.

Oxidation rate data were obtained by periodically removing the sample from the furnace and weighing on a microbalance with a sensitivity of ±2 μg. The structure of the growing oxide film was studied using scanning electron microscopy (SEM), x-ray diffraction, and infrared spectroscopy. A Cambridge Stereoscan Mark II was used in the emissive mode for the SEM work. X-ray diffraction scans were made of the initial silicide surface and of the growing oxide film. The diffraction patterns were obtained with a Norelco Geiger counter x-ray spectrometer using CuKα radiation. The surface of the wafer was usually scanned by inserting it directly in the sample holder, although a number of powder patterns were also prepared by

* Electrochemical Society Active Member.
[1] Present address: Semiconductor Research and Development Laboratories, Texas Instruments, Inc., Dallas, Texas 75222.
Key words: oxidation, titanium silicides, silica, titanium dioxide, diffusion.

grinding the finished wafer. Several powder patterns were also obtained on the oxide film.

A more detailed analysis of the amorphous region of the oxide film was performed by infrared spectroscopy using a Perkin-Elmer Micro Specular Reflectance Accessory in conjunction with a Perkin-Elmer 621 Spectrophotometer. The spectrum obtained was a 2X absorption spectrum which can be compared with literature data on amorphous silica and glasses.

Results

Sample quality.—The theoretical density of $TiSi_2$ as determined by x-ray diffraction is 4.13 g/cm^3 (7). Typical values obtained in the present study were 95-98% of the theoretical value. The surface quality of a polished and lightly etched wafer is indicated in Fig. 1. In addition to the $TiSi_2$, a small amount of a second phase identified as silicon was present at the grain boundaries. A few small pits are also present, the majority of them occurring in the silicon phase.

Kinetic data.—The major variable that was considered in the kinetic study was temperature. Unless otherwise indicated, the oxygen partial pressure of the gas phase was 0.2 atm although a limited number of experiments used pure oxygen as the ambient. In the initial phase of the study, alteration of the gas flow from 0 to 200 cc/min produced no change in oxidation rate.

Several $TiSi_2$ wafers were oxidized at 300°C in order to establish the lower level of observable oxidation. After 20 hr at temperature, a total weight gain of 25 μg was observed. After 320 hr, the weight increase was still only 112 μg.

Typical weight gain data obtained at 600°C are shown in Fig. 2 where the square of the weight gain

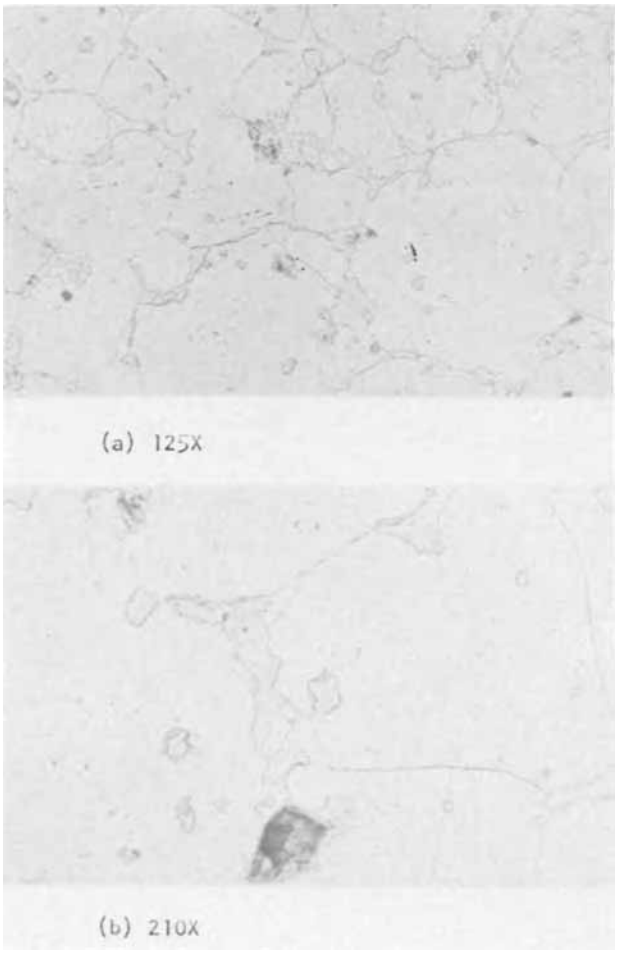

Fig. 1. Surface of polished and etched $TiSi_2$ wafer

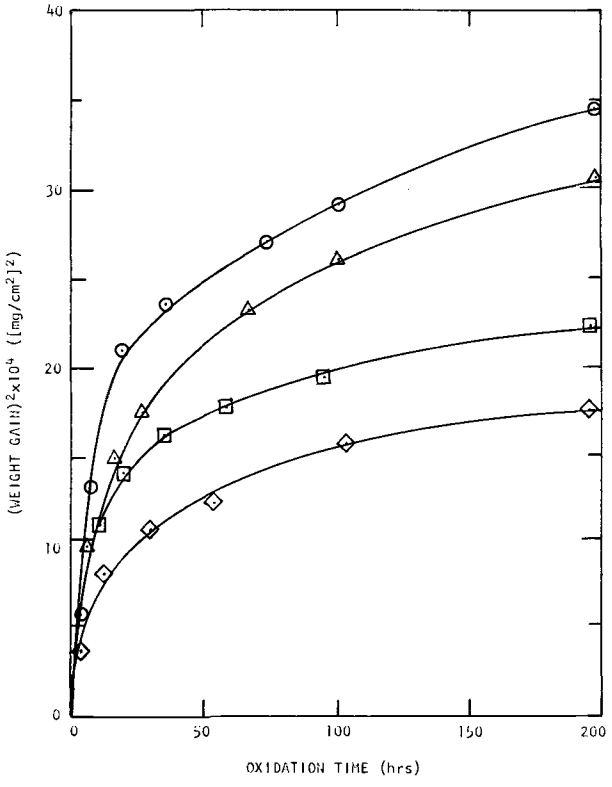

Fig. 2. Rate data for $TiSi_2$ oxidized at 600°C

is plotted against time of oxidation. The considerable variation in the data is caused by differences in surface quality. The greater the number of pits and size of the silicon phase, the higher the oxidation rate. The lower curve is typical of the best quality wafers. When the samples were oxidized in pure oxygen, within experimental error, no difference in rate was found. At 800°C, results similar to those obtained at 600°C were observed. Within experimental error, the magnitude of the observed weight gain for the first 50 hr was the same as that observed at 600°C. Beyond 50 hr, the weight gain at 800°C became greater.

Typical rate data obtained at 1000°C are shown in Fig. 3. Again, variation due to surface quality is evident. In this case, however, straight lines are obtained when the square of the weight gain is plotted against time. Similar straight lines were obtained at 1200° and 1300°C. Parabolic rate constants were determined at oxygen pressures of 0.2 atm and 1 atm. The constants for each run were obtained by the method of least squares and averaged over all runs at identical conditions. Only two short runs were made at 1300°C. The results are given in Table I.

A summary of the best data for intrinsic $TiSi_2$ is shown in Fig. 4. From the parabolic rate constants obtained at 1000°-1300°C an activation energy of 21.3 kcal/mole was obtained.

Character of the oxide film.—At 300°C, no visible continuous oxide film was observed after 300 hr at temperature. A few, very small, isolated, multicolored crystalline areas were visible under a light microscope. X-ray analysis indicated only the $TiSi_2$ substrate which remained unchanged during the oxidation pe-

Table I. Parabolic rate constant (mg/cm^2)^2/hr

Temp, °C	P_{O_2} = 0.2 atm	P_{O_2} = 1 atm
1000	$3.52 \pm 0.77 \times 10^{-4}$	4.06×10^{-4}
1200	$8.72 \pm 1.48 \times 10^{-4}$	10.03×10^{-4}
1300	17.4×10^{-4}	

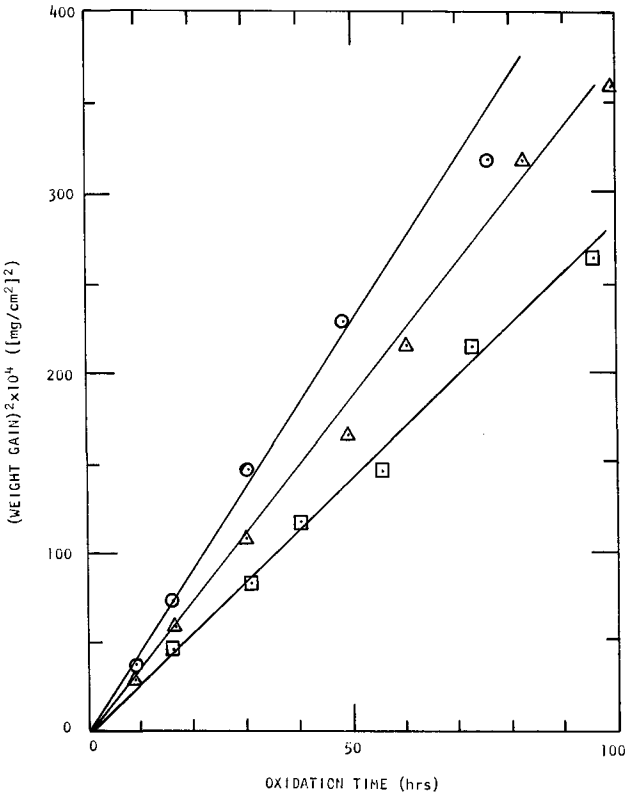

Fig. 3. Rate data for $TiSi_2$ oxidized at 1000°C

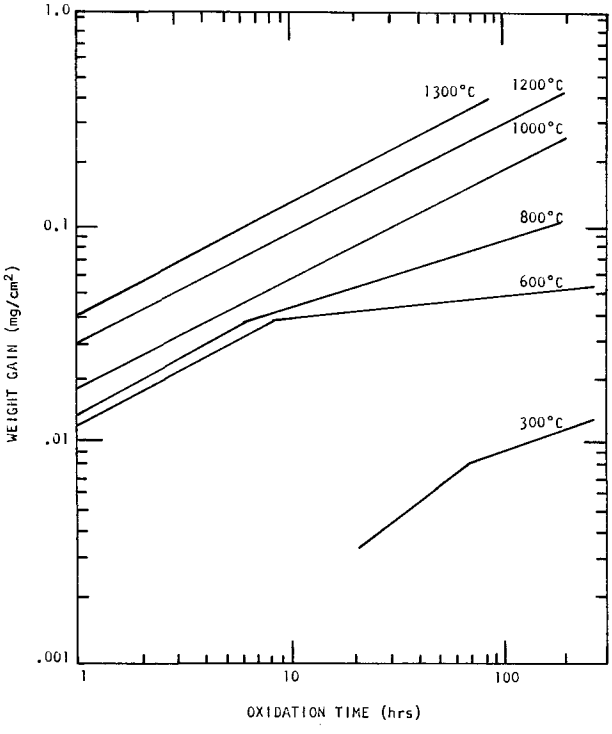

Fig. 4. Rate data for $TiSi_2$ oxidized at 300°-1300°C

riod. It is likely that the observed weight increase is due to the oxidation of small amounts of impurities such as iron and the formation of a thin, continuous silica layer. This is typically observed with single crystal silicon using ellipsometry (8), where, for example, 30Å of SiO_2 form on silicon standing at room temperature for several hours.

At 600°C, a transparent oxide film, exhibiting interference colors, was formed after one hour of oxidation. By incident light microscopy, it was found that the over-all color was a blend of several color regions. Each of the different colors corresponded roughly in size and shape to the $TiSi_2$ grain structure. The oxide formed over the separate silicon phase showed the same interference color throughout the specimen and from specimen to specimen. As the time of oxidation increased, the interference colors changed gradually until about 30 hr after which little change occurred. The color of the oxide on the silicon phase remained a tan to pale brown through the course of a run. Light microscopy of the oxide film revealed no crystalline regions after 300 hr of oxidation, but after 800 hr, a number of small, yellow crystalline islands were found near the holes originally observed in the surface. X-ray analysis showed only the $TiSi_2$ with parameters constant throughout the oxidation period.

Comparison of the infrared spectrum of the oxide with that obtained for silicon dioxide thermally grown on silicon provides considerable insight into the structure of the film. An extensive transmission infrared study of SiO_2 on silicon has been reported by Pliskin and Lehman (9). They found that a dense, thermally grown SiO_2 film with a thickness of 1 μm had absorption peaks at 1093, 805, and 455 cm^{-1}. The 1093 cm^{-1} peak is attributed to Si-O bond stretching and the 455 cm^{-1} peak to Si-O-Si bond bending. The exact nature of the other absorptions in unclear. The position and half-width of these absorptions, particularly the Si-O vibration at 1100 cm^{-1}, is strongly influenced by the structure of the SiO_2. A decrease in the oxide density causes a shift to lower absorption frequencies and an increase in the peak half-width.

The infrared spectrum of the oxide formed on $TiSi_2$ at 600°C has the characteristic absorption peaks of amorphous SiO_2. However, the major 1100 cm^{-1} Si-O peak was shifted to a lower frequency as was the Si-O-Si bond bending at 435 cm^{-1}. The 800 cm^{-1} peak appears to be in the same position as when found in dense, pure SiO_2 films. Based on the work of Zeitler and Brown (10), the observed absorption at 930 cm^{-1} is probably due to a Ti-O-Si vibration [Zeitler and Brown (10), studying the infrared spectra of organic-titanium-silicon compounds, reported an absorption at 920-925 cm^{-1} which they attributed to a Ti-O-Si bond]. These data, plus the observed shift in the Si-O vibration to a lower frequency indicates that the oxide film at 600°C is not pure SiO_2 but a titania-silica glass.

If a stoichiometric reaction occurred between the $TiSi_2$ and oxygen, the oxide should contain two atoms of silicon to each atom of titanium or 40 weight per cent (w/o) titanium. The phase diagram for the SiO_2-TiO_2 system (11) indicates a maximum solid solubility of about 10 w/o in SiO_2 at the eutectic temperature of 1540°C. The concentration of titanium in the glass formed on $TiSi_2$ at 600°C was not determined, but the mobility of the titanium in the oxide at 600°C is sufficiently low that a supersaturated solution of titanium in SiO_2 could be formed. Another possibility is that the oxide film contains approximately the 10 w/o TiO_2 solid solubility limit, with the remaining titanium having reacted to form a lower silicide. Typical reactions would be

$$2\,TiSi_2 + 4\,O_2 = TiO_2 + 3\,SiO_2 + TiSi$$

$$6\,TiSi_2 + 10\,O_2 = TiO_2 + 9\,SiO_2 + Ti_5Si_3$$

where the TiO_2 is in the form of a silica glass. The amount of Ti_5Si_3 could be too small to be observed by the x-ray.

Oxidation at 800°C produced a significant change in the structure of the growing oxide film. In the initial stage of oxidation, an amorphous film similar to that obtained at 600°C was produced, but the interference color was more uniform over the surface. However, after 3 hr, small clumps of crystalline islands were observed situated on top of the amorphous

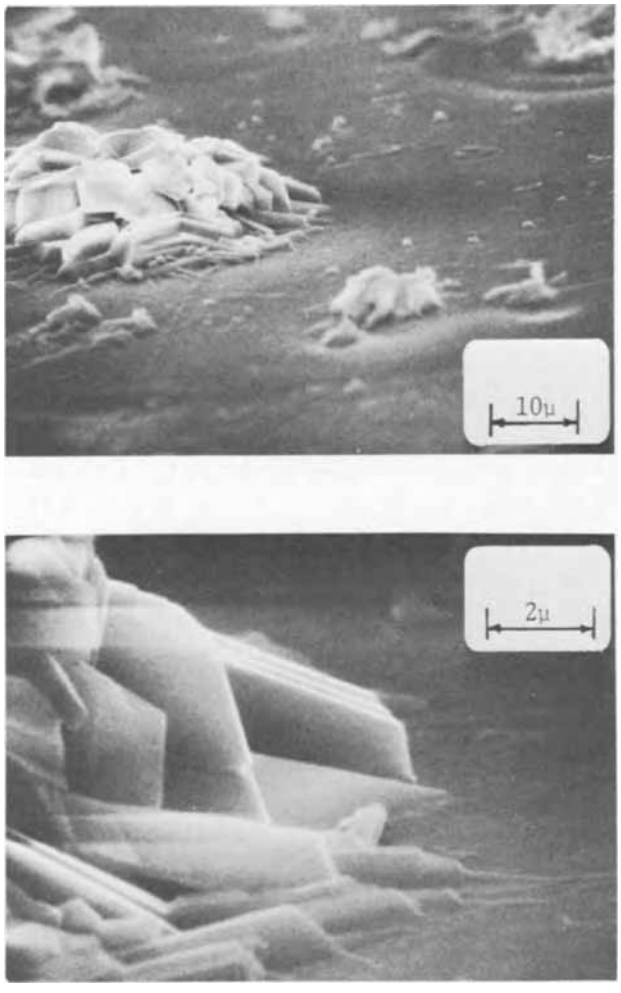

Fig. 5. Scanning electron micrographs of surface after oxidation at 800°C for 100 hr.

phase. A scanning electron micrograph of the surface after oxidation for 100 hr is shown in Fig. 5. Examination of a cleaved specimen in cross section showed that the crystalline region in most cases is separated from the substrate by the amorphous layer. In addition, as shown in Fig. 5, the outer region of the TiO_2 appears to have made intimate contact with the amorphous phase. X-ray diffraction identified TiO_2 in the rutile form. The crystalline islands were generally found at the phase boundary of the $TiSi_2$ and silicon phases, in particular where pits were present. As the oxidation time increased, more islands were formed while those formed earlier increased in size.

The oxide film formed at 1000°C was similar to that obtained at 800°C. X-ray and metallographic studies indicated an amorphous matrix with crystalline islands of TiO_2 (rutile). The crystallization occurred after only about 1 hr at reaction temperature as compared to the 3-7 hr required at 800°C. Most of the crystallization again occurred at the silicide grain boundaries. The TiO_2 clumps were more numerous and larger in size than those formed at 800°C for comparable oxidation times. The infrared spectrum of the oxide is more typical of the spectra observed when silicon is oxidized. The absorption at 930 cm^{-1} caused by titanium in the oxide is no longer present because TiO_2 has crystallized out. The frequency of the Si-O band is now 1060 cm^{-1}. This value is still not as high as the 1090-1100 cm^{-1} obtained for SiO_2 on silicon, indicating a less pure or lower density oxide.

At 1200°C, crystallization of the TiO_2 occurred within 0.5 hr at temperature. The major difference at this temperature was that α-cristobalite was also identified by x-ray after 0.5 hr. After 30 hr, the crystalline α-cristobalite regions could be observed with a light microscope in the amorphous SiO_2 matrix. The infrared spectrum obtained at 1200°C shows amorphous SiO_2 with additional vibrations at 1190, 950, and 535 cm^{-1}. The peaks are very much sharper than at lower temperatures, indicating a denser structure, but the major Si-O vibration is found at 1060 cm^{-1} indicating that the oxide is not as pure or dense as SiO_2 grown on silicon.

At 1350°C, the character of the oxide film was considerably changed. No interference colors were observed; the sample was a dark, dull gray covered with a glassy oxide which was thicker in the center of the sample. The wafer was distorted slightly.

At each of the temperatures studied, changing the oxygen partial pressure from 0.2 to 1.0 atm had no observable effect on the structure of the oxide film.

To explore the possible titanium content of the oxide grown on $TiSi_2$, a brief study was made of the x-ray and infrared characteristics of the TiO_2-SiO_2 system at elevated temperatures. Pellets formed from TiO_2 (rutile) and amorphous silica powders were fired at 1550°C for 15 min at 10^{-4} Torr. Cooling to below red heat was achieved in less than 2 min. When 10 w/o TiO_2 was used, x-ray analysis of the glassy-blue surface indicated that the material was amorphous. The infrared spectrum obtained using the KBr pellet technique was the same as that of the SiO_2 charged, with the exception of a broad absorption at 940 cm^{-1}. When the concentration of TiO_2 was increased to 20 w/o, TiO_2 was found in the x-ray analysis. The infrared spectrum was similar to that found for the 10 w/o TiO_2 sample. The existence of a true glass in this system up to 10.8 w/o titania has recently been confirmed by Evans (12).

Discussion

Effect of surface quality.—In order to obtain reliable oxidation rate data, it is necessary that the sample surface be both chemically and physically clean. However, it is difficult to prepare wafers that contain only a single compound and are free of macroscopic defects because there are three contiguous compounds (Ti_5Si_3, TiSi, $TiSi_2$) in the titanium-silicon system (13). When preparing $TiSi_2$, a small amount of a second phase is likely to be present. In this study, a slight excess of the stoichiometric amount of silicon was used in the preparation to offset any loss of silicon during vacuum sintering and also to insure that the second phase formed was silicon and not a lower silicide. In general, the lower silicides oxidize much more rapidly and it was felt that this would mask the $TiSi_2$ oxidation rate. Several wafers of TiSi and Ti_5Si_3 were fabricated and did show an oxidation rate which was an order of magnitude greater than $TiSi_2$.

On the other hand, the presence of more than 3% silicon causes a large increase in the oxidation rate. This appears to be due to an increase in the number of pits on the surface, most of which are in the silicon phase. During oxidation, these holes act as nucleation sites resulting in rapid localized oxidation. Nevertheless, it is significant that the physical and chemical defects do not prevent the formation of a protective oxide layer.

Kinetics of oxide growth.—Since the oxidation rate was independent of gas velocity and since it was highly dependent on film thickness, especially at low temperatures, it appears that some form of transport of one or both of the reacting species through the oxide film is the rate-controlling step.

The mechanism for the growth of the oxide film on $TiSi_2$ at 1000°-1300°C appears to be similar to that observed for silicon. In a detailed study on the oxidation of silicon, Deal and Grove (14) report parabolic

kinetics for the temperature range 1000°-1200°C. Earlier studies (15) had shown that the rate-controlling step was the diffusion of oxygen through the oxide film. The precise atomistic mechanism is not known although the rupture of Si-O bond appears to be required. The activation energy was measured at 28.5 kcal/mole (14) as compared with the value of 21.3 kcal/mole observed here for the oxidation of $TiSi_2$. The weight gained by $TiSi_2$ at 1000°C is approximately 1.6 to 2.0 times greater than that observed for silicon oxidized a comparable time. If diffusion of oxygen through the SiO_2 matrix is the rate-controlling step for $TiSi_2$ oxidation, the expected weight gain would be 1.5 times greater than for silicon because, assuming stoichiometric oxidation, 1 atom of titanium is oxidized in addition to the 2 atoms of silicon. As oxidation of the silicon occurs at the oxide-silicide interface, the titanium diffuses through the silica to the gas-oxide interface where TiO_2 clumps are formed.

A number of samples with many pits in the surface did not exhibit parabolic behavior in the initial few hours of oxidation at 1000°C. Instead, there was initial rapid oxidation at the pits because of their higher interfacial energy. As the oxidation proceeds, a barrier layer of amorphous SiO_2 forms slowing down the oxidation rate. It is likely that the rate in the localized region goes from surface-controlled to diffusion-controlled. It is difficult to formulate this result mathematically since the area involved in the changing kinetics is difficult to estimate as is the time required for the barrier layer to form.

The kinetic data at 600°C are characterized by a rapid initial oxidation rate followed by an extremely low rate. The variation of the interference color with orientation of the underlying $TiSi_2$ grains indicates that the rate of oxidation is a function of crystal orientation. This implies that in the initial period, bulk diffusion through the oxide is not the rate-controlling step. However, the data cannot be fitted to a linear or combination linear-parabolic mechanism. A possible controlling mechanism would be combination of surface reaction and diffusion with a variable diffusivity. In the initial phase, diffusion through short circuit paths in the oxide is rapid. As the time of oxidation increases, these paths become gradually blocked and bulk diffusion becomes rate controlling. Since the diffusion rate through a silica film at 600°C is small, the weight increase should drop off dramatically. This is what is observed. The mechanism that could account for a decrease in the diffusivity may be a pore closure model as described by Evans (16). While there is no evidence indicating pores in the oxide, the study of Ing *et al.* (17), on the structure of the oxide film formed on silicon indicates the presence of microchannels. This type of defect would be more likely to occur in the impure silica films formed on $TiSi_2$ at low temperatures where the mobilities of the atoms are quite low. The kinetic data for oxidation at 800°C show characteristics similar to those observed at 600°C.

Protective mechanism.—Polycrystalline $MoSi_2$ is highly oxidation-resistant at high temperatures (18), but deteriorates rapidly in the 300°-600°C range (19). This "pest" phenomenon has been attributed to the presence of MoO_3 in this range and its volatilization above 600°C. Microcracks in the substrate are also held to be responsible. Since TiO_2 is not volatile at any temperatures studied, the present work on $TiSi_2$ indicates that a protective film can be formed even when both oxides are present and when the surface has considerable imperfections. These results suggest that while the presence of cracks in the sample present high energy nucleation sites which increase the reaction rate, the compatibility of the oxides is a more fundamental requirement for the formation of a protective oxide. The fact that TiO_2 is partially soluble in SiO_2 appears to be quite significant. The ability of titanium to assume fourfold coordination and replace silicon in the SiO_2 network allows a protective titania-silica glass to be formed at low temperatures and increases the compatibility of the crystalline TiO_2 and amorphous SiO_2 at high temperatures. In the latter case, a dense, continuous transition region is most likely present between the two oxides. By contrast, the incompatibility of MoO_3 and SiO_2 may be due in part to the excess charge of the molybdenum ion. Considerably more work is required to present a clearer picture of oxidation protection by silicides.

Acknowledgments

The authors thank the Lewis Research Center of the National Aeronautics and Space Administration for its support under grant NGR 33-013-017 and Mr. R. Oldrieve who monitored the grant. They are also grateful to J. Bodnaruk and D. Marden for experimental assistance, and to L. Crosthwait and S. Swanson for the scanning electron micrographs.

Manuscript submitted March 2, 1971; revised manuscript received *ca.* July 14, 1971. This was Paper 108 presented at the Atlantic City Meeting of the Society, Oct. 4-8, 1970.

Any discussion of this paper will appear in a Discussion Section to be published in the June 1972 JOURNAL.

REFERENCES

1. J. W. Gadd, "Advancement of Protective Coating Systems for Columbium and Tantalum Alloys," Tech. Report AFML-TR-65-203 (1965).
2. R. T. Wimber and A. R. Stetson, "Development of Coatings for Tantalum Alloy Nozzle Vanes," Solar RDR 1396-2 for NASA, (May 1966).
3. A. R. Stetson, H. A. Cook, and V. S. Moore, "Development of Protective Coatings for Tantalum Base Alloys," Tech. Report AFML TR-65-205 (1965).
4. D. J. Bracco, P. Lublin, and L. Sama, "Identification of Microstructural Constituents and Chemical Concentration Profiles in Coated Refractory Metal Systems," AFML TR-66-126 (1966).
5. E. J. Felten, *Electrochem. Technol.*, **6**, 438 (1968).
6. G. V. Samsonov, "Silicides and Their Uses in Engineering," Translation from Russian FTD-TT-62 430 1 & 2 (July 1962).
7. G. V. Samsonov, Plenum Press Handbooks of High Temperature Materials—Properties Index (1964).
8. R. J. Archer, *This Journal*, **104**, 619 (1957).
9. W. A. Pliskin and H. S. Lehman, *ibid.*, **112**, 1013 (1965).
10. V. A. Zeitler and C. A. Brown, *J. Phys. Chem.*, **61**, 1174 (1957).
11. R. W. Ricker and F. A. Hummel, *J. Am. Ceram. Soc.*, **34**, (9), 271 (1951).
12. D. L. Evans, *ibid.*, **53**, (7), 418 (1970).
13. G. V. Samsonov, Plenum Press Handbooks of High Temperature Materials—Properties Index, p. 373 (1964).
14. B. E. Deal and A. S. Grove, *J. Appl. Phys.*, **36**, 3770 (1965).
15. W. A. Pliskin and P. Gnall, *This Journal*, **111**, 872 (1964).
16. U. R. Evans, "The Corrosion and Oxidation of Metals: Scientific Principles and Practical Applications," p. 833, St. Martin's Press, New York (1960).
17. S. W. Ing, R. E. Morrison, and J. E. Sandor, *This Journal*, **109**, 211 (1962).
18. C. D. Wirkus and D. R. Wilder, *J. Am. Ceram. Soc.*, **49**, (4), 173 (1966).
19. J. B. Berkowitz-Mattuck, *Trans. Met. Soc. AIME*, **233**, 1093 (1965).

The Kinetics and Morphological Development of the Oxide Scale on Nickel-Iron Alloys (0-25 w/o Fe) at 1000°C

A. D. Dalvi*,[1] and W. W. Smeltzer**

Department of Metallurgy and Materials Science, McMaster University, Hamilton, Ontario, Canada

ABSTRACT

The oxidation kinetics were determined for nickel alloys containing 0-25 w/o (weight per cent) iron in oxygen at 1000°C. The kinetics, which were obtained for periods up to 100 hr, followed a parabolic relationship at long times. The parabolic rate constant was obtained as a function of alloy composition; it increased in magnitude with addition of iron up to 5 w/o and subsequently decreased to a value approximately equal to that for pure nickel. The external scale on alloys containing up to 2 w/o iron was virtually single-phase nickel oxide. All other alloys exhibited scales consisting of an inner nickel oxide layer and an outer two-phase nickel oxide-spinel layer. All alloys oxidized internally, the internal oxide being an iron-nickel spinel, $Ni_xFe_{3-x}O_4$. Iron preferentially concentrated in the oxide phases. There was a large degree of iron depletion in the alloy towards the alloy/oxide interface where the iron concentration was less than 1 w/o. A schematic model based on thermodynamic and diffusion properties is advanced to account for the observed variation of the parabolic constant with alloy composition.

A survey of the high-temperature oxidation properties of Fe-Ni alloys has been presented by Foley (1). Recently, Wulf *et al.* (2) conducted an extensive investigation into the oxidation characteristics of these alloys over the entire composition range in pure oxygen at 1000°C. According to these authors Fe-Ni alloys can be divided into four major types: alloys containing up to 2 w/o Ni which exhibit scales similar to those found on iron; alloys containing approximately 2-30 w/o Ni which form scales devoid of wustite due to a large degree of nickel enrichment at the alloy/scale interface; alloys containing 30-75 w/o Ni which show formation of nickel oxide in the scales, the oxidation kinetics being governed primarily by the growth of a nickel containing spinel; and, alloys containing 75-100 w/o Ni which exhibit scales consisting of nickel oxide and spinel. All alloys show nickel enrichment at the alloy/scale interface and, in addition, exhibit subscale formation. Considerable recent information is also available on the oxidation properties of iron-rich alloys in pure oxygen and controlled atmospheres containing carbon dioxide and water as oxidizing reactants (3-14).

Information on the oxidation properties of nickel-rich alloys is not extensive and the results of kinetic studies have been neither reproducible nor of continuous pattern (15). Accordingly, we have carried out a detailed investigation of the oxidation kinetics of these alloys (0-25 w/o Fe) at 1000°C in conjunction with examination of the composition, structure, and the morphological development of the oxide scales.

Experimental

Electrolytic iron and nickel were used in preparation of the alloys. The compositions of the metals used are given in Table I. Portions of each material were accurately weighed to yield alloys nominally containing 2,4,5,6,8,10,15,20, and 25 w/o Fe. The actual alloy compositions are given in Table II. The melting operation was carried out in a nonconsumable arc furnace with a tungsten electrode and in an argon atmosphere. The samples were remelted to avoid long range segregation of the alloying elements. The buttons thus obtained were alternately cold rolled and vacuum annealed for 10 hr to obtain sheets approximately 1 mm thick. The surfaces of each sheet were cleaned by abrasion. Specimens for oxidation tests were plates, 1 cm × 2 cm. These were batch annealed in vacuum at 1000°C for 5 hr and then furnace-cooled to room temperature. This eliminated any stress and short range segregation in the samples and allowed them to attain an equilibrium grain size. The average grain diameter was in the range 100-300μ which corresponds to ASTM standard grain size No. 2.

Prior to oxidation, the specimens were metallographically polished by abrasion. This type of surface preparation was found to give the most reproducible oxidation kinetics and the scales were more adherent to the metal substrate as compared to electrochemical polishing. The plates were mounted flat in bakelite and polished through 240, 300, 400, and 600 grit silicon carbide papers using water as lubricant, followed by polishing on a wax lap impregnated with 15μ alumina to obtain a flat surface. The final polishing was done with 6μ and 1μ diamond abrasive on wheels with kerosene as lubricant. The samples were cleaned with petroleum ether and stored under acetone until re-

Table I. Spectrochemical analyses of iron and nickel

(in ppm)

	Al	Cd	Cr	Co	Cu	Fe	Mg	Mn	Mo	Si	Ti	V
Fe	tr	nd	tr	nd	10	—	30	tr	tr	30	tr	tr
Ni	12	20	54	tr	28	55	4	nd	tr	15	tr	tr

tr = trace.
nd = not detected.

Table II. Compositions of the investigated alloys based upon wet chemical analyses for nickel and iron

Nominal composition	Actual composition w/o Fe	w/o Ni
Ni-2% Fe	1.85	98.15
Ni-4% Fe	4.5	95.5
Ni-5% Fe	5.4	94.6
Ni-6% Fe	6.6	93.4
Ni-8% Fe	8.3	91.7
Ni-10% Fe	10.4	89.6
Ni-15% Fe	15.3	84.7
Ni-20% Fe	20.3	79.7
Ni-25% Fe	25.5	74.5

* Electrochemical Society Student Associate Member.
** Electrochemical Society Active Member.
[1] Present address: J. Roy Gordon Research Laboratory, The International Nickel Company of Canada Ltd., Sheridan Park, Clarkson, Ontario, Canada.
Key words: nickel, nickel-iron alloys, high-temperature oxidation, nickel oxide, spinel.

quired. Immediately before an experimental test a specimen was dried, weighed to ±2 μg, and its surface area computed by measuring the specimen dimensions with a micrometer. The specimen was then cleaned in dilute sulfuric acid, rinsed in distilled water, and dried in acetone.

The kinetics of the oxidation reaction were determined by means of a volumetric apparatus (16). A specimen was brought to the reaction temperature under a vacuum of 10^{-5} Torr. The reaction was initiated by admitting oxygen to the reaction cell and measuring the time thereon. Precision of measurement corresponded to ±0.3 mg. High purity research grade oxygen was used as the reacting gas, the total impurity content being less than 25 ppm. The oxidation reaction was carried out at 1000°C and 400 Torr pressure of oxygen. The temperature of the quartz reaction cell was controlled within ±2.5°C. After reacting a specimen for the desired interval, the reaction was discontinued by evacuating the reaction chamber and allowing the specimens to cool by removal of the furnace from around the reaction cell.

Metallographic examination, x-ray diffraction, and electron microprobe techniques were used in investigating morphology, structure, and compositions of a scale and the alloy substrate. The oxidized plates were cut into two pieces by a jeweller's saw: one-half of the plate was used in x-ray diffraction and the other half mounted for metallographic and electron probe studies. Specimens were mounted in room setting resin and kerosene was used as the lubricant throughout the polishing operations. Specimens were polished on silicon carbide papers 200 through 600 grit, then polished on a wax lap impregnated with 15μ alumina. This procedure resulted in the best retention of oxide grains and in obtaining a flat surface. The final polishing was done with 6μ and 1μ diamond as abrasive on wheels with napless cloths. It was necessary to etch the oxidized samples to reveal their grain structure. An aqueous etchant containing 16.7 v/o (volume per cent) of acetic acid and of hydrofluoric acid was used. Etching was done electrolytically at 300 mA under 10-15V with stainless steel as the cathode for a period of 1 min at 25°C. The techniques for oxide phase identification by x-rays and oxide and alloy compositions by the electron microprobe technique have been described in an earlier paper (17).

Results

Oxidation kinetics.—Typical oxidation curves for alloys containing 0-25% Fe are illustrated by the parabolic plots in Fig. 1 and 2, (weight gain per unit area)^2 *vs.* time. Although the period of oxidation was generally 50 hr, several specimens were exposed up to 100 hr. In each case more than one sample was oxidized to check the reproducibility of the kinetic curves, which was found to be within ±10%.

Oxidation of pure nickel was used as the basis of comparison for the kinetics. It was observed that continuous long time kinetics could be obtained for the alloys if careful metallographic preparation was followed. Parabolic kinetics were observed for pure nickel through the entire oxidation period. In the case of the alloys containing up to 20 w/o Fe an initial nonparabolic transient period of up to 15 hr was observed before onset of parabolic kinetics. The Ni-25 w/o Fe alloy showed two stage kinetics, the initial stage extending up to 45 hr (Fig. 2). The parabolic rate constants are given in Fig. 3. The oxidation rate of the alloys increases initially upon addition of iron and subsequently decreases to a nearly constant value. Composition of the alloy which yields the maximum oxidation rate corresponds to Ni-5 w/o Fe.

Oxide morphology and composition.—Only two oxide phases were identified. These were nickel oxide with dissolved iron, $Fe_xNi_{1-x}O$, and a spinel phase, $Ni_xFe_{3-x}O_4$, of variable compositions. The external scale formed on the 2 w/o Fe alloy consisted of nickel oxide with iron in solid solution. As illustrated by

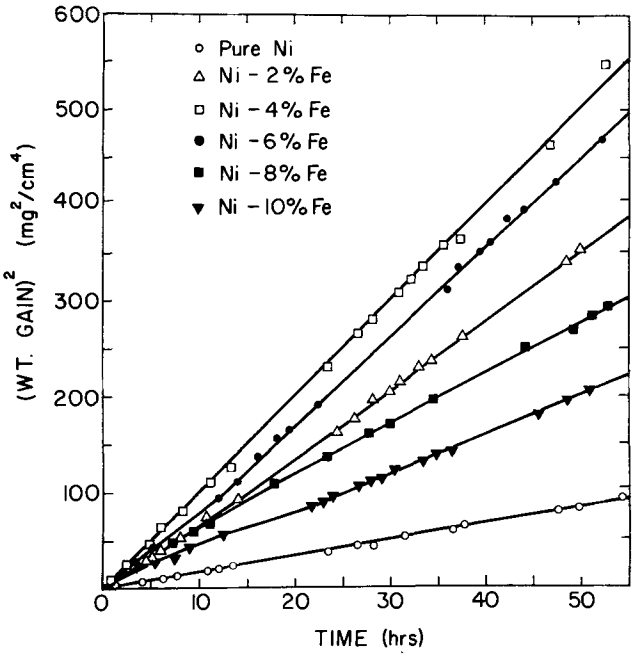

Fig. 1. Oxidation curves in parabolic form, $\left(\frac{\Delta m}{A}\right)^2$ *vs.* t, for nickel and nickel alloys containing up to 10 w/o Fe at 1000°C and 400 Torr oxygen pressure.

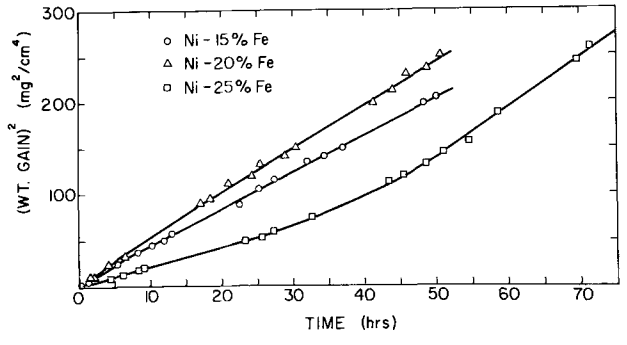

Fig. 2. Oxidation curves in parabolic form, $\left(\frac{\Delta m}{A}\right)^2$ *vs.* t, for Ni-Fe alloys containing 15-25 w/o Fe at 1000°C and 400 Torr oxygen pressure.

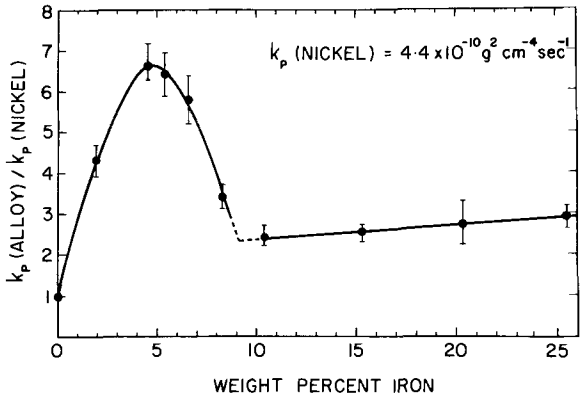

Fig. 3. Variation of the relative parabolic oxidation constant [k_p(alloy)/k_p(nickel)] with bulk alloy composition.

the micrograph in Fig. 4a no spinel growth could be detected in the scale. External scales formed on the remaining alloys consisted of two layers: an inner

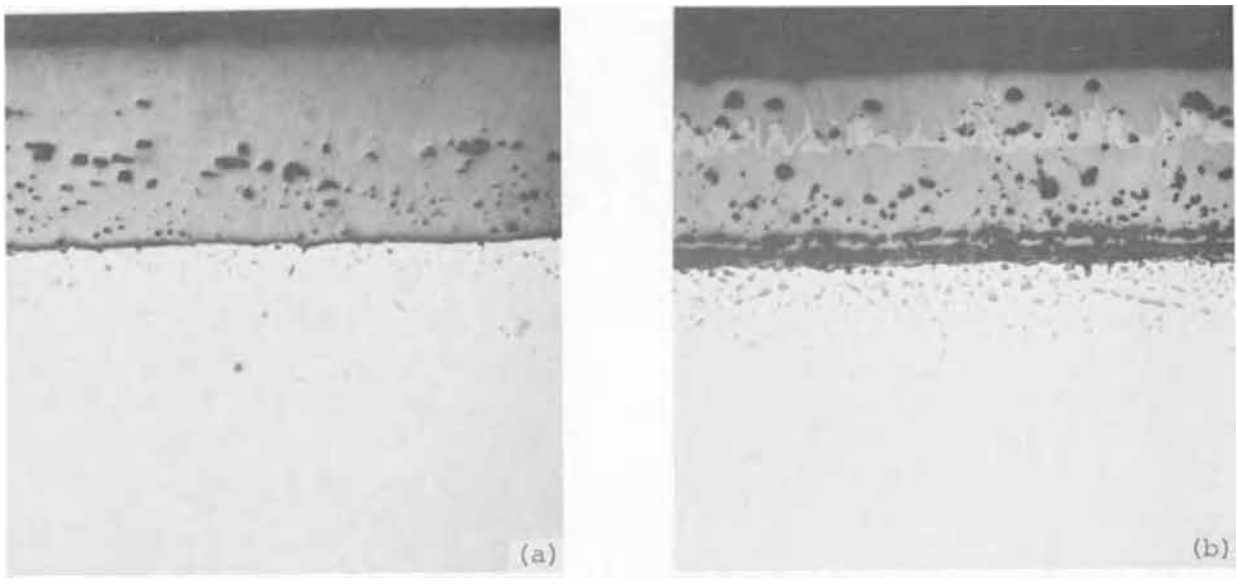

Fig. 4. Scale and internal oxidation zone in Ni-Fe alloys: (a) shows a nickel oxide scale and spinal internal precipitate for a Ni-2 w/o Fe alloy oxidized for 51.5 hr, (200×); (b) shows duplex scale and internal oxidation zone for a Ni-8 w/o Fe alloy oxidized for 48.5 hr, (200×). The external scale consists of an inner single-phase nickel oxide layer and an outer two-phase nickel oxide-spinel layer, the light precipitate phase in this latter layer being the spinel phase. The internal oxidation zone consists of spinel particles.

nickel oxide layer and an outer two-phase layer containing nickel oxide and spinel. The commencement of spinel growth and the consequent formation of the outer two-phase layer was observed in the scale on the alloy containing 4 w/o Fe. The spatial density of spinel phase in the scale increased with increasing iron content of the alloy. The composition of this spinel was found to correspond approximately to that of nickel ferrite, $NiFe_2O_4$. Figure 4b shows the duplex scale formed on an alloy containing 8 w/o Fe oxidized for 48.5 hr. The relative position of the spinel precipitation zone shifted inwards with increasing iron content of the bulk alloy. Grains of spinel started forming in the scale on the 10 w/o Fe alloy while the scale on the 25 w/o Fe alloy consisted of an inner nickel oxide layer which shaded into a predominantly spinel layer (Fig. 5). A continuous spinel layer, however, did not form since nickel oxide formed channels around the boundaries of the spinel grains. This structure agrees with the observations of Kennedy *et al.* (15).

Electrolytic etching of the scales revealed that the grain structure of the oxide formed on the Ni-2 w/o Fe alloy was columnar with small equiaxed grains at the alloy/oxide interface (Fig. 6a). The scales on alloys containing 4 to 8 w/o Fe structurally consisted of three zones (Fig. 6b). A zone containing small equiaxed grains, which exhibited a remarkably sharp boundary, existed at the alloy/oxide interface. Beyond this boundary a zone of medium sized elongated grains was observed up to the spinel precipitates in the scale. Beyond the spinel precipitates a zone of larger columnar grains extending up to the oxide/gas interface was observed (Fig. 6b). The spinel growths mainly occurred at the boundary between the outer zone of columnar grains and the middle zone of medium sized grains.

Internal oxidation.—Internal oxidation occurred in all the alloys and the oxide was identified as a nickel containing spinel, $Ni_xFe_{3-x}O_4$. The nickel content of the spinel appeared to increase from the bulk alloy towards the alloy/oxide interface. Only a qualitative analysis of the oxide composition could be done with the electron probe due to the very small spinel particle size which ranged from a fraction of a micron to about 10μ. The particle size appeared to depend on variables such as alloy composition, oxidation time, and the distance of the precipitate from the alloy/scale interface. The alloy grain boundaries appeared to provide preferential sites for the nucleation of the spinel (Fig. 7a); however, preferential penetration of oxide along the grain boundaries was not observed (Fig. 7b).

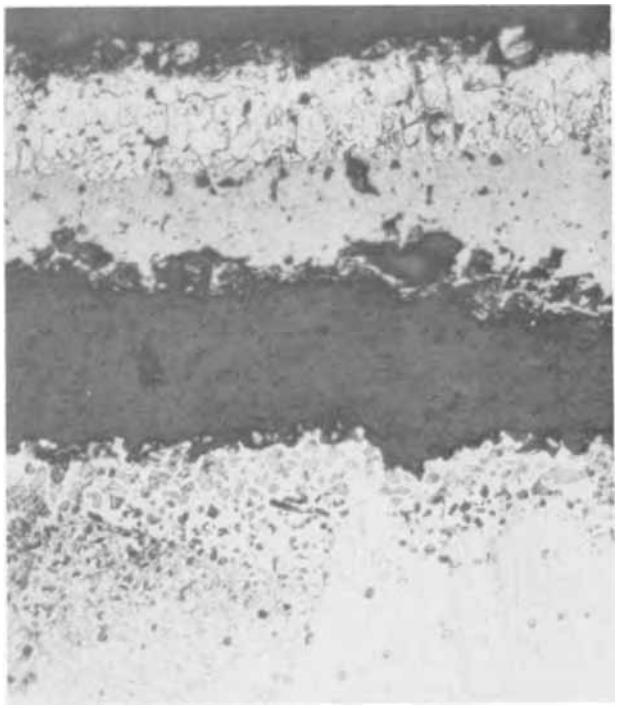

Fig. 5. Scale and internal oxidation zone in Ni-25 w/o Fe alloy oxidized for 61 hr (272×). The scale is of duplex structure consisting of an inner nickel oxide layer and an outer nickel oxide-spinel layer. The gap in the center of the micrograph separating the external scale from the alloy substrate is filled with the mounting plastic. Nickel oxide appears gray and the spinel white in the external scale.

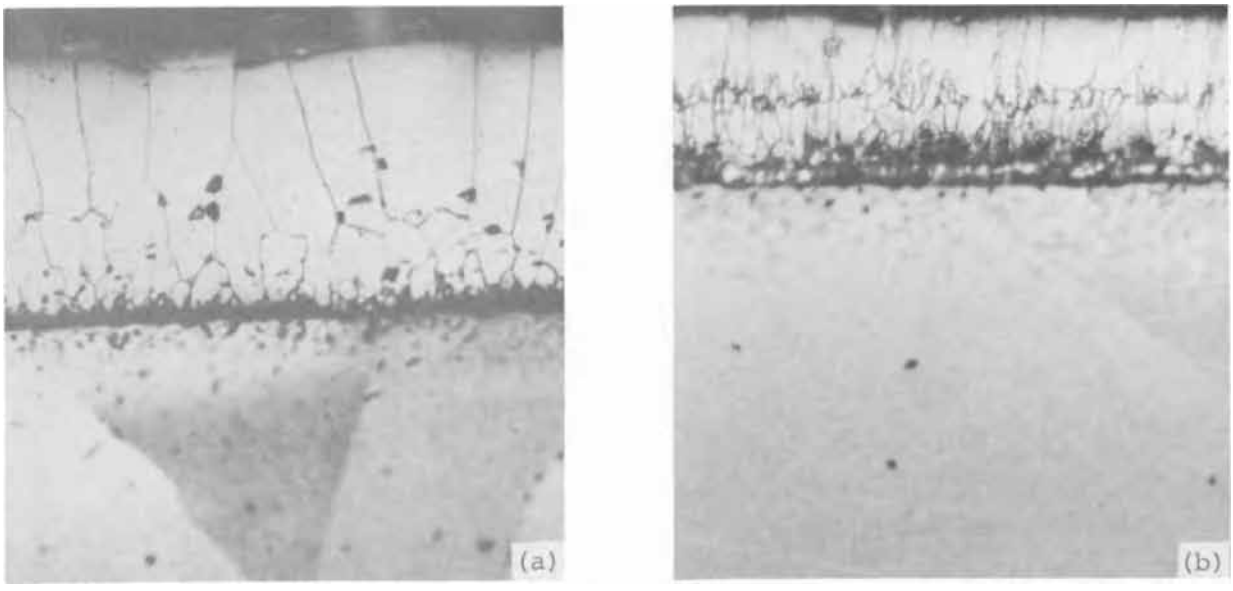

Fig. 6. Scale and internal oxidation zone in Ni-Fe alloys: (a) shows the typical grain structure of nickel oxide scales on alloys containing up to 2 w/o Fe (280×); (b) shows the typical grain structure for nickel oxide and spinel in scales formed on alloys containing between 4-8 w/o Fe (320×).

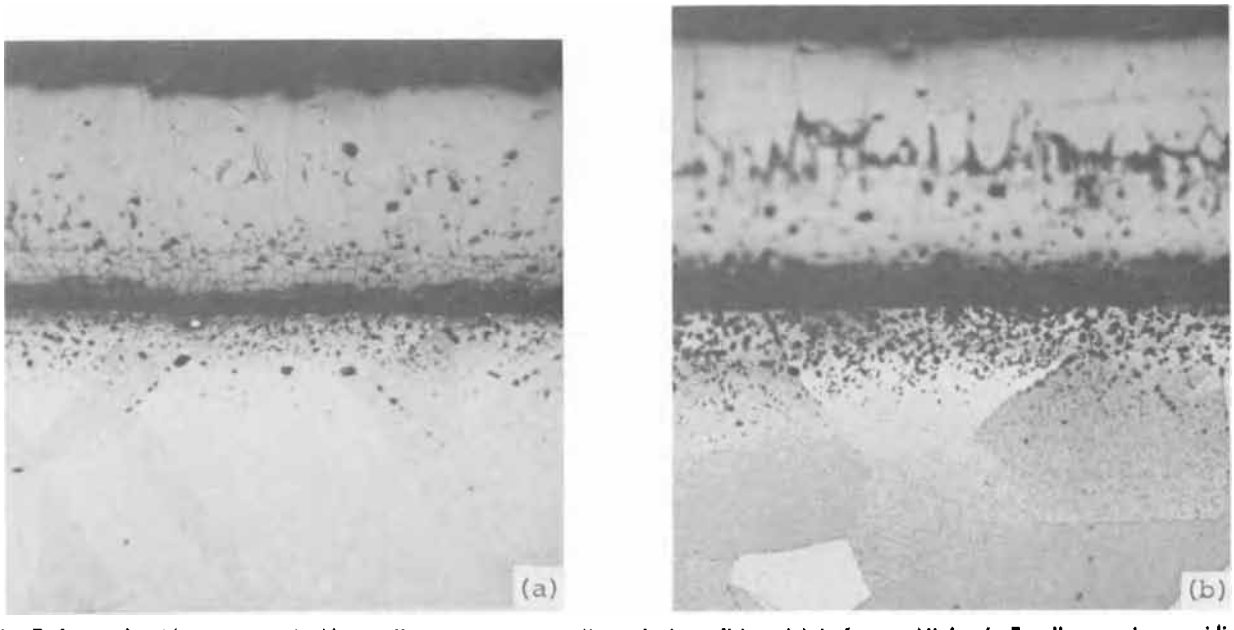

Fig. 7. Internal oxidation zones in Ni-Fe alloys in electrolytically etched condition: (a) is from a Ni-4 w/o Fe alloy specimen oxidized for 25.2 hr (200×); (b) is from a Ni-6 w/o Fe alloy specimen oxidized for 47.5 hr (200×).

Penetration of the internal oxidation zone and the size of the internal oxide particles increased with time. Figure 8 shows a photomicrograph of the internal oxidation zone in an alloy containing 6 w/o Fe oxidized for 47.5 hr which is typical of this zone in all alloys. Since the solubility product for the spinel phase is large, there is no discontinuity in either the concentration or its gradient at the interface between the zone of internal oxidation, and the unoxidized alloy (18). Accordingly, a sharp boundary defining this zone does not exist. Its approximate penetration as a function of time illustrated in Fig. 9 for various alloys shows that the penetration rate follows a parabolic dependence and that it is independent of the bulk alloy composition. However, since the particle density and size increased with increasing iron content of the bulk alloy, the amount of oxygen consumed in this zone also correspondingly increased. The rate constant for the internal oxidation zone as obtained from Fig. 8 is 3.7×10^{-10} cm²/sec.

Surface topography and the crystallographic orientation of the oxide scales.—The topographies of the specimens at various oxidation stages indicated that the grain boundaries and defect sites on the alloy substrate act as preferential growth sites for the external oxide scale during the initial stages (Fig. 10a). The small crystallites initially formed tended to coalesce and grow, forming bigger grains with a terraced structure (Fig. 10b). The preferred orientation as shown by the x-ray diffraction measurements was such that <110> directions are parallel to the oxide surface, The surface plane of the oxide scale was preferentially {111}.

It was observed for slow growing nickel oxide on pure nickel that its surface was smooth. As the oxidation rate increased with increasing iron content, a terraced structure appeared and was pronounced for the fastest growing oxide on the 5 w/o Fe alloy. As the oxidation rate decreased with addition of iron beyond 5 w/o, the terraced structure became less pronounced.

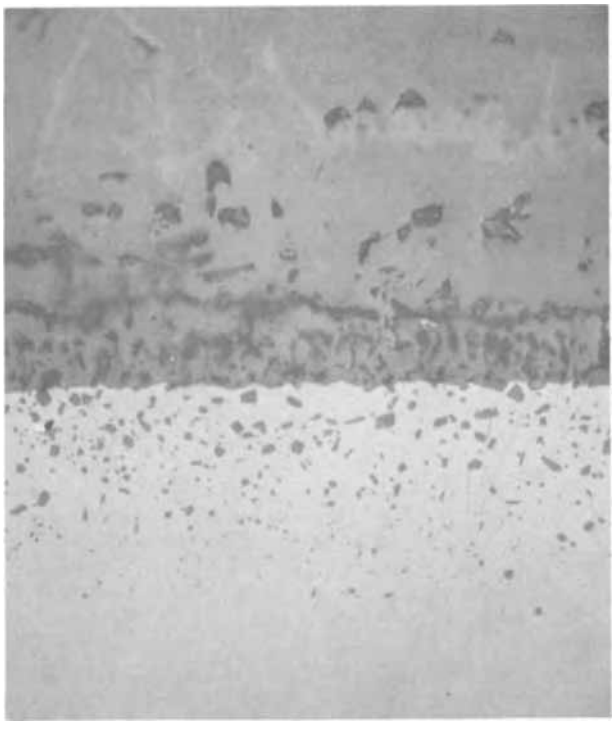

Fig. 8. Internal oxidation zone in a Ni-6 w/o Fe alloy oxidized for 47.5 hr, unetched (400×).

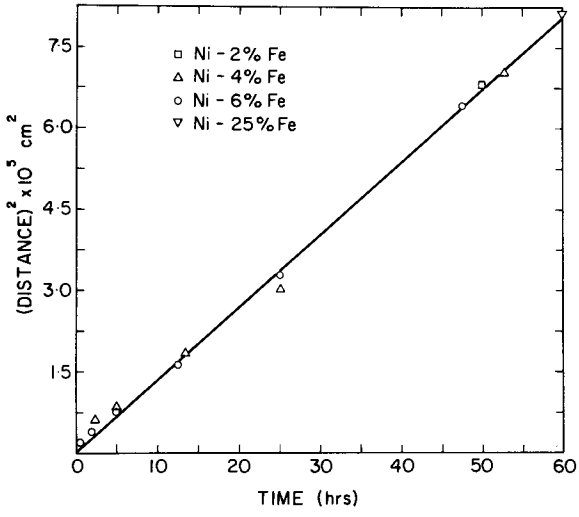

Fig. 9. Penetration of internal oxidation zone in Ni-Fe alloys containing 2-25 w/o Fe exposed at 1000°C to oxygen at 400 Torr pressure.

For slow growing nickel oxide on high iron content alloys, the surface was devoid of terraces as in the case of pure nickel.

Physical properties of the scales.—None of the scales on the oxidized specimens showed any tendency of breakaway during oxidation. The scales showed excellent adherence and the oxidation kinetics followed continuous curves. Scales formed on some alloys, however, showed a tendency to spall during quenching; the extent of spalling depended on the alloy composition and also on the time of oxidation. The tendency to spall appeared to decrease with increasing scale thickness.

The oxide scales formed on the alloys containing 2-6 w/o Fe showed excellent thermal shock resistance. Thus these scales were adherent even after quenching. Scales formed on the alloys containing 8 and 10 w/o Fe adhered to the alloy substrate fairly well after quenching. The scales formed on the 15 and 20 w/o Fe alloys, showed considerable tendency to spall whereas the scale on the Ni-25 w/o Fe alloy showed good adherence and spalling resistance.

The color of the nickel oxide scale was black at the oxide/gas interface and green at the alloy/oxide interface. The oxide scale surface on alloys containing up to 6 w/o Fe appeared black, glazy and with an orange peel texture. The surface of the oxide formed on alloys containing 8 and 10 w/o Fe showed dull and glazy areas. The appearance of the alloys containing 15 and 20 w/o Fe was dull. The 25 w/o Fe alloy showed a pronounced orange peel texture.

Scales formed on alloys containing up to 6 w/o Fe were relatively compact. Porosity was mainly observed at the alloy/oxide interface and it appeared to increase with increasing iron content of the alloy. Data were obtained on the rate of the external scale thickening by metallographic examination of specimens oxidized for different periods. Figures 11a and 11b show these curves for the alloys containing 2 and 4 w/o Fe. In the case of the first alloy, the thickening curve corresponds to the growth of a nickel oxide layer. The scale on the alloy containing 4 w/o Fe was of duplex structure consisting of an inner layer of nickel oxide and an

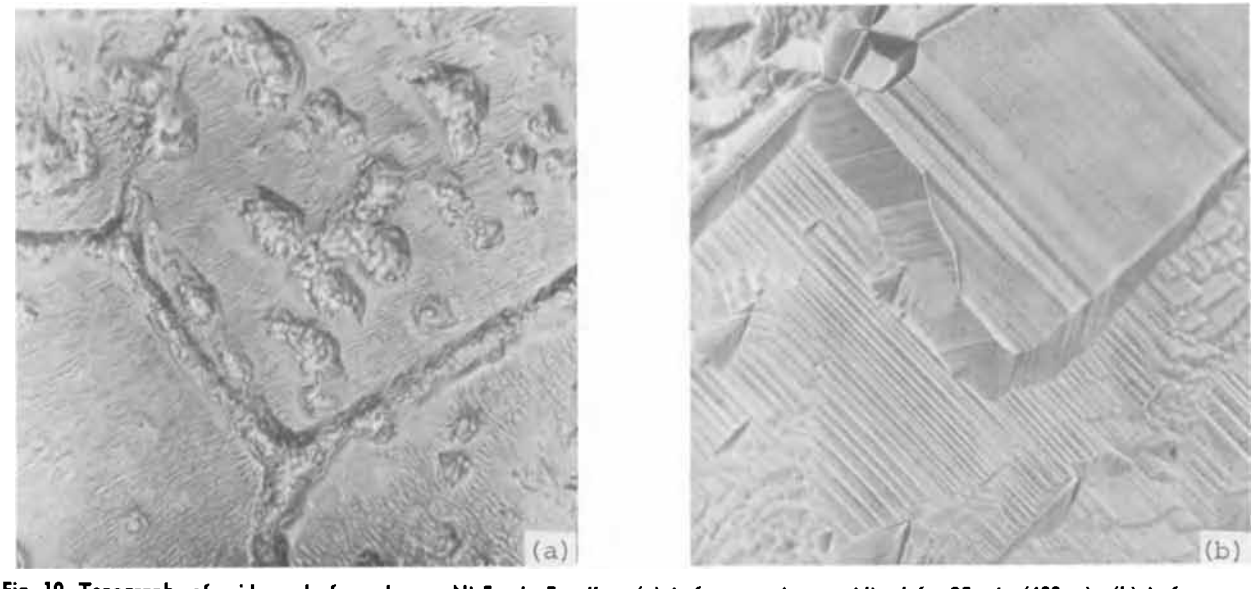

Fig. 10. Topography of oxide scale formed on a Ni-5 w/o Fe alloy: (a) is from specimen oxidized for 25 min (400×); (b) is from specimen oxidized for 18.5 hr (2000×).

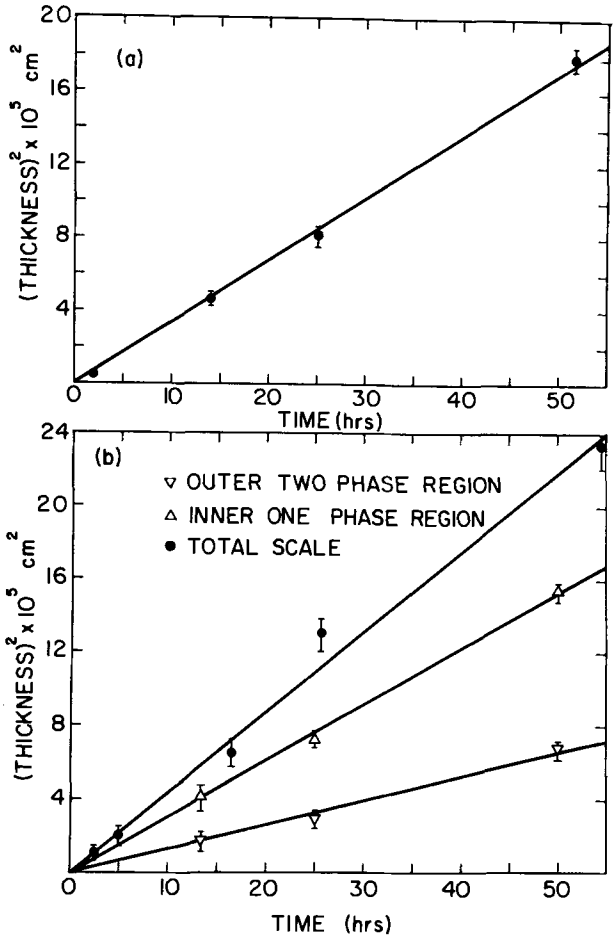

Fig. 11. Parabolic plots for scale growth: (a) the nickel oxide scale on a Ni-2 w/o Fe alloy; (b) the individual layers of nickel oxide, nickel oxide-spinel and the total duplex scale formed on a Ni-4 w/o Fe alloy.

outer layer composed of spinel growths in the nickel oxide matrix. Figure 11b gives the thickening of the individual layers as well as that of the total scale. It should be noted that the relative thicknesses of the two layers remain constant with time.

Iron and nickel distributions.—Several line scans were made for iron and nickel in the alloy and oxide phases in order to qualitatively determine their distributions. A line scan for iron and nickel in a Ni-8 w/o Fe alloy oxidized for 53 hr. is shown in Fig. 12. These metal profiles are typical for the alloys investigated, except that the alloy containing 2 w/o Fe did not show spinel formation in the external scale. It was observed from these profiles that iron tends to preferentially concentrate in the oxide phases. Thus there was a large degree of iron depletion in the alloy towards the alloy/oxide interface with a corresponding enrichment of nickel. The iron content of the alloy at the interface was sufficiently small for stabilization of nickel oxide in the external scale. Moreover, iron concentration in the inner single phase layer of the scale increased towards the oxide/gas interface.

Discussion

To the authors' knowledge, it has not been previously established that continuous and reproducible long time kinetic curves could be obtained for high-nickel alloys in dry oxygen. The present investigation shows that reproducible and continuous curves can be obtained. These findings should lead to a theoretical analysis for the oxidation properties of Ni-Fe alloys, and subsequent formulation of a mechanism for their oxidation kinetics based upon diffusional properties.

The results obtained in the present investigation demonstrated that nickel alloys containing up to 25 w/o Fe follow parabolic oxidation kinetics at 1000°C indicating that diffusion is probably the rate controlling mechanism. It is reasonable to assume that conditions of ambipolar diffusion and local equilibrium at interfaces would occur at this high temperature. The condition of local equilibrium is not satisfied, however, until constancy of composition at interfaces is attained. Thus, parabolic oxidation behavior was not found at short times, and it was only approached at long times.

Porosity in the oxide scales occurred mainly at the oxide/alloy interface, increasing with increasing iron content of the bulk alloy. However, the porosity was small and the oxide scales were essentially compact. Accordingly, one may postulate a mechanism based on diffusion through the different phases since the over-all reaction kinetics and growth of the individual reaction product layers followed a parabolic time dependence (Fig. 1, 2, 9, and 11).

As noted earlier, an iron-nickel spinel is formed both internally and externally during oxidation. A spinel, rich in iron, which has a comparatively low solubility product is precipitated within the alloy matrix. This precipitation is inferred to be brought about by oxygen supersaturation created within the alloy due to its high diffusivity (19, 20). Previous studies on the

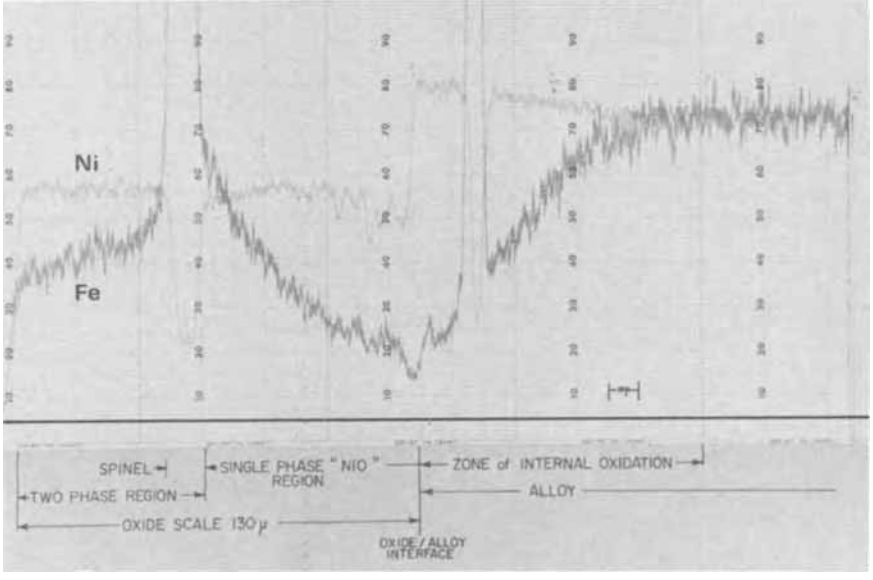

Fig. 12. Electron microprobe line scan for the distribution of iron and nickel in the alloy and oxide scale for a Ni-8 w/o Fe alloy oxidized for 53 hr at 1000°C and 400 Torr oxygen pressure. The datum for the x-ray intensities is indicated by the solid line at the bottom of the scale. Note that the scale for iron is approximately 10× that for nickel. The iron content of the alloy at the interface is less than 1 w/o.

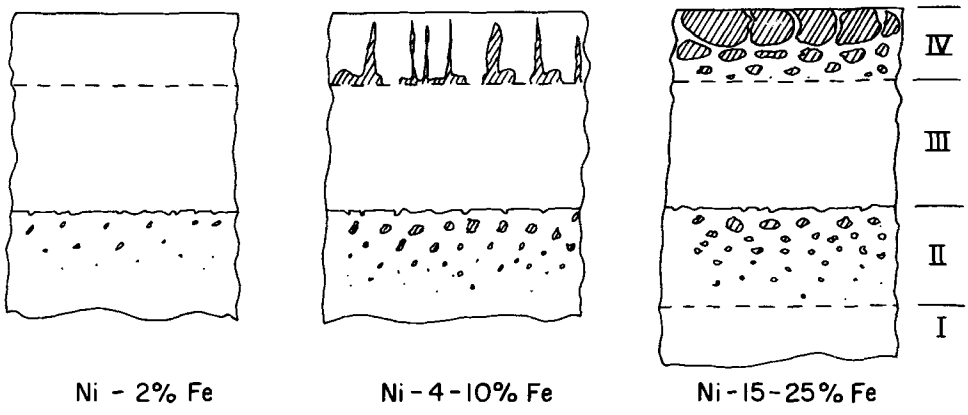

Fig. 13. Schematic representation of the scale and internal oxidation zone in nickel-iron alloys oxidized at 1000°C in oxygen at 400 Torr pressure.
I—unoxidized alloy
II—internal oxidation zone containing spinel precipitates
III—single-phase nickel oxide layer
IV—two-phase nickel oxide-spinel layer

Fe-Ni-O phase diagram at 1000°C have shown that a nickel oxide phase containing iron is stabilized for alloys containing greater than 99 w/o Ni (17). The electron probe results (Fig. 12) have shown that iron is intensively depleted in the alloy adjacent to the external scale. This depletion resulted from formation of iron containing spinel precipitates in the internal oxidation zone and dissolution of iron into the external scale. The occurrence of nickel oxide in the scale adjacent to the alloy/oxide interface is therefore consistent with the phase diagram.

The oxygen activity for these types of spinels increases with increasing nickel content. In fact, a spinel near the composition $NiFe_2O_4$ can coexist with oxygen near 1 atm pressure (17, 21). The spinel growths that occur within nickel oxide of the external oxide layer are high in nickel although quantitative analysis could not be carried out due to the small size of the particles. It is suggested that these particles coexisting with nickel oxide have not been merely carried into the external oxide layer from the zone of internal oxidation. Several observations may be advanced to support this viewpoint. Firstly, spinel particles could be detected almost up to the alloy/oxide interface within the alloy matrix; however, no spinel particles were detected within the scale at the alloy/oxide interface. Also, no inhomogeneities to be associated with the presence of spinel growths at any time were observed within the inner layer of the external scale. These findings indicate that spinel was dissolved rapidly at the nickel oxide/alloy interface. On the other hand, the spinel precipitates in the outer layer of the scale were remarkably stable. Since they did not show any tendency to dissolve in the oxide matrix, spinel would appear to exist in local equilibrium with nickel oxide. Secondly, the relative position of the two-phase outer layer containing spinel was fixed with time in the external scale and the relative thickness of this layer to the total scale thickness was constant (Fig. 11). This is not expected if spinel precipitates are left behind in the oxide layer as the alloy interface recedes inwards.

A schematic model for the oxidation of the alloys may be advanced based on the experimental results and the above discussion. This model is illustrated in Fig. 13 and is summarized as follows:

1. Iron tends to preferentially concentrate in the oxide phases resulting in its depletion in the alloy. In all the alloys containing up to 25 w/o Fe the shift in the alloy composition at the alloy/oxide interface is beyond the value where nickel oxide can coexist with the alloy phase (>99 w/o Ni). Thus nickel oxide is only stabilized externally to the alloy/oxide interface. For low iron alloys (*e.g.* Ni-2 w/o Fe), the external scale is virtually single-phase nickel oxide.

2. Spinel occurs as a second phase in an outer layer of the external scale for alloys with iron contents larger than 2 w/o. The relative thickness of the two-phase outer layer containing spinel and nickel oxide increases with increasing iron content of the bulk alloy.

3. The oxidation rates increase with increasing iron content of the bulk alloy until the spinel phase begins to precipitate in the external scale in substantial proportion. Spinel forms a high resistance diffusion barrier since the diffusion rates of cations in this phase are lower than in iron doped nickel oxide (22, 23). Spinel in a scale becomes copious as the iron content of the bulk alloy is increased. This results in blocking the diffusion of cations and hence effective reduction in the cross section for diffusion.

4. The amount of internal oxide increases with increasing iron content of the bulk alloy. Spinel precipitates in the zone of internal oxidation may block oxygen and metal diffusion in the alloy (22).

5. The double blocking effect of spinel in the external scale and the internal oxidation zone effectively reduces the oxidation rates for these alloys. The diffusion fluxes in the external scale and the alloy are coupled at the alloy/oxide interface and a resistance to diffusion in any one phase would reduce the over-all flux and result in reduction of the oxidation rate. This coupled blocking effect to diffusion of reactants does not change significantly over the alloy composition range 10-25 w/o Fe.

The particular shape of the curve for the parabolic constant *vs.* the bulk alloy composition (Fig. 3) is therefore due to the combined effect of increasing diffusivities of cations in nickel oxide with increasing iron concentration and the increasing blocking effect of spinel growths in the external scale and internal oxidation zone with increasing iron content of the bulk alloy.

Acknowledgments

This work was carried out by A. D. Dalvi in partial fulfillment of the requirements for the award of the Ph.D. degree at McMaster University. He wishes to acknowledge the award of an International Nickel Company of Canada Fellowship for graduate research. This research was carried out under auspices of the National Research Council of Canada.

Manuscript submitted May 10, 1971; revised manuscript received *ca.* July 12, 1971. This was Paper 117 presented at the Atlantic City Meeting of the Society, Oct. 4-8, 1970.

Any discussion of this paper will appear in a Discussion Section to be published in the June 1972 JOURNAL.

REFERENCES

1. R. T. Foley, *This Journal*, **109**, 1202 (1962).
2. G. L. Wulf, T. J. Carter, and G. R. Wallwork, *Corrosion Sci.*, **9**, 689 (1969).
3. J. Benard and J. Moreau, *Rev. Met.*, **47**, 317 (1950).
4. P. K. Koh and B. Caugharty, *J. Appl. Phys.*, **23**, 427 (1952).
5. R. T. Foley, J. U. Druck, and R. G. Fryrell, *This Journal*, **102**, 440 (1955).
6. R. T. Foley, C. J. Guare, and H. R. Schmidt, *ibid.*, **104**, 413 (1957).
7. R. T. Foley and C. J. Guare, *ibid.*, **106**, 936 (1959).
8. R. T. Foley, *ibid.*, **108**, 216 (1961).
9. R. T. Foley, *ibid.*, **109**, 278 (1962).

10. M. J. Brabers and C. E. Birchenall, *Corrosion*, **14**, 179 (1958).
11. L. A. Morris and W. W. Smeltzer, *Acta Met.*, **15**, 1591 (1967).
12. L. A. Menzies and W. J. Tomlinson, *JISI*, **204**, 1239 (1966).
13. L. A. Menzies and W. J. Tomlinson, *J. Mater. Sci.*, **2**, 529 (1967).
14. L. A. Menzies and J. Lubkiewicz, *This Journal*, **117**, 1539 (1970).
15. S. W. Kennedy, L. D. Calvert, and M. Cohen, *Trans. AIME*, **215**, 64 (1959).
16. W. W. Smeltzer, E. L. Tollefson, and A. Cambron, *Can. J. Chem.*, **34**, 1046 (1956).
17. A. D. Dalvi and W. W. Smeltzer, *This Journal*, **117**, 1431 (1970).
18. L. S. Darken, *Trans. AIME*, **150**, 157 (1942).
19. J. Swisher and E. T. Turkdogan, *Trans. Met. Soc. AIME*, **239**, 626 (1967).
20. C. Wagner, *Corrosion Sci.*, **8**, 889 (1968).
21. H. Schmalzried, *Prog. Solid State Chem.*, **2**, 265 (1965).
22. R. H. Condit, M. J. Brabers, and C. E. Birchenall, *Trans. Met. Soc. AIME*, **218**, 768 (1960).
23. A. D. Dalvi, Ph.D. Thesis, McMaster University, January 1971.

Infrared Absorption of Chemical Vapor Deposited Borosilicate Glass Films

E. A. Taft

General Electric Research and Development Center, Schenectady, New York 12301

ABSTRACT

Diffusion sources of high-purity borosilicate films on silicon have been studied by infrared absorption over the full range of glass compositions. The relative strengths of the B-O and Si-O bands in the mixed glasses can be used as a monitor of the boron content of the films. The B-O absorption bands for glasses of high boron content show aging effects in moist air.

Infrared absorption will be shown to be a rapid, nondestructive test for boron concentration in deposited films of borosilicate glass. These films appear to be finding increasing use as diffusion sources for silicon processing (1-5). Older data on boron oxide glasses (6, 7) show the difficulty in removing water from the usual boric acid starting material, but different methods of preparation have shown infrared spectra to be characteristic of B_2O_3 (8). The spectra of the fully hydrated oxide, $B(OH)_3$, has been reasonably well established (9, 10). This paper shows the strengths of infrared absorption bands for pure borosilicate glass films of all compositions. Strong absorption due to the boron oxide in the film can be readily followed as the composition of the glass is changed.

The ratio of the strongest bands of B-O and of Si-O is used to monitor the concentration of boron oxide in the film. The effect of water absorption in the films is discussed.

Experimental Procedure

The reaction tube was made of 2¼ in. Pyrex and gases flowed downward over substrates sitting on a resistively heated substrate holder. The substrates were 1 in. wafers of 2 ohm-cm silicon. The holder temperature was 320°C, with argon carrier gas flowing at 4 CFH. One per cent silane in argon was normally used at 140 cm^3/min for deposition of SiO_2 films while oxygen was supplied at 20 cm^3/min. An adjustable flow of 1 per cent diborane in argon furnished the boron for the mixed oxide films. Growth rates depended on the gas ratios (5), but typical rates were on the order of 500 Å/min.

The infrared absorption of 0.5-1μ thick films was measured in transmission on a Perkin-Elmer 457 Grating Spectrophotometer. A clean silicon wafer was used in the reference beam. Thicknesses were observed by interference colors in reflection with occasional checks by ellipsometer measurements. The index of refraction of the glasses did not vary much from the value for silica of 1.47.

Key words: water, boron diffusion source, film stability.

Boron determinations were made on an Instrumentation Labs 153 Atomic Absorption Spectrophotometer; a Cahn Electrobalance was used for weighing the films.

Changes with time in the infrared absorption of films were observed under various constant humidity conditions.

Results

Infrared absorption.—The experimentally observed absorption coefficients of the principal bands in pure silicon oxide and in pure amorphous boron oxide films formed at these low temperatures are given in Fig. 1. The strongest band peak in SiO_2 at 1070 cm^{-1} (9.4μ) is about one-third smaller than that found in a thermally formed oxide, but it is slightly wider. Occasionally a small amount of hydrogen is seen in some films as is indicated by a broad weak absorption with absorption constant, $\alpha < 0.1 \times 10^4$ cm^{-1} at 3000-3640 cm^{-1} (3.3-2.75μ) and a sharper weak band at 880

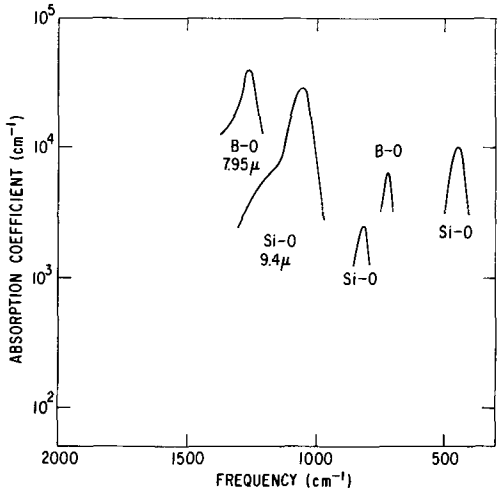

Fig. 1. The absorption coefficient of the major infrared bands in pure SiO_2 and in pure B_2O_3 pyrolytic films.

cm^{-1} (10.4μ) also with $\alpha < 0.1 \times 10^4$ cm^{-1}. The strongest band in B_2O_3 is the asymmetric mode at 1260 cm^{-1} (11) (7.95μ) with a peak absorption coefficient of 3.7 $\times$ 10^4 cm^{-1} making it about 1½ times as strong as the nearby SiO_2 band. The smaller symmetric band at 720 cm^{-1} (13.9μ) (11) has an absorption coefficient of 5 $\times$ 10^3 cm^{-1}. Several thicknesses of the same glass composition were employed to determine the background absorption.

In the mixed glasses there is some interaction of the boron and the silicon bonds within the oxygen lattice, but the two oxide networks do not greatly influence each other (12). Starting from pure SiO_2, as one adds small amounts of diborane to the gas mixture in making a glass film, weak bands of B-O begin to appear in addition to the normal Si-O absorptions. These bands first appear at 1390 cm^{-1}, 920 cm^{-1}, and 670 cm^{-1} (7.2μ, 10.9μ, and 15.4μ). With higher boron concentrations, the stronger Si-O bands clearly broaden and shift slightly in peak position. Figure 2 shows the shape and intensity of the infrared absorption regions in a glass containing approximately 15 (mole per cent) m/o of boron oxide. The arrows show the direction of the shifts in position and changes in intensity of the bands with increasing boron content. The Si-O peaks, of course, all decrease with decreasing silica content. The 720 cm^{-1} (13.9μ) symmetric vibrational mode of B-O does not initially appear at low boron concentrations. Instead it seems to be replaced by bands at 920 cm^{-1} (10.9μ) and 670 cm^{-1} (15.0μ). These bands increase to a maximum intensity as indicated in Fig. 2, then decrease as the boron content of the film continues to increase. As these two bands disappear the 720 cm^{-1} (13.9μ) absorption band appears at very high boron compositions. To further illustrate the behavior of the infrared absorption in the mixed glasses, the approximate absorption coefficients of the six major bands in this boron-silicate glass system are plotted in Fig. 3. The abscissa has been chosen as the ratio of the amount of diborane gas to the amount of diborane plus silane gas flowing through the reactor. The 15 m/o glass of Fig. 2 is found near a gas ratio of 25%.

Boron calibration.—As the B-O and Si-O absorptions remain separate, although slightly interacting, the boron content can be measured as a fraction of the silicon content in the oxide lattice. Using the ratio of the 1340 cm^{-1} (7.45μ) B-O peak absorption to the 1070 cm^{-1} (9.4μ) Si-O peak absorption, the sample thickness need not be determined in arriving at the glass composition. This ratio has been used by other

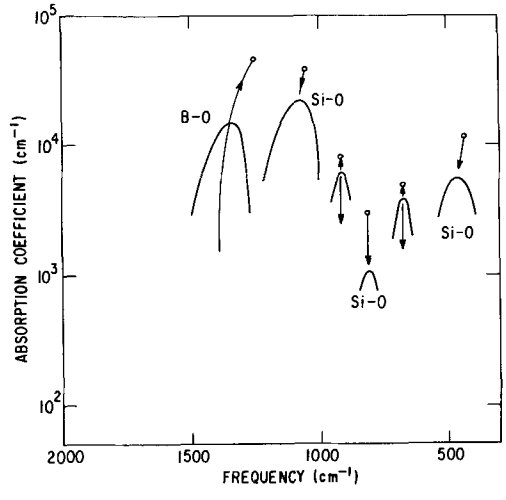

Fig. 2. Infrared bands appearing in a silicon oxide base glass containing approximately 15 m/o of boron oxide. The arrows indicate the direction of shift of the peaks with increasing boron oxide.

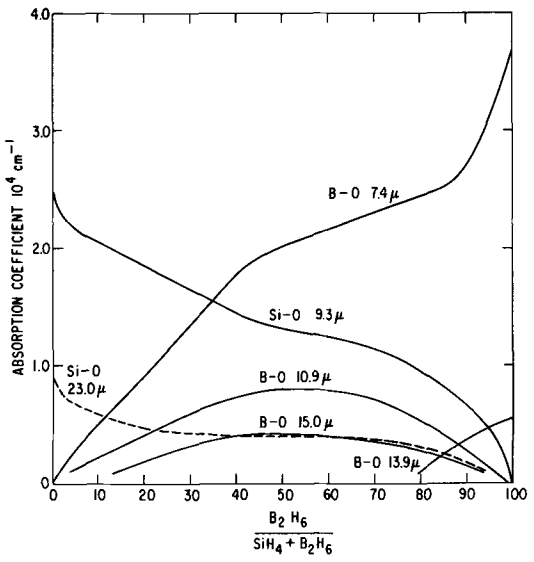

Fig. 3. Absorption coefficient of the major infrared bands in borosilicate glasses. The abscissa is the per cent of diborane gas to diborane plus silane gas flowing to the reactor.

workers with thin films (13-16). Films of from 1/2 to 1μ thickness and 300 μg weight were prepared; the film weight was determined by difference weighings on the 200 mg silicon wafers. The films were dissolved in a 10% HF solution and a 10 ml sample was aspirated in the flame spectrometer. The calibration of the boron content was obtained from standard solutions of boric acid. The mole per cent of B_2O_3 in the mixed glasses as a function of the infrared peak ratios is given in Fig. 4. The scatter in the data comes mostly from the boron determinations by the flame spectrometer. The glass of Fig. 2 while having a preparation gas ratio of nearly 25% B_2H_6 has about 15 m/o B_2O_3 in the finished film.

Water absorption.—Little change was noted in the glass of Fig. 2 after three days' exposure to room atmosphere. However, a pure boron oxide film even when covered with 2500Å of SiO_2 glass takes up a considerable amount of water during this same time. Without a cover, the pure boron oxide glass will show water absorption from the air within minutes after exposure.

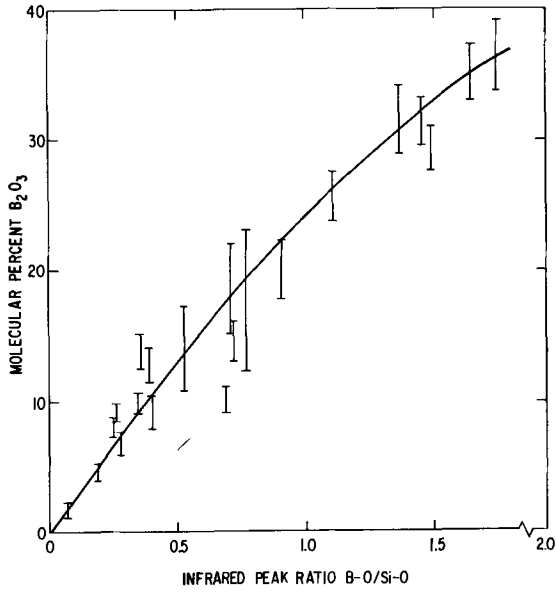

Fig. 4. A calibration of the m/o B_2O_3 in a borosilicate film against the infrared absorption peak ratio for the strongest B-O and Si-O bands at 1340 cm^{-1} and 1070 cm^{-1}.

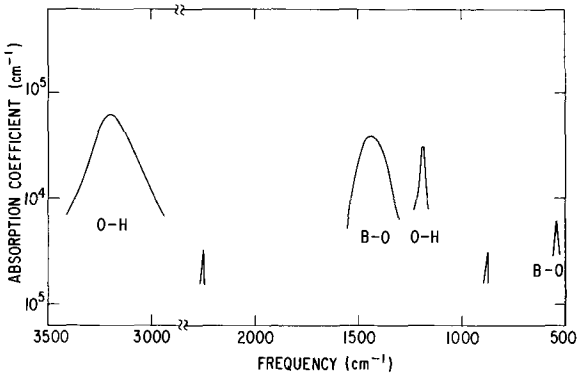

Fig. 5. Absorption coefficient of the infrared bands appearing in a highly hydrated B_2O_3 film.

This change in the film is observed in infrared absorption through the appearance of a number of B-O and O-H bands.

These new bands are identified with $B(OH)_3$ (9, 10); the approximate absorption coefficients of a hydrated boron oxide film are given in Fig. 5. The progress in the hydration of a pure B_2O_3 film can be observed through the infrared absorption changes. First to appear are the strong O-H band at 3220 cm^{-1} and a new B-O band at 1450 cm^{-1}. These bands of $B(OH)_3$ grow at the expense of the B-O bands of B_2O_3 which retain their wavelength positions. Also the new bands appear and increase in strength with no change in wavelength. These facts suggest that the film is two-layered with $B(OH)_3$ overlying the B_2O_3. Further hydration adds the sharp band at 1325 cm^{-1}, and the smaller sharp bands at 2250 and 540 cm^{-1} develop last.

In mixed B_2O_3-SiO_2 glasses the changes that take place in the film are slower. Observations of the stability of the films in controlled humidity tests indicate that water is taken from the air and incorporated in the film. In all deposited borosilicate glasses only a small absorption at 3570 cm^{-1} is originally observed—presumably caused by Si-O-H. Upon exposure of the glass to water vapor this absorption increases and absorption near 3340 cm^{-1} appears. Eventually the film exhibits a broad absorption beginning at 3640 cm^{-1} and tailing out beyond 2900 cm^{-1}. This band can be removed by heating the film for an hour at 400°C.

The main B-O absorption band near 1340 cm^{-1} decreases in amplitude upon exposure to water vapor. Heating the film at 400°C has no effect on this decreased value. The decrease with time in the B-O absorption band at two boron concentrations and at several relative humidities is shown in Fig. 6 and 7.

From Fig. 6, for films containing about 30 m/o B_2O_3, the infrared absorption ratio drops about 50% in two days at 50% relative humidity. From Fig. 7, 25% B_2O_3 films show a decrease of only 10% in two days at 50% relative humidity. The water sensitivity of the films is thus strongly dependent on the B_2O_3 content. The drop in the infrared ratios at 0% humidity is, no doubt, primarily caused by the short time exposures of the wafers to room air while measurements were made. A film containing 20% B_2O_3 has been exposed to normal laboratory atmosphere with relative humidities varying from 30 to 60%. As seen in Fig. 8, the infrared ratio is still dropping after more than a year's time. Also in Fig. 8 is a 10% B_2O_3 film which changes little with time even under 80% relative humidity.

A very rapid pickup of water occurs in borosilicate films of > 25% B_2O_3 content when they are exposed to relative humidities of > 50%. Within minutes after exposure the O-H band of $B(OH)_3$ appears at 3200 cm^{-1}. Often a visible haze appears on the wafer as the $B(OH)_3$ is formed in the borosilicate glass. The

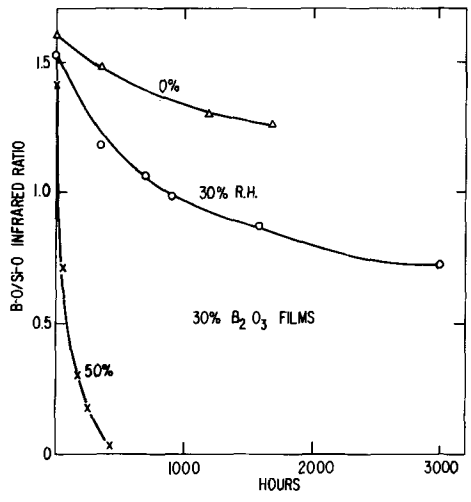

Fig. 6. The decrease with time of the B-O/Si-O infrared peak ratio for 30 m/o B_2O_3 in a borosilicate film exposed to various relative humidities in air.

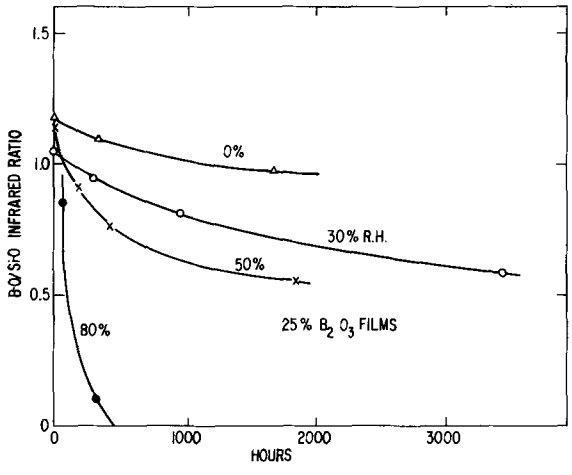

Fig. 7. The decrease with time of the B-O/Si-O infrared peak ratio for 25 m/o B_2O_3 in a borosilicate film exposed to various relative humidities in air.

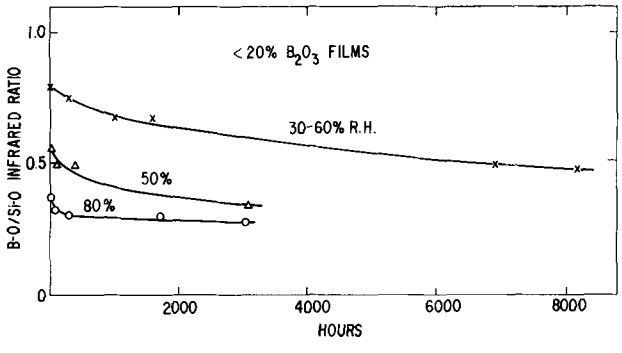

Fig. 8. The decrease with time of the B-O/Si-O infrared peak ratio of 20%, 14%, and 10% B_2O_3 borosilicate glass films exposed to various relative humidities in air.

1450 cm^{-1} band of $B(OH)_3$ also appears, usually as a shoulder on the nearby B_2O_3 absorption peak. The sharper band at 1180 cm^{-1} will also develop with time. Interestingly enough, these $B(OH)_3$ bands after maximum development with time will decrease in amplitude and essentially disappear. A film with this history is then not distinguishable from another film that has not shown the transient $B(OH)_3$ absorptions

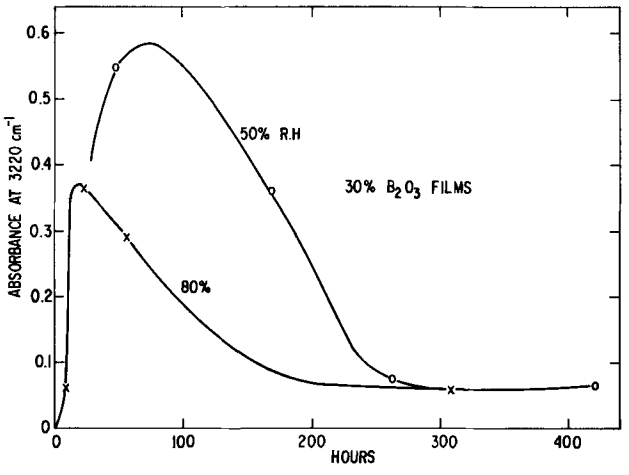

Fig. 9. The change with time in the B-O-H absorbance of a 30 m/o B_2O_3 borosilicate exposed to high relative humidity air.

but has, over a much longer period of time, also degraded insofar as the infrared absorption of B-O is concerned. The rise and decay of the 3200 cm^{-1} B-O-H band in high boron content films as a function of time is shown in Fig. 9 for two films exposed to different relative humidities. Heating of the films will remove the very broad residual absorption at 3640-3000 cm^{-1}, whereupon boron is no longer detected as either B-O or B-O-H. However, a diffusion step readily shows that much of the boron remains in the film presumably in a form which is not infrared active.

Densified films (those which have received a 10 min bake in argon at 800°C) are characterized by a decrease in the peak amplitude of the B-O absorption and an increase in the Si-O peak. The ratio of the peaks, for the same boron content of the film, drops some 30% depending on composition and the degree of heat treatment. The B_2O_3 calibration curve of Fig. 4, therefore, cannot be used for densified layers. However, the hydration in air of the densified films appears to be little different from that of the as-deposited glasses of the same boron content. Valletta *et al.* (14) also observed the water sensitivity.

The borosilicate films of Fisher (2) were covered by 3000Å of SiO_2. The densified films of Kern and Heim (15) were considered stable although the B_2O_3 content was stated to be 17%. Over long periods of time, water effects would no doubt be observed through infrared absorption in these films. For short periods, the water uptake will be delayed by SiO_2 glass overlayers. This modification is especially important for borosilicate glasses containing > 25% B_2O_3 (17).[1]

[1] J. W. Sprague uses thin SiO_2 covers to get short-term stabilization of high boron content films.

Conclusions

Borosilicate films on silicon wafers are readily identified as to boron content using infrared absorption characteristics. Once a calibration has been made, the ratio of the B-O to the Si-O absorption peak gives the molecular percentage of B_2O_3 in the film (18).[2] Water absorption at high humidities in films containing > 25 m/o B_2O_3 is rapid, but the pickup rate can be controlled in normal usage by the use of thin SiO_2 glass cover layers.

Acknowledgments

The help of P. R. Kennicott with the boron calibration and stimulating discussions with D. M. Brown are gratefully acknowledged. G. J. Charney prepared the glass films; R. F. Reihl measured the boron content of the films.

Manuscript submitted April 8, 1971; revised manuscript received June 30, 1971.

Any discussion of this paper will appear in a Discussion Section to be published in the June 1972 JOURNAL.

[2] The boron content of similar glass films has been checked by another method by A. S. Tenney. He has done intensive work on deposition of films and the boron analysis.

REFERENCES

1. J. Scott and J. Olmstead, *R C A Rev.*, **26**, 357 (1965).
2. A. W. Fisher, J. A. Amick, H. Hyman, and J. H. Scott, Jr., *ibid.*, **29**, 533 (1968).
3. M. L. Barry and P. Olofsen, *This Journal*, **116**, 854 (1969).
4. K. M. Whittle and G. L. Vick, *ibid.*, **116**, 645 (1969).
5. D. M. Brown and P. R. Kennicott, *ibid.*, **118**, 293 (1971).
6. S. Anderson, R. L. Bohon, and D. D. Kimpton, *J. Am. Ceram. Soc.*, **38**, 370 (1955).
7. W. J. Englert and F. A. Hummel, *J. Soc. Glass Technol.*, **39**, 121T (1955).
8. N. F. Borrelli, B. D. McSwain, and Gouq-Jen Su, *Phys. Chem. Glasses*, **4**, 11 (1963).
9. D. E. Bethell and N. Sheppard, *Trans. Faraday Soc.*, **51**, 9 (1955).
10. J. L. Parsons and M. E. Milberg, *J. Am. Ceram. Soc.*, **43**, 326 (1960).
11. N. F. Borrelli and Gouq-Jen Su, *Phys. Chem. Glasses*, **4**, 206 (1963).
12. A. H. Silver and P. J. Bray, *J. Chem. Phys.*, **29**, 984 (1958).
13. W. A. Pliskin, "Measurement Techniques for Thin Films," B. Schwartz and N. Schwartz, Editors, p. 280, The Electrochemical Society Softbound Symposium Series, New York (1967).
14. R. M. Valletta, W. A. Pliskin, D. W. Boss, and V. Y. Doo, Abstract No. 43, p. 111, Electrochemical Society, Extended Abstracts, Spring Meeting, New York, May 4-9, 1969.
15. W. Kern and R. C. Heim, *This Journal*, **117**, 568 (1970).
16. R. O. Schwenker, *ibid.*, **118**, 313 (1971).
17. J. W. Sprague, Private communication.
18. A. S. Tenney, Private communication; *This Journal*, **118**, 1658 (1971).

Electrical Properties of Anodic Oxide Films of Ta, Nb, Zr, Ti, W, and V Formed by the Ion-Cathode Method

D. Husted, L. Gruss, and T. Mackus

Pitman-Dunn Laboratories, Frankford Arsenal, Philadelphia, Pennsylvania 19137

ABSTRACT

Amorphous oxide films have been grown on Zr, Ti, W, Ta, Nb, and V by ionized gas anodization using the ion cathode as a source of negative ions. Films were grown on each metal at constant current to 175V followed by constant voltage for about 4 hr. Several electrical and optical properties were measured for the anodic films produced on these refractory metals. Resistivities of the anodic oxide films on Zr, Ti, W, Ta, Nb, and V ranged from 10^{14} to 10^{17} ohm-cm. Breakdown voltages with the refractory metal positive (gold contact negative) were of the order of 31V to 111V. Film capacitances for these metals varied between 0.031 and 0.050 μf/cm^2, and the dissipation factors averaged 0.015 for all the oxides except V which was 0.062. Thicknesses and refractive indices were obtained by ellipsometry for anodic films on Ta and Nb. Film thicknesses were respectively 0.61μ and 0.57μ for Ta and Nb whereas the refractive indices were 2.1 and 2.0. Dielectric constants calculated from capacitance measurements for these anodic films were 22 and 28, respectively. The properties of films prepared by the ion cathode method are compared with those produced by plasma and solution methods reported by others.

The technique for ionized gas anodization utilizing an ion cathode as the source of negative charge carriers was first devised and used at this laboratory for tantalum (1). O'Hanlon (2) re-emphasized the basic differences between our apparatus and those of others. In this method, anodization occurs outside of the concentrated ion plasma region so that the electron and positive ion density in the gaseous electrolyte near the anode is limited while the relative negative ion concentration is increased, with the advantages that anode temperatures out of the main discharge region are lower and film growth may be directly observed without the masking effects of a general discharge.

This paper reports an extension of the earlier work on tantalum (1) in which we attempted to optimize the film growth cycle and to improve film properties such as breakdown potential for thin film applications in electronics. In addition, ionized gas anodization using the ion cathode as a source of negative ions has been extended to Zr, Ti, W, Nb, and V metals. Plasma anodizations of some of these metals have been reported previously by others (2-5). Vratny (6) compared the properties of tantalum films obtained by vacuum techniques with those prepared in solution concluding that the latter films were superior with respect to growth rate and dielectric strength, but that in other respects such as uniformity of thickness and nonshort yield, the gas phase films were very promising. Plasma anodization results on tantalum and niobium by Lee *et al.* (4) stressed the analogy between gas and solution grown films, especially that two layers form in plasma grown films just as during ordinary solution anodization. They infer from this that both metal and oxygen ions are mobile in the solid phase during gas phase anodizations. Some other metals, for example V and Be, cannot be anodized in aqueous electrolytes because their oxidation products rapidly undergo dissolution. It follows that an alternative way to grow an anodic film on these metals would be in a nonaqueous media or by a plasma technique. In 1957, the growth of anodic oxide films on a series of metals including V in an aqueous boric acid-ammonia solution was studied by Johansen *et al.* (7). They concluded for V that either an extremely porous film forms or that the oxidation product is rapidly undergoing dissolution. Young (8) has suggested that anodic oxide films on V would probably best be studied in partly nonaqueous solutions. Keil and Salomon (9) found that uniform anodic V_2O_4 films can be grown on V in acetic acid-tetraborate solutions which contain small quantities of water and when the current densities exceed 450 μA/cm^2. To the best of our knowledge no previous work has been reported in the literature on the vapor phase or plasma anodization of V, nor for Ti and W except for some unpublished data referred to by O'Hanlon for these latter two elements (2). Successful preliminary results for Ti have been mentioned (10). We undertook this work in order to obtain films by the ion-cathode method with which to compare films obtained by other methods. Using techniques previously acquired with Ta (1), our hope was to apply the ion-cathode technique to obtain oxide films possessing high-breakdown voltages, electrical resistances and capacitances with low dissipation factors on other Group 5 and some Group 4 and 6 metals.

Key words: thin films, gas phase anodization, resistance, breakdown voltage, capacitance.

Experimental

The metal anodes were 99.5-99.8% pure except for Zr (98.0%). All of the metals, purchased in rod form with diameters of 2.4 cm, were cut to a length of 1.27 cm for use as anodes. Only one face of the metal disk was used in the anodization process. This surface was mechanically polished to a bright mirror-like finish, washed in warm tap water, rinsed with distilled water and spectrographic grade methanol, and then dried with a stream of dry nitrogen. The metal disk was then mounted in the anodization apparatus. The method of mounting and masking the anodes (Fig. 1) was described previously (11). The anodizations were carried out in an all metal, double base plate, ultra high vacuum system. Oxygen pressure was controlled by a variable leak. Details of the ion cathode have been described previously (1).

Prior to anodization the system was evacuated to 3 $\times$ 10^{-6} Torr and then backfilled with oxygen and held at a pressure of 85 milliTorr during the anodization process. The ion cathode current was maintained at 80 mA by the application of approximately -800V. Anode temperature was monitored using the thermocouple arrangement shown in Fig. 1. Since it is some

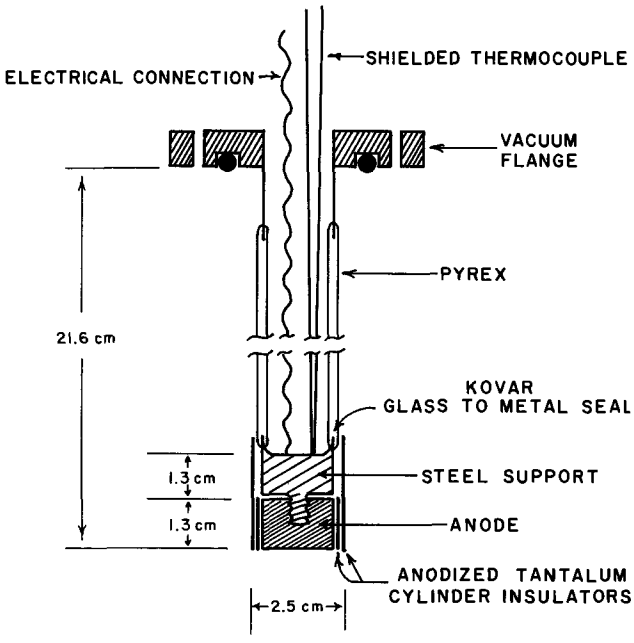

Fig. 1. Method of mounting and masking the metal anode

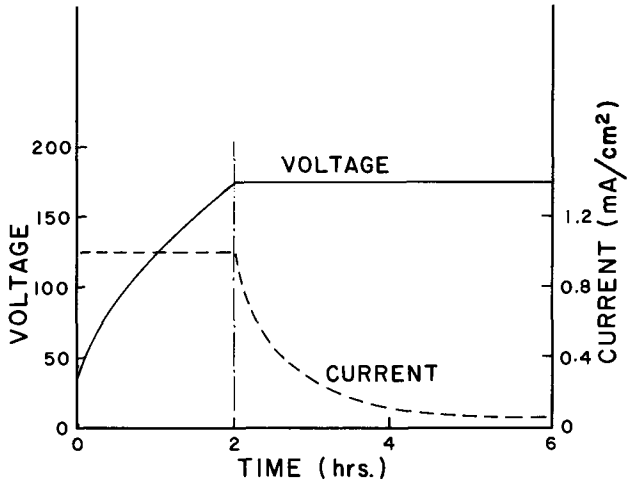

Fig. 2. Typical voltage, current, time relationships during the film growth cycle; current is held constant at 1.10 mA/cm² until the voltage reaches 175V, voltage is then held constant while the current decreases to a minimum value.

distance from the actual anode surface, the temperature measured by this thermocouple was checked against that of a thermocouple actually embedded in a hole drilled into the back of an anode to within 2 mm of the anode surface. The temperatures measured at both points were the same. Anode temperatures never exceeded 105°C.

In our earlier procedures (1) films were grown by anodizing at a constant anode current density to a preselected voltage at which point the anodization was stopped. This process produced films that were clear and uniform but with low breakdown voltages. In order to improve breakdown voltages, we experimented with extended film growth cycles. Being guided by our previous experiences in liquid phase anodization, we used the following cycle: the film growth potential was increased to its maximum value (max. = 175V due to leakage around the anode mask) maintaining a constant current density as the film grew. This operation was followed by a period of four hours during which the maximum potential was maintained while the leakage current fell to values of 0.08, 0.03, 0.08, 0.02, 0.09, and 0.15 mA for Zr, Ti, W, Ta, Nb, and V, respectively. Figure 2 shows an example of the growth cycle. This procedure resulted in improved breakdown voltages but at the expense of poor film uniformity. Anode current densities over the range 0.06-2.20 mA/cm² were investigated to determine the best growth conditions for attainment of uniform films. At 1.10 mA/cm² acceptable uniformity of oxide thicknesses resulted. Film uniformity was monitored by observation of interference colors. The typical film appears uniform in color indicating a uniform thickness across most of the surface of the specimen except for within approximately 3 mm of the anode edge.

Using the above procedure, films grown on Ta, Ti, Zr, Nb, W, and V exhibited strong interference colors, and were firmly adherent. Anodic films were grown on duplicate samples of each metal under identical conditions, and film resistance, capacitance, dissipation factor and breakdown voltage were measured. All measurements were in air, at room temperature, with the relative humidity limited to a maximum of 30%. After removal and exposure to air, gold contacts were vapor deposited onto the film surface using a suitable mask. Silver contact paint was then used to attach a copper wire to the gold contact. The contacts were circular, 0.021 cm² in area and arranged in a 3 row by 6 column array. Electrical properties of the anodic films could be measured through these contacts. The thickness and refractive index of the oxide films on Ta and Nb were measured using a Rudolph Ellipsometer. The dielectric constants of these films were calculated from capacitance measurements. Film resistance was measured using a Keithley Model 610B electrometer. Three contacts per sample were measured, using a potential of 4.0V, with the metal anode at a positive potential and the gold contact negative. Long polarization times were encountered during which the resistance increased with time. The mean final resistances are listed in Table I. The values reported are those

Table I. Breakdown potentials, resistance, capacitance, and dissipation factors of oxide films formed on ion-cathode anodized metals

Readings taken at relative humidity of 30% or less. (Standard deviation represents 68.27% confidence limits.)

Anodized metal	Film breakdown voltage, (volts) w/metal potential positive		Film breakdown voltage, (volts) w/metal potential negative		Film resistance (0.021 cm² contact area) (ohms)		Film capacitance at 1 kHz (μf/cm²)	Dissipation factor at 1 kHz
	Avg of 12 readings	Range of readings	Avg of 4 readings	Range of readings	Avg of 6 readings	Range of readings	Avg of readings (No. of contacts)	Avg of readings (No. of contacts)
Zr	111 ± 39	57-180	95 ± 29	63-124	(4.0 ± 2.1) × 10^{14}	1.8-8.0 × 10^{14}	0.04 ± 0.002 (17)	0.013 ± 0.001 (17)
Ti	83 ± 25	29-112	22 ± 5	18-29	(1.7 ± 1.7) × 10^{15}	0.04-4 × 10^{15}	0.036 ± 0.001 (19)	0.014 ± 0.004 (19)
W	66 ± 44	18-180	22 ± 5	18-29	(1.4 ± 0.2) × 10^{14}	1.1-1.8 × 10^{14}	0.046 ± 0.001 (17)	0.012 ± 0.002 (17)
Ta	50 ± 15	12-63	22 ± 13	6-35	(5.3 ± 3.8) × 10^{13}	1.10-1.1 × 10^{14}	0.031 ± 0.001 (20)	0.016 ± 0.001 (20)
Nb	49 ± 29	23-113	13 ± 6	6-22.5	(2.6 ± 1.4) × 10^{13}	1.3-5.3 × 10^{13}	0.041 ± 0.003 (21)	0.016 ± 0.001 (21)
V	31 ± 15	12-57	22 ± 13	6-35	(5.4 ± 5.0) × 10^{11}	0.10-1.5 × 10^{12}	0.050 ± 0.002 (19)	0.062 ± 0.016 (19)

recorded 210 min after the voltage was applied, by which time the resistance had stabilized. No attempt was made to determine whether or not this polarization was reversible by heating or by annealing. It would be necessary to heat tantalum oxide, for example to greater than 500°C (12) for effective annealing in order to determine whether the potentials were due to solid-state transitions or to a resistance polarization caused by semiconductor effects such as a lowering of acceptor density. A General Radio 716 C capacitance bridge was used to measure capacitance and dissipation factor at 1 kHz. Approximately ten contacts per sample were measured and the mean capacitance and dissipation factor for each film is shown in Table I.

Film breakdown voltage was determined by application of a d-c potential to the sample and monitoring the current. The procedure was to raise the voltage to a specific value while monitoring the current. If no current could be observed after 30 sec, the circuit was disconnected, the voltage raised by about 3-6V then the circuit was closed again and the procedure repeated. Breakdown was usually sharp and catastrophic, but in some measurements a significant leakage current would begin to occur before breakdown. In these cases the voltage at which current leakage reached 0.01 μA is reported as the breakdown voltage. This latter procedure is similar to that used by Schwartz and Gresh (13) and Vromen and Klerer (14). Self-healing breakdown would not be observed under our experimental conditions because the RC time constant of our circuit (the measuring circuit incorporated a one megohm resistor) was of the order of a millisecond while the characteristic time for self-healing is of the order of 1 μsec.

Results and Discussion

Using the results of earlier workers (2-6), we presumed that the films reported here are oxides and amorphous. Nevertheless we searched for evidence of crystallinity in the films by normal x-ray diffraction procedures and back-reflection techniques and by electron diffraction methods. These efforts failed to indicate any crystalline oxide. Low angle x-ray diffraction patterns were broad and diffuse. Electron diffraction results were confusing due to space charge effects. Efforts to minimize these effects by depositing a thin carbon film on the anodized film surface were helpful, but no pattern could be observed in any case. In addition, infrared absorption spectra in the range from 4000 to 250 cm^{-1} by the Attenuated Total Reflectance method proved only that the Nb films absorb at near 800 cm^{-1} as did both pure Nb_2O_5 and NbO_2 used as standards. Thus we can conclude only that the films are either amorphous oxides or composed of very small crystallites. The space charge effects observed in the electron diffraction study and their poor conductivity indicate that the surfaces of the anodized films were of higher oxides of the metal. Lower oxides, *e.g.* TaO_2, would possess extra "d" electrons, and hence they would be the more conductive oxides. This is not to say that the anodic films are purely higher oxides. Probably, anodic oxide films of a metal, for example Ta, are a mixture of Ta_2O_5 and TaO_2 as well as nonstoichiometric oxides.

Breakdown voltages (Table I) were measured on two films, each having 6 contacts with the metal side of the anode disk held at a positive potential and 2 contacts with the metal side negative. Breakdown voltage was higher for the metal positively charged for all the oxides (Table I). Several possible causes for this polarity have been suggested such as differing work functions of the contact metal (15), local inhomogeneities in the oxide, or the effects of moisture on conductivity in the anodic direction (13). The data in Table I show that high values of breakdown voltage and film resistance (corresponding to resistivities of the order of 10^{17} ohm-cm, if film thicknesses are about 0.6μ) may be obtained by the ion-cathode method. The large scatter of breakdown voltage measurements was to be expected based upon the experiences of others (16). The follow-up current in breakdown as measured in this work probably augments the initial melting and evaporation damage. Catastrophic breakdown was to be expected in view of the geometry and thickness of the electrodes, and the probable weak spots in the film aid in breakdown and contribute to the scatter in the data. Breakdown strengths of the order of 1×10^6 V-cm^{-1} for ion-cathode grown films on Ta may be compared with the breakdown strengths of tantalum oxide films obtained by aqueous methods (14) and by usual plasma techniques (6, 13, 14). The breakdown strengths of vapor-anodized niobium oxide films are also comparable (17). The breakdown voltages in a forward (metal positive) direction for oxide films grown on Zr, Ti, W, and V metals are 111, 83, 66, and 31V, respectively. If we assume that the thickness for each of these oxide films to be about 0.6μ then their breakdown strengths can be estimated accordingly. Breakdown strengths for plasma grown Zr oxide (5) and for vapor reaction Ti dioxide (18) are comparable to ours.

Breakdown voltages and film resistances for tantalum and niobium oxides appear to be greater than those obtained on vanadium oxide, while film capacitance and dissipation factor for vanadium oxide were greater. Higher resistances appear to be consistent with the bandgap energies obtained by spectroscopic means. Bandgap energies corresponding to the onset of electrical conduction are 3.72 eV for Ta_2O_5 (12), 3.03 eV for Nb_2O_5 (12) (19) compared to about 2.15 eV for V_2O_5 (19). For ZrO_2 (12) and TiO_2 (19) (20) the optical bandgap energies are 5.03 eV and 3.00 eV, respectively. However, because the films are probably a mixture of oxides, these data for higher oxides serve only to indicate the relative resistances of the films studied. For example, the anodic film of Ti may be a mixture of oxides including TiO_2 since its resistivity and breakdown voltage is higher than what would be expected on the basis of its optical bandgap. Similar data for W is unavailable. The dissipation factor of vanadium oxide was not only higher initially, but increased with time on standing. One V sample increased from 0.49 to 0.92 after standing at a relative humidity of $\leq$30% for 168 hr at room temperature. This could be due to absorption of water vapor by the oxide films. The other oxides increase in dissipation factors and capacitances with increasing relative humidity possibly also due to the adsorption of water into pores or flaws in the film. The changes are reversible. For example, in a sample of titanium oxide a large increase in relative humidity (from approximately 13% to 60%) caused the film capacitance to increase by 12% and the film dissipation factor to increase from 0.013 to 0.041 and decrease the same amount in dry atmosphere. Another indication of higher porosity may be the limiting current densities of the films, *i.e.* lower limiting current densities should correspond to a lower porosity. It is to be noted that V had the highest limiting current indicating that the film might possess a high porosity which may account for the higher dissipation factor and low resistance of the V film.

The ellipsometric thickness and refractive index measurements of the anodic films for Ta and Nb are given in Table II. Computations were performed using a program obtained from the National Bureau of Standards (21). In order to measure film thickness by ellipsometry it is necessary to know the optical constants of the film free substrate. However most metals, Au being the only exception (22), are thermodynamically unstable in the presence of oxygen at room temperature, and it is difficult to have a film free surface at the outset. For example, Ta in air, is typically covered by an oxide film about 70Å thick which leads to

Table II. Film thickness and refractive index as determined by ellipsometry

Dielectric constant calculated from capacitance measurement. Values are the mean for two films formed under identical conditions on ion cathode anodized metals.

	Film thickness (μ)	Refractive index at 5461Å at 25°C	Dielectric constant at 1 kHz
Tantalum	0.61	2.1	22
Niobium	0.57	2.0	28

large errors in the determination of the refractive index and extinction coefficient of the Ta metal base (23). The thickness and refractive index results for the films on Ta and Nb given in Table II are based upon the literature values of the optical constants obtained by the curve fitting technique for Ta and Nb metals (23, 24). The values of refractive index, 2.1 for tantalum oxide and 2.0 for niobium oxide, are somewhat lower than the values found in the literature for similar films prepared in an aqueous electrolyte. Kumagai and Young report 2.26 for tantalum oxide (23) and Young and Zobel report 2.37 for niobium oxide (24), both values being determined by ellipsometry. Lee *et al.* (4) found that oxides of Ta and Nb formed by gas anodization and ordinary anodization consisted of two layers with the layer closest to the metal surface being richer in metal atoms. The refractive indices obtained by Lee *et al.* for Ta were 2.22 for the inner layer and 1.89 for the outer layer. For Nb a value of 2.37 is found for the inner and 2.15 for the outer layer. Our data are consistent with Lee and co-workers if we assume that our films are like his outer films but that more time for migration of the ions has been allowed. The ionized gas oxide layer is probably richer in oxygen than inner oxide layers.

Anode glow was visible adjacent to the entire surface of each metal during anodization. The intensity of the glow seemed to remain constant up to the maximum voltage, but noticeably decreased during constant voltage anodization at 175V until at the limiting current, glow was either absent or at most barely visible. Glow is associated with the rate of oxide formation (1, 25). Although anode glow was visible over the wafer during anodization there was no evidence to indicate that film sputtering had occurred. However, Jennings and McNeill (11), working with the very same apparatus reported here, have observed Au film sputtering when the Au was biased positively with respect to the anode. They measured the sputtering rate of the Au to a maximum bias of 200V and showed that the Au sputtering is due to negative oxygen ion bombardment. This observation with Au serves to indicate that the metals studied here may also sputter but not by a significant amount.

Finally, the electrical properties of the anodic films formed in the ion cathode apparatus are consistent with those formed by other methods.

Resistance measurements given in Table I correspond to resistivities of the order of 1.40×10^{17}, 5.95×10^{17}, 4.90×10^{16}, 1.86×10^{16}, 9.1×10^{15}, and 1.89×10^{14} ohm-cm for Zr, Ti, W, Ta, Nb, and V respectively, again assuming thicknesses to be 0.6μ. These may be compared to resistivities of plasma anodized Ta (4, 6) and Nb (4, 24), vapor deposited Ti (18) and liquid phase oxide films of Ti (26), Ta (4), Nb (4), and oxides of vanadium (27). Capacitances and dissipation factors of the ion-cathode anodized metal films may be compared to the data obtained with films of Zr (28, 29), Ti (18, 26), Ta (30), Nb (31) anodized in solution, and with vapor anodized films on Ta (6) by reactive sputtering. The data for anodized films by various methods show inconsistencies but we can conclude with certainty that films deposited by the ion-cathode method are at least comparable in desirable electrical properties to those of solution and normal plasma anodization.

Acknowledgment

The authors gratefully acknowledge Dr. F. D. Verderame, for his helpful discussions and review of the manuscript.

Manuscript submitted Feb. 8, 1971; revised manuscript received *ca.* Aug. 23, 1971.

Any discussion of this paper will appear in a Discussion Section to be published in the June 1972 JOURNAL.

REFERENCES

1. T. A. Jennings, W. McNeill, and R. E. Salomon, *This Journal*, **114**, 1134 (1967).
2. J. F. O'Hanlon, *J. Vac. Sci. Technol.*, **7**, 330, (1970).
3. F. L. Miles and P. H. Smith, *This Journal*, **110**, 1240 (1963).
4. W. L. Lee, G. Olive, D. L. Pulfrey, and L. Young, *ibid.*, **117**, 1172 (1970).
5. N. Ramasubramanian, *ibid.*, **117**, 947 (1970).
6. F. Vratny, *J. Am. Ceram. Soc.*, **50**, 283 (1967).
7. H. A. Johansen, G. B. Adams, and P. Van Ryssel-berghe, *This Journal*, **104**, 339 (1957).
8. L. Young, "Anodic Oxide Films," p. 187, Academic Press Inc., New York (1961).
9. R. G. Keil and R. E. Salomon, *This Journal*, **115**, 628 (1968).
10. G. J. Tibol and R. W. Hull, *ibid.*, **111**, 1368 (1964).
11. T. A. Jennings and W. McNeill, *Appl. Phys. Letters*, **12**, 25 (1968).
12. Joseph Bendoraitis, Ph.D. Thesis, University Microfilms, Ann Arbor, Mich., Order No. 69-18,372.
13. N. Schwartz and M. Gresh, *This Journal*, **112**, 295 (1965).
14. B. Vromen and J. Klerer, Proc. of the Electronic Components Conference, Washington, D. C., May 1965.
15. V. F. Korzo, *Fiz. Tverdogo Tela (USSR)*, **9**, 2753 (1967).
16. N. Klein, *This Journal*, **116**, 963 (1969).
17. H. R. Brunner, F. P. Emmenegger, M.L.A. Robinson, and H. Rotschi, *This Journal*, **115**, 1287 (1968).
18. A. E. Feursinger, *Proc. I.E.E.E.*, **52**, 1463 (1964).
19. F. Vratny and J. J. Kokalas, *Appl. Spectry.*, **16**, 176 (1962).
20. R. H. Bube, "Photoconductivity of Solids," p. 234, John Wiley and Sons, Inc., New York (1960).
21. F. L. McCracken, *Nat. Bur. Std. (U.S.) Tech. Note* 479 (1969).
22. O. Kubaschewski and B. E. Hopkins, "Oxidation of Metals and Alloys," Butterworths, London (1953).
23. S. Kumagai and L. Young, *This Journal*, **111**, 1411 (1964).
24. L. Young and R. G. R. Zobel, *ibid.*, **113**, 277(1966).
25. J. R. Ligenza, *J. Appl. Phys.*, **36**, 2703 (1965).
26. M. E. Sibert, *This Journal*, **110**, 65 (1963).
27. G. A. Rosgonyi and W. J. Polito, *ibid*, **115**, 56 (1968).
28. P. J. Harrop and J. N. Wanklyn, *ibid.*, **111**, 1133 (1964).
29. N. J. M. Wilkins, *ibid.*, **109**, 998 (1962).
30. D. M. Smyth and T. B. Tripp, *ibid.*, **110**, 1271 (1963).
31. R. Hand, H. Ling, and T. Kolski, *ibid.*, **108**, 1023 (1961).

Conduction in Al_2O_3 Films and Charge Storage in MAOS Structures

C. A. T. Salama*

Department of Electrical Engineering, University of Toronto, Toronto 181, Ontario, Canada

ABSTRACT

The conduction characteristics of aluminum oxide films deposited by rf sputtering on silicon substrates and ranging from 400-600Å in thickness were measured over a range of temperatures. It was found that the current transport is essentially bulk limited and independent of the film thickness, the electrode material, and the polarity of the electrode. The three processes which affect the conduction through these films were found to be: Poole-Frenkel emission, field ionization, and trap hopping. The various parameters such as temperature and gate electrode affecting the charge storage in MAOS memory elements, were investigated using an automatic measurement set up and were related to the conduction characteristics of the two insulating layers. The memory elements consisted of 400-600Å thick Al_2O_3 films deposited by rf sputtering on thermally grown SiO_2 layers 50Å thick. The charging and memory retention characteristics of the MAOS structure were also investigated. The effect of charge transport across the silicon dioxide on the surface state density at the $Si-SiO_2$ interface was also observed.

The possibility of using charge storage in a dielectric, which forms the gate insulator of a field-effect transistor, in memory applications has attracted considerable interest and led to an intensive investigation of these structures. Most of the attention has been focused on charge storage in MNOS (metal-silicon nitride-thermally grown silicon dioxide-silicon) structures (1-11). The memory effect is characterized by a shift in the flat-band voltage of the MNOS capacitor under application of a stress field above a certain threshold. This threshold field is typically $1\text{-}3 \times 10^6$ Vcm^{-1} and causes sizable tunneling (3) or conduction (6), across the thin (20-300Å) silicon dioxide layer. The shift in the flat-band voltage is due to accumulation of charge in trapping centers at the interface between the two dielectrics or in the silicon nitride (3-5). The charge accumulation is semipermanent, and charge retention is limited only by current leakage across the dielectrics. The stable charge storage at the silicon nitride-silicon dioxide interface has led to the application of MNOS structures in alterable read-only semiconductor memories and digital circuits with nonvolatile storage capabilities.

The use of other dielectrics, like aluminum oxide instead of silicon nitride, has received relatively little attention. Nakanuma (12) reported the fabrication of a read-only memory consisting of MAS (metal-aluminum oxide-silicon) FET's (field effect transistors) which exhibited threshold voltages alterable both electrically and by radiation. The aluminum oxide films in these devices were deposited by hydrolysis of $AlCl_3$ at 850°C. The charge storage was characterized by positive shifts in the threshold voltage which occurred independently of the polarity of the applied stress bias, provided this bias was higher than a critical value. This phenomenon was explained by Tsujide (13) as being due to electron injection and trapping in the aluminum oxide. The trapped electrons have an extremely long lifetime, hence the good memory retention characteristics.

MAOS (metal-aluminum oxide-thermally grown silicon dioxide-silicon) structures using aluminum oxide films prepared by oxidation of trimethyl aluminum in an oxygen atmosphere at 450°C, as well as aluminum oxide prepared by plasma oxidation of an aluminum film, exhibited a memory behavior which was characterized by positive and negative shifts in the flat-band voltage for positive and negative applied stress bias respectively. The devices, however, exhibited poor reproducibility and high incidence of breakdown (4).

MAOS structures, in which the Al_2O_3 films were prepared from an $Al\,Br_3\text{-}NO\text{-}H_2$ mixture, exhibited positive flat-band voltage shifts for positive applied stress bias; while for negative bias, the flat-band voltage shift was positive at low voltages and became negative as the stress bias increased (14).

The object of this paper is to investigate the charge-storage properties of MAOS structures consisting of rf sputtered aluminum oxide films (15) deposited on a thin (50Å) layer of thermally grown silicon dioxide. The macroscopic model of the memory element, based on the differential conduction properties of the two insulators (6), is briefly reviewed here. The conduction characteristics of rf sputtered Al_2O_3 films are then investigated and related to the charge storage properties of the MAOS structures.

Theory

Macroscopic model of the memory effect.—A macroscopic model which predicts the charging and discharging behavior of the MNOS capacitor structure in terms of the field-dependent conduction characteristics and geometry of the two insulators was developed by Frohman-Bentchkowsky (6). This model has been used to verify the experimental characteristics of MNOS memory devices. The generality of the model makes it useful for any two insulators of arbitrary thickness on an arbitrary semiconductor, and it will be applied here to the MAOS structure.

Qualitatively the memory behavior can be understood as follows. When a stress voltage, V_c, is applied across two insulating layers having different field-dependant conductivities, particle currents will flow in both insulators. Charge accumulation at the insulators' interface will occur when the particle currents in the two layers differ in magnitude. The polarity of the charge depends on the relative magnitude of the two currents. As charge builds up at the interface, the field in each layer will change such that particle current in the layer of high conductivity will decrease while particle current in the layer of lower conductivity will increase. Charge accumulation will stop when the currents become equal. When the applied voltage, V_c, is removed, the field due to the stored charge sheet will cause the charge to leak off by a conduction mechanism appropriate to the individual insulating layer.

* Electrochemical Society Active Member.
Key words: dielectric, thin film, memory.

The value of the two insulator layer structure as a memory device lies in the highly nonlinear conductivity with applied voltage of one of the two layers (in this case aluminum oxide). Because of this, charging (writing) can be accomplished rapidly with relatively high applied voltages while the loss of the charge occurs very slowly at lower biases (during interrogation) or at zero bias (during storage).

The equations describing the memory behavior of the MAOS structure are

$$K_o E_o - K_a E_a = Q_i/\epsilon_o \quad [1]$$

$$X_o E_o + X_a E_a = V_c \quad [2]$$

$$J_o(V_c,t) - J_a(V_c,t) = \frac{\partial}{\partial t} Q_i(V_c,t) \quad [3]$$

where K_o, E_o, J_o, X_o and K_a, E_a, J_a, X_a are the relative dielectric constants, electric fields, current densities, and thicknesses of the silicon dioxide and the aluminum oxide layers respectively. ϵ_o is the permittivity of free space. Q_i is the charge stored at the two insulator interface and can be related to the flat-band voltage V_{fb} of the MAOS structure by the equation[1]

$$V_{fb} = \phi_{MS} - \frac{Q_{ss}}{C_t} - \frac{Q_i}{C_a} \quad [4]$$

in which

$$C_a^{-1} = \frac{X_a}{K_a\epsilon_o}, \quad C_o^{-1} = \frac{X_o}{K_o\epsilon_o}, \quad C_t^{-1} = C_o^{-1} + C_a^{-1} \quad [5]$$

and where C_a, C_o are the Al_2O_3, SiO_2 capacitances per unit area respectively, ϕ_{MS} is the metal-semiconductor work function, and Q_{ss} is the fixed oxide charge at the Si-SiO_2 interface. The data required to solve these equations are the dielectric constants and thicknesses of the two insulating layers as well as relationships describing the conduction mechanisms in each individual layer.

For thermally grown SiO_2 films, 50Å or thicker, the conduction mechanism was shown to be electrode limited due to Fowler-Nordheim emission (16). This mechanism leads to an exponential dependence of the current density J_o on the electric field across the oxide E_o according to the following expression

$$J_o = B_o E_o^2 \frac{\pi b k T/E_o}{\sin(\pi b k T/E_o)} \exp(-E_1/E_o) \quad [6]$$

where T is the temperature in °K, k is Boltzmann's constant, and E_1, B_o, b are characteristic constants depending on the barrier height of the interface, *i.e.* depending on whether injection occurs, in the particular case under consideration, from the silicon or the aluminum oxide. When the silicon dioxide thickness is reduced (below 50Å), to a value at which direct tunneling can occur, the following empirical relation between the oxide current density and the applied field has been shown to apply (17)

$$J_o = B_o' E_o^2 \exp -(E_1'/E_o) \quad [7]$$

where B_o' and E_1' are constants.

Aluminum oxide films prepared by hydrolysis of $AlCl_3$ (13) and decomposition of an aluminum trimethyl-nitrous oxide mixture (18) exhibited bulk-limited conduction characteristics due to field-enhanced thermal excitation of carriers from traps (Poole-Frenkel effect). Duffy (19) reported that the conduction in aluminum oxide films prepared by thermal decomposition of aluminum isopropoxide was controlled by the interfaces. Relatively little information is available on the conduction characteristics of rf sputtered aluminum oxide films. These characteristics are investigated here in order to apply the macroscopic model described above and explain charge storage effects in the specific MAOS structures under investigation.

[1] This equation neglects any possible contact potential at the interface between the two dielectrics (15).

Experimental Techniques

All of the electrical measurements were carried out on MAS or MAOS capacitor structures fabricated on silicon substrates. The silicon used in this work was in the form of polished circular slices (Monsanto), 2.5 cm in diameter, prepared by the Czochralski method. The slices used were n-type (phosphorus doped), (111) orientation of approximately 10 and 0.01 ohm-cm resistivities. The high resistivity slices were used for charge storage studies and the low resistivity ones were used for investigations of the conduction characteristics of the aluminum oxide films. The polished silicon wafers were degreased and cleaned thoroughly (20) prior to aluminum oxide deposition or silicon dioxide growth. The silicon dioxide was grown at 900°C in dry oxygen in a horizontal resistively-heated furnace provided with a quartz tube and alumina liner. The silicon dioxide was then annealed at the same temperature in nitrogen for 10 min. Both the oxygen and nitrogen gases were obtained from liquid sources. The silicon dioxide films were grown, as thin as reproducibly possible, approximately 50Å thick to reduce charging times and voltages in the MAOS memory elements (11). The thickness of the SiO_2 layer was measured using a spectrophotometric technique developed by Rand (21).

The apparatus used for the deposition of aluminum oxide films by rf sputtering has been described previously (15). The films were sputtered from a sintered aluminum oxide (99.97%) target 12.5 cm in diam and 1 cm thick. Ultrahigh purity argon (99.999%) was used as the sputtering gas. The argon pressure was kept at 5-7 $\times$ 10^{-3} Torr during the run. At this sputtering pressure a 3 cm target-to-substrate distance was found to be compatible with a self-sustained uniform discharge and satisfactory deposition rates. The sputtering power density used was approximately 1.5 W/cm^2 resulting in a deposition rate of 30Å/sec. The substrate temperature did not exceed 200°C. After deposition, the aluminum oxide films were annealed in nitrogen for 30 min at 300°C. The heat treatments were restricted to a temperature below 320°C because of the possible occurrence of the γ' phase of aluminum oxide above this temperature (22). The Al_2O_3 film thickness was measured using a Talystep capable of $\pm$ 20Å accuracy and ranged from 400 to 600Å.

The capacitor structures were completed by evaporating aluminum or gold (99.999%) field plates, 1000Å thick, 500 μm in diameter over the dielectric through a mask. Aluminum was also evaporated on the bare back-side of the silicon for contact. The aluminum evaporations were carried out from a resistively heated tungsten filament, and the gold was evaporated from a molybdenum boat. The vacuum during evaporation was kept below 10^{-6} Torr.

The conduction currents through the Al_2O_3 films were measured with a Keithley 602 electrometer or a Keithley 413 A micro-microammeter. All the electrical measurements were carried out in vacuum (<0.1 Torr) and the temperature was monitored using a copper-constantan thermocouple attached to the sample holder. Special care was taken to ensure that conduction measurements were made under equilibrium conditions.

Characterization of charge storage effects involve measurements of the shift in flat-band voltage after each stress voltage is applied. In order to speed-up the characterization of the MAOS structures, a system which stresses the capacitor, samples, and records the flat-band voltage *vs.* stress voltage automatically was used and has been described in detail previously (23).

The operation of the system is based on the fact that the flat-band capacitance remains constant for the MAOS structure at any flat-band voltage. The apparatus is shown in block diagram form in Fig. 1. It consists of a feedback system which can be operated in

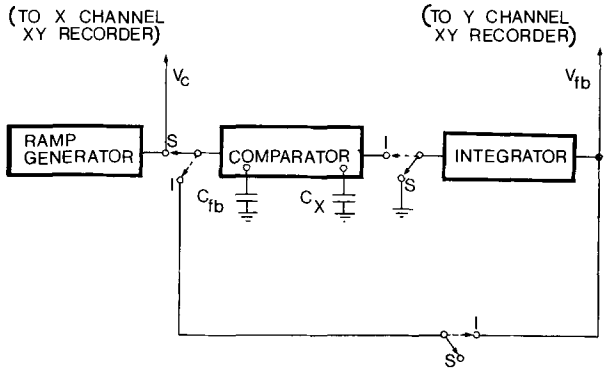

Fig. 1. Block diagram of automatic flat-band vs. stress voltage measurement system.

an open loop or stress (S) mode and a closed loop or integrating (I) mode. During the stress mode, a variable speed ramp generator applies a stress voltage to both the MAOS capacitor C_x and a fixed capacitor set at the appropriate flat-band capacitance value C_{fb}. A differential capacitance comparator (Boonton 71 A) is used to measure the difference between C_x and C_{fb} and produces a signal proportional to that difference. In the integrating mode, the ramp generator is disconnected and the loop is closed. The output of the comparator is applied to the integrator, whose output is in turn applied as a bias voltage to the two capacitors. When the output of the integrator reaches the flat-band voltage required to generate the correct flat-band capacitance, the output of the comparator is reduced to zero. Both the stress and the flat-band voltages are then recorded on an XY plotter. By replacing the ramp generator by a pulse generator, the system can be used to determine the flat-band voltage after application of a single stress pulse. It can also be used to monitor the flat-band voltage decay as a function of time.

The surface state density at the $Si-SiO_2$ interface was obtained from low-frequency C-V curves measured using the quasi-static technique as implemented by Kuhn (24). The method involves measurement of the MAOS capacitor displacement current density J_c in response to a linear gate voltage ramp $V_G = at$ where a is the ramp speed. The low frequency capacitance C_{LF} is related to the displacement current density by $J_c = a\,C_{LF}$.

Results and Discussion

Conduction in Al_2O_3 films.—Figure 2 shows the typical current density *vs.* square root of field for an $Al-Al_2O_3-Si$ structure at room temperature. The Al(+) and Al(−) curves refer to positive and negative aluminum electrodes. The two curves are almost identical and the slight difference in current density can be attributed to the presence of a thin layer of SiO_2 underneath the Al_2O_3 film (25).[2] Two regions can be distinguished on the curves. At high electric fields, the current varies exponentially with the square root of the field and at low fields the characteristic is ohmic. Similar results were obtained with Au electrodes deposited on the Al_2O_3 films. In general, the conduction characteristics were found to be independent of film thickness (for thicknesses in the range 400-600Å), electrode material and polarity of the electrodes. These results strongly suggest that the current is bulk controlled rather than electrode controlled.

Figure 3 shows plots of the current density *vs.* $1/T$ for two different fields for positive Al electrode. At low temperatures the current density becomes nearly independent of temperature.[3] At higher temperatures,

[2] In samples used for conduction measurements, special care was taken to minimize the thickness of the SiO_2 layer present on the silicon substrate prior to sputtering of the Al_2O_3 layer.

[3] At these low temperatures, log J_a exhibited a linear dependence on $1/E_a$.

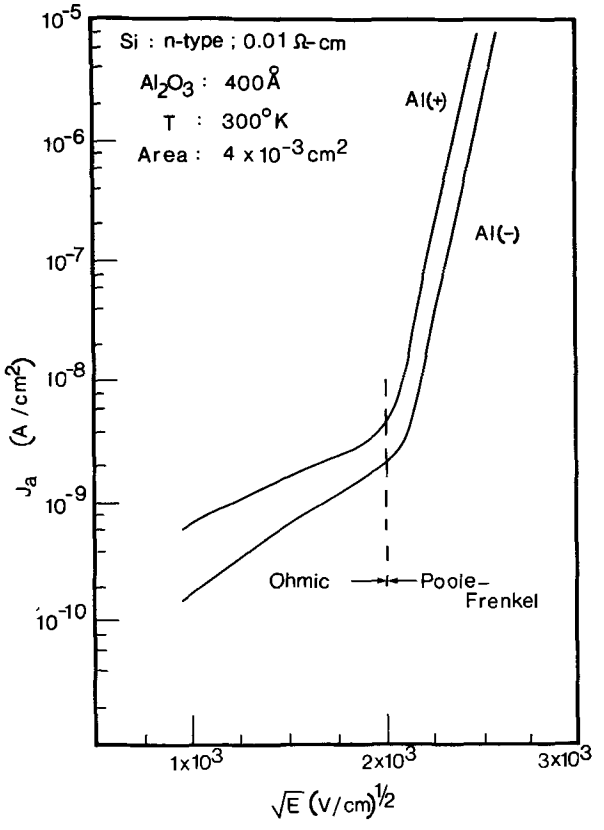

Fig. 2. Current density vs. square root of applied field for a MAS structure.

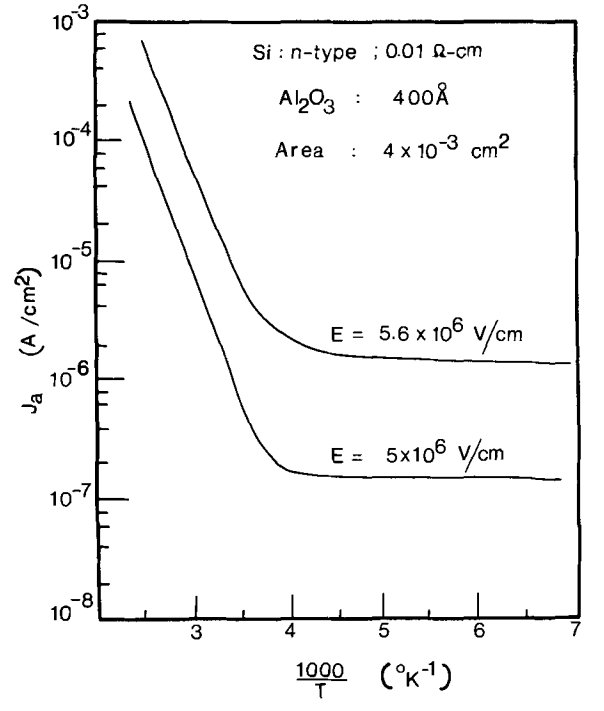

Fig. 3. Current density vs. 1000/T at two values of applied field for the same sample as in Fig. 2.

the current density exhibits a rapid increase. Based on these results and on the work of Mead (26) and Sze (27), the conduction current density J_a in the aluminum oxide films can be attributed to the sum of three contributions all bulk controlled

$$J_a = J_{a1} + J_{a2} + J_{a3} \qquad [8]$$

where

$$J_{a1} = C_1\,E_a \exp(-q\,\phi_a/kT) \exp q/kT\,(\beta E_a)^{1/2} \qquad [9]$$

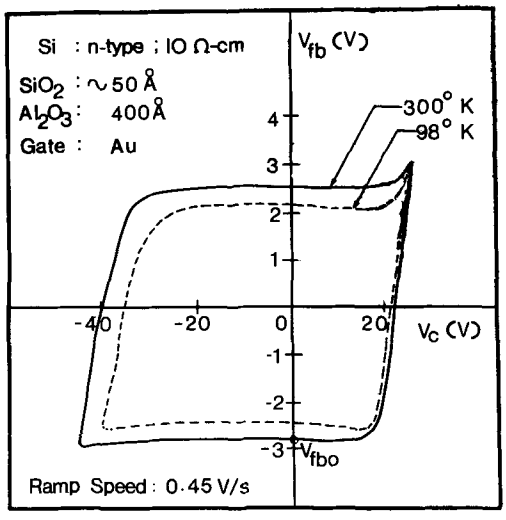

Fig. 4. Flat-band voltage *vs.* stress voltage hysteresis at two different temperatures for a MAOS structure.

$$J_{a2} = C_2 E_a^2 \exp(-E_2/E_a) \quad [10]$$

$$J_{a3} = C_3 E_a \exp(-q\phi_3/kT) \quad [11]$$

Current density J_{a1} is due to field enhanced thermal excitation of trapped electrons into the conduction band. This process is known as the Poole-Frenkel effect (26). In Eq. [9] C_1 is a constant, q is the electronic charge, ϕ_a is the barrier height, and $\beta = q/\pi K_a \epsilon_o$. Current density J_{a2} is due to field ionization of trapped electrons, this is a tunneling process essentially independent of temperature. Both C_2 and E_2 in Eq. [10] are constants (26). Current density J_{a3} is due to the hopping of thermally excited electrons from one isolated state to another (26). This process results in ohmic characteristics. In Eq. [11], C_3 and ϕ_3 are constants.

For the particular case illustrated in Fig. 2 and 3 for Al(+), the values of the constant terms in the current density equations were found to be as follows

$C_1 = 1.2 \times 10^{-6}$ A/V cm $\quad E_2 = 1 \times 10^8$ V/cm

$C_2 = 3 \times 10^{-13}$ A/V^2 $\quad \phi_3 = 0.15$ V

$C_3 = 3 \times 10^{-13}$ A/V cm $\quad \beta = 1.67 \times 10^{-7}$ V cm

$\phi_a = 1.35$ V

The value of β yields a self-consistent dynamic dielectric constant $K_a = 4.1$ for aluminum oxide. This value lies between the static value for the dielectric constant[4] 8 and the optical dielectric constant 2.89 (28) for aluminum oxide, as expected for Poole-Frenkel conduction (26).

The values of the constants were found to vary within a range of ± 10% for the various samples investigated. The magnitude of ϕ_a measured for the rf sputtered films is close to the value of 1.3V reported by Tsujide (13) but is much larger than the value of 0.5V reported by Hall (18).

In general, the results, reported above, are similar to those obtained on Si_3N_4 films except that the conduction current densities in the Al_2O_3 films are an order or two lower than those observed in pyrolitic Si_3N_4 (27). It follows that the charge storage characteristics of MAOS structures should be, qualitatively at least, similar to those of MNOS structures. These characteristics are discussed in the next section.

Charge storage in MAOS structures.—A typical flat-band voltage *vs.* stress voltage hysteresis loop, measured at room temperature (300°K), for a MAOS capacitor with gold gate electrode is shown in Fig. 4. The initial flat-band voltage is $V_{fbo} = -2.85$V. Knowing the value of $Q_{ss} \simeq 4 \times 10^{11}$ q/cm^2 (15), and $\phi_{MS} = -0.35$V (20) as well as the insulator capacitances, Eq. [4] can be used to estimate the initial charge $Q_i(0)$ stored at the Al_2O_3-SiO_2 interface. For the particular sample under investigation $Q_i(0)$ was found to be 3.3 $\times 10^{12}$ q/cm^2. This charge was positive for all the samples investigated and ranged from 3 $\times 10^{12}$ to 3.5 $\times 10^{12}$ q/cm^2. An asymmetry in the characteristics is observed in the figure. A larger negative than positive stress voltage is required to produce a fixed shift in V_{fb}. This asymmetry can be explained by the fact that the barrier height for injection from the Si into the SiO_2 under positive stress voltage, is smaller than the barrier height for injection from the Al_2O_3 into the SiO_2 under negative stress bias (6). Also shown in Fig. 4 is the hysteresis loop obtained on the same sample at 98°K under the same conditions. As expected, the flat-band voltage at 98°K is lower than that at 300°K, since some of the impurities in the substrate are not ionized at low temperatures thus reducing the fixed charge in the silicon depletion region. Under positive stress, the V_{fb} *vs.* V_c characteristics are almost identical at the two temperatures. This is due to the fact that most of the charging occurs through the thin silicon dioxide layer and that the conduction through this layer is almost independent of temperature[5] (see Eq. [6]). The area of the high temperature loop is larger than that of the low temperature one; this is an indication that Q_i increases with increasing temperature, as predicted by the theory, since the conductivity of the aluminum oxide film increases much faster than that of the silicon dioxide (6).

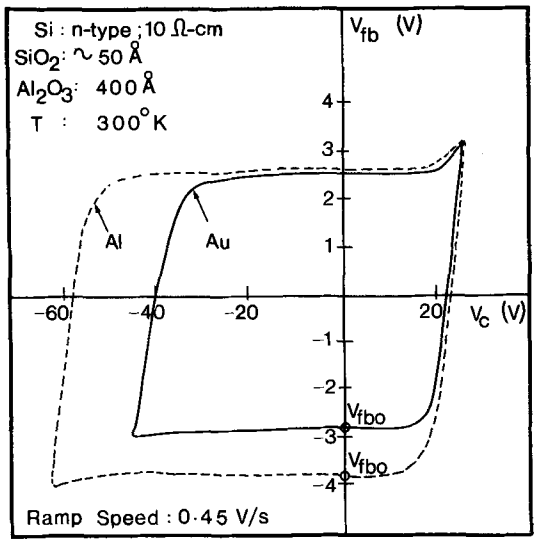

Fig. 5. Flat-band voltage *vs.* stress voltage hysteresis for a MAOS structure illustrating the effect of the gate electrode.

The effect of the gate electrode on the hysteresis characteristics is illustrated in Fig. 5 for Au and Al electrodes. The magnitude of the initial flat-band voltage is smaller for Au than for Al because of the difference in metal-semiconductor work function ϕ_{MS}. The V_{fb} *vs.* V_c curves under positive stress voltage are almost identical since the charging depends mostly on injection from the Si into the SiO_2. The flat-band voltage characteristics under negative stress are, however, different for Au and Al electrodes and this difference cannot be explained by the macroscopic theory, since it predicts that the characteristics should be independent of the gate electrode provided the conduction through the aluminum oxide is bulk controlled. This difference can, however, be attributed to electrode injection. At the very high fields encountered, injection from the aluminum electrode is quite plausible. In

[4] Measured at 1 MHz using a Boonton 71 A capacitance meter.

[5] The term $(\pi bkT/E_o)/\sin \frac{\pi bkT}{E_o}$ in Eq. [6] results in negligible temperature dependence.

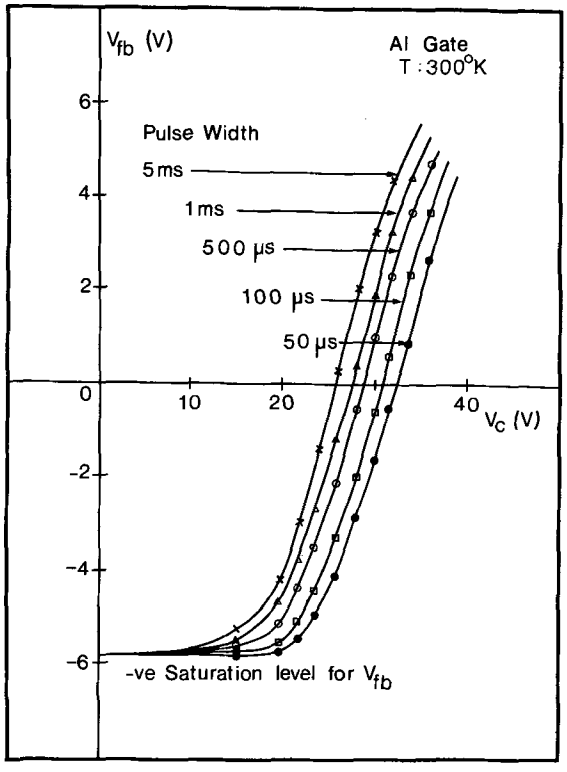

Fig. 6. Charging characteristics of a MAOS structure for various positive pulse widths.

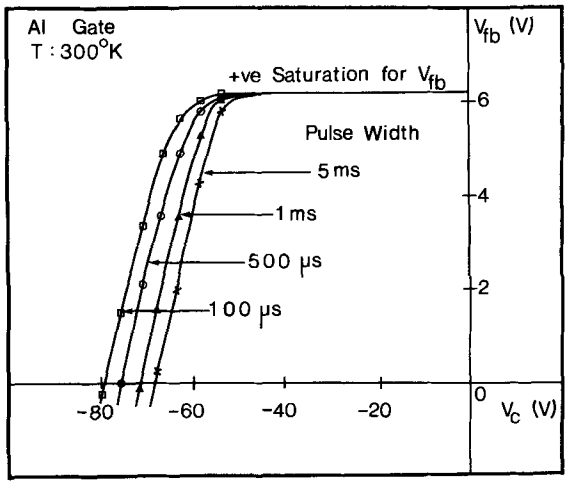

Fig. 7. Charging characteristics of a MAOS structure for various negative pulse widths.

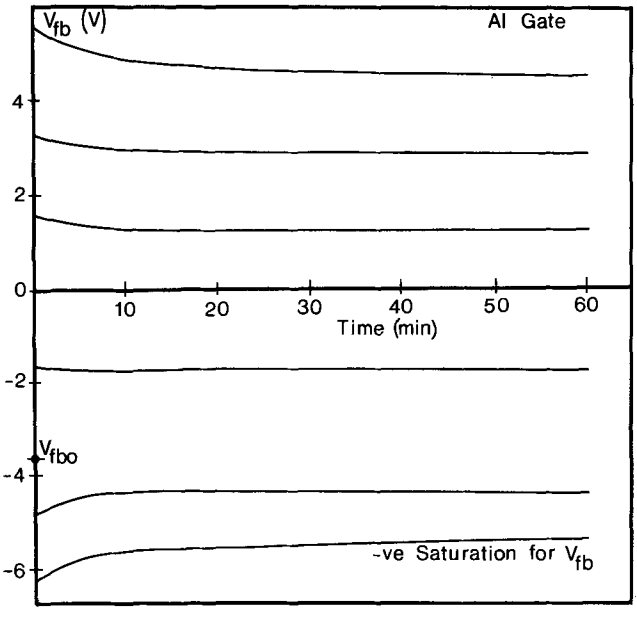

Fig. 8. Flat-band voltage *vs.* time illustrating charge retention characteristics of a MAOS structure.

the case of gold, this injection is transposed to much higher fields, due to the higher work function of gold (as compared to aluminum) (3), and is, therefore, ineffective.

The MAOS structures exhibited positive and negative saturation flat-band voltages at which increasing the magnitude of the stress voltage caused no further increase in the amount of stored charge. This maximum charge is of primary importance in the operation of the memory elements. For typical samples with a 400Å Al_2O_3 layer, a 50Å SiO_2 layer and an Al gate the maximum values of the stored charge as estimated from Eq. [4] are approximately $\pm$ 6.5 $\times$ 10^{12} q/cm^2.

In order to investigate the effect of pulse width and pulse amplitude on the charge transfer characteristics, the MAOS capacitor was first subjected to a large negative voltage typically -40V for 1 min. This voltage was sufficient to cause saturation of the flat-band voltage in the negative direction. A positive pulse of known amplitude and duration was then applied and the corresponding flat-band voltage was measured.[6] After each positive pulse, the flat-band voltage was returned to its saturation value and the procedure repeated. The resulting V_{fb} *vs.* V_c characteristics are shown in Fig. 6. The same procedure was repeated for negative pulses. The flat-band voltage in this case was first saturated in the positive direction prior to the application of the stress pulses. The V_{fb} *vs.* V_c characteristics for negative pulses are shown in Fig. 7. As seen from these curves, the flat-band voltage and therefore the charge stored Q_i depend on both the applied pulse voltage amplitude and its duration. As the pulses become shorter, their amplitude must be increased to shift the flat-band voltage by a given amount. Furthermore, the switching is asymmetric in that negative pulses must be larger than positive pulses for the same shift. Similar observations have been reported on MNOS structures by Frohman-Bentchkowsky (6) and Wallmark (4) and are predicted by the macroscopic theory.

[6] The flat-band voltage was measured 10 min after application of the pulse to avoid the fast initial discharge.

Of great importance to the practical application of MAOS memory structures is the long-term retention of the stored charge. This retention was measured in the following manner. The flat-band voltage was first saturated in the negative direction and positive pulses of various amplitude and 50 μsec duration were applied. The flat-band voltage was then monitored as a function of time in each case. Typical results are shown in Fig. 8. For this sample the initial flat-band voltage was $V_{fbo} = -3.80$V. A rapid rise in V_{fb} was observed whenever V_{fb} was smaller than V_{fbo}, while a rapid decay occurred whenever V_{fb} was larger than V_{fbo}. Most of the change occurred within the first 10 min and the flat-band voltage then reached an equilibrium value over the next 60 min. Any further change in V_{fb}, over a period of 72 hr, was observed to be less than 1%.[7] Similar results have been observed in MNOS structures (3, 11), and the dominant mechanism responsible for the initial loss of charge can be attributed to conduction through the thin SiO_2 layer.

The charge transfer across the silicon dioxide and aluminum oxide was found to affect the surface state density at the Si-SiO_2 interface. This effect was ob-

[7] Charge retention measurements were carried out under a vacuum of less than 0.1 Torr.

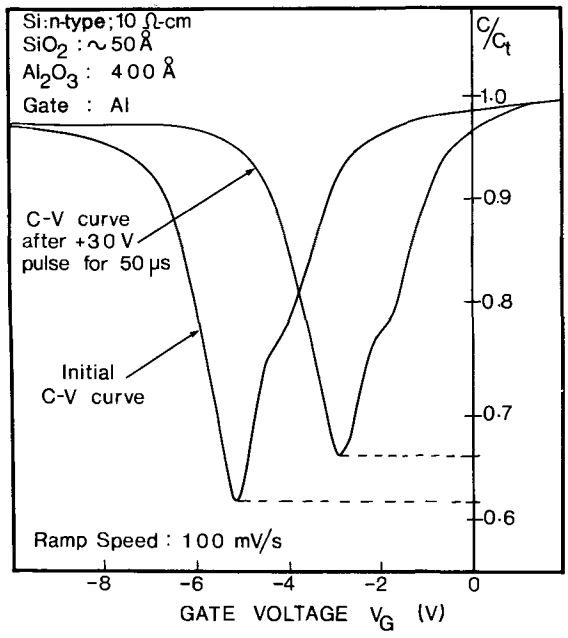

Fig. 9. Low-frequency C-V characteristic of a MAOS structure prior to and after a shift in flat-band voltage.

served by measuring the low-frequency C-V characteristics of the MAOS capacitors after application of a stress voltage large enough to cause a change in the flat-band voltage. The measurements were carried out using the quasi-static technique which has the advantage of allowing the direct determination of the surface state density independently of the charge stored in the dielectrics.

In order to obtain a quick estimate of the approximate surface state density N'_{st} near midgap, the minimum value of the experimental low frequency capacitance C'_{LF} per unit area can be related to N'_{st} by the expression (30)

$$qN'_{st} = \frac{C_t - C'_{FL}}{C_t - C'_{LF}} \left[C'_{LF} - \frac{C_t \; C'_{sc}}{C_t + C'_{sc}} \right] \quad [12]$$

where C'_{sc} is the minimum theoretical space charge capacitance (31) per unit area, C_t is the total capacitance per unit area of the MAOS structure, and the second term in the brackets in Eq. [12] is the minimum theoretical low frequency capacitance per unit area.

Figure 9 shows the typical experimental low-frequency C-V characteristics before and after application of a stress voltage. As observed in the figure the minimum value of the low-frequency capacitance and therefore the surface state density at the Si-SiO_2 interface increase with a change in the flat-band voltage. In the case under consideration, the surface state density N'_{st}, as obtained from Eq. [12], increased from 2.25×10^{12} cm^{-2} to 2.7×10^{12} cm^{-2} after application of a 50 μsec stress pulse with an amplitude + 30V which shifted the flat-band voltage by approximately 2V. The change in surface state density was permanent and was found to increase with increasing stress voltage.[8] This increase in surface-state density was observed in all the samples investigated and may affect the long term reliability of the MAOS memory elements.

Summary

The conduction in rf sputtered Al_2O_3 films deposited on silicon is bulk controlled and consists of three components as in the case of pyrolytic Si_3N_4. At high temperatures and high fields, the current is mainly due to field enhanced thermal excitation of carriers into the conduction band (Poole-Frenkel effect). At low temperatures and high fields, the current is mainly due to field ionization of carriers into the conduction band and at low fields and moderate temperatures the current is due to trap hopping.

The MAOS structures investigated exhibit charge storage and retention characteristics which are very similar to those observed in MNOS memory elements. Most of these characteristics can be explained in terms of the macroscopic theory developed by Frohman-Bentchkowsky (6). Two of the observed characteristics which cannot be explained using this theory, are the dependence of the flat-band voltage *vs.* stress voltage hysteresis on the gate electrode and the increase in the surface state density after a change in flat-band voltage.

The use of Al_2O_3 instead of Si_3N_4 in memory elements is expected to have certain advantages. The dielectric constant of Al_2O_3 ($K_a \sim 8$) is larger than that of Si_3N_4 ($K_N \sim 6.5$), this causes a higher proportion of the applied field to appear initially across the SiO_2 layer resulting in a large current flow, which causes rapid accumulation of charge at the Al_2O_3-SiO_2 interface. Furthermore, the lower conductivity of Al_2O_3 films at low fields as compared to Si_3N_4 films under similar conditions is expected to increase the memory retention time.

Acknowledgments

This work was supported by the Defense Research Board of Canada (Grant 5566-34) and by the National Research Council of Canada (Grant A-4408). The author wishes to thank V. V. Chettiar for assistance with the experimental work.

Manuscript submitted June 1, 1971; revised manuscript received *ca.* Aug. 1, 1971. This was Paper 172 presented at the Atlantic City Meeting of the Society, Oct. 4-8, 1970.

Any discussion of this paper will appear in a Discussion Section to be published in the June 1972 JOURNAL.

[8] To avoid fast discharge currents from affecting the quasi-static C-V measurements, the plots were made 60 min after stress occurred.

REFERENCES

1. H. C. Pao and M. O'Connel, *Appl. Phys. Letters*, **12**, 260 (1968).
2. F. A. Sewell, H. A. R. Wegener, and E. T. Lewis, *ibid.*, **14**, 45 (1969).
3. E. C. Ross and J. T. Wallmark, *RCA Rev.*, **30**, 366 (1969).
4. J. T. Wallmark and J. H. Scott, Jr., *ibid.*, **30**, 335 (1969).
5. E. C. Ross, M. T. Duffy, and A. M. Goodman, *Appl. Phys. Letters*, **15**, 408 (1969).
6. D. Frohman-Bentchkowsky and M. Lenzlinger, *J. Appl. Phys.*, **40**, 3307 (1969).
7. A. M. Goodman, E. C. Ross, and M. T. Duffy, *RCA Rev.*, **31**, 342 (1970).
8. E. C. Ross, A. M. Goodman, and M. T. Duffy, *ibid.*, **31**, 467 (1970).
9. M. Pulver and G. Dorda, *Phys. Status Solidi (a)*, **1**, 65 (1970).
10. G. Dorda and M. Pulver, *ibid.*, (a), **1**, 71 (1970).
11. D. Frohman-Bentchkowsky, *Proc. I.E.E.E.*, **58**, 1207 (1970).
12. S. Nakanuma, T. Tsujide, R. Tgarashi, K. Onoda, T. Wada, and M. Nakagiri, *I.E.E.E. J. Solid State Circuits*, **SC5**, 203 (1970).
13. T. Tsujide, S. Nakanuma, and Y. Ikushima, *This Journal*, **117**, 703 (1970).
14. P. Balk and F. Stephany, *NTZ*, **10**, 526 (1970).
15. C. A. T. Salama, *This Journal*, **117**, 913 (1970).
16. M. Lenzlinger and E. H. Snow, *J. Appl. Phys.*, **38**, 2951 (1967).
17. C. Svensson and I. Lundstrom, *Electron. Letters*, **6**, 645 (1970).
18. L. Hall and B. Robinette, *This Journal*, **117**, 107C (1970).
19. M. T. Duffy and A. G. Revesz, *ibid.*, **117**, 372 (1970).
20. W. Kern and D. Puotinen, *RCA Rev.*, **31**, 187 (1970).
21. M. J. Rand, *J. Appl. Phys.*, **41**, 787 (1970).
22. A. L. Dragoo and J. J. Diamond, *J. Am. Ceram. Soc.*, **50**, 568 (1967).
23. C. A. T. Salama and G. W. Taylor, *J. Phys. E*, **3**, 558 (1970).
24. M. Kuhn, *Solid-State Electron.*, **13**, 873 (1970).
25. R. B. Cavanagh, M.A.Sc. Thesis, University of Toronto (1971).

26. C. A. Mead, *Phys. Rev.*, **128**, 2088 (1962).
27. S. M. Sze, *J. Appl. Phys.*, **38**, 2951 (1967).
28. A. S. Barker, *Phys. Rev.*, **132**, 1474 (1963).
29. B. E. Deal, E. H. Snow, and C. A. Mead, *J. Phys. Chem. Solids*, **27**, 1873 (1966).
30. E. A. Fogels and C. A. T. Salama, *This Journal*, **118**, 2002 (1971).
31. D. R. Frankl, *Solid-State Electron.*, **2**, 71 (1961).

Random Substitution of Eu^{3+} for Y^{3+} in Y_2O_3:Eu^{3+}

H. Forest and G. Ban

Zenith Radio Corporation, Chicago, Illinois 60639

ABSTRACT

This paper is an investigation of whether trivalent europium occupies the two inequivalent yttrium sites (C_2 and S_6) in Y_2O_3 (C-form) randomly or preferentially. The distribution is found to be approximately random for concentrations greater than 1 atom per cent by comparing the $^7F_0 \rightarrow {}^5D_1$ reflection spectra of Y_2O_3:Eu^{3+} and C-form Eu_2O_3 powders. From the uncertainty of the measurements, an estimate is made for the ordering energy ($\sim$250 cm^{-1}) which is the maximum difference in the energy of Eu^{3+} located at the two sites.

The crystal structure of C-form Y_2O_3 contains two inequivalent yttrium sites with symmetries C_2 and S_6 which are in the ratio of three-to-one, respectively (see Fig. 1). In a previous paper (1), it has been shown that the narrow line emission and absorption spectra of Y_2O_3:Eu^{3+}, a well-known red emitting television phosphor, are due to Eu^{3+} situated at both sites. The different symmetry of each site results in two spectrally inequivalent and distinguishable Eu^{3+} centers. Table I lists the site assignments of the important Eu^{3+} transitions.

One interesting question is whether there is significant difference in the europium energy for either site (ordering energy) to produce a preferential substitution. For a random distribution the europium energies would be degenerate and, consequently, the substitution would occur for each site with the same probability. In some related studies on Y_2O_3:Eu^{3+} prepared by the oxalate procedure, it was found that the distribution was unaffected by annealing at temperatures between 1000°-1400°C for several hours. Commercially prepared Y_2O_3:Eu^{3+}, obtained from Sylvania, was found to have the same distribution as our phosphors. It seems at these firing temperatures that the ordering energy is small and the europium substitution is random, but this is only suggestive without actual knowledge of the distribution.

The present study was initiated in order to determine the distribution of Eu^{3+} between the two yttrium sites in Y_2O_3:Eu^{3+}. Our results indicate that the distribution can be determined from the relative intensities of the $^7F_0 \rightarrow {}^5D_1$ absorption spectrum which consists of C_2 and S_6 Eu^{3+} lines. From reflection measurements on powders, the relative intensities of the C_2 spectrum (see Table I, lines 2, 4, 5) to the S_6 spectrum (lines 1, 3) were found to be about the same as C-form from Eu_2O_3, where the ratio must be three-to-one, indicating a random distribution.

Key words: distribution, symmetry sites, ordering.

Table I. Site assignments for some Eu^{3+} transitions in Y_2O_3:Eu^{3+}

Transition	Wavelength (Å) C_2	S_6
$^7F_0 \rightarrow {}^5D_2$	4646.7	—
	4649.1	—
	4669.4	—
	4675.8	—
	4678.6	—
$^7F_0 \rightarrow {}^5D_1$	5257.7 (2)	5237.5 (1)
	5272.3 (4)	5262.0 (3)
	5278.5 (5)	—
$^7F_0 \rightarrow {}^5D_0$	5804.5	—
$^7F_1 \rightarrow {}^5D_0$	5873.7	5823.0
	5934.5	5924.5*
	5996.0	—
$^7F_2 \rightarrow {}^5D_0$	6112.9	—

* Resolved at 78°K.

Experimental

The Y_2O_3:Eu^{3+} phosphors were prepared by firing stoichiometric mixtures of the respective oxalates for 2 hr at 600°C followed by 2 hr at 1400°C under an O_2 atmosphere. C-form Eu_2O_3 was also prepared from the oxalates, but the firing temperature was selected so that no conversion to the higher temperature B-form occurred. The sample of Eu_2O_3 was analyzed by x-ray to insure that it was pure C-form with no trace of the high temperature B-form. From reflection spectra, it was found that commercially available Eu_2O_3 is a mixture of the C and B forms, in which the C-form is the major constituent.

Reflection measurements were made on loosely packed powders in planchettes with a 1-meter Jarrell Ash grating monochromator and a ribbon filament in-

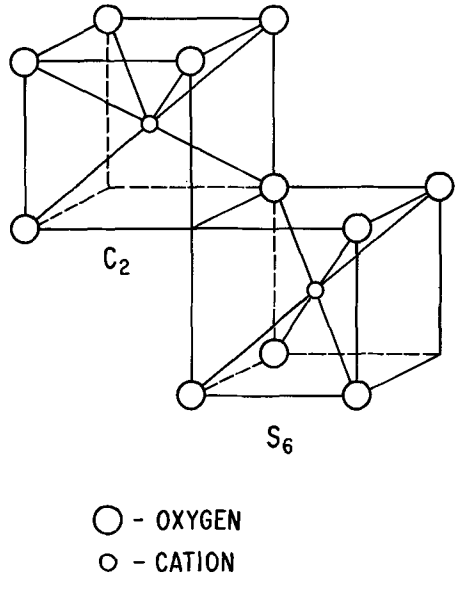

Fig. 1. C_2 and S_6 cation sites in C-form Y_2O_3. The major difference being the direction of the oxygen vacancies; it is along a body diagonal in S_6 and a face diagonal in C_2.

candescent lamp as the light source. The monochromator slit bandpass was set at 0.4Å which is 20% of the half-width of the narrowest line in the spectrum so that there was no significant broadening introduced by the instrument. An RCA 7265 photomultiplier was used as the detector. The reflection spectra reported in this paper are direct single beam measurements of the photomultiplier current *vs.* wavelength. No corrections were made for the response of the photomultiplier or the spectral distribution of the lamp since these were found to be minor for the narrow wavelength range of the $^7F_0 \rightarrow {}^5D_1$ transition. In order to maximize the absorption relative to the scattered light, the optics were arranged so that the focused image of the monochromator slit and light source did not superimpose on the phosphor, but were displaced slightly in a direction perpendicular to the optical axis of the monochromator. In this way the light entering the monochromator would undergo several reflections through the phosphor powder, thereby increasing the effective path length.

Absorption spectra were also taken on a single crystal of Y_2O_3:Eu^{3+} at room temperature with a Cary 14R spectrophotometer. The single crystal was prepared by a flame fusion technique at the Lockheed Palo Alto Research Laboratory.

Results

The five-line $^7F_0 \rightarrow {}^5D_1$ absorption spectrum of Y_2O_3:5% (atom per cent) Eu^{3+} single crystal is shown in Fig. 2. The number above each line corresponds to the symmetry assignment obtained from Table I. Figure 3 shows powder reflection spectra (absorptions appear as stalagtites) over the same wavelength range for Y_2O_3 with several practical Eu^{3+} concentrations, plus C-form Eu_2O_3. Although it is not obvious from the spectra, the amount of absorption does increase with europium concentration. The absorption due to Eu_2O_3 is shown to be less than the 5% sample due to a scale change, but actually it is much greater. No attempt was made to make the reflection spectra quantitative, since only the ratio of the C_2 to S_6 line intensities of each spectrum is important and will be compared. The lack of reproducible quantitative data is due to variations in the packing of the powders, which is of no consequence when taking ratios.

A relative absorption spectrum was obtained for the 5% powder by a point-by-point inversion of the reflection spectrum. The resulting spectrum has essentially the same relative line intensities as the single-crystal spectrum (Fig. 2), which indicates that the spectral corrections of the apparatus are minor. The other reflection spectra in Fig. 3 are also expected to be similar to absorption spectra measured on single crystals.

Discussion

Before proceeding to the comparison of the reflection spectra, a brief discussion of diffuse reflection theory will be necessary. Melamed (2) has calculated the diffuse reflectance of a powder[1] (for various indices of refraction) as a function of the unitless quantity kl, where k is the absorption coefficient in cm^{-1} and l is the particle diameter in cm. A family of curves is very nicely shown in ref. (3). The curves show that for a fixed particle diameter the diffuse reflectance does not vary linearly with absorption coefficient but tends to saturate beyond $kl = 0.50$. The saturation is more pronounced for higher values of the index of refraction. Therefore, when comparing line intensities of reflection spectra over a large concentration range, as we are doing in this paper (k will vary by a factor of 100), it is important to consider to what degree the reflectance nonlinearity will affect the spectra.

From Melamed's curves the nonlinearity of the reflectance spectra over a fixed range of k depends on the

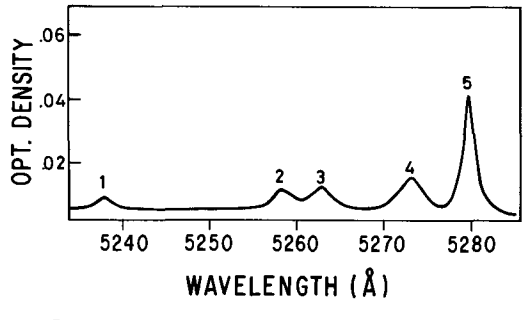

Fig. 2. $^7F_0 \rightarrow {}^5D_1$ absorption spectrum measured on a single crystal (Y_2O_3:Eu^{3+} 5%). The number above each line indicates the site assignment listed in Table I.

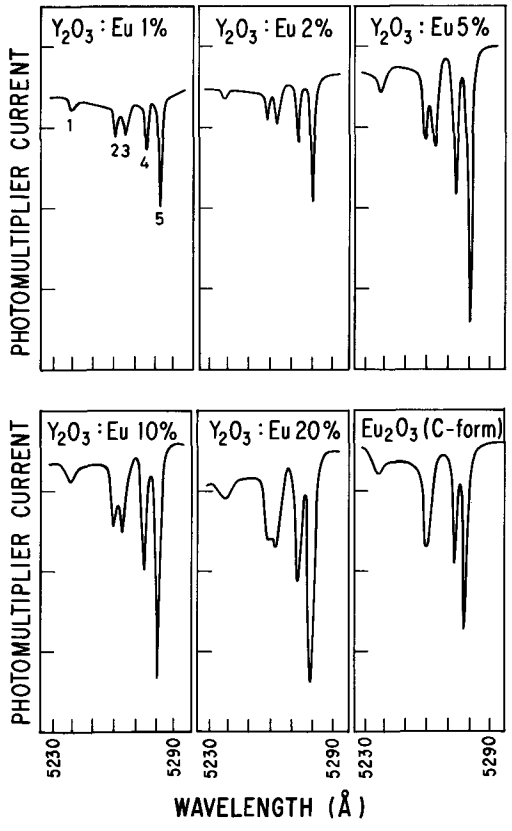

Fig. 3. $^7F_0 \rightarrow {}^5D_1$ reflection spectra for several concentrations of Y_2O_3:Eu^{3+}, including Eu_2O_3.

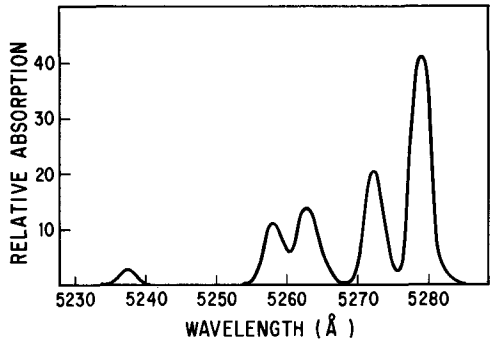

Fig. 4. Relative absorption spectrum obtained by a point-by-point inversion of the reflection spectrum for Y_2O_3:Eu^{3+} 5%. The ordinate is completely arbitrary and is labeled relative absorption only to qualitatively identify the spectrum.

[1] Melamed's model is for spherical particles.

Table II. Absorption coefficients (cm^{-1}) of $^7F_0 \rightarrow {}^5D_1$ transition

Line No.	Y_2O_3:Eu^{3+} 5%	Y_2O_3:Eu^{3+} 1%	Eu_2O_3
1	0.033	0.0067	0.67
2	0.064	0.013	1.3
3	0.076	0.015	1.5
4	0.092	0.018	1.8
5	0.38	0.076	7.6

magnitude of k and is less for low values of k. This means that lines 1 and 5 in Fig. 3 will be affected least and most, respectively, by the nonlinearity. Table II lists the range of the absorption coefficients of the five lines (columns 3 and 4) which were obtained from the single-crystal spectrum (column 2). The phosphor particle size is about 5μ so that kl for the strongest line, 5, varies from 3.8×10^{-5} — 3.8×10^{-3} which places the data on a section of Malamed's curve where the nonlinearity is low. However, examining Fig. 3, the relative intensity of line 5 does decrease slightly over the concentration range indicating some nonlinearity and therefore this line cannot be used to determine the ratio. Lines 2 and 3 have about the same absorption coefficient, but, unfortunately, they superimpose in the Eu_2O_3 spectrum. This leaves lines 1 and 4 for the comparison of the spectra and it will be assumed that their intensities are linear over the concentration range.

All of the spectra in Fig. 3 are similar and have essentially the same C_2 to S_6 line intensity ratio (*i.e.*, the ratio of line 4 to line 1 is 5.2 ± 1.0) indicating that the distribution of europium in Y_2O_3:Eu^{3+} is the same as in Eu_2O_3. This means that the substitution of europium for yttrium at either symmetry site proceeds with approximately equal probability and is independent of the europium concentration.

The major contribution to the uncertainty of the ratio (about 20%) is the determination of the baseline which is somewhat arbitrary and depends on the sample. There is no trend for the ratio to decrease with increasing europium concentration resulting from the nonlinearity of line 4 so that the assumption that the peak heights are linear with concentration appears to be valid.

However, there is a trend for the ratios to follow a trapezoidal dependence on europium concentration, *i.e.*, the ratio goes through a broad maximum at about 20% Eu^{3+} and is the same for 1% Eu^{3+} and Eu_2O_3. This is probably due to the broadening of the spectra which, as is discussed below, follows a similar dependence on europium concentration. The broadening of the spectra contributes to the uncertainty of the ratio, since taking peak heights as a measure of the line intensity implicitly assumes that the width of the C_2 and S_6 lines have the same europium concentration dependence, which may not be true.

The above result is semiquantitative at best, however, since the spectra are not identical and do show some gradual variations with europium concentration. As the europium concentration increases, the lines appear broader and shift by approximately 2Å to shorter wavelengths. As a result of the line shifts and broadening, the doublet at 5260Å formed by lines 2 and 3 is not resolved above 10% europium. We believe these minor variations in the spectra are due to crystal field effects rather than changes in the europium distribution for the following reason: since the atomic radius of Eu^{3+} is 0.95Å compared to 0.88Å for Y^{3+}, it is reasonable to expect some distortion of the crystal field by the substitution of europium into the lattice. Recently, it has been shown that the emissions from Eu^{3+} and Pr^{3+} in several oxysulfides shift to shorter wavelengths as the ionic radius of the host cation increases (4). In effect, the situation is the same for Eu_2O_3 relative to Y_2O_3:Eu^{3+}, since the ionic radius of europium is slightly larger than that of yttrium. For Gd_2O_3:Eu^{3+} where the ionic radius of the europium and gadolinium are very similar, the reflection spectrum, while not shown, is found to be closer to Eu_2O_3 than any of the Y_2O_3:Eu^{3+} spectra in Fig. 3.

The variation of the spectrum with ionic radius of the cation is also responsible for the Eu_2O_3 spectrum being narrower than the Y_2O_3:Eu^{3+} spectra above 5% Eu. The line broadening in the Y_2O_3:Eu^{3+} spectra results from variations of the local crystal field about each europium due to the presence of europium in one or more of the nearest neighbor yttrium positions. Only for Y_2O_3:Eu^{3+} at low europium concentrations, where each europium is surrounded only by yttrium, and for Eu_2O_3 are the europium symmetries unique and the spectra narrow. For intermediate concentrations, the spectra are composites of slightly different spectra and, consequently, appear broadened. Therefore, since the reflection spectra of Y_2O_3:Eu^{3+} are similar to Eu_2O_3 except for minor variations in the crystal field, it is concluded that the europium distribution between the two symmetry sites is random and the C_2 to S_6 ratio is 3.0 ± 0.6.

From the uncertainty of the distribution, the maximum energy difference between europium located at C_2 and S_6 sites can be calculated. The distribution between the two sites $(C_2)/(S_6)$ is given by

$$\frac{(C_2)}{(S_6)} = 3e^{-\Delta E/kT} \qquad [1]$$

where ΔE is the ordering energy and kT is the thermal energy. The factor 3 enters because there are three times as many C_2 sites as S_6 sites. If $(C_2)/(S_6)$ is taken as 2.4 and 3.6, which represents the uncertainty extremes of the distribution, then ΔE is $\sim \pm 250$ cm^{-1} for the 1400°C firing temperature used to prepare the phosphors. In Eq. [1], ΔE can be positive or negative depending on the relative stabilities of europium in the C_2 or S_6 yttrium sites, but at high firing temperatures (>1000°C) it is not possible to determine from the data which configuration is more stable. The ordering energy, which probably results from the distortion of the yttrium site by the presence of europium, is small enough to be insignificant when compared to the thermal energy. At temperatures about 500°C, however, some ordering may be detected and indicate the relative stability of each site.

Conclusion

It has been shown that europium is distributed randomly between the C_2 and S_6 yttrium sites in Y_2O_3 by comparing the reflection spectra with C-form Eu_2O_3. This is only true for the high temperatures (>1000°C) used to prepare the phosphors. At lower temperatures, however, some preferential substitution may be possible.

Manuscript submitted Oct. 12, 1970; revised manuscript received June 30, 1971. This was Paper 46 presented at the Los Angeles Meeting of the Society, May 10-15, 1970.

Any discussion of this paper will appear in a Discussion Section to be published in the June 1972 JOURNAL.

REFERENCES

1. H. Forest and G. Ban, *This Journal*, **116**, 474 (1969).
2. W. Wm. Wendlandt and H. G. Hecht, "Reflectance Spectroscopy," Interscience Publishers, New York (1966).
3. Ref. (2), p. 85.
4. L. Ozawa and P. Jaffe, *This Journal*, **118**, 1678 (1971); O. J. Sovars and T. Yoshioka, *J. Chem. Phys.*, **51**, 5330 (1969).

Characterization of Surface States at the Si-SiO_2 Interface Using the Quasi-Static Technique

E. A. Fogels and C. A. T. Salama*

Department of Electrical Engineering, University of Toronto, Toronto 5, Ontario, Canada

ABSTRACT

The quasi-static technique is used to investigate the effect of processing parameters on the surface-state density at the silicon-thermally grown silicon dioxide interface. The determination of the constant required for the evaluation of surface potential from equilibrium C-V data is discussed. A rapid method of estimating the midgap density of surface states is also described. The dependence of surface-state density on substrate orientation, type of oxide growth, high-temperature annealing in nitrogen, low-temperature heat treatment in forming gas, and temperature of oxide growth are discussed. The interdependence between the fixed oxide charge and the surface-state density is also investigated.

Several methods (1-4) have been developed for the extraction of surface-state properties at the Si-SiO_2 interface from measurements of the electrical characteristics of MOS (metal-oxide-semiconductor) capacitors. Among these is the integration method (3) which can be used in conjunction with low-frequency, thermal equilibrium MOS capacitance-voltage data to obtain the surface-state density distribution in energy. A particular advantage of this method is that the surface potential can be determined directly by a simple integration of the experimental results. Hence, the errors in surface-state densities arising from inaccuracies in doping or surface potential, or relating back to ideal curves, are greatly reduced. While not as accurate as the conductance method (4), the integration method results in the determination of surface-state densities over a wider region of the bandgap energy without the need for complex conductance measurements. Errors are also minimized because no graphical differentiation of experimental results is required as in the differential (1) and temperature (2) methods.

The successful implementation of any low-frequency, thermal equilibrium method is directly dependent on whether or not the bias and signal voltages are capable of creating and maintaining the semiconductor inversion layer and the interface surface-state charges in complete thermal equilibrium at all times. Deviations from thermal equilibrium, which are commonly observed at low temperatures or at high frequencies, would completely invalidate any results based on the integration method.

The original implementation of the integration method (3) used a phase-lock, low-frequency a-c technique. The difficulty with this implementation is due to the presence of drift in the phase sensitive detection system of the lock-in amplifier which introduces large errors in the output signal and therefore in the calculated surface-state density. Furthermore, the low-frequency cutoff of the lock-in amplifier restricts the measurement frequency used in this method to above 1.5 Hz. Such a frequency is often not sufficiently low to overcome the nonequilibrium effects that are apparent in samples having typical inversion layer response times of the order of a second or more.

A more desirable approach is to eliminate the instabilities associated with the lock-in amplifier and reduce the effective measuring frequency ω to such a point that $1/\omega$ is much greater than the time constants of the inversion layer and the surface-state charges, thus ensuring that thermal equilibrium conditions are satisfied. This has been achieved using the quasi-static technique. This technique was first suggested by Castagne (5, 6) and further investigated by Kuhn (7). It involves the measurement of the C-V characteristics of MOS capacitors under application of a very slow ramp bias voltage. This technique is ideally suited for surface-state measurements on thermally oxidized silicon structures possessing moderate surface-state densities. With a minimum amount of implementation and data processing, the method leads to the determination of the density of states over a considerable range of surface potentials extending from heavy inversion to heavy accumulation, with a sensitivity of about 10^{10} states/cm^2-eV for energies within 0.25 eV of midgap.

The basic equations used in conjunction with the quasi-static technique are briefly reviewed in this paper and particular emphasis is placed on the determination of the integration constant required for the evaluation of the surface potential from equilibrium C-V data. A rapid method of obtaining the approximate surface-state density near midgap is also described. The quasi-static technique is then used to investigate the effect of processing parameters on the surface-state density at the Si-SiO_2 interface. The effects of some of the processing parameters investigated here have been previously reported using other techniques of surface-state measurement which were restricted as to the energy range covered and the frequency of the measurement. Both of these limitations are minimized in the quasi-static technique. A correlation of the fixed oxide charge and the surface-state charge has been included, wherever possible, in order to investigate any common origin for these two charges. The advantage of the quasi-static technique in such an investigation is that it determines directly the surface-state density independently of the fixed oxide charge (7).

Analysis

The following analysis, due to Berglund (3), can be used to extract the surface potential and the surface-state density from the experimentally determined low-frequency (LF) C-V data obtained under thermal equilibrium conditions. The experimental variation of surface potential ψ_s with respect to the oxide voltage V_o is given by[1]

$$\left(\frac{d\psi_s}{dV_o}\right)_E = \frac{C_o}{C_{sc} + qN_{st}} = \frac{C_o}{C_{LF}} - 1 \qquad [1]$$

where C_o is the oxide capacitance for unit area, C_{sc} is the space charge capacitance per unit area, N_{st} is the density of surface states in cm^{-2}-eV^{-1}, q is the electronic charge, and C_{LF} is the low-frequency, equilibrium MOS capacitance per unit area. For an ideal capacitor with no surface states, Eq. [1] reduces to

* Electrochemical Society Active Member.

Key words: silicon, passivation, silicon dioxide, semiconductors.

[1] The surface potential ψ_s is given by $(E_F - E_i)/q$ where E_F and E_i are the Fermi and intrinsic energy levels respectively.

$$\left(\frac{d\psi_s}{dV_o}\right)_T = \frac{C_o}{C_{sc}} \quad [2]$$

For a known substrate doping and oxide capacitance, Eq. [2] can be evaluated theoretically for any ψ_s. The surface-state density can then be determined from the following equation

$$N_{st} = \frac{1}{q}\left[\frac{\left(\frac{d\psi_s}{dV_o}\right)_T}{\left(\frac{d\psi_s}{dV_o}\right)_E} - 1\right] C_{sc} \quad [3]$$

The surface potential $\psi_s(V_{g2})$ at any gate voltage V_{g2} can be determined within an additive constant $\psi_s(V_{g1})$ from the integral (3)[2]

$$\psi_s(V_{g2}) = \int_{V_{g1}}^{V_{g2}}\left(1 - \frac{C_{LF}}{C_o}\right) dV_g + \psi_s(V_{g1}) \quad [4]$$

The method of evaluating the constant, suggested by Berglund (3), is to match the experimental and theoretical $d\psi_s/dV_o$ curves in the accumulation region where the effect of surface states can be neglected. The matching points must be judiciously chosen to give accurate results. If the matching is attempted in a region of heavy accumulation where C_{sc} is very large, then $C_{LF} \simeq C_o$ and the value of $(d\psi_s/dV_o)_E$ becomes immeasurably small and is obscured by any error ΔC_{LF} in the measured value of C_{LF}. On the other hand, if matching is attempted in the region of light accumulation (near flat band), C_{sc} may be comparable to qN_{st} and again error in $\psi_s(V_{g1})$ may result. Assuming that the error in determining $\psi_s(V_{g1})$ is to be limited to $\Delta\psi_s$, then the optimum range of ψ_s useful for matching can be obtained by first solving the following equations for limits on C_{sc}

$$C_{sc}(\text{upper limit}) = \frac{C_{ox}\,\beta\,\Delta\psi_s}{2(\Delta C_{LF}/C_{LF})} \quad [5]$$

$$C_{sc}(\text{lower limit}) = \frac{2qN_{st}}{\beta\,\Delta\psi_s} \quad [6]$$

where $\beta = q/kT$.[3] Once the limits on C_{sc} are determined from Eq. [5] and [6], the corresponding values of ψ_s can be determined for an n-type semiconductor (in the heavy accumulation region) from (8)

$$C_{sc} \simeq \frac{\epsilon_s}{L_{De}} \exp\left(\frac{\beta(\psi_s - \psi_b)}{2}\right) \quad [7]$$

where L_{De} is the extrinsic Debye length and ϵ_s is the semiconductor dielectric constant. The bulk potential ψ_b is given by

$$\psi_b = \frac{1}{\beta}\ln\frac{N}{n_i} \quad [8]$$

where N is the bulk donor doping density and n_i is the intrinsic density.

The surface-state distribution in energy in our investigation is determined by a computer program[4] whose input consists of the substrate doping density N, the oxide capacitance C_o, and a point-by-point evaluation of the experimental LF capacitance-voltage characteristics. The program solves Eq. [1] and [2] for the experimental and theoretical values of $d\psi_s/dV_o$, matches these two curves over the range of surface potentials obtained from Eq. [5], [6], and [7], and determines an average value for the additive constant ψ_s (V_{g1}). The surface state density N_{st}, as a function of ψ_s, is then obtained from Eq. [3].

[2] Ideally, if Eq. [4] is evaluated from heavy accumulation to heavy inversion, the integral should give a value for $\psi_s(V_{g2}) - \psi_s(V_{g1})$ equal to, or slightly less than, the bandgap energy. A value greater than the energy gap indicates that gross nonuniformities are present either in the oxide or at the oxide-semiconductor interface and the analysis can no longer be applied (3).

[3] In Eq. [5], $(\Delta C_{LF}/C_{LF})$ is the effective accuracy in the measurement of C_{LF}. In Eq. [6], the value of N_{st} is set at $10N'_{st}$, where N'_{st} is the approximate density of states near midgap as determined from Eq. [10]. The value $10N'_{st}$ represents a worst case condition.

[4] Available on request.

Approximate Surface-State Density Near Midgap

For quality control purposes, it is often sufficient to obtain a single value of the surface-state density, N_{st}, at some point such as the minimum of the *LF* C-V characteristic and assume that this value is representative of the effective density.

Assuming a uniform surface-state density, the minima of the ideal (theoretical) and experimental low-frequency $C - \psi_s$ characteristics [curves (a) and (b) respectively in Fig. 1] occur at the same value, ψ'_s, of surface potential in the light inversion region near midgap.[5] The difference in the minimum capacitance between the two curves can be directly related to the surface-state density, N'_{st}. This observation allows the density of states near midgap (where they are most effective as recombination centers) to be evaluated using the following equations:

The minimum space charge capacitance C'_{sc} is given by Eq. [9]

$$C'_{sc} = \frac{\epsilon_s}{L_{Di}} \frac{[\cosh(\beta\psi_b)]^{1/2}}{1 + 0.542(\beta\psi_b) - 0.0115(\beta\psi_b)^2} \quad \text{for } (\beta\psi_b) < 21 \quad [9]$$

where L_{Di} is the intrinsic Debye length. From Eq. [1], the surface-state density N'_{st} at the minimum of the $C - \psi_s$ characteristic is then given by

$$qN'_{st} = \frac{C_o + C'_{sc}}{C_o - C'_{LF}}\left[C'_{LF} - \frac{C_o C'_{sc}}{C_o + C'_{sc}}\right] \quad [10]$$

where C'_{LF} is the minimum low-frequency capacitance obtained from the experimental C-V or $C - \psi_s$ characteristic. The second term in the brackets in Eq. [10] is the minimum theoretical low-frequency capacitance.

In general, the surface-state density is not uniform over the whole energy gap and the minima of the ideal and experimental $C - \psi_s$ curves will not coincide, as shown in Fig. 1. The value of surface-state density obtained from Eq. [10] then will be in error. However, for typical MOS devices, the surface-state distribution is fairly constant near midgap and good accuracy

[5] $\psi'_s = 1/\beta \cosh^{-1}\left(\frac{L_{Di} - C'_{sc}}{\epsilon_s}\right)^2$.

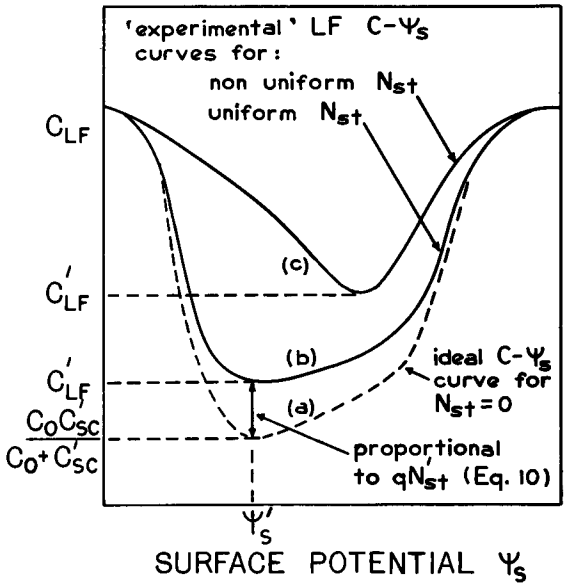

Fig. 1. Effect of uniform and nonuniform density of states on the C-ψ_s characteristics.

(within ± 10%) can be obtained. The validity of this method is illustrated in the following sections.

Experimental Techniques

The implementation of the quasi-static technique used in this investigation is similar to the one described by Kuhn (7). It involves the measurement of the MOS capacitor displacement current density, J_c, in response to a linear gate-voltage ramp, $V_g = at$. The low-frequency capacitance, C_{LF}, is related to the displacement current density by $J_c = aC_{LF}$.

Measurements of surface-state densities at the Si-SiO_2 interface were carried out on suitably prepared MOS capacitors. The silicon used in this work was in the form of polished circular slices (Monsanto), 2.5 cm in diameter, prepared by the Czochralski method. The dislocation count was specified to be less than 10^3 cm^{-2}. The slices used were n-type (phosphorus doped), of both (100) and (111) orientation, having resistivities ranging from 3 to 10 ohm-cm. The polished silicon wafers were degreased and carefully cleaned (10) prior to oxidation.

Oxidation was generally carried out immediately after cleaning. Dry or wet (95°C water) oxides were grown in a resistively heated furnace provided with a quartz tube and an alumina liner. Both the nitrogen and oxygen gases were derived from liquid sources. After oxidation and high-temperature annealing (if necessary), the slices were rapidly (< 3 sec) quenched to room temperature. Annealing was carried out either at the oxidation temperature, in the case of N_2, or at 450°C, in the case of forming gas. The thickness of the films was measured using a Talystep capable of ± 20Å accuracy. Typical oxide thicknesses used in this investigation ranged from 800 to 1500Å.

The MOS structures were completed by evaporating aluminum (99.999%) field plates, 1000Å thick, 500 μm in diameter, over the oxide through a metal mask. Aluminum was also evaporated on the bare back side of the silicon to produce an ohmic contact. The evaporations were carried out from a resistively heated, prefired, tungsten filament in a vacuum of 3×10^{-7} Torr.

After metallization, the over-all oxide quality was assessed by measuring the fixed oxide charge, Q_{ss}, and the mobile ionic charge, Q_o, using high-frequency (HF) C-V measurements and bias temperature (BT) stress techniques. All of the samples investigated exhibited minimal shift under BT stress at 150°C, + 10V for 10 min indicating no ionic contamination. The typical values of Q_{ss} observed ranged from 0.6×10^{11} to 4×10^{11} cm^{-2}, depending on the oxide growth and annealing temperatures. The HF C-V characteristics were also used to determine the effective substrate doping and the oxide capacitance.

After assessing the densities of extraneous charges, the surface-state density was determined. Figure 2 shows a typical C-V characteristic obtained at a bias sweep rate of 50 mV/sec. A factor of ten increase in the bias sweep rate resulted in negligible change in the C-V characteristics, indicating that the required equilibrium was obtained. For this particular sample, the matching of the experimental and theoretical $d\psi_s/dV_o$ was done for ψ_s between 0.375 and 0.430V, assuming $\Delta\psi_s < kT/2q$ and $\Delta C_{LF}/C_{LF} = 0.01$. The corresponding surface-state density is shown in Fig. 3.

The usefulness of the approximate method of determining near midgap surface-state densities was verified for this sample. The value of N'_{st} was 5.4×10^{10} states/cm^2-eV, which is within 10% of the midgap value of 6×10^{10} states/cm^2-eV obtained from computer calculations. For comparison purposes, some of the surface-state density plots in the next section show the estimated N_{st} as obtained from Eq. [10]. In most cases, good agreement between N'_{st} and the actual density of states was obtained.

Experimental Results and Discussion

A large number of MOS samples were prepared and the dependence of surface-state densities on the following processing parameters was investigated: (a) substrate orientation and type of oxide growth, (b) high-temperature annealing in nitrogen, (c) low-temperature heat treatment in forming gas, (d) temperature of oxide growth and fixed oxide charge, Q_{ss}.

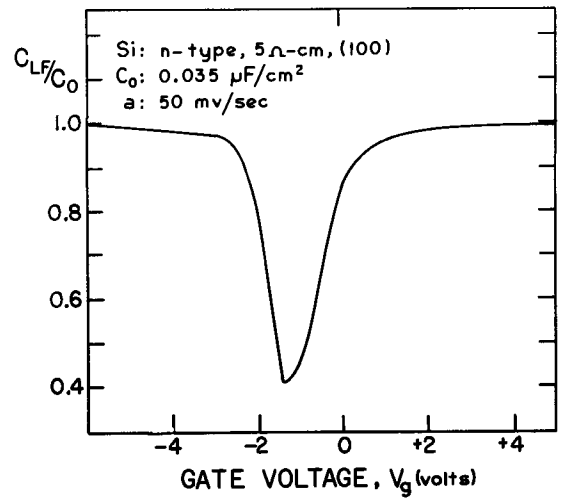

Fig. 2. LF thermal equilibrium C-V characteristics (oxide growth, dry; growth temperature, 1100°C; N_2 anneal, 1110°C for 30 min; H_2 anneal, 450°C for 30 min after metallization).

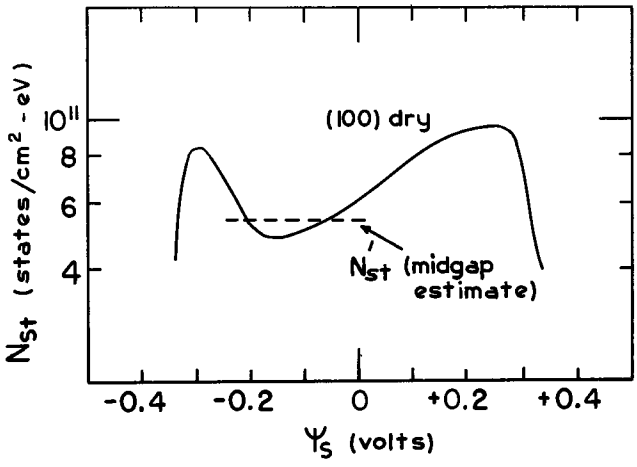

Fig. 3. Surface-state density vs. surface potential for the sample shown in Fig. 2.

The dependence of surface-state densities on orientation of the silicon substrate was evaluated using both dry and wet oxides. The typical surface-state densities obtained using dry oxides grown at 1100°C on (111) and (100) oriented slices are shown in Fig. 4 [curves (a) and (b)]. As expected, the (100) plane shows the lowest over-all density of states. Similar results were obtained using wet oxides, as shown in Fig. 4 [curves (c) and (d)]; however, in general the density of states was lower for wet than for dry oxides. The lower density of states in wet oxides is attributed to the annihilation of states by rapidly migrating and highly active hydrogen species originating from the water vapor. These results are in general agreement with those obtained by Brown (2), Nicollian (4), and Arnold (11).

The effect of nitrogen annealing at 1100°C on dry-grown oxides was investigated for both (100) and (111) oriented slices. Whereas previous to annealing the densities of surface states were quite different on (100) and (111) slices, as shown in Fig. 4, after annealing the densities were not only reduced considerably for both orientations but also approached approximately the same value near midgap, as shown in Fig. 5 [curves (a), (b)]. Furthermore, the midgap

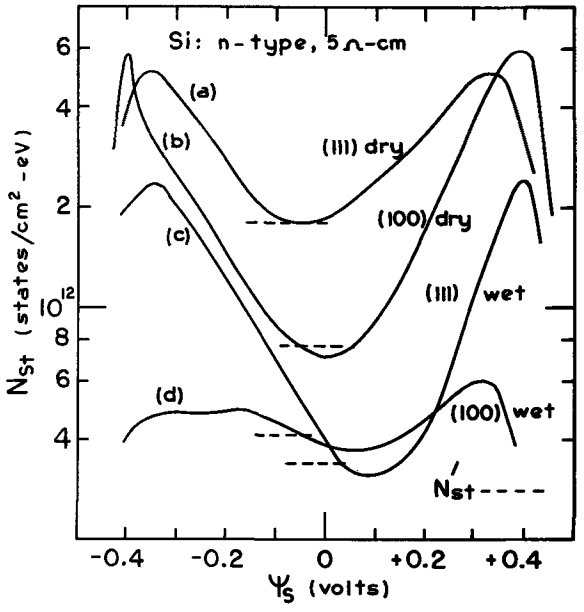

Fig. 4. Dependence of surface-state density vs. surface potential on orientation and type of oxide growth. (Oxide growth temperature, 1100°C; oxide thickness ≃ 1000Å; no annealing).

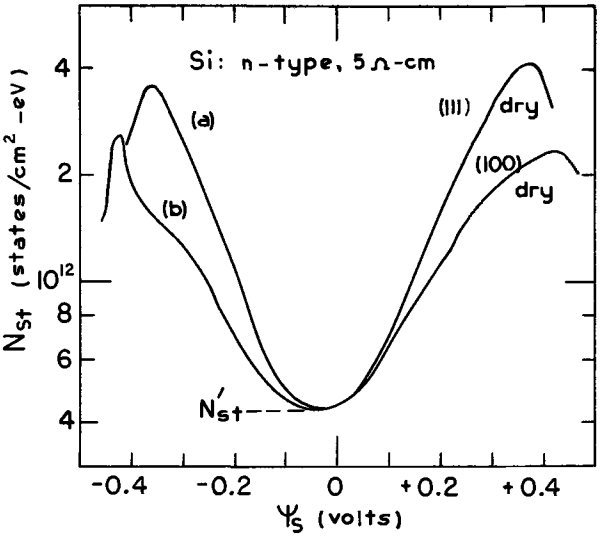

Fig. 5. Effect of N_2 annealing on surface-state density in dry grown oxides (oxide growth temperature, 1100°C; N_2 anneal at 1100°C for 30 min; oxide thickness ≃ 1000Å).

densities observed were close to those obtained on unannealed wet oxides of either orientation. However, the total density of states integrated over the bandgap was still lowest for wet, unannealed oxides on (100) orientation slices.

Nitrogen annealing was also observed to reduce the fixed oxide charge Q_{ss} (12) at the Si-SiO_2 interface. This reduction is the result of traps, induced by annealing (13, 14), competing with the oxide-silicon interface for electrons donated by the ionic silicon.[6] Trapped electrons effectively decrease the net fixed oxide charge Q_{ss} measured by the HF C-V technique.

The effect of low-temperature heat treatment of oxides in forming gas (5% H_2, 95% N_2) at 450°C was also investigated by comparing the surface-state densities observed on (100) oriented substrates under the

[6] These traps are also able to interact with sodium donor sites by trapping the sodium electrons and hence localizing any mobile sodium ions. This explains the experimentally observed improvement in stability of sodium-contaminated samples after nitrogen annealing, although the total sodium concentration in the sample remained fixed.

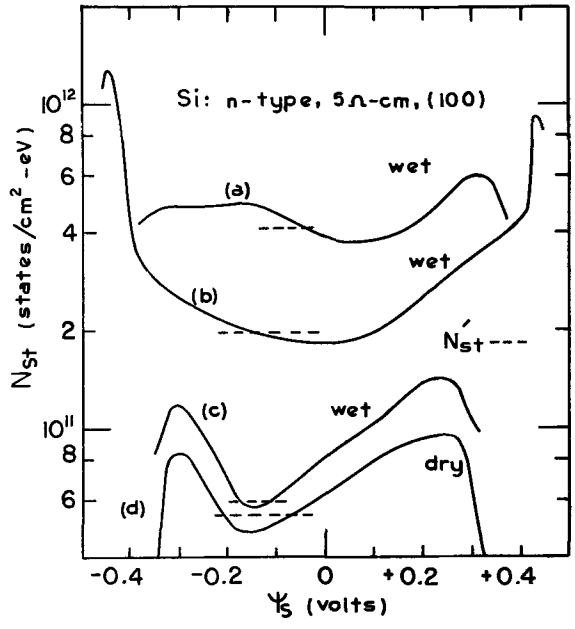

Fig. 6. Effect of annealing in forming gas (oxide growth temperature, 1100°C; oxide thickness ≃ 1000Å). (a) no anneal; (b) H_2 anneal, 450°C for 30 min prior to metallization, (c) H_2 anneal, 450°C for 30 min after metallization; (d) N_2 anneal, 1100°C for 30 min followed by H_2 anneal, 450°C for 30 min after metallization).

following conditions: (*a*) wet grown oxide + aluminum metallization, (*b*) wet grown oxide + forming gas heat treatment + aluminum metallization, (*c*) wet grown oxide + aluminum metallization + forming gas heat treatment.

Curves (a), (b) and (c) in Fig. 6 show that heat treatment of wet oxides in forming gas in the presence of a reactive metal such as aluminum is the most effective in reducing the surface-state density. The reduction in surface-state densities after forming-gas heat treatment is attributed to adsorption of active hydrogen at the Si-SiO_2 interface. The aluminum (15-17) causes a further reduction in surface-state density by reacting with water adsorbed at the oxide surface during the heat treatment. Hydrogen is released and migrates to the Si-SiO_2 interface. This hydrogen (atomic or ionic) is thus available for bonding to any uncompensated bonds which are believed to be a possible origin of fast states at that interface. As the dangling bonds are saturated, the density of fast states is reduced. It has been postulated (18) that ionic Si centers acting either as acceptor or donor states may be reduced according to the reaction

$$\mathrm{Si} + \mathrm{H} \rightleftarrows \mathrm{Si} - \mathrm{H}$$

However, Si—H bonds are not stable at elevated temperatures. This explains why low-temperature heat-treatments reduce the surface-state density even in wet-grown oxides where hydrogen is expected to be plentiful.

Also shown in Fig. 6, curve (d), is the surface-state density for a dry oxide grown at 1100°C and subjected to a nitrogen anneal at the growth temperature and then to a forming-gas anneal at 450°C after aluminum metallization. This combination of anneals resulted in the lowest midgap surface-state density (6×10^{10} cm^{-2}-eV^{-1}) as well as the lowest fixed oxide charge (6×10^{10} cm^{-2}) observed in this investigation and appears to be the optimum processing method of obtaining both low oxide charge and low surface-state density.

The effect of temperature of oxidation on the surface-state density was also investigated using dry oxides grown at 900°, 1000°, and 1100°C on (100) orien-

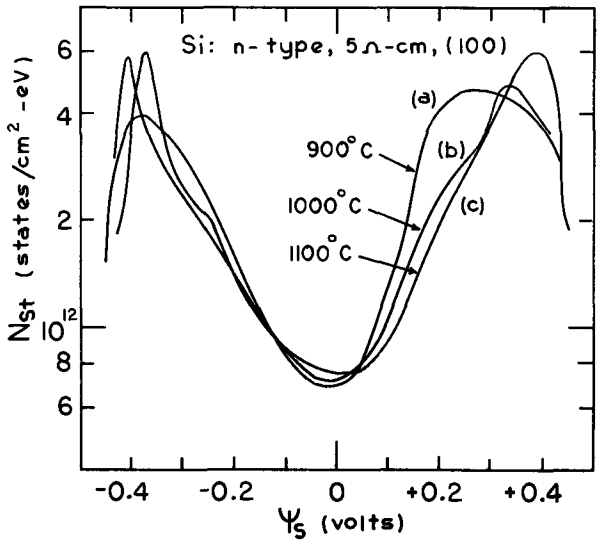

Fig. 7. Effect of dry oxide growth temperature on the surface state density (oxide thickness ≃ 1000Å; no anneal).

tated slices. The results, shown in Fig. 7, indicate no appreciable dependence of surface states on growth temperature. On the other hand, the fixed oxide charge, Q_{ss}, was observed to decrease with increasing temperature of oxidation in agreement with the results of Deal *et al.* (12).

Goetzberger *et al.* (19) have postulated a common origin for the fixed oxide charge and the surface-state charge. Evidence in favor of this postulate include:

(*a*) the fact that the surface-state density and the surface charge have the same crystallographic dependence as demonstrated by Arnold *et al.* (11), and
(*b*) the results obtained in this investigation with high-temperature nitrogen annealing which reduces both Q_{ss} and N_{st}.

However, hydrogen annealing, as shown, reduces the surface-state density without affecting the oxide charge. Similarly, the oxide growth temperature appears to have little affect on the surface-state density while reducing the oxide charge. Hence, it is evident that some processing parameters affect one charge without affecting the other. The lack of a more explicit correlation between the two charges suggests that they may not have a single common origin. It is perhaps possible that two or more discrete mechanisms contribute to the surface-state density, only one of which correlates with the fixed oxide charge (11).

Acknowledgments

This work was supported by the Defense Research Board of Canada (Grant 5566-34) and by the National Research Council of Canada (Grant A-4408). The authors wish to thank Mrs. S. Trettin for assistance in the sample preparation. Grateful acknowledgments are also made to the National Research Council of Canada for a postgraduate bursary awarded to one of the authors (E. A. F.).

Manuscript submitted Feb. 1, 1971; revised manuscript received *ca.* May 6, 1971.

Any discussion of this paper will appear in a Discussion Section to be published in the June 1972 JOURNAL.

REFERENCES

1. L. M. Terman, *Solid-State Electron.*, **5**, 285 (1962).
2. D. M. Brown and P. V. Gray, *This Journal*, **115**, 760 (1968).
3. C. N. Berglund, *IEEE Trans. ED*, **ED-13**, 701 (1966).
4. E. H. Nicollian and A. Goetzberger, *Bell Syst. Tech. J.*, **46**, 1055 (1967).
5. R. Castagne, *Compt. Rend. Acad. Sci. (Paris)*, **267**, 866 (1968).
6. R. Castagne, *ibid.*, **267**, 1000 (1968).
7. M. Kuhn, *Solid-State Electron.*, **13**, 873 (1970).
8. K. H. Zaininger, Semiconductor Surface Physics, in Field Effect Transistors, J. T. Wallmark and H. Johnson, Editors, Prentice Hall, Englewood Cliffs, N. J. (1963).
9. D. R. Frankl, *Solid-State Electron.*, **2**, 71 (1961).
10. W. Kern and D. Puotinen, *RCA Rev.*, **31**, 187 (1970).
11. E. Arnold, J. Ladell, and G. Abowitz, *Appl. Phys. Letters*, **13**, 413 (1968).
12. B. E. Deal, M. Sklar, A. S. Grove, and E. A. Snow, *This Journal*, **114**, 266 (1967).
13. F. M. Fowkes and T. E. Burgess, *ibid.*, **116**, 126C (1969).
14. F. M. Fowkes and T. E. Burgess, *Surface Sci.*, **13**, 184 (1969).
15. P. Balk, *This Journal*, **112**, 69C (1965).
16. P. L. Castro and B. E. Deal, *ibid.*, **118**, 280 (1971).
17. B. E. Deal, E. L. MacKenna, and P. L. Castro, *ibid.*, **116**, 997 (1969).
18. E. Kooi, *Phillips Res. Rept.*, **21**, 477 (1966).
19. A. Goetzberger, H. Heine, and E. H. Nicollian, *Appl. Phys. Letters*, **12**, 95 (1968).

Characterization of Multilevel Interconnection Defects

R. H. Cox* and H. Hentzschel*,[1]

Texas Instruments Incorporated, Dallas, Texas 75222

ABSTRACT

Scanning electron microscopy and metallurgical sectioning were combined to detect defects and potential reliability problems at crossovers and feedthroughs in multilevel circuits. The extremely large depth of field of the scanning electron microscope permitted "on-edge" examination of the sample surface topography, while metallurgical cross-sectioning allowed examination of buried layers. This method is a very powerful tool for characterizing multilevel integrated circuits.

The advent of large scale integration (LSI) has resulted in electronic components which have considerably greater functional capability than the basic integrated circuit. Conventional integrated circuits are the unit cells of an LSI array, and they are interconnected utilizing a multilevel system formed by interleaving layers of metal and insulation over the basic integrated circuit. Medium scale integration (MSI) lies in between integrated circuits and LSI in complexity. In some cases, MSI can be achieved with one level of interconnection, but frequently, a two-level interconnection system is employed. In order to achieve

* Electrochemical Society Active Member.
[1] Present address: Bosch, A.G., Germany.
Key words: multilevel interconnection defects, LSI (large scale integration), scanning electron microscopy, optical microscopy, metallography.

LSI, a multilevel interconnection system is required. At the present time, both two- and three-level systems are employed. The demands on this technology are more severe than on conventional integrated circuit passivation and metallization technology, for multilevel interconnection requires both that leads cross one another and that they feed through from one level to another. Crossovers are subject to both electrical shorts and opens, and interlevel feedthroughs are subject to electrical opens. Furthermore, the added processing problems of working with a multilevel construction can introduce multilevel defects which are potential reliability problems.

The purpose of this paper is to present two of the methods employed in this investigation and to discuss the defects which were identified and characterized using these techniques. Scanning electron microscopy of sample surfaces and optical microscopy of metallurgical sections were the two above-mentioned techniques. As is shown below, these two methods complement one another and, when they are used together, give a thorough characterization of the multilevel structure.

Experimental

Scanning electron microscopy possesses distinct advantages which can yield information quickly and accurately. A major advantage is that direct examination of the sample surface is possible, and the depth perception and magnification are much greater than that possible with the optical microscope.

Patterned multilevel structures are quite easy to examine in the scanning electron microscope. A particular advantage is the ability to study a slice "on edge," which gives an excellent perspective when searching for multilevel defects. This view is obtained by inclining the slice at a very shallow angle (10° to 30°) to the primary beam. Correspondingly, the secondary electron detector is located normal to the beam and at an 80°-60° angle to the sample. Although features parallel to the slice surface are greatly foreshortened in one direction, features normal to the slice surface are seen at nearly true size. Hence, the edges of patterned metal and the side walls of feedthroughs are seen clearly. These structural features cannot be examined at high magnifications using conventional optical microscopy. In this study, the SEM's emissive mode of operation was employed, utilizing a CRT display of secondary electrons produced by a 25 kV primary electron beam. Image contrast is produced by differences in secondary electron emission from the sample. The resultant image has a remarkable three-dimensional quality, especially when the sample is inclined at an angle to the electron beam.

The metallographic studies required considerable skill in sample preparation, but the results were equally rewarding. Although the depth perception and resolution (0.1-0.2 μm) of the optical microscope are less than the SEM, a major advantage is gained by an optical examination of a cross-sectioned sample. Because the different layers of thin films possessed distinct color and reflectivity differences, an optical examination of the metallographic section often yielded more information than an SEM examination of the same cross-sectioned sample.

The main problem in sectioning multilayer devices deposited on silicon is the rather low mechanical stability of the different layers, which may be as thin as 1000Å or less. Also the extreme difference in the hardness of the various materials involved causes the formation of steps during polishing. The optical microscope with its low depth of field cannot give clear pictures of the layers when steps exist between them. Yet, the goal of a flat, highly polished surface with no mechanical damage of the layers can be reached by the following technique: The sample is glued with the side carrying the devices to a glass plate; preferably, a thermosetting epoxy with a low viscosity in the uncured state is used. It is important to avoid the entrapment of bubbles during mixing. The curing is done at elevated temperatures to make a hard joint. This assembly is mounted in a plastic block in such a way that the multilayers are cut in the desired direction and plane. In the grinding, lapping, and polishing process, extreme care is taken to avoid a mechanical destruction of the various layers. Most of the different layers are visible in the optical microscope after polishing, without etching. It is well known that the etch rate of oxides deposited in different ways varies widely. So, a very slight oxide-etch can differentiate between different kinds of quartz. Now, the reflectivity of SiO_2 is quite low, especially at an oxide-oil interface when an oil-immersion objective is used. Therefore, an extremely thin film of evaporated metal is used to increase the reflectivity of the oxide and make it visible.

The majority of the multilevel structures presented in this paper employed Mo-Au metallization. A few examples of filament-evaporated Al metallization are presented as well. The insulating oxides were produced by RF sputtering and silane vapor-phase deposition.

Results and Discussion

The following photomicrographs were selected to illustrate the strength of the method of combining scanning electron microscopy and optical metallography for multilevel characterization. Both defective and good crossover and feedthrough structures are presented. The examples given represent neither the frequency of defect occurrence nor do they show all types of defects, but rather, they were selected because they were interesting photomicrographs and verified the usefulness of these two characterization tools when used together.

A schematic drawing of a multilevel crossover is given in Fig. 1. The first-level metals (Mo-Au-Mo) are deposited over the thermal oxide (SiO_2) which is grown on the Si substrate. After this first-level metallization is patterned by etching, insulating oxides (RF-sputtered and silane vapor-deposition oxides) are deposited over the entire wafer. Feedthrough holes to first-level metal are etched in the insulating oxide at appropriate locations. Finally, second-level metallization (Mo-Au) is deposited over the insulating oxide and through the feedthrough holes, and the second-level metal is patterned. One defect sometimes observed is an electrical open in the second-level metal.

Figure 2 presents SEM micrographs of defective crossovers with very thin, nearly open metal at the vertical edge of the step. Figure 2a represents Al metallization, and Fig. 2b represents Mo-Au metallization. The oxide-coated step runs from the upper-left to the lower-right part of each picture. The metallurgical cross section, Fig. 3, clearly shows the thin metal at the vertical edge of the step, and it confirms the existence of the defect suggested by the SEM inspection. The insulating oxides appear dark in the photomicrograph because of their low optical reflectivity. The top

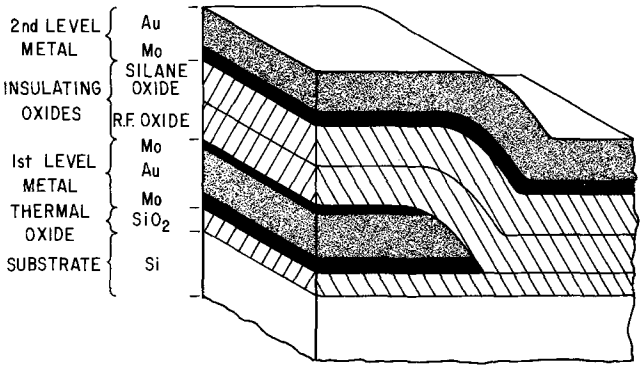

Fig. 1. Schematic drawing of a multilevel crossover

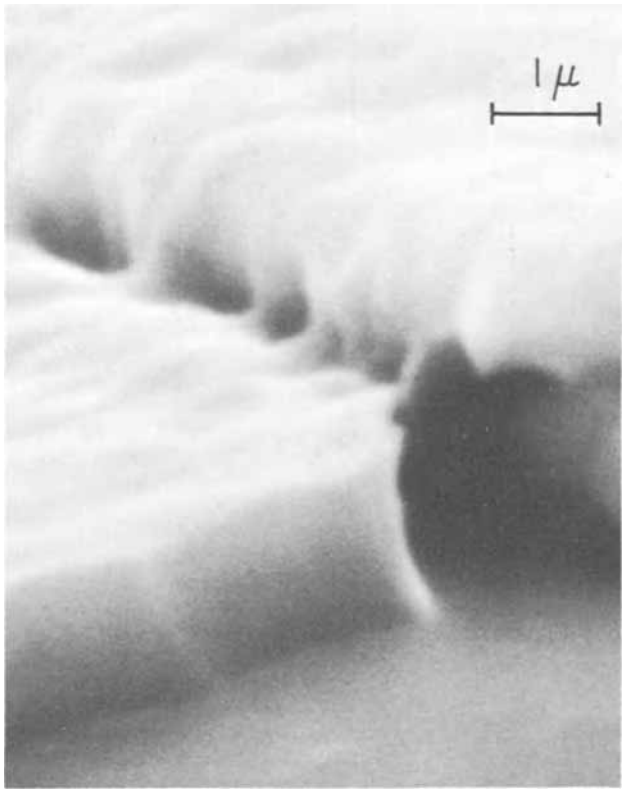

Fig. 2a. SEM micrograph of a defective Al crossover

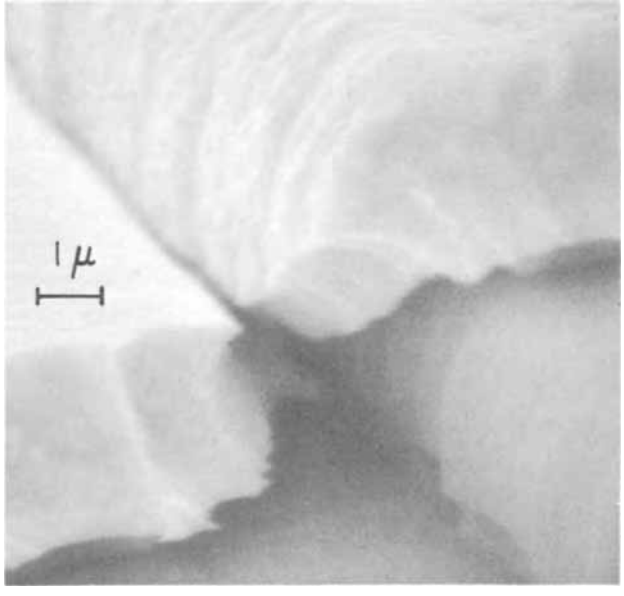

Fig. 2b. SEM micrograph of a defective Mo-Au crossover

Mo layer is very thin, and it is difficult to resolve in most of the figures. The bottom Mo layer shows much more clearly. A possible cause of the thin crossover metal is suggested by the vertical appearance of the edge of the first-level metal. Figures 4 and 5 illustrate the steps taken to produce a greatly improved crossover structure. Tapered Mo-Au-Mo coated with an insulating oxide layer is shown in Fig. 4. Note that the insulating oxide is clearly seen in this figure, as compared to the dark appearing, transparent oxide in Fig. 3. This improvement was achieved by coating the cross section with a very thin layer of evaporated Ge to increase the oxide reflectivity. Figure 5 shows a final Mo-Au crossover produced by tapering first-level metal. Note the second-level metal crosses over the step with no reduction in thickness. Figures 6a and 6b are SEM micrographs of good Mo-Au and Al crossovers, respectively. The slight darkening seen at the edge of the metal-oxide interface is caused by the charging of the oxide by the electron beam. As the beam sweeps over the oxide immediately adjacent to the highly conductive metal, a region of decreased secondary electron emission results. This effect can be troublesome where thick oxides are employed. However, excellent image quality can be gained easily by coating the entire sample with a thin layer of evaporated Au (< 250Å).

A schematic drawing of a multilevel feedthrough is given in Fig. 7; the first-level metallization and insulating oxide are produced in the same manner as explained in Fig. 1 (the multilevel crossover). Holes

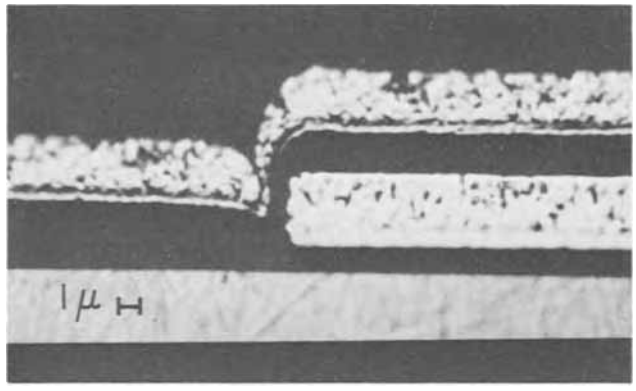

Fig. 3. Metallurgical cross section of a defective Mo-Au crossover.

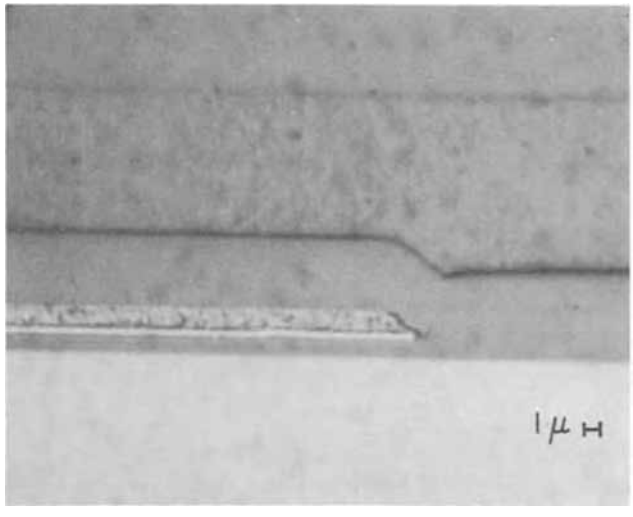

Fig. 4. Metallurgical cross section of tapered first-level Mo-Au metal coated with an insulating oxide.

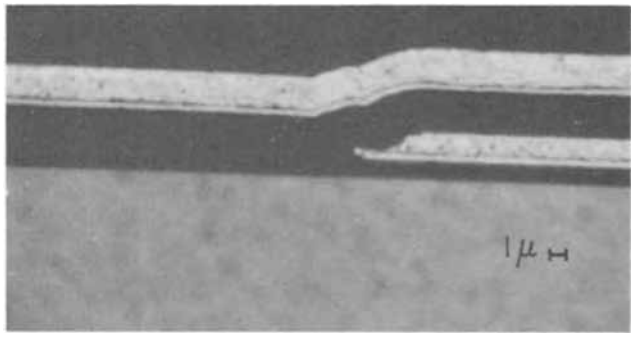

Fig. 5. Metallurgical cross section of a Mo-Au multilevel crossover produced by proper edge-tapering of first-level metal.

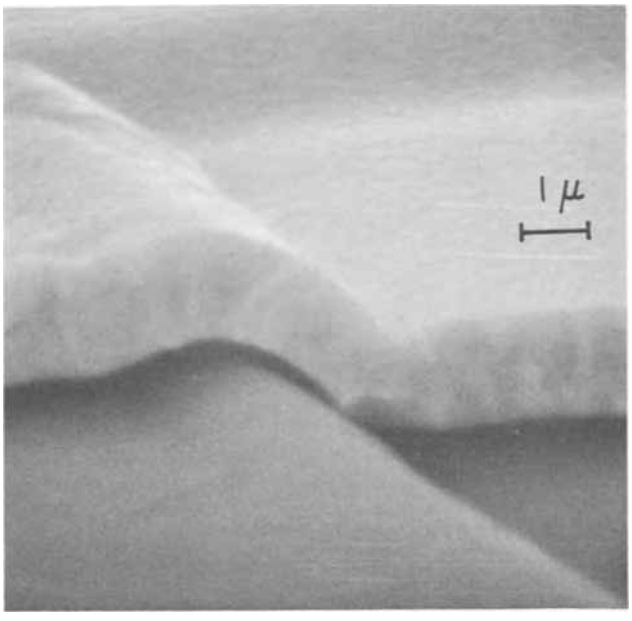

Fig. 6a. SEM micrograph of a good Mo-Au crossover

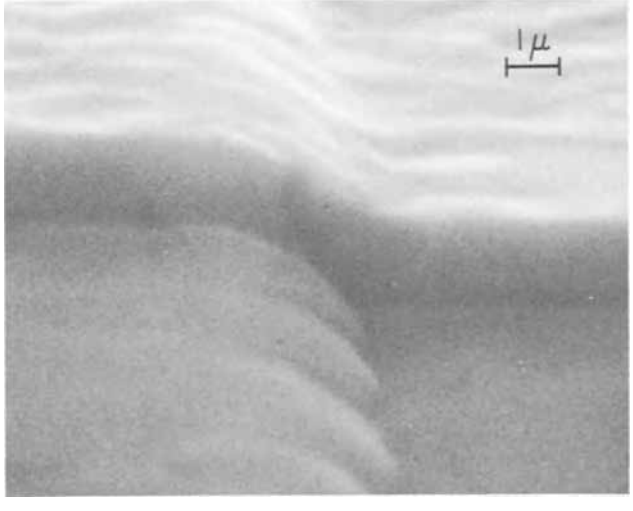

Fig. 6b. SEM micrograph of a good Al crossover

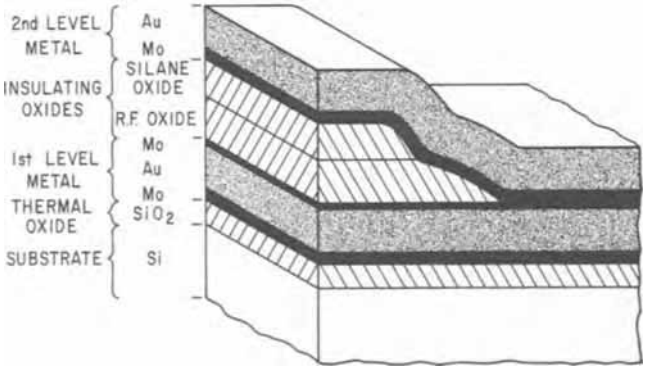

Fig. 7. Schematic drawing of a multilevel feedthrough

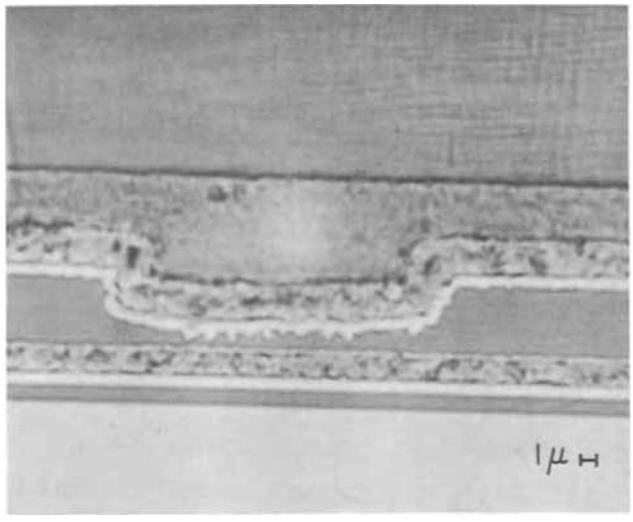

Fig. 8. Metallurgical cross section through a defective feedthrough. An open circuit resulted because the feedthrough hole was not etched all the way through.

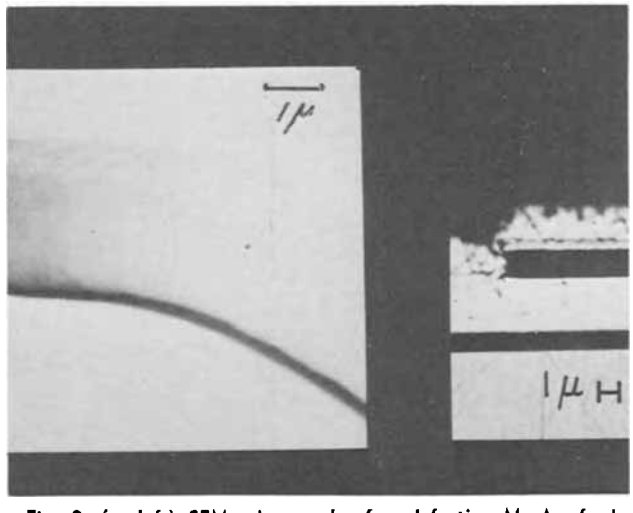

Fig. 9. (a, left) SEM micrograph of a defective Mo-Au feedthrough showing hairline crack at the base of the feedthrough; (b, right) metallurgical cross section of a defective Mo-Au feedthrough. Hairline crack is seen clearly.

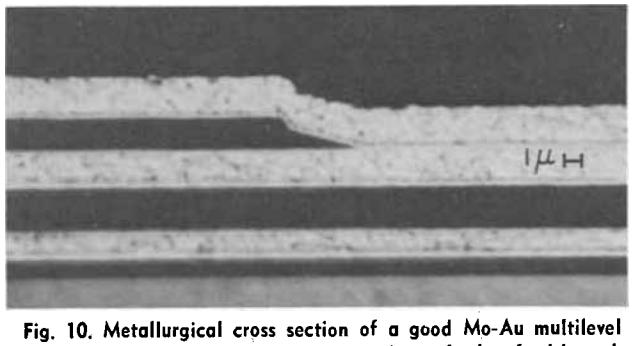

Fig. 10. Metallurgical cross section of a good Mo-Au multilevel feed-through produced by proper tapering of the feedthrough walls.

are etched in the oxide to produce the feedthrough interconnection, and the final metal is deposited and patterned. Causes of electrical open circuits are shown in the next photomicrographs. Figure 8 is a metallurgical cross section through a feedthrough. The failure to etch completely through the oxide is the obvious cause of the open circuit. In this case, scanning electron microscopy would not have indicated the defect. Figure 9 illustrates a second type of feedthrough defect. Figure 9a is a SEM photomicrograph showing an apparent

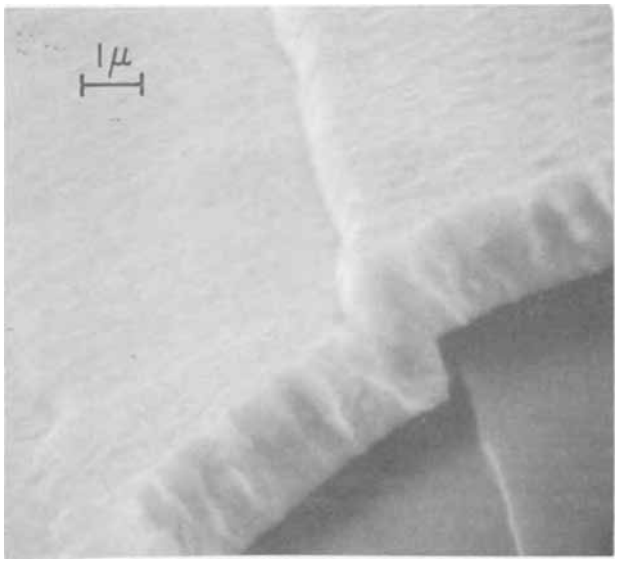

Fig. 11. SEM micrograph of a good Mo-Au feedthrough

hairline crack at the base of the vertical step of the Mo-Au feedthrough. Figure 9b is a cross section which confirms the presence of the hairline crack. The vertical sidewall of the oxide is likely to be the cause of the thin metal. Figure 10 is a cross section of a Mo-Au feedthrough produced by proper processing steps. The third-level metal connects to the second-level metal through a via hole etched in the oxide. The two slopes seen in the oxide wall are due to the difference in etch rates of the two oxides which compose the insulating layer. The top layer, made by silane deposition, etches more rapidly than the lower RF sputtered oxide layer. This feedthrough is excellent in quality, showing no reduction in metal thickness at the step. Figure 11 is a SEM photomicrograph of the same type feedthrough, showing the Mo-Au crossing the tapered oxide wall and connecting to the bottom of the feedthrough. The sharp silane-deposited oxide step runs from the upper center to the lower right-hand portion of the micrograph. The shallow RF deposited oxide step is the left-hand portion of the micrograph.

Conclusion

The combination of scanning electron microscopy and metallographic sectioning provided an excellent method of characterizing multilevel defects. The "on-edge" examination of multilevel crossovers was particularly revealing, and the exact location of metal opens were readily determined. Likewise, defects on the vertical walls of feedthroughs were quickly found. Optical microscopic data obtained from metallographic sections complemented the scanning electron microscope data. Defects in both crossover and feedthrough structures were shown with equal clarity when examined in cross section. The locations of both shorts and opens have been observed by optical microscopy. This investigation has resulted in an enhanced understanding of multilevel defects. Once this knowledge has been gained, it is an easier job to build higher reliability multilevel structures.

Acknowledgments

The authors would like to thank T. E. Hartman for his many valuable ideas and suggestions on this work. Thanks are also extended to Lucy Rascoe for the cross sectioning.

Manuscript submitted April 27, 1970; revised manuscript received *ca.* July 12, 1971. This was Paper 230RNP presented at the Detroit Meeting of the Society, Oct. 5-9, 1969.

Any discussion of this paper will appear in a Discussion Section to be published in the June 1972 JOURNAL.

Pseudo-Brewster Angle Determination of Carrier Concentration

W. A. Keenan and P. A. Schumann, Jr.*

IBM Component Division, East Fishkill Facility, Hopewell Junction, New York 12533

ABSTRACT

The Brewster angle has long been used to determine the index of refraction of nonabsorbing material. Semiconductors and other absorbing materials exhibit a nonzero minimum at a "pseudo-Brewster" angle which depends on the wavelength of incident light and the optical constants of the materials. Since semiconductor infrared optical constants are strongly dependent on the carrier density, the pseudo-Brewster angle is an indication of this density. An infrared, optical constant model for semiconductors has been used to calculate calibration curves relating carrier concentration in silicon to the pseudo-Brewster angle for several wavelengths, the range of carrier concentrations being limited by the wavelength employed. Experimental results for silicon are presented for a wavelength of 3.391 μm.

Optical techniques are very attractive for characterizing semiconductor materials, because they are both contactless and nondestructive. Infrared interference and plasma resonance are two very good examples of techniques used to measure the properties of processed semiconductors. Infrared interference is used to determine the thickness of epitaxial films. Plasma resonance is used to determine the carrier concentration of semiconductors.

For plasma resonance, a spectrophotometer is used to measure the reflectivity at a fixed angle of incidence on the semiconductor sample while the wavelength of the reflected light is scanned. The wavelength of minimum reflectivity is related to semiconductor carrier concentration by means of a calibration curve (1). In this technique no absolute quantities need be measured since only relative reflectivity is observed and

* Electrochemical Society Active Member.

Key words: semiconductor carrier concentration, polarized infrared light, silicon, Brewster angle, plasma resonance.

the wavelength corresponding to the reflectivity minimum determined.

In the above two techniques, a reflectivity minimum is observed by scanning the wavelength for a fixed angle of incidence. If, on the other hand, the polarized reflectivity is measured as a function of the angle of incidence for one wavelength, a minimum will again be observed. The angle at which this minimum is observed, the pseudo-Brewster angle, is related through the semiconductor optical constants to the carrier concentration of the material. Figure 1 shows calculated reflectivity curves for n-type silicon with an impurity concentration of 1×10^{19} cm^{-3} at a wavelength of 3.391 μm. This wavelength is put out by a He-Ne laser with special resonator windows used in the experimental work presented. R_s, the reflectivity for light polarized with its electric vector perpendicular to the plane of incidence, increases monotonically as the angle of incidence increases from 0 to 90 degrees. The parallel component of reflectivity (R_p), exhibits a minimum at an angle related to the optical constants of the semiconductor.

The approximate expressions (2) for the parallel, Eq. [1], and perpendicular, Eq. [2], components of linearly polarized, reflected light as a function of the angle of incidence are

$$R_p(\theta) = \frac{(n^2 + k^2)\cos^2\theta - 2n\cos\theta + 1}{(n^2 + k^2)\cos^2\theta + 2n\cos\theta + 1} \quad [1]$$

and

$$R_s(\theta) = \frac{(n^2 + k^2) - 2n\cos\theta + \cos^2\theta}{(n^2 + k^2) + 2n\cos\theta + \cos^2\theta} \quad [2]$$

where θ = angle of incidence, n = index of refraction, and k = extinction coefficient.

These approximations are valid for $(n^2 + k^2) >> 1$, which is the case for semiconductors in the infrared region of the spectrum. Setting the derivative of $R_p(\theta)$ with respect to cos θ equal to zero, the minimum in the parallel component of reflectivity is found to occur at

$$\cos\theta_B = \frac{1}{(n^2 + k^2)^{1/2}}$$

or

$$\theta_B = \cos^{-1}\frac{1}{(n^2 + k^2)^{1/2}} \quad [3]$$

where θ_B is defined as the pseudo-Brewster angle.

The Brewster angle for nonabsorbing material (3) (with a zero extinction coefficient) is defined as the angle at which the parallel reflectivity $R_p(\theta)$ goes to zero. For an absorbing material such as a semiconductor, with nonzero k, $R_p(\theta)$ attains a nonzero minimum at θ_B, the pseudo-Brewster angle. This angle is directly related to the optical constants of the material as shown in Eq. [3].

The free-carrier optical constant theory for a semiconductor derived by Schumann and Phillips (4) can be used to relate the index of refraction n and the extinction coefficient k at any wavelength to the impurity concentration of the material. The results are

$$n = \frac{1}{\sqrt{2}}\left[K_L - \frac{e^2\lambda^2 NJ(D)}{4\pi^2\epsilon_0 C^2 m^*}\right]^{1/2} \left\{1 \pm \left[1 + \frac{e^8\lambda^6 N^4\rho_0^2 g^2 [L(D)]^2}{64\pi^6\epsilon_0^2 C^6 m^{*4}\left[K - \frac{e^2\lambda^2 NJ(D)}{4\pi^2\epsilon_0 C^2 m^*}\right]^2}\right]^{1/2}\right\}^{1/2} \quad [4]$$

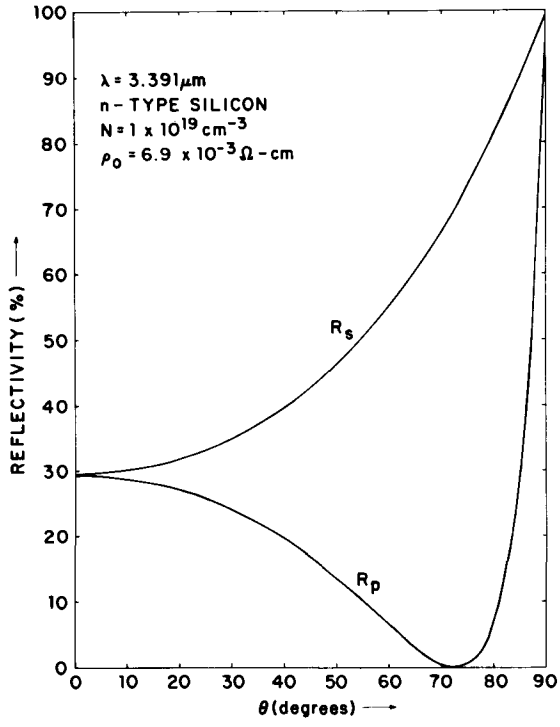

Fig. 1. Parallel and perpendicular reflectivity as a function of the angle of incidence at $\lambda = 3.391$ μm for n-type silicon; impurity concentration $N = 1 \times 10^{19}$ cm^{-3}.

where

$$J(D) = \frac{1}{\Gamma(5/2)}\int_0^\infty \frac{x^{9/2}e^{-x}\,dx}{x^3 + D}$$

$$L(D) = \int_0^\infty \frac{x^3 e^{-x}\,dx}{x^3 + D}$$

$$D = \frac{N^2 e^4 \lambda^2 \rho_0^2 \Gamma(4)\, g}{4\pi^2 C^2 m^{*2}}$$

$$g = \frac{\Gamma(4)}{[\Gamma(5/2)]^2} = 3.39$$

and

$$K_L = \frac{\epsilon_L}{\epsilon_0}$$

In the above equations ϵ_L = lattice dielectric constant, ϵ_0 = free space dielectric constant, $\Gamma(x)$ = gamma function of x, C = speed of light, m^* = effective mass, N = doping impurity concentration, e = electronic charge, λ = wavelength of light, and ρ_0 = d-c resistivity.

Since these equations relate n and k to N and ρ_0 and since θ_B is a function of n and k, θ_B can be used to determine the impurity concentration or resistivity of the semiconductor. In the theoretical curves presented in Fig. 1 through 8 for silicon, the calculations were made using Irvin's (5) curves to relate ρ_0 to N, an assumed value of 0.26 for the effective mass ratio for n-type silicon, and a relative lattice dielectric constant $K_L = 11.7$ (6).

In Fig. 1 the value of $R_p(\theta)$ appears to go to zero on the 100% scale used in the plot. Figure 2, a logarithmic plot of the same $R_p(\theta)$ curve, shows that the reflectivity attains a minimum of 3.63×10^{-4}% at a pseudo-Brewster angle of $\theta_B = 72.73°$. The angular width of

$$k = \frac{1}{\sqrt{2}}\left[K_L - \frac{e^2\lambda^2 NJ(D)}{4\pi^2\epsilon_0 C^2 m^*}\right]^{1/2} \left\{-1 \pm \left[1 + \frac{e^8\lambda^6 N^4\rho_0^2 g^2 [L(D)]^2}{64\pi^6\epsilon_0^2 C^6 m^{*4}\left[K_L - \frac{e^2\lambda^2 NJ(D)}{4\pi^2\epsilon_0 C^2 m^*}\right]^2}\right]^{1/2}\right\}^{1/2} \quad [5]$$

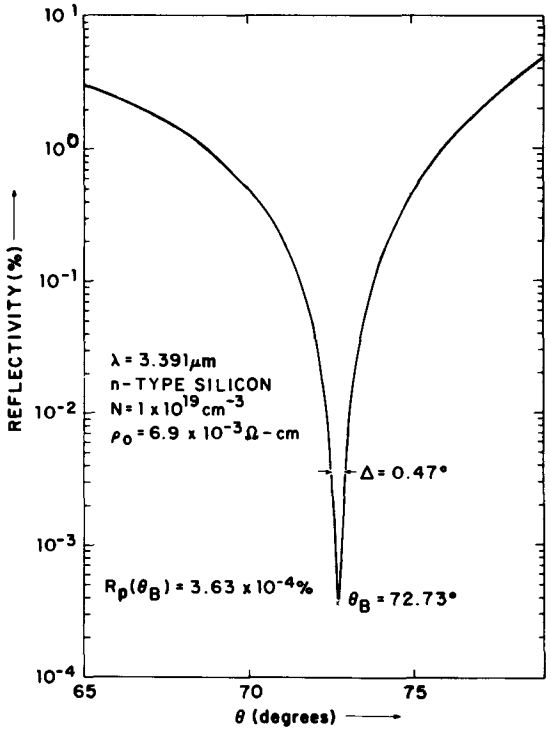

Fig. 2. Logarithm of parallel component of polarized reflectivity as a function of the angle of incidence at $\lambda = 3.391$ μm for n-type silicon; impurity concentration $N = 1 \times 10^{19}$ cm^{-3}.

this minimum is $\Delta = 0.47°$ at a value of R_p one order of magnitude greater than $R_p(\theta_B)$.

Figure 3 shows a logarithmic plot of $R_p(\theta)$ for n-type silicon with $N = 4 \times 10^{19}$ cm^{-3} using $\lambda = 3.391$ μm. Figure 2 is superimposed for comparison. Note that all three parameters [θ_B, $R_p(\theta_B)$, and Δ] that characterize the minimum change as concentration changes.

Calibration curves relating the impurity concentration N and the pseudo-Brewster angle θ_B, have been

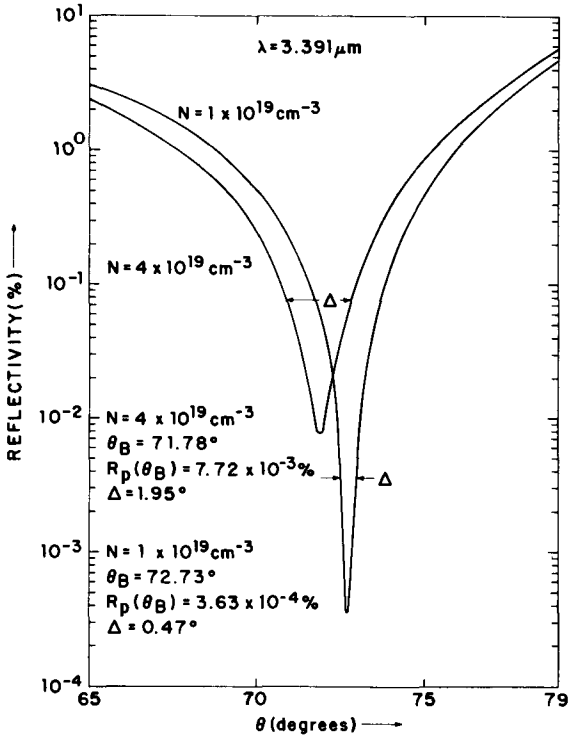

Fig. 3. Logarithmic plot of $R_p(\theta)$ at $\lambda = 3.391$ μm for impurity concentrations of $N = 4 \times 10^{19}$ cm^{-3} and $N = 1 \times 10^{19}$ cm^{-3}.

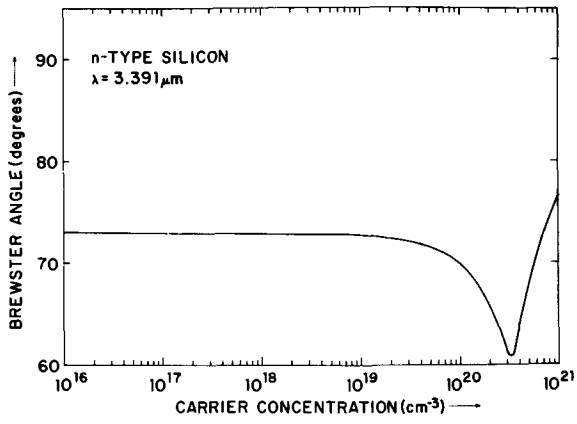

Fig. 4. Pseudo-Brewster angle calibration curve (θ_B vs. N) for n-type silicon at $\lambda = 3.391$ μm.

calculated using Eq. [3], [4], and [5]. Figure 4 shows the θ_B *vs.* N calibration curve for n-type silicon, and a wavelength $\lambda = 3.391$ μm. As the concentration decreases, θ_B approaches 73°, the value for intrinsic silicon. At higher concentrations θ_B is very sensitive to changes in concentration; unfortunately, for any angle less than 73° concentration is not a single-valued function of θ_B. For example, in Fig. 4, a pseudo-Brewster angle of 68.0 could correspond to a concentration of either $N = 1.45 \times 10^{20}$ cm^{-3} or $N = 5.0 \times 10^{20}$ cm^{-3}.

Since the semiconductor infrared optical constants, expressed in Eq. [4] and [5], are strongly dependent on the wavelength of light, the θ_B *vs.* N calibration curves are also strongly dependent on wavelength. A family of calibration curves for n-type silicon is shown in Fig. 5. Note that for short wavelengths, the sensitivity of θ_B to changes in concentration is great, but the range over which it is single valued is small. As wavelength is increased, the sensitivity of this angle to changes in concentration decreases, but the range over which it is single valued in concentration increases.

The fact that θ_B is not single valued in N for angles less than 73° can be resolved by measuring θ_B at two wavelengths. Alternately, if the magnitude of R_p is measured as the angle of incidence is varied around θ_B, then observing either $R_p(\theta_B)$ or the width Δ can resolve which N value is the correct one. Figure 6, showing calculated values of $R_p(\theta_B)$, indicates that it is a strong function of N; hence an order of magnitude measurement of $R_p(\theta_B)$ would suffice. Figure 7 shows that $\Delta = \theta_2 - \theta_1$ where $R_p(\theta_1) = R_p(\theta_2) \equiv 10R_p(\theta_B)$ is also a strong function of N.

Another technique for determining the correct value of N where θ_B is double valued is to measure the mag-

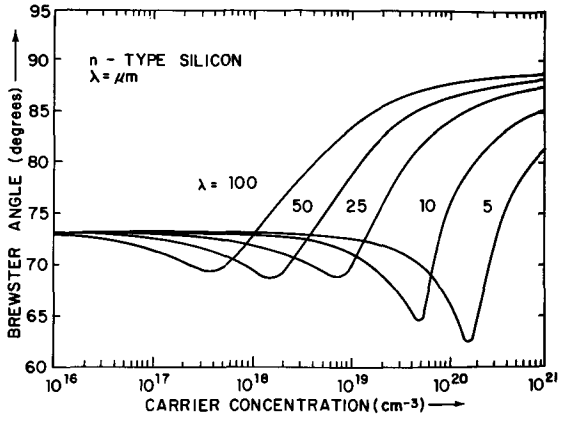

Fig. 5. θ_B calibration curves for n-type silicon at wavelengths of 5, 10, 25, 50, and 100 μm.

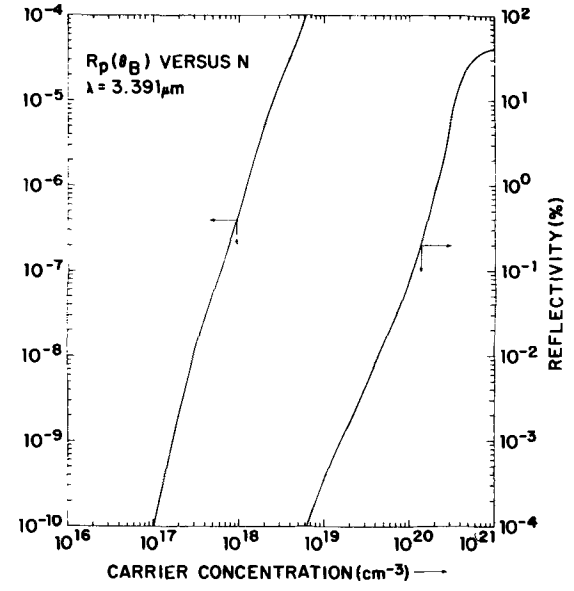

Fig. 6. Parallel component of polarized reflectivity at an angle of incidence equal to θ_B as a function of N for n-type silicon at $\lambda = 3.391$ μm.

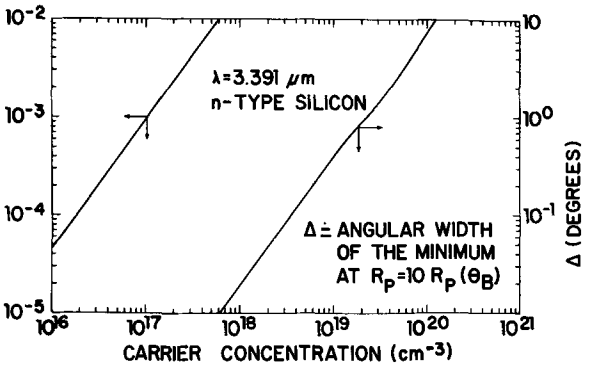

Fig. 7. Angular width of the parallel reflectivity minimum at $R_p = 10\ R_p(\theta_B)$ vs. N for n-type silicon at $\lambda = 3.391$ μm.

nitude of reflectivity of light incident at the pseudo-Brewster angle, but polarized perpendicular to the plane of incidence. This is done by rotating the plane of polarization while at the pseudo-Brewster angle. Figure 8 illustrates which of the double values of θ_B is correct for the sample concentration (N), using the perpendicular reflectivity $R_s(\theta_B)$. $R_s(\theta_B)$, calculated from the model and the calibration curve of θ_B is plot-

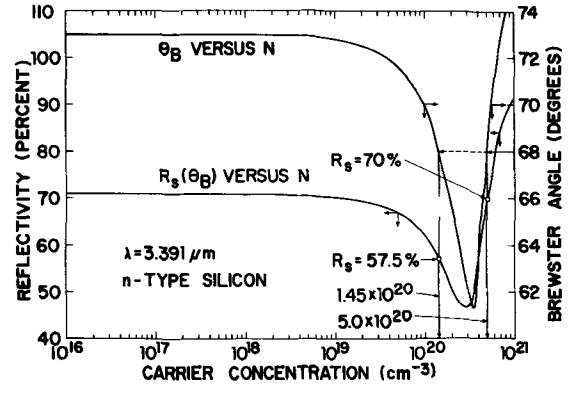

Fig. 8. Perpendicular reflectivity at θ_B vs. concentration and θ_B vs. N for n-type silicon at $\lambda = 3.391$ μm.

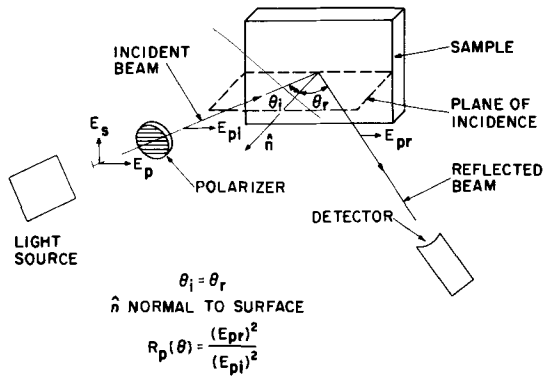

Fig. 9. Schematic of experimental setup to determine θ_B

ted *vs.* N for an assumed $\lambda = 3.391$ μm. As an example a specimen with θ_B measured at 68° would, from Fig. 8, correspond to $N = 1.45 \times 10^{20}$ cm^{-3} or $N = 5.0 \times 10^{20}$ cm^{-3}. Measurement would determine which of the corresponding values of $R_s(\theta_B)$, that is, 57.5% or 70%, obtains for this specimen, thus determining N.

An experimental setup to measure the polarized reflectivity and determine the pseudo-Brewster angle is shown schematically in Fig. 9. A Spectra-Physics He-Ne laser with 3.391 μm wavelength plane-polarized output served as the light source. The reflectivity was measured with a Golay infrared detector while a Siemens diffractometer simultaneously varied the angles of incidence and reflectance. An X-Y recorder (not indicated in Fig. 9) was used to plot R_p *vs.* the angle of incidence.

After orienting the laser for output polarized parallel to the plane of incidence of a test wafer, the angle was scanned to locate the reflectivity minimum. The polarization was adjusted to minimize the reflectivity and the angle was again scanned. This procedure was iterated until the reflectivity could no longer be reduced. The test wafer at its PBA served as an analyzer for adjusting the polarization of the laser.

Experimentally determined θ_B for several n-type silicon samples, both bulk and diffused wafers, are shown in Table I; the carrier concentration was determined from plasma resonance. The carrier concentration implied by the measured θ_B (shown in Table I) was determined using the theoretical calibration curve of Fig. 4. Figure 10 is a plot of the carrier concentrations determined by the two techniques. A least-square linear regression analysis yielded the straight line shown and a correlation coefficient of 0.992.

The concentrations derived from the PBA theoretical calibration curve fall below the plasma resonance concentrations. The excellent correlation implies that with the correct calibration curve, measurement of PBA could be used to determine N. The theoretical model (4) used to calculate the calibration curve assumes the

Table I. Experimentally determined θ_B for n-type silicon samples and the implied impurity concentration

Plasma resonance	Pseudo-Brewster angle	
N (cm^{-3})	θ_B (measured)	N (cm^{-3}) (from curve)
3.2×10^{19}	72.75	8.0×10^{18}
8.2×10^{19}	71.83	4.0×10^{19}
9.3×10^{19}	71.70	5.0×10^{19}
6.8×10^{19}	72.50	2.0×10^{19}
6.4×10^{19}	72.50	2.0×10^{19}
6.3×10^{20}	63.75	4.1×10^{20}
2.5×10^{20}	68.87	1.25×10^{20}
2.8×10^{20}	68.00	1.5×10^{20}
2.07×10^{20}	69.50	1.1×10^{20}
1.2×10^{20}	71.38	6.0×10^{19}
5.5×10^{20}	64.88	4.3×10^{20}
1.1×10^{20}	70.25	9.1×10^{19}
7.0×10^{20}	66.75	4.9×10^{20}
7.6×10^{20}	67.00	5.0×10^{20}
7.5×10^{19}	72.25	3.0×10^{19}
1.3×10^{20}	71.00	7.0×10^{19}

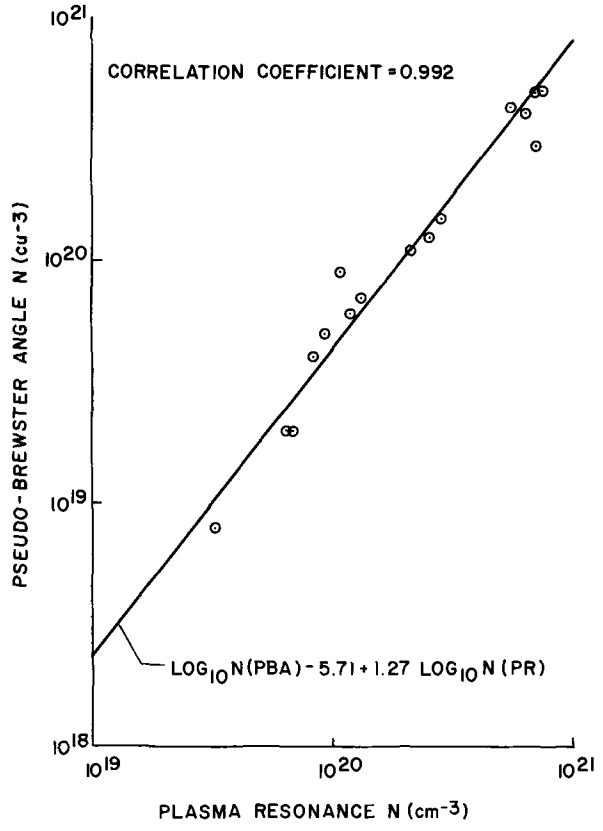

Fig. 10. Plot of PBA-determined concentration vs. concentration determined by plasma resonance.

Conwell-Weisskopf scattering and Maxwell-Boltzmann statistics. Recent work (7) has shown that while the model accurately predicts trends in the optical constants as a function of concentration and wavelength, the actual values are in error. A constant value of effective mass ratio was used in calculating the calibration curve although effective mass is known to vary with concentration. For application of the PBA technique at a particular wavelength an experimental calibration curve would have to be constructed.

The PBA technique for determination of carrier concentration offers several advantages over plasma resonance. It requires scanning the angle of incidence rather than wavelength. It has a sharp minimum which is easy to read, and which becomes sharper as concentration decreases (cf. Fig. 3). The lower limit to the concentration that can be measured with PBA depends only on the wavelength employed, the longer the wavelength the lower the detectable concentration limit. The availability of long wavelength infrared lasers as polarized light sources makes PBA attractive as an automated process monitoring technique.

Manuscript submitted May 1, 1970; revised manuscript received ca. July 21, 1971. This was Paper 117 presented at the Los Angeles Meeting of the Society, May 10-15, 1970.

Any discussion of this paper will appear in a Discussion Section to be published in the June 1972 JOURNAL.

REFERENCES

1. P. A. Schumann, Jr., *Solid-State Technol.*, p. 50, (January 1970).
2. O. S. Heavens, "Optical Properties of Thin Films," Dover Publications (1965).
3. J. D. Jackson, "Classical Electrodynamics," John Wiley & Sons, Inc., New York (1962).
4. P. A. Schumann, Jr. and R. P. Phillips, *Solid State Electron.*, **10**, 943 (1967).
5. J. C. Irvin, *Bell System Tech. J.*, **41**, 387 (1962).
6. P. W. Chapman, O. T. Tufte, J. D. Zook, and D. Long, *J. Appl. Phys.*, **34**, 3291 (1963).
7. P. A. Schumann, Jr., W. A. Keenan, A. H. Tong, H. H. Gegenwarth, and C. P. Schneider, *This Journal*, **118**, 145 (1971).

Partial Pressures in the Cd-Te and Zn-Te Systems

R. F. Brebrick*[1]

Lincoln Laboratory, Massachusetts Institute of Technology, Lexington, Massachusetts 02173

ABSTRACT

Partial pressures of Te_2, Cd, and Zn have been determined to within 10% for a number of compositions in the Cd-Te and Zn-Te systems by measuring the optical density of the vapor phase between 1990 and 7000A. For Te-saturated CdTe(c), the partial pressure of Te_2, p_2, reaches a maximum value of 0.188 atm near 915°C. For Cd-saturated CdTe(c), p_{Cd} is within a few per cent of that for pure Cd up to 840°C. At the 1092°C melting point, $p_2 = 5.5(10^{-3})$ and $p_{Cd} = 0.65$ atm. At 900°C the homogeneity range for CdTe(c) is shown to lie within outer limits of 49.0 and 50.5 a/o (atom per cent) Te and ΔG_f varies by less than 150 cal/g-atom between either Cd-saturated or Te-saturated and congruently subliming CdTe(c). Liquidus temperatures and the partial gram-atomic enthalpy and entropy are obtained for 55.0, 60.0, and 65.0 a/o Te melts. The liquidus points confirm the presence of an inflection point in the Te-rich liquidus and it is shown that this behavior is due primarily to the nonideal behavior of the Cd activity coefficient. Similarly, p_{Zn} for Zn-saturated ZnTe(c) has been determined to 900°C and p_2 for the Te-saturated ZnTe(c) to 1080°C. The homogeneity range at 900°C is bracketed between outer limits of 49.5 and 50.5 a/o Te corresponding to a maximum variation of ΔG_f of 190 cal/g-atom between either Zn-saturated or Te-saturated and congruently subliming ZnTe(c).

The liquidus line for CdTe has been determined by de Nobel (1), Kulwicki (2), Lorenz (3), and recently by Steininger *et al.* (4). The last three sets of data agree to within 10°C on the Cd-rich side of 50 a/o (atom per cent). The last two agree to within 20°C on the Te-rich side but are 10°C below the data of de Nobel and as much as 40°C below those of Kulwicki near 60 a/o Te. According to the last two determinations, the Te-rich liquidus temperature drops rapidly with increasing Te-content, being slightly concave out

* Electrochemical Society Active Member.
[1] Present address: Metallurgy and Materials Science, College of Engineering, Marquette University, Milwaukee, Wisconsin 53233.
Key words: phase diagram Cd-Te; thermodynamic properties Cd-Te, Zn-Te.

to 60-65 a/o where an inflection point occurs. The liquidus line is far removed from one calculated by assuming an ideal liquid phase in equilibrium with a compound CdTe(c) that melts at 1092°C with a heat of fusion of 12.01 kcal/mole. Partial pressures along the three-phase loop have been measured by de Nobel (1) and more extensively by Lorenz (3). Although the two determinations are in fair agreement on the partial pressure of Cd, p_{Cd}, along the Cd-rich leg of the loop, they are in poor agreement for that of Te_2, p_2, along the Te-rich leg. Recently Hall and conductivity measurements (5) on single crystal CdTe as a function of temperature and either p_{Cd} or p_2 indicate, on the basis of a simple point-defect model, that the homogeneity range for CdTe(c) includes, or is close to, the stoichiometric composition and is of the order of 10^{-5} a/o wide near 900°C. However, no direct measurements in terms of atom per cent have been made for the outer limits within which the homogeneity range must fall. Therefore, no upper bound has been placed on the variation of the Gibbs free energy of formation of CdTe(c) across its homogeneity range.

In this paper we report the results of optical density measurements which (*i*) give p_2 along the Te-rich leg of the three-phase loop up to the maximum melting point of 1092°C, (*ii*) give p_{Cd} along the Cd-rich leg up to 900°C, (*iii*) place outer limits of 49.0 and 50.5 a/o Te on the homogeneity range, and (*iv*) give liquidus temperatures for 55.0, 60.0, and 65.0 a/o Te. We also report similar measurements on ZnTe(c) that extend our earlier study (6).

Experimental

The experimental details of the optical density measurements between 1990 and 7000Å have been extensively described in an earlier study (6) on ZnTe(c). Essentially the experiment consists of measuring the optical density, $D = \log I_0/I$, of the vapor in a silica optical cell at a fixed temperature while a reservoir of a condensed phase, located at the end of a sidearm to the optical cell, is held at one of a series of lower temperatures. Since it was desired to determine pressures for reservoir temperatures approaching 1100°C, the optical cell was held fixed at 1100°C in some experiments, as well as at 1000°C in others, and calibration runs with pure Te and with pure Cd had to be made at 1100°C. For reservoir temperatures above 920°C, the Ag-liner used to help establish a uniform temperature over the reservoir zone was replaced by one of stainless steel. The temperature difference along the 5 cm reservoir zone was 2°-3°C or less in all measurements. The reservoir temperature was taken as that near the middle of the condensed phase in the reservoir zone and at the surface of the silica sidearm. It was measured using a Pt, 13% Rh thermocouple and an ice junction. The precision of measurement was ±0.1°C and, judging from calibrations at the melting point of Zn and Ag, the accuracy was better than ±0.5°C. The temperature difference across a 2 cm long optical cell at 1100°C was under 10°C. Both temperature differences were constant with time to within 0.5°C.

Spectroscopically pure elements (nominal 99.999% pure from Cominco American Inc., Spokane, Washington) were used to synthesize the samples by fusion. Generally, the Cd and Zn were first individually melted under 10^{-6} Torr vacuum, subjected to 600 Torr of H_2 for 5-10 min while molten, subjected to vacuum, and then quenched. In synthesizing the Cd-Te and Zn-Te samples, the elements were individually weighed to the nearest 0.1 mg to make a total near 3g, loaded into a silica test-tube, and outgassed for 4 hr at 140°C and pressures below 10^{-7} Torr. The sample was then sealed-off under vacuum, reacted with a hand torch, annealed 40 hr at 900°C, then 40 hr at 530°C, and quenched. The sample was removed from the silica test-tube, ground to pass a 1 mm opening, stainless steel sieve, and loaded into the carbon-coated sidearm of an optical cell. For five samples, 49.5 a/o Te Zn-Te, 49.0, 55.0, 60.0, and 65.0 a/o Te Cd-Te, the elements were loaded directly into the carbon-coated sidearm of an optical cell without pre-reaction. After outgassing the loaded cell for 4 hr at 140°C and 10^{-7} Torr, it was sealed-off. Optical cells used in an earlier study and containing 40.0 and 55.0 a/o Te Zn-Te were used again here. The optical cells were generally near 21 or 47 mm in optical path length (total length minus the thickness of two plane parallel windows). Windows that were 0.75 mm thick did not noticeably deform at 1100°C and total vapor pressures under 1 atm while 0.50 mm thick windows did deform over a period of 8-16 hr.

Results

Tellurium.—The qualitative features of the spectrum of $Te_2(g)$ at 1100°C are the same as at lower temperatures. [The optical density for a 1000°C optical cell is shown between 3100 and 4500Å in Fig. 2 of ref. (7) and between 2300 and 4000Å in Fig. 1 of ref. (8).] Since in the present study p_2 was in the 10^{-3} to 1 atm range, it was determined from the relatively weak absorption in the visible. A Te_2 band system extends from a minimum optical density near 3150Å through a maximum near 4100-5500Å and beyond, depending on the value of p_2. Vibronic bands are seen from 3870 to about 4500Å, the upper limit moving toward longer wavelengths with increasing partial pressure. The optical density at a number of wavelengths and for a 22.1 mm optical path length at 1100°C is plotted in Fig. 1 on a logarithmic scale against the reciprocal absolute temperature of the Te(l) reservoir. The line without points and near the middle of the figure gives the vapor pressure (9-11) of Te(l). The optical densities at 4357Å, an absorption band maximum, and at 5000 and 5500Å, in apparently structureless regions of the band system, have close to the same slope as the vapor pressure for optical densities greater than 0.1. When $D_{4357} \geq 0.1$, the relation between optical density and partial pressure is

$$p_2 = 0.320\, D_{4357}/L \qquad [1]$$

where L is the optical path length in millimeters. The optical densities at 2400 and 2800Å shown in Fig. 1 are at wavelengths where Cd(g) also absorbs. Except for two or three points, the straight lines in Fig. 1 fit the experimental points to better than 5% in optical density.

Cadmium.—Cd(g) has two prominent absorption peaks, the stronger at 2287Å, the weaker at 3257Å.

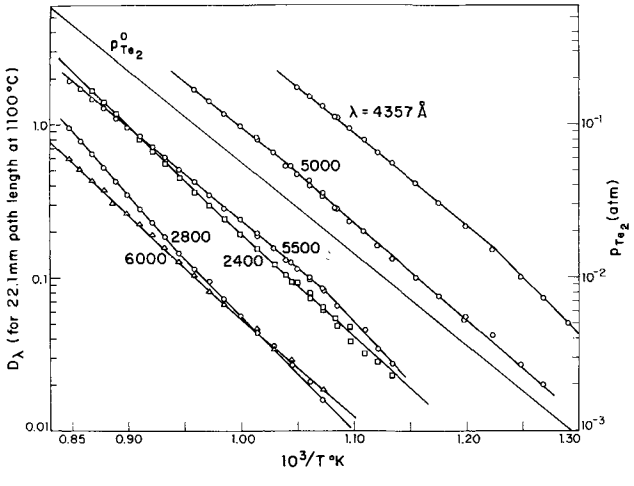

Fig. 1. The optical density of $Te_2(g)$, $D = \log (I^\circ_\lambda/I_\lambda)$, at a number of wavelengths for a 22.1 mm optical path at 1100°C plotted on a logarithmic scale against the reciprocal absolute temperature of a pure Te(l) reservoir. The solid line without points gives the vapor pressure of Te(l) as read with the right hand ordinate.

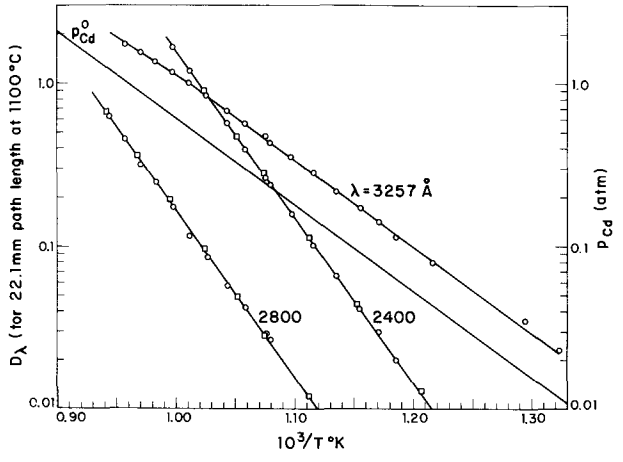

Fig. 2. Optical density of Cd(g) at a number of wavelengths for a 22.1 mm optical path at 1100°C plotted on a logarithmic scale against the reciprocal absolute temperature of a pure Cd(l) reservoir. The squares are normalized values obtained from a 47.5 mm optical-path cell. The line without points gives the vapor pressure of Cd(l) as read with the right hand ordinate.

With increasing pressure the 2287Å peak broadens extensively toward the red, as do the strongest peaks of Hg(g) (12, 13) and Zn(g) (6, 14). Figure 2 shows D_λ for a 22.1 mm path at 1100°C plotted against the reciprocal absolute temperature of the Cd(l) reservoir for a number of wavelengths. The line without points shows the vapor pressure of Cd(l) (15, 16). For the 10^{-2} to 1 atm range of pressure shown, D_{2287} is much greater than the upper limit of measurement, $D = 2$. In the long wavelength tail of this peak D_λ, shown in Fig. 2 for $\lambda = 2400$ and 2800Å, has a slope close to twice that of the vapor pressure, consistent with the statistical theory of self-broadening (17). For these two wavelengths, the plot also includes data obtained using an optical cell with a 47.5 mm path length and then normalized by multiplying by the factor (22.1/47.5). The two sets of points are in good agreement, showing that D depends linearly on the path length. Only the optical densities from the 22.1 mm cell are shown for the 3257Å peak. These are systematically larger than those obtained with a 47.5 mm cell after the latter are multiplied by (22.1/47.5). Thus D_{3257} depends on a fractional power of the path length rather than the first power. A similar behavior was noted (6) for the strong 2138Å Zn-line. Such behavior is to be expected (18) when the optical density at the peak of a narrow absorption line is measured, as is done here, using a spectral band-pass greater than the true half-width of the line.

The values of D at the 3257 and 2138Å peaks for Cd(g) and Zn(g), respectively, are sensitive to the spectrometer slit-width used and care was taken to hold these constant at a given wavelength for each spectral scan. Although D_{3257} has approximately the same temperature dependence as the vapor pressure of Cd(l), Fig. 2 itself was used to obtain p_{Cd} from the partial optical density of Cd(g), as is explained in the next section. Absorption of Cd(g) at 4357, 5000, and 5500Å is below 0.01 and negligible even at the highest values for p_{Cd} in Fig. 2. [The optical density at the strongest, 2287Å peak was used to determine p_{Cd} in a lower pressure range in an earlier study (19) on congruently subliming CdTe(c) using a 1000°C optical cell. The fact that the measured values of p_{Cd} and p_2 were in the ratio 2.00:1.00 attests to the accuracy attainable with this type of measurement as well as to the accuracy of the vapor pressures of Cd(l) and Te(l).]

Cadmium telluride.—For samples containing more than 50 a/o Te, the values of D_λ, $\lambda = 4357$, 5000, 5500Å, had the same relative magnitudes as observed with pure tellurium. As mentioned in the last section, the optical density due to Cd(g) is negligible at these wavelengths. Therefore, the observed value of D was multiplied by the factor, $22.1/L$, where L was the path length in millimeters, and Fig. 1 was used to determine p_2. Next the Te_2 contribution to the optical density at 2400 and 2800Å, where Cd(g) absorbs, was read from Fig. 1. The partial optical density of Cd(g) at each of these wavelengths was taken as the difference between the observed density and the Te_2 contribution. (The partial optical density of Cd(g) at 3257Å was taken as the difference between the observed optical density at 3257Å and an extrapolated value for the background at 3257Å that was obtained by drawing a straight line tangent to both sides of the peak on an optical density-wavelength trace.) The value of p_{Cd} corresponding to each of these partial optical densities was then read from Fig. 2.

The values of p_2 for samples containing more than 50 a/o Te are plotted on a logarithmic scale against the reciprocal absolute temperature in Fig. 3. The upper line without points gives the vapor pressure of Te(l), p^o_2 the vapor being essentially all Te_2(g). The lower line without points gives p_2 for congruently subliming CdTe(c) from an earlier study (19). Values of p_2 along the Te-rich leg of the three-phase loop fall along a parabola-like curve that approaches p^o_2 at low temperatures, reaches a maximum of 0.195 atm between 918° and 946°C, and then falls rapidly with increasing temperature. Near 946°C measurements were taken with both 1100° and 1000°C optical cells. The values obtained with the 1100°C cell are about 10% lower than those with the 1000°C cell, reaching a plateau of 0.180 atm at 940°C. Such a discrepancy could result from a relative error of 4° between the reservoir temperatures measured in the present calibration with a 1100°C cell and those measured in the calibration with a 1000°C cell (7, 8). At any rate, it introduces an uncertainty of 10% in the values reported here for the tellurium partial pressure. Since the values of p_2 agree for 50.5 and 55.0 a/o Te for $10^3/T \geqq 0.764$ and since p_2 for 50.5 a/o

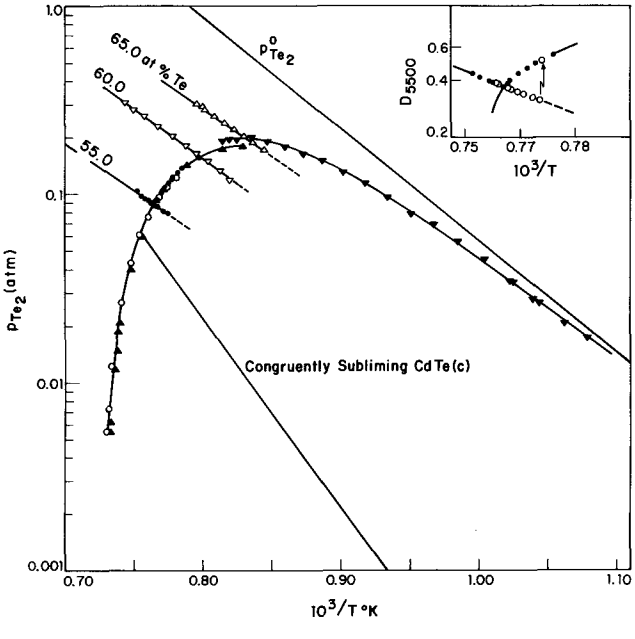

Fig. 3. Partial pressure of Te_2(g) in the Cd-Te system is plotted on a logarithmic scale against reciprocal absolute temperature. The vapor pressure of pure tellurium is given by the uppermost line without points. The lowest line without points gives $p_{Te_2} = p_2$ for congruently subliming CdTe(c) from ref. (19). ▼ 55.0 a/o Te, 1000°C cell; ● 55.0 a/o Te; ○, ▲ 50.5 a/o Te all with 1100°C cell. The inset in the upper right corner for a 55.0 a/o Te sample is described in the text.

Te drops rapidly with increasing temperature for $10^3/T < 0.764$, it appears that 50.5 a/o Te lies in the Te-rich three-phase field and outside the homogeneity range of CdTe(c). Smoothed values of p_2 along the Te-rich leg are given in Table I as a function of temperature. The smoothed values agree with those actually measured to within ±5%.

The three, short line segments cutting the three-phase curve in the upper left-hand portion of Fig. 3 give the p_2-$10^3/T$ relationship for liquids with the labeled compositions. The portions of these lines lying within the three-phase curve are for supercooled liquids. The intersection of these lines with the three-phase curve gives liquidus temperatures for the corresponding compositions, which are listed in Table II. (The 65.0 a/o Te sample was run with a 1000°C optical cell and the liquidus temperature is therefore taken at the intersection with the 1000°C data for the three-phase curve.) The lines are well enough defined that the relative, partial gram-atomic enthalpy and entropy of Te can be evaluated. These are also given in Table II.

Measurements on the 60.0 and 65.0 a/o Te samples were made only with decreasing temperatures and were not carried far enough to observe the termination of supercooling. Such a termination was observed with the 55.0 a/o Te sample as shown in the inset in Fig. 3, where D_{5500} (which is proportional to p_2 with good accuracy) is plotted on a logarithmic scale against $10^3/T$ on an expanded scale. The solid circles indicate points taken with increasing temperature and show that p_2 decreases with increasing temperature along the three-phase curve to the liquidus temperature, after which it increases along a straight line. The open circles indicate points taken with decreasing temperature. They show that the melt supercooled about 22° before crystallization of CdTe(c) commenced. At this time p_2 rose abruptly to a value on the three-phase curve (as indicated by the arrow) and there was a transient increase in temperature. Prior to crystallization, p_2 and T had been steady.

At the highest temperatures, p_{Cd} was obtained along the Te-rich leg of the three-phase curve as well as p_2. The pressure product, $p_{Cd}p_2^{1/2}$, is plotted on a logarithmic scale against the reciprocal absolute temperature in Fig. 4. The points near the upper end of the straight line are from the present study. The circles indicate that p_{Cd} was obtained from the partial optical density of Cd at its 3257Å peak, while the triangles indicate it was obtained from the partial optical density at 2400Å. These two determinations agree to within 15%. The squares at low temperatures along the lowest line are from an earlier study (19). The present results at the highest temperatures agree well with an extrapolation of the earlier results. The values of p_{Cd} in this range

Table I. Partial pressures of Te_2(g) and Cd(g) over Te-saturated CdTe(c)

$10^3/T$ (°K^{-1})	p_2 (atm)	$10^3/T$ (°K^{-1})	p_2 (atm)	$10^3/T$ (°K^{-1})	p_2 (atm)	p_{Cd} (atm)
1.07	0.017	0.81	0.180	0.755	0.60	—
1.05	0.025	0.80	0.160	0.748	0.042	0.19
1.00	0.046	0.79	0.148	0.74	0.023	0.31
0.95	0.082	0.78	0.125	0.735	0.012	0.48
0.90	0.135	0.77	0.102	0.732	0.068	0.68
0.85	0.188	0.764	0.088	0.731	0.056	—
0.83	0.188	0.76	0.075	—	—	—

Table II. Liquidus points and partial molar quantities for Te-rich Cd-Te melts

Te, a/o	55.0	60.0	65.0	100
T°C (This work)	1036 ± 2	980 ± 2	929 ± 2	—
T°C [Lorenz, ref. (3)]	1042	977	925	—
T°C [Steininger *et al.*, ref. (4)]	1027	967	—	—
h_{Te}-½h_{Te_2} (g, 1 atm); cal/g-atom	−11,500	−12,227	−11,660	−13,641
S_{Te}-½$S°_{Te_2}$ (g, 1 atm); cal/g-atom, deg	−6.384	−7.854	−8.087	−10.797

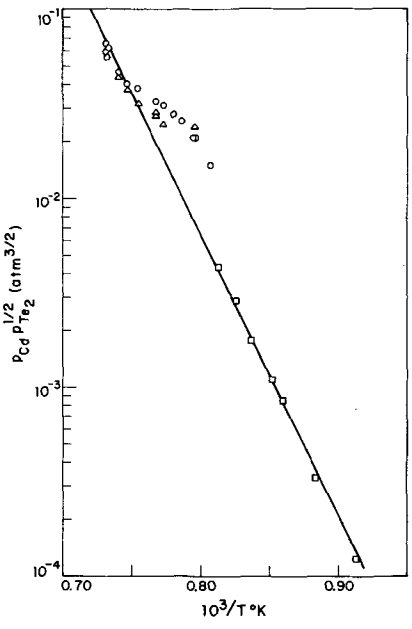

Fig. 4. Pressure product, $p_{Cd}p_2^{1/2}$, for CdTe(c) plotted on a logarithmic scale against the reciprocal absolute temperature. ○, p_{Cd} determined from the partial optical density of Cd(g) at 3257Å; △, p_{Cd} determined from the partial optical density at 2400Å; □, ref. (19).

are given in Table I. [At the melting point of 1092°C, $p_{Cd} = 0.65$ atm and $p_2 = 5.5(10^{-3})$ atm.] However, at the lowest temperature, $10^3/T = 0.81$, the pressure product obtained from the present measurements is high by a factor of three. It can be shown (20) thermodynamically, assuming only that the vapor is ideal, that at a given temperature, $p_{Cd}p_2^{1/2}$ is a maximum over a 50.00 a/o Te condensed phase. Since the present results near $10^3/T = 0.81$ give the pressure product not only for Te-saturated CdTe(c), but also for the 60 a/o Te melt in equilibrium with it (Fig. 3), the pressure product should not be higher than observed for congruently subliming CdTe(c). We, therefore, conclude that the present results at the lower temperatures are thermodynamically inconsistent with those obtained earlier and we believe them to be incorrect. Most likely the error lies in the measurement of p_{Cd} when p_2 is as much as five times larger. In particular, we speculate that under these circumstances our basic assumption is in error; namely, the total optical density is a linear superposition of contributions from Cd and Te_2 and does not depend on any terms of the form, $(p_{Cd})^m(p_2)^n$.

For 49.0 a/o Te, the only Cd-Te composition investigated with less than 50 a/o Te, the optical densities at 2500, 2800, and 2900Å are plotted on a logarithmic scale against $10^3/T$ along the upper three lines in Fig. 5. Also shown by the closed circles are data obtained with pure Cd. At each wavelength the points for these two compositions agree up to $10^3/T = 0.90$ (838°C) within an experimental error of about ±3%. Therefore, at least up to this temperature, 49.0 a/o Te lies outside the CdTe(c) homogeneity range. At higher temperatures, D_{2900} for the 49.0 a/o sample falls a little below that for pure Cd(l). Most likely, this means the Cd-rich liquidus composition is departing enough from pure Cd to cause a detectable decrease in the value of p_{Cd}. The line without points and near the bottom of Fig. 5 gives the vapor pressure of Cd(l) and, up to $10^3/T = 0.90$, also p_{Cd} for Cd-saturated CdTe(c). The points along the straight line branching away from the vapor pressure line at high temperatures give p_{Cd} for Cd-saturated CdTe(c) and were obtained from D_{2900}. At $10^3/T = 0.85$, $p_{Cd} = 3.24$ atm. At $10^3/T = 0.902$, $p_{Cd} = 2.0$ atm.

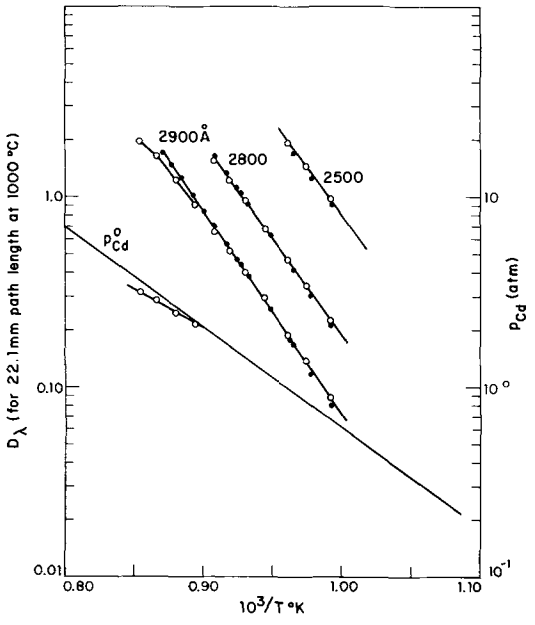

Fig. 5. Partial optical density of Cd(g) at the labeled wavelengths plotted on a logarithmic scale against reciprocal absolute temperature along the upper four lines. Open circles are for 49.0 a/o Te Cd-Te, closed circles for pure Cd(l). The line without points in the lower portion of the figures gives the vapor pressure of Cd(l). Points are shown for p_{Cd} of the 49.0 a/o sample only where they differ by at least 3% from the vapor pressure line of Cd(l).

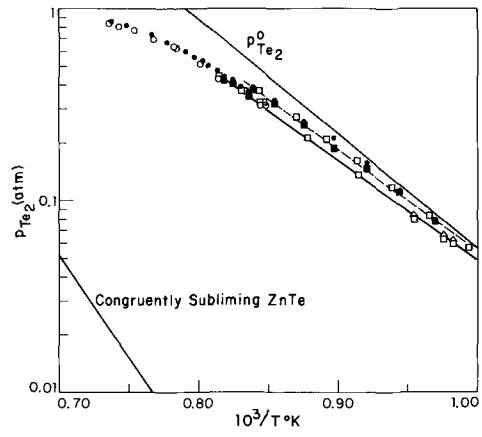

Fig. 6. Partial pressures of $Te_2(g)$ for Zn-Te samples with 50.5 a/o Te (open symbols) and 55.0 a/o Te (closed symbols) are plotted on a logarithmic scale against the reciprocal absolute temperature. Circles, squares, and triangles indicate p_2 was obtained from the optical density at 6000, 5500, and 5000Å, respectively. The lower line without points gives p_2 for congruently subliming ZnTe(c) from ref. (6).

Our first 49.0 a/o Te samples were prepared with as-received Cd and were pre-reacted and annealed before being loaded into the optical cell as described in the Experimental section. Optical density measurements indicated that although these samples were in the Cd-rich three-phase field at low temperatures as expected, they entered the CdTe(c) homogeneity range at 600°-700°C. It seemed likely that Cd had been lost either through reaction with oxygen or perhaps as an unrecovered film on the synthesis tubes. (A 40 mg loss of Cd would change an initially 3g, 49.0 a/o Te sample to a 50.0 a/o sample.) Therefore, the sample on which the results of Fig. 5 are based was prepared from hydrogen-reduced Cd, and the weighed elements were loaded directly into the optical cell without pre-reaction. The optical cell was mounted in the furnace and the Cd-Te heated to 833°C over a 4 hr period. At 680° and 833°C, p_2 (as indicated by D_{5500}) was on the Te-rich leg of the three-phase loop, *i.e.*, was appropriate for Te-saturated rather than Cd-saturated CdTe. When the reservoir temperature was increased to 898°C, the value of p_2 initially increased, then started to decrease. After 16 hr at 898°C the value of p_2 was too low to measure while p_{Cd} was nearly equal to the vapor pressure of pure Cd. The runs giving the data of Fig. 5 were then begun. The above observations show the kinetics of at least the last stages of the Cd-Te reaction are relatively slow, presumably because unreacted liquid Cd is effectively protected by a CdTe(c) film. They also indicate that the surface portion of the sample, which establishes the partial pressures, was eventually equilibrated, since it entered the Cd-rich field spontaneously after initially being in the Te-rich field. As discussed later, similar observations were made with the 49.5 a/o Te Zn-Te sample.

Zinc telluride.—The values of p_2 for Te-saturated ZnTe(c), obtained from the optical density data for samples with 50.5 and 55.0 a/o Te, are plotted on a logarithmic scale against $10^3/T$ in Fig. 6. The value of p_{Zn} was below our detectivity of about 10^{-5} atm. The upper line in Fig. 6 without points gives the vapor pressure of Te(l). The lowest line gives p_2 for ZnTe(c) in equilibrium with a stoichiometric vapor (50 a/o) and is taken from an earlier study (6). In the Discussion we argue that this can be considered to be p_2 for congruently subliming ZnTe(c). The experimental points along the Te-rich leg of the three-phase curve fall along two curves, the pressures obtained with a 1000°C optical cell being about 10-15% higher than those obtained with a 1100°C cell. (See the discussion on the similar discrepancy observed here with CdTe.) With increasing temperature the three-phase curve starts to flatten out and lies increasingly below the vapor pressure line for pure Te. The points for the 50.5 a/o Te sample (closed circles) are in close agreement with those for 55.0 a/o Te (open circles). Thus up to the highest temperature measured, 1086°C, the 50.5 a/o sample lies outside the homogeneity range of ZnTe(c). Smoothed values of p_2 from the 1100°C cell data are given in Table III. Straight line segments drawn through these smoothed values are within ±5% in p_2 of the actual experimental points.

The values of p_{Zn} for samples with 49.5, 40.0, and 0.00 a/o Te are plotted on a logarithmic scale against $10^3/T$ in Fig. 7. (The value of p_2 was below our level of detection of 10^{-6} atm.) Up to the highest temperature of measurement, 909°C, the value of p_{Zn} agrees for all three sample compositions within an experimental error of ±3%. Thus up to this temperature 49.5 a/o Te lies outside the homogeneity range of ZnTe(c). It is emphasized that the coincidence of p_{Zn} for the 49.5, 40.0, and 0.00 a/o Te depends on the coincidence of the optical densities observed and does not depend on the accuracy of the vapor pressure values for pure Zn(l).

Analogous to our observations with 49.0 a/o Te Cd-Te, 49.5 a/o Te Zn-Te samples which had been pre-reacted and annealed before being placed in the optical cell appeared Zn-saturated at the lowest temperatures as expected, but entered the ZnTe(c) homogeneity range between 600° and 700°C. The behavior was different for a 49.5 a/o Te sample prepared by using H_2-reduced Zn and by loading the weighed elements directly into the optical cell. When this sample was first heated, the optical density of the vapor phase indicated the surface layers were Te-saturated even after 40 hr at 899°C and also after 2 hr at 985°C. The temperature was then raised to 1066°C. After 20 min the tellurium pressure started to drop slowly. After 16

Table III. Partial pressure of $Te_2(g)$ over Te-saturated ZnTe(c)

$10^3/T$(°K^{-1})	0.95	0.90	0.85	0.80	0.78	0.76	0.74	0.735
p_2 (atm)	0.089	0.160	0.26	0.53	0.64	0.73	0.82	0.85

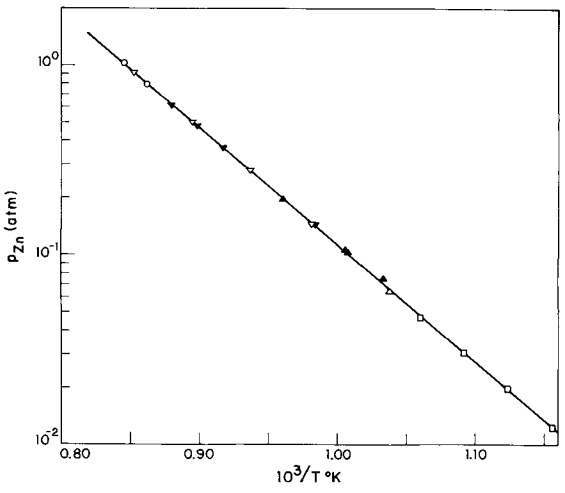

Fig. 7. Partial pressure of Zn(g) for Zn-Te samples with 49.5 a/o Te (open symbols), 40.0 a/o Te (closed symbols), and pure liquid Zn (straight line). Circles indicate p_{Zn} was obtained from D_λ at 2400 and 2500Å, the two values agreeing within ± 2%. Inverted triangles give the common value (to within ± 2%) of p_{Zn} obtained from D_λ at 2300, 2400, and 2500Å. Triangles and squares give p_{Zn} as obtained from D_λ at 2200 and 2150Å, respectively.

hr, p_2 was too low to measure. The reservoir temperature was then lowered to 970°C, the optical cell temperature was lowered to 1000°C, and measurements were taken with decreasing temperature and are shown in Fig. 7. Analogous to the case for CdTe, it appears that liquid Zn is protected from complete reaction with Te by an adhering layer of ZnTe, even when the value of p_{Zn} is well over 1 atm. The spontaneous transition of the surface layers of the sample from a composition in the Te-rich three-phase field to one in the Zn-rich field shows the latter condition to be characteristic of equilibrium for the 49.5 a/o Te sample.

Comparison with Other Work and Further Discussion

Cadmium telluride.—The values of p_2 shown in Fig. 3 for Te-saturated CdTe(c) are considerably below those reported by Lorenz (3), which range from 0.138 atm at 1092°C to 1.2 atm at 1079°C ($10^3/T = 0.740$). The three values reported by de Nobel for $0.786 \leq 10^3/T \leq 0.862$ reach a maximum of 0.168 atm at the lowest temperature but are below ours by 9-50%.

The three liquidus points obtained here for CdTe are close to those of Lorenz and those of Steininger *et al.* (4) as can be seen in Table II. Thus the liquidus temperatures given by Kulwicki (2) for this range of composition appear to be too high and the existence of an inflection point in the Te-rich liquidus is given support.

The activity coefficient for Te was calculated along the Te-rich liquidus using the values of p_2 in Table I and a smooth liquidus curve through the combined points from the present study, from the work of Lorenz, and from that of Steininger *et al.* The activity coefficient is already 0.80 at 60 a/o Te and is close to 1.0 between 80 and 100 a/o Te. The activity coefficient for Cd along the Te-rich liquidus can be obtained from the measured values of p_2 by taking $p_{Cd}p_2^{1/2} = K(T)$ as given by Eq. 8 of ref. (19) and shown here by the line in Fig. 4. This activity coefficient is 10^{-2} at 57 a/o Te, 10^{-3} at 78 a/o, and $2.4(10^{-4})$ at 91 a/o. Thus the behavior of Te in the melt is very nearly ideal between 80 and 100 a/o Te while that of Cd is far removed. Inspection of the "heat-of-fusion" liquidus equation (21) shows that it must be this nonideal behavior of Cd that is primarily responsible for the unusual Te-rich liquidus. As can be calculated from the values in Table II, the excess enthalpy and entropy of Te are about comparable in their contributions toward reducing the chemical potential of Te in melts in the 55-65 a/o Te range. At the maximum melting point of 1092°C both activity coefficients are 0.10.

Medvedev *et al.* (22) have determined p_2 over single crystals of CdTe by measuring the optical density at 4357Å using an optical cell at 815°C. From calibration experiments on pure Te they obtained the relation, $p_2 = 0.304\ D_{4357}/L(\text{mm})$. [For this same proportionality constant we had obtained values of 0.254 for a 755°C optical cell (11) and 0.320 for a 1000°C optical cell (8). Using our numbers the product of the proportionality constant and the reciprocal of the absolute optical cell temperature times 10^3 is 0.247 for a 755°C cell and 0.251 for a 1000°C cell, *i.e.*, the product is constant within experimental error. Thus in this temperature range the dependence of the proportionality constant on optical cell temperature is essentially through the reciprocal dependence of $Te_2(g)$ concentration on optical cell temperature, the product of the probability for the 4357Å transition and the fraction of $Te_2(g)$ molecules in the initial state for the 4357Å transition remaining constant. Taking an average value of 0.249 for the product, we calculate the proportionality constant is 0.271 for a 815°C optical cell. The value found by Medvedev *et al.* is only 12% higher.] Their values of p_2 for a high resistivity, near intrinsic crystal and for a strongly n-type crystal are parallel to our value of p_2 for congruently subliming CdTe(c) as shown in Fig. 3, but are higher by factors of 2.4 and 4.6, respectively. They believe a discrepancy exists and attribute it to our use of a coarse powder and/or inhomogeneities in a powder whose physicochemical properties are ill-defined. In disagreement, we see no obvious reason to conclude that the two sets of data are necessarily inconsistent. They merely show that the composition of our sample was more Cd-rich than that of either of the samples used by Medvedev *et al.* Further, the thermodynamic state of our sample was well defined at the temperatures of measurement since it was shown experimentally that the relation $p_{Cd} = 2p_2$ held. That is, the sample was shown to possess the congruently subliming composition, a unique composition at each temperature even if unknown in terms of atomic per cent or net electron concentration.

The present measurements allow upper limits to be placed on the change in the Gibbs free energy of CdTe(c), ΔG_f, in going from the congruently subliming composition to either that for Cd-saturation or that for Te-saturation at a given temperature. For any composition within the homogeneity range

$$\Delta G_f = (1 - x)RT \ln p_{Cd} + (x/2)RT \ln p_2 \qquad [2]$$

The ratio of p_2 for any two compositions can be related to that for p_{Cd} by an integration of the Gibbs-Duhem relation. Without knowing the detailed dependence of either partial pressure on x, the integration cannot be performed exactly. However, using the fact established here that $0.49 \leq x \leq 0.505$, for all compositions within the CdTe(c) homogeneity range, upper and lower limits can be obtained for the integral involved (7), giving the following inequalities

$$1.041 \ln (p'_{Cd}/p''_{Cd}) \geqq \tfrac{1}{2} \ln (p'_2/p''_2) \geqq 0.9801 \ln (p'_{Cd}/p''_{Cd}) \qquad [3]$$

Thus, if the prime refers to Cd-saturation and the double prime to the congruently subliming composition, then the one unmeasured partial pressure, p'_2, can be bracketed by using Eq. [3]. Upper limits for the difference in ΔG_f for these two compositions can then be calculated by taking $x' = 0.490$ and $x'' = 0.505$. A similar procedure can be followed in comparing Te-saturated and congruently subliming CdTe(c), in which case p''_{Cd} for Te-saturated CdTe is the unknown partial pressure and is bracketed by using Eq. [3]. A maximum value for the difference in ΔG_f for congruently subliming and Te-saturated CdTe is then ob-

tained by taking $x' = 0.490$ for the former and $x'' = 0.505$ for the latter. The result of both calculations is that at 900°C, ΔG_f for both Cd-saturated CdTe and for Te-saturated CdTe are within 150 cal/g-atom of that for congruently subliming CdTe(c). Since the value of p_{Cd} drops by a factor of 20 in going from the Cd-saturated to the congruently subliming composition, this demonstrates the very large curvature in the dependence of ΔG_f on x that is customarily assumed for compounds with a narrow homogeneity range.

Zinc telluride.—The lower line without points in Fig. 6 has been identified here as p_2 for congruently subliming ZnTe(c). Although it was shown (6) that this line gave p_2 for the ZnTe(c) composition in equilibrium with a stoichiometric vapor (50 a/o), the steady state achieved on progressive sublimation with increasing temperature was characterized by a value of 1.8 for the ratio, $R = p_{Zn}/p_2$, rather than the value of 2.0 expected for congruent sublimation. The value for R was based on optical density calibrations with the pure elements which used published values for the vapor pressure of Te (9, 10) and those tabulated by Hultgren *et al.* (23) for Zn just above its melting point. Recently, precision measurements (24) of the vapor pressure of Zn just below its melting point have given values for $p°_{Zn}$ that are higher than those tabulated by Hultgren *et al.* At the melting point the discrepancy is 20% in $p°_{Zn}$. If it is assumed that the tabulated values of $p°_{Zn}$ are also low by 10-20% in the 420°-520°C temperature range, then the corrected value for R is in the range 1.98-2.16. Within the experimental error of ± 0.1 in R, the steady state observed earlier with ZnTe(c) then corresponds to congruent sublimation.

Since we have established that the homogeneity range for ZnTe(c) must be within the 49.5 to 50.5 a/o Te range, outer limits for the change in ΔG_f with composition can be calculated from the present partial pressure measurements in the manner analogous to that used for CdTe(c) and discussed above. It is found that at 900°C the ΔG_f values for both Zn-saturated and Te-saturated ZnTe are within 190 cal/g-atom of that for congruently subliming ZnTe(c). In contrast, based on the measurements reported here, the chemical potential of Zn increases by 13,700 cal/g-atom in going from congruently subliming to Zn-saturated ZnTe(c) and the chemical potential of Te increases by 6300 cal/g-atom in going from congruently subliming to Te-saturated ZnTe(c). We, therefore, have experimental verification for an extremely strong curvature of the Gibbs free energy isotherm for ZnTe(c) as well as CdTe(c). Finally, with the above outer limits for the ZnTe(c) homogeneity range, the standard Gibbs free energy for formation of ZnTe(c) given by Eq. 8 of ref. (19) is changed by less than 1% if the composition dependent term, C, is set equal to zero.

Acknowledgment

The author takes pleasure in acknowledging the capable experimental assistance of Mr. R. N. Capes. He also wishes to express his thanks to Marquette University for providing the facilities to complete this paper. The work reported in this paper was sponsored by the Department of the Air Force.

Manuscript submitted April 7, 1971; revised manuscript received *ca.* July 30, 1971.

Any discussion of this paper will appear in a Discussion Section to be published in the June 1972 JOURNAL.

REFERENCES

1. D. de Nobel, *Philips Res. Repts.*, **14**, 361 (1959).
2. B. M. Kulwicki, Ph.D. Dissertation, University of Michigan (1963).
3. M. R. Lorenz, *J. Phys. Chem. Solids*, **23**, 939 (1962).
4. J. Steininger, A. J. Strauss, and R. F. Brebrick, *This Journal*, **117**, 1305 (1970).
5. F. T. J. Smith, *Metal Trans.*, **1**, 617 (1970).
6. R. F. Brebrick, *This Journal*, **116**, 1274 (1969).
7. R. F. Brebrick and A. J. Strauss, *J. Chem. Phys.*, **40**, 3230 (1964).
8. R. F. Brebrick, *ibid.*, **49**, 2584 (1968).
9. L. S. Brooks, *J. Am. Chem. Soc.*, **74**, 227 (1952).
10. A. A. Kudrysavtsev and G. P. Ustygov, *Russ. J. Inorg. Chem. (English Transl.)*, **6**, 1227 (1961).
11. R. F. Brebrick, *J. Phys. Chem.*, **72**, 1032 (1968).
12. H. Kuhn and K. Freudenberg, *Z. Phys.*, **76**, 38 (1932).
13. R. F. Brebrick and A. J. Strauss, *J. Phys. Chem. Solids*, **26**, 989 (1965).
14. F. L. Mohler and H. R. Moore, *J. Opt. Soc. Am.*, **15**, 74 (1927).
15. D. R. Stull and G. C. Sinke, "Thermodynamic Properties of the Elements," American Chemical Society, Washington, D. C. (1956).
16. W. van Gool, *Proc. Koninkl. Ned. Akad. Wetensch.*, **B66**, 209 (1963).
17. H. Kuhn, "Atomic Spectra," p. 395, Academic Press, New York (1962).
18. S. Brodersen, *J. Opt. Soc. Am.*, **43**, 877 (1953).
19. R. F. Brebrick and A. J. Strauss, *J. Phys. Chem. Solids*, **25**, 1441 (1964).
20. R. F. Brebrick, "Progress in Solid State Chemistry," Vol. III, p. 244, H. Reiss, Editor, Pergamon Press, Oxford and New York (1966).
21. L. J. Vieland, *Acta. Met.*, **2**, 137 (1963).
22. S. V. Medvedev, B. D. Kopylovskiy, and N. N. Sentyurina, "Cadmium Telluride," pp. 19-24, Nauka Press, Moscow (1968).
23. R. Hultgren, R. L. Orr, P. O. Andersen, and K. K. Kelley, "Selected Values of Thermodynamic Properties of Metals and Alloys," John Wiley and Sons, Inc., New York (1963).
24. J. R. McCreary and R. J. Thorn, *J. Chem. Phys.*, **50**, 3752 (1969).

Some Stability Considerations in Levitation Melting

Edward S. Bocian, Jr.,[1] and Frederick J. Young[2]

Department of Electrical Engineering, Carnegie-Mellon University, Pittsburgh, Pennsylvania 15213

ABSTRACT

Two types of instabilities are considered. First a circuit model for a levitation system is used to form linearized equations for the vertical motions of suspended metal samples. The basic inductive-resistive circuit model is dynamically stable, but capacitance in the circuit of the supporting coil can account for the self-oscillations of some practical levitation setups. Next, for an idealized coil arrangement, and in the case of negligible skin depth within a suspended molten sample, an upper bound on the mass of the sample is deduced. This result is a simple function of the metal density and surface tension, and of the order of 10g in favorable instances. Since the purely static considerations in this calculation yield an upper mass limit below what some investigators have tried to melt in levitation experiments, this model explains the rupture of such drops without resort to dynamic models of surface oscillations.

Levitation melting was first proposed in 1923 by Muck (1). The basic apparatus, derived from a simple transformer, uses a primary coil but substitutes a conducting sample for the secondary. An a-c coil current induces currents within the sample; there is a corresponding ohmic dissipation and, if the geometry is asymmetric, a net force between coil and sample. Combining these effects a levitation melting system can supply enough heat to melt a metallic sample, while the resultant electromagnetic force exactly balances its weight, and no mechanical support is necessary.

The coil arrangement used to suspend a sample may be a simple toroid, shaped like a nozzle (2), or in a case analogous to a magnetic mirror machine in plasma physics, it may consist of two coils—one below, a smaller one above, the unequal mmf's being necessary to balance the weight of the sample (3). Okress and Wroughton (4, 5), in particular, have experimented with a number of coil designs. Figure 1 shows some of the possibilities.

Levitation melting has been found suitable for casting metal buttons for hardness and corrosion tests, and for metallographic examination (2). An important advantage is that metals with high melting points may be melted out of contact with a crucible, preventing contamination by a refractory (2, 3). To further isolate a sample, a protective atmosphere can be used around reactive specimens (2, 4, 5). The system permits the addition of alloying ingredients while a sample is suspended, and then provides continuous agitation of the melt, insuring a homogeneous ingot (2, 3).

In actual practice, however, levitation is easier to achieve for solid than for molten samples, and instabilities can occur in either case. These unstable situations can be grouped roughly into three classes, though combinations of these mechanisms are certainly possible:

(*A*) A lateral drift of a sample, which continues until it is out of the influence of the coils and falling (3-5).

(*B*) A second gross instability of the suspension, in which the entire sample commences a growing vertical oscillation, leading to its eventual ejection, most likely straight down through the supporting coil (3, 6).

(*C*) A phenomenon limited to the liquid state, or perhaps to semimolten samples, in which surface ripples develop and culminate in a rupture of the suspended drop. The liquid pours down through the coil,

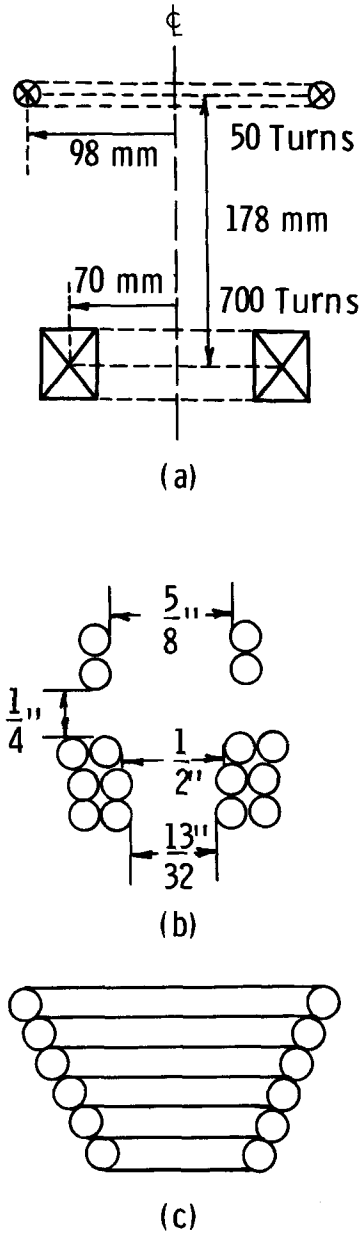

Fig. 1. Some experimental levitation coils; (a) used at 50 Hz by Mikel'son (3,6); (b) at 0.5 MHz by Weisberg (9); and (c) near 10 KHz by Okress (4), (5). The latter two employ ¼ in. OD copper tubing for the coils.

[1] Present address: Air Force Weapons Laboratory, Albuquerque, New Mexico 87103.

[2] Present address: Westinghouse Research Laboratory, Pittsburgh, Pennsylvania 15230.

Key words: electromagnetic levitations, surface stability.

usually near the axis where the induced current in the sample vanishes (3, 4).

The introduction of a restoring force towards the coil axis can prevent lateral drift. Several investigators (3, 6, 7) have found that a small stabilizing coil positioned above a suspended sample, and carrying current opposite in direction to that in the main coil, effectively solves this problem.

Remedies for the remaining instabilities, and the failure mechanisms themselves, are not so well understood. Kirko and Mikel'son (6) who have proposed a circuit model to explain vertical oscillation, conclude that operation of a levitation system above a certain frequency of excitation leads to instability, but later (3) successfully pass this limit with a high-frequency coil setup.

There are qualitative theories for the rupture of suspended liquid drops (3), but no means of predicting quantitatively how large a mass may be suspended in stable equilibrium. Most experimenters (3-5, 8) have noted such limitations in mass for their particular apparatuses, and both Polonis (2) and Weisberg (9) have recorded the suspicion that this limitation should be implicit in the system, and some function of mass density and surface tension.

This paper is concerned with supplying models for both unstable vertical oscillations of a suspended sample, and for the maximum mass of a molten specimen in stable suspension.

Vertical Stability of a Suspension

Like Kirko and Mikel'son (6) consider two coaxial inductors, one supported electromagnetically by the other, as a simple model for a levitation system (see Fig. 2). The lower coil is stationary; the upper restricted, by the coil form, to vertical motion. Reference directions are indicated. L_1, L_2, and M are self and mutual inductances, R_1 and R_2 coil resistances, V the applied voltage, and z_o the equilibrium co-ordinate of L_2. Write the circuit equation

$$L_1 \frac{dI_1}{dt} + R_1 I_1 + \frac{d}{dt}(MI_2) = V(t) \qquad [1]$$

$$L_2 \frac{dI_2}{dt} + R_2 I_2 + \frac{d}{dt}(MI_1) = 0 \qquad [2]$$

$$M = M_o - \beta(z - z_o) \qquad [3]$$

where M_o is the mutual inductance of the two coils at their equilibrium separation z_o, and the geometric parameter β specifies, to a linear approximation, the change of M with z. β is positive.

Next the equation of motion for the upper coil may be written

$$m\frac{d^2z}{dt^2} + r\frac{dz}{dt} = F_{sus}\left(z, \frac{dz}{dt}\right) - mg \qquad [4]$$

in terms of its mass m, some damping r, the gravitational constant g, and the electromagnetic force F_{sus}. Assuming oscillations of the sample occur at frequencies much lower than that of the excitation voltage, consider z and dz/dt as constants in the electrical equations. Using phasors $V(t) = Re\{\underset{\sim}{V}\, e^{j\omega t}\}$, these may be solved for the currents

$$\underset{\sim}{I}_1 = \frac{\underset{\sim}{V}(R_2 + L_2 j\omega)}{\left[(R_1 + L_1 j\omega)(R_2 + Lj\omega) - \left(Mj\omega - \beta\frac{dz}{dt}\right)^2\right]} \qquad [5]$$

$$\underset{\sim}{I}_2 = \frac{-\underset{\sim}{V}\left(Mj\omega - \beta\frac{dz}{dt}\right)}{\left[(R_1 + Lj\omega)(R_2 + Lj\omega) - \left(Mj\omega - \beta\frac{dz}{dt}\right)^2\right]} \qquad [6]$$

Now represent the electromagnetic force of suspension

$$F_{sus}\left(z, \frac{dz}{dt}\right) = \frac{k}{2} Re\{\underset{\sim}{I}_1 \underset{\sim}{I}_2{}^*\} \qquad [7]$$

with k a second geometric parameter. The asterisk denotes a complex conjugate. In static equilibrium

$$F_{sus}(z_o, 0) = mg = -\frac{k}{2}\frac{V^2\omega^2 L_2 M_o}{[R_1R_2 - \omega^2 L_1L_2 + \omega^2 M_o{}^2]^2 + [R_1L_2\omega + R_2L_1\omega]^2} \qquad [8]$$

and k is obviously negative for this equality to hold. Equation [8] shows the expected behavior at frequency extremes: $F_{sus} \to 0$ as $\omega \to 0$ and as $\omega \to \infty$ unless there is perfect coupling, $L_1L_2 = M_o{}^2$, in which case F_{sus} remains finite in the limit as $\omega \to \infty$.

In the more general dynamic case, the force expression is

$$F_{sus}\left(z, \frac{dz}{dt}\right) = \frac{-\frac{k}{2}V^2\left(\omega^2 L_2 M - R_2\beta\frac{dz}{dt}\right)}{\left[R_1R_2 - \omega^2L_1L_2 + \omega^2M^2 - \beta^2\left(\frac{dz^2}{dt}\right)\right]^2 + \left(R_1L_2\omega + R_2L_1\omega + 2M\omega\beta\frac{dz}{dt}\right)^2} \qquad [9]$$

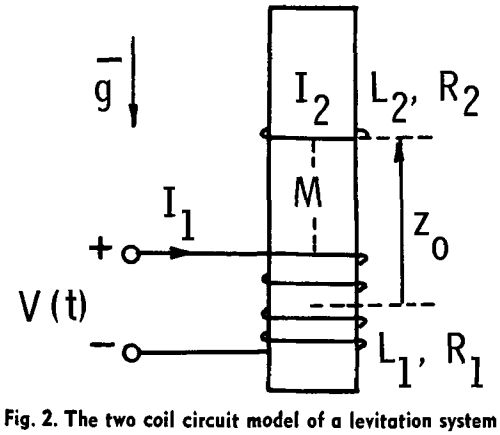

Fig. 2. The two coil circuit model of a levitation system

Since this formulation is valid, and principally of interest, for small departures from equilibrium, expand F_{sus} in a two-parameter Taylor series about the point $\left(z, \frac{dz}{dt}\right) = (z_o, 0)$, and truncate the result to exclude products of perturbations.

$$F_{sus}\left(z, \frac{dz}{dt}\right) \cong F_{sus}(z_o, 0) + (z - z_o)\left.\frac{\partial F_{sus}}{\partial z}\right|_{z_o} + \frac{dz}{dt}\left.\frac{\partial F_{sus}}{\partial \frac{dz}{dt}}\right|_{(z_o,0)} \qquad [10]$$

Use Eq. [9] to evaluate

$$\left.\frac{\partial F_{sus}}{\partial \frac{dz}{dt}}\right|_{(z_o,0)} = \frac{\frac{k}{2}\beta V^2}{\left\{(R_1R_2 - \omega^2L_1L_2 + \omega^2M_o^2)^2 + (R_1L_2\omega + R_2L_1\omega)^2\right\}} \left\{R_2 + \frac{4M_o^2\omega^4L_2(R_1L_2 + R_2L_1)}{(R_1R_2 - \omega^2L_1L_2 + \omega^2M_o^2)^2 + (R_1L_2\omega + R_2L_1\omega)^2}\right\} \quad [11]$$

Since $k < 0$, this entire expression is negative. In general, k is a function of z so $\partial F_{sus}/\partial z|_{(z_o,0)}$ is not available explicitly here. It must be obtained from a measured or calculated force curve, such as that in Fig. 3, obtained for a spherical sample and a simple toroid of N turns, modeled as a loop of vanishing cross section. Coil radius r_c, and the separation distance z_o of the sphere and coil centers are conveniently normalized with division by the sphere radius R_s.

Substituting Eq. [10] into the equation of motion [4] yields

$$m\frac{d^2(z-z_o)}{dt^2} + \frac{d(z-z_o)}{dt}\left\{r - \left.\frac{\partial F_{sus}}{\partial\left(\frac{dz}{dt}\right)}\right|_{(z_o,0)}\right\} + (z-z_o)\left\{-\left.\frac{\partial F_{sus}}{\partial z}\right|_{(z_o,0)}\right\} = 0 \quad [12]$$

Because of the sign associated with $\left.\frac{\partial F_{sus}}{\partial \frac{dz}{dt}}\right|_{(z_o,0)}$ in Eq. [11], the coefficient of velocity is always positive. If $\left.\frac{\partial F_{sus}}{\partial z}\right|_{(z_o,0)} < 0$ as it is for z_o/R_s beyond the peaks of the force curves in Fig. 3, the equilibrium at $z = z_o$ is stable; otherwise it is unstable. The coefficient of velocity in Eq. [12] does not change sign with increasing frequency, so this resistive-inductive model does not predict unstable motions where $\left.\frac{\partial F_{sus}}{\partial z}\right|_{(z_o,0)} < 0$ (10).

The introduction of a series capacitor C_1 into the primary modifies Eq. [5], [6], [9] and [11] as follows

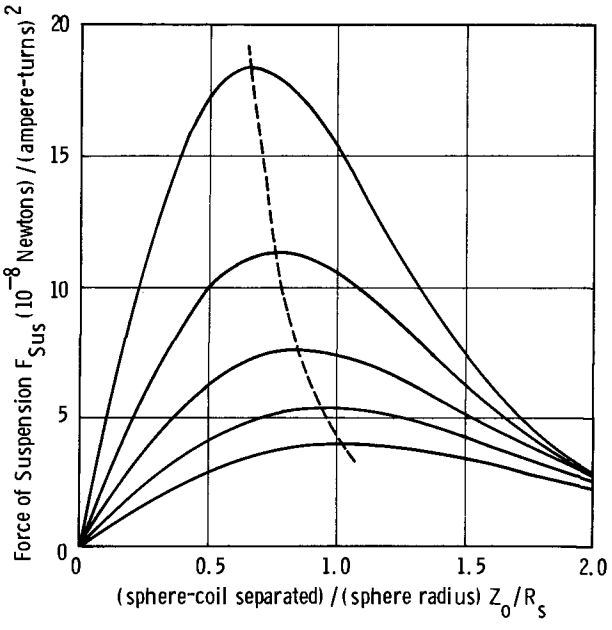

Fig. 3. Force of suspension is plotted vs. the separation of sphere and coil centers for a skin depth $R_s/32$, and in descending order of force magnitudes for r_c/R_s = 1.50, 1.75, 2.00, 2.25, 2.50. The dotted line denotes the limit of stable suspension.

$$\underset{\sim}{I_1} = \frac{\underset{\sim}{V}(R_2 + L_2j\omega)}{\left((R_1R_2 - \omega^2L_1L_2 + \omega^2M^2 + L_2/C_1 - \beta^2\left(\frac{dz}{dt}\right)^2\right) + \left(R_1L_2j\omega + R_2L_1j\omega + 2j\omega M\beta\frac{dz}{dt} + R_2/C_1j\omega\right)} \quad [13]$$

$$\underset{\sim}{I_2} = \frac{-\underset{\sim}{V}\left(j\omega M - \beta\frac{dz}{dt}\right)}{\left(R_1R_2 - \omega^2L_1L_2 + \omega^2M^2 + L_2/C_1 - \beta^2\left(\frac{dz}{dt}\right)^2\right) + \left(R_1L_2j\omega + R_2L_1j\omega + 2j\omega M\beta\frac{dz}{dt} + R_2/C_1j\omega\right)} \quad [14]$$

$$F_{sus}\left(z, \frac{dz}{dt}\right) = \frac{-\frac{k}{2}V^2\left(\omega^2L_2M - R_2\beta\frac{dz}{dt}\right)}{\left(R_1R_2 - \omega^2L_1L_2 + \omega^2M^2 - \beta^2\left(\frac{dz}{dt}\right)^2 + L_2/C_1\right)^2 + \left(R_1L_2\omega + R_2L_1\omega + 2\omega M\beta\frac{dz}{dt} - \frac{R_2}{C_1\omega}\right)^2} \quad [15]$$

$$\frac{\partial F_{sus}}{\partial\left(\frac{dz}{dt}\right)_{(z_o,0)}} = \frac{k}{2}\beta V^2 \frac{\left\{R_2 + \frac{4\omega^3L_2M_o^2(R_1L_2\omega + R_2L_1\omega - R_2/C_1\omega)}{[(R_1R_2 - \omega^2L_1L_2 + \omega^2M_o^2 + L_2/C_1)^2 + (R_2L_1\omega + R_1L_2\omega - R_2/C_1\omega)^2]}\right\}}{[(R_1R_2 - \omega^2L_1L_2 + \omega^2M_o^2 + L_2/C_1)^2 + (R_1L_2\omega + R_2L_1\omega - R_2/C_1\omega)^2]} \quad [16]$$

and, if C_1 is too small, the second term in the numerator may be negative. If the entire expression $\left.\frac{\partial F_{sus}}{\partial\left(\frac{dz}{dt}\right)}\right|_{(z_o,0)}$ is positive, self-oscillations occur and the suspension is unstable. This certainly cannot happen for $\omega^2 > \frac{R_2}{C_1(R_1L_2 + R_2L_1)}$, but the details of the frequency dependence of the damping coefficient are a function of the particular levitation circuit parameters.

Note that Eq. [12] specifies the undamped natural frequency of these oscillations as

$$\omega_{Mech} = \sqrt{-\frac{1}{m}\left.\frac{\partial F_{sus}}{\partial Z}\right|_{(Z_o,0)}}$$

which should be considerably less than ω for these equations to be valid. ω_{Mech} is, of course, a function of

the choice of equilibrium coordinate Z_o—again refer to Fig. 3 for an example.

Levitation of a Molten Sample

In practical applications of levitation melting, perhaps the most significant remaining unknown is the maximum size of a melt for which stable suspension is possible. The literature contains qualitative dynamic theories based on instabilities of a conducting surface in a magnetic field, and subject to perturbations in shape (3, 6). This section shows that an upper mass limit can be derived from purely static considerations, under certain restrictions, and that this mass limit is a function of the ratio ρ/σ_s of liquid metal mass density to surface tension.

First assume that the skin depth in a suspended metal sample is sufficiently small—the frequency of excitation is sufficiently large—so that the electromagnetic force of suspension is concentrated at the surface of the drop. This is certainly valid for experiments performed near 0.5 MHz (8, 9), and is a good approximation over a considerable range of lower frequencies. Then the electromagnetic force is the resultant of a magnetic pressure distribution, exerted on the surface of the drop, and directed normal to the surface at each point. The equation

$$\sigma_s\left\{\frac{-\frac{d^2r}{dh^2}}{\left[1+\left(\frac{dr}{dh}\right)^2\right]^{3/2}}+\frac{1}{r\left[1+\left(\frac{dr}{dh}\right)^2\right]^{1/2}}\right\}+\frac{B^2_{rms}}{2\mu_o}=\frac{2\sigma_s}{b}+\rho gh \quad [17]$$

describes the surface of such a drop in the coordinate system of Fig. 4. b is the radius of curvature at the top of the drop, B_{rms} the local magnetic field, and g the gravitational acceleration. In equilibrium, the drop has an axis of symmetry in common with the supporting coil system. Equation [17] is essentially a pressure balance: the pressure rise through the liquid surface at any height is equated to this same pressure rise through the top of the drop—where the magnetic field is zero with any axisymmetric coil system—plus the additional pressure of the standing liquid. The expressions in the large brackets are inverse principal radii of curvature of the liquid surface (11).

Equilibrium requires

$$F_{sus}=mg=2\pi\int_0^{h_{bot}}\frac{B^2_{rms}}{2\mu_o}\left(\frac{-dr}{dh}\right)dh \quad [18]$$

since the surface tension integrated over the surface of the drop contributes no net vertical force.

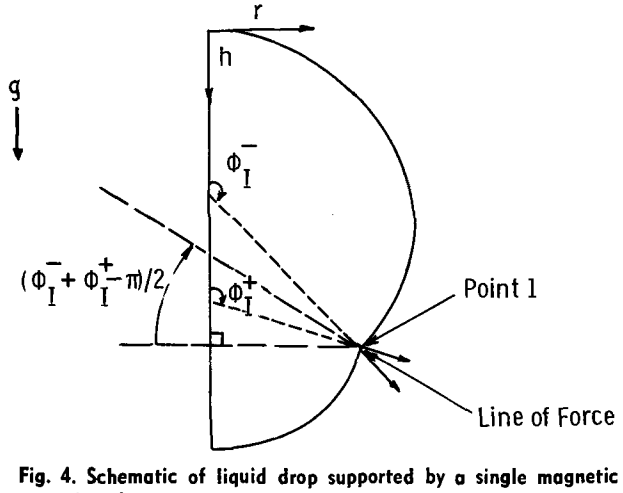

Fig. 4. Schematic of liquid drop supported by a single magnetic pressure impulse.

No analytic solution is known to Eq. [17] without the magnetic pressure term. Bashforth and Adams (11) considered numerical solutions to this simplified version in 1883. The complexity of simultaneous electromagnetic field and surface equation solutions may be circumvented by a second approximation. Model a coil system like the one in Fig. 1(a) with a single wire loop, of negligible cross section, and position it arbitrarily close to the surface of the drop. Then the electromagnetic force of suspension may be modeled as a delta function of force per unit length at a single cross-sectional point—the point of closest approach of coil to drop—and the situation is completely analagous to the purely mechanical problem of supporting a liquid drop with a fine wire ringstand (see Fig. 4).

With F the force per unit length due to the ring—a linear pressure—the surface Eq. [17] may be written

$$\frac{d\phi}{dS}+\frac{\sin\phi}{r}=\frac{2}{b}+\frac{\rho gh}{\sigma_S}-\frac{F}{\sigma_S}\delta(S-S_I);F>0 \quad [19]$$

where S is arc length along the surface from the top of the drop, ϕ the angle from the vertical to the outward surface normal ($\phi = 0$ at the top of the drop), and the subscript I denotes the point at which the idealized coil is located. Then the solution for $S \leq S_I$ is identical to that for a sessile drop (11). Integrating Eq. [19] through the ring of force yields

$$\phi(S_I^+)=\phi(S_I^-)-F/\sigma_S \quad [20]$$

The effect of the support is to introduce a discontinuous derivative to the surface curve, and to bend the surface about the supporting loop. On the average, the linear pressure is exerted along a line inclined at an angle midway between $\phi(S_I^+)$ and $\phi(S_I^-)$ since it must balance the surface tension forces at the point of discontinuity. If $\sigma_S \to \infty$, there is no discontinunity.

In an actual drop, waiving the assumption of infinite pressure also eliminates the discontinuity in ϕ, but the surface should undergo a rapid curvature very near the coil. One conclusion remains the same: a magnetic pressure push on the surface of a suspended drop requires the surface to curve outwards from the axis of symmetry.

From geometric considerations in Fig. 4

$$F_{sus}(S_I,F)=-2\pi r_I F\cos\left(\phi_{I-}-\frac{F}{2\sigma_S}\right) \quad [21]$$

and

$$\pi \geq \phi_{I-} > (\pi/2+F/2\sigma_S) \quad [22]$$

The upper limit is imposed by the set of sessile drop solutions, the lower by a requirement that $F_{sus} > 0$.

Now consider extrema of $F_{sus}(S_I,F)$ with respect to F. At $F = F_{MAX}$, and

$$\phi_{I-}=\pi+\frac{F_{MAX}}{2\sigma_S}-\sin^{-1}\left\{\frac{1}{\sqrt{1+\left(\frac{F_{MAX}}{2\sigma_S}\right)^2}}\right\} \quad [23]$$

the vertical force attains the maximum value

$$F_{sus}(S_I,F_{MAX})=\frac{4\pi\sigma_S r_I\left(\frac{F_{MAX}}{2\sigma_S}\right)^2}{\sqrt{1+(F_{MAX}/2\sigma_S)^2}} \quad [24]$$

If the vertical force of the ring is to support such a drop

$$mg=F_{sus}(S_I,F)\leq F_{sus}(S_I,F_{MAX}) \quad [25]$$

The nature of this force maximum is evident from Fig. 4. At $F = 0$, there is no vertical force; as F is increased, so is F_{sus}, but for larger and larger F, the net force on the drop is applied progressively nearer the horizontal, because of the discontinuity it induces in the surface direction; consequently F_{sus} decreases towards zero.

Next note that the weight of the entire drop must exceed that of the portion of the drop above the ring

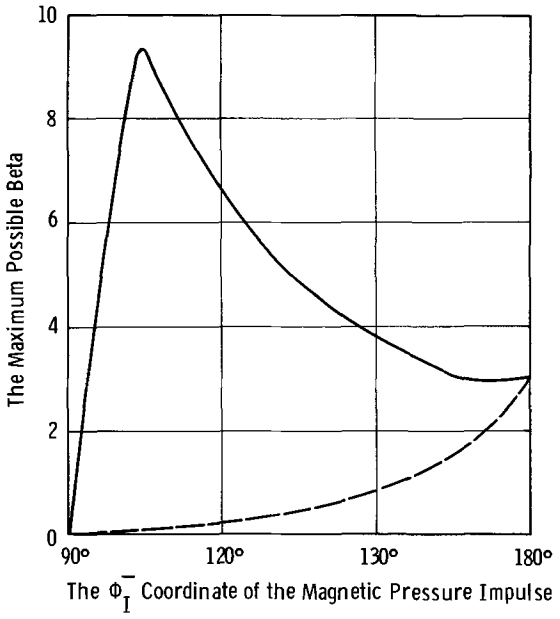

Fig. 5. The maximum β for static equilibrium: The solid line is the result for an infinite series of magnetic pressure impulses, the dotted line for a single magnetic pressure ring.

of magnetic pressure—a quantity available from sessile drop solutions which may be expressed parametrically as

$$\rho g V(\beta, b, \phi_I-) < mg \qquad [26]$$

where $\beta = \rho g b^2/\sigma_s$ is the parameter specifying the shape of a sessile drop (11). Combining this restriction with Eq. [24], [25], and sessile drop solutions produces a restriction $\beta < \beta_{max}(\phi_I-)$. This result is plotted as a dotted line in Fig. 5. The larger ϕ_I- permits the larger β, and the extremum occurs at $\phi_I- = 180°$, where the maximum permissible β is about 3. For any given liquid metal, a restriction on β is also a restriction on b.

The two bounds on the weight of liquid drop Eq. [25] and [26], in combination with the information $\beta_{max}(\phi_I-)$ in Fig. 5 yield numerical results

$$mg < 6.5\sqrt{\frac{\sigma_s^3}{\rho g}} \quad \text{or Volume} < 6.5\left(\frac{\sigma_s}{\rho g}\right)^{3/2} \qquad [27]$$

considered over the set of allowable sessile drop solutions.

The results, Eq. [25], are derived for a situation in which the magnetic pressure distribution is distinctly localized on the surface of the suspended drop.

To account for the distributed magnetic pressure expected in many small scale practical experiments, where the sample is small compared to the spatial extent of the supporting coil, some changes in this model are necessary.

One expedient is to model the magnetic pressure distribution with a sum of pressure impulses of the sort already described. Using an infinite sequence of such impulses, each applied at the same angle ϕ_I- (available after the drop surface has "recovered" from the previous impulse) leaves F_{MAX} unchanged. Under these conditions, the weight of a suspended drop may again be bounded

$$mg < 11.2\left(\frac{\sigma_s^3}{\rho g}\right); \quad \text{Volume} < 11.2\left(\frac{\sigma_s}{\rho g}\right)^{3/2} \qquad [28]$$

These are of the same form as Eq. [27] and again are extrema over the set of permissible combinations of β and ϕ_I-. The upper curve in Fig. 5 is the modified value $\beta_{max}(\phi_I-)$.

Table I summarizes the results of Eq. [28] for some metal elements and compares these calculations with some experimental data on small drops successfully melted in levitation. The largest entry of the calculated masses is some 13g for vanadium. It should be noted that the limitations, Eq. [27] and [28], can be temperature sensitive, and do not apply to only partially molten samples, or to samples with surface crusts due to oxidation or cooling by radiation.

Table I. The minimum mass of a levitated molten metal at its melting point

Element	Calculated mass, g	Experimental masses	References
Ag	3.2	4.5	(8)
Al	5.9	6, 10	(8), (4)
Au	1.1	4.5	(8), (9)
Co	10.7	8-12	(8)
Cr	9.1	8-12	(8)
Cu	5.9	8-12	(8)
Fe	11.4	near 5, 8-12	(2), (8)
Ga	2.9	4.5	(9)
In	1.8	4.5	(9)
Mo	11.7	13.5	(8)
Nb	10.8	13.5	(8)
Ni	9.8	near 5, 8-12	(2), (8)
Pb	1.1	less than 4.5	(9)
Pt	6.1	—	—
Sb	1.1	4.5	(9)
Sn	1.9	—	—
Ta	10.1	—	—
Ti	12.1	8, 8-12	(2), (8)
W	10.3	—	—
V	13.4	—	—
Zn	8.1	8-12	(8)

Conclusions

Instabilities resulting from vertical motions of a suspended metal sample should be attributed to the presence of impedance-matching capacitors in the coil circuit, or to capacitance in the output circuit of the power supply, rather than to the resistive and inductive circuit elements contributed by the coil arrangement and sample. Kirko and Mikel'son (6) reach the contrary conclusion only after several sign inversions and ignoring portions of the derivatives, Eq. [11] and [16].

The twin assumptions that: (*A*) a surface magnetic pressure distribution adequately accounts for the electromagnetic field distributions near a suspended drop, and (*B*) the supporting coil is reasonably modeled as a loop of negligible cross section placed very near the suspended sample require, for mechanical equilibrium, that a suspended liquid drop weigh less than an amount specified by its particular surface tension and density. A simple extension of this model, waiving the second assumption, leads to a similar formulation for this upper bound on the mass of a sample. The two versions are within a factor of two of one another, and predict a mass limit of the order of 10g or less for most metals considered. Further, there is enough accord with experimental data to conclude that requirements of static equilibrium are indeed responsible for the rupture, during melting, of larger specimens.

Manuscript submitted Nov. 16, 1970; revised manuscript received June 7, 1971.

Any discussion of this paper will appear in a Discussion Section to be published in the June 1972 JOURNAL.

REFERENCES

1. O. Muck, German Pat. 422004 (1923).
2. D. H. Polonis, R. G. Butters, and J. G. Parr, *Research*, **7**, 272 (1954).
3. I. M. Kirko, Magnetohydrodynamics of Liquid Metals, translated by Consultants Bureau, New York (1965).
4. E. C. Okress, D. M. Wroughton *et al.*, *J. Appl. Phys.*, **23**, 545 (1952).
5. D. M. Wroughton, E. C. Okress *et al.*, *This Journal*, **99**, 205 (1952).
6. I. M. Kirko and A. E. Mikel'son, translated in "Problems of Magnetohydrodynamics and Plasma Dynamics II," AFSC FTD-TT-62-1301, 587, Wright-Patterson AFB, Ohio (1963).

7. E. R. Laithwaite, "Induction Machines for Special Purposes," Chemical Publishing Co., New York (1966).
8. G. Comenetz and J. W. Salatka, *This Journal*, **105**, 673 (1958).
9. L. R. Weisberg, *Rev. Sci. Instrum.*, **30**, 135 (1959).
10. J. C. West and B. V. Jayavant, *Proc. I.E.E.*, **109(A)**, 292 (1962).
11. F. Bashforth and J. C. Adams, "An Attempt to Test the Theories of Capillary Action," Cambridge University Press (1883).

Technical Notes

Sensitivity of Cholesteric Films to Ultraviolet Exposure

James Adams and Werner Haas*

Xerox Research Laboratories, Webster, New York 14580

The pitch of a mixture of two or more cholesterics can be expressed in terms of an intrinsic property of each. The first insight into this relationship was provided by Friedel (1), who demonstrated that in binary mixtures of one right-handed and one left-handed constituent, there was one ingredient ratio for which the mixture exhibited nematic properties. Furthermore, for other ratios the cholesteric possessed the chirality of the dominant component. Much later, Cano (2, 3) demonstrated that in mixtures of certain cholesterics and nematics, the nematic acted as a passive element, and the influence of the cholesteric was essentially linear in proportion to its concentration.

Recently (4), it was shown that the pitch of two or more cholesterics can be expressed in terms of the linear influence of constituents. Thus, the functional form of pitch *vs.* composition is known for a wide variety of systems. In another recent observation (5), it was found that there is a strong connection between the sensitivity of pitch to certain stimuli, such as temperature, and the sensitivity of pitch to small compositional changes. In fact, it is possible to treat a variety of perturbations as if their effect were to change composition.

In those cases where the functional dependence of pitch on composition is known, it is possible to calculate the functional form for sensitivity to stimulus. We present here an experimental example of this principle. In this case the stimulus actually changes the composition of the cholesteric. The effect studied involves the change in pitch of a cholesteric film resulting from exposure to ultraviolet light (6-9).

Theory

In many mixed systems it has been shown that the pitch of the mixture, p, can be written as[1]

$$p = \left| \frac{1}{\Sigma \alpha_i \theta_i} \right| \qquad [1]$$

where α_i is the weight per cent of the i^{th} ingredient and θ_i is the effective rotary power (ERP) of the i^{th} ingredient (10). An example of a system which follows Eq. [1] over a wide compositional range is shown in Fig. 1. If the individual constituents have opposite chirality, the algebraic signs of the ERP's must be appropriately chosen. In general, the total differential change in pitch, dp, resulting from a change in composition and, simultaneously, a change in ERP caused by a differential stimulus, ds, is

$$\left| \frac{dp}{ds} \right| = \left| \Sigma \left(\frac{\partial p}{\partial \alpha_i} \frac{\partial \alpha_i}{\partial s} + \frac{\partial p}{\partial \theta_i} \frac{\partial \theta_i}{\partial s} \right) \right| \qquad [2]$$

or

$$\left| \frac{dp}{ds} \right| = p^2 \left| \Sigma \left(\theta_i \frac{\partial \alpha_i}{\partial s} + \alpha_i \frac{\partial \theta_i}{\partial s} \right) \right| \qquad [3]$$

subject to the constraint

$$\Sigma \alpha_i = 1 \qquad [4]$$

An example of a perturbation which changes composition is exposure to ultraviolet radiation or chemical vapor (8). In this case, the $\partial \theta_i / \partial s = 0$.

An example of a perturbation which changes only ERP's is heat; in which case, the $\partial \alpha_i / \partial s = 0$.

It is also possible to express the result of, for example, a stimulus which changes only ERP's in terms of an "effective" change in composition. Assume some differential stimulus, ds, actually changes only ERP.

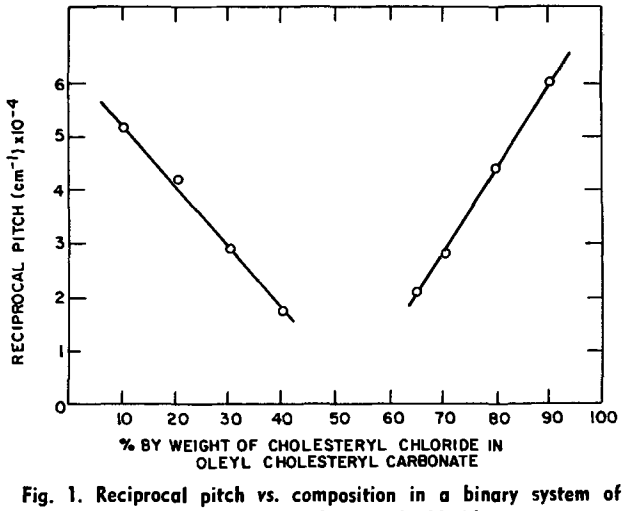

Fig. 1. Reciprocal pitch *vs.* composition in a binary system of oleyl cholesteryl carbonate and cholesteryl chloride.

* Electrochemical Society Active Member.

Key words: liquid crystals, pitch, effective rotary power.

[1] In this discussion we treat pitch as an intrinsically positive quantity and do not attempt to preserve the algebraic sign in derivatives. All calculations, therefore, predict only the magnitude of the system response to stimulus and not the direction. This is indicated by the absolute value signs. It is possible to solve this problem formally; however, the algebra is cumbersome and would obscure the main thrust of this paper.

Then

$$\left|\frac{dp}{ds}\right| = p^2 \left|\Sigma\alpha_i \frac{\partial\theta_i}{\partial s}\right| \qquad [5]$$

If this is treated as a change in composition instead, then

$$\left|\frac{dp}{ds}\right| = p^2 \left|\Sigma\theta_i \left(\frac{\partial\alpha_i}{\partial s}\right)_{\text{eff}}\right| \qquad [6]$$

Evidently,

$$\Sigma\alpha_i \left(\frac{\partial\theta_i}{\partial s}\right) = \Sigma\theta_i \left(\frac{\partial\alpha_i}{\partial s}\right)_{\text{eff}} \qquad [7]$$

In the case of a two-component system Eq. [7] has a unique solution (since $\alpha_2 = 1 - \alpha_1$) given by

$$\left(\frac{\partial\alpha}{\partial s}\right)_{\text{eff}} = \frac{\alpha}{(\theta_1 - \theta_2)}\left(\frac{\partial\theta_1}{\partial s}\right) + \frac{(1-\alpha)}{(\theta_1 - \theta_2)}\left(\frac{\partial\theta_2}{\partial s}\right) \qquad [8]$$

Let us turn now to the specific case of ultraviolet exposure, in which it is known that the actual composition is altered. Assuming that the light-sensitive molecule is the j^{th} species, whenever one of these molecules interacts with the light, it is destroyed and a new species [for example, the $(j + 1)$ species] is created. Evidently,

$$\frac{\partial\alpha_i}{\partial s} = k\alpha_i\left[-\delta_{i,j} + \delta_{i,j+1}\right] \qquad]9]$$

where

$$\delta_{a,b} = 0 \text{ for } a \neq b$$
$$= 1 \text{ for } a = b$$

and k is proportional to the probability of a conversion event.

Substituting into Eq. [3] with the condition that $\partial\theta_i/\partial s = 0$ yields

$$\left|\frac{dp}{ds}\right| = \left|kp^2\alpha_j\,(\theta_{j+1} - \theta_j)\right| \qquad [10]$$

The significance of the terms in Eq. [10] is clear: α_j determines the number of sensitive molecules; $(\theta_{j+1} - \theta_j)$ gives the relative influences of old and new molecules; and p^2 results from the form of Eq. [1]. If more than one species is created by the ultraviolet, it is still possible to characterize the collective role of all new molecules by a single ERP following arguments in Ref. (10). We now present experimental results which show close agreement with Eq. [10].

Experimental

The system chosen for study consisted of binary mixtures of cholesteryl nonanoate (CN) and cholesteryl iodide (CI). Chemicals were obtained from Eastman Kodak and used as received. All measurements were performed at room temperature. The compositional range varied from $\alpha = 25$ to $\alpha = 74$ where α is the per cent by weight of CI in a mixture of CI and CN. Pitch determinations were accomplished by dispersive reflection measurements (11) using a relationship derived by Fergason (12). Pitch *vs.* composition in unexposed films is shown in Fig. 2. In the region of $\alpha \geq 40$ this system is well described by Eq. [1], whereas for $\alpha < 40$ there is a deviation which becomes very strong as α decreases. We believe this relates to the tendency toward smectic of the nonanoate-rich films. This particular system is quite appropriate to our study since it offers a branch where Eq. [9] can be tested quantitatively and also a very anomalous branch which produces both highly sensitive regions ($\alpha \approx 26$) and highly insensitive regions ($\alpha \approx 30$).

The constituents were heated together in a crucible to the isotropic point and thoroughly mixed. An elliptical hole was cut in a two-mil Mylar spacer. The spacer was placed on a glass substrate and an amount of liquid crystal sufficient to fill the elliptical well was deposited in the center of the well. A cover slip was then dragged across the top of the Mylar several times producing a layer of approximately uniform thickness. These films were sufficiently thin to suppress the effect of thickness variation. Detailed absorption coefficient data were not taken; however, the effective coefficient was such that films over about 4 mils in thickness began to show thickness effects, resulting in less total shift for a given exposure, and in addition, the pitch band was broadened.

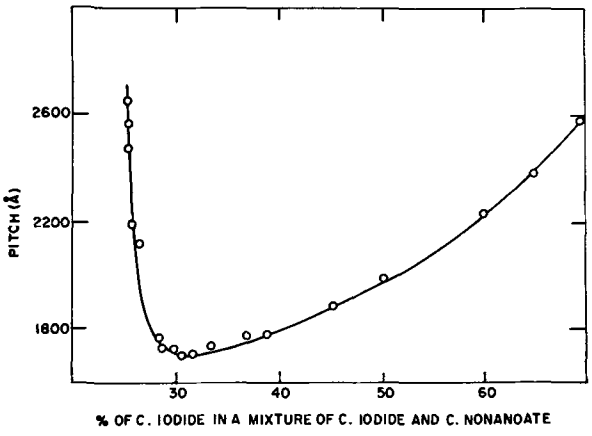

Fig. 2. Pitch *vs.* composition in a binary system of cholesteryl iodide and cholesteryl nonanoate.

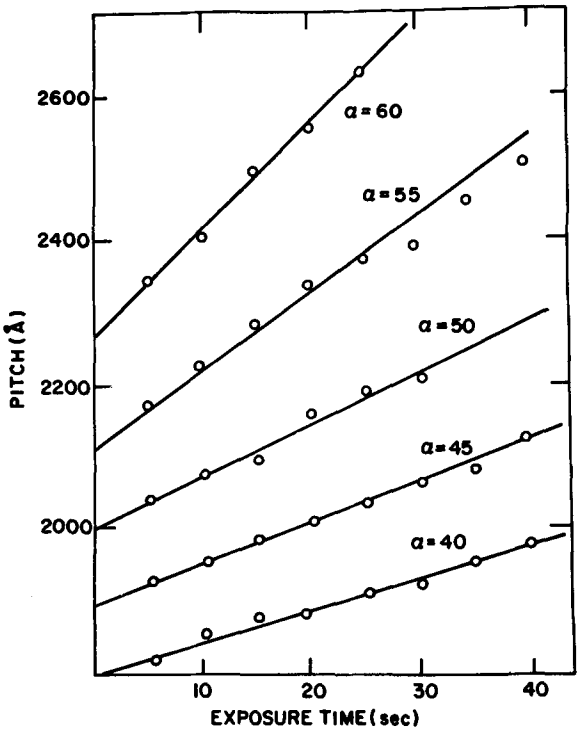

Fig. 3. Pitch *vs.* ultraviolet exposure in the region $dp/d\alpha > 0$

The two-mil films accorded a reproducibility of the order of $\epsilon = 0.1$ where $\epsilon = \delta\lambda/\Delta\lambda$; $\Delta\lambda$ was the pitch shift for a given exposure and $\delta\lambda$, the variation. Films were exposed to ultraviolet light produced by a BH-6 high-pressure, short-arc mercury lamp. Exposure was controlled by a shutter.

The results for several different starting ratios are shown in Fig. 3. The sensitivity is clearly a strong function of composition. A comparison between experimental results and the prediction of Eq. [10] is shown in Fig. 4. The agreement is well within experimental error. Small depletion effects were observed, principally in the region $dp/d\alpha < 0$. The results are shown in Fig. 5. In this case exposure tends to reduce the

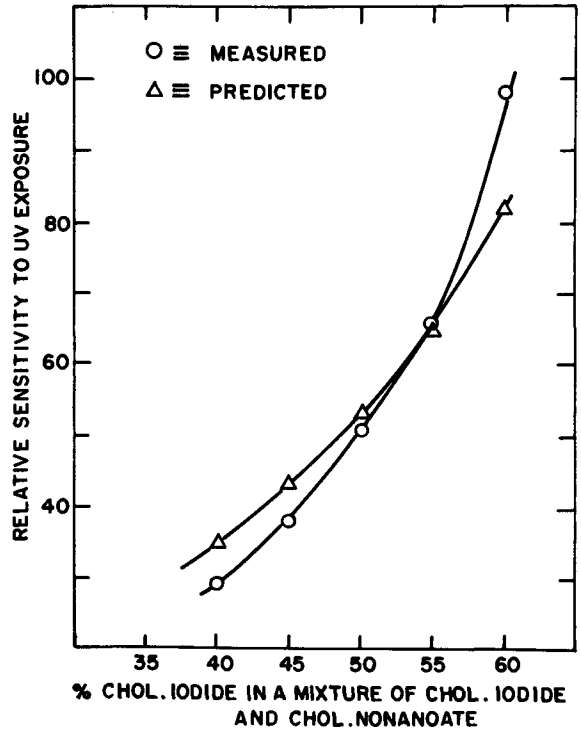

Fig. 4. Comparison of predicted and observed sensitivity

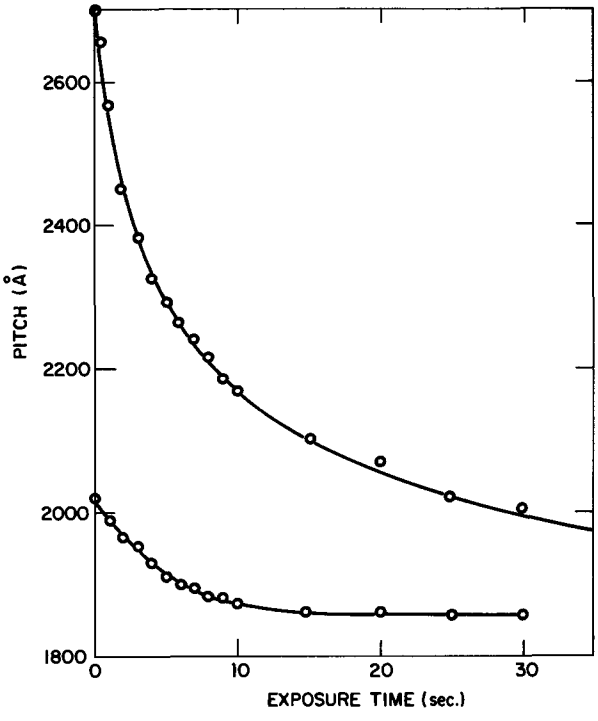

Fig. 5. Pitch vs. ultraviolet exposure in the region $dp/d\alpha < 0$

cholesteryl iodide content of a film and simultaneously shift the film into a region in which it is less sensitive to subsequent exposure. This is due to the shape of the curve in Fig. 3, *i.e.* where $dp/d\alpha < 0$ and $d^2p/d\alpha^2 > 0$. These two effects both decrease sensitivity. However, in the region $dp/d\alpha > 0$, although exposure does deplete cholesteryl iodide content, the film is shifted into a more sensitive composition area and the two effects tend to compensate.

Summary

The response of pitch to a wide variety of stimuli in mixed cholesteric systems can be predicted from compositional data. If the functional form of pitch *vs.* composition for a particular system is known, then it is possible to quantitatively calculate sensitivity. If the functional form is not known, it is still possible to gain qualitative information from the shape of the compositional curves.

Acknowledgment

The authors thank Bela Mechlowitz and David Trost for technical assistance.

Manuscript submitted Feb. 16, 1971; revised manuscript received July 9, 1971. This was Paper 159 presented at the Detroit, Michigan, Meeting of the Society, Oct. 5-9, 1969.

Any discussion of this paper will appear in a Discussion Section to be published in the June 1972 JOURNAL.

REFERENCES

1. G. Friedel, *Ann. Phys. (Paris)*, **18**, 274 (1922).
2. R. Cano and P. Chatelain, *Compt. Rend.*, **253**, 1815 (1961).
3. R. Cano, *Bull. Soc. Fran. Mineral. Crist.*, **90**, 333 (1967).
4. J. E. Adams, W. Haas, and J. J. Wysocki, *Bull Am. Phys. Soc.*, **14**, 739 (1969).
5. J. E. Adams, W. Haas, and J. J. Wysocki, *Phys. Rev. Letters*, **22**, 92 (1969).
6. "Investigation of Large Area Display Screen Using Liquid Crystals," by C. H. Jones, J. L. Fergason, J. A. Asars, I. Liberman, W. J. Harper, N. N. Goldberg, and W. C. Divens, RADC Report, TR 54-274 Dec. (1965).
7. W. Haas, J. E. Adams, and J. J. Wysocki, *Mol. Cryst.*, **7**, 371 (1969).
8. W. Haas, J. E. Adams, and J. J. Wysocki, *Appl. Opt. Suppl.*, **3**, 196 (1969).
9. J. E. Adams and W. Haas, *This Journal*, **116**, C298 (1969).
10. J. E. Adams, W. Haas, and J. J. Wysocki, *Liquid Crystals and Ordered Fluids*, pp. 463-475, J. F. Johnson and R. S. Porter, Editors, Plenum Press, New York (1970).
11. J. E. Adams, W. Haas, and J. J. Wysocki, *J. Chem. Phys.*, **50**, 2458 (1969).
12. J. Fergason, *Mol. Cryst.*, **1**, 293 (1966).

Characterization of CVD Molybdenum Thin Films

A.H. El-Hoshy[1]

General Electric Corporate Research and Development, Schenectady, New York 12301

Presently use is being made of CVD molybdenum thin films as an essential element of wafer processing in the manufacture of semiconductor field effect devices (1). In particular, the amount of boron diffused in the channel region of a field effect transistor may be largely determined by the thickness of the molybdenum film. For the purpose of process reproducibility it is necessary to characterize the physical properties of chemically vapor deposited molybdenum films. Previ-

[1] Present address: Integrated Circuits Project, General Electric Company, Electronics Park, Syracuse, New York 13201.

Key words: thin film, CVD molybdenum on silicon dioxide, grain size and orientation, resistance ratio.

ous work on the subject has not fully explored the influence of deposition parameters on film properties (2, 3).

Spark mass spectrometry and flame spectrophotometry have been used to trace certain elements in CVD Mo films (2, 4). The sensitivity of both methods is in the ppm range. These quantitative techniques are vital in detecting the presence of specific elements such as sodium as well as potential dopant impurities in silicon. However, they are not suited for qualitative estimates of the over-all impurity content, and they do not render information about the structure of the films.

In the present work, three techniques for characterizing CVD Mo films are described. Transmission electron microscopy and x-ray diffraction reveal details about the structure of the deposited metal while resistance ratio measurements give a relative estimate of the over-all purity.

Experiment

Polished silicon wafers of n-type 4 ohm-cm resistivity with a 900Å thermally grown oxide served as substrates for Mo deposition. The vapor deposition system used was supplied by Applied Materials Technology Inc. with a rotating graphite rf susceptor. Gaseous hydrogen acts as a carrier for $MoCl_5$; it also reaches the reaction chamber through a line that bypasses the $MoCl_5$ source. It then reduces $MoCl_5$ according to the following reaction (2)

$$MoCl_5 + H_2 \rightarrow HCl + Mo$$

Deposition conditions were varied in the following manner. Substrate temperature was controlled by the amount of rf power fed into the graphite susceptor, while the deposition rate at a fixed temperature was determined by the amount of carrier hydrogen passed over the $MoCl_5$ source. Since the deposition temperature and the deposition rate are interdependent, the first set of samples had the substrate temperature varied while the deposition rates were allowed to change accordingly. The second set of samples had a fixed deposition temperature and a deposition rate controlled by the amount of bleeder hydrogen over the $MoCl_5$ source. Table I lists the different samples tested and their corresponding deposition conditions. Three wafers were coated in each run. Film thickness was measured by a Tallysurf instrument while resistivities were determined by a four-point resistance probe.

Table I. Deposition parameters and resistivities for the molybdenum films

Run No.	Substrate temperature, °C	Molybdenum thickness, Å	Growth rate, Å/min	Resistivity, ohm-cm
1st Set				
229	500	2800	187	7.2×10^{-6}
240	600	3700	247	7.0×10^{-6}
228	700	4300	226	6.75×10^{-6}
241	800	2500	125	7.4×10^{-6}
2nd Set				
243	700	3050	87	7.56×10^{-6}
228	700	4300	226	6.75×10^{-6}
244	700	2800	350	7.2×10^{-6}

Transmission Electron Microscopy

The as-deposited Mo films were etched by immersion in a solution of 95 lactic acid, 5 nitric acid, and 1 hydrofluoric acid for times up to 90 sec. The films were then stripped from the wafers and mounted for direct electron transmission microscopy. Figures 1(a) and (b) are the micrographs obtained for samples 229 and 241 at 75,000 magnification. Using the intercept method on the micrographs, the grain surface area per unit volume was determined for each sample (5). Figure 2(a) shows the change in grain surface area per unit volume as a function of the deposition temperature. Except for the sample deposited at 500°C which has smaller grains, the grain size remained constant as the temperature was increased from 600° to 800°C. The variation in grain size with deposition rate at 700°C is shown in Fig. 2(b). The grain size was not affected by the increase in deposition rate from 87 to 226 Å/min; however, at a deposition rate of 350 Å/min the grain size was smaller. The influence of sample thickness on grain size is given in Fig. 3 where four samples of different thicknesses were deposited at 640°C. The variation in grain size is rather small for the thickness range of 2300-5100Å indicating that the observed changes in grain size as a function of deposition temperature and rate do not reflect a sample thickness effect.

Grain size expressed in surface area per unit volume is important for determining the area available for grain boundary diffusion. Since the maximum variation in grain boundary area was approximately a factor of two, the area available for grain boundary diffusion could not change by more than the ratios of the perim-

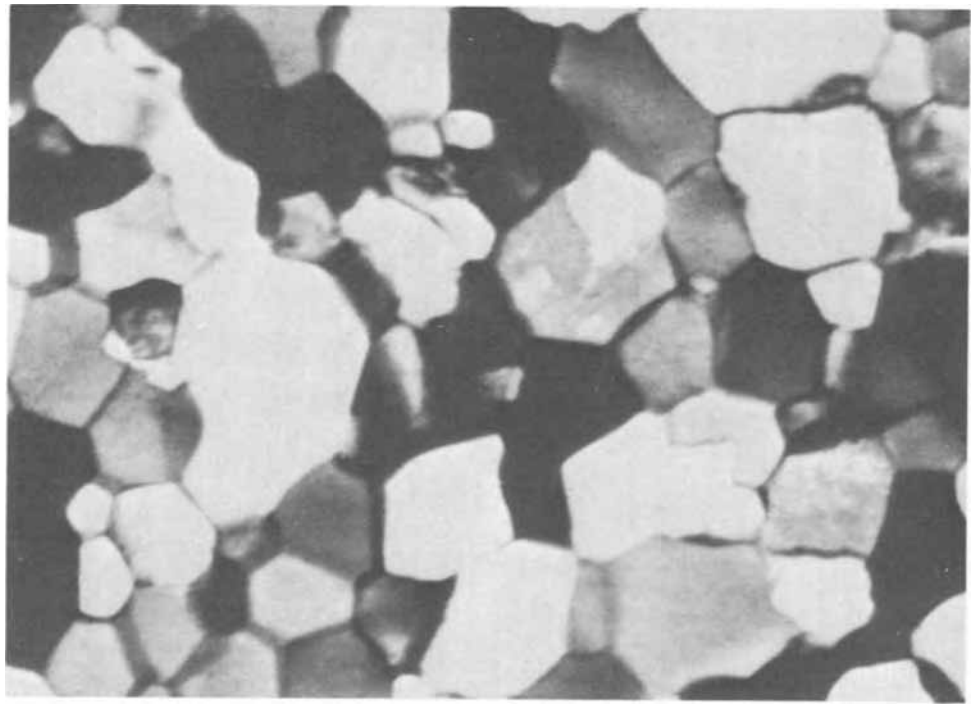

Fig. 1(a). Transmission electron-micrograph for sample No. 241. 75,000×.

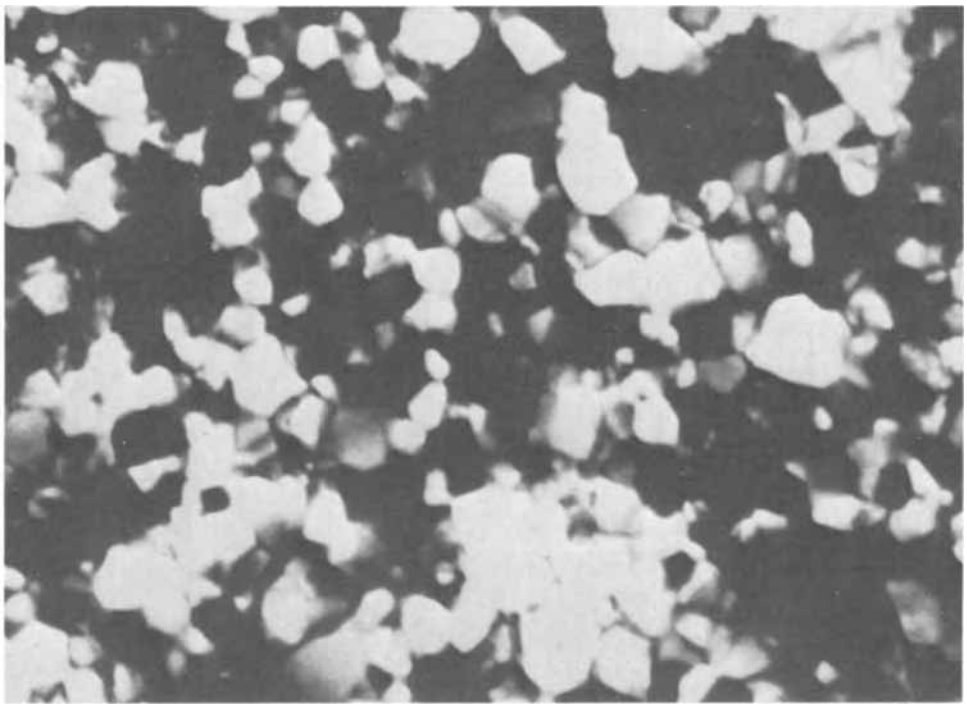

Fig. 1(b). Transmission electron micrograph for sample No. 229. 75,000×.

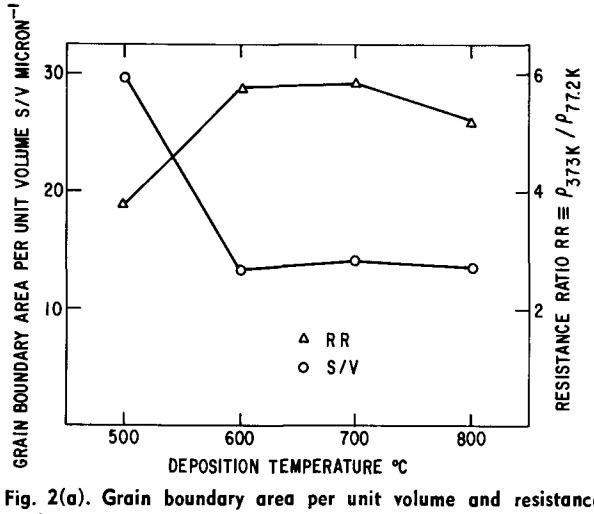

Fig. 2(a). Grain boundary area per unit volume and resistance ratio dependence on deposition temperature.

eters for a given volume, *i.e.* the flux of diffusants through grain boundaries would not increase by more than a factor of two. This seems rather small and should not influence appreciably the amount of diffusant through Mo films.

Resistance Measurements

Through a photoresist procedure, resistance patterns of 220 aspect ratio were created in the Mo films on the oxidized silicon wafers. The wafers were then scribed to obtain separate resistor pellets. These in turn were mounted on transistor headers and aluminum wires were ultrasonically bonded to join four pads on each resistor with corresponding posts on the header. Two wires served as current leads while the remaining two served as voltage leads. The headers were then hermetically sealed and resistance measurements were made using a stabilized current source and a digital voltmeter.

Figures 2(a) and (b) show the resistance measured at 373K divided by that at 77.2K as a function of the deposition parameters. Since previous measurements

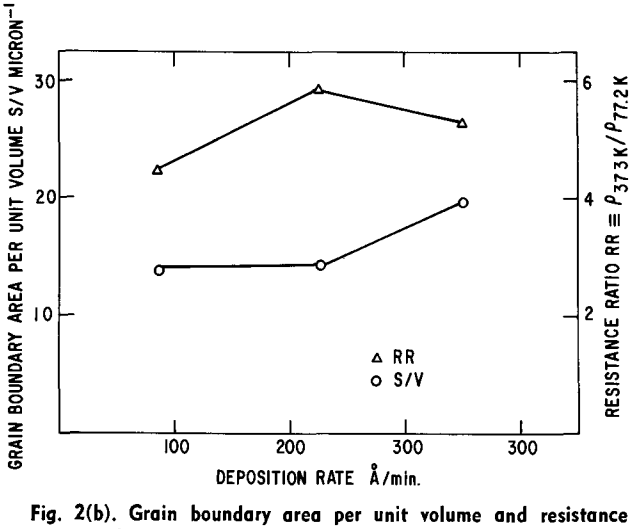

Fig. 2(b). Grain boundary area per unit volume and resistance ratio dependence on deposition rate at 700°C.

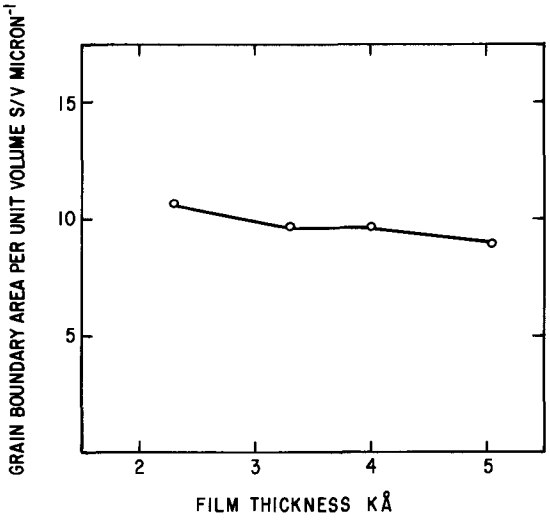

Fig. 3. Grain boundary area per unit volume dependence on film thickness at 640°C.

Table II. Effect of deposition conditions on grain orientation

Run No.	Substrate Temperature, °C	Growth rate, Å/min	(110)	(200)	(211)	(220)	(310)
ASTM			100	21	39	11	17
1st Set							
229	500	187	100	42.7	—	2.9	11.8
240	600	247	100	25.4	—	4.1	6.1
228	700	226	100	53.0	—	3.8	15.1
241	800	125	69.5	100	—	—	27.8
2nd Set							
243	700	87	61.5	100	13.8	17	7.7
228	700	226	100	53.0	—	3.8	15.1
244	700	350	27.5	100	—	—	12.1

(2, 6) indicate that the contribution of surface scattering to resistivity is quite small for Mo films of several thousand angstrom thickness at 77.2K, the resistance ratio $R_{373K}/R_{77.2K}$ can therefore be directly compared with bulk material. The most recently reported value for $R_{373K}/R_{77.2K}$ for single crystal zone-refined Mo of 99.999% purity is 15.2 (7). The difference between a maximum value of 5.85 obtained for CVD Mo films and 15.2 for bulk material can be attributed to the combined contribution of internal structural defects and the presence of impurities. Although resistance ratio measurement does not render specific details about either composition or structure; it can still serve as a means for detecting gross changes in the CVD Mo films. The resistance ratio can therefore provide a figure of merit for the over-all quality of the metal film, where the higher the resistance ratio the less structural defects and impurities present in the film.

X-Ray Diffraction

An x-ray diffractometer was used to examine the texture of the CVD Mo films. The effect of deposition conditions on grain orientation is shown in Table II. The intensities are normalized to the strongest reflection which is assigned a value of 100. When the relative intensities of reflections from the different crystallographic planes of CVD Mo films are compared with the ASTM (8) reference, a pronounced preferential orientation of the (200) planes is quite apparent. The relative intensities of the (110) and (200) reflections suggest that the amount of preferential orientation decreases as the deposition temperature is increased from 500° to 600°C. It then seems to increase with temperature for the range between 600° and 800°C. The dependence of grain orientation on deposition rate suggests a decrease in preferential orientation for the intermediate deposition rate of 226 Å/min.

Summary

Transmission electron micrographs, resistance ratios, and x-ray diffraction measurements have been used to characterize CVD Mo films for a deposition temperature range from 500° to 800°C and a deposition rate at 700°C that varies between 87 and 350 Å/min.

Acknowledgment

The author is thankful to M. Garfinkel for suggesting this study and to J. Sprague for providing the samples.

Manuscript submitted March 22, 1971; revised manuscript received ca. Aug. 13, 1971.

Any discussion of this paper will appear in a Discussion Section to be published in the June 1972 JOURNAL.

REFERENCES

1. A. El-Hoshy, D. M. Brown, and W. E. Engeler, *Appl. Phys. Letters*, **17**, 261 (1970).
2. Takuo Sugano, Hsun-Kwei Chou, Minoru Yoshida, and Tateki Nishi, *Japan J. Appl. Phys.*, **7**, 1028 (1968).
3. D. K. Seto, V. Y. Doo, and S. Dash in "Chemical Vapor Deposition," J. M. Blocher, Jr., and J. C. Withers, Editors, The Electrochemical Society Softbound Symposium Series, New York (1970).
4. P. R. Kennicott, Private communication.
5. C. S. Smith and L. Guttman, *J. Metals*, **5**, 81 (1953).
6. Yu. G. Ptushinskii and Z. V. Stasyuk, *Ukr. Fix. Zh.*, **13**, 221 (1968).
7. R. A. Holmwood and R. Glang, *J. Chem. Eng. Data*, **10**, 162 (1965).
8. ASTM File No. 4-809.

Brief Communication

Growth and Crystallographic Identification of MAg_4I_5 Single Crystals

M. R. Manning,* C. J. Venuto,* and D. P. Boden*

ESB Incorporated, Research Center, Yardley, Pennsylvania 19067

Compounds of the type MAg_4I_5 (M = K, NH_4, or Rb) have recently aroused considerable interest due to their unusually high ionic conductivities (1-3). It is very desirable to possess large single crystals of these compounds for fundamental physical studies. Previously, these materials have been produced by diffusing the powdered compounds MI and AgI together at a temperature between 100°C and 200°C in the correct molar ratio (4). Material produced by this method was mostly of the form MAg_4I_5, but it did contain small amounts of the compounds MI, AgI, and M_2AgI_3. Attempts at growing large single crystals by diffusion were unsuccessful, probably because of the disruptive effects of the presence of these impurities on the orderly rearrangement of atoms in a crystal structure. Fusion at a temperature above the eutectic points of the compounds MAg_4I_5 (5, 6) also failed to produce single large crystals in our labs for similar reasons.

Finally, a method involving crystallization from hydroiodic acid was successfully developed for growing large single crystals of these compounds. Octahedral crystals have been produced ranging in size from ⅜ to ½ in. in diameter. The technique described herein overcomes the two main obstacles to their successful growth from solution. These are (*a*) main-

* Electrochemical Society Active Member.
Key words: solid electrolytes, x-ray diffraction, solutions, ionic conductivity.

tenance of the correct relative concentrations of the cations incorporated into the structure of the desired compound and (b) retention of the degree of supersaturation necessary for a reasonable growth rate while keeping to a minimum the generation of extra seed crystals through spontaneous nucleation. It is believed that this is the first time that single crystals of any of the compounds $MAgI_5$ have been successfully isolated from solution.

Crystal Growth

During a series of attempts to produce suitable samples of the solid electrolytes MAg_4I_5 for electrochemical and physical investigations, it was found that appreciable quantities of both AgI and MI (M = K, NH_4, or Rb) were soluble in concentrated hydroiodic acid and that each of these could be crystallized from the HI solution. On this basis, it was decided to utilize aqueous HI as the solvent in an attempt to produce large single crystals of MAg_4I_5.

Preparation of the large single crystals included several steps. First, 57% hydroiodic acid was heated to 50°C, and to each gram of the warm acid, 0.805g AgI was added. Depending on the solid electrolyte desired, 0.166g RbI, 0.124g KI, or 0.108g NH_4I was added to the warm HI-AgI solution. The final solution was then allowed to cool to 30°C, 39°C, or 35°C (for M = Rb, K, or NH_4 respectively). During the cooling, dendritic orthorhombic crystals of the formula M_2AgI_3 appeared (7). The solution was then allowed to evaporate slowly at a temperature about 1 deg above the lowest temperature at which the compound MAg_4I_5 is stable, *i.e.* 27°, 36°, or 32° for M = Rb, K, or NH_4 respectively (3). During evaporation, the orthorhombic crystals continued to propagate until octahedral crystals began to appear, whereupon the solution was ready for production of the desired solid electrolyte crystals. At this point, most of the orthorhombic crystals were removed by coarse filtration, and the remainder dissolved by warming the solution 3°. The resulting solution will be referred to as growing solution.

The growing solution was then cooled at the rate of 1° every 12 hr. Octahedral seed crystals generally began to form within the first few hours. At the end of 36 hr, these seed crystals had attained a size of 1/8 to 3/16 in. They could then be separated from solution with the aid of Kel-F type plastic tweezers or by simple filtration through spun Fiberglas matting.

To minimize decomposition, the MAg_4I_5 crystals were quickly dried between two layers of asbestos cloth and stored over Drierite at 40°-50°C in an evacuated desiccator.

An individual crystal prepared as described above could be mounted on a glass filament for further growth if desired, as shown in Fig. 1. A glass "T" was suspended over the edges of a vial, 1 in. in diameter and 3 in. high, with the tip of the drawn glass filament heated to form a small bead for mounting. G. E. adhesive RTV-108 was used to hold the seed crystal to the glass bead. A Teflon disk was affixed to the filament as shown, to shield the growing crystal from falling seeds which may form at the surface of the solution. A piece of Fiberglas matting served as cover and evaporation shield.

The vial was then filled with freshly prepared growing solution, and the filament with attached crystal was lowered into it. The crystals grew to a diameter of ⅜ to ½ in. within 2-3 weeks. The temperature was held constant during this period to within half a degree. Figure 2 shows a crystal of $RbAg_4I_5$ grown by the described procedure.

It should also be noted that crystals of the form MAg_4I_5 could only be grown when the concentration of the M^+ ions was between 17.5 and 18.5% of the total cationic concentration, at the temperatures used (27°-40°C). Below this composition range only AgI crystals would appear; above it crystals of M_2AgI_3 or MI would grow. It was also found that below the temperatures of 27°, 36°, or 32°C, for M = Rb, K, or NH_4 respectively,

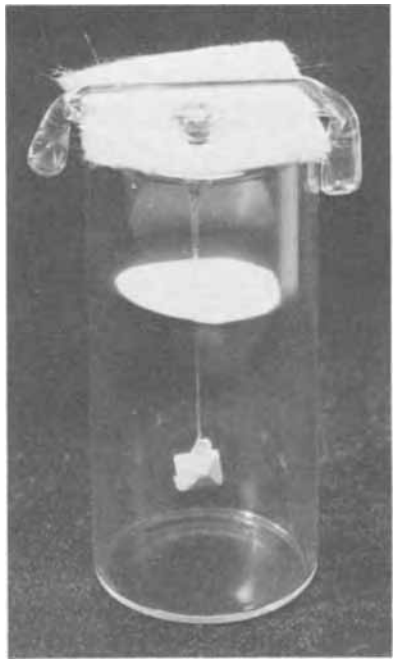

Fig. 1. Photograph showing a single crystal of $RbAg_4I_5$ mounted on glass filament.

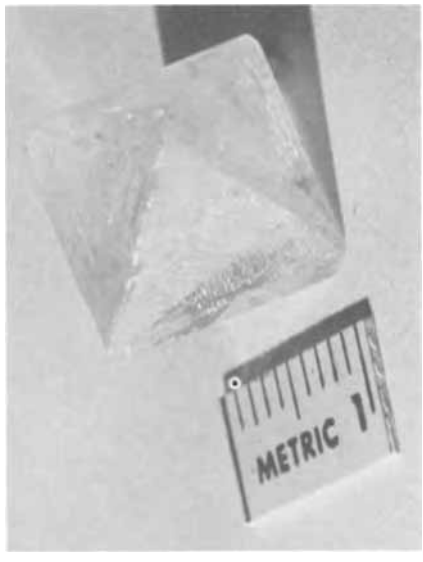

Fig. 2. Photograph of a single crystal of $RbAg_4I_5$. Size of crystal can be seen by reference to the one centimeter scale placed alongside.

no crystals of the type MAg_4I_5 could be formed. Indeed, when previously prepared ⅜ in. diam crystals of these solid electrolytes were inserted in the appropriate growing solutions at temperatures as little as one degree below those specified, they would be transformed within a few hours via the reaction

$$MAg_4I_{5(s)} \rightarrow 1/2\ M_2AgI_{3(s)} + 7/2\ AgI_{(aq)}$$

It was also found that when solutions containing reagent grade HI without the addition of H_3PO_4 as a preservative were used, molecular iodine became entrapped in the growing crystal. This free iodine, which colored the MAg_4I_5 crystals brown, could be removed, in the case of the Rb or K salt, by holding these crystals under vacuum at 100°C for about one week.

As an alternate method, the growing solution could be prepared by utilizing HI acid as sold commercially with 0.5 to 1.5% H_3PO_4 in it as a preservative. During preparation of the growing solution, it would turn brown with freed iodine but this could be removed

Table I. X-Ray data for $RbAg_4I_5$

	ESB-fused salt, cooled & ground (Diffractometer)		ESB-small single crystals, ground (Film)		Bradley and Greene observed (Film)		Calc'd
hkl	d, Å	I/I_1	d, Å	I	d, Å	I	d, Å
(110)	7.96	39	7.72	M	7.85	W	7.88
							6.44
							4.99
							4.55
							3.94
(221) (300)	3.75	47	3.70	MS	3.72	MS	3.72
(310)	3.55	5	3.52	VW	3.52	VW	3.53
(311)	3.39	100	3.35	S	3.36	S	3.36
(222)	3.24	16	3.21	MW	3.21	W	3.22
							3.09
(321)	3.00	3					2.98
							2.79
(411) (330)	2.65	13	2.63	MW	2.63	W	2.63
(331)	2.57	3					2.56
(420)	2.51	5	2.50	VW			2.49
(332)	2.39	13	2.38	MW	2.38	W	2.38
(422)	2.29	13	2.28	MW	2.28	MW	2.28
(500) (430)	2.24	18	2.23	M	2.23	MW	2.23
(510)	2.20	39	2.19	S	2.19	S	2.19
(511) (333)	2.16	5	2.15	W	2.15	VW	2.15
(520) (432)	2.09	21	2.08	MS	2.07	M	2.07
(521)	2.05	13	2.04	M	2.04	MW	2.04
(440)	1.987	11	1.977	MW	1.97	W	1.97
(522) (441)	1.959	5	1.949	MW	1.94	W	1.94
(530) (433)	1.927	3	1.920	VW			
(531)	1.903	3	1.888	VW			1.88
(600) (442)	1.873	5	1.868	VW			
(610)	1.846	5	1.839	VW			
(611) (532)	1.822	8	1.815	W			
(620)	1.779	3					
(621) (540) (443)	1.757	8	1.749	M			

by holding the solution at 96°C for 1-3 hr. The resulting straw-yellow solution could then be used as before without impairing crystal quality. Crystals so produced are semitransparent and do not exhibit the brownish tinge characteristic of free iodine. Transparency of the growing solution also aids in monitoring of the growth process.

Crystallographic Examination

A number of small single crystals of $RbAg_4I_5$ were chosen as representative specimens for crystallographic identification. These were ground to a powder for comparison with another powdered sample prepared by fusing RbI with AgI and subsequent cooling. Both samples were observed under the polarizing microscope and determined to be optically isotropic and without impurities.

Table II. Unit cell dimension for $RbAg_4I_5$

Author	Method	Unit cell
Bradley and Greene	Film (powder)	11.15Å
ESB	Film (powder)	11.16Å
ESB	Diffractometer (powder)	11.23Å
Bradley and Greene	Single crystal	11.22Å
Geller	Single crystal	11.24Å

X-ray diffraction powder data for the two samples of $RbAg_4I_5$ are presented in Table I. They agree well with the x-ray diffraction data published by Bradley and Greene (2). The 3.00, 2.57, 2.50, and 1.888 reflections were not observed by those authors. Their equivalents, however, were calculated by Bradley and Greene and are listed in the last column of Table I. All the lines in the ESB powder pattern using the Debye-Scherer method were indexed (column 1). The structure was determined to be cubic with a unit cell dimension of $a_o = 11.16$Å. A slightly larger unit cell of $a_o = 11.23$Å was obtained with the diffractometer method. The former unit cell size agrees with that obtained from powder data by Bradley and Greene, whereas the slightly larger cell agrees with single crystal data obtained by Bradley and Greene and by Geller (6) (Table II). The slight discrepancy is probably due to differences in x-ray method.

Manuscript received June 24, 1971.

Any discussion of this paper will appear in a Discussion Section to be published in the June 1972 JOURNAL.

REFERENCES

1. J. N. Bradley and P. D. Greene, *Trans. Faraday Soc.*, **63**, 424 (1967).
2. J. N. Bradley and P. D. Greene, *Trans. Faraday Soc.*, **63**, 2516 (1967).
3. L. E. Topol and B. B. Owens, *J. Phy. Chem.*, **72**, 2106 (1968).
4. J. N. Bradley and P. D. Greene, *Trans. Faraday Soc.*, **63**, 1023 (1967).
5. B. B. Owens and G. R. Argue, *Science*, **157**, 308 (1967).
6. S. Geller, *Science*, **157**, 310 (1967).
7. C. Brink and H. A. Stenfert Kroese, *Acta Cryst.*, **5**, 433 (1952).

DISCUSSION SECTION

This Discussion Section includes discussion of papers appearing in the *Journal of The Electrochemical Society*, Vol. 117, No. 12 and Vol. 118, No. 4, December 1970 and April 1971.

On the Redistribution of Boron in the Diffused Layer During Thermal Oxidization

J. S. T. Huang and L. C. Welliver (pp. 1577-1580, Vol. 117, No. 12)

M. G. Buehler[1]: The purpose of this note is to indicate that Huang and Welliver have failed to solve the problem they posed. The solution fails because the boundary condition imposed on the diffusive flow at the $Si-SiO_2$ boundary, Eq. [6], has been applied to just solution C_2. This condition should be applied to the total solution $C = C_1 + C_2$. An example of its failure can be seen by examining the special case, $k = m$. For this case, consider an infinitesimal growth of the oxide. Impurity atoms from the Si just converted to SiO_2 satisfy the impurity demands of the oxide with the result that there should be no diffusive flow at the $Si-SiO_2$ boundary. The solution for the impurity distribution in the Si, Eq. [11], does not satisfy the condition of no diffusive flow at the $Si-SiO_2$ boundary for $k = m$.

An additional observation is that the solution, Eq. [11], does not satisfy the diffusion equation because the constant A contains a "square root of time" term. To date, this problem has only been solved numerically,[2] and a closed-form solution is still being sought.

[1] Texas Instruments, Inc., Dallas, Texas.

J. S. T. Huang and L. C. Welliver: We would like to thank Dr. Buehler for his comment on our paper. It should have been pointed out that the model we proposed for boron redistribution is an approximation. The boundary condition, Eq. [6], is equivalent to the so-called radiation boundary condition encountered in heat conduction[3], *i.e.*

[2] T. Kato and Y. Nishi, *J. Appl. Phys. (Japan)*, **3**, 377 (1964).
[3] H. S. Carslaw and J. C. Jaeger, "Conduction of Heat in Solids," Clarendon Press, Oxford, England (1947).

$$D \frac{\partial C}{\partial X} \Big]_o = K\, C(o,t)$$

for which K is a constant. But in our case, K is a function of time due to the parabolic growth rate of thermal oxides. This fact makes the solution of the diffusion equation quite intractable. Even Kato and Nishi[4] in their numerical calculation had to resort to the approximation of K being a constant within a finite time interval. Essentially, our approximation lies in the solution of the second part, Eq. [7], which does not satisfy the diffusion equation but does satisfy the initial and boundary conditions.

The condition, Eq. [6], does apply to the total solution $C_1 + C_2$, since C_1 is approximately a Gaussian distribution, the term $D \frac{\partial C_1}{\partial X}$ evaluated at $X = 0$ vanishes for all times. In the special case for which $k = m$, Eq. [11] approaches a pure Gaussian distribution indicating an impermeable surface with no net diffusive flow across the Si-SiO_2 interface.

We believe that our approximate model is a good one, because it has been validated by extensive experimental results. Furthermore, this model gives considerable physical insight into the redistribution problem. We agree, however, with Dr. Buehler that a rigorous closed-form solution, if it exists, is still being sought.

Gas Phase Etching of Silicon with Chlorine

J. P. Dismukes and R. Ulmer (pp. 634-635, Vol. 118, No. 4)

S. E. Craig, Jr.[5]: Dismukes and Ulmer, in their paper, discussed a new and interesting technique for etching silicon with chlorine in a helium atmosphere. Their data are sufficient to prove that the rate limiting step is the rate of diffusion of reaction products from the surface, or that the reaction rate is mass transfer controlled.

For a mass transfer controlled reaction, the gas phase concentration at the gas-solid interface approaches the equilibrium value. These equilibrium concentrations can be calculated from the thermodynamic data in the JANAF tables[6]. At equilibrium, the concentration of Cl_2 is essentially zero. The only important equilibrium species are $SiCl_2$, $SiCl_4$, and He. The concentrations of these species at the interface are related by the equilibrium for the chemical reaction

$$Si(c) + SiCl_4 \rightleftarrows 2\ SiCl_2 \qquad [1]$$

A diffusion flux, J, for each of the species can be written in terms of a mass transport coefficient, k, and the difference between the inlet mole fraction and equilibrium mole fraction of the species[7]

$$J_{Cl_2} = k\ ([Cl_2] - 0) \qquad [2]$$

$$J_{SiCl_4} = k\ (0 - [SiCl_4]^*) \qquad [3]$$

$$J_{SiCl_2} = k\ (0 - [SiCl_2]^*) \qquad [4]$$

where bracketed quantities represent mole fractions of the indicated species,* indicates equilibrium values, while unstarred quantities represent feed values.

The total diffusion flux of silicon containing species away from the gas-solid interface is related to the etching rate, r, by the mass balance equation

$$\frac{r\rho_c}{M} = -\ (J_{SiCl_2} + J_{SiCl_4}) \qquad [5]$$

where ρ_c = density of solid Si = 2.33 g/cm^3 and M = molecular weight of Si = 28 g/mole. A combination of Eq. [3], [4], and [5] yields the complete rate expression[8].

$$= \frac{M}{\rho_c} k\ [Si]^* \qquad [6]$$

where $[Si]^* = [SiCl_4]^* + [SiCl_2]^*$.

Both k and $[Si]^*$ are functions of temperature. To facilitate comparison of the data with the theory, both sides of Eq. [6] are multiplied by k_o/k where k_o is the mass transfer coefficient computed at a standard reference temperature, T_o.

Graetz type solutions to the combined diffusion and flow problem usually give the Sherwood number, $kd/\mathcal{D}\rho$, as a function of a modified Graetz number, $W/\mathcal{D}\rho L$, where d and L are dimensions characteristic of the channel width and length, W is the molar flow rate of gas, $\mathcal{D}$ is the gas phase diffusivity and $\rho = P/RT$ is the molar density of the gas. These Graetz solutions show that the Sherwood number is proportional to the cube root of the Graetz number in the range of flows normally encountered. Since $\mathcal{D}$ is proportional to the 3/2 power of temperature, and ρ is inversely proportional to temperature, $k_o/k = (T_o/T)^{1/3}$.

Equation [6] becomes

$$r\,(T_o/T)^{1/3} = \frac{Mk_o}{\rho_c} [Si]^* \qquad [7]$$

[Si]* was calculated for the various feed compositions and reaction temperatures used by Dismukes and Ulmer. T_o was taken as 900°C (1173°K). A log-log plot of $r\,(T_o/T)^{1/3}$ *vs.* [Si]* is presented in Fig. 1. The data fit a straight line with a slope of 1 as the theory predicts.

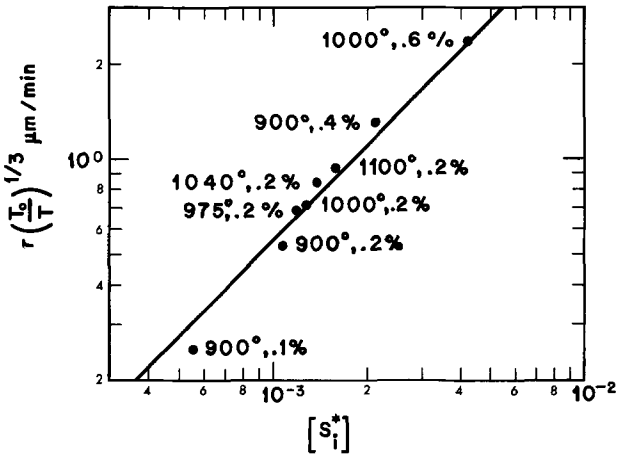

Fig. 1. Etch rate as a function of equilibrium gas phase mole fraction of silicon containing species. The reaction temperature in degrees C and the feed mole per cent (m/o) Cl_2 are shown for each data point. Solid line represents the theory for a mass transfer controlled reaction.

From Fig. 1, Mk_o/ρ_c is found to be 550 μm/min. This yields $k_o = 7.65 \times 10^{-5}$ moles/sec-cm^2. If we take $\mathcal{D} = 3.24$ cm^2/sec, $\rho = 1.04\ (10^{-5})$ moles/cm^3 and $d = 2$ cm, the Sherwood number, $k_o d/\mathcal{D}\rho = 4.6$. This value is typical of what one expects to find in a reactor of this type.

Activation Energy: The apparent activation energy, $\Delta E^\dagger_a$, is obtained by taking logarithms of Eq. [7] and differentiating with respect to $1/T$.

$$\Delta E^\dagger_a \equiv -R \frac{d \ln r}{d\left(\frac{1}{T}\right)} = \frac{RT}{3} - \frac{R\, d \ln [Si]^*}{d\left(\frac{1}{T}\right)} \qquad [8]$$

The first term on the right of Eq. [8] is the apparent activation energy due to the temperature dependence

[4] T. Kato and Y. Nishi, *J. Appl. Phys. (Japan)*, 3, 377 (1964).
[5] Arizona State University, Tempe, Arizona 85281.
[6] D. R. Stull *et al.*, JANAF Thermochemical Tables, Dow Chemical Co., Clearing House for Federal Scientific and Technical Information (1965).
[7] Because all active species are present in dilute concentrations, the increase in gas phase moles is neglected.
[8] For simplification, it is assumed that the mass transport coefficients are the same for all species.

of diffusion. This represents a small contribution and has a value of approximately 0.8 kcal/mole.

The second term on the right of Eq. [8] is the apparent activation energy due to the shift in equilibrium with temperature. For dilute solution this term becomes

$$\frac{-R\,d\ln[\mathrm{Si}]^*}{d(1/T)} = \frac{-R}{[\mathrm{Si}]^*\left(\frac{4}{2[\mathrm{Si}]^*-[\mathrm{Cl_2}]}+\frac{1}{[\mathrm{Cl_2}]-[\mathrm{Si}]^*}\right)}\,\frac{d\ln K}{d\left(\frac{1}{T}\right)} = \frac{\Delta H^o}{[\mathrm{Si}]^*\left(\frac{4}{2[\mathrm{Si}]^*-[\mathrm{Cl_2}]}+\frac{1}{[\mathrm{Cl_2}]-[\mathrm{Si}]^*}\right)} \quad [9]$$

where K and ΔH^o are the equilibrium constant and the heat of reaction for reaction Eq. [1].

At very low temperatures ($T < 900$°C), $SiCl_4$ is the dominant species at equilibrium and $[Si]^* \cong [SiCl_4] \cong [Cl_2]/2$. At these low temperatures, the equilibrium apparent activation energy is zero. The equilibrium apparent activation energy is also zero at very high temperatures ($T >$ melting point) where $SiCl_2$ is the dominant species and $[Si]^* \cong [SiCl_2]^* \cong [Cl_2]$.

The maximum value of the equilibrium apparent activation energy is obtained in the mid-range temperatures (1000°C $< T <$ 1100°C) where half the Cl_2 is in $SiCl_2$ and half is in $SiCl_4$. Under these conditions $[Si]^* = \frac{3}{4}\,[Cl_2]$ and the equilibrium apparent activation is $\Delta H^o/9 = 8.7$ kcal/mole[6]. When this is added to the apparent activation energy for diffusion, the total apparent activation energy of 9.5 kcal/mole is obtained. This is very close to the value of 10 kcal/mole reported in the paper under discussion.

This apparent activation energy is not a "true" activation energy but rather represents a shift in equilibrium with temperature. The rate is faster at high temperatures where $SiCl_2$ is the favored species than at low temperatures where $SiCl_4$ is the favored species because $SiCl_2$ is a more efficient transporter of silicon than is $SiCl_4$ (per atom of Cl).

Conclusion: Since the mass transport assumption correctly predicts all the trends in the kinetic behavior and also predicts the value of the etching rate, we conclude that the gross kinetics of etching Si with Cl_2 in He is indeed mass transfer controlled.

J. P. Dismukes[9] and F. W. Dittman[10]: We concur with Craig's conclusion that, in the etching of Si with Cl_2 in He atmosphere[11], mass transfer of Cl_2 to and of a mixture of $SiCl_2$ and $SiCl_4$ from the Si surface controls the rate of etching at a given temperature. Craig also correctly points out that the temperature dependence of the etch rate is related to a shift to the right of the equilibrium at the interface

$$\mathrm{Si(s)} + \mathrm{SiCl_4(g)} \leftrightarrow 2\mathrm{SiCl_2(g)} \quad [1]$$

rather than to a temperature dependent chemical kinetic process at the interface[11]. However, two additional comments are appropriate, the one with regard to the etching efficiency, which Craig did not discuss, and the other with regard to the preferred use of a Pohlhausen solution[12] rather than a Graetz solution[13] in the mass transfer analysis.

If mass transfer is indeed the rate limiting step, it has to account for the small observed efficiencies (2-4%) for reaction of Cl_2 with Si[11]. Since the mass transfer coefficient k can be more accurately calculated for Cl_2 than for a mixture of $SiCl_4$ and $SiCl_2$, we have estimated the mass transfer limited rate of etching of Si by Cl_2 using the relation

$$R = kAx_{\mathrm{Cl_2}}\frac{(1+\alpha)}{2} \quad [2]$$

where R = etch rate in gram moles Si/sec, A = area of Si in cm^2, x_{Cl_2} = mean unreacted mole fraction Cl_2, and α, calculated from thermochemical data, is the fraction of $SiCl_4$ converted to $SiCl_2$ in the reaction in Eq. [1] at equilibrium. For laminar flow across a plate, the Pohlhausen relation[12], which relates the Sherwood number to the product of the square root of the Reynolds number and the cube root of the Schmidt number

$$\frac{kL}{\rho D} = 0.664\left(\frac{Lv\rho}{\eta}\right)^{1/2}\left(\frac{\eta}{\rho D}\right)^{1/3} \quad [3]$$

was used to calculate k, where L = the length of the susceptor, v = the linear gas velocity, η = the gas viscosity, ρ = the molal density, and D = the diffusion coefficient. For 0.2%Cl_2, the calculated k values are 7.0×10^{-5} at 900°C and 6.5×10^{-5} at 1100°C, and the calculated R values are 4.0×10^{-7} at 900°C and 5.6×10^{-7} at 1100°C. The experimental R values[11], 3.7×10^{-7} at 900°C and 6.9×10^{-7} at 1100°C, show sufficient agreement with the calculated values to indicate that the etching of Si by Cl_2 is indeed mass transfer controlled.

A laminar flow mass transfer analysis using the Pohlhausen solution[12] for a flat plate, rather than the Graetz solution[13] for a tube, employed by Craig, is more meaningful for the actual geometry of the silicon wafer, susceptor, and reactor, as was previously pointed out for epitaxial growth[15] of Si by hydrogen reduction of $SiCl_4$. For the Pohlhausen case, and taking a more accurate temperature dependence of η and D[16], Craig's Eq. [7] becomes

$$r\,(T_o/T)^{0.447} = \frac{Mk_o}{\rho_c}[\mathrm{Si}]^* \quad [4]$$

A plot of this equation similar to Craig's Fig. 1 yields $k_o = 6.7 \times 10^{-5}$ for the mean mass transfer coefficient of the mixture of $SiCl_2$ and $SiCl_4$ at 900°C, compared to Craig's value of $k_o = 7.6 \times 10^{-5}$. For the present data, the difference between the Pohlhausen and Graetz solutions is not large, because the flow velocity was constant and the parameters of temperature and Cl_2 concentration did not vary widely. However, the Pohlhausen solution is the correct one for this type of reactor geometry.

[9] RCA Laboratories, Princeton, New Jersey 08540.
[10] Department of Chemical Engineering, Rutgers University, New Brunswick, New Jersey 08903.
[11] J. P. Dismukes and R. Ulmer, *This Journal*, **118**, 634 (1971).
[12] E. Pohlhausen, *Z.A.M.M.*, **1**, 115 (1921); C. O. Bennett and J. E. Myers, "Momentum, Heat, and Mass Transfer," pp. 298 ff, 471 ff, McGraw-Hill Book Co., New York (1962).
[13] L. Graetz, *Ann. Physik*, **18**, 79 (1883) and **25**, 737 (1885); Bennett and Myers, "Momentum, Heat, and Mass Transfer, pp. 305 ff., McGraw-Hill Book Co., New York (1962).
[14] H. Schäfer and J. Nickl, *Z. Anorg. u. Allgem. Chem.*, **274**, 250 (1953).
[15] R. W. Andrews, D. M. Rynne, and E. G. Wright, *Solid State Technol.*, **12**, 61 (1969).
[16] R. B. Bird, Stewart, and Lightfoot, "Transport Phenomena," pp. 21 ff, p. 505, John Wiley and Sons, New York (1960, 1964).

JOURNAL OF THE ELECTROCHEMICAL SOCIETY

ELECTROCHEMICAL TECHNOLOGY

DECEMBER 1971

Effect of Sulfur on the Corrosion Characteristics of Iron in Carbonated Beverage

Hideya Okada, Yuzo Hosoi, and Kazuo Yamamoto

Fundamental Research Laboratories, Nippon Steel Corporation, Kawasaki, Japan

ABSTRACT

The anodic polarization curve of sulfur-bearing iron was independent of pH in both sulfuric and phosphoric acids, whereas that of pure iron was influenced by pH. This pH-dependence of the polarization of pure iron was suppressed when SH^- or $S^=$ ions were added to the acid. By the addition of a small amount of cola beverage or "blue dye" (which plays a role similar to the organic substance in the cola beverage in the corrosion of iron) to the acid, anodic polarization of sulfur-bearing iron shifted in the more noble direction. A corrosion mechanism of sulfur-bearing iron in sulfuric acid and the inhibiting action of cola beverage on sulfur-bearing iron are discussed.

It is known that addition of sulfur to steel accelerates the corrosion rate in sulfuric acid (1) and hydrochloric acid (2). Recently, however, the corrosion resistance of steel in cola beverages was improved by alloying with sulfur (3). These two results imply that sulfur in steel plays a different role in corrosion reactions in mineral acids and cola beverages.

In this study, the effect of sulfur on the pH dependence of iron corrosion in both sulfuric acid and a cola beverage has been investigated and the role of sulfur in the corrosion of steel in the cola beverage is discussed.

Experimental

The polarization curve was obtained with the rapid galvanostatic method (4) which makes it possible to obtain a polarization curve within a few seconds (*ca.* 10^{-1} sec for each current density) without changing the surface state of the specimens in a corrosion system. Figure 1 shows the circuit diagram and the electrolytic cell used.

Acid solutions were prepared from analytical grade sulfuric acid and phosphoric acid. Coca Cola was used as the cola beverage. The blue dye test served as a corrosion testing method for estimating the corrosion behavior of steel in cola beverages. In this test, Brilliant Blue FCF (C. I. No. 42090) is used because it is expected to play a role similar to the organic substance contained in cola beverage (5). These solutions were saturated with purified nitrogen gas for more than one day, and kept at 25°C during the test.

Specimens were prepared as follows: (*i*) high frequency vacuum furnace melting, (*ii*) hot rolling or forging, (*iii*) machining, (*iv*) degreasing and chemical polishing [H_3PO_4-H_2O_2], (*v*) heat treatment 700°C, 1 hr], (*vi*) abrading with metallographic papers [0/2-0/4], (*vii*) chemical polishing [H_3PO_4-H_2O_2], (*viii*) acid pickling [1*N* HCl], and (*ix*) water rinse and drying with filter papers.

Chemical composition of materials used is listed in Table I. Electrolytic iron was used in an immersion corrosion test, and Puron was used for polarization measurement in order to avoid the effect of small amount of impurities on the polarization characteristic of iron.

Key words: inhibition, polarization, cola.

Results

Effect of sulfur on the pH-dependence of polarization of iron.—Table II indicates weight loss experiments of

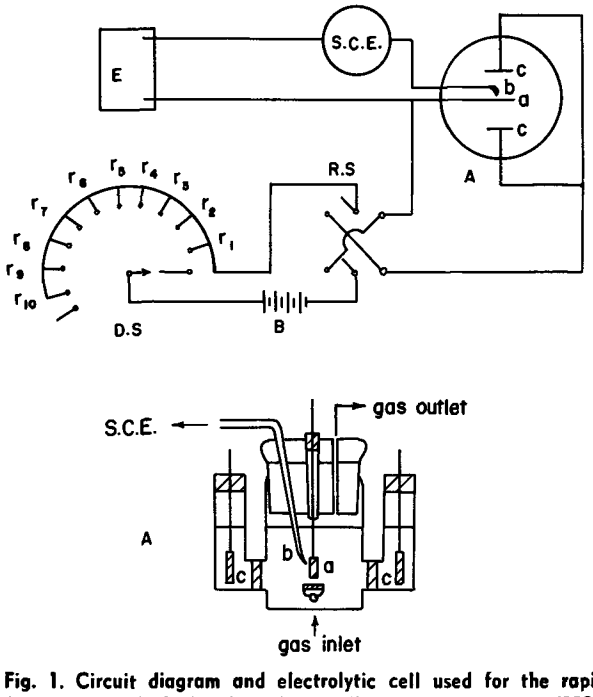

Fig. 1. Circuit diagram and electrolytic cell used for the rapid polarization method. A, electrolytic cell; B, current source (120V storage battery); D.S. dial switch; R.S., two way switch; E, synchroscope (Tektronix Type 545A); a, working electrode; b, Luggin capillary; c, counterelectrode (Pt); S.C.E., saturated calomel electrode.

Table I. Chemical compositions of materials used

	C	P	S	Si	Mn	Cu
Elec. iron	0.002	0.004	0.003	0.020	<0.01	<0.005
Puron	0.002	0.002	0.004	0.007	<0.01	<0.005

Table II. Weight losses of iron in sulfuric acid and that in cola beverage (CO_2 saturated, 25°C)

Immersion period: sulfuric acid 24 hr, cola beverage 48 hr

	Electrolytic iron (mg/cm²)	Sulfur-bearing* iron (mg/cm²)
0.1N H_2SO_4	1.40	8.57
Cola	0.70	0.37

* S = 0.05%.

the electrolytic iron and that of the sulfur-bearing iron in sulfuric acid and the cola beverage. It is noted that the corrosion rate of iron was markedly accelerated by addition of sulfur to iron in sulfuric acid; on the other hand, it was significantly decreased in the cola beverage.

Figure 2 shows the rapid polarization curves of Puron in sulfuric acid. The *p*H values were adjusted to 1.0, 1.9, and 2.7 by addition of sodium sulfate. As clearly shown in Fig. 2, both anodic and cathodic polarization curves were dependent on the *p*H values in this region. On the other hand, in the case of the sulfur-bearing iron, it is shown that anodic polarization curves were independent of the *p*H values. Both anodic and cathodic polarization were decreased as shown in Fig. 3. Similar results were also obtained by the steady-state polarization method (stationary-state method).

Since cola contains phosphoric acid, the anodic behavior of iron in an aqueous solution of phosphoric acid must be considered. Polarization of iron in phosphoric acid also indicated the same behavior as in sulfuric acid.

Effect of Brilliant Blue dye on polarization characteristics of iron in sulfuric acid.—In the case of Puron, there was no appreciable effect of the dye on anodic polarization. While in the case of the sulfur-bearing iron, anodic polarization increased by addition of Brilliant Blue dye (compare curves 1 and 2 with curves 1' and 2' in Fig. 4, respectively), and the *p*H-dependence appeared (see curves 1' and 2' in Fig. 4). Comparing curves 1' and 2' in Fig. 4 with the curves for *p*H 1.0 and for *p*H 2.7, respectively, it is noted that anodic polarization of sulfur-bearing iron is greater than that of Puron. Curve 3 in Fig. 4 shows the polarization of the sulfur-bearing iron in sulfuric acid (*p*H 2.7) to which 20 ml/liter of cola beverage was added.

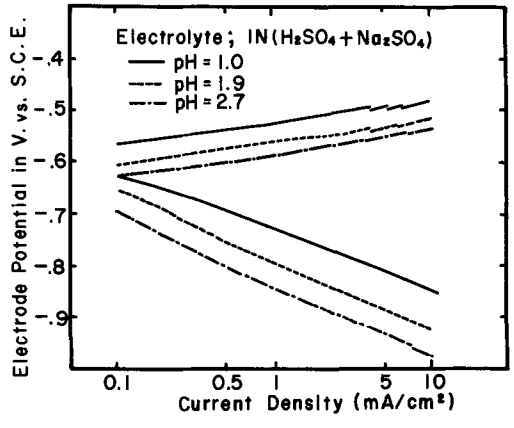

Fig. 2. Rapid polarization curves of Puron in sulfuric acid (N_2 saturated, 25°C).

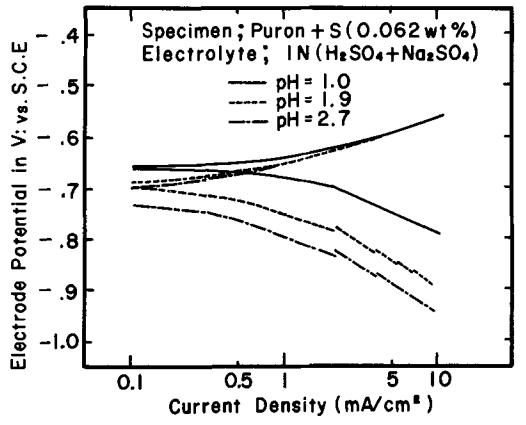

Fig. 3. Rapid polarization curves of sulfur-bearing iron in sulfuric acid (N_2 saturated, 25°C).

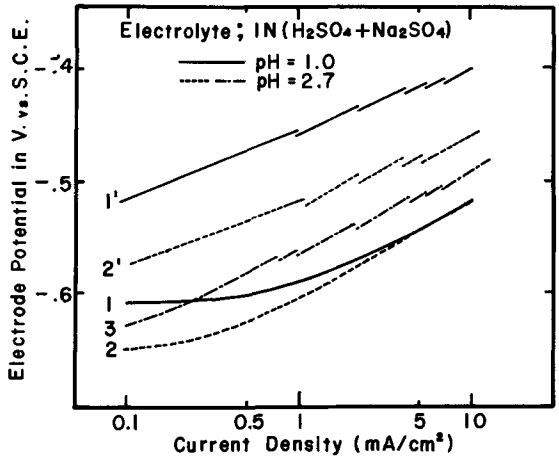

Fig. 4. Effect of Brilliant Blue FCF on anodic polarization of sulfur-bearing iron (N_2 saturated, 25°C). Lines 1,2; $SO_4^=$ solution. Lines 1', 2'; $SO_4^=$ solution containing FCF (1.44 g/liter). Line 3: $SO_4^=$ solution (180 ml) containing cola beverage (20 ml).

These results suggest that some interaction between sulfur and the dyestuff occurs during corrosion of iron.

Effect of SH^- ions on polarization characteristics of iron.—The results mentioned above suggest that the mechanism of the dissolution of the sulfur-bearing iron is somewhat different from that of the sulfur-free iron. It may be assumed that the corrosion of iron was probably affected by the formation of SH^- ions during the dissolution of sulfur-bearing iron. If this assumption is correct, the same behavior as the sulfur-bearing iron should be observed in a solution containing a small amount of sodium sulfide (5 ppm), even for the Puron. As expected, Puron tended to behave in the same manner as the sulfur-bearing iron in the above solution (Fig. 3) showing no detectable *p*H dependence in anodic polarization as shown in Fig. 5.

Discussion

It is well known that the corrosion of iron in acid solution is accelerated by addition of sulfur (1, 2, 6). Concerning the role of sulfur, several investigators (1, 7-9) have suggested that hydrogen sulfide produced by the dissolution of sulfur-bearing steel decreased anodic polarization and others (2) pointed out that sulfur in steel decreased cathodic polarization.

However, none investigated the effect of sulfur on the *p*H dependence of iron dissolution. It is emphasized in this study that the anodic polarization of iron becomes independent of the *p*H of the solution when sulfur is added to iron (Fig. 3).

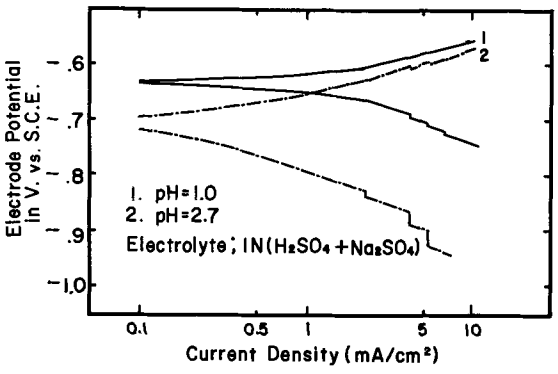

Fig. 5. Effect of the addition of Na_2S (5 ppm) on the rapid polarization curves of Puron in sulfuric acid (N_2 saturated, 25°C).

This fact implies that corrosion mechanism of sulfur-bearing iron is different than that of iron which exhibits pH dependence.

Reaction mechanisms of iron dissolution in acid solution have been presented by several investigators (10-16). Typically

$$Fe + OH^- \rightleftarrows (FeOH)_{ads} + e^- \quad [1]$$

$$Fe + OH^- + (FeOH)_{ads} \rightarrow (FeOH)^+ + (FeOH)_{ads} + 2e^- \quad [2]$$

$$(FeOH)^+ + H^+ \rightleftarrows Fe^{++} + H_2O \quad [3]$$

However, the dissolution reaction of sulfur-bearing iron is difficult to explain by the above reaction mechanism in which the adsorption of OH^- ions are involved, because anodic polarization of sulfur-bearing iron does not show the pH dependence. If SH^- ions exist in the solution, they are expected to be more easily adsorbed than OH^- ions. Thus, a reaction process in which SH^- ions (instead of OH^- ions) take part is introduced in the dissolution mechanism of sulfur-bearing iron.

Accordingly, the following reaction process may be presented

$$Fe + SH^- \rightleftarrows (FeSH)_{ads} + e^- \quad [4]$$

$$Fe + SH^- + (FeSH)_{ads} \rightarrow (FeSH)^+ + (FeSH)_{ads} + 2e^- \quad [5]$$

$$(FeSH)^+ + H^+ \rightleftarrows Fe^{++} + H_2S \quad [6]$$

Since the kinetic data are insufficient in this work, it is not clear whether the dissolution mechanism mentioned above is correct. However, this dissolution mechanism of sulfur-bearing iron is possible because the pH dependence does not appear in this mechanism.

Another important result is that the anodic reaction of sulfur-bearing iron is inhibited by addition of blue dye to the solution (Fig. 4, curves 1' and 2'), and the pH dependence of anodic polarization was observed. These facts suggest that there are some interactions between the dyestuff and the SH^- ions.

The role of dyestuff can be explained as follows: As mentioned above, SH^- ions are probably more easily adsorbed on the iron surface than OH^- ions. When the Brilliant Blue dye is added to the solution, it interacts with SH^- ions and forms a complex compound. Thus, the dissolution of sulfur-bearing iron is inhibited due to the adsorbed Brilliant Blue dye-SH^- complex, as schematically represented in Fig. 6. Under such conditions, OH^- ions contribute to the anodic dissolution of iron. Accordingly, the pH dependence of anodic polarization appears in sulfur-bearing iron when dyestuff is added to the solution (Fig. 4, curves 1' and 2').

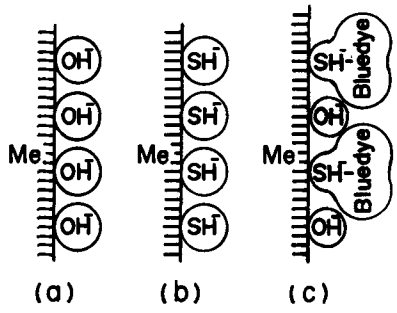

Fig. 6. Schematic representation of inhibition action of blue dyestuff (Brilliant Blue FCF) to SH^- ions. (a) Adsorption of OH^- ions in the dissolution process of pure iron, (b) adsorption of SH^- ions in the dissolution process of sulfur-bearing iron, (c) inhibition action due to SH^--blue dyestuff complex compound.

Conclusion

The corrosion rate of iron in cola beverage is decreased by the addition of sulfur to iron.

Polarization characteristics of iron and sulfur-bearing iron were measured in sulfuric acid, phosphoric acid, and the cola beverage to determine the effect of sulfur on the corrosion behavior of iron. Results were summarized as follows:

1. Polarization curves of sulfur-free iron in sulfuric or phosphoric acid, at pH values ranging from 1.0 to 2.7, depended on the pH, while for sulfur-bearing iron, polarization curves were independent of pH.
2. When SH^- or $S^=$ ions were added to the acid, the polarization curves of iron were independent of pH.
3. Anodic polarization curves of the sulfur-bearing iron shifted in the more noble direction, when Brilliant Blue dye was added to the acid. This effect also appeared when cola was added to the acid.
4. A corrosion mechanism for sulfur-bearing iron in acid is proposed which includes adsorption of SH^- ions.
5. Inhibition action of cola on sulfur-bearing iron was considered to be due to adsorption of a SH^--blue dye complex.

Manuscript submitted June 13, 1969; revised manuscript received Aug. 20, 1971.

Any discussion of this paper will appear in a Discussion Section to be published in the June 1972 JOURNAL.

REFERENCES

1. T. P. Hoar and H. Havenhand, *J. Iron Steel Inst. (London)*, **133**, 239 (1936).
2. Z. A. Foroulis and H. H. Uhlig, *This Journal*, **112**, 1177 (1965).
3. Jap. Pat. 42-23,700 (1967). U. S. Pat. 3,392,014 (1968).
4. G. Okamoto, M. Nagayama, and N. Sato *Proc. 8th Meeting CITCE, Madrid, 1956*, p. 72, Butterworth, London (1958).
5. *Steel*, **157**, No. 22, 66 (1965).
6. M. Stern, *This Journal*, **102**, 663 (1955).
7. A. C. Makrides and N. Hackerman, *Ind. Eng. Chem.*, **47**, 1773 (1955).
8. U. R. Evans, "The Corrosion and Oxidation of Metals," p. 315 (1960).
9. Z. A. Iofa and G. N. Tomashova, *Corrosion*, **19**, 12t (1963).
10. K. E. Heusler, *Z. Elektrochem.*, **62**, 582 (1958).
11. K. F. Bonhoeffer and K. E. Heusler, *Z. Physik. Chem., N.F.*, **8**, 390 (1956); *Z. Elektrochem.*, **61**, 122 (1958).
12. T. Hurlen, *Acta Chem. Scand.*, **14**, 1533 (1960).
13. K. A. Christiansen *et al.*, *ibid.*, **15**, 300 (1961).
14. J. O'M. Bockris *et al.*, *Electrochim. Acta*, **4**, 325 (1961).
15. W. J. Lorenz *et al.*, *Ber. Bunzenges. Physik. Chem.*, **62**, 582 (1958).
16. E. J. Kelly, *This Journal*, **112**, 124 (1965).

Dielectric Breakdown in Electrolytic Capacitors

F. J. Burger* and J. C. Wu

Sprague Electric of Canada Ltd., Toronto 337, Ontario, Canada

ABSTRACT

Starting with the known but unexplained fact that high-voltage electrolytic capacitors need operating electrolytes of high resistivity, breakdown (sparking) voltages of aluminum and tantalum anodes have been examined. If interfering side reactions are eliminated, breakdown voltage increases linearly with the logarithm of electrolyte resistivity and is insensitive to variations in electrolyte composition and to changes in temperature between 65°C and 95°C.

Guntherschulze and Betz, in their classic on electrolytic capacitors (1), considered ionic concentration of electrolytes to be the controlling factor of sparking voltage. They noted the linear dependence of sparking voltage on the logarithm of resistivity of the electrolyte. However, their experiments were limited to aqueous electrolytes and were done at or below room temperature which perhaps was not a good choice because anomalies in the formation process, *e.g.* etching, porous oxide formation and corrosion, are often experienced under those conditions. Some of their quantitative findings are open to doubt (2). Perhaps the phenomenon of sparking in electrolytic capacitors is still not well understood because side reactions may intervene during the formation process, and thus obscure whatever relationships may exist between sparking voltage and other relevant parameters. The reactions on aluminum in the ethylene glycol/borate system are characterized by electrochemical oxidation of the solvent (3), by metal corrosion and the appearance of a rust-colored solid corrosion product that adheres to the aluminum substrate. However, as will be shown, special measures can be taken to suppress these side reactions, particularly in the case of aluminum, with the result that a clear-cut relationship of wide applicability emerges, linking sparking voltages with the logarithm of electrolyte resistivity.

Experimental Technique

Constant current formations of foil specimens were carried out in a temperature-controlled, closed, reaction vessel, watching the rate of voltage rise and noting the voltage at which the sound of sparking could be clearly heard for the first time (at which point there occurs also an abrupt slowdown in the rate of voltage rise). All foil specimens, except when otherwise stated, were 3 cm wide and 5 cm long, the lead being formed by an integral central tab, 0.4 cm wide and 5 cm long which emerged from one of the 3 cm edges of the foil. The aluminum specimens were cut from 99.99% pure foil, either plain (0.0090 cm thick) or etched (0.0070 cm thick). Before anodization, the samples were given a pretreatment by immersing them first, at room temperature, in 1*N* NaOH solution, for 2 min in the case of plain, and for 30 sec in the case of etched foil. This was followed by rinsing in deionized water and then in absolute methanol before drying the specimens at 110°C for about 5 min. In the case of tantalum, plain capacitor grade, 0.0021 cm thick foil was used. The pretreatment here consisted of degreasing by boiling in trichloroethylene then air drying the specimens, and after rinsing them with deionized water, immersing them in 6*N* HNO_3 at 75°C for 1 min. This was followed by another rinse in deionized water, then absolute methanol, and, finally, drying them at 110°C for 5 min. The apparatus in which the formations were carried out was a three-necked 250-ml Pyrex distillation flask with a magnetic stirrer immersed in a temperature-controlled stirred bath of glycerine. One of the two side necks of the flask held a thermometer, the other held the cathode assembly. The cathode consisted of a piece of platinum foil 2 cm wide by 5 cm long by 0.005 cm thick to which was welded the lead, a platinum wire of 0.08 cm diam. The wire was sealed into the glass stopper of the flask and brought out to form the cathode terminal. The anode was suspended from its own tab which was held in a clip made from platinum wire, the other end of the wire passed through a glass tube and a Teflon seal to the outside to make contact with the anode terminal. The glass tube could be rotated and adjusted through a Teflon stopper sitting concentrically in, and closing off, the glass stopper of the large central neck of the flask. Care was taken to see that the specimen/platinum junction was always well above the electrolyte level and was kept dry during the progress of an experiment.

Details of the anodizing and measuring procedures follows. After bringing the electrolyte to the required temperature, the anodization was carried out at constant current densities of 0.5 mA/cm² in the case of plain foil (a total current of 15 mA) and 1.0 mA/cm² for the etched foil. By means of a VTVM connected across the cell terminals, the rise of voltage with time was followed and the voltage noted at which there was no further increase. The rate of rise for plain aluminum foil and the current densities as stated was mostly about 12.5 V/min; with tantalum, it was about 8.6 V/min. With the electrolytes employed, two kinds of voltage limitations were observed. One kind was due to a side reaction taking over from the formation proper and resulting in the appearance of corrosion spots on the foil surface. The other kind was due to the breakdown of the barrier film and characterized by sparking and a sound that was readily noted, especially if the thermometer bearing stopper was raised to facilitate listening. The voltage at which a side reaction or breakdown occurred could be determined with an accuracy of about 5V. Attempts were also made to detect the sparking voltage by counting breakdown pulses electronically, but this was abandoned since it did not result in any worthwhile improvement.

In order to determine the *IR* drop through the electrolyte, the cell constant of the anodization assembly was determined. This was done by substituting for the usual anode specimen a platinum foil electrode of the same shape and size and determining the impedance by an a-c (2.5 kHz) measurement, with electrolytes of known resistivity. The cell constant was thus found to be 7 cm. Hence, for an electrolyte resistivity of 1000 ohm-cm and using a total current of 0.015A the *IR* drop amounted to about 2.1V. The sparking voltage as referred to throughout this paper is defined as the voltage, corrected for the *IR* drop in the electrolyte, at which the sound of sparking is first heard in a formation experiment, the voltage being read by means of

* Electrochemical Society Active Member.

Key words: anodic oxidation, dielectric breakdown, electrolytic capacitors, sparking voltage.

a VTVM connected across the formation cell while the current is maintained at the initial value, *e.g.* 0.015A.

Results and Discussion

Before discussing sparking voltage, some detailed results are given concerning side reactions. When a plain aluminum foil anode was anodized at 85°C at 0.5 mA/cm² in an electrolyte consisting of a 32% by weight solution of ammonium pentaborate in ethylene glycol (ρ 85°C = 110 ohm-cm), a corrosion product formed on the surface of the foil at 280V and became plainly visible on maintaining the current at its initial value for about 15 min. The point of onset of the corrosion reaction was revealed by a sudden reduction to almost zero in the rate of voltage rise from its former value of about 12.5 V/min. The corrosion product was found to be distributed over the foil surface in plugs associated with the rolling marks of the foil.

When etched foil was substituted for plain aluminum foil, no corrosion occurred. Our belief is that the corrosion originates with metallic impurities picked up and rolled into plain foil during manufacture. Thus it is possible to produce this kind of corrosion at will by deliberately contaminating either a plain or etched foil. For instance, if the foil is struck with a hardened steel punch so as to produce a well-defined impression, corrosion will occur in the struck portion of the foil. If the foil is insulated against direct impact by the interposition of another thin Al foil between punch and specimen, no corrosion is observed. If a definite pattern is scratched onto the foil surface with a sharp piece of glass, no corrosion is observed. But, if the scratches are contaminated by exposing them to CrO_3 or $KMnO_4$ solution and heating them briefly to 100°C, then rinsing away the surplus after several minutes' contact, corrosion becomes evident very soon after formation has reached a certain voltage. Both chromium and manganese compounds show a specific ability to cause corrosion. Surprisingly, no effect was observed following contamination with iron or copper. However, attempts to make a positive identification of the contaminants normally present on the surface of plain foil have not been successful.

We have found that the corrosion causing side reactions can be suppressed by small additions of salicylic acid to the electrolyte, presumably because the acid is instrumental in removing corrosion centers by anodic etching during the formation process. The efficacy of salicylic acid addition in thus restoring proper formation conditions for aluminum can be demonstrated in organic solvent as well as in water-based electrolytes. If additions of salicylic acid are made in amounts insufficient to give complete suppression of side reactions, then tree-like etch patterns are seen to be formed on the foil surface as the result of the corrosion reaction. Two typical patterns are shown in Fig. 1 and 2. Figure 1 is a photomicrograph of a portion of a plain Al foil specimen (the actual field diameter is 1.2 mm) that had been formed at 85°C at a current density of 0.5 mA/cm² to the limit possible (400V) and kept at that voltage for 37 min during which time the tree pattern developed. In this case, the electrolyte was composed, in parts by weight, of 12 boric acid, 3.4 tributylamine, 88 ethylene glycol, and less than 0.1 salicylic acid. When the salicylic acid content was increased by a small amount, formation proceeded to 465V at which point sparking occurred, but neither corrosion nor tree formation. Figure 2 is a photograph taken of a 7 cm by 7 cm plain Al foil specimen formed because of its larger size in a 500 ml resin reaction jar at 85°C and 0.5 mA/cm² to the limiting voltage of 390V and kept at that voltage for about 33 min during which time the tree pattern developed. The electrolyte contained, in parts by weight, 12 boric acid, 2.5 ammonium pentaborate, 88 ethylene glycol, and less than 0.05 salicylic acid. Again, after the salicylic acid content was raised slightly, formation proceeded to 485V, where sparking was observed to take place, but

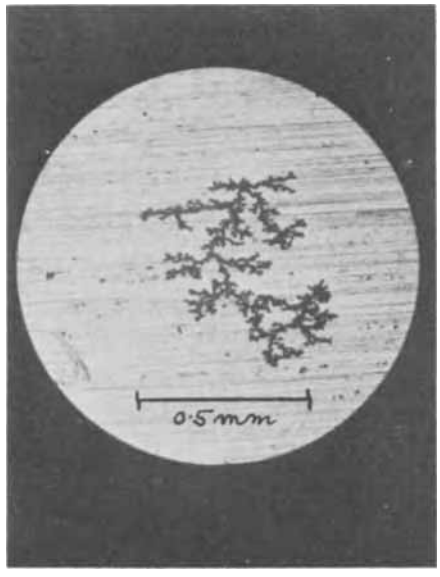

Fig. 1. Photomicrograph of "tree" corrosion pattern on aluminum anode; field diameter: 1.2 mm.

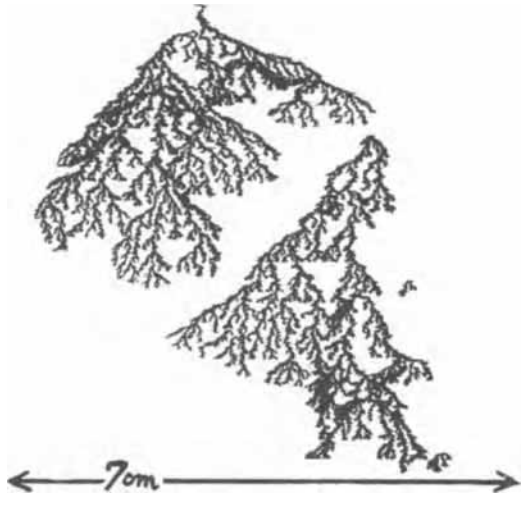

Fig. 2. Large "tree" corrosion pattern developed on aluminum anode specimen measuring 7 cm by 7 cm.

no corrosion or tree formation. The characteristic tree pattern as well as its association with the rolling marks in the foil is clearly evident from both illustrations. Somewhat similar, though possibly not as strikingly characteristic, structures have been reported as occurring in similar circumstances as a result of dielectric breakdown, in both aluminum and tantalum systems (3, 5).

If side reactions are suppressed, formations can proceed right up to the sparking voltage. Sparking voltages obtained by forming aluminum anodes with electrolytes A through I are recorded in Table I.[1] The sparking voltages listed have been corrected for *IR* drop. A plot of sparking voltages *vs.* log of resistivities is shown in Fig. 3. The experiments were done at three different temperatures, and the results are grouped accordingly. As will be seen, the sparking voltage depends linearly on the logarithm of resistivity. The dependence can be represented by a single line obeying the empirical equation

$$V_{Sp} = 123 \log_{10} \rho + 147$$

[1] pH values are as measured with a glass electrode.

Table I. Formation electrolytes for Al—composition, pH, resistivities, and sparking voltages

Composition	A	B	C	D	E	F	G	H	I
	(Parts by weight)								
Ammonium pentaborate	25	15	10	0.5	5	2.5		1	0.5
Dimethyl ammonium pentaborate							2.5		
Boric acid		10	10	5	10	10		10	10
Salicylic acid	0.24	0.18	0.14	0.02	0.1	0.08	0.01	0.06	0.02
Water	10			94.5					
Ethylene glycol	65	75	80		85	87.5	5	89	89.5
Dimethyl formamide							92.5		
pH	5.1	4.1	4.1	5.3	4.1	4.1	7.6	4.0	3.8
65°C Resistivity (ohm-cm)		250	300	330	470	760		1650	3060
V_{Sp} no preform		440	450	460	469	498		547	579
600V preform		475			504	523			
85°C Resistivity (ohm-cm)	77	160	190		300	510	990	1030	1950
V_{Sp} no preform	380	420	430		450	479	518	518	566
600V preform	430	460			485	504			
95°C Resistivity (ohm-cm)		130	160		250	420		900	1600
V_{Sp} no preform		410	420		440	469		508	537

Table II. Formation electrolytes for Ta—composition, pH, resistivities and sparking voltages (both at 85°C)

Composition	J	K	L	M	N	O	P
	(Parts by weight)						
Dimethyl ammonium pentaborate	8.6		4.66		2.5		0.86
Ammonium Di hydrogen phosphate	0.05		0.05		0.05		0.005
Phosphoric acid		0.1		0.03		0.01	
Water		99.9		99.97		99.99	
Ethylene glycol	16.3		9.3		5		1.63
Dimethyl formamide	75.1		86		92.5		97.5
pH	6.0	2.8	6.8	3.4	8.1	3.3	8.2
Operating temperature: 85°C							
Resistivity (ohm-cm)	300	300	490	720	890	1700	3000
V_{Sp}	410	410	439	458	468	506	544

where V_{Sp} = sparking voltage, in volts

and ρ = resistivity, in ohm-cm

Slight deviations from the rule involving aqueous and some organic electrolytes may occur at or near room temperature owing to anomalies in the formation process, but in all other cases experimental results follow the above equation irrespective of variations in electrolyte composition or temperature within the range of 65°C to 95°C. For example, it will be noted that of the aluminum electrolytes those bearing letters B, C, E, F, H, and I are based on ethylene glycol as the solvent, A on a mixture of ethylene glycol and water, D on water, and G on a mixture containing a major portion of dimethyl formamide and a minor portion of ethylene glycol. These electrolytes are typical of a much larger group that were found to confirm the validity of the rule stated above. From the examples listed in Table I and from Figure 3, the range of validity of the straight line relationship is seen to be from 77 to 3000 ohm-cm, corresponding to a voltage range from about 380 to about 580V, respectively. With resistivities greater than 5000 ohm-cm, the sound of sparking is less distinct than with the lower values and hence the measurement of V_{Sp} is somewhat more difficult and less accurate. However, the straight line relationship has been confirmed up to resistivities of 50,000 ohm-cm, the corresponding V_{Sp} being 720V. The results suggest that the sparking voltage/resistivity relationship is of quite fundamental nature. Consequently, the exceptional location of points below or above the straight line whenever it occurs should be taken to indicate an anomaly, either in respect to the anodizing process or to the composition or structure of the anodic oxide.

To test the effect of a pre-existing oxide layer, experiments were carried out with foils that had been preformed. These were first anodized to 600V at 85°C and of 0.5 mA/cm². The formation was continued at the constant voltage of 600V for 2 hr in an electrolyte of suitable resistivity (*e.g.* one very similar to but containing less ammonium pentaborate than electrolyte I of Table I) before determining their sparking voltages in the electrolyte (A, B, E, or F). The results of these experiments are included in Fig. 3 for comparison with those from aluminum anodes not so preformed. As can be seen, the sparking voltage of Al foil preformed to 600V again follows a semilog relationship with electrolyte resistivity. It runs at an angle to and above the standard line, merging into it at and near the 600V range.

Finally, results are given of anodization experiments done at 85°C with tantalum foil. Electrolyte particulars are shown in Table II[1] and the plot of sparking voltages *vs.* log of electrolyte resistivities is shown in Fig. 3 for comparison with the aluminum results. Thus the tantalum results also follow a semilogarithmic relationship. The tantalum line is parallel to that of aluminum, but displaced downward from it by about 40V. Hence, the voltage to which tantalum can be formed in a given electrolyte is always 40V below that of aluminum.

Attempts were also made to compare the behavior of other anodic metal oxides such as niobium and zirconium with that of aluminum and tantalum, but while generally confirming the findings of Alwitt and Vijh

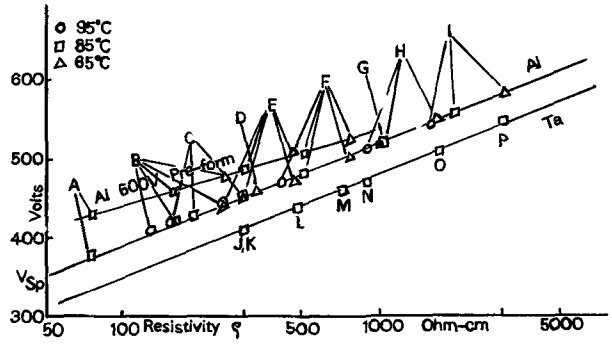

Fig. 3. Sparking voltages (V_{Sp}) *vs.* logarithm of electrolyte resistivities (log ρ): Al foil; Al foil preformed to 600V; Ta foil.

(4) as to the relative order of sparking voltages, namely V_{Sp} of Al > Zr > Ta > Nb, the results were inconclusive because of the scarcity of suitable electrolyte systems for Zr and Nb which permit flawless anodic oxides to be formed over an adequate voltage range.

The interpretation of the empirical semilogarithmic relationship between sparking voltage and electrolyte resistivity which is characterized by an unexpected insensitivity toward temperature changes presents difficulty. Guntherschulze (1) tried to link the phenomenon with the electrochemical potential which is a function of the logarithm of ion concentration, but this explanation is not acceptable today. Young's assumption (2) that the breakdown may not be a bulk phenomenon but may be taking place in electrolyte-filled fissures and flaws of the oxide is probably correct. However, it must be admitted that more work is needed before an adequate theory can be formulated.

Manuscript received Jan. 11, 1971. This was Paper 3 presented at the Los Angeles Meeting of the Society, May 10-15, 1970.

Any discussion of this paper will appear in a Discussion Section to be published in the June 1972 JOURNAL.

REFERENCES

1. A. Guntherschulze and H. Betz, "Elektrolyt-Kondensatoren," Technischer Verlag Herbert Cram, pp. 116-122, Berlin (1952).
2. L. Young, "Anodic Oxide Films," pp. 126-128, Academic Press, London and New York (1961).
3. R. W. Santway and R. S. Alwitt, *This Journal*, **117**, 1282 (1970).
4. R. S. Alwitt and A. K. Vijh, *ibid.*, **116**, 388 (1969).
5. G. Frade, G. Beranger, and P. Lacombe, Abstract No. 15, Electrochem. Soc. Extended Abstracts, Spring Meeting, New York, May 4-9, 1969.

Mössbauer Study of Tin(II) Sensitizer Deposits on Kapton

R. L. Cohen

Bell Telephone Laboratories, Incorporated, Murray Hill, New Jersey 07974

J. F. D'Amico

Western Electric Engineering Research Center, Princeton, New Jersey 08540

and K. W. West

Bell Telephone Laboratories, Incorporated, Murray Hill, New Jersey 07974

ABSTRACT

Mössbauer spectroscopy has been used to study tin(II) sensitizer deposits formed on Kapton films (du Pont polyimide) for use in the recently reported photoselective metal deposition (PSMD) process. Combined with previous results, this work shows that the sensitizer is present as a colloid in the sensitizing bath and is adsorbed on the substrate when it is dipped. This activation mechanism would be expected to apply to other insulating substrates as well. The photosensitive substance contains more tetravalent tin than divalent. The divalent tin is oxidized by exposure either to air or to the Pd activation bath. The photosensitive compound is not any well recognized tin oxychloride or hydroxide.

This paper presents the results of Mössbauer measurements on "tin oxide" sensitizer films as currently prepared and used in the Western Electric Engineering Research Center, Princeton, New Jersey, (ERC) photoselective metal deposition (PSMD) process (1-4). Mössbauer spectroscopy (MS) is a relatively new and powerful technique which can be used to study chemical structure and related properties. The results presented here were obtained using typical PSMD sensitizer deposits formed on Kapton (du Pont polyimide) substrates and supplement other sensitizer film research already in progress at ERC 4,5).

This paper is divided into two parts: The first part briefly discusses the applications of MS to the study of tin compounds and tin chemistry, and also gives, in a highly abbreviated fashion, the techniques and details of the PSMD process. The second section describes the results of the Mössbauer measurements on typical photosensitive layers on Kapton films and discusses the chemical intermediates involved in the sensitization and imaging. In addition, the material deposited on the Kapton film is shown to be similar to that present as a colloid in the solution before dipping.

We make no attempt here to develop a comprehensive discussion and introduction to MS principles and techniques, since a large number of books (6), journal articles, and reviews (7) are already available. However, we show some examples to illustrate the application of MS to already well-characterized tin compounds to give an idea of the possibilities and limitations of the technique. The over-all approach used here, of identifying compounds by distinctive spectral patterns, is a well-established one in many other forms of spectroscopy. For this investigation, the fact that MS is a relatively insensitive technique (in that only the immediate surroundings of the atom being studied affect the observed spectrum) is a definite advantage as it makes it possible to characterize compounds which have only very poorly maintained long-range order. Even highly nonstoichiometric and completely "amorphous" material such as tin atoms frozen into solutions can be studied conveniently.

The data are presented here in the format which has become standard for MS, that is, with "velocity" or

Key words: Mössbauer spectroscopy, electroless plating, sensitization, photochemistry.

Doppler energy shift along a horizontal scale and "counts transmitted" on the vertical scale, so that resonance absorption appears as a dip or a peak pointing downward. The observed lines have two significant parameters, namely their intensities and their positions relative to the zero of velocity. In all of the experiments shown, a source of tetravalent tin (Sn^{119m} in $BaSnO_3$) was used and all experiments were performed with source and absorber at 78°K. Standard MS techniques described in the literature were used. Since a tetravalent tin source was used, the isomer shift between the source and tetravalent tin in the absorber is relatively small, so that lines due to tetravalent tin in the absorber appear near zero velocity. The isomer shift between divalent tin and tetravalent tin is approximately 3-4 mm/sec (8). Thus, lines in the regions near 4 mm/sec can be identified as arising from divalent tin compounds. In both di- and tetravalent compounds, the absorption line can be split into two components of roughly equal intensity by the quadrupole splitting of the nuclear excited state level. This splitting tends to be much more pronounced for divalent tin than for tetravalent tin, because the hybridization of 5s electrons into 5p orbitals in the divalent ion produces a relatively large field gradient at the Sn^{119} nucleus. Variations in the isomer shift are generally attributed to the effects of covalency or of sp hybridization in the bonding of the tin atom.

Figure 1 shows spectra taken by us for a number of stannous compounds which can be considered "well characterized." These compounds are closely related to those used in the PSMD process and their spectra are shown primarily to demonstrate some of the possibilities and limitations of MS as applied to tin chemistry. For all three compounds shown the presence of divalent and tetravalent tin is readily observed and relatively small amounts of tetravalent tin can be seen by this technique (note the trace of tetravalent impurity in the figure). Since the spectrometer repeatability, resolution, and linearity are substantially better than 0.01 mm/sec, it is meaningful to determine line positions to this order of accuracy even though the linewidths are much broader. Figure 1 also shows the expected line positions [taken from a recent publication (9)] for a number of compounds relevant to the PSMD process chemistry. It can be seen that with proper data, the combination of isomer shift and quadrupole splitting provides a reasonably good basis for determining whether two compounds are identical. Thus the unknown may be identified if its spectrum corresponds to that of an already known compound. The compounds for which line positions are shown are all rather similar, being oxychlorides, hydroxides, and hydrated oxides, yet the spectra are obviously distinct.

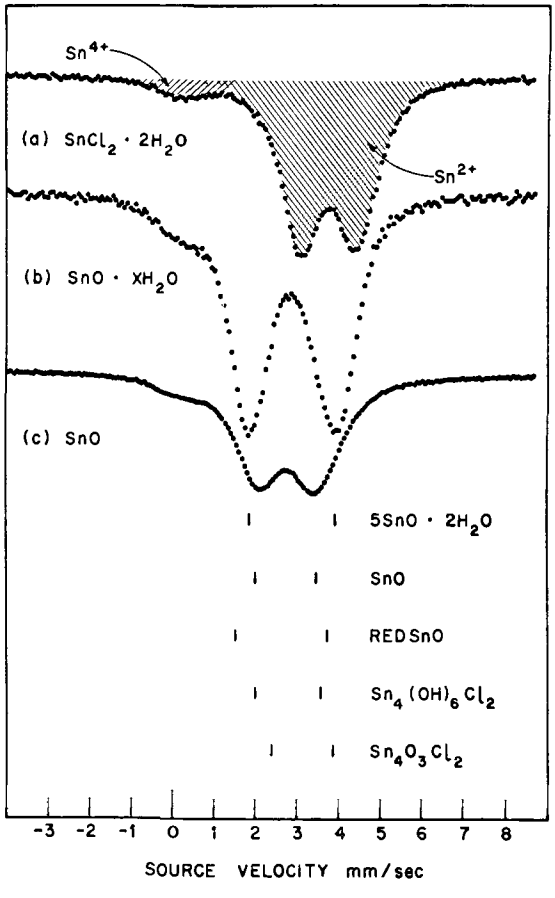

Fig. 1. Observed spectra of three stannous compounds. The $SnCl_2 \cdot 2H_2O$ was Baker, reagent grade; the other two were made in our laboratory by standard preparative techniques. Note the existence of a line due to Sn^{4+} in all samples. Line positions reported in ref. (9) for various well-characterized tin compounds are shown below the spectra.

The chemistry of the electroless metallization used in PSMD is similar to that used throughout the printed circuit industry. When one considers this chemistry in detail, the interest in studying the tin oxides, hydroxides, and hydroxychlorides is obvious. The substrate is dipped into a solution of tin chloride in water and HCl, then rinsed in water and partly dried. The sample is then placed in a dilute solution of palladium chloride in water and HCl, and is subsequently able to catalyze the deposition of copper from a electroless copper plating bath. Thus, it is a quite general technique for metallizing surfaces. The ability to selectively deposit comes from the fact that the sensitizer effectiveness for initiating electroless copper deposition can be destroyed by exposing the sample to ultraviolet light before it is placed in the palladium bath. By the use of appropriate masking it is possible to metallize in selected areas of the substrate and thus to make printed wiring boards and printed cables. Figure 2 shows the process as implemented for the continuous production of printed wiring on flexible substrates. This technique has a number of very obvious advantages for making wiring and cable.

At the initiation of our Mössbauer work, some important aspects of the sensitization process were rather speculative: *e.g.*, the chemical structure of the deposit on the substrate, its changes at various stages in the process chemistry, and the relation, if any, between the deposit and the contents of the sensitizer solution. In addition, it was not known exactly how the uv exposure altered the sensitizer, though it was clear from earlier work (1-5) that the imaging was in fact a light-induced tin oxidation. The use of Mössbauer spectroscopy on this problem offered the possibility of reaching many of these problems, providing a more positive identification of the photosensitive

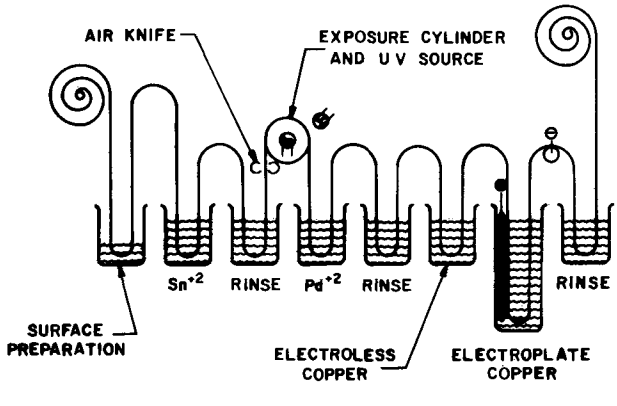

Fig. 2. Outline of the various steps in the PSMD production process [from ref. (4)].

species, and clarifying the results of the earlier ERC experiments.

The tin bath and rinse shown in Fig. 2 deposit on the substrate a thin layer of nominally divalent tin compound. This compound, when immersed in the palladium chloride, reduces palladium ions to their metallic state. The Pd layer on the substrate serves as the catalytic site for deposition of electroless copper. Where the substrate has been exposed to uv light, however, the divalent tin is converted to a tetravalent compound which is unable to reduce the palladium ions. Thus, at sites that have been exposed, no palladium metal is deposited and no copper plating occurs.

In the MS studies reported here, we have examined the sensitizer deposit at various stages in the imaging and metallization process to study the basic chemical processes.

Experimental

Deposits on Kapton.—Specimens were prepared by sensitizing 2 mil Kapton substrates using a solution containing 10g $SnCl_2 \cdot 2H_2O$ and 10 ml conc HCl per liter of deionized water.

Previous work (10) had shown that the amount of tin deposited and remaining on the substrate after the rinse operation was only on the order of a few micrograms per square centimeter. This is about 10,000 times less material than that desirable for an absorber in a tin MS experiment; typically layers containing from 10-50 mg of tin per square centimeter are desirable. This problem was alleviated somewhat by making absorbers from as many as 100 layers of Kapton foil. Each piece of Kapton was "sensitized" on both sides so that there was an increase by 200X in the effective absorber thickness. This increase to the range of 0.1 to 1 mg of tin per square centimeter made it possible to obtain reasonable spectra in about one or two days measuring time. (In contrast, satisfactory spectra of compounds available in bulk, *e.g.*, the spectra in Fig. 1, can be obtained in times from a few minutes to an hour.) Thus, the small amount of tin deposited was not a severe limitation in doing these experiments. The absorbers were prepared by punching ½ in. diameter disks out of the Kapton specimens with a small hand operated punch press and stacking these in a specially prepared absorber well.

To prevent possible sensitizer dehydration under vacuum, specimens were first cooled to ~120°K before pumpdown to 10^{-5} Torr, the pressure at which our MS measurements were made. Those specimens designated as freshly prepared and unexposed were, after sensitization, cooled, pumped down, and measured immediately to avoid air oxidation. The other specimens were stored under nitrogen during the time between their preparation and measurement.

Results

The spectra of the tin-sensitized Kapton foils at various stages of processing are given in Fig. 3 and 4. Figure 3 shows the Kapton foil under normal processing procedures. An inspection of the figure shows immediately that the layer deposited by the sensitization process contains roughly[1] two stannic ions for each stannous ion. We consider this deposit to consist of one substance, probably amorphous, containing both di- and tetravalent tin ions rather than a mixture of a stannous compound with a stannic compound. This is not established here.[2]

A careful examination of the divalent tin line positions shows that the divalent lines do not correspond exactly with line positions expected for any of the oxychloride or hydroxide phases shown in Fig. 1. We have also been able to make two other distinct crystalline phases of oxychloride and hydroxide materials

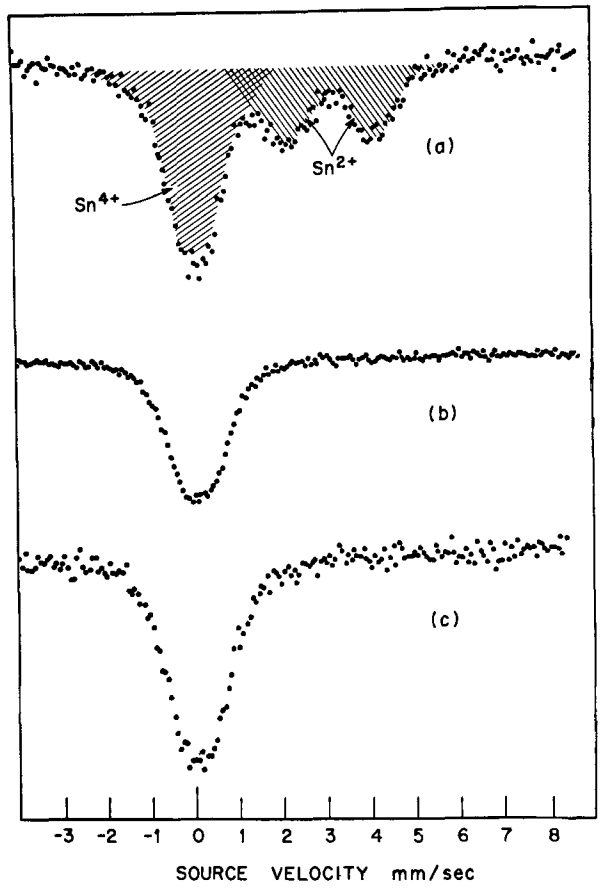

Fig. 3. Spectra of the tin layers on Kapton foil: (a), sensitized by tin bath and unexposed; (b), sensitized by tin bath and uv exposed; (c), sensitized by tin bath and then dipped in Pd solution. The relative amounts of di- and tetravalent tin can be estimated (see footnote 1) from the relative areas in the corresponding spectral lines.

of divalent tin by precipitation from HCl baths under slightly different conditions of *p*H. In no case did the positions of the divalent tin lines in these well-defined compounds correspond to the positions of the divalent tin lines observed in the material deposited on the Kapton. This lends support to the idea that the material deposited on the Kapton is not simply a microscopic mixture of already identified divalent and tetravalent tin compounds. The identification of the sensitizing material is discussed further in the next section and in ref. (11).

The second fact that is immediately clear from the spectra in Fig. 3 is that exposure to uv light oxidizes essentially all of the divalent tin to tetravalent tin. We can estimate roughly (from the lack of noticeable absorption in the region from 2-4 mm/sec) that no more than 10% of the divalent tin remains after uv exposure.

A third result which is evident from inspection of the spectra is that when the sensitized tin layer is placed in the palladium bath, once again essentially all the divalent tin is eliminated. Measurements[3] of tin and palladium on Kapton prepared and processed as we describe here show that (*a*) the amount of tin on the substrate is the same (~10 $\mu g/cm^2$) before and after the palladium treatment, and (*b*) the atomic ratio of tin to palladium on the substrate after the palladium step (plus a water rinse) is approximately 3.8:1. Within the accuracy of the Mössbauer measurements, this shows that the amount of palladium picked up corresponds to the amount of tin oxidized. This supports the picture of a redox reaction $Sn^{2+} + Pd^{2+} \rightarrow$

[1] We assume throughout that the "f value" (recoil-free fraction, related to the strength of the Mössbauer effect) is the same for both the di- and tetravalent tin ions. It is difficult to determine this ratio, and not very significant for the interpretation of the data, which is dependent primarily on the relative proportion of divalent tin under various conditions, rather than the absolute 2+/4+ ratio.

[2] A more extended discussion of the colloid and solution chemistry is given in ref. (11).

[3] Unpublished x-ray fluorescence measurements for palladium and tin on Kapton were made by D. A. Green, J. F. D'Amico, and M. A. De Angelo. Standardization was done by atomic absorption spectroscopy.

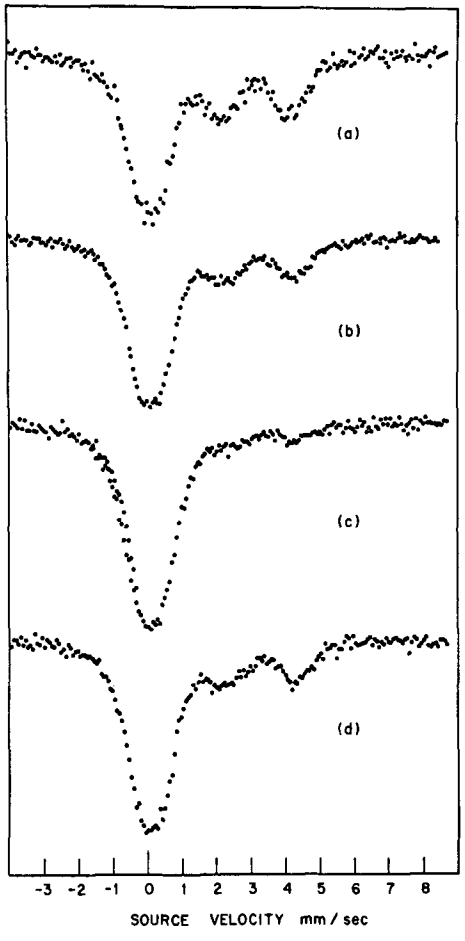

Fig. 4. Spectra of tin layers on Kapton after processing delays: (a), freshly sensitized layer; (b), after exposure to room light (1.5 hr each side, then kept in air for one week); (c), as in (b), but exposed to uv light just before the measurement; (d), as in (b), but after dipping in Pd solution.

Sn^{4+} + Pd, and excludes the possibility[4] that the Pd is picked up by adsorption.

Figure 3 shows the characteristics of the deposited layer at three critical points in the process: the sensitized layer, the exposed sensitized layer, and the layer treated with palladium solution. These samples were made under essentially ideal conditions of processing: fresh bath, careful handling, and negligible time between sensitization and the ultraviolet and palladium treatments.

Figure 4, in contrast, shows the effect on the photosensitive tin layer of such factors as a delay in processing, exposure to room light, or air oxidation. Such factors are known to alter the sensitizer's effectiveness for metallization. At the top of Fig. 4, the spectrum of the freshly sensitized Kapton foil is shown for reference. The second spectrum in Fig. 4 shows a substantial but far from complete oxidation of the divalent tin as a result of 1½ hr exposure to room light on each side plus an additional one week period kept in the dark but in ordinary laboratory air. It can be seen that this exposure substantially decreases, but does not completely remove, the divalent tin present in the sensitized layer. The result of exposure to uv light after this air aging is shown in the third spectrum in Fig. 4. It can be seen that the exposure to uv light after this air aging further decreases, but does not completely eliminate the remaining divalent tin.[5] Figure 4d shows that the spectrum of material dipped in the palladium solution after being exposed to air for one week does not change noticeably suggesting that little or no palladium is deposited. This observation is in accord with the known reduction in the palladium deposit as the photosensitive layer ages in air.[3] A reasonable explanation for this might be that the oxidation forms an impermeable skin of some oxide or hydroxide on the surface of the sensitizer and prevents access of the palladium ions to the remaining divalent tin.

Comparison of sensitizer vs. colloid spectra.—While the line positions for the sensitizer deposit do not match those of the identified compounds, they do closely match those obtained from MS measurements on colloid particles centrifuged from the sensitizer solutions. This result suggests that the deposit on the Kapton is in fact produced by adhesion of the colloid to the substrate at the time of immersion.

The presence of the colloid in sensitizer solutions has already been noted (5), and accordingly, the model used to describe sensitization included a colloid contribution to the total deposit. [The other contribution has been attributed (1-4) to the water rinse and hydrolysis of the soluble in species.] However, it was not possible to determine in the earlier results whether or not the substrate deposit was identical to, similar to, or perhaps quite different from the colloid species in the solution. In Fig. 5(a) we have replotted our results for a fresh tin deposit on Kapton and in Fig. 5(b) we present the Mössbauer results for colloid particles which were centrifuged from a fresh (*i.e.*, 2 hr old) standard tin solution. This separation was made using a field of 110,000G for 2 hr. (If the density of the colloid particles is 2 g/cc, particles > 60Å diameter are separated by this treatment.) Sard (13) has observed by electron microscopy the presence of particles of roughly this size range for deposits on evaporated carbon films from similar solutions. In Fig. 5(c) we show the spectrum obtained from measurements on the products of precipitation filtered from the solution after very long times (~600 hr). The line positions in both Fig. 5(b) and (c) are identical to those found for

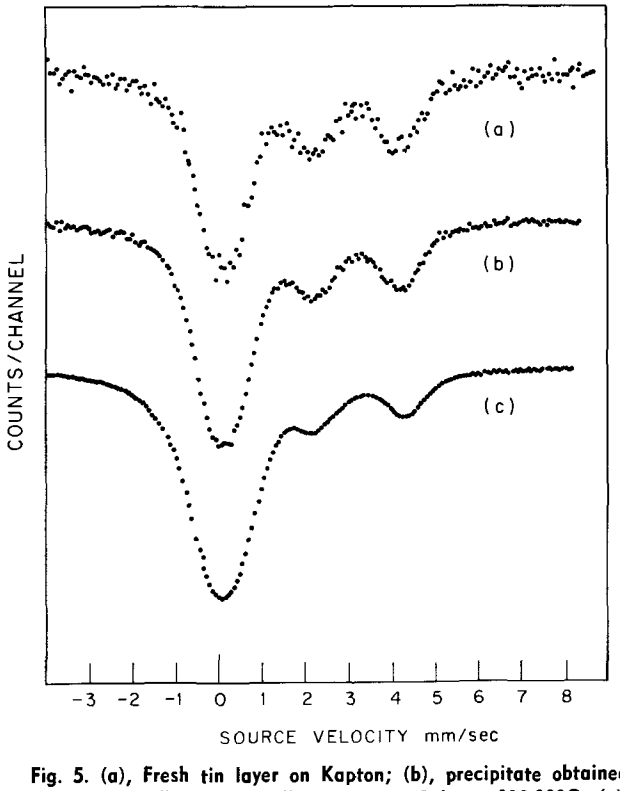

Fig. 5. (a), Fresh tin layer on Kapton; (b), precipitate obtained by centrifuging "standard tin" solution for 2 hr at 110,000G; (c), precipitate produced by aging solution 600 hr in contact with air.

[4] This alternative has been proposed, for example, by Goldie (12).
[5] This conclusion applies when light exposures sufficient to react freshly sensitized specimens are used. In aged specimens large overexposures are required for complete reaction.

the fresh Kapton deposits in (a), although the stannous component in (c), as expected, is greatly reduced.

The data of Fig. 5 suggest that the substrate deposit is in fact chemically identical to the colloid species in the solution at the time of substrate immersion. As the solution ages, the stannous component in solution diminishes.

If the solubility products[6] for the stannous and stannic hydroxides are used to estimate the respective equilibrium tin concentrations in solution, one finds that at $pH = 1$ the stannous solubility is at least 5M, while that of the stannic compound is only 10^{-4}M. Thus it would be reasonable to expect that the colloid is predominantly due to the stannic species, with the stannous ions incorporated by coprecipitation or adsorption onto the colloid (11). This analysis is compatible with the results reported here and in ref. (5).

Summary

Sensitizer deposits formed on Kapton from fresh tin chloride solutions contain roughly twice as much tetravalent tin as divalent. The Mössbauer spectrum of the deposited layer was distinctively different from that of any reported oxide, hydroxide, or oxychloride, and could not have arisen from a simple mixture of such compounds.

Specimens freshly sensitized with fresh solutions when exposed to uv light, or immersed in an acid palladium chloride solution, showed essentially quantitative conversion of the divalent tin component to the tetravalent form. On the other hand, similar specimens aged in laboratory light and air showed only a partial oxidation of divalent tin under these treatments. A possible explanation is that an impermeable barrier layer, which can inhibit the photo-oxidation or the deposition of palladium ions, is formed on standing.

The sensitizer deposit appears identical to the colloid species present in solution at the time of substrate immersion. Thus the adhesion of the colloid to the substrate appears to be a significant source of sensitization. This conclusion agrees with models previously proposed (2-5). In addition, any deposit due to water rinse and hydrolysis of the tin in the liquid layer appears to have the same chemical form. The sensitization mechanism described here would be expected to work for other insulating substrates as well, although no direct verification of this has been done.

[6] These estimates represent lower limits because they neglect the chloride complexing. Solubility products used were taken from Latimer and Hildebrand (14).

Acknowledgments

The authors gratefully acknowledge the technical assistance of M. A. DeAngelo for preparation and sensitization of the specimens. We also thank R. Sard for helpful discussions of the problem and M. W. Sagal for general encouragement. The colloid work was greatly aided by the use of the Biophysics Research Department's ultracentrifuge.

Manuscript submitted June 8, 1971; revised manuscript received Aug. 9, 1971.

Any discussion of this paper will appear in a Discussion Section to be published in the June 1972 JOURNAL.

REFERENCES

1. D. J. Sharp, *This Journal*, **116**, 143C (1969).
2. D. J. Sharp, J. F. Henrickson, J. F. D'Amico, and J. T. Kenney, *ibid.*, **116**, 295C (1969).
3. D. J. Sharp, J. F. Henrickson, J. F. D'Amico, and J. T. Kenney, 23rd Annual Conference, Photographic Science and Engineering, New York May 1970.
4. D. J. Sharp, *Proc. Third Plating in Electronics Industry Symposium*, American Electroplaters Society, Palo Alto, Calif., Feb. 1971, p. 103.
5. J. F. D'Amico, M. A. De Angelo, J. F. Henrickson, J. T. Kenney, and D. J. Sharp, *This Journal*, **118**, 1695 (1971).
6. G. K. Wertheim, "Mössbauer Effect: Principles and Applications," Academic Press, New York (1964).
7. R. H. Herber, in "Progress in Inorganic Chemistry," Vol. 8, p. 1, F. A. Cotton, Editor (1967).
8. M. Cordey-Hayes, *J. Inorg. Nucl. Chem.*, **26**, 915 (1964); V. I. Goldanskii, *At. Energy Rev.*, **4**, 3 (1963).
9. C. G. Davies and J. D. Donaldson, *J. Chem. Soc. (A)*, **1968**, 948.
10. P. Sewall, Masters Thesis, Lehigh University, June 1969.
11. R. L. Cohen and K. W. West, Submitted to *This Journal*.
12. W. Goldie, "Metallic Coating of Plastics," Vol. I, p. 51, Electrochemical Publication Ltd. (1968).
13. R. Sard, *This Journal*, **117**, 864 (1970).
14. W. M. Latimer and J. H. Hildebrand, "Reference Book of Inorganic Chemistry," 3rd ed., p. 562, MacMillan Co., New York (1951).

Calculations of Profitability in Electrolysis Installations

Alfred Schmidt[1]

Chemische Werke Hüls AG, Marl, Kreis Recklinghausen, Germany

ABSTRACT

Simple mathematical relationships, which can be used for all kinds of electrolysis installations, were derived by the methods of investment calculations. It is possible to calculate rapidly with these relations by means of a few characteristic numbers, the most economical current load of electrolysis cells, bus-bars, and electrodes, and to investigate the influence of the various cost factors on the optimum load, such as price of electric current, cell potential, cost of installation, lifetime, rate of interest on capital, and taxes on profits. The determination of the characteristic numbers and the use of the formulas are explained by means of examples of electrolytic chlorine production in mercury cells.

Optimum Load of Electrolysis Cells

In planning nonelectrochemical installations as a rule we use the smallest possible number of reactors of the largest possible size to keep the installation costs low. In order not to have too great a loss of production when a reactor breaks down, the economic and operating optimum ought to be at about 2-4 reactors. These considerations do not prove to be correct in the construction of electrolysis installations, because a minimum number of production units which is far larger than the numbers mentioned above is needed for tech-

[1] After retirement active as consulting engineer. Present address: 6241 Eppenhain/Ts, Im Birkenfeld 12, West Germany.

Key words: economics, optimization, mercury cell.

nical reasons (*e.g.* current rectification, limitation on the construction of larger electrolysis cells).

The modern development of the silicon and germanium rectifiers today permit an economic rectification of current, even at potentials down to 100V. Even at these potentials a minimum number of 10-25 cells is still necessary in electrolytic processes which normally operate with cell potentials in the range of about 4-10V.

In electrolytic processes the level of production of an electrolysis cell depends only upon the magnitude of the current, according to Faraday's law. Therefore, it must be decided in planning whether it is more economical to produce the desired capacity with a smaller number of cells at higher circuit currents or with a larger number at lower circuit currents. In the first case the installation costs of the cells are indeed smaller, but the costs of specific current consumption is higher. On the other hand in the second case we attain lower specific current consumption with higher installation costs. Thus for a given level of production two alternatives are possible:

Alternative 1. Equal current densities and thus equal potentials and equal specific energy consumption with the supposition of equal current efficiency. The installation is equipped with a few larger cells at a higher circuit current or with a larger number of smaller cells at lower circuit current. In Alternative 1, (see Fig. 1), the installation comprises a fewer number of larger cells, as compared to the base case with equal current density. The investment costs of the cells will be less, but the costs of the rectifier unit will be higher.

The most economical combination will be found by minimizing total costs of cells and rectifier installations. Above a certain minimum plant capacity, this generally leads to a choice of the fewest possible cells of the largest possible type.

Alternative 2. Different current densities and thus different cell potentials and different specific energy consumption at the same current efficiency. We use a smaller number of cells at higher current density or a larger number at lower current density. In Alternative 2 (see Fig. 1), the installation comprises a fewer number of cells of the same size, operating at a higher current density as compared to the base case. In this alternative, total installation cost is indeed lower, but the continuous operating costs increase considerably at higher current densities.

The object of this paper is to find, for a desired capacity, the optimum circuit current for a certain cell type and with it the number of cells required. The object is not to derive the optimal physical size of the cell type, which is dependent upon the desired production capacity and the limit of economic current rectification.

Chemical process reactors can be brought to higher capacity within the permissible limits with a relatively small additional consumption of energy (higher gas or liquid pressure, larger heat-exchanger surfaces, etc.). These installations as a rule operate more economically, the higher they are loaded, *i.e.* the more we produce with the installed capital. On the other hand, the higher load on electrolytic cells requires a higher cell potential in electrolysis processes and thus a quite important increase in the specific current costs, so that the question concerning the economical optimum of circuit current is here very much more difficult to determine.

In planning electrolysis installations the tendency today is to maximize the current density in order to produce as much as possible with minimum investment costs. In these attempts, the economic point of view should not be disregarded. The designer is faced with the question where the optimum current load for the cells lies. Whether, for example, it is more economical to attain the desired production capacity with a smaller number of cells at higher current density, or with a larger number of cells at lower current density. In addition to this, the load for the bus-bars, switches and for the electrodes must be optimized.

As a rule the profitability of an investment is judged by the level of interest on the invested capital or by the period of time in which the investment is returned. In the present problem we are dealing with only a relative comparison of alternatives for the same manufactured products at the same level of production and thus also with same proceeds for the products so that the proceeds could be disregarded here. In the same way, all of the costs that do not change for the various alternatives can remain outside of consideration. These are all of the costs, which arise from the manufacturing before and after electrolysis, and the costs within the electrolysis stage which are independent of the number of cells.

Several authors have already concerned themselves with the problem of the optimum design of electrolysis installations (1-7). In the following, simple mathematical relationships are developed. They shall help the designer to picture the optimal conditions of an electrolysis installation rapidly to himself by means of a few characteristic numbers (number and load of the cells, cross section of the bus-bars and the electrodes, etc.). These methods, like all investment calculations, could only be evaluated as approximations, since it is impossible to predict price and technical developments for years ahead. However, the results give a valuable reference point for deciding how the installation should be designed under the conditions which exist at the time of planning.

In the present method the optimal circuit current is determined, where for a given period of the investment return, and for a fixed rate of interest, the sum of investments including interests corresponds to the return of the yearly savings including interests (cash flow). The use of these methods remains limited to the planning of a uniform installation. Thus, for example, the question of whether it is more economical to load an existing installation higher or to establish a second new installation for a desired increased production, can be settled only from case to case on the basis of the existing situation. It is also not possible to consider with this method the intention to increase the capacity at a later date because the resulting factors are unknown and can therefore not be taken into consideration in the mathematical derivations. In this case the owner of the plant has to decide to what extent he will probably increase the capacity. If the probability is high, he has to decide if he will calculate the optimum for the intended end-capacity. If the probability is not high, he could decide to calculate the optimum for the first capacity or for a certain higher per cent of the possible end-capacity.

Example:	Fixed planned capacity	100,000 tons/year
	Possible demand in future	200,000 tons/year
	Calculations for the optimum load could be made for:	
		100,000 tons/year
		150,000 tons/year
		200,000 tons/year

The final decision is only in the hands of the owner and is his own risk. It depends upon the probability, the time, and to what extent the increase of the capacity will occur.

In order to design an installation for the desired capacity, we must first establish the size of cell (electrode surface). In this example a size of cell is chosen [see Fig. 1, Alternative 1] which permits operation in the lower potential region where the current rectification is still economical at the desired production capacity, *i.e.* the fewest possible number of cells of the largest possible size and used. The optimum current density is then calculated for this type of cell. The result of this calculation determines the number of

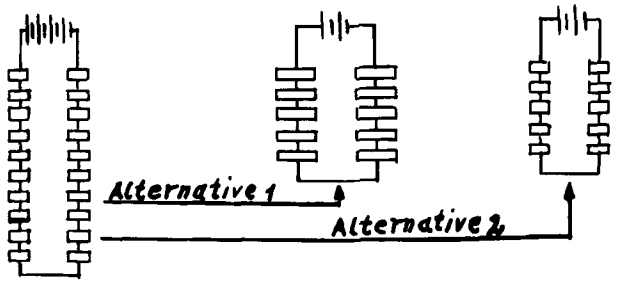

Fig. 1. Distribution of production by number of cells and current load.

Number: 2N cells	N cells	N cells
Load: I_T amperes	2 I_T amperes	2 I_T amperes
Electrode surface: S m²/cell	2 S m²/cell	S m²/cell

cells for the desired production capacity. In the following derivation a few simplifying assumptions have been made which however, do not significantly influence the result:

(a) Cell resistance does not change with the load (presuppositions: the same electrolyte temperature, the same electrolyte concentration, the same electrode distance, the same resistance of the current conductors, etc.).

(b) The current efficiency remains unchanged.

(c) Within the range of loading the current density and cell potential are linearly related.

(d) The life time of the cells shall be independent of the current density.

Not only the specific current costs change at a given level of production with the number of cells, but also the repair and operation costs. It should further be considered that the savings in current costs attained by higher investment costs are additional profits for the manufacturer and as such are subjected to taxation. Finally the investment costs of the rectifier plant are higher at the same electrical capacity if the available current intensity shall be higher.

For these various alternatives corresponding derivations are developed in stages as follows: (a) Only savings in electric current are considered. (b) Savings in electric current, repair and operation costs are considered. (c) Savings in electric current, repair and operation costs, and taxes on profits are considered. (d) The influence of the rectifier costs upon the optimum current load is examined.

Derivation of the optimum load under consideration of savings in current.—The equation for the current costs of an electrolysis installation (C_I) at a current load, I_T, polarization potential, V_p, the average specific resistance of the cells including the supply lines from the rectifier, R_r, time, t, current price, P_I, and the number of cells, N, is

$$C_I = (V_p + I_T \cdot R_r) \cdot I_T \cdot t \cdot P_I \cdot N \cdot 10^{-5} \quad [1]$$

At a constant-level of production the cell amps are constant

$$I_T \cdot N = \text{constant} = K, \quad \text{or } N = K/I_T \quad [2]$$

accordingly

$$C_I = (V_p + I_T \cdot R_r) \cdot t \cdot K \cdot P_I \cdot 10^{-5} \quad [3]$$

If the fixed amount of current cost is

$$F_I = V_p \cdot t \cdot K \cdot P_I \cdot 10^{-5} \quad [4]$$

and the factor of the varying part of cost is

$$b_I = R_r \cdot t \cdot K \cdot P_I \cdot 10^{-5} \quad [5]$$

then

$$C_I = F_I + b_I \cdot I_T \quad [6]$$

In this equation the fixed current cost F_I, is given by the polarization potential, V_p. b_I is defined by the slope of this line (increasing current costs with increasing current load). In case of investment costs, y_I, per cell the total investment costs of an electrolysis are

$$Y_i = y_T \cdot N \quad [7]$$

According to Eq. [2], it follows

$$Y_i = \frac{y_T \cdot K}{I_T} \quad [8]$$

If the electrochemical equivalent of the electrolysis product in g/A-hr is called e and the current efficiency, U, the constant, K, for a production of M_T tons/year product is calculated as follows

$$M_T = I_T \cdot t \cdot e \cdot \frac{U}{100} \cdot N \cdot 10^{-6} \quad [9]$$

From Eq. [2]

$$N = K/I_T \quad [10]$$

and

$$K = \frac{M_T \cdot 10^{-8}}{t \cdot e \cdot U} \quad [11]$$

follows.

To determine the optimum load, we calculate on one side the sum of the incremental change in current costs, when changing the circuit current; and on the other side the sum of the incremental change in investment costs, when changing the number of cells. All these costs include interest in full measure for a time of n years. We can calculate the optimum load, if these two sums have attained the same amount, as follows.

Between two current loads I_T and $I_T + \Delta I_T$:

1. the change in the current costs C_I, upon changing the current load I_T by ΔI_T is

$$\frac{\Delta C_I}{\Delta I_T} = \frac{F_I + b_I(I_T + \Delta I_T) - (F_I + b_I \cdot I_T)}{\Delta I_T} = b_I \quad [12]$$

and

2. the change in the expenditure for investment Y_i, with change of the current load I_T by ΔI_T is

$$\frac{\Delta Y_i}{\Delta I_T} = \frac{1}{\Delta I_T}\left(\frac{y_T \cdot K}{I_T} - \frac{y_T \cdot K}{I_T + \Delta I_T}\right) = \frac{y_T \cdot K}{I_T \cdot (I_T + \Delta I_T)} \quad [13]$$

The ratio in the change of the current costs to the change in the investment costs is then

$$\frac{\Delta C_I}{\Delta Y_i} = \frac{b_I}{y_T \cdot K} \cdot I_T(I_T + \Delta I_T) \quad [14]$$

The increased investment (Eq. [13]) is to be paid before the installation[2] is set into operation and interest is paid in full measure for this time. After $n + 1$ yr its sum is

$$\sum_0^n \frac{\Delta Y_i}{\Delta I_T} = \frac{\Delta Y_i}{\Delta I_T} \cdot Z^{(n+1)} \quad [15]$$

The savings in current (Eq. [12]) occurs annually[3] and it is likewise charged with interest correspondingly. After n years it amounts to

$$\sum_1^n \frac{\Delta C_I}{\Delta I_T} = \frac{\Delta C_I}{\Delta I_T} \cdot \frac{Z^n - 1}{Z - 1} \quad [16]$$

The capital is returned when the two sums have attained the same amount

$$\frac{\Delta C_I}{\Delta I_T} \cdot \frac{Z^n - 1}{Z - 1} = \frac{\Delta Y_i}{\Delta I_T} \cdot Z^{(n+1)}$$

The result is

[2] Since the investments are made before the savings occur, interest is paid on them for a full year previously in the following calculations. This corresponds to a construction time of about 2 yr.

[3] It is required that the level of savings remains constant. According to this, changes in costs are not taken into consideration.

Table I. W-Values for various interest factors, Z and years, n

n	Z = 1.050	Z = 1.060	Z = 1.070	Z = 1.075	Z = 1.080	Z = 1.090	Z = 1.100
5	0.243	0.252	0.261	0.266	0.270	0.280	0.290
10	0.136	0.144	0.152	0.157	0.161	0.170	0.179
15	0.101	0.109	0.117	0.122	0.126	0.135	0.145
20	0.084	0.092	0.101	0.105	0.110	0.119	0.129
25	0.075	0.083	0.092	0.096	0.101	0.111	0.121
30	0.068	0.077	0.086	0.091	0.096	0.106	0.117

$$\frac{\Delta C_I}{\Delta Y_i} = \frac{Z^{(n+1)}\,(Z-1)}{Z^n - 1} = W \qquad [17]$$

Equation [17] cannot be simplified any further mathematically, and we must therefore take the values for $W = C_I/Y_i$ for various values from n and Z from tables or curves. Values of W for various rates of interest are gives in Table I.

By combination of Eq. [14] and [17] we obtain

$$\frac{b_I}{y_T \cdot K} \cdot I_T(I_T + \Delta I_T) = W \qquad [18]$$

For a small value of I_T we obtain for the product $I_T \cdot (I_T + \Delta I_T) = I_T^2$ and with it the following relationship for the current intensity I_T

$$I_T = \sqrt{\frac{W \cdot y_T \cdot K}{b_I}} \qquad [19]$$

In this derivation the factor b_I, as the slope of the current cost line, takes into consideration only the savings in current costs with increasing investment, or the increased costs of current with decreasing investment. The personnel and repair costs, c_T, have not previously been taken into account. They change with the investment (number of cells). The influence of taxes on profit shall also be considered in the next sections.

Derivation of the optimum current intensity under consideration of savings in current, repair and operation costs.—The savings in current obtained with a larger number of cells are decreased by higher personnel and repair costs. The changes in these costs with the circuit current depend upon the number of cells, N, and are given by a hyperbolic function, like the investments.

Corresponding to Eq. [8] is

$$C_T = \frac{c_T \cdot K}{I_T} \qquad [20]$$

and according to Eq. [13] for the change of C_T with I_T

$$\frac{\Delta C_T}{\Delta I_T} = \frac{c_T \cdot K}{I_T(I_T + \Delta I_T)}$$

In Fig. 2 the installation costs, Y_i, the current costs, C_I, the personnel and repair costs, C_T, as well as the current costs minus the personnel and repair costs $(C_I - C_T)$ are plotted against the current intensity for the calculation example given later. The shape of the curves show that the factor b_T for the current costs modified by the personnel and repair costs is no longer constant like b_I but depends upon the current load, I_T

$$b_T = b_I - \frac{c_T \cdot K}{I_T(I_T + \Delta I_T)} \qquad [21]$$

Only at higher current intensities ($I_T > 150{,}000$A) the function, C_T, (curve ▲) again approaches a straight line, so that b_T is again approximately constant.

If we insert the equation for b_T in place of b_I in Eq. [19] we obtain

$$I_T = \sqrt{\frac{K(W \cdot y_T + c_T)}{b_I}} \qquad [22]$$

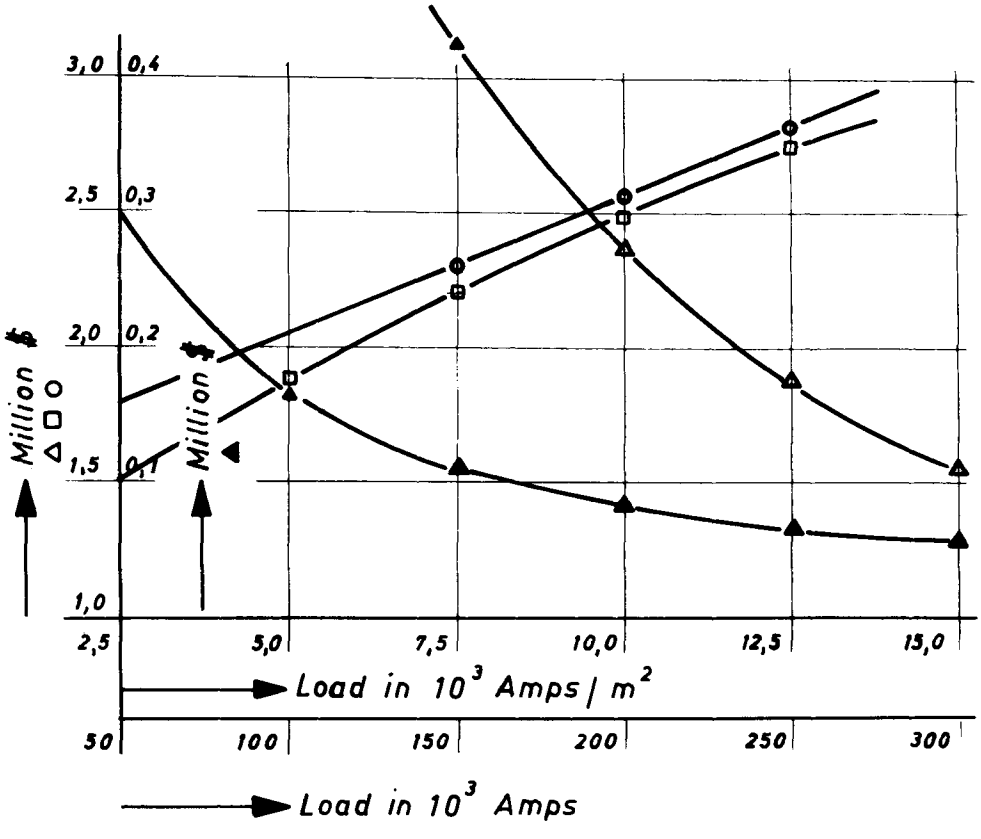

Fig. 2. The costs as function of current load. Curve ○, current costs $C_I = F_I + b_I \cdot I_T$; curve □, current costs minus personnel and repair costs $C_I - C_T$; curve △, investment costs Y_i (including mercury); curve ▲, personnel and repair costs C_T.

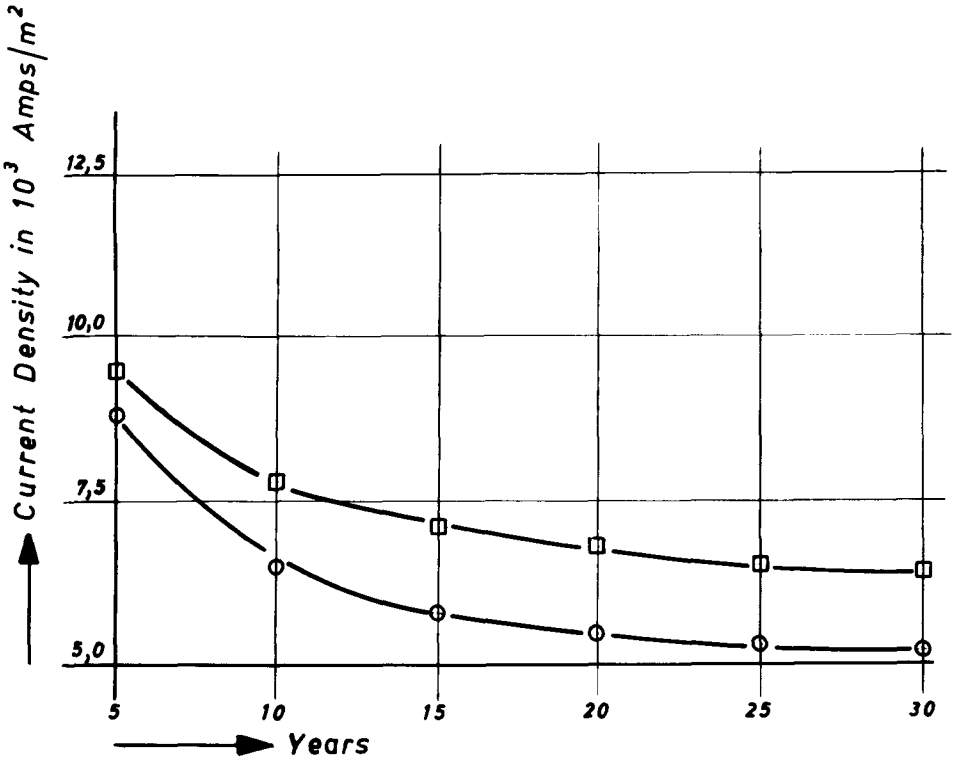

Fig. 3. Change in the optimum current load I_T with the operating time n Curve □ I_T calculated by Eq. [22] for a 20 m² cell. Curve ○ I_T calculated by Eq. [26] for a 20 m² cell.

From this simple relation we can calculate the optimum current load with a few characteristic numbers. As a rule in this type of calculation all of the dimensions (K,y_T,b_I,Z,c_T)[4] will be fixed so that only I_T and n remain as variables. The times in which the invested capital is returned may be fixed by the choice of n. The current density is plotted against the operation time in Fig. 3, for the calculated values of examples on page 2051. The smaller n is chosen the higher is the current load, I_T (fewer cells with a smaller installation cost).

Derivation of the optimum current density under consideration of savings in current, repair, and operation costs and taxes on profit.—In the derivation of Eq. [19] and [22], it has not been taken into consideration that the savings of current costs obtained with higher investment costs must in general be taxed by the company as additional profit. In this way the effective savings in current costs are reduced by the amount of taxes on profit. The slope b_p of the resulting cost curve is calculated from b_I with depreciation λ_i and a tax rate of P per cent[5]

$$b_p = \frac{(b_T - \lambda_i)(100 - P)}{100} + \lambda_i = b_T \cdot \frac{100 - P}{100} + \lambda_i \frac{P}{100} \quad [23]$$

According to Eq. [13] the depreciation λ_i of the incremental investment for a depreciation rate of i % is[6]

$$\frac{\Delta\lambda_i}{\Delta I_T} = \frac{y_T \cdot K \cdot i}{I_T(I_T + \Delta I_T) \cdot 10^2}$$

$$\lambda_i = \frac{y_T \cdot K \cdot i}{I_T^2 \cdot 10^2} \quad [24]$$

[4] Z and n are contained in W (see Eq. [17]).

[5] According to the "cash flow" method of calculation, only the amount of b_T decreased by the depreciation λ_i is taxed, so that the amount remaining after the subtraction of the taxes must again be increased by the depreciation λ_i.

[6] Here a linear depreciation is used to simplify the calculation.

If we introduce into Eq. [23] the term for

$$b_T = b_I - \frac{c_T \cdot K}{I_T^2} \quad [21] \text{ and for } \lambda_i = \frac{y_T \cdot K \cdot i}{I_T^2 \cdot 10^2} \quad [24]$$

we obtain

$$b_p = \frac{1}{100 \cdot I_T^2}(I_T^2 \cdot b_I(100 - P) - c_T \cdot K(100 - P) + y_T \cdot K \cdot P \cdot i \cdot 10^{-2})$$

According to the relation corresponding with Eq. [19], we obtain

$$b_p = \frac{W \cdot y_T \cdot K}{I_T^2}$$

From these two equations results for

$$I_T = \sqrt{\frac{K}{b_I(100 - P)}(100 \cdot W \cdot y_T + (100 - P)\, c_T - P \cdot y_T \cdot i \cdot 10^{-2})} \quad [25]$$

At a tax rate of $P = 50\%$ the equation simplifies to

$$I_T = \sqrt{\frac{2K}{b_I}[(W \cdot y_T + 0.5\,(c_T - y_T \cdot i \cdot 10^{-2})]} \quad [26]$$

In Eq. [25] and [26] the term, $y_T \cdot W$, stands for the interest on the whole investment capital, the term, $y_T \cdot i$, for the depreciation of the investment capital. If parts of the investment shall not be depreciated as for example mercury in a mercury cell chlorine plant, then y_T in the term, $y_T \cdot i$, must be decreased by this part of the investment.

Influence of the installation costs of the rectifier plant.—The costs of a rectifier installation are higher, the higher the circuit current. Figure 4 shows, for a rectifier installation of 50 MW, how much these costs depend on the circuit current, I_T. The plotted relation is a straight line, from which the equation for the installation costs, Y_E, may be deducted as

$$Y_E = F_E + b_E \cdot I_T \quad [27]$$

The optimum current load with consideration of the rectifier costs and the savings in current corresponding to Eq. [19] is then

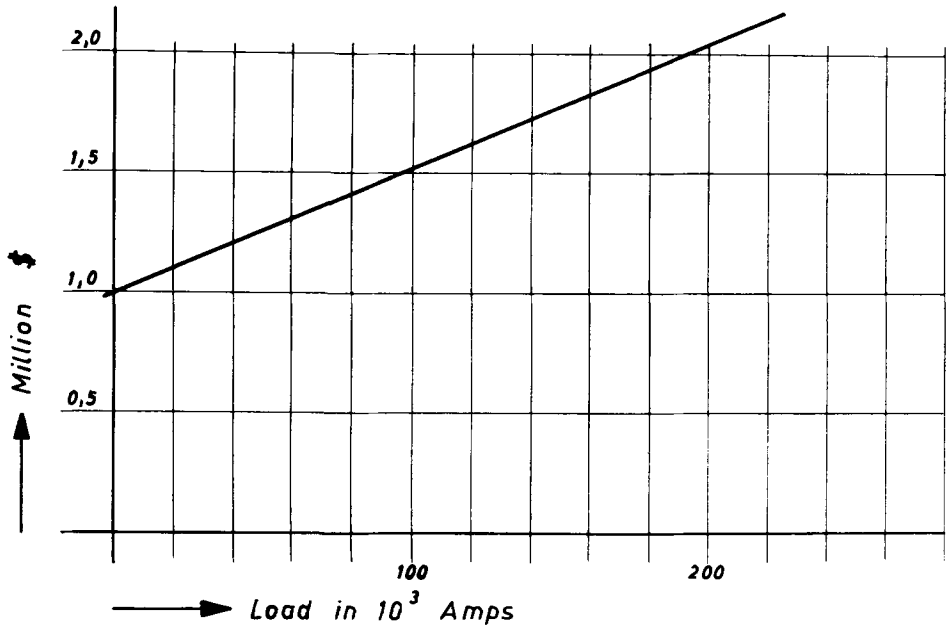

Fig. 4. Rectifier installation costs as function of current intensity for an installation of 50 MW.

$$I_T = \sqrt{\frac{W \cdot y_T \cdot K}{b_I + W \cdot b_E}} \qquad [28]$$

in which case $W \cdot b_E$ is the part of the variable installation costs for the rectifier per year. Figure 4 indicates a value of 5.37 for b_E.

Use in practice and calculation examples.—Using these relations in practice one proceeds as follows: (*a*) Look at the largest cell type, which can be used for the intended capacity, for the largest type will normally be the cheapest, related to its capacity. Thereby consider the lowest direct current voltage of the rectifier plant. (*b*) Determine all items, needed for Eq. [25] and [26] (compare the following examples) and calculate I_T. (*c*) I_T gives the production capacity of one cell, so that one can calculate the number of cells required for the desired production. (*d*) If the calculated optimum current intensity should be too low or too high for the chosen cell equipment (cell bottom, bus-bars, etc.) one may change y_T (cell type, equipment, etc.) and repeat the calculation.

The practical use shall be shown on the example of a chlorine electrolysis with amalgam-cells. The optimum current on circuit of an installation with a capacity of 60,000 tons chlorine/yr shall be determined.

The pretesting of this project shall have shown that the lowest limit of the rectifier voltage is 150V. At this potential an installation of 30-60 cells is needed to reach the desired production at current intensities of 90,000-150,000A. The suitable cell type for the current range is the 20 m² cell. Its average electrical resistance under operating conditions including all bus-bar losses beginning from the rectifiers shall be 11.0 x 10^{-6} ohm for each cell.

Moreover, the following numbers are used for the calculation:

t	= 1 year	8750 hours
U	= current efficiency	= 95%
R_r	= ohmic resistance of the cell	= $11.0 \cdot 10^{-6}$ ohm
c_T	= operation and repair costs per cell	= $3 \cdot 10^3$ \$/year
P_I	= electrical power price	= 1 \$/100 kWh
K		= $5.45 \cdot 10^6$ (Eq. [11])
b_I		= 5.28 \$ (Eq. [5])
Z_i	= rate of interest	= 7.5%
Z	= factor of interest $= \frac{100 + Z_i}{100}$	= 1.075
P	= tax on profits	= 50%
i	= depreciation/year	= 5%
n	= years after the startup of the plant	= 20
W	= for Z = 1.075 and n = 20	= 0.105

Example to 1: According to Eq. [19], we obtain

$$I_T = \sqrt{\frac{W \cdot y_T \cdot K}{b_I}} = \sqrt{\frac{0.105 \cdot 0.085 \cdot 10^6 \cdot 5.45 \cdot 10^6}{5.28}}$$

$$= I_T = \sqrt{92 \cdot 10^8} = 96.000\text{A}$$

Example to 2: According to Eq. [22], we obtain

$$I_T = \sqrt{\frac{K(W \cdot y_T + B)}{b_I}}$$

$$= \sqrt{\frac{5.45 \cdot 10^6 (0.085 \cdot 10^6 \cdot W + 3 \cdot 10^3)}{5.28}}$$

$$= \sqrt{1.23 \cdot 10^{10}} = 111.000\text{A}$$

Example to 3: According to Eq. [26], we obtain

$$I_T = \sqrt{\frac{2K}{b_I}[(W \cdot y_T + 0.5\ (c_T - y_c \cdot i \cdot 10^{-2})]}$$

$$= \sqrt{\frac{10.9 \cdot 10^6}{5.28}(W \cdot 0.085 \cdot 10^6 + 0.5\ (3 \cdot 10^3 - 0.065 \cdot 10^6 \cdot i \cdot 10^{-2})} = \sqrt{1.795 \cdot 10^{10}} = 135.000\text{A}$$

y_c	= costs per cell	= $0.065 \cdot 10^6$ \$[7]
y_m	= mercury costs per cell	= $0.020 \cdot 10^6$ \$
y_T	= total costs per cell	= $0.085 \cdot 10^6$ \$

[7] These costs proportionately cover all costs depending directly on the number of cells such as bus-bars, pipe lines, building of the cell room, etc.

In Table II the optimum current load I_T of the 20 m²-cell has been calculated for some other values of n, accordingly for i and W too.

These optimum current loads are the basis of the calculation for the three examples of Table II for a chlorine production of 60,000 tons/yr covering the values assembled in Table III for the number of the

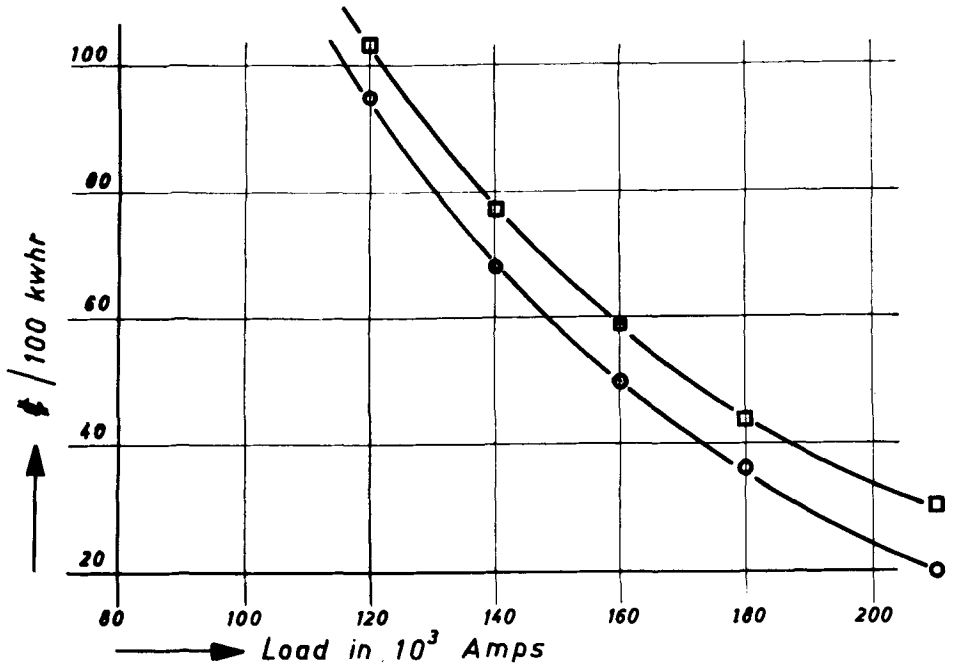

Fig. 5. Optimum load as function of current price. Curve ○, with rectifier costs; curve □, without rectifier costs.

cells N required (columns 2, 7, and 12), their production in tons/month chlorine (columns 3, 8, and 13), their average cell potential V (columns 4, 9, and 14), the direct current total potential (columns 5, 10, and 15) and the specific current consumption/100 kg chlorine (columns 6, 11, and 16).

Figure 5 represents the optimum current load for the values of the calculation Example 1 as a function of the current price with and without consideration of the installation costs of the rectifier. The course of both curves shows that these costs have no big influence unless the current prices are low.

Discussion of the Results

When examining the influence of the various parameters such as installation costs, mercury price, cell resistance, operating lifetime, installation costs for the rectifier on the optimum load by means of the derivations, it can be said that it fluctuates within comparatively narrow limits in the technical and economic fields in question.

Table II. The optimum current load I_T as a function of the operating years n

1	2	3	4	5	6
n	i	W	I_T	I_T	I_T
years	%	—	(Example 1) KA	(Example 2) KA	(Example 3) KA
5	20	0.266	153	162	191
10	10	0.157	117.5	130	154.5
20	5	0.105	96	111	135
30	3.3	0.091	89.5	103.5	131

The optimum current load is influenced considerably if we take into consideration the taxes on profit in the case of saved current costs. The comparison of the course of the curves □ and ○ in Fig. 3, shows that for the chosen example the optimum current load rises by about 25,000A, corresponding to a rise of current density from 1200 to 1300 A/m². For a lifeteime of 20 yr for the installation, we equal 6800 A/m², still considerably under the load of 10,000 A/m². At a current price of 75¢/100 kWhr, this load increases to 7500 A/m² and only at a price of 40¢/100 kWhr would we reach a specific load of 10,000 A/m².

In Eq. [19], [22], and [26] we can have at our disposal the two variables I_T and n (n is contained in W). The other items y_T, i, K, c_T, b_I, and Z are to be regarded as constant for a given installation. It is up to the company to define the time in which invested capital should be returned by the choice of n. In this case it should be taken into account that a short return time is purchased at the expense of a higher current load I_T, and with it higher specific costs. Also these higher current costs occur throughout the entire life time of the installation. Therefore n should be chosen corresponding to the entire life time of the installation, and n = 10-15 yr should come rather close to the practical situation.

The values of Table II and Fig. 3 show that with a return time $n > 15$ yr the optimum current load I_T changes only slightly with n.

Optimum Load of Bus-bars

The optimum load of bus-bars is calculated by the somewhat simpler method of cost comparison since the

Table III. Planning values for the optimum loads of Table II

1	2	3	4	5	6	7	8	9	10	11	12	13	14	15	16
		I_T for Example 1				I_T for Example 2					I_T for Example 3				
n	Number of cells	Prod. of Cl_2 p. cell	Cell potential	Total potential	Specific consumption of current	Number of cells	Prod. of Cl_2 p. cell	Cell potential	Total potential	Specific consumption of current	Number of cells	Prod. of Cl_2 p. cell	Cell potential	Total potential	Specific consumption of current
years	N	mt/ month	V	Volt	kWhr/ 100 kg	N	mt/ month	V	Volt	kWhr/ 100 kg	N	mt/ month	V	Volt	kWhr/ 100 kg
5	36	141.0	4.88	176	387	34	149	4.98	170	395	29	175	5.30	154	421
10	47	108.0	4.49	210	356	42	119	4.63	194	367	35	142	4.90	172	389
20	57	88.3	4.26	243	338	49	102	4.42	217	351	41	124	4.69	192	374
30	61	82.4	4.19	255	332	53	95	4.34	230	344	42	120	4.64	195	368

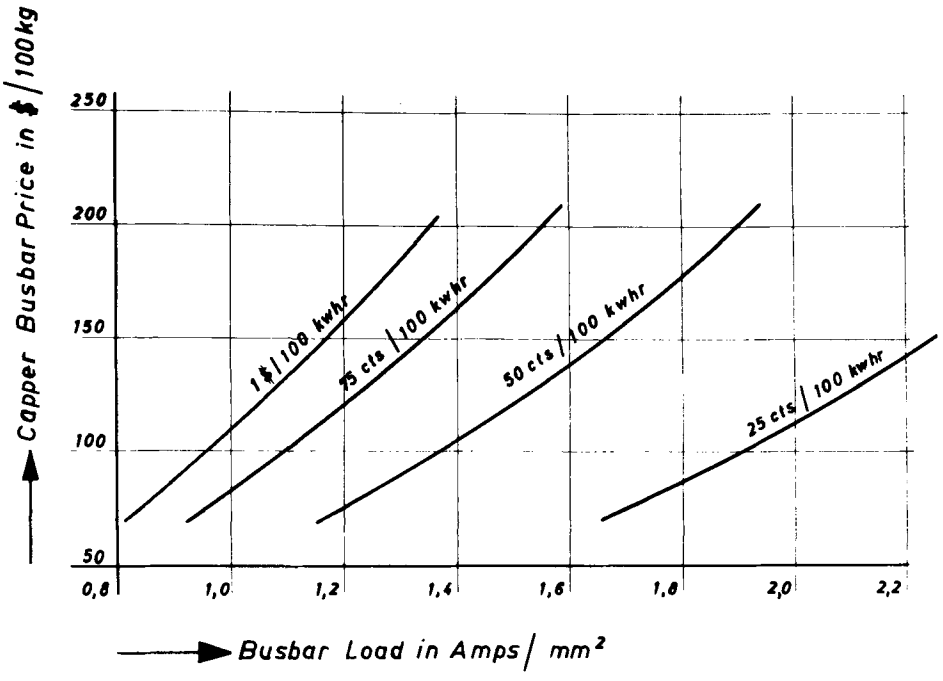

Fig. 6. Specific bus-bar load as function of copper price at different current prices.

influence of taxes on profits is insignificant on the result. The optimum lies where the sum of the costs for the current losses by ohmic resistance on the one hand, and the capital costs of the investment for the bus-bars on the other hand, reach a minimum.

This minimum is found by calculation if we represent the costs for the current losses $f_1(S_B)$ and for the capital costs $f_2(S_B)$ as functions of the bus-bars cross section S_B differentiate both functions with respect to S_B and set the sum of the differential quotients equal to 0

$$\frac{d f_1(S_B)}{d S_B} + \frac{d f_2(S_B)}{d S_B} = 0 \qquad [29]$$

The costs for the current losses are

$$C_B = f_1(S_B) = I_B^2 \cdot R_B \cdot \frac{L}{S_B} \cdot t \cdot 10^{-3} \cdot P_I \cdot 10^{-2} \qquad [30]$$

The part of the capital costs to be annually purchased for the bus-bars (depreciation and interest) depends on the depreciation period, (n), and the interest factor, Z. It corresponds to the value W (Table I).

The capital costs are

$$Y_B = f_2(S_B) = S_B \cdot L \cdot 10^{-3} \cdot \omega \cdot P_B \cdot W \qquad [31]$$

Differentiating Eq. [30] and [31] and setting the sum of the results = 0, we find for the specific load

$$\frac{I_B}{S_B} = \sqrt{\frac{\omega \cdot P_B \cdot W}{R_B \cdot t \cdot P_I}} \text{ A/mm}^2 \qquad [32][8]$$

Figure 6 shows the optimum specific load for copper bus-bars as a function of bus-bars-prices for various current prices.

Optimum Operating Time of Electrodes

This calculation principle for the solution of optimization problems in the electrolysis is also used to calculate the most favorable operating time of vertically arranged electrodes consumed during the electrolysis. As a consequence of the decrease in the cross section of the electrodes, higher potential losses occur. A condition for the following derivation is that the gap between anode and cathode is held nearly constant by continuous adjustment. The consumption of graphite anodes in a vertical mercury chlorine cell with rotating cathodes serves as an example for these calculations.

In this cell the graphite anodes are placed facing the two sides of the vertical rotating amalgamated iron cathode, as shown in cross section in Fig. 7. In this cell type the anodes are arranged as shown in the upper part of the cell, in which the brine is electrolyzed. The graphite anodes are adjusted every 2-3 days, to realize a nearly constant anode-cathode gap. Figure 7 shows the arrangement with new anodes and partly consumed anodes wherein the cross section is decreased and the voltage drop in the anodes increased.

The longer the anodes are in operation, the smaller are the specific graphite costs and the higher the specific current costs. From the economic point of view the most favorable time for renewing the anodes comes when the sum of the specific graphite costs and the specific current costs reaches a minimum. Other influences on the cell with increasing operating time, such as the change in the current efficiency etc. are not considered here.

We find this cost minimum by calculation when the specific current costs/100 kg chlorine, $f_1(t_c)$, and the specific graphite costs/100 kg chlorine, $f_2(t_c)$ are represented as a function of the operating time, t_c, of the anodes. Both functions are differentiated with respect to t_c and the sum of the differential quotients is set equal to 0

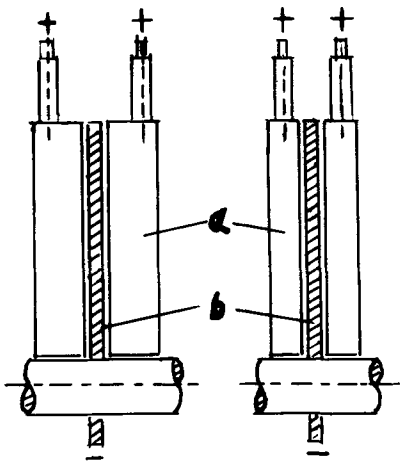

Fig. 7. Electrodes in a vertical chlorine cell; left, with new anodes, right, with anodes which are partly consumed. a, Fixed graphite anode; b, rotating iron cathode.

[8] As W refers to one year according to the definition, the number of hr/yr = 8750 must be inserted for t.

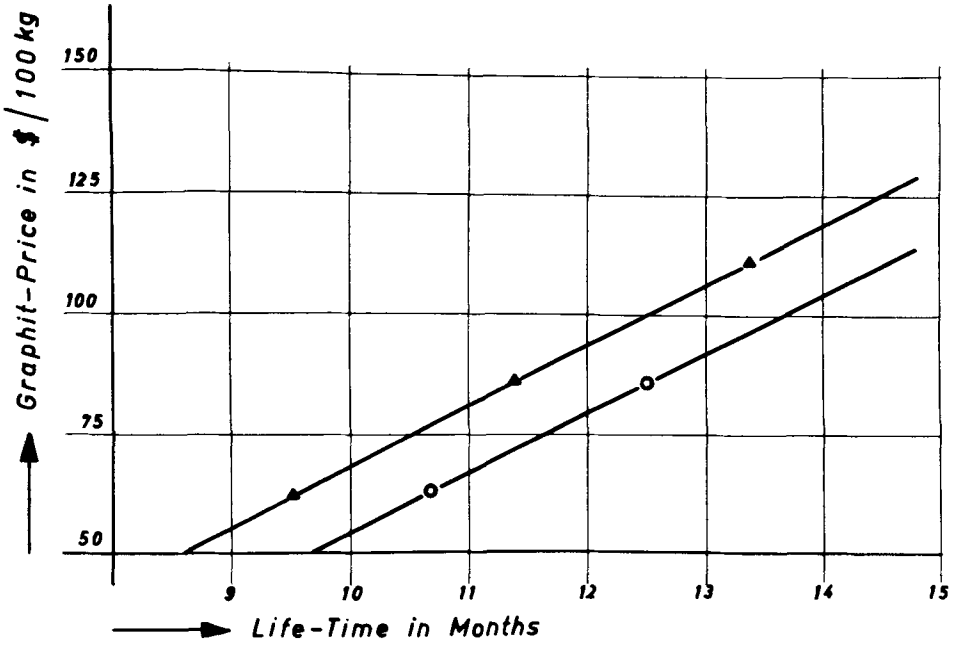

Fig. 8. Optimum operating time of graphite anodes as function of the price of graphite and current. Curve ○, 100¢/100 kWhr; curve △, 125¢/100 kWhr.

$$\frac{d f_1(t_c)}{d t_c} + \frac{d f_2(t_c)}{d t_c} = 0 \qquad [33]$$

The specific current costs for 100 kg chlorine during the operating time t_c are

$$c_I = f_1(t_c) = \frac{I_B \cdot P_I \cdot 720}{10^6 \cdot m \cdot t_c} [V_c + (V_c + v) + (V_c + 2v) + \ldots\ldots (V_c + t_c \cdot v)]$$

$$= \frac{I_B \cdot P_I \cdot 360}{10^6 \cdot m} (2V_c + v \cdot t_c) \quad \$/100\ \text{kg Cl}_2 \qquad [34]$$

The specific graphite costs are

$$c_G = f_2(t_c) = \frac{g \cdot P_G \cdot 10}{m \cdot t_c \cdot 10} \quad \$/100\ \text{kg Cl}_2 \qquad [35]$$

Differentiating these two equations with respect to t_c we obtain the most favorable operating time in months

$$t_c = \sqrt{\frac{g \cdot P_G \cdot 10^5}{I_B \cdot P_S \cdot 36 \cdot v}} \qquad [36]$$

In Fig. 8 there is graphically represented the optimum operating time, t_c, as a function of the graphite costs at various current prices for the example

m = 40 tons chlorine/month
g = 1.5 tons graphite
V_c = 4.5V
I_B = 45,000A
v = 0.05V
P_I = 1 and 1.25 $/100 kWhr

From the point of view of mechanical stability, the operating time of anodes of this type is about 9 to 10 months. At current prices below $1.25/100 kWhr, the price of graphite must be below $60/100 kg to justify removal before this time. At higher graphite prices or lower current costs, the optimum operating time is greater than the operating time which is technically possible, so that the anodes can be consumed as far as it is technically possible.

Manuscript submitted May 16, 1969; revised manuscript received ca. March 11, 1971.

Any discussion of this paper will appear in a Discussion Section to be published in the June 1972 JOURNAL.

TECHNICAL SYMBOLS

Optimum Load of Electrolysis Cells

I_T (A) = Circuit current of the electrolysis
t (hr) = Time
V_p (V) = Polarization potential
R_r (ohm) = Average specific resistance of one cell (including its share of the total bus-bar resistance beginning from the rectifier)
e (g/Ahr) = Electrochemical equivalent
U (%) = Current efficiency
K = Production constant (cell amperes)
M_T (mtons) = Quantity produced
N = Number of cells

Optimum Load of Bus-bars

S_B (mm²) = Bus-bar cross section
I_B (A) = Current intensity of the bus-bars or electrodes
R_B (ohm · mm² · m^{-1}) = Specific resistance of the bus-bar metal
L (m) = Length of the bus-bars
ω (g/cm³) = Specific weight of the bus-bar metal

Optimum Operating Time of Electrodes

t_c (months) = Operating time of the cell
V_c (V) = Total potential of the cell
v (V) = Average potential increase per cell and month
m (mtons) = Quantity produced per cell and month
g (mtons) = Weight of graphite anodes per cell

COST SYMBOLS

Optimum Load of Electrolysis Cells

y_T ($) = Investment cost per cell
c_T ($) = Personnel and repair costs per cell/year as well as all of the other operating costs which depend upon number of cells
F_I ($) = Fixed current costs (see Eq. [4])
Y_i ($) = Total investment costs ($y_T \cdot N$)[9]
C_I ($) = Total current costs/year
C_T ($) = Personnel and repair costs/year
Y_E ($) = Investment costs for rectifier
F_E ($) = Fixed share of costs for rectifier
b_I ($) = Factor for the variable cost of current (see Eq. [5])

[9] Including its share of the total installed investment costs of the complete cell house as building, cells, piping, bus-bars, switches, instrumentation, auxiliaries (*e.g.* mercury in mercury chlorine plants etc.), but without rectifier investment costs (Y_E).

b_T (\$) = Factor for the variable current costs, including the personnel and repair costs, as well as all of the other operating costs which depend upon the cell
b_p (\$) = Factor for the variable current costs including the personnel and repair costs + taxes on profits
b_E (\$) = Factor of the variable capital costs of the rectifier plant
Z_i (%) = Rate of interest
Z = Interest factor
n Years = Period of time after the installation has been put into operation
$W = \frac{Z^{(n+1)} \cdot (Z-1)}{Z^n - 1}$
i (%) = Rate of depreciation
λ_i (\$) = Depreciation/year
P (%) = Taxes on profits
P_I (\$/100 kWhr) = Direct current price

Optimum Load of Bus-bars

C_B (\$) = Current costs for bus-bar losses
Y_B (\$) = Capital costs for bus-bars
P_B (\$/100 kg) = Price for bus-bars

Optimum Operating Time of Electrodes

c_I (\$) = Specific current costs for 100 kg product
c_G (\$) = Specific graphite anode costs for 100 kg product
P_G (\$/100 kg) = Graphite price

REFERENCES

1. D. O. Hubbard, *Chem. Eng. Progr.*, **46**, 435 (1950).
2. R. B. Mac Mullin, *Electrochem. Technol.*, **1**, 5 (1963).
3. N. Ibl and E. Adam, *Chem. Ingr. Tech.*, **37**, 573 (1965).
4. H. Roscher, *Chem. Tech.*, **18**, 298 (1966).
5. A. Schmidt, *Chem. Ingr. Tech.*, **39**, 692 (1967).
6. F. Hine, *Electrochem. Technol.*, **6**, 69 (1968).
7. G. Seelmann, F. Glos, and D. Wagner, The Chemical Engineer, March 1968, CE 46.

Technical Note

Sodium Borohydride ($NaBH_4$) Initiation of Electroless Plating

Donald G. McBride and Gary P. Vlasak

International Business Machines Corporation, Systems Development Division, Endicott, New York 13760

The most widely used method for activating nonconductive materials prior to electroless plating consists of an acid solution of $SnCl_2$ as a sensitizer and an acid solution of $PdCl_2$ as an activator (1). This reaction is an oxidation-reduction as follows

$$Sn^{++} + Pd^{++} \rightarrow Sn^{+4} + Pd^{o}$$

The thin layer of deposited Pd acts as a catalyst and initiates electroless plating. A method of activation using a phosphorus system which forms an effective bond to the substrate has been reported (2). The reasons for investigating new methods of initiation were to obtain more complete metallic coverage, to improve adhesion of the metal to the substrate, and to eliminate permanent activation of the substrate with Pd. If a substrate on which a circuit has been provided is permanently activated, it is difficult to selectively electroless plate the circuitry without plating the total substrate.

A system has been developed using $NaBH_4$ (a strong reducing agent) which initiates metal plating on nonconductors but does not permanently activate the substrate. The primary criterion used for evaluation of the electroless metal deposits was adhesion. Electroless Cu, Ni, and Co on ceramic were evaluated. A sintering process was used to improve adhesion of Cu to ceramic. In addition, a comparison was made between Cu to ceramic using the $NaBH_4$ and sintering process *vs.* Cu to epoxy glass (laminated, and plated using both the $NaBH_4$ and $SnCl_2$-$PdCl_2$ methods of initiation).

Experimental Procedure

Materials.—The substrates were ceramic—American lava (96% alumina, ~ 20 μin. surface finish) and G-10 epoxy glass. The initiation solutions were stannous chloride, $SnCl_2$ 40 g/liter and HCl 40 cc/liter at room temperature; palladium chloride, $PdCl_2$ 0.15 g/liter and HCl 10 cc/liter at room temperature; and $NaBH_4$ = 19 g/liter. The plating solutions used were electroless Cu: copper sulfate, formaldehyde (37%), sodium potassium tartrate, NaOH, sodium carbonate, at room temperature, pH 11-12; electroless Ni: $NiCl_2$ 30 g/liter, sodium hypophosphite 10 g/liter, ammonium citrate 65 g/liter, ammonium chloride 50 g/liter, at boiling temperature, pH 3.0; electroless Co: cobalt chloride 75 g/liter, sodium hypophosphite 25 g/liter, ammonium citrate 163 g/liter, ammonium chloride 125 g/liter, 0.1M sodium borohydride 125 g/liter, ammonium hydroxide 125 g/liter, at boiling temperature, pH ~ 9-10.

Key words: electroless plating, nonconductor plating, initiation by $NaBH_4$.

Metallization.—The procedure for nonconductor metallization using $NaBH_4$ is (*a*) clean the substrate in an alkaline cleaner, (*b*) use deionized water rinse, (*c*) 30% (vol) HCl (37% wt), and (*d*) repeat deionized water rinse. Dip-coat the substrates in 0.5M $NaBH_4$. Electroless plate first in a "sludge pot" and then in a fresh solution. Finally, electrolytic plate 0.003 in Cu-Cu pyrophosphate.

The sludge pot is a separate electroless plating solution which decomposes because of the dragged in $NaBH_4$.

A thin layer of metal should be plated onto the substrate in the sludge pot; then further plating should be done in a fresh solution. The more difficult a substrate is to plate, the greater the concentration of $NaBH_4$ required, but the faster the sludge pot decomposes. An alternate method has been developed that eliminates the sludge pot technique. Substrates are dip coated in 0.5M $NaBH_4$ and subsequently sprayed with the electroless plating solution or a 10% solution of $NiCl_2$ or $AuCl_3$. Then they are placed in a standard electroless plating solution.

The $NaBH_4$ technique is not an activation of the substrate. It is just an adsorption of a reducing agent onto the substrate which reduces metal ions in solution at the substrate/plating solution interface. The metal then deposits onto the nearby substrate. If the $NaBH_4$ is rinsed off, the substrate remains unchanged

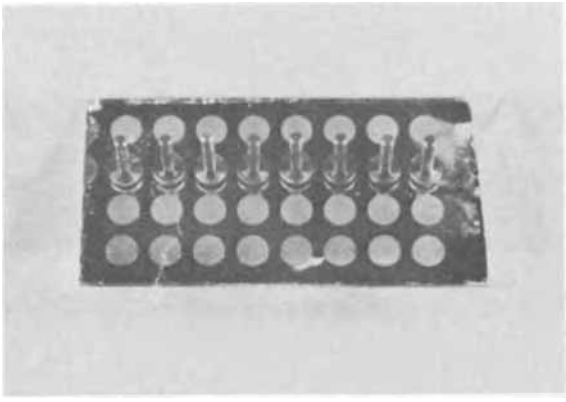

Fig. 1. Copper studs (150 mil diam)

and electroless plating will not occur—thus, no permanent activation occurs.

The procedure for nonconductor metallization using the $SnCl_2$-$PdCl_2$ system is (*i*) clean the substrates in an alkaline cleaner—deionized water, 30% HCl, deionized water; (*ii*) soak in $SnCl_2$ for 5 min, and rinse well with deionized water; (*iii*) soak in $PdCl_2$ for 2 min, and rinse well with deionized water; (*iv*) electroless plate; (*v*) electrolytic plate 0.003 in. Cu.

Sintering to improve adhesion.—Copper metallized ceramic substrates prepared by using both the $NaBH_4$ and $SnCl_2$-$PdCl_2$ processes were sintered for 45 min in an argon atmosphere in an attempt to improve adhesion. The sintering temperature was varied from 480°C to 1000°C to define the temperature which yielded the optimum adhesion.

Electroless Ni and Co metallized ceramic substrates using the $NaBH_4$ process were sintered at 800°C for 45 min in argon to compare their adhesion with that obtained with Cu.

Table I. Comparison of adhesion of Cu,* Ni, and Co to ceramic

Activation	Metal deposited	Avg. pull strength (lb/in.²)	Sintering temp (°C)
$SnCl_2$-$PdCl_2$	Cu	2060	None
$SnCl_2$-$PdCl_2$	Cu	2411	800
$NaBH_4$	Cu	1471	None
$NaBH_4$	Cu	2994	480
$NaBH_4$	Cu	>4244	600
$NaBH_4$	Cu	>4244	800
$NaBH_4$	Cu	>4244	1000
$NaBH_4$	Ni	198	800
$NaBH_4$	Co	170	800

* Accurate adhesion data of Cu to ceramics was not obtained for temperatures above 600°C because the ceramic broke in the fixture. Therefore, a small area was tested.

Table II. Optimization of sintering temperature

Sintering temperature (°C)	Avg. pull test (grams)
None	49
500	78
800	116
1000	43

Adhesion test.—The adhesion of the metals to the substrates was measured by three tests: 0.150 in. diam stud pull test (Fig. 1), 0.005 in. wire pull test, and 0.020 in. line peel test.

Using photolithographic and etching techniques, 0.150 in. diam pads, 0.005 in. lines, and 0.020 in. lines were etched on the metallized substrates. Then, a 0.150 in. stud, a 0.005 in. wire, or 0.020 in. wire was soldered to the Cu pad or line using 60/40 Sn/Pd solder. Pull testing was done on an Instron[1] tester at 90° to the substrate.

[1] Instron Corporation.

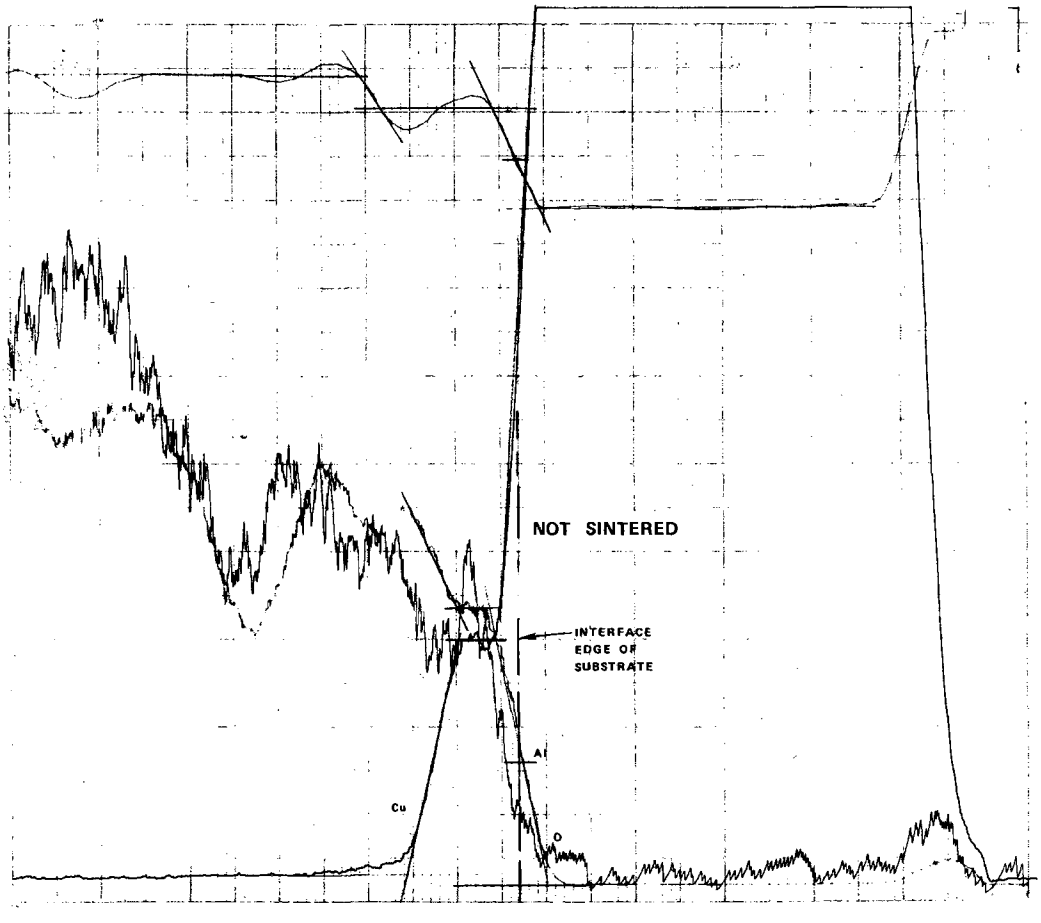

Fig. 2a. Cu plated plus CuO plus substrate (not sintered).

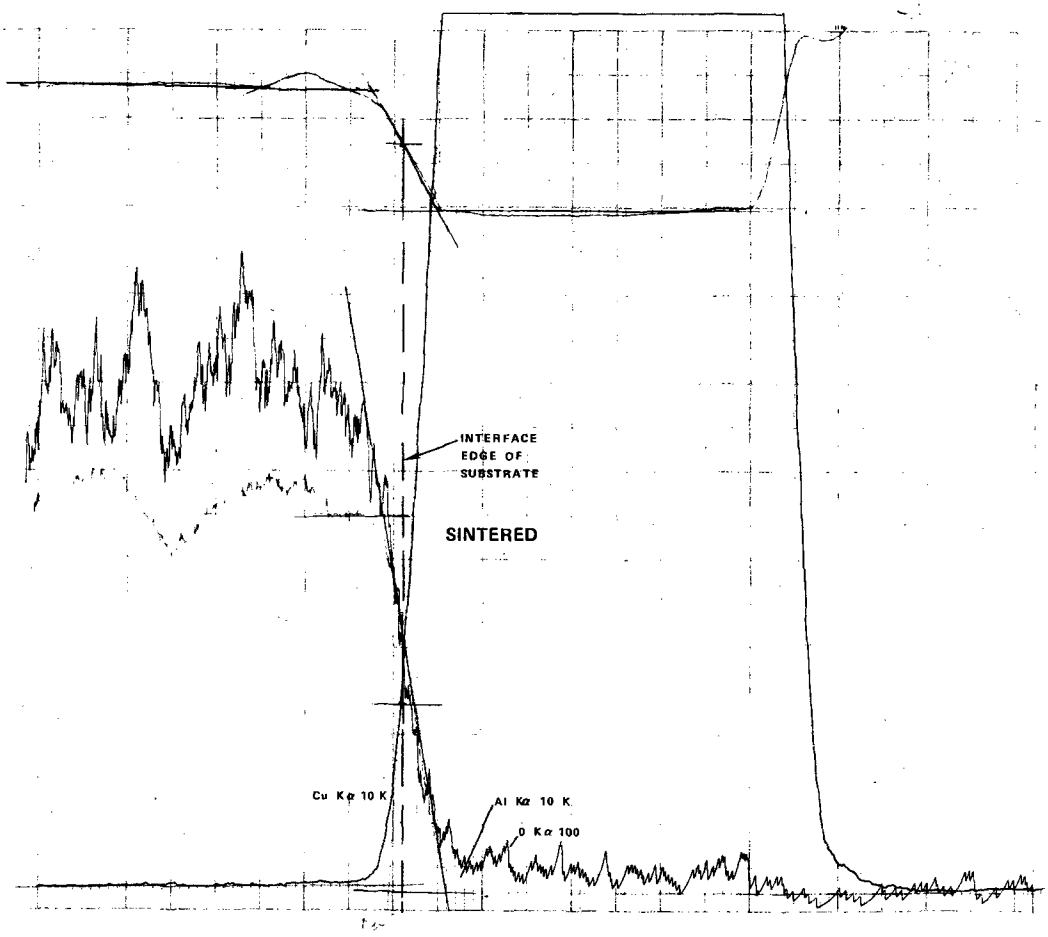

Fig. 2b. Cu plated plus CuO plus substrate (sintered).

Metallurgical evaluation.—X-ray and electron probe analysis was performed on substrates metallized using the $NaBH_4$ and sintering (800°C) process in an attempt to determine the mechanism of improved adhesion.

Results

Table I is a comparison of the adhesion of Cu, Ni, and Co to ceramic as determined by a 0.150 in. diam dot pull test.

Table II displays the pull test data obtained for a 0.005 in. wire soldered to a 0.005 in. Cu line, prepared using the $NaBH_4$ method of plating initiation and sintering at temperatures 500°-1000°C.

Electron probe analysis (Fig. 2a) indicates that prior to sintering Cu is approximately 4μ into the ceramic, at the left of the interface. The oxygen curve is on an expanded scale (100K) as opposed to Cu (10K). Thus, the Cu and O coincidence does not prove or disprove the presence of CuO. The slight peak (increased Cu) as the probe moves into the interior of the ceramic is probably an indication of irregular Cu because of the porous nature of the ceramic. Figure 2b indicates that after sintering the Cu has diffused away from the interior of the ceramic, to the right of the interface. This more abrupt junction obtained after sintering is probably the result of physical forces such as surface tension and stress relief, which are in operation at the sintering temperature (800°C).

A comparison was made between the adhesion of Cu to ceramic using the $NaBH_4$ and sintering at 800°C method and Cu to epoxy glass (laminated, and plated using both the $NaBH_4$ and $SnCl_2$-$PdCl_2$ methods of initiation). See Table III. Adhesion was measured using a 0.020 in. line peel test.

Table III. Adhesion of copper to ceramic vs. copper to epoxy glass

Substrate	Activation	Avg. peel strength (g)
Ceramic	$NaBH_4$	30-60
Epoxy glass	$NaBH_4$	20-30
Epoxy glass	$SnCl_2$-$PdCl_2$	50-70
Epoxy glass	Laminated	80-100

Qualitatively it has been observed that for difficult to metallize substrates, such as glazed ceramic, more complete coverage is obtained with the $NaBH_4$ initiation than with the $SnCl_2$-$PdCl_2$ method of activation. Also, $NaBH_4$ initiation does not permanently activate the surface as does $SnCl_2$-$PdCl_2$. This point is of considerable importance when one desires to selectively electroless plate circuitry on a substrate that has previously been activated.

Discussion

The initial Cu plate onto ceramics using $NaBH_4$ initiation appears to be Cu which immediately oxidizes into CuO from x-ray analysis. During sintering, Cu appears to diffuse into the ceramics. See Fig. 3. It is known (3) that several per cent of CuO wil diffuse into various glasses.

The improved adhesion may be the result of some shallow diffusion of CuO and Cu into the glass and ceramic. Also, a more homogeneous junction results (microprobe analysis) which may cause better interlocking of the Cu around the alumina. Reduced stress in the system should also lead to improved adhesion.

More recent work indicates that the adhesion obtained with the $NaBH_4$ and sintering method is substrate dependent. The difference obtained is probably the result of the different impurities (glass, etc.) used as a binder. Further investigation will be necessary to understand the observed phenomenon.

Conclusion

A new method of electroless plating initiation has been developed using $NaBH_4$. This method yields more complete coverage on difficult to metallize substrates, does not permanently activate the substrate, and leads

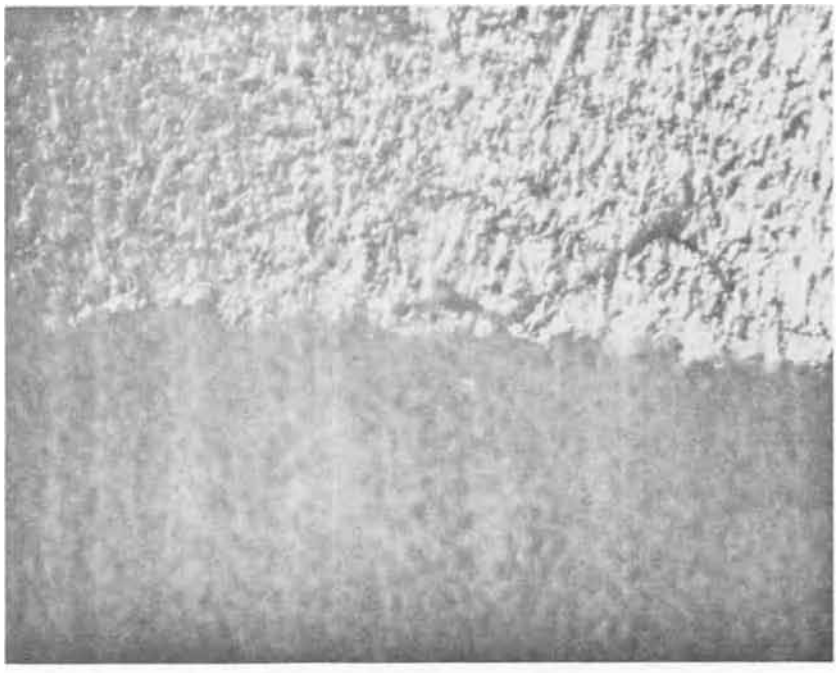

Fig. 3a. Ceramic (not sintered) (magnification: 1000X).

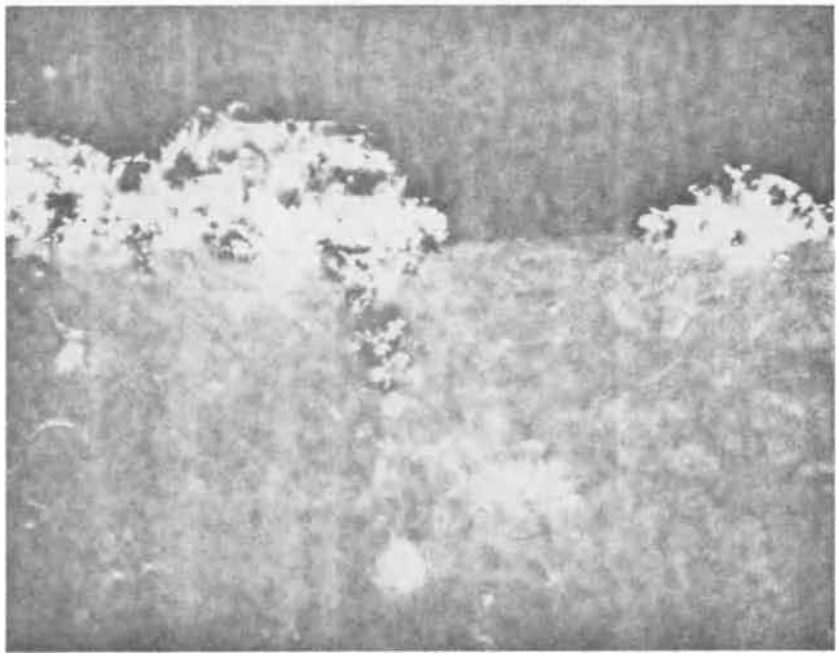

Fig. 3b. Ceramic (sintered) (magnification: 1000X).

to improved Cu to ceramic adhesion if the Cu is sintered into the ceramic at 800°C.

Manuscript submitted May 20, 1971; revised manuscript received *ca.* June 25, 1971.

Any discussion of this paper will appear in a Discussion Section to be published in the June 1972 JOURNAL.

REFERENCES

1. S. Wein, *Glass Ind.*, **38**, 625, 679 (1957).
2. G. T. Miller, J. K. MacKay, and W. R. Doty, The Electrochemical Society Extended Abstracts, Fall 1969, p. 361.
3. H. Hoagendoorn and B. Sunners, *Am. Ceram. Soc. Bull.*, **48**, 1125 (1969).

DISCUSSION SECTION

This Discussion Section includes discussion of the paper appearing in the *Journal of The Electrochemical Society*, Vol. 117, No. 11, November 1970.

Electrophoretic Deposition of Luminescent Materials

P. F. Grosso, R. E. Rutherford, and D. E. Sargent
(pp. 1456-1459, Vol. 117, No. 11)

E. I. Szabo and S. L. Gertsman: In the paper under discussion, the authors advocate the use of a multivalent ion to charge suspended particulates, since milling is claimed to have a deleterious effect on the light output efficiency of the phosphors.

While the authors acknowledge that the introduction of an ionic component results in a conductive suspension, and hence, gassing, they attempt to overcome the latter by including an organic depolarizer in the liquid vehicle.

We would comment, that while milling does indeed induce electrophoretic mobility in practically any solid/liquid combination, this is incidental, and is the result of the fresh, unoccupied sites generated. The deterioration in light output efficiency is the result of lattice distortion

Since the sole requirement to induce electrophoretic mobility in any suspended solid appears to be that of offering the atmosphere (preferably a polar liquid) an unoccupied site, this is easily accomplished by removing the adsorbates from the surface.

In practice, heating the powders to 400°C at a modest vacuum of 10^{-2} to 5 x 10^{-3} mm mercury, and holding there for 24-48 hr, was found sufficient. If the powders are to be stored for a time, backfilling with an inert gas, or maintaining the contents in a sealed container can retain the mobility of the powders.

JOURNAL OF THE ELECTROCHEMICAL SOCIETY

REVIEWS AND NEWS — OCTOBER 1971

Report of the Electrolytic Industries for the Year 1970[1]

Thomas C. Jeffery*

PPG Industries, Industrial Chemical Division, Lake Charles, Louisiana 70601

and L. C. Fuhrmeister*

Monsanto, Enviro-Chem Systems, Incorporated, Chicago, Illinois 60600

Chlorine-Caustic Soda

I. Production.—Another record high was set last year with the production of chlorine reaching 9,710,000 tons in the United States, a 3.0% increase over production in 1969. Canadian production was 852,500 tons, down approximately 4.1% from the preceding year. During the last ten years the growth rate in the U. S. has been about 8% and 11.5% in Canada (1).

From December 1, 1969, to December 1, 1970, U. S. daily chlorine capacity increased 800 tons to 29,002 tons while Canadian capacity remained constant at 2,631 tons. In 1970, U. S. producers operated at 92.6% of capacity, while Canadian facilities operated at 90.4%.

A summary of U. S. caustic soda capacity by producer is shown below (2):

Producer	Capacity, T/D
Alcoa	529
Allied	1,760
Diamond Shamrock	2,100
Dow	10,000
FMC	850
GAF	510
Goodrich	330
Hooker	1,820
Kaiser	500
Olin	1,630
Pennwalt	990
PPG Industries	3,330
Shell	275
Stauffer	810
Vulcan	470
Wyandotte	1,780
Paper Companies	715
Other	980
Total	29,620

Reflecting the short supply of caustic soda, price increases were announced on four separate occasions during the past few months (3-6). List prices for 50% and 73% now stand at $71/ton and $73/ton with dry flake and beads at $7/cwt. Anhydrous caustic is now available from PPG and Dow in the form of free-flowing beads. These dust-free prills have been well received.

A summary of Canadian chlor-alkali capacity by producer is shown below (7):

Producer	Capacity 1,000 tons/yr Chlorine	Caustic
Aluminum Co. of Canada	29	34
Canadian Industries Ltd.	135	156
Canso Chemicals	18	21
Domtar Group	35	41
Dow Chemical	394	455
Dryden Chemical	47	54
FMC Canada, Ltd.	36	40
Hooker Chemical	123	145
E. B. Eddy	8	9
Interprovincial Co-op.	35	40
Marathon Paper Co.	13	14
Standard Chemical, Ltd.	61	71
Totals	935	1,080

II. Expansions. (8-10)—

Company and Location	Type of cell	Capacity tons/day	Completion date
A. Shutdown			
Oxford Paper Div. Ethyl Corp. Rumford, Maine	Sorensen Mercury	13	August 1970
Dow Chemical Co. Plaquemine, La.	Solvay V-200 Mercury		December 1970
B. Production started			
Standard Chemical Ltd. Beauharnois, Quebec	Uhde Mercury	220	February 1971
Stauffer Chemical St. Gabriel, La.	Uhde 30m² Mercury	500	December 1970
C. Building or planned			
Dow Chemical Co. Dallesport, Wash.	Dow (Magnesium)	24,000 T/yr Magnesium, 40,000 T/yr Cl_2	Early 1972
Dow Chemical Co. Freeport, Texas	Dow Diaphragm	Expansion Bldg.	1971
Dow Chemical Co. Midland, Mich.	Dow Diaphragm	Moderniza-tion Planned	1971-1972
Hooker Chemical Corp. Taft, La.	Hooker S-4	120	1st Quarter 1971
Mobay Chemical Co. Cedar Bayou, Texas	HCl Electrolysis, Uhde	200	Late 1971
National Lead Co. Grantsville, Utah	BASF	45,000 T/yr Magnesium	Late 1971
PPG Industries, Inc. Guayanilla, Puerto Rico	DeNora Mercury	500	3rd Quarter 1971
PPG Industries, Inc. Lake Charles, La.	PPG-DeNora Bipolar	1,500	Not Announced

III. New developments.—A. Metal anodes.—Metal Anode Associates, a joint venture of Union Carbide Corporation and Engelhard Minerals and Chemicals Corporation, was formed in March, 1970, to produce and market metal anodes. The company combines Engelhard's years of experience producing and processing precious metals with those of Union Carbide in anode design and electrolytic operations. Engelhard is supplying the production facilities and Union Car-

[1] This report is sponsored by the Industrial Electrolytic Division of The Electrochemical Society. While it is primarily a summary of production and developments in the chlor-alkali industry, reports of other electrolytic industries are included.

The material presented herein has been gathered from many sources, as noted in the references, and does not necessarily represent the opinions of the authors.

* Electrochemical Society Active Member.

bide is serving as the marketing and technical service arm (11, 12).

As of this report, a number of chlor-alkali producers, both domestic and foreign, have been supplied with metal anodes by MAA.

Electrode Corporation, a joint venture of DeNora and Diamond Shamrock, continues as a leading supplier of the DSA for use in mercury cells. Titanium based anodes are now being used in many different types of mercury cells employing current densities from 4 to 14 kA/m^2.

Hooker Chemical Company signed an agreement with Electrode Corporation covering use of the DSA in Hooker cells. A new base assembly adapts this cell type to use of the DSA, eliminating the need of lead and asphalt (13, 14).

B. New cell designs.—A new diaphragm cell is being developed jointly between PPG Industries and Oronzio DeNora using a bipolar configuration and metal anode. The low investment per daily ton produced and lower operating cost will make the new cell attractive for large chlorine plants and installations where older cell technology has reduced profit margins. Electrode elements can be assembled into individual cell units that will produce up to 36 tons per day, more than double the capacity of most large mercury cells now in operations (15). PPG will market the cell in the U. S. and Canada, while deNora will market throughout the rest of the world.

C. Mercury.—Consumption, production, and imports of mercury were down in 1970. Decline in usage was due in part to the slowed pace of the U. S. economy and the problem of mercury pollution. Imports were down 20% and mine production was down slightly to 28,000 flasks (76 lbs each). California supplied 66% and Nevada 22% of domestic production with the balance split between Alaska, Arizona, Idaho, Oregon, and Texas. The value of primary production was estimated at 11 million dollars (16).

Canada furnished 80% of the imported mercury; Italy, 7%; and Spain, 7%, down significantly because of lower demand. The U. S. rate of duty on mercury imports dropped to $12.92/flask on January 1, 1970. The price per flask was $410 in 1970 compared to a $505 average in 1969. GSA reported that only 703 flasks were sold of 14,000 offered in January and Congressional hearings were cancelled on the bill to authorize release of 73,000 flasks from stockpile surplus. Several factors have contributed to the mercury price drop (17):

1. Controversy over mercury being a health hazard
2. State of U. S. economy
3. Massive new Canadian production

Several years ago mercury production was near zero. As world prices for mercury increased, Canadian companies, notably Cominco Ltd., were encouraged to develop their own plants. Within two years production has zoomed to between 20,000 and 25,000 flasks a year. To guarantee their markets, they signed long-term contracts guaranteeing 2-3% lower prices than U. S. quotes. This discounting clearly helped pull down the mercury prices.

The following is a breakdown of mercury consumption (18, 19):

76 lb. flasks	1969	1970	Estimated 1974-75
Agriculture	2,689	2,700	2,660
Catalysts	2,958	2,400	2,342
Dental preparations	3,053	2,000	3,795
Electrical apparatus	18,650	18,000	22,700
Chlorine and caustic*	20,720	16,000	22,840
General laboratory use	2,041	3,000	2,080
Industrial and control instruments	6,981	7,300	9,250
Mildew-proofing paint	9,486	9,000	10,700
Paper and pulp	558	725	237
Pharmaceuticals	724	650	658
Other	11,144	7,625	6,187
Total	79,104	70,000	83,500

* Quantities for chlorine cell startup included under "Other" uses.

Source: Bureau of Mines, CW estimates.

No attempt will be made in the limited space available here to discuss the mercury discharge problem faced by chlor-alkali producers; however, it is a safe guess to say that approximately $1,000-$1,500/daily ton of chlorine produced has been spent to reduce the amount previously discharged to essentially zero. Both in-plant recycling and effluent treatment have been used extensively.

Other Alkalis and Electrolytic Processes

Caustic potash.—Caustic potash facilities currently operable in the U. S. are shown below (20):

Producer	Capacity (short tons/yr)
Allied Chemical Co. Syracuse, N. Y.	30,000*
Diamond Shamrock Corp. Delaware City, Del.	16,000
Diamond Shamrock Corp. Muscle Shoals, Ala.	40,000
Hooker Chemical Corp. Niagara Falls, N. Y.	36,000*
International Minerals and Chemical Corp. Niagara Falls, N. Y.	23,000*
Monsanto Co. Sauget, Ill.	45,000
Pennwalt Corp. Calvert City, Ky.	25,000
PPG Industries, Inc. Corpus Christi, Texas	7,000*
PPG Industries, Inc. New Martinsville, W. Va.	8,000

* Includes solid or flake production.

Preliminary production figures for caustic potash total approximately 17,000 tons for 1970 (21).

Dow Chemical announced plans to dismantle its 10,000 ton/yr plant at Pittsburg, California, the only caustic potash plant on the West Coast (22). PPG announced a price increase on bulk 45% grade of $4/ton to $4/cwt. effective July 1, 1970. No changes were made in drummed liquid and dry caustic potash (23).

Soda ash.—National soda ash production in 1970 was 2.6 million tons valued at $53.3 million, an increase of 4% in quantity and 5% in value over 1969. The mines in Wyoming supplied the bulk of the total national output, the remaining amount came from dry lake beds in California (24). The production of synthetic soda ash, light, was 1,786,873 tons and synthetic, dense, was 2,477,490 tons (25).

Domestic alkali demand (25).—

Year	(1,000 Tons as Na_2O) NaOH	Na_2CO_3	Total
1960	4,734	5,196	9,930
1965	6,420	6,143	12,563
1969	8,845	6,674	15,519
1970	9,075	6,626	15,701
1975	12,450	7,300	19,750

With curtailed operations in 1970 in Aluminum and Pulp and Paper Industries, increased utilization of caustic soda was gained at the expense of soda ash which was down by 0.7% from 1969.

The growth rate of soda ash over the past five years has averaged 1.5% annually. In 1970, synthetic soda ash plants experienced problems with the government crackdown on pollution. Consequent reductions in synthetic soda ash and the over-all growth is forecasted at about 2%/yr.

Year end prices were quoted at $2.35 per 100 lb for light and $2.40 for dense, and $1.65 and $1.80 respectively in carload lots, f.o.b. production facility.

Sodium chlorate.—Facilities for the production of sodium chlorate in the U. S. are listed below (26):

Producer	Capacity (short tons/yr)
American Potash and Chemical Corp. Hamilton, Miss.	23,500
American Potash and Chemical Corp. Henderson, Nev.	30,000
Brunswick Pulp and Paper Co. Brunswick, Ga.	7,000
Georgia-Pacific Corp. Bellingham, Wash.	5,000
Hooker Chemical Corp. Columbus, Miss.	55,000
Hooker Chemical Corp. Niagara Falls, N. Y.	15,500
Reigel Paper Corp. Butler, Ala.	4,000
Reigel Paper Corp. Reigelwood, N. C.	7,000
Pacific Engineering and Production Co. Henderson, Nev.	6,000
Penn-Olin Chemical Co. Calvert City, Ky.	31,000
Pennwalt Corp. Portland, Oreg.	15,000
PPG Industries, Inc. Lake Charles, La.	15,000
	214,000

Hooker Chemical is building a 45,000 TPY sodium chlorate plant at Taft, Louisiana, with startup scheduled in 1972. An entirely new cell design will be employed (27).

The United States' production of sodium chlorate in 1970 was approximately 201,000 tons (28). The majority of production is consumed by the pulp and paper industry for the generation of chlorine dioxide for paper bleaching. Cotton defoliation and railroad rights-of-way cleaning account for most of the herbicide use while the production of perchlorates accounts for most of the balance.

Olin raised the price of sodium chlorate $20/ton to $150/ton while PPG raised the published price $10/ton (29).

Sodium.—The production of sodium metal set a new all-time high in 1970 of 171,220 tons (30, 31). This exceeded 1969 production of 164,588 tons by 4% and the previous high of 165,000 tons set in 1966 by 3.7%.

A dock strike in 1969 depressed sodium production resulting in a depletion of stocks. This in turn tended to increase 1970 production to replace stocks. Production was 10-12% higher during the first six months of 1970 than in the last half of the year when general economic conditions curtailed the purchase of gasoline.

Of the sodium produced, approximately 83% went to the manufacture of lead alkyls for gasoline additives, 6% to the production of titanium sponge, and 11% for miscellaneous uses (peroxide, sodium hydride, descaling of metals, chemical and drug intermediates, and as a coolant for nuclear power stations).

Publicity concerning air pollution resulting from lead additives in gasoline was of major interest in 1970. A number of articles discussed the problems (32-39). Considerable research is being done to find replacement additives. The only real problem for its removal is that it is not compatible with catalytic mufflers which the auto industry wants to put on the motor vehicles.

It appears that the oil industry is resigned to the fact that lead must come out of gasoline. This means that the 2.9% per year growth rate for lead additives (1960-1970) will decline about 17%/yr through 1975. Exports, which account for 9.7% of the gasoline additives, are expected to hold steady (31). Over-all, it appears the sodium producers will be forced to reduce production or find new uses for the metal in the next few years.

Aluminum.—Output of primary metal was estimated at 3,950,000 tons and inventories at reduction plants were said to have increased (40). The U. S. was a net exporter of aluminum products for the second consecutive year.

For the past 15 years, return on investment for the three major aluminum companies—Alcoa, Reynolds, and Kaiser—has rarely gotten above 6%, Even so, companies have continued to expand to increase their per cent of the market and have built a long-term debt equaling 40-50% of total capitalization (41). This trend was reversed somewhat in 1970 as some expansions were deferred, planned shutdowns brought forward, and unscheduled outages by Hurricane Celia (Reynolds, Corpus Christi) and strikes (Alcoa, Kitimat, B.C.) were lengthened, all combining to restrict production.

The price of primary ingot was raised 1¢/lb, bringing it to 29¢ and making a 3¢ total increase since January 1969 (42). Mill products, plate sheet, and extruded shapes average between 40-52¢/lb. Justification for these price increases was explained by the over-all aluminum situation. Consumption in the free world outside the U. S. was up 21%. In Japan consumption was up 33% over the 1968 level; in Germany 28%; in the European Economic Community as a whole, 24% (43). The use of aluminum in the U. S. is not declining; it just seems that way when compared to the rapid growth rate of foreign markets.

Approximately 66% of U. S. output is used by four industries: housing and mobile homes, 22%; transportation, 20%; electrical goods, 13.2%; and packaging, 10.2% (44).

Primary aluminum producers in the U.S. (45)

(Capacity in 1,000 short tons/yr)

	Jan. 1, 1970	Sites of new plant projects	Capacity being added	Projected capacity Dec. 31, 1973
Alcoa	1,325	Warrick, Ind. Alcoa, Tenn.	175	1,500
Reynolds	935	Troutdale, Ore Longview, Wash.	40	975
Kaiser	710	—	0	710
Anaconda	175	Sebree, Ky.	120	295
Intalco	265	—		265
Ormet	240	—	0	240
Harvey	91	Cliffs, Wash.	100	191
National-Southwire	7	Hawesville, Ky.	173	180
Amax	0	Warrenton, Ore.	150	150
Consolidated	140	—	0	140
Revere	0	Scottsboro, Ala.	112	112
Eastalco	0	Frederick, Md.	85*	85
Noranda	0	New Madrid, Mo.	75	75
Gulf Coast	0	Lake Charles, La.	35	35
Total U.S.	3,888	12 Projects	1,065	4,953

* First potline onstream Oct. 1970; second potline expected to be built by 1974.

Magnesium.—Production of primary magnesium in 1970 totaled 112,007 tons, up 12.2% over 1969. Shipments in 1970 were 118,693 tons, up only slightly from 1969. Imports for consumption in 1970 totaled 3,294 tons. Exports of magnesium metal and alloys in crude form and scrap, and in semi-fabricated forms were 35,731 tons, 31% higher than in 1969 (46).

Recovery of secondary magnesium was approximately 15,000 tons. Magnesite, brucite, and olivine production continued at about the same level as in 1969 (47).

On March 4, 1970, the Office of Emergency Preparedness abolished the stockpile objective for magnesium, which totaled 114,722 tons on March 31, 1970. Under authorization of Public Law 91-321, passed on July 10, 1970, the G.S.A. was authorized to sell 12,000 tons of magnesium (47).

Imports of refractory magnesium during the first ten months were 78,755 tons valued at $6,055,920. For the same period, imports of dead-burned and grain magnesium and periclase totaled 30,887 tons valued at $1,537,687 (47).

Manganese.—Domestic consumption of ore containing 35% or more manganese was estimated at 2.2 million short tons, approximately equal to the level of consumption of the two preceding years. The only mine in the U. S. (Nancy-Tower mine in Sacono County, N. M.) producing manganese ore containing 35% or more manganese, closed in October. Shipments continued to be made from inventory (48).

Approximately 1.8 million tons of manganese ore was imported from suppliers in Gabon and Brazil. Ferromanganese was imported at a slightly lower rate than in 1969, primarily from the Republic of South Africa and France. An increase in ocean freight rates was reflected in a price increase of ore containing 46 to 48% manganese from 49 to 53¢/ton to 56 to 59¢/ton.

Deepsea Ventures, Inc., a subsidiary of Tenneco, Inc., began pulling manganese ore from the floor of the ocean, 150 miles off the coast of Florida, in 3,000 ft of water (49). The presence of manganese-rich lumps or "nodules" scattered about on the ocean floor waiting to be gathered may be a new, competitive source of manganese. Nickel, cobalt, and copper also occur with the manganese in these nodules. Two, as yet unanswered, questions are: who owns rights to the ocean bottom and will a method that works in 3,000 ft of water be feasible at depths of two to three miles of water where some of the richest deposits lie?

Beryllium.—Beryl (a beryllium-aluminum-silicate) consumption leveled off in 1970 according to the Bureau of Mines and was about equal to the 6,000 tons reported for 1969. Actual figures remain classified due to the limited number of producers.

Production was reported from Colorado, Maine, New Mexico, South Dakota, and Utah. Successful operation of the Spur Mountain, Utah bertrandite (another beryllium-aluminum-silicate) mine will furnish a domestic source for beryllium, assure a more stable supply, and encourage use of the metal (50).

Imports in 1970 declined from 1969 with 3,575 tons valued at $1.4 million for 9 months. Midyear government stockpile inventories contained 22,990 tons of beryl (11% BeO equivalent), 7,387 tons of beryllium-copper master alloy, and 229 tons of beryllium metal. Through June the government disposed of 1,481 short tons of beryl. In September, 545 tons of beryl (5,500 short tons of BeO) sold for $207,625.

Kawecki Berylco Industries, Inc. installed one of the world's largest isostatic presses for use in powdered beryllium and other metals at Hazelton, Pennsylvania. The press has a 24-inch diameter by 96-inch long chamber capable of 80,000 psi and is expected to decrease the cost of finished beryllium parts because less machining is required with resultant less scrap.

Uses of beryllium in 1970 were the electronics industry—35%, transmission switchgear—25%, nuclear and space applications—20%, welding—10%, and other —10%.

Chromium.—Chemical-grade chromite sales for the first three quarters of the year totaled 184,000 tons while metallurgical-grade chromite shipments totaled 126,000 tons. Domestic consumption was about the same as in 1969, with a 2% increase in the metallurgical industry offset by a 6% decrease in use in the refractory industry (51).

Imports of chromite totaled nearly 1.2 million tons during the first 10 months, a 20% increase compared to the same period in 1969. GSA announced that no acceptable offers were received in response to its bid invitation for 803,000 tons of metallurgical-grade chromite stored at Nye, Montana.

Metallurgical-grade chromite prices rose for the fourth successive year as the United Nations economic sanctions against Southern Rhodesia remained in effect. Rhodesia was one of the principal suppliers of domestic requirements prior to 1967. Domestic production of chromite was last reported in 1961. Published prices for Turkish chromite ore/long ton, 3-1 ratio, 48% Cr_2O_3, delivered Atlantic ports, increased from $47.50-$48.50 in 1970 to $55-$57 for 1971 delivery. Quoted prices for Russian chromite, 54-56% Cr_2O_3, 4-1 ratio, was $55.10-$59.60/long ton.

Titanium.—In 1970, a total of 535,000 tons of titanium were consumed in the U.S. Ilmenite (Fe-Ti ore) was the source for 416,000 tons while 119,000 tons were from rutile (94-95% TiO_2 ore). Over 95% of the total went to nonmetal uses, primarily pigment. Approximately 27,000 tons of titanium from rutile went to titanium metal (52).

Metal production (short tons) (53, 54)				Consumption		
Type	1969 Classified	1970	% Change	1969	1970	% Change
Sponge	est. 19,500	est. 15,000	−23	20,124	16,413	−19.2
Ingot	28,490	24,728	−13.2			
Scrap				7,242		−4.3

Imports of titanium sponge totaled 6,565 tons. Of this, 6,240 was for consumption, 72% from Japan, 17% from Russia, and 11% from the United Kingdom. Exports of the metal sponge and scrap were expected to reach 3,100 tons (55). Sponge producers include: Titanium Metals Corp. of America, Henderson, Nevada; Reactive Metals, Inc., Astabula, Ohio; and Oregon Metallurgical Corp., Albany, Oregon. There are nine users of sponge, 14 of titanium scrap and 15 of ingot.

The demand for titanium metal was strong in the first three months of 1970, but decreased due to cutbacks in the space and aircraft industries.

The General Services Administration purchased 3,100 tons of titanium sponge during the first six months, increasing their stockpile to 33,859 tons, 25% of which is substandard grade.

Developments of interest are as follows:

1. Schlienger nonconsumable electrode arc furnace
2. Reactive Metals' new 60 in. wide alloy and pure titanium sheet
3. TMCA's stress free—completely flat alloy plate in sizes to 10 x 35 ft
4. Production of a 700 lb ball for a valve by Ti-Line

Domestic prices for titanium sponge (99.3% pure) remained at $1.32/lb. Prices of the same grade from Japan and the United Kingdom were quoted at $1.20-$1.25/lb.

Lithium.—As a result of trade sanctions, domestic imports from Southern Rhodesia were nil for the second consecutive year, and production of lithium minerals and lithium carbonate continued at a high rate. Processors of lithium raw materials to lithium primary products were: Foote Mineral Co., Sunbright, Virginia, and Silver Peak, Nevada; American Potash and Chemical Corp., Trona, California; and Lithium Corp. of America, Bessemer City, North Carolina.

Important new uses of lithium in increasing amounts were the use of lithium carbonate by the aluminum industry and the increased use of lithium hypochlorite for bleaches and as a sanitizing agent for swimming pools. Other domestic uses include ceramics and glass, greases, welding and brazing fluxes, air conditioning equipment, rubber, and pharmaceuticals (56).

Lithium metal was quoted at $8.18/lb in 1000 lb lots, which includes a 25¢/lb increase announced by Foote Mineral on April 1, 1970 (57). Lithium carbonate in carload lots was priced at $0.52/lb and lithium chloride $0.87/lb.

Copper.—The U. S. domestic copper industry set new production records in 1970. Mine production was 1.715 million tons, up 11% over 1969. Smelter output from domestic ores set a record at 1.606 million tons, up 3.8%. Refinery production was 1.514 MM tons from domestic ores, 0.238 MM from foreign ores to total 1.752 MM tons from primary plants. Secondary material production was 510,000 tons (58).

There was a dramatic reversal in copper markets from a short supply to a surplus situation. Consumption of primary refined copper was down from 1.683 MM tons in 1969 to 1.597 MM tons in 1970, down 5.1%. Total refined consumption was off 4% to 2.06 MM tons. The price reflected the market change. There was an increase in price in April followed by price reductions in October and December. The changed supply

situation led to the removal in September of export controls imposed in 1965. Consumption in the second half of 1970 was affected by the general slowdown in business activity and by the General Motors strike (58, 59).

Copper stocks (refined) increased 151% to 98,000 tons by year end. Imports were down slightly (465,893 tons-11 months 1970) and exports increased slightly (451,633 tons-11 months 1970). Fabricators' stocks of copper in all forms increased from 502,000 to 522,000 tons from the start of the year through October (58, 59).

The Duval Sierrita mine in Arizona, owned by Pennzoil United Corporation, was dedicated in June and achieved capacity production of 65,000 tons of ore/day in October (58).

Hydrometallurgical processing (leaching, reduction) of sulfide ores may soon compete with the conventional roasting, smelting reduction and electro-refining. Economics appear competitive or possibly better and the sulfur dioxide air pollution problem is eliminated. Several smelter operators are under fire by anti-pollution crusades. At least two processes for leaching and reduction are being tested. Anaconda is building a multi-million dollar pilot plant in Tucson, Arizona, based on a patent owned by Treadmill Corporation. Sheritt Gordon Mines, Ltd. (Toronto, Ontario) is working on another process (60).

The two-tier pricing for copper may be gone. A cabinet sub-committee appointed by President Nixon in January, decided the system was not justified and recommended steps to end it. Subsequently, congressional hearings were held. In the meantime, the surplus copper situation forced cuts in the world price determined by the London Metal Exchange. The two-tier system originated in 1964 when the LME, as high as 90¢/lb at one point, forced U. S. producers to set a lower price to prevent substitution of other metals. Copper was allocated under the system and some fabricators were unhappy. With the present surplus situation, political-economic problems are reduced. U. S. copper prices were at 53¢/lb with world prices just under 50¢/lb (61).

Nickel.—Nickel consumption, excluding secondary nickel, was approximately 320 million lb. Nickel imports were about 300 million lb with domestic mine production estimated at 18,000 tons of nickel from laterite ore. The year was marked by exceptionally rapid recovery of the industry from the severe shortage caused by the labor strike in Canadian mines in 1969 (62).

The four-year shortage of nickel is ending even though demand is expected to grow 7-8%/yr through 1975. World production of nickel totals about 1 billion lb, slightly under the estimated demand of 1.05 billion lb. Stainless steel consumes approximately 40% of the world's nickel production (63).

The nickel industry is virtually unique today in that the major economies of the West are uncomfortably dependent on the output of one company, International Nickel. INCO produces about 475 million lb annually, more than half of that consumed in the non-Communist world. Falconbridge, also based in Sudbury, has a capacity of about 90 million lb and Societe' Le Nickel produces 88 million lb annually from the Island of New Caledonia in the Western Pacific (64). When prices went from 77¾¢/lb in 1965 to $1.28 in 1969, the lower grade laterite ores became economical (65).

Falconbridge is investing $195 million in a new plant in the Dominican Republic where it is developing new sources of ferronickel, a combination of nickel and iron, especially suited for making stainless steel (66).

Russia will not be a major factor in the world's nickel supply, but through Greg-Gary International Corporation, the U. S. will import about 5,000 tons annually. By itself this represents a 50% increase in Soviet exports to the U. S. which amounted to only $52 million last year (67).

The development by United Aircraft Research Laboratories of a high-strength nickel based alloy was announced with a strength three times that of the widely used superalloys. The eutectic, a mixture of trinickel aluminide and trinickel columbium, was said to have tensile strength of 140 thousand psi at 2,000°F.

Zinc.—United States mine output of zinc in 1970 decreased slightly over 1969, 546,772 tons *vs.* 553,124 tons, down 1.1% (68). Of 21 states reporting production, 12 registered decreases and 9 showed increases relative to 1969. Tennessee continued to be the largest producer (69).

Smelter production of zinc slab dropped by 150,000 tons, from 1,111,150 tons in 1969 to 961,153 tons in 1970, off 13.4%, reflecting the general downward trend in industrial activity. Imports of ores and concentrates dropped from 602,120 tons in 1969 to 525,757 tons in 1970, off 12.3%. Imports of slab zinc dropped from 329,008 to 272,577 tons, down 17%. Exports of zinc slab dropped from 9,298 tons to 289 tons while exports of zinc scrap increased 1,989 tons to 3,113 tons.

Consumption of zinc was as indicated below:

Base-recoverable zinc content	(Tons) 1969	1970	Change—%
Zinc slab	1,368,323	1,164,622	−14.8
Ores	126,712	118,400	−6.6
Zinc base scrap	100,636	86,400	−14.2
Copper base scrap	194,356	134,400	−30.8
Al-Mg base scrap	7,083	6,000	−15.3
Total	1,797,110	1,509,822	−16.0

The automobile industry, which normally accounts for one-third of the total U. S. consumption of zinc for die castings, galvanized steel, brass and bronze, and zinc oxide, had its worst year since 1962. Appliance manufacturers, the second largest consumers of zinc die castings, and the construction industry which uses most of the galvanized steel, suffered sharp losses in demand and used substantially less zinc. Comparing broad use categories for 1970 with 1969, galvanizing was down 5%, brass and bronze 26%, zinc-base alloys 18%, rolled zinc 17%, other uses 17% and zinc oxide was up 12%. Consumers operated principally on a current delivery basis as their stocks were reduced approximately 15,000 tons during the year.

General Services Administration sales of zinc continued through the year but amounted to only 25 tons, leaving 22,583 tons in the existing disposal authorization. Sales to government agencies amounted to 20,049 tons. The Commodity Exchange suspended trading in zinc effective December 4, 1970, as a result of lack of activity. When buying and selling interest is revived, trading will be reinstituted.

Prime western zinc price was reduced ½¢ in August and was quoted at 15¢/lb at year end. The London Metal Exchange price fluctuated throughout the year and was 13½¢/lb at year end. Foreign producers established a price of 13.93¢/lb on January 2, 1970, which continued throughout the year.

Electrical Energy

U. S. generation.—The reported power consumption for the United States reached 1,638,000,000 kilowatt hours (kWhr) in 1970. The nation's electric utilities produced 1,530,000,000 kWhr, up 6.1% over 1969. Private industrial, self-generated power totaled 108,000,000 kWhr in 1970 (70).

Production by electric utilities (71)
(Million-kWhr)

Type	1969	1970	% Increase
Coal fired plants	706.0	709.1	0.4
Gas fired plants	333.0	369.5	11.0
Oil fired plants	137.0	180.9	32.0
Nuclear plants	13.9	21.8	56.8
Total—Fuel burning	1,192.0	1,282.3	7.6
Hydroelectric	250.2	247.3	−1.1
Total	1,442.2	1,529.6	6.1

Installed capacity—electrical utilities, kW (71)

Type plant	1969	1970	% Increase
Steam—electric[a]	246,297,381	265,493,023	7.8
Hydroelectric	52,753,126	55,059,406	4.4
Internal combustion	4,205,114	4,320,661	2.6
Gas turbine	10,093,724	15,480,183	43.9
Total	313,349,345	340,353,273	8.6

[a] Includes nuclear capacity of 3,979,975 in 1969 and 6,493,206 in 1970.

Fuel consumed for power production (71).—

	1970 Preliminary	1969
Coal—millions of tons	322.36	310.64
Oil—millions of Bbl	332.10	251.03
Gas—billions of cu ft	3,894.0	3,487.6
Coal and equivalent of oil and gas millions of tons	583.14	524.48
lb/kWhr	0.909	0.880

Peak demands for electric utilities in the United States will rise to 1,056,000,000 kW by 1990 and annual energy consumption will exceed 5.8 trillion kWhr according to FPC forecasts. The forecast covers all 50 states and are higher than comparative estimates issued in 1964. The annual rate of growth is expected to vary from a low of 6.2% in the northeast region to a high of 8.4% in the south central region. Industrial use is the largest category, accounting for 41% of the total national requirement in 1965 and is expected to grow at an annual rate of 7%. The new forecast takes into account the expanding national income with greater purchasing power and includes greater allowances for growth in air conditioning and space heating requirements. The following table shows the forecasts (72):

Forecast of electric utility power requirements by categories of use 1965-1990 (million kWhr)

Category of use	Actual 1965	Estimated 1970	1980	1990
Farm	26,974	36,718	60,471	96,790
Irrigation and drainage pumping	10,917	14,946	22,762	34,779
Residential (non farm)	255,281	381,262	758,849	1,416,623
Commercial	190,916	279,149	578,378	1,141,697
Industrial	436,434	613,550	1,260,145	2,392,820
Street and highway lighting	9,159	12,841	23,355	40,388
Electrified transportation	4,885	5,418	6,995	8,435
Other uses	33,004	48,280	106,350	216,242
Losses and unaccounted for	92,009	135,155	268,995	504,406
Total	1,059,579	1,527,319	3,086,300	5,852,180

Tight fuel supplies are being strained by an environment-conscious public. Electric utilities are being strained to meet a demand growing by 12%/yr. Low sulfur oil consumption increased by 35.7% in the last year. The industry burned 7.8 million more tons of coal than was excavated in 1969, the difference made up from stockpiles. The coal industry is reluctant to put money into new mines which could be pre-empted by nuclear energy in a few years. New technological advances are needed to meet sulfur and thermal pollution regulations. Yet, research and development has a low priority in electrical utility budgeting, accounting for 0.226% of operating revenues in 1969 (73).

Gas turbines may be an answer to the power crisis. Chlorine, magnesium, and aluminum producers are considering ways to switch out of the public utility systems which lack reserve capacities (74). The Dow Chemical Company at Freeport, Texas, will have a portion of its power supplied by a 300,000 mW power plant to be built on adjacent property by Salt Grass Power, Inc. and will incorporate the world's largest and most efficient gas turbines (75). The new Westinghouse turbines are about 96 ft long and provides 43,000 kW plus feedwater heat for boilers. The unit incorporates gas and steam turbines. Using the exhaust gas heat to help make steam to drive the steam turbines increases the over-all efficiency of the turbine-generator from 25.5% to 79.3%. The installation costs roughly $95/kW. Allis-Chalmers has announced it is getting back into the gas and steam turbine business to compete with Westinghouse and General Electric. North American Turbine Corporation was organized in April 1970, to manufacture and market industrial gas turbines, and turbine powered generator, pump, and compressor packages for industrial applications in the 1100-3000 hp range (76).

Nuclear power.—Nuclear power generating capacity in 1970 increased to 6,493,206 kW (up from 3,979,975 in 1969) or 1.8% of the national electrical energy total (77). These facilities produced 21,800,000,000 kWhr of electricity in 1970. By 1980 nuclear generating capacity is expected to be 150,000 Mwe. or nearly 25% of the national total capacity (78).

The growth rate of the atomic power segment of the nuclear industry showed a sharp rebound in 1970 and all indicators point to a strong and viable future (78). Nuclear plant orders to date are as follows:

Year	Units ordered	Installed capacity Mwe.
1970	14	14,336
1969	7	7,225
1968	16	14,791
1967	31	25,941
1966	20	16,306
Thru 1965	27*	8,435
Total	115*	87,064

* Includes 7 small plants no longer in operation or used for experimental work.

1. Twelve of the 1970 ordered plants will be located adjacent to previously ordered plants.
2. Of the 108 plants in operation, under construction or planned, there are 67 plant sites in 28 states; 33 of the sites will involve multiple units.
3. Assume six years to build a nuclear plant (79).

The Atomic Industrial Forum cited rising fossil fuel costs as a prime reason for the good showing of nuclear power in 1970. The cost of a nuclear plant was about $40/kW more than fossil-fueled plant. However, the cost of low sulfur coal has increased from 28¢ to 45¢/million BTUs in recent years compared to a stable 20¢/million BTUs for uranium fuels. The industry still faces problems with radioactive and thermal discharges and protracted licensing proceedings. The first delay in start-up, due to contested license hearings which affected two plants, occurred in 1970 (79).

The AEC is carrying out over 50 separate projects in the field of environmental and health related research. They have also entered into 40 agreements with other agencies for related studies. A thermal effects facility is being built at the Savannah River plant. The AEC claims an unprecedented safety record that there has not been a single radiation injury to the general public or any plant employee. While biological risks and many other environmental factors may be largely unknown, useful information on radiation is growing daily.

There are 155,000 people in the U. S. who depend on atomic energy for their *livelihood*. Government facilities employ 100,000 and private industry employs about 55,000. Most of these people are engaged in the manufacture, design and engineering of nuclear facilities. Approximately 3,000 utility employees are assigned to the operation, maintenance, and technical support of power reactors.

Allied Chemical and Gulf Oil formed a partnership for the recovery of nuclear fuel. Allied-Gulf Nuclear Services purchased 1,500 acres of land at Barnwell, S.C., to build the recovery plant (80). This plant was licensed to recover "spent" nuclear fuel on December 18, 1970, and is the nation's third such plant.

A science team at Princeton University claims they will bridge the technical gap between today's fission and tomorrow's fusion reactors. Today's reactors are based on fission reaction whereby the nuclei of atoms are split. They consume fuel such as uranium U-235 and create unwanted radioactive by-products. Fusion reactors would use energy released when atomic nuclei (derived from a virtually limitless supply of deuterium) are joined together. The process leaves no radioactive residue, but would require heating the nuclei to millions of degrees. Within a year the researchers hope to have answers to the basic questions with fusion reactors producing electricity forecasted by 1980 (81).

Manuscript received May 24, 1971. This report was presented at the Industrial Electrolytic Division Luncheon at the Washington, D.C., Meeting of the Society, May 9-13, 1971.

Any discussion of this report will appear in a Discussion Section to be published in the June 1972 JOURNAL.

REFERENCES

1. Robert F. Schultz, President, Chlorine Institute (Feb. 3, 1971).
2. *Oil, Paint and Drug Reporter*, Aug. 3, 1970.
3. *Wall Street Journal*, p. 10, March 11, 1970.
4. *Ibid.*, p. 6, Sept. 1, 1970.
5. *Chemical Week*, p. 41, Dec. 9, 1970.
6. *Ibid.*, p. 17, March 10, 1971.
7. *Ibid.*, p. 43, Sept. 9, 1970.
8. *European Chemical News*, p. 18, Jan. 1, 1971.
9. *Chem. Eng.*, p. 164, March 23, 1970.
10. *Chemical Week*, p. 11, Feb. 17, 1971.
11. *Ibid.*, p. 25, March 18, 1970.
12. *Wall Street Journal*, p. 4, March 10, 1970.
13. *Chem. Eng. News*, p. 39, Sept. 21, 1970.
14. *Ibid.*, p. 32, Nov. 9, 1970.
15. *Chemical Week*, p. 45, April 8, 1970.
16. Mineral Industry Surveys, U.S. Dept. of the Interior, Annual Preliminary, "Mercury in 1970."
17. *Wall Street Journal*, p. 14, July 6, 1970.
18. *Chemical Week*, p. 26, July 22, 1970.
19. *Chem. Eng. News*, Jan. 25, 1971.
20. PPG Industries, Verbal Communication.
21. Current Industrial Census, Inorganic Chemicals, U.S. Dept. of Commerce, Bureau of Census.
22. *Chemical Week*, p. 41, (April 22, 1970).
23. *Ibid.*, p. 31, June 10, 1970.
24. Mineral Industrial Surveys, U.S. Dept. of the Interior, Preliminary, "Sodium Compounds in 1970."
25. *Oil, Paint and Drug Reporter*, March 22, 1971.
26. *Ibid.*, Oct. 13, 1969.
27. *Chemical Processing*, p. 3, April 1971.
28. Current Industrial Census, Inorganic Chemicals, U.S. Dept. of Commerce, Bureau of Census.
29. *Chemical Week*, p. 22, Sept. 23, 1970.
30. Mr. W. L. Amos, Dept. of Commerce, Chemical Division.
31. *Oil, Paint and Drug Reporter*, March 22, 1971.
32. *Chemical Week*, p. 12, March 11, 1970.
33. *Chem. Eng. News*, p. 52, Nov. 9, 1970.
34. *Business Week*, p. 28, Sept. 26, 1970.
35. *Chem. Eng.*, p. 221, April 27, 1970.
36. *Finance*, p. 17, Aug. 1970.
37. *Business Week*, p. 21, Sept. 29, 1970.
38. *Chemical Week*, p. 14, Nov. 25, 1970.
39. *Ibid.*, p. 37, May 6, 1970.
40. Mineral Industry Surveys, U.S. Dept. of the Interior, Annual Preliminary, "Aluminum in 1970."
41. *Business Week*, p. 30, Nov. 14, 1970.
42. *Ibid.*, p. 26, April 18, 1970.
43. *Wall Street Journal*, p. 30, April 1, 1970.
44. *Chemical Week*, p. 89, May 6, 1970.
45. *Ibid.*, p. 17, Dec. 2, 1970.
46. Mineral Industry Surveys, U.S. Dept. of the Interior, Magnesium Quarterly (February 23, 1971).
47. Mineral Industry Surveys, U.S. Department of the Interior, Annual Preliminary, "Magnesium in 1970."
48. Mineral Industry Surveys, U.S. Dept. of the Interior, Annual Preliminary, "Manganese in 1970."
49. *Business Week*, p. 60, June 6, 1970.
50. Mineral Industry Surveys, U.S. Dept. of the Interior, Annual Preliminary, "Beryllium in 1970."
51. Mineral Industry Surveys, U.S. Dept. of the Interior, Annual Preliminary, "Chromium in 1970."
52. *American Metal Market*, June 15, 1970.
53. Mr. Frank Noe, U.S. Dept. of the Interior.
54. Mineral Industry Surveys, U.S. Dept. of the Interior, "Titanium in the Fourth Quarter 1970."
55. Mineral Industry Surveys, U.S. Dept. of the Interior, Annual Preliminary, "Titanium in 1970."
56. Mineral Industry Surveys, U.S. Dept. of the Interior, Annual Preliminary, "Lithium in 1970."
57. *Chemical Week*, p. 54, March 4, 1970.
58. Mineral Industry Surveys, U.S. Dept. of the Interior, Annual Preliminary, "Copper in 1970."
59. Mineral Industry Surveys, U.S. Dept. of the Interior, Copper Industry Annual Supplement, "Copper in 1970."
60. *Chem. Eng.*, p. 64, April 20, 1970.
61. *Forbes*, p. 33, Dec. 15, 1970.
62. Mineral Industry Surveys, U.S. Dept. of the Interior, Annual Preliminary, "Nickel in 1970."
63. *Chemical Week*, p. 16, Dec. 23, 1970.
64. *Fortune*, p. 100, March 1970.
65. *Forbes*, p. 52, June 1, 1970.
66. *Business Week*, p. 42, Nov. 28, 1970.
67. *Ibid.*, p. 44, April 18, 1970.
68. Mineral Industry Surveys, U.S. Dept. of the Interior, Zinc Industry Monthly, "Zinc Industry in December 1970."
69. Mineral Industry Surveys, U.S. Dept. of the Interior, Annual Preliminary, "Zinc in 1970."
70. Mr. P. Rederer, Edison Electrical Institute.
71. Federal Power Commission, News Release No. 17372, March 18, 1971.
72. *Ibid.*, News Release No. 16323, Sept. 24, 1970.
73. *Business Week*, p. 52, July 11, 1970.
74. *Chemical Week*, p. 17, May 13, 1970.
75. *Chem. Eng.*, p. 58, Feb. 9, 1970.
76. *Chemical Week*, p. 49-50, May 27, 1970.
77. Federal Power Commission, News Release No. 17372, March 18, 1971.
78. Annual Report to Congress of the Atomic Energy Commission for 1970.
79. *Chem. Eng. News*, p. 11, Jan. 11, 1971.
80. *Chemical Week*, p. 16, Aug. 26, 1970.
81. *Business Week*, p. 80, Sept. 12, 1970.